Regulation of Redox Signaling Involving Chemical Conjugation of Protein Thiols by Nitric Oxide and Electrophiles

Tomohiro Sawa,[†] Hirokazu Arimoto,[‡] and Takaaki Akaike*[,†]

Department of Microbiology, Graduate School of Medical Sciences, Kumamoto University, Kumamoto 860-8556, Japan, and Department of Biomolecular Chemistry, Graduate School of Life Sciences, Tohoku University, Sendai 981-8555, Japan.
Received September 9, 2009; Revised Manuscript Received January 6, 2010

Nitric oxide (NO), a gaseous free radical that is biologically synthesized by nitric oxide synthases, participates in a critical fashion in the regulation of diverse physiological functions including vascular and neuronal signal transduction, host defense, and cell death regulation. This article reviews the chemical and biochemical mechanisms of protein thiol modifications caused by NO and by electrophiles derived from NO metabolism. The classical NO signaling pathway involves formation of the second messenger guanosine 3′,5′-cyclic monophosphate (cGMP). Post-translational modifications of redox-sensitive protein thiols have also been shown to be important in this signaling pathway. For instance, redox-sensitive thiols are targets for NO conjugation and formation of *S*-nitrosothiols. Electrophiles generated by reactions of NO or reactive nitrogen oxide species and biomolecules (i.e., fatty acids) effect thiol conjugations through S-alkylation. Among this class of reactions, S-guanylation is particularly emphasized. S-Guanylation is a novel type of S-alkylation with nitrated cGMP that contributes to the cytoprotective effects of NO. Post-translational modifications of thiols affect protein structures and functions: allosteric effects may alter protein structure, modification of active centers of enzymes may suppress enzyme actions, and modifications may modulate protein−protein interactions. Better understanding of protein modification by NO-derived electrophiles and the molecular basis of NO signaling would be useful in the development of new diagnostic methods and treatment of diseases related to NO metabolism.

INTRODUCTION

Nitric oxide (NO) is a gaseous free radical that is synthesized by nitric oxide synthases (NOSs[1]). NOSs catalyze the oxidation of L-arginine to form NO and L-citrulline (*1*). In spite of its simple structure, NO participates in a critical fashion in the regulation of diverse physiological phenomena such as vascular and neuronal signal transduction, host defense, and cell death regulation (*2*−*5*). Signal transduction of NO primarily involves activation of soluble guanylate cyclase to form the second messenger molecule guanosine 3′,5′-cyclic monophosphate (cGMP) (*6*). cGMP thus formed binds to allosteric regulatory domains of target proteins, including protein kinases, ion channels, and phosphodiesterases (PDEs), with a variety of downstream biological consequences that allow cells to adapt to changes in environmental conditions and metabolic demands (*6*).

Post-translational modification (PTM) is the process that attaches functional groups such as acetate and phosphate to amino acid side chains of proteins. PTM plays major roles in regulating diverse biological processes through a wide variety of mechanisms that include changes in protein activities, interactions, and subcellular localizations (*7*−*9*). Accumulating evidence has suggested that PTM of redox-sensitive protein thiols contributes to the regulation of NO signaling via a cGMP-independent mechanism (*10*). A well-characterized example of PTM by NO is S-nitrosylation, i.e., the conjugation of an NO moiety to a reactive cysteine thiol to form an *S*-nitrosothiol (*11*−*13*). A number of proteins have been identified as targets for S-nitrosylation, and the functional impact of the PTM has been extensively studied (*13*−*15*). Recent studies have suggested the importance of electrophilic metabolites of NO in PTMs other than S-nitrosylation. Biomolecules such as fatty acids and nucleotides reacts with NO or other reactive nitrogen oxide species (RNOS) to form electrophilic metabolites, and these electrophiles modify protein thiols to regulate NO signaling. Thus, better understanding of the modification by NO-derived metabolites would contribute to the development of new diagnostic methods and treatments of NO-related diseases. In this review article, we discuss the chemical and biochemical mechanisms of protein thiol conjugation mediated by NO and electrophiles and the impact of such modification on redox signaling. We place particular emphasis on S-guanylation, a novel type of S-alkylation, which is involved in cytoprotective signaling mediated by NO (*16*−*19*).

TYPES OF PROTEIN THIOL MODIFICATIONS BY NITRIC OXIDE AND RELATED ELECTROPHILES

S-Nitrosylation. Although nitrosothiol is formed on exposure to NO in solution under aerobic conditions, possibly through the formation of the potent nitrosating agent N_2O_3 (*20*), its efficacy is drastically enhanced in the presence of Cu^{2+}-containing proteins such as ceruloplasmin (*11, 21*). Ceruloplas-

* Correspondence should be addressed to Dr. Takaaki Akaike, Department of Microbiology, Graduate School of Medical Sciences, Kumamoto University, Kumamoto 860-8556, Japan. Tel: 81-96-373-5100; Fax 81-96-362-8362; E-mail: takakaik@gpo.kumamoto-u.ac.jp.
[†] Kumamoto University.
[‡] Tohoku University.

[1]Abbreviations: ASK1, apoptotic signal-regulating kinase-1; cGMP, 3′,5′-cyclic monophosphate; GSH, glutathione; GAPDH, glyceraldehydes-3-phosphate dehydrogenase; HO-1, heme oxygenase-1; HIF-1, hypoxia-inducible factor 1; iNOS, inducible isoform of nitric oxide synthase; Keap1, Kelch-like ECH-associating protein 1; MTs, metallothioneins; Nrf2, NF-E2-related factor 2; NOSs, nitric oxide synthases; 8-nitro-cGMP, 8-nitroguanosine 3′,5′-cyclic monophosphate; ODD, oxygen-dependent degradation; PDE, phosphodiesterase; PTM, post-translational modification; PTP1B, protein tyrosine phosphatase 1B; RNOS, reactive nitrogen oxide species; ROS, reactive oxygen species; RSOH, sulfenic acid; Trx-1, thioredoxin-1; vHL, von Hipple-Lindau.

10.1021/bc900396u © 2010 American Chemical Society
Published on Web 03/12/2010

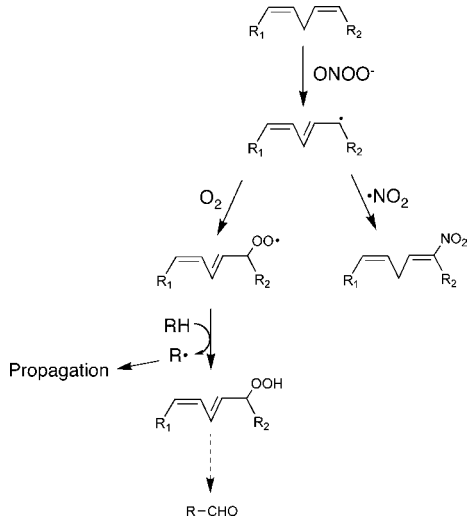


Figure 1. Proposed mechanisms for the peroxynitrite-induced formation of nitrated and oxidized fatty acids.

min catalyzes one-electron oxidation of NO to form the nitrosonium ion equivalent that favors electrophilic attack of thiols to form nitrosothiol.

Because deprotonation of thiols makes them more reactive toward NO, RNOS, and electrophiles (*22*, *23*), the pK_a value of the specific thiol defines the reactivity of a thiol-containing protein under physiological pH. The pK_a value of the thiol of cysteine is 8.33, and pK_a values of protein-associated cysteine thiols usually stay between 8.2 and 8.5 (*23*). The environment that surrounds cysteine thiols can modulate the pK_a: the pK_a value of the cysteine thiol is decreased when proximal to (a) basic amino acids such as histidine, lysine, and arginine; (b) aromatic amino acids such as tyrosine and tryptophan; or (c) metal centers such as heme−metal complexes (*13*, *23*). Allosteric regulators can also modulate the reactivity of cysteine thiols by affecting the accessibility of thiols and/or reactivity of cysteine thiols (*13*, *24*). In this context, we recently found that S-nitrosylation of human serum albumin by NO donors and low-molecular-weight nitrosothiols can be greatly enhanced by binding of endogenous ligands such as fatty acids and bilirubin to the protein (*25*). Thus, protein allostery may be a significant factor in the regulation of thiol modifications and warrants further investigation.

Oxidation and Disulfide Formation. Reaction of a thiol with an RNOS such as peroxynitrite, a coupling product of NO and superoxide (*26*), results in oxidation of the thiol to form sulfenic acid (RSOH) (*27*). RSOH can react with proximal thiol groups to form intra- or intermolecular disulfide bonds (*28*). Thus, RSOH may play an important role in glutathionylation, the covalent attachment of GSH to protein thiols via a mixed disulfide bond. Intra- or intermolecular disulfide bond formation can also be facilitated through formation of nitrosothiols (*28*).

S-Alkylation. In addition to direct modifications of protein thiols by RNOS, thiol S-alkylation caused by electrophilic secondary metabolites may also play an important role in the regulation of redox signaling. Examples of such electrophiles include nitrated fatty acids and nitrated guanine nucleotides.

Mechanisms of fatty acid nitration and oxidation by RNOS have been extensively studied by Freeman and colleagues (*29*). Carbon-centered radicals formed from hydrogen abstraction by oxidant react with nitrogen dioxide to form nitrated fatty acids (Figure 1). At low RNOS environment, however, lipid peroxidation proceeds predominantly to form peroxidation products including several electrophiles such as lipid aldehyde (e.g., 4-hydroxynonenal) rather than forming nitrated electrophiles (Figure 1).

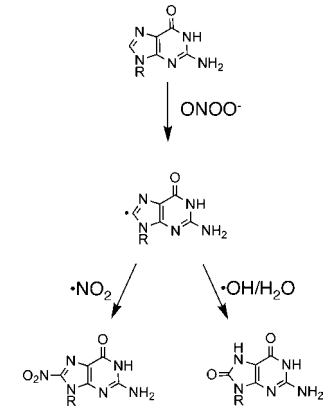


Figure 2. Proposed mechanisms for the peroxynitrite-induced formation of nitrated and oxidized guanine derivatives.

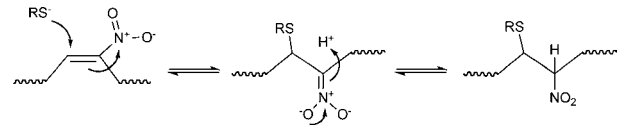


Figure 3. Michael addition reaction of nitroalkene derivatives with protein thiols (thiolates, RS-).

Peroxynitrite represents a biologically relevant oxidizing and nitrating agent. In physiological pH, peroxynitrite is rapidly converted to form nitrogen dioxide and hydroxyl radical; the latter can abstract hydrogen atom from guanine moiety to form guanine radical (Figure 2) (*30*, *31*). Guanine radical thus formed reacts with nitrogen dioxide or hydroxyl radical to form nitroguanine and hydroxyguanine, respectively (Figure 2). Physiologically relevant levels of carbon dioxide can facilitate peroxynitrite-mediated nitration of guanine derivatives (*32*), possibly through formation of nitrosoperoxycarbonate ($ONOOCO_2^-$) (*33*).

Biological formation of nitrated fatty acids has been reviewed recently (*29*). Other reports support the endogenous generation and presence of nitrated fatty acids (*34*, *35*). The first such nitrated fatty acid was observed in bovine papillary muscles: vicinal nitrohydroxyeicosatrienoic acid (*36*). Nitrolinoleate has been detected in human blood plasma, and cholesteryl nitrolinoleate has been found in human plasma and lipoproteins (*37*, *38*), with hyperlipidemic and postprandial conditions elevating plasma levels of nitrated fatty acids.

The nitrated fatty acids involve conjugated nitroalkene functions, and the electron-withdrawing nature of the nitro groups facilitates the Michael addition of thiols to the alkenes. The reaction of cysteine thiols (or corresponding thiolates) with nitrated fatty acids has been shown in vivo (S-nitroalkylation) (*39*) (Figure 3). The rate constants of those reactions exceed those with most fatty acid-derived electrophiles, with second-order rate constants of up to 355 M^{-1} s^{-1} at pH 7.4 and 37 °C (*40*). Those constants are orders of magnitude greater than those for the glutathione (GSH) reaction with H_2O_2 and electrophilic lipids such as 8-*iso*-prostaglandin A_2 and 15-deoxy-$\Delta^{12,14}$-prostaglandin J_2. It is noteworthy that S-nitroalkylation is reversible, and liberated nitroalkenes can react with thiols of other proteins or peptides (trans-alkylation) (*39*). Protein adducts of nitrated fatty acids have been detected in clinical environments, which is evidence of a metabolic and redox-sensitive mechanism for regulating protein distribution and function. Readers may refer to a review article by Freeman and colleagues for details of the chemistry and biology of nitrated fatty acid signaling (*29*).

Nitration products of guanine derivatives have been identified in various in vitro and in vivo settings, most of which were

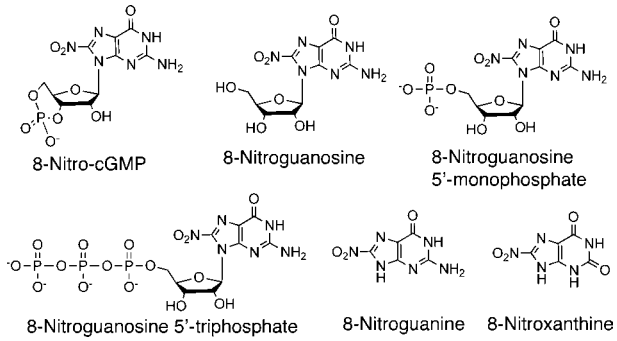


Figure 4. Chemical structures of 8-nitro-cGMP and related compounds.

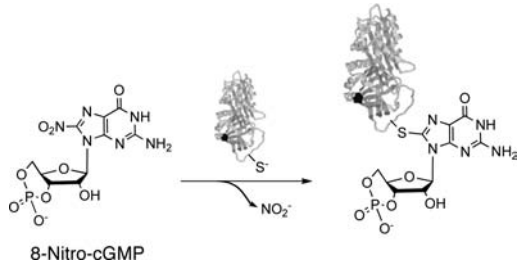


Figure 5. Schematic representation of protein S-guanylation. Nucleophilic protein thiolates attack the C8 carbon of 8-nitro-cGMP, which results in adduction of cGMP moieties to cysteine residues in proteins, with concomitant release of a nitrite anion.

associated with inflammatory conditions (*30, 41*−*48*). Detailed analyses of cell culture experiments revealed that nitrated cGMP (8-nitroguanosine 3′,5′-cyclic monophosphate [8-nitro-cGMP], Figure 4) was the major product formed in cells (*16*). 8-Nitro-cGMP was first identified in the mouse macrophage cell line RAW 264.7 when cells were stimulated with interferon-γ and lipopolysaccharide to produce NO via the inducible isoform of NO synthase (iNOS) (*16*). Infection with the gram-negative bacterium *Salmonella* facilitated the formation of 8-nitro-cGMP in mouse macrophages with the wild-type iNOS gene but not in iNOS-deficient macrophages. As another example, human hepatoma HepG2 cells treated with an NO donor under glucose starvation showed enhanced 8-nitro-cGMP formation (*16*).

8-Nitro-cGMP is the first endogenous cGMP derivative that forms a stable conjugate with cysteine thiols at the purine base. This conjugation reaction is called "protein S-guanylation" (*16*) and proceeds without enzymatic stimulation in vitro. The occurrence of S-guanylation in vivo was unambiguously proved by using a specific antibody and mass spectrometry. Figure 5 shows the mechanism of the reaction, in which the nitro group of 8-nitro-cGMP is replaced by a thiol group, with the release of NO_2^-. In contrast to S-nitrosylation and S-nitroalkylation (which are conjugations via addition), S-guanylation is believed to be irreversible under physiological conditions. Thus, as a signaling principle, deguanylation may be catalyzed by certain enzyme systems, which would be analogous to dephosphorylation catalyzed by phosphatases, and a search for such biological deguanylation mechanisms is warranted (*17*).

Kinetic analyses indicate that reactivity of 8-nitro-cGMP with cysteine thiols is moderate compared with that of other biological electrophiles (*16*). For instance, the reaction rate constants for GSH at pH 7.4 and 37 °C are 0.03, 0.7, 1.3, 183, and 355 M^{-1} s^{-1} for 8-nitro-cGMP, 15-deoxy-$\Delta^{12,14}$-prostaglandin J_2, 4-hydroxynonenal, nitrooleic acid, and nitrolinoleic acid, respectively. These data suggest that only proteins bearing highly nucleophilic reactive cysteine thiols as determined, for example, by low pK_a values, may be targets for S-guanylation.

MODULATION OF PROTEIN FUNCTIONS BY THIOL MODIFICATIONS

Modifications of cysteine thiols by NO, RNOS, and electrophiles have been reported to regulate the activity of numerous metabolic enzymes, including oxidoreductases, proteases, and protein kinases and phosphatases, as well as receptors, ion channels and transporters, transcription factors, and others (Table 1).

The best-characterized examples of protein function regulation include enzyme inhibition by modifications of active center thiols, thiol modifications that affect protein function and structure (allosteric regulation), and regulation of protein−protein interactions (*13, 49*).

Active Center Thiol Modification. Some enzymes contain cysteine residues at the active site that are involved in catalysis. Mannick et al. demonstrated that procaspase-3, an enzyme that executes apoptotic signals, is constitutively S-nitrosylated in situ at its active site thiol and that it is selectively denitrosylated after apoptotic stimulation by Fas (*50*). Phosphatases provide another example of thiol modifications associated with inhibition of enzyme activity. Protein tyrosine phosphatase 1B (PTP1B) is one of the protein tyrosine phosphatases that catalyze the removal of phosphate residues and regulate the activity of phosphotyrosyl proteins involved in numerous cell signaling pathways (*51*). The pK_a value of the active site thiol of PTP1B is reportedly 5.4, which suggests that the thiol may be susceptible to modification by NO and RNOS (*23*). Li and Whorton reported inhibition of PTP1B activity by *S*-nitrosothiols through modification of the active site cysteine of PTP1B, with a concomitant increase in the amount of phosphorylated epidermal growth factor receptor (*52*). This finding supports the idea that regulation of PTP1B activity through cysteine thiol modifications may contribute to regulation of phosphorylation-dephosphorylation signaling.

Allosteric Regulation. Thiol modifications can also affect protein functions by means of an allosteric mechanism. Cysteine residues that coordinate to metal ions, especially the nonoxidizable Zn^{2+}, have reduced pK_a values and are thereby susceptible to redox-based modification. Matrix metalloproteinases are enzymes that are critically involved in disintegration and remodeling of the extracellular matrix (*53*). Okamoto et al. demonstrated that matrix metalloproteinases can be activated through modification of Zn^{2+}-coordiated cysteine in a manner dependent on peroxynitrite and low-molecular-weight thiols such as GSH (*54*). Peroxynitrite was thus found to strongly activate matrix metalloproteinases in the presence of GSH. Mass spectrometric analyses revealed that *S*-nitroglutathione forms in the reaction of peroxynitrite with GSH, after which it forms mixed disulfide at the Zn^{2+}-coordinated cysteine, which leads to enzyme activation. Activation of metalloproteinases by NO via S-nitrosylation of Zn^{2+}-coordinated thiols has been reported for tumor necrosis factor α-converting enzyme, a member of a metalloproteinase−disintegrin family (*55*). Other experiments suggest, however, that NO donors or nitrosothiols such as *S*-nitrosoglutathione failed to induce direct activation of matrix metalloproteinases in spite of their ability to nitrosylate Zn^{2+}-coordiated cysteine (*56*). This may thus suggest that S-nitrosylation of matrix metalloproteinases is insufficient to activate the enzyme. Such a discrepancy observed for the impact of S-nitrosylation in the metalloproteinase activation may be explained by release of zinc ion from the zinc−thiolate complex as reported earliear (*56*).

A similar complicated mechanism for zinc release during S-nitrosylation of zinc-coordinated thiolate is described for

Table 1. Protein Targets for Thiol Modifications by NO, RNOS, and Electrophiles

protein[a]	effect[a]	modifications (refs)
procaspase-3	inhibition of enzyme activity	nitrosylation (*50*)
PTP1B	inhibition of enzyme activity	glutathionylation (*76*), nitrosylation (*52*)
proMMPs	activation of enzyme activity	glutathionylation (*54*)
Keap1	enhancement of Nrf2 translocation into the nucleus	alkylation (*16, 77*), oxidation (*78*)
HIF-1α	stabilization of HIF-1α via inhibition of vHL	nitrosylation (*71*)
GAPDH	promotion of GAPDH binding with Siah1, which leads to nuclear translocation and cell death inhibition of enzyme activity	nitrosylation (*73*), alkylation (*39*), glutathionylation (*79*)
Trx-1	inhibition of oxidoreductase activity and release of ASK1 by Cys32 and/or Cys35 modification	alkylation (*80*), nitrosylation (*74, 75*)
NMDA receptor	inhibition of excessive NMDA current	nitrosylation (*81, 82*)
TRP channels	activation of TRP channels (Ca^{2+} entry)	nitrosylation (*83*)
PDI	inhibition of enzyme activity	alkylation (*84*), nitrosylation (*85*)
NF-κB	inhibition of DNA binding by NF-κB	nitrosylation (*86, 87*)

[a] Abbreviations: PTP1B, protein tyrosine phosphatase 1B; proMMPs, precursors of matrix metalloproteinases; Keap1, Kelch-like ECH-associating protein 1; HIF-1α, hypoxia-inducible factor 1α; GAPDH, glyceraldehyde-3-phosphate dehydrogenase; Trx-1, thioredoxin-1; NMDA receptor, *N*-methyl-D-aspartate receptor; TRP channels, transient receptor potential channels; PDI, protein disulfide-isomerase; NF-κB, nuclear factor-κB; vHL, von Hippel-Lindau; ASK1, apoptotic signal-regulating kinase-1.

metallothioneins (MTs). MTs are a family of small (6−7 kDa) metal-binding proteins that bind seven divalent metal (Zn^{2+}, Cd^{2+}) via metal−thiolate coordination (*57*). Under aerobic conditions, NO via thiolate-nitrosylation induces the release of Zn^{2+} from MTs in vitro (*58*). Unbound, free zinc ion is known to activate gene expression and, hence, regulate cellular signaling, through activation of metal-response element-binding transcription factor-1 (*59*). Recent study has demonstrated that the NO-mediated zinc release may play a role in regulation of hypoxic pulmonary vasoconstriction (*60*). It is therefore conceivable that NO-mediated zinc release via thiolate modifications may participate in zinc-mediated redox signaling (*61*).

Regulation of Protein−Protein Interactions. Thiol modifications reportedly also control protein−protein interactions. Keap1 (Kelch-like ECH-associated protein 1) is a cysteine-rich redox-sensitive regulatory protein that binds to NF-E2-related factor 2 (Nrf2) and represses its transcriptional activity (*62, 63*). Modifications of Keap1 thiols by reactive oxygen species (ROS), RNOS, and electrophiles facilitate dissociation of Keap1 from Nrf2, which results in nuclear translocation of Nrf2 and transactivation of an array of genes involving antioxidant, anti-inflammatory, drug-metabolizing, and cytoprotective enzymes (*62, 63*). Mutation studies have suggested the importance of certain cysteine residues such as Cys151, Cys273, and Cys288 for the interaction of Keap1 and Nrf2 (*64*). Holland et al. recently reported that S-glutathionylation of Cys434 and Cys368 may cause marked alterations in the structure of Keap1 at the interface of the Nrf2-binding domain (*65*). Further study is needed to clarify the functional impact of thiol modification at cysteines other than Cys151, Cys273, and Cys288 in Keap1.

Similar regulatory mechanisms of inhibition of protein−protein interactions may also operate in stabilization of hypoxia-inducible factor 1 (HIF-1), a master transcriptional factor (*66*). HIF-1 is a heterodimeric protein that consists of the constitutively expressed HIF-1β/ARNT subunit and the highly regulated HIF-1α subunit (*67*). The overall activity of HIF-1 is determined by the intracellular HIF-1α level. Under normoxic conditions, HIF-1α is hydroxylated by oxygen-activated prolylhydroxylases at proline residues 402 and 564 in the oxygen-dependent degradation (ODD) domain (*68, 69*). This hydroxylation drives HIF-1α toward ubiquitylation by E3 ubiquitin protein ligase, which is part of the von Hippel-Lindau (vHL) tumor suppressor protein complex (*70*). Ubiquitylated HIF-1α is then rapidly degraded by the proteasome pathway. Li et al. demonstrated that NO can stabilize HIF-1α protein in cells (*71*). This HIF-1α stabilization is largely mediated by S-nitrosylation of the Cys533 in the ODD domain, which leads to inhibition of binding between the ODD domain and vHL (*71*).

Alternatively, thiol modification can facilitate protein−protein interactions. Glyceraldehyde-3-phosphate dehydrogenase (GAPDH) is a classic glycolytic enzyme, and accumulating evidence has suggested that GAPDH is a multifunctional protein (*72*). In particular, GAPDH plays an important role in regulating cell death mediated by NO. Hara et al. demonstrated that S-nitrosylation of GAPDH facilitates binding to Siah1, an E3 ubiquitin ligase with a nuclear localization signal (*73*). The GAPDH-Siah1 protein complex, in turn, translocates to the nucleus and mediates cell death.

Many proteins contain multiple cysteine residues that can be targets for thiol modifications. This information suggests that a single protein can be controlled in different ways by site-specific modifications. One well-characterized example is thioredoxin-1 (Trx-1). Trx-1 is an oxidoreductase that is essential for regulation of the cellular redox state, and it binds and inactivates apoptotic signal-regulating kinase-1 (ASK1). Haendeler et al. showed that Trx-1 is S-nitrosylated constitutively in endothelial cells at a single allosteric cysteine residue (Cys69) that lies outside the active site (which contains Cys32 and Cys35) and that S-nitrosylation of Cys69 is necessary for its basal antiapoptotic function in endothelial cells (*74*). However, treatment with *S*-nitrosoglutathione can reportedly induce S-nitrosylation of Trx-1 in intact cells and dissociate ASK1, possibly by targeting the active site Cys32 and/or Cys35. In contrast to S-nitrosylation of Cys69, S-nitrosylation of active site cysteine residues can affect apoptosis, perhaps through the release of ASK1 (*75*). Thus, the overall effect of thiol modifications may be regulated in a manner dependent on site-specific modifications, which may be determined by the amount and types of reactive metabolites that can modify thiols.

Table 1 includes other examples of thiol modifications that are not explained here in detail, and readers may refer to articles cited in Table 1 (*76*−*87*).

NITRIC OXIDE SIGNALING MEDIATED BY 8-NITRO-CGMP

8-Nitro-cGMP participates in the regulation of NO signaling in two ways. This molecule retains the activity of its parental cGMP and it possesses its own unique property: activation of a cytoprotective response. The latter was studied in a murine salmonellosis model (*19*). Production of NO by iNOS reportedly played an important role in cytoprotective responses in this model (*88, 89*), but the molecular mechanism of these responses has remained elusive. As mentioned earlier, 8-nitro-cGMP forms in cells infected with *Salmonella*, so the effect of this molecule in cell culture experiments using *Salmonella*-infected mouse macrophages was examined. 8-Nitro-cGMP clearly induced such a cytoprotective response (*19*). However, 8-bromoguanosine 3′,5′-cyclic monophosphate, a stable analogue of cGMP, did not provide such cytoprotection, which suggests that 8-nitro-

cGMP induces a cytoprotective response independent of cGMP-like activity. In macrophages that were infected with *Salmonella* and/or treated with 8-nitro-cGMP, marked induction of S-guanylation of Keap1 and associated overexpression of Nrf2-regulated cytoprotective genes including heme oxygenase-1 (HO-1) were seen, which may indicate that 8-nitro-cGMP can induce a cytoprotective response by activating the Keap1/Nrf2 system through protein S-guanylation. Similar activation of a cytoprotective response that depends on the Keap1/Nrf2 system was identified in HepG2 cells under conditions of glucose starvation and exposure to hydrogen peroxide (unpublished data). NO-induced activation of Nrf2 system has been reported previously (*78, 90*). Buckley et al. recently demonstrated the occurrence of thiol oxidation on intracellular Keap1 in response to NO donors (*78*). Thus, NO and RNOS exposure may induce several types of thiol modifications in Keap1, including S-guanylation, oxidation, and presumably nitrosylation. Further studies are warranted to clarify relative contribution of those thiol modifications in Nrf2 activation, particularly identification of modification sites and their impact on Keap1 function.

Consistent with those in vitro experiments, *Salmonella* infection of mice significantly increased the formation of 8-nitro-cGMP in the liver, with colocalization of HO-1 upregulation (*19*). Pharmacological intervention with an HO-1 inhibitor (pegylated zinc protoporphyrin IX) (*91*−*93*) further supported the importance of HO-1 upregulation in cytoprotective signaling mediated by NO in salmonellosis.

With regard to the regulation of vascular tone, 8-nitro-cGMP has unique biphasic effects: vasoconstriction at low concentrations and vasorelaxation at high concentrations (*16*). The vasorelaxation effect is mediated by the mechanism identical to that of the parental cGMP, which involves activation of cGMP-dependent protein kinase. However, vasoconstriction is caused by ROS formation secondary to NOS uncoupling (*41, 94*) caused by 8-nitro-cGMP (*16*).

Although the metabolic fate of 8-nitro-cGMP needs elucidation, this molecule may not undergo conventional cGMP metabolism because of its resistance to PDEs. PDEs are enzymes that catalyze hydrolysis of the 3′,5′-cyclic monophosphate moiety of cyclic nucleotides including cGMP and adenosine 3′,5′-cyclic monophosphate to form 5′-monophosphates of corresponding nucleotides (*95*). PDEs constitute members of a 21-gene family that are grouped into 11 different primary isoenzymes (with a total of 48 isoforms) on the basis of substrate affinity, selectivity, and regulation mechanisms (*95*). Of these enzymes, PDE5, PDE6, and PDE9 are highly selective for cGMP; PDE1, PDE2, and PDE11 have dual substrate affinity (*95*). In vitro experiments revealed that 8-nitro-cGMP was resistant to hydrolytic activity of PDE1 and PDE5 (*16*).

The GSH-dependent detoxification pathway may function as an alternative metabolic route for 8-nitro-cGMP. GSH is the most abundant nonprotein thiol in cells (*96, 97*). GSH protects cells against endogenous and exogenous toxins including ROS and RNOS (*96, 97*). ROS and RNOS are removed via nonenzymatic reduction with GSH. Conjugation of GSH with electrophilic compounds, in some cases, mediated the glutathione-S-transferases, and subsequent excretion of those conjugates from the cells also serves to regulate the levels of those electrophilic compounds (*96*). Our previous observation suggested that cellular formation of 8-nitro-cGMP was regulated partially by GSH (*16*). For example, depletion of cellular GSH by using an inhibitor for GSH biosynthesis, L-buthionine sulfoximine, resulted in moderate increase of the cellular 8-nitro-cGMP levels (*16*). This limited effect of GSH on 8-nitro-cGMP levels may be due to the moderate reactivity of 8-nitro-cGMP with GSH as mentioned above. In addition, our preliminary data shows that 8-nitro-cGMP is insensitive to glutathione-S-transferase-mediated glutathione conjugation (unpublished observation). These results are consistent with the finding that 8-nitro-cGMP gradually accumulates in cells during a long time period (∼11 h) after exposure to NO from endogenous and exogenous sources (*16*). Thus, with respect to temporal regulation, NO signaling mediated by 8-nitro-cGMP and NO signaling mediated by cGMP may differ. All these data together indicate that nitration of cGMP brings unique chemical and biological features to 8-nitro-cGMP including electrophilicity, redox activity, and PDE resistance, which establishes this molecule as a new cGMP messenger.

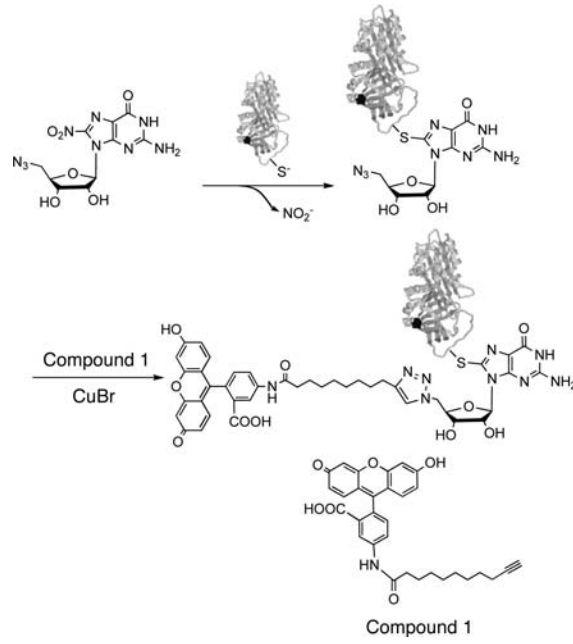


Figure 6. Click chemistry-based fluorescent labeling at sites of protein S-guanylation. 5′-Azido derivatives of 8-nitroguanosine undergo S-guanylation to introduce the azide group into proteins, with subsequent conjugation to fluorophores via the Huisgen reaction.

METHODOLOGIES TO DETECT PROTEIN S-GUANYLATION

Elucidation of temporal and spatial regulation of the formation of 8-nitro-cGMP and associated protein S-guanylation is important for understanding how protein S-guanylation contributes to the regulation of NO signaling. Anti-8-nitroguanine monoclonal antibodies were developed and used to localize the cellular formation of 8-nitroguanine derivatives. Among these antibodies, clone 1G6 exhibits the highest specificity against 8-nitro-cGMP compared with other 8-nitroguanine derivatives, with immunoreactivity decreasing in the order 8-nitro-cGMP > 8-nitroguanosine, 8-nitroguanosine 5′-monophosphate > nitrated RNA > 8-nitroguanosine 5′-triphosphate; no reactivity against 8-nitroguanine and 8-nitroxanthine was observed (*16*). Confocal laser microscopic analysis with the use of clone 1G6 and organelle-specific markers revealed immunostaining for 8-nitro-cGMP (1G6) mainly in the cytosol, with colocalization partly with mitochondria rather than endoplasmic reticulum (*16*). Mitochondrial localization of this nitrated derivative may implicate 8-nitro-cGMP in regulation of mitochondrial functions such as energy metabolism and cell death regulation, and further study related to this issue is ongoing.

Anti-8-thioalkoxy-cGMP antibodies that recognize the S-guanylation moiety have also been developed to detect protein S-guanylation by means of immunohistochemistry, Western blotting, and immunoaffinity purification coupled with chromatography (*16*). Western blotting of cell lysates obtained from

macrophages infected with *Salmonella* revealed multiple reactive bands except for S-guanylated Keap1 (*16*). Further characterization, via mass spectrometry, of the S-guanylation proteome is currently underway.

Appropriately labeled chemical probes are powerful tools that complement specific antibodies. Most important, the low molecular weight of the probes results in excellent membrane permeation that allows imaging of protein S-guanylation in living cells (*18*). We developed an azido derivative of 8-nitroguanosine for use in click chemistry-based fluorescent labeling of S-guanylated proteins (*18*) (Figure 6). This 5′-azido analogue efficiently upregulated HO-1 in a manner similar to that of 8-nitro-cGMP, which suggests that the azido analogue induces Keap1 S-guanylation and subsequently activates Nrf2 signaling. Proteins that are S-guanylated by this azido analogue can be labeled with fluorophore by means of click chemistry and can thus readily be detected by fluorescence scanning of electrophoresed gels. Prelabeling with a series of fluorophores is also possible with the azido derivatives, and the labeled 8-nitroguanosines have been shown to be incorporated into cells (unpublished data). This technique may allow analysis of the formation, localization, and metabolism of S-guanylated proteins in living cells with the use of organelle-specific markers and confocal microscopy.

CONCLUSIONS

Redox-sensitive protein thiols can become targets for chemical modifications caused by NO, RNOS, and electrophiles derived from reactions between RNOS and biomolecules, the result being formation of various protein thiol conjugates. Although those covalent modifications were previously regarded as nonspecific injurious changes to protein functions associated with oxidative stress, those modifications were recently recognized as involved in a critical fashion in regulation of diverse biological signaling processes (such as redox signaling). As mentioned earlier, chemical modification of redox-sensitive thiols affects protein functions through various mechanisms including modification of active center thiols, alteration of protein structure by allosteric effects, and modulation of protein−protein interactions, which in turn contribute to regulation of NO signaling. The total number of cysteine residues encoded in the human genome is estimated at approximately 214 000 (*49*). Among them, 21 000−42 000 residues (10−20% of the total) may be redox-sensitive (*49*). Thus, a number of proteins that possess redox-sensitive thiols remain to be discovered as redox-sensing targets in regulation of redox signaling.

The redox microenvironment that affects thiol reactivity may differ in each cell compartment. Hansen et al. reported that the relative redox states of these different compartments, which can be determined via the ratio of free thiols to thiols forming disulfide, from most reducing to most oxidizing are mitochondria > nuclei > cytoplasm > endoplasmic reticulum > extracellular space (*98*). In this context, mitochondrial proteins are assumed to be important targets of redox-dependent signaling through thiol modifications. Recent development of mass spectrometry-based proteomics may provide a powerful tool for identification of novel redox-sensitive protein targets and regulation of thiol modifications in each organelle. In fact, dozens of proteins that undergo S-nitrosylation and S-glutathionylation have been discovered (*14, 99*). Further analysis is now warranted to achieve comprehensive understanding of target proteins for S-alkylation reactions including S-guanylation and S-nitroalkylation.

Protein thiol modification is critically important in the regulation of physiological signaling. Impaired regulation of this modification, which results mainly from overproduction of reactive substances such as RNOS and ROS that are associated with oxidative stress, may contribute to development of diseases via disruption of well-organized signaling networks involving protein thiol modification (*100, 101*). Better understanding of the molecular mechanisms by which redox-sensitive thiol modifications regulate cell signaling will provide the basis for novel therapeutic approaches to restore normal signaling and control and thereby prevent pathological and toxicological consequences of oxidative stress.

ACKNOWLEDGMENT

We thank Judith B. Gandy for her excellent editing of the manuscript. This work was supported in part by Grants-in-Aid for Scientific Research (B, C: Nos. 21390097, 21590312) and for Exploratory Research (No. 20651056), and on Innovative Areas (Research in a Proposed Area: Nos. 20117001, 20117005, and 20117006) from the Ministry of Education, Culture, Sports, Science and Technology (MEXT) and grants-in-aid from the Ministry of Health, Labor and Welfare of Japan.

LITERATURE CITED

(1) Griffith, O. W., and Stuehr, D. J. (1995) Nitric oxide synthases: properties and catalytic mechanism. *Annu. Rev. Physiol. 57*, 707–736.
(2) Murad, F. (1986) Cyclic guanosine monophosphate as a mediator of vasodilation. *J. Clin. Invest. 78*, 1–5.
(3) Bredt, D. S., Hwang, P. M., and Snyder, S. H. (1990) Localization of nitric oxide synthase indicating a neural role for nitric oxide. *Nature 347*, 768–770.
(4) Nathan, C. (1992) Nitric oxide as a secretory product of mammalian cells. *FASEB J. 6*, 3051–3064.
(5) Patel, R. P., Moellering, D., Murphy-Ullrich, J., Jo, H., Beckman, J. S., and Darley-Usmar, V. M. (2000) Cell signaling by reactive nitrogen and oxygen species in atherosclerosis. *Free Radic. Biol. Med. 28*, 1780–1794.
(6) Madhusoodanan, K. S., and Murad, F. (2007) NO-cGMP signaling and regenerative medicine involving stem cells. *Neurochem. Res. 32*, 681–694.
(7) Walsh, C. T., Garneau-Tsodikova, S., and Gatto, G. J., Jr. (2005) Protein posttranslational modifications: the chemistry of proteome diversifications. *Angew. Chem., Int. Ed. Engl. 44*, 7342–7372.
(8) Spickett, C. M., Pitt, A. R., Morrice, N., and Kolch, W. (2006) Proteomic analysis of phosphorylation, oxidation and nitrosylation in signal transduction. *Biochim. Biophys. Acta 1764*, 1823–1841.
(9) Choudhary, C., Kumar, C., Gnad, F., Nielsen, M. L., Rehman, M., Walther, T. C., Olsen, J. V., and Mann, M. (2009) Lysine acetylation targets protein complexes and co-regulates major cellular functions. *Science 325*, 834–840.
(10) Martinez-Ruiz, A., and Lamas, S. (2009) Two decades of new concepts in nitric oxide signaling: from the discovery of a gas messenger to the mediation of nonenzymatic posttranslational modifications. *IUBMB Life 61*, 91–98.
(11) Akaike, T. (2000) Mechanisms of biological S-nitrosation and its measurement. *Free Radic. Res. 33*, 461–469.
(12) Stamler, J. S., Lamas, S., and Fang, F. C. (2001) Nitrosylation. The prototypic redox-based signaling mechanism. *Cell 106*, 675–683.
(13) Hess, D. T., Matsumoto, A., Kim, S. O., Marshall, H. E., and Stamler, J. S. (2005) Protein S-nitrosylation: purview and parameters. *Nat. Rev. Mol. Cell Biol. 6*, 150–166.
(14) Forrester, M. T., Thompson, J. W., Foster, M. W., Nogueira, L., Moseley, M. A., and Stamler, J. S. (2009) Proteomic analysis of S-nitrosylation and denitrosylation by resin-assisted capture. *Nat. Biotechnol. 27*, 557–559.
(15) Miyamoto, Y., Akaike, T., and Maeda, H. (2000) S-Nitrosylated human α_1-protease inhibitor. *Biochim. Biophys. Acta 1477*, 90–97.

(16) Sawa, T., Zaki, M. H., Okamoto, T., Akuta, T., Tokutomi, Y., Kim-Mitsuyama, S., Ihara, H., Kobayashi, A., Yamamoto, M., Fujii, S., Arimoto, H., and Akaike, T. (2007) Protein S-guanylation by the biological signal 8-nitroguanosine 3′,5′-cyclic monophosphate. *Nat. Chem. Biol. 3*, 727–735.

(17) Feelisch, M. (2007) Nitrated cyclic GMP as a new cellular signal. *Nat. Chem. Biol. 3*, 687–688.

(18) Saito, Y., Taguchi, H., Fujii, S., Sawa, T., Kida, E., Kabuto, C., Akaike, T., and Arimoto, H. (2008) 8-Nitroguanosines as chemical probes of the protein S-guanylation. *Chem. Commun.* 5984–5986.

(19) Zaki, M. H., Fujii, S., Okamoto, T., Islam, S., Khan, S., Ahmed, K. A., Sawa, T., and Akaike, T. (2009) Cytoprotective function of heme oxygenase 1 induced by a nitrated cyclic nucleotide formed during murine salmonellosis. *J. Immunol. 182*, 3746–3756.

(20) Forman, H. J., Fukuto, J. M., and Torres, M. (2004) Redox signaling: thiol chemistry defines which reactive oxygen and nitrogen species can act as second messengers. *Am. J. Physiol. Cell Physiol. 287*, C246–256.

(21) Inoue, K., Akaike, T., Miyamoto, Y., Okamoto, T., Sawa, T., Otagiri, M., Suzuki, S., Yoshimura, T., and Maeda, H. (1999) Nitrosothiol formation catalyzed by ceruloplasmin. Implication for cytoprotective mechanism in vivo. *J. Biol. Chem. 274*, 27069–27075.

(22) Eaton, P. (2006) Protein thiol oxidation in health and disease: techniques for measuring disulfides and related modifications in complex protein mixtures. *Free Radic. Biol. Med. 40*, 1889–1899.

(23) Winterbourn, C. C., and Hampton, M. B. (2008) Thiol chemistry and specificity in redox signaling. *Free Radic. Biol. Med. 45*, 549–561.

(24) Eu, J. P., Sun, J., Xu, L., Stamler, J. S., and Meissner, G. (2000) The skeletal muscle calcium release channel: coupled O_2 sensor and NO signaling fu nctions. *Cell 102*, 499–509.

(25) Ishima, Y., Akaike, T., Kragh-Hansen, U., Hiroyama, S., Sawa, T., Suenaga, A., Maruyama, T., Kai, T., and Otagiri, M. (2008) S-Nitrosylated human serum albumin-mediated cytoprotective activity is enhanced by fatty acid binding. *J. Biol. Chem. 283*, 34966–34975.

(26) Szabo, C., Ischiropoulos, H., and Radi, R. (2007) Peroxynitrite: biochemistry, pathophysiology and development of therapeutics. *Nat. Rev. Drug Discovery 6*, 662–680.

(27) Radi, R., Beckman, J. S., Bush, K. M., and Freeman, B. A. (1991) Peroxynitrite oxidation of sulfhydryls. The cytotoxic potential of superoxide and nitric oxide. *J. Biol. Chem. 266*, 4244–4250.

(28) Poole, L. B., Karplus, P. A., and Claiborne, A. (2004) Protein sulfenic acids in redox signaling. *Annu. Rev. Pharmacol. Toxicol. 44*, 325–347.

(29) Freeman, B. A., Baker, P. R., Schopfer, F. J., Woodcock, S. R., Napolitano, A., and d'Ischia, M. (2008) Nitro-fatty acid formation and signaling. *J. Biol. Chem. 283*, 15515–15519.

(30) Sawa, T., and Ohshima, H. (2006) Nitrative DNA damage in inflammation and its possible role in carcinogenesis. *Nitric Oxide 14*, 91–100.

(31) Niles, J. C., Wishnok, J. S., and Tannenbaum, S. R. (2001) A novel nitroimidazole compound formed during the reaction of peroxynitrite with 2′,3′,5′-tri-O-acetyl-guanosine. *J. Am. Chem. Soc. 123*, 12147–12151.

(32) Yermilov, V., Yoshie, Y., Rubio, J., and Ohshima, H. (1996) Effects of carbon dioxide/bicarbonate on induction of DNA single-strand breaks and formation of 8-nitroguanine, 8-oxoguanine and base-propenal mediated by peroxynitrite. *FEBS Lett. 399*, 67–70.

(33) Squadrito, G. L., and Pryor, W. A. (1998) Oxidative chemistry of nitric oxide: the roles of superoxide, peroxynitrite, and carbon dioxide. *Free Radic. Biol. Med. 25*, 392–403.

(34) Baker, P. R., Schopfer, F. J., Sweeney, S., and Freeman, B. A. (2004) Red cell membrane and plasma linoleic acid nitration products: synthesis, clinical identification, and quantitation. *Proc. Natl. Acad. Sci. U.S.A. 101*, 11577–11582.

(35) Baker, P. R., Lin, Y., Schopfer, F. J., Woodcock, S. R., Groeger, A. L., Batthyany, C., Sweeney, S., Long, M. H., Iles, K. E., Baker, L. M., Branchaud, B. P., Chen, Y. E., and Freeman, B. A. (2005) Fatty acid transduction of nitric oxide signaling: multiple nitrated unsaturated fatty acid derivatives exist in human blood and urine and serve as endogenous peroxisome proliferator-activated receptor ligands. *J. Biol. Chem. 280*, 42464–42475.

(36) Balazy, M., Iesaki, T., Park, J. L., Jiang, H., Kaminski, P. M., and Wolin, M. S. (2001) Vicinal nitrohydroxyeicosatrienoic acids: vasodilator lipids formed by reaction of nitrogen dioxide with arachidonic acid. *J. Pharmacol. Exp. Ther. 299*, 611–619.

(37) Lima, E. S., Di Mascio, P., and Abdalla, D. S. (2003) Cholesteryl nitrolinoleate, a nitrated lipid present in human blood plasma and lipoproteins. *J. Lipid Res. 44*, 1660–1666.

(38) Lima, E. S., Di Mascio, P., Rubbo, H., and Abdalla, D. S. (2002) Characterization of linoleic acid nitration in human blood plasma by mass spectrometry. *Biochemistry 41*, 10717–10722.

(39) Batthyany, C., Schopfer, F. J., Baker, P. R., Duran, R., Baker, L. M., Huang, Y., Cervenansky, C., Branchaud, B. P., and Freeman, B. A. (2006) Reversible post-translational modification of proteins by nitrated fatty acids in vivo. *J. Biol. Chem. 281*, 20450–20463.

(40) Baker, L. M., Baker, P. R., Golin-Bisello, F., Schopfer, F. J., Fink, M., Woodcock, S. R., Branchaud, B. P., Radi, R., and Freeman, B. A. (2007) Nitro-fatty acid reaction with glutathione and cysteine. Kinetic analysis of thiol alkylation by a Michael addition reaction. *J. Biol. Chem. 282*, 31085–31093.

(41) Akaike, T., Okamoto, S., Sawa, T., Yoshitake, J., Tamura, F., Ichimori, K., Miyazaki, K., Sasamoto, K., and Maeda, H. (2003) 8-Nitroguanosine formation in viral pneumonia and its implication for pathogenesis. *Proc. Natl. Acad. Sci. U.S.A. 100*, 685–690.

(42) Yoshitake, J., Akaike, T., Akuta, T., Tamura, F., Ogura, T., Esumi, H., and Maeda, H. (2004) Nitric oxide as an endogenous mutagen for Sendai virus without antiviral activity. *J. Virol. 78*, 8709–8719.

(43) Yasuhara, R., Miyamoto, Y., Akaike, T., Akuta, T., Nakamura, M., Takami, M., Morimura, N., Yasu, K., and Kamijo, R. (2005) Interleukin-1β induces death in chondrocyte-like ATDC5 cells through mitochondrial dysfunction and energy depletion in a reactive nitrogen and oxygen species-dependent manner. *Biochem. J. 389*, 315–323.

(44) Sawa, T., Tatemichi, M., Akaike, T., Barbin, A., and Ohshima, H. (2006) Analysis of urinary 8-nitroguanine, a marker of nitrative nucleic acid damage, by high-performance liquid chromatography-electrochemical detection coupled with immunoaffinity purification: association with cigarette smoking. *Free Radic. Biol. Med. 40*, 711–720.

(45) Terasaki, Y., Akuta, T., Terasaki, M., Sawa, T., Mori, T., Okamoto, T., Ozaki, M., Takeya, M., and Akaike, T. (2006) Guanine nitration in idiopathic pulmonary fibrosis and its implication for carcinogenesis. *Am. J. Respir. Crit. Care Med. 174*, 665–673.

(46) Ohshima, H., Sawa, T., and Akaike, T. (2006) 8-Nitroguanine, a product of nitrative DNA damage caused by reactive nitrogen species: formation, occurrence, and implications in inflammation and carcinogenesis. *Antioxid. Redox Signaling 8*, 1033–1045.

(47) Tazawa, H., Tatemichi, M., Sawa, T., Gilibert, I., Ma, N., Hiraku, Y., Donehower, L. A., Ohgaki, H., Kawanishi, S., and Ohshima, H. (2007) Oxidative and nitrative stress caused by subcutaneous implantation of a foreign body accelerates sarcoma development in *Trp53*$^{\pm}$ mice. *Carcinogenesis 28*, 191–198.

(48) Yoshitake, J., Kato, K., Yoshioka, D., Sueishi, Y., Sawa, T., Akaike, T., and Yoshimura, T. (2008) Suppression of NO production and 8-nitroguanosine formation by phenol-containing endocrine-disrupting chemicals in LPS-stimulated macrophages: involvement of estrogen receptor-dependent or -independent pathways. *Nitric Oxide 18*, 223–228.

(49) Jones, D. P. (2008) Radical-free biology of oxidative stress. *Am. J. Physiol. Cell Physiol. 295*, C849–868.

(50) Mannick, J. B., Hausladen, A., Liu, L., Hess, D. T., Zeng, M., Miao, Q. X., Kane, L. S., Gow, A. J., and Stamler, J. S. (1999) Fas-induced caspase denitrosylation. *Science 284*, 651–654.

(51) Li, L., and Dixon, J. E. (2000) Form, function, and regulation of protein tyrosine phosphatases and their involvement in human diseases. *Semin. Immunol. 12*, 75–84.

(52) Li, S., and Whorton, A. R. (2003) Regulation of protein tyrosine phosphatase 1B in intact cells by *S*-nitrosothiols. *Arch. Biochem. Biophys. 410*, 269–279.

(53) Visse, R., and Nagase, H. (2003) Matrix metalloproteinases and tissue inhibitors of metalloproteinases: structure, function, and biochemistry. *Circ. Res. 92*, 827–839.

(54) Okamoto, T., Akaike, T., Sawa, T., Miyamoto, Y., van der Vliet, A., and Maeda, H. (2001) Activation of matrix metalloproteinases by peroxynitrite-induced protein S-glutathiolation via disulfide S-oxide formation. *J. Biol. Chem. 276*, 29596–29602.

(55) Zhang, Z., Kolls, J. K., Oliver, P., Good, D., Schwarzenberger, P. O., Joshi, M. S., Ponthier, J. L., and Lancaster, J. R., Jr. (2000) Activation of tumor necrosis factor-α-converting enzyme-mediated ectodomain shedding by nitric oxide. *J. Biol. Chem. 275*, 15839–15844.

(56) McCarthy, S. M., Bove, P. F., Matthews, D. E., Akaike, T., and van der Vliet, A. (2008) Nitric oxide regulation of MMP-9 activation and its relationship to modifications of the cysteine switch. *Biochemistry 47*, 5832–5840.

(57) Otvos, J. D., and Armitage, I. M. (1980) Structure of the metal clusters in rabbit liver metallothionein. *Proc. Natl. Acad. Sci. U.S.A. 77*, 7094–7098.

(58) Kroncke, K. D., Fehsel, K., Schmidt, T., Zenke, F. T., Dasting, I., Wesener, J. R., Bettermann, H., Breunig, K. D., and Kolb-Bachofen, V. (1994) Nitric oxide destroys zinc-sulfur clusters inducing zinc release from metallothionein and inhibition of the zinc finger-type yeast transcription activator LAC9. *Biochem. Biophys. Res. Commun. 200*, 1105–1110.

(59) Cousins, R. J., Liuzzi, J. P., and Lichten, L. A. (2006) Mammalian zinc transport, trafficking, and signals. *J. Biol. Chem. 281*, 24085–24089.

(60) Bernal, P. J., Leelavanichkul, K., Bauer, E., Cao, R., Wilson, A., Wasserloos, K. J., Watkins, S. C., Pitt, B. R., and St Croix, C. M. (2008) Nitric-oxide-mediated zinc release contributes to hypoxic regulation of pulmonary vascular tone. *Circ. Res. 102*, 1575–1583.

(61) Krezel, A., Hao, Q., and Maret, W. (2007) The zinc/thiolate redox biochemistry of metallothionein and the control of zinc ion fluctuations in cell signaling. *Arch. Biochem. Biophys. 463*, 188–200.

(62) Itoh, K., Tong, K. I., and Yamamoto, M. (2004) Molecular mechanism activating Nrf2-Keap1 pathway in regulation of adaptive response to electrophiles. *Free Radic. Biol. Med. 36*, 1208–1213.

(63) Dinkova-Kostova, A. T., Holtzclaw, W. D., and Kensler, T. W. (2005) The role of Keap1 in cellular protective responses. *Chem. Res. Toxicol. 18*, 1779–1791.

(64) Yamamoto, T., Suzuki, T., Kobayashi, A., Wakabayashi, J., Maher, J., Motohashi, H., and Yamamoto, M. (2008) Physiological significance of reactive cysteine residues of Keap1 in determining Nrf2 activity. *Mol. Cell. Biol. 28*, 2758–2770.

(65) Holland, R., Hawkins, A. E., Eggler, A. L., Mesecar, A. D., Fabris, D., and Fishbein, J. C. (2008) Prospective type 1 and type 2 disulfides of Keap1 protein. *Chem. Res. Toxicol. 21*, 2051–2060.

(66) Semenza, G. L. (2003) Targeting HIF-1 for cancer therapy. *Nat. Rev. Cancer 3*, 721–732.

(67) Wang, G. L., and Semenza, G. L. (1995) Purification and characterization of hypoxia-inducible factor 1. *J. Biol. Chem. 270*, 1230–1237.

(68) Ivan, M., Kondo, K., Yang, H., Kim, W., Valiando, J., Ohh, M., Salic, A., Asara, J. M., Lane, W. S., and Kaelin, W. G., Jr. (2001) HIFα targeted for VHL-mediated destruction by proline hydroxylation: implications for O_2 sensing. *Science 292*, 464–468.

(69) Jaakkola, P., Mole, D. R., Tian, Y. M., Wilson, M. I., Gielbert, J., Gaskell, S. J., Kriegsheim, A., Hebestreit, H. F., Mukherji, M., Schofield, C. J., Maxwell, P. H., Pugh, C. W., and Ratcliffe, P. J. (2001) Targeting of HIF-α to the von Hippel-Lindau ubiquitylation complex by O_2-regulated prolyl hydroxylation. *Science 292*, 468–472.

(70) Maxwell, P. H., Pugh, C. W., and Ratcliffe, P. J. (2001) The pVHL-hIF-1 system. A key mediator of oxygen homeostasis. *Adv. Exp. Med. Biol. 502*, 365–376.

(71) Li, F., Sonveaux, P., Rabbani, Z. N., Liu, S., Yan, B., Huang, Q., Vujaskovic, Z., Dewhirst, M. W., and Li, C. Y. (2007) Regulation of HIF-1α stability through S-nitrosylation. *Mol. Cell 26*, 63–74.

(72) Hara, M. R., Cascio, M. B., and Sawa, A. (2006) GAPDH as a sensor of NO stress. *Biochim. Biophys. Acta 1762*, 502–509.

(73) Hara, M. R., Agrawal, N., Kim, S. F., Cascio, M. B., Fujimuro, M., Ozeki, Y., Takahashi, M., Cheah, J. H., Tankou, S. K., Hester, L. D., Ferris, C. D., Hayward, S. D., Snyder, S. H., and Sawa, A. (2005) S-Nitrosylated GAPDH initiates apoptotic cell death by nuclear translocation following Siah1 binding. *Nat. Cell Biol. 7*, 665–674.

(74) Haendeler, J., Hoffmann, J., Tischler, V., Berk, B. C., Zeiher, A. M., and Dimmeler, S. (2002) Redox regulatory and anti-apoptotic functions of thioredoxin depend on S-nitrosylation at cysteine 69. *Nat. Cell Biol. 4*, 743–749.

(75) Sumbayev, V. V. (2003) S-Nitrosylation of thioredoxin mediates activation of apoptosis signal-regulating kinase 1. *Arch. Biochem. Biophys. 415*, 133–136.

(76) Barrett, W. C., DeGnore, J. P., Konig, S., Fales, H. M., Keng, Y. F., Zhang, Z. Y., Yim, M. B., and Chock, P. B. (1999) Regulation of PTP1B via glutathionylation of the active site cysteine 215. *Biochemistry 38*, 6699–6705.

(77) Levonen, A. L., Landar, A., Ramachandran, A., Ceaser, E. K., Dickinson, D. A., Zanoni, G., Morrow, J. D., and Darley-Usmar, V. M. (2004) Cellular mechanisms of redox cell signalling: role of cysteine modification in controlling antioxidant defences in response to electrophilic lipid oxidation products. *Biochem. J. 378*, 373–382.

(78) Buckley, B. J., Li, S., and Whorton, A. R. (2008) Keap1 modification and nuclear accumulation in response to *S*-nitrosocysteine. *Free Radic. Biol. Med. 44*, 692–698.

(79) Mohr, S., Hallak, H., de Boitte, A., Lapetina, E. G., and Brune, B. (1999) Nitric oxide-induced S-glutathionylation and inactivation of glyceraldehyde-3-phosphate dehydrogenase. *J. Biol. Chem. 274*, 9427–9430.

(80) Fang, J., and Holmgren, A. (2006) Inhibition of thioredoxin and thioredoxin reductase by 4-hydroxy-2-nonenal in vitro and in vivo. *J. Am. Chem. Soc. 128*, 1879–1885.

(81) Choi, Y. B., Tenneti, L., Le, D. A., Ortiz, J., Bai, G., Chen, H. S., and Lipton, S. A. (2000) Molecular basis of NMDA receptor-coupled ion channel modulation by S-nitrosylation. *Nat. Neurosci. 3*, 15–21.

(82) Lipton, S. A., Choi, Y. B., Takahashi, H., Zhang, D., Li, W., Godzik, A., and Bankston, L. A. (2002) Cysteine regulation of protein function—as exemplified by NMDA-receptor modulation. *Trends Neurosci. 25*, 474–480.

(83) Yoshida, T., Inoue, R., Morii, T., Takahashi, N., Yamamoto, S., Hara, Y., Tominaga, M., Shimizu, S., Sato, Y., and Mori, Y. (2006) Nitric oxide activates TRP channels by cysteine S-nitrosylation. *Nat. Chem. Biol. 2*, 596–607.

(84) Carbone, D. L., Doorn, J. A., Kiebler, Z., and Petersen, D. R. (2005) Cysteine modification by lipid peroxidation products inhibits protein disulfide isomerase. *Chem. Res. Toxicol. 18*, 1324–1331.

(85) Uehara, T., Nakamura, T., Yao, D., Shi, Z. Q., Gu, Z., Ma, Y., Masliah, E., Nomura, Y., and Lipton, S. A. (2006) S-Nitrosylated protein-disulphide isomerase links protein misfolding to neurodegeneration. *Nature 441*, 513–517.

(86) Matthews, J. R., Botting, C. H., Panico, M., Morris, H. R., and Hay, R. T. (1996) Inhibition of NF-κB DNA binding by nitric oxide. *Nucleic Acids Res. 24*, 2236–2242.

(87) Reynaert, N. L., Ckless, K., Korn, S. H., Vos, N., Guala, A. S., Wouters, E. F., van der Vliet, A., and Janssen-Heininger, Y. M. (2004) Nitric oxide represses inhibitory κB kinase through *S*-nitrosylation. *Proc. Natl. Acad. Sci. U.S.A. 101*, 8945–8950.

(88) Alam, M. S., Akaike, T., Okamoto, S., Kubota, T., Yoshitake, J., Sawa, T., Miyamoto, Y., Tamura, F., and Maeda, H. (2002) Role of nitric oxide in host defense in murine salmonellosis as a function of its antibacterial and antiapoptotic activities. *Infect. Immun. 70*, 3130–3142.

(89) Alam, M. S., Zaki, M. H., Sawa, T., Islam, S., Ahmed, K. A., Fujii, S., Okamoto, T., and Akaike, T. (2008) Nitric oxide produced in Peyer's patches exhibits antiapoptotic activity contributing to an antimicrobial effect in murine salmonellosis. *Microbiol. Immunol. 52*, 197–208.

(90) Dhakshinamoorthy, S., and Porter, A. G. (2004) Nitric oxide-induced transcriptional up-regulation of protective genes by Nrf2 via the antioxidant response element counteracts apoptosis of neuroblastoma cells. *J. Biol. Chem. 279*, 20096–20107.

(91) Sahoo, S. K., Sawa, T., Fang, J., Tanaka, S., Miyamoto, Y., Akaike, T., and Maeda, H. (2002) Pegylated zinc protoporphyrin: a water-soluble heme oxygenase inhibitor with tumor-targeting capacity. *Bioconjugate Chem. 13*, 1031–1038.

(92) Fang, J., Sawa, T., Akaike, T., Akuta, T., Sahoo, S. K., Khaled, G., Hamada, A., and Maeda, H. (2003) In vivo antitumor activity of pegylated zinc protoporphyrin: targeted inhibition of heme oxygenase in solid tumor. *Cancer Res. 63*, 3567–3574.

(93) Fang, J., Sawa, T., Akaike, T., Greish, K., and Maeda, H. (2004) Enhancement of chemotherapeutic response of tumor cells by a heme oxygenase inhibitor, pegylated zinc protoporphyrin. *Int. J. Cancer 109*, 1–8.

(94) Sawa, T., Akaike, T., Ichimori, K., Akuta, T., Kaneko, K., Nakayama, H., Stuehr, D. J., and Maeda, H. (2003) Superoxide generation mediated by 8-nitroguanosine, a highly redox-active nucleic acid derivative. *Biochem. Biophys. Res. Commun. 311*, 300–306.

(95) Kass, D. A., Takimoto, E., Nagayama, T., and Champion, H. C. (2007) Phosphodiesterase regulation of nitric oxide signaling. *Cardiovasc. Res. 75*, 303–314.

(96) Dickinson, D. A., and Forman, H. J. (2002) Cellular glutathione and thiols metabolism. *Biochem. Pharmacol. 64*, 1019–1026.

(97) Martin, H. L., and Teismann, P. (2009) Glutathione--a review on its role and significance in Parkinson's disease. *FASEB J. 23*, 3263–3272.

(98) Hansen, J. M., Go, Y. M., and Jones, D. P. (2006) Nuclear and mitochondrial compartmentation of oxidative stress and redox signaling. *Annu. Rev. Pharmacol. Toxicol. 46*, 215−234.

(99) Martinez-Ruiz, A., and Lamas, S. (2007) Signalling by NO-induced protein S-nitrosylation and S-glutathionylation: convergences and divergences. *Cardiovasc. Res. 75*, 220–228.

(100) Rhee, S. G. (2006) Cell signaling. H_2O_2, a necessary evil for cell signaling. *Science 312*, 1882–1883.

(101) D'Autreaux, B., and Toledano, M. B. (2007) ROS as signalling molecules: mechanisms that generate specificity in ROS homeostasis. *Nat. Rev. Mol. Cell Biol. 8*, 813–824.

BC900396U

BF_2-Chelated Tetraarylazadipyrromethenes as NIR Fluorochromes

Mariusz Tasior and Donal F. O'Shea*

Centre for Synthesis and Chemical Biology, School of Chemistry and Chemical Biology, University College Dublin, Belfield, Dublin 4, Ireland. Received February 1, 2010; Revised Manuscript Received May 7, 2010

The synthesis and properties of a new visible red/near-infrared fluorochrome for bioconjugation via activated ester groups is described. Representative amine conjugations with amino acid lysine and proteins lysozyme and trypsin were successfully accomplished.

In recent years, there has been growing interest in near-infrared (NIR) fluorochromes (>700 nm) for qualitative and quantitative assays (*1*). Their simplicity of use coupled with high sensitivity ensures a continual expansion of their applications for in vitro and in vivo imaging (*2*). The inherent advantage of NIR fluorochromes over those that absorb in the shorter blue and green wavelengths lies in the dramatic reduction in background autofluorescence which leads to greatly improved sensitivity (*3*). In spite of these benefits, there are limited compound classes which have the desired absorption and emission properties, with cyanine dyes such as Cy5 **1a** and Cy5.5 **1b** remaining the most widely utilized visible red/NIR fluorescent probes for bioconjugation (Figure 1) (*4*−*8*). As such, a distinct need exists for new classes of NIR emitting fluorochromes, and thus, intensive efforts have recently been put into their development (*9*).

Our efforts have focused on the boron chelated tetraarylazadipyrromethene class **2**, as they are relatively easily synthesized, amenable to structural modification, and exhibit excellent spectral properties (*10*, *11*). For example, the tetraaryl analogue **2** has an absorption λ_{max} at 696 nm and emission at 727 nm in formulated aqueous solutions (Figure 2) (*11*). These promising photophysical characteristics have encouraged the adaption of this class to specific functions such as fluorescent sensors (*12*−*15*) and photodynamic therapeutic agents (*16*−*18*). In this paper, we present the synthesis and spectral properties of the first fluorochromes, based on this fluorophore scaffold, capable of amine conjugations. Our strategy was to exploit the bisphenol analogue **3** as a key synthetic starting point (*19*). Synthetic manipulation of the phenolic rings by differential oxygen alkylation would be utilized to introduce a water-solubilizing group on one ring and a conjugation group on the other (Figure 2).

For this first study, our approach was to impart partial aqueous solubility to the fluorophore by introducing a polyether on one phenol ring and a spacer-conjugatable activated ester group on the other. It was anticipated that a single polyether alone would not be sufficient to impart complete water solubility but perhaps sufficient to facilitate the conjugation reaction. While other charged solubilizing groups are currently under investigation, this approach offers the potential to produce an overall charge-neutral fluorochrome, which may limit the complications of noncovalent charge interactions of fluorophore and the conjugating biomolecule. Two different activated esters, *N*-hydroxysuccinimide and a sulfonated *N*-hydroxysulfosuccinimide sodium salt, were investigated; the latter would provide enhanced aqueous solubility without introducing charge directly onto the fluorophore.

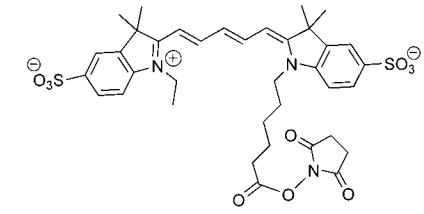


Figure 1. Structures of Cy5 and Cy5.5.

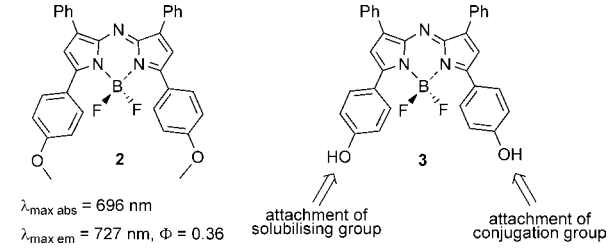


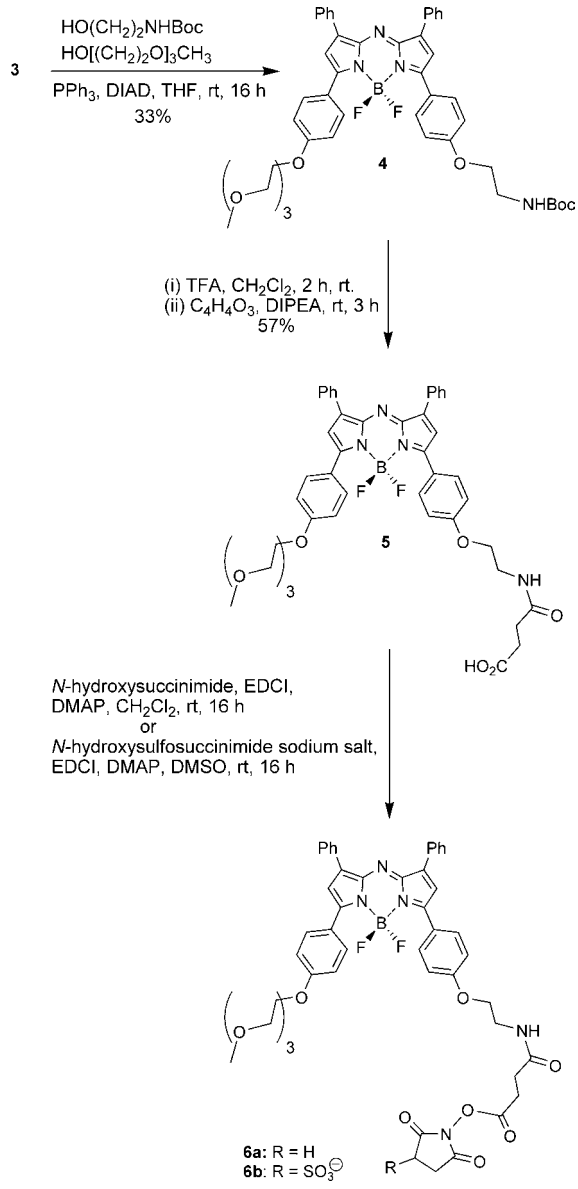
Figure 2. BF_2 Chelated Tetraarylazadipyrromethenes.

The synthetic challenge of functionalizing the equivalent phenols of **3** with differing substituents was achieved utilizing simultaneous Mitsunobu coupling of **3** with two different alcohols. It was found that rather than reacting the phenols in successive steps conditions were optimized to achieve this in a single operation. As such, desymmetrization of **3** was achieved in one step by condensation with the two different alcohols, the polyether triethylene glycol monomethyl ether and *N*-Boc protected ethanolamine under standard coupling conditions (Scheme 1). This afforded a mixture of a bis-polyether, a bis-*N*-Boc amine, and the desired product monopolyether, monoamine substituted product **4**. Chromatographic separation of **4** from unwanted symmetrical coupling products was achievable due to the large differences in retention factors on silica. This

* Tel: +353-(0)1-7162425; E-mail: donal.f.oshea@ucd.ie.

10.1021/bc100051p © 2010 American Chemical Society
Published on Web 06/10/2010

Scheme 1. Fluorochrome Synthesis



approach proved superior to a stepwise introduction of the different phenolic substituents due to poorer overall conversions and more difficult purifications. The introduction of a four-carbon spacer unit was achieved by the Boc-deprotection of **4** with TFA in CH_2Cl_2 and reaction with succinic anhydride to yield the carboxylic acid **5**. Subsequently, **5** was transformed into the activated ester **6a** or **6b** by coupling with *N*-hydroxysuccinimide or *N*-hydroxysulfosuccinimide respectively (Scheme 1, Supporting Information Figure S1). Fluorochrome **6a** was a bench-stable solid, and due to the higher reactivity of **6b**, it was directly used upon generation.

Spectroscopic analysis of **4** and **5** as representative constituent building blocks of the fluorescent probe showed very little variance in their properties with absorbance maxima at 688 and 691 nm, respectively, and fluorescence maxima at 714 nm for both (Table 1, Figure 3). Both had extinction coefficients in excess of 80 000 and good fluorescence quantum yields (Table 1). Their spectral features were also relatively insensitive to solvent polarity (Supporting Information, Figure S2).

Activated succinimide esters typically react with the *N*-terminus α-amino group and the amine of lysine constituent amino acids. Illustrative coupling of **6a** in organic and **6b** in aqueous solutions with N_ε-Boc-L-lysine rapidly gave amino acid

Table 1. Spectroscopic Properties[a]

entry	compound	λ_{max}abs nm[b]	ε M^{-1} cm^{-1}	λ_{max}emission nm[c,d,e]	Φ_f[f]
1	**4**	688	95 000	714	0.23
2	**5**	691	85 500	714	0.20
3	**7**	691	74 500	714	0.22

[a] In ethanol. [b] Conc 5×10^{-6} M. [c] Conc 5×10^{-7} M. [d] Excitation at 640 nm. [e] Slit widths 5 nm. [f] **2** used as standard.

substituted derivative **7** (Scheme 2). Encouragingly, the spectroscopic properties of **7** differed very little from those of its precursor **5** (Table 1, Figure 3).

Next, the conjugation of **6a** and **b** with the 14.4 kDa protein lysozyme was examined. Lysozyme was chosen as a representative substrate, as it has six potentially reactive lysine residues in addition to the *N*-terminal amine (*20, 21*). Conjugation of lysozyme with 5 equiv of **6a** was carried out in 1:1 water/DMSO and 4:1 water/THF mixtures and **6b** was coupled in pH 8.3 $NaHCO_3$ buffered water. Coupling was effectively achieved in all cases and confirmed by MALDI-TOF mass spectrometry and HPLC analysis (Supporting Information, Figure S3). Encouragingly, the MALDI analysis of the conjugates identified a distribution of mono to pentaconjugates from both **6a** and **6b** with each conjugate separated by an approximate mass of 800 amu (Figure 4 and Supporting Information Figure S3). As might be expected, the coupling of **6b** was superior to that of **6a** with the triconjugated protein being observed as the most abundant from coupling with 5 equiv of fluorochrome (Figure 4). The high loading achievable illustrates the effectiveness of the coupling reaction and reactive nature of the fluorochromes. The use of greater ratios of fluorochrome **6b** (10 and 20 equiv) to protein increased the loading levels with the tri to pentaconjugates being the most abundant (Supporting Information, Figure S3). A further confirmatory coupling of 10 equiv of **6b** with

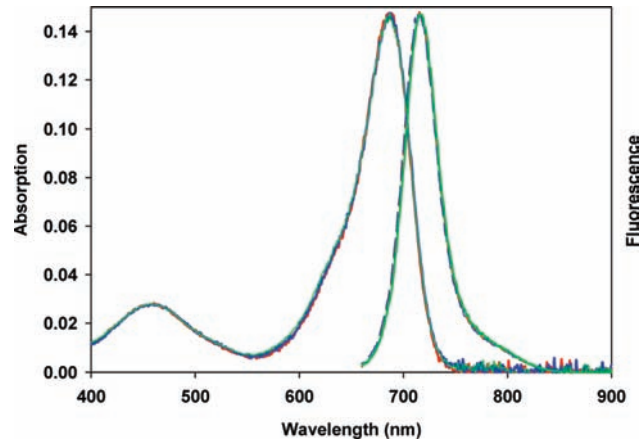
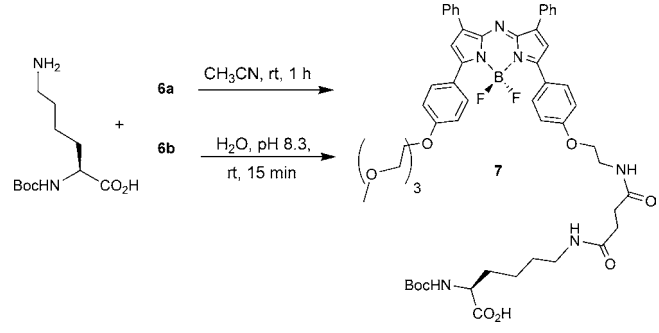


Figure 3. Normalized absorption (5×10^{-6} M) and emission (5×10^{-7} M) spectra of **4** (red line), **5** (blue line), and **7** (green line) in EtOH.

Scheme 2. Coupling of 6a and 6b with N_ε-Boc-L-lysine



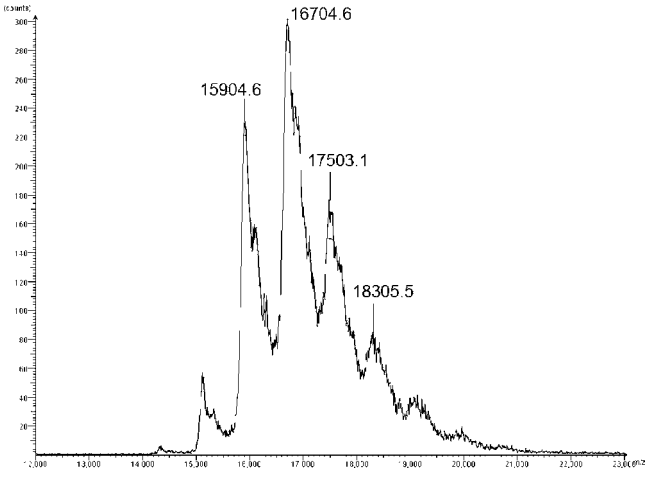
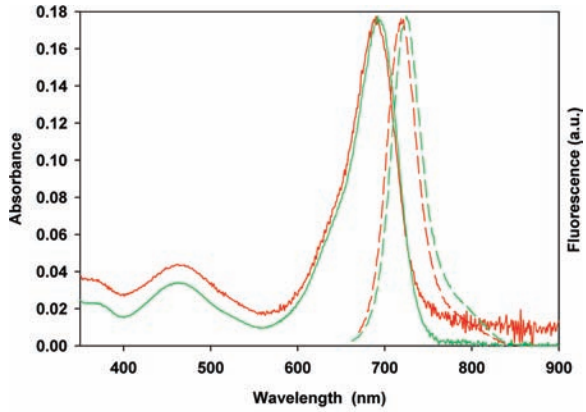


Figure 4. MALDI-MS of lysozyme conjugated with 5 equiv of **6b**. Diconjugate, 15 904; triconjugate, 16 704; tetraconjugate, 17 503; pentaconjugate, 18 305 *m/z*.



Entry	Conjugate	λ_{max}abs nm[a]	λ_{max}emiss nm[a,b,c]
1	lysozyme	690	720
2	trypsin	692	725

[a]PBS pH 7.0 with 0.4% SDS. [b] excitation at 640 nm. [c]slit widths 5 nm.

Figure 5. Normalized absorption (left) and emission (right) spectra of lysozyme (red line) and trypsin (green line) in aqueous PBS.

the 23.3 kDa protein trypsin in PBS at pH 7.5 gave a distribution of mono and difunctionalized enzyme (Supporting Information, Figure S4) (*22*).

Spectral analysis of the lysozyme and trypsin conjugates show that the attractive spectral features of this chromophore such as sharp absorption and emission bands are retained (Figure 5). Importantly, the emission maxima of both were above 720 nm.

In summary, we have outlined a short synthesis to a new NIR fluorchrome and illustrated its potential for effective amine conjugations with amino acids and proteins. Their application to in vivo use is currently under investigation and will be reported upon in due course. The development of further fluorochrome derivatives by combining different solubilizing groups (*23*) and conjugation methods is also ongoing.

EXPERIMENTAL SECTION

Synthesis of 4. Compound **3** (630 mg, 1.2 mmol), triethylene glycol monomethyl ether (294 μL, 1.8 mmol), *N*-Boc ethanolamine (285 μL, 1.8 mmol), and PPh_3 (1.257 g, 4 mmol) were dissolved in dry THF (100 mL). DIAD (969 μL, 4 mmol) in dry THF (5 mL) was slowly (20 min) added to the solution and the reaction mixture stirred at r.t. for 16 h. Solvent was removed under reduced pressure and dark green residue was chromatographed (silica, AcOEt/cyclohexane gradient of 1:1 to 4:1). Middle green fraction was isolated (R_f = 0.35, silica, AcOEt/cyclohexane, 4:1), evaporated and rechromatographed (silica, AcOEt/CH_2Cl_2, 1:4) to give **4** (321 mg, 33%) as a dark green solid. Mp = 51−53 °C. δ_H (500 MHz, $CDCl_3$): 1.47 (s, 9H), 3.38 (s, 3H), 3.54−3.58 (m, 4H), 3.67 (t, J = 4.6 Hz, 2H), 3.70 (t, J = 4.6 Hz, 2H), 3.76 (t, J = 4.6 Hz, 2H), 3.90 (t, J = 4.6 Hz, 2H), 4.11 (t, J = 4.6 Hz, 2H), 4.22 (t, J = 4.6 Hz, 2H), 4.99 (br s, 1H), 6.97−7.06 (m, 6H), 7.39−7.48 (m, 6H), 8.04−8.10 (m, 8H). δ_C (125 MHz, $CDCl_3$): δ 161.2, 160.8, 158.3, 157.8, 155.8, 145.4, 143.2, 132.4, 131.6, 129.2, 128.5, 124.5, 124.2, 118.7, 118.5, 114.8, 114.6, 79.6, 71.9, 70.9, 70.7, 70.6, 69.6, 67.6, 67.3, 59.0, 40.0, 28.4. HRMS (ES) calcd for $C_{46}H_{49}N_4O_7NaBF_2$ [M + Na^+]$^+$: 841.3560, found 841.3571. IR (KBr disk) cm^{-1}: 1504, 1603, 1710. λ_{abs} ($CHCl_3$, $\varepsilon \times 10^{-3}$) 689 (87.1), 450 (17.3), 367 (11.9), 318 (26.0) nm. λ_{emiss} ($CHCl_3$): 717 nm, Φ 0.36 (**2** used as standard Φ = 0.36).

Synthesis of 5. Compound **4** (164 mg, 200 μmol) was dissolved in CH_2Cl_2 (10 mL), TFA (1 mL) was slowly added and the reaction mixture was stirred at r.t. for 2 h. Saturated aqueous $NaHCO_3$ was added and the resulting suspension extracted with CH_2Cl_2 (2 × 30 mL). The combined organic phases were washed with water, dried over Na_2SO_4, and evaporated to dryness. The resulting green residue was dissolved in dry THF (10 mL), treated with succinic anhydride (24 mg, 240 μmol) and DIPEA (70 μL, 400 mmol), and stirred at r.t. for 3 h. Solvent was removed under reduced pressure and the residue chromatographed (silica, MeOH/CH_2Cl_2, 2:8) to give **5** (93 mg, 57%) as a dark green solid. Mp = 72−74 °C. δ_H (500 MHz, $CDCl_3$): 2.45 (t, J = 6.2 Hz, 2H), 2.65 (t, J = 6.2 Hz, 2H), 3.36 (s, 3H), 3.52−3.55 (m, 2H), 3.56−3.61 (m, 2H), 3.62−3.68 (m, 4H), 3.70−3.74 (m, 2H), 3.85 (t, J = 4.7 Hz, 2H), 4.01 (t, J = 4.7 Hz, 2H), 4.16 (t, J = 4.7 Hz, 2H), 6.45 (s, 1H), 6.87−7.01 (m, 6H), 7.34−7.44 (m, 6H), 7.92−8.08 (m, 8H). δ_C (100 MHz, $CDCl_3$): 26.9, 58.9, 66.5 (br), 67.5, 69.4, 70.4, 70.5, 70.7, 71.8, 114.5, 114.7, 118.4, 118.6, 124.1, 124.2, 128.3, 128.4, 129.0, 129.14, 129.17, 131.5 (br), 131.6 (br), 132.1, 132.4, 142.56, 142.59, 142.7, 145.0, 145.2, 157.5, 157.8, 160.7, 161.0. HRMS (ESI) calcd for $C_{45}H_{45}N_4O_8NaBF_2$ [M + Na^+]$^+$: 841.3196, found 841.3215. IR (KBr disk) cm^{-1}: 1509, 1602, 1655. λ_{abs} ($CHCl_3$) 689 nm. λ_{emiss} ($CHCl_3$): 717 nm.

Synthesis of 6a. Compound **5** (27 mg, 33 μmol), *N*-hydroxysuccinimide (5.2 mg, 45 μmol) and DMAP (cat.) were dissolved in dry DCM (5 mL). 1-Ethyl-3-(3′-dimethylaminopropyl)carbodiimide (EDCI) (8.8 mg, 45 μmol) was added at 0 °C and the resulting mixture stirred at r.t. for 16 h. The organic phase was washed with HCl (1 M, 1 mL), then water (2 mL), and dried over Na_2SO_4. Solvent was removed under reduced pressure to give **6a** (28 mg, 99%) as a dark green solid. δ_H (500 MHz, $CDCl_3$): 2.54 (t, J = 7 Hz, 2H), 2.57 (s, 4H), 2.91 (t, J = 7 Hz, 2H), 3.30 (s, 3H), 3.46−3.49 (m, 2H), 3.56−3.64 (m, 6H), 3.65−3.69 (m, 2H), 3.81 (t, J = 5 Hz, 2H), 4.01 (t, J = 5 Hz, 2H), 4.13 (t, J = 5 Hz, 2H), 6.18 (t, J = 5.6 Hz, 1H), 6.87−6.97 (m, 6H), 7.31−7.39 (m, 6H), 7.95−8.00 (m, 8H). HRMS (ESI) calcd for $C_{49}H_{48}BF_2N_5O_{10}Na$ [M + Na^+]$^+$: 938.3360, found 938.3886. IR (KBr disk) cm^{-1}: 1603, 3054.

Synthesis of 6b. Compound **5** (5 mg, 6.11 μmol), *N*-hydroxysulfosuccinimide sodium salt (1.4 mg, 6.4 μmol), 1-ethyl-3-(3′-dimethylaminopropyl)carbodiimide hydrochloride (1.2 mg, 6.2 μmol), and DMAP (cat.) were dissolved in dry in DMSO (200 μL) were stirred at r.t. for 16 h, under nitrogen. Monitoring the reaction by reverse-phase HPLC (C-18 column eluting with acetonitrile water 7:3) complete consumption of starting material. The solution was used directly for conjugation experiments. HRMS (ESI) calcd for $C_{49}H_{47}BF_2N_5O_{13}S$ [M − H^+]$^-$: 994.2952, found 994.2911.

Conjugation with N_ε-Boc-L-lysine, Synthesis of 7. Activated ester **6a** (11 mg, 12 μmol), Boc-lysine (6 mg, 24 μmol), and DIEA (4.3 μL, 24 μmol) were suspended in dry acetonitrile (5 mL) and stirred for 1 h under nitrogen. Solvent was removed, and the residue was chromatographed (silica, CH_2Cl_2/MeOH, 9:1 then 8:2, 7:3) affording **7** (9.5 mg, 76%) as green solid. A solution of activated ester **6b** (6.0 μmol) was added to Boc-lysine (3 mg, 12 μmol) solution in 0.1 M $NaHCO_3$ (1 mL, pH = 8.3). After 15 min, the resulting mixture was acidified with 2 M HCl and extracted with AcOEt. Subsequent chromatography (silica, CH_2Cl_2/MeOH, 7:3) afforded **7** as green solid (4 mg, 63%). ^{1}H NMR (500 MHz, $CDCl_3$) 1.26−1.46 (m, 4H), 1.39 (s, 9H), 1.55−1.65 (m, 2H), 1.70−1.80 (m, 2H), 2.25−240 (m, 2H), 2.46−2.54 (m, 2H), 3.12−3.18 (m, 2H), 3.34 (s, 3H), 3.52−3.55 (m, 2H), 3.50−3.53 (m, 2H), 3.60−3.66 (m, 4H), 3.68−3.71 (m, 2H), 3.82 (t, 2H), 3.95−4.02 (m, 3H), 4.10−4.16 (m, 2H), 5.83 (s, 1H), 6.83−6.97 (m, 6H), 7.05 (s, 1H), 7.22 (s, 1H), 7.29−7.40 (m, 6H), 7.90−8.05 (m, 8H). ^{13}C NMR (100 MHz, $CDCl_3$) δ: 173.2, 172.8, 161.1, 160.8, 157.8, 156.1, 145.2, 145.1, 142.9, 118.6, 114.7, 114.6, 71.8, 70.8, 70.5, 70.4, 69.5, 67.5, 66.6, 59.0, 28.5. HRMS (ESI) calcd for $C_{56}H_{65}BF_2N_6O_{11}Na$ $[M + Na^+]^+$: 1069.4670, found 1069.5371. IR (KBr disk) cm^{-1}: 1475, 1506, 1603, 1657, 3055.

ACKNOWLEDGMENT

We would like to thank Science Foundation Ireland and The Irish Research Council for Science, Engineering and Technology for financial support. Thanks to Dr. F. Paradisi for helpful discussions and Marco Grossi for technical assistance.

Supporting Information Available: Conjugation experimental procedures, UV−visible and fluorescence spectra, NMR spectra, MALDI-TOF data. This material is available free of charge via the Internet at http://pubs.acs.org.

LITERATURE CITED

(1) Ntziachristos, V., Ripoll, J., Wang, L. V., and Weissleder, R. (2005) Looking and listening to light: the evolution of whole-body photonic imaging. *Nat. Biotechnol. 23*, 313–20.

(2) De Grand, A. M., and Frangioni, J. V. (2006) An operational near-infrared fluorescence imaging system prototype for large animal surgery. *Technol. Can. Res. Treat. 2*, 553–62.

(3) Rudin, M., and Weissleder, R. (2003) Molecular imaging in drug discovery and development. *Nat. Rev. Drug Discovery 2*, 123–31.

(4) Mujumdar, R. B., Ernst, L. A., Mujumdar, S. R., Lewis, C. J., and Waggoner, A. S. (1993) Cyanine dye labeling reagents - sulfoindocyanine succinimidyl esters. *Bioconjugate Chem. 4*, 105–11.

(5) Mujumdar, S. R., Mujumdar, R. B., Grant, C. M., and Waggoner, A. S. (1996) Cyanine-labeling reagents: Sulfobenzindocyanine succinimidyl esters. *Bioconjugate Chem. 7*, 356–62.

(6) Buschmann, V., Weston, K. D., and Sauer, M. (2003) Spectroscopic study and evaluation of red-absorbing fluorescent dyes. *Bioconjugate Chem. 14*, 195–204.

(7) Veiseh, M., Gabikian, P., Bahrami, S.-B., Veiseh, O., Zhang, M., Hackman, R. C., Ravanpay, A. C., Stroud, M. R., Kusuma, Y., Hansen, S. J., Kwok, D., Munoz, N. M., Sze, R. W., Grady, W. M., Greenberg, N. M., Ellenbogen, R. G., and Olson, J. M. (2007) Tumor paint: A Chlorotoxin: Cy5.5 bioconjugate for intraoperative visualization of cancer foci. *Cancer Res. 67*, 6882–8.

(8) Bogdanov, A. A., Jr., Lin, C. P., and Kang, H.-W. (2007) Optical imaging of the adoptive transfer of human endothelial cells in mice using anti-human CD31 monoclonal antibody. *Pharm. Res. 24*, 1186–92.

(9) Yang, Y., Lowry, M., Xu, X., Escobedo, J. O., Sibrian-Vazquez, M., Wong, L., Schowalter, C. M., Jensen, T. J., Fronczek, F. R., Warner, I. M., and Strongin, R. M. (2008) Seminaphthofluorones are a family of water-soluble, low molecular weight, NIR-emitting fluorophores. *Proc. Natl. Acad. Sci. U.S.A. 105*, 8829–34.

(10) Killoran, J., Allen, L., Gallagher, J. F., Gallagher, W. M., and O'Shea, D. F. (2002) Synthesis of BF_2 chelates of tetraarylazadipyrromethenes and evidence for their photodynamic therapeutic behaviour. *Chem. Commun.* 1862–3.

(11) Gorman, A., Killoran, J., O'Shea, C., Kenna, T., Gallagher, W. M., and O'Shea, D. F. (2004) In vitro demonstration of the heavy-atom effect for photodynamic therapy. *J. Am. Chem. Soc. 126*, 10619–31.

(12) Hall, M. J., Allen, L. T., and O'Shea, D. F. (2006) PET modulated fluorescent sensing from the BF_2 chelated azadipyrromethene platform. *Org. Biomol. Chem. 4*, 776–80.

(13) McDonnell, S. O., and O'Shea, D. F. (2006) Near-infrared sensing properties of dimethlyamino-substituted BF_2-azadipyrromethenes. *Org. Lett. 8*, 3493–6.

(14) Gawley, R. E., Mao, H., Mahbubul Haque, M., Thorne, J. B., and Pharr, J. S. (2007) Visible fluorescence chemosensor for saxitoxin. *J. Org. Chem. 72*, 2187–91.

(15) Loudet, A., Bandichhor, R., Wu, L., and Burgess, K. (2008) Functionalized BF_2 chelated azadipyrromethene dyes. *Tetrahedron 64*, 3642–54.

(16) McDonnell, S. O., Hall, M. J., Allen, L. T., Byrne, A., Gallagher, W. M., and O'Shea, D. F. (2005) Supramolecular photonic therapeutic agents. *J. Am. Chem. Soc. 127*, 16360–1.

(17) Gallagher, W. M., Allen, L. T., O'Shea, C., Kenna, T., Hall, M., Killoran, J., and O'Shea, D. F. (2005) A potent nonporphyrin class of photodynamic therapeutic agent: cellular localisation, cytotoxic potential and influence of hypoxia. *Br. J. Cancer 92*, 1702–10.

(18) Byrne, A. T., O'Connor, A., Hall, M., Murtagh, J., O'Neill, K., Curran, K., Mongrain, H., Rousseau, J. A., Lecomte, R., McGee, S., Callanan, J. J., O'Shea, D. F., and Gallagher, W. M. (2009) Vascular-targeted photodynamic therapy with BF_2-chelated tetraaryl-azadipyrromethene agents: a multi-modality molecular imaging approach to therapeutic assessment. *Br. J. Cancer 101*, 1565–73.

(19) Murtagh, J., Frimannsson, D. O., and O'Shea, D. F. (2009) Azide conjugatable and pH responsive near-infrared fluorescent imaging probes. *Org. Lett. 11*, 5386–9.

(20) Teske, C. A., Simon, R., Niebisch, A., and Hubbuch, J. (2007) Changes in retention behavior of fluorescently labeled proteins during ion-exchange chromatography caused by different protein surface labeling positions. *Biotechnol. Bioeng. 98*, 193–200.

(21) Masuda, T., Ide, N., and Kitabatake, N. (2005) Effects of chemical modification of lysine residues on the sweetness of lysozyme. *Chem. Senses 30*, 253–64.

(22) Melchior, R., Quigley, J. P., and Armstrong, P. B. (1995) Alpha (2)-macroglobulin-mediated clearence of proteases from the plasma of the American horseshoe-crab, *Limulus Polyphemus*. *J. Biol. Chem. 270*, 13496–502.

(23) For alternative solubilizing approaches, see Tasior, M., Murtagh, J., Frimannsson, D. O., McDonnell, S. O., and O'Shea, D. F. (2010) Water-solubilised BF_2-chelated tetraarylazadipyrromethenes. *Org. Biomol. Chem. 8*, 522–5.

BC100051P

A Human Single Chain Transbody Specific to Matrix Protein (M1) Interferes with the Replication of Influenza A Virus

Ornnuthchar Poungpair,[†] Anek Pootong,[†] Santi Maneewatch,[‡,⊥] Potjanee Srimanote,[†] Pongsri Tongtawe,[†] Thaweesak Songserm,[§] Pramuan Tapchaisri,[†] and Wanpen Chaicumpa*[,‡]

Faculty of Allied Health Sciences, Thammasat University, Rangsit Center, Pathumthani 12120, Thailand, Department of Parasitology, Faculty of Medicine Siriraj Hospital, Mahidol University, Bangkok 10700, Thailand, and Department of Pathology, Faculty of Veterinary Medicine, Kasetsart University, Kampaengsaen Campus, Thailand. Received June 6, 2009; Revised Manuscript Received January 18, 2010

A cell penetrating format of human single chain antibody (HuScFv) specific to matrix protein (M1) of influenza A virus was produced by molecular linking of the gene sequence encoding the HuScFv (*huscfv*) to a protein transduction domain, i.e., penetratin (PEN) of the *Drosophila* homeodomain. DNA of a recombinant phagemid vector carrying the *huscfv* was used as a platform template in a three-step PCR for generating a nucleotide sequence encoding a 16 amino acid PEN peptide. The PEN-HuScFv had negligible cytotoxicity on living MDCK cells. They were readily translocated across the cell membrane and bound to native M1 in the A/H5N1-infected cells as revealed by immunofluorescent confocal microscopy. The PEN-HuScFv, when used to treat the influenza virus infected cells, reduced the number of viruses released from the cells. In conclusion, the cell penetrating M1-specific HuScFv, a transbody, produced in this study affected the influenza A virus life cycle in living mammalian cells. While the molecular mechanisms of the PEN-HuScFv need more investigation, the reagent warrants further testing in animals before developing it into a human immunotherapeutic anti-influenza formula.

INTRODUCTION

Antibodies have been used for treatment and intervention of diseases even before the discovery of the first antibiotics (*1*). However, most infectious diseases, especially bacterial infections, are currently treated by antimicrobial agents. Nevertheless, antibodies still have their niche in the treatment of viral infections and intoxications (*1*−*6*). For influenza, therapeutic antibodies that bind specifically to and interfere with the functions of the viral proteins should mitigate the problems of the unavailability of an effective broad-spectrum influenza vaccine, the inadequate supply of antiviral drugs, and drug-resistant influenza variants. Besides, the antibodies may be used as an adjunct of any drug to increase its efficacy for influenza treatment.

The matrix protein (M1) encoded by the RNA segment 7 of the influenza A viruses is conserved and has been used as a basis for the influenza virus classification into types A, B, and C (*7*). M1 is highly conserved among type A viruses. It plays an important role in various steps of the virus replication including the exit of the viral RNP (vRNP) from the endocytic vacuole to the host cytoplasm for further replication in the nucleus (*8*). M1 is believed to be essential in releasing the newly formed vRNP from the nuclear matrix (*9*). Thereafter, the M1 in conjunction with NEP (NS2 protein) encoded by the RNA segment 8 exports the vRNP from the nucleus to the cytosol for further viral assembly and budding (*8*−*12*). M1 also prevents the nuclear re-import of the newly synthesized vRNP (*13, 14*). Thus, both M1 and the M1-coding RNA segment are attractive targets for drug inhibitors, siRNA, and therapeutic antibodies (*15*−*17*).

Recently, fully human single chain antibody fragments (HuScFv) that bound specifically to the M1 of various influenza A subtypes including the highly pathogenic avian influenza (HPAI) H5N1, H1N1, and H3N2 and the less pathogenic avian influenza H8N4 viruses were produced using a human antibody phage display technology (*17*). HuScFv produced from one *E. coli* clone transformed with a recombinant phagemid carrying a DNA insert coding for the M1-specific HuScFv (*huscfv*) was found to inhibit the binding of recombinant M1 to vRNA in vitro (*17*). To interfere with the multiple biological functions of the M1, it is necessary that the HuScFv is able to access its intracellular target. Therefore, in this study, an M1-specific HuScFv was developed into a cell-penetrable format, i.e., a transbody, by using penetratin of the third helix of *Drosophila* homeodomain (*18*) as the HuScFv transduction domain. The transbody was then tested for its ability to interfere with the influenza virus infectivity via M1 interference.

EXPERIMENTAL PROCEDURES

Influenza A Virus. The influenza virus A/dog/Thailand/-Suphanburi/KU-08/2004 (H5N1) (*19*) was propagated in infected Mardin-Darby canine kidney (MDCK) cells grown in Dulbecco's modified Eagle's medium (DMEM; Invitrogen, USA) supplemented with 10% fetal bovine serum (FBS; HyClone, UK), streptomycin (100 μg/mL), and penicillin (100 U/mL), i.e., supplemented DMEM.

Gene Sequence Coding for HuScFv (*huscfv*) to the M1 of Influenza A Virus. An *E. coli* transformant harboring a recombinant *p*CANTAB5E phagemid with the *huscfv* has been established previously (*17*). HuScFv produced and purified from this transformed *E. coli* clone bound specifically to recombinant M1 of the highly pathogenic avian influenza virus, i.e., A/duck/Thailand/144/2005 (H5N1) (*17, 20*), as well as to native M1 of various influenza A viruses, i.e., H5N1 subtype (A/H5N1) of

* Corresponding author. Wanpen Chaicumpa, 2 Prannok Road, Bangkok-noi, Bangkok 10700. Phone: +66-02-4196491; Fax: +66-02-4196491; E-mail: tmwcc@mahidol.ac.th.

[†] Thammasat University.

[‡] Mahidol University.

[§] Kasetsart University.

[⊥] Present address: Department of Tropical Hygiene, Faculty of Tropical Medicine, Mahidol University, Bangkok 10400, Thailand.

10.1021/bc900251u © 2010 American Chemical Society
Published on Web 06/18/2010

Table 1. Primer Sequences Used in This Study

code	nucleotide sequence (5′→3′)
Reverse-*p*CAN-PEN1	ATT CTG GAA CCA AAT TTT GAT CTG GCG ATA GAA AGG AAC AAC TAA AGG AA
Reverse-*p*CAN-PEN2	TTT CTT CCA TTT CAT GCG ACG ATT CTG GAA CCA AAT TTT GAT
Reverse-PEN-*scfv*	GGC CGG CTG GGC CGC CTT TCT TCC ATT TCA TGC GAC G
Forward-*p*CANTAB	CAA GCT TTG GSG CCT TTT TTT T
*p*CANTAB-*R1*	CCA TGA TTA CGC CAA GCT TTG GAG CC
*p*CANTAB-*R2*	CGA TCT AAA GTT TTG TCG TCT TTC C
H5-Forward	ACA CAT GCY CAR ACA TAC T
H5-Reverse	CTY TGR TTY AGT GTT GAT GAT GT

different strains/clades/subclades, as well as to viruses belonging to other subtypes including A/H1N1, A/H3N2, and A/H8N4. The M1-specific HuScFv blocked the binding of M1 to vRNA (*17*).

MDCK Cell Monolayers. Monolayers of MDCK cells were grown in supplemented DMEM either in wells of 96- or 24-well tissue culture plates, or they were established on glass coverslips placed in wells of a 24-well tissue culture plate at 37 °C in a humidified 5% CO_2 incubator.

Construction of DNA Sequences Coding for Penetratin and Penetratin-HuScFv Fusion Protein. For constructing a DNA sequence coding for penetratin of the *Drosophila* homeodomain, a *p*CANTAB5E phagemid with *huscfv* (coding for M1 specific HuScFv) insert was used as platform template for incorporating the penetratin (PEN)-coding sequence into the vector by a three-step PCR using one forward primer (forward-*p*CANTAB) and three different reverse primers (reverse-*p*CAN-PEN1, reverse-*p*CAN-PEN2, and reverse-PEN-*scfv*) (Table 1). Each PCR reaction mixture contained 2.5 μL of 10× PCR buffer (Fermentas, Lithuania), 1.5 mM Mg^{2+}, 400 μM dNTPs, 0.4 μM of each primer, 1 unit of *Taq* DNA polymerase (Fermentas, Lithuania), 1 μL of DNA template, and sterile double-distilled water to a total volume of 25 μL. The thermal program was set to 94 °C for 5 min, 30 cycles of 94 °C for 50 s, 50 °C for 30 s, 72 °C for 30 s, and 72 °C for 5 min. The amplicons of the first- and second-step PCR were used as templates in the second- and third-step PCR cycles, respectively.

An amplicon from the third-step PCR (10 ng) was used as forward primer in a splice-overlapped extension PCR (SOE-PCR) to link the DNA encoding the penetratin to the *huscfv* located on the *p*CANTAB5E phagemid extracted from the transformed *E. coli* clone. The thermal cycles of the SOE-PCR were as follows: 94 °C for 5 min, 30 cycles of 94 °C for 1 min, 55 °C for 1 min, 72 °C for 1 min, and 72 °C for 5 min. The *PEN-huscfv*-coding sequence was then cloned into a cloning vector (*p*GEM-T Easy vector, Promega, USA) and the recombinant vector was introduced into chemically competent JM109 *E. coli*, respectively. Thereafter, the recombinant *PEN-huscfv* *p*GEM-T was extracted by the alkaline lysis method, doubly digested, and ligated to the *p*CANTAB5E precut with the *Hin*dIII and *Not*I restriction endonucleases (Fermentas, Lithuania). The ligated product was introduced into competent HB2151 *E. coli*. *E. coli* transformants were selected by growing them on a selective LB-Ampicillin (LB-A) agar plate and checking for the presence of the inserted *PEN-huscfv* by PCR using the *p*CANTAB-*R1* and *p*CANTAB-*R2* primers (Table 1). The sequence of the recombinant phagemid was verified by DNA sequencing.

Production of HuScFv and PEN-HuScFv. The M1-specific HuScFv was produced and purified from *huscfv*-*p*CANTAB5E transformed *E. coli* as previously described (*17*). Affinity of the HuScFv to full-length recombinant M1 was measured by indirect ELISA as previously described (*21*). The *PEN-huscfv* sequence in the *p*CANTAB5E phagemid was subcloned into the *p*ET23b+ expression vector (Novagen, USA) which was then introduced into the BL21(DE3) *E. coli* host. The *huscfv* without *PEN* sequence was also linked to the *p*ET23b+ expression vector and transformed into the BL21(DE3) *E. coli*. The PEN-HuScFv and HuScFv were produced by growing the respective *E. coli* transformants under 0.5 mM IPTG induction at 37 °C with shaking aeration for 3 h. Recombinant proteins were extracted and purified from the *E. coli* lysates using Ni-NTA agarose (Qiagen, Germany) according to the manufacturer's instruction. The proteins were dialyzed against 0.01 M PBS, pH 7.4, and kept at −20 °C until use.

Rabbit and Mouse Polyclonal Anti-M1 Antibodies. The polyclonal antibodies (PAb) to recombinant M1 of H5N1 influenza A virus were prepared as previously described (*17*).

Determination of the Cell Internalization of the PEN-HuScFv and Their Binding to M1 in the Influenza Virus Infected Cells. MDCK cells (50 000 cells) were added to the wells of a 24-well tissue culture plate which had a glass coverslip placed at the bottom of each well. The cells were allowed to grow for 48 h in supplemented DMEM. The cell monolayers on the glass coverslips were rinsed twice with PBS before incubation with an antibody solution, i.e., PEN-HuScFv/HuScFv (1 μM) or an antibody diluent (control) in a humidified chamber at 37 °C for 1 h. Thereafter, the cells were rinsed twice with PBS and fixed with 4% paraformaldehyde in PBS at 25 °C for 1 h. They were then permeabilized with 0.2% Triton X-100 for 15 min. After extensive washing with PBS, the cells were incubated with a blocking solution (2% FBS in PBS) at 25 °C for 1 h. Localization of the PEN-HuScFv/HuScFv was performed using mouse monoclonal anti 6×His as primary antibody and 1:500 diluted Alexa Fluor 488-labeled chicken antimouse immunoglobulins prepared in a blocking solution as the revelation solution. After extensive washing, the glass coverslips with the stained cells were individually placed right side down onto microscopic slides, mounted with 50% glycerol, and sealed with nail polish liquid. The cells were observed under a laser scanning confocal microscope (LSM 510 META, Carl Zeiss, Germany) for fluorescence emission.

To detect the binding of the PEN-HuScFv/HuScFv to native M1, MDCK cell monolayers previously infected with 100 TCID50 of A/dog/Thailand/-Suphanburi/KU-08/2004 (H5N1) for 3 h were prepared on the glass coverslips. The infected cells were washed and probed with the PEN-HuScFv or HuScFv, fixed with 4% paraformaldehyde, permeabilized with 0.2% Triton X-100, blocked, and incubated with a combination of mouse monoclonal anti 6×His antibody and 1:1000 diluted rabbit anti-M1 PAb (rPAb). The preparations were incubated with a mixture of 1:500 diluted Alexa Fluor 488-labeled chicken antimouse and 1:500 diluted Alexa Fluor 594-labeled goat antirabbit immunoglobulins. After mounting and sealing the glass coverslips, the cells were observed using the confocal microscopy as above.

Determination of the Effect of PEN-HuScFv on Normal Cells. The PEN-HuScFv was tested for toxicity to MDCK cells by the CytoTox 96 nonradioactive cytotoxicity assay (Promega, USA). The MDCK cells were seeded into the wells of a 96-well tissue culture plate and grown in supplemented DMEM for 24 h. Confluent monolayers were rinsed with PBS and incubated with various amounts of PEN-HuScFv (0.3−10 μM) at 37 °C for 1 h. Cells incubated with diluent and 10% sodium dodecyl sulfate (SDS) were included as negative and positive controls, respectively. Thereafter, the culture supernatant of each well was collected, and the amount of lactate dehydrogenase (LDH) in the fluids resulting from the membrane leakage/cell lysis was determined. The percent cytotoxicity was calculated as follows: (LDH release of test − LDH release of negative

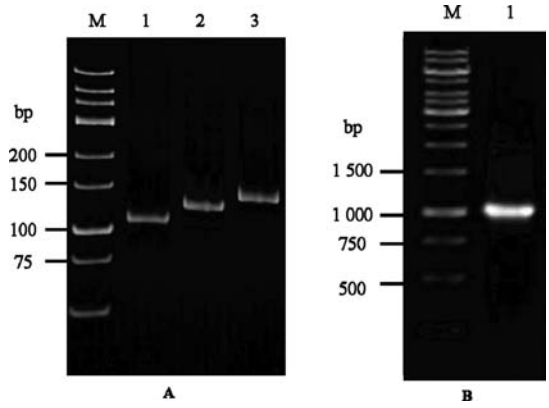


Figure 1. PCR amplicons of the Penetratin (PEN)-coding sequences (A) and the PEN-HuScFv-coding sequence (B). (A) The PEN-coding sequences were generated by the extension of nucleotide sequences via three-step PCR yielding three progressively longer amplicons at sizes of 107, 128, and 144 bp, respectively (lanes 1, 2, and 3, respectively). Lane M, low molecular weight DNA ladder. (B) The PEN-coding sequence was linked to the HuScFv-coding sequence by SOE-PCR in which the former acted as a megaprimer resulting in the *huscfv* with *PEN* at its 5′ end at a size of 1000 bp (lane 1). Lane M, GeneRuler 1 kb DNA ladder.

control)/(LDH release of positive control − LDH release of negative control) × 100. The percent cell viability was then calculated from 100 − % cytotoxicity of the test.

Neutralization of Influenza A Viral Infectivity by PEN-HuScFv/HuScFv. The ability of the PEN-HuScFv to interfere with the influenza A virus infectivity in comparison to the HuScFv was determined in MDCK cells using a plaque assay and semiquantitative RT-PCR. For the plaque assay, monolayers of MDCK cells in 24-well tissue culture plate were infected with A/dog/Thailand/-Suphanburi/KU-08/2004 (H5N1) as described above for 3 h. The extracellular virus in the culture fluid was removed, and the cells were rinsed. Antibody solutions, i.e., PEN-HuScFv/HuScFv (2.5 μM each) or 1:1000 rabbit anti-M1 (non-cell-penetrating antibody control) or diluent (negative antibody control) were separately added to the appropriate wells containing cells and the plate was incubated at 37 °C for 1 h. Thereafter, all fluids were aspirated, the cells were rinsed and further grown in 2% supplemented DMEM at 37 °C in a humidified 5% CO_2 incubator for 6 h. The number of progeny viruses in the culture supernatants was determined by plaque assay (*20, 22*). The antibody or control treated cells were grown in 2% supplemented DMEM medium for 24 h before the culture supernatants were collected, and the amount of the viruses contained in each supernatant was subjected to H5 gene RT-PCR using the primer sequences shown in Table 1 (*23*).

RESULTS

DNA Sequences Coding for Penetratin and Penetratin-HuScFv Fusion Protein. The coding sequences of penetratin (PEN) were generated via a three-step PCR. Lanes 1, 2, and 3 of Figure 1A show the PCR amplicons of the penetratin DNA sequences after the first, second, and third steps of PCR, at 107, 128, and 144 bp, respectively. The 144 bp amplicon encoding for penetratin was linked to *huscfv* encoding M1-specific HuScFv by SOE-PCR resulting in the *PEN-huscfv* fusion construct at ∼1000 bp (Figure 1B). The DNA was ligated to *p*CANTAB5E phagemid vectors before being introduced into HB2151 *E. coli*. The nucleotide sequence of the *PEN-huscfv* is shown in Figure 2. It was found that the *PEN* was in-frame and located at the 5′ end of the VH-coding sequence of the *huscfv* in the recombinant phagemid. The deduced amino acid sequence also revealed an incorporation of the 16-amino acid PEN peptide at the N-terminal of the HuScFv (Figure 2).

Production and Purification of the PEN-HuScFv and HuScFv. K_D value of the M1-specific HuScFv was deduced from a slope of Klotz plot calculated from a linear regression of ELISA. The HuScFv affinity to the full-length recombinant M1 was 8.6 nM. After subcloning the *PEN-huscfv* and *huscfv* from the phagemid vectors to *p*ET23b+ and introducing the respective recombinant plasmids into BL21(DE3) *E. coli* clones, the selected BL21(DE3) *E. coli* transformants were individually grown under IPTG induction. Figure 3A shows the Western blot patterns of the transformed BL21(DE3) *E. coli* lysate containing PEN-HuScFv (∼27 kDa) (lane 2) which is slightly larger than the HuScFv (lane 1). A high amount of PEN-HuScFv and HuScFv (approximately 5 mg/L) were produced from the *p*ET23b+ vector and from transformed BL21(DE3) *E. coli* in which the C-terminal E tag in the phagemid was replaced by a 6×His tag in the *p*ET23b+ for the detection and purification steps. Figure 3B illustrates the affinity-purified soluble PEN-HuScFv (lane 2) and HuScFv (lane 1).

Cell Internalization of the PEN-HuScFv. After incubating the MDCK cell monolayers with PEN-HuScFv or HuScFv, the PEN-HuScFv was found to localize inside the cells seen as apple green fluorescence (Figure 4, middle block), while there was no fluorescence emission from cells incubated with the HuScFv (Figure 4, left block), implying that the PEN peptide mediated cellular internalization of the HuScFv cargo protein. The intracellular localization of the PEN-HuScFv was confirmed by sectional laser confocal microscopy of MDCK cells after incubation with the PEN-HuScFv (Figure 5).

Binding of the PEN-HuScFv to M1 in the Influenza Virus Infected Cells. The upper panels of Figure 6 demonstrate the specific binding of the PEN-HuScFv to their intracellular target antigen, i.e., M1 protein in the influenza A virus infected MDCK cell monolayer. The M1-bound PEN-HuScFv (green fluorescence) was found to be colocalized with the rabbit polyclonal anti-M1 (red fluorescence). The infected cells incubated with HuScFv and rabbit polyclonal anti-M1 showed only the red fluorescence (Figure 6, lower panels). These results indicated not only that the PEN-HuScFv could penetrate the cells, but also that they specifically bound to the target antigen, i.e., the native M1, in the H5N1 influenza A virus-infected cells.

Determination of the Effect of PEN-HuScFv on Normal Cells. Figure 7 shows the % MDCK cell viability after incubation with various amounts of PEN-HuScFv. It was found that the cytotoxicity of the PEN-HuScFv was negligible even at a protein concentration as high as 10.0 μM.

PEN-HuScFv/HuScFv Mediated Neutralization of the Influenza A Viral Infectivity. In the plaque assay, both PEN-HuScFv and HuScFv were found to reduce the numbers of progeny viruses in the culture supernatants of the influenza virus A/dog/Thailand/-Suphanburi/KU-08/2004 (H5N1) infected MDCK cells compared to the infected cells treated with mouse polyclonal anti-M1 (mPAb) and the diluent controls (Figure 8). The results of the semiquantitative RT-PCR conformed to the results of the plaque assay. Under the same RT-PCR conditions, the amount of *H5* amplicons in the culture fluids of the infected cells incubated with PEN-HuScFv and HuScFv were markedly less than the amounts of the *H5* amplicons from the cells incubated with controls, i.e., non-cell-penetrable mouse polyclonal anti-M1 and diluent (Figure 9).

DISCUSSION

M1 is conserved among the type A influenza viruses (*7, 24*), and the protein has multiple pivotal roles in the virus replication (*8*−*14*). As such, an antibody specific to M1 that can penetrate into the virus-infected cells is envisaged to interfere with the virus replication. Such an antibody could also be a useful tool for studying the morphogenesis of different

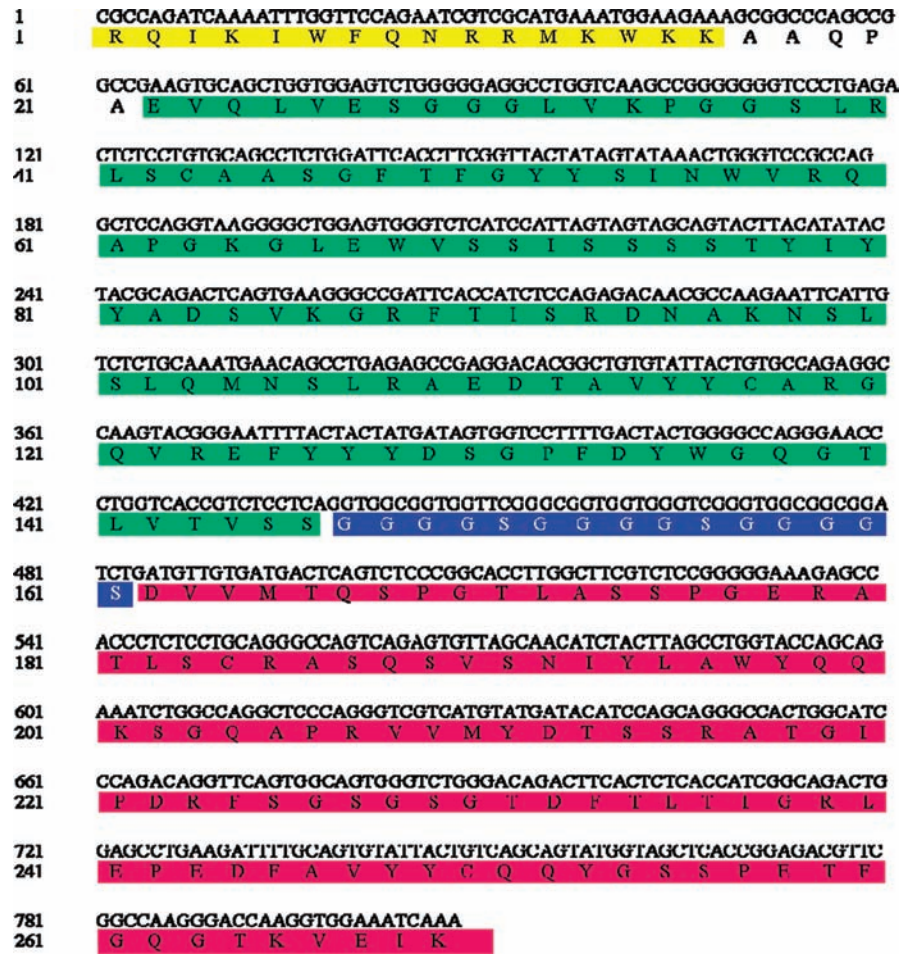


Figure 2. DNA sequence and deduced amino acid sequence of the *PEN-huscfv* amplicon. The penetratin-coding sequence is located at the 5′ terminus of the *huscfv*. Yellow, penetratin peptide; green, VH of HuScFv; blue, peptide linker; pink, VL of HuScFv. The numbers at the left are the positions of the nucleotides (upper) and the deduced amino acids (lower).

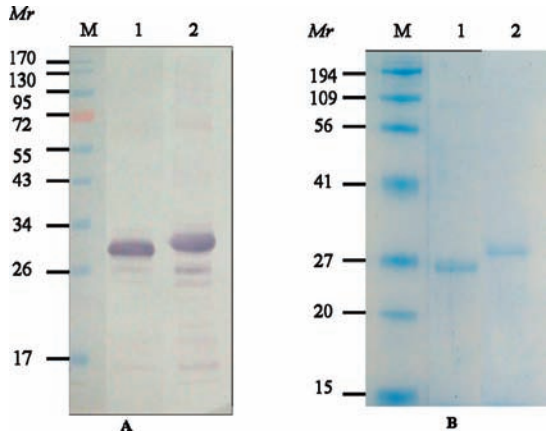


Figure 3. PEN-HuScFv and HuScFv produced from the respective recombinant BL21(DE3) *E. coli* clones. (A) The recombinant DNA construct of the *PEN-huscfv* was introduced into *p*ET23b+ and BL21(DE3) *E. coli*, respectively, for protein expression. The fusion PEN-HuScFv protein was produced and then detected by Western blot analysis using mouse anti-His tag antibody as the protein at a size of ~27 kDa (lane 2), which was slightly larger than the original HuScFv (lane 1). (B) The 6×His-tagged fusion proteins were purified by Ni-NTA agarose affinity chromatography. The purified SDS-PAGE separated-HuScFv and PEN-HuScFv proteins are shown in lanes 1 and 2, respectively. Lane M, a prestained broad-range protein marker.

subtypes of influenza viruses. Recently, HuScFv which could bind to the M1 protein of multiple influenza A virus subtypes was generated (*17*). The HuScFv inhibited the binding of M1 to vRNA in vitro. In order to further investigate the capability of the M1-specific HuScFv to interfere with the influenza virus infectious cycle, in this study, a cell-penetrable HuScFv was generated by molecular linking of the gene sequence coding for the M1-specific HuScFv (*huscfv*) to a self-constructed nucleotide sequence coding for a protein transduction domain, i.e., penetratin (PEN) of *Drosophila* homeodomain. The PEN-coding sequence was generated by means of a three-step PCR for extension of the nucleotide primers using *huscfv*-phagemid DNA as the platform. The complete *PEN* sequence then acted as a megaprimer for the fusion with *huscfv* via SOE-PCR. The fusion DNA construct in the *huscfv*-phagemid vector was verified by DNA sequencing and found to be in-frame with the open-reading frame of the *huscfv*. Deduced amino acids also showed the correct sequence of the PEN peptide implying the retention of the inherent membrane translocation activity of the synthesized PEN peptide (*18*). The PEN was chosen because several studies have demonstrated the membrane translocation activity not only for itself, but also for the cargo peptides (*25*). Molecular linking of the *PEN* with the *huscfv* was used to construct the fusion protein instead of chemical conjugation of the cell-penetrating peptide to the antibody via their thiol groups as previously performed (*26*), in order to avoid the reduction of the disulfide bond between the two peptides in the cytoplasm that might occur with the chemically conjugated PEN-cargo before the antibody has found the intracellular target antigen. Moreover, the expressed PEN-HuScFv was C-terminally tagged with 6×His during the molecular construction. This tag facilitated the subsequent purification of the fusion protein by

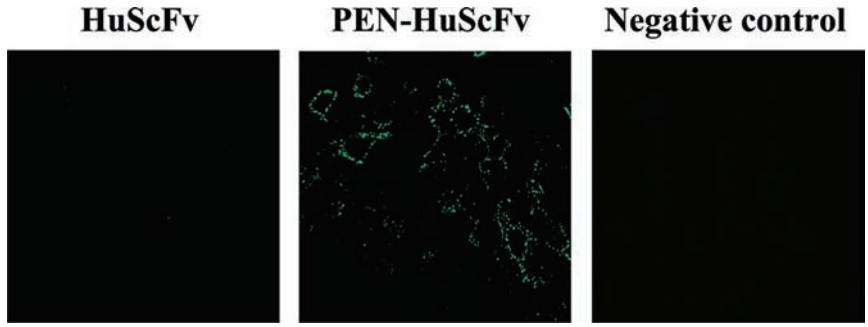


Figure 4. Immunofluorescence assay for determining the cell-penetrating ability of the PEN-HuScFv. Intact MDCK cells in a monolayer were treated with HuScFv (left block), PEN-HuScFv (middle block), and a negative antibody control (right block) before being permeabilized and probed with anti-His tag antibody and Alexa Fluor 488-labeled chicken antimouse immunoglobulin, respectively. The presence of intracellular PEN-HuScFv was determined by the green fluorescence only in the middle block.

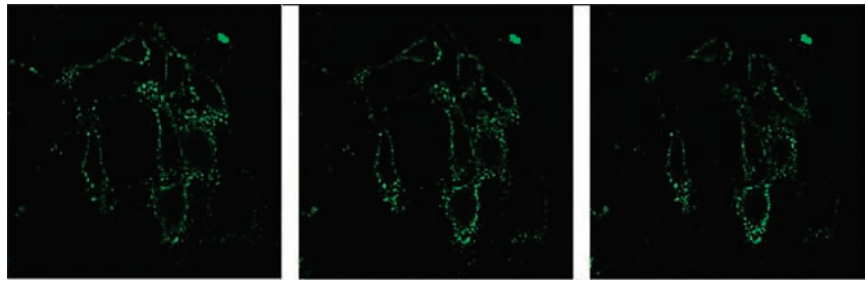


Figure 5. Sectional laser confocal microscopy of an MDCK cell monolayer after incubation with PEN-HuScFv as described in Figure 4. Three serial sections of 0.97 μm each from top to bottom are shown from left to right.

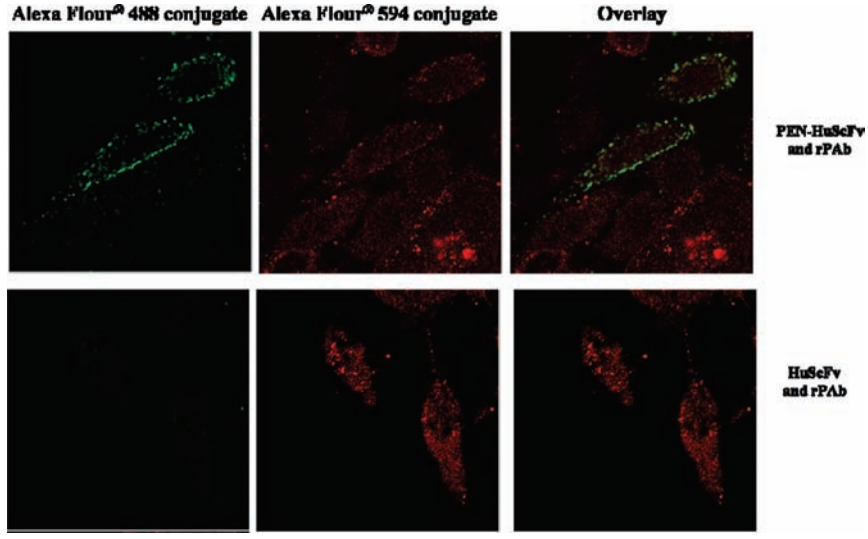


Figure 6. Localization of PEN-HuScFv in influenza virus A/H5N1-infected MDCK cell monolayers. After infection with the influenza virus A/H5N1, MDCK cell monolayers were incubated with either PEN-HuScFv or HuScFv for 1 h. The presence of intracellular M1-specific antibody was revealed by permeabilization of the fixed cells and staining with anti-His tag antibody and Alexa Fluor 488-labeled chicken antimouse Ig, which produced a green fluorescence of the 6×His-tagged PEN-HuScFv at the same area as the native M1 of the influenza virus, which exhibited red fluorescence produced by anti-M1 rPAb and Alexa Fluor 594-labeled goat antirabbit Ig, respectively.

affinity chromatography using a readily available commercial reagent (*27*). The PEN-HuScFv (25−30 kDa), which is 5 times smaller than the intact IgG antibody molecule (150 kDa), was purposely designed not only for minimizing the size of the cargo molecule across the membrane, but also because the mere binding of the HuScFv to the M1, either directly at the vRNA binding region of the molecule (*28*−*30*) or by interfering with the natural folding of the zinc finger motif outside the vRNA binding region of the protein, would be effective enough to inhibit the viral assembly and budding (*31*). The strategy used in this study could be universally applicable for any antibodies specific to any other intracellular target antigens.

According to the LDH leakage assay, 0.3−10 μM of the so-produced PEN-HuScFv added to the confluent MDCK cell monolayers in a 96-well plate did not cause any adverse effects to the living mammalian cells as the leakage of the cytosolic LDH was negligible, i.e., less than 10% (*32*). The experiment to demonstrate the membrane translocation activity of the PEN-HuScFv was performed in living MDCK cells incubated with only 1 μM. Thus, intracellular localization of the PEN-HuScFv found after fixing the PEN-HuScFv treated cells should not be an artifact (*33*). The intracellular PEN-HuScFv were seen as scattered fluorescence emissions only in the cytoplasm of the noninfected MDCK cells, which was more intense around the

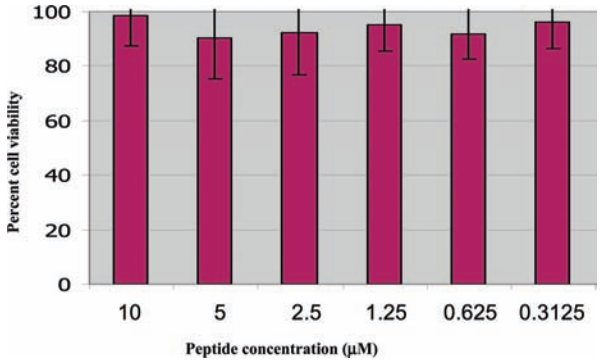


Figure 7. Percent MDCK cell viability after incubation with various amounts of PEN-HuScFv (10.0−0.3125 μM) determined by LDH leakage assay.

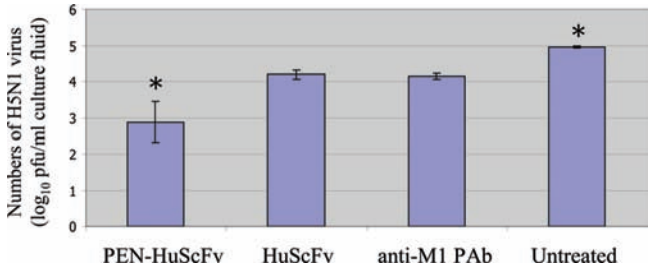


Figure 8. Inhibitory effect of the PEN-HuScFv on influenza A/H5N1 virus replication as determined by plaque assay. The bar graph (mean ± SEM of three experiments) shows the results of the plaque formation assay for determining the numbers of newly formed virus particles (pfu/mL) released from influenza A/H5N1 infected MDCK cell monolayers after incubation with M1-speicific PEN-HuScFv, non-cell-penetrating HuScFv, and controls, i.e., mPAb and negative antibody control. The number of plaques from infected cells treated with M1-speicific PEN-HuScFv was significantly less than the controls (* $p < 0.01$ by one-way ANOVA and Tukey's HSD test).

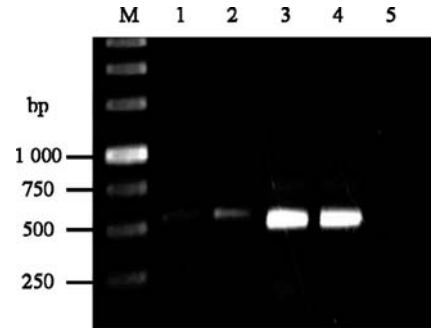


Figure 9. Inhibitory effect of the PEN-HuScFv on influenza A/H5N1 virus replication as determined by RT-PCR. Viral *H5* gene segments (~500 bp) were amplified using cDNA reverse-transcribed from virus particles released into the culture fluids as templates and analyzed by agarose gel electrophoresis. The PCR amplicons in the culture fluids of the infected MDCK cells after incubation with M1-specific PEN-HuScFv, M1-specific HuScFv, mPAb, and a negative antibody control are shown in lanes 1−4, respectively. The negative *H5* amplicon from the culture fluid of uninfected MDCK cells served as negative PCR control (lane 5). Lane M, GeneRuler 1 kb DNA ladder.

area underneath the inner lipid bilayer, and not in the nucleus (Figure 4). One possible reason to explain the submembranous aggregation of PEN-HuScFv was the positive charge of the PEN peptide, which caused the fusion molecules to attach to the negatively charged phospholipids of the inner leaflet of the plasma membrane after the peptide internalization (*34*, *35*). However, the intracellular patterns of the internalized CPP-cargo could also depend on the nature of the cargo molecules and the location of the intracellular ligand of the cargo protein as well as the rate of the intracytoplasmic CPP-cargo degradation (*36*). PEN-HuScFv incubated with the influenza virus-infected MDCK cells showed an intracellular distribution not much different from the pattern seen in the PEN-HuScFv treated noninfected MDCK cells (Figure 5). This happened probably because the newly produced M1, besides being free in the cytoplasm for vRNP nuclear export, were also localized at the inner surface of the plasma membrane for new progeny virus assembly (*37*−*39*). The PEN-HuScFv was not seen in the nucleus of the cells, maybe because the fusion protein was too large to passively enter via the nuclear pore and/or because the lipid composition/distribution of the nuclear membrane was incompatible with the nuclear internalization of the plasma membrane penetrating PEN-HuScFv.

The PEN-HuScFv reduced the number of influenza viruses in the culture fluids of the infected MDCK cells implying that the M1-specific HuScFv linked to the PEN were still functionally active. The result conformed to other studies in that antibodies translocated across the plasma membrane by CPP retained their original biological activity (*40*, *41*). The HuScFv has been shown previously to inhibit M1 binding to vRNA in vitro. This mechanism might as well operate in the influenza virus infected MDCK cells and thus interfere with the vRNP nuclear export. Because the PEN-HuScFv could not enter the nucleus, it was unlikely that the preparation interfered with the M1-mediated vRNP release from the nuclear matrix (*42*). Nevertheless, the binding of the PEN-HuScFv to M1 located juxtaposed to the inner surface of the plasma membrane could also interfere with the progeny virus assembly. Further experiments are needed to pinpoint the molecular mechanisms exerted by the PEN-HuScFv on the M1 and the virus replication. The finding that the nonpenetrating HuScFv could also reduce the viral shedding into the culture fluid of infected cells, although to a lesser magnitude than the PEN-HuScFv, was interesting. This effect might be due to the small size of the HuScFv, which could access the extracellular milieu at the immediate vicinity to the virus budding location and thus could obstruct the curvature formation of host cell membrane required for the budding process of the newly formed virus particles (*43*−*45*). This speculation needs further investigation.

In conclusion, the cell penetrating M1-specific HuScFv produced in this study affected the influenza A virus life cycle in living mammalian cells. The reagent warrants further testing in animals before developing it into a human immunotherapeutic anti-influenza virus formula.

CONCLUSION

In this study, M1-specific human single chain antibody fragments (HuScFv) that bound to matrix protein (M1) of various influenza A viruses produced previously were developed into a cell penetrating format by molecular linking of the gene sequence encoding the HuScFv (*huscfv*) to a protein transduction domain, i.e., penetratin (PEN), a 16-amino acid peptide, of the *Drosophila* homeodomain. The PEN-HuScFv had negligible cytotoxicity on living MDCK cells. They were readily transfered across the cell membrane and bound to native M1 in the A/H5N1-infected cells as revealed by immunofluorescent confocal microscopy. The PEN-HuScFv, when used to treat the influenza virus infected cells, reduced the number of viruses released from the cells. In conclusion, the cell penetrating M1-specific HuScFv, a transbody, produced in this study affected the influenza A virus life cycle in living mammalian cells. While the molecular mechanisms of the PEN-HuScFv need more investigation, the reagent warrants further testing in animals before developing it into a human immunotherapeutic anti-influenza formula.

ACKNOWLEDGMENT

The work was supported by the National Science and Technology Development Agency (NSTDA), and Commission of Higher Education (CHE). O.P.P. is a Royal Golden Jubilee Ph.D. scholar of the Thailand Research Fund (TRF). A.P.T. and P.S.M. are TRF grantees.

LITERATURE CITED

(1) Casadevall, A., Dadachova, E., and Pirofski, L. (2004) Passive antibody therapy for infectious diseases. *Nat. Rev. Microbiol. 2*, 695–703.

(2) Hayakawa, S., Uchida, T., Mekada, E., Moynihan, M. R., and Okada, Y. (1983) Monoclonal antibody against diphtheria toxin. Effect on toxin binding and entry into cells. *J. Biol. Chem. 258*, 4311–4317.

(3) Volk, W. A., Bizzini, B., Snyder, R. M., Bernhard, E., and Wagner, R. R. (1984) Neutralization of tetanus toxin by distinct monoclonal antibodies binding to multiple epitopes on the toxin molecule. *Infect. Immunol. 45*, 604–609.

(4) Zaccolo, M., Roggero, S., Armellini, D., Pegoraro, L., Rappuoli, R., and Malavasi, F. (1992) Generation of human monoclonal antibodies that confer protection against pertussis toxin. *Infect. Immunol. 60*, 1258–1260.

(5) Boyer, L. V., Seifert, S. A., and Cain, J. S. (2001) Recurrence phenomena after immunoglobulin therapy for snake envenomations: Part 2 Guidelines for clinical management with crotaline Fab antivenom. *Ann. Emerg. Med. 37*, 196–201.

(6) Bugli, F., Graffeo, R., Sterbini, F. P., Torelli, R., Masucci, L., Sali, M., Grasso, A., Rufini, S., Ricci, E., Fadda, G., and Pescatori, M. (2008) Monoclonal antibody fragment from combinatorial phage display library neutralizes alpha-latrotoxin activity and abolishes black widow spider venom lethality, in mice. *Toxicon 51*, 547–554.

(7) Lamb, R. A., and Lai, C. J. (1981) Conservation of the influenza virus membrane protein (M1) amino acid sequence and an open reading frame of RNA segment 7 encoding a second protein (M2) in H1N1 and H3N2 strains. *Virology 112*, 746–751.

(8) Bui, M., Whittaker, G. R., and Helenius, A. (1996) Effect of M1 protein and low pH on nuclear transport of influenza virus ribonucleoproteins. *J. Virol. 70*, 8391–8401.

(9) Bui, M., Wills, E. G., Helenius, A., and Whittaker, G. R. (2000) Role of the influenza virus M1 protein in nuclear export of viral ribonucleoproteins. *J. Virol. 74*, 1781–1786.

(10) Martin, K., and Helenius, A. (1991) Nuclear transport of influenza virus ribonucleoproteins: the viral matrix protein (M1) promotes export and inhibits import. *Cell 67*, 117–130.

(11) Gomez-Puertas, P., Albo, C., Perez-Pastrana, E., Vivo, A., and Portela, A. (2000) Influenza virus matrix protein is the major driving force in virus budding. *J. Virol. 74*, 11538–11547.

(12) Nayak, D. P., and Hui, E. K. W. (2002) Assembly and morphogenesis of influenza viruses. *Recent Res. Dev. Virol. 4*, 35–54.

(13) Whittaker, G. R., Bui, M., and Helenius, A. (1996) Nuclear trafficking of influenza virus ribonucleoproteins in heterokaryons. *J. Virol. 70*, 2743–2756.

(14) Whittaker, G. R., Bui, M., and Helenius, A. (1996) The role of nuclear import and export in influenza virus infection. *Trends Cell. Biol. 6*, 67–71.

(15) Kawaoka, M., Ochiai, H., Nakajima, K., and Niwayama, S. (1990) Inhibitory effect of protein kinase C inhibitor on the replication of influenza A virus. *J. Gen. Virol. 71*, 2149–2155.

(16) Hui, E. K. W., Yap, E. M., An, D. S., Chen, I. S., and, and Nayak, D. P. (2004) Inhibition of influenza virus matrix (M1) protein expression and replication by U6 promoter driven and lentivirus-mediated delivery of siRNA. *J. Gen. Virol. 85*, 1877–1884.

(17) Poungpair, O., Chaicumpa, W., Kulkeaw, K., Maneewatch, S., Thueng-in, K., Srimanote, P., Tongtawe, P., Songserm, T., Lekcharoensuk, P., and Tapchaisri, P. (2009) Human single chain monoclonal antibody that recognizes matrix protein of heterologous influenza A virus subtypes. *J. Virol. Methods 159*, 105–111.

(18) Derossi, D., Joliot, A. H., Chassaing, G., and Prochiantz, A. (1994) The third helix of Antennapedia homeodomain translocates through biological membranes. *J. Biol. Chem. 269*, 10444–10450.

(19) Songserm, T., Amonsin, A., Jam-on, R., Sae-Heng, N., Pariyothorn, N., Payungporn, S., Theamboonlers, A., Chutinimitkul, S., Thanawongnuwech, R., and Poovorawan, Y. (2006) Fatal avian influenza A H5N1 in a dog. *Emerg. Infect. Dis. 12*, 1744–1747.

(20) Simmons, C. P., Bernasconi, N. L., Suguitan, A. L., Jr., Mills, K., Ward, J. M., Chau, N. V. V., Hien, T. T., Sallusto, F., Ha, D. Q., Farrar, J., de Jong, M. D., Lanzavecchia, A., and Subbarao, K. (2007) Prophylactic and therapeutic efficacy of human monoclonal antibodies against H5N1 influenza. *PLoS Med. 4*, e178, 0928−0936.

(21) Friguet, B., Chaffotte, A. F., Djavadi-Ohaniance, L., and Goldberg, M. E. (1985) Measurements of the true affinity constant in solution of antigen-antibody complex by enzyme-linked immunosorbent assay. *J. Immunol. Methods 77*, 305–319.

(22) Maneewatch, S., Thanongsaksrikul, J., Songserm, T., Thueng-In, K., Kulkeaw, K., Thathaisong, U., Srimanote, P., Tongtawe, P., Tapchaisri, P., and Chaicumpa, W. (2009) Human single-chain antibodies that neutralize homologous and heterologous strains and clades of influenza A virus subtype H5N1. *Antivir. Ther. 14*, 221–230.

(23) Wei, H. L., Bai, G. R., Mweene, A. S., Zhou, Y. C., Cong, Y. L., and Pu, J. (2006) Rapid detection of avian influenza virus A and subtype H5N1 by single step multiplex reverse transcription-polymerase chain reaction. *Virus Genes 32*, 261–167.

(24) Ito, T., Gorman, O. T., Kawaoka, Y., Bean, W. J., and Webster, R. G. (1991) Evolutionary analysis of the influenza A virus M gene with comparison of the M1 and M2 proteins. *J. Virol. 65*, 5491–5498.

(25) Dietz, G. P. H., and Bahr, M. (2004) Delivery of bioactive molecules into the cell: the Trojan horse approach. *Mol. Cell. Neurosci. 27*, 85–131.

(26) Zhao, Y., Lou, D., Burkett, J., and Kohler, H. (2001) Chemical engineering of cell penetrating antibodies. *J. Immunol. Methods 254*, 137–145.

(27) Geoghegan, K. F., Dixon, H. B., Rosner, P. J., Hoth, L. R., Lanzetti, A. J., Borzilleri, K. A., Marr, E. S., Pezzullo, L. H., Martin, L. B., LeMotte, P. K., McColl, A. S., Kamath, A. V., and Stroh, J. G. (1999) Spontaneous alpha-N-6-phosphogluconoylation of a His tag in Escherichia coli: the cause of extra mass of 258 or 178 Da in fusion protein. *Anal. Biochem. 267*, 169–184.

(28) Ye, Z., Pal, R., Fox, J. W., and Wagner, R. R. (1987) Functional and antigenic domains of the matrix (M1) protein of influenza A virus. *J. Virol. 61*, 239–246.

(29) Ye, Z., Liu, T., Offringa, D. P., McInnis, J., and Levandowski, R. A. (1999) Association of influenza virus matrix protein with ribonucleoproteins. *J. Virol. 73*, 7467–7473.

(30) Baudin, F., Petit, I., Weissenhorn, W., and Ruigrok, R. W. H. (2001) In vitro dissection of the membrane and RNP binding activities of influenza virus M1 protein. *Virology 281*, 102–108.

(31) Nasser, E. H., Judd, A. K., Sanchez, A., Anastasiou, D., and Bucher, D. J. (1996) Antiviral activity of influenza virus M1 zinc finger peptides. *J. Virol. 70*, 8639–8644.

(32) Saar, M., Lindgren, M., Hansen, M., Eiriksdottir, E., Jiang, Y., Rosenthal-Aizman, K., Sassian, M., and Langel, U. (2005) Cell-penetrating peptides: a comparative membrane toxicity study. *Anal. Biochem. 345*, 55–65.

(33) Richard, J. P., Melikov, K., Vives, E., Ramos, C., Verbeure, B., Gait, M. J., Chernomordik, L. V., and Lebleu, B. (2003) Cell-penetrating peptides: a reevaluation of the mechanism of cellular uptake. *J. Biol. Chem. 278*, 585–590.

(34) Derossi, D., Calvet, S., Trembleau, A., Brunissen, A., Chassaing, G., and Prochiantz, A. (1996) Cell internalization of the third helix of the Antennapedia homeodomain is receptor-independent. *J. Biol. Chem. 271*, 18188–18193.

(35) El-Andaloussi, S., Holm, T., and Langel, U. (2005) Cell-penetrating peptides: mechanisms and applications. *Curr. Pharm. Des. 11*, 3597–3611.

(36) Palm, C., Jyamanne, M., Kjellander, M., and Hallbrink, M. (2007) Peptide degradation is a critical determinant for cell-penetrating peptide uptake. *Biochim. Biophys. Acta 1768*, 1769–1776.

(37) Hey, A. J. (1974) Studies on the formation of the influenza virus envelope. *Virology 60*, 398–418.

(38) Fujiyochi, Y., Kume, N. P., Sakata, K., and Sato, S. B. (1994) Fine structure of influenza A virus observed by electron cryomicroscopy. *EMBO J. 13*, 318–326.

(39) Zhang, J., and Lamb, R. A. (1996) Characterization of the membrane association of the influenza virus matrix protein in living cells. *Virology 225*, 255–266.

(40) Jain, M., Chauhan, S. C., Singh, A. P., Venkatraman, G., Colcher, D., and Batra, S. K. (2005) Penetratin improves tumor retention of single-chain antibodies: a novel step toward optimization of radioimmunotherapy of solid tumors. *Cancer Res. 65*, 7840–7846.

(41) Avignolo, C., Bagnasco, L., Biasotti, B., Melchiori, A., Tomati, V., Bauer, I., Salis, A., Chiossone, L., Mingari, M. C., Orecchia, P., Carnemolla, B., Neri, D., Zardi, L., and Parodi, S. (2008) Internalization via Antennapedia protein transduction domain of an scFv antibody toward c-Myc protein. *FASEB J. 22*, 1237–1245.

(42) Chen, Z., and Krug, R. M. (2000) Selective nuclear export of viral mRNAs in influenza virus-infected cells. *Trends Microbiol. 8*, 376–383.

(43) Lin, S., Naim, H. Y., Rodriguez, A. C., and Roth, M. G. (1998) Mutations in the middle of the transmembrane domain reverse the polarity of transport of the influenza virus hemagglutinin in MDCK epithelial cells. *J. Cell Biol. 142*, 51–57.

(44) Scheiffele, P., Roth, M. G., and Simons, K. (1997) Interaction of influenza virus hemagglutinin with sphingolipid-cholesterol membrane domains via its transmembrane domain. *EMBO J. 16*, 5501–5508.

(45) Scheiffele, P., Rietveld, A., Wilk, T., and Simons, K. (1999) Influenza viruses select ordered lipid domains during budding from the plasma membrane. *J. Biol. Chem. 274*, 2038–2044.

BC900251U

Effect of RGD-4C Position is More Important Than Disulfide Bonds on Antiangiogenic Activity of RGD-4C Modified Endostatin Derived Synthetic Polypeptide

Runting Yin, Heng Zheng, Tao Xi,* and Han-Mei Xu*

Department of Marine Pharmacy, College of Life Science and Technology, China Pharmaceutical University, Nanjing, 210009, P. R. China. Received July 10, 2009; Revised Manuscript Received January 24, 2010

ES-2 (IVRRADRAAVP), an endostatin-derived synthetic polypeptide, contains the amino acids 50−60 of endostatin from its N terminus, and it had no inhibitory effects on tumor growth in vivo. In order to increase the targeted delivery of ES-2 to tumors and further enhance the activity, the polypeptide RGD-4C (ACDCRGDCFC) was introduced into ES-2, and the effects of RGD-4C position and RGD-4C disulfide bonds on polypeptides activity were investigated. When RGD-4C polypeptides (with or without disulfide bonds) were introduced to the N-terminals of synthesized ES-2, the modified ES-2 showed significant antitumor activity in vivo. Cell proliferation and chicken chorioallantoic membrane (CAM) assay results showed that disulfide bonds had no significant effects on RGD-4C-modified ES-2 antiangiogenic activity. Furthermore, the target of modified peptides was integrin $\alpha 5\beta 1$, rather than integrin $\alpha v\beta 3$ as previous studies mentioned.

INTRODUCTION

Currently, angiogenesis has been widely recognized as an important factor controlling the growth of any solid tumor. Since endothelial cells that make up tumor vasculature are genetically stable, cancer treatment targeting at tumor endothelial cells exhibits less toxicity and rarely develops drug resistance compared with traditional chemotherapies. Great interest has been taken in targeting the tumor vasculature, and many efforts have been directed toward the development of antiangiogenic agents. One of the important endogenous angiogenesis inhibitors is endostatin (ES), a protein with a molecular weight of 20 kDa, which was isolated in the culture medium of rat vascular endothelial tumor cells by O'Reilly in 1997 (*1*). ES is the hydrolytic fragment of collagen XVIII. It can prevent blood vessel formation through specifically inhibiting endothelial cell proliferation and migration. Currently, ES is mainly produced by genetic engineering technology. For example, Xu (*2*) isolated soluble recombinant human ES with antiangiogenic effect expressed in *Escherichia coli* with molecular chaperone. Dhanabal (*3*) expressed human ES in *Pichia pastoris*. However, since ES contains multiple disulfide bonds, the renaturation process is difficult and complicated during manufacture. Thus, the expression product is not stable and the activity is affected after the in vitro refolding process. Furthermore, the potential targets of ES are not clear now. As such, the application of ES is limited (*4*).

In view of this, several groups have focused research on the active fragments of ES in order to identify smaller active units. Studies have shown that polypeptides corresponding to the partial sequence of ES exhibited higher biological activity (*5*). Wickström (*6*) found that the amino acids 50−60 of ES (ES-2) had higher antiangiogenic activity than the full-length ES. However, the in vivo activities were not investigated. Xu (*7*) established that the in vivo activity of ES-2 was not high. But after the introduction of the integrin-binding RGD into ES-2, the modified ES-2 showed significant antitumor results in vivo. Besides RGD, RGD-4C is another major integrin ligand, which exhibits higher specificity for integrin $\alpha v\beta 3$ than RGD (*8*). Integrin $\alpha v\beta 3$ is the molecular marker for angiogenesis, tumor growth, and metastasis (*9*). RGD-4C includes two pairs of disulfide bonds and the positions of the disulfide bonds play an important role in the activity of RGD-4C. The (1−4, 2−3) pairing patterns of the disulfide bonds exhibited the highest activity among different paring patterns (*10*).

In this study, ES-2 was modified by the addition of RGD-4C (without disulfide bonds or with (1−4, 2−3) pairing patterns for the disulfide bonds), resulting in the formation of 3 polypeptides, named AP, AP (O), and IC. Among those, AP and AP (O) refer to the polypeptides in which linear RGD-4C and RGD-4C containing disulfide bonds were attached to the amino terminus of ES-2, respectively, while IC refer to the polypeptides in which linear RGD-4C was attached to carboxyl terminus of ES-2. Four glycine residues were added between RGD (or RGD-4C) motif and ES-2 in an attempt to increase the flexibility. Therefore, we examined whether the position of RGD-4C and introduction of disulfide bonds will influence the activity of modified polypeptides using both in vivo and in vitro models.

MATERIALS AND METHODS

Materials. *Cell Lines, Animals, and Peptides.* B16F10 mouse melanoma cells (provided by Nanjing University), human hepatic carcinoma Bel-7402 cell line, and human breast cancer MCF-7 cell line were purchased from American type Cell Culture (ATCC, Shanghai, China) and maintained in Dulbecco's modified Eagle's medium (DMEM) with 10% fetal bovine serum and antibiotics. Bovine aorta endothelial (BAE) cells were isolated from newborn bovine aorta by trypsin treatment and maintained in Dulbecco's modified Eagle's medium (DMEM) with 20% fetal bovine serum and antibiotics. Mice were purchased from the Shanghai Laboratory Animal Center of the Chinese Academy of Sciences. Synthesis of the peptides was performed by GL Biochem (Shanghai) Ltd. All peptides were very soluble in water. The purity of the products was more than

* Correspondence to Department of of Marine Pharmacy, College of Life Science and Technology, China Pharmaceutical University, 24 Tongjiaxiang, Nanjing, 210009, P. R. China. (Tao Xi) Tel: 86-25-83271389. (Han-Mei Xu) Tel: 86-25-83271007; Fax: 86-25-83562576; E-mail: xuhanmei@yahoo.com.cn.

10.1021/bc900292y © 2010 American Chemical Society
Published on Web 06/01/2010

Table 1. Sequences and Disulfide Bridges of the Synthetic Peptides

Name	*Sequence*	*Disulfide bridge*
ES-2	IVRRADRAAVP	none
AP	ACDCRGDCFCGGGGIVRRADRAAVP	none
IC	IVRRADRAAVPGGGGACDCRGDCFC	none
AP (O)	ACDCRGDCFCGGGGIVRRADRAAVP	Two (1-4, 2-3)
P1	IVRRADRAAVPGGGGRGD	none
RGD-4C	ACDCRGDCFCG	none

92% analyzed by analytical high-performance liquid chromatography. Amino acid analysis and mass spectroscopy were conducted to confirm their compositions. N-terminal amino acid sequence analysis was performed at Fudan University (Shanghai, China). ES was purchased from Simcere pharmaceutical Co. Ltd. (Nanjing, Jiangsu province in China). Rabbit anti-integrin α5 polyclonal antibodies were purchased from Santa Cruz Biotechnology Company. Rabbit anti-integrin β1 polyclonal antibody and biotinylated goat antirabbit secondary antibody were purchased from Boster Biological Company (Wuhan, P. R. China).

Methods. *Polypeptide Synthesis and Determination of Disulfide Bond Position.* Polypeptides were synthesized using Fmoc-chemistry solid-phase synthesis methods according to the sequence of AP, AP (O), and IC, as well as the positions of disulfide bonds listed in Table 1. In order to obtain (1−4, 2−3) disulfide pairing pattern in polypeptides AP (O), Cys2 and Cys3 were protected with the S-acetamidomethyl (Acm) group while Cys1 and Cys4 were protected with trifluoroacetic acid (Trt) group. Reaction was performed in TFA solution (TFA/phenol/water/thioanisole/EDT, 9.0/0.3/0.3/0.2/0.2, v/v/v/v) for 3 h at room temperature. Protective group Trt was removed, and polypeptides were detached from the resin. Disulfide bond was formed between Cys1 and Cys4 by air oxidation. After that, reactions were carried out in acetic acid solution of iodine for 2 h at room temperature to remove Acm group and form disulfide bond between Cys2 and Cys3. Polypeptides were purified using HPLC and eluted with a 25 min gradient from 10% to 60% acetonitrile (0.1% TFA) in H_2O (containing 0.1% TFA). Products were purified by HPLC using C18 column after each cyclization step and analyzed by ESI LC-MS 2010A (Shimadzu) to identify the position of the disulfide bonds. The purity of obtained polypeptides was more than 92%. Polypeptides AP,IC and RGD-4C were synthesized directly without the formation of disulfide bonds.

Antitumor Activity of the Synthesized Peptides in Vivo. *Tumor Implantation.* B16F10 mouse melanoma cell line was grown in culture. Cell lines were washed with phosphate-buffered saline (PBS), dispersed in a 0.05% trypsin solution, and resuspended. After centrifugation at 1000 rpm for 5 min, the cell pellets were resuspended in PBS and adjusted to a concentration of 5×10^6 cells/mL. C57BL/6 female mice (5−6 weeks old) were implanted subcutaneously (s.c.) on the midright side with 5×10^5 B16F10 cells in 0.1 mL PBS.

C57BL/6 Female Mice Treatment. After the average tumor volume of B16F10 mouse melanoma reached 100−300 mm^3, mice were randomly divided into different groups with seven mice per group. At first, we compared activity of AP and IC. Group 1 received recombinant human ES at a dose of 10 mg/kg in 0.1 mL PBS, and group 2 was injected with equal volume of PBS. The other 6 groups were treated with AP and IC at doses of 5 mg/kg, 10 mg/kg, and 20 mg/kg each, in 0.1 mL PBS. Next, we compared activity of P1, AP, and RGD-4C. Group 1 received paclitaxel (Taxol, provided by Tai ji Pharmaceutical Co. Ltd., Chendu, in Sichuan province of China) at a dose of 10 mg/kg; group 2 received equal volume injections of PBS alone as control; group 3 was treated with AP at a dose of 20 mg/kg; group 4 was treated with RGD-4C at a dose of 9.11 mg/kg, which was the same number of moles as AP. All of the mice were injected subcutaneously distant from the tumor sites, once daily for 10 days.

Measurement of Tumor Growth. Tumors were measured individually with a vernier caliper. Volumes were determined using the formula: tumor volume = length × width^2 × 0.52. Therapeutic effects on tumor growth were expressed as mean tumor volume versus time, calculated as $(1 - T/C) \times 100\%$, where T = treated tumor volume and C = control tumor volume. For example, if the volume of the treated tumor was 40% of that of the control on a given day, tumor suppression in the treated group was regarded as 60%.

Histochemistry. Mice were euthanized 2 weeks post-treatment, and tumor tissue was collected, fixed with 4% formaldehyde, embedded in paraffin, and sectioned for hematoxylin and eosin (H&E) staining. H&E staining was performed according to standard histological procedures. Necrosis and vascularization in tumor tissue were observed under a light microscope.

Endothelial Cell Proliferation Assay. Bovine aorta endothelial (BAE) cells were cultured as previously described. Cell proliferation assays were performed as follows: Briefly, cells were washed with PBS and digested by trypsin solution. A cell suspension was made with culture medium, and the concentration was adjusted to 4×10^4 cells/mL. Cells were plated into 96-well culture plates (0.1 mL/well) and incubated at 37 °C in 5% CO_2 overnight. The cells were then treated with a series of indicated doses of samples (n = 5/group) for 72 h. After that, the cells were incubated with 3-(4,5-methylthiazol-2-yl)-2,5-diphenyl-tetrazolium bromide (MTT) 50 μg/well) for 4 h. Resulting formazan products were solubilized with 150 μL dimethyl sulfoxide (DMSO), and the optical density was measured at 570 nm. All experiments were performed in triplicate.

Chick Chorioallantoic Membrane Assay. To determine the antiangiogenic activity in vivo, CAM assay was performed. The in vivo CAM angiogenesis model used was initially described

by Folkman with some modifications according to Maragoudakis (*11*). All procedures were carried out in a laminar flow hood under sterile conditions. In 7-day chick embryos, after the air chamber was opened, the shell membrane was removed and sealed by a transparent tape to form a pseudoair chamber which also served as transparent observation windows. After a 1 day stabilization period, the transparent tape was cut open and a drug carrier plate with a 5 mm diameter was placed in the chamber. Ten microliter aliquots of each test reagent were added onto the plate. PBS and ES were used as negative and positive controls, respectively. The experimental groups were treated with AP and AP (O) at different indicated doses (1.25 nM for AP and 2.5 nM for AP (O), $n \geq 5$/group). After 72 h incubation at 37 °C, the pseudoair chambers of chick embryos were opened and fixed in the fixative (formaldehyde/acetone, 1:1) for 5 min. The chick embryo was subsequently removed, and the CAM was carefully peeled off from the egg shell and laid out flat for photography. The numbers of medium−small blood vessels within a radius of 5 mm from the center of the carrier plate were counted and subjected to statistical analysis. All experiments were performed in triplicate.

Western Blot Analysis. MCF-7 Cells were harvested, centrifuged, and the protein fractions separated. The protein was analyzed by 10% SDS-PAGE and further identified by Western blot analysis with PVDF Western blotting membranes (Millipore, USA) and rabbit polyclonal antibody.

Flow Cytometric Analysis of Peptide Binding Integrin. Bel-7402 cells expressing integrin $\alpha v\beta 3$ (*7*) and MCF-7 cells expressing integrin $\alpha 5\beta 1$ were grown in a 24-well plate until 80% confluency, harvested, and washed twice with ice-cold PBS. Before labeling, cells were resuspended in PBS plus 1% bovine serum albumin (BSA) for 30 min, then added with 1 μL fluorescein isothiocyanate (FITC)-labeled P1, which contained RGD domain (FITC-P1) together with 50-fold extra unlabeled peptides (AP and AP (O)) for Bel-7402 cells or 25-fold extra unlabeled peptides (AP, AP(O) and RGD-4C) for MCF-7 cells for an additional 1 h. Afterward, cells were collected and washed again with ice-cold PBS twice, resuspended in 400 μL PBS, and analyzed by flow cytometry (Becton Dickinson, Shanghai, China). To exclude nonviable cells, 1 μg/mL PI was added into the sample to exclude nonviable cells immediately before flow cytometric analysis. FITC fluorescence was measured in FL1 channel.

Three-Dimensional Modeling. Structure modeling of the composed peptides was performed using the InsightII (Accelrys Inc.)/CHARMm module. During the simulation, residues 1 to 11 of IC and residues 15 to 25 of AP and AP (O) were combined by the template which was the structure of residues 50 to 60 in human ES (PDB ID 1BNL). The modified protocol was performed by 500 steps of steepest descents (convergence was 0.1 kcal/mol) and 500 steps of conjugate gradients (convergence is 0.01 kcal/mol) under the CHARMM27 force field. Then, stimulation of the 3D structure was performed by molecule dynamics at 300 K.

Statistical Methods. Data are expressed as mean ± SD. Statistical significance was assessed using the Student's *t* test. For all statistical comparisons, treated groups were compared with PBS-treated controls. $P < 0.05$ was considered statistically significant.

RESULTS

Design of Cyclic Polypeptides and Orientation Synthesis of Disulfide Bonds. Table 1 lists the sequences of synthetic polypeptides and the position of disulfide bonds discussed in the present study. Polypeptides were synthesized using the solid-phase Fmoc-chemistry method. The purity of synthesized polypeptides was more than 92% as determined by HPLC and ESI mass spectrometry. Each reduction or oxidation step involved in the formation of disulfide bonds was identified by HPLC and ESI mass spectrometry. Any mismatch of disulfide bonds would cause decreased polypeptide purity and changes in peak shape. The results showed that disulfide bonds in the polypeptide AP (O) were (1−4, 2−3) paired.

Antitumor Activity of the Synthesized Peptides in Vivo. In in vivo study comparing the activity of AP and IC, the size of implanted mouse melanoma tumors in the group treated with synthesized peptide AP was significantly smaller than that in the PBS control group, and the inhibitory effect of AP on the tumor growth was dose-dependent (Figure 1A); no significant antitumor effects were observed at any doses of IC treatment groups (Figure 1B). A 48% inhibition of tumor volume after 10 day AP treatment ($P < 0.05$) was observed at the dose of 20 mg/kg (Figure 1C). While the IC-treated group showed no significant difference from the PBS-treated group regarding tumor size, even at the dose of 10−20 mg/kg, the tumor size of the IC-treated group was bigger than that of the PBS-treated group (Figure 1B). In in vivo study comparing activity of AP and RGD-4C, AP showed strong antitumor activity, which was higher than that of RGD-4C (Figure 1D).

Histochemistry. We also examined the effect of the peptides AP and RGD-4C on tumor tissue. AP displayed more severe tissue necrosis than RGD-4C (Figure 2A,B). RGD-4C displayed necrosis interspersed with viable tumor cells, whereas AP induced large areas of continuous necrosis within tumors. We then counted the number of visible blood vessels in H&E staining and found that AP significantly reduced the vessel density ($P < 0.01$ vs RGD-4C) (Figure 2C).

Inhibition of Endothelial Cell Proliferation. In vitro MTT method was applied to determine the inhibitory effects of polypeptides (AP and AP (O)) on endothelial cell proliferation. Passages 2 to 5 of primary endothelial cells isolated from bovine aorta were used in the experiment in order to maintain the primary characteristics of endothelial cells. Cells were treated with different doses of polypeptides (2.5 μg/mL, 5 μg/mL, and 10 μg/mL). The results showed that the two polypeptides could strongly inhibit the proliferation of endothelial cells in each dosage ($P < 0.01$) (Figure 3). At the dose of 10 μg/mL, AP exhibited higher inhibitory effect on endothelial cell proliferation than AP (O).

Chick Chorioallantoic Membrane Assay. Maragoudakis's study showed that collagen biosynthesis reached its peak on the first 8 to 11 days during chick embryo development, when angiogenesis also peaked (*11*). Thus, chick embryo on the eighth day of development was selected for drug treatment. Considering that there might be a certain limit for the diffusion of polypeptides from drug-loaded paper onto the chick chorioallantoic membrane, we only counted neovascular nuclei within the radius of 5 mm from the edge of paper. Each polypeptide was studied at different doses. At the concentration of 2.5 nM for the polypeptides, neovascular density and number were decreased significantly on CAM compared with PBS treated group ($P < 0.01$) (Figure 4). Maximum angiogenesis inhibition rates of polypeptides AP and AP (O) were 55.6% and 33.4%, respectively. In addition, polypeptide AP showed highly inhibitory effect at 2.5nM on angiogenesis in chick embryo, which was higher than that of AP (O).

Competitive Binding of the Polypeptides with the $\alpha 5\beta 1$ Integrin. The binding of the polypeptides with the targets was investigated using flow cytometry. Bel-7402 cells expressing integrin $\alpha v\beta 3$ (*7*) and MCF-7 expressing integrin $\alpha 5\beta 1$, which was proven by Western blotting were used (Figure 5B). We performed a competitive binding assay using FITC-P1, which showed binding affinity to integrin $\alpha v\beta 3$ in previous studies (*7*), to compete for binding to integrin $\alpha v\beta 3$. The results

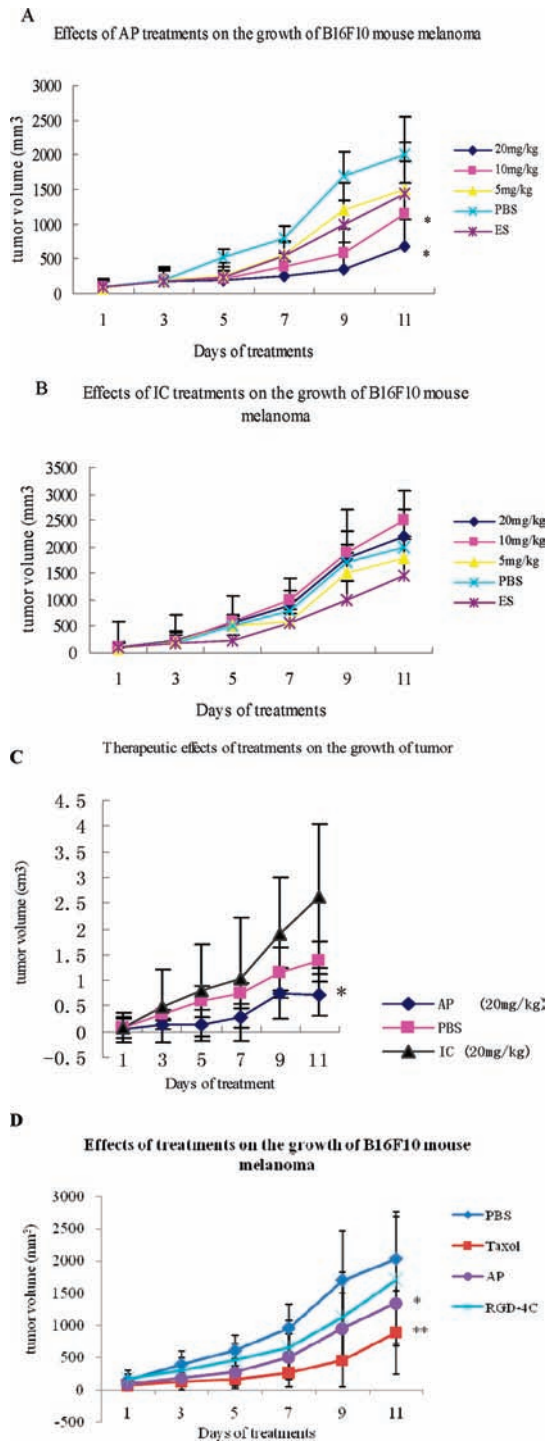


Figure 1. Therapeutic effects of peptides AP and IC on the growth of B16F10 mouse melanoma in vivo (A,B). The therapeutic effects of peptides AP and IC (20 mg/kg) on the growth of B16F10 mouse melanoma in vivo (C), AP (20 mg/kg), and RGD-4C (9.11 mg/kg) on the growth of tumor in vivo (D). Each point represents mean ± SD (* $P < 0.05$, ** $P < 0.01$).

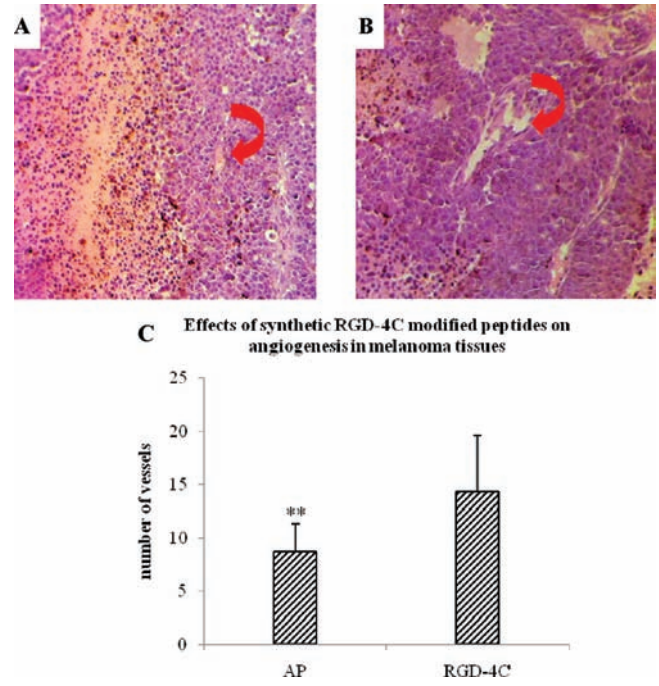


Figure 2. Necrosis areas within tumor and tumor blood vessel density (shown by H&E staining observed with light microscope; 40× original magnifications). (A) represents AP and (B) represents RGD-4C treatment, which exhibits incomplete tissue necrosis interspersed with viable tumor cells. Blood vessels were indicated with arrows. Results were expressed as mean ± SD of eleven regions of two sections per group (* $P < 0.05$; ** $P < 0.01$ vs RGD-4C group).

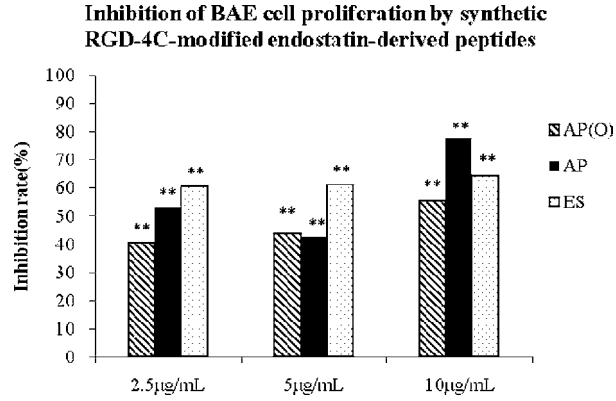


Figure 3. Inhibition of BAE cell proliferation by synthetic RGD-4C-modified endostatin-derived peptides. The optical density at 570 nm can reflect the survival of cells, and we defined the inhibition of cell proliferation (%) compared with PBS-treated control. The peptides showed strong antiproliferation activity($n = 5$, ** $P < 0.01$).

indicated that the two polypeptides (AP and AP (O)) did not bind to integrin $\alpha v\beta 3$ (Figure 5A). In MCF-7 cell binding assay, FITC-P1 could also bind to MCF-7 cells expressing integrin $\alpha 5\beta 1$, and the result of competition for binding to integrin $\alpha 5\beta 1$ showed the three polypeptides (AP, AP (O), and RGD-4C) could bind to this target (Figure 5C).

Three-Dimensional Modeling of the Polypeptides and Molecular Docking with the Integrin $\alpha v\beta 3$. In the simulation of polypeptide molecular structure, the coupling of RGD-4C to the N-terminus and C-terminus of the polypeptides formed different products, which might be due to different molecular folding of these two products. Three-dimensional modeling showed that the structure was closely related to the activity to some extent. Polypeptide IC folded in as expected manner, while AP was stretched. In addition, two functional domains of IC, ES-2 and RGD-4C, were closer to each other in space (Figure 6). In theory, such a structure might affect IC activity. On the basis of molecular modeling, polypeptides (AP and AP (O)) were docked onto the integrin $\alpha v\beta 3$. The docking procedure was performed on a Cluspro Server (http://nrc.bu.edu/cluster/) workstation, and docking results were analyzed using SWISS-PBD viewer (http://spdbv.vital-it.ch/) software. Analysis of the docking results obtained from the workstation indicated that both

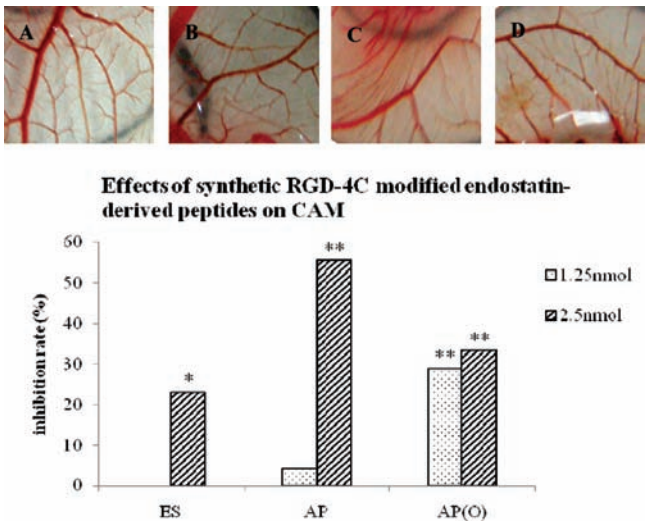


Figure 4. Effects of synthetic RGD-4C modified endostatin-derived peptides on chick chorioallantoic membrane angiogenesis (CAM). The chick embryos were treated with PBS (A); endostatin (B); peptide AP (C); and AP (O) (D), respectively. We defined the inhibition of angiogenesis (%) compared with PBS-treated control. The synthetic peptide showed strong antiangiogenic activity (*E*) ($n \geq 5$, * $P < 0.05$, ** $P < 0.01$).

of the two polypeptides (AP and AP (O)) could not bind to the αv integrin subunit.

DISCUSSION

RGD and RGD-4C are known ligands of integrin αvβ3, and studies have shown that RGD can be used as drug carrier to increase the drug targeting of tumor blood vessels (*12, 13*). Other research on the crystal structure of RGD and αvβ3 found that binding of the ligand occurred at the major interface between the αv and β3 subunits where the ligand made extensive contacts with both subunits (*14*).

However, RGD-4C, in theory, is more suitable as a drug carrier for tumor blood vessels according to the results of many studies in past years (*15, 16*). RGD-4C contains two pairs of disulfide bonds, resulting in a more complicated mechanism of activity. It has been indicated that RGD-4C displayed higher integrin-binding activity with the (1−4, 2−3) disulfide pairing pattern (*10*). However, considering that molecular behavior of RGD-4C-polypeptide complex might be different from that of RGD-4C, in the current study, we synthesized polypeptides AP, IC, and AP (O), AP (O) with the (1−4, 2−3) disulfide pairing pattern according to the previous report (*10*). The aim of this study was to identify whether the position of RGD-4C and introduction of disulfide bonds would influence the activity of modified polypeptides using both in vivo and in vitro models.

First, RGD-4C without disulfide bonds was coupled with N-/C-terminal of ES-2. In vivo antitumor activity study was conducted for the resulting polypeptides. The results showed that the coupling of RGD-4C to the N-terminal of ES-2 resulted in significant inhibitory effects on the tumor growth; otherwise, linear RGD-4C coupled to the C-terminal of ES-2 showed no inhibitory effects on the tumor growth and even caused opposite effects at higher dosage. Molecular modeling of polypeptides demonstrated that the molecular structure of IC was bent and the two domains ES-2 and RGD-4C were close to each other in space, resulting in relatively higher steric hindrance, thus preventing the binding of polypeptides to the targets. In contrast, AP was more stretched, and two functional domains will not interfere with each other, leading to significant in vivo and in vitro activity. Therefore, the position of RGD-4C has significant influence on the activity of the RGD-4C modified ES-2 peptides.

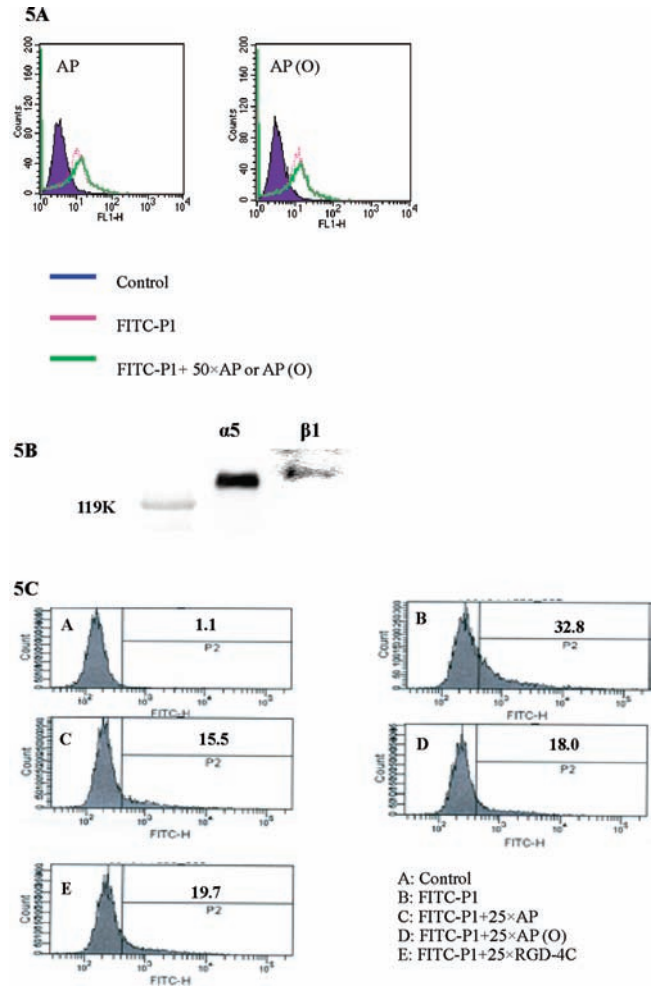


Figure 5. Western boltting and flow cytometric analysis of peptides binding to integrin. AP and AP (O) competed with FITC-P1 (contained RGD domain) for binding to the Bel-7402 cells. It showed that the two peptides did not affect the binding of FITC-P1 to integrin αvβ3 (A). Western blotting analysis of the expression of integrin α5 and β1 in human MCF-7 cells with rabbit antihuman integrin polyclonal antibody (B). AP (C), AP (O) (D), and RGD-4C (E) competed with FITC-P1 binding to the MCF-7 cells. It showed that the three peptides could affect the binding of FITC-P1 to integrin α5β1 (C).

However, further research is warranted to identify whether the disulfide bonds will affect the antiangiogenic activity of RGD-4C modified ES-2 peptides.

On the basis of the previous study, we focused on the peptides coupling of RGD-4C to the N-terminal of ES-2. Thus, AP (O) with disulfide bonds was synthesized to investigate the influence of the disulfide bond. No significant improvements were observed on polypeptide activity after the addition of disulfide bonds. Moreover, at some doses, non-disulfide polypeptides even showed higher activity than the disulfide-containing polypeptides. This might be caused by the fact that AP itself could also form a disulfide bond in solution or that this disulfide bond itself does not affect the activity of the modified peptides. In any case, the finding of this study has important significance for RGD-4C application. The synthesis of (1−4, 2−3) paired disulfide bonds is difficult, since mismatched disulfide pairs are very easy to form during synthesis; also, it is a high-cost process. However, if RGD-4C without disulfide bonds exhibits similar biological activity, cost and synthesis time could be greatly reduced, which is more conducive to the application.

The binding of the polypeptides with the targets was investigated using flow cytometry. As shown in the flow cytometry assay, FITC-P1 was applied to compete with AP and

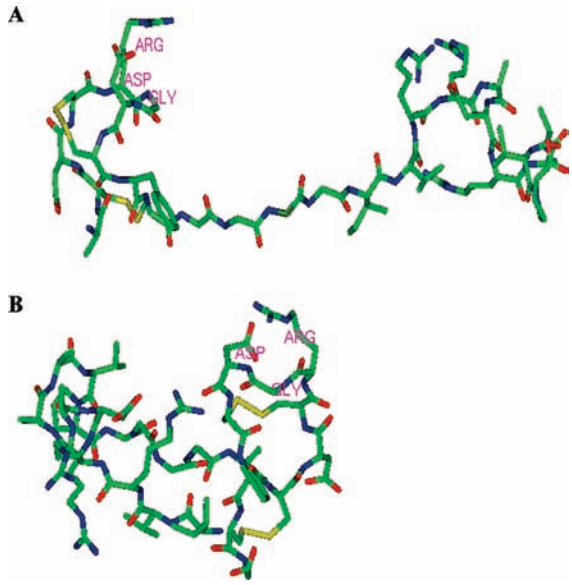


Figure 6. 3D modeling of the three peptide structures, AP (A) and IC (B). The 3D structure of AP was more extended than that of IC.

AP (O) for binding to integrin $\alpha v\beta 3$. The data showed that AP and AP (O) did not bind to $\alpha v\beta 3$. However, AP, AP (O), and RGD-4C could bind to integrin $\alpha 5\beta 1$. In previous studies, RGD-4C was shown to bind to the integrin αv subunit during screening by phage display technology (*17*). Such inconsistence might be caused by in vitro phage display technique and cannot represent the cytology or in vivo behavior of RGD-4C. Thus, RGD-4C and RGD-4C modified peptides may not bind to integrin $\alpha v\beta 3$ in vivo. To further illustrate this point, we docked these polypeptides with integrin $\alpha v\beta 3$ using ClusPro Server website. The docking results indicated that the polypeptides could not bind with the αv integrin subunit indeed. In this study, we found that the target of RGD-4C and RGD-4C modified peptides was integrin $\alpha 5\beta 1$. As such, our study might bring new insights into the investigation of RGD-4C and RGD-4C modified peptides targets. RGD-4C modified peptides might be applied to tumors with high expression of integrin $\alpha 5\beta 1$.

ACKNOWLEDGMENT

The authors are grateful to Dr. Yinwu (Department of Life Science, Nanjing University, Nanjing, 210008, P. R. China) for flow cytometric analysis. We thank Ying Wang (Department of Life Science and Technology, China Pharmaceutical University, Nanjing, 210009, P. R. China) for assistance of three-dimensional modeling of polypeptides and Mushowe (Department of Life Science and Technology, China Pharmaceutical University, Nanjing, 210009, P. R. China) for critical reading of the manuscript.

LITERATURE CITED

(1) O'Reilly, M. S., Boehm, T., Shing, Y., Fukai, N., Vasios, G., Lane, W. S., Flynn, E., Birkhead, J. R., Olsen, B. R., and Folkman, J. (1997) Endostatin: an endogenous inhibitor of angiogenesis and tumor growth. *Cell 88* (2), 277–85.

(2) Xu, H. M., Zhang, G. Y., Ji, X. D., Cao, L., Shu, L., and Hua, Z. C. (2005) Expression of soluble, biologically active recombinant human endostatin in *Escherichia coli*. *Protein Expr. Purif. 41* (2), 252–8.

(3) Dhanabal, M., Volk, R., Ramchandran, R., Simons, M., and Sukhatme, V. P. (1999) Cloning, expression, and *in vitro* activity of human endostatin. *Biochem. Biophys. Res. Commun. 258* (2), 345–52.

(4) Folkman, J. (2006) Antiangiogenesis in cancer therapy--endostatin and its mechanisms of action. *Exp. Cell Res. 312* (5), 594–607.

(5) Cattaneo, M. G., Pola, S., Francescato, P., Chillemi, F., and Vicentini, L. M. (2003) Human endostatin-derived synthetic peptides possess potent antiangiogenic properties *in vitro* and *in vivo*. *Exp. Cell Res. 283* (2), 230–6.

(6) Wickström, S. A., Alitalo, K., and Keski-Oja, J. (2004) An endostatin-derived peptide interacts with integrins and regulates actin cytoskeleton and migration of endothelial cells. *J. Biol. Chem. 279* (19), 20178–85.

(7) Xu, H. M., Yin, R., Chen, L., Siraj, S., Huang, X., Wang, M., Fang, H., and Wang, Y. (2008) An RGD-modified endostatin-derived synthetic peptide shows antitumor activity *in vivo*. *Bioconjugate Chem. 19* (10), 1980–6.

(8) Pasqualini, R., Koivunen, E., and Ruoslahti, E. (1997) Alpha v integrins as receptors for tumor targeting by circulating ligands. *Nat. Biotechnol. 15* (6), 542–6.

(9) Cai, W., and Chen, X. (2006) Anti-angiogenic cancer therapy based on integrin alphavbeta3 antagonism. *Anticancer Agents Med. Chem. 6* (5), 407–28.

(10) Assa-Munt, N., Jia, X., Laakkonen, P., and Rouslahti, E. (2001) Solution structures and integrin binding activities of an RGD peptide with two isomers. *Biochemistry 40* (8), 2373–8.

(11) Maragoudakis, M. E., Panoutsacopoulou, M., and Sarmonika, M. (1988) Rate of basement membrane biosynthesis as an index to angiogenesis. *Tissue Cell 20* (4), 531–9.

(12) Arap, W., Pasqualini, R., and Rouslahti, E. (1998) Cancer treatment by targeted drug delivery to tumor vasculature in a mouse model. *Science 279* (5349), 377–80.

(13) Kessler, T., Bieker, R., Padró, T., Schwöppe, C., Persigehl, T., Bremer, C., Kreuter, M., Berdel, W. E., and Mesters, R. M. (2005) Inhibition of tumor growth by RGD peptide-directed delivery of truncated tissue factor to the tumor vasculature. *Clin. Cancer Res. 11* (17), 6317–24.

(14) Xiong, J. P., Stehle, T., Zhang, R., Joachimiak, A., Frech, M., Goodman, S. L., and Arnaout, M. A. (2002) Crystal structure of the extracellular segment of integrin alphavbeta3 in complex with an Arg-Gly-Asp ligand. *Science 296* (5565), 151–5.

(15) Mitra, A., Mulholland, J., Nan, A., McNeill, E., Ghandehari, H., Line, B. R., Amitava, M., Justin, M., Anjan, N., Edwina, M. N., Hamidreza, G., and Bruce, R. L. (2005) Targeting tumor angiogenic vasculature using polymer-RGD conjugates. *J. Controlled Release 102* (1), 191–201.

(16) Wang, H., Yan, Z., Shi, J., Han, W., and Zhang, Y. (2006) Expression, purification, and characterization of a neovasculature targeted rmhTNF-α in *Escherichia coli*. *Protein Expr. Purif. 45* (1), 60–5.

(17) Koivunen, E., Arap, W., Rajotte, D., Lahdenranta, J., and Pasqualini, R. (1999) Identification of receptor ligands with phage display peptide libraries. *J. Nucl. Med. 40* (5), 883–8.

BC900292Y

Symmetrical Bisbenzimidazoles with Benzenediyl Spacer: The Role of the Shape of the Ligand on the Stabilization and Structural Alterations in Telomeric G-Quadruplex DNA and Telomerase Inhibition

Santanu Bhattacharya,*[,†,‡] Padmaparna Chaudhuri,[†] Akash K. Jain,[†] and Ananya Paul[†]

Department of Organic Chemistry, Indian Institute of Science, Bangalore 560 012, India, and Chemical Biology Unit, Jawaharlal Nehru Centre for Advanced Scientific Research, Bangalore 560 012, India. Received July 25, 2009; Revised Manuscript Received December 31, 2009

The extremities of chromosomes end in a G-rich single-stranded overhang that has been implicated in the onset of the replicate senescence. The repeated sequence forming a G-overhang is able to adopt a four-stranded DNA structure called G-quadruplex, which is a poor substrate for the enzyme telomerase. Small molecule based ligands that selectively stabilize the telomeric G-quadruplex DNA, induce telomere shortening eventually leading to cell death. Herein, we have investigated the G-quadruplex DNA interaction with two isomeric bisbenzimidazole-based compounds that differ in terms of shape (V-shaped angular vs linear). While the linear isomer induced some stabilization of the intramolecular G-quadruplex structure generated in the presence of Na^+, the other, having V-shaped central planar core, caused a dramatic structural alteration of the latter, above a threshold concentration. This transition was evident from the pronounced changes observed in the circular dichroism spectra and from the gel mobility shift assay involving the G-quadruplex DNA. Notably, this angular isomer could also induce the G-quadruplex formation in the absence of any added cation. The ligand−quadruplex complexes were investigated by computational molecular modeling, providing further information on structure−activity relationships. Finally, TRAP (telomerase repeat amplification protocol) experiments demonstrated that the angular isomer is selective toward the inhibition of telomerase activity.

INTRODUCTION

Telomeres are the noncoding regions of DNA at the end of the chromosomes (*1*). Their function is to counterbalance the function of the chromosome ends that occur with each replication cycle, and this prevents aberrant recombination and degradation by exonucleases (*2*). These are composed of tandem repeats of short G-rich sequences, as exemplified by the 5′-TTAGGG-3′ in human telomeric sequence. With the help of enzyme telomerase, a ribonucleoprotein, the cells are easily replicated indefinitely with reverse transcriptase activity. Telomerase is overexpressed in 85−90% of all cancer cells (*3–5*). Telomerase is therefore a potentially highly selective target for chemotherapeutic intervention cancer chemotherapy (*6, 7*).

Guanine-rich DNA sequence has the ability to form four-stranded inter- and intramolecular guanine quadruplex structures under high salt conditions. Since RNA template of telomerase requires a nonfolded telomeric DNA primer in order to affect telomere synthesis, the formation and the stabilization of G quadruplex structures results in the negative regulation of the telomerase function. To date, a number of families of compounds have been identified and their interactions with G-quadruplex have been extensively studied (*8, 9*), of which a few of them are in clinical use (*10, 11*).

G4 DNAs have several distinct structural features compared with duplex DNA, notably the possession of four quasi-equivalent grooves and a pronounced channel of negative electrostatic potential running through the center of the planes of the G-quate allowing metal ion to be coordinated between the planes in a bipyramidal antipoismatic manner (*12*). Due to these special features, a selective recognition of G-quadruplex by small molecule is possible (*13–15*). So, the design of new G-quadruplex stabilizing ligands involves an attractive strategy to develop new anticancer agents. Typical G-quadruplex binding ligands have planar aromatic molecules, capable of inducing interaction with guanine tetrads via $\pi-\pi$ interactions and also have side chains directed toward the quadruplex loops (*16, 17*). Certain triazole (*18*), indole (*19*), benzimidazole (*20*) and bisquinolinium (*21*) compounds having these properties have been tested.

We have previously reported duplex DNA binding (*22−24*), DNA cleaving (*25−28*) and DNA-dependent topoisomerase inhibiting properties (*29*). We have also reported the effect of symmetric benzimidazoles on the stability and topology of quadruplex DNA made from *Tetrahymena thermophilla* (*30*). These molecules were derived from 1,3-substituted symmetrical phenylene bisbenzimidazole system and exerted significant influence on the stability of quadruplex DNA depending on the nature of substitution on the aromatic skeleton.

A few G-quadruplex stabilizing small molecules have been designed and investigated, and it was found that isomers which differ in shape and geometry have different binding affinities toward G-quadruplex DNA (*31, 32*). Herein, we examine comparative quadruplex formation, stabilization, and telomerase inhibition by two isomeric symmetrical bisbenzimidazoles, ***p*-Phenbbim** and ***m*-Phenbbim**, which are devoid of any substitution at the aromatic core (Figure 1). The molecule ***p*-Phenbbim** is based on 1,4-substituted symmetrical phenylene bisbenzimidazole which differs in shape from its 1,3-substituted counterpart (***m*-Phenbbim**). Earlier reports suggest that 1,4-substituted phenylene bisbenzimidazole analogues (*33, 34*) may

* To whom correspondence should be addressed. Also J. C. Bose Fellow, Department of Science & Techonology (DST), New Delhi. E-mail: sb@orgchem.iisc.ernet.in, Phone: (91)-80-22932664; Fax: (91)-80-2360-0529.

† Indian Institute of Science.

‡ Jawaharlal Nehru Centre for Advanced Scientific Research.

10.1021/bc9003298 © 2010 American Chemical Society
Published on Web 06/10/2010

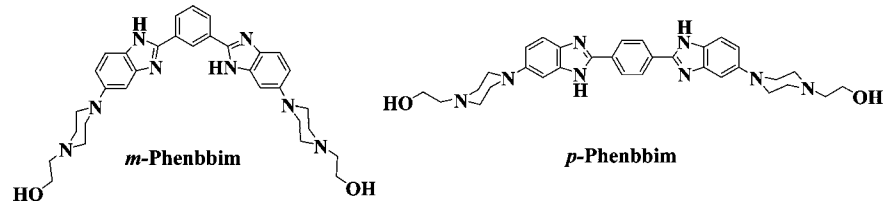


Figure 1. Chemical structures of ***m*-Phenbbim** and ***p*-Phenbbim**.

also have affinity toward quadruplex structures. So, we have decided to compare the quadruplex recognition properties of these two isomeric molecules.

In this study, we have utilized telomeric oligonucleotide $d[T_2G_4]_4$ related to the sequence *Tetrahymena thermophilia*, which is capable of forming both intramolecular and intermolecular conformations stabilized by either K^+ or Na^+ ions. This sequence was shown to exhibit an interesting range of structural polymorphism depending on whether the G-quadruplex was formed in the presence of either K^+ or Na^+ ions (*30, 35–38*). We discuss comparative G-quadruplex formation, stabilization, and structural alteration of $d[T_2G_4]_4$ quadruplex in the presence of either isomeric compound. We have also reported here the relative efficiencies to inhibit the telomerase activity as indicated by the TRAP[1]assay.

EXPERIMENTAL SECTION

All starting compounds were procured from Sigma, Aldrich, or E-Merck. All solvents were from Merck, and they were distilled and/or dried prior to use whenever necessary.

General Spectrometric Characterizations. NMR spectra were recorded on a Bruker AMX (300 or 400 MHz) spectrometer. IR spectra were recorded on an FTIR Perkin-Elmer Spectrum GX spectrometer. Mass spectra were recorded on a Micromass Q-TOF Micro TM spectrometer.

5-(4-(2-Hydroxyethyl)-1-piperazinyl)-2-nitroaniline (1). 5-Chloro-2-nitroaniline (2 g, 11.6 mmol) was taken in dry DMF (5 mL). To this, 1-(2-hydroxyethyl)-piperazine (1.8 g, 13.8 mmol) and K_2CO_3 (2.5 g, 18 mmol) were added. It was then heated at 110 °C for 12 h until TLC showed the disappearance of 5-chloro-2-nitroaniline. The crude compound was suspended in water, and the product was extracted with ethyl acetate. The organic layer was washed twice with water, dried over anhydrous Na_2SO_4, and concentrated to get 5-(4-(2-hydroxyethyl)-1-piperazinyl)-2-nitroaniline, which was purified by column chromatography using neutral alumina with a solvent system of increasing polarity from $CHCl_3$ to 2% MeOH in $CHCl_3$. The pure product was isolated as a bright yellow solid (2.7 g, 90% yield). ^{1}H NMR (300 MHz, $CDCl_3$) δ ppm = 2.59−2.65 (m, 6H), 3.7 (t, 2H), 3.8 (t, 4H), 5.95 (d, J = 2.7 Hz, 1H), 6.1 (bs, 2H, NH_2), 6.29 (dd, J = 9.3, J = 2.7, 1H), 8.02 (d, J = 9.3, 1H).

5-(4-(2-Hydroxyethyl)-1-piperazinyl)-1,2-phenylenediamine (2). Compound **1** (0.2 g, 0.66 mmol) was added to a stirred suspension of 10% Pd−C (50 mg) in methanol. The mixture was then stirred at room temperature for 24 h under H_2 at 1 atm pressure. It was then filtered and evaporated to get **2** and put for the next step without further purification.

2,2′-(1,4-Phenylene)-bis-[5-(4-(2-hydroxyethyl)-1-piperazinyl)-1*H*-benzimidazole] (*p*-Phenbbim). To a methanolic solution of **2** (380 mg, 1.6 mmol), 15 mL of nitrobenzene and 0.5 equiv of 1,4-benzene dialdehyde **5** (115 mg, 0.8 mmol) were added. The resulting solution was heated at 65 °C for 1 h when a bright red precipitate appeared. After cooling the reaction mixture to room temperature, the precipitate was filtered and washed with methanol. The precipitate was subsequently taken in dry nitrobenzene and heated at 150 °C for 3 h. The reaction mixture was cooled and the product precipitated out upon addition of petroleum ether. A yellow solid so obtained was washed repeatedly with petroleum ether until TLC confirmed 100% purity of the material. This was then dried to obtain 370 mg of ***p*-Phenbbim** in 70% yield. FTIR (KBr) (ν cm^{-1}): 3488, 3455, 3054, 2925.6, 1614, 1492, 1440 cm^{-1}. ^{1}H NMR ($C_{32}H_{38}N_8O_2$.HCl) (400 MHz, DMSO-d_6) δ ppm: 3.37 (t, 4H), 3.80 (bs, 4H), 3.99 (t, 8H), 3.42 (t, 8H), 7.37 (bs, 2H), 7.47 (dd, J = 9.1 Hz, J = 1.96 Hz, 2H), 7.78 (d, 2H, J = 9.1), 8.42 (s, 4H). ^{13}C NMR (DMSO-d_6) δ ppm: 45.56, 50.94, 54.23, 57.36, 98.47, 113.9, 117.75, 126.13, 127.74, 132.78, 145.91, 148.88. MALDI-TOF: 568.3129 (found), 568.3196 (calcd. for $[M + H]^+$. Elemental Analysis: calcd. For $C_{32}H_{38}N_8O_2 \cdot 1.5\ H_2O$: C, 64.7; H, 6.9; N, 18.8. Found: C, 64.6; H, 6.5; N, 18.5.

Benzene-1,3-dicarboxaldehyde (4). α,α′-Dichloro-*m*-xylene **3** (970 mg, 5.54 mmol) and hexamethylenetetramine (1.55 g, 11.08 mmol) were dissolved separately in dry $CHCl_3$ (20 mL), and the mixture was refluxed for 3 h. A white precipitate, which resulted in the salt formation, was filtered and dried. The salt was dissolved in 25 mL water and refluxed for 4 h. The reaction mixture was filtered when hot and the filtrate was cooled in an ice bath, which resulted in the separation of white crystals. It was filtered, washed with cold water, and then dried to get pure aldehyde **4** (370 mg, 50%). ^{1}H NMR (300 MHz, $CDCl_3$) δ ppm: 7.74 (t, 1H), 8.27 (d, J = 7.8 Hz, 2H), 8.39 (s, 1H), 10.13 (s, 2H). FTIR (KBr) (ν cm^{-1}) = 1686 (C═O str.).

2,2′-(1,3-Phenylene)-bis-[5-(4-(2-hydroxyethyl)-1-piperazinyl)-1*H*-benzimidazole] (*m*-Phenbbim). To a methanolic solution of **2** (350 mg, 1.5 mmol), 15 mL of nitrobenzene and 0.5 equiv of benzene-1,3-dicarboxaldehyde (100 mg, 0.74 mmol) were added, and the mixture was refluxed for 1 h. A yellow precipitate formed, which was filtered and suspended in nitrobenzene (6 mL) and heated at 150 °C for 3 h. The reaction mixture was cooled to rt, and petroleum ether was added to precipitate out the product as a yellow−green solid. The precipitate was repeatedly washed with petroleum ether to remove nitrobenzene to get 100 mg of the pure compound as judged by TLC (50% yield). IR: 3490, 3458, 3053.5, 2927, 1619, 1450, 1436 cm^{-1}. ^{1}H NMR (300 MHz, CD_3OD): δ 2.7 (t, 4H), 2.8 (t, 8H), 3.28 (t, 8H), 3.75 (t, 4H), 7.08 (d, J = 8.1 Hz, 2H), 7.64−7.74 (m, 3H), 8.15 (d, J = 8.1), 8.25 (d, J = 9.0 Hz, 2H), 8.5 (s, 1H). ^{13}C NMR (DMSO-d_6) δ ppm: 45.27, 48.57, 53.71, 56.76, 98.36, 113.74, 116.63, 124.67, 125.52, 126.63, 129.70, 132.90, 146.30, 147.96. MALDI-TOF: 568.3214 (found), 568.3196 (calcd. for $[M + H]^+$). Elemental Analysis: calcd. for $C_{32}H_{38}N_8O_2 \cdot 1.5\ H_2O$: C, 64.7; H, 6.9; N, 18.8. Found: C, 64.4; H 6.8; N, 18.5.

Oligonucleotides. HPLC purified oligodeoxyribonucleotides (ODN) $d[T_2G_4]_4$ and dT_{20} were purchased from Sigma Genosys, Bangalore. Their purity was confirmed using high-resolution sequencing gel. The molar concentration of each ODN was determined from absorbance measurements at 260

[1]Abbreviations: hTERT, telomerase reverse transcriptase; DMSO-d_6, dimethyl sulfoxide (deuterated); HRMS, high-resolution mass spectrometry; CD, circular dichroic spectropolarimetry; PAGE, polyacrylamide gel electrophoresis; T_{20}, 5′-TTT TTT TTT TTT TTT TTT TT-3′; MD, molecular dynamics simulation; TRAP, telomerase repeat amplification protocol.

nm based on their molar extinction coefficients (ε_{260}) 229 000 and 148 400, respectively, for d[T_2G_4]$_4$ and d T_{20} markers.

Quadruplex Formation. For quadruplex formation from 5′-$T_2G_4T_2G_4T_2G_4T_2G_4$-3′, the following technique was used: the oligonucleotide in buffer (10 mM Tris-HCl at pH = 7.4, 0.1 mM EDTA, and 100 mM NaCl or 100 mM KCl) was heated at 95 °C for 10 min and then snap-chilled, after which the ligands were added in appropriate proportions and incubated at 37 °C for 24 h. To form a quadruplex in the absence of ligands, the same procedure was followed, but the compounds were not added prior to incubation. To check secondary structure formation in the absence of Na^+ or K^+, again the same technique was followed but the buffer contained no NaCl or KCl.

Circular Dichroism. CD spectra were recorded on a JASCO J-810 spectropolarimeter at a scan speed of 50 nm/min and over the wavelength range 220−400 nm. The samples were taken in quartz cuvettes of 1 cm path-length. CD spectra of quadruplex formed in the presence of ligands (at [DNA]:[ligand] ratios = 1:1, 1:2, 1:4) in buffer (10 mM Tris−HCl, pH = 7.4, 0.1 mM EDTA) containing 100 mM NaCl were measured. For another series of experiments, the compounds were titrated into preformed Na^+-induced DNA quadruplex in buffer. Between each drug addition, an interval of 20 min was allowed. For experiments carried out in the absence monovalent cations, the compounds were titrated into single-stranded 5′-$T_2G_4T_2G_4T_2G_4T_2G_4$-3′ in buffer, not containing NaCl or KCl. The concentration of DNA was maintained at 2 μM in all cases. CD melting for uncomplexed and complexed quadruplex (2 μM) was examined at 295 nm with 1 °C/min ramp.

Melting Temperature Measurements. The stability of G-quadruplex DNA was measured by examining the melting temperature (T_m) of the folded structures. T_m measurements were performed by following the change in absorbance at 295 nm as a function of temperature. Experiments were carried out in quartz cuvettes stoppered with Teflon caps on a Beckman model 640 spectrophotometer attached with a programmable temperature controller. Concentration of DNA was kept at 2 μM. Uncomplexed DNA quadruplex and quadruplex structure formed in the presence of ligand molecules were investigated. Samples were heated at the rate of 1.0 °C/min and the absorbance recorded for every 1.0 °C rise in sample temperature. The melting temperatures (T_m) were determined from a first derivative analysis of the heating scans.

Absorption Titration Experiments. Binding assays were performed with preformed d[T_2G_4]$_4$ quadruplex in 10 mM Tris−HCl, having 100 mM KCl and 0.1 mM EDTA buffer, and with d[(5′-$CGT_{13}GC$-3′)/(5′-$GCA_{13}CG$-3′)] duplex in 10 mM Tris−HCl, having 100 mM NaCl and 0.1 mM EDTA buffer at pH 7.4. Ligand solution (50 μM, 500 μL) was titrated by stepwise addition of aliquots of DNA solution (4 μM). After each addition, the mixture was incubated at 25 °C for 15 min before measurement. The fractional decrease in absorbance at 325 nm for each [DNA]/[ligand] ratio was normalized using

$$\Delta A = (A_{free} - A)/(A_{free} - A_{sat})$$

where A_{free} and A_{sat} are the absorbances for the free and fully bound (saturated) ligands. The fraction of bound drug α (on a 0−1 scale) at each intermediate titration position is given directly by the relative ΔA hypochromicity term (*39*). The concentration of free ligand has been calculated using

$$C_f = (1 - \alpha)C$$

where C is the total ligand concentration (fixed at 50 μM) and can be used to determine the binding ratio r, defined as $(C - C_f)$/[DNA]. Titration data were cast into the form of Scatchard plots of r/C_f versus r for analysis where K_D is the intrinsic equilibrium binding constant and n is an exclusion parameter that defines the number of ligand molecules bound per DNA quadruplex. Data were also fitted using the simpler, linear Scatchard equation

$$r/C_f = K_a(n - r) \quad (1)$$

Native Gel Electrophoresis. The single-stranded d[T_2G_4]$_4$ and dT_{20} marker (10 pmol/μL each) were 5′-^{32}P labeled using [γ-^{32}P]-ATP (Amersham) using protocol given by the supplier, and purified by chromatography on Sephadex G-50. For G-quadruplex constructs, labeled DNA (10 000 CPM tracer) mixed with unlabeled single-stranded DNA to a concentration of 5 μM (20 μL reaction volume) containing 100 mM NaCl, Tris, and 1 mM EDTA buffer, pH 7.4. Resulting solution was heated at 95 °C for 10 min and then snap-chilled after which the individual ligands was added in appropriate quantities and incubated at 37 °C for 24 h. Finally, the ligand incubation with DNA was terminated by the addition of 5 μL gel loading buffer (30% glycerol, 0.1% bromophenol blue, and 0.1% xylene cyanol). Ten microliters of the subsequent ligand−quadruplex complexes were analyzed on a 12% native PAGE (the gel was pre-run for 30 min). Electrophoresis was carried out for 3 h at 4 °C using 80 V in 0.5× TBE buffer (pH = 7.4) containing 20 mM NaCl. Gels were dried and then visualized on a phosphor imager.

Computational Methods. All calculations were performed using the *Gaussian 03* suite program (*40*). Each conformer of the two isomers was optimized at B3LYP/6-31G* level of theory. For each system studied, vibrational frequency calculations were carried out to confirm that they converged to true minima. The Mulliken atomic charges of the optimized ligands obtained from the calculation used for docking studies. The distance (Å) for the all conformers of each isomer was calculated, which is essential for understanding the drug−DNA interaction.

Docking studies were performed using the *AUTODOCK 4.0* program (*41*). Using ADT, nonpolar hydrogens of telomeric G-quadruplex were merged to their corresponding carbons and atomic charges were assigned (*42*). The nonpolar hydrogens of the ligands were merged, and rotatable bonds were assigned. The intramolecular G-quadruplex structure was used as an input for the AUTOGRID program. AUTOGRID performed a precalculated atomic affinity grid map for each atom type in the ligand plus an electrostatics map and a separate desolvation map present in the molecule. The dimensions of the active site box that was placed at the center of the macromolecule were set to 110 Å × 110 Å × 110 Å with a grid spacing of 0.375 Å. Docking calculations were carried out using the Lamarckian genetic algorithm (LGA). Initially, we used a population of random individuals (population size: 150), a maximum number of 2 500 000 energy evaluations, a maximum number of generations of 27 000, and a mutation rate of 0.02. Fifty independent docking runs were done for each ligand. The resulting positions were performed according to a root-mean-square criterion of 0.5 Å.

Molecular dynamics simulations were performed using the sander module of the *AMBER 9.0* program suite and the nucleic acids studied were as treated using the parm99 parameters (*43*). Partial atomic charges for the ligand molecules were derived using the HF/6-31G* basis set followed by RESP calculation, while force-field parameters

were taken from the generalized Amber force field (GAFF) (*44*) using the ANTECHAMBER module. K^+ radius was kept at 2.025 Å (*45, 46*). Periodic boundary conditions were applied with the particle-mesh Ewald (PME) method (*47*) used to treat long-range electrostatic interactions. The quadruplex and ligand complexes were solvated in a rectangular box of TIP3P (*48*), water molecules with solvent layers 10 Å and the potassium counterions were added to neutralize the complexes. The hydrogen bonds were constrained using SHAKE (*49*). For the nonbonded interactions, a residue-based cutoff of 10 Å was used. The solvated structures were subjected to initial minimization to equilibrate the solvent and counter cations. The system was then heated from 0 to 300 K in a 100 ps simulation and followed by a 100 ps simulation to the equilibrate the density of the system. Afterward, constant pressure MD simulation of 8 ns was then performed in an NPT ensemble at 1 atm and 300 K. The output and trajectory files were saved every 0.1 and 1 ps for the subsequent analysis, respectively. All trajectory analysis was done with the Ptraj module in the *AMBER 9.0* suite and examined visually using the VMD software package (*50*).

Telomerase Inhibition. An aliquot of 5×10^6 A549 (human lung carcinoma cell line) cells in exponential phase of growth was pelleted and lysed for 30 min on ice using 200 μL of 1 $\times$ CHAPS lysis buffer (10 mM Tris-HCl, pH 7.5, 1 mM $MgCl_2$, 1 mM EGTA, 0.1 mM benzamidine, 5 mM β-mercaptoetanol, 0.5% CHAPS 10% glycerol in 8200 μL volume). The lysate was centrifuged at 12 000 rpm for 30 min at 4 °C and the supernatant collected, stored at −80 °C, and used as the telomerase source. Telomerase activity was assayed using a modified telomere repeat amplification protocol (TRAP) assay. Briefly, an appropriate primer TS (5′-AATCCGTC-GAGCAGAGTT-3′) has been 5′-labeled with [γ-^{32}P]-ATP and T4 polynucleotide kinase. After enzyme inactivation (85 °C for 5 min), a 120 μL TRAP reaction mix (50 μM of dNTPs, 0.2 μg of labeled TS, 0.1 μg of return primer ACX, 500 ng of protein extract, 2 U *Taq* polymerase) was prepared in the presence/absence of increasing drug concentration in 20 mM Tris-HCl pH 8.3, 68 mM KCl, 1.5 mM $MgCl_2$, 1 mM EGTA, 0.05% v/v Tween-20. An internal control template (0.01 mmol TSNT) with its return primer (1 ng) was added to the reaction mixture. Then, the telomerase elongation step has been performed (30 min at 30 °C), followed by a PCR amplification step (30 cycles of 30 s at 94 °C and 30 s at 59 °C). The reaction products were loaded onto a 10% polyacrylamide gel (19:1) in TBE 0.5×. Gels were transferred to Whatman 3 mm paper, dried under vacuum at 80 °C, and read using a Phosphorimager 840 (Amersham). Measurements were made in triplicate with respect to a negative control run using the equivalent TRAP-PCR conditions but omitting the protein extract, thus ensuring that the ladders observed were not due to artifacts of the PCR reaction.

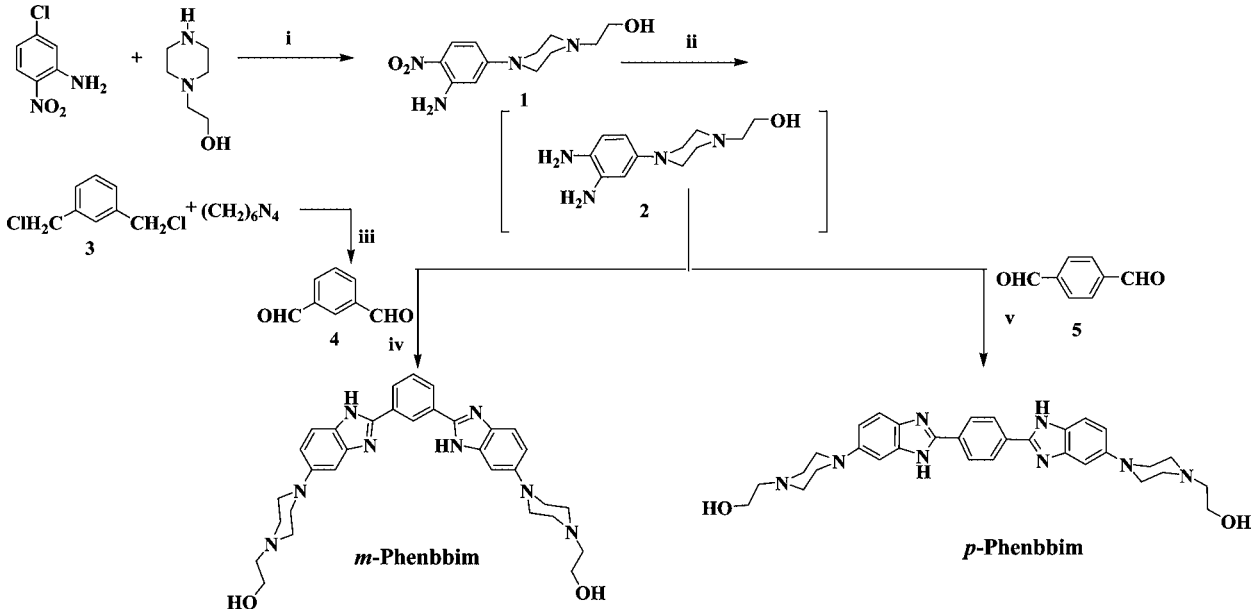
RESULTS AND DISCUSSION

Owing to the interesting array of structural variations exhibited by the telomeric repeats of *Tetrahymena thermophilia*, we selected the single-stranded telomeric repeat $d[T_2G_4]_4$ as a model G-tract for the present study. The sequence $d[T_2G_4]_4$ has been shown to exhibit a wide range of interesting structural polymorphism depending upon whether quadruplex DNA formation occurs in the presence of Na^+ or K^+ (*35, 36*). Due to its structural polymorphism, *Tetrahymena* quadruplex has been used as a model system by other researchers also to probe ligand−DNA interactions (*37, 51, 52*). We were interested to compare the interaction of the two new isomeric benzimidazoles with the various structural polymorphs of the quadruplex structure.

The hybrid quadruplex formed in Na^+ solution bears a circular dichroism (CD) spectral profile with approximately equal intensity maxima around 295 nm (antiparallel characteristics) and 260 nm (parallel) and a minimum around 237 nm (*35, 53*). In contrast, the mixture of multistranded intermolecular and intramolecular quadruplex species formed in K^+ solution was marked by the development of an intense positive band at 265 nm, shoulder at 295 nm, and a minimum around 242 nm (*53*). Among these, the intramolecular quadruplexes are less stable, and their structures may be easily altered by interacting with appropriate ligands or proteins, and so forth.

The benzimidazole nucleus is a constituent of many of the bioactive heterocyclic compounds that are of wide interest

Scheme 1[a]



[a] Reagents, conditions, and yields: (i) Anhydrous K_2CO_3, dry DMF, 110 °C, 12 h, 90%; (ii) H_2 (1 atm), 10% Pd−C, MeOH, rt, 24 h; (iii) dry $CHCl_3$, reflux, 3 h then water, reflux 4 h, 50% (overall); (iv) compound **2**, $PhNO_2$/MeOH, 65 °C, 1 h, then $PhNO_2$, 150 °C, 3 h, 50%; (v) compound **2**, $PhNO_2$/MeOH, 65 °C, 1 h, then $PhNO_2$, 150 °C, 2 h, 70%.

because of their diverse biological and clinical applications (*54*). Moreover, benzimidazoles are structural isosteres of natural nucleotides (purines), which allows them to interact easily with the biopolymers of the living system. Besides having these properties, bisbenzimidazole compounds are known to have cell and nuclear membrane permeability and are being used in cytometry and in nuclear chromosomal staining in cell culture (*55–58*). With these factors taken together, we have synthesized two isomeric bisbenzimidazoles ***p*-Phenbbim** and ***m*-Phenbbim** having central symmetrical and planar core, extended delocalized π-electron system, and side chain tertiary amines, which will develop positive charge via protonation under physiological conditions (pH = 7.4). These molecules also possess groups that are able to form hydrogen bonds with the DNA bases and phosphate backbone of loops, the properties required for the stabilization of G-quadruplex structure (*57, 58*).

Synthesis. For the synthesis of the bisbenzimidazoles, commercially available 5-chloro-2-nitroaniline was chosen as the key starting material. It was reacted with 1-(2-hydroxyethyl)piperazine to produce compound **1**. The next step involved catalytic hydrogenation of **1** over 10% Pd−C to afford the diamine **2**. Subsequent oxidative condensation of **2** with 1,3- or 1,4-benzene-dicarboxaldehydes afforded the required ***m***- and ***p*-Phenbbim**, respectively, in good yields (Scheme 1).

Circular Dichroism Spectroscopy. To investigate the ability of the above molecules toward the stabilization of G-quadruplex structure, quadruplex DNA formation was explored in the presence of ***m*-Phenbbim** and ***p*-Phenbbim**, at [DNA]:[compound] ratios of 1:1, 1:2, and 1:4, in buffer containing 100 mM NaCl. CD spectral data showed that preincubation with ***p*-Phenbbim** formed a structure in which the characteristic CD signatures of a Na^+-stabilized quadruplex, i.e., two positive maxima at 295 and 260 nm, respectively, were retained (*35*). However, there was a hypochromism of both the bands implying some kind of interaction between ***p*-Phenbbim** and G-quadruplex (Figure 2A).

With ***m*-Phenbbim** on the other hand, a very interesting phenomenon was observed. At [DNA]:[drug] ratios 1:1 and 1:2, there was a decrease in the 260 nm CD band along with a concomitant enhancement in the 295 nm band (Figure 2B) However, at [DNA]:[drug] ratio of 1:4, there was a dramatic increase in the 260 nm band along with a red-shift to 265 nm. The intensity of the 295 nm band was reduced; also, the minima at 235 nm became more negative and shifted to 239 nm (Figure 2B).

Next, to examine if ***m*-Phenbbim** could induce such a change in preformed G-quadruplex structure, we first formed a DNA quadruplex in 100 mM NaCl and titrated the molecule against this. As seen in the previous section, up to [DNA]:[drug] ratio 1:2, the 260 nm CD band reduced in intensity and the 295 nm band increased (Supporting Information). At [DNA]:[drug] ratio of ~1:3, there was a dramatic reversal in the CD profile (Supporting Information). The 260 nm band increased in intensity accompanied by a marked red-shift to 265 nm, while the 295 nm band intensity decreased. Finally, at [DNA]:[drug] ratio of 1:6, the 295 nm band appeared as a shoulder to the pronounced 265 nm band. Also, the negative band at 235 nm was red-shifted to 240 nm (Supporting Information). The results were similar to that observed in the previous case where quadruplex structure was formed in the presence of ***m*-Phenbbim**.

Next, we wanted to check the kind of DNA secondary structure these drugs induced in the absence of any added monovalent cations like Na^+ or K^+. This is important, as

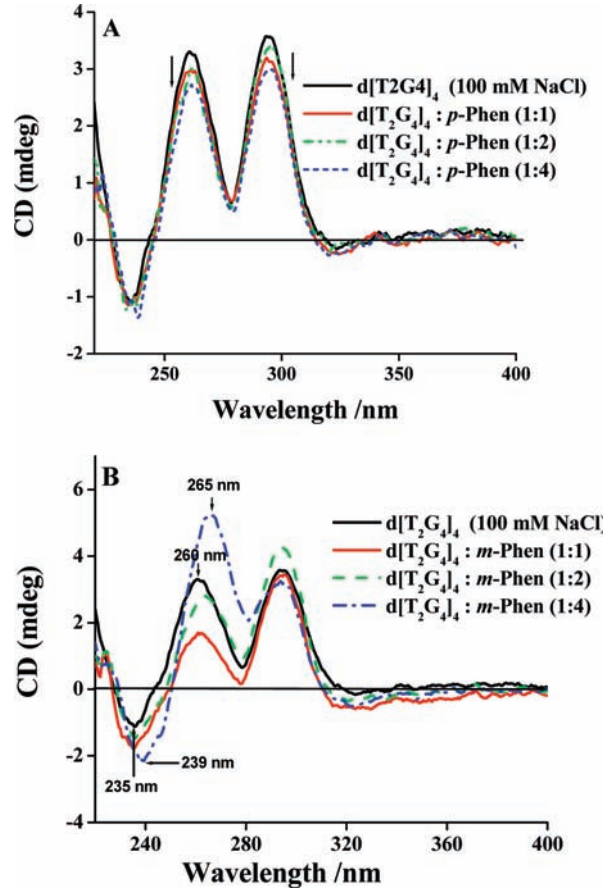


Figure 2. CD profile of quadruplex DNA structure formed in buffer containing 100 mM NaCl in the presence of ligands (A) ***p*-Phenbbim** and (B) ***m*-Phenbbim**, at [DNA]/[Drug] ratio of 1:1, 1:2, and 1:4. The DNA concentration was 2 μm in each case.

only a few ligands are currently known that are capable of inducing the quadruplex formation in the absence of any added cation (*14, 30*). To single-stranded DNA, which had no specific secondary structure (Figure 3, dotted line), compound ***m*-Phenbbim** was titrated. Addition of drug caused a pronounced red-shift of the DNA, i.e., from 256 nm to 265 nm, along with a marked enhancement in the intensity of the said band. Initially, at [DNA]: [drug] = 1:2, there were two bands, one at 265 nm and another, a pronounced hump, at 293 nm. As the drug concentration was increased, the 265 nm maxima increased in intensity and the 293 nm band decreased. The shallow minimum at 235 nm became more intense and shifted to 240 nm. There were two clear isodichroic points at 252 and 282 nm, respectively (Figure 3, solid lines). The final CD signature at [DNA]:[drug] ratio of 1:8 resembled the CD profile of K^+-quad (Figure 3B).

Titration of ***p*-Phenbbim** to randomly structured ss-DNA also led to changes in CD signature of DNA, but the changes were different and less pronounced than that observed with ***m*-Phenbbim** (Supporting Information). However, either of the compounds could not cause any structural alterations of the K^+-quad (Supporting Information).

Specific secondary structure formation was evident from the development of characteristic CD bands. From the CD signature, a structure similar to that formed in the presence of KCl was interpreted. An important feature was the persistence of isodichroic points at 252 and 282 nm throughout the titration. The presence of these two isodichroic points signifies an equilibrium involving at least two species. Hence, the molecule ***m*-Phenbbim** not only caused structural transition of preformed

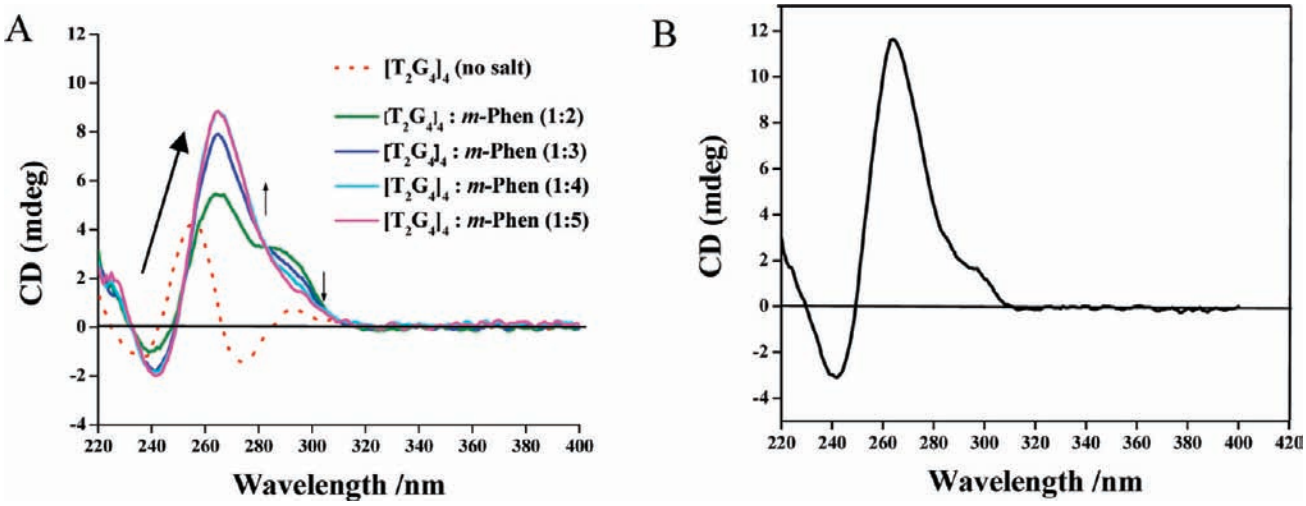


Figure 3. (A) Compound ***m*-Phenbbim** titrated into single-stranded d$[T_2G_4]_4$ (2 μM), in buffer in the absence of KCl or NaCl. The dotted line shows the CD profile of DNA alone. Solid lines show the CD profile of DNA on incremental addition of the compound. Arrows indicate the change in CD bands. (B) The CD profile of quadruplex structure formed in 100 mM KCl.

Table 1. Melting Temperature (T_m) of DNA Quadruplex[a] by Monitoring Absorbance at 295 nm

	T_m (°C)	ΔT_m (°C)[b]
DNA (buffer)	53.4	
DNA (buffer)[c]	36	
DNA + ***p*-Phenbbim** (1:4)	57.1	3.7
DNA + ***m*-Phenbbim** (1:2)	58.5	5.1
DNA + ***m*-Phenbbim**(1:5)[c,d]	48	12

[a] Quadruplex (2 μM strand conc.) formed in buffer (10 mM Tris−HCl at pH = 7.4, 0.1 mM EDTA, and 100 mM NaCl) in the presence of the individual ligands. [b] ΔT_m values represent the differences in melting temperatures for the ligand-bound and free quadruplex. [c] CD melting in buffer (10 mM sodium cacodylate at pH 7.4, 0.1 mM EDTA, and 100 mM LiCl), for DNA alone at 295 nm. [d] CD melting in buffer for ligand-bound complex at 265 nm.

Na^+ stabilized quadruplex, but also induced secondary structure formation from a randomly structured single-stranded DNA in the absence of any monovalent cation.

Melting Temperature Measurements (T_m). Melting of intramolecular quadruplex structure was accompanied by a hypochromicity of the 295 nm absorption band (*15*). Thermal denaturation of the quadruplex, formed in the presence of 100 mM NaCl, showed hypochromicity of the 295 nm absorption band. Next, the melting of secondary structures formed in the presence of the two compounds in 100 mM NaCl buffer was examined. The molecule ***p*-Phenbbim**, at various [DNA]:[drug] ratios (1:1, 1:2, and 1:4), induced stabilization of the intramolecular quadruplex structure. Reversible melting profiles were obtained when the absorption at 295 nm *vs.* temperature was monitored (Supporting Information, only the heating scans are shown). With ***m*-Phenbbim**, at [DNA]:[drug] ratio 1:2, secondary structure dissociation was accompanied by a hypochromism of the 295 nm absorption band, and heating/cooling profiles were almost reversible (Supporting Information).

From the CD titrations and thermal melting data, it is apparent that ***p*-Phenbbim**, at all concentrations, stabilizes Na^+-induced intramolecular quadruplex structure without causing any major structural changes in the latter. The melting temperature enhancement of the drug-bound quadruplex (compared to the uncomplexed quadruplex) indicates stabilization of the DNA secondary structure by the molecule (Table 1).

On the other hand, ***m*-Phenbbim** retained the intramolecular Na^+-induced quadruplex structure only at low concentrations. However, at higher drug concentrations a dramatic reversal of the DNA CD profile occurred and at [DNA]:[***m*-Phenbbim**] of ~1:8, the DNA CD signatures resembled that of K^+-quad, with an intense positive band at 265 nm, a shoulder at 290 nm, and a negative peak at 240 nm. When the drug was titrated into preformed Na^+-quad, similar structural transition was observed, and at [drug]/[DNA] ratios of ≥4:1, the CD signatures resembled that of a K^+-quad. The most dramatic results were seen when the drug was titrated into single-stranded d$[T_2G_4]_4$ in the absence of K^+ or Na^+ in buffer. Compound ***p*-Phenbbim** provided weaker stabilization to the quadruplex than ***m*-Phenbbim**.

Quadruplex has a positive CD signal at 295 nm, which is intensified after interacting with the added compounds. We performed CD melting at 295 nm to again confirm the effect of ligand on the stability of quadruplex and to rule out any confusion in the results obtained from UV melting experiments. At [DNA]:[drug] ratio 1:5, ***m*-Phenbbim** gave a stabilization of 12 °C (Figure 4) (T_m for quadruplex alone at 295 nm was 36 °C, and with ligand, it was 48 °C) in 10 mM sodium cacodylate buffer having 100 mM LiCl (Supporting Information) (Li^+ is known to help the formation of quadruplex but does not stabilize it) (*61*). Hence ***m*-Phenbbim** have high affinity for the quadruplex DNA.

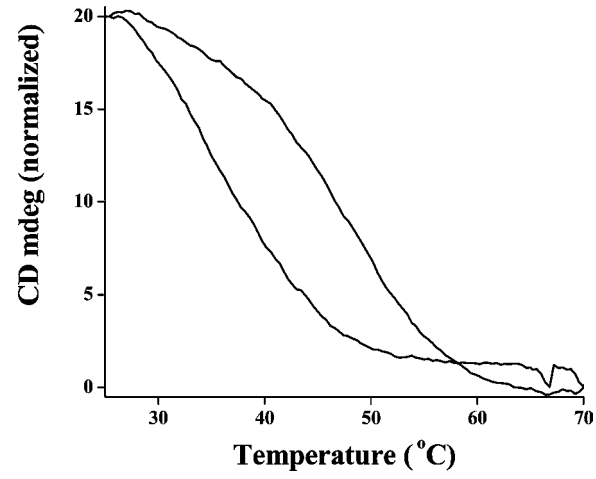


Figure 4. Normalized CD melting profiles of *Tetrahymena* d$[T_2G_4]_4$ quadruplex (2 μM strand conc.) in LiCl buffer (10 mM sodium cacodylate having 100 mM LiCl) at 295 nm and with 10 μM of ***m*-Phenbbim**.

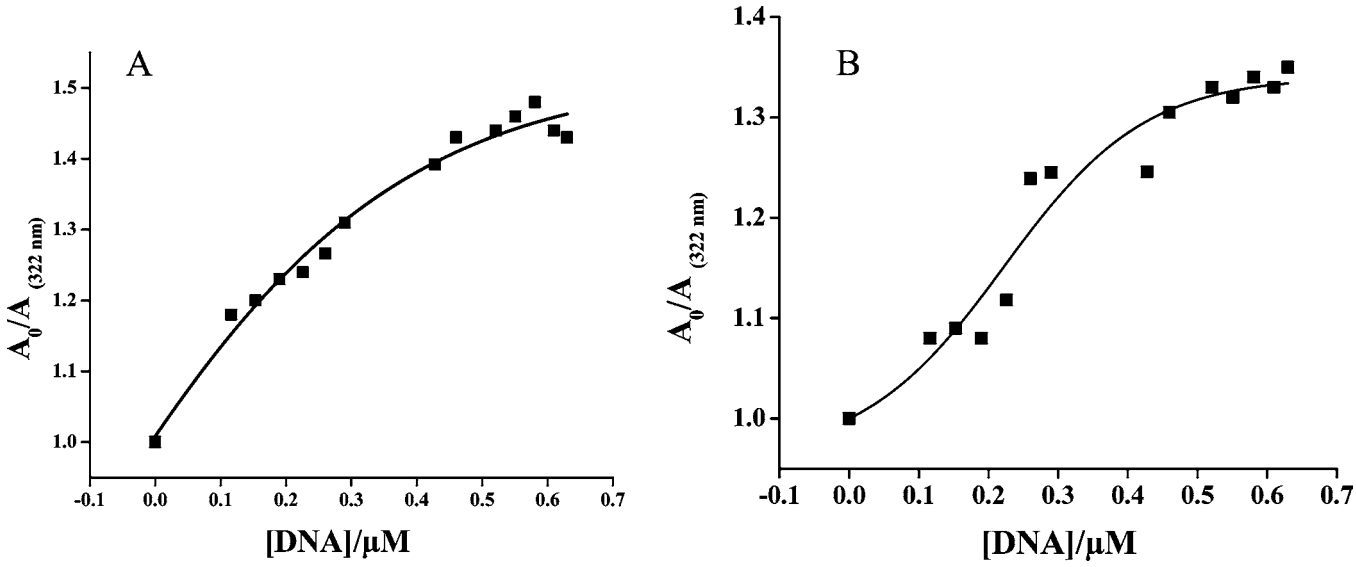


Figure 5. UV−vis titration of ***m*-Phenbbim** (A) and ***p*-Phenbbim** (B) upon addition of preformed G-quadruplex DNA in 10 mM Tris-HCl, 100 mM KCl, and 0.1 mM EDTA buffer solution at pH = 7.4. The saturation plot obtained upon plotting A_0/A against [DNA] expressed in base molarity change.

Table 2. Dissociation Constant (K_D) of *m*-Phenbbim and *p*-Phenbbim to Preformed *Tetrahymena* Quadruplex Sequence in 100 mM KCl Buffer and [(5′-CGT$_{13}$GC-3′)/(5′-GCA$_{13}$CG-3′)] Duplex[a]

	K_D (10^5 M^{-1})	
ligand	d[T_2G_4]$_4$	duplex
***m*-Phenbbim**	4.22 ± 0.8	0.058 ± 0.03
***p*-Phenbbim**	1.76 ± 0.6	0.089 ± 0.12
berberine	5.64 ± 0.3	0.12 ± 0.03

[a] Binding assays were performed with preformed d(T_2G_4)$_4$ quadruplex in 10 mM Tris-HCl, having 100 mM KCl and 0.1 mM EDTA buffer, and with [(5′-CGT$_{13}$GC-3′)/(5′-GCA$_{13}$CG-3′)] duplex in 10 mM Tris-HCl, having 100 mM NaCl and 0.1 mM EDTA buffer at pH 7.4.

The UV−vis titration spectra of both ***m*-Phenbbim** and ***p*-Phenbbim** were preformed with G-quadruplex in 100 mM KCl solution (Figure 5A,B), which resulted in hypochromicity, indicating a specific binding and strong stacking interaction between either ligands and G-quadruplex DNA. The UV−vis titration results were converted into Scatchard plots (Supporting Information), and the dissociation constants (K_D) were determined by linear fitting. Compound ***m*-Phenbbim** binds to the G-quadruplex DNA showing a dissociation constant (K_D) of 4.22×10^5 M^{-1}, while ***p*-Phenbbim** presents a relatively lower binding constant with a K_D of 1.76×10^5 M^{-1} (Table 2). The natural product berberine binds with G-quadruplex DNA with a binding constant K_D of 5.64×10^5 M^{-1}, which is comparable to that of ***m*-Phenbbim**.

Native Gel Electrophoresis. Electrophoresis on 12% native polyacrylamide gel showed the emergence of a new band after interaction with ***m*-Phenbbim** and ***p*-Phenbbim** (Figure 6). Compound ***m*-Phenbbim** showed complete conversion at [DNA]:[drug] of ∼1:12, while other isomers could not completely convert at this ratio. A second band also emerged from ***p*-Phenbbim** giving rise to a heterogeneous mixture of electrophoretic bands.

Taken together from the CD titration and electrophoresis data, it appears that ***m*-Phenbbim** is able to convert antiparallel intramolecular quadruplex into parallel intramolecular quadruplex. An intermolecular structure formation would cause even greater retardation in the electrophoretic mobility. Indeed, a similar observation was reported with human telomeric sequence when quadruplex was formed in the presence of PEG (*62*). These authors proposed the conversion from hybrid structure to parallel propeller structure. ***p*-Phenbbim** also induces similar topological conversion but only at higher [drug]:[DNA] ratio. In our case, both original quadruplex band and the band emerging after interaction with the compounds had significantly higher mobility than that of the T_{20} marker. It is well-documented that the intramolecular quadruplex formed by the sequence d[T_2G_4]$_4$ (in K^+ solution) has mobility corresponding to the T_{15} marker. Hence, our results unambiguously indicate that the difference in mobility of the drug−DNA complex is due to the change in the topology of the quadruplex after interacting with the compound and not due to any aggregation. Compound ***m*-Phenbbim** thus converts the hybrid intramolecular quadruplex into a parallel-stranded intramolecular quadruplex more efficiently than its linear isomer, ***p*-Phenbbim**.

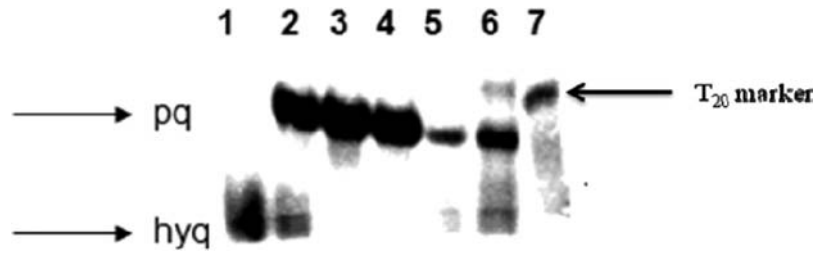


Figure 6. Electrophoresis of *Tetrahymena* d[T_2G_4]$_4$ quadruplex with ligands in 100 mM NaCl. Lane 1: 5 μM strand. Lanes 2, 3, and 4: 5 μM strand +30, 40, and 60 μM of ***m*-Phenbbim**. Lanes 5 and 6: 5 μM strand +30 and 60 μM ***p*-Phenbbim**. Lane 7: T_{20} marker. The notation "hyq" means hybrid intramolecular quadruplex and "pq" means parallel intramolecular quadruplex.

Molecular Modeling Studies. To gain more understanding on the nature of interactions that prevail between bisbenzimidazole derivatives with the telomeric G-quadruplex, an approach that combined a molecular docking and MD simulations were performed. The solution structure of *Tetrahymena* $d[T_2G_4]_4$ G-quadruplex in Na^+ solution is already known on the basis of NMR (PDB-186D) studies, which indicates that this sequence adopts a unique folding topology. Molecular docking studies were first carried out to predict the possible interactions between the ligand and G-quadruplex DNA. It has been previously shown that G-quadruplex binders can stack on the surface of the G-quartet planes. It was not possible to dock the ligands on the G-quartet planes because these were covered with loops. Interaction energies would be much lower if the ligands could be docked between G-quartet plane and loop of the quadruplex DNA. While the molecule ***p*-Phenbbim** has a linear-shaped central aromatic core, ***m*-Phenbbim** consists of a V-shaped central aromatic core. The end-to-end length of the central core of ***m*-Phenbbim** as calculated from energy-minimized calculation is 19.89 Å (Supporting Information), which is almost equal to the distances (20.18 Å; Supporting Information) of one of the grooves of the *Tetrahymena* G-quadruplex parallel structure. The molecular organization of the central core (internal H-bonds) and electronic/electrostatic properties (two benzimidazole system and piparazine side arms) make ***m*-Phenbbim** perfectly fit for the recognition of the quadruplex target. On the other hand, for the linear ***p*-Phenbbim** the end-to-end length is almost 23 Å, which is considerably longer than the length of the groove (Supporting Information). The interaction energy (free energy, ΔG) and docking energy of ***p*-Phenbbim** with quadruplex DNA were found to be higher than that of ***m*-Phenbbim** (Supporting Information). This again suggests that, while both compounds could stabilize G-quadruplex DNA, but ***m*-Phenbbim** provides more stabilization to the G-quadruplex DNA than ***p*-Phenbbim**.

On the other hand, the X-ray-crystal structure of *Oxytricha nova* telomeric quadruplex (PDB 3EM2) has similar sequence to that of *Tetrahymena* G-quadruplex. Here, each quadruplex contains two strands of the sequence d[5′-GGGGTTTTGGGG-3′] with a diagonal fold topology, in which the thymine loops are lying diagonally across the top and bottom of the stack of the guanine quartets and strands of each sequence are antiparallel to each other. The quadruplex shows an alternating syn−anti arrangement of guanine glycosidic torsion angles along the strand and syn−syn and anti−anti arrangement within the quartet. One base in each of the terminal quartet is slightly more tilted than the others. This stacks effectively with the 3′-thymine residue from the loop. The diagonal topology of the structure results in one wide, two medium, and one narrow groove (*63*).

A close examination of the crystal structure of 22AG (1KF1, RCSB Protein Data Bank) shows that a G-quartet can be considered a square aromatic surface whose dimensions (13.6 Å and 10.9 Å) are closely related to that of the conformation ***m*-Phenbbim** (Supporting Information Figure S9; Table 4), which indicates good coplanarity of the molecule with G-quartet plane, and hence, this could explain the high stabilization properties of quadruplex by this ligand. Using Autodock, we have docked our two ligands in between G-quartet plane and T4 loop of *Oxytricha nova* telomeric quadruplex DNA. On the basis of the docking results, MD simulation (8 ns) were performed on the two complexes formed by G-quadruplex DNA (*Oxytricha nova*) with ligands ***m*-Phenbbim** and ***p*-Phenbbim** in the binding mode of intercalation between G-quartet and T4 loop. All of the models were quite stable during the dynamics runs. During the simulation runs, it has been found that the complex with ***m*-Phenbbim** was giving much lower rmsd than the complex with ***p*-Phenbbim** (Figure 7). It also has been found that due to the V-shape and bond flexibility of the ***m*-Phenbbim** ligand two positively charged side chains are going toward the groove and forming strong hydrogen bonding with the phosphate backbone and NH_2 hydrogen of the guanine residue (Figure 7). Recently, a crystal structure of BRACO-19 with bimolecular human quadruplex has been published showing the binding of the side chains of the compounds in the grooves of the quadruplex DNA (*64*). The molecular organization of the central core (internal H-bonds) and π-stacking interaction (3.4 Å) and electronic/electrostatic properties (two benzimidazole system and piparazine side arms) make derivatives perfectly fitted for the recognition of the quadruplex target.

For ***m*-Phenbbim** at higher [drug]/[DNA] ratio of >10:1, we indeed observe an induced CD signal (ICD) possibly due to groove binding (Supporting Information). On the other hand, due to the linear shape of *p*-**Phenbbim** its side chains were not properly fitted in the grooves. This again suggests that, while both compounds could stabilize G-quadruplex DNA, ***m*-Phenbbim** provides more stabilization to the G-quadruplex DNA than ***p*-Phenbbim**.

One problem encountered during G-quadruplex recognition may be the interference caused by duplex DNA when compounds are injected *in vivo*. Intercalation and minor groove binding are the two possible binding modes with duplex DNA. Intercalators are known to increase the viscosity of DNA solution (*29*). Viscometric titrations with CT DNA indicate that ***m*-Phenbbim** is a considerably poorer intercalator than ethidium bromide (EtBr) **(**Table 5, Supporting Information). It also shows a very low increment in the melting temperature (T_m) of CT-DNA when compared with that of a classical minor groove binder Hoechst-33258 (Table 5, Supporting Information) indicating its insignificant affinity toward duplex DNA at drug:DNA ratio of 0.5. This observation is consistent with a report in which a structural analogue of ***m*-Phenbbim** was shown to have very low affinity with duplex DNA as compared to Hoechst 33258 (*28*). Hence, ***m*-Phenbbim** has weak binding with duplex DNA in either mode (intercalation or minor groove binding), and it has significant quadruplex affinity, as suggested by CD titrations and thermal denaturation experiments.

Telomerase Inhibition (TRAP assay). Finally, we have examined the telomerase inhibition ability of these two compounds. In this paper, we have presented the binding studies with a nonhuman quadruplex DNA sequence (*Tetrahymena*). At the same time, it is of interest to examine whether these ligands may also work as possible anticancer agents. Indeed, several potential quadruplex ligands, e.g., porphyrins (TMPyP4), telomestatin, BRACO 19, and so forth, which inhibit the enzyme telomerase in telomerase repeat amplification protocol (TRAP) assay, also demonstrate antitumor activity (*17, 65, 66*). The modified TRAP assay provides an estimate of the telomerase inhibition by small molecules (*67*). Accordingly, as a first step both of the compounds have been tested using TRAP assay at concentrations ranging from 2.5 μM to 30 μM. Compound ***m*-Phenbbim** inhibited telomerase activity at 10 μM concentration; on the other hand, for ***p*-Phenbbim** there was no significant inhibition of the telomerase activity even at 30 μM (Figure 8). These results indicate that ***m*-Phenbbim** may have higher affinity toward the G-quadruplex structures

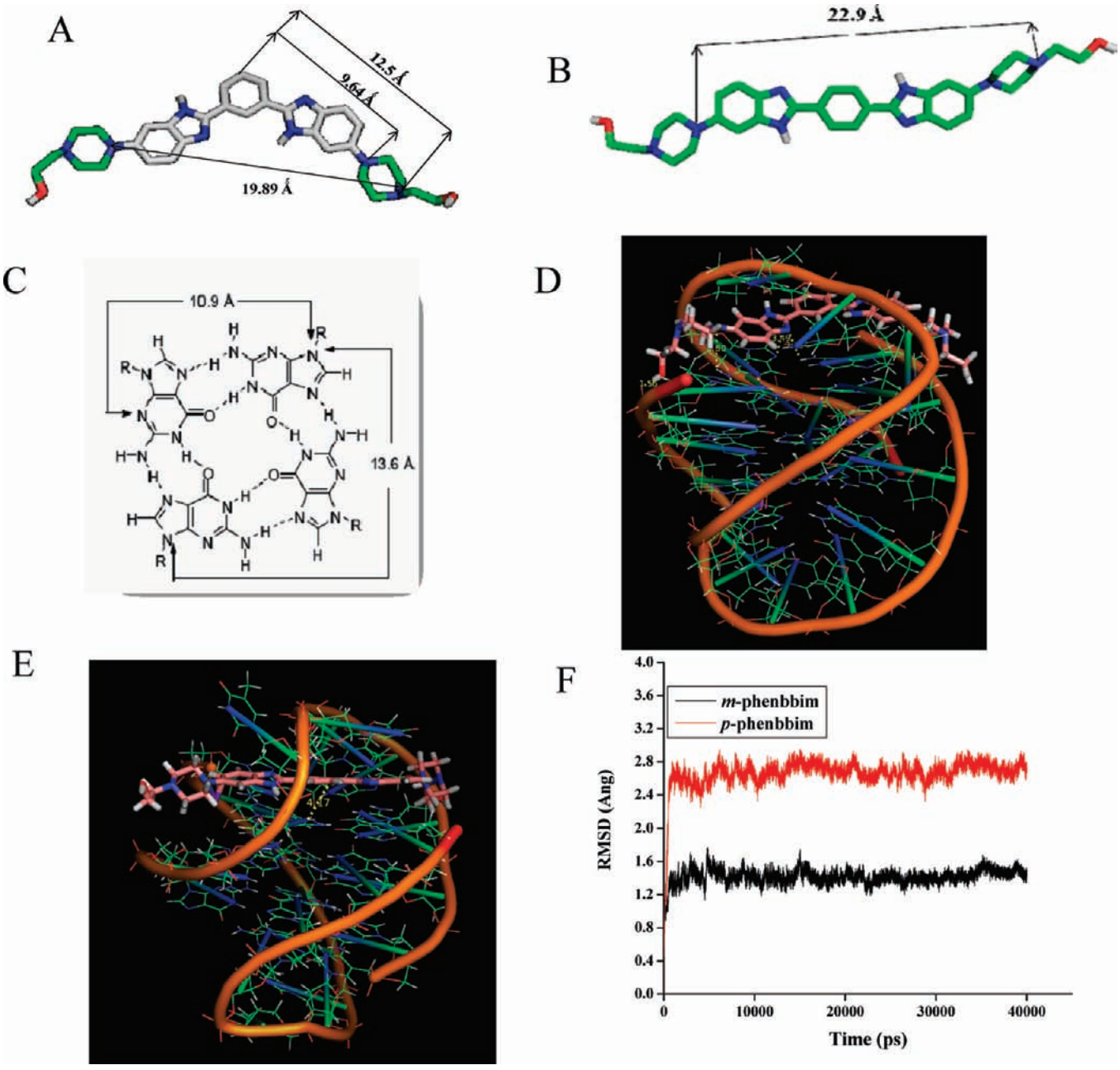


Figure 7. (A,B) Optimized structures at the B3LYP/6-31G* level of theory of ***m*-Phenbbim** and ***p*-Phenbbim**, respectively. (C) Structures of the G-tetrad; model of ligand−quadruplex complex. (D,E) ***m*-Phenbbim** stacking on the surface of G-quartet (D) and ***p*-Phenbbim** stacking on the surface of G-quartet (E). (F) Plots following the stability of the models during the dynamics runs (rmsd plots with time).

formed by human telomeric DNA sequence than its counterpart ***p*-Phenbbim**.

CONCLUSION

In summary, we have developed two new isomeric bisbenzimidazole-based compounds, both showing stabilization of the G-quadruplex DNA structure. The affinity of the compounds toward the G-quadruplex is dependent on the shape of the molecule. While the linear isomer stabilized the Na^+-induced intramolecular quadruplex, the other (V-shaped) isomer caused a remarkable structural transition of the latter above a certain threshold ligand concentration. The latter also showed higher affinity toward the G-quadruplex. The final CD signature of DNA and retardation on 12% native acrylamide gel suggested possible switching of antiparallel intramolecular quadruplex into intramolecular parallel quadruplex. Interestingly, even in the absence of any monovalent cation like Na^+ or K^+, the same isomer induced specific secondary structure formation from randomly oriented single-stranded DNA.

Compound ***m*-Phenbbim** has comparable molecular size and geometry to that of the G-quartet, and hence, it could stack over three guanine residues of the quartet and thus provides high stabilization (comparable to that of natural quadruplex stabilizing ligand berberine) of the quadruplex and induce structural switching, while, being linear, ***p*-Phenbbim** could stack only with two guanine residues of the quartet. The differential interaction of the two isomers with the quadruplex DNA forming sequence opens up interesting possibilities where drug−DNA recognition can be fine-tuned by minor alteration of the molecular structure of the ligand. Finally, there are only a few examples known

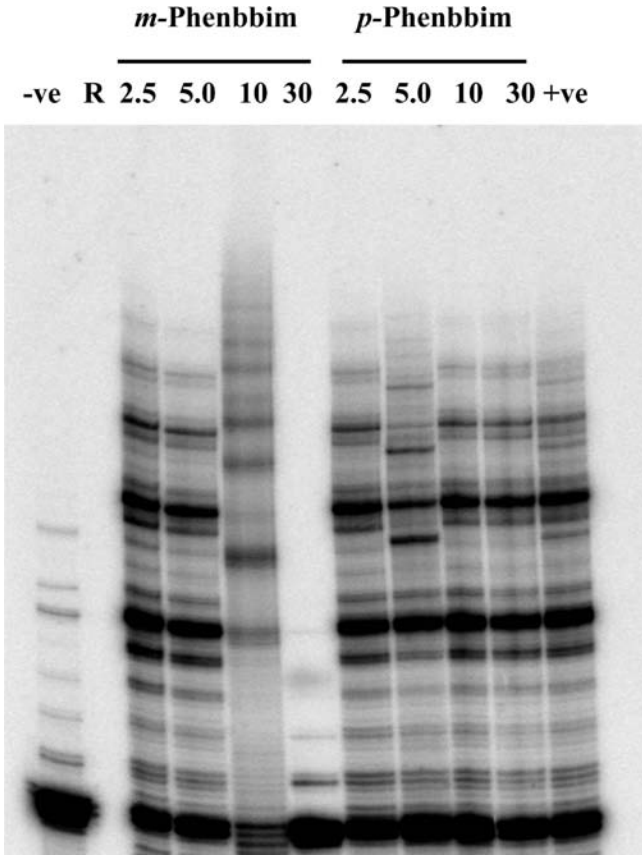


Figure 8. Representative experiments for the determination of telomerase inhibitory properties by the bisbenzimidazole derivatives. TRAP assay performed with increasing concentrations of ***m*-Phenbbim** and ***p*-Phenbbim**. Lane 1: (−) *ve* control (absence of enzyme and drug). Lane 2: R = PCR control. Lane 3, 4, 5, and 6: TRAP reaction mixture + (2.5, 5, 10, and 30 μM of ***m*-Phenbbim**). Lanes 7, 8, 9, and 10: TRAP reaction mixture + (2.5, 5, 10, and 30 μM of ***p*-Phenbbim**). Lane 11: (+) *ve* control (absence of drug).

where a small organic molecule has been shown to induce quadruplex DNA formation from randomly oriented single-stranded DNA in the absence of other mono- or divalent cations. The TRAP experiment further demonstrated that the *m*-isomer is highly active toward telomerase activity.

ACKNOWLEDGMENT

This work was supported by a grant from Department of Science and Technology, New Delhi, India. AKJ is thankful to DBT for a Postdoctoral Fellowship.

Supporting Information Available: CD titrations other than those given in the manuscript, calculations on gas-phase conformation and effects of salvation, schematic representation of molecular staking on G-quartet and interatomic distances, docking structure and energies, comparison of duplex binding properties of ***m*-Phenbbim**. This material is available free of charge via the Internet at http://pubs.acs.org.

LITERATURE CITED

(1) Blackburn, E. H. (1991) Structure and function of telomeres. *Nature 350*, 569–573.
(2) Harley, C. B., Futcher, A. B., and Greider, C. W. (1990) Telomeres shorten during ageing of human fibroblasts. *Nature 345*, 458–460.
(3) Gowan, S. M., Harrison, J. R., Patterson, Valenti, L. M., Read, M. A., Neidle, S., and Kelland, L. R. (2002) A G-quadruplex-interactive potent small-molecule inhibitor of telomerase exhibiting in vitro and in vivo antitumor activity. *Mol. Pharmacol. 61*, 1154–1162.
(4) Cech, T. R. (2000) Life at the end of the chromosome: Telomeres and telomerase. *Angew. Chem. Int. Ed. 39*, 34–43.
(5) Kerwin, S. M. (2000) G-quadruplex DNA as a target for drug design. *Curr. Pharmacol. Des. 6*, 441–478.
(6) Perry, P. J., and Kell, L. R. (1998) Telomeres and telomerase: targets for cancer chemotherapy. *Exp. Opin. Ther. Patents 8*, 1567–1586.
(7) Franceschin, M. (2009) G-Quadruplex DNA structures and organic chemistry: More than one connection. *Eur. J. Org. Chem.* 2225–2238.
(8) Kim, M. Y., Vankayalapati, H., Shin-Ya, K., Wierzba, K., and Hurley, L. H. (2002) Telomestatin, a potent telomerase inhibitor that interacts quite specifically with the human telomeric intramolecular G-quadruplex. *J. Am. Chem. Soc. 124*, 2098–2099.
(9) Barbieri, C. M., Srinivasan, A. R., Rzuczek, S. G., Rice, J. E., LaVoie, E. J., and Pilch, D. S. (2007) Defending the mode, energetic and specificity with which a macrocyclic hexaoxazole binds to human telomeric G-quadruplex DNA. *Nucleic Acids Res. 35*, 3272–3286.
(10) Hurley, L. H. (2002) DNA and its associated processes as targets for cancer therapy. *Nat. Rev. Cancer 2*, 188–200.
(11) Pindur, U., and Fischer, G. A. (1996) DNA complexing minor groove-binding ligands: Antitumour and antimicrobial drug design. *Curr. Med. Chem. 3*, 379–406.
(12) Phillips, K., Dauter, Z., Murchie, A. I. H., Lilley, D. M. J., and Luisi, B. (1997) The crystal structure of a parallel-stranded guanine tetraplex at 0.95 Å resolution. *J. Mol. Biol. 273*, 171–182.
(13) Tang, C. F., and Shafer, R. H. (2006) Engineering the quadruplex fold: Nucleoside conformation determines both folding topology and molecularity in guanine quadruplexes. *J. Am. Chem. Soc. 128*, 5966–5973.
(14) Rodriguez, R., Pantos, G. D., Goncalvs, D. P. N., Sanders, J. K. M., and Balasubramanian, S. (2007) Ligand induced-driven G-quadruplex conformational switching by using an unusual mode of interaction. *Angew. Chem. Int. Ed. 46*, 5405–5407.
(15) Mergny, J. L., Phan, A. T., and Lacroix, L. (1998) Following G-quartet formation by UV-spectroscopy. *FEBS Lett. 435*, 74–78.
(16) Han, H., and Hurley, L. H. (2000) G-quadruplex DNA: A potential target for anti-cancer drug design. *Trends Pharmacol. Sci. 21*, 136–141.
(17) Burger, A. M., Schultes, Dai, F., Reszka, C. M., Moore, A. P., Double, J. A., and Neidle, S. (2005) The G-Quadruplex-interactive molecule BRACO-19 inhibits tumour growth, consistent with telomere targeting and interference with telomerase function. *Cancer Res. 65*, 1489–1496.
(18) Moorehouse, A. D., Santos, A. M., Gunaratnam, M., Moore, M., Neidle, S., and Mosses, J. E. (2006) Stabilization of G-quadruplex DNA by highly selective ligands via click chemistry. *J. Am. Chem. Soc. 128*, 15972–15973.
(19) Dash, J., Shirude, P. S., and Balasubramanian, S. (2008) Quadruplex recognition by bis-indole carboxamides. *Chem. Commun.* 3055–3057.
(20) Li, G., Huang, J., Zhang, M., Zhou, Y., Zhang, D., Wu, Z., Wang, S., Weng, X., and Zhou, X. Y. (2008) G. Bis(benzimidazole)pyridine derivative as a new class of G-quadruplex inducing and stabilizing ligand. *Chem. Commun.* 4564–4566.
(21) Monchaud, D., Yang, P., Lacroix, L., Teulade-Fichou, M. P., and Mergny, J. L. (2008) A metal-mediated conformational switch controls G-quadruplex binding affinity. *Angew. Chem., Int. Ed. 47*, 4858–4861.
(22) Bhattacharya, S., and Thomas, M. (2000) Facile synthesis of oligopeptide distmycin analogs devoid of hydogen bond donors or acceptors at the N-terminus: Sequence-specific duplex DNA binding as a function of peptide chain length. *Tetrahedron Lett. 41*, 5571–5575.
(23) Thomas, M., Varshney, U., and Bhattacharya, S. (2002) Distamycin analogs without leading amide at their N-termini

comparative binding properties to AT- and GC-rich DNA sequences. *Eur. J. Org. Chem.* 3604–3615.

(24) Ghosh, S., Defrancq, E., Lhomme, J. H., Dumy, P., and Bhattacharya, S. (2004) Efficient conjugation and characterization of distamycin based peptides with selected oligonucleotide stretches. *Bioconjugate Chem. 15*, 520–529.

(25) Bhattacharya, S., and Mandal, S. S. (1995) Ambient oxygen activating water soluble cobalt-salen complex for DNA cleavage. *J. Chem. Soc. Chem. Commun.* 2489–2490.

(26) Mandal, S. S., Kumar, N. V., Varshney, U., and Bhattacharya, S. (1996) Metal-ion dependent oxidative DNA cleavage by transition metal complex of a new water soluble salen derivative. *J. Inorg. Biochem. 63*, 265–272.

(27) Bhattacharya, S., and Mandal, S. S. (1996) DNA cleavage by intercalatable cobalt-bispicolylamine complexes activated by visible light. *Chem. Commun.* 1515–1516.

(28) Mandal, S. S., Varshney, U., and Bhattacharya, S. (1997) Role of central metal ion and ligand charge in the DNA binding and modification by metallosalen complexes. *Bioconjugate Chem. 8*, 798–812.

(29) Chaudhuri, P., Majumder, H. K., and Bhattacharya, S. (2007) Synthesis, DNA binding, and *Leishmania* topoisomerase inhibition activities of a novel series of anthra[1, 2*d*]imidazole-6,11-dione derivatives. *J. Med. Chem. 50*, 2536–2540.

(30) Jain, A. K., Reddy, V. V., Paul, A., Muniyappa, K., and Bhattacharya, S. (2009) Synthesis and evaluation of a novel class of G-quadruplex-stabilizing small molecules based on the 1,3-phenylene-bis(piperazinyl benzimidazole) system. *Biochemistry 48*, 10693–10704.

(31) Drewe, W. C., Nanjunda, R., Gunaratnam, M., Beltran, M., Parkinson, G. N., Reszka, A. P., Wilson, D., and Neidle, S. (2008) Rational design of substituted diarylureas: A scaffold for binding to G-quadruplex motifs. *J. Med. Chem. 51*, 7751–7767.

(32) Muller, S., Pantos, G. D., Rodriguez, R., and Balasubramanian, S. (2009) Controlled-folding of a small molecule modulates DNA G-quadruplex recognition. *Chem. Commun.* 80–82.

(33) Bathini, Y., Rao, K. E., Shea, R. G., and Lown, W. (1990) Molecular recognition between ligands and nucleic acids: novel pyridine- and benzoxazole-containing agents related to Hoechst 33258 that exhibit altered DNA sequence specificity deduced from footprinting analysis and spectroscopic studies. *Chem. Res. Toxicol. 3*, 268–280.

(34) Hori, Y., Bichenkova, E. V., Wilton, A. N., El-Attug, M. N., Sadat-Ebrahimi, S., Tanaka, T., Kikuchi, Y., Araki, M., Sugiura, Y., and Douglas, K. T. (2001) Synthetic inhibitors of the processing of pretransfer RNA by the ribonuclease P ribozyme: Enzyme inhibitors which act by binding to substrate. *Biochemistry 40*, 603–608.

(35) Hardin, C. C., Henderson, E., Watson, T., and Prosser, J. K. (1991) Monovalent cation induced structural transitions in telomeric DNAs: G-DNA folding intermediates. *Biochemistry 30*, 4460–4472.

(36) Chen, F. M. (1992) Strontium (2^+) facilitates intermolecular G-quadruplex formation of telomeric sequences. *Biochemistry 31*, 3769–3776.

(37) Murashima, Sakiyama, T. D., Miyoshi, D., Kuriyama, M., Yamada, T., Miyazawa, T. and, and Sugimoto, N. (2008) Cationic porphyrin induced a telomeric DNA to G-quadruplex form in water. *Bioinorg. Chem. Appl.* 1–5.

(38) Wang, Y., and Patel, D. J. (1994) Solution structure of the *Tetrahymena* telomeric repeat d $(T_2G_4)_4$ G-tetraplex. *Structure 2*, 1141–1156.

(39) Peacocke, A. R., and Skerrett, J. N. H. (1956) The interaction of aminoacridines with nucleic acids. *J. Chem. Soc., Faraday Trans. 52*, 261–279.

(40) Frisch, M. J., Trucks, G. W., Schlegel, H. B., Scuseria, G. E., Robb, M. A., Cheeseman, J. R., Montgomery, J. A., Vreven, T., Kudin, K. N., Burant, J. C., and Milliam, J. M. *Gaussian 03*, Gaussian, Inc., Wallingford, CT.

(41) Morris, G. M., Goodsell, D. S., Halliday, R. S., Huey, R., Hart, W. E., Belew, R. K., and Olson, A. J. (1998) Automated docking using a Lamarckian genetic algorithm and an empirical binding free energy function. *J. Comput. Chem. 19*, 1639–1662.

(42) Sanner, M. F. (1999) Python: a programming language for software integration and development. *J. Mol. Graph. Model. 17*, 57–61.

(43) Cornell, W. D., Cieplak, P., Bayly, C. I., Gould, I. R., Merz, K. M., Jr., Ferguson, D. M., Spellmeyer, D. C., Fox, T., Caldwell, J. W., and Kollman, P. A. (1995) A second generation force field for the simulation of proteins, nucleic acids, and organic molecules. *J. Am. Chem. Soc. 117*, 5179–5197.

(44) Wang, J., Wolf, R. M., Caldwell, J. W., Kollman, P. A., and Case, D. A. (2004) Development and testing of a general Amber force field. *J. Comput. Chem. 25*, 1157–1174.

(45) Hazel, P., Huppert, J., Balasubramanian, S., and Neidle, S. (2004) Loop-length-dependent folding of G-quadruplex. *J. Am. Chem. Soc. 126*, 16405–16415.

(46) Hazel, P., Parkinson, G. N., and Neidle, S. (2006) Predictive modelling of topology and loop variations in dimeric DNA quadruplex structures. *Nucleic Acids Res. 34*, 2117–2127.

(47) Darden, T., York, D., and Pedersen, L. (1993) Particle mesh Ewald: an $N \log(N)$ method for Ewald sums in large systems. *J. Chem. Phys. 98*, 10089–10092.

(48) Jorgensen, W. L., Chandrasekhar, J., Madura, J. D., Impey, R. W., and Klein, M. L. (1983) Comparison of simple potential functions for simulating liquid water. *J. Chem. Phys. 79*, 926–935.

(49) Ryckaert, J. P., Ciccotti, G., and Berendsen, H. J. C. (1977) Numerical integration of the Cartesian equations of motion of a system with constraints: molecular dynamics of *n*-alkanes. *J. Comput. Phys. 23*, 327–41.

(50) Humphrey, W., Dalke, A., and Schulten, K. (1996) VMD: visual molecular dynamics. *J. Mol. Graph. 14*, 33–8, plates 27−28.

(51) Pagano, B., Virno, A., Mattia, C. A., Mayol, L., Randazzo, A., and Giancola, C. (2008) Targeting DNA quadruplexes with distamycin A and its derivatives: An ITC and NMR study. *Biochimie 90*, 1224–1232.

(52) Wei, C., Lihua, Wang, L., Jia, G., Jun, Z. J., Han, G., and Li, C. (2009) The binding mode of porphyrins with cation side arms to $(TG_4T)_4$ G-quadruplex: Spectroscopic evidence. *Biophys. Chem. 143*, 79–84.

(53) Rezler, E. M., Seenisamy, J., Bashyam, J. S., Kim, M. Y., White, E., Wilson, W. D., and Hurley, L. H. (2005) Telomestatin and diseleno sapphyrin bind selectively to two different forms of the human telomeric G-quadruplex structure. *J. Am. Chem. Soc. 127*, 9439–9447.

(54) Bhattacharya, S., and Chaudhuri, P. (2008) Medical implications of benzimidazole derivatives as drugs designed for targeting DNA and DNA associated processes. *Curr. Med. Chem. 15*, 1762–1777.

(55) Stokke, T., and Steen, H. B. (1985) Multiple binding modes for Hoechst 33258 to DNA. *J. Histochem. Cytochem. 33*, 333–338.

(56) Latt, S. A., and Wohlleb, J. C. (1975) Optical studies of the interaction of 33258 Hoechst with DNA, chromatin, and metaphase chromosomes. *Chromosoma 52*, 297–316.

(57) Chaudhuri, P., Ganguly, B., and Bhattacharya, S. (2007) An experimental and computational analysis on the differential role of the positional isomers of symmetric bis-2-(pyridyl)-1*H*-benzimidazoles as DNA binding agents. *J. Org. Chem. 72*, 1912–1923.

(58) Tawar, U., Jain, A. K., Dwarakanath, B. S., Chandra, R., Singh, Y., Chaudhury, N. K., Khaitan, D., and Tandon, V. (2003) Influence of phenyl ring disubstitution on bisbenzimidazole and terbenzimidazole cytotoxicity: synthesis and biological evaluation as radioprotectors. *J. Med. Chem. 46*, 3785–3792.

(59) Kieltyka, R., Fakhoury, J., Moitessier, N., and Sleiman, H. F. (2008) Platinum phenanthroimidazole complexes as G-quadruplex DNA selective binders. *Chem.—Eur. J. 14*, 1145–1154.

(60) Arora, A., Balasubramanian, C., Kumar, N., Agrawal, S., Ojha, R. P., and Maiti, S. (2008) Binding of berberine to human telomeric quadruplex - spectroscopic, calorimetric and molecular modeling studies. *FEBS J. 275*, 3971–3983.

(61) De. Cian, A., Guittat, L., Kaiser, M., Sacca, B., Amrane, S., Bourdoncle, A., Albrtti, P., Teulade-Fichou, M. P., Lacriox, L., and Mergny, J. L. (2007) Fluorescence-based melting assays for studying quadruplex ligands. *Methods 42*, 183−195.

(62) Xue, Y., Kan, Z. Y., Wang, Q., Yao, Y., Liu, J., Hao, Y.-H., and Tan, Z. (2007) Human telomeric DNA forms parallel-stranded intramolecular G-quadruplex in K^+ solution under molecular crowding condition. *J. Am. Chem. Soc. 129*, 11185–11191.

(63) Haider, S. M., Parkinson, G. N., and Neidle, S. (2003) Structure of a G-quadruplex-ligand complex. *J. Mol. Biol. 326*, 117–125.

(64) Campbell, N. H., Parkinson, G. N., Reszka, A. P., and Neidle, S. (2008) Structural basis of DNA quadruplex recognition by an acridine drug. *J. Am. Chem. Soc. 130*, 6722–6724.

(65) Gomez, D., Aouali, N., Renaud, A., Douarre, Ce.-T., Shinya, K., Tazi, J., Martinez, S., Trentesaux, C., Morjani, H., and ois Riou, J.-F. (2003) Resistance to senescence induction and telomere shortening by a G-quadruplex ligand inhibitor of telomerase. *Cancer Res. 63*, 6149–6153.

(66) Mikami-Terao, Y., Akiyama, M., Yuza, Y., Yanagisawa, T., Yamada, O., and Yamada, H. (2008) Antitumor activity of G-quadruplex-interactive agent TMPyP4 in K562 leukemic cells. *Cancer Lett. 261*, 226–234.

(67) Read, M. J., Gunaratnam, M., Beltran, A. P., Reszka, R. V., and Neidle, S. (2008) TRAP-LIG, a modified telomere repeat amplification protocol assay to quantitate telomerase inhibition by small molecules. *Anal. Biochem. 380*, 99–105.

BC9003298

Surface Ligand Effects on Metal-Affinity Coordination to Quantum Dots: Implications for Nanoprobe Self-Assembly

Allison M. Dennis,[||,†] David C. Sotto,[†] Bing C. Mei,[∞,‡] Igor L. Medintz,[§] Hedi Mattoussi,[▼,‡] and Gang Bao*[,†]

Department of Biomedical Engineering, Georgia Institute of Technology and Emory University, Atlanta, Georgia 30332, Division of Optical Sciences, Code 5611, and Center for Bio/Molecular Science and Engineering, Code 6900, U.S. Naval Research Laboratory, Washington, DC 20375. Received November 14, 2009; Revised Manuscript Received April 13, 2010

The conjugation of biomolecules such as proteins and peptides to semiconductor quantum dots (QD) is a critical step in the development of QD-based imaging probes and nanocarriers. Such protein−QD assemblies can have a wide range of biological applications including in vitro protein assays and live-cell fluorescence imaging. One conjugation scheme that has a number of advantages is the self-assembly of biomolecules on a QD surface via polyhistidine coordination. This approach has been demonstrated using QDs that have different coating types, resulting in different interactions between the biomolecule and QD surface. Here, we report the use of a fluorescence resonance energy transfer (FRET) assay to evaluate the self-assembly of fluorescent proteins on the surface of QDs with eight distinct coatings, including several used in commercial preparations. The results of this systematic comparison can provide a basis for rational design of self-assembled biomolecule−QD complexes for biomedical applications.

INTRODUCTION

Since quantum dots (QDs) were first rendered water-soluble, thereby making them available for biological applications (*1, 2*), extensive studies have been performed using QD-based approaches for imaging, biosensing, and cellular delivery (*3*−*6*). However, assembly of biomolecule−QD constructs has proven to be a challenge even as orthogonal bioconjugation techniques become available (*7*). An optimal bioconjugation strategy would be quick and facile with high affinity, would not require subsequent purification, and would enable control over the conjugate valence, all while not disrupting the biological function of the biomolecule. Standard protocols include chemical coupling with covalent bonds (*7*), noncovalent interactions exploiting ligand−receptor affinities such as biotin−avidin binding (*8*), and more general affinity-driven self-assemblies using electrostatic interactions (*9, 10*) or metal chelation (*11*−*16*). Each of these techniques has advantages and disadvantages that must be assessed when choosing the bioconjugation method for a particular design of the biomolecule-QD construct.

Covalent coupling provides the most durable attachment of a biomolecule to a QD with carbodiimide (EDC) chemistry being the most commonly utilized. However, this often causes nanoparticle aggregation, may result in a relatively low number of biomolecules per nanoparticle compared to the reaction ratios, and often requires purification steps that are also a source of loss, depressing the overall yield of the functional construct (*7*). In addition, the heterogeneous conjugation may cause proteins to attach in an unproductive manner or to lose activity. Streptavidin−biotin binding is a common and useful coupling mechanism that utilizes exceptionally simple protocols, provided the constituent components are already functionalized with the required streptavidin and biotin moieties. With femtomolar binding affinities, the streptavidin−biotin interaction is often considered to be effectively as stable as a covalent bond (*17*). In some applications, however, the advantages of the streptavidin−biotin interaction may be overshadowed by the tetrameric nature of streptavidin, which can result in multiple binding events and induce aggregation, two undesired and detrimental outcomes (*18*). The addition of multiple streptavidin molecules (with a molecular weight of ca. 53 kD) to a single QD adds considerably to the overall size of the nanoparticle construct. This extra protein bulk could be detrimental in applications where the increase in size may impair function. Optical biosensors based on fluorescence resonance energy transfer (FRET), for example, require short distances between their fluorescent donors and acceptors. As the efficiency of energy transfer is inversely related to the donor−acceptor distance to the sixth power (*19*), the additional separation by a few nanometers due to the size of streptavidin can dramatically reduce FRET efficiency.

An alternative conjugation strategy could exploit the affinities between specific biomolecule domains and various substrates. These range in strength and specificity from electrostatic interactions to metal chelation to interactions culled from phage display. Although the binding affinities of these reactions cannot rival that of avidin−biotin, advantages arising because the minimal affinity tag can often be naturally incorporated into the biomolecule of interest and bind to the QD without necessitating additional functionalization of the nanoparticle. Self-assembly based coupling requires only small tags, is facile, is typically not intrusive on the other components of the nanoparticle system, is orthogonal to most biological structures and activity, provides reasonable control over the relative component stoichiometries, and utilizes well-established pro-

* To whom correspondence should be addressed. Telephone 404-385-0373; Fax 404-385-3856; E-mail gang.bao@gatech.edu.

[||] Present address: Physical Chemistry and Spectroscopy, Los Alamos National Laboratories, Los Alamos, New Mexico 87545.

[∞] Present address: Avon Products, Inc., Suffern, New York 10901.

[▼] Present address: Department of Chemistry and Biochemistry, Florida State University, Tallahassee, FL 23306.

[†] Georgia Institute of Technology and Emory University.

[‡] Division of Optical Sciences, Code 5611, U.S. Naval Research Laboratory.

[§] Center for Bio/Molecular Science and Engineering, Code 6900, U.S. Naval Research Laboratory.

10.1021/bc900500m © 2010 American Chemical Society
Published on Web 06/22/2010

tocols. This is highly desirable since it fulfills many of the characteristics of ideal nanoparticle bioconjugation chemistry.

A specific example of one such small affinity tag is the polyhistidine sequence (his-tag), which has an affinity for divalent cations. It was discovered that his-tag chelation of metal ions, such as Ni^{2+}, Zn^{2+}, or Cu^{2+}, could be used to purify recombinant proteins using immobilized metal affinity chromatography (IMAC) (*20*). More recently, his-tags have been used to bind a range of biomolecules to CdSe-ZnS core−shell QDs which inherently display zinc ions on their surface (*11*−*16*). Although this coupling technique has been used with success in several QD-based sensing applications, the characteristics of the QD−polyhisitidine interaction appear to vary depending on the particular organic coating used to confer water solubility of the QDs (*21*).

Conjugation of biomolecules (including proteins) to inorganic nanoparticles plays an essential role in the development and application of nanomedicine; thus, a more thorough understanding of the factors that affect his-tag mediated bioconjugation and self-assembly may enable the optimal design of biomolecule−nanoparticle hybrids for a broad range of applications. For example, in molecular imaging applications, it is critical to establish robust protocols for conjugating purified proteins to the surface of QDs with high affinity. His-tag mediated bioconjugation is very attractive as a his-tag is often already incorporated into the protein backbone for purification purposes. However, the applicability of this conjugation strategy depends on the specific coating on QDs, and the comparison of his-tag binding to different QDs will provide important insight. Further, the development of quantum dot-fluorescent protein biosensors will be greatly facilitated by a better understanding of the effects of surface ligand on metal-affinity coordination to quantum dots. In addition to expanding our knowledge of his-tag based self-assembly strategy, our demonstration of how fluorescent proteins can be used in FRET assays to study biomolecule−QD association may have a significant implication to the design of other nanoparticle bioconjugates.

In this study, we systematically evaluated the his-tag-mediated self-assembly of biomolecules onto the surface of CdSe/ZnS QDs using a FRET-based assay (Figure 1). The QDs studied here have several different coatings, including phospholipid-PEG and amphiphilic block copolymers (both rely on hydrophobic interactions to passivate the QD surface), and DHLA-based moieties, which bind the ZnS surface with a thiolate during ligand-exchange. The advantages and disadvantages of using each QD coating scheme in nanoprobe self-assembly are discussed.

EXPERIMENTAL PROCEDURES

Materials.

In-House Synthesis and Coating of QDs. CdSe/ZnS QDs were synthesized and surface modified with DHLA (QD1), DHLA-PEG_{600}-OH (DHLA-PEG; QD2), or DHLA-PEG_{750}-OCH_3 (DHLA-mPEG; QD3) as previously described (*22*−*24*). The inorganic core/shell QDs were synthesized in a stepwise reaction using organometallic precursors (e.g., trioctylphosphine selenium (TOP:Se), cadmium acetylacetonate, diethylzinc, and hexamethyldisilathiane) at high temperatures (*25*−*28*). Since these nanoparticles are grown and coated with a mixture of trioctylphosphine, trioctylphosphine oxide, and hexadecylamine, they are water-insoluble. In order to render them water-soluble, the native ligands (TOP/TOPO/HDA) were replaced with the DHLA-based ligands (*29*).

Commercially Available QDs. Commercial CdSe/ZnS quantum dots (QDs) were acquired from two sources. Qdot 545 nm ITK carboxyl (QD4) and amino-PEG (QD5) quantum dots were bought from Invitrogen (now Life Technologies, Carlsbad, CA).

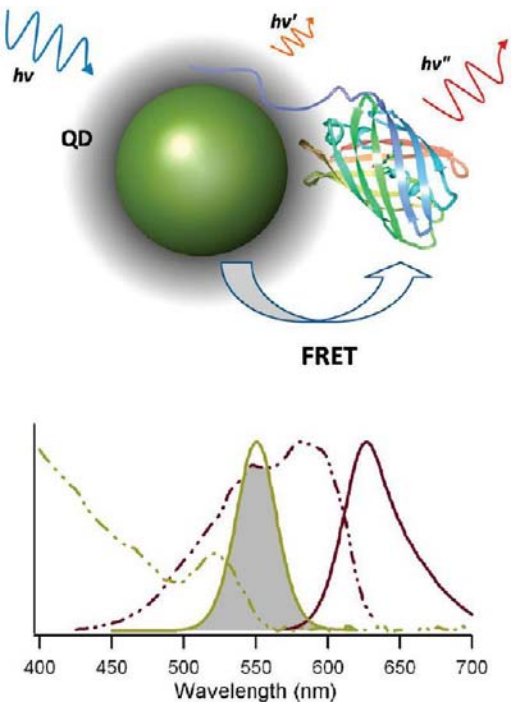


Figure 1. FRET-based assessment of QD-FP self-assembly. Top: Schematic of the FRET assay used to investigate the his-tag self-assembly on quantum dots. An N-terminal polyhistidine sequence is used to assemble mCherry (PDB 2H5Q) on the surface of the quantum dot. If assembly is successful, the proximity of the QD and FP will facilitate energy transfer and a measurable FRET signal will be detected. Bottom: Absorbance (dashed lines) and emission (solid lines) spectra of a quantum dot (540 nm T2-MP carboxyl-functionalized EviTag (QD6) shown in green) and mCherry (in red). The shaded area depicts the spectral overlap of the donor emission and acceptor absorbance.

Three varieties of the T2-MP EviTags were purchased from Evident Technologies (Troy, NY). The carboxyl-functionalized (QD6), amine-functionalized (QD7), and nonfunctionalized EviTags (QD8) vary only in their lipid-PEG terminal group (Note: EviTags are now sold as eFluor Nanocrystals by eBioscience in San Diego, CA).

Rhodamine 6G was acquired from Invitrogen. Luria−Bertani (LB) agar, LB broth, ampicillin (Amp), chloramphenicol (Cam), and isopropyl-β-D-thiogalactoside (IPTG) were purchased from U.S. Biological (Swampscott, MA). Borax, Tris-EDTA (TE) buffer, and $NiCl_2$ were procured from Sigma Aldrich (St. Louis, MO).

Quantum Dot Characterization. The hydrodynamic diameter and zeta potential of all eight of the QD varieties were measured, as was their quantum yield (QY). Dynamic light scattering (DLS) was used to measure the hydrodynamic diameter and zeta potential using the Nicomp 280 from Particle Sizing Systems (PSS; Goleta, CA). Each QD stock solution was diluted with distilled water and filtered through a 0.22 μm syringe filter before the hydrodynamic diameter was measured. The same sample was then further diluted with distilled water for measurement of the zeta potential at pH 7. Subsequently, a KOH solution in water was added to the sample to raise the pH to 9.5 before the zeta potential was measured again.

The QD quantum yields were measured against rhodamine 6G in water. Absorption and emission spectra of the QDs were measured using an Ultrospec 2100 *pro* UV−vis Spectrophotometer (GE Healthcare, Piscataway, NJ) and a Tecan Safire^2 multiplate reader (Männedorf, Switzerland), respectively.

Mutagenesis, Expression, and Purification of the Fluorescent Protein mCherry. Engineering and production of the fluorescent protein (FP) mCherry proceeded as previously described (*11*).

A pRSET-B plasmid containing the insert for the fluorescent protein mCherry was kindly provided by Roger Tsien's laboratory at the University of California, San Diego. This plasmid was modified using PCR mutagenesis to produce the control mCherry, which lacks a polyhistidine sequence, and His6-mCherry, which contains six N-terminal histidines linked to the fluorescent protein with three glycines. Both mutagenesis reactions, which were performed using Phusion High-Fidelity Master Mix (New England Biolabs, Ipswich, MA) in PCR reactions with primers custom synthesized by Integrated DNA Technologies, Inc. (IDT; Coralville, IA), also removed any unnecessary amino acids from the original pRSET-B plasmid, including an existing 6×His, an Xpress Epitope, an enterokinase site, and extra amino acids arising from the multiple cloning site. The His6-mCherry plasmid was also mutated to create a protein with three site-mutations, S148C I165N Q167M, resulting in a nonfluorescent, nonchromogenic GFP-like protein termed His6-mCherry-NF.

Plasmids coding for mCherry, His6-mCherry, and His6-mCherry-NF were expressed in Rosetta 2 (DE3)s using IPTG induction. Protein purification was performed on an ÄKTAprime plus system (GE Healthcare). The his-tagged proteins were purified on a 1 mL HisTrap HF column, while the untagged protein was purified with a hydrophobic column (HiPrep 16/10 Butyl FF) followed by size-exclusion chromatography (HiPrep 16/60 Sephacryl S-300 HR). The purified proteins were concentrated and buffer-exchanged into PBS using centrifugal filtration devices (Centricon Plus-20; Millipore, Billerica, MA). The proteins were aliquoted into PCR tubes and snap-frozen in liquid nitrogen as previously described (*30*). Protein purity was checked with SDS-PAGE, and protein concentrations were determined using a BCA Assay (Pierce, Rockford, IL).

Calculation of the Spectral Overlap Integrals and Förster Distance. Igor Pro was used as previously described to calculate the overlap integral and Förster distances for each of the possible FRET pairs (*19, 31*). The spectral overlap integral

$$J = \int F_{\text{D-corr}}(\lambda)\varepsilon_{\text{A}}(\lambda)\lambda^4 \, \text{d}\lambda \tag{1}$$

describes the degree of coincidence between the donor emission and the acceptor absorption, where $F_{\text{D-corr}}$ designates the normalized emission spectrum of the donor, ε_{A} is the molar extinction coefficient of the acceptor, and λ is the wavelength in nanometers. Once the overlap integral was calculated, the Förster distance, R_0, or the distance between the donor and acceptor at which the FRET efficiency is 50%, was determined using the equation

$$R_0^6 = 8.785 \times 10^{-5} k^2 Q_{\text{D}} J / {n_{\text{D}}}^4 \tag{2}$$

where κ^2 is the dipole orientation factor, assumed to be 2/3, Q_{D} is the quantum yield of the donor, and n_{D} is the refractive index of the medium.

FRET Assays. Assays assessing the binding of his-tagged mCherry to diverse QDs were conducted by measuring the FRET efficiency of the various pairs in black, flat-bottomed, nonbinding 384-well plates (Corning). QDs and FPs were mixed directly in the well plates with a final QD concentration of 50 nM and 0 to 12 molar equivalents of protein per QD in either 10 mM tetraborate buffered saline, pH 9.5, or 10 mM tetraborate buffer, 1 M NaCl, pH 9.5, as indicated. After allowing at least 15 minutes for self-assembly, the emission spectra of each FRET pair was measured in a Tecan Safire^2 multiplate reader with an excitation wavelength of 400 nm, excitation bandwidth of 10 nm, emission bandwidth of 5 nm, integration time of 100 μs, and a step size of 2 nm. All of the assays were performed in triplicate, as were FP-only controls. For measurements involving the use of supplemented Ni^{2+}, the spectra were measured first with just the QDs and FPs present; then, 1 μL of 20 mM $NiCl_2$ was added to the 80 μL reaction volume, resulting in a final Ni^{2+} concentration around 250 μM. The solutions were incubated at room temperature for at least 15 minutes to allow binding to reach equilibrium, and then the emission spectra were again measured. In this study, the donor−acceptor distance is assumed to be the distance between the center of the QD and the fluorescent protein chromophore. Since FRET signal is generated only when the QD and fluorescent proteins are within ~20 nm, unbound fluorescent proteins contribute little to the overall signal and thus were not removed from the sample prior to measuring the FRET signal.

The background emission resulting from detector gain and any direct excitation of mCherry was subtracted from each of the FRET spectra at that same mCherry concentration. Each background-subtracted spectrum was then deconvolved using *PeakFit* software (v4.12, Systat, San Jose, CA); the symmetrical quantum dot emission was fit to a Voigt Area peak, while an exponentially modified Gaussian (EMG) curve was used to account for the tailing resulting from the asymmetrical mCherry emission. The areas under the QD peaks were normalized to the area under the QD spectrum in the absence of mCherry. The resulting normalized QD emissions were plotted relative to the acceptor concentrations. FRET efficiencies were calculated using the equation

$$E = 1 - \frac{F_{\text{DA}}}{F_{\text{D}}} \tag{3}$$

where F_{DA} is the fluorescence of the donor in the presence of the acceptor and F_{D} is the fluorescence of the donor in the absence of the acceptor. The method of estimating the donor−acceptor distance (R) has been described before (*11, 16, 32*) and is outlined in the Supporting Information.

RESULTS AND DISCUSSION

As shown in Table 1, QDs with eight different organic coatings from three distinct sources were evaluated using a FRET assay to determine their capacity for self-assembly to biomolecules via polyhistidine (metal-affinity) coordination. These three major categories of QDs consist of (1) QDs coated using ligand exchange with DHLA (QD1), DHLA-PEG_{600}-OH (QD2), and DHLA-PEG_{750}-OCH_3 (or DHLA-mPEG) (QD3); (2) Invitrogen Qdots, which are coated with an amphiphilic block copolymer, including carboxyl Qdots (QD4) and amino-PEG Qdots (QD5); and (3) lipid-PEG coated QDs, specifically carboxyl-functionalized (QD6), amine-functionalized (QD7), and nonfunctionalized (QD8) T2-MP EviTags from Evident Technologies. In order to relate the results of the FRET assay to the fundamentals of the interaction between the his-tagged fluorescent protein and the QD, basic QD properties, such as photoluminescence emission, hydrodynamic diameter, zeta potential, and quantum yield, were first characterized and compared.

Quantum Dot Properties. All eight of the QDs tested exhibit emission peaks between 540 and 550 nm (Table 1 and Figure S1 of the Supporting Information). These similar emission spectra translate into comparable spectral overlap integrals with the mCherry acceptor (J; Table 1), but significant differences are seen in the Förster distances, R_0, calculated for each of the FRET pairs because of variations in the quantum yields of the distinct QDs. At identical donor−acceptor (QD−protein) distances, QDs with higher QYs, and therefore larger Förster distances, will exhibit increased FRET efficiencies. Thus, when determining conjugate conformation, it is important to utilize

Table 1. Summary of Quantum Dot Properties

QD type	water-soluble coating		peak emission (nm)	QY[a]	hydrodynamic diameter (nm)[b]	zeta potential at pH 7 (mV)[c]	zeta potential at pH 9.5 (mV)[c]
dihydrolipoic acid (DHLA) coated QDs	DHLA	(QD1)	550	0.11	9.8 ± 0.3	−29.8 ± 1.8	−23.3 ± 2.6
	DHLA-PEG_{600}-OH	(QD2)	548	0.10	12.2 ± 0.9	−12.9 ± 1.3	−34.6 ± 2.0
	DHLA-PEG_{750}-OCH_3	(QD3)	550	0.12	12.9 ± 0.5	−2.8 ± 0.5	−18.2 ± 0.6
Invitrogen: Qdot 545 ITK	Polymer (-COOH)	(QD4)	544	0.75	13.0 ± 0.3	−3.4 ± 0.8	−31.0 ± 1.3
	Polymer (-PEG_{2000}-NH_2)	(QD5)	550	0.74	15.9 ± 0.8	−2.3 ± 0.7	−4.8 ± 1.2
Evident Technologies: T2-MP EviTags	Lipid-PEG_{2000}-COOH	(QD6)	548	0.29	14.9 ± 1.7	−0.6 ± 0.2	−26.5 ± 0.8
	Lipid-PEG_{2000}-NH_2	(QD7)	540	0.77	20.8 ± 0.5	−4.0 ± 0.6	−31.8 ± 0.5
	Lipid-PEG_{2000}-OCH_3	(QD8)	542	0.39	23.2 ± 0.7	−10.0 ± 0.5	−15.5 ± 1.3

[a] QY measured relative to Rhodamine 6G in water. [b] Hydrodynamic diameter values are the mean ± standard deviation of the volume-weighted size distribution. [c] Zeta potential values are means ± standard deviations of $n = 3$ or $n = 4$ measurements.

Table 2. Summary of FRET Pair Specifications and Key Parameters

FRET donor (acceptor: His6-mCherry)		J (10^{-15} M^{-1} cm^3)	R_0 (Å)	E at 1:1 QD/FP	max E
(QD1)	DHLA 550 nm QDs	4.73	44.9	0.15	0.48
(QD2)	DHLA-PEG 550 nm QDs	4.57	43.8	0.02	0.18
(QD3)	DHLA-mPEG 550 nm QDs	4.76	45.2	0.01	0.17
(QD4)	Qdot 545 ITK carboxyl quantum dots	4.56	61.1	<0.01 (0.09)[a]	0.21 (0.47)[a]
(QD5)	Qdot 545 ITK amino (PEG) quantum dots	5.10	62.1	N/A	N/A
(QD6)	Carboxyl-functionalized 540 nm T2-MP EviTag	4.77	52.6	0.51	0.76
(QD7)	Amine-functionalized 540 nm T2-MP EviTag	3.82	59.6	0.37	0.64
(QD8)	Nonfunctionalized 540 nm T2-MP EviTag	4.20	53.9	N/A	N/A

[a] Ni^{2+} added to enhance QD-FP interaction.

donor−acceptor distances extracted from the empirical FRET results in addition to the relative FRET efficiency.

Because emission wavelength is a property of the QD core size (*33*), based on their similar emission wavelengths, the eight QDs examined here have similar nanoparticle dimensions (~4 nm according to technical support from Evident and Invitrogen). Significant differences in the hydrodynamic diameter were, however, apparent in the DLS measurements (Table 1), which reflect subtle differences in the contribution of the hydrated organic coatings to the hydrodynamic interactions.

Ligand-Exchange Coated QDs. DHLA-coated QDs (QD1) were the only nanoparticles that exhibited sub-10 nm hydrodynamic diameters, which can be attributed to the small DHLA-based moieties and removal of the native TOP/TOPO surfactant during the aqueous phase transfer (*10, 34*). DHLA, among the smallest molecules capable of conferring water solubility to QDs (*3*), binds the ZnS capping layer via bidentete thiols and contains a carboxylic acid that holds the QD in suspension as a colloid when deprotonated. Although this thin organic coating is ideal for minimizing the donor−acceptor distance, which is critical for achieving high FRET efficiencies, colloidal stabilization based on electrostatic repulsion is vulnerable to changes in the environment and the protonation state of the carboxyl groups, i.e., pH. For example, compared to the other seven QDs used in this study, we measured a progressive decrease in photoluminescence over time for the DHLA-coated QDs (QD1) in the presence of 1 M NaCl (Supporting Information Figure S2), which can be attributed in aggregation build up in the solution; DHLA-coated QDs are also known to be more stable in alkaline solutions than at acidic pHs (*34*).

The other two QD varieties coated using ligand-exchange, the DHLA-PEG (QD2; coated with DHLA-PEG_{600}-OH) and DHLA-mPEG (QD3; coated with DHLA-PEG_{750}-OCH_3) QDs, exhibit 25% and 32% increases in hydrodynamic diameter over the DHLA coating, respectively (Table 1, see ref *35*). The increase in size is accompanied by enhanced colloidal stability since solubility is mediated by the ethylene glycol repeats. These QDs also exhibited less variation in the photoluminescent output over time, including under high salt conditions (Supporting Information Figure S2).

Ligand exchange with these molecular-scale caps decreases the QY of the QDs relative to the starting QDs in organic solvents. For example, all three of the ligand-exchanged QDs had quantum yields between 0.10 and 0.12. The exact value depends on the nature of the starting TOP/TOPO-capped nanocrystals; higher yields (0.2−0.3) have been reported for these materials (*34*).

QDs Coated with Amphiphilic Block Copolymers. The amphiphilic block copolymer coated carboxyl Qdots from Invitrogen (QD4) exhibited the smallest hydrodynamic diameter (13 nm) of the commercially available QDs (Table 1), a value in good agreement with previously reported measurements (*35*). The hydrophobic region of the amphiphilic poly(acrylic acid) polymer interdigitates with the TOP/TOPO layer and presents a high density of carboxylic acids at the QD−solvent interface. While the hydrophilic carboxylic acids confer water solubility to the QDs similarly to those on the small molecule DHLA, the larger, more neutral polymer does appear to improve the QD passivation as well, providing the Qdot with relatively reliable photoluminescence over time, even in high salt conditions (Supporting Information Figure S3). This coating type preserves the high QY of the QDs even in aqueous solution, consistently producing batches with QYs greater than 0.70. The amino-PEG Qdots (QD5) add another layer to the same coating scheme used for the carboxyl Qdots. The amine-terminated PEG_{2000} chains that are conjugated to the carboxyl groups on the surface of the carboxyl Qdots add almost 3 nm to the hydrodynamic diameter of the Qdots (Table 1), but the hydration of the PEG molecules results in a QD surface that significantly reduces nonspecific interactions (*36*).

Lipid−PEG Coated QDs. The three EviTags exhibited rather different hydrodynamic diameters although they used the same core−shell structure and lipid−PEG coating scheme (Table 1). Each coating consists of a micelle-like shell of amphiphilic 1,2-distearoyl-*sn*-glycero-3-phosphoethanolamine-*N*-[carboxy(poly(ethylene glycol))-2000], i.e., DSPE-PEG_{2000}, from Avanti Polar Lipids, Inc. (Alabaster, AL), terminated with a carboxyl, amine, or methoxy group (Table 2). The reduction in hydrodynamic diameter as the PEG terminal group changes from -OCH_3 to -NH_2 to -COOH does not correlate with a decrease in photoluminescence (PL) stability, even under high salt conditions (Supporting Information Figure S4). These differences in the hydrodynamic diameter may indicate variations in the density and orientation of the lipid-PEG coating.

A previous report on thickness measurements of DSPE-PEG_{2000} Langmuir−Blodgett monolayer films, using neutron reflectivity, indicated that a densely packed monolayer of DSPE-PEG_{2000} could reach a thickness of 10.7 nm, but smaller thicknesses were measured for less densely packed monolayers. In that case, the decrease in the monolayer thickness was found to be related to the brush height of the PEG polymer; the lipid demonstrated no density-dependent variation in its geometry (*37*). This effect may be even more pronounced on a nanoparticle, where surface curvature inherently increases the lateral space available for PEG molecules. The difference in hydrodynamic sizes measured for these various nanocrystals may thus be attributed to differences in the contributions of the end-functionalized PEG (-COOH, $-NH_2$, and $-OCH_3$) to the coating quality and hydrodynamic structure. The zeta potential measurement results also signal surprising differences between the three coating types that are not consistent with the surface charge that would be expected on the basis of the lipid−PEG terminal group. This is a further indication of the differences in the structure of the coatings beyond the functional moiety. We should also note that, while the variation in coating thickness does not appear to affect PL stability of QDs, it does seem to influence polyhistidine self-assembly, as discussed below.

His-Tag-Mediated Self-Assembly. FRET assays were performed to determine under what conditions and to what extent the his-tag mediates self-assembly of fluorescent proteins to QDs. The FRET-based assay is particularly useful here because it both confirms the proximity of the nanoparticle and biomolecule and allows the derivation of a separation distance due to its strong distance dependence. This provides insight into both self-assembly and the overall conjugate structure. In all cases, a non-his-tagged fluorescent protein mCherry was used as a negative control in order to ascertain that the his-tag was necessary to induce the interaction between the donor (QD) and acceptor (FP). Self-assembly was also attempted under high salt conditions (1 M NaCl) in cases where the QD PL was stable under these buffer conditions (see Supporting Information). The extreme salt concentration is disruptive to electrostatic interactions and therefore can be used to test whether the interaction is metal chelation-based or mediated electrostatically. His-based metal chelation to Ni-NTA, for example, can tolerate extreme conditions and the presence of denaturing agents including 5% SDS, 6 M guanidine, 8 M urea, and greater than 1 M NaCl (*7, 15, 20*). In addition, supplementation with $NiCl_2$ was included to determine if the presence of additional chelating ions would affect QD−protein binding.

Ligand-Exchange Coated QDs. Our FRET assays revealed that, of the three DHLA-based organic coatings, only QDs coated with DHLA (QD1) (the smallest ligand of the three) demonstrated a good capacity for self-assembly via polyhistidine coordination (Figure 2). The spectra collected from the DHLA-QDs incubated with His6-mCherry show a clear and progressive decrease in the QD emission with a concomitant dose-dependent increase in the sensitized emission of the fluorescent protein, with an isosbestic point around 580 nm (Figure 2A). It was not possible to test self-assembly with these QDs under high salt conditions because DHLA QDs exhibit reduced stability in those conditions (Supporting Information Figure S2), but the addition of the divalent cation (Ni^{2+}) did not appear to enhance binding (Figure 2B). The approximately 6 nm donor−acceptor distance extracted for the DHLA-coated QD and His6-mCherry implies that the FP barrel structure is indeed very close to the QD surface. These findings are consistent with previously reported kinetic data on the binding of his-tagged biomolecules to DHLA-coated QDs, which indicated that the his-tag binds directly to the ZnS capping layer of the QD (*15*).

It has been previously documented that the polyhistidine-mediated coordination of a nonfluorescent protein such as maltose-binding protein (MBP) to the DHLA-coated can QDs result in a photoluminescence (PL) increase of up to 20% (*38*). This was attributed to the passivation of surface defects in the DHLA coating by his-tags, thereby reducing the emission loss in aqueous media. This effect could be problematic for the analysis of the FRET assays described above, since his-tag binding could increase the QD emission concomitantly as the QD emission is being reduced by energy transfer to the His6-mCherry proteins. The effect of his-tag binding on QD PL was examined for all eight QDs, and the two that seemed to be affected by the presence of the his-tagged protein, the DHLA QDs and the carboxyl-functionalized EviTags (Supporting Information Figure S8), were tested in an alternative FRET assay format. The modified FRET assay, in which the total number of proteins was fixed while the ratio of fluorescent to nonfluorescent proteins was varied, was explored to see if the inclusion of the nonfluorescent protein would increase the overall FRET efficiency of the system. In this particular experimental protocol, the modified conjugate configuration did not improve the conjugate FRET efficiency (see Supporting Information Figure S9).

Both PEG-conjugated DHLA moieties (QD2 and QD3) exhibited marginal QD PL quenching when mixed with His6-mCherry (Figures 2C and 2E), demonstrating an inability of the his-tag to stably interact with the nanoparticles. DHLA-PEG-capped QDs, though not amenable to his-driven conjugation with proteins (due to the steric hindrance from the PEG coating), have been shown to tightly bind his-terminated peptides, as these are able to penetrate the PEG brush and interact directly with the QD Zn-rich surface. QD-peptide assemblies made using these QDs have been employed in enzymatic assays and conjugate uptake by live cells, where the improvements in colloidal stability were beneficial (*39*).

QDs Coated with Amphiphilic Block Copolymers. The carboxyl Qdots from Invitrogen (QD4) showed only a limited capacity to self-assemble with the His6-tagged mCherry in borate buffered saline, and this subtle interaction was disrupted in the presence of 1 M NaCl (Figures 3A and 3B). However, a stronger FRET signal was observed following supplementation with $NiCl_2$. The Ni^{2+}-dependent FRET signal was also reduced in the presence of 1 M NaCl, but not eliminated as in the non-Ni^{2+}-dependent case (Figures 3C and 3D). In the absence of the supplemented Ni^{2+}, we found that the limited interaction between the fluorescent protein and the carboxyl Qdot is nonspecific and electrostatically mediated, and can be disrupted with high salt concentrations. The supplemented Ni^{2+}, however, appears to complex with the high density of carboxyl groups on the Qdot surface, enabling the interaction with the protein via Ni^{2+} chelation. The same interaction was observed in another study when his-tagged luciferase molecules were incubated with carboxyl Qdots in the presence of Ni^{2+} (*40*). Other divalent ions including Ca^{2+}, Mg^{2+}, and Mn^{2+} were tested in that study as well, but Ni^{2+} was the most effective one in inducing the interaction between the his-tagged protein and the Qdot, while maintaining protein functionality (*40*). Calculation of the corrected donor−acceptor distance yielded a median separation of 94 nm between the QD core and the FP fluorophore (see Table S1 in Supporting Information). This distance is significantly larger than the hydrodynamic radius of 65 nm measured for the QDs (Table 1) and is consistent with the model in which the FPs bind to the outer surface of a solid polymer coating that surrounds the QD.

In contrast, the amino-PEG ITK Qdots (QD5) showed no difference in QD emission regardless of whether his-tagged or control mCherry was used (Figure 4B), and addition of $NiCl_2$

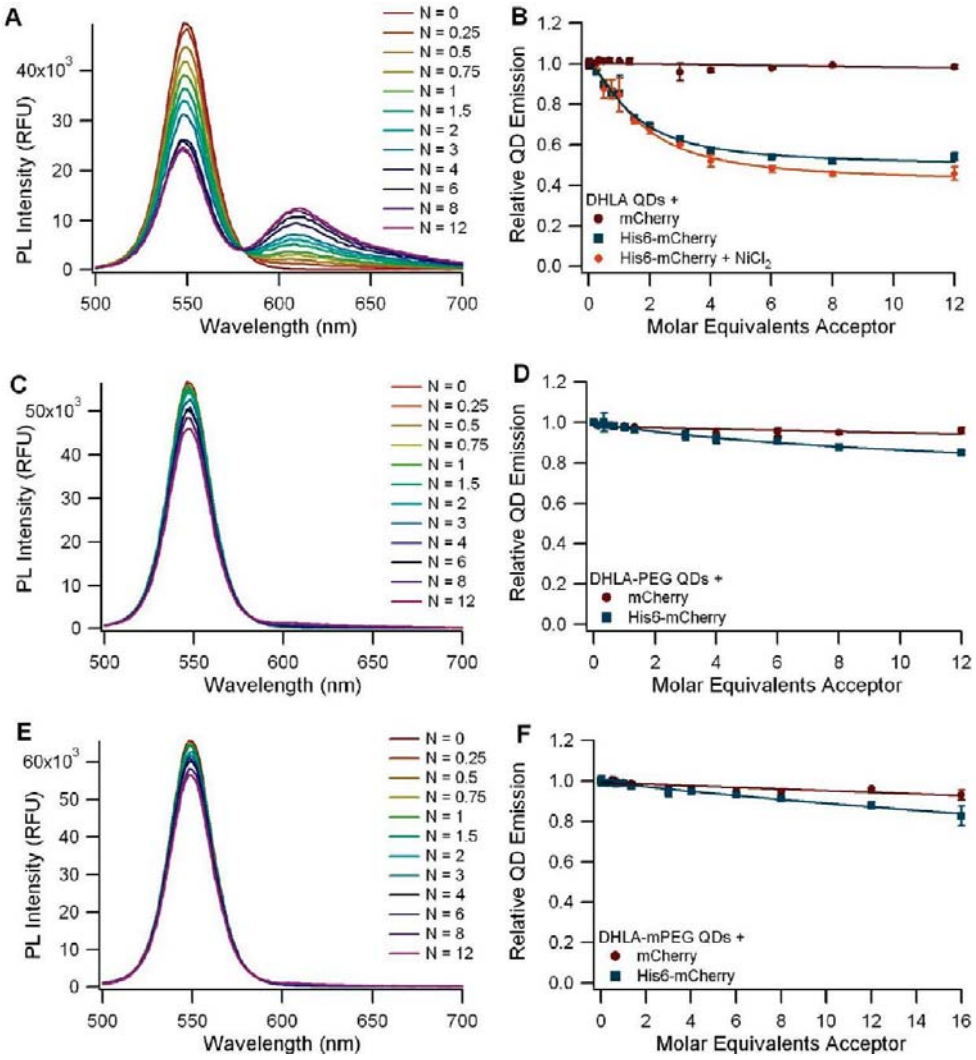


Figure 2. FRET assay using 550 nm QDs coated with (A,B) DHLA (QD1), (C,D) DHLA-PEG$_{600}$-OH (QD2), or (E,F) DHLA-PEG$_{750}$-OCH$_3$ (QD3). A, C, and E: Spectra of QDs incubated with varying ratios (*N*) of His6-mCherry monomers per QD. B, D, and F: Graph of the normalized QD emission relative to the number of acceptor molecules per QD. Circles (•) represent QDs incubated with a nonhis-tag control mCherry, squares (■) represent experiments with His6-mCherry as the acceptor, and the diamonds (♦) represent experiments with His6-mCherry following supplementation with Ni^{2+}. All points are mean ± standard deviation with $n = 3$.

did not increase the level of interaction (Figure 4D). We attribute this to the presence of the amino-PEG moieties on the Qdot surface, which shield the nanoparticles from interacting with the protein (even nonspecifically, as seen with the carboxyl Qdots) and prevent the immobilization of Ni^{2+} ions on the nanoparticle surface. The zeta potential measurements showed that the carboxyl Qdots are highly negatively charged while the amino-PEG Qdots have a near neutral zeta potential, supporting the finding that the carboxyl Qdots are primed for both electrostatic interactions and metal chelation, whereas the amino-PEG Qdots are not.

It is worth noting that the carboxyl Qdots (QD4) produce minimal sensitized emission from the his-tagged mCherry even when FRET quenching is significant (Figure 3C). In fact, the relative intensity of the sensitized emission from the protein is the largest in the case of the DHLA QDs (QD1) (Figure 2A), even though there is more FRET quenching observed for the carboxyl-functionalized EviTags (QD2) (Figure 5A). This difference in sensitized emission between the samples arises because different detector-gain settings are necessary to accommodate the large range in QD brightnesses. The Qdots (QD4 and QD5) required dramatically lower fluorimeter gain settings compared to the EviTags (QD6, QD7, QD8), which still had lower gains than applied for the DHLA QDs (QD1, QD2, QD3), because of their significantly enhanced relative brightness. Protein emission intensity may have paled in comparison to the brightness of the Qdots. Because it was necessary to optimize gain settings to the QD-type under examination, the relative intensities of the peaks should only be compared within one type of QD, not from figure to figure.

Lipid-PEG Coated QDs. The interaction between the His6-mCherry and the EviTags was found to be dependent on the terminal functional group present in the lipid-PEG coating. The carboxyl-functionalized EviTags (QD6) were shown to be excellent FRET donors with 70% quenching of the QD emission at a donor to acceptor ratio of 1:3 (Figures 5A and 5B). His-tag binding to carboxyl-functionalized EviTags proceeded in both saline and high salt and was not enhanced by the addition of Ni^{2+}. This indicates that the interaction was neither electrostatically driven nor dependent on the chelation of free divalent cations by the carboxyl groups, as is the case with the carboxyl Qdots. The incubation of the carboxyl-functionalized EviTags with nonfluorescent his-tagged proteins resulted in a mild increase in the QD PL (Supporting Information Figure S8), indicating that these EviTags may have surface defects similar to those described for the DHLA QDs. As with the DHLA QDs, the modified conjugate configuration designed to account for

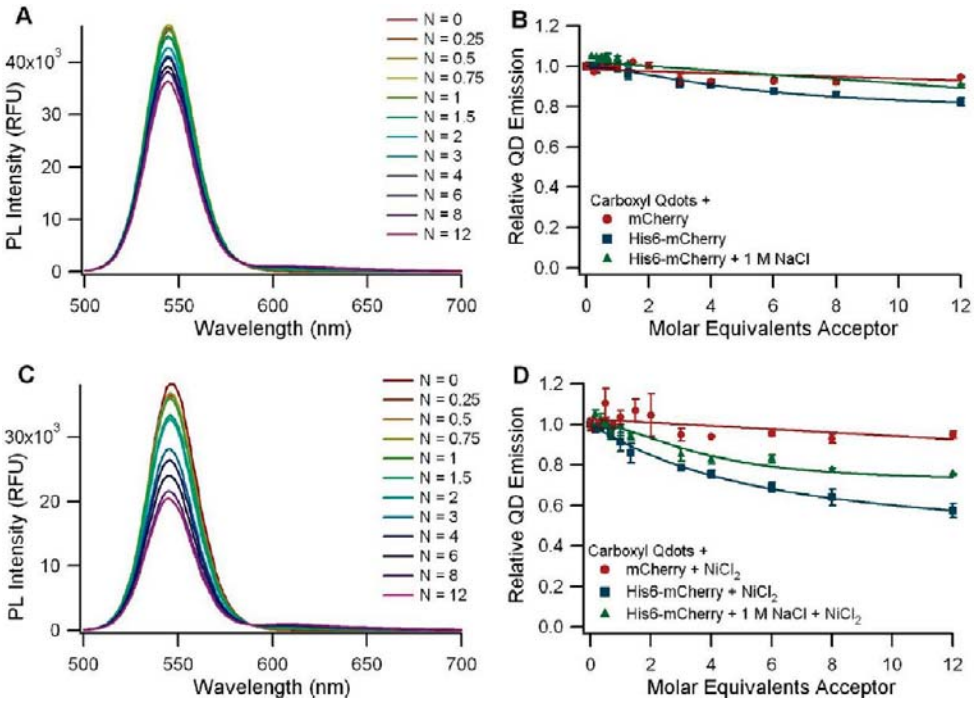


Figure 3. FRET assay using 545 nm Invitrogen ITK Carboxyl Qdots (QD4) before (A,B) and after (C,D) supplementation with Ni^{2+}. A and C: Spectra of carboxyl Qdots (QD4) incubated with varying ratios (*N*) of His6-mCherry per QD. B and D: Graphs of the normalized QD emission with respect to the ratio of acceptor molecules per QD. Circles (•) represent a nonhis-tagged mCherry control, squares (■) represent the His6-mCherry acceptor, and triangles (▲) represent the addition of His6-mCherry in the presence of 1 M NaCl to diminish the effect of electrostatic interactions.

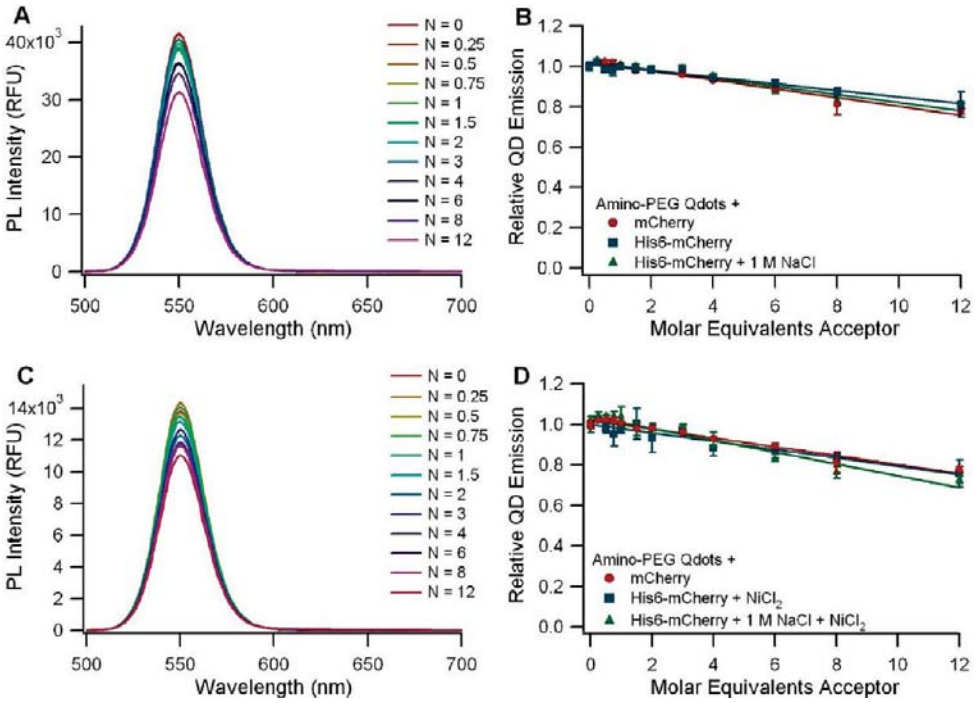


Figure 4. FRET assay using 545 nm Invitrogen ITK Amino-PEG Qdots (QD5) before (A,B) and after (C,D) supplementation with Ni^{2+}. A and C: Spectra of amino-PEG Qdots (QD5) incubated with varying ratios (*N*) of His6-mCherry per QD. B and D: Graph of the normalized QD emission with respect to the number of acceptor molecules per QD. Circles (•) represent QDs incubated with a nonhis-tagged mCherry control, squares (■) represent the His6-mCherry acceptor, and triangles (▲) represent the addition of His6-mCherry in the presence of 1 M NaCl to diminish the effect of electrostatic interactions.

the increase in PL due to protein binding did not yield improved FRET efficiencies (Supporting Information Figure S9).

Amine-functionalized EviTags (QD7) also showed a capacity for the polyhistidine-mediated self-assembly (Figures 5C and 5D), but this interaction was more susceptible to disruption from high salt concentrations. Not only was the extent of QD quenching lessened in the high salt buffer, but the shape of the dose-dependent quenching curve was altered as well, indicating that the mechanism of the interaction between the amine-functionalized EviTags and His6-mCherry likely contains an electrostatic component, where transient nonspecific interactions between the amines in the coating and the fluorescent protein

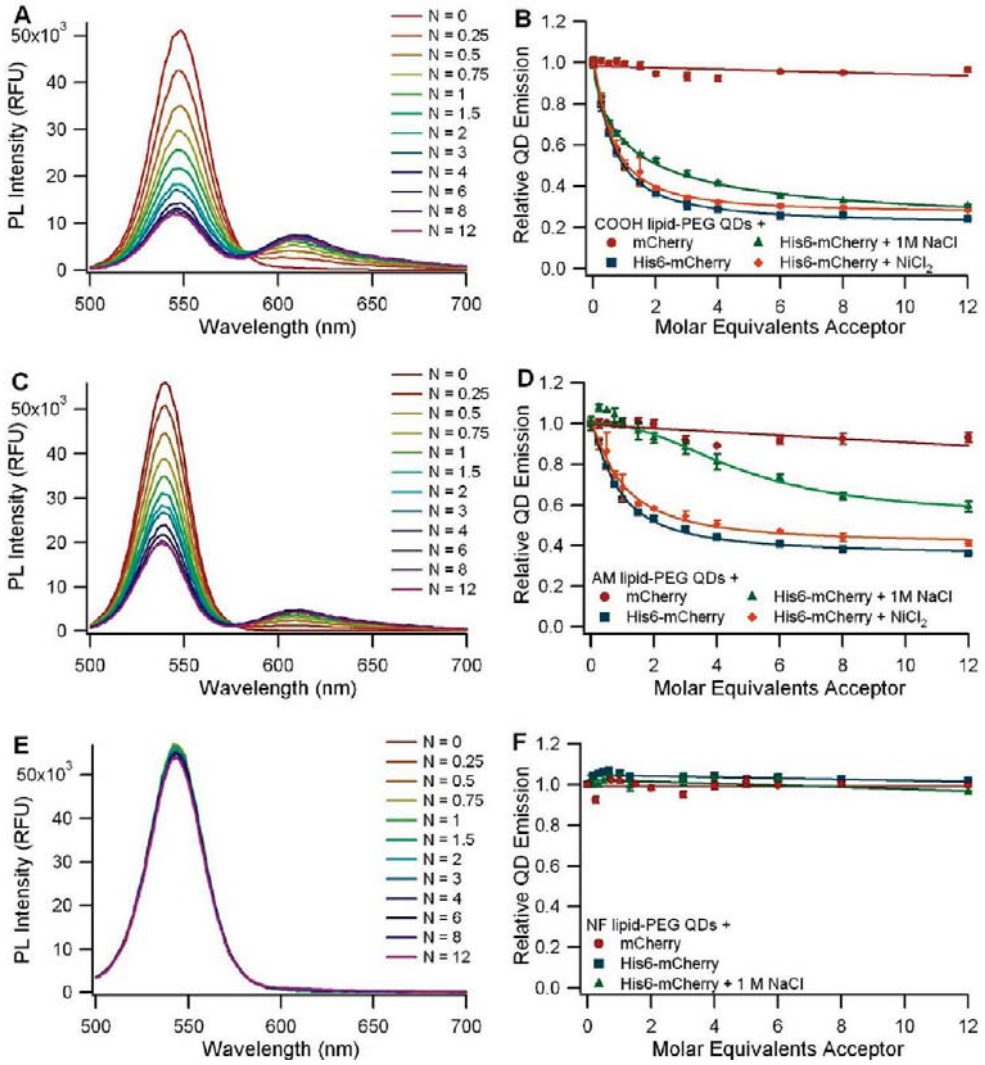


Figure 5. FRET assay using 540 nm (A,B) carboxyl- (QD6), (C,D) amine- (QD7), and (E,F) nonfunctionalized (QD8) T2-MP EviTags. A, C, and E: Background-subtracted spectra of EviTags incubated with various ratios (*N*) of His6-mCherry molecules per QD. B, D, and F: Graph of the normalized QD emission relative to the number of acceptor molecules per QD. Circles (•) represent EviTags incubated with a nonhis-tagged mCherry control, squares (■) represent QDs incubated with the His6-mCherry acceptor, triangles (▲) represent experiments with His6-mCherry in the presence of 1 M NaCl, and diamonds (♦) represent experiments with His6-mCherry following supplementation with Ni^{2+}.

may provide the opportunity for close proximity between the his-tag and the QD surface. Although these nonspecific associations do appear to contribute to the probe assembly in this case, the presence of some conjugate formation in the high salt solution implies the incidence of polyhistidine-derived metal chelation as well.

Nonfunctionalized EviTags (QD8), in contrast, showed no capacity for polyhistidine-mediated self-assembly (Figures 5E and 5F), perhaps in part due to the lack of electrostatic attraction, but more likely due to hindrance from a dense lipid−PEG coating.

The significant differences in the quenching effect of the three EviTag QDs are surprising given that the only difference between the three QD types is the functional group at the terminal end of the lipid−PEG coating moiety. However, it may be explained, in part, by the hydrodynamic diameter measurements. If the large diameter of the nonfunctionalized EviTags is indeed indicative of a coating with closely packed lipid−PEG molecules that are extended brush-like, then this coating may be impenetrable to the his-tagged FP, similarly to what was reported for DHLA-PEG-capped QDs. If the 35% decrease in the hydrodynamic diameter of the carboxyl-functionalized EviTags, in contrast, reflects a less dense, or even patchy, lipid−PEG coating, then some regions of the QD surface may be exposed and thus amenable to the binding of the polyhistidine tag. It is unclear, however, what role the TOP/TOPO layer that passivated the surface following the inorganic synthesis plays in this scenario. The amine-functionalized EviTags exhibited a behavior between the two discussed above, in both hydrodynamic diameter and the extent of FRET. In fact, given the much higher quantum yield of the amine-functionalized EviTag, one would expect a greater quenching than that with the carboxyl-functionalized EviTag, if the fluorescent proteins were bound to the QDs in the same amount and positioned at the same distance from the QD core. Instead, we found that quenching was reduced with the amine-functionalized EviTags. Calculations of the corrected donor−acceptor distances yielded median *R* values of 5.6 nm and 7.1 nm for the carboxyl- and amine-functionalized EviTags, respectively (Supporting Information Table S1). Both of these donor−acceptor distances are shorter than half of the hydrodynamic diameter of the QDs, as measured with DLS (Table 1), suggesting that in both cases the fluorescent proteins may be embedded in the coating layer rather than outside of the PEG corona. The flexibility of the hydrated PEG chains, particularly when not close-packed into a dense brush-like conformation, could permit this physical arrangement. Furthermore, the difference in the donor−acceptor distance for carboxyl-functionalized or amine-functionalized EviTags could

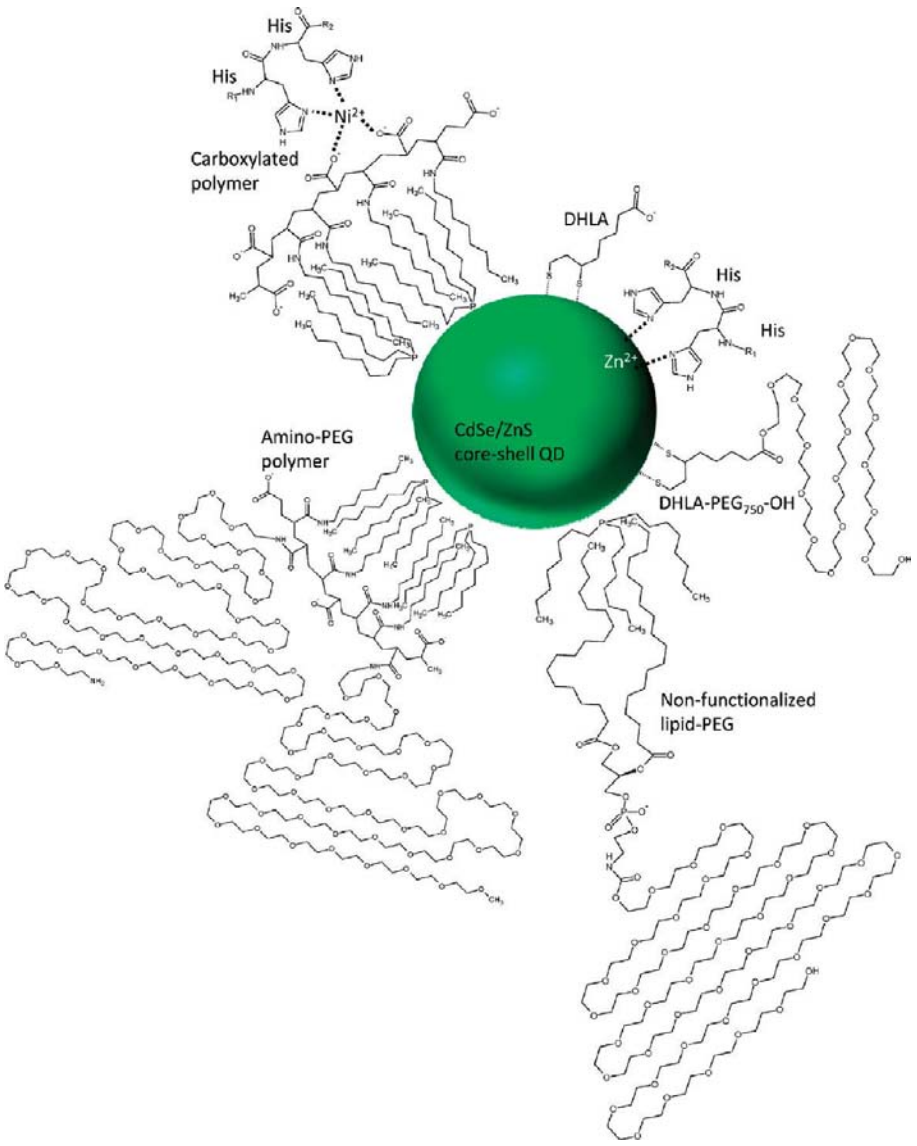


Figure 6. Schematic of various QD coatings and his-tag interactions. The organic coating moieties and their interaction with the polyhisitidine sequence are depicted. Where the his-tag can access the QD surface, coordination of the Zn^{2+} ions in the ZnS capping layer facilitates self-assembly. In the case of the carboxylated polymer, a divalent cation is chelated by both the carboxyl groups on the polymer surface and the histidine.

arise if the amino acid linker region between the his-tag and the FP barrel structure is fully extended when the protein is bound to the amine-functionalized EviTag due to the differences in their PEG conformations.

To ensure that the results of the EviTag FRET assays are not dependent on the particular batches of QDs, self-assembly experiments were repeated many times with different coating batches and QD emission wavelengths (paired with alternative GFP-like FPs to ensure appropriate spectral overlap where necessary) utilizing QDs purchased during the past few years, making it likely that multiple batches of Avanti's lipid−PEG were involved for each coating type as well. Our general observation of strong quenching of the carboxyl-functionalized EviTags (QD6), moderate quenching of the amine-functionalized EviTags (QD7), and no quenching of the nonfunctionalized EviTags (QD8) was consistent for all experiments conducted (data not shown). Our previous results indicated that carboxyl-functionalized EviTags with three different coating batches all showed considerable quenching when bound to FPs via polyhistidine-mediated coordination (*11*). Thus, these results demonstrate the utility of polyhistidine coordination for the bioconjugation of biomolecules to QDs coated with carboxyl-functionalized lipid−PEG molecules even though the technique does not extend to all lipid−PEG-based coatings.

In this study, we compared QDs with eight different coatings using three different coating schemes and determined their capacity for polyhistidine coordination as a means to conjugate biomolecules to nanoparticles by self-assembly. Polyhistidine coordination is highly desirable for the assembly of nanoparticle-based imaging probes and delivery systems because of its technical simplicity; it has also been applied to self-assembling histidine-modified DNA to QDs (*16*). Our results demonstrate the importance of accessibility for his-tag-mediated coordination. Successful self-assembly depends on enabling access either with small ligand coatings like DHLA or with porous polymeric coatings like the carboxyl-functionalized lipid-PEG (Figure 6). DHLA-coated QDs (QD1) exhibited effective his-tag mediated binding and short donor−acceptor distances but exhibit some environmental sensitivity and pH-dependent colloidal instability. Using QDs coated with PEGylated DHLA (QD2 and QD3) improved the stability and environmental sensitivity, making them advantageous for certain applications including intracellular imaging, but steric hindrance precluded his-tagged proteins from penetrating to the QD surface, even in cases where his-

tagged peptides had been able to bind. The ZnS surface of the carboxyl- (QD4) and amino-PEG (QD5) Qdots was similarly inaccessible for his-tag binding, but chelation of supplemented Ni^{2+} to the high density of carboxyl groups on the carboxyl Qdot polymer coating did allow for Ni^{2+}-mediated association of the protein with the Qdot, similar to the way in which a his-tagged protein binds to a Ni^{2+}-containing metal affinity chromatography column. While the added distance between the donor and acceptor resulting from this binding scheme may make the strategy suboptimal for FRET-based assays, it would nonetheless be useful for labeling Qdots with proteins for applications where the protein should be completely exposed at the QD surface to maintain functionality. Finally, the lipid−PEG-coated EviTags demonstrated a range of his-tag binding permissiveness, depending on the specific functional group at the PEG terminus. Lipid-PEGs terminated with a methoxy group (QD6) generated a thick, impenetrable coating, while coatings with terminal carboxyl groups (QD7) were much thinner and susceptible to his-tag binding. Amine-functionalized EviTags (QD8) performed in between the two.

In summary, this study systematically compares the capacity of eight QD types for self-assembly with his-tagged proteins. The FRET assay employed was particularly useful for studying the conjugate properties as both the presence of binding and an estimation of the distance between the QD and the protein can be extracted from the experimental results. We found that the accessibility of the ZnS surface is paramount to metal coordination and that this nanoparticle characteristic can vary dramatically with subtle changes to the organic coating of the colloid. While the results of this screening for materials compatible with his-tag binding is of general interest for QD−biomolecule hybrid device design, it is particularly important for biosensing applications as this self-assembly method produces compact conjugates that are very suitable for FRET-based assays.

ACKNOWLEDGMENT

The authors gratefully acknowledge laboratory support from Andrea Fernandez and Annie Zheng as well as helpful discussions with Drs. Steven Dublin and Charles Glaus. This work was supported by NIH through a Nanomedicine Development Center award (1PN2EY018244 to G.B.), a Program of Excellence in Nanotechnology award (HL80711 to G.B.), a Center of Cancer Nanotechnology Excellence award (CA119338 to G.B.), and a National Defense Science and Engineering Graduate (NDSEG) Fellowship (to A.M.D.). B.M.C., I.M., and H.M. acknowledge support from DTRA, ONR, and the NRL-NSI.

Supporting Information Available: Results of the calculation of the donor−acceptor distance, assessment of QD stability, characterization of His6-mCherry-NF, evaluation of the QD PL change due to his6 binding, and application of the modified FRET assay. This material is available free of charge via the Internet at http://pubs.acs.org.

LITERATURE CITED

(1) Chan, W. C., and Nie, S. (1998) Quantum dot bioconjugates for ultrasensitive nonisotopic detection. *Science 281*, 2016–2018.
(2) Bruchez, M., Moronne, M., Gin, P., Weiss, S., and Alivisatos, A. P. (1998) Semiconductor nanocrystals as fluorescent biological labels. *Science 281*, 2013–2016.
(3) Medintz, I. L., Uyeda, H. T., Goldman, E. R., and Mattoussi, H. (2005) Quantum dot bioconjugates for imaging, labelling and sensing. *Nat. Mater. 4*, 435–446.
(4) Chan, W. C. W., Maxwell, D. J., Gao, X. H., Bailey, R. E., Han, M. Y., and Nie, S. M. (2002) Luminescent quantum dots for multiplexed biological detection and imaging. *Curr. Opin. Biotechnol. 13*, 40–46.
(5) Medintz, I. L., and Mattoussi, H. (2009) Quantum dot-based resonance energy transfer and its growing application in biology. *Phys. Chem. Chem. Phys. 11*, 17–45.
(6) Sapsford, K. E., Pons, T., Medintz, I. L., and Mattoussi, H. (2006) Biosensing with luminescent semiconductor quantum dots. *Sensors 6*, 925–953.
(7) Hermanson, G. T. (2008) *Bioconjugate Techniques*, 2nd ed.;Academic Press, San Diego.
(8) Howarth, M., Takao, K., Hayashi, Y., and Ting, A. Y. (2005) Targeting quantum dots to surface proteins in living cells with biotin ligase. *Proc. Natl. Acad. Sci. U.S.A. 102*, 7583–7588.
(9) Lingerfelt, B. M., Mattoussi, H., Goldman, E. R., Mauro, J. M., and Anderson, G. P. (2003) Preparation of quantum dot-biotin conjugates and their use in immunochromatography assays. *Anal. Chem. 75*, 4043–4049.
(10) Mattoussi, H., Mauro, J. M., Goldman, E. R., Green, T. M., Anderson, G. P., Sundar, V. C., and Bawendi, M. G. (2001) Bioconjugation of highly luminescent colloidal CdSe-ZnS quantum dots with an engineered two-domain recombinant protein. *Phys. Stat. Solidi B 224*, 277–283.
(11) Dennis, A. M., and Bao, G. (2008) Quantum dot-fluorescent protein pairs as novel fluorescence resonance energy transfer probes. *Nano Lett. 8*, 1439–1445.
(12) Liu, W., Howarth, M., Greytak, A. B., Zheng, Y., Nocera, D. G., Ting, A. Y., and Bawendi, M. G. (2008) Compact biocompatible quantum dots functionalized for cellular imaging. *J. Am. Chem. Soc. 130*, 1274–1284.
(13) Lu, H., Schops, O., Woggon, U., and Niemeyer, C. M. (2008) Self-assembled donor comprising quantum dots and fluorescent proteins for long-range fluorescence resonance energy transfer. *J. Am. Chem. Soc. 130*, 4815–4827.
(14) Medintz, I. L., Clapp, A. R., Mattoussi, H., Goldman, E. R., Fisher, B., and Mauro, J. M. (2003) Self-assembled nanoscale biosensors based on quantum dot FRET donors. *Nat. Mater. 2*, 630–638.
(15) Sapsford, K. E., Pons, T., Medintz, I. L., Higashiya, S., Brunel, F. M., Dawson, P. E., and Mattoussi, H. (2007) Kinetics of metal-affinity driven self-assembly between proteins or peptides and CdSe-ZnS quantum dots. *J. Phys. Chem. C 111*, 11528–11538.
(16) Medintz, I. L., Berti, L., Pons, T., Grimes, A. F., English, D. S., Alessandrini, A., Facci, P., and Mattoussi, H. (2007) A reactive peptidic linker for self-assembling hybrid quantum dot-DNA bioconjugates. *Nano Lett. 7*, 1741–1748.
(17) Green, N. M. (1990) Avidin and streptavidin. *Methods Enzymol. 184*, 51–67.
(18) Howarth, M., Chinnapen, D. J. F., Gerrow, K., Dorrestein, P. C., Grandy, M. R., Kelleher, N. L., El-Husseini, A., and Ting, A. Y. (2006) A monovalent streptavidin with a single femtomolar biotin binding site. *Nat. Methods 3*, 267–273.
(19) Lakowicz, J. R. (2006) *Principles of Fluorescence Spectroscopy*, 3rd ed.; Springer, New York.
(20) Sulkowski, E. (1985) Purification of proteins by Imac. *Trends Biotechnol. 3*, 1–7.
(21) Dennis, A. M., and Bao, G. (2008) Förster resonance energy transfer (FRET) between a fluorescent protein and commercially available quantum dots: a comparison. *Proc. SPIE 6866*, 1–11.
(22) Mei, B. C., Susumu, K., Medintz, I. L., and Mattoussi, H. (2009) Polyethylene glycol-based bidentate ligands to enhance quantum dot and gold nanoparticle stability in biological media. *Nat. Protoc. 4*, 412–423.
(23) Susumu, K., Mei, B. C., and Mattoussi, H. (2009) Multifunctional ligands based on dihydrolipoic acid and polyethylene glycol to promote biocompatibility of quantum dots. *Nat. Protoc. 4*, 424–436.
(24) Mei, B. C., Susumu, K., Medintz, I. L., Delehanty, J. B., Mountziaris, T. J., and Mattoussi, H. (2008) Modular poly(ethylene glycol) ligands for biocompatible semiconductor and gold nanocrystals with extended pH and ionic stability. *J. Mater. Chem. 18*, 4949–4958.
(25) Dabbousi, B. O., RodriguezViejo, J., Mikulec, F. V., Heine, J. R., Mattoussi, H., Ober, R., Jensen, K. F., and Bawendi, M. G.

(1997) (CdSe)ZnS core-shell quantum dots: Synthesis and characterization of a size series of highly luminescent nanocrystallites. *J. Phys. Chem. B 101*, 9463–9475.

(26) Hines, M. A., and Guyot-Sionnest, P. (1996) Synthesis and characterization of strongly luminescing ZnS-Capped CdSe nanocrystals. *J. Phys. Chem. 100*, 468–471.

(27) Peng, Z. A., and Peng, X. G. (2001) Formation of high-quality CdTe, CdSe, and CdS nanocrystals using CdO as precursor. *J. Am. Chem. Soc. 123*, 183–184.

(28) Clapp, A. R., Goldman, E. R., and Mattoussi, H. (2006) Capping of CdSe-ZnS quantum dots with DHLA and subsequent conjugation with proteins. *Nat. Protoc. 1*, 1258–1267.

(29) Susumu, K., Uyeda, H. T., Medintz, I. L., Pons, T., Delehanty, J. B., and Mattoussi, H. (2007) Enhancing the stability and biological functionalities of quantum dots via compact multifunctional ligands. *J. Am. Chem. Soc. 129*, 13987–13996.

(30) Deng, J., Davies, D. R., Wisedchaisri, G., Wu, M., Hol, W. G., and Mehlin, C. (2004) An improved protocol for rapid freezing of protein samples for long-term storage. *Acta Crystallogr., Sect. D 60*, 203–204.

(31) Hink, M. A., Visser, N. V., Borst, J. W., van Hoek, A., and Visser, A. J. W. G. (2003) Practical use of corrected fluorescence excitation and emission spectra of fluorescent proteins in Forster resonance energy transfer (FRET) studies. *J. Fluoresc. 13*.

(32) Medintz, I. L., Clapp, A. R., Brunel, F. M., Tiefenbrunn, T., Uyeda, H. T., Chang, E. L., Deschamps, J. R., Dawson, P. E., and Mattoussi, H. (2006) Proteolytic activity monitored by fluorescence resonance energy transfer through quantum-dot-peptide conjugates. *Nat. Mater. 5*, 581–589.

(33) Qu, L., and Peng, X. (2002) Control of photoluminescence properties of CdSe nanocrystals in growth. *J. Am. Chem. Soc. 124*, 2049–2055.

(34) Uyeda, H. T., Medintz, I. L., Jaiswal, J. K., Simon, S. M., and Mattoussi, H. (2005) Synthesis of compact multidentate ligands to prepare stable hydrophilic quantum dot fluorophores. *J. Am. Chem. Soc. 127*, 3870–3878.

(35) Pons, T., Uyeda, H. T., Medintz, I. L., and Mattoussi, H. (2006) Hydrodynamic dimensions, electrophoretic mobility, and stability of hydrophilic quantum dots. *J. Phys. Chem. B 110*, 20308–20316.

(36) Bentzen, E. L., Tomlinson, I. D., Mason, J., Gresch, P., Warnement, M. R., Wright, D., Sanders-Bush, E., Blakely, R., and Rosenthal, S. J. (2005) Surface modification to reduce nonspecific binding of quantum dots in live cell assays. *Bioconjugate Chem. 16*, 1488–1494.

(37) Bianco-Peled, H., Dori, Y., Schneider, J., Sung, L. P., Satija, S., and Tirrell, M. (2001) Structural study of langmuir monolayers containing lipidated poly(ethylene glycol) and peptides. *Langmuir 17*, 6931–6937.

(38) Clapp, A. R., Medintz, I. L., Mauro, J. M., Fisher, B. R., Bawendi, M. G., and Mattoussi, H. (2004) Fluorescence resonance energy transfer between quantum dot donors and dye-labeled protein acceptors. *J. Am. Chem. Soc. 126*, 301–310.

(39) Medintz, I. L., Pons, T., Delehanty, J. B., Susumu, K., Brunel, F. M., Dawson, P. E., and Mattoussi, H. (2008) Intracellular delivery of quantum dot-protein cargos mediated by cell penetrating peptides. *Bioconjugate Chem. 19*, 1785–1795.

(40) Yao, H., Zhang, Y., Xiao, F., Xia, Z., and Rao, J. (2007) Quantum dot/bioluminescence resonance energy transfer based highly sensitive detection of proteases. *Angew. Chem., Int. Ed. 46*, 4346–4349.

BC900500M

Comparative Evaluation of Three ^{64}Cu-Labeled *E. coli* Heat-Stable Enterotoxin Analogues for PET Imaging of Colorectal Cancer

Dijie Liu,[†,⊥] Douglas Overbey,[⊥] Lisa D. Watkinson,[⊥] Charles J. Smith,[†,‡,⊥] Said Daibes-Figueroa,[†,‡,⊥] Timothy J. Hoffman,[†,§,⊥] Leonard R. Forte,[†,||,⊥] Wynn A. Volkert,[†,‡,⊥] and Michael F. Giblin*[,†,‡,⊥]

Harry S. Truman Memorial Veterans Administration Hospital, 800 Hospital Drive, Columbia, Missouri 65201, and Department of Radiology, Department of Internal Medicine, Department of Medical Pharmacology and Physiology, and Radiopharmaceutical Sciences Institute, University of Missouri-Columbia, Columbia, Missouri 65211. Received November 20, 2009; Revised Manuscript Received March 28, 2010

Analogues of the *E. coli* heat-stable enterotoxin (STh) are currently under study as both imaging and therapeutic agents for colorectal cancer. Studies have shown that the guanylate cyclase C (GC-C) receptor is commonly expressed in colorectal cancers. It has also been shown that STh peptides inhibit the growth of tumor cells expressing GC-C. The ability to determine GC-C status of tumor tissue using in vivo molecular imaging techniques would provide a useful tool for the optimization of GC-C-targeted therapeutics. In this work, we have compared receptor binding affinities, internalization/efflux rates, and in vivo biodistribution patterns of an STh analogue linked to N-terminal DOTA, TETA, and NOTA chelating moieties and radiolabeled with Cu-64. The peptide F^{19}−STh(2−19) was N-terminally labeled with three different chelating groups via NHS ester activation and characterized by RP-HPLC, ESI-MS, and GC-C receptor binding assays. The purified conjugates were radiolabeled with Cu-64 and used for in vitro internalization/efflux, in vivo biodistribution, and in vivo PET imaging studies. In vivo experiments were carried out using SCID mice bearing T84 human colorectal cancer tumor xenografts. Incorporation of DOTA-, TETA-, and NOTA-chelators at the N-terminus of the peptide F^{19}-STh(2−19) resulted in IC_{50}s between 1.2 and 3.2 nM. In vivo, tumor localization was similar for all three compounds, with 1.2−1.3%ID/g at 1 h pi and 0.58−0.83%ID/g at 4 h pi. The principal difference between the three compounds related to uptake in nontarget tissues, principally kidney and liver. At 1 h pi, ^{64}Cu-NOTA-F^{19}-STh(2−19) demonstrated significantly ($p < 0.05$) lower uptake in liver than ^{64}Cu-DOTA-F^{19}-STh(2−19) (0.36 ± 0.13 vs 1.21 ± 0.65%ID/g) and significantly ($p < 0.05$) lower uptake in kidney than ^{64}Cu-TETA-F^{19}-STh(2−19) (3.67 ± 1.60 vs 11.36 ± 2.85%ID/g). Use of the NOTA chelator for coordination of Cu-64 in the context of *E. coli* heat-stable enterotoxin analogues results in higher tumor/nontarget tissue ratios at 1 h pi than either DOTA or TETA macrocycles. Heat-stable enterotoxin-based radiopharmaceuticals such as these provide a means of noninvasively determining GC-C receptor status in colorectal cancers by PET.

INTRODUCTION

Colorectal cancer is an enormous problem within the United States, with an estimated 148 000 new cases diagnosed and almost 50 000 deaths in 2008 alone (*1*). Of patients diagnosed with colorectal cancer, the majority will at some time during the course of the disease develop distant metastases (*2*). The liver is the most common site of colorectal cancer metastasis, and patients with liver metastases in general have a poor prognosis, with 5-year survival rates of 25−40% following resection with curative intent (*2*). Recent research has resulted in the approval of several new agents for the treatment of metastatic colorectal cancer. While fluorouracil/leucovorin therapy was formerly the standard treatment regimen, advances made within the past decade have added the topoisomerase I inhibitor irinotecan (Camptosar, Pfizer) and the alkylating agent oxaliplatin (Eloxatin, Sanofi-Aventis) to combination therapy protocols (*3, 4*). More recently, monoclonal antibodies targeted against the epidermal growth factor receptor (EGFR) and the vascular endothelial growth factor (VEGF) have received FDA approval for treatment of metastatic colorectal cancer (*3, 4*). Both EGFR-targeted Cetuximab (Erbitux, ImClone Systems/Bristol-Myers Squibb) and the α-VEGF mAb Bevacizumab (Avastin, Genentech/Roche) have been shown to synergize with existing chemotherapy protocols and lengthen duration of response (*5, 6*). Additionally, EGFR-targeted Panitumumab (Vectibix; Amgen) has been recently approved for treatment of chemotherapy-refractory metastatic CRC expressing wild-type KRAS (*7*). Despite these advances, however, the median life expectancy for people with advanced colorectal cancer is approximately 20 months, suggesting that new forms of treatment are still required (*4*).

Guanylate cyclase C (GC-C) is a type I transmembrane glycoprotein overexpressed on colorectal cancer cells. Recent clinical trials have shown a correlation between expression of the GUY2C mRNA for the GC-C protein in lymph nodes of CRC patients and disease recurrence (*8*). GC-C agonists such as the *E. coli* heat-stable enterotoxin (STh) and uroguanylin have been shown to have antiproliferative effects on human colorectal cancer cells (*9, 10*) and have demonstrated efficacy in the treatment of colorectal cancers in animal models (*11*). Mecha-

* Corresponding author. Michael F. Giblin, Ph.D., Department of Radiology, University of Missouri-Columbia, A004 Research Service, HSTMVH, 800 Hospital Dr., Columbia, MO 65201. Phone: (573) 814-6000 x53669. Fax: (573) 882-1663. E-mail: giblinm@health.missouri.edu.

[†] Harry S. Truman Memorial Veterans Administration Hospital.

[‡] Department of Radiology, University of Missouri-Columbia.

[§] Department of Internal Medicine, University of Missouri-Columbia.

[||] Department of Medical Pharmacology and Physiology, University of Missouri-Columbia.

[⊥] Radiopharmaceutical Sciences Institute, University of Missouri-Columbia.

10.1021/bc900513u © 2010 American Chemical Society
Published on Web 06/10/2010

nistically, agonist binding to GC-C stimulates production of intracellular cyclic guanosine 3′,5′-monophosphate (cGMP), which can lead to either cell cycle arrest (*9*) or apoptosis (*11*). A substantial body of experimental evidence supports the concept that the intracellular signaling pathway regulated by the second messenger molecule cGMP may be a therapeutic target for the treatment of colon cancer as well as other malignant tumors (*12*−*15*). STh-based imaging agents could therefore be useful for assessment of GC-C receptor status in colorectal cancer metastases, thus defining subsets of patients who may benefit from GC-C agonist-based adjuvant therapy.

Although ^{111}In- and ^{99m}Tc-labeled GC-C agonists have shown promise as SPECT imaging agents (*16*−*18*), peptides in this class have not as yet been exploited for PET imaging. Existing previously characterized constructs have employed an N-terminal DOTA macrocycle for coordination of ^{111}In (*17, 18*) and could easily be employed for M^{2+} or M^{3+} PET radionuclides such as ^{64}Cu, ^{86}Y, and ^{68}Ga. In the case of ^{64}Cu, extensive research using diverse targeting vectors has documented some degree of in vivo instability of ^{64}Cu-DOTA complexes, giving rise to observations of increased uptake in nontarget tissues such as liver (*19, 20*). The azomacrocyclic chelator TETA has often been used in ^{64}Cu radiopharmaceuticals in preference to DOTA, since the larger TETA macrocycle forms a more stable Cu(II) complex (*19, 21*). However, ^{64}Cu-TETA complexes have also demonstrated in vivo instability, resulting in uptake of free ^{64}Cu by cytosolic proteins such as superoxide dismutase (*22*−*24*). These findings have catalyzed continuing research into the development of ^{64}Cu chelators with increased stability in vivo (*20, 22*−*25*). In this study, we have compared three different macrocyclic chelating systems for the coordination of ^{64}Cu combined with an analogue of the *E. coli* heat-stable enterotoxin, to address the hypothesis that ^{64}Cu-labeled GCC agonists could be effective PET agents for in vivo imaging of GC-C receptor status.

MATERIALS AND METHODS

Reagents. The peptide F^{19}-STh(2−19) was obtained from Bachem (King of Prussia, PA) and used as received. 1,4,8,11-Tetraazacyclododecane-*N*,*N*′,*N*″,*N*‴-tetraacetic acid (TETA) and the NHS ester of 1,4,7,10-tetraazacyclododecane-*N*,*N*′,*N*″,*N*‴-tetraacetic acid (DOTA) were obtained from Macrocyclics, Inc. 1,4,7-Triazacyclononane-*N*,*N*′,*N*″-triacetic acid (NOTA) was synthesized as previously described (*25*). All solvents were either ACS certified or HPLC-grade solvents obtained from Fischer Scientific and used as received. MALDI-TOF mass spectral analyses were performed by the Proteomics Center at the University of Missouri-Columbia. ^{64}Cu ($T_{1/2}$ 12.7 h, β^+, 17.4%, $E_{\beta+\max}$, 656 keV; β^-, 39%, $E_{\beta-\max}$, 573 keV) was obtained from Trace Life Sciences or from the cyclotron facility at the University of Wisconsin-Madison. T-84 human colon cancer cells were obtained from American Type Culture Collection (ATCC) and maintained and grown for use in these studies in the University of Missouri Cell and Immunology Core facilities.

Synthesis and Purification of Chelator-Peptide Conjugates. Folded *E. coli* heat-stable enterotoxin analogues were N-terminally labeled with the DOTA chelating moiety via incubation with the NHS ester of DOTA at 100-fold molar excess at 4 °C overnight in 0.3 M HEPES, pH 8.5. TETA and NOTA conjugations were performed by in situ formation of the activated esters using a 100-fold molar excess of EDC and sulfo-NHS in 0.2 M sodium phosphate buffer, pH 8.0. Polyaminocarboxylate-conjugated peptides were purified by reversed-phase high-performance liquid chromatography (RP-HPLC). HPLC was performed using a Shimadzu system with SCL-10A controller, LC-20AT pumps, and in-line SPD-20A UV−vis/NaI solid crystal scintillation detectors. Column temperature was maintained at 37 °C using an Eppendorf TC-50 column heater, and data acquisition took place with *EZstart* software version 7.4 (Shimadzu). HPLC solvents consisted of H_2O containing 0.1% trifluoroacetic acid (Solvent A) and acetonitrile containing 0.1% trifluoroacetic acid (Solvent B). Conditions: A Phenomenex Jupiter C-18 (5 μm, 300 Å, 4.6 × 250 mm) column was used with a flow rate of 1.5 mL/min. Gradient purification of compounds is achieved during a linear 30 min ramp from 23% B to 33% B, followed by column rinse and reequilibration. Masses of each peptide conjugate were confirmed postpurification by MALDI-TOF MS analysis (DOTA-F^{19}-STh(2−19) $(M+H)^+$ Calc. = 2297.6, Obs. = 2297.8; TETA-F^{19}-STh(2−19) $(M+H)^+$ Calc. = 2325.6, Obs. = 2325.9; NOTA-F^{19}-STh(2−19) $(M+H)^+$ Calc. = 2196.6, Obs. = 2196.8.).

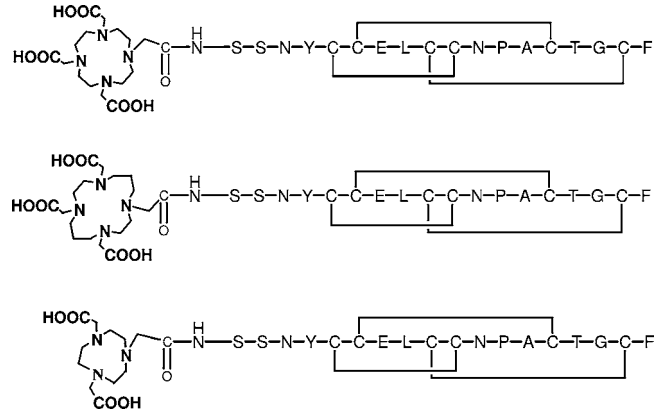


Figure 1. Structures of STh analogues. Top: DOTA-F^{19}-STh(2−19). Middle: TETA-F^{19}-STh(2−19). Bottom: NOTA-F^{19}-STh(2−19).

Radiolabeling. F^{19}-STh(1−19) was iodinated by a modified lactoperoxidase method. Briefly, 2 μg peptide was suspended in 50 μL 100 mM sodium phosphate buffer, pH 7.5, containing 2 μg lactoperoxidase and 10−20 MBq Na^{125}I. The reaction was initiated by addition of 2 μL of a 1:10 000 dilution 30% H_2O_2. The reaction was incubated 30 min at room temperature with occasional mixing, then diluted with dH_2O and purified to homogeneity by RP-HPLC.

For the synthesis of ^{64}Cu-labeled peptides, aliquots of $^{64}CuCl_2$ (7.4−74 MBq, 4−40 μL) were added to solutions of DOTA-, TETA-, and NOTA-F^{19}-STh(2−19) (2−5 μg) in 0.4 M ammonium acetate (200 μL). The pH of the reaction mixture was adjusted to 6.0. The reaction mixture was incubated for 1 h at 80 °C. After 1 h, an aliquot of 2 mM EDTA (50 μL) was added to the reaction mixture to complex unreacted $^{64}Cu^{2+}$. Radiochemical yields were typically >70%, with higher yields obtainable with increasing peptide concentration in the reaction mix. The resulting radiolabeled conjugates were purified to homogeneity by RP-HPLC. All purified ^{64}Cu-STh conjugates were then concentrated by passing through a 3M Empore C-18 HD high performance extraction disk (7 mm/3 mL) cartridge and eluting with 50% ethanol in 0.1 M NaH_2PO_4 buffer (500 μL). The concentrated fractions were then reduced in volume under a stream of $N_{2(g)}$, and finally diluted with 0.1 M NaH_2PO_4 buffer, pH 7.0, to a final activity of approximately 74 kBq/100 μL. Calculated specific activities of ^{64}Cu-radiotracers ranged between 240 and 1200 Ci/mmol.

In Vitro Cell Binding Studies. IC_{50}s of DOTA-, TETA-, and NOTA-F^{19}-STh(2−19) were determined by a competitive displacement cell binding assay using ^{125}I−F^{19}-STh(1−19). Briefly, 3 × 10^6 cells suspended in DMEM/F-12 media containing 15 mM MES and 0.2% BSA, pH 5.5, were incubated at 37 °C for 1 h in the presence of approximately 20 000 cpm ^{125}I-tracer and increasing concentrations of STh peptides. After the incubation, the reaction medium was aspirated and cells were

washed three times with media. The radioactivity bound to the cells was counted in a Wallac Wizard 1480 gamma counting system. The percentage of $^{125}I-F^{19}$-STh(1−19) bound to cells was plotted vs increasing concentrations of peptides to determine the respective IC_{50} values. For statistical considerations, three separate in vitro cell-binding experiments with each analogue were performed in duplicate. IC_{50} calculations were performed using the four-parameter logistic model within *GraphPad Prism*.

In vitro studies to measure rates of internalization and efflux of labeled compounds in T-84 human colon carcinoma cells were carried out as described previously (*17*). For internalization measurements, 3×10^6 cells suspended in DMEM/F-12 media containing 15 mM MES and 0.2% BSA, pH 5.5, were incubated for varying times at 37 °C with 30 000−60 000 cpm ^{64}Cu-labeled peptides. At designated times, binding media was aspirated, and cells were washed 3× with 4 °C binding media, then washed 2× with 4 °C acid/saline solution (0.5 M NaCl, 1.2% CH_3COOH). The activity of the acid/saline rinse and the cell pellet were determined and represent surface and internalized activity, respectively. For efflux experiments, all samples were initially incubated for 1 h under the above conditions, then washed 3× with 37 °C binding media to remove free label. The initial ($t = 0$) sample was then washed 3× with 4 °C binding media, then 2× with 4 °C acid/saline wash. Subsequent time points were treated identically, with surface and internalized activity determined as above.

Biodistribution Studies. Four- to five-week-old female ICR SCID (severe combined immunodeficient) outbred mice were obtained from Taconic (Germantown, NY). The mice were housed four animals per cage in sterile micro isolator cages in a temperature- and humidity-controlled room with a 12 h light/12 h dark schedule. The animals were fed sterile rodent chow (Ralston Purina Company, St. Louis, MO) and water ad libitum. Animals were housed one week prior to inoculation of tumor cells and anesthetized for injections with isoflurane (Minrad, Inc.) at a rate of 2.5% with 0.4 L/min oxygen through a nonrebreathing anesthesia vaporizer.

Human T-84 colorectal carcinoma cells were injected on the subcutaneous (s.c.) flank with $(5-10) \times 10^6$ cells in a suspension of 100 μL 3:1 phosphate buffered saline/matrigel (BD Biosciences) per injection site. T-84 cells were allowed to grow in vivo four to six weeks postinoculation, developing tumors ranging in sizes from 0.06 to 0.30 g. Mice (average weight, 25 g) were injected with aliquots (50−100 μL) of radiolabeled peptide solutions (55−90 kBq) via the tail vein. To demonstrate the specificity of tumor localization, blocking studies were carried out in which ^{64}Cu-NOTA-F^{19}-STh(2−19) was coinjected with 2 mg/kg unlabeled F^{19}-STh(2−19). Tissues, organs, and tumors were excised from animals sacrificed at 1 and 4 h p.i., weighed, and counted. Radioactivity was measured in a Wallac 1480 automated gamma counter and the percent injected dose per gram tissue was calculated. Differences in organ uptake between labeled constructs were analyzed by Student's *t* test. Differences at the 95% confidence level ($P < 0.05$) were considered significant. Animal studies were conducted in accordance with the highest standards of care as outlined in the NIH guide for Care and Use of Laboratory Animals and the Policy and Procedures for Animal Research at the Harry S. Truman Memorial Veterans' Hospital and according to approved protocols.

MicroPET/microCT Imaging. MicroPET imaging was performed using a MOSAIC small-animal PET unit (Philips, USA). The unit has a gantry port diameter of 21 cm, a transverse field of view (FOV) of 12.8 cm and an axial length of 11.6 cm. The microPET scanner operates in a 3D volume imaging acquisition mode facilitating measurements of relative changes in radiotracer pharmacokinetics in vivo either as in frame, sequential, or dynamic scanning capabilities. Small animals are frequently laser-aligned at the center of the scanner FOV for subsequent imaging. SCID mice bearing T84 human colorectal cancer tumor xenografts were injected intravenously with 10.1 MBq, 36.4 MBq, and 13.9 MBq ^{64}Cu-DOTA-, ^{64}Cu-TETA-, and ^{64}Cu-NOTA-F^{19}-STh(2−19), respectively. 0.8, 2.1, and 1.0 MBq of activity remained in each animal, respectively, at the time of image acquisition (1 h pi). Tumor bearing mice were imaged and data collected using an emission scan protocol, and image reconstruction was performed with the use of a 3D row action maximum likelihood algorithm (RAMLA) without tissue attenuation correction. The MicroPET data were filtered with a 1.1 mm Gaussian fwhm filter. The MicroCT unit (MicroCAT II CT/SPECT, Siemens Pre-Clinical Solutions, Knoxville, TN) consists of a CCD X-ray detector and an 80 kVp microfocus X-ray source (40 μm focal spot). MicroCT imaging was performed preceding microPET imaging for the purpose of anatomic/molecular data fusion and concurrent microCT image reconstruction was achieved with the use of a Fanbeam (Feldkamp) Filtered back projection algorithm. Co-registration, visualization, and image analysis of PET/CT data was achieved with the use of the *Amira 3.1* software package (TGS, Germany).

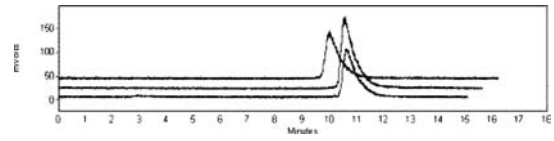


Figure 2. C18 RP-HPLC chromatograms of purified ^{64}Cu-labeled peptides. Upper: ^{64}Cu-NOTA-F^{19}-STh(2−19), Tr = 10.0 min. Middle: ^{64}Cu-DOTA-F^{19}-STh(2−19), Tr = 10.5 min. Lower: ^{64}Cu-TETA-F^{19}-STh(2−19), Tr = 10.6 min.

RESULTS

The polyaminocarboxylate chelating moieties DOTA, TETA, and NOTA were appended to the N-terminus of F^{19}-STh(2−19) via NHS ester activation. The addition of DOTA was carried out using a commercially available NHS ester of DOTA, while TETA and NOTA were appended via in situ NHS ester activation using a 100-fold excess of sulfo NHS and EDC in aqueous solution. Addition of TETA and DOTA to the N-terminus of F^{19}-STh(2−19) resulted in 0.5−0.6 min shifts to earlier retention times, respectively, while addition of NOTA resulted in a retention time of 0.4 min later, as assessed by C18 RP-HPLC. The identity of each conjugate was confirmed postpurification by MALDI-TOF mass spectral analyses.

Each peptide conjugate was subsequently radiolabeled with ^{64}Cu and purified by C18 RP-HPLC (Figure 2). Radiolabeling efficiencies observed for each peptide were typically in the range 70−80%, with quantitative radiolabeling achievable with the use of higher concentrations of peptide substrate. Coordination of ^{64}Cu by DOTA and TETA macrocycles resulted in radiolabeled STh analogues, which coeluted with unlabeled peptides, while ^{64}Cu-labeling of the NOTA peptide resulted in a retention time 1.3 min earlier than the unlabeled NOTA-peptide.

Affinities of each conjugate for GC-C were measured in vitro in a competitive radioligand binding assay using $^{125}I-F^{19}$-STh(1−19) and intact T84 human colorectal cancer cells. Incorporation of each chelating macrocycle at the N-terminus of the targeting peptide had minimal impact on measured receptor binding affinities (Figure 3). Binding affinities for the three peptide conjugates were 3.2 ± 1.9, 2.0 ± 0.5, and 1.2 ± 0.4 nM for DOTA-, TETA-, and NOTA-F^{19}-STh(2−19), respectively, similar to the previously reported value of 2.2 ± 0.4 nM for the unmodified F^{19}-STh(2−19) molecule (*18*).

Internalization and efflux studies were also performed with each ^{64}Cu-labeled peptide. The fraction of internalized radio-

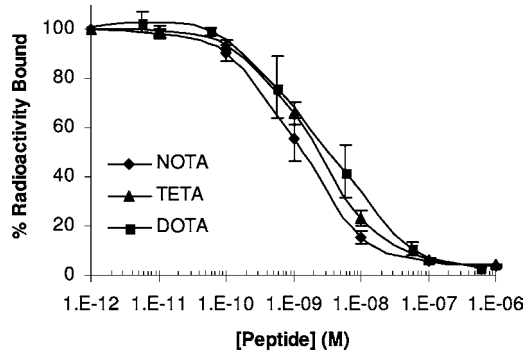


Figure 3. Measurement of F^{19}-STh(2−19) peptide conjugate IC_{50} values in a competitive receptor-binding assay with ^{125}I−F^{19}-STh(1−19) using cultured T84 human colorectal cancer cells.

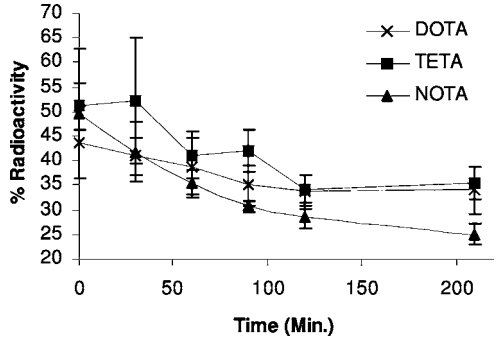


Figure 4. Determination of % efflux of radioactivity from T-84 human colon carcinoma cells for ^{64}Cu-DOTA-F^{19}-STh(2−19), ^{64}Cu-TETA-F^{19}-STh(2−19), and ^{64}Cu-NOTA-F^{19}-STh(2−19).

Table 1. Biodistribution of ^{64}Cu-DOTA-, ^{64}Cu-TETA-, and ^{64}Cu-NOTA-F^{19}-STh(2−19) (%ID/g (±SD), $N = 4$) at 1 h pi in SCID Mice Bearing T-84 Human Colorectal Cancer Tumor Xenografts

organ	DOTA	TETA	NOTA
blood	0.57 (0.21)	0.76 (0.25)	0.48 (0.22)
heart	0.28 (0.14)	0.25 (0.08)	0.20 (0.10)
lung	0.79 (0.33)	0.82 (0.18)	1.00 (0.73)
liver	1.21 (0.65)	0.49 (0.15)	0.36 (0.13)
spleen	0.29 (0.30)	0.20 (0.11)	0.10 (0.09)
intestine	0.98 (0.49)	0.64 (0.13)	0.59 (0.20)
kidney	6.52 (2.74)	11.36 (2.85)	3.67 (1.60)
muscle	0.11 (0.05)	0.12 (0.06)	0.09 (0.03)
bone	0.08 (0.17)	0.05 (0.05)	0.06 (0.09)
tumor	1.33 (0.52)	1.37 (0.27)	1.18 (0.40)

activity for each ^{64}Cu-labeled peptide was similar over time, with 45.1 ± 7.2%, 43.6 ± 3.6%, and 49.1 ± 2.7% of total cell-associated radioactivity internalized at 100 min for DOTA, NOTA, and TETA constructs, respectively. The degree of residualization of ^{64}Cu within cells was also not significantly different between DOTA- and TETA-labeled peptides. However, ^{64}Cu-NOTA-F^{19}-STh(2−19) demonstrated an increased rate of efflux from T84 cells in vitro (Figure 4).

Biodistribution studies of ^{64}Cu-labeled peptides were conducted in SCID mice bearing T84 human colorectal cancer tumor xenografts. At 1 h pi, all three bioconjugates showed rapid elimination via the renal/urinary route, with 88.6 ± 4.3%, 85.1 ± 5.8%, and 91.7 ± 2.6% ID in urine for DOTA, TETA, and NOTA peptides, respectively. Tumor uptake of all three peptides was similar, with 1.18−1.37%ID/g in tumor tissue. At 1 h pi, uptake in tumor for each construct was higher than for all other normal tissues with the exception of kidney (Table 1). Blocking studies, carried out by coadministration of unlabeled F^{19}-STh(2−19), reduced accumulation of the NOTA conjugate in tumor tissue by ∼42% ($p < 0.05$), comparable to previous results obtained for this class of peptides (*17, 18*). Kidney uptake values at 1 h pi for the NOTA conjugate (3.7 ± 1.6%ID/g) were lower than for either the DOTA (6.5 ± 2.7%ID/g) or TETA (11.4 ± 2.9%ID/g) constructs (Table 1, Figure 5). Uptake in liver was also lower for the NOTA conjugate (0.36 ± 0.13%ID/g) than for either the DOTA (1.21 ± 0.67%ID/g) or TETA (0.49 ± 0.15%ID/g) constructs (Table 1, Figure 5). Resulting tumor/normal tissue ratios for the three conjugates ranged 1.8−2.5 for blood, 11.4−13.1 for muscle, 1.1−3.3 for liver, and 0.12−0.32 for kidney, with the NOTA conjugate yielding the highest ratio in each instance.

At 4 h pi, >94% of all three ^{64}Cu-labeled peptides had been excreted into urine. Kidney uptake for all three compounds was significantly ($p < 0.05$) reduced, with 57−62% lower uptake relative to 1 h pi. Tumor and blood %ID/g values for both the TETA- and NOTA-peptides were significantly lower than at 1 h pi, while these values for the DOTA-peptide were not ($p < 0.05$). Tumor uptake of the three labeled peptides ranged 0.58−0.83%ID/g. Tumor/blood, tumor/muscle, and tumor/liver ratios for the three conjugates ranged 3.5−11.8, 15−29, and 0.8−1.5, respectively.

The results of small-animal microPET/microCT imaging experiments performed on SCID mice bearing hind flank T84 human colorectal cancer tumor xenografts are shown in Figure 6. Images obtained using DOTA, TETA, and NOTA conjugates at 1 h pi demonstrate their potential as site-directed PET agents for in vivo characterization of GC-C-expressing colorectal cancers. These images visually recapitulate the in vivo biodistribution results at the same time point, with tumor uptake clearly visualized in each case. Uptake in nontarget tissues is also evident to varying extents, with uptake in liver most evident for the DOTA conjugate, as predicted from biodistribution data (Table 1).

DISCUSSION

Stable in vivo complexation of ^{64}Cu in the context of receptor-targeted radiopharmaceuticals is essential for minimization of off-target uptake in normal tissues such as liver and kidneys with concomitant maximization of receptor-mediated tumor uptake. While the cyclam- and cyclen-based chelating backbones, TETA and DOTA have been most commonly used for ^{64}Cu-coordination in targeted radiopharmaceuticals, other polyaminocarboxylate macrocycles have been extensively studied for their increased kinetic inertness to both H^+-mediated Cu(II) dissociation and protein transchelation (*24*). Among these alternative chelators, both cross-bridged DOTA- and TETA-based chelators and the nine-membered NOTA macrocycle have been found to offer increased resistance to in vitro and in vivo ^{64}Cu demetalation (*22, 25, 26*).

Characterization of the three ^{64}Cu-labeled heat-stable enterotoxin peptides demonstrated significantly earlier elution of the NOTA compound from a C18 RP-HPLC column relative to the DOTA and TETA peptides. In the ^{64}Cu-NOTA peptide, each of two carboxylate arms is thought to be involved in metal coordination, resulting in a neutral complex (*25*). DOTA and TETA peptides, by contrast, each possess a free carboxylate arm, resulting in metal centers with an overall net −1 charge (*21, 27*).

Several differences exist between in vivo biodistribution patterns of ^{64}Cu-DOTA-F^{19}-STh(2−19) and the previously described ^{111}In-complex of this DOTA-peptide (*18*). At 1 h pi, tumor uptake of ^{64}Cu-DOTA-F^{19}-STh(2−19) was significantly lower than that of ^{111}In-DOTA-F^{19}-STh(2−19) (1.33 ± 0.52%ID/g vs 2.35 ± 0.43%ID/g, respectively). Simultaneously, the liver uptake of the ^{64}Cu-labeled peptide was higher than for the ^{111}In-complex (1.21 ± 0.65 vs 0.2 ± 0.09, respectively). At 4 h pi, both ^{111}In- and ^{64}Cu-DOTA-F^{19}-STh(2−19) were retained in tumor to a similar degree (0.74 ± 0.1%ID/g vs 0.83 ± 0.3%ID/

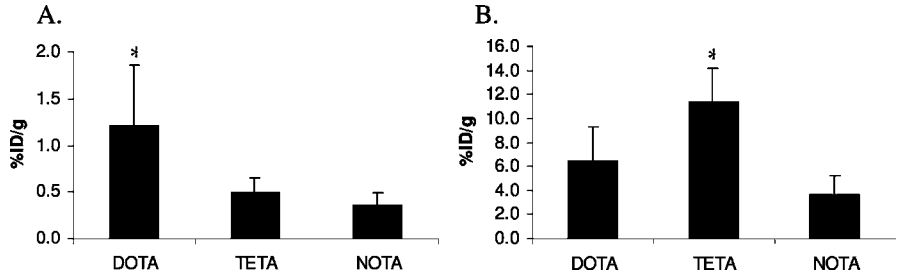


Figure 5. Differences in (A) liver and (B) kidney uptake among ^{64}Cu-DOTA-, ^{64}Cu-TETA-, and ^{64}Cu-NOTA-F^{19}-STh(2−19) at 1 h pi (* $p < 0.05$ vs NOTA).

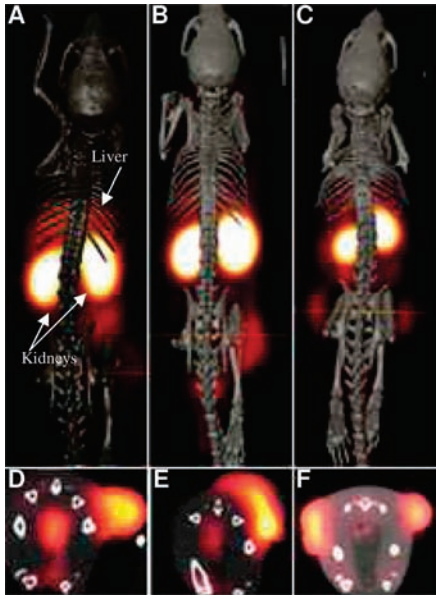


Figure 6. PET/CT images of SCID mice bearing hind flank T84 human colorectal cancer tumor xenografts 1 h postinjection of 10−36 MBq labeled peptides in three-dimensional views (A−C) and as transaxial sections (D−F). ^{64}Cu-DOTA-F^{19}-STh(2−19) (A,D), ^{64}Cu-TETA-F^{19}-STh(2−19) (B,E), and ^{64}Cu-NOTA-F^{19}-STh(2−19) (C,F). Pictured data has been normalized to the highest pixel intensity within each image. Axial cross sections through tumor xenografts are shown as red horizontal lines in A−C.

Table 2. Biodistribution of ^{64}Cu-DOTA-, ^{64}Cu-TETA-, and ^{64}Cu-NOTA-F^{19}-STh(2−19) (%ID/g (±SD), $N = 3$) at 4 h pi in SCID Mice Bearing T-84 Human Colorectal Cancer Tumor Xenografts

organ	DOTA	TETA	NOTA
blood	0.24 (0.24)	0.07 (0.03)	0.05 (0.01)
heart	0.21 (0.17)	0.06 (0.01)	0.04 (0.06)
lung	0.54 (0.35)	0.28 (0.13)	0.17 (0.04)
liver	1.07 (0.80)	0.47 (0.13)	0.40 (0.06)
spleen	0.26 (0.29)	0.08 (0.11)	0.15 (0.12)
intestine	0.69 (0.37)	0.48 (0.12)	0.57 (0.04)
kidney	2.81 (1.37)	4.34 (0.10)	1.47 (0.37)
muscle	0.03 (0.03)	0.02 (0.01)	0.04 (0.04)
bone	0.15 (0.25)	0.04 (0.03)	0.002 (0.003)
tumor	0.83 (0.30)	0.58 (0.12)	0.59 (0.11)

g, respectively). This was due to slower washout of ^{64}Cu-labeled peptides from tumor tissue—42−62% of 1 h ^{64}Cu activity remained in tumor at 4 h pi, contrasted with only 31% of ^{111}In activity. Uptake in liver of the ^{111}In-labeled peptide at 4 h pi was only 0.07 ± 0.01%ID/g, while 88% of ^{64}Cu activity in liver tissue at 1 h pi remained at 4 h pi (1.07 ± 0.8%ID/g, Table 2). The 6−15-fold higher accumulation of the ^{64}Cu-DOTA-labeled peptide in liver is likely due to instability of the ^{64}Cu-DOTA complex, with transchelation of ^{64}Cu by proteins such as superoxide dismutase, ceruloplasmin, serum albumin, and metallothionein (*22*). Similar results have previously been observed in the context of other peptide radiopharmaceuticals (*20*, *28*), and great effort has been put toward the development of alternate Cu-chelating frameworks (*19*−*25*).

The major distinguishing characteristic among the ^{64}Cu-DOTA, ^{64}Cu-TETA, and ^{64}Cu-NOTA peptides in vivo relates not to tumor uptake, but to uptake in nontarget tissues such as liver and kidney (Figure 5, Figure 6). The ^{64}Cu-NOTA conjugate displays significantly lower liver uptake at 1 h pi than the ^{64}Cu-DOTA conjugate. Although experiments to characterize products of in vivo metabolism were not carried out in this work, one possible explanation for this could be increased in vivo kinetic stability of the ^{64}Cu-NOTA complex (*25*, *26*). Previously published studies have demonstrated similar effects in the context of other receptor-targeted radiopharmaceuticals containing cross-bridged macrocyclic chelators for the coordination of Cu-64 (*20*, *23*, *24*). The ^{64}Cu-NOTA conjugate also displays lower kidney uptake at 1 and 4 h pi than either the ^{64}Cu-TETA or the ^{64}Cu-DOTA conjugates. This difference is most probably due to the differences in formal charge between these species. ^{64}Cu-TETA and ^{64}Cu-DOTA conjugates possess an additional negatively charged carboxylate group at physiological pH relative to ^{64}Cu-NOTA conjugates, which can increase tubular reabsorption of radiolabeled peptides following glomerular filtration (*29*). Previous studies have also shown higher kidney uptake for ^{64}Cu-DOTA/^{64}Cu-TETA peptides in comparison with ^{64}Cu-TETA peptides, which again is correlated with the formal charge of the Cu complexes (*20*, *23*).

MicroPET/CT images obtained with each radioconjugate at 1 h pi (Figure 6) essentially recapitulate the in vivo biodistribution results. T84 tumor xenografts are clearly visualized in the normalized images, with only kidney uptake more clearly evident. Both ^{64}Cu-TETA and ^{64}Cu-NOTA conjugates display decreased liver uptake with respect to the ^{64}Cu-DOTA conjugate. Similarly, the markedly reduced kidney uptake of the ^{64}Cu-NOTA conjugate relative to the ^{64}Cu-TETA conjugate in the normalized images also reflects the in vivo biodistribution results.

CONCLUSION

This study demonstrates the utility of ^{64}Cu-labeled heat-stable enterotoxin analogues as PET imaging agents for the in vivo detection of colorectal cancers expressing GC-C. Employment of the NOTA chelator in this context gave superior tumor/liver and tumor/kidney ratios relative to DOTA- and TETA-functionalized peptides, respectively. This class of PET imaging agents could prove useful in stratification of subpopulations of individuals who may benefit from treatment with GC-C-targeted therapeutics.

ACKNOWLEDGMENT

This material is the result of work supported with resources and the use of facilities at the Harry S. Truman Memorial Veterans' Administration Hospital, Columbia, MO 65201, and

the University of Missouri-Columbia School of Medicine Department of Radiology, Columbia, MO 65211. This work was supported by a United States Department of Veterans' Affairs VA Merit Award, and by a National Cancer Institute Center grant (1 P50 CA103130-01).

LITERATURE CITED

(1) Jemal, A., Siegel, R., Ward, E., Hao, Y., Xu, J., Murray, T., and Thun, M. J. (2008) Cancer Statistics, 2008. *CA Cancer J. Clin. 58*, 71–96.

(2) Gruenberger, B., Tamandl, D., Schueller, J., Scheithauer, W., Zielinski, C., Herbst, F., and Gruenberger, T. (2008) Bevacizumab, capecitabine, and oxaliplatin as neoadjuvant therapy for patients with potentially curable metastatic colorectal cancer. *J. Clin. Oncol. 26*, 1830–1835.

(3) Kelly, H., and Goldberg, R. M. (2005) Systemic therapy for metastatic colorectal cancer: current options, current evidence. *J. Clin. Oncol. 23*, 4553–4560.

(4) Meyerhardt, J. A., and Mayer, R. J. (2005) Systemic therapy for colorectal cancer. *N. Engl. J. Med. 352*, 476–487.

(5) Ellis, L. M. (2005) Bevacizumab. *Nat. Rev. Drug Discovery 4*, S8–S9.

(6) Goldberg, R. M. (2005) Cetuximab. *Nat. Rev. Drug Discovery 4*, S10–S11.

(7) Peeters, M., Price, T., and Van Laethem, J. L. (2009) Anti-epidermal growth factor receptor monotherapy in the treatment of metastatic colorectal cancer: where are we today? *Oncologist 14*, 29–39.

(8) Waldman, S. A., Hyslop, T., Schulz, S., Barkun, A., Nielsen, K., Haaf, J., Bonaccorso, C., Li, Y., and Weinberg, D. S. (2009) Association of GUCY2C expression in lymph nodes with time to recurrence and disease-free survival in pN0 colorectal cancer. *JAMA 301*, 745–752.

(9) Pitari, G. M., Di Guglielmo, M. D., Park, J., Schulz, S., and Waldman, S. A. (2001) Guanylyl cyclase C agonists regulate progression through the cell cycle of human colon carcinoma cells. *Proc. Natl. Acad. Sci. U.S.A. 98*, 7846–7851.

(10) Pitari, G. M., Zingman, L. V., Hodgson, D. M., Alekseev, A. E., Kazerounian, S., Bienengraeber, M., Hajnóczky, G., Terzic, A., and Waldman, S. A. (2003) Bacterial enterotoxins are associated with resistance to colon cancer. *Proc. Natl. Acad. Sci. U.S.A. 100*, 2695–2699.

(11) Shailubhai, K., Yu, H. H., Karunanandaa, K., Wang, J. Y., Eber, S. L., Wang, Y., Joo, N. S., Kim, H. D., Miedema, B. W., Abbas, S. Z., Boddupalli, S. S., Currie, M. G., and Forte, L. R. (2000) Uroguanylin treatment suppresses polyp formation in the ApcMin/+ mouse and induces apoptosis in human colon adenocarcinoma cells via cyclic GMP. *Cancer Res. 60*, 5151–5157.

(12) Liu, L., Li, H., Underwood, T., Lloyd, M., David, M., Sperl, G., Pamukcu, R., and Thompson, W. J. (2001) Cyclic GMP-dependent protein kinase activation and induction by exisulind and cp461 in colon tumor cells. *J. Pharmacol. Exp. Ther. 299*, 583–592.

(13) Goluboff, E. T., Shabsigh, A., Saidi, J. A., Weinstein, I. B., Mitra, N., Heitjan, D., Piazza, G. A., Pamukcu, R., Buttyan, R., and Olsson, C. A. (1999) Exisulind (sulindac sulfone) suppresses growth of human prostate cancer in a nude mouse xenograft model by increasing apoptosis. *Urology 53*, 440–445.

(14) Vesely, D. L., Clark, L. C., Garces, A. H., McAfee, Q. W., Soto, J., and Gower, W. R., Jr. (2004) Novel therapeutic approach for cancer using four cardiovascular hormones. *Eur. J. Clin. Invest. 24*, 674–682.

(15) Pitari, G. M., Baksh, R. I., Harris, D. M., Li, P., Kazerounian, S., and Waldman, S. A. (2005) Interruption of homologous desensitization in cyclic guanosine 3′5′-monophosphate signaling restores colon cancer cytostasis by bacterial enterotoxins. *Cancer Res. 65*, 11129–11135.

(16) Wolfe, H. R., Mendizabal, M., Lleong, E., Cuthbertson, A., Desai, V., Pullan, S., Fujii, D. K., Morrison, M., Pither, R., and Waldman, S. A. (2002) In vivo imaging of human colon cancer xenografts in immunodeficient mice using a guanylyl cyclase C-specific ligand. *J. Nucl. Med. 43*, 392–399.

(17) Giblin, M. F., Gali, H., Sieckman, G. L., Owen, N. K., Hoffman, T. J., Forte, L. R., and Volkert, W. A. (2004) In vitro and in vivo comparison of human Escherichia coli heat-stable peptide analogues incorporating the ^{111}In-DOTA group and distinct linker moieties. *Bioconjugate Chem. 15*, 872–880.

(18) Giblin, M. F., Sieckman, G. L., Watkinson, L. D., Figueroa, S. D., Hoffman, T. J., Forte, L. R., and Volkert, W. A. (2006) Selective targeting of E. coli heat-stable enterotoxin analogs to human colon cancer cells. *Anticancer Res. 26*, 3243–3251.

(19) Jones-Wilson, T. M., Deal, K. A., Anderson, C. J., McCarthy, D. W., Kovacs, Z., Motekaitis, R. J., Sherry, A. D., Martell, A. E., and Welch, M. J. (1998) The in vivo behavior of copper-64-labeled azamacrocyclic complexes. *Nucl. Med. Biol. 25*, 523–530.

(20) Garrison, J. C., Rold, T. L., Sieckman, G. L., Figueroa, S. D., Volkert, W. A., Jurisson, S. S., and Hoffman, T. J. (2007) In vivo evaluation and small-animal PET/CT of a prostate cancer mouse model using 64Cu bombesin analogs: side-by-side comparison of the CB-TE2A and DOTA chelation systems. *J. Nucl. Med. 48*, 1327–1337.

(21) Anderson, C. J., Wadas, T. J., Wong, E. H., and Weisman, G. R. (2008) Cross-bridged macrocyclic chelators for stable complexation of copper radionuclides for PET imaging. (2008). *Q. J. Nucl. Med. Mol. Imaging 52*, 185–192.

(22) Boswell, C. A., Sun, X., Niu, W., Weisman, G. R., Wong, E. H., Rheingold, A. L., and Anderson, C. J. (2004) Comparative in vivo stability of copper-64-labeled cross-bridged and conventional tetraazamacrocyclic complexes. *J. Med. Chem. 47*, 1465–1474.

(23) Sprague, J. E., Peng, Y., Sun, X., Weisman, G. R., Wong, E. H., Achilefu, S., and Anderson, C. J. (2004) Preparation and biological evaluation of copper-64-labeled tyr3-octreotate using a cross-bridged macrocyclic chelator. *Clin. Cancer Res. 10*, 8674–8682.

(24) Wadas, T. J., Wong, E. H., Weisman, G. R., and Anderson, C. J. (2007) Copper chelation chemistry and its role in copper radiopharmaceuticals. *Curr. Pharm. Des. 13*, 3–16.

(25) Prasanphanich, A. F., Nanda, P. K., Rold, T. L., Ma, L., Lewis, M. R., Garrison, J. C., Hoffman, T. J., Sieckman, G. L., Figueroa, S. D., and Smith, C. J. (2007) [64Cu-NOTA-8-Aoc-BBN(7−14)NH2] targeting vector for positron-emission tomography imaging of gastrin-releasing peptide receptor-expressing tissues. *Proc. Natl. Acad. Sci. U.S.A. 104*, 12462–12467.

(26) Pippen, C. G., Kumar, K., Mirzadeh, S., and Gansow, O. A. (1991) Kinetics of the isotopic exchange between copper (II) and copper (II) 1,4,7-triazacyclononane-N, N′, N″ triacetate. *J. Labelled Cmpds. Radiopharm. 30*, 221.

(27) Eiblmaier, M., Andrews, R., Laforest, R., Rogers, B. E., and Anderson, C. J. (2007) Nuclear uptake and dosimetry of 64Cu-labeled chelator somatostatin conjugates in an SSTr2-transfected human tumor cell line. *J. Nucl. Med. 48*, 1390–1396.

(28) Hoffman, T. J., Gali, H., Smith, C. J., Sieckman, G. L., Hayes, D. L., Owen, N. K., and Volkert, W. A. (2003) Novel series of ^{111}In-labeled bombesin analogs as potential radiopharmaceuticals for specific targeting of gastrin-releasing peptide receptors expressed on human prostate cancer cells. *J. Nucl. Med. 44*, 823–831.

(29) Vegt, E., van Eerd, J. E. M., Eek, A., Oyen, W. J., Wetzels, J. F., de Jong, M., Russel, F. G., Masereeuw, R., Gotthardt, M., and Boerman, O. C. (2008) Reducing renal uptake of radiolabeled peptides using albumin fragments. *J. Nucl. Med. 49*, 1506–1511.

BC900513U

Site Specific and Reversible Protein Immobilization Facilitated by A DNA Binding Fusion Tag

Meng Zhong, Jun Fang, and Yinan Wei*

Department of Chemistry, University of Kentucky, Lexington, Kentucky 40506-0055. Received December 6, 2009; Revised Manuscript Received June 15, 2010

Due to the complexity and diversity of protein structures, site-specific protein immobilization has always been challenging. On the contrary, DNA immobilization is straightforward with well established chemical methods. Single-strand DNA binding protein (SSB) binds tightly to single-stranded DNA (ssDNA). Herein, we investigated the feasibility of using SSB as a fusion tag to facilitate site-specific and reversible immobilization of target proteins. As a model system, we constructed a fusion protein by joining a superfolder green fluorescent protein (sfGFP) with SSB. The fluorescence emission and ssDNA binding affinity of the fusion protein were compared separately with those of the individual modules. Both modules fully retained their properties in the fusion construct. Next, we covalently attached ssDNA (dT_{37}) to a supporting matrix through either amine or thiol functionalization. The attached ssDNA mediated reversible sfGFP-SSB immobilization. The immobilized protein could be released through changes of conditions including pH, concentration of divalent cations, and the presence of the complementary dA_{35} oligonucleotide.

INTRODUCTION

Protein immobilization is an important first step for many applications including the construction of biosensors and protein microarrays, development of immunoassay methods, and employment of enzymes in biotechnology procedures (*1*−*4*). Protein immobilization methods can be categorized as nonspecific and site-specific. Nonspecific immobilization is usually achieved by physical adsorption or direct chemical reactions with amine, carboxyl, or thiol groups in the protein (*5, 6*). Because there are usually multiple copies of a given functional group in the target protein, it is difficult to control the extent of immobilization and orientation of the immobilized protein. In addition, chemical modification of functional groups within a protein may have negative impact on the protein's structure and function. This effect has been demonstrated by the decrease of protein activities upon immobilization in many cases (*7, 8*). On the other hand, physical adsorption is facilitated by the van der Waals, electrostatic and hydrophobic interactions (*9*). Such interactions are weak, which usually result in protein leaching.

A procedure that can produce a homogeneous, stable, and active protein layer on a specific surface is highly desirable. Many studies have investigated the use of affinity tags and fusion proteins for the purpose of site-specific and oriented protein immobilization. Proteins bind to specific affinity matrixes after being modified with the corresponding binding domains or tags. The polyhistidine tag (histag) is a popular choice and has been used in the immobilization of proteins on the metal affinity resins (*9*−*11*). However, there are limitations of the binding specificity of the metal affinity resin. For example, at least three *E. coli* endogenous proteins bind to the nickel nitrilotriacetic acid (Ni-NTA) resin (*12*). This limited selectivity could complicate the immobilization procedure. Other fusion tags have also being used to immobilize target proteins, including the glutathione S-transferase, maltose binding protein, chitin binding protein, streptag and metal binding peptide (*13*−*15*).

Compared to protein, oligonucleotides have simpler structure and chemical composition, which make them easier to modify in order to facilitate specific immobilization. Creation of DNA microarrays is an established and commercialized technique. The usage of DNA arrays to direct the assembly of proteins has attracted many research interests. In most of these studies, a ssDNA was first connected to the target protein, and then the DNA−protein conjugate was attached to a matrix modified with the complementary strand of that ssDNA (*15*−*19*). The DNA−protein conjugates have been obtained through direct covalent attachment (*20*−*25*), a biotin-streptavidin bridge (*26*), or the expressed protein ligation (*27*). RNA-protein fusions have also been constructed for site specific protein immobilization (*28, 29*). The formation of the DNA/RNA-protein conjugate requires chemical modification, which may have a negative impact on the protein activity. In a more recent study, protein capture by a DNA functionalized matrix was accomplished through the coiled-coil association of an engineered pair of heterodimeric leucine zippers. One helix of the zipper was chemically linked to the DNA, and the other helix was expressed as a fusion tag to the protein (*30*).

To eliminate the need of chemical modification of the target protein, we investigated the incorporation of a DNA binding protein as the fusion tag to direct the immobilization of the protein of interest. Recently Gang and co-workers had shown that surface-bound DNA could serve as anchoring sites to immobilize DNA binding proteins (*31*). Herein, we describe the construction of a fusion protein containing an N-terminus superfolder green fluorescent protein (sfGFP) and a C-terminus single-strand DNA binding protein (SSB). In this work, sfGFP was used as a reporter group to facilitate convenient characterization of protein immobilization, while SSB facilitated high affinity binding toward single-stranded DNA. The fusion protein sfGFP-SSB retained the properties from both domains, being fluorescent and binding to single stranded DNA. Next, we demonstrated that SSB could be used as a fusion tag to facilitate fast and convenient protein immobilization through the coupling

* To whom correspondence should be addressed. 305 Chemistry-Physics Building, University of Kentucky, Lexington, KY 40506-0055. Telephone: (859) 257-7085. Fax: (859) 323-1069. E-mail: yinan.wei@uky.edu.

10.1021/bc9005392 © 2010 American Chemical Society
Published on Web 06/28/2010

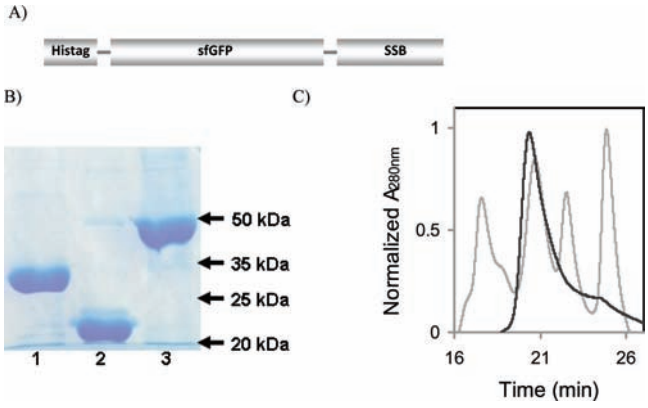


Figure 1. (A) The construct of the fusion protein, which contains a N-terminus histag, followed by sfGFP, and a C-terminus SSB. (B) SDS-PAGE analysis of purified sfGFP (lane 1), SSB (lane 2), and the sfGFP-SSB fusion protein (lane 3). Positions of the molecular weight markers are indicated by arrows. (C) Size exclusion chromatography analysis of the fusion protein (black trace). The gray trace is the molecular weight standard. From left to right, the peaks correspond to 670, 158, 44, and 17 kDa, respectively.

with a ssDNA modified surface. The bound protein could be eluted from the matrix without suffering from denaturation, and the DNA-modified surface could be regenerated.

EXPERIMENTAL PROCEDURES

Cloning, Protein Expression, and Purification. The SSB gene was amplified by polymerase chain reaction (PCR) using the *E. coli* genomic DNA as the template and primers 5′-GTACGGATCCATGGCCAGCAGAGGCGTAAACAAGGT-3′ (forward) and 5′-GTACCTCGAGTCAGAACGGAATGT-CATCATCAAAG-3′ (reverse). The PCR product was digested using *Bam*HI and XhoI, gel purified, and inserted into a similarly digested pET28a vector to generate plasmid pET28a-SSB. The sfGFP plasmid was obtained from Theranostech Inc. (Albuquerque, NM, USA). Gene encoding sfGFP was excised from the plasmid using restriction enzymes NdeI and *Bam*HI, and cloned into similarly digested pET28a or pET28a-SSB to generate pET28a-sfGFP and pET28a-sfGFP-SSB (Figure 1). All protein constructs contain a histag at the N-terminus of the proteins. The sequences of all cloned constructs were confirmed by DNA sequencing (Retrogen, CA, USA).

Plasmids pET28a-sfGFP-SSB, pET28a-sfGFP, and pET28a-SSB were used to transform *E. coli* strain ER2566 for protein production. The cells were grown at 37 °C in LB medium containing 100 μg/mL kanamycin to an $OD_{600\ nm}$ of 0.6, and then induced with 1 mM isopropyl-D-thiogalactopyranoside (IPTG). Three hours after induction, the cells were harvested by centrifugation at 7000 rpm for 10 min. The cell pellets were resuspended in a binding buffer (100 mM Tris-HCl, 0.5 M NaCl, and 10% glycerol, pH 8.1) and lysed by sonication on ice for 10 min with 10 s on−off intervals. The cell debris was removed by centrifugation at 12 000 rpm for 15 min. DNaseI was added to the cleared lysate to digest DNA at room temperature for 30 min. The cleared lysate was incubated with Ni-NTA resin (Qiagen, Huntsville, AL) with shaking at room temperature for 45 min before being loaded to an empty column. The resin was then washed with a buffer containing 100 mM Tris-HCl, 0.5 M NaCl, 10% glycerol, and 50 mM imidazole (pH 8.1). Finally, the protein was eluted with a buffer containing 100 mM Tris-HCl buffer, 0.5 M NaCl, 10% glycerol, and 500 mM imidazole (pH 8.1). Purified sfGFP-SSB, sfGFP, and SSB were dialyzed extensively against the binding buffer to remove excess imidazole.

The purified proteins were analyzed using the sodium dodecyl sulfate−polyacrylamide gel electrophoresis (SDS-PAGE) and visualized with Coomassie Blue stain. Protein concentrations were determined using the Bradford protein assay.

Fluorescence Spectroscopy. Fluorescence emission spectra were collected using a Perkin-Elmer LS-55 fluorescence spectrometer (PerkinElmer, Waltham, MA) at 20 °C. Fluorescence quenching titration was used to measure the binding affinity between sfGFP-SSB and ssDNA dT_{37}. All oligonucleotides were obtained from Integrated DNA Technology (San Diego, CA), including dT_{37}, dA_{35}, the 5′ amine-derivatized dT_{37} (H_2N-dT_{37}), and the 5′ thiol-derivatized dT_{37} (RSS-dT_{37}). dT_{37} was titrated into the protein solution and the tryptophan fluorescence was monitored at excitation and emission wavelengths of 282 and 357 nm, respectively. To measure the fluorescence of sfGFP, the excitation wavelength was 490 nm.

Protein Immobilization. H_2N-dT_{37} was attached to the N-hydroxysuccinimidyl-Sepharose resin (NHS resin) (Sigma-Aldrich, St. Louis, MO). The NHS resin was first washed with 100 mM sodium phosphate buffer (pH 7.4) and then incubated with H_2N-dT_{37} (25 μmol/L) at room temperature for 2 h. Finally, Tris-HCl buffer was added to a final concentration of 20 mM to quench the unreacted NHS groups. The modified resin was washed 3 times with 10 bed volume of 100 mM Tris-HCl buffer (pH 8.1) each time.

RSS-dT_{37} was attached to the DVS-A activated resin (Adar Biotech LTD, Rehovot, Israel). Before DNA immobilization, the resin was washed using a sodium phosphate buffer (100 mM, pH 7.4). RSS-dT_{37} was first reduced to form free thiols using 10 mM tris(2-carboxyethyl)phosphine (TCEP) in a HAc-NaAc buffer (100 mM, pH 5.4) and then incubated with the DVS-A resin at room temperature for 2 h in the above sodium phosphate buffer. Next, the reaction was quenched using 20 mM DTT. The DNA modified resin was washed using the same phosphate buffer.

To examine site-specific protein immobilization, sfGFP-SSB or sfGFP (used as a negative control) was incubated with the DNA-modified resins for 15 min in a Tris buffer (100 mM Tris-HCl, 100 mM NaCl, pH 8.1). Then, the resin was collected through centrifugation and washed 3 times with 10 bed volumes of the same Tris-HCl buffer each time. Protein bound to the resin was quantified by subtracting the amount of protein left unbound from the total amount of protein added. After protein immobilization and washing, the resins were also examined directly under a fluorescent microscope (Nikon Eclipse 55i, Nikon Instrument Inc., Elgin, IL).

Reversibility of Protein Immobilization. After sfGFP-SSB was immobilized on NHS-dT_{37} and DVS-A-dT_{37} activated resins, the effect of different pHs on protein−substrate dissociation was examined. HAc-NaAc buffer was used for pHs 4, 4.5, and 5.0. Sodium phosphate buffer was used for pHs 5.5, 6, 6.5, and 7. Tris−HCl buffer was used for pHs 7.5, 8, and 8.5. Sodium-glycine buffer was used for pHs 9, 9.5, 10, and 10.5. The indicated buffer (at 100 mM) was added to sfGFP-SSB modified resin and incubated at room temperature for 30 min. The protein in the supernatant was quantified to determine the effectiveness of elution.

RESULTS AND DISCUSSION

Aiming at developing a reversible and site specific method for protein immobilization, we examined the prospect of immobilizing proteins through a DNA binding fusion tag. We created a fusion protein containing the protein of interest and a ssDNA binding module. To facilitate convenient detection and characterization, we have chosen sfGFP as the model target protein. sfGFP was fused with SSB at the C-terminus. Furthermore, a histag was introduced at the N-terminus of the fusion protein to facilitate convenient purification (Figure 1A). We expressed and purified the fusion protein as well as the

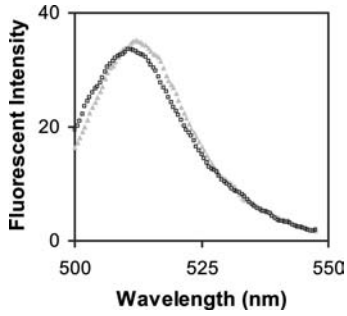


Figure 2. Fluorescent emission spectra of sfGFP (open square) and sfGFP-SSB (filled triangle) measured with the excitation wavelength of 490 nm. The concentration of both proteins was 45 nM. The maximum emission wavelengths of sfGFP-SSB and sfGFP are 512 and 510 nm, respectively.

individual modules, sfGFP and SSB, in high yield. Figure 1B showed the SDS-PAGE analysis of all three proteins. The calculated molecular weights of the histagged proteins are 29.0 kDa (sfGFP), 22.5 kDa (SSB), and 48.1 kDa (sfGFP-SSB). The experimental results are consistent with the calculated molecular weights. SSB is a tetramer, which is critical for its interaction with ssDNA. We examined the quaternary structure of the fusion protein using the size exclusion chromatography (SEC) (Figure 1C). The retention time of the fusion protein was around 20.4 min, slightly shorter than the molecular weight standard of 158 kDa (20.7 min). This result suggests that the fusion protein is a tetramer. To examine the influence of fusing on the properties of each individual module, we measured the fluorescence emission, as well as the ssDNA binding affinity of the fusion protein.

We first compared the fluorescent emissions of sfGFP and sfGFP-SSB. There is a small red shift of the emission peak, from 510 nm for sfGFP to 512 nm for sfGFP-SSB (Figure 2). The fluorescence intensities of the two proteins were comparable. Next, we examined the ssDNA binding affinity of sfGFP-SSB. Previous studies showed that, when SSB bound to dT_{37}, the tryptophan fluorescence of the protein decreased (*32*). On the basis of the percentage of fluorescent quenching, the binding affinity between SSB and dT_{37} could be determined. sfGFP has one tryptophan, W57. When excited at 282 nm, the intrinsic fluorescence emission of sfGFP at 357 nm was approximately 3% of the intensity of the SSB emission (Figure 3A). Furthermore, the addition of dT_{37} had no effect on the emission of sfGFP (Figure 3A). Finally, we titrated dT_{37} into samples containing either sfGFP-SSB or SSB and monitored their tryptophan fluorescence emission (Figure 3B). The fluorescence quenching curves of the two proteins superimposed well in the concentration range examined (between $10^{-9.5}$ M to 10^{-7} M) and matched the result from the literature for SSB (*33*). This result indicates that the ssDNA binding affinity of SSB was not affected in the fusion protein.

Interaction between SSB and ssDNA was highly dependent on pH and cation concentrations (*34*−*36*). We expect the binding of sfGFP-SSB to dT_{37} to be sensitive to changes of pH and cationic concentration as well. Therefore, we characterized their interaction at different pHs (pH 8.1 and pH 10), as well as different NaCl and $MgCl_2$ concentrations, aiming at identifying conditions that could enable reversible protein immobilization/elution. There are two major binding modes between SSB and dT_{37}, known as $(SSB)_{35}$ and $(SSB)_{65}$. The subscripts refer to the length of the oligonucleotides that interact with each SSB tetramer during binding (*19*). In the $(SSB)_{35}$ binding mode, ssDNA only interacts with two out of the four SSB subunits in a tetramer. On the other hand, in the $(SSB)_{65}$ binding mode, all four subunits participate in DNA binding. The switch between

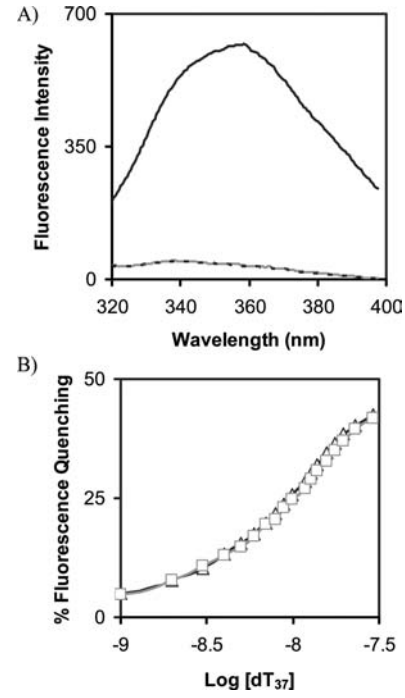


Figure 3. (A) Tryptophan fluorescence spectra of sfGFP (gray), SSB (black), and sfGFP after the addition of 100 nM dT_{37} (dotted black line) when excited at 282 nm. (B) Fluorescence quenching of sfGFP-SSB (gray) and SSB (black) in the presence of dT_{37}. The excitation and emission wavelengths are 282 and 357 nm, respectively. The concentrations of both proteins were 4.2×10^{-7} M.

the two binding modes is sensitive to changes in pH, temperature, and cation concentrations. For example, when the concentration of Na^+ is less than 10 mM, the main binding mode is the $(SSB)_{35}$ mode, and $(SSB)_{65}$ mode is the main binding mode when Na^+ concentration is higher than 200 mM. For $MgCl_2$, such a switch happens at a much lower Mg^{2+} concentration. We examined the effect of NaCl and $MgCl_2$ on the ssDNA binding of the fusion protein. We found that sfGFP-SSB behaved very much like the free SSB. ssDNA titration experiment using dT_{37} showed that fluorescence quenching reached a plateau at 60% in 1 mM NaCl, while in the presence of 2.5 mM $MgCl_2$, 90% of the tryptophan emission was quenched (Figure 4A). These results indicate that the fusion protein also has two binding modes, similar to the two binding modes of SSB. There are two binding sites per SSB tetramer (each binding site contains two SSB subunits). A negative cooperation exists between bindings at these two sites (*21*). As salt concentration decreases, this negative cooperation increases. This explains why the percentage fluorescence quenching upon binding was different in the presence of 1 mM NaCl (one site binding, or $(SSB)_{35}$ mode) or 2.5 mM $MgCl_2$ (two sites binding, or $(SSB)_{65}$ mode).

Next, we examined a series of pH and cation concentrations and their combinations to identify a condition that minimized the interaction between sfGFP-SSB and dT_{37}. This condition could be used potentially as the elution condition during protein immobilization experiments. We first determined the effect of pH on the tryptophan fluorescence of the fusion protein (Figure 4B). Spectra were collected at pH 6.9 with 2.5 $MgCl_2$ (dark gray) and pH 10 with 1 mM NaCl (light gray). At the higher pH, the tryptophan fluorescence emission decreased by approximately 10%. We found that, while the fusion protein bound efficiently with dT_{37} over a broad range of conditions (pH 7−8, >100 mM NaCl or 2.5 mM $MgCl_2$), the combination of high pH and low salt concentration disrupts such interaction. In the presence of 100 nM dT_{37}, sfGFP-SSB binding had reached

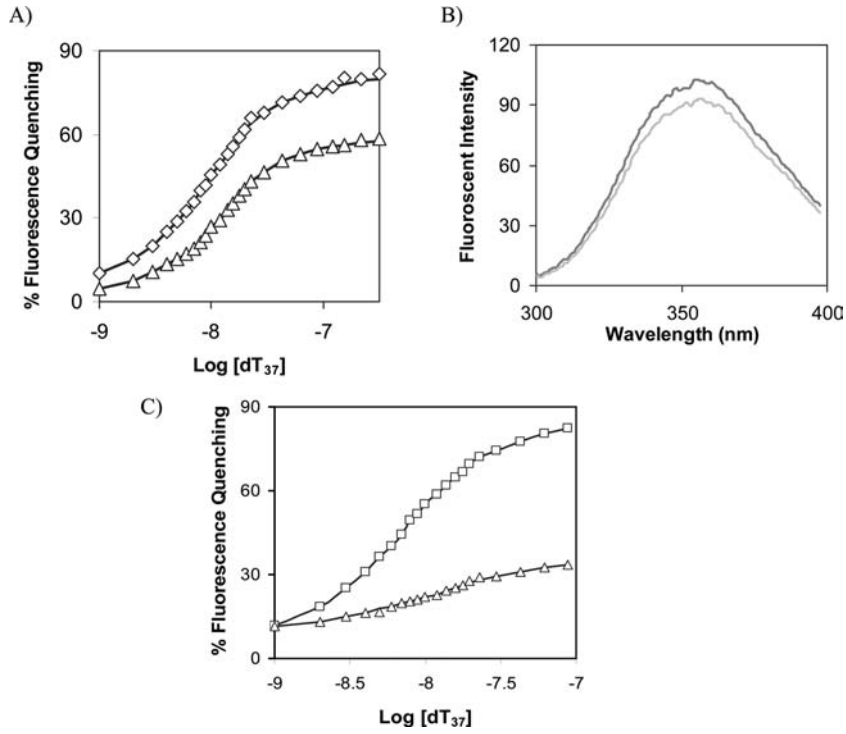


Figure 4. (A) sfGFP-SSB and dT_{37} binding monitored as tryptophan fluorescence quenching in the presence of 1 mM NaCl, 25 mM Tris-HCl, pH 8.1 (triangle) or 2.5 mM $MgCl_2$, 25 mM Tris-HCl, pH 8.1 (diamond). The concentration of sfGFP-SSB was 1.4×10^{-7} M. (B) sfGFP-SSB tryptophan fluorescence emission measured at pH 6.9 with 2.5 mM $MgCl_2$ (dark gray) or pH 10 with 1 mM NaCl (light gray). (C) sfGFP-SSB and dT_{37} binding at pH 6.9 with 2.5 mM $MgCl_2$ (square) or pH 10 with 1 mM NaCl (triangle).

saturation at pH 6.9 with 2.5 mM $MgCl_2$ (square), while much less protein bound at pH 10 with 1 mM NaCl (triangle) (Figure 4C).

To examine the binding of sfGFP-SSB with immobilized ssDNA, we first covalently attached chemically derivatized dT_{37} to a solid matrix. Two kinds of chemical reactions were tested: amine-derivatized ssDNA to NHS functionalized resin and thiol-derivatized ssDNA to DVS-A activated resin. After the modification, the resins were washed extensively to remove the unreacted ssDNA. Next, sfGFP-SSB or sfGFP were incubated under the same experimental condition with the modified resins. We used sfGFP as a negative control to examine the effect of nonspecific interaction between the protein and the beads. After incubation, the resins were separated from excess proteins by centrifugation and washed extensively using the binding buffer. The difference in colors of the modified resins incubated with sfGFP-SSB and sfGFP indicated that nonspecific binding of sfGFP was very weak compared to the SSB facilitated specific binding (Figure 5A). Panels a and b were NHS-T_{37} and DVS-A-T_{37} resins, respectively. The tube on the left in each panel contained sfGFP-SSB treated resins, while the tube on the right contained sfGFP treated resins. Next, fluorescent microscope was used to further characterize both types of resins incubated with sfGFP or sfGFP-SSB (Figure 5B). The control resins were not fluorescent, further confirming the lack of nonspecific interaction. The amount of sfGFP-SSB immobilized to the resins was determined as described in the experimental procedures. Approximately 2.6 or 1.8 mg proteins was bound in each milliliter of drained NHS-dT_{37} or DVS-A-dT_{37} resin.

Reversibility of the immobilization procedure provides the possibility to recycle the functional proteins and regenerate the supporting matrix. We evaluated two approaches to elute the protein off the resins without affecting its activity: addition of the complementary dA_{35} oligonucleotide and change of pH/salt concentration. We first examined the reversibility of sfGFP-SSB interaction with the immobilized dT_{37} through the addition

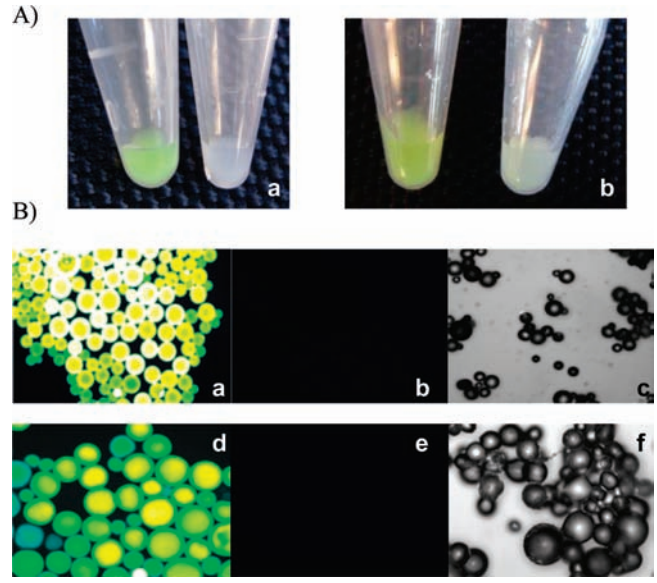


Figure 5. (A) Protein immobilization on NHS-dT_{37} (a) or DVS-A-dT_{37} (b) resins. In each panel, the resins in the microcentrifuge tubes were incubated with sfGFP-SSB (left) or sfGFP (right) and then washed extensively. (B) Protein modified NHS-dT_{37} (a,b,c) and DVS-A-dT_{37} (d,e,f) imaged using fluorescent light (a,b,d,e) or normal white light (c,f). Resins in panels a and d were treated with sfGFP-SSB. Resins in panels b, c, e and f were treated with sfGFP.

of dA_{35}. Binding of the two oligonucleotides generated double-stranded DNA, which did not bind to SSB. In the presence of 125 μM dA_{35}, 82.4% of bound protein was eluted within the first 10 min of incubation (Figure 6A). In addition, the resin could be regenerated by the treatment of free dT_{37}, which competitively bound to dA_{35} and removed them from the resin.

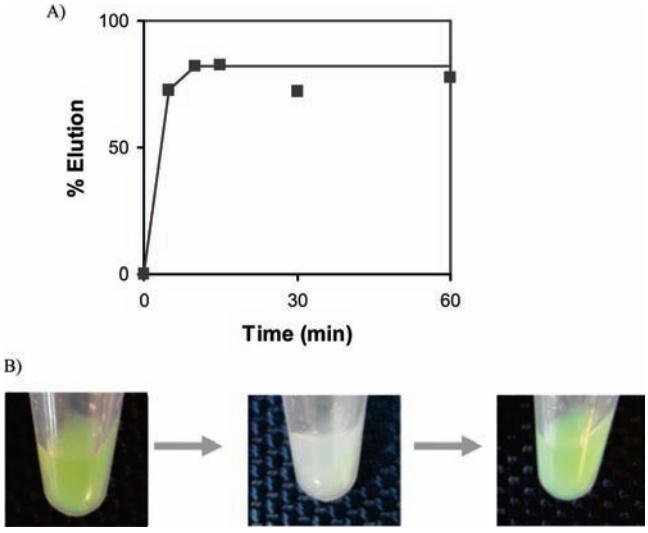


Figure 6. (A) Effect of incubation time on protein elution by dA_{35}. (B) NHS-dT_{37} resins modified with sfGFP-SSB (left), eluted using dA_{35} (middle), and then regenerated and incubated with fresh sfGFP-SSB (right).

The regenerated resins bound to sfGFP-SSB, as revealed by their color change after incubated with fresh sfGFP-SSB (Figure 6B).

To identify a more convenient method to release the fusion protein from the resin, we examined the effect of pH/salt concentration on the elution of the fusion protein. We found that 68.4% of sfGFP-SSB could be eluted by the condition identified above (Na-glycine buffer, 1 mM NaCl, pH 10). To examine the reversibility of binding, the protein eluate was adjusted to pH 8.1 and mixed with fresh resins. In parallel, fresh sfGFP-SSB was added to the resin after pH mediated elution and re-equilibration. In both cases, sfGFP-SSB bound to the resins.

In summary, we have demonstrated that SSB could serve as a versatile fusion tag to facilitate ssDNA-mediated protein immobilization. SSB is very stable and shows no negative impact on the overall expression level and stability of the fusion protein. The binding between SSB and ssDNA is very tight, with nanomolar affinity. Yet, such interaction can be attenuated through the change of pH/salt concentration, which could serve as a convenient method to elute the immobilized protein and regenerate the surface without denaturing the fusion protein. In comparison to other DNA- or RNA-mediated protein immobilization methods, our approach has the advantage of not requiring additional chemical modification. Thus, potential complications related to chemical modifications of the target proteins are avoided. The binding between SSB and ssDNA is not site specific. We speculate that incorporation of site specific DNA-binding proteins as fusion tags will introduce an additional level of control over the assembly of protein arrays based on DNA array templates.

LITERATURE CITED

(1) Katz, E., and Willner, I. (2003) Probing biomolecular interactions at conductive and semiconductive surfaces by impedance spectroscopy: Routes to impedimetric immunosensors, DNA-sensors, and enzyme biosensors. *Electroanalysis 15*, 913–47.

(2) Kohn, M. (2009) Immobilization strategies for small molecule, peptide and protein microarrays. *J. Pept. Sci. 15*, 393–7.

(3) Yamaguchi, H., Miyazaki, M., Honda, T., Briones-Nagata, M. P., Arima, K., and Maeda, H. (2009) Rapid and efficient proteolysis for proteomic analysis by protease-immobilized microreactor. *Electrophoresis 30*, 3257–64.

(4) Wu, B. Y., Hou, S. H., Huang, L., Yin, F., Zhao, Z. X., Anzai, J. I., and Chen, Q. (2008) Oriented immobilization of immunoglobulin G onto the cuvette surface of the resonant mirror biosensor through layer-by-layer assembly of multilayer films. *Mater. Sci. Eng. C 28*, 1065–9.

(5) Tan, Y. H., Liu, M., Nolting, B., Go, J. G., Gervay-Hague, J., and Liu, G. Y. (2008) A nanoengineering approach for investigation and regulation of protein immobilization. *ACS Nano 2*, 2374–84.

(6) Batalla, P., Fuentes, M., Mateo, C., Grazu, V., Fernandez-Lafuente, R., and Guisan, J. M. (2008) Covalent immobilization of antibodies on finally inert support surfaces through their surface regions having the highest densities in carboxyl groups. *Biomacromolecules 9*, 2230–6.

(7) Rao, S. V., Anderson, K. W., and Bachas, L. G. (1998) Oriented immobilization of proteins. *Mikrochim. Acta 128*, 127–43.

(8) Cha, T. W., Guo, A., and Zhu, X. Y. (2005) Enzymatic activity on a chip: the critical role of protein immobilization. *Proteomics 5*, 416–9.

(9) Hochuli, E., Bannwarth, W., Dobeli, H., Gentz, R., and Stuber, D. (1988) Genetic approach to facilitate purification of recombinant proteins with a novel metal chelate adsorbent. *Nat. Biotechnol. 6*, 1321–5.

(10) Khan, F., He, M. Y., and Taussig, M. J. (2006) Double-hexahistidine tag with high-affinity binding for protein immobilization, purification and detection on Ni-nitrilotriacetic acid surfaces. *Anal. Chem. 78*, 3072–9.

(11) Fischer, N. O., Blanchette, C. D., Chromy, B. A., Kuhn, E. A., Segelke, B. W., Corzett, M., Bench, G., Mason, P. W., and Hoeprich, P. D. (2009) Immobilization of His-tagged proteins on nickel-chelating nanolipoprotein particles. *Bioconjugate Chem. 20*, 460–5.

(12) Hengen, P. N. (1995) Purification of His-tag fusion proteins from Escherichia coli. *Trends Biochem. Sci. 20*, 285–6.

(13) Shao, W. H., Zhang, X. E., Liu, H., and Zhang, Z. P. (2000) Anchor-chain molecular system for orientation control in enzyme immobilization. *Bioconjugate Chem. 11*, 822–6.

(14) Kacar, T., Zin, M. T., So, C., Wilson, B., Ma, H., Gul-Karaguler, N., Jen, A. K. Y., Sarikaya, M., and Tamerler, C. (2009) Directed self-immobilization of alkaline phosphatase on micro-patterned substrates via genetically fused metal-binding peptide. *Biotechnol. Bioeng. 103*, 696–705.

(15) Rusmini, F., Zhong, Z. Y., and Jan, F. J. (2007) Protein immobilization strategies for protein biochips. *Biomacromolecules 8*, 1775–89.

(16) Niemeyer, C. M. (2002) The developments of semisynthetic DNA-protein conjugates. *Trends Biotechnol. 20*, 395–401.

(17) Weng, S., Gu, K., Hammond, P. W., Lohse, P., Rise, C., Wagner, R. W., Wright, M. C., and Kuimelis, R. G. (2002) Generating addressable protein microarrays with PROfusion (TM) covalent mRNA-protein fusion technology. *Proteomics 2*, 48–57.

(18) Hendrickson, E. R., Haffield-Truby, T. M., Joerger, R. D., Majarian, W. R., and Ebersole, R. C. (1995) A sensitivity multianalyte immunoassay using covalent DNA-labeled antibodies and polymerase chain reaction. *Nucleic Acids Res. 23*, 522–9.

(19) Schweitzer, B., Wiltshire, S., Lambert, J., O'Malley, S., Kukanskis, K., Zhu, Z., Kingsmore, S. F., Lizardi, P. M., and Ward, D. (2000) Immunoassays with rolling circle DNA amplification: A versatile platform for ultrasensitive antigen detection. *Proc. Natl. Acad. Sci. U.S.A. 97*, 10113–9.

(20) Howorka, S., Cheley, S., and Bayley, H. (2001) Sequence-specific detection of individual DNA strands using engineered nanopores. *Nat. Biotechnol. 19*, 636–9.

(21) Kozlov, I. A., Melnyk, P. C., Stromsborg, K. E., Chee, M. S., Barker, D. L., and Zhao, C. (2004) Efficient strategies for the conjugation of oligonucleotides to antibodies enabling highly sensitive protein detection. *Biopolymers 73*, 621–30.

(22) Glynou, K., Ioannou, P. C., and Christopoulos, T. K. (2003) Affinity capture-facilitated preparation of aequorin-oligonucle-

otide conjugates for rapid hybridization assays. *Bioconjugate Chem. 14*, 1024–9.
(23) Boozer, C., Ladd, J., Chen, S., Yu, Q., Homola, J., and Jiang, S. (2004) DNA directed protein immobilization on mixed ssDNA/oligo(ethylene glycol) self-assembled monolayers for sensitive biosensors. *Anal. Chem. 76*, 6967–72.
(24) Boozer, C., Ladd, J., Chen, S., and Jiang, S. (2006) DNA-directed protein immobilization for simultaneous detection of multiple analytes by surface plasmon resonance biosensor. *Anal. Chem. 78*, 1515–9.
(25) Schlapak, R., Pammer, P., Armitage, D., Zhu, R., Hinterdorfer, P., Vaupel, M., Fruhwirth, T., and Howorka, S. (2006) Glass surfaces grafted with high-density poly(ethylene glycol) as substrates for DNA oligonucleotide microarrays. *Langmuir 22*, 277–85.
(26) Niemeyer, C. M., Boldt, L., Ceyhan, B., and Blohm, D. (1999) DNA-directed immobilization: Efficient, reversible, and site-selective surface binding of proteins by means of covalent DNA-streptavidin conjugates. *Anal. Biochem. 268*, 54–63.
(27) Takeda, S., Tsukiji, S., and Nagamune, T. (2004) Site-specific conjugation of oligonucleotides to the C-terminus of recombinant protein by expressed protein ligation. *Bioorg. Med. Chem. Lett. 14*, 2407–10.
(28) Roberts, R. W., and Szostaks, J. W. (1997) RNA-peptide fusions for the in vitro selection of peptides and proteins. *Proc. Natl. Acad. Sci. U.S.A. 94*, 12297–302.
(29) Biyani, M., Husimi, Y., and Nemoto, N. (2006) Solid-phase translation and RNA-protein fusion: a novel approach for folding quality control and direct immobilization of proteins using anchored mRNA. *Nucleic Acids Res. 34*, e140.
(30) Schweller, R. M., Constantinou, P. E., Frankel, N. W., Narayan, P., and Diehl, M. R. (2008) Design of DNA-conjugated polypeptide-based capture probes for the anchoring of proteins to DNA matrices. *Bioconjugate Chem. 19*, 2304–7.
(31) Lee, S. K., Maye, M. M., Zhang, Y. B., Gang, O., and Van der Lelie, D. (2009) Controllable g5p-protein-directed aggregation of ssDNA-gold nanoparticles. *Langmuir 25*, 657–60.
(32) Meyer, R. R., and Laine, P. S. (1990) The single-stranded DNA-binding protein of Escherichia coli. *Microbiol. Rev. 54*, 342–80.
(33) Lohman, T. M., and Bujalowski, W. (1988) Negative cooperativity within individual tetramers of Escherichia coli single strand binding protein is responsible for the transition between $(SSB)_{35}$ and $(SSB)_{56}$ DNA binding modes. *Biochemistry 27*, 2260–5.
(34) Lohman, T. M., and Ferrari, M. E. (1994) Escherichia coli single stranded DNA-binding protein: Multiple DNA-binding modes and cooperativities. *Annu. Rev. Biochem. 63*, 527−70.
(35) Overman, L. B., Bujalowski, W., and Lohman, T. M. (1988) Equilibrium binding of Escherichia coli single-strand binding protein to single-stranded nucleic acids in the $(SSB)_{65}$ binding mode. Cation and anion effects and polynucleotide specificity. *Biochemistry 27*, 456–71.
(36) Raghunathan, S., Kozlov, A. G., Lohman, T. M., and Waksman, G. (2000) Structure of the DNA binding domain of E. coli SSB bound to ssDNA. *Nat. Struct. Biol. 7*, 648–52.

BC9005392

Hybrid PET/CT for Noninvasive Pharmacokinetic Evaluation of Dynamic PolyConjugates, a Synthetic siRNA Delivery System

Sarah R. Mudd,[†] Vladimir S. Trubetskoy,*[,‡] Andrei V. Blokhin,[‡] Jamey P. Weichert,[§] and Jon A. Wolff[‡]

Department of Pharmaceutical Sciences, University of Wisconsin - Madison, 777 Highland Ave., Madison, Wisconsin 53705, Roche Madison Inc., 465 Science Dr., Madison, Wisconsin 53711, Department of Radiology, University of Wisconsin - Madison, 600 Highland Ave., Madison, Wisconsin 53792. Received December 15, 2009; Revised Manuscript Received May 25, 2010

Positron emission tomography/computed tomography (PET/CT) hybrid imaging can be used to gain insights into a synthetic siRNA delivery system targeted to the liver. Either siRNA or the delivery vehicle was labeled with ^{64}Cu via 1, 4, 7, 10- tetraazacyclododecane- 1, 4, 7, 10- tetraacetic acid (DOTA) chelation. This study confirmed that the siRNA delivery system was successfully targeted to the liver. Incorporation of the siRNA into the delivery system protected the siRNA from renal filtration long enough so that the siRNA could be delivered to the liver. PET/CT imaging was important for confirming biodistribution and for determining differences in the distribution of labeled siRNA, siRNA incorporated into the delivery system, and the delivery system without siRNA.

INTRODUCTION

The delivery of short interfering RNA (siRNA) into cells is a powerful approach to selectively inhibit gene expression (*1*). For therapeutic application in humans, a variety of approaches are being developed to deliver the siRNA to the appropriate target cells *in vivo*. These include siRNA-conjugates and a variety of lipid- and polymer-based delivery systems (*2*). We recently developed a new polymer-based delivery system, termed dynamic polyconjugates (DPCs), for delivering siRNA to hepatocytes and other cells *in vivo* (*3*). A key element of this new approach is the use of masked endosomolytic polymers that improve the release of nucleic acids from endosomes. When the masked endosomolytic polymers enter the acidic environment of the endosome, a pH-labile bond is broken, releasing the agent's endosomolytic capability. This approach enables polyethylene glycol (PEG) and targeting ligands to be attached to the polymer without disturbing its endosomolytic function, while still enabling *in vivo* delivery and targeting. In its current version for hepatocyte delivery, the endosomolytic polymer is an amphipathic poly vinyl ether composed of butyl and amino vinyl ethers termed PBAVE. The asialoglycoprotein receptor ligand N-acetylgalactosamine (NAG) is used to target the DPC to hepatocytes. PEG is used to discourage nonspecific interactions. Both the NAG and the PEG are attached to the PBAVE via pH-labile bonds. The siRNA is covalently attached to the PBAVE via a labile disulfide bond. The resulting DPC is 10 ± 2 nm (*3*).

We were interested in studying the tissue distribution and kinetics of DPCs in mice. Advances in animal and human imaging techniques have made it possible to refine the process of modern drug discovery, specifically in assessing the delivery of an experimental drug to its targeted and nontargeted tissues (*4*). Of particular interest was evaluating the distribution of both the endosomolytic polymer PBAVE and siRNA components using a similar procedure. While hybridization- and PCR-based methods have been used to track siRNA (*5*), such an approach would not be applicable for following the distribution of a synthetic polymer such as PBAVE. Also, a hybridization or PCR-based method only detects relatively intact siRNA, while a label-based method can assess total accumulation independently of the intactness of the siRNA over a certain time period, assuming slow removal of the label from the target tissue. Furthermore, a quantitative imaging procedure provides additional information about distribution that would not be available from procedures that rely upon the use of tissue extracts. A disadvantage of a label-based procedure is that parent and metabolites cannot be distinguished *in vivo*. To address this concern somewhat, a chemically modified siRNA sequence that was relatively resistant to nuclease degradation was used. In addition, a tissue imaging procedure cannot delineate the subtissue cellular distribution and must be coupled with microscopy studies. Our previous study using confocal microscopy showed that the DPCs delivered fluorescently labeled siRNA predominantly to hepatocytes within the liver (*3*).

Prior siRNA *in vivo* imaging studies have used PET, SPECT, and planar gamma camera imaging. Labeling of siRNA has been achieved using the positron emitters ^{18}F and ^{64}Cu; SPECT has been done using ^{125}I, ^{111}In, and ^{99}m Tc (*6*−*11*). The first report of siRNA delivery assessment using nuclear imaging was done using PET with ^{64}Cu chelated by DOTA (*6*). Planar gamma camera imaging techniques were ineffective for quantitative biodistribution studies because internal organs overlap in the same plane making the precise uptake in each unknown. For example, liver and kidney activities were reported together as a sum (*8*). Because siRNA kinetics are very rapid, an imaging technique must be chosen that is quantitative and has good temporal resolution. PET has superior sensitivity compared to SPECT, which allows for improved image quality as well as improved temporal resolution. This allows for many short frames to be obtained in a dynamic image series (*12*). Thus, we chose PET imaging for our studies.

We designed the present study to examine the whole body biodistribution of therapeutically relevant doses of DPCs containing siRNA targeted to hepatocytes *in vivo* using micro-PET/CT hybrid imaging with ^{64}Cu DOTA-labeled DPCs. The half-life of ^{64}Cu is 12.7 h, which is reasonable for imaging

* Corresponding Author: Vladimir S. Trubetskoy, Address: 465 Science Dr., Madison, WI 53711. E-mail: Vladimir.trubetskoy@roche.com, Telephone number: (608)316-3925, Fax number: (608)441-0741.

[†] Department of Pharmaceutical Sciences, University of Wisconsin − Madison.

[‡] Roche Madison Inc.

[§] Department of Radiology, University of Wisconsin − Madison.

10.1021/bc900558z © 2010 American Chemical Society
Published on Web 06/16/2010

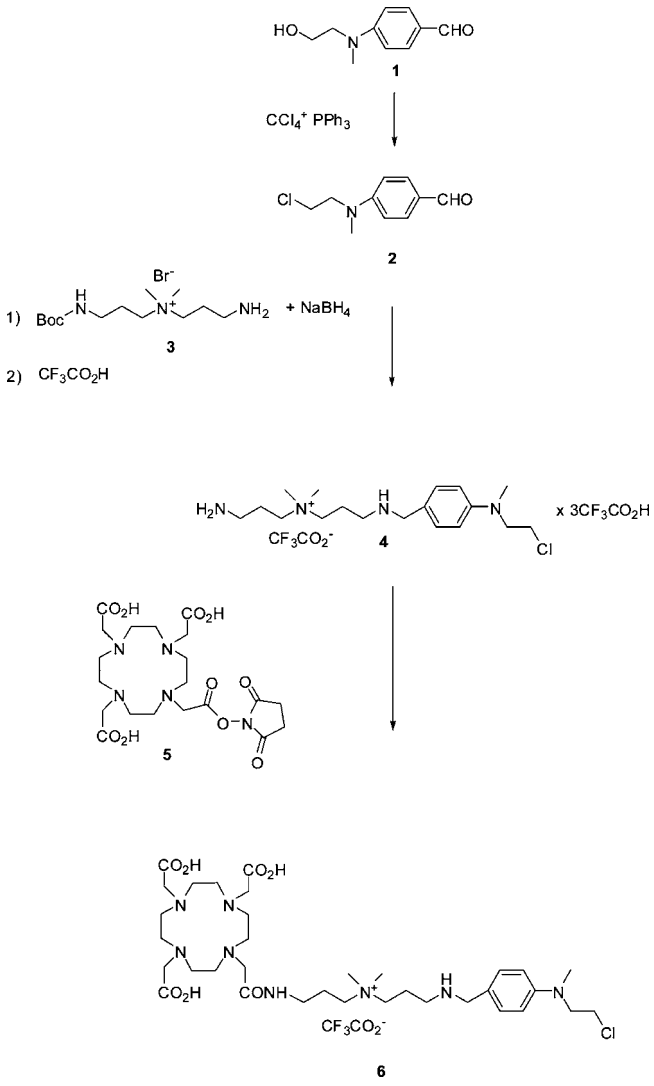


Figure 1. Preparation of DOTA-NM.

siRNA kinetics. Because the DPC system consists of two main components, the siRNA (payload) and an excess of the polymer PBAVE (carrier), the primary objective was to image the kinetics of tissue distribution of both components *in vivo*. This study also incorporated several modifications of existing procedures. A new DOTA-labeling reagent was synthesized that enables the attachment of the chelated ^{64}Cu to siRNA after its synthesis. A CT contrast reagent was utilized to ensure accurate liver definition and coregistration with the PET scans. In addition, we used a stabilized siRNA containing 2′*O*-methyl modified nucleotides and phosphorothioate linkages in this study (*13*), while previous imaging studies used less stabilized siRNAs (*6, 8, 10*).

MATERIALS AND METHODS

Materials. Primary amine modified ApoB-2 siRNA sequence (*13*) was ordered from Ambion (Austin, TX) (*13*). DOTA-NHS-ester 5 was purchased from Macrocyclics (Dallas, TX). 4-[N-(2-Hydroxyethyl)-N-methyl]aminobenzaldehyde **1** (Figure 1) was purchased from Sigma-Aldrich. Compounds **3** and **4** (Figure 1) were prepared by a known procedure (*14*). ^{64}Cu chloride was provided by the University of Wisconsin cyclotron facility (Madison, WI). Sephadex G50, G75 and QAE columns were purchased from GE Healthcare (Piscataway, NJ).

Methods. *Preparation of DOTA-nitrogen mustard (DOTA-NM).* In preparation of precursor **4** we utilized reductive alkylation of amine **3** with 4-[(N-(2-chloroethyl)-N-methyl]aminobenzaldehyde **2** followed by Boc-deprotection with CF_3CO_2H (Figure 1) (*14, 15*). Aldehyde **2** was prepared from 4-[N-(2-hydroxyethyl)-N-methyl]aminobenzaldehyde **1** (27.9 mmol) by reaction with triphenylphospine (58.6 mmol) in $CCl_4/CHCl_3$ (2:1, 75 mL) mixture under Ar at 55 °C for 1 h. The solvent was evaporated *in vacuo* and the product **2** was purified on a silica gel column (hexane:EtOAc 8:2). The structure was verified by ^{1}H NMR.

N-(3-aminopropyl)-N-[3-[[[4-[(2-chloroethyl)methylamino]phenyl]methyl]amino]propyl]-N,N-dimethylammonium tetrakis(trifluoroacetate) **4** (0.096 mmol) was dissolved in DMF before being combined with DOTA-NHS-ester **5** (0.1 mmol) and diisopropylamine (0.46 mmol). The mixture was stirred for 4 h at 20 °C under Ar. The product, N-(3-DOTA-amidopropyl)-N-[3-[[[4-[(2-chloroethyl)methylamino]phenyl]methyl]amino]propyl]-N,N-dimethylammonium trifluoroacetate **6** was precipitated in 10 mL of Et_2O and purified by HPLC on a Gemini C-18, 5 μm, 110 Å column, 260 × 21.2 mm (Phenomenex). The mobile phase was CH_3OH(TFA 0.1%)-H_2O(TFA 0.1%), 15 mL/min and the organic gradient was 12% (4.5 min), 12−32% (25 min), 32−95% (5 min), 95% (10 min), 90−12% (1 min). UV monitoring was done at 210 nm.

Modification of siRNA. The siRNA used with both the DOTA-PBAVE DPC and DOTA-siRNA experiments was modified with succinimidyl-S-acetylthioacetate (SATA) as previously described by Rozema, et al. (*3*). To make DOTA-siRNA, the siRNA was treated with DOTA-NM (2:1 w/w) in 5 mM TAPS, pH 9.0 for 2 h at 37 °C. The final product was purified from the excess of chelate by 3x ethanol precipitation.

Preparation of DOTA-PBAVE. PBAVE polymer was modified with DOTA-NHS ester by incubating the polymer and the activated ester in 20 mM HEPES buffer, pH 8.0 for 1 h at room temperature. Polymer concentration was 10 mg/mL, molar ratio of the activated ester to the polymer amines was 2%. The modified polymer was purified using QAE-Sephadex column in water and freeze-dried.

^{64}Cu labeling. The ^{64}Cu chloride was mixed with 0.5 M sodium acetate buffer at pH 5.5 and DOTA-siRNA or activated DOTA-PBAVE at a ratio of approximately 4 mCi:75 μg DOTA-siRNA or 500 μg activated DOTA-PBAVE. The siRNA mixture was incubated at 40 °C for one hour; if activated DOTA-PBAVE was used, the mixture was incubated at room temperature for 30 min. To remove the unconjugated ^{64}Cu, size exclusion chormatography was performed using Sephadex G-50 columns for siRNA labeled product and QAE columns for PBAVE labeled product. Centrifugation was performed in a Beckman TJ-6 centrifuge (Fullerton, CA) for 2 min at 2000 rpm.

Dynamic Polyconjugate Synthesis and Formulation. The polyconjugate was synthesized and formulated according to previously published procedures at an siRNA/PBAVE ratio of 1:10 (w/w) (*3*). A ratio of 2:1 of PEG:NAG was used to modify the PBAVE, which contains no more than one siRNA covalently attached. To remove unconjugated siRNA, a Sephadex G-75 column was used for 5 min at 1000 rpm.

Radio-Thin Layer Chromatography Studies. Radio-TLC studies were performed using EMD Merck Silica Gel 60 TLC plates and methanol: 5% ammonium acetate (1:1 v/v) mobile phase. The plates were scanned using Bioscan AR 2000 Imaging Scanner (Washington, DC).

Animal studies. Female, ICR mice were obtained from Harlan (Indianapolis, IN). The number of animals per group and naming scheme used in the figures is as follows: n = 3 for free ^{64}Cu (^{64}Cu), n = 4 for ^{64}Cu DOTA siRNA (labeled siRNA), n = 4 for ^{64}Cu DOTA siRNA DPC (DPC), and n = 3 for ^{64}Cu DOTA PBAVE/DPC (PBAVE/DPC). All animal studies were performed in accordance with all guidelines and were approved

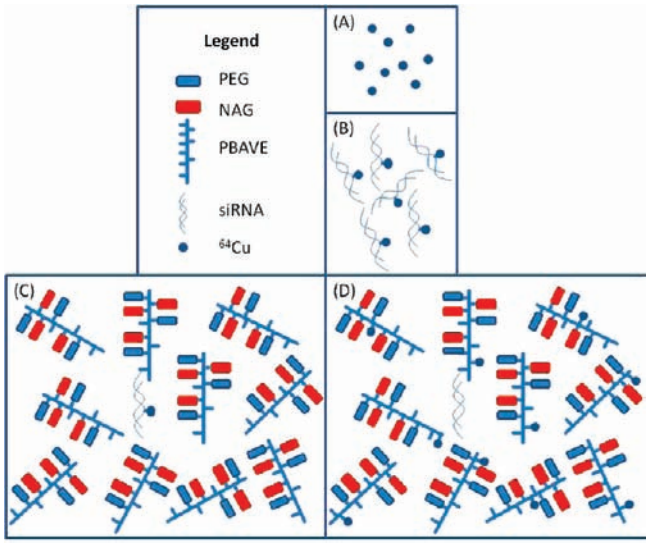


Figure 2. Schematic representations of (A) Labeled ^{64}Cu (^{64}Cu), (B) ^{64}Cu DOTA siRNA (Labeled siRNA), (C) ^{64}Cu DOTA siRNA DPC (DPC), and (D) ^{64}Cu DOTA PBAVE:DPC (PBAVE/DPC).

by the University of Wisconsin-Madison and Roche Madison animal care and use committees.

In vivo imaging using microPET/CT. All images were acquired on a Siemens Inveon microPET/CT scanner (Knoxville, TN). Approximately 3 h prior to the start of the CT scan, mice were injected with 120 μL of eXIA 160 (Binitio, Ottawa, Canada) liver CT contrast agent in order to accurately define the liver. Mice were anesthetized using 1 mg/kg body weight of medetomidine and 75 mg/kg body weight of ketamine prior to the injection of radiotracer and imaging procedures. Between 250 − 300 μCi, 100 − 250 μL, of the selected ^{64}Cu labeled agent was injected via catheter in the tail vein while the animal was on the scanner. Dynamic PET scans were started at the time of injection and acquired for one hour post-injection and reconstructed using an OSEM 2D reconstruction algorithm. Listmode data were binned into sinograms of dimensions 1, 4, 10, 25, 45, and 75 s frames and 2, 4, 8, 12, 20, 30, 40, 50, and 60 min frames; all frames were decay corrected during reconstruction. CT scans were acquired at 80 kVp and 1000 μA and reconstructed using a filtered back projection algorithm with a Shepp-Logan filter. Scatter correction and attenuation correction, based on CT imaging, were done for all PET images.

Image analysis and registration was performed using Inveon Research Workplace (IRW) (Knoxville, TN). All images displayed have the same PET window leveling to ensure accurate comparison. All regions of interest (ROIs) were drawn in the CT field of view to ensure accurate organ definition; CT contrast was utilized to ensure accurate liver definition. The injected dose was determined by creating a 3D ROI for the entire mouse. Ellipsoid regions of interest were drawn over the liver, kidneys, bladder, heart, spleen, and lungs to obtain tracer ^{64}Cu concentration values in units of μCi/mL, which were normalized to percent injected dose per mL. One region of interest per organ was drawn to include the maximum volume possible without including nonROI organ tissue. Percent injected dose per organ (%ID) values were calculated based on average organ volumes (*16*). The organ volumes for a 20 g animal were scaled based on the weight of the animals used. Average values with standard deviation are reported.

3D Movies. 3D movies were made using Amira (San Diego, CA) software for one representative animal per group. The 3D movies show the CT image with the dynamic PET data (see online Supporting Information).

RESULTS AND DISCUSSION

^{64}Cu Labeling. The ^{64}Cu chelator DOTA-NHS ester has shown to be a convenient method of labeling synthetic polymers for testing various bioconjugates *in vivo* (*17*). The DOTA moiety (1,4,7,10-tetraazacyclododecane-N,N′,N″,N‴-tetraacetic acid)

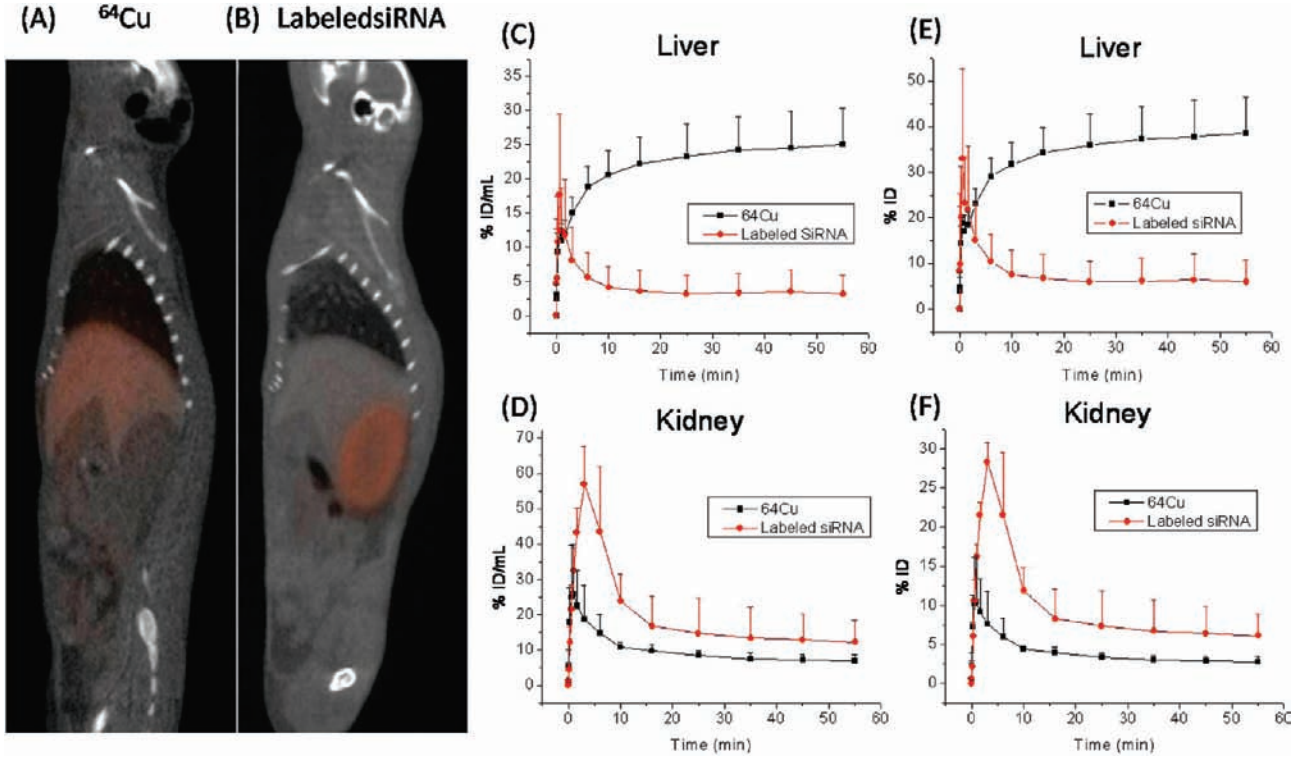


Figure 3. PET/CT images of (A) free ^{64}Cu and (B) ^{64}Cu-labeled siRNA (Labeled siRNA) at 60 min post-injection and corresponding time-activity curves for the (C) liver and (D) kidneys shown as percent injected dose per mL and (E) liver and (F) kidney shown as percent injected dose.

chelates ^{64}Cu while the N-hydroxysuccinamide (NHS) moiety reacts with amines. Accordingly, this strategy was chosen for labeling the primary amines of PBAVE with ^{64}Cu. In order to attach the DOTA group to siRNA, the nucleic acid-reactive DOTA-based chelation reagent, DOTA-NM, was synthesized (Compound 6, Figure 1). It contains the DOTA chelator and an alkylating moiety that reacts with nucleic acid bases randomly. Both labeling procedures were carried out in 2% DOTA, which corresponds to 0.75 mol DOTA/mol siRNA.

The incorporation of ^{64}Cu into DOTA was performed using a standard method of transchelation from slightly acidic acetate or citrate buffers at elevated temperatures. The purification of the labeled species prior to injection was performed by centrifugation on G50 or QAE columns. Successful labeling of both siRNA and PBAVE was confirmed by labeling with ^{64}Cu in which approximately 50 - 85% of ^{64}Cu was conjugated to DOTA siRNA or DOTA PBAVE. It was confirmed that free ^{64}Cu remained in the column after centrifugation by measuring radioactivity in a dose calibrator.

The stability of the ^{64}Cu DOTA complex on PBAVE modified with PEG and NAG was confirmed *in vitro* using radioTLC analysis. It is possible that the carboxyl groups on the carboxy dimethylmaleic anhydride (CDM) derivatives, containing PEG or NAG, could potentially chelate the free ^{64}Cu or strip the ^{64}Cu from the DOTA. However, there was no association of free ^{64}Cu with CDM-modified PBAVE without the presence of DOTA on the PBAVE. ^{64}Cu remained bound to the DOTA-modified PBAVE (data not shown).

The tissue distribution of a variety of ^{64}Cu-labeled molecules and DPC complexes was studied and is depicted in Figure 2. These include free ^{64}Cu (^{64}Cu; Figure 2A), siRNA (labeled siRNA; Figure 2B), ^{64}Cu-labeled siRNA within DPC complexes containing mostly siRNA covalently linked to the PBAVE polymer (DPC; Figure 2C), and ^{64}Cu-labeled PBAVE within unpurified DPC complexes (PBAVE/DPC Figure 2D). The percent conjugation of siRNA to PBAVE was not measured for these experiments, but values typically range from 70 − 90% of the input siRNA (*3*).

Free ^{64}Cu Imaging Studies. Given the possible dissociation of free ^{64}Cu from the polymer and siRNA complexes, the tissue distribution of free ^{64}Cu, unassociated with any other molecule, was determined (Figure 3). Free ^{64}Cu was mainly taken up by the liver after intravenous administration (Figure 3A) in agreement with a previous report (*6*). The concentration in the liver steadily increased and then reached a plateau approximately 30 min after administration (Figure 3C and E). Liver-associated radioactivity for all experiments was confirmed by coregistration of the PET and CT images; the liver was contrast enhanced in the CT. At one hour post-injection 25.1 ± 5.3% injected dose/mL or 38.6 ± 7.8% injected dose of free ^{64}Cu was present in the liver. The only organ, other than the liver, with substantial amount of radioactivity was the kidney (Figure 3D and F). The peak concentration of ^{64}Cu in the kidneys was 25.9 ± 14.2% injected dose/mL at 1.25 min postinjection. At one hour post-injection only 4.3 ± 2.6% of the total injected dose was present in the bladder. Because very little of the ^{64}Cu was present in the bladder and the peak in kidney concentration was seen soon after injection, the peak concentration seen in the kidneys at 1.25 min post-injection was most likely due to ^{64}Cu in the blood and not in the kidney tissue. Free copper normally enters hepatocytes to be used in the synthesis of proteins in the liver (ceruloplasmin) or to be eliminated via biliary excretion (*18*).

^{64}Cu-Labeled siRNA (Labeled siRNA) Imaging Studies. The distribution of ^{64}Cu-labeled siRNA was very different from that of free ^{64}Cu (Figure 3). At the end of 60 min, labeled siRNA accumulated much less in the liver: less than 10% of the injected dose was present in the liver as compared to almost 40% with

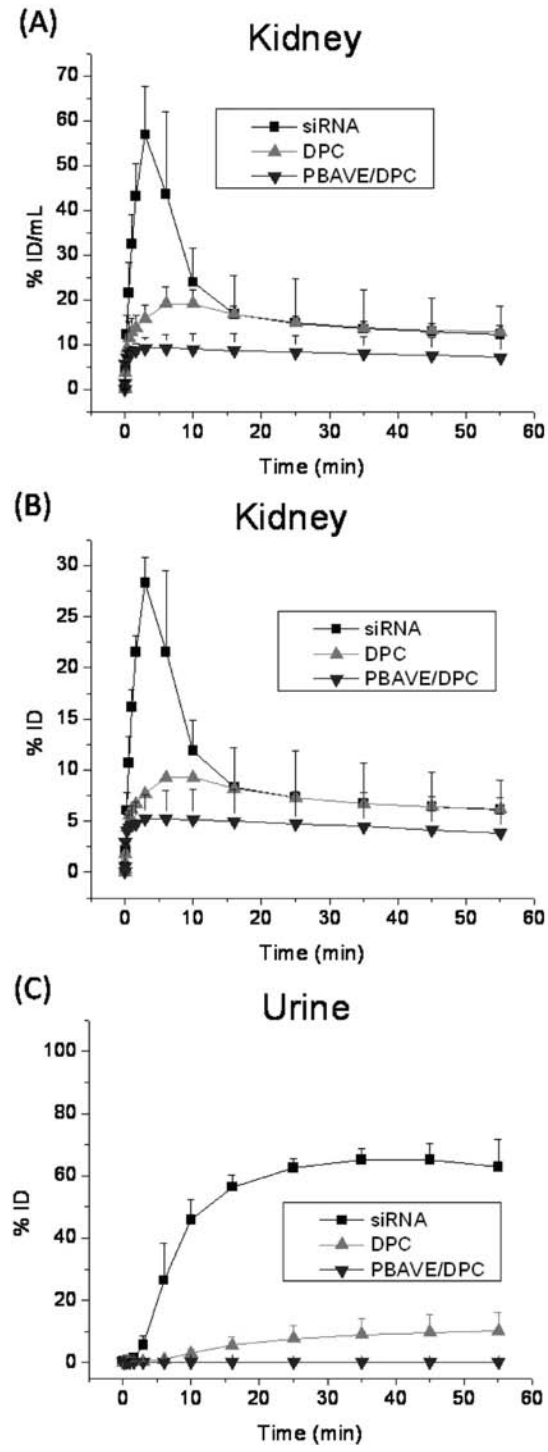


Figure 4. Time activity curves for (A) kidney as percent injected dose per milliliter and (B) kidney as percent injected dose, and (C) urine as percent injected dose for ^{64}Cu-labeled siRNA (labeled siRNA), ^{64}Cu DOTA siRNA DPC (DPC), and ^{64}Cu DOTA PBAVE/DPC (PBAVE/DPC).

free ^{64}Cu. However, the peak amount of labeled siRNA in the liver was 32.9 ± 19.8% of the total injected dose, which occurred 45 s after injection. It cannot be determined whether this is due to siRNA in the blood or actual uptake and degradation in the liver tissue. However, considering the timing of the peak, a large fraction of this was most likely due to labeled siRNA that was still in the blood.

In comparison to free ^{64}Cu, more of the labeled siRNA-associated radioactivity appeared in the kidneys, especially at the early time points (Figure 3B,D,F). The maximum labeled

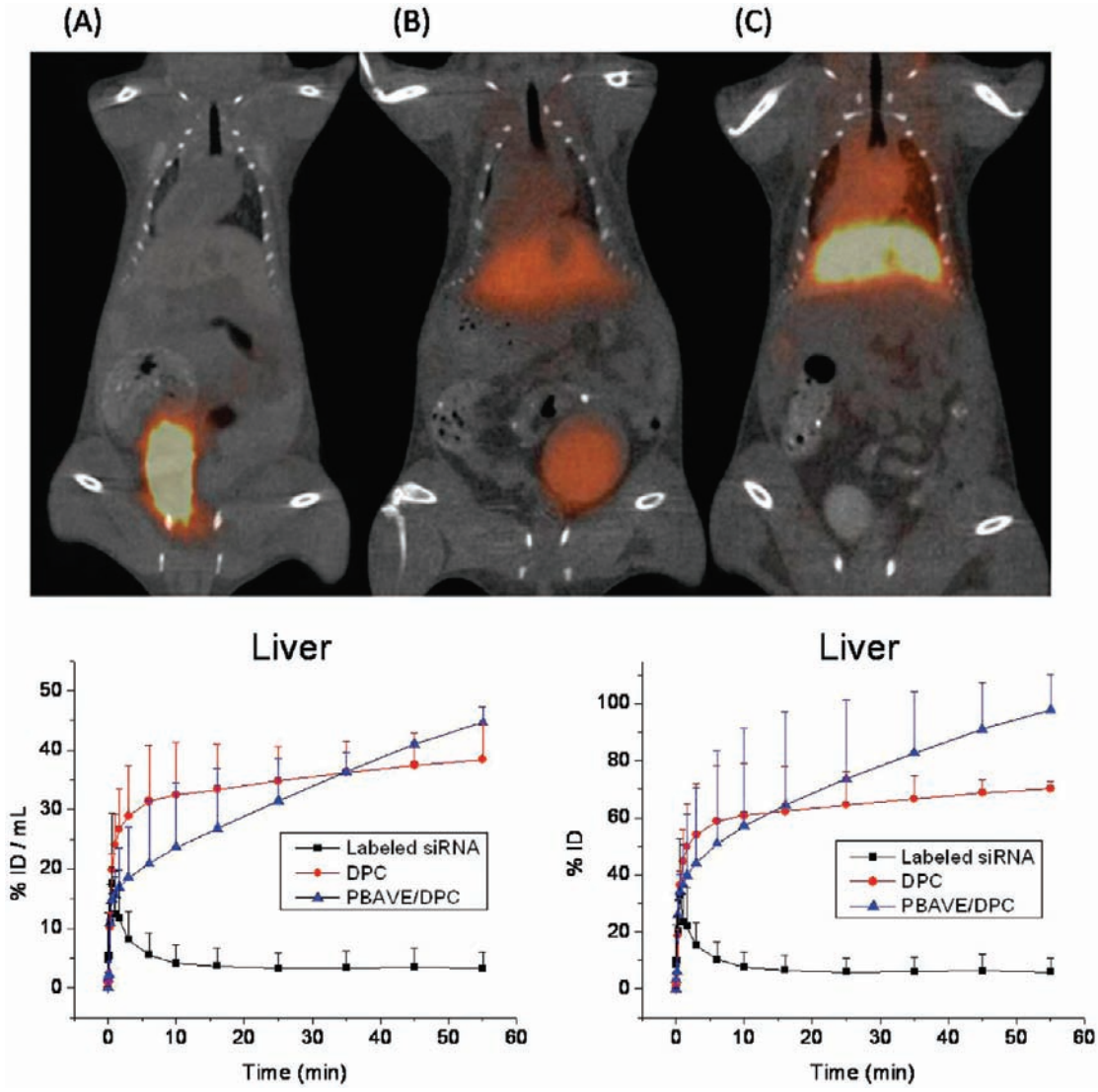


Figure 5. PET/CT images of (A) naked ^{64}Cu DOTA siRNA (siRNA), (B) ^{64}Cu DOTA siRNA DPC (DPC), and (C) ^{64}Cu DOTA PBAVE/DPC (PBAVE/DPC) at 60 min post-injection and corresponding time−activity curve for the liver as (D) percent injected dose per milliliter and (E) percent injected dose.

siRNA seen in the kidneys was 56.9 ± 10.8% injected dose/mL or 28.3 ± 2.5% of the injected dose at 4 min post-injection. At later times, the amount of radioactivity decreased in the kidneys and accumulated in the bladder (Figures 4A,B,C and 5A). At one hour after injection, 62.9 ± 8.7% of the injected dose was present in the bladder (Figure 4C).

Using imaging techniques to study biodistribution, Davis et al. and Braasch et al. reported uptake of siRNA by the liver and kidney in the mouse one hour postinjection with more activity being present in the liver (*6, 11*). However, van de Water et al. reported minimal uptake of siRNA by the liver compared to the kidneys in rats. The differences in van de Water et al.'s reported values and Braasch et al.'s were attributed to the sequence of siRNA, labeling method, or differences in species (*10*). Since the labeling method presented in this paper is similar to the method used by Davis et al., the most likely explanation for the differences in liver uptake may be due to differences in chemical modification, the sequence of siRNA, or differences in animal breeds.

^{64}Cu-Labeled siRNA DPC (DPC) Imaging Studies. With the DPC preparation, a much larger percentage of the injected siRNA accumulated in the liver and a smaller percentage accumulated in the bladder compared with labeled siRNA (Figures 4 and 5B,D,E). A rapid peak followed by a plateau was observed in the liver. One hour after injection of DPC, 38.4 ± 6.0% injected dose/mL or 70.1 ± 2.5% of the injected dose accumulated in the liver.

With the siRNA labeled DPC preparation, the concentration in the kidney peaked 8 min after injection at 19.1 ± 3.1% injected dose/mL or 9.3 ± 2.0% injected dose. At one hour post-injection, 10.1 ± 6.1% of the radioactivity was present in the bladder.

This is the highest siRNA delivery efficiency to the liver yet reported. Kissel et al. reported 15% of the injected dose of PEI/siRNA complexes delivered to the liver, and Morrissey et al. noted 28% of the injected dose of siRNA delivered to the liver using stable nucleic acid−lipid particles (SNALP) (*8, 19*). With both of these studies, the delivery vehicle is not targeted to a specific cell type. For delivery to the liver, SNALP relies on the liver's ability to clear particles of a certain size, and uptake by Kupffer cells is observed (*20*). Thus, it is likely that a significant portion of the siRNA delivered using PEI and SNALP is not taken up by hepatocytes. In contrast, we have previously demonstrated using confocal microscopy that the majority of the liver uptake following DPC siRNA delivery is

in hepatocytes (*3*). This is consistent with receptor ligand mediated uptake of DPC.

^{64}Cu-Labeled PBAVE/DPC (PBAVE/DPC) Imaging Studies. The DPC contains an excess of the NAG-targeted PBAVE not conjugated with siRNA. Thus, the tissue distribution ^{64}Cu-labeled PBAVE (Figures 4 and 5) is of interest in order to gain insight into how the PBAVE behaves *in vivo*. One hour after injection, 44.7 ± 2.7% injected dose/mL or 97.9 ± 12.5% of the injected dose was in the liver. This is substantially more than the ~70% of the injected signal that accumulated in the liver after injection of labeled siRNA in the DPC (Figure 5D). Furthermore, the kinetics of liver accumulation were different between the DPCs that had either the siRNA or PBAVE labeled (Figure 5D,E). As previously noted, the DPC rapidly reached a plateau by 4 min after injection, while the PBAVE/DPC also quickly accumulated by 4 min but kept rising for the duration of the 60 min study (Figure 5D,E).

Also, in contrast to siRNA-labeled DPC, PBAVE/DPC underwent minimal renal filtration (Figure 4). The peak concentration in the kidneys was 9.2 ± 2.4% injected dose/mL or 5.2 ± 2.8% injected dose at 4 min after injection. It is likely that this peak corresponds to radioactivity that is in the blood and not actually being filtered by the kidneys. Only 0.1 ± 0.07% of the injected dose was present in the bladder at one hour.

Accumulation in Other Organs. The total radioactivity associated with the liver, kidneys, bladder, heart, spleen, and lungs accounted for 64% to 100% of the total injected dose for all samples, suggesting that these were the most important organs involved in the biodistribution of the labeled molecules (data not shown). The sum of the activity in these organs was 75.3 ± 11.6% for labeled siRNA, 89.4 ± 6.0% for DPC, and 105.2 ± 16.3% for PBAVE/DPC. Because the %ID per organ calculations were based on scaled organ volumes, these calculations contain more error than the %ID/mL, which are derived from direct measurements. The sum of the %ID per organ being above 100% can be attributed to this error. In addition, less than 2% of the injected label from any of the complexes accumulated in the spleen (data not shown).

CONCLUSION

PET/CT imaging provided a wealth of qualitative and quantitative information about the biodistribution and kinetics of the delivery system without the use of lengthy, invasive tissue distribution studies. One advantage of the *in vivo* imaging method is that it allows one to visualize biodistribution three-dimensionally throughout the entire body. The DPC delivery system effectively delivered a significant portion of its conjugated siRNA, ~70% of the total injected dose, to the liver, the organ of interest. The PBAVE polymer behaved differently from the siRNA in the DPC in that even more accumulated in the liver, ~98% of the injected dose, but at a slower rate. Approximately 10% of the injected DPC-conjugated siRNA accumulated in the bladder, but practically none of the PBAVE-associated signal could be detected there. Further studies are in progress to understand these differences in targeting of DPC-associated siRNA and PBAVE.

ACKNOWLEDGMENT

The authors would like to thank Dave Rozema and Darren Wakefield for helpful discussions, Mark Noble and Alice Nomura for their help with experiments, and John Floberg for help with 3D movies. The authors would also like to thank Christine Wooddell and Hans Herweijer for critically reading the manuscript.

Supporting Information Available: Three movies depicting the first 60 min of postinjection dynamics for the ^{64}Cu-labeled free siRNA, DPC with the ^{64}Cu-labeled PBAVE and DPC with the ^{64}Cu-labeled conjugated siRNA were prepared as indicated in Materials and Methods section. This material is available free of charge via the Internet at http://pubs.acs.org.

LITERATURE CITED

(1) Meister, G., and Tuschl, T. (2004) Mechanisms of gene silencing by double-stranded RNA. *Nature 431*, 343–9.

(2) Whitehead, K. A., Langer, R., and Anderson, D. G. (2009) Knocking down barriers: advances in siRNA delivery. *Nat. Rev. Drug Discovery 8*, 129–38.

(3) Rozema, D. B., Lewis, D. L., Wakefield, D. H., Wong, S. C., Klein, J. J., Roesch, P. L., Bertin, S. L., Reppen, T. W., Chu, Q., Blokhin, A. V., Hagstrom, J. E., and Wolff, J. A. (2007) Dynamic PolyConjugates for targeted in vivo delivery of siRNA to hepatocytes. *Proc. Natl. Acad. Sci. U.S.A. 104*, 12982–7.

(4) Boss, D. S., Olmos, R. V., Sinaasappel, M., Beijnen, J. H., and Schellens, J. H. (2008) Application of PET/CT in the development of novel anticancer drugs. *Oncologist 13*, 25–38.

(5) Abrams, M. T., Koser, M. L., Seitzer, J., Williams, S. C., Dipietro, M. A., Wang, W., Shaw, A. W., Mao, X., Jadhav, V., Davide, J. P., Burke, P. A., Sachs, A. B., Stirdivant, S. M., and Sepp-Lorenzino, L. (2009) Evaluation of efficacy, biodistribution, and inflammation for a potent siRNA nanoparticle: effect of dexamethasone co-treatment. *Mol. Ther.*

(6) Bartlett, D. W., Su, H., Hildebrandt, I. J., Weber, W. A., and Davis, M. E. (2007) Impact of tumor-specific targeting on the biodistribution and efficacy of siRNA nanoparticles measured by multimodality in vivo imaging. *Proc. Natl. Acad. Sci. U.S.A. 104*, 15549–54.

(7) Viel, T., Boisgard, R., Kuhnast, B., Jego, B., Siquier-Pernet, K., Hinnen, F., Dolle, F., and Tavitian, B. (2008) Molecular imaging study on in vivo distribution and pharmacokinetics of modified small interfering RNAs (siRNAs). *Oligonucleotides 18*, 201–12.

(8) Merkel, O. M., Librizzi, D., Pfestroff, A., Schurrat, T., Behe, M., and Kissel, T. (2009) In vivo SPECT and real-time gamma camera imaging of biodistribution and pharmacokinetics of siRNA delivery using an optimized radiolabeling and purification procedure. *Bioconjugate Chem. 20*, 174–82.

(9) Merkel, O. M., Librizzi, D., Pfestroff, A., Schurrat, T., Buyens, K., Sanders, N. N., De Smedt, S. C., Behe, M., and Kissel, T. (2009) Stability of siRNA polyplexes from poly(ethylenimine) and poly(ethylenimine)-g-poly(ethylene glycol) under in vivo conditions: Effects on pharmacokinetics and biodistribution measured by fluorescence fluctuation spectroscopy and single photon emission computed tomography (SPECT) imaging. *J. Controlled Release*.

(10) van de Water, F. M., Boerman, O. C., Wouterse, A. C., Peters, J. G., Russel, F. G., and Masereeuw, R. (2006) Intravenously administered short interfering RNA accumulates in the kidney and selectively suppresses gene function in renal proximal tubules. *Drug Metab. Dispos. 34*, 1393–7.

(11) Braasch, D. A., Paroo, Z., Constantinescu, A., Ren, G., Oz, O. K., Mason, R. P., and Corey, D. R. (2004) Biodistribution of phosphodiester and phosphorothioate siRNA. *Bioorg. Med. Chem. Lett. 14*, 1139–43.

(12) Rahmim, A., and Zaidi, H. (2008) PET versus SPECT: strengths, limitations and challenges. *Nucl. Med. Commun. 29*, 193–207.

(13) Zimmermann, T. S., Lee, A. C., Akinc, A., Bramlage, B., Bumcrot, D., Fedoruk, M. N., Harborth, J., Heyes, J. A., Jeffs, L. B., John, M., Judge, A. D., Lam, K., McClintock, K., Nechev, L. V., Palmer, L. R., Racie, T., Rohl, I., Seiffert, S., Shanmugam, S., Sood, V., Soutschek, J., Toudjarska, I., Wheat, A. J., Yaworski, E., Zedalis, W., Koteliansky, V., Manoharan, M., Vornlocher, H. P., and MacLachlan, I. (2006) RNAi-mediated gene silencing in non-human primates. *Nature 441*, 111–4.

(14) Slattum, P. M., Wolff, J. A., Hagstrom, J. E., and Budker, V. G. (2008), United States of America Patent No. 7,326,780.

(15) Wolff, J. A., Hagstrom, J. E., Slattum, P. M., and Budker, V. G. (2003), United States of America Patent No 6,593,465.

(16) Davies, B., and Morris, T. (1993) Physiological parameters in laboratory animals and humans. *Pharm. Res. 10*, 1093–5.

(17) Xu, J., Sun, G., Rossin, R., Hagooly, A., Li, Z., Fukukawa, K. I., Messmore, B. W., Moore, D. A., Welch, M. J., Hawker, C. J., and Wooley, K. L. (2007) Labeling of polymer nanostructures for medical imaging: importance of crosslinking extent, spacer length, and charge density. *Macromolecules 40*, 2971–2973.

(18) Owen, C. A., Jr., and Orvis, A. L. (1970) Release of copper by rat liver. *Am. J. Physiol. 218*, 88–91.

(19) Morrissey, D. V., Lockridge, J. A., Shaw, L., Blanchard, K., Jensen, K., Breen, W., Hartsough, K., Machemer, L., Radka, S., Jadhav, V., Vaish, N., Zinnen, S., Vargeese, C., Bowman, K., Shaffer, C. S., Jeffs, L. B., Judge, A., MacLachlan, I., and Polisky, B. (2005) Potent and persistent in vivo anti-HBV activity of chemically modified siRNAs. *Nat. Biotechnol. 23*, 1002–7.

(20) Morrissey, D. V., Blanchard, K., Shaw, L., Jensen, K., Lockridge, J. A., Dickinson, B., McSwiggen, J. A., Vargeese, C., Bowman, K., Shaffer, C. S., Polisky, B. A., and Zinnen, S. (2005) Activity of stabilized short interfering RNA in a mouse model of hepatitis B virus replication. *Hepatology 41*, 1349–56.

BC900558Z

Functionalized Congeners of $P2Y_1$ Receptor Antagonists: 2-Alkynyl (*N*)-Methanocarba 2′-Deoxyadenosine 3′,5′-Bisphosphate Analogues and Conjugation to a Polyamidoamine (PAMAM) Dendrimer Carrier

Sonia de Castro,[†] Hiroshi Maruoka,[†] Kunlun Hong,[||] S. Michael Kilbey II,[||] Stefano Costanzi,[§] Béatrice Hechler,[⊥] Garth G. Brown, Jr.,[▼] Christian Gachet,[⊥] T. Kendall Harden,[‡] and Kenneth A. Jacobson*[,†]

Molecular Recognition Section and Laboratory of Biological Modeling, National Institute of Diabetes and Digestive and Kidney Diseases, NIH, Bethesda, Maryland, PerkinElmer Inc., 940 Winter Street, Waltham, Massachusetts 02451, Department of Pharmacology, University of North Carolina, School of Medicine, Chapel Hill, North Carolina, Center for Nanophase Materials Sciences, Oak Ridge National Laboratory, Oak Ridge, Tennessee 37831, and UMR_S949 Inserm-Université de Strasbourg, EFS-Alsace, Strasbourg, France. Received December 21, 2009; Revised Manuscript Received March 26, 2010

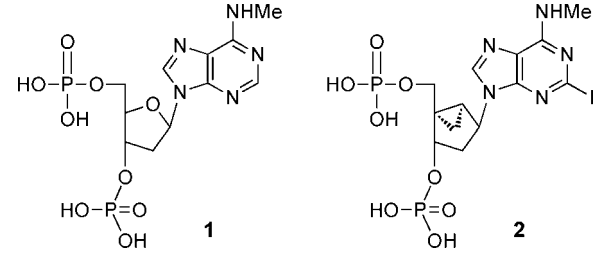
The $P2Y_1$ receptor is a prothrombotic G protein-coupled receptor (GPCR) activated by ADP. Preference for the North (N) ring conformation of the ribose moiety of adenine nucleotide 3′,5′-bisphosphate antagonists of the $P2Y_1$ receptor was established by using a ring-constrained methanocarba (a bicyclo[3.1.0]hexane) ring as a ribose substitute. A series of covalently linkable N^6-methyl-(*N*)-methanocarba-2′-deoxyadenosine-3′,5′-bisphosphates containing extended 2-alkynyl chains was designed, and binding affinity at the human (h) $P2Y_1$ receptor determined. The chain of these functionalized congeners contained hydrophilic moieties, a reactive substituent, or biotin, linked via an amide. Variation of the chain length and position of an intermediate amide group revealed high affinity of carboxylic congener **8** (K_i 23 nM) and extended amine congener **15** (K_i 132 nM), both having a 2-(1-pentynoyl) group. A biotin conjugate **18** containing an extended ε-aminocaproyl spacer chain exhibited higher affinity than a shorter biotinylated analogue. Alternatively, click coupling of terminal alkynes of homologous 2-dialkynyl nucleotide derivatives to alkyl azido groups produced triazole derivatives that bound to the $P2Y_1$ receptor following deprotection of the bisphosphate groups. The preservation of receptor affinity of the functionalized congeners was consistent with new $P2Y_1$ receptor modeling and ligand docking. Attempted $P2Y_1$ antagonist conjugation to PAMAM dendrimer carriers by amide formation or palladium-catalyzed reaction between an alkyne on the dendrimer and a 2-iodopurine-derivatized nucleotide was unsuccessful. A dialkynyl intermediate containing the chain length favored in receptor binding was conjugated to an azide-derivatized dendrimer, and the conjugate inhibited ADP-promoted human platelet aggregation. This is the first example of attaching a strategically functionalized P2Y receptor antagonist to a PAMAM dendrimer to produce a multivalent conjugate exhibiting a desired biological effect, i.e., antithrombotic action.

INTRODUCTION

The family of P2Y receptors consists of eight subtypes of G protein-coupled receptors (GPCRs) that respond to extracellular purine and pyrimidine nucleotides. Native ligands of these receptors include ATP, ADP, UTP, UDP, and UDP-glucose (*1, 2*). Two subfamilies have been delineated on the basis of second messengers and sequence homology, i.e., a cluster of $P2Y_1$, $P2Y_2$, $P2Y_4$, $P2Y_6$, and $P2Y_{11}$ receptors, which activate phospholipase C-β via G_q, and a smaller cluster of $P2Y_{12}$, $P2Y_{13}$, and $P2Y_{14}$, which inhibit adenylyl cyclase via G_i.

$P2Y_1$ receptors are involved in activation of platelets and other hematopoietic cells (*3*−*6*), vascular function (*7*), apoptotic events (*8*), inflammation, glial cell differentiation and function (*9*−*11*), and development of vision (*12*). Activation of a $P2Y_1$ receptor expressed in brain astrocytes participates in cytoprotection, as indicated in a forebrain model using hydrogen peroxide, one of the main reactive oxygen species generated by traumatic brain injury, ischemic stroke, and various neurodegenerative diseases (*10, 11*). On the surface of platelets, simultaneous activation of the $P2Y_1$ and $P2Y_{12}$ receptors by ADP induces aggregation (*3, 4*). The $P2Y_1$-mediated response is associated with the initial shape change and rapid aggregation, and the $P2Y_{12}$ receptor is associated with amplification of aggregation. $P2Y_{12}$ receptor antagonists are used extensively as antithrombotic agents, and new antagonists are currently under development (*13*).

Chart 1. Prototypical Nucleotide Antagonists of the $P2Y_1$ Receptor



A prototypical competitive antagonist of the $P2Y_1$ receptor, bisphosphate derivative MRS2179 **1** (Chart 1) widely used as

* Corresponding author. Laboratory of Bioorganic Chemistry, National Institutes of Diabetes and Digestive and Kidney Diseases, NIH, Bldg. 8A, Rm. B1A-19, Bethesda, MD 20892-0810, USA. E-mail: kajacobs@helix.nih.gov. Phone: 301-496-9024. Fax: 301-480-8422.

[†] Molecular Recognition Section, National Institute of Diabetes and Digestive and Kidney Diseases.

[§] Laboratory of Biological Modeling, National Institute of Diabetes and Digestive and Kidney Diseases.

[▼] PerkinElmer Inc.

[‡] University of North Carolina, School of Medicine.

[||] Oak Ridge National Laboratory.

[⊥] UMR_S949 Inserm-Université de Strasbourg.

10.1021/bc900569u © 2010 American Chemical Society
Published on Web 06/21/2010

a pharmacological probe, has a K_B of 102 nM (*14*). Newer and more potent and selective $P2Y_1$ receptor antagonists, such as the conformationally locked North (N)-methanocarba nucleotide MRS2500 **2** ((1′*R*,2′*S*,4′*S*,5′*S*)-4-(2-iodo-6-methylamino-purin-9-yl)-1-[(phosphato)-methyl]-2-(phosphato)-bicyclo[3.1.0]hexane, K_i 0.79 nM), which contains a bicyclo[3.1.0]hexane ring system in place of ribose, have been designed and shown to have promise in preclinical studies as antithrombotic agents (*5, 15*−*18*). This novel drug concept is also supported by studies of mice in which the $P2Y_1$ receptor has been genetically deleted (*19, 20*).

While most substitutions at positions other than C2 of adenine in this family of (N)-methanocarba nucleotides related to MRS2500 decrease antagonist potency at the $P2Y_1$ receptor, 2-alkynyl substitution preserves or enhances antagonist potency (*18*). Structure−activity relationship (SAR) analysis indicated that hydrophobic substituents at the C2 position are favored. In the present study, we have extended our search for antagonists of the $P2Y_1$ receptor by modifying the C2 position with novel alkynyl substituents. We have generated new $P2Y_1$ antagonists using a conceptual approach for covalently linking GPCR ligands to carrier molecules while preserving the receptor interactions, i.e., the functionalized congener approach (*21*). Carrier molecules may include small molecules, biopolymers, or synthetic polymers that are biocompatible. The linkage used between the nucleotide pharmacophore and a carrier moiety was explored systematically in a series of small model compounds that contain typical linking moieties that may be used for tethering to the polymer, and thus can be evaluated for effects on receptor recognition. These model compounds incorporated groups such as a carboxylic acid, an amine, or a terminal alkyne that allow introduction of hydrophilic or chemically reactive substituents or link to a carrier. A terminal alkyne-derivatized nucleotide was coupled by a "click" reaction (*22*) to a polymeric carrier, a polyamidoamine (PAMAM)[1] dendrimer that had been derivatized with terminal azide groups. The most biologically favorable chain length among the resulting triazole derivatives was incorporated in a covalent conjugate with the dendrimer. The resulting multivalent conjugate displayed antithrombotic activity characteristic of $P2Y_1$ antagonists in a human platelet preparation (*5, 16*). Attempted conjugation of the nucleotides to dendrimers by alternate routes, e.g., amide formation or palladium-catalyzed reaction between an alkyne on the dendrimer and an iodoaryl-derivatized nucleotide, was unsuccessful.

EXPERIMENTAL PROCEDURES

Chemical Synthesis. *Materials and Instrumentation.* Methylamine, PAMAM dendrimer (G3, 20 wt % solution in methanol; G4, 5 wt % solution in methanol) with an ethylenediamine core, and other reagents and solvents were purchased from Sigma-Aldrich (St. Louis, MO). Dialysis membranes (Spectra/Pore Membrane, MWCO 3500, flat width 18 mm) were purchased from Spectrum Laboratories, Inc. (Rancho Dominguez, CA). Compound **25** was synthesized as reported from the starting material **24** (Organomed Corp., Coventry, RI) (*15*). Azido dendrimer derivative **51** was prepared as described (*23*). ^{1}H NMR spectra of monomeric derivatives were obtained with a Varian Gemini 300 spectrometer using $CDCl_3$ and CD_3OD as solvents. Chemical shifts are expressed in δ values (ppm) with tetramethylsilane ($\delta = 0.00$) for $CDCl_3$ and water (δ 3.30) for CD_3OD. TLC analysis was performed using aluminum sheets precoated with silica gel F_{254} (0.2 mm) from Aldrich. The nucleotide derivatives were purified by HPLC (Agilent 1100 series) before biological testing, and the purity of each was shown to be >95%. The mobile phases consisted of System A, linear gradient solvent system of CH_3CN/triethyl ammonium acetate from 5/95 to 60/40 in 20 min, flow rate 1.0 mL/min; System B, linear gradient solvent system of CH_3CN/tetrabutyl ammonium phosphate from 20/80 to 60/40 in 20 min, flow rate 1.0 mL/min; *For systems A and B*: Zorbax Eclipse 5 μ XDB-C18 analytical column (250 × 4.6 mm; Agilent Technologies, Palo Alto, CA). System C, linear gradient solvent system of CH_3CN/tetrabutyl ammonium phosphate from 20/80 to 60/40 in 13 min, flow rate 0.5 mL/min with a Zorbax SB-Aq 5 μ analytical column (50 × 4.6 mm; Agilent); System D, with a Luna 5 L RP-C18(2) semipreparative column (250 × 10.0 mm; Phenomenex, Torrance, CA) and using the following conditions: flow rate of 2 mL/min; 10 mM triethylammonium acetate (TEAA)-CH_3CN from 100:0 to 0:100 in 10 min and held at 0:100 for 10 min; and System E, a Luna 5 L RP-C18(2) semipreparative column (250 × 10.0 mm; Phenomenex, Torrance, CA) using the following conditions: flow rate of 2 mL/min; 10 mM triethylammonium acetate (TEAA)-CH_3CN from 100:0 to 60:40 in 30 min. HRMS measurements were performed on a proteomics optimized Q-TOF-2 (Micromass-Waters) using external calibration with polyalanine, unless noted. Observed mass accuracies are those expected, based on the known performance of the instrument as well as trends in masses of standard compounds observed at intervals during the series of measurements. Reported masses are observed masses uncorrected for this time-dependent drift in mass accuracy.

General Procedure for 2-(Methoxycarbonylalkynyl) Derivatives 26−28. A solution of **25** (30 mg, 0.038 mmol) in DMF (5 mL) containing Et_3N (7.6 μL) was treated with $(PPh_3)_2PdCl_2$ (2.63 mg, 0.0038 mmol) and CuI (1.5 mg, 0.0076 mmol) (*13*). Then, the appropriate acetylene derivative (0.076 mmol, 2 equiv) was subsequently added dropwise to the reaction mixture, which was then stirred under argon at room temperature for 7 h. The solvent was removed under reduced pressure, and the residue was purified by flash chromatography to obtain the desired compounds as solids.

*(1′R,2′S,4′S,5′S)-Phosphoric Acid Di-tert-butylester 1-(Di-tert-butoxy-phosphoryloxymethyl)-4-{2-[(methoxycarbonyl)-1-propynyl]-6-methylaminopurin-9-yl}-bicyclo[3.1.0]hex-2-yl Ester (**26**).* Yield: 28.40 (90%). ^{1}H NMR ($CDC1_3$) δ 8.10 (s, 1H), 5.26 (dd, 1H, J = 14.2, 7.9 Hz), 5.10 (d, 1H, J = 6.9 Hz), 4.58 (dd, 1H, J = 11.1, 4.7 Hz), 3.80 (dd, 1H, J = 11.1, 6.3 Hz), 3.64 (s, 3H), 3.15 (c, 3H, J = 7.5 Hz), 2.67 (m, 4H), 2.23 (dd, 1H, J = 15.3, 8.4 Hz), 2.02 (m, 1H), 1.70 (m, 1H), 1.43, 1.41, 1.40, 1.39 (4s, 36H), 1.04 (m, 1H), 0.90 (m, 1H); HRMS (ESI MS *m*/*z*) calculated for $C_{35}H_{58}N_5O_{10}P_2^+$ $(M+H)^+$ 770.3653; found 770.3658.

*(1′R,2′S,4′S,5′S)-Phosphoric Acid Di-tert-butylester 1-(Di-tert-butoxy-phosphoryloxymethyl)-4-{2-[(methoxycarbonyl)-1-pentynyl]-6-methylaminopurin-9-yl}-bicyclo[3.1.0]hex-2-yl Ester (**27**).* Yield: 34 mg (85%). ^{1}H NMR ($CDC1_3$) δ 8.10 (s, 1H), 5.26 (dd, 1H, J = 8.7, 2.4 Hz), 5.12 (d, 1H, J = 7.2 Hz), 4.59 (dd, 1H, J = 11.4, 4.8 Hz), 3.77 (dd, 1H, J = 11.7, 6.3 Hz), 3.61 (s, 3H),

[1]Abbreviations: A3P5P, adenosine-3′,5′-bisphosphate; cAMP, adenosine 3′,5′-cyclic phosphate; CHO, Chinese hamster ovary; EDC, *N*-ethyl-*N*′-dimethylaminopropylcarbodiimide; DCM, dichloromethane; DIEA, diisopropylethylamine; DMEM, Dulbecco's modified Eagle's medium; DMF, *N*,*N*-dimethylformamide; EDTA, ethylenediaminetetraacetic acid; EtOAc, ethyl acetate; G_i, GTP-binding protein containing α_i subunit; G_q, GTP-binding protein containing α_q subunit; GPCR, G protein-coupled receptor; HATU, 2-(1*H*-7-azabenzotriazol-1-yl)-1,1,3,3-tetramethyl uronium hexafluorophosphate methanaminium; HEK, human embryonic kidney; HEPES, 4-(2-hydroxyethyl)-1-piperazineethanesulfonic acid; HPLC RT, high performance liquid chromatography retention time; HRMS, high resolution mass spectroscopy; MeOH, methanol; MRS2179, N^6-methyl-2′-deoxyadenosine-3′,5′-bisphosphate; MRS2500, ((1′*R*,2′*S*,4′*S*,5′*S*)-4-(2-iodo-6-methylamino-purin-9-yl)-1-[(phosphato)-methyl]-2-(phosphato)-bicyclo[3.1.0]hexane); PAMAM, polyamidoamine; PBS, phosphate-buffered saline; PDB, Protein Data Bank; PKC, protein kinase C; TEA, triethylamine; TEAA, triethylammonium acetate; TFA, trifluoroacetic acid; TLC, thin layer chromatography.

3.15 (m, 3H), 2.47 (m, 2H), 2.38 (m, 1H), 2.24 (m, 1H), 1.92 (m,1H), 1.82 (m, 3H),1.42, 1.41, 1.40, 1.38 (4s, 36 H), 1.04 (m, 1H), 0.90 (m, 1H); HRMS (ESI MS *m*/*z*) calculated for $C_{36}H_{60}N_5O_{10}P_2^+$ $(M+H)^+$ 784.3815; found 784.3794.

*(1′R,2′S,4′S,5′S)-Phosphoric Acid Di-tert-butylester 1-(Di-tert-butoxy-phosphoryloxymethyl)-4-{2-[(methoxycarbonyl)-1-hexynyl]-6-methylaminopurin-9-yl}-bicyclo[3.1.0]hex-2-yl Ester (**28**).* Yield: 29 mg (95%). ^{1}H NMR ($CDC1_3$) δ 8.07 (s, 1H), 5.26 (dd, 1H, J = 14.7, 8.7 Hz), 5.12 (d, 1H, J = 6.9 Hz), 4.57 (dd, 1H, J = 11.1, 4.6 Hz), 3.76 (dd, 1H, J = 11.4, 6.3 Hz), 3.60 (s, 3H), 3.14 (c, 3H, J = 7.2 Hz), 2.40 (t, 2H, J = 7.2 Hz), 2.29 (t, 2H, J = 7.2 Hz), 2.18 (m, 1H), 2.02 (m, 1H), 1.68 (m, 4H), 1.41, 1.39, 1.37 (3s, 36H), 1.04 (m, 1H), 0.88 (m, 1H); HRMS (ESI MS *m*/*z*) calculated for $C_{37}H_{62}N_5O_{10}P_2^+$ $(M+H)^+$ 798.3966; found 798.3953.

General Procedure for 2-(Methoxycarbonylalkynyl) Derivatives 5−7. A mixture of the appropriate ester **26**−**28** (0.012 mmol) in CH_2C1_2 (1 mL) was treated with trifluoroacetic acid (TFA, 29 μL), and the reaction mixture was stirred at room temperature for 3 h. After removal of the solvent, the crude product was purified by HPLC with System E and isolated in the triethylammonium salt form to obtain the desired compounds as solid.

*(1′R,2′S,4′S,5′S)-4-{2-[(Methoxycarbonyl)-1-propynyl]-6-methylaminopurin-9-yl}-1-[(phosphato)-methyl]-2-(phosphato)-bicyclo[3.1.0]hexane (**5**).* Yield: 8.3 mg (73%). ^{1}H NMR (D_2O) δ 8.52 (s, 1H), 5.23 (dd, 1H, J = 13.8, 6.8 Hz), 5.02 (d, 1H, J = 6.0 Hz), 4.59 (dd, 1H, J = 11.7, 5.1 Hz), 3.79 (s, 3H), 3.71 (dd, 1H, J = 11.4, 4.5 Hz), 3.12 (s, 3H), 2.82 (m, 4H), 2.29 (dd, 1H, J = 15.1, 7.9 Hz), 2.04 (m, 1H), 1.70 (m, 1H), 1.24 (m, 1H), 1.04 (m, 1H); ^{31}P NMR (D_2O) δ 0.90 (s), 0.40 (s); HRMS (ESI MS *m*/*z*) calculated for $C_{19}H_{24}N_5O_{10}P_2^-$ $(M-H)^-$ 544.1004; found 544.0998; HPLC RT 6.9 min (98%) in solvent System A, 15.1 min (99%) in System B.

*(1′R,2′S,4′S,5′S)-4-{2-[(Methoxycarbonyl)-1-pentynyl]-6-methylaminopurin-9-yl}-1-[(phosphato)-methyl]-2-(phosphato)-bicyclo[3.1.0]hexane (**6**).* Yield: 9.3 mg (82%). ^{1}H NMR (D_2O) δ 8.53 (s, 1H), 5.22 (m, 1H), 5.05 (m, 1H), 4.59 (m, 1H), 3.79 (s, 3H), 3.68 (m, 1H), 3.12 (s, 3H), 2.64 (t, 4H, J = 7.5 Hz), 2.58 (t, 1H, J = 6.9 Hz), 2.29 (m, 1H), 1.99 (m, 2H), 1.24 (m, 1H), 1.04 (m, 1H); ^{31}P NMR (D_2O) δ 0.87 (s), 0.23 (s); HRMS (ESI MS *m*/*z*) calculated for $C_{20}H_{26}N_5O_{10}P_2^-$ $(M-H)^-$, 558.1160; found, 558.1135; HPLC RT 7.5 min (98%) in solvent System A, 15.7 min (99%) in System B.

*(1′R,2′S,4′S,5′S)-4-{2-[(Methoxycarbonyl)-1-hexynyl]-6-methylaminopurin-9-yl}-1-[(phosphato)-methyl]-2-(phosphato)-bicyclo[3.1.0]hexane (**7**).* Yield: 8.3 mg (71%). ^{1}H NMR (D_2O) δ 8.55 (s, 1H), 5.21 (m, 1H), 5.05 (m, 1H), 4.60 (m, 1H), 3.73 (s, 3H), 3.68 (m, 1H), 3.13 (s, 3H), 2.55 (t, 4H, J = 6.8 Hz), 2.52 (t, 1H, J = 7.3 Hz), 2.26 (m, 1H), 1.95 (m, 2H), 1.54 (m, 1H), 1.72 (m, 1H), 1.26 (m, 1H), 1.05 (m, 1H); ^{31}P NMR (D_2O) δ 0.92 (s), 0.41 (s); HRMS (ESI MS *m*/*z*) calculated for $C_{21}H_{28}N_5O_{10}P_2^-$ $(M-H)^-$ 572.1317; found 572.1286; HPLC RT 8.2 min (98%) in solvent System A, 16.4 min (99%) in System B.

General Procedure for 2-(Carboxyalkynyl) Derivatives 8−10. Aqueous KOH (0.5 mL of a 0.25 M solution) was added to a solution of the appropriate ester **5**−**7** (0.008 mmol) in water (1 mL), and the mixture was stirred overnight at room temperature. After removal of the solvent, the crude product was purified by HPLC with System E and isolated in the triethylammonium salt form to obtain the desired compounds as solids.

*(1′R,2′S,4′S,5′S)-4-{2-[Hydroxycarbonyl]-1-propynyl]-6-methylaminopurin-9-yl}-1-[(phosphato)-methyl]-2-(phosphato)-bicyclo[3.1.0]hexane (**8**).* Yield: 5.2 mg (69%). ^{1}H NMR (D_2O) δ 8.49 (s, 1H), 5.16 (dd, 1H, J = 15.0, 9.0 Hz), 5.01 (d, 1H, J = 6.6 Hz), 4.55 (dd, 1H, J = 10.2, 5.1 Hz), 3.70 (dd, 1H, J = 11.4, 4.7 Hz), 3.09 (s, 3H), 2.70 (dd, 4H, J = 18.1, 5.8 Hz), 2.25 (m. 1H), 1.94 (m, 2H), 1.08 (t, 1H, J = 7.5 Hz); ^{31}P NMR (D_2O) δ 0.63 (s), 0.16 (s); HRMS (ESI MS *m*/*z*) calculated for $C_{18}H_{22}N_5O_{10}P_2^-$ $(M-H)^-$ 530.0847; found 530.0347; HPLC RT 5.5 min (98%) in solvent System A, 15.6 min (99%) in System B.

*(1′R,2′S,4′S,5′S)-4-{2-[Hydroxycarbonyl]-1-pentynyl]-6-methylaminopurin-9-yl}-1-[(phosphato)-methyl]-2-(phosphato)-bicyclo[3.1.0]hexane (**9**).* Yield: 5.0 mg (64%). ^{1}H NMR (D_2O) δ 8.48 (s, 1H), 5.19 (m, 1H), 5.00 (m, 1H), 4.55 (m, 1H), 3.68 (m, 1H), 3.09 (s, 3H), 2.52 (t, 4H, J = 7.2 Hz), 2.44 (t, 1H, J = 7.2 Hz), 2.24 (m, 1H), 1.92 (m, 2H), 1.03 (m, 1H); ^{31}P NMR (D_2O) δ 0.70 (s), 0.31 (s); HRMS (ESI MS *m*/*z*) calculated for $C_{19}H_{24}N_5O_{10}P_2^-$ $(M-H)^-$ 544.1004; found 544.0998; HPLC RT 5.0 min (98%) in solvent System A, 15.4 min (99%) in System B.

*(1′R,2′S,4′S,5′S)-4-{2-[Hydroxycarbonyl]-1-hexynyl]-6-methylaminopurin-9-yl}-1-[(phosphato)-methyl]-2-(phosphato)-bicyclo[3.1.0]hexane (**10**).* Yield: 2.6 mg (60%). ^{1}H NMR (D_2O) δ 8.56 (s, 1H), 5.23 (m, 1H), 6.00 (m, 1H), 4.56 (m, 1H), 3.65 (m, 1H), 3.13 (s, 3H), 2.53 (t, 4H, J = 6.2 Hz), 2.27 (t, 1H, J = 6.6 Hz), 2.03 (m, 1H), 1.89 (m, 2H), 1.70 (m, 1H), 1.21 (m, 1H), 0.99 (m, 1H); ^{31}P NMR (D_2O) δ 1.94 (s), 1.29 (s); HRMS (ESI MS *m*/*z*) calculated for $C_{2O}H_{26}N_5O_{10}P_2^-$ $(M-H)^-$ 558.1160; found 558.1155; HPLC RT 5.2 min (98%) in solvent System A, 16.0 min (99%) in System B.

General Procedure for 2-(Aminoalkylamino-carbonylalkynyl) Derivatives 29−34. A solution of the appropriate phosphate-protected ester derivative **26**−**28** (0.0135 mmol) in methanol (12 μL) was treated with ethylenediamine (0.22 mL, 3.2 mmol) or its homologue. The reaction mixture was stirred overnight at room temperature. The residue was purified by flash chromatography EtOAc/MeOH (5:1) to obtain the desired compounds as solids.

*(1′R,2′S,4′S,5′S)-Phosphoric Acid Di-tert-butylester 1-(Di-tert-butoxy-phosphoryloxymethyl)-4-{2-[(2-aminoethylaminocarbonyl)-1-propynyl]-6-methylaminopurin-9-yl}-bicyclo[3.1.0]hex-2-yl Ester (**29**).* Yield from **26** and ethylenediamine: 7.4 mg (69%). ^{1}H NMR ($CDC1_3$) δ 8.24 (s, 1H), 5.47 (dd, 1H, J = 15.0, 8.1 Hz), 5.08 (d, 1H, J = 7.2 Hz), 4.58 (dd, 1H, J = 11.4, 5.1 Hz), 4.02 (dd, 1H, J = 11.1, 6.3 Hz), 3.14 (br s, 3H), 2.80 (t, 2H, J = 7.2 Hz), 2.61 (t, 2H, J = 7.2 Hz), 2.40 (dd, 1H, J = 15.3, 8.4 Hz), 2.22 (m, 1H), 1.90 (m, 1H), 1.41, 1.37, 1.36 (3s, 36H), 1.23 (m, 1H), 1.13 (m, 1H); HRMS (ESI MS *m*/*z*) calculated for $C_{36}H_{62}N_7O_9P_2^+$ $(M+H)^+$ 798.4079; found 798.4035.

*(1′R,2′S,4′S,5′S)-Phosphoric Acid Di-tert-butylester 1-(Di-tert-butoxy-phosphoryloxymethyl)-4-{2-[(2-aminoethylaminocarbonyl)-1-pentynyl]-6-methylaminopurin-9-yl}-bicyclo[3.1.0]hex-2-yl Ester (**30**).* Yield from **27** and ethylenediamine: 7.4 mg (68%). ^{1}H NMR ($CDC1_3$) δ 8.07 (s, 1H), 6.66 (br s, 1H), 5.83 (m, 1H), 5.43 (dd, 1H, J = 14.1, 7.5 Hz), 5.11 (d, 1H, J = 6.9 Hz), 4.69 (dd, 1H, J = 10.8, 5.0 Hz), 3.97 (dd, 1H, J = 10.8, 6.3 Hz), 3.33 (c, 2H, J = 5.7 Hz), 3.25 (m, 3H), 2.84 (t, 2H, J = 6.0 Hz), 2.54 (t, 2H, J = 6.6 Hz), 2.47 (t, 2H, J = 7.2 Hz), 2.31 (dd, 1H, J = 15.6, 8.4 Hz), 2.11 (c, 1H, J = 7.5 Hz), 2.01 (t, 1H, J = 7.2 Hz), 1.43, 1.40, 1.35 (3s, 36H), 1.08 (m, 1H), 1.00 (m, 1H); HRMS (ESI MS *m*/*z*) calculated for $C_{37}H_{64}N_7O_9P_2^+$ $(M+H)^+$ 812.4235; found 812.4221.

*(1′R,2′S,4′S,5′S)-Phosphoric Acid Di-tert-butylester 1-(Di-tert-butoxy-phosphoryloxymethyl)-4-{2-[(2-aminoethylaminocarbonyl)-1-hexynyl]-6-methylaminopurin-9-yl}-bicyclo[3.1.0]hex-2-yl Ester (**31**).* Yield from **28** and ethylenediamine: 8.1 mg (73%). ^{1}H NMR ($CDC1_3$) δ 8.04 (s, 1H), 5.29 (dd, 1H, J = 14.4, 7.5 Hz), 5.08 (d, 1H, J = 7.2 Hz), 4.59 (dd, 1H, J = 11.1, 4.5 Hz), 3.80 (dd, 1H, J = 10.9, 6.5 Hz), 3.25 (c, 3H, J = 5.5 Hz), 3.17 (s, 1H), 2.77 (t, 2H, J = 6.0 Hz), 2.48 (t, 2H, J = 6.7 Hz), 2.24 (t,

2H, $J = 7.3$ Hz), 2.22 (m, 1H), 2.01 (m, 1H), 1.40, 1.32, 1.33 (3s, 36H), 1.04 (m, 1H), 0.90 (m, 1H); HRMS (ESI MS *m*/*z*) calculated for $C_{38}H_{66}N_7O_9P_2^+$ $(M+H)^+$ 826.4392; found 826.4434.

*(1′R,2′S,4′S,5′S)-Phosphoric Acid Di-tert-butylester 1-(Di-tert-butoxy-phosphoryloxymethyl)-4-{2-[(3-aminopropylaminocarbonyl)-1-propynyl]-6-methylaminopurin-9-yl}-bicyclo[3.1.0]hex-2-yl Ester (**32**).* Yield from **26** and 1,3-diaminopropane: 10.4 mg (95%). ^{1}H NMR ($CDC1_3$) δ 8.09 (s, 1H), 5.39 (dd, 1H, $J = 14.0$, 7.2 Hz), 5.09 (d, 1H, $J = 7.2$ Hz), 4.66 (dd, 1H, $J = 10.8$, 4.2 Hz), 3.93 (dd, 1H, $J = 10.5$, 6.0 Hz), 3.43 (m, 2H), 3.19 (br s, 3H), 3.11 (m, 1H), 3.05 (m, 1H), 2.97 (m, 2H), 2.85 (t, 2H, $J = 7.2$ Hz), 2.60 (m, 2H), 2.13 (m, 1H), 1.88 (m, 2H), 1.76 (m, 1H), 1.41, 1.39, 1.37 (3s, 36H), 1.28 (m, 1H), 1.22 (m, 1H); HRMS (ESI MS *m*/*z*) calculated for $C_{37}H_{64}N_7O_9P_2^+$ $(M+H)^+$ 812.4235; found 812.4225.

*(1′R,2′S,4′S,5′S)-Phosphoric Acid Di-tert-butylester 1-(Di-tert-butoxy-phosphoryloxymethyl)-4-{2-[(4-aminobutylaminocarbonyl)-1-propynyl]-6-methylaminopurin-9-yl}-bicyclo[3.1.0]hex-2-yl Ester (**33**).* Yield from **26** and 1,4-diaminobutane: 7.8 mg (70%). ^{1}H NMR ($CDC1_3$) δ 8.17 (s, 1H), 5.39 (m, 1H), 5.11 (t, 1H, $J =$ 6.3 Hz), 4.94 (m, 1H), 4.67 (dd, 1H, $J = 11.4$, 5.4 Hz), 3.97 (m, 1H), 3.03 (m, 2H), 3.22 (m, 2H), 3.10 (s, 1H), 2.77 (t, 2H, $J = 7.2$ Hz), 2.57 (t, 2H, $J = 6.9$ Hz), 2.38 (m, 2H), 2.31 (c, 2H, $J = 7.5$ Hz), 2.15 (m, 1H), 2.05 (m, 1H), 1.42, 1.39, 1.36 (3s, 36H), 1.84−1.54 (m, 2H), 1.10 (m, 1H), 0.94 (m, 1H); HRMS (ESI MS *m*/*z*) calculated for $C_{38}H_{66}N_7O_9P_2^+$ $(M+H)^+$ 826.4392; found 826.4452.

*(1′R,2′S,4′S,5′S)-Phosphoric Acid Di-tert-butylester 1-(Di-tert-butoxy-phosphoryloxymethyl)-4-{2-[(6-aminohexylaminocarbonyl)-1-propynyl]-6-methylaminopurin-9-yl}-bicyclo[3.1.0]hex-2-yl Ester (**34**).* Yield from **26** and 1,6-diaminohexane: 7.8 mg (68%). ^{1}H NMR ($CDC1_3$) δ 8.20 (s, 1H), 5.36 (m, 1H), 5.13 (d, 1H, $J =$ 6.9 Hz), 4.68 (dd, 1H, $J = 15.9$, 6.9 Hz), 3.88 (dd, 1H, $J =$ 11.1, 6.3 Hz), 3.31 (m, 2H), 2.99 (m, 1H), 2.76 (t, 2H, $J = 8.0$ Hz), 2.57 (t, 2H, $J = 8.0$ Hz), 2.32 (m, 2H), 2.18 (m, 1H), 1.75 (m, 2H), 1.49, 1.478, 1.26 (3s, 36H), 1.10 (m, 1H), 0.94 (m, 1H); HRMS (ESI MS *m*/*z*) calculated for $C_{40}H_{70}N_7O_9P_2^+$ $(M+H)^+$ 854.4705; found 854.4731.

General Procedure for 2-(Aminoalkylamino-carbonylalkynyl) Derivatives 11−16. A mixture of the appropriate phosphate-protected derivatives **29**−**34** (0.0045 mmol) in CH_2C1_2 (0.5 mL) was treated with TFA (11 μL) and the reaction mixture was stirred at room temperature for 3 h. After removal of the solvent, the crude product was purified by HPLC with System E and isolated in the triethylammonium salt form to obtain the desired compounds as solids.

*(1′R,2′S,4′S,5′S)-4-{2-[(2-Aminoethylaminocarbonyl)-1-propynyl]-6-methylaminopurin-9-yl}-1-[(phosphato)-methyl]-2-(phosphato)-bicyclo[3.1.0]hexane (**11**).* Yield from **29**: 3.1 mg (71%). ^{1}H NMR (D_2O) δ 8.63 (s, 1H), 5.09 (dd, 1H, $J = 16.2$, 9.0 Hz), 4.92 (d, 1H, $J = 6.3$ Hz), 4.50 (dd, 1H, $J = 11.4$, 4.2 Hz), 3.63 (m, 1H), 3.58 (t, 3H, $J = 6.3$ Hz), 2.82 (t, 2H, $J = 6.7$ Hz), 2.67 (t, 2H, $J = 6.6$ Hz), 2.25 (dd, 1H, $J = 14.7$, 7.6 Hz), 1.95 (m, 1H), 1.18 (m, 1H), 1.00 (m, 1H); ^{31}P NMR (D_2O) δ 3.19 (s), 2.60 (s); HRMS (ESI MS *m*/*z*) calculated for $C_{20}H_{28}N_7O_9P_2^-$ $(M-H)^-$ 572.1429; found 572.1412. HPLC RT 5.3 min (98%) in solvent System A, 5.6 min (99%) in System B.

*(1′R,2′S,4′S,5′S)-4-{2-[(2-Aminoethylaminocarbonyl)-1-pentynyl]-6-methylaminopurin-9-yl}-1-[(phosphato)-methyl]-2-(phosphato)-bicyclo[3.1.0]hexane (**12**).* Yield from **30**: 3.0 mg (68%). ^{1}H NMR (D_2O) δ 8.54 (s, 1H), 5.15 (dd, 1H, $J = 15.9$, 8.6 Hz), 4.94 (d, 1H, $J = 6.6$ Hz), 4.55 (dd, 1H, $J = 11.5$, 5.6 Hz), 3.7 (dd, 1H, $J = 11.4$, 4.5 Hz), 5.7 (t, 2H, $J = 5.7$ Hz), 3.17 (t, 2H, $J = 6.0$ Hz), 3.09 (br s, 3H), 2.55 (m, 2H), 2.24 (dd, 1H, $J =$ 14.5, 7.6 Hz), 1.97 (m, 3H), 1.21 (m, 1H), 1.00 (m, 1H); ^{31}P NMR (D_2O) δ 2.02 (s), 1.58 (s); HRMS (ESI MS *m*/*z*) calculated for $C_{21}H_{30}N_7O_9P_2^-$ $(M-H)^-$ 586.1580; found 586.1592. HPLC RT 5.9 min (98%) in solvent System A, 5.8 min (99%) in System B.

*(1′R,2′S,4′S,5′S)-4-{2-[(2-Aminoethylaminocarbonyl)-1-hexynyl]-6-methylaminopurin-9-yl}-1-[(phosphato)-methyl]-2-(phosphato)-bicyclo[3.1.0]hexane (**13**).* Yield from **31**: 3.3 mg (73%). ^{1}H NMR (D_2O) δ 8.55 (s, 1H), 5.18 (dd, 1H, $J = 11$, 7.2 Hz), 5.00 (d, 1H, $J = 6.3$ Hz), 4.57 (dd, 1H, $J = 11.4$, 5.7 Hz), 3.66 (dd, 1H, $J = 11.1$, 4.8 Hz), 3.52 (t, 2H, $J = 6.0$ Hz), 3.16 (t, 2H, $J = 6.0$ Hz), 3.11 (s, 3H), 2.55 (t, 2H, $J = 6.9$ Hz), 2.40 (t, 2H, $J = 7.5$ Hz), 2.26 (m, 1H), 2.00 (m, 1H), 1.94 (m, 1H), 1.84 (m, 2H), 1.69 (m, 2H), 1.21 (m, 1H), 1.00 (m, 1H); ^{31}P NMR (D_2O) δ 1.92 (s), 1.43 (s); HRMS (ESI MS *m*/*z*) calculated for $C_{22}H_{32}N_7O_9P_2^-$ $(M-H)^-$ 600.1737; found 600.1735. HPLC RT 6.4 min (98%) in solvent System A, 6.3 min (99%) in System B.

*(1′R,2′S,4′S,5′S)-4-{2-[(3-Aminopropylaminocarbonyl)-1-propynyl]-6-methylaminopurin-9-yl}-1-[(phosphato)-methyl]-2-(phosphato)-bicyclo[3.1.0]hexane (**14**).* Yield from **32**: 2.2 mg (50%). ^{1}H NMR ($CDC1_3$) δ 8.75 (s, 1H), 5.05 (m, 1H), 5.03 (m, 1H), 4.96 (m, 1H), 4.47 (m, 1H), 3.64 (m, 1H), 3.35 (t, 2H, $J = 5.1$ Hz), 3.11 (s, 2H), 2.81 (t, 2H, $J = 6.3$ Hz), 2.61 (t, 2H, $J = 6.3$ Hz), 2.24 (m, 1H), 1.93 (m, 2H), 1.85 (m, 2H), 1.65 (m, 1H), 1.16 (m, 1H), 0.99 (m, 1H); HRMS (ESI MS *m*/*z*) calculated for $C_{21}H_{30}N_7O_9P_2^-$ $(M-H)^-$ 586.1580; found 586.1594. ^{31}P NMR (D_2O) δ 1.90 (s), 1.19 (s); HPLC RT 5.5 min (99%) in solvent System A, 5.0 min (99%) in System B.

*(1′R,2′S,4′S,5′S)-4-{2-[(4-Aminobutylaminocarbonyl)-1-propynyl]-6-methylaminopurin-9-yl}-1-[(phosphato)-methyl]-2-(phosphato)-bicyclo[3.1.0]hexane (**15**).* Yield from **33**: 2.2 mg (49%). ^{1}H NMR ($CDC1_3$) δ 8.55 (s, 1H), 5.11 (dd, 1H, $J = 10.5$, 6.9 Hz), 4.94 (d, 1H, $J = 7.2$ Hz), 4.53 (dd, 1H, $J = 12.0$, 6.0 Hz), 3.59 (dd, 1H, $J = 13.2$, 6.0 Hz), 3.07 (m, 2H), 2.78 (t, 2H, $J = 6.3$ Hz), 2.56 (m, 4H), 2.18 (m, 1H), 2.00 (m, 4H), 1.91 (m, 2H), 1.54, 1.44 (m, 4H), 1.17 (m, 1H), 0.96 (m, 1H); ^{31}P NMR (D_2O) δ 1.99 (s), 1.63 (s); HRMS (ESI MS *m*/*z*) calculated for $C_{22}H_{32}N_7O_9P_2^-$ $(M-H)^-$ 600.1737; found 600.1763. HPLC RT 5.8 min (98%) in solvent System A, 5.4 min (99%) in System B.

*(1′R,2′S,4′S,5′S)-4-{2-[(6-Aminohexylaminocarbonyl)-1-propynyl]-6-methylaminopurin-9-yl}-1-[(phosphato)-methyl]-2-(phosphato)-bicyclo[3.1.0]hexane (**16**).* Yield from **34**: 2.9 mg (63%). ^{1}H NMR ($CDC1_3$) δ 8.55 (s, 1H), 6.03 (bs, 1H), 5.15 (m, 1H), 5.03 (m, 1H), 4.48 (m, 1H), 3.71 (m, 1H), 3.65 (m, 2H), 3.44 (m, 2H), 3.15 (s, 2H), 2.99 (t, 2H, $J = 7.8$ Hz), 2.66 (m, 1H), 2.29 (m, 1H), 1.98 (m, 1H), 1.88 (m, 1H), 1.69 (m, 1H), 1.43 (m, 1H), 1.15 (m, 1H), 0.97 (m, 1H); ^{31}P NMR (D_2O) δ 3.09 (s), 2.48 (s); HRMS (ESI MS *m*/*z*) calculated for $C_{24}H_{36}N_7O_9P_2^+$ $(M+H)^+$ 628.2055; found 628.2070. HPLC RT 7.4 min (99%) in solvent System A, 6.6 min (98%) in System B.

*(1′R,2′S,4′S,5′S)-Phosphoric Acid Di-tert-butylester 1-(Di-tert-butoxy-phosphoryloxymethyl)-4-{2-[(6-(6-oxo-6-(2-(5-(2-oxohexahydro-1H-thieno[3,4-d]imidazol-4-yl)pentanamido)ethylamino)hex-1-ynyl)-1-propynyl]-6-methylaminopurin-9-yl}-1-[(phosphato)-methyl]-2-(phosphato)-bicyclo[3.1.0]hexane (**35**).* HATU (2.8 mg, 0.0074 mmol, 1.2 equiv) was added to a solution of **30** (5 mg, 0.0062 mmol), biotin (1.67 mg, 0.0068 82 mmol, 1.1 equiv), and DIEA (1.4 μL, 0.008 mmol, 1.3 equiv) in DMF (0.5 mL), and the resulting mixture was stirred overnight at room temperature. The residue was purified by flash chromatography EtOAc/MeOH (10:1 to 3:1) to give 3.9 mg of **35** (61%) as a solid. ^{1}H NMR ($CDC1_3$) δ 8.07 (s, 1H), 5.73 (m, 2H), 5.02 (m, 4H,), 4.69 (m, 1H), 4.51 (m, 1H), 4.25 (m, 4H), 3.80 (m, 1H), 3.44 (m, 4H), 3.30 (m, 3H), 3.20 (m, 2H), 2.82 (m, 1H), 2.52 (m, 2H), 1.62 (m, 6H), 1.43, 1.40, 1.35 (3s, 36H), 1.08 (m, 1H); HRMS (ESI MS *m*/*z*) calculated for $C_{47}H_{78}N_9O_{11}P_2S^+$ $(M+H)^+$ 1038.5011; found 1038.5016.

*(1′R,2′S,4′S,5′S)-Phosphoric Acid Di-tert-butylester 1-(Di-tert-butoxy-phosphoryloxymethyl)-4-{2-[6-(6-oxo-6-(2-(6-(5-(2-oxohexahydro-1H-thieno[3,4-d]imidazol-4-yl)pentanamido)hexanamido)ethylamino)hex-1-ynyl)]-6-methylaminopurin-9-yl}-1-[(phosphato)-methyl]-2-(phosphato)-bicyclo[3.1.0]hexane (**36**).* A solution of **30** (5 mg, 0.0062 mmol) and biotinamidohexanoic acid 3-sulfo-*N*-hydroxysuccinimide ester sodium salt (5.18 mg, 0.0093 mmol, 1.5 equiv) in DMF (1 mL) was treated with bicarbonate buffer (0.002 M Na_2CO_3, 0.048 M $NaHCO_3$, 0.15 M NaCl) until pH 8.5. The mixture was stirred overnight at room temperature. The residue was purified by flash chromatography using EtOAc/MeOH (10:1 to 3:1) to give 5.6 mg of **36** (78%) as a solid. ^{1}H NMR ($CDC1_3$) δ 8.08 (s, 1H), 5.44 (dd, 1H, J = 14.4, 7.8 Hz), 5.08 (d, 1H, J = 6.9 Hz), 4.69 (dd, 1H, J = 11.1, 5.1 Hz), 4.51 (m, 2H), 4.36 (m, 2H), 4.14 (t, 1H, J = 7.2 Hz), 4.01 (dd, 1H, J = 11.1, 6.0 Hz), 3.38 (m, 3H), 3.32 (m, 2H), 2.92 (m, 2H), 2.53 (t, 2H, J = 6.6 Hz), 2.46 (t, 2H, J = 7.5 Hz), 2.22 (m, 1H), 1.92 (m, 6H), 1.63, 1.49, 1.47, 1.46 (3s, 36H), 1.27 (m, 1H), 1.12 (m, 1H); HRMS (ESI MS *m*/*z*) calculated for $C_{53}H_{89}N_{10}O_{12}P_2S^+$ $(M+H)^+$ 1151.5952; found 1151.5901.

*(1′R,2′S,4′S,5′S)-4-{2-[(6-(6-Oxo-6-(2-(5-(2-oxohexahydro-1H-thieno[3,4-d]imidazol-4-yl)pentanamido)ethylamino)hex-1-ynyl)-1-propynyl]-6-methylaminopurin-9-yl}-1-[(phosphato)-methyl]-2-(phosphato)-bicyclo[3.1.0]hexane (**17**).* A solution of **35** (3 mg, 0.0029 mmol) in CH_2C1_2 (0.3 mL) was treated with TFA (9 μL), and the reaction mixture was stirred at room temperature for 3 h. After removal of the solvent, the crude product was purified by HPLC with System E to give 0.6 mg of **17** (20%, isolated in the triethylammonium salt form) as a solid. ^{1}H NMR ($CDC1_3$) δ 8.68 (s, 1H), 5.00 (m, 4H,), 4.88 (m, 1H), 4.48 (m, 1H), 4.23 (m, 4H), 3.83 (m, 1H), 3.59 (m, 4H), 3.33 (m, 3H), 3.12 (m, 2H), 3.01 (m, 1H), 2.82 (m, 1H), 2.52 (c, 2H, J = 6.7 Hz), 2.23 (t, 2H, J = 7.8 Hz), 1.97 (m, 2H), 1.58 (m, 1H), 0.44 (m, 1H); HRMS (ESI MS *m*/*z*) calculated for $C_{31}H_{44}N_9O_{11}P_2S^-$ $(M-H)^-$ 812.2362; found 812.2358. RT 6.7 min (98%) in solvent System A, 12.4 min (98%) in System B.

*(1′R,2′S,4′S,5′S)-4-{2-[6-(6-Oxo-6-(2-(6-(5-(2-oxohexahydro-1H-thieno[3,4-d]imidazol-4-yl)pentanamido)hexanamido)ethylamino)hex-1-ynyl)]-6-methylaminopurin-9-yl}-1-[(phosphato)-methyl]-2-(phosphato)-bicyclo[3.1.0]hexane (**18**).* A solution of **36** (5 mg, 0.0043 mmol) in CH_2C1_2 (0.3 mL) was treated with TFA (10 μL), and the reaction mixture was stirred at room temperature for 3 h. After removal of the solvent, the crude product was purified by HPLC with System E to give 1.58 mg of **18** (36%, isolated in the triethylammonium salt form) as a solid. ^{1}H NMR (D_2O) 8.65 (s, 1H), 5.24 (dd, 1H, J = 14.4, 7.8 Hz), 5.04 (d, 1H, J = 6.0 Hz), 4.60 (m, 1H), 4.48 (dd, 2H, J = 8.1, 4.3 Hz), 4.39 (m, 2H), 3.66 (m, 3H), 3.16 (m, 2H), 3.04 (m, 2H), 2.57 (t, 2H, J = 6.9 Hz), 2.52 (t, 2H, J = 7.5 Hz), 2.30 (m, 1H), 1.59 (m, 6H), 1.45 (m, 1H); ^{31}P NMR (D_2O) δ 2.78 (s), 2.13 (s); HRMS (ESI MS *m*/*z*) calculated for $C_{37}H_{55}N_{10}O_{12}P_2S^-$ $(M-H)^-$ 925.3102; found 925.3126. HPLC RT 7.24 min (99%) in solvent System A, 12.3 min (99%) in System B.

*(1′R,2′S,4′S,5′S)-4-{2-[(6-(6-(4-(Fluorosulfonyl)phenethylamino)-6-oxohex-1-ynyl)]-6-methylaminopurin-9-yl}-1-[(phosphato)-methyl]-2-(phosphato)-bicyclo[3.1.0]hexane (**19**).* HATU (2.8 mg, 0.0074 mmol, 1.2 equiv) was added to a solution of **9** (2 mg, 0.0021 mmol), 4-(2-aminoethyl)benzenesulfonyl fluoride hydrochloride **37** (1.67 mg, 0.006 82 mmol, 1.1 equiv), and DIEA (1.4 μL, 0.008 mmol, 1.3 equiv) in DMF (0.5 mL), and the resulting mixture was stirred overnight at room temperature. The crude product was purified by HPLC with System E to give 0.6 mg of **19** (25%, isolated in the triethylammonium salt form) as a solid. ^{1}H NMR (D_2O) δ 8.53 (s, 1H), 8.17 (s, 1H), 8.12 (d, 2H, J = 8.3 Hz), 7.73 (d, 2H, J = 8.3 Hz), 5.21 (m, 1H), 4.92 (m, 1H), 3.48 (m, 1H), 3.25 (s, 3H), 2.97 (m, 4H), 2.31 (m, 1H), 2.28 (m, 1H), 2.17 (m, 2H), 1.31 (m, 1H); HRMS (ESI MS *m*/*z*) calculated for $C_{27}H_{33}N_6O_{11}P_2S^-$ $(M-F)^-$ 711.1403; found 711.1498; HPLC RT 10.9 min (96%) in solvent System A, 17.6 min (96%) in System B.

*(1′R,2′S,4′S,5′S)-Phosphoric Acid Di-tert-butylester 1-(Di-tert-butoxyphosphoryloxymethyl)-4-{2-(1,5-hexadiyn-1-yl)-6-methylaminopurin-9-yl}-bicyclo[3.1.0]hex-2-yl Ester (**38**).* To a solution of **25** (10 mg, 0.013 mmol) in DMF (0.2 mL), 1,5-hexadiyne (50% in pentane, 12 mL, 0.13 mmol), tetrakis(triphenylphosphine)-palladium(0) (2.9 mg, 0.0025 mmol), copper(I) iodide (1.0 mg, 0.0051 mmol), and triethylamine (3.5 mL, 0.025 mmol) were added. The mixture was stirred overnight at room temperature. The residue was concentrated and purified by flash chromatography using $CHCl_3$/EtOAc (1:1) to $CHCl_3$/EtOAc/MeOH (5:5:1) and purified again by HPLC with System D to give 5.0 mg of **38** (53%) as a pale yellow oil. ^{1}H NMR ($CDC1_3$) δ 8.16 (s, 1H), 5.90−5.77 (br, 1H), 5.33 (dd, 1H, J = 14.4, 7.8 Hz), 5.19 (d, 1H, J = 6.9 Hz), 4.68 (dd, 1H, J = 11.1, 4.8 Hz), 3.83 (dd, 1H, J = 11.1, 6.3 Hz), 3.23 (brs, 3H), 2.72 (t, 2H, J = 7.5 Hz), 2.61−2.53 (m, 2H), 2.29 (dd, 1H, J = 15.0, 8.1 Hz), 2.15−2.03 (m, 2H), 1.50, 1.49, 1.47 (3s, 36H), 1.13 (dd, 1H, J = 5.7, 4.5 Hz), 0.96 (dd, 1H, J = 8.4, 6.3 Hz); HRMS (ESI MS *m*/*z*) calculated for $C_{35}H_{56}N_5O_8P_2^+$ $(M+H)^+$ 736.3604; found 736.3604.

*(1′R,2′S,4′S,5′S)-Phosphoric Acid Di-tert-butylester 1-(Di-tert-butoxyphosphoryloxymethyl)-4-{2-(1,6-heptadiyn-1-yl)-6-methylaminopurin-9-yl}-bicyclo[3.1.0]hex-2-yl Ester (**39**).* To a solution of **25** (10 mg, 0.013 mmol) in DMF (0.2 mL), 1,6-heptadiyne (15 mL, 0.13 mmol), tetrakis(triphenylphosphine)palladium(0) (2.9 mg, 0.0025 mmol), copper(I) iodide (1.0 mg, 0.0051 mmol), and triethylamine (3.5 mL, 0.025 mmol) were added. The mixture was stirred overnight at room temperature. The residue was concentrated and purified by flash chromatography using $CHCl_3$/EtOAc (1:1) to $CHCl_3$/EtOAc/MeOH (5:5:1) and purified again by HPLC with System D to give 4.8 mg of **39** (50%) as pale yellow oil. ^{1}H NMR ($CDC1_3$) δ 8.15 (s, 1H), 5.89−5.78 (br, 1H), 5.35 (dd, 1H, J = 14.4, 7.8 Hz), 5.20 (d, 1H, J = 6.9 Hz), 4.67 (dd, 1H, J = 11.1, 4.8 Hz), 3.83 (dd, 1H, J = 11.1, 6.3 Hz), 3.24 (brs, 3H), 2.60 (t, 2H, J = 7.2 Hz), 2.39 (dt, 2H, J = 7.2, 2.7 Hz), 2.30 (dd, 1H, J = 15.3, 8.1 Hz), 2.17−2.04 (m, 1H), 1.98 (t, 1H, J = 2.7 Hz), 1.91 (dt, 2H, J = 7.2, 7.2 Hz), 1.50, 1.49, 1.47, 1.46 (4s, 36H), 1.09 (dd, 1H, J = 8.4, 6.9 Hz), 0.96 (dd, 1H, J = 8.1, 6.6 Hz); HRMS (ESI MS *m*/*z*) calculated for $C_{36}H_{58}N_5O_8P_2^+$ $(M+H)^+$ 750.3761; found 750.3761.

*(1′R,2′S,4′S,5′S)-Phosphoric Acid Di-tert-butylester 1-(Di-tert-butoxyphosphoryloxymethyl)-4-{2-(1,7-octadiyn-1-yl)-6-methylaminopurin-9-yl}-bicyclo[3.1.0]hex-2-yl Ester (**40**).* To a solution of **25** (10 mg, 0.013 mmol) in DMF (0.2 mL), 1,7-octadiyne (17 mL, 0.13 mmol), tetrakis(triphenylphosphine)palladium(0) (2.9 mg, 0.0025 mmol), copper(I) iodide (1.0 mg, 0.0051 mmol), and triethylamine (3.5 mL, 0.025 mmol) were added. The mixture was stirred overnight at room temperature. The residue was concentrated and purified by flash chromatography using $CHCl_3$/EtOAc (1:1) to $CHCl_3$/EtOAc/MeOH (5:5:1) and purified again by HPLC with System D to give 3.7 mg of **40** (38%) as pale yellow oil. ^{1}H NMR ($CDC1_3$) δ 8.15 (s, 1H), 5.86−5.73 (br, 1H), 5.33 (dd, 1H, J = 15.0, 8.4 Hz), 5.21 (d, 1H, J = 6.9 Hz), 4.68 (dd, 1H, J = 10.8, 4.5 Hz), 3.83 (dd, 1H, J = 11.1, 6.3 Hz), 3.24 (brs, 3H), 2.50 (t, 2H, J = 6.9 Hz), 2.30−2.22 (m, 2H), 2.10 (dd, 1H, J = 15.0, 7.8 Hz), 1.96 (t, 1H, J = 2.7 Hz), 1.82−1.65 (m, 4H), 1.50, 1.49, 1.47, 1.46 (4s, 36H), 1.13 (dd, 1H, J = 6.0, 4.2 Hz), 0.97 (dd, 1H, J = 7.8, 4.2 Hz); HRMS (ESI MS *m*/*z*) calculated for $C_{37}H_{60}N_5O_8P_2^+$ $(M+H)^+$ 764.3917; found 764.3917.

*(1′R,2′S,4′S,5′S)-Phosphoric Acid Di-tert-butylester 1-(Di-tert-butoxyphosphoryloxymethyl)-4-{2-(1,8-nonadiyn-1-yl)-6-methylaminopurin-9-yl}-bicyclo[3.1.0]hex-2-yl Ester (**41**).* To a solution of

25 (10 mg, 0.013 mmol) in DMF (0.2 mL), 1,8-nonadiyne (19 mL, 0.13 mmol), tetrakis(triphenylphosphine)palladium(0) (2.9 mg, 0.0025 mmol), copper(I) iodide (1.0 mg, 0.0051 mmol), and triethylamine (3.5 mL, 0.025 mmol) were added. The mixture was stirred overnight at room temperature. The residue was concentrated and purified by flash chromatography using $CHCl_3$/EtOAc (1:1) to $CHCl_3$/EtOAc/MeOH (5:5:1) and purified again by HPLC with System D to give 5.4 mg of **41** (55%) as pale yellow oil. ^{1}H NMR ($CDC1_3$) δ 8.16 (s, 1H), 5.90−5.77 (br, 1H), 5.33 (dd, 1H, J = 14.4, 7.8 Hz), 5.19 (d, 1H, J = 6.9 Hz), 4.68 (dd, 1H, J = 11.1, 4.8 Hz), 3.83 (dd, 1H, J = 11.1, 6.3 Hz), 3.23 (brs, 3H), 2.72 (t, 2H, J = 7.5 Hz), 2.61−2.53 (m, 2H), 2.29 (dd, 1H, J = 15.0, 8.1 Hz), 2.15−2.03 (m, 2H), 1.50, 1.49, 1.47 (3s, 36H), 1.13 (dd, 1H, J = 5.7, 4.5 Hz), 0.96 (t, 1H, J = 7.5 Hz); HRMS (ESI MS *m*/*z*) calculated for $C_{38}H_{62}N_5O_8P_2^+$ $(M+H)^+$ 778.4074; found 778.4074.

General Procedure for *tert*-Bu-Protected Triazole Derivatives 42−45. Freshly prepared aqueous sodium ascorbate (1 M, 1 mmol equiv) was added to a mixture of the appropriate *tert*-Bu-protected dialkyne derivative (compounds **38**−**41**, 1.66 mmol equiv) and *N*-(2-azidoethyl)acetamide (*24*) (3.4 mmol equiv) in a mixture of THF (46 mL per mmol equiv) and water (46 mL per mmol equiv), followed by addition of 7.5% aqueous copper(II) sulfate pentahydrate (3.2 μL per mmol equiv). The reaction mixture was stirred at room temperature overnight, and the reaction mixture was concentrated. The crude product was used in the next reaction without purification.

*(1′R,2′S,4′S,5′S)-Phosphoric Acid Di-tert-butylester 1-(Di-tert-butoxyphosphoryloxymethyl)-4-{2-[(4-(2-acetamidoethyl)-1H-1,2,3-triazol-4-yl)-but-1-yn-1-yl]-6-methylaminopurin-9-yl}-bicyclo[3.1.0]hex-2-yl Ester (**42**).* Prepared according to the general procedure from compound **38** (5.0 mg, 6.8 mmol).

*(1′R,2′S,4′S,5′S)-Phosphoric Acid Di-tert-butylester 1-(Di-tert-butoxyphosphoryloxymethyl)-4-{2-[(5-(2-acetamidoethyl)-1H-1,2,3-triazol-4-yl)-pent-1-yn-1-yl]-6-methylaminopurin-9-yl}-bicyclo[3.1.0]hex-2-yl Ester (**43**).* Prepared according to the general procedure from compound **39** (4.8 mg, 6.4 mmol).

*(1′R,2′S,4′S,5′S)-Phosphoric Acid Di-tert-butylester 1-(Di-tert-butoxyphosphoryloxymethyl)-4-{2-[(6-(2-acetamidoethyl)-1H-1,2,3-triazol-4-yl)-hex-1-yn-1-yl]-6-methylaminopurin-9-yl}-bicyclo[3.1.0]hex-2-yl Ester (**44**).* Prepared according to the general procedure from compound **40** (2.1 mg, 2.7 mmol).

*(1′R,2′S,4′S,5′S)-Phosphoric Acid Di-tert-butylester 1-(Di-tert-butoxyphosphoryloxymethyl)-4-{2-[(7-(2-acetamidoethyl)-1H-1,2,3-triazol-4-yl)-hept-1-yn-1-yl]-6-methylaminopurin-9-yl}-bicyclo[3.1.0]hex-2-yl Ester (**45**).* Prepared according to the general procedure from compound **41** (5.4 mg, 6.9 mmol).

General Procedure for Phosphate-Deprotected Triazole Derivatives 20−23. A solution of a *tert*-Bu-protected triazole derivative prepared above (compounds **42**−**45**, crude) in CH_2C1_2 (0.21 mL) was treated with TFA (0.07 mL), and the reaction mixture was stirred at room temperature for 3 h. After removal of the solvent, the crude product was purified by HPLC with a Luna 5 L RP-C18(2) semipreparative column (250 × 10.0 mm; Phenomenex, Torrance, CA) and using the following conditions: flow rate of 2 mL/min; 10 mM triethylammonium acetate (TEAA)-CH_3CN from 100:0 to 70:30 in 20 min to give the desired products **20**−**23** as white amorphous solids (triethylammonium salt form).

*(1′R,2′S,4′S,5′S)-4-{2-[(5-(2-Acetamidoethyl)-1H-1,2,3-triazol-4-yl)-pent-1-yn-1-yl]-6-methylaminopurin-9-yl}-1-[(phosphato)-methyl]-2-(phosphato)-bicyclo[3.1.0]hexane (**21**).* Prepared according to the general procedure from compound **43** to give 3.6 mg of **21** (65% in 2 steps, isolated as triethylammonium salt form). ^{1}H NMR (D_2O) δ 8.70−8.55 (br, 1H), 7.89 (s, 1H), 5.33−5.18 (br, 1H), 5.08−5.01 (m, 1H), 4.70−4.55 (br, 1H), 4.48 (t, 2H, J = 5.7 Hz), 3.73−3.65 (m, 1H), 3.59 (t, 2H, J = 5.7 Hz), 3.13 (brs, 3H), 2.95 (t, 2H, J = 6.6 Hz), 2.52 (t, 2H, J = 6.6 Hz), 2.37−2.21 (m, 1H), 2.10−1.97 (m, 3H), 1.93 (s, 3H), 1.26−1.19 (m, 1H), 1.06−0.97 (m, 1H); ^{31}P NMR (D_2O) δ 4.0−1.0 (br); HRMS (ESI MS *m*/*z*) calculated for $C_{24}H_{32}N_9O_9P_2^-$ $(M-H)^-$ 652.1804; found 638.1798. RT 7.9 min (98%) in solvent System C.

*(1′R,2′S,4′S,5′S)-4-{2-[(6-(2-Acetamidoethyl)-1H-1,2,3-triazol-4-yl)-hex-1-yn-1-yl]-6-methylaminopurin-9-yl}-1-[(phosphato)-methyl]-2-(phosphato)-bicyclo[3.1.0]hexane (**22**).* Prepared according to the general procedure from compound **44** to give 1.1 mg of **22** (44% in 2 steps, isolated as triethylammonium salt form). ^{1}H NMR (D_2O) δ 8.63−8.50 (br, 1H), 7.83 (s, 1H), 5.31−5.18 (br, 1H), 5.06−5.02 (m, 1H), 4.67−4.50 (m, 1H), 4.51 (t, 1H, J = 6.0 Hz), 3.71−3.63 (m, 1H), 3.62 (t, 1H, J = 6.0 Hz), 3.12 (brs, 3H), 2.81 (t, 2H, J = 6.6 Hz), 2.54 (t, 2H, J = 6.6 Hz), 2.36−2.23 (m, 1H), 2.08−1.93 (m, 1H), 1.93−1.82 (m, 3H), 1.89 (s, 3H), 1.75−1.62 (m, 2H), 1.26−1.21 (m, 1H), 1.05−0.97 (m, 1H); ^{31}P NMR (D_2O) δ 2.2−0.2 (br); HRMS (ESI MS *m*/*z*) calculated for $C_{25}H_{34}N_9O_9P_2^-$ $(M-H)^-$ 666.1960; found 666.1955. RT 8.2 min (98%) in solvent System C.

*(1′R,2′S,4′S,5′S)-4-{2-[(7-(2-Acetamidoethyl)-1H-1,2,3-triazol-4-yl)-hept-1-yn-1-yl]-6-methylaminopurin-9-yl}-1-[(phosphato)-methyl]-2-(phosphato)-bicyclo[3.1.0]hexane (**23**).* Prepared according to the general procedure from compound **45** to give 3.6 mg of **23** (59% in 2 steps, isolated as triethylammonium salt form). ^{1}H NMR (D_2O) δ 8.65−8.50 (br, 1H), 7.78 (s, 1H), 5.34−5.16 (br, 1H), 5.07−5.00 (m, 1H), 4.69−4.51 (m, 1H), 4.36 (t, 2H, J = 6.3 Hz), 3.75−3.68 (m, 1H), 3.49 (t, 2H, J = 6.0 Hz), 3.11 (br s, 3H), 2.78 (t, 2H, J = 6.0 Hz), 2.51 (t, 2H, J = 6.6 Hz), 2.36−2.21 (m, 1H), 2.10−1.96 (m, 1H), 1.96−1.88 (m, 1H), 1.89 (s, 3H), 1.80−1.63 (m, 4H), 1.58−1.48 (2H, m), 1.27−1.21 (m, 1H), 1.07−0.98 (m, 1H); ^{31}P NMR (D_2O) δ 2.0−1.0 (br); HRMS (ESI MS *m*/*z*) calculated for $C_{26}H_{36}N_9O_9P_2^-$ $(M-H)^-$ 680.2117; found 680.2111. RT 8.5 min (98%) in solvent System C.

PAMAM Dendrimer Derivatives. Dialysis was performed using Spectra/Por Dialysis membrane (molecular weight cutoff of 3500) purchased from Spectrum Laboratories, Inc. (Rancho Dominguez, CA, USA). NMR spectra were recorded on a Bruker DRX-600 spectrometer at 25 °C under an optimized parameter setting for each sample, unless otherwise mentioned. ^{1}H NMR chemical shifts were measured relative to the residual solvent peak at 2.50 ppm in DMSO-d_6 and at 4.80 ppm in D_2O. Complete NMR peak assignments were made possible with 2D COSY and NOESY experiments. Each PAMAM dendrimer conjugate was not unimolecular, and thus, the characterization by NMR represented the average value from its polymeric distribution. The integration values were reported only for the peaks clearly resolved (i.e., with a relatively good baseline separation) in the ^{1}H NMR spectra and to two decimal places.

*G3 PAMAM, Conjugated with 4-Pentynoic Acid (**47**).* HATU (20.6 mg, 55 μmol, 38 equiv) was added to a mixture of **46** (10 mg, 1.44 μmol), 4-pentynoic acid (5 mg, 50 μmol, 35 equiv), and DIEA (10 μL, 60 μmol, 42 equiv) in DMF (0.5 mL). The reaction mixture was stirred at room temperature overnight, and the product was purified by dialysis in water. The mixture was lyophilized to give compound **47** (7.6 mg, 70%) as a white foamy solid, which was determined to contain 8 moieties of 4-pentynoic acid per G3 dendrimer. MALDI-MS: calcd. 7545; found 7536.

*G4 PAMAM, Conjugated with tert-Bu-Protected $P2Y_1$ Antagonist **38** (**52**).* Freshly prepared aqueous sodium ascorbate (1 M, 10 μL, 10 μmol) was added to a mixture of compound **51** (1.0 mg, 0.06 μmol) and compound **38** (0.2 mg, 0.3 μmol) in a mixture of *t*-butanol (0.1 mL) and water (0.1 mL), followed by addition of 7.5% aqueous cupric sulfate (17 μL, 5.0 μmol). The reaction mixture was stirred at room temperature overnight, and

the product was purified by dialysis in water. The mixture was lyophilized to give compound **52** (0.57 mg, 43%) as a white amorphous. ^{1}H NMR (D_2O, 400 MHz) δ 8.30 (brs), 5.30−5.25 (br), 5.17−5.13 (br), 4.36−4.30 (br), 4.03−3.90 (m), 3.87−3.03 (m), 2.28−2.20 (br), 2.09−2.00 (br), 1.47−1.36 (br), 1.30−1.00 (m), 1.18 (s), 1.16 (s), 0.80−0.67 (m).

*G4 PAMAM, Conjugated with P2Y$_1$ Antagonist (**53**).* TFA (10 μL) was added to a solution of compound **52** (0.21 mg, 0.01 μmol) in CH_2Cl_2 (10 μL). The reaction mixture was stirred at room temperature overnight and concentrated. The product was purified by dialysis in water. The mixture was lyophilized to give compound **53** (0.15 mg, 78%) as a white amorphous solid. ^{1}H NMR (D_2O, 400 MHz) δ 4.00−1.70 (br). MALDI-MS: calcd. 19,458; found 19,601.

Pharmacological Testing. 2-MeSADP was purchased from Sigma (St. Louis, MO). The affinities of bisphosphate analogues for the hP2Y$_1$ receptor were directly determined by using [^{125}I]MRS2500 **2** in a radioligand binding assay, as we recently described in detail (*25, 26*). Binding and functional parameters were estimated using GraphPAD *Prism* software (GraphPAD, San Diego, CA).

Binding of [^{125}I]MRS2500, 2. *P2Y$_1$ Receptor Expression in Sf9 Insect Cells.* Sf9 insect cell membranes expressing recombinant hP2Y$_1$ receptors were prepared as described in detail previously (*25*). Briefly, suspension cultures of Sf9 insect cells grown to a density of 1.4×10^6 cells/mL were infected with empty vector or recombinant baculovirus encoding the hP2Y$_1$ receptor. Cells were harvested after two days by low-speed centrifugation, and the cells were lysed using a Parr cavitation apparatus. A membrane fraction was isolated by high-speed centrifugation, and the membranes were resuspended at a concentration of ~3.5 mg/mL in 20 mM Tris, pH 8.0, 250 mM sucrose, 2 mM 2-mercaptoethanol, 100 μg/mL phenylmethanesulfonylfluoride, 100 μM benzamidine, and 50 μg/mL tosylphenylalanyl chloromethyl ketone. Membranes were stored at −80 °C and diluted approximately 50-fold for binding assays as described below.

Binding Assay at the hP2Y$_1$ Receptor. Assays with membranes isolated from P2Y$_1$ receptor-expressing Sf9 insect cells typically were with 0.2−0.5 nM [^{125}I]MRS2500 (*26*) and 100−300 ng of membranes in assay buffer (20 mM HEPES, 145 mM NaCl, 5 mM $MgCl_2$, pH 7.5) in a total volume of 25 μL. All incubations were carried out in 12 × 75 mm conical tubes at 4 °C and were terminated after 30 min by the addition of 3.5 mL of ice-cold assay buffer followed by vacuum filtration over Whatman GF/A glass microfiber filters. The filters were washed with 7 mL of ice-cold assay buffer and radioactivity on each filter was quantified in a gamma counter. Specific binding was defined as total [^{125}I]MRS2500 bound minus binding occurring in the presence of 30 μM 2-MeSADP or 10 μM MRS2179. Radioactivity was determined in a Beckman 5500B γ-counter.

Statistical Analysis. Binding and functional parameters were calculated using *Prism 4.0* software (GraphPAD, San Diego, CA). IC_{50} values obtained from competition curves were converted to K_i values using the Cheng-Prusoff equation (*27*). Data were expressed as the mean ± standard error. Statistical analysis was performed using analysis of variance (ANOVA) with post hoc test or Student's *t* test where appropriate with *p* values less than 0.05 being considered significant.

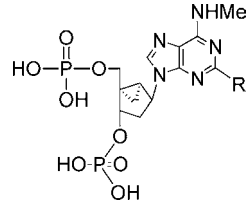
Studies of Human Washed Platelets. *Preparation.* Human washed platelets were prepared as previously described (*28*). Briefly, fresh blood obtained from healthy donors was centrifuged at 175 × *g* for 15 min at 37 °C. Then, platelet-rich plasma was removed and centrifuged at 1570 × *g* for 15 min at 37 °C. The platelet pellet was washed twice in Tyrode's buffer (137 mM NaCl, 2 mM KCl, 12 mM $NaHCO_3$, 0.3 mM NaH_2PO_4, 1 mM $MgCl_2$, 2 mM $CaCl_2$, 5.5 mM glucose, 5 mM Hepes, pH 7.3) containing 0.35% human serum albumin. The final resuspension was at a density of 3×10^5 platelets/μL in Tyrode's buffer containing 0.02 U/mL of apyrase (adenosine 5′-triphosphate diphosphohydrolase, EC 3.6.1.5), a concentration sufficient to prevent desensitization of platelet P2Y receptors during storage. Platelets were kept at 37 °C throughout all experiments.

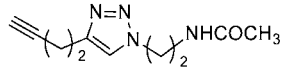
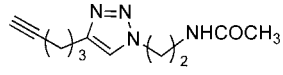
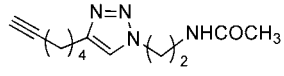
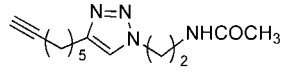
Platelet Aggregation Studies. Aggregation was measured at 37 °C by a turbidimetric method in a dual-channel Payton aggregometer (Payton Associates, Scarborough, Ontario, Canada). The stock solutions for platelet aggregation studies were 1.5 mM solutions of dendrimer **53** or MRS2500 **2** in water (HPLC grade, Aldrich), to give final concentrations of 1 or 4 μM **53** and 1 μM **2**. An aliquot of platelet suspension (450 μL) was stirred at 1100 rpm and activated by addition of ADP (5 mM stock solution to give a final concentration of 5 μM), in the presence or absence of a monomeric or dendrimeric P2Y$_1$ antagonist and in the presence of human fibrinogen (0.8 mg/mL), in a final volume of 500 μL. The extent of aggregation was estimated quantitatively by measuring the maximum curve height above the baseline level.

Molecular Modeling. The homology model of the P2Y$_1$ receptor has been constructed in MOE (*MOE* [2008.10] 2008, Chemical Computing Group Inc.) using a two-template strategy. In particular, our established rhodopsin-based P2Y$_1$ homology model (*1*) has been for the construction of almost the entirety of the receptor, while the A_{2A} adenosine receptor (PDB ID: 3EML) (*29*) has been used as the template for the construction of the second extracellular loop (EL2)—alignment shown in Figure S1 of the Supporting Information (page S19). In this way, we obtained a model closely resembling our previous one (*18*), but with a more solvent-exposed EL2. In particular, the A_{2A} receptor was used as the template to model only the portion of EL2 downstream of Cys 202. The remaining portion of the loop, for which the published crystal structures of GPCRs suggest a greater variability among the receptors, was instead modeled without the use of a template. The Charmm27 force field and the Born model for implicit solvation were employed. The level of energy minimizations for the intermediate and final models was set to medium. This setting employed an MOE internal protocol, which allows only for restrained energy minimizations that do not prevent the model from drifting far away from the template.

Molecular Docking. The remainder of the modeling was performed with the Schrödinger package through the Maestro interface (*Maestro* [9.0] 2009, Schrödinger, LLC). The structure of **2** was taken from the previously published model (*18*). Compound **20** was sketched in Maestro from **2**, and its susbtituent at the 2-position was then subjected to 500 steps of energy minimization with the MacroModel engine (*MacroModel* [9.7] 2009, Schrödinger, LLC) using the MMFF, force field and the GBSA implicit model for solvation. The homology model of the receptor was subjected to the Protein Preparation Wizard workflow. This added hydrogens, which were subsequently minimized, and also optimized the protonation state of His residues and the orientation of hydroxyl groups, Asn residues, and Gln residues. The molecular docking was performed with Glide (*Glide* [5.5] 2009, Schrödinger, LLC) using the XP protocol and the extended sampling. A docking grid with a side of 30 Ang was centered on the centroid of Arg 128, Lys 280, and Arg 310, which are known to be involved in nucleotide binding. Additionally, the docking of the phosphate moieties was directed within a sphere of 3.4 Å radius centered on the centroids of Arg 128, Lys 280, and Arg 310. No scaling factors were used for the van der Waals (vdW) radii of the P2Y$_1$ receptor atoms, while a scaling factor of 0.5 was applied to the vdW radii of the ligand atoms with partial charge lower than 0.15. All the hydroxyl groups within the binding pocket were

Table 1. Pharmacological Data for Inhibition of Radioligand Binding at the $hP2Y_1$ Receptor by the Novel Nucleotide Derivatives



Compound	R	Binding, K_i, nM[a,b]
2	I	0.78 ± 0.08 (*18*)
3	C≡CH	95 ± 39 (*18*)
4	$C{\equiv}C(CH_2)_3CH_3$	430 ± 200 (*18*)
5	$C{\equiv}C(CH_2)_2COOCH_3$	363 ± 18
6	$C{\equiv}C(CH_2)_3COOCH_3$	2200 ± 770
7	$C{\equiv}C(CH_2)_4COOCH_3$	649 ± 57
8	$C{\equiv}C(CH_2)_2COOH$	23 ± 3
9	$C{\equiv}C(CH_2)_3COOH$	376 ± 101
10	$C{\equiv}C(CH_2)_4COOH$	350 ± 139
11	$C{\equiv}C(CH_2)_2CONH(CH_2)_2NH_2$	1440 ± 30
12	$C{\equiv}C(CH_2)_3CONH(CH_2)_2NH_2$	1150 ± 100
13	$C{\equiv}C(CH_2)_4CONH(CH_2)_2NH_2$	3960 ± 960
14	$C{\equiv}C(CH_2)_2CONH(CH_2)_3NH_2$	3580 ± 140
15	$C{\equiv}C(CH_2)_2CONH(CH_2)_4NH_2$	132 ± 17
16	$C{\equiv}C(CH_2)_2CONH(CH_2)_6NH_2$	2410 ± 460
17	$C{\equiv}C(CH_2)_3CONH(CH_2)_2$NH-biotin	>10,000
18	$C{\equiv}C(CH_2)_3CONH(CH_2)_2NHCO(CH_2)_5$NH-biotin	1210 ± 230
19	$C{\equiv}C(CH_2)_3CONH(CH_2)_2$-(4-$SO_2F$)-Ph	>10,000
20		300 ± 200
21		2700 ± 600
22		8300 ± 1500
23		6300 ± 2000

[a] Affinities determined by using [^{125}I]MRS2500 **2** in a radioligand binding assay, except for **2**−**4**, which were determined using [^{3}H]MRS2279. The $hP2Y_1$ receptor was expressed to high levels in Sf9 insect cells with a recombinant baculovirus. Membranes prepared from these cells were incubated for 30 min at 4 °C in the presence of ~1 nM [^{125}I]MRS2500 **2**. [b] Mean ± standard error given for three separate determinations. [c] **2**, MRS2500; **8**, MRS2816; **15**, MRS2900; **20**, MRS2939.

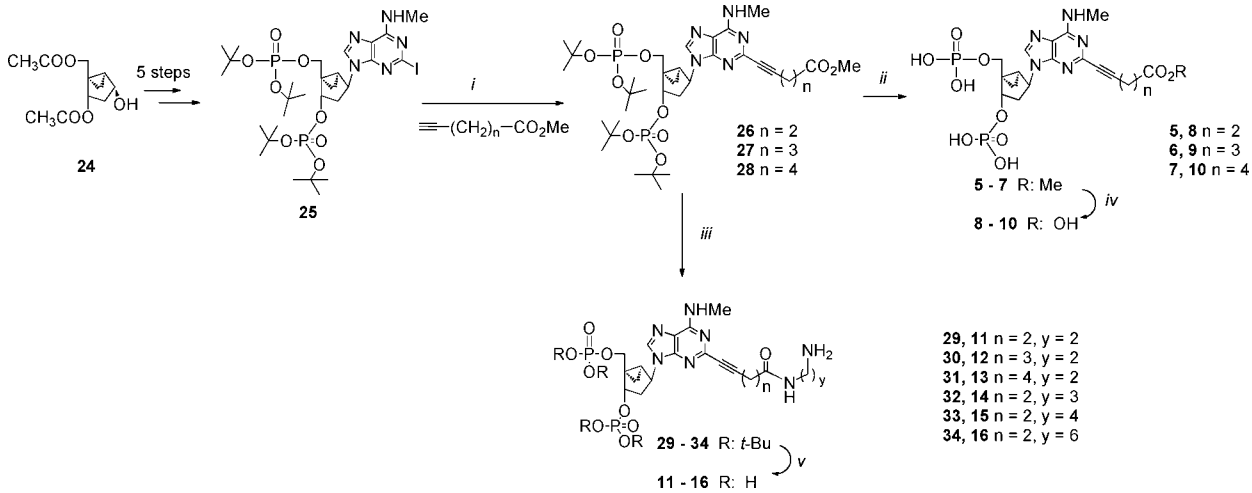
considered rotatable. A maximum of 50 poses per ligand were generated, all of which were subjected to a postdocking energy minimization. The highest scoring complexes were then subjected to a 500 steps of energy minimization with the MacroModel engine, using the MMFFs force field and the GBSA implicit model for solvation.

Systematic Torsional Sampling. Conformational analyses were performed with the Systematic Pseudo-Monte Carlo (SPMC) method, as implemented in MacroModel,[4] using the MMFFs force field and the GBSA implicit model for solvation. The torsion samping level was set to extended, the number of search steps to 5000, and the number of minimization steps to 500 per search step.

RESULTS

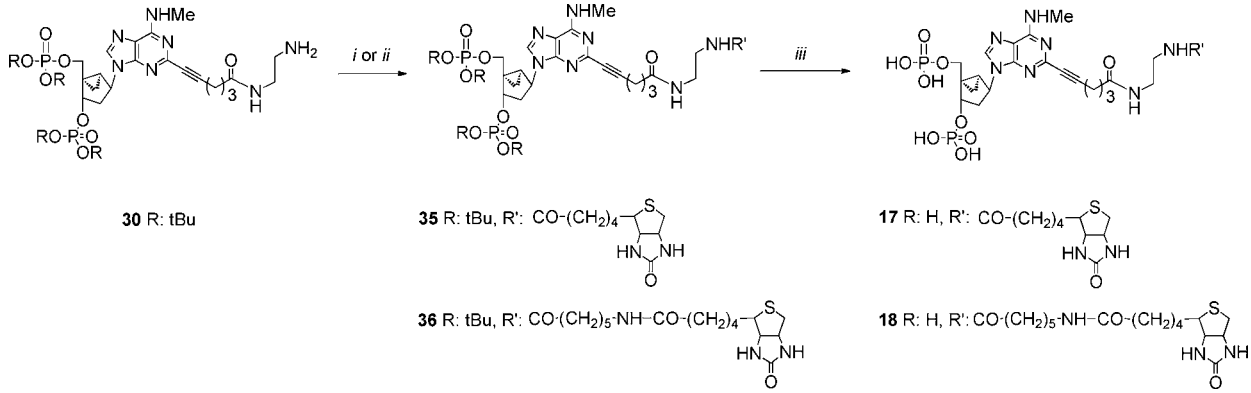
Chemical Synthesis. Novel (N)-methanocarba $P2Y_1$ receptor antagonist derivatives (Table 1) containing C2 chains with terminal ester **5**−**7**, carboxylic acid **8**−**10**, and amino **11**−**16** groups were synthesized by the routes shown in Scheme 1 (*15, 16, 30*). A functionalized chain at the 2-position of the adenine ring was formed by a Sonogashira reaction (*31*) of the

Scheme 1. Synthesis of C2 Derivatives of $P2Y_1$ Receptor Antagonists Containing Terminal Ester 5−7, Carboxylic Acid 8−10, and Amino 11−16 Groups[a]



[a] Reagents and conditions: (i) CuI, $(Ph_3P)_2PdCl_2$,TEA, DMF, rt; (ii) TFA, CH_2Cl_2, rt; (iii) ethylenediamine, MeOH, rt; (iv) KOH, H_2O, rt; (v) TFA, CH_2Cl_2, rt.

Scheme 2. Preparation of Biotin Derivatives of a $P2Y_1$ Receptor Antagonist for Avidin Complexation[a]



[a] Reagents and conditions: (i) biotin, DIEA, HATU, DMF, rt; (ii) biotinamidohexanoic acid 3-sulfo-*N*-hydroxysuccinimide ester sodium salt, bicarbonate buffer, DMF, rt; (iii) TFA, CH_2Cl_2.

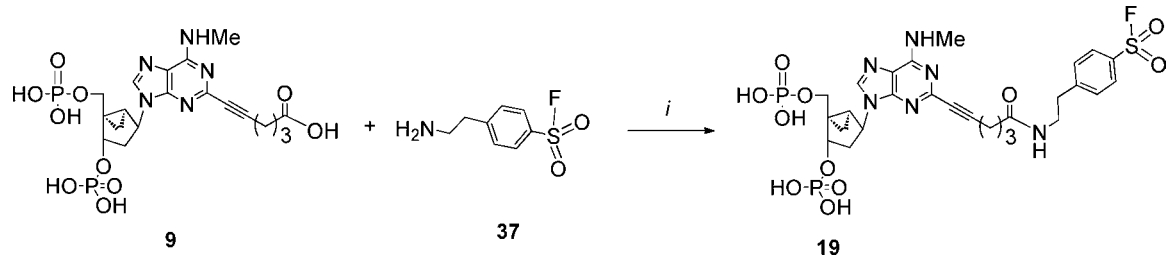
protected 2-iodo derivative **25** with $(PPh_3)_2PdCl_2$, CuI and the appropriate acetylene. The deprotection of *t*-butyl protecting groups of the phosphates in derivatives **26**−**28** with TFA provided the ester derivatives **5**−**7**. Each of the terminal ester groups was then hydrolyzed with aqueous KOH to yield the corresponding carboxylic acid **8**−**10**. Alternatively, the ester group was directly aminolyzed using 1,2-diaminoethylene, 1,3-diaminopropane, or 1,4-diaminobutane to provide, after deprotection with TFA, amine congeners **11**−**16**.

Ligands intended for irreversible receptor binding and avidin complexation were synthesized by attaching an appropriate prosthetic group to the functionalized chains at the C2 position. Biotin conjugates of varying length **17** and **18** were synthesized by amide coupling of the phosphate-protected intermediate amine **30** (Scheme 2), which was the precursor of amine congener **12**. Amine derivative **12** was found to be the most potent of the aminoethyl congeners in the series **11**−**13** (see below). The biotin conjugate **17** was prepared by a HATU coupling with biotin via protected intermediate **35**, and the extended chain analogue **18** was prepared from the corresponding biotin-ε-aminocaproyl active ester via protected intermediate **36**. In the final step, the phosphate groups were cleanly deprotected by reaction with TFA to provide **17** and **18**.

Sulfonyl fluoride derivatives have been used as covalently binding affinity labels of GPCRs (*32, 33*). To prepare the sulfonyl fluoride derivative **19**, we tried to use a phosphate-protected free carboxylic acid derivative as starting material. Unfortunately, the reaction to deprotect ester derivative **27** with base, using either KOH at room temperature or LiOH at 4 °C, failed to afford the desired protected phosphate compound, and a mixture containing the deprotected phosphate ester and deprotected carboxylic acid was recovered in a very low yield. Finally, the condensation of phosphate-unprotected carboxylic acid **9** with the corresponding amine **37** (containing the preformed arylsulfonyl fluoride) in DMF in the presence of HATU and DIEA afforded the amine derivative **19** (Scheme 3). The presence of the free phosphate groups in **9** did not interfere with this coupling reaction.

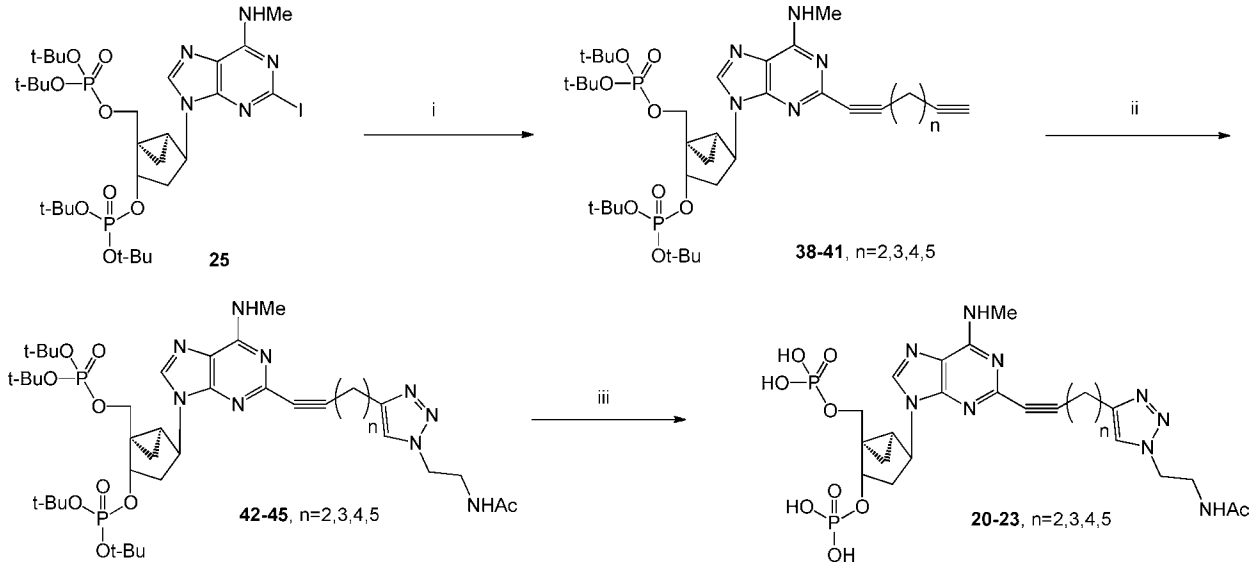
The functionalized congeners **5**−**16** are designed for amide coupling schemes. Alternately, we introduced dialkyne groups on an extended adenine C2 substituent, as synthetic intermediates leading to selective $P2Y_1$ antagonists. The proximal alkyne was intended to promote receptor recognition, and the distal alkynes reacted with azides to form triazole derivatives through click chemistry (*22*). The synthesis of the phosphate-protected dialkynyl intermediates **38**−**41** was performed using a Sonogashira coupling (*31*) on the corresponding 2-iodo intermediate **25** (Scheme 4). We then used Cu(I)-catalyzed [3 + 2] cycloaddition (click reaction) of *N*-(2-azidoethyl)acetamide (*24*) and the terminal acetylene group of dialkynyl nucleotide intermediates **38**−**41** to provide protected triazole derivatives **42**−**45**. The reactions are generally selective for the terminal and least

Scheme 3. Preparation of a Sulfonyl Fluoride Derivative 19 of a $P2Y_1$ Receptor Antagonist[a]



[a] Reagents and conditions: (i) DIEA, HATU, DMF, rt.

Scheme 4. Use of Click Chemistry to Couple $P2Y_1$ Antagonists to Small Azido-Bearing Molecules $AcNH(CH_2)_2$ Present in the Final Products 20−23 as a Group to Serve As a Model for the Attachment to a PAMAM Dendrimer[a]



[a] Reagents and conditions: (i) diyne, CuI, $(Ph_3P)_2PdCl_2$,TEA, DMF, rt; (ii) $AcNHCH_2CH_2N_3$, $CuSO_4$ aq., sodium ascorbate; (iii) TFA.

hindered alkyne when more than one alkyne is present in a reactant (*34*), which was confirmed in this series. Subsequent deprotection of the 3′- and 5′-phosphate groups with TFA provided biologically active triazole-containing nucleotides **20**−**23**.

The optimal chain length for preservation of receptor recognition was found to be two methylene groups between the alkynyl groups, i.e., the product of intermediate **38**. This dialkyne was used in subsequent reactions to maintain the $P2Y_1$ receptor binding affinity.

Three approaches were attempted to couple functionalized $P2Y_1$ receptor antagonists to PAMAM dendrimers. In Scheme 5A, a Sonogashira reaction was used in an attempt to couple compound **25** to an alkyne-derivatized PAMAM dendrimer **47**. The isolated material was insoluble in DMSO and likely was a cross-linked polymeric side product. We also attempted to condense the short-chain amine congener **11** (in its phosphate-protected form **29**) with a G2.5 (32 terminal carboxylic acid groups) PAMAM dendrimer **49** using DIEA, HATU, in DMF at room temperature overnight, but the desired protected conjugate **50** was not obtained (Scheme 5B).

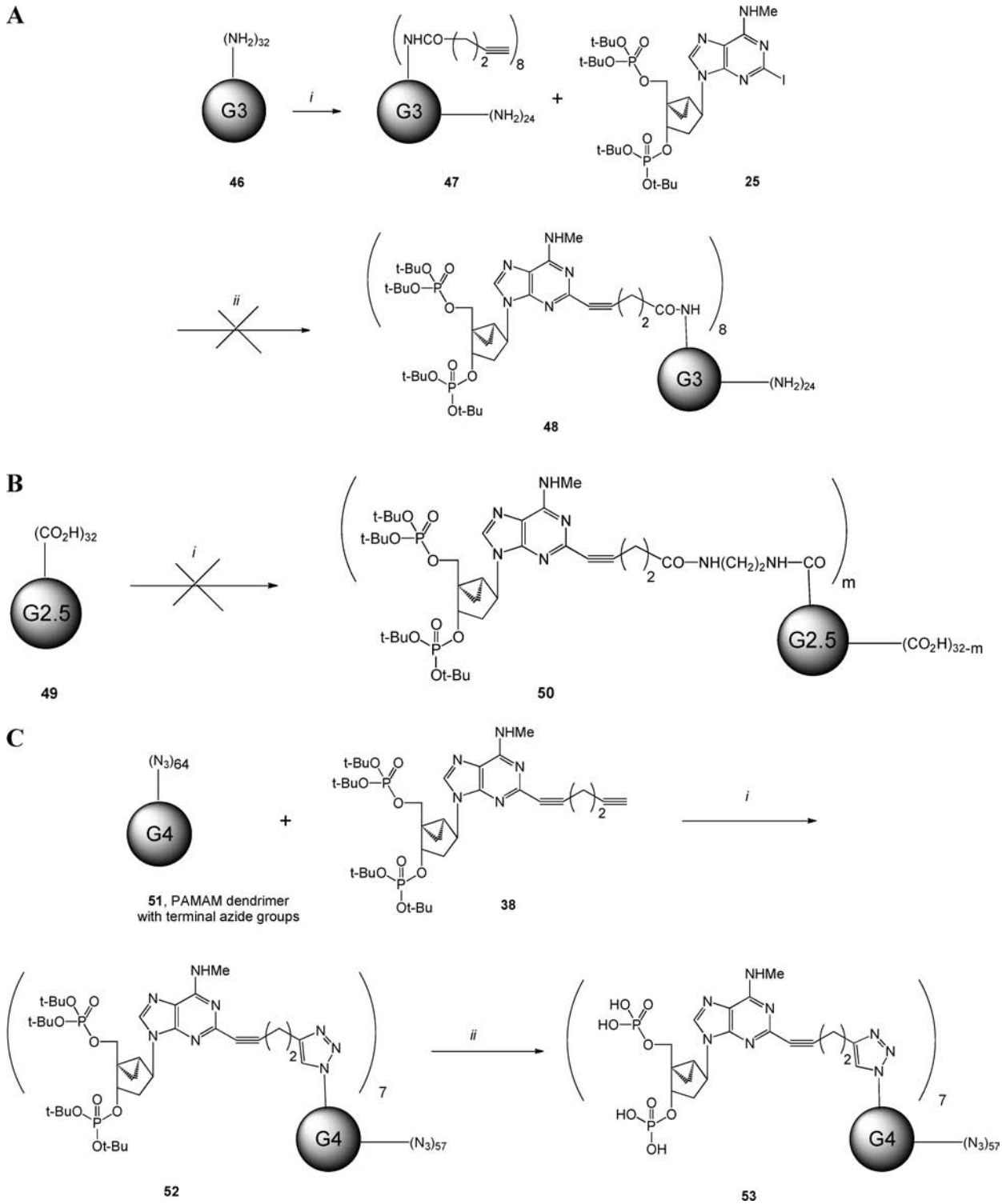
A third synthetic approach (Scheme 5C) consisted of a click reaction on a PAMAM dendrimer of Generation 4 (G4) containing terminal azido groups (*23*) that were suitable for the conjugation of $P2Y_1$ receptor antagonists. The azido groups of **51** were first coupled to the nucleotide intermediate **38**, which provided the biologically optimal chain length of the C2 chain. The bisphosphate-protected dendrimer conjugate **52** was then deprotected using TFA to provide a dendrimeric nucleoside bisphosphate derivative **53** that was expected to act as a multivalent $P2Y_1$ receptor antagonist. This conjugate contained an average of 7 nucleotide moieties on each dendrimer structure out of 64 theoretical terminal groups, as determined by mass spectrometry.

Pharmacological Evaluation. The novel bisphosphate monomeric nucleotide derivatives **4**−**23** were evaluated in radioligand binding experiments using the new radiotracer [^{125}I]MRS2500 **2** (Table 1) (*26*). The three terminal ester derivatives **5**−**7** displayed micromolar affinity at the $hP2Y_1$ receptor. The shortest analogue **5**, having two methylenes in the alkynyl chain, was slightly more potent than the longer analogues. The carboxylic acid derivatives **8**−**10** were more potent than the corresponding ester derivatives. There was a clearly favored analogue among the carboxylic acid derivatives **8**−**10**, i.e., compound **8** with a K_i of 23 nM. A comparison of the hexynyl derivative **4** with the corresponding carboxylic acid derivative **8** indicates a gain of approximately 40-fold in affinity due to the presence of the terminal carboxylate group.

The K_i values of the corresponding ethylenediamine derivatives **11**−**13**, derived from the three homologous carboxylic derivatives, were all slightly higher than 1.0 μM. Thus, affinity enhancement was observed by addition of a negatively charged group to the chain, but not a positively charged terminal ethylamino group.

Therefore, we extended the alkylamino moiety of compound **11** to empirically locate an optimal chain length in the terminal amino series. Compounds **14**−**16** were all prepared as extended amine derivatives of the carboxylic acid **8**. The highest affinity (K_i = 132 nM) among the amine derivatives was observed for compound **15**. The isomeric compound **13**, which differed from

Scheme 5. Coupling of $P2Y_1$ Receptor Antagonists to PAMAM Dendrimers in a Manner That Preserves the Interaction with the Receptor[a]



[a] (A) Attempted use of the Sonogashira reaction to couple a 2-iodoadenine derivative to a terminal alkyne G3 dendrimer. Reagents and conditions: (i) HATU, 4-pentynoic acid, DIEA, DMF; (ii) CuI, $(Ph_3P)_2PdCl_2$,TEA, DMF, rt. (B) Attempted coupling of a 2-amine derivatized nucleotide to a terminal carboxylic acid G2.5 dendrimer. Reagents: (i) Compound **30**, HATU, DIEA, DMSO. (C) Successful use of click chemistry to couple an alkyne-functionalized, protected nucleotide derivative to a terminal azido-bearing G4 dendrimer to yield dendrimer conjugate **53** (MRS2966). Reagents: (i) $CuSO_4$ aq., sodium ascorbate; (ii) TFA.

15 only in the position of the intermediate amide group within the chain, displayed a K_i of 3.96 μM. Biotin conjugate **18** containing an extended ε-aminocaproyl spacer chain was more potent in binding than the shorter analogue **17**. The sulfonyl fluoride derivative **19** was not appreciably potent in binding to the $P2Y_1$ receptor.

Receptor binding affinities of terminal triazole derivatives **20**−**23** in the $P2Y_1$ receptor-antagonist series prepared as model compounds for linking to carriers by click chemistry showed a great dependence on the chain length. The shortest homologue **20** having two methylenes in the spacer group was the most potent with a K_i value of 300 nM, and the two longest

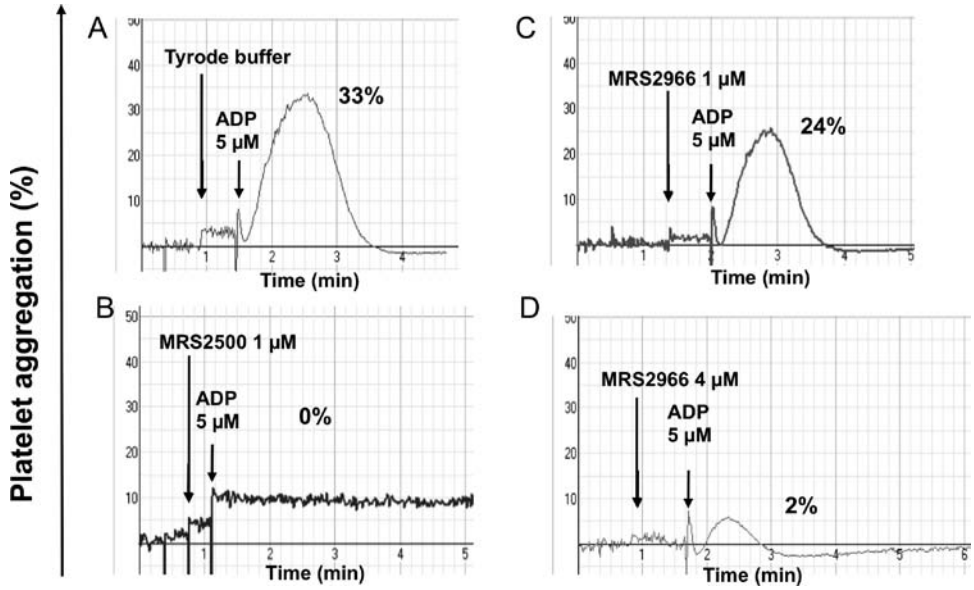


Figure 1. Aggregation of human platelets induced by ADP (A) is inhibited by $P2Y_1$ receptor antagonists: (B) the potent, small molecule antagonist MRS2500 **2** and (C,D) dendrimer derivative **53** (MRS2966). The concentration of the dendrimer−ligand complex **53** was measured as the concentration of the dendrimer, not the nucleotide moiety. The results are representative of two separate determinations.

homologues, **22** and **23**, were 20−30-fold weaker in binding. Therefore, the precursor compound **38** was used in the dendrimer conjugation reactions to achieve the biologically optimal linkage.

We tested the dendrimer derivative **53** on aggregation of human platelets induced by ADP (Figure 1). Compound **53** (MRS2966, 1, and 4 μM) inhibited platelet aggregation induced by ADP (5 μM) in a concentration-dependent fashion. However, the inhibition by 4 μM **53** was not total (2% residual aggregation compared to 33% in the ADP control), and the dendrimer conjugate **53** was less potent than MRS2500, which completely inhibited aggregation at 1 μM.

Molecular Modeling. We have successfully used rhodopsin-based homology modeling to explain the SAR of the P2Y receptors and design mutagenesis experiments (*1, 18, 35*). However, the solution of the crystal structure of the β-adrenergic (*36*−*38*) and the adenosine A_{2A} receptors (*29*), as well as controlled homology modeling experiments (*39, 40*), revealed that the second extracellular loop (EL2) of rhodopsin is not a good template for modeling the corresponding regions of other GPCRs because it hovers singularly low over the binding pocket, occluding its entrance from the extracellular space. For this reason, here we modified our established rhosopsin-based $P2Y_1$ model by substituting the EL2 with a model based on the A_{2A} adenosine receptor (*29*). More specifically, we modeled on the basis of the A_{2A} receptor only the portion of EL2 downstream of the conserved Cys involved in the disulfide bridge with the third transmembrane domain (TM3), while the remaining residues were modeled without the use of a template, due to the large structural variability revealed by the published crystal structures for this region. Clearly, the lack of a template is detrimental for the accuracy of this portion of the model; however, since this region appears to be further away from the putative ligand binding pocket it is not likely to affect the docking results.

The molecular docking of **2** into the binding pocket of our revised $P2Y_1$ model confirmed the well-established binding mode that fits well with the experimental data (Figure 2, panels A and B) (*1, 35*). Notably, we have shown that this binding mode can explain in a quantitative manner the SAR of $P2Y_1$ antagonists based on the general scaffold of adenosine-3′,5′-bisphosphate (A3P5P) (*18*). Briefly, the phosphate moieties dock between TM3, TM6, and TM7, and are coordinated by Arg 128, Lys 280, and Arg 310, three cationic residues that have been experimentally found to be a key component of ligand recognition. Around the glycosidic bond, the nucleobase was arranged in an *anti* conformation with respect to the pseudosugar moiety, resulting in the substituent at the 2-position of the purine ring pointing toward the space between TM1 and TM7, and oriented toward the core of the receptor. The exocyclic amino group was engaged in a hydrogen bond with Gln 307 in TM7, another key interaction supported by the experiments. In agreement with this docked conformation, in 80% of the crystal structures found in the PDB, A3P5P is found in an *anti* conformation (see Table S1 of Supporting Information, page S20).

However, for the triazole model compound **20**, the results of our molecular docking experiments suggested docking of the nucleoside with the nucleobase oriented in a *syn* conformation with respect to the sugar moiety, because of the large substituent at the 2-position (Figure 2, panels C and D). This allowed for the maintenance of all the key interactions, including not only those of the phosphate moieties with the three key cationic residues, but also that of the exocyclic amino group with the Gln in TM7, because of a concomitant 180° rotation of the latter. As is evident from Figure 2, the *syn* conformation of the nucleobase allowed the substituent to point toward the extracellular space, thus explaining the possibility of coupling the structural equivalent of **20** to PAMAM dendrimers, while maintaining antagonistic activity. Notably, the terminal amido group of the substituent established a favorable interaction with Asp 116 in the first extracellular loop (EL1). Although the modeling of the loops generally yields less accurate results than that of the transmembrane domains (*40*), the short nature of EL1 conferred a relatively high confidence on the accuracy of this model.

We subjected to systematic torsional sampling six nucleotides (**2**, **5**, **8**, **11**, **17**, **20**) bearing different substituents at the 2-position and having different receptor affinities. For all of these nucleotides, including compound **20**, the *syn* conformation was slightly disfavored over *anti*, with an energy content that was 0.20−0.25% higher (see Table S2 of the Supporting Information, page S21). This suggests that the putative ability of some of the compounds with large appendages at the 2-position to bind to the $P2Y_1$ receptor in the *syn* conformation is not due to the

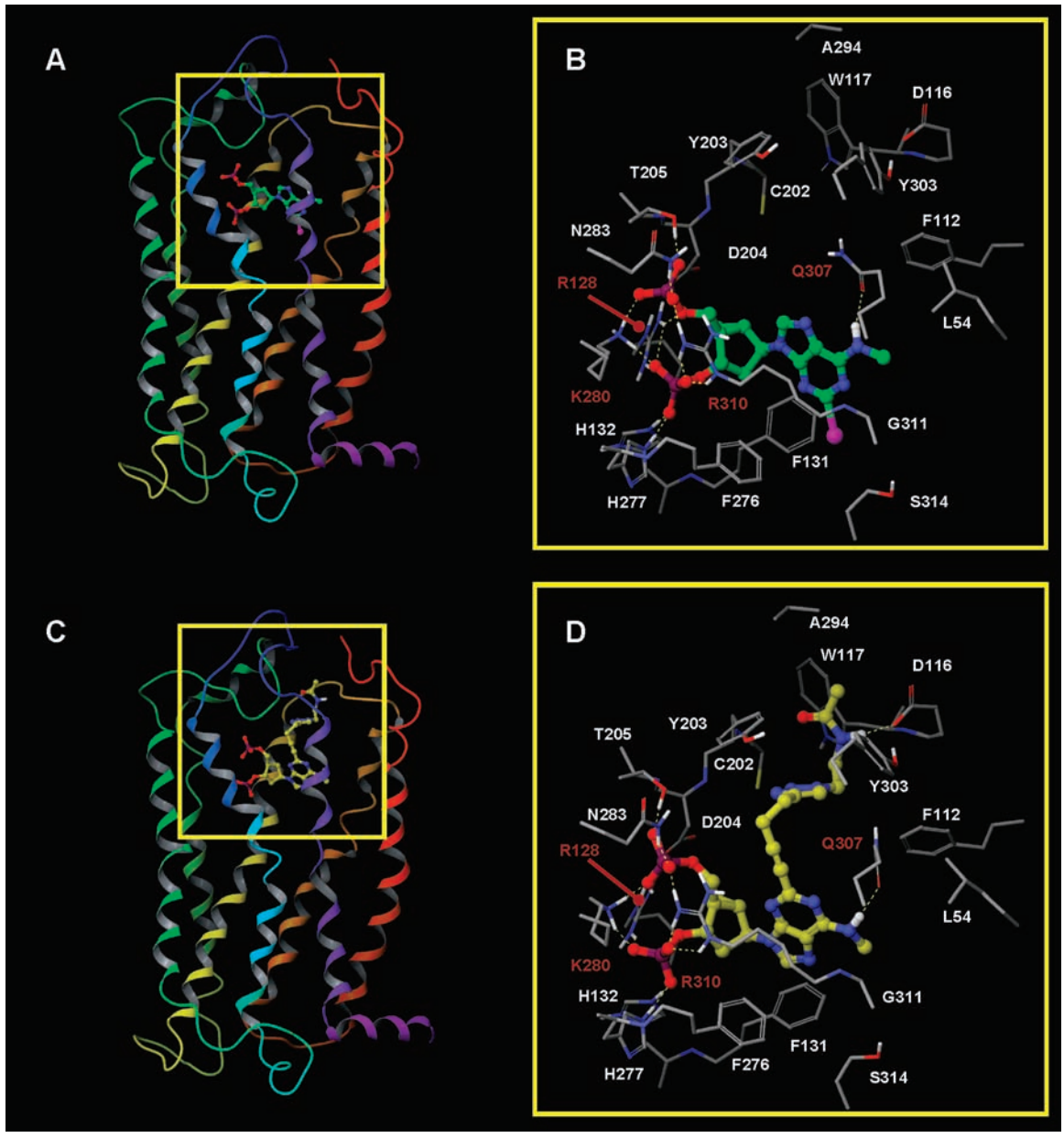


Figure 2. Molecular models of the hP2Y receptor in complex with compound **2** (panels A and B) and compound **20** (panels C and D), as obtained through molecular docking at the homology model of the receptor. Panels A and C show the receptor−ligand complexes from the plane of the membrane, while panels B and D offer a more detailed view of the ligand binding site, with the intermolecular hydrogen bonds indicated by yellow dotted lines. The backbone structure of the receptor is represented as a ribbon with the colors of the rainbow: TM1, orange; TM2, orange/yellow; TM3, yellow; TM4, green; TM5, green/blue; TM6, cyan; TM7, purple. The carbon atoms are colored gray for the receptor, green for compound **2**, and yellow for compound **20**. The residue numbering according to a standard GPCR indexing system (*47*) for the residues shown is L54(1.35), F112(2.65), D116(EL1), W117(EL1), R128(3.29), F131(3.32), H132(3.33), C202(EL2), Y203(EL2), D204(EL2), T205(EL2), F276(6.51), H277(6.52), N283(6.58), A294(EL3), Y303(7.32), Q307(7.36), G311(7.40), and S314(7.43). For both ligands, a schematic representation of the interactions with the receptor is given in the Supporting Information (Figure S2, pages S22−S23).

conformational preferences of the compounds in solution, but rather to steric fit and the establishment of favorable interactions with the receptor. The absence of good templates for the modeling of the loops prevented us from accurately establishing the nature of these interactions. However, as mentioned, our model suggested a hydrogen bond between compound **20** and Asp 116 in EL1.

DISCUSSION

MRS2500 (**2**) contains a bicyclo[3.1.0]hexane ring, i.e., methanocarba ring system constrained in the (N)-conformation (2′-exo), which is preferred in the receptor binding site (*15*). This high-affinity antagonist has been radiolabeled, and its application for quantification of the $P2Y_1$ receptor underscores the utility of this chemical series as molecular probes of this important signaling protein. MRS2500 is also sufficiently stable for in vivo use, and its antithrombotic properties have been demonstrated against thrombus formation induced by laser or ferric chloride and in systemic thromboembolism. The presence of the methanocarba ring in MRS2500 impedes the action of 5′-nucleotidase to cleave the 5′-monophosphate and other ectonucleotidases that otherwise would greatly limit the half-life in vivo (*5*). Thus, this series of $P2Y_1$ receptor antagonists has potential for use as research tools in vitro and in vivo or perhaps as therapeutic agents.

Molecular modeling, based on homology of the receptor to the high-resolution structure of rhodopsin, and ligand docking have played a role in studies of the SAR at the $P2Y_1$ receptor (*1, 35*). The recognition of the phosphate group(s) in the putative binding site is associated with three conserved cationic residues, which serve as a ligand anchor in the modeling. Another key interaction is established between Gln 307 in TM7 and the exocyclic amino group. Combining docking and QSAR, we generated a consensus model correlating antagonist structures with their apparent binding affinities (*18*). A QSAR model of the $P2Y_1$ receptor antagonists based on alignment of 45 docked nucleotide antagonists was constructed using comparative molecular field analysis (CoMFA), comparative molecular similarity indices analysis (CoMSIA), and molecular descriptors. Consensus scoring of free binding energy based on multiple models predicted accurately the potency of 75% of a test set. This experimentally supported model, in which the adenine ring is oriented in the *anti* conformation with respect to the pseudosugar moiety, suggests the tolerance for only small substituents at the 2-position. However, the results obtained in the present study suggest that, when the pseudonucleotides bear large substituents at the 2 position, the adenine ring adopts the *syn* conformation upon binding to the receptor. Thus, the 2-position of the adenine ring is oriented toward extracellular space, allowing the presence of a large appendage. Large substituents in some (e.g., **20**) but not all (e.g., **17** and **19**) of the dervatives presented here are tolerated in receptor binding. The preservation of receptor affinity in many of the functionalized congeners and the $P2Y_1$ receptor antagonistic activity of the macromolecular conjugate **53** are consistent with this proposed new binding mode.

A series of small molecule congeners of N^6-methyl-(N)-methanocarba-2′-deoxyadenosine-3′,5′-bisphosphates containing extended 2-alkynyl chains was synthesized and tested in radioligand binding at the $hP2Y_1$ receptor. The chains of these functionalized congeners contained hydrophilic moieties, a reactive substituent, or biotin, linked via an amide. Although the functionalized congeners are thought to be chain functionalized in a region that is insensitive in the receptor binding, only intermediate $P2Y_1$ receptor affinity was achieved in these compounds. Variation of the chain length and position of an intermediate amide group revealed high affinity of both a carboxylic congener **8** (K_i 23 nM) and an extended amine congener **15** (K_i 132 nM), both of which contained a 2-(1-pentynoyl) group. The terminal carboxylic acid or amino groups of the model compounds allowed incorporation of hydrophilic or chemically reactive substituents. These were intended as general sites for conjugation to groups such as fluorescent reporter groups. Thus, a consistent pattern of SAR depending on chain length and terminal functionality was observed. Although **17** and **19** were weak in binding to the receptor, their activities illustrate that the distal regions of the chain can have a major effect on the receptor interaction. Not all chain-extended derivatives anchored on the purine core with a 2-alkynyl group are suitable probes of the $P2Y_1$ receptor.

PAMAM dendrimers are tree-like polymers that have wide application in drug delivery in vivo (*41, 42*). Their advantages as peptide-like biocompatible drug carriers are the ability to control the size, functionality, and degree of substitution. We recently reported the first example of using a PAMAM dendrimer scaffolding for the polyvalent, nanoscale presentation of nucleosides to selectively activate adenosine receptors to induce intracellular signal transduction (*43*−*45*). The effective inhibition of ADP-induced platelet aggregation was previously demonstrated using PAMAM dendrimers with multiple copies of an A_{2A} adenosine receptor agonist (*43, 46*).

Different approaches to synthesize dendrimer conjugates were compared here. Conjugation of $P2Y_1$ receptor antagonists to dendrimers by amide formation or palladium-catalyzed reaction between an alkyne on the dendrimer and an iodoaryl-derivatized nucleotide was unsuccessful. Only click coupling to an azide-containing PAMAM dendrimer was successful. The resulting multivalent nucleotide conjugate, which had a chain length that in model compounds was favored in receptor binding, inhibited human platelet aggregation. Thus, click chemistry was an efficient synthetic approach to attaching a purinergic antagonist to a PAMAM dendrimer, and this linkage containing a triazole moiety maintained the interaction with the receptor.

In conclusion, this study is the first example of attaching multiple ligands to PAMAM dendrimers that target the P2Y receptors to produce a desired biological effect, i.e., antithrombotic action of $P2Y_1$ antagonists. Although the potency of **53** in inhibition of ADP-induced platelet aggregation was less than the high-affinity antagonist **2**, at 4 μM it inhibited aggregation by >90%. Thus, this multivalent nucleotide dendrimer conjugate provides an initial approach to novel antithrombotic agents. The preservation of receptor interaction of the functionalized congeners was also consistent with new $P2Y_1$ receptor modeling and ligand docking. The model proposed a conformation change in the angle of the nucleobase to explain the availability of the 2-alkynyl group for conjugation to carriers. In the future, we will explore structural modification of the spacer group to enhance potency. The multivalent conjugates may now be examined in in vivo testing to determine bioavailability and pharmacokinetic characteristics.

ACKNOWLEDGMENT

This research was supported by the Intramural Research Program of the NIH, National Institute of Diabetes and Digestive and Kidney Diseases, and a grant (GM38213) from the National Institute of General Medical Sciences. We thank Dr. John Lloyd and Dr. Noel Whittaker (NIDDK) for the mass spectral determinations. Research conducted at the Center for Nanophase Materials Sciences at Oak Ridge National Laboratory is sponsored by the Scientific User Facilities Division, Office of Basic Energy Sciences, U.S. Department of Energy. S. de Castro thanks Ministerio de Educación y Ciencia (Spain) for financial support. H. Maruoka thanks Asubio Pharmaceuticals for financial support.

Supporting Information Available: HPLC traces of monomeric compounds submitted for biological testing, sequence alignment for P2Y receptors, documentation of the *anti* conformation in crystal structures, and schematic representations of the receptor−ligand interactions. This material is available free of charge via the Internet at http://pubs.acs.org.

LITERATURE CITED

(1) Costanzi, S., Mamedova, L., Gao, Z. G., and Jacobson, K. A. (2004) Architecture of P2Y nucleotide receptors: structural comparison based on sequence analysis, mutagenesis, and homology modeling. *J. Med. Chem. 47*, 5393–5404.

(2) Abbracchio, M. P., Burnstock, G., Boeynaems, J. M., Barnard, E. A., Boyer, J. L., Kennedy, C., Knight, G. E., Fumagalli, M., Gachet, C., Jacobson, K. A., and Weisman, G. A. (2006) International Union of Pharmacology LVIII: update on the P2Y G protein-coupled nucleotide receptors: from molecular mechanisms and pathophysiology to therapy. *Pharmacol. Rev. 58*, 281–341.

(3) Gachet, C. (2006) Regulation of platelet functions by P2 receptors. *Annu. Rev. Pharmacol. Toxicol. 46*, 277–300.

(4) Jin, J., and Kunapuli, S. P. (1998) Coactivation of two different G protein-coupled receptors is essential for ADP-induced platelet aggregation. *Proc. Natl. Acad. Sci. U.S.A. 95*, 8070–8074.

(5) Hechler, B., Nonne, C., Roh, E. J., Cattaneo, M., Cazenave, J. P., Lanza, F., Jacobson, K. A., and Gachet, C. (2006) MRS2500 [2-iodo-N^6-methyl-(N)-methanocarba-2′-deoxyadenosine-3′,5′-bisphosphate], a potent, selective, and stable antagonist of the platelet $P2Y_1$ receptor with strong antithrombotic activity in mice. *J. Pharmacol. Exp. Ther. 316*, 556–563.

(6) Paredes-Gamero, E. J., Leon, C. M. M. P., Borojevic, R., Oshiro, M. E. M., and Ferreira, A T. (2008) Changes in intracellular Ca^{2+} levels induced by cytokines and P2 agonists differentially modulate proliferation or commitment with macrophage differentiation in murine hematopoietic cells. *J. Biol. Chem. 283*, 31909–31919.

(7) Hechler, B., Freund, M., Ravanat, C., Magnenat, S., Cazenave, J. P., and Gachet, C. (2008) Reduced atherosclerotic lesions in $P2Y_1$/apolipoprotein E double-knockout mice: the contribution of non-hematopoietic-derived $P2Y_1$ receptors. *Circulation 118*, 754–763.

(8) Sellers, L. A., Simon, J., Lundahl, T. S., Cousens, D. J., Humphrey, P. P., and Barnard, E. A. (2001) Adenosine nucleotides acting at the human $P2Y_1$ receptor stimulate mitogen-activated protein kinases and induce apoptosis. *J. Biol. Chem. 276*, 16379–16390.

(9) Amadio, S., Vacca, F., Martorana, A., Sancesario, G., and Volonté, C. (2007) $P2Y_1$ receptor switches to neurons from glia in juvenile versus neonatal rat cerebellar cortex. *BMC Developmental Biol. 7*, 1–17.

(10) Tonazzini, I., Trincavelli, M. L., Montali, M., and Martini, C. (2008) Regulation of A_1 adenosine receptor functioning induced by $P2Y_1$ purinergic receptor activation in human astroglial cells. *J. Neurosci. Res. 86*, 2857–2866.

(11) Fujita, T., Tozaki-Saitoh, H., and Inoue, K. (2009) $P2Y_1$ receptor signaling enhances neuroprotection by astrocytes against oxidative stress via IL-6 release in hippocampal cultures. *Glia 57*, 244–257.

(12) Massé, K., Bhamra, S., Eason, R., Dale, N., and Jones, E. A. (2007) Purine-mediated signalling triggers eye development. *Nature 449*, 1058–1062.

(13) Shalito, I., Kopyleva, O., and Serebruany, V. (2009) Novel antiplatelet agents in development: Prasugrel, ticagrelor, and cangrelor and beyond. *Am. J. Ther.* (Feb 28), PMID: 19262362.

(14) Boyer, J. L., Mohanram, A., Camaioni, E., Jacobson, K. A., and Harden, T. K. (1998) Competitive and selective antagonism of $P2Y_1$ receptors by N^6-methyl 2′-deoxyadenosine 3′,5′-bisphosphate. *Br. J. Pharmacol. 124*, 1–3.

(15) Kim, H. S., Ohno, M., Xu, B., Kim, H. O., Choi, Y., Ji, X. D., Maddileti, S., Marquez, V. E., Harden, T. K., and Jacobson, K. A. (2003) 2-Substitution of adenine nucleotide analogues containing a bicyclo[3.1.0]hexane ring system locked in a northern conformation: enhanced potency as $P2Y_1$ receptor antagonists. *J. Med. Chem. 46*, 4974–4987.

(16) Cattaneo, M., Lecchi, A., Ohno, M., Joshi, B. V., Besada, P., Tchilibon, S., Lombardi, R., Bischofberger, N., Harden, T. K., and Jacobson, K. A. (2004) Antiaggregatory activity in human platelets of potent antagonists of the $P2Y_1$ receptor. *Biochem. Pharmacol. 68*, 1995–2002.

(17) Houston, D., Ohno, M., Nicholas, R. A., Jacobson, K. A., and Harden, T. K. (2006) [^{32}P]2-iodo-N^6-methyl-(N)-methanocarba-2′-deoxyadenosine-3′,5′-bisphosphate ([^{32}P]MRS2500), a novel radioligand for quantification of native $P2Y_1$ receptors. *Br. J. Pharmacol. 147*, 459–467.

(18) Costanzi, S., Tikhonova, I. G., Ohno, M., Roh, E. J., Joshi, B. V., Colson, A. -O., Houston, D., Maddileti, S., Harden, T. K., and Jacobson, K. A. (2007) $P2Y_1$ antagonists: combining receptor-based modeling and QSAR for a quantitative prediction of the biological activity based on consensus scoring. *J. Med. Chem. 50*, 3229–3241.

(19) Léon, C., Hechler, B., Freund, M., Eckly, A., Vial, C., Ohlmann, P., Dierich, A., LeMeur, M., Cazenave, J. P., and Gachet, C. (1999) Defective platelet aggregation and increased resistance to thrombosis in purinergic $P2Y_1$ receptor-null mice. *J. Clin. Invest. 104*, 1731–1737.

(20) Léon, C., Freund, M., Ravanat, C., Baurand, A., Cazenave, J. P., and Gachet, C. (2001) Key role of the $P2Y_1$ receptor in tissue factor-induced thrombin-dependent acute thromboembolism: studies in $P2Y_1$-knockout mice and mice treated with a $P2Y_1$ antagonist. *Circulation 103*, 718–723.

(21) Jacobson, K. A. (2009) Functionalized congener approach to the design of ligands for G protein-coupled receptors (GPCRs. *Bioconjugate Chem. 20*, 1816–1835.

(22) Kolb, H. C., and Sharpless, K. B. (2003) The growing impact of click chemistry on drug discovery. *Drug Discovery Today 8*, 1128–1137.

(23) Tosh, D. K., Yoo, L. S., Chinn, M., Hong, K., Kilbey, S. M., Barrett, M. O., Fricks, I. P., Harden, T. K., Gao, Z. G., and Jacobson, K. A. (2010) Polyamidoamine (PAMAM) dendrimer conjugates of "clickable" agonists of the A_3 adenosine receptor and coactivation of the $P2Y_{14}$ receptor by a tethered nucleotide. *Bioconjugate Chem. 21*, 372–384.

(24) Saito, S., Tamai, H., Usui, Y., Inaba, M., and Moriwake, T. (1984) Efficient synthesis of secondary carboxamides with ω-substituted ethyl and propyl groups on nitrogen atom by nucleophilic ring opening of cyclic imidates. *Chem. Lett. 7*, 1243–1246.

(25) Waldo, G. L., Corbitt, J., Boyer, J. L., Ravi, G., Kim, H. S., Ji, X. D., Lacy, J., Jacobson, K. A., and Harden, T. K. (2002) Quantitation of the $P2Y_1$ receptor with a high affinity radiolabeled antagonist. *Mol. Pharmacol. 62*, 1249–1257.

(26) Ohlmann, P., de Castro, S., Gachet, C., Jacobson, K. A., Harden, T. K. Quantification of recombinant and platelet $P2Y_1$ receptors utilizing a [^{125}I]-labeled high affinity antagonist 2-iodo-N^6-methyl-(*N*)-methanocarba-2′-deoxyadenosine-3′,5′-bisphosphate ([^{125}I]MRS2500). *Pharmacol. Res.*, in press.

(27) Cheng, Y, and Prusoff, W. H. (1973) Relationship between the inhibition constant (Ki) and the concentration of inhibitor which causes 50% inhibition (I50) of an enzymatic reaction. *Biochem. Pharmacol. 22*, 3099–3108.

(28) Cazenave, J. P., Ohlmann, P., Cassel, D., Eckly, A., Hechler, B., and Gachet, C. (2004) Preparation of washed platelet suspensions from human and rodent blood. *Methods Mol. Biol. 272*, 13–28.

(29) Jaakola, V. P., Griffith, M. T., Hanson, M. A., Cherezov, V., Chien, E. Y. T., Lane, J. R., IJzerman, A. P., and Stevens, R. C. (2008) The 2.6 angstrom crystal structure of a human A_{2A} adenosine receptor bound to an antagonist. *Science 322*, 1211–1207.

(30) Yoshimura, Y., Moon, H. R., Choi, Y., and Marquez, V. E. (2002) Enantioselective synthesis of bicyclo[3.1.0]hexane carbocyclic nucleosides via a lipase-catalyzed asymmetric acetylation. Characterization of an unusual acetal byproduct. *J. Org. Chem. 67*, 5938–5945.

(31) Chincshilla, R., and Nájera, C. (2007) The Sonogashira reaction: A booming methodology in synthetic organic chemistry. *Chem. Rev. 107*, 874–922.

(32) Shryock, J. C., Snowdy, S., Baraldi, P. G., Cacciari, B., Spalluto, G., Monopoli, A., Ongini, E., Baker, S. P., and Belardinelli, L. (1998) A_{2A}-Adenosine receptor reserve for coronary vasodilation. *Circulation 98*, 711–718.

(33) Scammells, P. J., Baker, S. P., Belardinelli, L., and Olsson, R. A. (1994) Substituted 1,3-dipropylxanthines as irreversible antagonists of A_1 adenosine receptors. *J. Med. Chem. 37*, 2704–2712.

(34) Bock, V. D., Hiemstra, H., and van Maarseveen, J. H. (2006) Cu^I-Catalyzed alkyne-azide click cycloadditions from a mechanistic and synthetic perspective. *Eur. J. Org. Chem.* 51–68.

(35) Ohno, M., Costanzi, S., Kim, H. S., Kempeneers, V., Vastmans, K., Herdewijn, P., Maddileti, S., Gao, Z. G., Harden, T. K., and Jacobson, K. A. (2004) Nucleotide analogues containing 2-oxa-bicyclo[2.2.1]heptane and l-alpha-threofuranosyl ring systems: interactions with P2Y receptors. *Bioorg. Med. Chem. 12*, 5619–5630.

(36) Cherezov, V., Rosenbaum, D. M., Hanson, M. A., Rasmussen, S. G. F., Thian, F. S., Kobilka, T. S., Choi, H. J., Kuhn, P.,

Weis, W. I., Kobilka, B. K., and Stevens, R. C. (2007) High-resolution crystal structure of an engineered human β_2-adrenergic G protein-coupled receptor. *Science 318*, 1258–1265.

(37) Rosenbaum, D. M., Cherezov, V., Hanson, M. A., Rasmussen, S. G. F., Thian, F. S., Kobilka, T. S., Choi, H. J., Yao, X. J., Weis, W. I., Stevens, R. C., and Kobilka, B. K. (2007) GPCR engineering yields high-resolution structural insights into β_2-adrenergic receptor function. *Science 318*, 1266–1273.

(38) Warne, T., Serrano-Vega, M. J., Baker, J. G., Moukhametzianov, R., Edwards, P. C., Henderson, R., Leslie, A. G. W., Tate, C. G., and Schertler, G. F. X. (2008) Structure of a β1-adrenergic G-protein-coupled receptor. *Nature 454*, 486–491.

(39) Costanzi, S. (2008) On the applicability of GPCR homology models to computer-aided drug discovery: a comparison between in silico and crystal structures of the β2-adrenergic receptor. *J. Med. Chem. 51*, 2907–2914.

(40) Michino, M., Abola, E., GPCR Dock 2008 participants, Brooks, C. L., Dixon, J. S., Moult, J., and Stevens, R. C. (2009) Community-wide assessment of GPCR structure modelling and ligand docking: GPCR Dock 2008. *Nat. Rev. Drug. Discov. 8*, 455–463.

(41) Nwe, K., and Brechbiel, M. W. (2009) Growing applications of "click chemistry" for bioconjugation in contemporary biomedical research. *Cancer Biother. Radiopharm. 24*, 289–302.

(42) Tomalia, D. A., Reyna, L. A., and Svenson, S. (2007) Dendrimers as multi-purpose nanodevices for oncology drug delivery and diagnostic imaging. *Biochem. Soc. Trans. 35*, 61–67.

(43) Kim, Y., Hechler, B., Klutz, A., Gachet, C., and Jacobson, K. A. (2008) Toward multivalent signaling across G protein-coupled receptors from poly(amidoamine) dendrimers. *Bioconjugate Chem. 19*, 406–411.

(44) Klutz, A. M., Gao, Z. G., Lloyd, J., Shainberg, A., and Jacobson, K. A. (2008) Enhanced A_3 adenosine receptor selectivity of multivalent nucleoside-dendrimer conjugates. *J. Nanobiotechnol. 6*, 12.

(45) Das, A., Zhou, Y., Ivanov, A. A., Carter, R. L., Harden, T. K., and Jacobson, K. A. (2009) Enhanced potency of nucleotide-dendrimer conjugates as agonists of the $P2Y_{14}$ receptor: Multivalent effect in G protein-coupled receptor recognition. *Bioconjugate Chem. 20*, 1650–1659.

(46) Kim, Y., Hechler, B., Gao, Z. G., Gachet, C., and Jacobson, K. A. (2009) PEGylated dendritic unimolecular micelles as versatile carriers for ligands of G protein-coupled receptors. *Bioconjugate Chem. 20*, 1888–1898.

(47) Ballesteros, J. A., and Weinstein, H. (1995) Integrated methods for the construction of three-dimensional models and computational probing of structure-function relations in G-protein coupled receptors. *Methods Neurosci. 25*, 366–428.

BC900569U

Liposomal Cu-64 Labeling Method Using Bifunctional Chelators: Poly(ethylene glycol) Spacer and Chelator Effects

Jai Woong Seo, Lisa M. Mahakian, Azadeh Kheirolomoom, Hua Zhang, Claude F. Meares,[†] Riccardo Ferdani,[‡] Carolyn J. Anderson,[‡] and Katherine W. Ferrara*

Department of Chemistry and Department of Biomedical Engineering, University of California, Davis, California 95616, and Mallinckrodt Institute of Radiology, Washington University School of Medicine, St. Louis, Missouri 63110. Received January 11, 2010; Revised Manuscript Received May 12, 2010

Two bifunctional Cu-64 chelators (BFCs), (6-(6-(3-(2-pyridyldithio)propionamido)hexanamido)benzyl)-1,4,8,11-tetraazacyclotetradecane-1,4,8,11-tetraacetic acid (TETA-PDP) and 4-(2-(2-pyridyldithioethyl)ethanamido)-11-carboxymethyl-1,4,8,11-tetraazabicyclo(6.6.2)hexadecane (CB-TE2A-PDEA), were synthesized and conjugated to long-circulating liposomes (LCLs) via attachment to a maleimide lipid. An in vitro stability assay of ^{64}Cu-TETA, ^{64}Cu-TETA-PEG2k, and ^{64}Cu-CB-TE2A-PEG2k liposomes showed that more than 86% of the radioactivity remains associated with the liposomal fraction after 48 h of incubation with mouse serum. The in vivo time activity curves (TAC) for the three liposomal formulations showed that ~50% of the radioactivity cleared from the blood pool in 16−18 h. As expected, the in vivo biodistribution and TAC data obtained at 48 h demonstrate that the clearance of radioactivity from the liver slows with the incorporation of a poly(ethylene glycol)-2k (PEG2k) brush. Our data suggest that ^{64}Cu-TETA and ^{64}Cu-CB-TE2A are similarly stable in the blood pool and accumulation of radioactivity in the liver and spleen is not related to the stability of Cu-64 chelator complex; however, clearance of Cu-64 from the liver and spleen are faster when injected as ^{64}Cu-TETA-chelated liposomes rather than ^{64}Cu-CB-TE2A-chelated liposomes.

INTRODUCTION

Liposomes, spherical vehicles composed of a lipid bilayer with an aqueous interior, have been investigated for more than 40 years as a promising drug carrier (*1*−*3*). When coated by poly(ethylene glycol), liposomal circulation time in blood increased with a decrease in reticuloendothelial system (RES) uptake (*4*−*6*). Currently, 90−100-nm-diameter liposomes entrapping anticancer or antifungal drugs are approved and used for passively targeting the relatively leaky vasculature of tumors (*7*, *8*). Advanced liposomal technology exploits peptide (*9*, *10*), antibody (*11*, *12*), and small molecule ligands (*13*, *14*) by attaching these ligands on the surface of liposomes to maximize the retention at the target site. In addition, triggered drug release by ultrasound (*15*, *16*) or a laser (*17*, *18*) and in a low pH environment (*19*) has been explored for local delivery.

Noninvasive imaging techniques using SPECT and PET have been developed to evaluate the pharmacokinetics and biodistribution of liposomes in vivo (*20*−*22*). Previous studies have utilized liposomes with radionuclides such as technetium-99m (*23*−*27*), gallium-67 (*28*), and indium-111 (*29*, *30*) for single photon emission computed tomography (SPECT) and fluorine-18 (*31*−*33*), iodine-124 (*34*), oxygen-15 (*35*), and copper-64 (*36*) for positron emission tomography (PET), where radionuclides were applied with three distinct schemes involving entrapment, insertion, and chelation. In the entrapment method, radionuclides such as indium-111 ($t_{1/2}$ = 2.8 days), gallium-67 ($t_{1/2}$ = 3.3 days), and technetium-99m ($t_{1/2}$ = 6.01 h) were coordinated with membrane permeable lipophilic chelators and loaded into the aqueous liposomal core with a change to a hydrophilic chelator (*25*, *26*, *28*, *30*). As an insertion method, radiolabeled lipids, 3-[^{18}F]fluoro-1,2-dipalmitoylglycerol ([^{18}F]-FDP) or [^{18}F]-labeled amphiphilic lipids, were incorporated into the liposomal bilayer (*31*, *33*). Surface chelation methods, the most convenient method, were also developed with technetium-99m or copper-64 ($t_{1/2}$ = 12.7 h) by covalently attaching the chelator on the surface of the liposome (*27*, *36*) or conjugating ^{18}F-labeled PEG-acetylene with an azide group on the liposome via a "click" reaction (*37*).

The previous labeling approaches were focused on obtaining a stable conjugation of a radionuclide and liposome to quantify the liposomal activity in target tissues over days to weeks without the radionuclide undergoing metabolism or becoming decomplexed. We previously developed a liposomal Cu-64 labeling method using 6-[*p*-(bromoacetamido)benzyl]-1,4,8,11-tetraazacyclotetradecane-*N*,*N*′,*N*″,*N*‴-tetraacetic acid (BAT) conjugated lipid (6-BAT-lipid) and successfully measured the liposomal circulation time in blood over 48 h (*36*). However, liposomes with high molar concentrations of peptide have shown a lower radiolabeling yield. CB-TE2A, which forms a highly stable complex with Cu-64, has not previously been explored in a liposomal study using a postlabeling method because the chelation of Cu-64 should be performed at a temperature above 80 °C, which may affect liposomal stability due to the intrinsic transition temperature of the liposome (*38*, *39*).

Recent studies of targeted nanoparticles combine antibodies, peptides, small molecules, and polymers on the surface to optimize and personalize targeting (*9*−*14*). For this reason, it is important to optimize radiochemistry techniques for specific surface architectures, and therefore, alternative postlabeling methods and CB-TE2A are explored. Herein, we developed and evaluated a Cu-64 labeling method using a maleimide lipid and

* To whom correspondence should be addressed. Prof. Katherine W. Ferrara, Dept. of Biomedical Engineering, 451 East Health Sciences Drive, University of California, Davis, Davis, CA 95616. Phone 530-754-9436, fax (530)754-5739, e-mail: kwferrara@ucdavis.edu.

[†] Department of Biomedical Engineering, University of California, Davis.

[‡] Washington University School of Medicine.

10.1021/bc100018n © 2010 American Chemical Society
Published on Web 06/22/2010

bifunctional chelator (BFC). Stability in vitro and in vivo is then compared for liposomes labeled with TETA-PDP and CB-TE2A-PDEA and with varied spacer lengths between the lipid and the chelator.[1]

Materials. HSPC, DSPE-PEG2k-maleimide, cholesterol, DSPE-PEG2k-OMe, were purchased from Avanti Polar Lipids (Alabaster, AL), and DSPE-maleimide was purchased from NOF America Corporation (White Plains, NY). Sulfo-LC-SPDP (sulfosuccinimidyl 6-[3-(2-pyridyldithio)-propionamido]hexanoate) was purchased from Thermo Scientific (Rockford, IL). *S*-(2-Aminoethyl)dithio-2-pyridine hydrochloride was purchased from Toronto Research Chemicals (North York, ON). Solvents and other agents were all of analytical purity and purchased from Sigma-Aldrich (Milwaukee, WI) and VWR (Brisbane, CA). $^{64}CuCl_2$ was purchased from Isotrace (St. Louis, MO) under a protocol controlled by the University of California, Davis. PBS was purchased from Invitrogen Corporation (Carlsbad, CA). Mouse serum was purchased from Innovative research (Novi, MI).

EXPERIMENTAL SECTION

Synthesis of TETA-PDP (*2*). (6-(6-(3-(2-Pyridyldithio)propionamido)hexanamido)benzyl)-1,4,8,11-tetraazacyclotetradecane-1,4,8,11-tetraacetic acid (TETA-PDP, **2**) was synthesized from aminobenzyl-TETA (**1**) based on a previously reported method (*40*, *41*). To a solution of **1** (18 mg, 34 μmol) in DI water (2 mL, pH 7) was added sulfosuccinimidyl-6-[3′-(2-pyridyldithio)-propionamido]hexanoate (22 mg, 42 μmol). The mixture was stirred at room temperature for 4 h. Reaction progress was monitored by a semipreparative HPLC (column, Jupiter 10 μ proteo, 250 × 10 mm; flow rate, 3 mL/min; eluent, A - MeOH, B - 0.05% TFA in triple-distilled water; gradient, 0−15 min (40−80% A), 15−30 min (80−100% A)) and retention time was 11 min. Coupled product **2** was isolated by preparative HPLC (column, Jupiter 10 μ, 250 × 21.2 mm; flow rate, 10 mL/min; eluent, A - MeOH, B - 0.05% TFA in triple-distilled water; gradient, 0−15 min (40−80% A), 1−30 min (80−100% A); retention time, 13.3 ± 0.36 min) and lyophilized as a white solid (25 mg, 87%). ^{1}H NMR (500 MHz, D_2O): 8.48 (d, J = 5.5 Hz, 1H), 8.12 (t, J = 8.0 Hz, 1H), 7.91 (d, J = 8.5 Hz, 1H), 7.55 (t, J = 6.0 Hz, 1H), 7.36 (d, J = 7.5 Hz, 2H), 7.30 (d, J = 8.0 Hz, 2H), 3.35−3.65 (m, 12H), 0.2.95−3.32 (m, 16H), 2.61 (t, J = 6.5 Hz, 2H), 2.55−2.45 (m, 3H), 2.08 (bs, 1H), 1.78 (bs, 1H), 1.73 (m, 2H), 1.54 (m, 2H), 1.39 (m, 2H); MS (ESI) m/z 848.4 ($M+H^+$).

Synthesis of CB-TE2A-PDEA (*4*). 4-(2-(2-Pyridyldithioethyl)ethanamido)-11-carboxymethyl-1,4,8,11-tetraazabicyclo-(6.6.2)hexadecane (CB-TE2A-PDEA, **4**) was synthesized from CB-TE2A (*3*) as in refs 42, 43. To a solution of **3** (68 mg, 0.1 mmol) in DMF (4 mL) was added *N*-(3-dimethylaminopropyl)-*N*′-ethylcarbodiimide hydrochloride (EDCI·HCl, 9.6 mg, 50 μmol), *N*-hydroxybenzotriazole (HOBt, 8.1 mg, 60 μmol), and *N*,*N*-diisopropylethylamine (DIPEA, 52 μL, 0.3 mmol). After stirring for 30 min at room temperature, *S*-(2-aminoethyl)dithio-2-pyridine hydrochloride (11 mg, 50 μmol) was added and the reaction mixture was stirred overnight. The solvent was removed under high vacuum, and residual oil was injected into the preparative HPLC after dilution of oil with a 0.05% TFA solution (column, Jupiter 10 μ, 250 × 21.2 mm; flow rate, 10 mL/min; eluent, A - acetonitrile, B - 0.05% TFA in triple-distilled water; gradient, 0−15 min (20−25% A), 15−30 min (25−90% A); retention time, 9.3 ± 0.35 min). The collected product fraction was lyophilized and **4** obtained as a white powder (19 mg, 74%). ^{1}H NMR (500 MHz, D_2O): 8.58 (d, J = 5.0 Hz, 1H), 8.23 (t, J = 8.5 Hz, 1H), 8.13 (d, J = 8.5 Hz, 1H), 7.64 (t, J = 6.5 Hz, 1H), 4.22 (d, J = 15.5 Hz, 1H), 4.02 (d, J = 16.0 Hz, 1H), 3.76−3.62 (m, 3H), 3.62−3.51 (m, 2H), 3.50−3.34 (m, 4H), 3.25−2.90 (m, 15H), 2.75 (bd, J = 13.5 Hz, 1H), 2.75 (dd, J = 13.5, 2.0 Hz, 1H), 2.45−2.31 (m, 2H), 1.75 (t, J = 16.5 Hz, 2H); MS (ESI) m/z 511.5 ($M+H^+$, 100).

HPLC Analysis of Cu-64 Chelation with CB-TE2A-PDEA. A few microliters of $^{64}CuCl_2$ were buffered with 0.1 M ammonium citrate (100 μL). CB-TE2A-PDEA (1 mM, 2 μL) dissolved in ammonium citrate buffer (0.1 M, pH 5.5) was added into a buffered $^{64}CuCl_2$ solution, and the mixture was incubated at 85 °C. Samples for HPLC analysis were acquired at 0, 30, and 60 min and kept in an ice bath until they were injected into the HPLC. Freshly prepared TCEP (10 mM, 2 μL) in PBS was then added, and the mixture was held at room temperature for 10 min and applied to an HPLC column (Jupiter, C12, 250 × 4.6 mm, flow rate, 1 mL/min; eluent, A - 0.5% TFA in deionized water, B - 0.5% TFA in acetonitrile, 0−10 min (10−20% B), 10−20 min (20−100% B), 20−24 min (100% B), 24−25 min (100−10% B)).

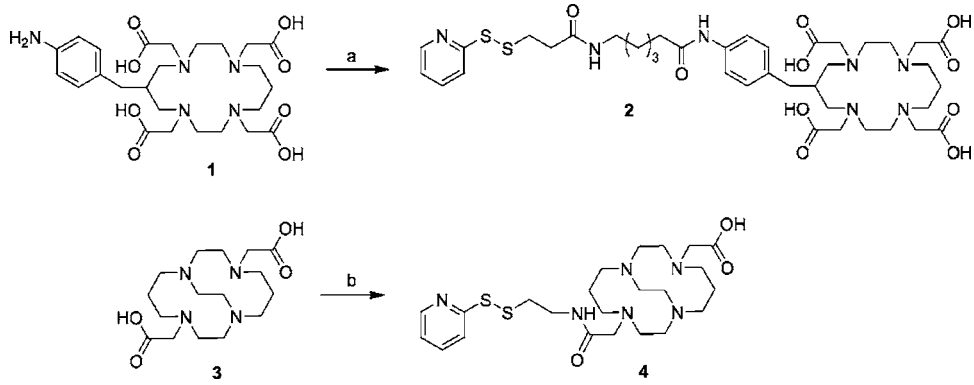
Preparation of Maleimide Liposomes. Commercially available lipids (10 mg of HSPC, cholesterol, DSPE-PEG2k-OMe, and 1 mol % DSPE-PEG2k-maleimde or DSPE-maleimide) in chloroform were mixed in a test tube. Chloroform was evaporated by a gentle stream of nitrogen with a vortex. After drying overnight in a lyophilizer, lipids were suspended in PBS (1×). The lipid solution was incubated at 60 °C for 5 min, drawn into the 1 mL syringe, and extruded at 60 °C by a mini extruder unit with 100 nm filters. Immediately after extrusion, the size was measured using a NICOMP 380 ZLS (Particle Sizing Systems, CA), and liposomes were labeled with Cu-64 labeled bifunctional chelators. The average liposomal diameter was 123.6 ± 13.0 nm.

Labeling of Maleimide Liposomes with BFCs. All labeling procedures were controlled under a protocol of the University of California, Davis. $^{64}CuCl_2$ (0.55−5 mCi, [18.5−185 MBq]) was buffered with 0.1 M ammonium citrate (100 μL). TETA-PDP or CB-TE2A-PDEA (1 mM, 10−2 μL) in an ammonium citrate buffer (0.1 M, pH 5.5) was added into a $^{64}CuCl_2$ solution, which was incubated for 40 min at 30 °C or 1.5 h at 85 °C, respectively. The reaction progress was monitored by radio TLC (silica backed plate, eluent 10% (w/w) ammonium acetate and methanol (1:1, v/v)) or radio HPLC. After the addition of 10× excess of 0.1 M Tris(2-carboxylethyl)phosphine hydrochloride (TCEP·HCl) dissolved in PBS, the solution was incubated for 5 min at room temperature. Freshly prepared maleimide liposomes (10, 5, 2.5, and 1 mg) in PBS (0.4 mL) were added to the reduced bifunctional chelator mixture. The pH was adjusted with 5.6% (v) ammonium hydroxide solution, and the liposomal mixture was incubated for 40 min at 30 °C. After cooling of the liposomal mixture, unreacted maleimide on the surface of the liposomes was quenched by an excess (maleimide/ethanethiol = 1:10, mol/mol) of freshly prepared 0.1 M ethanethiol solution by incubating for 10 min. Lastly, nonspecific binding of Cu-64 was removed by 0.1 M EDTA (20 μL) incubation for 5−10 min. Liposomes were purified by size exclusion chromatography with PBS.

In Vitro Stability Test. ^{64}Cu-labeled liposomes (^{64}Cu-TETA, ^{64}Cu-TETA-PEG2k, and ^{64}Cu-CB-TE2A-PEG2k liposomes, 1 mg, 10.1−12.28 MBq) were added to 0.5 mL of mouse serum and PBS, and the mixture was incubated for 48 h at 37 °C. After cooling, a portion of the liposomal serum mixture (100 μL) was hand-loaded onto a preconditioned Sephacryl-300HR

[1]Abbreviations: HSPC, hydrogenated soy L-α-phosphatidylcholine; DSPE, 1,2-distearoyl-*sn*-glycero-3-phosphoethanolamine; DSPE-PEG2k-OMe, 1,2-distearoyl-*sn*-glycero-3-phosphoethanolamine-*N*-[methoxy-(polyethylene glycol)-2000]; MI, maleimide; HOBt, *N*-hydroxybenzotriazole; EDCI, (3-(dimethylamino)propyl)ethyl carbodiimide; DIPEA, diisopropylethylamine.

Scheme 1. Synthesis of Bifunctional Chelators (BFCs) Bearing TETA and CB-TE2A[a]



[a] Reagents: (a) Sulfo-LC-SPDP (sulfosuccinimidyl-6-[3′-(2-pyridyldithio)propionamido]hexanoate), DI water, rt, 4 h. (b) *S*-(2-Aminoethyl)dithio-2-pyridine hydrochloride, HOBt, EDCI, DIPEA, DMF, rt, 6 h.

(GE Healthcare, NJ) packed column (15 mm i.d., 250 mm height) and separated with PBS at 2 psi. Fractions (1.5 mL/fraction) were collected into test tubes, and the radioactivity was measured with the 1470 Automatic Gamma Counter (Perkin-Elmer Life Sciences, MA). After the radioactive decay, the absorbance of all fractions was measured at 280 nm. The radio TLC assay was run on aluminum-backed silica gel sheets (silica gel 60 F254, EMD, NJ), developed with chloroform/methanol/H_2O (50:40:6, v/v/v) and recorded by a radio-TLC Imaging Scanner (Bioscan, NW).

Biodistribution Study. All animal studies were conducted under a protocol approved by the University of California, Davis, Animal Use and Care Committee. A total of 13 animals (female FVB mice, 12−19 weeks, 25−30 g, Charles River, MA) were examined over the course of this study. For each image, 4 or 5 mice per group were anesthetized with 3.5% isoflurane and maintained at 2.0−2.5%. ^{64}Cu-TETA liposomes (38 ± 0.7 mg/kg, 313 ± 19 μCi [11.58 ± 0.70 MBq]/animal), ^{64}Cu-TETA-PEG2k liposomes (43 ± 6.7 mg/kg, 332 ± 55 μCi [12.28 ± 2.03 MBq]/animal), and ^{64}Cu-CB-TE2A-PEG2k liposomes (34 ± 1.6 mg/kg, 272 ± 9.2 μCi [10.06 ± 0.34 MBq]/animal) in PBS (pH 7.4) were administered to the mice on a PET scanner bed by catheterized tail vein injection. After scanning over 48 h, the mice were euthanized by cervical dislocation, and organs of interest were harvested and weighed. Radioactivity was measured using a 1470 Automatic Gamma Counter.

PET Scans and Time−Activity Curves (TAC). Two mice were placed on one bed, and each set of PET scans was conducted with the microPET Focus (Concorde Microsystems, Inc., TN) over 30 min. Mice were scanned at an initial time point ($t = 0$), and 6, 18, 28, and 48 h. Filtered backprojection (FBP) reconstruction was obtained with *ASIPro* software (CTI Molecular Imaging). TACs were obtained with region-of-interest (ROI) analysis using *ASIPro* software and expressed as the percentage of injected dose per cubic centimeter (%ID/cc).

Statistical Analysis. *Prism* (GraphPad Software Inc., San Diego, CA) was used for statistical analysis. One-phase exponential blood clearance curves were generated via a curve fit. The data analysis was performed using one-way analysis of variance (ANOVA).

RESULTS

Synthesis of TETA-PDP (*2*). Aminobenzyl TETA **1**, precursor of TETA-PDP, was achieved in 5 steps from 4-nitrobenzyl bromide as previously reported (*40, 41*). Critical steps in determining the yield were cyclization, where the resulting yield was 40% with *N*,*N*-bis(2-aminoethyl)-1.3-propanediamine, and alkylation, where the resulting yield was 41% with benzylbromoacetate. To reduce the contamination from trace metals, aminobenzyl TETA **1** was coupled with sulfosuccinimidyl-6-[3′-(2-pyridyldithio)propionamido]hexanoate in distilled water at pH 7 (Scheme 1). The product was isolated by preparative HPLC with retention time on average 13.3 min, and overall synthesis yield was 10%. The final product was validated by ^{1}H NMR spectral analysis and electrospray ionization−mass spectrometry in a positive mode. A single charged peak (20%) at 848 and a double charged peak (100%) at 425 were detected.

Synthesis of CB-TE2A-PDEA (*4*). A half equivalent of *S*-(2-aminoethyl)dithio-2-pyridine hydrochloride and CB-TE2A was treated with HOBt, EDCI, and DIPEA in DMF to obtain the carboxylic acid-coupled product (Scheme 1). DMF was removed under high vacuum to achieve a consistent retention time of 9.3 min on preparative HPLC. Lyophilization of the product fractions yielded 74% CB-TE2A-PDEA. The product was also validated by ^{1}H NMR spectral analysis and electrospray ionization−mass spectrometry in a positive mode. A single charged peak was detected at 511 (100%).

Radio HPLC Analysis of Cu-64 Incorporation into CB-TE2A-PDEA and Formation of Active Sulfhydryl Group. Incorporation of Cu-64 with TETA is performed at room temperature within 1 h. On the other hand, CB-TE2A requires heating (>80 °C) for incorporation of Cu-64. First, we evaluated the stability of CB-TE2A-PDEA under the chelation conditions at 85 °C. Freshly prepared 2 nmol of 1 mM CB-TE2A-PDEA **4** in ammonium acetate buffer (pH 5.5, 100 μL) was incubated with a few hundred μCi of Cu-64 at 85 °C. The reaction progress and decomposition of Cu-64 incorporated BFC were monitored by HPLC analysis. After the addition of $^{64}CuCl_2$ into the CB-TE2A-PDEA solution, the radiochromatogram showed that only Cu-64 peak was eluted at 3 min (**a**, Figure 2). After incubation for 30 and 60 min, 69% and 96% of the radioactivity was observed with a retention time of 15 min, respectively (**b** and **c**, Figure 2), which indicated that Cu-64 was completely incorporated into CB-TE2A-PDEA without decomposition. After the Cu-64 chelation, ^{64}Cu-CB-TE2A-PDEA solution was cooled to room temperature for 10 min, and the addition of a 10× excess amount of TCEP (10 mM, 2 μL) as a reducing reagent selectively cleaved the disulfide bond (*44*). Incubation for 10 min converted all Cu-64-incorporated-CB-TE2A-PDEA into the peak at 8 min. Thus, the pyridyldithiol **6** was rapidly reduced to the sulfhydryl group **7** (**d**, Figure 2) with more than 99% yield, which was confirmed by the conversion of retention time of **6** to **7**.

BFC Conjugation Study with Maleimide Liposome. Liposomes (average diameter: 119 ± 12 nm) were prepared from HSPC, DSPE-PEG2k-OMe, cholesterol, and DSPE-maleimide

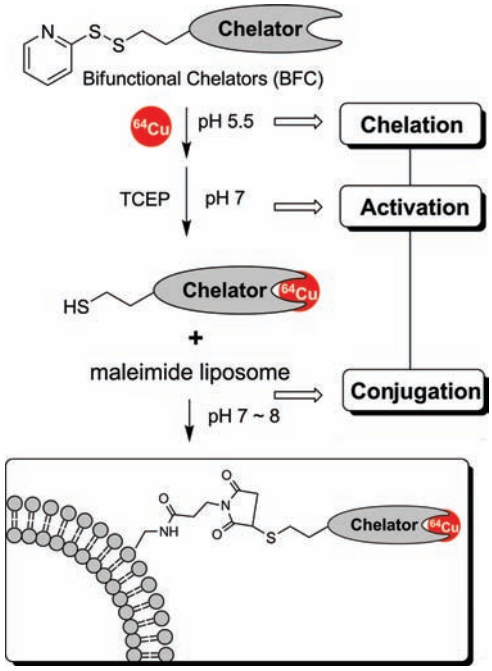


Figure 1. General scheme of liposomal postlabeling with (BFC).

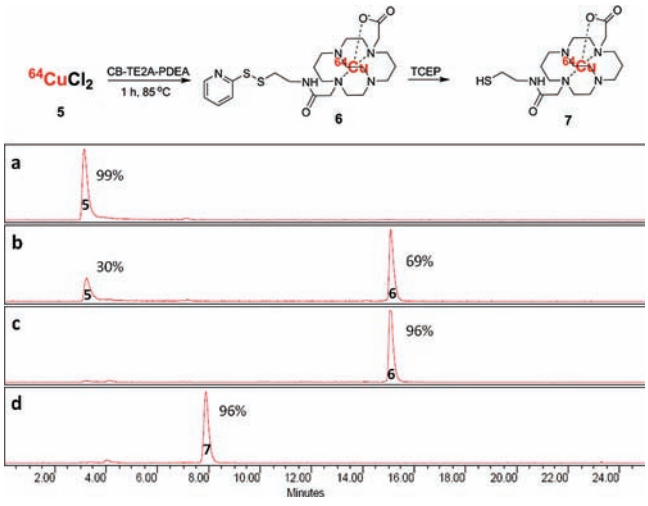
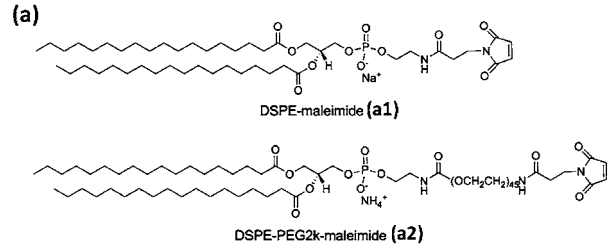


Figure 2. HPLC radio chromatogram: (a) immediately after mixing $^{64}CuCl_2$ and CB-TE2A-PDEA at room temperature; (b) after 30 min incubation at 85 °C; (c) after 60 min incubation at 85 °C; (d) after addition of 10 equiv of tris-(2-carboxyethyl)phosphine (TCEP) at room temperature.

(molar ratio 55/5/39/1) and HSPC, DSPE-PEG2k-OMe, cholesterol, and DSPE-PEG2k-maleimide (molar ration 56/4/39/1) (Figure 3) as described in the experimental procedure. The incorporation of Cu-64 (0.2−1 mCi [7.4−37 MBq]) into TETA-PDP **2** (2 nmol) at 30 °C was successful (>99%), which was confirmed by the R_f value of radio TLC ($^{64}CuCl_2$, R_f 0; ^{64}Cu-TETA-PDP, R_f 0.45). Treatment by TCEP (10 equiv/TETA-PDP), which reduces a disulfide over a wide pH range (*45*), converted pyridyldithiol **8** to the sulfhydryl compound **9** with more than 99% yield within 10 min (data not shown but similar to Figure 2). To increase the nucleophilicity of the thiols, the pH was adjusted to 7.0−7.5. The conjugation yield of ^{64}Cu-TETA-thiol **9** was assessed with 0.5, 1.25, and 2.5 mg of maleimide liposomes which have 7, 17, 35, and 70 nmol of maleimide on the surface of liposome, respectively. The corresponding liposomal conjugation yields were 16 ± 2%, 43 ± 14%, 91 ± 3%, and 93 ± 3% (n = 4) for 1 mol % maleimide



(b)

Liposomes	Formulation (mol%)			
	HSPC	DSPE-PEG2k-OMe	Chol[a]	Maleimide lipid
Long circulating liposome	56	5	39	-
1 mol% maleimide liposome	55	5	39	**1 (a1)**
1 mol% maleimide-PEG2k liposome	56	4	39	**1 (a2)**

Figure 3. (a) Structure of maleimide lipids with and without PEG. (b) Formulations of long circulating liposomes and modified formulations. Two different 1 mol % maleimide lipids were included.

liposomes, and 20 ± 4%, 47 ± 17%, 92 ± 3%, and 94 ± 3% (n = 4) for 1 mol % maleimide-PEG2k-liposomes (Figure 5). The radiochemical purity checked by the separated liposomal fraction was more than 99% on radio TLC. The specific activity of Cu-64 labeled liposomes in this in vivo study was 20.8 ± 1.6 mCi/μmol maleimide lipid.

In Vitro Stability Test. The in vitro stability of BFC conjugated maleimide liposomes was assessed with ^{64}Cu-TETA, ^{64}Cu-TETA-PEG2k, and ^{64}Cu-CB-TE2A-PEG2k liposomes (each 1 mg) in PBS/mouse serum (1/1, v/v) after 48 h incubation at 37 °C. After size exclusion chromatography (n = 3), we obtained 84 ± 2% of the total radioactivity in 50 fractions (75 mL) from all liposomes. Liposomal fractions eluted from fraction 8 to 15 contain 89% (^{64}Cu-TETA liposomes), 86% (^{64}Cu-TETA-PEG2k liposomes), and 86% (^{64}Cu-CB-TE2A-PEG2k liposomes) of total eluted radioactivity (Figure 6). Radiochemical purity, monitored by radio TLC, of each liposomal fraction was more than 98%.

In Vivo PET Images and Time−Activity Curves (TAC). In vivo imaging with ^{64}Cu-BFC-labeled liposomes from 30 min scans at 0, 6, 18, and 28 h after intravenous injection demonstrated long circulation of the ^{64}Cu-TETA liposomes (1.0 mg, 313 ± 19 μCi [11.58 ± 0.70 MBq]), ^{64}Cu-TETA-PEG2k liposomes (1.2 mg, 332 ± 56 μCi [12.28 ± 2.03 MBq]), and ^{64}Cu-CB-TE2A-PEG2k liposomes (1.0 mg, 272 ± 9.2 μCi [10.06 ± 0.34 MBq]) (Figure 7). Liposomal activity was high in the blood pool from 0 to 6 h and slowly cleared out through the reticuloendothelial system. Time activity curves (TAC) corresponding to blood, liver, and spleen are shown in Figure 8. For ^{64}Cu-TETA liposomes, radioactivity in the blood pool decreased to 41 ± 1.2%, 34 ± 1.6%, 20 ± 0.5%, 13 ± 1.0%, and 8.4 ± 0.6%ID/cc at 30 min and 6, 18, 28, and 48 h, respectively (Figure 8b). At the same time points, with ^{64}Cu-TETA-PEG2k liposomes, the radioactivity in the blood pool was 41 ± 3.8%, 31 ± 3.3%, 20 ± 2.0%, 13 ± 2.3%, and 7.6 ± 0.6%ID/cc, for ^{64}Cu-CB-TE2A-PEG2k liposomes, 39 ± 1.1%, 28 ± 2.3%, 18 ± 2.1%, 11 ± 1.0%, and 6.4 ± 1.6%ID/cc at 30 min and 6, 18, 28, and 48 h, respectively (Figure 8b). Exponential curve-fitting of three liposomal formulations showed one-phase exponential clearance from the blood pool. TAC data obtained from the blood pool was simulated with one-phase exponential decay as shown in Table 2.

For the three liposomal preparations, estimated radioactivity in the liver was 10.5 ± 0.8%, 13.3 ± 0.6%, 12.1 ± 0.9%, 8.7 ± 0.1%, and 6.7 ± 0.2%ID/cc (^{64}Cu-TETA liposomes), 8.1 ±

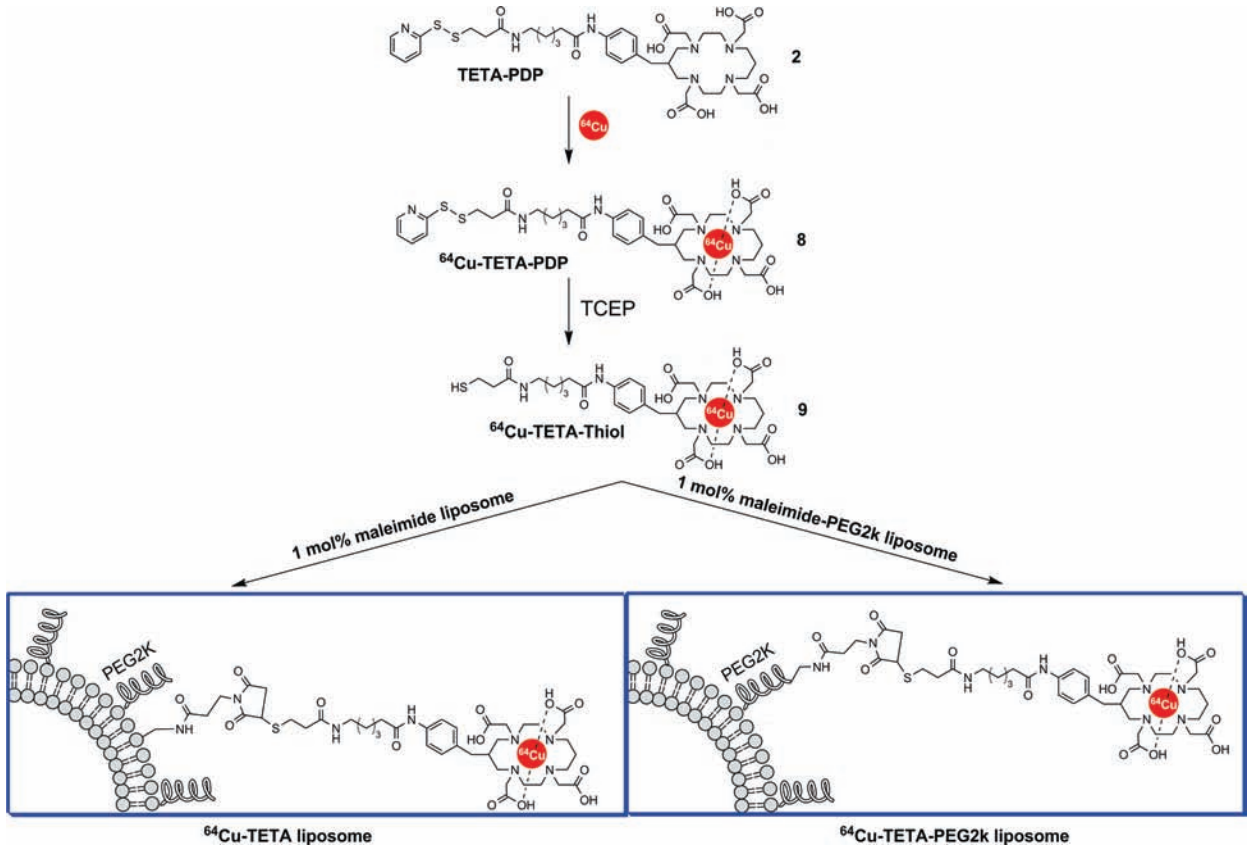


Figure 4. Liposomal labeling model with ^{64}Cu-TETA-PDP and two maleimide liposomes.

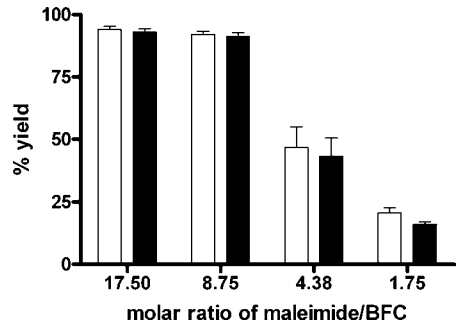


Figure 5. Labeling yield ($n = 4$) of maleimide (1 mol %) liposomes with various molar ratios of Cu-64-incorporated TETA-BFC at pH 7 (black bar, 1 mol % maleimide liposomes; white bar, 1 mol % maleimide-PEG2k liposomes).

1.5%, 14.3 ± 1.0%, 15.1 ± 0.9%, 13.7 ± 1.3%, and 11.0 ± 0.8%ID/cc (^{64}Cu-TETA-PEG2k liposomes), and 7.4 ± 0.9%, 13.5 ± 2.0%, 16.5 ± 2.2%, 15.4 ± 2.0%, and 15.7 ± 1.7%ID/cc (^{64}Cu-CB-TE2A-PEG2k liposomes) at 30 min, and 6, 18, 28, and 48 h, respectively (Figure 8c). Estimated radioactivity in the spleen was 6.0 ± 1.7%, 8.1 ± 4.1%, 8.1 ± 1.0%, 4.8 ± 1.3%, and 4.2 ± 0.9%ID/cc (^{64}Cu-TETA liposomes), 7.5 ± 0.8%, 9.6 ± 1.2%, 10.2 ± 2.1%, 9.4 ± 2.4%, and 8.3 ± 2.0%ID/cc (^{64}Cu-TETA-PEG2k-liposomes), and 6.9 ± 0.6%, 10.8 ± 1.3%, 14.8 ± 3.6%, 13.2 ± 4.5%, and 10.4 ± 2.7%ID/cc (^{64}Cu-CB-TE2A-PEG2k liposomes) at 30 min, 6, 18, 28, and 48 h, respectively (Figure 8d).

Biodistribution. The biodistribution at 48 h confirmed the TAC estimates (Table 1). There was no significant difference in blood radioactivity (8.71 ± 0.38%, 8.35 ± 1.10%, and 6.85 ± 1.66%ID/g) at 48 h after administration of ^{64}Cu-TETA liposomes, ^{64}Cu-TETA-PEG2k liposomes, and ^{64}Cu-CB-TE2A-PEG2k liposomes, respectively. For ^{64}Cu-TETA liposome-injected mice, radioactivity in the liver (6.88 ± 0.96%ID/g) and spleen (12.26 ± 0.70%ID/g) was significantly lower than that of the liver (15.2 ± 1.23%ID/g, 22.9 ± 4.42%ID/g) and spleen (20.3 ± 2.49%ID/g, 30.4 ± 5.25%ID/g) of ^{64}Cu-TETA-PEG2k and ^{64}Cu-CB-TE2A-PEG2k liposome-injected mice, respectively. Other organs showed a similar biodistribution for the three liposomal formulations (Table 1).

DISCUSSION

The first aim of this study was to develop a liposomal conjugation method using a Cu-64 and thiol-reactive bifunctional chelator. Since the conjugation of peptides on the liposomal surface has utilized the reaction of thiol with maleimide within 5 to 60 min at 25 °C (*46*−*48*), liposomal conjugation with a thiol-activable Cu-64-incorporated bifunctional chelator was considered to be a promising approach. On the basis of this aim, we proposed the scheme outlined in Figure 1.

The incorporation of Cu-64 to TETA-PDP was performed under mild conditions (30 °C) within an hour, and the reaction progress could easily be confirmed by radio TLC (R_f 0.45 with 10% ammonium acetate and methanol (1:1, v/v)). However, the reaction progress of **4** could not be monitored by radio-TLC due to the similar retention factor (both R_f = 0) of ^{64}CuCl (*5*) and ^{64}Cu-CB-TE2A-PDEA (*6*). In addition, the stability of pyridine dithiol in CB-TE2A-PDEA (*4*) during chelation at 85 °C was a concern. Accordingly, the reaction progress was assessed by HPLC analysis (Figure 2). Radio HPLC analysis demonstrated that the chelation of Cu-64 into CB-TE2A-PDEA (*4*) was completed within 1 h, and the conversion of **6** to thiol (*7*) succeeded without decomplexation of Cu-64 from the chelators or decomposition of **6** and **7** (Figure 2).

Next, we moved forward to the optimization of labeling yield, as outlined in Figure 4. For this study, 1 mol % maleimide and

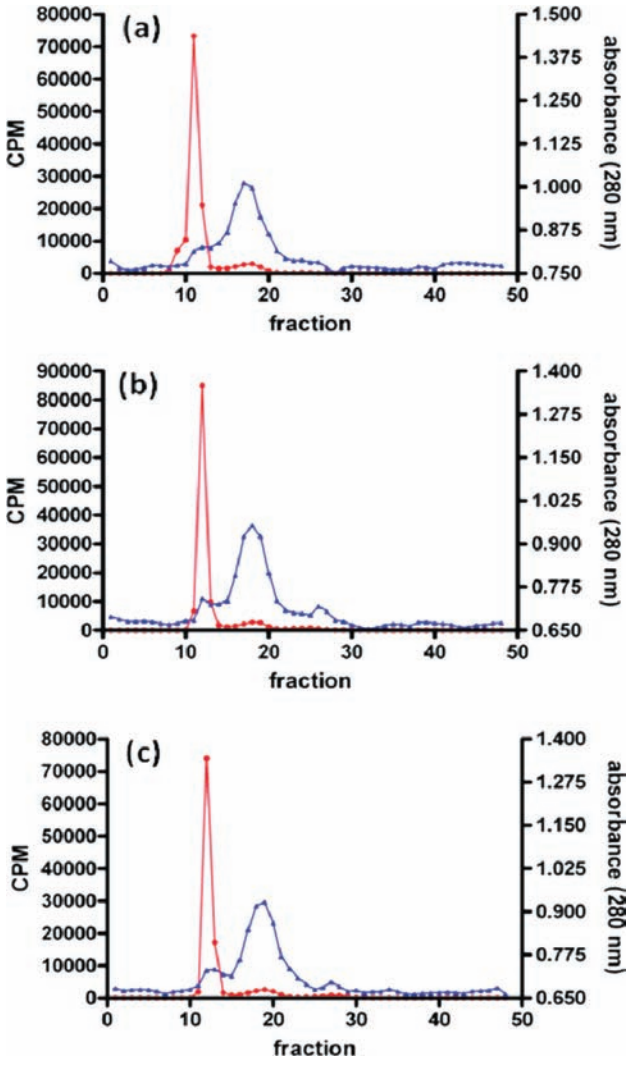


Figure 6. In vitro assay of Cu-64-labeled maleimide liposomes. Chromatograms were obtained after 48 h incubation in mouse serum and PBS (1:1, v/v) bearing (a) ^{64}Cu-TETA liposomes; (b) ^{64}Cu-TETA- PEG2k liposomes; and (c) ^{64}Cu-CB-TE2A-PEG2k liposomes. Red line represents radioactivity of liposomes detected by a gamma counter and blue line represents serum proteins detected by UV-absorbance at 280 nm.

1 mol % maleimide-PEG2k liposomes were employed to compare the labeling efficiency and to determine whether the PEG2k brush decreases the conjugation (Figure 3). In order to maintain 5 mol % PEG2k on the surface of the liposomes, which facilitates long circulation of liposomes in the blood pool, either 5 mol % DSPE-PEG2k-OMe or a combination of 4 mol % DSPE-PEG2k-OMe and 1 mol % DSPE-PEG2k maleimide were incorporated within our formulations (Figure 3). The labeling study (measured in four molar ratios of maleimide lipid versus TETA-PDP (*2*)) showed that at least an 8-fold lower molar concentration of **2** should be incubated with both liposomes to obtain greater than 90% yield (pH 7, 40 min incubation) (Figure 5). The BFC is fully accessible with similar labeling efficiency whether the maleimide sits under the PEG2k-brush or at the end of the PEG2k lipid.

In general, more than 6000 mCi/μmol maleimide lipids could be obtained from Cu-64 generated from a Ni-64 target (*49*) under the assumption of 100% chelation of Cu-64 with the BFC and 100% conjugation of ^{64}Cu-BFC to the maleimide lipid. However, due to the excess BFC (10 times more than Cu-64) and maleimide (7 times more than ^{64}Cu-BFC), the specific activity calculated from maleimide lipids was 20.8

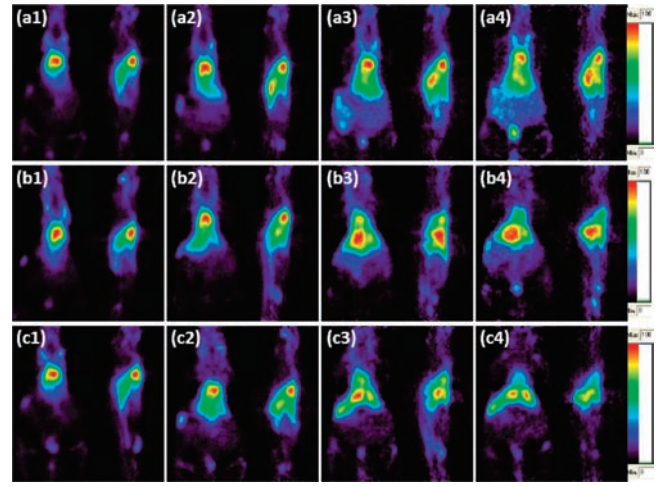


Figure 7. Micro-PET images (left, coronal; right, sagittal) acquired after injection of ^{64}Cu-TETA liposomes (a1−4); ^{64}Cu-TETA-PEG2k liposomes (b1−4); and ^{64}Cu-CB-TE2A-PEG2k liposomes (c1−4) immediately after injection (a1−c1); 6 h later (a2−c2); 18 h later (a3−c3); and 28 h later (a4−c4). All images were acquired after reconstruction by filtered backprojection.

mCi/μmol maleimide lipids. Preclinical studies of Doxil (long circulating liposomes) typically use 2.5−20 mg lipids/kg mouse for the treatment of tumor-bearing mice (*7*). In our model, approximately 40 mg/kg lipids were administered for the Cu-64 labeled liposomal study, and a high signal-to-noise ratio was achieved. The liposome dose can be reduced if imaging with Cu-64 labeled liposomes shows tumor accumulation at a lower liposome dose, and particularly if the Cu-64 has a high effective specific activity (>6000 mCi/μmol Cu-64) (*49*).

Previously, ^{99m}Tc-BMEDA encapsulated liposomes (*50*) and ^{99m}Tc-HYNIC surface-labeled liposomes (*26*) have been considered stable labeling methods for liposomal SPECT studies. For liposomal PET studies, our prior labeling method showed sufficient stability to represent liposomal behavior in vivo (*36*). In this connection, the second step of the study was to evaluate the liposomal stability in vitro and in vivo after the conjugation of different bifunctional chelators (**6** and **8**). The stability of 1 mol % maleimide-PEG2k liposomes was compared after the conjugation with ^{64}Cu-TETA-PDP and ^{64}Cu-CB-TE2A-PDEA to evaluate the effect of the chelator. Maleimide and maleimide-PEG2k liposomes were compared after labeling with ^{64}Cu-TETA-PDP to determine whether the conjugated ^{64}Cu-TETA-PDP is stable under a PEG2k brush or the end of a PEG2k lipopolymer. To answer those questions, the stability of three liposomal formulations (^{64}Cu-TETA, ^{64}Cu-TETA-PEG2k, and ^{64}Cu-CB-TE2A-PEG2k liposomes) was examined in vitro and vivo.

In vitro assays performed with ^{64}Cu-TETA, ^{64}Cu-TETA-PEG2k, and ^{64}Cu-CB-TE2A-PEG2k liposomes showed that 89%, 86%, and 86% radioactivity are still associated with the liposomal fraction, respectively, at 48 h (Figure 6). This result was similar to that obtained in our previous study (in which 88% of the radioactivity was in the liposomal fraction) (*36*). The radiochemical purity of each liposomal fraction determined with radio TLC was more than 98%.

A normal rat study performed by Bao et al. using ^{99m}Tc-BMEDA encapsulated liposomes reported a two-phase blood clearance of liposomes (*50*). Forty percent of activity remained in the blood pool at 18 h based on the decay function in their study ($y = 36.4 \times e^{-0.315 \times t} + 63.7 \times e^{-0.0264 \times t}$, y = % activity in blood, t = time (h)). *S. aureus* infected rats studied by Laverman et al. using ^{99m}Tc-HYNIC surface-

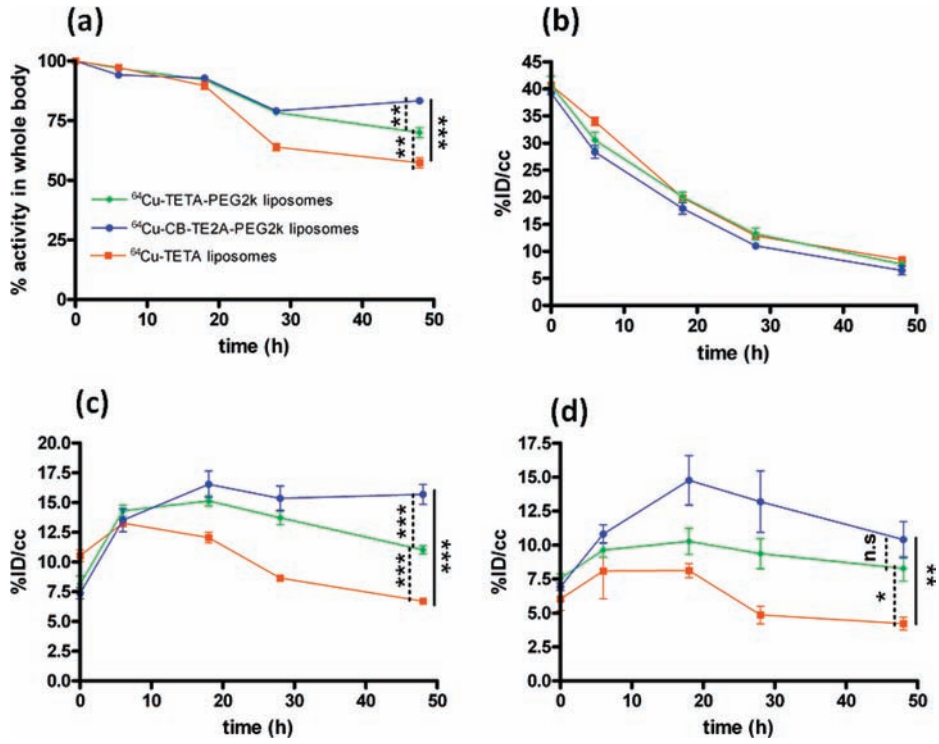


Figure 8. (a) Whole body activity clearance (decay-corrected). Time activity curves (TACs, %ID/cc) of heart (b), liver (c), and spleen (d) (n = 4−5) obtained from microPET by drawing regions of interest (ROI) after the injection of ^{64}Cu-TETA liposomes (orange square), ^{64}Cu-TETA-PEG2K liposomes (green diamond), and ^{64}Cu-CB-TE2A-PEG2k liposomes (blue round). ANOVA followed by Tukey's multiple comparison test was performed (error bars, mean ± STD; n.s., not significant; *P < 0.05; **P < 0.01; ***P < 0.001).

Table 1. Biodistribution of ^{64}Cu-TETA Liposomes (n = 4), ^{64}Cu-TETA-PEG2K Liposomes (n = 5), and ^{64}Cu-CB-TE2A-PEG2k Liposomes (n = 4) in Mice at 48 h after Injection[a]

	^{64}Cu-TETA liposomes (n = 4)		^{64}Cu-TETA-PEG2k liposomes (n = 5)		^{64}Cu-CB-TE2A-PEG2k liposomes (n = 4)	
	%ID/g ± SD	A	%ID/g ± SD	C	%ID/g ± SD	B
blood	8.71 ± 0.38	n.s.	8.35 ± 1.11	n.s.	6.85 ± 1.47	n.s.
spleen	12.26 ± 0.70	*	20.25 ± 2.50	**	30.41 ± 1.40	***
lungs	3.14 ± 0.25	n.s.	3.57 ± 0.20	**	2.24 ± 0.27	*
diaphragm	1.28 ± 0.16	n.s.	1.41 ± 0.15	n.s.	1.18 ± 0.43	n.s.
heart	2.89 ± 0.50	n.s.	3.34 ± 0.74	*	2.21 ± 0.40	n.s.
liver	6.88 ± 0.97	**	15.15 ± 1.24	**	22.92 ± 1.94	***
left kidney	6.14 ± 0.43	*	7.85 ± 1.17	*	5.80 ± 0.34	n.s.
right kidney	6.03 ± 0.52	n.s.	7.60 ± 1.20	*	5.63 ± 0.33	n.s.
duodenum	4.83 ± 0.57	n.s.	5.63 ± 0.14	n.s.	4.74 ± 0.23	n.s.
jejunum	3.66 ± 0.63	n.s.	4.55 ± 0.61	*	2.79 ± 0.99	n.s.
muscle	0.31 ± 0.06	n.s.	0.31 ± 0.09	n.s.	0.27 ± 0.03	n.s.

[a] One-way analysis of variance followed by Tukey's multiple comparison test was performed. (A: ^{64}Cu-TETA liposomes vs ^{64}Cu-TETA -PEG2k liposomes; B:^{64}Cu-TETA liposomes vs ^{64}Cu-CB-TE2A-PEG2k liposomes; C:^{64}Cu-TETA-PEG2k liposomes vs ^{64}Cu-CB-TE2A-PEG2k liposomes, n.s., not significant. * P < 0.05. ** P < 0.01. *** P < 0.001.

Table 2. One-Phase Exponential Decay Curves[a] of Liposomal Clearance from the Blood Pool in Mice

liposomes	$t_{1/2}$[b] (h)	span	k
^{64}Cu-TETA liposomes (n = 4)	18.22	41.10	0.03805
^{64}Cu-TETA-PEG2k liposomes (n = 5)	18.15	39.82	0.03819
^{64}Cu-CB-TE2A-PEG2k liposomes (n = 4)	16.20	38.32	0.04280

[a] Exponential decay curves were obtained from TAC of heart (Y = span × $e^{-k\times t}$). [b] Half clearance time.

labeled liposomes yielded 40% of the initial blood-pool activity at 24 h (*27*). In our study, the TAC data simulated with a one-phase exponential decay showed that the 60% clearance times were 24 h (^{64}Cu-TETA liposomes), 24 h (^{64}Cu-TETA-PEG2k liposomes), and 21 h (^{64}Cu-CB-TE2A-PEG2k liposomes) (Figure 8b). There was no significant difference in the time required for 60% clearance between ^{64}Cu-TETA liposomes and ^{64}Cu-TETA-PEG2k liposomes. Given the slow release and the anticipated reduction in Cu-64 transchelation with ceruloplasmin and superoxide dismutase (SOD) with CB-TE2A as the Cu-64 chelator, we had hypothesized that the accumulation of Cu-64 in the liver and spleen would be lower than that observed using TETA (*51, 52*). The TAC obtained here illustrated that liver accumulation at 48 h (P < 0.001) was higher for ^{64}Cu-CB-TE2A-PEG2k liposomes than for ^{64}Cu-TETA and ^{64}Cu-TETA-PEG2k liposomes (Figure 8c). The lipophilicity of ^{64}Cu-labeled CB-TE2A and negative charge of ^{64}Cu-TETA may contribute to the comparatively larger RES accumulation of ^{64}Cu-CB-TE2A-PEG2k liposomes. Due to the slow clearance and high uptake of ^{64}Cu-CB-TE2A-PEG2k liposomes in the liver (Figure 8c) and spleen (Figure 8d), the decay-corrected whole body activity (^{64}Cu-CB-TE2A-PEG2k liposome) at 48 h was also higher than other formulations (^{64}Cu-CB-TE2A-PEG2k liposomes vs ^{64}Cu-TETA liposomes, p < 0.001; ^{64}Cu-CB-TE2A-PEG2k liposomes vs ^{64}Cu-TETA-PEG2k liposomes, p < 0.01; Figure 8a).

Similar to the TAC data, the liver ($P < 0.001$) and spleen ($P < 0.001$) biodistribution at 48 h (Table 1) showed that the properties of all three liposomal formulations differed, while a small but insignificant difference in accumulation was observed in the kidneys, lung, heart, blood, intestine, and muscle. At 48 h postinjection, liposomal accumulation of ^{64}Cu-TETA liposomes in the liver was 3.3-fold lower as compared with that of ^{64}Cu-CB-TE2A-PEG2k liposomes ($P < 0.001$), and 2.2× less than that of ^{64}Cu-TETA-PEG2k liposomes ($P < 0.001$). Accumulation in the spleen also varied in the order ^{64}Cu-CB-TE2A-PEG2k liposomes > ^{64}Cu-TETA-PEG2k liposomes > ^{64}Cu-TETA liposomes (Table 1). According to the previous literature, ^{64}Cu-CB-TE2A showed lower uptake in the liver and higher resistance to transchelation than ^{64}Cu-TETA (*51, 52*), but these reports involve the pharmacokinetics of chelators with (*53*) or without (*52*) conjugation to a peptide. The comparison of ^{18}F-labeled RGD peptides with a PEG spacer ([^{18}F]FB-PEG-RGD) or without PEG ([^{18}F]FB-RGD), reported by Chen et. al, did not show a difference in accumulation of radioactivity in the liver, although the blood clearance of [^{18}F]FB-PEG-RGD was slower than that of [^{18}F]FB-RGD (*4, 54*). In contrast, the liver and spleen accumulation of [^{125}I]PEG-DPDPE was greater than that of [^{125}I]DPDPE (*55*). In ref *54*, F-18 was labeled at the end of the PEG chain and, in ref *55*, I-125 was labeled on the tyrosine residue between DPDPE and the PEG chain. Both results indicate that the presence of a PEG spacer is not necessarily correlated with the accumulation of radioactivity in the liver and spleen. The labeling position and molecular structure is also likely to affect the RES accumulation of activity. In our study, the radiolabel was at the end of the lipid or PEG.

The differences in liver radioactivity observed here between formulations may in part be due to the protective effect of the PEG2k spacer brush while liposomes are passing through the perisinusoidal space and sinusoids. In our previous liposomal study using 6-BAT-lipid with PEG1.2k as a spacer between the lipid and the chelator, 6.21 ± 0.66%ID/g remained in the liver and 13.61 ± 6.19 in the spleen at 48 h (*36*); here, with ^{64}Cu-TETA liposomes, 6.88 ± 0.97%ID/g remained in the liver and 12.26 ± 0.70%ID/g in the spleen (Table 1). Those values are smaller than radioactivity in the liver and spleen resulting from both ^{64}Cu-TETA-PEG2k and ^{64}Cu-CB-TE2A-PEG2k liposomes (Table 1). ^{64}Cu-chelator complexes of 6-BAT liposomes (*36*) and ^{64}Cu-TETA liposomes are likely to be hidden under the PEG2k brush, while ^{64}Cu-chelator complexes of ^{64}Cu-TETA-PEG2k liposomes and ^{64}Cu-CB-TE2A-PEG2k liposomes are exposed at the end of the PEG2k brush.

Verkade et al. reported that hepatic processing and biliary secretion of liposome-associated phosphatidylcholine (PC) is predominantly determined by the degradation of PC in the liver (*56*). The degraded products are partially secreted into bile (*56*). The similar radioactivity in the duodenum and jejunum of mice administered with the three formulations (Table 1) may result in part from the slow release of radioactivity from the liver through the bile duct. Radioactivity in the kidney was also similar for the three formulations at 48 h irrespective of the presence of the PEG spacer and the specific chelator. Similarities in the size, primary lipid species, and surface charge of the three formulations contributes to similarities in the accumulation of radioactivity.

In summary, we have synthesized two thiol-reactive bifunctional chelators, TETA-PDP and CB-TE2A-PDEA, and developed a liposomal labeling method using maleimide lipid with those BFCs. An in vitro assay with mouse serum showed a similar liposomal stability for the three liposomal formulations. Liposomes labeled with the BFCs were stable in the blood pool over 48 h, and the 60% clearance time was 21−24 h. The presence of the PEG spacer between the chelator and the lipid did not significantly alter the labeling efficiency and the clearance rate of liposomes from the blood pool. The location of the ^{64}Cu-chelator complex influences the liposomal uptake in liver and spleen. The bifunctional chelator as a postlabeling method is applicable for liposomal labeling as well as labeling of antibodies and other nanoparticle formulations.

ACKNOWLEDGMENT

We thank the staff in the CMGI (Center for Molecular and Genomic Imaging, UC Davis) for handling ^{64}Cu and imaging studies. We appreciate the support of NIH R01 CA016861, R01 CA103828, and R01 CA134659, and NCI 5R01 CA93375.

LITERATURE CITED

(1) Medina, O. P., Zhu, Y., and Kairemo, K. (2004) Targeted liposomal drug delivery in cancer. *Curr. Pharm. Des. 10*, 2981–2989.

(2) Torchilin, V. P. (2005) Recent advances with liposomes as pharmaceutical carriers. *Nat. Rev. Drug Discovery 4*, 145–160.

(3) Andresen, T. L., Jensen, S. S., and Jorgensen, K. (2005) Advanced strategies in liposomal cancer therapy: Problems and prospects of active and tumor specific drug release. *Prog. Lipid Res. 44*, 68–97.

(4) Klibanov, A. L., Maruyama, K., Torchilin, V. P., and Huang, L. (1990) Amphipathic polyethyleneglycols effectively prolong the circulation time of liposomes. *FEBS Lett. 268*, 235–237.

(5) O'Shaughnessy, J. A. (2003) Pegylated liposomal doxorubicin in the treatment of breast cancer. *Clin. Breast Cancer 4*, 318–328.

(6) Torchilin, V. P., Omelyanenko, V. G., Papisov, M. I., Bogdanov, A. A., Jr., Trubetskoy, V. S., Herron, J. N., and Gentry, C. A. (1994) Poly(ethylene glycol) on the liposome surface: on the mechanism of polymer-coated liposome longevity. *Biochim. Biophys. Acta 1195*, 11–20.

(7) Gabizon, A., Shmeeda, H., and Barenholz, Y. (2003) Pharmacokinetics of pegylated liposomal Doxorubicin: review of animal and human studies. *Clin. Pharmacokinet. 42*, 419–436.

(8) Barratt, G., and Legrand, P. (2005) Comparison of the efficacy and pharmacology of formulations of amphotericin B used in treatment of leishmaniasis. *Curr. Opin. Infect. Dis. 18*, 527–530.

(9) Lestini, B. J., Sagnella, S. M., Xu, Z., Shive, M. S., Richter, N. J., Jayaseharan, J., Case, A. J., Kottke-Marchant, K., Anderson, J. M., and Marchant, R. E. (2002) Surface modification of liposomes for selective cell targeting in cardiovascular drug delivery. *J. Controlled Release 78*, 235–247.

(10) Mamot, C., Drummond, D. C., Greiser, U., Hong, K., Kirpotin, D. B., Marks, J. D., and Park, J. W. (2003) Epidermal growth factor receptor (EGFR)-targeted immunoliposomes mediate specific and efficient drug delivery to EGFR- and EGFRvIII-overexpressing tumor cells. *Cancer Res. 63*, 3154–3161.

(11) Park, J. W., Kirpotin, D. B., Hong, K., Shalaby, R., Shao, Y., Nielsen, U. B., Marks, J. D., Papahadjopoulos, D., and Benz, C. C. (2001) Tumor targeting using anti-her2 immunoliposomes. *J. Controlled Release 74*, 95–113.

(12) Lukyanov, A. N., Elbayoumi, T. A., Chakilam, A. R., and Torchilin, V. P. (2004) Tumor-targeted liposomes: doxorubicin-loaded long-circulating liposomes modified with anti-cancer antibody. *J. Controlled Release 100*, 135–144.

(13) Lu, Y., and Low, P. S. (2002) Folate-mediated delivery of macromolecular anticancer therapeutic agents. *Adv. Drug Delivery Rev. 54*, 675–693.

(14) Gabizon, A., Shmeeda, H., Horowitz, A. T., and Zalipsky, S. (2004) Tumor cell targeting of liposome-entrapped drugs with phospholipid-anchored folic acid-PEG conjugates. *Adv. Drug Delivery Rev. 56*, 1177–1192.

(15) Ferrara, K. W., Borden, M. A., and Zhang, H. (2009) Lipid-shelled vehicles: engineering for ultrasound molecular imaging and drug delivery. *Acc. Chem. Res. 42*, 881–892.

(16) Schroeder, A., Honen, R., Turjeman, K., Gabizon, A., Kost, J., and Barenholz, Y. (2009) Ultrasound triggered release of cisplatin from liposomes in murine tumors. *J. Controlled Release 137*, 63–68.

(17) Wu, G. H., Milkhailovsky, A., Khant, H. A., Fu, C., Chiu, W., and Zasadzinski, J. A. (2008) Remotely triggered liposome release by near-infrared light absorption via hollow gold nanoshells. *J. Am. Chem. Soc. 130*, 8175–8177.

(18) Mackanos, M. A., Larabi, M., Shinde, R., Simanovskii, D. M., Guccione, S., and Contag, C. H. (2009) Laser-induced disruption of systemically administered liposomes for targeted drug delivery. *J. Biomed. Opt. 14*, 044009.

(19) Simoes, S., Moreira, J. N., Fonseca, C., Duzgunes, N., and de Lima, M. C. (2004) On the formulation of pH-sensitive liposomes with long circulation times. *Adv. Drug Delivery Rev. 56*, 947–965.

(20) Hamoudeh, M., Kamleh, M. A., Diab, R., and Fessi, H. (2008) Radionuclides delivery systems for nuclear imaging and radiotherapy of cancer. *Adv. Drug Delivery Rev. 60*, 1329–1346.

(21) Oku, N. (1999) Delivery of contrast agents for positron emission tomography imaging by liposomes. *Adv. Drug Delivery Rev. 37*, 53–61.

(22) Phillips, W. T., Goins, B. A., and Bao, A. (2009) Radioactive liposomes. *Wiley Interdiscip. Rev.: Nanomed. Nanobiotechnol. 1*, 69–83.

(23) Tilcock, C., Ahkong, Q. F., and Fisher, D. (1994) ^{99m}Tc-labeling of lipid vesicles containing the lipophilic chelator PE-DTTA: effect of tin-to-chelate ratio, chelate content and surface polymer on labeling efficiency and biodistribution behavior. *Nucl. Med. Biol. 21*, 89–96.

(24) Ahkong, Q. F., and Tilcock, C. (1992) Attachment of ^{99m}Tc to lipid vesicles containing the lipophilic chelate dipalmitoylphosphatidylethanolamine-DTTA. *Int. J. Rad. Appl. Instrum. B 19*, 831–840.

(25) Bao, A., Goins, B., Klipper, R., Negrete, G., Mahindaratne, M., and Phillips, W. T. (2003) A novel liposome radiolabeling method using ^{99m}Tc-"SNS/S" complexes: in vitro and in vivo evaluation. *J. Pharm. Sci. 92*, 1893–1904.

(26) Phillips, W. T., Rudolph, A. S., Goins, B., Timmons, J. H., Klipper, R., and Blumhardt, R. (1992) A simple method for producing a technetium-99m-labeled liposome which is stable in vivo. *Int. J. Rad. Appl. Instrum. B 19*, 539–547.

(27) Laverman, P., Dams, E. T., Oyen, W. J., Storm, G., Koenders, E. B., Prevost, R., van der Meer, J. W., Corstens, F. H., and Boerman, O. C. (1999) A novel method to label liposomes with ^{99m}Tc by the hydrazino nicotinyl derivative. *J. Nucl. Med. 40*, 192–197.

(28) Gabizon, A., and Papahadjopoulos, D. (1988) Liposome formulations with prolonged circulation time in blood and enhanced uptake by tumors. *Proc. Natl. Acad. Sci. U.S.A. 85*, 6949–6953.

(29) Harrington, K. J., Mohammadtaghi, S., Uster, P. S., Glass, D., Peters, A. M., Vile, R. G., and Stewart, J. S. (2001) Effective targeting of solid tumors in patients with locally advanced cancers by radiolabeled pegylated liposomes. *Clin. Cancer Res. 7*, 243–254.

(30) Hwang, K. J., Merriam, J. E., Beaumier, P. L., and Luk, K. F. (1982) Encapsulation, with high efficiency, of radioactive metal ions in liposomes. *Biochim. Biophys. Acta 716*, 101–109.

(31) Marik, J., Tartis, M. S., Zhang, H., Fung, J. Y., Kheirolomoom, A., Sutcliffe, J. L., and Ferrara, K. W. (2007) Long-circulating liposomes radiolabeled with [^{18}F]fluorodipalmitin ([^{18}F]FDP). *Nucl. Med. Biol. 34*, 165–171.

(32) Oku, N., Tokudome, Y., Tsukada, H., and Okada, S. (1995) Real-time analysis of liposomal trafficking in tumor-bearing mice by use of positron emission tomography. *Biochim. Biophys. Acta 1238*, 86–90.

(33) Urakami, T., Akai, S., Katayama, Y., Harada, N., Tsukada, H., and Oku, N. (2007) Novel amphiphilic probes for [^{18}F]-radiolabeling preformed liposomes and determination of liposomal trafficking by positron emission tomography. *J. Med. Chem. 50*, 6454–6457.

(34) Mougin-Degraef, M., Jestin, E., Bruel, D., Remaud-Le Saec, P., Morandeau, L., Faivre-Chauvet, A., and Barbet, J. (2006) High-activity radio-iodine labeling of conventional and stealth liposomes. *J. Liposome Res. 16*, 91–102.

(35) Awasthi, V., Yee, S. H., Jerabek, P., Goins, B., and Phillips, W. T. (2007) Cerebral oxygen delivery by liposome-encapsulated hemoglobin: a positron-emission tomographic evaluation in a rat model of hemorrhagic shock. *J. Appl. Physiol. 103*, 28–38.

(36) Seo, J. W., Zhang, H., Kukis, D. L., Meares, C. F., and Ferrara, K. W. (2008) A novel method to label preformed liposomes with ^{64}Cu for positron emission tomography (PET) imaging. *Bioconjugate Chem. 19*, 2577–2584.

(37) Devaraj, N. K., Keliher, E. J., Thurber, G. M., Nahrendorf, M., and Weissleder, R. (2009) ^{18}F labeled nanoparticles for in vivo PET-CT imaging. *Bioconjugate Chem. 20*, 397–401.

(38) Wadas, T. J., Wong, E. H., Weisman, G. R., and Anderson, C. J. (2007) Copper chelation chemistry and its role in copper radiopharmaceuticals. *Curr. Pharm. Des. 13*, 3–16.

(39) Smith, S. V. (2004) Molecular imaging with copper-64. *J. Inorg. Biochem. 98*, 1874–1901.

(40) Moran, J. K., Greiner, D. P., and Meares, C. F. (1995) Improved synthesis of 6-[p-(bromoacetamido)benzyl]-1,4,8,11-tetraazacyclotetradecane- N, N′, N″, N″-tetraacetic acid and development of a thin-layer assay for thiol-reactive bifunctional chelating agents. *Bioconjugate Chem. 6*, 296–301.

(41) Moreau, P., Tinkl, M., Tsukazaki, M., Bury, P. S., Griffen, E. J., Snieckus, V., Maharajh, R. B., Kwok, C. S., Somayaji, V. V., Peng, Z., Sykes, T. R., and Noujaim, A. A. (1997) Synthesis of the bifunctional chelating agent 6-(4-aminobenzyl)-1,4,8,11-tetra-azacyclotetradecane-N, N′, N″, N‴-tetra acetic acid (H_2NBn-TETA). *Synthesis* 1010–1012.

(42) Weisman, G. R., Wong, E. H., Hill, D. C., Rogers, M. E., Reed, D. P., and Calabrese, J. C. (1996) Synthesis and transition-metal complexes of new cross-bridged tetraamine ligands. *Chem. Commun.* 947–948.

(43) Wong, E. H., Weisman, G. R., Hill, D. C., Reed, D. P., Rogers, M. E., Condon, J. S., Fagan, M. A., Calabrese, J. C., Lam, K. C., Guzei, I. A., and Rheingold, A. L. (2000) Synthesis and characterization of cross-bridged cyclams and pendant-armed derivatives and structural studies of their copper(II) complexes. *J. Am. Chem. Soc. 122*, 10561–10572.

(44) Burns, J. A., Butler, J. C., Moran, J., and Whitesides, G. M. (1991) Selective reduction of disulfides by tris(2-carboxyethyl) - phosphine. *J. Org. Chem. 56*, 2648–2650.

(45) Han, J. C., and Han, G. Y. (1994) A procedure for quantitative determination of tris(2-carboxyethyl)phosphine, an odorless reducing agent more stable and effective than dithiothreitol. *Anal. Biochem. 220*, 5–10.

(46) Frisch, B., Boeckler, C., and Schuber, F. (1996) Synthesis of short polyoxyethylene-based heterobifunctional cross-linking reagents. Application to the coupling of peptides to liposomes. *Bioconjugate Chem. 7*, 180–186.

(47) Roth, A., Espuelas, S., Thumann, C., Frisch, B., and Schuber, F. (2004) Synthesis of thiol-reactive lipopeptide adjuvants. Incorporation into liposomes and study of their mitogenic effect on mouse splenocytes. *Bioconjugate Chem. 15*, 541–553.

(48) Schelte, P., Boeckler, C., Frisch, B., and Schuber, F. (2000) Differential reactivity of maleimide and bromoacetyl functions with thiols: Application to the preparation of liposomal diepitope constructs. *Bioconjugate Chem. 11*, 118–123.

(49) McCarthy, D. W., Shefer, R. E., Klinkowstein, R. E., Bass, L. A., Margeneau, W. H., Cutler, C. S., Anderson, C. J., and Welch, M. J. (1997) Efficient production of high specific activity 64Cu using a biomedical cyclotron. *Nucl. Med. Biol. 24*, 35–43.

(50) Bao, A., Goins, B., Klipper, R., Negrete, G., and Phillips, W. T. (2004) Direct ^{99}mTc labeling of pegylated liposomal doxorubicin (Doxil) for pharmacokinetic and noninvasive imaging studies. *J. Pharmacol. Exp. Ther. 308*, 419−425.

(51) Sun, X., Wuest, M., Weisman, G. R., Wong, E. H., Reed, D. P., Boswell, C. A., Motekaitis, R., Martell, A. E., Welch, M. J., and Anderson, C. J. (2002) Radiolabeling and in vivo behavior of copper-64-labeled cross-bridged cyclam ligands. *J. Med. Chem. 45*, 469–477.

(52) Boswell, C. A., Sun, X., Niu, W., Weisman, G. R., Wong, E. H., Rheingold, A. L., and Anderson, C. J. (2004) Comparative in vivo stability of copper-64-labeled cross-bridged and conventional tetraazamacrocyclic complexes. *J. Med. Chem. 47*, 1465–1474.

(53) Sprague, J. E., Peng, Y., Sun, X., Weisman, G. R., Wong, E. H., Achilefu, S., and Anderson, C. J. (2004) Preparation and biological evaluation of copper-64-labeled tyr3-octreotate using a cross-bridged macrocyclic chelator. *Clin. Cancer Res. 10*, 8674–8682.

(54) Chen, X., Park, R., Hou, Y., Khankaldyyan, V., Gonzales-Gomez, I., Tohme, M., Bading, J. R., Laug, W. E., and Conti, P. S. (2004) MicroPET imaging of brain tumor angiogenesis with ^{18}F-labeled PEGylated RGD peptide. *Eur. J. Nucl. Med. Mol. Imaging 31*, 1081–1089.

(55) Witt, K. A., Huber, J. D., Egleton, R. D., Roberts, M. J., Bentley, M. D., Guo, L., Wei, H., Yamamura, H. I., and Davis, T. P. (2001) Pharmacodynamic and pharmacokinetic characterization of poly(ethylene glycol) conjugation to met-enkephalin analog [D-Pen2, D-Pen5]-enkephalin (DPDPE). *J. Pharmacol. Exp. Ther. 298*, 848–856.

(56) Verkade, H. J., Derksen, J. T., Gerding, A., Scherphof, G. L., Vonk, R. J., and Kuipers, F. (1991) Differential hepatic processing and biliary secretion of head-group and acyl chains of liposomal phosphatidylcholines. *Biochem. J. 275*, 139–144.

BC100018N

Well-Defined, Size-Tunable, Multifunctional Micelles for Efficient Paclitaxel Delivery for Cancer Treatment

Juntao Luo,*,† Kai Xiao,† Yuanpei Li,† Joyce S. Lee,† Lifang Shi,‡ Yih-Horng Tan,‡ Li Xing,§ R. Holland Cheng,§ Gang-Yu Liu,‡ and Kit S. Lam*,†

Division of Hematology and Oncology, University of California, Davis Cancer Center, Sacramento, California 95817, Department of Chemistry and Department of Molecular and Cellular Biology, University of California Davis, Davis, California 95616. Received January 13, 2010; Revised Manuscript Received May 17, 2010

We have developed a well-defined and biocompatible amphiphilic telodendrimer system (PEG-*b*-dendritic oligocholic acid) which can self-assemble into multifunctional micelles in aqueous solution for efficient delivery of hydrophobic drugs such as paclitaxel. In this telodendrimer system, cholic acid is essential for the formation of stable micelles with high drug loading capacity, owing to its facial amphiphilicity. A series of telodendrimers with variable length of PEG chain and number of cholic acid in the dendritic blocks were synthesized. The structure and molecular weight of each of these telodendrimers were characterized, and their critical micellization concentration (CMC), drug-loading properties, particle sizes, and cytotoxicity were examined and evaluated for further optimization for anticancer drug delivery. The sizes of the micelles, with and without paclitaxel loading, could be tuned from 11.5 to 21 nm and from 15 to 141 nm, respectively. Optical imaging studies in xenograft models demonstrated preferential uptake of the smaller paclitaxel-loaded micelles (17−60 nm) by the tumor and the larger micelles (150 nm) by the liver and lung. The toxicity and antitumor efficacy profiles of these paclitaxel-loaded micelles in xenograft models were found to be superior to those of Taxol and Abraxane.

INTRODUCTION

Abraxane and Doxil are the first two FDA-approved nanotherapeutic agents for cancer treatment. These two agents are not likely to be able to penetrate deeply into a tumor mass due to the relatively large sizes (130 and 150 nm, respectively) (*1*−*3*). In order to take the full advantage of the enhanced permeability and retention (EPR) effect (*4*, *5*) for the tumor-targeting drug delivery and to ensure deep tumor penetration, the size of the nanocarriers ought to be smaller. The optimal therapeutic nanocarriers should have the following properties (*6*−*8*): high drug loading capacity, narrow polydispersity, well-defined structure and multifunctionality, good physical and chemical stability, biocompatibility, and biodegradability. Polymeric micelles with small particle size (20−100 nm) have shown great promise as nanocarriers for efficient drug delivery (*9*−*11*). It has been reported that the size of the blank polymeric micelles can be tuned by adjusting the ratio of the hydrophobic and hydrophilic segments in the diblock copolymers (*12*). In some of these micelle systems, the particle size varies relative to the preparing conditions, such as the initial polymer concentration in the organic solvent prior to the dilution in aqueous solution (*12*, *13*), making it difficult to control in a clinical setting. The random chain propagation, chain transfer, and chain termination reactions in polymerizations, especially for radical polymerization, often lead to polydispersed polymer chains (*14*). Therefore, it is difficult to prepare polymeric materials, with precise structures and possessing orthogonal functional groups at specific sites, for the generation of well-defined multifunctional nanocarriers displaying targeting ligands, fluorescent probes, or radionuclides.

Linear−dendritic copolymer has a well-defined and engineerable dendritic block structure at one or both ends of a linear polymer chain (*15*, *16*). There are a few examples in the literature in which hydrophobic molecules were introduced to the periphery of the dendritic segments of PEG-dendritic copolymers, generating amphiphilic linear−dendritic copolymers that could form micelles in aqueous solution (*17*−*20*). However, the application of these linear−dendritic copolymers in drug delivery has rarely been reported (*21*, *22*). This is probably due to the lack of suitable building blocks to form the copolymers with superior properties. Cholic acid is one of the major bile acids produced in the human liver. Its unique facial amphiphilicity makes it a very useful building block for synthesizing biocompatible polymers for drug delivery (*23*). Linear cholic acid−PEG conjugate (CA-PEG) (*24*) and star-shaped cholic acid-centered PEG conjugate (CA-PEG_4) (*25*) have been reported to aggregate in water and form micelles. However, the drug-loading capacities of these micelles are very limited. Oligomers of CA have been employed as functional molecular containers for caging hydrophobic molecules (*26*−*28*); however, their application in drug delivery is very limited mainly due to the small and unstable cavities and poor water solubility. To develop cancer therapeutic nanocarriers with optimal properties, we have designed and synthesized a new linear−dendritic block copolymer (named a telodendrimer) using three biocompatible building blocks: poly(ethylene glycol) (PEG), L-lysine, and cholic acid (CA).

Paclitaxel (PTX) is one of the most effective anticancer drugs for the treatment of a wide spectrum of cancers. However, it has very poor solubility in water (1 μg/mL). The commercially available paclitaxel (Taxol) is formulated in an oily solution (Cremophor EL/absolute ethanol, 1:1 v/v), which has been associated with severe hypersensitivity reactions. Therefore, premedications with acetaminophen, steroid, and histamine

* Corresponding authors: Juntao Luo, Ph.D. Fax: (+01)916-734-6415; E-mail: juntao.luo@ucdmc.ucdavis.edu. Prof. Kit S. Lam, M.D., Ph.D. Fax: (+01)916-734-7946; E-mail: kit.lam@ucdmc.ucdavis.edu.

† University of California, Davis Cancer Center.

‡ Department of Chemistry, University of California Davis.

§ Department of Molecular and Cellular Biology, University of California Davis.

10.1021/bc1000033 © 2010 American Chemical Society
Published on Web 06/10/2010

blockers are almost always required prior to PTX administration (*29*). Several polymeric micelle systems have been developed for PTX delivery, but many of them had low drug loading capacity and poor stability (*30, 31*). Although Me-PEG-b-PDLLA micelles had shown an impressive PTX loading level of 25% w/w, they are stable for only 24 h (*32*). We have recently reported (*33*) the design and synthesis of a telodendrimer, $PEG^{5k}CA_8$, with a dendritic oligomer of cholic acid conjugated on one end of linear PEG, which forms a stable micelle in water and can load paclitaxel (PTX) as high as 36.5% of drug/polymer ratio (w/w). The *in vivo* antitumor efficacy of our PTX-loaded $PEG^{5k}CA_8$ micelles (*33*) were tested in both subcutaneous and intraperitoneal ovarian cancer mouse models, and it exhibited superior toxicity profile and antitumor effects, compared with the clinical formulations of PTX, such as Taxol and Abraxane.

One major advantage of this telodendrimer system is the easily engineered and well-defined structures, which lead to its tunable properties. In this report, we describe the design and synthesis of a series of related telodendrimers so that we can better define the relation between the structures of the telodendrimers and their physicochemical properties for drug delivery. By varying the PEG chain length and the number of cholic acid in the dendritic core, we were able to prepare a series of stable micelle systems with tunable particle sizes that have superior PTX loading capacities. The structure, micelle formation, drug-loading properties, and *in vitro* cytotoxicity of the telodendrimers were characterized. The size effects of the nanoparticles on their *in vivo* biodistribution in the xenograft model were also studied. Different from our previous study (*33*), we were able to achieve complete cure in the group of nude mice bearing small ovarian tumor xenograft implants by giving them five consecutive doses instead of three consecutive doses of PTX-loaded $PEG^{5k}CA_8$ micelles.

EXPERIMENTAL SECTION

Materials and Instruments. Paclitaxel was purchased from AK Scientific Inc. (Mountain View, CA). Monomethyl-terminated poly(ethylene glycol) monoamine (MeO-PEG-NH_2, M_w = 2, 3, 5, and 10 kDa, respectively) were purchased from Rapp Polymere (Tübingen, Germany). (Fmoc)lysine(Fmoc)OH was purchased from NeoMPS INC (San Diego, CA, USA), cholic acid, cholesterol chloroformate, lithocholic acid, heptadecanoic acid, Cremphor EL, and MTT [3-(4,5-dimethyldiazol-2-yl)-2,5-diphenyl tetrazolium bromide] were purchased from Sigma-Aldrich. Hydrophobic near-infrared fluorescence (NIRF) dye DiD (1,1′-dioctadecyl-3,3,3′,3′-tetramethylindodicarbocyanine perchlorate, D-307) was purchased from Invitrogen. Taxol (Mayne Pharma, Paramus, NJ) and Abraxane (Abraxis Bioscience, LA, CA) were obtained from a hospital pharmacy. The proton NMR spectra were collected on a Bruck Avance 500 spectrometer. The mass spectra of the telodendrimer were collected on ABI 4700 MALDI TOF/TOF mass spectrometer using α-cyano-4-hydroxycinnamic acid as a matrix. The fluorescence analysis for the critical micelle concentration (CMC) study and the colorimetric measurement in MTT assays were performed on a SpectraMaX M2 (Molecular Devices) microplate reader. The sizes of the micelles were analyzed on a Zetatrac DLS particle sizer (Macrotrac).

Synthesis of Telodendrimer. The telodendrimers were synthesized via solution-phase condensation reactions from MeO-PEG-NH_2 with a certain molecular weight. Typical procedure for synthesis of PEG^{5k}-CA_8: (Fmoc)lysine(Fmoc)-OH (2 equiv) was coupled onto the N-terminal of PEG using diisopropyl carbodimide (DIC, 2 equiv) and *N*-hydroxybenzotriazole (HOBt, 2 equiv) as coupling reagents in DMF overnight. The completion of the coupling was confirmed by Kaiser test: yellow color indicates no amino group left, blue color indicates the presence of amino groups. PEGylated molecules were precipitated by adding ice-cold ether and washed with ice-cold ether twice. Fmoc groups were removed by the treatment with 20% piperidine in DMF, and the PEGylated molecules were precipitated and washed three times by cold ether. White powder precipitate was dried under vacuum and two additional repeat couplings of (Fmoc)lysine(Fmoc)-OH were carried out to generate a third generation of dendritic polylysine on one end of PEG. Cholic acid NHS ester, prepared according to the literature (*34*), was coupled to the terminal end of dendritic polylysine, resulting in PEG^{5k}-CA_8. The telodendrimer was precipitated and washed by cold ether and dissolved in water. The telodendrimer solution was filtered and then dialyzed against 4 L water in a dialysis tube with MWCO of 3.5 KDa; reservoir water was refreshed completely four times in 24 h. Finally, the telodendrimer was lyophilized.

Typical synthesis of the multifunctional telodendrimer N_3-PEG^{5k}-(BocNH)-CA_8: 3-azidopropylamine (2 equiv), prepared following the procedure in the literature (*35*), was coupled onto a carboxylic group of the FmocNH-PEG-COOH (5000 Da) using HOBt (2 equiv)/DIC (2 equiv) as coupling agents in DMF overnight, then the polymer was precipitated and washed with cold ether. After removal of the Fmoc with the treatment of 20% piperidine solution in DMF, (Fmoc)Lys(Boc)-OH (2 equiv) was coupled onto the N-terminal of PEG using DIC and HOBt as coupling reagents until a negative Kaiser test result was obtained, indicating completion of the coupling reaction. The PEGylated compounds were then precipitated and washed with cold ether. The dendritic structure of lysine was achieved by the three repeated coupling of (Fmoc)Lys(Fmoc)-OH following the above Fmoc peptide synthesis procedure. After removal of Fmoc group, cholic acid NHS ester (*34*) (16 equiv) was used to react with the amino groups on the third generation of dendritic polylysine to generate N_3-PEG^{5k}-(BocNH)-CA_8. This telodendrimer was subsequently dialyzed and lyophilized to yield a white powder.

Loading of Paclitaxel and Fluorescence Dye into Micelles. Paclitaxel (6 mg) and telodendrimer (20 mg) were first dissolved in chloroform (4 mL) in a 10 mL flask. The organic solvent was rotoevaporated under vacuum to form a thin film, which was further dried under high vacuum for 30 min to remove residual organic solvents. PBS buffer solution (1 mL) was added into the flask, followed by the sonication for 2 h to disperse the polymer−drug conjugates into water. Finally, the micelle solution was filtered through a 0.22 μm filter to remove bacteria prior to *in vitro* and *in vivo* studies. The coloading of paclitaxel with the hydrophobic near-infrared dye, DiD, followed the same procedure above. In order to encapsulate same concentration of DiD into micelles with different sizes, 1 mg of DiD (a hydrophobic near-infrared (NIR) cyanine dye) and PTX (4 mg, 4 mg, and 3 mg, respectively) were coloaded into 20 mg of PEG^{2k}-CA_4, PEG^{5k}-CA_8, and PEG^{3k}-CA_4, respectively, and dispersed in 1 mL PBS solution. The loading of the PTX in micelles is measured by HPLC: 10 μL aqueous solution of the PTX-loaded micelle was diluted with 90 μL of DMSO to break the micelle prior to the injection into HPLC, equipped with a UV−vis detector. The gradient eluting solution, composed of water (A) and acetonitrile (B), was used: 1−7 min (A to B); 7−9 min (B); 9−9.5 min (B to A); 9.5−13 min (A). The column was Xterra MS C18 5 μm, 46 × 150 mm column.

CMC Measurement. A series concentration of the telodendrimers in PBS (100 μL) were prepared in a 96-well plate in the range from 1 μg/mL to 5 mg/mL. One microliter of a stock solution of the pyrene in methanol was added into the micelle solution to make a final concentration of pyrene of 2 μM. The solution was mildly shaken for equilibrium for 2 h. Then, the fluorescence emissions of the pyrene at 391 nm were collected,

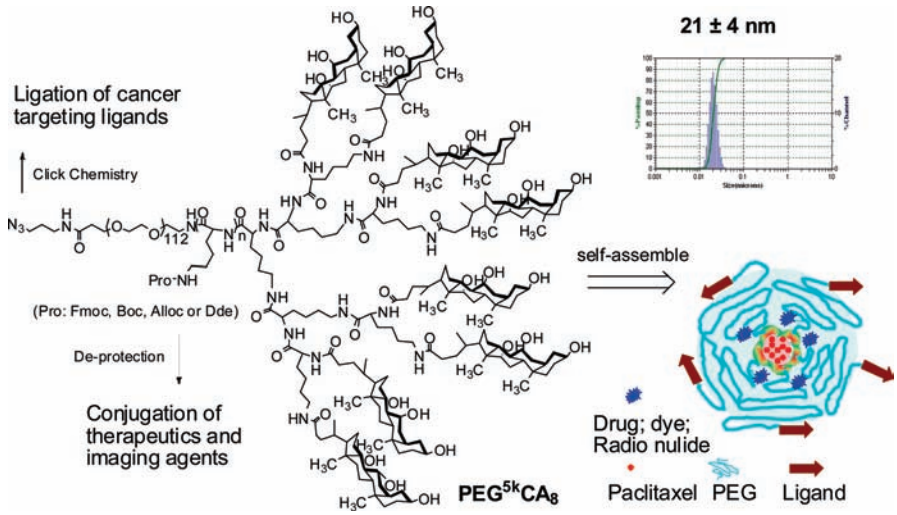


Figure 1. Chemical structure of PEG^{5k}-CA$_8$ with multiple functional groups and its size measured by DLS particle sizer; the cartoon illustrates the functionalized micelles formed by telodendrimers.

respectively, at the excitation of 332 and 336 nm. The ratios of the intensity at 336 to 332 nm were plotted vs the concentration of the telodendrimers, as reported in the literature (*36*), to calculate the CMC. The CMC is determined by the threshold concentration, where the intensity ratio I_{336}/I_{332} begins to increase markedly.

Drug Release. The *in vitro* paclitaxel release profile was studied by dialysis technique. Aliquots of the paclitaxel-loaded micelle solution (3 mL, with a PTX concentration of 2 mg/mL) were injected into a dialysis cartridge (Pierce Chemical Inc.) with a 3.5 KDa MWCO. The cartridge was dialyzed against 1 L of PBS media under different conditions: (a) The PBS media was kept unchanged; (b) PBS media was refreshed at each time point for sampling; (c) PBS media was kept unchanged with 10 g/L of BSA; and (d) PBS media was kept unchanged with 10 g/L of charcoal. The dialysis was kept at 37 °C and swirled at 100 rpm. The concentration of paclitaxel remained in the dialysis cartridge at various time points was measured by HPLC. Values were reported as the means for each triplicate samples.

MTT Assay. MTT growth inhibition method was performed briefly as follows: cells were seeded in 96-well plates 24 h before treatment at a density of 3000 cells/well. After 72 h of incubation with different concentrations of telodendrimers and various formulations of paclitaxel in a humidified 37 °C, 5% CO_2 incubator, MTT was added to each well at a final concentration of 0.5 mg/mL and further incubated for 4 h at 37 °C. To stop the reaction, the MTT medium was removed and a 100 μL of detergent mixture (0.04 N HCl in absolute isopropanol) was added and incubated for 30 min at room temperature. The absorbances at 570 and 660 nm were detected using a microplate ELISA reader (SpectraMax M2, Molecular Devices, USA). Results were displayed as the cell viability [$(OD_{treat} - OD_{blank})/(OD_{control} - OD_{blank}) \times 100\%$] by three independent experiments. The IC_{50} value was calculated as the concentration of agents that inhibited the growth of cells by 50%.

Xenograft Mouse Model. Female athymic nude mice (Nu/Nu strain), 6−8 weeks age, were purchased from Harlan (Livermore, CA) and kept under pathogen-free conditions according to AAALAC guidelines and were allowed to acclimatize for at least 4 days prior to any experiments. SKOV-3 ovarian cancer cells transfected with luciferase gene (7×10^6) in a 100 μL of mixture of PBS and Matrigel (1:1 v/v) without fetal bovine serum (FBS) were injected subcutaneously into nude mice to form subcutaneous nodules.

Fluorescence Optical Imaging. SKOV-3 tumor bearing mouse was injected via tail vein with the PBS solution (100 μL) of micelles with different sizes coloaded with the same concentration of DiD (hydrophobic dye) together with paclitaxel. Mice were anesthetized and optically imaged with a Kodak Image Station 2000MM at 30 min, 1 h, 2 h, 4 h, and 24 h. At the end of the experiment, the animal was sacrificed and all the major organs and tumor were excised for ex vivo imaging.

Therapeutic Studies. Nude mice bearing human SKOV3-luc (transfected with luciferase gene) ovarian cancer tumor (50 mm^3) were treated (five mice per group) with various formulations of paclitaxel at days 0, 4, 8, 12, and 16 for 5 consecutive doses. Abraxane and Taxol at maximum tolerated dose (MTD) of 30 mg/kg and 15 mg/kg, respectively, were given intravenously. PTX-loaded PEG^{5k}CA$_8$ was administered at two dose levels of 15 and 45 mg/kg, in which the latter dose is the MTD. One day after the last treatment, blood was obtained for blood counts and serum chemistries. Digital calipers were used to measure the length and width of the tumor twice a week, and the tumor sizes were calculated using the following formula: (width^2 × length)/2. A luciferin kinetic study was performed for each animal to determine the peak signal time. Briefly, 150 mg/kg D-luciferin was injected intraperitoneal (i.p.), and mice were anesthetized with pentobarbital (i.p., 60 mg/kg); the bioluminescence imaging was obtained at 15 min after luciferin injection using Kodak imaging station 2000 MM.

RESULTS AND DISCUSSION

The chemical structure of PEG^{5k}-CA$_8$, a representative telodendrimer, is shown in Figure 1. According to our nomenclature, "5k" represents the molecular weight of PEG (i.e., 5000 Da) and "8" indicates the number of CA subunits in the telodendrimer. PEG^{5k}-CA$_8$ is soluble in water and self-assembles into micelles with a size of 21 ± 4 nm. More importantly, it is capable of encapsulating hydrophobic drugs such as PTX. Bifunctional FmocNH-PEG-COOH is used as the starting material to construct the multifunctional telodendrimers (Figure 1), and the azide group is introduced at the distal C-terminal of PEG and can be conveniently used for the ligation of cell surface targeting ligands (*37*) or antibodies. The Boc-protected amino groups adjacent to the dendritic core are reserved for the conjugation of fluorescent dyes, radionuclides, or drug molecules to the micelles, and hydrophobic drugs or probes can be physically encapsulated inside the micelles as shown in the cartoon in Figure 1.

To study the physical properties of various telodendrimers and their effects on the *in vivo* passive tumor targeting effects

Table 1. Physical Properties of Telodendrimers with Different PEG Chain Length and Number of Cholic Acids and Lipophilic Molecules

telodendrimers	M_w (theo.)	M_w[a] (MS)	M_w[b] (NMR)	CMC (μM)[c]	size (nm)[d]	size with PTX (nm)[d]	PTX[e] (mg/mL)
PEG^{2k}-CA_4	3914	4105	4511	7.9	11.5	15	5.2
PEG^{3k}-CA_4	5250	5606	5251	12.5	15	141	5.6
PEG^{5k}-CA_4	6644	6313	6082	67	10	131	2.3
PEG^{2k}-CA_8	5986	5985	6127	1.3	302/6000	96/348/1863	N/D
PEG^{3k}-CA_8	7322	7624	8025	5.9	20	58	4.7
PEG^{5k}-CA_8	8716	8814	8805	5.3	21	61	7.3
PEG^{10k}-CA_{16}	8172	N/D	N/D	0.97	42.7/2163	102/602/2435	0.6
PEG^{5k}-CF_8[f]	8909	N/D	N/D	0.4	122/280/827	134/388/905	N/D
PEG^{5k}-LA_8[g]	8460	N/D	N/D	1.8	73/6000	67/450/872	0.8
PEG^{5k}-HA_8[h]	7620	N/D	N/D	1.5	55/322	97/5990	N/D

[a] Obtained via MALDI-TOF MS analysis, α-cyano-hydroxyl-cinnamic acid as a matrix compound. [b] Obtained via ^{1}H NMR method. Given the molecular weights of the starting PEGs by MALDI-TOF MS (Figure S-1 in Supporting Information), the molecular weight was calculated based on the ratio of proton signals of the methyl groups on cholic acid to the proton signals of the PEG in the ^{1}H NMR spectra. [c] CMC was measured by fluorescence spectrometry using pyrene (2×10^{-6} M) as a probe. [d] Measured by dynamic light scattering particle sizer (Nanotrac). [e] PTX loading, in the presence of 20 mg/mL of telodendrimers, were measured by HPLC after passing through an 0.45 μm filter. N/D means not detectable. [f] CF = cholesterol formate. [g] LA = lithocholic acid. [h] HA = heptadecanoic acid.

of the resulting nanoparticles, monofunctionalized MeO-PEG-NH_2 with different PEG chain lengths (2−10 kDa) were used for linking various number of CA (4, 8, and 16) to the dendritic block to prepare a series of telodendrimers (Table 1). Representative structure of the inert telodendrimer is shown in Scheme S-1 in the Supporting Information. The molecular weights of the telodendrimers were measured with MALDI-TOF mass spectrometry. The monodispersed mass traces were detected for the starting PEG and the telodendrimers. The molecular weight shifts between the telodendrimers and the corresponding starting PEG were almost identical to the mass increase by the conjugation of the oligo-cholic acids (Figure S-1 in Supporting Information). The molecular weights of the telodendrimers from MALDI-TOF MS (Table 1) were very similar to the theoretical value. The molecular weights of the telodendrimers were also determined by NMR spectrometry, based on the ratio of the proton signals of the three methyl groups on cholic acid (0.6−1.1 ppm) to the proton signals of the PEG (3.5−3.65 ppm) in the ^{1}H NMR spectra of the telodendrimers in $CDCl_3$ (Figure 4a). The molecular weights obtained from NMR method were also very close to the theoretical values (Table 1), indicating the well-defined structures of telodendrimers. These telodendrimers were prepared via the well-established stepwise Fmoc peptide chemistry. The soluble PEG-supported conjugation reactions can be driven to completion by adding excess amount of reagents. Subsequently, the PEGylated intermediate and products can be easily isolated and purified via the precipitation and washing with cold ether, thus ensuring that the structures of the telodendrimers are well-defined. As shown Figure 1, another advantage of this stepwise synthesis is that the structure of the telodendrimer can be easily engineered, and multiple functional groups can be introduced into the polymer at particular density and at the specific sites.

The critical micelle concentration (CMC) of the telodendrimers was measured with a standard fluorescence technique using pyrene as the probe (*36*). As shown in Figure 2, the CMCs of the telodendrimers with different PEG chain length and number of the cholic acid vary from 8 μg/mL to 250 μg/mL, corresponding to 0.97 μM to 67 μM (Table 1), due to the changes of the amphiphilicity. We found that the telodendrimers with larger numbers of cholic acids, such as PEG^{2k}-CA_8 and PEG^{10k}-CA_{16}, had low CMCs of ~1 μM and yielded larger micelles with a heterogeneous size distribution. After loading with PTX, significant precipitation was observed. Very low or undetectable PTX loading was observed after the removal of precipitates (Table 1). Micelles prepared from telodendrimers with medium CMC values (5−7.9 μM), such as PEG^{2k}-CA_4, PEG^{3k}-CA_8, and PEG^{5k}-CA_8, were found to be very stable and homogeneous in size before and after PTX loading. Those telodendrimers composed of fewer cholic acid molecules (PEG^{3k}-CA_4 and

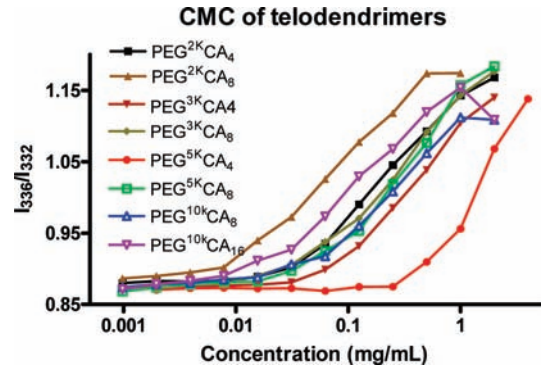


Figure 2. CMC studies of the telodendrimers via fluorescence technique using pyrene as a probe molecule. The emissions of pyrene at 391 nm were collected through the excitation at 332 and 336 nm, respectively. The ratios of I_{336}/I_{332} are plotted vs the concentration of the telodendrimers. [pyrene] is 2×10^{-6} M, and the data were the averages of triplicate measurements.

PEG^{5k}-CA_4) and with high CMCs (12.5 and 67 μM, respectively) were found to form smaller micelles (10 and 15 nm, respectively) prior to drug loading. After PTX loading, the micelles increased in size up to 131 and 141 nm, respectively, at relatively low PTX loading level, however, remaining very stable and homogeneous in size. While more PTX was added (>10% w/w drug/polymer), significant precipitation occurred for PEG^{5k}-CA_4.

Most of telodendrimers discussed above, except PEG^{2k}-CA_8 and PEG^{10k}-CA_{16}, can be readily dissolved in water at concentration up to 200 mg/mL. In the micelle characterization, PTX loading, and *in vivo* xenograft studies, we decided to keep the concentration of the telodendrimers at 20 mg/mL, which provided sufficient PTX concentration and exhibited the low viscosity needed for tail vein injection of the nanotherapeutics in the *in vivo* animal experiments. After adjusting the PEG chain length and the number of CA subunits in the telodendrimers, the particle sizes of the PTX loaded micelles can be tuned into the range 15−141 nm. Among them, PEG^{5k}-CA_8 has a medium particle size of 61 nm and the highest PTX loading capacity (7.3 mg PTX loaded in 20 mg PEG^{5k}-CA_8/mL), which is equivalent to 36.5% (w/w) of drug/polymer ratio (Figure 3a). The final particle size of PTX-loaded PEG^{5k}-CA_8 (with CMC around 5 μM) showed a modertate increase in size, while other telodendrimers, such as PEG^{3k}-CA_4 (CMC at 12.5 μM), produced a significant size increase at high drug loading level (Figure 3b). Our telodendrimer micelle systems can also effectively deliver other therapeutic agents including etoposide, a topoisomerase II inhibitor for cancer treatment, at an etopside/polymer ratio of 18.5% in PEG^{5k}-CA_8 (Figure 3d). By increasing

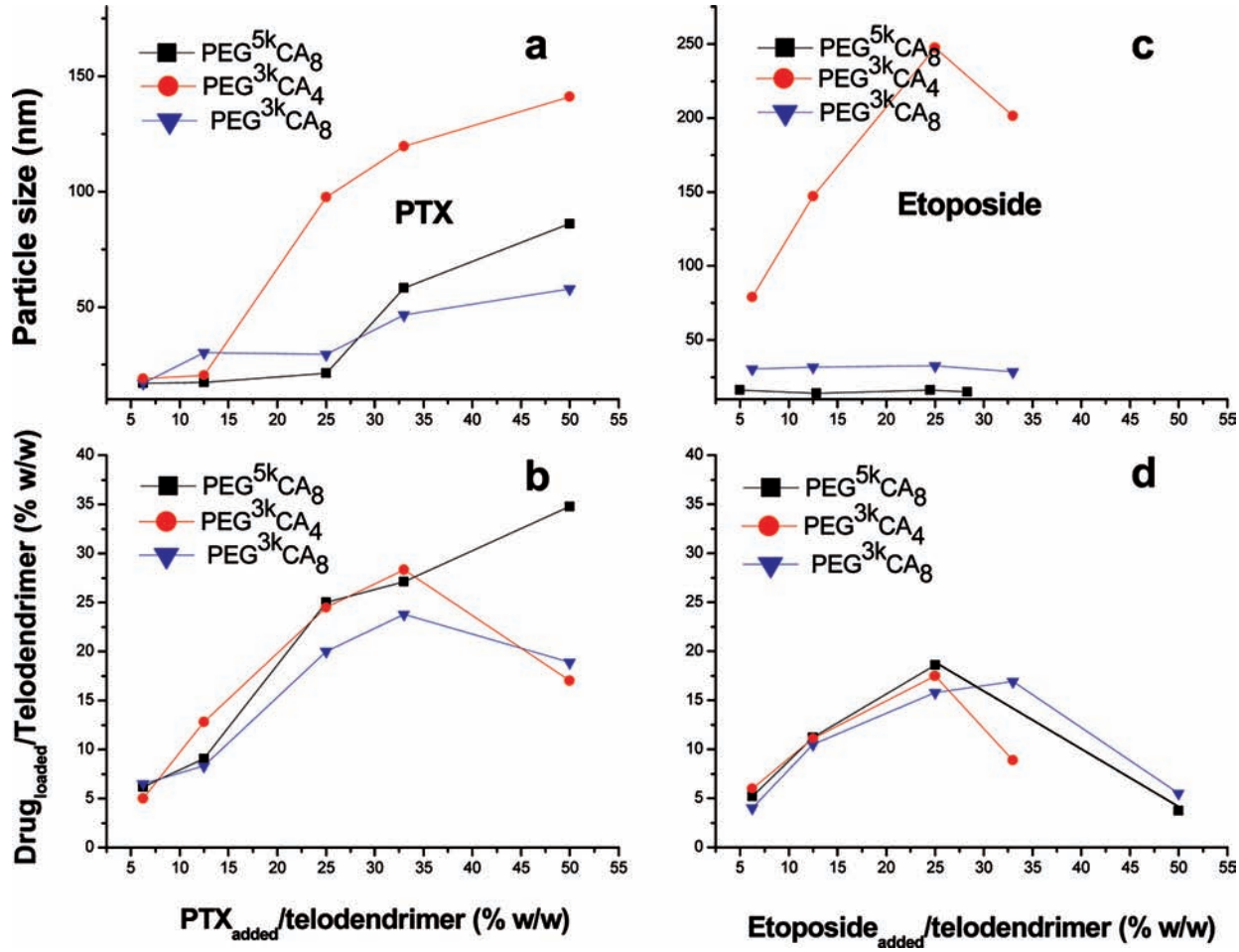


Figure 3. Relationships of the particle size of the PTX and etoposide loaded micelles formed by different telodendrimers (a, c) and the drug/telodendrimer ratios in drug loaded micelles (b, d) vs the feed ratios of drug/telodendrimers during the drug loading, respectively. The concentrations of telodendrimers were 20 mg/mL.

the amount of drug added, the etoposide-loaded micelles exhibited very similar changes in sizes: PEG^{3k}-CA$_8$ and PEG^{5k}-CA$_8$ maintain their small particle sizes with high drug loading capacities, while and the size of etopside-PEG^{3k}-CA$_4$ micelles increases dramatically with the increased drug loading (Figure 3c).

We have also substituted cholic acid in PEG^{5k}-CA$_8$ with other natural lipophilic molecules such as cholesterol formate (CF), lithocholic acid (LA) (both with planar steroid scaffold), and heptadecanoic acid (HA) (linear fatty acid). The resulting telodendrimers, with low CMCs at approximately 1 μM, tend to form precipitate in aqueous solution, and their PTX loading capacities are rather low (Table 1). The above studies indicate that cholic acid is essential to form stable telodendrimer micelles. Presumably, under aqueous environment, the facial amphiphilic cholic acids in the dendritic core can arrange their hydrophobic convex surfaces to the interior of micelle and place the opposite hydrophilic surfaces against the aqueous environment to lower the energy, and, together with PEG, stabilize the hydrophobic components inside the micelles. Additionally, some of the cholic acids might be randomly packed inside the hydrophobic core and their hydroxyl groups may form hydrogen bonds with the hydrophilic groups in PTX; such interactions may contribute to the good drug loading capacity of these micelles (*38*).

^{1}H NMR spectra of PEG^{5k}-CA$_8$ in CDCl$_3$ revealed the expected structure of the telodendrimer. However, when the ^{1}H NMR spectrum was collected in deuterated water, the cholane signals (0.6−2.2 ppm) were greatly suppressed (Figure 4a), indicating that the dendritic oligo-CA was tightly packed in the core of the micelles with high microviscosity. Similar phenomena were also reported in other micelle systems (*32*, *36*, *39*). In the cryoTEM study (Figure 4b), PTX was loaded into PEG^{5k}-CA$_8$ micelles (7.3 mg PTX/mL) in order to increase the density of the core and enhance the contrast against the background. Spherical micelles were observed with in situ sizes ranging from 30 to 60 nm calibrated with tobacco mosaic virus (18 nm in width), which is consistent with the DLS measurement (61 ± 21 nm, Table 1). Blank micelles (16 ± 4 nm by DLS) and PTX-loaded micelles (6.4 mg PTX/mL, 23 ± 8 nm by DLS) prepared from thiol-functionalized HS-PEG^{5k}-CA$_8$ (Scheme S-2 in the Supporting Information) were immobilized on gold surfaces for atomic force microscopy (AFM) scanning. Tapping-mode AFM topographs were obtained in aqueous solution. Both the empty and drug-loaded micelles appeared as individually immobilized nanoparticles with average sizes of 15 and 26 nm, respectively (Figure 4c−f), which were close to the particle sizes obtained by DLS measurement.

The morphology of the aggregates formed by other telodendrimers was studied by TEM. As mentioned above, PEG^{3k}-CA$_4$ and PEG^{5k}-CA$_4$ when loaded with hydrophobic molecules such as PTX tend to form large nanoparticles. Interestingly, rod-shaped aggregates (40 nm in width and several hundreds of nanometers in length) were observed under TEM imaging of the PTX-PEG^{5k}-CA$_4$ sample (Figure 5a). PEG^{2k}CA$_4$, on the other hand, was observed to form gel or gel particles at high concentration (30 mg/mL) upon storage. After loading with hydrophobic payloads, such as NIR dye (DiD) or PTX, the micelle solution became more viscous upon storage overnight

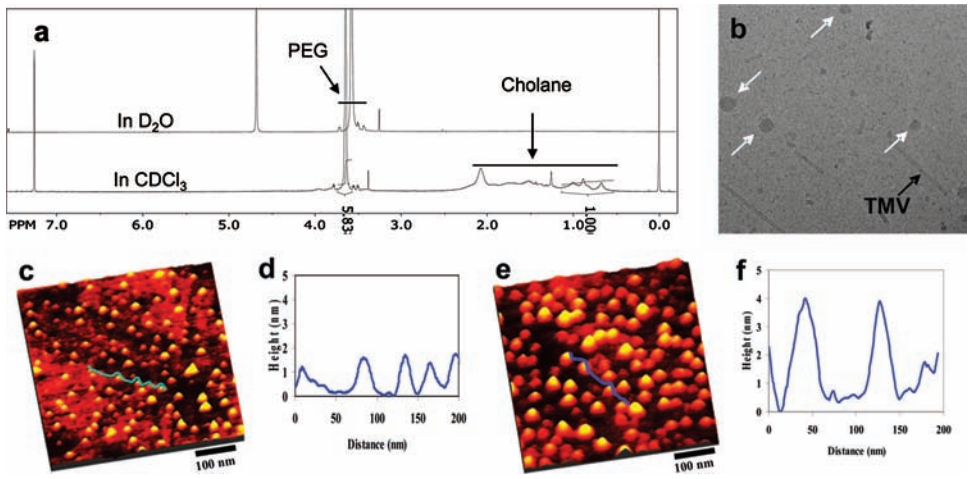


Figure 4. (a) ^{1}H NMR spectra of PEG^{5k}-CA$_8$ were recorded in $CDCl_3$ and D_2O; the suppression of cholic acid signals in D_2O indicates the entanglement of cholanes in water by the formation of micelles; (b) CryoTEM images of PEG^{5k}-CA$_8$ loaded with PTX in the presence of tobacco mosaic virus (TMV) as calibration standard (18 nm in width); tapping-mode AFM topographs of (c) the HS-PEG^{5K}-CA$_8$ micelles and (e) PTX-loaded HS-PEG^{5K}-CA$_8$ micelles on gold surfaces, and the corresponding cursor profiles are represented in (d) and (f), respectively, to review the 3D sizes.

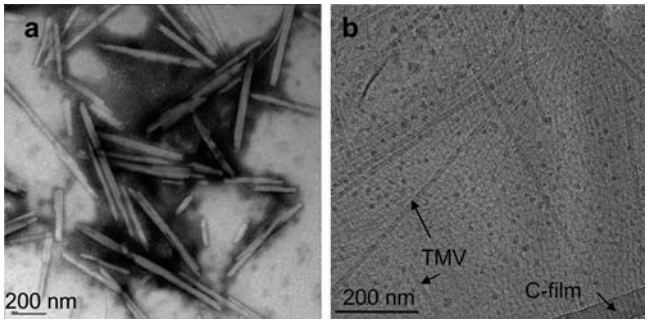


Figure 5. (a) TEM images of the PTX-loaded PEG^{5k}-CA$_4$ (20% w/w) solutions. The rod-like aggregates were observed with 40 nm in width and several hundreds of nanometers in length. (b) CryoTEM images of DiD loaded PEG^{2k}-CA$_4$ in the presence of tobacco mosaic virus (TMV) as calibration standard (18 nm in width); the spherical micelles (15 nm) and thin nanofibers (2 nm in thickness) were observed.

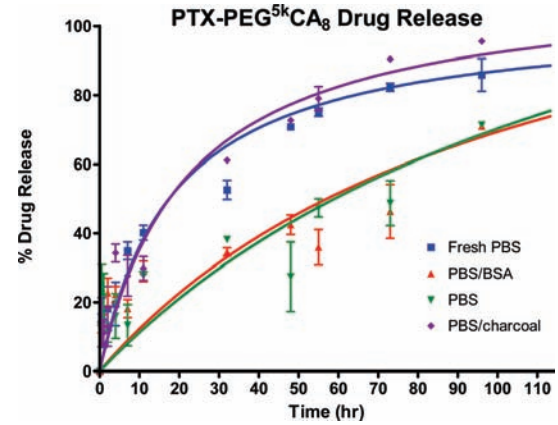


Figure 6. Accumulative paclitaxel released from micelles formed by PEG^{5k}-CA$_8$ in PBS (pH 7.4) at 37 °C with different sink conditions: unchanged PBS; refreshed PBS; unchanged PBS with 10 mg/mL of BSA and charcoal, respectively. The concentrations of PTX were 2 mg/mL. The data points were the average of three measurements.

at room temperature. Spherical micelles (15 nm) and nanofibers (about 2 nm thickness) were observed under CryoTEM (Figure 5b). This indicates that the morphology could change from the spherical micelles (low viscosity) to fibers (high viscosity) during storage. The morphological outcome is probably determined by the structure as well as the amphiphilic balance of the telodendrimers. The packing parameters (ratio of hydrophobic/hydrophilic blocks) have been widely used to predict the morphology of the micelles formed by linear amphiphilic copolymers (*40, 41*). However, the same rule may not apply to our telodendrimers with facial amphiphilicity and bulky cluster of cholic acids. Work is currently underway in our laboratory to study the relationship between the packing parameters and morphological outcome of the telodendrimer-based micelles.

The stability of the PTX-loaded PEG^{5k}-CA$_8$ micelles were followed by the DLS particle sizer. The particle size of these PTX-loaded micelles in aqueous solution was found to be highly stable at 4 °C for over 6 months, no further aggregations and no needle crystals of PTX were observed. In contrast, most of the PTX-loaded polymeric micelles reported in the literature lack stability (from a few hours to days) (*30*−*32*). Even Abraxane, the FDA-approved albumin nanoparticle-bound PTX, tends to precipitate 24 h after reconstituted with saline (Supporting Information, Figure S-2). Upon dilution with PBS to 125-fold to mimic the dilution by the blood pool through intravenous (iv) injection, needle-like crystals of PTX were observed in the diluted Taxol (Cremophor formulation of PTX) solution within a month. In contrast, this was not observed in the diluted PTX-loaded PEG^{5k}-CA$_8$ micelle solutions even for 12 months, indicating that the PTX complex inside these micelles is very stable.

Upon dialysis in a cassette (MWCO 3500 Da) against PBS with different sink conditions over time, PTX can diffuse out from the micelle systems, but no burst release was observed (Figure 6). Under the condition of frequently refreshed PBS during sampling, the drug release was much faster than that in the unchanged PBS. The condition with charcoal in the PBS reservoir (without changing PBS) allowed efficient absorption of the released PTX, which mimics the *in vivo* protein binding and cellular uptake of drug; the drug release was even more faster than that in the refreshed PBS. Bovine serum albumin (BSA) was found to be inefficient for absorbing the released free PTX, resulting in a slow drug release rate, which is very similar to that in the unchanged PBS condition. In addition, PTX needle crystals were observed in the dialysate in the unchanged PBS and in BSA solution conditions, which leads to some variations in the measurements. However, the needle crystals were not found in the dialysates in the conditions of refreshed PBS and in the unchanged PBS with charcoal. Approximately 50% of the loaded PTX was released from the micelles after 24 h in the sink conditions, and no burst release

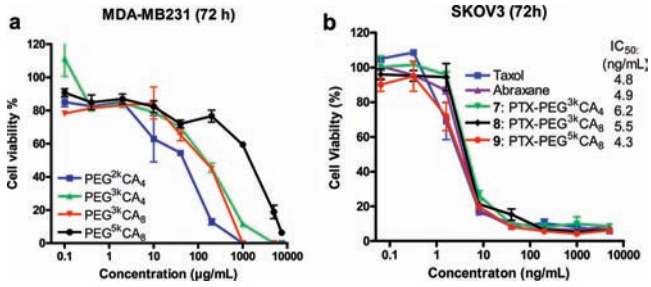


Figure 7. (a) Cytotoxicity of empty telodendrimer micelles against the MDA-MB-231 breast cancer cells; no significant toxicity for PEG^{5k}-CA_8 was observed at 1 mg/mL concentration; telodendrimers with short PEG chains show moderate toxicity at high concentrations (50−150 μg/mL). (b) Tumor cell killing of the PTX-loaded micelles in the SKOV-3 ovarian cancer cells, very similar IC_{50} values were observed for all the formulations in in vitro tumor cell killing.

was observed during the fist few hours. Interestingly, we found that the PTX release rates of the samples, which had been prepared and stored for two months, were lower compared to the freshly loaded samples, and the release pattern was in a linear mode (Supporting Information, Figure S-3). One possible explanation for this observation is the crystallization of PTX inside the core of the micelle or the crystallization of hydrophobic segments of the telodendrimer over time. To address this question, X-ray diffraction (XRD) studies were performed on these samples. Distinct PEG crystalline peaks were identified at 19.1° and 23.3° (*42*, *43*) (Supporting Information, Figure S-4); however, no crystalline peaks for PTX (*42*) or hydrophobic moieties (cholic acid) were detected in the XRD spectra. Instead, the typical diffraction curve of the amorphous polymer was observed from 10° to 30°, indicating that the micellar core loaded with PTX was amorphous. The XRD studies of these old samples indicate that the slow PTX release was not caused by the crystallization of PTX or the hydrophobic segments inside the micelles. The DSC (differential scanning colorimetry) analysis revealed an increased T_g (glass transition temperature, 200 °C) of the cholane core for a PTX-$PEG^{5k}CA_8$ sample lyophilized after storage for 55 days at 4 °C, compared with the same sample lyophilized at earlier time point, such as day 5 (T_g: 179 °C) (Supporting Information, Figure S-5). Thus, the slow PTX release from the old PTX-loaded samples may be due to the more compact core structures formed by the rearrangement of the dendritic cholane segments during storage.

The cytotoxicity of the telodendrimers in cell culture was evaluated via the MTT assays. As shown in Figure 7a, at up to 1 mg/mL of $PEG^{5k}CA_8$ in the cell culture media, no significant cytotoxicity was observed on MDA-MB-231 breast cancer cells (IC_{50}: 1.5 mg/mL). However, the telodendrimers with shorter PEG chain lengths (2 and 3 kDa) exhibited cytotoxic effects at relatively lower concentrations, and the IC_{50} values of $PEG^{2k}CA_4$, $PEG^{3k}CA_4$, and $PEG^{3k}CA_8$ were 45, 126, and 150 μg/mL, respectively. $PEG^{5k}CA_8$ remained rather nontoxic, compared to other telodendrimers with shorter PEG chains, to other cancer cell types including SKOV-3 (ovarian cancer) and HT29 (colon cancer). This may be explained by the extra stereohindrance of the longer PEG preventing the interaction between the micelles and cells. The cell-killing efficacies of PTX-loaded telodendrimers, such as PEG^{5k}-CA_8, $PEG^{3k}CA_4$, and $PEG^{3k}CA_8$ and the two clinical formulations of PTX (Taxol and Abraxane) on SKOV-3 cells were found to be comparable, and the IC_{50} ranged from 4.3 to 6.2 ng/mL, after 72 h of continuous incubation with the drugs (Figure 7b). The corresponding concentrations of the telodendrimers at the IC_{50} of PTX formulations are 20−30 ng/mL, which are far less than the IC_{50} of the blank telodendrimers (45−1500 μg/mL), indicating the potential clinical applications of these telodendrimers for delivery of PTX. The IC_{50} values of PTX and PTX-loaded $PEG^{5k}CA_8$ on the MDA-MB-231 cells were observed to be higher than that in SKOV3 cells at 45 ng/mL and 17 ng/mL, respectively, over 72 h of continuous drug exposure.

To study the effects of particle size on the *in vivo* biodistribution of nanoparticles, DiD (a hydrophobic near-infrared (NIR) cyanine dye, 1 mg/mL) was coloaded with PTX (4 mg/mL, 4 mg/mL, and 3 mg/mL, respectively) into 20 mg/mL micelle solutions of PEG^{2k}-CA_4, PEG^{5k}-CA_8, and PEG^{3k}-CA_4, to form three fluorescence-labeled micelle preparations with distinct sizes of 17, 64, and 154 nm, respectively (Figure 8a). Each of these three formulations of DiD-loaded micelles was incubated with Raw 264.7 macrophage cells for 2 h. The cells were then washed three times with PBS, fixed with 70% ethanol, and observed under confocal fluorescence microscope. As shown in Figure 8b, the larger micelles (154 nm), compared to the two smaller ones, were preferentially taken up by the macrophages, which was subsequently confirmed by the flow cytometry

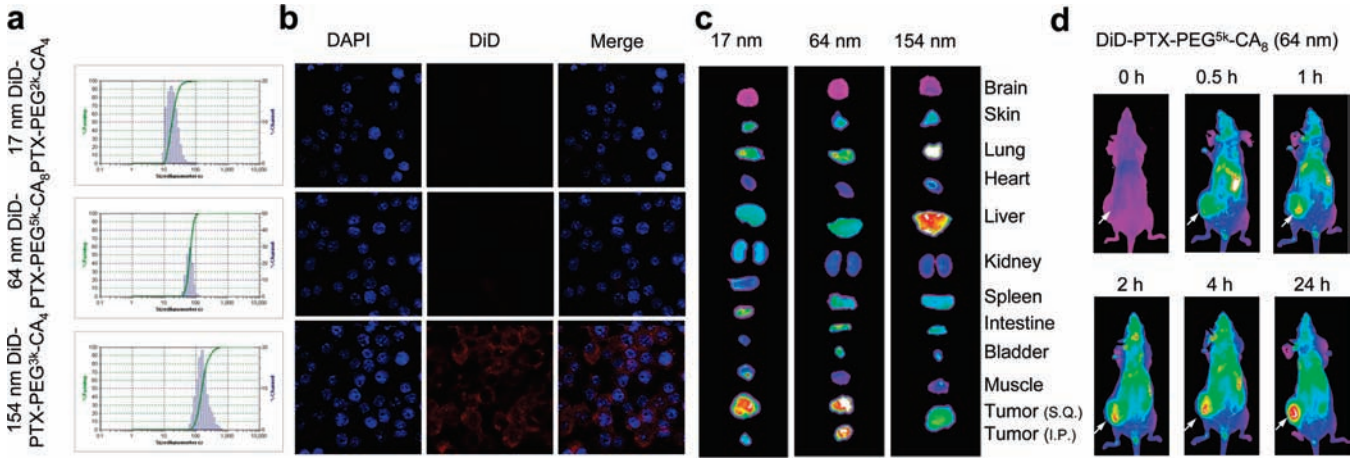


Figure 8. (a) Three micelles, each with a different size after coloading with PTX and DiD, were measured with DLS particle sizer. (b) Raw 264.7 macrophage cells were incubated with each of the three micelle preparations and then imaged under a confocal fluorescence microscope. The nuclei of the cells were stained with DAPI; the red DiD signals indicated that the 154 nm micelles, compared to the smaller micelles (17 and 64 nm), were preferentially taken up by the macrophages. (c) Ex vivo biodistribution of the micelles (three different sizes) in the SKOV-3 ovarian cancer xenograft bearing mice at 24 h after tail vein injection. (d) In vivo NIR fluorescence imaging of the tumor bearing mice after i.v. injection with the DiD-PTX-$PEG^{5k}CA_8$ over time; passive accumulation of the micelles in the S.Q. implanted xenograft (arrow) was observed from 2 to 24 h after injection.

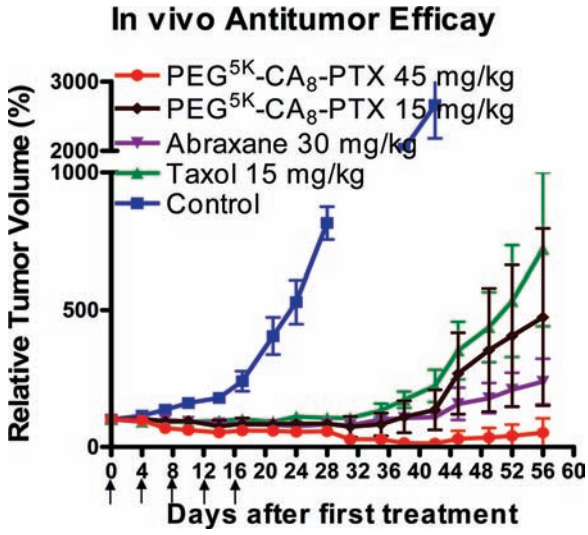


Figure 9. Antitumor efficacy of different PTX formulations in nude mice bearing human SKOV3-luc ovarian cancer xenograft. PBS (control). Taxol, Abraxane, and the PTX-PEG^{5k}-CA$_8$ preparations were administered i.v. on days 0, 4, 8, 12, and 16 (marked with arrows) when tumor volume reached about 50 mm^3.

analysis (data were not shown). NIR fluorescent imaging was used to evaluate the *in vivo* biodistribution of the three micelles with different sizes in nude mice bearing the SKOV-3 ovarian cancer xenografts (subcutaneous implants). The mice were injected via the tail vein with the same volume of the above three PTX-DiD-loaded micelle preparations in PBS. Ex vivo imaging of the excised organs and tumors was performed at 24 h after injection. As shown in Figure 8c, the larger nanoparticles (154 nm) clearly exhibited the highest fluorescence intensity in the liver and the lungs, likely due to nonspecific uptake by macrophages in those organs; moreover, the fluorescent uptake by the tumor was very low. In contrast, tumor uptake of the smaller micelles (17 and 64 nm) was much higher than that of normal organs. The duplicated images in a different set of mice showed similar size effects on the biodistributions (Figure S-6 in Supporting Information). The *in vivo* NIR images of a tumor-bearing mouse treated with the DiD-PTX-PEG^{5k}CA$_8$ was recorded over time (Figure 8d). It is evident that the accumulation of the DiD loaded micelles at the tumor site via the EPR effect began at 2 h after injection and continued to increase over the next 24 h period. In contrast, tumor targeting was not found in the tumor-bearing mice treated with the free dye (*33*). Consistent with imaging study of the size effect, PTX-loaded PEG^{5k}-CA$_8$ have been shown to be superior to Abraxane and Taxol in the treatment of both subcutaneous and intraporitoneal xenograft ovarian cancer murine models (*33*). We believe PTX-PEG^{2k}-CA$_4$, with smaller micelle sizes (17 nm), will be able to penetrate more deeply into the solid tumor and potentially result in better antitumor effects in tumor xenograft models. This study is currently ongoing in our laboratory.

In our previous report (*33*), we were able to demonstrate that PTX-loaded PEG^{5k}-CA$_8$ (3 consecutive doses every 4 days) slowed down the growth of ovarian cancer xenograft (100−200 mm^3) considerably; however, the tumors eventually progressed and complete cure was never achieved. In this study, we treated 5 groups of mice with 5 consecutive doses of drugs given i.v. every 4 days when the xeongraft implants reached 50 mm^3 in size. As expected, rapid tumor growth was observed beginning on day 16 in the control group treated with PBS (Figure 9). In contrast, no tumor growth was detected in mice treated with each of these five PTX regimens until day 35 when the tumors began to grow in the Taxol group at 15 mg/kg (MTD dosage for five consecutive treatment (*44*)). By day 40, tumor growth also began in the Abraxane group at 30 mg/kg (MTD dosage for five consecutive treatment (*44*)) and the low dose PEG^{5k}-CA$_8$ (15 mg/kg) group. For the high dose PEG^{5k}-CA$_8$ group at 45 mg/kg (MTD dosage for five consecutive treatment), the luciferase signal was undetectable by day 42 (Supporting Information Figure S-7) and there was no sign of palpable tumor over 3 months, which indicated that there was no residual disease and complete cure was achieved. Unlike Taxol and Abraxane, myelosuppression from the PTX-loaded PEG^{5k}-CA$_8$ was minimal (Supporting Information Figure S-8). No weight loss was observed in mice treated with these new nanoformulations (Supporting Information Figure S-9), while consistent weight loss was observed in those treated with Taxol.

In summary, we have developed a well-defined, engineerable and multifunctional telodendrimer system, which can self-assemble to form micelles in aqueous condition. By optimizing the structures of the telodendrimers, biocompatible nanocarriers have been obtained with tunable sizes and efficient PTX and etoposide loading properties. We have found that the size of the micelles can greatly influence their *in vivo* biodistribution. The smaller drug-loaded micelles (17 and 64 nm) were more readily and efficiently able to carry the loaded hydrophobic anticancer drugs to the tumor sites via EPR effects. In contrast, micelles with larger sizes (154 nm) were found to have very high uptake in liver and lung, but low uptake in tumor. In the *in vivo* antitumor efficacy studies in nude mice bearing early stage tumor xenografts, the toxicity profile and antitumor effects for PTX-loaded PEG^{5k}-CA$_8$ were observed to be superior to those of Abraxane and Taxol, and the cure of the disease was achieved in the group treated with PTX-loaded PEG^{5k}-CA$_8$ at its MTD dosage.

ACKNOWLEDGMENT

The authors thank the editorial assistance provided by Mr. Joel Kugelmass and the financial support from NIH U19CA113298, R21CA128501, RO1CA115483, and CIRM TG2-01163. We also thank Dr. Mullen and Prof. Weiss at The Pennsylvania State University for their insightful information with respect to displacement in 1-adamantanethiol SAM. This work was also supported by the Institute for Complex Adaptive Matter (ICAM) (postdoctoral fellowship to (L.S.)), the University of California at Davis (CHE 0809977), and the National Institutes of Health (R21GM77850-01).

Supporting Information Available: The experimental details of AFM studies, structures of telodendrimers, drug release, and stability of the PTX loaded micelles and the duplicated *in vitro* imaging for the size effects. This material is available free of charge via the Internet at http://pubs.acs.org.

LITERATURE CITED

(1) Unezaki, S., Maruyama, K., Hosoda, J.-I., Nagae, I., Koyanagi, Y., Nakata, M., Ishida, O., Iwatsuru, M., and Tsuchiya, S. (1996) Direct measurement of the extravasation of polyethyleneglycol-coated liposomes into solid tumor tissue by *in vivo* fluorescence microscopy. *Int. J. Pharm. 144*, 11–17.

(2) Oku, N. (1999) Anticancer therapy using glucuronate modified long-circulating liposomes. *Adv. Drug Delivery Rev. 40*, 63–73.

(3) Senior, J. H. (1987) Fate and behavior of liposomes *in vivo*: a review of controlling factors. *Crit. Rev. Ther. Drug Carrier Syst. 3*, 123–93.

(4) Maeda, H. (2001) The enhanced permeability and retention (EPR) effect in tumor vasculature: the key role of tumor-selective macromolecular drug targeting. *Adv. Enzyme Regul. 41*, 189–207.

(5) Jain, R. K. (1990) Vascular and interstitial barriers to delivery of therapeutic agents in tumors. *Cancer Metastasis Rev. 9*, 253–66.

(6) Cho, K., Wang, X., Nie, S., Chen, Z. G., and Shin, D. M. (2008) Therapeutic nanoparticles for drug delivery in cancer. *Clin. Cancer Res. 14*, 1310–6.
(7) Ferrari, M. (2005) Cancer nanotechnology: opportunities and challenges. *Nat. Rev. Cancer 5*, 161–171.
(8) Peer, D., Karp, J. M., Hong, S., Farokhzad, O. C., Margalit, R., and Langer, R. (2007) Nanocarriers as an emerging platform for cancer therapy. *Nat. Nanotechnol. 2*, 751–60.
(9) Trubetskoy, V. S. (1999) Polymeric micelles as carriers of diagnostic agents. *Adv. Drug Delivery Rev. 37*, 81–88.
(10) Liu, J., Lee, H., and Allen, C. (2006) Formulation of drugs in block copolymer micelles: drug loading and release. *Curr. Pharm. Des. 12*, 4685–701.
(11) Tong, R., and Cheng, J. (2007) Anticancer polymeric nanomedicines. *Polym. Rev. 47*, 345–381.
(12) Riley, T., Stolnik, S., Heald, C. R., Xiong, C. D., Garnett, M. C., Illum, L., Davis, S. S., Purkiss, S. C., Barlow, R. J., and Gellert, P. R. (2001) Physicochemical evaluation of nanoparticles assembled from poly(lactic acid)-poly(ethylene glycol) (PLA-PEG) block copolymers as drug delivery vehicles. *Langmuir 17*, 3168–3174.
(13) Letchford, K., Liggins, R., Wasan, K. M., and Burt, H. (2009) *In vitro* human plasma distribution of nanoparticulate paclitaxel is dependent on the physicochemical properties of poly(ethylene glycol)-block-poly(caprolactone) nanoparticles. *Eur. J. Pharm. Biopharm. 71*, 196–206.
(14) Hirao, A., Hayashi, M., Loykulnant, S., Sugiyama, K., Ryu, S. W., Haraguchi, N., Matsuo, A., and Higashihara, T. (2005) Precise syntheses of chain-multi-functionalized polymers, star-branched polymers, star-linear block polymers, densely branched polymers, and dendritic branched polymers based on iterative approach using functionalized 1,1-diphenylethylene derivatives. *Prog. Polym. Sci. 30*, 111–182.
(15) Chapman, T. M., Hillyer, G. L., Mahan, E. J., and Shaffer, K. A. (1994) Hydraamphiphiles: novel linear dendritic block copolymer surfactants. *J. Am. Chem. Soc. 116*, 11195–6.
(16) van Hest, J. C. M., Delnoye, D. A. P., Baars, M. W. P. L., van Genderen, M. H. P., and Meijer, E. W. (1995) Polystyrene-dendrimer amphiphilic block copolymers with a generation-dependent aggregation. *Science 268*, 1592–5.
(17) Gillies, E. R., Jonsson, T. B., and Frechet, J. M. (2004) Stimuli-responsive supramolecular assemblies of linear-dendritic copolymers. *J. Am. Chem. Soc. 126*, 11936–43.
(18) Chang, Y., Kwon, Y. C., Lee, S. C., and Kim, C. (2000) Amphiphilic linear PEO-dendritic carbosilane block copolymers. *Macromolecules 33*, 4496–4500.
(19) Gitsov, I., Wooley, K. L., Hawker, C. J., Ivanova, P. T., and Frechet, J. M. J. (1993) Synthesis and properties of novel linear-dendritic block copolymers. Reactivity of dendritic macromolecules toward linear polymers. *Macromolecules 26*, 5621–7.
(20) Iyer, J., Fleming, K., and Hammond, P. T. (1998) Synthesis and solution properties of new linear-dendritic diblock copolymers. *Macromolecules 31*, 8757–8765.
(21) Gillies, E. R., and Frechet, J. M. (2005) pH-Responsive copolymer assemblies for controlled release of doxorubicin. *Bioconjugate Chem. 16*, 361–8.
(22) Lee, C. C., Gillies, E. R., Fox, M. E., Guillaudeu, S. J., Frechet, J. M., Dy, E. E., and Szoka, F. C. (2006) A single dose of doxorubicin-functionalized bow-tie dendrimer cures mice bearing C-26 colon carcinomas. *Proc. Natl. Acad. Sci. U.S.A. 103*, 16649–54.
(23) Zhu, X.-X., and Nichifor, M. (2002) Polymeric materials containing bile acids. *Acc. Chem. Res. 35*, 539–546.
(24) Kim, I. S., and Kim, S. H. (2001) Evaluation of polymeric nanoparticles composed of cholic acid and methoxy poly(ethylene glycol). *Int. J. Pharm. 226*, 23–9.
(25) Luo, J., Giguere, G., and Zhu, X. X. (2009) Asymmetric poly(ethylene glycol) star polymers with a cholic acid core and their aggregation properties. *Biomacromolecules 10*, 900–906.
(26) Zhao, Y. (2007) Facial amphiphiles in molecular recognition: From unusual aggregates to solvophobically driven foldamers. *Curr. Opin. Colloid Interface Sci. 12*, 92–97.
(27) Janout, V., and Regen, S. L. (2009) Bioconjugate-based molecular umbrellas. *Bioconjugate Chem. 20*, 183–192.
(28) Chen, Y., Luo, J., and Zhu, X. X. (2008) Fluorescence study of inclusion complexes between star-shaped cholic acid derivatives and polycyclic aromatic fluorescent probes and the size effects of host and guest molecules. *J. Phys. Chem. B 112*, 3402–9.
(29) Weiss, R. B., Donehower, R. C., Wiernik, P. H., Ohnuma, T., Gralla, R. J., Trump, D. L., Baker, J. R., Jr., Van Echo, D. A., Von Hoff, D. D., and Leyland-Jones, B. (1990) Hypersensitivity reactions from taxol. *J. Clin. Oncol. 8*, 1263–8.
(30) Liggins, R. T., and Burt, H. M. (2002) Polyether-polyester diblock copolymers for the preparation of paclitaxel loaded polymeric micelle formulations. *Adv. Drug Delivery Rev. 54*, 191–202.
(31) Le Garrec, D., Ranger, M., and Leroux, J.-C. (2004) Micelles in anticancer drug delivery. *Adv. Drug Delivery Rev. 2*, 15–42.
(32) Zhang, X., Jackson, J. K., and Burt, H. M. (1996) Development of amphiphilic diblock copolymers as micellar carriers of taxol. *Int. J. Pharm. 132*, 195–206.
(33) Xiao, K., Luo, J., Fowler, W. L., Li, Y., Lee, J. S., Xing, L., Cheng, R. H., Wang, L., and Lam, K. S. (2009) A self-assembling nanoparticle for paclitaxel delivery in ovarian cancer. *Biomaterials 30*, 6006–16.
(34) Pandey, P. S., Rai, R., and Singh, R. B. (2002) Synthesis of cholic acid-based molecular receptors: head-to-head cholaphanes. *J. Chem. Soc., Perkin Trans. 1* 918–923.
(35) Lampkins, A. J., O'Neil, E. J., and Smith, B. D. (2008) Bioorthogonal phosphatidylserine conjugates for delivery and imaging applications. *J. Org. Chem. 73*, 6053–6058.
(36) Kim, C., Lee, S. C., Kang, S. W., Kwon, I. C., Kim, Y.-H., and Jeong, S. Y. (2000) Synthesis and the micellar characteristics of poly(ethylene oxide)-deoxycholic acid conjugates. *Langmuir 16*, 4792–4797.
(37) Aina, O. H., Liu, R., Sutcliffe, J. L., Marik, J., Pan, C. X., and Lam, K. S. (2007) From combinatorial chemistry to cancer-targeting peptides. *Mol. Pharm. 4*, 631–51.
(38) Lee, J., Cho, E. C., and Cho, K. (2004) Incorporation and release behavior of hydrophobic drug in functionalized poly(D,L-lactide)-block-poly(ethylene oxide) micelles. *J. Controlled Release 94*, 323–35.
(39) Weimer, M. W., Scherman, O. A., and Sogah, D. Y. (1998) Multifunctional initiators containing orthogonal sites. one-pot, one-step block copolymerization by simultaneous free radical and either cationic ring-opening or anionic ring-opening polymerization. *Macromolecules 31*, 8425–8428.
(40) Antonietti, M., and Foerster, S. (2003) Vesicles and liposomes: A self-assembly principle beyond lipids. *Adv. Mater. 15*, 1323–1333.
(41) Christian, D. A., Cai, S., Bowen, D. M., Kim, Y., Pajerowski, J. D., and Discher, D. E. (2009) Polymersome carriers: From self-assembly to siRNA and protein therapeutics. *Eur. J. Pharm. Biopharm. 71*, 463–474.
(42) Guo, X. D., Tan, J. P., Kim, S. H., Zhang, L. J., Zhang, Y., Hedrick, J. L., Yang, Y. Y., and Qian, Y. (2009) Computational studies on self-assembled paclitaxel structures: templates for hierarchical block copolymer assemblies and sustained drug release. *Biomaterials 30*, 6556–63.
(43) Kang, N., Perron, M. E., Prud'homme, R. E., Zhang, Y., Gaucher, G., and Leroux, J. C. (2005) Stereocomplex block copolymer micelles: core-shell nanostructures with enhanced stability. *Nano Lett 5*, 315–9.
(44) Desai, N., Trieu, V., Yao, Z., Louie, L., Ci, S., Yang, A., Tao, C., De, T., Beals, B., Dykes, D., Noker, P., Yao, R., Labao, E., Hawkins, M., and Soon-Shiong, P. (2006) Increased antitumor activity, intratumor paclitaxel concentrations, and endothelial cell transport of cremophor-free, albumin-bound paclitaxel, ABI-007, compared with cremophor-based paclitaxel. *Clin. Cancer Res. 12*, 1317–24.

BC1000033

Design and Synthesis of Bis-Biotin-Containing Reagents for Applications Utilizing Monoclonal Antibody-Based Pretargeting Systems with Streptavidin Mutants

D. Scott Wilbur,[*,†,§] Steven I. Park,[†,‡,#] Ming-Kuan Chyan,[§] Feng Wan,[‡,§] Donald K. Hamlin,[§] Jaideep Shenoi,[#] Yukang Lin,[#] Shani M. Wilbur,[#] Franz Buchegger,[‡,#] Anastasia Pantelias,[‡,#] John M. Pagel,[||,#] and Oliver W. Press[||,⊥,#]

Departments of Radiation Oncology, Medicine, and Biological Structure, University of Washington, Seattle, Washington, and Clinical Research Division, Fred Hutchinson Cancer Research Center, Seattle, Washington. Received January 15, 2010; Revised Manuscript Received May 15, 2010

Previous studies have shown that pretargeting protocols, using cancer-targeting fusion proteins, composed of 4 anti-CD20 single chain Fv (scFv) fragments and streptavidin ($scFv_4$-SAv), followed by a biotinylated dendrimeric *N*-acetyl-galactosamine blood clearing agent (CA), **1**, then a radiolabeled DOTA-biotin derivative (a monobiotin), **3a**, can provide effective therapy for lymphoma xenografts in mouse models. A shortcoming in this pretargeting system is that endogenous biotin may affect its efficacy in patients. To circumvent this potential problem, we investigated a pretargeting system that employs anti-CD20 $scFv_4$-SAv mutant fusion proteins with radioiodinated bis-biotin derivatives. With that combination of reagents, good localization of the radiolabel to lymphoma tumor xenografts was obtained in the presence of endogenous biotin. However, the blood clearance reagents employed in the studies were ineffective, resulting in abnormally high levels of radioactivity in other tissues. Thus, in the present investigation a bis-biotin-trigalactose blood clearance reagent, **2**, was designed, synthesized, and evaluated in vivo. Additionally, another DOTA−biotin derivative (a bis-biotin), **4a**, was designed and synthesized, such that radiometals (e.g., ^{111}In, ^{90}Y, ^{177}Lu) could be used in the pretargeting protocols employing $scFv_4$-SAv mutant fusion proteins. Studies in mice demonstrated that the CA **2** was more effective than CA **1** at removing [^{125}I]$scFv_4$-SAv-S45A mutant fusion proteins from blood. Another in vivo study compared tumor targeting and normal tissue concentrations of the new reagents (**2** and [^{111}In]**4b**) with standard reagents (**1** and [^{111}In]**3b**) used in pretargeting protocols. The study showed that lymphoma xenografts could be targeted in the presence of endogenous biotin when anti-CD20 fusion proteins containing SAv mutants ($scFv_4$-SAv-S45A or $scFv_4$-SAv-Y43A) were employed in combination with CA **2** and [^{111}In]**4b**. Importantly, normal tissue concentrations of [^{111}In]**4b** were similar to those obtained using the standard reagents (**1** and [^{111}In]**3b**), except that the blood and liver concentrations were slightly higher with the new reagents. While the reasons for the higher blood and liver concentrations are unknown, the differences in the galactose structures of the clearance agents **1** and **2** may play a role.

INTRODUCTION

Radioimmunotherapy (RIT[1]) employing radiolabeled anti-CD20 monoclonal antibodies (mAb) has proven to be efficacious as a treatment for patients with B-cell lymphomas (*1*). While it seems likely that changes being evaluated in the current RIT treatment regimens will increase efficacy and/or decrease toxicity (*2*−*4*), newer approaches to RIT, such as cancer "pretargeting" (*5*−*7*), may provide more significant improvements in the treatment of lymphoma. One of the pretargeting approaches being investigated uses monoclonal antibody−streptavidin (mAb-SAv) conjugates (*8*−*10*), or related $scFv_4$-SAv fusion proteins, in protocols where they are administered in an initial step, followed in subsequent steps by administration of a blood clearance agent, then a biotin derivative labeled with a therapeutic radionuclide. In preclinical investigations, it has been conclusively shown that pretargeting protocols in mouse models using mAb-SAv conjugates or fusion proteins, reactive with CD20 (*11*), or other lymphoma cell surface antigens (*12, 13*), either alone or in combinations (*14*), provides a more efficacious therapy than obtained with conventional RIT.

Although the mAb-SAv/radiolabeled biotin pretargeting approach benefits from the very high affinity of the biotin-SAv binding pair, a potential limitation in the approach is the fact that patient serum contains significant amounts of biotin (*15*). On the basis of animal studies (*16*), it is possible that endogenous biotin in patient blood can bind with administered mAb-SAv conjugates or fusion proteins to block the binding of subsequently administered blood clearance and radiolabeled biotin derivatives. To circumvent this problem, new mAb-SAv/

* Address correspondence to D. Scott Wilbur, Ph.D., Department of Radiation Oncology, University of Washington, Box 355016, 616 N.E. Northlake Place, Seattle, WA 98105, Phone: 206-616-9246, E-mail: dswilbur@u.washington.edu.

† These investigators contributed equally to this manuscript.

‡ Current Addresses: Steven I. Park, M.D., Division of Hematology/Oncology, University of North Carolina, Chapel Hill, NC 27599-7305; Feng (Connie) Wan, Ph.D., Intellectual Ventures, 11235 SE 6th St., Suite A 200, Bellevue, WA 98004; Franz Buchegger, M.D., University Hospital of Lausanne, CH-1011 Lausanne, Switzerland; Anastasia Pantelias, Bill and Melinda Gates Foundation, Seattle, WA.

§ Department of Radiation Oncology, University of Washington.

|| Department of Medicine, University of Washington.

⊥ Department of Biological Structure, University of Washington.

Fred Hutchinson Cancer Research Center.

[1] Abbreviations: ASOR, asialoorosomucoid protein; CA, blood clearance agent; CDI, carbonyldiimidazole; DCC, *N,N*′-dicyclohexylcarbodiimide; DOTA, 1,4,7,10-tetraazacyclododecane tetraacetic acid; EDC, 1-ethyl-3-(3-dimethylaminopropyl)carbodiimide; FP, fusion protein; HOBT, 1-hydroxybenztriazole; mAb, monoclonal antibody; PEG, poly(ethylene glycol); Ra/Ni, Raney-Nickel; RIP, relative inhibitory power; RIT, radioimmunotherapy; RB, radiolabeled biotin; SAv, streptavidin; scFv, single chain fusion of light and heavy chains in variable region of mAb; TCDI, thiocarbonyldiimidazole; TFA, trifluoroacetic acid; TFP-OTFA, 2,3,5,6-tetrafluorophenyl-O-trifluoroacetate; WT, wild-type (native) protein sequence

10.1021/bc100030q © 2010 American Chemical Society
Published on Web 07/02/2010

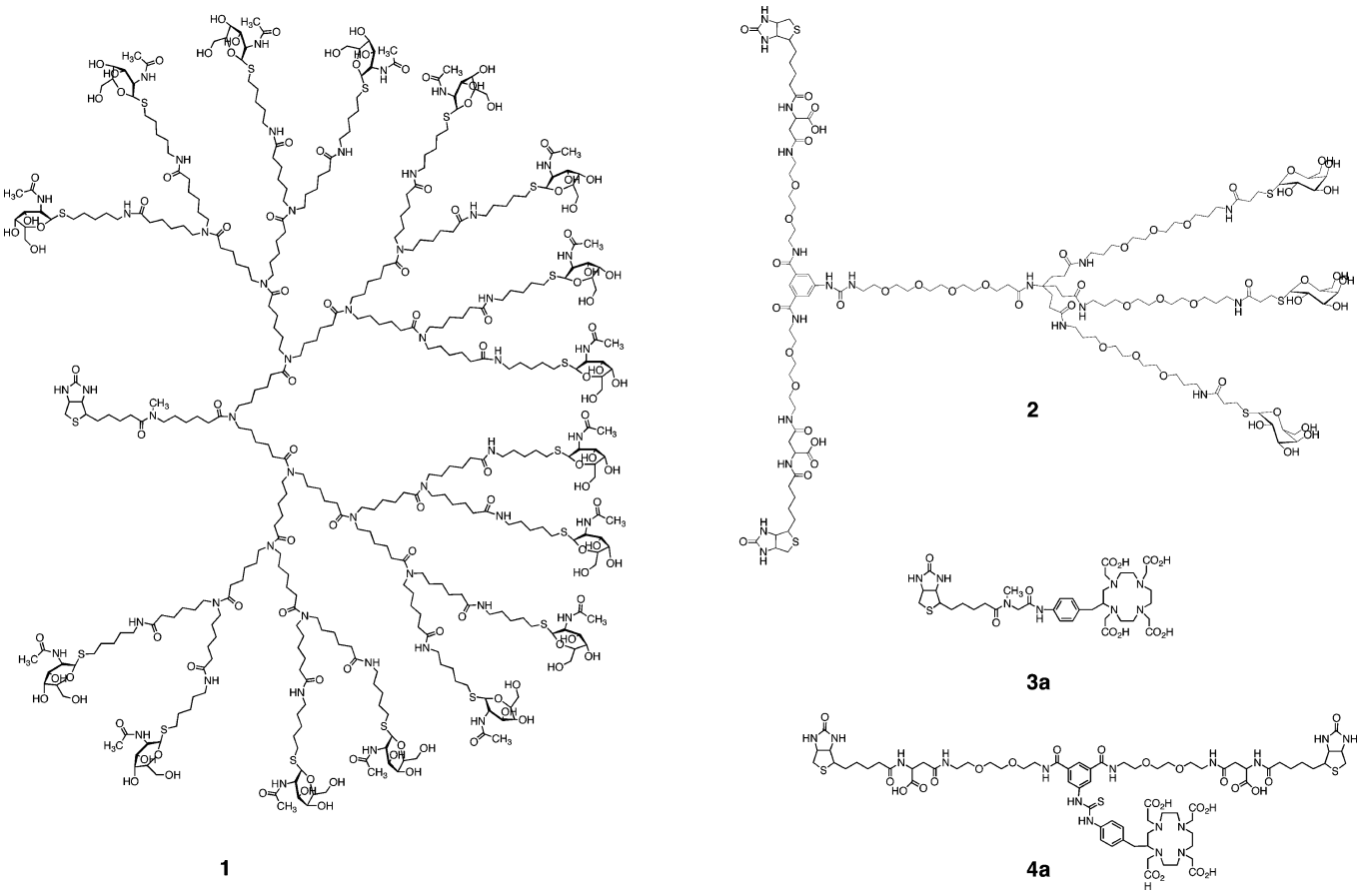


Figure 1. Chemical structures for monobiotin- and bis-biotin-blood clearance agents (**1**, **2**) and nonmetalated DOTA-biotin derivatives (**3a**, **4a**).

biotin binding pairs were designed and prepared. Site-directed mutations of the biotin-binding pocket in streptavidin (SAv) were performed to prepare SAv mutants that have decreased binding with biotin (*17*). Subsequently, those SAv mutants were used to prepare $scFv_4$-SAv mutant fusion proteins (*18*). It was hypothesized that the decrease in biotin binding in the SAv mutants could be offset by using bis-biotin derivatives, which would have increased binding due to dual binding with a single SAv molecule (*19*) and an avidity effect (*20*). Therefore, a series of bis-biotin derivatives were synthesized and their binding with SAv mutants was assessed. Importantly, it was demonstrated that the bis-biotin derivatives could bind with the SAv mutants in the presence of biotin (*21*). Later pretargeting studies demonstrated that tumor xenografts could be effectively targeted using $scFv_4$-SAv mutant fusion proteins, a blood clearance agent, and a radioiodinated bis-biotin derivative, even when the mice were placed on a normal (biotin-containing) diet (*22*). While the studies successfully demonstrated that a mAb-SAv/biotin-based pretargeting approach targeted tumors in the presence of endogenous biotin, the concentrations of radioactivity in normal tissues were much higher than those obtained in other pretargeting studies. The higher normal tissue concentrations appeared to be caused by a lack of efficient blood clearance when using either of the two blood clearing agents studied. Those agents included [1] a monobiotin-hexadecyl-*N*-acetylgalactose derivative, **1**, (Figure 1) and [2] a galactosylated and bis-biotinylated human serum albumin derivative (*22*).

In the current studies, two new reagents, **2** and **4a** (Figure 1), were synthesized for use in pretargeting protocols with scFv4-SAv mutant fusion proteins. A new biotin-containing blood clearance agent, **2**, was designed and synthesized to evaluate the hypothesis that the unacceptably high concentrations of a radioiodinated bis-biotin derivative in normal tissues previously obtained was due to ineffective blood clearance of the antibody-SAv mutant fusion protein. Additionally, a bis-biotin derivative containing the metal chelation moiety DOTA, **4a**, was designed and synthesized due to our interest in using radiometals, such as indium-111 (^{111}In) and yttrium-90 (^{90}Y) in pretargeting protocols. The bis-biotin-DOTA derivative, **4a**, was designed to be similar to the bis-biotin-iodobenzoyl derivative previously shown to bind selectively with SAv mutants in the presence of biotin (*21*). In addition to syntheses of the new reagents, studies were conducted in mice to demonstrate that the new reagents functioned as designed. A study was conducted in mice to compare the blood clearance of a $scFv_4$-SAv mutant fusion in the presence of endogenous biotin when the clearing agents **1** and **2** were employed. Another study was conducted to evaluate whether ^{111}In-labeled **4a**, [^{111}In]**4b**, could successfully target tumors in athymic mice bearing Ramos lymphoma. In that study, an anti-CD20 $scFv_4$-SAv mutant fusion protein was administered, followed by blood clearance with **2**, then administration of an ^{111}In-labeled biotin derivative. For comparison, the biodistribution of [^{111}In]**4b** alone was evaluated in mice. The results obtained in the synthesis of **2** and **4a**, preparation of radiolabeled biotin derivatives, [^{111}In]**3a**/[^{111}In]**4a**, and use of those reagents in animal studies are described herein.

EXPERIMENTAL PROCEDURES

General. Chemicals purchased from commercial sources were analytical grade or better, and were used without further purification. Di-*tert*-butyl-dicarbonate, 2,2′-(ethylenedioxy)bis-(ethylamine), nitromethanetrispropionic acid, acetobromo-α-D-galactose (2,3,4,6-tetra-*O*-acetyl-α-D-galactopyranosyl bromide), 3-iodopropionic acid, 1,1′-carbonyldiimidazole (CDI), 1,1′-thiocarbonyldiimidazole (TCDI), Amberlite IR120 (hydrogen form), and most other chemicals were obtained from Sigma-Aldrich (Milwaukee, WI). L-Aspartic acid α-*t*-butyl ester, **10**,

was obtained from Novabiochem (AMD Biosciences, Inc., San Diego, CA). D-Biotin, **9**, *N*-Boc-trioxatridecanediamine, **16**, and *N*-(phthalimido)amino-dPEG$_4$-acid, **19**, were gifts from Quanta BioDesign, Powell, OH; aminobenzyl-DOTA (*S*-2-(4-Aminobenzyl)-1,4,7,10-tetraazacyclododecane tetraacetic acid), **31**, was obtained from Macrocyclics, Inc. (Dallas, TX). Biotin-sarcosine-aminobenzyl-DOTA, **3a**, was prepared as previously described (*23*) (currently available from Macrocyclics, Inc., Dallas, TX). 2,3,5,6-Tetrafluorophenyl trifluoroacetate, TFP-OTFA, was prepared as previously described (*24*). Sephadex LH-20 gel filtration resin was obtained from Fluka (Sigma-Aldrich, Milwaukee, WI). Melting points were obtained in open capillary tubes on a Mel-Temp II apparatus with a Fluke 51 K/J electronic thermometer and are uncorrected.

Radioactive Materials. All radioactive materials were handled according to approved protocols at the University of Washington and Fred Hutchinson Cancer Research Center. Standard methods for safely using radioactive materials were employed (*25*). Sodium [^{125}I]iodide and [^{111}In]indium chloride were purchased from PerkinElmer Life Sciences (Billerica, MA). Measurement of ^{125}I and ^{111}In was conducted on a Capintec CRC-15R Radioisotope Calibrator using calibration numbers provided by the manufacturer. Samples containing ^{125}I or ^{111}In were counted in a Packard Cobra II gamma counter (PerkinElmer Life and Analytical Services, Waltham, MA). Radioactivity counts were imported into an Excel Spreadsheet (Microsoft Corp., Redmond, WA) where calculations of percent injected dose (%ID) and percent injected dose per gram (%ID/g) were made.

Spectral Analyses. ^{1}H NMR spectra were obtained on a Bruker AV 500 (500 MHz) instrument. Proton chemical shifts are expressed as ppm using tetramethylsilane as an internal standard ($\delta = 0.0$ ppm). Low-resolution mass spectral (LRMS) and high-resolution mass spectral (HRMS) data were obtained on a Bruker APEX III 47e Fourier transform mass spectrometer using electrospray ionization. For analysis, the samples were dissolved in 50/50 MeOH/H_2O and were introduced by an integral syringe infusion pump (Cole Parmer series 74900).

Chromatography. All synthetic reactions were monitored by HPLC. Samples were assessed on a system that contained a Hewlett-Packard quaternary 1050 gradient pump, a variable wavelength UV detector (254 nm), and a Varex ELSD MKIII or an Alltech ELSD 2000 evaporative light-scattering detector. Analyses of HPLC data were conducted using Hewlett-Packard HPLC ChemStation software. Reversed-phase HPLC chromatography was carried out on an Alltech Altima C-18 column (5 μm, 250 × 4.5 mm) using a gradient solvent system at a flow rate of 1 mL/min. A gradient of MeOH and H_2O/0.1% HOAc was used. Starting with 40% MeOH, the initial solvent mixture was held for 2 min, then the gradient was increased to 100% MeOH over the next 10 min, then held at 100% MeOH for 8 min. Retention times (t_R) under these conditions for compounds are provided with the compound experimental.

Some synthesized compounds were purified from crude reaction mixtures using a Biotage SP Flash Purification System (Charlottesville, VA) on a reversed-phase C18 FLASH 25+M column. The purification used a gradient mixture composed of MeOH and 0.1% aqueous HOAc solution (pH 3.25). The gradient started with 25% MeOH/75% HOAc/H_2O, and that mixture was held for 2 min. Following that, the % MeOH was increased linearly to 100% over the next 10 min, then held at 100% for 8 min. Fractions were collected based on UV detection at 215 or 254 nm. Fractions containing pure products were determined by analytical HPLC and were combined, solvent evaporated, and isolated to provide the yields listed.

The ^{111}In-labeling reactions of biotin derivatives **3a** and **4a**, to prepare [^{111}In]**3b** and [^{111}In]**4b**, were followed by radio-HPLC, and the products were purified by isolation from the HPLC effluent. The HPLC equipment used consisted of a Hewlett-Packard quaternary 1050 gradient pump, Waters 601 UV detector, and a Beckman model 170 radioisotope detector. Analysis of the HPLC data was conducted on Hewlett-Packard HPLC ChemStation software. The separations used a C-18 column (Altima C-18, 5 mm, 250 × 4.5 mm; Alltech, Deerfield, IL) with a gradient eluting at a flow rate of 1 mL/min. The gradient was composed of MeOH as solvent A and 0.1% HOAc in water as solvent B. The gradient started at 60% B, which was held for 2 min, then the percent of MeOH was increased linearly to 100% over the next 10 min. After reaching 100% MeOH, it was held there for 8 min.

5-*N*-(*tert*-Butyloxycarbonyl)aminoisophthalate-1,3-bis-*O*-(2,3,5,6-tetrafluorophenyl) Ester, 6. This compound was prepared from aminoisophthalic acid, **5**, by reaction with di-*tert*-butyl dicarbonate in basic DMF/H_2O solution, followed by esterification with tetrafluorophenol and EDC in DMF as previously reported (*21*).

N-(*tert*-Butyloxycarbonyl)-3,6-dioxa-1,8-octanediamine, 7. To a solution of 2,2′-(ethylenedioxy)bis(ethylamine) (403 mL, 2760 mmol) in 200 mL of dichloromethane, di-*tert*-butyl dicarbonate (20 g, 91.6 mmol) with 200 mL of dichloromethane was added dropwise over 4 h. After the addition was completed, the reaction solution was allowed to stir at room temperature for 1 h. Dichloromethane was evaporated by rotoevaporator under vacuum, and then the residue was dissolved in water (200 mL) and washed with hexanes (2 × 200 mL). The aqueous solution was then extracted with dichloromethane (3 × 100 mL). The fractions of dichloromethane were combined and washed with water (3 × 100 mL), dried over anhydrous Na_2SO_4, and then evaporated under vacuum on a rotoevaporator to yield 14.11 g (62%) of **7** as a colorless oil (used without further purification). ^{1}H NMR ($CDCl_3$, 500 MHz): δ 1.45 (s, 9H), 1.57 (s, 2H), 2.88 (t, $J = 5.4$ Hz, 2H), 3.32 (q, $J = 5.2$ Hz, 2H), 3.54 (q, $J = 5.5$ Hz, 4H), 3.62 (s, 4H), 5.18 (br s, 1H). HPLC: $t_R = 4.1$ min. (Alternate syntheses have been previously reported *26, 27*).

***N*,*N*′-Bis(*N*-(*tert*-butyloxycarbonyl)-*N*-(8-amino-3,6-dioxaoctanylamino)-5-(*N*-*tert*-butyloxycarbonyl)aminoisophthalamide, 8.** A 1.25 g (5.09 mmol) quantity of **7** was added to a solution containing **6** (1.50 g, 2.42 mmol), Et_3N (1.01 mL, 7.27 mmol), and anhydrous CH_3CN (150 mL). The resultant solution was stirred at room temperature for 30 min, and then evaporated to dryness under vacuum on a rotoevaporator. The crude product was purified by silica gel column (2.5 cm ×25 cm) eluting with 10% MeOH/EtOAc to yield 1.57 g (81%) of **8** as a colorless, tacky solid. ^{1}H NMR ($CDCl_3$, 500 MHz): δ 1.41 (s, 18H), 1.53 (s, 9H), 3.28−3.31 (m, 4H), 3.55 (t, $J = 5.3$ Hz, 4H), 3.64 (s, 8H), 3.67 (s, 8H), 5.23 (s, 2H), 7.10 (s, 2H), 7.87 (s, 1H), 7.99 (s, 1H), 8.17 (s, 2H). HRMS (ES^+) calcd for $C_{35}H_{60}N_5O_{12}$ $(M+H)^+$: 764.4052. Found: 764.4030. HPLC: $t_R = 13.7$ min.

2-(*N*-Biotinoyl)-L-aspartate-1-*O*-*tert*-butyl Ester, 11. This compound was prepared from biotin, **9**, by reaction with 2,3,5,6-tetrafluorophenyl trifluoroacetate (TFP-OTFA) in an initial step, followed by reaction of the intermediate biotin tetrafluorophenyl ester with L-aspartic acid α-*tert*-butyl ester, **10**, as previously reported (*28*).

4-(*O*-Tetrafluorophenyl)-2-(*N*-Biotinoyl)-L-aspartate-1-*O*-*tert*-butyl Ester, 12. This compound was prepared by reaction of **11** with TFP-OTFA following a previously reported procedure (*28*).

***N*,*N*′-Bis(*N*-(biotinyl)-β-*N*-(*tert*-butyloxycarbonyl)-*N*-(8-amino-3,6-dioxaoctanyl)aspartamidyl)-5-aminoisophthalamide, 13.** A 1.50 g (2.02 mmol) quantity of **8** was stirred with trifluoroacetic acid (10 mL) at room temperature for 10 min. Excess trifluoroacetic acid was evaporated under a stream of argon, and then the residue was washed with ethyl acetate (2

× 40 mL) and dried under vacuum for 3 h. The deprotected aniline derivative was dissolved in anhydrous DMF (20 mL), and then Et_3N (1.13 mL, 8.09 mmol) and **12** (2.34 g, 4.14 mmol) were added, respectively. The resultant solution was stirred at room temperature for 1 h. After solvents were evaporated under vacuum on a rotoevaporator, the crude product was purified by silica gel column (2.5 cm ×25 cm) eluting with 50% MeOH/EtOAc to yield 1.84 g (74%) of **13** as a colorless tacky solid. ^{1}H NMR (CD_3OD, 500 MHz): δ 1.38−1.43 (m, 4H), 1.44 (s, 18H), 1.51−1.75 (m, 8H), 2.19−2.28 (m, 4H), 2.62−2.72 (m, 6H), 2.89−2.92 (m, 2H), 3.15−3.19 (m, 2H), 3.33−3.35 (m, 4H), 3.53 (t, J = 5.4 Hz, 4H), 3.56 (t, J = 5.4 Hz, 4H), 3.61−3.67 (m, 12H), 4.29 (dd, J = 4.8, 8.0 Hz, 2H), 4.47 (dd, J = 4.8, 8.0 Hz, 2H), 4.61 (t, J = 6.6 Hz, 2H), 7.24 (s, 2H), 7.49 (s, 1H). LRMS (ES^+) calcd for $C_{56}H_{90}N_{11}O_{16}S_2$ $(M+H)^+$: 1236.6. Found: 1236.8. HPLC: t_R = 11.0 min.

Nitromethane-tris(3-propionate-*O*-2,3,5,6-tetrafluorophenyl ester), 15. A 5.0 g (18.1 mmol) quantity of nitromethane-trispropionic acid, **14**, was dissolved in 10 mL of anhydrous DMF under argon atmosphere. To that solution was added 10.4 mL (7.29 g, 72.2 mmol) of Et_3N, followed by addition of 12.5 mL (18.9 g, 72.2 mmol) of TFP-OTFA at 0 °C. The reaction was allowed to come to room temperature and was stirred for an additional 30 min. A portion of the DMF was removed under vacuum, and the resultant light brown liquid was poured into 200 mL cold water (ice bath) with stirring. The colorless solid was collected and dried to give 12.28 g (96%) of **15**. mp 133.4−134.4 °C. ^{1}H NMR ($CDCl_3$, 500 MHz): δ 2.52 (t, J = 7.9 Hz, 6H), 2.82 (t, J = 7.9 Hz, 6H), 7.00−7.06 (m, 3H). HRMS (ES^+) calcd for $C_{28}H_{15}F_{12}NNaO_8$ $(M+Na)^+$: 744.0504. Found: 744.0518. HPLC: t_R = 15.2 min.

Nitromethane-tris(*N*-(4,7,10-trioxa-13-tridecaneamino)-*N*-(tert-butyloxycarbonyl)-3-propionylamine), 17. A 8.40 g (26.2 mmol) quantity of *N*-(*tert*-butyloxycarbonyl)-4,7,10-trioxa-1,13-tridecanediamine, **16**, was dissolved in 70 mL anhydrous THF. The solution was cooled to −78 °C using a dry ice acetone bath. Then, 5.64 g (8.0 mmol) of **15** was added. The reaction mixture changed from yellow to clear while it was allowed to come to room temperature with stirring overnight. The THF was removed on a rotary evaporator and the residue was dissolved in 100 mL EtOAc, washed with 1 N HCl (2 × 50 mL), 1 N Na_2CO_3 (3 × 50 mL), and brine (50 mL). The EtOAc was evaporated by rotary evaporator, and the residue was dried under vacuum to give 8.65 g (92%) of **17** as a yellow oil. ^{1}H NMR ($CDCl_3$, 500 MHz): δ 1.43 (s, 27H), 1.73−1.79 (m, 12H), 2.13 (t, J = 7.9 Hz, 6H), 2.25 (t, J = 7.9 Hz, 6H), 3.21 (q, J = 5.8 Hz, 6H), 3.33 (q, J = 5.9 Hz, 6H), 3.52−3.57 (m, 12H), 3.58−3.61 (m, 12H), 3.63−3.66 (m, 12H), 5.08 (br s, 3H), 6.65 (br s, 3H). HRMS (ES^+) calcd for $C_{55}H_{105}N_7NaO_{20}$ $(M+Na)^+$: 1206.7312. Found: 1206.7245. HPLC: t_R = 13.2 min.

Aminomethane-tris(*N*-(4,7,10-trioxa-13-amino)-*N*-(tert-butyloxycarbonyl)-3-propionylamine), 18. A 0.95 g (0.83 mmol) quantity of **17** was dissolved in 30 mL of absolute EtOH. To that solution was added 3 g of a 50% RaNi/H_2O slurry with stirring. The mixture was put under hydrogen (45 psi) and was stirred overnight. Hydrogen pressure dropped from 45 to 40 psi. Hydrogen was removed with a H_2O aspirator vacuum, and argon was introduced to the mixture; this procedure was repeated 3×, and then the EtOH solution was filtered through a Celite column. The solvent was removed from the filtrate to yield 0.95 g (99%) of **18** as colorless oil. ^{1}H NMR ($CDCl_3$, 500 MHz): δ 1.44 (s, 27H), 1.66 (t, J = 7.9 Hz, 6H), 1.73−1.79 (m, 12H), 2.05 (br s, 2H), 2.21 (t, J = 7.8 Hz, 6H), 3.22 (q, J = 5.8 Hz, 6H), 3.32 (q, J = 6.0 Hz, 6H), 3.54 (q, J = 6.0 Hz, 12H), 3.58−3.61 (m, 12H), 3.63−3.66 (m, 12H), 5.14 (br s, 3H), 6.59 (br s, 3H). HRMS (ES^+) calcd for $C_{55}H_{108}N_7O_{18}$ $(M+H)^+$: 1154.7751. Found: 1154.7754. HPLC: t_R = 11.6 min.

15-*N*-(Phthalimido)-(3,6,9,12-tetraoxa)pentadecanoic acid, 19. This compound was obtained from Quanta BioDesign (Powell, OH) and was used without further purification. ^{1}H NMR ($CDCl_3$, 500 MHz): δ 2.62 (t, J = 6.4 Hz, 2H), 3.57−3.63 (m, 10H), 3.65−3.67 (m, 2H), 3.74−3.77 (m, 4H), 3.91 (t, J = 5.8 Hz, 2H), 7.72 (dd, J = 3.2, 5.4 Hz, 2H), 7.85 (dd, J = 3.2, 5.4 Hz, 2H), 9.38 (br s, 1H).

1-(15-*N*-(Phthalimido)-(3,6,9,12-tetraoxa)pentadecanoylamino)methane-tris(*N*-(4,7,10-trioxa-13-amino)-*N*-(*tert*-butyloxycarbonyl)-3-propionylamine), 20. A 0.30 g (0.77 mmol) quantity of **19** was dissolved in 50 mL of anhydrous DMF. To that solution was added 0.89 g (0.77 mmol) of **18**, 0.32 g (1.54 mmol) of DCC and catalytic amount of HOBT. This solution was stirred at room temperature over a weekend. Et_3N was added to neutralize the residual TFA in the acid (from removal of tBu ester). When the acid and DCC were mixed, a white precipitate was noted immediately. To purify, the solvent was removed under vacuum and the residue loaded onto a silica gel column and eluted with a gradient of 100% EtOAc to 50% MeOH/EtOAc to yield 0.85 g (72%) of **20** as a pale yellow oil. ^{1}H NMR ($CDCl_3$, 500 MHz): δ 1.43 (s, 27H), 1.73−1.78 (m, 12H), 1.99 (t, J = 7.8 Hz, 6H), 2.19 (t, J = 7.8 Hz, 6H), 2.38 (t, J = 5.9 Hz, 2H), 2.43 (br s, 1H), 3.21 (q, J = 5.9 Hz, 6H), 3.29 (q, J = 6.0 Hz, 6H), 3.52−3.55 (m, 12H), 3.57−3.60 (m, 22H), 3.63−3.66 (m, 14H), 3.72 (t, J = 5.8 Hz, 2H), 3.73 (t, J = 5.8 Hz, 2H), 3.90 (t, J = 5.9 Hz, 2H), 5.13 (br s, 3H), 6.53 (br s, 3H), 7.73 (dd, J = 3.2, 5.4 Hz, 2H), 7.85 (dd, J = 3.2, 5.4 Hz, 2H). HRMS (ES^+) calcd for $C_{74}H_{130}N_8NaO_{25}$ $(M+Na)^+$: 1553.9045. Found: 1553.8990. HPLC: t_R = 14.2 min.

***N*-(15-Amino-(3,6,9,12-tetraoxa)pentadecanoylamino)methane-tris(*N*-(4,7,10-trioxa-13-amino)-*N*-(*tert*-butyloxycarbonyl)-3-propionylamine), 21.** Hydrazine (106 mg, 3.3 mmol) was added to a solution of **20** (245 mg, 0.16 mmol) in absolute EtOH (20 mL) and stirred at room temperature overnight. The solvent was removed under vacuum, and the residue was dissolved in MeOH. The solution was filtered to remove precipitates and then loaded onto a Sephadex LH-20 gel filtration column for purification. Combined fractions yielded 0.18 g (78%) of **21** as pale yellow oil. ^{1}H NMR ($CDCl_3$, 500 MHz): δ 1.43 (s, 27H), 1.73−1.79 (m, 12H), 1.99 (t, J = 7.6 Hz, 6H), 2.21 (t, J = 7.6 Hz, 6H), 2.45 (t, J = 5.9 Hz, 2H), 3.05 (br s, 2H), 3.22 (q, J = 6.0 Hz, 6H), 3.28 (q, J = 6.1 Hz, 6H), 3.53 (q, J = 6.3 Hz, 12H), 3.58−3.61 (m, 18H), 3.62−3.68 (m, 22H), 3.72 (t, J = 5.8 Hz, 2H), 5.12 (br s, 3H), 7.07 (br s, 3H), 7.51 (s, 1H). HRMS (ES^+) calcd for $C_{66}H_{129}N_8O_{23}$ $(M+H)^+$: 1401.9165. Found: 1401.9122. HPLC: t_R = 12.0 min.

2,3,4,6-Tetra-*O*-acetyl-galactopyranosyl-1-β-pseudothiourea Hydrobromide, 23. This compound was prepared by reaction of 2,3,4,6-tetra-*O*-acetyl-α-D-galactopyranosyl bromide, **22**, to form thiourea intermediate, **23**, in a procedure similar to that previously described (*29*). To a solution of 2.02 g (0.026 mol) of thiourea in 24 mL acetone was added 10 g (0.024 mol) of 2,3,4,6-tetra-*O*-acetyl-α-D-galactopyranosyl bromide, **22**. The mixture was refluxed for 20 min, then cooled on ice. The solid was collected and rinsed with 10 mL of ice-cold acetone. The collected solid was suspended in 20 mL ice-cold acetone, then refluxed for 15 min, cooled on ice, and filtered. The solid was rinsed with 10 mL of ice-cold acetone, air-dried, and then dried under vacuum to yield 4.15 g (69%) of **23** as a colorless solid. This compound was used in the next step without further purification.

2,3,4,6-Tetra-*O*-acetyl-galactopyranosyl-1-β-(3′-thiopropionic acid), 24. This compound was prepared from the pseudothiourea intermediate, **23**, as previously described (*30*). Briefly, a mixture of 0.9 g (1.85 mmol) **23**, 0.37 g (1.99 mmol) 3-iodopriopionic acid, 0.32 g (167 mmol) $Na_2S_2O_5$, and 0.30 g (2.15 mmol) potassium carbonate in 1.5 mL acetone/1.5 mL

H_2O was stirred at room temperature for 45 min. To the mixture was added 7 mL of HCl (5%) and 7 mL of $CHCl_3$. The $CHCl_3$ layer was separated, washed with H_2O, dried with $MgSO_4$, and evaporated to give 0.77 g (96%) of **24** as an oil. This compound was used in the next step without further purification.

2,3,4,6-Tetra-*O*-acetyl-galactopyranosyl-1-α-(3′-thiopropionate-*O*-2,3,5,6-tetrafluorophenyl ester), 25. To a solution of **24** (772 mg, 1.77 mmol) in anhydrous DMF (15 mL) at 0 °C, was added dropwise TFP-OTFA (0.448 mL, 2.6 mmol), followed by addition of Et_3N (0.362 mL, 2.6 mmol). The mixture was stirred in an ice bath for 1 h. Then, half of the solvent was removed under vacuum, and the remaining solution was extracted with EtOAc (3 × 100 mL). The EtOAc solution was dried with $MgSO_4$ and evaporated by rotary evaporator under vacuum to afford 1.038 g (100%) of **25** as a pale yellow oil. ^{1}H NMR ($CDCl_3$, 500 MHz): δ 2.00 (s, 3H), 2.05 (s, 3H), 2.08 (s, 3H), 2.17 (s, 3H), 2.98−3.04 (m, 1H), 3.09−3.12 (m, 2H), 3.13−3.19 (m, 1H), 3.99 (t, J = 6.5 Hz, 1H), 4.14−4.19 (m, 2H), 4.60 (d, J = 10.0 Hz, 1H), 5.08 (dd, J = 3.4, 10.0 Hz, 1H), 5.28 (t, J = 9.9 Hz, 1H), 5.46 (d, J = 3.5 Hz, 1H), 7.01−7.08 (m, 1H). HRMS (ES$^+$) $C_{23}H_{24}F_4NaO_{11}S$ (M+Na)$^+$ calcd: 607.0873. Found: 607.0865. HPLC: t_R = 16.3 min.

***N*-(15-(*N*,*N*′-Bis(*N*-(biotinyl)-*β*-*N*-(*tert*-butyloxycarbonyl)-*N*-(8-amino-3,6-dioxaoctanyl)aspartamidyl)-5-aminoisophthalamido)-(3,6,9,12-tetraoxa)pentadecanoylamino)methane-tris(*N*-(4,7,10-trioxa-13-amino)-*N*-(*tert*-butyloxycarbonyl)-3-propionylamine), 27.** A solution of **13** (135 mg, 0.109 mmol), 1,1′-carbonyldiimidazole (35.4 mg, 0.218 mmol) and anhydrous DMF (8 mL) was stirred at room temperature for 1 h. The solution was triturated with 10% EtOAc/hexanes (50 mL). The solution was decanted, and the residue, containing **26**, was washed with EtOAc (2 × 10 mL), then dried under vacuum for 2 h. A solution containing **21** (104 mg, 0.74 mmol), Et_3N (20.6 μL, 0.148 mmol), and anhydrous DMF (8 mL) was added to the flask containing **26**, and the resultant solution was stirred at room temperature overnight. The volatile materials were removed by rotary evaporation under vacuum, and the crude residue was purified by Sephadex LH-20 gel filtration column to yield 173 mg (88%) of **27**. ^{1}H NMR (CD_3OD, 500 MHz): δ 1.42 (s, 27H), 1.43 (s, 9H), 1.44 (s, 9H), 1.52−1.77 (m, 24H), 1.97 (t, J = 7.6 Hz, 6H), 2.15−2.27 (m, 10H), 2.41 (t, J = 6.0 Hz, 2H), 2.62−2.72 (m, 6H), 2.88−2.93 (m, 2H), 3.11 (t, J = 6.8 Hz, 6H), 3.14−3.19 (m, 2H), 3.24 (t, J = 6.9 Hz, 6H), 3.33−3.35 (m, 4H), 3.42 (t, J = 5.2 Hz, 2H), 3.48−3.52 (m, 12H), 3.53−3.72 (m, 60H), 4.30 (dd, J = 4.9, 7.9 Hz, 2H), 4.48 (dd, J = 4.9, 7.9 Hz, 2H), 4.61 (t, J = 6.3 Hz, 2H), 7.86 (s, 1H), 7.99 (s, 1H), 8.12 (s, 1H). HRMS (ES$^+$) $C_{123}H_{215}N_{19}Na_2O_{40}S_2$ (M+2Na)$^{2+}$ calcd: 1354.2300. Found: 1354.2239. HPLC: t_R = 13.7 min.

***N*-(15-(*N*,*N*′-Bis(*N*-(biotinyl)-*β*-*N*-(*tert*-butyloxycarbonyl)-*N*-(8-amino-3,6-dioxaoctanyl)aspartamidyl)-5-aminoisophthalamido)-(3,6,9,12-tetraoxa)pentadecanoylamino)methane-*tris*(*N*-(4,7,10-trioxa-13-amino)-3-propionylamine), 28.** A 139 mg (0.052 mmol) quantity of **27** was stirred in 2 mL of TFA for 45 min. The excess TFA was removed under a stream of air. The residue was washed with diethyl ether and was placed under high vacuum overnight. The crude residue was dissolved in H_2O and was purified over a Sephadex LH-20 gel filtration column to yield 92.8 mg (0.036 mmol; 69%) of **28**. This compound was used in the next step without further characterization.

***N*-(15-(*N*,*N*′-Bis(*N*-(biotinyl)-*β*-*N*-(*tert*-butyloxycarbonyl)-*N*-(8-amino-3,6-dioxaoctanyl)aspartamidyl)-5-aminoisophthalamido)-(3,6,9,12-tetraoxa)pentadecanoylamino)methane-*tris*(*N*-(4,7,10-trioxa-13-amino)-*N*-(2,3,4,6-tetra-*O*-acetyl-galactose-1-α-(3′-thiopropionylamine), 29.** A solution, containing **28** (42.3 mg, 0.019 mmol), Et_3N (21 mL, 0.15 mmol), and anhydrous DMF (2 mL), was added dropwise to a solution of **25** (54.9 mg, 0.094 mmol) in anhydrous DMF (2 mL). The resultant solution was stirred at room temperature overnight. Volatile materials were removed by rotary evaporator under vacuum, and then the crude product was dissolved in 50% MeOH/water and purified by flash chromatography (Biotage). After purification, a 60 mg (0.017 mmol; 91%) quantity of **29** was obtained as a colorless oil. ^{1}H NMR (CD_3OD, 500 MHz): δ 1.38−1.46 (m, 4H), 1.52−1.65 (m, 8H), 1.72−1.78 (m, 12H), 1.95 (s, 9H), 1.96−2.00 (m, 6H), 2.03 (s, 9H), 2.04 (s, 9H), 2.15 (s, 9H), 2.16−2.24 (m, 10H), 2.51−2.55 (m, 6H), 2.66−2.71 (m, 4H), 2.86−3.01 (m, 15H), 3.16−3.29 (m, 15H), 3.41 (t, J = 5.1 Hz, 2H), 3.50−3.54 (m, 12H), 3.57−3.72 (m, 63H), 4.13 (s, 6H), 4.28−4.31 (m, 2H), 4.44−4.50 (m, 4H), 4.76 (d, J = 9.6 Hz, 3H), 5.10−5.17 (m, 6H), 5.43 (d, J = 2.9 Hz, 3H), 7.38 (s, 1H), 7.86 (s, 1H), 7.87 (s, 1H). LRMS (ES$^+$) $C_{151}H_{242}KN_{19}NaO_{64}S_5$ (M+H+Na+K)$^+$ calc 3567.4. Found 3567.5. HPLC: t_R = 11.2 min.

***N*-(15-(*N*,*N*′-Bis(*N*-(biotinyl)-*β*-*N*-(*tert*-butyloxycarbonyl)-*N*-(8-amino-3,6-dioxaoctanyl)aspartamidyl)-5-aminoisophthalamido)-(3,6,9,12-tetraoxa)pentadecanoylamino)methane-tris(*N*-(4,7,10-trioxa-13-amino)-*N*-(galactose-1-α-(3′-thiopropionylamine), 2.** A 83 mg (0.024 mmol) quantity of **29** was added to a clear solution of Na metal (0.55 mg; 0.024 mmol) in anhydrous MeOH (1 mL). The resultant solution was stirred for 2 h at room temperature. The mixture was loaded onto an Amberlite IR120 ion-exchange resin (H^+ form) and eluted slowly. The fractions containing **2** were combined, and the solvent was removed under vacuum to yield 67.5 mg (0.022 mmol; 94%) as a pale yellow oil. ^{1}H NMR (CD_3OD, 500 MHz): δ 1.38−1.46 (m, 4H), 1.54−1.66 (m, 8H), 1.73−1.79 (m, 12H), 1.96−2.00 (m, 6H), 2.17−2.30 (m, 10H), 2.42 (t, J = 5.7 Hz, 2H), 2.55 (t, J = 6.9 Hz, 6H), 2.68−2.79 (m, 4H), 2.88−2.93 (m, 4H), 2.97−3.03 (m, 4H), 3.16−3.29 (m, 15H), 3.42 (t, J = 5.1 Hz, 2H), 3.46−3.56 (m, 25H), 3.57−3.72 (m, 63H), 3.77 (dd, J = 7.4 Hz, 11.4 Hz, 3H), 3.87 (d, J = 2.0 Hz, 3H), 4.28−4.31 (m, 2H), 4.34 (d, J = 7.3 Hz, 2H), 4.47−4.50 (m, 2H), 4.72−4.74 (m, 2H), 7.37 (s, 1H), 7.88 (s, 1H), 7.93 (s, 1H). HRMS (ES$^+$) $C_{127}H_{218}N_{19}O_{52}S_5$ (M+H)$^+$ calc: 3001.3602. Found: 3001.3223. HPLC: t_R = 8.4 min.

***N*,*N*′-Bis(*N*-(biotinyl)-*β*-*N*-(butyloxycarbonyl)-*N*-(8-amino-3,6-dioxaoctanyl)aspartamidyl-5-*N*-(DOTA-benzylamido)aminoisophthalamide, 32.** A solution of **13** (170 mg, 0.137 mmol), thiocarbonyldiimidazole (40.8 mg, 0.206 mmol), and anhydrous DMF (4 mL) was stirred at room temperature for 1 h. After the solution was washed with 10% EtOAc/hexanes (5 × 15 mL), the volatile materials were removed under vacuum on a rotoevaporator, and the isothiocyanate **30** was dried under vacuum for 2 h. The crude **30** was dissolved in anhydrous DMF (4 mL), and then aminobenzylDOTA, HCl salt, **31** (100 mg, 0.137 mmol), and pyridine (111 μL, 1.374 mmol) were added, respectively. The resultant solution was stirred at room temperature for 16 h. Volatile materials were evaporated under vacuum on a rotoevaporator. The residue was dissolved in DMF/MeOH/water (5 mL, 1/2/2) and purified by flash chromatography (Biotage). Fractions containing product were combined and solvent removed to yield 185 mg (75%) of **32** as a colorless solid. ^{1}H NMR (CD_3OD, 500 MHz): δ 1.37−1.42 (m, 4H), 1.44 (s, 18H), 1.51−1.75 (m, 8H), 2.26 (t, J = 7.2 Hz, 4H), 2.69 (t, J = 7.1 Hz, 4H), 2.74 (d, J = 12.9 Hz, 2H), 2.95 (dd, J = 4.4, 12.9 Hz, 2H), 3.00−3.19 (m, 6H), 3.22−3.26 (m, 3H), 3.31−3.42 (m, 11H), 3.58−3.76 (m, 26H), 3.85−3.98 (m, 5H), 4.36 (dd, J = 4.5, 7.5 Hz, 2H), 4.56 (dd, J = 4.5, 7.5 Hz, 2H), 4.59 (t, J = 6.5 Hz, 2H), 7.36 (d, J = 8.3 Hz, 2H), 7.42 (d, J = 8.3 Hz, 2H), 8.04 (s, 2H), 8.10 (s, 1H). HRMS (ES$^+$) calcd for $C_{80}H_{123}N_{16}O_{24}S_3$ (M+H)$^+$: 1787.8053. Found: 1787.8137. HPLC: t_R = 10.4 min.

***N,N′*-Bis(*N*-biotinyl-*N*-(8-amino-3,6-dioxaoctanyl)aspartamidyl-5-*N*-(DOTA-benzylamido)aminoisophthalamide, 4a.** A solution containing **32** (185 mg, 0.103 mmol) and trifluoroacetic acid (4 mL) was stirred at room temperature for 20 min. Excess trifluoroacetic acid was evaporated under a stream of argon, and then the residue was dissolved in 50% MeOH/water and purified by flash chromatography (Biotage). Fractions containing product were combined and solvent removed to yield 165 mg (95%) of **4a** as a colorless solid. mp 211−213 °C. ^{1}H NMR (CD_3OD, 500 MHz): δ 1.33−1.41 (m, 4H), 1.47−1.71 (m, 8H), 2.23 (t, J = 7.2 Hz, 4H), 2.66−2.78 (m, 6 H), 2.92 (dd, J = 4.9, 13.0 Hz, 2H), 2.97−3.17 (m, 6H), 3.19−3.23 (m, 3H), 3.33 (t, J = 5.3 Hz, 4H), 3.56 (t, J = 5.1 Hz, 4H), 3.62−3.74 (m, 28H), 3.90−4.21 (m, 6H), 4.33 (dd, J = 4.8, 7.5 Hz, 2H), 4.53 (dd, J = 4.9, 7.4 Hz, 2H), 4.69 (t, J = 6.4 Hz, 2H), 7.32−7.43 (m, 4H), 8.00 (s, 2H), 8.07 (s, 1H). LRMS (ES^+) calcd for $C_{72}H_{107}N_{16}O_{24}S_3$ $(M+H)^+$: 1675.6. Found: 1675.5. HPLC: t_R = 6.3 min.

Preparation of [^{111}In]indium-labeled 3a, [^{111}In]3b. The radiolabeling reactions were conducted with metal free reagents and labware. Methods for demetalation have been previously described (*31*). To a 7−17 μL aliquot of a 3 mg/mL (20−50 μg) solution of **3a** in H_2O was added 80−100 μL 500 mM NH_4OAc solution, pH 5.3 (demetalated), followed by 2−4 μL (0.63−1.22 mCi) of [^{111}In]indium chloride. This mixture was placed in a heat block at 85 °C for 30−60 min, then purified by radio-HPLC to give 72−95% isolated yield from a peak at 4.5 min. Following isolation from the HPLC, the eluant solvents were removed by evaporation under vacuum (90−100%), and the predetermined amount of PBS was added to make the animal injectate. Radiochemical purity was determined by an avidin bead assay. In that assay, the preparations had 95−99% of the [^{111}In]**3b** bound with avidin.

Preparation of [^{111}In]Indium-labeled 4a, [^{111}In]4b. This reaction was conducted in a manner similar to preparation of [^{111}In]**3b**. To a 27−33 μL aliquot of 3 mg/mL (80−100 μg) **4a** in H_2O was added 80−100 μL 500 mM NH_4OAc solution, pH 5.3 (demetalated) followed by 6−10 μL (1.42−2.81 mCi) of [^{111}In]indium chloride. This mixture was placed in a heat block at 85 °C for 30 min, then purified by HPLC to give 45−94% isolated yields from a peak at 7.5 min. Following isolation from the HPLC, the eluant solvents were removed by evaporation under vacuum (90−100%) and the predetermined amount of PBS was added to make the animal injectate. Analyses by avidin bead assay showed that 85−95% of the [^{111}In]**4b** bound with avidin.

Avidin Bead Assay. The avidin beads were prepared for use by the following procedure. A solution of avidin−agarose from the manufacturer (Sigma-Aldrich #A9207−5 mL or ImmunoPure Immobilized Avidin Gel, Pierce Biotechnology, Inc. Rockford, IL), was vortexed, and then a 300 μL aliquot of the suspended avidin−agarose beads was added to a microcentrifuge filter (Fisher #07−200−387; 0.45 mm cellulose acetate spin column with centrifuge tube filter). The filter was placed in a microcentrifuge and spun at 1000 *g* for 1 min. The filtrate was discarded.

The binding assay was conducted as follows. A 300 μL aliquot of PBS was added to filter (with avidin−agarose) and vortexed to thoroughly mix. The beads were spun at 1000 *g* for 1 min, and then the PBS filtrate was discarded. The PBS washing step was repeated, and then an aliquot (up to 2 μL) of ^{111}In-labeled biotin ([^{111}In]**3b** or [^{111}In]**4b**) was added to the suspended beads, and this suspension was vortexed to mix thoroughly. The ^{111}In-labeled biotin was incubated with the beads for 10 min at room temperature. The mixture was vortexed to mix, then placed in microcentrifuge and spun at 1000 *g* for 1 min. The filtrate was set aside, and 300 μL of PBS was added to the avidin−agarose beads as a wash. The filter was vortexed to mix, then was placed in a microcentrifuge and spun at 1000 *g* for 1 min. The filtrate was combined with the previous filtrate. The microcentrifuge filter containing avidin−agarose beads was placed in a tube, and then that tube and the tube containing the combined filtrates were counted in a gamma counter. The quantity of ^{111}In-labeled biotin derivative remaining in the filter (% bound) was calculated as [radioactivity in filter]/[radioactivity in filter] + [radioactivity in filtrates] × 100.

Lymphoma Cell Line. The human Ramos B lymphoma cell line (American Type Culture Collection, Bethesda, MD) was maintained in log-phase growth in RPMI-1640 medium supplemented with 10% heat-inactivated fetal calf serum in a 5% CO_2 incubator.

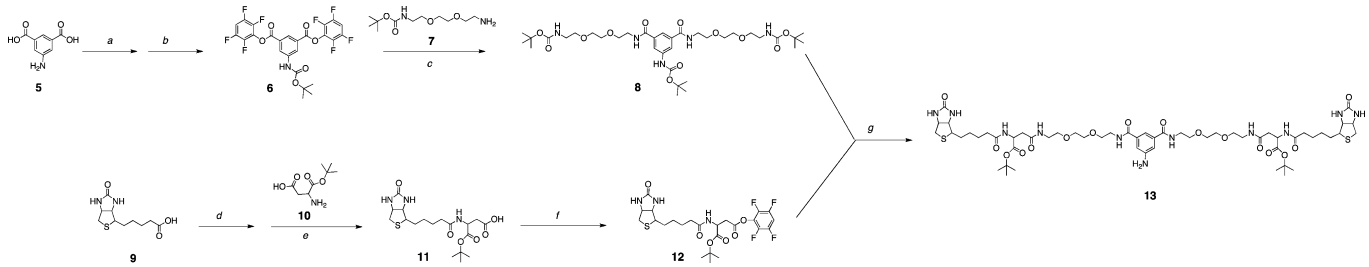
Synthesis and Purification of anti-CD20 1F5 scFv$_4$-SAv Fusion Proteins. The production and purification of 1F5 scFv$_4$-SAv-WT fusion protein and the related site-directed SAv mutant fusion proteins, 1F5 scFv$_4$-SAv-S45A and 1F5 scFv$_4$-SAv-Y43A, have been previously described (*17, 18*). Briefly, scFv-SAv fusion genes were produced by molecularly fusing the single-chain variable regions (scFv) of the murine anti-CD20 1F5 antibody to either the full-length SAv wild-type gene or SAv mutant genes. The resultant fusion proteins were expressed in the periplasmic space of *E. coli* and spontaneously formed stable soluble tetramers of 1F5 scFv$_4$-SAv with a molecular weight of 174 kDa. The 1F5-SAv fusion proteins were formulated at a concentration of 3 mg/mL in phosphate buffered saline (PBS) containing 5% sorbitol.

Preparation of 1F5 [^{125}I]scFv$_4$-SAv-S45A Fusion Protein. Fusion proteins were radioiodinated with Na[^{125}I]I (PerkinElmer, Waltham, MA) by the chloramine-T method in a manner similar to that previously published (*32*). Briefly, 50 μL of a 1 mg/mL solution of chloramine-T (Sigma-Aldrich, St. Louis, MO) was added to 500 μL fusion protein. Next, the Na[^{125}I]I was added and the solution vortexed. Following a 1 min incubation at room temperature, 5 μL of a 1 mg/mL solution of sodium metabisulfite was added, and the solution was vortexed. The contents were pipetted onto a prewashed PD10 column and eluted with PBS, collecting 600 μL fractions. The amount of radioactivity in each fraction was measured in a Capintec CRC-7 Radioisotope Calibrator, and early fractions with the highest activity were pooled to obtain the labeled fusion protein.

Blood Clearance of 1F5 [^{125}I]scFv$_4$-SAv Fusion Protein. Female FoxN1^{NU} athymic nude mice, aged 6−8 weeks, were obtained from Harlan Sprague−Dawley (Indianapolis, IN) and housed under protocols approved by the Fred Hutchinson Cancer Research Institute Institutional Animal Care and Use Committee. Mice were fed a standard diet (containing biotin) and separated into three groups of 4 mice each. Mice were injected intravenously with 500 μg (2.8 nmol) of 1F5 [^{125}I]scFv$_4$-SAv-S45A fusion protein. After 24 h, mice were injected intravenously with equimolar doses of **1** (5.8 nmol; 50 μg) or **2** (5.8 nmol; 17.4 μg). Blood samples were drawn at serial time points before and after injection of **1** or **2**, and the blood samples were counted in a gamma counter. The percent of injected dose per gram of blood (%ID/g) was calculated, and the mean values were plotted using *KaleidaGraph* software (Synergy Software, Reading, PA). A tabulation of the blood clearance data is provided as Table S1 in the Supporting Information.

Biodistributions of [^{111}In]3b and [^{111}In]4b in Tumor-Bearing Mice Pretargeted with 1F5 scFv$_4$-SAv Fusion Proteins. Female FoxN1^{NU} athymic nude mice were separated into four groups and were fed either a standard diet (group 1) or biotin-free diet (Harlan Teklad, Madison, WI) (groups 2−4). Ramos cells (10×10^6) were injected subcutaneously in the right flank of each mouse. Mice were monitored until palpable tumor nodules appeared (7−10 days) and mice with tumors of

Scheme 1. Synthetic Steps to Prepare the Bis-Biotin Derivative 13, Used for Syntheses of Bis-Biotin Clearing Agent, 2, and Bis-Biotin-DOTA Derivative, 4[a]



[a] (a) DMF, H_2O, NaOH, di-tBu-dicarbonate, 0 °C to rt, 30 h; (b) DMF, tetrafluorophenol, EDC, rt, 16 h; (c) Et_3N, CH_3CN, 7, rt, 30 min, 81%; (d) TFP-OTFA, Et_3N, rt, 10 min; (e) H_2O, acetone, $NaHCO_3$, **10**, rt, 6 h; (f) TFP-OTFA, DMF, Et_3N, 0 °C, 30 min; (g) TFA, rt, 10 min, evap, DMF, Et_3N, rt, 1 h, 74%.

similar sizes (5−10 mm^3) were selected for the experiment. Groups of 5 mice were injected intravenously with 500 μg (2.9 nmol) of 1F5 $scFv_4$-Sav-WT (groups 1 and 2) or one of the SAv mutant fusion proteins, 1F5 $scFv_4$-SAv-S45A (group 3) or 1F5 $scFv_4$-SAv-Y43A (group 4). After 20 h, the mice were injected with either 50 μg (5.8 nmol) of **1** (groups 1 and 2) or 17.5 μg (5.8 nmol) of **2** (groups 3 and 4). Four hours after administration of clearing agent, 20 μCi on 1.2 nmol (∼1 μg **3a** or ∼2 μg of **4a**) of the ^{111}In-labeled biotin derivatives, [^{111}In]**3b** (groups 1 and 2) or [^{111}In]**4b** (groups 3 and 4), were administered. Mice were euthanized, and tumors and normal organs were harvested 24 h after injection of radioactivity. Selected tissues and tumors were weighed and counted in a gamma counter. Counts were corrected for decay using standard aliquots of the injectate. The percent injected dose per gram (%ID/g) values for tissues and tumor xenografts were calculated. The mean values and standard deviations were plotted for each tissue. A tabulation of the pretargeting data is provided as Table S2 in the Supporting Information.

Biodistributions of [^{111}In]4b. Female FoxN1^{NU} athymic nude mice, aged 6−8 weeks, were obtained from Harlan Sprague−Dawley (Indianapolis, IN) and housed under protocols approved by the Fred Hutchinson Cancer Research Institute Institutional Animal Care and Use Committee. Mice were fed a standard diet (containing biotin) and separated into three groups of 5 mice each. Mice were injected intravenously with ∼30 μCi on 2 μg of [^{111}In]**4b**. Groups of mice were euthanized at 1, 4, and 24 h post injection of [^{111}In]**4b**, and preselected tissues were harvested and counted in a gamma counter. The percent of injected dose per gram (%ID/g) of blood or tissue was calculated. A tabulation of the biodistribution data is provided as Table S3 in the Supporting Information.

RESULTS

Synthesis of the Blood Clearance Agent, 2. The synthesis of **2** utilized a convergent approach, combining a bis-biotin component, a tetrafunctional poly(ethylene glycol) (PEG) component, and a galactosyl component. The syntheses of the individual components are shown in Schemes 1−3. The synthetic steps to prepare the bis-biotin derivative **13** are shown in Scheme 1. In the synthesis, aminoisophthalic acid, **5**, was modified with di-*tert*-butyl-dicarbonate, and then tetrafluorophenol and EDC were used to prepare N-Boc-aminoisophthalate ditetrafluorophenyl ester, **6**. Reaction of **6** with mono-Boc protected diamino-dioxaoctane, **7**, and triethylamine in anhydrous DMF provided the tri-N-Boc protected aminoisophthalic acid derivative, **8**. After removal of the N-Boc groups on **8** with neat TFA, the resulting alkyl amines were reacted with the tetrafluorophenyl ester of the biotin-aspartate adduct **12**, which was prepared from biotin, **9**, as previously described (*28*). That reaction provided the anilino-bis-biotin derivative **13** in 74% yield. It should be noted that the synthesis was conducted in this manner so that the aspartate carboxylates remained as *tert*-butyl esters in bis-biotin derivative **13**, since that is required to prepare the isocyanate functionality in a later step of the synthesis.

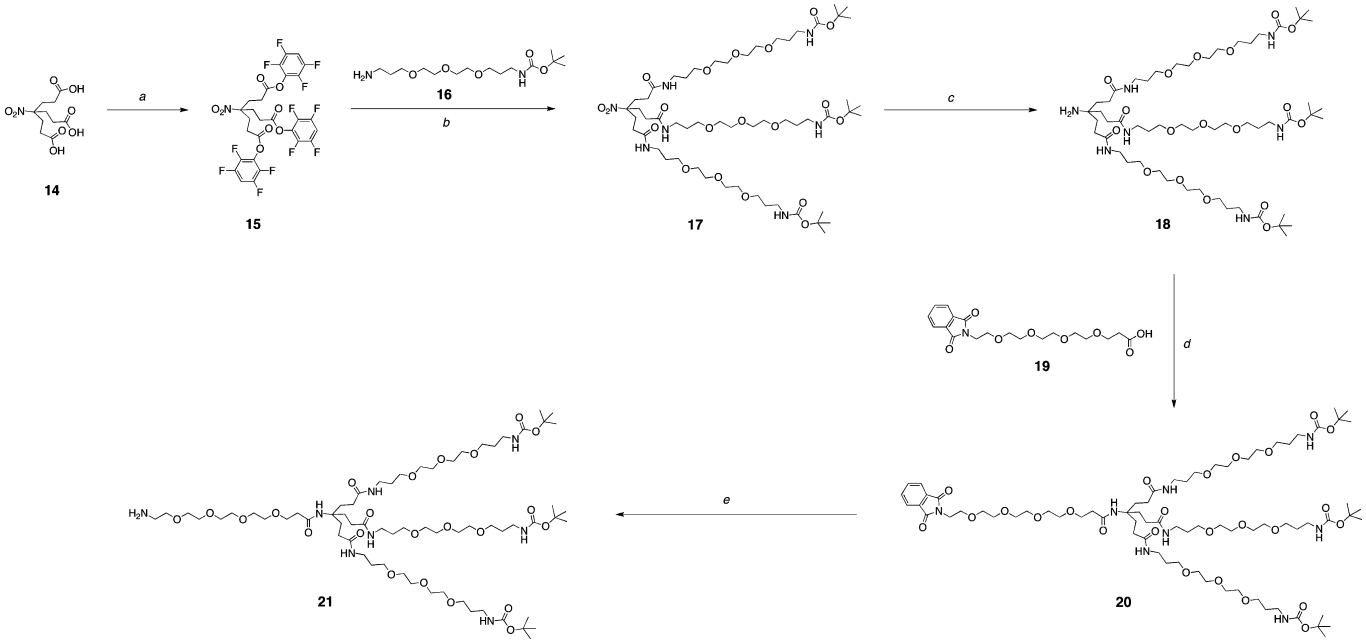
A key part of the design of the blood-clearing agent **2** was the inclusion of three galactosyl groups at the termini of poly(ethylene glycol) (PEG) spacer arms. A PEG-containing tetrafunctional molecule, **21**, was utilized as a core for the branched galactosyl portion of **2**. The synthesis to prepare **21** is shown in Scheme 2. In the synthesis, nitromethane-tris-propionic acid, **14**, was converted to the tris-tetrafluorophenyl ester **15** in 96% yield by reaction with tetrafluorophenyl-*O*-trifluoroacetate (TFP-OTFA) and triethylamine in DMF. Reaction of **15** with an excess of N-Boc-trioxatridecanediamine, **16**, provided the adduct **17** in 92% yield. Reduction of the nitro group in **17** by hydrogenation over Raney-Nickel gave nearly a quantitative yield of the amino derivative **18**. Reaction of the hindered amine in **18** with the phthalimido-protected amino-dPEG$_4$-acid, **19**, and DCC/HOBT in DMF at room temperature for 72 h provided a 72% yield of adduct **20**. Removal of the phthalimide protecting group using hydrazine in ethanol for 16 h provided a 78% yield of the tetra-functional intermediate, **21**.

The tetra-O-acetyl-galactose derivative **25** used in the synthesis of **2** was prepared as shown in Scheme 3. Nucleophilic displacement of the bromine in acetylbromo-α-D-galactose, **22**, by reaction of thiourea in refluxing acetone produced the β-pseudothiourea derivative **23** in 69% yield. Reaction of **23** with 3-iodopropionic acid in a basic acetone/water mixture gave a 96% yield of the galactose−thiopropionic acid derivative, **24**. Preparation of the tetrafluorophenyl ester derivative, **25**, was achieved in nearly quantitative yield by reaction of **24** with TFP-OTFA.

The final sequence of reactions, which combined the three components to produce **2**, is shown in Scheme 4. The reaction sequence began with conversion of the bis-biotin derivative **13** to the phenylisocyanate, **26**, by reaction with carbonyldiimidazole (CDI). Reaction of **26** with **21** provided the adduct **27** in 88% yield. Deprotection of the N-Boc and *tert*-butyl esters in **27** was accomplished in one step by reaction in neat trifluoroacetic acid to provide a 69% yield of intermediate **28**. Reaction of **28** with the tetra-O-acetyl-galactose derivative **25** provided **29** in 91% yield. In the final step, the acetyl protecting groups were removed from **29** using an acid form of an ion exchange column to provide a 94% yield of the targeted blood clearance agent **2**.

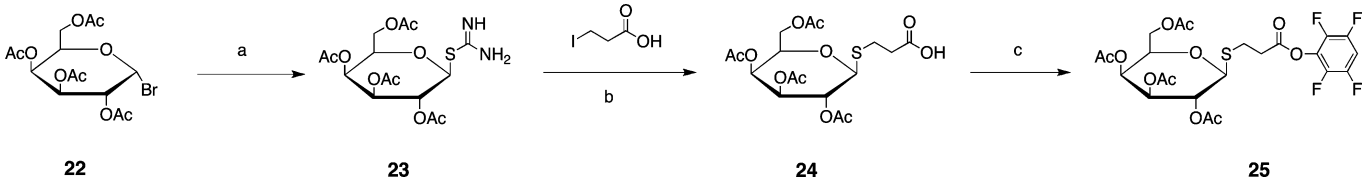
Syntheses of the Bis-Biotin-DOTA Derivative, 4a. Partial synthesis of the radiometal-binding bis-biotin derivative **4a** is shown in Scheme 5. The initial steps of the synthesis involved preparation of bis-biotin derivative **13**, as described previously (and shown in Scheme 1). Conversion of the aniline in **13** to

Scheme 2. Synthetic Steps to Prepare the Branched Polyethylene Glycol (PEG) Core, 21, Used in Synthesis of Bis-Biotin Clearing Agent, 2[a]



[a] (a) TFP-OTFA, DMF, Et_3N, 0 °C, 30 min, 96%; (b) **16**, THF, −78 °C − rt, 92%; (c) RaNi, H_2, EtOH, H_2O, 16 h, 99%; (d) **19**, DMF, DCC, HOBT, rt, 72 h, 72%; (e) NH_2NH_2, EtOH, rt, 16 h, 78%.

Scheme 3. Synthetic Steps to Prepare the Galactosyl Derivative, 25, Used in Synthesis of Bis-Biotin Clearing Agent, 2[a]



[a] (a) Thiourea, acetone, Δ, 20 min, 69%; (b) iodopropionic acid, K_2CO_3, acetone, H_2O, rt, 45 min, HCl, 96%; (c) TFP-OTFA, Et_3N, DMF, 0 °C, 1 h, 100%.

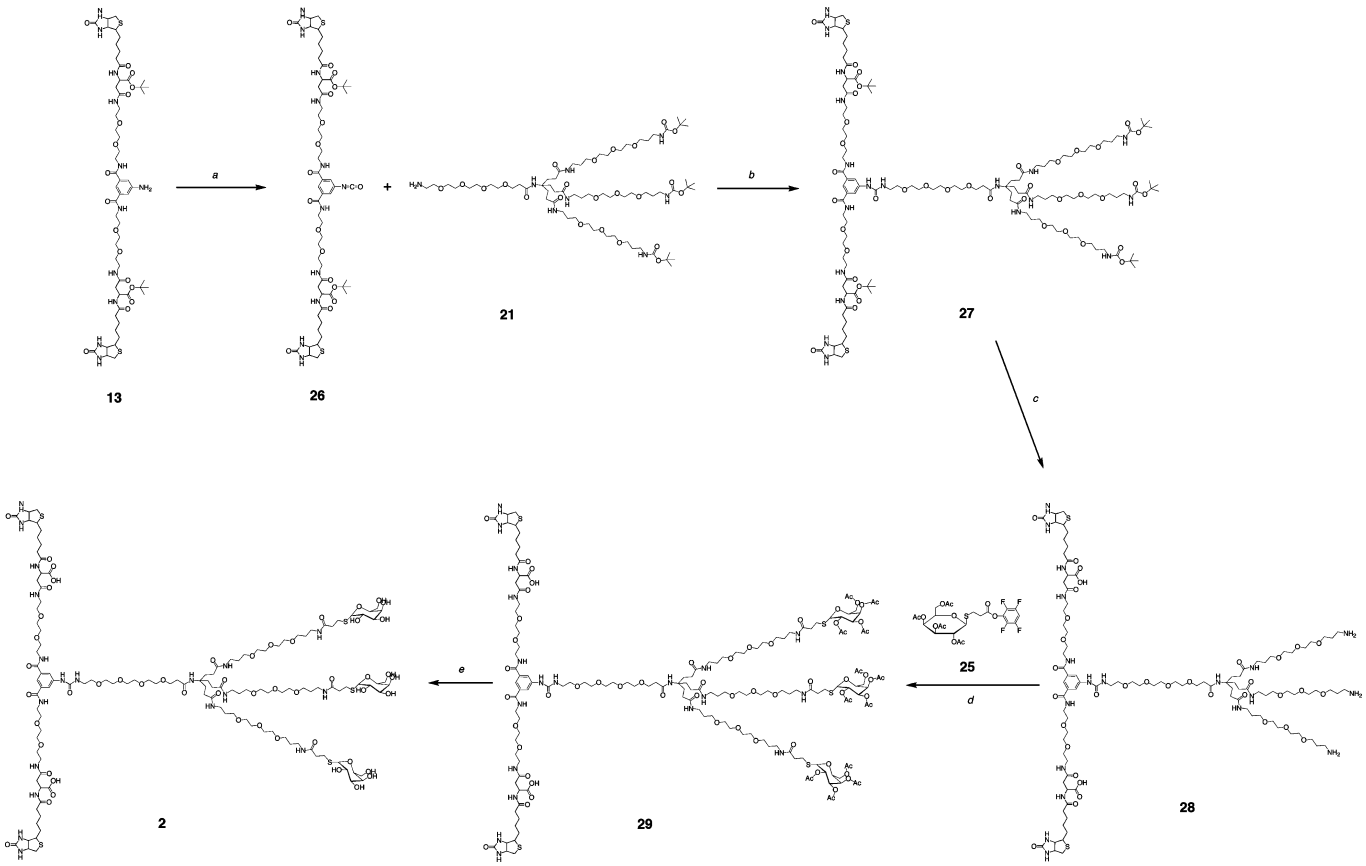
the phenylisothiocyanate functionality in **30** was accomplished by reaction with thiocarbonyldiimidazole (TCDI). The isothiocyanate derivative, **30**, was prepared and used in this coupling reaction, rather than the phenylisocyanate, **26**, due to the low reactivity of the aniline. Reaction of **30** with aminobenzylDOTA, **31**, using pyridine as the base, provided the adduct **32** in 75% yield. Removal of the *tert*-butyl esters in **32** was accomplished in neat TFA to provide the bis-DOTA-biotin compound **4a** in 95% yield.

Radiolabeling. The 1F5 $scFv_4$-SAv-S45A mutant fusion protein was radioiodinated in a standard protocol using chloramine-T as the oxidant. Several ^{111}In-labeling reactions of the biotin derivative **3a** conducted for these studies provided isolated radiochemical yields (72−95%) of [^{111}In]**3b**, with radiochemical purities of 95−99% being obtained as measured in an avidin binding assay. It should be noted that the labeling yields reported are for the isolated product, and in some examples, not all of the [^{111}In]**3b** was isolated from the HPLC eluant making the radiolabeling yields appear lower. In labeling optimization studies, radiolabeling yields of 97+% were obtained for [^{111}In]**3b** under a variety of reaction conditions studied.

Radiolabeling reactions of **4a** with ^{111}In were more variable, providing ranges of isolated radiochemical yields from 45% to 94% under the reaction conditions used. The radiolabeled product was purified by radio-HPLC. Analysis of the radiochemical purity of [^{111}In]**4b**, as determined by the avidin bead assay, was 85−95% for the preparations (some were HPLC purified). In subsequent labeling optimization studies, it was found that consistently high ^{111}In-labeling yields (90+%) could be obtained for the reaction of **4a** by conducting the reactions in 0.5 M ammonium acetate buffer at pH 5.3 and lowering the reaction temperature to 45 °C (from 85 °C).

Comparison of Blood Clearance with 1 and 2. An experiment was conducted to determine the effectiveness of **1** and **2** for decreasing 1F5 $scFv_4$-SAv-S45A mutant fusion protein concentration in blood. In the experiment, the blood concentrations were assessed in three groups of four athymic FoxN1^{Nu} mice after administration of 1F5 [^{125}I]$scFv_4$-SAv-S45A. Serial blood samples were obtained and counted to assess the blood concentrations. A logarithmic plot of the blood concentrations of 1F5 [^{125}I]$scFv_4$SA-S45A in the three groups of mice, as a function of time, is provided in Figure 2 (data are provided as Table S1 in Supporting Information). One group of mice did not receive a blood clearance agent (group 1, red line). Mice in the second and third groups received a single dose of either **1** or **2** given intravenously 24 h after 1F5 [^{125}I]$scFv_4$-SAv-S45A administration. Administration of the bis-biotin-trigalactose reagent, **2**, removed 70% of 1F5 [^{125}I]$scFv_4$-SAv-S45A from the bloodstream within 2 h of injection (group 3, green line). However, only a 29% reduction in blood concentrations of 1F5 [^{125}I]$scFv_4$-SAv-S45A was observed at the same time point when **1** was used (group 2, blue line). Similar blood clearance data were obtained in mice administered the fusion protein, 1F5 [^{125}I]$scFv_4$-SAv-Y43A (data not shown).

Scheme 4. Synthetic Steps Combining Bis-Biotin Derivative, 13, with PEG Core, 21, and Galactosyl Derivative, 25, in the Preparation of Bis-Biotin Clearing Agent, 2[a]



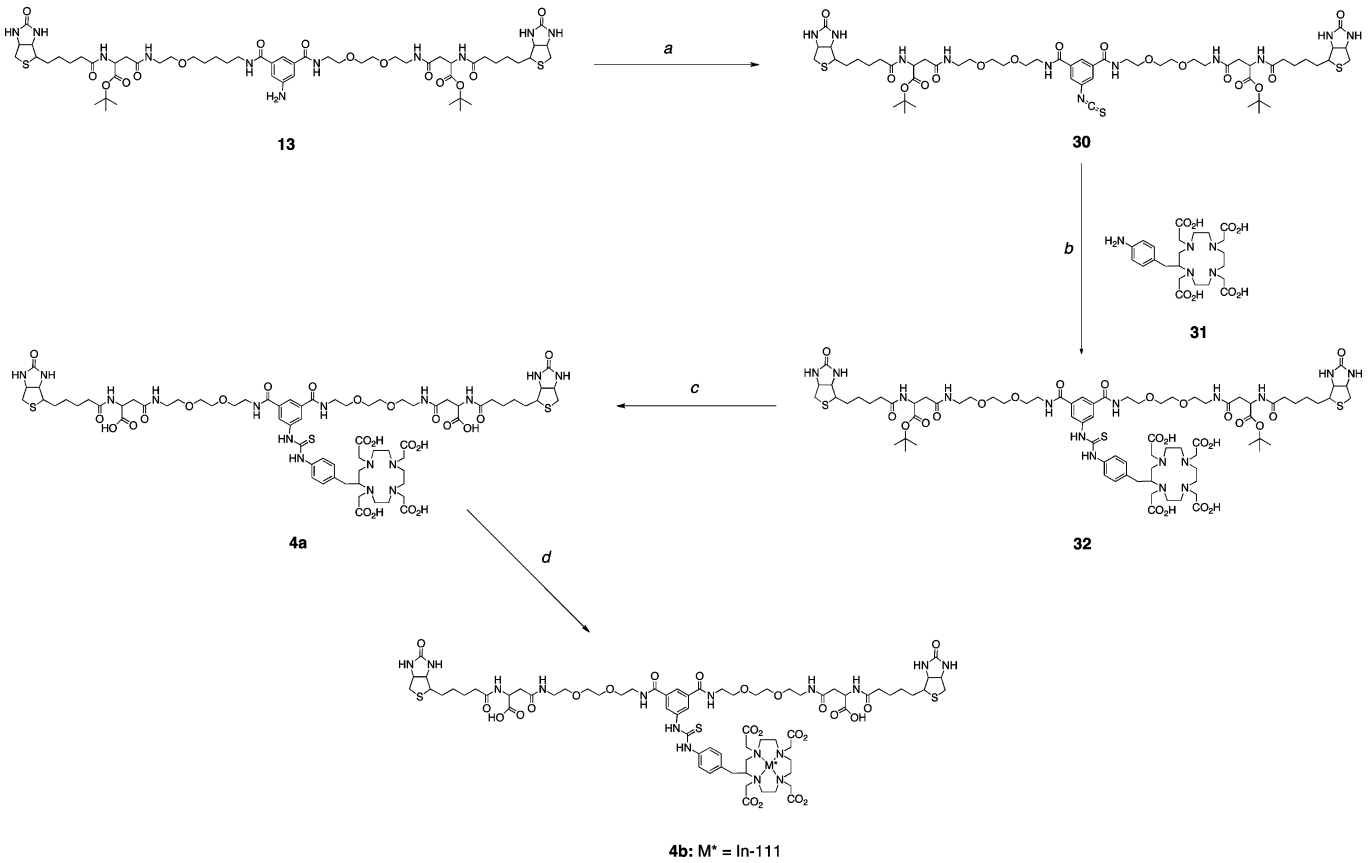
[a] (a) CDI, DMF, rt, 1 h; (b) Et3N, DMF, rt, 16−20 h, 88% [from **13**]; (c) TFA, 45 min, 69%; (d) Et3N, DMF, rt, 16−20 h, 91%; (e) MeOH, Amberlite IR-120 [H^+ form], 94%.

Biodistributions of [^{111}In]3b or [^{111}In]4b in Tumor-Bearing Mice Pretargeted with 1F5 scFv$_4$-SAv Fusion Proteins. A pretargeting experiment was conducted to determine if the new clearing agent **2** was effective in decreasing normal tissue concentrations of [^{111}In]**4b** and to determine if [^{111}In]**4b** could be used in a pretargeting protocol to effectively target tumor xenografts in the presence of endogenous biotin. The biodistribution study did not include groups of mice on biotin-deficient diets when scFv$_4$-SAv mutant fusion proteins were administered, as no difference in tumor concentration was seen previously in pretargeting experiments using the same fusion proteins in mice placed on biotin-deficient diets or standard diets (*22*).

In the pretargeting experiment, four groups of female FoxN1^{NU} athymic nude mice (5 mice/group) bearing Ramos lymphoma xenografts were administered the fusion proteins (FP), blood clearance agents (CA), and radiolabeled biotin derivatives (RB) as depicted in Scheme 6. Group 1 was fed a biotin-deficient diet and groups 2 through 4 were fed standard diets. Twenty hours after anti-CD20 fusion protein administration, the mice received a blood clearing agent, either **1** or **2**, followed 4 h later by either [^{111}In]**3b** or [^{111}In]**4b**. Mice were sacrificed 24 h after administration of [^{111}In]**3b** or [^{111}In]**4b**, and selected tissues were harvested. The tissues were counted in a gamma counter, and the concentration of ^{111}In in each tissue was calculated as %ID/g. A bar graph showing the concentrations in tumor xenografts and selected tissues is provided as Figure 3 (data is provided as Table S2 in Supporting Information). An additional biodistribution study was conducted in athymic mice injecting [^{111}In]**4b** alone. In that biodistribution, the only tissue that had more than 1% ID/g was kidney (1.57 ± 0.10, 1.54 ± 0.11, and 1.03 ± 0.20 at 1, 4, and 24 h pi, respectively), and most tissue concentrations were less than 0.2%ID/g (Table S3 in Supporting Information).

Figure 3 shows the dramatic effect that endogenous biotin can have on tumor concentrations of radiolabeled biotin in pretargeting protocols. The tumor and tissue concentrations after administration of wild-type SAv fusion protein (1F5 scFv$_4$-SAv-WT), the blood clearance agent **1**, and ^{111}In-labeled DOTA-biotin, [^{111}In]**3b**, are represented as groups 1 (red bars) and 2 (blue bars). Significant tumor concentrations (8.6 ± 1.2% ID/g) of [^{111}In]**3b** were obtained when the mice were fed biotin-free diets (group 1), whereas when mice were on normal diets (group 2), the concentrations of [^{111}In]**3b** in tumor (0.25 ± 0.1%ID/g) were very low, indicating that little or no tumor targeting was attained. Furthermore, the substitution of **2** for **1**, or [^{111}In]**4b** for [^{111}In]**3b**, did not significantly change the concentration of radioactivity in tumor xenografts when pretargeted with 1F5 scFv$_4$SA-WT (data not shown). In contrast, pretargeting using the SAv mutant fusion proteins, scFv$_4$-SAv-S45A or scFv$_4$-Y43A, in mice fed a standard diet exhibited high concentrations of radioactivity (8.52 ± 4.4% ID/g and 6.71 ± 1.3% ID/g, respectively) in tumor xenografts. These results demonstrate that the blocking of radiolabeled biotin by endogenous biotin observed with the 1F5-SAv-WT can be overcome by using the lower-affinity SAv mutants. The tissue concentrations of [^{111}In]**3b** and [^{111}In]**4b** were of a similar magnitude for the three fusion proteins, except in the blood and liver. The blood concentrations in the groups administered SAv mutant fusion proteins, scFv$_4$-SAv-S45A and scFv$_4$-SAv-Y43A, were much higher (0.18 ± 0.06%ID/g and 0.58 ± 0.13%ID/g) than in the groups administered scFv4-SAv-WT (0.008 ± 0.002%ID/g and 0.004 ± 0.001%ID/g), indicating that CA **2** was less efficient at clearing the SAv mutant fusion proteins than CA **1**

Scheme 5. Synthetic Steps to Prepare Bis-Biotin-DOTA Derivative, 4a, and Radiolabeling to Obtain [^{111}In]4b[a]



[a] (a) TCDI, DMF, rt, 1 h; (b) **31**, pyridine, rt, 16 h, 75%; (c) TFA, rt, 20 min, 95%; (d) [^{111}In]$InCl_3$, NH_4OAc, H_2O, pH 5.3, 85 °C, 30 min, 45−94%.

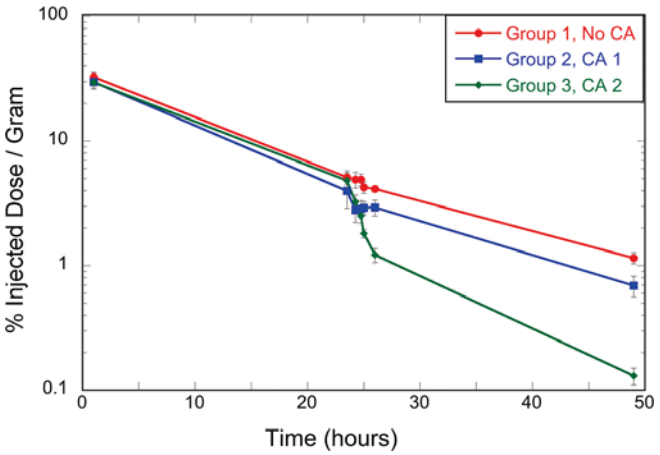
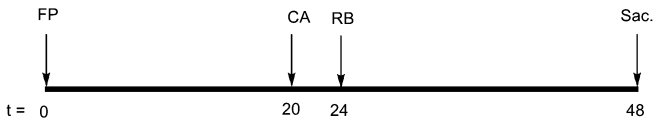


Figure 2. Blood clearance of 1F5 [^{125}I]scFv$_4$-SAv-S45A fusion protein after administration of **1** or **2**. Graph (log scale) of 1F5 [^{125}I]scFv$_4$-SAv-S45A fusion protein concentration (%ID/g) when no blood clearance agent was used (group 1; red line), or after administration of one of the biotinyl-galactosyl-blood clearance agents, **1** (group 2, blue line) or **2** (group 3, green line). In the experiment, three groups of athymic FoxN1^{Nu} mice (n = 4 per group) were injected intravenously at t = 0 with 2.8 nmol of 1F5 [^{125}I]scFv$_4$-SAv-S45A fusion protein, followed 24 h later with an intravenous injection of 5.8 nmol of either **1** or **2**. Serial blood samples were obtained from the tail vein, and ^{125}I was counted in a gamma counter. The %ID/g was calculated based on separately counted injection standards. Average %ID/g values are plotted with error bars representing ± standard deviation. The plotted data are provided as Table S1 in the Supporting Information.

was with the SAv WT fusion protein. Similarly, liver concentrations in the groups administered SAv mutant fusion proteins, scFv$_4$-SAv-S45A and scFv$_4$-SAv-Y43A, were somewhat higher

Scheme 6. Schematic Depicting the Time Course of Reagent Injections (Panel A) and the Reagents Used in Each Study Group (Panel B) in the Pretargeting Experiment[a]

A: Timeline (in hours) for administration of reagents to mice and their sacrifice



B: Diet and reagents used in study groups

Group #	Mouse Diet	Fusion Protein	CA	^{111}In-biotin
1	Biotin Deficient	scFv$_4$-SAv-WT	**1**	[^{111}In]**3b**
2	Normal	scFv$_4$-SAv-WT	**1**	[^{111}In]**3b**
3	Normal	scFv$_4$-SAv-S45A	**2**	[^{111}In]**4b**
4	Normal	scFv$_4$-SAv-Y43A	**2**	[^{111}In]**4b**

[a] In the experiment, the reagents outlined in the table (panel B) were administered to 4 groups of mice (n = 5/group) following the timeline shown (panel A). The fusion protein (FP) was initially injected (t = 0 h), followed 20 h later by a clearing agent (CA, **1** or **2**). Four hours later, the radiolabeled biotin (RB) derivative, [^{111}In]**3b** or [^{111}In]**4b**, was administered. Mice were sacrificed at 48 h post the fusion protein. Tumor xenografts and selected tissues were harvested and counted to determine concentrations (%ID/g) of ^{111}In-labeled biotin derivative in the tissues.

(1.77 ± 0.4% ID/g and 3.99 ± 0.8% ID/g, respectively) than were obtained in groups administered the scFv$_4$-SAv-WT fusion protein (0.43 ± 0.1% ID/g and 0.36 ± 0.18%ID/g).

DISCUSSION

The ultimate goal of our studies is to develop a pretargeting protocol based on the streptavidin/biotin binding pair that

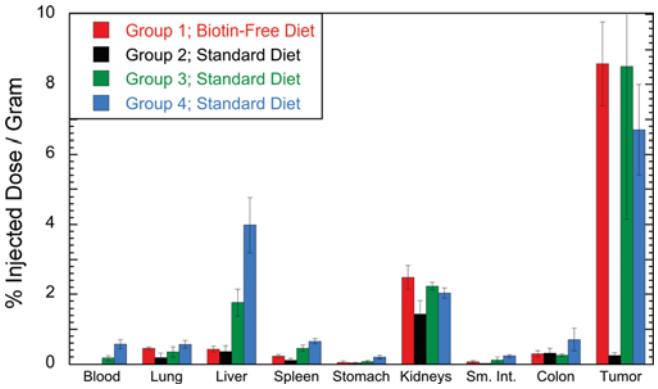


Figure 3. Biodistribution of ^{111}In-labeled biotin derivatives in tumor-bearing mice pretargeted with anti-CD20 scFv$_4$-SAv fusion proteins. Bar graph depicting tissue concentrations (%ID/g) of ^{111}In-labeled biotin derivatives [^{111}In]**3b** or [^{111}In]**4b** in mice bearing Ramos lymphoma xenografts after administration of the following pretargeting reagents and diets. Group 1 (red bars): 1F5 scFv$_4$-SAv-WT, CA **1**, [^{111}In]**3b**, biotin-deficient diet. Group 2 (black bars): 1F5 scFv$_4$-SAv-WT, CA **1**, [^{111}In]**3b**, standard diet. Group 3 (green bars): 1F5 scFv$_4$-SAv-S45A, CA 2, [^{111}In]**4b**, standard diet. Group 4 (blue bars): 1F5 scFv$_4$-SAv-Y43A, CA 2, [^{111}In]**4b**, standard diet. In the pretargeting protocol, a 2.8 nmol quantity of the fusion protein was injected; then after 24 h, 5.8 nmol of either blood clearance agent, **1** or **2**, was injected, followed 4 h later by injection of 1.2 nmol of the ^{111}In-labeled biotin derivative, [^{111}In]**3b** or [^{111}In]**4b**. Mice were euthanized 24 h after ^{111}In-labeled biotin injection; and blood, tumor, and selected normal tissues were harvested, weighed, and counted to determine %ID/g. Average %ID/g values are shown ± standard deviation. The plotted data are provided as Table S2 in the Supporting Information.

provides good tumor targeting of therapeutic radionuclides in the presence of endogenous biotin, while having minimal localization of the radionuclides in normal tissues. Although endogenous biotin has not precluded the use of antibody−streptavidin conjugates or fusion proteins in clinical studies (*33*), it has the potential to significantly diminish the blood clearance and tumor targeting of the radiolabeled biotin derivatives in patients. In the pretargeting approach being investigated, a recombinant tetrameric fusion protein, combining the scFv portion of the anti-CD20 antibody 1F5 with streptavidin mutants that have decreased binding for biotin, is used in combination with a bis-biotin derivative that is radiolabeled with a diagnostic or therapeutic radionuclide. Due to its bivalency, bis-biotin derivatives have higher binding avidities than biotin, allowing their preferential binding with SAv mutants in the presence of endogenous biotin. The SAv mutants used in this investigation have a serine or tyrosine in the biotin-binding pocket replaced with an alanine residue (S45A and Y43A, respectively (*17*)). In initial proof-of-principle studies, the SAv-Y43A mutant was found to have a 67-fold lower affinity for biotin compared to the wild-type (WT) SAv, and the off-rate for the bis-biotin was found to be 640 times slower than that of biotin when binding SAv-Y43A (*21*). This combination of reagents was previously found to target radionuclides to lymphoma xenografts in the presence of endogenous biotin, but normal tissues had significant concentrations of the radionuclides (*22*). Thus, the primary goal of this investigation was to design and synthesize a galactose-containing bis-biotin reagent that would bind in vivo with a scFv$_4$-SAv fusion protein, such that more efficient blood clearance of the fusion proteins could be attained. In addition to preparation of an effective clearing agent, a bis-biotin derivative that could be radiolabeled with ^{111}In and ^{90}Y was prepared such that those radiometals could be used in the pretargeting protocols with mutant SAv fusion proteins.

The majority of our pretargeting investigations have used the biotin-hexadecyl-galactosamine reagent, **1** (also referred to as N-acetylgalactosamine-biotin or NAGB; note: the N-acetylgalactosamine-biotin reagent, **1**, was designed and synthesized at NeoRx Corporation, Seattle, WA, and was provided as a gift), to affect clearance of the wild-type SAv conjugates of, or fusion proteins with, antibodies. The asialoglycoprotein receptors, also referred to as Ashwell receptors, are hepatic plasma membrane receptors responsible for regulating the concentrations of circulating glycoproteins (*34, 35*). This regulation is controlled by removal of sialic acid termini on glycoproteins to expose terminal galactose residues, allowing binding with the asialoglycoprotein receptor. It has been shown that asialogycoproteins are bound to liver membranes by a saturable, calcium-dependent process. Bis-biotin blood-clearance reagent **2** was designed to bind with SAv in antibody conjugates or fusion proteins in the blood, then bind with the asialoglycoprotein receptors in the liver to clear them from blood. The structure of **2** was designed based on information provided in several literature reports. Studies by Lee et al. reported that conjugation of different monosacharides to proteins resulted in varying binding affinities with isolated rabbit liver membranes (*36*). In those studies, it was demonstrated that proteins conjugated with thio-D-galactose moieties were effective at inhibiting binding of a standard, [^{125}I]iodo-asialoorosomucoid ([^{125}I]ASOR). Indeed, depending on the number of thio-D-galactosyl moieties conjugated, measured relative inhibitory power (RIP) values were as high as 10 000× the [^{125}I]ASOR. The studies also demonstrated that a nine-atom linker between the sugar and protein provided a higher RIP then when there was a two- or five-atom linker. Those early studies set a basis for the use of galactosyl conjugates for removal of proteins from blood using the asialoglycoprotein receptors and began to define some of the structural requirements of the conjugates for efficient binding.

The difficulty in synthesizing a bis-biotin counterpart to the large clearing agent **1** led us to consider whether the 16 galactosyl moieties were required for effective blood clearance. There are literature reports suggesting that as few as 3 galactosyl moieties may be effective. In early studies, Lee recognized that a number of biological systems require clustering of glycosides for biological activity, and that such clustering was often obtained from branched structures, so he prepared a number of triglucose and trigalactose derivatives for study (*37*). Evaluation of mono-, bis-, and tris-galactosyl derivatized bovine serum albumin binding with rabbit liver membrane demonstrated that the tris-galactosyl conjugates were better at inhibiting binding of [^{125}I]ASOR than the bis-galactose conjugate, which was better than the monogalactose conjugate (*38*). In another study, Lee et al. demonstrated that the number of branched galactose moieties provided dramatic differences in inhibitory potency, with tetra > tris→bis→mono (*39*). The 50% inhibitory value was ∼1 mM for the monogalactose conjugate, whereas it was ∼1 nM for the trigalactose conjugate. This large difference in binding inhibition based on the number of galactose residue in branched chains was also noted by Bezouska et al. (*40*). It was noted by Baenziger and Maynard that the galactose residues may bind two sites simultaneously and speculated that the sites might be 25−30 Å apart (*41*). In a later study, Lee et al. synthesized "cluster ligands" with 1, 2, 3, 4, or 6 terminal galactose moieties (*42*). They found that the highest binding was obtained with the highest number of galactose moieties (i.e., 6 moieties), but that the binding affinity increased only a modest amount for the compounds containing 4 or 6 galactose moieties relative to the high binding of the compound that had 3 galactose moieties in a "flexible" structure. On the basis of their results, it was hypothesized that there are three galactose binding sites in the asialoglycoprotein receptor and the binding occurs in a triangle configuration with distances between binding sites of 15, 22, and 25 Å. Some years later, Biessen et al. added

hydrophilic poly(ethylene glycol) spacers of varying lengths (4, 9, 10, 13, and 20 Å) between galactose moieties and the branch point in trigalactose derivatives (or 38 Å between anomeric oxygen atoms on galactose residues) and evaluated their competitive binding vs [^{125}I]ASOR to isolated parenchymal liver cells (*43*). They found that the binding affinity of the trigalactose cluster compounds was strongly correlated with the length of the spacer between the galactosyl residues and the branching point of the galactoside, with a factor of 2000× higher affinity with the 20 Å spacer vs the 4 Å spacer.

The information from the literature provided the basis for the structure of galactose-containing portion of **2**. Our previous studies demonstrating successful in vivo targeting of tumor xenografts with a radioiodinated bis-biotin derivative led us to retain the main structural features of that portion of the compound. Those structural features included (1) appropriate functional groups to provide a distance between biotin carboxyate carbonyl functionalities of ∼40 Å, (2) carboxylate groups on the carbon alpha to the biotinamide functionalities, and (3) diamino-dioxaoctane spacer arms to increase aqueous solubility of compound. The distance between biotin moieties was chosen as the distance that was adequate to readily bind the two biotin-binding pockets on one face of the streptavidin mutants (*19*). The addition of the carboxylates alpha to the biotinamide provided protection from in vivo cleavage of the biotinamide bonds by the enzyme biotinidase (*28*). The structural properties that were previously shown to bind asialoglycoprotein receptors in liver were combined with the bis-biotin structural properties desired for binding with streptavidin mutants to design blood clearance agent **2**.

An investigation of pretargeting using bis-biotin derivatives **2** and [^{111}In]**4b** was conducted in mice. The quantities of bis-biotin clearing agent **2** (5.8 nmol) and radiolabeled bis-biotin [^{111}In]**4b** (1.2 nmol) used in this investigation were the same as in the previous studies employing fusion proteins constructed with wild-type (WT) SAv, the NAGB clearing agent, **1**, and radiolabeled DOTA-biotin, [^{111}In]**3b**. The quantity of those reagents and the times for their administration were optimized in a series of experiments (*18, 44*). Those optimization studies were not repeated in this investigation; instead, a limited series of experiments varying the doses of mutant SAv fusion protein and **2** within a more narrow range were conducted. Those studies verified that the quantities previously optimized also worked optimally with the new reagents.

A blood clearance study demonstrated that the fusion protein 1F5 [^{125}I]scFv4-S45A could be more efficiently cleared from blood in mice after administration of **2** than when **1** was administered. This is shown in Figure 2. Importantly, use of **2** in a pretargeting study, where both 1F5 scFv4-SAv-S45A and 1F5 scFv4-SAv-Y43A fusion proteins (in separate groups) were evaluated with bis-biotin [^{111}In]**4b**, resulted in normal tissue concentrations that were much lower than obtained in our previous pretargeting studies employing those fusion proteins with CA **1** and a radioiodinated bis-biotin derivative. The tissue concentration data obtained in the pretargeting study are shown as a bar graph in Figure 3. The most striking differences between [^{111}In]**4b** and [^{111}In]**3b** concentrations in tissues were found in the blood and liver. The higher blood concentrations are most likely brought about by less efficient blood clearance using **2**; however, it is unclear why the liver concentrations of [^{111}In]**4b** are somewhat higher. There may be several possible contributing factors to the observed differences in liver concentrations. For example, a contributing factor may be the difference in the nature of the galactose derivative in the clearing agents, **1** and **2**. In **1**, the galactose derivative is an *N*-acetyl-galactosamine moiety, whereas in **2**, it is a galactose moiety. Although most literature relating to developing ligands for binding to asialoglycoprotein receptor is directed at galactose derivatives, it has been reported that the avidity of agents with terminal N-acetylgalactosamine moieties is greater than those terminated with galactose moieties (*41*). Indeed, studies have shown that tris-*N*-acetyl-D-galactosamine derivatives can have subnanomolar binding with the asialoglycoprotein receptor (*45*). Another possible contributing factor is higher denticity (i.e., more galactosamine residues), which could increase the rate of cell internalization (*20*). Yet another possible contributing factor is the binding avidity of the bis-biotin with the mutant fusion protein. It seems likely that the difference in the binding of **1** with the mutant proteins contributes to the higher liver concentrations, as the liver concentration of [^{111}In]**4b** at the time of sacrifice was about 2× higher when the fusion protein 1F5 scFv$_4$-SAv-Y43A was used than when 1F5 scFv$_4$-SAv-S45A was used. It is not possible to determine the reason for the differences in liver concentrations with the data obtained, particularly with the complexity of the internalization process (*46*) and receptor/ligand recycling that has been observed (*47, 48*). Further studies need to be conducted to understand which parameters affect the observed higher liver concentrations.

In conclusion, the pretargeting approach using a combination of SAv mutant fusion proteins, bis-biotin-trigalactose blood clearance agent **2**, and ^{111}In-labeled DOTA-bis-biotin, [^{111}In]**4b**, was found to target lymphoma tumor xenografts in high concentrations, resulting in far superior biodistributions compared with the 1F5 scFv$_4$-SAv-WT conjugate system in the presence of endogenous biotin. While the new blood clearance agent, **2**, has been shown to greatly decrease the radioactivity concentrations in most normal tissues relative to CA **1**, the fact that higher blood and liver concentrations were obtained indicates that the structure of **2** is not optimal. Optimization of the structure of **2** might include use of N-acetylgalactosamine residues in the place of galactose residues and incorporation of a higher number of galactosamine residues (i.e., 4−6). While CA **2** is not optimized, we believe the results obtained are adequate to support investigation of **2** and **4a** in pretargeting therapy studies using scFv$_4$-SAv mutant fusion proteins in tumor-bearing mice fed standard diets.

ACKNOWLEDGMENT

We thank Quanta BioDesign (Powell, Ohio) for providing D-biotin, **9**, N-Boc-trioxatridecanediamine, **16**, and N-(phthalimido)amino-dPEG$_4$-acid, **19**, used in the studies. We thank Dr. Patrick Stayton (Bioengineering, University of Washington, Seattle, WA) for assistance in the preparation and purification of the fusion proteins containing mutant streptavidins S45A and Y43A. We thank NIH (P01 CA44991, R01 CA76287, R01 109663, R01 136639, R01 CA113431, and K08 CA095448) and Lymphoma Research Foundation (Postdoctoral Fellowship Grant # 82360) for funding the studies.

Supporting Information Available: Tables S1 and S2 provide the data plotted to prepare Figures 2 and 3, and Table S3 provides biodistribution data for [^{111}In]**4b**. This material is available free of charge via the Internet at http://pubs.acs.org.

LITERATURE CITED

(1) Press, O. W. (2008) Evidence mounts for the efficacy of radioimmunotherapy for B-cell lymphomas. *J. Clin. Oncol. 26*, 5147–50.

(2) Press, O. W. (2003) Radioimmunotherapy for non-Hodgkin's lymphomas: a historical perspective. *Semin. Oncol. 30*, 10–21.

(3) Sharkey, R. M., Press, O. W., and Goldenberg, D. M. (2009) A re-examination of radioimmunotherapy in the treatment of non-Hodgkin lymphoma: prospects for dual-targeted antibody/radioantibody therapy. *Blood 113*, 3891–5.

(4) Buchegger, F., Press, O. W., Delaloye, A. B., and Ketterer, N. (2008) Radiolabeled and native antibodies and the prospect of cure of follicular lymphoma. *Oncologist 13*, 657–67.
(5) Green, D. J., Pagel, J. M., Pantelias, A., Hedin, N., Lin, Y., Wilbur, D. S., Gopal, A., Hamlin, D. K., and Press, O. W. (2007) Pretargeted radioimmunotherapy for B-cell lymphomas. *Clin. Cancer Res. 13*, 5598s–5603s.
(6) Sharkey, R. M., Karacay, H., Cardillo, T. M., Chang, C. H., McBride, W. J., Rossi, E. A., Horak, I. D., and Goldenberg, D. M. (2005) Improving the delivery of radionuclides for imaging and therapy of cancer using pretargeting methods. *Clin. Cancer Res. 11*, 7109s–7121s.
(7) Goodwin, D. A., and Meares, C. F. (1997) Pretargeting: General Principles. *Cancer (Suppl.) 80*, 2675–2680.
(8) Axworthy, D. B., Fritzberg, A. R., Hylarides, M. D., Mallett, R. W., Theodore, L. J., Gustavson, L. M., Su, F.-M., Beaumier, P. L., and Reno, J. M. (1994) Preclinical evaluation of an anti-tumor monoclonal antibody/streptavidin conjugate for pretargeted ^{90}Y radioimmunotherapy in a mouse xenograft model. *J. Immunother. 16*, 158.
(9) Axworthy, D. B., Reno, J. M., Hylarides, M. D., Mallett, R. W., Theodore, L. J., Gustavson, L. M., Su, F., Hobson, L. J., Beaumier, P. L., and Fritzberg, A. R. (2000) Cure of human carcinoma xenografts by a single dose of pretargeted yttrium-90 with negligible toxicity. *Proc. Natl. Acad. Sci. U.S.A. 97*, 1802–7.
(10) Theodore, L. J., Fritzberg, A. R., Schultz, J. E., and Axworthy, D. B. (2000) Evolution of a pretarget radioimmunotherapeutic regimen, in *Radioimmunotherapy of Cancer* (Abrams, P. G., and Fritzberg, A. R., Eds.) pp 195−221, Marcel Dekker, New York.
(11) Press, O. W., Corcoran, M., Subbiah, K., Hamlin, D. K., Wilbur, D. S., Johnson, T., Theodore, L., Yau, E., Mallett, R., Meyer, D. L., and Axworthy, D. (2001) A comparative evaluation of conventional and pretargeted radioimmunotherapy of CD20-expressing lymphoma xenografts. *Blood 98*, 2535–2543.
(12) Pagel, J. M., Pantelias, A., Hedin, N., Wilbur, S., Saganic, L., Lin, Y., Axworthy, D., Hamlin, D. K., Wilbur, D. S., Gopal, A. K., and Press, O. W. (2007) Evaluation of CD20, CD22, and HLA-DR targeting for radioimmunotherapy of B-cell lymphomas. *Cancer Res. 67*, 5921–8.
(13) Pagel, J. M., Hedin, N., Subbiah, K., Meyer, D., Mallet, R., Axworthy, D., Theodore, L. J., Wilbur, D. S., Matthews, D. C., and Press, O. W. (2003) Comparison of anti-CD20 and anti-CD45 antibodies for conventional and pretargeted radioimmunotherapy of B-cell lymphomas. *Blood 101*, 2340–8.
(14) Pagel, J. M., Orgun, N., Hamlin, D. K., Wilbur, D. S., Gooley, T. A., Gopal, A. K., Park, S. I., Green, D. J., Lin, Y., and Press, O. W. (2009) A comparative analysis of conventional and pretargeted radioimmunotherapy of B-cell lymphomas by targeting CD20, CD22, and HLA-DR singly and in combinations. *Blood 113*, 4903–13.
(15) Baker, H. (1985) Assessment of biotin status: clinical implications. *Ann. N.Y. Acad. Sci. 447*, 129–132.
(16) Rusckowski, M., Fogarasi, M., Virzi, F., and Hnatowich, D. J. (1995) Influence of endogenous biotin on the biodistribution of labelled biotin derivatives in mice. *Nucl. Med. Commun. 16*, 38–46.
(17) Klumb, L. A., Chu, V., and Stayton, P. S. (1998) Energetic roles of hydrogen bonds at the ureido oxygen binding pocket in the streptavidin-biotin complex. *Biochemistry 37*, 7657–7663.
(18) Lin, Y., Pagel, J. M., Axworthy, D., Pantelias, A., Hedin, N., and Press, O. W. (2006) A genetically engineered anti-CD45 single-chain antibody-streptavidin fusion protein for pretargeted radioimmunotherapy of hematologic malignancies. *Cancer Res. 66*, 3884–92.
(19) Wilbur, D. S., Pathare, P. M., Hamlin, D. K., and Weerawarna, S. A. (1997) Biotin reagents for antibody pretargeting. 2. synthesis and in vitro evaluation of biotin dimers and trimers for crosslinking of streptavidin. *Bioconjugate Chem. 8*, 819–832.
(20) Mammen, M., Chio, S.-K., and Whitesides, G. M. (1998) Polyvalent interactions in biological systems: implications for design and use of multivalent ligands and inhibitors. *Angew. Chem., Int. Ed. 37*, 2755–2794.
(21) Hamblett, K. J., Kegley, B. B., Hamlin, D. K., Chyan, M. K., Hyre, D. E., Press, O. W., Wilbur, D. S., and Stayton, P. S. (2002) A streptavidin-biotin binding system that minimizes blocking by endogenous biotin. *Bioconjugate Chem. 13*, 588–98.
(22) Hamblett, K. J., Press, O. W., Meyer, D. L., Hamlin, D. K., Axworthy, D., Wilbur, D. S., and Stayton, P. S. (2005) Role of biotin-binding affinity in streptavidin-based pretargeted radioimmunotherapy of lymphoma. *Bioconjugate Chem. 16*, 131–8.
(23) Yau, E. K., Theodore, L. J., and Gustavson, L. M. (1996) Pretargeting Methods and Compounds, U. S. Patent 5,541,287.
(24) Gamper, H. B., Reed, M. W., Cox, T., Virosco, J. S., Adams, A. D., Gall, A. A., Scholler, J. K., and Meyer, R. B., Jr. (1993) Facile preparation of nuclease resistant 3′ modified oligodeoxynucleotides. *Nucleic Acids Res. 21*, 145–50.
(25) Wilbur, D. S., Hamlin, D. K., Vessella, R. L., Stray, J. E., Buhler, K. R., Stayton, P. S., Klumb, L. A., Pathare, P. M., and Weerawarna, S. A. (1996) Antibody fragments in tumor pretargeting. Evaluation of biotinylated Fab' colocalization with recombinant streptavidin and avidin. *Bioconjugate Chem. 7*, 689–702.
(26) Sigal, G. B., Mammen, M., Dahmann, G., and Whitesides, G. M. (1996) Polyacrylamides bearing pendant asialoside groups strongly inhibit agglutination of erythrocytes by influenza virus: the strong inhibition reflects enhanced binding through cooperative polyvalent interactions. *J. Am. Chem. Soc. 118*, 3789–3800.
(27) Braun, M., Camps, X., Vostrowsky, O., Hirsch, A., Endress, E., Bayerl, T. M., Birkert, O., and Gauglitz, G. (2000) Synthesis of a biotinylated lipofullerene as a new type of transmembrane anchor. *Eur. J. Org. Chem.* 1173–1182.
(28) Wilbur, D. S., Hamlin, D. K., Chyan, M. K., Kegley, B. B., and Pathare, P. M. (2001) Biotin reagents for antibody pretargeting. 5. Additional studies of biotin conjugate design to provide biotinidase stability. *Bioconjugate Chem. 12*, 616–23.
(29) Theodore, L. J., and Axworthy, D. B. (2001) Cluster clearing agents, U.S. Patent 6,172,045.
(30) Ponpipom, M. M., Bugianesi, R. L., Robbins, J. C., Doebber, T. W., and Shen, T. Y. (1981) Cell-specific ligands for selective drug delivery to tissues and organs. *J. Med. Chem. 24*, 1388–95.
(31) Sandmaier, B. M., Bethge, W. A., Wilbur, D. S., Hamlin, D. K., Santos, E. B., Brechbiel, M. W., Fisher, D. R., and Storb, R. (2002) Bismuth 213-labeled anti-CD45 radioimmunoconjugate to condition dogs for nonmyeloablative allogeneic marrow grafts. *Blood 100*, 318–26.
(32) Press, O. W., Eary, J. F., Badger, C. C., Martin, P. J., Appelbaum, F. R., Levy, R., Miller, R., Brown, S., Nelp, W. B., Krohn, K. A., Fisher, D., DeSantes, K., Porter, B., Kidd, P., Thomas, E. D., and Berstein, I. D. (1989) Treatment of refractory non-Hodgkin's lymphoma with radiolabeled MB-1 (Anti-CD37) antibody. *J. Clin. Oncol. 7*, 1027–2038.
(33) Knox, S. J., Goris, M. L., Tempero, M., Weiden, P. L., Gentner, L., Breitz, H., Adams, G. P., Axworthy, D., Gaffigan, S., Bryan, K., Fisher, D. R., Colcher, D., Horak, I. D., and Weiner, L. M. (2000) Phase II trial of yttrium-90-DOTA-biotin pretargeted by NR-LU-10 antibody/streptavidin in patients with metastatic colon cancer. *Clin. Cancer Res. 6*, 406–414.
(34) Ashwell, G., and Morell, A. G. (1974) The role of surface carbohydrates in the hepatic recognition and transport of circulating glycoproteins. *Adv. Enzymol. 41*, 99–128.
(35) Ashwell, G., and Harford, J. (1982) Carbohydrate-specific receptors of the liver. *Annu. Rev. Biochem. 51*, 531–54.
(36) Lee, R. T., and Lee, Y. C. (1980) Preparation and some biochemical properties of neoglycoproteins produced by reductive amination of thioglycosides containing an omega-aldehydoaglycon. *Biochemistry 19*, 156–63.
(37) Lee, Y. C. (1978) Synthesis of some cluster glycosides suitable for attachment to proteins or solid matrices. *Carbohydr. Res. 67*, 509–514.
(38) Kawaguchi, K., Kuhlenschmidt, M., Roseman, S., and Lee, Y. C. (1980) Synthesis of some cluster galactosides and their

effect on the hepatic galactose-binding system. *Arch. Biochem. Biophys. 205*, 388–95.
(39) Lee, Y. C., Townsend, R. R., Hardy, M. R., Lonngren, J., Arnarp, J., Haraldsson, M., and Lonn, H. (1983) Binding of synthetic oligosaccharides to the hepatic Gal/GalNAc lectin. Dependence on fine structural features. *J. Biol. Chem. 258*, 199–202.
(40) Bezouska, K., Táborsky, O., Kubrycht, J., Pospisil, M., and Kocourek, J. (1985) Carbohydrate-structure dependent recognition of desialylated serum glycoproteins in the liver and leucocyes. *Biochem. J. 227*, 345–354.
(41) Baenziger, J. U., and Maynard, Y. (1980) Human hepatic lectin. Physiochemical properties and specificity. *J. Biol. Chem. 255*, 4607–13.
(42) Lee, R. T., Lin, P., and Lee, Y. C. (1984) New synthetic cluster ligands for galactose/N-acetylgalactosamine-specific lectin of mammalian liver. *Biochemistry 23*, 4255–61.
(43) Biessen, E. A. L., Beuting, D. M., Roelen, H. C. P. F., van de Marel, G. A., Van Boom, J. H., and Van Berkel, T. J. C. (1995) Synthesis of cluster galactosides with high affinity for the hepatic asialoglycoprotein receptor. *J. Med. Chem. 38*, 1538–46.
(44) Pagel, J. M., Lin, Y., Hedin, N., Pantelias, A., Axworthy, D., Stone, D., Hamlin, D. K., Wilbur, D. S., and Press, O. W. (2006) Comparison of a tetravalent single-chain antibody-streptavidin fusion protein and an antibody-streptavidin chemical conjugate for pretargeted anti-CD20 radioimmunotherapy of B-cell lymphomas. *Blood 108*, 328–36.
(45) Lee, R. T., and Lee, Y. C. (1987) Preparation of cluster glycosides of N-acetylgalactosamine that have subnanomolar binding constants towards the mammalian hepatic Gal/GalNAc-specific receptor. *Glycoconjugate J. 4*, 317–328.
(46) Wall, D. A., Wilson, G., and Hubbard, A. L. (1980) The galactose-specific recognition system of mammalian liver: the route of ligand internalization in rat hepatocytes. *Cell (Cambridge, Mass.) 21*, 79–93.
(47) Oka, J. A., and Weigel, P. H. (1983) Recycling of the asialoglycoprotein receptor in isolated rat hepatocytes. Dissociation of internalized ligand from receptor occurs in two kinetically and thermally distinguishable compartments. *J. Biol. Chem. 258*, 10253–62.
(48) Townsend, R. R., Wall, D. A., Hubbard, A. L., and Lee, Y. C. (1984) Rapid release of galactose-terminated ligands after endocytosis by hepatic parenchymal cells: evidence for a role of carbohydrate structure in the release of internalized ligand from receptor. *Proc. Natl. Acad. Sci. U. S. A. 81*, 466–70.

BC100030Q

Targeted DNA Methylation by a DNA Methyltransferase Coupled to a Triple Helix Forming Oligonucleotide To Down-Regulate the Epithelial Cell Adhesion Molecule

Bernardina T. F. van der Gun,[†] Maria Maluszynska-Hoffman,[‡] Antal Kiss,[§] Alice J. Arendzen,[†] Marcel H. J. Ruiters,[||] Pamela M. J. McLaughlin,[†] Elmar Weinhold,[‡] and Marianne G. Rots*[,†]

Epigenetic Editing, Department of Pathology and Medical Biology, University Medical Center Groningen, University of Groningen, Hanzeplein 1, 9713 GZ Groningen, The Netherlands, Institute of Organic Chemistry, RWTH Aachen University, Landoltweg 1, D-52056 Aachen, Germany, Institute of Biochemistry, Biological Research Center of the Hungarian Academy of Sciences, Temesvári krt. 62, 6726 Szeged, Hungary, and Synvolux Therapeutics Inc., L. J. Zielstraweg 1, 9713 GX Groningen, The Netherlands. Received January 19, 2010; Revised Manuscript Received May 20, 2010

The epithelial cell adhesion molecule (EpCAM) is a membrane glycoprotein that has been identified as a marker of cancer-initiating cells. EpCAM is highly expressed on most carcinomas, and transient silencing of EpCAM expression leads to reduced oncogenic potential. To silence the EpCAM gene in a persistent manner via targeted DNA methylation, a low activity mutant (C141S) of the CpG-specific DNA methyltransferase M.SssI was coupled to a triple-helix-forming oligonucleotide (TFO−C141S) specifically designed for the EpCAM gene. Reporter plasmids encoding the green fluorescent protein under control of different EpCAM promoter fragments were treated with the TFO−C141S conjugate to determine the specificity of targeted DNA methylation in the context of a functional EpCAM promoter. Treatment of the plasmids with TFO−C141S resulted in efficient and specific methylation of the targeted CpG located directly downstream of the triple helix forming site (TFS). No background DNA methylation was observed neither in a 700 bp region of the EpCAM promoter nor in a 400 bp region of the reporter gene downstream of the TFS. Methylation of the target CpG did not have a detectable effect on promoter activity. This study shows that the combination of a specific TFO and a reduced activity methyltransferase variant can be used to target DNA methylation to predetermined sites with high specificity, allowing determination of crucial CpGs for promoter activity.

INTRODUCTION

The epithelial cell adhesion molecule (EpCAM) is a membrane glycoprotein that is highly expressed on most carcinomas. Recently, EpCAM has gained renewed interest as a signal transducer in carcinogenesis (*1*) and has been identified as a marker of cancer-initiating cells in breast (*2*), pancreatic (*3*), hepatocellular (*4*) and colon cancer (*5*). In the clinical setting, EpCAM has become a target for carcinoma directed immunotherapy (*6*). Transient silencing of EpCAM expression utilizing antisense or siRNA led to reduced proliferation, migration, and invasiveness (*7*−*10*), illustrating the therapeutic potential of EpCAM inhibition. However, as mRNA molecules are constantly produced, RNA-based approaches require repeated administration of the inactivating reagent. This study aims to develop a tool to silence the EpCAM gene in a more persistent manner via targeted DNA methylation.

It has been shown that the EpCAM promoter is differentially methylated in lung adenocarcinoma (*11*), oral squamous cell carcinoma (*12*), and colon cancer (*13*) and that EpCAM expression is associated with the methylation status of the promoter (*11, 13, 14*). For several cell lines, we and others have demonstrated that treatment with DNA methyltransferase inhibitors like 5-aza-2-deoxycytidine up-regulates the expression of EpCAM (*11, 14, 15*). Moreover, after delivery of the CpG-specific prokaryotic DNA (cytosine-5) methyltransferase M.SssI into EpCAM positive ovarian carcinoma cells, methylation of the EpCAM gene resulted in sustained repression of EpCAM expression (*14*). However, if DNA methylation can be targeted with high specificity to predetermined sites in the genome, DNA methylation-mediated gene silencing can be fully exploited as a research tool and further developed as a therapeutic approach. Application of targeted DNA methylation to silence EpCAM expression would have many advantages over transient silencing by siRNA. First, the maintenance DNA methyltransferases in the cell will copy the new methylation mark in the absence of the exogenous methyltransferase, so a single hit is expected to be sufficient to silence the EpCAM gene in a permanent way. Second, targeted DNA methylation needs to affect just two copies of the EpCAM gene rather than the numerous copies of mRNA present in each cell.

Targeted DNA methylation, pioneered by Xu and Bestor (*16*), traditionally employed DNA methyltransferases genetically fused to sequence specific DNA binding proteins, zinc finger proteins, which acted as targeting domains (*16*−*19*). As an alternative to zinc finger proteins, triple-helix-forming oligonucleotides (TFO) can be used as targeting domains. TFOs binding by sequence-specific Hoogsteen hydrogen bonds in the major groove of double-stranded DNA have been used to target cleaving (*20*), cross-linking reagents (*21*) or anticancer agents (*22*) to unique target sequences. The advantages of TFOs relative to zinc finger proteins are the easy synthesis and low cost. The drawbacks are the requirements for an in vitro coupling step to covalently link the effector protein to the TFO and the limitation of binding to oligopurine−oligopyrimidine sequences. However, the latter limitation is mitigated by the over-representation of

* To whom correspondence should be addressed. E-mail: M.G.Rots@med.umcg.nl. Phone: +31-50-361 0153. Fax: +31-50-361 9911.
[†] University of Groningen.
[‡] RWTH Aachen University.
[§] Biological Research Center of the Hungarian Academy of Sciences.
[||] Synvolux Therapeutics Inc.

10.1021/bc1000388 © 2010 American Chemical Society
Published on Web 07/02/2010

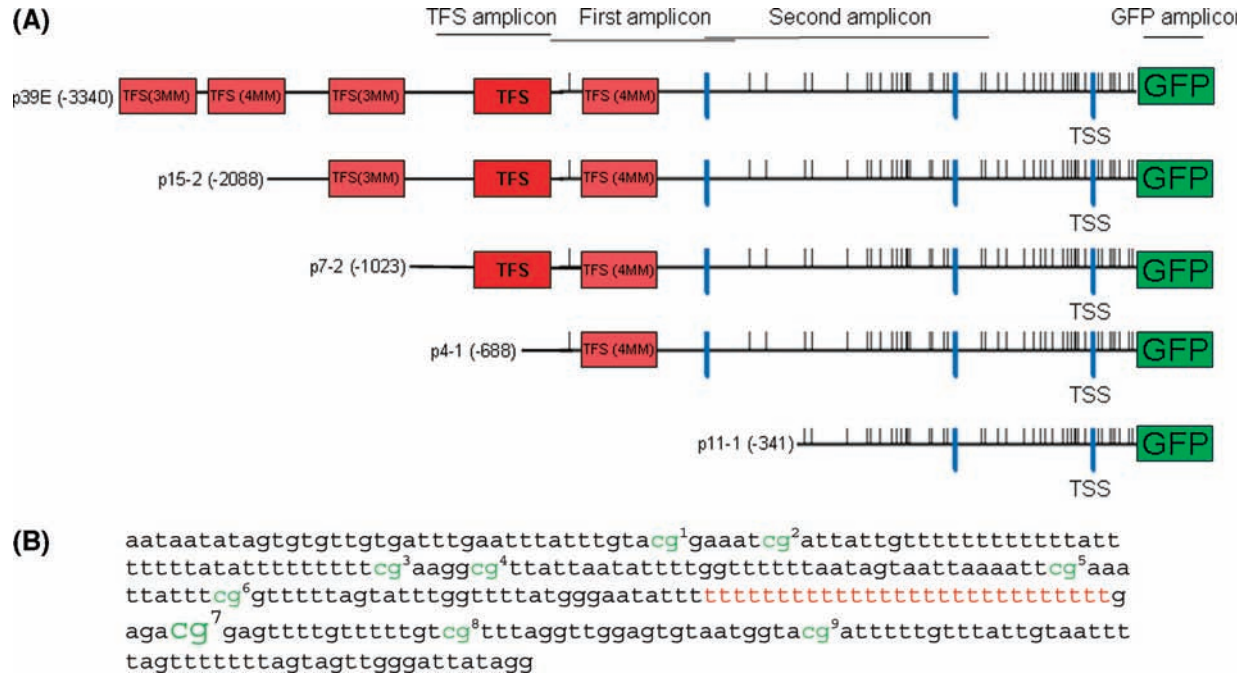


Figure 1. Schematic overview of EpCAM promoter fragments in the GFP reporter plasmids. (A) Plasmid p39E encompasses the GFP gene under control of 3.4 kb of the EpCAM promoter. The Triple helix Forming Site (TFS) and sequences differing from the targeted TFS by only three or four mismatches (3MM or 4MM) are indicated. CpGs are depicted by vertical bars. The transcription start site (TSS) corresponds to position +1. The location of the amplicons analyzed for DNA methylation are indicated (not drawn to scale). (B) Sequence of one strand of bisulfite converted, fully methylated DNA of the TFS amplicon. All cytosines in CpG combination are assumed to be methylated and therefore not converted by bisulfite treatment. The CpGs are numbered and depicted in green. The TFS is shown in red, containing three Cs that have been converted to Ts. CpG number 7 is the targeted CpG.

oligopurine−-oligopyrimidine stretches in promoter regions of human genes (*23*−*25*). Recently, we and others have shown that coupling of a TFO to the restriction enzymes scPvuII (*20*) and Mun-I is feasible (Geel et al., manuscript in preparation).

To explore the possibility of targeting methylation to specific DNA sequences using a TFO as targeting domain, we coupled a variant of the methyltransferase M.SssI to a TFO specifically designed for the EpCAM gene (*26*). This M.SssI variant, named C141S throughout this paper, carried the C141S and C368A substitutions and a C-terminal 6xHis-Cys tag. In this variant the internal cysteines were thus replaced and the C-terminal Cys was introduced to allow coupling of the methyltransferase to the TFO. Although one of the replaced cysteines (C141S) is the active site cysteine, the C141S mutation does not fully abolish the methyltransferase activity; the mutant enzyme has 2−5% of the wild type (WT) activity (*27*). DNA binding affinity of the C141S variant is similar to that of the WT enzyme (*28*). Coupling of C141S to the TFO did not affect activity of the enzyme, and binding specificity of the TFO−C141S conjugate to the DNA was dominated by the TFO. Site-specific methylation by the TFO−C141S conjugate was demonstrated using a plasmid containing a 43 bp segment of the EpCAM promoter encompassing the TFS and a target CpG (*26*). To investigate targeted methylation in the context of a functional EpCAM promoter, reporter plasmids encoding the Green Fluorescent Protein (GFP) under control of different EpCAM promoter fragments (*29*) were treated with the TFO−C141S conjugate and assayed for DNA methylation and gene expression.

In this study we demonstrate that a TFO coupled to a reduced activity DNA methyltransferase can be directed to a predetermined site to induce targeted methylation, allowing determination of crucial CpGs for promoter activity.

EXPERIMENTAL PROCEDURES

Methylation of Plasmids with TFO−C141S. The p39E plasmid and its promoter deletion derivatives (*29*) are schematically depicted in Figure 1A. These plasmids encode GFP under control of a 3.4 kb fragment of the EpCAM promoter. Construction of the plasmids expressing WT M.SssI or C141S, purification of the enzymes (*14*) and coupling of the 5′-TTTTTTTTTTTTTTTCTCTCTTTT-3′ TFO to M.SssI(C141S) were done as described (*26*). Plasmids were incubated with 5-fold molar excess of TFO−C141S, M.SssI, C141S, or TFO in a buffer containing 20 mM Tris, 50 mM NaCl, 10 mM $MgCl_2$, pH 7.9, with or without 640 μM *S*-adenosylmethionine (SAM) (New England Biolabs, Ipswich, MA) at 30 °C. The reaction was terminated after 20 h by heat inactivation at 65 °C for 20 min, and plasmids were purified by Qiagen PCR purification kit (Qiagen, Benelux B.V., Venlo, The Netherlands).

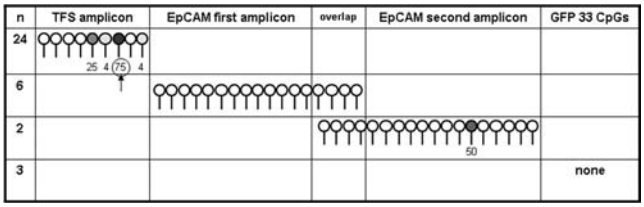
To test the involvement of enzyme activity in TFO−C141S-induced relaxation of supercoiled plasmid DNA, C141S and TFO−C141S were heat-inactivated by incubation at 65 °C for 20 min. Plasmid p39E was incubated with active or inactivated C141S or TFO−C141S for 15 or 30 min or 1, 2.5, 5, or 20 h at 30 °C. Then the reaction was stopped by 10% SDS and digestion with proteinase K.

Transfection. The SKOV3 (HTB-77) cell line was purchased from ATCC (Manasas, VA) and cultured according to ATCC recommendations. SKOV3 cells were seeded 100000/well in 24-wells plates, and transfection was performed at 60−80% confluency using SAINT-2:DOPE (SD, 0.75 mM) (Synvolux Therapeutics, Groningen, The Netherlands) (*30*). Pretreated plasmid DNA (250 ng) in 25 μL of Hanks balanced salt solution was added to 5 μL of SD filled up with 20 μL of HBS. Within 15 min the complex was diluted in 200 μL of serum-free culture medium and added directly to the cells. After 3 h of incubation at 37 °C, in 5% CO_2, serum containing medium was added. After 48 h, cells were harvested and GFP expression was measured by flow cytometry (Beckton Dickenson Bioscience Calibur, San Jose, CA).

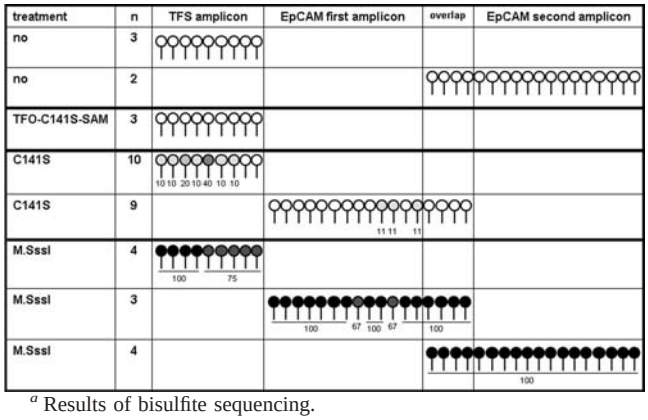
DNA Methylation Analysis. Plasmid DNA (250 ng) methylated in vitro by TFO−C141S was treated with sodium

Table 1. Targeted DNA Methylation of p39E by TFO−C141S

(A) Methylation Status of Bisulfite Amplicons for p39E Treated with TFO−C141S and the Methyl Donor SAM[a]



(B) Methylation Status of Bisulfite Amplicons for p39E Treated with the Controls As Indicated



[a] Results of bisulfite sequencing.

bisulfite to convert unmethylated cytosines to uracils using the EZ DNA Methylation-Gold kit (Zymo, Baseclear Lab Products, Leiden, The Netherlands). Bisulfite specific primers void of any CpG were used to obtain amplification products (amplicons) unbiased for the methylation status. Primer sequences for the TFS amplicon were 5′-AATAATATAGTGTGTTGTGATTT-3′ (forward) and 5′-CCTATAATCCCAACTACTAA-3′ (reverse). (The PCR product is shown in Figure 1B.) Two overlapping amplicons were selected to cover a 700 bp region directly downstream of the TFS in the EpCAM promoter. Primer sequences for the first amplicon were 5′-ACCTCCCCAATAAC-TAAAATTAC-3′ (forward) and 5′-TTGAAGATTTTGTGT-TGAGATTT-3′ (reverse). For the second one, they were 5′-AGTGTTTTGGAAGGTTTTTTGT-3′ (forward) and 5′-AAATTAAAAAAATAAATAAACTCCC-3′ (reverse). Primers used for the GFP amplicon were 5′-GGGGTGGTGTT-TATTTTG-3′ (forward) and 5′-CTCCAACTTATACCCCAAAAT-3′ (reverse). The location of the amplicons in the plasmids is indicated in Figure 1A. PCR conditions were as follows: 95 °C for 15 min, followed by 35 cycles of 95 °C for 45 s, 53−56 °C for 45 s, 72 °C for 45 s, and finished with 72 °C for 10 min. PCR fragments were purified from gels using the DNA extraction kit (Qiagen) and cloned into pCR 2.1-TOPO TA vector (Invitrogen, Breda, The Netherlands). Following transformation, plasmids were isolated from individual bacterial colonies using the Qiaprep Spin Miniprep kit (Qiagen) and subjected to restriction analysis. Clones with the expected structure were sequenced.

RESULTS

Targeted DNA Methylation of the EpCAM Promoter in p39E. To test the targeting specificity of the TFO−C141S conjugate in the context of a functional EpCAM promoter, p39E containing the 3.4 kb EpCAM promoter was treated with TFO−C141S. Three independent TFO−C141S treatments resulted in 57% ($n = 7$), 89% ($n = 9$), and 75% ($n = 8$) methylation of CpG7 (Figure 1B) located directly downstream the TFS (Table 1A). Of the 24 clones analyzed, 18 showed methylation of CpG7. Only three clones were devoid of methylation. One clone showed methylation only of CpG9, and two clones showed methylation only of CpG5 located ∼40 bp upstream of the TFS. Four of the 18 positive clones showed methylation of CpG5 and CpG7, and one of these clones also showed methylation of CpG6. CpG1, -2, -3, -4, and -8 within the TFS amplicon (Figure 1B) were not methylated in the clones sequenced. Importantly, apart from one sporadic methylation event, no methylation was observed downstream of the TFS neither in the EpCAM promoter (EpCAM first and second amplicon, Table 1A) nor in the part of the GFP gene (GFP amplicon). In the control samples, obtained by treating p39E with WT M.SssI, all CpGs analyzed were methylated (Table 1B), whereas treatment with the less active C141S variant resulted in random methylation.

GFP Expression from the EpCAM Promoter after Pretreatment with TFO−C141S. After observing that the TFO−C141S conjugate induced targeted DNA methylation, we tested if methylation of this single CpG (CpG7) is sufficient to inhibit EpCAM promoter activity. Hence, all treated plasmids were transfected in SKOV3 cells to determine GFP expression. The three independent treatments of p39E with TFO−C141S showed 46% ± 20 ($n = 3$), 48% ± 16 ($n = 3$), and 57% ± 6 ($n = 2$) GFP down-regulation (see Figure 2A for a representative experiment). Transfection of plasmids treated with untargeted M.SssI or untargeted C141S resulted in 91% ± 1 and 27% ± 1 GFP down-regulation, respectively, whereas treatment with just the TFO did not influence GFP expression. Transfection of p39E treated with a 100-fold excess of TFO in the presence of TFO−C141S (competition sample in Figure 2A) showed 24% ± 17 down-regulation of GFP, which is approximately 33% less than the value obtained with TFO−C141S only, indicating that targeting was dependent on the TFO. These observations suggested that methylation of a single CpG was sufficient to reduce EpCAM promoter activity.

Down-Regulation of GFP Gene Expression by TFO−C141S in the Absence of TFS or Methyl Donor. To investigate if the reduction in GFP expression was indeed due to targeted DNA methylation, deletion derivatives of p39E (*29*) (p15-2, p7-2, p4-1, and p11-1) (Figure 1A) were treated with TFO−C141S and transfected in SKOV3 cells to determine GFP expression. Plasmids p15-2 and p7-2 contained the TFS, whereas plasmids p4-1 and p11-1 lacked this sequence. In addition to the targeted TFS, the EpCAM promoter region contains four sites, which differ from the targeted TFS only by three or four mismatches (3MM or 4MM, as indicated in Figure 1A). Plasmids p7-2 and p4-1 treated with TFO−C141S showed 51% ± 4 and 46% ± 8 GFP down-regulation, respectively (Figure 2B). The latter result was unexpected, as plasmid p4-1 lacked the TFS. To exclude the possibility that down-regulation was caused by binding of TFO−C141S to the TFS 4MM site (Figure 1A) present in p4-1, plasmids p15-2 and p11-1 were treated with TFO−C141S and transfected into SKOV3 cells. Plasmid p15-2 contains the TFS and two TFS-like sites, whereas from p11-1 all potential binding sites had been deleted (Figure 1A). Both pretreated plasmids showed approximately 45% reduction of GFP expression compared to their untreated controls (data not shown).

To exclude that the reduction in GFP expression was not caused by a specific DNA methylation, the methylation status of the deletion derivatives of p39E was analyzed. Treatment of p15-2 with TFO−C141S resulted in 36% methylation of CpG7 (5/14 clones), and one clone showed methylation of CpG5 (Table 2). Apart from one sporadic event, deletion derivatives p7-2 and p4-1 and p11-1 did not show methylation in the downstream amplicons. These results confirm the specificity of targeted methylation by TFO−C141S.

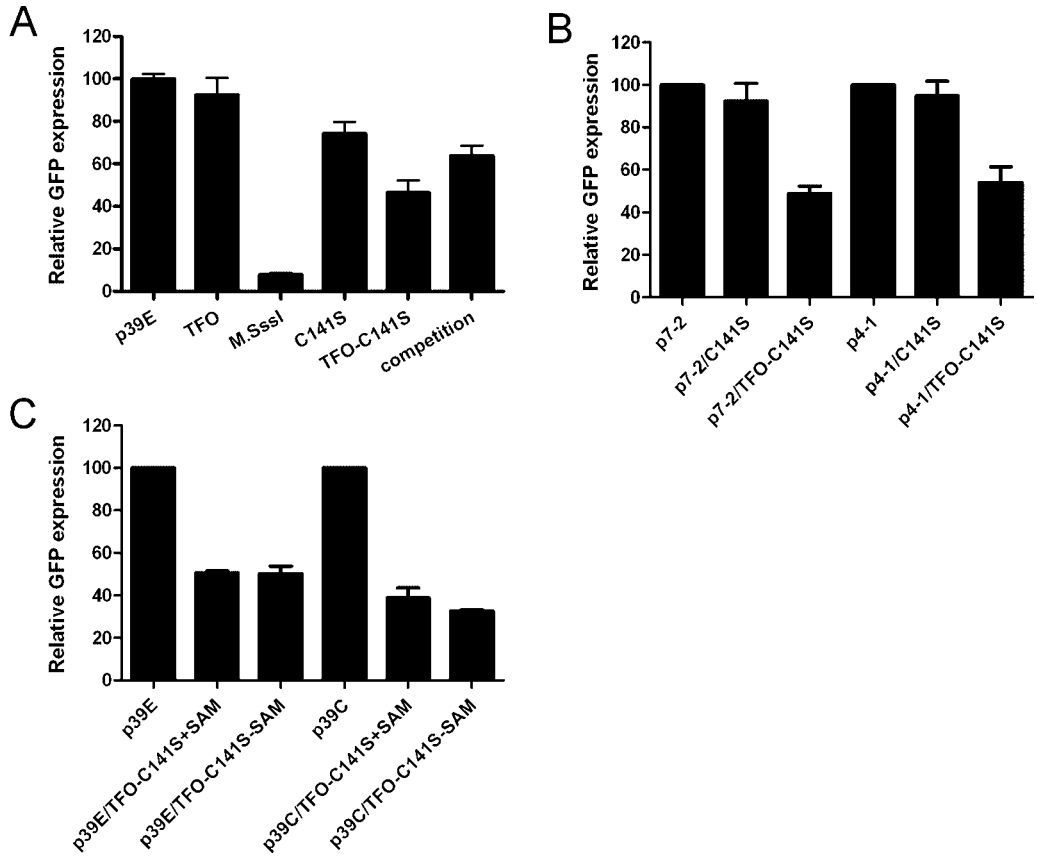
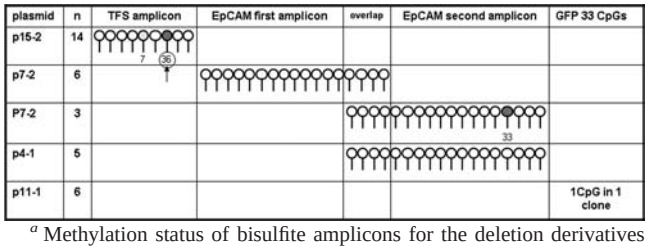


Figure 2. Effect of TFO−C141S treatment on GFP expression in EpCAM positive SKOV3 cells. (A) Relative GFP expression measured 48 h after transfection of pretreated p39E. Plasmid p39E was treated as indicated: p39E = treatment without TFO−C141S, treated with TFO only, with untargeted M.SssI or C141S, with the TFO−C141S conjugate or with 100-fold excess of TFO and TFO−C141S (=competition). The value obtained with p39E without TFO−C141S was taken as 100%. Shown is the average GFP expression (±SD) of one representative transfection performed in triplicate. (B) Relative GFP expression measured 48 h after transfection of pretreated deletion derivatives p7-2 and p4-1. For each derivative, the values obtained with samples treated without TFO−C141S were taken as 100%. Shown is the average GFP expression (±SEM) of the mean of three independent transfections performed in triplicate. (C) Relative GFP expression was measured 48 h after transfection of pretreated p39E or p39C. Treatments were as indicated: (+) or (−) indicates the presence or absence of the methyl donor (SAM). Shown is the average GFP expression (±SEM) of the mean of three independent transfections performed in triplicate.

Table 2. Targeted DNA Methylation of p39E Deletion Derivatives by TFO−C141S[a]



[a] Methylation status of bisulfite amplicons for the deletion derivatives p39E treated with TFO−C141S and the methyl donor SAM. Shown are the results of bisulfite sequencing. *n* = number of clones analyzed. Below the lollipop: the percentage of clones of which the CpG was methylated. Open lollipop: 0% methylated CpG. Black lollipop: 100% methylated CpG.

To exclude that reduction in GFP expression was the result of the conjugate still being attached to the plasmid, p39E was also treated with TFO−C141S in the absence of *S*-adenosylmethionine (SAM). No difference in reduction of GFP expression was observed between samples treated with or without the methyl donor (Figure 2C). To confirm that reduction in GFP expression was not caused by aspecific DNA methylation, plasmid p39C encoding GFP under control of the CMV promoter without a TFS-like sequence was subjected to TFO−C141S treatment. Also for p39C, GFP expression was reduced while no difference was observed between treatments in the presence or in the absence of SAM (Figure 2C).

TFO−C141S Induced Relaxation of Supercoiled Plasmids. Because GFP expression from the transfected pretreated plasmids seemed to be independent of their methylation status, we examined the conformation of the pretreated plasmids. Treatment of p39E with TFO−C141S with or without methyl donor led to relaxation of the supercoiled plasmid (Figure 3A, lanes 6, 7). The deletion plasmid p11-1 behaved in the same way; treatment with TFO−C141S caused relaxation (lane 12), whereas treatment with only the TFO, M.SssI, or C141S did not affect conformation of the plasmid. Interestingly, the presence of excess TFO seemed to protect to some extent the plasmid from conversion into the relaxed form (lane 8).

The phenomenon of conformation change appeared to be general: treatment of p39C, p7-2, and p4-1 with TFO−C141S also caused a conversion to the relaxed form (data not shown). To exclude the possibility that the slower electrophoretic mobility was caused by TFO−C141S still being attached to the plasmid, the TFO−C141S treated samples were digested with proteinase K. No difference in conformation was observed between the plasmids with and without proteinase K treatment (data not shown), indicating that C141S was not attached to the plasmid.

Because it has been reported that M.SssI can display topoisomerase activity (*31*), TFO−C141S was heat-inactivated before treatment of p39E. Treatment of the plasmid p39E with heat-inactivated TFO−C141S did not result in conformation change, whereas treatment with active TFO−C141S led to

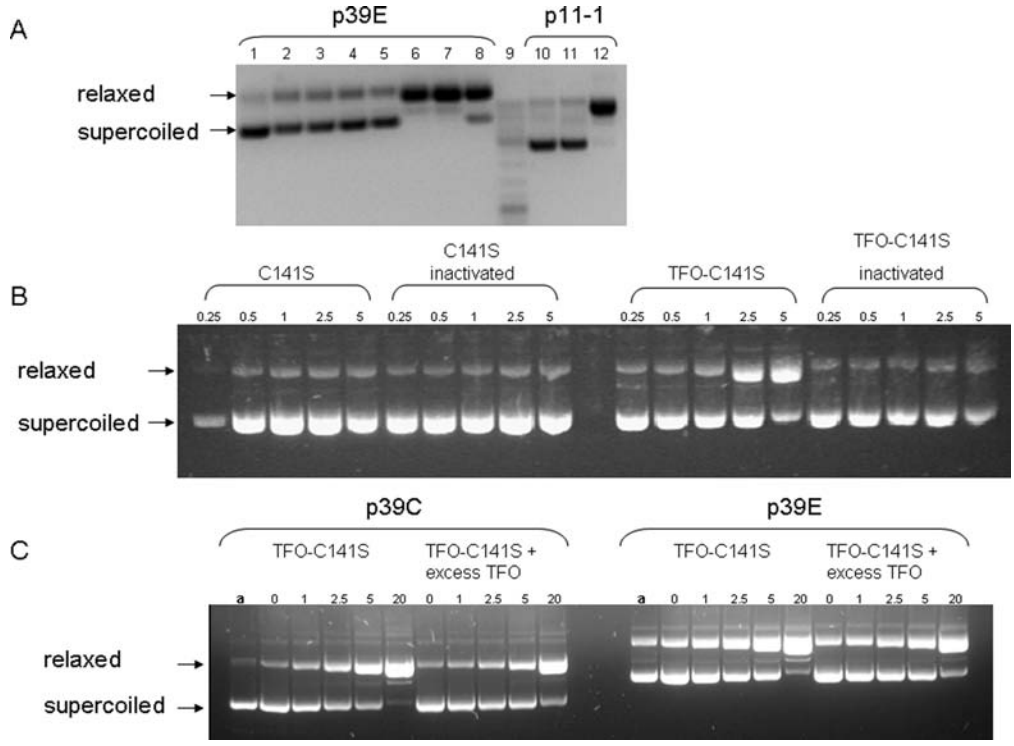


Figure 3. Effect of TFO-141S treatment on plasmid conformation. (A) Agarose gel electrophoresis of plasmids p39E and p11-1 treated with the TFO, WT M.SssI, C141S, or the TFO−C141S conjugate: lane 1, untreated; lane 2, without TFO−C141S; lane 3, TFO; lane 4, M.SssI; lane 5, C141S; lane 6, TFO−C141S; lane 7, TFO- C141S without SAM; lane 8, 100-fold excess of TFO and TFO−C141S; lane 9, marker; lane 10, without TFO−C141S; lane 11, C141S; lane 12, TFO−C141S. (B) Agarose gel electrophoresis of plasmid p39E treated with active and heat-inactivated C141S and TFO−C141S. The supercoiled plasmid was incubated at 30 °C for different time points as indicated above the lanes (hours). Then the samples were deproteinized before electrophoresis as described in Experimental Procedures. (C) Agarose gel electrophoresis of plasmid p39C and p39E treated with the TFO−C141S conjugate only or in the presence of 100-fold excess of TFO. Plasmids were incubated as in part B. Lane a is purified plasmid.

conversion from the supercoiled into the relaxed form (Figure 3B). This change in conformation was dependent on the duration of the treatment; i.e., longer treatment resulted in a less supercoiled and a more relaxed conformation. Treatment of p39E with C141S or heat-inactivated C141S showed no conformation change.

On the basis of the observation that excess TFO could protect the p39E plasmid from TFO−C141S mediated relaxation (Figure 3A, lanes 6, 7, 8), we investigated this protection in more detail. Treatment of p39E, as well as p39C with TFO−C141S only, showed efficient relaxation already after 2.5 h of treatment (Figure 3C). In the presence of excess TFO, again both plasmids showed relaxation although the efficiency was somewhat less (Figure 3C). To further prove that the presence of the TFS is not necessary for relaxation, plasmids with a different backbone were subjected to TFO−C141S treatment. Although the backbones did not contain any TFS-like sequences, we again observed an increase in the relaxed conformation when the incubation time with TFO−C141S was increasing (data not shown).

DISCUSSION

In this study, we demonstrated that a DNA methyltransferase can be directed to a predetermined site by a covalently attached TFO and that TFO-mediated targeting can be used to induce targeted methylation. Because the TFO binds antiparallel to the sense strand of the TFS in the EpCAM promoter and C141S is coupled to the 5′-end of the TFO, C141S should orient downstream of the TFS. We therefore expected CpG7 (Figure 1B) to be the main target for C141S. Indeed, treatment of reporter plasmids with TFO−C141S resulted in efficient (18/24 clones) and specific (14/21 clones) methylation of CpG7 located directly downstream the TFS. These results indicate that binding specificity of TFO−C141S is dominated by the TFO.

The 24 nucleotide long TFO used in this study contains three cytosines. Specific binding of the TFO requires protonation of the three cytosines to form the C+·GC triplets (pH < 6) (*21*). However, treatment of the plasmids with TFO−C141S was performed under conditions optimal for methylation (pH 7.9), i.e., at a pH higher than required for efficient formation of C+·GC triplets. Despite the suboptimal annealing conditions, efficient DNA methylation was observed at the target site.

The 3.4 kb EpCAM promoter encompasses four sites that are similar to the targeted TFS (i.e., differing only at three or four positions); hence, they would be expected to be potential sites of nontargeted binding and methylation. To test this possibility, deletion derivatives of p39E containing (p15-2, p7-2) or lacking the TFS (p4-1, p11-1) were treated with TFO−C141S. Despite the presence of a possible binding site in amplicon 1, CpG7 was preferentially methylated (18/24 clones), whereas no methylation was observed for amplicon 1 in all treated plasmids. Moreover, deletion derivatives lacking the TFS (p4-1, p11-1) displayed no methylation in the analyzed areas. We thus conclude that the TFO directs C141S only to its predetermined site.

Next, we investigated if this site-specific DNA methylation in the EpCAM promoter is sufficient to induce inhibition of gene expression. It has been shown that methylation of one or a few CpGs within a promoter might be sufficient to repress transcription. Transfection of a reporter plasmid under control of the p53 promoter in which a single CpG was methylated in vitro by HhaI showed 85% down-regulation of the reporter gene (*32*). Unexpectedly, in our experiments TFO−C141S treatment of all GFP reporter plasmids resulted in lower GFP expression,

and this phenomenon was independent of the methylation status of the transfected plasmid. Gel electrophoresis revealed that TFO−C141S treatment, in contrast to treatment with the enzyme or TFO only, led to relaxation of the supercoiled plasmid, explaining the observed GFP repression (*33*). Since plasmid treatment with heat-inactivated TFO−C141S did not cause a conformation change of the plasmid, we might conclude that the observed relaxation is probably caused by topoisomerase activity of C141S. Matsuo et al. described that M.SssI contains both methylase and topoisomerase activities (*31*). However, the observed topoisomerase activity was only displayed by the TFO−C141S conjugate and not after treatment with the TFO only or with C141S only. Independent of the presence of the TFS, all plasmids treated with the TFO−C141S conjugate showed relaxation of the plasmid: the observed ratio of supercoiled versus relaxed plasmid conformation was decreasing when the treatment time was prolonged. Somehow, the chemical coupling of the TFO with the enzyme seems to change the conformation of the enzyme, thereby uncovering the catalytic topoisomerase domain. It requires further research to determine which amino acid should be replaced to abolish this activity.

A puzzling observation of this study was that there was no significant difference in GFP down-regulation between plasmids treated in the presence or absence of the methyl donor. A possible explanation might be that the CpGs targeted in this study do not play a role in the epigenetic regulation of the EpCAM gene. Indeed, recent observations (*11*, *14*, *15*) suggest that the CpGs, which display differential methylation, are located further downstream (approximately −400 to +280 bps) of the TFS, which is located around −917. Currently, we are investigating which CpGs are crucial in regulating EpCAM gene expression. The important CpGs can then be targeted for induced DNA methylation.

In summary, the data obtained with the TFO−C141S conjugate offer a novel approach for targeted DNA methylation. The combination of a specific TFO and the reduced methyltransferase activity of the M.SssI mutant C141S allowed us to target methylation predominantly to a specific DNA sequence without significant background methylation. Because of the flexibility provided by the use of TFOs as targeting domain, this approach appears to be a promising tool in both research and therapeutic areas.

ACKNOWLEDGMENT

This work was supported by Grants QRLT-2001-0448 and COOP-CT-2005-017984 of the European Commission's Fifth and Sixth Framework Programmes, respectively. We thank Dr. Bill Jack (New England Biolabs) for the original plasmid with the M.SssI gene and Burcu Duycu for technical assistance.

LITERATURE CITED

(1) Maetzel, D., Denzel, S., Mack, B., Canis, M., Went, P., Benk, M., Kieu, C., Papior, P., Baeuerle, P. A., Munz, M., and Gires, O. (2009) Nuclear signalling by tumour-associated antigen EpCAM. *Nat. Cell Biol. 11*, 162–171.

(2) Al-Hajj, M., Wicha, M. S., Benito-Hernandez, A., Morrison, S. J., and Clarke, M. F. (2003) Prospective identification of tumorigenic breast cancer cells. *Proc. Natl. Acad. Sci. U.S.A. 100*, 3983–3988.

(3) Li, C., Heidt, D. G., Dalerba, P., Burant, C. F., Zhang, L., Adsay, V., Wicha, M., Clarke, M. F., and Simeone, D. M. (2007) Identification of pancreatic cancer stem cells. *Cancer Res. 67*, 1030–1037.

(4) Yamashita, T., Forgues, M., Wang, W., Kim, J. W., Ye, Q., Jia, H., Budhu, A., Zanetti, K. A., Chen, Y., Qin, L. X., Tang, Z. Y., and Wang, X. W. (2008) EpCAM and {alpha}-fetoprotein expression defines novel prognostic subtypes of hepatocellular carcinoma. *Cancer Res. 68*, 1451–1461.

(5) Dalerba, P., Dylla, S. J., Park, I. K., Liu, R., Wang, X., Cho, R. W., Hoey, T., Gurney, A., Huang, E. H., Simeone, D. M., Shelton, A. A., Parmiani, G., Castelli, C., and Clarke, M. F. (2007) Phenotypic characterization of human colorectal cancer stem cells. *Proc. Natl. Acad. Sci. U.S.A. 104*, 10158–10163.

(6) Baeuerle, P. A., and Gires, O. (2007) EpCAM (CD326) finding its role in cancer. *Br. J. Cancer 96*, 417–423.

(7) Munz, M., Kieu, C., Mack, B., Schmitt, B., Zeidler, R., and Gires, O. (2004) The carcinoma-associated antigen EpCAM upregulates c-myc and induces cell proliferation. *Oncogene 23*, 5748–5758.

(8) Osta, W. A., Chen, Y., Mikhitarian, K., Mitas, M., Salem, M., Hannun, Y. A., Cole, D. J., and Gillanders, W. E. (2004) EpCAM is overexpressed in breast cancer and is a potential target for breast cancer gene therapy. *Cancer Res. 64*, 5818–5824.

(9) Yanamoto, S., Kawasaki, G., Yoshitomi, I., Iwamoto, T., Hirata, K., and Mizuno, A. (2007) Clinicopathologic significance of EpCAM expression in squamous cell carcinoma of the tongue and its possibility as a potential target for tongue cancer gene therapy. *Oral Oncol. 43*, 869–877.

(10) Du, W., Ji, H., Cao, S., Wang, L., Bai, F., Liu, J., and Fan, D. (2009) EpCAM: a potential antimetastatic target for gastric cancer. *Dig. Dis. Sci.* 1033–1038.

(11) Tai, K. Y., Shiah, S. G., Shieh, Y. S., Kao, Y. R., Chi, C. Y., Huang, E., Lee, H. S., Chang, L. C., Yang, P. C., and Wu, C. W. (2007) DNA methylation and histone modification regulate silencing of epithelial cell adhesion molecule for tumor invasion and progression. *Oncogene 26*, 3989–3997.

(12) Shiah, S. G., Chang, L. C., Tai, K. Y., Lee, G. H., Wu, C. W., and Shieh, Y. S. (2009) The involvement of promoter methylation and DNA methyltransferase-1 in the regulation of EpCAM expression in oral squamous cell carcinoma. *Oral Oncology 45*, e1–e8.

(13) Yu, G., Zhang, X., Wang, H., Rui, D., Yin, A., Qiu, G., and He, Y. (2008) CpG island methylation status in the EpCAM promoter region and gene expression. *Oncol. Rep. 20*, 1061–1067.

(14) van der Gun, B. T., Wasserkort, R., Monami, A., Jeltsch, A., Rasko, T., Slaska-Kiss, K., Cortese, R., Rots, M. G., de Leij, L. F., Ruiters, M. H., Kiss, A., Weinhold, E., and McLaughlin, P. M. (2008) Persistent downregulation of the pancarcinoma-associated epithelial cell adhesion molecule via active intranuclear methylation. *Int. J. Cancer 123*, 484–489.

(15) Spizzo, G., Gastl, G., Obrist, P., Fong, D., Haun, M., Grunewald, K., Parson, W., Eichmann, C., Millinger, S., Fiegl, H., Margreiter, R., and Amberger, A. (2007) Methylation status of the Ep-CAM promoter region in human breast cancer cell lines and breast cancer tissue. *Cancer Lett. 246*, 253–261.

(16) Xu, G., and Bestor, T. (1997) Cytosine methylation targetted to pre-determined sequences. *Nat. Genet. 17*, 376–378.

(17) Li, F., Papworth, M., Minczuk, M., Rohde, C., Zhang, Y., Ragozin, S., and Jeltsch, A. (2007) Chimeric DNA methyltransferases target DNA methylation to specific DNA sequences and repress expression of target genes. *Nucleic Acids Res. 35*, 100–112.

(18) Nomura, W., and Barbas, C. F. (2007) In vivo site-specific DNA methylation with a designed sequence-enabled DNA methylase. *J. Am. Chem. Soc. 129*, 8676–8677.

(19) Smith, A. E., and Ford, K. G. (2007) Specific targeting of cytosine methylation to DNA sequences in vivo. *Nucleic Acids Res. 35*, 740–754.

(20) Eisenschmidt, K., Lanio, T., Simoncsits, A., Jeltsch, A., Pingoud, V., Wende, W., and Pingoud, A. (2005) Developing a programmed restriction endonuclease for highly specific DNA cleavage. *Nucleic Acids Res. 33*, 7039–7047.

(21) Duca, M., Vekhoff, P., Oussedik, K., Halby, L., and Arimondo, P. B. (2008) The triple helix: 50 years later, the outcome. *Nucleic Acids Res. 36*, 5123–5138.

(22) Vekhoff, P., Halby, L., Oussedik, K., Dallavalle, S., Merlini, L., Mahieu, C., Lansiaux, A., Bailly, C., Boutorine, A., Pisano,

C., Giannini, G., Alloatti, D., and Arimondo, P. B. (2009) Optimized synthesis and enhanced efficacy of novel triplex-forming camptothecin derivatives based on gimatecan. *Bioconjugate Chem. 20*, 666–672.

(23) Wu, Q., Gaddis, S. S., Macleod, M. C., Walborg, E. F., Thames, H. D., DiGiovanni, J., and Vasquez, K. M. (2007) High-affinity triplex-forming oligonucleotide target sequences in mammalian genomes. *Mol. Carcinog. 46*, 15–23.

(24) Goni, J. R., de la Cruz, X., and Orozco, M. (2004) Triplex-forming oligonucleotide target sequences in the human genome. *Nucleic Acids Res. 32*, 354–360.

(25) Goni, J., Vaquerizas, J., Dopazo, J., and Orozco, M. (2006) Exploring the reasons for the large density of triplex-forming oligonucleotide target sequences in the human regulatory regions. *BMC Genomics 7*, 63.

(26) Maluszynska-Hoffman, M. (2009) Super-specificDNA methyltion by a DNA methyltransferase coupled with a triple helix-forming oligonucleotide. Dissertation. RWTH Aachen University, Aachen, Germany. http://darwin.bth.rwth-aachen.de/opus3/volltexte/2009/2854/.

(27) Rathert, P., Rasko, T., Roth, M., Slaska-Kiss, K., Pingoud, A., Kiss, A., and Jeltsch, A. (2007) Reversible inactivation of the CG specific SssI DNA (cytosine-C5)-methyltransferase with a photocleavable protecting group. *ChemBioChem 8*, 202–207.

(28) Darii, M. V., Cherepanova, N. A., Subach, O. M., Kirsanova, O. V., Rasko, T., Slaska-Kiss, K., Kiss, A., ville-Bonne, D., Reboud-Ravaux, M., and Gromova, E. S. (2009) Mutational analysis of the CG recognizing DNA methyltransferase SssI: insight into enzyme−DNA interactions. *Biochim. Biophys. Acta 1794*, 1654–1662.

(29) McLaughlin, P. M., Trzpis, M., Kroesen, B. J., Helfrich, W., Terpstra, P., Dokter, W. H., Ruiters, M. H., de Leij, L. F., and Harmsen, M. C. (2004) Use of the EGP-2/Ep-CAM promoter for targeted expression of heterologous genes in carcinoma derived cell lines. *Cancer Gene Ther. 11*, 603–612.

(30) van der Gun, B. T., Monami, A., Laarmann, S., Rasko, T., Slaska-Kiss, K., Weinhold, E., Wasserkort, R., de Leij, L. F., Ruiters, M. H., Kiss, A., and McLaughlin, P. M. (2007) Serum insensitive, intranuclear protein delivery by the multipurpose cationic lipid SAINT-2. *J. Controlled Release 123*, 228–238.

(31) Matsuo, K., Silke, J., Gramatikoff, K., and Schaffner, W. (1994) The CpG-specific methylase SssI has topoisomerase activity in the presence of Mg^{2+}. *Nucleic Acids Res. 22*, 5354–5359.

(32) Pogribny, I. P., Pogribna, M., Christman, J. K., and James, S. J. (2000) Single-site methylation within the p53 promoter region reduces gene expression in a reporter gene construct: possible in vivo relevance during tumorigenesis. *Cancer Res. 60*, 588–594.

(33) Remaut, K., Sanders, N. N., Fayazpour, F., Demeester, J., and De Smedt, S. C. (2006) Influence of plasmid DNA topology on the transfection properties of DOTAP/DOPE lipoplexes. *J. Controlled Release 115*, 335–343.

BC1000388

One-Step, Acid-Mediated Method for Modification of Glass Surfaces with *N*-Hydroxysuccinimide Esters and Its Application to the Construction of Microarrays for Studies of Biomolecular Interactions

Sungjin Park, Jaeyoung Pai, Eun-Hee Han, Chul-Ho Jun,* and Injae Shin*

Center for Biofunctional Molecules, Department of Chemistry, Yonsei University, Seoul 120-749, Korea. Received January 21, 2010; Revised Manuscript Received June 5, 2010

Microarray technologies have received considerable attention owing to the fact that they serve as powerful tools for the high-throughput analysis of biomolecular interactions and the identification of bioactive substances that bind to biomolecules. Most of the current methods used to construct microarrays rely on the immobilization of substances on properly derivatized surfaces. Among various functional groups used for this purpose, the *N*-hydroxysuccinimide (NHS) ester group has been largely employed because it can be readily reacted with amine or hydrazide functionalities in substances of interest. However, the NHS ester group is usually introduced onto the surface of a glass slide by employing inconvenient and time-consuming multistep processes. In recent studies, we have developed an efficient, single step method for derivatization of glass surfaces with NHS ester groups that takes advantage of an acid-mediated reaction of NHS ester functionalized dimethallylsilanes with silanols on the glass surface. Conditions for the surface modification procedure that utilize TfOH rather than $Sc(OTf)_3$ were found to be superior. Protein and RNA-binding experiments show that glass surfaces modified by employing this method are suitable for efficient immobilization of various substances that are appended by amine, hydrazide, and alcohol functionalities. The microarrays, generated in this way, are applicable to procedures for rapid analysis of protein−protein, protein−glycan, protein−small molecule, and peptide−RNA interactions, as well as for profiling enzyme activities. The newly developed acid-mediated, glass surface modification method should be generally applicable to the preparation of various functional group-modified surfaces.

INTRODUCTION

Since the discovery of peptide microarrays in 1991 (*1*), technologies based on DNA, peptide, protein, and carbohydrate microarrays have attracted enormous attention as powerful and sensitive tools for genomics, transcriptomics, proteomics, and glycomics research (*2*−*8*). The microarrays are composed of diverse probes that are orderly and densely immobilized on a single chip. Microarray-based technologies have gained prominence over other conventional analytic methods because they can be used to assess simultaneously large numbers of recognition events employing only small amounts of samples. These beneficial features make microarray technologies suitable for the rapid analysis of biomolecular interactions such as those taking place in DNA−RNA/DNA−DNA, peptide−protein, protein−protein, and protein−glycan systems (*9*−*14*). This technology is also applicable to the rapid identification of bioactive molecules that selectively interact with proteins or act as substrates for enzymes (*15*−*18*).

Microarrays are generally prepared by covalent or noncovalent immobilization of (bio)molecules on appropriate solid surfaces. Glass slides are most extensively used as the surface material as a result of ease of manipulation and low cost. Another advantage of glass slides is that they are amenable to applications that involve optical detection of events. Most of the existing modification methods rely on the reaction of piranha solution-treated glass surfaces with alkoxysilane-appended aldehydes, carboxylic acids, or amines (*19*, *20*). The resulting slides are directly used for attachment of (bio)molecules, or they are further derivatized with functional groups, such as thiol, maleimide, alkyne, *N*-hydroxysuccinimide (NHS) ester, epoxide, hydrazide, aminooxy, fluoroalkyl, and photoreactive groups, which can be used for attachment of samples (*21*−*35*).

Among the various functionalities used for immobilization on solid surfaces, the NHS ester group has been the most utilized to construct microarrays because it readily reacts with amine or hydrazide functional groups in substances at pH 8−9 (*25*−*27*). However, the NHS ester group is usually introduced onto glass slides by employing multistep modification processes, which often lack efficiency and are time-consuming. As a consequence, the development of simple, facile, and efficient methods for derivatization of glass surfaces with NHS esters is a significant pursuit.

Recently, we developed a procedure for $Sc(OTf)_3$-mediated silylation of hydroxyl groups for the purpose of derivatizing silica surfaces (*36*). In this process, easily prepared and stable methallylsilanes undergo facile reaction with alcohols in the presence of acid catalysts. This catalyst-mediated process has advantages associated with controllability and experimental simplicity. Below, we report the results of a study in which this chemistry has been adapted to an efficient, one-step surface modification method to prepare the NHS ester-derivatized glass slides. The strategy relies on the use of an acid-mediated reaction of an NHS ester functionalized dimethallylsilane with silanols on glass surfaces and avoids the need for laborious surface derivatization. To validate the utility of the surface modification approach, microarrays containing various substances, such as proteins, peptides, sugars, and small molecules, were constructed by printing on NHS ester-coated glass slides, generated by the one-step process. The microarrays were applied to the analysis of carbohydrate−protein, protein−protein, RNA−peptide, and

* To whom correspondence should be addressed. Phone: +82-2-2123-2631. Fax: +82-2-364-7050. E-mail: injae@yonsei.ac.kr, junch@yonsei.ac.kr.

10.1021/bc100042j © 2010 American Chemical Society
Published on Web 06/22/2010

small molecule−protein interactions. The results of these studies are described and discussed below.

MATERIALS AND METHODS

General. All chemical and biochemical products were of analytical grade and purchased from commercial suppliers: lectins from Vector Laboratories (Peterborough, U.K.) and Sigma-Aldrich (St. Louis, MO); protein G from *Streptococcus* sp. and goat anti-mouse FITC-labeled IgG from Sigma-Aldrich; Cy3-streptavidin from Amersham Pharmacia biotech (Piscataway, NJ); β-1,4-galactosyltransferase (β-1,4-GalT) and UDP-Gal from Calbiochem (Gibbstown, NJ); carbohydrates from Sigma-Aldrich, Calbiochem (Gibbstown, NJ), TCI Corp. (Tokyo, Japan), and Acros (Morris Plains, NJ); anti-dextran antibody from Stemcell Technologies Inc. (Vancouver, BC, Canada); microscope glass slide from Corning (Lowell, MA); Dy547-RRE from Thermo Fisher Scientific (Lafayette, CO). The solutions of probes were printed on the surface with a MicroSys 5100 from Cartesian Technologies Inc. (Irvine, CA). Microarrays probed with fluorescent dye labeled proteins and RNA were scanned with an ArrayWoRx biochip reader from Applied Precision (Northwest Issaquah, WA).

Synthesis of 3-Chloropropyldimethallylmethylsilane (2a). A solution of $H_2PtCl_6 \cdot xH_2O$ (10.4 mg, 0.02 mmol) in 2-propanol (0.2 mL) and dichloromethylsilane (26 mL, 250 mmol) was added in a round-bottom flask, and the mixture was stirred until it became homogeneous. Diethyl ether (10 mL) was added into the reaction vessel, and the reaction temperature was raised to 40 °C by an oil bath. After dropwise addition of allyl chloride (20 mL, 250 mmol), the mixture was stirred for 6 h at 80 °C. After the reaction, all volatiles were evaporated under the reduced pressure. The crude product, 3-chloropropyldichloromethylsilane, was used in the next step without further purification.

The crude 3-chloropropyldichloromethylsilane was added dropwise into methallylmagnesium chloride (1.1 equiv) solution in 300 mL of THF at 0 °C, and the reaction mixture was stirred for 6 h at 0 °C. After the reaction, saturated aqueous NH_4Cl was added to the reaction mixture, and the mixture was extracted with diethyl ether three times. The collected organic layers were dried over anhydrous $MgSO_4$ and filtered through Celite pad. The crude mixture was purified by flash column chromatography (*n*-hexane; $R_f = 0.6$) to give **2a** in 70% yield (40 g): ^{1}H NMR (250 MHz, $CDCl_3$) δ 4.57 (d, $J = 30.7$ Hz, 4 H), 3.50 (t, $J = 13.9$ Hz, 2 H), 1.86−1.76 (m, 2 H), 1.73 (s, 6 H), 1.60 (s, 4 H), 0.73−0.68 (m, 2 H), 0.09 (s, 3 H); ^{13}C NMR (62.9 MHz, $CDCl_3$) δ 143.3, 109.3, 48.1, 27.7, 25.8, 25.6, 11.9, 4.2; IR spectrum (neat) 3083, 2966, 2914, 1644, 1450, 1748, 1378, 1280, 1168, 871, 840 cm^{-1}. Anal. Calcd for $C_{12}H_{23}ClSi$: C, 62.43; H, 10.04. Found: C, 62.48; H, 9.93.

Synthesis of 3-Azidopropyldimethallylmethylsilane (3a). 3-Chloropropyldimethallylmethylsilane (**2a**, 10 g, 43.2 mmol) and sodium azide (5.63 g, 86.58 mmol) was added to 100 mL of DMF and stirred for 4 h at 80 °C. After the reaction, saturated aqueous NH_4Cl solution was added. The solution was extracted with diethyl ether three times. The collected organic layers were dried over anhydrous $MgSO_4$ and filtered through Celite pad. The crude mixture was purified by flash column chromatography (*n*-hexane/ethyl acetate = 10:1, $R_f = 0.6$) to give **3a** in 92% yield (9.5 g): ^{1}H NMR (250 MHz, $CDCl_3$) δ 4.57 (d, $J = 28.5$ Hz, 4 H), 3.23 (t, $J = 7.0$ Hz, 2 H), 1.78 (s, 6 H), 1.77−1.60 (m, 2 H), 1.58 (s, 4 H), 0.66−0.60 (m, 2 H), 0.07 (s, 3 H); ^{13}C NMR (62.9 MHz, $CDCl_3$) δ 143.3, 109.3, 54.7, 25.8, 25.6, 23.8, 11.4, 4.2; IR spectrum (neat) 3079, 2971, 2922, 2876, 2102, 1748, 1636, 1459, 1378, 1282, 1255, 1170, 873, 846 cm^{-1}. Anal. Calcd for $C_{12}H_{23}N_3Si$: C, 60.71; H, 9.76; N, 17.70. Found: C, 60.68; H, 9.72; N, 16.78.

Synthesis of 11-Chloroundecyldimethallylmethylsilane (2b). A solution of $H_2PtCl_6 \cdot xH_2O$ (10.4 mg, 0.02 mmol) in 2-propanol (0.2 mL) and dichloromethylsilane (5 mL, 48 mmol) was added in a round-bottom flask, and the mixture was stirred until it became homogeneous. Diethyl ether (10 mL) was added into the reaction vessel, and the reaction temperature was raised to 40 °C by an oil bath. After dropwise addition of 11-chloroundec-1-ene (10 g, 52.98 mmol), the mixture was stirred for 6 h at 80 °C. After the reaction, unreacted 11-chloroundec-1-ene was removed by distillation. The remaining crude product, dichloro-11-chloroundecylmethylsilane, was used in the next step without further purification.

The crude dichloro-11-chloroundecylmethylsilane was added dropwise into methallylmagnesium chloride (1.1 equiv) solution in 300 mL of THF at 0 °C, and the reaction mixture was stirred for 6 h at 0 °C. After the reaction, saturated aqueous NH_4Cl was added to the reaction mixture, and the mixture was extracted with diethyl ether three times. The collected organic layers were dried over anhydrous $MgSO_4$ and filtered through Celite pad. The crude mixture was purified by flash column chromatography (*n*-hexane; $R_f = 0.8$) to give **2b** in 65% yield (10.71 g): ^{1}H NMR (250 MHz, $CDCl_3$) δ 4.74 (d, $J = 26.6$ Hz, 4 H), 3.70 (t, $J = 6.74$ Hz, 2 H), 2.04−1.91 (m, 8 H), 1.64−1.48 (m, 18 H), 0.77−0.74 (m, 2 H), 0.25 (s, 3 H); ^{13}C NMR (62.9 MHz, $CDCl_3$) δ 143.4, 108.9, 45.0, 33.9, 32.9, 29.7, 29.6, 29.4, 29.1, 27.1, 26.3, 25.9, 25.5, 23.9, 14.3, 4.2; IR spectrum (neat) 3073, 2924, 2853, 1636, 1448, 1279, 1250, 870 cm^{-1}. Anal. Calcd for $C_{20}H_{39}ClSi$: C, 70.02; H, 11.46. Found: C, 70.08; H, 11.79.

Synthesis of 11-Azidoundecyldimethallylmethylsilane (3b). 11-Chloroundecyldimethallylsilane (**2b**, 5.5 g, 16.7 mmol) and sodium azide (2.18 g, 33.5 mmol) were added to 100 mL of DMF and stirred for 4 h at 80 °C. After the reaction, saturated aqueous NH_4Cl solution was added. The solution was extracted with diethyl ether three times. The collected organic layers were dried over anhydrous $MgSO_4$ and filtered through Celite pad. The crude mixture was purified by flash column chromatography (*n*-hexane/ethyl acetate = 10:1, $R_f = 0.6$) to give **3b** in 78% yield (4.56 g): ^{1}H NMR (250 MHz, $CDCl_3$) δ 4.51 (d, $J = 27.3$ Hz, 4 H), 3.22 (t, $J = 6.9$ Hz, 2 H), 1.68 (s, 6 H), 1.58 (m, 6 H), 1.24 (s, 18 H), 0.54 (t, $J = 7.8$ Hz, 2 H), 0.01 (s, 3 H); ^{13}C NMR (62.9 MHz, $CDCl_3$) δ 143.7, 108.9, 51.7, 33.9, 30.0, 29.8, 29.5, 29.4, 29.1, 26.9, 25.9, 25.6, 23.9, 14.3, −4.3; IR spectrum (neat) 3072, 2921, 2851, 2094, 1636, 1454, 1373, 1279, 1250, 1166, 998, 971, 868, 839, 722 cm^{-1}. Anal. Calcd for $C_{20}H_{39}N_3Si$: C, 68.71; H, 11.24; N, 12.02. Found: C, 68.60; H, 12.15; N, 12.15.

Synthesis of 2,5-Dioxopyrrolidin-1-yl-1-(3-(methylbis(2-methylallyl)silyl)propyl)-1*H*-1,2,3-triazole 4-Carboxylate (1a). A solution of propiolic acid (2.1 mL, 34.0 mmol), *N*-hydroxysuccinimide (4.0 g, 34.8 mmol), and *N*,*N*′-dicyclohexylcarbodiimide (8.6 g, 41.7 mmol) in 80 mL of dimethoxyethane was stirred for 18 h at room temperature. After the reaction, the mixture was filtered through Celite pad to remove dicyclohexylurea, and all volatiles were evaporated under the reduced pressure. The crude product, 2,5-dioxopyrrolidin-1-yl propiolate, was used in the next step without further purification. To a solution of crude 2,5-dioxopyrrolidin-1-yl propiolate in 50 mL of THF was added $CuSO_4 \cdot 5H_2O$ (0.43 g, 1.74 mmol), sodium ascorbate (0.69 g, 3.48 mmol) in 50 mL of H_2O, and 3-azidopropylmethyldimethallylsilane (**3a**, 4.13 g, 17.38 mmol). The reaction mixture was stirred for 4 h at room temperature. After the reaction, saturated aqueous NH_4Cl was added, and the resulting mixture was extracted with diethyl ether three times. The collected organic layers were dried over anhydrous $MgSO_4$ and filtered through Celite pad, then purified by flash column chromatography (*n*-hexane/ethyl acetate = 1:1, $R_f = 0.3$) to give **1a** in 60% yield (4.21 g): ^{1}H NMR (250 MHz, $CDCl_3$) δ 8.33

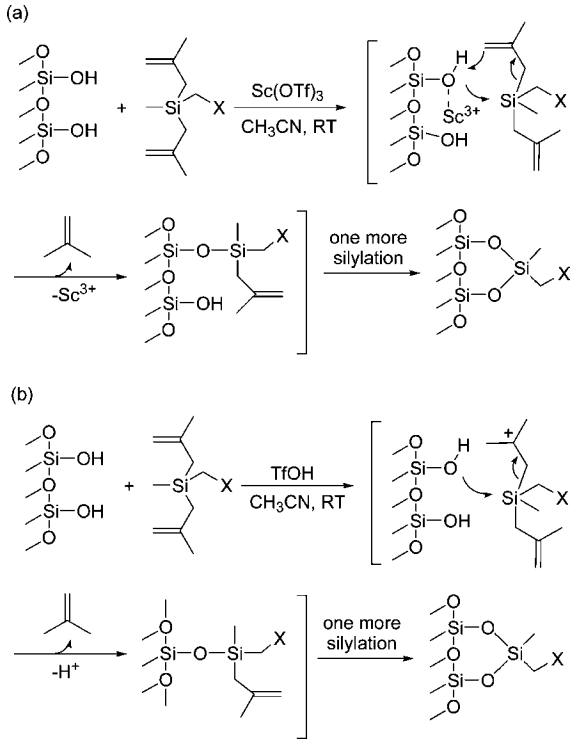
(s, 1 H), 4.56 (d, $J = 16.5$ Hz, 4 H), 4.44 (t, $J = 4.8$ Hz, 2 H), 2.93 (s, 4 H), 1.98 (m, 2 H), 1.70 (s, 6 H), 1.59 (s, 4 H), 0.59 (m, 4 H), 0.08 (s, 3 H); ^{13}C NMR (62.9 MHz, $CDCl_3$) δ 169.3, 155.9, 143.0, 129.3, 54.0, 25.8, 25.6, 25.5, 25.2, 10.9, 4.3; IR spectrum (neat) 3149, 3071, 2935, 2252, 1815, 1793, 1742, 1636, 1535, 1466, 1450, 1437, 1374, 1278, 1254, 1202, 1168, 1074, 958, 907, 839, 732, 649 cm^{-1}; HR-MS (TOF) calcd for $C_{19}H_{28}N_4O_4SiNa$ ($M + Na^+$) 427.1778, found 427.1774. Anal. Calcd for $C_{12}H_{23}N_3Si$: C, 56.41; H, 6.98; N, 13.85. Found: C, 56.94; H, 6.96; N, 13.09.

Synthesis of 2,5-Dioxopyrrolidin-1-yl 1-(11-(methylbis(2-methylallyl)silyl)undecyl)-1*H*-1,2,3-triazole 4-Carboxylate (1b). A solution of propiolic acid (2.1 mL, 34.0 mmol), *N*-hydroxysuccinimide (4.0 g, 34.8 mmol), and *N*,*N*′-dicyclohexylcarbodiimide (8.6 g, 41.7 mmol) in 80 mL of dimethoxyethane was stirred for 18 h at room temperature. After the reaction, the mixture was filtered through a Celite pad to remove dicyclohexylurea, and all volatiles were evaporated. The crude product, 2,5-dioxopyrrolidin-1-yl propiolate, was used in the next step without further purification. To a solution of crude 2,5-dioxopyrrolidin-1-yl-propiolate in 50 mL of THF was added 11-azidoundecyldimethallylmethylsilane (6.08 g, 17.38 mmol) and catalyst mixture of $CuSO_4 \cdot 5H_2O$ (0.43 g, 1.74 mmol) and sodium ascorbate (0.69 g, 3.48 mmol) in 50 mL of H_2O, and the reaction mixture was stirred for 4 h at room temperature. After the reaction, saturated aqueous NH_4Cl was added, and the mixture was extracted with diethyl ether three times. The collected organic layers were dried over anhydrous $MgSO_4$, then filtered through a Celite pad and purified by flash column chromatography (*n*-hexane/ethyl acetate = 1:1, $R_f = 0.3$) to give **1b** in 50% yield (4.2 g): ^{1}H NMR (250 MHz, $CDCl_3$) δ 8.24 (s, 1 H), 4.56 (d, $J = 28.6$ Hz, 2 H), 4.45 (t, $J = 7.2$ Hz, 2 H), 2.91 (s, 4 H), 1.98−1.93 (m, 2 H), 1.71 (s, 3 H), 1.57 (s, 2 H), 0.56−0.53 (m, 2 H), 0.03 (s, 3 H); ^{13}C NMR (62.9 MHz, $CDCl_3$) δ 169.0, 155.9, 143.7, 134.9, 129.1, 108.8, 51.1, 33.8, 30.2, 29.6, 29.5, 29.4, 29.1, 26.5, 25.9, 25.8, 25.5, 23.9, 14.3, 4.2; IR spectrum (neat) 3515, 3347, 3137, 3073, 2920, 2853, 1811, 1785, 1636, 1536, 1465, 1370, 1202, 1078, 870 cm^{-1}; HR-MS (TOF) calcd for $C_{27}H_{44}N_4O_4SiNa$ ($M + Na^+$) 539.3030, found 539.3032. Anal. Calcd for $C_{27}H_{44}N_4O_4Si$: C, 62.76; H, 8.58; N, 10.84. Found: C, 62.32; H, 8.69; N, 10.69.

Preparation of NHS Ester-Functionalized Glass Slides. The microscope slides (2.5 cm × 7.5 cm) were immersed in a "piranha" solution (a mixture of 70% volume of concentrated sulfuric acid and 30% volume of a 30% hydrogen peroxide solution) for 12 h at room temperature. (*Caution:* Piranha solution should be handled with extreme caution because of its high oxidizing power and risk of explosion. Experimenters should wear protective clothes and safety goggles.) The cleaned glass slides were carefully removed from the piranha solution, washed extensively with deionized water, and dried by purging with argon gas. The cleaned slides were kept in a custom slide reaction vessel containing a solution of **1a** or **1b** (3% or 6%) in the presence of $Sc(OTf)_3$ (0.1 equiv) or TfOH (0.1 equiv) as a acid catalyst in 1:1 toluene/acetonitrile for 8 h. The reaction vessel was closed to prevent evaporation of solvent during reaction. After washing with acetonitrile three times, the slides were dried by purging with argon gas. The derivatized slides can be stored at room temperature in a desiccator for several weeks.

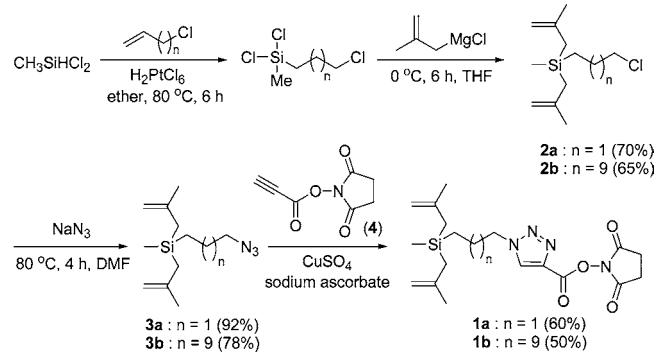
Printing of Samples on the NHS-Ester Functionalized Glass Surface. Carbohydrates, small molecules, proteins, and peptides were dissolved in 50 mM sodium phosphate buffer (pH 8.0) containing 40% glycerol. A solution of samples (1 nL) from a 384-well plate was printed in predetermined places on the NHS-ester functionalized glass slide with a distance of 270 μm between the centers of adjacent spots. After completion

Scheme 1. Mechanism for Acid-Mediated Silylation of Silanols on a Glass Surface[a]



[a] (a) $Sc(OTf)_3$ and (b) TfOH are used as acid catalysts.

Scheme 2. Preparation of NHS-Ester Functionalized Dimethallylsilanes 1a and 1b



of printing, the slide was placed into a humidity chamber (60%) at room temperature for 3−5 h. The spotted slide was divided into several blocks by using a compartmentalized plastic film that was coated with adhesive on one side (thickness: 0.1−0.2 mm) to avoid cross-contamination. The slide was washed with PBS (pH 7.4) containing 0.1% Tween 20, and a solution possessing 1% 2-aminoethanol in 50 mM sodium phosphate buffer (pH 8.0) was dropped in the blocks to remove unreacted NHS esters on the surface. After incubation for 0.5 h, the slide was washed with PBS (pH 7.4) containing 0.1% Tween 20, rinsed with water, and dried by purging with argon gas.

Detection of (Bio)Molecular Interactions. The printed slides were probed with fluorescent dye-labeled proteins (1−20 μg/mL) in PBS (pH 7.4) containing 0.1% Tween 20 or Dy547-RRE RNA (10 μM) in 20 mM HEPES (pH 7.4) containing 1 mM $MgCl_2$, 5 mM KCl, and 140 mM NaCl for 1 h at room temperature. For ConA binding, $MnCl_2$ and $CaCl_2$ were added at final concentrations of 1 mM. The unbound proteins and RRE were then removed by washing with the same buffer and rinsed with water. After drying by purging with argon gas, the slide treated with fluorescent dye-labeled proteins and RRE was

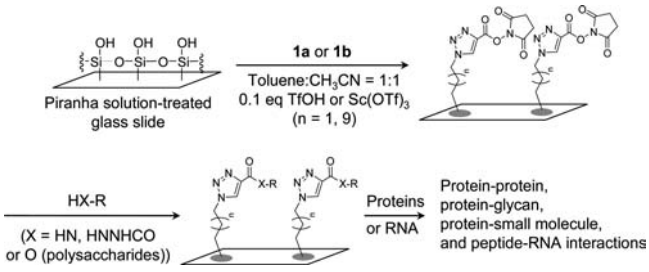


Figure 1. Fabrication of microarrays using NHS-ester derivatized glass slides and its application in studies of (bio)molecular interactions.

scanned by using an ArrayWoRx scanner. The slide probed with unlabeled antibody was further treated with FITC-labeled goat IgG and then scanned by using a microarray scanner. Fluorescence intensity was analyzed using ImaGene 6.1 software from BioDiscovery.

Enzymatic Glycosylation on Microarrays by β-1,4-GalT. A solution of β-1,4-galactosyltransferase (1 mU, a final concentration of 0.5 μM), $MnCl_2$ (10 mM), and UDP-Gal (1 mM) in 50 mM HEPES buffer (pH 7.5) was dropped into each block on the spotted slide, and the slide was placed in a temperature- and humidity-controlled incubator (80% humidity) at 37 °C for 3 h. The slide was washed with PBS buffer containing 0.1% Tween 20 (3 × 3 min). After drying by purging with Ar gas, the slide was probed with Cy3-RCA_{120} at room temperature for 1 h. The unbound protein was removed with PBS buffer containing 0.1% Tween 20 (3 × 3 min) by gentle shaking and rinsed with water. After drying by purging with Ar gas, the slide was scanned by using an ArrayWorx microarray scanner.

RESULTS AND DISCUSSION

The identification of efficient reactions that can be used for derivatization is a prerequisite for developing a single step method to introduce NHS esters on glass surfaces as part of the construction of microarrays. We hypothesized that Si−O−Si bond formation, using moisture-stable silylating reagents, could be employed to carry out a one-step glass surface modification process in which NHS esters are introduced. Pertinent to this proposal are recent observations we have made in studies of $Sc(OTf)_3$-mediated silylation reactions of silanols (*36*). We envisaged that NHS ester-containing methallylsilanes could be utilized for this purpose owing to their ready preparation, high stability, and the ease with which they react with alcohols in the presence of acid catalysts.

A mechanism for glass surface modification through an acid-mediated silylation of silanol groups is shown in Scheme 1. NHS-ester functionalized dimethallylsilanes are reacted with glass surface silanols at room temperature in the presence of $Sc(OTf)_3$ or trifluoromethanesulfonic acid (TfOH) as catalysts. Two different tether lengths (**1a** for C3 and **1b** for C11) were created in order to examine the effects on surface modification efficiency and subsequent protein binding. NHS-functionalized dimethallylsilanes **1a** and **1b**, employed in this methodology, were prepared on a large scale by the route delineated in Scheme 2. Briefly, the pathway involves conversion of dichloromethylsilane to the azide-containing dimethallylsilanes **3a** (C3 tether)

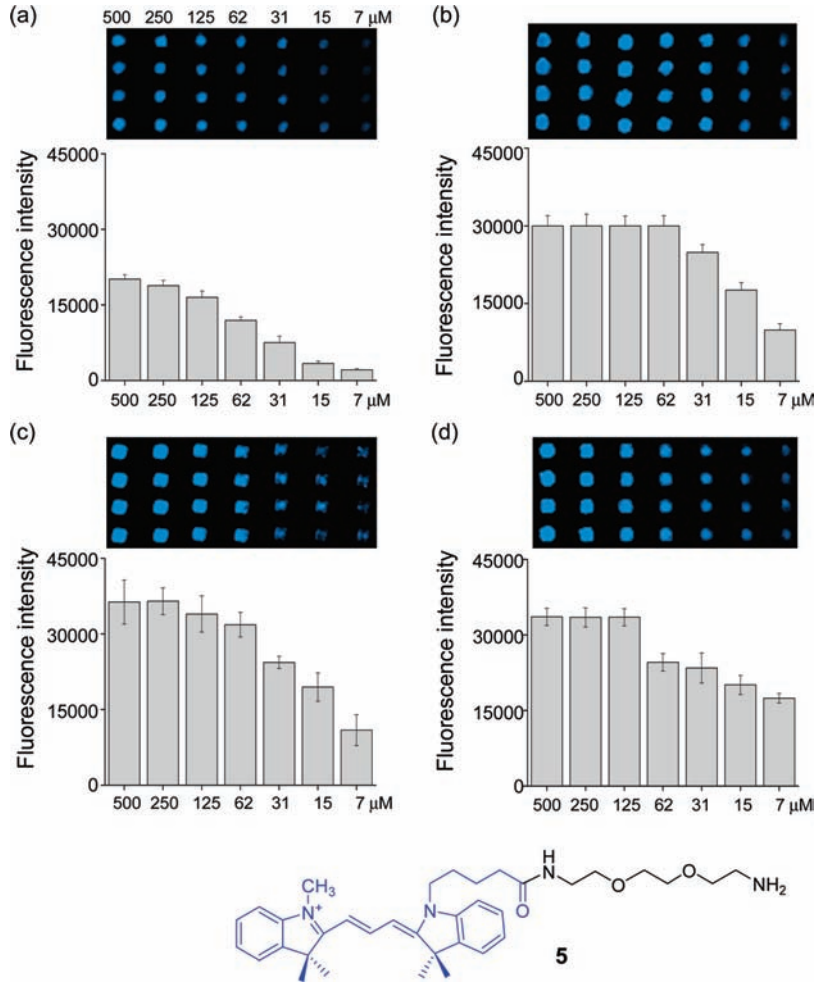


Figure 2. Immobilization of amine-linked Cy3 (**5**) (7−500 μM) on NHS-ester coated glass slides, prepared by using (a) 3% **1a** and 0.1 equiv of $Sc(OTf)_3$, (b) 3% **1a** and 0.1 equiv of TfOH, (c) 6% **1a** and 0.1 equiv of TfOH, and (d) 3% **1b** and 0.1 equiv of TfOH.

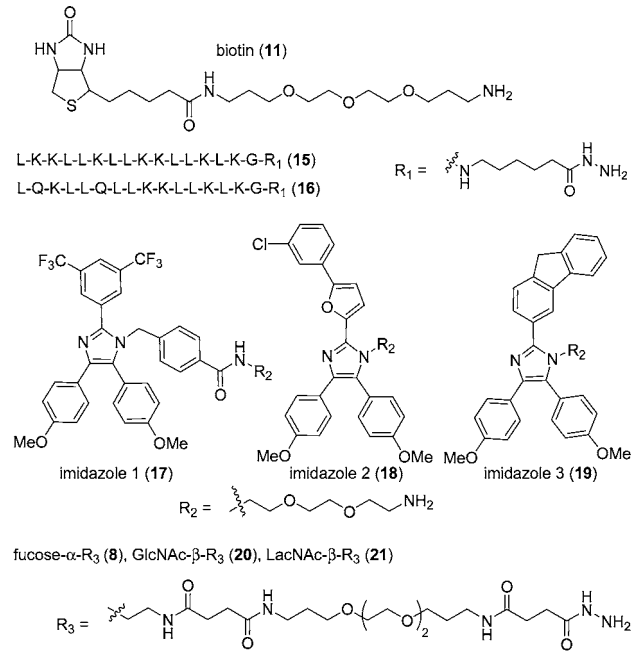
and **3b** (C11 tether) via sequential platinum-catalyzed hydrosilylation, Grignard reaction with methallyl magnesium chloride, and substitution of Cl for N_3. Finally, copper(I)-catalyzed [2 + 3] cycloaddition of **3a** and **3b** with NHS propiolate ester (**4**), generated in situ from *N*-hydroxysuccinimide and propiolic acid under *N*,*N*′-dicyclohexylcarbodiimide (DCC), was used to produce **1a** and **1b**.

Microarrays were prepared by treating glass slides with **1a** or **1b** in a 1:1 mixture of toluene and acetonitrile in the presence of 0.1 equiv of $Sc(OTf)_3$ or TfOH, followed by printing with amine-, hydrazide-, or hydroxy-conjugated (bio)molecules on the NHS ester derivatized surfaces (Figure 1). The constructed microarrays were probed by using fluorophore-conjugated proteins or RNA for analysis of biomolecular interactions.

Initially, optimized surface derivatization conditions were explored using amine-conjugated Cy3 (**5**). The piranha solution-treated slide was incubated with dimethallylsilanes **1a** (3% or 6%) or **1b** (3%) in the presence of 0.1 equiv of $Sc(OTf)_3$ or TfOH for 8 h at room temperature. Various concentrations (7−500 μM) of **5** in 50 mM sodium phosphate buffer (pH 8.0) containing 40% glycerol were printed on the NHS ester-derivatized substrates by using a robotic pin-type microarrayer (*37*). The extent of probe immobilization was determined by measuring the fluorescence intensities of Cy3 in spots on the surfaces. It was found that the fluorescence intensities of spots on microarrays, fabricated using 0.1 equiv of $Sc(OTf)_3$, were reproducibly lower than those generated by using 0.1 equiv of TfOH (Figure 2a,b) as the catalyst. This finding shows that TfOH is a more efficient catalyst than $Sc(OTf)_3$ for the key Si−O−Si bond forming reaction. However, an increase in the amount of **1a** used in the modification reaction from 3% to 6% led to a slight improvement in the surface derivatization efficiency (Figure 2b,c). Interestingly, the length of tether (**1a** versus **1b**) has little effect on the surface modification efficiency (Figure 2b,d).

To further probe this surface modification/microarray methodology, various concentrations of proteins, carbohydrates, and small molecule samples (protein G, fucose, biotin, and mannan in 50 mM sodium phosphate buffer (pH 8.0) containing 40% glycerol, Figure 3) were printed on NHS ester coated slides, prepared by treatment with **1a** (3% or 6%) or **1b** (3%) in the presence of 0.1 equiv of $Sc(OTf)_3$ or TfOH. The microspotted slides were kept in a humidity chamber at room temperature for 3−5 h and were divided into several blocks by using an incubation blocker to avoid cross-contamination. Probing the microarrays with Cy5-*Aleuria aurantia* (Cy5-AA, a fucose-binding lectin), Cy3-streptavidin, and FITC-ConA (an α-mannose/α-glucose binding lectin) shows that the microarrays prepared using TfOH exhibit higher fluorescence intensities than those obtained using $Sc(OTf)_3$ (Figure 4a). It was also found that both the amount of **1a** (3% or 6%) used in the surface derivatization process and the length of tether (**1a** versus **1b**) have little influence on the surface derivatization efficiency and protein binding (Figure 4b,c). Therefore, surface derivatization conditions using 3% **1a** and 0.1 equiv of TfOH were used throughout the remainder of this study.

Prior to developing applications of this surface derivatization procedure for the fabrication of microarrays, the number of molecules immobilized on the NHS ester coated surface prepared with 3% **1a** and 0.1 equiv of TfOH was determined. To this end, various concentrations (7−500 μM) of **5** were printed on the NHS ester slide and the fluorescence intensities of the printed spots were measured before and after washing. The maximum density of the molecule immobilized on the surface was determined to be $(2-8) \times 10^{15}$ molecules/cm^2 (see Supporting Information), which is a little higher than that for an array prepared by using the conventional multistep approach (*33*,*38*).



6: protein G, **7:** fetuin, **8:** fucose-CONHNH$_2$, **9:** mannan, **10:** dextran, **11:** biotin-NH$_2$, **12:** proteinase K, **13:** collagenase, **14:** insulin, **15:** peptide 1-CONHNH$_2$ **16:** peptide 2-CONHNH$_2$, **17:** imidazole 1-NH$_2$, **18:** imidazole 2-NH$_2$, **19:** imidazole 3-NH$_2$, **20:** GlcNAc-CONHNH$_2$, **21:** LacNAc-CONHNH$_2$, **22:** asialo-fetuin.

Figure 3. Structures of substances used for immobilization on NHS-ester derivatized glass surfaces.

This result shows that glass surfaces are more efficiently derivatized with NHS esters when the single step process is employed.

To demonstrate the utility of the new surface derivatization method, various concentrations of the 17 substances shown in Figure 3 (1 nL in 50 mM sodium phosphate buffer (pH 8.0) containing 40% glycerol) were printed in duplicate on a NHS ester-derivatized glass slide, prepared by using 3% **1a** and 0.1 equiv of TfOH. The microarrays were divided into blocks in order to examine several biomolecular interactions with a single microarray. The substances used for printing are comprised of proteins (**6**, **7**, **12**−**14**, **22**), peptides (**15**, **16**), simple carbohydrates (**8**, **20**, **21**), polysaccharides (**9**, **10**), and small molecules (**11**, **17**−**19**). In the microarray, proteins and small molecules (*39*, *40*) are attached to the surface via amide bonds formed between amines and NHS esters on the surface. Peptides (*41*) and simple carbohydrates are immobilized on the surface through reactions of hydrazides with NHS esters (*28*). However, polysaccharides are attached to the surface via ester bonds between alcohols and NHS esters.

Glycan−protein interactions that play a critical role in a variety of physiological and pathological processes (*42*) were investigated initially by probing with fluorophore-labeled carbohydrate-binding proteins (five lectins and one antibody). Fluorescence data, obtained after incubating the microarrays with carbohydrate-binding proteins, are shown in Figure 5a−f. The findings show that Cy5-AA and FITC-ConA interact with fucose (**8**) and mannan (**9**), respectively (Figure 5a,b). The microarrays treated with sialic acid-binding proteins, such as Cy5-*Sambucus nigra* lectin (SNA, a α-2,6-linked sialic acid binding protein) and Cy3-*Maackia amurensis* lectin II (MAL II, a α-2,3-linked sialic acid binding protein), exhibit binding to fetuin (**7**), which is a glycoprotein containing NeuNAcα2,3Gal and NeuNAcα2,6Gal residues (Figure 5c,d) (*43*). However, these lectins do not interact with asialofetuin (**22**), which lacks sialic acid residues (*44*). In addition, the binding specificity of a carbohydrate-

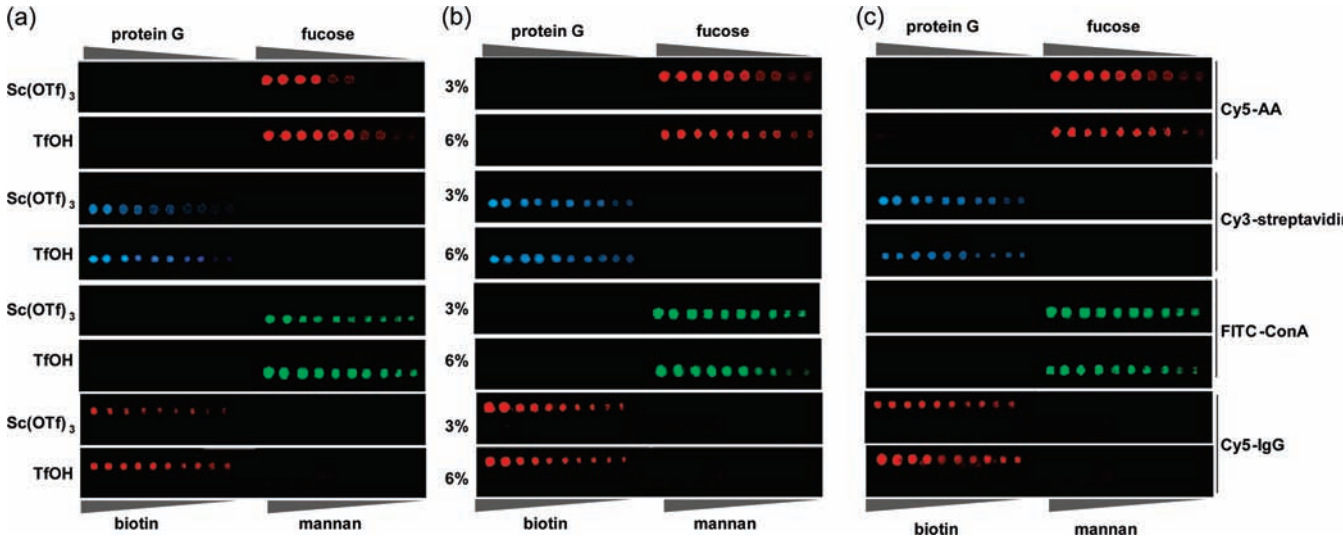


Figure 4. Immobilization of various concentrations of protein G (**6**) (15, 7.5, 3.75, 1.88, 0.94 μM), mannan (**9**) (10, 5.0, 2.5, 1.25, 0.65 mg/mL), fucose (**8**), and biotin (**11**) (2.0, 1.0, 0.5, 0.25, 0.125 mM) on the NHS-ester coated glass surface prepared under (a) 3% **1a** in the presence of 0.1 equiv of $Sc(OTf)_3$ or TfOH, (b) 3% or 6% **1a** in the presence of 0.1 equiv of TfOH, (c) 3% **1a** or 3% **1b** in the presence of 0.1 equiv of TfOH. The prepared microarrays were probed with Cy5-AA, Cy3-streptavidin, FITC-ConA, and Cy5-IgG (see Supporting Information for quantitative fluorescence intensity data).

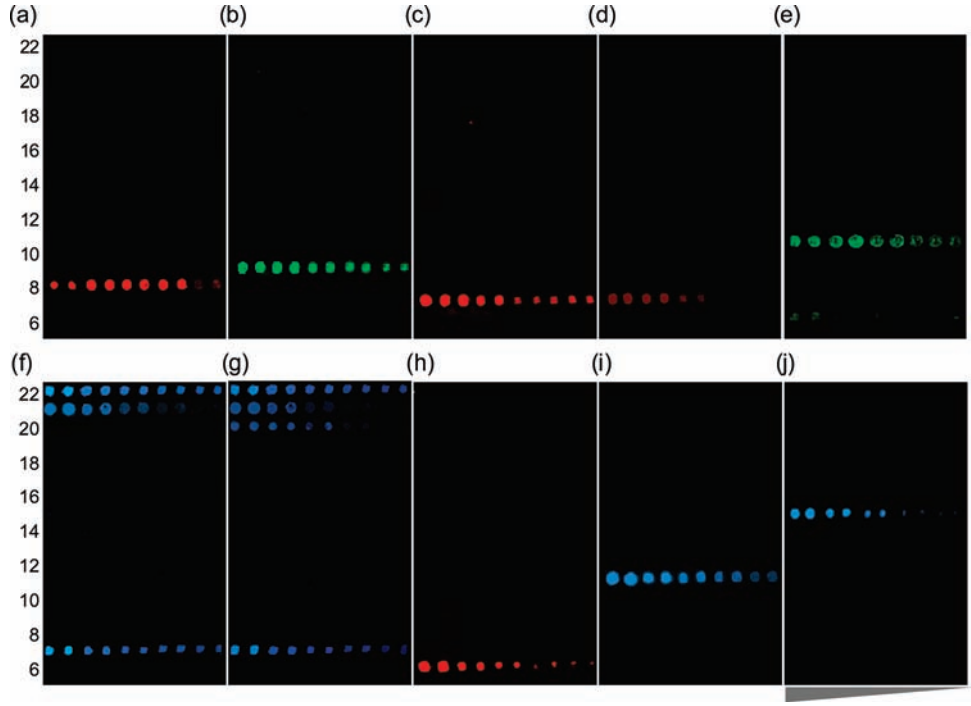


Figure 5. Fluorescence images of microarrays containing 17 substances (**6**−**22**) after probing with (a) Cy5-AA, (b) FITC-ConA, (c) Cy5-SNA, (d) Cy3-MAL II, (e) dextran-antibody followed by incubation with FITC-labeled anti-antibody, (f) Cy3-RCA_{120}, (g) Cy3-RCA_{120} after enzymatic reaction with β-1,4-GalT, (h) Cy5-IgG, (i) Cy3-streptavidin, and (j) Dy547-RRE. Concentrations of samples used for immobilization: proteins (**6**, **7**, **12**, **13**, **14**, **22**) 15, 7.5, 3.75, 1.88, 0.94 μM; polysaccharides (**9**, **10**) 10, 5.0, 2.5, 1.25, 0.65 mg/mL; small molecules, peptides and simple carbohydrates (**8**, **11**, **15**−**21**) 2.0, 1.0, 0.5, 0.25, 0.125 mM. See Supporting Information for quantitative fluorescence intensity data.

binding antibody was analyzed by using the microarrays. The results of experiments, in which the microarrays were probed with anti-dextran antibody followed by treatment with FITC-labeled goat IgG, show that anti-dextran antibody recognizes dextran (**10**) (Figure 5e). Since goat FITC-IgG was used as a secondary antibody to detect anti-dextran antibody, the spots containing protein G (**6**) also exhibit fluorescence.

The binding specificity of a galactose binding protein Cy3-*Ricinus communis* agglutinin 120 (Cy3-RCA_{120}) was determined by using the microarrays. The results indicate that RCA_{120} binds to galactose-containing substances, such as fetuin (**7**), LacNAc (**21**), and asialofetuin (**22**) (Figure 5f). Next, in order to profile β-1,4-GalT activity, the microarrays were incubated with 1 mU β-1,4-GalT (final concentration of 0.5 μM), 10 mM Mn^{2+}, and 1 mM UDP-Gal in 50 mM HEPES buffer (pH 7.5) at 37 °C. After a 3 h incubation period, the microarray slides were probed with Cy3-RCA_{120} in order to detect galactose moieties transferred by β-1,4-GalT (*18*). Notably, even when washing with hot SDS solution under sonication is not employed, a step that is normally (*18*, *45*) employed to reduce background fluorescence signals, the arrays do not display high background fluorescence signals. Probing the enzyme-treated microarrays

with Cy3-RCA_{120} leads to fluorescence patterns that show the conversion of GlcNAc to LacNAc catalyzed by this enzyme. The observations made in this effort demonstrate that the microarrays prepared by the new acid-mediated, one-step modification method can be effectively employed to assess carbohydrate-binding properties of proteins and to profile enzyme activities.

Attention next turned to the question of whether or not the fabricated microarrays could be used to study protein−protein and protein−small molecule interactions. For this purpose, the microarrays were incubated with IgG and streptavidin. The spots containing protein G (**6**) and biotin (**11**) were found to display fluorescence after being subjected to the respective IgG and streptavidin probes, respectively (Figure 5h,i). Finally, the microarrays were used to identify peptides or small molecules that interact with hairpin RNA, a motif often targeted by therapeutic agents (*46, 47*). For these studies, microarrays were treated with 10 μM 5′-Dy547-RRE (the HIV-1 Rev response element; see Supporting Information for its structure), a substance that forms a hairpin secondary structure that interacts with its natural partner the Rev peptide (*48*). The results show that the hairpin RRE RNA binds to the amphiphilic peptide **15**. However, peptide **16**, in which two lysines at the 2 and 6 positions are replaced with glutamines, is not recognized by RRE. This finding is consistent with studies that show that the 2- and 6-lysines are important elements for RRE recognition (*49*). The observations made in the RNA−peptide interaction studies demonstrate that the new microarrays can be applied in efforts aimed at the discovery of peptide-based drugs that target hairpin RNA.

CONCLUSIONS

The investigation described above has led to the development of a one-step, simple, and efficient method for the surface derivatization of glass as part of procedures for the construction of microarrays. The technique utilizes acid-mediated reactions of NHS ester functionalized dimethallylsilanes with the silanols present on glass surfaces. The surface modification process that employs TfOH as an acid catalyst was found to be superior to the one using $Sc(OTf)_3$. The results of protein and RNA-binding investigations show that glass surfaces modified by using this method are suitable for efficient immobilization of various substances, including proteins, peptides, carbohydrates, and small molecules, which are appended by amine, hydrazide, and alcohol functionalities. Microarrays, generated in this manner, are applicable to the rapid analysis of protein−protein, protein−glycan, protein−small molecule, and peptide−RNA interactions and profiling enzyme activities. The acid-mediated glass surface modification procedure developed in this effort should be applicable to the preparation of various functional group-modified surfaces that are utilized in the construction of various types of microarrays.

ACKNOWLEDGMENT

This work was supported by grants from the National Creative Research Initiative Program, NRF (Grant 2009-0059013), WCU (Grant R32-2008-000-10217-0), and CBMH programs (Project KOSEF/MEST).

Supporting Information Available: Measurement of the density of an immobilized molecule and quantitative analysis of fluorescence intensity of microarrays probed with biomolecules. This material is available free of charge via the Internet at http://pubs.acs.org.

LITERATURE CITED

(1) Fodor, S. P. A., Read, J. L., Pirrung, M. C., Stryer, L., Lu, A. T., and Solas, D. (1991) Light-directed, spatially addressable parallel chemical synthesis. *Science 251*, 767–773.

(2) Pease, A. C., Solas, D., Sullivan, E. J., Cronin, M. T., Holmes, C. P., and Fodor, S. P. A. (1994) Light-generated oligonucleotide arrays for rapid DNA sequence analysis. *Proc. Natl. Acad. Sci. U.S.A. 91*, 5022–5026.

(3) MacBeath, G., and Schreiber, S. (2000) Printing proteins as microarrays for high-throughput function determination. *Science 289*, 1760–1763.

(4) Zhu, H., Klemic, J. F., Chang, S., Bertone, S. P., Casamayor, A., Klemic, K. G., Smith, D., Gerstein, M., Reed, M. A., and Snyder, M. (2000) Analysis of yeast protein kinases using protein chips. *Nat. Genet. 26*, 283–289.

(5) Park, S., and Shin, I. (2002) Fabrication of carbohydrate chips for studying protein−carbohydrate interactions. *Angew. Chem., Int. Ed. 41*, 3180–3182.

(6) Wang, D., Liu, S., Trummer, B. J., Deng, C., and Wang, A. (2002) Carbohydrate microarrays for the recognition of cross-reactive molecular markers of microbes and host cells. *Nat. Biotechnol. 20*, 275–281.

(7) Fukui, S., Feizi, T., Galustian, C., Lawson, A. M., and Chai, W. (2002) Oligosaccharide microarrays for high-throughput detection and specificity assignments of carbohydrate−protein interactions. *Nat. Biotechnol. 20*, 1011–1017.

(8) Houseman, B. T., and Mrksich, M. (2002) Carbohydrate arrays for the evaluation of protein binding and enzymatic modification. *Chem. Biol. 9*, 443–454.

(9) Koch, W. H. (2004) Technology platforms for pharmacogenomic diagnostic assays. *Nat. Rev. Drug Discovery 3*, 749–761.

(10) Villeneuve, D. J., and Parissenti, A. M. (2004) The use of DNA microarrays to investigate the pharmacogenomics of drug response in living systems. *Curr. Top. Med. Chem. 4*, 1329–1345.

(11) Zhu, H., and Snyder, M. (2003) Protein chip technology. *Curr. Opin. Chem. Biol. 7*, 55–63.

(12) Uttamchandani, M., and Yao, S. Q. (2008) Peptide microarrays: next generation biochips for detection, diagnostics and high-throughput screening. *Curr. Pharm. Des. 14*, 2428–2438.

(13) Park, S., Lee, M.-R., and Shin, I. (2008) Carbohydrate microarrays as powerful tools in studies of carbohydrate-mediated biological processes. *Chem. Commun.* 4389–4399.

(14) Tomizaki, K. Y., Usui, K., and Mihara, H. (2005) Protein-detecting microarrays: current accomplishments and requirements. *ChemBioChem 6*, 782–799.

(15) Salisbury, C. M., Maly, D. J., and Ellman, J. A. (2002) Peptide microarrays for the determination of protease substrate specificity. *J. Am. Chem. Soc. 124*, 14868–14870.

(16) Sun, H., Lu, C. H., Shi, H., Gao, L., and Yao, S. Q. (2008) Peptide microarrays for high-throughput studies of Ser/Thr phosphatases. *Nat. Protoc. 3*, 1485–1493.

(17) Kuruvilla, F. G., Shamji, A. F., Sternson, S. M., Hergenrother, P. J., and Schreiber, S. L. (2002) Dissecting glucose signalling with diversity-oriented synthesis and small-molecule microarrays. *Nature 416*, 653–657.

(18) Park, S., and Shin, I. (2007) Carbohydrate microarrays for assaying galactosyltransferase activity. *Org. Lett. 9*, 1675–1678.

(19) Moon, J. H., Shin, J. W., Kim, S. Y., and Park, J. W. (1996) Formation of uniform aminosilane thin layers: an imine formation to measure relative surface density of the amine group. *Langmuir 12*, 4621–4624.

(20) MacBeath, G., Koehler, A. N., and Schreiber, S. L. (1999) Printing small molecules as microarrays and detecting protein−ligand interactions en masse. *J. Am. Chem. Soc. 121*, 7967–7968.

(21) Park, S., and Shin, I. (2002) Fabrication of carbohydrate chips for studying protein−carbohydrate interactions. *Angew. Chem., Int. Ed. 41*, 3180–3182.

(22) Park, S., Lee, M. R., Pyo, S. J., and Shin, I. (2004) Carbohydrate chips for studying high-throughput carbohydrate−protein interactions. *J. Am. Chem. Soc. 126*, 4812–4819.

(23) Adams, E. W., Ratner, D. M., Bokesch, H. R., Mcmahon, J. B., O'Keefe, B. R., and Seeberger, P. H. (2004) Oligosaccharide and glycoprotein microarrays as tools in HIV glycobi-

ology: glycan-dependent gp120/protein interactions. *Chem. Biol. 11*, 875–881.
(24) Sun, X.-L., Stabler, C. L., Cazalis, C. S., and Chaikof, E. L. (2006) Carbohydrate and protein immobilization onto solid surfaces by sequential Diels−Alder and azide−alkyne cycloadditions. *Bioconjugate Chem. 17*, 52–57.
(25) Blixt, O., Head, S., Mondala, T., Scanlan, C., Huflejt, M. E., Alvarez, R., Bryan, M. C., Fazio, F., Calarese, D., Stevens, J., Razi, N., Stevens, D. J., Skehel, J. J., van Die, I., Burton, D. R., Wilson, I. A., Cummings, R., Bovin, N., Wong, C.-H., and Paulson, J. C. (2004) Printed covalent glycan array for ligand profiling of diverse glycan binding proteins. *Proc. Natl. Acad. Sci. U.S.A. 101*, 17033–17038.
(26) de Paz, J. L., Noti, C., and Seeberger, P. H. (2006) Microarrays of synthetic heparin oligosaccharides. *J. Am. Chem. Soc. 128*, 2766–2767.
(27) Lee, M.-R., Park, S., and Shin, I. (2006) Protein microarrays to study carbohydrate-recognition events. *Bioorg. Med. Chem. Lett. 16*, 5132–5135.
(28) Lee, M.-R., and Shin, I. (2005) Fabrication of chemical microarrays by efficient immobilization of hydrazide-linked substances on epoxide-coated glass surfaces. *Angew. Chem., Int. Ed. 44*, 2881–2884.
(29) Park, S., Lee, M.-R., and Shin, I. (2007) Fabrication of carbohydrate chips and their use to probe protein−carbohydrate interactions. *Nat. Protoc. 2*, 2747–2758.
(30) Manimala, J. C., Li, Z., Jain, A., VedBrat, S., and Gildersleeve, J. C. (2005) Carbohydrate array analysis of anti-Tn antibodies and lectins reveals unexpected specificities: implications for diagnostic and vaccine development. *ChemBioChem 6*, 2229–2241.
(31) Lee, M.-R., and Shin, I. (2005) Facile preparation of carbohydrate microarrays by site-specific, covalent immobilization of unmodified carbohydrates on hydrazide-coated glass slides. *Org. Lett. 7*, 4269–4272.
(32) Zhi, Z. L., Powell, A. K., and Turnbull, J. E. (2006) Fabrication of carbohydrate microarrays on gold surfaces: direct attachment of nonderivatized oligosaccharides to hydrazide-modified self-assembled monolayers. *Anal. Chem. 78*, 4786–4793.
(33) Park, S., Lee, M.-R., and Shin, I. (2009) Construction of carbohydrate microarrays by using one-step, direct immobilizations of diverse unmodified glycans on solid surfaces. *Bioconjugate Chem. 20*, 155–162.
(34) Ko, K. S., Jaipuri, F. A., and Pohl, N. L. (2005) Fluorous-based carbohydrate microarrays. *J. Am. Chem. Soc. 127*, 13162–13163.
(35) Angeloni, S., Ridet, J. L., Kusy, N., Gao, H., Crevoisier, F., Guinchard, S., Kochhar, S., Sigrist, H., and Sprenger, N. (2005) Glycoprofiling with micro-arrays of glycoconjugates and lectins. *Glycobiology 15*, 31–41.
(36) Yeon, Y.-R., Park, Y. J., Lee, J.-S., Park, J.-W., Kang, S.-G., and Jun, C.-H. (2008) $Sc(OTf)_3$-mediated silylation on hydroxy functional groups on a solid surface: a catalytic grafting method operating at room temperature. *Angew. Chem., Int. Ed. 47*, 109–112.
(37) Lee, M.-R., Jung, D.-W., Williams, D., and Shin, I. (2005) Efficient solid-phase synthesis of tifunctional probes and their application to the detection of carbohydrate-binding proteins. *Org. Lett. 7*, 5477–5480.
(38) Liang, P.-H., Wang, S.-K., and Wong, C.-H. (2007) Quantitative analysis of carbohydrate−protein interactions using glycan microarrays: determination of surface and solution dissociation constants. *J. Am. Chem. Soc. 128*, 13668–13669.
(39) Williams, D. R., Lee, M.-R., Song, Y.-A., Ko, S.-K., Kim, G.-H., and Shin, I. (2007) Synthetic small molecules that induce neurogenesis in skeletal muscle. *J. Am. Chem. Soc. 129*, 9258–9259.
(40) Williams, D. R., Ko, S.-K., Park, S., Lee, M.-R., and Shin, I. (2008) An apoptosis-inducing small molecule that binds to heat shock protein 70. *Angew. Chem., Int. Ed. 47*, 7466–7469.
(41) Yang, S.-J., Tian, X., and Shin, I. (2009) Nondestructive, colorimetric monitoring of amines and thiols on a solid support. *Org. Lett. 11*, 3438–3441.
(42) Park, S., Lee, M.-R., and Shin, I. (2008) Chemical tools for functional studies of glycans. *Chem. Soc. Rev. 37*, 1579–1591.
(43) Nilsson, B., Norden, N. E., and Svensson, S. (1979) Structural studies on the carbohydrate portion of fetuin. *J. Biol. Chem. 254*, 4545–4553.
(44) Townsend, R. R., Hardy, M. R., Wong, T. C., and Lee, Y. C. (1986) Binding of N-linked bovine fetuin glycopeptides to isolated rabbit hepatocytes: Gal/GalNAc hepatic lectin discrimination between Gal beta(1,4)GlcNAc and Gal beta(1,3)GlcNAc in a triantennary structure. *Biochemistry 25*, 5716–5725.
(45) Eppinger, J., Funeriu, D. P., Miyake, M., Denizot, L., and Miyake, J. (2004) Enzyme microarrays: on-chip determination of inhibition constants based on affinity-label detection of enzymatic activity. *Angew. Chem., Int. Ed. 43*, 3806–3810.
(46) Hermann, T. (2005) Drugs targeting the ribosome. *Curr. Opin. Struct. Biol. 15*, 355–366.
(47) Gallego, J., and Varani, G. (2001) Targeting RNA with small-molecule drugs: therapeutic promise and chemical challenges. *Acc. Chem. Res. 34*, 836–843.
(48) Gosser, Y., Hermann, T., Majumdar, A., Hu, W., Frederick, R., Jiang, F., Xu, F., and Patel, D. J. (2001) Peptide-triggered conformational switch in HIV-1 RRE RNA complexes. *Nat. Struct. Biol. 8*, 146–150.
(49) Lee, S. J., Hyun, S., Kieft, J. S., and Yu, J. (2009) An approach to the construction of tailor-made amphiphilic peptides that strongly and selectively bind to hairpin RNA targets. *J. Am. Chem. Soc. 131*, 2224–2230.

BC100042J

Optimized Avidin Nucleic Acid Nanoassemblies by a Tailored PEGylation Strategy and Their Application as Molecular Amplifiers in Detection

Mauro Pignatto, Nicola Realdon, and Margherita Morpurgo*

Department of Pharmaceutical Sciences, University of Padova, Via Marzolo, 5, 35131 Padova, Italy. Received January 22, 2010; Revised Manuscript Received April 15, 2010

Avidin was recently found to display the ability to interact with high affinity with nucleic acids. In this work, we investigated how this property is affected by the protein modification with poly(ethylene glycol) (PEG). More precisely, we studied the influence of the size and geometry of the polymer and of the mode of anchorage to the protein surface. To this end, we synthesized five PEG derivatives capable of PEGylating avidin either through covalent attachment to its lysine primary amines or by exploiting its biotin binding pockets. Several differently PEGylated avidin derivatives were then obtained, which were later tested for their affinity for plasmid DNA by means of the electrophoretic mobility assay. The results show that covalent PEGylation reduces the affinity for DNA in a dose-dependent manner, whereas PEG anchoring through the biotin binding sites does not, even when bulky and high MW biotin-PEG derivatives are used. We then investigated how the size and molecular weight of the biotin-PEG affects the solubility and stability of avidin-nucleic acid nanoassemblies in physiological buffer. Among the biotin-PEG derivatives synthesized in this work, the branched forms were more efficient in protecting particle surface and preventing their aggregation. Full nanoparticle solubility was achieved by saturating 30% of the biotin binding sites with a 2 × 5 kDa branched derivative. the optimized avidin nucleic acid nanoassemblies (ANANAS) were employed in a model analytical test where they showed at least 40-fold higher efficiency than monomeric avidin in recognizing biotinylated surface immobilized IgGs. The results pave the way toward the application of this novel nanosystem in biomedicine.

INTRODUCTION

Avidin is a tetrameric glycoprotein known mainly for its ability to bind to four molecules of biotin with very high affinity ($K_d \approx 10^{-15}$ M), a property that forms the basis for its use as a molecular tool in a large number of biotechnological applications (the avidin−biotin technology) (*1*−*5*). The most common applications are in research and diagnostics, in the functionalization of surfaces, and in drug delivery for the targeting of drugs or diagnostic elements to defined locations in the body after parenteral administration (*6*−*10*). However, the classical avidin−biotin technology is somehow limited by the maximum number (four) of biotins that can be brought together by the individual avidin molecule which forms the central nucleus of the system. Having a core unit with greater biotin loading capacity can improve the potential of this technology, and this can be obtained by joining together several avidin molecules into a single unit (a "poly-avidin unit"). To this end, several approaches for obtaining polyavidins are described in the literature. The strategies most commonly adopted are based on the coating of micro- or nanospheres (polymer or metal-based) with several avidin molecules by exploiting nonspecific adsorption processes. Alternatively, several avidin units can be united either by chemical cross-linking or by using polybiotinylated spacers as bridging functions (*11*−*13*). All of these methods share the common drawbacks of leading to polydisperse systems with some degree of avidin inactivation. In practical terms, avidin inactivation is translated into a diminished total biotin binding capacity, whereas polydispersivity is translated into poly avidin assemblies with statistically rather than precisely defined properties. In addition, in most cases the components used for the assembly (namely, the chemical linkers or the polymeric particle cores) are not of natural origin or are potentially toxic, and this limits their use in in vivo biomedical applications.

Another possibility to obtain polyavidin particles is by taking advantage of an additional property of avidin that has been recently brought to light, namely, its ability to bind the nucleic acids with high affinity (*14*). In fact, secondary to this interaction, avidin self-assembles onto the DNA molecule in an organized manner, giving rise to stable agglomerates where the nucleic acid is coated by avidin molecules in a precisely defined stoichiometric ratio. This binding is stable at high dilutions and in physiological buffers and apparently does not directly involve the biotin binding site, since the affinity for DNA is higher in the presence of biotin (*14*).

However, the practical exploitation of these assemblies depends on the possibility to obtain them in the form of reproducible, solution stable and poorly polydispersed particles. In fact, from the macroscopic point of view, the avidin−nucleic acid assemblies assume various shapes and geometries depending on the conditions in which they are obtained (*14*). For example, by mixing avidin and nucleic acids in a buffered aqueous environment, the assembly process gives rise to agglomerates of large size (>1 μm), which are poorly soluble, highly polydispersed, and of undefined geometry, and therefore unusable from the practical viewpoint. Conversely, it was shown that, in a salt-free environment and under specific conditions of concentration and ratio of nucleic acids to protein, nanoparticulate structures of toroid or rod shape are obtained, in which a single nucleic acid molecule is surrounded by several avidin molecules. In this case, the nanoassemblies are poorly polydispersed and their size depends solely on the type and length of the nucleic acid used (*14*). However, when these nanoparticles are transferred into a buffered solution, they undergo a rapid process of aggregation subsequent to which polydispersed macro-aggregates are again obtained, unusable for practical purposes. Therefore, in order to exploit the avidin nucleic acid

* E-mail: margherita.morpurgo@unipd.it, Phone: (+39)-049-827-5339; Fax: (+39)-049-827-5366.

10.1021/bc100044u © 2010 American Chemical Society
Published on Web 06/08/2010

nanoassemblies (ANANAS) for practical application, it is necessary to find a way to prevent their aggregation in physiological buffers. One possibility is to protect their surface with the use of hydrophilic polymers, for example, poly(ethylene glycol) (PEG). The modification of bioactive elements with PEG is a well-known technology used since the 1970s (*15*, *16*) to biocompatilize protein drugs and protect them from undesired nonspecific interactions. The same strategy is also used to modify the surface of nanoparticles to improve their solution properties and/or their pharmacokinetic and immunogenic profiles (*17*−*19*), as is the case of the commercial doxorubicin liposome formulation DOXIL (or Caelyx) or of the fluorescent quantum dots (*20*). However, it is known that the type and amount of PEG linked to the surface is a critical point. For example, in the case of proteins, an excessive amount can impair the biological activity; on the other hand, if the amount is too low, it may not be sufficient to improve the pharmacokinetic or pharmacodynamic properties of either proteins or nanoparticles or to prevent them from nonspecific interactions. Therefore, the amount of PEG, the size and shape of the polymer, as well as the chemistry of conjugation are all important variables that need to be optimized (*21*−*23*).

In the case of avidin, two strategies can be adopted to link the PEG chains. On one hand, the polymer can be linked to the protein by classic covalent coupling. On the other hand, it can be attached to the protein by exploiting its biotin binding sites. In any case, the size, geometry, and amount of polymer must be optimized not to affect the twofold protein biological activity, namely, its ability to bind with high affinity both biotin and DNA. In this work, we first investigated the effect of PEG grafting on the ability of avidin to bind the nucleic acids. More precisely, we tested the influence of the amount of PEG and of the mode of grafting to the protein surface, covalent versus the biotin bridging. We then studied the influence of the size, the geometry, and the amount of PEG added to the surface of the nanoparticles on their aggregation in physiological buffer. The results clearly show the importance of identifying the best strategy of surface modification to achieve optimal results. The applicability of the optimized surface-protected nanoparticles in a model analytical assay demonstrate for the first time the potentialities of the avidin−nucleic acid nanoassemblies as novel tools in biomedicine.

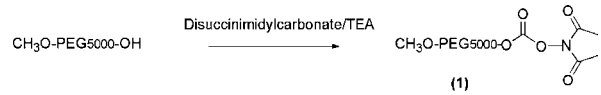
EXPERIMENTAL PROCEDURES

Materials and Instrumentation. Glycosylated chicken egg avidin was obtained from Belovo Chemicals, Belgium. Plasmid pEGFP-C1, 4.7 kb, was from Clontech. Water was Milli-Q or double-distilled (dd-H_2O) grade.

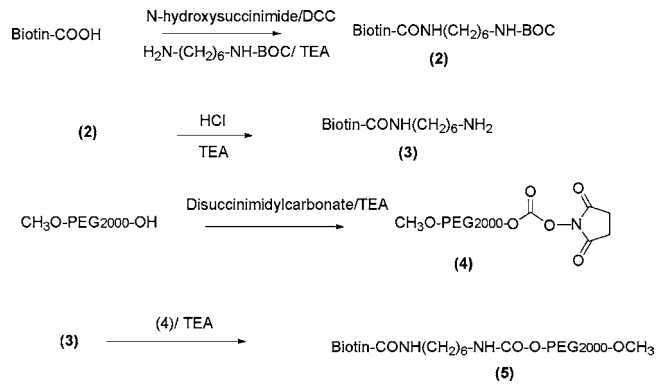
O-Methyl-poly(ethylene glycol) (2 kDa and 5 kDa, methyl-PEG2000-OH and methyl-PEG5000-OH), *O*-(2-aminoethyl)-*O*′-methyl-poly(ethylene glycol) (5 kDa, methyl-PEG5000-NH_2), α-biotin-ω-carboxy-succinimidyl ester poly(ethylene glycol) (5 kDa, biotin-PEG5000-CO-OSu, 5 kDa) was purchased from IRIS Biotech Gmbh (Marktredwitz, Germany), biotinamidocaproate *N*-hydroxysuccinimidyl ester and *N*,*N*′-di-Boc-L-lysine hydroxysuccinimidyl ester, horseradish peroxidase (Tpe VI), and all other reagents were purchased from Sigma-Aldrich (St. Louis, MI, USA); normal goat IgG was purchased from KPL (Gaithersburg, MA, USA); biotin-AlexaFluor^{546} was from Molecular probes (Invitrogen Corporation, USA). All other chemicals were from Sigma-Aldrich.

NMR analysis was carried out using a Bruker AMX 300 MHz. Agarose gel electrophoresis analysis was performed using the Biorad GEL DOC XR trans-illuminator; UV spectra were recorded on a Varian cary 50 UV−vis spectrophotometer; fluorescence was determined using a JASCO FP-6200 spectrofluorimeter. Dynamic light scattering measurements were performed using an in-house assembled system as further described in the Experimental Procedures. Biotinyl derivatives were detected by spraying the TLC plate with an acidic dimethylamino cinnamaldehyde solution (*24*); NH-containing compounds were detected using ninhydrin (*25*, *26*). Primary amines in solution were detected and quantified by the trinitrobenzenesulfonic acid assay (TNBSA) according to Habeeb (*27*, *28*). Biotin in solution was quantified by the 2-(4′-hydroxyazobenzene) benzoic acid (HABA) assay (*29*). PEG in solution was detected and quantified by the iodine method (*28*).

Scheme 1



Scheme 2



Synthesis of PEG Derivatives. *O-(N-Hydrosuccinimidyl-carbonate)-O′-methyl-poly(ethylene glycol)5000 (**1**, Scheme 1).* A similar procedure as the one described by Miron et al. (*30*) was followed. *O*-Methyl-poly(ethylene glycol)5000 (5 g, 1 mmol) was dried by azeotropic distillation in toluene and then redissolved in an anhydrous mixture of chloroform/toluene (1:3) (40 mL) containing disuccinimidylcarbonate (DSC) (1.02 g; 4 equiv) and triethylamine (TEA) (556 μL; 4 equiv). The reaction was stirred for 12 h at room temperature; the product was precipitated in anhydrous diethyl ether, recovered by filtration, and dried in vacuo. It was then purified by hot−cold crystallization in absolute ethanol, filtered, rinsed with ether, and dried in vacuo.

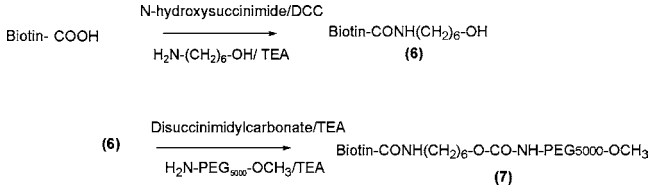
^{1}H NMR (d_6-DMSO, 300 MHz) δ 4.46 and 3.38 ppm (t, 2H, -O-CO-OC$\underline{H}_2$-CH), δ 3.38 ppm (s, 3H, $-CH_2CH_2-O-C\underline{H}_3$-). The degree of conversion was 95%; yield 92%.

*N-BOC-biotinamidohexylamine (**2**, Scheme 2).* Biotin (0.5 g; 2 mmol) was dissolved in dry dimethylformamide (DMF, 12 mL); then, *N*-hydroxysuccinimide (259 mg; 1.1 equiv) and dicyclohexylcarbodiimide (DCCI, 464 mg; 1.1 equiv) were added. The reaction was carried out at room temperature and was monitored by TLC (chloroform/methanol 80/20). After 12 h, the dicyclohexyl urea formed was removed by filtration and *N*-BOC-1,6-diaminohexane (517 mg; 1 equiv) and TEA (286 μL; 1 equiv) were added. After 2 h at room temperature, the product (*N*-BOC-biotinamidohexylamine, compound **2**) was precipitated by adding cold water, it was isolated by filtration and rinsed with cold HCl 0.1 N and anhydrous diethyl ether, dried in vacuo, and the purity assessed by ^{1}H NMR. The degree of conversion was 100%; yield 90%.

^{1}H NMR (d_6-DMSO, 300 MHz) δ 4.29 and 413 ppm (m, 2H, NH-C$\underline{H}$R-C$\underline{H}$R-NH in biotin ring), δ 1.37 ppm (s, 9H, C(C$\underline{H}_3$)$_3$).

Biotinamidohexylamine (3, Scheme 2). Compound **2** was dissolved in methanol saturated with HCl. After 15 min, the solvent was evaporated and the product was redissolved in the

Scheme 3



minimum amount of chloroform, and TEA was added to obtain biotinamidohexylamine as the free base. The insoluble product was isolated by filtration; it was rinsed with chloroform and cold diethyl ether and dried in vacuo. The degree of conversion was 100%; yield 52%.

^{1}H NMR (d_6-DMSO, 300 MHz) of **2**: δ 4.29 and 4.12 ppm (m, 2H, -NH-CHR-CHR-NH in biotin ring), δ 3.03 ppm (m, 2H, -CO-NH-CH$_2$-).

*O-(N-Hydrosuccinimidylcarbonate)-O′-methylpoly(ethylene glycol)2000 (**4**, Scheme 2).* This compound was synthesized through the same protocol as compound **1** (*30*) using methyl-PEG2000 instead of methyl-PEG5000.

^{1}H NMR (d_6-DMSO, 300 MHz) δ 4.46 and 3.38 ppm (t, 2H, -O-CO-OCH$_2$-CH), δ 3.38 ppm (s, 3H -CH$_2$CH$_2$-O-CH$_3$-). The degree of conversion was100%; yield 83%.

*O-Biotinamidohexylamate,O′-methyl-PEG2000 (methyl-PEG2000-biotin, **5**, Scheme 2).* Compound **3** (10 mg; 0.03 mmol) was dissolved in anhydrous dimethylsulfoxyde (DMSO, 1.5 mL), and compound **4** (200 mg; 3 equiv) and TEA (4.2 μL; 1 equiv) were added. The reaction was stirred for 2 h at room temperature, and the product was then precipitated in diethyl ether, filtered, and dried under vacuum. After hot−cold crystallization in absolute ethanol, the product was rinsed with diethyl ether and dried in vacuo. It was analyzed by ^{1}H NMR; the absence of unreacted biotinamidohexylamine was also confirmed by TNBSA assay. Biotin titer in the final product was measured by the HABA assay.

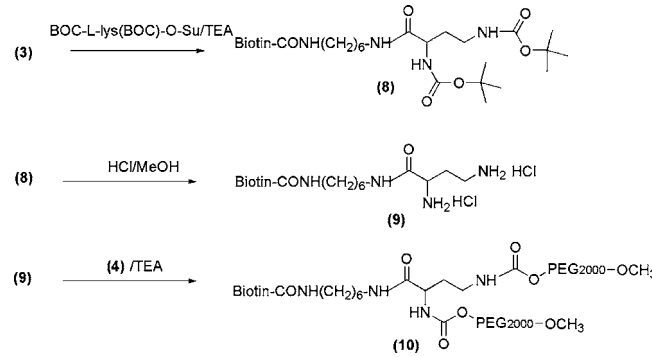
^{1}H NMR (*d*-chloroform, 300 MHz) δ 4.51 and 4.32 ppm (m, 2H, -NH-CHR-CHR-NH in biotin ring); δ 4.04 ppm (m, 2H, -CO-O-NH-CH$_2$-CH$_2$-O-), δ 3.64 ppm (wide s, about 180 -O-CH$_2$-CH$_2$-O-, PEG chain). The degree of amine conversion was 100%; yield 90%.

Biotinamidohexanol (6, Scheme 3). This product was synthesized through a similar procedure as the one followed to obtain compound **2**. 6-Aminohexanol was used instead of *N*-BOC-1,6-diaminohexane. It was isolated upon filtration after precipitation with cold, diluted HCl. It was then rinsed with diethyl ether and dried in vacuo.

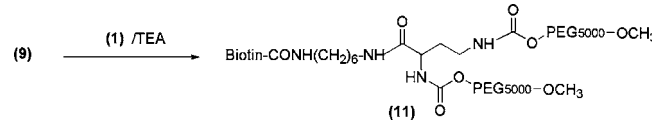
^{1}H NMR (d_6-DMSO, 300 MHz) δ 7.71 ppm (t, 1H, -CH$_2$-OH), δ 4.31 and 4.12 ppm (m, 2H, -NH-CHR-CHR-NH in biotin ring). The degree of biotin conversion was 100%; yield 56%.

*O-Biotinamidohexanolamate,O′-methyl-poly(ethylene glycol)5000 (methyl-PEG5000-biotin) (**7**, Scheme 3).* Compound **6** (150 mg; 0.43 mmol) was dissolved in anhydrous DMF (5 mL) and DSC (243 mg; 2.2 equiv) and TEA (150 μL; 2.5 equiv) were then added. After stirring overnight at room temperature, the solution was mixed with *O*-(2-aminoethyl)-*O′*-methyl-poly(ethylene glycol) (5 kDa, 500 mg; 0.23 equiv) previously dehydrated by azeotropic distillation in toluene. The reaction was monitored by TLC (chloroform/methanol 80/20) until the polymer amino groups were no longer detectable by ninhydrin assay. The product was extracted in chloroform, washed with diluted HCl, then with diluted Na_2CO_3, and, finally, with water. The organic phase was dried over $MgSO_4$, concentrated by rotavapor, and the product precipitated in anhydrous cold diethyl ether, filtered, and dried in vacuo. It was analyzed by ^{1}H NMR; its biotin titer was also confirmed by HABA assay.

Scheme 4



Scheme 5



^{1}H NMR (*d*-chloroform, 300 MHz) Biotin-mPEG5000 δ 4.53 and 4.35 ppm (m, 2H, -NH-CHR-CHR-NH in biotin ring), δ 4.03 ppm (m, 2H, -CO-O-NH-CH$_2$-CH$_2$-O-), δ 3.63 ppm wide s, about 450 -O-CH$_2$-CH$_2$-O-, PEG chain). The degree of amine modification was 100%, yield 82%.

*Biotinamidohexylamido-L-lys·(HCl)$_2$ (**9**, Scheme 4).* Compound **3** (203 mg, 0.594 mmol) was dissolved in of 4 mL of dry DMF. This solution was added of 290 mg of *N*,*N′*-di-Boc-L-lysine hydroxysuccinimide ester (0.653 mmol, 1.1 equiv), previously dissolved in 3 mL of dry DMF, followed by 82.6 μL of TEA (0.594 mmol, 1 equiv). The reaction was stirred for one hour at room temperature. The product (**8**) was precipitated by the addition of cold, dry diethyl ether, then washed with cold aqueous diluted Na_2CO_3 in H_2O, the diluted citric acid in H_2O, and finally water. It was then redissolved in HCl-saturated chloroform to remove the BOC group. The reaction was monitored by TLC, and after 30 min, biotin-L-lys·(HCl)$_2$ (**9**) was precipitated by the addition of diethyl ether; it was then isolated by filtration and dried in vacuo.

^{1}H NMR (*d*-chloroform, 300 MHz) δ 4.30 and 4.14 ppm (m, 2H, -NH-CHR-CHR-NH in biotin ring), δ 3.74 ppm (m, 1H, CO-CHR-NH$_2$·HC in lysine). The degree of biotinamidohexylamine conversion was 100%; yield 47%.

*Biotinamidohexylamido-L-lys·(methyl-PEG2000)$_2$ (biotin-L-lys-(methyl-PEG2000)$_2$, **10**, Scheme 4).* Compound **9** (8.2 mg, 0.015 mmol) was dissolved in anhydrous dimethylsulfoxide (DMSO) (1.5 mL). Compound **4** was added in several aliquots, each time followed by the same number of equivalents of TEA. One hour after each addition, a small portion of the solution was tested for primary amine content by TNBSA assay. This was repeated until no more free amines could be detected. Due to the large excess of compound **4** used, the final mixture was composed of the desired product together with the hydrolyzed excess of methyl-PEG2000-OH. The PEG mixture was isolated by diethyl ether precipitation and purified by hot−cold crystallization in absolute ethanol, filtered, and dried in vacuo. The amount of biotin-L-lys-(methyl-PEG2000)$_2$ in the final powder was determined on the basis of its biotin titer using the HABA assay. The absence of unreacted primary amines was verified by TNBSA assay. The degree of amine coupling was 100%, PEG product recovery 80%.

*Biotinamidohexylamido-L-lys·(methyl-PEG5000)$_2$ (**11**, Scheme 5).* Compound **9** (13.2 mg, 0.024 mmol) was dissolved in anhydrous DMSO (5 mL), followed by Compound **1** and TEA in a similar fashion as described above for compound **10**. In

Table 1. Properties of Covalent Methyl-PEG5000−Avidin Conjugates

sample name	PEG/avidin in the reaction (mol/mol)	mean number PEG molecules per protein
avidin-$(mPEG5000)_1$	20	1.2
avidin-$(mPEG5000)_{2.1}$	40	2.1
avidin-$(mPEG5000)_{3.6}$	80	3.6

this case, the final mixture was composed of the desired product together with the hydrolyzed excess of mPEG−OH5000. It was isolated by ether precipitation and purified by hot−cold crystallization in absolute ethanol, filtered, and dried under vacuum. The amount of the biotin-L-lys-$(methyl\text{-}PEG5000)_2$ in the mixture was determined on the basis of its biotin titer using the HABA assay. The absence of unreacted primary amines was verified by TNBSA assay.

The degree of amine coupling was 100%, PEG product recovery 87%.

PEGylation of Avidin. *Covalent PEGylation.* We obtained three avidin−PEG covalent conjugates by mixing the protein (10 mg/mL), dissolved in 0.1 M borate pH 8.0, with different amounts of **1**. The polymer/avidin molar ratio in the reaction mixtures was 20, 40, and 80 (15 mg, 30 mg, and 60 mg of compound **1** every milliliter of avidin solution). Each solution was gently mixed for 2 h at room temperature, and the products were purified by ultrafiltration using a polyethersulfone filter membrane (cutoff 30 kDa). Removal of unbound PEG was verified by testing the eluate by iodine assay. Protein concentration in the final solution was determined by UV absorbance ($E_{0.1\%}$ at 280 nm = 1.54). The mean number of polymer chains bound to the protein was determined by both TNBSA and iodine assays. The properties of the resulting products are summarized in Table 1.

PEGylation via Biotin Bridge. PEGylated avidins at controlled PEG/avidin ratios were obtained using compounds **5**, **7**, **10**, and **11** by exploiting the high affinity of avidin for the biotin moiety. Avidin was dissolved in PBS buffer and the biotin-PEG derivative was then added at the desired biotin/avidin molar ratio. We assumed that all of the biotin residues added to the solution would stably bind to avidin. No purification was necessary.

Other Biotinylated Proteins. *Biotin-PEG-Horseradish Peroxidase.* Horseradish peroxidase type VI (HRP) was dissolved in 0.1 borate buffer pH 8.0 (1 mg/1 mL) and biotin-PEG5000-CO-OSu (1.2 mg) was added (PEG/HRP molar ratio = 10). The solution was gently mixed for 1 h at room temperature. The product was purified by ultrafiltration using a polyethersulfone filter membrane (MWCO 30 kDa). HRP concentration in the final solution was determined by UV absorbance ($E_{0.1\%}$ at 403 nm = 2.5). The mean number of biotin−PEG chains bound to the protein was determined by both HABA and "iodine" assays using standard curves obtained with the corresponding polymer. The PEG/HRP molar ratio in the final product was 1.2:1.

Biotin-Immunoglobulin G (IgG). Normal goat IgG was dissolved in 10 mM phosphate, 150 mM NaCl, pH 7.4 (PBS) buffer at 3 mg/mL and added of 2.7 μL of a DMSO solution of biotinamidocaproate *N*-hydroxysuccinimidyl ester (5 mg/mL, biotin/IgG = 1.5:1). The solution was gently mixed for 1 h at room temperature. The product was purified from low-molecular-weight side products by gel filtration using a Sephadex G25 resin. The degree of biotinylation was determined by means of the HABA assay after trypsin digestion according to standard procedures. The biotin/IgG molar ratio in the final product was 1.3:1.

Interaction of the PEGylated Avidins with Plasmid DNA. The ability of avidin and of its PEGylated derivatives to interact with plasmid DNA was assessed by electrophoretic mobility assay (EMSA) on an agarose gel (*14*). Unmodified avidin (with or without biotin), covalently PEGylated avidin (with or without biotin), and avidin previously saturated with different amounts of selected biotin-PEGs or biotin-PEG-peroxidase were tested. Experiments were carried out by mixing constant amounts of a DNA in PBS to equal volumes of avidin solutions (in PBS) at increasing concentration according to the desired molar (or charge) ratios. The final DNA concentration in all mixtures was 6.25 μg/mL. Twenty-four microliter aliquots of each final solution were then loaded on 0.8% agarose gels and run for about 60 min at 80 mV voltage. DNA in the gel was visualized by fluorescence (ethidium bromide) using a GEL DOC XR trans-illuminator (Biorad), and band fluorescence intensity was quantified with *ImageJ* software. For quantitative analysis, the time of exposure to UV light was controlled in order to prevent signal saturation. The linearity of fluorescence intensity versus DNA concentration was verified by means of calibration curves built in parallel to each experiment (serial dilutions from 6.25 μg/mL to 24 ng/mL dissolved in the same buffer).

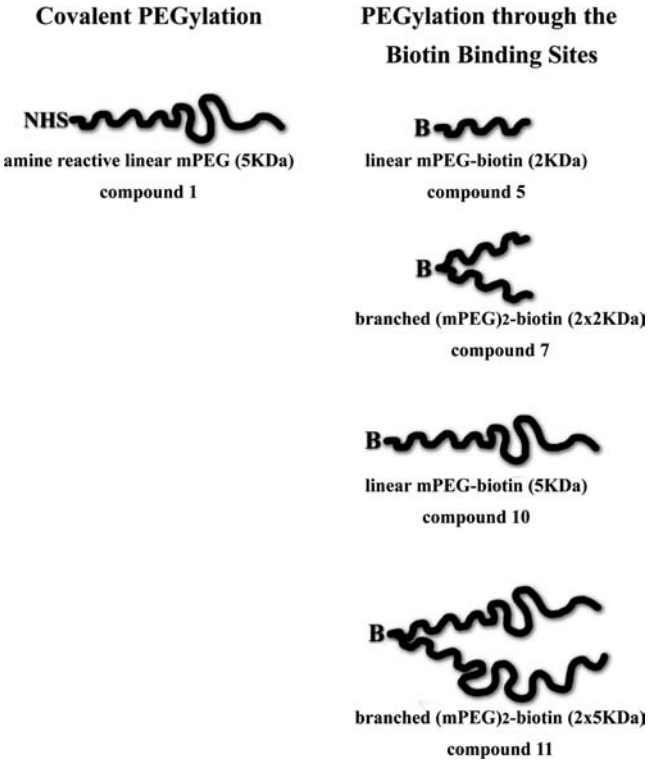
Preparation of Nanoassembled Avidin−Nucleic Acid Complexes. DNA (430 μg/mL) and avidin (20 μg/mL) were dissolved in double-distilled water (dd-H_2O) and cooled in an ice bucket. Equal volumes of each solution were then mixed while vortexing. Vortexing was maintained for 10 s after mixing, and then samples were kept in an ice bucket until further use.

Aggregation Studies. Nanoassembly aggregation was tested by following the increase in time of the average particles size via dynamic light scattering measurements (DLS). These experiments were carried out with core nanoparticles obtained as described above and upon addition of different amounts of each of the biotin-PEG synthesized. DLS measurements were carried out on samples after preparation in dd-H_2O and after the addition of 0.1 vol of 10× PBS buffer. Measurements were repeated every 5−10 min for up to 2 h or until precipitation occurred.

Light scattering measurements were performed using an in-house assembled system. Samples (300 μL) were placed in thin-walled cylindrical borosilicate glass cuvettes (1 cm diameter) and placed in a vat filled with toluene as the index matching fluid. During the course of the measurements, the vat temperature was kept at 25 °C. The light source was a Spectra Physics Stabilite 2017 laser (λ = 632.8 nm), and photons scattered by the sample were collected by a photomultiplier tube mounted on the goniometer arm at 90° to the direction of the incident radiation. The photoelectron count-time autocorrelation function was measured with a Pacific Scientific NICOMP 370 correlator. Applying the Stokes−Einstein equation to the translation diffusion coefficients provides an intensity-weighted distribution of hydrodynamic sizes (*31*).

Optimized Nanoassemblies in a Model Analytical Test. Nanoassemblies were obtained in dd H_2O at charge ratio of ±3 as previously described (calculated on the basis of the number of basic and acid residues on avidin that give rise to a net positive charge of 24 at pH 7.4 (*14*)), using a stock avidin solution where 2% of the total biotin binding sites had been saturated with biotin-$AlexaFluor^{546}$. Compound **11** was then added in order to cover 30% of the total biotin binding sites. After 1 h, the excess of avidin unbound to the DNA was removed using a cross-flow filtration cartridge (Vivaspin 50, Sartorius Stedim Biotech S.A., Aubagne Cedex, France) with a membrane with 100 kDa cutoff and water as the flowthrough buffer. The amount of avidin in the eluting buffer was quantified through the $AlexaFluor^{546}$ fluorescent signal (λ_{exc} 556; λ_{emiss} 573). The retained solution containing the nanoassembled avidin was analyzed by dynamic light scattering and used in a dot blot assay described as follows.

Scheme 6



Various amount of biotinylated goat IgG (99 ng to 0.02 ng in 0.2 μL) were spotted on a nitrocellulose membranes, which were then soaked 60 min in a blocking solution (10% skimmed milk in PBS). Avidin as a monomer or in the form of the ANANAS assembly was added to the block solution to a final concentration of 4 μg/mL. After 60 min, the membranes were thoroughly washed with PBS and incubated for 60 min with biotin-PEG-HRP dissolved in 10% skim milk/PBS (4 μg/mL). After washing, detection was carried out by adding a 3,3′-diaminobenzidine (DAB)/H_2O_2 solution in PBS (0.03% and 0.015%, respectively). The reaction was stopped after 10 min by washing the membrane twice with dd-H_2O. The intensity of the signal generated on the membrane was quantified after air drying upon recording the membrane image with a digital camera and using the NIH *ImageJ* software.

RESULTS

Synthesis of the PEG Derivatives for Avidin PEGylation. PEGylation of avidin was achieved either through covalent bonding at the protein primary amines or through the addition of biotinylated PEGs. All PEGylating derivatives were synthesized within this work. More precisely (Scheme 6), we obtained one amine reactive derivative of methyl-PEG having 5000 Da MW (**1**) that was used for covalent coupling and four biotin-PEG derivatives (compounds **5**, **7**, **10**, **11**) (Schemes 2−5) with different sizes (from 2000 to 10 000 Da) and geometry (linear or branched) for high-affinity attachment through the biotin binding pockets. In all biotin derivatives, a 6 carbon atom spacer between biotin and the polymer chain was introduced to maximize the interaction with the protein (*32*).

The PEG reagent for covalent modification (**1**) was synthesized according to a protocol already described in the literature (*30*). The same compound was also used as an intermediate for the preparation of two of the four biotin-PEG derivatives. The latter were obtained either (a) by generating primary amine-containing derivatives of biotin (compounds **3** or **9**), which were reacted with an excess of amine-reactive PEG, or (b) by synthesizing an amine-reactive derivative of biotin (DSC derivative of compound **6**) which was reacted with biotin-PEG-amine. All syntheses have been carried out in such a way to guarantee the final product would not contain any biotin derivative of low or intermediate molecular weight. In fact, this was fundamental for later experiments, which required the preparation of avidin/biotin-PEG complexes with polymer/protein molar ratios precisely defined. All product mixtures were therefore characterized for their biotin and primary amine titers using the HABA and TNBSA assays, respectively. The composition of the four product mixtures is shown in Table 2.

In order to achieve full biotin modification through the first synthetic strategy, (compounds **5**, **10**, and **11**), excess of amine-reactive PEGs had to be used. As a consequence, the final reaction products were composed of mixtures of the desired biotinylated-PEG together with the excess of hydrolyzed polymer reagent. Even if this impurity is inert and does not interfere with the avidin−DNA interaction, the exact composition of the product had to be precisely determined.

In the case of the linear derivatives, two distinct synthetic strategies were adopted, which lead to derivatives with an inverted chemistry within the six-carbon spacer between the biotin and PEG moieties. The choice of using the two strategies was made in order to compare them in terms of reaction efficacy and cost. We assumed that small differences in this region of the conjugate would have no influence on the final properties of the PEGylated avidin. As opposed to the first synthetic strategy described, quantitative PEG biotinylation was achieved by reacting the amine-PEG with an excess of amine-reactive biotin. The excess of low-molecular-weight biotin derivative was removed through the washing steps, and the final product (compound **7**) was composed of the sole biotin-PEG. This strategy was indeed more straightforward than the previous one. However, it required the use of methyl-PEG-amine, which is more expensive than the hydroxyl derivative.

Effect of PEGylation on the Affinity of Avidin for Plasmid DNA. The interaction of DNA with any DNA binding agent can be followed by gel retardation assay (EMSA). The assay is based on the rationale that the electrophoresis mobility of a biomolecule in a nondenaturing gel depends on both its charge and molecular weight. If a DNA-binding agent is added to the DNA prior to its loading on the gel, the electrophoresis mobility of DNA will vary depending on the size and charge of the resulting complex. In the assay, the binding agent is mixed with DNA at different molar ratios and loaded in the gel. Qualitative and quantitative information on the interaction can be obtained by measuring the intensity of the band relative to the unbound (free) DNA. Quantitative information may also be obtained from the intensity and position of the band(s) relative to the bound DNA.

In this work, the assay was used to estimate the relative affinity of avidin differently PEGylated either through covalent attachment to its surface lysines or by adding stoichiometrically controlled

Table 2. Biotin Titer, Primary Amine, and Unmodified Methyl-PEG Content in 1 g of Biotin-mPEG Compounds 1, 7, 10, and 11

	PEGylated biotins (moles × 10^{-5})	primary amines (moles ×10^{-5})	unmodified mPEG (moles ×10^{-4})
Methyl-PEG2000-biotin (**5**)	13.10	0	3.50
Methyl-PEG5000-biotin (**7**)	16.50	0	0
Biotin-L-lys-(methyl-PEG2000)$_2$ (**10**)	4.83	0	3.96
Biotin-L-lys-(methyl-PEG5000)$_2$ (**11**)	1.57	0	1.67

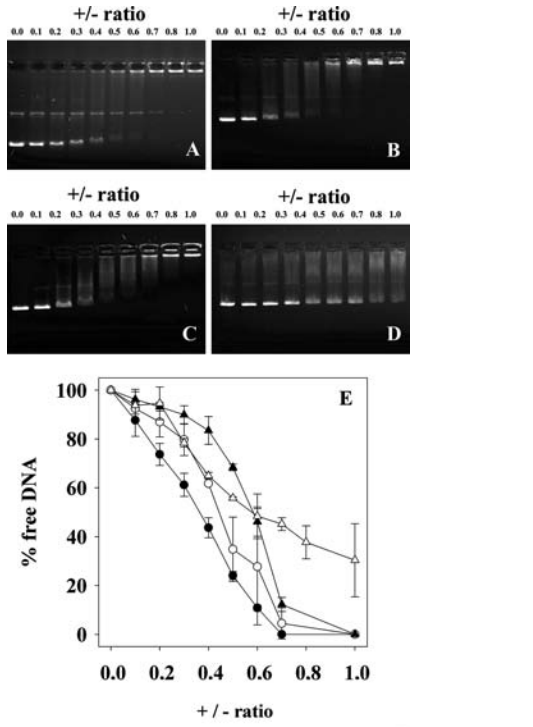


Figure 1. Electrophoretic mobility assay of plasmid DNA upon interaction with avidin covalently modified with increasing amounts of methyl-PEG5000 (see methods): (A) native avidin; (B) methyl-PEG 5000/avidin = 1.2; (C) methyl-PEG 5000/avidin = 2; (D) methyl-PEG 5000/avidin = 3.6; (E) binding curves obtained measuring the intensity of band relative to the free DNA; experiments were carried out in duplicate: (•) native avidin; (°) methyl-PEG 5000/avidin = 1.2; (▲) methyl-PEG 5000/avidin = 2; (Δ) methyl-PEG 5000/avidin = 3.6.

amounts of biotinylated-PEGs. The experiments were performed on agarose gels, and the amount of free DNA in each sample was quantified by measuring the fluorescence intensity of the ethidium bromide-stained bands. Binding curves were derived as a function of the protein/plasmid molar ratio. Since avidin is a basic protein characterized by a large excess of positively charged residues (12 acid vs 17 basic amino acids + 1α-NH_2/subunit), the same data can be plotted by substituting the protein/plasmid molar ratio with the corresponding (±) charge ratio, a parameter that is commonly used when evaluating DNA binding proteins that have a positive charge in physiological buffer.

Figure 1 shows the images of the DNA electrophoretic mobility assay carried out with avidin covalently modified with increasing amounts of methyl-PEG5000. The binding curves obtained from the quantitative analysis of band intensity are also reported. The results indicate that, when PEG is covalently bound to avidin, its affinity for DNA decreases in a dose-dependent manner. At one PEG per avidin, the loss of affinity is of minor intensity; however, at higher polymer loading it becomes dramatic.

In order to evaluate the effect of the mode of PEGylation, avidins with the same total PEG load attached either through covalent binding or via biotin bridge were tested in parallel. Figure 2A and B shows the results of the EMSA carried out with avidin in its native form or PEGylated with 1 or 4 molecules of methyl-PEG5000 attached either covalently (compound **1**) or through the biotin bridge (compound **7**).

PEGylation through biotin bridging has no impact on the affinity for DNA that remains totally preserved. Since it is known that the affinity of avidin for plasmid DNA increases upon addition of biotin (*14*), the covalently PEGylated avidins were also tested upon addition of free biotin at equimolar amounts as the PEG molecules covalently bound. The loss in affinity caused by covalent attachment is only partially reversed by the presence of biotin.

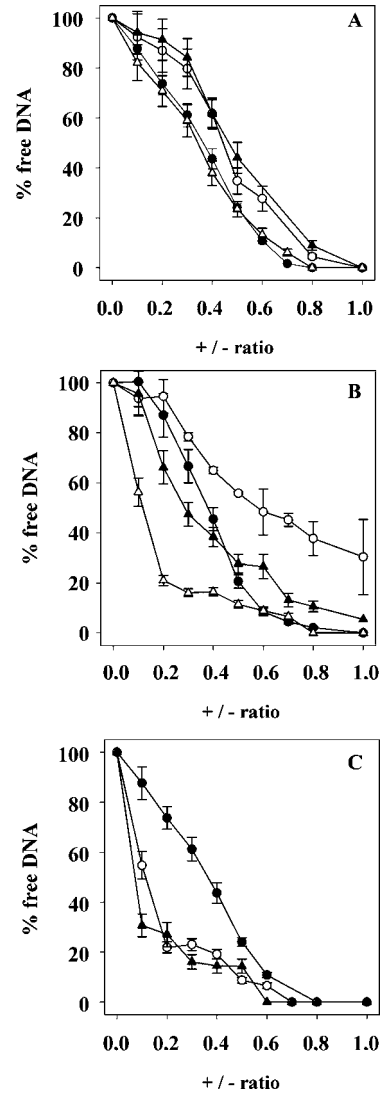


Figure 2. Electrophoretic mobility assay of plasmid DNA upon interaction with avidin differently PEGylated through the covalent or the biotin-bridge strategy. Binding curves obtained by measuring the intensity of band relative to the free DNA. (A) Low degree of PEGylation using linear 5000 MW polymers (•) native avidin; (○) covalent PEGylation with 1.2 methyl-PEG5000; (▲) covalent PEGylation with 1.2 methyl-PEG5000 + 1 biotin; (Δ) PEGylation with 1 linear biotin-PEG5000 (compound **7**). (B) High degree of PEGylation using linear 5000 MW polymers: (•) native avidin + 4 free biotins; (○) covalent PEGylation with 3.6 methyl-PEG5000; (▲) PEGylation with 3.6 methyl-PEG5000 + 4 free biotins; (Δ) PEGylation with 4 biotin-PEG5000 (compound **7**). (C) Very high degree of PEGylation using bulky biotin-PEG derivatives: (•) native avidin + 4 free biotins; (○) PEGylation with 3 molecules of biotin-PEG5000-HRP; (▲) PEGylation with 4 molecules of compound **11**. All experiments were carried out in duplicate.

Figure 2C shows the results of the EMSA carried out using avidin PEGylated to a large extent with highly bulky biotin derivatives, namely, compound **11** and biotinylated-PEG-HRP. Interestingly, in this case the affinity for DNA seems higher than that of native avidin.

Effect of the Amount of PEG on the Size of the Nanossemblies and on Their Aggregation Behavior. Avidin-plasmid DNA nanoassemblies were obtained in double-distilled water as described by Morpurgo et al. (*14*). This procedure leads to discrete nanoparticles of defined sizes (about 100 nm) and composed of individual DNA filaments covered by several avidin molecules. Even though the interaction between the protein and DNA is not affected by the presence of salts or buffers, when the nanoparticles are transferred to a buffered

Table 3. Size of the Avidin-DNA Nanoassemblies in Water as a Function of Type and Amount of Biotin-PEG Used for Their Surface Coating

	mean diameter (nm)			
% BBS occupied	methyl-PEG2000-biotin (**5**)	biotin-L-lys-(methyl-PEG2000)$_2$ (**7**)	methyl-PEG5000-biotin (**10**)	biotin-L-lys-(methyl-PEG5000)$_2$ (**11**)
no biotin-PEG	97 ± 10.7	97 ± 10.7	97 ± 10.7	97 ± 10.7
20	88.5 ± 0.7	101 ± 14.8	95.5 ± 6.4	93.5 ± 9.2
30	93 ± 2.8	99 ± 11.3	93.5 ± 7.8	95 ± 7.1
40	86 ± 1.4	90 ± 11.3	94 ± 5.7	99.5 ± 0.7
50	88.5 ± 0.7	91 ± 2.8	93.5 ± 7.8	100 ± 1.4
60	91.5 ± 0.7	109 ± 19.1	99 ± 4.2	98 ± 2.8

solution they undergo rapid aggregation. This phenomenon can be followed by measuring the size of the nanoassemblies at regular time intervals after buffer addition.

Since anchorage through the biotin binding sites is the only PEGylation strategy that does not alter the protein DNA binding affinity, the effect of the amount of PEG on the aggregation of avidin-plasmid DNA assemblies has been investigated with the biotin-PEG derivatives only.

In order to evaluate and quantitate the effect of biotin-PEGylation on aggregation, the four biotin-PEGs were added to the particles at precisely defined polymer/protein ratios in order to cover increasing percentages of their biotin binding sites (between 20% and 60% of the total amount). The size of the particles was initially measured in dd-H_2O and then at regular times after mixing with the buffer solution. As seen in Table 3 and Figure 3, the presence of biotin-PEG does not affect the particle's size in dd-H_2O but reduces their aggregation behavior in a dose-dependent manner. The four biotin-PEG derivatives behave differently: the two linear ones slow down the aggregation in a dose-dependent manner, but at the concentrations tested, only the highest-molecular-weight one (5 KDa) was capable of preventing it completely, namely, when 60% of the biotin binding sites were occupied. The branched biotin-PEGs were more effective than the linear ones. However, in the case of the lower MW derivative (MW = 2 KDa × 2), the size of the particles increased up to about 200 nm in ~10 min independently of the amount of polymer added. After this initial phase, the aggregation process slowed down significantly, and at the highest polymer concentration investigated, it stopped completely. In the case of the branched high MW derivative (5 KDa × 2), aggregation was detectable only when low amounts of PEG were added: 30% biotin binding sites (BBS) coverage was enough to stabilize the particles indefinitely. In fact, the size of the particles was re-analyzed 24 h after their preparation and it remained unchanged.

Application of the Optimized Assemblies in Detection. The potential usefulness of the optimized assembly prepared upon protecting the particle surface with 30% of the BBS with compound **11** was assessed by means of a simple analytical test. This was carried out after removing the excess of free avidin resulting from the preparation process. Purification was carried out by tangential flow filtration (TFF) using 100 kDa cutoff filters, and the efficiency of the purification step was measured through two parameters: (a) the amount of protein recovered and (b) the size of the particles in the retained solution.

The time necessary to run the purification was about 1 h, with 500−700 mL total filtered volume. After purification, avidin recovery was quantitative, as calculated from the UV absorbance of the filtered and retained solutions. Dynamic light scattering analysis of the retained sample (intensity-weighted Nicomp distribution) indicated the presence of two different particle populations, one of 130 nm size and the other of 600−800 nm. The first one, representing 96% of the total number, had about the same size of the nanoassemblies before TFF, whereas the second population was of larger size. This suggests that that, upon removal of the excess of avidin, either aggregation occurs partially or the DNA loosens its condensed architecture and unrolls, at least to some extent, into a nonglobular shape. If this were the case, the particles might still exist as individual and discrete objects, but the DLS technique would not be the best tool to analyze their size, as the algorithm it uses is based on the assumption that the particles are of spherical geometry. Only the sample ultrastructure analysis could clarify which phenomenon underlies the change of sample size registered after purification. However, from a practical viewpoint the fact that total avidin recovery was

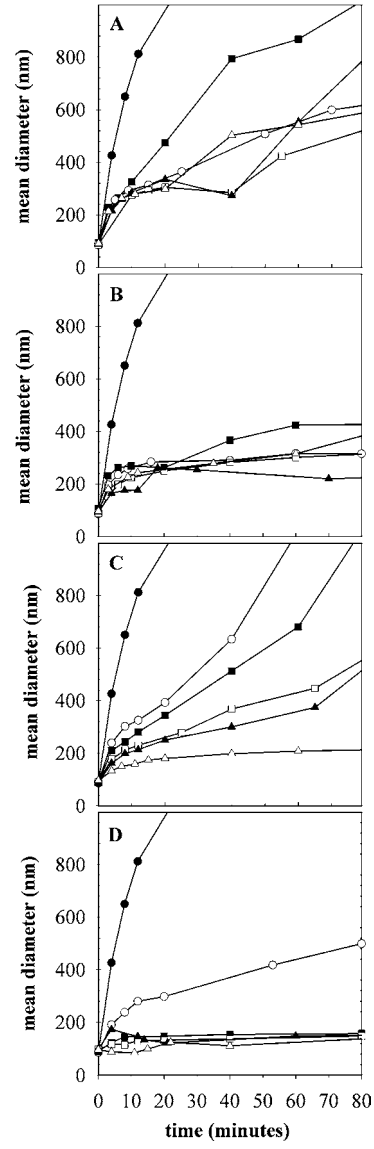


Figure 3. Aggregation in PBS buffer of avidin-DNA nanoassemblies PEGylated through the use of different amounts of the four biotin-PEG polymers. (A) methyl-PEG2000-biotin (**5**); (B) biotin-L-lys-(methyl-PEG2000)$_2$ (**10**), (C) methyl-PEG5000-biotin (**7**), or (D) biotin-L-lys-(methyl-PEG5000)$_2$ (**11**). Biotin-PEG derivatives were added in order to occupy increasing percentages of the total biotin binding sites (BBS) available: 0% (•), 20% (○), 30% (■), 40% (□), 50% (▲), and 60% (Δ). Standard deviations have been omitted for clarity purposes, as they increased together with the increase of particle's size.

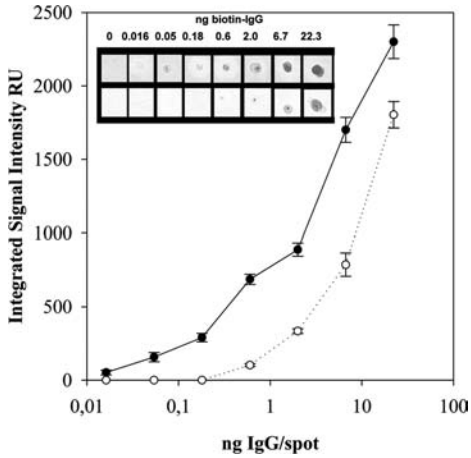


Figure 4. Integrated signal of biotin-HRP/DAB based dot-blot on a nitrocellulose membrane spotted with a biotinylated model IgG and incubated with monomer (○) or nanoassembled (•) avidin. The DAB substrate generated spot intensities were quantified with *ImageJ* software. The assay was carried out in duplicate.

achieved indicates that, even if in a larger size, the purified product remains in solution and can be used as an analytical tool in solution assays.

The results of the first analytical test are shown in Figure 4. In the test, different amounts of a biotinylated sample protein were spotted on a nitrocellulose membrane and detected upon adding the nanoassemblies followed by biotinylated-HRP and development using DAB substrate. In order to evaluate if the nanoassemblies were capable of improving the performance of the classical avidin−biotin system, the assay was carried out in parallel with monomer avidin. Figure 4 shows the intensity of the signal generated upon recognition of decreasing amounts of a biotinylated protein spotted on a nitrocellulose membrane. Both signal intensity and onset of detection improved when using the purified nanoassemblies as compared to monomer avidin. Signal intensity was higher at all analyte concentrations tested. In addition, the limit of detection (LOD) observed with the nanoassemblies was lower by more than 40-fold than that with monomer avidin: in fact, monomer avidin failed to detect the biotin-analyte below 0.6 ng/spot, whereas the nanoassemblies gave rise to a positive signal even when the biotinylated IgG was as low as 0.016 ng/spot.

DISCUSSION

The idea of exploiting for biomedical applications a double self-assembly process driven by nature-dictated affinities is a fascinating one and was the driving force behind this work. However, the applicability of the ordered polyavidin nanoassemblies generated from the high-affinity interaction of avidin with the nucleic acids depends primarily on the possibility of generating solution-stable nanoassemblies capable of remaining as such when diluted in physiological buffers. In this respect, the nature-driven process moves in the opposite direction to the one required by applicative science: the avidin-nucleic acid assemblies are insoluble in buffer solution, and this is probably because of the natural role of the interaction which is presumably to segregate undesired exogenous DNA when it enters the egg (*14*). In any case, aggregation is a common phenomenon occurring with nanosized particles, largely related to the large surface area exposed with its peculiar characteristics of charge type and density, and hydrophobicity−hydrophilicity balance. Hydrophilic polymers, covalently bound or adsorbed onto the particle surface, are often used to avoid or slow down aggregation of otherwise solution-unstable nanoparticles (*20, 33*). Their effectiveness in preventing nonspecific interactions between different surfaces (and hence also between nanoparticles) to which they are attached is related to two parameters: (a) polymer chain length and (b) its grafting density (*17, 34*−*36*). For each system, the same efficacy of aggregation prevention is achievable by varying each or both of the above parameters. Despite the common general rules dictating the efficacy of hydrophilic polymers surface protection, each individual nanosystem, being characterized by unique size, surface properties, and curvature angle, has to be optimized individually. In the case of the avidin-nucleic acid assemblies, an additional property that needs to be taken into consideration is the fact that the particles exist only secondary to a high-affinity phenomenon whose likelihood depends on the ability to preserve the DNA binding site on the protein surface. Avidin covalent PEGylation has been described by some authors, whose main objective was to increase the protein in vivo half-life and to reduce its immunogenicity. In those works, it was shown that the protein ability to bind biotin is affected by covalent modification in a dose-dependent manner (*37*) unless a site protection strategy is adopted to prevent it (*38*). However, the effect of covalent PEGylation on the more recently discovered property of avidin of binding the nucleic acids has not yet been described. This second property is the key element that drives the formation of the avidin-nucleic acids described here, because a diminished or lost affinity would impair the assemblies stability and therefore their applicability.

The results show that when PEG is covalently bound to avidin, its affinity for DNA decreases in a dose-dependent manner. At one PEG per avidin the loss of affinity is of minor intensity, however, at higher polymer loading it becomes dramatic. It was shown previously that the affinity for plasmid DNA is higher when the protein biotin binding pockets are occupied by biotin (*14*). Therefore, in order to better compare biotin-PEGylated samples with the covalently PEGylated ones, the latter have been tested also upon addition of 1 equiv of biotin/each covalent PEG chain attached to the protein. Nevertheless, the original affinity was not recovered, indicating that the loss in affinity is nonreversible. Even though covalently PEGylated avidins are still capable of interacting with DNA at the concentrations used in the EMSA assay, the results suggest that the loss of affinity induced is likely to affect the solution stability of the avidin-DNA assemblies at lower concentrations regimes. Data from our laboratory (manuscript in preparation) indicate that the affinity between native avidin and double-stranded DNA is in the nanomolar range, but no information is yet available on the PEGylated protein. It must be pointed out that the agarose gel retardation assays of this work and the aggregation tests have been carried out at relatively high concentrations (micromolar range). Therefore, losses in affinity of 1 or 2 orders of magnitude are likely to remain undetected by both assays, while they might induce instability at lower concentrations, thus reducing the application potential of the assemblies. As a matter of fact, some authors tried, without success, to use covalently PEGylated avidin-nucleic acid assemblies as cell transfecting systems (*39*). In that work, short-term (up to ten minutes) aggregation kinetics had been carried out demonstrating the particle solution stability at the concentration tested. However, the aggregation assays had been carried out at higher concentrations than that later used in the cell assays, so the loss in DNA affinity might have had a negative impact on the biological activity pursued.

On the other hand, PEGylation through biotin bridging has no impact on the affinity for DNA, which remains totally preserved. In reality, the data obtained with avidin PEGylated to a large extent with highly bulky biotin-PEG derivatives (compound **11** and biotinylated-PEG-HRP) indicate an increase in affinity. This is difficult to explain: it could be related to the fact that biotinylated avidin has a higher affinity for DNA that

the apo form. However, higher affinity in the presence of biotin is observable only at ionic strength conditions higher that those used in this work (*14*), and indeed, no difference in affinity was detected upon saturating native avidin with free biotin (Figure 2A vs B). The increase in affinity could therefore be related to an interaction between the PEG chains, but the nature of this phenomenon is yet to be investigated.

In any case, the EMSA data show clearly that the use of the biotin binding sites as the anchoring points for polymer attachment is the best strategy to achieve surface protection of the nanoassemblies. On the basis of these data and taking into account that aggregation studies on covalently PEGylated avidin have been described by other authors (*39*), the effect of the amount of PEG on the aggregation has been investigated here with the biotin derivatives only. In fact, the next questions that needed to be answered were how much and what kind of biotin-PEG should be used. This is not a trivial matter, as the use of too much biotin-PEG would, on one hand, reduce the assemblies cargo capability and, on the other hand, possibly affect their ability to interact with further biotinylated functions. On the contrary, amounts of PEG that are too low would not be enough to protect them from aggregation. The four PEG-biotin derivatives described in this work differed in the biotin/PEG-monomer ratio and/or the polymer geometry: two of them (**1** and **7**) were of linear geometry and two (**10** and **11**) had a Y-shape, similar to the amine-reactive Tween-PEG described by Monfardini (*40*). Monfardini's Y-shaped polymer is capable of inducing higher surface protection than that induced by two individual molecules of linear PEG having half its molecular weight, with the advantage of generating minor protein perturbation and loss of biological activity. Similarly, the Y-shaped biotin-PEGs synthesized in this work (compounds **10** and **11**) were more efficient than the linear ones (compounds **1** and **7**) in preventing sample aggregation. As a matter of fact, total protection from aggregation was achieved by saturating 30% of the total biotin binding sites with the Y-shaped 2×5 kDa MW compound or 60% of the BBS with the linear 5 kDa MW one. Therefore, the amount of PEG/surface area necessary to totally prevent the aggregation is the same. However, the use of the branched compound allows the majority (70%) of the original biotin binding sites to remain available for further interactions, and this translates into a more powerful nanoassembly. The results can also be discussed in terms of PEG size and degree of surface coverage as a function of polymer chain distance. According to the literature, the calculated radii of gyration (R_g) of the 2, 4, 5, and 10 kDa PEGs are about 1.7, 2.5, 2.8, and 4.2 nm, respectively (*41*), and the theoretical distances between two adjacent polymer chains necessary to achieve maximal surface protection are, respectively, 3.8, 5.5, 6.1, and 8.9 nm (*34, 35, 42*−*47*). On the basis of the information available from the avidin crystallography data (*48*), the distance between two biotin binding sites on an individual avidin molecule (or between two biotin binding sites in two adjacent avidins) can vary between about 3 and 6 nm, depending on the biotin binding sites considered. Even if the precise information regarding the distance between the biotin binding sites in the nanoassembly can only be obtained by ultrastructure investigation, these numbers suggest that the 2 kDa and the Y-shaped 4 kDa PEGs should not always be able to provide maximal surface protection even at 100% BBS coverage, and this is in agreement with our observations. On the contrary, the 5 kDa and the Y-shaped 10 kDa polymers are large enough to provide maximal protection.

The next questions we wanted to answer were if the optimized and stabilized assemblies were still capable of recognizing biotinylated molecules once immobilized on a surface, and consequently, if they were capable of acting as signal amplifiers with respect to the avidin monomer. This was indeed verified by a simple dot blot assay that demonstrated that the particles are capable of generating a higher signal as compared to monomer avidin and to improve the limit of detection by at least 40-fold. This result demonstrates for the first time that the optimized assemblies can indeed be used as molecular amplifiers in detection, therefore paving the way toward further application where a higher sensitivity such as the one obtained by the classical avidin−biotin technology might be of use.

CONCLUSIONS

The results demonstrate for the first time the possibility of exploiting the avidin-DNA high-affinity interaction to obtain solution-stable nanoassemblies with improved detection capabilities as compared to monomeric avidin. This was achieved by fine-tuning the surface protection strategy of the assemblies so that neither the biotin- nor the DNA-binding properties are impaired upon PEGylation. In fact, covalent PEGylation partially reduces the affinity for DNA, whereas PEG anchoring through the biotin binding sites does not. The full potential of this new system is yet to be explored. However, as compared to other polyavidin systems described in the literature, the ANANAS particles have the additional advantages of (a) being stoichiometrically defined and (b) being composed of biocompatible or biodegradable elements only, and (c) having the full biotin binding potentials preserved. These are fundamental features that allow for envisioning their potential application in further areas of investigation, among which are in vivo diagnostics and drug delivery.

ACKNOWLEDGMENT

This work was funded by the University of Padova 2007 "Progetto di Ateneo" and the Italian Ministry of Education (ex 60% funds). The authors are grateful to Meir Wilchek for his constant support, especially in the early stages of this work.

LITERATURE CITED

(1) Wilchek, M., and Bayer, E. A. (1988) The avidin-biotin complex in bioanalytical applications. *Anal. Biochem. 171*, 1–32.
(2) Wilchek, M., and Bayer, E. A. (1990) Introduction to avidin-biotin technology. *Methods Enzymol. 184*, 5–13.
(3) Wilchek, M., and Bayer, E. A. (1990) Avidin-biotin mediated immunoassays: overview. *Methods Enzymol. 184*, 467–9.
(4) Wilchek, M., and Bayer, E. A. (1990) Applications of avidin-biotin technology: literature survey. *Methods Enzymol. 184*, 14–45.
(5) Wilchek, M., Bayer, E. A., and Livnah, O. (2006) Essentials of biorecognition: the (strept)avidin-biotin system as a model for protein-protein and protein-ligand interaction. *Immunol. Lett. 103*, 27–32.
(6) Goldenberg, D. M., Sharkey, R. M., Paganelli, G., Barbet, J., and Chatal, J. F. (2006) Antibody pretargeting advances cancer radioimmunodetection and radioimmunotherapy. *J. Clin. Oncol. 24*, 823–34.
(7) Mamede, M., Saga, T., Ishimori, T., Higashi, T., Kobayashi, H., Konishi, J., and Brechbiel, M. W. (2002) Radiolabeling of Avidin with very high specific activity for internal radiation therapy of intraperitoneally disseminated tumors. *J. Nucl. Med. 43*, 270p–70p.
(8) Hytonen, V. P., Laitinen, O. H., Grapputo, A., Kettunen, A., Savolainen, J., Kalkkinen, N., Marttila, A. T., Nordlund, H. R., Nyholm, T. K., Paganelli, G., and Kulomaa, M. S. (2003) Characterization of poultry egg-white avidins and their potential as a tool in pretargeting cancer treatment. *Biochem. J. 372*, 219–25.
(9) Chinol, M., De Cobelli, O., Trifiro, G., Scardino, E., Bartolomei, M., Verweij, F., Papi, S., Matei, D. V., and Paganelli, G. (2003) Localization of avidin in superficial bladder cancer: a potentially new approach for radionuclide therapy. *Eur. Urol. 44*, 556–9.

(10) Laverman, P., Zalipsky, S., Oyen, W. J., Dams, E. T., Storm, G., Mullah, N., Corstens, F. H., and Boerman, O. C. (2000) Improved imaging of infections by avidin-induced clearance of 99mTc-biotin-PEG liposomes. *J. Nucl. Med. 41*, 912–8.
(11) Hsu, S. M., Raine, L., and Fanger, H. (1981) Use of avidin-biotin-peroxidase complex (ABC) in immunoperoxidase techniques: a comparison between ABC and unlabeled antibody (PAP) procedures. *J. Histochem. Cytochem. 29*, 577–80.
(12) Li, H., Ha Park, S., Reif, J., LaBean, T., and Yan, H. (2004) DNA-templated self-assembly of protein and nanoparticle linear arrays. *J. Am. Chem. Soc. 126*, 418–19.
(13) Kazuyuki, S., Nobuhiro, H., Hiroki, T., and Satoshi, F. (2004) Complexes containing crosslinked avidin, analytical method with the use of crosslinked avidin and analytical reagents and kits., Iatron Laboratories, Inc., Tokyo (JP), Kikkoman Corporation, Chiba, Japan, U.S. Patent 6,787,325, EP Patent 1052510/B1.
(14) Morpurgo, M., Radu, A., Bayer, E. A., and Wilchek, M. (2004) DNA condensation by high-affinity interaction with avidin. *J. Mol. Recognit. 17*, 558–66.
(15) Abuchowski, A., McCoy, J. R., Palczuk, N. C., van Es, T., and Davis, F. F. (1977) Effect of covalent attachment of polyethylene glycol on immunogenicity and circulating life of bovine liver catalase. *J. Biol. Chem. 252*, 3582–6.
(16) Abuchowski, A., van Es, T., Palczuk, N. C., and Davis, F. F. (1977) Alteration of immunological properties of bovine serum albumin by covalent attachment of polyethylene glycol. *J. Biol. Chem. 252*, 3578–81.
(17) Torchilin, V. P., Omelyanenko, V. G., Papisov, M. I., Bogdanov, A. A., Jr., Trubetskoy, V. S., Herron, J. N., and Gentry, C. A. (1994) Poly(ethylene glycol) on the liposome surface: on the mechanism of polymer-coated liposome longevity. *Biochim. Biophys. Acta 1195*, 11–20.
(18) Immordino, M. L., Dosio, F., and Cattel, L. (2006) Stealth liposomes: review of the basic science, rationale, and clinical applications, existing and potential. *Int. J. Nanomed. 1*, 297–315.
(19) Owens, D. E., 3rd, and Peppas, N. A. (2006) Opsonization, biodistribution, and pharmacokinetics of polymeric nanoparticles. *Int. J. Pharm. 307*, 93–102.
(20) Dubertret, B., Skourides, P., Norris, D. J., Noireaux, V., Brivanlou, A. H., and Libchaber, A. (2002) In vivo imaging of quantum dots encapsulated in phospholipid micelles. *Science 298*, 1759–62.
(21) Morpurgo, M., Pasut, G., and Veronese, F. M. (2006) Pegylated proteins as cancer therapeutics in *Delivery of Protein and Peptide Drugs in Cancer* (Torchilin, V., Ed.) Imperial College Press, London.
(22) Zhai, Y., Zhao, Y., Lei, J., Su, Z., and Ma, G. (2009) Enhanced circulation half-life of site-specific PEGylated rhG-CSF: optimization of PEG molecular weight. *J. Biotechnol. 142*, 259–66.
(23) Treetharnmathurot, B., Ovartlarnporn, C., Wungsintaweekul, J., Duncan, R., and Wiwattanapatapee, R. (2008) Effect of PEG molecular weight and linking chemistry on the biological activity and thermal stability of PEGylated trypsin. *Int. J. Pharm. 357*, 252–9.
(24) Renz, C., and Loew, K. (1903) Ueber a-Methyl-Indol. *Ber. Deuts. Chem. Ges. 36*, 4326–30.
(25) Kaiser, E., Colescott, R. L., Bossinger, C. D., and Cook, P. I. (1970) Color test for detection of free terminal amino groups in the solid-phase synthesis of peptides. *Anal. Biochem. 34*, 595–8.
(26) Harding, V., and Warneford, F. (1916) The ninhidrin reaction with amino-acids and amonium salts. *J. Biol. Chem.* 25.
(27) Habeeb, A. (1966) Determination of free amino groups in proteins by trinitrobenzensulphonic acid. *Anal. Biochem. 14*, 328–36.
(28) Morpurgo, M., and Veronese, F. M. (2004) Conjugates of peptides and proteins to polyethylene glycols. *Methods Mol. Biol. 283*, 45–70.
(29) Green, N. M. (1965) A spectrophotometric assay for avidin and biotin based on binding of dyes by avidin. *Biochem. J. 94*, 23C–24C.
(30) Miron, T., and Wilchek, M. (1993) A simplified method for the preparation of succinimidyl carbonate polyethylene glycol for coupling to proteins. *Bioconjugate Chem. 4*, 568–9.
(31) Finsy, R. (1994) Particle sizing by quasi-elastic light scattering. *Adv. Colloid Interface Sci.* 79–143.
(32) Cuatrecasas, P., Wilchek, M., and Anfinsen, C. B. (1968) Selective enzyme purification by affinity chromatography. *Proc. Natl. Acad. Sci. U.S.A. 61*, 636–43.
(33) Cattel, L., Ceruti, M., and Dosio, F. (2003) From conventional to stealth liposomes: a new frontier in cancer chemotherapy. *Tumori 89*, 237–49.
(34) Jeon, S. I., and Andrade, J. D. 1991b Protein surface interactions in the presence of polyethylene oxide 0.2. effect of protein size. *J. Colloid Interface Sci. 142*, 159–66.
(35) Jeon, S. I., Lee, J. H., Andrade, J. D., and Degennes, P. G. 1991a Protein surface interactions in the presence of polyethylene oxide 0.1. simplified theory. *J. Colloid Interface Sci. 142*, 149–58.
(36) Sofia, S. J., Premnath, V., and Merrill, E. W. (1998) Poly(ethylene oxide) grafted to silicon surfaces: Grafting density and protein adsorption. *Macromolecules 31*, 5059–70.
(37) Caliceti, P., Chinol, M., Roldo, M., Veronese, F. M., Semenzato, A., Salmaso, S., and Paganelli, G. (2002) Poly(ethylene glycol)-avidin bioconjugates: suitable candidates for tumor pretargeting. *J. Controlled Release 83*, 97–108.
(38) Salmaso, S., Semenzato, A., Bersania, S., Chinol, M., Paganelli, G., and Caliceti, P. (2005) Preparation and characterization of active site protected poly(ethylene glycol)-avidin bioconjugates. *Biochim. Biophys. Acta Gen. Subj. 1726*, 57–66.
(39) Segura, T., and Shea, L. D. (2002) Surface-tethered DNA complexes for enhanced gene delivery. *Bioconjugate Chem. 13*, 621–9.
(40) Monfardini, C., Schiavon, O., Caliceti, P., Morpurgo, M., Harris, J. M., and Veronese, F. M. (1995) A branched monomethoxypoly(ethylene glycol) for protein modification. *Bioconjugate Chem. 6*, 62–69.
(41) Kenausis, G. L., Voros, J., Elbert, D. L., Huang, N. P., Hofer, R., Ruiz-Taylor, L., Textor, M., Hubbell, J. A., and Spencer, N. D. (2000) Poly(L-lysine)-g-poly(ethylene glycol) layers on metal oxide surfaces: Attachment mechanism and effects of polymer architecture on resistance to protein adsorption. *J. Phys. Chem. B 104*, 3298–309.
(42) Jeon, Y. T., Lee, C. P., and Mariano, P. S. (1991) Radical cyclization reactions of alpha-silyl amine alpha, beta-unsaturated ketone and ester systems promoted by single electron-transfer photosensitization. *J. Am. Chem. Soc. 113*, 8847–63.
(43) Palegrosdemange, C., Simon, E. S., Prime, K. L., and Whitesides, G. M. (1991) Formation of self-assembled monolayers by chemisorption of derivatives of oligo(ethylene glycol) of structure Hs(Ch2)11(Och2ch2)Meta-Oh on Gold. *J. Am. Chem. Soc. 113*, 12–20.
(44) Du, H., Chandaroy, P., and Hui, S. W. (1997) Grafted poly-(ethylene glycol) on lipid surfaces inhibits protein adsorption and cell adhesion. *Biochim. Biophys. Acta 1326*, 236–48.
(45) Lu, H. B., Campbell, C. T., and Castner, D. G. (2000) Attachment of functionalized poly(ethylene glycol) films to gold surfaces. *Langmuir 16*, 1711–18.
(46) Yang, Z. H., Galloway, J. A., and Yu, H. U. (1999) Protein interactions with poly(ethylene glycol) self-assembled monolayers on glass substrates: diffusion and adsorption. *Langmuir 15*, 8405–11.
(47) Harder, P., Buck, M., Zolk, M., Lampert, A., Pertsin, A., and Grunze, M. (1998) Interaction of water with ethylene glycol terminated self-assembled monolayers. *Abstr. Pap. Am. Chem. Soc. 215*, U212–U12.
(48) Livnah, O., Bayer, E. A., Wilchek, M., and Sussman, J. L. (1993) Three-dimensional structures of avidin and the avidin-biotin complex. *Proc. Natl. Acad. Sci. U.S.A. 90*, 5076–80.

BC100044U

Sensitive Quantification of PEGylated Compounds by Second-Generation Anti-Poly(ethylene glycol) Monoclonal Antibodies

Yu-Cheng Su,[†,‡] Bing-Mae Chen,[‡] Kuo-Hsiang Chuang,[§] Tian-Lu Cheng,*[,||] and Steve R. Roffler*[,‡]

Institute of Microbiology and Immunology, National Yang-Ming University, Taipei, 11529, Taiwan, Institute of Biomedical Sciences, Academia Sinica, Taipei, 11529, Taiwan, and Institute of Medicine and Department of Biomedical Science and Environmental Biology, MedicoGenomic Research Center, Kaohsiung Medical University, Kaohsiung, 80708, Taiwan. Received February 3, 2010; Revised Manuscript Received May 12, 2010

Poly(ethylene glycol) (PEG) is often attached to compounds to increase serum half-life, reduce immunogenicity, and enhance bioavailability. Accurate and sensitive quantification of PEG conjugates is critical for product development, pharmacokinetic measurements, and efficacy studies. However, PEGylated compounds can be difficult to quantify due to epitope masking by PEG. We previously generated two monoclonal antibodies to PEG (AGP3, IgM and E11, IgG) for quantitative detection of PEGylated proteins. We now report the identification of two second-generation mAbs to PEG (AGP4, IgM and 3.3, IgG) that bind to the repeating subunits of the PEG backbone and facilitate more sensitive quantification of a wider range of PEGylated compounds. A sandwich ELISA in which AGP4/3.3-biotin was employed as the capture/detection antibodies allowed quantification of PEG-Qdot 525 with 14−50-fold greater sensitivity than the original AGP3/E11 combination. Pegasys (PEG-interferon alpha-2a), PEG-Intron (PEG-interferon alpha-2b), Neulasta (PEG-G-CSF), and Lipo-Dox (PEGylated liposomal doxorubicin) could also be quantified with low ng/mL detection limits. The assay tolerated the presence of 50% human serum or 20% free PEG molecules. These new anti-PEG antibodies appear useful for qualitative and quantitative analysis of a wide range of PEGylated compounds.

INTRODUCTION

Covalent attachment of poly(ethylene glycol) (PEG) to peptides, proteins, and nanoparticles can enhance their stability, solubility, and circulation life. A wide range of PEGylated protein drugs is under development (*1*−*7*). More recently, PEG has been conjugated to nanoparticles, such as superparamagnetic iron oxide (SPIO) (*8, 9*), quantum dots (PEG-Qdot) (*10, 11*), and liposomes to enhance their biocompatibility and diminish uptake by the reticuloendothelial system. Several PEGylated compounds have been approved for clinical use by the FDA including Pegasys (PEG-interferon alpha-2a) (*12, 13*), PEG-Intron (PEG-interferon alpha-2b) (*14*), Somavert (PEG-human growth hormone receptor antagonist) (*15*), Cimzia (certolizumab pegol, pegylated antihuman TNF-alpha Fab') (*16*), Neulasta (pegfilgrastim, PEG-G-CSF) (*17, 18*), and Lipo-Dox (Pegylated liposomal-doxorubicin) (*19, 20*). PEG modification will likely facilitate clinical utilization of more imaging reagents, therapeutic proteins, and small molecule drugs.

Although PEGylation is a promising technology to improve the pharmacokinetic properties of compounds, effective approaches to quantify PEGylated conjugates in complex samples are limited. Sandwich ELISA is commonly used to measure the protein component of PEGylated proteins, but shielding antibody epitopes with bulky PEG chains, which is advantageous for reducing protein immunogenicity, may also limit assay sensitivity. Chromatographic methods are complicated by peak broadening due to the polydispersity of PEG conjugates and strong peak tailing due to nonspecific adhesion to the stationary phase (*21*). LC-MS/MS approaches can be sensitive but usually require complex multistep sample processing steps to reduce sample complexity before analysis (*22*). Solid-phase extraction and multiple analyses are also typically required to measure total, free, and encapsulated drug concentrations in PEGylated liposomes due to the difficulty of directly assaying liposomes in serum samples (*23*). Therefore, the successful development of a sensitive anti-PEG sandwich ELISA may provide a simple and universal tool for quantifying PEGylated compounds. Previously, we described a sandwich ELISA system using monoclonal anti-PEG antibodies (APG3/IgM and E11/IgG) to measure PEGylated compounds in vitro and in vivo (*24*). We recently generated additional second-generation monoclonal antibodies against PEG. Here, we show that two of these antibodies (AGP4 and 3.3) allow much more sensitive detection of a broader range of PEGylated compounds including PEG-interferon α (Pegasys and PEG-Intron), PEG-Qdot 525, and Lipo-Dox.

EXPERIMENTAL PROCEDURES

Reagents and Animals. Methoxy-PEG_{750}-NH_2, methoxy-PEG_{2000}-NH_2, hydroxy-PEG_{5000}-NH_2, methoxy-$PEG_{10,000}$-NH_2, methoxy-$PEG_{20,000}$-NH_2 (750, 2000, 5000, 10 000 and 20 000 Da, respectively), NH_2-PEG_{3000}-NH_2, methoxy-PEG_{5000}-COOH, and 4-arm poly(ethylene oxide)$_{10,000}$-NH_2 were purchased from Sigma-Aldrich Chemical Co. (St. Louis, MO). EZ-link NHS-LC-Biotin was purchased from Pierce (Rockford, IL). PEG-Qdot 525 (Qdot 525 ITK amino (PEG) quantum dots), a nanocrystal semiconductor material coated with multiple linear

* Correspondence to Dr. Steve Roffler, Room N232, Institute of Biomedical Sciences, Academia Sinica, Academia Road, Section 2, No. 128, Taipei 11529, Taiwan. Tel: (886)-2-2652-3079; Fax: (886)-2-2782-9142; E-mail: sroff@ibms.sinica.edu.tw. Dr. Tian-Lu Cheng, Room N930, Department of Biomedical Science and Environmental Biology, Kaohsiung Medical University, Shiquan First Road, No. 100, Kaohsiung 80708, Taiwan. Tel: (886)-7-3121-1101ext. 2697; Fax: (886)-7-3227-508; E-mail: tlcheng@kmu.edu.tw.

[†] National Yang-Ming University.

[‡] Academia Sinica.

[§] Institute of Medicine, Kaohsiung Medical University.

[||] Department of Biomedical Science and Environmental Biology, MedicoGenomic Research Center, Kaohsiung Medical University.

10.1021/bc100067t © 2010 American Chemical Society
Published on Web 06/10/2010

2 kDa amino-PEG molecules, was purchased from Invitrogen (Carlsbad, CA). Lipo-Dox was from Taiwan Tung Yang Biopharm (TTY Biopharm Company Ltd., Taipei, Taiwan). Pegasys and PEG-Intron were from Roche (Nutley, NJ, CA) and Schering-Plough (Kenilworth, NJ, CA), respectively. Neulasta (pegylated G-CSF) was a gift from Amgen (Thousand Oaks, CA). Specific pathogen-free BALB/c mice were obtained from the National Laboratory Animal Center, Taipei, Taiwan.

Antibodies. Hybridomas secreting AGP3, AGP4 (IgM mAb against PEG), 1E8 (IgG_1 mAb against *E. coli* βG, eβG), E11, and 3.3 (IgG_1 mAbs against PEG) were generated by immunizing female BALB/c mice with PEG-derived proteins as described previously (*25*). Briefly, mice were i.v. injected with 200 μg of RH1-eβG-PEG_{5000}, a conjugate formed between a murine antibody and PEG-derivatized eβG. The mice were i.p. injected with 100 μg RH1-eβG-PEG_{5000} one week later and then s.c. injected at weekly intervals with 50 μg of eβG-PEG_{5000} in complete Freund's adjuvant, 30 μg of eβG-PEG_{5000} in incomplete adjuvant, 30 μg of BSA-PEG_{5000} in incomplete adjuvant, and 10 μg of BSA-PEG_{5000} in incomplete adjuvant. Three days before fusion with FO myeloma cells, the mice were i.p. injected with 30 μg of BSA-PEG_{5000} in PBS. Hybridomas were generated by fusing spleen cells with FO myeloma cells and then screening culture media by ELISA in 96-well microtiter plates coated with 1 μg/well βG or βG-PEG_{5000}. Hybridomas were cloned 3 times by limiting dilution in 96-well microtiter plates containing thymocyte feeder cells in HT medium supplemented with 15% fetal calf serum. Anti-PEG rabbit mAb PEG-B-47 was from Epitomics (Burlingame, CA). B139 M and B141 M mouse anti-PEG mAbs were from Meridian Life Science, Inc. (Saco, ME). Horseradish peroxidase (HRP)-conjugated goat antimouse IgM μ-chain antibody, HRP-conjugated donkey antimouse IgG Fc, HRP-conjugated goat antimouse Ig, and HRP-conjugated streptavidin were from Jackson ImmunoResearch Laboratories (Westgrove, PA).

Antibody Biotinylation. Antibodies (3.3, E11, AGP3, and AGP4) in PBS at 2 mg/mL were mixed with a 25-fold molar excess of EZ-link NHS-LC-Biotin (dissolved in DMSO) for 2 h at room temperature to produce 3.3-biotin, E11-biotin, AGP3-biotin, and AGP4-biotin. One-tenth volume of a saturated glycine solution was added to stop the reaction. Free biotin was removed by dialysis in PBS at 4 °C. Antibody concentration was evaluated by the bicinchoninic acid assay (Pierce, Rockford, IL) with bovine serum albumin used as the reference protein.

Antibody ELISA. Maxisorp 96-well microplates (Nalge-Nunc International, Roskilde, Denmark) were coated with 0.5 μg/well CH_3-PEG_{750}-NH_2, CH_3-PEG_{2000}-NH_2, NH_2-PEG_{3000}-NH_2, CH_3-PEG_{5000}-NH_2, CH_3-$PEG_{10,000}$-NH_2, or CH_3-$PEG_{20,0000}$-NH_2 in 50 μL/well 0.1 M $NaHCO_3/Na_2CO_3$ (adjusted to pH 8.0 with HCl) for 3 h at 37 °C and then blocked with 200 μL/well dilution buffer (2% skim milk in PBS) at 4 °C overnight. Graded concentrations of antibodies in 50 μL 2% skim milk were added to the plates at RT for 1 h. The plates were washed with PBS-T (PBS containing 0.05% Tween-20) three times and with PBS two times. HRP-conjugated goat antimouse IgM μ chain (2 μg/mL) or HRP-conjugated donkey antimouse IgG Fc (2 μg/mL) in 50 μL dilution buffer were added for 1 h at room temperature. The plates were washed as described above, and bound peroxidase activity was measured by adding 100 μL/well TMB substrate solution (BioLegend, San Diego, CA) for 30 min at room temperature. After adding stop buffer (2 N H_2SO_4, 50 μL/well), the absorbance (450 nm) of wells was measured in a microplate reader (Molecular Device, Menlo Park, CA).

Immunoblotting. Samples of Pegasys (0.5 μg), PEG-Intron (0.5 μg) or Neulasta (0.5 μg) were electrophoresed in a 10% SDS-PAGE gel under reducing conditions before overnight transfer to nitrocellulose paper by capillary diffusion in blotting buffer (50 mM NaCl, 2 mM EDTA, 0.5 mM 2-mercaptoethanol, 10 mM Tris-HCl, pH 7.5). Blots were blocked for 1 h with 5% skim milk in PBS and incubated for 1 h at RT with 1 μg/mL AGP3, AGP4, 3.3, or E11 in dilution buffer. The blots were washed 3 times with PBS-T and twice with PBS before incubation with goat antimouse Ig-HRP for 1 h at RT. After washing three times with PBS-T and twice with PBS, specific bands were visualized by ECL detection according to the manufacturer's instructions (Pierce, Rockford, IL), then detected by a LAS-3000 mini Fujifilm imaging system (FujiFilm, Tokyo, Japan).

Sandwich ELISA. Maxisorp 96-well microplates were coated with 50 μL/well of AGP3, AGP4, E11, 3.3, B139M, B141 M, or PEG-B-47 (5 or 20 μg/mL) in 0.1 M $NaHCO_3/Na_2CO_3$ (adjusted to pH 8.0 with HCl) for 4 h at 37 °C and then at 4 °C overnight. The plates were blocked with 200 μL/well 2% skim milk in PBS for 2 h at room temperature and then washed with PBS three times. Graded concentrations of PEG-Qdot 525, Lipo-Dox, Pegasys, PEG-Intron, or Neulasta in dilution buffer were added to wells for 2 h at room temperature. Defined amounts of human serum or free PEG molecules (methoxy-PEG-NH_2, 2000 or 10 000 Da) were added with samples in some experiments. After washing with PBS-T three times and PBS twice (unless B139 M or B141 M antibodies were assayed, in which case Tween-20 was omitted from all washing steps to prevent competition of the antibodies with detergent), the plates were sequentially stained with 50 μL/well detection antibody (5 μg/mL 3.3-biotin, AGP4-biotin, AGP3-biotin, B141M-biotin, or PEG-B-47-biotin) and 1 μg/mL HRP-conjugated streptavidin. The plates were washed with PBS-T six times and with PBS two times and 100 μL/well ABTS solution (0.4 mg/mL 2,2′-azino-di(3-ethylbenzthiazoline-6-sulfonic acid), 0.003% H_2O_2, 100 mM phosphate citrate, pH 4.0) was added for 30 min at room temperature. The absorbance of the wells at 405 nm was measured on a microplate reader.

Statistical Analysis. The detection limit in ELISAs was defined as the lowest concentration of PEGylated compound that produced a statistically higher signal than the blank. Statistical significance was calculated using *Graphpad Prism 5.0* with the *t*-test. Data were considered significant at $p \leq 0.05$. The relative sensitivities of antibody combinations in ELISA were also compared by interpolating the concentration of analyte that produced an absorbance reading of 1.5 units.

RESULTS

Comparison of Antibody Binding to Immobilized PEG. The binding specificity of anti-PEG antibodies to different lengths of free linear PEG (MW 750, 2000, 3000, 5000, 10 000, and 20 000 Da) and branched PEG (4-arm poly(ethylene oxide), 10 000 Da) was examined by coating NH_2-PEG molecules on microtiter plates and then performing ELISA. Both first-generation (E11, AGP3) and second-generation (3.3 and AGP4) antibodies bound to methoxy-PEG-NH_2, hydroxyl-PEG-NH_2, and diamino PEG demonstrated that the antibodies did not bind to terminal methoxy or hydroxyl groups in PEG (Figure 1). E11, AGP3, and AGP4 bound to both large and small PEG molecules. mAb 3.3, on the other hand, bound PEG molecules longer than 2000 Da but did not bind well to CH_3-PEG_{750}-NH_2. Longer PEG chains resulted in enhanced binding of all antibodies, although E11 binding displayed less sensitivity to PEG size. AGP3, AGP4, and 3.3 bound to long PEG chain (MW $\geq$ 10 000 Da) with similar apparent avidities, whereas E11 bound with ~10-fold lower avidity.

Immunoblot Analysis of PEG and PEGylated Proteins. The ability of the anti-PEG antibodies to recognize various PEGylated compounds in immunoblots was determined. AGP3,

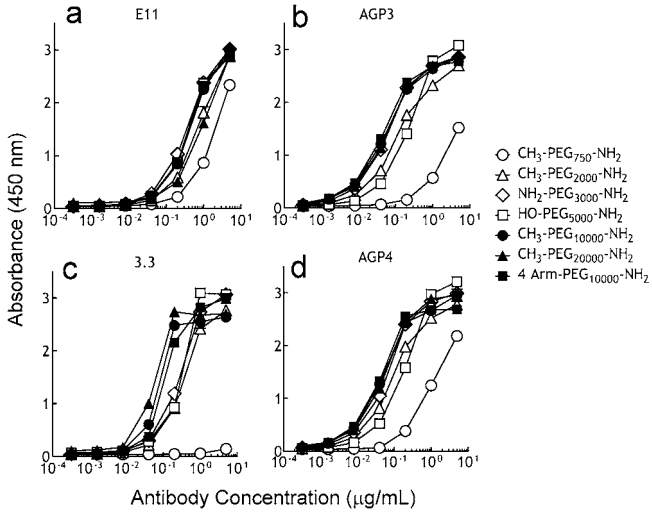


Figure 1. Antibody binding to adsorbed PEG molecules. Graded concentrations of E11 (a), AGP3 (b), 3.3 (c), or AGP4 (d) were added to microplate wells coated with the indicated amino-PEG molecules. After 1 h, the wells were washed and antibody binding was determined by adding HRP-conjugated goat antimouse IgM μ chain or HRP-conjugated donkey antimouse IgG Fc antibodies, followed by adding TMB substrate. The mean absorbance values (450 nm) of triplicate determinations are shown. Bars, SD.

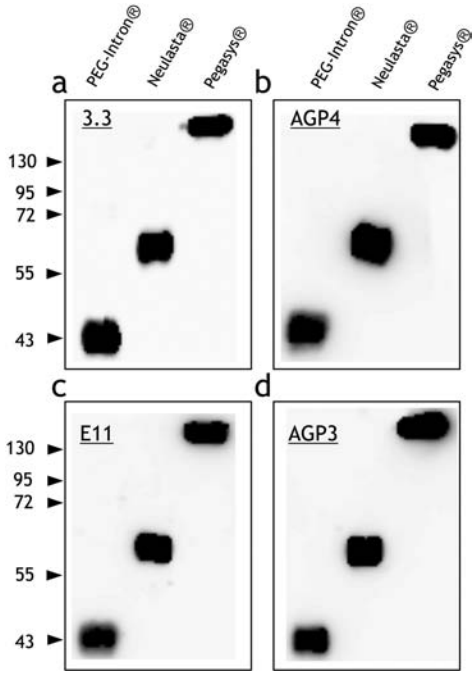


Figure 2. Immunoblot of PEGylated proteins. PEG-Intron, Neulasta, and Pegasys were electrophoresed on a 10% reduced SDS-PAGE gel, transferred to nitrocellulose paper, and probed with mAb 3.3 (a), AGP4 (b), E11 (c), or AGP3 (d) antibodies as described in Experimental Procedures. Lane 1, PEG-INTRON; lane 2, Neulasta; lane 3, Pegasys, molecular mass in thousands.

AGP4, E11, and 3.3 bound to PEGylated proteins, including PEG-Intron (lane 1), Neulasta (lane 2), and Pegasys (lane 3) (Figure 2). The predicted molecular weights of PEG-Intron (methoxy-$PEG_{12\ kDa}$-interferon alpha-$2b_{19\ kDa}$), Neulasta (methoxy-$PEG_{20\ kDa}$-$G\text{-}CSF_{19\ kDa}$), and Pegasys (methoxy-$PEG_{43\ kDa}$-interferon alpha-$2a_{19\ kDa}$) are 31 kDa, 39 kDa, and 62 kDa. However, PEG-Intron, Neulasta, and Pegasys migrated with apparent molecule weights of 43 kDa, 60 kDa, and 170 kDa. The higher apparent molecule weights are likely due to the large hydrodynamic volume of PEG in SDS-PAGE gels (*26*).

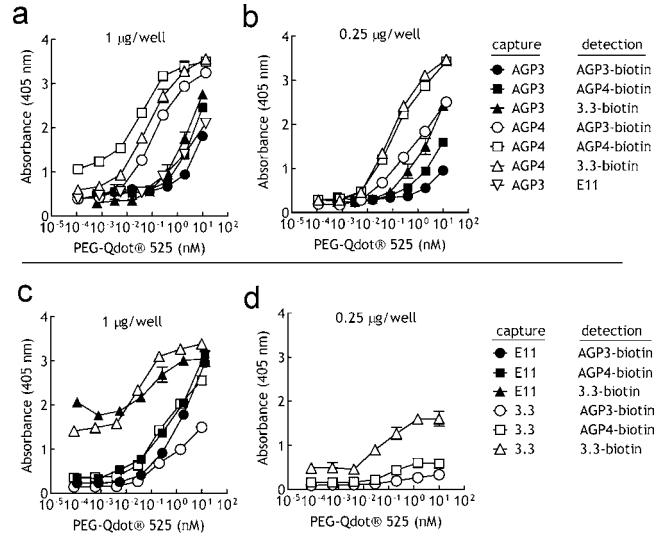


Figure 3. Comparison of first- and second-generation anti-PEG antibodies for detection of PEG-Qdot 525 by sandwich ELISA. Graded concentrations of PEG-Qdot 525 were assayed in triplicate in a sandwich ELISA in which 1 μg/well (left panels) or 0.25 μg/well (right panels) anti-PEG IgG (3.3 and E11) or IgM (AGP3 and AGP4) antibodies were coated in wells as capture antibodies. PEG-Qdot 525 was detected with 0.25 μg/well E11 followed by anti-IgG-HRP or by 0.25 μg/well AGP3-biotin, AGP4-biotin, or 3.3-biotin followed by streptavidin-HRP. Bars, SD.

Comparison of First- and Second-Generation Antibodies for Sandwich ELISA. We compared different combinations of the first- and second-generation anti-PEG antibodies (capture/detection antibodies) to measure PEGylated compounds by sandwich ELISA. High (1 μg/well) and low (0.25 μg/well) amounts of capture antibodies were examined. Assay sensitivities were compared by determining the concentration of analyte (PEG-Qdot 525) that produced an optical absorbance reading of 1.5 units. The best combinations of first generation antibodies (1 μg/well E11 for capture and AGP3-biotin for detection or 1 μg/well AGP3 for capture and E11 for detection) produced a 1.5 absorbance reading at 1.4 nM and 3.5 nM PEG-Qdot 525, respectively (Figure 3a and c). E11-biotin could not be used in assays because biotinylation destroyed its activity. By contrast, lower concentrations of the second-generation antibodies (AGP4 for capture (0.25 μg/well) with AGP4-biotin or 3.3-biotin for detection) produced absorbance readings at 0.1 and 0.07 nM PEG-Qdot 525, respectively (Figure 3b). Coating higher concentrations of AGP4 produced excessive background readings (Figure 3a). 3.3 performed relatively poorly as a capture antibody for PEG-Qdot 525 (Figure 3c,d). By contrast, the combination of 3.3/3.3-biotin for capture/detection showed the best sensitivity for Neulasta detection (Figure 4c and d). However, the AGP4/3.3-biotin combination produced well-behaved dose−response curves with better sensitivity than when AGP3 or E11 were used as capture antibodies (Figure 4a and b). The combination of 0.25 μg AGP4 for capture and 3.3-biotin for detection appeared to represent a good choice for sensitive detection of PEGylated compounds.

Quantitative Sandwich ELISA of PEGylated Compounds. To further investigate the utility of AGP4/3.3-biotin and AGP4/AGP4-biotin sandwich ELISAs for the detection of PEGylated compounds, a range of PEGylated compounds were analyzed. Both formats allowed detection of a wide range of PEGylated compounds, although AGP4/3.3-biotin tended to produce lower background levels with good detection limits of 0.79 pM for PEG-Qdot 525, 0.32 ng/mL for Lipo-Dox, 0.32 ng/mL for Pegasys, 4.12 ng/mL for PEG-Intron, and 1.22 ng/mL for

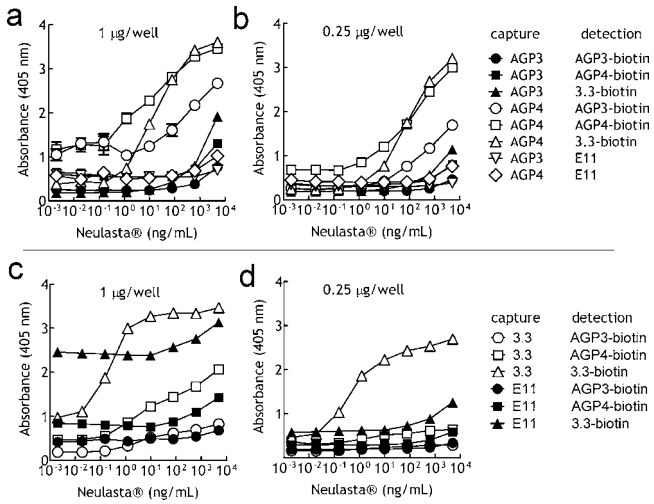


Figure 4. Comparison of first- and second-generation anti-PEG antibodies for detection of Neulasta by sandwich ELISA. Graded concentrations of Neulasta were assayed in triplicate in a sandwich ELISA in which 1 μg/well (left panels) or 0.25 μg/well (right panels) anti-PEG IgG (3.3 and E11) or IgM (AGP3 and AGP4) antibodies were coated in wells as capture antibodies. Neulasta was detected with 0.25 μg/well E11 followed by anti-IgG-HRP or by 0.25 μg/well AGP3-biotin, AGP4-biotin, or 3.3-biotin followed by streptavidin-HRP. Bars, SD.

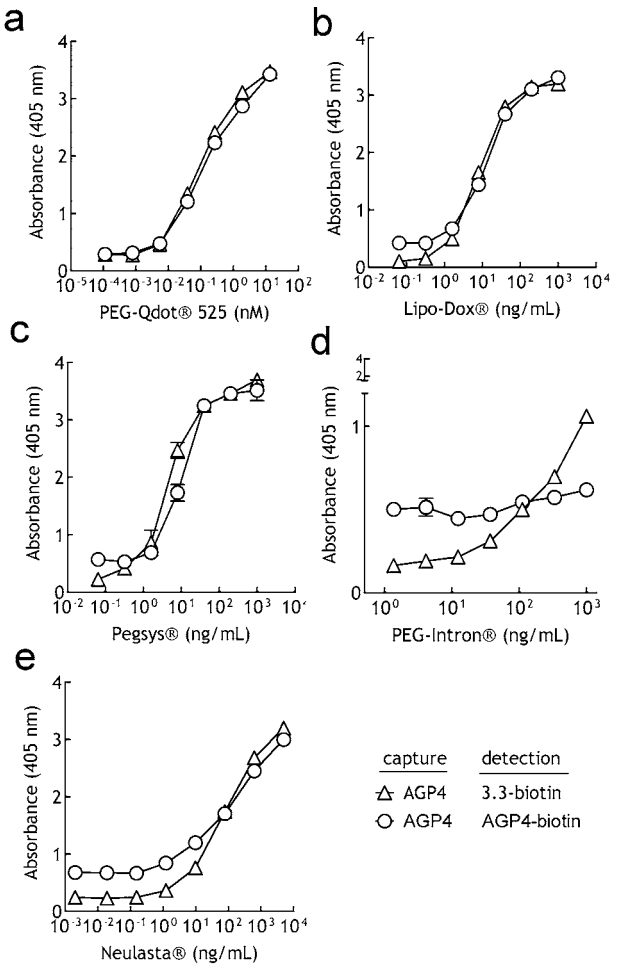


Figure 5. Quantitative analysis of PEGylated compounds by sandwich ELISA. Results of a sandwich ELISA in which 0.25 μg/well AGP4 was used as a capture antibody to measure the concentrations of PEG-Qdot 525 (a), Lio-Dox (b), Pegasys (c), PEG-Intron (d), and Neulasta (e), respectively, with 0.25 μg/well AGP4-biotin (○) or 3.3-biotin (Δ) as detection antibodies. Results show mean values of triplicate determination. Bars, SD.

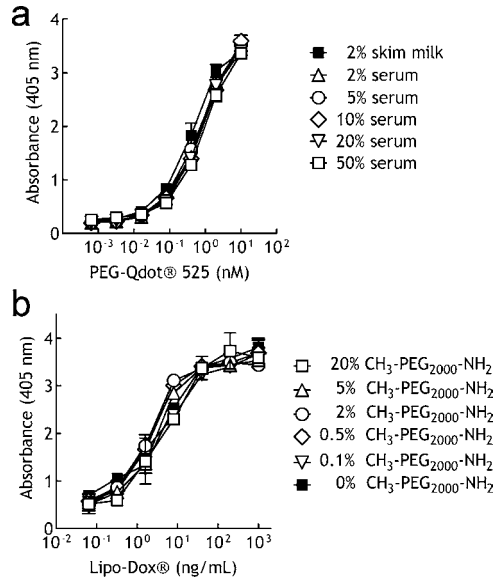


Figure 6. The influence of human serum and free PEG in the AGP4/3.3-biotin sandwich ELISA. (a) Sandwich ELISA in which AGP4/3.3-biotin were employed as the capture/detection antibodies to measure PEG-Qdot 525 in the presence of 2% skim milk or 2−50% human serum. (b) Lipo-Dox was spiked with the indicated amounts of free CH_3-PEG2000-NH_2 before serial dilutions were measured by a sandwich ELISA in which AGP4/3.3-biotin were used as capture/detection antibodies, respectively. Bars, SD.

Neulasta, respectively (Figure 5). AGP4/3.3-biotin was the only combination that allowed quantification of PEG-Intron (Figure 5d).

Effect of Serum and Free PEG on Anti-PEG Sandwich ELISA. Compared with the control, addition of up to 50% human serum did not affect the quantitative assay of PEG-Qdot 525 (Figure 6a). Likewise, spiking samples with up to 20% free CH_3-PEG_{2000}-NH_2 did not interfere with the detection of Lipo-Dox (Figure 6b).

Comparison of Commercial Antibodies for Anti-PEG Sandwich ELISA. Several anti-PEG antibodies were compared for detection of five PEGylated compounds by sandwich ELISA (Figure 7). An assay using B141 M for capture and 3.3-biotin for detection successfully quantified four of five PEGylated compounds. The combination of B141M/B141M-biotin for capture/detection, on the other hand, did not produce detectable signals for any of the compounds (Table 1). B139 M did not produce useful signals when employed as a capture antibody for any of the tested substances (Figure 7a−e). PEG-B-47 worked well as a capture antibody when combined with PEG-B-47-biotin for quantification of Lipo-Dox, but was relatively insensitive for the detection of the other four PEGylated compounds. Use of AGP4 for capture in combination with PEG-B-47-biotin for detection extended the utility of the assay to both Lipo-Dox and Pegasys (Figure 7b,c). The combination of AGP4/3.3-biotin for capture/detection, respectively, allowed sensitive detection of all five PEGylated compounds (Table 1).

DISCUSSION

In this report, we describe two new second-generation anti-PEG monoclonal antibodies, 3.3 and AGP4, that specifically bind to the repeating (OCH_2CH_2) subunits of PEG and allow more sensitive detection of PEGylated compounds as compared to our first-generation E11 and AGP3 antibodies (*24*). Utilization of AGP4 and 3.3-biotin in a sandwich ELISA as capture and detection antibodies, respectively, also allowed more sensitive detection of Pegasys, PEG-Intron, Neulasta, PEG-Qdot 525, and Lipo-Dox as compared to commercially available anti-PEG

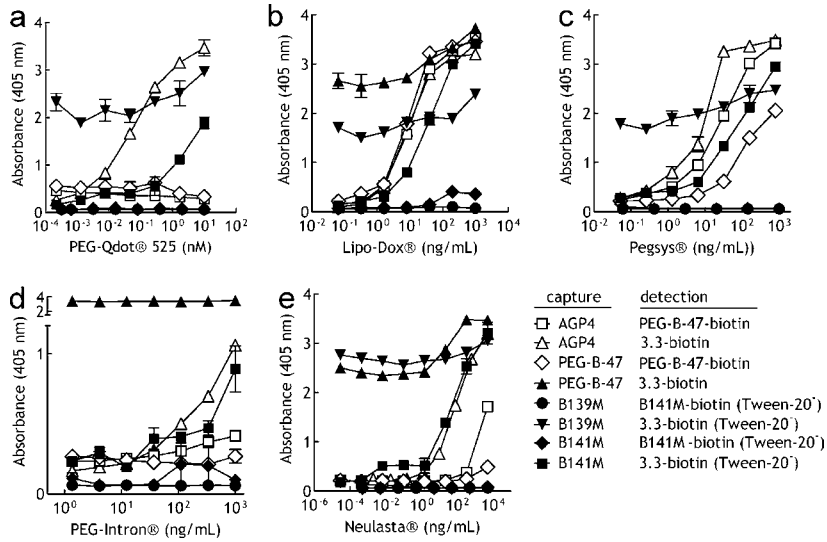


Figure 7. Comparison of anti-PEG antibodies for sandwich ELISA of PEGylated compounds. Graded concentrations of PEG-Qdot 525 (a), Lipo-Dox (b), Pegasys (c), PEG-Intron, and Neulasta were assayed in a sandwich ELISA in which 0.25 μg/well AGP4, PEG-B-47, B139 M, or B141 M were used as capture antibodies and 0.25 μg/well 3.3-biotin, PEG-B-47-biotin, or B141M-biotin were employed as detection antibodies. Bars, SD.

Table 1. Comparison of Anti-PEG Antibodies for the Quantification of PEGylated Compounds by Sandwich ELISA[a]

		assay sensitivity (analyte concentration that produces an absorbance value of 1.5 units)				
capture antibody (0.25 μg/well)	detection antibody (0.25 μg/well)	PEG-Qdot 525 (pM)	Lipo-Dox (ng/mL)	Pegasys (ng/mL)	PEG-Intron (ng/mL)	Neulasta (ng/mL)
AGP4	3.3-biotin	40	7.2	8.1	1800	61.2
AGP4	PEG-B-47-biotin	>10 000	7.6	20.6	>2000	4300
PEG-B-47	3.3-biotin	>10 000	NM	>10 000	NM	NM
PEG-B-47	PEG-B-47-biotin	>10 000	6.5	170	>2000	>10 000
B139M	3.3-biotin	NM[b]	NM	NM	ND[c]	NM
B139M	B141M-biotin	>10 000	>10 000	>10 000	>2000	>10 000
B141M	3.3-biotin	5800	29.4	59.2	>2000	54.6
B141M	B141M-biotin	>10 000	>10 000	>10 000	>2000	>10 000

[a] Results show the concentration of PEGylated compound that can produce an absorbance reading (A_{280}) of 1.5 in a sandwich ELISA using the indicated capture and detection antibodies. [b] NM, not meaningful, high background reading at all concentrations. [c] ND, not determined.

antibodies. AGP4 and 3.3 antibodies should be useful for the quantification of a wide range of PEG conjugates.

A plethora of PEGylated compounds is under development or already approved for medical use such as Oncaspar (PEG-asparaginase) for leukemia (*27*−*29*), Macugen (PEG-anti VEGF aptamer) for age-related macular degeneration (*30*), and Adagen (PEG-adenosine deaminase) for severe combined immunodeficiency disease (SCID) (*31, 32*). PEGylation may also improve the properties of novel agents entering clinical testing such as PEGylated polyethylenimine (PEI) for in vivo DNA delivery (*33*), PEGylaed Zn-protoporphyrin for photodynamic tumor therapy (*34*), PEGylated SWENTs (single-walled carbon nanotubes) with ultralong blood circulation for drug delivery (*35*), and PEGylated aptamers that act as agonists or antagonists (*36*). The large number of PEG-conjugates under development will require qualitative and quantitative detection in preclinical and clinical studies to determinate their pharmacokinetic properties. Sandwich ELISA is a well-established technique to quantify analytes in serum samples and biological fluids due to its high sensitivity and specificity.

In this study, we examined the detection of five commercially available PEG conjugates. PEG-Qdot 525 is a nanocrystal semiconductor material coated with multiple linear 2 kDa amino-PEG molecules, Lipo-Dox is liposomal doxorubicin decorated with multiple linear 2 kDa methoxy-PEG-distearoyl phosphatidyl ethanolamine molecules (*37*), Pegasys is an interferon alpha-2a conjugated with a single 40 kDa branched-chain methoxy PEG (*38*), PEG-Intron is an interferon alpha-2b conjugated with a single 12 kDa methoxy PEG (*39*), and Neulasta is a G-CSF conjugated with a single 20 kDa monomethoxy PEG (*40*).

Our results demonstrated that AGP4 and 3.3 can both serve as capture/detection antibodies to quantify all five PEGylated compounds investigated. The combination of AGP4/3.3-biotin was preferable to 3.3/AGP4-biotin for capture/detection because this combination produced equal detection sensitivity with lower background readings (Figure 5). When compared with first-generation anti-PEG antibodies (E11 and AGP3), one-fourth the amount of AGP4 (0.25 μg/well vs 1 μg/well for first-generation antibodies) allowed effective capture of PEGylated compounds in sandwich ELISA assays with 14−50-fold enhanced sensitivity (Figures 3 and 4). The sandwich ELISA using AGP4/3.3-biotin also allowed sensitive quantification of Lipo-Dox in the presence of free PEG molecules (Figure 6). For reasons not well understood, anti-PEG antibodies bind best when PEG is linked to a molecule (i.e., protein, liposome, nanoparticles) or adsorbed on a surface (i.e., nitrocellulose paper in immunoblots or plastic in direct ELISA). Free PEG therefore had little effect on the assay of PEGylated compounds because of the much greater sensitivity of the sandwich ELISA for PEG-conjugates as compared to free PEG. Interestingly, membrane-tethered anti-PEG antibodies expressed on 3T3 fibroblasts can bind to soluble PEG molecules much more effectively than anti-PEG antibodies coated in 96-well microtiter plates (*41*). Likewise, human serum did not affect the assay of PEG-Qdot 525. Of note, the sandwich ELISA could detect conjugates possessing

a single PEG molecule, although detection sensitivity was greatly enhanced for conjugates containing a longer PEG chain (Neulasta vs PEG-Intron) or a branched-chain PEG (Pegasys). Conjugates with multiple PEG chains (PEG-Qdot 525 and Lipo-Dox) afforded the most sensitive detection by anti-PEG sandwich ELISA (Table 1).

AGP4 and 3.3-biotin appeared to offer advantages compared with other anti-PEG antibodies. PEG-B-47 is a rabbit monoclonal antibody that binds to terminal methoxy-PEG moieties. This explains why only compounds containing branched-chain methoxy-PEG (Pegasys, Figure 7e) or multiple methoxy-PEG molecules (Lipo-Dox, Figure 7b) could be detected by PEG-B-47/PEG-B-47-biotin in sandwich ELISA format. Mouse monoclonal anti-PEG antibodies (B139 M and B141M) bound amino-PEG molecules that were immobilized on plastic (data not show). Binding of both these antibodies to PEG was blocked by Tween 20 (results not shown), indicating that B139 M and B141 M can recognize the short repeating (OCH_2CH_2) subunits present in Tween-20. Even though all assays with these antibodies were performed without Tween-20 in the wash buffers, B139 M did not produce usable signals in sandwich ELISAs. On the other hand, B141 M in combination with 3.3-biotin was able to quantify PEG-Qdot 525, Lipo-Dox, Pegasys, and Neulasta, although generally with less sensitivity than AGP4/3.3-biotin (Figure 7 and Table 1).

In summary, the combination of AGP4 for capture and 3.3-biotin for detection in a sandwich ELISA format allowed sensitive measurement of PEGylated proteins, nanoparticles, and liposomes with minimal interference from free PEG or human serum. These characteristics should allow universal and simple measurement of the increasing numbers of novel PEG-conjugates for pharmacological and pharmacokinetic studies. Although AGP4/3.3-biotin provided versatile detection of PEGylated compounds, the ideal antibody format for ELISA may vary from compound to compound.

ACKNOWLEDGMENT

This study was supported by a grant from the Academia Sinica, Taipei, Taiwan (AS-98-TP-B09).

LITERATURE CITED

(1) Ensor, C. M., Holtsberg, F. W., Bomalaski, J. S., and Clark, M. A. (2002) Pegylated arginine deiminase (ADI-SS PEG20,000 mw) inhibits human melanomas and hepatocellular carcinomas in vitro and in vivo. *Cancer Res. 62*, 5443–50.

(2) Sun, X., Yang, Z., Li, S., Tan, Y., Zhang, N., Wang, X., Yagi, S., Yoshioka, T., Takimoto, A., Mitsushima, K., Suginaka, A., Frenkel, E. P., and Hoffman, R. M. (2003) In vivo efficacy of recombinant methioninase is enhanced by the combination of polyethylene glycol conjugation and pyridoxal 5′-phosphate supplementation. *Cancer Res. 63*, 8377–83.

(3) Yamamoto, Y., Tsutsumi, Y., Yoshioka, Y., Nishibata, T., Kobayashi, K., Okamoto, T., Mukai, Y., Shimizu, T., Nakagawa, S., Nagata, S., and Mayumi, T. (2003) Site-specific PEGylation of a lysine-deficient TNF-alpha with full bioactivity. *Nat. Biotechnol. 21*, 546–52.

(4) Baker, D. P., Lin, E. Y., Lin, K., Pellegrini, M., Petter, R. C., Chen, L. L., Arduini, R. M., Brickelmaier, M., Wen, D., Hess, D. M., Chen, L., Grant, D., Whitty, A., Gill, A., Lindner, D. J., and Pepinsky, R. B. (2006) N-terminally PEGylated human interferon-beta-1a with improved pharmacokinetic properties and in vivo efficacy in a melanoma angiogenesis model. *Bioconjugate Chem. 17*, 179–88.

(5) Zappe, H., Snell, M. E., and Bossard, M. J. (2008) PEGylation of cyanovirin-N, an entry inhibitor of HIV. *Adv. Drug Delivery Rev. 60*, 79–87.

(6) Kronman, C., Cohen, O., Mazor, O., Ordentlich, A., Raveh, L., Velan, B., and Shafferman, A. (2009) Next generation OP-bioscavengers: A circulatory long-lived 4-PEG hypolysine mutant of F338A-HuAChE with optimal pharmacokinetics and pseudo-catalytic characteristics. *Chem. Biol. Interact.*, 10.1016/j.cbi.2009.12.004.

(7) Freitas, D. D., Spencer, P. J., Vassao, R. C., and Abrahao-Neto, J. (2010) Biochemical and biopharmaceutical properties of PEGylated uricase. *Int. J. Pharm. 387*, 215–222.

(8) Zhang, Y., Sun, C., Kohler, N., and Zhang, M. (2004) Self-assembled coatings on individual monodisperse magnetite nanoparticles for efficient intracellular uptake. *Biomed. Microdevices 6*, 33–40.

(9) Lee, H., Yu, M. K., Park, S., Moon, S., Min, J. J., Jeong, Y. Y., Kang, H. W., and Jon, S. (2007) Thermally cross-linked superparamagnetic iron oxide nanoparticles: synthesis and application as a dual imaging probe for cancer in vivo. *J. Am. Chem. Soc. 129*, 12739–45.

(10) Kim, S., Lim, Y. T., Soltesz, E. G., De Grand, A. M., Lee, J., Nakayama, A., Parker, J. A., Mihaljevic, T., Laurence, R. G., Dor, D. M., Cohn, L. H., Bawendi, M. G., and Frangioni, J. V. (2004) Near-infrared fluorescent type II quantum dots for sentinel lymph node mapping. *Nat. Biotechnol. 22*, 93–7.

(11) Gao, X., Cui, Y., Levenson, R. M., Chung, L. W., and Nie, S. (2004) In vivo cancer targeting and imaging with semiconductor quantum dots. *Nat. Biotechnol. 22*, 969–76.

(12) Heathcote, E. J., Shiffman, M. L., Cooksley, W. G., Dusheiko, G. M., Lee, S. S., Balart, L., Reindollar, R., Reddy, R. K., Wright, T. L., Lin, A., Hoffman, J., and De Pamphilis, J. (2000) Peginterferon alfa-2a in patients with chronic hepatitis C and cirrhosis. *N. Engl. J. Med. 343*, 1673–80.

(13) Reddy, K. R., Wright, T. L., Pockros, P. J., Shiffman, M., Everson, G., Reindollar, R., Fried, M. W., Purdum, P. P., 3rd, Jensen, D., Smith, C., Lee, W. M., Boyer, T. D., Lin, A., Pedder, S., and DePamphilis, J. (2001) Efficacy and safety of pegylated (40-kd) interferon alpha-2a compared with interferon alpha-2a in noncirrhotic patients with chronic hepatitis C. *Hepatology 33*, 433–8.

(14) Manns, M. P., McHutchison, J. G., Gordon, S. C., Rustgi, V. K., Shiffman, M., Reindollar, R., Goodman, Z. D., Koury, K., Ling, M., and Albrecht, J. K. (2001) Peginterferon alfa-2b plus ribavirin compared with interferon alfa-2b plus ribavirin for initial treatment of chronic hepatitis C: a randomised trial. *Lancet 358*, 958–65.

(15) Goffin, V., and Touraine, P. (2002) Pegvisomant. Pharmacia. *Curr. Opin. Invest. Drugs (Thomson Sci.) 3*, 752–7.

(16) Schreiber, S., Khaliq-Kareemi, M., Lawrance, I. C., Thomsen, O. O., Hanauer, S. B., McColm, J., Bloomfield, R., and Sandborn, W. J. (2007) Maintenance therapy with certolizumab pegol for Crohn's disease. *N. Engl. J. Med. 357*, 239–50.

(17) Molineux, G. (2004) The design and development of pegfilgrastim (PEG-rmetHuG-CSF, Neulasta). *Curr. Pharm. Des. 10*, 1235–44.

(18) Lyman, G. H. (2005) Pegfilgrastim: a granulocyte colony-stimulating factor with sustained duration of action. *Expert Opin. Biol. Ther. 5*, 1635–46.

(19) Gordon, A., Fleagle, J., Guthrie, D., Parkin, D., Gore, M., and Lacave, A. (2001) Recurrent epithelial ovarian carcinoma: a randomized phase III study of pegylated liposomal doxorubicin versus topotecan. *J. Clin. Oncol. 19*, 3312.

(20) Park, J. (2002) Liposome-based drug delivery in breast cancer treatment. *Breast Cancer Res. 4*, 95–99.

(21) Gaberc-Porekar, V., Zore, I., Podobnik, B., and Menart, V. (2008) Obstacles and pitfalls in the PEGylation of therapeutic proteins. *Curr. Opin. Drug Discovery Dev. 11*, 242.

(22) Yang, Z., Ke, J., Hayes, M., Bryant, M., and Tse, F. (2009) A sensitive and high-throughput LC-MS/MS method for the quantification of pegylated-interferon-alpha (2a) in human serum using monolithic C (18) solid phase extraction for enrichment. *J. Chromatogr., B: Anal. Technol. Biomed. Life Sci.*

(23) Zamboni, W., Ramalingam, S., Friedland, D., Edwards, R., Stoller, R., Strychor, S., Maruca, L., Zamboni, B., Belani, C., and Ramanathan, R. (2009) Phase I and pharmacokinetic study of pegylated liposomal CKD-602 in patients with advanced malignancies. *Clin. Cancer Res. 15*, 1466–1472.

(24) Cheng, T. L., Cheng, C. M., Chen, B. M., Tsao, D. A., Chuang, K. H., Hsiao, S. W., Lin, Y. H., and Roffler, S. R. (2005) Monoclonal antibody-based quantitation of poly(ethylene glycol)-derivatized proteins, liposomes, and nanoparticles. *Bioconjugate Chem. 16*, 1225–31.

(25) Cheng, T. L., Wu, P. Y., Wu, M. F., Chern, J. W., and Roffler, S. R. (1999) Accelerated clearance of polyethylene glycol-modified proteins by anti-polyethylene glycol IgM. *Bioconjugate Chem. 10*, 520–8.

(26) Kurfurst, M. M. (1992) Detection and molecular weight determination of polyethylene glycol-modified hirudin by staining after sodium dodecyl sulfate-polyacrylamide gel electrophoresis. *Anal. Biochem. 200*, 244–8.

(27) Graham, M. L. (2003) Pegaspargase: a review of clinical studies. *Adv. Drug Delivery Rev. 55*, 1293–302.

(28) Panetta, J. C., Gajjar, A., Hijiya, N., Hak, L. J., Cheng, C., Liu, W., Pui, C. H., and Relling, M. V. (2009) Comparison of native E. coli and PEG asparaginase pharmacokinetics and pharmacodynamics in pediatric acute lymphoblastic leukemia. *Clin. Pharmacol. Ther. 86*, 651–8.

(29) Silverman, L. B., Supko, J. G., Stevenson, K. E., Woodward, C., Vrooman, L. M., Neuberg, D. S., Asselin, B. L., Athale, U. H., Clavell, L., Cole, P. D., Kelly, K. M., Laverdiere, C., Michon, B., Schorin, M., Schwartz, C. L., O'Brien, J. E., Cohen, H. J., and Sallan, S. E. (2009) Intravenous PEG-asparaginase during remission induction in children and adolescents with newly diagnosed acute lymphoblastic leukemia. *Blood 7*, 1351–1353.

(30) Ng, E. W., Shima, D. T., Calias, P., Cunningham, E. T., Jr., Guyer, D. R., and Adamis, A. P. (2006) Pegaptanib, a targeted anti-VEGF aptamer for ocular vascular disease. *Nat. Rev. Drug Discovery 5*, 123–32.

(31) Booth, C., and Gaspar, H. B. (2009) Pegademase bovine (PEG-ADA) for the treatment of infants and children with severe combined immunodeficiency (SCID). *Biologics 3*, 349–58.

(32) Liu, P., Santisteban, I., Burroughs, L. M., Ochs, H. D., Torgerson, T. R., Hershfield, M. S., Rawlings, D. J., and Scharenberg, A. M. (2009) Immunologic reconstitution during PEG-ADA therapy in an unusual mosaic ADA deficient patient. *Clin. Immunol. 130*, 162–74.

(33) Burke, R. S., and Pun, S. H. (2008) Extracellular barriers to in Vivo PEI and PEGylated PEI polyplex-mediated gene delivery to the liver. *Bioconjugate Chem. 19*, 693–704.

(34) Regehly, M., Greish, K., Rancan, F., Maeda, H., Bohm, F., and Roder, B. (2007) Water-soluble polymer conjugates of ZnPP for photodynamic tumor therapy. *Bioconjugate Chem. 18*, 494–9.

(35) Prencipe, G., Tabakman, S. M., Welsher, K., Liu, Z., Goodwin, A. P., Zhang, L., Henry, J., and Dai, H. (2009) PEG branched polymer for functionalization of nanomaterials with ultralong blood circulation. *J. Am. Chem. Soc. 131*, 4783–7.

(36) Cosmi, B. (2009) ARC-1779, a PEGylated aptamer antagonist of von Willebrand factor for potential use as an anticoagulant or antithrombotic agent. *Curr. Opin. Mol. Ther. 11*, 322–8.

(37) Hong, R. L., and Tseng, Y. L. (2001) Phase I and pharmacokinetic study of a stable, polyethylene-glycolated liposomal doxorubicin in patients with solid tumors: the relation between pharmacokinetic property and toxicity. *Cancer 91*, 1826–33.

(38) Bailon, P., Palleroni, A., Schaffer, C. A., Spence, C. L., Fung, W. J., Porter, J. E., Ehrlich, G. K., Pan, W., Xu, Z. X., Modi, M. W., Farid, A., Berthold, W., and Graves, M. (2001) Rational design of a potent, long-lasting form of interferon: a 40 kDa branched polyethylene glycol-conjugated interferon alpha-2a for the treatment of hepatitis C. *Bioconjugate Chem. 12*, 195–202.

(39) Wang, Y. S., Youngster, S., Grace, M., Bausch, J., Bordens, R., and Wyss, D. F. (2002) Structural and biological characterization of pegylated recombinant interferon alpha-2b and its therapeutic implications. *Adv. Drug Delivery Rev. 54*, 547–70.

(40) Curran, M. P., and Goa, K. L. (2002) Pegfilgrastim. *Drugs 62*, 1207–13.

(41) Chuang, K., Tzou, S., Cheng, T., Kao, C., Tseng, W., Shiea, J., Liao, K., Wang, Y., Chang, Y., and Huang, B. (2010) Measurement of poly(ethylene glycol) by cell-based anti-poly (ethylene glycol) ELISA. *Anal. Chem. 82*, 2355–2362.

BC100067T

Effect of Molecular Weight and Degree of Substitution of Quaternized Cellulose on the Efficiency of Gene Transfection

Yongbo Song, Huiyuan Wang, Xuan Zeng, Yunxia Sun, Xianzheng Zhang, Jinping Zhou,* and Lina Zhang

Department of Chemistry and Key Laboratory of Biomedical Polymers, Ministry of Education, Wuhan University, Wuhan 430072, China. Received February 8, 2010; Revised Manuscript Received March 22, 2010

Quaternized celluloses (QCs) with different molecular weight (M_w) and degree of cationic substitution (DS) were homogeneously synthesized in NaOH/urea aqueous solutions and were studied as gene carriers. QCs were evaluated for efficacy of nanoparticle formation, DNA binding efficiency, morphology, and in vitro gene transfection efficiency. The factors affecting the transfection efficiency, e.g., M_w, DS, and N/P ratios, have been evaluated. The cytotoxicity of QCs and QC/DNA complexes were evaluated in 293T cells and were found to be relatively low compared with 25 kDa PEI and PEI/DNA complex, which increased slightly with increasing of M_w and DS. All QCs obtained could bind DNA efficiently, and QC/DNA complexes exhibited effective transfection in comparison to the naked DNA. More importantly, the QC/DNA complexes, were stable and the transfection efficiency was not inhibited in the presence of serum. The results revealed an important combined effect between M_w and DS of QCs in determining transgene expression, and QCs with M_w of about 8×10^4 g/mol and DS of about 0.6 displayed relatively higher transfection efficiencies attributed to the intermediate stability.

INTRODUCTION

Among the various polycations used in nonviral gene delivery and transfection vectors, cationic polysaccharides have been receiving more and more attention and been considered the most attractive candidates (*1*−*4*). They are natural, renewable, nontoxic, biodegradable, and biocompatible materials with low immunogenicity (*3*−*9*). The cationic polysaccharides investigated as gene carriers include cationized schizophyllan (*4, 10*), pullulan (*5, 11*), pectin (*12*), dextran (*13*−*21*), and chitosan and chitosan derivatives (*22*−*27*). The advantages of cationic polysaccharides, over other cationic polymers, are the presence of groups that can be simply modified for the improvement of the physicochemical properties and the cell internalization possibly accelerated by a sugar-recognition receptor on the cell surface (*5*).

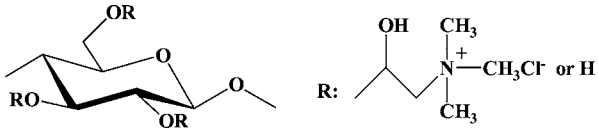
It is well-recognized that the formulation parameters of cationic polysaccharides, such as molecular weight (M_w) and degree of cationic substitution (DS) (or degree of deacetylation (DD) for chitosan), as well as N/P ratio, have a major influence on the stability of the cationic polysaccharides/DNA complex, the efficiency of cell uptake, and the dissociation of DNA from the complex after endocytosis and, therefore, affect the level of gene expression of cationic polysaccharides/DNA complexes (*5, 7, 28, 29*). For example, Domb et al. (*14*−*20*) studied more than 300 different polycations prepared starting from various polysaccharides of different molecular weights and oligoamines having 2−4 amine groups. Although most of these conjugates formed stable complexes with DNA, only the dextran-spermine (D-SPM) polycations of defined molecular weights were found to be active in transfecting a wide range of cell lines in vitro. Sato et al. (*30*) reported that the tranfection efficiency mediated by chitosan with M_w >100 kDa was less than that by chitosan with 15 and 52 kDa. Huang et al. (*31*) suggested that chitosan DD had a greater influence than M_w on the uptake and cytotoxicity of chitosan nanoparticles because of its effect on the zeta potential of the nanoparticles. Decreasing either the polymer M_w or DD will lead to decreasing protection of the condensed DNA and less efficient cellular uptake, causing low transfection efficiency (*32*). Lavertu et al. (*33*) revealed an important coupling between DD and M_w of chitosan in determining transgene expression. Maximum expression was obtained with a certain combination of DD and M_w that depended on N:P ratio and the pH, but similar expression levels could be achieved by simultaneously lowering M_w and increasing DD or lowering DD and increasing M_w. Zhang et al. (*34*) reported that the molecular weight of polyethylenimine (PEI) grafted N-maleated chitosan (NMC-g-PEI) has an important effect on cytotoxicity and transfection activity, and low-molecular-weight NMC-g-PEI had a good potential as efficient nonviral gene vectors.

Cationic cellulose derivatives are large-scale commercial products, having many useful characteristics, such as hydrophilicity, biodegradability, biocompatibility, and antibacterial properties (*35, 36*). They have been found numerous applications in a variety of fields including the food, cosmetics, chemical, pharmaceutical, and paper and textile industries. Recently, the transfection properties of cationic hydroxyethylcelluloses (HECs)/plasmid DNA (pDNA) nanoparticles were investigated (*37*). Although the cationic HECs/pDNA nanoparticles transfected cells to a much less extent than the PEI-based pDNA nanoparticles, tailoring the nature and extent of cationic side chains on the cationic HECs may be promising to further enhance their DNA delivery properties. More recently, well-defined comb-shaped copolymers composed of hydroxypropylcellulose (HPC) backbones and cationic poly((2-dimethyl amino)ethyl methacrylate) side chains were prepared and studied as novel nonviral gene vectors (*3*). In our previous study (*38*), a novel water-soluble cationic cellulose derivative, namely, quaternized cellulose (QC, chemical structure as shown in Chart 1), was homogeneously synthesized in NaOH/urea aqueous solutions by reacting cellulose directly with 3-chloro-2-hydroxypropyltrimethylammonium chloride (CHPTAC) and was studied as a gene carrier for the first time. QCs have showed elevated potential as gene carrier by efficient DNA condensation and mediated a higher level of gene transfection with negligible

* Corresponding author. Tel.: 86-27-8721 9274. Fax: 86-27-6875 4067. E-mail addresses: zhoujp325@whu.edu.cn (J. Zhou).

10.1021/bc100068f © 2010 American Chemical Society
Published on Web 06/03/2010

Chart 1. Chemical Structure of the Quaternized Cellulose (QC)



cytotoxicity in human embryonic kidney transformed (293T) cells. To provide more important information of scientific values to the utilization of this novel cationic polysaccharide, in the present work, QC with different molecular weight (M_w) and degree of substitution (DS) were synthesized homogeneously in NaOH/urea aqueous solutions, and the effect of M_w and DS of QCs on DNA binding efficiency, QC/DNA complex formation and morphology, and in vitro gene transfection efficiency was investigated.

EXPERIMENTAL PROCEDURES

Materials. Cellulose (cotton linter pulp) was supplied by Hubei Chemical Fiber Group Ltd. (Hubei, China), and the viscosity-average molecular weight (M_η) of the cellulose was determined by viscometry to be 3.7, 5.0, 7.8, and 11.2 $\times$ 10^4 g/mol, respectively. CHPTAC was purchased from Guofeng Fine Chemical Co. Ltd. (Shandong, China) and was used as etherifying reagent without further purification. Branched polyethylenimine (PEI), with a molecular weight of 25 kDa, was purchased from Sigma-Aldrich. Dulbecco's Modified Eagle's Medium (DMEM), 3-[4,5-dimethylthiazol-2-yl]-2,5-diphenyltetrazolium bromide (MTT), fetal bovine serum (FBS), penicillin−streptomycin, trypsin, and Dulbecco's phosphate-buffered saline (PBS) were purchased from Invitrogen Corp. All other reagents were of analytical grade and were used without further purification.

Quaternization of Cellulose. QCs with different M_w and DS were prepared according to the previous work (*38*). Briefly, a certain amount of CHPTAC aqueous solution was added dropwise into the 100 g cellulose solution (2 wt %, in NaOH/urea aqueous solutions), and the mixture was stirred at 25 °C for 24 h. The reaction product was neutralized with aqueous HCl and dialyzed with regenerated cellulose tubes (M_w cutoff 8000) against distilled water for 7 days. The solution was finally freeze−dried with lyophilizer to obtain the purified cellulose derivative. According to Table 1, eight quaternized cellulose derivatives were prepared by changing the molecular weight of cellulose and the molar ratio of CHPTAC to the anhydroglucose unit (AGU).

Characterization of QCs. Nitrogen contents (N%) of QCs were measured with an elemental analyzer (CHN-O-Rapid, Foss Hera us GmbH, Hanau, Germany). Chlorine contents (Cl%) of QCs were measured with an ion chromatograph (ICS 2500, Dionex, USA). The DS_N and DS_{Cl} values of QCs were determined by nitrogen and chlorine contents, respectively, and calculated according to the following equations:

$$DS_N = 162 \times N\%/(14-151.5 \times N\%)$$

$$DS_{Cl} = 162 \times Cl\%/(35.5 - 151.5 \times Cl\%)$$

The weight-average molecular weight (M_w) of QC was determined with static light scattering. The light-scattering intensities were measured with a modified commercial light scattering spectrometer (ALV/SP-125, ALV, Germany) equipped with an ALV-5000/E multi-τ digital time correlator and a He−Ne laser (λ = 632.8 nm) in an angular range from 30° to 150° at 10° intervals at 25 °C. The test QC solutions were prepared in 0.15 M NaCl aqueous solution and made optically clean by filtration through 0.22 μm Millipore filters. The specific refractive-index increments (d*n*/d*c*) of QC in 0.15 M NaCl aqueous solution were measured on an Optilab refractometer (Wyatt Technology) at 632.8 nm and 25 °C and were found to be 0.135 cm^3/g.

ζ-Potential of the QCs in distilled water ($c_{polymer}$ = 1 mg/mL) was performed on a Nano-ZS ZEN3600 (Malven Instruments, U.K.) at 25 °C.

Cell Culture. Human embryonic kidney transformed (293T) cells were incubated in DMEM containing 10% FBS and 1% antibiotics (penicillin−streptomycin, 10 000 U/mL) at 37 °C in a humidified atmosphere containing 5% CO_2.

Amplification and Purification of Plasmid DNA. pGL-3 and pEGFP-C1 plasmids DNA were used in this study. The former one as the luciferase reporter gene was transformed in *E. coli* JM109 and the latter one as the green fluorescent protein gene was transformed in *E. coli* DH5α. Both plasmids were amplified in broth media at 37 °C overnight at 300 rpm. Then, the purified plasmid was diluted by TE buffer solution and stored at −20 °C. The integrity of plasmid was confirmed by agarose gel electrophoresis. The purity and concentration of plasmid were determined by ultraviolet (UV) absorbance at 260 and 280 nm.

Agarose Gel Electrophoresis Assay. QC/DNA complexes at different N/P ratios ranging from 0.25 to 5 were prepared by adding appropriate volume of QC (in 0.15 M NaCl solution) to 96 ng pGL-3 DNA (in 40 mM Tris-HCl buffer solution). The complexes were diluted by 0.15 M NaCl solution to 8 μL, and then the complexes were incubated at 37 °C for 30 min. After that, the complexes were subjected to electrophoresis on the 0.7% (W/V) agarose gel containing GelRed and with Tris-acetate (TAE) running buffer at 80 V for 80 min. DNA was visualized with a UV lamp using a Vilber Lourmat imaging system.

Characterization of QC/DNA Complexes. Particle size and ζ-potential of QC/DNA complexes were measured by Nano-ZS ZEN3600 (Malvern Instruments, U.K.) at 25 °C. The complexes at various N/P ratios ranging from 1 to 20 were prepared by adding appropriate volume of QCs solution (in 0.15 M NaCl solution) to 1 μg of pGL-3 DNA solution (in 40 mM Tris-HCl buffer solution). The complexes were incubated at 37 °C for 30 min. After that, the complexes were diluted by 0.15 M NaCl solution to 1 mL prior to measurement.

Table 1. Homogeneous Quaternization of Cellulose with CHPTAC in NaOH/Urea Aqueous Solutions and Molecular Parameters of the QCs

Code	$M_{\eta,\ cellulose} \times 10^{-4}$ (g/mol)	molar ratio[a]	N (wt %)	Cl (wt %)	DS_N[b]	DS_{Cl}[c]	$M_w \times 10^{-4}$ (g/mol)	ζ (mV)
QC1	3.7	12	3.311	8.135	0.60	0.57	4.51	33.90
QC2	5.0	12	3.280	8.239	0.59	0.58	6.11	36.50
QC3	7.8	12	3.320	8.339	0.60	0.59	8.36	35.70
QC4	11.2	12	3.318	8.281	0.60	0.58	14.29	35.05
QC5	7.8	6	1.856	4.682	0.27	0.27	−	28.85
QC6	7.8	9	2.509	6.048	0.40	0.37	−	30.43
QC7	7.8	12	3.217	7.452	0.57	0.50	8.13	34.95
QC8	7.8	15	3.514	8.774	0.66	0.64	8.38	40.35

[a] The molar ratio of CHPTAC to the anhydroglucose unit (AGU) of cellulose. [b] DS_N, DS calculated from the nitrogen content. [c] DS_{Cl}, DS calculated from the chloride content.

The morphologies of QC/DNA complexes at N/P ratio 6 were observed by a transmission electron microscopy (TEM, JEM-100CX II, Japan). The complexes were prepared by adding an appropriate volume of QC solution to an appropriate volume of pGL-3 solution. The complexes were diluted to a total volume of 100 μL by 0.15 M NaCl solution and then incubated at 37 °C for 30 min. A TEM sample was prepared by dipping a copper grid with Formvar film into the freshly prepared nanoparticle solution. After the deposition, the aqueous solution was blotted away with a strip of filter paper and dried in air.

In Vitro Cytotoxicity Assay. The cytotoxicity of polymer as well as polymer/DNA complexes was examined by MTT assay. The 293T cells were seeded in a 96-well plate at 6000 cells/well and cultured for 1 day in 200 μL of DMEM containing 10% FBS. After incubation for 24 h, polymer solutions were added to the culture medium, while QC/DNA complexes (N/P ratio 20) and 25 kDa PEI/DNA complexes (N/P ratio 10) were added to each well of the culture medium at 1 μg DNA/well. Cell viability was tested after the addition of polymer or polymer/DNA complexes for 48 h. After incubation, 20 μL MTT (5 mg/mL) solution in phosphate-buffered saline (PBS, pH = 7.4) was added to each well and further incubated in 5% CO_2 incubator at 37 °C for 4 h. After removal of the MTT containing medium, 150 μL DMSO was added to dissolve the formazan crystals formed in live cells. The absorbance was measured at 570 nm using a microplate reader (Bio-Rad, model 550, USA). The relative cell viability was calculated as cell viability (%) = $(OD_{570\ (samples)}/OD_{570\ (control)}) \times 100$. Where $OD_{570\ (control)}$ was obtained in the absence of polymer or polymer/DNA complexes and $OD_{570\ (samples)}$ was obtained in the presence of polymer or polymer/DNA complexes.

In Vitro Transfection Assay. For the in vitro transfection studies, the 25 kDa PEI/DNA at N/P ratio of 10 and naked pGL-3 DNA (1 μg) were, respectively, used as the positive and negative control. 293T cells were seeded at a density of 6×10^4 cells/well in 24-well plate with 1 mL DMEM containing 10% FBS and incubated at 37 °C for 24 h. The QC/DNA complexes at N/P ratios ranging from 2 to 20 were prepared by adding appropriate volume of QC to 1 μg of pGL-3 DNA solution and then diluted by 0.15 M NaCl solution to 100 μL and incubated at 37 °C for 30 min. Before transfection, the cells were washed by PBS, and then the QC/DNA complexes, PEI/DNA complexes, and naked DNA were added with serum-free or 10% serum-containing culture medium, respectively, for 4 h at 37 °C. Then, the medium was replaced with fresh medium containing 10% serum and incubated for 48 h. The luciferase assay was performed according to manufacture's protocols. Relative light units (RLUs) were measured with chemiluminometer (Lumat LB9507, EG&G Berthold, Germany). The total protein was measured according to a BCA protein assay kit (Pierce). Luciferase activity was expressed as RLU/mg protein. Data were shown as mean ± standard deviation (SD) based on three independent measurements.

In order to directly visualize the infected cells expressing pEGFP-C1 DNA, enhanced green fluorescent protein in 293T cells were also evaluated and were directly observed by fluorescent microscope (Olympus IX 70). The microscopy images were obtained at the magnification of 100× and recorded using CoolSNAP-Pro (4.5.1.1) software.

Cellular Uptake Study. Live cell confocal microscopy was used to image QC/pDNA complex uptake into 293T cells. 10 μM YOYO-1 water stock solution (green molecular probe) was used to tag pGL-3 and 10 mg/mL Hoechst 33258 water stock solution (blue molecular probe) was used to stain nuclei. Cells were seeded into LabTek chamber slide dishes at a density of 5.0×10^4 cells/well with 1 mL of DMEM containing 10% FBS and incubated at 37 °C for 24 h. One microgram of pGL-3 plasmid was mixed with 2.5 μL YOYO-1 solution and incubated for 15 min at 37 °C. Then, the complexes were prepared at an N/P ratio of 15 by adding an appropriate volume of QC solution to the YOYO-1 labeled pGL-3 and incubating for 30 min at 37 °C. After the complexes were added into the wells of a cell plate and incubated in serum-free DMEM for 4 h at 37 °C, the serum-free DMEM was removed, the cells in each well were washed twice with PBS, and then 200 μL DMEM (with FBS) with 20 μL Hoechst 33258 solution was added and incubated for 20 min at 37 °C. Finally, the solution was removed, cells in each well were washed with PBS twice, and 1 mL fresh DMEM (with FBS) was added. The fluorescent images of cells were observed under excitation at 488 nm using confocal laser scanning microscopy (Nikon C1-si TE2000, Japan). All confocal images were slice images to distinguish QC internalized from that adherent to the outside cellular membrane. The whole preparation process should avoid exposure to strong light in order to protect the fluorescent dyes.

RESULTS AND DISCUSSION

Molecular Parameters of Quaternized Celluloses. Table 1 summarizes the reaction conditions and results of the homogeneous quaternization of cellulose in NaOH/urea aqueous solutions. The reaction was mild and performed at room temperature, and the solution kept its transparent nature and remained completely homogeneous as the reaction proceeded. All the QC samples have good solubility in aqueous solutions, and their structures (shown in Chart 1) were proven by FT-IR and liquid ^{13}C NMR measurements (data not shown), consistent with the previous work (*38*). As shown in Table 1, QCs with DS_N values of 0.27 to 0.66 were obtained by changing the molar ratio of CHPTAC to the anhydroglucose unit (AGU) of cellulose from 6 to 15. Moreover, the DS values calculated from the nitrogen content were in good agreement with those calculated from the chloride content of the samples, and ζ-potential value increased with increasing of DS values.

Figure 1 shows the Zimm plots of QC3 and QC5 in 0.15 M NaCl aqueous solution at 25 °C. Because of the introduction of the quaternary ammonium salt group on cellulose backbone, QCs with $DS_N > 0.57$ could form dilute "truly" solution in 0.15 M NaCl aqueous. Therefore, the M_w of single chain for QCs with $DS_N > 0.57$ could be determined by laser-light scattering and are listed in Table 1. QCs were produced with M_w from 4.51×10^4 g/mol to 14.29×10^4 g/mol by beginning with cellulose of different M_η. The polydispersity index ($d = M_w/M_n$) of the QCs were determined to be 1.2−1.4 by size exclusion chromatography combined with laser light scattering (SEC-LLS) measurements. Attributed to the strong hydrogen bonding of the residual −OH groups within the AGU unit of the derivatives (*38*), QC5 and QC6 with relatively lower DS values formed large aggregates in aqueous solutions. For example, the M_w of QC5 was determined to be 3.29×10^7 g/mol, which was much larger than its calculated value from its DS value and the M_η of the native cellulose (7.8×10^4 g/mol). Therefore, the M_w values of QC5 and QC6 for their single chain were not detected.

Interactions of QCs and pDNA. The binding capability of polycations to pDNA is a prerequisite as the gene vectors. The polycations can condense pDNA into compact structures and reduce the electrostatic repulsion between DNA and cell surface by neutralizing the negative charge, which facilitates the uptake of the complex to negatively charged cell membrane constituents, leading to a higher rate of uptake. When pDNA is condensed by polycations, it also can be better protected against enzymatic degradation by nucleases in serum and extracellular fluids (*19*). To investigate the binding capability of QCs to pDNA and determine the optimal complexation conditions adequately, solutions of QCs and pDNA were electrophoresed

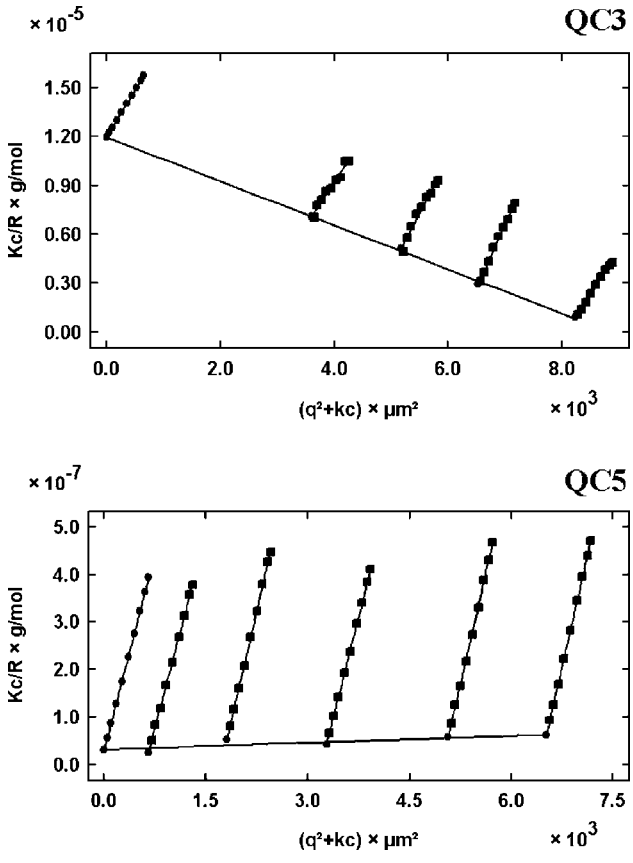


Figure 1. Zimm plots of QC3 and QC5 in 0.15 M NaCl aqueous solution at 25 °C.

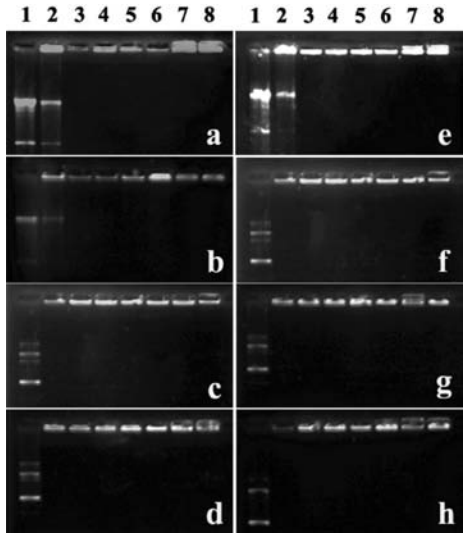


Figure 2. Agarose gel electrophoresis retardation assay of QC/DNA complexes. (a−h) QC1−QC8. Plasmid DNA was mixed with QCs at different N/P ratios: 1 (0), 2 (0.25), 3 (0.5), 4 (1), 5 (2), 6 (3), 7 (4), and 8 (5).

on an agarose gel containing ethidium bromide. The results of gel electrophoresis measurements are shown in Figure 2. Clearly, at N/P ratio of 0.25, QC3−4 and QC6−8 were already able to bind the pDNA, whereas at N/P ratio of 0.5 and higher, all QCs bound the pDNA completely and prevented its migration under electrophoretic conditions. The results revealed that DNA binding capability was dependent on both the M_w and the DS of QC used. At similar DS values, higher M_w of QCs were superior to lower M_w in enhanced DNA binding; lower M_w of QCs required higher N/P ratio to completely bind the pDNA.

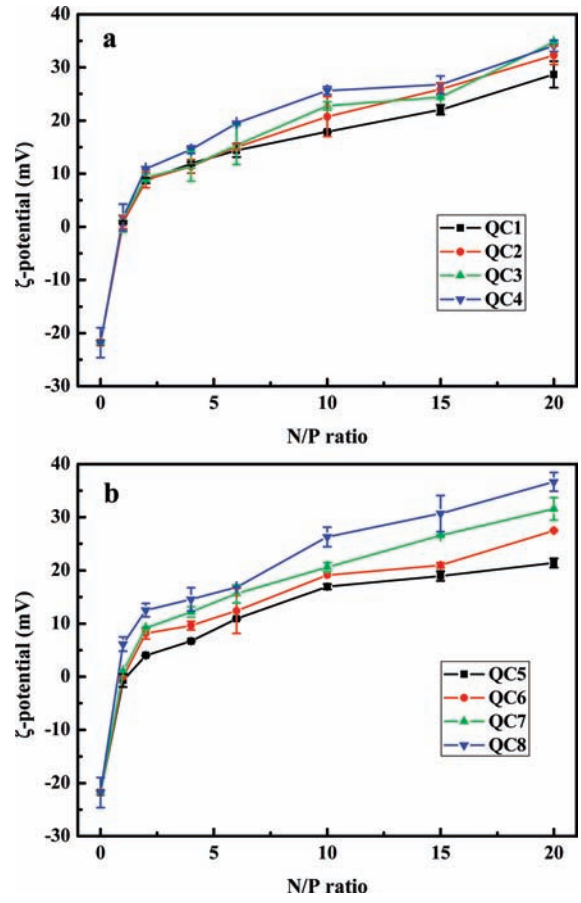


Figure 3. ζ-potential of QC/DNA complexes at N/P ratios ranging from 0 to 20. Data are shown as mean ± SD (n = 3).

This could be observed by comparing the gels from the left column of Figure 2. Higher M_w of QCs (QC3 and QC4) bound pDNA at N/P ratio of 0.25, whereas lower M_w of QCs (QC1 and QC2) required N/P ratio of 0.5 to completely bind the pDNA. The influence of M_w in DNA binding could be attributed to the chain entanglement effect. Longer polymer chains in the higher M_w QCs more easily entangled free DNA once the initial electrostatic interaction had occurred (*28*). Similarly, at constant M_w, the DNA binding ability of higher DS of QCs was stronger than that of lower DS of QCs because of the relatively higher density of positive charge. When DS decreased, the DNA binding capacity was decreased, i.e., higher N/P ratio was required to completely bind the DNA. This could be observed by comparing the gels from the right column of Figure 2. QCs with higher DS (QC6−8) bound pDNA at N/P ratio of 0.25, while QC with lower DS (QC5) required N/P ratio of 0.5 to completely bind the pDNA.

The charge and particle size of the polymer/DNA complexes are very important for polycations used as gene vectors, playing an important role in the endosomal uptake, the cytoplasmatic transport, and the migration through the nucleopore complexes, which mediate the bidirectional transport between cytoplasm and nucleus (*19*). In the present study, the ζ-potential and particle sizes of QC/DNA complexes at various N/P ratios ranging from 1 to 20 were measured by adding QC solutions to DNA at physiological ionic strength condition (in 0.15 M NaCl solution). Figure 3 shows the ζ-potential values of QC/DNA complexes at N/P ratios ranging from 1 to 20. Initially, the ζ-potential of the complexes increased with the increase of N/P ratios. At high N/P ratios, the ζ-potential appeared to reach a maximum plateau as observed. Lowering the DS of QC caused the zeta potential of the complex to fall (Figure 3b), which was

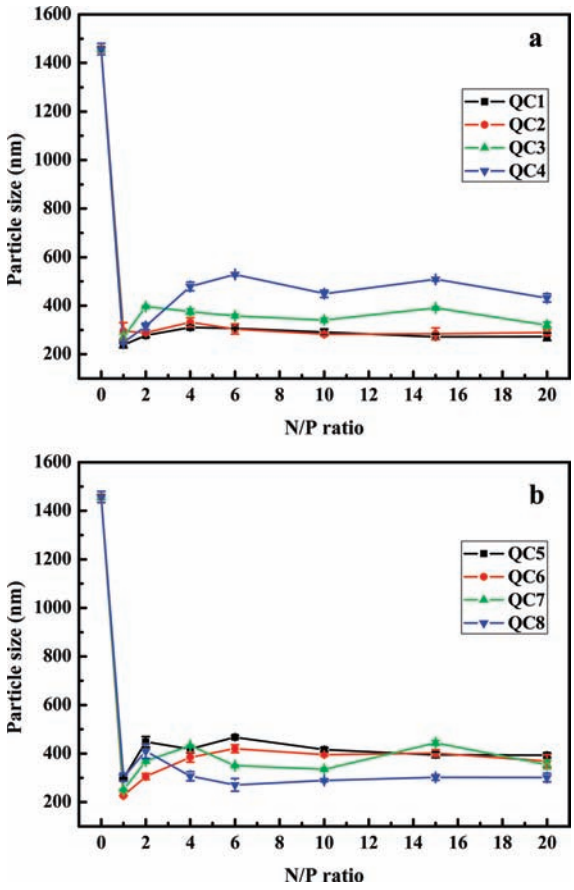


Figure 4. Particle size of QC/DNA complexes at N/P ratios ranging from 0 to 20. Data are shown as mean ± SD ($n = 3$).

attributed to the relative lower ζ-potential value (as shown in Table 1). Molecular weight did not significantly affect the ζ-potential, and no noticeable differences were observed (Figure 3a), which agreed well with the previous observations (*25*, *31*).

As shown in Figure 4, the particle size of the DNA molecule was about 1457 nm. As QCs were added, the particle sizes of the QC/DNA complexes decreased sharply as a result of the electrostatic interaction and then hardly changed with further increase of N/P ratios. The particle size of QC/DNA complexes had similar trends (in the range of 227 and 529 nm) at various N/P ratios ranging from 1 to 20. The particle size of QC/DNA complexes was dependent on M_w and DS of QCs. Lowering the M_w of QC caused the mean particle size of the complex to fall (Figure 4a), because that shorter polymer chains of the lower M_w QCs could form QC/DNA complexes with smaller size. Size of the complexes was found to increase with decreasing of QCs DS (Figure 4b). This was because of the relatively lower ζ-potential value, the reduction of ζ-potential of QC decreasing its condensing affinity to DNA.

To know better the formation of QC/DNA complex nanoparticles, the representative morphologies of QC/DNA nanoparticles at N/P ratio 6 were observed by transmission electron microscopy (Figure 5). All the nanoparticles displayed uniform nanospheres with sizes of about 150−500 nm, which were consistent with the particle sizes measured by Nano-ZS ZEN3600 (Figure 4). Apparently, QCs with relatively higher DS values formed dense particles with DNA attributed to the stronger condensing affinity to DNA; QC5 formed loose complexes with DNA for its relatively lower DS value.

In Vitro Cytotoxicity. One of the major requirements of the cationic polymer vectors for use in gene delivery is the low cytotoxicity. The cytotoxicity of QCs was evaluated in 293T cells by MTT assay, and the 25 kDa PEI was used as the control.

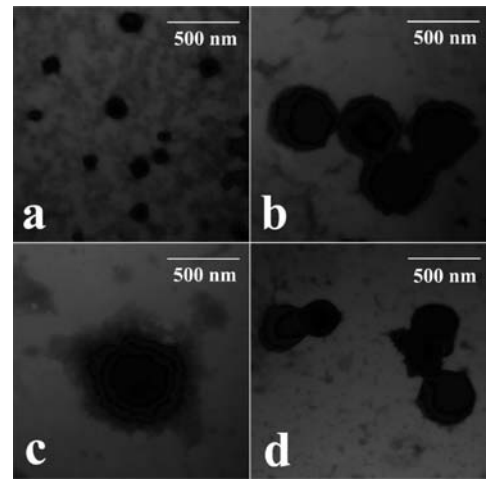


Figure 5. TEM images of QC/DNA complexes at N/P ratios 6: (a) QC1, (b) QC4, (c) QC5, and (d) QC8.

Cytotoxicity of QC was related to the molecular weight (Figure 6a). At similar DS values, lower M_w QCs appeared to be less cytotoxic compared to those with higher M_w. This could be explained by each individual shorter chain of the lower M_w QCs having fewer contact points with the cell components (*25*). As shown in Figure 6b, the cytotoxicity of QCs increased gradually with increase of the concentrations and DS values due to the presence of a higher amount of cationic cellulose damaging the cellular membranes. However, the QCs exhibited much lower cytotoxicity in comparison with 25 kDa PEI, the most popular "gold standard" of cationic polymer transfection (*39*). On the basis of the results of cytotoxicity, while the QC/DNA complexes at the maximum N/P ratio studied of 20 (the maximum concentration of 43 μg/mL for QC5), all the 293T cells hade viability above 90%. In addition, when combined with DNA, the QC/DNA complexes exhibited much lower toxicity on cell viability, and PEI/DNA complexes also showed decreased cytotoxicity (Figure 6c). The reason might be that the positive charge of polymers was counterbalanced by negative charge of DNA, which minimized the direct contact of polycations to cellular membrane. It was demonstrated that QC/DNA complexes were safe at the maximum concentration used in the succeeding in vitro transfection assay.

In Vitro Transfection. The achievement of high gene transfection efficiency is a final goal for the development of novel gene carriers. Among the factors in determining the gene transfection efficiency, the stability of cationic polymer/DNA complexes is already well-recognized as the key factor (*33*). Usually, complexes not sufficiently stable will dissociate too early, showing little or no transgene expression; highly stable complexes could not release DNA once inside the cells or will release DNA slowly, which resulted in low or delayed expression (*40*, *41*). Thus, a fine balance must be achieved and an intermediate stability is desired. In this case, QC with different M_w and DS were compounded with DNA at various N/P ratios (ranging from 2 to 20) to investigate the optimal conditions for gene transfection. The plasmid pGL-3 DNA and 293T cells were used. Figure 7 shows the transfection efficiency of QC/DNA complexes in the absence of serum. Although the transfection efficiency was relatively lower than that of 25 kDa PEI/DNA complexes, QC/DNA complexes exhibited much higher transfection efficiency compared with the naked DNA. The level of transfection efficiency was significantly influenced by M_w and DS of QC, as well as N/P ratios. At similar DS values (Figure 7a), the QC with lower M_w had the higher optimal N/P ratio, while QC with higher M_w had the lower optimal N/P ratio. This was because complexes formed with low M_w QC at

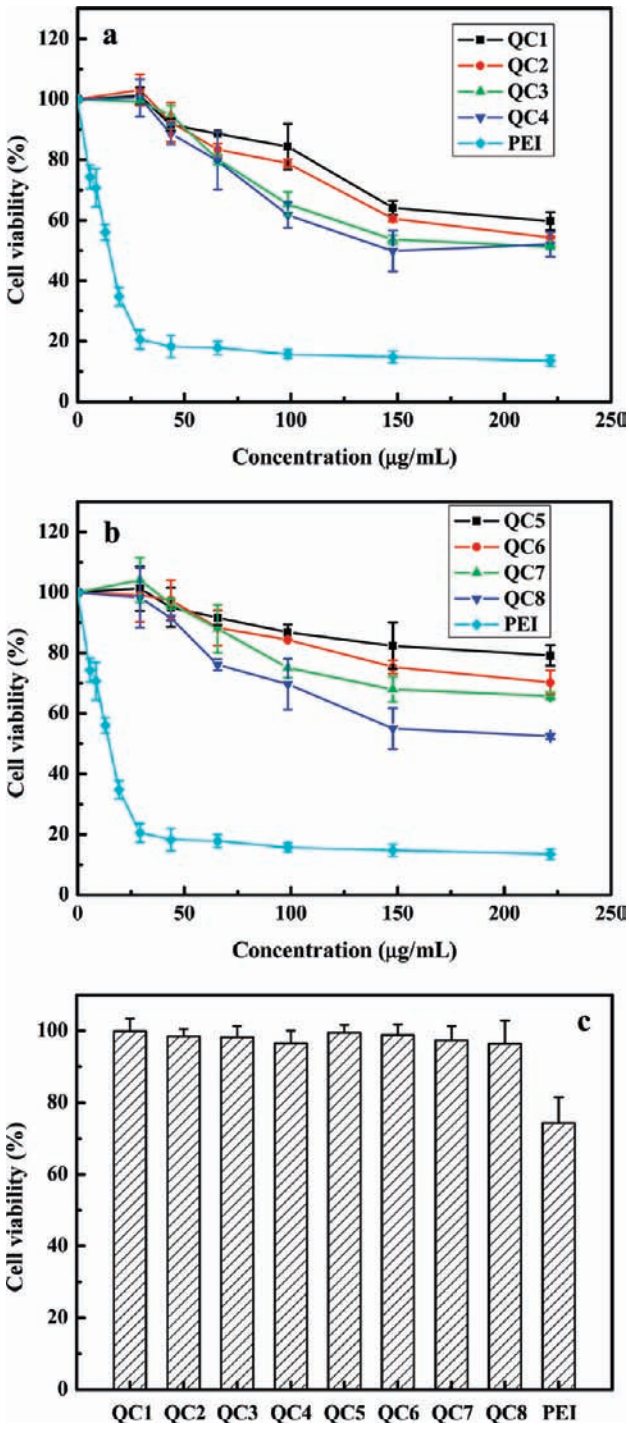


Figure 6. Cell viabilities of 293T cells in the presence of QCs and 25 kDa PEI (a,b), as well as QC/DNA (N/P ratio 20) and PEI/DNA (N/P ratio 10) complexes (c). Data are shown as mean ± SD (n = 3).

low N/P ratio were not sufficiently stable to transfect cells efficiently. On the other hand, complexes formed with high M_w, at higher N/P ratio, were too stable and led to low transfection. Moreover, QC3 showed relatively higher transfection efficiencies than the other three samples. Figure 7b shows the influence of DS and N/P ratios. When M_w values were kept constant (QC5−QC8), there also was an optimal N/P ratio value for each particular DS, indicating a combined effect between DS and N/P ratio. The QC with lower DS had the higher optimal N/P ratio value, because complexes formed with low DS QC at low N/P ratio were not sufficiently stable to transfect cells efficiently, while complexes formed with high DS, at higher N/P ratio, were

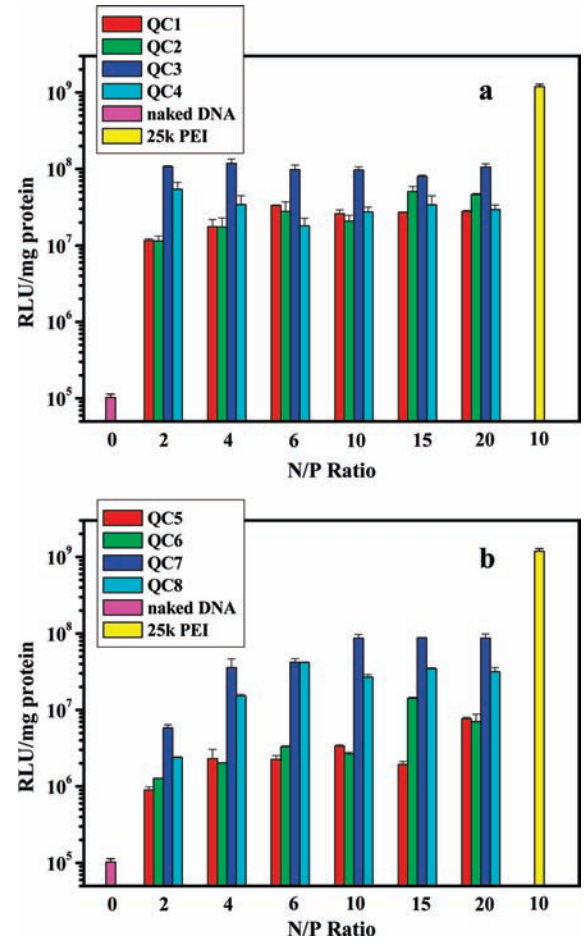


Figure 7. Luciferase expression in 293T cells transfected by QC/DNA complexes in the absence of serum at different N/P ratios. Transfection efficiencies of the naked DNA and 25 kDa PEI are shown as controls. Data are shown as mean ± SD (n = 3).

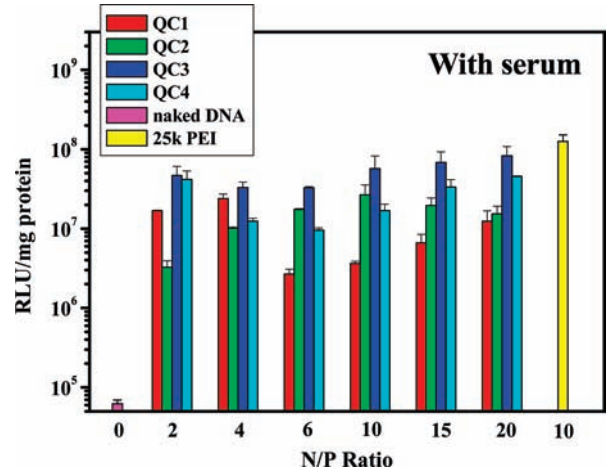


Figure 8. Luciferase expression in 293T cells transfected by QC/DNA complexes in the presence of 10% serum at different N/P ratios. Transfection efficiency of the naked DNA and 25 kDa PEI are shown as control. Data are shown as mean ± SD (n = 3).

too stable and led to low transfection. QC7 displayed relatively higher transfection efficiencies than the other three samples.

The development of gene vectors that are stable even in serum after coagulation of blood is very important for practical applications (*7, 42*). In this study, the effect of serum on the transfection efficiency of PEI/DNA and QC/DNA complexes was further evaluated. As shown in Figure 8, 25 kDa PEI

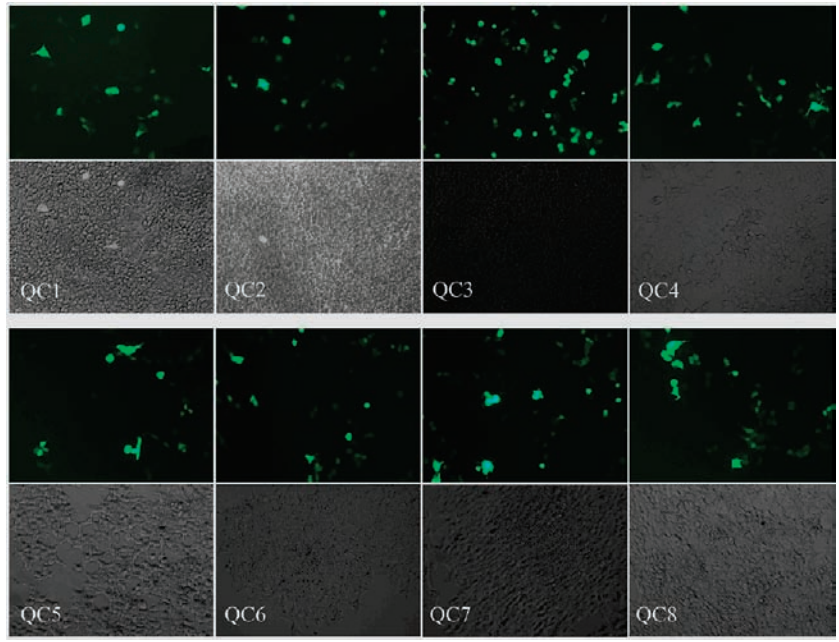


Figure 9. Fluorescent (top) and bright field (bottom) images of enhanced green fluorescent protein expression by QC/DNA complexes at N/P ratio 10 in 293T cells. The images were obtained by a fluorescent microscope at the magnification of 100×.

showed dramatically reduced transfection efficiency of DNA in the presence of serum. However, in contrast, the transfection efficiency of QC/DNA complexes was not inhibited apparently in comparison with that in the absence of serum. Even in some conditions, the existence of serum slightly increased the transfection efficiency of QC/DNA complexes, and the transfection efficiency mediated by QC was comparable to that of PEI. It has been reported that the polysaccharide polymers could prevent the serum-mediated aggregation in serum through steric stabilization (*13, 43*−*45*). Therefore, we speculate that the saccharide ring chains of QCs may play an important role in these QC/DNA complexes to resist the inhibition of serum. Thus, QC had a distinct advantage and maintained a similar level of DNA tansfection efficiency regardless of the serum present in media, indicating that QC will have great potential as a safe and efficient nonviral vector in the presence of serum.

Moreover, pEGFP-C1 was employed as another reporter gene so that the transgene expression level of complexes can be directly visualized by the inverted microscope. The number of green fluorescent cells was observed at N/P ratio 10 for QC/DNA complexes. The result shown in Figure 9 was also in accordance with those of the luciferase assay. Therefore, it could be concluded that QCs with M_w of about 8×10^4 g/mol and DS of about 0.6 displayed relatively highest transfection efficiencies attributed to the intermediate stability.

Cellular Uptake. The cellular internalization of polymer/DNA complex is essential to gene delivery. To illuminate the cellular uptake of QC/DNA complexes in 293T cells, molecular probes (YOYO-1 and Hoechst 33258) were used to tag DNA and nucleus. Turquoise fluorescence (overlapped by blue and green fluorescence) can be seen in Figure 10, which demonstrated that YOYO-1 labeled QC/DNA complexes were accumulated in the nucleus of cells and the transfection had occurred. It is known that the positively charged complexes electrostatically interact with the negatively charged cellular membrane (*10, 46*). Then, endocytosis is generally involved in the cellular uptake of plasmid DNA using nonviral vectors (*4, 42*). In our study herein, QC/DNA complexes were internalized in the cells through the endocytosis pathway. Moreover, the role of complex-cellular membrane fusion might be to trigger and/or facilitate the uptake of the large QC/DNA complex particles

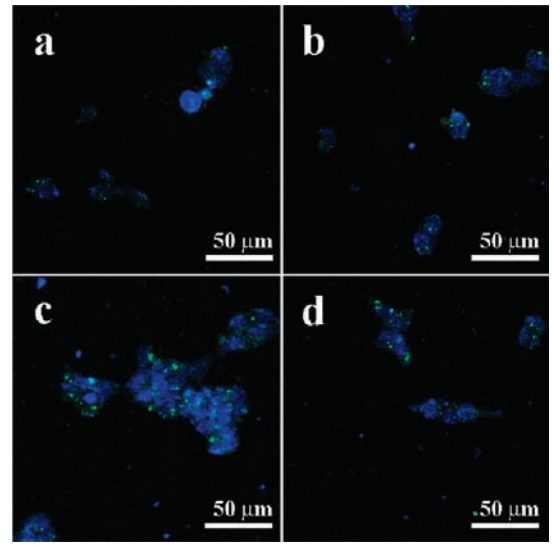


Figure 10. Confocal overlapped images of 293T cells after incubation with the complexes of pGL-3 DNA and QCs. (a) QC1, (b) QC2, (c) QC3, and (d) QC4. pGL-3 plasmids are stained green by YOYO-1. Nucleus of cells is stained blue by Hoechst 33258.

(*47*). As shown in Figure 10c, much more turquoise fluorescence could be observed, which indicated that the cellular uptake of QC3/pDNA complexes was significantly higher compared with that of other QC/pDNA complexes. The qualitative results from fluorescent microscopy studies are in good agreement with the quantitative results obtained from above luciferase assay.

CONCLUSIONS

Quaternized celluloses with different M_w and DS values were synthesized successfully and were studied as gene carriers. The results revealed that all QC derivatives could bind DNA efficiently. DNA binding efficacy depended on both M_w and DS of QCs. QC/DNA complexes exhibited effective transfection in compared to the naked DNA in 293T cells. The level of transfection efficiency was significantly influenced by M_w and DS of QC as well as N/P ratios. The stability of QC/DNA

complexes was the key factor in gene transfection and an intermediate stability was desired. QCs with M_w of about 8×10^4 g/mol and DS of about 0.6 displayed relatively highest transfection efficiencies. Moreover, QCs displayed relatively lower cytotoxicity as compared with 25 kDa PEI, and their cytotoxicity slightly increased with increasing M_w and DS. QC had a distinct advantage and maintained a similar level of DNA tansfection efficiency regardless of the serum present in the media. These studies provided important information of scientific value for further development of QC use as safe and efficient nonviral vectors.

ACKNOWLEDGMENT

This work was financially supported by the National Basic Research Program of China (973 Program, 2010CB732203), the National Natural Science Foundation of China (20674057 and 50973085), the Fundamental Research Funds for the Central Universities (2081005), and the Foundation of Key Laboratory of Cellulose and Lignocellulosic Chemistry, Chinese Academy of Sciences, China.

LITERATURE CITED

(1) Dang, J. M., and Leong, K. W. (2006) Natural polymers for gene delivery and tissue engineering. *Adv. Drug Delivery Rev. 58*, 487–499.

(2) De Smedt, S. C., Demeester, J., and Hennink, W. E. (2000) Cationic polymer based gene delivery systems. *Pharm. Res. 17*, 113–126.

(3) Xu, F. J., Ping, Y., Ma, J., Tang, G. P., Yang, W. T., Li, J., Kang, E. T., and Neoh, K. G. (2009) Comb-shaped copolymers composed of hydroxypropyl cellulose backbones and cationic poly((2-dimethyl amino)ethyl methacrylate) side chains for gene delivery. *Bioconjugate Chem. 20*, 1449–1458.

(4) Nagasaki, T., Hojo, M., Uno, A., Satoh, T., Koumoto, K., Mizu, M., Sakurai, K., and Shinkai, S. (2004) Long-term expression with a cationic polymer derived from a natural polysaccharide: schizophyllan. *Bioconjugate Chem. 15*, 249–259.

(5) Jo, J., Ikai, T., Okazaki, A., Yamamoto, M., Hirano, Y., and Tabata, Y. (2007) Expression profile of plasmid DNA by spermine derivatives of pullulan with different extents of spermine introduced. *J. Controlled Release 118*, 389–398.

(6) Lv, H., Zhang, S., Wang, B., Cui, S., and Yan, J. (2006) Toxicity of cationic lipids and cationic polymers in gene delivery. *J. Controlled Release 114*, 100–109.

(7) Borchard, G. (2001) Chitosans for gene delivery. *Adv. Drug Delivery Rev. 52*, 145–150.

(8) Kim, T. H., Jiang, H. L., Jere, D., Park, I. K., Cho, M. H., Nah, J. W., Choi, Y. J., Akaike, T., and Cho, C. S. (2007) Chemical modification of chitosan as a gene carrier in vitro and in vivo. *Prog. Polym. Sci. 32*, 726–753.

(9) Liu, Z., Jiao, Y., Wang, Y., Zhou, C., and Zhang, Z. (2008) Polysaccharides-based nanoparticles as drug delivery systems. *Adv. Drug Delivery Rev. 60*, 1650–1662.

(10) Mizu, M., Koumoto, K., Anada, T., Matsumoto, T., Numata, M., Shinkai, S., Nagasaki, T., and Sakurai, K. (2004) A polysaccharide carrier for immunostimulatory CpG DNAs to enhance cytokine secretion. *J. Am. Chem. Soc. 126*, 8372–8373.

(11) Thakor, D. K., Teng, Y. D., and Tabata, Y. (2009) Neuronal gene delivery by negatively charged pullulan-spermine/DNA anioplexes. *Biomaterials 30*, 1815–1826.

(12) Katav, T., Liu, L. S., Traitel, T., Goldbart, R., Wolfson, M., and Kost, J. (2008) Modified pectin-based carrier for gene delivery: Cellular barriers in gene delivery course. *J. Controlled Release 130*, 183–191.

(13) Tseng, W. C., and Jong, C. M. (2003) Improved stability of polycationic vector by dextran-grafted branched polyethylenimine. *Biomacromolecules 4*, 1277–1284.

(14) Azzam, T., Raskin, A., Makovitzki, A., Brem, H., Vierling, P., Lineal, M., and Domb, A. J. (2002) Cationic polysaccharides for gene delivery. *Macromolecules 35*, 9947–9953.

(15) Farber, I. Y., Yanay, C., Azzam, T., Linial, M., and Domb, A. J. (2005) Quaternary ammonium polysaccharides for gene delivery. *Bioconjugate Chem. 16*, 1196–1203.

(16) Eliyahu, H., Joseph, A., Azzam, T., Barenholz, Y., and Domb, A. J. (2006) Dextran-spermine-based polyplexes—Evaluation of transgene expression and of local and systemic toxicity in mice. *Biomaterials 27*, 1636–1645.

(17) Hosseinkhani, H., Azzam, T., Tabata1, Y., and Domb, A. J. (2004) Dextran-spermine polycation: an efficient nonviral vector for in vitro and in vivo gene transfection. *Gene Ther. 11*, 194–203.

(18) Azzam, T., Eliyahu, H., Shapira, L., Linial, M., Barenholz, Y., and Domb, A. J. (2002) Polysaccharide-oligoamine based conjugates for gene delivery. *J. Med. Chem. 45*, 1817–1824.

(19) Farber, I. Y., and Domb, A. J. (2007) Cationic polysaccharides for gene delivery. *Mater. Sci. Eng., C 27*, 595–598.

(20) Azzam, T., Eliyahu, H., Makovitzki, A., Linial, M., and Domb, A. J. (2004) Hydrophobized dextran-spermine conjugate as potential vector for in vitro gene transfection. *J. Controlled Release 96*, 309–323.

(21) Sun, Y., Xiao, W., Cheng, S., Zhang, X., and Zhuo, R. (2008) Synthesis of (Dex-HMDI)-g-PEIs as effective and low cytotoxic nonviral gene vectors. *J. Controlled Release 128*, 171–178.

(22) Gao, Y., Zhang, Z., Chen, L., Gu, W., and Li, Y. (2009) Synthesis of 6-N, N, N-Trimethyltriazole chitosan via "click chemistry" and evaluation for gene delivery. *Biomacromolecules 10*, 2175–2182.

(23) Fuente, M., Seijo, B., and Alonso, M. J. (2008) Design of novel polysaccharidic nanostructures for gene delivery. *Nanotechnology 19*, 075105−075113.

(24) Mao, H. Q., Roy, K., Troung-Le, V. L., Janes, K. A., Lin, K. Y., Wang, Y., August, J. T., and Leong, K. W. (2001) Chitosan-DNA nanoparticles as gene carriers: synthesis, characterization and transfection efficiency. *J. Controlled Release 70*, 399–421.

(25) Kean, T., Roth, S., and Thanou, M. (2005) Trimethylated chitosans as non-viral gene delivery vectors: Cytotoxicity and transfection efficiency. *J. Controlled Release 103*, 643–653.

(26) Opanasopit, P., Sajomsang, W., Ruktanonchai, U., Mayen, V., Rojanarata, T., and Ngawhiirunpat, T. (2008) Methylated N-(4-pyridinylmethyl) chitosan as a novel effective safe gene carrier. *Int. J. Pharm. 364*, 127–134.

(27) Gao, Y., Zhang, Z., Chen, L., Gu, W., and Li, Y. (2009) Chitosan N-betainates/DNA self-assembly nanoparticles for gene delivery: In vitro uptake and transfection efficiency. *Int. J. Pharm. 371*, 156–162.

(28) Kiang, T., Wen, J., Lim, H. W., and Leong, K. W. (2004) The effect of the degree of chitosan deacetylation on the efficiency of gene transfection. *Biomaterials 25*, 5293–5301.

(29) Romóren, K., Pedersen, S., Smistad, G., Evensen, O., and Thu, B. J. (2003) The influence of formulation variables on in vitro transfection efficiency and physicochemical properties of chitosan-based polyplexes. *Int. J. Pharm. 261*, 115–127.

(30) Sato, T., Ishii, T., and Okahata, Y. (2001) In vitro gene delivery mediated by chitosan. Effect of pH, serum, and molecular mass of chitosan on the transfection efficiency. *Biomaterials 22*, 2075–2080.

(31) Huang, M., Khor, E., and Lim, L. Y. (2004) Uptake and cytotoxicity of chitosan molecules and nanoparticles: Effects of molecular weight and degree of deacetylation. *Pharm. Res. 21*, 344–353.

(32) Huang, M., Fong, C. W., Khor, E., and Lim, L. Y. (2005) Transfection efficiency of chitosan vectors: Effect of polymer molecular weight and degree of deacetylation. *J. Controlled Release 106*, 391–406.

(33) Lavertu, M., Methot, S., Tran-Khanh, N., and Buschmann, M. D. (2006) High efficiency gene transfer using chitosan/DNA nanoparticles with specific combinations of molecular weight and degree of deacetylation. *Biomaterials 27*, 4815–4824.

(34) Lu, B., Xu, X., Zhang, X., Cheng, S., and Zhuo, R. (2008) Low molecular weight polyethylenimine grafted N-maleated chitosan for gene delivery: properties and in vitro transfection studies. *Biomacromolecules 9*, 2594–2600.

(35) Rodríguez, R., Alvarez-Lorenzo, C., and Concheiro, A. (2001) Rheological evaluation of the interactions between cationic celluloses and Carbopol 974p in water. *Biomacromolecules 2*, 886–893.

(36) Rodríguez, R., Alvarez-Lorenzo, C., and Concheiro, A. (2003) Cationic cellulose hydrogels: kinetics of the cross-linking process and characterization as pH-/ion-sensitive drug delivery systems. *J. Controlled Release 86*, 253–265.

(37) Fayazpour, F., Lucas, B., Alvarez-Lorenzo, C., Sanders, N. N., Demeester, J., and De Smedt, S. C. (2006) Physicochemical and transfection properties of cationic hydroxyethylcellulose/DNA nanoparticles. *Biomacromolecules 7*, 2856–2862.

(38) Song, Y., Sun, Y., Zhang, X., Zhou, J., and Zhang, L. (2008) Homogenous quaternization of cellulose in NaOH/urea aqueous solutions as gene carriers. *Biomacromolecules 9*, 2259–2264.

(39) Merdan, T., Kopecek, J., and Kissel, T. (2002) Prospects for cationic polymers in gene and oligonucleotide therapy against cancer. *Adv. Drug Delivery Rev. 54*, 715–758.

(40) Koping-Hoggard, M., Tubulekas, I., Guan, H., Edwards, K., Nilsson, M., Varum, K. M., and Artursson, P. (2001) Chitosan as a nonviral gene delivery system. Structure-property relationships and characteristics compared with polyethylenimine in vitro and after lung administration in vivo. *Gene Ther. 8*, 1108–1121.

(41) MacLaughlin, F. C., Mumper, R. J., Wang, J., Tagliaferri, J. M., Gill, I., Hinchcliffe, M., and Rolland, A. P. (1998) Chitosan and depolymerized chitosan oligomers as condensing carriers for in vivo plasmid delivery. *J. Controlled Release 56*, 259–272.

(42) Jeong, J. H., Kim, S. W., and Park, T. G. (2007) Molecular design of functional polymers for gene therapy. *Prog. Polym. Sci. 32*, 1239–1274.

(43) Lu, B., Sun, Y., Li, Y., Zhang, X., and Zhuo, R. (2009) N-Succinyl-chitosan grafted with low molecular weight polyethylenimine as a serum-resistant gene vector. *Mol. BioSyst. 5*, 629–637.

(44) Srinivasachari, S., Liu, Y., Zhang, G., Prevette, L., and Reineke, T. M. (2006) Trehalose click polymers inhibit nanoparticle aggregation and promote pDNA delivery in serum. *J. Am. Chem. Soc. 128*, 8176–8184.

(45) Maruyama, A., Ishihara, T., Kim, J. S., Kim, S. W., and Araike, T. (1997) Nanoparticle DNA carrier with poly(L-lysine) grafted polysaccharide copolymer and poly(D, L-lactic acid). *Bioconjugate Chem. 8*, 735–742.

(46) Erbacher, P., Remy, J. S., and Behr, J. P. (1999) Gene transfer with synthetic virus-like particles via the integrin-mediated endocytosis pathway. *Gene Ther. 6*, 138–145.

(47) Almofti, M. R., Harashima, H., Shinohara, Y., Almofti, A., Baba, Y., and Kiwada, H. (2003) Cationic liposome-mediated gene delivery: Biophysical study and mechanism of internalization. *Arch. Biochem. Biophys. 410*, 246–253.

BC100068F

Synthesis, Cell-Surface Binding, and Cellular Uptake of Fluorescently Labeled Glucose−DNA Conjugates with Different Carbohydrate Presentation

Begoña Ugarte-Uribe,[†] Sonia Pérez-Rentero,[‡] Ricardo Lucas,[§] Anna Aviñó,[‡] José J. Reina,[§] Itziar Alkorta,[†] Ramón Eritja,[‡] and Juan C. Morales*[,§]

Unidad de Biofísica, Centro Mixto CSIC-UPV/EHU, Universidad del País Vasco, 48080 Bilbao, Spain, Institute for Research in Biomedicine (IRB Barcelona), Institute for Advanced Chemistry of Catalonia (IQAC−CSIC), Networking Centre on Bioengineering, Biomaterials and Nanomedicine (CIBER-BBN), Edifici Helix, Baldiri Reixac 15, E-08028 Barcelona, Spain, and Instituto de Investigaciones Químicas, CSIC - Universidad de Sevilla, 49 Americo Vespucio, 41092 Sevilla, Spain. Received February 9, 2010; Revised Manuscript Received May 17, 2010

Oligonucleotide conjugates carrying carbohydrates at the 5′-end have been prepared. Glucose, fucose, and saccharides containing glucose at the nonreducing end were attached to DNA strands using the classical phosphoramidite chemistry. Two types of spacers and a dendron scaffold helped to obtain a diversity of sugar presentations in the DNA conjugates. Cellular surface adsorption and cellular uptake of carbohydrate oligonucleotide antisense sequences were measured using flow cytometric analysis. Conjugates with the glucose moiety linked through long spacers (15 to 18 atom distances) were internalized better than those with short linkers (4 atom distance) and than DNA control strands without sugar modification. Conjugates with tetravalent presentation of glucose did not improve cell uptake.

INTRODUCTION

In the past two decades, new compounds based on the use of small synthetic nucleic acids have shown promising results as potential drugs (*1, 2*). Oligonucleotides have been used for the inhibition of a specific gene by blocking gene translation or gene transcription or by stimulating the degradation of a particular mRNA. Several strategies have been developed for this purpose. In the antisense strategy, synthetic oligonucleotides complementary to the mRNA of a given gene have been used to inhibit translation of mRNA to protein (*3, 4*). In the antigene strategy, triplex-forming oligonucleotides may interact with double-stranded DNA inhibiting DNA transcription (*5*−*7*). More recently, in the siRNA strategy, small RNA duplexes complementary to mRNA sequences bind a protein complex named RISC. The complex formed by the antisense or guide RNA strand and RISC is able to catalyze the efficient degradation of a specific mRNA, lowering the amount of target protein (*8*−*10*).

Among the problems found during the development of oligonucleotides as drugs are their degradation by nucleases under physiological conditions, and particularly their low cell uptake mainly due to the highly negative charge of the phosphate backbone that results in a large repulsion from the cell membrane. Most of the improvements in the design of nucleic acid derivatives have been directed to enhance stability against nucleases and/or to improve cellular uptake without hindering the hybridization properties that are vital for the efficient gene inhibitory properties of the oligonucleotides. Conjugation of siRNA to different delivery carriers such as liposomes (*11*), antibodies (*12*), lipids (*13*), polymers (*14, 15*), or peptides (*16*) has been reported for improved delivery of siRNA. Moreover, cationic carriers are among the most efficient strategies for cell uptake, although many of them exhibit severe cytotoxicity (*17*). At the same time, covalent conjugation of oligonucleotides to peptides or to hydrophobic moieties has been used to facilitate internalization (*18, 19*). For example, cholesterol−DNA and siRNA conjugates have shown improved inhibitory properties (*20*−*22*).

A possible alternative to enhance oligonucleotide uptake is the preparation of carbohydrate oligonucleotide conjugates (COCs) that may use sugar binding membrane receptors to mediate cell entry. Different COCs have been synthesized up to the present day (*18, 23, 24*), but only a few have been experimentally tested. Recently, antisense oligonucleotides conjugated to multivalent hyaluronan disaccharide did not show higher or more specific uptake than unconjugated oligonucleotides in a cell line expressing the hyaluronan receptor CD44 (*25*). In contrast, Mahato et al. has utilized mannose 6-phosphate-bovine serum albumin and galactose poly(ethylene glycol) conjugated to oligonucleotides for site-specific delivery into hepatic cells when injected into rats (*26, 27*). Also, siRNA carrying lactose linked through a poly(ethylene glycol) branch at the 5′-end of the sense strand immersed in a polyionic complex micelle has been shown to enhance gene silencing in hepatoma cells (*28*).

Glucose is essential for cell survival, and its transport is facilitated by members of the GLUT protein family. We reasoned that oligonucleotide conjugates carrying glucose moieties could bind to GLUT receptors and facilitate internalization via receptor-mediated endocytosis. In the present work, we have prepared oligonucleotides modified at the 5′-end with glucose or glucose-containing saccharides at the nonreducing end (Figure 1). Two types of spacers and a dendron scaffold have been used to probe a diversity of sugar presentations. A carbohydrate−oligonucleotide conjugate containing a fucose unit was also prepared as a negative control. We have covalently bound the carbohydrate moieties to a single-stranded oligodeoxynucleotide antisense sequence and finally added a fluorescence tag. The corresponding labeled carbohydrate−oligonucleotide conjugates have been used to study their cell-surface binding

* Author e-mail address: jcmorales@iiq.csic.es.
[†] Universidad del País Vasco.
[‡] CIBER-BBN.
[§] Universidad de Sevilla.

10.1021/bc100079n © 2010 American Chemical Society
Published on Web 06/30/2010

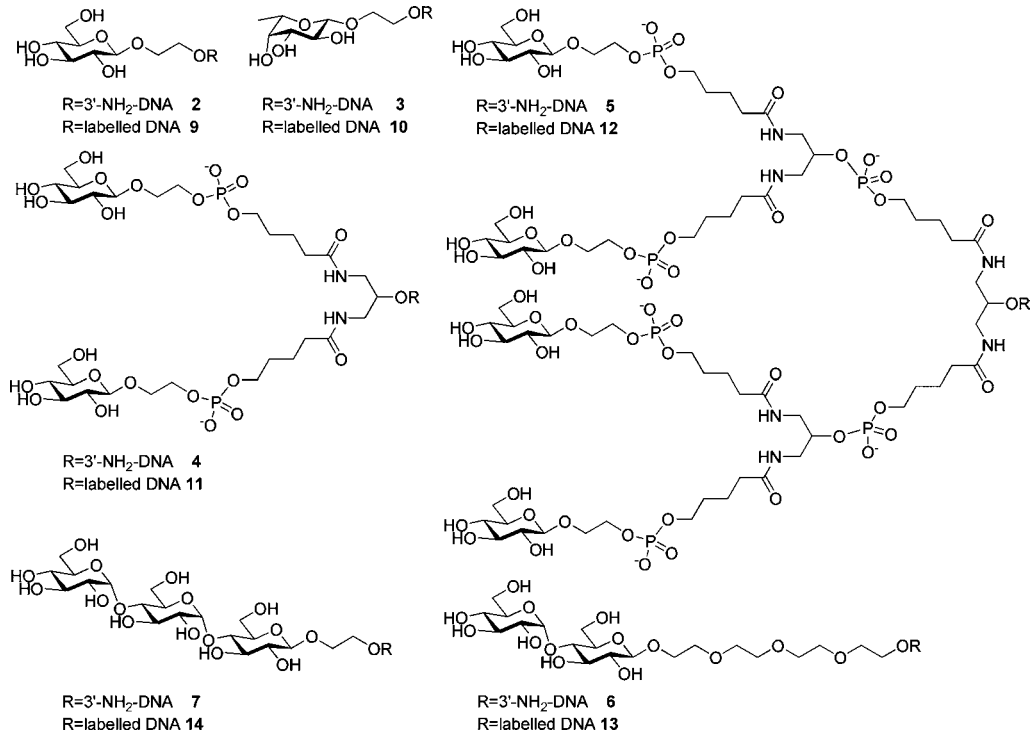


Figure 1. Carbohydrate oligonucleotide conjugates prepared (**2**−**7** and **9**−**14**). "3′-NH_2-DNA" strands correspond to -OPO_2^--GEM91-3′-NH_2 sequence (GEM91 = CTCTCGCACCCATCTCTCTCCTTCT); the corresponding DNA control **1** is the sequence GEM91−3′-NH_2. "Labeled DNA" corresponds to GEM91 strands with Alexa 488 coupled at the 3′-end; the corresponding labeled DNA control **8** is the sequence GEM91-3′-NHCO-Alexa 488.

and their cellular uptake in HeLa and U87.CD4.CXCR4 cell lines using flow cytometric analysis.

EXPERIMENTAL PROCEDURES

General Methods and Materials. All chemicals were obtained from chemical suppliers and used without further purification, unless otherwise noted. All reactions were monitored by TLC on precoated silica gel 60 plates F254 and detected by heating with Mostain (500 mL of 10% H_2SO_4, 25 g of $(NH_4)_6Mo_7O_{24}\cdot 4H_2O$, 1 g $Ce(SO_4)_2\cdot 4H_2O$). Products were purified by flash chromatography with silica gel 60 (200−400 mesh). NMR spectra were recorded on either a Bruker AVANCE 300 or ARX 400 MHz [300 or 400 MHz (^{1}H), 75 or 100 (^{13}C)] spectrometer, at room temperature for solutions in $CDCl_3$. Chemical shifts are referred to the solvent signal and are expressed in ppm. 2D NMR experiments (COSY, TOCSY, ROESY, and HMQC) were carried out when necessary to assign the corresponding signals of the new compounds. Low-resolution electrospray mass spectral analyses were obtained on a Bruker Esquire 6000 ion trap mass spectrometer. High-resolution FAB (+) mass spectral analyses were obtained on a Micromass AutoSpec-Q spectrometer.

11-Hydroxy-3,6,9-trioxaundecyl-*O*-2,3,6,2′,3′,4′,6′-hepta-*O*-acetyl-*β*-D-maltopyranoside (18). To a solution of hepta-*O*-acetyl-maltopyranosyl bromide (**17**) (0.80 g, 1.146 mmol) (*29*) and tetraethylene glycol (4.0 mL, 22.92 mmoL, 20 equiv) previously dried over molecular sieves, under argon atmosphere, in anhydrous THF (30 mL) Ag_2CO_3 (3.15 g, 11.46 mmol, 10 equiv) was added, and stirring was continued for 22 h (TLC/Hex−EtOAc, 2:3). The mixture was filtered, diluted with CH_2Cl_2 (100 mL), washed with water (3 × 100 mL), dried over anh $MgSO_4$, and the solvent evaporated under reduced pressure. The product was purified by silica gel column chromatography using as eluent pure EtOAc to EtOAc with 3% methanol to give compound **18** (0.46 g, 50%) as a syrup. ^{1}H NMR (300 MHz, $CDCl_3$): δ = 5.34 (d, 1H, J = 3.5 Hz, H-1′), 5.29 (t, 1H, J = 10.0 Hz, H-3′), 5.19 (t, 1H, J = 9.3 Hz, H-3), 4.98 (t, 1H, J = 9.9 Hz, H-4′), 4.81−4.72 (m, 2H, H-2, H-2′), 4.58 (d, 1H, J = 7.8 Hz, H-1), 4.42 (dd, 1H, J = 2.4 and 12.0 Hz, H-6a), 4.21−4.13 (m, 2 H, H-6b, H-6′a), 4.00−3.81 (m, 4 H, H-5, H-5′, H-6′b, H-4), 3.71−3.52 (m, 16 H, 4 × OCH_2CH_2O), 2.64 (br s, 1 H, OH), 2.10−1.93 (6s, 21H, OCO*C*H_3) ppm. ^{13}C NMR (75 MHz, $CDCl_3$): δ = 170.5, 170.4, 170.2, 170.0, 169.7, 169.4 (C═O), 96.6 (C-1), 94.3 (C-1′), 76.7, 74.4, 73.2, 72.4, 71.1, 70.5, 70.3, 69.0, 69.1, 68.2, 67.0, 62.8, 63.4, 61.5, 21.7, 21.6, 21.4, 21.3, 20.0, 19.9, 19.7, 19.6 ppm. $[\alpha]_D^{22}$ +34.5 (c 1 in $CHCl_3$). MS (ES^+) Calcd. for $C_{34}H_{52}O_{22}N_2Na$: 835.3. Found: 835.5.

11-(2,3,6,2′,3′,4′,6′-Hepta-*O*-acetyl-*β*-D-maltopyranosyloxy)-3,6,9-trioxaundecyl (2-cyanoethyl) (*N*,*N*-diisopropyl) phosphoramidite (19). To a solution of 11-hydroxy-3,6,9-trioxaundecyl-*O*-2,3,6,2′,3′,4′,6′-hepta-*O*-acetyl-*β*-D-maltopyranoside (**18**) (0.30 g, 0.36 mmol) in dry CH_2Cl_2 (2 mL), DIEA (235 μL, 1.35 mmol), and 2-cyanoethyl-*N*,*N*′-diisopropylaminochlorophosphoramidite (120 μL, 0.54 mmoL) were added at room temperature under argon atmosphere. After 2 h, the solution was diluted with EtOAc (25 mL), and the organic phase was washed with brine (3 × 25 mL), dried over anh $MgSO_4$, filtered, and the solvent evaporated to dryness. The product was purified by silica gel column chromathography using as eluent Hex−EtOAc, 1:1 with 5% of NEt_3 to give compound **19** (360 mg, 98%) as a syrup. ^{1}H NMR (300 MHz, $CDCl_3$) (mix of isomers): δ = 5.39 (d, 1H, J = 3.5 Hz, H-1′), 5.33 (t, 1H, J = 10.0 Hz, H-3′), 5.23 (t, 1H, J = 9.0 Hz, H-3), 5.03 (t, 1H, J = 10.0 Hz, H-4′), 4.85−4.78 (m, 2H, H-2, H-2′), 4.59 (d, 1H, J = 8.0 Hz, H-1), 4.46 (m, 1H, H-6a), 4.25−4.18 (m, 2 H, H-6b, H-6′a), 4.03−3.57 (m, 24 H, 4xOCH_2CH_2O, H-5, H-5′, H-6′b, H-4, O*C*H_2CH_2CN, CHisopropyl), 2.65 (m, 2 H, OCH_2CH_2CN), 2.15−2.00 (6s, 21H, OCO*C*H_3), 1.16 (t, 12 H, CH_3isopropyl) ppm. ^{13}C NMR (75 MHz, $CDCl_3$) (mix of isomers): δ = 170.5, 170.4, 170.2, 170.0, 169.7, 169.4 (C═O), 117.7 (CN), 100.0 (C-1), 95.3 (C-1′), 75.3, 72.7, 72.1, 71.2,

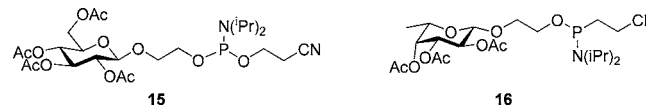
70.7, 70.6, 70.5, 70.4, 70.1, 70.0, 69.3, 69.1, 68.5, 68.0, 62.8, 62.6, 62.5, 61.5, 58.6, 58.4, 43.1, 42.9, 24.6, 24.5, 20.9, 20.8, 20.7, 20.6, 20.3, 20.2 ppm. ^{31}P NMR (101 MHz, $CDCl_3$): δ = 149.8, 149.7. MS (ES^+) Calcd. for $C_{43}H_{69}O_{23}N_2PNa$: 1035.4. Found: 1035.0.

2-Hydroxyethyl-*O*-(2,3,4, 6-tetra-*O*-acetyl-α-D-glucopyranosyl-(1→4)-*O*-(2,3,6-tri-*O*-acetyl-α-D-glucopyranosyl)-(1→4)-2,3,6-tri-*O*-acetyl-*β*-D-glucopyranoside (21). To a solution of the deca-*O*-acetyl-maltotriopyranosyl bromide (**20**) (1.69 g, 1.75 mmol) (*30*, *31*) and ethylene glycol (0.98 mL, 17.5 mmoL, 10 equiv) previously dried over molecular sieves, under argon atmosphere, in anhydrous CH_2Cl_2 (20 mL) was added Ag_2CO_3 (965 mg, 3.5 mmol, 2.1 equiv). The reaction was then stirred for 24 h. The mixture was then filtered over Celite and washed with CH_2Cl_2. The solvent were then removed, and the crude was purified by flash column chromatography (hexane/ethyl acetate from 1:3 to 0:1) to afford **21** (1.16 g, 68%) as a glassy solid. ^{1}H NMR (500 MHz, $CDCl_3$): δ = 5.34−5.32 (m, 3H, H_{1C}, H_{1B}, H_{3A}), 5.30−5.26 (m, 2H, $H_{3B,}$ H_{4B}), 5.08 (t, 1H, J = 10.0 Hz, H_{4C}), 4.88−4.82 (m, 2H, H_{2A}, H_{2C}), 4.75 (dd, 1H, J = 4.0 and 10.0 Hz, H_{2B}), 4.59 (d, 1H, J = 8.0 Hz, H_{1A}), 4.55 (dd, 1H, J = 2.4 and 12.1 Hz, H_{6A}), 4.49−4.46 (m, 1H, H_{6B}), 4.29−4.24 (m, 2H, $H_{6'A,}$ $H_{6'B}$), 4.21 (dd, 1H, J = 3.4 and 12.3 Hz, H_{6C}), 4.06 (m, 1H, $H_{6'C}$), 4.00−3.92 (m, 4H, H_{5A}, $H_{4A,}$ $H_{5B,}$ H_{5C}), 3.85−3.72 (m, 5H, CH_2O-, CH_2OH, OH), 2.18, 2.16, 2.11, 2.06, 2.04, 2.03, 2.02, 2.015, 2.01, 2.00 (10s, 30H. OCOCH_3) ppm. ^{13}C NMR (125 MHz, $CDCl_3$): δ = 170.7, 170.6, 170.55, 170.5, 170.4, 170.1, 169.9, 169.8, 169.7, 169.4 (C═O), 100.9 (C_{1B}), 95.8 (C_{1A}), 95.7 (C_{1C}), 75.1 (C_{4A}), 73.8, 72.5, 72.3, 72.2, 71.7, 70.4, 70.0, 69.4, 69.0, 68.5, 67.9 (*C*H), 65.8, 62.8, 62.3, 61.9, 61.8 (C_{6A}, C_{6B}, C_{6C}, OCH_2CH_2OH), 20.9, 20.85, 20.8, 20.7, 20.6, 20.5 (OCO*C*H$_3$) PPM. $[\alpha]_D^{22}$ + 39.0 (c 1 in $CHCl_3$). HRMS (ES^+) Calcd. for $C_{37}H_{57}O_{20}N_2Na$: 903.3140. Found: 903.3146.

2-[(2,3,4,6-Tetra-*O*-acetyl-α-D-glucopyranosyl-(1→4)*O*-(2,3,6-tri-*O*-acetyl-α-D-glucopyranosyl)-(1→4)-2,3,6-tri-*O*-acetyl-*β*-D-glucopyranosyloxy)]ethyl(2-cyanoethyl)(*N*,*N*-diisopropyl)phosphoramidite (22). DIEA (132 μL, 0.75 mmol) and 2-cyanoethyl-*N*,*N*′-diisopropylaminochlorophosphoramidite (70 μL, 0.31 mmoL) were added to a solution of compound **21** (200 mg, 0.20 mmol) in anhydrous CH_2Cl_2 (4 mL) at room temperature under an argon atmosphere. After 2.0 h, no starting material was observed. Solvents were then removed, and the crude was purified by silica gel column chromatography by using Hex/EtOAc (1:3 with 5% of NEt_3) to give compound **22** (197 mg, 84%) as a syrup. ^{1}H NMR (500 MHz, $CDCl_3$): δ = 5.39−5.17 (m, 5H, H_{1C}, H_{1B}, H_{3A},$H_{3B,}$ H_{4B}), 5.03 (t, 1H, J = 9.9 Hz, H_{4C}), 4.84−4.74 (m, 2H, H_{2A}, H_{2C}), 4.70 (dd, 1H, J = 3.9 and 10.5 Hz, H_{2B}), 4.59 (m, 1H, H_{1A}), 4.44−4.40 (m, 1H, $H_{6A,}$ H_{6B}), 4.30−3.44 (m, 16H, $H_{6'A,}$ $H_{6'B}$, H_{6C}, $H_{6'C}$, H_{5A}, $H_{4A,}$ $H_{5B,}$ H_{5C}, CH_2O-, CH_2CH$_2$CN, CH_2OH, $CH_{isopropyl}$), 2.60 (m, 2 H, OCH$_2$CH_2CN), 2.14, 2.12, 2.06, 2.01, 1.99, 1.98, 1.96, 1.94 (8s, 30H. OCOCH_3), 1.20−1.14 (m, 12 H, CH_3isopropyl) ppm. ^{13}C NMR (125 MHz, $CDCl_3$): δ = 170.5, 170.5, 170.4, 170.3, 170.1, 169.8, 169.7, 169.4 (C═O), 117.7 (CN), 100.2 (C_{1B}), 95.7 (C_{1A}), 95.6 (C_{1C}), 75.3 (C_{4A}), 73.8, 72.4, 72.0, 71.7, 70.4, 70.0, 69.4, 69.3, 68.8, 68.4, 67.8 (*C*H), 63.0, 62.3, 61.3, 58.6, 58.3 (C_{6A}, C_{6B}, C_{6C}, OCH_2CH_2OH), 45.1, 45.0, 43.1, 42.9, 24.7, 24.6, 24.5, 22.9, 20.9, 20.8, 20.7, 20.6 (OCO*C*H$_3$) PPM. ^{31}P NMR (101 MHz, $CDCl_3$): δ = 149.8, 149.6. HRMS (ES^+) Calcd. for $C_{49}H_{74}N_2O_{28}P$ (M+H): 1169.4166. Found: 1169.4188.

Synthesis of Carbohydrate Oligonucleotide Conjugates. Oligodeoxynucleotides carrying carbohydrates at the 5′-end were prepared in a DNA synthesizer (Applied Biosystems 3400) using standard 2-cyanoethyl phosphoramidites and the appropriate carbohydrate phosphoramidites (Schemes 1 and 2). The syntheses were carried out on controlled-pore glass (CPG) supports

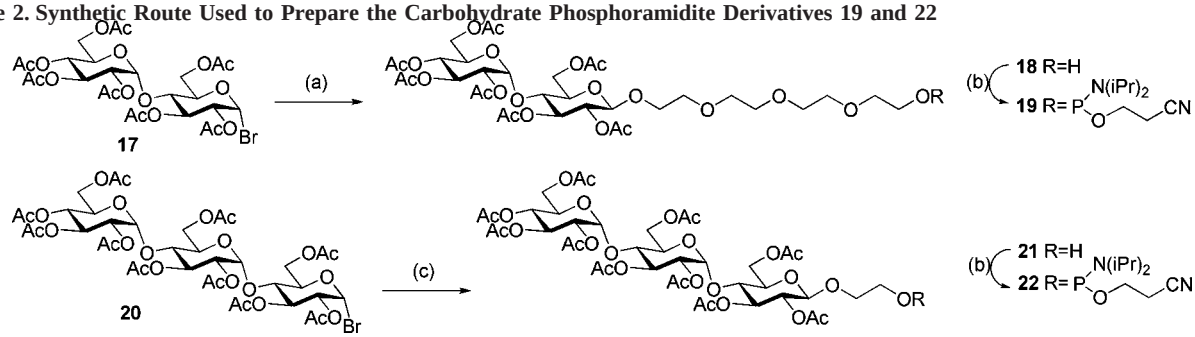
Scheme 1. Carbohydrate Phosphoramidites 15 and 16



carrying the 2-(*N*-[9*H*-fluoren-9-yl-methoxycarbonyl]-4-aminobutyl)propane-1,3-diol linker (Glen Research) to yield oligonucleotides carrying an aliphatic amino group a the 3′-end (*32*). The following sequences were prepared: Sequence **1**: CTCTCGCACCCATCTCTCTCCTTCT-3′-NH_2. Sequence **2**: Glucose-C2-5′-CTCTCGCACCCATCTCTCTCCTTCT-3′-NH_2, (C2 stands for $-CH_2CH_2-OPO_2^-$). Sequence **3**: Fucose-C2-5′-CTCTCGCACCCATCTCTCTCCTTCT-3′-NH_2. Sequence **4**: (Glucose-C2)$_2$-DB-CTCTCGCACCCATCTCTCTCCTTCT-3′-NH_2 (DB stands for the symmetric doubler phosphoramidite obtained from commercial sources (Glen Research)). Sequence **5**: (Glucose-C2)$_4$-DB-DB-CTCTCGCACCCATCTCTCTCCT-TCT-3′-NH_2. Sequence **6**: Maltose-PEG4-5′-CTCTCGCAC-CCATCTCTCTCCTTCT-3′-NH_2 (PEG4 stands for -$(OCH_2CH_2)_4$-OPO_2^--). Sequence **7**: Maltotriose-C2-5′-CTCTCG-CACCCATCTCTCTCCTTCT-3′-NH_2. After ammonia deprotection (overnight, 55 °C), the resulting oligodeoxynucleotides were purified by HPLC (see conditions below). The purified products were analyzed by MALDI-TOF mass spectrometry. Sequence **1** [M] = 7603.6 (Calcd. for $C_{244}H_{327}N_{73}O_{159}P_{25}$ M = 7601.0). Yield (1 μmol scale synthesis) was 118 OD units at 260 nm (580 nmol, 58%). Sequence **2** [M] = 7888.4 (Calcd. for $C_{252}H_{341}N_{73}O_{168}P_{26}$ M= 7886.2). Yield (1 μmol scale synthesis) was 83 OD units at 260 nm (410 nmol, 41%). Sequence **3** [M] = 7870.7 (Calcd. for $C_{252}H_{3241}N_{73}O_{167}P_{26}$ M = 7870.2). Yield (1 μmol scale synthesis) was 98 OD units at 260 nm (480 nmol, 48%). Sequence **4** [M] = 8524.4 (Calcd. for $C_{273}H_{382}N_{75}O_{184}P_{28}$ M = 8525.7). Yield (0.5 μmol scale synthesis) was 31 OD units at 260 nm (155 nmol, 31%). Sequence **5** [M] = 9793.9 (Calcd. for $C_{315}H_{462}N_{79}O_{216}P_{32}$ M = 9802.7). Yield (0.5 μmol scale synthesis) was 23 OD units at 260 nm (115 nmol, 23%). Sequence **6** [M] = 8182.7 (Calcd. for $C_{264}H_{363}N_{73}O_{176}P_{26}$ M = 8180.5). Yield (0.5 μmol scale synthesis) was 22.5 OD units at 260 nm (110 nmol, 22%). Sequence **7** [M] = 8209.4 (Calcd. for $C_{264}H_{360}N_{73}O_{178}P_{26}$ M = 8209.4). Yield (0.5 μmol scale synthesis) was 28 OD units at 260 nm (140 nmol, 28%).

Synthesis of Carbohydrate Oligonucleotide Conjugates Carrying Fluorescent Label. The following sequences were prepared: Sequence **8**: CTCTCGCACCCATCTCTCTCCTTCT-3′-NHCO-Alexa488. Sequence **9**: Glucose-C2-5′-CTCTCG-CACCCATCTCTCTCCTTCT-3′-NHCO-Alexa488. Sequence **10**: Fucose-C2-5′-CTCTCGCACCCATCTCTCTCCTTCT-3′-NHCO-Alexa488. Sequence **11**: (Glucose-C2)$_2$-DB-CTCTCG-CACCCATCTCTCTCCTTCT-3′-NHCO-Alexa488. Sequence **12**: (Glucose-C2)$_4$-DB-DB-CTCTCGCACCCATCTCTCTCCT-TCT-3′-NHCO-Alexa488. Sequence **13**: Maltose-PEG4-5′-CTCTCGCACCCATCTCTCTCCTTCT-3′-NHCO-Alexa488. Sequence **14**: Maltotriose-C2-5′-CTCTCGCACCCATCTCTCTC-CTTCT-3′-NHCO-Alexa488. Carbohydrate oligonucleotide conjugates carrying the fluorescent label at the 3′- end were prepared by reaction of the corresponding 3-amino oligonucleotides (**1**−**7**) with Alexa Fluor 488 tetrafluorophenyl (5-TPF) ester obtained from commercial sources (Invitrogen). The corresponding 3′amino oligonucleotide was dissolved with 50 μL of an aqueous solution of 0.2 M $NaHCO_3$ (pH = 9). Then, 1.1 equiv of Alexa Fluor 488 5-TPF dissolved in 30 μL DMF was added to the solution and left to react overnight at room temperature. The mixture was concentrated to dryness, and the residue was dissolved in H_2O. The residue was dissolved with 1 mL H_2O and was purified with Sephadex G-25 (NAP-10 Column), and the oligonucleotide fraction was analyzed by HPLC (see

Scheme 2. Synthetic Route Used to Prepare the Carbohydrate Phosphoramidite Derivatives 19 and 22



(a) Tetraethylene glycol, Ag_2CO_3, THF, r.t., 22 h, 50%; (b) 2-cyanoethyl-*N*,*N*′-diisopropylaminochlorophosphoramidite, DIEA, CH_2Cl_2, r.t., 2 h, 84−98%; (c) ethylene glycol, Ag_2CO_3, CH_2Cl_2, r.t., 18h, 68%.

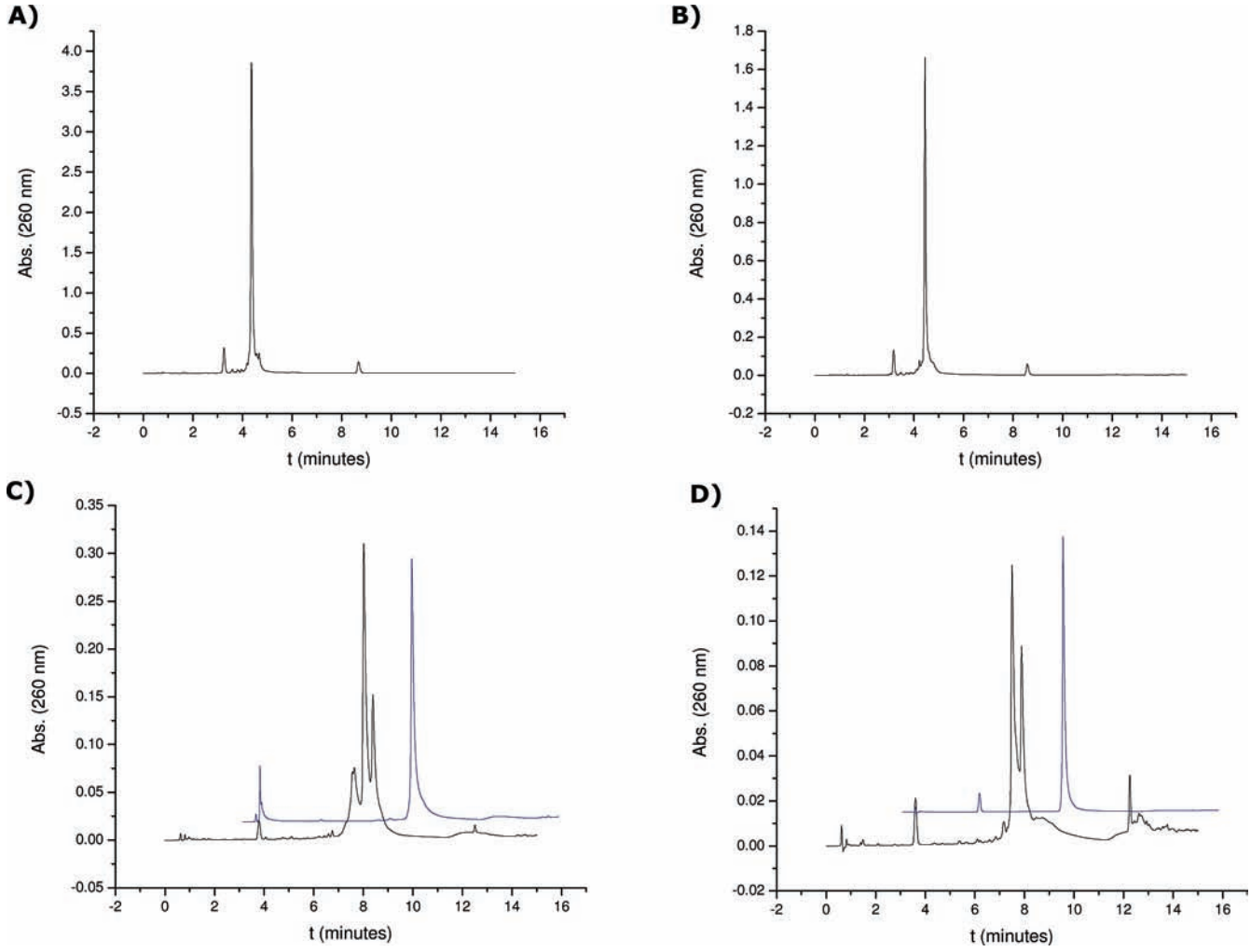


Figure 2. HPLC profiles of 3′-amino 5′-carbohydrate oligonucleotide conjugates: (A) glucose conjugate **2**, (B) fucose conjugate **3**, (C) diglucose conjugate **4**, and (D) tetraglucose conjugate **5**. Insets in (C) and (D) correspond to the analytical HPLC profiles of purified conjugates using X-Bridge TMOST C18 columns.

conditions below). The purified products were analyzed by MALDI-TOF mass spectrometry. Sequence **8** [M] = 8117.4 (Calcd. for $C_{265}H_{340}N_{75}O_{169}P_{25}S_2$ M = 8118.5). Yield (0.23 μmol scale) was 43 OD units at 260 nm (93%). Sequence **9** [M] = 8400.0 (Calcd. for $C_{273}H_{355}N_{75}O_{178}P_{26}S_2$ M = 8404.7). Yield (0.21 μmol scale) was 42 OD units at 260 nm (93%). Sequence **10** [M] = 8385.6 (Calcd. for $C_{273}H_{355}N_{75}O_{177}P_{26}S_2$ M = 8388.7). Yield (0.25 μmol scale) was 44 OD units at 260 nm (86%). Sequence **11** [M] = 9040.5 (Calcd. for $C_{294}H_{395}N_{77}O_{194}P_{28}S_2$ M = 9043.1). Yield (0.07 μmol scale synthesis) was 15 OD units at 260 nm (67%). Sequence **12** [M] = 10320.0 (Calcd. for $C_{336}H_{475}N_{81}O_{226}P_{32}S_2$ M = 10320.1). Yield (0.07 μmol scale) was 23 OD units at 260 nm (87%). Sequence **13** [M] = 8696.2 (Calcd. for $C_{285}H_{377}N_{75}O_{186}P_{26}S_2$ M = 8698.9). Yield (0.06 μmol scale) was 13 OD units at 260 nm (61%). Sequence **14** [M] = 8730.4 (Calcd. for $C_{285}H_{374}N_{75}O_{188}P_{26}$ S_2 M = 8727.9). Yield (0.1 μmol scale) was 19 OD units at 260 nm (90%).

HPLC Purification Conditions. Column: Nucleosil 120C_{18} (10 μm, 200 × 10 mm). Flow rate: 3 mL/min. Conditions: 20 min linear gradient 0−50% B. The purity of the resulting oligonucleotides was analyzed as follows: Column: X-Bridge ^{TM}OST C_{18} (2.5 μm, 4.6 × 50 mm). Flow rate: 1 mL/min.

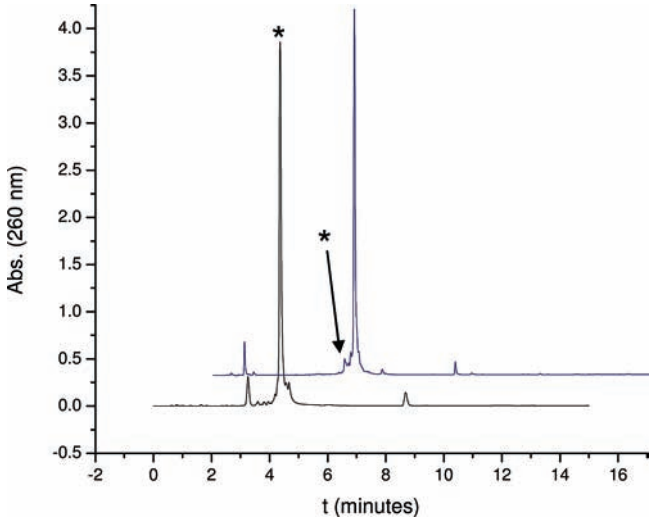


Figure 3. HPLC profiles of glucose conjugate **2** (below), and reaction mixture of **2** with Alexa 488 (above) showing the formation of the 3′-Alexa 5′-glucose conjugate **9**. The asterisk indicates the position of the starting amino oligonucleotide **2**. Column: X-Bridge TMOST C18 (2.5 mm, 4.6 × 50 mm). Flow rate: 1 mL/min. Conditions: 10 min linear gradient 0−30%.

Conditions: 10 min linear gradient 0−30% B). In both cases, solvent A is 5% acetonitrile in 100 mM triethylammonium acetate (pH = 7) and solvent B is 70% acetonitrile in 100 mM triethylammonium acetate (pH = 7).

Mass Spectrometry. MALDI-TOF spectra were performed using a Perseptive Voyager DETMRP mass spectrometer, equipped with nitrogen laser at 337 nm using a 3 ns pulse. The matrix used contained 2,4,6-trihydroxyacetophenone (THAP, 10 mg/mL in ACN/water 1:1) and ammonium citrate (50 mg/mL in water).

Cell Cultures. HeLa (cervical carcinoma) and U87.CD4.CXCR4 cells lines were kindly provided by Prof. Alfredo Berzal (Instituto de Parasitología y Biomedicina "López-Neyra", CSIC, Granada, Spain). Cells were cultured as exponentially growing subconfluent monolayers and maintained in Dulbecco's modified Eagle's medium (DMEM, PAA Laboratories GMBH) supplemented with 10% fetal bovine serum (FBS, Invitrogen), 4 mM L-Glutamine (Sigma), Mycokill AB (PAA Laboratories GMBH), and penicillin/streptomycin (100 units/mL and 100 μg/mL, respectively) (Invitrogen) in a humidified atmosphere consisting of 5% CO_2 and 95% air. Human astroglioma U87.CD4.CXCR4 cells were also supplemented with 1 μg/mL puromicine (Sigma) and 300 μg/mL Geneticin (G-418 sulfate) (Invitrogen).

Cell-Surface Adsorption Studies by Flow Cytometric analysis. Cells were seeded into 24-well plates 48 h prior to treatment in DMEM supplemented with 10% FBS, in the absence or presence of glucose (5.5 mM glucose). Then, cells were incubated on ice serum-free DMEM containing 5 μM of different Alexa 488-labeled oligonucleotides, in the absence or presence (5.5 mM) of glucose for 1 h, washed twice with ice-cold phosphate-buffered saline (PBS), harvested, and resuspended in ice-cold PBS, followed by a flow cytometry analysis (FACSCalibur, Beckton Dickinson).

Cellular Uptake Studies by Flow Cytometric analysis. Cells were seeded into 24-well plate prior to treatment in DMEM supplemented with 10% FBS and 5.5 mM glucose. Then, cells were incubated with 2 μM of different Alexa 488-labeled oligonucleotides at 37 °C in the presence or absence of glucose for 2, 6, and 24 h. After incubation, cells were completely dissociated in 0.5% Trypsin−EDTA (Invitrogen). Trypsin treated cells were washed by centrifugation at 520 *g* for 10 min and then resuspended into ice-cold 1× PBS, followed by a flow cytometry analysis. The fluorescence of Alexa-labeled oligonucleotides remaining at the cellular surface was quenched with 0.2% Trypan Blue (final concentration), and subsequently, the fluorescence corresponding to the internalized oligonucleotides was measured.

Statistical Analyses. Statistical analyses were performed using Student's *t* test as appropriate, with the level of significance set at $P < 0.05$.

RESULTS AND DISCUSSION

Synthesis of Carbohydrate Phosphoramidites (15, 16, 19, 22). Among the different approaches described to prepare carbohydrate oligonucleotide conjugates (COCs) (*23*), we selected one of the most straightforward methodologies based on the coupling of a sugar phophoramidite to oligonucleotides on a solid support. This approach has been previously used to introduce sugars linked through the primary alcohol (*33, 34*) where the anomeric position was methylated. Our group (*35*) and others (*36*) have used this methodology to introduce sugars linked through the anomeric position. We have extended this approach to prepare COCs that possess a glucose moiety with different presentations. With this purpose, we have attached sugars to DNA strands through two types of spacers (ethylene glycol, C2, or tetraethyleneglycol, PEG4) and a commercially available symmetric dendrimer (symmetric doubler phosphoramidite). Glucose and fucose phosphoramidites (**15** and **16**, respectively) carrying the short spacers were recently synthesized in two steps (*35*): classical glycosylation from their corresponding bromo peracetylated sugars and ethylene glycol and subsequent standard phosphoramidite chemistry (Scheme 1). Following the same strategy, maltose and maltotriose phosphoramidites have been prepared carrying tetraethylene glycol and ethylene glycol spacers, respectively (compounds **19** and **22**, Scheme 2). Glycosylation was carried out using silver carbonate as the promoter to obtain moderate yields of intermediates **18** and **21** (50% and 68%, respectively). The resulting alcohols were reacted with 2-cyanoethyl-*N*,*N*-diisopropylchlorophosphoramidite and *N*-diisopropylethylamine to yield the carbohydrate phosphoramidite derivatives **19** and **22** (84% and 98%, respectively).

Synthesis of Carbohydrate Oligonucleotide Conjugates (2−7). Oligodeoxynucleotides carrying carbohydrates at the 5′-end were prepared using the appropriate carbohydrate phosphoramidites (Schemes 1 and 2) and the commercial dendrimer symmetric doubler phosphoramidite. We selected the well-known antisense oligonucleotide sequence GEM91 (5′-CTCTCG-CACCCATCTCTCTCCTTCT) that was targeted to the translational initiation site of the Gag mRNA of HIV (*37*). We designed oligonucleotide sequences that carried an amino group at the 3′-end so that a carboxyl-activated fluorescent label could be attached at a subsequent step. We selected the commercially available 3′-amino-modifier C7 CPG for the amino modification of the COC's. The oligonucleotide glycoconjugates (**2**−**7**) contained the following carbohydrates covalently linked to the GEM91 oligonucleotide with different spacers: glucose−ethylene glycol, fucose−ethylene glycol as control, maltose−tetraethylene glycol, maltotriose−ethylene glycol, diglucose−doubler dendrimer, and tetraglucose−doubler−doubler dendrimer, respectively. Additionally, a nonconjugated 3-amino oligonucleotide (**1**) was synthesized for reference. Oligonucleotides **1**, **2**, and **3** show a single peak (Figure 2) that had the expected mass and they were used in the next reaction without further purification (41−58% yield). Oligonucleotides **4**−**7** presented a major peak with some impurities (Figure 2) that were easily separated by HPLC obtaining the desired conjugates in a 22−31% yield after HPLC purification. The side products from the synthesis of the branched oligonucleotides **4** and **5** were collected and analyzed

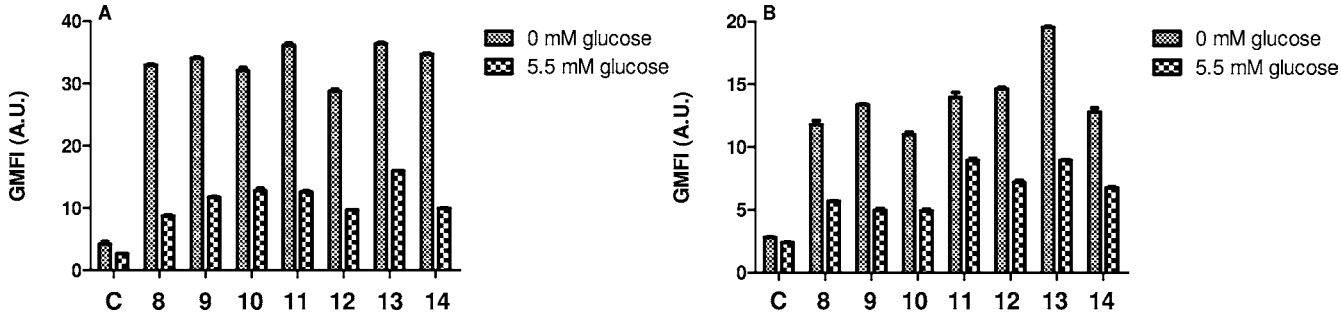


Figure 4. Cell-surface adsorption of Alexa 488-labeled carbohydrate oligonucleotide conjugates (**9**−**14**) and control Alexa 488-labeled DNA oligonucleotide **8**. (A) HeLa cells and (B) U87.CD4.CXCR4 cells were cultured in the absence or presence of glucose for 48 h at 37 °C. Then, the medium was replaced and cells were incubated with 5 μM bioconjugate for 1 h at 4 °C in the absence or presence of glucose. After incubation, cells were washed three times, resuspended in ice-cold PBS, and analyzed by flow cytometry. C represents cell basal fluorescence intensity. GMFI corresponds to Geometric mean of fluorescence intensity. Measurements from two independent experiments were averaged. Error bars indicate SD. All the results obtained were $P < 0.001$.

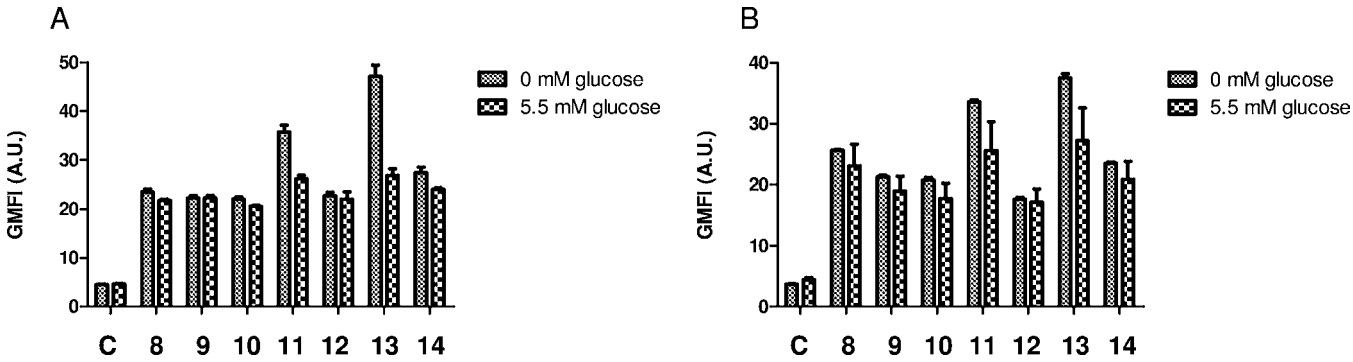


Figure 5. Cellular uptake of Alexa 488-labeled carbohydrate oligonucleotide conjugates (**9**−**14**) and control Alexa 488-labeled DNA oligonucleotide **8**. (A) HeLa cells and (B) U87.CD4.CXCR4 cells were cultured until preconfluency at 37 °C. Then, the medium was replaced, and cells were incubated with 2 μM bioconjugate for 2 h at 37 °C in the absence or presence of glucose. After incubation, cells were washed three times, resuspended in ice-cold PBS and analyzed by flow cytometry. C represents cell basal fluorescence intensity. GMFI corresponds to geometric mean of fluorescence intensity. Measurements from three independent experiments were averaged. Error bars indicate SD. All the results obtained were $P < 0.05$.

by MS and gel electrophoresis showing that these side products lack one or two glucose residues. This confirms that phosphoramidite couplings after branching are somehow less efficient according to literature (*38, 39*), but this fact did not prevent us from obtaining pure oligonucleotide conjugates with two and four glucose units.

Synthesis of Carbohydrate Oligonucleotide Conjugates Carrying a Fluorescent Label (9−14). For the cellular uptake studies, six 3′-end fluorescently labeled oligonucleotide glycoconjugates (**9**−**14**) were prepared. We selected Alexa 488 as the fluorescent tag mainly due to its photostability and brightness compared to other common fluorescent labels, its fluorescent lifetime, and the hydrolytic stability of the corresponding amine-reactive Alexa 488 derivative. These compounds contained the same carbohydrate moieties presented above. Carbohydrate oligonucleotide conjugates (**2**−**7**) dissolved in 0.1−0.2 M sodium bicarbonate buffer (pH 8.3) were reacted with Alexa Fluor 488 tetrafluorophenyl ester dissolved in DMF for 1 h at room temperature. In all cases, a major peak was obtained (Figure 3) and the desired fluorescently labeled oligonucleotides were isolated in good yields (67−93%). Finally, a control labeled DNA oligonucleotide (**8**) was prepared using the same conditions described above.

Cell-Surface Adsorption and Uptake by Flow Cytometric analysis. We measured cell-surface adsorption of the carbohydrate oligonucleotide conjugates (**9**−**14**, Figure 1) and the control labeled DNA oligonucleotide (**8**, Figure 1) in both the presence and absence of glucose in the medium. HeLa cells and U87.CD4.CXCR4 cells were seeded on 24-well culture plates, in the presence (5.5 mM) or absence of glucose for 48 h until preconfluency at 37 °C. Then, the medium was replaced, and cells were incubated with 5 μM bioconjugate for 1 h at 4 °C in the presence or absence of glucose. Note that incubation at 4 °C allows oligonucleotide adsorption onto the cell-surface but not endocytosis-dependent cellular internalization (*40*). After incubation, cells were washed and resuspended in ice-cold PBS and analyzed by flow cytometry (Figure 4). In the absence of glucose, an overall increase in fluorescence intensity is observed for all the oligonucleotides analyzed in comparison to the data observed when glucose was present in the medium. This behavior was similar for both HeLa and U87.CD4.CXCR4 cells, and it could be due to the starving conditions suffered by the cells during long periods of time (i.e., 48 h). In the absence of glucose in the medium, glucose-containing oligonucleotides **11**, **13**, and **14** were better adsorbed to the surface than oligonucleotide control **8** and glucose− and fucose−oligonucleotide conjugates **9** and**10** in HeLa cells. In contrast, all the glucose conjugates showed a better cell-surface adsorption than **8** with a strong adsorption for **13** for U87.CD4.CXCR4 cells. Tetravalent glucose oligonucleotide conjugate **12** behaved differently for each cell type, showing worse adsorption than the other glucose conjugates and control **8** in HeLa cells, whereas in U87 cells, its adsorption was better than that of the control **8**. In the presence of glucose, all the carbohydrate oligonucleotide conjugates were adsorbed better than control **8**, except conjugates **12** and **14** in HeLa cells and conjugates **9** and **10** in U87 cells. In general, the differences found in cell-surface adsorption of the conjugates were small, with oligonucleotides **11** and **13** showing a slight increase in fluorescence, for both cell types in the presence or absence of glucose.

To determine the influence of glucose units in the oligonucleotide and the relevance of the different spatial presentation

in the cellular uptake, the carbohydrate oligonucleotide conjugates labeled with Alexa 488 (**9**−**14**, Figure 1) and the control labeled DNA oligonucleotide (**8**, Figure 1) were incubated with HeLa cells and U87.CD4.CXCR4 cells. The incubation was performed under standard conditions with 2 μM oligonucleotide for 2 h at 37 °C, both in the absence and in the presence of glucose (5.5 mM). After washing, the fluorescence intensity was determined by flow cytometry (Figure 5). Flow cytometry revealed that, in the absence of glucose, the fluorescence intensity of the cells was higher for DNA glycoconjugates **11** and **13** than for glycoconjugates **9**, **10**, **12**, and **14** and the control labeled DNA oligonucleotide without sugar modification **8**. This behavior was observed in both HeLa and U87.CD4.CXCR4 cells (Figure 5A,B). These differences diminished quite considerably when glucose was present in the medium, most probably due to the large difference in concentration between glucose (5.5 mM) and the oligonucleotide conjugates (2 μM). It seems that oligonucleotides with the glucose moiety linked through longer spacers (15 and 18 atom distance in COCs **11** and **13**, respectively) showed better incorporation into the target cell than those with glucose linked through shorter spacers (4 atom distance in COC **9**). Moreover, high multivalency of glucose, as in glycoconjugate **14**, seems to hinder cell uptake, maybe due to its high structural volume.

CONCLUSIONS

We have efficiently synthesized carbohydrate oligonucleotide conjugates with sugar moieties bound at the 5′-end of the DNA strand obtaining good yields and purities. Two types of spacers, ethylene glycol and tetraethylene glycol, and a doubler dendrimer were used to construct DNA glycoconjugates with different glucose presentations. Cellular uptake of oligonucleotides containing a terminal glucose unit linked through a long tetraethylene glycol spacer or just one doubler dendrimer was more efficient than the other glycoconjugates and the unconjugated control. In contrast, the conjugate containing four glucose units showed lower cell uptake, in both HeLa and U87.CD4.CXCR4 cells. These results indicate that keeping a certain distance (15 to 18 atoms) between DNA and sugar modification could be important for a better incorporation of the oligonucleotide conjugate into the target cell. In fact, this strategy seems promising for further DNA conjugate design.

ACKNOWLEDGMENT

This work was supported by Consejo Superior de Investigaciones Científicas (PIF06-045); Spanish Ministry of Science (grants BFU2007-63287, BFU2007-62062, CTQ2006-01123, CTQ2009-13705), Generalitat de Catalunya (2009/SGR/208), and Instituto de Salud Carlos III (CIBER-BNN, CB06_01_0019). RL thanks CSIC for a JAE contract.

Supporting Information Available: NMR spectral data for compounds **18**, **19**, **21**, and **22**. This material is available free of charge via the Internet at http://pubs.acs.org.

LITERATURE CITED

(1) Braasch, D. A., and Corey, D. R. (2002) Novel antisense and peptide nucleic acid strategies for controlling gene expression. *Biochemistry 41*, 4503–10.

(2) Fabani, M. M., Turner, J. J., and Gait, M. J. (2006) Oligonucleotide analogs as antiviral agents. *Curr. Opin. Mol. Ther. 8*, 108–14.

(3) Aboul-Fadl, T. (2005) Antisense oligonucleotides: the state of the art. *Curr. Med. Chem. 12*, 2193–214.

(4) Chan, J. H., Lim, S., and Wong, W. S. (2006) Antisense oligonucleotides: from design to therapeutic application. *Clin. Exp. Pharmacol. Physiol. 33*, 533–40.

(5) Frank-Kamenetskii, M. D., and Mirkin, S. M. (1995) Triplex DNA structures. *Annu. Rev. Biochem. 64*, 65–95.

(6) Praseuth, D., Guieysse, A. L., and Helene, C. (1999) Triple helix formation and the antigene strategy for sequence-specific control of gene expression. *Biochim. Biophys. Acta 1489*, 181–206.

(7) Sun, J. S., Garestier, T., and Helene, C. (1996) Oligonucleotide directed triple helix formation. *Curr. Opin. Struct. Biol. 6*, 327–33.

(8) Bumcrot, D., Manoharan, M., Koteliansky, V., and Sah, D. W. Y. (2006) RNAi therapeutics: a potential new class of pharmaceutical drugs. *Nat. Chem. Biol. 2*, 711–719.

(9) de Fougerolles, A., Manoharan, M., Meyers, R., and Vornlocher, H. P. (2005) RNA interference in vivo: toward synthetic small inhibitory RNA-based therapeutics. *Methods Enzymol. 392*, 278–96.

(10) Sioud, M., and Iversen, P. O. (2005) Ribozymes, DNAzymes and small interfering RNAs as therapeutics. *Curr. Drug Targets 6*, 647–53.

(11) Zimmermann, T. S., Lee, A. C., Akinc, A., Bramlage, B., Bumcrot, D., Fedoruk, M. N., Harborth, J., Heyes, J. A., Jeffs, L. B., John, M., Judge, A. D., Lam, K., McClintock, K., Nechev, L. V., Palmer, L. R., Racie, T., Rohl, I., Seiffert, S., Shanmugam, S., Sood, V., Soutschek, J., Toudjarska, I., Wheat, A. J., Yaworski, E., Zedalis, W., Koteliansky, V., Manoharan, M., Vornlocher, H. P., and MacLachlan, I. (2006) RNAi-mediated gene silencing in non-human primates. *Nature 441*, 111–4.

(12) Liu, B. (2007) Exploring cell type-specific internalizing antibodies for targeted delivery of siRNA. *Brief Funct. Genom. Proteom. 6*, 112–119.

(13) Santel, A., Aleku, M., Keil, O., Endruschat, J., Esche, V., Durieux, B., Loffler, K., Fechtner, M., Rohl, T., Fisch, G., Dames, S., Arnold, W., Giese, K., Klippel, A., and Kaufmann, J. (2006) RNA interference in the mouse vascular endothelium by systemic administration of siRNA-lipoplexes for cancer therapy. *Gene Ther. 13*, 1360–1370.

(14) Kim, S. H., Mok, H., Jeong, J. H., Kim, S. W., and Park, T. G. (2006) Comparative evaluation of target-specific GFP gene silencing efficiencies for antisense ODN, synthetic siRNA, and siRNA plasmid complexed with PEI-PEG-FOL conjugate. *Bioconjugate Chem. 17*, 241–4.

(15) Urban-Klein, B., Werth, S., Abuharbeid, S., Czubayko, F., and Aigner, A. (2004) RNAi-mediated gene-targeting through systemic application of polyethylenimine (PEI)-complexed siRNA in vivo. *Gene Ther. 12*, 461–466.

(16) Mok, H., and Park, T. G. (2008) Self-crosslinked and reducible fusogenic peptides for intracellular delivery of siRNA. *Biopolymers 89*, 881–888.

(17) Park, T. G., Jeong, J. H., and Kim, S. W. (2006) Current status of polymeric gene delivery systems. *Adv. Drug Delivery Rev. 58*, 467–486.

(18) Lonnberg, H. (2009) Solid-phase synthesis of oligonucleotide conjugates useful for delivery and targeting of potential nucleic acid therapeutics. *Bioconjugate Chem. 20*, 1065–94.

(19) Jeong, J. H., Mok, H., Oh, Y. K., and Park, T. G. (2009) siRNA conjugate delivery systems. *Bioconjugate Chem. 20*, 5–14.

(20) LeDoan, T., Etore, F., Tenu, J. P., Letourneux, Y., and Agrawal, S. (1999) Cell binding, uptake and cytosolic partition of HIV anti-gag phosphodiester oligonucleotides 3′-linked to cholesterol derivatives in macrophages. *Bioorg. Med. Chem. 7*, 2263–9.

(21) Soutschek, J., Akinc, A., Bramlage, B., Charisse, K., Constien, R., Donoghue, M., Elbashir, S., Geick, A., Hadwiger, P., Harborth, J., John, M., Kesavan, V., Lavine, G., Pandey, R. K., Racie, T., Rajeev, K. G., Rohl, I., Toudjarska, I., Wang, G., Wuschko, S., Bumcrot, D., Koteliansky, V., Limmer, S., Manoharan, M., and Vornlocher, H. P. (2004) Therapeutic silencing of an endogenous gene by systemic administration of modified siRNAs. *Nature 432*, 173–8.

(22) Zelphati, O., Wagner, E., and Leserman, L. (1994) Synthesis and anti-HIV activity of thiocholesteryl-coupled phosphodiester antisense oligonucleotides incorporated into immunoliposomes. *Antivir. Res. 25*, 13–25.
(23) Yan, H., and Tram, K. (2007) Glycotargeting to improve cellular delivery efficiency of nucleic acids. *Glycoconjugate J. 24*, 107–23.
(24) Zatsepin, T. S., and Oretskaya, T. S. (2004) Synthesis and applications of oligonucleotide-carbohydrate conjugates. *Chem. Biodivers. 1*, 1401–17.
(25) Karskela, M., Virta, P., Malinen, M., Urtti, A., and Lonnberg, H. (2008) Synthesis and cellular uptake of fluorescently labeled multivalent hyaluronan disaccharide conjugates of oligonucleotide phosphorothioates. *Bioconjugate Chem. 19*, 2549–58.
(26) Ye, Z., Cheng, K., Guntaka, R. V., and Mahato, R. I. (2005) Targeted delivery of a triplex-forming oligonucleotide to hepatic stellate cells. *Biochemistry 44*, 4466–76.
(27) Zhu, L., Ye, Z., Cheng, K., Miller, D. D., and Mahato, R. I. (2008) Site-specific delivery of oligonucleotides to hepatocytes after systemic administration. *Bioconjugate Chem. 19*, 290–8.
(28) Oishi, M., Nagasaki, Y., Itaka, K., Nishiyama, N., and Kataoka, K. (2005) Lactosylated poly(ethylene glycol)-siRNA conjugate through acid-labile beta-thiopropionate linkage to construct pH-sensitive polyion complex micelles achieving enhanced gene silencing in hepatoma cells. *J. Am. Chem. Soc. 127*, 1624–5.
(29) Brauns, D. H. (1929) Optical rotation and atomic dimension VIII. Halogen-hepta-acetul derivatives of melibiose and maltose. The structures of bioses and cellulose. *J. Am. Chem. Soc. 51*, 1820–1831.
(30) Barker, S. A., and Bourne, E. J. (1952) The oligosaccharides synthesised from maltose by Escherichia coli. *J. Chem. Soc.* 209–214.
(31) Nigam, V. N., and Giri, K. V. (1960) Enzymatic synthesis of oligosaccharides from maltose by germinated green gram (phaseolus radiatus). *J. Biol. Chem. 235*, 947–950.
(32) Nelson, P. S., Kent, M., and Muthini, S. (1992) Oligonucleotide labeling methods 3. Direct labeling of oligonucleotides employing a novel, non-nucleosidic, 2-aminobutyl-1,3-propanediol backbone. *Nucleic Acids Res. 20*, 6253–6259.
(33) Katajisto, J., Heinonen, P., and Lonnberg, H. (2004) Solid-phase synthesis of oligonucleotide glycoconjugates bearing three different glycosyl groups: orthogonally protected bis(hydroxymethyl)-N,N'-bis(3-hydroxypropyl)malondiamide phosphoramidite as key building block. *J. Org. Chem. 69*, 7609–15.
(34) Wang, Y., and Sheppard, T. L. (2003) Chemoenzymatic synthesis and antibody detection of DNA glycoconjugates. *Bioconjugate Chem. 14*, 1314–22.
(35) Morales, J. C., Reina, J., J., Díaz, I., Aviñó, A., Nieto, P. M., and Eritja, R. (2008) Experimental measurement of carbohydrate-aromatic stacking in water by using a dangling-ended DNA model system. *Chem.—Eur. J. 14*, 7828–7835.
(36) Akhtar, S., Routledge, A., Patel, R., and Gardiner, J. M. (1995) Synthesis of mono- and dimannoside phosphoramidite derivatives for solid-phase conjugation to oligonucleotides. *Tetrahedron Lett. 36*, 7333–7336.
(37) Lisziewicz, J., Sun, D., Weichold, F. F., Thierry, A. R., Lusso, P., Tang, J., Gallo, R. C., and Agrawal, S. (1994) Antisense oligodeoxynucleotide phosphorothioate complementary to Gag mRNA blocks replication of human immunodeficiency virus type 1 in human peripheral blood cells. *Proc. Natl. Acad. Sci. U.S.A. 91*, 7942–7946.
(38) Aviñó, A., Grimau, M. G., Frieden, M., and Eritja, R. (2004) Synthesis and triple-helix-stabilization properties of branched oligonucleotides carrying 8-aminoadenine moieties. *Helv. Chim. Acta 87*, 303–316.
(39) Grimau, M. G., Iacopino, D., Aviñó, A., de la Torre, B. G., Ongaro, A., Fitzmaurice, D., Wessels, J., and Eritja, R. (2003) Synthesis of branched oligonucleotides as templates for the assembly of nanomaterials. *Helv. Chim. Acta 86*, 2814–2826.
(40) Nishi, K., and Saigo, K. (2007) Cellular internalization of green fluorescent protein fused with herpes simplex virus protein VP22 via a lipid raft-mediated endocytic pathway independent of caveolae and Rho family GTPases but dependent on dynamin and Arf6. *J. Biol. Chem. 282*, 27503–17.

BC100079N

Protease-Activatable Organometal−Peptide Bioconjugates with Enhanced Cytotoxicity on Cancer Cells

Katrin Splith,[†] Wanning Hu,[‡] Ulrich Schatzschneider,[‡] Ronald Gust,[§] Ingo Ott,[||] Liliane A. Onambele, Aram Prokop,[⊥] and Ines Neundorf*,[†]

Institut für Biochemie, Fakultät für Biowissenschaften, Pharmazie und Psychologie, Brüderstr. 34, D-04103 Leipzig, Germany, Lehrstuhl für Anorganische Chemie I-Bioanorganische Chemie, Ruhr-Universität Bochum NC 3/74, Universitätsstr. 150, D-44801 Bochum, Germany, Institut für Pharmazie, Freie Universität Berlin, Königin-Luise-Str. 2 + 4, D-14195 Berlin, Germany, Institut für Pharmazeutische Chemie, Technische Universität Braunschweig, Beethovenstr. 55, D-38106 Braunschweig, Germany, and Kinderklinik der Stadt Köln, Amsterdamerstr. 59, D- 50735 Köln, Germany. Received February 16, 2010; Revised Manuscript Received April 25, 2010

Over the past years, numerous promising new metalorganic lead structures have been developed exhibiting highly active cytostatic properties. However, the efficiency of such chemotherapeutics in the treatment of tumors is often limited by their low therapeutic index due to their short half-life, lack of tumor selectivity, and associated side effects. Furthermore, the membrane barrier often restricts their cellular uptake by passive diffusion. In this contribution, we describe the synthesis, cellular uptake, and biologic activity of a series of cymantrene−peptide conjugates. Cymantrene $CpMn(CO)_3$ is a robust organometallic group, which is stable in air and water and easy to functionalize. In this work, some new cymantrene derivatives with different linkers between the half-sandwich complex and the carboxylate group were attached to the cell-penetrating peptide sC18 that should act as a transporter for the metal moiety. All conjugates were characterized for their cytotoxic activity on human breast adenocarcinoma cells (MCF-7) and human colon carcinoma cells (HT-29). We found that bioconjugates bearing two cymantrene groups were more active than the monofunctionalized ones. By the introduction of a cathepsin B cleavage site next to the organometallic group, the biologic activity could be in increased even further. Fluorescence microscopy studies and apoptosis assays gave preliminary hints on the mode of action of these systems.

INTRODUCTION

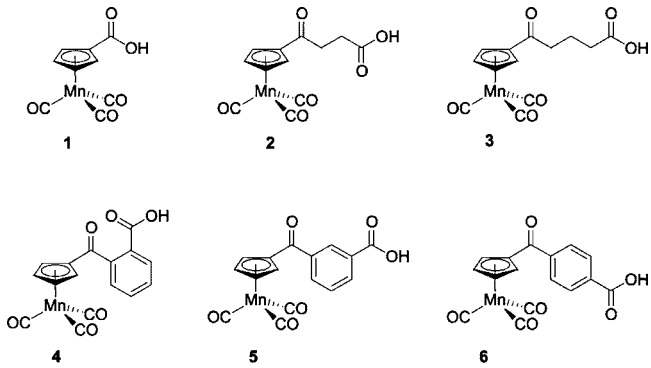
In addition to the surgical removal of tumor tissue, an efficient tumor treatment is very often based on chemo-, radio-, or immunotherapy. Currently, there exist a wide range of chemotherapeutic agents that come from different sources and can be classified as alkylating agents, DNA intercalators, antimetabolites, plant alkaloids, anthracyclines, or protein kinase inhibitors. They normally affect cell division or DNA synthesis leading to inhibition of cell growth. In addition to these purely organic compounds, those incorporating an active metal moiety are also of growing interest for the pharmaceutical industry (*1*). A very prominent representative in clinical use for some decades is the inorganic complex cisplatin, which is widely used for the treatment of a variety of tumors (*2*). However, due to severe side-effects and problems with increasing resistancies, research now also focuses on the further development of cisplatin analogues and the design of new generations of platinum compounds (*3*−*6*). During the past years, numerous promising new metalorganic lead structures have been developed exhibiting high cytostatic activity. The most well explored ones are ruthenium complexes (*7*, *8*), but other metals have also come into focus such as iron (*9*−*11*), rhodium (*12*−*14*), titanium (*15*, *16*), or cobalt (*17*). From a general view, the efficiency of antitumor chemotherapeutics is greatly limited by their low therapeutic index that is mainly caused by their short half-life, lack of tumor selectivity, and such associated side effects. Furthermore, the membrane barrier often restricts their cellular uptake by passive diffusion. One approach to circumvent the above-mentioned limitations is based on using peptides that act as delivery vehicles for the metal organic drug (*18*) and also improve properties such as water solubility.

We have recently reported on the attachment of so-called cell-penetrating peptides (CPP) to bioactive cymantrene complexes to enhance the bioavailability of the whole metal complex−peptide bioconjugate (*19*). Cell-penetrating peptides are known to act as transporters for a wide range of different substances (*20*, *21*). They can cross the lipid−membrane without the need of a transporter or receptor molecule. By coupling CPP to a metal complex, the uptake of the bioactive substance into the cell can be increased, and furthermore, an improved solubility as well as an increased chemical or enzymatic stability might result. To further extend the duration of effect of a drug and to minimize side effects, a targeted release of the bioactive compound from an intact prodrug would be beneficial. Several approaches exist to deliver drugs to cellular target structures where they exert their biological effect (*22*, *23*). Since many diseases are characterized by deregulated protease expression, advantage can be taken of up-regulated proteolysis to assist in therapeutic and diagnostic applications (*24*−*28*). The rationale behind prodrug approaches is to improve the bioactivity and bioavailability of therapeutic molecules. For instance, the tissue peptidase cathepsin B is proposed as an activator for conjugated peptide−substrates containing Gly-Phe-Leu-Gly as the protease sensitive cleavage site (*29*, *30*). Several examples of successful substrate release based on this approach have been reported (*31*).

* Corresponding author. Phone: +49 (0) 341 97 36832. Fax: +49 (0) 341 97 36909. E-mail: neundorf@uni-leipzig.de.
[†] Institut für Biochemie.
[‡] Lehrstuhl für Anorganische Chemie I-Bioanorganische Chemie.
[§] Freie Universität Berlin.
[||] Technische Universität Braunschweig.
[⊥] Kinderklinik der Stadt Köln.

10.1021/bc100089z © 2010 American Chemical Society
Published on Web 06/29/2010

Scheme 1. Functionalized Cymantrene Carboxylic Acids for Coupling to the Cell-Penetrating Peptide sC18[a]



[a] For synthesis details see ref *37*.

Metal-based building blocks have promising features for applications in diagnosis and therapy. They have been coupled to antibodies, saccharides, and steroids to create new derivatives with promising activities (*32*, *33*). In addition to metallocenes, cymantrene $CpMn(CO)_3$ has been recognized as a robust organometallic group, which is stable in air and water and easy to functionalize (*34*−*36*). Recently, we have reported on some new cymantrene derivatives with different linkers between the half-sandwich complex and the carboxylate group used for attachment to the peptide (*37*) (Scheme 1). We expected that due to these different linkers, different cytotoxic activities of the metal−peptide conjugates prepared might result. For an efficient cellular uptake, they are coupled to the cell-penetrating peptide sC18. This CPP is derived from the cationic antimicrobial peptide CAP18 and has been identified to efficiently translocate into different cell lines (*38*). Initial biological data pointed to a promising cytotoxic profile. The aim of the present study is to elucidate in more detail the uptake and biologic activities of all new cymantrene−sC18 conjugates and determine potential structure−activity relationships.

MATERIALS AND METHODS

Materials. Fmoc amino acid derivatives were purchased from Iris Biotech (Marktredwitz, Germany) and Novabiochem (Läufelfingen, Switzerland). 1-Hydroxybenzotriazole (HOBt) and 4-(2′,4′-dimethoxyphenyl-Fmoc-aminomethyl)-phenoxymethyl-linked polystyrene (Rink amide) were obtained from Novabiochem (Läufelfingen, Switzerland). *N*,*N*-diisopropylethylamine (DIEA), piperidine, 5(6)-carboxyfluorescein (CF), trypan blue, and *O*-(7-azabenzotriazol-1-yl)-1,1,3,3-tetramethyluronium hexafluorophosphate (HATU) were purchased from Fluka (Taufkirchen, Germany). Dichloromethane (DCM) and *N*,*N*-dimethylformamide (DMF) were Biosolve (Valkenswaard, Netherlands) products. Diisopropylcarbodiimide (DIC) was obtained from Iris Biotech (Marktredwitz, Germany), and trifluoroacetic acid (TFA), 1,3-dimethoxybenzene (DMB), and the resazurin-based in vitro toxicology assay kit were from Sigma-Aldrich (Taufkirchen, Germany). Gradient-grade high-performance liquid chromatography (HPLC) solvent acetonitrile (ACN) was from VWR (Darmstadt, Germany). All of the reagents and solvents were used without purification as provided from the commercial suppliers.

The following media and supplements were used for cell cultures: Dulbecco's modified Eagle's medium (DMEM)/Ham's F12 (without L-glutamine), RPMI 1640 (with L-glutamine), heat-inactivated fetal bovine serum (FBS), L-glutamine (Q), Dulbecco's phosphate buffered saline (PBS) (without calcium and magnesium), and Trypsin/EDTA were purchased from PAA (Pasching, Austria). OptiMEM was an Invitrogen Gibco (Karlsruhe, Germany) product. Hoechst3342, MitoTracker Red FM, and LysoTracker Red DND-99 were obtained from Invitrogen Molecular Probes (Karlsruhe, Germany). Cell culture flasks (75 cm^2), 24-well plates, and 96-well plates were from TPP (Trasadingen, Switzerland) and 8-well plates from ibidi (Martinsried, München Germany).

Synthesis of Cymantrene−sC18 Bioconjugates. Automated peptide synthesis was performed on a multiple peptide synthesizer (Syro II, MultiSyntech, Witten, Germany). All peptides were prepared as C-terminal amides using a Rink amide resin as the solid support, following Fmoc-strategy utilizing *in situ* activation with HOBt/DIC. The amino acids were dissolved in 0.5 M HOBt in DMF and added in 10-fold excess. Functionalized cymantrene acids **1** to **6** were manually coupled to the N-terminus of the carrier peptide sC18 as previously reported (*37*).

The synthesis of conjugates **7** to **19** was achieved by an orthogonal protecting group strategy. First, Fmoc-Lys(Dde)-OH was manually coupled at position 109 of an sC18 fragment assembled before. Then, the peptide was extended automatically. For the CF-labeled peptides, 5,6-carboxyfluorescein was coupled and protected with a trityl group. Afterward, the Dde-protecting group was cleaved by treating the preswollen resin with a 2% hydrazine/DMF solution (v/v) for 10 min (10 repetitions). Then, the respective cymantrene carboxylic acids were coupled by the above-mentioned protocol. Synthesis of conjugates **18** and **19** was done by coupling of one cymantrene moiety to the N-terminus of sC18 and the other to the ε-amino group of Lys^{109}. After Dde-cleavage, a 2-fold excess of cymantrene carboxylic acid was coupled to the two free amino groups. The final cleavage of bioconjugates **7** to **19** from the resin was achieved by treatment with a mixture of DMB (50 μL) and TFA (950 μL) or in the case of the Cym4 bioconjugates with a mixture of water (50 μL) and TFA (950 μL). The peptide was then precipitated by the addition of ice-cold diethyl ether. The precipitate was centrifuged and washed with diethylether (five repetitions). Afterward, the peptide pellet was dried and then dissolved in a 1:3-mixture (v/v) of *tert*-butanol and water. The solution was subsequently frozen and the solvent removed by lyophilization. If the purity of the peptides was below 95%, the bioconjugates were purified with semipreparative or preparative HPLC.

All peptides were analyzed by MALDI-TOF and electrospray mass spectrometry using a Bruker Daltonics Ultraflex III and a Bruker HCT mass spectrometer.

Analytical HPLC was performed using a Merck-Hitachi system with a Grace Vydac 218TP54 column, and semipreparative or preparative HPLC was carried out using a Chromatopac Shimadzu system with a Vydac 208MS510 C18 column/Vydac 218TP1022 C18 column. A linear gradient of 0.1% TFA in H_2O (A) and 0.08% TFA in methanol (B) from 20% to 70% B in A over 30 min or from 40% to 90% B in A over 40 min was used. The flow rates were 0.6 mL/min and 4 mL/min/10 mL/min, respectively.

Cell Culture. MCF-7 (human breast adenocarcinoma) cells were procured in 2004 from the University Hospital for Children and Adolescents, University of Leipzig, and HT-29 (human Caucasian colon adenocarcinoma grade II) cells were purchased from the ATTC. Cells were grown at 37 °C and 5% CO_2 under a humidified atmosphere in 75 cm^2 cell culture flasks. MCF-7 cells were cultivated in DMEM/Ham's F12 with 10% FBS (v/v) and 2 mM Q. HT-29 cells were cultivated in RPMI1640 (with Q) with 10% FBS (v/v). All cells were grown to subconfluency before use.

Fluorescence Microscopy. For internalization studies with MCF-7 and HT-29 cells, 60.000 cells per well were seeded into an 8-well plate and grown to 70% confluency. Cells were incubated for 30 min at 37 °C with 20 μM (MCF-7) or 50 μM

(HT-29) solutions of CF-labeled sC18 or Cym3-sC18 in OptiMEM. After 20 min of incubation time, 1 μg/mL Hoechst33342 nuclear dye was added to each well. In addition, 0.1 μL of a MitoTracker Red FM solution (1 mM) or a LysoTracker Red-DND 99 solution (1 mM) was added after 15 min to stain the mitochondria. Then, the medium was removed, and the cells were incubated with 300 μM trypan blue solution (in glycine buffer, pH 4.5) for 1 min to quench extracellular fluorescence. Afterward, all wells were washed twice with OptiMEM, and HBSS was added. Fluorescence images were obtained using a Zeiss AxioObersver Z1 fluorescence microscope including an Apotome unit and a 63×/1.4 oil immersion objective.

Cellular Uptake by Atomic Absorption Spectroscopy. Subconfluent MCF-7 and HT-29 cells were washed and replaced by the addition of Trypsin/EDTA. Cells were counted, and pellets out of 2.5 mio. cells were prepared, which were incubated for 1 h at 37 °C with 20 μM solutions of the organometallic peptide conjugates. Then cells were washed two times with PBS, and the remaining peptide was detached with Trypsin/EDTA.

The cell pellets were resuspended in 1 mL of doubly destilled water, lysed with a sonotrode, and appropriately diluted using doubly destilled water. An aliquot was removed for protein quantification by the Bradford method. (Cellular uptake is expressed as nmol manganese per mg cell protein.) Prior to manganese quantification by AAS (see below), to each 200 μL of the cell suspensions 20 μL of Triton X-100 (1%) and nitric acid (13%) was added. A Vario-6 graphite furnace atomic absorption spectrometer (AnalytikJena AG) was used for the manganese determination. Manganese was detected at a wavelength of 279.5 nm with a bandpass of 0.2 nm. A deuterium lamp was used for background correction. Probes were injected at a volume of 20 μL into graphite tubes. Heating procedures in the graphite furnace were as previously reported (*39*). The graphite tube was purged with a constant flow of argon gas, which was only halted during the zeroing and atomization steps. The mean AUC (area under curve) absorptions of duplicate injections were used throughout the study. Serial aqueous dilutions of **7** were used for calibration purposes. The mean manganese background concentration of blank cell pellets was subtracted from the data obtained with the probes. All experiments were carried out two times in triplicate.

Cell Viability Assays. MCF-7 or HT-29 cells were seeded in 96-well plates (30.000 or 40.000 cells per well). After reaching 60−80% confluency, the medium was removed, and cells were incubated at 37 °C for 24 h with the substances at different concentrations ranging from 1 to 1000 μM. Therefore, the respective stock solution (1 mM) was diluted with cell medium to a total volume of 100 μL. As a negative control, untreated cells were used. Cell viability of MCF-7 cells was tested using a resazurin-based toxicology assay. After 24 h, MCF-7 cells were washed twice with cell medium and incubated for 2 h at 37 °C with 10% resazurin in the cell medium (v/v). The positive control was additionally treated with 70% ethanol (100 μL) for 10 min before resazurin addition.

To examine the viability of HT-29 cells, after 24 h of incubation with the peptide solution CytoTOX-ONE (100 μL) reagent was added and incubated for 10 min at room temperature. The positive control had previously been treated with lysis solution (2 μL).

Finally, in both cases, fluorescence was measured using TECAN Spectra Fluor Plus at 595 nm with an excitation wavelength of 550 nm. All experiments were done with n (number of experiments) $\geq$ 2 in triplicate.

Annexin V/Propidium Iodide Assay. MCF-7 or HT-29 cells were seeded in 24-well plates (150.000 or 200.000 cells per well). After reaching 60−80% confluency, the medium was removed, and cells were incubated at 37 °C for 24 h with the substances in different concentrations ranging from 10 to 100 μM. The respective stock solution (1 mM) was diluted with cell medium to a total volume of 300 μL. As a negative control, untreated cells were used, and as a positive control, cells were treated with staurosporine (7 μM). Cells were washed with PBS, harvested, and the solutions were combined and centrifuged (7.5 min, 1000 rpm). Then the cell pellet was washed with PBS again, and the cells were resuspended in annexin-binding buffer (10 mM HEPES, 140 mM NaCl, and 2.5 mM CaCl, pH 7.4). Afterward, 5 μL of the annexin V conjugate was added to each sample as well as 4 μL of FDA staining solution (10 μg/mL) and 5 μL of PI staining solution (1 μg/mL). Cells were incubated at room temperature for 15 min, then diluted with PBS, and kept on ice. As soon as possible, the samples were analyzed with a Partec CyFlow ML FCM system.

Concentration Dependent Effects on Human B-Cell Leukemia Cells. The following human cell line and its chemoresistant subline were used in this study: leukemia B-cell precursor (Nalm-6) and its vincristin (VCR) resistant subline Nalm-6/VCR. Both cell lines were cultured in RPMI 1640 supplemented with 10% fetal calf serum.

For the determination of cell concentration and cell viability, CASY Cell Counter + Analyzer System of Schaerfe System GmbH (Reutlingen, Germany) was used. Settings were specifically defined for the requirements of the cells used. With this system, the cell concentration is analyzed simultaneously in three different size ranges: cell debris, dead cells, and viable cells were determined in one measurement. Nalm-6 cells were seeded at a density of 1×10^5 cells/mL and treated with different concentrations of **9** or **19**, nontreated cells served as controls (Co). After 24 h of incubation, cells were resuspended properly and 100 μL of each well was diluted in 10 mL CASYton (ready-to-use isotonic saline solution) for an immediate automated count of the cells.

Apoptotic cell death was determined by a modified cell cycle analysis, which detects DNA fragmentation at the single cell level. For measurement of DNA fragmentation cells were seeded at a density of 1×10^5cells/mL and treated with different concentrations of **9** or **19**. After 72 h of incubation, cells were collected by centrifugation at 300*g* for 5 min, washed with PBS at 4 °C, and fixed in PBS/2% (v/v) formaldehyde on ice for 30 min. After fixation, cells were incubated with ethanol/PBS (2:1, v/v) for 15 min, pelleted, and resuspended in PBS containing 40 μg/mL RNase A. After incubation for 30 min at 37 °C, cells were pelleted again and finally resuspended in PBS containing 50 μg/mL propidium iodide. Nuclear DNA fragmentation was then quantified by flow cytometric determination of hypodiploid DNA. Data were collected and analyzed using FACScan (Becton Dickinson, Heidelberg, Germany) equipped with the CELLQuest software. Data are given in % hypoploidy (subG1), which reflects the number of apoptotic cells.

RESULTS

Synthesis of Cymantrene−Peptide Bioconjugates. Recently, we reported on the solid phase synthesis of cymantrene−sC18 peptide conjugates **7** to **12** (*37*). The attachment of the functionalized cymantrene acids **1** to **6** to sC18 was easily achieved by HOBt/DIC activation directly on the solid support. Interestingly, we found out that cleavage of the metal complex−peptide conjugates from the solid support led to several byproducts depending on the cleavage mixture used. We observed inappropriate decomposition of the Rink amide linker leading on the one hand to N-alkylated C-terminal peptide amides and on the other hand to the formation of reactive carbocationic species that specifically alkylated the cymantrene linker when a phenyl was present. With these results in mind,

Table 1. Cymantrene−Peptide Conjugates: Names, Amino Acid Sequences, Molecular Weights, and IC_{50} Values (as Determined in MCF-7 and HT-29 Cells)[a]

number	name	sequence	MW [Da]	IC_{50} [μM] MCF-7	IC_{50} [μM] HT-29
7	Cym1-sC18	Cym1-GLRKRLRKFRNKIKEK	2298.4	59.5 ± 6.7	>100
8	Cym2-sC18	Cym2-GLRKRLRKFRNKIKEK	2354.5	63.0 ± 4.3	>100
9	Cym3-sC18	Cym3-GLRKRLRKFRNKIKEK	2368.5	64.8 ± 15.4	>100
10	Cym4-sC18	Cym4-GLRKRLRKFRNKIKEK	2402.5	57.4 ± 15.3	>100
11	Cym5-sC18	Cym5-GLRKRLRKFRNKIKEK	2402.5	55.1 ± 3.8	>100
12	Cym6-sC18	Cym6-GLRKRLRKFRNKIKEK	2402.5	65.8 ± 5.7	>100
13	CF-sC18(Cym3)	CF-GLRK(Cym3)RLRKFRNKIKEK	2726.8	61.5 ± 1.2	n.d.
14	$(Cym2)_2$-sC18	Cym2-GLRK(Cym2)RLRKFRNKIKEK	2641.6	45.9 ± 7.9	n.d.
15	$(Cym3)_2$-sC18	Cym3-GLRK(Cym3)RLRKFRNKIKEK	2668.6	42.5 ± 5.3	n.d.
16	$(Cym4)_2$-sC18	Cym4-GLRK(Cym4)RLRKFRNKIKEK	2736.7	49.5 ± 0.4	n.d.
17	Cym3-RR-sC18	Cym3-RRGLRKRLRKFRNKIKEK	2680.7	38.2 ± 2.2	n.d.
18	Cym3-GFL-sC18	Cym3-GFLGLRKRLRKFRNKIKEK	2685.7	28.9 ± 4.2	n.d.
19	$(Cym3\text{-}GFLG)_2$-sC18	Cym3-GFLGGLRK(GLFG-Cym3)RLRKFRNKIKEK	3417.3	15.2 ± 1.8	35.0 ± 3.7

[a] n.d.: not determined.

the synthesis of the newly designed metal−peptide conjugates, **13** to **19** (see Table 1 for amino acid sequence and point of attachment of the organometallic moiety), was achieved by the use of the appropriate cleavage mixture. Table 1 gives an overview of all cymantrene−peptide bioconjugates prepared by this method. All compounds were obtained in >95% purity and characterized by analytical HPLC as well as MALDI-TOF mass spectrometry.

Internalization Studies in MCF-7 and HT-29 Cells. First, we evaluated the cellular uptake of the cymantrene−peptide conjugates for some representative systems. This was achieved by following two different strategies: on the one hand, the intracellular manganese content was determined by using graphite-furnace atomic absorption spectroscopy (GF-AAS). On the other hand, carboxyfluorescein-labeled peptides were visualized by fluorescence microscopy.

In the first case, human breast cancer (MCF-7) as well as human colon carcinoma (HT-29) cells were incubated with solutions of peptide conjugates **7** to **10**, and after cell lysis, the manganese content was determined and related to the overall protein content of the cells. Values do not vary much between the different conjugates and cell lines studied but indicate an increased manganese content compared to that of untreated cells for both cell lines tested (Figure 1A). On the basis of distinct cellular parameters such as the mean diameter and mean protein content, the cellular molar concentrations can be estimated from the measured nmol/mg values (*40*, *41*). Accordingly, the measured values corresponded to 31−108 μM in HT-29 cells and to 12−36 μM in MCF-7 cells. It can be concluded that the cellular concentrations did not exceed the extracellular concentrations (exposure concentration of >20 μM) more than 5-fold, which is in good agreement with previous studies on metal peptide derivatives (*42*, *43*).

Additionally, we investigated the subcellular distribution of the CF-labeled compounds by fluorescence microscopy. MCF-7 or HT-29 cells were incubated for 30 min at 37 °C with a 20 μM concentration of the cymantrene−sC18 conjugate **13**, which was labeled with carboxyfluorescein. Interestingly, a much higher concentration of **13** was required to detect this conjugate in HT-29 cells than in MCF-7 cells (50 μM versus 20 μM). Under these conditions, a dot-like distribution pattern with vesicles near the nucleus was observed for both cell-lines (Figure 1B), pointing to an endosomal uptake pathway. This is in agreement with our previous results obtained for the unmodified carrier peptide sC18 (*38*). Also, no uptake into the nucleus was detected, different from our observation made for **4** coupled to another CPP (*19*). No uptake into the nucleus was observed of the CF-labeled compounds **10** to **12** too that bear structurally different cymantrene carboxylic acids (data not shown). Thus,

A

Compound	Cellular uptake nmol Mn/mg cell protein MCF-7	HT-29
7	0.32 ± 0.23	0.17 ± 0.08
8	0.21 ± 0.09	0.16 ± 0.11
9	0.10 ± 0.03	0.17 ± 0.12
10	0.29 ± 0.04	0.55 ± 0.50

B

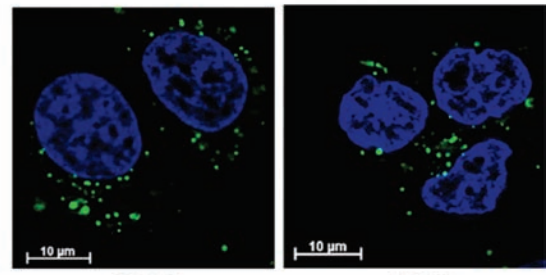


Figure 1. (A) Accumulation of manganese in MCF-7 and HT-29 cells after incubation with compounds **7** to **10** as determined by using GF-AAS. (B) Fluorescence microscopic images of MCF-7 and HT-29 cells after incubation with a 20 μM (MCF-7) or 50 μM (HT-29) solution of CF-labeled substance **13**.

we assume that the intracellular distribution is determined by the CPP and not the organometallic group attached to it.

Cytotoxicity Studies. Next, the cytotoxic profiles of the cymantrene−sC18 conjugates were studied to elucidate the influence of different peptide-to-metal complex linkers. All cymantrene carboxylic acids investigated so far did not exhibit any cytotoxicity by themselves when incubated with the human breast cancer cell line MCF-7 (*4*, *24*, *25*). We found that this is also the case for compounds **1** to **6** not only when tested for MCF-7 but also for HT-29 cells. Even after incubating the cells with concentrations of up to 200 μM, no cytotoxicity was observed (data not shown). The reason might be that the cells do not efficiently take them up. Since the water solubility of compounds **1** to **6** was limited, higher concentrations could not be tested. Also, the cell-penetrating peptide sC18 itself was shown to be nontoxic when incubated with several different cell lines (*38*).

In contrast, bioconjugates **7** to **12**, obtained after attachment of the different cymantrene carboxylic acids **1** to **6** to sC18, led to a concentration dependent reduction of cell viability for both MCF-7 and HT-29 cells (Figure 2A and B).

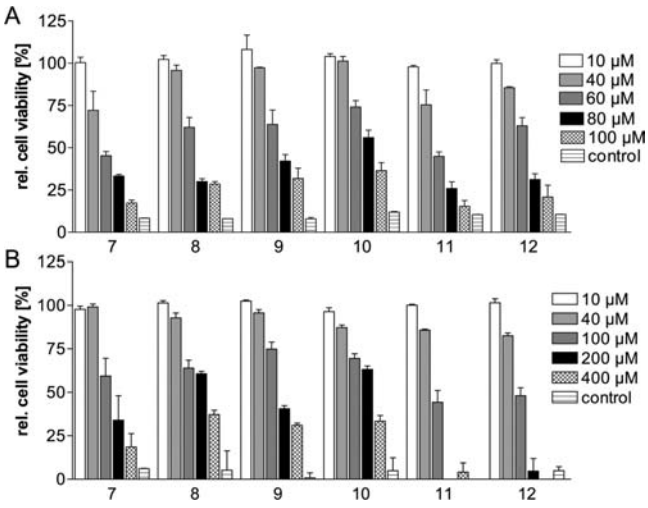


Figure 2. Relative cell viability of MCF-7 (A) and HT-29 (B) cells after treatment for 24 h with compounds **7** to **12**, respectively. Cells incubated with 70% ethanol for 10 min served as positive control for cytotoxicity. Data are normalized to untreated cells (100% viability). For IC_{50} values, see Table 1.

The cytotoxic activity of the cymantrene−peptide conjugates **7** to **12** on MCF-7 cells was more pronounced, with IC_{50} values in the range of 55 to 65 μM (Table 1). In contrast, for HT-29 cells the activity was much lower, with IC_{50} values above 100 μM. This is likely due to the lower uptake efficiency in this cell line as reported above. All six cymantrene−peptide derivatives had rather similar IC_{50} values of around 60 μM, indicating that there is no effect on the activity due to the different linkers (aliphatic vs aromatic, *ortho*- vs *meta*- vs *para*-phenylene) between the cyclopentadienyl ring and the peptide. We also investigated the effect of increasing the payload of cymantrene groups on the peptide. Thus, conjugates **14** to **16** were prepared that carry two units of **2**, **3**, and **4**, respectively. Interestingly, this led to a decrease of the IC_{50} values on MCF-7 cells by a factor of 1.2 to 1.5 (Table 1). We take this as a clear indication that the organometallic cymantrene group is vital for the observed biological activity.

Mechanistic Insights. To elucidate the mechanism of action of the peptide conjugates, compound **9** was selected as a representative example and incubated with MCF-7 cells to assess whether necrotic or apoptotic pathways are involved in tumor growth inhibition. Therefore, apoptotic cells were labeled with annexin V (*44*). Soon after apoptosis induction, membrane phophatidylserine (PS) is translocated from the inner side of the cell membrane to the cell surface. Annexin V is a protein with high affinity to PS and can thus be used to detect PS exposure. Additional staining with fluorescein diacetate (FDA) and propidium iodide (PI) was used to label viable and dead cells, respectively. Thus, differences between necrosis and early stages of apoptosis can be detected by dye exclusion from intact cells (annexin $V^-/PI^-/FDA^+$), apoptotic cells (annexin $V^+/PI^-/FDA^+$), and necrotic cells (annexin$^+/PI^+/FDA^-$). MCF-7 as well as HT-29 cells were incubated for 24 h at 37 °C with conjugate **9** using concentrations in the range of 10 to 100 μM. Then, cells were stained with annexin V−PacificBlue conjugate, PI, and FDA and analyzed via flow cytometry. In addition to significant necrotic events, cells undergoing early apoptosis could also be detected after the treatment of MCF-7 cells with compound **9**. Figure 3 (left bars) displays dead and viable cells, which are identified by PI and FDA staining, respectively. In addition, apoptotic cells are identified by PI dye exclusion and staining with FDA and annexin V (right bars in light gray). The results demonstrate that at a lower concentration of compound **9** early apoptotic events are involved, whereas at higher concentrations, mainly necrotic events are detectable. In contrast, when incubating HT-29 cells with a 100 μM solution of compound **9**, mainly some necrotic events could be detected.

Since apoptotis-inducing proteins can also affect the mitochondria, we were interested in the intracellular fate and distribution of the cymantrene−sC18 conjugates after cell uptake. Therefore, we used fluorescence markers to stain different cell components, in this case mitochondria and lysosomes. Either MCF-7 or HT-29 cells were incubated for 30 min at 37 °C with a 20 μM (MCF-7) or 50 μM (HT-29) concentration of conjugate **13**, the CF-labeled analogue of **9**, and stained with either MitoTracker or LysoTracker. We did not observe any colocalization of **13** and MitoTracker (Figure 4A and B), indicating no accumulation in the mitochondria. However, since only the peptide and not the organometallic moiety itself was fluorescently labeled, it cannot be ruled out that the bioactive cymantrene moiety is cleaved from the peptide after internalization and that both components then distribute differently inside the cell. In fact, most of the peptide seems to end up in lysosomes located near the nucleus as indicated by the merged fluorescence of the CF-labeled peptide and LysoTracker (Figure 4C and D).

Protease-Cleavable Metal Complex−Peptide Bioconjugates. Since the uptake of the cymantrene−sC18 conjugates seems to occur by endocytosis, we looked for a strategy to enhance the endosomal escape of the cargo-CPP construct, which is expected to increase the cytotoxic effect of the conjugates. One method is to introduce enzymatic cleavage sites to the peptide, preferably for enzymes that are overexpressed in target cells. Therefore, we introduced an Arg-Arg and a Gly-Phe-Leu-Gly peptide sequence, both recognized by the endopeptidase cathepsin B, between the N-terminal end of the sC18 sequence and the cymantrene unit. The latter is more specific for cathepsin B recognition, and the introduction of this GFLG sequence is often described as an efficient tool to liberate the cargo after uptake into the tumor cell (*31*, *45*, *46*). As indicated in Figure 5, the new conjugates **17** and **18** exhibited an enhanced cytotoxic effect on the MCF-7 cells with a nearly 2-fold decrease of the IC_{50} value compared to that of the cymantrene peptides not containing an enzymatic cleavage site (Table 1). Furthermore, when combining this strategy with an increase in the number of cymantrene units attached to the peptides as in **19**, the IC_{50} value decreased further by a factor of about three compared to that of **15** and reached a value of 15.2 ± 1.8 μM. This effect could also be observed for HT-29 cells. Here, after incubation with compound **19**, an IC_{50} value of 35.0 ± 3.7 μM was calculated.

This very promising compound **19** was further tested on human B-cell leukemia (Nalm-6) cells. For comparison, we also tested substance **9** that contains no enzymatic cleavage sites and only one cymantrene unit. Figure 6A and B demonstrate that both compounds exhibited reduced proliferation and lowered cell viability after an incubation period of 24 h, confirming the above-described cytotoxic potential of the conjugates. Furthermore, we quantified the induction of apoptosis via flow cytometric measurements of the DNA fragments after incubating Nalm-6 cells for 72 h with **9** and **19**. Significant DNA fragmentation is observed for both compounds, but even at very low concentrations of the cytotoxic cymantrene−peptide conjugate, **19** proving once more its higher cytotoxic effect (Figure 6C and D). Sixty percent of the treated cells were apoptotic after treatment with 40 μM **9**, whereas already after treatment with 20 μM **19**, the same effect could be observed. For testing the ability of **19** to overcome drug resistance, we used the vincristine (VCR) resistant cell line Nalm-6/VCR. Compound **19** as well as the reference compound **9** could induce apoptosis in both cell lines. Interestingly, this effect was more pronounced for compound **9** where the apoptotic effect in the resistant

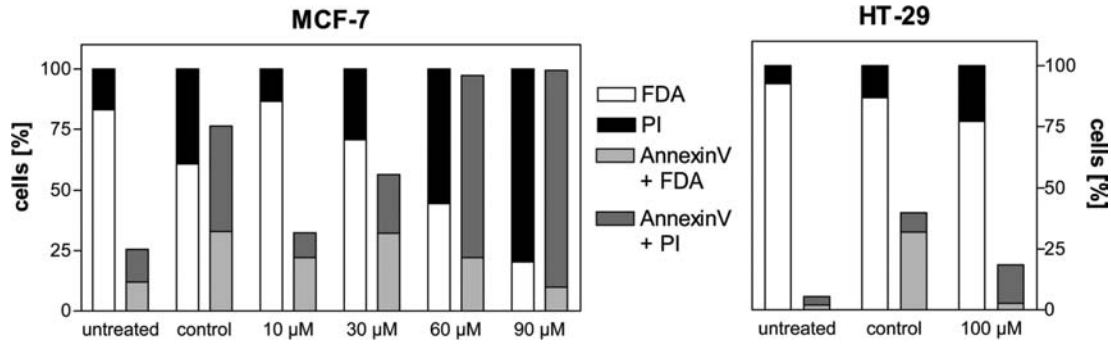


Figure 3. Investigation of the apoptosis rate with the fragmentation-independent annexin-V/propidium iodide binding assay by using flow cytometry. MCF-7 as well as HT-29 cells were incubated with compound **9** for 24 h. As the negative control, untreated cells were used. As the positive control, cells incubated with the apoptosis-inducing substance staurosporine (7 μM) were used.

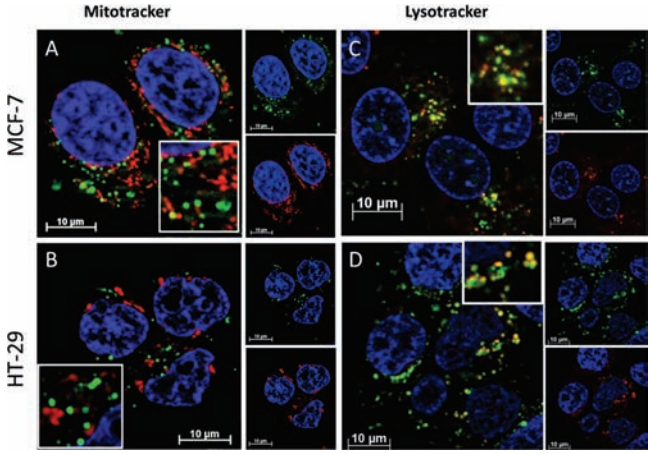


Figure 4. Investigation of the intracellular fate of compound **13** after cellular uptake in MCF-7 (top) or HT-29 cells (bottom). Cells were incubated for 30 min at 37 °C with a 20 μM (MCF-7) or 50 μM (HT-29) concentration of conjugate **13** and stained either with MitoTracker Red FM and LysoTracker Red DND-99 conjugates, respectively. Nuclei are stained with Hoechst 33342.

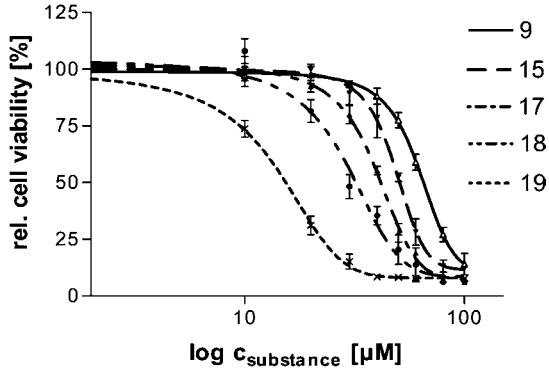


Figure 5. Representative IC_{50}curves after incubating MCF-7 cells with compounds **9**, **15**, **17**, **18**, and **19**. Conjugate **19** turned out to exhibit very promising effects on MCF-7 cells with an IC_{50} value of about 15.2 ± 1.8 μM. Data are normalized to untreated cells (100% viability).

Nalm-6 cells was even higher than in the nonresistant cells Nalm-6 (Figure 6E) at least for low concentrations. The Nalm-6/VCR cells treated with **19** were also strongly affected but less than the nonresistant cells (Figure 6F).

DISCUSSION

During the past years, there has been increasing attention on the combination of peptides with metal complexes (*47*−*51*). On the one hand, the metal ion may have a structural role in bringing together discrete elements of peptide secondary structure. On the other hand, it may also serve a functional role, for example in the biological activity of the conjugate. Also, peptide attachment may support stability and solubility of the metal moiety and may act as a transport system for membrane translocation.

In recent works, we have identified cymantrene−peptide bioconjugates as promising lead structures. The cymantrene carboxylic acid **4** was attached to a cell-penetrating peptide derived from human calcitonin (*19*). Evaluation of the cytotoxic activity on MCF-7 cells gave an IC_{50} value of about 35 μM. Interestingly, we found out that coupling of the cymantrene moiety affected the cytosolic distribution of the cell-penetrating peptide. In comparison to the unmodified CPP, the metal complex−CPP construct was distributed throughout the cytosol and not in a vesicular distribution pattern. These findings prompted us to investigate the influence of other CPP sequences on the bioactivity of cymantrene−peptide conjugates. We chose the membrane-active sC18 peptide that we recently identified to be a very efficient CPP for several cell lines tested (*38*). Furthermore, the influence of the metal-to-peptide linker was studied by using a series of new cymantrene carboxylic acids prepared in our groups (*37*). Our aim was to elucidate (i) if another CPP would be affected in the same way concerning its cellular uptake and distribution, (ii) whether a different linker structure between the cymantrene moiety and the peptide would lead to different biological effects, and (iii) how it would be possible to increase the cytotoxicity and selectivity of the new metal−peptide conjugates.

The synthesis of all new conjugates was achieved by a method recently described (*37*). In this previous study, we found out that attachment of the metal complex leads to a nonstandard cleavage of the Rink amide linker during the cleavage procedure, resulting in peptide amides that were N-alkylated at the C-terminus. Depending on the type of cymantrene moiety attached, the formation of reactive carbocations was also facilitated, which result from decomposition of the resin linker and alkylate the metal complex moiety. However, cleavage mixtures for efficient elimination of this byproduct formation could be identified. Thus, synthesis of the new conjugates **13** to **19** was conducted using this improved cleavage protocol. All constructs were obtained in a purity of >95% and analyzed by mass spectrometry and analytical HPLC.

First, we explored the cellular uptake of substances **7** to **10** that were chosen as representatives by GF-AAS studies. Although the overall metal content was similar in both investigated cells, at least for all compounds studied we proved an increased manganese content pointing to successful intracellular uptake of the intact bioconjugates. Furthermore, the values are similar to recently reported results in HT-29 cells

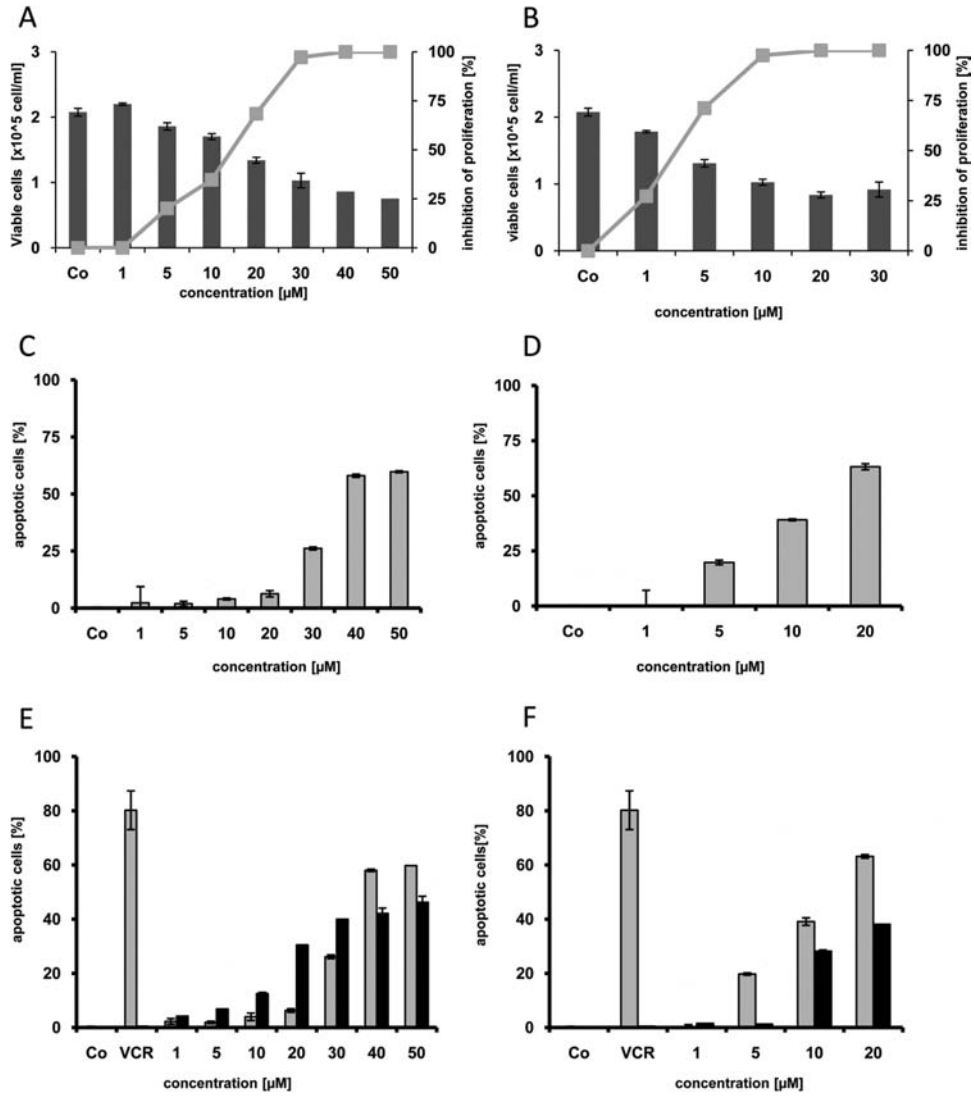


Figure 6. (A,B) Inhibition of proliferation: Nalm-6 cells were treated with different concentrations of **9** (A) or **19** (B). After 24 h of incubation, proliferation was measured using the casyCount System. Values are given as the percentage of the inhibition of cells proliferation ± SD ($n = 3$). (C,D) Apoptosis induction: Nalm-6 cells were treated with different concentrations of **9** (C) or **19** (D). After 72 h of incubation, DNA fragmentation was measured by cytometric analysis of cellular DNA content. Values are given as percentage of cells with hypodiploid DNA ± SD ($n = 3$). (E,F) Overcoming of vincristine resistance in Nalm-6 cells: wild type (gray bars) and vincristine resistant Nalm-6/VCR cells (black bars) were treated with different concentrations of **9** (E) or **19** (F) for 72 h. Then, DNA fragmentation was measured by flow cytometric analysis of cellular DNA content. Values are given as the percentage of cells with hypodiploid DNA ± SD ($n = 3$).

(*43*). Additionally, we conducted fluorescence microscopic studies with fluorescently labeled conjugates and could verify their cellular uptake. However, we could not observe any cytosolic distribution or any accumulation in the nucleus but a distribution in a vesicular pattern pointing to an endosomal uptake pathway. This observation differs from our recent investigation on the cellular uptake of an hCT-based cymantrene−peptide conjugate (*19*). One reason could be that the studies presented here were conducted in concentrations below the IC_{50} value of the cymantrene−sC18 conjugates, whereas the fluorescence microscopy experiments for the hCT-based cymantrene−peptide conjugate were examined close to the IC_{50} value of this compound.

The cytotoxic activity of compounds **7** to **12** was tested in MCF-7 and HT-29 cells. The MCF-7 cells were more sensitive toward the compounds, which is likely due to the more efficient internalization compared to the HT-29 cell line. IC_{50} values were in the range of 55 to 65 μM. Thus, the different metal complex-to-peptide linkers have no influence on the biological activity of the cymantrene−sC18 conjugates. The cytotoxicity could be increased when incorporating more than one cymantrene unit to the peptide, as in **14** to **16**, and IC_{50} values decreased to about 40 to 50 μM. Apparently, it is the amount of cymantrene shuttled into cells and not the peptide itself which is important for the biological activity. Recently, similar effects have been reported for a polymer−drug conjugate with a triple payload of paclitaxel (*52*). Moreover, the cytotoxicity of our compounds could be further increased by the introduction of an enzymatic cleavage site. Especially, the presence of the GFLG peptide sequence that is obviously more specifically recognized by cathepsin B leads to a significant decrease of the IC_{50} value to 15 μM in **19**, which incorporates two such Cym-GFLG building blocks.

The mechanism of action of our newly designed conjugates is unclear at present. However, the involvement of cymantrene tricarbonyl compounds themselves in pulmonary activation and toxicity has been described recently (*53*). Flow cytometric investigations with annexin V, fluorescein diacetate, and propidium iodide staining point to fast necrotic events, although early apoptotic events could also be observed when incubating MCF-7 cells in lower concentrations with compound **9**.

Additional fluorescence microscopic studies provided some more insight into the intracellular distribution of the metal−peptide

conjugates. It has been speculated that an interaction with mitochondria might be important since apoptotic proteins can affect mitochondrial activity. However, we did not observe any colocalization with the mitochondria. Rather, the peptides seem to end up in lysosomes after cellular uptake. This would be in good agreement with the high activity of compounds **18** and **19**, which contain an additional enzymatic cleavage site and are expected to be activated by the presence of cathepsin B in the lysosomes. However, one has to keep in mind that only the peptide or peptide fragments still having the carboxyfluorescein attached can be detected by fluorescence microscopy.

The high cytotoxic potential of compound **19** could be further confirmed by incubation with the human B-cell leukemia cell line Nalm-6, where it mediates strong proliferation inhibition and specific apoptosis. Interestingly, the effects to the vincristine resistant Nalm-6/VCR cell line were reduced compared to those of compound **9**. For the Nalm-6/VCR cells an overexpression of p-glycoprotein (P-GP) could be shown. P-GP is a plasma membrane protein that has been shown to pump substrates out of tumor cells through an ATP-dependent mechanism in a unidirectional fashion (*54*). Thus, the reduced effect of compound **19** is probably due to reduced intracellular drug concentration caused by the more efficient endosomal release of the cytotoxic drug into the cytoplasma.

All in all, these new organometallic peptide conjugates offer several advantages: first, the GFLG sequence allows for a targeted delivery approach to tumor cells overexpressing the cathepsin B protease. Second, our sC18-CPP is now firmly established as an efficient transporter for organometallic groups.

CONCLUSIONS

In summary, we have studied a series of cymantrene−peptide conjugates for their cytotoxic activity on human cancer cells and obtained insight into the details of their biological mode of action and intracellular distribution after uptake. New cymantrene−CPP conjugates bearing a protease-cleavable GFLG linker were prepared that also allowed attachment of two molecules of the metal complex. This strategy led to new metal complex−peptide conjugates with promising antitumor activity.

ACKNOWLEDGMENT

We thank K. Löbner for help in cell culture and R. Reppich-Sacher for help in MALDI and ESI mass spectrometry. This work was supported by the Deutsche Forschungsgemeinschaft (DFG) within the project FOR 630 “Biological function of organometallic compounds”. I.N. thanks Professor Dr. A. G. Beck-Sickinger (Leipzig) for generous access to all facilities of the institute.

LITERATURE CITED

(1) Storr, T., Thompson, K. H., and Orvig, C. (2006) Design of targeting ligands in medicinal inorganic chemistry. *Chem. Soc. Rev. 35*, 534–544.

(2) Lippert, B. (1999) *Cisplatin, Chemistry and Biochemistry of a Leading Anticancer Drug*, Wiley-VCH, Weinheim, Germany.

(3) Cossa, G., Gatti, L., Zunino, F., and Perego, P. (2009) Strategies to improve the efficacy of platinum compounds. *Curr. Med. Chem. 16*, 2355–2365.

(4) Farrell, N., Ha, T. T., Souchard, J. P., Wimmer, F. L., Cros, S., and Johnson, N. P. (1989) Cytostatic trans-platinum(II) complexes. *J. Med. Chem. 32*, 2240–2241.

(5) Jodrell, D. I., Evans, T. R., Steward, W., Cameron, D., Prendiville, J., Aschele, C., Noberasco, C., Lind, M., Carmichael, J., Dobbs, N., Camboni, G., Gatti, B., and De Braud, F. (2004) Phase II studies of BBR3464, a novel tri-nuclear platinum complex, in patients with gastric or gastro-oesophageal adenocarcinoma. *Eur. J. Cancer 40*, 1872–1877.

(6) Lovejoy, K. S., Todd, R. C., Zhang, S., McCormick, M. S., D’Aquino, J. A., Reardon, J. T., Sancar, A., Giacomini, K. M., and Lippard, S. J. (2008) cis-Diammine(pyridine)chloroplatinum(II), a monofunctional platinum(II) antitumor agent: Uptake, structure, function, and prospects. *Proc. Natl. Acad. Sci. U.S.A. 105*, 8902–8907.

(7) Hartinger, C. G., Zorbas-Seifried, S., Jakupec, M. A., Kynast, B., Zorbas, H., and Keppler, B. K. (2006) From bench to bedside--preclinical and early clinical development of the anticancer agent indazolium trans-[tetrachlorobis(1H-indazole)ruthenate(III)] (KP1019 or FFC14A). *J. Inorg. Biochem. 100*, 891–904.

(8) Alessio, E., Mestroni, G., Bergamo, A., and Sava, G. (2004) Ruthenium antimetastatic agents. *Curr. Top. Med. Chem. 4*, 1525–1535.

(9) Michard, Q., Jaouen, G., Vessieres, A., and Bernard, B. A. (2008) Evaluation of cytotoxic properties of organometallic ferrocifens on melanocytes, primary and metastatic melanoma cell lines. *J. Inorg. Biochem. 102*, 1980–1985.

(10) Hillard, E., Vessieres, A., Thouin, L., Jaouen, G., and Amatore, C. (2005) Ferrocene-mediated proton-coupled electron transfer in a series of ferrocifen-type breast-cancer drug candidates. *Angew. Chem., Int. Ed. 45*, 285–290.

(11) Franke, J. C., Plotz, M., Prokop, A., Geilen, C. C., Schmalz, H. G., and Eberle, J. (2010) New caspase-independent but ROS-dependent apoptosis pathways are targeted in melanoma cells by an iron-containing cytosine analogue. *Biochem. Pharmacol. 79*, 575–586.

(12) Dobroschke, M., Geldmacher, Y., Ott, I., Harlos, M., Kater, L., Wagner, L., Gust, R., Sheldrick, W. S., and Prokop, A. (2009) Cytotoxic rhodium(III) and iridium(III) polypyridyl complexes: structure-activity relationships, antileukemic activity, and apoptosis induction. *ChemMedChem 4*, 177–187.

(13) Bieda, R., Ott, I., Dobroschke, M., Prokop, A., Gust, R., and Sheldrick, W. S. (2009) Structure-activity relationships and DNA binding properties of apoptosis inducing cytotoxic rhodium(III) polypyridyl complexes containing the cyclic thioether [9]aneS(3). *J. Inorg. Biochem. 103*, 698–708.

(14) Harlos, M., Ott, I., Gust, R., Alborzinia, H., Wolfl, S., Kromm, A., and Sheldrick, W. S. (2008) Synthesis, biological activity, and structure-activity relationships for potent cytotoxic rhodium(III) polypyridyl complexes. *J. Med. Chem. 51*, 3924–3933.

(15) Guo, M., Guo, Z., and Sadler, P. J. (2001) Titanium(IV) targets phosphoesters on nucleotides: implications for the mechanism of action of the anticancer drug titanocene dichloride. *J. Biol. Inorg. Chem. 6*, 698–707.

(16) Tshuva, E. Y., and Peri, D. (2009) Modern cytotoxic titanium(IV) complexes; Insights on the enigmatic involvement of hydrolysis. *Coord. Chem. Rev. 253*, 2098–2115.

(17) Ott, I., Kircher, B., Bagowski, C. P., Vlecken, D. H., Ott, E. B., Will, J., Bensdorf, K., Sheldrick, W. S., and Gust, R. (2009) Modulation of the biological properties of aspirin by formation of a bioorganometallic derivative. *Angew. Chem., Int. Ed. 48*, 1160–1163.

(18) Noor, F., Kinscherf, R., Bonaterra, G. A., Walczak, S., Wolfl, S., and Metzler-Nolte, N. (2009) Enhanced cellular uptake and cytotoxicity studies of organometallic bioconjugates of the NLS peptide in Hep G2 cells. *ChemBioChem 10*, 493–502.

(19) Neundorf, I., Hoyer, J., Splith, K., Rennert, R., Peindy N’dongo, H W., and Schatzschneider, U. (2008) Cymantrene conjugation modulates the intracellular distribution and induces high cytotoxicity of a cell-penetrating peptide. *Chem. Commun.* 5604–5606.

(20) Joliot, A., and Prochiantz, A. (2004) Transduction peptides: from technology to physiology. *Nat. Cell Biol. 6*, 189–196.

(21) Pujals, S., Fernandez-Carneado, J., Lopez-Iglesias, C., Kogan, M. J., and Giralt, E. (2006) Mechanistic aspects of CPP-mediated intracellular drug delivery: relevance of CPP self-assembly. *Biochim. Biophys. Acta 1758*, 264–279.

(22) Chari, R. V. (2008) Targeted cancer therapy: conferring specificity to cytotoxic drugs. *Acc. Chem. Res. 41*, 98–107.

(23) Reddy, L. H. (2005) Drug delivery to tumours: recent strategies. *J. Pharm. Pharmacol. 57*, 1231–1242.

(24) Law, B., and Tung, C. H. (2009) Proteolysis: a biological process adapted in drug delivery, therapy, and imaging. *Bioconjugate Chem. 20*, 1683–1695.

(25) Kratz, F., Muller, I. A., Ryppa, C., and Warnecke, A. (2008) Prodrug strategies in anticancer chemotherapy. *ChemMedChem 3*, 20–53.

(26) Weissleder, R., Tung, C. H., Mahmood, U., and Bogdanov, A., Jr. (1999) In vivo imaging of tumors with protease-activated near-infrared fluorescent probes. *Nat. Biotechnol. 17*, 375–378.

(27) Funovics, M., Weissleder, R., and Tung, C. H. (2003) Protease sensors for bioimaging. *Anal. Bioanal. Chem. 377*, 956–963.

(28) Jiang, T., Olson, E. S., Nguyen, Q. T., Roy, M., Jennings, P. A., and Tsien, R. Y. (2004) Tumor imaging by means of proteolytic activation of cell-penetrating peptides. *Proc. Natl. Acad. Sci. U.S.A. 101*, 17867–17872.

(29) Foekens, J. A., Kos, J., Peters, H. A., Krasovec, M., Look, M. P., Cimerman, N., Meijer-van Gelder, M. E., Henzen-Logmans, S. C., van Putten, W. L., and Klijn, J. G. (1998) Prognostic significance of cathepsins B and L in primary human breast cancer. *J. Clin. Oncol. 16*, 1013–1021.

(30) Strojnik, T., Kos, J., Zidanik, B., Golouh, R., and Lah, T. (1999) Cathepsin B immunohistochemical staining in tumor and endothelial cells is a new prognostic factor for survival in patients with brain tumors. *Clin. Cancer Res. 5*, 559–567.

(31) Miller, K., Erez, R., Segal, E., Shabat, D., and Satchi-Fainaro, R. (2009) Targeting bone metastases with a bispecific anticancer and antiangiogenic polymer-alendronate-taxane conjugate. *Angew. Chem., Int. Ed. 48*, 2949–2954.

(32) van Staveren, D. R., and Metzler-Nolte, N. (2004) Bioorganometallic chemistry of ferrocene. *Chem. Rev. 104*, 5931–5985.

(33) Husken, N., Gasser, G., Koster, S. D., and Metzler-Nolte, N. (2009) ″Four-potential″ ferrocene labeling of PNA oligomers via click chemistry. *Bioconjugate Chem. 20*, 1578–1586.

(34) Hromadova, M., Salmain, M., Fischer-Durand, N., Pospisil, L., and Jaouen, G. (2006) Electrochemical microbead-based immunoassay using an (eta5-cyclopentadienyl)tricarbonyl-manganese redox marker bound to bovine serum albumin. *Langmuir 22*, 506–511.

(35) I Lavastre, J. B., Brossier, P., and Moise, C. (1990) The synthesis of metallocene-labelled drugs for biological assays. *Appl. Organomet. Chem. 4*, 9–17.

(36) Salmain, M., Fischer-Durand, N., Cavalier, L., Rudolf, B., Zakrzewski, J., and Jaouen, G. (2002) Transition metal-carbonyl labeling of biotin and avidin for use in solid-phase carbonyl metallo immunoassay (CMIA). *Bioconjugate Chem. 13*, 693–698.

(37) Splith, K., Neundorf, I., Hu, W., N'Dongo, H., Vasylyeva, V., Merz, K., and Schatzschneider, U. (2010) Influence of the metal complex-to-peptide linker on the synthesis and properties of bioactive CpMn(CO)3 peptide conjugates. *Dalton Trans. 39*, 2536–2545.

(38) Neundorf, I., Rennert, R., Hoyer, J., Schramm, F., Löbner, K., Kitanovic, I., and Wölfl, S. (2009) Fusion of a short HA2-derived peptide sequence to cell-penetrating peptides improves cytosolic uptake, but enhances cytotoxic activity. *Pharmaceuticals 2*, 49–65.

(39) Niesel, J., Pinto, A., Peindy N'Dongo, H. W., Merz, K., Ott, I., Gust, R., and Schatzschneider, U. (2008) Photoinduced CO release, cellular uptake and cytotoxicity of a tris(pyrazolyl) -methane (tpm) manganese tricarbonyl complex. *Chem. Commun.* 1798–1800.

(40) Gust, R., Schnurr, B., Krauser, R., Bernhardt, G., Koch, M., Schmid, B., Hummel, E., and Schonenberger, H. (1998) Stability and cellular studies of [rac-1,2-bis(4-fluorophenyl)-ethylenediamine][cyclobutane-1,1- dicarboxylato]platinum(II), a novel, highly active carboplatin derivative. *J. Cancer Res. Clin. Oncol. 124*, 585–597.

(41) Ott, I., Scheffler, H., and Gust, R. (2007) Development of a method for the quantification of the molar gold concentration in tumour cells exposed to gold-containing drugs. *ChemMedChem 2*, 702–707.

(42) Kirin, S. I., Ott, I., Gust, R., Mier, W., Weyhermuller, T., and Metzler-Nolte, N. (2008) Cellular uptake quantification of metalated peptide and peptide nucleic acid bioconjugates by atomic absorption spectroscopy. *Angew. Chem., Int. Ed. 47*, 955–959.

(43) Peindy N'dongo, H. W., Ott, I., Gust, R., and Schatzschneider, U. (2009) Microwave-assisted solid-phase synthesis, cellular uptake, and cytotoxicity studies of cymantrene−peptide bioconjugates. *J. Organomet. Chem. 694*, 823–827.

(44) Vermes, I., Haanen, C., Steffens-Nakken, H., and Reutelingsperger, C. (1995) A novel assay for apoptosis. Flow cytometric detection of phosphatidylserine expression on early apoptotic cells using fluorescein labelled Annexin V. *J. Immunol. Methods 184*, 39–51.

(45) Chipman, S. D., Oldham, F. B., Pezzoni, G., and Singer, J. W. (2006) Biological and clinical characterization of paclitaxel poliglumex (PPX, CT-2103), a macromolecular polymer-drug conjugate. *Int. J. Nanomedicine 1*, 375–383.

(46) Lutgens, S. P., Cleutjens, K. B., Daemen, M. J., and Heeneman, S. (2007) Cathepsin cysteine proteases in cardiovascular disease. *FASEB J. 21*, 3029–3041.

(47) Sardesai, N. Y., Lin, S. C., Zimmerman, K., and Barton, J. K. (1995) Construction of coordinatively saturated rhodium complexes containing appended peptides. *Bioconjugate Chem. 6*, 302–312.

(48) Pinto, A., Hoffmanns, U., Ott, M., Fricker, G., and Metzler-Nolte, N. (2009) Modification with organometallic compounds improves crossing of the blood-brain barrier of [Leu5]-enkephalin derivatives in an in vitro model system. *ChemBioChem 10*, 1852–1860.

(49) Noor, F., Wustholz, A., Kinscherf, R., and Metzler-Nolte, N. (2005) A cobaltocenium-peptide bioconjugate shows enhanced cellular uptake and directed nuclear delivery. *Angew. Chem., Int. Ed. 44*, 2429–2432.

(50) Miklan, Z., Szabo, R., Zsoldos-Mady, V., Remenyi, J., Banoczi, Z., and Hudecz, F. (2007) New ferrocene containing peptide conjugates: synthesis and effect on human leukemia (HL-60) cells. *Biopolymers 88*, 108–114.

(51) Cosgrave, L., Devocelle, M., Forster, R. J., and Keyes, T. E. (2010) Multimodal cell imaging by ruthenium polypyridyl labelled cell penetrating peptides. *Chem. Commun. 46*, 103–105.

(52) Erez, R., Segal, E., Miller, K., Satchi-Fainaro, R., and Shabat, D. (2009) Enhanced cytotoxicity of a polymer-drug conjugate with triple payload of paclitaxel. *Bioorg. Med. Chem. 17*, 4327–4335.

(53) Blanchard, K. T., Clay, R. J., and Morris, J. B. (1996) Pulmonary activation and toxicity of cyclopentadienyl manganese tricarbonyl. *Toxicol. Appl. Pharmacol. 136*, 280–288.

(54) Krishna, R., and Mayer, L. D. (2000) Multidrug resistance (MDR) in cancer. Mechanisms, reversal using modulators of MDR and the role of MDR modulators in influencing the pharmacokinetics of anticancer drugs. *Eur. J. Pharm. Sci. 11*, 265–283.

BC100089Z

Optical Imaging of Bacterial Infection in Living Mice Using Deep-Red Fluorescent Squaraine Rotaxane Probes

Alexander G. White, Na Fu, W. Matthew Leevy, Jung-Jae Lee, Michael A. Blasco, and Bradley D. Smith*

Department of Chemistry and Biochemistry and the Notre Dame Integrated Imaging Facility, 236 Nieuwland Science Hall, University of Notre Dame, Notre Dame, Indiana 46556. Received February 21, 2010; Revised Manuscript Received April 26, 2010

Two structurally related fluorescent imaging probes allow optical imaging of bacterial leg infection models in living athymic and immunocompetent mice. Structurally, the probes are comprised of a deep-red fluorescent squaraine rotaxane scaffold with two appended bis(zinc(II)-dicolylamine) (bis(Zn-DPA)) targeting ligands. The bis(Zn-DPA) ligands have high affinity for the anionic phospholipids and related biomolecules that reside within the bacterial envelope, and they are known to selectively target bacterial cells over the nearly uncharged membrane surfaces of healthy mammalian cells. Planar, whole-animal optical imaging studies showed that intravenous dosing of either probe (10 nmol) allowed imaging of localized infections of Gram-positive *Staphylococcus aureus* and Gram-negative *Salmonella enterica* serovar typhimurium. High selectivity for the infected target leg (T) over the contralateral nontarget leg (NT) was reflected by T/NT ratios up to six. The infection imaging signal was independent of mouse humoral immune status, and there was essentially no targeting at a site of sterile inflammation induced by injection of λ-carrageenan. Furthermore, the fluorescent probe imaging signal colocalized with the bioluminescence signal from a genetically engineered strain of *S. enterica* serovar typhimurium. Although not highly sensitive (the localized infection must contain at least $\sim 10^6$ colony forming units for fluorescence visualization), the probes are remarkably selective for bacterial cells considering their low molecular weight (<1.5 kDa) and simple structural design. The more hydrophilic of the two probes produced a higher T/NT ratio in the early stages of the imaging experiment and washed out more rapidly from the blood clearance organs (liver, kidney). Therefore, it is best suited for longitudinal studies that require repeated dosing and imaging of the same animal. The results indicate that fluorescent probes based on squaraine rotaxanes should be broadly useful for in vivo animal imaging studies, and they further validate the ability of imaging probes with bis(Zn-DPA) ligands to selectively target bacterial infections in living animals.

INTRODUCTION

Optical imaging continues to undergo major advances that produce landmark contributions to biomedical science (*1*−*4*). Concurrent with technical improvements in the design and operation of fluorescence microscopes and whole-animal imaging stations, there is an ongoing effort to develop new types of fluorescent molecular probes (*5, 6*). Organic fluorophores are the most common components in the bioimaging probe toolbox; however, they are well-known for performance drawbacks like photobleaching, self-quenching, and chemical decomposition (*7*). These problems are especially prevalent with organic probes with excitation/emission wavelengths in the deep-red and near-infrared, a wavelength region that is preferred for biological imaging because there is maximal light penetration through skin and tissue with minimal scattering (*8*). Of the few available deep-red and near-infrared fluorophores, the most popular are the carbocyanine dyes (*9*). In addition to the photochemical drawbacks listed above, the photophysical properties of long-wavelength carbocyanine dyes are known to vary with solvent polarity and the presence of blood serum proteins (*10*). Together, these problems make it difficult to develop methods for quantitative whole-animal optical imaging. The need for new families of deep-red and near-infrared organic fluorophores is reflected by the ongoing international effort to prepare and evaluate new structural classes (*11*).

Our research group has invented a novel family of deep-red fluorescent dyes called squaraine rotaxanes (*12*−*20*). Squaraines were discovered almost fifty years ago and they exhibit narrow and intense absorption/emission bands. Squaraine dyes and their conjugates have been prepared and evaluated for various types of in vitro imaging applications (*21*−*23*); however, to the best of our knowledge they have never been reported for in vivo imaging in living animals. The most likely reason for this absence is their inherent chemical reactivity. The central squaraine ring is electrophilic and susceptible to attack by biological nucleophiles; thus, unprotected squaraine dyes are susceptible to decomposition during in vivo imaging. Squaraine rotaxanes circumvent this stability problem by encapsulating the squaraine fluorophore inside a protective macrocycle. We have demonstrated that squaraine rotaxanes are chemically and photochemically stable and very useful for many types of in vitro cell culture imaging applications (*12*−*20*). Two examples are the squaraine rotaxane probes **1** (*19*) and **2** (*24*) in Figure 1. They both contain the same squaraine fluorophore with conjugated bis(zinc(II)-dicolylamine) (bis(Zn-DPA)) targeting ligands at each end. The bis(Zn-DPA) ligands have high affinity for anionic cell membranes, and they are known to selectively target bacterial cells over the nearly uncharged membrane surfaces of healthy mammalian cells (*19, 25*−*27*). The bis(Zn-DPA) ligands associate with the anionic phospholipids and related amphiphilic structures that reside within the bacterial envelope (*28, 29*). Preliminary fluorescence microscopy studies of probes **1** and **2** have shown that they stain both Gram-positive and Gram-negative bacteria without inducing an antibiotic effect. The probes are extremely photostable and permit real-time imaging studies of live cell process like bacterial fission. The difference between probes **1** and **2** is the structure of the surrounding macrocycle. The macrocycle in probe **1** has two

* smith.115@nd.edu, ph: +1 (574) 631 8632, fax: +1 (574) 631 6652.

10.1021/bc1000998 © 2010 American Chemical Society
Published on Web 06/10/2010

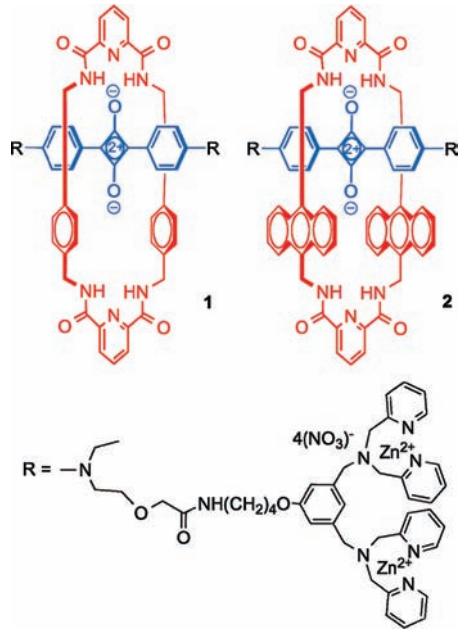


Figure 1. Chemical structures of fluorescent probes.

phenylene units that hardly effect the photophysical properties of the encapsulated squaraine fluorophore, such that probe **1** exhibits excitation/emission wavelengths of 653/675 nm that match the common Cy5 filter set on microscopes and imaging stations. The macrocycle in probe **2** has two anthrylene units that lead to red-shifted excitation/emission of 664/709 nm that match the Cy5.5 filter set.

In this current study, we report that probes **1** and **2** can be used to optically image bacterial infection and that they do not respond to sterile inflammation in living mice. We find that the more hydrophilic probe **1** produces a higher ratio of target to nontarget signals in the early stages of the imaging experiment and appears to be the better infection imaging probe for longitudinal studies that require rapid probe wash out and repeated imaging of the same animal. Our results indicate that fluorescent probes based on squaraine rotaxanes should be broadly useful for in vivo animal imaging studies, and they further validate the ability of imaging probes with bis(Zn-DPA) ligands to selectively target bacterial infections in living animals.

EXPERIMENTAL PROCEDURES

Materials. The probes **1** (5 μM in water, ex: 653 nm, em: 675 nm, log ε 5.1, quantum yield 0.20 in water) and **2** (5 μM in water, ex: 664 nm, em: 709 nm, log ε 5.3, quantum yield 0.22) were prepared as previously reported (*19, 24*). These previous reports also include the excitation and emission spectra. Luria−Bertani (LB) broth purchased from BD Medical Supplies (Sparks, MD). Kanamycin, λ-carrageenan, and ATP were purchased from Sigma (St. Louis, MO). Isoflurane was purchased from Butler Animal Health Supply (Dublin, OH). Animals were purchased from Taconic Farms, Inc. (Hudson, NY). *Salmonella enterica* serovar typhimurium FL6 and AM3 were gifts from the laboratory of Professor David Piwnica-Worms (Washington University, School of Medicine, St. Louis, MO) (*30*).

In Vitro Fluorescence Microscopy. Fluorescence microscopy was conducted on a Nikon Eclipse TE-2000 U epifluorescence microscope equipped with Cy5 (exciter: HQ620/60X, dichroic: 660LP, emitter: HQ700/75 m) filter. Images were acquired using *Metamorph* software (v 6.2 Molecular Devices, Sunnyvale, CA) and a Photometrics 512 B black and white digital camera (1500×) at 100 ms acquisition time. The data was processed with *ImageJ* v 1.42q software (available for free download at http://rsb.info.nih.gov/ij) as previously described (*26*).

In Vitro Cell Staining. *S. enterica* serovar typhimurium AM3 was cultured in LB broth containing 30 μg/mL kanamycin after transfer from a preserved agar plate stored at 4 °C. *Staphylococcus aureus* NRS11, *Escherichia coli* K12, *Escherichia coli* UTI89, *Klebsiella pneumoniae* (ATCC #33495), *Proteus vulgaris* (ATCC #49132), and *Pseudomonas aeruginosa* (ATCC #27853) were cultured in LB broth containing no antibiotic after transfer from a preserved agar plate stored at 4 °C. Cells were allowed to grow overnight by incubating at 37 °C and a shaker speed of 200 rpm. *Salmonella* cells were centrifuged at 10 000 rpm for 5 min, while all other bacterial strains were centrifuged at 5000 rpm for 5 min. Growth media were removed, and the cells resuspended in 5 mM TES buffer (145 mM NaCl buffer, pH 7.4). Separate samples of 10^8 colony forming units (CFU) were treated with 10 nmol of probe **1** or **2**, and the mixture was incubated in the dark for 15 min at room temperature. After centrifugation at the above speeds for 5 min, the media were discarded and the pellet resuspended in 5 mM TES buffer with vortexing. The stained cells were rinsed with TES buffer by repeating the centrifugation/resuspension cycle.

ATP inhibition of cell staining by probe **1** was performed by adding specific volumes of ATP from a stock solution prior to incubating bacteria and probe for 15 min. Region-of-interest (ROI) analysis using *ImageJ* software produced average pixel intensity for an individual cell. The fluorescence intensities in the bottom of Figure 3 are the average of twenty random bacterial cells in each staining sample.

Minimum inhibitory concentration for probes **1** and **2** against the Gram-positive *S. aureus* NRS11 and Gram-negative *E. coli* UTI89 were determined using a previously described procedure (*28*).

Animal Preparation. All animal care and procedures were approved by the Notre Dame Institutional Advisory Committee of Animal Care. All animals were anesthetized using 2−3% v/v isoflurane before infection, probe injection, and imaging. Anesthesia during imaging was maintained at 1.5−2% v/v isoflurane. Athymic nude mice (strain NCr Foxn1^{nu}) required no additional preparation before imaging. Immunocompetent mice (strain ICr) were anesthetized, and hair was removed from the lower quarter of the body by clippers followed by depilatory cream.

In Vivo Leg Infection/Inflammation Model. An aliquot of *Staphylococcus aureus* NRS11 (~10^8 CFU) in 50 μL of LB growth media was injected into the muscles that overlay the tibia bone in a posterior leg of an athymic or immunocompetent mouse. This anatomical location is not the thigh, which is closer to the body of the mouse. The same location on the contralateral leg was injected with 50 μL of LB media as a vehicle control. For inflammation response, immunocompetent ICr mice were injected with 50 μL of 1% λ-carrageenan solution into the left posterior leg muscle and injected with 50 μL of a sterile saline solution in the right posterior leg muscle. The mice were then allowed to recover for 6 h before intravenous injection with fluorescent probe via the tail vein. A complete probe toxicity study was not conducted, but both the athymic and immunocompetent mice easily tolerated the single doses (10 nmol) of probes **1** or **2** as judged by their continued grooming and nesting activities.

In Vivo Planar Imaging. Fluorescence dorsal images were acquired using a Xenogen IVIS Lumina (Caliper Life Sciences, Alameda, CA) for 5 s (ex 640 ± 25, em 732 ± 37 nm, binning 2 × 2, f/stop 2, field-of-view 125 mm). IVIS Lumina imaging was controlled by *Living Image* software (v 3.0) and employed 16-bit TIFF format files. Fluorescence ventral images were

acquired using a Kodak Multispectral In Vivo Imaging System FX Pro (Carestream Health, New Haven, CT) for 30 s (ex 630 ± 10 nm, em 700 ± 17.5 nm, no binning, f/stop 2.51, focal plane 11.2 mm, field-of-view 160 mm). Kodak multispectral imaging was controlled by *Carestream Molecular Imaging Software* (v 5.0.2.30). Image files were saved as BIP format and converted to 16-bit TIFF format. X-ray acquisition used a 120 s exposure (no binning, f/stop 2.5, focal plane 12.31 mm, field-of-view 160 mm).

S. enterica serovar typhimurium FL6 is a genetically engineered strain with the *lux*CDABE genes from *Photorhabdus luminescens*, which expresses bacterial luciferase and the enzymes for production of its substrate, decanal. The cells continuously emit light, and in vivo bioluminescence images were acquired for 3 min (open filter, 16 × 16 binning, f/stop 2.51, field-of-view 160 mm).

In Vivo Image Processing. The 16-bit TIFF images were sequentially opened using the *ImageJ* software and then converted to an image stack using the "convert images to stack" software command. The stack of images was background subtracted using the rolling ball algorithm (radius 500 pixels). Next, the image stack was set to the "Fire" fluorescence intensity scale (under "Lookup Tables" menu) which color-codes the fluorescence counts contained in each pixel. The stack of images was converted into a montage using the "convert stack to montage" command. A calibration bar was added to the montage using the "calibration bar" command, and the resulting RGB image saved as a TIFF file. ROI analysis was performed by selecting a free-hand ROI from the *ImageJ* tool bar and circling the appropriate anatomical location of each mouse. The average pixel intensity of the target (T), nontarget (NT), and whole animal was measured, and statistical analysis of the cohort produced an average ratio for T/NT with a standard error of the mean.

Biodistribution Analysis. After imaging studies, the mice were anesthetized by isoflurane inhalation (2−3%) and euthanized by cervical dislocation. The major organs were dissected, placed on low reflectance paper, and imaged as described above. The biodistribution image was analyzed in *ImageJ* by first subtracting the background using the rolling ball method (radius 500 pixels). Free-hand ROIs were drawn around each organ, and average intensity values were measured. Statistical analysis of the cohort produced an average pixel intensity relative to the uninfected leg for each organ with a standard error of the mean. Each excised organ attenuates probe signal intensity to a slightly different degree, depending on tissue thickness and pigmentation. Therefore, the biodistribution analysis focused on a comparison of the average intensities for probe **1** and **2** in each organ and assumed that they suffer equal amounts of signal attenuation.

RESULTS

In Vitro Studies. The generality of probe targeting for various bacterial genera was tested by conducting in vitro microscopy experiments using probe **1** and cultures of planktonic *S. aureus*, *E. coli*, *S. enterica* serovar typhimurium AM3, *P. aeruginosa*, *K. pneumoniae*, and *P. vulgaris*. In each case, separate samples of ~10^8 CFU were treated for 15 min with probe **1** (10 μM) in TES, a nonphosphate buffer, which does not inhibit probe binding to the bacteria. After probe treatment, the bacterial cells were rinsed twice to ensure high-contrast microscopy images. As expected, strong fluorescence staining of all genera was observed, although staining of the Gram-negative strains was typically less intense, indicating some steric protection by the second, outer membrane. Shown in Figure 2 are typical images obtained with Gram-positive *S. aureus* NRS11 and Gram-negative *S. enterica* serovar typhimurium AM3 using a standard, deep-red Cy5 filter set. In agreement with previous studies of fluorescent bis(Zn-DPA) probes, the fluorescence emission is localized in the bacterial envelope. Each image shows examples of bacterial cells captured in the process of cell division with bright fluorescence indicating a septum across circular *S. aureus* and a pinched equator for dividing *Salmonella*.

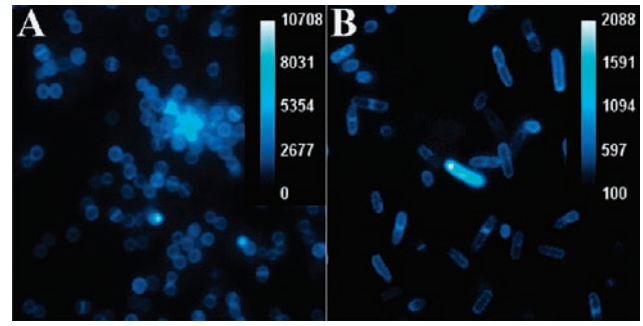


Figure 2. Epifluorescence microscopy of planktonic *S. aureus* NRS11 (panel A) and *S. enterica* serovar typhimurium AM3 (panel B) after incubation of ~10^8 CFU with probe **1** (10 μM). Images viewed at 1500× magnification and show pixel intensity with scale bar in arbitrary units.

Bis(Zn-DPA) probes are well-known to associate with polyphosphorylated biomolecules and anionic vesicle membranes (*31*), and the most likely explanation for bacterial staining is coordination of the zinc(II) cations with the phospholipids and phosphorylated amphiphiles in the bacterial envelope. The structural complexity and multifarious components of the bacterial envelope makes it quite challenging to unambiguously prove the cell association mechanism. Imaging studies using the apo-ligands (that is, probe **1** or **2** without the zinc(II) cations) are not possible, since they are not soluble in water. Indirect evidence that the bacterial staining is due to association of the bis(Zn-DPA) units with phosphorylated sites in the bacterial envelope was gained by conducting staining inhibition studies with probe **1**. The triphosphate unit in ATP is known to have a strong affinity for bis(Zn-DPA) ligands (*32*), and as shown in Figure 3, the addition of ATP inhibits, in a dose-dependent manner, the staining of *S. aureus* NRS11 or *E. coli* K12 cells by probe **1**.

Measurements of minimum inhibitory concentrations showed that probes **1** and **2** do not halt the growth of Gram-positive *S. aureus* NRS11 until the probe concentration is 60 μg/mL and they are even less active against Gram-negative *E. coli* UTI89. This agrees with previous studies indicating that imaging probes with bis(Zn-DPA) ligands have a very weak antibiotic effect (*27*).

Imaging Leg Infection Model in Athymic Mice. *Comparison of Probes* **1** *and* **2** *to Image S. aureus Infection.* The in vivo imaging performances of probes **1** and **2** were compared under the same conditions in a leg infection model using two different planar optical imaging stations. Separate cohorts of athymic nude mice were infected by intramuscular injection of ~10^8 CFU of *S. aureus* NRS11 into the left posterior leg, and as a control, the same volume (50 μL) of sterile growth media was injected into the contralateral leg. Six hours after inoculation, the anesthetized mice were given intravenous doses of imaging probes **1** or **2** (10 nmol) and then imaged periodically by illuminating with deep-red light and capturing the resulting fluorescence using a CCD camera. Shown in Figure 4 are typical whole-animal planar fluorescence images (false colored to show average pixel intensity) of two infected mice at 0, 3, and 12 h after the probe dosage. The probes exhibit quite different pharmacokinetics. With probe **1**, the average pixel intensity at the infection site increased rapidly over the first three hours. The appearance was sufficiently fast that it could be followed

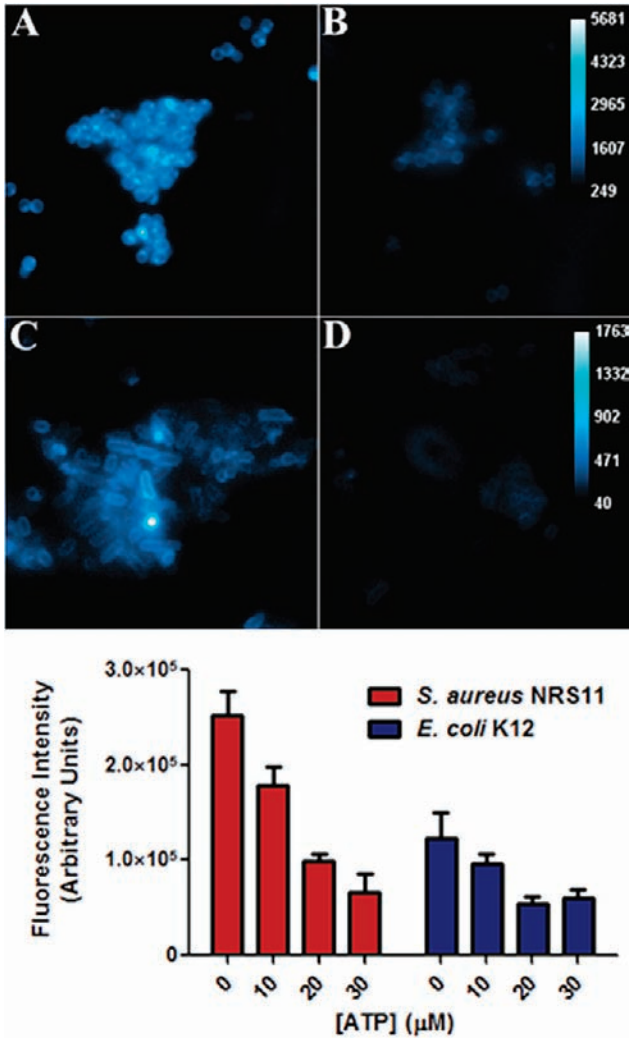


Figure 3. (top) Fluorescence micrographs showing intensity of probe **1** (10 μM) staining of *S. aureus* NRS11 in the absence (panel A) and presence of 30 μM ATP (panel B), and intensity of *E. coli* K12 staining in the absence (panel C) and presence of 30 μM ATP (panel D). (bottom) Change in probe **1** staining intensity of bacteria as a function of added ATP.

in real time while the mouse remained under anesthesia. The Supporting Information contains a movie showing a typical change in whole-animal fluorescence pixel intensity over the first three hours with probe **1**.

The mouse imaging data was analyzed by region-of-interest (ROI) methods that calculated the ratio of pixel intensities for the infected target leg (T) over the contralateral nontarget leg (NT). The intensity scales for different mice cannot be directly compared, however; T/NT ratios account for the differences in intrinsic brightness and allow a comparison of probe signal clearance. At three hours after probe injection, the T/NT ratio for probe **1** was close to six and significantly higher than the value of four for probe **2** (Figure 5a); however, at 21 h postinjection the T/NT ratios for both probes were about the same. Shown in Figure 5b are plots of the change in average pixel intensity at the infection site and for the whole animal. These plots show that signal contrast at the infection site develops in two different probe-dependent ways. With probe **1**, there is a rapid and large absolute increase in pixel intensity at the infection site, with a concomitant slower rate of clearance from the entire animal. With probe **2**, there is little intensity change at the infection site, with signal contrast developing, because probe clearance from the rest of the animal is faster than from the site of infection.

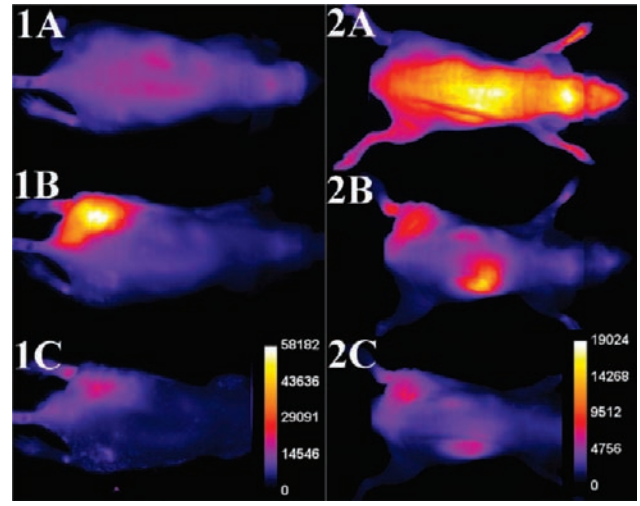


Figure 4. Typical infection imaging montages. Nude, athymic mice were injected with *S. aureus* (~10^8 CFU) in LB broth (50 μL) in the left leg and sterile LB broth (50 μL) in the right leg. Six hours later, 10 nmol of probe **1** (series 1) or probe **2** (series 2) was injected via the tail vein, and whole-animal dorsal images were acquired at (A) 0, (B) 3, and (C) 12 h after probe dosage. The intensity scale bars (a.u.) apply to all images in each series.

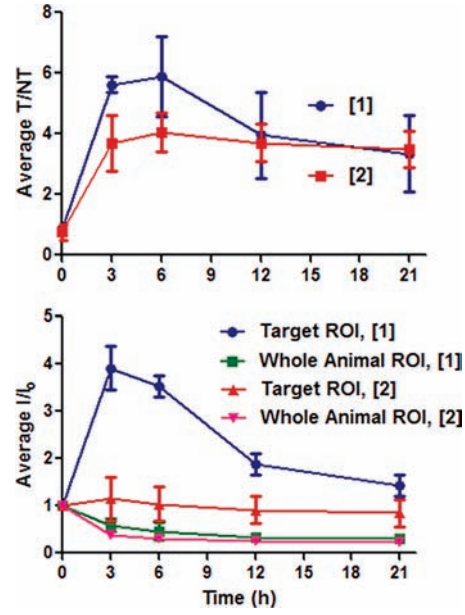


Figure 5. Region-of-interest analysis of nude mouse infected with *S. aureus* and treated with probes **1** or **2**. (top) Ratio of signals for infected target leg (T) to uninfected nontarget leg (NT). (bottom) Change in intensity for infected target leg and whole animal. Error bars reflect the standard error of the mean. $N = 4$ for probe **1**; $N = 3$ for probe **2**.

Imaging Bioluminescent S. enterica Serovar Typhimurium Infection. The ability of probe **1** to target Gram-negative bacterial infection in athymic mice was evaluated using a bioluminescent strain of *Salmonella*. A cohort of mice were injected with ~10^8 CFU of *S. enterica* serovar typhimurium (strain FL6) in the left leg followed by treatment with 10 nmol of probe **1** via the tail vein six hours later. *S. typhimurium* FL6 is genetically engineered to express bacterial luciferase and its substrate, thus allowing continuous light production. The goal was to determine how much the bacterial bioluminescence colocalized with the fluorescence signal from probe **1**. Shown in Figure 6A,B are overlaid images of the planar X-ray with the bioluminescence and fluorescence emissions, respectively. The images were acquired three hours after animal dosing with probe **1**, which in turn was delivered six hours after infection.

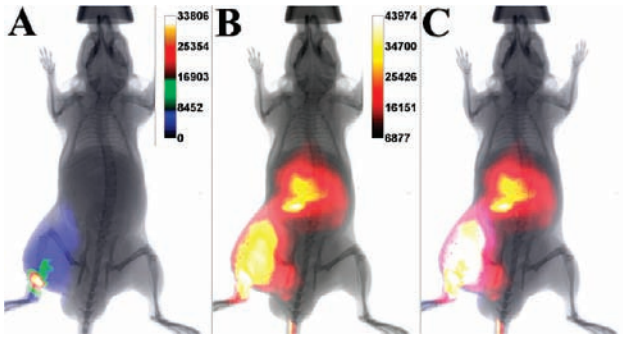


Figure 6. Typical optical imaging of athymic mouse containing a Gram-negative bacterial infection. Overlaid ventral images of planar X-ray and (A) bioluminescence intensity from genetically altered *S. enterica* serovar typhimurium FL6; (B) fluorescence intensity from molecular probe **1** at three hours after probe dosage; (C) bioluminescence and fluorescence intensities. $N = 3$.

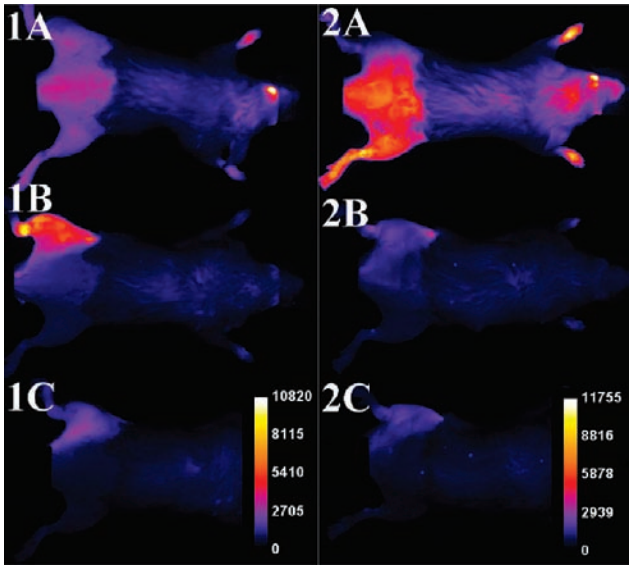


Figure 7. Typical infection imaging montages. Immunocompetent mice were injected with *S. aureus* ($\sim 10^8$ CFU) in LB broth (50 μL) in the left leg and sterile LB broth (50 μL) in the right leg. Six hours later, 10 nmol of probe **1** (series 1) or probe **2** (series 2) was injected via the tail vein, and whole-animal dorsal images were acquired at (A) 0, (B) 3, and (C) 12 h after probe dosage. The intensity scale bars (a.u.) apply to all images in each series. $N = 3$.

The bioluminescent signal is quite diffuse and indicates some migration of the bacteria away from the initial injection site. As shown in Figure 6C, which is an overlay of panels A and B, there is a considerable colocalization of the bioluminescence and fluorescence signals. As expected, there is also a strong fluorescence signal from the liver which is a major pathway for probe **1** clearance from the animal. Imaging did not continue beyond the three hour time point because the *Salmonella* bacteria were quite virulent, and the mice were euthanized.

Imaging Leg Infection in Immunocompetent Mice. *Comparison of Probes* **1** *and* **2** *to Image S. aureus Infection.* Separate cohorts of immunocompetent mice were inoculated by injection of *S. aureus* NRS11 ($\sim 10^8$ CFU) into the left posterior leg, and an equal volume (50 μL) of sterile growth media was injected as a control into the contralateral leg. Six hours later, the mice were given intravenous doses of imaging probes **1** or **2** (10 nmol). Shown in Figure 7 are whole-animal images of an infected mouse at 0, 3, and 12 h after the probe dosage. The imaging montages are quite similar to that obtained with the athymic mice. As shown in Figure 8, the T/NT ratio with probe **1** reached a maximum of six and then returned to a value of four, whereas the T/NT ratio with probe **2** steadily

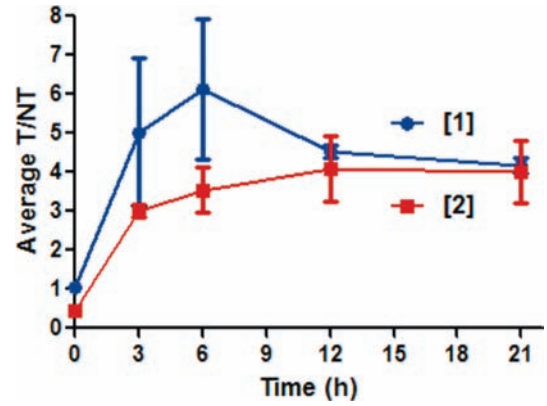


Figure 8. Region-of-interest analysis of immunocompetent mice infected with *S. aureus* and treated with probe **1** or **2**. (left) Ratio of signals for infected target leg (T) to uninfected nontarget leg (NT). Error bars are indicative of the standard error of the mean. $N = 3$ for both probes.

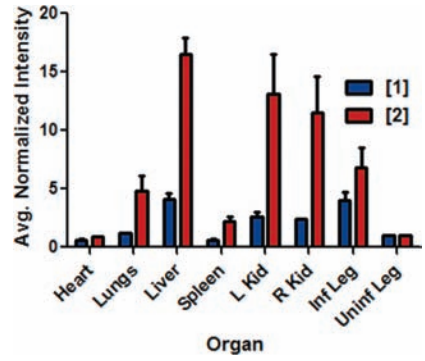


Figure 9. Bar graph comparing the fluorescence of organs harvested from ICr mice that were infected in the left posterior leg with *S. aureus* NRS11 and treated with probe **1** or probe **2**. The animals were sacrificed at 21 h after probe dosage. All data are normalized to the fluorescence of the uninfected posterior leg in each animal. Error bars reflect the standard error of the mean. $N = 3$ for each group.

rose to the same final value over the 21 h period. Compared to immunocompetent mice, athymic mice have an attenuated humoral immune system; however, both mice strains have innate immunity, which is the predominant host defense within the time frame of the experiment. This explains why there was no measurable difference between in vivo T/NT ratios (compare Figures 5 and 8).

After in vivo imaging was complete, the mice were euthanized and the excised organs were imaged to establish probe biodistribution. Shown in Figure 9 is a comparison of the probe fluorescence (average pixel intensity) from each organ, relative to the uninfected leg muscle which was set to a value of one. The bar graph shows that probe **2** was retained more strongly in all organs than the more hydrophilic probe **1**. There was more of probe **2** in the excised infected leg muscle than probe **1**, even though the in vivo T/NT ratios at the time point immediately before sacrifice were essentially equal. This suggests that more of probe **1** partitions into the extracellular fluid that surrounds the infection site and that this fluid is lost upon necropsy.

The in vivo detection limit using probe **1** for *S. aureus* infection in immunocompetent mice was determined by injecting serially diluted inoculations and keeping the probe dose (10 nmol) constant. Infections generated by injecting 10^6 CFU could be detected using the above whole-animal imaging protocol, whereas injections of 10^5 CFU could not (data not shown).

The ability of probe **1** to localize in a site of sterile inflammation was evaluated using a model of inflammation induced by the seaweed-derived irritant λ-carrageenan (*33*). Three cohorts of three immunocompetent mice were injected

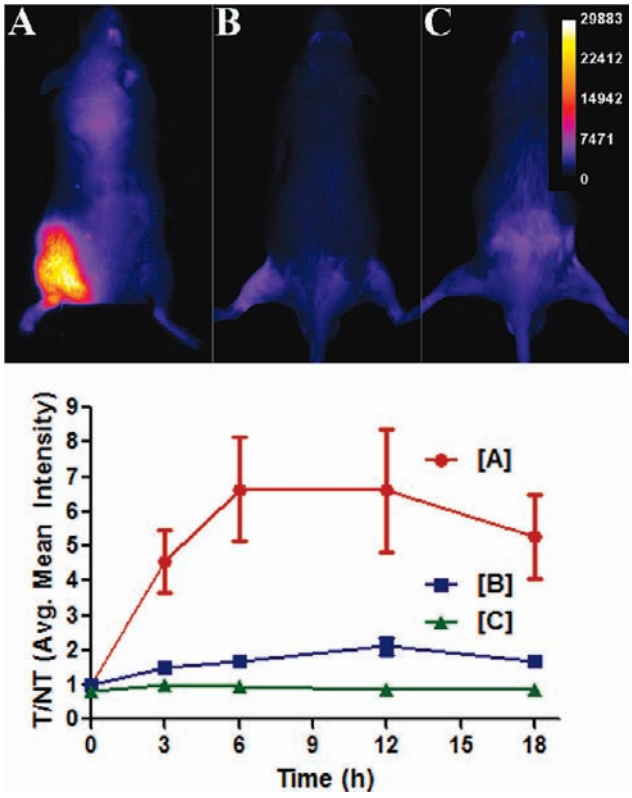


Figure 10. Probe **1** targets bacterial infection and not sterile inflammation in immunocompetent mice (strain ICr). (top) Mice were treated with 10 nmol of probe **1** six hours after the left posterior leg was injected with $\sim 10^8$ CFU of *S. aureus* NRS11 (A), 50 μL of a 1% λ-carrageenan solution (B), or 50 μL of a sterile saline solution (C). The dorsal images were acquired at 12 h post injection of probe. (bottom) Graph depicts the change in target-to-nontarget ratios (T/NT) obtained via ROI analyses of images. Error bars represent standard error of the mean. $N = 3$ for each group.

in the left leg with 50 μL doses containing (a) $\sim 10^8$ CFU of *S. aureus* in LB broth, (b) 1% λ-carrageenan solution, or (c) saline. Six hours later, each mouse was dosed with 10 nmol of probe **1** via the tail vein and then imaged periodically over the following 18 h. The λ-carrageenan induced considerable swelling, as judged by physical observation. However, as shown in Figure 10, the imaging signal from this inflammation site was quite small compared to the signal for *S. aureus* infection, although slightly higher than the imaging signal obtained with saline injection.

DISCUSSION

Most of the published whole-animal optical imaging studies of bacterial infection in small animals have employed bioluminescent bacteria and explored questions concerning migration and colonization of the bacteria or they have developed an in vivo model for testing the efficacy of drug candidates (*34*, *35*). The value of bioluminescent infection models is undisputed, but the method has some limitations. The signal is dependent on local ATP and oxygen levels and thus is not appropriate for bacteria in hypoxic conditions. The technique requires genetically modified bacteria which is often not possible or requires extensive time and biotechnology resources. The development of optical probes that can target all genera of bacterial infection is a complementary technology that can be employed in situations where bioluminescence is not applicable. In addition, there is the possibility of developing the synthetic probes for use in humans. Optical probes should be useful for imaging of shallow-tissue infections or fluorescence guided surgery, and it should be possible to replace the fluorophore with a reporter group that enables deep-tissue imaging. At present, the standard method for deep-tissue imaging of bacterial infection is to look for the associated inflammation response (*36*), but inflammation is a clinically ambiguous parameter that can lead to a false positive diagnosis. Despite the efforts of many international imaging groups, several recent review articles have concluded that there is currently no validated bacterial imaging probe that can distinguish infection from sterile inflammation (*37*−*41*). Over the past twenty years, various bacterial affinity ligands have been examined including antibiotic drugs (*42*), antimicrobial peptides (*43, 44*), sugars (*45*), bacteria-binding peptides (*46*), antibodies (*47*), and enzyme substrates (*48*). While a few radiotracer probes for bacteria have advanced to large-scale human clinical trials, the evidence for clear success is not compelling (*36*−*41*). New classes of targeting ligands are needed, and synthetic zinc coordination complexes are a promising new lead. The results reported in this study further demonstrate the remarkably selective bacterial targeting capabilities of bis(Zn-DPA) affinity ligands.

The deep-red fluorescent squaraine rotaxane probes **1** or **2** can readily target model leg infections in living mice but at least 10^6 CFU is needed for in vivo optical visualization. The high selectivity for infected target leg over the contralateral nontarget leg is reflected by T/NT ratios high as six (Figures 5 and 8), which compares favorably with the results of other infection imaging probes in the literature (*49*). The bis(Zn-DPA) ligands have a moderate affinity for polyphosphorylated molecules such as pyrophosphate and ATP, which are present in serum at micromolar concentrations (*50*−*52*). Nonetheless, the probes are apparently transferred from carrier serum proteins and phosphorylated molecules in the bloodstream/extracellular matrix to phosphorylated sites in the bacterial envelope. Our previous histological analyses of infected leg muscles that have been targeted by bis(Zn-DPA) probes indicate that the probes selectively associate with the bacterial cells (*26*). Furthermore, we have previously demonstrated that a control dye lacking a bis(Zn-DPA) ligand does not target the infection site (*26*). This current study provides additional evidence for high bacterial selectivity by showing that the imaging signal from probe **1** closely colocalizes with the bioluminescence signal from genetically engineered *S. enterica* serovar typhimurium (Figure 6) and it does not strongly target a site of sterile inflammation (Figure 10). The ability to distinguish between infection and sterile inflammation is one of the major applications of infection imaging and imaging probes with this selective targeting capability are quite rare and highly coveted.[1]

Probe **1** is more hydrophilic than probe **2**, and this is likely a major reason for the differences in probe clearance rates. The in vivo signal intensity for probe **1** at the infection site increases substantially during the first few hours after probe injection and then washes out, whereas the in vivo signal intensity for probe **2** at the infection site hardly changes over this time period (Figure 5). At the end of the 21 h imaging experiment, the in vivo T/NT ratios for probes **1** and **2** are equal (Figures 5 and 8), yet ex vivo analysis of the organs indicates that there is more of probe **2** in the infected leg muscle. Taken together, these results suggest that the relatively hydrophilic probe **1** partitions more into the extracellular fluid that surrounds the swollen infection site, and because it is closer to the surface of the body, there is an increase in fluorescence signal. This explains both the apparent build up of in vivo imaging signal at the infection site over three hours and the partial loss of probe mass from the infected leg muscle after necropsy.

[1] As discussed previously (*26*, *27*), bis(Zn-DPA) probes preferentially target the small and highly anionic surfaces of bacterial cells in preference to the nearby apoptotic and necrotic host mouse cells whose larger surfaces are also anionic but more diffusely charged.

It is worth comparing the in vivo imaging performance of squaraine rotaxane probes **1** and **2** with the performance of our previously reported probe that contained a cyanine dye and a single bis(Zn-DPA) affinity ligand (*26*). The cyanine probe exhibits near-IR excitation/fluorescence wavelengths of 794/810 nm that are within the optimal window for maximum penetration of light through skin and tissue; however, its brightness can be attenuated by self-quenching. Although the deep-red absorption/fluorescence wavelengths of probes **1** and **2** have poorer tissue penetration than the cyanine probe, they nonetheless could be employed at almost 10-fold lower concentrations and still produce more intense signals in the same leg infection models. The ability to employ lower probe doses is a major benefit because there is less concern with probe toxicity, both to the animal and to the bacterial infection. This latter point is especially important if the goal is to develop an infection imaging method for assessing in vivo efficacy of drug candidates (*53*−*55*). Clearly, this type of application requires that the probe not interfere with the course of the infection. Another advantage with the deep-red fluorescence of probes **1** and **2** is that it can be seen with the naked eye and thus is quite convenient for in vitro microscopy studies (*19*). Therefore, exactly the same probe can be employed for both in vitro and in vivo imaging studies. Yet another attractive practical feature with probes **1** and **2** is high water solubility, which facilitates formulation and intravenous delivery. A final point is that the different wavelengths of the above three bacterial imaging probes can be readily distinguished by the filter sets and spectral unmixing algorithms on modern microscopes and imaging stations, thus enabling fluorescence imaging experiments that label and track separate populations of bacteria in the same sample.

CONCLUSIONS

Squaraine rotaxanes are a new family of deep-red fluorophores that exhibit extremely high chemical and photochemical stability. The results of this study show that they can be converted into effective in vivo imaging probes for optical imaging in rodents. The fluorescent imaging probes **1** and **2** contain two bis(Zn-DPA) affinity ligands that allow targeting of localized bacterial infections over healthy host tissue in living mice. Although not highly sensitive (the infection must contain at least $\sim 10^6$ CFU for optical visualization), the probes are remarkably selective for bacterial cells considering their low molecular weight (<1.5 kDa) and simple structural design. The in vivo signal contrast from probe **1** is higher than that from probe **2** and it clears more rapidly from uninfected organs; thus, probe **1** is probably the best suited for most types of small animal imaging applications. Regarding possible translation to human medicine, the limited tissue penetration of deep-red light means that these probes can only be employed for shallow-tissue imaging, or infection sites that can be observed using endoscopes. Another possible application is fluorescence-guided surgery, where the surgeon employs the probes in conjunction with suitable imaging technology to identify and completely remove all bacterial cells.

ACKNOWLEDGMENT

This study was supported by the NIH, the University of Notre Dame, the Notre Dame Integrated Imaging Facility, and the Freimann Life Sciences Center. We thank Kelly Flentie and the laboratory of Professor Piwnica-Worms, Washington University, School of Medicine, St. Louis, MO, for the generous gift of *Salmonella* bacteria.

Supporting Information Available: Movie in .avi format showing the real-time change in imaging pixel intensity over three hours for a nude athymic mouse infected with *S. aureus* and treated with probe **1**. This material is available free of charge via the Internet at http://pubs.acs.org.

LITERATURE CITED

(1) Demchenko, A. P. (2009) *Introduction to Fluorescence Sensing*, Springer, New York.

(2) Hilderbrand, S. A., and Weissleder, R. (2009) Near-infrared fluorescence: application to in vivo molecular imaging. *Curr. Opin. Chem. Biol. 14*, 71–79.

(3) Levitt, J. A., Matthews, D. R., Ameer-Beg, S. M., and Suhling, K. (2009) Fluorescence lifetime and polarization-resolved imaging in cell biology. *Curr. Opin. Biotechnol. 20*, 28–36.

(4) Tuchin, V. V. (2007) *Tissue optics: light scattering methods and instruments for medical diagnosis*, 2nd ed., SPIE/International Society for Optical Engineering, Bellingham, WA.

(5) Kobayashi, H., Ogawa, M., Alford, R., Choyke, P. L., and UranoY. New strategies for fluorescent probe design in medical diagnostic imaging, *Chem. Rev.* 2010. [Online early access]., DOI: 10.1021/cr900263j.

(6) Terai, T., and Nagano, T. (2008) Fluorescent probes for bioimaging applications. *Curr. Opin. Chem. Biol. 12*, 515–521.

(7) Resch-Genger, U., Grabolle, M., Cavaliere-Jaricot, S., Nitschke, R., and Nann, T. (2008) Quantum dots versus organic dyes as fluorescent labels. *Nat. Methods 5*, 763–775.

(8) Licha, K. (2002) Contrast agents for optical imaging. *Top. Curr. Chem. 222*, 1–29.

(9) Mishra, A., Behera, R. K., Behera, P. K., Mishra, B. K., and Behera, G. B. (2000) Cyanines during the 1990s: a review. *Chem. Rev. 100*, 1973–2011.

(10) Yuan, B. H., Chen, N. G., and Zhu, Q. (2004) Emission and absorption properties of indocyanine green in Intralipid solution. *J. Biomed. Opt. 9*, 497–503.

(11) Escobedo, J. O., Rusin, O., Lim, S., and Strongin, R. M. (2009) NIR dyes for bioimaging applications. *Curr. Opin. Chem. Biol. 14*, 64–70.

(12) Arunkumar, E., Forbes, C. C., Noll, B. C., and Smith, B. D. (2005) Squaraine-derived rotaxanes: Sterically protected fluorescent near-IR dyes. *J. Am. Chem. Soc. 127*, 3288–3289.

(13) Arunkumar, E., Fu, N., and Smith, B. D. (2006) Squaraine-derived rotaxanes: Highly stable, fluorescent near-IR dyes. *Chem.—Eur. J. 12*, 4684–4690.

(14) Arunkumar, E., Sudeep, P. K., Kamat, P. V., Noll, B. C., and Smith, B. D. (2007) Singlet oxygen generation using iodinated squaraine and squaraine-rotaxane dyes. *New J. Chem. 31*, 677–683.

(15) Fu, N., Baumes, J. M., Arunkumar, E., Noll, B. C., and Smith, B. D. (2009) Squaraine rotaxanes with boat conformation macrocycles. *J. Org. Chem. 74*, 6462–6468.

(16) Fu, N., Gassensmith, J. J., and Smith, B. D. (2009) Effect of stopper size on squaraine rotaxane stability. *Supramol. Chem. 21*, 118–124.

(17) Gassensmith, J. J., Barr, L., Baumes, J. M., Paek, A., Nguyen, A., and Smith, B. D. (2008) Synthesis and photophysical investigation of squaraine rotaxanes by "clicked capping. *Org. Lett. 10*, 3343–3346.

(18) Gassensmith, J. J., Baumes, J. M., and Smith, B. D. (2009) Discovery and early development of squaraine rotaxanes. *Chem. Commun. 42*, 6329–6338.

(19) Johnson, J. R., Fu, N., Arunkumar, E., Leevy, W. M., Gammon, S. T., Piwnica-Worms, D., and Smith, B. D. (2007) Squaraine rotaxanes: Superior substitutes for Cy-5 in molecular probes for near-infrared fluorescence cell imaging. *Angew. Chem., Int. Ed. 46*, 5528–5531.

(20) Xiao, S. Z., Fu, N., Peckham, K., and Smith, B. D. (2010) Efficient synthesis of fluorescent squaraine rotaxane dendrimers. *Org. Lett. 12*, 140–143.

(21) Jisha, V. S., Arun, K. T., Hariharan, M., and Ramaiah, D. (2006) Site-selective binding and dual mode recognition of serum albumin by a squaraine dye. *J. Am. Chem. Soc. 128*, 6024–6025.

(22) Thomas, J., Sherman, D. B., Amiss, T. J., Andaluz, S. A., and Pitner, J. B. (2007) Synthesis and biosensor performance of a near-IR thiol-reactive fluorophore based on benzothiazolium squaraine. *Bioconjugate Chem. 18*, 1841–1846.
(23) Umezawa, K., Cittierio, D., and Suzuki, K. (2008) Water-soluble NIR fluorescent probes based on squaraine and their application for protein labeling. *Anal. Sci. 24*, 213–217.
(24) Lee, J. J., White, A. G., Baumes, J. M., and Smith, B. D. (2010) Microwave-assisted slipping synthesis of fluorescent squaraine rotaxane probe for bacterial imaging. *Chem. Commun. 46*, 1068–1069.
(25) Leevy, W. M., Gammon, S. T., Jiang, H., Johnson, J. R., Maxwell, D. J., Jackson, E. N., Marquez, M., Piwnica-Worms, D., and Smith, B. D. (2006) Optical imaging of bacterial infection in living mice using a fluorescent near-infrared molecular probe. *J. Am. Chem. Soc. 128*, 16476–16477.
(26) Leevy, W. M., Gammon, S. T., Johnson, J. R., Lampkins, A. J., Jiang, H., Marquez, M., Piwnica-Worms, D., Suckow, M. A., and Smith, B. D. (2008) Noninvasive optical imaging of staphylococcus aureus bacterial infection in living mice using a bis-dipicolylamine-zinc(II) affinity group conjugated to a near-infrared fluorophore. *Bioconjugate Chem. 19*, 686–692.
(27) Leevy, W. M., Johnson, J. R., Lakshmi, C., Morris, J., Marquez, M., and Smith, B. D. (2006) Selective recognition of bacterial membranes by zinc(II)-coordination complexes. *Chem. Commun. 15*, 1595–1597.
(28) DiVittorio, K. M., Leevy, W. M., O'Neil, E. J., Johnson, J. R., Vakulenko, S., Morris, J. D., Rosek, K. D., Serazin, N., Hilkert, S., Hurley, S., Marquez, M., and Smith, B. D. (2008) Zinc(II) coordination complexes as membrane-active fluorescent probes and antibiotics. *ChemBioChem 9*, 286–293.
(29) Ganesh, V., Bodewits, K., Bartholdson, S. J., Natale, D., Campopiano, D. J., and Mareque-Rivas, J. C. (2009) Effective binding and sensing of lipopolysaccharide: combining complementary pattern recognition receptors. *Angew. Chem., Int. Ed. 48*, 356–360.
(30) Flentie, K. N., Qi, M., Gammon, S. T., Razia, Y., Lui, F., Marpegan, L., Manglik, A., Piwnica-Worms, D., and McKinney, J. S. (2008) Stably integrated luxCDABE for assessment of Salmonella invasion. *Mol. Imaging 7*, 222–233.
(31) O'Neil, E. J., and Smith, B. D. (2006) Anion recognition using dimetallic coordination complexes. *Coord. Chem. Rev. 250*, 3068–3080.
(32) Hanshaw, R. G., Hilkert, S. M., Hua, J., and Smith, B. D. (2004) An indicator displacement system for fluorescent detection of phosphate oxyanions under physiological conditions. *Tetrahedron Lett. 45*, 8721–8724.
(33) Yvonne Wan, Y. J., and Badr, M. Z. (2006) Inhibition of carrageenan-induced cutaneous inflammation by PPAR agonists is dependent on hepatocyte-specific retinoid X receptor alpha, *PPAR Res.* Article ID 96341.
(34) Hutchens, M., and Luker, G. D. (2007) Applications of bioluminescence imaging to the study of infectious diseases. *Cell. Microbiol. 9*, 2315–2322.
(35) Leevy, W. M., Serazin, N., and Smith, B. D. (2007) Optical imaging of bacterial infection models. *Drug Discovery Today: Disease Models 4*, 91–97.
(36) Goldsmith, S. J., and Vallabhajosula, S. (2009) Clinically proven radiopharmaceuticals for infection imaging: mechanisms and applications. *Sem. Nucl. Med. 39*, 2–10.
(37) Chianelli, M., Boerman, O. C., Malviya, G., Galli, F., Oyen, W. J. G., and Signore, A. (2008) Receptor binding ligands to image infection. *Curr. Pharm. Des. 14*, 3316–3325.
(38) Gemmel, F., Dumarey, N., and Welling, M. (2009) Future diagnostic agents. *Semin. Nucl. Med. 39*, 11–26.
(39) Oyen, W. J., Corstens, F. H., and Boerman, O. C. (2005) Discriminating infection from sterile inflammation: can radiolabelled antibiotics solve the problem? *Eur. J. Nucl. Med. Mol. Imaging 32*, 151–152.
(40) Signore, A., D'Alessandria, C., Lazzeri, E., and Dierckx, R. (2008) Can we produce an image of bacteria with radiopharmaceuticals? *Eur. J. Nucl. Med. Mol. Imaging 35*, 1051–1055.
(41) Welling, M., Stokkel, M., Balter, J., Sarda-Mantel, L., Meulemans, A., and Le Guludec, D. (2008) The many roads to infection imaging. *Eur. J. Nucl. Med. Mol. Imaging 35*, 848–849.
(42) Britton, K. E., Wareham, D. W., Das, S. S., Solanki, K. K., Amaral, H., Bhatnagar, A., Katamihardja, A. H., Malamitsi, J., Moustafa, H. M., Soroa, V. E., Sundram, F. X., and Padhy, A. K. (2002) Imaging bacterial infection with (99m)Tc-ciprofloxacin (Infecton). *J. Clin. Pathol. 55*, 817–823.
(43) Lupetti, A., Welling, M. M., Pauwels, E. K. J., and Nibbering, P. H. (2003) Radiolabelled antimicrobial peptides for infection detection. *Lancet Inf. Dis. 3*, 223–229.
(44) Saeed, M., Iqbal, J., Khan, M. A., Irfanullah, J., Jehangir, M., Khan, B., ul-Haq, I., Muhammad, M. P. G., Nadeem, M. A., Shehzad, M., and Imran, M. B. (2004) Tc-99m-labeled antimicrobial peptide ubiquicidin (29−41) accumulates less in Escherichia coli infection than in Staphlococcus aureus infection. *J. Nucl. Med. 45*, 849–856.
(45) Qu, L. W., Luo, P. G., Taylor, S., Lin, Y., Huang, W. J., Anyadike, N., Tzeng, T. R. J., Stutzenberger, F., Latour, R. A., and Sun, Y. P. (2005) Visualizing adhesion-induced agglutination of Escherichia coli with mannosylated nanoparticles. *J. Nanosci. Nanotechnol. 5*, 319–322.
(46) Dhayal, B., Henne, W. A., Doorneweerd, D. D., Reifenberger, R. G., and Low, P. S. (2006) Detection of Bacillus subtilis spores using peptide-functionalized cantilever arrays. *J. Am. Chem. Soc. 128*, 3716–3721.
(47) Zhao, X. J., Hilliard, L. R., Mechery, S. J., Wang, Y. P., Bagwe, R. P., Jin, S. G., and Tan, W. H. (2004) A rapid bioassay for single bacterial cell quantitation using bioconjugated nanoparticles. *Proc. Nat. Acad. Sci. U.S.A. 101*, 15027–15032.
(48) Bettegowda, C., Foss, C. A., Cheong, I., Wang, Y., Diaz, L., Agrawal, N., Fox, J., Dick, J., Dang, L. H., Zhou, S., Kinzler, K. W., Vogelstein, B., and Pomper, M. G. (2005) Imaging bacterial infections with radiolabeled 1-(2′-deoxy-2′-fluoro-β-D-arabinofluranosyl)-5-iodouracil. *Proc. Nat. Acad. Sci. U.S.A. 102*, 1145–1150.
(49) Welling, M. M., Lupetti, A., Balter, H. S., Lanzzeri, S., Souto, B., Rey, A. M., Savio, E. O., Paulusma-Annema, A., Pauwels, E. K., and Nibbering, P. H. (2001) 99mTc-labeled antimicrobial peptides for detection of bacterial and Candida albicans infections. *J. Nucl. Med. 42*, 788–794.
(50) Gorman, M. W., Feigl, E. O., and Buffington, C. W. (2007) Human plasma ATP concentration. *Clin. Chem. 53*, 318–325.
(51) Preston, C. J., Noorwali, A., Challa, A., Paterson, A. D., Beard, D. J., Kanis, J. A., and Russell, R. G. G. (1982) Intracellular inorganic-phosphate and ATP levels in human-blood erythrocytes, leukocytes and platelets in normal subjects and in diseases associated with altered phosphate-metabolism. *Adv. Exp. Med. Biol. 151*, 147–155.
(52) Ryan, L. M., Rachow, J. W., McCarty, B. A., and McCarty, D. J. (1996) Adenosine triphosphate levels in human plasma. *J. Rheu. 23*, 214–219.
(53) Hoffman, R. M., and Zhao, M. (2006) Whole-body imaging of bacterial infection and antibiotic response. *Nat. Protoc. 1*, 2988–2994.
(54) Mortin, L. I., Li, T., Van Praagh, A. D. G., Zhang, S., Zhang, X., and Alder, J. D. (2007) Rapid bactericidal activity of daptomycin against methicillin-resistant and methicillin-susceptible staphylococcus aureus peritonitis in mice as measured with bioluminescent bacteria. *Antimicrob. Agents Chemother. 51*, 1787–1794.
(55) Zhang, H., Kalweri, G., Mani, N., and Grossman, T. H. (2008) Development and validation of a multi-dose neutropenic rat thigh model using real-time monitoring of staphylococcus aureus growth in vivo. *In Vivo 22*, 667–672.

BC1000998

Bioconjugation of Hydroxylated Semiconductor Nanocrystals and Background-Free Biomolecule Detection

Yongwook Kim, Wonjung Kim, Hye-Joo Yoon,* and Seung Koo Shin*

Bio-Nanotechnology Center, Department of Chemistry, Pohang University of Science and Technology, San 31 Hyojadong Namgu, Pohang, Kyungbuk 790-784, Korea. Received March 2, 2010; Revised Manuscript Received June 1, 2010

Semiconductor nanocrystals emerge as fluorescent bioprobes for long-term imaging and multiplexed assays; however, there is a challenge of making nanocrystals biocompatible without nonspecific bindings to background molecules. Here, we report the bioconjugation of small-sized, hydroxylated nanocrystals, enabling highly sensitive detection of various biomolecules with little or no nonspecific binding. Zinc-blende CdSe/ZnS nanocrystals were passivated with 3-mercapto-1-propanol (MPO) and activated to amine-reactive succinimidyl carbonate derivatives and then covalently linked to amine-functionalized biomolecules, such as biotin, DNA, and hemagglutinin peptide, by forming a carbamate linkage. Tris(3-hydroxypropyl)phosphine was added to stabilize the zinc−thiolate linkage on nanocrystals. For comparison, CdSe/ZnS nanocrystals were passivated with 3-mercaptopropionic acid (MPA) and conjugated with aminated biomolecules. Photoluminescence properties of organic, water-soluble, and bioconjugated nanocrystals were characterized. Significantly, the bioconjugates of hydroxylated (CdSe/ZnS−MPO) nanocrystals exhibited brighter photoluminescence with longer lifetimes than those of carboxylated (CdSe/ZnS−MPA) nanocrystals. Specific and nonspecific interactions between nanocrystals and biomolecules were examined by incubating nanocrystal−bioconjugates with avidin−agarose beads, anti-hemagglutinin affinity matrix, DNA glass slide, or avidin glass slide. CdSe/ZnS−MPO nanocrystals showed little or no nonspecific binding to both agarose beads and glass slides, whereas CdSe/ZnS−MPA nanocrystals exhibited significant nonspecific binding due to the carboxyl−amine interactions. Notably, CdSe/ZnS−MPO bioconjugates yield about 20 times brighter images than CdSe/ZnS−MPA bioconjugates in both DNA hybridization and biotin−streptavidin binding. Hydroxylated nanocrystals stabilized by hydroxyphosphine are small, bright, and photostable in physiological conditions, and their bioconjugates afford background-free detection of specific biomolecular interactions, positioning them for an ideal fluorescent probe to biological settings.

INTRODUCTION

Core/shell CdSe/ZnS nanocrystals are a new class of fluorescent probes for biological studies (*1, 2*), from long-term imaging (*3, 4*) and tracking of biomolecules (*5, 6*) to biochip sensors (*7, 8*). Fluorescent semiconductor nanocrystals offer several advantages over organic dyes (*7, 9*), including size-tunable, narrow, and symmetric emission, broad excitation wavelengths, and strong resistance to photobleaching. However, organic-soluble CdSe/ZnS nanocrystals prepared by colloidal synthesis (*10−13*) are not directly compatible with biological settings (*14−16*). A nanocrystal surface must be made water-soluble and functionalized for bioconjugation. In recent years, organic-soluble nanocrystals have been made biocompatible in two ways: (1) direct ligand exchange with bifunctional hydrophilic thiols (*17−19*); (2) functional surface encapsulation using silica (*20, 21*), amphiphilic polymers (*6, 22*), or amphiphilic lipids (*23*). The surface encapsulation results in physiologically stable nanocrystals with multiple functionalities, but their hydrodynamic sizes are rather large and sometimes even larger than typical biomolecules (*14−16, 24*), thus hindering the transport and activity of conjugated biomolecules (*14, 25*). On the other hand, the ligand exchange with hydrophilic thiols yields nanocrystals with a small hydrodynamic size, but the resulting nanocrystals tend to aggregate into clusters over time and/or nonspecifically bind to biomolecules (*26, 27*), thereby obscuring the detection of specific biomolecular interactions (*24*). For instance, carboxylic acid-terminated nanocrystals with mercaptoalkanoic acid or dihydrolipoic acid nonspecifically bind to various biological surfaces presenting positively charged functional groups (*28*).

To reduce the nonspecific binding to biological surfaces, nanocrystals have been functionalized with hydroxyl groups: Thompson and co-workers have shown little nonspecific binding of hydroxylated nanocrystals to DNA (*19*). Nie and co-workers (*28*) have minimized nonspecific binding to cellular membranes by functionalizing polymer-encapsulated nanocrystals with the hydroxyl group. Although the hydroxyl group is very promising in reducing nonspecific binding, the previously reported bioconjugation procedure for hydroxylated nanocrystals (*19*) is not as efficient as that for carboxylated nanocrystals (*29−31*). Carboxylic acid-terminated nanocrystals have been typically activated to the *O*-succinimide (OSu) esters in water and subsequently linked to amine-functionalized biomolecules (*16*). Meanwhile, hydroxyl-terminated nanocrystals have been activated to the imidazole carbamates in dioxane and conjugated with aminated biomolecules in dioxane/water (*19*). The OSu esters of carboxylated nanocrystals are highly soluble in water (*2*), but the imidazole carbamates of hydroxylated nanocrystals are sparingly soluble in dioxane/water (*19*). This solubility difference leads to a significant difference in reaction efficiency between the two bioconjugation procedures. Thus, the hydroxyl group is rarely used for direct conjugation with biomolecules. For instance, Klenerman and co-workers (*29*) have employed 11-meraptoundecyl-tri(ethylene glycol)acetic acid to covalently link probe oligonucleotides to nanocrystals and 11-meraptoundecyl-tri(ethylene glycol) alcohol to reduce nonspecific binding to target oligonucleotides. Obviously, there is a strong need for

* To whom correspondence should be addressed. For H.-J. Y.: e-mail, hjyoon@postech.ac.kr. For S. K. S.: e-mail, skshin@postech.ac.kr.

10.1021/bc100114q © 2010 American Chemical Society
Published on Web 06/28/2010

efficient bioconjugation of hydroxylated nanocrystals. Herein, we present the bioconjugation of CdSe/ZnS core/shell nanocrystals capped with 3-mercapto-1-propanol (MPO), enabling background-free fluorescent detection of biomolecules.

Recently, our group has reported synthesis and characterization of zinc blende (ZB) CdSe/ZnS core/shell nanocrystals and their high luminescence in water (*13*). Specifically, the ZB lattice structure has been used as a template for the uniform, epitaxial growth of the ZnS shell, and the ligand exchange with 3-mercaptopropionic acid (MPA) has resulted in ~50% photoluminescence (PL) quantum efficiency (QE) in water (*13*). Using both organic- and water-soluble ZB CdSe/ZnS nanocrystals, we have further characterized the surface ligands by mass spectrometric imaging (*32*) and studied ligand- and shell-dependent blinking of single nanocrystals (*33, 34*). In this paper, we established an efficient bioconjugation strategy for hydroxylated (CdSe/ZnS−MPO) nanocrystals by employing ZB core/shell nanocrystals. To compare with hydroxylated nanocrystals, carboxylated (CdSe/ZnS−MPA) nanocrystals were also prepared. Both CdSe/ZnS−MPO and CdSe/ZnS−MPA nanocrystals were conjugated with amine-functionalized biomolecules, such as biotin, hemagglutinin (HA) peptide, and DNA.

We characterized the lattice structure, size distribution, and optical properties of organic- and water-soluble nanocrystals and studied the effect of tris(3-hydroxypropyl)phosphine (THP) on the long-term stability of hydroxylated nanocrystals exposed to room light. Optical properties of nanocrystal−bioconjugates were also characterized. To examine specific and nonspecific interactions between nanocrystals and biomolecules, we incubated biotinylated, DNA-conjugated, and HA peptide-tagged nanocrystals with avidin−agarose beads/avidin glass slide, cDNA glass slide, and anti-HA affinity matrix, respectively. Our results demonstrate that CdSe/ZnS−MPO nanocrystals and their bioconjugates carry outstanding optical properties and thus offer highly sensitive and nonspecific interaction-free signals for biomolecule detection.

MATERIALS AND METHODS

Materials. MPO (95%), MPA (99%), tetramethylammonium hydroxide (25% w/v in methanol), *N*,*N*-diisopropylethylamine (DIPEA, 99.5%), dimethyformamide (DMF, anhydrous, 99.8%), 4-morpholineethanesulfonic acid (MES, 99%), β-mercaptoethanol (98%), hydroxylamine (50% w/v in water), propylamine (98%), sodium bicarbonate (100%), magnesium chloride (99.5%), and dimethyl sulfoxide (DMSO, 99.8%) were purchased from Sigma-Aldrich. HPLC-grade methanol, acetone, chloroform, and ethyl acetate were from J. T. Baker. THP (80%) was obtained from Strem Chemicals. *N*,*N*′-Disuccinimidyl carbonate (DSC, ≥95%) was from Fluka. *N*-Ethyl-*N*′-(3-dimethylaminopropyl)-carbodiimide hydrochloride (EDC), sulfo-*N*-hydroxysuccinimide (sulfo-NHS), amine-functionalized biotin [(+)-biotinyl-3,6-dioxaoctanediamine], streptavidin (affinity purified), D-Salt dextran desalting column, and avidin agarose beads were purchased from Thermo Scientific. Anti-HA agarose beads were from Roche Applied Science. Amine-functionalized DNA was obtained from Bionics. HA peptide (YPYDVPDYA) was from Peptron. NSB27-amine and NSB27-*N*-hydroxysuccinimide (NSB27-NHS) slides were purchased from Nano Surface Biosciences (NSB). Both NSB27 slides have 6−7 nm lateral spacing between surface functional groups (*35*).

Preparation of Hydroxylated and Carboxylated Nanocrystals. Organic-soluble CdSe/ZnS core/shell nanocrystals were prepared, as presented in Supporting Information (SI), and characterized, as shown in Figures S1 and S2 (SI). Organic-soluble nanocrystals were converted to water-soluble ones by dissolving nanocrystal powder into a methanol solution containing MPA or MPO (0.1 M) for 3 h at 60 °C (*32, 33*). The solution pH was adjusted to >10 with tetramethylammonium hydroxide. Both CdSe/ZnS−MPO and CdSe/ZnS−MPA nanocrystals were precipitated and washed with ethyl acetate, harvested by centrifugation, and dried under vacuum. The hydrodynamic size distribution of water-soluble nanocrystals (~1 μM) was measured in distilled water by dynamic light scattering (DLS) at 632.8 nm (Zetasizer Nano S, Malvern Instruments). The pH-dependent solubility of water-soluble nanocrystals was tested at 10 different pH values between 3.5 and 8.0 using three buffer systems: propionate (pH 3.5−5.5), MES (pH 5.5−7.0), and phosphate buffered saline (PBS) (pH 7.0−8.0), as described in SI.

Effects of THP on the Stabilization of Hydroxylated Nanocrystals. THP (260 nmol) was added to an aqueous solution (1 mL) containing CdSe/ZnS−MPO nanocrystals (0.1 μM). The amount of THP was 5 times the calculated amount of surface atoms on nanocrystals. The nanocrystal solution was sealed in a cuvette under argon in the presence or absence of THP and stored for several days at room temperature (rt) under room light. The hydrodynamic size distribution was measured over time by DLS, and fluorescent images were taken with a hand-held UV (365 nm) lamp using a digital camera.

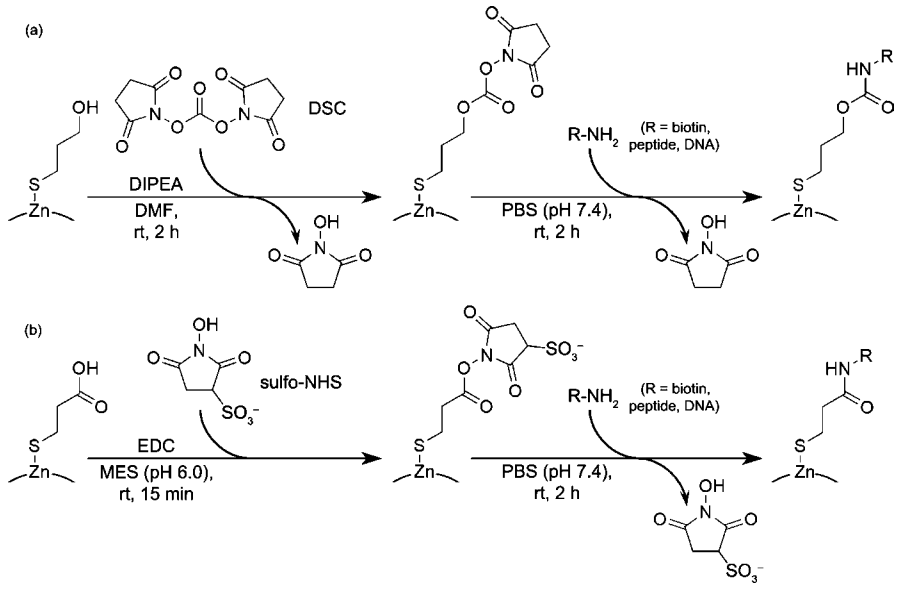
Bioconjugation of Water-Soluble Nanocrystals. Biomolecules were conjugated to CdSe/ZnS−MPO nanocrystals through DSC coupling (*36*), as shown in Scheme 1a, or to CdSe/ZnS−MPA nanocrystals through EDC/sulfo-NHS coupling (*37*), as illustrated in Scheme 1b. CdSe/ZnS−MPO powder (0.3 nmol) was dispersed into DMF, and the mixture was incubated with DSC (250 nmol) and DIPEA (500 nmol) for 2 h at rt to activate the hydroxyl groups to the succinimidyl carbonate derivatives. Then DSC-activated nanocrystals were precipitated and washed with diethyl ether, dried under vacuum, and dissolved in PBS (pH 7.4). CdSe/ZnS−MPA powder (0.3 nmol) was dissolved in water containing 0.1 M MES (pH 6.0), and the solution was incubated with EDC (2 μmol) and sulfo-NHS (5 μmol) for 15 min at rt to activate the carboxyl groups to the OSu esters. Excess EDC was quenched with β-mercaptoethanol (1.4 μL), and the reaction buffer was changed to PBS by using a dextran desalting column equilibrated with PBS to remove organic byproducts from the activated nanocrystals.

Amine-functionalized biomolecules (3 nmol) such as biotin, HA peptide, and DNA (amine-C_6-5′-GATCCAAATAAGTCA-CATGATGATA-3′) were reacted with the activated nanocrystals for 2 h at rt, and the reaction was quenched with hydroxylamine (10 μmol). The reaction mixture was passed through a dextran desalting size-exclusion column equilibrated with PBS. Nanocrystal−bioconjugates were stored at 4 °C in the dark.

Specific and Nonspecific Bindings of Nanocrystal−Bioconjugates to Protein Beads and Functionalized Surfaces. Both avidin and anti-HA agarose beads were used as protein beads. They were washed three times with PBS, incubated with nanocrystals (10 nmol) in PBS for 1 h at rt, and washed twice with water. To examine specific binding, we incubated biotinylated nanocrystals with avidin beads and incubated HA-tagged nanocrystals with anti-HA beads. To examine nonspecific binding, both CdSe/ZnS−MPO and CdSe/ZnS−MPA nanocrystals were also separately incubated with agarose beads. Fluorescent images were taken with a microscope (Nikon, Eclipse 80i) using a mercury lamp as a light source. A band-pass filter (Omega 365WB50), a dichroic mirror (Omega 400DCLP), a long-pass filter (Omega 435ALP), and a color CCD camera (Nikon DXM1200F) were used for fluorescent detection.

Both NSB27-amine and alkylated NSB27-NHS slides were employed as functionalized surfaces. The alkylated slide was prepared by conjugating propylamine (1 mM) onto a NSB27-

Scheme 1. Activation and Bioconjugation of (a) CdSe/ZnS−MPO and (b) CdSe/ZnS−MPA Nanocrystals



NHS slide in sodium bicarbonate buffer (pH 8.5) for 7 h at rt. Both CdSe/ZnS−MPO and CdSe/ZnS−MPA nanocrystals were separately dissolved in PBS to 0.1 μM, and aliquots (1 μL each) were loaded on either an amine or alkyl surface. The slide was incubated in a humidity (100%) chamber for 1 h at rt, washed with PBST (0.1% Tween 20 in PBS, v/v) for 3 min, and rinsed twice with water. Fluorescent images of the glass slides were obtained using a gel imaging system (VersaDoc 5000MP, Bio-Rad).

DNA Hybridization and Biotin−Streptavidin Binding. Amine-functionalized target DNA (amine-C_6-5′-TATCATCAT-GTGACTTATTTGGATC-3′) or biotin was dissolved to 1 mM in a buffer solution (pH 8.5) containing 25 mM sodium bicarbonate, 10 mM magnesium chloride, and 10% (v/v) DMSO (*35*). An aliquot (1 μL) of each solution was loaded on a NSB27-NHS slide. The spot size was ∼2.5 mm in diameter. The slide was incubated in a humidity (100%) chamber for 12 h at rt and washed with PBST and water. NHS groups outside the spotted area were alkylated, as described above. For DNA hybridization, an aliquot (1 μL) of nanocrystal−DNA conjugates (0.1 μM) in PBS was placed on the target DNA-spot, and the slide was incubated in a humidity (100%) chamber for 1 h at 45 °C and then for 12 h at rt. For biotin−avidin binding, an aliquot (1 μL) of streptavidin (1 mg/mL) in PBS was loaded on the biotin-spot, and the slide was incubated in a humidity (100%) chamber for 1 h at rt and washed sequentially with PBST and water. Then an aliquot (1 μL) of nanocrystal−biotin conjugates (0.1 μM) in PBS was loaded on the streptavidin−biotin-spot, and the slide was incubated again in a humidity (100%) chamber for 1 h at rt. Fluorescent images of the glass slides were recorded with a gel imaging system after washing with PBST and water and were processed with ImageJ software (NIH, Bethesda, MD).

RESULTS AND DISCUSSION

Size Distribution and Optical Properties of Water-Soluble Nanocrystals. The hydrodynamic size distributions of water-soluble CdSe/ZnS−MPO and CdSe/ZnS−MPA nanocrystals are presented in parts a and b of Figure 1, respectively. Their average size is 9.8 ± 1.6 and 11.7 ± 2.1 nm, respectively. CdSe/ZnS−MPO nanocrystals appear to be smaller than CdSe/ZnS−MPA nanocrystals. Nonetheless, both CdSe/ZnS−MPO and CdSe/ZnS−MPA nanocrystals display no indication of clusters larger than 20 nm.

Both the absorption/emission spectra and the PL decay of water-soluble nanocrystals are compared with organic-soluble ones in parts c and d of Figure 1, respectively. The band-edge absorption (λ_{abs}) occurs at 529 nm for CdSe/ZnS nanocrystals in chloroform and at 518 and 524 nm for CdSe/ZnS−MPO and CdSe/ZnS−MPA nanocrystals in water, respectively. The emission maxima (λ_{em}) appear at 549 nm for organic-soluble CdSe/ZnS nanocrystals and at 542 and 547 nm for water-soluble CdSe/ZnS−MPO and CdSe/ZnS−MPA nanocrystals, respectively, with full width at half-maximum (fwhm) of 30−32 nm. The QE decreases from 74% of CdSe/ZnS nanocrystals in chloroform to 56% and 51% after ligand exchange with MPO and MPA, respectively. The effective PL lifetime (τ_{eff}) is 16.9 ns for CdSe/ZnS nanocrystals in chloroform and 12.9 and 10.9 ns for CdSe/ZnS−MPO and CdSe/ZnS−MPA nanocrystals in water, respectively. These optical properties (λ_{abs}, λ_{em}, fwhm, QE, and τ_{eff}) are listed in Table S1 (SI). The thiolate capping

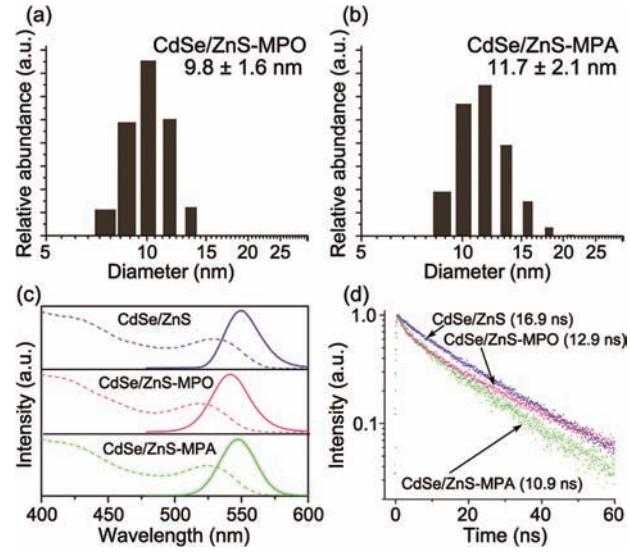


Figure 1. Hydrodynamic size distributions (average of 15 measurements) of (a) CdSe/ZnS−MPO and (b) CdSe/ZnS−MPA nanocrystals (1 μM) in water. (c) Absorption (dashed line) and emission (solid line) spectra of CdSe/ZnS nanocrystals in chloroform and of CdSe/ZnS−MPO and CdSe/ZnS−MPA nanocrystals in water. (d) PL decay and effective PL lifetime of CdSe/ZnS nanocrystals in chloroform and of CdSe/ZnS−MPO and CdSe/ZnS−MPA nanocrystals in water.

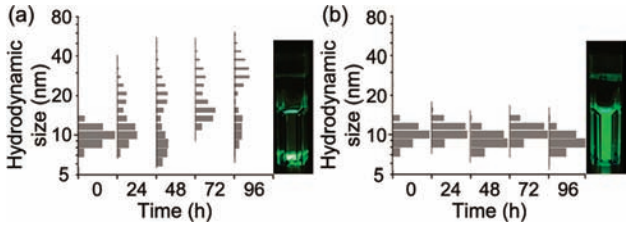


Figure 2. Hydrodynamic size distributions of CdSe/ZnS−MPO nanocrystals (a) in the absence and (b) in the presence of THP over 96 h under exposure to room light. Insets show fluorescent images of nanocrystals in a cuvette after 96 h. Highly luminescent nanocrystals are precipitated at the bottom in the absence of THP (a) but uniformly dispersed in water in the presence of THP (b).

over the ZnS shell slightly changes optical properties of CdSe/ZnS nanocrystals. Significantly, the MPO capping results in a longer PL lifetime than the MPA capping.

CdSe/ZnS−MPO nanocrystals were stable (fluorescent and soluble) in water in the tested pH range from 3.5 to 8.0, whereas CdSe/ZnS−MPA nanocrystals were stable only at pH above 5.5, as shown in Figure S3 (SI). Below pH 5.0, CdSe/ZnS−MPA nanocrystals were neutralized and precipitated because of intermolecular hydrogen bonding. Above pH 5.5, however, the carboxyl groups on CdSe/ZnS−MPA nanocrystals were ionized to become soluble in water. Nonetheless, both CdSe/ZnS−MPO and CdSe/ZnS−MPA nanocrystals were stable for 2 years in buffer as long as they were kept in the dark at 4 °C.

Hydroxyphosphine (THP) Stabilization of Hydroxylated Nanocrystals. Although both CdSe/ZnS−MPO and CdSe/ZnS−MPA nanocrystals are typically stable for the long-term in the dark at 4 °C, they tend to form aggregates over time when exposed to light. Between the two water-soluble nanocrystals, CdSe/ZnS−MPO nanocrystals are more sensitive to light than CdSe/ZnS−MPA nanocrystals. Hydrophilic thiols are reported to undergo photochemical oxidation to disulfides that dissolve into the solution (*26*). As the water-soluble ligands dissociate from the nanocrystal surface, nanocrystals become less and less soluble in water and assemble into clusters. By suppression of disulfide bond formation, nanocrystals could be kept from aggregation. Water-soluble hydroxyphosphine has been reported to reduce disulfides (*38*) more efficiently than tris(2-carboxyethyl)phosphine (*39*). Thus, we tested the effect of THP on the stability of CdSe/ZnS−MPO nanocrystals. The hydrodynamic size distribution and the PL intensity of hydroxylated nanocrystals were monitored in water in the absence or the presence of THP. Nanocrystals were exposed to room light under argon for 4 days. Fresh CdSe/ZnS−MPO nanocrystals exhibit a narrow hydrodynamic size distribution with no indication of clustering in water, as displayed in Figure 2 (time 0). They form aggregates that slowly precipitate over time in the absence of THP (Figure 2a). As the light induces the formation of disulfide bonds, nanocrystals keep losing thiolates from the surface, thereby precipitating out of the solution. In the presence of THP (Figure 2b), however, CdSe/ZnS−MPO nanocrystals undergo no aggregation or precipitation. Remarkably, THP stabilizes the zinc−thiolate linkage on CdSe/ZnS−MPO nanocrystals. THP also increases the stability of CdSe/ZnS−MPA nanocrystals, as supported by the absence of aggregates over time (data not shown). Most recently, we have shown that the tertiary phosphine binds to and stabilizes the chalcogen atoms on CdSe semiconductor nanocrystals (*40*). THP seems to stabilize the surface chalcogen atoms on the CdSe/ZnS nanocrystals and suppress the disulfide formation of thiolate ligands. Besides, addition of THP hardly modifies the optical properties (λ_{abs}, λ_{em}, fwhm, QE, and τ_{eff}) of water-soluble CdSe/ZnS core/shell nanocrystals (data not shown). Also, THP has been shown to be biocompatible under physiological conditions (*39, 41*). Therefore, we routinely added THP to nanocrystal preparations, particularly when nanocrystal probes were used for long-term bioimaging.

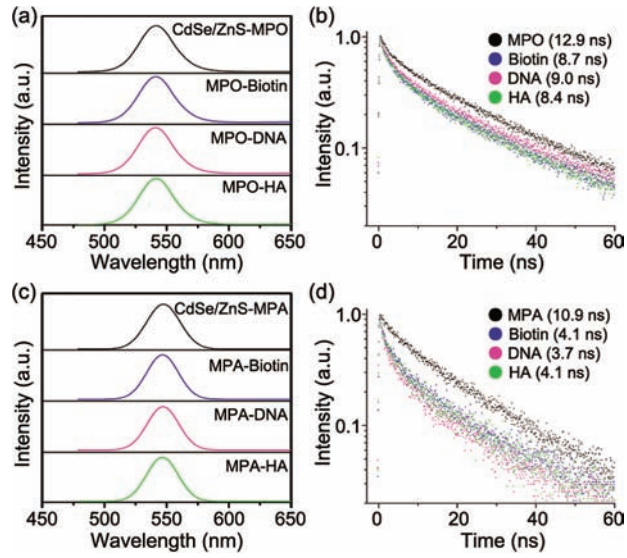


Figure 3. (a) Emission spectra and (b) PL decay of CdSe/ZnS−MPO nanocrystals in water and their bioconjugates with biotin, DNA, and HA peptide in PBS. (c) Emission spectra and (d) PL decay of CdSe/ZnS−MPA nanocrystals in water and their bioconjugates in PBS. λ_{em}, fwhm, and τ_{eff} are listed in Table S1 (SI).

Bioconjugation of Hydroxylated Nanocrystals. Both CdSe/ZnS−MPO and CdSe/ZnS−MPA nanocrystals are activated to the succinimidyl derivatives and conjugated with biomolecules, as shown in Scheme 1. Although the previously reported imidazole carbamate derivatives of hydroxylated nanocrystals are sparingly soluble in dioxane/PBS, the succinimidyl carbonate derivatives are highly soluble in PBS. Consequently, the subsequent conjugation reaction with amine-functionalized biomolecules readily proceeds in PBS to near completion.

The emission spectra and the PL decay of nanocrystal−bioconjugates are presented in Figure 3. For all nanocrystals, the emission spectra look almost identical before and after bioconjugation. However, the PL lifetime decreases after bioconjugation from 12.9 to 8.4−9.0 ns for CdSe/ZnS−MPO nanocrystals and from 10.9 to 3.7−4.1 ns for CdSe/ZnS−MPA nanocrystals. To find out the origin of this lifetime shortening, we examined the optical properties of the succinimidyl derivatives of nanocrystals before and after DNA conjugation. The emission spectra and the PL decay obtained from another batch of nanocrystals are depicted in Figure S4 (SI). The activation of water-soluble nanocrystals to the succinimidyl derivatives reduces the emission intensity by ∼50% for CdSe/ZnS−MPO and by ∼90% for CdSe/ZnS−MPA.

Meanwhile, the PL lifetime of CdSe/ZnS−MPO slightly increases, whereas that of CdSe/ZnS−MPA decreases. The subsequent DNA conjugation barely reduces the emission intensity of both nanocrystal−DNA conjugates with little change in lifetime. Evidently, the formation of the succinimidyl derivatives primarily reduces the emission intensity, whereas the subsequent bioconjugation induces little change in emission properties.

Fluorescent Detection of Biomolecules Using Nanocrystal Probes. We applied nanocrystals to the fluorescent detection of biomolecules. In biological applications of fluorescent nanocrystals, nonspecific interactions between biomolecules and nanocrystals are one of the most serious problems (*8, 14, 28*). Thus, we first studied specific and nonspecific bindings between nanocrystal−bioconjugates and protein−agarose beads to detect

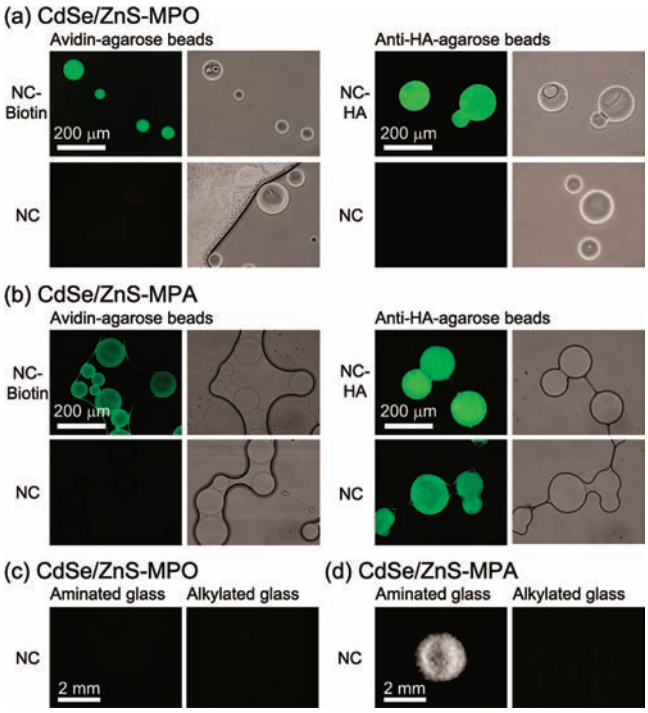


Figure 4. Fluorescence microscope images of protein-immobilized agarose beads probed with (a) CdSe/ZnS−MPO-bioconjugates or (b) CdSe/ZnS−MPA-bioconjugates. Avidin−agarose beads were incubated with biotinylated nanocrystals (NC−biotin, top), and anti-HA-agarose beads were incubated with HA-tagged nanocrystals (NC−HA, top). CdSe/ZnS−MPO or CdSe/ZnS−MPA nanocrystals before bioconjugation were used as control (NC, bottom). Bright-field images (right) corresponding to the fluorescent images (left) are also shown. Nonspecific interaction between (c) CdSe/ZnS−MPO or (d) CdSe/ZnS−MPA nanocrystals and the amine-functionalized glass slide (aminated glass, left) is shown. The amine surface was passivated with propylamine through DSC coupling to make the surface uncharged and hydrophobic (alkylated surface, right).

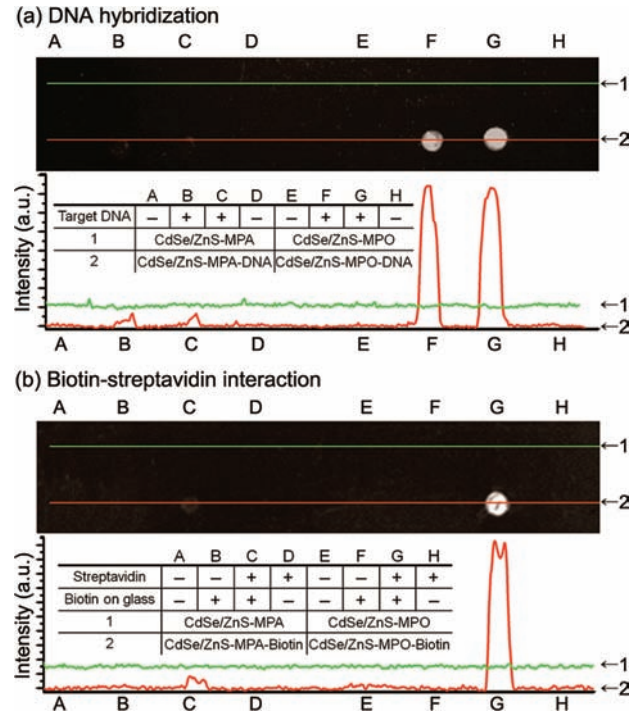


Figure 5. Fluorescent images (top) and intensity profiles (bottom) of (a) DNA hybridization and (b) biotin−streptavidin interaction on glass slides using nanocrystal−bioconjugate probes.

well-known biomolecular interactions, such as biotin−avidin and antigen−antibody recognition. Specific binding was examined by incubating biotinylated nanocrystals with avidin-immobilized agarose beads and incubating HA antigen-tagged nanocrystals with anti-HA antibody agarose beads. Nonspecific binding was tested by incubating the protein−agarose beads with water-soluble (both CdSe/ZnS−MPO and CdSe/ZnS−MPA) nanocrystals unconjugated with biomolecules.

Fluorescence microscope images of agarose beads are presented in Figure 4. Both CdSe/ZnS−MPO−biotin and CdSe/ZnS−MPA−biotin yield bright images by binding to avidin beads. HA-tagged nanocrystals also result in bright images by binding to anti-HA beads. In control experiments, CdSe/ZnS−MPO nanocrystals show no fluorescent images with both avidin and anti-HA beads, indicating the absence of nonspecific interactions (Figure 4a, bottom). On the other hand, CdSe/ZnS−MPA nanocrystals exhibit bright images with anti-HA beads but no fluorescence with avidin beads, suggesting the presence of nonspecific interactions between carboxylated nanocrystals and anti-HA beads (Figure 4b, bottom). Although the functional groups on the surface of protein−agarose beads are not well characterized, the positively charged amine groups on agarose beads could interact with the negatively charged carboxyl groups on nanocrystals in PBS (pH 7.4).

To further examine nonspecific interactions between water-soluble nanocrystals and amine functional groups, we spotted nanocrystals on an amine-functionalized glass slide (NSB27-amine) (*35*). As presented in Figure 4d, CdSe/ZnS−MPA nanocrystals indeed display a bright fluorescent image on the amine surface at pH 7.4 (left), manifesting nonspecific interactions between the carboxyl groups on nanocrystals and the amine groups on the glass surface in PBS. In contrast, CdSe/ZnS−MPO nanocrystals exhibit no fluorescent image (Figure 4c, left), confirming the absence of nonspecific binding to the amine surface. To solve the carboxyl−amine interaction problem, we modified the amine-functionalized glass surface with propylamine through DSC coupling. The propylamine passivation makes the glass surface hydrophobic with no charged functional groups. Consequently, CdSe/ZnS−MPA nanocrystals no longer bind to the alkylated surface (Figure 4d, right). CdSe/ZnS−MPO nanocrystals again show no binding affinity to the hydrophobic surface (Figure 4c, right). This alkyl passivation of the amine surface is a simple and easy way to reduce the background noise when carboxylated nanocrystals are used as fluorescent probes.

To broaden biological applications of our nanocrystal probes, we tested both CdSe/ZnS−MPO and CdSe/ZnS−MPA nanocrystals for the detection of DNA hybridization as well as biotin−streptavidin binding on NHS-functionalized glass chips (NSB27-NHS). Both DNA and biotin were immobilized on the NSB27-NHS slide, and then the unspotted area was passivated with propylamine to block nonspecific interaction between water-soluble nanocrystals and the glass surface. Fluorescent images and intensity profiles on the glass slide are displayed in Figure 5. The intensity profile across the horizontal line (green or red) is displayed below the image. In the case of DNA hybridization (Figure 5a), eight spots were tested for each type of nanocrystal. Of them, two spots, B2 and C2 for CdSe/ZnS−MPA nanocrystals and F2 and G2 for CdSe/ZnS−MPO nanocrystals, have both target and probe DNA. The other six spots lack either one or both. Of the 16 spots for both nanocrystals, only those 4 spots having both target and probe DNA show fluorescent signals, demonstrating specific detection of DNA hybridization without nonspecific interactions. In the case of biotin−streptavidin binding (Figure 5b), of the eight spots tested for each type of nanocrystals, only one spot, C2 for CdSe/ZnS−MPA nanocrystals and G2 for CdSe/ZnS−MPO

nanocrystals, contains all three complementary components, biotin on the glass surface, streptavidin as a linker, and biotin on the nanocrystal. The other spots lack at least one component. Of the 16 spots for both nanocrystals, only C2 and G2 spots show fluorescent signals, and all other spots yield no fluorescence, manifesting background-free detection of biotin−streptavidin binding. Notably, CdSe/ZnS−MPO nanocrystal−bioconjugates show the integrated signals about 20 times stronger than CdSe/ZnS−MPA nanocrystal−bioconjugates in both binding studies.

In conclusion, the bioconjugates of CdSe/ZnS−MPO nanocrystals show higher photoluminescence intensities and longer lifetimes than those of CdSe/ZnS−MPA nanocrystals. Unlike CdSe/ZnS−MPA nanocrystals, CdSe/ZnS−MPO nanocrystals show no nonspecific binding to protein-immobilized agarose beads or to amine-functionalized glass slides. Nonspecific interactions between carboxylated nanocrystals and amine-functionalized surface are minimized by alkylating the amine surface with propylamine. As a result, both CdSe/ZnS−MPO and CdSe/ZnS−MPA nanocrystals are applicable to fluorescent detection of biomolecules immobilized on glass slides with little or no nonspecific binding. CdSe/ZnS−MPO nanocrystals yield about 20 times stronger specific binding signals on the glass chip. Notably, tris(3-hydroxypropyl)phosphine greatly stabilizes the zinc−thiolate linkage on both CdSe/ZnS−MPO and CdSe/ZnS−MPA nanocrystals. Addition of THP to CdSe/ZnS−MPO nanocrystals and their bioconjugates allows long-lasting, background-free fluorescent detection of biomolecules without aggregation of nanocrystals. CdSe/ZnS nanocrystals hydroxylated with 3-mercapto-1-propanol are a promising fluorescent probe in biological settings, which offers the small hydrodynamic size, high photoluminescence quantum yield, long-term photostability, and nonspecific interaction-free signals.

ACKNOWLEDGMENT

We are thankful for the support from the Advanced Scientific Analysis Instruments Development Project administered by the Korea Research Institute of Standards and Science and the Nano Research and Development Program through the National Research Foundation of Korea funded by the Ministry of Education, Science, and Technology (Grant No. 2008-04540).

Supporting Information Available: Synthesis and characterization of CdSe core and CdSe/ZnS core/shell nanocrystals, powder X-ray diffraction patterns, high-resolution transmission electron microscope images, optical properties and pH-dependent solubility of nanocrystals, and fitting parameters of PL decay. This material is available free of charge via the Internet at http://pubs.acs.org.

LITERATURE CITED

(1) Bruchez, M., Jr., Moronne, M., Gin, P., Weiss, S., and Alivisatos, A. P. (1998) Semiconductor nanocrystals as fluorescent biological labels. *Science 281*, 2013–2016.

(2) Chan, W. C. W., and Nie, S. (1998) Quantum dot bioconjugates for ultrasensitive nonisotopic detection. *Science 281*, 2016–2018.

(3) Chan, W. C. W., Maxwell, D. J., Gao, X., Bailey, R. E., Han, M., and Nie, S. (2002) Luminescent quantum dots for multiplexed biological detection and imaging. *Curr. Opin. Biotechnol. 13*, 40–46.

(4) Jaiswal, J. K., Mattoussi, H., Mauro, J. M., and Simon, S. M. (2003) Long-term multiple color imaging of live cells using quantum dot bioconjugates. *Nat. Biotechnol. 21*, 47–51.

(5) Alivisatos, A. P. (2004) The use of nanocrystals in biological detection. *Nat. Biotechnol. 22*, 47–52.

(6) Gao, X., Cui, Y., Levenson, R. M., Chung, L. W. K., and Nie, S. (2004) In vivo cancer targeting and imaging with semiconductor quantum dots. *Nat. Biotechnol. 22*, 969–976.

(7) Shin, S. K., Yoon, H.-J., Jung, Y. J., and Park, J. W. (2006) Nanoscale controlled self-assembled monolayers and quantum dots. *Curr. Opin. Chem. Biol. 10*, 423–429.

(8) De, M., Ghosh, P. S., and Rotello, V. M. (2008) Applications of nanoparticles in biology. *Adv. Mater. 20*, 4225–4241.

(9) Resch-Genger, U., Grabolle, M., Cavaliere-Jaricot, S., Nitschke, R., and Nann, T. (2008) Quantum dots versus organic dyes as fluorescent labels. *Nat. Methods 5*, 763–775.

(10) Hines, M. A., and Guyot-Sionnest, P. (1996) Synthesis and characterization of strongly luminescing ZnS-capped CdSe nanocrystals. *J. Phys. Chem. 100*, 468–471.

(11) Dabbousi, B. O., Rodriguez-Viejo, J., Mikulec, F. V., Heine, J. R., Mattoussi, H., Ober, R., Jensen, K. F., and Bawendi, M. G. (1997) (CdSe)ZnS core-shell quantum dots: synthesis and characterization of a size series of highly luminescent nanocrystallites. *J. Phys. Chem. B 101*, 9463–9475.

(12) Yang, Y. A., Wu, H., Williams, K. R., and Cao, Y. C. (2005) Synthesis of CdSe and CdTe nanocrystals without precursor injection. *Angew. Chem., Int. Ed. 44*, 6712–6715.

(13) Lim, S. J., Chon, B., Joo, T., and Shin, S. K. (2008) Synthesis and characterization of zinc-blende CdSe-based core/shell nanocrystals and their luminescence in water. *J. Phys. Chem. C 112*, 1744–1747.

(14) Jaiswal, J. K., and Simon, S. M. (2004) Potentials and pitfalls of fluorescent quantum dots for biological imaging. *Trends Cell Biol. 14*, 497–504.

(15) Michalet, X., Pinaud, F. F., Bentolila, L. A., Tsay, J. M., Doose, S., Li, J. J., Sundaresan, G., Wu, A. M., Gambhir, S. S., and Weiss, S. (2005) Quantum dots for live cells, in vivo imaging, and diagnostics. *Science 307*, 538–544.

(16) Medintz, I. L., Uyeda, H. T., Goldman, E. R., and Mattoussi, H. (2005) Quantum dot bioconjugates for imaging, labeling and sensing. *Nat. Mater. 4*, 435–446.

(17) Mitchell, G. P., Mirkin, C. A., and Letsinger, R. L. (1999) Programmed assembly of DNA functionalized quantum dots. *J. Am. Chem. Soc. 121*, 8122–8123.

(18) Mattoussi, H., Mauro, J. M., Goldman, E. R., Anderson, G. P., Sunder, V. C., Mikulec, F. V., and Bawendi, M. G. (2000) Self-assembly of CdSe−ZnS quantum dots bioconjugates using an engineered recombination protein. *J. Am. Chem. Soc. 122*, 12142–12150.

(19) Pathak, S., Choi, S.-K., Arnheim, N., and Thompson, M. E. (2001) Hydroxylated quantum dots as luminescent probes for in situ hybridization. *J. Am. Chem. Soc. 123*, 4103–4104.

(20) Gerion, D., Pinaud, F., Williams, S. C., Parak, W. J., Zanchet, D., Weiss, S., and Alivisatos, A. P. (2001) Synthesis and properties of biocompatible water-soluble silica-coated CdSe/ZnS semiconductor quantum dots. *J. Phys. Chem. B 105*, 8861–8871.

(21) Parak, W. J., Gerion, D., Zanchet, D., Woerz, A. S., Pellegrino, T., Micheel, C., Williams, S. C., Seitz, M., Bruehl, R. E., Bryant, Z., Bustamante, C., Bertozzi, C. R., and Alivisatos, A. P. (2002) Conjugation of DNA to silanized colloidal semiconductor nanocrystalline quantum dots. *Chem. Mater. 14*, 2113–2019.

(22) Wu, X., Liu, H., Liu, J., Haley, K. N., Treadway, J. A., Larson, J. P., Ge, N., Peale, F., and Bruchez, M. P. (2003) Immunofluorescent labeling of cancer marker Her2 and other cellular targets with semiconductor quantum dots. *Nat. Biotechnol. 21*, 41–46.

(23) Dubertret, B., Skourides, P., Norris, D. J., Noireaux, V., Brivanlou, A. H., and Libchaber, A. (2002) In vivo imaging of quantum dots encapsulated in phospholipid micelles. *Science 298*, 1759–1762.

(24) Smith, A. M., Duan, H., Rhyner, M. N., Ruan, G., and Nie, S. (2006) A systematic examination of surface coatings on the optical and chemical properties of semiconductor quantum dots. *Phys. Chem. Chem. Phys. 8*, 3895–3903.

(25) Choi, H. S., Ipe, B. I., Misra, P., Lee, J. H., Bawendi, M. G., and Frangioni, J. V. (2009) Tissue- and organic-selective biodistribution of NIR fluorescent quantum dots. *Nano Lett. 9*, 2354–2359.
(26) Aldana, J., Wang, Y. A., and Peng, X. (2001) Photochemical instability of CdSe nanocrystals coated by hydrophilic thiols. *J. Am. Chem. Soc. 123*, 8844–8850.
(27) Aldana, J., Lavelle, N., Wang, Y., and Peng, X. (2005) Size-dependent dissociation pH of thiolate ligands from cadmium chalcogenide nanocrystals. *J. Am. Chem. Soc. 127*, 2496–2504.
(28) Kairdolf, B. A., Mancini, M. C., Smith, A. M., and Nie, S. (2008) Minimizing nonspecific cellular binding of quantum dots with hydroxyl-derivatized surface coatings. *Anal. Chem. 80*, 3029–3034.
(29) Zhou, D., Ying, L., Hong, X., Hall, E. A., Abell, C., and Klenerman, D. (2008) A compact functional quantum dot−DNA conjugate: preparation, hybridization, and specific label-free DNA detection. *Langmuir 24*, 1659–1664.
(30) Gerion, D., Parak, W. J., Williams, S. C., Zanchet, D., Micheel, C. M., and Alivisatos, A. P. (2002) Sorting fluorescent nanocrystals with DNA. *J. Am. Chem. Soc. 124*, 7070–7074.
(31) Veronese, F. M. (2001) Peptide and protein PEGylation: a review of problems and solutions. *Biomaterials 22*, 405–417.
(32) Min, H., Kim, Y., Yu, H., Moon, D. W., Lim, S. J., Yoon, H.-J., Lee, T. G., and Shin, S. K. (2008) Probing the surface of organic and bioconjugated nanocrystals by using mass spectrometric imaging. *Chem.−Eur. J. 14*, 8461–8464.
(33) Kim, Y., Song, N. W., Yu, H., Moon, D. W., Lim, S. J., Kim, W., Yoon, H.-J., and Shin, S. K. (2009) Ligand-dependent blinking of zinc-blende CdSe/ZnS core/shell nanocrystals. *Phys. Chem. Chem. Phys. 11*, 3497–3502.
(34) Chon, B., Lim, S. J., Kim, W., Seo, J., Kang, H., Joo, T., Hwang, J., and Shin, S. K. Shell- and ligand-dependent blinking of zinc-blende CdSe-based core/shell nanocrystals. *Phys. Chem. Chem. Phys.* [Online early access]. DOI: 10.1039/b924917F.
(35) Hong, B. J., Sunkara, V., and Park, J. W. (2005) DNA microarrays on nanoscale-controlled surface. *Nucleic Acids Res. 33*, e106.
(36) Miron, T., and Wilchek, M. (1993) A simplified method for the preparation of succinimidyl carbonate polyethylene glycol for coupling to protein. *Bioconjugate Chem. 4*, 568–569.
(37) Staros, J. V., Wright, R. W., and Swingle, D. M. (1986) Enhancement by *N*-hydroxysulfosuccinimide of water-soluble carbodiimide-mediated coupling reactions. *Anal. Biochem. 156*, 220–222.
(38) Levison, M. E., Josephson, A. S., and Kirschenbaum, D. M. (1969) Reduction of biological substance by water-soluble phosphine: gamma-globulin (IgG). *Experientia 25*, 126–127.
(39) Cline, D. J., Redding, S. E., Brohawn, S. G., Psathas, J. N., Schneider, J. P., and Thorpe, C. (2004) New water-soluble phosphine as reductants of peptide and protein disulfide bonds: reactivity and membrane permeability. *Biochemistry 43*, 15195–15203.
(40) Kim, W., Lim, S. J., Jung, S., and Shin, S. K. (2010) Binary amine−phosphine passivation of surface traps on CdSe nanocrystals. *J. Phys. Chem. C 114*, 1539–1546.
(41) Hansen, R. E., Roth, D., and Winther, J. R. (2009) Quantifying the global cellular thiol−disulfide status. *Proc. Natl. Acad. Sci. U.S.A. 106*, 422–427.

BC100114Q

Acetylated Hyaluronic Acid/Photosensitizer Conjugate for the Preparation of Nanogels with Controllable Phototoxicity: Synthesis, Characterization, Autophotoquenching Properties, and *in vitro* Phototoxicity against HeLa Cells

Fangyuan Li, Byoung-chan Bae, and Kun Na*

Department of Biotechnology, The Catholic University of Korea, 43-1 Yeokkok2-dong, Wonmi-gu, Bucheon-si, Gyeonggi-do 420-743, Republic of Korea. Received March 6, 2010; Revised Manuscript Received June 1, 2010

A proposal is herein examined for a novel yet simple design of a polymeric nanogel, with tumor targeting properties and a controllable phototoxicity, utilizing a low molecular weight-hyaluronic acid (HA_{LM})/photosensitizer conjugate. HA_{LM} was acetylated prior to being dissolved in DMSO (Ac-HA_{LM}) and then was conjugated with different amounts of pheophorbide a (Pba), resulting in the formulation of self-organizing nanogels in aqueous solutions (Ac−HA−Pba 1, 2, and 3). The nanogels observed were below 200 nm in size, with a monodispersed size distribution. The nanogels displayed auto photoquenching qualities in PBS, while their fluorescent intensity strongly correlated with the amount of Pba in the organic solvent (DMSO or DMF). The critical self-quenching concentration (CQC) of the conjugates was found to have decreased as the content of Pba rose. Although Pba was conjugated with HA, the nanogel's photoactivity, in terms of fluorescent properties, singlet oxygen generation, and photocytotoxicity, was approximately maintained. Confocal imaging and FACS analysis showed that Ac−HA−Pba nanogels were rapidly internalized into HeLa cells via an HA-induced endocytosis mechanism, a process which could be blocked with the application of an excess of HA polymer. The results of the study indicate that HA-based nanogels can potentially be applied in photodynamic therapy (PDT).

INTRODUCTION

Photodynamic therapy (PDT), a promising therapeutic modality for cancer treatment, involves the administration of photosensitizers (PSs) coupled with specific wavelengths of light irradiation, having the effect of significantly increasing production of cytotoxic singlet oxygen, as well as other reactive oxygen species (ROS), causing malignant cell death (*1, 2*). However, problems with water-insolubility and nonspecific distribution after intravenous injection of most PSs limit the range of application in spite of their great efficacy and compel researchers to overcome these hurdles in order to make fuller use of the technique.

To date, a variety of polymer vehicles have been extensively investigated for use with hydrophobic PSs with the objective of achieving not only stable aqueous dispersion but also site-specific delivery. In previous studies, it was shown that the attachment of polyethylene glycol to a conjugate between poly L-lysine and $chlorin_{e6}$ was able to reduce the aggregation of PS and increase tumor targeting (*3*). In addition, two water-soluble polymer conjugates of Zn-protoporphyrin, ZnPP-poly(styrene-maleicacid) and ZnPP-poly(ethylene glycol), were synthesized to make ZnPP water-soluble and investigated for use as an aqueous solution (*4*). Lee et al. also reported enhanced tumor targeting activity in self-assembled chitosan-based nanoparticles encapsulating water-insoluble protophorphyrin IX (*5*). The passive targeting of these polymeric nanoparticles is referred to as the enhanced permeability and retention (EPR) effect, with theory based on the high permeability of blood vessels at tumor sites. However, this targeting modality may release a considerable quantity of drugs before any substantial uptake by malignant cells. To further enhance selective accumulation of PSs into target cells, surface modification, using monoclonal antibodies or specific tumor-seeking molecules, has been attached to PS loaded nanoparticles (*6*−*8*). Although antibody targeting is regarded as a promising strategy, there have been reports that antibody targeting does not increase tumor localization (*9, 10*) and does not address the difficulty in further conjugation without a subsequent decrease in binding capabilities.

Hyaluronic acid (HA), the only nonsulfated glycosaminoglycan composed of repeating disaccharide units of *N*-acetyl-D-glucosamine and D-glucuronic acid (*11*), highlights itself as a potential drug carrier due to its unique properties: to render an appropriate size alongside aqueous stability for passive targeting tumor tissues using the EPR effect; to control active targeting to tumor cells through the selective interaction between HA and its receptors; and to release drugs in targeted cells with enhanced therapeutic efficacy. Naturally occurring HA is widely present in the extracellular matrix (ECM), connective tissues, and bodily fluids and plays a vital role in many pathophysiological processes including cell adhesion, proliferation, and migration. It is also known that HA specific receptors such as CD44 (*12*−*14*) and RHAMM (*15*) overexpress on the surface of various tumor cells, enhancing the binding and internalization of HA. As a result, HA has found success in an extraordinarily broad range of biomedical applications such as molecular imaging (*16, 17*), drug delivery (*18, 19*), and tissue engineering (*20*).

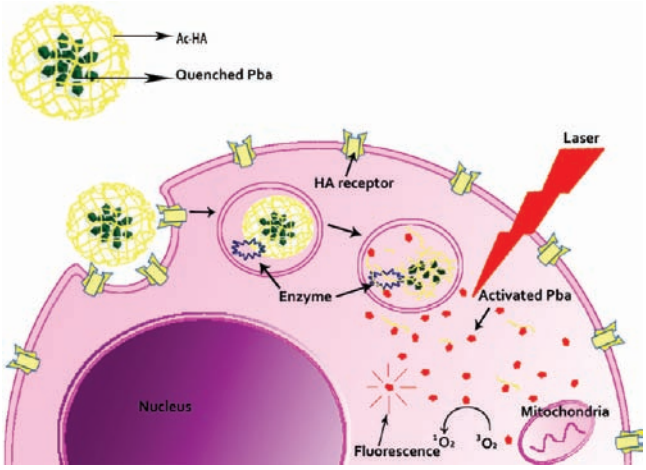
Unfortunately, the strong hydrophility of HA renders itself unpopular for conjugation with hydrophobic drugs, as a result of chemical reactions in polar organic solvents. Some physiochemical methods have been developed to solve this problem (*18, 19*). However, most synthesis approaches using carboxyl groups of HA probably affect the interaction between HA/CD44 and specific receptor-mediated endocytosis of cancer cells (*21, 22*).

Pheophorbide a (Pba), chosen as an attractive second-generation PS, absorbs at longer wavelengths and rapidly exudes

* Corresponding author. Tel: (82) (2) 2164-4832. Fax: (82) (2) 2164-4865. E-mail: kna6997@catholic.ac.kr.

10.1021/bc100116v © 2010 American Chemical Society
Published on Web 06/29/2010

Scheme 1. Schematic Diagram of the PDT Strategy of Ac−HA−Pba[a]



[a] Ac−HA−Pba nanogels in aqueous solution intelligently quenched both the dye's fluorescence and singlet oxygen generation as a result of the hydrophobic ($\pi-\pi$) interaction between Pba's themselves, known as the fluorescence resonance energy transfer effect (FRET). However, the dequenching behavior of nanogels destroyed cancer cells under illumination after internalization due to the cleavage of the HA backbone caused by various intracellular enzymes in cellular compartments.

a very high singlet oxygen yield (*23*). It has been reported that Pba exhibits strong antitumor effects on human lung cancers cells (*24*), hepatoma carcinoma cells (*25*), and uterine sarcoma cells (*26*). The resulting Ac−HA−Pba nanogel, in an aqueous solution, quenched both the dye's fluorescence and singlet oxygen generation through a hydrophobic ($\pi-\pi$) interaction between Pbas themselves, such as the fluorescence resonance energy transfer (FRET) effect. However, the dequenching behavior of the nanogel destroyed cancer cells under illumination after internalization as a result of cleavage of the HA backbone, caused by various intracellular enzymes in cellular compartments (*27*) and reactive oxygen species (*28, 29*) (Scheme 1).

In this study, we synthesized Ac−HA−Pba utilizing a simple two-step reaction method: (1) the acetylation of HA (Ac-HA) capable of being dissolved in both distilled water (DW) and anhydrous dimethyl solfoxide (DMSO) and (2) the conjugation of Ac-HA and Pba through a conventional carbodiimide reaction, in which hydroxyl groups of HA were arranged to be substituted. Physicochemical properties, such as particle size and zeta potential, were then examined. We also detected the photoquenching properties of the Ac−HA−Pba nanogel, target-specific activities, as well as *in vitro* phototoxicity with HeLa cells.

EXPERIMENTAL PROCEDURES

Materials. Oligo hyaluronic acid (HA_{LM}, MW 5800 Da) was kindly provided by the Bioland Company (Cheonan, Korea). Pba was obtained from Frontier Scientific Inc. (Salt Lake City, UT). Acetic anhydride (AA), pyridine, 1, 3-dicyclohexyl carbodiimide (DCC), 4-dimethylaminopyridine (DMAP), formamide, *N*,*N*-dimethylformamide (N,N-DMF), and anhydrous dimethyl sulfoxide (DMSO) were purchased from the Sigma-Aldrich Co. (St. Louis, MO, USA). The dialysis membrane was sourced from Spectrum Laboratories Inc. (Rancho Dominguez, CA). Dulbecco's modified Eagle's medium (DMEM), fetal bovine serum (FBS), antibiotics (penicillin/streptomycin), and Dulbecco's phosphate buffer saline (DPBS) were obtained from GibcoBRL (Invitrogen Corp., Carlsbad, CA). The Live/Dead assay kit containing two fluorescent probes, ethidium homodimer-1 (EthD-1), and CalceinAM were purchased from the Molecular Probe Inc. (Eugene, OR, USA). All other chemicals and solvents were of analytical grade.

Preparation of Ac−HA−Pba Conjugates. In order to prepare the amphiphilic HA_{LM} polymer, acetyl moieties were chemically introduced to HA. HA_{LM} (0.5 g) was dissolved in 10 mL of formamide via vigorous stirring. After adding pyridine (55 μL) and AA (50 μL), the mixture was stirred for a further 12 h. The reactant mixture was placed in a molecular porous dialysis membrane (molecular weight cutoff size 3.5 kDa) against distilled water for three days. The white HA_{LM}-acetate (Ac-HA_{LM}) was obtained by lyophilization. The conjugation of Pba into Ac-HA_{LM} was conducted via a conventional carbodiimide reaction: three different concentrations of Pba (10 mg, 5 mg, and 2.5 mg) were separately added to 10 mL of anhydrous DMSO containing 50 mg of Ac-HA_{LM}. The mixtures were vigorously stirred for 48 h followed by the addition of predetermined amounts of DCC and DMAP. Using distilled water, the reactants were then filtered and dialyzed for three days with a dialysis membrane (MWCO 10 kDa). The dialysis was repeated 3 times to remove unreacted Pba. The final green products were obtained by lyophilization. All of the above reactions were carried out at room temperature. The synthesized Ac−HA−Pba conjugations were analyzed through ^{1}H NMR spectroscopy.

Characterization of the Ac−HA−Pba Nanogel. Self-organized nanogels were prepared by the dispersion of the conjugates into aqueous solution. After filtration with a 0.45 μm syringe filter, the particle size and zeta potential of each sample (1 mg/mL) were determined utilizing a dynamic light scattering instrument (Zetasizer 3000, Malvern Instruments Ltd., UK). The particle production yield was shown to be approximately 75%. As a means of observing the morphology of the nanogel, a droplet of nanogel suspension in distilled water (DW) was deposited on carbon stickers and the water evaporated in a vacuum oven. The dried sample was visualized with a Pt-coating by a field emission scanning electron microscope (FE-SEM; S-4700, Hitachi, Japan). Average size was also assessed by measuring the diameter of particles in the SEM images.

Measurement of the Critical Self-Quenching Concentration. The critical self-quenching concentration (CQC) of Ac−HA−Pba nanogels was measured using a fluorescence probe technique. Pyrene dissolved in acetone was diluted in distilled water to give a concentration of 12×10^{-7} M. Acetone was removed by distillation under vacuum at 60° for 1 h. The acetone-free pyrene solution and each nanogel solution of different concentrations were mixed and incubated for 6 h without light. The final pyrene in each sample solution was 6×10^{-7} M. The excitation spectra of the pyrene were measured at a fixed emission wavelength of 390 nm, and the excitation wavelength was set at 339 nm for the emission spectra of pyrene which were recorded on a RF spectrofluorometer (RF-5301PC, Shimadzu, Japan). The slit width was 10 nm for both excitation and emission.

Optical Spectroscopy. The absorption spectra were acquired using a UV/visible spectrophotometer (UV-2450, Shimadzu, Japan) in a quartz cuvette of 1 cm path length to compare Ac−HA−Pba conjugates with free Pba in DMSO. To estimate the self-quenching effect, Ac−HA−Pba was dissolved in DMSO or PBS, and Pba concentrations were adjusted to 20, 10, 5, 2, 1, 0.5, 0.2, and 0.1 μg/mL. The fluorescence spectra were taken at room temperature in 1 cm × 1 cm optical quartz cells using a Xenon short arc lamp (XBO 150, Ushino, Japan) in a spectrofluorephotometer. All samples were then plated onto 96-well plates to take direct fluorescence images utilizing KODAK Image Station.

To measure the fluorescence quantum yield (FOY), six Ac−HA−Pba suspensions in DMSO with different Pba concentrations of 10, 5, 2, 1, 0.5, and 0.2 μg/mL were prepared to plot a graft of integrated fluorescence intensity against absorbance. Absorbance at the excitation wavelength was recorded from the UV/vis absorbance spectrum and marked as X data, whereas integrated fluorescence intensity, obtained from the fully corrected fluorescence spectrum, was tabled as Y data. The FQY of Ac−HA−Pba conjugates was calculated using free Pba with a known FQY value, according to the following equation:

$$\Phi_X=\Phi_{ST}(Grad_X/Grad_{ST})(\eta_X^2/\eta_{ST}^2)$$

where the subscripts ST and X denote standard and test, respectively, Φ_X is the FQY, Grad is the gradient from the plot of integrated fluorescence intensity against absorbance, and η is the refractive index of the solvent.

Singlet Oxygen Generation. The generation of singlet oxygen ($^1O_2$) was observed chemically by the detection of 9,10-dimethylanthracene (DMA) utilizing fluorescent spectroscopy as an independent method. It is known that DMA reacts irreversibly with $^1O_2$ in many organic solvents and water, which causes a decrease in the intensity of the DMA absorption band at 360 nm (*30*−*32*). Twenty micromolars of DMA was mixed with each solution (N,N-DMF, or DW) of Ac−HA−Pba. The solutions were irradiated with a 670 nm laser source (Institute of Electronics) at 10mW/cm^2. Singlet oxygen-induced reduction of DMA fluorescence intensity (Ex 360 nm and Em 380−550 nm) was recorded at 0, 10, 20, 30, 40, 50, 60, 70, 80, 90, 100, 110, and 120 s using an RF-spectrofluorometer. Singlet oxygen quantum yields ($\Phi\Delta$) were then calculated according to the gradient from the curve of DMA fluorescent intensity (or DMA concentration) against the time of light exposure, utilizing the following equation:

$$\Phi\Delta_U=\Phi\Delta_{ST}(S_U/S_{ST})$$

where U and St denote unknown and standard, respectively, and *S* represents the slope. Free Pba was used as the standard.

Ac−HA−Pba Nanogels in the Cell Culture System. *Cell Culture.* HeLa cells were cultured in suspension in DMEM medium supplemented with 10% FBS and 1% antibiotics at 37° in a balanced air humidified incubator with an atmosphere of 5% CO_2. Cells were maintained in an exponential growth phase through periodic dilutions with fresh medium.

Confocal Microscopy. To observe cellular uptake, HeLa cells were seeded at a density of 1.0×10^5 cells per well on 18 × 18 mm sterile cover glasses inserted into 12-well plates. The medium was replaced with serum-free DMEM containing Ac−HA−Pba or free Pba (Pba concn 15 μg/mL). After 6 h, the cells were rinsed with DPBS, fixed with 4% paraformaldehyde solution for 10 min, and stained with 4, 6-diamidino-2-phenylindole (DAPI 1 μL, 3.63 mM) for 2 min. Cover glasses were then placed on the slide glasses. Internalization of Pba into live cells was monitored by fluorescence using a confocal laser scanning microscope (Zeiss, LSM 510 Meta, Germany). Fluorescence images were analyzed using LSM image browser software (Zeiss, Germany).

Fluorescence Activated Cell Sorting (FACS). To confirm the competitive inhibition of cellular uptake, HeLa cells were exposed to HA polymer (3 mg/mL) and Ac−HA−Pba (Pba concn 0.3 μg/mL) simultaneously and compared with those exposed only to Ac−HA−Pba. The cells were incubated for 1 h, washed, harvested, and resuspended with DPBS. Flow cytometry was performed using a FACScan flow cytometer (Beckman, San Jose, CA, USA). Ten thousand cells (gated events) were counted for each sample, and free Pba fluorescence was detected with logarithmic settings (FL4; Em = 670 nm). Cells were counted as positive if their fluorescence (FL4) was higher than that of cells from an untreated cell suspension. Each experiment was analyzed statistically using the CXP Analysis Program.

Near-Infrared (NIR) Fluorescent Images. HeLa cells were grown in a 96-well culture plate at 1×10^4 cells per well in a 200 μL culture medium. Ac−HA−Pba with two different concentrations were treated to HeLa cells or serum-free DMEM at predetermined incubation times of 0 min, 20 min, 1 h, 6 h, and 12 h, and the plates were observed through NIR fluorescence emissions on the KODAK Image Station.

MTT Assay. HeLa cells at 1×10^4 HeLa cells per well were seeded in 200 μL of cell culture medium in 96-well plates. After cell attachment, the medium were replaced with a serum-free culture. The cells were treated with Ac−HA−Pba or equivalently free Pba and incubated for 6 h. The medium were replaced again with serum-free DMEM, followed by light illumination. The cells were divided into three groups under distinctly different conditions: (1) no irradiation; (2) irradiation for 1 min with a 1 mW/cm^2 laser; (3) irradiation for 5 min with a 1 W/cm^2 laser. Cell viability was determined following incubation for 24 h using 3-[4,5-dimethylthiazol-2-yl]-3,5-diphenyltetrazolium bromide dye (MTT dye, 2 mg/mL) uptake at 570 nm on an ELISA reader. Dark toxicity of Ac−HA−Pba and free Pba was also assessed against HeLa cells incubated for 72 h in a completely lightproof plate.

Live/Dead Viability/Cytotoxicity Assay. A two-color fluorescence cell viability assay was used to measure two recognized parameters of cell viability−intracellular esterase activity and plasma membrane integrity. It is known that nonfluorescent CalceinAM is converted into a green-fluorescent calcein after acetoxymethyl ester hydrolysis by intracellular esterases in live cells and that EthD-1 marks the nuclei by staining dead cells red once the integrity of the cell membrane is compromised (*33*). HeLa cells on glass coverslips were removed from the culture medium, rinsed carefully with Hanks1× balanced salt solution, and placed in the microscope chamber at 37 °C. The cells were then covered with Hanks1× balanced salt solution (2 mL) containing 10 mM pH buffer HEPES (4-(2-hydroxyethyl)piperazine-1-ethanesulfonic acid), 2 μM CalceinAM, 4 μM EthD-1, and Ac−HA−Pba (Pba concn 0.15 μg/mL). The cells were exposed at a small location for 10 min to a 670 nm laser with a power intensity of 1 mW/cm^2. Finally, confocal microscopic images were taken with an oil immersion 60× objective lens in two channels (488-nm excitation of the calcein converted from CalceinAM, 568-nm excitation of the EthD-1), allowing for the concurrent comparison of cells exposed to light alongside those without exposure.

RESULTS AND DISCUSSION

Synthesis of Ac−HA−Pba Conjugates. HA, a linear polysaccharide widely used in drug delivery systems, was selected for the production of PS-conjugated nanogels, from various block copolymers, due to its biocompatibility, biodegradability, and tumor-targeting receptors. However, the possibilities for chemosynthesis of HA, with hydrophobic drugs or other polymers in a single organic phase, are severely limited due to the poor solubility of HA in most organic solvents. To increase the hydrophobicity of HA, partially acetylated derivatives were prepared in formamide through the reaction between the hydroxyl groups of HA and acetic anhydride (AA), while adding pyridine as a catalyzer (Figure 1). Previously, we have described acetylated modification with other polysaccharides, such as pullulan, to increase hydrophobicity (*34*−*36*). By changing the feeding amount of AA for the reaction, control of the degree of AA modification in polymer-acetate could be achieved (*37*). In the present study, acetylation was confined to

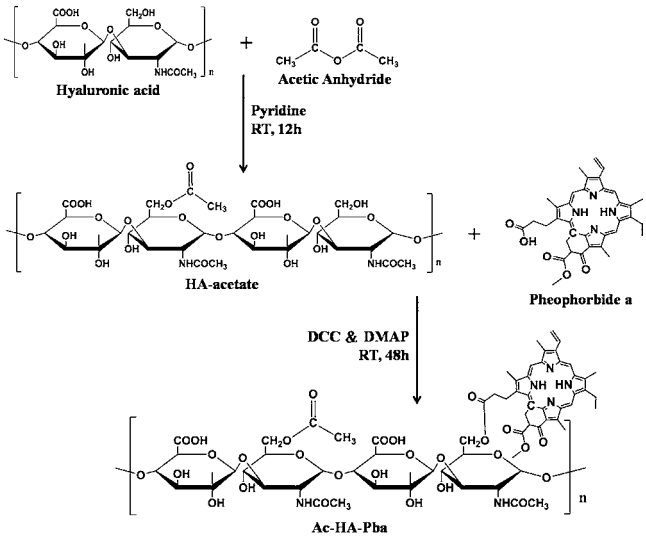


Figure 1. Synthetic scheme of AC-HA-Pba conjugates.

Table 1. Ac−HA−Pba Conjugates with Three Different Pba Contents Were Synthesized, Showing the Characteristics of Self-Organized Ac−HA−Pba Nanogels in an Aqueous Solution

	Pba content[a]	average size (nm)[b]	potential (mV)[c]	CQC ($\times 10^{-6}$ M)[d]
Ac−HA−Pba1	0.31	125.1 ± 1.1	−33.8 ± 0.8	0.26
Ac-HA-*Pba*2	0.17	139.1 ± 0.5	−27.1 ± 1.6	0.83
Ac−HA−Pba3	0.08	150.4 ± 1.5	−21.2 ± 1.0	2.10

[a] The degree of substitution of Pba molecules per 1 unit (2 glucose rings) of HA. [b] Mean diameter (intensity average) measured by dynamic light scattering. [c] Potential detected by zeta potential. [d] Critical self-quenching concentration determined using pyrene.

a low extent because the conversion of HA to HA-acetate (Ac-HA) was required merely to make HA soluble in DMSO for the second conjugation of HA and Pba. Typically, the proton signal of the acetamido methyl group in disaccharide units of HA polymer was observed at $\delta = 1.9$ ppm ($-CH_3$) in the ^{1}H NMR spectrum. Because of the introduction of acetyl groups, the signals from AC-HA slightly increased when compared with those of native HA. Thus, by a comparison of the intensities of peaks from $\delta = 1.9$ ppm from HA and Ac-HA in D_2O, the degree of acetylation was determined as 0.4 acetyl groups per unit (2 glucose rings) of HA. The synthesis of Ac-HA with Pba was successfully carried out using carbodiimide coupling chemistry as schematically shown in Figure 1. The chemical structures of Ac−HA−Pba conjugates were confirmed by ^{1}H NMR. The characteristic peaks of Pba such as ═CH- from 4 pyrrole subunits were identified, while the methyl resonance of the acetamido moiety of HA was 2 ppm (Figure S1, Supporting Information). The degrees of substitution of Pba molecules per unit (2 glucose rings) of HA are in the range of 0.31 to 0.08 (Table 1). Many researchers have reported that most synthesis protocol designs of HA nanoparticles are based on there carboxyl groups, which may impair the binding of HA to its receptors when tumor targeting (*22*). Also, Petra et al. reported that after the hydroxyl groups were modified, the degradation rate of HA derivates is almost the same for the original HA (*38*). From this paper, we considered that the modification of hydroxyl groups in HA is better than that of the carboxyl groups to maintain the nature of HA. It should be noted that the simple two-step reaction scheme utilized in the current study was based on the hydroxyl group of HA.

Size Distribution and Morphology. Ac−HA−Pba conjugates showed self-organizing behavior in aqueous solutions due to the strong hydrophobicity of grafted Pba, the driving force

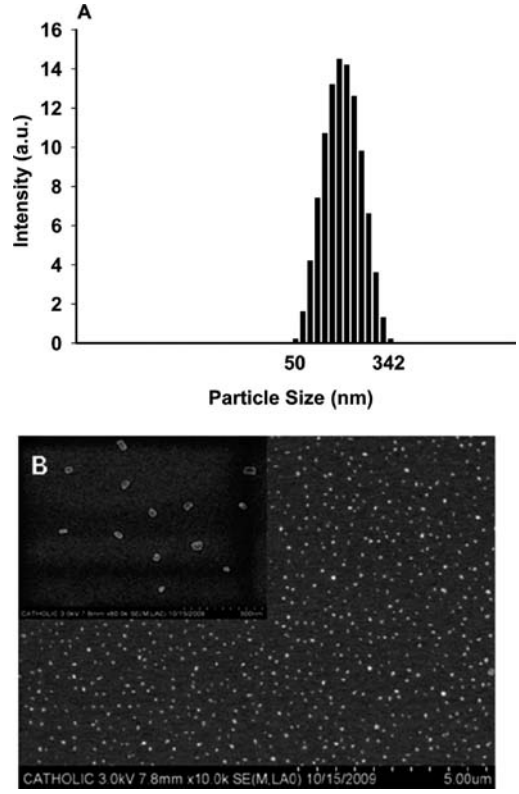


Figure 2. Size distribution histogram measured by dynamic light scattering (A) and morphology observed by a field-emission scanning electron microscope (B) of Ac−HA−Pba1 nanogels.

of aggregation. It is likely that Pba self-organized to form a hydrophobic inner core surrounded by a hydrophilic outer shell of HA. The mean particle size of Ac−HA−Pba1 nanogels was 125 nm with a monodispersed size distribution (Figure 2A). The samples showed a decreasing particle size with increasing Pba content (Table 1). The size of the tumor vascular pore openings has been reported to be significantly larger than those observed along vessels in normal tissues (*39*). The average size of tumor vascular pores is generally 400−600 nm (*40*). Therefore, the greater pore size leads to prolonged retention of Ac−HA−Pba nanogels in tumors. The negative charge, determined by zeta potential measurement, confirmed the presence of HA at the surface of the nanogels (Table 1). This negative surface charge may also help the enhancement of retention times within the body. The FE-SEM images of Ac−HA−Pba1 nanogels revealed that they were homogeneously distributed in spherical shapes with sizes of 40−80 nm (Figure 2B). The smaller size of Ac−HA−Pba1 nanogels when observed through FE-SEM, rather than DLS data, indicates that Ac−HA−Pba1 nanogels have huge water retention properties.

Critical Self-Quenching Concentration (CQC). Pyrene, as a fluorescence probe, was used to investigate the CQCs of Ac−HA−Pba nanogels (*41*). The excitation and emission spectra of pyrene were recorded by an RF spectrofluorometer (Figure 3). In general, changes in pyrene intensity and (0,0) band shift as a function of material concentration were employed to measure critical micelle concentrations (CMC) and critical aggregation concentrations (CAC). Polymers with high concentrations spontaneously formed nanoparticles in an aqueous solution, and pyrene could partition into the polycore of the nanoparticles due to its hydrohopicity, resulting in an increase in pyrene intensity. At the dilution of the polymer suspension, excitation and emission were more weakly exhibited, in line with a reduction of naonoparticle formations. When the

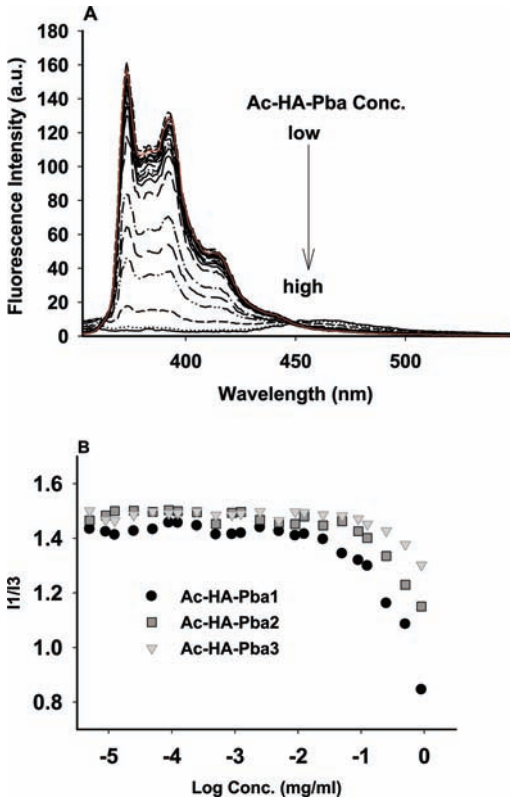


Figure 3. Critical self-quenching concentration (CQC) of Ac−HA−Pba measured by pyrene: emission spectra of pyrene in Ac−HA−Pba1 suspension (A) and the plot of intensity ratio of I_1/I_3 as a function of the logarithm of concentration (B).

concentration was adjust below the CAC, excitation and emission dropped to their lowest levels, both in suspension and in DW.

Interestingly, in the case of Ac−HA−Pba suspensions, the excitation and emission spectra of pyrene were the reverse of the general result (Figure 3). The emission intensity of pyrene gradually decreased with an increase in Ac−HA−Pba1 concentration, while in DW, these were shown to be at their highest levels (the red line in Figure 3A). It is assumed that Pba located in the hydrophobic core interfered with the fluorescent intensity of pyrene due to the strong quenching effect of the hydrophobic interaction between Pba and pyrene, known as the fluorescence resonance energy transfer effect (FRET). Thus, we designated a new term, the critical self-quenching concentration (CQC) (Figure 3B). Table 1 shows that the CQC values of Ac−HA−Pba nanogels decreased alongside an increased Pba content.

Photoactivities of Ac−HA−Pba1 Nanogels. As regards photophysical and photochemical properties, the typical absorption spectra of Ac−HA−Pba conjugates in DMSO were overlapped by that of free Pba with the same Pba concentration of 10 μg/mL (Figure S2, Supporting Information). Also, the fluorescent intensity of Ac−HA−Pba dissociated in DMSO clearly declined alongside a decrease in dye concentration (Figure 4A), whereas in DW it was unclear (Figure 4B), as a likely result of the fact that Ac−HA−Pba begins to form nanogels in DW, while the close geometry between conjugated Pba in the core of nanogels creates the self-quenching effect (*42*).

Combining the absorbance and the emission intensity in DMSO, the fluorescence quantum yield of Ac−HA−Pba conjugates was found to be almost the same when compared with that of standard Pba (Figure S3, Supporting Information). This demonstrates that the conjugation of Ac-HA and Pba does not affect any fluorescent properties of free Pba.

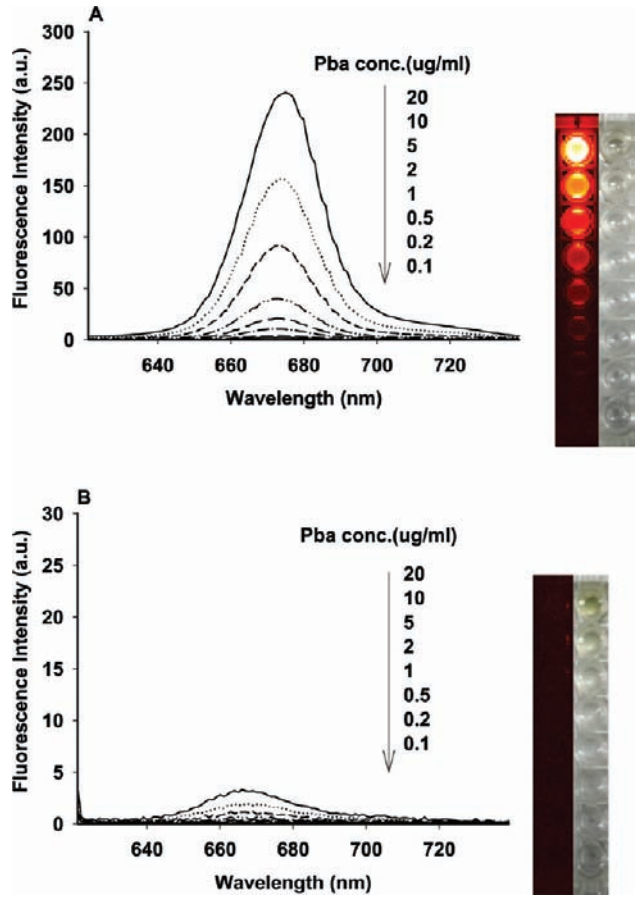


Figure 4. Fluorescence spectra, near-infrared fluorescence images, and optical images of Ac−HA−Pba1 in DMSO (A) and PBS (B).

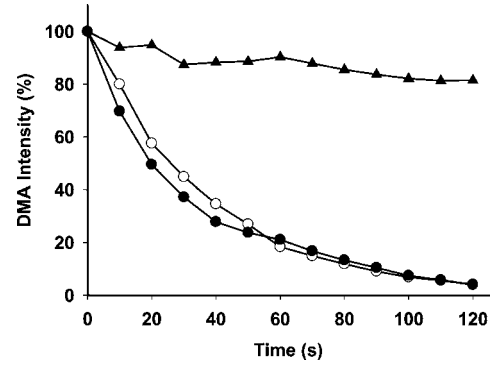


Figure 5. Changes in DMA fluorescent intensity according to time in the presence of Ac−HA−Pba1 conjugates in N,N-DMF (●) or DW (▲), as well as the same concentration of free Pba in N,N-DMF (○). All irradiations were performed using 670 nm light at a fluorescence-rate of 10 mW/cm^2.

DMA was used in the experiment as a detector to evaluate singlet oxygen generation (Figure S4, Supporting Information, and Figure 5). Ac−HA−Pba completely dissolved in DMF resulting in a sharp decline in DMA fluorescent intensity, indicating the rapid generation of singlet oxygen upon laser irradiation. The experiment mixed DMA with free Pba dispersed in N,N-DMF was used as the standard. Singlet oxygen quantum yields ($\Phi\Delta$) of Ac−HA−Pba1, 2, and 3 were calculated as 0.552, 0.550, and 0.546, respectively, by a comparison of the slope for Ac−HA−Pba with the corresponding slope for free Pba ($\Phi = 0.56$). However, singlet oxygen generation can significantly change in a different medium. As self-assembly of Ac−HA−Pba in an aqueous solution leads to fluorescent

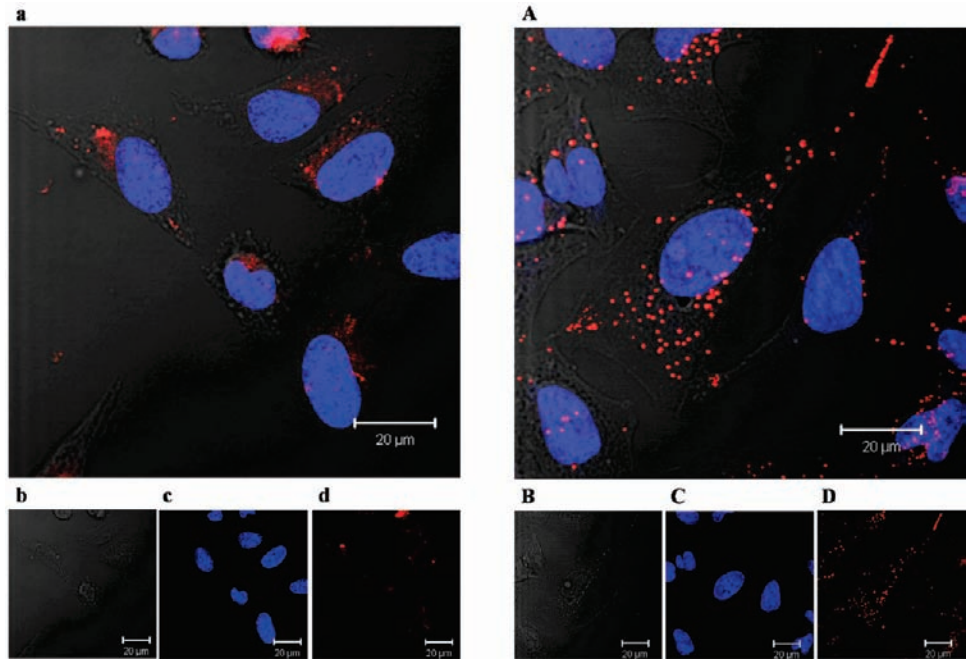


Figure 6. Confocal microscopy images of fixed HeLa cells incubated with Ac−HA−Pba (A−D) or free Pba (a−d) for 6 h. (A,a) Merged image of panels B/C or b/c; (B,b) DIC image; (C,c) DAPI image; (D,d) Pba image. The scale length of each picture is 20 μm.

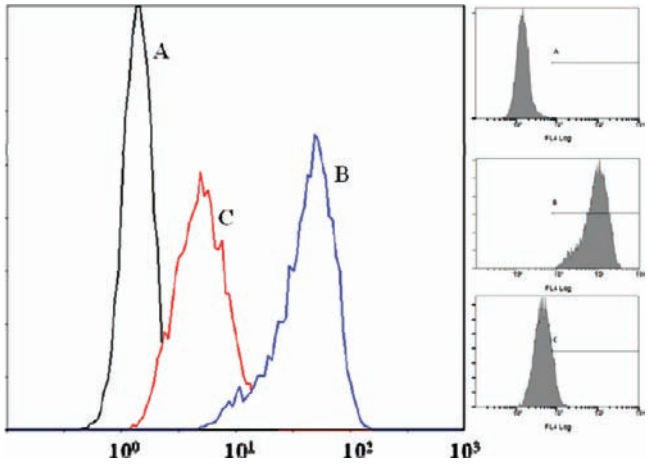


Figure 7. Flow cytometry results of nontreated control cells (A), Ac−HA−Pba treated cells (B), and HA polymer and Ac−HA−Pba cotreated cells (C).

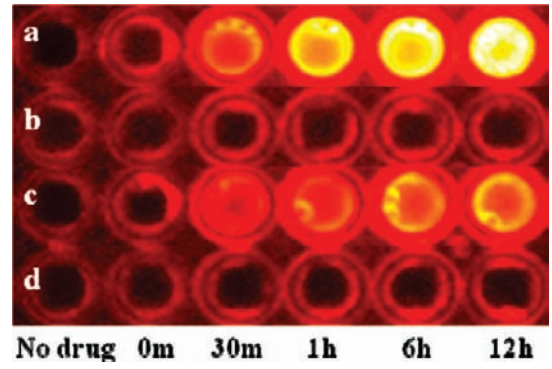


Figure 8. *In vitro* fluorescent image of Ac−HA−Pba induced by time-dependent cellular uptake and degradation of HA: Ac−HA−Pba was exposed to HeLa cells (a, c) or culture medium (b, d) for a predetermined incubation time. Pba concns are 1.0 μg/mL (a, b) or 0.5 μg/mL (c, d), respectively.

quenching, the Ac−HA−Pba nanogels could not be activated into the triplet state by mutual energy transfer, resulting in the concealment of the ability to generate ROS (*43*).

The absence of differences in absorption/fluorescence/singlet oxygen generation for Ac−HA−Pba and free Pba denotes that conjugation with HA maintains the PDT effect of Pba. Though the three samples show similar properties of fluorescence and efficiency of singlet oxygen generation, Ac−HA−Pba1 was chosen for further *in vitro* studies due to it being of the smallest size and the lowest CQC. A small size and lower CQC allow for easier tumor cellular targeting and reduced side effects from photosensitizers.

Cell Uptake of Ac−HA−Pba Nanogels. The cellular uptake behavior of Ac−HA−Pba was monitored by confocal microscopy following incubation for 6 h (Figure 6). The internalization and passive diffusion of Ac−HA−Pba nanogels and Pba, into HeLa cells, were very rapid and effective. The red fluorescence of free Pba induced the formulation of ambiguous clusters, while Ac−HA−Pba appeared as perinuclear punctuate spots in the cytoplasm, suggesting that Ac−HA−Pba was internalized via endocytosis.

To confirm whether the uptake of Ac−HA−Pba nanogels is involved with HA-receptors, competition inhibition studies were performed with an HA polymer with strong binding properties to specific HA-receptors on the surface of tumor cells, potentially reducing the uptake of Ac−HA−Pba nanogels into HeLa cells (*44*, *45*). As shown in Figure 7, HeLa cells incubated with Ac−HA−Pba for 1 h showed a high fluorescence of 99.38%. However, with competition as a result of excess HA polymer (non acetylated HA), the peak of the fluorescence shifted, and the value dropped to 14.90%. The results suggest a significantly greater cellular uptake of Ac−HA−Pba (Figure 7B) than that of Ac−HA−Pba added with HA polymer (Figure 7C), as a consequence of HA receptor-mediated endocytosis. Thus, HA-based nanogels not only selectively target cancer cells but also improve the internalization of photosensitizers within targeted cancer cells.

The Ac−HA−Pba nanogel was designed for internalization within cancer cells via HA receptor−mediator endocytosis. The

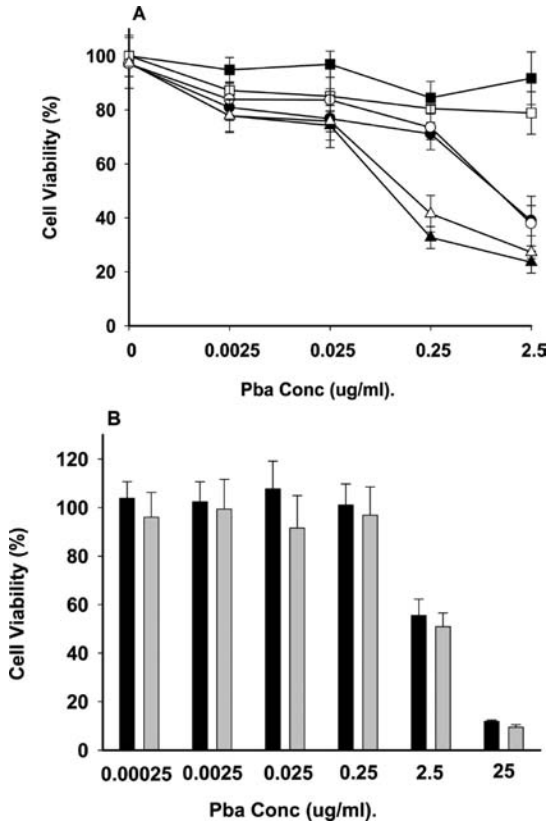


Figure 9. Viability of HeLa cells treated with Ac−HA−Pba (□, ○, Δ) and Pba (■, ●, ▲) after photoirradiation for 0 min (□, ■), 1 min (○, ●), or 5 min (Δ, ▲) using 670 nm light at a fluorescence rate of 1 mW/cm^2 (A). Dark toxicity of Ac−HA−Pba (black bar) and free Pba (gray bar) (B).

internalized nanogel goes to the lysozome, which has a lot of enzymes passing through the endosome for polysaccharide cleavage, and at last, photoactivity appears in the lysozome as a result of the removal of the FRET effect (Scheme 1). In an attempt to prove this theory, nanogels were coincubated with HeLa cells, and the fluorescence image as a function of time was observed with a KODAK image station (Figure 8). As incubation time increased, the fluorescence became more pronounced due to an increase in Pba concentrations. The results of confocal images and FACS indicate that the cellular uptake of Ac−HA−Pba nanogels correlated well with the theory. However, the nanogels incubated in a cell culture medium without cells showed no fluorescence. Form the above results, we conclude that Ac-HA-based nanogels are internalized by HA receptor-mediated endocytosis and then disintegrated by enzymes in the intracellular microenvironment, leading to the release of fluorescence exhibiting Pba.

Phototoxicity of Ac−HA−Pba against Cancer Cell Lines. The efficacy of Ac−HA−Pba nanogels as PDT agents depends on the production of singlet oxygen (*46*). As the singlet oxygen quantum yield is similar to that of free Pba, tumor cells treated with Ac−HA−Pba may not show a significant difference from those treated with Pba. As shown in Figure 9A, the group with no light and no drug treatment was set as 100%, and the other data were normalized for comparison. The nanogel samples of different Pba concentrations (0.0025, 0.0250, 0.2500, and 2.5000 μg/mL) showed a cytotoxicity similar to that of free Pba in each group with laser treatment. An increase in Pba concentrations or the prolongation of illumination time brought about higher cell death. However, samples treated only with Ac−HA−Pba nanogels or laser excitation did not cause cytotoxicity against HeLa cells. The dark toxicity was also evaluated by the MTT assay. With a long incubation time of 72 h, Ac−HA−Pba nanogels went inside HeLa cells, causing intracellular HA degradation and releasing Pba. Thus, Ac−HA−Pba nanogels displayed a slightly lower dark toxicity than that of free Pba in the range of the concentrations used (Figure 9B).

To further assess the phototoxicity of Ac−HA−Pba naonogels, their tumor cell killing activity was also determined by the live and dead assay. Stained live and dead cells treated with CalceinAM and EthD-1 were visualized as green and red light emissions, respectively, through fluorescence microscopy (Figure 10). No toxicity was found in the control cells treated with light only. Unlike the control, HeLa cells treated by Ac−HA−Pba showed small, bright, red dots where also treated by a laser (Figure 9A). It was clearly evident that the combination of treatment with Ac−HA−Pba nanogels and exposure to laser light resulted in selected cell death.

CONCLUSIONS

A HA/photosensitizer conjugate system has seldom been reported as a potential photosensitizer carrier for photodynamic

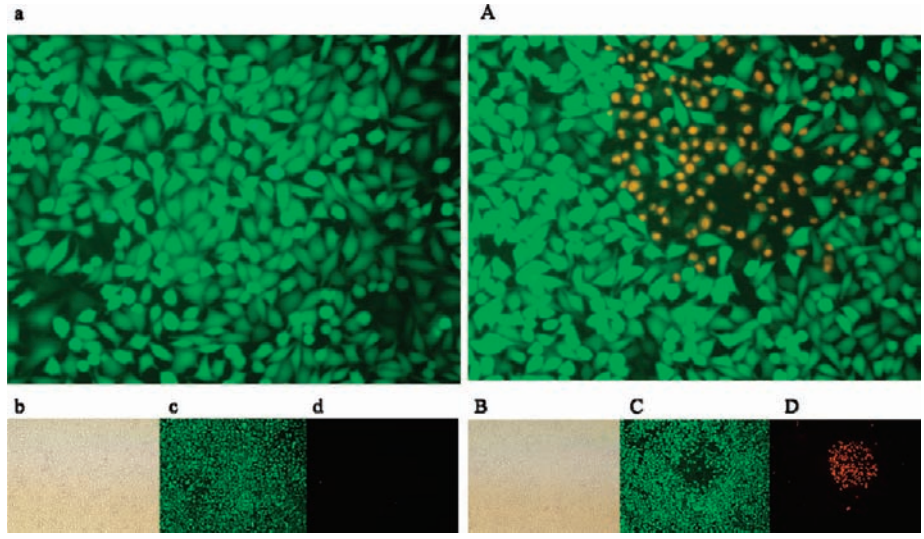


Figure 10. Detection of photodamage by fluorescence microscopy with fluorescent probes (double-staining with CalceinAM and EthD-1: the Ac−HA−Pba group (A−D) and the control group without drug treatment (a−d) were irradiated with a 1 mW/cm^2 laser for 10 min at a small dot, in which the red dead cells might appear. (A,a) Compound pictures of c/d or C/D; (B,b) optical images; (C,c) control living cells without irradiation; green fluorescence of CalceinAM; (D,d) dead cells after PDT treatment; red fluorescence of EthD-1.

therapy. In this study, we introduced a simple method for the solubilization of HA_{LM} in an organic solvent. The method was utilized to conjugate Pba to HA_{LM} (Ac−HA−Pba conjugate) and self-organized nanogels, with the diameter below 150 nm, was prepared by simple dispersion in an aqueous solution. The results displayed autoquenching properties on photoactivity. As the nanogel was incubated with cells, the autoquenching behavior disappeared due to the degradation of the HA backbone by attacks from enzymes in the presence of intracellular compartments such as the endosome and lysosome. The nanogels also show HA-induced tumor homing properties, resulting in a rapid internalization rate. Moreover, the cytotoxicity of the nanogel is similar to that of free Pba with light, while the nanogel reveals very low cytotoxicity against cancer cells without light. Therefore, Ac−HA−Pba nanogels may be instrumental in the design of new photodynamic therapies utilizing a minimum of unfavorable phototoxicity.

ACKNOWLEDGMENT

This work was financially supported by Fundamental R&D Program for Core Technology of Materials, Ministry of Knowledge Economy, Republic of Korea.

Supporting Information Available: Additional data associated with this article. Figure S1 showing ^{1}H NMR spectra, Figure S2 showing absorption spectra, Figure S3 showing fluorescence quantum yields, and Figure S4 showing singlet oxygen generation. This material is available free of charge via the Internet at http://pubs.acs.org.

LITERATURE CITED

(1) Dolmans, D. E., and Dai Fukumura, R. K. J. (2003) Photodynamic therapy for cancer. *Nature Rev. Cancer 3*, 380–387.
(2) Brown, S. B., Brown, E. A., and Walker, I. (2004) The present and future role of photodynamic therapy in cancer treatment. *Lancet Oncol. 5*, 497–508.
(3) Hamblin, M., Miller, J., Rizvi, I., Ortel, B., Maytin, E., and Hasan, T. (2001) Pegylation of a chlorine6 polymer conjugate increases tumor targeting of photosensitizer. *Cancer Res. 61*, 7155.
(4) Regehly, M., Greish, K., Rancan, F., Maeda, H., Bohm, F., and Roder, B. (2007) Water-soluble polymer conjugates of ZnPP for photodynamic tumor therapy. *Bioconjugate Chem. 18*, 494–499.
(5) Lee, S., Park, K., Oh, Y., Kwon, S., Her, S., Kim, I., Choi, K., Kim, H., and Lee, S. (2009) Tumor specificity and therapeutic efficacy of photosensitizer-encapsulated glycol chitosan-based nanoparticles in tumor-bearing mice. *Biomaterials 30*, 2929–2939.
(6) Konan, Y. N., Gurny, R., and Allémann, E. (2002) State of the art in the delivery of photosensitizers for photodynamic therapy. *J. Photochem. Photobiol., B 66*, 89–106.
(7) Allison, R. R., Mota, H. C., Bagnato, V. S., and Sibata, C. H. (2008) Bio-nanotechnology and photodynamic therapy—State of the art review. *Photodiagn. Photodyn. Ther. 5*, 19–28.
(8) Chatterjee, D., Fong, L., and Zhang, Y. (2008) Nanoparticles in photodynamic therapy: an emerging paradigm. *Adv. Drug Delivery Rev. 60*, 1627–1637.
(9) Kirpotin, D., Drummond, D., Shao, Y., Shalaby, M., Hong, K., Nielsen, U., Marks, J., Benz, C., and Park, J. (2006) Antibody targeting of long-circulating lipidic nanoparticles does not increase tumor localization but does increase internalization in animal models. *Cancer Res. 66*, 6732.
(10) Hatakeyama, H., Akita, H., Ishida, E., Hashimoto, K., Kobayashi, H., Aoki, T., Yasuda, J., Obata, K., Kikuchi, H., and Ishida, T. (2007) Tumor targeting of doxorubicin by anti-MT1-MMP antibody-modified PEG liposomes. *Int. J. Pharm. 342*, 194–200.
(11) Necas, J., Bartosikova, L., Brauner, P., and Kolar, J. (2008) Hyaluronic acid (hyaluronan): a review. *Veterinarni Medicina 53*, 397–411.
(12) Aruffo, A., Stamenkovic, I., Melnick, M., Underhill, C., and Seed, B. (1990) CD44 is the principal cell surface receptor for hyaluronate. *Cell 61*, 1303–1313.
(13) Culty, M., Nguyen, H., and Underhill, C. (1992) The hyaluronan receptor (CD44) participates in the uptake and degradation of hyaluronan. *J. Cell Biol. 116*, 1055.
(14) Underhill, C. (1992) CD44: the hyaluronan receptor. *J. Cell Sci. 103*, 293–298.
(15) Entwistle, J., Hall, C., and Turley, E. (1996) HA receptors: regulators of signalling to the cytoskeleton. *J. Cell. Biochem. 61*, 569–577.
(16) Bhang, S., Won, N., Lee, T., Jin, H., Nam, J., Park, J., Chung, H., Park, H., Sung, Y., and Hahn, S. (2009) Hyaluronic acid-quantum dot conjugates for in vivo lymphatic vessel imaging. *ACS Nano 3*, 1389–1398.
(17) Lee, H., Choi, S., and Park, T. (2006) Direct visualization of hyaluronic acid polymer chain by self-assembled one-dimensional array of gold nanoparticles. *Macromolecules 39*, 23–25.
(18) Luo, Y., and Prestwich, G. (1999) Synthesis and Selective Cytotoxicity of a Hyaluronic Acid- Antitumor Bioconjugate. *Bioconjugate Chem. 10*, 755–763.
(19) Lee, H., Lee, K., and Park, T. (2008) Hyaluronic acid-paclitaxel conjugate micelles: synthesis, characterization, and antitumor activity. *Bioconjugate Chem. 19*, 1319–1325.
(20) Ohri, R., Hahn, S., Hoffman, A., Stayton, P., and Giachelli, C. (2004) Hyaluronic acid grafting mitigates calcification of glutaraldehyde-fixed bovine pericardium. *J. Biomed. Mater. Res. 70*, 328–334.
(21) Christner, J., Brown, M., and Dziewiatkowski, D. (1977) Interaction of cartilage proteoglycans with hyaluronic acid. The role of the hyaluronic acid carboxyl groups. *Biochem. J. 167*, 711.
(22) Peach, R., Hollenbaugh, D., Stamenkovic, I., and Aruffo, A. (1993) Identification of hyaluronic acid binding sites in the extracellular domain of CD44. *J. Cell Biol. 122*, 257.
(23) Hajri, A., Wack, S., Meyer, C., Smith, M., Leberquier, C., Kedinger, M., and Aprahamian, M. (2002) In vitro and in vivo efficacy of Photofrin® and pheophorbide a, a bacteriochlorin, in photodynamic therapy of colonic cancer cells. *Photochem. Photobiol. 75*, 140–148.
(24) Yin, X., Zhou, J., Jie, C., Xing, D., and Zhang, Y. (2004) Anticancer activity and mechanism of *Scutellaria barbata* extract on human lung cancer cell line A549. *Life Sci. 75*, 2233–2244.
(25) Chan, J., Tang, P., Hon, P., Au, S., Tsui, S., Waye, M., Kong, S., Mak, T., and Fung, K. (2006) Pheophorbide a, a major antitumor component purified from *Scutellaria barbata*, induces apoptosis in human hepatocellular carcinoma cells. *Planta Med. 72*, 28.
(26) Tang, P., Liu, X., Zhang, D., Fong, W., and Fung, K. (2009) Pheophorbide a based photodynamic therapy induces apoptosis via mitochondrial-mediated pathway in human uterine carcinosarcoma. *Cancer Biol. Ther.* 8.
(27) Toole, B. (2004) Hyaluronan: from extracellular glue to pericellular cue. *Nature Rev. Cancer 4*, 528–539.
(28) Soltes, L., Mendichi, R., Kogan, G., Schiller, J., Stankovska, M., and Arnhold, J. (2006) Degradative action of reactive oxygen species on hyaluronan. *Biomacromolecules 7*, 659–668.
(29) Frati, E., Khatib, A. M., Front, P., Panasyuk, A., Aprile, F., and Mitrovic, D. R. (1997) Degradation of hyaluronic acid by photosensitized riboflavin in vitro. Modulation of the effect by transition metals, radical quenchers, and metal chelators. *Free Radical Biol. Med. 22*, 1139–1144.
(30) Corey, E., and Taylor, W. (1964) A study of the peroxidation of organic compounds by externally generated singlet oxygen molecules. *J. Am. Chem. Soc. 86*, 3881–3882.
(31) Usui, Y. (1973) Determination of quantum yield of singlet oxygen formation by photosensitization. *Chem. Lett. 2*, 743–744.

(32) Wilkinson, F., Helman, W., and Ross, A. (1995) Rate constants for the decay and reactions of the lowest electronically excited singlet state of molecular oxygen in solution. An expanded and revised compilation. *J. Phys. Chem. Ref. Data 24*, 663–1022.
(33) King, M. (2000) Detection of dead cells and measurement of cell killing by flow cytometry. *J. Immunol. Methods 243*, 155–166.
(34) Na, K., Bum Lee, T., Park, K., Shin, E., Lee, Y., and Choi, H. (2003) Self-assembled nanoparticles of hydrophobically-modified polysaccharide bearing vitamin H as a targeted anti-cancer drug delivery system. *Eur. J. Pharm. Sci. 18*, 165–173.
(35) Na, K., Lee, K., and Bae, Y. (2004) pH-sensitivity and pH-dependent interior structural change of self-assembled hydrogel nanoparticles of pullulan acetate/oligo-sulfonamide conjugate. *J. Controlled Release 97*, 513–525.
(36) Na, K., Seong Lee, E., and Bae, Y. (2003) Adriamycin loaded pullulan acetate/sulfonamide conjugate nanoparticles responding to tumor pH: pH-dependent cell interaction, internalization and cytotoxicity in vitro. *J. Controlled Release 87*, 3–13.
(37) Yang, H., Park, I., and Na, K. (2009) Biocompatible microspheres based on acetylated polysaccharide prepared from water-in-oil-in-water (W1/O/W2) double-emulsion method for delivery of type II diabetic drug (exenatide). *Colloids Surf., A 340*, 115–120.
(38) Petra, M., Slavomir, B., Bohumil, S., Eva, M., Vladimir, V., and Martin, K. (2006) Synthesis and characterization of new biodegradable hyaluronan alkyl derivatives. *Biopolymers 82*, 74–79.
(39) Campbell, R. (2006) Tumor physiology and delivery of nanopharmaceuticals. *Anti-Cancer Agents Med. Chem. (Formerly Curr. Med. Chem.) 6*, 503–512.
(40) Maeda, H., Wu, J., Sawa, T., Matsumura, Y., and Hori, K. (2000) Tumor vascular permeability and the EPR effect in macromolecular therapeutics: a review. *J. Controlled Release 65*, 271–284.
(41) Kalyanasundaram, K., and Thomas, J. (1977) Environmental effects on vibronic band intensities in pyrene monomer fluorescence and their application in studies of micellar systems. *J. Am. Chem. Soc. 99*, 2039–2044.
(42) Lakowicz, J., and Masters, B. (2008) Principles of fluorescence spectroscopy. *J. Biomed. Optics 13*, 029901.
(43) Choi, Y., Weissleder, R., and Tung, C. (2006) Selective antitumor effect of novel protease-mediated photodynamic agent. *Cancer Res. 66*, 7225.
(44) Lee, H., Ahn, C., and Park, T. (2008) Poly [lactic-co-(glycolic acid)]-grafted hyaluronic acid copolymer micelle nanoparticles for target-specific delivery of doxorubicin. *Macromol. Biosci. 9*, 336–342.
(45) Luo, Y., Ziebell, M., and Prestwich, G. (2000) A hyaluronic acid-taxol antitumor bioconjugate targeted to cancer cells. *Biomacromolecules 1*, 208–218.
(46) Nilsson, R., Merkel, P., and Kearns, D. (1972) Unambiguous evidence for the participation of singlet oxygen in photodynamic oxidation of amino acids. *Photochem. Photobiol. 16*, 117–124.

BC100116V

Kinetic Analysis of His-Tagged Protein Binding to Nickel-Chelating Nanolipoprotein Particles

Craig D. Blanchette,[†] Nicholas O. Fischer,[†] Michele Corzett,[†] Graham Bench,[‡] and Paul D. Hoeprich*[,†]

Physical and Life Sciences Directorate, and Center for Accelerator Mass Spectrometry, Lawrence Livermore National Laboratory, Livermore, California 94551. Received March 8, 2010; Revised Manuscript Received April 23, 2010

Nanolipoprotein particles (NLPs) are discoidal self-assembling membrane mimetics that have been primarily used as a platform for the solubilization and stabilization of membrane proteins. Nickel-chelating nanolipoprotein particles (NiNLPs) containing nickel-chelating lipids (Ni-lipid) for the targeted immobilization of His-tagged proteins hold promise as carriers of hydrophilic biological molecules for a range of applications. The effect of protein loading (i.e., the number of proteins bound per NiNLP) and Ni-lipid content on the time scales and kinetics of binding are important to various applications such as vaccine development, diagnostic imaging, and drug delivery. We have immobilized hexa-His-tagged LsrB, a *Yersinia pestis* transport protein, onto NiNLPs to examine the effect of protein binding stoichiometry and Ni-lipid content on the time scales and kinetics of protein binding by surface plasmon resonance (SPR). Data indicate that the dissociation half-time increases with Ni-lipid content up to a molar concentration of 35% and decreases as the number of bound protein per NiNLP increases. These findings indicate that the kinetics of protein binding are highly dependent on both the number of bound protein per NiNLP and Ni-lipid content.

INTRODUCTION

Purified apolipoproteins and lipids self-assemble *in vitro* to form discoidal bilayer patches that are stabilized by binding of the lipoproteins to the hydrophobic perimeter of the lipid bilayer (*1*−*10*). These nanolipoprotein particles (NLPs), also referred to as reconstituted high density lipoproteins (rHDLs) and nanodiscs, have been primarily used as a platform for the solubilization and stabilization of membrane proteins (*6, 7, 9, 11, 12*). Indeed, a wide range of different membrane proteins have been incorporated into and solubilized by NLPs, including bacterial rhodopsin (*8, 9, 11*−*13*), hydrogenases (*6*), cytochrome P450 (*14, 15*), β(2)-adrenergic receptor (*16, 17*), a membrane spanning fragment of CD4 (*18*), human mitochondrial voltage-dependent anion channel (VDAC-1) (*19*), and human monoamine oxidase A (*20*). In addition to this application, NLPs have been used as drug delivery platforms (*21*−*26*) and diagnostic imaging particles (*27*). The use of NLPs in these applications has been primarily based on hydrophobic interactions between the particle core (i.e., the hydrophobic interior of the lipid bilayer) and the molecule of interest. Although this type of interaction is vital for applications requiring the solubilization of membrane proteins, it is not necessarily the only mode of associating a molecule of interest to the NLP. In fact, restricting the interaction to simply hydrophobic molecules greatly limits the potential range of NLP applications since hydrophilic molecules are excluded under these conditions.

The primary reason why hydrophobic interactions have been used to incorporate biological molecules into the NLP is that the NLP has no other inherent functionality for molecular conjugation. However, by utilizing functionalized lipid materials during NLP assembly, one can readily impart novel functionality into the assembled particle, such as utilizing lipids with functionalized head groups. In fact, the diversity in both protein and lipid components that have been successfully used to assemble NLPs (*1, 3, 28*−*32*) demonstrates the robust nature of the assembly process and hints at facile NLP functionalization by incorporating modified starting materials. The resulting functionalized NLPs can be used to capture recombinant proteins, peptides, drugs, and oligonucleotides. These NLP−cargo complexes can then be used for a range of applications, including vaccine development, drug targeting and delivery, therapeutic imaging, and the study of receptor/antigen interactions.

With this goal in mind, we previously demonstrated the facile preparation of nickel-chelating nanolipoprotein particles (NiNLPs) for the targeted immobilization of any His-tagged protein (*33*). This conjugation scheme was based on the highly characterized reversible interaction between His-tagged proteins and chelated nickel (*34, 35*). Recombinant engineering of His-tagged proteins is a common practice in molecular biology and proteomics, and is readily achievable in a variety of protein expression systems. As such, a substantial library of recombinant His-tagged proteins is available for NiNLP immobilization. In this previous study, NLPs containing various different helper lipids were assembled in the presence of a nickel-chelating lipid, 1,2-dioleoyl-*sn*-glycero-3-{[*N*(5-amino-1-carboxypentyl) iminodiacetic acid] succinyl}(nickel salt) (from herein referred to as Ni-lipid), at a lipid molar percentage of 10%. The resultant NiNLPs were used successfully to conjugate several His-tagged proteins, including bacteriocin pesticin (Pst) from *Y. pestis*, the *Y. pestis* quorum sensing protein lsrG, and the light chain of botulinum neurotoxin A (*36*).

This initial study was highly valuable in demonstrating both the ability to assemble NiNLPs and to conjugate His-tagged proteins to the assembled NiNLP. However, the effect of Ni-lipid concentration on the maximal His-tagged protein binding stoichiometry (i.e., the maximal number of proteins/NiNLP) and NiNLP-His-tagged protein kinetics was not investigated. The interaction between chelated nickel and polyhistidine tags is reversible, and both the affinity and dissociation half-time of this interaction are strongly dependent on the density and availability of chelated nickel on the immobilizing surface

* To whom correspondence should be addressed. E-mail: hoeprich2@llnl.gov.

[†] Physical and Life Sciences Directorate.

[‡] Center for Accelerator Mass Spectrometry.

10.1021/bc100129s © 2010 American Chemical Society
Published on Web 06/29/2010

(*37*−*39*). Thus, a better understanding of the effects of Ni-lipid concentration on NiNLP/His-tagged protein binding and kinetics will be necessary to understand the time scales and protein loading capacity of the NiNLP for the aforementioned *in vivo* and *in vitro* applications.

In this study, NLPs functionalized with varying ratios of Ni-lipid were prepared, purified, and evaluated in terms of His-tagged protein immobilization. Different ratios of a Ni-lipid were doped into NiNLP assembly reactions that consisted of dimyristoyl-*sn*-glycero-3-phosphocholine (DMPC), the 22 kDa N-terminal truncation of human apolipoprotein E4 (apoE422K) (*7, 8, 28*) and sodium cholate. The Ni-lipid molar ratio was varied from 0 to 40%, and the resulting NiNLPs were characterized by size exclusion chromatography (SEC), nondenaturing gradient gel electrophoresis (NDGGE), proton induced X-ray emission (PIXE), and atomic force microscopy (AFM). In addition, analytical SEC (aSEC) and surface plasmon resonance (SPR) were used to assess the effect of Ni-lipid concentration on the maximal number of His-tagged proteins that could bind to a single NiNLP. Furthermore, SPR was used to examine the effect of protein binding density and Ni-lipid concentration on the protein binding kinetics between His-tagged proteins and NiNLPs. Hexa-His-tagged LsrB (herein referred to as LsrB), a *Y. pestis* protein involved in the ABC transporter complex, was used as a model His-tagged protein.

MATERIALS AND METHODS

Materials. 1,2-Dimyristoyl-*sn*-glycero-3-phosphocholine (DMPC) and 1,2-dioleoyl-*sn*-glycero-3-{[*N*(5-amino-1-carboxypentyl)iminodiacetic acid] succinyl}(nickel salt) (Ni-lipid) were purchased from Avanti Polar Lipids (Alabaster, AL). All other reagents were ordered from Sigma-Aldrich (St. Louis, MO).

Protein Expression and Purification. The expression clone for the 22 kDa N-terminal fragment of apolipoprotein E4 (apoE422K, kindly provided by Dr. Karl Weisgraber) featuring a cleavable His-tag (26) was expressed and purified as previously described (*28*). The expression clone for the *Y. pestis* protein used in this study, LsrB, was generated by amplification from genomic DNA (*Y. pestis* KIM D27) and the full length ORFs were directly cloned into a modified pETBlue expression plasmid encoding a C-terminal hexa-His tag. Plasmids were subsequently transformed into BL21(DE3)pLacI competent cells (Novagen, Madison, WI). Cells were grown in LB media with 50 μg/mL ampicillin, pelleted, and lysed using a high-pressure homogenizer (Emulsiflex-C5, Avestin, Ottawa, Canada). Insoluble material was pelleted, and soluble His-tagged protein was purified with a HisTrap HP column (GE, Piscataway, NJ). Immobilized protein was eluted with imidazole and further purified by SEC using a HiLoad 26/60 Superdex 75 prep-grade column (GE Healthcare, Piscataway, NJ).

NiNLP Assemblies. NiNLPs were assembled according to a previously reported procedure (*33*) with slight modifications. Briefly, lipids were either prepared or obtained in chloroform and aliquoted into glass vials. The appropriate amount of Ni-lipid and DMPC were determined prior to the experiment and added to a glass reaction. Total lipid-to-apoE422K molar ratios were varied from 180 to 125 depending on the Ni-lipid molar fraction: 180:1 (0% Ni-lipid), 180:1 (5% Ni-lipid), 170:1 (10% Ni-lipid), 162:1 (15% Ni-lipid), 157:1 (20% Ni-lipid), 150:1 (25% Ni-lipid), 141:1 (30% Ni-lipid), 132:1 (35% Ni-lipid), and 125:1 (40% Ni-lipid). Chloroform was then removed using a stream of N_2 under agitation to form a thin lipid film, which was further dried under vacuum for at least 2 h. Lipids were then solubilized in TBS buffer (10 mM Tris and 150 mM NaCl, pH 7.4) using 20 mM sodium cholate. After the addition of apoE422K (150 μM in final assembly volume), samples were incubated at 23.8 °C for at least 2 h. Assemblies were dialyzed overnight against TBS to remove cholate and then filtered using a 0.22 μm spin filter to remove any particulates. Samples were subsequently analyzed and purified by SEC (Superdex 200, 10/300 GL column, GE Healthcare, Piscataway, NJ) in TBS buffer (0.5 mL/min flow rate). The exclusion limit of the column was determined with Blue Dextran 2000. Two hundred fifty microliter SEC fractions were collected every 30 s, and NLP homogeneity in each fraction was assessed by NDGGE. For NDGGE analysis, 4−20% Tris-glycine polyacrylamide gels were used (Invitrogen, Carlsbad, CA) and subsequently stained with SyproRuby (BioRad, Hercules, CA) and imaged using Typhoon 9410 Variable Mode Imager (GE Healthcare). SEC fractions containing homogeneous NLP populations of the appropriate size, as assessed by native gel analysis (i.e., the presence of a single band at the correct MW), were concentrated using 50k molecular weight cutoff (MWCO) spin concentrators (Agilent Technologies, Santa Clara, CA). The apoE422K concentration was determined using Advanced Protein Assay Reagent (Cytoskeleton Inc., Denver, CO), where BSA was used as the standard. The concentrated NiNLP samples were then stored at 4 °C until further use.

NiNLP Component Analysis. To determine the component ratios of assembled NiNLPs, phospholipid and nickel content were quantified. Phospholipid content was determined using an enzymatic method to detect choline (Phospholipids C Assay kit, Wako Diagnostics, Richmond, VA). Nickel content was quantified using the X-ray fluorescence technique proton induced X-ray emission (PIXE) at the nuclear microprobe facility within Lawrence Livermore National Laboratory (*40*). For PIXE analysis, NiNLP samples were dialyzed into 10 mM ammonium acetate. The samples (0.5 μL) were spotted onto polycarbonate polyvinylpyrrole-free membranes (10 μm thick) (GE Osmonics, Minnetonka, MN) and subsequently dried prior to analysis. X-ray spectra were analyzed using the PIXE spectrum fitting code PIXEF to extract characteristic X-ray peak areas (or yields) for Ni and to convert Ni X-ray yields to concentrations (*41*).

AFM Analysis of NLPs. AFM images were acquired using a MFP-3D-CF AFM (Asylum Research, Santa Barbara, CA). Details of the imaging parameters have been described elsewhere (*8, 10*).

LsrB-NiNLP Binding Quantified by Analytical SEC. Because of the significant size difference between the NiNLPs and LsrB, aSEC was used as a quantitative tool to measure the number of proteins bound per NiNLP as a function of Ni-lipid content. NiNLPs were purified to homogeneity with diameters averaging 23.5 nm. Previously, computational modeling of apoE422K containing NLPs indicated that NLPs 23.5 nm in diameter have 6 apoE422K per NLP (*8*). Therefore, in these experiments, the NiNLP concentration was calculated on the basis of the apoE422K concentration by assuming that each NiNLP contained 6 apoE422K scaffold proteins (*8*). LsrB was incubated with NiNLPs at different LsrB/NiNLP ratios for 30 min and then subjected to aSEC analysis (Superdex PC 3.2/30 column, GE Healthcare, Piscataway, NJ) in TBS buffer. A flow rate of 0.15 mL/min was used to ensure no overlap in the elution of unbound LsrB and NiNLP bound LsrB. The area under each SEC peak was determined using the software program Origin Pro 7.0 to quantify the number of LsrB proteins/NiNLP.

LsrB-NiNLP Binding Kinetics Quantified by Surface Plasmon Resonance (SPR). Binding kinetics were determined by SPR using a Biacore 3000 instrument (Biacore AB, Uppsala, Sweden). TBS (10 mM Tris and 150 mM NaCl, pH 7.4) was used as the running buffer. All buffers were filtered (0.22 μm) and thoroughly degassed prior to SPR experiments. NLPs were immobilized on the lipophilic L1 sensor chip purchased from Biacore (Piscataway, NJ). Four milligram/milliliter of the NiNLPs and non-nickel containing NLPs were injected over

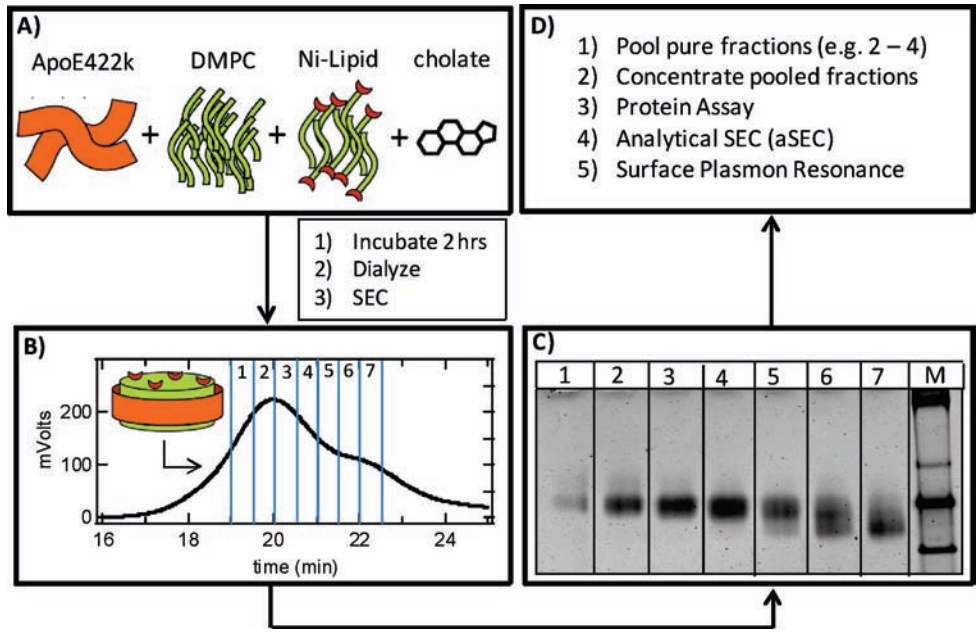


Figure 1. Assembly and purification of NiNLPs. (A) Purified apolipoprotein, DMPC, Ni-lipids, and cholate were mixed in TBS buffer at 23.8 °C for 2 h. NiNLP self-assembly was initiated by dialysis to remove cholate. (B) SEC chromatogram of the NiNLP peaks. The two peaks indicate that assembly did not result in homogeneous NiNLPs. Blue lines indicate collected SEC fractions. (C) NDGGE of the seven fractions collected by SEC (refer to SEC chromatogram in B). A single band was observed in lanes 2−4 indicating a monodisperse NiNLP population. Fractions 5−7 exhibited multiple bands indicative of a polydisperse NiNLP population. (D) Outline of subsequent steps to assess the homogeneity of different NiNLP fractions purified by SEC.

the sample and reference flow cell, respectively, at a flow rate of 10 μL/min for 70 s. This was followed by an injection of LsrB at a flow rate of 40 μL/min for 375 s across both the reference cell and sample cell. After 375 s, TBS buffer not containing LsrB continued flowing over the cell to monitor the dissociation of the interaction. The chip surface was then regenerated by two 30 s pulses of 20 mM CHAPS in TBS buffer. This treatment stripped off the bound NiNLPs and LsrB, which was then recoated for subsequent binding experiments. Analysis of LsrB binding was quantitatively assessed after subtracting the reference curve (non-nickel containing NLPs) from the sample curve (NiNLPs). SPR binding experiments were conducted over a range of LsrB concentrations to assess the effect of the number of bound LsrB proteins per NiNLP on LsrB−NiNLP dissociation. The dissociation kinetics were fit to a 1:1 binding model using the Biacore software, BIAevaluation.

RESULTS

NiNLP Assembly and Purification. The primary objective of this work was to examine the effect of Ni-lipid content in NLPs on the kinetics and stoichiometry of His-tagged protein binding. As such, the assembly of homogeneous NiNLP populations was a prerequisite for direct comparison across different NiNLP compositions. To achieve homogeneous or monodisperse NiNLPs, NiNLPs were assembled at different lipid-to-scaffold protein ratios, and the homogeneity of the resulting assembly was analyzed by both SEC and NDGGE (data not shown). While a completely pure NLP population was not achievable prior to SEC purification, regardless of the lipid-to-protein ratio, a dominant SEC peak was always identified. NDGGE analysis of the SEC fractions was subsequently used to assess NLP homogeneity. A typical purification protocol for NLPs prepared with 10% Ni-lipid and 90% 1,2-dimyristoyl-*sn*-glycero-3-phosphocholine (DMPC) (10% NiNLPs) is outlined in Figure 1. As can be clearly seen in Figure 1B, the SEC chromatogram contained a dominant peak at ~19.6 min and a smaller peak at ~22.5 min. Since these peaks partially overlapped, each fraction was further analyzed by NDGGE. As shown in Figure 1C, only a single band was observed in fractions 2−4, whereas a second band of increased electrophoretic mobility was evident in fractions 5−7, indicating the presence of two different NiNLP populations. For subsequent studies, only fractions that appeared homogeneous by NDGGE were pooled, concentrated, and quantified (Figure 1D).

Characterization of NiNLP Size by SEC, NDGGE, and AFM and Composition by PIXE. NiNLPs were assembled at molar Ni-lipid concentrations ranging from 5%−40%, using DMPC as the helper lipid in all assemblies. The lipid-to-apoE422K ratios used for each Ni-lipid concentration are described in Material and Methods. The NiNLPs were purified as described above. To assess the effect of Ni-lipid content on NiNLP size, the purified NiNLP populations were subjected to SEC, NDGGE, and AFM analysis (Figure 2). The SEC traces were nearly identical for each assembly (Figure 2A) with retention times varying only from 19.5−19.7 min (Table 1). On the basis of the NDGGE analysis, the electrophoretic mobility of the NiNLP gradually increased as the Ni-lipid content increased (Figure 2B and Table 1). This gradual increase in mobility at increased Ni-lipid incorporation could be attributed either to a decrease in NiNLP molecular weight (due to a decrease in particle diameter) or to the attenuation of charge at the NiNLP lipid bilayer surface. The Ni-lipid used in this study was uncharged, while the DMPC helper lipid was zwitterionic. Thus, an increase in Ni-lipid percentage in the NiNLP lipid bilayer and the concomitant decrease in charged DMPC will impact the migration of the NiNLP during NDGGE. To address this issue, the purified NiNLPs were assessed by AFM.

NiNLPs were analyzed at the single particle level by AFM to elucidate particle diameter, height, and discoidal morphology. After purification, NiNLPs were incubated on a mica surface as described in the Materials and Methods section. An exemplary image of 10% NiNLPs is shown in Figure 2C. The average NiNLP diameter did not change as a function of Ni-lipid content when purified using the protocol outlined above (Figure 2C and

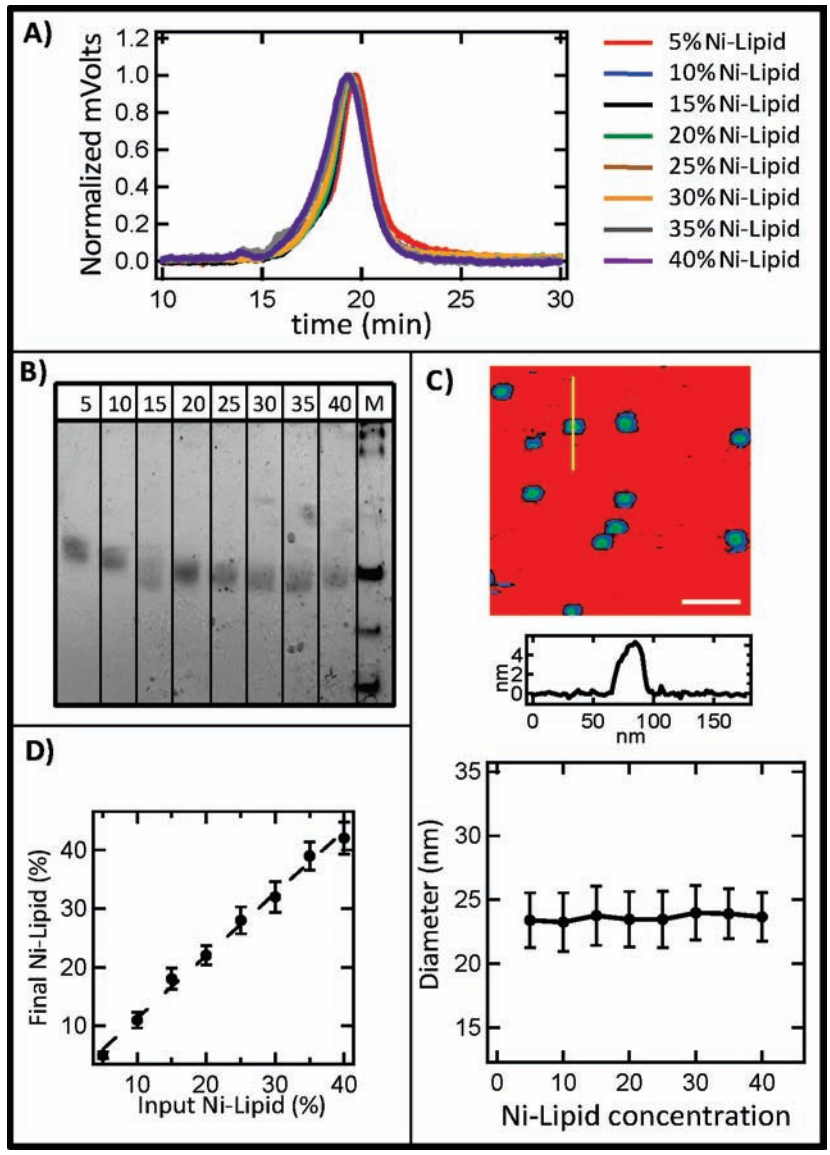


Figure 2. SEC, NDGGE, AFM, and PIXE analyses of NiNLP size and composition. (A) SEC chromatograms of NiNLPs assembled with an input Ni-lipid content ranging from 5 to 40%. (B) NDGGE of NiNLPs assembled with an input Ni-lipid content ranging from 5 to 40%. (C) AFM cross-sectional analysis of NLP diameter for NiNLPs assembled with an input Ni-lipid content ranging from 5 to 40%. Image: typical AFM image of NiNLPs (10% NiNLPs). The scale bar is 100 nm. The graph below the image represents the cross-section of the yellow line displayed in the AFM image. Bottom graph: NiNLP diameter as a function of Ni-lipid content. (D) PIXE analysis of the fraction of incorporated Ni-lipid in NiNLP as a function of the fraction of Ni-lipid used in the assembly.

Table 1. NiNLP Retention Time, MW, and Diameter as Assessed by SEC, NDGGE and AFM, Respectively

% Ni-Lipid	SEC (min)	NDGGE (kDa)	AFM (nm)
5	19.7	619	23.4 ± 2.1
10	19.5	597	23.2 ± 2.3
15	19.5	588	23.8 ± 2.3
20	19.5	582	23.5 ± 2.2
25	19.5	578	23.5 ± 2.2
30	19.5	573	24.0 ± 2.1
35	19.3	570	23.9 ± 1.9
40	19.4	570	23.7 ± 1.9

Table 1). On the basis of this analysis, the average particle diameter was ~23.5 nm.

Analysis of the kinetics and binding stoichiometry of His-tagged proteins to NiNLP required quantitation of the DMPC and Ni-lipid content in the purified NiNLPs after assembly. DMPC concentrations were assessed using a commercially available kit. Nickel concentrations were determined by proton-induced X-ray emission (PIXE), an analytically quantitative elemental analysis technique. PIXE was used to measure the Ni-lipid content in the NiNLP at a given input ratio for NiNLPs assembled with a Ni-lipid concentration ranging from 0−40% (Figure 2D). Using these analyses, the input Ni-lipid content was found to accurately reflect the Ni-lipid content in the NiNLP after assembly, where the slope of the linear fit to the final Ni-lipid % versus input Ni-lipid % was ~1 with an r^2 value of 0.993. These results demonstrate that the input ratio of Ni-lipid to DMPC was mirrored in the final NiNLP composition.

Quantitative Analysis of the Number of Bound LsrB per NiNLP as a Function of Ni-lipid Concentration by Analytical SEC (aSEC). His-tagged protein binding at different protein-to-NiNLP molar ratios was quantitatively analyzed at different Ni-lipid concentrations by aSEC using His-tagged LsrB. The aSEC chromatograms of LsrB alone and NiNLP alone are shown in Figure 3A and B, respectively. The retention time of LsrB alone was ~11.7 min (Figure 3A), and the retention time of NiNLP alone was ~7.8 min (Figure 3B). When LsrB and

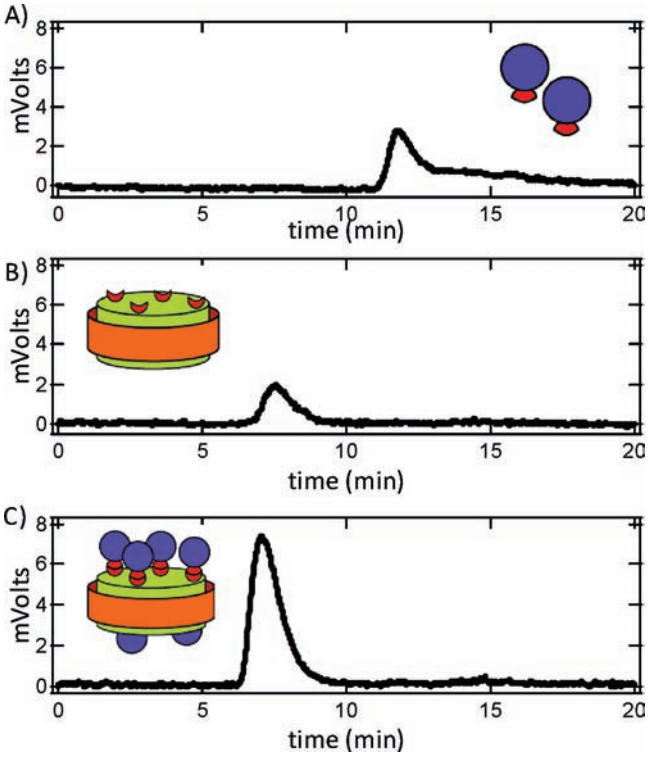


Figure 3. Monitoring LsrB binding to NiNLPs by aSEC. aSEC traces of (A) 1.6 μM LsrB alone, (B) 0.2 μM 10% NiNLPs alone, and (C) 0.2 μM 10% NiNLPs incubated with 1.6 μM LsrB for 30 min. Successful LsrB−NiNLP conjugation is indicated by the increase in intensity and decreased retention time of the NiNLP/LsrB peak in addition to the absence of a protein peak.

NiNLP were incubated together at the same concentrations shown in Figure 3A and B, a single, larger peak at ~7 min was observed (Figure 3C). The shift in retention time, the increase in signal intensity, and the absence of an LsrB peak were all indicative of His-tagged LsrB binding to the NiNLP to form a larger complex.

To determine the stoichiometry of the immobilized LsrB to the NiNLP, NiNLPs were mixed with LsrB at varying molar ratios and subjected to aSEC analysis. Using previously reported MD simulations, the ~23.5 diameter NiNLPs were expected to contain six apoE422K scaffold proteins per particle (*8*). The NiNLP molar concentration could hence be calculated from the molar apoE422K concentration ([NiNLP] = [E4]/6). As the LsrB/NiNLP ratio was increased for 10% NiNLPs, the intensity of the NiNLP/LsrB aSEC peak continued to increase up to a ratio of 15:1 (Figure 4A). At higher ratios, no further increase in intensity of the NiNLP/LsrB peak was observed, whereas a second peak corresponding to LsrB alone (retention time ~11.7 min) appeared. These results indicate that at LsrB/NiNLP ratios lower than 15:1, all LsrB was bound to the NiNLP and that at ratios higher than 15:1, a fraction of the LsrB did not bind to the NiNLP. To quantitatively evaluate these aSEC traces, the integrated area under the NiNLP/LsrB peak was analyzed as a function of the LsrB/NiNLP ratio. As shown in the inset of Figure 4A, the area under the main NiNLP/LsrB peak increased at higher LsrB/NiNLP ratios and eventually saturated. The point of saturation was determined by doubling the LsrB/NiNLP ratio where the integrated area of the NiNLP/LsrB peak was half the maximal value, which was determined as a fitting parameter to a sigmoidal function. Using this approach, the saturation molar ratio for LsrB to 10% NiNLPs was determined to be ~12, i.e., at this Ni-lipid composition, the maximal number of LsrB proteins that could bind to a single 10% NiNLP (maximal #LsrB/NiNLP) was ~12.

These experiments were repeated with NiNLPs containing a Ni-lipid content varying from 5−35%. The integrated area of the NiNLP/LsrB peak as a function of LsrB/NiNLP ratios at these different Ni-lipid concentrations is shown in Figure 4B. At all Ni-lipid concentrations, the integrated area under the NiNLP/LsrB peak increased up to a saturation molar ratio, and the maximal #LsrB/NiNLP was shown to increase as a function of Ni-lipid content up to a Ni-lipid concentration of 30% (Figure 4C). The maximal #LsrB/NiNLP at a Ni-lipid concentration of 30% was determined to be ~30 LsrB proteins per NiNLP.

Quantitative Determination of the Number of Bound LsrB per NiNLP as a Function of Ni-Lipid Concentration by Surface Plasmon Resonance (SPR). LsrB binding to NiNLPs as a function of Ni-lipid content was qualitatively analyzed by SPR (*42*). NiNLPs were immobilized on a commercially available lipophilic SPR chip (L1 chip), which has been extensively used for immobilization of lipid vesicles (*43*−*46*). Clear binding responses were observed upon sequential injection of NiNLPs and LsrB (Figure 5A). The stability of the SPR response units (RU) after NiNLP injection indicated tight association of the NiNLPs with the L1 chip surface. The decrease in the LsrB signal after injection was indicative of LsrB desorption from the NiNLP surface (Figure 5A). To qualitatively assess the LsrB binding capacity of NiNLPs, increasing concentrations of LsrB were injected over a fixed amount of immobilized NiNLPs (2500 RU). SPR sensograms from a typical LsrB titration for 20% NiNLPs are shown in Figure 5B. Solutions of increasing LsrB concentration were injected for a fixed time (375 s). The ratio of LsrB RU at the end of injection (black circles, Figure 5B) and NiNLP RU immediately prior to LsrB injection (black arrow, Figure 5B) (LsrB RU/NiNLP RU) was measured quantitatively as a function of injected LsrB concentration (Figure 5B, inset). This ratio gradually increased up to a maximal saturation point (red dashed line, inset of Figure 5B). Thus, the maximal LsrB RU/NiNLP RU could be used as a qualitative measure of maximal LsrB binding. This analysis was repeated for all NiNLPs (0, 10, 20, 25, 30, 35, and 40%). The maximal LsrB RU/NiNLP RU values for each NiNLP are plotted in Figure 5C. The maximal LsrB loading density increased as a function of Ni-lipid content until a plateau was reached at a Ni-lipid concentration of 30%.

Since the number of LsrB molecules per NiNLP could not be empirically determined by SPR, the qualitative measure of LsrB RU/NiNLP RU was converted to the number of LsrB molecules bound to the NiNLPs using the aSEC data. The SPR response increases linearly with the mass immobilized on the chip surface; thus, the LsrB RU/NiNLP RU was assumed to be linearly related to the #LsrB/NiNLP through the following relationship: #LsrB/NiNLP = $Fc \times$ LsrB RU/NiNLP RU, where Fc is a correction factor. Under this assumption, the calculated Fc value between the maximal #LsrB/NiNLPs determined by aSEC and the maximal LsrB RU/NiNLP RU determined by SPR should remain constant at each Ni-lipid concentration. The Fc value was calculated for all Ni-lipid concentrations and varied only slightly (between 14.8 and 16), validating the initial assumption that the #LsrB/NiNLP was linearly related to LsrB RU/NiNLP RU. Therefore, an average Fc value of 15.5 was used to convert the LsrB RU/NiNLP RU into #LsrB/NiNLP. When this was done, the maximal #LsrB/NiNLP determined by aSEC and the maximal #LsrB/NiNLP determined by SPR using the Fc closely matched (Figure 5D). It is important to note that only one face of the NiNLP was available for binding during SPR since the NiNLPs were immobilized on the lipophilic chip, whereas both faces were available in the solution based aSEC experiments. Therefore, the actual #LsrB/NiNLP

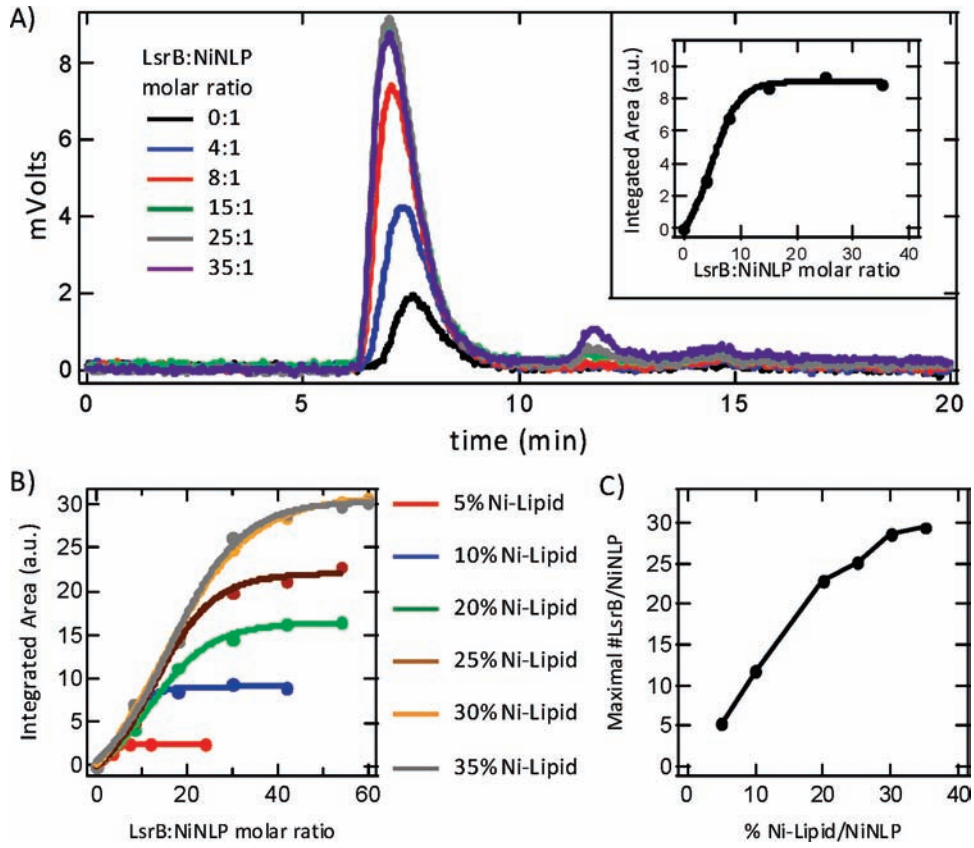


Figure 4. Quantitative analysis by aSEC of LsrB binding to NiNLPs as a function of Ni-lipid content. (A) Representative aSEC chromatograms of 10% NiNLPs incubated with increasing molar ratios of LsrB. An increase in molar ratio resulted in an increase in integrated peak area. This increase eventually saturated, concomitant with the appearance of a free, unbound protein (~12 min). Inset: integrated area of the NiNLP/LsrB peak as a function of the LsrB/NiNLP molar ratio. (B) Integrated area of the NiNLP/LsrB peak as a function of the LsrB/NiNLP molar ratio for NiNLPs containing different Ni-lipid concentrations. (C) Maximal number of LsrB protein molecules able to bind to a single NiNLP as a function of Ni-lipid content. These values were determined from the sigmoidal fits to B.

during the SPR experiments was half the value shown in Figure 5D. Since the NiNLP is a symmetric particle and the binding properties of both faces are expected to be identical, the SPR values were normalized by multiplying by a factor of 2 to allow a direct comparison to be made between SPR and aSEC. This calibration constant was subsequently used to evaluate the kinetics of binding as a function of the #LsrB/NiNLP.

Dissociation Half-Times between NiNLPs and LsrB as a Function of #LsrB/NiNLP and Ni-Lipid Content. The dissociation kinetics between LsrB and NiNLPs were analyzed as a function of the number of bound LsrB molecules per NiNLP and Ni-lipid content. An example demonstrating the method used to determine the dissociation kinetics as a function of #LsrB/NiNLP for 20% NiNLPs is shown in Figure 6A. Since the actual binding kinetics between LsrB and NiNLPs are expected to be dependent on the #LsrB/NiNLP due to the multivalent nature of this interaction, the dissociation half-time ($t_{1/2}$) was determined by fitting only small regions of the LsrB dissociation curves to the 1:1 Langmuir binding model (Figure 6A). Increasing concentrations of LsrB were injected over a fixed amount of immobilized NiNLPs, and the LsrB RU/NiNLP RU was calculated at the point where the dissociation kinetics was fit (LsrB RU, black circles; NiNLP RU, black arrow in Figure 6A). The LsrB RU/NiNLP RU at each injected LsrB concentration was converted to #LsrB/NiNLP using the correction factor described above. The k_{off} values were then used to calculate the dissociation half-time ($t_{1/2} = 0.693 \times k_{off}$) (Figure 6A, top inset) as a function of #LsrB/NiNLP. It is worth noting that the actual binding kinetics between LsrB and NiNLPs were multivalent since the hexa-His-tag on the LsrB could bind to multiple Ni-lipids. However, modeling this multivalent interaction was precluded by the fact that the number of interactions occurring at each condition could not be empirically elucidated. Therefore, we utilized the 1:1 Langmuir binding model, which resulted in good fits over short segments of the dissociation curve and has also been used in other previous studies that characterized Ni-polyhistidine binding by SPR (*47*). In addition, to limit any errors associated with this procedure, identical time periods during dissociation (Figure 6A) were fit to the 1:1 Langmuir binding kinetics for all curves. These experiments were repeated for NiNLPs functionalized with different Ni-lipid concentrations (10, 20, 30, 35, and 40%) (Figure 6B). At all Ni-lipid compositions, the $t_{1/2}$ value decreased as the amount of LsrB bound to the NiNLP increased. In addition, for a given #LsrB/NiNLP, the $t_{1/2}$ increased significantly as the Ni-lipid content increased up to a concentration of 35%. No further increase in $t_{1/2}$ was observed at a Ni-lipid concentration above 35%, as indicated by the overlap in $t_{1/2}$ values between 35% NiNLPs and 40% NiNLPs. For example, at a #LsrB/NiNLP of ~5 the $t_{1/2}$ value increased from 10.6 to 240 min as the Ni-lipid content increased from 10% to 35%.

DISCUSSION

NLPs have been used to solubilize hydrophobic molecules such as membrane proteins (*6*, *7*, *9*, *11*, *48*) and drugs (*49*, *50*). While hydrophobic interactions have been used successfully to incorporate a limited number of biomolecules into the NLPs, the lack of readily available functional elements on the NLP has precluded more diverse biomolecule incorporations. However, by utilizing functionalized starting materials during NLP

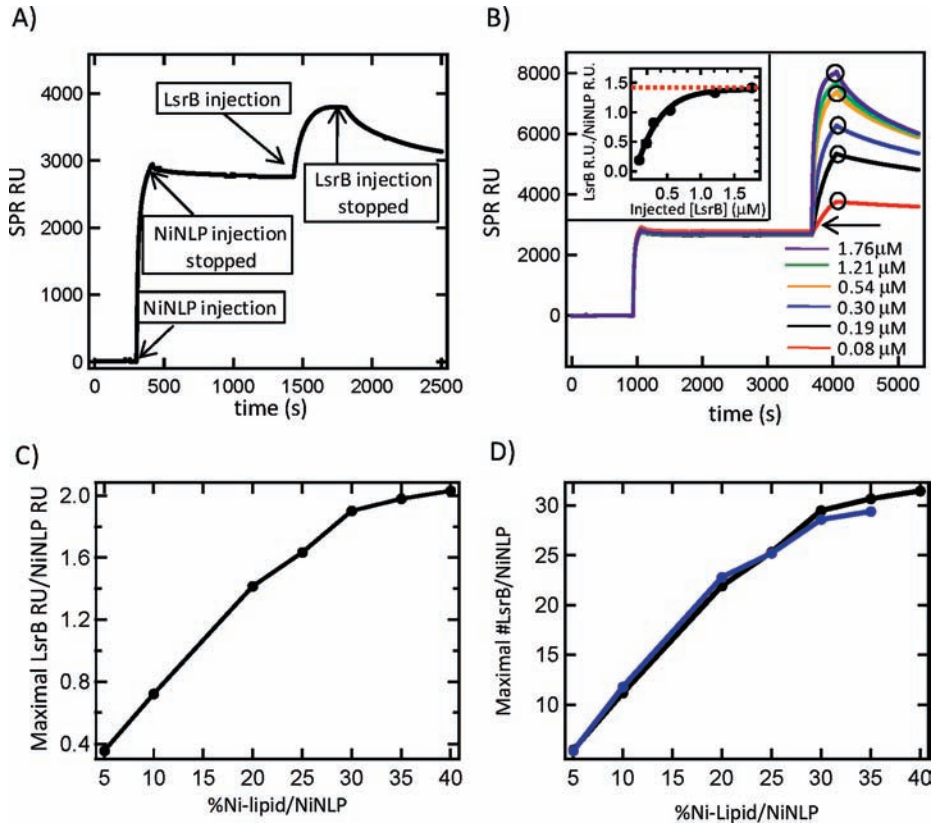


Figure 5. Quantitative analysis of LsrB binding as a function of Ni-lipid content by SPR. (A) Exemplary SPR sensogram of NiNLP immobilization on the L1 chip and subsequent binding of LsrB to the immobilized NiNLPs. (B) SPR sensograms of 20% NiNLP deposition and LsrB−NiNLP binding at different LsrB injection concentrations. NiNLP RU quickly reached a steady state, at which point LsrB was injected. The LsrB RU at the end of injection (●) increased as the concentration of injected LsrB increased up to a maximal saturation point. Inset: LsrB RU/NiNLP RU as a function of the concentration of injected LsrB. (C) The maximal LsrB RU/NiNLP RU as a function of Ni-lipid composition determined from analysis of the SPR sensograms. (D) The maximal #LsrB/NiNLP as a function of Ni-lipid concentration determined by aSEC (blue line) and the maximal #LsrB/NiNLP determined by SPR using *Fc* (black line).

assembly, one can readily impart novel functionality into the assembled particle, such as utilizing lipids with functionalized headgroups. The resulting functionalized NLPs can then be used to capture recombinant proteins, peptides, drugs, or oligonucleotides for a range of applications, including vaccine development, biomolecule targeting and delivery, diagnostic imaging, and the study of receptor/ligand interactions.

We have previously introduced the concept of functionalized NLPs by incorporating a nickel-chelating lipid into the NLP bilayer and demonstrated both the ability to assemble NiNLPs and to conjugate His-tagged proteins to the NiNLP. In this study, an in-depth analysis of the effect of Ni-lipid concentration on His-tagged protein binding and dissociation was investigated to better understand the His-tagged protein binding and loading capacity of the NiNLP for *in vivo* and *in vitro* applications.

aSEC was used to quantify the effect of Ni-lipid content on the maximal number of LsrB molecules that could bind to a single NiNLP. We found that the maximal #LsrB/NiNLP linearly increased with Ni-lipid content, with ca. 30 LsrB molecules immobilized on 30% NiNLPs. Only minimal increases in the #LsrB/NiNLP were observed at higher Ni-lipid concentrations. These results were mirrored when LsrB binding to NiNLPs was analyzed by SPR. These results correlate well with theoretical calculations that ∼37 LsrB molecules could bind a NiNLP that is 23.5 nm in diameter, based on the assumption that LsrB (37 kDa) is a globular protein with a diameter of ∼5.0 nm (based on the known size of streptavidin) and assuming that a bilayer area of one face of the NiNLP is 363 nm^2 (based on the 23.5 nm diameter minus 2 nm for the thickness of the scaffold (*8*)).

An understanding of the time scales and kinetics of binding between His-tagged proteins and NiNLPs is important for *in vivo* applications of this technology. The binding kinetics between the NiNLPs and His-tagged protein are dependent on avidity, i.e., the synergistic binding affinity of multiple interactions between a protein and ligand. Although the affinity between a single chelated Ni atom and a polyhistidine tag is relatively low (K_D ∼10 μM) (*51*−*53*), the binding affinity is significantly increased when multiple Ni atoms are available for binding to a single His-tag. Since two histidines are coordinated by a single Ni, a 6X-His-tag can accommodate three Ni atoms. Thus, the density of chelated Ni (i.e., density of Ni-lipid) greatly impacts the avidity effect, resulting in an increased apparent affinity between the His-tagged protein and the NiNLP when multiple Ni-lipids are clustered in close proximity to bind the same His-tag. In this study, LsrB−NiNLP dissociation was characterized as a function of the #LsrB/NiNLP and Ni-lipid content by SPR. At any given #LsrB/NiNLP, the $t_{1/2}$ value drastically increased as the Ni-lipid content increased up to a concentration of 35%. As the density of the chelated Ni on the bilayer surface increased, the rate of dissociation decreased since the His-tag has a greater likelihood of interacting with multiple Ni atoms, hence increasing avidity. No further change in the dissociation rate was observed above Ni-lipid concentrations of 35%. This can be attributed, most likely, to rotational mobility on the part of the nitrilotriacetic acid (NTA) headgroup. Assuming a DMPC molecular area of 0.52 nm^2 (*54*) and an area of Ni-NTA rotational freedom of ca. 2 nm^2, the Ni groups could potentially cover almost the entire surface area of the bilayer at a 35% Ni-lipid concentration (see schematic in Figure

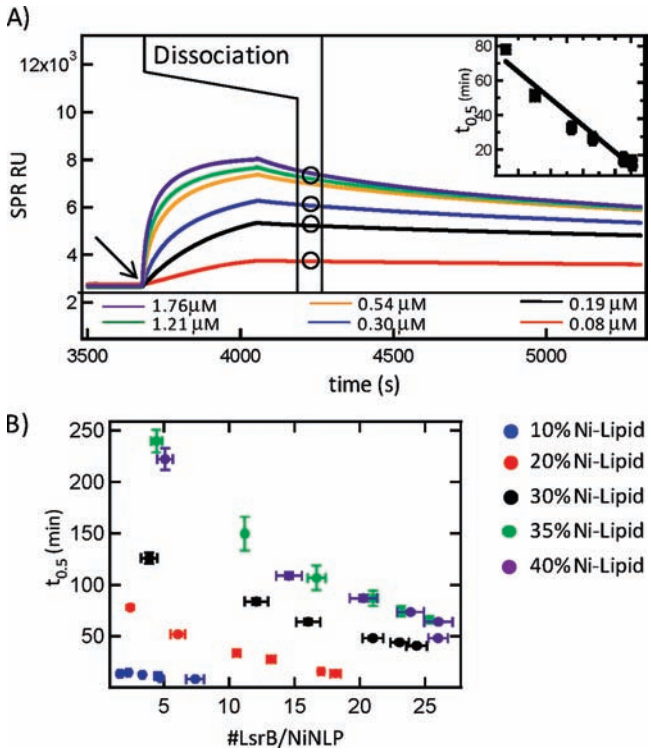


Figure 6. Analysis of the dissociation between LsrB and NiNLP as a function of #LsrB/NiNLP and Ni-Lipid concentration. (A) SPR sensograms of LsrB binding to 20% NiNLPs at different LsrB injection concentrations. The k_{off} value between LsrB and 20% NiLNPs was determined by fitting the region between the lines marked dissociation with a 1:1 Langmuir binding model. For each curve, the #LsrB/NiNLP where k_{off} was fit was determined by dividing the LsrB RU at that point (●) by the NiNLP RU (black arrow) and multiplying this value by the correction factor, *Fc*. The determined k_{off} values were used to calculate the dissociation half-time ($t_{1/2}$) (inset) as a function of #LsrB/NiNLP. (B) The $t_{1/2}$ value as a function of #LsrB/NiNLP for NiNLPs containing differing amounts of Ni-lipid.

7). Thus, higher concentrations of Ni-lipid, i.e., >35% Ni-lipid, would not increase the effective area density of the Ni groups or the accessibility of the Ni groups for binding to His-tagged proteins.

We also found that the dissociation half-time was dependent on the #LsrB/NiNLP at all Ni-lipid concentrations. This trend in binding kinetics is related to the effect of occupied Ni-lipid groups on the overall avidity of binding between the NiNLP and polyhistidine tag of LsrB. As the number of bound LsrB increases, there is a concomitant decrease in the number of available free Ni groups (i.e., those not interacting with bound protein) to recapture individual histidine residues in the polyhistidine tag upon dissociation. However, a decrease in the density of bound LsrB molecules ensures that unoccupied Ni groups are available for the LsrB His-tag to rebind before complete dissociation. It is worth noting that as proteins dissociate from the particle, the K_d of the remaining bound proteins changes. As such, multiple rate constants would be needed to fit the entire dissociation curve; for this reason, only small regions of the dissociation curve were fit to the Langmuir model.

On the basis of the kinetic analysis conducted in this study, the dissociation kinetics were shown to be highly dependent on both the Ni-lipid content and number of bound LsrB molecules per NiNLP. If this functional scheme is to be used for protein attachment, one must be mindful of the time scale required for the desired application. The longest attainable dissociation time was ~240 min (35% Ni-lipid and ~5 LsrB/NiNLP); therefore, if the protein is required to be immobilized for longer durations, alternative functional schemes may be required. One approach to achieve more durable immobilization is to utilize a longer polyhistidine tag. Several expression vectors are available that allow attachment of a 10× His-tag rather than the hexa-His-tag used in this study. The dissociation time may also be dramatically increased if one uses a double hexa-His-tag (*55*). In fact, when NiNLP experiments were conducted with a hexa-His-tag protein that formed a dimer, the dissociation half-time increased by an order of magnitude for the 35% NiNLPs (~2400 min) (data not shown). Another method of increasing the dissociation time would be the use of lipids containing multiple nitrilotriacetic acid (NTA) moieties. Previous studies have demonstrated that the affinity between His-tagged proteins and surfaces containing di- or tri-NTA moieties was significantly higher than that when mono-NTA moieties were used (*47, 56*). Another possible method of eliminating the issues associated with protein dissociation is to utilize a covalent functional scheme. We are currently examining these different functional schemes to increase the dissociation time and/or to eliminate the issue of reversibility in protein attachment.

CONCLUSIONS

In this study, we characterized the binding kinetics between a hexa-His-tagged protein (LsrB) and NLPs functionalized with Ni-lipids (NiNLPs) using SPR and aSEC. On the basis of the kinetic analysis, we found that the binding kinetics were strongly dependent on the Ni-lipid concentration in the NiNLP and the number of bound LsrB per NiNLP, where the dissociation time increased at higher Ni-lipid concentrations up to 35% and decreased as the #LsrB/NiNLP molecules increased. The results presented in this study will prove valuable in assessing the Ni-lipid composition and protein density that will be needed for a

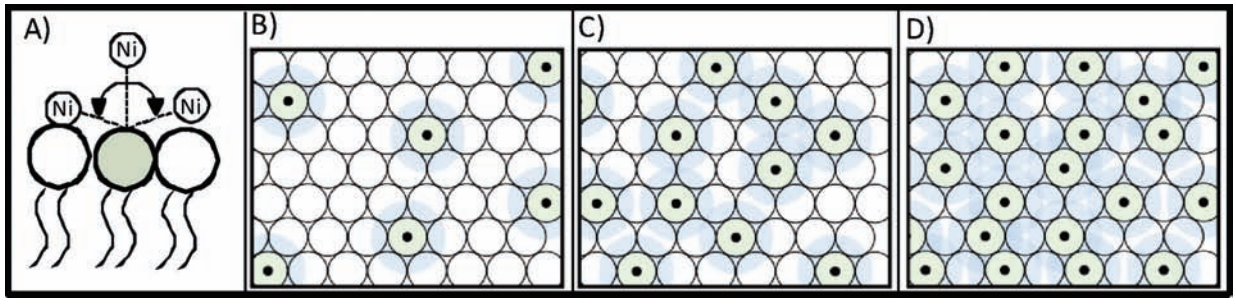


Figure 7. Schematic of the potential range of motion of the Ni groups over the surface of the lipid bilayer. (A) Cross-sectional schematic demonstrating that due to the flexible 0.77 nm spacer the Ni group can rotate and be present above adjacent lipids. (B) Top view of NiNLPs containing 10% Ni-lipid. (C) Top view of NiNLPs containing 20% Ni-lipid. (D) Top view of NiNLPs containing 35% Ni-lipid. Because of the length and flexible nature of the carbon spacer, the Ni groups have access to almost the entire surface area of the NiNLP at a Ni-lipid concentration of 35%. Light green, Ni-lipid; white, DMPC; light-blue circles, the range the Ni group can access.

given application, which will depend on the time scale the proteins need to be retained on the NiNLP. The longest attainable dissociation half-time was ~240 min at a Ni-lipid concentration of 35% and #LsrB/NiNLP of 5. For applications that require a longer association time, alternative conjugation schemes may be required, such as utilizing multiple or longer polyhistidine tags, multiple NTA moieties, or covalent immobilization of the protein onto NLPs.

ACKNOWLEDGMENT

This work was performed under the auspices of the U.S. Department of Energy by Lawrence Livermore National Laboratory under Contract DE-AC52-07NA27344 with support from Lawrence Livermore National Laboratory (LDRD 09-LW-077 awarded to C.D.B.). LLNL-JRNL-425115.

LITERATURE CITED

(1) Garda, H. A., Arrese, E. L., and Soulages, J. L. (2002) Structure of apolipophorin-III in discoidal lipoproteins - Interhelical distances in the lipid-bound state and conformational change upon binding to lipid. *J. Biol. Chem. 277*, 19773–19782.

(2) Jonas, A. (1986) Reconstitution of high-density-lipoproteins. *Methods Enzymol. 128*, 553–582.

(3) Jonas, A., Sweeny, S. A., and Herbert, P. N. (1984) Discoidal complexes of a and C apolipoproteins with lipids and their reactions with lecithin-cholesterol acyltransferase. *J. Biol. Chem. 259*, 6369–6375.

(4) Lu, B., Morrow, J. A., and Weisgraber, K. H. (2000) Reorganization of the four-helix bundle of human apolipoprotein E in binding to phospholipid. *J. Biol. Chem. 275*, 20775–20781.

(5) Wald, J. H., Krul, E. S., and Jonas, A. (1990) Structure of apolipoprotein-a-I in 3 homogeneous, reconstituted high-density-lipoprotein particles. *J. Biol. Chem. 265*, 20037–20043.

(6) Baker, S. E., Hopkins, R. C., Blanchette, C. D., Walsworth, V. L., Sumbad, R., Fischer, N. O., Kuhn, E. A., Coleman, M., Chromy, B. A., Letant, S. E., Hoeprich, P. D., Adams, M. W. W., and Henderson, P. T. (2009) Hydrogen production by a hyperthermophilic membrane-bound hydrogenase in water-soluble nanolipoprotein particles. *J. Am. Chem. Soc. 131*, 7508–7509.

(7) Blanchette, C. D., Cappuccio, J. A., Kuhn, E. A., Segelke, B. W., Benner, W. H., Chromy, B. A., Coleman, M. A., Bench, G., Hoeprich, P. D., and Sulchek, T. A. (2009) Atomic force microscopy differentiates discrete size distributions between membrane protein containing and empty nanolipoprotein particles. *Biochim. Biophys. Acta 1788*, 724–731.

(8) Blanchette, C. D., Law, R., Benner, W. H., Pesavento, J. B., Cappuccio, J. A., Walsworth, V., Kuhn, E. A., Corzett, M., Chromy, B. A., Segelke, B. W., Coleman, M. A., Bench, G., Hoeprich, P. D., and Sulchek, T. A. (2008) Quantifying size distributions of nanolipoprotein particles with single-particle analysis and molecular dynamic simulations. *J. Lipid Res. 49*, 1420–1430.

(9) Cappuccio, J. A., Blanchette, C. D., Sulchek, T. A., Arroyo, E. S., Kralj, J. M., Hinz, A. K., Kuhn, E. A., Chromy, B. A., Segelke, B. W., Rothschild, K. J., Fletcher, J. E., Katzen, F., Peterson, T. C., Kudlicki, W. A., Bench, G., Hoeprich, P. D., and Coleman, M. A. (2008) Cell-free co-expression of functional membrane proteins and apolipoprotein, forming soluble nanolipoprotein particles. *Mol. Cell. Proteomics 7*, 2246–2253.

(10) Chromy, B. A., Arroyo, E., Blanchette, C. D., Bench, G., Benner, H., Cappuccio, J. A., Coleman, M. A., Henderson, P. T., Hinz, A. K., Kuhn, E. A., Pesavento, J. B., Segelke, B. W., Sulchek, T. A., Tarasow, T., Walsworth, V. L., and Hoeprich, P. D. (2007) Different apolipoproteins impact nanolipoprotein particle formation. *J. Am. Chem. Soc. 129*, 14348–14354.

(11) Bayburt, T. H., Grinkova, Y. V., and Sligar, S. G. (2006) Assembly of single bacteriorhodopsin trimers in bilayer nanodiscs. *Arch. Biochem. Biophys. 450*, 215–222.

(12) Katzen, F., Fletcher, J. E., Yang, J. P., Kang, D., Peterson, T. C., Cappuccio, J. A., Blanchette, C. D., Sulchek, T., Chromy, B. A., Hoeprich, P. D., Coleman, M. A., and Kudlicki, W. (2008) Insertion of membrane proteins into discoidal membranes using a cell-free protein expression approach. *J. Proteome Res. 7*, 3535–42.

(13) Bayburt, T. H., and Sligar, S. G. (2003) Self-assembly of single integral membrane proteins into soluble nanoscale phospholipid bilayers. *Protein Sci. 12*, 2476–2481.

(14) Bayburt, T. H., and Sligar, S. G. (2002) Single-molecule height measurements on microsomal cytochrome P450 in nanometer-scale phospholipid bilayer disks. *Proc. Natl. Acad. Sci. U.S.A. 99*, 6725–30.

(15) Bayburt, T. H., Carlson, J. W., and Sligar, S. G. (1998) Reconstitution and imaging of a membrane protein in a nanometer-size phospholipid bilayer. *J. Struct. Biol. 123*, 37–44.

(16) Leitz, A. J., Bayburt, T. H., Barnakov, A. N., Springer, B. A., and Sligar, S. G. (2006) Functional reconstitution of beta2-adrenergic receptors utilizing self-assembling Nanodisc technology. *Biotechniques 40*, 601–602.

(17) Whorton, M. R., Bokoch, M. P., Rasmussen, S. G., Huang, B., Zare, R. N., Kobilka, B., and Sunahara, R. K. (2007) A monomeric G protein-coupled receptor isolated in a high-density lipoprotein particle efficiently activates its G protein. *Proc. Natl. Acad. Sci. U.S.A. 104*, 7682–7.

(18) Gluck, J. M., Wittlich, M., Feuerstein, S., Hoffmann, S., Willbold, D., and Koenig, B. W. (2009) Integral membrane proteins in nanodiscs can be studied by solution NMR spectroscopy. *J. Am. Chem. Soc. 131*, 12060–12061.

(19) Raschle, T., Hiller, S., Yu, T. Y., Rice, A. J., Walz, T., and Wagner, G. (2009) Structural and functional characterization of the integral membrane protein VDAC-1 in lipid bilayer nanodiscs. *J. Am. Chem. Soc. 131*, 17777–17779.

(20) Cruz, F., and Edmondson, D. E. (2007) Kinetic properties of recombinant MAO-A on incorporation into phospholipid nanodisks. *J. Neural. Transm. 114*, 699–702.

(21) Redmond, K. A., Nguyen, T. S., and Ryan, R. O. (2007) All-trans-retinoic acid nanodisks. *Int. J. Pharm. 339*, 246–250.

(22) Tufteland, M., Ren, G., and Ryan, R. O. (2008) Nanodisks derived from amphotericin B lipid complex. *J. Pharm. Sci. 97*, 4425–4432.

(23) Oda, M. N., Hargreaves, P. L., Beckstead, J. A., Redmond, K. A., van Antwerpen, R., and Ryan, R. O. (2006) Reconstituted high density lipoprotein enriched with the polyene antibiotic amphotericin B. *J. Lipid Res. 47*, 260–267.

(24) Nguyen, T. S., Weers, P. M., Raussens, V., Wang, Z., Ren, G., Sulchek, T., Hoeprich, P. D., Jr., and Ryan, R. O. (2008) Amphotericin B induces interdigitation of apolipoprotein stabilized nanodisk bilayers. *Biochim. Biophys. Acta 1778*, 303–312.

(25) Nikanjam, M., Gibbs, A. R., Hunt, C. A., Budinger, T. F., and Forte, T. M. (2007) Synthetic nano-LDL with paclitaxel oleate as a targeted drug delivery vehicle for glioblastoma multiforme. *J. Controlled Release 124*, 163–171.

(26) Rensen, P. C., de Vrueh, R. L., Kuiper, J., Bijsterbosch, M. K., Biessen, E. A., and van Berkel, T. J. (2001) Recombinant lipoproteins: lipoprotein-like lipid particles for drug targeting. *Adv. Drug Delivery Rev. 47*, 251–276.

(27) Frias, J. C., Ma, Y., Williams, K. J., Fayad, Z. A., and Fisher, E. A. (2006) Properties of a versatile nanoparticle platform contrast agent to image and characterize atherosclerotic plaques by magnetic resonance imaging. *Nano Lett. 6*, 2220–2224.

(28) Chromy, B. A., Arroyo, E., Blanchette, C. D., Bench, G., Benner, H., Cappuccio, J. A., Coleman, M. A., Henderson, P. T., Hinz, A. K., Kuhn, E. A., Pesavento, J. B., Segelke, B. W., Sulchek, T. A., Tarasow, T., Walsworth, V. L., and Hoeprich, P. D. (2007) Different apolipoproteins impact nanolipoprotein particle formation. *J. Am. Chem. Soc. 129*, 14348–14354.

(29) Zorich, N., Jonas, A., and Pownall, H. J. (1985) Activation of lecithin-cholesterol acyltransferase by human apolipoprotein-E in discoidal complexes with lipids. *J. Biol. Chem. 260*, 8831–8837.

(30) Gursky, O., Ranjana, and Gantz, D. L. (2002) Complex of human apolipoprotein C-1 with phospholipid: thermodynamic or kinetic stability. *Biochemistry 41*, 7373–7384.

(31) Wientzek, M., Kay, C. M., Oikawa, K., and Ryan, R. O. (1994) Binding of insect apolipophorin-III to dimyristoylphosphatidylcholine vesicles: evidence for a conformational change. *J. Biol. Chem. 269*, 4605–4612.

(32) Herscovitz, H., Hadzopoulou cladaras, M., Walsh, M. T., Cladaras, C., Zannis, V. I., and Small, D. M. (1991) Expression, secretion, and lipid-binding characterization of the N-terminal 17-percent of apolipoprotein-B. *Proc. Natl. Acad. Sci. U.S.A. 88*, 7313–7317.

(33) Fischer, N. O., Blanchette, C. D., Chromy, B. A., Kuhn, E. A., Segelke, B. W., Corzett, M., Bench, G., Mason, P. W., and Hoeprich, P. D. (2009) Immobilization of His-tagged proteins on nickel-chelating nanolipoprotein particles. *Bioconjugate Chem. 20*, 460–465.

(34) Arnold, F. H. (1991) Metal-affinity separations: a new dimension in protein processing. *Biotechnology (N.Y.) 9*, 151–156.

(35) Khan, F., He, M., and Taussig, M. J. (2006) Double-hexahistidine tag with high-affinity binding for protein immobilization, purification, and detection on ni-nitrilotriacetic acid surfaces. *Anal. Chem. 78*, 3072–3079.

(36) Fischer, N. O., Blanchette, C. D., Chromy, B. A., Kuhn, E. A., Segelke, B. W., Corzett, M., Bench, G., Mason, P. W., and Hoeprich, P. D. (2009) Immobilization of His-tagged proteins on nickel-chelating nanolipoprotein particles. *Bioconjugate Chem. 20*, 460–465.

(37) Sigal, G. B., Bamdad, C., Barberis, A., Strominger, J., and Whitesides, G. M. (1996) A self-assembled monolayer for the binding and study of histidine-tagged proteins by surface plasmon resonance. *Anal. Chem. 68*, 490–497.

(38) Nieba, L., Nieba-Axmann, S. E., Persson, A., Hamalainen, M., Edebratt, F., Hansson, A., Lidholm, J., Magnusson, K., Karlsson, A. F., and Pluckthun, A. (1997) BIACORE analysis of histidine-tagged proteins using a chelating NTA sensor chip. *Anal. Biochem. 252*, 217–228.

(39) Dorn, I. T., Pawlitschko, K., Pettinger, S. C., and Tampe, R. (1998) Orientation and two-dimensional organization of proteins at chelator lipid interfaces. *Biol. Chem. 379*, 1151–1159.

(40) Roberts, M. L., Grant, P. G., Bench, G. S., Brown, T. A., Frantz, B. R., Morse, D. H., and Antolak, A. J. (1999) The stand-alone microprobe at Livermore. *Nucl. Instrum. Methods Phys. Res., Sect. B 158*, 24–30.

(41) Antolak, A. J., and Bench, G. S. (1994) PIXEF: the Livermore PIXE Spectrum Analysis Package. *Nucl. Instrum. Methods Phys. Res., Sect. B 90*, 596–601.

(42) Borch, J., Torta, F., Sligar, S. G., and Roepstorff, P. (2008) Nanodiscs for immobilization of lipid bilayers and membrane receptors: kinetic analysis of cholera toxin binding to a glycolipid receptor. *Anal. Chem. 80*, 6245–6252.

(43) Cooper, M. A., Hansson, A., Lofas, S., and Williams, D. H. (2000) A vesicle capture sensor chip for kinetic analysis of interactions with membrane-bound receptors. *Anal. Biochem. 277*, 196–205.

(44) Kim, K., Cho, S. P., Park, J. H., Byun, Y. R., Chung, H., Kwon, I. C., and Jeong, S. Y. (2004) Surface plasmon resonance studies of the direct interaction between a drug/intestinal brush border membrane. *Pharm. Res. 21*, 1233–1239.

(45) Anderluh, G., Besenicar, M., Kladnik, A., Lakey, J. H., and Macek, P. (2005) Properties of nonfused liposomes immobilized on an L1 Biacore chip and their permeabilization by a eukaryotic pore-forming toxin. *Anal. Biochem. 344*, 43–52.

(46) Erb, E. M., Chen, X. Y., Allen, S., Roberts, C. J., Tendler, S. J. B., Davies, M. C., and Forsen, S. (2000) Characterization of the surfaces generated by liposome binding to the modified dextran matrix of a surface plasmon resonance sensor chip. *Anal. Biochem. 280*, 29–35.

(47) Huang, Z. H., Hwang, P., Watson, D. S., Cao, L. M., and Szoka, F. C. (2009) Tris-nitrilotriacetic acids of subnanomolar affinity toward hexahistidine tagged molecules. *Bioconjugate Chem. 20*, 1667–1672.

(48) Leitz, A. J., Bayburt, T. H., Barnakov, A. N., Springer, B. A., and Sligar, S. G. (2006) Functional reconstitution of beta(2)-adrenergic receptors utilizing self-assembling Nanodisc technology. *Biotechniques 40*, 601–602.

(49) Cruz, F., and Edmondson, D. E. (2007) Kinetic properties of recombinant MAO-A on incorporation into phospholipid nanodisks. *J. Neural Transm. 114*, 699–702.

(50) Nguyen, T. S., Weers, P. M. M., Raussens, V., Wang, Z., Ren, G., Sulchek, T., Hoeprich, P. D., and Ryan, R. O. (2008) Amphotericin B induces interdigitation of apolipoprotein stabilized nanodisk bilayers. *Biochim. Biophy. Acta 1778*, 303–312.

(51) Dorn, I. T., Neumaier, K. R., and Tampe, R. (1998) Molecular recognition of histidine-tagged molecules by metal-chelating lipids monitored by fluorescence energy transfer and correlation spectroscopy. *J. Am. Chem. Soc. 120*, 2753–2763.

(52) Kapanidis, A. N., Ebright, Y. W., and Ebright, R. H. (2001) Site-specific incorporation of fluorescent probes into protein: Hexahistidine-tag-mediated fluorescent labeling with (Ni2+: Nitrilotriacetic acid)(n)-fluorochrome conjugates. *J. Am. Chem. Soc. 123*, 12123–12125.

(53) Guignet, E. G., Hovius, R., and Vogel, H. (2004) Reversible site-selective labeling of membrane proteins in live cells. *Nat. Biotechnol. 22*, 440–444.

(54) Denisov, I. G., Grinkova, Y. V., Lazarides, A. A., and Sligar, S. G. (2004) Directed self-assembly of monodisperse phospholipid bilayer nanodiscs with controlled size. *J. Am. Chem. Soc. 126*, 3477–3487.

(55) Khan, F., He, M. Y., and Taussig, M. J. (2006) Double-hexahistidine tag with high-affinity binding for protein immobilization, purification, and detection on Ni-nitrilotriacetic acid surfaces. *Anal. Chem. 78*, 3072–3079.

(56) Lata, S., Reichel, A., Brock, R., Tampe, R., and Piehler, J. (2005) High-affinity adaptors for switchable recognition of histidine-tagged proteins. *J. Am. Chem. Soc. 127*, 10205–10215.

BC100129S

Improved ^{18}F Labeling of Peptides with a Fluoride-Aluminum-Chelate Complex

William J. McBride,*[,†] Christopher A. D'Souza,[†] Robert M. Sharkey,[§] Habibe Karacay,[§] Edmund A. Rossi,[‡] Chien-Hsing Chang,[‡] and David M. Goldenberg[§]

Immunomedics, Inc., Morris Plains, New Jersey 07950, IBC Pharmaceuticals, Inc., Morris Plains, New Jersey 07950, and Garden State Cancer Center, Center for Molecular Medicine and Immunology, Belleville, New Jersey 07109. Received March 17, 2010; Revised Manuscript Received May 10, 2010

We reported previously the feasibility to radiolabel peptides with fluorine-18 (^{18}F) using a rapid one-pot method that first mixes $^{18}F^-$ with Al^{3+} and then binds the $(Al^{18}F)^{2+}$ complex to a NOTA ligand on the peptide. In this report, we examined several new NOTA ligands and determined how temperature, reaction time, and reagent concentration affected the radiolabeling yield. Four structural variations of the NOTA ligand had isolated radiolabeling yields ranging from 5.8% to 87% under similar reaction conditions. All of the $Al^{18}F$ NOTA complexes were stable in vitro in human serum, and those that were tested in vivo also were stable. The radiolabeling reactions were performed at 100 °C, and the peptides could be labeled in as little as 5 min. The IMP467 peptide could be labeled up to 115 GBq/μmol (3100 Ci/mmol), with a total reaction and purification time of 30 min without chromatographic purification.

INTRODUCTION

^{18}F is the most commonly used isotope for positron-emission tomography (PET), due to its nearly ideal imaging properties ($\beta+$ 0.635 MeV 97%, $T_{1/2}$ 110 min). Conventionally, ^{18}F is attached to peptides by binding it to a carbon atom (*1–4*), but attachments to silicon (*5, 6*) and boron (*7*) also have been reported. Binding to carbon usually involves multistep syntheses, in some instances taking several hours to complete, which can be problematic for an isotope with a 110 min half-life.

The most common use of ^{18}F-labeled peptides is to image receptor sites in vivo (*2*). The number of receptor sites is usually limited, so a high specific activity is necessary to avoid blocking target receptors with the excess unlabeled peptide. In most ^{18}F-peptide applications, the final peptide must be purified by high-pressure liquid chromatography (HPLC) to separate the unlabeled peptide from the radiolabeled peptide in order to obtain the specific activity needed for imaging. In one case (*8*), the radiolabeled peptide was generated with a high specific activity and an excellent yield (79%) without the need for HPLC purification. However, most of the ^{18}F-peptide radiolabeling processes are complicated, take several reaction steps, and require specialized equipment and highly trained personnel. For example, Table 1 lists the properties of several of the more commonly reported fluorination procedures. Peptide labeling through carbon often involves ^{18}F-binding to a prosthetic group through nucleophilic substitution, usually in 2 or 3 steps, where the $^{18}F^-$ is first boiled to dryness in the presence of $KHCO_3$ and Kryptofix 2.2.2 (K222), then mixed with acetonitrile and dried 2 more times (dry-down step). The prosthetic group is then labeled with $^{18}F^-$ in the presence of excess precursor. The ^{18}F-prosthetic group is purified, attached to the targeting peptide, and then purified again. This method has been used to attach prosthetic groups through amide bonds, aldehydes, and "click chemistry" (*8–12*).

The most common amide bond-forming reagent has been *N*-succinimidyl 4-^{18}F-fluorobenzoate (^{18}F-SFB), but a number of other groups have been tested (*1–3*). In some cases, such as when ^{18}F-labeled active ester amide-forming groups are used, it may be necessary to protect certain groups on a peptide during the coupling reaction, after which they are cleaved. The synthesis of the ^{18}F-SFB reagent and subsequent conjugation to the peptide requires many synthetic steps and takes about 1.5−3 h (*11, 12*).

A simpler, more efficient ^{18}F-peptide labeling method was developed by Poethko et al. (*10*), where a 4-^{18}F-fluorobenzaldehyde reagent was conjugated to a peptide through an oxime linkage in about 75 min, including the dry-down step. The newer "click chemistry" method attaches ^{18}F-labeled molecules onto peptides with an acetylene or azide in the presence of a copper catalyst (*8, 9*). The reaction between the azide and acetylene groups forms a triazole connection, which is quite stable and forms very efficiently on peptides without the need for protecting groups. Click chemistry produces the ^{18}F-labeled peptides in good to excellent yield (∼50−79%) in about 30−90 min, including the dry-down step.

A more recent method of binding ^{18}F to silicon uses isotopic exchange to displace ^{19}F with ^{18}F (*5*). Performed at room temperature in 10 min, this reaction produces the ^{18}F-prosthetic aldehyde group with high specific activity (225−680 GBq/μmol; 6100−18 400 Ci/mmol). The ^{18}F-labeled aldehyde is subsequently conjugated to a peptide and purified by HPLC, and the purified labeled peptide is obtained within 40 min (including dry-down) with ∼55% yield. The ^{18}F-silicon approach was modified subsequently to a single-step process by incorporating the silicon into the peptide before the labeling reaction (*6*). Biodistribution studies in mice with an ^{18}F-silicon-bombesin derivative showed increasing bone uptake over time (1.35 ± 0.47% injected dose (ID)/g at 0.5 h vs 5.14 ± 2.71% ID/g at 4.0 h), suggesting a release of ^{18}F from the peptide, since unbound ^{18}F is known to localize in bone. HPLC analysis of urine showed a substantial amount of ^{18}F activity in the void volume, which may be due to $^{18}F^-$ released from the peptide.

* Corresponding author. William J. McBride. E-mail bmcbride@immunomedics.com. Immunomedics, Inc., 300 American Road, Morris Plains, NJ 07950; Phone 973-605-8200ext. 233. Fax 973-605-1340.
† Immunomedics, Inc.
‡ IBC Pharmaceuticals, Inc.
§ Garden State Cancer Center.

10.1021/bc100137x © 2010 American Chemical Society
Published on Web 06/14/2010

Table 1. Summary of Selected ^{18}F-Peptide Labeling Methods

author/ref	Schirrmacher *5*	Höhne *6*	Marik *8*	Glaser *9*	Poethko *10*	Wester/Mäding (*11, 12*)	Becaud *13*	McBride
attachment	silicon	silicon	click	click	aldehyde/oxime	amide	direct-substitution	aluminum complex
Rx steps	2	1	2	2	2	many	1	1
process time (min)[a]	40	115−155	30	65[b]	75	60$^+$	35	30[c]
yield (%)[d]	55	13	79	50	40	10	57	51
HPLC-purification steps	1	1	distillation + Sep-Pak	1 + distillation	1	2	1	SPE
specific activity (GBq/μmol)	225−680	62	>35	high	high	high	74	115

[a] Includes dry-down step. [b] Estimated. [c] Dry-down step is not required. [d] Decay-corrected.

Substantial hepatobiliary excretion also was reported, attributed to the lipophilic nature of the ^{18}F-silicon-binding substrate, and requiring future derivatives to be more hydrophilic. Methods of attaching ^{18}F to boron also have been explored; however, the current process produces conjugates with low specific activity (*7*).

A direct ^{18}F-labeling method has also been explored (*13*). Here, the peptide contains a trimethylammonium-leaving group attached to an aromatic ring containing an electron-withdrawing group. The $^{18}F^-$ is dried down (10 min) with K222/K_2CO_3 or Cs_2CO_3 and heated (50−90 °C) with the peptide for 15 min to substitute the ^{18}F for the trimethylammonium group. The reaction mixture is then purified by HPLC (∼10 min) to produce the high-specific-activity ^{18}F-labeled peptide (74 GBq/μmol) in 20−57% isolated yield. The radiolabeled peptide was stable in vitro in mouse plasma.

In contrast to these multistep, time-consuming procedures, antibodies and peptides are radiolabeled routinely with radiometals typically in 15 min and in quantitative yields (*14, 15*). For PET imaging, copper-64 and, more recently, gallium-68 have been bound to peptides via a chelate, and have shown reasonably good PET-imaging properties (*16*). Since fluoride binds to most metals (*17*), we sought to determine if an ^{18}F-metal complex could be bound to a chelate on a targeting molecule. We focused on the binding of an $(Al^{18}F)^{2+}$ complex, since the aluminum−fluoride bond is one of the strongest fluoride−metal bonds and the $(AlF)^{2+}$ complex was known to bind to ligands (*18*). The AlF_n complex is stable in vivo, since this is part of the mechanism that the body uses to incorporate fluoride into tooth enamel, and thus, low doses of AlF_n should be compatible for human use (*19, 20*). We reported previously initial studies that showed the feasibility of this approach, using an ^{18}F-labeled peptide for in vivo targeting of cancer with a bispecific antibody (bsMAb) pretargeting system (*21*), a procedure that was shown to be a highly sensitive and specific technique for localizing cancer, in some cases better than ^{18}F-FDG (fluorodeoxyglucose) (*22–30*). In this initial report, we found that an $(Al^{18}F)^{2+}$ complex could bind stably to a 1,4,7-triazacyclononane-1,4,7-triacetic acid (NOTA) ligand, but the yields were low and the labeled peptide had to be purified by HPLC to obtain the specific activity needed for the imaging study.

As shown in this report, we have improved the radiolabeling yields and specific activity of this NOTA ligand, but have also prepared several new NOTA ligands to determine if structural changes would yield further improvements. Our goal is to develop a one-pot radiolabeling method that provides the radiolabeled peptide with a specific activity greater than 37 GBq/μmol with no more than a simple filtration-type solid-phase extraction (SPE) purification needed before formulation for injection. Three new NOTA ligands were chosen: the NODA-GA ligand (IMP460), because it was commercially available in a form suitable for peptide synthesis; a simple NOT2A derivative (IMP461) because our experience with IMP449 suggested that only two carboxyl groups of the NOTA were needed for the Al^{18}F-NOTA complex (*21*); and the *C*-NETA-containing peptide, IMP467, because the literature had indicated that this NOTA ligand could have increased binding kinetics for metals (*31*). As shown herein, IMP467 proved to be the best of the 4 NOTA ligands we have evaluated to date, and thus, additional studies were performed to assess optimal labeling conditions for IMP467.

EXPERIMENTAL PROCEDURES

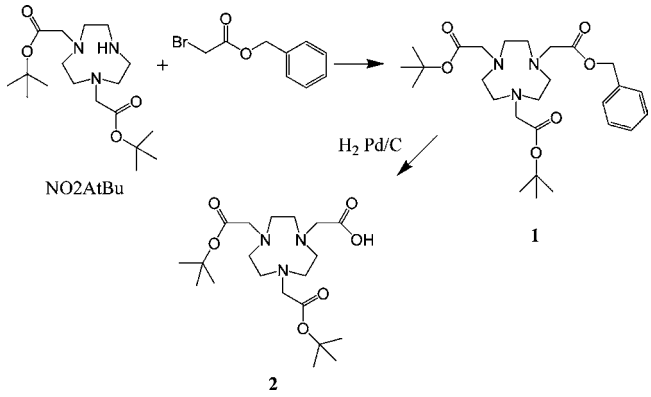
Materials. The *p*-SCN-Bn-NOTA and TACN were purchased from Macrocyclics, Inc. (Dallas, TX). The DiBocTACN, NODA-GA(tBu)$_3$, and NO2AtBu were obtained from CheMatech (Dijon, France). Protected amino acids, other peptide synthesis reagents, and resins were procured from Creosalus (Louisville, KY), Chem Impex (Wood Dale, IL), Bachem (Torrance, CA), and EMD Biosciences (San Diego, CA). The peptides were synthesized by the Fmoc method either manually or on a Protein Technologies, Inc. (Tucson, AZ) peptide synthesizer. The aluminum chloride hexahydrate was acquired from Sigma-Aldrich (Milwaukee, WI). The remaining solvents and reagents were obtained from Fisher Scientific (Pittsburgh, PA) or Sigma-Aldrich. The analytical and preparative reverse-phase HPLC (RP-HPLC) columns were bought from Phenomenex (Torrance, CA) and Waters Corp. (Milford, MA). The Sep-Pak Light Waters Accell Plus QMA and CM cartridges used to purify the $^{18}F^-$ and Waters Oasis HLB 1 cm^3 flangeless cartridges, which were used to purify the radiolabeled peptides, were purchased from Waters Corp. The size exclusion HPLC (SE-HPLC) column and the AG 1-X8 resin were from Bio-Rad (Hercules, CA). The Tricorn 5/20 Column was acquired from GE Healthcare (Piscataway, NJ). $^{18}F^-$ was supplied by IBA Molecular (Somerset, NJ). Female nude mice (NCr nu-m), 23.1 ± 2.3 g, were obtained from Taconic Farms, Germantown, NY.

The recombinant, humanized, tri-Fab bsMAb, TF2, was provided by IBC Pharmaceuticals, Inc. (Morris Plains, NJ). TF2 binds divalently to carcinoembryonic antigen (CEACAM5 or CD66e) and monovalently to the synthetic hapten, HSG (histamine-succinyl-glycine) (*30*). The bsMAb was >95% immunoreactive against CEACAM5 and the divalent-HSG NOTA-peptide, IMP449, using a SE-HPLC method described previously (*30*).

^{1}H and ^{13}C NMR spectra were obtained using a Varian Inova NMR Spectrometer (Varian Inc., Palo Alto, CA) at 500 MHz for ^{1}H and 125.7 MHz for ^{13}C at Rutgers University Chemistry Department (Newark, NJ). Chemical shifts were referenced to tetramethyl silane. High-resolution mass spectra (HRMS) were obtained on an Agilent ESI-TOF instrument at the Scripps Center for Mass Spectrometry (La Jolla, CA) or at Immunomedics, Inc. (Morris Plains, NJ).

Methods. *Synthesis of IMP460: NODA-GA-D-Ala-D-Lys(HSG)-D-Tyr-D-Lys(HSG)-NH$_2$.* The peptide was synthesized on Sieber

Scheme 1. Synthesis of Bis-t-butyl NOTA



amide resin with the amino acids and other agents added in the following order: Aloc-D-Lys(Fmoc)-OH, Trt-HSG-OH, Aloc removal, Fmoc-D-Tyr(But)-OH, Aloc-D-Lys(Fmoc)-OH, Trt-HSG-OH, Aloc removal, Fmoc-D-Ala-OH, and NODA-GA(t-Bu)$_3$. The peptide was then cleaved and purified by HPLC. HRMS $C_{61}H_{92}N_{18}O_{18}$ MH^+ calcd 1365.6909, found 1365.6912.

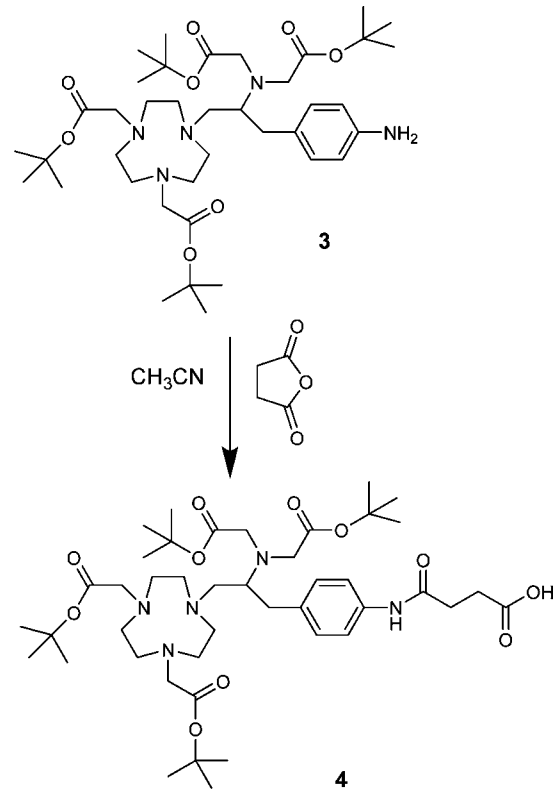
Synthesis of IMP461: NOT2A-D-Ala-D-Lys(HSG)-D-Tyr-D-Lys-(HSG)-NH$_2$ 2-{4,7-bis-tert-butoxycarbonylmethyl-[1,4,7] triazocyclononan-1-yl }-acetic acid (Bis-t-butyl-NOTA). The NO2AtBu (Scheme 1) (0.501 g 1.4×10^{-3} mol) was dissolved in 5 mL anhydrous acetonitrile. The benzyl-2-bromoacetate (0.222 mL, 1.4×10^{-3} mol) was added to the solution followed by 0.387 g of anhydrous K_2CO_3. The reaction was stirred at room temperature overnight, then filtered and concentrated to obtain 0.605 g (86% yield) of the benzyl ester conjugate (*1*). The crude product was dissolved in 50 mL of isopropanol, mixed with 0.2 g of 10% Pd/C (under Ar), and placed under 50 psi H_2 for 3 days. The product was then filtered and concentrated under vacuum to obtain 0.462 g of the desired product (*2*). HRMS $C_{20}H_{37}N_3O_6$ MH^+ calcd 416.2755, found 416.2759. ^{1}H NMR (500 MHz, $CDCl_3$, 25 °C, TMS) δ 1.45 (s, 18 H), 2.8−3.3 (m, 12 H), 3.44 (s, 4 H), 3.67 (s, 2 H); ^{13}C (125.7 MHz, $CDCl_3$) δ 28.15, 49.75, 52.43, 53.54, 57.25, 58.99, 81.56, 168.77, 170.68.

Synthesis of IMP461. The peptide was synthesized as described above with Bis-t-butyl-NOTA-OH added last. The peptide was then cleaved and purified by HPLC to obtain the product. HRMS $C_{58}H_{88}N_{18}O_{16}$ MH^+ calcd 1293.6698, found 1293.6707.

*Synthesis of IMP467: tert-Butyl {4-[2-(Bis-tert-butyoxycarbonylmethylamino-3-(4-succinylamidophenyl)propyl]-7-tert-butyoxycarbonylmethyl-[1,4,7]triazacyclononan-1-yl}acetate (Succinyl-C-NETA) (***4***).* To a solution of **3** (*31*) (Scheme 2) (148.1 mg, 0.202 mmol) in anhydrous CH_3CN (3 mL) was added (21.1 mg, 0.210 mmol) succinic anhydride. After 3 h, the solvent was evaporated and the reaction was purified by preparative RP-HPLC to yield pure **4** (137.7 mg, 82%) as dark brown oil. HRMS $C_{43}H_{71}N_5O_{11}$ MH^+ calcd 834.5223, found 834.5221. ^{1}H NMR (500 MHz, $CDCl_3$, 25 °C, TMS) δ 1.43 (s, 18 H), 1.44 (s, 18 H), 2.65−2.66 (m, 4 H), 2.85−2.88 (m, 5 H), 3.18−3.32 (m, 10 H), 3.43−3.46 (m, 10 H), 6.99 (d, 2H), 7.44 (d, 2H); ^{13}C (125.7 MHz, $CDCl_3$) δ 27.95, 28.05, 29.96,31.58, 33.36, 58.10, 58.74, 58.77, 60.69, 81.93, 82.40, 120.76, 129.20, 132.21, 137.26, 170.19, 170.21, 171.61, 171.75, 175.10.

Synthesis of IMP467: C-NETA-succinyl-D-Lys(HSG)-D-Tyr-D-Lys(HSG)-NH$_2$. IMP467 was made on a Sieber amide resin, as described above, except when the last Aloc was cleaved, the *tert*-butyl{4-[bis-(*tert*-butoxycarbonylmethyl)amino)-3-(4-succinylamidophenyl)propyl]-7-*tert*-butoxycarbonylmethyl[1,4,7]-triazanonan-1-yl}acetate (**4**) was added. The peptide was then cleaved from the resin and purified by RP-HPLC to yield 6.3 mg of IMP 467. HRMS $C_{70}H_{101}N_{19}O_{20}$ MH^+ calcd 1528.7543, found 1528.7565.

Scheme 2. Synthesis of Succinyl C-NETA Ligand (4)



Preparation of Aluminum Acetate Stock Solution. An aluminum acetate buffer solution was prepared by dissolving $AlCl_3 \cdot 6H_2O$ in a 0.1 M, pH 4, sodium acetate solution to provide a 2 mM Al-stock solution.

Concentration and Purification of $^{18}F^-$. Radiochemical-grade $^{18}F^-$ needs to be purified and concentrated before use. We examined four different SPE purification procedures to process the $^{18}F^-$ prior to its use.

Most of the radiolabeling procedures were performed using $^{18}F^-$ prepared by a conventional process (*32*). The $^{18}F^-$ in 2 mL of water was loaded onto a Sep-Pak Light, Waters Accell QMA Plus Cartridge that was prewashed with 10 mL of 0.4 M $KHCO_3$, followed by 10 mL water. After loading the $^{18}F^-$ onto the cartridge, it was washed with 5 mL water to remove any dissolved metal and radiometal impurities. The isotope was then eluted with ~1 mL of 0.4 M $KHCO_3$ in several fractions to isolate the fraction with the highest concentration of activity. The eluted fractions were neutralized with 5 μL of glacial acetic acid per 100 μL of solution to adjust the eluent to pH 4−5.

In the second process, the QMA cartridge was washed with 10 mL pH 8.4, 0.5 M NaOAc followed by 10 mL DI H_2O. $^{18}F^-$ was loaded onto the column as described above and eluted with 1 mL, pH 6, 0.05 M KNO_3 in 200 μL fractions with 60−70% of the activity in one of the fractions. No pH adjustment of this solution was needed.

In the third process, the QMA cartridge was washed with 10 mL pH 8.4, 0.5 M NaOAc followed by 10 mL DI H_2O. The $^{18}F^-$ was loaded onto the column as described above and eluted with 1 mL, pH 5−7, 0.154 M commercial normal saline in 200 μL fractions with 80% of the activity in one of the fractions. No pH adjustment of this solution was needed.

Finally, we devised a method to prepare a more concentrated and high-activity $^{18}F^-$ solution, using tandem ion exchange. Briefly, Tygon tubing (1.27 cm long, 0.64 cm OD) was inserted into a Tricorn 5/20 column and filled with ~200 μL of AG 1-X8 resin, 100−200 mesh. The resin was washed with 6 mL 0.4 M K_2CO_3 followed by 6 mL H_2O. A Sep-Pak light Waters

Accell Plus CM cartridge was washed with DI H_2O. Using a syringe pump, the crude $^{18}F^-$ that was received in a 5 mL syringe in 2 mL DI H_2O flowed slowly through the CM cartridge and the Tricorn column over ~5 min followed by a 6 mL wash with DI H_2O through both ion-binding columns. Finally, 0.4 M K_2CO_3 was pushed through only the Tricorn column in 50 μL fractions. Typically, 40−60% of the eluted activity was in one 50 μL fraction. The fractions were collected in 2.0 mL free-standing screw-cap microcentrifuge tubes containing 5 μL glacial acetic acid to neutralize the carbonate solution. The elution vial with the most activity was then used as the reaction vial.

Comparison of Al^{18}F Radiolabeling Yields of IMP449, IMP460, IMP461, and IMP467. Three microliters of 2 mM Al^{3+} stock solution was added to 60 μL of $^{18}F^-$ (44 MBq) followed by the addition of 10 μL of 0.05 M peptide solution in pH 4.1, 0.5 M NaOAc. The four reaction mixtures were formulated and placed in a 103 °C heating block for 19 min. The reaction mixtures were purified by an HLB column, as described above, to determine the radiochemical reaction yield. All of the reaction yields noted in this work are isolated radiochemical yields.

Kinetics of ^{18}F-IMP467 Radiolabeling. Three microliters of 2 mM Al^{3+} stock solution was mixed with 40 μL of $^{18}F^-$ followed by the addition of 20 μL of 2 mM IMP467 in 0.1 M, pH 4, acetate buffer. Four reaction mixtures were formulated and placed in a 107 °C heating block for 5, 10, 15, and 30 min. The crude products were each purified on a Waters Oasis HLB 1 cm^3 (30 mg) Flangeless Cartridge. Briefly, 200 μL of water was added to the reaction solution, which was then removed via pipet and drawn into the HLB column. The reaction solution was drawn into the column. The reaction vessel was rinsed with 1 mL of H_2O, which was then transferred and drawn into the column. The column was eluted with 2 × 200 μL portions of 1:1 EtOH/H_2O, with the product being isolated in a 3 mL vial that contained 15 mg of ascorbic acid that was adjusted to pH 6 and previously lyophilized. The yield was determined by measuring the activity left in the reaction vessel, remaining on the HLB column, in the water wash, and in the 1:1 EtOH/H_2O. The amount of activity in the 1:1 EtOH/H_2O fraction divided by the total activity from the other fractions gave the isolated radiochemical yield. The radiolabeled peptides were then analyzed by RP-HPLC, which showed that the unbound $^{18}F^-$ was removed in all cases.

Comparison of ^{18}F-IMP467 Reaction Yield vs Moles of Peptide Used. Three microliters of 2 mM Al^{3+} stock solution was added to 40 μL of $^{18}F^-$ (24 MBq) followed by the addition of 5, 10, 15, or 20 μL of 2 mM IMP467 in 0.1 M, pH 4.1 acetate buffer and 15, 10, 5, or 0 μL of water, respectively. The reaction solutions were heated to 99 °C for 15 min, then purified by HLB column as described above to determine the isolated radiochemical yield.

Comparison of ^{18}F-IMP467 Reaction Yield Vs Reaction pH. A CM cartridge (to remove metals) was washed with H_2O and placed upstream from the QMA cartridge. The $^{18}F^-$ was purified by the nitrate method described above. The peptide and $AlCl_3$ were both dissolved in pH 4, 0.1 M NaOAc. The peptide was radiolabeled with the purified $^{18}F^-$ in duplicate over the pH range 4−7.2. Each sample was labeled by mixing 20 μL of $^{18}F^-$, 2 μL of 0.01 M $AlCl_3$ in 0.05 M NaOAc pH 4.9, 20 μL 2 mM IMP467 in 0.1 M NaOAc pH 6, and 158 μL of 0.1 M reaction buffer. One sample was purified and the duplicate was allowed to decay while sealed. The pH of the decayed sample was measured with a calibrated pH meter equipped with a Calomel glass microcombination pH electrode.

Radiolabeling of IMP467 with Carbonate-Eluted ^{18}F-Fluoride. ^{18}F-fluoride (5.39 GBq) in 50 μL 0.4 M K_2CO_3 was neutralized with 5 μL glacial acetic acid and then mixed with 1 μL 0.01 M ($AlCl_3 \cdot 6H_2O$) in 0.1 M NaOAc (pH 4), followed by 2 μL 0.01 M IMP467 (20 nmol) in 0.1 M NaOAc (pH 4), and incubated in a 105 °C heating block for 17 min. The solution was cooled briefly and diluted with 1 mL H_2O, and then placed in an HLB 1-cc (30 mg) cartridge. The solution was eluted under vacuum into an empty crimp-sealed vial as follows. The reaction vessel and the column were rinsed with 2 × 1 mL portions of H_2O. The column was moved to a vial containing lyophilized ascorbic acid (15 mg, buffered at pH 5.5) and eluted with 2 × 200 μL of 1:1 ethanol/water.

Radiolabeling of IMP467 Using Saline-Eluted ^{18}F-Fluoride Ion. ^{18}F-fluoride ion (70.3 MBq) in 50 μL saline was mixed with 2 μL 0.01 M ($AlCl_3 \cdot 6H_2O$) in 0.1 M NaOAc (pH 4) followed by 20 μL IMP467 (2 mM, 40 nmol) in 0.1 M NaOAc (pH 4), and incubated in a 105 °C heating block for 15 min. The solution was cooled briefly, diluted with 1 mL PBS (pH 7.4), and then placed in a HLB cartridge. The solution was purified as described above to obtain 48.3 MBq of the radiolabeled product in 85% isolated yield. The total reaction and purification time was 30 min.

Synthesis and Characterization of ^{19}F-IMP467. The ^{19}F-IMP467 was prepared by mixing 20 μL of 2 mM IMP467 in 2 mM NaOAc buffer, pH 4.18, with 50 μL of 2 mM $AlCl_3$ and 100 μL of 2 mM NaF in the same acetate buffer in a 2 mL screwcap microcentrifuge vial and heated (sealed) for 5 min at 101 °C. The sample was then examined by HPLC on a Waters 2695 HPLC system equipped with a Phenomenex Gemini C_{18} reverse-phase column (250 × 4.6 mm, 5 μm, 110 Å), using a linear gradient of 90% A (0.1% TFA) to 20% B (90% acetonitrile, 10% water, 0.1% TFA) over 20 min at a flow rate of 1 mL/min, absorbance was detected at 254 nm using Waters PDA 2996 detector. The ^{19}F-IMP467 forms two complexes (12.92 and 14.84 min), which were isolated by HPLC. The isolates were stored in the eluent buffer and reinjected 0.5, 1, 1.5, and 2 h after isolation. The complexes were examined by HPLC on the Agilent ESI-TOF.

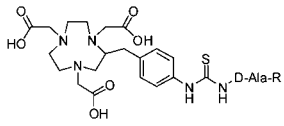
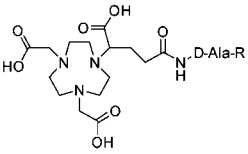
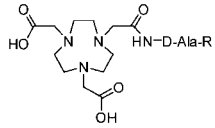
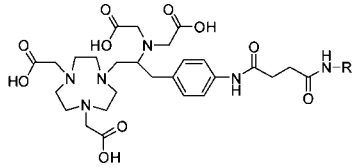
HPLC Separation of ^{19}F-IMP467 from Unreacted Peptide. The unreacted peptide could be separated from the ^{19}F or ^{18}F-peptide by using a Phenomenex Kinetex C-18 column, 50 × 4.60 mm, 2.6 μ, 100A and eluting at 0.6 mL/min using 0.01% formic acid in 5% acetonitrile/water as Buffer A and 0.01% formic acid in 90% acetonitrile as Buffer B. The gradient ran for 1 min with 100% Buffer A, then to 80:20 A/B over 6 min. Under these conditions, the Al-peptide and the unreacted peptide were eluted before the fluoride-bound peptides. These were the HPLC conditions used to examine the peptide reaction mixture on the Agilent ESI-TOF.

Stability of ^{18}F-IMP467 in Phosphate-Buffered Saline (PBS) and Human Serum. The purified radiolabeled peptide in 50 μL 1:1 EtOH/H_2O was mixed with 150 μL of human serum and placed in the HPLC autosampler heated to 37 °C. Another sample of ^{18}F-IMP467 was diluted in the same manner with PBS and heated to 37 °C. The samples were analyzed by RP-HPLC.

Biodistribution and in Vivo Stability of ^{18}F-IMP467. All animal studies were approved in advance by the Institutional Animal Care and Use Committee of the Center for Molecular Medicine and Immunology.

The stability of ^{18}F-IMP467 was examined by comparing HPLC elution profiles of the peptide prior to injection to that found in the urine at 0.5 and 1.5 h after the intravenous injection ^{18}F-IMP467 (18.5 MBq (500 μCi), 2.67 × 10^{-10} mol in 1% human serum albumin) in nude mice. The materials were analyzed by RP-HPLC and by SE-HPLC alone and in the presence of TF2 anti-CEACAM5 × anti-HSG tri-Fab bsMAb,

Table 2. NOTA Ligands and Maximum Isolated Yields after Radiolabeling with 500 nmol Peptide (R = D-Lys(HSG)-D-Tyr-D-Lys(HSG)-NH_2)

PEPTIDE	Structure	Maximum ^{18}F-Labeling Yield
IMP449		44%
IMP460		5.8%
IMP461		31%
IMP467		87%

which was used to illustrate the continued association of the HSG-hapten with the ^{18}F-IMP467 as an indication of product stability.

Biodistribution studies were performed in nude mice bearing subcutaneous LS174T human colon cancer xenografts. Mice in the pretargeting group received 163 μg (1 nmol) of TF2 intravenously, followed with ^{18}F-IMP467 (3.91 MBq (105 μCi), 0.05 nmol in 1% human serum albumin) 16 h later. Mice were necropsied 1 and 3 h post-peptide injection, and the tissues were weighed and co-counted in a gamma scintillation counter with standards prepared from the injected product. The data are expressed as the percent-injected dose per gram (% ID/g).

RESULTS

IMP449, a benzyl-NOTA derivative (Table 2) of a peptide used for pretargeting, was the first chelate that formed a stable complex with $(Al^{18}F)^{2+}$ suitable for in vivo targeting (*21*). IMP449 was labeled previously by mixing 6 nmol of Al^{3+} with $^{18}F^-$ in a pH 4 sodium acetate buffer to form $(Al^{18}F)^{2+}$, then mixed with 521 nmol of IMP449 (total volume 213 μL) and heated for 15 min at ~100 °C. Labeling yields were between 5% and 20% after HPLC purification. We found subsequently that radiolabeling yields with this derivative could be improved to as much as 44% by reducing the reaction volume (73 μL) by one-third. Several products also were observed by RP-HPLC after radiolabeling the IMP449 peptide. Adding ascorbic acid to the reaction mixture markedly reduced these side products (not shown).

Three new NOTA and NOT2A derivatives were synthesized as part of a pretargeting peptide in an attempt to find a ligand that would improve labeling yields and maintain stability of the $Al^{18}F$-NOTA complex. Table 2 shows the maximum radiolabeling yields obtained with the three new ligands using the same conditions that enabled 44% yields with IMP449. One of the derivatives, IMP460, had only 5.8%, while another, IMP461, had a 31% yield. However, radiolabeling yields nearly doubled to 87% with IMP467. The reported improved binding properties of the ligand may be responsible for the increased labeling yield (*33*). While all of these products were tested and found to be stable in human serum, further studies focused on IMP467 to assess the impact that other aspects of the radiolabeling procedure might have on the yield and specific activity.

Table 3. ^{18}F-IMP467 Yield as a Function of pH

reaction buffer pH	final reaction pH	isolated yield (%)
2.88	3.96	54
3.99	4.27	70
	4.25	77
5.00	5.05	70
	4.25	69
6.00	6.04	41
7.30	7.23	3.0

Decreasing the amount IMP467 in the reaction mixture from 500 nmol to 40 nmol reduced the labeling yield to 65−75%, which was still better than the 44% yield achieved with 500 nmol of IMP449. When the amount of peptide added to the reaction was varied from 40 to 20 nmol (at concentrations from 0.63 to 0.32 mM), the yields remained fairly constant at around 75−82%, but decreased to 49% when only 10 nmol was used at a concentration of 0.16 mM. Other studies found that binding was nearly complete within 5 min at 107 °C (5 min, 68%; 10 min, 61%; 15 min, 71%; and 30 min, 75%), with only moderate increases in isolated yield with reaction times as long as 30 min, but no binding was achieved with labeling at 50 °C.

In an effort to enhance the specific activity further, we devised a procedure for purifying and concentrating $^{18}F^-$, starting with substantially higher levels of $^{18}F^-$ than were employed in all previous studies. When using only 20 nmol of IMP467 with 5.39 GBq (145.6 mCi) of $^{18}F^-$, the labeling yield was 52% (isolated radiochemical yield, without correcting for decay, 51% decay-corrected). Thus, this process further improved the specific activity of the preparation [i.e., the isolated peptide contained 2.29 GBq (61.9 mCi) of the purified peptide, with an effective specific activity of 115 GBq/μmol (3100 Ci/mmol)], albeit at the expense of somewhat reduced, but acceptable, yields. This radiolabeled product was prepared in 28 min ($^{18}F^-$ post purification delay = 6 min; reaction time = 17 min; purification time = 5 min). A second experiment using 7 min heating afforded a similar yield and specific activity in only 14 min. Overall, these studies confirmed that increasing the concentration of reagents improves the reaction kinetics and the specific activity of the labeled product, with some reduction in labeling efficiency.

We next assessed how the concentration of Al^{3+} might impact the labeling yields. When IMP467 (40 nmol) was labeled in the presence of increasing amounts of Al^{3+} (0, 5, 10, 15, 20 μL of 2 mM Al in pH 4 acetate buffer and keeping the total volume constant), yields of 3.5%, 80%, 77%, 78%, and 74%, respectively, were achieved. These results indicated that (a) nonspecific binding of $^{18}F^-$ to this peptide in the absence of Al^{3+} was low, (b) 10 nmol of Al^{3+} was sufficient to allow for maximum ^{18}F-binding, and (c) higher amounts of Al^{3+} did not reduce binding substantially, indicating that there was sufficient chelation capacity at this peptide concentration.

The optimal pH for labeling was between 4.3 and 5.5 (Table 3). The process could be expedited by eluting the $^{18}F^-$ from the anion exchange column with nitrate or chloride ion instead of carbonate ion, which eliminates the need to adjust the eluent to pH 4 with glacial acetic acid before mixing with the $AlCl_3$.

RP-HPLC showed unlabeled IMP467 elutes as a single peak at 13.454 min (Figure 1A), but when radiolabeled, ^{18}F-IMP467 elutes as two peaks 13.399 and 15.388 min (Figure 1B), suggesting that the aluminum fluoride forms two complexes with the peptide. To examine this further, we prepared and characterized cold ^{19}F-IMP467 by RP-HPLC (UV) and HPLC-mass spectroscopy (ESI-TOF). The HPLC of the ^{19}F-IMP467 (Figure 1C) confirmed that the ^{19}F-IMP467 peaks 12.927 and 14.887

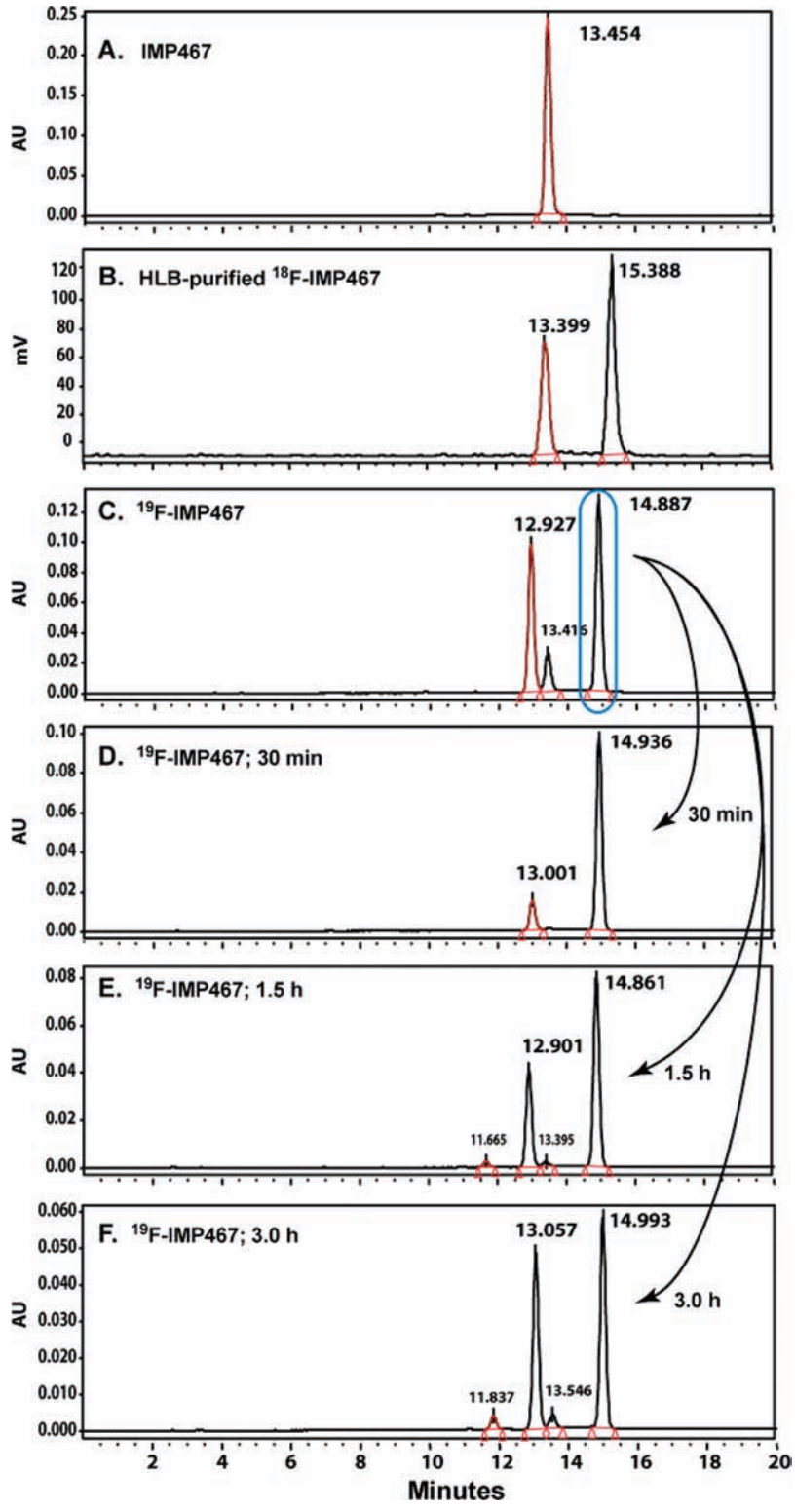


Figure 1. RP-HPLC analysis of IMP467, ^{18}F-IMP467, and ^{19}F-IMP467. The unlabeled peptide elutes as a single peak (A), but when radiolabeled with Al^{18}F (^{18}F-IMP467), two peaks are observed (B). ^{19}F-IMP467 also showed two main peaks (C) [13.4 min peak is unlabeled peptide as seen in (A)]. The 14.9 min peak was isolated and evaluated over time (D−F), showing the equilibration of the isomeric counterpart (∼13.0 min).

min corresponded to the same peaks seen with the ^{18}F-IMP467 with the retention times of the radiometric detector being slightly later since it is downstream from the UV detector. When this reaction mixture was analyzed by HPLC-mass spectrometry (high resolution), the results confirmed that each of the two peaks contained the peptide, one aluminum, and one fluorine (ESI-TOF $C_{70}H_{99}FN_{19}O_{20}Al$ calcd 1571.7113 found 786.8635 $[M+2H]^{2+}$).

The individual ^{18}F and ^{19}F peaks could be isolated by HPLC. Over time, the isolated isomers interconvert, as shown in Figure 1C−F, where the ∼14.9 min ^{19}F-IMP467 product was isolated and then re-evaluated over 3 h. This interconversion also was seen previously with the simple NOT2A ligand (*34*). Under the HPLC conditions shown in Figure 1, the unlabeled peptide is eluted between the two ^{19}F-IMP467 complexes (∼13.4 min). This peak also was seen to develop over the 3 h evaluation of

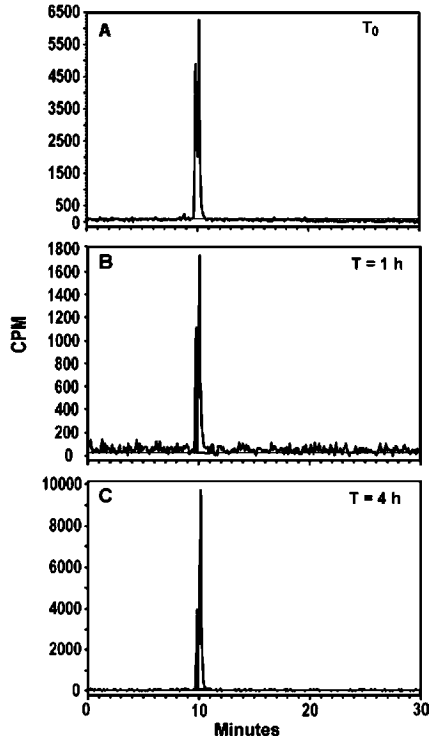


Figure 2. Serum stability of IMP467 as analyzed by RP-HPLC: (A) ^{18}F-IMP467 in serum at time-zero, (B) ^{18}F-IMP467 in serum after 1 h, (C) ^{18}F-IMP467 in serum after 4 h.

the isolated 14.9 min ^{19}F-IMP467 peak, suggesting some loss of Al^{19}F from the product over time when held in 0.1% TFA buffer. Al-peptide complexes are eluted before these peaks (i.e., between 9.8 and 12.2 min). If a different C-18 column is used (Phenomenex Kinetex C-18), the Al peptide complexes and the unreacted peptide are eluted first followed by the ^{18}F- or ^{19}F-complexed peptide. The purification on the Kinetex column would permit isolation of the labeled peptide if further increases in effective specific activity were desired (data not shown).

Stability studies with ^{18}F-IMP467 were performed in PBS and initially, in previously frozen human serum. At time zero, both samples showed no detectable $^{18}F^-$ above background at the void volume of the column. At 5.5 h, the PBS sample had 2.3% of the $^{18}F^-$ activity in the void volume. At 1 and 4 h, there was no detectable activity in the void volume, but the ratio of the two radiolabeled peaks changed over time, with a higher portion found in the second peak (Figure 2). The serum stability study was later repeated in fresh human serum at 37 °C for 5 h and the RP-HPLC indicated that 0.5% of the injected activity was present at the void volume of the column (not shown). ^{18}F-IMP467 analyzed by SE-HPLC showed that nearly all of the activity shifted to a shorter retention time on addition of TF2, indicating that the binding of the Al^{18}F complex did not compromise the binding of the HSG hapten (Figure 3).

In order to confirm the suitability of ^{18}F-IMP467 for in vivo use, biodistribution studies were performed in nude mice using the peptide alone or in a pretargeting setting (*21*). The peptide eliminated in the urine had an identical RP-HPLC elution profile as the ^{18}F-IMP467 that was injected, and SE-HPLC further showed the labeled peptide contained the HSG-hapten used to bind the bsMAb (Figure 4). These results indicate that the peptide was excreted intact, indicating no dissociation of the radionuclide. As shown in Table 4, the peptide cleared quickly from the blood (~0.1% ID/g at 1 h), with little residual activity in the tissues and low renal retention (~2% ID/g). Bone uptake was also low, averaging 0.4−0.5%, as compared to 6% and 9% ID/g that were reported previously for ^{18}F and Al^{18}F at 1

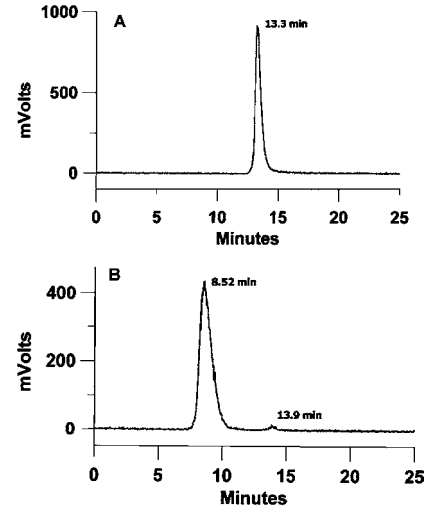


Figure 3. Binding of ^{18}F-IMP467 to TF2 by SE-HPLC: (A) ^{18}F-IMP467 after HLB purification, alone, or (B) mixed with TF2 anti-CEA × anti-HSG bsMAb.

and 3 h, respectively (*21*). Tumor uptake in the pretargeted animals 1 h after injection of the ^{18}F-IMP467 was nearly 50× higher than that observed with the ^{18}F-IMP467 alone, providing tumor/nontumor ratios of ~100:1 for the blood, liver, and other tissues, and even 5:1 for the kidney, indicating the suitability of this method to prepare functionally active and stable ^{18}F-labeled peptides for immunoPET imaging.

DISCUSSION

Molecular imaging has become an important priority, with far-reaching implications in many fields of biomedical research and clinical practice. PET imaging represents one of the more sensitive imaging modalities, with the ability to view the whole-body distribution of a radiotagged compound. A number of different positron-emitting radionuclides have been used for PET imaging, but ^{18}F is preferred because of its ideal imaging properties, and it is also widely available and relatively inexpensive because of the extensive use of ^{18}F-fluorodexoyglucose in oncology and neurobiology. However, coupling ^{18}F to compounds has been a challenge. Currently, there are a number of groups exploring ^{68}Ga, because products can be prepared at high specific activities, and also because this radionuclide can be readily coupled to compounds through simple chelation chemistry that has been widely used for radiometal labeling over the past 25 years (*14–16*). We envisioned that a similar process could be applied to metal−fluorine complex that would permit more facile radiolabeling of compounds with ^{18}F and reported previously the initial success of this approach applied to a NOTA-containing peptide used in a pretargeting procedure (*21*). However, radiolabeling yields were low (5−20%), and HPLC purification was required to isolate the ^{18}F-peptide from the unlabeled peptide.

We now report improvements to this radiolabeling procedure by changing the structure of the core NOTA compound and the reaction conditions. This method can be performed by simply mixing Al^{3+}(6−40 nmol) with $^{18}F^-$ in pH 4−5.5 acetate buffer with a 5 min incubation, followed by an HLB cartridge purification to remove unbound $^{18}F^-$ and ($AlF_n{}^{18}F$). Using these improvements, we have been able to label IMP467 with a specific activity as high as 115 GBq/μmol (3100 Ci/mmol) in ≤30 min without HPLC purification, but this required a more concentrated and high-activity $^{18}F^-$ than what is commonly supplied by the commercial vendor and resulted in somewhat lower yields. Purification of the $^{18}F^-$ to remove trace metals is important here, as well as in other methods. Importantly, the

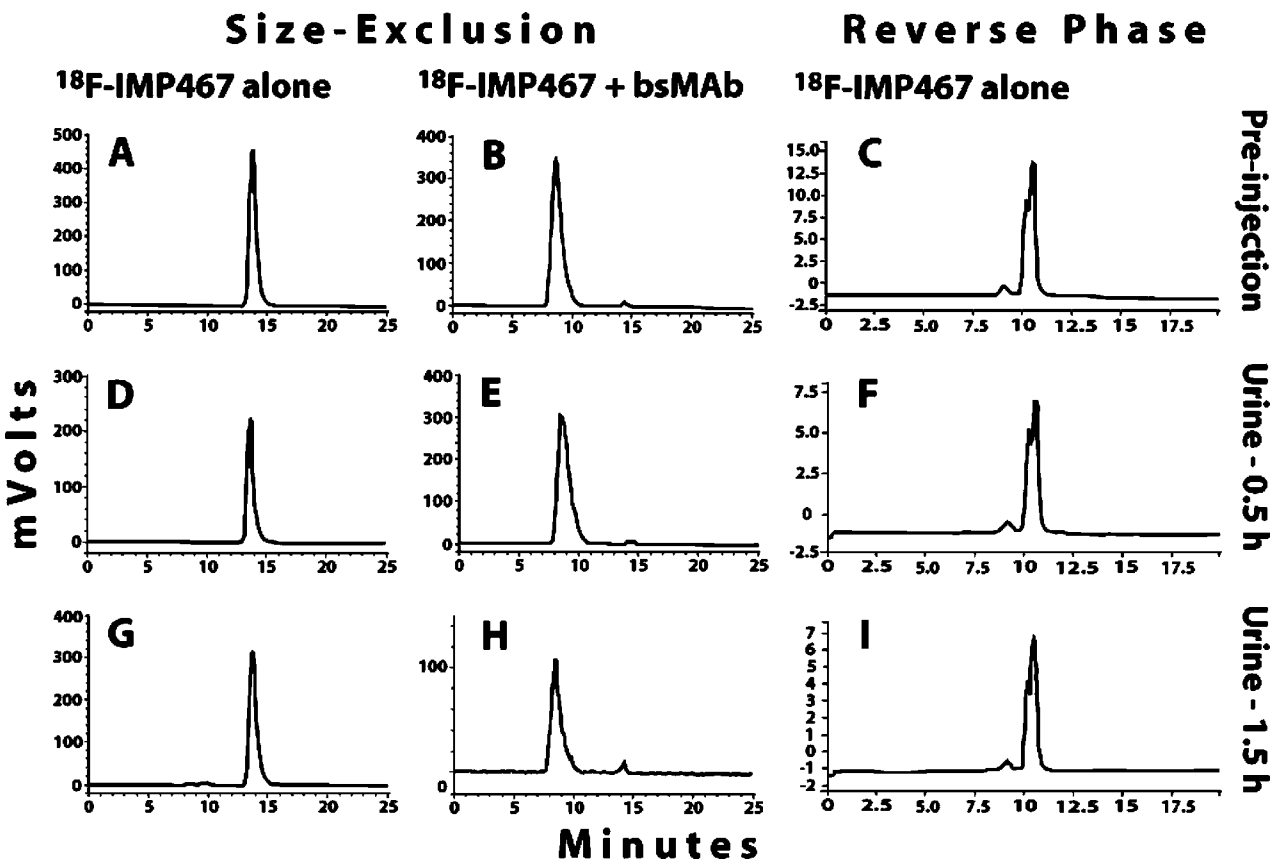


Figure 4. In vivo stability of ^{18}F-IMP467. SE- and RP-HPLC analysis of ^{18}F-IMP467 before injection and in urine samples taken from mice 0.5 and 1.5 h postinjection. RP-HPLC shows the same elution profile in the original product and in the urine, while SE-HPLC was performed to show ^{18}F-IMP467 eliminated in urine continued to retain binding to the TF2 anti-CEACAM5 × anti-HSG bsMAb.

Table 4. Biodistribution of ^{18}F-IMP467 Alone or Pretargeted by TF2 Anti-CEACAM5 × Anti-HSG bsMAb[a]

	percent-injected dose per gram tissue (mean ± SD; $N = 5$)			
tissue	TF2-pretargeted ^{18}F-IMP467 1 h	TF2-pretargeted ^{18}F-IMP467 3 h	^{18}F-IMP467 1 h alone	^{18}F-IMP467 3 h alone
LS174T	11.8 ± 2.97	8.16 ± 4.83	0.23 ± 0.11	0.09 ± 0.05
liver	0.29 ± 0.32	0.09 ± 0.02	0.07 ± 0.01	0.06 ± 0.01
spleen	0.26 ± 0.19	0.11 ± 0.04	0.05 ± 0.01	0.03 ± 0.01
kidney	2.28 ± 0.47	1.98 ± 0.35	2.47 ± 0.56	1.96 ± 0.55
lung	0.29 ± 0.18	0.08 ± 0.02	0.12 ± 0.02	0.06 ± 0.01
blood	0.12 ± 0.06	0.02 ± 0.01	0.08 ± 0.05	0.01 ± 0.00
stomach	0.13 ± 0.06	0.05 ± 0.04	0.03 ± 0.02	0.03 ± 0.01
small intestine	0.46 ± 0.12	0.12 ± 0.03	0.21 ± 0.05	0.13 ± 0.04
large intestine	0.11 ± 0.09	0.27 ± 0.11	0.07 ± 0.02	0.20 ± 0.09
scapula	0.57 ± 0.13	0.41 ± 0.08	0.40 ± 0.11	0.44 ± 0.14
muscle	0.54 ± 0.88	0.03 ± 0.04	0.03 ± 0.01	0.02 ± 0.01
brain	0.02 ± 0.00	0.02 ± 0.02	0.01 ± 0.00	0.01 ± 0.00

[a] Nude mice bearing LS174T human colonic cancer xenografts were necropsied 1 and 3 h after ^{18}F-IMP467 injection (TF2 given 16 h earlier).

labeling process could be performed by eluting ^{18}F-fluoride with commercial sterile saline, with optimal yields occurring when mixing 71 MBq of purified $^{18}F^-$ with 20 nmol Al and 40 nmol IMP467 in a pH 4.3−5.5 acetate buffer in a total volume of 100 μL, heating to 90 to 110 °C for 15 min, and performing SPE separation to remove unbound $^{18}F^-$ from the radiolabeled peptide.

As mentioned, the specific activity and yields are contingent on the concentration of the reaction mixture, but HPLC purification also could be used to isolate the Al^{18}F-labeled peptide from the Al-peptide/peptide if higher specific activities are necessary. In the case of IMP449, Al-IMP449 had about the same HPLC retention time as the ^{18}F-IMP449, but it could be purified to a specific activity of about 1300 Ci/mmol, which provided highly favorable tumor localization with the pretargeting method (*21*). Some of the new peptides developed for this work had a much greater separation between the Al-peptide and the Al^{18}F peptide, making the HPLC purification to obtain high-specific-activity ^{18}F-peptides somewhat easier. More recently, NOT2A-octreotide (*34*) and NOT2A-bombesin (*35*) derivatives bearing the same simple NOT2A ligand as IMP461 were prepared and labeled with $(Al^{18}F)^{2+}$. As with IMP461, radiolabeling yields were in the same range, and in both of these situations, HPLC purification was able to separate radiolabeled from unlabeled peptide to improve the specific activity, but we suspect that higher specific activities may be possible by modifying the NOTA ligand. As indicated herein, radiolabeling yields vary from as low as 6% to as high as 87%, based on the NOTA ligand. The higher labeling yield (87%) observed for IMP467 may be due to the increased binding kinetics of the ligand (*33*).

In our initial studies, many known metal-binding ligands were examined for their suitability for complexing $(Al^{18}F)^{2+}$ (*21*). Diethylenetriaminepenatacetic acid-(DTPA-Al^{18}F) complexes were formed in >90% yield, but they were not stable in vitro. Other ligands known to bind Al^{3+} were tested but also were unsuitable. André et al. reported that the Al-NOTA complex was stable (*36*), and in our testing, all the NOTA-Al^{18}F compounds tested to date showed a high level of stability in serum, and both IMP449 and IMP467 were stable in vivo. A recent study also found the targeting of ^{18}F-IMP449 was similar to the same peptide radiolabeled with ^{68}Ga, attesting to the stability of the ^{18}F-product (*29*). While the HPLC analysis of the 14.9 min peak from the ^{19}F-IMP467 showed some formation of the unlabeled peptide (peak ~13.4 min) over time, this product was isolated in 0.1% TFA buffer, which is certainly not the condition in which ^{18}F-IMP467 would be held for in

vivo use. Indeed, in PBS, only ~2% loss of ^{18}F occurred, and when held in serum over 4 h, no detectable loss of ^{18}F was observed, but there was a noticeable change in the proportion of the product in the early eluting peak to the later-eluting peak. The in vivo studies also clearly support the suitability of the product's stability, with very low uptake in bone.

All of the $Al^{18}F$ peptide complexes formed two peaks (diastereomeric products), and with IMP467, the ratio of the two peaks changed over time, but this isomerization did not result in the loss of ^{18}F. Al^{3+} forms octahedral complexes with four binding sites in a plane and two axial binding sites. Many isomer possibilities with the NOTA ligands exist, but it may be that the two complexes arise from a fluoride−aluminum bond in the plane in one complex and a fluoride−aluminum bond in the axial position in the other complex. Further studies will be needed to determine the exact nature of the complexes.

CONCLUSION

In conclusion, *C*-NETA-containing peptides, as exemplified by IMP467, can be labeled with ^{18}F rapidly (15−30 min) and in high yield (up to 85%) via Al-bound ^{18}F at a specific activity of up to 115 GBq/μmol, without requiring HPLC purification. The resulting ^{18}F-IMP467 is stable in human serum and suitable for in vivo pretargeting applications. The use of the $^{18}F^-$ saline as a source of purified ^{18}F-fluoride simplifies the labeling process. We anticipate that similar results can be achieved with a broad spectrum of peptides derivatized with *C*-NETA. This labeling method provides a simple procedure for obtaining high-specific-activity ^{18}F-labeled peptides using conventional equipment and is amenable to the development of a kit formulation, requiring only the addition of $^{18}F^-$ to a peptide−aluminum mixture. Such a simple, inexpensive labeling process should expand the use of ^{18}F-radiolabeled peptides for research and clinical use.

ACKNOWLEDGMENT

This work was funded in part by NIH grants 9R44 RR028018 and 2R44CA123985. Disclaimer: WJM, CAD, EAR, C-HC, and DMG are employed or have financial interest in Immunomedics, Inc., or IBC Pharmaceuticals, Inc. RMS and HK have disclosed no financial conflicts.

LITERATURE CITED

(1) Miller, P. W., Long, N. J., Vilar, R., and Gee, A. D. (2008) Synthesis of ^{11}C, ^{18}F, ^{15}O, and ^{13}N radiolabels for positron emission tomography. *Angew. Chem., Int. Ed. 47*, 8998–9033.

(2) Wester, H. J., and Schottelius, M. (2007) Fluorine-18 labeling of peptides and proteins. In *PET chemistry-the driving force in molecular imaging* (Schubiger, P. A., Lehmann, L., and Friebe, M., Eds.) pp 79−111.

(3) Cai, L., Lu, S., and Pike, V. W. (2008) Chemistry with [^{18}F]fluoride ion. *Eur. J. Org. Chem.* 2853–2873.

(4) Mamat, C., Ramenda, T., and Weust, F. R. (2009) Recent applications of click chemistry for the synthesis of radiotracers for molecular imaging. *Mini-Rev. Org. Chem. 6*, 21–34.

(5) Schirrmacher, E., Wängler, B., Cypryk, M., Bradtmöller, G., Schäfer, M., Eisenhut, M., Jurkschat, K., and Schirrmacher, R. (2007) Synthesis of *p*-(di-*tert*-butyl[^{18}F]fluorosilyl)benzaldehyde ([^{18}F] SiFA-A) with high specific activity by isotopic exchange: a convenient labeling synthon for the ^{18}F-labeling of N-aminooxy derivatized peptides. *Bioconjugate Chem. 18*, 2085–2089.

(6) Höhne, A., Mu, L., Honer, M., Schubiger, P. A., Ametamey, S. M., Graham, K., Stellfeld, T., Borkowski, S., Berndorff, D., Klar, U., Voigtmann, U., Cyr, J. E., Friebe, M., Dinkelborg, L., and Srinivasan, A. (2008) Synthesis, ^{18}F-labeling, and *in vitro* and *in vivo* studies of bombesin peptides modified with silicon-based building blocks. *Bioconjugate Chem. 19*, 1871–1879.

(7) Ting, R., Harwig, C., Keller, U. A. D., McCormick, S., Austin, P., Overall, C. M., Adam, M. J., Ruth, T. J., and Perrin, D. M. (2008) Toward [^{18}F]-labeled aryltrifluoroborate radiotracers: in vivo positron emission tomography imaging of stable aryltrifluoroborate clearance in mice. *J. Am. Chem. Soc. 130*, 12045–12055.

(8) Marik, J., and Sutcliffe, J. L. (2006) Click for PET: rapid preparation of [^{18}F]fluoropeptides using Cu^I catalyzed 1,3-dipolar cycloaddition. *Tetrahedron Lett. 27*, 6681–6684.

(9) Glaser, M., and Årstad, E. (2007) Click labeling" with 2-[^{18}F]fluoroethylazide for positron emission tomography. *Bioconjugate Chem. 18*, 989–993.

(10) Poethko, T., Schottelius, M., Thumshirn, G., Hersel, U., Herz, M., Henriksen, G., Kessler, H., Schwaiger, M., and Wester, H.-J. (2004) Two-step methodology for high-yield routine radiohalogenation of peptides: 18F-labeled RGD and octreotide analogs. *J. Nucl. Med. 45*, 892–902.

(11) Wester, H. J., Hamacher, K., and Stocklin, G. (1996) A comparative study of N.C.A. fluorine-18 labeling of proteins via acylation and photochemical conjugation. *Nucl. Med. Biol. 23*, 365–372.

(12) Mäding, P., Füchtner, F., and Wüst, F. (2005) Module-assisted synthesis of the bifunctional labeling agent N-succinimidyl 4-[^{18}F]fluorobenzoate ([^{18}F]SFB). *Appl. Radiat. Isot. 63*, 329–332.

(13) Becaud, J., Mu, L., Schubiger, P. A., Ametamey, S. M., Graham, K., Stellfeld, T., Lehmann, L., Borkowski, S., Berndorf, D., Dinkelborg, L., Srinivasan, A., Smits, R., and Koksch, B. (2009) Direct one-step ^{18}F-Labeling of peptides via nucleophilic aromatic substitution. *Bioconjugate Chem. 20*, 2254–2261.

(14) Meares, C. F., and Wensel, T. G. (1984) Metal chelates as probes of biological systems. *Acc. Chem. Res. 17*, 202–209.

(15) Scheinberg, D. A., Strand, M., and Gansow, O. A. (1982) Tumor imaging with radioactive metal chelates conjugated to monoclonal antibodies. *Science 215*, 1511–1513.

(16) Heppeler, A., Froidevaux, S., Eberle, A. N., and Maecke, H. R. (2000) Receptor targeting for tumor localisation and therapy with radiopeptides. *Curr. Med. Chem. 7*, 971–994.

(17) Tewson, T. J. (1989) Procedures, pitfalls and solutions in the production of [^{18}F]2-deoxy-2-fluoro-D-glucose: a paradigm in the routine synthesis of fluorine-18 radiopharmaceuticals. *Nucl. Med. Biol. 16*, 533–551.

(18) Martin, R. B. (1996) Ternary complexes of Al^{3+} and F^- with a third ligand. *Coord. Chem. Rev. 141*, 23–32.

(19) Li, L. (2003) The biochemistry and physiology of metallic fluoride: action, mechanism, and implications. *Crit. Rev. Oral Biol. Med. 14*, 100–114.

(20) Antonny, B., and Chabre, M. (1992) Characterization of the aluminum and beryllium fluoride species which activate transducin. *J. Biol. Chem. 267*, 6710–6718.

(21) McBride, W. J., Sharkey, R. M., Karacay, H., D'Souza, C. A., Rossi, E. A., Laverman, P., Chang, C.-H., Boerman, O. C., and Goldenberg, D. M. (2009) A novel method of ^{18}F radiolabeling for PET. *J. Nucl. Med. 50*, 991–998.

(22) Karacay, H., McBride, W. J., Griffiths, G. L., Sharkey, R. M., Barbet, J., Hansen, H. J., and Goldenberg, D. M. (2000) Experimental pretargeting studies of cancer with a humanized anti-CEA x murine anti-[In-DTPA] bispecific antibody construct and a ^{99m}Tc-/^{188}Re-labeled peptide. *Bioconjugate Chem. 11*, 842–854.

(23) Sharkey, R. M., Karacay, H., Litwin, S., Rossi, E. A., McBride, W. J., Chang, C.-H., and Goldenberg, D. M. (2008) Improved therapeutic results by pretargeted radioimmunotherapy of non-Hodgkin's lymphoma with a new recombinant, trivalent, anti-CD20, bispecific antibody. *Cancer Res. 68*, 5282–5290.

(24) Gold, D. V., Goldenberg, D. M., Karacay, H., Rossi, E. A., Chang, C.-H., Cardillo, T. M., McBride, W. J., and Sharkey, R. M. (2008) A novel bispecific, trivalent antibody construct for targeting pancreatic carcinoma. *Cancer Res. 68*, 4819–4826.

(25) Sharkey, R. M., Cardillo, T. M., Rossi, E. A., Chang, C.-H., Karacay, H., McBride, W. J., Hansen, H. J., Horak, I. D., and Goldenberg, D. M. (2005) Signal amplification in molecular imaging by pretargeting a multivalent, bispecific antibody. *Nat. Med. 11*, 1250–1255.

(26) Sharkey, R. M., Karacay, H., Cardillo, T. M., Chang, C.-H., McBride, W. J., Rossi, E. A., Horak, I. D., and Goldenberg, D. M. (2005) Improving the delivery of radionuclides for imaging and therapy of cancer using pretargeting methods. *Clin. Cancer Res. 11*, 7109s–7121s.

(27) McBride, W. J., Zanzonico, P., Sharkey, R. M., Norén, C., Karacay, H., Rossi, E. A., Losman, M. J., Brard, P.-Y., Chang, C.-H., Larson, S. M., and Goldenberg, D. M. (2006) Bispecific antibody pretargeting PET (immunoPET) with an ^{124}I-labeled hapten-peptide. *J. Nucl. Med. 47*, 1678–1688.

(28) Sharkey, R. M., Karacay, H., Vallabhajosula, S., McBride, W. J., Rossi, E. A., Chang, C.-H., Goldsmith, S. J., and Goldenberg, D. M. (2008) Metastatic human colonic carcinoma: molecular imaging with pretargeted SPECT and PET in a mouse model. *Radiology 246*, 497–507.

(29) Schoffelen, R., Sharkey, R. M., Goldenberg, D. M., Franssen, G., McBride, W. J., Rossi, E. A., Chang, C.-H., Laverman, P., Disselhorst, J. A., Eek, A., van der Graaf, W. T. A., Oyen, W. J. G., and Boerman, O. C. (2010) Pretargeted immunoPET imaging of CEA-expressing tumors with a bispecific antibody and a ^{68}Ga and ^{18}F-labeled hapten-peptide in mice with human tumor xenografts. *Mol. Cancer Ther. 9*, 1019–1027.

(30) Rossi, E. A., Goldenberg, D. M., Cardillo, T. M., McBride, W. J., Sharkey, R. M., and Chang, C.-H. (2006) Stably tethered multifunctional structures of defined composition made by the dock and lock method for use in cancer targeting. *Proc. Natl. Acad. Sci. U.S.A. 103*, 6841–6846.

(31) Chong, H.-S., Song, H. A., Ma, X., Milenic, D. E., Brady, E. D., Lim, S., Lee, H., Baidoo, K., Cheng, D., and Brechbiel, M. W. (2008) Novel bimodal bifunctional ligands for radioimmunotherapy and targeted MRI. *Bioconjugate Chem. 19*, 1439–1447.

(32) Kim, H. W., Jeong, J. M., Lee, Y.-S., Chi, D. Y., Chung, K.-H., Lee, D. S., Chung, J.-K., and Lee, M. C. (2004) Rapid synthesis of [^{18}F]FDG without an evaporation step using an ionic liquid. *Appl. Radiat. Isot. 61*, 1241–1246.

(33) Chong, H.-S., Garmestani, K., Ma, D., Milenic, D. E., Overstreet, T., and Brechbiel, M. W. (2002) Synthesis and biological evaluation of novel macrocyclic ligands with pendent donor groups as potential yttrium chelators for radioimmunotherapy with improved complex formation kinetics. *J. Med. Chem. 45*, 3458–3464.

(34) Laverman, P., McBride, W. J., Sharkey, R. M., Eek, A., Joosten, L., Oyen, W. J. G., Goldenberg, D. M., and Boerman, O. C. (2010) A novel facile method of labeling octreotide with ^{18}F-fluorine. *J. Nucl. Med. 51*, 454–461.

(35) Karacay, H., McBride, W. J., Sharkey, R. M., Cardillo, T. M., Smith, C. J., and Goldenberg, D. M. (2009) ^{18}F labeling of a peptide for PET imaging of receptor expressing tumors. *J. Nucl. Med. 50*, 318P.

(36) André, J. P., Mäcke, H., Kaspar, A., Künnecke, B., Zehnder, M., and Macko, L. (2002) In vivo and in vitro ^{27}Al NMR studies of aluminum(III) chelates of triazacyclononane polycarboxylate ligands. *J. Inorg. Biochem. 88*, 1–6.

BC100137X

Detection of *Escherichia coli* Enoyl-ACP Reductase Using Biarsenical-Tetracysteine Motif

Hang Yang, Jin He,* Fen Hu, Cao Zheng, and Ziniu Yu

State Key Laboratory of Agricultural Microbiology and National Engineering Research Center of Microbial Pesticides, Huazhong Agricultural University, Wuhan, Hubei 430070, P. R. China. Received March 28, 2010; Revised Manuscript Received May 24, 2010

Although the tetracysteine (TC) motif has been used as a tag, the binding stability between TC motif and biarsenical reagent against extreme conditions as well as its capacity as a quantitative tag remains not well developed. To reveal these problems, we chose enoyl−acyl carrier protein reductase (FabI), which was involved in the final step of elongation in the bacterial fatty acid biosynthesis, to be tagged by the TC motif. Taking enhanced green fluorescent protein (EGFP) tagged FabI as a control, we investigated the activities of various TC tagged FabIs (N-terminus, C-terminus, or both N- and C-terminus TC motif). The results showed that all the TC tagged FabIs had high enzyme activities while the EGFP tagged FabI exhaustively lost the activity. Beside this, the characteristics of the tag, including labeling stability against extreme conditions, capacity for quantitative analysis, and ability for in-cell labeling, were also investigated. We demonstrated for the first time that the binding between FlAsH reagent and TC motif was stable against high pressure, high field strength, high temperature, and ultrasound. Furthermore, we verified the potential of TC motif for quantitative analysis of target protein by different approaches, including SDS−PAGE, spectrofluorometry (SPF), and capillary zone electrophoresis (CZE).

INTRODUCTION

Analysis of target proteins within living cells is of fundamental importance for detailed understanding of their molecular mechanisms and biological processes (*1, 2*). Most strategies aimed at realizing this objective are based on the usage of biological or chemical tags that could image or quantify target proteins in living cells or tissues, directly or indirectly (*3*).

Green fluorescent protein (GFP) and its variants are the most classic biological tags that have been widely used (*4*−*6*). Fusion of a protein of interest with an autofluorescent protein is a widely adopted strategy for live cell imaging (*7, 8*). However, this strategy has several limitations. First, since the GFP size is relatively large (up to 25 kDa), it may affect the physiological function of the fused proteins, especially the small proteins (*9*). Another disadvantage is that the spectral properties of each autofluorescent protein have been restricted to the fluorophores and require optical forms of readout (*10*), and their modest photostability has not matched well with the requirement of some applications (*11*). To overcome these drawbacks, researchers have been increasingly employing the quantum dots as an alternative because of their high quantum yields, wide spectral range, enhanced photostability, and long fluorescence lifetime (*12*). However, as nanoparticles, the quantum dots are less biocompatible and are too large for the proper functions of relative small proteins. Furthermore, because they are nongenetic, they would be diluted along with the fast cell division from one generation to another (*13, 14*). Therefore, much effort had been made to exploit smaller molecular tags that would label proteins with minimal functional perturbation (*15, 16*).

Many selective small molecule chemical tags for labeling of proteins in living cells have been developed recently, including O6-alkylguanine-DNA alkyltransferase (hAGT) tag, peptide carrier proteins (PCPs) tag, and acyl carrier proteins (ACPs) tag. Although they are advantageous because of the availability of many commercial fluorescent reagents, they still exhibit certain disadvantages. For examples, the human hAGT tag is among the most promising emerging fluorescent tags for cellular imaging in vivo and in vitro, but its usage has been limited by difficulties in obtaining of hAGT-deficient cell lines (*17, 18*). The employing of PCPs (*19*) as well as ACPs (*20*) as tags to monitor the changes in living cells is of considerable current interest, but their usage is restricted to cell surface studies (*21*). To circumvent these drawbacks, the biarsenical-tetracysteine (TC) system first developed by Roger Tsien and co-workers appears to be particularly promising (*22*). It is based on the subnanomolar affinity between a biarsenical variant fluorescein compound such as 4′,5′-bis(1,3,2-dithioarsolan-2-yl)fuorescein (FlAsH) or resorufin (ReAsH) and a genetically encoded short TC motif of only six amino acids (CCXXCC), where C presents cysteine and X is any amino acid except cysteine (*23*). In its freedom situation, the biarsenical dye is premixed with an excess of 1,2-ethanedithiol (EDT). And in its active situation, it becomes highly fluorescent by binding to the cysteines of the TC motif. The main shortcoming of this tag may come from the cell toxicity of biarsenical dye (*24*) and the relatively high background fluorescence (*25*). However, it has displayed outstanding advantages over other large fusion tags attributing to its relatively small size and potential to avoid loss of bioactivity or structural obstruction (*26*). More importantly, the TC motif is so small that it can be introduced into either terminus of target protein directly through cloning primers (*27*).

Although TC-fusion protein has been used as detectors for in-cell research (*28, 29*), the binding stability between TC motif and biarsenical reagent against extreme conditions and its capacity as a quantitative tag has been rarely reported. Herein, much effort has been done surrounding these problems relying on the enoyl−acyl carrier protein (ACP) reductase (FabI) from *Escherichia coli*, which is involved in the final step of elongation in the bacterial fatty acid biosynthesis (*30*) and is an attractive target for the development of new antibacterial agents (*31*). FabI is the only enoyl-ACP reductase in *E. coli* fatty acid synthesis, and the activity of this enzyme displays a prominent role in the cycle of fatty acid elongation. The understanding of its real-

* To whom correspondence should be addressed. E-mail address: hejin@mail.hzau.edu.cn. Fax: +86 27 87280670.

10.1021/bc1001533 © 2010 American Chemical Society
Published on Web 06/28/2010

Table 1. Bacterial Strains, Plasmids, and Oligonucleotides Used in This Work

strain/plasmid	relevant characteristics	source or reference
E. coli strain		
MG1655	*Escherichia coli* K12 wild type	lab collection
BL21(DE3)	*omp*T *hsd*S B (rB$^-$ mB$^-$) (λ DE3)	Invitrogen
Hh31	BL21(DE3) expressing strain, which contains pET-Wt-FabI	this work
Hh32	BL21(DE3) expressing strain, which contains pET-Nt-FabI	this work
Hh33	BL21(DE3) expressing strain, which contains pET-Ct-FabI	this work
Hh34	BL21(DE3) expressing strain, which contains pET-Bt-FabI	this work
Hh35	BL21(DE3) expressing strain, which contains pET-Gt-FabI	this work
plasmid		
pBAD24	Amp*R* cloning vector for introduction of TC motif encoding sequence	ref *33*
pEGFP	Amp*R egfp* cassette vector	Invitrogen
pET28a(+)	Kan*R* expressing vector with a T7 promoter	Novagen
pB-lumio[a]	annealed oligonucleotides (pB-lumio-S and pB-lumio-A), which contains a TC motif and a *Nde*I recognition site, was ligated into the *EcoR*I and *Nco*I sites of pBAD24	this work
pB-lu-FabI	MG1655 FabI cloned into the *Nde*I and *Nco*I sites of pB-*lumio* with primers pB-*lu-FabI*-F and pB-*lu-FabI*-R	this work
pET-Wt-FabI	FabI was excised from pB-lu-FabI and inserted in the *Nde*I and *Sal*I sites of pET28a(+)	this work
pET-Nt-FabI	lu-FabI was excised from pB-lu-FabI with *EcoR*I and *Sal*I and inserted in pET28a(+)	this work
pET-Ct-FabI	lu-FabI was amplified from pB-lu-FabI with primers Ctag-F and Ctag-R[b] and inserted in the *Nde*I and *Sal*I sites of pET28a(+)	this work
pET-Bt-FabI	lu-FabI was amplified from pB-lu-FabI with primers Ctag-F and Ctag-R and inserted in the *EcoR*I and *Sal*I sites of pET28a(+)	this work
pET-Gt-FabI	*egfp* was amplified from pEGFP with primers GL-F and GL-R and inserted in the *Nde*I and *Nhe*I sites of pET-Nt-FabI	this work

oligonucleotide	sequence (5′−3′)
pB-lumio-S	AAAGAATTCATGTGTTGTCCTGGCTGTTGCCATATGCTCGAGCCATGGAA
pB-lumio-A	TTCCATGGCTCGAGCATATGGCAACAGCCAGGACAACACATGAATTCTTT
pB-lu-FabI-F	ATTAA ACATA TGGGT TTTCT TTCCG
pB-lu-FabI-R	CATCT AGATT ATTTC AGTTC GAGTT CG
Ctag-F	TCTCC ATACC CGTTT TTTTG GGCTA GC
Ctag-R	AAAGTCGACTTAGCAACAACCAGGGCAACAAAATTTCAGTTCGAGTTCGTTC
GL-F	AATCG CTAGC ATGGT GAGCA AGGG
GL-R	GGCCG AATTC CTTGT ACAGC TCGTC

[a] lumio represents TC motif (-CCPGCC-) encoding sequence TGTTGTCCTGGCTGTTGC. [b] Ctag-R contains another TC motif (-CCPGCC-) encoding sequence GCAACAACCAGGGCAACA.

time activity and content within living cells is of considerable importance for mastering the status of bacterial growth and multiplication and developing correct administration strategy. In the current study, we investigated the enzyme activity and quantization of FabI from *E. coli*, employing the biarsenical-tetracysteine system. Furthermore, the properties of the tag, including labeling stability against extreme conditions, capacity for quantitative analysis, and ability for in-cell labeling, were also investigated comprehensively for the first time.

EXPERIMENTAL SECTION

Materials. The restriction endonuclease *Nde*I, *Nco*I, *EcoR*I, *Xba*I, *Hind*III, *Sal*I, and *Nhe*I were purchased from TaKaRa (Dalian, Liaoning, China). The PCR cleanup kit, plasmid miniprep kit, and DNA gel extraction kit were purchased from AxyGen (Hangzhou, Zhejiang, China). Primers for PCR amplification and sequencing verification were obtained from Sunbiotech (Beijing, China). The lumio green in-gel detection kit was purchased from Invitrogen (Carlsbad, CA). The Ni-NTA resin for His6 affinity purification was purchased from GenScript (Nanjing, Jiangsu, China). All other chemicals were the purest grade commercially available.

Construction of Recombinant FabIs. FabI was genetically fused with six amino acids (CCPGCC), which was the optimized motif of CCXXCC (*32*). The recombinant proteins employed in this work were engineered with N-terminus or C-terminus or both N- and C-terminus TC motif or N-terminus EGFP tag or without any tag. The five corresponding expression plasmids pET-Nt-*fabI*, pET-Ct-*fabI*, pET-Bt-*fabI*, pET-Gt-*fabI*, pET-Wt-*fabI* were constructed (Table 1). The creation procedures are detailed in Figures S-1−S-6, and the sequence of each recombinant proteins is detailed in Supporting Information (SI). The recombinant proteins were overexpressed in the *E. coli* strain BL21(DE3) and utilized for further research in vitro and in vivo.

Protein Expression and Purification. The recombinant protein was expressed in the *E. coli* strain BL21(DE3) in standard LB medium. Protein expression was induced with 1 mM isopropyl β-D-thiogalactoside (IPTG) when an optical density of 0.6−0.8 was reached and incubated for another 4 h to allow expression. Purification was achieved by using its His6 tag following the general protocol of nickel nitrilotriacetic acid column and washing and eluting in an imidazole concentration of 20 and 250 mM, respectively. Collected fractions were dialyzed against 20 mM Tris-Cl, pH 8.0, containing 1 mM DTT, concentrated in the Bradford assay using BSA as a standard, and then stored in −70 °C.

In Vitro FlAsH Labeling. The labeling procedure for TC-tagged FabIs closely followed the method described previously with a few modifications (*32*). The FlAsH reagent (the structure is shown in Figure S-7) was supplied precomplexed to 1,2-ethanedithiol (EDT), which not only decreased the nonspecific binding of As(III) to endogenous thiols but also stabilized and solubilized the biarsenical reagent. TC-tagged FabIs were dissolved in 20 mM Tris-Cl, pH 8.0, containing 1 mM DTT which was used to keep deoxidation of the thiol group in the cysteine residues and improve labeling efficiency. The TC-tagged FabIs were reacted with 1 μM FlAsH-EDT$_2$ reagent at room temperature for 2 h to ensure complete labeling. The

labeled samples were analyzed by kinetic assay, high performance liquid chromatography (HPLC), and capillary electrophoresis (CE). For SDS−PAGE and spectrofluorometer analysis, the labeling procedure was replaced by heating at 70 °C for 10 min, which was not only time-saving but also efficient.

In Vivo FlAsH Labeling. Intracellular FlAsH labeling of TC-tagged protein was carried out according to the protocol described by Kottegoda et al. (*34*) with some modifications. The BL21(DE3) cells expressing the TC-tagged proteins were washed twice with extracellular buffer (ECB, 135 mM NaCl, 5 mM KCl, 10 mM HEPES, 2 mM $MgCl_2$, 2 mM $CaCl_2$, pH 7.4) before FlAsH labeling. Then the cells were incubated at 37 °C for 2 h in the presence of 1 μM FlAsH reagent. The labeling efficiency was confirmed by LSM 510 META (Carl Zeiss, Jena, Germany) confocal system after washing the FlAsH labeled cells twice with the ECB buffer. The cells were then lysed in lysis buffer (50 mM NaH_2PO_4, 300 mM NaCl, 10 mM imidazole, pH 8.0) for CE analysis. As a control, wild-type BL21(DE3) cells were also labeled with FlAsH reagent in parallel.

Kinetic Assay of Tagged FabIs. The kinetic assay of tagged FabIs was performed to explore the distinction of different tags. Kinetic parameters were studied for pro- and post-FlAsH-labeled FabIs. The reaction system for enzyme assay was prepared strictly as described (*35*) with a few modifications. Control experiments for both pro- and post-FlAsH-labeling were conducted simultaneously in identical conditions. After completion of both labeling and enzyme assay, samples were stored in −70 °C prior to further analysis.

Fluorescence Scan. After FlAsH labeling, the TC tagged protein underwent fluorescence scan analysis. Continuous scanning was carried out by fixing excitation wavelength at 505 nm and reading the fluorescence intensity from 519 to 560 nm.

HPLC Analysis of TC-Tagged FabIs. A HPLC system (Waters Ltd., Watford, Hertfordshire, U.K.) with a photodiode array (PDA) detector in tandem with a fluorescence detector was used to analyze the TC-tagged FabIs. An injection of 10 μL of reaction mixture was analyzed on a Proteomix SAX-NP5 column (Sepax, Shanghai, China) using online gradient programming from 100% solution A (20 mM phosphate, containing 1 mM DTT, pH 8.0) to 100% solution B (20 mM phosphate, containing 1 mM DTT and 0.5 M NaCl, pH 8.0) in 30 min with a delay of 20 min.

Capillary Electrophoresis Analysis of TC-Tagged FabIs. A CE system (Beckman Coulter, Fullerton, CA) with a laser-induced fluorescence (LIF) detector was used for analyzing the FlAsH labeled samples. All the separations were completed in an uncoated silica capillary, with 75 μm i.d., effective length of 50 cm with an overall length of 62 cm, at voltage strength of 25 kV. Separations were performed by capillary zone electrophoresis (CZE) for all the samples with an injection pressure of 0.5 psi for 5 s. The running buffer consisted of 1 mM DTT and 20 mM borate at pH 8.4. The presence of DTT in the running buffer is to maintain a reducing environment during the electrophoresis. The LIF detector condition is Ex/Em = 488 nm/535 nm.

SDS−PAGE Analysis. The fact that the TC motif can function with high specificity and affinity opened the way for the development of an in vitro system for quick monitoring of the integrity of target proteins in traditional denaturing gel electrophoresis (*36*). The FlAsH labeled recombinant proteins were mixed with SDS−PAGE loading buffer before electrophoresis. Then the TC-tagged protein complexes were visualized directly under UV illumination (Syngene Gene Genius, Frederick, MD), followed by Coomassie blue staining to visualize the total proteins.

RESULTS AND DISCUSSION

Stability of FlAsH Labeling. We first tested the stability of FlAsH reagent binding to TC motif because it is one of the most important attributes of a tag that can be used in the labeling study. A strong and stable binding force could ensure high reproducibility and credibility. Herein, the binding stability between FlAsH reagent and TC motif was examined for the first time under various extreme conditions including high electric field strength, high pressure, high temperature, and ultrasonic and microwave treatments.

Capillary electrophoresis has been proved to be a powerful tool for investigation of protein and polypeptides (*37*). Moreover, the excitation and emission wavelengths of the TC-tagged complex (Ex/Em = 505 nm/535 nm) were compatible with commonly used detection schemes of CE-LIF (Ex/Em = 488 nm/535 nm). Therefore, a CE-LIF system was employed to test the binding force between FlAsH reagent and TC motif in the condition of high electric field strength. We first tested the Nt-FabI, which was labeled with FlAsH followed by being injected into a capillary and electrophoresed immediately. The resulting electropherograms revealed a singlet at 4.017 ± 0.021 min (n = 13, RDS = 0.52%), while the parallel electropherograms of Nt-FabI and the FlAsH reagent alone produced no corresponding peaks (Figure 1A). And the corresponding peak areas of the repeated injections were found to be $(3.50 \pm 0.10) \times 10^6$ (RDS = 2.8%). These data suggested that the binding of FlAsH reagent with Nt-FabI is strong enough to survive under high field strength. This result also indicated that the capillary zone electrophoresis was a useful tool for the analysis of TC-tagged protein with high resolution and low background signal.

To examine the binding stability against high temperature, the FlAsH labeled FabIs were heated at 70 °C for 10 min before spectrofluorometric (SPF) analysis. Figure 1B showed that the heating procedure did not change the optical qualities of the TC-tagged FabIs/FlAsH complex (for detailed information, see Table S-1), which was consistent with the claim of Invitrogen Co. The influence of microwave and ultrasound on the stability of the fluorescent complex was also tested. The reaction mixture was incubated at 70 °C for 10 min to allow complete labeling, and then microwave (wp750L23-6, Galanz Ltd., Foshan, Guangdong, China) and ultrasound (KQ-100DE, Kunshan, Jiangsu, China) procedures following a time gradient strategy were carried out. The power of the microwave oven was set at 750 W, and the parameters for ultrasound treatment were controlled at 25 °C and 80 W. The scanning results showed that the ultrasonic treatment did not affect the fluorescent complex (Figure 1C), while the microwave displayed a time-dependent destruction effect to the complex (Figure 1D). The destruction effect was very weak when treatment time was shorter than 5 min. When the treatment was extended to 15 min, the emission spectrum of the fluorescent complex changed greatly and the maximum emission wavelength was generalized.

HPLC was used to examine the binding force between the FlAsH reagent and the TC motif against high pressure. The resulting chromatograms revealed a peak area of $(7.17 \pm 0.36) \times 10^6$ μV·s on the PDA detector (RDS = 5.0%) and $(6.27 \pm 0.31) \times 10^8$ μV·s on the fluorescence detector (n = 5, RDS = 4.8%). Those results indicated that the FlAsH dye could keep conjugating to the TC motif stably under high pressure of up to 760 ± 15 psi (Figure 1E). In the study, a fluorescence detector was placed in tandem after a PDA detector, so the singlet observed on the fluorescence detector was delayed compared with that of PDA detector (Figure 1F). Taken together, the above data indicated that the binding between FlAsH reagent and TC

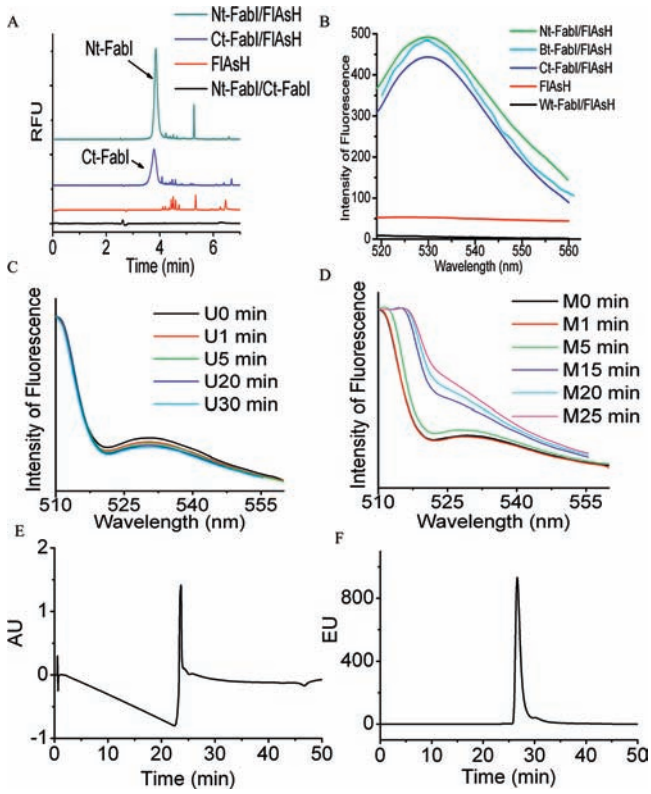


Figure 1. Stability of TC-tagged FabI/FlAsH complex. (A) The TC-tagged FabIs/FlAsH complex was stable under high electric field strength conditions on CZE. The TC-tagged Nt-FabI and Ct-FabI were labeled with FlAsH reagent for up to 2 h at room temperature, and then the samples were analyzed on CE. The separation of all the samples were conducted in an uncoated silica capillary, 75 μm i.d., effective length 50 cm with an overall length of 62 cm. run buffer, 20 mM borate buffer with 1 mM DTT, pH 8.4; voltage, 25 kV; LIF detection condition, Ex/Em = 488 nm/535 nm. (B) The TC-tagged FabIs/FlAsH complex was examined by fluoroscence scanning after being incubated at 70 °C for 10 min. The excitation wavelength was fixed at 505 nm, and each sample got five repeats. The influence of ultrasound treatment (C) and microwave (D) on the binding stability of the Nt-FabI/FlAsH complex was then tested. The graph showed that the ultrasonic treatement did not have an obvious influence on the stability of the fluorescent complex ($p < 0.01$), while the destructive effects of microwave increaseed greatly along with the elongation of the treating time. (E) HPLC separation of the Nt-FabI obtained from PDA detector at 214 nm and (F) the corresponding chromatogram obtained from fluorescence detector under the condition of Ex/Em = 505 nm/535 nm. All the samples labeled with FlAsH reagent were analyzed on a Proteomix SAX-NP5 column (5 μm, 4.6 mm × 50 mm, Sepax, Shanghai, China) by linear gradient elution at a flow rate of 0.75 mL min^{-1}. Mobile-phase composition was changed from 100% solution A (20 mM phosphate, containing 1 mM DTT, pH 8.0) to 100% solution B (20 mM phosphate, containing 1 mM DTT and 0.5 M NaCl, pH 8.0) in 30 min with a delay of 20 min.

motif was stable under extreme conditions, such as high field strength, high temperature, high pressure, and strong ultrasonic treatment.

Influence of Different Tags on the Enzyme Activity. It is critical to choose a proper optical molecular tag for a detailed understanding of the protein dynamics both in vitro and in vivo. To this end, current studies take it as the key criterion for checking whether the structure and function of the target protein are compatible with the tag or affected by the tag. We investigated the influence of the TC tag on the structure and function of the FabI by assaying its enzyme activity in vitro, taking EGFP tag as a control. The activities of TC-tagged FabI with crotonoyl-CoA as substrate were determined at various pH ranging from 6.0 to 8.5. We found that the FabI showed the highest activity at pH 7.6, which was adopted for all subsequent kinetic measurements. The typical kinetic curves for the FabI catalyzed reaction before FlAsH labeling are shown in Figure S-8. Detailed Michaelis−Menten constants κ_{cat} and K_m were determined for the modified FabIs under the same conditions (Table 2). Before FlAsH labeling, all of the TC tagged FabIs exhibited much higher enzyme activity than the EGFP tagged FabI. This suggests that the larger-sized EGFP tag imposed a greater disturbance on tagged FabI than the smaller-sized TC tag. Among the TC tagged FabIs, little variance of the κ_{cat} values was observed, and the K_m values varied smoothly. Compared with the K_m value observed for Wt-FabI, the κ_{cat} value was 2-fold smaller for Nt-FabI and nearly 1-fold greater for Bt-FabI, respectively. The κ_{cat} values have a slight tendency to decrease after the labeling procedure. In contrast, the K_m values tended to increase to a small extent. These data indicated that the presence of the biarsenical dye exhibits very little impact to the reaction mediated by FabI. After the FlAsH labeling, the K_m values of TC tagged FabIs were similar. However, the κ_{cat} value of Ct-FabI was slightly greater than that of Nt-FabI and Bt-FabI by about 0.68-fold and 0.90-fold, respectively. As expected, the reagent imposed a greater effect on Wt-FabI, resulting in a 2.59-fold greater K_m value than that of control, which may due to the higher concentration of nomadic dye in the reaction mixture (*24*). Previous studies evaluating the influence of the TC tag on an enzyme involved in bacterial fatty acid synthesis have indicated that these short peptides did not prevent the bioactivity of FabI from catalyzing the last step reaction of elongation. Furthermore, different modes of introducing the TC tag into the target protein displayed similar effectiveness. The smaller-sized six-amino acid TC tag, labeled or not labeled, displayed tiny disturbance on the structure of target protein. In contrast, the EGFP tagged FabI exhibited a total loss of activity. Therefore, the TC tag is a better protein tag than EGFP because of the smaller size.

Quantitative Analysis of TC Motif FabIs. Although more and more attention has been paid to use the TC motif to study complicated and delicate dynamics in living cells (*38*), little attention has been paid to develop its capacities for quantitative analysis. To expand the application of this system instead of merely being used for living cell imaging, in the current study, we made the first effort to investigate the capacity of TC tag for quantitative analysis comprehensively. The FabI involved in the synthesis cycle of fatty acid in *E. coli* is an important enzyme composed of 263 amino acids with a p*I* of 5.58 and a molecular weight of 27.8 kDa. The final recombinant proteins Nt-FabI, Ct-FabI, and Bt-FabI possessed molecular masses of 28.6, 28.5, and 29.3 kDa, respectively. The TC-tagged FabIs were purified by His6 tag and then labeled with FlAsH reagent. SDS−PAGE analysis was performed to confirm that the biarsenical reagent remained binding to its motif with high specificity (Figure 2A). Experiments to assess the sensitivity of labeling in denaturant gel indicated that the TC tag could specifically bind to the TC motif with high sensitivity over competing proteins under the complicated matrix. The lowest quantity of labeled protein that can be detected directly in gel was less than 1 ng (about 3.49×10^{-11} M), while 25 ng of Coomassie blue stained protein was needed to be detected in the same gel (Figure 2B). SDS−PAGE was regarded to be a fast and convenient way for protein quantitative analysis with different staining strategies, such as silver staining (*39*), negative staining (*40*), and fluorescence staining (*41*). It has been reported that the TC motif exhibited drawbacks for quantitative analysis in gel, including unspecific binding to endogenous cysteine-rich proteins (*42*) and unspecific binding of arsenites for either mono- or dithiol compounds (*43*, *44*), even when the TC motif was separated as two moieties in the folded interior of a protein (*45*). However, these problems were not present in our

Table 2. Steady-State Kinetic Parameters of FabI Enzymes with Different Modification Pre- and Post-FlAsH Labeling

	pre-FlAsH labeling			labeling control			post-FlAsH labeling		
name	$\kappa_{cat} \times 10^{-3}$ S^{-1}	$K_m \times 10^3$ M	$\kappa_{cat}/K_m \times 10^{-6}$ S^{-1} M^{-1}	$\kappa_{cat} \times 10^{-3}$ S^{-1}	$K_m \times 10^4$ M	$\kappa_{cat}/K_m \times 10^{-6}$ S^{-1} M^{-1}	$\kappa_{cat} \times 10^{-3}$ S^{-1}	$K_m \times 10^4$ M	$\kappa_{cat}/K_m \times 10^{-6}$ S^{-1} M^{-1}
Wt-FabI	2.1 ± 0.10	1.08	1.98 ± 0.09	1.52 ± 0.07	3.65	4.17 ± 0.19	1.05	9.46	1.11
Nt-FabI	3.32 ± 0.20	0.29	11.16 ± 0.68	2.52 ± 0.18	6.92	3.64 ± 0.26	2.12	8.23	2.57
Ct-FabI	5.67 ± 0.15	0.71	7.98 ± 0.02	4.02 ± 0.25	6.35	6.32 ± 0.39	3.55	8.39	4.23
Bt-FabI	2.37 ± 0.23	2.00	1.18 ± 0.12	2.26 ± 0.16	6.67	3.39 ± 0.27	1.87	8.76	2.14
Gt-FabI	nd[a]	nd[a]	nd[a]	nd[a]	nd[a]	nd[a]	nd[a]	nd[a]	nd[a]

[a] nd: not detected.

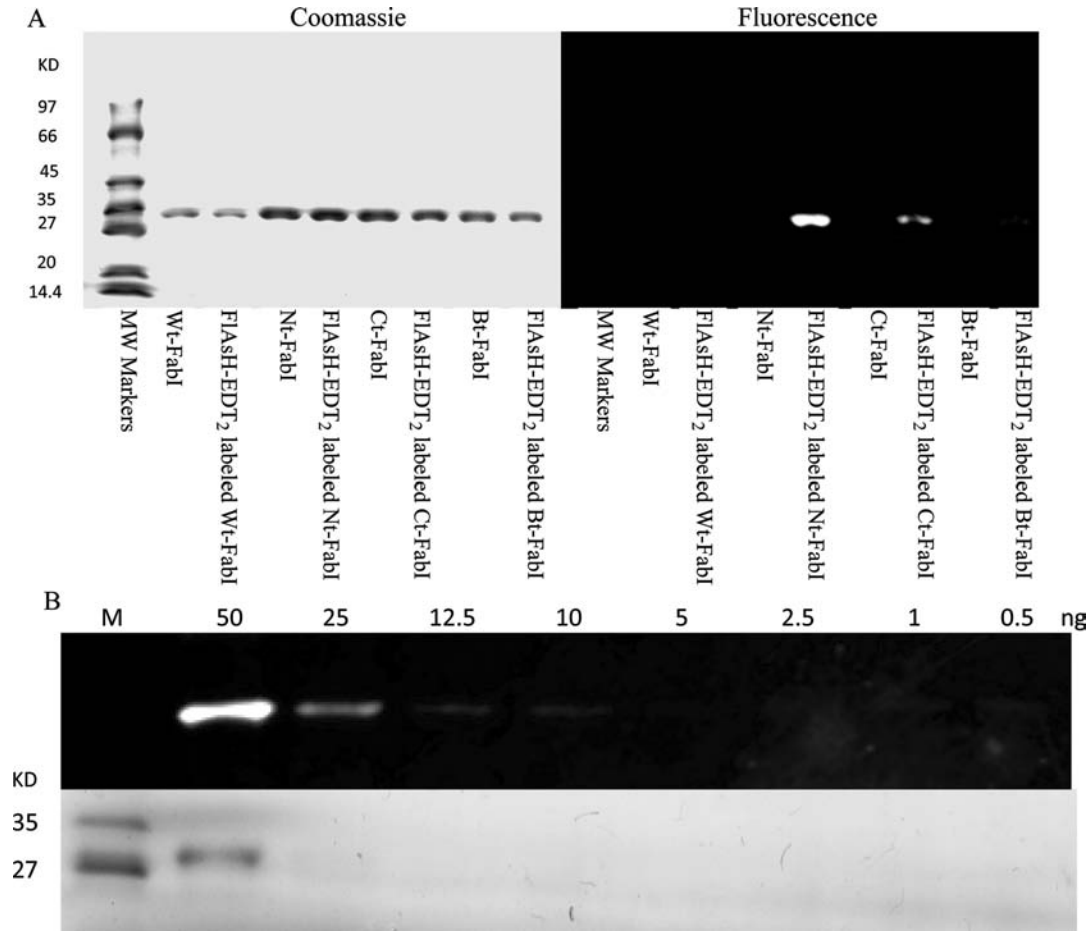


Figure 2. Specificity and sensitivity of TC-tagged FabIs labeled with FlAsH-EDT_2 revealed by SDS−PAGE. (A) Proteins eluted from the Ni-NTA column were labeled directly with FlAsH-EDT_2 reagent in a sample buffer for SDS−PAGE. When the electrophoresis was completed, the gel was visualized first by a 302 nm transilluminator to obtain a fluorescence image and then stained with Coomassie blue. (B) The sensitivity of FlAsH labeling was assayed in SDS−PAGE gel. Dosages of 50, 25, 12.5, 10, 5, 2.5, 1, 0.5 ng labeled Nt-FabI were injected. An injection dosage of as low as 0.5 ng was detected in the gel directly (B, top, the last lane), exhibiting a vivid comparison with the results discovered by the coomassie stained gel (B, bottom).

investigation with purified FabIs. The cysteines within FabI are not adjacently located and could not form closely located parallel pairs in space structure.

On the basis of our previous work, the detection limits for Nt-FabI and Ct-FabI were tested on CZE (Figure 1A). The presence of a single TC motif ensured a better interpreting of its capacity for protein labeling and detection on CE-LIF system. The electropherograms of Ct-FabI displayed an obvious peak at 3.887 ± 0.021 min ($n = 13$, RDS = 0.54%). And the corresponding peak areas of the repeated injections were found to be $(4.31 \pm 0.06) \times 10^5$ (RDS = 1.4%). In contrast, a sample of the FlAsH reagent alone was also injected into the CE column. The resulting electropherogram revealed no corresponding peaks at that time point but displayed many small background peaks. No fluorescence peaks appeared in the analysis of unlabeled TC-tagged FabIs. Assuming complete reactions were achieved, the detection was found to be linear over a range of 2.00×10^{-12} to 1.21×10^{-10} M for Nt-FabI and 1.32×10^{-12} to 1.25×10^{-10} M for Ct-FabI. The detection limits for the TC-tagged FabIs/FlAsH complex were found to be 3.49×10^{-16} M for the Nt-FabI/FlAsH complex and 8.51×10^{-16} M for the Ct-FabI/FlAsH complex which is somewhat higher than that of other researchers obtained by using synthesized peptides (*34*). Although these values were calculated based on the broadened peaks which should be further improved by optimization of the separation conditions, these data demonstrated that the TC motif was a feasible and reliable labeling tag for protein analysis on CZE. The ability of TC tag for quantitative assay was also tested according to the fluorescence intensity by fixing the excitation wavelength at 505 nm on a spectrofluorometer. In this experiment, the labeling procedure was reinforced by incubating at 70 °C for 10 min. The results

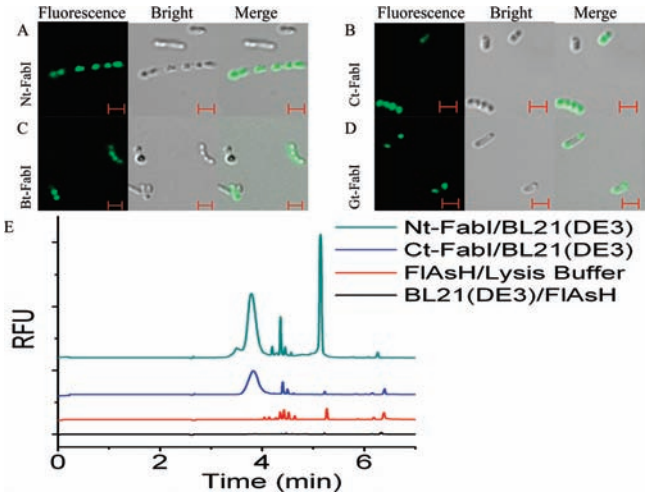


Figure 3. In vivo FlAsH labeled cells displayed minimum cellular background fluorescence. FabI protein was fused with TC-tag at its N-terminus, C-terminus, both N- and C-terminus, or fused with EGFP-tag at its N-terminus. *E. coli* BL21(DE3) cells expressing fusion proteins were grown to logarithmic phase and labeled with FlAsH-EDT_2 reagent at room temperature, followed by imaging with a LSM 510 META confocal microscope system. The BL21(DE3) cells expressing EGFP-tagged protein were microscoped directly. (A) image of cells expressing Nt-FabI; (B) image of cells expressing Ct-FabI; (C) image of cells expressing Bt-FabI; (D) image of cells expressing Gt-FabI. Bar, 2 μm. (E) Electropherograms of FlAsH labeled cell lysate. After confocal imaging, the BL21(DE3) cells expressing the TC-tagged FabIs were lysed and the 100-fold dilution of cell lysate samples were analyzed on the CE system. Cell lysate of wild-type BL21 (DE3) cells preincubated with FlAsH was used as control.

showed that the detection limit of the TC-tagged FabIs in either terminus was degraded for about one order of magnitude by adding another TC tag, and correspondingly, the linear range was extended for a number of folds. That was, the detection limits for Nt-FabI, Ct-FabI and Bt-FabI were $(7.33 \pm 0.38) \times 10^{-12}$ molar, $(6.32 \pm 0.14) \times 10^{-12}$ molar and $(3.41 \pm 0.07) \times 10^{-13}$ molar, and the linear ranges for the three were from 2.42×10^{-11} to 7.34×10^{-9} molar, from 2.49×10^{-11} to 3.12×10^{-9} molar and from 3.41×10^{-11} to 5.72×10^{-19} molar, respectively.

Efficiency and Life Span of FlAsH Labeling in Vivo. The property that the nonfluorescent small biarsenical dye can penetrate through cellular membrane freely along with its various available colors makes it a powerful multicolor and multiuse toolbox for assessing protein location and function (*46*, *47*). On the basis of our observation that the TC motif can be used in the detection of the tagged protein in vitro with high specificity, we hypothesize that specific FlAsH labeling of a target protein in vivo is also controllable. As expected, an efficient FlAsH labeling was observed with uniform fluorescence throughout cells when we performed in-cell FlAsH labeling (Figure 3A−D), which was further confirmed by CE analysis of the cell lysate (Figure 3E). To our surprise, no cellular toxicity was observed after labeling with FlAsH reagent for up to 16 days; at this time point the fluorescence still existed and the cells were still alive (data not shown).

The BL21(DE3) cells, after confocal imaging, were then lysed and sampled by 100-fold dilution for CE analysis. The electropherograms of the wild-type cells labeled with the FlAsH reagent and the reagent alone did not display definitive peaks ($n = 4$). In contrast, the electropherograms obtained from the FlAsH labeled cell lysate samples of BL21(DE3) expressing the TC-tagged proteins exhibited a major peak ($n = 6$). In addition, the electropherogram of cell lysate sample of BL21(DE3) expressing Nt-FabI was similar to that of purified Nt-FabI in Figure 1A. The doublet peak for the Nt-FabI/FlAsH complex was the isomeric complex, for the two As(III) atoms of the FlAsH reagent can be bound in more than one orientation with the four thiols of the TC motif (*23*, *32*). We also showed that the electropherograms of cell lysate samples from BL21(DE3) expressing Nt-FabI and Ct-FabI were very similar, which may be a result of the similar mass and charge of the two TC-tagged FabIs. Therefore, the data from cell lysate demonstrated the feasibility of employing the CZE technique to analyze TC-tagged protein without purification. To understand whether there is any difference when fusing the TC tag to a different terminus of the protein genetically, we found that the Nt-FabI and Ct-FabI have similar kinetic parameters (see Table 2), which indicated that the two TC-tagged FabIs are similar in many aspects. In other words, the TC tag fused to either terminus of the enzyme exhibited similar minor perturbance on the conformation and functions of fused proteins. Taken together, all these data demonstrated that the TC motif, fused to either terminus of the target protein, could function well with minimal disturbance and background fluorescence during the analysis on CZE.

CONCLUSIONS

In the present study, we demonstrated that the cell-permeable color-facultative small dye kept adhering covalently to the TC motif under extreme conditions. We have also displayed that the small TC tag was more suitable for nondestructive protein labeling than the EGFP tag. It was clear that the small tag could function quite well in target protein quantitative analysis, which may trigger a large number of applications. A capillary zone electrophoresis system equipped with a laser-induced fluorescence detector had a detection limit of 10^{-16} M for the labeled proteins. The attempt to expand the utility of TC tag associated with the HPLC system was of critical dominance, which offered another powerful tool for the detection of tagged proteins. In a word, the biarsenical-tetracysteine motif would have promising prospects for protein labeling and detection both in vitro and in vivo.

ACKNOWLEDGMENT

This work was funded by the Fundamental Research Funds for the Central Universities of China (Grant 2009PY019) and the Major S&T Projects on the Cultivation of New Varieties of Genetically Modified Organisms (Grant 2009ZX08009-120B). The authors thank Dr. Hongping Wei at Wuhan Institute of Virology, Chinese Academy of Sciences, for his assistance in quantitative analysis and Dr. Jingming Wu at the Center for Advanced Water Technology, PUB Consultants, Singapore, for her kind advice and help in the manuscript preparation.

Supporting Information Available: Sequences of recombinant proteins, plasmid construction procedures, structure of FlAsH reagent, and kinetics data and SPF analysis of FabIs. This material is available free of charge via the Internet at http://pubs.acs.org.

LITERATURE CITED

(1) Miller, L. W., and Cornish, V. W. (2005) Selective chemical labeling of proteins in living cells. *Curr. Opin. Chem. Biol. 9*, 56–61.
(2) Machleidt, T., Robers, M., and Hanson, G. T. (2007) Protein labeling with FlAsH and ReAsH. *Methods Mol. Biol. 356*, 209–220.
(3) Bonasio, R., Carman, C. V., Kim, E., Sage, P. T., Love, K. R., Memp, T. R., Springer, T. A., and von Andrian, U. H. (2007) Specific and covalent labeling of a membrane protein with

organic fluorochromes and quantum dots. *Proc. Natl. Acad. Sci. U.S.A. 104*, 14753–14758.
(4) Heim, R., Prashert, D., and Tsien, R. Y. (1994) Wavelength mutations and posttranslational autoxidation of green fluorescent protein. *Proc. Natl. Acad. Sci. U.S.A. 91*, 12501–12504.
(5) Cubitt, A. B., Heim, R., Adams, S. R., Boyd, A. E., Gross, L. A., and Tsien, R. Y. (1995) Understanding, improving and using green fluorescent proteins. *Trends Biochem. Sci. 20*, 448–455.
(6) Dickson, R. M., Cubitt, A. B., Tsien, R. Y., and Moerner, W. E. (1997) On/off blinking and switching behaviour of single molecules of green fluorescent protein. *Nature 388*, 355–358.
(7) Haseloff, J., and Amos, B. (1995) GFP in plants. *Trends Genet. 11*, 328–329.
(8) Tsien, R. Y. (1998) The green fluorescent protein. *Annu. Rev. Biochem. 67*, 509–544.
(9) Hoffmann, C., Gaietta, G., Bünemann, M., Adamas, S. R., Oberdorff-Maass, S., Behr, B., Vilardaga, J. P., Tsien, R. Y., Ellisman, M. H., and Lohse, M. J. (2005) A FlAsH-based FRET approach to determine G protein coupled receptor activation in living cells. *Nat. Methods 2*, 171–177.
(10) Shaner, N. C., Campbell, R. E., Steinbach, P. A., Giepmans, B. N., Palmer, A. E., and Tsien, R. Y. (2004) Improved monomeric red, orange and yellow fluorescent proteins derived from Discosoma sp. red fluorescent protein. *Nat. Biotechnol. 22*, 1567–1572.
(11) Steinmeyer, R., Noskov, A., Krasel, C., Weber, I., Dees, C., and Harms, G. S. (2005) Improved fluorescent proteins for single-molecule research in molecular tracking and co-localization. *J. Fluoresc. 15*, 707–721.
(12) Michalet, X., Pinaud, F. F., Bentolila, L. A., Tsay, J. M., Doose, S., Li, J. J., Sundaresan, G., Wu, A. M., Gambhir, S. S., and Weiss, S. (2005) Quantum dots for live cells, in vivo imaging, and diagnostics. *Science 28*, 538–544.
(13) Dubertret, B., Skourides, P., Norris, D. J., Noireaux, V., Brivanlor, A. H., and Livchaver, A. (2002) In vivo imaging of quantum dots encapsulated in phospholipid micelles. *Science 298*, 1759–1762.
(14) Wu, X., Liu, H., Liu, J., Haley, K. N., Treadway, J. A., Larson, J. P., Ge, N., Peale, F., and Bruchez, M. P. (2002) Immunofluorescent labeling of cancer marker Her2 and other cellular targets with semiconductor quantum dots. *Nat. Biotechnol. 21*, 41–46.
(15) Maxwell, D., Chang, Q., Zhang, X., Barnett, E. M., and Piwnica-Worms, D. (2009) An improved cell-penetrating, caspase-activatable, near-infrared fluorescent peptide for apoptosis imaging. *Bioconjugate Chem. 20*, 702–709.
(16) Lin, M. Z., Glenn, J. S., and Tsien, R. Y. (2008) A drug-controllable tag for visualizing newly synthesized proteins in cells and whole animals. *Proc. Natl. Acad. Sci. U.S.A. 105*, 7744–7749.
(17) Keppler, A., Gendreizig, S., Gromemeyer, T., Pick, H., Vogel, H., and Johnsson, K. (2003) A general method for the covalent labeling of fusion proteins with small molecules in vivo. *Nat. Biotechnol. 21*, 86–89.
(18) Keppler, A., Pick, H., Arrivoli, C., Vogel, H., and Johnsson, K. (2004) Labeling of fusion proteins with synthetic fluorophores in live cells. *Proc. Natl. Acad. Sci. U.S.A. 101*, 9955–9959.
(19) Yin, J., Lin, A. J., Buckett, P. D., Resnick, M. W., Golan, D. E., and Walsh, C. T. (2005) Single-cell FRET imaging of transferrin receptor trafficking dynamics by Sfp-catalyzed, site-specific protein labeling. *Chem. Biol. 12*, 999–1006.
(20) Zhou, Z., Koglin, A., Wang, Y., McMahon, A. P., and Walsh, C. T. (2008) An eight residue fragment of an acyl carrier protein suffices for post-translational introduction of fluorescent pantetheinyl arms in protein modification in vitro and in vivo. *J. Am. Chem. Soc. 130*, 9925–9930.
(21) George, N., Pick, H., Vogel, H., Johnsson, N., and Johnsson, K. (2004) Specific labeling of cell surface proteins with chemically diverse compounds. *J. Am. Chem. Soc. 126*, 8896–8897.
(22) Grifin, B. A., Adams, S. R., Jones, J., and Tsien, R. Y. (2000) Fluorescent labeling of recombinant proteins in living cells with FlAsH. *Methods Enzymol. 327*, 565–578.
(23) Griffin, B. A., Adams, S. R., and Tsien, R. Y. (1998) Specific covalent labeling of recombinant protein molecules inside live cells. *Science 281*, 269–272.
(24) Langhorst, M. F., Genisyuerek, S., and Stuermer, C. A. O. (2006) Accumulation of FlAsH/Lumio green in active mitochondria can be reversed by beta-mercaptoethanol for specific staining of tetracysteine-tagged proteins. *Histochem. Cell Biol. 125*, 743–747.
(25) Hearps, A. C., Pryor, M. J., Kuusisto, H. V., Rawlinson, S. M., Piller, S. C., and Jans, D. A. (2007) The biarsenical dye Lumio (TM) exhibits a reduced ability to specifically detect tetracysteine-containing proteins within live cells. *J. Fluoresc. 17*, 593–597.
(26) Andresen, M., Schmitz-Salue, R., and Jakobs, S. (2004) Short tetracysteine tags to beta-tubulin demonstrate the significance of small labels for live cell imaging. *Mol. Biol. Cell 15*, 5616–5622.
(27) Taguchi, Y., Shi, Z. D., Ruddy, B., Dorward, D. W., Greene, L., and Baron, G. S. (2009) Specific biarsenical labeling of cell surface proteins allows fluorescent- and biotin-tagging of amyloid precursor protein and prion proteins. *Mol. Biol. Cell 20*, 233–244.
(28) Tour, O., Adams, S. R., Kerr, R. A., Meijer, R. M., Sejnowski, T. J., Tsien, R. W., and Tsien, R. Y. (2007) Calcium green FlAsH as a genetically targeted small-molecule calcium indicator. *Nat. Chem. Biol. 3*, 423–431.
(29) Nakanishi, J., Maeda, M., and Umezawa, Y. (2004) A new protein conformation indicator based on biarsenical fluorescein with an extended benzoic acid moiety. *Anal. Sci. 20*, 273–278.
(30) Massengo-Tiassé, R. P., and Cronan, J. E. (2009) Diversity in enoyl-acyl carrier protein reductases. *Cell. Mol. Life Sci. 66*, 1507–1517.
(31) Yao, J., Zhang, Q., Min, J., He, J., and Yu, Z. (2010) Novel enoyl-ACP reductase (FabI) potential inhibitors of *Escherichia coli* from Chinese medicine monomers. *Bioorg. Med. Chem. Lett. 20*, 56–59.
(32) Adams, S. R., Campbell, R. E., Gross, L. A., Martin, B. R., Walkup, G. K., Yao, Y., Llopis, J., and Tsien, R. Y. (2002) New biarsenical ligands and tetracysteine motifs for protein labeling in vitro and in vivo: synthesis and biological applications. *J. Am. Chem. Soc. 124*, 6063–6076.
(33) Wang, H., and Cronan, J. E. (2004) Functional replacement of the FabA and FabB proteins of *Escherichia coli* fatty acid synthesis by *Enterococcus faecalis* FabZ and FabF homologues. *J. Biol. Chem. 279*, 34489–34495.
(34) Kottegoda, S., Aoto, P. C., Sims, C. E., and Allbritton, N. L. (2008) Biarsenical-tetracysteine motif as a fluorescent tag for detection in capillary electrophoresis. *Anal. Chem. 80*, 5358–5366.
(35) Banerjee, T., Sharma, S. K., Surolia, N., and Surolia, A. (2008) Epigallocatechin gallate is a slow−tight binding inhibitor of enoyl-ACP reductase from *Plasmodium falciparum*. *Biochem. Biophys. Res. Commun. 377*, 1238–1242.
(36) Feldman, G., Bogoev, R., Shevirov, J., Sartiel, A., and Margalit, L. (2004) Detection of tetracysteine-tagged proteins using a biarsenical fluorescein derivative through dry microplate array gel electrophoresis. *Electrophoresis 25*, 2447–2451.
(37) Haes, A. J., Giordano, B. C., and Collins, G. E. (2006) Aptamer-based detection and quantitative analysis of ricin using affinity probe capillary electrophoresis. *Anal. Chem. 78*, 3758–3764.
(38) Gousset, K., Ablan, S. D., Coren, L. V., Ono, A., Soheilian, F., Nagashima, K., Ott, D. E., and Freed, E. O. (2008) Real-time visualization of HIV-1 GAG trafficking in infected macrophages. *PloS Pathog. 4*, e1000015.
(39) Shevchenko, A., Wilm, M., Vorm, O., and Mann, M. (1996) Mass spectrometric sequencing of proteins from silver-stained polyacrylamide gels. *Anal. Chem. 68*, 850–858.

(40) Candiano, G., Porotto, M., Lanciotti, M., and Ghiggeri, G. M. (1996) Negative staining of proteins in polyacrylamide gels with methyl trichloroacetate. *Anal. Biochem. 243*, 245–248.

(41) Stasyk, T., Morandel, S., Bakry, R., Feuerstein, I., Huck, C. W., Stecher, G., Bonn, G. K., and Huber, L. A. (2005) Quantitative detection of phosphoproteins by combination of two-dimensional difference gel electrophoresis and phosphospecific fluorescent staining. *Electrophoresis 26*, 2850–2854.

(42) Stroffekova, K., Proenza, C., and Beam, K. G. (2001) The protein-labeling reagent FLASH-EDT2 binds not only to CCXX-CC motifs but also non-specifically to endogenous cysteine-rich proteins. *Pfluegers Arch. 442*, 859–866.

(43) Spuches, A. M., Kruszyna, H. G., Rich, A. M., and Wilcox, D. E. (2005) Thermodynamics of the As(III)−thiol interaction: arsenite and monomethylarsenite complexes with glutathione, dihydrolipoic acid, and other thiol ligands. *Inorg. Chem. 44*, 2964–2972.

(44) Rey, N. A., Howarth, O. W., and Pereira-Maia, E. C. (2004) Equilibrium characterization of the As(III)-cysteine and the As(III)-glutathione systems in aqueous solution. *J. Inorg. Biochem. 98*, 1151–1159.

(45) Krishnan, B., and Gierasch, L. M. (2008) Cross-strand split Tetra-Cys motifs as structure sensors in a beta-sheet protein. *Chem. Biol. 15*, 1104–1115.

(46) Giepmans, B. N. G., Adams, S. R., Ellisman, M. H., and Tsien, R. Y. (2006) The fluorescent toolbox for assessing protein location and function. *Science 312*, 217–224.

(47) Gaietta, G., Deerinck, T. J., Adams, S. R., Bouwer, J., Tour, O., Laird, D. W., Sosinsky, G. E., Tsien, R. Y., and Ellisman, M. H. (2002) Multicolor and electron microscopic imaging of connexin trafficking. *Science 296*, 503–507.

BC1001533

Novel Nanoassemblies Composed of Squalenoyl−Paclitaxel Derivatives: Synthesis, Characterization, and Biological Evaluation

Franco Dosio,*[,‡] L. Harivardhan Reddy,[†,§] Annalisa Ferrero,[‡] Barbara Stella,[‡] Luigi Cattel,[‡] and Patrick Couvreur[§]

Università degli Studi di Torino, Facoltà di Farmacia, Dipartimento di Scienza e Tecnologia del Farmaco, 10125 Torino, Italy, and Université Paris-Sud XI, Faculté de Pharmacie, UMR CNRS 8612, 92296 Châtenay-Malabry Cedex, France. Received March 29, 2010; Revised Manuscript Received June 2, 2010

Using the anticancer compound paclitaxel as a model drug, this study investigates the potential of the *squalenoylation* technology (i.e., bioconjugation with the natural lipid squalene) in addressing the drug ability and delivery issues of poorly soluble therapeutic agents. In this view, a variety of novel squalene-based prodrugs of the anticancer compound paclitaxel were synthesized, which produced nanoparticles in water. These prodrugs were obtained by covalent coupling of the paclitaxel 2′-hydroxyl group as direct ester, as well as with a succinate or a diglycolate ester as cleavable linker to the 1,1′,2-tris-norsqualenoic acid. The hydrophilicity of these paclitaxel bioconjugates was increased by placing poly(ethylene glycol) chains of different lengths between paclitaxel and the squalenoyl moiety. All these prodrugs self-assembled into nanosized aggregates in aqueous solution as characterized by dynamic light scattering, atomic force microscopy, and transmission electron microscopy. The critical aggregation concentration was very low, ranging from 0.09 to 0.4 mg/L. Zeta potential measurements revealed that all squalenoyl−paclitaxel nanoassemblies (NA) held a global negative charge and appeared stable in water for several weeks as determined by particle size measurement. The release of paclitaxel from NA was evaluated in different conditions and in the presence of serum and depended on the nature of the linker used. Preliminary biological assessment showed that these squalenoyl−paclitaxel NA induced the formation of microtubule bundles in HT-29 and KB-31 cells, and additionally displayed notable cytotoxicity on a lung tumor cell line. Furthermore, the cytotoxic activity of these different prodrugs correlated closely with the observed linker stability. Overall, the squalenoylation nanotechnology opens up interesting perspectives for the development of injectable prodrugs of poorly soluble therapeutic compounds by addressing the associated physicochemical and biopharmaceutical challenges.

INTRODUCTION

Nanotechnology now plays an important part in developing drug delivery methods. These nanodevices can be tailormade with particular functionalities and exploited for therapeutic purposes to transport the drug in the body in a controlled manner from the site of administration to the therapeutic target. Nanomedicine can improve drug properties in various ways: by controlling release and distribution, by enhancing drug absorption by mucosa or cells and by protecting the drug from degradation. Therefore, they offer many possibilities of improving the specificity of drug treatment. Despite this, there is still no universal platform, which is suitable for the delivery of all kinds of drugs and current nanotechnologies have important limitations. As a consequence of the poor drug loading (usually less than 5% of the transported drug versus the carrier material), the quantity of the administered drug may be insufficient to reach a pharmacologically active concentration in the body or the amount of the carrier material which has to be administered, is too high, leading to toxicity or side effects. The rapid release (so-called "burst release") of the encapsulated drug after administration, generally corresponding to the drug fraction which is simply adsorbed at the surface of the nanocarrier, is another important limitation, since a significant fraction of the drug will be released before reaching the pharmacological target in the body, leading also to low activity and side effects. Finally, the difficulty of designing synthetic materials which combine low toxicity, lack of immunogenicity, and biodegradability and do not accumulate in cells or tissues represents an important challenge, which explains the limited number of marketed nanomedicines. There is, therefore, an urgent need to introduce better and safer (bio)materials for drug targeting purposes to load more efficiently and to release in a controlled manner a large number of challenging drugs, for which no effective delivery system is yet available.

As candidates for this application, terpenoids (or isoprenoids) are a group of compounds that are extraordinarily diverse in chemistry, structure, and function. More than 30 000 isoprenoid compounds have been characterized, constituting the largest group of natural products (*1*). As suggested earlier by Ourisson (*2*), their lipophilic character and widespread presence in all living organisms have led to the hypothesis that the most primitive lipids involved in the formation of membranes were exclusively polyterpenoids. Surprisingly, although numerous natural terpenoids are flexible and biocompatible biopolymers, possessing a wide range of physicochemical characteristics able to adapt to a wide variety of biologically active compounds, they have never been used previously in the nanomedicine world for drug delivery and targeting purposes, except very recently by us to design squalene-based nanomedicines (*3*).

Our concept is to chemically link a terpenoid to a biologically active drug molecule in order to create a bioconjugate, which can self-aggregate as nanoassemblies in water. In other words,

* Corresponding author. Franco Dosio, Dipartimento di Scienza e Tecnologia del Farmaco, v. Giuria, 9, 10125 Torino, Italy. franco.dosio@unito.it, tel ++390116707697, fax ++390112367697.

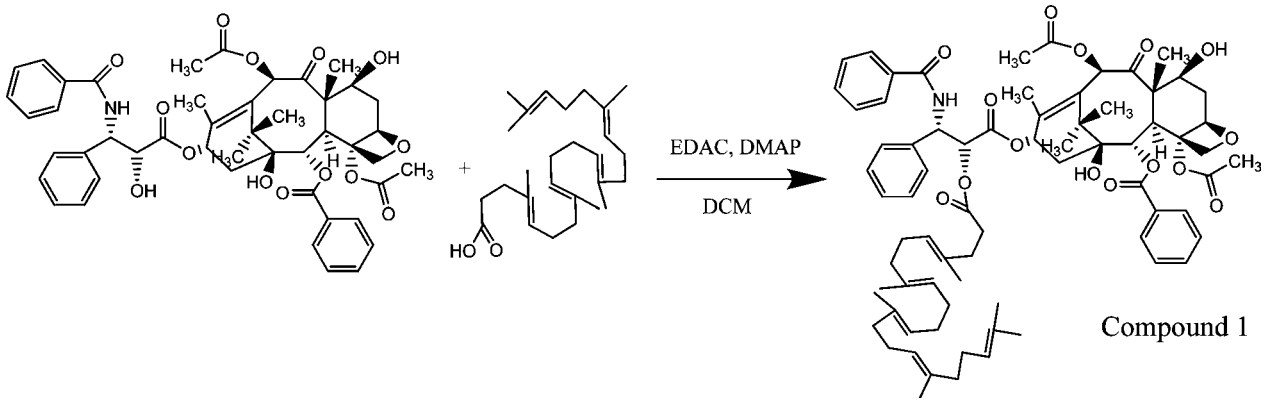
[†] Current address: Sanofi-aventis, 13 Quai Jules-Guesdes, 94403 Vitry-sur-Seine, France.

[‡] Università degli Studi di Torino.

[§] UMR CNRS 8612.

10.1021/bc100154g © 2010 American Chemical Society
Published on Web 07/02/2010

Scheme 1



the prodrug will form the nanomedicine by self-assembling without the need of any other transporter material. The proof of concept of this unique approach has been given using squalene as the polyterpenoid moiety and gemcitabine as a model anticancer nucleoside analogue (*4*, *5*). The gemcitabine−squalene bioconjugate self-aggregated in water as nanoassemblies (with a diameter of about 100 nm) with hexagonal molecular packing, resulting from the stacking of cylinders (*6*). The ability of squalene to form nanoassemblies when linked with gemcitabine was explained by the amphiphilic character of the bioconjugate, the squalene corresponding to the lipophilic moiety, whereas the gemcitabine represented the hydrophilic part of the molecule. Thus, it was expected that this approach only applied to hydrophilic compounds. We show here that, unexpectedly, the "squalenoylation" may also be appropriate to design nanomedicines loaded with hydrophobic compounds with very low water solubility, like paclitaxel (PTX), one of the leading anticancer drugs in clinical use today. Paclitaxel is efficient to treat patients with breast, ovarian, lung, head, and neck cancers, and Kaposi's sarcoma (*7*–*11*). Nevetheless, the reduced solubility of this compound requires the use of the micelle-forming vehicle Cremophor EL which has been shown to cause hypersensitivity reactions and neuropathy (*12*). Thus, it represents a relevant model of poorly water soluble compound, difficult to be administered intravenously.

In the current study, we show that the conjugation of paclitaxel to squalene led to the construction of nanoassemblies with high drug loading and absence of burst release also avoiding the use of Cremophor. The design, synthesis, and characterization of a series of novel paclitaxel−squalenoyl derivatives were assessed. The stability of the resulting nanoassemblies and release of paclitaxel were evaluated in different conditions and in the presence of serum. Preliminary biological behavior and cytotoxic activity of the different prodrugs were investigated too.

EXPERIMENTAL PROCEDURES

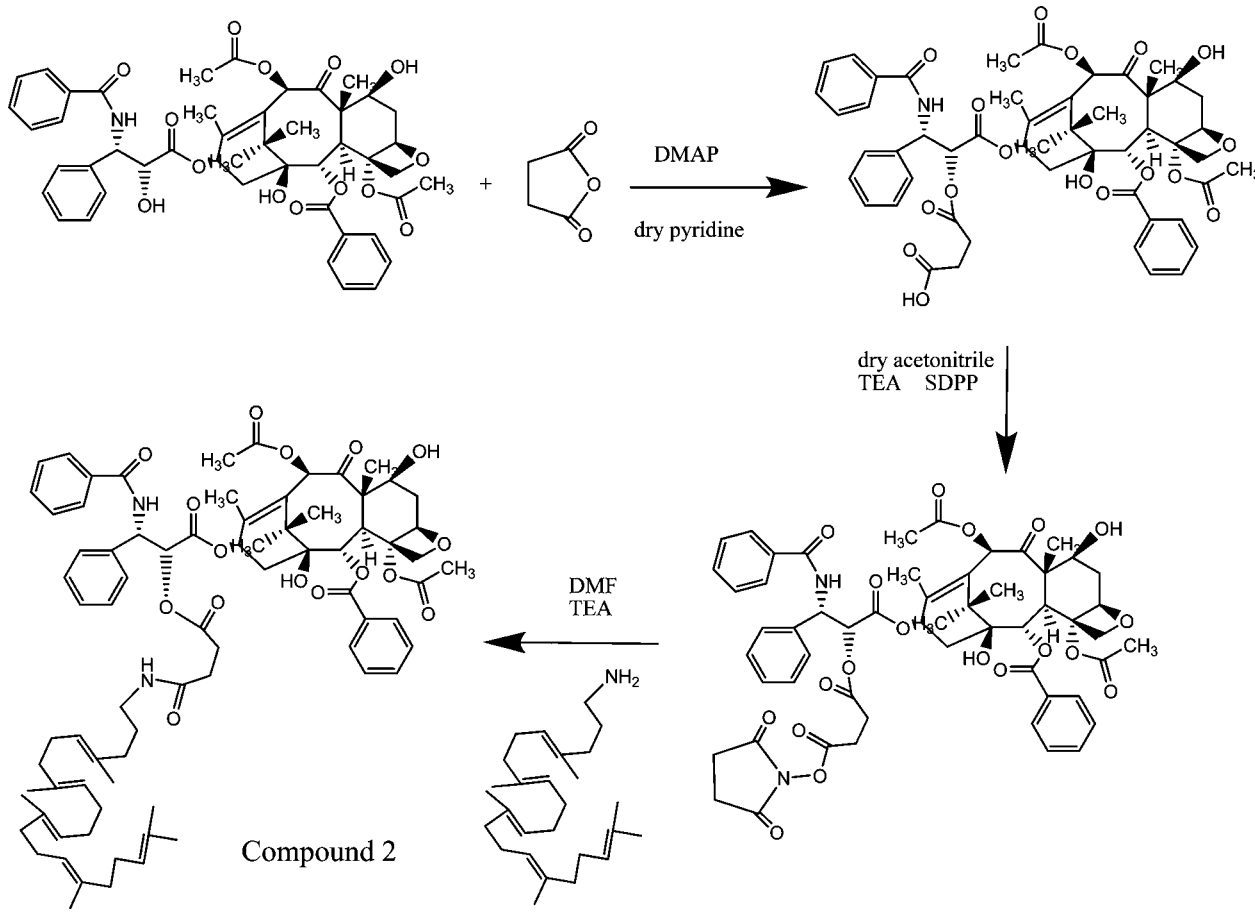
Paclitaxel was purchased from Indena (Milan, Italy). PEG derivatives were purchased from Quanta BioDesign (Powell, OH), and all other reagents were purchased from Aldrich (Milwaukee, WI) and used without further purification. 1,1′,2-*Tris*-norsqualenoic acid and 1,1′,2-tris-norsqualene alcohol were prepared following a published method (*13*) starting from squalene and via the intermediates squalene monobromohydrine and squalene 2,3-epoxide. Squalene amine was prepared by the method described by Duriatti (*14*) by reductive amination of 1,1′,2-tris-norsqualene aldehyde using sodium cyanoborohydride at pH 6.0.

The NMR spectra were recorded using a NMR Bruker Avance 300 spectrometer. Elemental analyses were carried out by Redox Snc (Monza, Italy). Quasi-elastic light scattering (QELS) and zeta potential measurements were carried out using a 90 Plus Particle Size Analyzer (Brookhaven Instruments, Co.) photometer. The UV−vis spectra were recorded using a Beckman 730 spectrophotometer with a temperature controller. Mass spectra were recorded with a Finnigan Mat TSQ700 and Waters Micromass ZQ (ESCI and APCI sources). Fluorescence spectra were recorded on a FluoroLog Horiba Jobin Yvon spectrofluorophotometer (Milan, Italy). All HPLC analyses were performed on a Merck-Hitachi L-6200 liquid chromatograph equipped with L5000 LC controller (Merck, Milan, Italy) and the eluting fractions containing PTX were monitored at 227 nm using an L-4200 UV detector.

Synthesis of Squalenoyl−Paclitaxel 2′ Esters with Different Linkers. *2′-Tris-norsqualenoyl-paclitaxel Ester (Compound* **1***).* (Scheme 1) Paclitaxel (1.2 g, 1.4 mmol), dissolved in 30 mL of dichloromethane (DCM), was reacted with EDAC (*N*-ethyl-*N*′-(3-dimethylaminopropyl) carbodiimide) (0.6 equiv), in the presence of DMAP (4-dimethylamino pyridine (0.2 equiv) and 1,1′,2-tris-norsqualenoic acid (0.6 equiv) previously dissolved in DCM at room temperature. After 3 h, the reaction was stopped with water and extracted with brine. The crude mixture was purified by chromatography on SiO_2 eluted with a gradient (from 95:5 to 80:20) of DCM/ethyl acetate to give the pure compound **1** (yield 65%). TLC control DCM/ethanol (97:3) Rf 0.55. The purity of compound **1** was checked by HPLC on a RP-18 reverse phase column (LiChrospher 100 RP 18e 5 μm, Merck) eluted with an acetonitrile/water mixture (40:60 and, after 5 min, gradient up to 100% acetonitrile, 20 min), elution time 19.23 min. Purity by HPLC was above 92%. Characterization: ^{1}H NMR (300 MHz, $CDCl_3$): 8.13 (d, 2H, C23, C27ArH), 7.75 (d, 2H, C39, C43 ArH), 7.62 (t, 1H, C25 ArH), 7.53−7.49 (band, 3H, C24, C26, C41 ArH), 7.43−7.35 (band, 7H, C33, C34, C35, C36, C37, C40, C42 ArH), 6.91 (d,1H, 4′NH), 6.35 (s, 1H, C(10)-H), 6.24 (m, 1H, C(13)-H), 5.99 (dd, 1H, C(3′)-H), 5.69 (d, 1H, C(2)-H), 5.53 (d, 1H, C(2′)-H), 5.20 (m, 5H, C(SQ-H)), 4.97 (d, 1H, C(5)-H), 4.44 (m, 1H, C(7)-H), 4.33 (d, 1H, C(20)-H_a), 4.20 (d, 1H, C(20)-H_b), 3.85 (d, 1H, C(3)-H), 2.55 (m 1H, C(6)-H_a), 2.49 (s, 3H, C(29)-H), 2.45 (m, 2H,$\underline{CH_2}$-CH_2-CO SQ), 2.30 (t, 2H, CH_2-$\underline{CH_2}$-CO SQ), 2.23 (s, 3H, C(31)-H), 2.09 (s, 3H, C(18)-H), 2.00 (m, 16H, CH_2 SQ), 1.97 (m, 1H, C(6)-H_b), 1.70 (m, 1H, C(14)-H_a), 1.67 (s, 3H, C(19)-H), 1.61 (m, 18H, C(SQ)-CH_3), 1,25 (m, 1H, C(14)-H_b), 1.21 (s, 3H, C(16)-H), 1.13 (s, 3H, C(17)-H). ESI-MS calculated for $C_{74}H_{93}NO_{15}$: 1235.65. Found 1237.24 (MH+). Elemental Analysis calculated: C 71.88%, H 7.58%, N 1.13%. Measured: C 71.99%, H 7.63%, N 1.19%.

2′-O-Tris-norsqualenoylamido-succiniloyl Paclitaxel (Compound **2***).* (Scheme 2) Paclitaxel-2′-hemisuccinate was prepared

Scheme 2



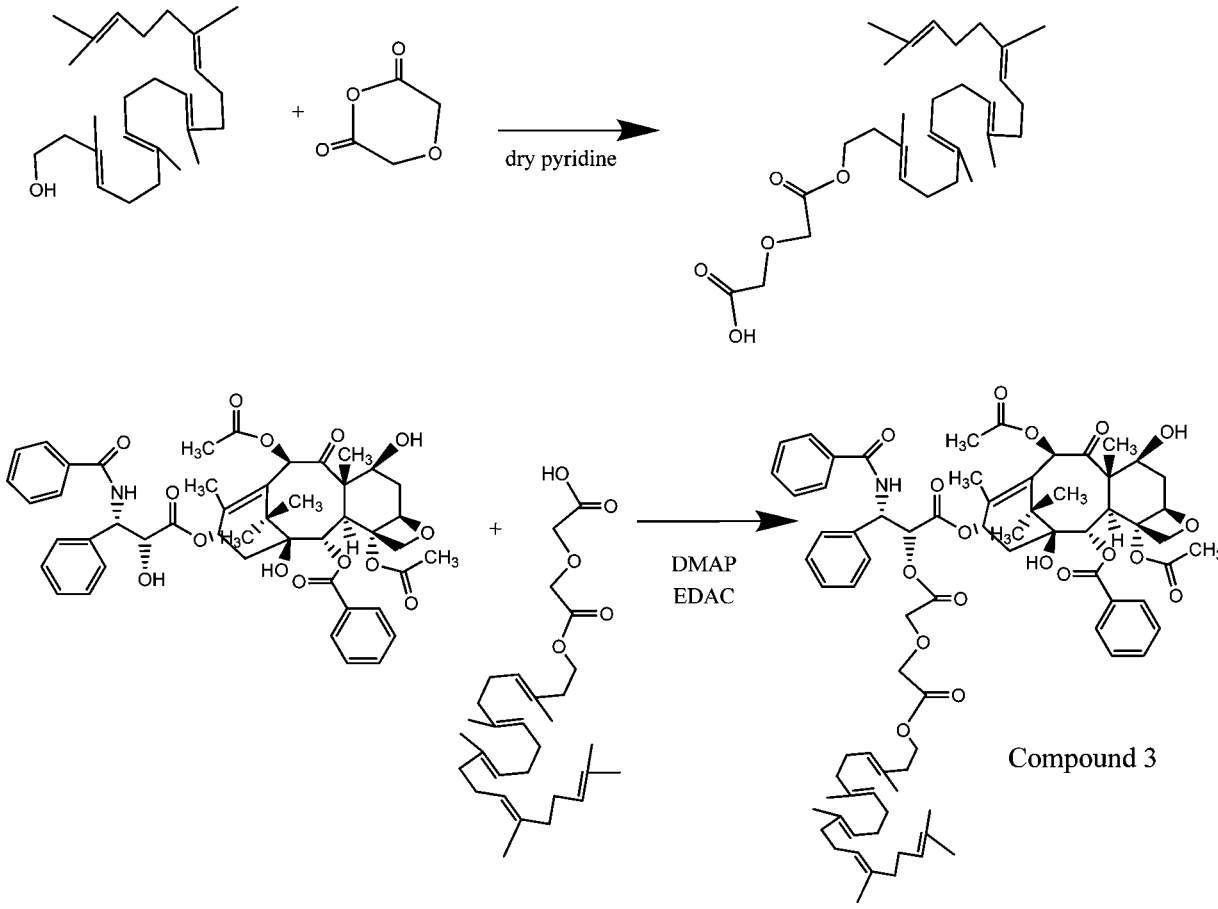
as described by Dosio (*15*). Paclitaxel (1.2 g, 1.4 mmol) was added to DMAP (0.1 equiv) and succinic anhydride (2 equiv) and dried for 2 h under vacuum. After addition of dry pyridine (12 mL), the reaction was stirred for 3 h at RT. Paclitaxel-2′-hemisuccinate was purified on silica gel (DCM/ethyl acetate). The yield was 88%. Paclitaxel-2′-hemisuccinate-*N*-hydroxysuccinimide ester (NHS) was prepared essentially by following the method of Luo (*16*). *N*-Hydroxysuccinimido diphenyl phosphate (SDPP) was prepared starting from diphenylphosphoryl chloride, *N*-hydroxysuccinimide, and triethylamine (TEA) in DCM (*17*). Crude SDPP was triturated with ether, dissolved in ethyl acetate, washed with water, dried, and concentrated under vacuum to give SDPP at 95% yield. To a solution of paclitaxel-2′-hemisuccinate (300 mg, 0.314 mmol), SDPP (1.5 equiv) was added, dissolved in acetonitrile with triethylamine (4 equiv). The reaction was stirred for 6 h at room temperature and then concentrated under vacuum. The crude reaction mixture was dissolved in ethyl acetate and extracted with brine and did not require any further purification (yield 85%). ESI-MS calculated for $C_{55}H_{58}N_2O_{19}$: 1051.05. Found: 1052.15 (MH+).

Paclitaxel-2′-succinyl-NHS (300 mg, 0.285 mmol) dissolved in 4 mL of dry dimethylformamide (DMF) was reacted with 1,1′,2-tris-norsqualene amine (1 equiv) previously dissolved in dry DMF, in the presence of triethylamine (1 equiv). After 8 h at RT and overnight reaction at 5 °C, the mixture was extracted with brine and purified on SiO_2 gel, eluted with DCM−ethyl acetate (80:20 to 50:50). TLC control DCM−ethanol (97:3). Rf 0.42. The purity was checked by HPLC (85%); elution time 18.61 min. ^{1}H NMR (300 MHz, $CDCl_3$): 8.0 (s, 1H, NH-SQ), 5.20 (m, 5H, C(SQ-H), 3.15 (m, 2H, SQ CH_2-NH), 2.82 (m, 2H, CH_2-CO-NH succinic), 2.63 (m, 2H, CH_2-COO succinic), 2.45 (m, 2H,$\underline{CH_2}$-CH_2-CH_2-NH SQ), 2.00 (m, 16H, CH_2 SQ), 1.80 (m, 2H, CH_2-$\underline{CH_2}$-NH SQ), 1.61 (m, 18H, C(SQ)-CH_3). ESI-MS calculated for $C_{74}H_{93}NO_{15}$: 1321.36. Found: 1322.45 (MH+). Elemental Analysis calculated: C 70.88%, H 7.63%, N 2.12%. Measured: C 71.02%, H 7.68%, N 2.45%.

2′-O-(5″-O-Tris-norsqualenoyldiglicoloyl)-paclitaxel (Compound **3***).* (Scheme 3) 1,1′,2-Tris-norsqualene alcohol (500 mg, 1.34 mmol) was mixed with diglycolic anhydride (2.5 equiv) in 6 mL of dry pyridine at room temperature overnight under stirring. The solvent was removed and the residue extracted from dilute hydrochloric acid and brine with DCM. Conversion to the appropriate compound, monitored by TLC, was approximately 100%. The resultant product was dried under vacuum, and the acid was used without further purification. Squalene−diglycolic acid (400 mg, 0.82 mmol) was dissolved in 4 mL of DCM, and then, paclitaxel (1 equiv) and DMAP (3 equiv), previously dissolved in DCM, were added. After 10 min, EDAC (1.3 equiv) was added and the solution stirred at room temperature for 2 h. After removal of the solvent, the crude product was purified on SiO_2 gel, eluted with DCM−ethyl acetate (80:20 to 50:50). TLC control DCM−ethanol (97:3) Rf 0.62. Purity by HPLC was above 92%, elution time 19.33 min. ^{1}H NMR (300 MHz, $CDCl_3$): 5.20 (m, 5H, C(SQ-H)), 4.12 (s, 4H, CH_2 diglycolyl), 4.07 (m, 2H, CH_2-O SQ), 2.15 (m, 2H, $\underline{CH_2}$-CH_2-O SQ), 2.00 (m, 16H, CH_2 SQ), 1.61 (m, 18H, C(SQ)-CH_3). ESI-MS calculated for $C_{78}H_{99}NO_{18}$: 1338.62. Found: 1339.43 (MH+). Elemental Analysis calculated: C 69.99%, H 7.45%, N 1.05%. Measured: C 70.02%, H 7.49%, N 1.12%.

2′-O-(4″-N-(Tris-norsqualen-PEG$_3$ Amido) Succiniloyl) Paclitaxel (Compound **4***).* (Scheme 4) Paclitaxel-2′-hemisuccinate-NHS, previously prepared (200 mg, 0.19 mmol), was dissolved in 8 mL of DCM, and *N*-*t*-boc-4,7,10-trioxadecane-13-amine (tBoc-NH-PEG_3-NH_2) (1 equiv) in DCM was added under stirring. TEA (0.5 equiv) was added at 4 °C, and the reaction was maintained at 20 °C for 5 h. The crude reaction

Scheme 3



mixture was extracted with HCl 0.1 N and then with brine. The paclitaxel-succinyl-PEG_3-NH-tBoc obtained (204 mg, 0.16 mmol) was dissolved in 20 mL of dry DCM, and 0.5 mL of trifluoroacetic acid (TFA) was added under stirring at 20 °C. After 2 h, the reaction was complete, and the mixture was extracted with sodium acetate solution and then with brine until neutral. Squalene *N*-hydroxysuccinimide ester (60 mg, 0.12 mmol), previously prepared by reaction of 1,1′,2-trisnorsqualenoic acid with NHS, in the presence of EDAC, was added to paclitaxel-succinyl-PEG_3-amine (1 equiv). TEA (0.3 equiv) was added, and the reaction was stirred at room temperature for 6 h. After removal of solvent, the crude product was purified on SiO_2 gel, eluted with DCM−ethanol (99:1 to 90:10). TLC control DCM−ethanol (94:6). Rf 0.52.

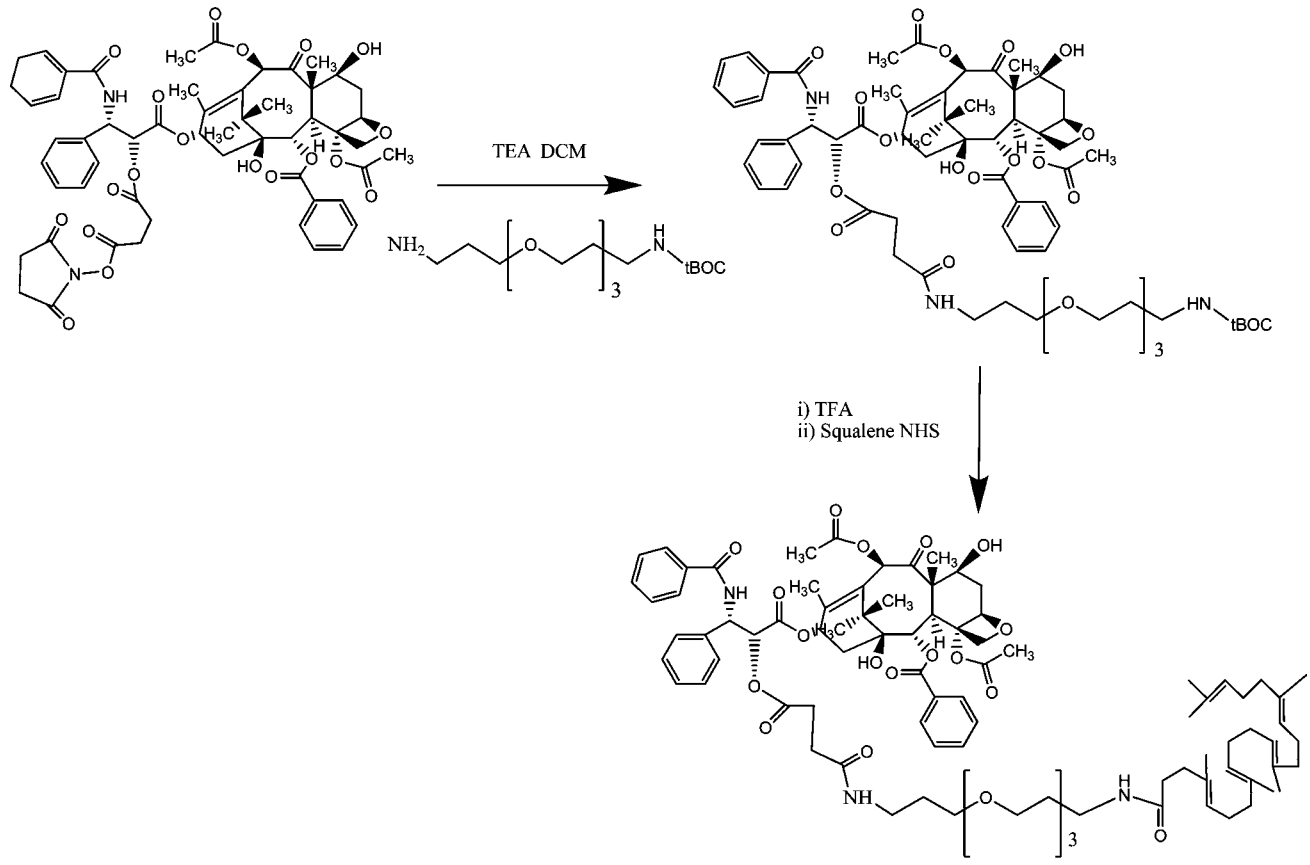
Purity by RP-HPLC (conditions as for compound **1**, with the addition of 0.1% TFA) was above 85%, elution time 14.23 min. ^{1}H NMR (300 MHz, $CDCl_3$): 8.0 (s, 1H, NH-SQ), 5.20 (m, 5H, C(SQ-H)), 3.60 (m, 12H, CH_2-O PEG), 3.13 (m, 4H, CH_2-NH PEG), 2.82 (m, 2H, CH_2-CO-NH succinic), 2.63 (m, 2H, CH_2-COO succinic), 2.40 (m, 2H,$\underline{CH_2}$-CH_2-CO SQ), 2.30 (t, 2H, CH_2-$\underline{CH_2}$-CO SQ), 1.61 (m, 18H, C(SQ)-CH_3). ESI-MS calculated for $C_{88}H_{119}N_3O_{20}$: 1538.89. Found: 1540.00 (MH+), 1562.08 (M+Na). Elemental Analysis calculated: C 68.68%, H 7.79%, N 2.73%. Measured: C 68.72%, H 7.69%, N 2.80%.

2′-O-(4″-N-(Tris-norsqualen-PEG_{11} Amido) Succiniloyl) Paclitaxel (Compound **5***).* (Scheme 5) Paclitaxel-2′-hemisuccinate-NHS, previously prepared, was dissolved in DCM and *N*-*t*-boc-3,6,9,12,15,18,21,24,27,30,33-undecaoxapentatriacontane-1,35-diamine (tBoc-NH-PEG_{11}-NH_2) (1 equiv) in DCM was added under stirring. TEA (0.5 equiv) was added at 4 °C, and the reaction was maintained at 20 °C for 5 h. The crude reaction mixture was extracted with HCl 0.1 N and then with brine. Paclitaxel-succinyl-PEG_{11}-NH-tBoc was dissolved in 20 mL of dry DCM, and 0.5 mL of TFA was added under stirring at 20 °C. After 2 h, the reaction was complete, and the mixture was extracted with sodium acetate solution and then with brine until neutral.

Squalene *N*-hydroxysuccinimide ester (1.3 equiv), previously prepared, was added to paclitaxel-succinyl-PEG_{11}-amine. TEA (0.3 equiv) was added, and the reaction was stirred at room temperature for 6 h. After removal of solvent, the crude product was purified on a silica gel column using a DCM/ethanol gradient, obtaining the purified prodrug. Purity by HPLC was above 80%, elution time 12.32 min. ^{1}H NMR (300 MHz, $CDCl_3$): 8.0 (s, 1H, NH-SQ), 5.20 (m, 5H, C(SQ-H)), 3.30−3.70 (m, 48H, CH_2-O PEG and CH_2-NH PEG), 2,82 (m, 2H, CH_2-CO-NH succinic), 2.63 (m, 2H, CH_2-COO succinic), 2.40 (m, 2H,$\underline{CH_2}$-CH_2-CO SQ), 2.30 (t, 2H, CH_2-$\underline{CH_2}$-CO SQ), 2.00 (m, 16H, CH_2 SQ, 1.61 (m, 18H, C(SQ)-CH_3). ESI-MS calculated for $C_{102}H_{147}N_3O_{28}$: 1863.26. Found: 1864.77 (MH+), 1886.26 (M+Na). Elemental Analysis calculated: C 65.75%, H 7.95%, N 2.26%. Measured: C 65.82%, H 7.99%, N 2.30%.

Measurement of Theoretical and Experimental Hydrophobicity. The lipophilic character of the synthesized compounds was determined using a chromatographic Rm method (*18*). Solutions of the compounds were spotted 1 cm above the bottom of silanized silica gel TLC plates (20 × 20 cm, Bracco-Merck) prepared as described by Csermely (*19*). The plates were developed with seven mixtures of water−methanol (from 80% to 95% of methanol), then dried and exposed to iodine vapors. The Rm were calculated from the following expression: $Rm = \log[(1/Rf) - 1]$ where Rf is the distance traveled by the compound by that of the solvent front. The Rm values, plotted versus increasing concentrations of methanol, were interpolated with a straight line of equation $y = (R_{m0} + ax)$. The values reported are the mean values of 3 different chromatographic

Scheme 4



Compound 4

runs for each PTX derivative with correlation coefficient values ranging from 0.987 to 0.992.

Three-dimensional molecular models were built starting from SMILES strings with the *MOE* modeling suite (*MOE* v 2009.10, Chemical Computing Group Inc., Montreal, QC). Initial geometries were optimized with the MMFF94s force-field using a Generalized Born implicit solvent model with no cutoff for nonbonded interactions. A Monte Carlo conformational search was carried out with the ConfSearch module implemented in *MOE*, to find all stable conformers in a 7 kcal range from the global minimum. The distance between the 2′-hydroxyl oxygen moiety and the α-carbon atom of the squalenic acid residue was measured as the Boltzmann-weighted mean distance among all conformers.

Theoretical logP was calculated using the software *ALOGPS 2.1* (*20*) available on the Web site http://www.vcclab.org/lab/alogps/start.html.

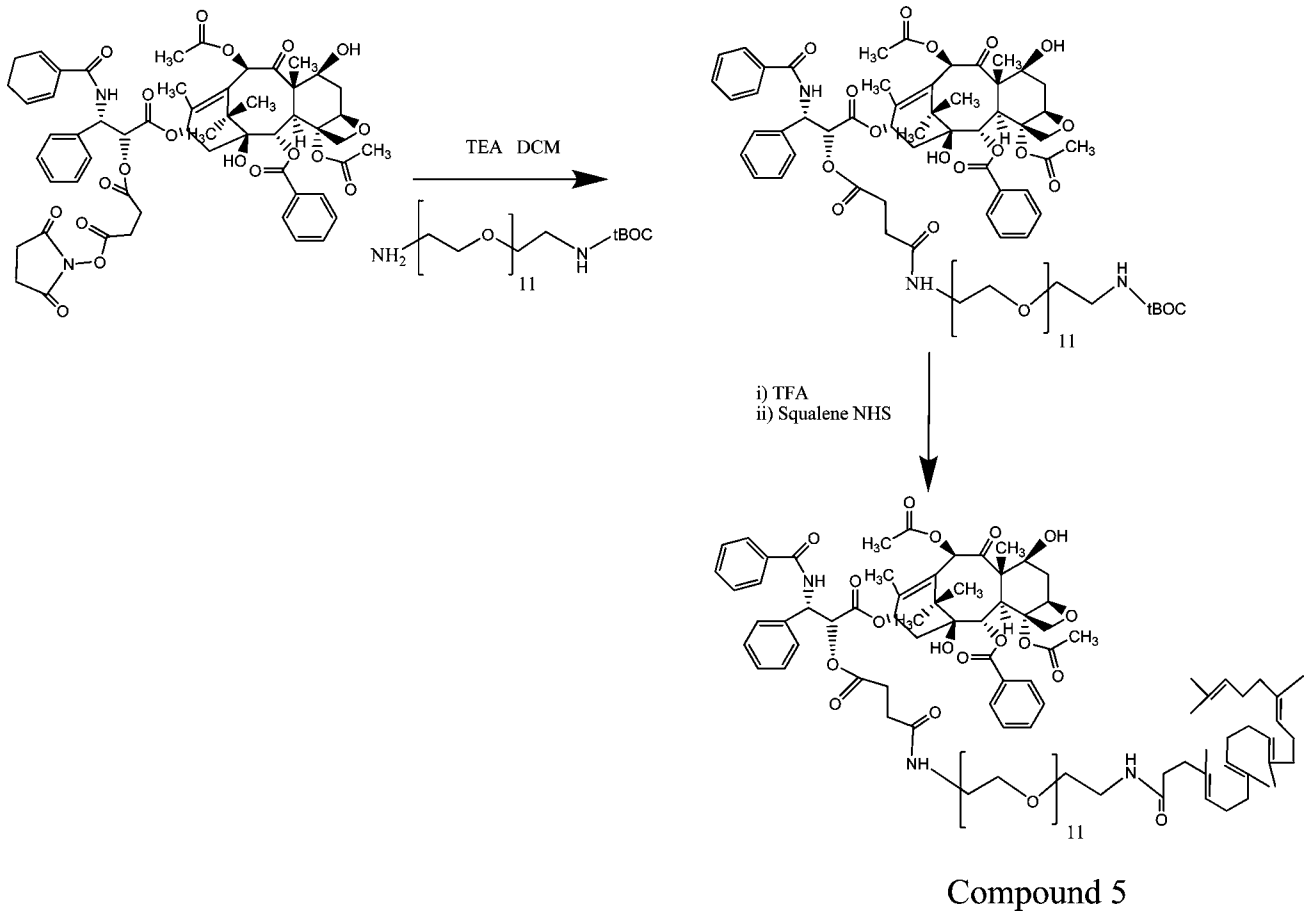
Preparation of Nanoassemblies. Nanoassemblies (NAs) were prepared by first dissolving the paclitaxel−squalene conjugates in ethanol, acetone, or THF (4−6 mg/mL), followed by dropwise addition of the organic solution under stirring into Milli-Q grade water (for compound **3**) or in 5% aqueous dextrose solution. Finally, the organic solvent was completely evaporated using Rotavapor at 37 °C under vacuum or under nitrogen flow, to obtain an aqueous suspension of squalenoyl−paclitaxel NAs. In a typical nanoassemblies preparation, a final concentration of 2 mg/mL squalenoyl−paclitaxel was obtained.

Size and Zeta Potential Measurements. The average diameter and polydispersity index of the nanoassemblies was determined using quasi-elastic light scattering (QELS) at a fixed angle of 90 °C and at a temperature of 25 °C. The NA dispersions were diluted 1:20 with Milli-Q water before analysis. Each value reported is the average of five measurements. To determine the electrophoretic mobility, the NA samples were diluted with 0.1 mM KCl and placed in the electrophoretic cell, where an electric field of 15.24 V/cm was established. Each sample was analyzed in triplicate. The zeta potential values were calculated using the Smolochowski equation.

Transmission Electron Microscopy Characterization. Droplets (20 μL) of NA suspensions were placed on parafilm and brought into contact with a copper grid for 2−3 min at room temperature. After adhesion, the grids were washed with four droplets of distilled water before being placed onto a drop of uranyl acetate (2%) for 2 min. Finally, the grids were dried at room temperature after removing the excess liquid. Transmission electron microscopy was performed with a Philips CM10 (Philips Co., Amsterdam, The Netherlands) using 80 kV acceleration voltage. Film was used for imaging, and an Epson 4990 Photo flat-bed scanner was then used to generate high-quality digital images from the film.

Atomic Force Microscopy Characterization. AFM observation was done following the procedure described by Ruozi (*21*) using a Park Autoprobe atomic force microscope (Park Instruments, Sunnyvale, CA, USA). AFM images were obtained by measurement of the interaction forces between the tip and the sample surface. The experiments were conducted under water at room temperature (20 °C) and at atmospheric pressure (760 mmHg) operating in noncontact mode (NCAFM), in which the space between the tip and the sample is between 10 and 100 Å, and the total force is very low. A triangular silicon tip

Scheme 5



Compound 5

was used for this analysis. The resonant frequencies of this cantilever were found to be about 250 kHz. Higher resonant frequencies of the cantilever were necessary to minimize the sensitivity to vibrational noise. In order to visualize the samples, the noncontact mode was found more appropriate, because the vesicles were only slightly susceptible to the load forces applied. Immediately before the analysis, the samples were diluted in water (1:10 v/v) to obtain a less sticky fluid to analyze. Droplets of constant volume (20 μL) of NAs were deposited onto a small mica disk with a diameter of 1 cm. After 2 min, excess water was removed using a paper filter. Two kinds of images were obtained: topographical images and those indicated as "error signal". This error signal was obtained by comparing two signals: the first, a direct signal, represented the amplitude of the vibrations of the cantilever, and the second represented the amplitude of a reference point. The images obtained by this method revealed small surface variations of the specimen examined. Images were flattened using second-order fitting to remove sample tilt.

Self-Aggregation Behavior of Paclitaxel Prodrugs. The critical aggregation concentration test (CAC) was performed by steady-state fluorescence spectra: a solution of pyrene (1.0×10^{-4} M) in acetone was diluted in water, and then, the acetone was evaporated to obtain a pyrene concentration of 12×10^{-7} M. Eleven samples of the NAs in water, with concentrations ranging from 0.1 μg/L to 0.5 g/L, were prepared and left to equilibrate with a constant pyrene concentration of 6×10^{-7} M for 12 h at room temperature under stirring. Fluorescence emission spectra were recorded from 360 to 550 nm at an integration time of 0.1 s, using 343 nm excitation wavelength. Excitation and emission bandwidths were set at 14.7 and 1.5 nm, respectively. In the emission spectra of unstacked pyrene, the intensity ratio of the first band (I373) to the third band (I384) was analyzed as a function of NA concentration. A CAC value was determined from the intersection of the tangent to the curve at the inflection with the horizontal tangent through the points at low concentration (*22*).

Stability Assessment of Squalenoyl−Paclitaxel Conjugates and NAs in Aqueous Dispersion and in Serum. The stability of NAs (at a concentration of 2 mg/mL) was evaluated at different pH values by analyzing the mean particle size after incubation for 24 h at room *T* (20 °C); the pH value of the sample solution was adjusted from 4 to 9 using 0.1 M solutions of NaOH or HCl.

In order to investigate the chemical stability of squalenoyl−paclitaxel conjugates, the corresponding NAs (1 mg/mL) were diluted at a concentration of 0.2 mg/mL with sodium acetate buffer 0.1 M (pH 4.5), sodium phosphate buffer 0.1 M (pH 7.4), or sodium borate buffer 0.1 M (pH 9.0) and incubated at 37 °C in a plate-shaker. At selected time intervals (1 h to 96 h), aliquots (40 μL) were removed and diluted in acetonitrile to 300 μL. In order to avoid hydrolysis during sample workup, all the samples were maintained at −20 °C and warmed only prior to analysis. The chemical stability of the squalenoyl conjugate was determined by HPLC analysis. 100 μL aliquots of the obtained solutions were injected into a LiChrospher 100 RP 18e (4.6 × 250 mm, 5 μm) equipped with a C18 column guard. The column was eluted with acetonitrile and 0.05% trifluoroacetic acid in water (40:60 and, after 5 min, linear gradient to 100% acetonitrile, 20 min) at flow rate 1 mL/min, and the column effluent was detected at 227 nm. The assay was linear over the tested concentration range (1−50 μg as paclitaxel). Eluted peaks were also characterized using a Waters HPLC-MS Micromass ZQ with ESI detector, eluting the column with methanol and 0.05% trifluoroacetic acid in water, with the same gradient as described above.

The stability of the squalenoyl−paclitaxel conjugates with different linkers was also analyzed in the presence of serum. Incubation in human serum was performed at 37 °C with a final concentration of NAs of 0.33 mg/mL. Aliquots (60−80 μL) were removed at different time intervals (0.5 to 72 h), and 1 μg of the internal standard, freshly prepared *N*-octylbenzamide, was added to each aliquot. After addition of 0.8 mL of acetonitrile, the aliquots were centrifuged, and the solution was analyzed as above. All the tests were repeated thrice.

Immunofluorescence Assay. Human nasopharyngeal epidermal carcinoma KB-31 cells and colorectal carcinoma HT-29 cells were grown to subconfluence on glass coverslips in 35 mm plastic Petri dishes and then incubated with the drugs for 14 h. Cells were extracted with 0.5% Triton X-100 in PEM microtubule stabilizing buffer [100 mM PIPES, 2 mM EGTA, and 2 mM $MgCl_2$ (pH 6.8)] for 4 min, fixed in 3% formaldehyde in PEM for 40 min, blocked with 20% normal fetal calf serum for 30 min, and incubated with 1:200 fluorescein isothiocyanate (FITC) conjugated antitubulin monoclonal antibody for 1 h (Sigma). The presence of microtubule bundles after treatment with 0.1 μM of paclitaxel, or with 5 μM of paclitaxel NAs, was determined by observation under a Leica TCS SP2 confocal microscope (Wetzlar, Germany) equipped with an Apo 40× 0.80 objective, λ exc 497 nm, λ emission 555 nm.

Cytotoxicity Assay. The cytotoxicity assay of squalenoyl−paclitaxel conjugates was carried out on M109 murine lung carcinoma cell line. Cell culture medium was used as dilution medium to make relevant dilutions of the nanoassemblies for this assay. Cytotoxicity was evaluated by incubating the cells with different concentrations of nanoassemblies for 72 h at 37 °C/5% CO_2. For comparison purposes, paclitaxel and a freshly prepared mixture of paclitaxel, 1,1′,2-tris-norsqualenoic acid (SQCOOH) and 1,1′,2-tris-norsqualene-MePEG (SQPEG) were used as a control. In brief, M109 murine lung carcinoma cells were cultured in RPMI 1640 supplemented with 10% fetal calf serum, 50 U/mL penicillin, 50 μg/mL streptomycin, and 2 mM L-glutamine. The cytotoxicity of paclitaxel and squalenoyl−paclitaxel NAs was determined using the 3-[4,5-dimethylthiazol-2-yl]-3,5-diphenyl tetrazolium bromide (MTT) test, measuring mitochondrial dehydrogenase activity. Cells in the exponential growth phase were seeded into 96-well plates and preincubated for 24 h at 37 °C in a humidified atmosphere of 5% CO_2 in air. Different dilutions of paclitaxel and squalenoyl−paclitaxel NAs were added to the cells in the culture medium. After 72 h at 37 °C, 200 μL of MTT solution in cell culture medium (0.5 mg/mL) were added to each well. After incubation for 2.5 h at 37 °C/5% CO_2, the culture medium was removed following centrifugation, and the resultant formazan crystals were dissolved in 200 μL dimethylsulfoxide. The absorbance of the converted dye, which is proportional to the number of viable cells, was measured at 570 nm using a microplate reader (Metertech Σ 960, Fisher Bioblock, Illkirch, France). The percentage of surviving cells was calculated as the absorbance ratio of treated to untreated cells. The experiment was repeated thrice in triplicate for each concentration of the tested compounds.

RESULTS AND DISCUSSION

Many of the novel and potent anticancer class of compounds emerging from drug discovery are hydrophobic drugs posing drugability issues, thus necessitating the use of solubilizers and/or surfactants for developing injectable formulations. However, such solubilizing compositions are often toxic, they frequently limit the injectable payload of the drugs, and they may concurrently lead to hypersensitivity reactions in patients following intravenous injection. Thus, the formulation of hydrophobic drugs by avoiding toxic excipients is a real pharmaceutical challenge.

Table 1. Theoretical and Experimental Characteristics of Squalenoyl Derivatives of Paclitaxel

compound[a]	R_{m0}[b]	*A* LogPs [c]	theoretical distance PTX and SQ (Å)[d]
PTX	8.76	3.20	
1 PTXSQ	14.35	7.30	2.35
2 PTXsuccSQ	14.32	7.15	5.49
3 PTXdiglSQ	14.28	7.30	5.94
4 $PTXPEG_3SQ$	13.50	7.01	6.27
5 $PTXPEG_{11}SQ$	12.80	6.11	23.34

[a] PTX, paclitaxel; PTXSQ, squalenoyl−paclitaxel; PTXsuccSQ, squalenoyl-succinyl-paclitaxel; PTXdiglSQ, squalenoyl-diglolyl-paclitaxel; PTXPEGSQ, squalenoyl-poly(ethylene glycol)-paclitaxel. [b] Lipophilicity values for paclitaxel and squalenoyl−paclitaxel derivatives was determined by reversed-phase TLC (R_{m0}). [c] Theoretical analysis was performed with A*LOGPS 2.1* (logP). [d] Theoretical analysis was performed with *MMFF94s* software (mean distance).

Earlier, the squalenoylation platform discovered by our group was employed to design self-assembling nanomedicines of hydrophilic therapeutic agents, such as gemcitabine, 2′,3′-dideoxycytidine, and 2′,3′-dideoxyinosine (*23, 24*). However, it was not known if this technology platform could also be applied to poorly water-soluble therapeutic agents such as paclitaxel. Therefore, a series of paclitaxel-based bioconjugates composed of the squalenoyl moiety and different linkages were developed and characterized. Moreover, the influence on paclitaxel release and efficacy of iterative changes to the anchor-linker-drug structural motif was evaluated.

Prodrug Synthesis. The prodrugs used in this study were based on the generalized structured paclitaxel-linker-squalene. The anchor, 1,1′,2-trisnorsqualenoic acid, length 27 carbon atoms, was maintained constant, so as to evaluate the possibility of obtaining NAs at increasing hydrophilicity of the linker (e.g., with PEG) (Schemes 1−5). All derivatives were obtained by conjugation to the 2′-hydroxyl group of paclitaxel; it is noteworthy that most of the previously synthesized taxoid prodrugs were generated by linking to the 2′-hydroxyl position of paclitaxel or docetaxel (*25–27*). Derivatives (esters, carbamates, etc.) obtained by linkage at this position are much more accessible to various enzymes in the body and are able to undergo hydrolysis so as to release the active drug. In a small number of cases, derivatives obtained by alterations at 10-acyl and 7-hydroxyl position of the taxoids have also been reported; however, they have been shown to be more stable to enzymatic degradation than 2′-esters (*28*).

In the present study, the conjugation of squalene to paclitaxel was approached from a hydrolytic perspective, to allow the release of paclitaxel in vivo following intravenous injection. Thus, different linkages have been designed using direct ester linkage between paclitaxel and squalenic acid (compound **1**), succinic (compounds **2**,**4**,**5**) or diglycolic (compound **3**) spacers using, as reagents, suitable squalene amine, PEG amines, and squalene alcohol.

PEG spacers were also used in order to investigate the influence of water access on paclitaxel release, since PEG chain increases the hydrophilicity between the two very hydrophobic moieties of the conjugate (i.e., squalene and paclitaxel). PEG spacers were, indeed, previously reported to improve the biological activity of paclitaxel by reducing the steric hindrance (16 or 40 atoms) (*29*) (*30*). In this study, we selected two PEG derivatives of different chain lengths (3 and 11 ethyl-oxy frame). Thus, the distance between paclitaxel and the hydrophobic chain of squalene was increased from 2.35 Å (compound **1**) to 6.27 Å (compound **4**) or 23.34 Å (compound **5**), measured as the Boltzmann-weighted mean distance among all stable conformers (Table 1).

The 3-oxa moiety of compound **3** was intended to increase the susceptibility to hydrolysis of the 2′-acyl group of the cross-

Table 2. Physicochemical Chatacterization and Stability of Squalenoyl−Paclitaxel Nanoassemblies[a]

compound	size (nm)[b]	P.I.[b]	ζ potential (mV)[b]	CAC (mg/L)[c]	NA stability (size, nm) after 24 h, 20 °C[d] (water 30 d)	pH 4	pH 7	pH 9
1 PTXSQ	117.7 ± 7	0.087	−36.88	0.2	128.4 ± 6	120.9 ± 4	120.0 ± 5	121.4 ± 8
2 PTXsuccSQ	140.7 ± 11	0.097	−44.33	0.09	143.9 ± 12	149.1 ± 8	147.1 ± 9	144.8 ± 10
3 PTXdiglSQ	121.3 ± 13	0.129	−38.03	0.2	122.8 ± 10	126.7 ± 9	124.7 ± 11	1251 ± 9
4 PTXPEG$_3$SQ	285.2 ± 13	0.245	−41.42	0.3	288.0 ± 19	291.0 ± 13	289.4 ± 16	285.1 ± 9
5 PTXPEG$_{11}$SQ	293.4 ± 21	0.317	−40.88	0.4	297.9 ± 18	294.7 ± 20	298.7 ± 17	303.8 ± 28

[a] All formulations were prepared using nanoprecipitation technique at a concentration of 2 mg/mL aqueous nanodispersions. [b] Particle mean diameter, polydispersity index (P.I.) and charge were determined using a Brookhaven Nanosizer. [c] Critical aggregation concentration (CAC) measurement by pyrene was obtained from a ratio between I373 and I384 as a function of concentration. [d] Stability was assessed by measuring the size of samples diluted with water (checked after one month at 5 °C) and in acidic (pH 4), neutral, and basic (pH 9) conditions at 20 °C for 24 h. Abbreviations as in Table 1.

linker, relative to the succinic analogues, by increasing the distance between paclitaxel and squalene and so the accessibility to the linkage.

The 2′-acyl paclitaxel derivatives (**1** or paclitaxel−succinate intermediate) were prepared selectively by exploiting the difference in reaction rates between the paclitaxel 2′- and 7-hydroxyl groups (*27*). Under the reaction conditions used here, the majority of paclitaxel was consumed before significant levels of the 2′,7-diacyl product had been generated. High yield of disubstituted prodrug were only obtained by increasing the molar ratio of 1,1′,2-tris-norsqualenoic acid and of the condensing agent (data not shown). Prodrugs with the succinic spacer were synthesized using the reactive paclitaxel-succinyl-NHS ester and the corresponding amine, whereas the prodrug with 2′-diglycolate spacer was synthesized by reaction of the squalene alcohol with diglycolic anhydride before reaction with the condensing agent and paclitaxel.

Lipophilic Behavior. The squalenoyl−paclitaxel derivatives were further characterized by evaluating the relative lipophilicity factor (Rm), following the procedure described by Biagi (*18*) where the Rm value was extrapolated to 100% water (R_{m0}). The partitioning of paclitaxel derivatives between a nonpolar stationary and a polar phase is a function of their structure in the medium, and under these conditions, Rm values were very similar among the different derivatives (Table 1). The addition of PEG chains has significantly increased the hydrophilic nature of the conjugates. This experimental evaluation was compared with theoretical logP values. Thus, it has been observed that squalene moiety (SQ) dramatically increased the lipophilicity of paclitaxel, and even the presence of a long hydrophilic spacer (PEG_{11}) did not greatly lower the logP value. Furthermore, a substantial agreement was observed between the theoretical and experimental evaluations (linear regression slope 1.98, sd 0.07), which confirmed the goodness of computational approach even for highly hydrophobic compounds.

Nanoassemblies: Preparation and Characterization. The squalenoyl−paclitaxel prodrugs were formulated into nanoassemblies in water, using simple nanoprecipitation technique without the aid of surfactants. These aqueous NA suspensions were found to be physically stable as measured by particle size, at a standard concentration of 2 mg/mL.

It is noteworthy that all the squalenoyl−paclitaxel derivatives formed NAs in water after solvent displacement. This was a priori unexpected with regard to the dramatic lipophilicity and absence of amphiphilicity of the different conjugates. Interestingly however, the paclitaxel derivatives not containing squalene moiety (i.e., paclitaxel, paclitaxel−succinate, and PEG derivatives) failed to form NAs but precipitated into macro-aggregates when processed using the same conditions. It is hypothesized that the ability of the squalenoyl−paclitaxel conjugates to spontaneously form NAs in water resulted from the irreplaceable squalene's molecular flexibility and dynamically folded conformation, unlike from the single amphiphilicity of the conjugates that was previously suggested for squalenoyl−gemcitabine (*23*). In this context and for comparison, a physical mixture of paclitaxel (1 mg) dissolved in ethanol, 1,1′,2-trisnorsqualene-MePEG (M_w 2200) (5 mg), and 1,1′,2-trisnorsqualenoic acid (10 mg) was also prepared by nanoprecipitation; however, these nanoparticles were unstable and underwent rapid aggregation.

This unique ability of the squalenoyl−paclitaxel derivatives to form NAs in water was further confirmed by the critical aggregation concentration (CAC) measurement, using pyrene

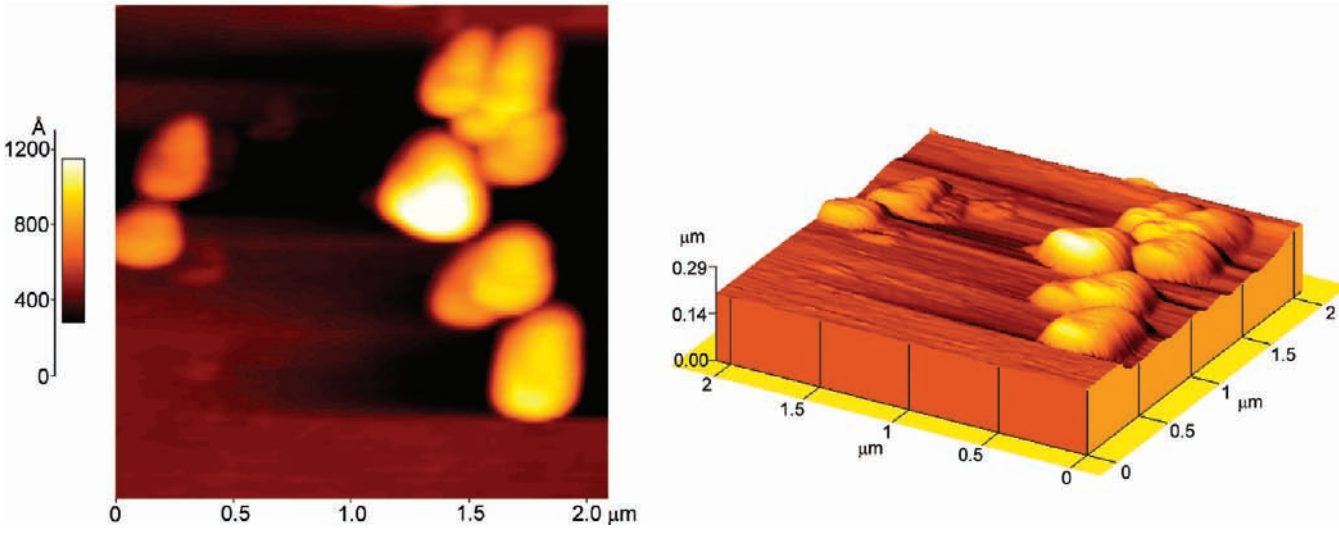


Figure 1. AFM images underwater by noncontact mode of 2′-tris-norsqualenoyl−paclitaxel (**1**) nanoassemblies after sample deposition on mica support: topography on the left and 3D view on right.

as hydrophobic fluorescent probe. In the emission spectra of pyrene, the value of I373/I384 emission intensity ratio was found to be very sensitive to the polarity of the medium surrounding the pyrene molecules. The higher this value was, the higher the polarity of the medium. From the plot of fluorescence intensity ratio (I373/I384) versus concentration, an abrupt decrease of this ratio was observed at a critical concentration (CAC), indicating the formation of aggregates and the transfer of pyrene into the hydrophobic core of the aggregates (*22*). Table 2 shows that the CAC value of the different NAs varied from 0.09 to 0.4 mg/L, which permits their use in very dilute aqueous media such as body fluids. This was an interesting finding demonstrating that all the very hydrophobic squalenoyl−paclitaxel conjugates resulted in the effective formation of nanosized self-assemblies, composed of a more rigid part (paclitaxel) and regions having some degree of flexibility (squalenoyl− or PEG−squalenoyl domains). It has to be noted that the observed CAC values were lower than those of polymeric micelles used for drug delivery purposes, such as poly(L-lactic acid) grafted chondroitin sulfate (5.0 mg/L) (*31*), PLGA grafted poly(L-lysine) (1.0−9.6 mg/L) (*32*), hyaluronic acid−paclitaxel conjugate (7.8 mg/L) (*33*) and similar to lactose-functionalized ribavirin-conjugating amphiphilic random copolymer (*34*).

With the respective contribution of the molecular weights of paclitaxel and squalene in the different synthesized derivatives, the paclitaxel loading into the NAs ranged from 45% to 69% of the entire mass. Thus, drug loading in these nanoassembly formulations is considerably higher than with other currently available nanocarriers such as liposome (3%) (*35*), tocopherol nanoemulsion (8%) (*36*), Abraxane (10%) (*37*), and Genexol-PM (20%) (*38*). NAs with high drug loading could be of considerable importance where small administration volume is allowed, such as intra-arterial administration for locoregional treatments (*39*).

The morphology of NAs was investigated by atomic force microscopy (AFM) and transmission electron microscopy (TEM). A topography AFM image and the related 3D reconstruction of compound **1**, as reference, is presented in Figure 1. As evident from the images, spherical soft structures with a certain degree of aggregation appeared. The observed topographical changes (slightly deformed structures) could have been influenced by different factors as previously described for other "soft" delivery systems such as liposomes (*21*), particularly the interaction between the sample and the substrate, and the vertical force applied by the tip on the sample during the scanning procedure. The noncontact mode was employed, since it had less probability in damaging the samples than the tapping mode, owing to the elimination of the possible dragging of the sample when the tip moved across the NA. Nevertheless, the vertical force applied by the tip on the vesicles during the scanning procedure could induce deformation of squalenoyl−paclitaxel NA.

The TEM image provided evidence for the spherical morphology and dimension (∼100 nm) of the nanoassemblies (Figure 2). Slight differences in morphology were seen for the other prodrug compositions (data not shown).

As represented in Table 2, the NA size increased progressively with the increase in molecular mass of the conjugate, ranging from about 110 to 300 nm, but in all the cases with a prevailing unimodal size distribution. As the PEG length increased, the mean size and polydispersity of the nanoassemblies increased. The zeta potential measurement revealed a global negative charge for all NA formulations (from −30 to −45 mV) predicting long-term stability of the nanosuspensions, due to particle electrostatic repulsion.

From these observations, the influence of the squalenoyl moiety on the ability of paclitaxel conjugates to spontaneously form nanoassemblies became evident. This may be explained by the fact that squalene, a natural acyclic molecule, has the unique property of being transformed into the cyclic derivative lanosterol (a precursor of the cholesterol) by spontaneously passing through a highly coiled, compact conformation, without the aid of either coenzymes or biochemical energy (ATP). The flexibility of squalene molecule and the possibility of assuming many different conformations with similar stability certainly help this molecule in reaching the hydrophobic pocket of the enzyme (i.e., oxidosqualene cyclase) in which the cyclization occurs (*40*). We assume that this unique folded molecular conformation of the squalene help in the nanoparticle formation. Noteworthy, it was previously shown that the conjugation of gemcitabine to squalene let to a supramolecular organization as inverted hexagonal phases (*41*), whereas the conjugation of 2′,3′-dideoxycytidine to squalene formed nanoparticles of similar sizes but with a cubic structure (*6*). It has to be noted that these bioconjugates were highly amphiphilic, which may explain the observed structures. This is not the case for the squalenoyl−paclitaxel conjugates (except when using PEG as a spacer arm), which are totally lipophilic. Additional experiments by means of high-resolution synchrotron X-ray diffraction are required to investigate in more detail the supramolecular organization of squalenoyl−paclitaxel NA.

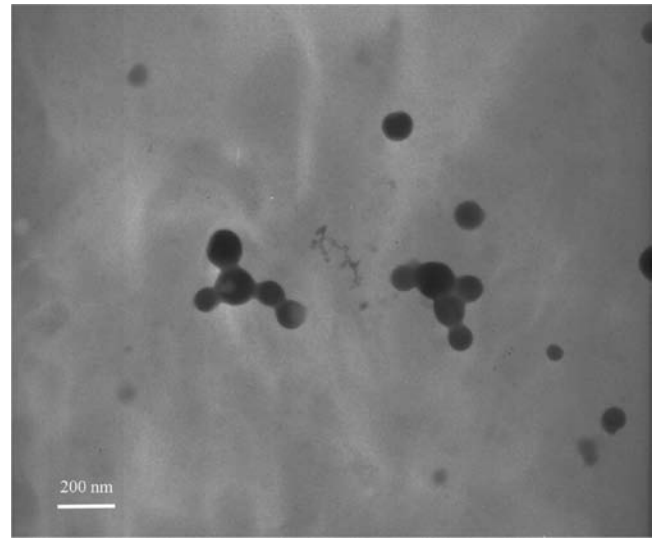


Figure 2. Transmission electron micrograph of 2′-tris-nor-squalenoyl−paclitaxel (compound **1**) nanoassemblies obtained at 18 000× magnification.

Stability of NA and Bioconjugates. The physical stability of the squalenoyl−paclitaxel bioconjugate NAs and paclitaxel release from these NAs were assessed in different media, varying the pH values, while the stability of the linkage was also tested in human serum. The NAs formed from various types of the synthesized bioconjugates were found to be remarkably stable in water, and the aqueous NA suspensions of 2−4 mg/mL were stable at 5 °C for a three-month period without any significant size modification. Moreover, the size of the NAs of all the conjugates remained unchanged upon dilution into water (data not shown). The NAs suspensions, at a concentration of 2 mg/mL, remained physically stable also in both acidic and basic media for 24 h at room temperature (Table 2). To evaluate the chemical stability of the ester linkage (direct or via succinate or diglycolate spacers) of the bioconjugates, the NAs were diluted at different pH as well as in serum (Figure 3) and incubated at 37 °C. These experimental conditions allowed investigation of the different hydrolytic behaviors derived by the spacer moiety. Compound **1**, paclitaxel 2′-squalenoyl ester, demonstrated very high stability in all the media studied, with

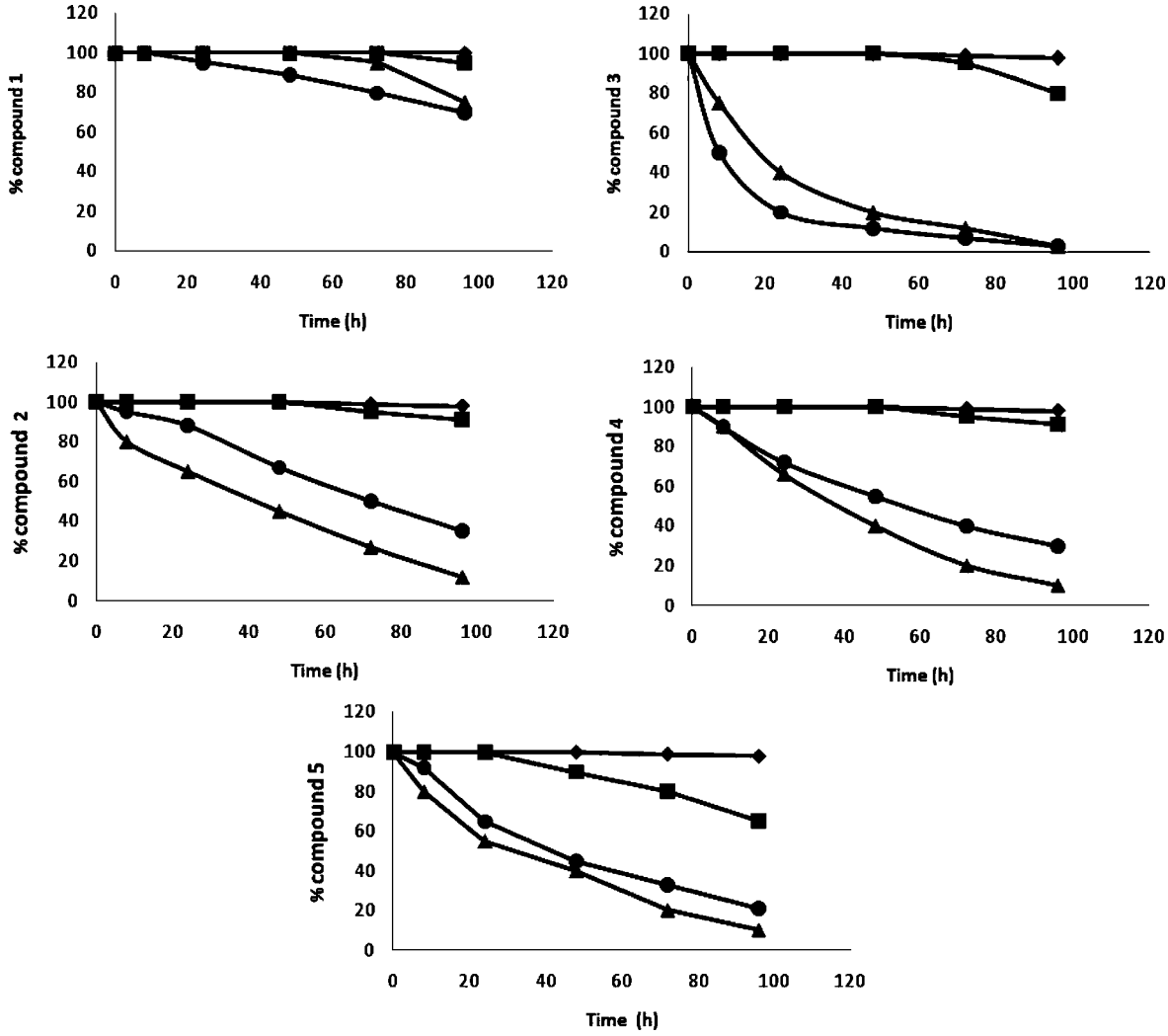


Figure 3. Stability of squalenoyl−paclitaxel prodrugs under various conditions: sodium acetate buffer (♦) pH 4.5, sodium phosphate buffer (■) pH 7.4, sodium borate buffer (▲) pH 9.0, and human serum (•) at 37 °C for different times.

no more than 40% of the conjugate being hydrolyzed after 96 h. The diglycolate linkage (compound **3**) was found to be more susceptible to hydrolysis than the succinate linkage (compound **2**) as reported by Nicolaou (*42*); indeed, the diglycolate prodrug was rapidly hydrolyzed in serum, and only 20% of the initial quantity of the conjugate remained intact after 24 h, whereas the succinate prodrug was cleaved to the same extent only after 4 days of incubation. Hydrolysis was not observed when the samples were incubated at pH 4.5 or pH 7.4. Only in mild borate basic media (pH 9.0) was a progressive release of paclitaxel observed (Figure 4), confirmed by HPLC-MS analysis.

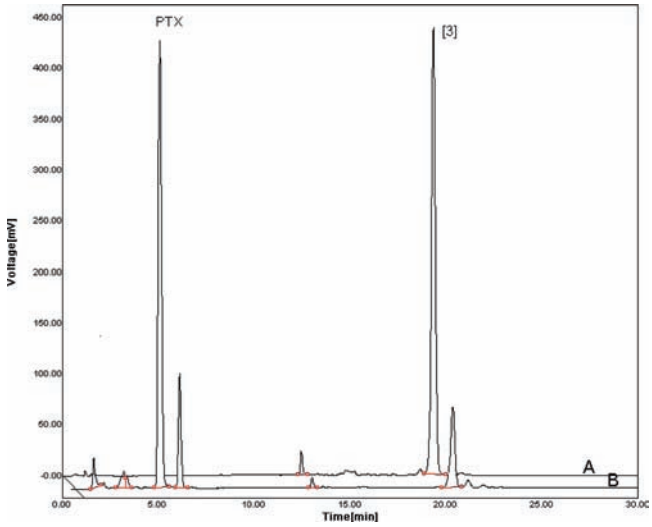


Figure 4. Example of the stability measurement of a squalenoyl−paclitaxel prodrug and release of free paclitaxel (PTX) after incubation in buffer and in serum. HPLC profile of compound **3** (squalenoyl-diglycoloyl-paclitaxel) before (A) and after (B) incubation in BSB for 48 h at 37 °C.

The release of paclitaxel from the bioconjugates following incubation in serum is attributed to the hydrolysis caused by the esterases activity of serum. Indeed, the paclitaxel 2′-esters and carbonates demonstrated to be good substrates for these enzymes (*43*).

Regarding the synthesis of the conjugates containing PEG, we used only succinate linker as a spacer, because diglycolate may give rise to extreme instability of paclitaxel C-2′ derivatives (*44*) even in acidic media. It has been observed that, in comparison to the succinate prodrug (compound **2**), the addition of a PEG chain (compounds **4** and **5**) increased the hydrolysis rate of the conjugates, both in basic medium and in serum; this behavior was accentuated if a longer PEG spacer was used (Figure 3).

Microtubule Bundle Formation as Determined by Immunofluorescence. Because microtubules are the major target for the antimitotic paclitaxel, a test based on microtubule

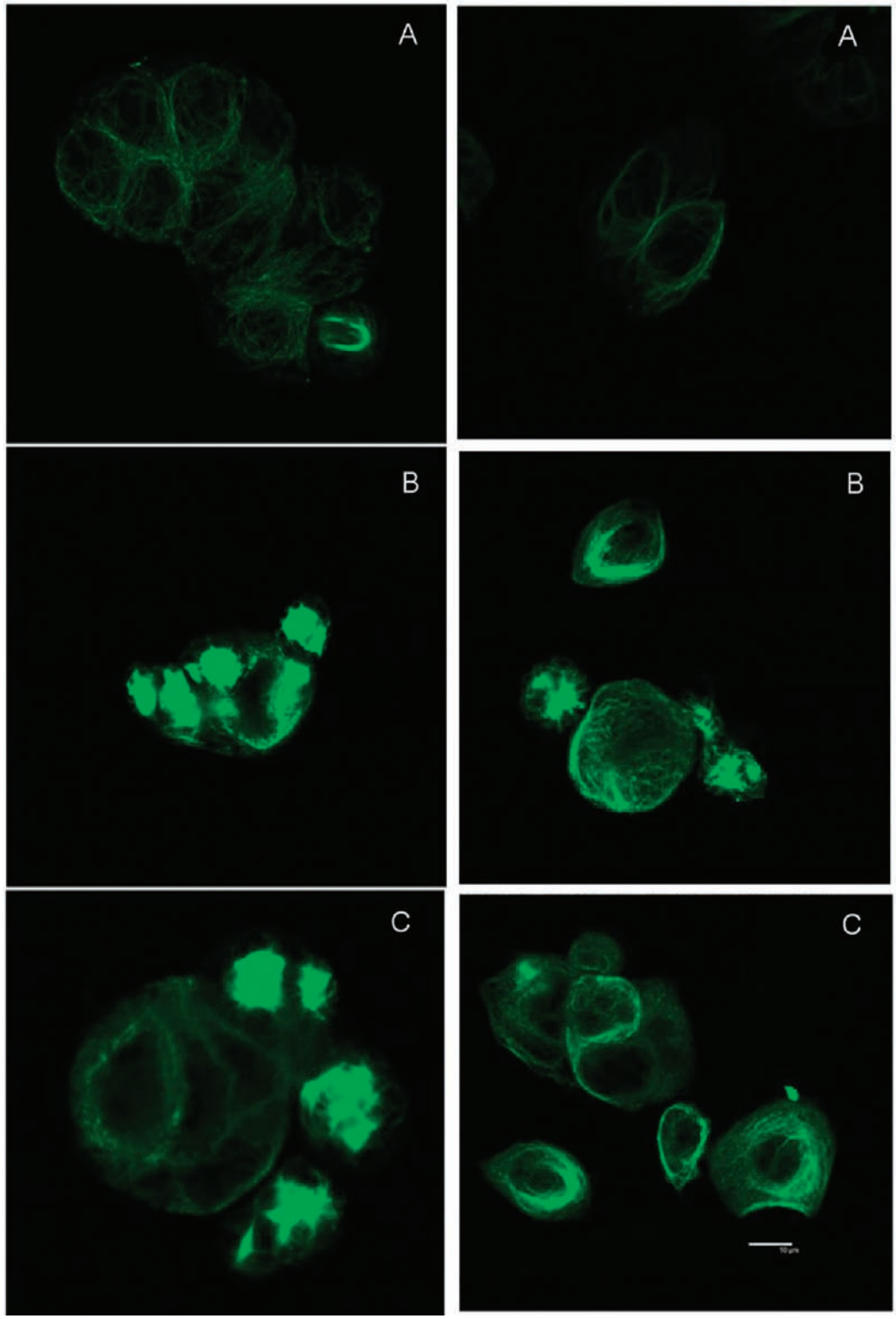


Figure 5. Microtubule bundle formation induced by paclitaxel and 2′-tris-norsqualenoyl−paclitaxel (compound **1**) in cultured HT-29 cells (left) and KB-31 (right). Cells were incubated with FITC antitubulin antibody after exposure to paclitaxel 100 nM (panel B) and compound **1** at 5 μM (panel C) for 14 h. Panel A, control (solvent).

bundle formation was carried out. Indeed, paclitaxel stabilizes the intrinsically unstable microtubule polymer, promotes assembly, and suppresses microtubule dynamics (*45*). In addition, paclitaxel affects the structure by decreasing protofilament and increasing microtubule flexibility (*46*).

A proliferating culture of HT-29 and KB-31 cells was treated with 0.1 μM paclitaxel or 5 μM compound **1** and examined for microtubule bundle formation, essentially as described by Bradley (*47*). As shown in Figure 5C, exposure of the cells to compound **1** resulted in the formation of extensive microtubule bundles in both cell lines, which were similar to the changes induced by paclitaxel (Figure 5B). Since the pharmacological activity of the prodrug occurred at a dose 50 times higher than paclitaxel, it is assumed that only the fraction of paclitaxel that was released from the conjugate nanoparticles could induce microtubule bundle formation. It is, indeed, unlikely that the bioconjugate by itself could promote bundle formation. Similar observation has been reported for Taxoprexin (DHA−paclitaxel

Table 3. In Vitro Anticancer Activity of Squalenoyl−Paclitaxel Nanoassemblies on M109 Murine Lung Carcinoma Cell Line (MTT Test)[a]

compound	IC_{50}(nM)
PTX	9.0 ± 2.65
PTX+SQCOOH+SQPEG mix	14.0 ± 3.0
3 PTXdiglSQ	175.0 ± 5.51
2 PTXsuccSQ	365.0 ± 5.3
4 $PTXPEG_3SQ$	490.0 ± 4.58
5 $PTXPEG_{11}SQ$	6450.0 ± 7.0
1 PTXSQ	16500.0 ± 7.81

[a] The cells were incubated with various concentrations of PTX-SQ nanoassemblies for 72 h. Abbreviations as in Table 1.

conjugate), a very promising slow-release conjugate currently in phase II clinical trials. In both cases, cell metabolism is necessary to convert the conjugates to paclitaxel in order to induce microtubule bundle formation (*47*).

In Vitro Activity. Squalenoyl-paclitaxel nanoassemblies cytotoxicity was evaluated using the M109 murine lung carcinoma cell line (Table 3). For comparison purposes, paclitaxel and a freshly prepared mixture of paclitaxel, 1,1′,2-trisnorsqualenoic acid (SQCOOH) and 1,1′,2-trisnorsqualene-MePEG (SQPEG) were used as a control.

Comparison of the dose−response curves obtained for paclitaxel and squalenoyl−paclitaxel nanoassemblies revealed that the conjugation of paclitaxel to squalene decreased the cytotoxicity toward M109 cell line (Table 3). Whereas paclitaxel displayed efficient cytotoxicity (IC_{50} of 9 nM), the various squalenoyl−paclitaxel conjugates exhibited different IC_{50} values (Table 3). The cytotoxicity of compound **1** was in the micromolar range (mention IC_{50} value), an activity comparable to that of Taxoprexin (*48*), formulated using 10% Cremophor EL-P/10% ethanol/80% normal saline.

A progressive increase in the cytotoxicity of squalenoyl−paclitaxel conjugates was evident in the order of PEG derivatives, succinyl linkage, and diglycolate linkage. The succinate-linked prodrug (compound **2**) was found to be approximately 30 times less potent than paclitaxel free against M109 cells. This lower cytotoxicity of the succinate-linked prodrug was likely due to the resistance of the succinate group to hydrolysis. By increasing the length of the spacer with PEG moieties (comparison of compounds **2**, **4**, and **5**) and maintaining the same succinyl linkage on squalenoyl−paclitaxel, a further decrease in cytotoxicity occurred, respectively, of 1.3 and 18 times (for compounds **4** and **5**, as compared to compound **2**). As envisaged, the squalenoyl−paclitaxel NAs with the diglycolate linker moiety (compound **3**), which was expected to be more susceptible to hydrolysis because of the presence of the 3-oxa group, displayed the best cytotoxicity comparatively to the other conjugates tested, but was 1 order of magnitude less potent than free paclitaxel. These results are consistent with the reports on hydrolyzable hydrophobic taxane derivatives (*49*). Contrarily, the cytotoxicity of the control mixture of paclitaxel, 1,1′,2-trisnorsqualenoic acid, and 1,1′,2-trisnorsqualenoyl-PEG displayed an IC_{50} value very close to that of paclitaxel, revealing that the squalene component neither enhanced nor significantly reduced the in vitro activity of the free drug in this mixture.

CONCLUSIONS

This study demonstrated that the conjugation of a hydrophobic drug such as paclitaxel to squalene resulted in bioconjugates capable of self-assembling into nanoparticles in aqueous media, despite their marked hydrophobic character. It was noteworthy that these NA, which were characterized by impressively high drug loading (from 45% to 69%) did not require any added surface-active agent, which, from a toxicological point of view, would be a major advantage for intravenous administration of the conjugated drugs. The most promising cytotoxicity displayed by diglycolate linker-based prodrug compared to that of the other prodrugs synthesized suggests its candidature for further in vivo assays. In a nutshell, squalenoylation represents a new option to facilitate the drugability of poorly soluble therapeutic agents as injectable nanoparticles.

ACKNOWLEDGMENT

The research leading to these results has received funding from the Italian Ministry of University and Research (PRIN) and European Research Council under the European Community's Seventh Framework Programme FP7/2007-2013 Grant Agreement no. 249835. The authors are thankful to Barbara Ruozi for atomic force microscopy analysis and to Paolo Tosco for computation analysis.

LITERATURE CITED

(1) Penuelas, J., and Munne-Bosch, S. (2005) Isoprenoids: an evolutionary pool for photoprotection. *Trends Plant Sci. 10*, 166–169.
(2) Ourisson, G. (1989) The evolution of terpenes to sterols. *Pure Appl. Chem. 61*, 345–348.
(3) Couvreur, P., Stella, B., Reddy, L. H., Hillaireau, H., Dubernet, C., Desmaele, D., Lepetre-Mouelhi, S., Rocco, F., Dereuddre-Bosquet, N., Clayette, P., Rosilio, V., Marsaud, V., Renoir, J.-M., and Cattel, L. (2006) Squalenoyl nanomedicines as potential therapeutics. *Nano Lett. 6*, 2544–2548.
(4) Reddy, L. H., Dubernet, C., Mouelhi, S. L., Marque, P. E., Desmaele, D., and Couvreur, P. (2007) A new nanomedicine of gemcitabine displays enhanced anticancer activity in sensitive and resistant leukemia types. *J. Controlled Release 124*, 20–27.
(5) Reddy, L. H., Khoury, H., Paci, A., Deroussent, A., Ferreira, H., Dubernet, C., Decleves, X., Besnard, M., Chacun, H., Lepetre-Mouelhi, S., Desmaele, D., Rousseau, B., Laugier, C., Cintrat, J. C., Vassal, G., and Couvreur, P. (2008) Squalenoylation favorably modifies the in vivo pharmacokinetics and biodistribution of gemcitabine in mice. *Drug Metab. Dispos. 36*, 1570–1577.
(6) Bekkara-Aounallah, F., Gref, R., Othman, M., Reddy, L. H., Pili, B., Allain, V., Bourgaux, C., Hillaireau, H., Lepetre-Mouelhi, S., Desmaele, D., Nicolas, J., Chafi, N., and Couvreur, P. (2008) Novel PEGylated nanoassemblies made of self-assembled squalenoyl nucleoside analogues. *Adv. Funct. Mater. 18*, 3715–3725.
(7) Crown, J., O'Leary, M., and Ooi, W.-S. (2004) Docetaxel and paclitaxel in the treatment of breast cancer: a review of clinical experience. *Oncologist 9*, 24–32.
(8) Dhillon, T., Stebbing, J., and Bower, M. (2005) Paclitaxel for AIDS-associated Kaposi's sarcoma. *Expert Rev. Anticancer Ther. 5*, 215–219.
(9) Ramalingam, S., and Belani, C. P. (2004) Paclitaxel for non-small cell lung cancer. *Expert Opin. Pharmacother. 5*, 1771–1780.
(10) Thomas, H., and Rosenberg, P. (2002) Role of weekly paclitaxel in the treatment of advanced ovarian cancer. *Crit. Rev. Oncol. Hematol. 44*, S43–S51.
(11) Rosenthal, D. I., Harris, J., Forastiere, A. A., Weber, R. S., Ridge, J. A., Myers, J. N., Garden, A. S., Kuettel, M. R., Sidhu, K., Schultz, C. J., Trotti, A., and Ang, K. K. (2009) Early postoperative paclitaxel followed by concurrent paclitaxel and cisplatin with radiation therapy for patients with resected high-risk head and neck squamous cell carcinoma: report of the phase II trial RTOG 0024. *J. Clin. Oncol. 27*, 4727–32.
(12) Gelderblom, H., Verweij, J., Nooter, K., and Sparreboom, A. (2001) Cremophor EL: the drawbacks and advantages of vehicle selection for drug formulation. *Eur. J. Cancer 37*, 1590–1598.
(13) Ceruti, M., Balliano, G., Viola, F., Cattel, L., Gerst, N., and Schuber, F. (1987) Synthesis and biological activity of aza-squalenes, bis-azasqualenes and derivatives. *Eur. J. Med. Chem. 22*, 199–208.
(14) Duriatti, A., Bouvier-Nave, P., Benveniste, P., Schuber, F., Delprino, L., Balliano, G., and Cattel, L. (1985) In vitro inhibition of animal and

higher plants 2,3-oxidosqualene-sterol cyclases by 2-aza-2,3- dihydrosqualene and derivatives, and by other ammonium-containing molecules. *Biochem. Pharmacol. 34*, 2765–2777.

(15) Dosio, F., Brusa, P., Crosasso, P., Arpicco, S., and Cattel, L. (1997) Preparation, characterization and properties in vitro and in vivo of a paclitaxel-albumin conjugate. *J. Controlled Release 47*, 293–304.

(16) Luo, Y., and Prestwich, G. D. (2001) Hyaluronic acid-N-hydroxysuccinimide: A useful intermediate for bioconjugation. *Bioconjugate Chem. 12*, 1085–1088.

(17) Ogura, H., Nagai, S., and Takeda, K. (1980) A novel reagent (N_succinimidyl diphenylphosphate) for synthesis of active ester and peptide. *Tetrahedron Lett. 21*, 1467–1468.

(18) Biagi, G. L., Guerra, M. C., and Barbaro, A. M. (1970) Relation between lipophilic character and hemolytic activity of testosterone and testosterone esters. *J. Med. Chem. 13*, 944–948.

(19) Csermely, T., Kalasz, H., Deak, K., Hasan, M. Y., Darvas, F., and, and Petroianu, G. (2008) Lipophilicity determination of some ACE inhibitors by TLC. *J. Liq. Chromatogr. Relat. Technol. 31*, 2019–2034.

(20) Tetko, I. V., Gasteiger, J., Todeschini, R., Mauri, A., Livingstone, D., Ertl, P., Palyulin, V., Radchenko, E., Zefirov, N. S., Makarenko, A. S., Tanchuk, V. Y., and Prokopenko, V. V. (2005) Virtual computational chemistry laboratory - design and description. *J. Comput.-Aided Mol. Des. 19*, 453–463.

(21) Ruozi, B., Tosi, G., Forni, F., Fresta, M., and Vandelli, M. A. (2005) Atomic force microscopy and photon correlation spectroscopy: Two techniques for rapid characterization of liposomes. *Eur. J. Pharm. Sci. 25*, 81–89.

(22) Kalyanasundaram, K., and Thomas, J. K. (1977) Environmental effects on vibronic band intensities in pyrene monomer fluorescence and their application in studies of micellar systems. *J. Am. Chem. Soc. 99*, 2039–2044.

(23) Couvreur, P., Stella, B., Reddy, L. H., Hillaireau, H., Dubernet, C., Desmaele, D., Lepetre-Mouelhi, S., Rocco, F., Dereuddre-Bosquet, N., Clayette, P., Rosilio, V., Marsaud, V., Renoir, J. M., and Cattel, L. (2006) Squalenoyl nanomedicines as potential therapeutics. *Nano Lett. 6*, 2544–2548.

(24) Reddy, L. H., and Couvreur, P. (2008) Novel approaches to deliver gemcitabine to cancers. *Curr. Pharm. Des. 14*, 1124–1137.

(25) Greenwald, R. B., Gilbert, C. W., Pendri, A., Conover, C. D., Xia, J., and Martinez, A. (1996) Drug delivery systems: water soluble taxol 2′-poly(ethylene glycol) ester prodrugs design and in vivo effectiveness. *J. Med. Chem. 39*, 424–431.

(26) Magri, N. F., and Kingston, D. G. (1988) Modified taxols, 4. Synthesis and biological activity of taxols modified in the side chain. *J. Nat. Prod. 51*, 298–306.

(27) Deutsch, H. M., Glinski, J. A., Hernandez, M., Haugwitz, R. D., Narayanan, V. L., Suffness, M., and Zalkow, L. H. (1989) Synthesis of congeners and prodrugs. 3. Water-soluble prodrugs of taxol with potent antitumor activity. *J. Med. Chem. 32*, 788–92.

(28) Liu, C. H., Strobl, J. S., Bane, S., Schilling, J. K., McCracken, M., Chatterjee, S. K., Rahim-Bata, R., and Kingston, D. G. I. (2004) Design, synthesis, and bioactivities of steroid-linked taxol analogues as potential targeted drugs for prostate and breast cancer. *J. Nat. Prod. 67*, 152–159.

(29) Takahashi, T., Tsukamoto, H., and Yamada, H. (1998) Design and synthesis of a water-soluble taxol analogue: Taxol-sialyl conjugate. *Bioorg. Med. Chem. Lett. 8*, 113–116.

(30) Greenwald, R. B., Pendri, A., and Bolikal, D. (1995) Highly water soluble taxol derivatives: 7-polyethylene glycol carbamates and carbonates. *J. Org. Chem. 60*, 331–336.

(31) Lee, C. T., Huang, C. P., and Lee, Y. D. (2006) Preparation of amphiphilic poly(L-lactide)-graft-chondroitin sulfate copolymer self-aggregates and its aggregation behavior. *Biomacromolecules 7*, 1179–1186.

(32) Wei, H., Zhang, X. Z., Cheng, C., Cheng, S. X., and Zhuo, R. X. (2007) Self-assembled, thermosensitive micelles of a star block copolymer based on PMMA and PNIPAAm for controlled drug delivery. *Biomaterials 28*, 99–107.

(33) Lee, H., Lee, K., and Park, T. G. (2008) Hyaluronic acid-paclitaxel conjugate micelles: synthesis, characterization, and antitumor activity. *Bioconjugate Chem. 19*, 1319–1325.

(34) Li, X., Wu, Q., Chen, Z., Gong, X., and Lin, X. (2008) Preparation, characterization and controlled release of liver-targeting nanoparticles from the amphiphilic random copolymer. *Polymer 49*, 4769–4775.

(35) Sharma, A., and Straubinger, R. M. (1994) Novel taxol formulations- preparation and characterization of taxol-containing liposomes. *Pharm. Res. 11*, 889–896.

(36) Constantinides, P. P., Lambert, K. J., Tustian, A. K., Schneider, B., Lalji, S., Ma, W. W., Wentzel, B., Kessler, D., Worah, D., and Quay, S. C. (2000) Formulation development and antitumor activity of a filter-sterilizable emulsion of paclitaxel. *Pharm. Res. 17*, 175–182.

(37) Ibrahim, N. K., Desai, N., Legha, S., Soon-Shiong, P., Theriault, R. L., Rivera, E., Esmaeli, B., Ring, S. E., Bedikian, A., Hortobagyi, G. N., and Ellerhorst, J. A. (2002) Phase I and pharmacokinetic study of ABI-007, a cremophor-free, protein-stabilized, nanoparticle formulation of paclitaxel. *Clin. Cancer Res. 8*, 1038–1044.

(38) Lee, K. S., Chung, H. C., Im, S. A., Park, Y. H., Kim, C. S., Kim, S. B., Rha, S. Y., Lee, M. Y., and Ro, J. (2008) Multicenter phase II trial of Genexol-PM, a Cremophor-free, polymeric micelle formulation of paclitaxel, in patients with metastatic breast cancer. *Breast Cancer Res. Treat. 108*, 241–250.

(39) Damascelli, B., Cantu, G., Mattavelli, F., Tamplenizza, P., Bidoli, P., Leo, E., Dosio, F., Cerrotta, A. M., Di Tolla, G., Frigerio, L. F., Garbagnati, F., Lanocita, R., Marchiano, A., Patelli, G., Spreafico, C., Ticha, V., Vespro, V., and Zunino, F. (2001) Intraarterial chemotherapy with polyoxyethylated castor oil free paclitaxel, incorporated in albumin nanoparticles (ABI-007) - Phase I study of patients with squamous cell carcinoma of the head and neck and anal canal: Preliminary evidence of clinical activity. *Cancer 92*, 2592–2602.

(40) Pogliani, L., Milanesio, M., Ceruti, M., and Viterbo, D. (1999) Conformational and dynamical study of squalene derivatives. III: azasqualenes and solvated squalene. *Chem. Phys. Lipids 103*, 81–93.

(41) Couvreur, P., Reddy, L. H., Mangenot, S., Poupaert, J. H., Desmaele, D., Lepetre-Mouelhi, S., Pili, B., Bourgaux, C., Amenitsch, H., and Ollivon, M. (2008) Discovery of new hexagonal supramolecular nanostructures formed by squalenoylation of an anticancer nucleoside analogue. *Small 4*, 247–253.

(42) Nicolaou, K. C. R., C., Kerr, M. A., Rideout, D., and Wrasidlo, W. (1993) Design, synthesis and biological activity of protaxols. *Nature 364*, 464–466.

(43) Tanino, T., Nawa, A., Miki, Y., and Iwaki, M. (2008) Enzymatic stability of 2′-ethylcarbonate-linked paclitaxel in serum and conversion to paclitaxel by rabbit liver carboxylesterase for use in prodrug/enzyme therapy. *Biopharm. Drug Dispos. 29*, 259–269.

(44) Jae Wook Lee, J. Y. L., P. S., and Low Fuchs, P. L. (2002) Synthesis and evaluation of taxol-folic acid conjugates as targeted antineoplastics. *Bioorg. Med. Chem. 10*, 2397–2414.

(45) Howard, W. D., and Timasheff, S. N. (1988) Linkages between the effects of taxol, colchicine, and GTP on tubulin polymerization. *J. Biol. Chem. 263*, 1342–1346.

(46) Dye, R. B., Fink, S. P., and Williams, R. C. (1993) Taxol-induced flexibility of microtubules and its reversal by MAP-2 and Tau. *J. Biol. Chem. 268*, 6847–6850.

(47) Bradley, M. O., Webb, N. L., Anthony, F. H., Devanesan, P., Witman, P. A., Hemamalini, S., Chander, M. C., Baker, S. D., He, L. F., Horwitz, S. B., and Swindell, C. S. (2001) Tumor targeting by covalent conjugation of a natural fatty acid to paclitaxel. *Clin. Cancer Res. 7*, 3229–3238.

(48) Shashoua V. E. S. C. E., Webb N.L., and Bradley M. O. (2004) DHA-pharmaceutical agent conjugates of taxanes, U.S. Patent 4,180,949.

(49) Ali, S., Ahmad, I., Peters, A., Masters, G., Minchey, S., Janoff, A., and Mayhew, E. (2001) Hydrolyzable hydrophobic taxanes: synthesis and anti-cancer activities. *Anti-Cancer Drugs 12*, 117–128.

BC100154G

Near-Infrared Fluorescent Probe for Imaging of Pancreatic β Cells

Thomas Reiner,[†] Rainer H. Kohler,[†] Chong Wee Liew,[‡] Jonathan A. Hill,[‡,§] Jason Gaglia,[‡,§] Rohit N. Kulkarni,[‡] and Ralph Weissleder*[,†,||]

Center for Systems Biology, Massachusetts General Hospital, 185 Cambridge Street, CPZN 5206, Boston, Massachusetts 02114, Department of Medicine, Joslin Diabetes Center, Harvard Medical School, Boston, Massachusetts 02215, Department of Pathology, Harvard Medical School, 77 Avenue Louis Pasteur, Boston, Massachusetts 02115, Department of Systems Biology, Harvard Medical School, 200 Longwood Avenue, Boston, Massachusetts 02115. Received April 19, 2010; Revised Manuscript Received June 4, 2010

The ability to image and ultimately quantitate β-cell mass in vivo will likely have far reaching implications in the study of diabetes biology, in the monitoring of disease progression or response to treatment, and for drug development. Here, using animal models, we report on the synthesis, characterization, and intravital microscopic imaging properties of a near-infrared fluorescent exendin-4 analogue with specificity for the GLP-1 receptor on β cells ($E4_{K12}$-Fl). The agent demonstrated subnanomolar EC_{50} binding concentrations, with high specificity and binding that could be inhibited by GLP-1R agonists. Following intravenous administration to mice, pancreatic islets were readily distinguishable from exocrine pancreas, achieving target-to-background ratios within the pancreas of 6:1, as measured by intravital microscopy. Serial imaging revealed rapid accumulation kinetics (with initial signal within the islets detectable within 3 min and peak fluorescence within 20 min of injection), making this an ideal agent for in vivo imaging.

INTRODUCTION

β-Cell mass (BCM) and the functional state of islets are critical measures when assessing the magnitude of autoimmune destruction in type 1 diabetes (T1D). Progressive loss of BCM is also believed to be causative in the secondary failure of many therapies in type 2 diabetes. Serum tests such as stimulated insulin or C-peptide do not reliably correlate with BCM, particularly at the extremes of BCM (*1*). The gold standard continues to be the laborious task of measurement at autopsy via morphometric methods. It is now believed that imaging technologies could ultimately be exploited to (a) better understand the history and pathophysiology of diabetes, (b) enable earlier diagnosis of T1D perhaps while in the occult phase, (c) allow monitoring of therapeutic efficacy and durability (including islet transplantation), and (d) facilitate the discovery of new therapies. Unfortunately, the necessary tools for reliably quantifying BCM in vivo have remained elusive.

A number of imaging agents with putative β cell specificity have been investigated, partly based on known markers/functions of these cells (e.g., glucose transporters or sulfonylurea receptors) and partly based on profiling studies (reviewed in *refs* 2−4). Many of the imaging studies to date have relied on isotope-labeled compounds including compounds targeting sulfonylurea receptors (*5*), neuroreceptors such as the presynaptic vesicular acetylcholine transporter (*6*), the vesicular monoamine transporter (VMAT2) using the neurotracer ^{11}C-dihydroterabenazine (^{11}C-DTBZ) (*7*−*10*), or an antibody against a pancreatic islet antigen (IC-2) (*11*). Unfortunately, these agents have not been proven effective for in vivo islet imaging, most likely on account of their failure to achieve the required high binding ratios necessary for macroscopic imaging or a lack of understanding of the physiology of the underlying target (*5*, *12*). Alternatively, to image at higher spatial resolution than possible with isotopic imaging techniques, a variety of fluorescent compounds have also been suggested. Labeled glucoses (*13*), fluorescent streptozotocin analogues (*14*), and Zn chelators (which bind zinc-rich insulin vesicles) (*15*), antibodies (*12*), or activatable fluorescent substrates for dipeptidyl peptidase 4 (DPP4) (*16*) have all been utilized. Many of these probes have been tested primarily in insulinoma or in other cells expressing high levels of glucose transporter 2 (GLUT2), where they have shown some success in vitro but not in vivo. However, it is not until recently that intravital imaging approaches have emerged as a method to validate the behavior of labeled agents in the pancreas in vivo (*17*−*20*). Indeed, when tested under rigorous conditions in NOD MIP-GFP (non-obese diabetic mouse insulin promoter-green fluorescent protein) mice using intravital imaging, we found that the majority of the above fluorescent agents failed to show the required target-to-background ratio (unpublished data).

On the basis of the recent success of therapeutic targeting of the glucagon-like peptide-1 receptor (GLP-1R) in the clinic with agonists (*21*, *22*), we hypothesized that certain fluorescent exendin-4 analogues could be used to image β cells in vivo but that detailed investigations would be necessary to ensure target binding of putative key compounds. In this report, we systematically investigated several analogues and characterized the most promising candidates before performing in vivo validation studies including intravital imaging. Our results demonstrated high islet specificity within the pancreas in vivo with the compound ($E4_{K12}$-Fl).

EXPERIMENTAL METHODS

Materials. All reagents were purchased from Sigma-Aldrich (St. Louis, MO) and used without further purification unless otherwise noted. Exendin-4 was obtained from Prospec (Reho-

* To whom correspondence should be addressed. Address: Center for Systems Biology, Massachusetts General Hospital, 185 Cambridge Street, CPZN 5206, Boston, MA 02114. Phone: 617-726-8226. E-mail: rweissleder@mgh.harvard.edu.

[†] Massachusetts General Hospital.

[‡] Joslin Diabetes Center, Harvard Medical School.

[§] Department of Pathology, Harvard Medical School.

[||] Department of Systems Biology, Harvard Medical School.

10.1021/bc100184w © 2010 American Chemical Society
Published on Web 06/29/2010

vot, Israel). Near-infrared fluorochrome Vivotag-680 (VT680-NHS ester) was purchased from VisEn (Bedford, MA). LC−ESI-MS analysis and HPLC purifications were performed on a Waters (Milford, MA) LC−MS system. For LC−ESI-MS analyses, a Waters XTerra C18 5 μm column was used. For preparative runs, an Atlantis Prep T3 OBD 5 μM column was used. MALDI-MS spectra were collected on a Voyager-DE Biospectrometry workstation spectrometer (Applied Biosystems, Foster City, CA).

Preparation of 11-Azido-3,6,9-trioxaundecan-1-amide-Fl. To a solution of 10 mg (46 μmol) of 11-azido-3,6,9-trioxaundecan-1-amine in 300 μL of 10× PBS, 2.5 mg (2 μmol) VivoTag 680 was added. The reaction solution was stirred at room temperature in the dark for 2 h. The crude mixture was directly subjected to HPLC purification, yielding 1.5 mg (1.1 μmol, 56%) of the title compound as a blue solid. LC−ESI-MS *m/z* (%) = 1342 $[M + H^+]^+$.

Preparation of $E4_{40}$-Fl. To a solution of 0.8 mg (0.2 μmol) of exendin-4 (40-Pra) in 400 μL of a 25 mM Tris-buffered aqueous solution (pH 7.2), 50 μL of a 50 mM solution of L-ascorbic acid in H_2O and 50 μL of a 50 mM aqueous $CuSO_4$ solution in H_2O were added. Then 0.4 mg (0.3 μmol) of 11-azido-3,6,9-trioxaundecan-1-amide-VT680 in 500 μL of 2× PBS solution was then added, and the reaction mixture was gently stirred at room temperature in the dark overnight. The crude mixture was diluted with 2 mL of 1× PBS and purified using an Amicon Ultra 3 kDa (Millipore, Carrigtwohill, Ireland) centrifugal filter, before it was subjected to HPLC purification, yielding 0.3 mg (0.05 μmol, 25%) of the title compound as a blue film. LC−ESI-MS *m/z* (%) = 1405 $[M - 4H^+]^{4-}$ (100); 1873 $[M - 3H^+]^{3-}$ (*14*).

Preparation of $E4_{K12}$-Fl. To a solution of 250 μg (0.06 μmol) of exendin-4 in 3.6 mL of a 25 mM Tris-buffered aqueous solution (pH 7.2), 1 mg of VivoTag 680 (0.8 μmol) was added. The reaction mixture was stirred at room temperature in the dark for 3 h. The mixture was subjected to HPLC purification, yielding the title compound as a blue solid (100 μg, 0.02 μmol, 33%). LC−ESI-MS *m/z* (%) = 1769 $[M - 3H^+]^{3-}$ (100).

MALDI MS Spectra. To a suspension of sinapinic acid (5 μL, 10 mg/mL, AcN/H_2O = 1/1, 0.5% TFA), 5 μL of protein sample (approximately 100 μM in H_2O) was added. The carefully mixed solution was purified via ZipTips (Millipore, Billercia, MA) prior to measurement. Each sample was also run with adrenocorticotropic hormone fragment 18−39 (ACTH fragment 18−39) as a calibration standard.

Tryptic Digest. To a solution of $E4_{K12}$-Fl (10.5 μL, approximately 10 μg), 15 μL of $NaHCO_3$ (50 mM) and 1.5 μL of dithiothreitol (DTT, 100 mM) were added. The mixture was incubated at 95 °C for 5 min. Subsequently, 3 μL of IAA (100 mM) was added, and the sample was incubated at room temperature for 20 min before 1 μL of activated trypsin (100 ng/μL, Pierce, Rockford, IL) was added. This was followed by an incubation at 37 °C for 3 h. An additional 1 μL of activated trypsin (100 ng/μL) was then added, and the sample was further incubated at 37 °C for 2 h before being purified using ZipTips (Millipore, Billerica, MA) and subjected to MALDI-MS analysis.

Cell Culture. Mouse insulinoma-derived MIN6 cells, courtesy of Dr. Miyazaki (*23*), were used between passages 26 and 40 and grown in high-glucose DMEM containing 15% (v/v) heat-inactivated FBS, 50 U/mL penicillin, and 10 μg/mL streptomycin as reported previously (*24*). HEK 293 cells, stably expressing human GLP-1R (HEK/hGLP-1R) (*25*), were grown in high glucose DMEM containing 10% (v/v) heat-inactivated FBS, 50 U/mL penicillin, 10 μg/mL streptomycin, 1 mM sodium pyruvate, and 150 μg/mL G418. NIH-3T3 fibroblasts (ATCC) were grown in high glucose DMEM containing 10% (v/v) heat-inactivated FBS, 50 U/mL penicillin, and 10 μg/mL streptomycin.

Western Blot. MIN6, HEK/hGLP-1R, or NIH-3T3 cells seeded into six-well plates were washed twice with ice-cold PBS and lysed on ice with 200 μL of ice-cold RIPA lysis buffer. Protein concentrations were determined using bicinchoninic acid (BCA) protein assays (Pierce, Rockford, IL). Cell lysates (50 μg) were subjected to SDS−PAGE, followed by immunoblotting using a specific anti-GLP-1R antibody (Abcam), and detection with chemiluminescence (Pierce, Rockford, IL).

Cellular Imaging. MIN6 (2×10^5 cells/well), HEK/hGLP-1R (7.5×10^4 cells/well), or NIH-3T3 (7.5×10^4 cells/well) cells were seeded into eight-well chamber slides (LabTek, Rochester, NY) and incubated for 48 h before incubation with 100 nM $E4_{K12}$-Fl for 30 min at 37 °C. Cells were washed three times with PBS before subjected to imaging. MIN6, HEK/hGLP-1R, and NIH 3T3 cells were imaged on an Olympus FluoView1000 confocal laser scanning microscope with an Olympus XLPan N 25× (NA. 1.1) water immersion objective and the FluoView 1000, version 2.1a program. $E4_{K12}$-Fl was imaged using a 635 nm laser, dichroic mirrors DM405/488/559/635 and SDM640, and a barrier filter BA655-755.

Dose-Response Assays. MIN6 (1×10^5 cells/well), HEK/hGLP-1R (3×10^4 cells/well), or NIH-3T3 (3×10^4 cells/well) cells were seeded into 96-well plates and incubated for 48 h before adding different concentrations of $E4_{K12}$-Fl. After incubating for 1 h at 37 °C, cells were washed three times with PBS and the fluorescence levels were measured with a SynergyMx plate reader (Biotek) with excitation at 620 nm and emission at 690 nm. Following fluorescence measurement, proteins were extracted using RIPA lysis buffers (*24*) and quantified using BCA (Pierce, Rockford, IL).

Blocking Experiments. MIN6 (1×10^5 cells/well), HEK/hGLP-1R (3×10^4 cells/well), or NIH-3T3 (3×10^4 cells/well) cells were seeded into 96-well plates and incubated for 48 h before incubation either with exendin-4 (100 nM) for 1 h at 37 °C and subsequently $E4_{K12}$-Fl (10 nM) for 1 h at 37 °C or with just $E4_{K12}$-Fl (10 nM) for 1 h at 37 °C. Following the incubation, cells were washed three times with PBS and the fluorescence levels were measured with a SynergyMx plate reader (Biotek) with excitation at 620 nm and emission at 690 nm. Following fluorescence measurement, proteins were extracted using RIPA lysis buffers (*24*) and quantified using BCA (Pierce, Rockford, IL).

Animals. NOD MIP-GFP mice (NOD.Cg-Tg(Ins-EGFP)Hara/QtngJ) that express the fluorescent protein EGFP within the islets under the mouse insulin 1 promoter were obtained from The Jackson Laboratory (Bar Harbor, ME). All procedures and animal protocols were approved by the subcommittee on Research Animal care at Massachusetts General Hospital.

Animal Preparation. Nondiabetic male NOD MIP-GFP mice were anesthetized with 2% isoflurane and 2 L/min O_2. The peritoneal cavity was opened with a transverse incision in the disinfected abdominal wall. The gastric−splenic ligament was dissected and the pancreas carefully exteriorized. Robust blood flow was observed in the pancreatic arteries for the duration of each experiment, and pancreas perfusion was confirmed by observation of a circulating fluorescent vascular agent (Angiosense 750, VisEn, Bedford, MA). The exteriorized pancreas was completely submerged in temperature-controlled lactated Ringer's solution. Temperature near the spleen was carefully monitored using an Omega HH12A thermometer with fine wire thermocouples (Omega Engineering Inc., Stamford, CT) and kept at 37 °C. A tail vein catheter, made using a 30G × $^1/_2$ in. needle inserted into CLAY ADAMS polyethylene 10 tubing, was inserted prior to surgery. Subsequently, 200 μL (4 nmol/200 μL) of $E4_{K12}$-F1 and 10 min after the initial injection, another 200 μL (4 nmol/200 μL) of $E4_{K12}$-Fl was injected via the tail vein catheter.

Name	Abbreviation	Amino Acid sequence	Length (aa)	NIRF mod	MW (kDa)
Glucagon-like peptide-1	GLP1	HAEGTFTSDVSSYLEGQAAKEFIAWLVKGR	30	none	3299
Exendin-4	E4	HGEGTFTSDLSKQMEEEAVRLFIEWLKNGGPSSGAPPPS	39	none	4188
Exendin-4(40-Pra)	$E4_{40}$-Pra	HGEGTFTSDLSKQMEEEAVRLFIEWLKNGGPSSGAPPPSX	40	none	4282
Exendin-4(40-Fl)	$E4_{40}$-Fl	HGEGTFTSDLSKQMEEEAVRLFIEWLKNGGPSSGAPPPSX(NIRF)	40	Pra40	5623
Exendin-4(K12Fl)	$E4_{K12}$-Fl	HGEGTFTSDLSK(NIRF)QMEEEAVRLFIEWLKNGGPSSGAPPPS	39	K12	5311

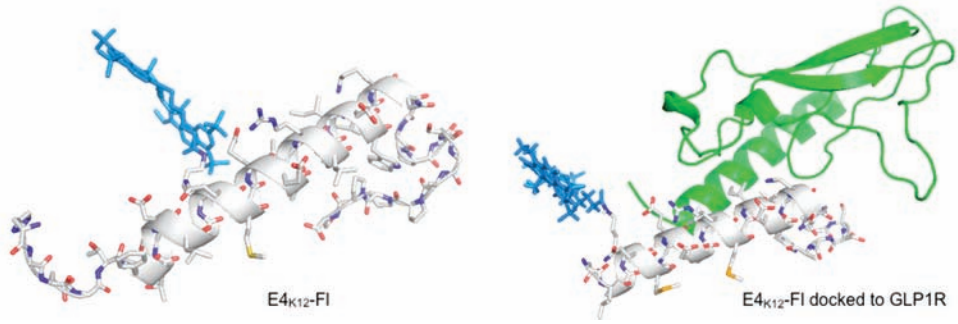


Figure 1. Top: Amino acid sequences, molecular weight and structures of synthesized fluorescent exendin-4 based compounds. Bottom left: Molecular model of exendin-4-like NIR fluorochrome, $E4_{K12}$-Fl, is based on the nuclear magnetic resonance (NMR)-structure, 1JRJ (*33*). Bottom right: Molecular model of exendin-4-like NIR fluorochrome $E4_{K12}$-Fl (amino acids 9−39) complexed with the extracellular domain of GLP-1R is based on the crystal structure 3C59 (*30*).

Intravital Laser Scanning Microscopy. Images were collected with a prototypical intravital laser scanning microscope (IV100, Olympus Corp., Tokyo, Japan) (*26*) using an Olympus 4× (UplanSApo NA 0.16) and 20× (UplanFL NA 0.5) objective and the Olympus FluoView FV300, version 4.3, program. Samples were excited at 488 nm with an air-cooled argon laser (Melles Griot, Carlsbad, CA) for visualization of the GFP expressing islet cells, at 633 nm with a HeNe-R laser (model 05LHP925, Melles Griot) for visualization of $E4_{K12}$-Fl and at 748 nm with a red diode laser (model FV10-LD748, Olympus Corp., Tokyo, Japan) for visualization of the blood pool agent (AngioSense-780, VisEn Medical, MA). Light was collected using custom-built dichroic mirrors SDM-560, SDM640, and SDM-750 and with emission filters BA 505-550, BA660-730, and BA 770 nm IF (Olympus Corp., Tokyo, Japan). The $E4_{K12}$-Fl signal was collected sequentially to the other channels to avoid bleed-through into the VT680 channel. A prototypical tissue stabilizer (Olympus Corp., Tokyo, Japan) was used to reduce motion and to stabilize the focal plane. The stabilizer was attached to the objective, and its *z*-position was finely adjusted using a micrometer screw to apply soft pressure on the tissue.

Histology. Nondiabetic male NOD MIP-GFP mice were cannulated with a tail vein catheter, made using a 30G × $^1/_2$ in. needle inserted into CLAY ADAMS polyethylene 10 tubing. Subsequently, 200 μL (4 nmol/200 μL) of $E4_{K12}$-Fl was injected via the tail vein catheter. Mice were sacrificed 2 h after the initial injection, and the pancreas was harvested and frozen in OCT compound (Sakura, Finetek, Torrance, CA) with isopentane on dry ice. The frozen tissues were sectioned (thickness, 6 μm) and mounted on microscope slides. Without further processing, tissue samples were excited with an EXFO X-CiteTM 120 light source (EXFO Photonic Solutions Inc. Ontario, Canada) and imaged with a Nikon Eclipse 80i microscope with either a 10× Plan Fluor NA 0.3 or a 20× Plan Apo 0.75 objective (Nikon Corp.). GFP fluorescence was observed with a Chroma HQ FITC filter cube (HQ480/40x EX, dichroic Q505LP BS, and emission filter HQ535/50m EM) and exendin-VT680 fluorescence with a Chroma Cy5.5 filter cube (HQ650/45x EX, dichroic Q680LP BS, and emission filter HQ710/50m EM; Chroma Technology Corp., VT). Images were captured with a Cascade model 512B camera (Roper Scientific, Tucson, AZ). Validation of fluorescence signals employed immunohistochemistry for insulin (insulin (H-86), Santa Cruz Biotechnology, Santa Cruz, CA) using the avidin−biotin peroxidase method. The reaction was visualized with a 3-amino-9-ethylcarbazole substrate (AEC, Sigma Chemical, Saint Louis, MO). Adjacent sections treated with nonimmune IgG provided controls for antibody specificity.

RESULTS

Near-infrared fluorescent exendin-4 analogues were created via two different strategies (Figure 1). In the first strategy, an alkyne-modified artificial amino acid (*S*)-2-amino-4-pentynoic acid was attached to the C-terminal end of exendin-4, yielding the peptide exendin-4-Pra. To this peptide, an azide-modified near-infrared (NIR) fluorochrome 11-azido-3,6,9-trioxaundecan-1-amide-Fl was covalently attached using standard copper catalyzed click-chemistry protocols, yielding the exendin-4-like NIR-fluorochrome, $E4_{40}$-Fl. 11-aAzido-3,6,9-trioxaundecan-1-amide-Fl was generated in good yields (56%) by conjugation of 11-azido-3,6,9-trioxaundecan-1-amine to the commercially available NIR fluorochrome VT680-NHS ester in the presence of triethylamine. The structural identity of the exendin-like NIR-fluorochrome $E4_{40}$-Fl was confirmed using liquid chromatography−mass spectrometry (LC/MS) analysis, which confirmed the expected mass of 5623 g/mol (*m*/*z* (%) = 1405 $[M - 4H^+]^{4-}$ (100); 1873 $[M - 3H^+]^{3-}$ (*14*)). The second approach was based on the direct reaction of VT680-NHS ester with exendin-4, facilitated in a Tris-HCl buffered aqueous solution. Although exendin-4 offers multiple nucleophilic sites, which can all theoretically react with NHS esters at one or multiple sites, only three reaction products were detected in the crude reaction mixture via LC/MS under current reaction conditions. All of the products had the same mass of 5311 g/mol (*m*/*z* (%) =1769 $[M - 3H^+]^{3-}$ (100); Figure 2b), which corresponded to the addition of a single fluorochrome per exendin-4. Three products were observed in ratios of 5/5/90. The major product (90%) was isolated using preparative HPLC, yielding the exendin-4-like NIR fluorochrome $E4_{K12}$-Fl (Figure 1).

The mass of $E4_{K12}$-Fl was analyzed using matrix assisted laser desorption ionization mass spectrometry (MALDI-MS), which

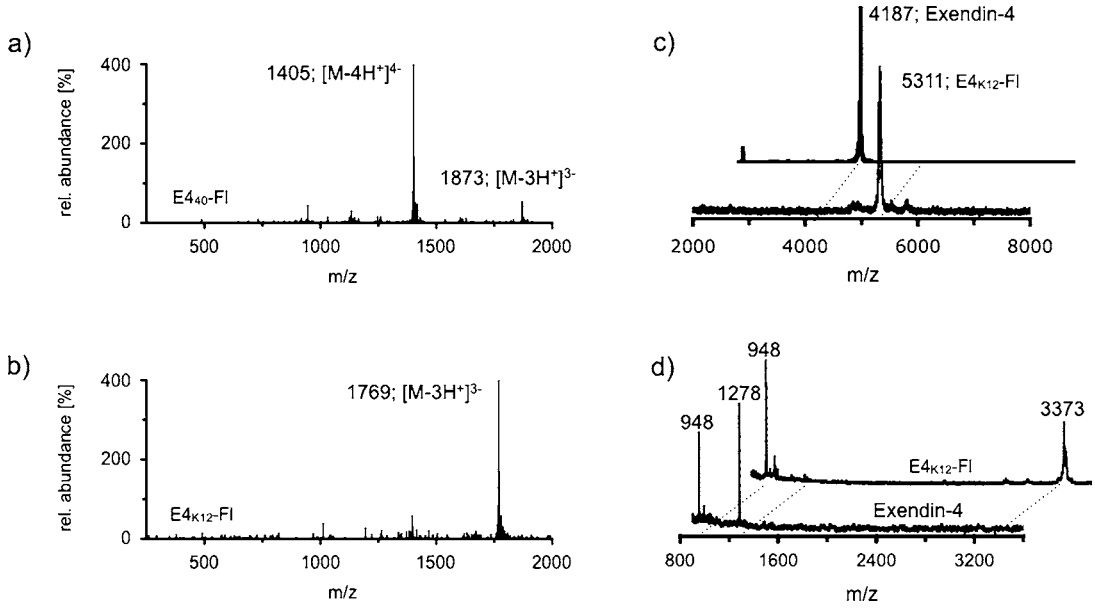


Figure 2. (a) ESI-MS trace of E4$_{40}$-Fl. (b) ESI-MS trace of E4$_{K12}$-Fl. (c) MALDI-MS traces of exendin-4 and E4$_{K12}$-Fl. (d) MALDI-MS traces of tryptic digest fragments of exendin-4 and E4$_{K12}$-Fl.

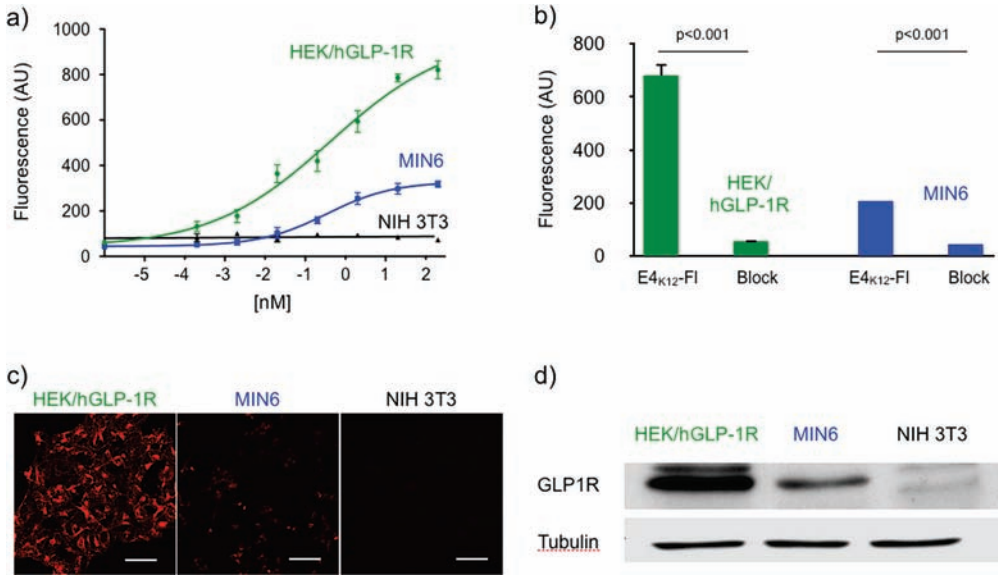


Figure 3. (a) Dose-response curves of E4$_{K12}$-Fl, where GLP-1R is either overexpressed (HEK/hGLP-1R) or naturally expressed (MIN6), and of a GLP-1R negative (NIH 3T3) cell line. (b) Blocking of E4$_{K12}$-Fl (10 nM) with exendin-4 (100 nM). (c) Live cell microscopy. HEK/hGLP-1R, MIN6, or NIH 3T3 cells were treated with E4$_{K12}$-Fl (100 nM) and then imaged. Scale bar: 50 μm. (d) Western blot of HEK/hGLP-1R, MIN6, and NIH 3T3 cell lines against GLP-1R and tubulin.

confirmed the exendin-4-like NIR fluorochrome to be composed of exendin-4 and a single fluorochrome molecule ($m/z = 5311$, Figure 2c). Structural analysis of the compound was determined by tryptic digestion of both E4$_{K12}$-Fl and exendin-4. Whereas exendin-4 displayed two strongly ionizing fragments at 1278 Da (H1-K12) and 948 Da (L21-K27), tryptic digest of E4$_{K12}$-Fl did not result in the formation of a 1278 Da fragment but showed a dominant peak at 3373 Da (Figure 2d). The fragment corresponded to amino acids H1-R20 (2251 Da) plus the mass of the fluorochrome (1123 Da). Observation of a peak at 3373 Da for E4$_{K12}$-Fl but not for exendin-4 indicated that the fluorochrome was part of that fragment and that it was conjugated to amino acid K12. If the fluorochrome were not conjugated to K12, the fragment would have been digested by trypsin at the K12-position into two smaller fragments. The predominant attachment of the fluorochrome to K12 compared to other nucleophilic residues (e.g., K27 or the N-terminus) is likely explained by either sterically or electronically favored conformations of K12.

In order to determine accumulation of E4$_{K12}$-Fl on GLP-1R expressing cells, we tested the compounds against human GLP1-R overexpressing HEK/hGLP-1R cells (HEK/hGLP-1R), GLP-1R naturally expressing MIN6, and against GLP-1R negative NIH 3T3 cells (Figure 3). The expression levels of GLP-1R were then analyzed by staining the respective cell lysates with an anti-GLP-1R antibody, and equal cell lysate concentrations were analyzed by staining against tubulin in Western blots (Figure 3). Western blotting confirmed GLP-1R to be absent in NIH 3T3 cells and overexpressed in transformed HEK/hGLP-1R cells. Each cell line was incubated with different concentrations of E4$_{K12}$-Fl for 1 h. The cells were later washed, and their fluorescence was measured. The fluorescent signal was normalized to the number of cells present in each well. GLP-1R overexpressing HEK/hGLP-1R cells displayed the highest

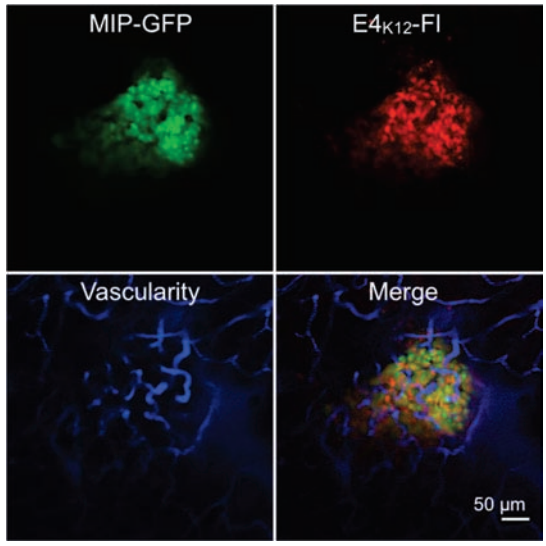


Figure 4. In vivo imaging of $E4_{K12}$-Fl in a pancreatic islet of a live NOD MIP-GFP mouse: green, GFP-expressing pancreatic β cells; red, $E4_{K12}$-Fl accumulation (dose, 0.4 nmol/g); blue, fluorescent vascular agent. All images were acquired with 20× objective in anesthetized live mice. Scale bar: 50 μm.

fluorescence, followed by insulinoma-derived MIN6 cells. GLP-1R negative NIH 3T3 cells did not show any discernible fluorescence (Figure 3a). For HEK/hGLP-1R cells, a binding EC_{50} of 0.3 ± 0.2 nM was determined, and for MIN6 cells, the observed EC_{50} was 0.5 ± 0.3 nM. These findings were corroborated using confocal microscopy (Figure 3c). Blocking experiments with nonfluorescent exendin-4 were subsequently conducted. Pretreated HEK/hGLP-1R cells were observed to have a 12-fold lower fluorescence and pretreated MIN6 cells a 5-fold lower fluorescence. Finally, we also tested the terminally labeled $E4_{40}$-Fl (as in a previous study (*19*)) which did not show strong preferential accumulation in GLP-1R expressing cell lines.

In order to evaluate the performance of $E4_{K12}$-Fl in vivo, NOD MIP-GFP mice were anesthetized and the pancreas exteriorized onto a heated chamber for real-time multichannel confocal imaging. Microvasculature was imaged in the 750 nm channel after injection of AngioSense-750, a long circulating blood pool agent, and islets were identified in the 488 nm channel via their GFP expression. Following this, 8 nmol of $E4_{K12}$-Fl in 200 μL of PBS was injected, and accumulation of the probe in the islets and surrounding tissue was monitored (Figure 4). Intravital imaging confirmed that prior to imaging no signal corresponding to a pancreatic islet was observable in the $E4_{K12}$-Fl channel

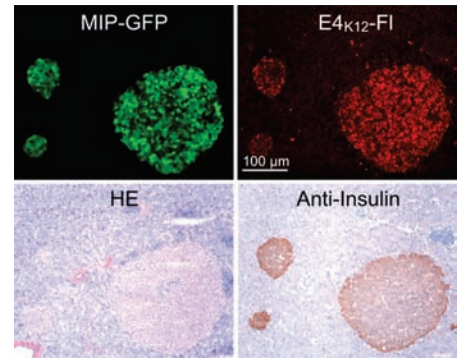


Figure 6. Immuno- and fluorescence histology of adjacent pancreas sections from a MIP-GFP mouse injected with $E4_{K12}$-Fl: (top left) GFP channel, (green) pancreatic islets, 10×; (top right) $E4_{K12}$-Fl accumulation, (red) pancreatic islets, 10×; (bottom left) HE; (bottom right) anti-insulin staining. Scale bar: 100 μm.

(Figure 5, 0 min). However, after 3 min, accumulation of $E4_{K12}$-Fl could be observed in the pancreatic islets, and this fluorescence increased during the observation time of 20 min, after which steady state was reached (target-to-background ratio of 6:1, Figure 5). Ninety minutes after injection, the signal still displayed a ratio of 6:1. Following comparison of imaging results from the vasculature and the GFP islets, it was confirmed that $E4_{K12}$-Fl colocalized in the pancreatic β cells and did not simply extravasate from the vasculature that traverses the islets. During the time of measurement, no increase in background noise from surrounding tissue was observed. The target-to-background ratio of islets over exocrine pancreas was 6.0 ± 0.5 in steady state. To further confirm that probe accumulation occurs in pancreatic β cells, we performed additional immuno- and fluorescence histology (Figure 6). These studies also demonstrated exclusive accumulation of $E4_{K12}$-Fl in the islets and specifically in the pancreatic β cells expressing insulin and GLP-1R. Biodistribution studies show renal excretion of non-localized agent and intracellular degradation in endosomal compartments.

DISCUSSION

T1D is a classic example of an organ-specific autoimmune disease. It has two stages. The first is an occult phase, termed insulitis, in which a mixed population of leukocytes invades the islets of Langerhans of the pancreas. This, in turn, eventually provokes specific destruction of the insulin-producing β cells. The second stage is the overt phase (diabetes), in which the bulk of β cells have been destroyed and insulin production is no longer sufficient to regulate blood-glucose levels. This

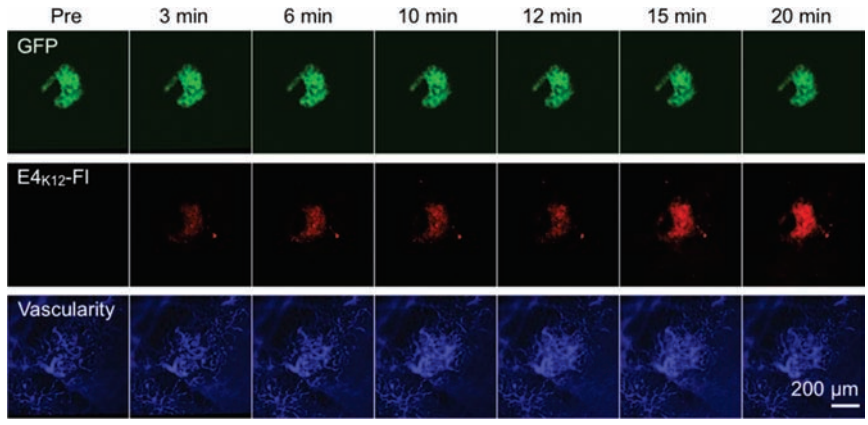


Figure 5. In vivo time course imaging of probe accumulation in an islet: (a) GPF channel (488 nm); (b) E4k12-Fl channel (680 nm); (c) vasculature (750 nm). All images were acquired with 10× objectives. Scale bar: 200 μm.

eventually results in hyperglycemia. To date, a major hindrance to both research on and treatment of T1D has been the inability to directly visualize β cells during disease progression. Our goal has therefore been to develop robust, noninvasive methods to image BCM (both experimentally in mouse models and clinically). Thus far, we have tested most of the published fluorescent probes in vivo in MIP-GFP mice but with little or modest success. On the basis of profiling studies, we also investigated a number of novel targets including carboxypeptidase E (CPE), proprotein convertase subtilisin/kexin 2 (PCSK2), and islet amyloid polypeptide (IAPP), among others. This study now reports on the first selective fluorophore-based probe for in vivo imaging of pancreatic β cells, and we confirm its potency in biochemical assays, in in vitro assays, by histology and by in vivo imaging.

The islets of Langerhans, encompassing the endocrine pancreas, represent approximately 1−2% of the pancreatic mass. They are also scattered throughout the pancreas, which is likely the underlying reason for the previous difficulties in visualizing BCM with macroscopic imaging techniques (*5*). Within each islet, there are five major endocrine cell types: insulin-producing β cells (60−80% of the islet), glucagon-producing α cells (15−20% of the islet), somatostatin-producing δ cells (5−10% of the islet), pancreatic-polypeptide-producing (PP) cells (15−20% of the islet), and ghrelin-producing ε cells (<1%).

The adult mouse pancreas contains about 3000 islets, with about 2×10^6 β cells (*27*). The human pancreas contains about 10^6 islets. These pancreatic islets measure 50−300 μm in diameter and are highly vascularized, with one to five arterioles branching into numerous capillaries. Capillaries are fenestrated and are therefore highly permeable. It has been estimated that islets receive 10−20% of pancreatic blood flow, which is disproportionally large for an area that assumes 1−2% of pancreatic volume and <0.005% of body weight. This feature, however, creates a favorable environment for the delivery of imaging agents. In our studies, we used intravital confocal microscopy to study islet microvascularity and were able to show rapid delivery of the $E4_{K12}$-Fl agent to the pancreatic islets with high spatial overlap with EGFP labeled β cells.

In the pancreas of mice, rats, and humans, the GLP-1R is highly expressed within the islets and to a lesser extent within some ducts. Within the islets the GLP-1R protein almost exclusively colocalizes with insulin and is highly restricted to pancreatic β cells (*28*). This distribution makes the GLP-1R a good target for measuring BCM. Glucagon-like peptide-1 (GLP-1) is secreted by intestinal L cells as a gut hormone, and its secretion is dependent on the presence of nutrients in the small intestine. The physiological functions of GLP-1 include potentiation of insulin secretion in a glucose dependent manner as well as influencing a number of gastric functions (slowing gastric emptying and inhibiting acid secretion). GLP-1 analogues are a new class of drugs for the treatment of diabetes because they have a low risk of causing hypoglycemia (*29*). Exenatide (Byetta), the first FDA approved GLP-1 analogue, is a synthetic version of exendin-4, a hormone found in the saliva of the Gila monster. It has 53% sequence homology with GLP-1 (*30*). A recent crystal structure shows that exendin-4 binds to the extracellular domain of GLP-1R (*30*). From this crystal structure, it follows that the amino acid K12 is not involved in GLP-1R binding (Figure 1) and explains its efficacy as an imaging agent. Conversely, other modifications with fluorochromes do alter binding.

In this study, we focused on the exendin-4 analogue $E4_{K12}$-Fl. There are, however, several other pharmaceutical analogues of GLP-1 that are currently in development or in clinical use, including liraglutide, albiglutide, and taspoglutide, each of which have variable substitutions and modifications that alter their pharmacokinetics (*21*). It is entirely possible that we will be able to further optimize probe development by using some of these newer GLP-1 analogues as platforms. Another potential avenue for probe development would be to use the peptide as a targeting ligand for the delivery of multimodal, nanoparticle based constructs for imaging (*31*) and or therapeutics (*32*). We believe that the featured $E4_{K12}$-Fl, and possibly similar derivatives, will prove to be useful agents for the selective visualization of β cells. Finally, it appears reasonable that more immediately one should be able to use the described agent in the imaging of often difficult to localize insulinomas, possibly via positron emission tomography (PET) tracers, via magnetic resonance imaging (MRI) with agents based on this peptide, or by intraoperative imaging of fluorescent compounds as described.

ACKNOWLEDGMENT

We would especially like to thank Christophe Benoist and Diane Mathis for many helpful discussions. We acknowledge the help of George Holz for providing reagents, Yoshiko Iwamoto for histology and Rostic Gorbatov for surgery. The work was supported in part by NIH Grants P01 AI54904, RO1 67536, U24 CA092782, an NIH Interdisciplinary training grant (1RL9EB008539-01) (SysCODE) for C.W.L., fellowships from the Canadian Institutes of Health Research and the Canadian Diabetes Association for J.A.H. and a grant from the Deutsche Akademie der Naturforscher Leopolina (German Academy of Sciences Leopoldina) to T.R.

LITERATURE CITED

(1) McCulloch, D. K., Koerker, D. J., Kahn, S. E., Bonner-Weir, S., and Palmer, J. P. (1991) Correlations of in vivo beta-cell function tests with beta-cell mass and pancreatic insulin content in streptozocin-administered baboons. *Diabetes 40*, 673–679.

(2) Malaisse, W. J., Louchami, K., and Sener, A. (2009) Noninvasive imaging of pancreatic beta cells. *Nat. Rev. Endocrinol. 5*, 394–400.

(3) Mathis, D., Gaglia, J. (2010) Autoimmune diabetes. In *Molecular Imaging* (Weissleder, R., Ross, B. D., Rehemtulla, A., Gambhir, S. S., Eds.) People's Medical Publishing House-USA, Shelton, CT.

(4) Maffei, A., Liu, Z., Witkowski, P., Moschella, F., Del Pozzo, G., Liu, E., Herold, K., Winchester, R. J., Hardy, M. A., and Harris, P. E. (2004) Identification of tissue-restricted transcripts in human islets. *Endocrinology 145*, 4513–4521.

(5) Sweet, I. R., Cook, D. L., Lernmark, A., Greenbaum, C. J., Wallen, A. R., Marcum, E. S., Stekhova, S. A., and Krohn, K. A. (2004) Systematic screening of potential beta-cell imaging agents. *Biochem. Biophys. Res. Commun. 314*, 976–983.

(6) Clark, P. B., Gage, H. D., Brown-Proctor, C., Buchheimer, N., Calles-Escandon, J., Mach, R. H., and Morton, K. A. (2004) Neurofunctional imaging of the pancreas utilizing the cholinergic PET radioligand [^{18}F]4-fluorobenzyltrozamicol. *Eur. J. Nucl. Med. Mol. Imaging 31*, 258–260.

(7) Souza, F., Simpson, N., Raffo, A., Saxena, C., Maffei, A., Hardy, M., Kilbourn, M., Goland, R., Leibel, R., Mann, J. J., Van Heertum, R., and Harris, P. E. (2006) Longitudinal noninvasive PET-based beta cell mass estimates in a spontaneous diabetes rat model. *J. Clin. Invest. 116*, 1506–1513.

(8) Simpson, N. R., Souza, F., Witkowski, P., Maffei, A., Raffo, A., Herron, A., Kilbourn, M., Jurewicz, A., Herold, K., Liu, E., Hardy, M. A., Van Heertum, R., and Harris, P. E. (2006) Visualizing pancreatic beta-cell mass with [^{11}C]DTBZ. *Nucl. Med. Biol. 33*, 855–864.

(9) Souza, F., Freeby, M., Hultman, K., Simpson, N., Herron, A., Witkowsky, P., Liu, E., Maffei, A., and Harris, P. E. (2006) Current

progress in non-invasive imaging of beta cell mass of the endocrine pancreas. *Curr. Med. Chem. 13*, 2761–2773.

(10) Harris, P. E., Ferrara, C., Barba, P., Polito, T., Freeby, M., and Maffei, A. (2007) VMAT2 gene expression and function as it applies to imaging beta-cell mass. *J. Mol. Med. 86*, 5–16.

(11) Moore, A., Bonner-Weir, S., and Weissleder, R. (2001) Noninvasive in vivo measurement of beta-cell mass in mouse model of diabetes. *Diabetes 50*, 2231–2236.

(12) Ueberberg, S., Meier, J. J., Waengler, C., Schechinger, W., Dietrich, J. W., Tannapfel, A., Schmitz, I., Schirrmacher, R., Koller, M., Klein, H. H., and Schneider, S. (2009) Generation of novel single-chain antibodies by phage-display technology to direct imaging agents highly selective to pancreatic beta- or alpha-cells in vivo. *Diabetes 58*, 2324–2334.

(13) Yamada, K., Nakata, M., Horimoto, N., Saito, M., Matsuoka, H., and Inagaki, N. (2000) Measurement of glucose uptake and intracellular calcium concentration in single, living pancreatic beta-cells. *J. Biol. Chem. 275*, 22278–22283.

(14) Ran, C., Pantazopoulos, P., Medarova, Z., and Moore, A. (2007) Synthesis and testing of beta-cell-specific streptozotocin-derived near-infrared imaging probes. *Angew. Chem., Int. Ed. 46*, 8998–9001.

(15) Denis, M. C., Mahmood, U., Benoist, C., Mathis, D., and Weissleder, R. (2004) Imaging inflammation of the pancreatic islets in type 1 diabetes. *Proc. Natl. Acad. Sci. U.S.A. 101*, 12634–12639.

(16) Ho, N. H., Weissleder, R., and Tung, C. H. (2006) Development of a dual fluorogenic and chromogenic dipeptidyl peptidase IV substrate. *Bioorg. Med. Chem. Lett. 16*, 2599–2602.

(17) Kelly, K. A., Bardeesy, N., Anbazhagan, R., Gurumurthy, S., Berger, J., Alencar, H., Depinho, R. A., Mahmood, U., and Weissleder, R. (2008) Targeted nanoparticles for imaging incipient pancreatic ductal adenocarcinoma. *PLoS Med. 5*, e85.

(18) Mukai, E., Toyoda, K., Kimura, H., Kawashima, H., Fujimoto, H., Ueda, M., Temma, T., Hirao, K., Nagakawa, K., Saji, H., and Inagaki, N. (2009) GLP-1 receptor antagonist as a potential probe for pancreatic beta-cell imaging. *Biochem. Biophys. Res. Commun. 389*, 523–526.

(19) Gotthardt, M., Lalyko, G., van Eerd-Vismale, J., Keil, B., Schurrat, T., Hower, M., Laverman, P., Behr, T. M., Boerman, O. C., Goke, B., and Behe, M. (2006) A new technique for in vivo imaging of specific GLP-1 binding sites: first results in small rodents. *Regul. Pept. 137*, 162–167.

(20) Martinic, M. M., and von Herrath, M. G. (2008) Real-time imaging of the pancreas during development of diabetes. *Immunol. Rev. 221*, 200–213.

(21) Ahren, B. (2009) Islet G protein-coupled receptors as potential targets for treatment of type 2 diabetes. *Nat. Rev. Drug Discovery 8*, 369–385.

(22) Doyle, M. E., McConville, P., Theodorakis, M. J., Goetschkes, M. M., Bernier, M., Spencer, R. G., Holloway, H. W., Greig, N. H., and Egan, J. M. (2005) In vivo biological activity of exendin (1−30). *Endocrine 27*, 1–9.

(23) Miyazaki, J., Araki, K., Yamato, E., Ikegami, H., Asano, T., Shibasaki, Y., Oka, Y., and Yamamura, K. (1990) Establishment of a pancreatic beta cell line that retains glucose-inducible insulin secretion: special reference to expression of glucose transporter isoforms. *Endocrinology 127*, 126–132.

(24) Borowiec, M., Liew, C. W., Thompson, R., Boonyasrisawat, W., Hu, J., Mlynarski, W. M., El Khattabi, I., Kim, S. H., Marselli, L., Rich, S. S., Krolewski, A. S., Bonner-Weir, S., Sharma, A., Sale, M., Mychaleckyj, J. C., Kulkarni, R. N., and Doria, A. (2009) Mutations at the BLK locus linked to maturity onset diabetes of the young and beta-cell dysfunction. *Proc. Natl. Acad. Sci. U.S.A. 106*, 14460–14465.

(25) Gromada, J., Rorsman, P., Dissing, S., and Wulff, B. S. (1995) Stimulation of cloned human glucagon-like peptide 1 receptor expressed in HEK 293 cells induces cAMP-dependent activation of calcium-induced calcium release. *FEBS Lett. 373*, 182–186.

(26) Alencar, H., Mahmood, U., Kawano, Y., Hirata, T., and Weissleder, R. (2005) Novel multiwavelength microscopic scanner for mouse imaging. *Neoplasia 7*, 977–983.

(27) Park, S. Y., Wang, X., Chen, Z., Powers, A. C., Magnuson, M. A., Head, W. S., Piston, D. W., and Bell, G. I. (2005) Optical imaging of pancreatic beta cells in living mice expressing a mouse insulin I promoter-firefly luciferase transgene. *Genesis 43*, 80–86.

(28) Tornehave, D., Kristensen, P., Romer, J., Knudsen, L. B., and Heller, R. S. (2008) Expression of the GLP-1 receptor in mouse, rat, and human pancreas. *J. Histochem. Cytochem. 56*, 841–851.

(29) Lin, F., and Wang, R. (2009) Molecular modeling of the three-dimensional structure of GLP-1R and its interactions with several agonists. *J. Mol. Model. 15*, 53–65.

(30) Runge, S., Thogersen, H., Madsen, K., Lau, J., and Rudolph, R. (2008) Crystal structure of the ligand-bound glucagon-like peptide-1 receptor extracellular domain. *J. Biol. Chem. 283*, 11340–11347.

(31) Nahrendorf, M., Keliher, E., Marinelli, B., Waterman, P., Feruglio, P. F., Fexon, L., Pivovarov, M., Swirski, F. K., Pittet, M. J., Vinegoni, C., and Weissleder, R. (2010) Hybrid PET-optical imaging using targeted probes. *Proc. Natl. Acad. Sci. U.S.A. 107*, 7910–7915.

(32) Weissleder, R., and Pittet, M. J. (2008) Imaging in the era of molecular oncology. *Nature 452*, 580–589.

(33) Neidigh, J. W., Fesinmeyer, R. M., Prickett, K. S., and Andersen, N. H. (2001) Exendin-4 and glucagon-like-peptide-1: NMR structural comparisons in the solution and micelle-associated states. *Biochemistry 40*, 13188–13200.

BC100184W

Chemical Modification of M13 Bacteriophage and Its Application in Cancer Cell Imaging

Kai Li,[†,‡] Yi Chen,[‡] Siqi Li,[‡] Huong Giang Nguyen,[‡] Zhongwei Niu,[‡] Shaojin You,[§] Charlene M. Mello,[||] Xiaobing Lu,[†] and Qian Wang*[,†]

State Key Laboratory of Fine Chemicals, Dalian University of Technology (DUT), Dalian, P. R. China, Department of Chemistry and Biochemistry and Nanocenter, University of South Carolina, Columbia, South Carolina 29208, Atlanta Research & Educational Foundation, Atlanta VA Medical Center 1670, Clairmont Road, Decatur, Georgia 30033, and Botulinum Research Center, University of Massachusetts, Dartmouth, 285 Old Westport Road, Dartmouth, Massachusetts 02747. Received September 14, 2009; Revised Manuscript Received April 12, 2010

The M13 bacteriophage has been demonstrated to be a robust scaffold for bionanomaterial development. In this paper, we report on the chemical modifications of three kinds of reactive groups, i.e., the amino groups of lysine residues or N-terminal, the carboxylic acid groups of aspartic acid or glutamic acid residues, and the phenol group of tyrosine residues, on M13 surface. The reactivity of each group was identified through conjugation with small fluorescent molecules. Furthermore, the regioselectivity of each reaction was investigated by HPLC-MS-MS. By optimizing the reaction condition, hundreds of fluorescent moieties could be attached to create a highly fluorescent M13 bacteriophage. In addition, cancer cell targeting motifs such as folic acid could also be conjugated onto the M13 surface. Therefore, dual-modified M13 particles with folic acid and fluorescent molecules were synthesized via the selective modification of two kinds of reactive groups. Such dual-modified M13 particles showed very good binding affinity to human KB cancer cells, which demonstrated the potential applications of M13 bacteriophage in bioimaging and drug delivery.

INTRODUCTION

In this paper, we report on our recent progress in fully screening the reactivity of three different reactive groups of the P8 coat protein of M13 phage. In addition, we also report on a potential application of the M13 phage in cell imaging to demonstrate how improved knowledge of its specific reactivity can be practically applied. M13 bacteriophage is a rod-like virus (880 nm long and 6.6 nm wide for wild-type) composed of a circular, single-stranded DNA that is encapsulated by approximately 2700 copies of the major coat protein P8 and capped with 5 copies of four different minor coat proteins (P9, P7, P6, and P3) on the ends (Figure 1) (*1, 2*). The functionality of these subunit proteins can be engineered to identify and display peptides that have a good binding affinity and specificity for essentially any target analyte through a technique called phage display (*3*). On the basis of this technology, a great number of M13 mutations were selected for many interesting applications, such as high-power phage batteries (*2, 4, 5*), tissue regenerating materials (*6*), metal nanowire catalysts (*7*), biological sensors and cell-targeting agents (*8*−*11*), gene transfer vectors (*12, 13*), and targeted cancer therapies (*14*). Furthermore, M13 bacteriophage has been used as a template to align inorganic, organic, and biological nanomaterials to generate different nanostructures, such as nanorings (*15*), nanowires (*16, 17*), films (*18*−*22*), nanofibers (*1, 23*), semiconductors (*24*), and metal hybrid materials (*25*). Although phage display is a powerful technology, it relies entirely on peptide expressions and selection. If the needed functionalities were beyond peptide modification, the genetic tools would fail to address the requirements.

Orthogonal bioconjugation techniques have permeated fundamental virus chemistry, decorating addressable amino acids with a variety of molecules ranging from small molecules, such as fluorescent dyes, to large particles, such as quantum dots (*26*). As another simple way to generate functionalities, M13 bacteriophage has been chemically addressed with drugs (*27*−*30*), RGD peptides (*31*), near-infrared fluorescent dyes (*32, 33*), carboxylic acid groups (*34*), and other fluorophores (*35, 36*) for a variety of applications. Although these examples clearly showed that the P8 coat protein of M13 bacteriophage could be easily modified using simple bioconjugation methods, the detailed reactivity and regioselectivity of the reactive residues have not been reported yet. Therefore, it is necessary to fully investigate those two properties of all reactive groups on the M13 surface to further widen its potential application.

Virus and virus-like particles (VLPs) have been currently used as scaffolds for bioimaging applications (*37, 38*). These bionanoparticles have the advantages of nanoscale size, high solubility, and the capability for multivalent and orthogonal display. Multivalency is important, since both the targeting and the signaling motifs could be displayed throughout the viral surface to significantly increase cellular uptake and signal intensity, respectively (*39*). Here, we showed that M13 phage could be modified simultaneously with multiple functional units, which could be used as a probe for cancer cell imaging.

EXPERIMENTAL SECTION

General. Reactive fluorescein (FL) *N*-hydroxysuccinimidyl (NHS) ester and *N*,*N*,*N*′,*N*′-tetramethylrhodamine (TMR) NHS ester, Modified Lowry Protein Assay Kit, and Pierce Biotin Quantification Kit were purchased from Pierce and used without further purification. The other chemicals were purchased from

* Correspondence to Qian Wang, Ph.D., Department of Chemistry and Biochemistry, University of South Carolina, Columbia, SC 29208. Phone: ++001-803-777-8436. Fax: ++001-803-777-9521. E-mail: wang@mail.chem.sc.edu.

[†] DUT.

[‡] University of South Carolina.

[§] Atlanta VA Medical Center.

[||] University of Massachusetts.

10.1021/bc900405q © 2010 American Chemical Society
Published on Web 05/25/2010

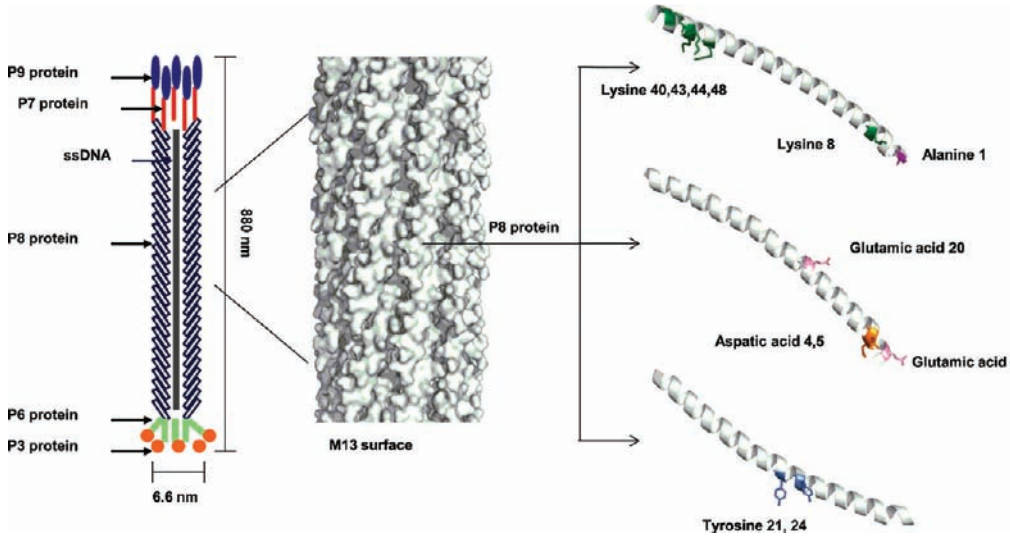


Figure 1. (Left) Schematic depiction of M13 bacteriophage. (Middle) Surface crystal structure of M13 bacteriophage. (Right) The structure of M13 P8 protein subunit with target amino acid residues highlighted (*59*).

VWR and were used as received. Dialysis tubing of 300 000 molecular weight cutoff (MWCO) biotech was purchased from Spectrum Laboratories. TEM analyses were carried out by depositing 20 μL aliquots of each sample at a concentration of 0.1 mg/mL onto 100-mesh carbon-coated copper grids for 2 min. The grids were then stained with 20 μL of 2% uranyl acetate and viewed with a Hitachi H-8000 TEM electron microscope. Fluorescent microscopy was performed on Olympus IX 86 with 20× and 60× oil immersion objective lenses.

MALDI-TOF MS of M13 P8 Subunit. A solution of M13 (1 mg/mL, 24 μL) was denatured by incubating with guanidinium chloride (6.0 M, 6 μL) for 5 min at RT, using Millipore $ZipTip_{\mu\text{-}C18}$ tips to remove the salts. The denatured protein was spotted onto a MALDI plate. These spots were analyzed by a Bruker Ultra-Flex I TOF/TOF mass spectrometer. MS-grade 2,5-dihydroxybenzoic acid with 0.1% TFA was used as the matrix.

HPLC-MS/MS Study. The mass spectra were acquired in the positive ion mode using a Micromass Q TOF spectrometer (Waters, MA) equipped with an electrospray source. The source temperature was held constant at 100 °C. The desolvation temperature was set at 350 °C. The capillary voltage was 3 kV. Full-scan spectra were collected from *m*/*z* 100 to 4000. The collision energy in the collision cell was set around 45 V. *Masslynx 4.0* was used for data acquisition and analysis.

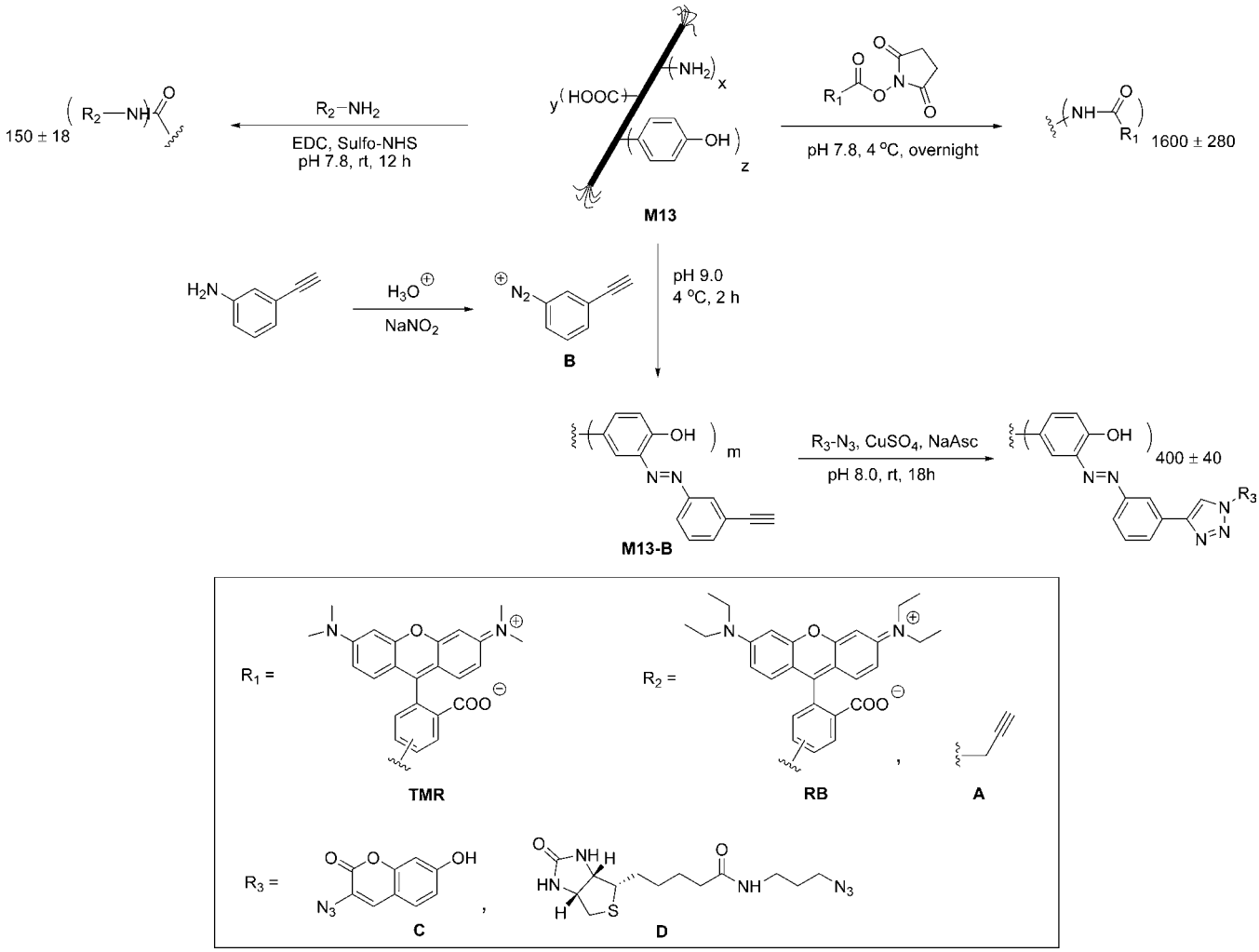
Reactivity Screening of M13 Bacteriophage. The reactivity of the amino groups of M13 bacteriophage was screened by incubating with varying concentrations of TMR-NHS at a phage concentration of 1.0 mg/mL in a mixed solution of buffer and dimethyl sulfoxide (DMSO) (v/v = 80:20). The reactions were performed at 4 °C for 24 h. Reactions were purified by four dialysis steps of 5 h each against 2 L of potassium phosphate buffer (pH 7.8, 10 mM). The carboxylic acid groups of M13 bacteriophage were screened for reactivity by incubating with varying concentrations of Rhodamine B amine (RB), 1-ethyl-3-(3-dimethylaminopropyl) carbodiimide (EDC) (10 mM), and *N*-hydroxysulfosuccinimide (Sulfo-NHS) (30 mM) in potassium phosphate buffer (pH 7.8, 10 mM) at room temperature for 12 h and purified by dialysis. The loading of dyes per phage was determined by UV−visible spectroscopy. Wild-type phage concentrations were determined by measuring the absorbance at 269 nm; virus at 0.1 mg/mL gives a standard absorbance of 0.38 (*40*). Modified phage concentrations were determined by Modified Lowry Protein Assay Kit from Pierce. The average molecular weight of the M13 bacteriophage is 1.64×10^7 Da (*34*). Dye concentrations were obtained by measurement of absorbance at λ_{max} (517 nm for TMR, 559 nm for RB), with molar absorptivity calibrated for each use by mixing known quantities of dye with M13 (1.0 mg/mL). The integrity of the modified M13 bacteriophage was determined by TEM. Reactive residues were identified by using HPLC-MS/MS.

Reactions on Tyrosine Residues. The 3-ethynylbenzenediazonium (100 mM, 500 μL) was prepared by incubating *p*-toluenesulfonic acid (0.35 M, 400 μL) and 3-ethynylaniline (78 mg/mL, 75 μL), $NaNO_2$ (207 mg/mL, 25 μL) on ice for 1 h. The diazo linkage was created by incubating M13 bacteriophage (20 mg/mL, 250 μL) with 20 μL of the 3-ethynylbenzenediazonium (0.1 M) in borate buffer (0.1 M, 4.73 mL, pH 9.0) for 2 h on ice. The reaction was purified by dialysis against Tris buffer (10 mM, pH 8.0). A following Cu(I)-catalyzed azide−alkyne cycloaddition (CuAAC) reaction can efficiently conjugate small molecules such as coumarin to the tyrosine residues. For a standard CuAAC reaction, azide (100 mM, 79 μL) and the solution of modified M13 bacteriophage (4 mg/mL, 250 μL) were mixed with $CuSO_4$ (100 mM, 10 μL) and NaAsc (200 mM, 10 μL) in Tris buffer (10 mM, 651 μL, pH = 8.0) and incubated at room temperature for 18 h. Next, phage precipitates were removed by centrifugation for 20 min at 13 500 rcf at 4 °C. The suspension was collected and purified by dialysis. The number of biotins per phage was obtained by the Pierce Biotin Quantification Kit. The integrity of the modified M13 bacteriophage was determined by TEM. Reactive residues were identified using HPLC-MS-MS.

Dual Modification of M13 Bacteriophage. M13 bacteriophage (20 mg/mL, 200 μL) was first incubated with FL-NHS (0.2 M, 20 μL) in a mixed solution of phosphate buffer (pH 7.8, 10 mM) and DMSO (v/v = 80:20) to generate a 190 dye/phage nanoparticle (M13-FL). After dialysis, the dye-modified M13 was further modified with folate-azide (synthesis can be found in Supporting Information) by the tyrosine conjugation method mentioned above. TEM results showed that dual-modified M13 (FL-M13-FA) was still kept intact after the reaction.

Cell Culture. HeLa contaminant cell line-KB cells were obtained from ATCC. They were grown continuously as a monolayer by using folate-free RPMI 1640 media with 10%

Scheme 1. Modification of M13 Bacteriophage



FBS, penicillin (50 units/mL), streptomycin (50 μg/mL), and 2 mM L-glutamine at 37 °C in a 5% CO_2/95% air humidified atmosphere.

Cell Imaging Study. Cells were seeded into a 12-well plate containing 18 mm sterile glass coverslips at approximately 1 $\times$ 10^5 cells/well. After overnight incubation, the cells were exposed to FL-M13 (37 μL, 2.7 mg/mL), FL-M13-Folate (37 μL, 2.7 mg/mL), or FA-FL (37 μL, 2.7 mg/mL) (synthesis can be found in Supporting Information), respectively, with 963 μL of culture media from 1 to 24 h. Following incubation, cells were washed 3 times with folate-free media to remove unbound phage and then fixed with 4% paraformaldehyde in Dulbecco-modified phosphate buffer saline (DPBS) for 10 min. After fixing, the cells were washed 3 times with DPBS buffer and then stained with 4′,6-diamidino-2-phenylindole (DAPI) (5 μg/mL, 1 mL) for 10 min. The cells were washed 3 times with DPBS and then mounted with GVA mount (VWR) on glass slides. The cells were examined with an Olympus IX 86 confocal microscope.

RESULTS AND DISCUSSION

Reactivity of Amine Conjugation. M13 was purified in high yield from *Escherichia coli* cells (*34*). The integrity of virus through the purification was confirmed by TEM analysis (Supporting Information Figure S7A). TMR-NHS, which was selected for reactions with amino groups of protein, was utilized to study the reactivity of M13 bacteriophage (Scheme 1). Lysine reactive NHS chemistry was used. The reaction occurs via a nucleophilic attack by an unprotonated amine on the ester, followed by an amide bond formation and release of NHS (*41*). For the protein labeling reaction, pH range 7.0−9.2 could be considered optimal conditions (*42*). Here, pH 7.8 buffer was selected for the reaction.

In order to screen the reactivity of amino groups on M13 bacteriophage, different concentrations of TMR-NHS (40 μM to 8 mM) were used. The reactions were purified via dialysis and analyzed with UV−vis spectroscopy. The modified M13 bacteriophages were stable and remained intact as confirmed by TEM (Supporting Information Figure S7B). The normal absorption spectrum of free TMR is shown in Figure 2E (blue line). Compared to free dye, the modified bacteriophage (M13-TMR) displays two absorption peaks around 517 and 555 nm (red line). Whereas the 555 nm peak corresponds to the rhodamine monomers, the peak around 517 nm is caused by the formation of the tetramethylrhodamine dimers (*43*). The absorbance of free TMR at 280 nm gave noticeable differences in the spectra of wild-type M13 (black line) and M13-TMR complex (red line). The UV−vis measurements were used to calculate the dye per particle ratios based on the molar absorptivity of the dye and of the virus. When different concentrations of TMR-NHS were used, up to 1600 rhodamine units could be attached on to M13 bacteriophage, which gave a very high local concentration of fluorescent dye (Figure 2A). Since the fluorescent dyes were covalently linked to the virus particles at the defined position, we expected that the virus scaffold could prevent possible

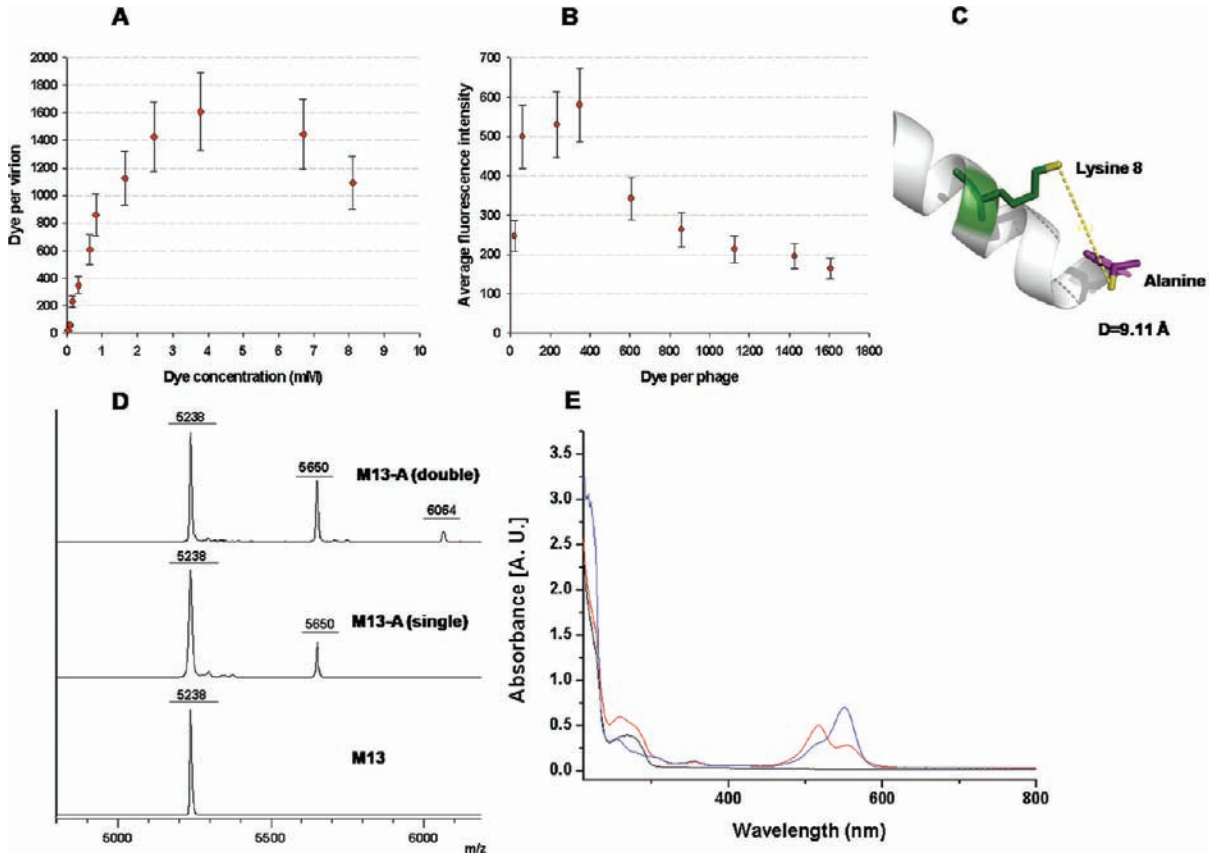


Figure 2. (A) Loading of TMR on M13 bacteriophage related to concentration of reagents in the reaction mixture. The loading of dye units per phage plateaus at a TMR-NHS ester concentration greater than 4 mM. Every data point displayed in this figure was based on multiple repeated experiments. The error bars in this figure represent the average values of standard deviations of all data points. (B) Overall fluorescence intensity vs dye loading for M13-TMR. The concentration of the phage in all samples in this study was controlled at 0.2 mg/mL. (C) The distance between the amino groups of alanine 1 and lysine 8 is 9.11 Å (Distance was measured by Pymol with a protein structure PDB file 1ifj). (D) MALDI-TOF MS of whole P8 subunit of M13 and M13-TMR. WT-M13: wild-type M13 coat protein, *m/z* 5,238. M13-TMR (single): monomodified M13 coat protein, *m/z* 5650. M13-TMR (double): double-modified M13 coat protein, *m/z* 6064 (the theoretical mass difference upon modification with TMR = 412 Da). (E) UV−vis spectra showing bacteriophage absorbance of M13 (black curve), M13-TMR (red curve), and free dye TMR-NHS (blue curve) in solution. The viral concentrations were comparable for M13 and M13-TMR. The concentration of dye TMR-NHS was comparable for M13-TMR.

fluorescence quenching. Unfortunately, an obvious fluorescence quenching was detected. As shown in Figure 2B, the overall fluorescence intensity of M13-A began to decrease upon anchorage of more than ~400 dye units per phage particle. Compared to similar amounts of the free dyes in solution, the fluorescence intensity of the M13-TMR complexes was lower (data not shown). The fluorescence intensity of M13-TMR was reduced because of the self-quenching that might have been caused by the close distance between rhodamine moieties, which could form nonfluorescent dimers (*44*). The proximity (9.11 Å) of two available modification cites (alanine 1 and lysine 8) could be a factor contributing to the formation nonfluorescent dimers (see the following discussion and Figure 2C) (*45*).

The MALDI-TOF mass spectra showed the intense peak of protonated coat proteins of wild-type M13 at *m/z* 5238 (Figure 2D). At a lower level of modification (340 dyes per phage), single showed two major peaks, one at *m/z* 5238 from wild-type M13 and another at *m/z* 5650 resulting from the protonated monomodified coat protein of M13 with TMR (M13-TMR). The 412 *m/z* mass difference between wild-type M13 and M13-TMR was consistent with the theoretical mass of newly added TMR unit (Figure 2D). At a higher level of modification (600 dyes per phage), a third peak at *m/z* 6064 was observed, suggesting that some P8 proteins were doubly modified by TMR. As shown in Figure 1, one P8 subunit of M13 bacteriophage contains five lysine groups (Lys 8, 40, 43, 44, 48) and one N-terminal amine on Ala 1. On the basis of the previous works reported on bioconjugation of bionanoparticles, it is usually regarded that amine modifications happen at exposed amine groups (*28, 31, 34, 46−49*). Thus, HPLC−MS/MS was employed to identify the modification sites. The MS data showed that at the lower levels of modifications only Ala-1 could be modified; however, at the higher levels of modification both Ala-1 and Lys-8 could be modified (detailed discussions can be found in the Supporting Information).

Reactivity of Carboxylic Acid Residues. Four carboxylic acid groups are found on one P8 subunit: they are Glu 2 and 20 and Asp 4 and 5 (Figure 1). The reactivity of the carboxylic acid groups of M13 bacteriophage was screened by treating the viral particle with RB dye activated with EDC and sulfo-NHS (Scheme 1). Up to 150 carboxyl groups were derivatized after 12 h incubation (Figure 3B). As shown in Figure 3A, after conjugation, the modified bacteriophage (M13-RB) gave a dye absorbance at 559 nm. The MALDI-TOF mass spectra pointed to successful modification, represented by the peak of M13-RB at *m/z* 5677 (Figure 3C). The modified M13 bacteriophages were stable and remained intact as confirmed by TEM (Supporting Information Figure S7C).

Compared to amine conjugation, the carboxylic acid groups on M13 showed relatively low levels of activities toward RB, which made it harder to identify the reactive residues using

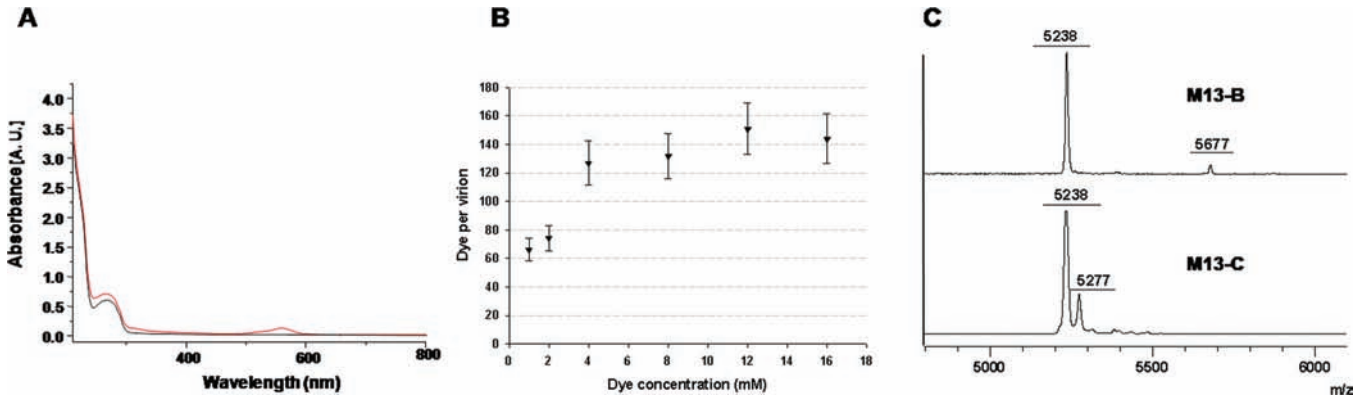


Figure 3. (A) UV−vis spectra showing bacteriophage absorbance of wild-type M13 (black curve) and M13-RB (red curve) after purification. (B) Loading of RB on M13 bacteriophage as related to concentration of reagents in the reaction mixture. Every data point displayed in this figure was based on multiple repeated experiments. The error bars in this figure represent the average values of standard deviations of all data points. (C) MALDI-TOF MS of whole subunit of wild-type M13 (*m*/*z* 5238), M13-RB (*m*/*z* 5677), and M13-A (*m*/*z* 5277).

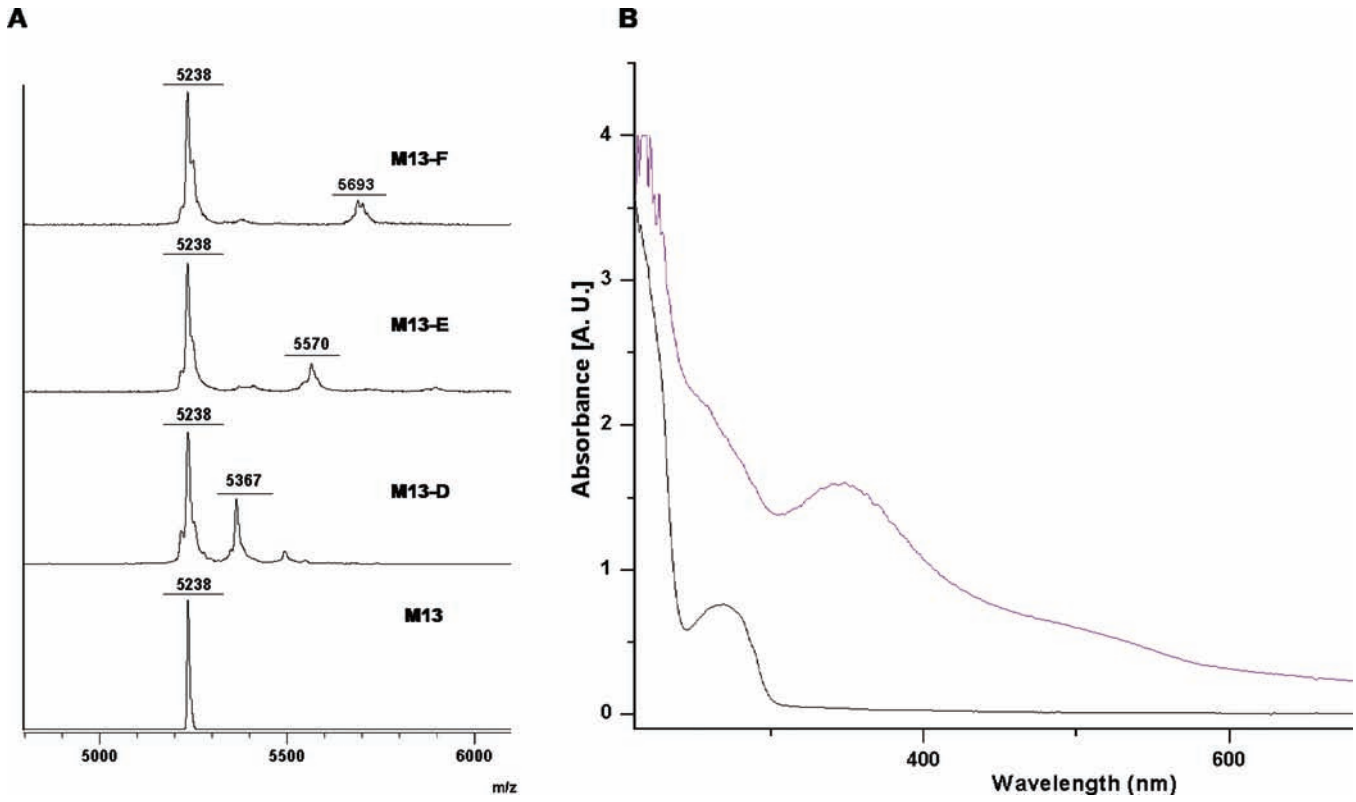


Figure 4. (A) MALDI-TOF MS of whole subunit of wild-type M13 and M13-B (*m*/*z* 5367), and a following conjugation with compound C (M13-C: *m*/*z* 5570) or compound D (M13-D: *m*/*z* 5693). (B) UV−vis spectra showing bacteriophage absorbance of wild-type M13 (black curve) and M13-C (purple curve). M13-C gives a strong absorbance at 340 nm.

HPLC-MS/MS. In order to solve this problem, prop-2-yn-1-amine (compound A), a smaller molecule with better water solubility, was used in the reaction. The MALDI-TOF mass spectra of the coupling products can be found in Figure 3C. Similarly, HPLC-MS/MS was employed to uncover the specific reactive sites. Among all carboxylic acid groups, Glu-2 was reactive and Glu-20 was too "buried" to be modified. Asp-4/Asp-5 could also be modified, but it was difficult to determine which residue(s) contributed to the reactivity due to their proximity. Detailed analysis of the MS results can be found in Supporting Information.

Tyrosine Conjugation. There are two tyrosine residues (Tyr 21 and Tyr 24) on the P8 protein (Figure 1). In order to test the possibility of tyrosine conjugation on M13 bacteriophage, a diazonium coupling reaction with compound B was applied (Scheme 1) (*50*−*52*). As shown in Figure 4A, the modified peak can be found at *m*/*z* 5367, which indicates that the P8 protein was decorated with the alkyne moiety (M13-B). Although it was well-known that diazonium groups were able to react with a variety of protein functional groups, including tyrosine, histidine, or lysine residues (*53*−*55*), the HPLC-MS/MS data indicated that the modifications only took place at tyrosine residues and both Tyr 21 and 24 were modified (See Supporting Information). A CuAAC reaction was then performed to conjugate azides to the alkynyl groups. As shown in Figure 4A, coumarin (compound C) and biotin (compound D) were successfully conjugated onto M13 surface based on MALDI MS analyses (M13-C at *m*/*z* 5570;

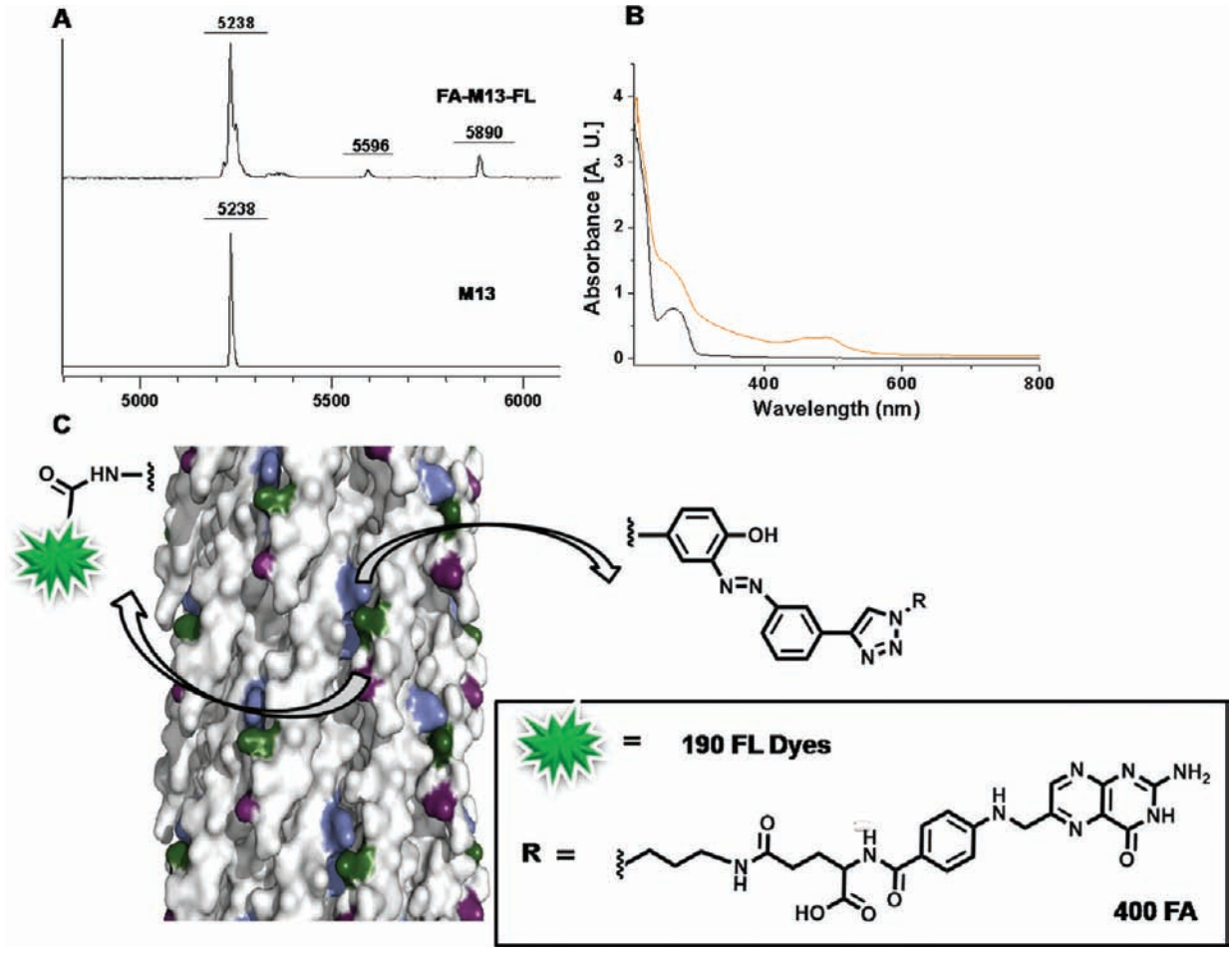


Figure 5. (A) MALDI-TOF MS of whole subunit of WT-M13 and M13 after dual modification with FL-NHS and folic acid. Wild-type M13 (WT-M13): peak = *m*/*z* 5238; the sequential modifications show the peaks of *m*/*z* 5596 and *m*/*z* 5890, respectively, indicating the fluorescein and then folic acid conjugation. (B) UV−vis spectra showing bacteriophage absorbance of wild-type M13 (black curve) and dual-modified M13 bacteriophage (orange curve) after purification. Dual-modified M13 bacteriophage shows an absorbance at 494 nm. (C) The surface structure of M13 bacteriophage with highlighting amine and tyrosine conjugations.

M13-D at *m*/*z* 5693). The biotin concentration was calculated using a Pierce Biotin Quantitation Kit, and around 400 biotins were conjugated per phage. The coumarin clicked compound can be easily monitored by UV−visible absorption at 340 nm (Figure 4B).

Dual Modification on M13 Bacteriophage and Cell Imaging Study. Vitamin folic acid (FA) is one of the most common ligands for cancer cell targeting. It plays an important role in tissue growth and, at the cellular level, in cell division and DNA synthesis. Uptake of FA into cells is mediated by the folate receptor (FR), which is particularly overexpressed in many cancers compared to the limited distribution found on normal cells (*56*). On the basis of the preliminary conjugation analysis, the amino groups and tyrosine groups were chosen as reactive sites for the dual-modification M13 bacteriophage with fluorescent dyes and folic acid motifs. The two reactive groups were chosen because of their higher reactivities, and possible cross-linking caused by EDC chemistry could be avoided. Here, by combining amine and tyrosine bioconjugation, folic acid and fluorescent dye modified M13 bacteriophage could be readily prepared for application in cancer cell imaging. M13 was first treated with FL-NHS to get a 190-fluorescein-unit tailored bacteriophage. After purification, the dye-modified M13 could be further modified with azide-folate via a two-step tyrosine reaction. As shown in Figure 5A, the *m*/*z* 5596 peak indicated the fluorescent dye modification, and the peak at *m*/*z* 5890 indicated the dye and folate dual modified peak. On the basis of the intensity of MS, it was estimated that around 400 folic acid molecules were successfully conjugated onto the M13 surface. The modified M13 bacteriophages were stable and remained intact as confirmed by TEM (Supporting Information Figure S7D).

The dual-modified M13 bacteriophage was investigated for its potential application in tumor cell targeting. HeLa contaminant KB cells were used for the targeting study. Before the imaging study, the KB cells were cultured in the folate-free media to promote the overexpression of the folate-binding proteins. The cellular uptake of M13 bacteriophages in KB cells was analyzed using fluorescence microscopy. Besides dual-modified M13 bacteriophage (FA-M13-FL), two controls, M13-FL and small molecular probe FA-FL, were used. After 1, 8, and 24 h incubation of each sample with KB cells, the cells were fixed and images taken. As shown in Figure 6, the blue color represents cell nuclei, which were labeled with DAPI, and the green color came from different fluorescein-modified samples (M13-FL, FA-FL, and FA-M13-FL). As expected, FA-M13-FL (Figure 6C) showed higher cellular uptake than the M13 bacteriophage that was only modified with fluorescein (M13-FL, Figure 6B). Furthermore, compared with FA-M13-FL particles, the small molecule probe, fluorescein−folate conjugate (FA-FL), only showed weak signals (Figure 6A). The cellular uptake of dual-modified M13 bacteriophage showed a significant increase after longer incubation time. Although the cytoplasm of the

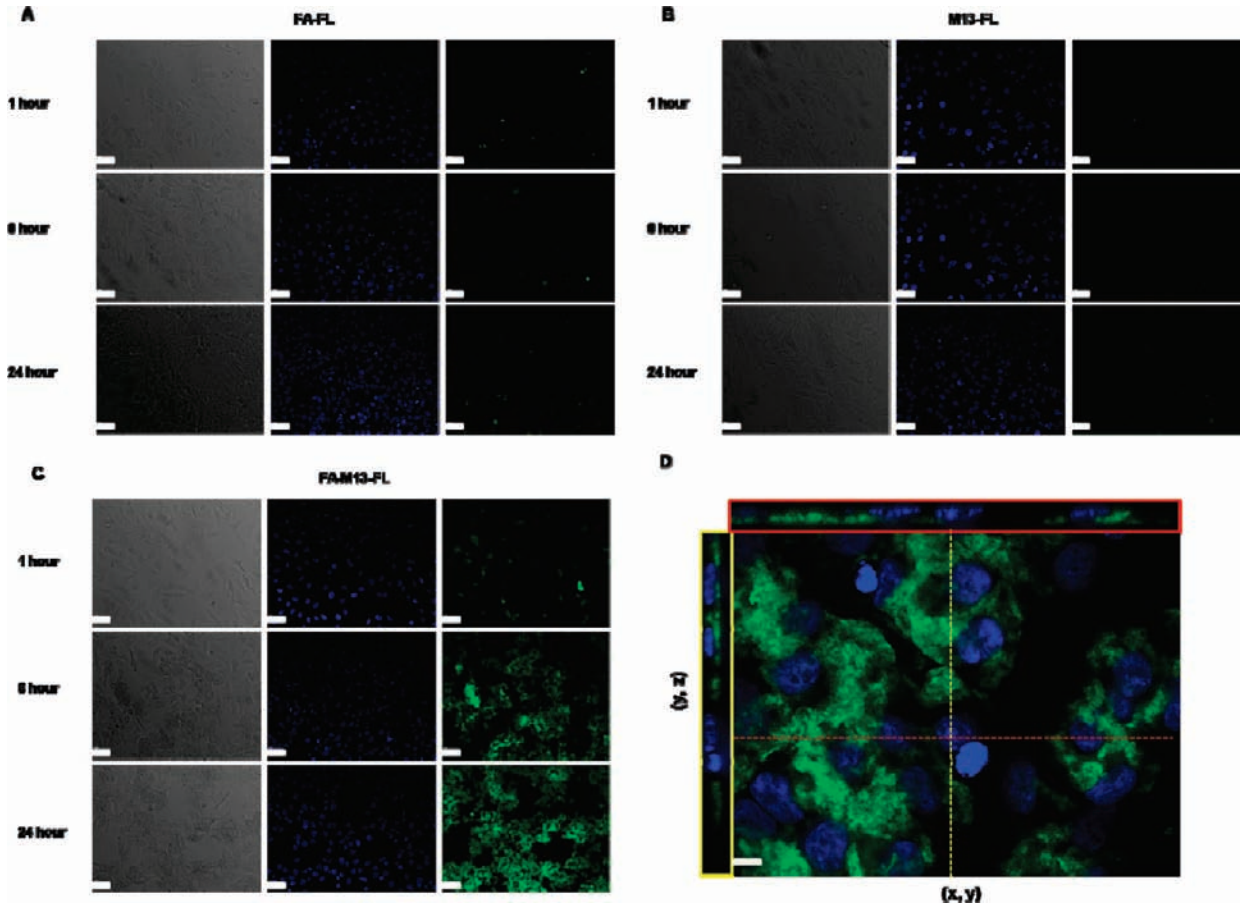


Figure 6. (A−C) Binding and internalization images of FA-FL, M13-FL, and FA-M13-FL into KB cells during different time periods. From left to right, images represent different fluorescent channels. Scale bar: 40 μm (confocal setting, 20×/0.85 oil lens; gain, 0; ND, 1; exposure time: cDAPI, 110 ms; cFITC, 500 ms). (D) Three-dimensional view of FA-M13-FL cell image. The top and left columns show the *z*-axis images. Scale bar: 10 μm (confocal setting, 60×/1.35 oil lens; gain, 0; ND, 1; exposure time: cDAPI, 30 ms; cFITC, 500 ms).

cells were not specifically stained, three-dimensional imaging indicated that the M13 bacteriophage might be located in the cytoplasm of KB cells (Figure 6D). Full *z*-stack 3D rendered rotational video images from confocal imaging are available in the Supporting Information.

CONCLUSION

In conclusion, we fully screened the reactivity of three different reactive groups on the M13 surface by traditional bioconjugation methods. Amine-NHS coupling chemistry led to functionalization at N-terminus and Lys-8 residues, which was confirmed by LC-MS/MS, while the N-terminal amino group showed significantly higher reactivity than the amino group of the Lys-8 residue, which may be attributed to their different pK_a (N-terminal α-amine: 7.6−8.0; ε-amine of lysine: 9.3−9.5) (*57*). As reported, the lower pK_a value of N-terminal amine groups (relative to lysines) can be selectively modified in a lower pH reaction (*58*). Carboxylic acid groups and tyrosine residues of M13 could also be modified at a relatively lower level compared to amine group. For a tyrosine modification, a following "click" reaction could easily conjugate different small molecules onto the M13 surface. After the chemical modifications, the M13 particles were still kept intact, which was confirmed by TEM analysis. Through dual modification of M13 with fluorescent dyes and a cell targeting motif, such as folic acid, the newly functionalized biological particle could be used as fluorescent probe for human KB cancer cell imaging.

ACKNOWLEDGMENT

We are grateful for the financial support from the US NSF (CAREER program and DMR-0706431), US DoD (W911NF-09-1-0236), the Alfred P. Sloan Scholarship, the Camille Dreyfus Teacher Scholar Award, DoD-BCRP, and the W. M. Keck Foundation. We thank L. Andrew Lee and Elizabeth Balizan for the assistance of confocal images, and Laying Wu for the assistance of TEM images. Kai Li would like to thank the Scholarship from the China Scholarship Council. Huong Giang Nguyen would like to thank the Magellan Scholar Program from USC Research Foundation. We are also grateful for all constructive suggestions given by all reviewers.

Supporting Information Available: MALDI spectra of wild-type M13 and chemically derivatized M13, and the MS/MS spectra of wild-type M13 with most of b-ions and y-ions marked, discussions of the site specificity and MS data, synthesis of all small molecules, and TEM images of M13 and its derivatives. This material is available free of charge via the Internet at http://pubs.acs.org.

LITERATURE CITED

(1) Chiang, C.-Y., Mello, C. M., Gu, J., Silva, E. C. C. M., Van Vliet, K. J., and Belcher, A. M. (2007) Weaving genetically engineered functionality into mechanically robust virus fibers. *Adv. Mater. 19*, 826–832.

(2) Nam, K. T., Kim, D.-W., Yoo, P. J., Chiang, C.-Y., Meethong, N., Hammond, P. T., Chiang, Y.-M., and Belcher, A. M. (2006) Virus-enabled synthesis and assembly of nanowires for lithium ion battery electrodes. *Science 312*, 885–888.
(3) Smith, G. P., and Petrenko, V. A. (1997) Phage display. *Chem. Rev. 97*, 391–410.
(4) Nam, K. T., Wartena, R., Yoo, P. J., Liau, F. W., Lee, Y. J., Chiang, Y.-M., Hammond, P. T., and Belcher, A. M. (2008) Stamped microbattery electrodes based on self-assembled M13 viruses. *Proc. Natl. Acad. Sci. U.S.A. 105*, 17227–17231.
(5) Lee, Y. J., Yi, H., Kim, W.-J., Kang, K., Yun, D. S., Strano, M. S., Ceder, G., and Belcher, A. M. (2009) Fabricating genetically engineered high-power lithium-ion batteries using multiple virus genes. *Science 324*, 1051–1055.
(6) Merzlyak, A., Indrakanti, S., and Lee, S.-W. (2009) Genetically engineered nanofiber-like viruses for tissue regenerating materials. *Nano Lett. 9*, 846–852.
(7) Avery, K. N., Schaak, J. E., and Schaak, R. E. (2009) M13 bacteriophage as a biological scaffold for magnetically-recoverable metal nanowire catalysts: combining specific and nonspecific interactions to design multifunctional nanocomposites. *Chem. Mater. 21*, 2176–2178.
(8) Yang, L. M. C., Diaz, J. E., McIntire, T. M., Weiss, G. A., and Penner, R. M. (2008) Covalent virus layer for mass-based biosensing. *Anal. Chem. 80*, 933–943.
(9) Yang, L. M. C., Diaz, J. E., McIntire, T. M., Weiss, G. A., and Penner, R. M. (2008) Direct electrical transduction of antibody binding to a covalent virus layer using electrochemical impedance. *Anal. Chem. 80*, 5695–5705.
(10) Yang, L. M. C., Tam, P. Y., Murray, B. J., McIntire, T. M., Overstreet, C. M., Weiss, G. A., and Penner, R. M. (2006) Virus electrodes for universal biodetection. *Anal. Chem. 78*, 3265–3270.
(11) Souza, G., Christianson, D., Staquicini, F., Ozawa, M., Snyder, E., Sidman, R., Miller, J., Arap, W., and Pasqualini, R. (2006) Networks of gold nanoparticles and bacteriophage as biological sensors and cell-targeting agents. *Proc. Natl. Acad. Sci. U.S.A. 103*, 1215–1220.
(12) Kassner, P., Burg, M., Baird, A., and Larocca, D. (1999) Genetic selection of phage engineered for receptor-mediated gene transfer to mammalian cells. *Biochem. Biophys. Res. Commun. 264*, 921–928.
(13) Larocca, D., and Baird, A. (2001) Receptor-mediated gene transfer by phage-display vectors: applications in functional genomics and gene therapy. *Drug Discovery Today 6*, 793–801.
(14) Nielsen, U., and Marks, J. (2000) Internalizing antibodies and targeted cancer therapy: direct selection from phage display libraries. *Pharm. Sci. Technol. Today 3*, 282–291.
(15) Nam, K. T., Peelle, B. R., Lee, S.-W., and Belcher, A. M. (2004) Genetically driven assembly of nanorings based on the M13 virus. *Nano Lett. 4*, 23–27.
(16) Mao, C., Flynn, C. E., Hayhurst, A., Sweeney, R., Qi, J., Georgiou, G., Iverson, B., and Belcher, A. M. (2003) Viral assembly of oriented quantum dot nanowires. *Proc. Natl. Acad. Sci. U.S.A. 100*, 6946–6951.
(17) Mao, C., Solis, D. J., Reiss, B. D., Kottmann, S. T., Sweeney, R. Y., Hayhurst, A., Georgiou, G., Iverson, B., and Belcher, A. M. (2004) Virus-based toolkit for the directed synthesis of magnetic and semiconducting nanowires. *Science 303*, 213–217.
(18) Lee, S.-W., Lee, S. K., and Belcher, A. M. (2003) Virus-based alignment of inorganic, organic, and biological nanosized materials. *Adv. Mater. 15*, 689–692.
(19) Ni, J., Lee, S.-W., White, J. M., and Belcher, A. M. (2004) Molecular orientation of a ZnS-nanocrystal-modified M13 virus on a silicon substrate. *J. Polym. Sci., Part B: Polym. Phys. 42*, 629–635.
(20) Lee, S.-W., Wood, B. M., and Belcher, A. M. (2003) Chiral smectic C structures of virus-based films. *Langmuir 19*, 1592–1598.
(21) Yoo, P. J., Nam, K. T., Belcher, A. M., and Hammond, P. T. (2008) Solvent-assisted patterning of polyelectrolyte multilayers and selective deposition of virus assemblies. *Nano Lett. 8*, 1081–1089.
(22) Yoo, P. J., Nam, K. T., Qi, J., Lee, S.-K., Park, J., Belcher, A. M., and Hammond, P. T. (2006) Spontaneous assembly of viruses on multilayered polymer surfaces. *Nat. Mater. 5*, 234–240.
(23) Lee, S.-W., and Belcher, A. M. (2004) Virus-based fabrication of micro- and nanofibers using electrospinning. *Nano Lett. 4*, 387–390.
(24) Flynn, C. E., Mao, C., Hayhurst, A., Williams, J. L., Georgiou, G., Iverson, B., and Belcher, A. M. (2003) Synthesis and organization of nanoscale II-VI semiconductor materials using evolved peptide specificity and viral capsid assembly. *J. Mater. Chem. 13*, 2414–2421.
(25) Lee, S.-K., Yun, D. S., and Belcher, A. M. (2006) Cobalt ion mediated self-assembly of genetically engineered bacteriophage for biomimetic Co-Pt hybrid material. *Biomacromolecules 7*, 14–17.
(26) Lee, L., Niu, Z., and Wang, Q. (2009) Viruses and virus-like protein assemblies-Chemically programmable nanoscale building blocks. *Nano Res. 2*, 349–364.
(27) Yacoby, I., Bar, H., and Benhar, I. (2007) Targeted drug-carrying bacteriophages as antibacterial nanomedicines. *Antimicrob. Agents Chemother. 51*, 2156–2163.
(28) Yacoby, I., Shamis, M., Bar, H., Shabat, D., and Benhar, I. (2006) Targeting antibacterial agents by using drug-carrying filamentous bacteriophages. *Antimicrob. Agents Chemother. 50*, 2087–2097.
(29) Bar, H., Yacoby, I., and Benhar, I. (2008) Killing cancer cells by targeted drug-carrying phage nanomedicines. *BMC Biotechnol. 8*, 37.
(30) Yacoby, I., and Benhar, I. (2008) Targeted filamentous bacteriophages as therapeutic agents. *Expert Opin. Drug Delivery 5*, 321–329.
(31) Rong, J. H., Lee, L. A., Li, K., Harp, B., Mello, C. M., Niu, Z. W., and Wang, Q. (2008) Oriented cell growth on self-assembled bacteriophage M13 thin films. *Chem. Commun.* 5185–5187.
(32) Hilderbrand, S. A., Kelly, K. A., Weissleder, R., and Tung, C.-H. (2005) Monofunctional near-infrared fluorochromes for imaging applications. *Bioconjugate Chem. 16*, 1275–1281.
(33) Hilderbrand, S. A., Kelly, K. A., Niedre, M., and Weissleder, R. (2008) Near infrared fluorescence-based bacteriophage particles for ratiometric pH imaging. *Bioconjugate Chem. 19*, 1635–1639.
(34) Niu, Z., Bruckman, M., Harp, B., Mello, C., and Wang, Q. (2008) Bacteriophage M13 as a scaffold for preparing conductive polymeric composite fibers. *Nano Res. 1*, 235–241.
(35) Goldman, E. R., Pazirandeh, M. P., Mauro, J. M., King, K. D., Frey, J. C., and Anderson, G. P. (2000) Phage-displayed peptides as biosensor reagents. *J. Mol. Recog. 13*, 382–387.
(36) Jaye, D. L., Geigerman, C. M., Fuller, R. E., Akyildiz, A., and Parkos, C. A. (2004) Direct fluorochrome labeling of phage display library clones for studying binding specificities: applications in flow cytometry and fluorescence microscopy. *J. Immunol. Methods 295*, 119–127.
(37) Lewis, J. D., Destito, G., Zijlstra, A., Gonzalez, M. J., Quigley, J. P., Manchester, M., and Stuhlmann, H. (2006) Viral nanoparticles as tools for intravital vascular imaging. *Nat. Med. 12*, 354–360.
(38) Singh, P., Destito, G., Schneemann, A., and Manchester, M. (2006) Canine parvovirus-like particles, a novel nanomaterial for tumor targeting. *J. Nanobiotechnol. 4*, 2.
(39) Destito, G., Yeh, R., Rae, C. S., Finn, M. G., and Manchester, M. (2007) Folic acid-mediated targeting of cowpea mosaic virus particles to tumor cells. *Nanomed. Nanotechnol. Biol. Med. 3*, 349–349.
(40) Newman, J., Swinney, H. L., and Day, L. A. (1977) Hydrodynamic properties and structure of Fd virus. *J. Mol. Biol. 116*, 593–603.
(41) Hermanson, G. T. (2008) Bioconjugate Techniques, 2nd ed., pp 171−172, Academic Press, Inc., London.

(42) Mujumdar, R. B., Ernst, L. A., Mujumdar, S. R., Lewis, C. J., and Waggoner, A. S. (2002) Cyanine dye labeling reagents: Sulfoindocyanine succinimidyl esters. *Bioconjugate Chem. 4*, 105–111.

(43) Hamman, B. D., Oleinikov, A. V., Jokhadze, G. G., Bochkariov, D. E., Traut, R. R., and Jameson, D. M. (1996) Tetramethylrhodamine dimer formation as a spectroscopic probe of the conformation of Escherichia coli ribosomal protein L7/L12 dimers. *J. Biol. Chem. 271*, 7568–7573.

(44) Grama, L., Somogyi, B., and Kellermayer, M. S. Z. (2001) Global configuration of single titin molecules observed through chain-associated rhodamine dimers. *Proc. Natl. Acad. Sci. U.S.A. 98*, 14362–14367.

(45) Gruber, H. J., Hahn, C. D., Kada, G., Riener, C. K., Harms, G. S., Ahrer, W., Dax, T. G., and Knaus, H.-G. (2000) Anomalous fluorescence enhancement of Cy3 and Cy3.5 versus anomalous fluorescence loss of Cy5 and Cy7 upon covalent linking to IgG and noncovalent binding to avidin. *Bioconjuate Chem. 11*, 696–704.

(46) Gillitzer, E., Willits, D., Young, M., and Douglas, T. (2002) Chemical modification of a viral cage for multivalent presentation. *Chem. Commun.* 2390–2391.

(47) Wang, Q., Kaltgrad, E., Lin, T. W., Johnson, J. E., and Finn, M. G. (2002) Natural supramolecular building blocks: Wild-type cowpea mosaic virus. *Chem. Biol. 9*, 805–811.

(48) Taylor, D. J., Wang, Q., Bothner, B., Natarajan, P., Finn, M. G., and Johnson, J. E. (2003) Correlation of chemical reactivity of Nudaurelia capensis omega virus with a pH-induced conformational change. *Chem. Commun.* 2770–2771.

(49) Chatterji, A., Ochoa, W. F., Paine, M., Ratna, B. R., Johnson, J. E., and Lin, T. W. (2004) New addresses on an addressable virus nanoblock: Uniquely reactive lys residues on cowpea mosaic virus. *Chem. Biol. 11*, 855–863.

(50) Wu, P., Feldman, A. K., Nugent, A. K., Hawker, C. J., Scheel, A., Voit, B., Pyun, J., Fréchet, J. M. J., Sharpless, K. B., and Fokin, V. V. (2004) Efficiency and fidelity in a click-chemistry route to triazole dendrimers by the copper(I)-catalyzed ligation of azides and alkynes. *Angew. Chem., Int. Ed. 43*, 3928–3932.

(51) Bruckman, M. A., Kaur, G., Lee, L. A., Xie, F., Sepulvecla, J., Breitenkamp, R., Zhang, X., Joralemon, M., Russell, T. P., Emrick, T., and Wang, Q. (2008) Surface modification of tobacco mosaic virus with "Click" chemistry. *ChemBioChem 9*, 519–523.

(52) Schlick, T. L., Ding, Z., Kovacs, E. W., and Francis, M. B. (2005) Dual-surface modification of the tobacco mosaic virus. *J. Am. Chem. Soc. 127*, 3718–3723.

(53) Howard, A. N., and Wild, F. (1957) Reactions of diazonium compounds with amino acids and proteins. *Biochem. J. 65*, 651–659.

(54) Eagle, H., and Vickers, P. (1936) The nature of the reaction between diazotized sulfanilic acid and proteins. *J. Biol. Chem. 114*, 193–197.

(55) Meares, C. F., Goodwin, D. A., Leung, C. S., Girgis, A. Y., Silvester, D. J., Nunn, A. D., and Lavender, P. J. (1976) Covalent attachment of metal chelates to proteins:the stability in vivo and in vitro of the conjugate of albumin with a chelate of 111indium. *Proc. Natl. Acad. Sci. U.S.A. 73*, 3803–3806.

(56) Low, P. S., Henne, W. A., and Doorneweerd, D. D. (2008) Discovery and development of folic-acid-based receptor targeting for Imaging and therapy of cancer and inflammatory diseases. *Acc. Chem. Res. 41*, 120–129.

(57) Natarajan, S. K., Assadi, M., and Sadegh-Nasseri, S. (1999) Stable peptide binding to MHC class II molecule is rapid and is determined by a receptive conformation shaped by prior association with low affinity peptides. *J. Immunol. 162*, 4030–4036.

(58) Baker, D. P., Lin, E. Y., Lin, K., Pellegrini, M., Petter, R. C., Chen, L. L., Arduini, R. M., Brickelmaier, M., Wen, D., Hess, D. M., Chen, L., Grant, D., Whitty, A., Gill, A., Lindner, D. J., and Pepinsky, R. B. (2005) N-Terminally PEGylated human interferon-β-1a with improved pharmacokinetic properties and in vivo efficacy in a melanoma angiogenesis models. *Bioconjugate Chem. 17*, 179–188.

(59) Marvin, D. A., Hale, R. D., Nave, C., and Helmer-Citterich, M. (1994) Molecular models and structural comparisons of native and mutant class I filamentous bacteriophages Ff (fd, f1, M13), If1 and IKe. *J. Mol. Biol. 235*, 260–286.

BC900405Q

"One-Step" Detection of Matrix Metalloproteinase Activity Using a Fluorogenic Peptide Probe-Immobilized Diagnostic Kit

Ju Hee Ryu,[†,‡] Aeju Lee,[†,‡] Seulki Lee,[‡] Cheol-Hee Ahn,[§] Jong Woong Park,[||] James F. Leary,[⊥] Sangjin Park,[‡] Kwangmeyung Kim,[‡] Ick Chan Kwon,[‡] In-Chan Youn,*[,‡] and Kuiwon Choi*[,‡]

Biomedical Research Center, Korea Institute of Science and Technology, Seongbuk-Gu, Seoul, South Korea, Research Institute of Advanced Materials (RIAM), Department of Materials Science and Engineering, Seoul National University, San 56-1 Sillim, Gwanak, Seoul, 151-744, South Korea, Department of Orthopaedic Surgery, College of Medicine, Korea University, Seoul, South Korea, and Weldon School of Biomedical Engineering, Purdue University, West Lafayette, Indiana. Received January 5, 2010; Revised Manuscript Received March 5, 2010

Matrix metalloproteinases (MMPs) have been shown to be abundant in pathological conditions such as cancer, osteoarthritis (OA), and rheumatoid arthritis (RA). The extent of MMPs detected in biological samples provides important clinical information for diagnosis, prognosis, and therapeutic monitoring of various diseases relating with MMPs. Herein, we developed a new high-throughput MMP diagnostic kit (MMP-D-KIT) based on a 96-well plate by immobilizing MMP-13 specific fluorogenic peptide probes (MMP peptide probe), which is a pair consisting of a near-infrared (NIR) fluorophore (Cy5.5) and a quencher (BHQ-3), onto the biocompatible glycol chitosan (GC) polymer anchored 96-well plate. When MMP enzymes were simply added and incubated in a MMP-D-KIT, the fluorescence of each well was recovered and the fluorescence intensity showed distinct difference within minutes through NIR fluorescence imaging system. The fluorescence was recovered not only by MMP-13 activity, but also by other MMPs activity. Furthermore, recovery of NIR fluorescent signals in MMP-D-KIT was proportional to concentrations of immobilized MMP peptide probe−GC conjugates and, importantly, MMP concentration. The MMP-D-KIT is most specific for target MMP, compared with other enzymes including caspase-3 and 20s proteasome. Additionally, the MMP-D-KIT was used to detect MMP activity in biological samples such as synovial fluid from 12 OA patients (grades 1−4 based on the Kellgren-Lawrence grading scale). It was found that the fluorescence intensity measured using MMP-D-KIT decidedly correlates with the progression of OA. The MMP-D-KIT could be applicable in detecting MMP activities in various biological samples and evaluating the effects of MMP inhibitors in a rapid and easy fashion.

INTRODUCTION

Matrix metalloproteinases (MMPs) are a class of secretory proteinases that are capable of degrading extracellular matrix (ECM) components in physiological and pathophysiological turnover of tissues (*1*). In particular, MMPs have been shown to be overexpressed in pathological situations such as cancer, atherosclerosis (*2, 3*), rheumatoid arthritis (RA), and osteoarthritis (OA) (*4*). The amount of MMP expression has been found to be associated with tumor stage, invasiveness, and metastasis (*5*−*7*). Therefore, the detection of MMP activity in biological samples provides important information for diagnosis, prognosis, and therapeutic monitoring of various diseases.

Numerous attempts have been made to detect activities of MMPs in biological samples by natural or synthetic substrate-based methods (*8*−*10*). Natural substrate-based methods included radiolabeled gelatin and zymography. The radiolabeled gelatin method detects only degraded products small enough to be soluble in 20% trichloroacetic acid ($Mr < 5000$), which consequently deteriorate the reliability of the assay (*11*). In addition, zymography, the most commonly used natural substrate method, is superior in its detection of MMPs in terms of sensitivity. Gelatin zymography can detect MMP-2 and -9 at low level, but might not be suitable to detect MMP-13 activity.

Nonetheless, they are unsuitable for rapid high-throughput screening of potential MMP inhibitors because of its time-consuming and cumbersome to perform and, furthermore, limitation in specificity (*12*). Some synthetic substrate-based methods include the use of internally quenched fluorogenic substrates that comprise a fluorophore, a quencher, and short peptide substrates. In normal condition, the emitting light from the fluorophore is absorbed into the quencher by resonance energy transfer. Once target enzymes like MMPs cleave specific peptide substrates, separating fluorophore from the quencher, the extent of fluorescence increases remarkably. In order to maximize this phenomenon, great efforts have been made to prepare an efficient pair of a fluorophore and a quencher (*13, 14*). Advantages of using internally quenched fluorogenic substrates include increased selectivity and applicabilty for high-throughput analysis and allow for rapid and continuous measurement of enzyme activity (*15, 16*). Previously, we developed a highly efficient fluorogenic probe for the visual detection of MMP-13 in an OA-induced rat model (*17*). A pair of a fluorophore (Cy5.5) and a quencher (black hole quencher-3; BHQ-3) showed low fluorescence background and significant fluorescent signal recovery, enabling a highly sensitive visual detection in vitro and in vivo.

Herein, we rationally designed a new MMP activity diagnostic kit (MMP-D-KIT) for high-throughput screening of the bioac-

* To whom correspondence should be addressed. (Dr. I. C. Youn) Tel: +82-2-958-5913; Fax: +82-2-958-5909; E-mail: iyoun@kist.re.kr. (Dr. K Choi) Tel: +82-2-958-5921; Fax: +82-2-958-5909; E-mail: choi@kist.re.kr.

[†] These authors contributed equally to this paper.

[‡] Korea Institute of Science and Technology.

[§] Seoul National University.

[||] Korea University.

[⊥] Purdue University.

10.1021/bc100008b © 2010 American Chemical Society
Published on Web 06/24/2010

tivity of MMPs in a rapid and simple fashion. To construct the MMP-D-KIT, first, MMP-13 specific fluorogenic peptide probe (MMP peptide probe) consisted of NIR fluorophore, MMP-13 specific peptide, and black hole quencher were chemically conjugated to glycol chitosan (GC) polymer, resulting in MMP peptide probe−GC conjugates. Second, MMP peptide probe−GC conjugates were effectively immobilized onto the maleic anhydride group-terminated 96-well plate, resulting in MMP-D-KIT. On the basis of this polymer surface modification method, MMP peptide probes were successfully chemically conjugated onto the plate surface, wherein MMP peptide probes can maintain their excellent fluorogenicity against target MMP-13, due to the three-dimensional support of biocompatible GC polymers (*18*−*22*). Further, we investigated whether this new MMP-D-KIT can effectively monitor MMP activity using an NIR fluorescence imaging system, when MMP enzymes or synovial fluids from OA patients were simply added into the MMP-D-KIT.

EXPERIMENTAL METHODS

Preparation of MMP-13 Specific Fluorogenic Peptide Probe (MMP Peptide Probe). MMP peptide probe was prepared by conjugating NIR fluorochrome, Cy5.5 (ex/em; 675/695 nm) and black hole quencher-3 (BHQ-3, abs. 650 nm) to MMP-13 specific substrate (Gly-*Pro-Leu-Gly-Val-Arg*(pbf)-Gly-Lys(boc)-Gly-Gly) (*23*), wherein the cleavage site between Gly and Val was synthesized using standard solid-phase Fmoc peptide chemistry (Peptron, Daejeon, Korea). First, Cy5.5 mono *N*-hydroxysuccinamide ester (8.4 μmol; GE Healthcare, Piscateway, NJ) was chemically conjugated to the N-terminus of the MMP-13 specific peptide (4.0 μmol) in anhydrous dimethylformamide (DMF, 200 μL; Sigma) containing *N*-methyl morpholine (NMM, 52 μmol; Sigma) and 4-dimethylaminopyridine (2.5 μmol; Sigma) at room temperature in the dark with shaking for 2 h. The Cy5.5-MMP-13 specific peptide was precipitated by adding ethyl ether (Sigma). The precipitate was washed with ethyl ether and dried in vacuum, and the side chain protecting groups were removed by incubating in 1 mL of trifluoroacetic acid (TFA; Sigma)/distillated water (DW)/anisole (Sigma) (95:2.5:2.5, v/v). The TFA was evaporated on the rotary evaporator and an additional 1 mL of DW containing 0.1% TFA/acetonitrile containing 0.1% TFA (1:1, v/v) was then added to the product in the rotary evaporator. The dissolved product in the rotary evaporator was purified by C18 semipreparative reversed-phase HPLC; 22% to 40% acetonitrile containing 0.1% TFA versus DW containing 0.1% TFA over 20 min at a flow rate of 4.0 mL/min. Purity (>95%) was confirmed by HPLC. The appropriate fractions were collected and lyophilized. Next, the BHQ-3 mono *N*-hydroxysuccinamide ester (0.90 μmol; Biosearch Technologies, Inc., Novato, CA) was coupled to the primary amine of the lysine of the Cy5.5-Gly-Pro-Leu-Gly-Val-Arg-Gly-Lys-Gly-Gly (0.90 μmol) in anhydrous DMF (30 μL) containing NMM (9.7 μmol) and 4-dimethylaminopyridine (1.0 μmol) at room temperature in the dark with shaking overnight. The product was purified by C18 semipreparative reversed-phase HPLC; 30% to 70% acetonitrile containing 0.1% TFA versus DW containing 0.1% TFA over 20 min at a flow rate of 4.0 mL/min. Purity (>95%) was confirmed by HPLC. The appropriate fractions were collected and lyophilized.

Synthesis of MMP Peptide Probe−GC Conjugates. Dark-quenched MMP peptide probe of Cy5.5-MMP-13-substrate-BHQ-3 was chemically conjugated to the GC polymer, as follows. MMP peptide probe (0.88 μmol) dissolved in dimethyl sulfoxide (DMSO, 100 μL; Sigma)/phosphate buffered saline (PBS, 100 μL, pH 6.0; Sigma) was mixed with 1-[3-(dimethylamino)propyl]-3-ethylcarbodiimide hydrochloride (EDC, 5.2 μmol; Sigma) and *N*-hydroxysulfosuccinimide (Sulfo-NHS, 5.2 μmol; Pierce, Rockford, IL) dissolved in PBS (100 μL, pH 6.0) for 15 min. The mixture was then added to GC (250 kDa, 0.04 μmol; Sigma) and dispersed in PBS (14 mL, pH 7.4). The reaction was performed at room temperature in the dark with shaking overnight. Unreacted MMP peptide probes were removed for 3 days by dialysis (molecular weight cutoff = 12−14K, Spectrum Laboratories, Inc., Rancho Dominguez, CA). The product was subsequently lyophilized.

UV Measurements of MMP Peptide Probe−GC Conjugates. In order to obtain a standard curve for calculation of the amounts of MMP peptide probes conjugated to GC polymer, UV absorbance of MMP peptide probe−GC conjugates (1.10 μM) was recorded from 450 to 800 nm using UV/vis spectrophotometer (Optizen 2120, Mecasys, Daejeon, Korea). MMP peptide probes at various concentrations (1.5, 2.6, 5.5, 11.0, and 22.0 μM, respectively) were served as standard. Standard curve was achieved using the UV absorption spectra data at 690 nm.

Enzyme Specificity of the MMP Peptide Probe−GC Conjugates. The MMP-13 specific fluorogenic property of the MMP peptide probe−GC conjugates (20 nM) was examined by incubating in the reaction buffer (50 mM Tris·HCl, 10 mM $CaCl_2 \cdot 2H_2O$, 0.15 M NaCl, 0.05% Brij35, pH 7.8) containing 15 nM of activated MMP-2, MMP-3, MMP-7, MMP-9, MMP-13 (R&D Systems, Inc., Minneapolis, MN), and MMP-13 with inhibitor (*N*-hydroxy-1,3-di-(4-methoxybenzenesulfonyl)-5,5-dimethyl-[1,3]-piperazine-2-carboxamide) (Calbiochem, San Diego, CA), respectively. MMP-2, MMP-3, MMP-7, and MMP-13 enzymes were activated by incubating them with 2.5 mM of *p*-aminophenyl mercuric acid in 0.1% NaOH buffer for 1 h at 37 °C before initiation of the assay. Fluorescence intensity was monitored using a spectrofluorometer (F-7000 Fluorescence Spectrophotometer, Hitach, Tokyo, Japan) every 10 min at 37 °C using a 1 mL of cuvette. The excitation wavelength was set at 675 nm and emission spectra recorded from 676 to 800 nm. The same experimental conditions were applied to various concentrations of activated MMP-13 (0.5, 1.9, 3.8, 7.5 nM) in the presence of a fixed concentration of MMP peptide probe−GC conjugates (20 nM).

Immobilization of MMP Peptide Probe−GC Conjugates onto 96-well Plate (MMP-D-KIT). MMP peptide−GC conjugates (10 μM) in PBS/DMSO (7:3, 100 μL) were directly immobilized on each well of maleic anhydride-activated 96-well plates (Pierce) and another MMP peptide−GC conjugates (10 μM) in PBS/DMSO (7:3, 100 μL) were placed on each well of usual 96-well plates. After incubating for 12 h at room temperature while shaking, the MMP peptide−GC conjugate solutions from maleic anhydride-activated 96-well plate and usual 96-well plate were diluted 10-fold, respectively, and UV absorbance was measured. The difference of UV absorbance between the MMP peptide−GC conjugate solutions from maleic anhydride-activated 96-well plate and usual 96-well plate were calculated to concentration of immobilized MMP probes, comparing with standards of known concentration of MMP peptide−GC conjugates. Various concentrations of MMP peptide−GC conjugates (0.1, 0.25, 0.5, 1.0, 2.5, 5.0, 7.5, 10, 20, and 40 μM) in PBS/DMSO were directly immobilized on each well of maleic anhydride-activated 96-well plates. After incubating for 12 h at room temperature while shaking, the MMP peptide−GC conjugate solution was removed from each well. The plates were blocked by addition of 0.5% bovine serum albumin in PBS for 1 h at room temperature, after which the plates were washed three times with washing buffer (50 mM Tris·HCl, 10 mM $CaCl_2 \cdot 2H_2O$, 0.15 M NaCl, 0.05% Brij35, pH 7.8).

Fluorescence Quantitative Analysis of the MMP-D-KIT. Activated MMP-13 enzyme (15 nM) was added to each well and incubated for 1 h at 37 °C. After the incubation, MMP-D-

KIT was imaged using a Kodak Image Station 4000MM. The NIR fluorescent images of MMP-D-KIT were obtained using a 12-bit CCD camera (Kodak, Japan) equipped with a special C-mount lens and a Cy5.5 bandpass emission filter (680 to 720 nm; Omega Optical, Brattleboro, VT). Simultaneously, the emission spectrum of each sample at the excitation wavelength (675 nm) was obtained to quantify the NIR fluorescence intensity. To confirm that visual detection of the MMP-D-KIT was dependent on the amount of MMPs, 96-well plates immobilized of MMP peptide probe−GC conjugates (10 μM) were prepared under the same experimental conditions. Serial dilutions of activated MMP-13 enzyme (1.0, 1.8, 3.7, 7.5, 15, 30 nM) was added to each well and incubated for 1 h at 37 °C. To confirm the specificity of the MMP-D-KIT, it was incubated with activated MMP-13 (15 nM), activated MMP-13 (15 nM) with inhibitor, caspase-3 (70 nM; R&D Systems), and 20s proteasome (1 nM, Boston Biochem, Cambridge, MA). 20s proteasome in working buffer (50 mM HEPES, pH 7.6, 100 mM NaCl, 1 mM dithiothreitol) was activated by adding sodium dodecyl sulfate (0.035%) for 20 min at 37 °C. Activated 20s proteasome and caspase-3 in working buffer (25 mM HEPES, pH 7.5, 0.1% CHAPS, 10 mM dithiothreitol) were added to each MMP-D-KIT and incubated for 1 h at 37 °C, and the fluorescence image and intensity were measured using Kodak Image Station and fluorescence spectofluorometer. Data were obtained from three samples per group and expressed as the mean ± standard deviation.

Screening the MMP Activity from Osteoarthritis (OA) Patients. Twelve OA patients were divided into four groups according to the severity of OA based on the Kellgren-Lawrence grading scale: grade 1, doubtful narrowing of joint space and possible osteophytic lipping; grade 2, definite osteophytes, definite narrowing of joint space; grade 3, moderate multiple osteophytes, definite narrowing of joints space, some sclerosis and possible deformity of bone contour; grade 4, large osteophytes, marked narrowing of joint space, severe sclerosis, and definite deformity of bone contour (*24*). The severity of OA was separately scored and statistically confirmed by four physicians using the cross-validation method. The synovial fluid (3−21 mL) was harvested from the knee joint of OA patients and aliquoted in 2 mL samples and stored at −70 °C before use. Finally, each sample was diluted 10-fold in TCNB buffer solution, and it was added to the MMP-D-KIT and incubated for 1 h at 37 °C to measure the MMP activity. Therefore, TCNB buffer was regarded as controls. After the incubation, MMP-D-KIT was imaged using a 12-bit CCD camera (Kodak, Japan) equipped with a special C-mount lens and a Cy5.5 bandpass emission filter (680 to 720 nm; Omega Optical, Brattleboro, VT). The fluorescence intensity was measured using a fluorescence spectofluorometer. Data were obtained from three synovial fluids per group and expressed as the mean ± standard deviation.

RESULTS AND DISCUSSION

In order to prepare a high-throughput MMP-D-KIT, first, MMP peptide probes were chemically conjugated to GC polymer (MMP peptide probe−GC conjugates), which act as polymeric linker between MMP peptide probe and 96-well plate. Second, MMP peptide probe−GC conjugates were directly immobilized onto the maleic anhydride group-terminated 96-well plate, wherein the maleic anhydride group likely reacts with primary amine of GC, resulting in MMP-D-KIT (Figure 1).

The MMP fluorogenic peptide probe (MMP peptide probe) was prepared by conjugating near-infrared (NIR) fluorophore, Cy5.5, and black hole quencher, BHQ-3, to the MMP-13 specific peptide substrate of *GPLGVRGKGG*, in resulting Cy5.5-MMP-13 substrate-BHQ-3 (*17, 23*). The MMP peptide probe of Cy5.5-MMP-13 substrate-BHQ-3 was optimized by modeling the X-ray crystal structure of hMMP-13 (*17*), wherein a short peptide sequence, *GPLGVRGKGG*, was specifically cleaved by MMP-13 (the MMP-13 specific cleavage site is between G and V). This MMP peptide probe showed a minimal NIR fluorescence signal at normal condition, because black hole quencher, BHQ-3, is able to quench emitting fluorophores of Cy5.5, resulting in significantly low fluorescent backgrounds without MMP-13 enzyme. However, it was reported that the dark-quenched fluorogenic MMP peptide probe presented strong fluorescent signal by the addition of target MMP-13 (*17*).

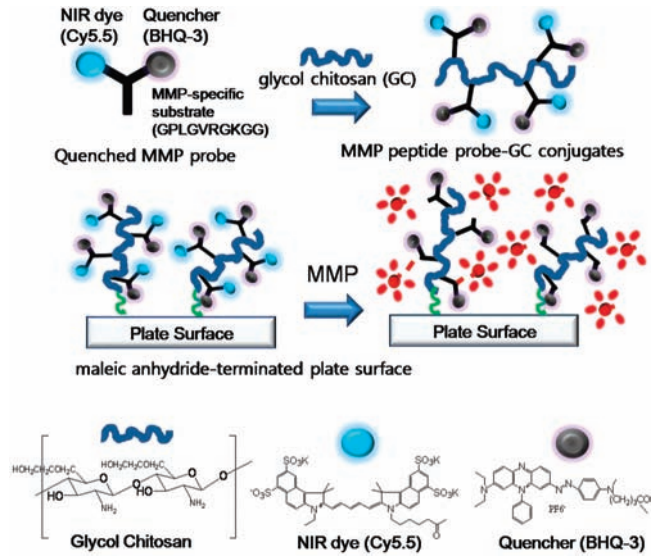


Figure 1. Schematic diagram of MMP diagnostic kit (MMP-D-KIT) for "one step" detection of MMP acitivity. First, MMP peptide probe consisted of Cy5.5-MMP-13 substrate-BHQ-3 was conjugated to GC polymer (MMP peptide probe−GC conjugates). Second, MMP peptide probe−GC conjugates were immobilized on each well of maleic anhydride-terminated 96-well plates (MMP-D-KIT). The MMP-D-KIT was quenched before treatment of MMPs, resulting in no fluorescent signals, but active MMP could recover the NIR fluorescent signal.

To give a biocompatible and three-dimensional support of MMP peptide probes on the surface of 96-well plate, we introduced a polymer support of GC polymer (M_w = 250 kDa) by chemical coupling reaction between MMP peptide probes and GC polymer, in resulting MMP peptide probe−GC conjugates. It has been reported that this three-dimensional support of biocompatible polymers may minimize the steric hindrance of MMP peptide probes against MMP enzymes on the solid surface (*20*−*22*). The MMP peptide probes in the flexible polymer conjugates may freely access the target MMP enzymes with high specificity and sensitivity. The optimal reaction ratio of MMP peptide probes in the GC conjugate was confirmed with UV absorbance, wherein most MMP peptide probes were successfully chemically conjugated to GC polymer. UV absorbance of serial dilutions of MMP fluorogenic probes (1.5 to 11 μM) and MMP peptide probe−GC conjugate (1.10 μM) were observed at 690 nm (Figure 2A). The standard curve was plotted according to the MMP peptide probe concentration, and this graph showed a linear relationship ($R^2 > 0.999$) (Figure 2B). On the basis of the UV measurement, the UV absorbance of MMP peptide probe−GC conjugate (1.10 μM) corresponds to that of MMP peptide probe (10.6 μM) in the standard curve, indicating that approximately 10 molecules of MMP peptide probe were conjugated to 1 molecule of GC polymer.

Furthermore, when the MMP peptide−GC conjugate was incubated with different MMP enzymes (MMP-2, MMP-3, MMP-7, MMP-9, and MMP-13), it showed different NIR fluorescent signals at 695 nm over the reaction time at 37 °C

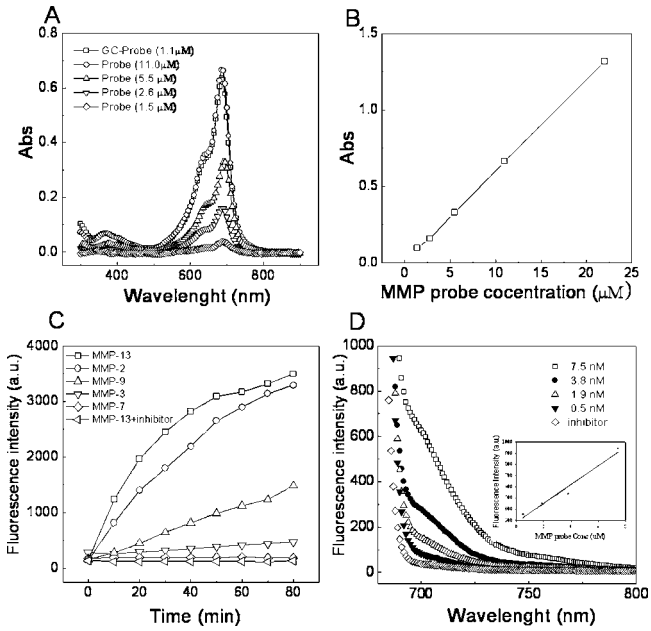


Figure 2. Characterization of MMP peptide probe−GC conjugates. (A) UV absorbance of MMP peptide probe−GC conjugates (1.10 μM) and various concentrations of MMP peptide probes (1.5, 2.6, 5.5, 11.0 μM). (B) Standard curve for calculation of the amounts of MMP peptide probes conjugated to GC polymer. (C) Fluorescence intensity of MMP peptide probe−GC conjugates in solution (20 nM) in the presence of various stimuli (MMP-2, -3, -7, -9, -13, and MMP-13 with inhibitor) as a function of time following incubation for 80 min at 37 °C. (D) Fluorescence emission spectra of MMP peptide probe−GC conjugates in the presence of various concentrations of MMP-13 following incubation for 60 min at 37 °C. Inset: standard curve of MMP peptide probe−GC conjugates.

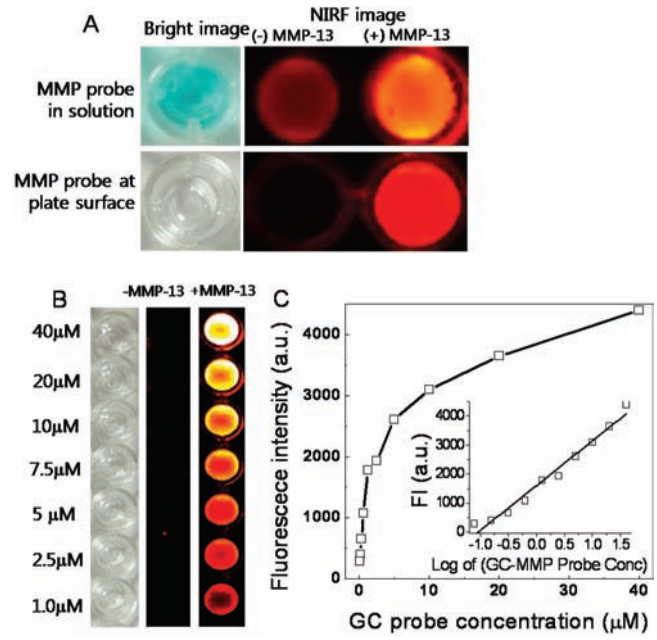


Figure 3. Immobilization of MMP peptide probe−GC conjugates onto 96-well plates. (A) Bright and NIR fluorescent images of 96-well plates containing MMP peptide probe−GC conjugates in the immobilized phase (MMP-D-KIT) and those in the solution, respectively. (B) Bright and NIR fluorescent images of MMP-D-KIT where various concentrations of MMP peptide probe−GC conjugates were immobilized. (C) Graph of corresponding fluorescence intensity of MMP-D-KIT versus the concentration of MMP peptide probe−GC conjugates. Inset: standard curve of MMP concentration.

(Figure 2C). No detectable change was found in the fluorescence signal of polymer conjugates treated by MMP-3 and MMP-7, which meant that MMP-3 and MMP-7 were less effective in cleaving MMP peptide probe−GC conjugates than any other tested MMP enzymes. A small amount of recovery of the NIR fluorescent intensity occurred in the polymer conjugates treated by MMP-9. Noticeably, 25-fold and 22-fold increases in NIR fluorescent intensity occur in the polymer conjugates treated by MMP-2 and MMP-13 after 80 min of incubation, respectively. This result indicates that MMP-13 specific peptide probe−GC conjugates are very specific to target MMP-2 and MMP-13. It was also reported that some overlapping substrate specificity in MMPs was observed, due to the similar homology of MMP enzymes (*25*). As a control experiment, NIR fluorescent signal of the polymer conjugates was not observed by adding MMP-13 inhibitor, indicating the higher specificity of MMP peptide probe−GC conjugates against MMP-13. To test the sensitivity of the polymer conjugates against target enzyme of MMP-13, MMP peptide probe−GC conjugates were incubated with various concentrations of MMP-13 for 1 h at 37 °C (Figure 2D). At the lower MMP-13 concentration of 1.9 nM, substantial NIR fluorescent signal was observed, indicating the higher sensitivity of the polymer conjugates against active MMP-13. Also, the polymer conjugates showed the linear proportional fluorescent signals according to MMP-13 concentrations (R^2 = 0.95) (inset image in Figure 2D). Approximately 2.4-, 3.1-, 3.7-, and 6.4-fold increases in NIR fluorescent intensity occur according to the 0.5, 1.9, 3.8, 7.5 nM of active MMP-13, respectively. It suggests that chemically conjugated MMP peptide probes in the GC polymer conjugates still maintained their fluorogenic enzyme activity against target MMP-13 protease with the higher specificity and sensitivity.

To prepare the MMP-D-KIT, MMP peptide probe−GC conjugates (10 μM) were directly immobilized onto the maleic anhydride group-terminated 96-well plate by simply adding the polymer conjugate solution. At 12 h postreaction, unreacted polymer conjugates were removed from the plate, and the reaction was blocked by addition of 0.5% bovine serum albumin in PBS for 1 h. The freshly prepared MMP-D-KIT was completely washed with 50 mM Tris·HCl washing buffer and further used for in vitro assay. As shown in Figure 3A, at the normal state without MMP-13, MMP-D-KIT presented a completely quenched background, compared to MMP peptide probe−GC conjugate solution with the same MMP peptide probe concentration. It is deduced that surface immobilized MMP peptide probe−GC conjugates may present an additional intermolecular quenching effect of MMP peptide probes on the 96-well plate surface, due to the short distance between MMP peptide probes at the two-dimensional solid surface, compared to the polymer conjugates in solution. In particular, MMP-D-KIT recovered 90% of NIR fluorescent intensity by adding active MMP-13 (15 nM), compared to the MMP peptide probe−GC conjugate solution. It means that the surface-immobilized MMP peptide probes on the GC polymer layer can be freely exposed to the target enzymes. Therefore, this excellently quenched and highly reactive MMP-D-KIT may be applicable in detecting target MMP activity in a rapid and easy fashion.

Before treatment of active MMP-13, the different MMP-D-KIT, treated with different MMP peptide probe−GC conjugate concentrations from 1 μM to 40 μM, presented the same quenched state at normal condition (Figure 3B), due to the complete quenching effect of MMP peptide probes. However, at 1 h postincubation with active MMP 13 (15 nM), the NIR fluorescence signal proportionally increased according to the MMP peptide probe−GC conjugate solution concentration. On the basis of the fluorescence spectrofluo-

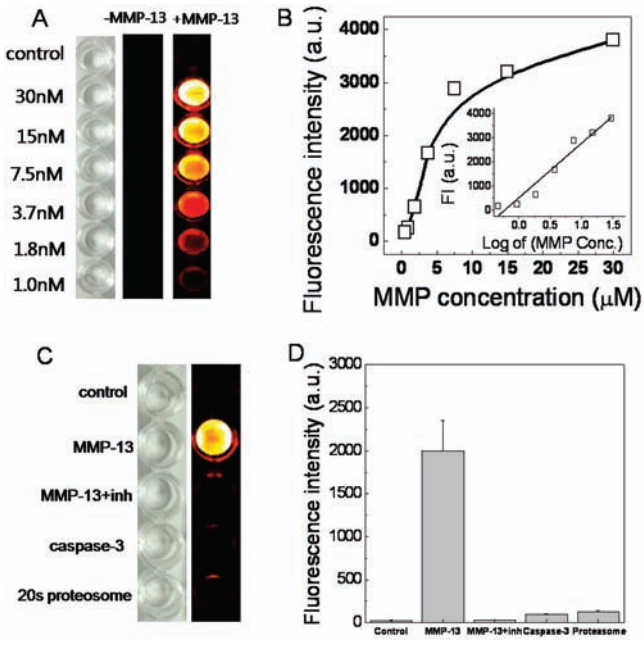


Figure 4. Fluorescence quantitative analysis of the MMP-D-KIT. (A) Bright and NIR fluorescent images of MMP-D-KIT in which various concentrations of MMP-13 were treated. (B) Graph of corresponding fluorescence intensity of MMP-D-KIT versus MMP concentration. (C) Bright and NIRF images of MMP-D-KIT where various proteases (MMP-13, MMP-13 with inhibitor, caspase-3, and 20s proteosome) were treated. (D) NIR fluorescent intensity of various proteases-treated MMP-D-KIT (MMP-13, MMP-13 with inhibitor, caspase-3, and 20s proteosome).

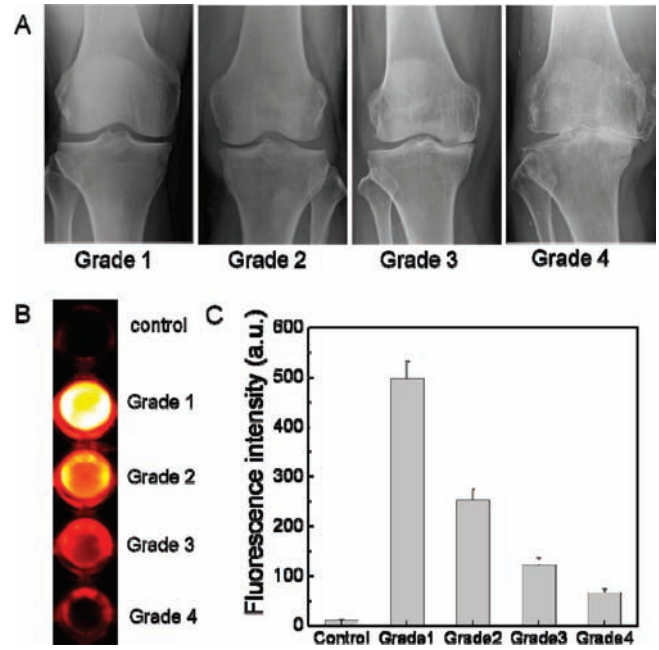


Figure 5. Application of MMP-D-KIT to synovial fluids from OA patients. (A) X-ray data of OA patients. (B) NIR fluorescent image of OA patient's synovial fluid-treated MMP-D-KIT. (C) Fluorescent intensity of OA patient's synovial fluid-treated MMP-D-KIT. TCNB buffer serves as control.

rometer data, a plot of average fluorescence intensity versus probe concentration revealed a hyperbola curve (Figure 3C). The fluorescence signal was further replotted against the logarithm of MMP peptide probe concentration, and it showed a linear relationship, with a good correlation coefficient (R^2 = 0.97, inset image in Figure 3C). This result indicated that the concentration of MMP peptide probes in the MMP-D-KIT can be easily controlled by adding MMP peptide probe solution with a predetermined concentration. In order to assay the extremely small enzyme activity, we optimized the polymer conjugate concentration to 10 μM, wherein the nanomolar MMP activity could be detectable with the higher specificity and sensitivity. Under this optimized condition, recovery of NIR fluorescent signals in the detection kit was proportional to the nanomolar MMP concentration (Figure 4A). At the nanomolar MMP concentration in the range 1−30 nM, the MMP-D-KIT exhibited distinguishable color differences in a 96-well plate after 1 h postincubation at 37 °C, enabling facile visual comparison of relative bioactivity of MMP. The MMP-D-KIT for "one-step" detection of MMP is capable of measuring up to 1 nM (0.5 ng/mL) of MMP-13. There are other detection methods such as radiolabeled gelatin and zymography for MMP-2 and MMP-9. Interestingly, the detection limit of MMP-D-KIT is similar with that of radiolabeled gelatin assay or gelatin zymograpy assay for MMP-2 and MMP-9 (*27*). Furthermore, detection of MMP using MMP-D-KIT is a rapid and simple process compared with other detection methods. As predicted, control MMP-D-KIT without active MMP-13 gave no detectable NIR fluorescent signal.

This proportional relationship between NIR fluorescent signal and MMP concentration was quantitatively confirmed by a spectrofluorometer measurement. A plot of average fluorescence intensity against MMP concentrations demonstrated a MMP concentration-dependent hyperbola curve (Figure 4B). The fluorescence signal was further replotted against a logarithm of MMP enzyme concentration, and it shows a linear relationship with a good correlation coefficient (R^2 = 0.96, inset image in Figure 4B). On the basis of the optimal MMP activity assay, our new MMP-D-KIT could assay the nanomolar MMP activity by "one-step" fluorescence imaging without any additional procedure. Furthermore, our MMP-D-KIT is most specific for target MMP-13, compared with the other proteases including caspase-3 and 20s proteasome (Figure 4C,D). Within 1 h after protease addition, the MMP-D-KIT containing MMP-13 exhibited distinguishable change in the NIR fluorescence signal, wherein an 80-fold increase in NIR fluorescence intensity was observed, compared to the MMP-D-KIT without MMP-13. As a control experiment, the wells containing 20s proteasome and caspase-3 exhibited little to no detectable fluorescence change after protease reaction. The near-recovery of fluorescence signal of the MMP-13 treated detection kit was inhibited in the presence of the MMP inhibitor, suggesting that the detection kit has a reasonable specificity for MMP-13.

For clinical application, the MMP-D-KIT was used to detect MMP-13 activity in synovial fluid from OA patients (Figure 5A). It was previously reported that significantly high MMP-13 activity was monitored in synovial fluid harvested from the knee joint of OA patients (*26*). In order to assay the OA grade-dependent MMP activity, OA patients were divided into four different groups based on the original Kellgren-Lawrence radiographic grading scale, which emphasizes patellofemoral joint space narrowing and presence of osteophytes (grades 1−4, with 1 being early stage of OA and 4 severe OA). When the 10-fold diluted synovial fluid (100 μL) with different OA grades (1−4 grades) were simply incubated in the MMP-D-KIT at 37 °C, each showed distinct NIR fluorescent signal differences at 1 h postincubation, indicating OA grade-dependent MMP activities. TCNB buffer serving as control exhibited little to no detectable fluorescence change.

Interestingly, the synovial fluid sample of early-stage OA patients (grade 1) presented the strongest NIR fluorescent signal,

compared to those of other OA patients (grades 2−4), wherein 50-fold increased NIR fluorescent signal was observed (Figure 5B,C). As the OA grades increased from 2 to 3, the NIR fluorescent signals rapidly decreased, indicating the decrease of MMP-13 activity in late-stage OA patients. The results suggested that the expression of MMP-13 in OA patients may be closely related to the development stages of OA patients. Therefore, our results confirmed the diagnostic feasibility of our MMP-D-KIT for detection and visualization of overexpressed MMP-13 activity in OA patients. We are currently conducting experiments to analyze MMP activity in synovial fluids from a statistically significant number of OA patients with the MMP-D-KIT. In our experimental design, we carried out measurements of MMP activity with synovial fluid of OA patients and TCNB buffer used as a control group, because it is ethically difficult to harvest synovial fluid from individuals without any clinical sign of arthritis. It would be meaningful to compare MMP activity in the synovial fluid of OA patients with that of individuals without any sign of arthritis.

In summary, this study showed that the new fluorogenic peptide-immobilized MMP detection kit based on a 96-well plate could monitor protease activity in a rapid and easy fashion. Fluorogenic peptide probe−GC conjugates were easily immobilized on a 96-well plate, and fluorogenic peptide probes were freely exposed to target MMP-13 enzyme in three-dimensional support GC polymer layer. When target MMP enzyme was simply added and incubated in the MMP detection kit, recovery of NIR fluorescent signals within minutes was proportional to the MMP concentration. The MMP detection kit was also applied to detect MMP activity in synovial fluids from OA patients and showed the fluorescence intensity to correlate with the stage of OA development. The detection kit can be utilized to detect MMP activity in various biological samples and evaluate the effects of MMP inhibitors in a rapid and easy fashion. Additionally, the detection kit can be extended to other proteases simply by changing the specific peptide substrate linker between the fluorophore and black hole quencher.

ACKNOWLEDGMENT

This work was financially supported by the Real-Time Molecular Imaging Project, 2009K 001594, and GRL Program, Pioneer Research Center (2009-0081523) of MEST and by grant to the Intramural Research Program (Theragnosis) of KIST, by a grant of by Advanced Medical Technology Cluster for Diagnosis and Prediction at Kyungpook National University from MOCIE.

LITERATURE CITED

(1) Christopher, M. (2002) Molecular determinants of metalloproteinase substrate specificity: matrix metalloproteinase substrate binding domains, modules, and exosites. *Mol. Biotechnol. 22*, 51–86.

(2) Thompson, R. W., and Baxter, B. T. (1999) MMP inhibition in abdominal aortic aneurysms. Rationale for a prospective randomized clinical trial. *Ann. N. Y. Acad. Sci. 878*, 159–178.

(3) McCawley, L. J., and Matrisian, L. M. (2000) Matrix metalloproteinases: multifunctional contributors to tumor progression. *Mol. Med. Today 6*, 149–156.

(4) Martel-Pelletier, J., McCollum, R., Fujimoto, N., Obata, K., Cloutier, J. M., and Pelletier, J. P. (1994) Excess of metalloproteases over tissue inhibitor of metalloprotease may contribute to cartilage degradation in osteoarthritis and rheumatoid arthritis. *Lab. Invest. 70*, 807–815.

(5) Egeblad, M., and Werb, Z. (2002) New functions for the matrix metalloproteinase in cancer progression. *Nat. Rev. Cancer 2*, 161–174.

(6) Stearns, M. E., and Wang, M. (1993) Type IV collagenase (M(r) 72,000) expression in human prostate: benign and malignant tissue. *Cancer Res. 53*, 878–883.

(7) Turpeenniemi-Hujanen, T. (2005) Gelatinases (MMP-2 and -9) and their natural inhibitors as prognostic indicators in solid cancers. *Biochimie 87*, 287–297.

(8) Koivunen, E., Arap, W., Valtanen, H., Rainisalo, A., Medina, O. P., Heikkilä, P., Kantor, C., Gahmberg, C. G., Salo, T., Konttinen, Y. T., Sorsa, T., Ruoslahti, E., and Pasqualini, R. (1999) Tumor targeting with a selective gelatinase inhibitor. *Nat. Biotechnol. 17*, 768–774.

(9) Yang, J., Zhang, Z., Lin, J., Lu, J., Liu, B. F., Zeng, S., and Luo, Q. (2007) Detection of MMP activity in living cells by a genetically encoded surface-displayed FRET sensor. *Biochim. Biophys. Acta 1773*, 400–407.

(10) Lauer-Fields, J. L., Nagase, H., and Fields, G. B. (2004) Development of a solid-phase assay for analysis of matrix metalloproteinase activity. *J. Biomol. Technol. 15*, 305–316.

(11) Seltzer, J. L., Adams, S. A., Grant, G. A., and Eisen, A. Z. (1981) Purification and properties of a gelatin-specific neutral protease from human skin. *J. Biol. Chem. 256*, 4662–4668.

(12) Law, B., Hsiao, J. K., Bugge, T. H., Weissleder, R., and Tung, C. H. (2005) Optical zymography for specific detection of urokinase plasminogen activator activity in biological samples. *Anal. Biochem. 338*, 151–158.

(13) Melo, R. L., Alves, L. C., Del Nery, E., Juliano, L., and Juliano, M. A. (2001) Synthesis and hydrolysis by cysteine and serine proteases of short internally quenched fluorogenic peptides. *Anal. Biochem. 293*, 71–77.

(14) Grahn, S., Ullmann, D., and Jakubke, H. (1998) Design and synthesis of fluorogenic trypsin peptide substrates based on resonance energy transfer. *Anal. Biochem. 265*, 225–231.

(15) Carvalho, K. M., Boileau, G., Camargo, A. C., and Juliano, L. (1996) A highly selective assay for neutral endopeptidase based on the cleavage of a fluorogenic substrate related to Leu-enkephalin. *Anal. Biochem. 237*, 167–173.

(16) Miners, J. S., Verbeek, M. M., Rikkert, M. O., Kehoe, P. G., and Love, S. (2007) Immunocapture-based fluorometric assay for the measurement of neprilysin-specific enzyme activity in brain tissue homogenates and cerebrospinal fluid. *J. Neurosci. Methods 167*, 229–236.

(17) Lee, S., Park, K., Lee, S. Y., Ryu, J. H., Park, J. W., Ahn, H. J., Kwon, I. C., Youn, I. C., Kim, K., and Choi, K. (2008) Dark quenched matrix metalloproteinase fluorogenic probe for imaging osteoarthritis development in vivo. *Bioconjugate Chem. 19*, 1743–1747.

(18) Park, S., Lee, K. B., Choi, I. S., Langer, R., and Jon, S. (2007) Dual functional, polymeric self-assembled monolayers as a facile platform for construction of patterns of biomolecules. *Langmuir 23*, 10902–10905.

(19) Soper, S. A., Hashimoto, M., Situma, C., Murphy, M. C., McCarley, R. L., Cheng, Y. W., and Barany, F. (2005) Fabrication of DNA microarrays onto polymer substrates using UV modification protocols with integration into microfluidic platforms for the sensing of low-abundant DNA point mutations. *Methods 37*, 103–113.

(20) Rubina, A. Y., Kolchinsky, A., Makarov, A. A., and Zasedatelev, A. S. (2008) Why 3-D? Gel-based microarrays in proteomics. *Proteomics 8*, 817–831.

(21) Fouque, B., Brachet, A. G., Getin, S., Pegon, P., Obeid, P., Delapierre, G., and Chatelain, F. (2007) Improvement of yeast biochip sensitivity using multilayer inorganic sol-gel substrates. *Biosens. Bioelectron. 22*, 2151–2157.

(22) Oillic, C., Mur, P., Blanquet, E., Delapierre, G., Vinet, F., and Billon, T. (2007) DNA microarrays on silicon nanostructures: optimization of the multilayer stack for fluorescence detection. *Biosens. Bioelectron. 22*, 2086–2092.

(23) Lee, S., Ryu, J. H., Park, K., Lee, A., Lee, S. Y., Youn, I. C., Ahn, C. H., Yoon, S. M., Myung, S. J., Moon, D. H., Chen, X.,

Choi, K., Kwon, I. C., and Kim, K. (2009) Polymeric nanoparticle-based activatable near-infrared nanosensor for protease determination in vivo. *Nano Lett. 9*, 4412–4416.

(24) Abe, M., Takahashi, M., Naitou, K., Ohmura, K., and Nagano, A. (2003) Investigation of generalized osteoarthritis by combining X-ray grading of the knee, spine and hand using biochemical markers for arthritis in patients with knee osteoarthritis. *Clin. Rheumatol. 22*, 425–431.

(25) Turk, B. E., Huang, L. L., Piro, E. T., and Cantley, L. C. (2001) Determination of protease cleavage site motifs using mixture-based oriented peptide libraries. *Nat. Biotechnol. 19*, 661–667.

(26) Andereya, S., Streich, N., Schmidt-Rohlfing, B., Mumme, T., Müller-Rath, R., and Schneider, U. (2006) Comparison of modern marker proteins in serum and synovial fluid in patients with advanced osteoarthrosis and rheumatoid arthritis. *Rheumatol. Int. 26*, 432–438.

(27) Zucker, S., Mancuso, P., DiMassimo, B., Lysik, R. M., Conner, C., and Wu, C. L. (1994) Comparison of techniques for measurement of gelatinases/type IV collagenases: enzyme-linked immunoassays versus substrate degradation assays. *Clin. Exp. Metastasis 12*, 13–23.

BC100008B

Multimodality Nuclear and Fluorescence Tumor Imaging in Mice Using a Streptavidin Nanoparticle

Minmin Liang,[†,‡] Xinrong Liu,[†] Dengfeng Cheng,[†] Guozheng Liu,[†] Shuping Dou,[†] Yi Wang,[†] Mary Rusckowski,[†] and Donald J. Hnatowich*[,†]

Department of Radiology, University of Massachusetts Medical School, Worcester, Massachusetts 01655, and National Laboratory of Biomacromolecules, Institute of Biophysics, Chinese Academy of Sciences, 15 Datun Road, Beijing 100101, China. Received February 9, 2010; Revised Manuscript Received May 17, 2010

Combining two or more different imaging modalities in the same agent can be of considerable value in molecular imaging. We describe the use of streptavidin nanoparticle-based complexes as multimodality imaging agents to achieve tumor detection in a mouse model by both fluorescence and nuclear imaging. Up to four biotinylated functionalities can be readily attached to these streptavidin nanoparticles without apparent influence on their properties and with reasonable pharmacokinetics and therefore may be ideally suited for multimodality imaging. By binding a biotinylated anti-Her2 Herceptin antibody to provide tumor targeting, a biotinylated DOTA chelator labeled with ^{111}In and a biotinylated Cy5.5 fluorophore to a streptavidin nanoparticle, we demonstrated multimodality imaging in SUM190 (Her2+) tumor bearing mice on both an IVIS fluorescence camera and a NanoSPECT/CT small animal nuclear camera. The imaging results show high tumor accumulation and strong tumor-to-normal tissue contrast by both fluorescence and nuclear imaging. The subsequent biodistribution study confirmed the specific tumor accumulation in that tumor accumulation of radioactivity at 40 h was 21 ID%/g and therefore much higher than all other tissues including liver, heart, kidney, spleen, and muscle that accumulated 8.7, 2.5, 6.9, 7.2, and 1.9 ID%/g, respectively. In conclusion, the streptavidin nanoparticle under development in this laboratory was used effectively for multimodality imaging of tumor in mice by fluorescence and nuclear detection. Presumably, other imaging modalities could also be considered.

INTRODUCTION

Optical imaging is a relatively new imaging modality that provides rapid, low-cost, and real-time screening for surface lesions such as breast cancer (*1*−*3*). However, optical imaging suffers from limited sensitivity with tissue depth due to light absorption and scatter and as yet has limited ability to provide quantitative and tomographic information (*4*−*7*). By contrast, nuclear imaging offers excellent sensitivity regardless of tissue depth and readily provides both tomographic as well as quantitative information but at a considerably higher cost (*8*−*10*). Thus, the coupling of nuclear and optical imaging in the same agent could overcome the shortcomings of each and combine the benefits of each modality.

In the past several years, many conjugates have been developed by integrating antibodies, peptides, ligands, gene complexes, or small molecule probes with radioactive and optical agents using covalent conjugation (*11*−*15*). This laboratory is developing a nanoparticle based on streptavidin to which up to four biotinylated functionalities can be readily attached without apparent influence on their properties and with reasonable pharmacokinetics (*16*−*18*). The nanoparticle therefore appears to be ideally suited for multimodality imaging. In this study, we developed a trifunctional dual-modality nanoparticle to achieve tumor detection in a mouse model by both fluorescence and nuclear imaging. The nanoparticle consisted of the biotinylated anti-Her2 Herceptin antibody to provide tumor targeting, a biotinylated DOTA chelator labeled with ^{111}In and a biotinylated Cy5.5 fluorophore, each linked via streptavidin. The antitumor antibody, Herceptin, binds to the extracellular segment of the Her2 receptor and is widely used in the clinic in combination with chemotherapy to increase both survival and response rate in breast cancer patients (*19*−*22*). The streptavidin nanoparticles are easily prepared by simple mixing and therefore allow ready replacement of functionalities on the streptavidin core. To our knowledge, no streptavidin-based dual-modality nuclear-fluorescence imaging agents have been reported.

MATERIALS AND METHODS

Chemicals. The clinical-grade anti-Her2 antibody trastuzumab (Herceptin) was manufactured by Genentech, Inc. (South San Francisco, CA, USA). The *N*-hydroxysuccinimide ester of Cy5.5 (NHS-Cy5.5) was obtained from GE Healthcare (Piscataway, NJ). The biotinylation reagent biocytin was from Sigma (St. Louis, MO, USA) and used to biotinylate NHS-Cy5.5; sulfosuccinimidyl-6-[biotinamido]-6-hexanamido hexanoate (sulfo-NHS-LC-LC-biotin) was from Pierce (Rockford, IL, USA) and used to biotinylate Herceptin. The streptavidin was purchased from Sigma (St. Louis, MO, USA). The human breast cancer cell line SUM190 (Her2+) was obtained from Asterand Co. (Detroit, MI, USA) and was grown in Ham's F-12 medium with 5 μg/mL insulin, 1 μg/mL hydrocortisone, 5 mM ethanolamine, 5 μg/mL transferrin, 10 nM triiodothyronine, 50 nM sodium selenite, and 1 g/L bovine serum albumin. The biotinylated DOTA derivative was obtained from Macrocyclics Inc. (Dallas, TX, USA) and $^{111}InCl_3$ was from Perkin-Elmer Life Science Inc. (Boston, MA, USA). All other chemicals were of reagent grade and used without purification.

Size-exclusion HPLC analyses were performed on a Superose 12 (Amersham Pharmacia Biotech, Piscataway, NJ, USA) installed on a Waters 515 solvent delivery system (Waters, Milford, MA, USA) equipped with an in-line radioactivity detector and a Waters UV2487 dual wavelength absorbance

[†] University of Massachusetts Medical School.
[‡] Institute of Biophysics, Chinese Academy of Sciences.

10.1021/bc100081h © 2010 American Chemical Society
Published on Web 06/17/2010

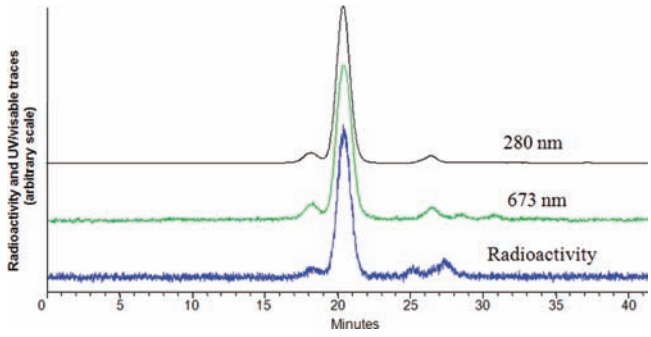


Figure 1. Size-exclusion HPLC traces of the Cy5.5/streptavidin/DOTA-^{111}In nanoparticle by in-line UV detection at 280 nm (streptavidin) and 673 nm (Cy5.5) and radioactivity detection.

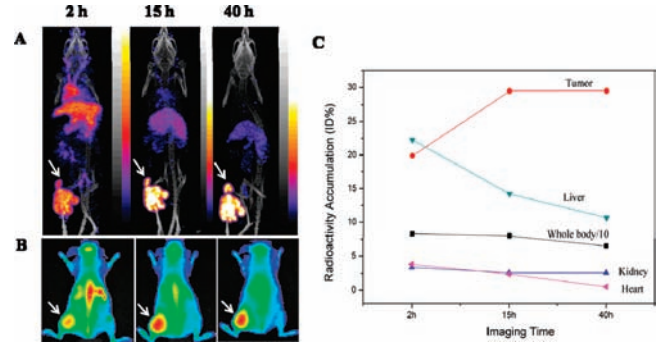


Figure 2. In vivo imaging of a representative tumored mouse at 2, 15, and 40 h post-administration of the Cy5.5/Herceptin/DOTA-^{111}In nanoparticle by SPECT/CT (A) and fluorescence imaging (B). Arrows mark the tumor location. Also presented is radioactivity quantitation by imaging in percent injected dose (%ID) in tumor, liver, kidney, heart, and whole body (C).

detector. The running solution was 20% acetonitrile in 0.1 M Tris-HCl, pH 8.0, at a flow rate of 0.6 mL/min.

Biotinylation of Herceptin Antibody. Herceptin from a reconstituted commercial vial was purified from histidine by dialyzing against 0.1 M $NaHCO_3$ solution, pH 8.5, overnight. The dialyzed Herceptin was added to a nonstick microfuge tube containing sulfo-NHS-LC-LC-biotin at a molar ratio of Herceptin to sulfo-NHS-LC-LC-biotin of approximately 1:4.6. The longer LC-LC linker was used in the antibody conjugation in place of the shorter LC linker to help avoid steric hindrance when bound to streptavidin. The preparation was mixed by gentle agitation for 1 h at room temperature and then dialyzed again against phosphate-buffered saline (PBS) overnight. The conjugated antibody was stored in PBS at 4 °C.

Labelings and Nanoparticle Preparations. The NHS-Cy5.5 was biotinylated by the following procedure. The NHS-Cy5.5 was dissolved in dry dimethylformamide and added to biocytin in 0.1 M $NaHCO_3$, pH 8.5, at a 10-fold molar excess to ensure that free biocytin was effectively consumed. The solution was gently vortexed for 1 h at room temperature in the dark and then stored overnight to hydrolyze the unreacted NHS ester on Cy5.5 to the free acid. The solution was then added very slowly and with vigorous agitation to streptavidin dissolved in 0.15 M saline at a biocytin to streptavidin molar ratio of 1:1. After 30 min of incubation in the dark, the product was purified on a polyacrylamide column (Thermo Scientific, Rockford, IL, USA, MWCO 6000) using 0.1 M PBS, pH 7.2, as eluant to remove the free Cy5.5. The Cy5.5-labeled streptavidin (Cy5.5/streptavidin) was analyzed by HPLC that showed only a single absorbance peak in the UV trace at 280 nm (streptavidin) corresponding to a single absorbance peak in the visible at 673 nm (Cy5.5). The Cy5.5 concentration was determined by measuring the absorbance at 673 nm and the concentration of streptavidin was determined using a BCA protein assay reagent kit (Pierce, Rockford, IL, USA). The Cy5.5:streptavidin molar ratio was calculated to be 1.1:1.

The preparation of the Cy5.5/streptavidin/DOTA nanoparticle was accomplished by mixing the Cy5.5/streptavidin complex with the biotinylated DOTA at a molar ratio of 1:1 with vigorous agitation for 30 min at room temperature. The $^{111}InCl_3$ stock solution in 0.05 M HCl was mixed with an equal volume of 0.5 M sodium acetate buffer, resulting in a final pH 5.5 and 500 μCi was then added to the prepared Cy5.5/streptavidin/DOTA complex and allowed to incubate at 43 °C for 1 h. The labeled product Cy5.5/streptavidin/DOTA-^{111}In was analyzed on a size-exclusion HPLC with a Superose 12 column. As shown in Figure 1, the appearance of a single peak in the UV trace at 280 nm (streptavidin) corresponding to a single peak at 673 nm (Cy5.5), and the single peak in the radioactivity trace (^{111}In) was taken as evidence of complete complexation at specific radioactivity of about 10 μCi/μg. Radioactivity recoveries were in all cases 90% or better. Finally, the biotinylated Herceptin was added and the product was incubated at room temperature for an additional 30 min in the same manner. The final Cy5.5/Herceptin/^{111}In-DOTA nanoparticle was drawn into a 1 mL U-100 insulin syringe for injection.

Animal Studies. All animal studies were performed with the approval of the UMMS Institutional Animal Care and Use Committee. Female nude mice (NIH Swiss, Taconic Farms, Germantown, NY, USA, 25−30 g) at 7 weeks of age were each injected subcutaneously in the left thigh with a 0.1 mL suspension containing 10^6 SUM190 cells mixed with 5 mg of Matrigel per milliliter. Mice were used for imaging studies 14 days later when the tumors reached 0.4−0.6 cm in diameter and were placed on a chlorophyll-free diet (AIN-93G Purified Diet, Harlan Teklad, Madison, WI) for 5 days prior to imaging.

Mice with SUM190 tumor xenografts were intravenously administered Cy5.5/Herceptin/DOTA-^{111}In nanoparticles containing 50 μg streptavidin, 139 μg Herceptin, 500 μCi of ^{111}In, and 1 nmol of Cy5.5 in 200 μL of saline. Mice were imaged on an IVIS 100 small-animal imaging system using a Cy5.5 filter set (Xenogen, Alameda, CA) at 2, 15, and 40 h post-intravenous administration under anesthesia by inhalation of oxygen−isofluorane. The mice were also imaged at approximately the same time points on a NanoSPECT/CT small animal nuclear camera (Bioscan, Washington, DC, USA) with region-of-interest (ROI) analysis using *InVivoScope 1.37* software (Bioscan). After the last image at 40 h, the mice were immediately sacrificed by cervical dislocation under anesthesia by isoflurance inhalation for biodistribution. Samples of blood and organs were removed, weighed, and counted for radioactivity in a dose calibrator.

RESULTS

Four nude mice each bearing SUM190 tumors in the left thigh received an injection of the multimodality Cy5.5/Herceptin/DOTA-^{111}In nanoparticle and were imaged on both an IVIS fluorescence scanner and a NanoSPECT/CT small animal nuclear scanner for comparison at 2, 15, and 40 h. A typical set of SPECT/CT acquisition are shown in Figure 2A, and for the same animal, a set of IVIS fluorescence images in the dorsal view at the corresponding time points are shown in Figure 2B. Figure 2C presents the percent of the injected radioactivity at each time point in several organs measured by volume of interest (VOI) analyses using *InVivoScope* software.

Figure 3 shows the biodistribution of radioactivity at 40 h postinjection. Tumor accumulation was 21 ID%/g and therefore

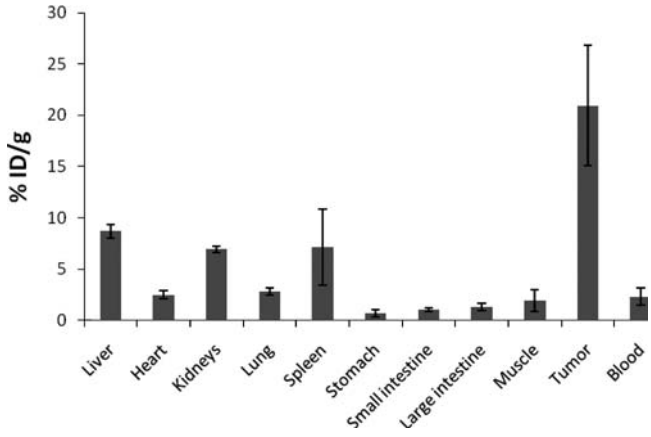


Figure 3. Biodistribution of the trifunctional multimodality nanoparticle by radioactivity (% ID/g) in tumor and selected organs at 40 h postinjection by sacrifice and dissection. ($N = 3$, error bars represent one standard deviation.)

much higher than all normal tissues such as liver, heart, kidneys, spleen, and muscle that accumulated 8.7, 2.5, 7.0, 7.2, and 1.9 ID%/g, respectively.

DISCUSSION

With the benefits of molecular imaging becoming increasingly apparent in many fields of medical research, it is also becoming increasingly apparent that no one imaging modality will serve all needs. Accordingly, an ability to couple two or more imaging modalities within the same agent could be useful. This laboratory is developing a nanoparticle based on streptavidin that is ideally suited to multimodality imaging, since up to four biotinylated functionalities can be readily combined without apparent influence on their properties and with reasonable pharmacokinetics (*16*−*18*). We had previously established that the noncovalent bond between streptavidin and biotin is sufficiently stable in vivo, that different biotinylated components (antibodies, cell penetrating peptides, DNA, and MORF oligomers) on streptavidin within the nanoparticle apparently exhibit preserved function, and that the nanoparticle exhibits favorable pharmacokinetics (*16*−*18*, *25*, *26*). Finally, we had previously shown that the nanoparticle is capable of accumulating in tumor by specific mechanisms. In our earliest studies, the nanoparticle was labeled with ^{99m}Tc or Cy3 and studied in SUM190 (Her2+) and SUM149 (Her2−) cells in culture (*18*). The nanoparticle accumulation was significantly higher in SUM190 vs SUM149 cells (10% vs 2% at 7 h). When the Herceptin was omitted from the nanoparticle, accumulation dropped to that of controls (<2%) and the difference in accumulation between SUM190 and SUM149 cells disappeared. The nanoparticle has also been incubated in these cells while labeled with ^{99m}Tc or Lissamine. Accumulations were again significantly higher in SUM190 vs SUM149 cells (11% vs 0.2% at 12 h) and the immunofluorescence results confirmed the much higher accumulation in the Her2+ cells (*26*). When administered to SUM190 tumor-bearing mice, accumulation reached 17%ID/g at 9 h and therefore similar to the 21%ID/g at 40 h in this multimodality study, a value that could not be achieved by any conceivable nonspecific mechanism. In a direct comparison of our nanoparticle labeled with ^{111}In with that of ^{111}In-labeled Herceptin in SUM190 tumors, both the images and the necropsy results were remarkably similar (*16*). For example, at 8 h, tumor accumulation was 10% vs 12% ID/g. In this case, the ^{111}In was on the MORF oligomer that clears rapidly through the kidneys and does not accumulate in tumor unless coupled to Herceptin. When the Herceptin is omitted from the nanoparticle, the tumor accumulation falls to about 3% ID/g at 21 h (*17*). These results show conclusively that our nanoparticle accumulates specifically in Her2+ tumors due to the presence of the Herceptin. Although not pertinent to this study, several of these reports also present results showing conclusively that accumulation is significantly higher when the nanoparticle is incubated with the radiolabeled antisense oligomer compared to the radiolabeled control oligomer, as further evidence of specific binding.

As shown in Figure 2A and B, the tumor is evident in both the fluorescent and nuclear images at all times, confirming that the streptavidin nanoparticle successfully delivered all three components to the tumor target such that each component could perform its function. The high tumor accumulation is due to the antitumor Herceptin antibody carried by the nanoparticle to the tumor, while the images are due to the nuclear and fluorescent labels also delivered to the tumor by the nanoparticle.

The nuclear images obtained on a SPECT/CT camera located the tumor with relatively high resolution (Figure 2A) and provided quantitative information on accumulations in tumor and in several normal organs (Figure 2C). Fluorescence imaging obtained on the IVIS scanner provides a relatively inexpensive and complementary approach to real-time tumor screening (Figure 2B). Despite the tissue absorption and lower resolution inherent in these fluorescent images, the two modelities have provided images that are remarkably similar and in which the tumor kinetics of the nanoparticle could have been estimated by either method with equal effectiveness.

CONCLUSION

Both the fluorescent and nuclear images confirm that each component of the Cy5.5/Herceptin/DOTA-^{111}In nanoparticle has performed as expected. The obvious accumulation in the Her2+ tumor and the impressive tumor/normal tissue ratios is a result of the presence of a functioning Herceptin within the nanoparticle. That this favorable biodistribution was observed by both fluorescence and nuclear imaging confirms that the Cy5.5 fluorophore and the ^{111}In along with its DOTA chelator remained bound to the antibody throughout the imaging period. Thus, the streptavidin nanoparticle under development in this laboratory was used effectively for multimodality imaging of tumor in mice by fluorescence and nuclear detection. Presumably, other imaging modalities could also be considered.

LITERATURE CITED

(1) Massoud, F. T., and Gambhir, S. S. (2003) Molecular imaging in living subjects: seeing fundamental biological processes in a new light. *Gene. Dev. 17*, 545–580.
(2) Liu, X., Wang, Y., Nakamura, K., Liu, G., Dou, S., Kubo, A., Rusckowski, M., and Hnatowich, D. J. (2007) Optical antisense imaging of tumor with fluorescent DNA duplexes. *Bioconjugate Chem. 18*, 1905–1911.
(3) Liang, M., Liu, X., Cheng, D., Nakamura, K., Wang, Y., Dou, S., Liu, G., Rusckowski, M., and Hnatowich, D. J. (2009) Optical antisense tumor targeting in vivo with an improved fluorescent DNA duplex probe. *Bioconjugate Chem. 20*, 1223–1227.
(4) Alfano, R. R., Demos, S. G., and Gayen, S. K. (1997) Advances in optical imaging of biomedical media. *Ann. N. Y. Acad. Sci. 820*, 248–270.
(5) Kaijzel, E. L., Pluijm, G., and Löwik, C. W. G. M. (2007) Whole-body optical imaging in animal models to assess cancer development and progression. *Clin. Cancer Res. 13*, 3490–3497.
(6) Cheng, Z., Levi, J., Xiong, Z., Gheysens, O., Keren, S., Chen, X., and Gambhir, S. S. (2006) Near-infrared fluorescent deoxyglucose analogue for tumor optical imaging in cell culture and living mice. *Bioconjugate Chem. 17*, 662–669.
(7) Ntziachristos, V., Bremer, C., and Weissleder, R. (2003) Fluorescence imaging with near-infrared light: new technological

advances that enable in vivo molecular imaging. *Eur. Radiol. 13*, 195–208.

(8) Weissleder, R., and Mahmood, U. (2001) Molecular imaging. *Radiology 219*, 316–333.

(9) Rosenthal, M. S., Cullom, J., Hawkins, W., Moore, S. C., Tsui, B. M., and Yester, M. (1995) Quantitative SPECT imaging: A review and recommendations by the focus committee of the society of nuclear medicine computer and instrumentation council. *J. Nucl. Med. 36*, 1489–1513.

(10) Chatziioannou, A. F. (2002) Molecular imaging of small animals with dedicated PET tomographs. *Eur. J. Nucl. Med. 29*, 98–114.

(11) Blasberg, G. R. (2003) in vivo molecular-genetic imaging: multi-modality nuclear and optical combinations. *Nucl. Med. Biol. 30*, 879–888.

(12) Bhushan, R. K., Misra, P., Liu, F., Mathur, S., Lenkinski, R., and Frangioni, V. J. (2008) Detection of breast cancer microcalcifications using a dual-modality SPECT/NIR fluorescent probe. *J. Am. Chem. Soc. 130*, 17648–17649.

(13) Cao, Q., Cai, W., Gang, N., He, L., and Chen, X. (2008) Multimodality imaging of IL-18-binding protein-Fc therapy of experimental lung metastasis. *Clin. Cancer Res. 14*, 6137–6145.

(14) Ponomarev, V., Doubrovin, M., Serganova, I., Vider, J., Shavrin, A., Beresten, T., Ivanova, A., Ageyeva, L., Tourkova1, V., Balatoni, J., Bornmann, W., Blasberg, R., and Gelovani, T. J. (2004) A novel triple-modality reporter gene for whole-body fluorescent, bioluminescent, and nuclear noninvasive imaging. *Eur. J. Nucl. Med. Mol. Imaging 31*, 740–751.

(15) Culver, J., Akers, W., and Achilefu, S. (2008) Multimodality molecular imaging with combined optical and SPECT/PET modalities. *J. Nucl. Med. 49*, 169–172.

(16) Liu, X., Wang, Y., Nakamura, K., Kawauchi, S., Akalin, A., Cheng, D., Chen, L., Rusckowski, M., and Hnatowich, D. J. (2009) Auger radiation-induced, antisense-mediated cytotoxicity of tumor cells using a three-component streptavidin delivery nanoparticle with 111In. *J. Nucl. Med. 50*, 582–590.

(17) Wang, Y., Liu, X., Nakamura, K., Chen, L., Rusckowski, M., and Hnatowich, D. J. (2009) In vivo delivery of antisense MORF oligomer by MORF/carrier streptavidin nanoparticles. *Cancer Biother. Radiopharm. 24*, 573–578.

(18) Liu, X., Wang, Y., Nakamura, K., Kubo, A., and Hnatowich, D. J. (2008) Cell studies of a three-component antisense MORF/tat/herceptin nanoparticle designed for improved tumor delivery. *Cancer Gene Ther. 15*, 126–132.

(19) Nahta, R., and Esteva, F. J. (2003) HER2-targeted therapy: lessons learned and future directions. *Clin. Cancer Res. 9*, 5078–5084.

(20) Piccart-Gebhart, M. J., Procter, M., Leyland-Jones, B., Goldhirsch, A., Untch, M., and Smith, I. (2005) Trastuzumab after adjuvant chemotherapy in HER2-positive breast cancer. *N. Engl. J. Med. 353*, 1659–1672.

(21) Bange, J., Zwick, E., and Ullrich, A. (2001) Molecular targets for breast cancer therapy and prevention. *Nat. Med. 7*, 548–552.

(22) Weissleder, R. (1999) Molecular imaging: exploring the next frontier. *Radiology 212*, 609–614.

(23) Cai, W., Gambhir, S., and Chen, X. (2005) Multimodality tumor imaging targeting integrin $\alpha v\beta 3$. *Bio. Techniques 39*, S6–S17.

(24) Christophe, M. D., Abhijit, D., Andreas, M. L., Patrick, L. C., Pritha, R., Arion, F. C., and Sanjiv, S. G. (2007) Multimodality imaging of tumor Xenografts and metastases in mice with combined small-animal PET, small-animal CT, and bioluminescence imaging. *J. Nucl. Med. 48*, 295–303.

(25) Wang, Y., Nakamura, K., Liu, X., Kitamura, N., Kubo, A., and Hnatowich, D. J. (2007) Simplified preparation via streptavidin of antisense oligomers/ carriers nanoparticles showing improved cellular delivery in culture. *Bioconjug. Chem. 18*, 1338–1343.

(26) Wang, Y., Liu, X., Chen, L., Cheng, D., Rusckowski, M., and Hnatowich, D. J. (2009) Tumor delivery of antisense oligomer using trastuzumab within a streptavidin nanoparticle. *Eur J. Nucl. Mol. Imaging 36*, 1977–1986.

BC100081H

Groove Binding Ligands for the Interaction with Parallel-Stranded *ps*-Duplex DNA and Triplex DNA

Akash K. Jain[†] and Santanu Bhattacharya*[,†,‡]

Department of Organic Chemistry, Indian Institute of Science, Bangalore 560012, India, Chemical Biology Unit, Jawaharlal Nehru Centre for Advanced Scientific Research, Bangalore 560012, India. Received June 5, 2009; Revised Manuscript Received January 23, 2010

DNA adopts different conformations not only based on novel base pairs, but also with different chain polarities. Besides several duplex structures (*A, B, Z,* parallel stranded (*ps*)-DNA, etc.), DNA also forms higher-order structures like triplex, tetraplex, and *i*-motif. Each of these structures has its own biological significance. The *ps*-duplexes have been found to be resistant to certain nucleases and endonucleases. Molecules that promote triple-helix formation have significant potential. These investigations have many therapeutic advantages which may be useful in the regulation of the expression of genes responsible for certain diseases by locking either their transcription (antigene) or translation (antisense). Each DNA minor groove binding ligand (MGBL) interacts with DNA through helical minor groove recognition in a sequence-specific manner, and this interferes with several DNA-associated processes. Incidentally, these ligands interact with some non-*B*-DNA and with higher-order DNA structures including *ps*-DNA and triplexes. While the design and recognition of minor grooves of duplex DNA by specific MGBLs have been a topic of many reports, limited information is available on the binding behavior of MGBLs with nonduplex DNA. In this review, we summarize various attempts of the interaction of MGBLs with *ps*-DNA and DNA triplexes.

INTRODUCTION

The "central dogma" of molecular biology states that genetic information flows first from DNA to RNA and then to proteins (*1*). The right-handed double-helical structure, called the *B*-form of DNA, consisting of two strands, having a common helical axis, running in opposite directions (one along 5′→3′ and the other along 3′→5′) was demonstrated for the first time by Watson and Crick in 1953 (*2*). This is the most well-known and has been considered one of the most biologically relevant DNA structure, since this structure could explain how the DNA molecule could code for and transmit the genetic information. The DNA molecule, however, could exhibit intrinsic, as well as environmentally induced, structural polymorphism. Various DNA structures that have been characterized are *A*-DNA, *B*-DNA, *C*-DNA, and so forth, and there is even a DNA structure associated with 18 other letters of the English alphabet. Only the letters F, Q, U, V, and Y have been left to choose from (*3*). The main DNA structural families that have been widely studied are the *A, B,* and *Z* double-helical polymorphs. The nucleic acid bases have multiple donor and acceptor sites for hydrogen bonding. This allows DNA (and RNA) to adopt several unusual conformations like single-stranded hairpins (*4*), parallel-stranded (*ps*) DNA (*5*−*8*), triplexes (*9*−*12*), tetraplexes (or quadruplexes) (*13*−*15*), and *i*-motif (*16*). These structures are involved in the activation/inhibition of several biological processes.

Ligands, especially proteins, act on double-stranded DNA and control a variety of fundamental cellular processes such as replication, transcription, and translation. Elucidation of the mechanism of recognition of the DNA conformation and the base sequence by cellular proteins is a prerequisite for understanding the biologically important regulatory processes at the molecular level (*17, 18*). Low molecular mass DNA-binding ligands are useful tools to elucidate essential elements involved in the recognition process of DNA. Because of the complex double-helical organization of DNA, different binding modes are possible for the drug−DNA interactions. Both covalent and noncovalent interactions are involved in the two modes of drug−DNA interactions. Covalent interactions are irreversible. The DNA alkylating agents like nitrogen mustards (*19*), cis-platin (*20*), and so forth fall into this category. These compounds inhibit transcription, translation, and replication of DNA and also block the progression of DNA polymerase (*21, 22*). Cis-platin and its less toxic derivatives are used widely as anticancer drugs and in combination chemotherapy (*20*).

Intercalative and non-intercalative drugs represent the major classes of noncovalently interacting DNA binding molecules (*23*). Intercalators are typically made of a planar polyaromatic system, which position between the layers of nucleic acid base pairs and grossly disrupt the organization of the DNA double-helix. This disruption prevents replication and transcription. Intercalation typically untwists the DNA (*15, 24*). Intercalators generally do not show sequence-specific DNA binding and are often used in cancer treatment (*15*). Non-intercalative molecules on the other hand bind with duplex-DNA through its grooves. The major and minor grooves of DNA differ in electrostatic potential, hydrogen bonding characteristics, steric effects, hydration, and microenvironmental polarity (*25*). Most of the proteins bind with the major grooves, while small molecules can bind with either groove, although they often prefer the minor groove of the double-helical DNA (*26*).

DNA minor groove binding ligands (MGBL) possess common structural motifs that allow them to adopt a "crescent shape". Such a shape matches with the turn of the DNA double-helix, and these ligands bind the minor groove in a sequence-

* To whom correspondence should be addressed. Also, J. C. Bose Fellow, Department of Science and Technology (DST), New Delhi. E-mail: sb@orgchem.iisc.ernet.in Phone: (91)-80-2293-2664; Fax: (91)-80-2360-0529.

[†] Indian Institute of Science.

[‡] Jawaharlal Nehru Centre for Advanced Scientific Research.

10.1021/bc900247s © 2010 American Chemical Society
Published on Web 05/28/2010

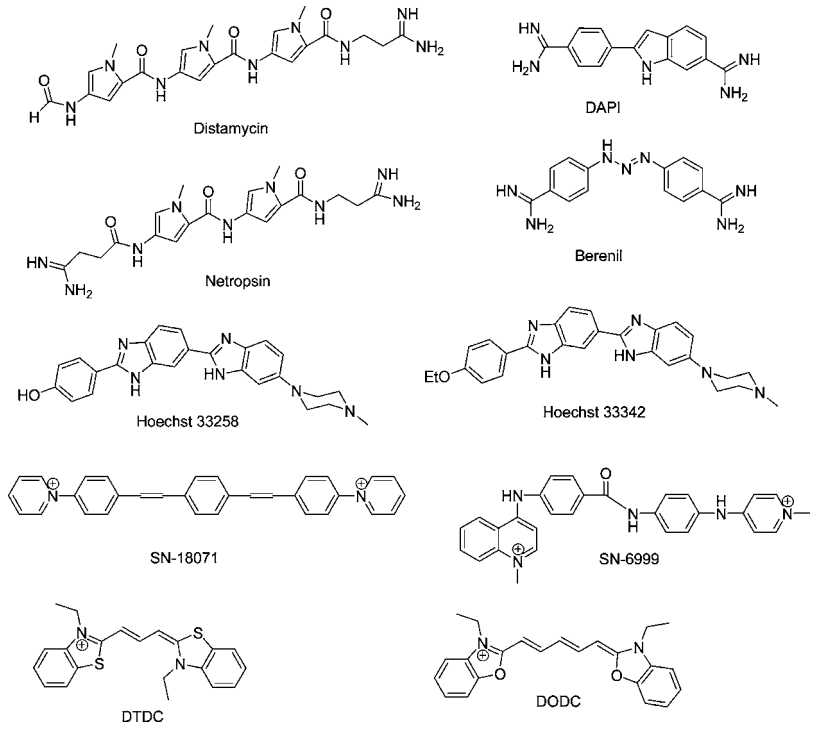


Figure 1. Chemical structures of some DNA minor groove binding ligands.

specific manner. These ligands have a wide range of biological applications. For instance, they are useful as fluorescent DNA stains, and they are potential agents for the modulation of gene expression (*27*−*32*). Moreover, DNA binding studies of such compounds provide fundamental information about the nucleic acid recognition properties, and they continue to act as important models in the study of drug−DNA complexes (*33*−*48*). A lot of structural and/or computational studies have been performed with MGBL-DNA complexes, but a molecular-level understanding of DNA minor groove recognition by small organic ligands requires detailed studies including thermodynamic information (*33*−*36, 49*−*54*).

Oligopeptides such as netropsin and distamycin, benzimidazoles (Hoechst 33258, Hoechst 33342), DAPI, berenil, bisquaternary cations (SN 6999, SN 7167, SN 18071), and cyanine dyes (DTDC, DODC) represent some of the important minor groove binding ligands (Figure 1). These ligands recognize approximately 3 to 5 base pairs, and some of their analogues recognize even longer contiguous stretches (*44, 45*). It is expected that those agents capable of recognizing longer sequences will exhibit greater specificity. However, many of these agents when targeted to longer sequences often lack in this binding specificity because of "imperfect" DNA recognition and conformational "mismatch" in solution (*55*−*58*). A series of novel distamycin-based oligopeptide conjugates of deoxyoligonucleotides (ODN) has been synthesized, and their hybridization with complementary ODN and thermal denaturation have been investigated (*59*). Self-recognition of distamycin units by the duplex ODN offers possibilities to design unnatural, folded cyclic DNA duplex systems.

MGBLs bind with non-*B*-DNA too. Studies of the complexes of MGBLs with quadruplex DNA have been reported (reviewed in ref *14*). In the present review, we give an overview of MGBL interaction studies with *ps*-DNA and triplex DNA. Since these structures are involved in several important cellular functions, the studies of these complexes offer possibilities to design effective chemotherapeutic agents.

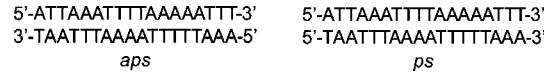


Figure 2. Example of antiparallel-stranded (*aps*) duplex DNA and parallel-stranded (*ps*) duplex DNA.

PARALLEL STRANDED (*PS*)-DNA AND ITS BIOLOGICAL IMPORTANCE

Double-stranded DNA generally consists of two strands running in opposite directions (one is in the direction 5′→3′, and the other one is in the direction of 3′→5′, antiparallel stranded, *aps*-duplex). However, single-stranded DNA may also adopt a parallel-stranded *ps*-duplex conformation in which both strands adopt the 5′→3′ orientation (Figure 2) (*5*−*8, 60*−*63*). The construction of two-stranded *ps*-DNA duplexes requires a selection of sequences that are perfectly complementary in the parallel orientation but which at the same time are poorly matched toward the function of other possible alternative, potentially competitive antiparallel homo- and heteroduplexes. Such *ps*-DNA has the potential to play an important role in the regulation of replication, transcription, genetic recombination, chromosomal folding, mutational processes, biosynthesis, and RNA splicing (*5, 64*). The *ps*-duplexes have shown resistance to certain nucleases and to restriction endonucleases, e.g., *Dra I*, *Ssp I*, and *Mse I* (*65*). *DNase I* and exonuclease III exhibit much lower activity in presence of *ps*-DNA compared to that with the *aps*-DNA. Parallel complementary stretches of DNA in different genomes have also been evidenced by in vitro studies. Thus, a parallel complementary region has been reported to exist between two *Drosophila* DNA sequences, fragments of the suffix and a 5′-noncoding sequence of the alcohol dehydrogenase gene (*66*). The *ps*-duplexes made of purine-pyrimidine bases, also called the Hoogsteen duplexes, are part of pyrimidine motif triplexes, and hence, their studies are helpful

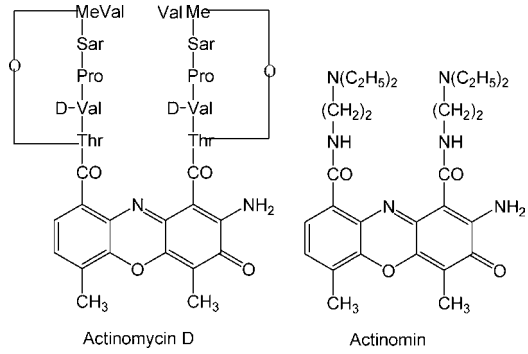


Figure 3. Chemical structures of actinomycin D and actinomin.

to understand the properties of triplexes and triplex−ligand interactions (*60*).

Stability of *ps*-DNA. The thermodynamic stability of the *ps*-DNA when formed exclusively with A-T base pairs is only slightly lower than that of the *aps*-DNA. However, the incorporation of GC base pairs in such parallel-stranded DNA largely destabilizes them. At neutral pH, the parallel duplexes can be stabilized by noncanonical reverse Watson−Crick GC and AT hydrogen-bonded base pairs (*67*). This is also called Donohue base pairs, with the glycoside bonds in trans orientation, and in this situation, the two grooves are equivalent (*62*). The *ps*-duplexes can also be stabilized by Hoogsteen AT and C^+G base pairing (*7, 63, 68*). Parallel-stranded purine-pyrimidine stretches are also part of the RNA triplexes, DNA and RNA tetraplexes, and *H*-type DNA structures (*11, 63, 68*−*70*). The *ps*-duplexes may form via two categories of base pairing, homobase pairs (AA^+, TT, GG, and CC^+) (*71, 72*) and heterobase pairs (complementary or mismatched) (*73, 74*).

The *ps*-duplexes can be formed both in hairpin and in linear form (*60, 75, 76*). Several synthetic methods are known which allow preparation of *ps*-duplexes in vitro. These can be achieved by polarity reversal using a 3′/3′ or 5′/5′ linkage (*76*), using modified oligodeoxynucleotides (ODNs) (*77, 78*), or via the use of modified backbone (*79*). Recently, FTIR studies have been utilized to follow the formation of parallel-stranded DNA duplexes incorporating isoG or m^5isoC bases and their base pairing schemes have also been determined (*80*).

Interaction of ps-DNA with Organic Ligands. There are only a few reports that describe the interaction of *ps*-duplex DNA with small organic ligands. Hoogsteen base paired *ps*-DNA has been stabilized by the presence of Mg^{2+} ions (*68*). The *ps*-duplexes are often stabilized by intercalators as well (*81*). In comparison, the *ps*-DNA contains grooves that are of about equal sizes (*60*). Thus, the nature of molecular recognition of *ps*-DNA by intercalating molecules is quite different from the duplex DNA with antiparallel strand orientation. Benzopyridoindole derivatives were shown to induce the formation and stabilization of Hoogsteen paired *ps*-duplexes (*67, 81*). The stabilization of these complexes was found to depend on pH. Actinomycin D (Figure 3), a drug, is made of an intercalatable central polyaromatic part and minor groove binding pentapeptide side chains. This molecule binds weakly with the *ps*-duplexes having normal GC base pairs, but it stabilizes *ps*-duplexes with modified base pairs. On the contrary, an actinomycin D analogue actinomin, which possesses positively charged side chains instead of chiral peptide rings, stabilize both *aps*- and *ps*-duplexes (*82*).

MGBLs generally destabilize the *ps*-duplexes. Hoechst 33258 exhibited a little increase in fluorescence emission in the presence of *ps*-hairpins but a significantly enhanced emission with antiparallel hairpins (*60*). In contrast, the intercalator ethidium bromide formed fluorescent complexes with all types of hairpins, the intensity of which was even higher for the *ps*-species (*60*).

Infrared and fluorescence studies of the complexes of netropsin, distamycin, and Hoechst 33258 with *ps*-duplexes and *aps*-duplexes have been performed. These ligands induce cooperative dissociation of *ps*-duplex and rearrangement of the strands to form imperfectly matched *aps*-duplexes (*83*). Other reports suggest destabilization of *ps*-duplexes induced by Hoechst 33258 and DAPI (*80, 84*).

Some bisbenzimidazoles (including Hoechst 33258) and terbenzimidazoles having different substitutions on the phenyl ring have been evaluated to probe their effect on the stability of *ps*-DNA duplexes and triplexes (*85*). None of the bisbenzimidazole was found to destabilize the *ps*-DNA under the experimental conditions (pH 5.2), and the terbenzimidazoles were in fact found to stabilize the *ps*-DNA. Stabilization of *ps*-DNA occurs probably due to the protonation of nitrogens and amines of the benzimidazoles at pH 5.2, which compensate for the negative charge of the phosphate backbone of DNA reducing the repulsion between the DNA strands (*85*). Hence, groove binding ligands having positively charged side chains may be important for achieving stabilization of *ps*-DNA.

TRIPLE HELICES

In triple helices, a third strand, also called the triplex-forming ODN (TFO), binds within the major groove of the duplex DNA via Hoogsteen (or reverse Hoogsteen) type hydrogen bonding with the exposed groups on the base pairs (Figure 4) (*11, 86*). The binding of the third strand is highly sequence-specific, and this property of sequence specificity forms the basis of the triplex-based applications that aim to bind a single-stranded DNA (TFO) to a specific target site in duplex DNA, which is known as "Antigene Strategy" (*87*). Triplexes can be prepared from either RNA or DNA chains or their combinations, and these can be either intramolecular or intermolecular. Different configurations (circular, alternate strand, and so forth) of the triplexes and the numerous geometrical modes of triplex formation have been described (*9*). Some general principles based on which TFOs recognize DNA sequences have evolved (*88*−*91*). TFO can bind either in a parallel or an antiparallel fashion along the major groove of the duplex DNA.

The parallel or antiparallel mode of TFO binding has different DNA-recognition codes. When a TFO (containing pyrimidine bases) binds in parallel with respect to the purine-rich target strand, it does so according to the so-called "pyrimidine motif" (*92*−*94*). In this motif, the adenine and guanine residues of the purine-rich target strand are, respectively, recognized through Hoogsteen-type hydrogen bonds with the thymines and cytosines (hence "pyrimidine motif", Figure 4) of the TFO. A requirement for the triplex formation by the pyrimidine motif TFOs is the protonation of N3 of the cytosine residue. Thus, formation of such triplexes is favorable under acidic conditions (*12, 95*). The pyrimidine motif triplexes contain T.A:T and C^+.G:C triplets (: = Watson−Crick H-bonding;. = Hoogsteen H-bonding).

In case of the antiparallel binding mode, the TFO binds to the target strand according to the so-called "purine motif" (*92, 93, 96*). Here, the adenines and guanines of the purine-rich target strand are, respectively, recognized through reverse Hoogsteen hydrogen bonds by adenines and guanines (hence "purine motif", Figure 4) of the TFO. The purine motif triplexes generally contain G.G:C and A.A:T triads. Some reports also include a T.A:T triad (*97*−*100*). Sometimes, the stability of the triplexes consisting of alternating G.G:C and T.A:T triads is higher than that of the triplexes made of G.G:C and A.A:T triads (*97*). The stability of the purine motif triplexes depends significantly on the presence of bivalent metal cations (*101*). Third strand

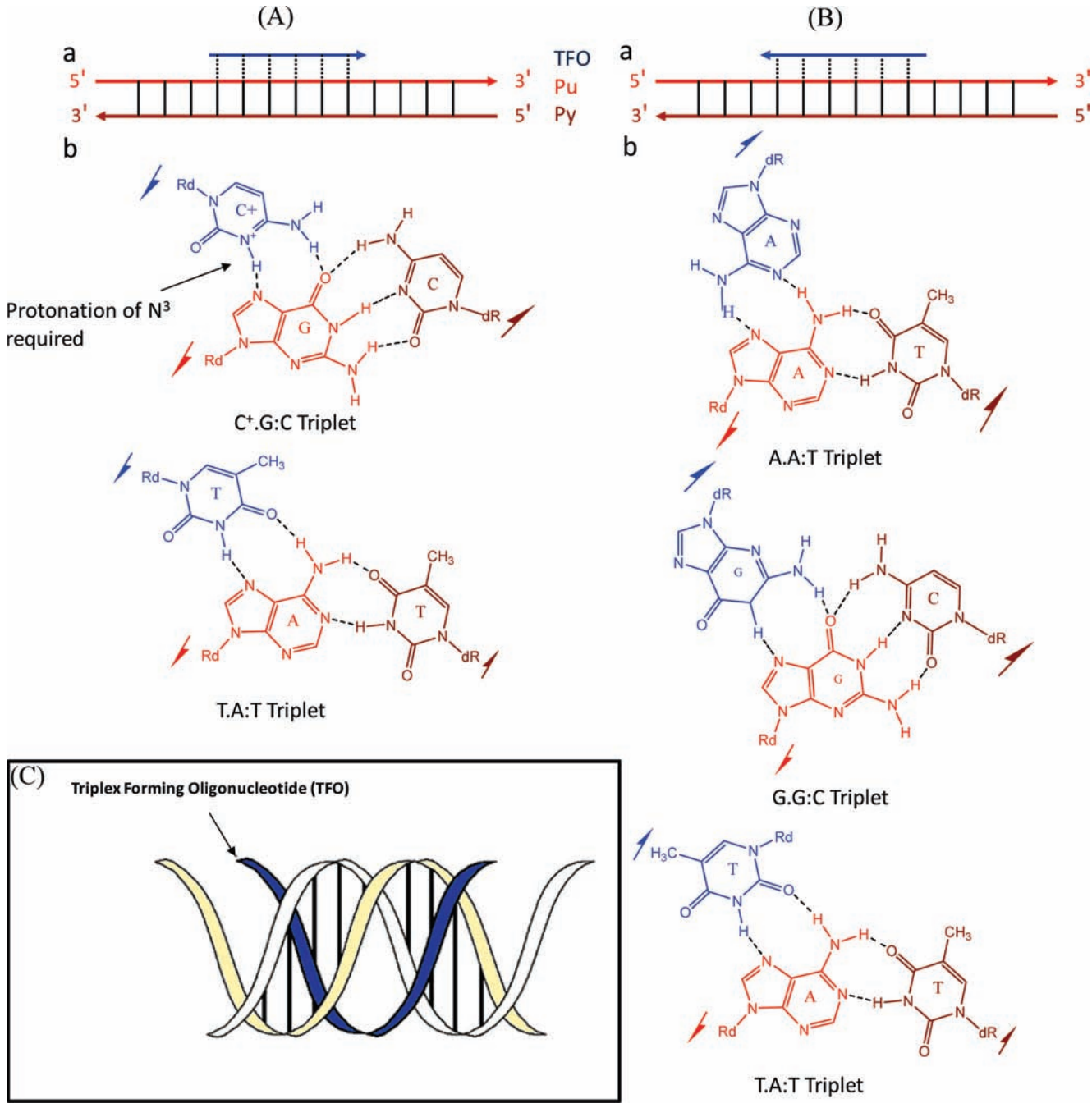


Figure 4. (A) The pyrimidine motif for the triple helix. (a) The third strand is parallel in terms of 5′→3′ orientation with respect to the purine-rich strand of the duplex target. (b) Base triplets formed in the pyrimidine motif and an illustration of the Hoogsteen hydrogen bond. (B) The purine motif for the triple helix. (a) The third strand is oriented antiparallel in terms of 5′→3′ direction with respect to the purine-rich strand of the duplex target. (b) Base triplets formed in the purine motif and an illustration of the reverse Hoogsteen hydrogen bonds. (C) A depiction of a DNA triple helix, with the third strand binding in the major groove of the target duplex. (TFO, Triplex Forming Oligonucleotide; Pu, Poly purine strand of duplex; Py, Poly pyrimidine strand of duplex.)

orientation in G.G:C triplexes is usually considered to be antiparallel, although parallel orientation has also been suggested on the basis of X-ray diffraction studies (*102*). It depends on the number of GpT and TpG steps and the stretches of T (*103*).

Despite the above-mentioned differences, both motifs are quite similar in most of their fundamental features. Thus, the duplex involved in the triplex formation must have a homopurine sequence in one strand, and the orientation of the two chemically homologous strands should be antiparallel.

The structural features of DNA triplexes have been studied using different techniques like chemical and enzymatic probing, affinity cleavage, and electrophoresis (*86*, *97*, *104*, *105*). The first attempt to deduce the structure of a poly(dT).poly(dA).poly(dT) triplex using X-ray fiber diffraction was performed in 1974 (*106*). The structures of DNA and RNA triplexes having T.A:T and U.A:U triplets were proposed on the basis of X-ray fiber diffraction data (*107*, *108*). A model for the $[C^+.G:C]_n$ triple helix derived from observation of the $[C^+.G:C]$ base triplet in a crystal structure of an ODN−drug complex, between netropsin and the decanucleotide $d(CGCAATTGCG)_2$ has been proposed (*109*). Two different crystal morphologies of the sequence d(TGGCCTTAAGG) have been obtained by the hanging-drop vapor diffusion method recently (*110*). The triplexes were also extensively studied by NMR spectroscopy (*106*, *111*−*114*).

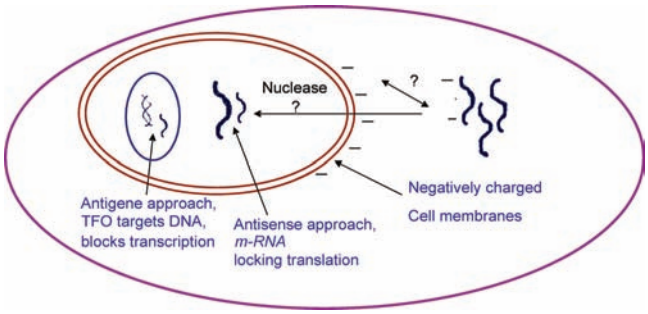


Figure 5. A schematic presentation of antigene and antisense therapeutics.

H-DNA is another class of DNA triple helix which is formed under negatively superhelical conditions. There is an entire family of *H*-DNA-like structures (*101*). This structure is formed by sites sensitive to S1 nuclease and formed under acidic conditions (*101, 115, 116*). The structure is called the *H* form because it is clearly stabilized by hydrogen ions, and therefore, this is a protonated structure. It consists of an intramolecular triple helix and its *H*−*Y3* and *H*−*Y5* isoforms have been described (*9, 117, 118*). These isoforms are named based on that half (according to strand polarity) of the homopurine strand which is donated to the triplex (*9*).

Biological Importance of the Triple Helices. An original approach involving the use of DNA as a possible therapeutic agent has emerged in medicinal chemistry during the past decade. This is based on the principle of regulation of expression of genes that are responsible for the synthesis of protein/enzyme for specific diseases by locking their transcription (antigene) or translation (antisense) pathways (Figure 5). In this context, the specific duplex DNA targeting by TFO provides an attractive strategy for genetic manipulation with the ultimate goal of repairing genetic defects (site-directed mutagenesis, site-directed recombination, etc.) in human cells (*118*). TFO may also induce site-specific mutagenesis (*120, 121*). The ability to target mutations may work as a technique for genetic engineering applications (*122*). Triplex-bound TFOs are able to increase the recombinogenic processes around their binding sites (*123, 124*).

Certain genetic mutations can be repaired by utilizing the induction of a homologous recombination between an exogenous DNA, called donor DNA, and the target gene (*125*). A TFO that binds to a site close to a mutated sequence of a pathogenic gene may function to place a wild-type donor DNA sequence which can induce recombination leading to the correction of the targeted gene. Such effects have indeed been shown with episomal and chromosomal sequences (*125, 126*).

TFOs can also be used for the sequence-specific positioning of DNA-reactive groups. For instance, TFOs may be used to direct validated anticancer drugs to genes carrying cancer-specific mutations or translocations thereby inducing DNA damage selectively to tumor cells (*127*−*129*). Other DNA-reactive groups positioned by TFOs have been described for alkylating group mustards (*130*). One can exploit DNA cleaving agents, and other classes of DNA modifying agents (like organometallic complexes) in this context (*131*−*136*). Positioning of DNA-damaging radio isotopes to specific sites is known as "antigene radiotherapy" (*137*). In dermatology, psoralens and UVA are used to treat psoriasis and other inflammatory or malignant skin diseases (*138*). Site-specific positioning of psoralen may also reduce side effects caused by the formation of random photoadducts that are observed in this therapy (*139*).

The other application includes intercellular gene targeting, identification of genes that are responsible for the cell growth and malignant transformation (*140, 141*). Triplex-mediated

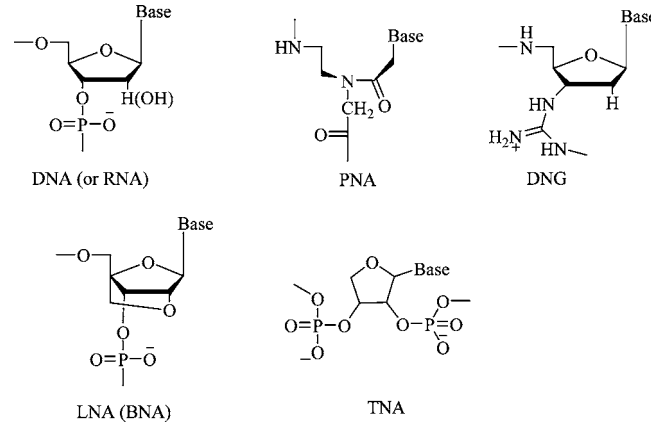


Figure 6. Chemical structures of nucleotides in DNA, RNA, PNA, DNG, LNA, and TNA.

inhibition of transcription may be achieved by interfering with the transcription initiation (competition of TFOs with transcription factors at the promoter) or by interfering with the transcription elongation (RNA synthesis arrest at triplex structures) (*142, 143*). Interestingly, the TFOs were also shown to function as transcription activators (*144*). Circular TFOs are of particular interest, since these are not substrates for degradation by exonucleases (*145, 146*). Several diseases like cancer, HIV, influenza, HSC, trypanosoma, and Alzheimer's disease can be controlled with the use of DNA therapeutics (*147*). Despite this vital role of DNA therapeutics, cell permeability of TFOs and their stability from nucleases remain as unresolved problems. To address these issues, several modifications have been reported in TFOs, which are discussed in the next section.

Stability of the Triple Helices. The utility of TFOs is limited because of its relatively weak binding to the underlying duplex. This is partially due to the charge repulsion between the three adjacent polyatomic DNA strands. In addition, the TAT triplet is less stable than C^+.G:C triplet, possibly because it lacks a positive charge (*148*). A minimum of 15 bases of poly(purine/pyrimidine) are necessary to form an intramolecular triplex, and more than 12 residues of poly(purine/pyrimidine) are required to form a stable intermolecular triple helix (*149*). Numerous studies were aimed at achieving the stabilization of DNA triplexes at physiological conditions. Most of the studies involving pyrimidine motif triplexes have concentrated on overcoming the pH dependency. It was found that the polyamines, specifically spermine and spermidine, favor both inter- and intramolecular pyrimidine motif triplexes under physiological pH (*150*−*152*). Millimolar levels of polyamine concentration found in the nuclei of eukaryotic cells raise hope for the stability of triplexes in vivo (*153*). The requirement for cytosine protonation could be overcome by several chemical means (using modified bases) (*154*−*158*). Recently, silver ion mediated stabilization of parallel-motif triplexes having CG.C^+ has been reported at neutral and acidic pH. The silver ion is expected to displace an N3 proton of a cytosine in the CG.C^+ base triplet to form a CG.CAg^+ triplet (*159*). A number of TFOs containing the nucleotide analogue 5-dimethylaminopropargyl deoxyuridine (DMAPdU) in place of thymidine were synthesized. These were found to enhance the triplex stability relative to thymidine (*160*).

The phosphodiester backbone of DNA has also been modified. These include the peptide nucleic acid (PNA) (*161*) and deoxyribonucleic guanidine (DNG) (*162*), in which the entire phosphodiester backbone of the nucleic acid is replaced by either neutral polypeptide or positively charged DNG backbone (Figure 6). The DNG oligomers were found to be nuclease resistant. Such DNA analogues show enhanced binding with the DNA counterpart. Replacement of some nucleotides of TFO with

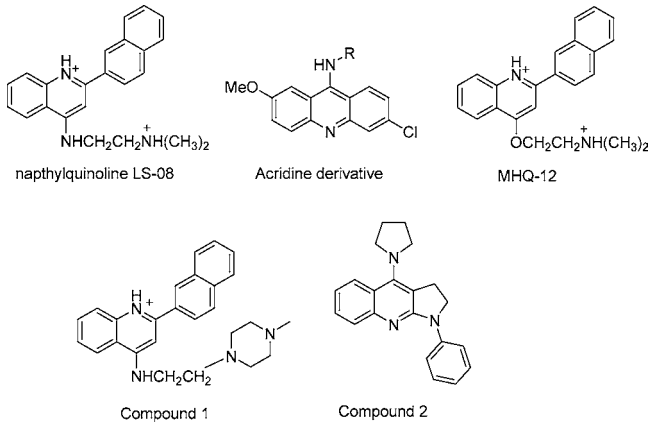


Figure 7. Molecular structures of triple-helix specific compounds LS-08, acridine derivatives, MHQ-12, 4-(4-methylpiperazino-2-ethyl-(2-naphthyl)quinoline, compound **1**, and 1-phenyl-4-pyrrolidino-2,3-dihydro-1*H*-pyrrolo [2,3-*b*]quinoline, compound **2**.

locked nucleic acid (LNA, also sometimes called "bridged" nucleic acid, BNA) was also carried out to achieve enhanced binding (*163*, *164*). A review regarding some of these approaches has been published (*165*). Use of threofuranosyl-(3′-2′) nucleic acid (TNA) is a relatively new approach (*166*). Recently, nucleoside analogue 2′-*O*-(2-aminoethyl)-5-(3-amino-1-propynyl)uridine has also been used to enhance the stability of TAT triplets (*167*). End-linked ODNs have also been used (*168*).

Properties of the Triple-Helix Specific Organic Ligands. Organic ligands were also employed to enhance the stability of the triple helices. The required properties of a triplex specific ligand have been described. The minimum criterion of such a ligand should be cationic, although the positive charge may be unfavorable for the stabilization of C^+.G:C triplets due to charge repulsion. It should have an aromatic surface, and it should also have an unfused aromatic system with torsional flexibility (*169*). The general structure of such type of compound, LS-08, is shown in Figure 7. Recently, this compound and its derivatives (MHQ-12, compound **1** and compound **2**) were used to stabilize the triple helix (*170*, *171*). In all of these compounds, the positively charged side chains might be located in the DNA grooves. Most of the triplex stabilizing compounds are generally intercalators. Acridine (Figure 7) and its derivatives stabilize the triple helix (*170*). Benzopyridoindoles and benzopyridoquinoxalines were the first molecules reported to bind to a triplex DNA more tightly than that with a duplex, thus providing a strong stabilization of triple helix involving the pyrimidine motif (*172*).

Several other intercalators were investigated for achieving triplex stabilization (*165*). In this context, the most extensively studied compounds include benzopyridoindole derivatives, coralyne, naphthylquinoline compounds, and disubstituted anthraquinones. Recently, interaction of some intercalators with duplexes and triplexes was studied using electrospray tandem mass spectrometry (*173*).

Intermolecular triplexes could be additionally stabilized if the third strand represented an ODN−intercalator conjugate. This was first demonstrated for a homopyrimidine ODN linked with an acridine derivative (*174*) and later shown for other ODN and intercalators. A review describing some of these efforts has been published in 1999 (*175*). Recently, a few camptothecin (CPT)-TFO conjugates and CPT-minor groove binder conjugates have been synthesized to target topoisomerases (*176*). Some gitmatecan-based camptothecin derivatives, conjugated with TFO, also have been synthesized recently (*177*). Excimer and exciplex triplexes were formed using the conjugated intercalator (*178*).

Triple Helices and DNA Groove Binders. As triplex formation results from the binding of a third TFO strand within the major groove (M) of the host duplex, this groove is bisected to form two daughter grooves, one major−major groove (MM) and the other one minor−major groove (mM) (Figure 8), although the host minor groove (m) remains essentially unaltered (*9*, *64*, *179*). These three groove conduits differ in complexion given their origins and disposition of the hydrogen-bond acceptor/donor centers on the bases and the nature and the dimensions of the grooves. NMR-based investigations and molecular modeling studies of oligopurine triplexes suggest that the MM channel resembles a regular minor groove, although the walls are dominated by hydrophobic residues presented by the pyrimidine C5-Me/H groups leaving the polar C4-carbonyl/amino groups buried (*179*).

A number of studies have addressed the ability of various nonintercalative minor groove binders to complex with the triplex DNA. Most of these studies were limited to short pyrimidine.purine.pyrimidine triple helices (less than 20 bp long) comprising primarily poly [$d(T)_n.d(A)_n.d(T)_n$] triplex sequences. The majority of these studies have also utilized artificial triplex-forming sequences as opposed to the naturally occurring gene-specific triplex-forming sequences.

In general, binding of the minor groove binders is associated with a decrease in the thermal stability of the triple helices unlike the double-helical DNA. However, there were several exceptions. Some minor groove binding ligands were shown to induce the formation of triplex structures that would not otherwise form. These include the binding of berenil, DAPI, and netropsin, which induced the formation of Poly(rA).Poly(rA).Poly(rT) and Poly(dT).Poly(rA).Poly(dT) triplexes (*180*), thereby overcoming the practical limitation to the formation of DNA.RNA.DNA triplex with a purine RNA strand.

In another report, berenil was shown to bind with poly(dA).2poly(dT).DNA and poly(rA).2poly(rT).RNA triplexes without displacing the major groove-bound third strand (*181*). The magnitude and even the direction of the impact of berenil binding on the thermal stability of the DNA triplex depends on both the Na^+ concentration and the drug binding density (the [base triplet]/[total berenil] ratio). There was a stabilization of the triplex at lower Na^+ concentration and a destabilization at higher Na^+ concentrations. Berenil binding to either the DNA or the RNA triplex is enthalpically more favorable than berenil binding to the corresponding duplex. Also, berenil binding to both triplexes decreases the cooperativity of the triplex to duplex melting event (*181*).

Netropsin has also been shown to bind with Poly(dT).Poly(dA).Poly(dT) triplexes, giving rise to an induced CD signal at around 320 nm. Netropsin binding to the triplex is enthalpically favorable over the binding of netropsin to the corresponding duplex (*182*). Netropsin binding with intramolecular triplex $(dT)_{12}$-x-$(dA)_{12}$-x-$(dT)_{12}$ (where x is a hexaethylene glycol based spacer) has been investigated (*183*). Spectral analysis suggests that the bound drug exhibits a conformation and an environment similar to that in a double-stranded and triple-stranded structure. However, the binding constant to the triple-stranded structure is found to be smaller than the binding constant with the double-stranded DNA, and there was a destabilization for the triplex. Hoechst 33258 was also shown to destabilize the same triplex (*184*). DAPI was also shown to destabilize triplex having TAT triplets (*180*). It appears from most of the data that minor groove binders can modulate the affinity and selectivity of the interaction of the major groove-bound third strand (*180, 181, 185*). With the TAT triplex, DAPI gives an isosbestic point at 345 nm suggesting the involvement of two species, e.g., free and bound DAPI (*185*), in equilibrium with triplex DNA.

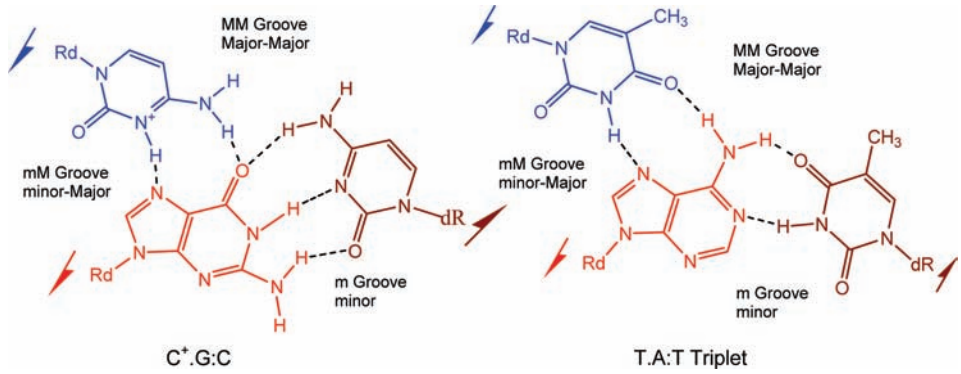


Figure 8. Three grooves of the triplets of parallel triplexes. Bifurcated H-bond centers present in the MM groove where the C5-Me/H groups comprise the hydrophobic walls, but the minor groove (m) resembles the host duplex (*179*).

In another report, netropsin has been shown to bind in a 2:1 stoichiometry with the intramolecular triplex as evidenced from circular dichroism (CD) spectroscopy, melting, and isothermal titration calorimetry (ITC) techniques, while with the intramolecular duplex, the stoichiometry has been ~1:1 (*186*). The binding of the second netropsin is accompanied by only ~15% change in the induced CD signal of the first ligand, indicating binding of the ligand most likely to a different environment (*187*). Thus, there was a destabilization of the triplex.

NMR and IR spectroscopy were used to show that distamycin binds to the triplex poly(dA).[poly(dT)]$_2$ (*187*, *188*). Distamycin is known to bind highly selectively to the minor groove of the *B*-form DNA, but not to the *A*-form of DNA (*189*). The fact that it binds to the poly(dA).[poly-(dT)]$_2$ triplex suggests that the triplex does indeed adopt a *B*-form conformation in solution. The binding of netropsin and berenil to the intramolecular T.A.T triplex has been comparatively studied by CD and thermal denaturation (*183*, *190*). These studies lead to the conclusions that the ligand-bound duplex and triplex DNA exhibit a similar conformation to that observed with netropsin (which destabilizes the third strand) or with berenil, which could either stabilize (when no NaCl is present) or destabilize (in the presence of 1 M NaCl) the third strand.

Minor groove binders (netropsin, DAPI, and Hoechst-33258) and threading molecules (which intercalates, but have some groove binding arms, e.g., NiP4, nogalamycin, etc.) along with a few intercalators were investigated for their interaction with the triplexes (*191*). DAPI has shown some stabilization effect, but Hoechst-33258 and netropsin have induced destabilization of triplexes. The threading molecules had little effect on the triplex stability.

Recently, some benzimidazole derivatives have been shown to stabilize the DNA triplex. The stabilization was pH-dependent, and there was a considerably high stabilization at pH 5.2 suggesting that the stabilization was due to electrostatic forces (*85*). Modeling studies showed that these molecules bind to the Watson−Crick minor groove of the triplex, which can exert a profound impact on the properties of the host triplex. CD binding studies indicate that nearly 5.77 base triplets/ligand is an apparent binding site size for bis-benzimidazoles and 8.66 for the terbenzimidazoles (*85*).

GC- and AT-specific minor groove ligands, e.g., mithramycin (a GC-specific, RNA synthesis inhibitor, and an antineoplastic agent, Figure 9), distamycin, and berenil (both AT-specific), were shown to differentially affect the intermolecular pur.pur:pyr triplex formed by the human c-K_i-ras promoter by using *DNase I* footprinting and gel shift assays (*192*). Mithramycin binding with the c-K_i-ras promoter completely abolishes the triplex formation. Furthermore, the addition of mithramycin to preformed triplex by c-K_i-ras promoter displaces the major-groove-bound ODN. Neither distamycin nor berenil, however, prevents

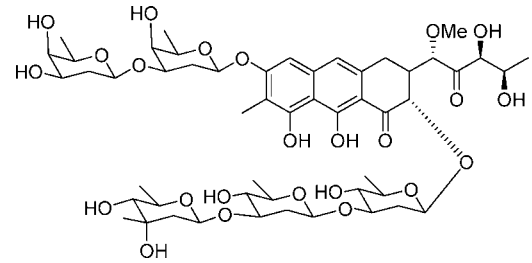


Figure 9. Molecular structure of mithramycin.

the triplex formation, and furthermore, the addition of either distamycin or berenil to the preformed triplex structure did not displace the major-groove-bound third strand (*192*). On the other hand in another report, on the basis of *DNase I* footprinting studies, distamycin and mithramycin were shown to abolish the triplex formation (*193*).

DAPI was reported to exhibit properties characteristic of intercalation. Thus, it enhances the thermal stability when complexed with the poly(rA).2poly(dT) triplex, while providing evidence of the ability of such a ligand to alter dramatically the affinity and specificity of a third strand toward its host duplex (*194*). Such triplexes do not form in the absence of any ligand (*194*).

Interactions of distamycin A and DAPI along with the intercalators like ethidium bromide, 8-methoxypsoralen, and the **Δ** and **Λ** enantiomers of Ru(phen)$_2$-dppz^{2+} were investigated using PNA-DNA duplexes and a PNA$_2$/DNA triplex on the basis of optical spectroscopic methods (*195*). No significant intercalative binding was detected for any of the DNA intercalators with triple helical poly(dA)/(H-T$_{10}$-Lys-NH$_2$)$_2$. DAPI was found to exhibit a CD with a positive sign, and its amplitude was consistent with a minor groove binding (*195*). Distamycin showed no significant binding with the PNA$_2$/DNA triplex. Both DAPI and distamycin showed minor groove binding with DNA triplex.

Interaction of netropsin with parallel and antiparallel intramolecular DNA triple helices formed by the ODNs d(G$_4$A$_4$G$_4$[T$_4$]C$_4$T$_4$C$_4$[T$_4$]G$_4$T$_4$G$_4$) and d(G$_4$T$_4$G$_4$[T$_4$]G$_4$A$_4$G$_4$[T$_4$]C$_4$T$_4$C$_4$) was examined. Netropsin binds to the central site A$_4$/T$_4$ of the duplex or triplex in an equimolar stoichiometry. Its association constant, *K*, is smaller for the parallel triplex than for the antiparallel one (*196*). In contrast to the antiparallel structure, netropsin binding has no apparent effect on the thermal stability of the parallel triple helix (*196*).

The changes in volume and adiabatic compressibility, were determined that accompanied with the binding of netropsin to the poly(dA.dT).poly(dA.dT) triplex and poly(dA).poly(dT) duplex, as well as to the poly(dT).poly(dA):poly(dT) triplex (*197*). Netropsin binding to the triplex causes changes in both

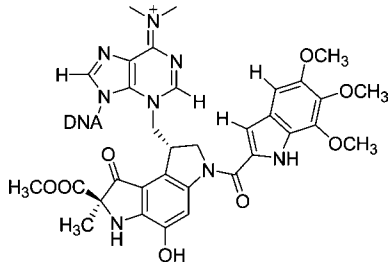


Figure 10. Molecular structure of duocarmycin A covalently linked with the N3 of adenine.

volume and compressibility that are nearly twice as large as those observed when netropsin binds to the poly(dA).poly(dT) duplex. Netropsin binding induces the release of about 53 water molecules from the hydration shell of the poly-(dT).poly-(dA).poly(dT) triplex (*197*).

The interaction of a series of bis-quaternary ammonium heterocycles (BQA) with the triple helix of poly(dA). Two poly(dT) was investigated. The ionic strength dependence of the triplex stability at increasing ligand concentration was analyzed by phase diagrams. These results demonstrated that certain BQA ligands promote triplex formation under low ionic strength and lower the affinity of the major groove-bound third strand of the triplex at high ionic strength (*198*). Compound SN-6999 (Figure 1) destabilizes the triplex structure strongly but stabilizes the DNA duplex, while SN-16814 (Figure 1) shows no effect at all on the triplex stability. In contrast, SN-18071 (Figure 1) promotes triplex formation exclusively and is one of the most potent triplex stabilizers of the BQA ligand investigated, which is also more effective than spermine (*199*).

SN-18071 stabilized DNA triple-helix containing TAT triplets as reported earlier, while SN-6999 induced destabilization of the triple helix under the comparable ionic strength conditions (*199*). This may be due to the fact that SN-18071 is devoid of functional groups that form hydrogen bonds, and such ligand molecules may stabilize the triple-helical grooves by electrostatic interactions. A carbocyanine dye, 3,3′-diethyloxadicarbocyanine (DODC), was also shown to stabilize the triplexes having TAT triplets. The stabilization was found to depend on concentration of the ligand (*200*).

A quantitative chemical-probing assay was been reported that involved protection of duplex guanines in a homopyrimidine-homopurine (Py-Pu) sequence from dimethyl sulfate modification. This was carried out to study the effects of basic oligopeptides, e.g., Lys-Gly-Lys-Gly-Lys, Lys-Ala-Lys-Ala-Lys, and Lys-Lys-Lys-Lys-Lys on the stability of triplex (*201*). Cationic amino acid residues of the basic peptides might neutralize the phosphate groups of triple-helical nucleic acids through salt formation. Since the major groove of the duplex target would be occupied by the third strand of the triplex, such oligopeptides might bind in the minor groove and/or in the new grooves formed by a third strand and two duplex strands (*201*). Of the basic peptides studied, pentalysine (Lys-Lys-Lys-Lys-Lys) was the most effective triplex stabilizer.

Duocarmycin A (Figure 10) is a DNA-alkylating agent which covalently binds to the N3 of adenine in a sequence-specific manner in the minor groove of duplex DNA. In order to generate a site-specifically and covalently bound duocarmycin A to the minor groove N3 atom of a single adenine of a pyrimidine-purine-pyrimidine DNA triplex and to monitor the potential groove cross-talks between the duocarmycin A and the third pyrimidine strand, it was added for interaction with intramolecular C^+GC triplex (*202*). The covalently bound duocarmycin A in the minor groove did not expel the pyrimidine third strand from the major groove of the triplex at low temperature and acidic pH. However, it affects the pH-dependent triplex−duplex equilibrium, which reflects protonation of the third strand cytidines involved in C^+GC triple formation and it lowers the pK_a for protonation of third strand cytidines in the major groove by 1.8 pH units in the complex (*202*).

A major groove binding ligand, methyl green (Figure 11), was also studied with triplexes having TAT triplets by linear dichroism (LD) spectroscopy. In contrast to other minor groove binding ligands (such as DAPI and Hoechst 33258), methyl green was found to be excluded from binding to the triple-helical poly(dA).two poly(dT) in which the major groove was filled by the third strand (*203*).

Molecular modeling studies and molecular mechanics calculations on polyamine−DNA interactions have suggested a binding mode involving the docking of the polyamines in either the major or minor groove of duplex DNA (*204*). Experimental evidence for either mode of interaction is, however, rather rare. Single-crystal X-ray crystallography of ODN−spermine complexes showed a complex mode of interaction involving the binding of the amino groups of spermine in the major groove of DNA (*205*). There are also other reports of triplex stabilization by the polyamines (*150*−*153*, *206*, *207*).

Traditional RNA binders, e.g., aminoglycosides, were found to be another class of triple-helical nucleic acid-stabilizing ligands. Out of all aminoglycosides, neomycin (Figure 11) has shown the most significant effects in stabilizing DNA, RNA, and hybrid triple helices (*208*, *209*). It is a groove binder and binds at the larger Watson-Hoogsteen groove of the triple helix (*210*). Triplex stabilization by neomycin is salt-dependent (increased KCl and $MgCl_2$ concentrations decrease neomycin's binding effectiveness, at a fixed drug concentration) and pH-dependent (increased pH decreases neomycin's interaction, at a fixed drug concentration).

Neomycin conjugates with triplex binding intercalators such as pyrene and benzo[*f*]quino[3,4-*b*]quinoxaline (BQQ, Figure 11) were synthesized (*211*, *212*). Neomycin−BQQ conjugates were shown to provide very high stabilization of the triplexes

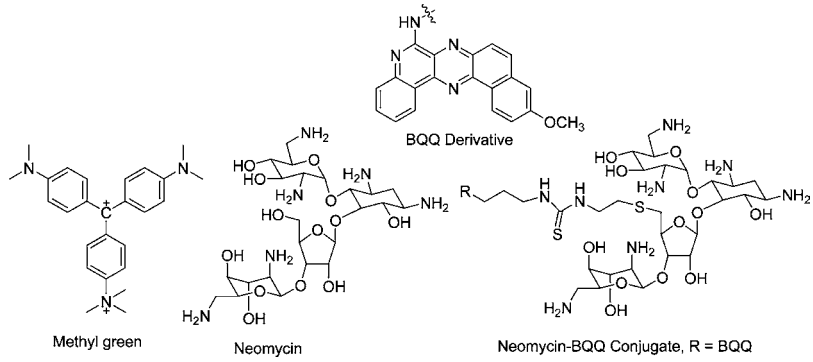


Figure 11. Chemical structures of methyl green, aminoglycoside neomycin, BQQ derivative, and neomycin−BQQ conjugate.

Table 1. Groove Binding Ligands Having Destabilizing Effect on Triplexes

ligands	triplex	effect/comment	reference
Netropsin	DNA, Intramolecular	2:1 binding, destabilization	(*186*)
Hoechst 33258	DNA (TAT), Intramolecular	Destabilization	(*184*)
DAPI	DNA (TAT), Intermolecular	Two kind of binding	(*185*)
Hoechst 33258, Netropsin	DNA (TAT), Intermolecular	Destabilization	(*191*)
Mithramycin	DNA (c-Ki-ras promoter)	Abolishes triplex formation	(*192*)
Distamycin	$(PNA)_2$/DNA	No significant binding	(*195*)
DAPI	$(PNA)_2$/DNA	Binding	(*195*)
SN-6999	DNA (TAT)	Destabilization	(*198, 199*)
Methyl green	DNA (TAT), Intermolecular	Triplex does not form	(*203*)

Table 2. Stabilizing Effect of Groove Binding Ligands on Triplexes and Conditions

ligands	triplex	effect/comment	reference
Berenil	DNA (TAT) and RNA (TAT), Intermolecular	Salt concentration (NaCl) dependant stabilization	(*181*)
Netropsin, Berenil	DNA (TAT), Intramolecular	Netropsin has similar bound drug environment in duplex and triplex, Berenil induce salt dependant stabilization	(*183, 190*)
Netropsin	DNA, Intramolecular	Stabilization of anti-parallel triplex, no effect on parallel triplex	(*196*)
DAPI	dT.rA.dT, Intermolecular	Stabilization	(*194*)
DAPI	DNA (TAT), Intermolecular	Some stabilization	(*191*)
Terbenzimidazoles	DNA (TAT, C^+GC mix), Intermolecular	pH dependant stabilization	(*85*)
SN-18071	DNA (TAT)	Stabilization	(*199*)
DODC	DNA (TAT)	Ligand concentration dependant stabilization	(*200*)
Oligopeptide	DNA (TAT, C^+GC mix), Intermolecular	Stabilization	(*201*)
Polyamines	DNA, Intermolecular	Stabilization	(*150−153, 206, 207*)
Aminoglycosides (neomycin etc.)	DNA, RNA	Salt, pH and drug concentration dependant stabilization	(*208, 209*)
Neomycin-BQQ conjugates	DNA	High stabilization	(*211, 212, 215*)
MGBL-DNA conjugates	DNA	Stabilization	(*216, 222*)

Table 3. Groove Binding Ligands Promoting Triplex Formation (But No Stabilization)

ligands	triplex	effect/comment	reference
Berenil, Netropsin, DAPI	RNA (AAT and TAT), Intermolecular	Induction of RNA triplex formation	(*180*)
Netropsin	DNA (TAT), Intermolecular	Enthalpically favorable binding	(*182*)
Netropsin	DNA, Intramolecular	Stabilization of anti-parallel triplex, no effect on parallel triplex	(*196*)
Netropsin	DNA (TAT), Intermolecular	Compress triplex due to dehydration	(*197*)
Distamycin	DNA (TAT), Intermolecular	Favorable binding	(*185*)
Distamycin, Berenil	DNA (c-Ki-ras promoter)	Formation of triplex	(*192*)
DAPI	$(PNA)_2$/DNA	Binding	(*195*)
Doucarmycin A	DNA (TAT, C^+GC mix), Intermolecular	Lower the *p*Ka for protonation	(*202*)
Neomycin-Hoechest 33258 conjugate	DNA	Binding	(*214, 215*)

(*211*). Aminoglycoside−DNA conjugates were also synthesized to target nucleic acid sequences (*213*). Synthesis of a neomycin−Hoechst 33258 conjugate was reported. The conjugate combines the ligands known to selectively bind with the duplex and the triplex groove. The conjugate stabilizes duplex DNA over DNA triplex (*214*). A review regarding triplex-stabilizing properties of aminoglycosides addresses this issue in greater detail (*215*).

Minor groove binding ligands and polyamines, when conjugated to the third strand of a triple helix, were found to be very effective in providing additional triplex stabilization (*216−218*). An oligonucleotide-maleimide-bisbenzimidazole conjugate has been synthesized to stabilize triplexes recently (*219*). These conjugates stabilize the triple helix by simultaneous major and minor groove binding. The MGBL remains bound with the duplex DNA after opening the triple helix and increases the melting temperature of the duplex to coil transition. These types of conjugates have potential for developing transcription factor inhibitor. A deoxynucleic guanidine (DNG)−Hoechst 33258 conjugate and PNA−bisbenzimidazole conjugate have also been used to stabilize triple helix and double helix (*220, 221*). It has been reported that minor groove binders are comparable with the intercalators in the degree of stabilization of the triple helix, especially when two ligand molecules are attached in a parallel orientation to the same terminal phosphate of a triplex-forming ODN (*222*).

A TFO-tethered MGBL can bind with the minor groove of triplex itself and also in the minor groove of adjacent duplex. TFO-tethered MGBL preferably binds in the minor groove of the adjacent duplex when it has the binding site (*217, 218*). However, TFO-tethered MGBL binds with the triplex region when the adjacent duplex is devoid of a binding site (*218, 220*). Similarly, a TFO-tethered MGBL can share the binding site of duplex and triplex regions; e.g., for the triplex used in the reference (*219*), having a 14mer-long TFO tethered with a bisbenzimidazole, the binding site (for bisbenzimidazole) in the duplex near the tethering end could be a d(5′-AAGAA-3′)/d(3′-TTCTT-5′) sequence in the 14-triplet-long triple helix region and it could be d(5′-TTAAGAA-3′)/d(3′-AATTCTT-5′) if the base pairs outside the triplex region were also considered.

There are contradictory reports regarding the interaction of minor groove binders with DNA/RNA triplexes. Some reports state that the binding of MGBLs with the triplex DNA is associated with triplex destabilization (Table 1), while others claim that MGBLs either provide conditional stabilization of triplexes (Table 2) or promote the triplex formation for the systems in which it is otherwise not possible (Table 3). Ligands having positively charged groups/atoms may have impact triplex stability, since Ag^+ ion has been shown to stabilize CGC triplex (at neutral pH (*159*)) and benzimidazole derivatives were shown to stabilize triplex at acidic pH (*85*). It has been further suggested that groove-directed triplex stabilization may be more efficient

if the stabilizing agent has little or no inherent affinity for the underlying duplex in order to prevent the intergroove cross talk and consequent binding induced displacement of a strand. On the basis of molecular modeling, crystal coordinates, and X-ray fiber diffraction data, a series of analogues of antitrypanosomal agent berenil, ω-aminoalkyl ester-functionalized 1,3-diaryltriazines have been proposed as potential triplex stabilizing agents (*179*). Hence, it may be possible in principle to design and synthesize more effective triplex-stabilizing minor groove binding ligands.

CONCLUDING REMARKS

Parallel-stranded duplex-DNA offers new opportunities for the design of unique hybridization probes or antisense constructs. Therefore, the binding selectivity of ligands (dyes, antibiotics, etc.) with *ps*-DNA is of considerable interest. The specific interaction of DNA binding drugs with the naturally occurring triplex target sequences is important for a number of reasons. First, a DNA binding drug might interact preferentially with a triplex DNA, as opposed to a duplex DNA, enhancing the stability of the triplex structure. Second, the combined exposure to ODN and "triplex-specific" DNA binding drugs may increase their ability to inhibit specific genes. Finally, the identification of a drug which can cause the "dis"-association of triplex DNA may have application in the study of structure and function of the intramolecular triplex (*H*-DNA) in vivo. Ligand-induced formation of new classes of hybrid triplexes may have implications in the recognition of RNA-DNA duplexes by cellular and viral proteins, such as ribonuclease H and reverse transcriptase. Triplex formation at protein recognition sites may provide a viable means of achieving specific control of the protein function. In this article, we have highlighted the potential use of the minor groove binding ligands along with the major groove binding ligands to achieve modulation of the affinities and specificities of the third strands for their duplex targets. In this way, novel antisense, antigene, antiviral, and diagnostic strategies could be designed with far greater degrees of specificity and perhaps even significantly enhanced clinical efficacy.

ACKNOWLEDGMENT

This work was supported by a grant from the Department of Science and Technology, New Delhi, India. A.K.J. is thankful to DBT for a Post Doctoral Fellowship.

LITERATURE CITED

(1) Lehninger, A. L. (1970) The molecular basis of cell structure and function. In *Biochemistry*, 2nd ed., pp 398−399, Worth Publishers, Inc., New York.

(2) Watson, J. D., and Crick, F. H. C. (1953) Molecular structure for nucleic acids: A structure for deoxyribose nucleic acid. *Nature 171*, 737–738.

(3) Bansal, M. (2003) DNA structure: Revisiting the Watson-Crick double helix. *Curr. Sci. 85*, 1556–1563.

(4) Orbons, L. P. M., van der Marcel, G. A., van Boom, A. H., and Altona, C. (1986) Hairpin duplex formation of the octamer d(m5C-G-m5C-G-T-G-m5C-G) in solution. An NMR study. *Nucleic Acids Res. 14*, 4187–4196.

(5) Shchyolkina, A. K., Borisova, O. F., Livshits, M. A., and Jovin, T. M. (2003) Parallel-stranded DNA with natural base sequences. *Mol. Biol. 37*, 223–231.

(6) Parvathy, V. R., Bhaumik, S. R., Chary, K. V. R., Govil, G., Liu, K., Howard, F. B., and Miles, H. T. (2002) NMR structure of a parallel-stranded DNA duplex at atomic resolution. *Nucleic Acids Res. 30*, 1500–1511.

(7) Raghunathan, G., Miles, H. T., and Sasisekharan, V. (1994) Parallel nucleic acid helices with Hoogsteen base pairing: symmetry and structure. *Biopolymers 34*, 1573–1581.

(8) Pattabiraman, N. (1986) Can the double helix be parallel? *Biopolymers 25*, 1603–1606.

(9) Frank-Kamenetskii, M. D., and Mirkin, S. M. (1995) Triplex DNA structures. *Annu. Rev. Biochem. 64*, 65–95.

(10) Minsky, A. (2004) Information content and complexity in the high-order organization of DNA. *Annu. Rev. Biophys. Biomol. Struct. 33*, 317–342.

(11) Felsenfeld, G., Davies, D. R., and Rich, A. (1957) Formation of a three-stranded polynucleotide molecule. *J. Am. Chem. Soc. 79*, 2023–2024.

(12) Lee, J. S., Johnson, D. A., and Morgan, A. R. (1979) Complexes formed by $(Pyrimidine)_n.(Purine)_n$ DNAs on lowering the pH are three stranded. *Nucleic Acids Res. 6*, 3073–3091.

(13) Blackburn, E. H., and Szostak, J. W. (1984) The molecular structure of centromeres and telomeres. *Annu. Rev. Biochem. 53*, 163–194.

(14) Kerwin, S. M. (2000) G-quadruplex DNA as a target for drug design. *Curr. Pharm. Des. 6*, 441–478.

(15) Hurley, L. H. (2002) DNA and its associated processes as targets for cancer therapy. *Nat. Rev. Cancer 2*, 188–200.

(16) Volker, J., Klump, H. H., and Breslauer, K. J. (1997) The energetics of *i*-DNA tetraplex structures formed intermolecularly by $d(TC_5)$ and intramolecularly by $d[(C_5T_3)_3C_5]$. *Biopolymers 86*, 136–147.

(17) Von Hippel, P. H. (1979) The molecular bases of the specificity of interaction of transcriptional proteins with genome DNA. *Biological regulation and development* (Goldberger, R., Ed.) pp 279−347, Plenum Press, New York.

(18) Helene, C., and Lancelot, G. (1982) Interactions between functional groups in protein-nucleic acid associations. *Prog. Biophys. Mol. Biol. 39*, 1–68.

(19) Bauer, G. B., and Povrik, L. F. (1997) Specificity and kinetics of interstrand and intrastrand bifunctional alkylation by nitrogen mustards at a G-G-C sequence. *Nucleic Acids Res. 25*, 1211–1218.

(20) Wang, K., Lu, J., and Li, R. (1996) The events that occur when cisplatin encounters cells. *Coord. Chem. Rev. 151*, 53–88.

(21) Masta, A., Gray, P. J., and Phillips, D. R. (1995) Nitrogen mustard inhibits transcription and translation in a cell free system. *Nucleic Acids Res. 23*, 3508–3515.

(22) Fuertes, M. A., Castilla, J., Alonso, C., and Perez, J. M. (2002) Novel concepts in the development of platinum antitumor drugs. *Curr. Med. Chem. - Anti-Cancer Agents 2*, 539–551.

(23) Neidle, S. (1981) The molecular bases for the action of some DNA-binding drugs. *Prog. Med. Chem. 16*, 151–221.

(24) Graves, D. E., and Velea, L. M. (2000) Intercalative binding of small molecules to nucleic acids. *Curr. Org. Chem. 4*, 915–929.

(25) Blackburn, G. M. (1996) DNA and RNA structure. *Nucleic Acids in Chemistry and Biology*, 2nd ed. (Blackburn, G. M., and Gait, M. J., Eds.) pp 15−81, Oxford University Press, New York.

(26) Praveen Reddy, B. S., Sondhi, S. M., and Lown, J. W. (1999) Synthetic DNA minor groove-binding drugs. *Pharmacol. Ther. 84*, 1–111.

(27) Bhattacharya, S., and Chaudhuri, P. (2008) Medical implications of benzimidazole derivatives as drugs designed for targeting DNA and DNA associated processes. *Curr. Med. Chem. 15*, 1762–1777.

(28) Dervan, P. B., Poulin-Kerstien, A. T., Fechter, E. J., and Edelson, B. S. (2005) Regulation of gene expression by synthetic DNA-binding ligands. *Top. Curr. Chem. 253*, 1–31.

(29) Geierstanger, B. H., and Wemmer, D. E. (1995) Complexes of the minor groove of DNA. *Annu. Rev. Biophys. Biomol. Struct. 24*, 463–493.

(30) Reddy, B. S., Sharma, S. K., and Lown, J. W. (2001) Recent developments in sequence selective minor groove effectors. *Curr. Med. Chem. 8*, 475–508.

(31) Neidle, S. (2002) *Nucleic Acid Structure and Recognition*, pp 89−137, Oxford University Press, Oxford.

(32) Wemmer, D. E. (2000) Designed sequence-specific minor groove ligands. *Annu. Rev. Biophys. Biomol. Struct. 29*, 439–461.
(33) Chaires, J. B. (1997) Energetics of drug-DNA interactions. *Biopolymers 44*, 201–215.
(34) Haq, I. (2002) Thermodynamics of drug-DNA interactions. *Arch. Biochem. Biophys. 403*, 1–15.
(35) Mazur, S., Tanious, F. A., Ding, D., Kumar, A., Boykin, D. W., Simpson, I.J., Neidle, S. and, and Wilson, W. D. (2000) A thermodynamic and structural analysis of DNA minor-groove complex formation. *J. Mol. Biol. 300*, 321–337.
(36) Haq, I., Ladbury, J. E., Chowdhry, B. Z., Jenkins, T. C., and Chaires, J. B. (1997) Specific binding of Hoechst 33258 to the $d(CGCAAATTTGCG)_2$ duplex: calorimetric and spectroscopic studies. *J. Mol. Biol. 271*, 244–257.
(37) Lah, J., and Vesnaver, G. (2004) Energetic diversity of DNA minor groove recognition by small molecules displayed through some model ligand-DNA systems. *J. Mol. Biol. 342*, 73–89.
(38) Lah, J., and Vesnaver, G. (2000) Binding of distamycin A and netropsin to the 12mer DNA duplexes containing mixed AT-GC sequences with at most five or three successive AT base pairs. *Biochemistry 39*, 9317–9326.
(39) Lah, J., Carl, N., Drobnak, I., Sumiga, B., and Vesnaver, G. (2006) Competition of some minor groove binders for a single DNA binding site. *Acta Chim. Slov. 53*, 284–291.
(40) Zimmer, C., and Wahnert, U. (1986) Non-intercalating DNA-binding ligands: specificity of the interaction and their tools in biophysical, biochemical and biological investigations of the genetic material. *Prog. Biophys. Mol. Biol. 47*, 31–112.
(41) Abu-Daya, A., and Fox, K. R. (1997) Interaction of minor groove binding ligands with long AT tracts. *Nucleic Acids Res. 25*, 4962–4969.
(42) Bostock-Smith, C. E., Harris, S. A., Laughton, C. A., and Searle, M. S. (2001) Induced fit DNA recognition by a minor groove binding analogue of Hoechst 33258: fluctuations in DNA. A tract structure investigated by NMR and molecular dynamics simulations. *Nucleic Acids Res. 29*, 693–702.
(43) Tawar, U., Jain, A. K., Dwarakanath, B. S., Chandra, R., Singh, Y., Chaudhury, N. K., Khaitan, D., and Tandon, V. (2003) Influence on phenyl ring disubstitution on bisbenzimidazole and terbenzimidazole cytotoxicity: Synthesis and biological evaluation as radioprotectors. *J. Med. Chem. 46*, *18*, 3785–3792.
(44) Tawar, U., Jain, A. K., Chandra, R., Singh, Y., Dwarakanath, B. S., Chaudhury, N. K., Good, L., and Tandon, V. (2003) Minor groove binding DNA ligands with expanded A/T sequence length recognition, selective binding to bent DNA regions and enhanced fluorescent properties. *Biochemistry 42*, 13339–13346.
(45) Jain, A. K., Gupta, S. K., and Tandon, V. (2009) Evaluation of electronic effect of phenyl ring substituents on the DNA minor groove binding properties of novel bis and terbenzimidazoles: Synthesis and spectroscopic studies of ligand-DNA interaction. *Oligonucleotides 19*, 329–340.
(46) Ghosh, S., Usharani, D., Paul, A., De, S., Jemmis, E. D., and Bhattacharya, S. (2008) Design, synthesis, and DNA binding properties of photoisomerizable azobenzene-distamycin conjugates: An experimental and computational study. *Bioconjugate Chem. 19*, 2332–2345.
(47) Ghosh, S., Usharani, D., De, S., Jemmis, E. D., and Bhattacharya, S. (2008) Photophysical and duplex-DNA binding properties of distamycin dimers based on 4, 4′ and 2, 2′-dialkoxyazobenzenes as the core. *Chem. Asian J. 3*, 1949–1961.
(48) Thomas, M., Rao, A. R., Varshney, U., and Bhattacharya, S. (2001) Unusual DNA binding exhibited by synthetic distamycin analogs lacking the N-terminal amide unit under high salt conditions. *J. Biomol. Str. Dyn. 18*, 858–871.
(49) Kakkar, R., Suruchi, and Grover, R. (2005) Theoretical study of molecular recognition by Hoechst 33258 derivatives. *J. Biomol. Str. Dyn. 23*, 37–47.
(50) Dolenc, J., Oostenbrink, C., Koller, J., and van Gunsteren, W. F. (2005) Molecular dynamics simulations and free energy calculations of netropsin and distamycin binding to an AAAAA DNA binding site. *Nucleic Acids Res. 33*, 725–733.
(51) Thomas, M., Varshney, U., and Bhattacharya, S. (2002) Distamycin analogs without leading amide at their N-terminii-comparative binding properties to AT- and GC-rich DNA sequences. *Eur. J. Org. Chem.* 3604–3615.
(52) Chaudhuri, P., Ganguly, B., and Bhattacharya, S. (2007) An experimental and computational analysis on the differential role of the positional isomers of symmetric bis-2-(pyridyl)-1*H*-benzimidazoles as DNA binding agents. *J. Org. Chem. 72*, 1912–1923.
(53) Chaudhuri, P., Majumder, H. K., and Bhattacharya, S. (2007) Synthesis, DNA binding, and leishmania topoisomerase inhibition activities of a novel series of anthra[1,2*d*]imidazole-6,11-dione derivatives. *J. Med. Chem. 50*, 2536–2540.
(54) Bhattacharya, S., and Chaudhuri, P. (2007) Metal-ion-mediated tuning of duplex DNA binding by bis[2-(2-pyridyl)-1H-benzimidazole]. *Chem. Asian J. 2*, 648–655.
(55) Turner, J. M., Baird, E. E., and Dervan, P. B. (1997) Recognition of seven base pair sequences in the minor groove of DNA by ten-ring pyrrole-imidazole polyamide hairpins. *J. Am. Chem. Soc. 119*, 7636–7644.
(56) Bhattacharya, S., and Thomas, M. (2000) Facile synthesis of oligopeptide distamycin analogs devoid of hydrogen bond donors or acceptors at the N-terminus: Sequence-specific duplex DNA binding as a function of peptide chain length. *Tetrahedron Lett. 41*, 5571−5575.
(57) Staz, A. L., and Bruice, T. C. (2000) Recognition of nine base pairs in the minor groove of DNA by a tripyrrole-peptide-Hoechst conjugate. *J. Am. Chem. Soc. 123*, 2469–2477.
(58) Bhattacharya, S., and Thomas, M. (2001) DNA recognition by the first *tail-to-tail* linked distamycin-like oligopeptide dimers. *Chem. Commun.* 1464–1465.
(59) Ghosh, S., Defrancq, E., Lhomme, J. H., Dumy, P., and Bhattacharya, S. (2004) Efficient conjugation and characterization of distamycin based peptides with selected oligonucleotide stretches. *Bioconjugate Chem. 15*, 520–529.
(60) van de Sande, J. H., Ramsing, N. B., Germann, M. W., Elhorst, W., Kalisch, B. W., vonKitzing, E., Pon, R. T., Clegg, R. C., and Jovin, T. M. (1988) Parallel stranded DNA. *Science* 551–557.
(61) Rippe, K., and Jovin, T. M. (1992) Parallel stranded duplex DNA. *Methods Enzymol. 211*, 199–220.
(62) Saha, T., and Roy, K. B. (1999) A novel parallel-stranded DNA duplex with non-canonical A-T and G-C base pairing in synthetic dodacamers. *Curr. Sci. 77*, 436–453.
(63) Liu, K., Miles, H. T, Frazier, J., and Sasisekharan, V. (1993) A Novel DNA duplex: A parallel stranded DNA helix with Hoogsteen base pairing. *Biochemistry 32*, 11802–11809.
(64) Soyfer, V. N., and Potaman, V. N. (1996) The discovery of triple stranded nucleic acids. In *Triple-Helical Nucleic Acids* pp 1−46, Springer-Verlag, New York.
(65) Rippe, K., and Jovin, T. M. (1989) Substrate properties of 25-nt parallel-stranded linear DNA duplexes. *Biochemistry 28*, 9542–9549.
(66) Tchurikov, N. A., Chernov, B. K., Golov, Y. B., and Nechipurenko, Y. D. (1989) Parallel DNA: generation of a duplex between two *Drosophila* sequences *in vitro*. *FEBS Lett. 257*, 415–418.
(67) Otto, C., Thomas, G. A., Rippe, K., Jovin, T. M., and Peticolas, W. L. (1991) The hydrogen-bonding structure in parallel-stranded duplex DNA is reverse-Watson-Crick. *Biochemistry 30*, 3062–3069.
(68) Escude, C., Mohammadi, S, Sun, J.-S., Nguyen, C.-H., Bisagni, E., Liquier, J, Taillandier, E., Carestier, T., and Helene, C. (1996) Ligand induced formation of Hoogsteen-paired parallel DNA. *Chem. Biol. 3*, 57–65.
(69) Hoogsteen, K. (1963) The crystal and molecular structure of a hydrogen bonded complex between 1-methylthymene and 9-methyl thymine. *Acta Crystallogr. 16*, 907–916.
(70) Smith, F. W., and Feigon, J. (1992) Quadruplex structure of *Oxitrycha* telomeric DNA oligonucleotides. *Nature 356*, 126–131.
(71) Suda, T., Mishima, Y., Asakura, H., and Kominami, R. (1995) Formation of a parallel-stranded DNA homoduplex by (CGA) repeat oligonucleotides. *Nucleic Acid Res. 23*, 3771–3777.

(72) Wand, Y., and Patel, D. J. (1994) Solution structure of the d(T-C-G-A) duplex at acidic pH. A parallel-stranded helix containing C:C^+, G:G and A:A^+ base pairs. *J. Mol. Biol. 242*, 508–526.

(73) Fortsch, I., Fritzsche, H., Birch-Hirschfeld, E, Evertsz, E, Klement, R, Jovin, T. M., and Zimmer, C. (1996) Parallel-stranded duplex DNA containing dA.dU base pairs. *Biopolymers 38*, 209–220.

(74) Dolinnaya, N., Ulku, A., and Fresco, J. R. (1997) Parallel-stranded linear homoduplexes of $d(A^+\text{-}G)_{n>10}$ and $d(A\text{-}G)_{n>10}$ manifesting the contrasting ionic strength sensitivities of poly (A^+A^+) and DNA. *Nucleic Acid Res. 25*, 1100–1107.

(75) Ramsing, N. B., Rippe, K., and Jovin, T. M. (1989) Helix-coil transition of parallel-stranded DNA. Thermodynamics of hairpin and linear duplex oligonucleotides. *Biochemistry 28*, 9528–9535.

(76) Lancelot, G., Guesnet, J. L., and Vovelle, F. (1989) Solution structure of the parallel-stranded duplex oligonucleotide α-d(TCTAAAC)-βd(AGATTTG)via complete relaxation matrix analysis of the NOE effects and molecular mechanics calculations. *Biochemistry 28*, 7871–7878.

(77) Ishikawa, F., Frazier, J., Howard, F. B., and Miles, H. T. (1972) Polydenylate polyuridylate helices with non-Watson-Crick hydrogen bonding. *J. Mol. Biol. 70*, 475–490.

(78) Yang, X.-L., Sugiyama, H., Ikeda, S., Saito, I., and Wang, A. H. J. (1998) Structural studies of a stable parallel-stranded duplex incorporating isoguanine:cytocine and isocytocine:guanine base pairs by nuclear magnetic resonance spectroscopy. *Biophys. J. 75*, 1163–1171.

(79) Praseuth, D., Chassignol, M., Takasugi, M., Doan, T. L., Thuong, N. T., and Helene, C. (1987) Double helices with parallel strands are formed by nuclease resistant oligo-[α]-deoxynucleotides covalently linked to an intercalating agent with complementary oligo-[β]-deoxynucleotides. *J. Mol. Biol. 196*, 939–942.

(80) Geinguenaud, F., Mondragon-Sanchez, J. A., Liquier, J., Shchyolkina, A. K., Klement, R., Arndt-Jovin, D. J., Jovin, T. M., and Taillandier, E. (2005) Parallel DNA double helices incorporating isoG or m^5isoC bases studied by FTIR, CD and molecular modeling. *Spectrochim. Acta, Part A 61*, 579–587.

(81) Jovin, T. M. (1991) In *Nucleic Acids and Molecular Biology Vol.* (Eckstein, F., and Lilley, D. M., Eds.), pp 25−52, Vol *5*, Springer-Verlag, Berlin.

(82) Le, H., Peng, X., Leonard, P., and Seela, F. (2006) Binding of actinamycin C_1 (D) and actinomin to base modified oligonucleotide with parallel chain orientation. *Bioorg. Med. Chem. 14*, 4089–4100.

(83) Fritzsche, H., Akhebat, A., Taillandier, E., Rippe, K., and Jovin, T. M. (1993) Structure and drug interactions of parallel-stranded DNA studied by infrared spectroscopy and fluorescence. *Nucleic Acids Res. 21*, 5085–5091.

(84) Jovin, T. M., Rippe, K., Ramsing, N. B., Kelment, R., Elhorst, W., and Vojtisova, M. (1990) Parallel stranded DNA. *Structures and methods, Vol 3: DNA and RNA* (Sharma, R. H., and Sharma, M. H., Eds.) pp 155−174, Adenine Press, Schenectady, NY.

(85) Jain, A. K., Tawar, U., Gupta, S. K., Dogra, S. K., and Tandon, V. (2009) Benzimidazoles: A minor groove binding ligand mediated stabilization of triple helix. *Oligonucleotides 19*, 53–62.

(86) Moser, H. E., and Dervan, P. B. (1987) Sequence specific cleavage of double helical DNA by triple helix formation. *Science 238*, 645–650.

(87) Helene, C. (1991) The anti-gene strategy: control of gene expression by triplex forming oligonucleotides. *Anti Cancer Drug Des. 6*, 569–584.

(88) Faria, M., and Giovannangeli, C. (2001) Triplex-forming molecules: from concepts to applications. *J. Gene Med. 3*, 299–310.

(89) Faria, M., and Ulrich, H. (2002) The use of synthetic oligonucleotides as protein inhibitors and anticode drugs in cancer therapy: accomplishments and limitations. *Curr. Cancer Drug Targeting 2*, 355–368.

(90) Knauert, M. P., and Glazer, P. M. (2001) Triplex forming oligonucleotides: sequence-specific tools for gene targeting. *Hum. Mol. Genet. 10*, 2243–2251.

(91) Vasquez, K. M., and Glazer, P. M. (2002) Triplex-forming oligonucleotides: principles and applications. *Q. Rev. Biophys. 35*, 89–107.

(92) Letai, A. G., Palladino, M. A., Fromm, E., Rizzo, V., and Fresco, J. R. (1988) Specificity in formation of triple-stranded nucleic acid helical complexes: studies with agarose-linked polyribonucleotide affinity columns. *Biochemistry 27*, 9108–9112.

(93) Vasquez, K. M., and Wilson, J. H. (1998) Triplex-directed modification of genes and gene activity. *Trends Biochem. Sci. 23*, 4–9.

(94) Fossella, J. A., Kim, Y. J., Shih, H., Richards, E. G., and Fresco, J. R. (1993) Relative specificities in binding of Watson-Crick base pairs by third strand residues in a DNA pyrimidine triplex motif. *Nucleic Acids Res. 21*, 4511–4515.

(95) Morgan, A. R., and Wells, R. D. (1968) Specificity of the three stranded complex formation between double stranded DNA and single stranded RNAcontaining repeating nucleotide sequences. *J. Mol. Biol. 37*, 63–80.

(96) Hardenbol, P., and Van Dyke, M. W. (1996) Sequence specificity of triplex DNA formation: analysis by a combinatorial approach, restriction endonuclease protection selection and amplification. *Proc. Natl. Acad. Sci. U.S.A. 93*, 2811–2816.

(97) Beal, P. A., and Dervan, P. B. (1991) Second structural motif for recognition of DNA by oligonucleotide directed triple helix formation. *Science 251*, 1360–1363.

(98) Keppler, M. D., Neidle, S., and Fox, K. R. (2001) Stabilization of TG- and AG-containing triplexes by triplex binding ligands. *Nucleic Acids Res. 29*, 1935–1942.

(99) Mills, M., Arimondo, P. B., Lacroix, L., Garestier, T., Helene, C., Klump, H., and Mergny, J.-L. (1999) Energetics of strand-displacement reactions in triple helices: a spectroscopic study. *J. Mol. Biol. 291*, 1035–1054.

(100) Vekhoff, P., Ceccaldi, A., Polverari, D., Pylouster, J., Pisano, C., and Arimondo, P. B. (2008) Triplex formation on DNA targets: How to choose the oligonucleotide. *Biochemistry 47*, 12277–12289.

(101) Mirkin, S. M., and Frank-Kamenetskii, M. D. (1994) H-DNA and related structures. *Annu. Rev. Biophys. Biomol. Struct. 23*, 541–576.

(102) Vlieghe, D., Meervelt, L. V., Dautant, A., Gallois, B., Précigoux, G., and Kennard, O. (1996) Parallel and antiparallel $(G\cdot GC)_2$ triple helix fragments in a crystal structure. *Science 273*, 1702–1705.

(103) Khomyakova, E. B., Gousset, H., Liquier, J., Huynh-Dinh, T., Gouyette, C., Takahashi, M., Florentiev, V. L., and Taillandier, E. (2000) Parallel intramolecular DNA triple helix with G and T bases in the third strand stabilized by Zn^{2+} ions. *Nucleic Acids Res. 28*, 3511–3516.

(104) Jayasena, S. D., and Johnston, B. H. (1993) Sequence limitations of triple helix formation by alternate-strand recognition. *Biochemistry 32*, 2800–2807.

(105) Lyamichev, V. I., Mirkin, S. M., Frank-Kamenetskii, M. D., Charles, R., and Cantor, C. R. (1988) A stable complex between homoprimidine oligomers and the homologous regions of duplex DNA. *Nucleic Acid Res. 16*, 2165–2187.

(106) Aruott, S., and Selsing, E. (1974) Structures for the polynucleotide complexes poly(dA) · poly(dT) and poly(dT) · poly(dA) · poly(dT). *J. Mol. Biol. 88*, 509–512.

(107) Raghunathan, G., Miles, H. T., and Sasisekharan, V. (1995) Symmetry and structure of RNA and DNA triple helices. *Biopolymers 36*, 333–343.

(108) Liu, K., Sasisekharan, V., Miles, H. T., and Raghunathan, G. (1996) Structure of Py. Pu. Py DNA triple helices. Fourier transforms of fiber-type X-Ray diffraction of single crystals. *Biopolymers 39*, 573–589.

(109) Nunn, C. M., Trent, J. O., and Neidle, S. (1997) A model for the $[C^+.G.C]_n$ triple helix derived from observation of the

[C^+.G.C] base triplet in a crystal structure. *FEBS Lett. 416*, 86–89.
(110) Han, Z.-J., Rhee, S., Liu, K., Miles, H. T., and Davies, D. R. (2000) Crystallization and preliminary crystallographic study of triple-helical DNA. *Acta Crystallogr., Sect. D 56*, 104–105.
(111) Rajagopal, P., and Feigon, J. (1989) Triple-strand formation in the homopurine: homopyrimidine DNA oligonucleotides d(G-A)$_4$ and d(T-C)$_4$. *Nature 339*, 637–640.
(112) Haner, R., and Dervan, P. B. (1990) Single-strand DNA triple-helix formation. *Biochemistry 29*, 9761–9765.
(113) Raghunathan, G., Mires, H. T., and Sasisekharan, V. (1993) Symmetry and molecular structure of a DNA triple helix. *Biochemistry 32*, 455–462.
(114) Radhakrishnan, I., and Patel, D. J. Solution structure of a purine·purine·pyrimidine DNA triplex containing G·GC and T·AT triples. *Structure 1*, 135−152.
(115) Radhakrishnan, I., de los Santos, C., and Patel, D. J. (1993) Nuclear magnetic resonance structural studies of A · AT base triple alignments in intramolecular purine · purine · pyrimidine DNA triplexes in solution. *J. Mol. Biol. 234*, 188–197.
(116) Hentehel, C. C. (1982) Homocopolymer sequences in the spacer of sea urchin histone gene repeat are sensitive to S1 nuclease. *Nature 295*, 714–716.
(117) Lyamichev, V. I., Mirkin, S. M., and Frank-Kamenetskii, M. D. (1986) Structures of homopurine-homopyrimidine tract in superhelical DNA. *J. Biomol. Struct. Dyn. 3*, 667–669.
(118) Htun, H., and Dahlberg, J. E. (1989) Topology and formation of triple stranded H-DNA. *Science 243*, 1571–1576.
(119) Panas Scaria, P. V., and Shafer, R. H. (1991) Binding of ethidium bromide to a DNA triple helix. Evidence for intercalation. *J. Biol. Chem. 266*, 5417–5423.
(120) Vasquez, K. M., Wang, G., Havre, P. A., and Glazer, P. M. (1999) Chromosomal mutations induced by triplex-forming oligonucleotides in mammalian cells. *Nucleic Acids Res. 27*, 1176–1181.
(121) Majumdar, A., Puri, N., Cuenoud, B., Natt, F., Martin, P., Khorlin, A., Dyatkina, N., George, A. J., Miller, P. S., and Seidman, M. M. (2003) Cell cycle modulation of gene targeting by a triple helix-forming oligonucleotide. *J. Biol. Chem. 278*, 11072–11077.
(122) Nagatsugi, F., Sasaki, S., Miller, P. S., and Seidman, M. M. (2003) Site-specific mutagenesis by triple-helix forming oligonucleotides containing a reactive nucleoside analogue. *Nucleic Acids Res. 31*, e31=.
(123) Faruqi, A. F., Seidman, M. M., Segal, D. J., Carroll, D., and Glazer, P. M. (1996) Recombination induced by triple-helix-targeted DNA damage in mammalian cells. *Mol. Cell. Biol. 16*, 6820–6828.
(124) Luo, Z., Macris, M. A., Faruqi, A. F., and Glazer, P. M. (2000) High-frequency intrachromosomal gene conversion induced by triplex-forming oligonucleotides microinjected into mouse cells. *Proc. Natl. Acad. Sci. U.S.A. 97*, 9003–9008.
(125) Chan, P. P., Lin, M., Faruqi, A. F., Powell, J., Seidman, M. M., and Glazer, P. M. (1999) Targeted correction of an episomal gene in mammalian cells by a short DNA fragment tethered to a triplex-forming oligonucleotide. *J. Biol. Chem. 274*, 11541–11548.
(126) Culver, K. W., Hsieh, W. T., Huyen, Y, Chen, V, Liu, J, Khripine, Y, and Khorlin, A. (1999) Correction of chromosomal point mutations in human cells with bifunctional oligonucleotides. *Nat. Biotechnol. 17*, 989–993.
(127) Arimondo, P. B., Boutorine, A., Baldeyrou, B., Bailly, C., Kuwahara, M., Hecht, S. M., Sun, J.-S., Garestier, T., and Helene, C. (2002) Design and optimization of camptothecin conjugates of triple helix-forming oligonucleotides for sequence-specific DNA cleavage by *Topoisomerase I*. *J. Biol. Chem. 277*, 3132–3140.
(128) Povsic, T. J., Strobel, S. A., and Dervan, P. B. (1992) Sequence-specific double-strand alkylation and cleavage of DNA mediated by triple-helix formation. *J. Am. Chem. Soc. 114*, 5934–5941.
(129) Strobel, S. A., Doucette-Stamm, L. A., Riba, L., Housman, D. E., and Dervan, P. B. (1991) Site-specific cleavage of human chromosome 4 mediated by triple-helix formation. *Science 254*, 1639–1642.
(130) Ziemba, A J., Reed, M. W., Raney, K. D., Byrd, A. B., and Ebbinghaus, S. W. (2003) A bis-alkylating triplex forming oligonucleotide inhibits intracellular reporter gene expression and prevents triplex unwinding due to helicase activity. *Biochemistry 42*, 5013–5024.
(131) Marchand, C., Nguyen, C. H., Ward, B., Sun, J.-S., Bisagni, E., Garestier, T., and Helene, C. (2000) A new family of sequence-specific DNA-cleaving agents directed by triple-helical structures: benzopyridoindole-EDTA conjugates. *Chem.—Eur. J. 6*, 1559–1563.
(132) Bhattacharya, S., and Mandal, S. S. (1995) Ambient oxygen activating water soluble cobalt-salen complex for DNA cleavage. *J. Chem. Soc. Chem. Commun.* 2489–2490.
(133) Bhattacharya, S., and Mandal, S. S. (1996) DNA cleavage by intercalatable cobalt-bispicolylamine complexes activated by visible light. *Chem. Commun.* 1515–1516.
(134) Mandal, S. S., Varshney, U., and Bhattacharya, S. (1997) Role of the central metal ion and ligand charge in the DNA binding and modification by metallosalen complexes. *Bioconjugate Chem. 8*, 798–812.
(135) Dreyer, G. B., and Dervan, P. B. (1985) Sequence-specific cleavage of single-stranded DNA: Oligodeoxynucleotide-EDTA·Fe(II). *Proc. Natl. Acad. Sci. U.S.A. 82*, 968–972.
(136) Mandal, S. S., Kumar, N. V., Varshney, U., and Bhattacharya, S. (1996) Metal-ion dependent oxidative DNA cleavage by transition metal complex of a new water soluble salen derivative. *J. Inorg. Biochem. 63*, 265–272.
(137) Sedelnikova, O. A., Karamychev, V. N., Panyutin, I. G., and Neumann, R. D. (2002) Sequence-specific gene cleavage in intact mammalian cells by 125I-labeled triplex-forming oligonucleotides conjugated with nuclear localization signal peptide. *Antisense Nucleic Acid Drug Dev. 12*, 43–49.
(138) Honigsmann, H., Szeimies, R. M., Knobler, R., Fitzpatrick, T. B., Pathak, M. A., and Wolff, K. (2003) Photochemotherapy and photodynamic therapy. *Fitzpatrick's dermatology in general medicine* (Freedberg, I. M., Eizen, A. Z., Wolff, K., Austen, K. F., Goldsmith, L. A., and Katz, S. I., Eds.) pp 2477−2493, McGraw-Hill, New York.
(139) Besch, R., Marschall, C., Schuh, T., Giovannangeli, C., Kammerbauer, C., and Degitz, K. (2004) Triple helix-mediated inhibition of gene expression is increased by PUVA. *J. Invest. Dermatol. 122*, 1114–1120.
(140) Fearon, E. R., and Dang, C. V. (1999) Cancer genetics: tumor suppressor meets oncogene. *Curr. Biol. 9*, R62–R65.
(141) Hahn, W. C., Counter, C. M., Lundberg, A. S., Roderick, L., Beijersbergen, R. L., Mary, W., Brooks, M. W., Robert, A., and Weinberg, R. A. (1999) Creation of human tumor cells with defined genetic elements. *Nature 400*, 464–468.
(142) Bailey, C., and Weeks, D. L. (2000) Understanding oligonucleotide-mediated inhibition of gene expression in *Xenopus laevis* oocytes. *Nucleic Acids Res. 28*, 1154–1161.
(143) Faria, M., Wood, C. D., Nelson, J. S., Winter, A., White, M. R. H., Helene, C., and Giovannangeli, C. (2000) Targeted inhibition of transcription elongation in cells mediated by triplex-forming oligonucleotides. *Proc. Natl. Acad. Sci. U.S.A. 97*, 3862–3867.
(144) Wang, G., Xu, X., Pace, B., Dean, D. A., Glazer, P. M., Chan, P., Goodman, S. R., and Shokolenko, I. (1999) Peptide nucleic acid (PNA) binding-mediated induction of human gamma-globin gene expression. *Nucleic Acids Res. 27*, 2806–2813.
(145) Kool, E. (1991) Molecular recognition by circular oligonucleotides: increasing the selectivity of DNA binding. *J. Am. Chem. Soc. 113*, 6265–6266.
(146) Prakash, G., and Kool, E. (1992) Structural effects in the recognition of DNA by circular oligonucleotides. *J. Am. Chem. Soc. 114*, 523–529.

(147) Nayak, A., Khare, P., Chourasia, M. K., Silakari, O., and Kohli, D. V. (2006) DNA triple helix formation: A potential tool for genetic repair. *Indian J. Pharm. Sci. 68*, 697–704.
(148) James, P. L., Brown, T., and Fox, K. R. (2003) Thermodynamic and kinetic stability of intermolecular triple helices containing different proportions of CGC and TAT triplets. *Nucleic Acids Res. 31*, 5598–5606.
(149) Ghosh, M. K., Katyal, A., Brahmachari, V., and Chandra, R. (2002) Design and Structural analysis of hairpin-TFO for transcriptional activation of genes in S. cerevisiae. *J. Biomol. Str. Dyn. 20*, 265–274.
(150) Potaman, V. N., and Soyfer, V. N. (1994) Divalent metal cations upon coordination on the N-7 of purines differentially stabilize the PyPuPu DNA triplex due to unequal Hoogsteen type hydrogen bond. *J. Biomol. Str. Dyn. 11*, 1035–1040.
(151) Hampel, K. J., Crosson, P., and Lee, J. S. (1991) Polyamines favor DNA triplex formation at neutral pH. *Biochemistry 30*, 4455–4459.
(152) Hampel, K. J., Burkholder, G. D., and Lee, J. S. (1993) Plasmid dimerization mediated by triplex formation between polypyrimidine-polypurine repeats. *Biochemistry 32*, 1072–1077.
(153) Tabor, C. W., and Tabor, H. (1984) Polyamines. *Annu. Rev. Biochem. 53*, 749–790.
(154) Lee, J. S., Woodsworth, M. L., Latimer, L. J. P., and Morgan, A. R. (1984) Poly(pyrimidine). poly (purine) synthetic DNAs containing 5- methylcytosine form stable triplexes at neutral pH. *Nucleic Acid Res. 12*, 6603–6614.
(155) MaherIII, L. J., Wold, B. O., and Dervan, P. B. (1989) Inhibition of DNA binding protines by oligonucleotide directed triple helix formation. *Science 245*, 725–730.
(156) Krawczyk, S. H., Milligan, J. F., Wadwani, S, Moulds, C,B,C, Froehler, B. C., and Matteucci, M. D. (1992) Oligonucleotide-mediated triple helix formation using an N^3-protonated deoxycytidine analog exhibiting pH-independent binding within the physiological range. *Proc. Natl. Acad. Sci. U.S.A. 89*, 3761–3764.
(157) Jetter, M. C., and Hobbs, F. W. (1993) 7, 8-Dihydro-8-oxoadenine as a replacement for cytosine in the third strand of triple helixes. Triplex formation without hypochromicity. *Biochemistry 32*, 3249–3254.
(158) Koh, J. S., and Dervan, P. B. (1992) Design of a non-natural deoxyribonucleoside for recognition of GC base pairs by oligonucleotide-directed triple helix formation. *J. Am. Chem. Soc. 114*, 1470–1478.
(159) Ihara, T., Ishii, T., Araki, N., Wilson, A. W., and Akinori Jyo, A. (2009) Silver ion unusually stabilizes the structure of a parallel-motif DNA triplex. *J. Am. Chem. Soc. 131*, 3836–3827.
(160) Rusling, D. A., Peng, G., Srinivasan, N., Fox, K. R., and Brown, T. (2009) DNA triplex formation with 5-dimethylaminopropargyl deoxyuridine. *Nucleic Acids Res. 37*, 1288–1296.
(161) Nielsen, P. E., Egholm, M., Berg, R. H., and Buchardt, O. (1993) Oligonucleotide analogs with a polyamide backbone. In *Antisense Research and Applications* (Crooke, S. T., and Lebleu, B., Eds.) pp 363−373, CRC Press, Boca Raton, FL.
(162) Linkletter, B. A., Szabo, I. E., and Bruice, T. C. (2001) Solid-phase synthesis of ologopurine deoxynucleic guanidine (DNG) and analysis of binding with DNA oligomers. *Nucleic Acids Res. 29*, 2370–2376.
(163) Torigoe, H., Hani, Y., Sekiguchi, M., Obika, S., and Imanishi, T. (2001) 2′-*O*, 4′-C-Methylene bridged nucleic acid modification promotes pyrimidine motif triplex DNA formation at physiological pH. Thermodynamic and kinetic studies. *J. Biol. Chem. 276*, 2354–2360.
(164) Kaur, H., Babu, B. R., and Maiti, S. (2007) Perspectives on chemistry and therapeutic applications of locked nucleic acid (LNA). *Chem. Rev. 107*, 4672–4697.
(165) Escude, C., and Sun, J.-S. (2005) DNA major groove binders: Triple helix-forming oligonucleotides, triple helix-specific DNA ligands and cleaving agents. *Top. Curr. Chem. 253*, 109–148.
(166) Ichida, J. K., Zou, K., Horhota, A., Yu, B., McLaughlin, L. W., and Szostak, J. W. (2005) An in vitro selection system for TNA. *J. Am. Chem. Soc. 127*, 2802–2803.
(167) Rusling, D. A., Broughton-Head, V. J., Tuck, A., Khairallah, H., Osborne, S. D., Brown, T., and Fox, K. R. (2008) Kinetic studies on the formation of DNA triplexes containing the nucleoside analogue 2′-*O*-(2-aminoethyl)-5-(3-amino-1-propynyl)uridine. *Org. Biomol. Chem. 6*, 122–129.
(168) Ueno, Y., Shibata, A., Matsuda, A., and Kitade, Y. (2003) Synthesis of 3′-3′-linked oligonucleotides branched by a pentaerythritol linker and the thermal stabilities of the triplexes with single-stranded DNA or RNA. *Bioconjugate Chem 14*, 684–689.
(169) Wilson, W. D., Tanious, F. A., Mizan, S., Yao, S., Kiselyov, A. S., Zon, G., and Strekowski, L. (1993) DNA Triple-helix specific intercalators as antigene enhancers: unfused aromatic cations? *Biochemistry 32*, 10614–10621.
(170) Cassidy, S. A., Strekowski, L., Wilson, W. D., and Fox, K. R. (1994) Effect of a triplex-binding ligand on parallel and antiparallel DNA triple helixes using short unmodified and acridine-linked oligonucleotides. *Biochemistry 33*, 15338–15347.
(171) Holt, P. A., Ragazzon, P., Strekowski, L., Chaires, J. B., and Trent, J. O. (2009) Discovery of novel triple helical DNA intercalators by an integrated virtual and actual screening platform. *Nucleic Acids Res. 37*, 1280–1287.
(172) Mergny, J. L., Duval-Valentin, G., Nguyen, C. H., Perrouault, L., Faucon, B., Rougee, M., Montenay-Garestier, T., Bisagni, E, and C. Helene, C. (1992) Triple helix specific ligands. *Science 256*, 1681–1684.
(173) Rosu, F., Nguyen, C-H, De Pauw, E., and Gabelica, V. (2007) Ligand binding mode to duplex and triplex DNA assessed by combining electrospray tandem mass spectrometry and molecular modeling. *J. Am. Soc. Mass Spectrom. 18*, 1052–1062.
(174) Sun, J. S., Giovannangeli, C., Francois, J. C., Kurfurst, R., Montenay-Garestier, T., Asseline, U., Saison-Behmoaras, T., Thuong, N. T., and Helene, C. (1991) Triple-helix formation by α-oligodeoxynucleotides and α-oligodeoxynucleotide-intercalator conjugates. *Proc. Natl. Acad. Sci. U.S.A. 88*, 6023–6027.
(175) Praseuth, D., Guieysse, A. L., and Helene, C. (1999) Triple helix formation and the antigene strategy for sequence-specific control of gene expression. *Biochim. Biophys. Acta 1489*, 181–206.
(176) Paola, B., Arimondo, P. B., Thomas, C. J., Oussedik, K., Baldeyrou, B., Mahieu, C., Halby, L., Guianvarch, D., Amelie Lansiaux, A., Hecht, S. H., Bailly, C., and Giovannangeli, C. (2006) Exploring the cellular activity of camptothecin-triple-helix-forming oligonucleotide conjugates. *Mol. Cell. Biol. 26*, 324–333.
(177) Vekhoff, P., Halby, L., Oussedik, K., Dallavalle, S., Merlini, L., Mahieu, C., Lansiaux, A., Bailly, C., Boutorine, A., Pisano, C., et al. (2009) Optimized synthesis and enhanced efficacy of novel triplex-forming camptothecin derivatives based on gimatecan. *Bioconjugate Chem. 20*, 666–672.
(178) Trkulja, I., and Haner, R. (2007) Triple-helix mediated excimer and exciplex formation. *Bioconjugate Chem. 18*, 289–292.
(179) Jenkins, T. C. (2000) Targeting multi-stranded DNA structures. *Curr. Med. Chem. 7*, 99–115.
(180) Pilch, D. S., and Breslauer, K. J. (1994) Ligand induced formation of nucleic acid triple helices. *Proc. Natl. Acad. Sci. U.S.A. 91*, 9332–9336.
(181) Pilch, D. S., Kirolos, M. A., and Breslauer, K J. (1995) Berenil binding to higher ordered nucleic acid structures: complexation with a DNA and RNA triple helix. *Biochemistry 34*, 16107–16124.
(182) Park, Y. W., and Breslauer, K. J. (1992) Drug binding to higher ordered DNA structures: netropsin complexation with a nucleic acid triple helix. *Proc. Natl. Acad. Sci. U.S.A. 92*, 6653–6657.
(183) Durand, M., Thuong, N. T., and Maurizot, J. C. (1992) Binding of netropsin to a DNA triple helix. *J. Biol. Chem. 267*, 24394–24399.
(184) Durand, M., Thuong, N. T., and Maurizot, J. C. (1994) Interaction of Hoechst 33258 with a DNA triple helix. *Biochemie 76*, 181–186.
(185) Kim, H. K., Kim, J. M., Kim, S. K., Rodge, R A., and Norden, B. (1996) Interactions of intercalative and minor groove

binding ligands with triplex poly(dA) ·[poly(dT)]$_2$ and with duplex poly(dA) ·poly(dT) and poly[d(A-T)]$_2$ studied by CD, LD, and normal absorption. *Biochemistry 35*, 1187–1194.
(186) Rentzeperis, D., and Marky, L. A. (1995) Ligand binding to the Hoogsteen-WC groove of TAT base triplets: thermodynamic contribution of the thymine methyl group. *J. Am. Chem. Soc. 117*, 5423–5424.
(187) Umemoto, K., Sarma, M. H., Gupta, G., Luo, J., and Sarma, R. H. (1990) Structure and stability of a DNA triple helix in solution: NMR studies on d (T)$_6$.d (A)$_6$.d(T)$_6$ and its complex with a minor groove binding drug. *J. Am. Chem. Soc. 112*, 4539–4545.
(188) Howard, F. B., Todd Miles, H., Liu, K., Frazier, J., Raghunathan, G., and Sasisekharan, V. (1992) Structure of d(T)$_n$.d(A)$_n$.d(T)$_n$: the DNA triple helix has B-form geometry with C2′-endo sugar pucker. *Biochemistry 31*, 10671–10677.
(189) Zimmer, Ch., and Wahnert, U. (1986) Non-intercalating DNA-binding ligands: specificity of the interaction and their use as tools in biophysical, biochemical and biological investigations of the genetic materials. *Prog. Biophys. Mol. Biol. 41*, 31–112.
(190) Durand, M., Thuong, N. T., and Maurizot, J. C. (1994) Berenil complexation with a nucleic acid triple helix. *J. Biomol. Struct. Dyn. 11*, 1191–1202.
(191) Wilson, W. D., Mizan, S., Tanious, F. A., and Yao, S. (1994) The interaction of intercalators and groove-binding agents with DNA triple-helical structures: the influence of ligand structure, DNA backbone modifications and sequence. *J. Mol. Recognit. 7*, 89–98.
(192) Vigneswaran, N., Mayfield, C. A., Rodu, B., James, R., Kim, H.-G., and Miller, D. M. (1996) Influence of GC and AT specific DNA minor groove binding drugs on intermolecular triplex formation in the human c-Ki-ras promoter. *Biochemistry 35*, 1106–1114.
(193) Stonehouse, T. J., and Fox, K. R. (1994) DNase I footprinting of triple helix formation at polypurine tracts by acridine-linked oligopyrimidines: stringency, structural changes and interaction with minor groove binding ligands. *Biochim. Biophys. Acta 1218*, 322–330.
(194) Xu, Z., Pilch, D. S., Srinivasan, A. R., Olson, W. K., Geacintov, N. E., and Breslauer, K. J. (1997) Modulation of nucleic acid structure by ligand binding: Induction of a DNA.RNA.DNA hybrid triplex by DAPI intercalation. *Bioorg. Med. Chem. 5*, 1137–1147.
(195) Wittung, P., Kim, S. K., Buchardt, O., Nielsen, P. and, and Norden, B. (1994) Interactions of DNA binding ligands with PNA-DNA hybrids. *Nucleic Acids Res. 22*, 5371–5377.
(196) Gondeau, C., Maurizot, J. C., and Durand, M. (1998) Circular dichroism and UV melting studies on formation of an intramolecular triplex containing parallel T*A:T and G*G:C triplets: netropsin complexation with the triplex. *Nucleic Acids Res. 26*, 4996–5003.
(197) Chalikian, T. V., Plum, G. E., Sarvazyan, A. P., and Breslauer, K. J. (1994) Influence of drug binding on DNA hydration: acoustic and densitometric characterizations of netropsin binding to the Poly(dA-dT)*Poly(dA-dT) and Poly (dA)*Poly (dT) duplexes and the Poly (dT).Poly (dA)*Poly(dT) triplex at 25 °C. *Biochemistry 33*, 8629–8640.
(198) Fortsch, I., Baguley, B., and Zimmer, C. (1998) Structure-dependent effects of minor groove binders on the DNA triple helix motif poly(dA).2poly(dT): influence of antitumor active non-intercalative bisquaternary ammonium heterocycles. *Anti-Cancer Drug Des. 13*, 417–429.
(199) Fortsch, I., Birch-Hirschfild, E., Schutz, H, and Zimmer, C. (1996) Different effects of non-intercalative antitumor drugs on triple helix stability: SN-18071 promotes triple helix formation. *J. Biomol. Struct. Dyn. 14*, 317–329.
(200) Ren, J., and Chaires, J. B. (2000) Preferential binding of 3, 3′-diethyloxadicarbocyanine to triplex DNA. *J. Am. Chem. Soc. 122*, 424–425.
(201) Potaman, V. N., and Sinden, R. R. (1995) Stabilization of triple-helical nucleic acids by basic oligopeptides. *Biochemistry 34*, 14885–14892.
(202) Lin, C. H., and Patel, D. J. (1992) Site-specific covalent duocarmycin A-intramolecular DNA triplex complex. *J. Am. Chem. Soc. 114*, 10658–10660.
(203) Kim, S. K., and Norden, B. (1993) Methyl green A DNA major-groove binding drug. *FEBS Lett. 315*, 61–64.
(204) Feuerstein, B. G., Pattabiraman, N., and Marton, L. J. (1986) Spermine-DNA interactions: a theoretical study. *Proc. Natl. Acad. Sci. U.S.A. 83*, 5948–5952.
(205) Egli, M., Williams, L. D., Gao, Q., and Rich, A. (1991) Structure of the pure-spermine form of Z-DNA (magnesium free) at 1-Å resolution. *Biochemistry 30*, 11388–11402.
(206) Thomas, T., and Thomas, T. J. (1993) Selectivity of polyamines in triplex DNA stabilization. *Biochemistry 32*, 14068–14074.
(207) Pallan, P. S., and Ganesh, K. N. (1996) DNA Triple helix stabilization by bisguanidinyl analogues of biogenic polyamines. *Biophys. Biochem. Res. Commun. 222*, 416–420.
(208) Arya, D. P., and Coffee, R. L. (2000) DNA triple helix stabilization by aminoglycoside antibiotics. *Bioorg. Med. Chem. Lett. 10*, 1897–1899.
(209) Arya, D. P., Coffee, R. L., Jr., Willis, B., and Abramovitch, A. I.,. (2001) Aminoglycoside-nucleic acid interactions: remarkable stabilization of DNA and RNA triple helices by neomycin. *J. Am. Chem. Soc. 123*, 5385–5395.
(210) Arya, D. P., Micovic, L., Charles, I., Jr., Willis, B., and Xue, L. (2003) Neomycin binding to Watson-Hoogsteen (W-H) DNA triplex groove: A model. *J. Am. Chem. Soc. 125*, 3733–3744.
(211) Xue, L., Charles, I., and Arya, D. P. (2002) Pyrene-neomycin conjugate: dual recognition of a DNA triple helix. *Chem. Commun.* 70–71.
(212) Arya, D. P., Xue, L., and Tennant, P. (2003) Combining the best in triplex recognition: Synthesis and nucleic acid binding of a BQQ-neomycin conjugate. *J. Am. Chem. Soc. 125*, 8070–8071.
(213) Charles, I., Xue, L., and Arya, D. P. (2002) Synthesis of aminoglycoside-DNA conjugates. *Bioorg. Med. Chem. Lett. 12*, 1259–1262.
(214) Arya, D. P., and Willis, B. (2003) Reaching into the major groove of B-DNA: Synthesis and nucleic acid binding of a neomycin-Hoechst 33258 conjugate. *J. Am. Chem. Soc. 125*, 12398–12399.
(215) Xi, H., and Arya, D. P. (2005) Recognition of triple helical nucleic acids by aminoglycosides. *Curr. Med. Chem. Anti-cancer Agents 5*, 327–538.
(216) Tung, C. H., Breslauer, K. J., and Stein, S. (1993) Polyamine-linked oligonucleotides for DNA triple helix formation. *Nucleic Acids Res. 21*, 5489–5494.
(217) Szewczyk, J. W., Baird, E. E., and Derven, P. B. (1996) Cooperative triple-helix formation via a minor groove dimerization domain. *J. Am. Chem. Soc. 118*, 6778–6779.
(218) Robles, J., and McLaughlin, L. W. (1997) DNA triplex stabilization using a tethered minor groove binding Hoechst analogue. *J. Am. Chem. Soc. 119*, 6014–6021.
(219) Jain, A. K., Awasthi, S. K., and Tandon, V. (2006) Triple helix stabilization by covalently linked DNA-bisbenzimidazole conjugate synthesized by maleimide-thiol coupling chemistry. *Bioorg. Med. Chem. 14*, 6444–6452.
(220) Reddy, P. M., and Bruice, T. C. (2004) Solid phase synthesis of positively charged deoxynucleic guanidine (DNG) tethering a Hoechst 33258 analogue: triplex and duplex stabilization by simultaneous minor groove binding. *J. Am. Chem. Soc. 125*, 3736–3747.
(221) Nielsen, P. E., Frederiksen, K., and Behrens, C. (2005) Extended target sequence specificity of PNA-minor-groove binder conjugates. *ChemBioChem 6*, 66–68.
(222) Sinyakov, A. N., Ryabinin, V. A., Grimm, G. N., and Boutorine, A. S. (2001) Stabilization of DNA triple helices using conjugates of oligonucleotides and synthetic ligands. *Mol. Biol. (Moscow) 35*, 251–260.

BC900247S

Photocleavable Polyethylene Glycol for the Light-Regulation of Protein Function

Wesleigh E. Georgianna, Hrvoje Lusic, Andrew L. McIver, and Alexander Deiters*

Department of Chemistry, North Carolina State University, Raleigh, North Carolina 27695. Received February 10, 2010; Revised Manuscript Received July 12, 2010

PEGylation is commonly employed to enhance the pharmacokinetic properties of proteins, but it can interfere with natural protein function. Protein activity can thus be abrogated through PEGylation, and a controllable means to remove the polyethylene glycol (PEG) group from the protein is desirable. As such, light affords a unique control over biomolecules through the application of photosensitive groups. Herein, we report the synthesis of a photocleavable PEG reagent (PhotoPEG) and its application to the light-regulation of enzyme activity.

Poly(ethylene glycol) (PEG) groups have been used extensively in biological and pharmaceutical applications to improve the pharmacokinetic properties of biomolecules (*1*−*3*). PEG bioconjugates provide enhanced *in vivo* stability and are nontoxic and nonimmunogenic (*4*−*6*). They are typically generated from proteins through a process termed PEGylation, which involves the surface installation of PEG groups through a covalent reaction with amino functionalities, e.g., the ε-NH_2 groups of reagent-accessible lysines. PEGylation greatly enhances the solubility, half-life, cellular uptake, and bioavailability of proteins in cells and organisms (*1*, *7*, *8*). A number of PEGylated therapeutics have been approved by the FDA and are currently on the market (*9*−*11*), demonstrating the growing interest in PEGylation chemistry toward drug delivery and protein stabilization.

However, the PEGylation of proteins can negatively impact their biological activity and lead to complete inhibition of protein function, e.g., through steric blocking of the active site of an enzyme (*12*). The bulk of the PEG polymer wraps around the protein, thus providing the desired protective effects by sterically blocking it without perturbing the conformation and dynamics of the protein native fold (*13*, *14*). For this reason, PEGs containing an ester linkage for tethering to the biomolecule have been developed that are susceptible to spontaneous hydrolysis and provide a slow release pathway for protein delivery (*12*, *15*). While hydrolyzable linkers facilitate general release of the active therapeutic over time, a means to obtain precise spatial and temporal control over bioavailability without compromising stability or cellular uptake would be greatly advantageous.

* E-mail alex_deiters@ncsu.edu.

Due to our interest in the photochemical control of biological processes (*16*−*23*), we sought to accomplish such control over protein function using light. Light affords a noninvasive tool for modulating biological function, as it can be modified in amplitude, duration, and location to achieve a high level of spatiotemporal resolution. We reasoned that the installation of a photolabile PEG directly onto a protein would provide a PEG photocage that can inhibit protein activity (Figure 1A). Upon irradiation with non-phototoxic UV light, the PEG photocage will be removed from the protein, thus restoring its native activity. Since UV irradiation can be precisely controlled with high spatial and temporal resolution, this methodology provides a fundamentally new approach to achieve spatiotemporal control over protein activity. Herein, we describe the first photocleavable PEG reagent (PhotoPEG). In addition, we demonstrate that it provides photochemical control over the activity of a Photo-PEGylated enzyme.

In order to demonstrate the applicability of our approach, we selected lysozyme as a target. Lysozyme is a 14.7 kDa protein that catalyzes the hydrolysis of 1,4-β-linkages in peptidoglycans and chitodextrins, thus destroying the cell walls of bacteria and protecting tissue from bacterial invasion (*24*). For this reason, lysozyme has been extensively studied (*25*−*27*), its crystal structure has been solved (*28*), and assays to assess its enzymatic activity have been developed (*29*, *30*). Importantly, in addition to its N-terminus, lysozyme contains six solvent-accessible lysine residues (Figure 1B) and is thus readily PEGylated, which has previously been shown to inhibit its catalytic activity (*30*).

We designed a lysozyme–photocleavable linker−PEG conjugate (Scheme 1) that is stable to hydrolysis and wholly abrogates enzymatic activity until a brief UV irradiation at 365

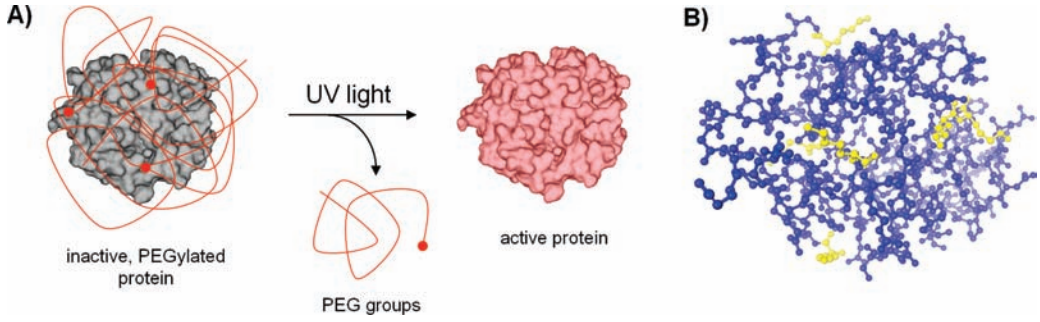
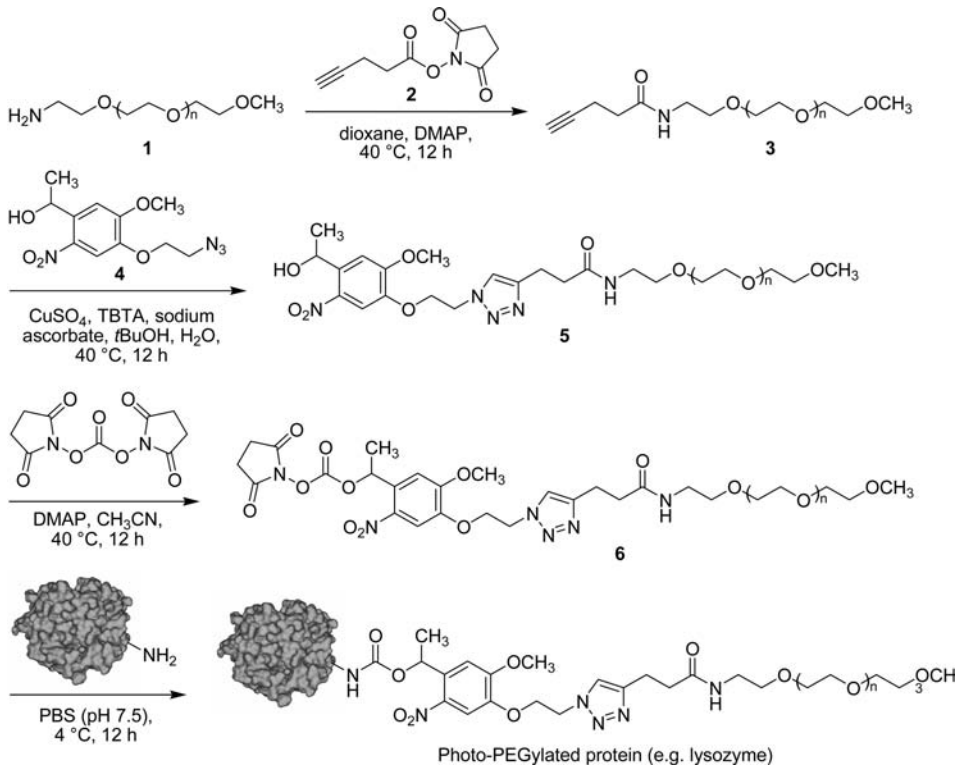


Figure 1. (A) Light-induced removal of PEG groups enables photochemical control of protein function. (B) X-ray structure of lysozyme with the six solvent-accessible lysine residues highlighted in yellow (PDB 2VB1).

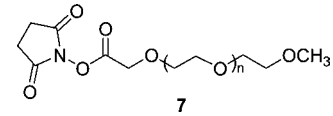
10.1021/bc100084n © 2010 American Chemical Society
Published on Web 07/22/2010

Scheme 1. Synthesis of the 5000 Da, Lysine-Reactive, Photocleavable PEG Reagent 6 (PhotoPEG), and Its Application in the PEGylation of Lysozyme (Only One NH_2 Group Is Shown)



nm cleaves the linker and releases free, active lysozyme. The photolabile linker is covalently attached to PEG (MW 5000 Da) and is comprised of an *ortho*-nitrobenzyl core that confers light sensitivity. The *ortho*-nitrobenzyl functionality has traditionally been used to provide photocontrol over proteins, nucleic acids, and small molecules (*16*−*23*). Reagent **6** also bears a terminal *N*-hydroxysuccinimide (NHS) ester that makes the PEG-linker moiety susceptible to nucleophilic attack by a primary amine. The PhotoPEG **6** was synthesized by reacting $mPEG_{5000}$-NH_2 (**1**, Laysan Bio, Inc.) with the alkynyl *N*-hydroxysuccinimide ester **2** to give the alkyne PEG reagent **3**. Using Cu(I)-catalyzed "click" chemistry (*31*, *32*), the alkyne PEG **3** was then connected to the novel azido-bearing caging group **4**. The difunctional molecule **4** (see Supporting Information for a detailed synthesis) represents a photocleavable linker that can be used in a wide range of applications, since its two functional groups, hydroxyl and azido, have completely orthogonal reactivity and thus can be employed in the linking of a wide range of substrates. Here, the alcohol **5** was subsequently activated as an NHS ester using NHS carbonate in the presence of DMAP to yield **6**.

Hen egg white lysozyme (EMD Chemicals) was first incubated with increasing equivalents of the non light-cleavable *N*-hydroxysuccinimide (NHS)-PEG_{5000} **7** (Jenkem Technology) overnight at 4 °C in phosphate buffered saline (PBS), pH 7.5. One equivalent of **7** (Figure 2, lane 2) produced a singly PEGylated protein; however, a substantial amount of non-PEGylated wild-type enzyme remained. Increasing the amount of **7** from 5 to 25 equiv led to a total consumption of wild-type lysozyme (lanes 3−5) but produced multiple PEGylated protein species which still displayed enzymatic activity (data not shown). PEGylation with 50 equiv of **7** (lane 6) completely abolished lysozyme activity. Thus, we employed 50 equiv of the PhotoPEG **6** in the PEGylation of lysozyme (lane 7), followed by dialysis into PBS (pH 7.5) using a dialysis membrane with a cutoff of 50 kDa in order to remove excess PEG reagent. Irradiation of the PhotoPEG-modified enzyme with UV light of 365 nm (25 W, 30 min) released all PEG groups, regenerating wild-type lysozyme as shown by SDS PAGE analysis (lane 8).



7

Lysozyme assays were performed as previously reported (*29*). The amount of purified PEGylated lysozyme was determined by a Bradford assay (*33*). The lyophilized gram-positive substrate *Micrococcus lysodeikticus* (Sigma) was suspended in 66 mM sodium phosphate, pH 6.24, to achieve a starting optical density of approximately $OD_{450} = 1$. Lysozyme or PEGylated lysozyme in 100 μL PBS was added to 100 μL of cell suspension for a final enzyme concentration of 3 μM. The OD_{450} was measured after a 20 min reaction time. Active wild-type

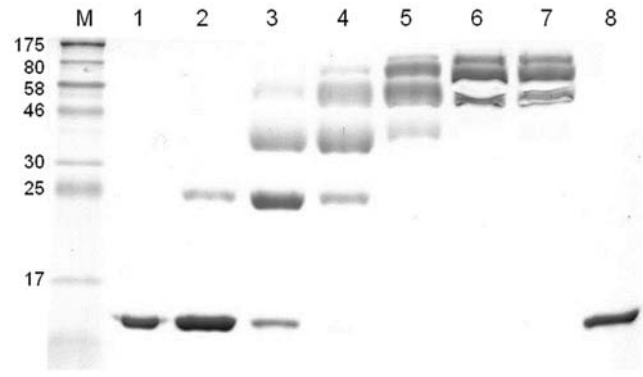


Figure 2. SDS-PAGE analysis of lysozyme PEGylation. M, protein maker (in kDa); lane 1, wild-type lysozyme; lanes 2−6, PEGylation with 1, 5, 10, 25, and 50 equiv of NHS-PEG **7**, respectively; lane 7, PEGylation with 50 equiv PhotoPEG **6**; lane 8, PhotoPEG-modified lysozyme from lane 7 after UV exposure (365 nm, 25 W, 30 min).

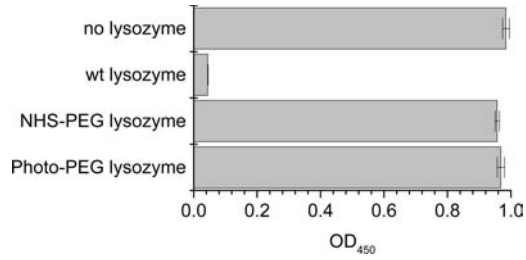


Figure 3. *Micrococcus lysodeikticus* exposed to different lysozymes for 20 min, followed by an optical density (OD_{450}) measurement. Wild-type lysozyme leads to complete cell lysis. In contrast, lysozymes PEGylated with the NHS-PEG **7** or the PhotoPEG **6** are completely inactive, thus inducing no cell lysis. Error bars represent standard deviations from three independent experiments.

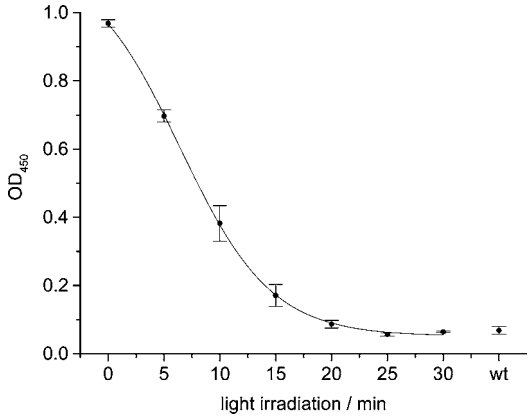


Figure 4. *Micrococcus lysodeikticus* exposed to lysozyme modified with Photo-PEG **6**, followed by an optical density (OD_{450}) measurement after 20 min. The Photo-PEGylated lysozyme is completely inactive before irradiation (0 min); however, activity was restored to the level of wild-type lysozyme (wt) through UV irradiation (365 nm; 25 W; 5−30 min). Error bars represent standard deviations from three independent experiments.

lysozyme induces cell lysis, leading to a reduction in optical density (Figure 3). In contrast, the lysozyme PEGylated with the classical NHS-PEG reagent **7** (from Figure 2, lane 6), and the lysozyme modified with the photocleavable PEG **6** (from Figure 2, lane 7) were completely inactive, since no change in the OD_{450} was observed, as in the absence of lysozyme (Figure 3).

Next, we investigated the photochemical activation of enzyme function through a light-induced removal of the PEG groups. The completely inactive PhotoPEG-modified lysozyme was irradiated for 0−30 min, and substrate lysis was determined as described above. As expected, in the absence of UV irradiation (0 min) no enzymatic activity was observed, resulting in an OD_{450} of 0.98 after 20 min, identical to the OD_{450} at the beginning of the assay. However, UV irradiation for 5, 10, 15, and 20 min led to increasing enzymatic activity resulting in the reduction of the final optical density of the cell suspension due to cell lysis. Optimal light-activation of the enzyme was observed after irradiation for 25 and 30 min, since the measured OD_{450} values were identical to the value for wild-type lysozyme (Figure 4). This observation is in agreement with the gel-based assessment of complete photochemical PEG removal after 30 min of UV irradiation (Figure 2, lane 8). Furthermore, we conducted time-course studies of the lysis assay (see Supporting Information) and found that the 30 min UV irradiation of the PhotoPEGylated lysozyme restored 50% of the maximal enzymatic velocity of wild-type lysozyme. An incomplete restoration of enzymatic activity is not uncommon in the light-activation of biological processes (*22*) and can be easily augmented by increasing the amount of the caged biological molecule and/or extending the time of the process under study. Importantly, the PhotoPEG-modified lysozyme fulfills the crucial criterion of complete inactivity prior to irradiation.

In summary, we have developed a photocleavable PEG reagent (PhotoPEG) and applied it successfully in the photochemical regulation of enzyme activity. This light-removable PEGylation represents the first example of a literal protein photocage, as the polyethylene glycol chains surround the enzyme and prohibit any interaction with its substrate (*34*). The PEGylated enzyme is completely inactive, and irradiation with UV light of 365 nm removes the otherwise stable PEG groups and restores enzymatic activity. Lysine PEGylation with the developed reagent is rapid and facile; the installation of caging-PEG groups on the protein can be easily assessed by standard gel electrophoresis, which, if necessary, also facilitates purification of the caged protein from noncaged protein. This methodology combines the advantages of protein PEGylation (increased protein solubility, intracellular stability, and circulation time) with the advantages of light-activation of protein function (spatial and temporal activity control with high precision). Due to the simplicity of the necessary manipulations, the developed methodology has a wide range of potential applications in the study of protein function in cell culture and whole organisms, as well as activation of protein therapeutics, with the only requirement being the presence of a suitable number of reactive lysine residues on the protein of interest.

ACKNOWLEDGMENT

This work was financially supported by the Research Corporation (Cottrell Scholar Award to AD) and the Beckman Foundation (Beckman Young Investigator Award to AD).

Supporting Information Available: Synthesis of the azide **4** and the PhotoPEG **6**, lysozyme PEGylation and assay protocols, assay timecourse. This material is available free of charge via the Internet at http://pubs.acs.org.

LITERATURE CITED

(1) Hamidi, M., Azadi, A., and Rafiei, P. (2006) Pharmacokinetic consequences of pegylation. *Drug Delivery 13*, 399–409.
(2) Ryan, S. M., Mantovani, G., Wang, X., Haddleton, D. M., and Brayden, D. J. (2008) Advances in PEGylation of important biotech molecules: Delivery aspects. *Expert Opin. Drug Delivery 5*, 371–383.
(3) Veronese, F. M., and Mero, A. (2008) The impact of PEGylation on biological therapies. *BioDrugs 22*, 315–329.
(4) *Poly(ethylene glycol) chemistry: Biotechnical and biomedical applications* (Harris, J. M., Ed.) (1992) pp 1−408, Springer, New York
(5) Greenwald, R. B., Choe, Y. H., McGuire, J., and Conover, C. D. (2003) Effective drug delivery by PEGylated drug conjugates. *Adv. Drug Delivery Rev. 55*, 217–250.
(6) Jain, A., and Jain, S. K. (2008) PEGylation: An approach for drug delivery. A review. *Crit. Rev. Ther. Drug Carrier Syst. 25*, 403–447.
(7) Inada, Y., Matsushima, A., Hiroto, M., Nishimura, H., and Kodera, Y. (1994) Modification of proteins with polyethylene glycol derivatives. *Methods Enzymol. 242*, 65–90.
(8) Bailon, P., and Won, C. Y. (2009) PEG-modified biopharmaceuticals. *Expert Opin. Drug Delivery 6*, 1–16.
(9) Barnard, D. L. (2001) Pegasys (hoffmann-la roche). *Curr. Opin. Invest. Drugs 2*, 1530–1538.
(10) Castineiras, I., Almagro, M., Rodriguez-Lozano, J., Fernandez-Jorge, B., Paradela, S., Pozo, J. D., and Fonseca, E. (2006) Disseminated classic Kaposi's sarcoma. Two cases with excellent response to pegylated liposomal doxorubicin. *J. Dermatol. Treat. 17*, 377–380.

(11) Dinndorf, P. A., Gootenberg, J., Cohen, M. H., Keegan, P., and Pazdur, R. (2007) FDA drug approval summary: Pegaspargase (oncaspar) for the first-line treatment of children with acute lymphoblastic leukemia (ALL). *Oncologist 12*, 991–998.
(12) Filpula, D., and Zhao, H. (2008) Releasable PEGylation of proteins with customized linkers. *Adv. Drug Delivery Rev. 60*, 29–49.
(13) Digilio, G., Barbero, L., Bracco, C., Corpillo, D., Esposito, P., Piquet, G., Traversa, S., and Aime, S. (2003) NMR structure of two novel polyethylene glycol conjugates of the human growth hormone-releasing factor, hGRF(1−29)-NH2. *J. Am. Chem. Soc. 125*, 3458–3470.
(14) Gonnelli, M., and Strambini, G. B. (2009) No effect of covalently linked poly(ethylene glycol) chains on protein internal dynamics. *Biochim. Biophys. Acta 1794*, 569–576.
(15) Lin, C. C., and Anseth, K. S. (2009) PEG hydrogels for the controlled release of biomolecules in regenerative medicine. *Pharm. Res. 26*, 631–643.
(16) Lawrence, D. S. (2005) The preparation and in vivo applications of caged peptides and proteins. *Curr. Opin. Chem. Biol. 9*, 570–575.
(17) Mayer, G., and Heckel, A. (2006) Biologically active molecules with a "light switch. *Angew. Chem., Int. Ed. 45*, 4900–4921.
(18) Tang, X., and Dmochowski, I. J. (2007) Regulating gene expression with light-activated oligonucleotides. *Mol. Biosyst. 3*, 100–110.
(19) Casey, J. P., Blidner, R. A., and Monroe, W. T. (2009) Caged siRNAs for spatiotemporal control of gene silencing. *Mol. Pharm. 6*, 669–685.
(20) Lee, H. M., Larson, D. R., and Lawrence, D. S. (2009) Illuminating the chemistry of life: Design, synthesis, and applications of "caged" and related photoresponsive compounds. *ACS Chem. Biol. 4*, 409–427.
(21) Deiters, A. (2009) Light activation as a method of regulating and studying gene expression. *Curr. Opin. Chem. Biol. 13*, 678–686.
(22) Deiters, A. (2010) Principles and applications of the photochemical control of cellular processes. *ChemBioChem 11*, 47–53.
(23) Young, D. D., and Deiters, A. (2007) Photochemical control of biological processes. *Org. Biomol. Chem. 5*, 999–1005.
(24) Fischer, B., Perry, B., Phillips, G., Sumner, I., and Goodenough, P. (1993) Physiological consequence of expression of soluble and active hen egg white lysozyme in escherichia coli. *Appl. Microbiol. Biotechnol. 39*, 537–540.
(25) Sava, G. (1996) Pharmacological aspects and therapeutic applications of lysozymes. *EXS 75*, 433–449.
(26) Van Dael, H. (1998) Chimeras of human lysozyme and alpha-lactalbumin: An interesting tool for studying partially folded states during protein folding. *Cell. Mol. Life Sci. 54*, 1217–1230.
(27) Masschalck, B., and Michiels, C. W. (2003) Antimicrobial properties of lysozyme in relation to foodborne vegetative bacteria. *Crit. Rev. Microbiol. 29*, 191–214.
(28) Wang, J., Dauter, M., Alkire, R., Joachimiak, A., and Dauter, Z. (2007) Triclinic lysozyme at 0.65 A resolution. *Acta Crystallogr., Sect. D: Biol. Crystallogr. 63*, 1254–1268.
(29) Shugar, D. (1952) The measurement of lysozyme activity and the ultra-violet inactivation of lysozyme. *Biochim. Biophys. Acta 8*, 302–309.
(30) Roberts, M. J., and Harris, J. M. (1998) Attachment of degradable poly(ethylene glycol) to proteins has the potential to increase therapeutic efficacy. *J. Pharm. Sci. 87*, 1440–1445.
(31) Wang, Q., Chan, T. R., Hilgraf, R., Fokin, V. V., Sharpless, K. B., and Finn, M. G. (2003) Bioconjugation by copper(I)-catalyzed azide-alkyne (3 + 2) cycloaddition. *J. Am. Chem. Soc. 125*, 3192–3193.
(32) Moses, J. E., and Moorhouse, A. D. (2007) The growing applications of click chemistry. *Chem. Soc. Rev. 36*, 1249–1262.
(33) Bradford, M. M. (1976) A rapid and sensitive method for the quantitation of microgram quantities of protein utilizing the principle of protein-dye binding. *Anal. Biochem. 72*, 248–254.
(34) Reference added in proof, describing an alternative light-cleavable protein PEGylation approach: Serwa, R., Horstman, B., Majkut, P., Swiecicki, J.-M., Gerrits, M., Krause, E., Hackenberger, C.P.R. (2010) Site-specific PEGylation of proteins by a Staudinger-phosphite reaction. *Chem. Sci.* DOI: 10.1039/c0sc00324g.

BC100084N

Supporting Information

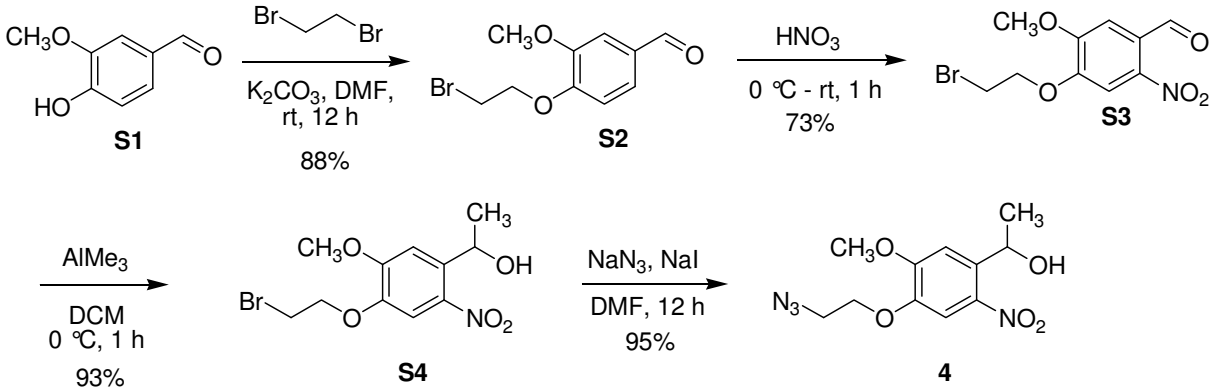
Photocleavable Polyethylene Glycol for the Light-Regulation of Protein Function

Wesleigh E. Georgianna, Hrvoje Lusic, Andrew L. McIver, and Alexander Deiters*

Department of Chemistry, North Carolina State University, Raleigh, NC 27695

SYNTHESIS OF THE AZIDE 4

The synthesis of 1-[4-(2-azidoethoxy)-5-methoxy-2-nitrophenyl]ethanol (**4**) was accomplished in four steps starting with commercially available vanillin (**S1**). The bromide intermediate **S2** was prepared by alkylating the phenol functionality of **S1** with dibromoethane in the presence of a base (K_2CO_3, DMF; 88% yield). Subsequent nitration of **S2** to **S3** was achieved in 73% yield using concentrated HNO_3. The aldehyde **S3** was subsequently methylated to the secondary alcohol **S4** using $AlMe_3$ (DCM, 0 °C; 93% yield). The azide caging group **4** was obtained in 95% yield by nucleophilic substitution of the bromine with sodium azide (NaN_3, NaI, DMF). This molecule is very versatile since its azido and hydroxy groups can be reacted in an orthogonal fashion in order to covalently link two different molecules (e.g. a protein and a PEG), which can then be separated again using a brief light irradiation at 365 nm.



EXPERIMENTAL PROCEDURES

Synthesis of 4-(2-Bromoethoxy)-3-Methoxybenzaldehyde (S2). 1,2-Dibromoethane (7.4g, 3.4 mL, 39.3 mmol) was added to a solution of vanillin (**S1**) (2g, 13.1 mmol) in DMF (30 mL), containing K_2CO_3 (5.4g, 39.3 mmol). The reaction was stirred for 12 h at r.t. Subsequently, the reaction was filtered, diluted with ethyl ether (200 mL), and washed with 1 M NaOH (200 mL), water (2 × 200 mL), and brine (200 mL). The organic layer was dried over Na_2SO_4 and the volatiles were evaporated, affording 4-(2-bromoethoxy)-3-methoxybenzaldehyde (**S2**) in 88% yield as a white solid (2.99 g, 11.5 mmol). The analytical data matched previously reported data (^{1}H NMR, ^{13}C NMR, HRMS) [(1)].

Synthesis of 4-(2-Bromoethoxy)-5-methoxy-2-nitrobenzaldehyde (S3). 4-(2-Bromoethoxy)-3-methoxybenzaldehyde (**S2**) (3 g, 11.5 mmol) was suspended in 60 mL of ice-cold HNO_3. The solution was slowly warmed to room temperature, and the reaction was stirred until all of the material

dissolved. The solution was then poured onto ice and the precipitate was filtered off then washed with cold water. The product was recrystallized from boiling EtOH (approximately 30 mL), affording 4-(2-bromoethoxy)-5-methoxy-2-nitrobenzaldehyde (**S3**) in 73% yield as a yellow solid (2.55 g, 8.4 mmol). ^{1}H NMR (300 MHz, $CDCl_3$): δ = 3.69 (q, *J* = 6.3 Hz, 2 H), 4.01 (s, 3 H), 4.47 (q, *J* = 6.3 Hz, 2 H), 7.41 (s, 1 H), 7.61 (s, 1 H), 10.43 (s, 1 H). ^{13}C NMR (75 MHz, $CDCl_3$): δ = 28.0, 57.0, 69.6, 108.1, 110.6, 126.5, 143.7, 151.0, 153.9, 187.9. HRMS: *m/z* calcd for $C_{10}H_{10}NO_5Br$ $[M+H]^+$: 302.9742; found: 302.9743.

Synthesis of 1-[4-(2-Bromoethoxy)-5-methoxy-2-nitrophenyl]ethanol (S4). Trimethylaluminum (2.4 mL, 4.8 mmol; 2 M solution in hexanes) was added dropwise over 20 min to a solution of 4-(2-bromoethoxy)-5-methoxy-2-nitrobenzaldehyde (**S3**) (1 g, 3.18 mmol) in DCM (20 mL), at 0 ºC. The reaction was stirred at 0 ºC for 1 h and quenched with 2 mL of ice-cold water. 20 mL of 1 M NaOH were added and the mixture was stirred for 30 min. The reaction was taken into DCM (100 mL) and washed with 1 M NaOH (100 mL) and brine (100 mL). The organic layer was dried over Na_2SO_4 and the volatiles were evaporated, giving 1-[4-(2-bromoethoxy)-5-methoxy-2-nitrophenyl]ethanol (**S4**) in 93% yield as a yellow solid (946 mg, 2.95 mmol). ^{1}H NMR (300 MHz, $CDCl_3$): δ = 1.54 (d, *J* = 6.3 Hz, 3 H), 3.67 (t, *J* = 6.6 Hz, 2 H), 3.98 (s, 3 H), 4.38 (t, *J* = 6.6 Hz, 2 H), 6.43 (q, *J* = 6.3 Hz, 1 H), 7.32 (s, 1 H), 7.58 (s, 1 H). ^{13}C NMR (75 MHz, $CDCl_3$): δ = 24.5, 28.5, 56.7, 65.9, 69.5, 109.4, 110.5, 126.2, 138.1, 146.3, 154.6. HRMS: *m/z* calcd for $C_{11}H_{14}NO_5Br$ $[M+H]^+$: 319.0055; found: 319.0054.

Synthesis of 1-[4-(2-azidoethoxy)-5-methoxy-2-nitrophenyl]ethanol (4). Sodium azide (100 mg, 1.56 mmol) and catalytic amounts of NaI (spatula tip) were added to a solution of 1-[4-(2-bromoethoxy)-5-methoxy-2-nitrophenyl]ethanol (**S4**) (50 mg, 0.156 mmol) in DMF (1 mL), and the reaction mixture was heated to 60 ºC for 16 h. After cooling to room temperature, the reaction mixture was filtered and diluted with EtOAc (5 mL). The reaction was washed with water (3 × 5 mL) and brine (5 mL). The organic layer was dried over Na_2SO_4 and the volatiles were evaporated, affording the azide 1-[4-(2-azidoethoxy)-5-methoxy-2-nitrophenyl]ethanol (**4**) as a yellow solid in 95% yield (42 mg, 0.148 mmol). ^{1}H NMR (300 MHz, $CDCl_3$): δ = 1.54 (d, *J* = 6.3 Hz, 3 H), 3.67 (t, *J* = 5.4 Hz, 2 H), 3.97 (s, 3 H), 4.22 (t, *J* = 5.1 Hz, 2 H), 7.31 (s, 1 H), 7.57 (s, 1 H). ^{13}C NMR (75 MHz, $CDCl_3$): δ = 24.5, 50.2, 56.6, 65.9, 68.6, 109.2, 110.0, 138.1, 139.5, 146.6, 154.6. HRMS: *m/z* calcd for $C_{11}H_{14}N_4O_5$ $[M+H]^+$: 282.0964; found: 282.0970.

Synthesis of photocleavable PEG reagent 6. The *N*-hydroxysuccinimide ester of pentynoic acid **2** (58.5 mg, 0.3 mmol)[(2)] and DMAP (spatula tip) were added to a solution of $mPEG_{5000Da}$-NH_2 (**1**, 300 mg, 0.06 mmol; LaysanBio) in dioxane (3 mL). The reaction was stirred at 40 °C for 12 h, and was then precipitated into Et_2O (30 mL). The suspension was centrifuged, the supernatant was poured off, and was repeated three times. Alkyne PEG **3** (302 mg, ~0.06 mmol) was obtained as a white solid, and directly dissolved in DMSO (1 mL). The azide caging reagent **4** (84 mg, 0.297 mmol), TBTA (15.6 mg, 0.0295 mmol), $CuSO_4$•$5H_2O$ (1.5 mg, 0.0059 mmol), and sodium ascorbate (13 mg, 0.068 mmol) were added. The reaction was stirred at 40 °C for 12 h, the DMSO was concentrated and the residue was re-dissolved in DCM (2mL). Et_2O (30 mL) was added and the suspension was centrifuged, the supernatant was poured off, and was repeated three times to afford PEG **5** (234 mg, ~0.044 mmol) as a tan solid. PEG reagent **5** (234 mg, 0.044 mmol) was subsequently dissolved in CH_3CN (2.6 mL) in the presence of cat. DMAP (spatula tip) and to the solution was added *N,N′*-disuccinimidyl carbonate (56 mg, 0.22 mmol). The reaction was stirred at 40 °C for 12 h, the CH_3CN was concentrated and the residue was re-dissolved in DCM (1mL). Et_2O (30 mL) was added and the suspension was centrifuged, the supernatant was poured off, and was repeated three times giving the activated PEG **6** (232 mg, ~0.044 mmol) as a tan solid.

Lysozyme PEGylation. Hen egg white lysozyme was dissolved in phosphate buffered saline (PBS, pH 7.5) to a final concentration of 450 µM. 50 equivalents of (NHS)-PEG_{5000Da} **7** or the photocleavable PEG reagent **6** were added as a solid to 100 µL of the lysozyme solution, and the reaction mixture was incubated overnight at 4 °C. The solution was then dialyzed (50 kDa MWCO, SpectraPor) over two days into PBS (pH 7.5) at 4 °C. The concentration of PEGylated lysozyme after dialysis was determined by a standard Bradford assay (3).

Lysozyme Assays. The lyophilized lysozyme substrate *Micrococcus lysodeikticus* (Sigma) was suspended in 66 mM sodium phosphate, pH 6.24, to an optical density at 450 nm of approximately 2.0, providing a 2× cell suspension stock. Wild-type or PEGylated lysozyme (100 µL of 6 µM enzyme solution in PBS) was added to the cell suspension (100 µL) for a final concentration of 3 µM enzyme. Prior to the assay, the Photo-PEG lysozyme was kept in the dark or was selectively irradiated in one well of a 96-well plate on a transilluminator (365 nm, 25 W, 5-30 min) pre-chilled to 0 °C with an ice pack. Wild type lysozyme was also irradiated in the same manner and showed no decrease in activity, indicating that irradiation causes no discernible photodamage to the enzyme. A_{450} values were measured every 12 seconds for 20 minutes (SpectraMax Plus^{384} UV plate reader, Molecular Devices), and all assays were performed in triplicate. Additionally, assays were performed with decreasing percentages of wild-type lysozyme to determine the percent activity restoration of Photo-PEGylated lysozyme. A_{450} values were then measured every 12 seconds for 20 minutes (Figure S1), and the V_{max} values calculated from the initial slope of each reaction (first 72 sec, linear regression resulted in $R > 0.998$) for wild-type lysozyme and PhotoPEGylated lysozyme activated by the optimal UV irradiation (365 nm, 25 W, 30 min). The obtained velocities were: V_{max}(wild-type) = $(263 \pm 6)\times10^{-5}$ s^{-1} and V_{max}(PhotoPEG+UV) = $(132 \pm 4)\times10^{-5}$ s^{-1}. Thus, the light-activation of Photo-PEGylated lysozyme was found to be 50% of wild-type lysozyme activity.

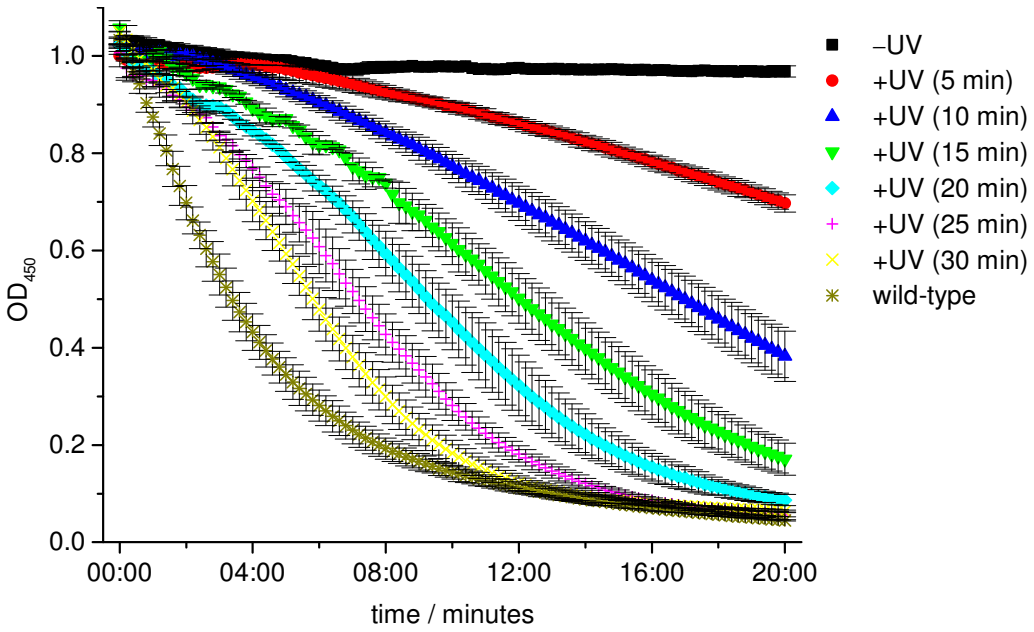


Figure S1. Time-course of the lysozyme assay for PEGylated and UV irradiated protein, as described above.

SDS-PAGE Analysis. To ensure complete cleavage of Photo-PEG upon irradiation, PEGylated lysozyme was analyzed by denaturing polyacrylamide electrophoresis (SDS-PAGE). 100 ng wild-type and PEGylated lysozyme (non-irradiated and irradiated) were mixed with 4× SDS loading buffer (final concentration 10% (v:v) glycerol, 62.5 mM Tris-HCl, pH 6.8, 2% (w:v) SDS, 0.01 mg/mL bromophenol blue, and 5% ethanethiol) and separated on a 13% SDS-PAGE running gel overlaid with a 4% stacking gel at 8 mA until the buffer loading dye was clear of the stacking gel, then at 14 mA for 45 minutes. The low amperage was determined to provide more compact protein bands and eliminate streakiness of the highly PEGylated proteins. The gel was then stained (0.006 g coomassie brilliant blue, 100 mL glacial acetic acid and 900 mL H_2O) for two hours, followed by incubation in the destaining solution (100 mL glacial acetic acid and 900 mL H_2O) for at least two hours.

REFERENCES

1 Ryu, E. K., Choe, Y. S., Lee, K., Choi, Y. and Kim, B. (2006) Curcumin and dehydrozingerone derivatives: Synthesis, radiolabeling, and evaluation for β-amyloid plaque imaging. *J. Med. Chem.* **49**, 6111-6119

2 Slater, M., Snauko, M., Svec, F. and Frechet, J. M. (2006) "Click chemistry" in the preparation of porous polymer-based particulate stationary phases for μ-HPLC separation of peptides and proteins. *Anal. Chem.* **78**, 4969-4975

3 Bradford, M. M. (1976) A rapid and sensitive method for the quantitation of microgram quantities of protein utilizing the principle of protein-dye binding. *Anal. Biochem.* **72**, 248-254

Immobilization of Iron Oxide Magnetic Nanoparticles for Enhancement of Vessel Wall Magnetic Resonance Imaging—An *Ex Vivo* Feasibility Study

Binh Thai Nguyen,[†,#] Praveen Kumar Vemula,[†,‡,§,||] Dimitrios Mitsouras,[⊥] Peng Yu,[#] Ming Tao,[#] Christina Campagna,[#] Robert V. Mulkern,[⊥] Frank J. Rybicki,[⊥] Jeffrey M. Karp,*[,§,||] and C. Keith Ozaki*[,#]

Department of Medicine, Brigham and Women's Hospital, Harvard Medical School, Harvard-MIT Division of Heath Sciences &Technology, 65 Landsdowne Street, Cambridge, Massachusetts 02139, Harvard Stem Cell Institute, Harvard Medical School, and Applied Imaging Science Laboratory, Department of Radiology, and Department of Surgery, Brigham and Women's Hospital, Harvard Medical School, 75 Francis Street, Boston, Massachusetts 02115. Received March 15, 2010; Revised Manuscript Received June 1, 2010

Emerging data supports a role for negative wall remodeling in the failure of vascular interventions such as vein grafts, yet clinicians/researchers currently lack the ability to temporally/efficiently investigate adventitial surface topography/total vascular wall anatomy in vivo. We established a strategy of immobilizing commercially available iron oxide magnetic nanoparticles (Fe-NPs) onto the surface of human vein conduits to facilitate high-throughput total vascular wall demarcation with magnetic resonance (MR). Binding of activated Fe-NPs to amine groups on the surface of the veins induced a thin layer of negative contrast that differentiated the adventitia from surrounding saline signal in all MR images, enabling delineation of total wall anatomy; this was not possible in simultaneously imaged unlabeled control veins. Under the conditions of this ex vivo experiment, stable covalent binding of Fe-NPs can be achieved (dose-dependent) on human vein surface for MR detection, suggesting a potential strategy for enhancing the ability of MRI to investigate total wall adaptation and remodeling in vein graft failure.

Over half a million vein grafts are implanted in the United States each year, and yet the task of maintaining vein graft patency continues to represent a major challenge for cardiac and vascular clinicians. Almost 40% of lower extremity vein bypass grafts develop occlusive lesions or fail within a year (*1*), and almost half of cardiac bypass patients will lose (>75% stenosis) a vein graft within the first year (*2*). This manifests as significant morbidity and mortality for patients and contributes to the enormous cost of cardiovascular health care related expenses. For decades, researchers have sought to understand the clinical, biological, and hemodynamic factors that contribute to neointimal hyperplasia, the presumed primary pathophysiology for early (1−18 months postimplantation) vein graft failure. Vein wall thickening and neointimal hyperplasia develop as an adaptive response to the arterial environment; luminal loss seen directly with angiography, or indirectly as increased velocity detected by duplex sonography, has traditionally been viewed as a pathological dysregulation of this process. However, with the increasing recognition of entire vessel wall negative vein graft remodeling as a significant contributor to vein graft failure (*3*−*6*), there exists an opportunity and need for advances in vascular imaging techniques to study total vein graft wall adaptations and remodeling.

Magnetic resonance imaging (MRI) is a powerful noninvasive diagnostic technique and a well-validated modality for vessel wall (and surrounding soft tissue) imaging (*7*). However, it is limited to modest spatial resolutions (e.g., $0.4 \times 0.4 \times 4$ mm^3) that, while adequate to study atherosclerosis in medium to large arteries, are largely inadequate for small-caliber vessels such as human vein grafts (*8*). Even achieving such comparatively high (by MR standards) spatial resolution poses a further limitation with respect to attainable craniocaudal coverage. For example, at clinical 1.5−3 T MRI magnetic field strengths, a 10 min scan suffices to image a 3−12 cm portion of a vessel (*8*−*10*). Lower resolutions require less imaging time and can enable increased coverage, but accurate delineation of the anatomy of the tissue interfaces becomes increasingly difficult to achieve due to partial voluming of the different tissues (i.e., one voxel containing multiple tissues presents a signal intensity that is the average of those of the underlying tissues).

One approach to overcome these challenges would be to coat vein grafts with an implantable contrast agent at the time of original surgical placement that can be readily identified by MRI, thereby facilitating efficient longitudinal imaging of the vessel wall with reduced reliance on imaging resolution. Vein grafts are often present on the operating room back table for up to thirty minutes, a time that has been utilized for other graft wall modifications (*1*). Superparamagnetic magnetic nanoparticles (Fe-NPs) have been widely used as ultrasensitive negative contrast agents for a wide range of applications such as stem cell tracking and early detection of cancers (*11*−*13*). Over the past decade, Fe-NPs have been explored for biomedical applications such as molecular imaging of cardiovascular disease, gene delivery, magnetic drug targeting, nanomedicine, and regenerative medicine (*14*, *15*). These Fe-NPs provide an attractive alternative to other commercially available contrast agents because they are nontoxic and biocompatible, can undergo selective magnetization only when exposed to a magnetic field, and also allow a targetable delivery with particle localization in a specific area (*16*). Utilizing these advantages, we have developed a method to attach Fe-NPs on the surface of human veins, that can be performed under physiological

* Corresponding authors. Jeffrey M. Karp, Ph.D., Tel: 617-817 9174, Fax: 617-768-8338, E-mail: jkarp@rics.bwh.harvard.edu. C. Keith Ozaki, M.D., Tel: 857-307-1920, Fax: 857-307-1922, E-mail: CKOzaki@partners.org.

† Authors contributed equally.

‡ Kauffman Foundation Entrepreneur Postdoc Fellow.

§ Harvard-MIT Division of Heath Sciences &Technology.

|| Harvard Stem Cell Institute.

⊥ Department of Radiology, Brigham and Women's Hospital.

Department of Surgery, Brigham and Women's Hospital.

10.1021/bc100138c © 2010 American Chemical Society
Published on Web 07/07/2010

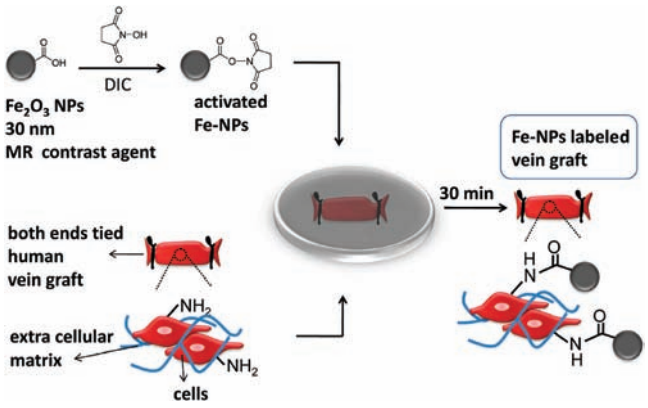


Figure 1. Schematic representation of the immobilization of Fe-NPs on human vein. Incubation of the vein in an activated Fe-NPs solution produces binding of Fe-NPs on its surface. Particles could bind to amine groups on the cell surface as well as the extracellular matrix.

conditions, and could potentially serve as a durable vein graft adventitial label to facilitate and enhance MR imaging.

Previously, we have demonstrated that *N*-hydroxysuccinamide esters of small target molecules could be covalently attached to amine groups that are present on the cell surface (*17*). Human mesenchymal stem cells modified through this method did not alter the inherent cell properties such as cell viability, proliferation, adhesion kinetics, and their stem cell phenotype. This suggests that covalent modification could be performed under conditions that have minimal impact on live cells. Thus, we adopted a similar strategy to covalently immobilize Fe-NPs on the surface of human veins. The current project capitalizes on the innovative synergy of commercially available Fe-NPs (modified to covalently bind to human tissue), and high spatial resolution MRI to enhance visualization of the entire vessel wall ex vivo. Specifically, we test the hypothesis that Fe-NPs can be covalently immobilized onto the external wall of human vein conduits and subsequently enable enhanced delineation of the adventitia through MR imaging.

Amine groups are present in abundance on the surface of various tissues (*18*) and are available to react with *N*-hydroxysuccinamide. After appropriate institutional approvals, freshly discarded human vein segments from bypass surgeries and major amputations were collected and "labeled" with commercially available Fe-NPs via a two-step reaction (Figure 1). Briefly, carboxylic groups that are on the magnetic nanoparticles' surface were activated by reacting with *N*-hydroxysuccinamide esters. Subsequently, the activated particles were immediately used for coating the vein graft adventitia. With the luminal side protected via ligatures on either end, the test human vein sample was placed in a PBS filled Petri dish. The activated magnetic particles (in PBS) were added and incubated for 30 min at room temperature (for detailed synthesis methods, see Supporting Information). As a non-label control experiment, a vein segment was incubated in PBS (without Fe-NPs). Finally, all vein segments were individually and thoroughly rinsed thrice with PBS to remove unbound Fe-NPs. The current technique was applied with thirty minutes of incubation time, and this resulted in significant Fe-NP deposition on the vein; future optimization of the reaction conditions (e.g., pH, temperature) may accelerate this process.

Fe-NP labeled veins were thoroughly characterized using scanning electron microscopy (SEM) and energy dispersive X-ray analysis (EDAX). SEM images of labeled and unlabeled veins clearly show the presence of Fe-NPs on the surface of labeled veins (Figure 2). Results obtained from elemental mapping analysis (SEM-EDAX) show that Fe-NP coatings covered the majority of the labeled vein surface (Figure 3). In

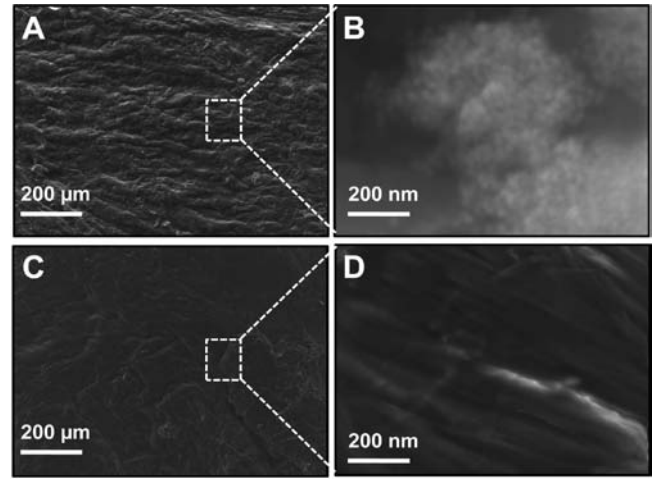


Figure 2. SEM images of the outer surface of the human veins with immobilized Fe-NPs (A and B) and without Fe-NPs (C and D).

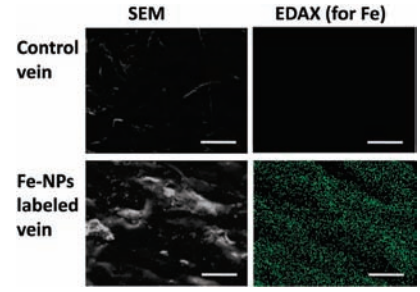


Figure 3. SEM micrograph (left) and Fe elemental mapping using EDAX (right) of unlabeled control (top row) and Fe-NPs labeled (bottom row) surface of the human veins. EDAX was positive (colored) for Fe on the Fe-NPs labeled portions only. In all images, scale bar represents 20 μm.

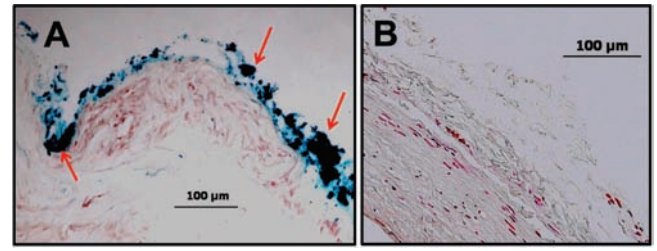


Figure 4. Iron histochemistry. Perl's Prussian blue staining images of (A) Fe-NPs labeled and (B) unlabeled human veins. Presence of Fe is confirmed by the appearance of dark blue/black colored areas (shown by red arrows in panel A).

addition, absence of Fe-NPs on the surface of unlabeled veins was confirmed (Figure 3). Iron histochemistry of labeled vein cross sections, using Perl's Prussian Blue protocol (see methods in Supporting Information), was also performed to visualize the location of Fe-NPs on the outer surface of the vein. Dark blue/black stains in the polarized microscopy images are attributed to the presence of Fe, suggesting that Fe is confined to the vein surface (Figure 4).

Prior to EDAX and histochemistry, MR imaging was employed to validate our strategy of utilizing the magnetic properties of Fe-NPs to readily delineate the vein surface from any surrounding MR signal-generating environment. Vein segments were immersed in saline to accomplish this task. Fe-NPs create a large dipolar magnetic field gradient that acts on the water molecules that diffuse close to the particles (*19*). They have a very large transverse to longitudinal relaxitivity ratio, thus creating a predominant T2* effect resulting in MR signal

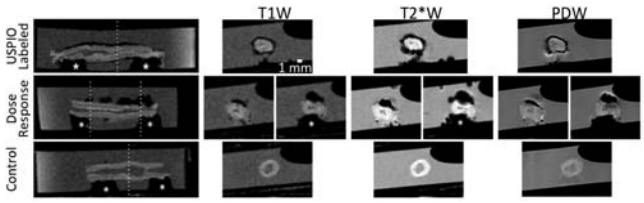


Figure 5. T1-weighted, T2*-weighted, and PD-weighted MR images ($0.3 \times 0.3 \times 0.5$ mm^3 resolution) obtained at 3 T of three segments of the same saphenous vein: a segment circumferentially labeled with activated Fe-NPs as described in the text (top row); a segment with 4 equal drops of cyanoacrylate adhesive, each containing different concentration of Fe-NPs (middle row); the unlabeled control vein segment (bottom row). A sagittal curved multiplanar reformation of the T1W acquisition is shown in the first column; the dashed vertical lines indicate the locations of the axial images shown in the other columns. The concentration of Fe-NPs shown in the middle row of the sagittal reformation is 6, 12.5, 25, and 50 μg, from left to right. All vein segments were imaged immersed in Petri dishes filled with saline and mounted on polystyrene scaffolds (white stars in images) to suspend them within the fluid.

hypointensity (i.e., darker), as well as generating contrast in T1-, T2-, and T2*-weighted images (*20*).

T1-weighted (T1W), T2*-weighted (T2*W), and proton density-weighted (PDW) high-resolution (spatial resolution 0.3 $\times$ 0.3 $\times$ 0.5 mm^3) MR imaging of labeled and control vein specimens was performed on a clinical 3 T MRI scanner (HDx, General Electric, Milwaukee, WI) equipped with 40 mT/m gradients (150 T/m/s slew rate) (Figure 5). For detailed MRI methods, see Supporting Information. In addition, the MRI dose−response to different Fe-NPs concentrations was explored: four concentrations of Fe-NPs (50, 25, 12.5, and 6 μg) were each mixed with a drop of Cyanoacrylate adhesive and placed on the adventitia of an unlabeled vein prior to imaging. All three vein segments were imaged simultaneously (Figure 5). Additional experiments confirmed that Cyanoacrylate adhesive had no measurable effect for those image contrast weightings (not shown).

Quantitative assessment of the ability of the Fe-NPs to enhance delineation of the vein wall from surrounding signal was performed by direct planimetry of the vessel wall and surrounding signal voids caused by the Fe-NPs using region-of-interest (ROI) measurements; for detailed methods, see Supporting Information. In brief, three ROIs were drawn on each of the control and labeled samples in T1W images: a central ROI delineated the lumen, a second ROI delineated the outer extent of the vein-wall tissue, and a third ROI was used to delineate the region surrounding the vein. For the labeled vein, this encompassed the outer extent of the iron oxide susceptibility-induced signal void. In the control vein segment, this region was a similarly sized ROI containing some of the surrounding saline around the control specimen (Figure 6). ROI areas were used to deduce the average thickness of the vessel wall and surrounding Fe-NP label, as well as the relative signal characteristics of the vein wall tissue and label.

First, we tested the hypothesis that the vessel wall thickness could be accurately measured despite the presence of the iron oxide particles. The average wall thickness of the unlabeled control vein segment was 1.47 $\pm$ 0.06 mm, while that of the labeled segment was 1.36 $\pm$ 0.08 mm. The 0.11 mm difference in wall thickness was statistically significant (*t*-test, $p < 0.0001$). There were no apparent trends in wall thickness with slice location for either vein segment (Figure 7). Since both vein segments were obtained from consecutive portions of the same donor vein (1.5 cm length ea.), the observed difference in wall thickness was most likely due to the signal nulling effect of the Fe-NP on the labeled vein. This difference, however, is much

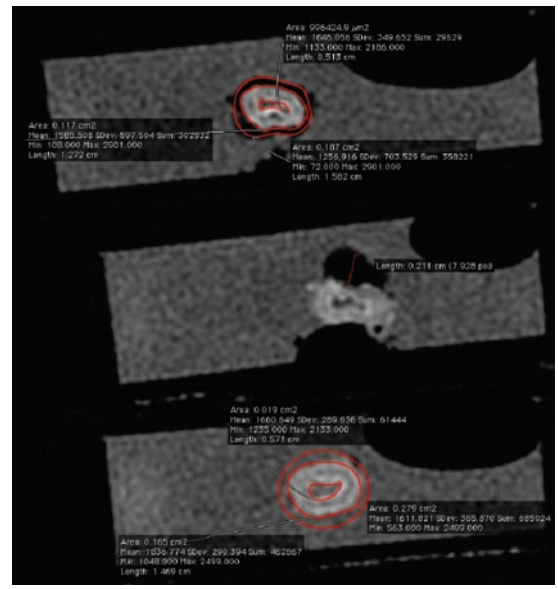


Figure 6. Definition of ROIs and lengths used for quantitative analyses; for each axial slice analyzed, a lumen ROI was first delineated for both the labeled and control segment. Next, a wall ROI was delineated for both segments. Finally, a third ROI extending to the edge of the Fe-NP label, or a corresponding similar region in the saline, was delineated for the labeled and control vein specimens, respectively. These ROIs were used to determine the average thickness of the vessel wall, the average thickness of the Fe-NP label, and the CNR between vessel wall and surrounding label or saline as appropriate. Finally, for the dose−response experiment, the maximal width of the signal void was measured for each axial slice along a line orthogonal to the vessel wall.

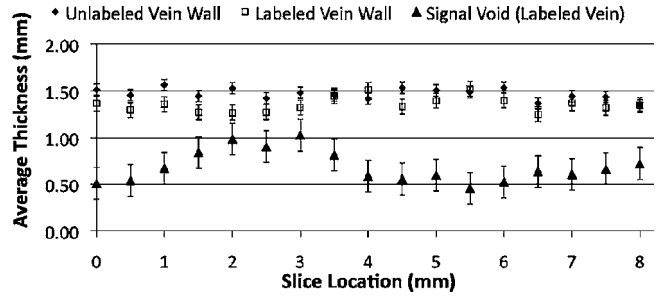


Figure 7. Average wall thickness of labeled and control vein segments in each slice analyzed along the length of the specimens, and average thickness of the iron-oxide susceptibility-induced signal void around the labeled vein. Error bars indicate the standard deviation of measurements across all slices.

lower than in vivo MR imaging resolutions and thus is unlikely to impact our ability to perform accurate wall thickness measurements. At present, the highest published resolution used for vein graft imaging is 0.312 mm in-plane (*8*−*10*), while most in vivo MRI is performed at resolutions higher than 0.5 mm due to scan time constraints at clinically used field strengths of 1.5−3 T.

A second analysis was performed to determine the ability of the Fe-NP label to enhance the delineation of the vessel wall boundary in comparison to the surrounding MR signal-generating environment. In general, this is a combination of the size of the structure to be delineated (e.g., Fe-NP label) compared to the image resolution, as well as the contrast to noise ratio of the structure (e.g., imposed between the wall tissue and the Fe-NP label).

For our ex vivo experiment, each of these two metrics was assessed separately. The average thickness of the Fe-NP label obtained from ROI measurements was 0.68 $\pm$ 0.17 mm (Figure

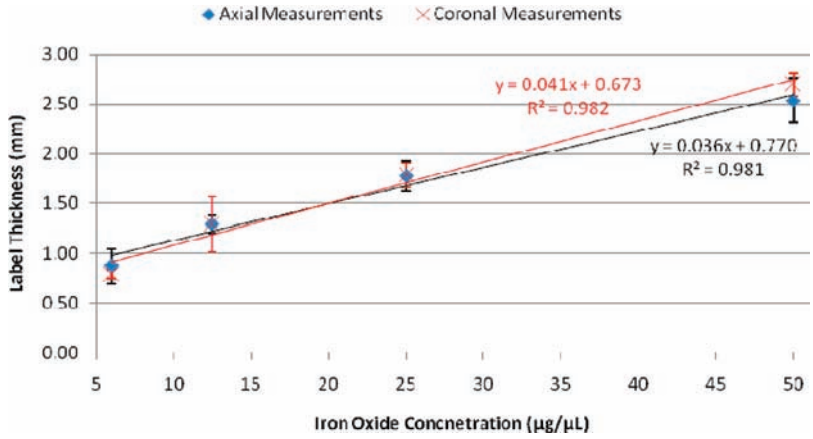


Figure 8. Correlation between label thickness and Fe-NP load observed in the dose−response experiment. Measurements were performed independently in both raw axial images, as well as coronal/sagital multiplanar reformations.

7), well within the limits of in vivo MRI resolutions. In addition, the CNR between the vessel wall and surrounding label was 20.3 ± 2.4. Such high CNR values observed with the Fe-NP label are uncommon in vessel wall MRI; the highest CNR values encountered are near 10, and represent signal differences between the vessel wall and the signal void within the lumen in black-blood MRI (*21*). CNRs are much lower between the vessel wall and surrounding signal-generating tissues for in vivo T1W vein graft imaging. Values near zero are often encountered when the vein wall is surrounded by muscle or scar tissues. Thus, the finding of this preliminary study is that the Fe-NP label produces an effect that is global (encompassing the entire vein wall irrespective of the surrounding signal) and that can be readily detected (high CNR) within the limitations of current in vivo MR imaging (extent greater than or equal to a single pixel).

While multiplanar reformation of the vein segment with the four concentrations of Fe-NP-loaded adhesive (50, 25, 12.5, and 6 μg) demonstrated a clear dose−response of the susceptibility-induced signal void (Figure 5), a final analysis was performed to determine the correlation between Fe-NP concentration and the thickness of the resulting label. As expected, there exists a strong linear relationship between the width of the Fe-NP susceptibility-induced signal void (Figure 6) and the iron oxide load of the cyanoacrylate adhesive (Figure 8). Careful control of the Fe-NP concentration will be critical, since at higher concentrations (above 12.5 μg), the signal void induced by the Fe-NPs interferes with visualization of the vein wall (Figure 5). Nonetheless, the linear response of the label to Fe-NP loading suggests that this adverse effect can be minimized by optimization of the reaction conditions to employ sufficiently low Fe-NP quantities with which to label the vein wall.

An interesting effect observed in this study is underscored by the "asymmetry" of the label thickness measurements in light of the wall thickness difference between labeled and control vein segments. Specifically, while the label measured nearly 0.7 mm thick, it only encroached 0.11 mm within the vessel wall. This anisotropic effect of the Fe-NPs (namely, the preferential nulling of signals outside the vessel wall rather than equally affecting the vein wall tissue signal) is likely explained by the increased mobility of the water protons in the saline compared to those in the vessel wall. As a result, we can postulate that in an in vivo environment the thickness of the label will likely be lower at the same concentration. Nonetheless, given current in vivo imaging resolutions and the large CNR attainable by the Fe-NP label developed in this work, this study suggests that sufficient label thicknesses ($\geq$0.3 mm) can be readily achieved to delineate the label without affecting measurement of the vein wall tissue.

Data obtained from our ex vivo studies highlight the potential application of Fe-NPs to enhance vein graft wall visualization in vivo. By enhancing the sensitivity of MRIs to clearly delineate the entire vessel wall, the relationship between vein wall remodeling and early events (first four weeks post implantation) may eventually be investigated longitudinally and more efficiently. Such studies to date have required invasive imaging techniques. External wall labeling with Fe-NPs may serve to enhance the sensitivity of MRI by helping to more readily delineate the vessel adventitia; this would be potentially useful in the in vivo setting, where improving cranial caudal coverage within clinical scan time remains a challenge. Since negative wall remodeling (permanent constriction of the vein graft) stands as an important etiology of failure (*3*−*6*), more sensitive delineation of early negative remodeling may also enable timely clinical interventions to halt the process.

The vein conduit labeling techniques can be expanded to include other contrast agents such as gadolinium metal complexes that can provide enhanced graft wall MR signals, thus further improving the efficacy and resolution of MRI as a tool to investigate vein grafts (and other solid organ surfaces). On the basis of these promising ex vivo results, we are in the process of evaluating the stability and toxicity of this agent and strategy using in vivo animal models. The potential long-term effects of Fe-NPs localization on the surface of vein grafts, as well as other distant organs such as liver and kidneys will be investigated. The present strategy may also be combined with molecular/biologically based contrast agents to provide a better understanding of vascular wall remodeling mechanisms and improve our understanding of vein graft failure.

ACKNOWLEDGMENT

The authors would like to thank Prof. Frederick J. Schoen, M.D., Ph.D., and Dr. Sivapriya Kirubakaran for helpful discussions. J.M.K. acknowledges American Heart Association grant #0970178N and NIH R01HL095722 for financial support. P.K.V. would like to thank the Ewing Marion Kauffman Foundation for Entrepreneur Postdoc Fellowship. C.K.O. acknowledges NIH grant #1R01HL079135 and 5T32HL007734-16 for financial support.

Supporting Information Available: Detailed materials and methods. This material is available free of charge via the Internet at http://pubs.acs.org.

LITERATURE CITED

(1) Conte, M. S., Bandyk, D. F., Clowes, A. W., Moneta, G. L., Seely, L., Lorenz, T. J., Namini, H., Hamdan, A. D., Roddy,

S. P., Belkin, M., Berceli, S. A., DeMasi, R. J., Samson, R. H., and Berman, S. S. (2006) Results of PREVENT III: a multicenter, randomized trial of edifoligide for the prevention of vein graft failure in lower extremity bypass surgery. *J. Vasc. Surg. 43*, 742–751, discussion 751.

(2) Alexander, J. H., Hafley, G., Harrington, R. A., Peterson, E. D., Ferguson, T. B., Jr., Lorenz, T. J., Goyal, A., Gibson, M., Mack, M. J., Gennevois, D., Califf, R. M., and Kouchoukos, N. T. (2005) Efficacy and safety of edifoligide, an E2F transcription factor decoy, for prevention of vein graft failure following coronary artery bypass graft surgery: PREVENT IV: a randomized controlled trial. *JAMA 294*, 2446–2454.

(3) Lau, G. T., Ridley, L. J., Bannon, P. G., Wong, L. A., Trieu, J., Brieger, D. B., Lowe, H. C., Freedman, B. S., and Kritharides, L. (2006) Lumen loss in the first year in saphenous vein grafts is predominantly a result of negative remodeling of the whole vessel rather than a result of changes in wall thickness. *Circulation 114*, I435–40.

(4) Owens, C. D. (2009) Adaptive changes in autogenous vein grafts for arterial reconstruction: Clinical implications. *J. Vasc. Surg.*

(5) Wu, J., and Zhang, C. (2009) Neointimal hyperplasia, vein graft remodeling, and long-term patency. *Am. J. Physiol. 297*, H1194–5.

(6) Jiang, Z., Tao, M., Omalley, K. A., Wang, D., Ozaki, C. K., and Berceli, S. A. (2009) Established neointimal hyperplasia in vein grafts expands via TGF-beta-mediated progressive fibrosis. *Am. J. Physiol. 297*, H1200–7.

(7) Yuan, C., and Kerwin, W. S. (2004) MRI of atherosclerosis. *J. Magn. Reson. Imaging 19*, 710–9.

(8) Mitsouras, D., Mulkern, R. V., Owens, C. D., Conte, M. S., Ersoy, H., Luu, T. M., Whitmore, A. G., Creager, M. A., and Rybicki, F. J. (2008) High-resolution peripheral vein bypass graft wall studies using high sampling efficiency inner volume 3D FSE. *Magn. Reson. Med. 59*, 650–4.

(9) Crowe, L. A., Gatehouse, P., Yang, G. Z., Mohiaddin, R. H., Varghese, A., Charrier, C., Keegan, J., and Firmin, D. N. (2003) Volume-selective 3D turbo spin echo imaging for vascular wall imaging and distensibility measurement. *J. Magn. Reson. Imaging 17*, 572–80.

(10) Koktzoglou, I., Chung, Y. C., Carroll, T. J., Simonetti, O. P., Morasch, M. D., and Li, D. (2007) Three-dimensional black-blood MR imaging of carotid arteries with segmented steady-state free precession: initial experience. *Radiology 243*, 220–8.

(11) Bulte, J. W., Zhang, S., van Gelderen, P., Herynek, V., Jordan, E. K., Duncan, I. D., and Frank, J. A. (1999) Neurotransplantation of magnetically labeled oligodendrocyte progenitors: magnetic resonance tracking of cell migration and myelination. *Proc. Natl. Acad. Sci. U.S.A. 96*, 15256–61.

(12) Josephson, L., Tung, C. H., Moore, A., and Weissleder, R. (1999) High-efficiency intracellular magnetic labeling with novel superparamagnetic-Tat peptide conjugates. *Bioconjugate Chem. 10*, 186–91.

(13) Lee, H., Lee, E., Kim do, K., Jang, N. K., Jeong, Y. Y., and Jon, S. (2006) Antibiofouling polymer-coated superparamagnetic iron oxide nanoparticles as potential magnetic resonance contrast agents for in vivo cancer imaging. *J. Am. Chem. Soc. 128*, 7383–9.

(14) McCarthy, J. R., and Weissleder, R. (2008) Multifunctional magnetic nanoparticles for targeted imaging and therapy. *Adv. Drug Delivery Rev. 60*, 1241–51.

(15) Weissleder, R., Kelly, K., Sun, E. Y., Shtatland, T., and Josephson, L. (2005) Cell-specific targeting of nanoparticles by multivalent attachment of small molecules. *Nat. Biotechnol. 23*, 1418–23.

(16) Gupta, A. K., Naregalkar, R. R., Vaidya, V. D., and Gupta, M. (2007) Recent advances on surface engineering of magnetic iron oxide nanoparticles and their biomedical applications. *Nanomed. (London, England) 2*, 23–39.

(17) Sarkar, D., Vemula, P. K., Teo, G. S., Spelke, D., Karnik, R., Wee le, Y., and Karp, J. M. (2008) Chemical engineering of mesenchymal stem cells to induce a cell rolling response. *Bioconjugate Chem. 19*, 2105–9.

(18) Artzi, N., Shazly, T., Baker, A. B., Bon, A., and Edelman, E. R. (2009) Aldehyde-amine chemistry enables modulated biosealants with tissu-specific adhesion. *Adv. Mater. 21*, 3399–3403.

(19) Winter, P. M., Caruthers, S. D., Yu, X., Song, S. K., Chen, J., Miller, B., Bulte, J. W., Robertson, J. D., Gaffney, P. J., Wickline, S. A., and Lanza, G. M. (2003) Improved molecular imaging contrast agent for detection of human thrombus. *Magn. Reson. Med. 50*, 411–6.

(20) Tang, T. Y., Muller, K. H., Graves, M. J., Li, Z. Y., Walsh, S. R., Young, V., Sadat, U., Howarth, S. P., and Gillard, J. H. (2009) Iron oxide particles for atheroma imaging. *Arterioscler. Thromb. Vasc. Biol. 29*, 1001–8.

(21) Balu, N., Chu, B., Hatsukami, T. S., Yuan, C., and Yarnykh, V. L. (2008) Comparison between 2D and 3D high-resolution black-blood techniques for carotid artery wall imaging in clinically significant atherosclerosis. *J. Magn. Reson. Imaging 27*, 918–24.

BC100138C

Supporting Information for:

Immobilization of Iron Oxide Magnetic Nanoparticles for Enhancement of Vessel Wall Magnetic Resonance Imaging – An *Ex Vivo* Feasibility Study

Binh Thai Nguyen,[†,≠] Praveen Kumar Vemula,[‡,¶,≠,ǂ] Dimitrios Mitsouras,[§] Peng Yu,[†] Ming Tao,[†] Christina Campagna,[†] Robert V. Mulkern,[§] Frank J. Rybicki,[§] Jeffrey M. Karp,[‡,¶,*] C. Keith Ozaki[†,*]

[‡]Department of Medicine, Brigham and Women's Hospital, Harvard Medical School, Harvard-MIT Division of Heath Sciences & Technology
65 Landsdowne Street, Cambridge, MA 02139, USA

[¶]Harvard Stem Cell Institute, Harvard Medical School

[§]Applied Imaging Science Laboratory
Department of Radiology, Brigham and Women's Hospital, Harvard Medical School,
75 Francis Street, Boston, MA 02115

[†]Department of Surgery, Brigham and Women's Hospital, Harvard Medical School,
75 Francis Street, Boston, MA 02115

[ǂ] Kauffman Foundation Entrepreneur Postdoc Fellow

[≠]Authors contributed equally

**Co-corresponding Author*

Jeffrey M. Karp, Ph.D
Tel: 617-817 9174
Fax: 617-768-8338
Email: jkarp@rics.bwh.harvard.edu

C. Keith Ozaki, M.D
Tel: 857-307-1920
Fax: 857-307-1922
Email: CKOzaki@partners.org

METHODS

Acquisition of vein specimens and vein conduit labeling: Fresh discarded human vein segments (n=3) from bypass surgeries and major amputations were collected by following approved institutional protocols and used for labeling experiments. The sample size used in this proof of principle experiment (n=3 total) is small, and has largely been limited by the scarcity of adequately sized fresh discarded human vein specimens.

Fe-NPs that have carboxylic groups on the surface (~ 30 nm) were purchased from Ocean Nanotech LLC USA. The surface carboxylic groups have been activated through *N*-hydroxysuccinamide ester reaction as follows: 50 µL of Fe-NPs were (5 mg/mL water) diluted with 150 µL of double distilled water (ddH_2O). The particle solution was centrifuged at 13,000 rpm for 6 min. The supernatant was removed and 200 µL of dimethyl formamide (DMF) was added, then the solution was vortexed and centrifuged for 6 min. The supernatant was again removed, and the pellet re-dispersed in 200 µL of DMF containing *N, N'*-diisopropylcarbodiimide (DIC, 1 mmol/L) and *N*- hydroxysuccinamide (1 mmol/L). The reaction continued at room temperature overnight. The activated particles were then spun down and washed with DMF (200 µL). The particles were finally re-dispersed in phosphate buffer saline (PBS) and used immediately for coating the vein graft adventitia. With the luminal side protected via ligatures on either end, the test human vein sample (n=1) was placed in a PBS filled Petri-dish. The activated Fe-NPs (200 µL in PBS) were added and incubated for 30 minutes at room temperature. The procedure was repeated for the unlabeled control vein segment (n=1), but incubated with plain PBS without the addition of Fe-NPs. Finally, all vein segments were thoroughly rinsed thrice with PBS to remove nonspecifically bound nanoparticles. Different sets of instruments were employed for each study group to avoid cross contamination.

Dose-responsive samples: To non-covalently fixate different concentrations of Fe-NPs on the vein, four concentrations of Fe-NPs (50, 25, 12.5 and 6 μg) were each mixed with a drop of Cyanoacrylate adhesive and placed on the adventitia of a segment of unlabeled vein (n=1) prior to imaging. This method resulted in non-covalent localization of Fe-NPs on the vein.

Evaluation of contrast localization—SEM and EDAX: Scanning Electron Microscopy (SEM) with energy dispersive spectroscopy (EDAX) was used to map the presence of Fe-NPs on the surface of the vein following MR imaging. The Fe-NP-coated vein segments were mounted on an aluminum stub with carbon tape, and directly examined using Environmental SEM (FEI/Phillips XL30 FEG-ESEM) operated at 10 kV. EDAX and elemental mapping analysis data was also collected from the same samples at 10 kV using X-ray detector (Torr Scientific Ltd., UK) coupled with FEI/Phillips XL30 FEG-ESEM.

MR Imaging: T1-weighted (T1W), T2*-weighted (T2*W), and proton density-weighted (PDW) high resolution MR Imaging of labeled, control, and dose-response vein specimens was performed on a clinical 3 T MRI scanner (HDx, General Electric, Milwaukee, WI) equipped with 40 mT/m gradients (150 T/m/s slew rate). T1-weighted contrast images were obtained using a standard 3D spoiled gradient recalled echo sequence using the following parameters: 30° flip angle, 12.8 ms TR, 3.5 ms TE, ±32 kHz receiver bandwidth, 224×224×84 image matrix, 0.5 mm slice thickness and 6.8 cm field-of-view. T2*-weighted contrast images were obtained using the same sequence except with 5 ms TE, 100 ms TR, 160×160×68 image matrix and 4.8 cm field-of-view. Proton density-weighted images were obtained using a high sampling efficiency 3D fast

spin echo (FSE) sequence with 1800 ms TR, 9 ms TE, ±16 kHz receiver bandwidth, 150×150×92 image matrix, 0.5 mm slice thickness and 4.5 cm field-of-view. Spatial resolution was 0.3×0.3×0.5 mm^3 for all imaging experiments.

Quantitative MR Image Analysis: Three regions-of-interest (ROI) were drawn using direct planimetry for each of the control and labeled samples in T1W images for 17 consecutive image sections (8.5 mm longitudinal extent) sufficiently away from the Petri dish mounting setup. First, a central ROI was used to delineate the lumen. A second ROI was used to delineate the outer extent of the vessel wall tissue. Finally, the third ROI was used to delineate the region surrounding the vein. For the labeled vein, this ROI was used to delineate the outer extent of the Fe-NP susceptibility-induced signal void. For the control vein segment, this ROI was used to delineate a similar sized region containing the saline surrounding the vein (Figure 6). These ROIs were used to perform two analyses; the first analysis was aimed at testing the hypothesis that the vessel wall thickness could be accurately measured despite the presence of the Fe-NPs. For this analysis, the two inner-most ROIs (lumen and vessel wall ROIs) were assumed to represent ideal disks in order to obtain average radii as $r = \sqrt{\text{ROI area}/\pi}$. The average vessel wall thickness was then calculated by subtracting the radius corresponding to the lumen ROI from the radius corresponding to the vessel wall ROI. The unpaired t-test was used to compare the average vessel wall thickness of the labeled versus the unlabeled vein segments. This comparison was based on the assumption that the wall thickness of the two short (appx. 1.5 cm extent) vein segments did not vary significantly in thickness given that they were harvested from consecutive portions of the same donor vein.

The second analysis was aimed at assessing the ability of the Fe-NP label to effectively enhance the delineation of the vessel wall boundary in comparison to surrounding tissues. First, we measured the average thickness of the iron oxide label, as this places a limit on the image resolution required to detect it. This analysis was similar to that described for the wall thickness, except using the wall and outer region ROIs. Second, we measured the contrast-to-noise-ratio (CNR) achieved using the label. This analysis was performed by comparing the average signal in the vessel wall ROI to the average signal in the ROI surrounding the vessel wall. Average signal in each ROI was calculated by subtracting the total signal in the inner ROI from the total signal in the enclosing ROI, divided by the number of pixels in the enclosing ROI minus that in the enclosed ROI. For example, the average vessel wall signal was obtained as the total signal in the vessel wall ROI minus the total signal in the lumen ROI, divided by the number of pixels in vessel wall ROI minus the number of pixels in the lumen ROI. CNR was then computed as $CNR = \frac{(\text{average vessel wall signal} - \text{ average surrounding signal})}{\sigma_{\text{noise}}}$, where σ_{noise} the noise standard deviation measured in an ROI placed in empty space.

A final quantitative analysis was performed for the dose-response experiment in order to determine the correlation between tissue Fe-NP concentration, and label width. For this analysis we measured the length of the susceptibility-induced signal void orthogonal to the vessel wall for each axial image containing one of the drops of the Fe-NP-loaded adhesive (Figure 6). The lengths of the signal voids were additionally measured on a single sagittal reformat of the 3D volume in order to ensure that axial slice measurements were not significantly biased by the angle of the vein segment relative to the image plane. Linear regression was used to correlate the measured widths of the Fe-NP label to the label concentration.

Evaluation of contrast localization—Iron histochemistry: Perl's Prussian Blue protocol was used to detect the presence of iron bound to the vein adventitia. Sections from the Fe-NPs labeled vein conduit were incubated with 2% aqueous potassium ferrocyanide-hydrochloic acid incubating solution (composed of equal volumes of 4% aqueous potassium ferrocyanide and 4% aqueous hydrochloric acid) for 15 minutes. The sections were washed twice for 2 minutes with ddH_2O, and then counterstained for 2 minutes with 1% Neutral Red. Subsequently, these slides were rinsed with ddH_2O (2 washes for 2 minutes each) and then dehydrated rapidly using increasing concentrations of ethanol (70%, 95%, 100%; 10 seconds each). They were then examined under polarized microscopy.

Stable Gold Nanoparticle Conjugation to Internal DNA Positions: Facile Generation of Discrete Gold Nanoparticle−DNA Assemblies

Yongqiang Wen, Christopher K. McLaughlin, Pik Kwan Lo, Hua Yang, and Hanadi F. Sleiman*

Department of Chemistry, McGill University, 801 Sherbrooke Street West, Montreal, Quebec H3A 2K6, Canada. Received March 31, 2010; Revised Manuscript Received July 6, 2010

A straightforward strategy to stably anchor one or more gold nanoparticles (AuNPs) at both the internal and terminal positions of single-stranded DNA is presented. Discrete DNA−AuNP conjugates are isolated using a noncovalent extension strand strategy, that helps to resolve prepared species by agarose gel electrophoresis (AGE). These are used to assemble well-defined AuNP squares and rectangles. Two complementary bis-AuNP-labeled DNA conjugates are then prepared. One of these places two smaller (5 nm) AuNPs at defined internal positions within a DNA strand, and the other places two larger (13 nm) AuNPs at each of its terminal positions. We show the self-assembly of these bis-AuNP conjugates into a tapered tetrameric gold nanoparticle "antenna" structures of direct relevance to engineered "hot spots" and surface enhanced Raman scattering (SERS) substrates.

Gold nanoparticle assemblies have recently attracted considerable interest as a class of materials with novel optical, electronic, catalytic, and sensing applications (*1, 2*). In particular, their ability to exhibit single electron transport and to act as plasmon "antennae" for focusing light to nanoscale volumes may lead to their incorporation in future nanoelectronic and nanophotonic devices and as sensitive reporters in biodetection and bioimaging strategies (*3*). These properties arise directly from the geometric arrangement of the particles within the assembly (*1, 4*−*10*). In order to investigate these phenomena and to incorporate nanoparticles into devices and biosensing schemes, methods to systematically organize gold particles (AuNPs) into well-defined assemblies are essential.

Toward this goal, the DNA-directed organization of AuNPs can provide a high degree of control, due to its programmable self-assembly parameters (*4, 11*−*24*). However, the 1:1 conjugation of a DNA strand onto a gold nanoparticle is still synthetically challenging. It typically relies on bringing together gold nanoparticles with a DNA strand that is end-labeled with a single thiol unit, in a 1:1 ratio. This leads to a statistical mixture of unlabeled, singly labeled, and multiply labeled nanoparticles that are usually difficult to separate, unless the DNA strand is very long (e.g., >80 bases). Moreover, because the conjugation is through a single gold−thiol bond, these conjugates are typically labile and tend to lose their DNA labels in a relatively short time. Finally, strategies to conjugate nanoparticles to internal positions of a DNA strand in a stable manner are necessary, in order to expand the range of gold−DNA assemblies. Solutions have been put forward to address some of these problems individually (*25*−*32*); however, there remains a need for a single strategy that gives ready access to these conjugates with stability, ease of separation, and internal conjugation, and as a result increases their applications range.

We report here the first example of site-specific and stable conjugation of gold nanoparticles at any internal position within DNA strands. This is achieved through incorporation of a cyclic disulfide group (**D**, inset Figure 1A) within a DNA strand, which serves as a chelating anchor to stably position AuNPs. Moreover, we achieved ready separation and purification of the AuNP−DNA conjugates through the use of a noncovalent extension strategy. This involves hybridization with a partially cDNA strand (**EXT**) that helps to increase the separation between conjugated and unconjugated nanoparticles by electrophoresis, followed by strand displacement of **EXT** (Figure 1). Thus, AuNP monoconjugates can be isolated even when the DNA strand is relatively short.

Using this strategy, we designed an internally bis-labeled DNA strand that can capture two AuNPs within a single DNA sequence **2** (Figure 1B). This creates AuNP dimers that can now be used for further self-assemby. By combining bis-AuNP labeling at internal and terminal (**3**) positions, we can create a nanoparticle "antenna" tapered structure, containing two larger nanoparticles at its two ends and two smaller particles in the middle. Such tapered structures have been predicted to exhibit strong focusing of light in their middle gap through plasmon coupling (*7*), with a number of applications in nanophotonics and as surface enhanced Raman scattering substrates. However, they have not been previously generated. Thus, the stable anchoring of gold nanoparticles on any position within a DNA strand can be achieved and gives access to gold nanoparticle groupings with programmability, stability, and positional and geometric control.

Oligonucleotides $\mathbf{1}_{\mathbf{a\text{-}d}}$, **2**, and **3** containing gold nanoparticle anchoring units were obtained in high yields by standard automated solid-phase synthesis, with site-specific incorporation of a chelating cyclic disulfide **D** as its commercially available phosphoramidite precursor (Figure 1 inset). AuNP conjugation methods were first developed using the singly modified DNA strands $\mathbf{1}_{\mathbf{a\text{-}d}}$ that had **D** placed in the middle of the sequence space (Figure 1A). As an example, sequence $\mathbf{1}_{\mathbf{a}}$ was added to 5 nm AuNPs in different molar ratios and left overnight at room temperature in a phosphate buffered saline (PBS) solution. Samples were analyzed by agarose gel electrophoresis (AGE) to determine product composition (Figure 2a). These (lanes 1−4) resulted in diffuse bands of only slightly reduced mobility compared to the 5 nm AuNP marker (lane M). While it was possible that no reaction had taken place between the AuNP and **D** under these conditions, we hypothesized that gold conjugates were formed but may have been inadequately separated by electrophoresis. Previous approaches have used longer conjugating DNA strands to help resolve AuNP−DNA

* E-mail: hanadi.sleiman@mcgill.ca.

10.1021/bc100160k © 2010 American Chemical Society
Published on Web 07/28/2010

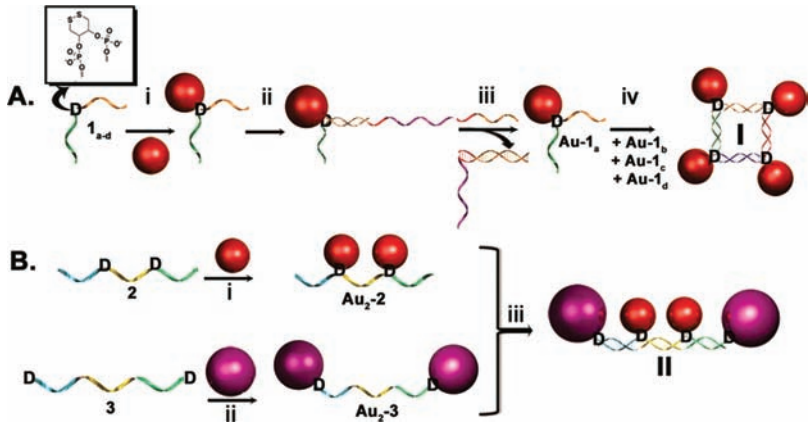


Figure 1. Site-specific conjugation of AuNPs to internal and external DNA positions using a cyclic disulfide: (A) Sequence 1a, modified internally with cyclic disulfide **D** (inset), is conjugated to AuNPs (step i). Upon addition of extension strand (step ii), the conjugate can be isolated by electrophoresis, and a displacement strand (step iii) is used to obtain the DNA−AuNP conjugate. Four such monoconjugates **Au-1$_{a-d}$** are annealed to give discrete AuNP tetramer **I** (step iv). (B) Selective functionalization of **D**-modified strands **2** (step i) and **3** (step ii) with two different sizes of nanoparticles generate dimers that can be further assembled into linear tetrameric structure **II**.

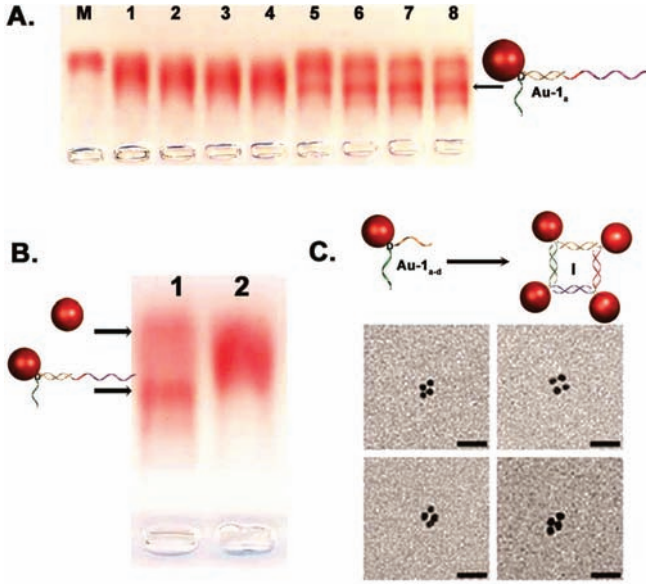


Figure 2. AuNP conjugation to internal singly-**D** modified DNA: (A) 3% agarose gel electrophoresis (AGE, 0.5× TBE) analysis of conjugation between AuNPs (5 nm) and **1$_a$** at various molar ratios (**1$_a$**/AuNP) in the absence (lanes 1−4) and presence (lanes 5−8) of **EXT-1$_a$**. Lane M, 5 nm AuNP; lane 1, 1:1 ratio **1$_a$**/AuNP; lane 2, 2:1 ratio; lane 3, 3:1 ratio; lane 4, 4:1 ratio. Lanes 5−8 contain same ratios of **1$_a$**/AuNP, respectively, except the correct ratio of **EXT-1$_a$** was added prior to AGE analysis. (B) 3% AGE analysis of **1$_a$**/**EXT-1$_a$**/AuNP mixture (2:2:1) in the absence (lane 1) and presence (lane 2) of **DISP-1$_a$**. (C) Representative TEM fields of view of square structure I assembled from **Au-1$_{a-d}$**. Scale bars are 20 nm.

conjugates with electrophoresis (*12*) or anion-exchange HPLC separation (*20*).

Here, we used a noncovalent method for lengthening the conjugating DNA strands. A partially complementary extension (**EXT**) strand is designed to hybridize to the DNA sequence on the gold nanoparticles (Figure 1A). This temporarily increases the size of the DNA strand on the nanoparticle and allows better electrophoretic separation of the monoconjugates from the unconjugated gold nanoparticle (*16*). After separation by AGE, the extension strand can be removed by the addition of displacement (**DISP**) strand that possesses a larger region of complementarity. Addition of the appropriate **EXT-1$_a$** sequence to each sample prior to AGE analysis results in the formation of two discrete bands (Figure 2a, lanes 5−8), one with the same mobility as unconjugated AuNPs and one with retarded mobility, that is assigned to the **Au-1$_a$** monoconjugate.

To test the displacement strategy, we conjugated **1$_a$** to 5 nm AuNPs in a 2:1 (DNA/AuNP) molar ratio and added the **EXT-1$_a$**. After a 10 min incubation period, half of the sample was loaded directly onto a 3% agarose gel. This sample showed two well-separated bands for the unconjugated and the monoconjugated AuNPs (Figure 2b, Lane 1), consistent with temporary lengthening of the conjugating DNA strand. To the second half was added **DISP-1$_a$**, which is fully complementary to **EXT-1$_a$**. This results in a single diffuse band of increased mobility (Figure 2b, lane 2), consistent with displacement of **EXT-1$_a$** from the conjugate and reduced resolution of the unconjugated and the monoconjugated AuNPs.

To confirm the gel band assignment and demonstrate the ability of the internal AuNP monojugates to undergo further organized assembly, we designed an additional set of **D**-labeled sequences (**1$_{b-d}$**), which, once conjugated to AuNPs, could be hybridized together to yield square particle grouping **I** (Figure 1A). Conjugation of these sequences to AuNPs and isolation of monoconjugates **Au-1$_{a-d}$** was carried out as above. Quantification of these isolated products **Au-1$_{a-d}$** was based on the AuNP absorbance at 520 nm, and samples were then mixed in an approximate stoichiometric fashion (1:1:1:1). Characterization of the resulting gold nanoparticle assembly **I** by transmission electron microscopy (TEM) (Figure 2c) revealed a number of discrete particle groupings with the expected cyclic tetramer geometry, formed in a yield of ∼40%. The TEM analysis in Figure 2c reveals some distortion of the AuNP groupings from the expected square geometry. Unlike our previous system where a rigid organic vertex helps to define the DNA junctions (*16*), the vertices in this design are more flexible, leading to increased conformational mobility in the DNA−AuNP conjugates. In addition, structural distortions of DNA−nanoparticle assemblies have been previously noted during TEM imaging on hydrophobic substrates (*23*). Using a similar strategy, we also created DNA strands where the **D**-label was asymmetrically positioned in the sequence, such that its AuNP conjugate carries two DNA arms of different lengths. These conjugates were used to generate rectangular particle groupings with the same efficiency as the square groupings above (Supporting Information, Figure S7). In this manner, a variety of discrete gold nanoparticle assemblies can be readily obtained, using the site-specific insertion of a single **D** group within the interior sequence space of single-stranded DNA components.

To test whether a single DNA strand could selectively conjugate to two gold nanoparticles, we designed doubly labeled

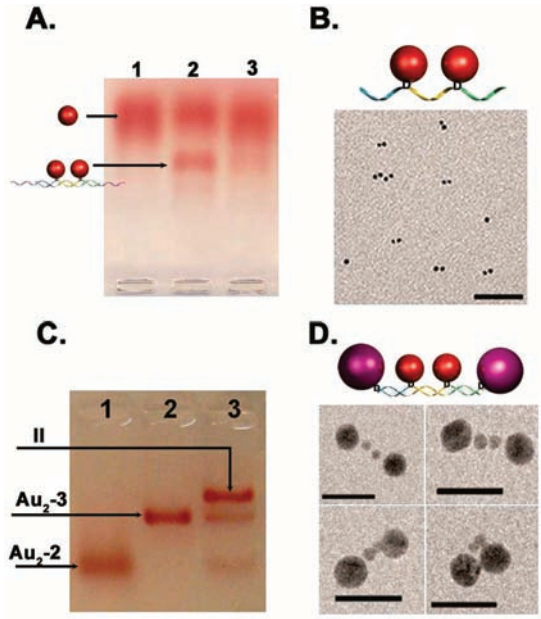


Figure 3. Characterization of **Au_2-2** conjugation and assembled nanostructure II: (A) AGE analysis (3%, 0.5× TBE) of doubly-**D** modified **2** conjugation with AuNPs (5 nm) (**2**/AuNP ratio is 2:1) in the absence (lane 1) and presence (lane 2) of **EXT-2**. Lane 3 shows the mobility after addition of the correct amount of **DISP-2**. (B) Representative TEM field of view for **Au_2-2** (scale bar = 100 nm). (C) AGE analysis (2.5%, 0.5× TBE) of isolated structures **Au_2-2** (lane 1), **Au_2-3** (lane 2), and assembled tetrameric AuNP nanostructure **II** (lane 3). (D) Representative TEM field of view for **II** (scale bar = 20 nm).

sequence **2** (Figure 1B), which is capable of binding two 5 nm AuNPs. As an example, incubation of **2** with 5 nm AuNPs in a 2:1 ratio (AuNP/DNA) produced a band of reduced electrophoretic mobility upon addition of the extension strand **EXT-2** (Figure 3a, lane 1), which we assigned to the AuNP dimer. Isolation of this band, followed by removal of extension strand **EXT-2** with added **DISP-2**, gave **Au_2-2**. This dimer contains one internal DNA single strand between the two nanoparticles, as well as two external single-stranded DNA sections on each particle, that are available for further hybridization (Figure 1B). After isolation of this band, TEM analysis was used to confirm the **Au_2-2** dimer assignment. A typical TEM field of view for **Au_2-2** is shown in Figure 2b, which reveals a number of dimer structures that are formed in high yield (∼75%). Additional evidence for the formation of these single-stranded DNA−AuNP dimers came from testing the assembly of two such dimers, containing complementary external DNA strands, into a AuNP square structure (Supporting Information, Figure S8). Thus, by placing the cyclic disulfide group **D** within each sequence, access to stable, AuNP modified DNA strands can be achieved. More importantly, the relative position of each AuNP can be easily tuned on the DNA strand, as is the case when comparing structures **Au-1** and **Au_2-2** (Figure 1), while retaining single-stranded regions that can now be used to further hybridize materials in a site-specific and programmable manner.

Interestingly, in the case of internal DNA modification with AuNPs such as for **Au-1** and **Au_2-2**, increasing the relative ratio of DNA/AuNP from 1:1 to 3:1 did not appear to generate distinct polyconjugated structures as is normally observed when thiol modifications are made at the termini of DNA (*12*).

With selective control over the position of AuNPs at internal positions within a DNA sequence, we next attempted to introduce a higher degree of complexity in the assembled nanostructures. Specifically, we designed DNA sequence **3**, the complementary sequence of **2**, to contain **D** at both the 3′- and 5′-positions. In this way, we could conjugate 13 nm nanoparticles to the two ends of this sequence to form AuNP dimers **Au_2-3**. **Au_2-3** is expected to hybridize with **Au_2-2** to form linear tetrameric structure **II**, containing two large 13 nm particles on its two ends and two smaller 5 nm particles in internal positions (Figure 1B). Motivation for this "antenna" structure came from recent simulations that have shown that tapered structures such as **II** are expected to exhibit strong focusing of light in their middle gap through plasmon coupling (*7*), with important implications in engineered "hot spots" for surface-enhanced Raman scattering (SERS) (*6*).

In a similar fashion to the conjugation of **1** and **2**, doubly 5′−3′ **D**-modified **3** was conjugated to 13 nm AuNPs, resulting in a band of reduced electrophoretic mobility (see Supporting Information, Figure S2). After isolation of this band, TEM imaging was used to confirm assignment of the AuNP dimer **Au_2-3**. Typical TEM fields of view for **Au_2-3** (see Supporting Information, Figure S4) reveal a significant number of dimer products with yields of ∼75%. Reanalysis of structures **Au_2-2** and **Au_2-3** by AGE (Figure 3c, lanes 1 and 2, respectively) showed the clean isolation of each product.

Hybridization of discrete structures **Au_2-2** and **Au_2-3** in a 1:1 ratio generated the desired "antenna" tetrameric architecture **II** in good yield, as evidenced by the band of reduced mobility in Figure 3c, lane 3. Direct evidence of the tapered structure by TEM analysis (Figure 3d) indeed reveals the formation of tetramer structure **II** in ∼38% yield and shows the arrangement of the 5 nm AuNPs placed on the interior and two 13 nm AuNPs that book-end the construct. Similar to the TEM analysis of **I**, distortion in some of the AuNP assemblies **II** is observed, due to the drying conditions on the hydrophobic TEM substrate. It should be noted here that, while bulk optical measurements on these assemblies would yield ensemble averages for all conformations, single-molecule optical measurements on individual assemblies (e.g., surface enhanced Raman scattering) coupled with TEM imaging are expected to provide a better correlation between individual structures and optical activity (*9*).

Unlike other DNA-based systems for arranging AuNPs, the stability afforded by the cyclic disulfide insertion, in conjunction with the ability to easily isolate site-specifically labeled AuNP-DNA constructs that contain single-stranded regions, introduces a high degree of programmability and modularity into this approach. In this way, fewer restrictions exist in comparison to end-monoconjugation, and the stable dimer products can be readily isolated by electrophoresis and further assembled into any number of spatial arrangements via their single-stranded regions.

In conclusion, we have introduced a facile method to stably and site-specifically append one or more AuNPs to either the interior sequence space, or to terminal (5′ or 3′) positions of single-stranded DNA. Insertion of this anchoring group within a DNA sequence led to the generation of AuNP−DNA constructs that contain single-stranded regions, which can be designed to assemble into discrete polygons of spatially well-defined AuNPs. This method was further explored to generate a tetrameric linear construct that contains well-defined positioning of two different sizes of AuNPs (5 and 13 nm). This facile conjugation strategy has the potential to enable the construction of any number of discrete metal nanoparticles, with varied sizes and spatial arrangements, based on the preparation of stably held conjugated AuNP−DNA synthons and their programmed self-assembly. Such discrete structures will be valuable model systems for fundamental physics investigations of optical and electronic properties of nanoparticles and for the generation of surface-enhanced Raman scattering substrates for sensitive biological detection.

ACKNOWLEDGMENT

The authors thank CIFAR, NSERC, CFI, and CSACS for financial support, Thomas Szkopek and Peter Grutter for helpful discussions, and G. Hamblin for help in preparing graphical illustrations. H. F. Sleiman is a Cottrell scholar of the Research Corporation.

Supporting Information Available: Detailed experimental preocedures pertaining to AuNP-DNA conjugation and characterization. This material is available free of charge via the Internet at http://pubs.acs.org.

LITERATURE CITED

(1) Nie, Z., Petukhova, A., and Kumacheva, E. (2010) Properties and emerging applications of self-assembled structures made from inorganic nanoparticles. *Nat. Nanotechnol. 5*, 15–25.

(2) Sperling, R. A., Gil, P. R., Zhang, F., Zanella, M., and Parak, W. J. (2008) Biological applications of gold nanoparticles. *Chem. Soc. Rev. 37*, 1896–1908.

(3) Wilson, R. (2008) The use of gold nanoparticles in diagnostics and detection. *Chem. Soc. Rev. 37*, 2028–2045.

(4) Mirkin, C. A., Letsinger, R. L., Mucic, R. C., and Storhoff, J. J. (1996) A DNA-based method for rationally assembling nanoparticles into macroscopic materials. *Nature 382*, 607–609.

(5) Reinhard, B. M., Siu, M., Argarwal, H., Alivisatos, A. P., and Liphardt, J. (2005) Calibration of dynamic molecular rulers based on plasmon coupling between gold nanoparticles. *Nano Lett. 5*, 2246–2252.

(6) Ghosh, S. K., and Pal, T. (2007) Interparticle coupling effect on the surface plasmon resonance of gold nanoparticles: from theory to applications. *Chem. Rev. 107*, 4797–4862.

(7) Chien, W.-Y., and Szkopek, T. (2008) Multiple-multipole simulation of optical nearfields in discrete metal nanosphere assemblies. *Opt. Express 16*, 1820–1835.

(8) Li, W., Camargo, P. H. C., Lu, X., and Xia, Y. (2009) Dimers of silver nanospheres: Facile synthesis and their use as hot spots for surface-enhanced Raman scattering. *Nano Lett. 9*, 485–490.

(9) Lim, D.-K., Jeon, K.-S., Kim, H. M., Nam, J.-M., and Suh, Y. D. (2010) Nanogap-engineerable raman-active nanodumbbells for single-molecule detection. *Nat. Mater. 9*, 60–67.

(10) Myroshnychenko, V., Rodríguez-Fernández, J., Pastoriza-Santos, I., Funston, A. M., Novo, C., Mulvaney, P., Liz-Marzánb, L. M., and de Abajo, F. J. G. (2008) Modeling the optical response of gold nanoparticles. *Chem. Soc. Rev. 37*, 1792–1805.

(11) Alivisatos, A. P., Johnsson, K. P., Peng, X. G., Wilson, T. E., Loweth, C. J., Bruchez Jr, M. P., and Schultz, P. G. (1996) Organization of 'nanocrystal molecules' using DNA. *Nature 382*, 609–611.

(12) Zanchet, D., Micheel, C. M., Parak, W. J., Gerion, D., and Alivisatos, A. P. (2001) Electrophoretic isolation of discrete Au nanocrystal/DNA conjugates. *Nano Lett. 1*, 32–35.

(13) Deng, Z. X., Tian, Y., Lee, S. H., Ribbe, A. E., and Mao, C. D. (2005) DNA-encoded self-assembly of gold nanoparticles into one-dimensional arrays. *Angew. Chem., Int. Ed. 44*, 3582–3585.

(14) Zheng, J., Constantinou, P. E., Micheel, C., Alivisatos, A. P., Kiehl, R. A., and Seeman, N. C. (2006) Two-dimensional nanoparticle arrays show the organizational power of robust DNA motifs. *Nano Lett. 6*, 1502–1504.

(15) Aldaye, F. A., and Sleiman, H. F. (2006) Sequential self-assembly of a DNA hexagon as a template for the organization of gold nanoparticles. *Angew. Chem., Int. Ed. 45*, 2204–2209.

(16) Aldaye, F. A., and Sleiman, H. F. (2007) Dynamic DNA templates for discrete gold nanoparticle assemblies: control of geometry, modularity, write/erase and structural switching. *J. Am. Chem. Soc. 129*, 4130–4131.

(17) Lee, J. H., Wernette, D. P., Yigit, M. V., Liu, J. W., Wang, Z. D., and Lu, Y. (2007) Site-specific control of distances between gold nanoparticles using phosphorothioate anchors on DNA and a short bifunctional molecular fastener. *Angew. Chem., Int. Ed. 46*, 9006–9010.

(18) Lee, J. S., Lytton-Jean, A. K. R., Hurst, S. J., and Mirkin, C. A. (2007) Silver nanoparticle-oligonucleotide conjugates based on DNA with triple cyclic disulfide moietie. *Nano Lett. 7*, 2112–2115.

(19) Bidault, S., de Abajo, F. J. G., and Polman, A. (2008) Plasmon-based nanolens assembled on a well-defined DNA template. *J. Am. Chem. Soc. 130*, 2750–2751.

(20) Claridge, S. A., Liang, H. W., Basu, S. R., Fréchet, J. M. J., and Alivisatos, A. P. (2008) Isolation of discrete nanoparticle-DNA conjugates for plasmonic applications. *Nano Lett. 8*, 1202–1206.

(21) Park, S. Y., Lytton-Jean, A. K. R., Lee, B., Weigand, S., Schatz, G. C., and Mirkin, C. A. (2008) DNA-programmable nanoparticle crystallization. *Nature 451*, 553–556.

(22) Nykypanchuk, D., Maye, M. M., van der Lelie, D., and Gang, O. (2008) DNA-guided crystallization of colloidal nanoparticles. *Nature 451*, 549–552.

(23) Mastroianni, A. J., Claridge, S. A., and Alivisatos, A. P. (2009) Pyramidal and chiral groupings of gold nanocrystals assembled using DNA scaffolds. *J. Am. Chem. Soc. 131*, 8455–8459.

(24) Sharma, J., Chhabra, R., Cheng, A., Brownell, J., Liu, Y., and Yan, H. (2009) Control of self-assembly of DNA tubules through integration of gold nanoparticles. *Science 323*, 112–116.

(25) Letsinger, R. L., Elghanian, R., Viswanadham, G., and Mirkin, C. A. (2000) Use of a steroid cyclic disulfide anchor in constructing gold nanoparticle-oligonucleotide conjugates. *Bioconjugate Chem. 11*, 289–291.

(26) Li, Z., Jin, R. C., Mirkin, C. A., and Letsinger, R. L. (2002) Multiple thiol-anchor capped DNA-gold nanoparticle conjugates. *Nucleic Acids Res. 30*, 1558–1562.

(27) Dougan, J. A., Karlsson, C., Smith, W. E., and Graham, D. (2007) Enhanced oligonucleotide-nanoparticle conjugate stability using thioctic acid modified oligonucleotides. *Nucleic Acid Res. 35*, 3668–3675.

(28) Sharma, J., Chhabra, R., Andersen, C. S., Gothelf, K. V., Yan, H., and Liu, Y. (2008) Toward reliable gold nanoparticle patterning on self-assembled DNA nanoscaffold. *J. Am. Chem. Soc. 130*, 7820–7821.

(29) Sharma, J., Chhabra, R., Yan, H., and Liu, Y. (2008) A facile in situ generation of dithiocarbamate ligands for stable gold nanoparticle-oligonucleotide conjugates. *Chem. Commun.* 2140–2142.

(30) Stakenborg, T., Peeters, S., Reekmans, G., Laureyn, W., Jans, H., Borghs, G., and Imberechts, H. (2008) Increasing the stability of DNA-functionalized gold nanoparticles using mercaptoalkanes. *J. Nanopart. Res. 10*, 143–152.

(31) Mei, B. C., Oh, E., Susumu, K., Farrell, D., Mountziaris, T. J., and Mattoussi, H. (2009) Effects of ligand coordination number and surface curvature on the stability of gold nanoparticles in aqueous solutions. *Langmuir 25*, 10604–10611.

(32) Suzuki, K., Hosokawa, K., and Maeda, M. (2009) Controlling the number and positions of oligonucleotides on gold nanoparticles. *J. Am. Chem. Soc. 131*, 7518–7519.

BC100160K

Supporting Information

Stable Gold Nanoparticle Conjugation to Internal DNA Positions: Facile Generation of Discrete Gold Nanoparticle-DNA Assemblies

*Yongqiang Wen, Christopher K. McLaughlin, Pik Kwan Lo, Hua Yang, Hanadi F. Sleiman**

Department of Chemistry, McGill University, 801 Sherbrooke Street West, Montreal, Quebec H3A 2K6, Canada.

E-mail: hanadi.sleiman@mcgill.ca

Contents

I. General
II. Instrumentation
III. DNA Synthesis
IV. Confirmation of Hybridized Structures by Non-denaturing PAGE
V. DNA-AuNP conjugation and Characterization
VI. References

I. General

Tris(hydroxymethyl)-aminomethane (Tris), boric acid, acetic acid, ethylenediamine-tetraacetic acid, NaCl, $MgCl_2.6H_2O$, StainsAll®, formamide, and ethidium bromide were purchased from Aldrich. 1,2-Dithiane-4-O-Dimethoxytrityl-5-[(2-cyanoethyl)- N,N-diisopropyl]-phosphoramidite (DTPA) was purchased form Glen Research Corporation. 5-ethylthiotetrazole, CPG and reagents used for automated DNA synthesis were purchased from ChemGenes. Sephadex G-25 (super fine DNA grade), was purchased from Amersham Biosciences. Microcon® size-exclusion centrifugal filter devices were purchased from Millipore. Citrate coated gold nanoparticles were either made in-house or purchased from Ted Pella. The ligand bis(*p*-sulfonatophenyl) phenylphosphine dihydrate dipotassium salt (BSPP) was purchased from Strem Chemicals. 400 mesh Formvar-carbon coated copper grids for transmission electron microscopy imaging were purchased from Electron Microscopy Sciences.

II. Instrumentation

Standard automated oligonucleotide solid-phase synthesis was performed on either a Perspective Biosystems Expedite 8900 DNA synthesizer or MM6 Mermade Synthesizer (Bioautomation). UV-vis experiments were conducted on a Varian Cary 300 biospectrophotometer. Gel electrophoresis experiments were carried out on an acrylamide 20 × 20 cm vertical Hoefer 600 electrophoresis unit or 7 × 8 cm horizontal Owl separation minigel system. Transmission electron microscopy (TEM) images were obtained using a Philips CM 200 200 kV electron microscope.

III. DNA Synthesis

Modified oligonucleotides were constructed on CPG supports (1000 Angstrom) using conventional phosphoramidite chemistry. Products were cleaved from the support by treatment with concentrated NH_4OH for 16 h at 55 °C. The NH_4OH solution was carefully pipetted out and dried down to yield the crude DNA mixture. The crude mixture was purified on 24% polyacrylamide/7 M urea gels using 0.09 M Tris-borate-EDTA buffer (pH 8.3). Gels were illuminated briefly with UV light to visualize DNA bands which were excised, crushed and incubated in 10 mL of sterile water at 55°C (16 hours). The tubes were then vortexed and briefly centrifuged to condense acyrlamide. The supernatant was removed and the volume brought to ca. 1 mL under heat/reduced pressure in a speedvac system. DNA samples were then desalted using Sephadex G-25 size exclusion media. Quantification was estimated based on UV-vis absorbance at 260 nm.

For the sequences modified by one or more **D** inserts in the middle, the first arm, of appropriate sequence, was initially grown on the solid support using standard automated solid phase oligonucleotide synthetic protocols. **D** was then incorporated using a modified protocol in which the coupling and deprotection times were extended to ten and two minutes, respectively. Subsequently, the second arm was synthesized using standard synthetic protocols.

DNA Sequences used for AuNP Conjugation Experiments

All sequences written 5′ → 3′

1$_a$: AATTGATATGTCACGAATAACACAAATCGGTCAGTAATCT**D**CT
TGAAGGTAGCAAACGACAGGTCCAAATGAAGATACGAA
1$_b$: TCATTGCTTCAGTATCTAAGTAGTAGTGACCACTAGCTCT**D**TT
CGTATCTTCATTTGGACCTGTCGTTTGCTACCTTCAAC

1_c: AGAGCTAGTGGTCACTACTACTTAGATACTGAAGCAATGA**D**T
GAGGCAGATAAGGATAGGACTTTTGGAGACTACGACGGA
1_d: AGATTACTGACCGATTTGTGTTATTCGTGACATATCAATT**D**TC
CGTCGTAGTCTCCAAAAGTCCTATCCTTATCTGCCTCA
EXT-1_a:
TTTTTTTTTTTTTTTTTTTTTTTTTTTTTTTTTTTTTTTTTTAGAGCTAGTGGTCA
CTTCGTATCTTCATTTG GACCT
DISP-1_a: AGGTCCAAATGAAGATACGAAGTGACCACTAGCTCT
2: TCAGTATCGTATCTTT**D**TCCTTGGACCTGTCGTGTTT**D**TTGCCTTCTCTACTTC
EXT-2:
TTTTTTTTTTTTTTTTTTTTTTTTTTTTTTTTTATCCACACGACAGGTCCAACGGCA
TTTTTTTTTTTTTTTTTTTTTTTTTTTTTTT
DISP-2: TGCCGTTGGACCTGTCGTGTGGAT
3:
DTTGAAGTAGAGAAGGCATTTAACACGACAGGTCCAAGGTTTAAGATACGATAC
TGATT**D**
EXT-3: TTTTTTTTTTTTTTTTTTTTATCCAGAACACGACAGGTCCAAGGTCGGCA
TTTTTTTTTTTTTTTTTTT
DISP-3: TGCCGACCTTGGACCTGTCGTGTTCTGGAT

IV. Confirmation of Hybridized Structures by Non-Denaturing PAGE

Annealed structures **I** and **II** were initially verified by polyacrylamide gel electrophoresis (PAGE) under non-denaturing conditions. In a typical experiment, samples of each building block in the correct molar ratios (final assembly 1.2×10^{-10} moles; 30 μL PBS) were added in PBS (pH 7.4, 10mM, 100 mM NaCl) and incubated at room temperature for 10 minutes. All of the final assemblies were characterized using 7 % native polyacrylamide gel (run at constant current of 10 mA, 4 °C and visualized using StainsAll®). As an example, Figure S1 shows the hybrdization of both square structure **I** and linear tetra-**D** mfunctionalized **II**. Strand **1_a** alone showed a band of relatively high mobility (Fig. S1a, lane 1). The assemblies of two, three, and four building blocks showed well-defined, single bands of steadily decreasing mobility. This behavior is consistent with the clean and quantitative formation of discrete duplex assemblies containing the desired number of building blocks in each case. The addition of the fourth building block is expected to result in both duplex formation and subsequent cyclization (lane 4 in Figure S1a). In addition, a second band of low mobility was detected, suggesting the concomitant formation of a small amount of higher order oligomeric species.

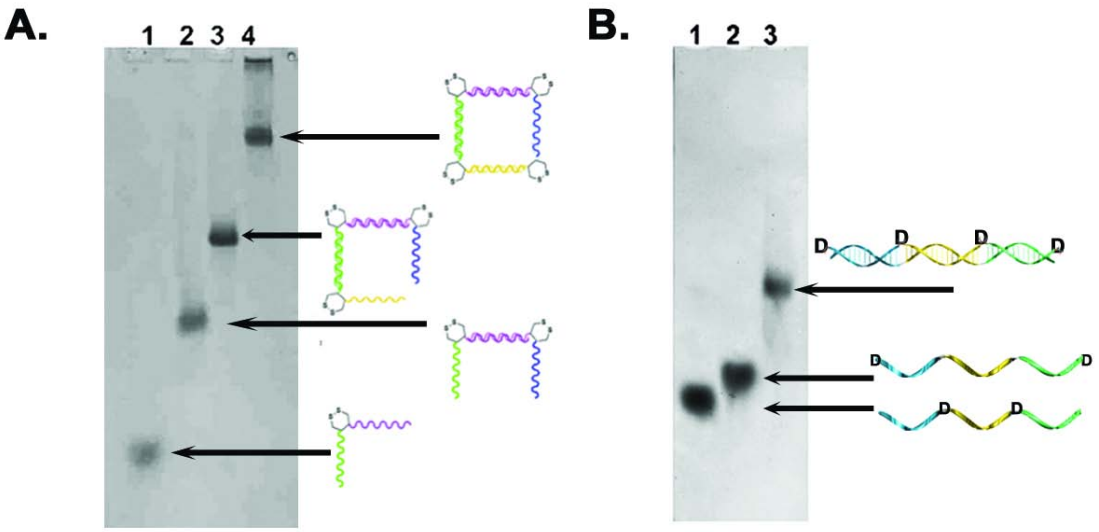


Figure S1 Native polyacrylamide gel (7%, 1x TAEMg) analysis of the assembly products. (a) Structure **I** was assembled by the sequential addition of $\mathbf{1}_{\mathbf{a\text{-}d}}$ (lanes 1-4, respectively) in PBS solution at room temperature . (b) Sequences **2** and **3** are annealed at room temperature in PBS solution to yield the tetra-subsituted nanostructure **II** in an excellent yield.

V. DNA-AuNP Conjugation and Characterization

Preparation and Phosphination of AuNPs

AuNPs were prepared by citrate reduction methods in the presence (5 nm)[S1] or absence (13 nm)[S2] of tannic acid as co-reductant. Both types of citrate coated AuNPs were further stabilized against aggregation via addition of BSPP.[S2] Briefly, 20 mg of BSPP was added to the 10 mL of AuNP solution and left overnight on a vortex mixer at low speed. Sodium Chloride (solid) was added slowly to the colloidal gold solutions until a colour change was observed from burgundy to purple. Resulting mixtures were centrifuged at 4000 rpm for 30 min and the supernatant removed and discarded. The pelleted AuNPs were then resuspended in 100 μL of a BSPP solution (2.5 mM). AuNPs were quantified by assaying the optical absorbance at 520 nm.

General Protocol for AuNP-DNA Conjugation

In general, 1 x 10^{-11} moles of AuNPs (3.3 uM) were used in conjugation experiments for both 5 and 13 nm AuNPs. Varying molar ratios of DNA based on the above moles of AuNPs were used for conjugation experiments to account for any inaccuracy in the quantified AuNP solutions. Typically, appropriate DNA volumes, based on the required moles, were taken from stock solutions and dried to completion. The DNA was then resuspended in an appropriate volume of PBS (10 mM, 100mM NaCl) that would bring the AuNP concentration to 3.3 uM. AuNPs were added to the resuspended DNA with slight mixing and samples were

left overnight at room temperature. The resulting AuNP-DNA conjugates were loaded onto an agarose gel (3% for 5 nm and 2.5% for 13 nm) and run at 10V/cm in 0.5x TBE running buffer. In the case of conjugates requiring extension strands, the appropriate **EXT** strand was added in the correct molar ratio (initially dried down and resuspended in a minimal volume of PBS) with slight mixing and left to stand at room temperature for 10 minutes prior to being loaded onto an agarose gel. Monoconjugate bands were isolated after AGE by electroelution into glass fiber backed with dialysis membrane (MWCO 10000). After removal of the dialysis membrane, the glass fiber containing the AuNP conjugates were placed into a 0.6 μL centrifuge tube that had a small hole fitted in the bottom with a syringe needle. This centrifuge tube was then placed into a 1.5 mL centrifuge tube and spun at 500 rpm for 5 minutes. The AuNP-DNA conjugates were then carefully pipetted into a clean centrifuge tube. Quantification of monoconjugates was estimated by obtaining the absorbance at 520 nm and samples stored at 4 ^{o}C. If necessary, monoconjugate solutions were further concentrated using microcon filtration devices (MWCO 3000). From the estimated concentrations, the correct molar ratio of the appropriate displacement strand could be calculated that is required to remove the extension strands.

Agarose Gel Electrophoresis (AGE) Analysis of Au_2-3

Sequence **3**, modifed with **D** at both the 5′ and 3′ positions, was conjugated with 13 nm AuNPs in a similar fashion as outlined in the above section. One modification was that only 1/6 the volume of AuNP conjugates were loaded onto the agarose gel. Due to an approximate 10-fold increase in the extinction coefficient, it is easier to visualize the larger particles by AGE. As revealed in the agarose gel found in Figure S4, incubation of **3** with AuNPs in a number of molar ratios (DNA:AuNP- 1:1-lane 1, 2:1-lane 2, 3:1-lane 3) generated a discrete product band upon addition of **EXT-3**. This band was then isolated and quantified as outlined in the previous section.

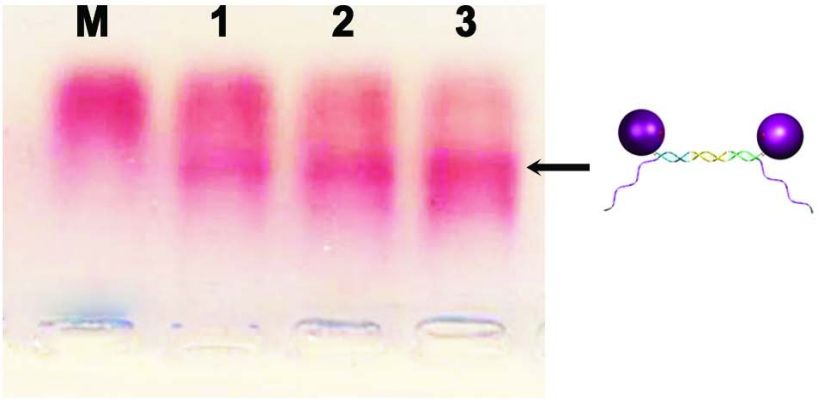


Figure S2 Characterization of Au_2-3 conjugation. AGE analysis (2.5%, 0.5x TBE) of doubly-**D** modified **3** conjugated with AuNPs (15 nm) with **3**:AuNP ratios of 1:1 (lane 1), 2:1 (lane 2) and 3:1 (lane 3). **EXT-3** has been added to each experiment prior to separation. Unconjugated 15 nm AuNPs were run as a control (lane M).

Transmission electron microscopy (TEM)

TEM was performed using a Philips CM 200 kV electron microscope. 3 - 5 μL of dilute sample in 0.5xTBE buffer was spotted on the surface of Formvar-coated copper TEM grids. The sample was left on the grid for 3 min to allow particles to adsorb to the surface before touching the edge of the grid with a filter paper to wick off excess moisture and salts. Grids were then allowed to air-dry prior to analysis. Additional TEM support for all hybridized AuNP structures can be found in Figures S3-S8.

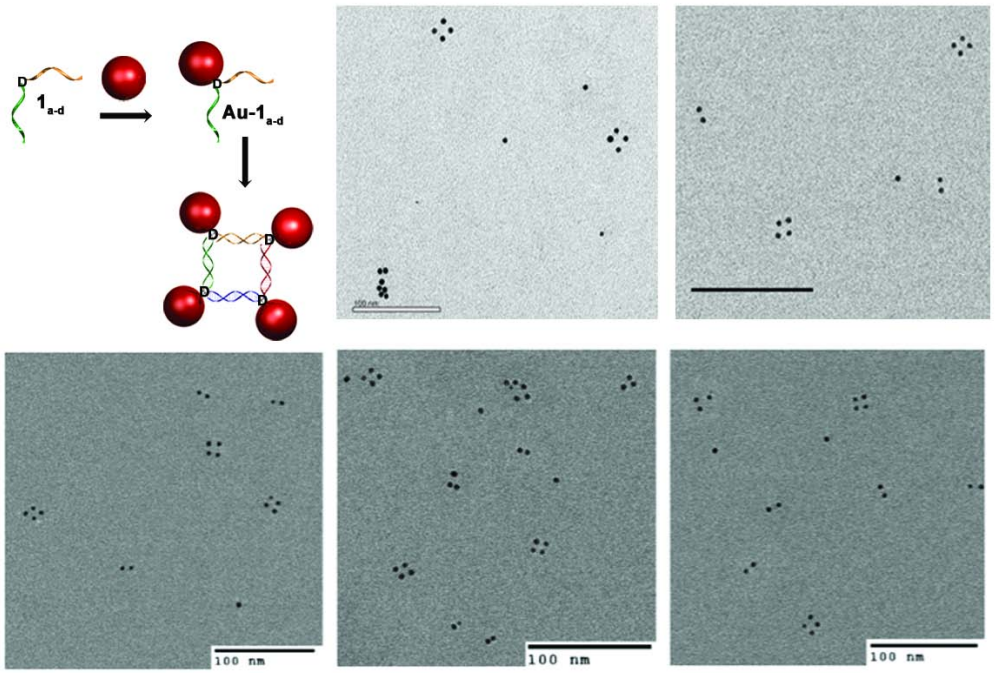


Figure S3 Additional TEM fields of view obtained for I. Square **I** was produced from **Au-1_{a-d}** in ca. 41% yield.

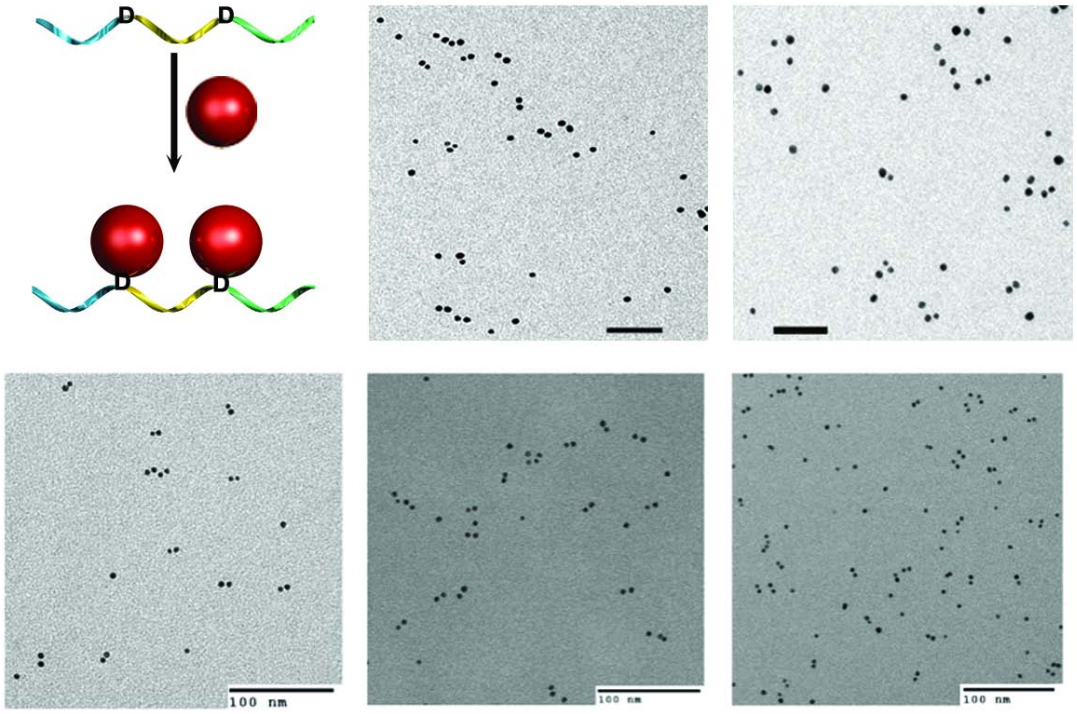


Figure S4 Additional TEM fields of view obtained for Au_2-2. The dimer of 5 nm AuNPs **Au_2-2** was produced in ca. 75% yield.

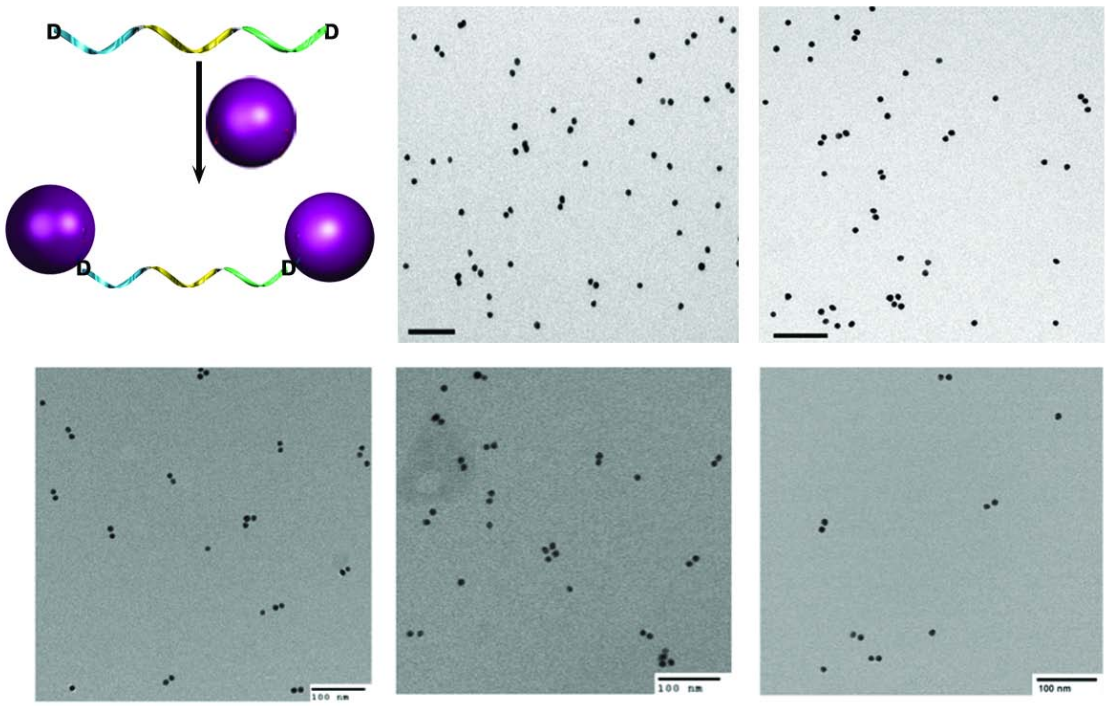


Figure S5 Additional TEM fields of view obtained for Au_2-3. The dimer of 15 nm AuNPs **Au_2-3** was produced in ca. 75% yield.

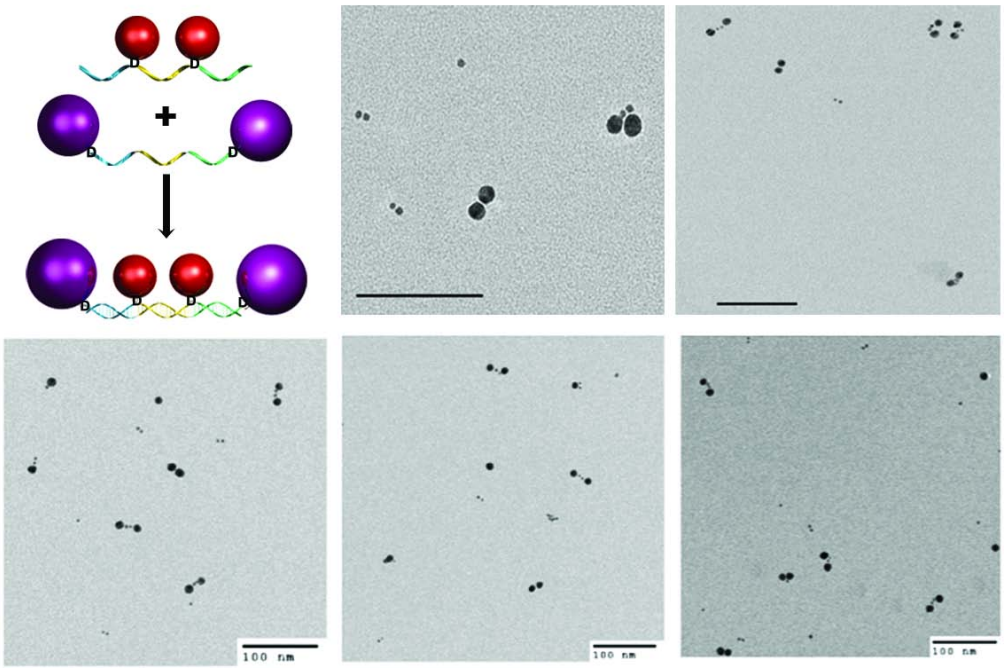


Figure S6 Additional TEM fields of view obtained for structure II. The tetrameric mixed AuNP structure **II**, prepared from **Au_2-2** and **Au_2-3**, was produced in ca. 38% yield.

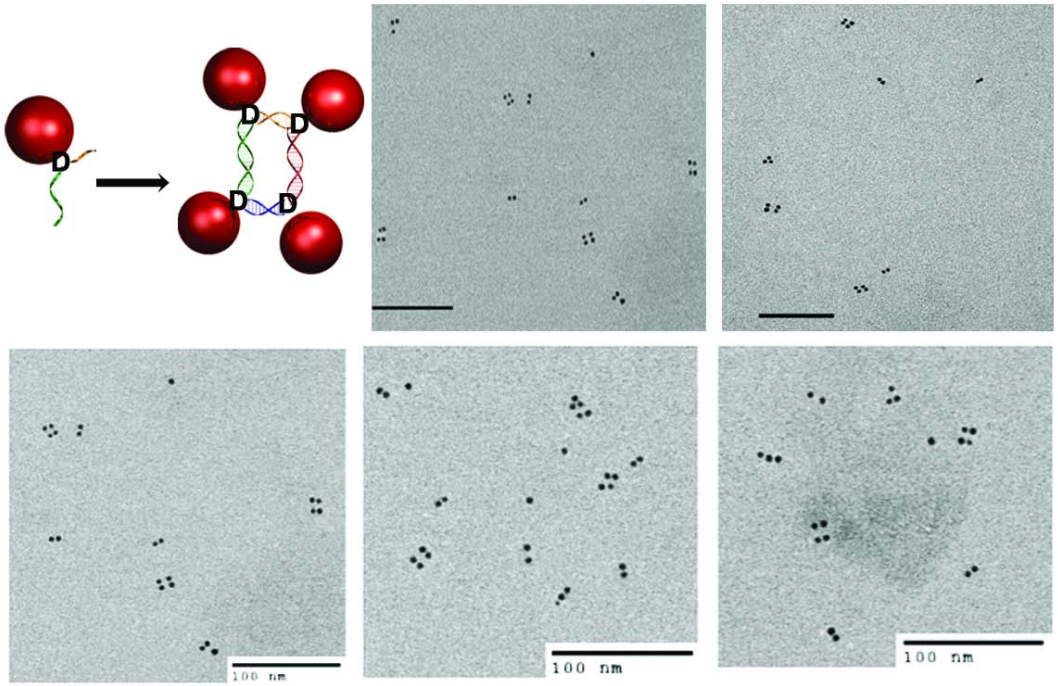


Figure S7 Additional TEM fields of view obtained for structure III. The rectangular AuNP structure **III** was prepared in ca. 37% yield.

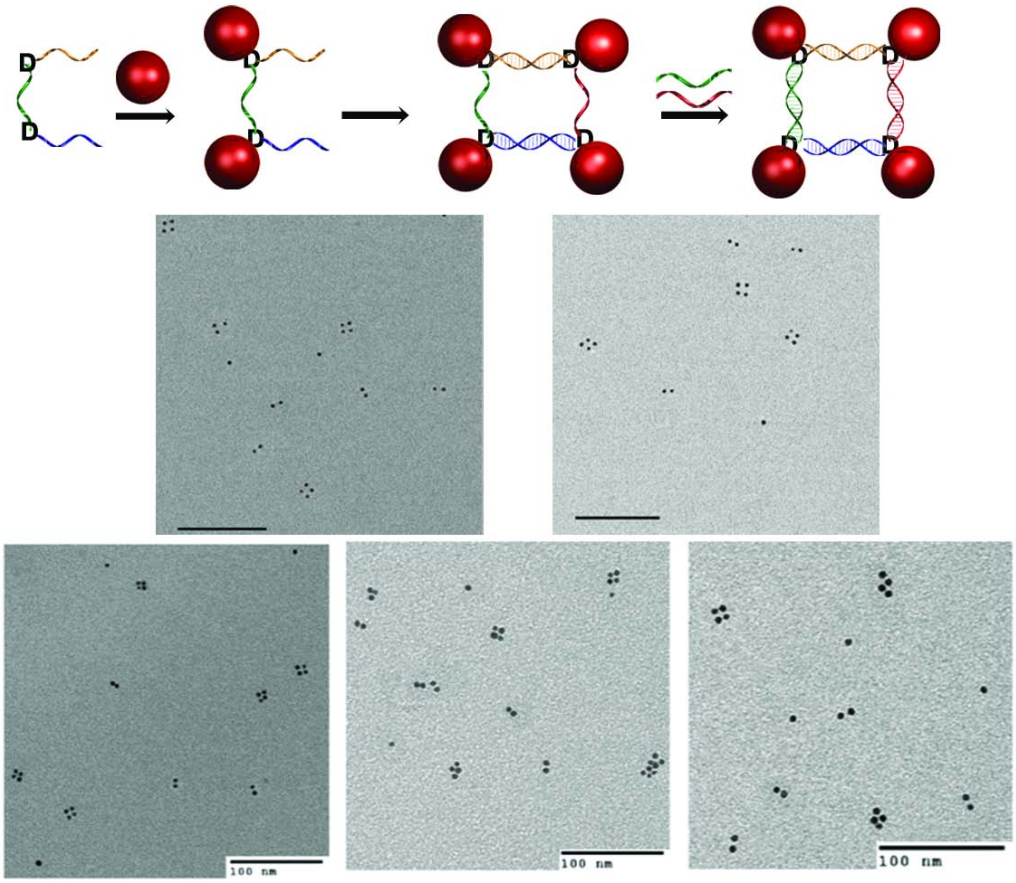


Figure S8 Additional TEM fields of view obtained for structure IV. The square AuNP structure **IV** was prepared in ca. 48% yield.

Reference:

(1) D. A. Handley (1989) *Colloidal Gold: Principles, Methods and Applications Vol. 1* (Hayat, M. A., Ed.) pp 13-22, Academic press, San Diego.

(2) T.A. Taton (2002) Preparation of Gold Nanoparticle–DNA Conjugates. *Current Protocols in Nucleic Acid Chemistry*. pp 12.2.1-12.2.12.

Evaluation of Copper-64 Labeled AmBaSar Conjugated Cyclic RGD Peptide for Improved MicroPET Imaging of Integrin $\alpha_v\beta_3$ Expression

Hancheng Cai, Zibo Li, Chiun-Wei Huang, Anthony H. Shahinian, Hui Wang, Ryan Park, and Peter S. Conti*

Molecular Imaging Center, Keck School of Medicine, University of Southern California, Los Angeles, California 90033.
Received December 5, 2009; Revised Manuscript Received July 13, 2010

Recently, we have developed a new cage-like bifunctional chelator 4-((8-amino-3,6,10,13,16,19-hexaazabicyclo [6.6.6] icosane-1-ylamino) methyl) benzoic acid (AmBaSar) for copper-64 labeling and synthesized the positron emission tomography (PET) tracer ^{64}Cu-AmBaSar-RGD. In this study, we further evaluate the biological property of this new AmBaSar chelator by using ^{64}Cu-AmBaSar-RGD as the model compound. *In vitro* and *in vivo* stability, lipophilicity, cell binding and uptake, microPET imaging, receptor blocking experiments, and biodistribution studies of ^{64}Cu-AmBaSar-RGD were investigated, and the results were directly compared with the established radiotracer ^{64}Cu-DOTA-RGD. The ^{64}Cu-AmBaSar-RGD was obtained with high radiochemical yield (≥95%) and purity (≥99%) under mild conditions (pH 5.0−5.5 and 23−37 °C) in less than 30 min. For *in vitro* studies, the radiochemical purity of ^{64}Cu-AmBaSar-RGD was more than 97% in PBS or FBS and 95% in mouse serum after 24 h of incubation. The log *P* value of ^{64}Cu-AmBaSar-RGD was −2.44 ± 0.12. For *in vivo* studies, ^{64}Cu-AmBaSar-RGD and ^{64}Cu-DOTA-RGD have demonstrated comparable tumor uptake at selected time points on the basis of microPET imaging. The integrin $\alpha_v\beta_3$ receptor specificity was confirmed by blocking experiments for both tracers. Compared with ^{64}Cu-DOTA-RGD, ^{64}Cu-AmBaSar-RGD demonstrated much lower liver accumulation in both microPET imaging and biodistribution studies. Metabolic studies also directly supported the observation that ^{64}Cu-AmBaSar-RGD was more stable *in vivo* than ^{64}Cu-DOTA-RGD. In summary, the *in vitro* and *in vivo* evaluations of the ^{64}Cu-AmBaSar-RGD have demonstrated its improved Cu-chelation stability compared with that of the established tracer ^{64}Cu-DOTA-RGD. The AmBaSar chelator will also have general applications for ^{64}Cu labeling of various bioactive molecules in high radiochemical yield and high *in vivo* stability.

INTRODUCTION

The advancement of molecular imaging based on positron emission tomography (PET) is mainly driven by the discovery of imaging biomarkers and targeted molecules labeled with positron emitting radioisotopes (*1*−*3*). PET tracers have been widely applied in molecular imaging as these agents exhibit high binding affinity toward various promising biological targets, such as receptors or enzymes expressed during different phases of tumor growth or in other uncontrolled diseases (*3, 4*). Targeted copper-64 labeled molecules have shown promise for diagnostic PET imaging, as well as for radiotherapy, due to the favorable nuclear characteristics of the isotope ($t_{1/2}$ = 12.7 h, β^+ 17.4%, E_{max} = 0.656 MeV, β^- 39%, E_{max} = 0.573 MeV) and its availability with high specific activity (*5*). The half-life of ^{64}Cu is more suitable for developing biomolecule-based PET tracers, which usually require longer circulation times to achieve optimal targeting and uptake. Furthermore, ^{64}Cu-based PET tracers may be used to provide *in vivo* pharmacokinetic profiles of radiopharmaceuticals which contain the therapeutic radionuclide copper-67 ($t_{1/2}$ = 61.5 h, β^- 100%, E_{max} =0.121 MeV) (*6*). *In vivo* stable attachment of $^{64}Cu^{2+}$ to targeted biomolecules requires the use of a bifunctional chelator (BFC) (*7*). More and more ligands have been investigated as BFCs to complex $^{64}Cu^{2+}$ due to the development of copper coordination chemistry. Three of the most common chelators for $^{64}Cu^{2+}$ labeling are the macrocyclic ligands 1,4,7,10-tetraazacyclododecane-*N*,*N*′,*N*″,*N*‴-tetraacetic acid (DOTA), 1,4,8,11-tetraazacyclotetradecane-*N*,*N*′,*N*″,*N*‴-tetraacetic acid (TETA), and cross-bridged TETA ligands (*2, 5, 7, 8*). It is well known that DOTA, TETA, and their derivatives for $^{64}Cu^{2+}$ labeling have limited stability *in vivo* due to the dissociation of $^{64}Cu^{2+}$ from these BFCs, leading to high retention in the liver. A class of cross-bridged TETA derivatives has been developed that form stable complexes with $^{64}Cu^{2+}$ and are less susceptible to *in vivo* transchelation than their nonbridged TETA analogues (*9*). However, harsh $^{64}Cu^{2+}$ radiolabeling conditions (e.g., incubation at 85 °C under basic conditions) for cross-bridged TETA derivatives may result in the denaturation and hydrolysis of some biomolecules (*10*). Recently, a new class of bifunctional chelators has been synthesized on the basis of the sarcophagine (3,6,10,13,16,19-hexaazabicyclo [6.6.6] icosane, also called Sar) for $^{64}Cu^{2+}$ radiolabeling, resulting in extraordinarily stable ^{64}Cu-Sar based complexes *in vitro* and *in vivo* under physiological conditions (*11, 12*). The carboxylate and amino derivatives of the diamSar have also been developed by our group and Smith's group, respectively (*13*−*16*). These derivatives allow them to be readily cross-linked to amine or carboxyl residues on peptides and antibody molecules through amide bonds, yielding PET probes with improved pharmacokinetics, and dynamics due to the increased stability (*1, 15*).

The integrin $\alpha_v\beta_3$ receptor has been the attractive target of intensive research given its major role in several distinct processes, such as tumor angiogenesis and metastasis, and osteoclast mediated bone resorption (*17, 18*). The molecular imaging of integrin $\alpha_v\beta_3$ expression will allow the detection of cancer and other angiogenesis related diseases, patient stratification, and treatment monitoring of antiangiogenesis based therapy (*19, 20*). Although we and others have successfully developed various DOTA conjugated RGD peptides for multimodality imaging of integrin $\alpha_v\beta_3$ expression (*19*−*23*), the loss of ^{64}Cu from the chelator has led to unfavorable high

* To whom correspondence should be addressed. E-mail: pconti@usc.edu.

10.1021/bc900537f © 2010 American Chemical Society
Published on Web 07/28/2010

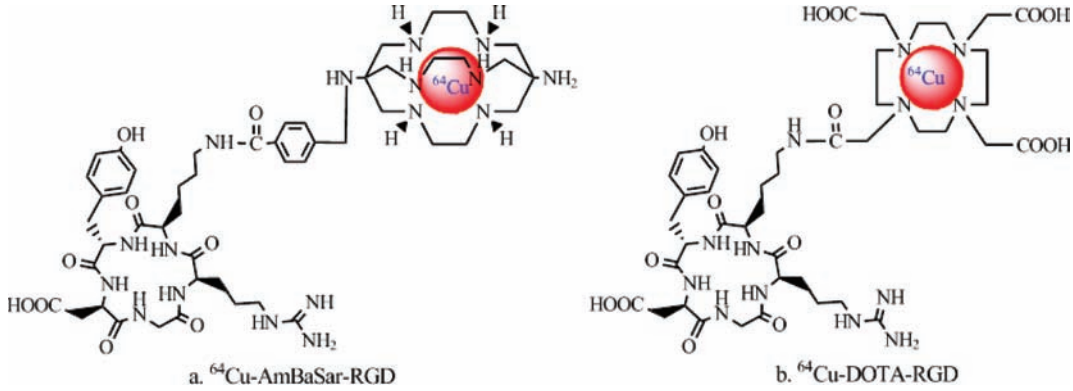


Figure 1. Chemical structures of ^{64}Cu-AmBaSar-RGD and ^{64}Cu-DOTA-RGD.

retention in the liver, resulting in high background. Therefore, the choice of a more stable BFC is preferred. As we mentioned above, we have developed a carboxylate derivative of diamSar, 4-((8-amino-3,6,10,13,16,19-hexaazabicyclo [6.6.6] icosane-1-ylamino) methyl) benzoic acid (AmBaSar) (*15, 16*), which could be conjugated to the primary amines in biomolecules through amide bonds. We also reported the synthesis of a new PET tracer ^{64}Cu-AmBaSar-RGD (Figure 1a). In this study, we further evaluated the conjugation and labeling conditions of ^{64}Cu-AmBaSar-RGD. Moreover, the *in vitro* and *in vivo* stability, lipophilicity, cell uptake, microPET imaging, and biodistribution studies of ^{64}Cu-AmBaSar-RGD and the established ^{64}Cu-DOTA-RGD (Figure 1b) were investigated to obtain a direct comparison of the two agents.

EXPERIMENTAL PROCEDURES

General. All reagents and solvents were purchased from Sigma-Aldrich Chemicals (St. Louis, MO, USA) and used without further purification unless otherwise stated. *N*,*N*-Diisopropylethylamine (DIPEA), 1-hydroxy-7-azabenzotriazole (HOAt), *O*-(7-azabenzotriazol-1-yl)-1,1,3,3-tetramethyluronium hexafluorophosphate (HATU), and Chelex 100 resin (50−100 mesh) were obtained from the Sigma-Aldrich Chemical Co. The c(RGDyK) peptide was purchased from Peptides International, Inc. (Louisville, KY, USA). DOTA was purchased from Macrocyclics (Dallas, TX, USA). The chelator AmBaSar was prepared following a method developed in our laboratory (*16*). $^{64}CuCl_2$ solution was ordered from University of Wisconsin (Madison, WI) or Washington University School of Medicine (St. Louis, MO), which both were produced through the ^{64}Ni(p,n)^{64}Cu nuclear reaction. Water was purified using a Milli-Q ultrapure water system from Millipore (Milford, MA, USA), followed by passing through a Chelex 100 resin before bioconjugation and radiolabeling.

Analytic and semipreparative reversed phase high performance liquid chromatography (HPLC) were accomplished on two Waters 515 HPLC pumps, a Waters 2487 absorbance UV detector, and a Ludlum Model 2200 radioactivity detector, which were operated by Waters Empower 2 software. The purification of AmBaSar, DOTA conjugated c(RGDyK) peptides, and ^{64}Cu-labeled peptides were performed on a Phenomenex Luna C18 reversed phase column (5 μm, 250 × 10 mm). The flow rate was 3 mL/min for semipreparative HPLC, with the mobile phase starting from 98% solvent A (0.1% TFA in water) and 2% solvent B (0.1% TFA in acetonitrile) (0−2 min) to 60% solvent A and 40% solvent B at 40 min. The separation was monitored using a radiodetector and UV at 218 and 254 nm. The analytic HPLC was performed with the same mobile phase gradient system and detection, except that a Phenomenex Luna C18 reversed phase analytic column (5 μm, 250 × 4.6 mm) was used at a flow rate of 1 mL/min. For the *in vivo* stability study, analytical HPLC was operated at the same conditions with a Rainin Microsorb-MV C18 column (5 μm, 250 × 4.6 mm) and the mobile phase starting from 98% solvent A and 2% solvent B (0−2 min) to 50% solvent A and 50% solvent B at 25 min. Radio-TLC was performed on MKC18 silica gel 60 Å plates (Whatman, NJ) with MeOH/20% NaOAc = 3:1 as the eluent. The plates were read with a Bioscan AR2000 imaging scanner (Washington, DC) and Winscan 2.2 software. Mass spectrometry using LC-MS was operated by the Proteomics Core Facility of the USC School of Pharmacy.

Syntheses of AmBaSar-RGD and DOTA-RGD. AmBaSar could be activated and conjugated to the c(RGDyK) peptide in a water-soluble procedure as reported earlier (*15*). The conjugation can also be performed in organic phase according to literature procedures (*24, 25*). Briefly, the solution of AmBaSar (4.5 mg, 0.01 mmol), HATU (3.8 mg, 0.01 mmol), HOAt (1.4 mg, 0.01 mmol), and dimethyl sulfoxide (DMSO, 0.5 mL) were stirred at room temperature for 10 min. Seven equivalents of DIPEA (9.1 mg, 0.07 mmol) and c(RGDyK) (1.2 mg, 0.002 mmol) in 300 μL of DMSO were then added to the mixture at 0 °C. The mixture was stirred for 3 h at room temperature, and the solvent removed *in vacuo*. The residue was dissolved in acetonitrile/water (1:3) containing 0.1% TFA and purified by semipreparative HPLC. AmBaSar-RGD was obtained as a white solid material after lyophilization. DOTA was activated and conjugated to c(RGDyK) as reported earlier (*23*). DOTA-RGD was also purified by semipreparative HPLC and confirmed by mass spectrometry. AmBaSar-RGD and DOTA-RGD conjugates were dissolved in 0.1 N ammonium acetate buffer solution (pH 5−5.5) and stored at −20 °C for future use in radiolabeling reactions.

Copper-64 Labeling and Formulation. The ^{64}Cu-AmBaSar-RGD was prepared using a method developed in our laboratory (*15*) with minor modifications as follows: [^{64}Cu]Acetate ($^{64}Cu(OAc)_2$) was prepared by adding 37−111 MBq of $^{64}CuCl_2$ in 0.1 N HCl into 300 μL of 0.1 N ammonium acetate buffer (pH 5.0−5.5), followed by mixing and incubating for 15 min at room temperature. The AmBaSar-RGD (about 2−5 μg in 100 μL 0.1 N ammonium acetate buffer) was added to the above $^{64}Cu(OAc)_2$ solution. The resulting mixture was incubated at a temperature of 23−37 °C for 30 min. The ^{64}Cu-AmBaSar-RGD was determined and purified by semipreparative HPLC. The radioactive peak containing ^{64}Cu-AmBaSar-RGD was collected and concentrated by rotary evaporation to remove organic solvent, and the radioactivity was reconstituted in 500−800 μL of phosphate buffered saline (PBS) and passed through a 0.22 μm Millipore filter into a sterile dose vial for use in the experiments below.

Details of the ^{64}Cu-labeling DOTA-RGD procedure were reported earlier (*23*). Briefly, 37−111 MBq of $^{64}CuCl_2$ in 0.1 N HCl was diluted in 300 μL of 0.1 N ammonium acetate buffer

(pH 5.5) and added to the DOTA-RGD solution (about 2−5 μg in 100 μL of 0.1 N ammonium acetate buffer). The reaction mixture was incubated at 45 °C for 45 min. The radiochemical yield was determined by radio-TLC and HPLC. ^{64}Cu-DOTA-RGD was then purified by semipreparative HPLC, and the radioactive peak containing the desired product was collected. After removal of the solvent by rotary evaporation, the residue was reconstituted in 500−800 μL of PBS and passed through a 0.22 μm Millipore filter into a sterile multidose vial for use in the following experiments.

Determination of log *P* Value. The partition coefficient value was expressed as log *P*. log *P* of ^{64}Cu-AmBaSar-RGD was determined by measuring the distribution of radioactivity in 1-octanol and PBS. A 5 μL sample of ^{64}Cu-AmBaSar-RGD in PBS was added to a vial containing 1 mL each of 1-octanol and PBS. After vigorously vortexing for 10 min, the vial was centrifuged for 5 min to ensure the complete separation of layers. Then, 3 × 10 μL of each layer was pipetted into other test tubes, and radioactivity was measured using a gamma counter (Perkin-Elmer Packard Cobra). The measurement was repeated three times, and log *P* values were calculated according to a known formula.

***In Vitro* Stability Assay.** The *in vitro* stability of ^{64}Cu-AmBaSar-RGD and ^{64}Cu-DOTA-RGD was studied at different time points. Briefly, 3.7 MBq of ^{64}Cu-AmBaSar-RGD and ^{64}Cu-DOTA-RGD was pipetted into 1 mL of PBS, fetal bovine serum (FBS), and mouse serum, respectively. After incubation at 37 °C for 3, 18, and 24 h, an aliquot of the mixture was removed from the PBS solution and the radiochemical purity was determined with HPLC. For the solution of FBS and mouse serum, the aliquots were added to 100 μL of PBS with 50% TFA. After centrifugation, the upper solution was taken and filtered for HPLC analysis.

Integrin Receptor Binding Assay and Cell Uptake Study. U87MG human glioblastoma cell line (integrin $\alpha_v\beta_3$-positive) was obtained from the American Type Culture Collection (ATCC, Manassas, VA) and maintained under standard conditions according to ATCC as follows: the U87MG glioma cells were grown in Gibco's Dulbecco's medium supplemented with 10% fetal bovine serum (FBS), 100 IU/mL penicillin, and 100 μg/mL streptomycin (Invitrogen Co, Carlsbad, CA), at 37 °C in humidified atmosphere containing 5% CO_2. The U87MG glioma cells were grown in culture until sufficient cells were available.

The *in vitro* integrin-binding affinity and specificity of AmBaSar-RGD and RGD were assessed via competitive cell binding assays using ^{125}I-echistatin as the integrin $\alpha_v\beta_3$-specific radioligand by a minor modification of a method previously described (*26*, *27*). In detail, U87MG cells were harvested, washed three times with PBS, and resuspended (2×10^6 cells/mL) in the binding buffer. Filter multiscreen DV plates (96-well, pore size, 0.65 μm, Millipore) were seeded with 10^5 cells and incubated with ^{125}I-echistatin (0.74 kBq/well) in the presence of increasing concentrations of different RGD peptide analogues (0−1,000 nmol/L). The total incubation volume was adjusted to 200 μL. After the cells were incubated for 2 h at room temperature, the plates were filtered through a multiscreen vacuum manifold and washed three times with binding buffer. The hydrophilic polyvinylidenedifluoride (PVDF) filters were collected, and the radioactivity was determined using a gamma counter. The best-fit 50% inhibitory concentration (IC_{50}) values for U87MG cells were calculated by fitting the data with nonlinear regression using GraphPad Prism (GraphPad Software, Inc.). Experiments were performed on triplicate samples.

The cell uptake study was performed as described with some modifications (*25*). Cells were incubated with ^{64}Cu-AmBaSar-RGD (37 kBq/well) or ^{64}Cu-DOTA-RGD at 37 °C for 30 min, 60 min, and 120 min. The blocking experiment was performed by incubating U87MG cells with ^{64}Cu-AmBaSar-RGD (37 kBq/well) in the presence of 2 μg of c(RGDyK). The tumor cells were then washed three times with chilled PBS and harvested by 0.1 N NaOH solution containing 0.5% sodium dodecyl sulfate (SDS). The cell suspensions were collected and measured in a gamma counter.

Animal Model. Athymic nude mice (about 10−20 weeks old, with a body weight of 25−35 g) were obtained from Harlan (Charles River, MA). All animal experiments were performed according to a protocol approved by the University of Southern California Institutional Animal Care and Use Committee. The U87MG human glioma xenograft model was generated by a subcutaneous injection of 5×10^6 U87MG human glioma cells into the front flank of athymic nude mice. The tumors were allowed to grow 3−5 weeks until 200−500 mm^3 in volume. Tumor growth was followed by caliper measurements of the perpendicular dimensions.

MicroPET Imaging and Blocking Experiment. MicroPET scans and imaging analysis were performed using a rodent scanner (microPET R4; Siemens Medical Solutions) as previously reported (*26*). About 11.1 MBq of ^{64}Cu-AmBaSar-RGD or ^{64}Cu-DOTA-RGD was intravenously injected into each mouse under isoflurane anesthesia. Ten minute static scans were acquired at 1, 2, 4, and 20 h post-injection. The images were reconstructed by a 2-dimensional ordered-subsets expectation maximum (OSEM) algorithm. For each microPET scan, regions of interest were drawn over the tumor, normal tissue, and major organs on the decay-corrected whole-body coronal images. The radioactivity concentration (accumulation) within the tumor, muscle, liver, and kidneys were obtained from the mean value within the multiple regions of interest and then converted to % ID/g. For the receptor blocking experiment, mice bearing U87MG tumors were scanned (10 min static) at the 2 h time point after the coinjection of 11.1 MBq of ^{64}Cu-AmBaSar-RGD or ^{64}Cu-DOTA-RGD with 10 mg/kg c(RGDyK) per mouse.

Biodistribution Studies. The U87MG tumor bearing nude mice ($n = 3$) were injected with 0.37 MBq of ^{64}Cu-AmBaSar-RGD or ^{64}Cu-DOTA-RGD to evaluate the biodistribution of these tracers. All mice were sacrificed and dissected at 20 h after the injection of the tracers. Blood, U87MG tumor, major organs, and tissues were collected and weighed wet. The radioactivity in the tissues was measured using a gamma counter. The results were presented as the percentage injected dose per gram of tissue (% ID/g). For each mouse, the radioactivity of the tissue samples was calibrated against a known aliquot of the injected activity. The mean uptake (% ID/g) for each group of animals was calculated with standard deviations.

Metabolic Stability. The metabolic stabilities of ^{64}Cu-AmBaSar-RGD and ^{64}Cu-DOTA-RGD were evaluated in an athymic nude mouse bearing a U87MG tumor. Sixty minutes after the intravenous injection of 11.1 MBq of ^{64}Cu-AmBaSar-RGD or ^{64}Cu-DOTA-RGD, the mouse was sacrificed, and the relevant organs were harvested. The blood was collected immediately and centrifuged for 5 min at 14,000 rpm. Then, 50% TFA in 100 μL of PBS was added to the upper serum solution, followed by mixing and centrifugation for 5 min. The upper solution was then taken and injected for HPLC analysis. The liver, kidneys, and tumor were homogenized using a homogenizer, suspended in 1 mL of PBS buffer, and then centrifuged for 5 min at 14,000 rpm. For each sample, after the removal of the supernatant, 50% TFA in 100 μL PBS was added to the solution, followed by mixing and centrifugation for 5 min. The upper solution was then taken and injected for HPLC analysis. The eluent was collected with a fraction collector (1.5 min/fraction), and the radioactivity of each fraction was measured with a gamma counter.

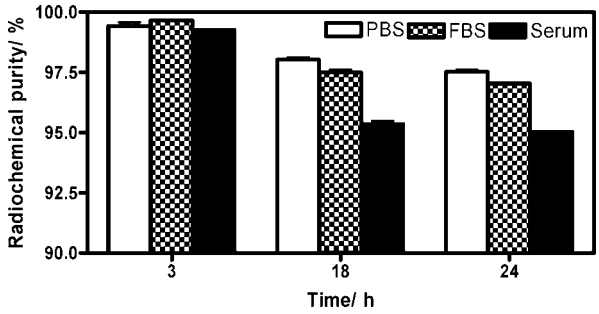


Figure 2. *In vitro* stability of ^{64}Cu-AmBaSar-RGD in PBS (pH 7.4), FBS, and mouse serum for incubation under 37 °C for 3, 18, and 24 h.

Statistical Analysis. Quantitative data were expressed as the mean ± SD. Means were compared using one-way ANOVA and Student'S *t* test. *P* values <0.05 were considered statistically significant.

RESULTS

Chemistry and Radiolabeling. The identity of AmBaSar-RGD and DOTA-RGD conjugates was confirmed by HPLC and mass spectrometry as previously reported (*15, 23*). The AmBaSar-RGD conjugate was obtained in about 80% yield after HPLC purification for both aqueous and organic phase procedures. The ^{64}Cu-labeling ($n = 7$) was achieved in more than 95% decay-corrected yield for ^{64}Cu-AmBaSar-RGD with a radiochemical purity of >99% and 80% radiochemical yield for ^{64}Cu-DOTA-RGD with a radiochemical purity >98%. ^{64}Cu-AmBaSar-RGD and ^{64}Cu-DOTA-RGD were analyzed and purified by HPLC. The HPLC retention times of ^{64}Cu-AmBaSar-RGD and ^{64}Cu-DOTA-RGD were 26.5 and 21.5 min, respectively, under the analytical conditions. For radio-TLC analysis, the free $^{64}Cu^{2+}$ remained at the origin of the TLC plate, while the R_f values of ^{64}Cu-DOTA-RGD and ^{64}Cu-AmBaSar-RGD were about 0.8−1.0. The specific activity of ^{64}Cu-DOTA-RGD and ^{64}Cu-AmBaSar-RGD was estimated to be about 10.1−22.2 GBq/μmol. Both tracers were used immediately after the formulation.

log *P* Value and *in Vitro* Stability. The octanol/water partition coefficients (log *P*) for ^{64}Cu-AmBaSar-RGD and ^{64}Cu-DOTA-RGD were −2.44 ± 0.12 and −2.80 ± 0.04, respectively (*23*), which demonstrated that both tracers are rather hydrophilic. The *in vitro* stability of ^{64}Cu-AmBaSar-RGD was also studied in PBS (pH 7.4), FBS, and mouse serum for different time intervals (3, 18, and 24 h) at physiological temperature of 37 °C. The stability was presented as the percentage of intact ^{64}Cu-AmBaSar-RGD on the basis of the HPLC analysis, and the results are shown in Figure 2. After 24 h of incubation, more than 97% of ^{64}Cu-AmBaSar-RGD remained intact in the PBS and FBS, and more than 95% of ^{64}Cu-AmBaSar-RGD remained intact in mouse serum. We also found that ^{64}Cu-DOTA-RGD demonstrated similar stability results *in vitro* under the above experimental conditions (data not shown).

***In Vitro* Cell Binding Affinity and Uptake.** We compared the receptor-binding affinity of AmBaSar-RGD and c(RGDyK) using a competitive cell-binding assay (Figure 3A). All peptides inhibited the binding of ^{125}I-echistatin to $\alpha_v\beta_3$ integrin-positive U87MG cells in a dose-dependent manner. The IC_{50} value for AmBaSar-RGD (53.26 ± 0.51 nmol/L) was comparable to that of c(RGDyK) (36.55 ± 0.65 nmol/L). These results had shown that chelator (such as AmBaSar or DOTA) conjugation had a minimal effect on the receptor-binding avidity (*27*).

The cell uptake study of ^{64}Cu-AmBaSar-RGD or ^{64}Cu-DOTA-RGD was performed on U87MG tumor cells, and the cell uptake was expressed as radioactivity (cpm) per 10^6 cells after decay correction as shown in Figure 3B. The cell uptake study revealed that both ^{64}Cu-AmBaSar-RGD and ^{64}Cu-DOTA-RGD could bind to U87MG tumor cells, but relatively low amounts of activity (only about 0.1−0.4% was internalized). However, this binding could be efficiently blocked by an excess amount of cold c(RGDyK) peptide, which demonstrated the binding specificity of the radiolabeled ligands.

MicroPET Imaging. The tumor-targeting efficacy and biodistribution patterns of ^{64}Cu-AmBaSar-RGD and ^{64}Cu-DOTA-RGD were evaluated in nude mice bearing U87MG human glioma xenograft tumors ($n = 3$) at multiple time points (1, 2, 4, and 20 h) with static microPET scans. Representative decay-corrected coronal images at different time points were shown in Figure 4A. The U87MG tumors were clearly visualized with high tumor-to-background contrast for both tracers. The uptake of ^{64}Cu-AmBaSar-RGD in U87MG tumors was 2.04 ± 0.14, 1.85 ± 0.16, 1.87 ± 0.11, and 0.97 ± 0.05% ID/g at 1, 2, 4, and 20 h p.i., respectively. ^{64}Cu-DOTA-RGD demonstrated similar tumor uptake with the value of 2.03 ± 0.10, 1.97 ± 0.05, 1.88 ± 0.29, and 0.88 ± 0.07% ID/g at the above time points, respectively (Figure 4B). However, the biodistribution patterns of ^{64}Cu-AmBaSar-RGD and ^{64}Cu-DOTA-RGD were significantly different, especially in the kidneys and liver. The renal uptake of ^{64}Cu-AmBaSar-RGD were 2.83 ± 0.77, 2.68 ± 0.55, 2.49 ± 0.50, and 1.43 ± 0.35% ID/g at 1, 2, 4, and 20 h p.i., respectively, while the corresponding uptake for ^{64}Cu-DOTA-RGD was 1.52 ± 0.46, 1.33 ± 0.23, 1.55 ± 0.61, and 1.58 ± 0.13% ID/g, respectively. This was lower than that of ^{64}Cu-AmBaSar-RGD from 1 to 4 h, and reached comparable levels at the 20 h time point. The liver uptake for ^{64}Cu-AmBaSar-RGD was 0.89 ± 0.13, 0.76 ± 0.13, 0.75 ± 0.14, and 0.64 ± 0.06% ID/g at 1, 2, 4, and 20 h p.i.. The corresponding uptake value for ^{64}Cu-DOTA-RGD was 2.28 ±

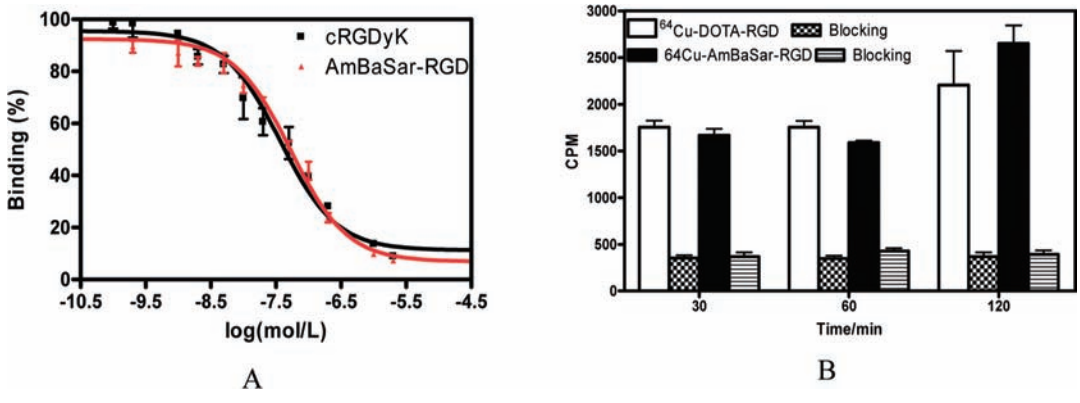


Figure 3. *In vitro* cell integrin receptor binding assay and cell uptake study. (A) *In vitro* inhibition of ^{125}I-echistatin binding to integrin on U87MG cells by c(RGDyK), AmBaSar-RGD, and DOTA-RGD; (B) U87MG cell uptake of ^{64}Cu-AmBaSar-RGD and ^{64}Cu-DOTA-RGD at 0.5, 1, and 2 h in the absence/presence of an excess amount of c(RGDyK) peptide.

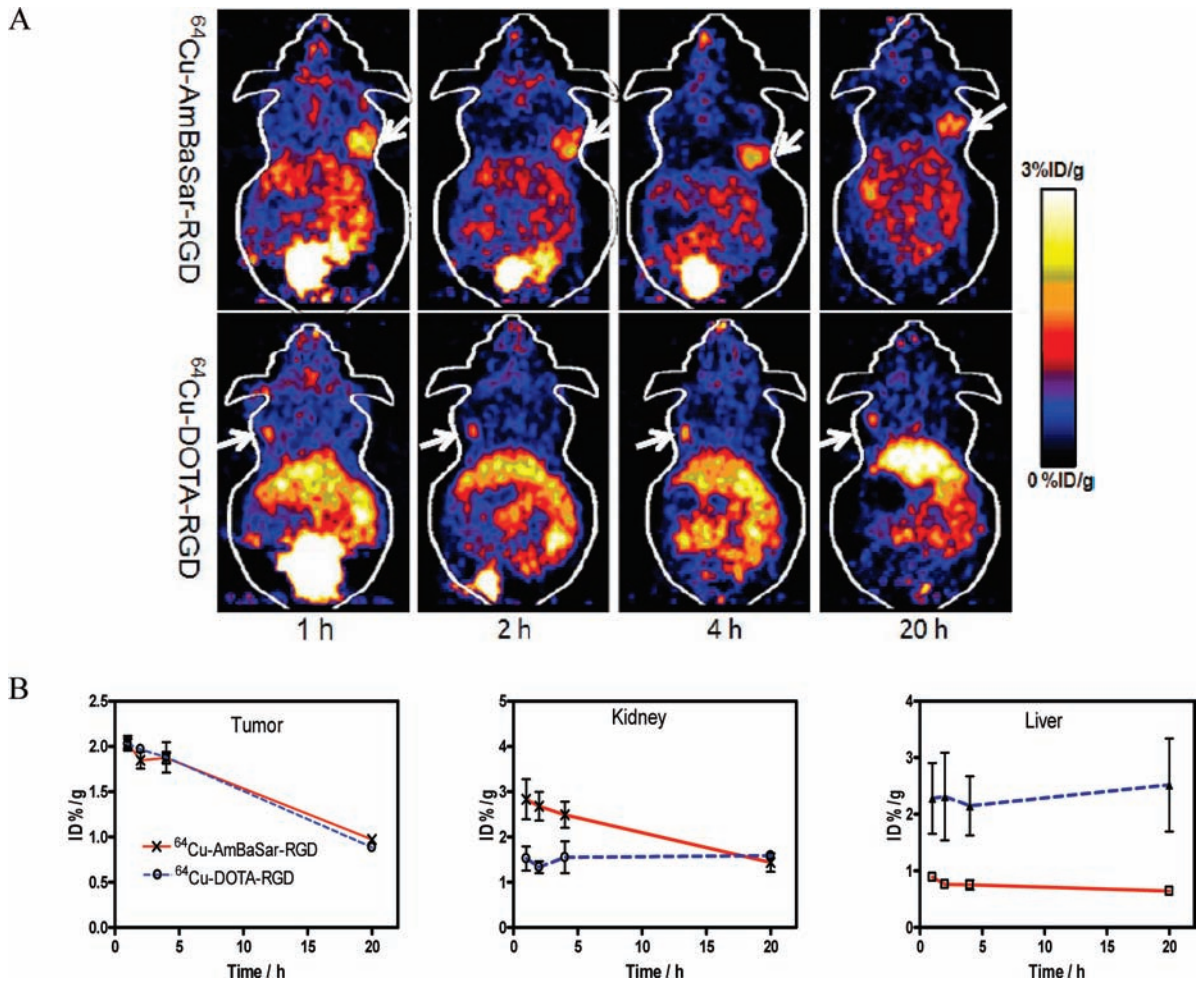


Figure 4. MicroPET study of U87MG tumor-bearing mice. (A) Coronal images of nude mice bearing the U87MG tumor at 1, 2, 4, and 20 h p.i. of ^{64}Cu-AmbaSar-RGD and ^{64}Cu-DOTA-RGD; (B) time activity curves of ^{64}Cu-AmBaSar-RGD and ^{64}Cu-DOTA-RGD in the U87MG tumor, liver, and kidneys ($n = 3$). Tumors are indicated by arrows.

1.08, 2.31 ± 1.34, 2.15 ± 0.90, and 2.52 ± 1.43% ID/g, respectively, which were significantly higher than those of ^{64}Cu-AmBaSar-RGD at all time points.

Blocking Experiment. The integrin $\alpha_v\beta_3$ receptor specificity of ^{64}Cu-AmBaSar-RGD was confirmed by a blocking experiment where the tracers were coinjected with the c(RGDyK) peptide (10 mg/kg). As can be seen from Figure 5, the U87MG tumor uptake in the presence of nonradiolabeled c(RGDyK) peptide (0.09 ± 0.03% ID/g) is significantly lower than that without c(RGDyK) peptide blocking (1.85 ± 0.16% ID/g) ($P < 0.05$) at 2 h p.i. The uptake of ^{64}Cu-AmBaSar-RGD in other organs (heart, intestine, kidneys, lungs, liver, and spleen) was also significantly decreased, which correlates well with previous references (*23*). Similarly, the integrin $\alpha_v\beta_3$ specificity of ^{64}Cu-DOTA-RGD was confirmed by blocking experiments (Figure 5).

Biodistribution Studies. To validate the accuracy of small animal PET quantification, we also performed a biodistribution experiment by using the direct tissue sampling technique. The data shown as the percentage administered activity (injected dose) per gram of tissue (% ID/g) in Figure 6A. Both ^{64}Cu-AmBaSar-RGD and ^{64}Cu-DOTA-RGD mainly accumulated in the kidneys, liver, stomach, intestine, and tumor. After 20 h p.i., the kidneys and liver uptake reached 1.51 ± 0.27 and 0.55 ± 0.06% ID/g for ^{64}Cu-AmBaSar-RGD and 0.98 ± 0.40 and 2.16 ± 0.85% ID/g for ^{64}Cu-DOTA-RGD, respectively. This difference was consistent with the excretion pattern from the microPET imaging results. On the basis of the biodistribution results, we also calculated the contrast of the tumor to main organs, which is shown in Figure 6B. For ^{64}Cu-AmBaSar-RGD, the ratio of tumor uptake to muscle, heart, lung, liver, and kidney uptake was 14.20 ± 3.84, 7.33 ± 1.55, 3.34 ± 0.70, 1.18 ± 0.05, and 0.43 ± 0.06, respectively, while the corresponding values for ^{64}Cu-DOTA-RGD were 5.97 ± 2.25, 1.78 ± 0.37, 1.27 ± 0.37, 0.33 ± 0.09, and 0.66 ± 0.04, respectively.

Metabolic Stability of ^{64}Cu-AmBaSar-RGD and ^{64}Cu-DOTA-RGD. The metabolic stability of ^{64}Cu-AmBaSar-RGD and ^{64}Cu-DOTA-RGD were determined in mouse blood and in liver, kidney, and tumor homogenates at 1 h after the intravenous injection of the radiotracer into a U87MG tumor-bearing mouse according to the literature procedures (*28*, *29*). The radioactivity of each sample was analyzed by HPLC, and the representative radio-HPLC profiles were shown in Figure 7. There was only one major radiolabeled metabolite with a retention time between 3.0 to 6.0 min. It has been well demonstrated that the cylic-RGDyk peptide is stable *in vivo*. Therefore, it is highly possible that this solvent front peak corresponds to free Cu. Nonetheless, its identity needs to be confirmed in our future studies. The amount of intact tracer in the blood, tumor, liver, and kidneys were approximately 88%, 95%, 98%, and 98% for ^{64}Cu-AmBaSar-RGD and 38%, 87%, 34%, and 74% for ^{64}Cu-DOTA-RGD at 1 h post-injection, respectively.

DISCUSSION

The established BFC DOTA is the most widely used Cu chelation ligand for molecular imaging and radiotherapy (*4*, *7*, *30*). DOTA has been conjugated to various macromolecules includ-

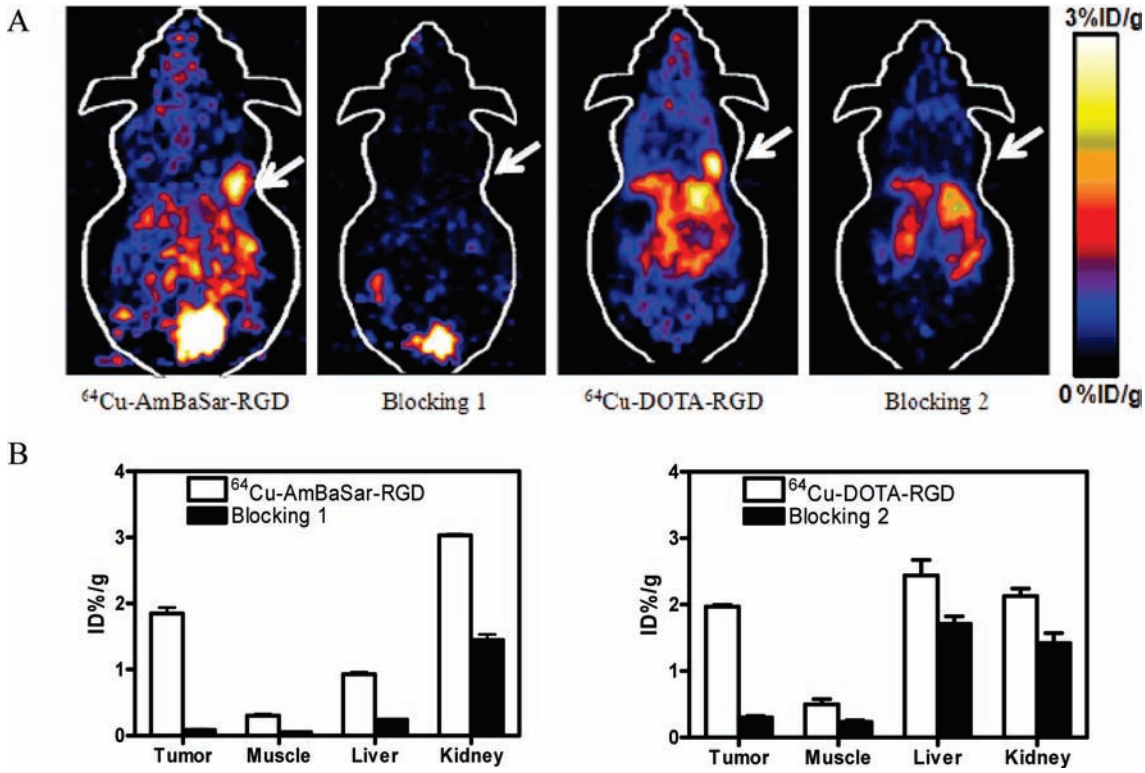


Figure 5. MicroPET imaging of ^{64}Cu-AmBaSar-RGD and ^{64}Cu-DOTA-RGD on the U87MG xenograft mouse model at 2 h p.i. with/without a blocking dose of c(RGDyK) peptide: (A) microPET coronal images. (B) Quantitative analyses of microPET imaging of the U87MG tumor, muscle, liver, and kidneys ($n = 3$). Arrows indicate the tumor positions.

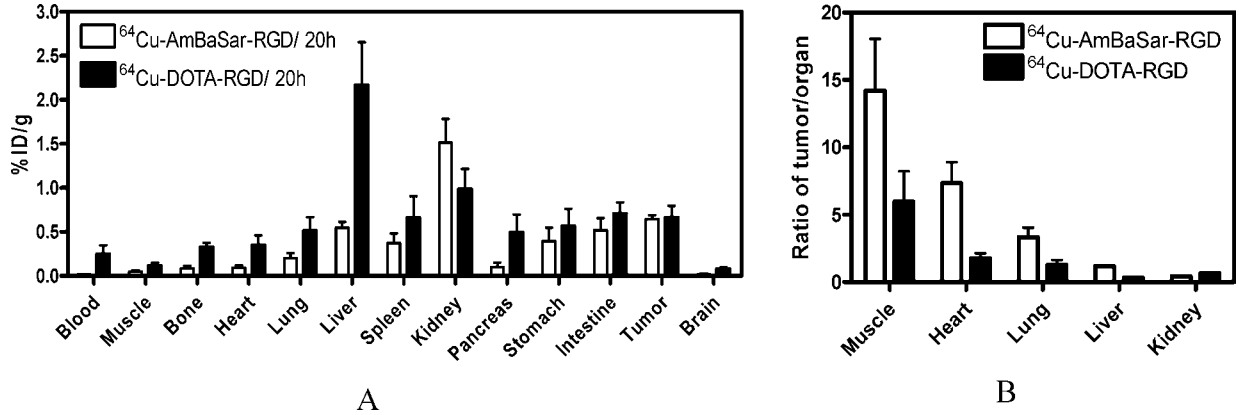


Figure 6. (A) Biodistribution data for ^{64}Cu-AmBaSar-RGD and ^{64}Cu-DOTA-RGD in mice bearing U87MG glioma xenografts (mean ± SD, $n = 3$) at 20 h p.i.; (B) the ratios of tumor to main organ uptake of ^{64}Cu-AmBaSar-RGD and ^{64}Cu-DOTA-RGD.

ing proteins (*31*), antibodies (*32*), peptides (*30*), as well as nanoparticles to track their distributions *in vivo* (*33, 34*). However, under physiological conditions, Cu may be removed from the Cu-DOTA complex and transferred to copper-binding proteins. The significant loss of Cu from the conjugate could lead to high uptake in the liver and fail to reflect the real distribution of the macromolecules. Therefore, the limited stability of the copper chelate *in vivo* has hindered its further applications (*5*). For example, although we have demonstrated that ^{64}Cu-DOTA-RGD could be a suitable tracer for PET imaging of integrin $\alpha_v\beta_3$ expression in breast cancer (*23*), unfavorable hepatobiliary excretion was also observed due to $^{64}Cu^{2+}$ dissociation from the DOTA-RGD conjugate *in vivo*. Recently, we have developed a new cage-like BFC AmBaSar for $^{64}Cu^{2+}$ labeling and demonstrated that this ^{64}Cu-complexing moiety is a superior ligand for imaging application and targeted radiotherapy due to its improved Cu-chelation stability compared with that of DOTA (*16*). We also reported the synthesis of a new PET tracer ^{64}Cu-AmBaSar-RGD that could be possibly used for imaging integrin $\alpha_v\beta_3$ expression (*15*). The objective of this study is to evaluate the $^{64}Cu^{2+}$ labeling and imaging ability of AmBaSar-RGD conjugates and compare the results with the established chelator DOTA using the DOTA-RGD peptide as the standard compound. These studies have demonstrated that ^{64}Cu-AmBaSar-RGD and ^{64}Cu-DOTA-RGD have comparable *in vitro* stability, lipophilicity, and tumor uptake. However, ^{64}Cu-AmBaSar-RGD did demonstrate improved *in vivo* stability and biodistribution pattern compared with those of ^{64}Cu-DOTA-RGD.

From the chemistry point of view, there were no obvious differences between the AmBaSar and DOTA conjugation to the c(RGDyK) peptide. Both chelators used a carboxylate group to directly conjugate with the lysine amine in the c(RGDyK) peptide in high yield. However, for radiochemistry, the $^{64}Cu^{2+}$ labeling condition of AmBaSar-RGD was more favorable, and the ^{64}Cu-AmBaSar-RGD could be obtained with higher radiochemical yield (≥95%) and purity (≥99%) under mild conditions (pH 5.0−5.5, 23−37 °C) in less than 30 min, compared

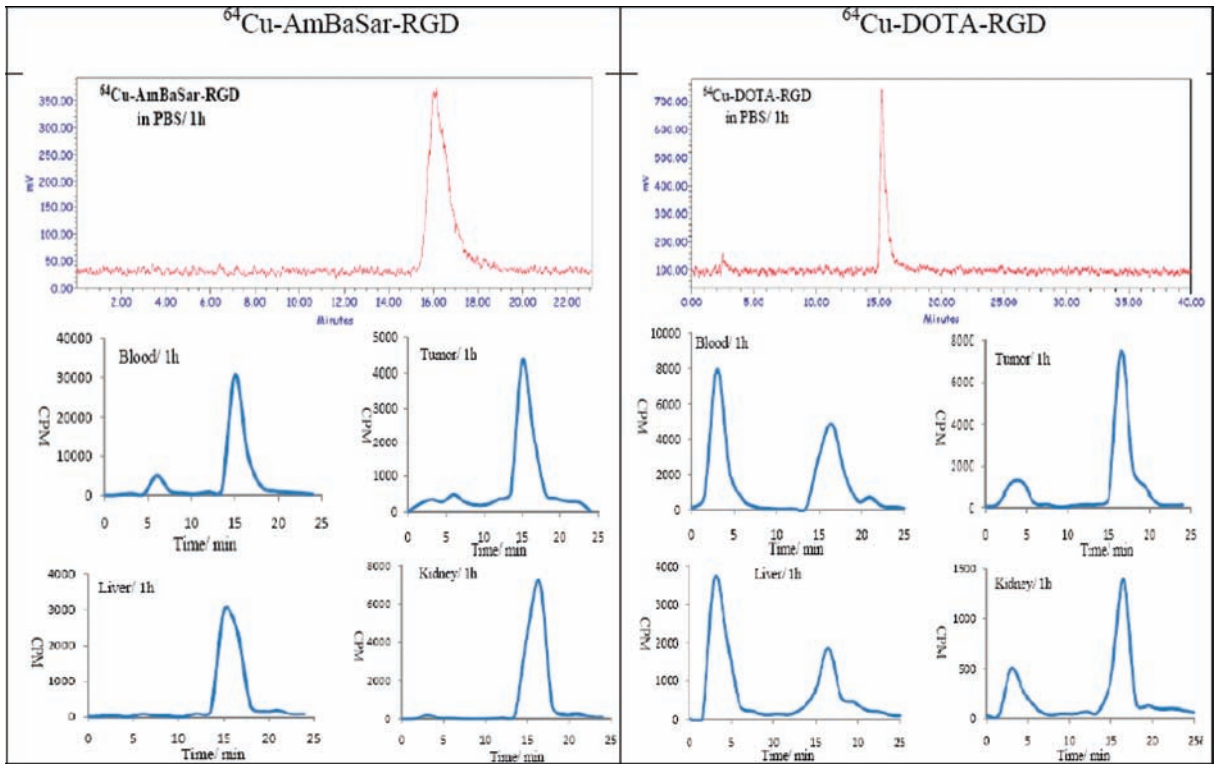


Figure 7. Metabolic stability of ^{64}Cu-AmBaSar-RGD and ^{64}Cu-DOTA-RGD in the mouse blood sample and in the liver, kidney, and U87MG tumor homogenates at 1 h post-injection. The HPLC profiles of pure ^{64}Cu-AmBaSar-RGD and ^{64}Cu-DOTA-RGD (standard) are also shown.

with 90% radiochemical yield for ^{64}Cu-DOTA-RGD after incubation at 45 °C for 45 min.

Under *in vitro* conditions, both ^{64}Cu-AmBaSar-RGD and ^{64}Cu-DOTA-RGD were very stable in PBS, FBS, and mouse serum solutions at physiological temperature. The log *P* value is a very useful parameter that can be used to understand the behavior of drug molecules and predict the distribution of a drug compound in a biological system in combination with other parameters (*35*). The log *P* values of ^{64}Cu-AmBaSar-RGD and ^{64}Cu-DOTA-RGD indicated that both tracers are rather hydrophilic and that they should show rapid blood clearance and preferential renal excretion if the Cu-chelation is stable *in vivo*. However, compared with ^{64}Cu-AmBaSar-RGD, ^{64}Cu-DOTA-RGD had significantly higher liver uptake (∼2−3 times) on the basis of the microPET imaging and biodistrbution studies, which indicated that ^{64}Cu-DOTA-RGD is less stable than ^{64}Cu-AmBaSar-RGD *in vivo*. In microPET studies, the U87MG tumor uptake of ^{64}Cu-AmBaSar-RGD and ^{64}Cu-DOTA-RGD were comparable at selected time points, and the binding specificity was proven by the blocking experiment. The biodistribution study was consistent with the microPET studies. Similar tumor uptake of both tracers may be attributed to their comparable hydrophilicity and the minimal impact of chelators on the integrin binding affinity of c(RGDyK) peptides (*36*). ^{64}Cu-AmBaSar-RGD cleared rapidly from the blood and predominantly through the kidneys, and ^{64}Cu-DOTA-RGD mainly cleared through both kidneys and liver. This difference might be because the Cu-chelation in ^{64}Cu-AmBaSar-RGD is more stable *in vivo* compared with that in ^{64}Cu-DOTA-RGD, which would result in reduced nonspecific binding. To further confirm this statement, we also studied the metabolic stability of ^{64}Cu-AmBaSar-RGD and ^{64}Cu-DOTA-RGD in blood, liver, kidneys, and tumors in nude mice bearing U87MG glioma xenografts after 1 h p.i. Our study clearly demonstrated that the amount of intact ^{64}Cu-AmBaSar-RGD was much higher than that of ^{64}Cu-DOTA-RGD in blood, tumor, liver, and kidneys. To the best of our knowledge, this is the first study that directly demonstrates that a Sar-type chelator, such as AmBaSar, forms a more stable Cu complex *in vivo* than the established chelator DOTA through direct comparison of their metabolic stability. We would also like to point out that the rapid renal clearance of ^{64}Cu-AmBaSar-RGD, as opposed to the mixed renal and hepatic clearance of ^{64}Cu-DOTA-RGD is preferred as it will provide better somatic contrast from the imaging perspective and potentially reduce radiation exposure.

CONCLUSIONS

^{64}Cu-AmBaSar-RGD was obtained in high yield under mild conditions for PET imaging of integrin $\alpha_v\beta_3$ expression. This tracer exhibited good tumor-targeting efficacy, excellent metabolic stability, as well as favorable *in vivo* pharmacokinetics. *In vitro* and *in vivo* evaluation of the ^{64}Cu-AmBaSar-RGD has demonstrated its improved *in vivo* Cu-chelation stability compared with that of the established tracer ^{64}Cu-DOTA-RGD. The AmBaSar chelator will also have a general application for ^{64}Cu labeling of various bioactive molecules in high radiochemical yield and high *in vivo* Cu-chelation stability for future PET applications.

ACKNOWLEDGMENT

This work was supported partially by research grant DE-SC0002353 from the Department of Energy, the USC Department of Radiology, and the Provost's Biomedical Imaging Science Initiative.

LITERATURE CITED

(1) Voss, S. D., Smith, S. V., DiBartolo, N., McIntosh, L. J., Cyr, E. M., Bonab, A. A., Dearling, J. L., Carter, E. A., Fischman, A. J., Treves, S. T., Gillies, S. D., Sargeson, A. M., Huston, J. S., and Packard, A. B. (2007) Positron emission tomography (PET) imaging of neuroblastoma and melanoma with ^{64}Cu-SarAr immunoconjugates. *Proc. Natl. Acad. Sci. U.S.A. 104*, 17489–17493.

(2) Shokeen, M., and Anderson, C. J. (2009) Molecular imaging of cancer with copper-64 radiopharmaceuticals and positron emission tomography (PET). *Acc. Chem. Res. 42*, 832–841.
(3) Eckelman, W. C., Reba, R. C., and Kelloff, G. J. (2008) Targeted imaging: an important biomarker for understanding disease progression in the era of personalized medicine. *Drug Discovery Today 13*, 748–759.
(4) Tanaka, K., and Fukase, K. (2008) PET (positron emission tomography) imaging of biomolecules using metal-DOTA complexes: a new collaborative challenge by chemists, biologists, and physicians for future diagnostics and exploration of in vivo dynamics. *Org. Biomol. Chem. 6*, 815–828.
(5) Wadas, T. J., Wong, E. H., Weisman, G. R., and Anderson, C. J. (2007) Copper chelation chemistry and its role in copper radiopharmaceuticals. *Curr. Pharm. Des 13*, 3–16.
(6) Blower, P. J., Lewis, J. S., and Zweit, J. (1996) Copper radionuclides and radiopharmaceuticals in nuclear medicine. *Nucl. Med. Biol. 23*, 957–980.
(7) Liu, S. (2008) Bifunctional coupling agents for radiolabeling of biomolecules and target-specific delivery of metallic radionuclides. *Adv. Drug Delivery Rev. 60*, 1347–1370.
(8) Smith, S. V. (2004) Molecular imaging with copper-64. *J. Inorg. Biochem 98*, 1874–1901.
(9) Anderson, C. J., Wadas, T. J., Wong, E. H., and Weisman, G. R. (2008) Cross-bridged macrocyclic chelators for stable complexation of copper radionuclides for PET imaging. *Q. J. Nucl. Med. Mol. Imaging 52*, 185–192.
(10) Ferreira, C. L., Yapp, D. T., Lamsa, E., Gleave, M., Bensimon, C., Jurek, P., and Kiefer, G. E. (2008) Evaluation of novel bifunctional chelates for the development of Cu-64-based radiopharmaceuticals. *Nucl. Med. Biol. 35*, 875–882.
(11) Sargeson, A. M. (1996) The potential for the cage complexes in biology. *Coord. Chem. Rev. 151*, 89–114.
(12) Smith, S. V. (2008) Sarar technology for the application of Copper-64 in biology and materials science. *Q. J. Nucl. Med. Mol. Imaging 52*, 193–202.
(13) DiBartolo, N., Sargeson, A. M., Donlevy, T. M., and Smith, S. V. (2001) Synthesis of a new cage ligand, SarAr, and its complexation with selected transition metal ions for potential use in radioimaging. *J. Chem. Soc., Dalton Trans.* , 2303–2309.
(14) DiBartolo, N., Sargeson, A. M., and Smith, S. V. (2006) New^{64}Cu PET imaging agents for personalised medicine and drug development using the hexa-aza cage, SarAr. *Org. Biomol. Chem. 4*, 3350–3357.
(15) Cai, H., Fissekis, J., and Conti, P. S. (2009) Synthesis of a novel bifunctional chelator AmBaSar based on sarcophagine for peptide conjugation and ^{64}Cu radiolabelling. *Dalton Trans.* , 5395–5400.
(16) Cai, H., Li., Z., Huang, C., Park, R., Shahinian, A., and Conti, P. S. (2010) An improved synthesis and biological evaluation of a new caged-like bifunctional chelator 4-((8-amino-3, 6, 10, 13, 16, 19- hexaazabicyclo [6.6.6] icosane-1-ylamino) methyl) benzoic acid (AmBaSar) for ^{64}Cu-radiopharmaceuticals. *Nucl. Med. Biol. 37*, 57–65.
(17) Varner, J. A., and Cheresh, D. A. (1996) Tumor angiogenesis and the role of vascular cell integrin $\alpha_v\beta_3$. *Important Adv. Oncol.* 69–87.
(18) Wadas, T. J., Deng, H., Sprague, J. E., Zheleznyak, A., Weilbaecher, K. N., and Anderson, C. J. (2009) Targeting the $\alpha_v\beta_3$ integrin for small-animal PET/CT of osteolytic bone metastases. *J. Nucl. Med. 50*, 1873–1880.
(19) Cai, W., and Chen, X. (2008) Multimodality molecular imaging of tumor angiogenesis. *J. Nucl. Med. 49* (2), 113S–128S.
(20) Schottelius, M., Laufer, B., Kessler, H., and Wester, H. J. (2009) Ligands for mapping $\alpha_v\beta_3$-integrin expression in vivo. *Acc. Chem. Res. 42*, 969–80.
(21) Liu, S. (2006) Radiolabeled multimeric cyclic RGD peptides as integrin $\alpha_v\beta_3$ targeted radiotracers for tumor imaging. *Mol. Pharmaceutics 3*, 472–487.
(22) Haubner, R., and Wester, H. J. (2004) Radiolabeled tracers for imaging of tumor angiogenesis and evaluation of anti-angiogenic therapies. *Curr. Pharm. Des. 10*, 1439–1455.
(23) Chen, X., Park, R., Tohme, M., Shahinian, A. H., Bading, J. R., and Conti, P. S. (2004) MicroPET and autoradiographic imaging of breast cancer α_v-integrin expression using ^{18}F- and ^{64}Cu-labeled RGD peptide. *Bioconjugate Chem. 15*, 41–49.
(24) Achilefu, S., Bloch, S., Markiewicz, M. A., Zhong, T., Ye, Y., Dorshow, R. B., Chance, B., and Liang, K. (2005) Synergistic effects of light-emitting probes and peptides for targeting and monitoring integrin expression. *Proc. Natl. Acad. Sci. U.S.A. 102*, 7976–7981.
(25) Decristoforo, C., Hernandez Gonzalez, I., Carlsen, J., Rupprich, M., Huisman, M., Virgolini, I., Wester, H. J., and Haubner, R. (2008) ^{68}Ga- and ^{111}In-labelled DOTA-RGD peptides for imaging of $\alpha_v\beta_3$ integrin expression. *Eur. J. Nucl. Med. Mol. Imaging 35*, 1507–1515.
(26) Li, Z., Cai, W., Cao, Q., Chen, K., Wu, Z., He, L., and Chen, X. (2007) ^{64}Cu-labeled tetrameric and octameric RGD peptides for small-animal PET of tumor $\alpha_v\beta_3$ integrin expression. *J. Nucl. Med. 48*, 1162–1171.
(27) Chen, X., Hou, Y., Tohme, M., Park, R., Khankaldyyan, V., Gonzales-Gomez, I., Bading, J. R., Laug, W. E., and Conti, P. S. (2004) Pegylated Arg-Gly-Asp peptide: ^{64}Cu labeling and PET imaging of brain tumor alphavbeta3-integrin expression. *J. Nucl. Med. 45*, 1776–1783.
(28) Juran, S., Walther, M., Stephan, H., Bergmann, R., Steinbach, J., Kraus, W., Emmerling, F., and Comba, P. (2009) Hexadentate bispidine derivatives as versatile bifunctional chelate agents for copper(II) radioisotopes. *Bioconjugate Chem. 20*, 347–359.
(29) Shi, J., Kim, Y. S., Zhai, S., Liu, Z., Chen, X., and Liu, S. (2009) Improving tumor uptake and pharmacokinetics of ^{64}Cu-labeled cyclic RGD peptide dimers with Gly_3 and PEG_4 linkers. *Bioconjugate Chem. 20*, 750–759.
(30) De Leon-Rodriguez, L. M., and Kovacs, Z. (2008) The synthesis and chelation chemistry of DOTA-peptide conjugates. *Bioconjugate Chem. 19*, 391–402.
(31) Wang, H., Chen, K., Cai, W., Li, Z., He, L., Kashefi, A., and Chen, X. (2008) Integrin-targeted imaging and therapy with RGD4C-TNF fusion protein. *Mol. Cancer Ther. 7*, 1044–1053.
(32) Eiblmaier, M., Meyer, L. A., Watson, M. A., Fracasso, P. M., Pike, L. J., and Anderson, C. J. (2008) Correlating EGFR expression with receptor-binding properties and internalization of ^{64}Cu-DOTA-cetuximab in 5 cervical cancer cell lines. *J. Nucl. Med. 49*, 1472–1479.
(33) Jarrett, B. R., Gustafsson, B., Kukis, D. L., and Louie, A. Y. (2008) Synthesis of ^{64}Cu-labeled magnetic nanoparticles for multimodal imaging. *Bioconjugate Chem. 19*, 1496–1504.
(34) Rossin, R., Muro, S., Welch, M. J., Muzykantov, V. R., and Schuster, D. P. (2008) In vivo imaging of ^{64}Cu-labeled polymer nanoparticles targeted to the lung endothelium. *J. Nucl. Med. 49*, 103–111.
(35) Valko, K. (2004) Application of high-performance liquid chromatography based measurements of lipophilicity to model biological distribution. *J. Chromatogr., A 1037*, 299–310.
(36) Wei, L., Ye, Y., Wadas, T. J., Lewis, J. S., Welch, M. J., Achilefu, S., and Anderson, C. J. (2009) ^{64}Cu-labeled CB-TE2A and diamsar-conjugated RGD peptide analogs for targeting angiogenesis: comparison of their biological activity. *Nucl. Med. Biol. 36*, 277–285.

BC900537F

A Metal-Free DNA Nuclease Based on a Cyclic Peptide Scaffold

Shadad Alkhader,[†] Aviva Ezra,[†] Jana Kasparkova,[‡] Viktor Brabec,[‡] and Eylon Yavin*[,†]

The Institute for Drug Research, The School of Pharmacy, The Hebrew University of Jerusalem, Hadassah Ein-Karem, Jerusalem 91120, Israel, and Institute of Biophysics, Academy of Sciences of the Czech Republic, v.v.i., 61265 Brno, Czech Republic.
Received December 9, 2009; Revised Manuscript Received May 5, 2010

The ability to cleave DNA with the aid of chemical nucleases has been a challenge in the scientific community, particularly in the absence of a redox active metal ion. Inspired by structural characterization of the active site found in Staphylococcal nuclease, we have designed a series of organic molecule comprising cyclic pentapeptides conjugated to a DNA intercalator (e.g., anthraquinone). The cyclic peptide is designed to cleave the phosphodiester backbone, whereas the intercalator is expected to improve binding affinity to the substrate (DNA). Our lead compound (**1-AQ**), composed of the cyclic peptide cyc-D-Lys-Gly-Arg-Ser-Arg conjugated to anthraquinone, degrades DNA into small fragments at physiologically relevant conditions (i.e., 37 °C, pH = 7.4). We find that **1-AQ** is highly effective in degrading duplex DNA at micromolar concentrations as corroborated by agarose and polyacrylamide gel electrophoresis. Changing the DNA intercalator to acridine (**1-Ac**) renders the compound comparable in nuclease activity to **1-AQ**. In comparison to control compounds (**Lin-1** and **1**) that lack either the cyclic scaffold or the DNA intercalator, our lead compound (**1-AQ**) is found to be significantly more active as a DNA chemical nuclease. We have studied the importance of the triad (Arg-Ser-Arg) as the designed module for DNA cleavage. Changing L-Ser to L-Glu (cyc-D-Lys-Gly-Arg-Glu-Arg, **Glu-AQ**) results in an inactive compound, whereas the cyclic peptide **Gly-AQ** (cyc-D-Lys-Gly-Arg-Gly-Arg, where glycine replaces L-serine) has similar DNA nuclease activity to **1-AQ**. In addition, changing the stereochemistry from D-lysine to L-lysine results in a cyclic peptide (**1-L-AQ**) exerting weak DNA nuclease activity, highlighting the importance of the cyclic backbone conformation for efficient DNA nuclease activity. The addition of ROS scavengers does not reduce DNA nuclease activity; an observation that supports a hydrolytic cleavage mechanism. Finally, we have estimated the kinetics of DNA cleavage of a 15-mer duplex DNA substrate by compound **1-AQ**. By monitoring DNA duplex degradation by following the change in absorbance (hyperchromicity) at various **1-AQ** concentrations, we report a maximal k_{obs} value (as an underestimation of k_{max}) of 1.62 h^{-1} at a 7.5-fold of **1-AQ**. We have also compared the other two active peptide conjugates, namely, **1-Ac** and **Gly-AQ** to that of **1-AQ**. Both compounds exert similar nuclease activity to that of **1-AQ**. To the best of our knowledge, this is the most active metal-free DNA nuclease reported to date that exerts its DNA nuclease activity at biologically relevant conditions.

INTRODUCTION

In recent years, there has been considerable interest in designing synthetic small organic molecules as catalysts that hydrolyze the phosphodiester bond (*1, 2*). Such compounds, when targeted to certain DNA/RNA sequences, might lead to the development of highly specific artificial restriction enzymes, as well as potential therapeutic molecules for specific gene silencing. Several research groups have been working on the development of DNA cleavage agents that are metal-free and hydrolytic in nature (*1*−*10*). The absence of a redox active metal ion has the advantage of avoiding complications such as metal dissociation and uncontrolled redox chemistry. Nonetheless, ligand-based hydrolytic DNA cleavage remains a challenge, as it is well-known that the DNA phosphodiester bond is very stable under physiological conditions with a half-life hydrolysis rate of about 200 million years (*3*).

Various peptides have been used as metal-free DNA nucleases (*1, 3*−*6*); however, DNA cleavage was typically observed at high peptide concentration (e.g., 10 mM) (*5*) or at non-physiological conditions (e.g., 50 °C) (*4*). Another synthetic approach is based on utilizing macrocyclic compounds as scaffolds to which various ligands (e.g., guanidine) are appended (*7*−*10*). In several cases, hydrolytic DNA cleavage was achieved at physiological conditions (pH 7.5, 37 °C) though ligand concentration was relatively high (100−200 μM) (*7, 8*). In a recent report, DNA cleavage was shown to be promoted by 2,6-pyridinecarboxamide substituted with two guanidine groups (*11*). As in the previous cases, a relatively high concentration of ligand was required for metal-free DNA hydrolytic cleavage.

Staphylococcal nuclease from *Staphylococcus aureus* is a Ca^{2+} dependent extracellular enzyme that is secreted by these bacteria as a defense mechanism against viral DNA and RNA (*12*). This enzyme has been exploited for achieving site-specific DNA and RNA cleavage by it is conjugation to triplex-forming oligonucleotides (*13, 14*). Inspired by the detailed mechanistic and structural characterization of this enzyme (*12, 15*−*24*) indicating several amino acid residues (e.g., L-Arg and L-Glu) as well as Ca^{2+} as key players in the hydrolysis of the phosphodiester bond, we set out to prepare a cyclic pentapeptide scaffold presenting such amino acids. On the basis of extensive studies by the Kessler group (*25, 26*) on cyclic RGD peptides arranged in a βII′/γ-turn, we synthesized several cyclic pentapeptides (cRSRG<u>K</u>, cRSRGK, cRERG<u>K</u>, and cRGRG<u>K</u> where <u>K</u> = D-lysine) to which DNA intercalators (anthraquinone = AQ or acridine = Ac) were conjugated via the ε-amine of (D or L) lysine (Scheme 1).

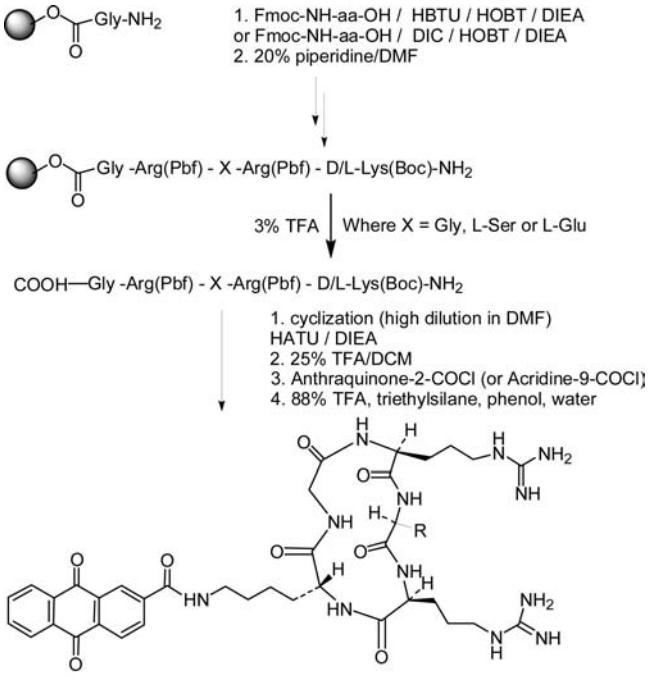
* Corresponding author. The Institute for Drug Research, The School of Pharmacy, The Hebrew University of Jerusalem, Hadassah Ein-Karem, Jerusalem 91120, Israel. E-mail: eylony@ekmd.huji.ac.il, Tel: 972-2-6758692, Fax: 972-2-6757076.

[†] The Hebrew University of Jerusalem.

[‡] Academy of Sciences of the Czech Republic.

10.1021/bc900543b © 2010 American Chemical Society
Published on Web 07/19/2010

Scheme 1. Synthesis of Cyclic Pentapeptides Conjugated to DNA Intercalators (Anthraquinone or Acridine)



Intercalator	R group	Title compond
AQ	CH_2OH	1-AQ
AQ	$(CH_2)_2COOH$	Glu-AQ
AQ	H	Gly-AQ
Ac	CH_2OH	1-Ac
AQ	CH_2OH	1-L-AQ*

* D-Lys is replaced with L-Lys

These cyclic peptides were designed to bring about the following properties: (1) Three amino acid side chains (Arg-Ser-Arg, Arg-Gly-Arg, or Arg-Glu-Arg) as a triad (γ-turn) are designed to bind to the phosphodiester backbone and potentially cleave DNA; (2) the D-Lysine is then oriented to allow conjugation of a DNA binding moiety (intercalators AQ or Ac) affording a βII′/γ-turn arrangement with D-lysine at the $i + 1$ position (*25*, *26*). Herein, we report on DNA nuclease activity of these peptide−conjugates highlighting the various chemical features that are required for efficient DNA degradation by such metal-free DNA cutters.

MATERIALS AND METHODS

All commercially available chemical reagents were used without further purification. The solvents DMF, DCM, and MeOH were purchased from Acros (dry under molecular sieves) and used for peptide synthesis without further purification. Phosphoramidites and reagents for DNA synthesis were purchased from Biolab (Jerusalem, Israel) and used as received. Fmoc-6-aminocaproic acid (Fmoc-Ahx) (*27*), anthraquinone-2-cabonyl chloride (AQ-Cl), and acridine-9-carbonyl chloride (*28*) were synthesized according to the literature.

Thin-layer chromatography (TLC) was performed on aluminum sheets Merck silica gel 60 F_{254}. Compounds were visualized by UV absorption at 254 nm and stained with 3% ninhydrin solution in 97% EtOH to monitor the presence of free amines. Semipreparative RP-HPLC separations were performed on a Shimadzu instrument (LC-2010C) by using a Phenomenex C_{18} column (300A^0, 5 μm, 250 mm × 20 mm) with a flow rate of 4 mL/min^{-1}. The eluent was a linear gradient from 95% water (with 0.1% TFA) to 30% acetonitrile over 5 min followed by a gradient of 30% to 80% acetonitrile over 25 min. The detection was performed at 255 nm. ESI-MS spectra were carried out either on an Orbi-trap mass spectrometer (Thermo Finnigan) using a nanospray attachment or on a ThermoQuest Finnigan LCQ Duo MS. Preparative normal-phase CombiFlash separations were performed on a Mercury instrument. The eluent was a linear gradient from 0% MeOH to 20% MeOH (in DCM).

General Procedures for Solid-Phase Peptide Synthesis. *Ia. Coupling with HBTU/HOBt (used for Ser/Gly/Glu/Lys Amino Acids and Ahx).* Fmoc-amino acid (4 equiv), 2-(1*H*-benzotriazole-1-yl)-1,1,3,3-tetramethyluronium hexafluorophosphate (HBTU, 4 equiv), 1-hydroxybenzotriazole (HOBt, 4 equiv), and *N*,*N*-diisopropylethylamine (DIEA, 7 equiv) were dissolved in DMF (5 mL) to give a reaction mixture which was added to the 2-chlorotrityl-Gly resin (0.5 g, theoretical loading 0.55 mmol g^{-1}, 0.275 mmol). The reaction mixture was shaken at room temperature (2 × 90 min) and washed with DMF (3 × 5 mL) and DCM (3 × 5 mL). 90% average yield/amino acid based on monitoring Fmoc removal by UV−vis spectroscopy ($\varepsilon^{300} = 7800$ cm^{-1} M^{-1}).

Ib. Coupling with DIC/HOBt (used for Arg Amino Acid). Fmoc-amino acid (4 equiv), *N*,*N*-diisopropylcarbodiimide (DIC, 4 equiv), HOBt (4 equiv), DIEA (7 equiv), and 4-(dimethylamino)-pyridine (DMAP, 0.1 equiv) were dissolved in DMF to give a clear solution which was added to the resin. The reaction mixture was shaken at room temperature for 90 min, and then a fresh solution (of the above mixture) was added to the resin and shaken overnight. The resin was washed with DMF (3 × 5 mL), DCM (3 × 5 mL). Typically 85% yield.

II. Fmoc Deprotection. The Fmoc-protected resin was suspended in a solution of 20% piperidine in DMF (5 mL) for 2 × 10 min. The resin was washed with DMF (3 × 5 mL) and DCM (3 × 5 mL).

III. Peptide Cleavage from Resin by TFA Treatment. The resin was washed with DCM (3 × 5 mL) and treated with a solution of 3% TFA/DCM (5 mL) for 2 × 10 min. After removal of the resin by filtration, the filtrates were combined and the product was precipitated by the addition of cold Et_2O (25 mL). After filtration, the product was obtained as a white powder.

IV. Cyclization of the Linear Pentapeptide. The linear pentapeptide was dissolved in DMF (high dilution, $C = 2 \times 10^{-3}$ M). After addition of 2-(1*H*-7-azabenzotriazol-1-yl)-1,3,3-tetramethyluranium hexafluorophosphate methanaminium (HATU, 2 equiv) and DIEA (7 equiv), the suspension was stirred for 12 h at room temperature. After the solution was concentrated under vacuum to a minimum volume of DMF, the cyclic peptide was precipitated by the addition of water.

V. Pbf and OtBu Deprotection with TFA. The protected peptide was dissolved in TFA/H_2O/Et_3SiH/phenol (88:5:2:5). After 3 h, Et_2O was added to the reaction mixture and a white precipitate was collected by filtration. The final product was HPLC purified using conditions stated above.

Synthesis of Compound 1-AQ. *Linear-Gly-Arg(Pbf)-Ser(tBu)-Arg(Pbf)-D-Lys(Boc).* The linear peptide GRSRK was initially synthesized on the solid support as described in the general procedures (sections I−III). 235 mg of crude linear peptide was subsequently cyclized without purification.

Cyclic-Gly-Arg(Pbf)-Ser(tBu)-Arg(Pbf)-D-Lys(Boc). The linear peptide was cyclized according to general procedure (section IV). The cyclic peptide was purified by column chromatography (CombiFlash) using conditions described in materials and equipment. Yield: 164 mg (0.13 mmol, 70%) of cyclic peptide.

Cyclic-Gly-Arg(Pbf)-Ser(tBu)-Arg(Pbf)-D-Lys. Boc Deprotection with TFA: The protected cyclic peptide was dissolved in 25% TFA/DCM for 30 min at room temperature. After addition of cold Et_2O, the white precipitate was collected by filtration.

Cyclic- Gly-Arg(Pbf)-Ser(tBu)-Arg(Pbf)-D-Lys(AQ). Coupling of cyclic peptide with AQ-Cl: Cyclic peptide cGRSRK (0.13 mmol), DIEA (4 eq (0.52 mmol)), and AQ-Cl (0.14 mmol) were dissolved in 10 mL dry DCM under an argon atmosphere. The reaction mixture was stirred at room temperature for 2 h. The reaction progress was monitored by TLC and was terminated by disappearance of the starting material (cyclic peptide).

Deprotection of Cyclic-Gly-Arg-Ser-Arg-D-Lys(AQ). Final deprotection of Pbf and tBu protecting groups was carried out as described in general procedures (section V). Total yield of coupling to AQ-Cl and deprotection was 5.4 μmol (4%). MS: [M+1] (Observed) = 820.01; [M+1] (expected) = 819.88.

Synthesis of Compound Glu-AQ. *Linear-Gly-Arg(Pbf)-Glu(tBu)-Arg(Pbf)-D-Lys(Boc).* The cyclic peptide cRERGK was initially synthesized on the solid support as described in the general procedures (sections I−III). 181 mg of crude linear peptide were subsequently cyclized without purification.

Cyclic-Gly-Arg(Pbf)-Glu(tBu)-Arg(Pbf)-D-Lys(Boc). Peptide cyclization: The linear peptide was cyclized according to general procedure (section IV). The cyclic peptide was purified by column chromatography (CombiFlash) using conditions described in materials and equipment. Yield: 126 mg (0.1 mmol, 70%) of cyclic peptide.

Cyclic-Gly-Arg(Pbf)-Glu(tBu)-Arg(Pbf)-D-Lys. Boc deprotection with TFA: The protected cyclic peptide was dissolved in 25% TFA/DCM for 30 min at room temperature. After addition of cold Et_2O, the white precipitate was collected by filtration.

Cyclic-Gly-Arg(Pbf)-Glu(tBu)-Arg(Pbf)-D-Lys(AQ). Coupling of cyclic peptide with AQ-Cl: Cyclic peptide cGRSRK (0.1 mmol), DIEA (4 equiv (0.4 mmol)) and AQ-Cl (0.11 mmol) were dissolved in 10 mL dry DCM under an argon atmosphere. The reaction mixture was stirred at room temperature for 2 h. The reaction progress was monitored by TLC and was terminated by disappearance of the starting material (cyclic peptide).

Deprotection of Cyclic-Gly-Arg-Glu-Arg-D-Lys(AQ). Final deprotection of Pbf and tBu protecting groups was carried out as described in general procedures (section V). Total yield of coupling to AQ-Cl and deprotection was 4.5 μmol (5%). MS: [M+1] (observed) = 861.75; [M+1] (expected) = 861.92.

Synthesis of Compound 1-L-AQ. Cyclic-Gly-Arg-Ser-Arg-Lys(AQ) was synthesized as described for compound **1-AQ**. 290 mg of crude linear peptide was subsequently cyclized without purification. Yield: 223 mg (0.179 mmol, 78%) of cyclic peptide. Total yield of coupling to AQ-Cl and final deprotection was 10 μmol (6%). MS: [M/2] (observed) = 410.3; [M+1] (expected) = 819.88.

Synthesis of Compound 1-Ac. Cyclic-Gly-Arg-Ser-Arg-Lys(Ac) was synthesized as described for compound **1-AQ**. 210 mg of crude linear peptide were subsequently cyclized without purification. Yield: 170 mg (0.136 mmol, 82%) of cyclic peptide. Total yield of coupling to Ac-Cl and final deprotection was 13.9 μmol (10%). MS: [M/2] (observed) = 395.93; [M+1] (expected) = 789.88.

Synthesis of compound Gly-AQ. *Linear-Gly-Arg(Pbf)-Gly-Arg(Pbf)-D-Lys(Boc).* The linear peptide GRGRK was initially synthesized on the solid support as described in the general procedures (sections I−III). 230 mg of crude linear peptide was subsequently cyclized without purification.

Cyclic-Gly-Arg(Pbf)-Gly-Arg(Pbf)-D-Lys(Boc). The linear peptide was cyclized according to general procedure (section IV). The cyclic peptide was purified by column chromatography (CombiFlash) using conditions described in materials and equipment. Yield: 190 mg (0.164 mmol, 84%) of cyclic peptide.

Cyclic-Gly-Arg(Pbf)-Gly-Arg(Pbf)-D-Lys. Boc deprotection with TFA: The protected cyclic peptide was dissolved in 25% TFA/DCM for 30 min at room temperature. After addition of cold Et_2O, the white precipitate was collected by filtration.

Cyclic-Gly-Arg(Pbf)-Gly-Arg(Pbf)-D-Lys(AQ). Coupling of cyclic peptide with AQ-Cl: Cyclic peptide cGRGRK (0.13 mmol), DIEA (4 eq (0.52 mmol)), and AQ-Cl (0.14 mmol) were dissolved in 10 mL dry DCM under an argon atmosphere. The reaction mixture was stirred at room temperature for 2 h. The reaction progress was monitored by TLC and was terminated by disappearance of the starting material (cyclic peptide).

Deprotection of Cyclic-Gly-Arg-Gly-Arg-D-Lys(AQ). Final deprotection of Pbf and tBu protecting groups was carried out as described in general procedures (section V). Total yield of coupling to AQ-Cl and deprotection was 7.8 μmol (5%). MS: [M/2] (observed) = 395.3; [M+1] (expected) = 788.85.

Synthesis of Compound 1 (Without Intercalator). *Cyclic-Gly-Arg-Ser-Arg-Gly.* The cyclic control peptide GRSRG was synthesized on the solid support as described in the general procedures (sections I−IV). 205 mg of linear peptide was subsequently cyclized without purification.

Cyclic peptide was purified by column chromatography (CombiFlash) using the conditions described in materials and equipment. Total yield of cyclization was 170 mg (0.158 mmol, 84%).

Deprotection of Cyclic Peptide. Final deprotection of Pbf and tBu protecting groups was carried out as described in general procedures (section V). MS: [M/2] (observed) = 257.64; [M+1] (expected) = 513.55.

Synthesis of Compound Lin-1. *Linear-Gly-Arg-Ser-Arg-Ahx-(AQ).* The linear peptide GRSR-Ahx was initially synthesized on the solid support (150 mg Rink Amide resin, L = 0.5 mmol/g) as described in general procedures (sections I−II).

Coupling of AQ-Cl to Resin-Bound Linear Peptide. AQ-Cl (4 equiv) and DIEA (7 equiv) dissolved in dry DCM (3 mL) were added to the linear peptide GRSRAhx (on the solid support) and shaken for 90 min. Cleavage from the resin and removal of the protecting groups were carried out as described in general procedures (section V). 6.5 mg of compound **Lin-1** were obtained (7.9 μmol, 10% yield). MS: [M/2] (observed) = 411.2; [M] (expected) = 820.89.

DNA Cleavage Monitored by Agarose Gel Electrophoresis. DNA cleavage experiments were performed using 95 ng DNA (PCR product or plasmid) per reaction. DNA (dissolved in 50 mM Tris-HCl/10 mM $CaCl_2$ buffer, pH = 7.4) was incubated (in the dark) at 37 °C with the various peptides. After incubation, 1.5 μL of the loading buffer (30 mM EDTA, 0.05% (w/v) glycerol, 36% (v/v) bromophenol blue) was added to each sample followed by loading samples (total volume = 15 μL) on a1% agarose gel containing 1.0 μg/mL ethidium bromide. Electrophoresis was carried out at 90 V for 1.5 h in 0.5 M TAE buffer. Bands were visualized by UV light and photographed.

DNA Cleavage Monitored by Polyacrylamide Gel Electrophoresis. Double-stranded oligonucleotide (50 bp), 5′-end labeled at the top strand, was incubated at 37 °C with **1-AQ** in a 50 mM Tris, in 10 mM $CaCl_2$ buffer (pH 7.4), and in the dark. The aliquots were withdrawn at various time intervals, and the reaction was stopped by placing samples on dry ice. DNA cleavage products were resolved by polyacrylamide gel electrophoresis under denaturing conditions (20% PAA/8 M urea). The autoradiograms were visualized by using the bioimaging analyzer BAS-2500 (Fuji Photo Film Co. Ltd., Tokyo, Japan) and Aida image analyzer software (Raytest GmbH, Strauben, Germany).

DNA Synthesis. Oligonucleotides (15-mer 5′-CGCGATGACTGTACT and its complementary sequence) were synthesized on an Applied Biosystems 3400 DNA/RNA synthesizer, purified by reverse-phase HPLC (Phenomenex, Clarity 5 μ oligo RP), and characterized by MALDI-TOF MS.

DNA Cleavage as Monitored by Hyperchromicity. A 60 μL quartz cuvette was loaded with 1.8 μM dsDNA (15 mer-5′-CGCGATGACTGTACT and its complementary sequence) dissolved in Tris buffer (50 mM Tris, 10 mM $CaCl_2$, pH 7.4). The peptide conjugate (at a given concentration between 1.8 μM to 18 μM) was added, and the adsorption of the sample at 260 nm was monitored by UV−vis spectroscopy every 5 min.

Binding Affinity of Inactive Peptide Conjugate (Glu-AQ) to CT-DNA as Determined by EtBr Displacement. A 1 mL four-sided quartz cuvette was loaded with ethidium bromide (1.3 μM) dissolved in Tris buffer (50 mM Tris, 10 mM NaCl, pH 7.4). The fluorescence was measured (ex. 545 nm, em. 595 nm, RT). Next, CT-DNA was added (254 μM) in aliquots (2 μL), and the increase in fluorescence was measured after the continuous addition of CT-DNA. This procedure was continued until no change in fluorescence was noticed (saturation). Finally, a solution of **Glu-AQ** (4 μM) was added in aliquots of 2.6 μL, and fluorescence quenching was measured. The binding affinity of **Glu-AQ** was estimated according to

$$K_{app} = (K_{EB}X[EB])/[\text{Glu-AQ}]_{50}$$

where $K_{EB} = 1 \times 10^7\ M^{-1}$, $[EB] = 1.3 \times 10^{-6}$ M, and $[\text{Glu-AQ}]_{50}$ = concentration of **Glu-AQ** where 50% reduction in fluorescence is achieved (*29*).

RESULTS AND DISCUSSION

Structural Considerations. On the basis of the active site found in Staphylococcal nuclease which consists of two L-Arg (Arg35 and Arg87) that electrostatically bind and activate the phosphodiester bonds toward hydrolysis by an activated water as nucleophile, several cyclic pentapeptides were synthesized (Scheme 1) with the following variations: Triads of the type Arg-X-Arg (where X = L-Ser, Gly, or L-Glu) positioned on the γ-turn (*25, 26*) as mediators of DNA cleavage were studied. The choice of X = L-serine (compounds **1-AQ** and **1-Ac**) stems from the potential of the hydroxyl group to act as a nucleophile; attacking the phosphodiester bond that is more susceptible to nucleophilic attack due to it is electrostatic interactions with two L-Arg.

In the case of L-Glu (compound **Glu-AQ**), the carboxyl side chain of this amino acid is designed to activate a water molecule (as elucidated in the enzyme's active site) that, in turn, would then attack the susceptible phosphodiester bond. Positioning Gly (compound **Gly-AQ**) between two L-Arg should determine whether it is necessary to have a nucleophile at position X, as H_2O may provide this role.

In addition, we have synthesized a cyclic pentapeptide conjugated to AQ (**1-L-AQ**, *vide post*) where L-lysine replaces D-Lys. This change in stereochemistry should dramatically change the cyclic backbone conformation, thus allowing assessment of the importance of the designed cyclic peptides (with the βII′/γ-turn arrangement *25, 26*) to DNA nuclease activity.

Chemical Synthesis. The synthesis of the cyclic pentapeptides (Scheme 1) was carried out by synthesizing the linear peptide (GRSR<u>K</u>, GRSRK, GRGR<u>K</u>, and GRER<u>K</u>, where <u>K</u> = D-lysine) on the solid support (2-chlorotrityl Gly resin) followed by C- to N-terminus peptide cyclization in a diluted DMF solution using HATU as a coupling reagent.

After cyclization, peptides were purified by column chromatography and the BOC protected ε-amine was removed by treating the cyclic peptides with 25% TFA (in DCM) for 30 min at room temperature. Anthraquinone-2-carbonyl chloride or acridine-9- carbonyl chloride (obtained by reflux of the acid in neat $SOCl_2$) was then added to the peptides and stirred for 2 h in dry DCM in the presence of excess base (DIEA). The crude products were dried in vacuo and redissolved in the deprotection solution (88:2:5:5 TFA/triethylsilane/water/phenol) for 3 h. All final cyclic compounds were precipitated in cold diethyl ether and HPLC purified on a C18 column.

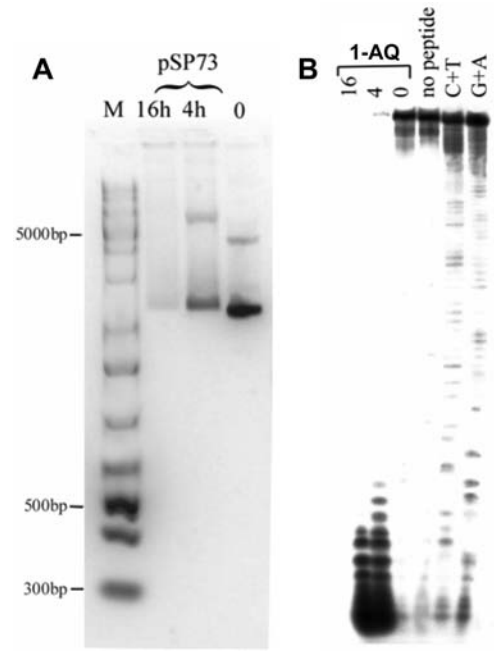


Figure 1. (A) Agarose gel (1%) electrophoresis of supercoiled DNA (pSP73 plasmid, superhelical density = −0.063) incubated for 4 and 16 h with **1-AQ** at 37 °C. Lanes: 0, 4, 16 h = DNA incubated with **1-AQ** for 0, 4, and 16 h, respectively; M = 1 kb DNA ladder. (B) DNA nuclease activity of **1-AQ** on a ^{32}P-labeled 50-mer DNA duplex as corroborated on a 20% polyacrylamide/8 M urea gel. Lanes: C+T and G+A = Maxam−Gilbert sequencing reactions; no peptide = control, no peptide added; 0, 4, and 16 = DNA incubated with **1-AQ** for 0, 4, and 16 h, respectively. For both gels: Incubation temperature = 37 °C, [peptide]:[DNA in bp] = 1:1, final peptide concentration = 20 μM. All samples were kept in the dark. Incubation buffer: [Tris] = 50 mM, $[CaCl_2]$ = 10 mM, pH = 7.4.

DNA Nuclease Activity of Cyclic Peptides. Chemical nuclease activity was initially evaluated in a phosphate buffer after incubating both **1-AQ** and **Glu-AQ** (20 μM) with plasmid DNA (pSP73) in the dark to avoid UV-induced DNA photocleavage by AQ (*27, 28*). At 37 °C, no activity of either cyclic pentapeptide was seen. However, at 50 °C, **1-AQ** was extremely active (Figures S15−S16, Supporting Information).

Taking into account that a high concentration of phosphate ions (phosphate buffer) might interfere with the nuclease activity of the cyclic pentapeptides, we decided instead to incubate the cyclic pentapeptides in a TRIS buffer. In this buffer (50 mM TRIS, 10 mM $CaCl_2$, pH = 7.4), incubation of **1-AQ** with plasmid DNA at 37 °C leads to complete disappearance of the band after overnight incubation (Figure 1A). To verify that this observation is due to DNA cleavage, a 50-mer ^{32}P-radiolabeled duplex was incubated with **1-AQ**. As shown in Figure 1B, small DNA fragments are observed already after 4 h of incubation. On the contrary, **Glu-AQ** is completely inactive (data not shown).

The inactivity of **Glu-AQ** might be a consequence of an electrostatic interaction between the guanidine group(s) of L-Arg (positively charged at pH = 7.4) and the carboxylate group of L-Glu. Thus, the designed activity for both L-Arg and L-Glu might be hampered by such an electrostatic interaction.

As **Glu-AQ** showed no DNA nuclease activity, it was exploited in order to estimate the apparent binding affinity of this class of peptide conjugates to dsDNA. An EtBr displacement experiment was conducted (see experimental section for details). By following the reduction in EtBr fluorescence (when excluded from CT-DNA by **Glu-AQ**), we have determined a

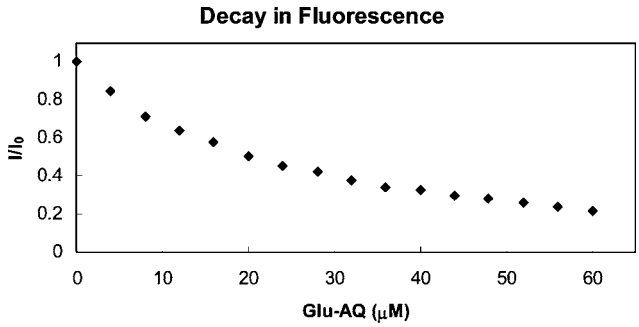
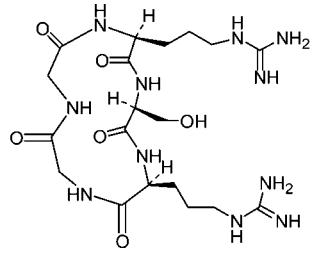
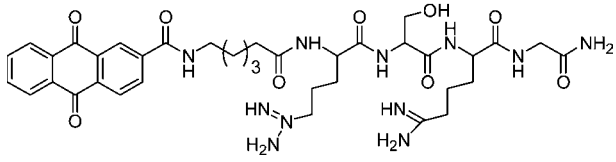


Figure 2. Fluorescence decay of EtBr bound to CT-DNA after the addition of **Glu-AQ**. The estimated binding affinity ($K_{app} = 5.4 \times 10^5$ M^{-1}) of **Glu-AQ** to dsDNA was determined according to the amount of **Glu-AQ** required for a 50% decrease in fluorescence (see text for formula).

Scheme 2. Chemical Structures of Control Peptides Lin-1 and 1



compound **1**: Cyclic peptide lacking DNA intercalator



compound **Lin-1**: linear version of compound **1-AQ**

K_{app} value of 5.4×10^5 M^{-1} (Figure 2). This value is in the range of the intrinsic binding constants reported for peptidyl anthraquinones (*30*).

Several control peptides were synthesized (Scheme 2). Compound **Lin-1** is a linear version of the cyclic peptide where a 6-aminocaproic acid (Ahx) linker is used to separate AQ from the triad (Arg-Ser-Arg). Compound **1** (Scheme 2) is a cyclic pentapeptide that lacks AQ. Both compounds were incubated with a PCR product (591 bp's) and compared to the DNA nuclease activity of the parent compound **1-AQ** (Figure 3). Both compounds **Lin-1** and **1** were considerably less active. Thus, it is apparent that both cyclic scaffold and DNA intercalator are required for the superior DNA nuclease activity exerted by compound **1-AQ**.

In order to gain some insight into the importance of the triad (Arg-Ser-Arg), a cyclic peptide was synthesized where glycine replaces L-Serine. The title compound (cRGRGK conjugated

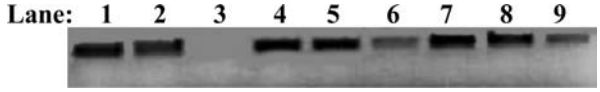


Figure 3. DNA nuclease activity of compounds **1-AQ**, **1**, and **Lin-1** in [Tris] = 50 mM, [$CaCl_2$] = 10 mM, pH = 7.4 buffer at 37 °C as corroborated on an agarose gel. In all lanes: 95 ng PCR product (591 bp). Lane 1, control (without peptide); lane 2, 4 μM of **1-AQ**; lane 3, 16 μM of **1-AQ**; lane 4, 16 μM of **1**; lane 5, 48 μM of **1**; lane 6, 144 μM of **1**; lane 7, 16 μM of **Lin-1**; lane 8, 48 μM of **Lin-1**; lane 9, 144 μM of **Lin-1**. DNA incubated with all peptides for 4 h. All samples were kept in the dark.

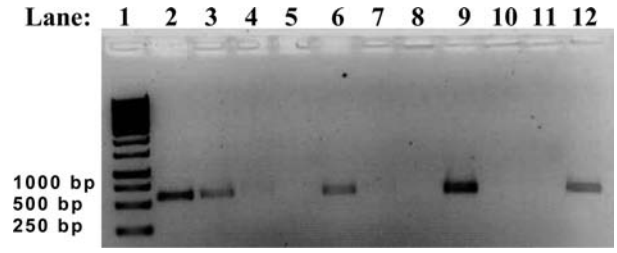


Figure 4. DNA nuclease activity of compounds **1-AQ**, **Gly-AQ**, **1-Ac**, and **1-L-AQ** in [Tris] = 50 mM, [$CaCl_2$] = 10 mM, pH = 7.4 buffer at 37 °C as corroborated on an agarose gel. In lanes 2−12: 95 ng PCR product (591 b.p.). Lane 1, DNA ladder; lane 2, DNA control (without peptides); lanes 3−5, **1-AQ** at 4, 16, and 64 μM, respectively; lanes 6−8, **Gly-AQ** at 4, 16, and 64 μM, respectively; lanes 9−11, **1-Ac** at 4, 16, and 64 μM, respectively; lane 12, 16 μM of **1-L-AQ**. DNA incubated with all cyclic peptides for 4 h. All samples were kept in the dark.

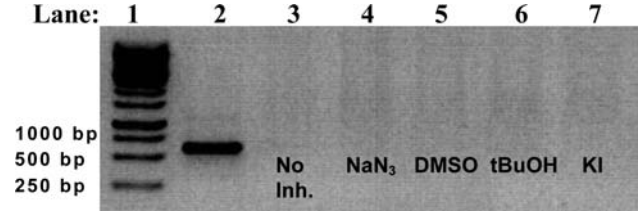


Figure 5. DNA nuclease activity of **1-AQ** in the presence of ROS scavengers. 95 ng PCR product (591 bp) was incubated with **1-AQ** (20 μM) for 4 h at 37 °C. Lane 1, DNA ladder; lane 2, only DNA; lane 3, no inhibitor added; lane 4, 10 mM NaN_3; lanes 5−6, 1 mM of DMSO and tBuOH, respectively; and lane 7, 10 mM KI. All samples were kept in the dark during incubation. Incubation buffer: [Tris] = 50 mM, [$CaCl_2$] = 10 mM, pH = 7.4.

to AQ, **Gly-AQ**) has two L-arginine amino acids for phosphodiester binding and activation; however, it lacks a nucleophile. DNA nuclease activity of such a conjugate would suggest that a water molecule acts as a nucleophile. Indeed, we observe that **Gly-AQ** exerts similar DNA nuclease activity to that of **1-AQ** (Figure 4, lanes 6−8). The high DNA nuclease activity observed for these conjugates also coincides with water as a nucleophile. In such a scenario, phosphodiester cleavage would regenerate the chemical nuclease providing catalytic activity to such conjugates.

DNA nuclease activity of both cyclic peptides with the Arg-Ser-Arg triad but with different DNA intercalators (AQ and Ac) were compared (Figure 4, compounds **1-AQ** and **1-Ac**, lanes 9−11). No significant difference in activity was observed, highlighting the versatility of such cyclic peptide−DNA intercalator conjugates as metal-free chemical nucleases.

L-Lysine was introduced into the cyclic pentapeptide (cRSRGK, **1-L-AQ**) replacing D-lysine. This is expected to bring about a dramatic change in the conformation of the cyclic peptide's backbone. As shown in Figure 4 (lane 12), a concentration of 16 μM of **1-L-AQ** results only in modest DNA nuclease activity (as corroborated by the weakened DNA band) in comparison to complete disappearance of the DNA band obtained with **1-AQ**, **1-Ac**, and **Gly-AQ** at the same concentration.

Mechanism and Potency of DNA Cleavage. To gain evidence that supports a hydrolytic mechanism of cleavage by the active cyclic pentapeptides, ROS scavengers were added to incubated samples (**1-AQ** + DNA) in order to exclude an oxidative mechanism for DNA cleavage. As shown in Figure 5, the addition of a singlet oxygen quencher (NaN_3), hydroxyl radical scavengers (DMSO or tBuOH), and a superoxide scavenger (KI) had no effect on **1-AQ**'s DNA nuclease activity. In all cases, the plasmid is cleaved as observed for the control sample (lane 3) without inhibitor.

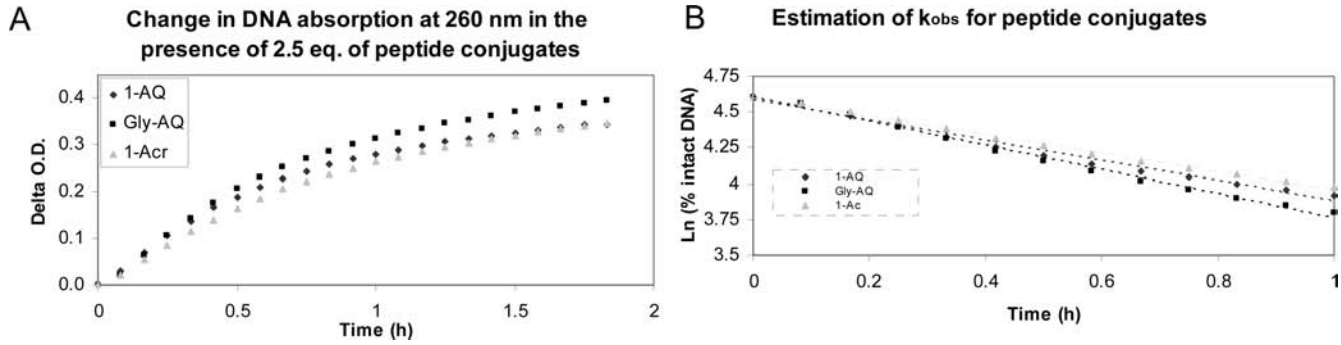


Figure 6. (A) Hyperchromicity of 15-mer dsDNA substrate after the addition of peptide conjugates **1-AQ**, **Gly-AQ**, and **1-Ac** at 2.5 molar excess concentrations. (B) Estimated k_{obs} values of 0.70 h^{-1}, 0.85 h^{-1}, and 0.65 h^{-1} for peptide conjugates **1-AQ**, **Gly-AQ**, and **1-Ac**, respectively. k_{obs} values were extracted form the linear fit (slope = k_{obs}) for all three peptides conjugates.

The fact that DNA cleavage of plasmid DNA or duplex DNA (591 bp) by **1-AQ** (and other active cyclic peptides) yielded either DNA smears or complete disappearance of the parent band precluded the straightforward analysis of cleavage kinetics (i.e., nicking (form II-coiled) and double strand breaks (form III-linear)). Thus, we decided to monitor DNA cleavage of the active peptide conjugates by following DNA degradation by monitoring the change in absorbance at 260 nm (hyperchromicity). A synthetic 15-mer DNA duplex was chosen as a DNA substrate. The various peptide conjugates were added to this 15-mer duplex DNA substrate, and the change in adsorption was followed at 260 nm. Degradation of dsDNA to ssDNA and to further single bases is expected to lead to an increase in absorption (hyperchromicity) (*31, 32*). As we have observed complete degradation of the radiolabeled 50-mer duplex (Figure 1B), we assume that the change in adsorption on a longer time scale in which the change in O.D. is negligible (e.g., 2 h) represents a good approximation for complete degradation of the DNA substrate. Accordingly, we have estimated the amount of intact DNA as follows:

$$\% \text{ intact DNA} = 100 - (\text{O.D.}_t - \text{O.D.}_0/\text{O.D.}_\infty)$$

where O.D._t = measured adsorption, O.D._0 = measured adsorption at $t = 0$, and O.D._∞ = measured adsorption at the end of the reaction (plateau region). By plotting the logarithm of this value as a function of time (within the first hour of kinetics), we obtain a linear fit where the slope is an estimation for k_{obs}.

Figure 6 presents the hyperchromicity data (change in O.D.) related to the initial DNA nuclease activity (within 2 h) and the linear plots of the three active peptide conjugates, namely, **1-AQ**, **1-Ac**, and **Gly-AQ** at 2.5 equiv peptide conjugate to dsDNA substrate. On the basis of the k_{obs} values that range 0.65−0.85 h^{-1}, all three peptide conjugates seem to be similarly active. The peptide conjugate (**Gly-AQ**) that has no bulky group situated between the two L-Arg in its triad (Gly instead of L-Ser) seems to be the most active of all three compounds. We speculate that the introduction of L-Ser at this position diminishes DNA nuclease activity perhaps due to steric hindrance. However, further peptide analogues are required in order to verify this argument. The small differences in k_{obs} between **1-AQ** and **1-Ac** are attributed to the DNA intercalator (anthraquinone vs acridine), as this is the only difference in structure between these peptide conjugates.

We have also repeated these experiments with one of the active compounds (**1-AQ**) at various peptide-conjugate concentrations. Table 1 lists the k_{obs} values determined for this peptide conjugate (see Supporting Information Figure S17 for kinetic profiles of **1-AQ** at various concentrations). Interestingly, we find that at a high peptide conjugate concentration (10 equiv) the k_{obs} value is reduced. Thus, an optimal value is obtained at

Table 1. Kinetics of DNA Cleavage by 1-AQ as Determined by Hyperchromicity at 260 nm

fold of **1-AQ**	k_{obs} (h^{-1})
1	0.26
2.5	0.70
5	1.13
7.5	1.62
10	0.53

7.5 equiv of **1-AQ**. It is possible that, at higher concentrations, compound **1-AQ** forms aggregates in buffer by π-stacking of the appended anthraquinone moieties on each D-Lys of the cyclic peptide.

At 7.5 equiv of **1-AQ**, a k_{obs} of 1.62 h^{-1} is found based on the hyperchromicity measurements. To the best of our knowledge, this value is by an order of magnitude higher than the most efficient metal-free DNA nucleases reported to date (at physiological conditions).

In summary, we have synthesized a family of metal-free DNA nucleases that exert high DNA nuclease activity at physiological conditions and at micromolar concentrations. It was found that both amino acid composition as well as conjugation of the cyclic pentapeptide to DNA binders (intercalators) are essential features required for such activity. As DNA intercalators such as anthraquinone (*33*) have been shown to exert some sequence specificity when bound to short peptides, it is possible to exploit this discrimination for selective DNA cleavage. Alternatively, the conjugation of a triplex-forming oligonucleotides (TFO) in place of a DNA intercalator now has the potential to bring about sequence-specific DNA cleavage by such cyclic peptide−TFO conjugates; a goal that we are currently pursuing.

ACKNOWLEDGMENT

We thank the authority for R&D of the Hebrew U. and the Alex Grass Center for Drug Design for financial support. This research was also supported by the Academy of Sciences of the CR (IAA400040803), the Ministry of Education of the CR (MSMT LC06030, ME08017, OC08003), the Academy of Sciences of the CR (Grants KAN200200651, AV0Z50040507). J.K. is the international research scholar of the Howard Hughes Medical Institute.

Supporting Information Available: Gel electrophoresis of compounds **1-AQ** and **Glu-AQ** in phosphate buffer, MS and HPLC chromatograms of compounds **1-AQ**, **1-L-AQ**, **1-Ac**, **Gly-AQ**, **Glu-AQ**, **1**, and **Lin-1**, and kinetics plots of **1-AQ** at various concentrations. This material is available free of charge via the Internet at http://pubs.acs.org.

LITERATURE CITED

(1) Ma, Y., Chen, X., Sun, M., Wan, R., Zhu, C., Li, Y., and Zhao, Y. (2008) DNA cleavage function of seryl-histidine dipeptide and its application. *Amino Acids 35*, 251–256.

(2) Razkin, J., Lindgren, J., Nilsson, H., and Baltzer, L. (2008) Enhanced complexity and catalytic efficiency in the hydrolysis of phosphate diesters by rationally designed helix-loop-helix motifs. *ChemBioChem 9*, 1975–1984.

(3) Cheng, C. T., Lo, V., Chen, J., Chen, W. C., Lin, C. Y., Lin, H. C., Yang, C. H., and Sheh, L. (2001) Synthesis and DNA nicking studies of a novel cyclic peptide: Cyclo[Lys-Trp-Lys-Ahx-]. *Bioorg. Med. Chem. 9*, 1493–1498.

(4) Feng, Y. P., Cao, S. L., Xiao, A. S., Xie, W. J., Li, Y. M., and Zhao, Y. F. (2006) Studies on cleavage of DNA by N-phosphoryl branched peptides. *Peptides 27*, 1554–1560.

(5) Li, Y. S., Zhao, Y. F., Hatfield, S., Wan, R., Zhu, Q., Li, X. H., McMills, M., Ma, Y., Li, J., Brown, K. L., He, C., Liu, F., and Chen, X. Z. (2000) Dipeptide seryl-histidine and related oligopeptides cleave DNA, protein, and a carboxyl ester. *Bioorg. Med. Chem. 8*, 2675–2680.

(6) Schmuck, C., and Dudaczek, J. (2007) Screening of a combinatorial library reveals peptide-based catalysts for phosphorester cleavage in water. *Org. Lett. 9*, 5389–5392.

(7) Sheng, X., Lu, X. M., Chen, Y. T., Lu, G. Y., Zhang, J. J., Shao, Y., Liu, F., and Xu, Q. (2007) Synthesis, DNA-Binding, cleavage, and cytotoxic activity of new 1,7-dioxa-4,10-diazacyclododecane artificial receptors containing bisguanidinoethyl or diaminoethyl double side arms. *Chem.—Eur. J. 13*, 9703–9712.

(8) Sheng, X., Lu, X. M., Zhang, J. J., Chen, Y. T., Lu, G. Y., Shao, Y., Liu, F., and Xu, Q. (2007) Synthesis and DNA cleavage activity of artificial receptor 1,4,7-triazacyclononane containing guanidinoethyl and hydroxyethyl side arms. *J. Org. Chem. 72*, 1799–1802.

(9) Wan, S. H., Liang, F., Xiong, X. Q., Yang, L., Wu, X. J., Wang, P., Zhou, X., and Wu, C. T. (2006) DNA hydrolysis promoted by 1,7-dimethyl-1,4,7,10-tetraazacyclododecane. *Bioorg. Med. Chem. Lett. 16*, 2804–2806.

(10) Zhao, Y. C., Zhang, J., Huang, Y., Wang, G. Q., and Yu, X. Q. (2007) DNA cleavage promoted by 2,9-dimethyl-4,7-diazadecane-2,9-dithiol (DDD) derivatives. *Bioorg. Med. Chem. Lett. 17*, 2745–2748.

(11) Shao, Y., Sheng, X., Li, Y., Jia, Z.-L., Zhang, J.-J., Liu, F., and Lu, G. Y. (2008) DNA binding and cleaving activity of the new cleft molecule N,N′-bis(guanidinoethyl)-2,6-pyridinedicarboxamide in the absence or in the presence of copper(II). *Bioconjugate Chem. 19*, 1840–1848.

(12) Cotton, F. A., Hazen, E. E., and Legg, M. J. (1979) Staphylococcal nuclease - proposed mechanism of action based on structure of enzyme-thymidine 3′,5′-bisphosphate-calcium ion complex at 1.5-Å resolution. *Proc. Natl. Acad. Sci. U.S.A. 76*, 2551–2555.

(13) Pei, D. H., Corey, D. R., and Schultz, P. G. (1990) Site-specific cleavage of duplex DNA by a semisynthetic nuclease via triple-helix formation. *Proc. Natl. Acad. Sci. U.S.A. 87*, 9858–9862.

(14) Zuckermann, R. N., and Schultz, P. G. (1989) Site-selective cleavage of structured RNA by a staphylococcal nuclease DNA hybrid. *Proc. Natl. Acad. Sci. U.S.A. 86*, 1766–1770.

(15) Cole, H. B. R., Sparks, S. W., and Torchia, D. A. (1988) Comparison of the solution and crystal-structures of staphylococcal nuclease with C-13 and N-15 chemical-shifts used as structural fingerprints. *Proc. Natl. Acad. Sci. U.S.A. 85*, 6362–6365.

(16) Deiters, J. A., Gallucci, J. C., and Holmes, R. R. (1982) Pentacoordinated molecules 0.41. computer-simulation of staphylococcal nuclease action on thymidine 3′,5′-bis(phosphate) (Pdtp). *J. Am. Chem. Soc. 104*, 5457–5465.

(17) Leung, K. W., Liaw, Y. C., Chan, S. C., Lo, H. Y., Musayev, F. N., Chen, J. Z. W., Fang, H. J., and Chen, H. M. (2001) Significance of local electrostatic interactions in staphylococcal nuclease studied by site-directed mutagenesis. *J. Biol. Chem. 276*, 46039–46045.

(18) Libson, A. M., Gittis, A. G., and Lattman, E. E. (1994) Crystal-structures of the binary Ca^{2+} and Pdtp complexes and the tertiary complex of the Asp(21) -] Glu mutant of staphylococcal nuclease - implications for catalysis and ligand-binding. *Biochemistry 33*, 8007–8016.

(19) Serpersu, E. H., Shortle, D., and Mildvan, A. S. (1986) Kinetic and magnetic-resonance studies of effects of genetic substitution of a Ca^{-2+}-liganding amino-acid in staphylococcal nuclease. *Biochemistry 25*, 68–77.

(20) Shan, L., Tong, Y. F., Xie, T., Wang, M., and Wang, J. F. (2007) Restricted backbone conformational and motional flexibilities of loops containing peptidyl-proline bonds dominate the enzyme activity of staphylococcal nuclease. *Biochemistry 46*, 11504–11513.

(21) Ting, A. Y., Shin, I., Lucero, C., and Schultz, P. G. (1998) Energetic analysis of an engineered cation-pi interaction in staphylococcal nuclease. *J. Am. Chem. Soc. 120*, 7135–7136.

(22) Wall, M. E., Ealick, S. E., and Gruner, S. M. (1997) Three-dimensional diffuse x-ray scattering from crystals of Staphylococcal nuclease. *Proc. Natl. Acad. Sci. U.S.A. 94*, 6180–6184.

(23) Wang, J. F., Hinck, A. P., Loh, S. N., Lemaster, D. M., and Markley, J. L. (1992) Solution studies of staphylococcal nuclease H124l 0.2. H-1, C-13, and N-15 chemical-shift assignments for the unligated enzyme and analysis of chemical-shift changes that accompany formation of the nuclease thymidine 3′,5′-bisphosphate calcium ternary complex. *Biochemistry 31*, 921–936.

(24) Weber, D. J., Libson, A. M., Gittis, A. G., Lebowitz, M. S., and Mildvan, A. S. (1994) NMR docking of a substrate into the X-Ray structure of the Asp-21 -] Glu mutant of staphylococcal nuclease. *Biochemistry 33*, 8017–8028.

(25) Haubner, R., Gratias, R., Diefenbach, B., Goodman, S. L., Jonczyk, A., and Kessler, H. (1996) Structural and functional aspects of RGD-containing cyclic pentapeptides as highly potent and selective integrin alpha(v)beta(3) antagonists. *J. Am. Chem. Soc. 118*, 7461–7472.

(26) Kessler, H., Gratias, R., Hessler, G., Gurrath, M., and Muller, G. (1996) Conformation of cyclic peptides. Principle concepts and the design of selectivity and superactivity in bioactive sequences by 'spatial screening'. *Pure Appl. Chem. 68*, 1201–1205.

(27) Khandazhinskaya, A. L., Kukhanova, M. K., and Jasko, M. V. (2005) New nonnucleoside substrates for terminal deoxynucleotidyl transferase: Synthesis and dependence of substrate properties on structure. *Russ. J. Bioorg. Chem. 31*, 352–356.

(28) Tierney, M. T., and Grinstaff, M. W. (2000) Synthesis and characterization of fluorenone-, anthraquinone-, and phenothiazine-labeled oligodeoxynucleotides: 5′-probes for DNA redox chemistry. *J. Org. Chem. 65*, 5355–5359.

(29) Begum, M. S. A., Saha, S., Nethaji, M., and Chakravarty, A. R. (2010) Iron(III) schiff base complexes of arginine and lysine as netropsin mimics showing AT-selective DNA binding and photonuclease activity. *J. Inorg. Biochem. 104*, 477–484.

(30) Gatto, B., Zagotto, G., Sissi, C., Cera, C., Uriarte, E., Palù, G., Capranico, G., and Palumbo, M. (1996) Peptidyl anthraquinones as potential antineoplastic drugs: Synthesis, DNA binding, redox cycling and biological activity. *J. Med. Chem. 39*, 3114–3122.

(31) Tataurov, A. V., You, Y., and Owczarzy, R. (2008) Predicting ultraviolet spectrum of single stranded and double stranded deoxyribonucleic acids. *Biophys. Chem. 133*, 66–70.

(32) See website: http://www.owczarzy.net/extinct.htm.

(33) Gatto, B., Zagotto, G., Sissi, C., and Pulambo, M. (1997) Preferred interaction of D peptidyl-anthraquinones with double-stranded B-DNA. *Int. J. Biol. Macromol. 21*, 319–326.

BC900543B

A Metal-Free DNA Nuclease Based on a Cyclic Peptide Scaffold

Shadad Alkhader[†], Aviva Ezra[†], Jana Kasparkova[‡], Viktor Brabec[‡] and Eylon Yavin[†,*]

The Institute for Drug Research[†], The School of Pharmacy, The Hebrew University of Jerusalem, Hadassah Ein-Karem, Jerusalem 91120, Israel.
Institute of Biophysics[‡], Academy of Sciences of the Czech Republic, v.v.i., 61265 Brno, Czech Republic.

[*] Corresponding author, e-mail: eylony@ekmd.huji.ac.il, Tel: 972-2-6758692, Fax: 972-2-6757076

Tables of contents:

HPLC and MS characterization of **1-AQ, Glu-AQ, 1, lin-1, 1-Ac, Gly-AQ, 1-L-AQ** 3-9

Gel electrophoresis (agarose and polyacrylamide) in phosphate buffer with compounds **1-AQ** and **Glu-AQ** 10-11

Kinetic profiles of **1-AQ** 12

All HPLC chromatograms were monitored at **255 nm** except for that of compound **1** (Fig. S5, monitored at **210 nm**).

Compound **1-AQ** purification and characterization: HPLC + MS

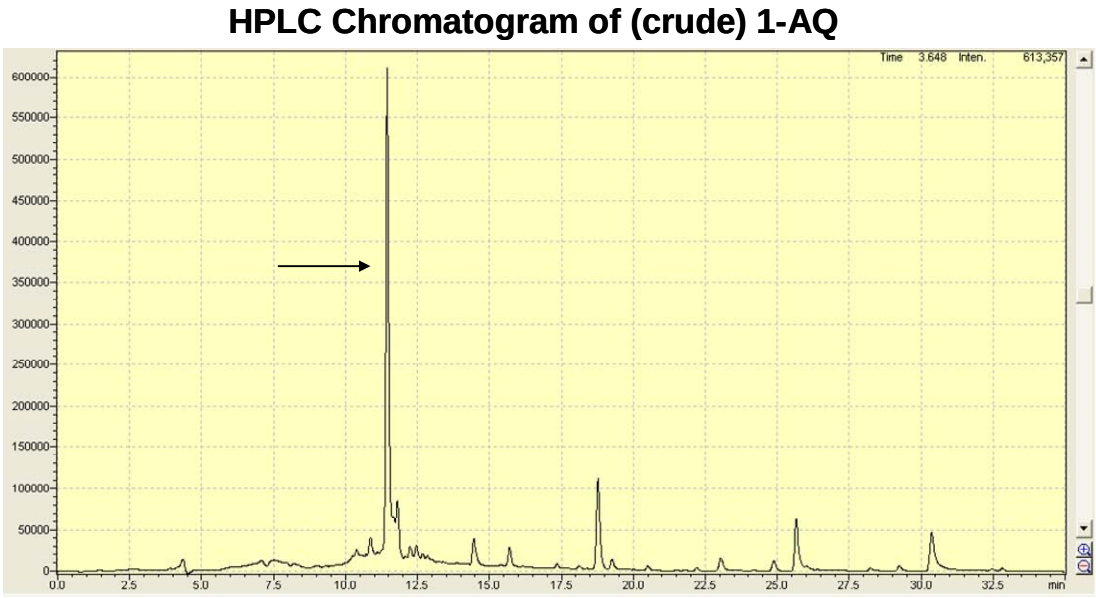


Figure S1: HPLC chromatogram of compound **1-AQ** (crude). HPLC conditions: linear gradient from 95% water (with 0.1% TFA) to 30% acetonitrile over 5 min followed by a gradient of 30% to 80% acetonitrile over 25 min. Arrow designates product.

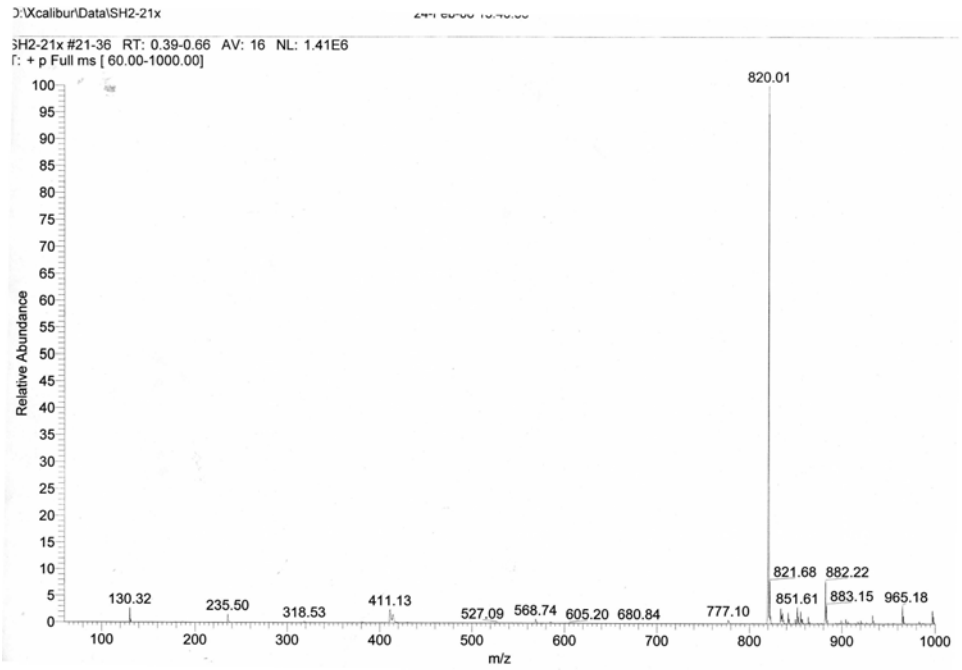


Figure S2: Mass Spectrometry of HPLC purified cyclic pentapeptide cGRSRK-AQ (compound **1-AQ**). [M+1] (Observed) = 820.01; [M+1] (expected) = 819.88.

Compound **Glu-AQ** purification and characterization: HPLC + MS

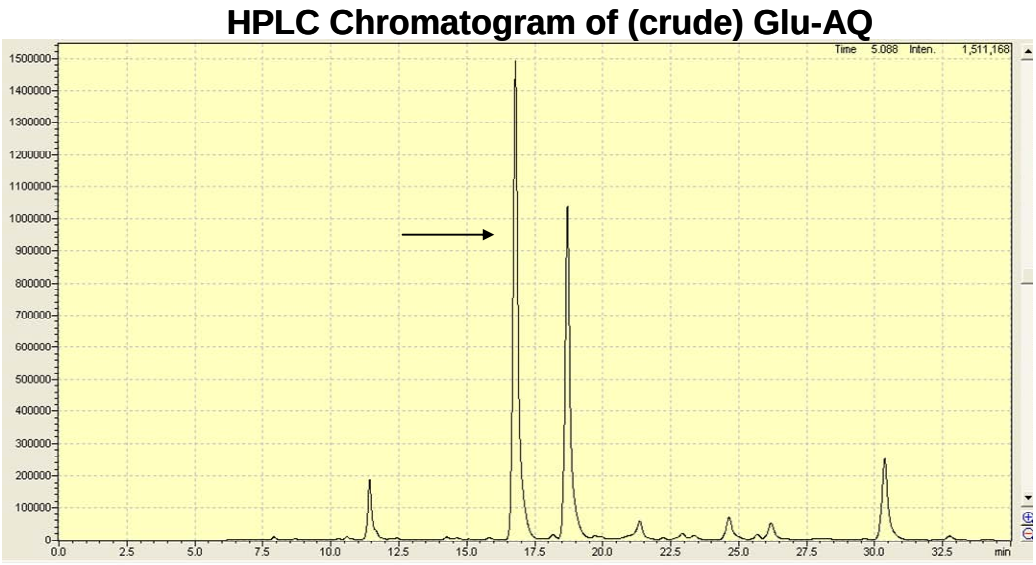


Figure S3: HPLC chromatogram of compound **Glu-AQ** (crude). HPLC conditions: linear gradient from 95% water (with 0.1% TFA) to 30% acetonitrile over 5 min followed by a gradient of 30% to 80% acetonitrile over 25 min. Arrow designates product.

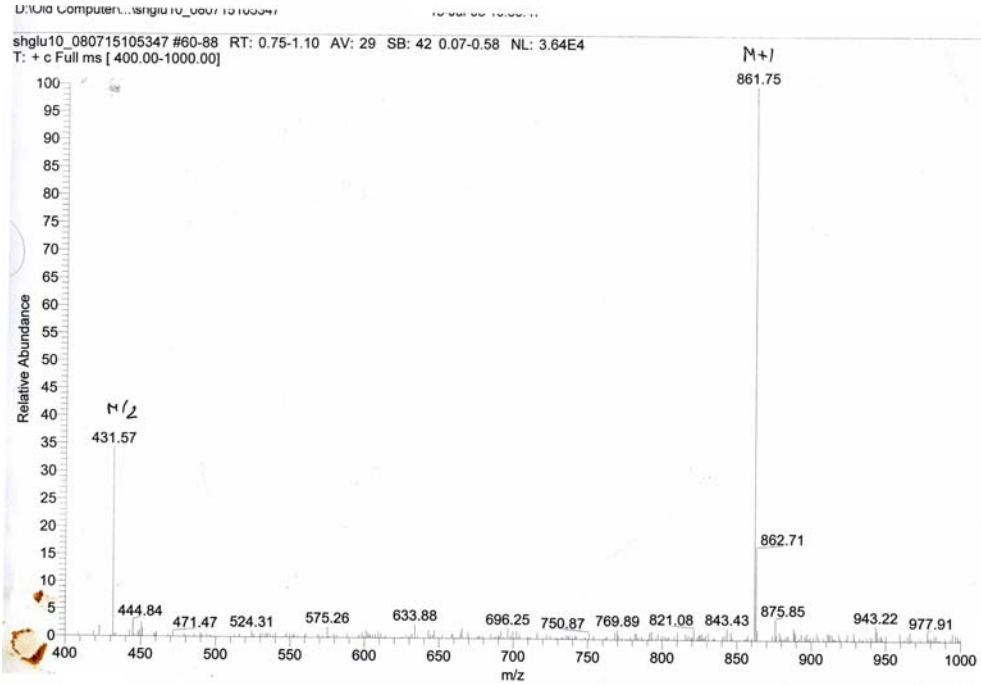


Figure S4: Mass Spectrometry of HPLC purified cyclic pentapeptide cGRERK-AQ (compound Glu-AQ). [M+1] (Observed) = 861.75; [M+1] (expected) = 861.92.

Compound **1** purification and characterization: HPLC + MS

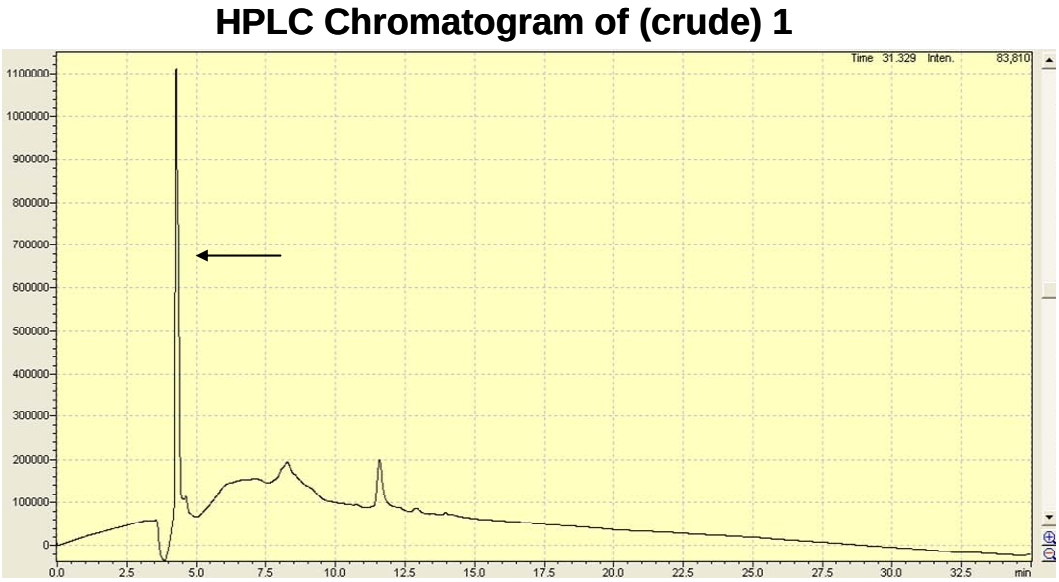


Figure S5: HPLC chromatogram of compound **1** (crude). HPLC conditions: linear gradient from 95% water (with 0.1% TFA) to 30% acetonitrile over 5 min followed by a gradient of 30% to 80% acetonitrile over 25 min. Arrow designates product.

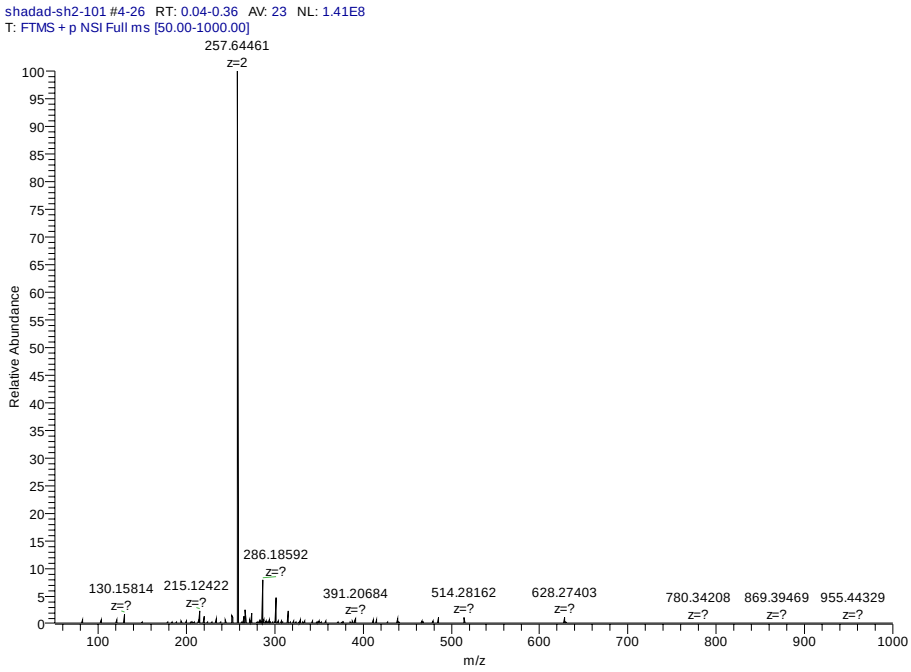


Figure S6: Mass Spectrometry of control cyclic pentapeptide cGRSRG (compound **1**). [M/2] (Observed) = 257.64 (M = 515.28); [M+1] (expected) = 513.55.

Compound **Lin-1** purification and characterization: HPLC + MS

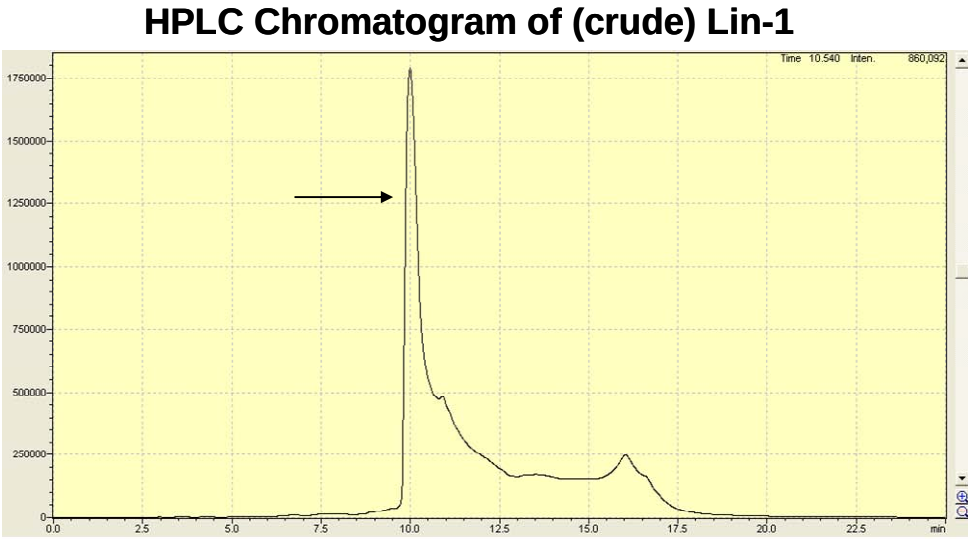


Figure S7: HPLC chromatogram of compound **Lin-1** (crude). HPLC conditions: linear gradient from 95% water (with 0.1% TFA) to 30% acetonitrile over 5 min followed by a gradient of 30% to 80% acetonitrile over 25 min. Arrow designates product.

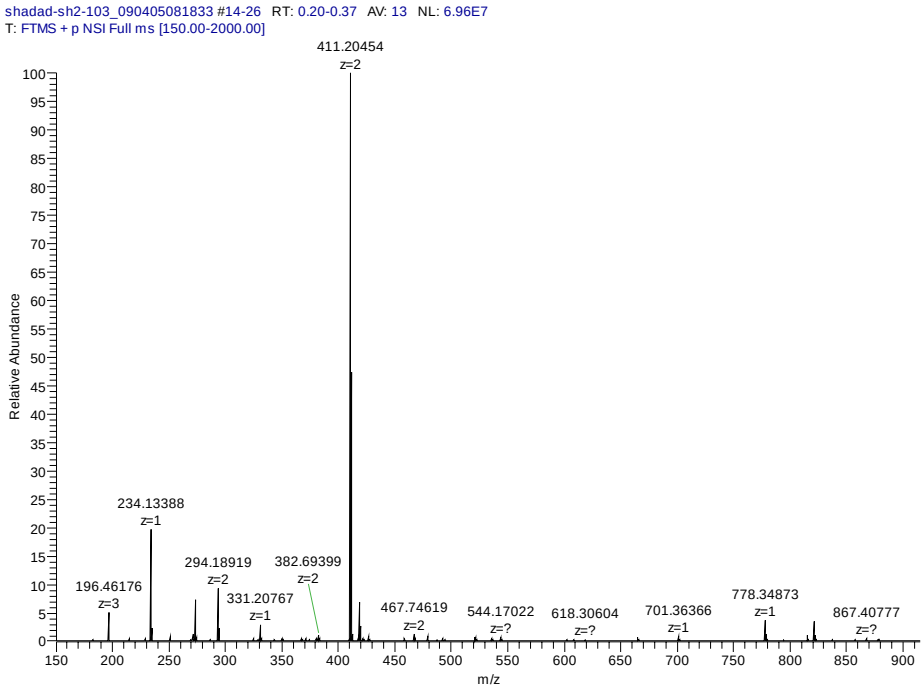


Figure S8: Mass Spectrometry of HPLC purified linear pentapeptide GRSR-Ahx-AQ (compound **Lin-1**). [M/2] (Observed) = 411.2 (M = 822.4); [M] (expected) = 820.89.

Compound **1-Ac** purification and characterization: HPLC + MS

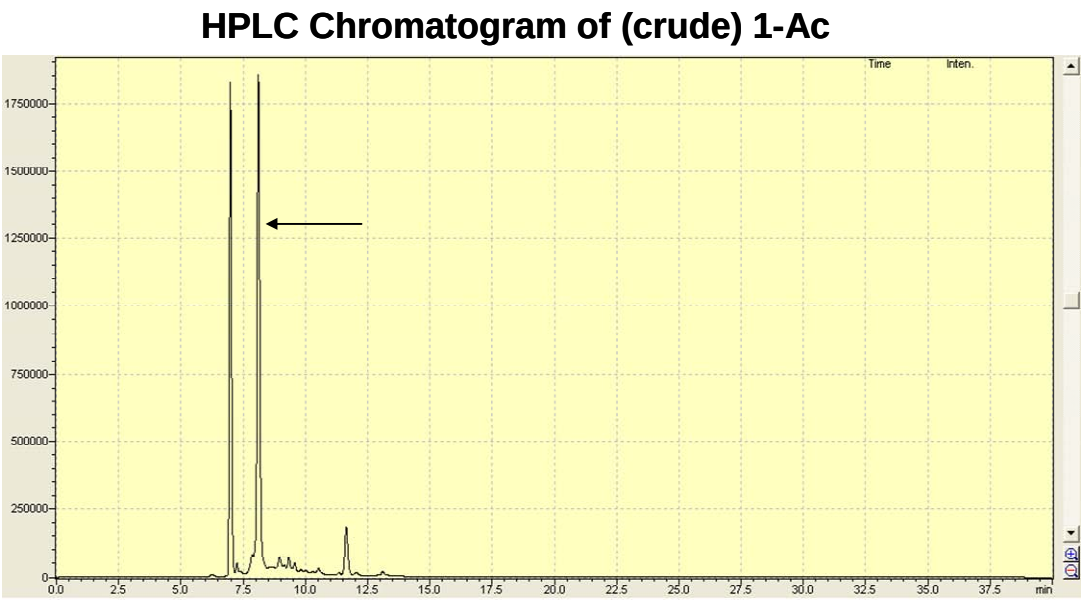


Figure S9: HPLC chromatogram of compound **1-Ac** (crude). HPLC conditions: linear gradient from 95% water (with 0.1% TFA) to 30% acetonitrile over 5 min followed by a gradient of 30% to 80% acetonitrile over 25 min. Arrow designates product.

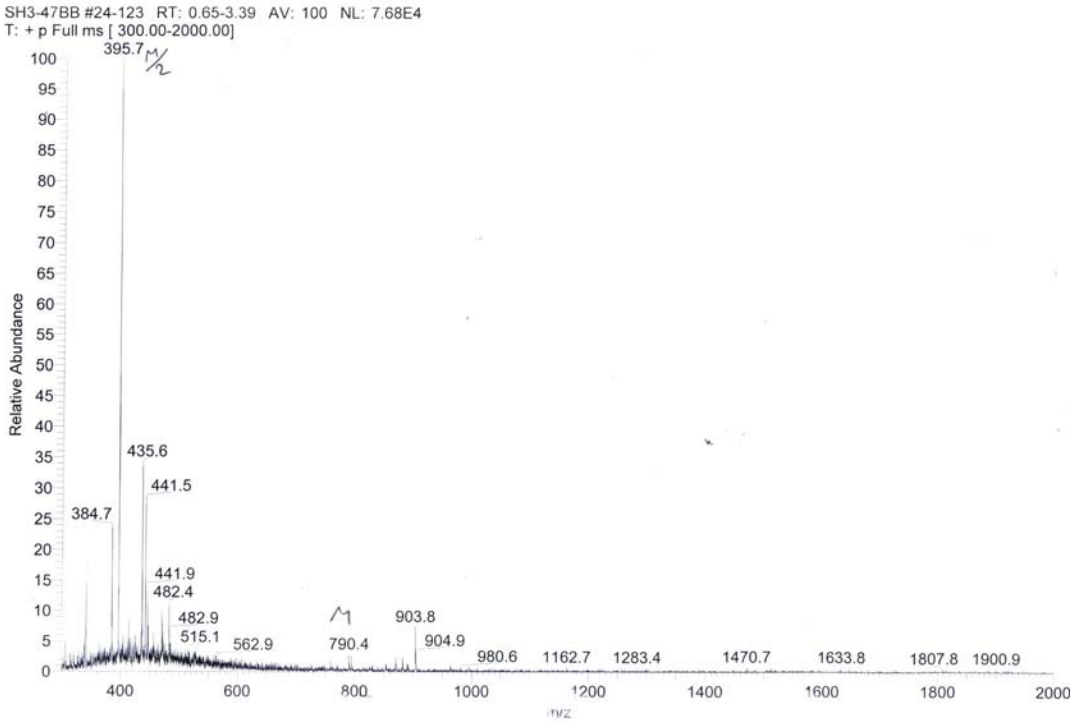


Figure S10: Mass Spectrometry of HPLC purified cyclic pentapeptide GRSRK-Ac (compound **1-Ac**). [M/2] (Observed) = 395.7 (M = 790.4); [M] (expected) = 789.88.

Compound **Gly-AQ** purification and characterization: HPLC + MS

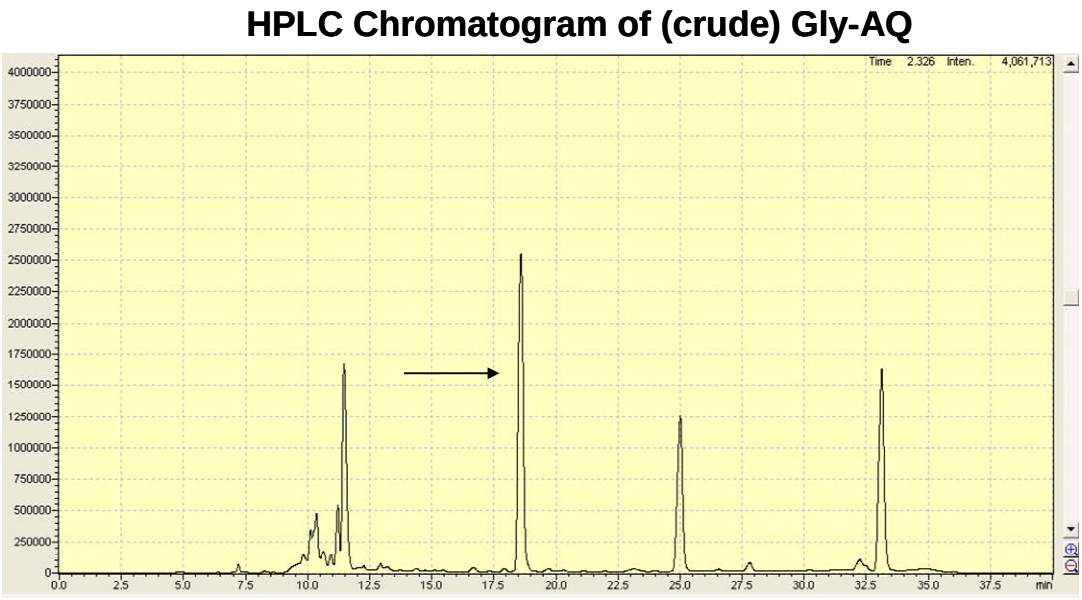


Figure S11: HPLC chromatogram of compound **Gly-AQ** (crude). HPLC conditions: linear gradient from 95% water (with 0.1% TFA) to 30% acetonitrile over 5 min followed by a gradient of 30% to 80% acetonitrile over 25 min. Arrow designates product.

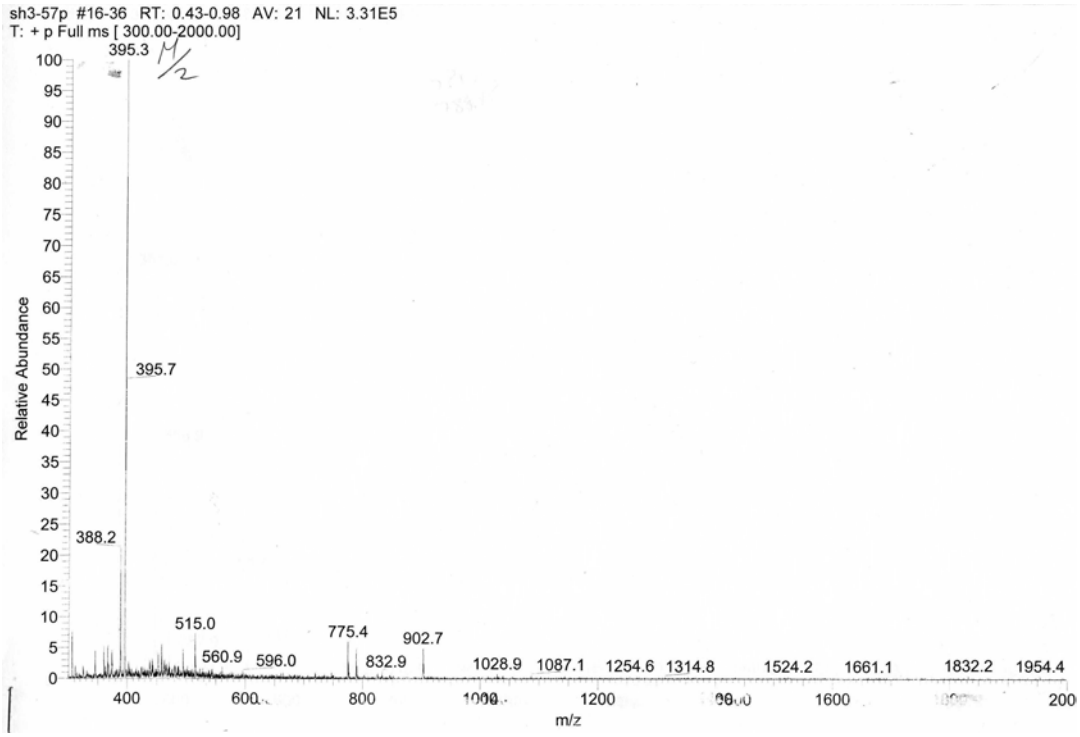


Figure S12: Mass Spectrometry of HPLC purified cyclic pentapeptide GRGRK-AQ (compound **Gly-AQ**). [M/2] (Observed) = 395.3 (M = 790.6); [M+1] (expected) = 788.85.

Compound **1-L-AQ** purification and characterization: HPLC + MS

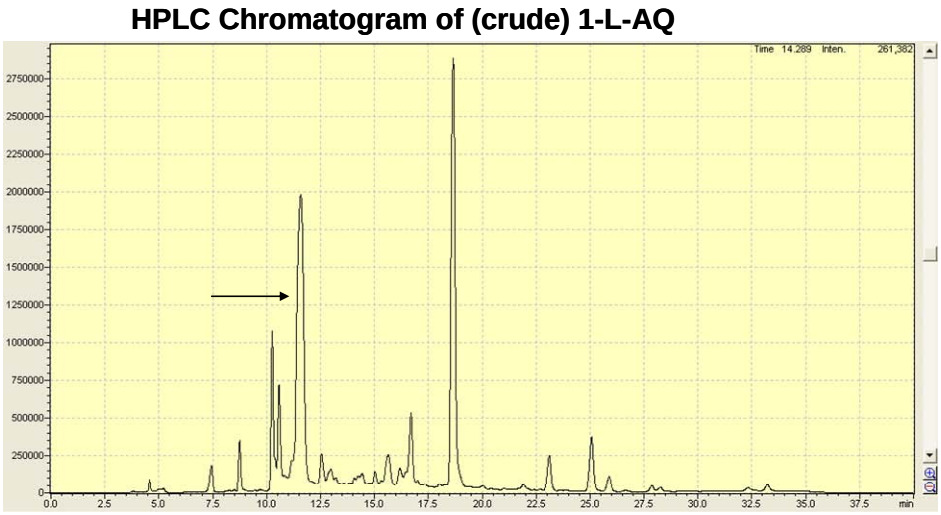


Figure S13: HPLC chromatogram of compound **1-L-AQ** (crude). HPLC conditions: linear gradient from 95% water (with 0.1% TFA) to 30% acetonitrile over 5 min followed by a gradient of 30% to 80% acetonitrile over 25 min. Arrow designates product.

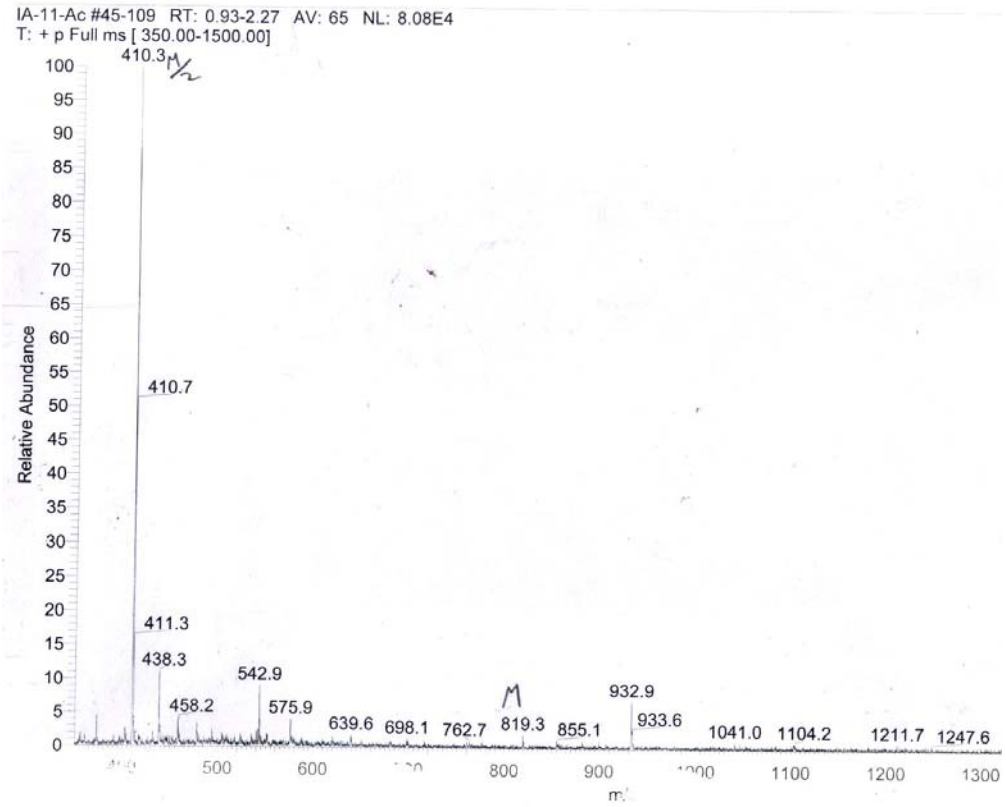


Figure S14: Mass Spectrometry of HPLC purified cyclic pentapeptide GRGRK-AQ (compound **1-L-AQ**). [M/2] (Observed) = 410.3 (M = 820.6); [M+1] (expected) = 819.88.

Gel Electrophoresis of Compounds **1-AQ** and **Glu-AQ** in phosphate buffer:

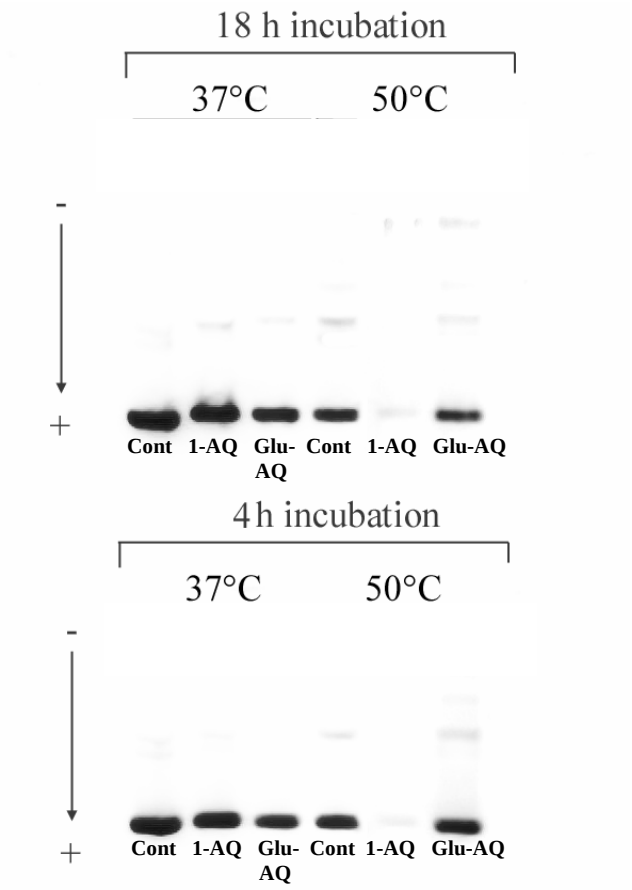


Figure S15: Agarose gel (1%) electrophoresis of supercoiled DNA (pSP73 plasmid) incubated for 4 and 16 hours with compounds **1-AQ** and **Glu-AQ** at 37°C and 50°C. [Peptide]:[DNA in base pairs] = 1:1. Cont = control (no peptide). Final peptide concentration = 20 μM. All samples were kept in the dark during incubation.

Incubation buffer: [NaPi] = 50 mM, [$CaCl_2$] = 10 mM, pH = 7.4.

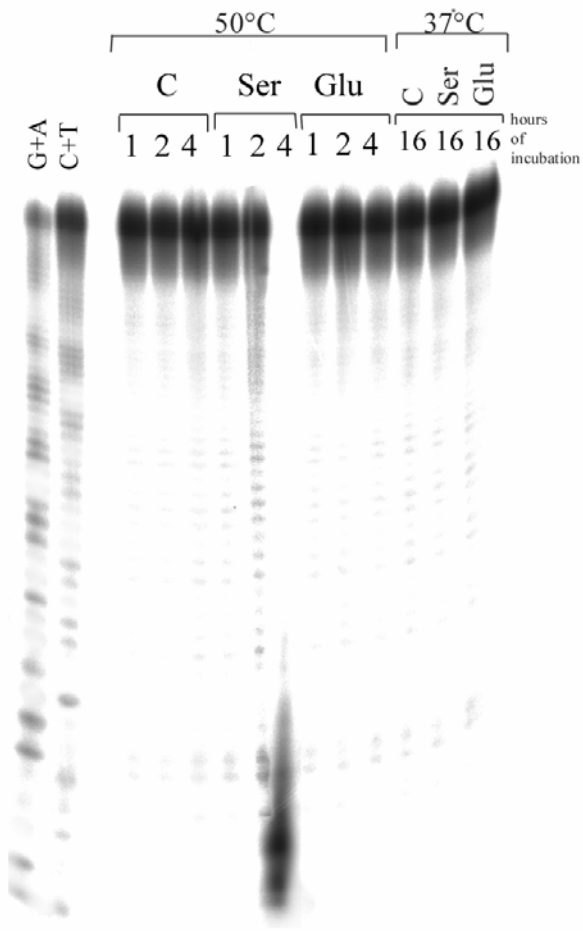


Figure S16: Polyacrylamide gel electrophoresis (20% polyacryamide/8M urea) of 50-mer duplex DNA (^{32}P-labeled) incubated for 1, 2 and 4 hours with compounds **1-AQ** and **Glu-AQ** at 50°C and 16 hours at 37°C. [peptide]:[DNA in base pairs] = 1:1. C = control (no peptide), **Ser** = compound **1-AQ**, **Glu** = compound **Glu-AQ**. C+T and G+A = Maxam-Gilbert sequencing reactions. Final peptide concentration = 20 μM. All samples were kept in the dark during incubation. Incubation buffer: [NaPi] = 50 mM, [$CaCl_2$] = 10 mM, pH = 7.4.

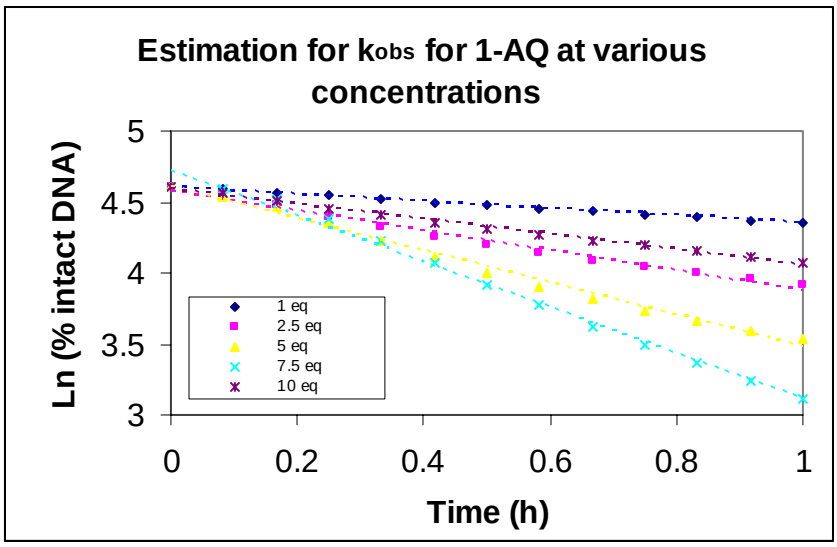


Figure S17: Estimated k_{obs} values for **1-AQ** based on hyperchromicity studies using a 15-mer dsDNA substrate. Based on linear fit for each **1-AQ** concentration, k_{obs} values were 0.26 h^{-1}, 0.70 h^{-1}, 1.13 h^{-1}, 1.62 h^{-1} and 0.53 h^{-1} for 1, 2.5, 5, 7.5 and 10 equivalents of **1-AQ**, respectively.

Stable GM_3 Lactone Mimetic Raises Antibodies Specific for the Antigens Expressed on Melanoma Cells

Annarosa Arcangeli,*[,†] Lucio Toma,*[,‡] Luca Contiero,[§] Olivia Crociani,[†] Laura Legnani,[‡] Carlotta Lunghi,[§] Elisa Nesti,[†] Gloriano Moneti,[||] Barbara Richichi,[§] and Cristina Nativi*[,§,⊥]

Dipartimento di Patologia e Oncologia Sperimentali, Universita' di Firenze, Firenze, Italy, Dipartimento di Chimica Organica, Universita' di Pavia, Pavia, Italy, Dipartimento di Chimica, Universita' di Firenze, Firenze, Italy, Dipartimento di Farmacologia, Universita' di Firenze, Firenze, Italy, and FiorGen, Universita' di Firenze, Firenze, Italy. Received December 17, 2009; Revised Manuscript Received June 23, 2010

Immunotherapy of tumors and of melanoma in particular has a long history, and recently this therapeutic approach found a reliable scientific rationale. This biological therapy aims to teach the patient's immune system to recognize the antigens expressed on tumor cells and destroy them, leaving normal cells intact. The success of this therapy highly depends on the selection of target antigens that are essential for tumors growth and progression. The overexpression of GM_3 ganglioside **1** and especially the expression of its metabolite GM_3 lactone **2** characterize murine and human melanomas, playing an important role in tumor progression and making such self-antigens potential targets for the immunotherapy of these neoplasms. Although more immunogenic than its precursor, GM_3 lactone **2** is unsuitable to be used in immunotherapy as a melanoma-associated antigen (MAA) because it is unstable under physiological conditions. We designed and synthesized the hydrolytically stable mimetic **3**, which is remarkably simpler than the native lactone **2**; after conjugation of **3** to the protein carrier keyhole-limpet hemocyanin (KLH), the obtained glycoprotein **5** was used as the immunogen *in vivo* to successfully elicit specific antimelanoma antibodies. In fact, no appreciable binding to GM_1 was observed. Capitalizing on the stability and on the reduced structural complexity of mimetic **3**, the immunostimulant **5** we report represents a new promising synthetic glycoconjugate for the immunotherapy of melanoma.

INTRODUCTION

Oncogenic transformations are accompanied by biochemical and functional changes. In particular, qualitative and quantitative changes in carbohydrate composition of the glycocalix during cell differentiation and proliferation have been observed and seem to reflect the state of malignant transformation of a variety of human tumors (*1*−*4*). Although the biological significance of such changes has not been elucidated yet, it is widely accepted that they contribute to or trigger an uncontrolled cellular adhesion, making the cell potentially metastatic. In recent years, a variety of monoclonal antibodies have been developed to specifically recognize carbohydrate epitopes that result from these faulty glycosylation processes. These epitopes (*5*−*8*), known as tumor associated antigens (TAAs), have been successfully used as markers of tumor progression and include carbohydrates expressed on normal tissues but which are accumulated in high density on the surface of tumor cells (*5*). Gangliosides are sialic acid containing glycosphingolipids composed of a complex carbohydrate moiety linked to a hydrophobic ceramide portion. Embedded within the outer leaflet of the cell membrane, the carbohydrate chain is exposed to the extracellular matrix. GM_3 ganglioside **1** (Figure 1), a glycosphingolipid found in essentially all types of cells and tissues, is the major ganglioside in normal melanocytes and is overexpressed in melanoma cells with metastatic potential (*9, 10*). The corresponding GM_3 lactone **2** (Figure 1) has also been found in melanoma as a minor component (*11, 12*); its formation is likely promoted by the lower pH environment of tumor cells (*13*) and, possibly, by a different conformation of GM_3 ganglioside induced on the tumor cell surface as a result of its local high density (*12*). GM_3 ganglioside has been widely investigated as a potential vaccine against cancer, although with scarce success since the majority of melanoma associated antigens (MAAs) are weakly immunogenic, owing to their nature and tissue distribution (*14*). Nevertheless, as metastatic melanoma appears to be resistant even to the most recent molecularly targeted agents, immunotherapeutic strategies continue to be used in an attempt to improve the results of the last 10 years of clinical investigations both in active and adoptive immune therapy. Indeed, vaccines prepared by using specific tumor antigens have recently lead to the commercial availability of the first tumor immunotherapeutic agents, which are usually employed in the postsurgery treatment of removed tumors, to stimulate the patient to develop the appropriate immune defenses, in order to inhibit the recruitment of the same tumor and avoid far more invasive chemo- or radiotherapeutic agents (*12, 15*). To date, a large repertoire of MAAs are available, most of which are extensively studied for their possible use in immunotherapy (*16*).

Recent findings showing relevant clinical responses in metastatic melanoma patients proved the principle that, under appropriate conditions, even large tumor masses can be made to regress by immune interventions (*17*).

Although more immunogenic than GM_3 ganglioside **1**, GM_3 lactone **2** (Figure 1) also failed as an immunostimulant because, under physiological conditions, the amount of lactone is below

* To whom correspondence should be addressed. Prof. A. Arcangeli: Tel, +39 0554598206; Fax, +39 0554598900; E-mail, annarosa.arcangeli@unifi.it. Prof. L. Toma: Tel, +39 0382987843; Fax, +39 0382987323; E-mail, lucio.toma@unipv.it. Prof. C. Nativi: Tel, +39 0554573540, Fax, +39 0554573570; E-mail, cristina.nativi@unifi.it.

† Dipartimento di Patologia e Oncologia Sperimentali, Universita' di Firenze.

‡ Universita' di Pavia.

§ Dipartimento di Chimica, Universita' di Firenze.

|| Dipartimento di Farmacologia, Universita' di Firenze.

⊥ FiorGen, Universita' di Firenze.

10.1021/bc900557v © 2010 American Chemical Society
Published on Web 07/29/2010

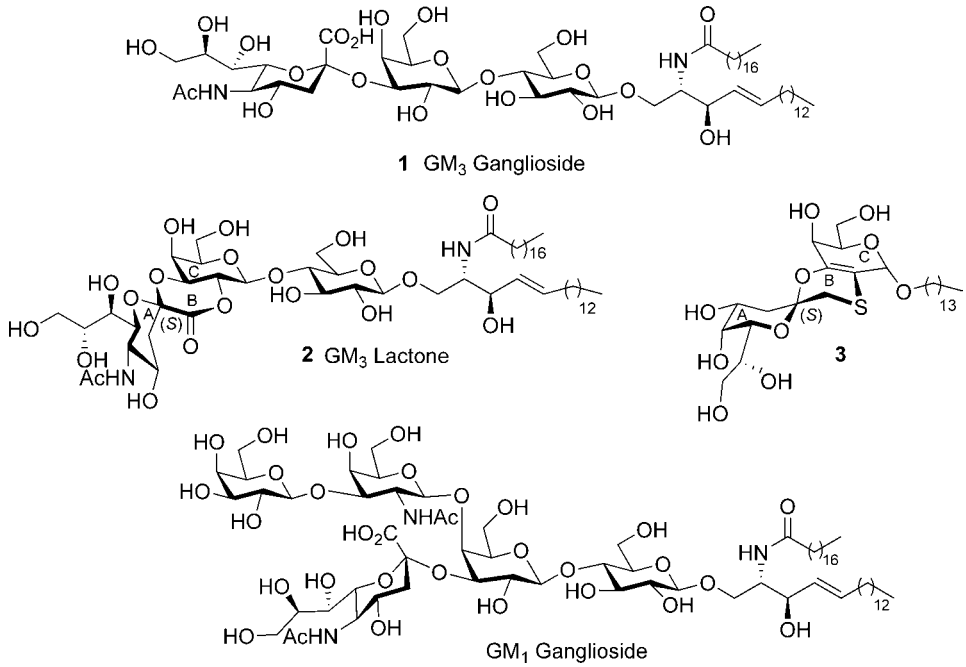


Figure 1. Structure of GM_3 ganglioside **1**, GM_3 lactone **2**, thioether mimetic **3**, and GM_1 ganglioside.

the recognition threshold. In this context and due to the advantage represented by nonpeptidic immunostimulants (*18*), hydrolytically stable analogues of GM_3 lactone are extremely attractive molecules to replace the native lactone as potential immunostimulants (*19*, *20*).

We recently reported (*21*) the totally diasteroselective synthesis of a thioether-bridged mimetic of GM_3 lactone, compound **3** (Figure 1), which is stable under physiological conditions and is structurally simpler than the endogenous lactone **2**. The structure of **3** presents a deoxy manno residue replacing the sialic portion, whereas the ceramidic residue is replaced by an aliphatic chain. A striking shape similarity between GM_3 lactone **2** and GM_3 thioether **3** was revealed; indeed, **3** presents the folded shape characteristic of the lactone structure which might be responsible for the enhanced immunogenicity of **2** compared to that of the parent GM_3 ganglioside **1**.

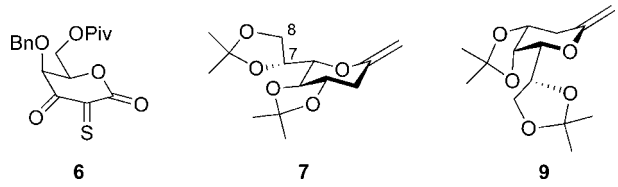
However, unlike proteins, saccharidic antigens are poorly immunogenic (*22*); thus, the synthesis of glycosyl derivative **4** (see Scheme 3) and of the corresponding keyhole-limpet hemocyanin (KLH) (*23*) conjugate **5** was realized and is here described together with the computational approach that allowed the proper choice of the synthetic precursors. The use of KLH-conjugate **5** as an immunogen *in vivo* to raise antibodies that cross-reacted with antigens expressed on melanoma cells is also reported.

EXPERIMENTAL PROCEDURES

Computational Methods. All of the calculations were carried out using the Gaussian 03 program package through optimizations in the gas phase at the B3LYP/6-311+G(2df,p) level for the S atom and 6-311+G(d,p) level for the other atoms to correctly describe the geometries and the electronic properties of compounds that contain a sulfur atom (*24*, *25*). Vibrational frequencies were computed at the same level of theory to define the optimized structures as minima or transition states, which present an imaginary frequency corresponding to the forming bonds. The solvent effects were considered by single-point calculations, at the same level as that above, on the gas-phase optimized geometries, using a self-consistent reaction field (SCRF) method based on the polarizable continuum model (PCM) (*26*−*28*).

Representative Procedure for Glycosylation. *Azido glycoside* **17.** To a mixture of **15** (160 mg, 0.25 mmol), bis(cyclopentadienyl)hafnium(IV) dichloride (Cp_2HfCl_2) (170 mg, 0.45 mmol), AgOTf (250 mg, 0.97 mmol), and 6-azido-1-hexanol (70 mg, 0.5 mmol) cooled to −40 °C, dry CH_2Cl_2 (30 mL) was added. After 40 min at −40 °C, the solution was neutralized with NEt_3 and filtered through a pad of Celite, and the filtrate was washed with a saturated solution of $NaHCO_3$ (1 × 50 mL), then with brine (1 × 50 mL). The organic phase was dried over Na_2SO_4 and concentrated to dryness to give 200 mg of crude product. The crude product was purified by flash column chromatography on silica gel (petroleum ether/EtOAc 1:1) to give **20** (150 mg, 80%), as a glassy solid. ^{1}H NMR (400 MHz, $CDCl_3$): δ 5.37 (d, 1H, $J_{d\text{-}e}$ = 2.4 Hz), 5.32 (bs, 1H), 5.26−5.21 (m, 1H), 5.12−5.09 (m,1H), 4.97 (s, 1H), 4.50−4.46 (m, 1H), 4.25−4.16 (m, 2H), 4.18−4.14 (X part of an AXY system, 1H, J_{XA} = 6.4 Hz, J_{XY} = 11.6 Hz), 4.11−4.06 (Y part of an AXY system, 1H, J_{YA} = 7.6 Hz, J_{YX} = 11.6 Hz), 3.96 (ad, 1H, J_{5-6} = 10.0 Hz), 3.75−3.69 (m, 1H), 3.53−3.47 (m 1H), 3.24 (t, 2H, J = 7.2 Hz), 3.02−2.98 (A part of an AB system, 1H, J_{AB} = 13.0 Hz), 2.97−2.94 (B part of an AB system, 1H, J_{BA} = 13.0 Hz), 2.15 (s, 3H), 2.10 (s, 3H), 2.07 (s, 3H), 2.02 (s, 3H), 2.00 (s, 3H), 1.99−1.98 (m 2H), 1.95 (s, 3H), 1.62−1.56 (m, 4H), 1.43−1.36 (m, 4H). ^{13}C NMR (50 MHz, $CDCl_3$): δ 170.8, 170.2, 170.1, 169.6, 169.5 (2C), 137.4, 109.0, 95.7, 93.0, 68.6, 68.0, 67.4, 67.3, 66.4, 64.4 (2C), 62.0, 61.7, 51.3, 33.8, 33.6, 29.3, 28.7, 26.4, 25.7, 20.7 (3C), 20.6 (3C). $[\alpha]_D^{23}$ +22.31 (c 1.09, CH_2Cl_2). Elem. Anal. for $C_{32}H_{45}N_3O_{16}S$: Calcd. C 50.59, H 5.97, N 5.53. Found: C 50.62, H 6.01, N 5.42; ESI-MS 782.2 $[M + Na]^+$, 798.2 $[M + K]^+$. To a stirred solution of **20** (120 mg, 0.158 mmol) in CH_3OH (3.2 mL), MeONa (2 mg, 0.032 mmol) was added. The mixture was stirred at RT for 2.5 h, then the pH adjusted to neutrality with HCl (10% in MeOH). Evaporation of the solvent under vacuum gave a crude product which was purified by flash chromatography on silica gel (EtOAc/CH_3OH 5:1) to give **17** (72 mg, 90%) as a glassy solid. ^{1}H NMR (400 MHz, CD_3OD): δ 4.97 (s, 1H), 4.17−4.12 (m, 1H), 4.09−4.06 (m, 1H), 4.02 (dd, 1H, J_{4-3} = 3.2 Hz, J_{4-5} = 1.2 Hz), 3.94 (dd, 1H, J_{5-6} = 9.6 Hz, J_{5-4} = 1.2 Hz), 3.84−3.79 (A part of an ABX_2 system, 1H, $J_{A\text{-}B}$ = 10.0 Hz, $J_{A\text{-}X}$ = 6.4 Hz), 3.77−3.62 (m, 6H), 3.52−3.47 (B part of an ABX_2 system, 1H, $J_{B\text{-}A}$ = 10.0 Hz, $J_{B\text{-}X}$ = 6.4 Hz), 3.31−3.28 (m, 2H), 3.05−3.01 (A part of an AB system, 1H, J_{AB} = 13.0 Hz), 2.99−2.96 (B part of an AB system, 1H, J_{BA} = 13.0 Hz),

Chart 1. Structure of Heterodiene 6 and Dienophiles 7 and 9



1.94−1.92 (m, 2H), 1.64−1.57 (m, 4H), 1.46−1.41 (m, 4H). ^{13}C NMR (50 MHz, CD_3OD): δ 141.6, 106.4, 96.3, 92.3, 72.6, 70.9, 68.5, 67.8, 66.5, 66.3, 64.6, 62.8, 61.1, 51.1, 36.3, 33.4, 29.2, 28.6, 26.3, 25.6. $[\alpha]_D^{23}$ +51.64 (c 0.25, CH_3OH). ESI-MS 530.3 $[M + Na]^+$.

Immunization and Fusion. Two female, 8 week old BALB/c mice (Ce.S.A.L., Firenze) were immunized with intraperitoneal (mouse A) and intravenous (mouse B) injections with antigen−KLH conjugate solution four times, twice a week. In the first immunization, the antigen was injected as a 1:1 (v/v) emulsion in Freund's complete adjuvant (mouse A) to a final volume of 0.2 mL and as a 1:1 (v/v) solution in sterile PBS (mouse B) to a total volume of 0.2 mL. The second and third immunizations were performed in the same way, except that an incomplete Freund's adjuvant was used in mouse A. The final immunization was given 3 days prior to cell fusion, through intravenous injection in both mice A and B. On the day of fusion, the mice were euthanized by cervical dislocation, spleens were harvested, and 1×10^8 cells were collected and used for each fusion. Spleen cells were fused with a hypoxanthine−aminopterin−thymidine (HAT) sensitive mouse myeloma cell line, NS0, by the polyethylene glycol (PEG) method (*29*). NS0 cells were maintained in DMEM with 10% Fetalclone I (HyClone) and split 1:2 the day before fusion. NS0 cells (1×10^8) were mixed in serum-free DMEM, centrifuged, and, after removing the supernatant, were placed in a water bath at 37 °C. Then, 1 mL of prewarmed PEG (Sigma-Aldrich) was added dropwise. At the end of PEG addition, prewarmed serum-free medium was added, and the tube was centrifuged to remove the supernatant. The fusion product was resuspended in DMEM containing 20% Fetalclone I and 1× HAT, and the ensuing cell suspension was plated in 24 well plates; cells were incubated at 37 °C in a CO_2 incubator.

ELISA Procedures. Hybridoma supernatants were screened for binding to the GM_3 ganglioside by enzyme-linked immunosorbent assay (ELISA). The ELISA 96 well plate (Corning) was first treated with 100 μL of GM_3 (30 μg/mL in 100% ethanol) overnight at room temperature. To minimize nonspecific adsorption, 300 μL of PBS containing 0.05% Tween (TPBS) and 3% BSA were added for 1 h and washed three times with TPBS. Hybridoma culture supernatants (100 μL/well) were added to the coated plate and incubated at room temperature for 2 h. Subsequently, the plate was washed and incubated with secondary antibody (peroxidase-labeled antimouse, 1:500 in TPBS) for 1 h. The plate was washed three times with TPBS, then 100 μL of tetramethylbenzidine (TMB, Sigma) was added to each well. The plate was further incubated for 5 min, and hence, the reaction was stopped with 0.5 M HCl. Absorbance was measured using a microplate reader (ELX800, Bio-Tek Instruments, Inc.) at 450 nm.

Table 1. Relative Reaction and Activation Energies for the Cycloaddition Reaction of 6A to 7A and 9A Giving, Respectively, the Diastereoisomeric Cycloadducts 8-*S*/8-*R* and 10-*S*/10-*R*

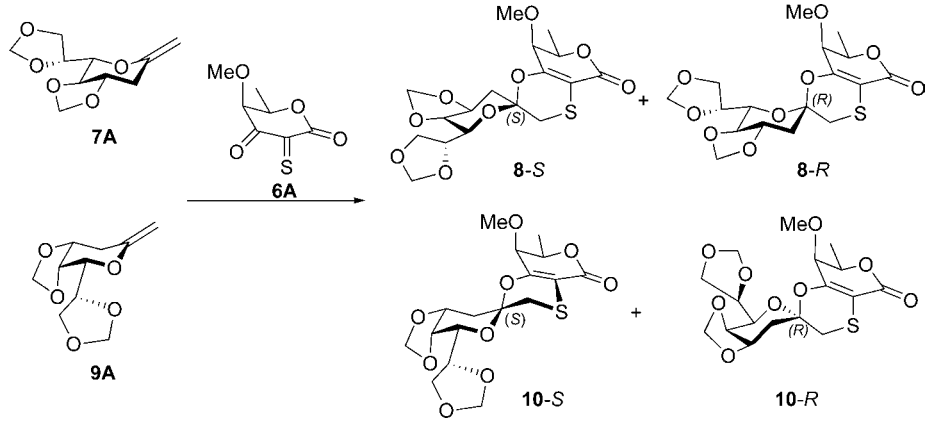
compound	$\Delta\Delta E$ (kcal/mol)	$\Delta\Delta E^{\ddagger}$(kcal/mol)
8-*S*	3.77	0.85
8-*R*	0.00	0.00
10-*S*	0.00	0.00
10-*R*	5.07	10.85

DISCUSSION

Molecular Modeling. The entirely diasteroselective synthesis of mimetics **3** and **4** is based on an inverse electron demand [4 + 2] cycloaddition between the α-thiono-β-keto-δ-lactone **6** (Chart 1) and an appropriate exoenitol obtained from a commercially available monosaccharide. Considering the configuration of the stereogenic centers of the structure of the sialic acid moiety of **2** (ring A, Figure 1), we envisaged exoenitol **7**, easily obtainable from D-galactose, as an electron rich dienophile featuring the correct orientation of the substituents at C4−C8, although the native acetamido group at C5 is replaced by an oxygenated function.

The synthetic scheme may be effective if the spiranic stereocenter rising from cycloaddition would be formed with the correct stereochemistry, i.e., with the same *S* configuration as that of GM_3 lactone **2**. DFT calculations (*24*, *25*) were performed on the simplified structure **7A**, in which the isopropylidene methyl groups of **7** (Chart 1) were replaced by hydrogen atoms, and **6A**, in which the benzyl and the pyvaloyloxymethyl groups of **6** (Chart 1) were both replaced by methyl groups. These simplifications do not alter the basis structural elements of cycloaddends but allow reasonable computational times. In Scheme 1, diene **6A**, exoenitol **7A**, and the corresponding diastereoisomeric cycloadducts **8**-*S* and **8**-*R* are depicted. The reaction was investigated both from the thermodynamic and the kinetic points of view. In particular, the relative stability of **8**-*S* and **8**-*R* and that of the corresponding transition states (TSs) was studied (*30*) and is reported in Table 1. It is easily appreciated that the energetically preferred diasteroisomer **8**-*R* corresponded to the incorrect *R* configuration of the spiro

Scheme 1. Structures of Model Exoenitols 7A and 9A, Model Diene 6A, and of the Corresponding Cycloadducts 8-*S* and 8-*R*, and 10-*S* and 10-*R*



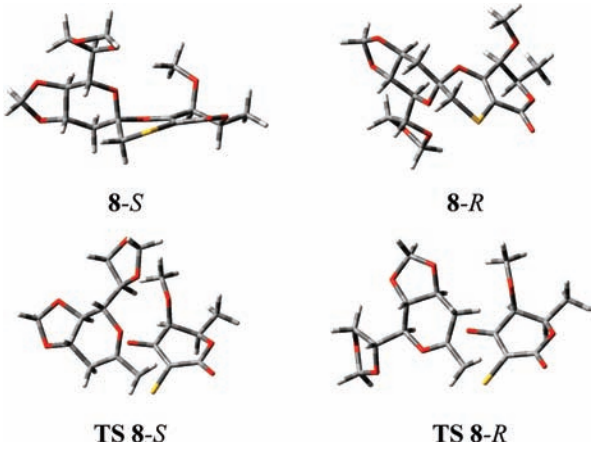


Figure 2. Three-dimensional plots of the preferred conformations of the diastereoisomeric cycloadducts **8**-*S* and **8**-*R* and of the corresponding TSs.

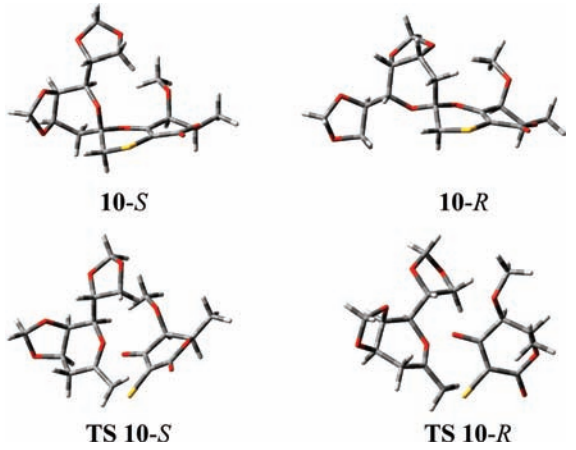


Figure 3. Three-dimensional plots of the preferred conformations of the diastereoisomeric cycloadducts **10**-*S* and **10**-*R* and of the corresponding TSs.

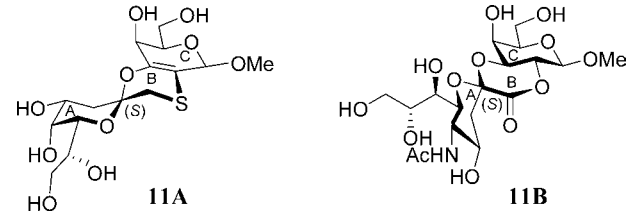


Figure 4. Structure of model compounds **11A** and **11B**.

center (see Figure 2), suggesting that exoenitol **7** is the incorrect precursor for the desired mimetic.

We therefore moved to exoenitol **9** (Chart 1), easily available from D-mannose, which may react with **6** to give the tricyclic cycloadduct with *S* configuration at the spiro center. Indeed, when the reaction of the simplified dienophile **9A** (Scheme 1) was investigated using a DFT computational approach at the same level of theory previously employed, thermodynamic and kinetic preference for the adduct **10**-*S* over the adduct **10**-*R* could neatly be appreciated (Scheme 1, Table 1, and Figure 3), indicating that a mimetic of **2** of the correct configuration could be obtained by the described synthetic strategy.

Actually, when **6** was reacted with **9**, the predicted stereochemical outcome was confirmed (see below), and the reaction afforded a cycloadduct (**12**, Scheme 2) with a tricyclic moiety presenting a double bond at the junction between the B and C rings. To evaluate the effects of this insaturation, the conformational properties of the model structure **11A** were investigated through DFT calculations in comparison with the saturated portion of GM_3 lactone **11B** (Figure 4). The energies of all of the conformers were recalculated in water, to reflect the actual situation in solution. Calculations confirmed the preference for a boat-like conformation of the lactone ring of **11B** (*31*) and showed a very similar geometry of the most stable conformation of **11A**. Figure 5 shows the global minimum conformations of **11A** and **11B** and their good superimposition, although their A rings differ in the configuration of two stereocenters. Moreover, experimentally determined ^{1}H NMR coupling constants of

Scheme 2. Synthesis of Thioether Mimetic 3

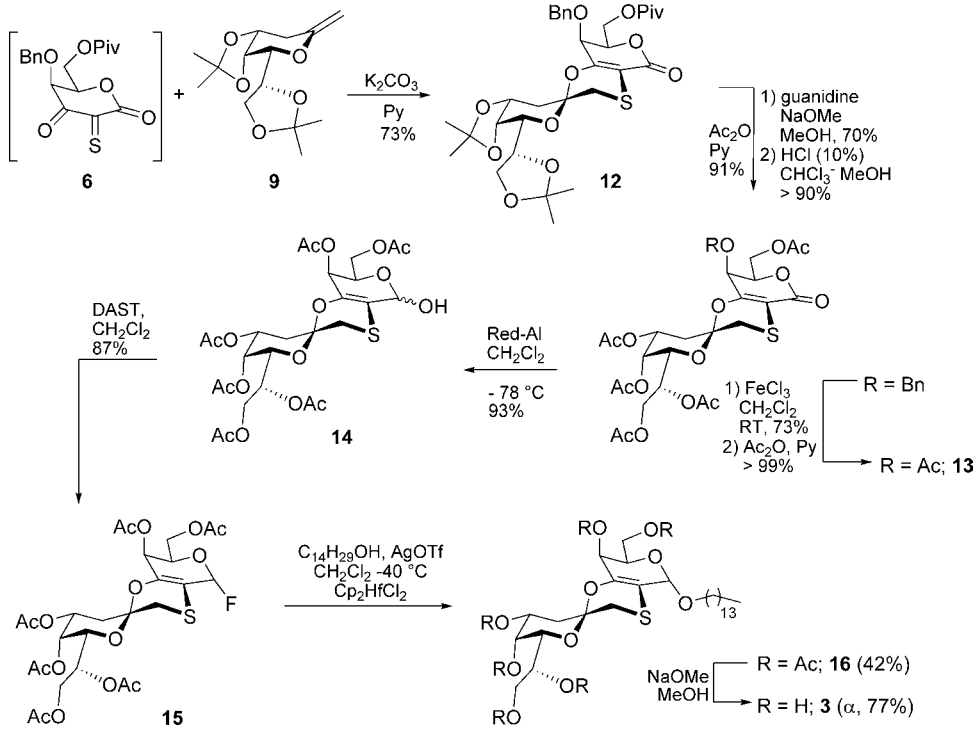
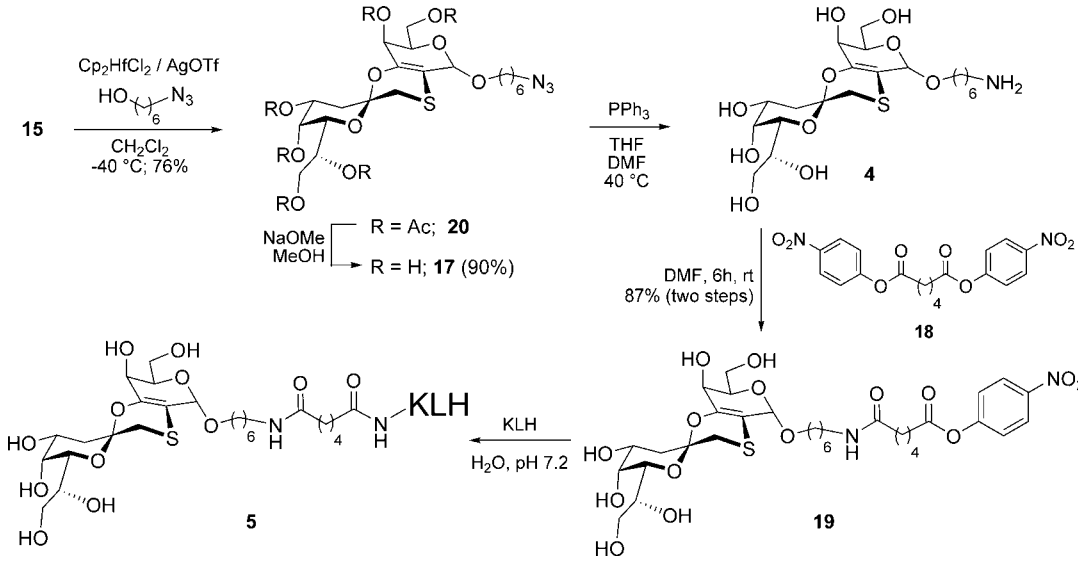




Figure 5. Three-dimensional plots of the preferred conformations of **11A** and **11B** and their superimposition.

Scheme 3. Synthesis of the KLH-Conjugate Mimetic 5



significant vicinal hydrogen atoms in the tricyclic moiety are in agreement with the preferred geometry of **11A** depicted in Figure 5 (see $J_{5,6}$, $J_{3,4}$, and $J_{4,5}$ of compounds **17** and **20** in the Experimental Procedures section).

Diasteroselective Synthesis. [4 + 2] Cycloaddition between α-thiono-*β*-keto-*δ*-lactone **6** (*32*) and exoenitol **9** (*21, 33*) was performed in $CHCl_3$ at 40 °C in the presence of pyridine and potassium carbonate affording the desired product (Scheme 2) with complete diasteroselectivity (*21*). The configuration of the spiranic stereocenter of cycloadduct **12** (73% over two steps) was unambiguously assigned by X-ray crystal structure determination (*21*). Sequential removal of protecting groups and acetylation of free hydroxyl groups under standard conditions gave the peracetylated derivative **13**. Reduction of the lactonic function with freshly prepared sodium bis(2-methoxyethoxy)-aluminum (RedAl, 1.06 M toluene) afforded the hemiacetalic derivative **14** (93%). Activation of **14** as fluorinated glycoside with diethylaminosulfotrifluoride (DAST) in CH_2Cl_2 allowed the isolation of **15** as a pseudoalpha anomer in 87% yield which, in turn, was treated with tetradecanol under Ley's glycosylation conditions (*34*) to afford **16** (42%). Deacetylation of pseudo-α-glycoside **16** gave the desired thioether **3** in 77% yield (Scheme 2). The hydrolytic stability of **3** at pH ∼7 (1 month at room temperature) and at pH 5−6 (15 days, room temperature) was monitored by ^{1}H NMR analysis.

In order to use thioether **3** as an immunogen to raise polyclonal and monoclonal antibodies, considering the known low immunogenicity of saccharidic antigens (*35*), the *ω*-amino glycosyl derivative **4** (Scheme 3) was prepared from the fluoro derivative **15** by treatment with azido hexanol under Ley's glycosylation conditions (*34*). The pseudo-α azido derivative **17** obtained after the removal of acetyl groups underwent a Staudinger reduction to give **4**, which was reacted with bis-*p* nitrophenyl adipic ester **18** (*36*) and gave **19** (87%, over two steps) as an activated carboxylic derivative (Scheme 3). Finally, **19** was coupled to the protein carrier KLH (*23, 35*).

The thioether−KLH conjugate **5** was prepared by mixing **19** with KLH (phosphate buffer, room temperature, 20 h). Saccharide molecule/KLH loading was determined by the trinitrobenzensulfonic (TNBS) test (*37*) to be ∼27%.

Biological Tests. To determine the immunogenicity of mimetic **5**, BALB/c mice were immunized with the KLH conjugate. Following Galfrè's procedure (*29*) for the production of monoclonal antibodies, after sequential immunizations spleen cells from immunized mice were collected and fused with a HAT sensitive mouse myeloma cell line (NS0). The ensuing hybridomas were screened by testing supernatants for binding to GM_3 ganglioside **1** by an enzyme-linked immunosorbent assay (ELISA). The supernatant displaying the highest absorbance (IV1:4C5C4) was then chosen for further analyses. An ELISA test aimed at isotype determination was also performed. The IV1:4C5C4 supernatant turned out to be composed by two isotypes: IgM and IgG3, with the IgM quantitatively prevailing on the IgG3 (Figure 6).

The immunoreactivity of the IV1:4C5C4 supernatant toward either GM_3- or GM_1-ganglioside was then screened through an ELISA test. Results (Figure 7) clearly indicated that the supernatant indeed binds GM_3, whereas no appreciable binding to GM_1 was observed.

In order to demonstrate the potential use as an immunostimulant of a newly synthesized thioether-bridged mimetic of GM_3 lactone, we described here the procedure and the results obtained from the production and the first step of characterization of monoclonal antibodies raised against the saccharidic antigen. To this purpose, three BALB-C mice were immunized by multiple injections of the conjugated KLH−antigen (*38, 39*) every two-three weeks. We periodically measured the antibody

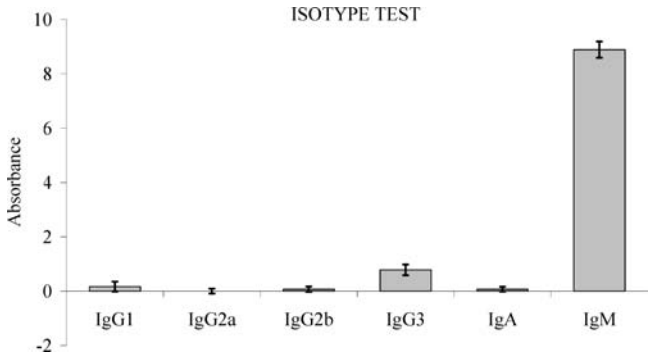


Figure 6. ELISA test performed for isotype determination. The hybridoma IV1:4C5C4 supernatant was composed of two isotypes: IgM and IgG3.

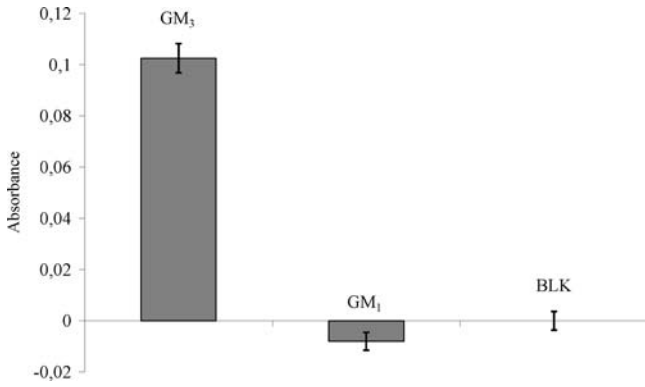


Figure 7. ELISA test to compare antibody immunoreactivity toward either GM_3- or GM_1-ganglioside.

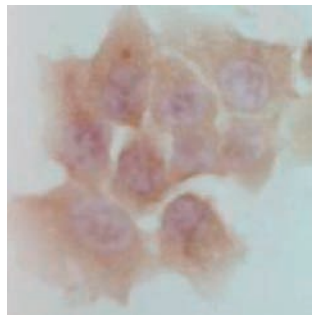


Figure 8. Human HCT116 cell line: staining with polyclonal serum obtained from mice immunized with the GM_3 mimetic.

titer in mice serum, and we proceeded to the sacrifice and splenic explants only after reaching a good polyclonal titer (1:10000). Such results were obtained after three months from the first inoculum. The serum specificity for GM_3 was confirmed by ELISA, using microtiter plate wells coated with 3 μg/well of GM_3 antigen in ethanol, incubated overnight at room temperature. To evaluate the cross-reactivity of the polyclonal serum for the human GM_3, it was also checked by immunocytochemistry on human colon cancer cells HCT116 expressing the GM_3 antigen. As we expected, the results reported below indicate a clear positivity of the cell line tested, evidenced by the brown staining. Note that there is no detectable signal at the nuclear level (Figure 8).

The same protocols were performed on melanoma cells expressing or not expressing the GM_3 antigen with the hybridoma population IV1:4C5C4 supernatant, obtaining a staining of good intensity and specificity (Figure 9).

The specificity of the signal is demonstrated by the absence of staining in the negative cell line (WM-266-4) and by the focal staining at the plasma membrane level of GM_3 expressing cells (A375). Note that the signal obtained with the hybridoma supernatant is more localized at the cell periphery with respect to polyclonal one.

These latter results can encourage further cloning of the IV1:4C5C4 hybridoma and purification of the IV1:4C5C4 supernatant to obtain a monoclonal antibody against GM_3 to be used in the future for the immunotherapy of melanoma.

CONCLUSIONS

In conclusion, the rational design and the diasteroselective synthesis of a novel thioether-bridged mimetic of GM_3 lactone, characterized by the replacement of the sialic ring by a manno residue and the stability under physiological conditions, were reported. Conjugation to the proteic carrier KLH gave glycoconjugate **5**, which was employed for the immunization of Balb/c mice. Hybridoma IV1:4C5C4, obtained after immunization, was screened for binding to GM_3 by ELISA and ICC tests. The results obtained demonstrated that **5** is immunogenic and able to raise the production of antibodies that bind GM_3 expressed on melanoma cells. The reduced structure complexity of the mimetic with respect to the native antigen, its stability *in vivo*, as well as the notable ability of the KLH−glycoconjugate **5** to induce a specific immune response against melanoma suggest that it possesses significant advantages over the known compounds and represents a new promising synthetic glycoconjugate for the immunotherapy of melanoma.

ACKNOWLEDGMENT

We thank Professor Lucio Luzzatto (Istituto Toscano Tumori (ITT), Italy) and Professor Gabriele Mugnai (University of

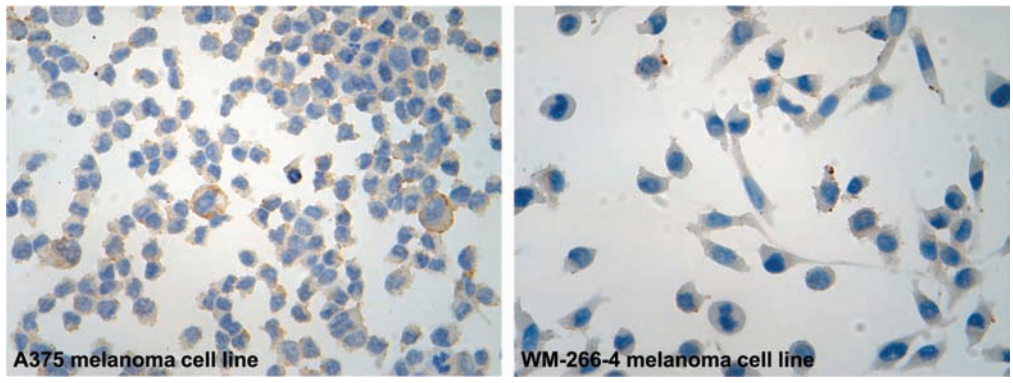


Figure 9. Human melanoma cell lines expressing (A375) and not expressing (WM-266-4) GM_3 antigen. Signals were obtained using the hybridoma population IV1:4C5C4 supernatant.

Florence) for fruitful discussions. Finantial support was provided by Ministero Universita' e Ricerca (MiUR), Italy, (PRIN 2006) and Ente Cassa di Risparmio di Firenze.

Supporting Information Available: Synthesis and characterization of compounds **5** and **19** and immunocitochemistry. This material is available free of charge via the Internet at http://pubs.acs.org.

LITERATURE CITED

(1) Feizi, T. (1985) Demonstration by monoclonal antibodies that carbohydrate structures of glycoproteins and glycolipids are oncodevelopmental antigens. *Nature 314*, 53.

(2) Hakomori, S.-I., and Zhang, Y. (1997) Glycosphingolipid antigens and cancer therapy. *Chem. Biol. 4*, 97.

(3) Kim, Y. J., and Varki, A. (1997) Perspectives on the significance of altered glycosylation of glycoproteins in cancer. *Glycoconjugate J. 14*, 569.

(4) Mannori, G., Cecconi, O., Mugnai, G., and Ruggieri, S. (1990) Role of glycolipids in the metastatic process: characteristics of neutral glycolipids in clones with different metastatic potentials isolated from a murine fibrosarcoma cell line. *Int. J. Cancer 45*, 984.

(5) Singhal, A., and Hakomori, S. (1990) Molecular changes in carbohydrate antigens associated with cancer. *BioEssay 12*, 223.

(6) Muramatsu, T. (1993) Carbohydrate signals in metastasis and prognosis of human carcinomas. *Glycobiology 3*, 291.

(7) Buck, C. A., Glick, M. C., and Warren, L. (1971) Glycopeptides from the surface of control and virus-transformed cells. *Science 172*, 169.

(8) Wickus, G. G., and Robbins, P. W. (1973) Plasma membrane proteins of normal and Rous sarcoma virus-transformed chick-embryo fibroblasts. *Nat. New Biol. 245*, 65.

(9) Harada, Y., Sakatsume, M., and Nores, G. A. (1989) Density of GM3 with normal primary structure determines mouse melanoma antigenicity; a new concept of tumor antigen. *Jpn. J. Cancer Res. 80*, 988.

(10) Tardif, M., Coulumbe, J., and Souliers, D. (1996) Gangliosides in human uveal melanoma metastatic process. *Int. J. Cancer 68*, 97.

(11) Nores, G. A., Dohi, T., and Taniguchi, M. (1987) Density-dependent recognition of cell surface GM3 by a certain anti-melanoma antibody, and GM3 lactone as a possible immunogen: requirements for tumor-associated antigen and immunogen. *J. Immunol. 139*, 3171.

(12) Harada, Y., Sakatsume, M., and Taniguchi, M. (1990) Induction of mouse anti-melanoma cytotoxic and suppressor T cells in vitro by an artificial antigen, GM3-lactone. *Jpn. J. Cancer Res. 81*, 383.

(13) Kawashima, I., Kotani, M., and Ozawa, H. (1994) Generation of monoclonal antibodies specific for ganglioside lactones: Evidence of the expression of lactone on human melanoma cells. *Int. J. Cancer 58*, 263.

(14) Pan, Y., Chefalo, P., and Nagy, N. (2005) Synthesis and immunological properties of N-modified GM3 antigens as therapeutic cancer vaccines. *J. Med. Chem. 48*, 875.

(15) Jarvis, L. M. (2006) Body, heal thyself. After false starts, cancer immunotherapies tiptoe toward commercialization. *Chem. Eng. News 84*, 23.

(16) Parmiani, G., De Filippo, A., Novellino, L., and Castelli, U. (2007) Unique human tumour antigens: immunobiology and use in clinical trials. *J. Immunol. 178*, 1975.

(17) Dudley, M. E., Wunderlich, J. R., and Yang, J. C. (2005) Adoptive cell transfer therapy following non-myeloablative but lymphodepleting chemotherapy for the treatment of patients with refractory metastatic melanoma. *J. Clin. Oncol. 23*, 2346.

(18) Riker, A. I., Radfar, S., Liu, S. H., Wang, Y., and Khong, H. T. (2007) Immunotherapy of melanoma: a critical review of current concepts and future strategies. *Expert Opin. Biol. Ther. 7*, 1.

(19) Wilstermann, M., Kononov, L. O., Nilsson, U., Ray, A. K., and Magnusson, G. (1995) Synthesis of ganglioside lactams corresponding to GM1-, GM2-, GM3-, and GM4-ganglioside lactones. *J. Am. Chem. Soc. 117*, 4742.

(20) Tietze, L. F., Keim, H., Janβen, C. O., Tappertzhofen, J., and Olschimke, J. (2000) Synthesis of a novel ether-bridged GM_3-lactone analogue as a target for an antibody-based cancer therapy. *Chem.—Eur. J. 6*, 2801.

(21) Toma, L., Di Cola, E., Ienco, A., Legnani, L., Lunghi, C., Moneti, G., Richichi, B., Ristori, S., Dell'Atti, D., and Nativi, C. (2007) Synthesis, conformational studies, binding assessment and liposome insertion of a thioether-bridged mimetic of the antigen GM_3 ganglioside lactone. *ChemBioChem 8*, 1646.

(22) Tzianabos, A. O. (2000) Polysaccharide immunomodulators as therapeutic agents: structural aspects and biological function. *Clin. Microbiol. Rev. 13*, 523.

(23) Danishefsky, S. J., and Allen, J. R. (2000) From the laboratory to the clinic: a retrospective on fully synthetic carbohydrate-based anticancer vaccines. *Angew. Chem., Int. Ed. 39*, 836.

(24) Becke, A. D. (1993) Density-functional thermochemistry. III. The role of exact exchange. *J. Chem. Phys. 98*, 5648.

(25) Lee, C., Yang, W., and Parr, R. G. (1988) Development of the Colle-Salvetti correlation-energy formula into a functional of the electron density. *Phys. Rev. B 37*, 785.

(26) Cancés, E., Mennucci, B., and Tomasi, J. (1997) A new integral equation formalism for the polarizable continuum model: Theoretical background and applications to isotropic and anisotropic dielectrics. *J. Chem. Phys. 107*, 3032.

(27) Cossi, M., Barone, V., Cammi, R., and Tomasi, J. (1996) Ab initio study of solvated molecules: a new implementation of the polarizable continuum model. *Chem. Phys. Lett. 255*, 327.

(28) Barone, V., Cossi, M., and Tomasi, J. (1998) A new integral equation formalism for the polarizable continuum model: theoretical background and applications to isotropic and anisotropic dielectrics. *J. Comput. Chem. 19*, 404.

(29) Galfrè, G., and Milstein, C. (1981) Preparation of monoclonal antibodies: strategies and procedures. *Methods Enzymol. 73* (Pt B), 3–46.

(30) All the degrees of conformational freedom of the ground state structures **8**-*S* and **8**-*R* as well as of the corresponding TSs were taken into consideration by performing several optimizations in each case.

(31) Ray, A. K., Nilsson, U., and Magnusson, G. (1992) Synthesis and conformational analysis of GM3 lactam; a hydrolytically stable analog of GM3 ganglioside lactone. *J. Am. Chem. Soc. 114*, 2256.

(32) Bartolozzi, A., Pacciani, S., Benvenuti, C., Cacciarini, M., Liguori, F., Menichetti, S., and Nativi, C. (2003) Totally Stereoselective synthesis of 1,3-disaccharides through Diels-Alder reactions. *J. Org. Chem. 68*, 8529.

(33) Haudrechy, A., and Sinaÿ, P. (1992) Cyclization of hydroxy enol ethers: a stereocontrolled approach to 3-deoxy-D-manno-2-octulosonic acid containing disaccharides. *J. Org. Chem. 57*, 4142.

(34) Baeschlin, D. K., Green, L. G., Hahn, M. G., Hinzen, B., Ince, S. J., and Ley, S. V. (2000) Rapid assembly of oligosaccharides: 1,2-diacetal-mediated reactivity tuning in the coupling of glycosyl fluorides. *Tetrahedron: Asymmetry 11*, 173.

(35) Hermanson, G. T. (1996) *Bioconjugate Technique*, pp 421—427, Academic Press, Orlando, FL.

(36) Wu, X., Ling, C.-C., and Bundle, D. (2004) A new homobifunctional *p*-nitro phenyl ester coupling reagent for the preparation of neoglycoproteins. *Org. Lett. 6*, 4407.

(37) Habeeb, F. S. A. (1966) Determination of free amino groups in proteins by trinitrobenzenesulfonic acid. *Anal. Biochem. 14*, 328.

(38) Bitton, R. J., Guthmann, M. D., Gabri, M. R., Carnero, A. J. L., Alonso, D. F., Fainboim, L., and Gomez, D. E. (2002) Cancer vaccines: an update with special focus on ganglioside antigens (review). *Oncol. Rep. 9*, 267.

(39) Gabri, M. R., Mazorra, Z., Rispoli, G. V., Mesa, C., Fernandez, L. E., Gomez, D. E., and Alonso, D. F. (2006) Complete antitumor protection by perioperative immunization with GM3/VSSP vaccine in a preclinical mouse melanoma model. *Clin. Cancer Res. 12*, 7092.

BC900557V

Supporting Informations

A Stable GM_3 Lactone Mimetic Raises Antibodies Specific for the Antigens Expressed on Melanoma Cells

Annarosa Arcangeli,[*,∫] *Lucio Toma*[*,≠] *Luca Contiero,*[¥] *Olivia Crociani,*[∫] *Laura Legnani,*[≠] *Carlotta Lunghi,*[¥] *Elisa Nesti,*[∫] *Gloriano Moneti,*[¶] *Barbara Richichi*[¥] *and Cristina Nativi*[*¥~]

Dipartimento di Patologia e Oncologia Sperimentali, Universita' di Firenze; Dipartimento di Chimica Organica, Universita' di Pavia; Dipartimento di Chimica, Universita' di Firenze; Dipartimento di Farmacologia, Universita' di Firenze; FiorGen, Universita' di Firenze.

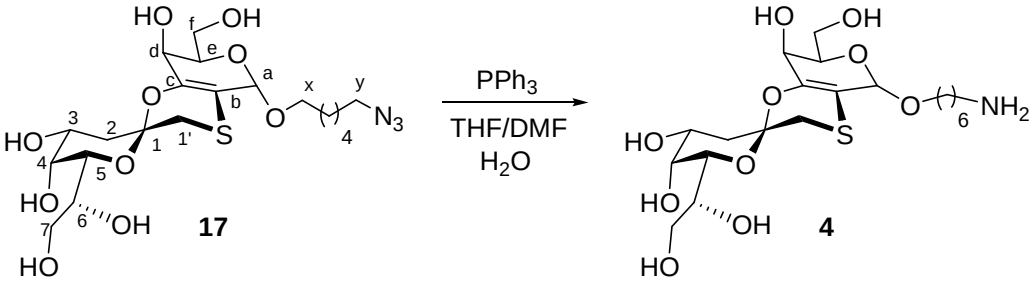
cristina.nativi@unifi.it

Synthesis of compound 19 S3

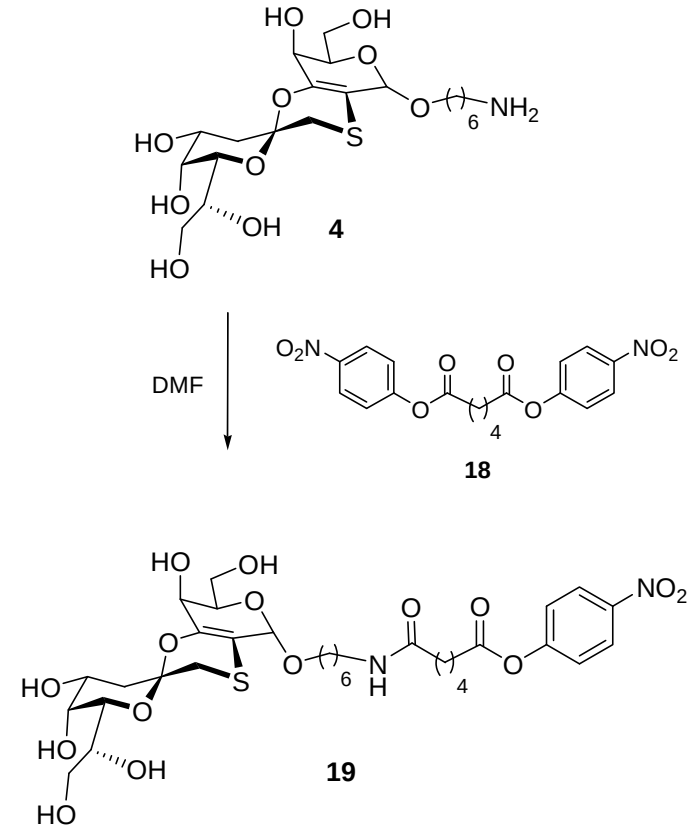
Synthesis of compound 5 S4

Immunocitochemistry (ICC) S5

Synthesis of compound 19



To a stirred solution of **17** (13.2 mg, 0.026 mmol) in a mixture of dry THF (1 mL) and dry DMF (0.1 mL), Ph_3P (13.6 mg, 0.052 mmol) and H_2O (2.3 μL, 0.13 mmol) were added. The reaction mixture was warmed to 40 °C and stirred for 18 h. Evaporation of the solvent under vacuum gave the crude **4** which was used without purification for the following reaction.

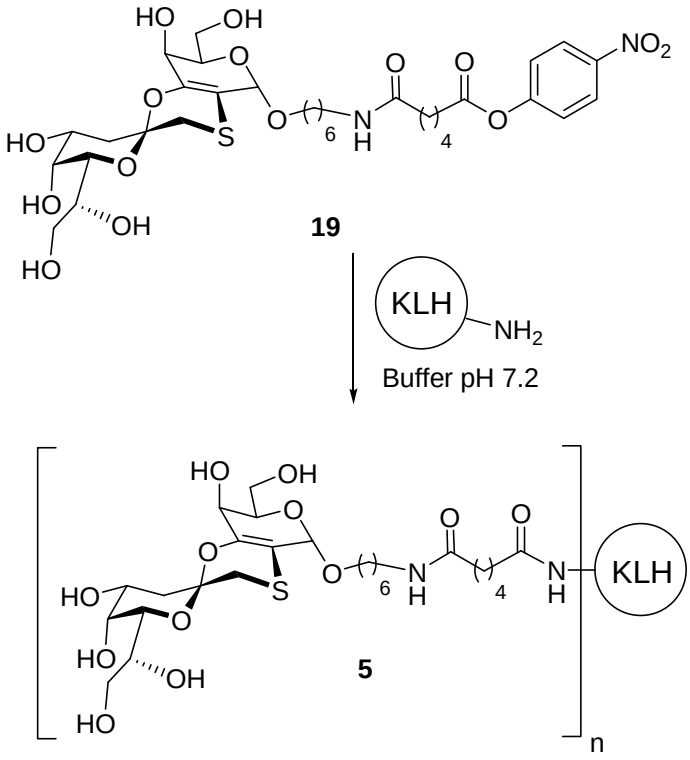


To a stirred solution of **4** in dry DMF (1 mL), **18** (50 mg, 0.130 mmol) was added and the reaction mixture was stirred at RT for 6 h. Evaporation of the solvent under vacuum gave a crude which was purified by flash chromatography on silica gel (CH_2Cl_2/CH_3OH 2:1) to give **19** (16.5 mg, 87%) as glassy solid.

^{1}H NMR (400MHz, CD_3OD): δ 8.30-8.29 (AA' part of an AA'MM' system, 2H, $J_{A\text{-}M}$ = 4.8 Hz, Ph), 7.38-7.37 (MM' part of an AA'MM' system, 2H, $J_{M\text{-}A}$ = 4.8 Hz, Ph), 4.96 (s, 1H, H_a), 4.15 (adt, 1H, $J_{3\text{-}4}$ = 2.8 Hz, $J_{3\text{-}2}$ = $J_{3\text{-}2'}$ = 8.8 Hz, H_3), 4.09-4.05 (m, 1H, H_e), 4.03-4.02 (dd, 1H, $J_{4\text{-}3}$ = 2.8 Hz, $J_{4\text{-}5}$

= 0.8 Hz, H_4), 3.94 (dd, 1H, $J_{5\text{-}6}$ = 9.6 Hz, $J_{5\text{-}4}$ = 0.8 Hz, H_5), 3.82-3.77 (A part of an ABX_2 system, 1H, $J_{A\text{-}B}$ = 10.0 Hz, $J_{A\text{-}X}$ = 6.4 Hz, H_x), 3.76-3.61 (m, 6H, H_d, H_6, H_7, $H_{7'}$, H_f, $H_{f'}$), 3.51-3.45 (B part of an ABX_2 system, 1H, $J_{B\text{-}A}$ = 10.0 Hz, $J_{B\text{-}X}$ = 6.4 Hz, $H_{x'}$), 3.184 (t, 2H, J = 7.0 Hz, CH_{2y}), 3.03-3.00 (A part of an AB system, 1H, $J_{A\text{-}B}$ = 13.0 Hz, $H_{1'a}$), 2.98-2.95 (B part of an AB system, 1H, $J_{B\text{-}A}$ = 13.0 Hz, $H_{1'b}$), 2.67 (t, 2H, J = 7.0 Hz, CH_2CO), 2.25 (t, 2H, J = 7.0 Hz, CH_2CO), 1.93-1.91 (m, 2H, H_2, $H_{2'}$), 1.78-1.72 (m, 4H, CH_2CH_2), 1.62-1.49 (m, 4H, CH_2CH_2), 1.44-1.33 (m, 4H, CH_2CH_2). ^{13}C NMR (50MHz, CD_3OD): δ 174.2, 171.1, 155.7, 141.7, 124.7 (2C), 122.5 (2C), 106.4, 96.3, 92.3, 72.5, 70.8, 68.4, 67.8, 66.4, 66.2, 64.5, 62.7, 60.9, 38.9, 36.1, 35.2, 33.2, 33.1, 29.2, 28.9, 26.3, 25.5, 24.8, 23.8. Elem. Anal. for $C_{32}H_{46}N_2O_{15}S$: Calc. C 52.59, H 6.34, N 3.83. Found: C 52.79, H 6.61, N 5.51; ESI-MS 753.3 $[M+Na]^+$.

Synthesis of compound 5:



To a solution of KLH (20 mg) in 20 mL of buffer (0.1 M sodium phosphate and 0.15 M sodium chloride, pH 7.2) **19** (15 mg, 0.020 mmol) was added and the mixture was stirred overnight at RT. The solution was lyophilized and the solid was dialysed to give 18.5 mg of glycoconjugate **5**.

Thioether-protein ratios were evaluated by determination of free lysine amino groups before and after conjugation by titration with trinitrobenzensulfonic acid.[S1]

Immunocitochemistry (ICC)

ICC was performed on B16F1 melanoma. Cultured B16 melanoma cells were grown in DMEM supplemented with 10% FCS and 2 mM L-glutamine. Cells were mounted on polylysine-coated slides and fixed with formaline solution. After blocking endogenous peroxidases, cells were treated with proteinase K (Roche; 5 g/ml in PBS) and UltraVBlock solution (LabVision) and then incubated with the primary antibody (hybridomas supernatant) and with the anti-GM3 antibody (M2590) diluted 1:100 in PBS-UltraVBlock (10:1 v/v) overnight at 4°C. Immunostaining was carried out using a commercially available kit (PicTure Plus kit; Zymed). For the negative control hybridomas medium replacing the primary antibody was used.[S2]

S1) F.S.A. Habeeb, *Anal. Biochem.* **1966**, *14*, 328-336.

S2) G, Galfrè; C. Milstein "Preparation of monoclonal antibodies: strategies and procedures" *Methods Enzymol*. 1981; 73(Pt B), 3-46.

Thiopalmitoylated Peptides from the Peripheral Nervous System Myelin P0 Protein: Synthesis, Characterization, and Neuritogenic Properties

Wissam Beaino and Elisabeth Trifilieff*

Laboratoire d'Imagerie et de Neurosciences Cognitives (LINC), Université de Strasbourg/CNRS. Received January 19, 2010; Revised Manuscript Received July 9, 2010

Thiopalmitoylation (i.e., the covalent attachment of palmitic acid via a thioester linkage to cysteine residues in the polypeptide backbone) is a common post-translational modification of proteins. Several proteins that have been identified as putative autoantigens in a variety of T-cell mediated autoimmune diseases are thiopalmitoylated, and thus, we have hypothesized that endogenous thiopalmitoylated peptides released during tissue breakdown may play a role in the development and chronicity of autoimmune diseases. To investigate this, we have studied the effect of thiopalmitoylation on the immunogenic and neuritogenic properties of P0, the major peripheral nervous system (PNS) myelin protein, which is thiopalmitoylated at cysteine 153, and described as a canditate autoantigen in Guillain-Barré syndrome (GBS), a human inflammatory demyelinating disease of the PNS. This paper describes the synthesis of palmitoylated peptide P0(180−199) and P0(152−171) by on-resin acylation using specific cysteine side-chain protecting groups: Mmt (labile in diluted acid) and StBu (labile in the presence of tributylphosphine). Our results show that the thiol protecting group had to be adjusted to the peptide sequence: Mmt was efficiently used for P0(180−199) thioacylation, but it was not suitable for thiopalmitoylation of P0(152−171) because of a premature deprotection of the Boc protecting group on the ε-NH_2 Lys in the presence of 2% TFA, leading to dipalmitoylation. Palmitoylated P0(152−171) was successfully obtained by using StBu as the thiol protecting group. We could show by circular dichroism that palmitoylation has no influence on the structuration of the peptide in solution but palmitoylation increased the stability of the peptide in the presence of serum. Using EAN (experimental autoimmune neuritis), the rat model of GBS, we have compared the immunological properties of palm and non-palm P0 peptides and showed that thiopalmitoylation has indeed a great influence on their neuritogenic and immunogenic properties. This study provides further support for our hypothesis concerning the role of thiopalmitoylation in the development and chronicity of inflammatory demyelinating diseases and confirms that thiopalmitoylation of peptides may provide a simple means to increase MHC class II restricted responses.

INTRODUCTION

Thiopalmitoylation (i.e., the covalent attachment of palmitic acid via a thioester linkage to cysteine residues in the polypeptide backbone) is a common post-translational modification of proteins that had been implicated in the process of protein trafficking and in the segregation of proteins in membrane compartments (*1*). Of particular interest is the role that thiopalmitoylated antigens might play in autoimmunity, since several proteins that have been identified as putative autoantigen in a variety of T-cell mediated autoimmune diseases are palmitoylated (*2*−*4*).

In our previous work, we have shown that thiopalmitoylation of encephalitogenic T-cell epitopes of central nervous myelin proteolipid protein (PLP), as occur naturally in vivo (*5*), enhanced immune responses as well as the development and chronicity of experimental autoimmune encephalomyelitis (EAE), an animal model of the human inflammatory demyelinating disease, multiple sclerosis (MS) (*6*). The lability of the thioester bond between the peptide and the palmitic chain was important for induction of encephalitogenic (disease inducing) $CD4^+$ T helper cells, as PLP peptides synthesized with the fatty acid attached via an amide linkage at the N-terminus were not encephalitogenic and induced a greater proportion of $CD8^+$ T cells. We showed also that the lipopeptides are taken up more efficiently in antigen presenting cells than the non-palm peptides and that their route of uptake is dependent on the type of bond between lipid chain and peptide (*7*). These results suggest that the immune response induced by endogenous thioacylated peptides that are released during myelin breakdown may play a role in the development and chronicity of autoimmune inflammatory demyelinating diseases.

To confirm this hypothesis, we decided to study the effects of thiopalmitoylation on the immunogenic and neuritogenic properties of P0 protein, the major protein of peripheral nervous system (PNS) myelin. P0 protein is post-translationally acylated by covalent attachment of palmitic acid to Cys^{153} via a thioester linkage (*8*) and is a candidate autoantigen in AIDP (acute inflammatory demyelinating polyradiculoneuropathy), the most common subtype of Guillain-Barré syndrome (GBS), a human inflammatory demyelinating disease of the PNS (*9*). Valuable insights in the immunopathogenic mechanism of GBS have been gained from the animal model, experimental autoimmune neuritis (EAN), that can be induced in Lewis rats by injection of the whole P0 protein or the immunodominant neuritogenic epitope peptide P0(180−199) (*10*). Previously, no P0 peptides that contain the Cys^{153} residue have been reported to be neuritogenic in the EAN model. EAN induced by P0(180−199) is characterized by a single spontaneously resolving episode of neuritis, similar to the AIDP form of GBS. At present, however, there is no reliable animal model for CIDP (chronic inflammatory demyelinating neuropthy), the chronic form of GBS (*11*). Because we have previously shown that thiopalmitoylation of PLP encephalitogenic epitopes enhanced the chronicity of EAE

* Corresponding author's address: LINC, Institut de Physique Biologique Faculté de Médecine, 4 rue Kirschleger, 67085 Strasbourg Cedex, France, e-mail address: elisabeth.trifilieff@linc.u-strasbg.fr, Telephone: + 33 (0) 368 85 40 83, Fax: + 33 (0) 368 85 40 84.

10.1021/bc100039u © 2010 American Chemical Society
Published on Web 07/27/2010

(*6*), in the current study we have injected thiopalmitoylated P0(180−199) into Lewis rats to determine if this could induce a chronic form of EAN.

This paper describes the solid-phase synthesis, characterization (secondary structure, stability) of thiopalmitoylated and non-palmitoylated P0(152−171)Cys^{153} and P0(180−199)Cys^{181} peptides and the study of their immunogenic and neuritogenic properties after injection into Lewis rats. Our results show that thiopalmitoylation has indeed important effects on the immunogenicity and neuritogenicity of P0 antigens.

EXPERIMENTAL PROCEDURES

Materials. Fmoc-L-amino acids and Boc-L-amino acids were purchased from Novabiochem (Merck chemical Ltd., France). Preloaded Wang resins and BOP were obtained from Novabiochem. Tri-*n*-butylphosphine (tBu_3P), trifluoroacetic acid (TFA), triisopropylsilane (TIS), and dimethylformamide (DMF) were purchased from Sigma-Aldrich (St-Quentin Fallavier, France). Palmitic acid was purchased from Fluka (St-Quentin Fallavier, France). Dichloromethane and piperidine were purchased from SDS (Peypin, France). *N*-Ethyldiisopropylamine (DIEA) was purchased from Merck (Briare Le Canal, France). All other chemicals were of the purest grade available.

Peptide Synthesis. Peptides (0.2 mmol) were synthesized manually on a Wang resin using the Fmoc/tBu strategy and BOP as coupling reagent. Typically, successive single couplings were performed with 3 equiv of Fmoc amino acid and were monitored with the Kaiser color test. Fmoc amino acid side-chain protecting groups were Arg(PbF), Asp(OtBu), Cys(Mmt), Cys(StBu), Glu(OtBu), Gln(Trt), His(Trt), Lys(Boc), Ser(tBu), Thr(tBu), Trp(Boc), and Tyr(tBu). Boc-Ala-OH and Boc-Tyr(tBu)−OH were coupled as N-terminal amino acids.

Peptides were cleaved from the resin with the low-odor mixture (87.5% trifluoroacetic acid (TFA, 5% phenol, 5% H_2O, 2.5% triisopropylsilane (TIS)) for non-palmitoylated peptides and (95% trifluoroacetic acid (TFA), 2.5% triisopropylsilane (TIS), 2.5% H_2O) for palmitoylated peptides. After evaporation of TFA, peptides were precipitated in ethyl ether and lyophilized after solubilization in 10% acetic acid.

Deprotection of the S-(Mmt) Cysteinyl Residue. The peptide−resin (200 mg) was treated with a solution of 2% TFA in dichloromethane (DCM) containing 5% TIS for 10 min in a glass reaction vessel equipped with a sintered glass filter using nitrogen for mixing. After filtration, the peptide−resin was washed with DCM. The deprotection and washing steps were repeated seven times. The peptide−resin was finally washed with DCM and DMF.

Deprotection of the S-(StBu) Cysteinyl Residue. The peptide−resin (200 mg) was introduced in a glass reaction vessel equipped with a sintered glass filter using nitrogen for mixing. A freshly prepared mixture of tributylphosphine (100 equiv) and H_2O (400 equiv) DMF/DCM (1/1) (1 mL) was added. The suspension was mixed for 3 h and maintained overnight under nitrogen atmosphere. The peptide−resin was finally washed 6 times with DCM and DMF.

Palmitoylation of the Free SH Group on the Solid Support. In a glass reaction vessel equipped with a sintered glass filter, the free thiol peptide−resin (200 mg) was suspended in DMF (3 mL) containing palmitic acid (20 equiv) and BOP (20 equiv). DIEA (60 equiv) was then added. After 90 min of reaction at room temperature, the peptide−resin was filtered off; washed with DMF, DCM, and ether; and then dried in a vacuum.

Peptide Characterization. *Analytical HPLC.* Non-palmitoylated peptides were analyzed by RP-HPLC on an analytical Nucleosil C18 column (300 Å pore size, 5 μm particle size, 3.9 × 150 mm) using a Waters HPLC system. Solvent A was H_2O/0.1% TFA and solvent B was CH_3CN/H_2O (80/20)/0.09% TFA. Elution was conducted at a flow rate of 1 mL/min, and detection was performed at 214 nm. The peptides were analyzed using a stepwise gradient from 10% to 60% B over 20 min.

Table 1. Yields of Crude and Purified Peptides

peptide designation	crude peptide yield	purified peptide yield
P0(180−199)	80%	41%
Palm P0(180−199)	66%	30%
P0(152−171)	91%	42%
Palm P0(152−171)	77%	37%

Palmitoylated peptides were analyzed by RP-HPLC on an analytical Nucleosil C18 column (300 Å pore size, 5 μm particle size, 3.9 × 150 mm) using a Waters HPLC system. Solvent A was H_2O/0.1% TFA and solvent B was CH_3CN/H_2O (95/5)/0.09% TFA. Elution was conducted at a flow rate of 1 mL/min, and detection was performed at 214 nm. The peptides were analyzed using a stepwise gradient from 20% to 100% B over 20 min.

Palmitoylated Peptides Purification. The crude palmitoylated peptides were purified on a semipreparative Nucleosil C4 column (300 Å pore size, 7 μm particle size, 250 × 10 mm) using a Waters HPLC system. Solvent A was H_2O/0.1% TFA and solvent B was CH_3CN/H_2O (95/5)/0.09% TFA. Elution was conducted at a flow rate of 6 mL/min, and detection was performed at 214 nm. Peptides were purified using a stepwise gradient from 30% to 80% B for palm P0(152−171) or 20% to 60% B for palm P0(180−199) over 20 min. The crude palm peptides (20 mg) were usually solubilized in the initial eluent.

Yield data are in Table 1.

Mass Spectrometry. Peptides were characterized on a Bruker-Daltonics matrix-assisted laser desorption time-of-flight mass spectrometer (MALDI-TOF) equipped with laser SCOUT. The drop-drying method was applied using a solution of α-cyano-4-hydroxycinnamic acid in H_2O/CH_3CN (1:1).

Determination of the PLP (152−171) Palmitoylation Sites. *Acetylation with Acetic Anhydride (Ac_2O).* In a glass reaction vessel equipped with a sintered glass filter, the 2% TFA treated peptide−resin P0(152−171)Cys^{153}(StBu) (100 mg) was suspended in minimum DMF containing acetic anhydride (500 μL) and DIEA (700 μL). After 20 min of reaction at room temperature, the peptide−resin was filtered off; washed with DMF, DCM, and ether; and then dried in a vacuum. The peptide−resin was then cleaved with concentrated TFA to give the crude acetylated peptide. The crude peptide was analyzed by RP-HPLC on an analytical Nucleosil C18 column (300 Å pore size, 5 μm particle size, 3.9 × 150 mm) using a stepwise gradient from 35% to 80% in 20 min. Each peak was collected and lyophilized.

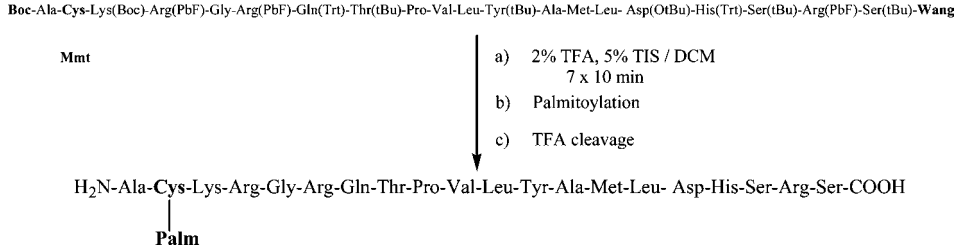
Trypsin Digestion. Each acetylated peptide (200 μg) was solubilized in 0.5 mL of 0.1 M Tris-HCl pH 8. TPCK-treated Trypsin was added as protease/peptide ratio 1/50 and incubated for 90 min at 37 °C. The reaction was stopped by addition of acetic acid. The digest was then injected in RP-HPLC on an analytical Nucleosil C18 column (300 Å pore size, 5 μm particle size, 3.9 × 150 mm) using a stepwise gradient from 1% to 60% in 20 min, then to 100% in 10 min. Each peak was collected and identified by mass spectrometry.

Circular Dichroism. Circular dichroism measurements were performed using a Jasco (Tokyo, Japan) J-810 spectropolarimeter, which was calibrated with ammonium-D-camphor-10-sulfonate as described in the instruction manual. The CD data were recorded in a 1 mm quartz cell at 25 °C between 250 and 190 nm and were expressed in terms of ellipticity units per mole of peptide residue (Θ in deg/cm^2/dmol). Stock peptide solutions were made up in Millipore-purified (Molsheim, France) water (pH 6), and the peptide concentrations were determined by UV

Table 2. Sequences of Peptides Used in This Study

peptide designation	sequence	calculated MH^+ monoisotopic mass
P0(180−199) C^{181}	ACKRGRQTPVLYAMLDHSRS	2289.17
Palm P0(180−199)	A**C(Palm)**KRGRQTPVLYAMLDHSRS	2527.37
P0(152−171)	YCWLRRQAALQRRLSAMEKG	2436.29
Palm P0(152−171)	Y**C(Palm)**WLRRQAALQRRLSAMEKG	2674.49
Dipalm P0(152−171)	Y**C(Palm)**WLRRQAALQRRLSAME**K(Palm)**G	2912.69

Scheme 1. Solid-Phase Synthesis of Thiopalmitoylated P0(180−199) Using Mmt as the Thiol Protecting Group



spectroscopy according to the Van Iersel method (*15*). CD spectra were recorded in the absence and presence of TFE (10%, 30%, and 60%). The percentage of α-helix was calculated from "calculate from ellipticity" within the *DICHROPROT* software package.

Peptides and Lipopeptides Stability in Serum. The peptide (500 μg) was dissolved in 900 μL of 0.05 M phosphate buffer (pH 7.2) containing 1% acetonitrile. Fetal calf serum (10% serum, v/v) was added (100 μL). The reaction mixture was incubated at 37 °C. At different incubation times, a 100 μL aliquot was collected, and protease activities were blocked by adding of 2 vol of acetonitrile (200 μL). After centrifugation at 3000 rpm for 5 min, the supernatant was analyzed by RP-HPLC. In these conditions, no peptide precipitated. A control sample was run in the absence of peptide.

Induction of EAN and Assessment of Clinical Signs. Male Lewis rats, 8 weeks old, weighing 230−250 g, purchased from Charles River (Domaine des oncins, L'Arbresele, France), were used in the present study. Groups of four rats were immunized with peptides P0(180−199), palm P0(180−199), P0(152−171), and palm P0(152−171), by s.c. injection at the base of the tail of 200 μL of an inoculum containing 200 μg of peptide and 0.5 mg of *Mycobacterium tuberculosis* (strain H37 RA, Difco, Detroit, Michigan, USA) emulsified in 100 μL saline and 100 μL Freund's incomplete adjuvant (SIGMA-Aldrich, St-Quentin Fallavier, France). Two noninjected rats were used as negative control. Body weights and clinical scores were assessed daily until 62 days postimmunization (dpi). Severity of paresis was graded as follows: 0 = no illness; 1 = flaccid tail; 2 = moderate paraparesis; 3 = severe paraparesis; 4 = tetraparesis; 5 = death; intermediate scores of 0.5 increments were given to rats with intermediate signs. All experiments were conducted according to protocol approved by the animal experimentation ethical committee of Univeristé de Strasbourg.

Enzyme-Linked Immunosorbent Assay (ELISA). Sera sample of all rats collected at 21, 31, and 62 dpi were tested for anti P0(180−199) and anti P0(152−171) using ELISA. Pure P0(180−199) or P0(152−171) was coated onto 96-well Maxisorb ELISA plates (NUNC) at 20 μg/mL in a volume of 100 μL of 0.05 M carbonate−bicarbonate buffer solution (pH 9.6). The plates were incubated for 1 h at 37 °C followed by three washings with PBS + 0.05% Tween 20. Nonspecific binding was blocked with 0.1% bovine serum albumin for 1 h at 37 °C. After three washings of the plates, serum samples diluted at 1/4000 were added to the wells and incubated for 1 h at 37 °C. After three additional washings, plates were incubated with mouse antirat IgG coupled to peroxidase (AbD Serotec) for 1 h at 37 °C. The reaction was visualized with *o*-phenylenediamine dihydrochloride (OPD) (SIGMA) substrate and read at 450 nm.

RESULTS

Peptide Sequences and Sites of Thiopalmitoylation. P0(180−199), the immunodominant neuritogenic epitope in the Lewis rat, will be used as the control peptide (*10*). As native P0(180−199) does not contain a Cys residue for palmitoylation, we substituted Ser181 by a Cys residue, which is the isoelectronic counterpart, in order to have the palmitoylation site at residue N-1 like in P0(152−171).

In P0(152−171), Cys153 is the site of palmitoylation described for P0 (*8*). A 20-residue-long peptide was synthesized for homogeneity with the neuritogenic peptide P0(180−199). The sequences of the peptides used in this study are given in Table 2.

Peptide Synthesis. Previously (*12*), we showed that the highly acid labile methoxytrityl (Mmt) group (*13*) was the more versatile protecting group of the thiol for use in the on-resin synthesis of thiopalmitoylated PLP peptides, compared to the *t*-butylsulfenyl (StBu) protecting group (*14*). Here, however, we show that Mmt was not suitable for thiopalmitoylation of P0(152−171), because a side deprotection reaction occurred leading to dipalmitoylation. On the other hand, Mmt could be efficiently used for P0(180−199) thioacylation.

P0(180−199)Cys181 Palm and Non-Palm. The synthesis of peptide P0(180−199)Cys181 was performed manually on a preloaded Wang resin using the Fmoc/tBu strategy with BOP as coupling reagent. Cys181 was coupled as Fmoc-Cys(Mmt)-OH in order to allow the on-resin palmitoylation. Boc-Ala-OH was coupled as N-terminal amino acid in order to protect the N-terminus during palmitoylation (Scheme 1).

The non-palm peptide was obtained by cleavage of the peptide−resin with concentrated TFA and the HPLC analysis of the crude peptide showed a major peak (Rt = 19.5 min) (Figure 1) that was purified by RP-HPLC and characterized by MALDI-TOF mass spectrometry (MH^+ = 2289.02).

For on-resin palmitoylation, the Mmt group was removed from the resin-bound peptide with 2% TFA, and the Cys thiol group was acylated using palmitic acid activated with BOP. After cleavage from the resin, the crude peptide was analyzed by HPLC and showed the presence of a major peak (Rt = 17.9 min) (Figure 2) which could be purified by preparative RP-HPLC at greater than 95% purity with a yield of purification of 30%. The mass measured by MALDI-TOF mass spectrometry (MH^+ = 2527.23 Da) confirmed the identity of palmitoylated P0(180−199).

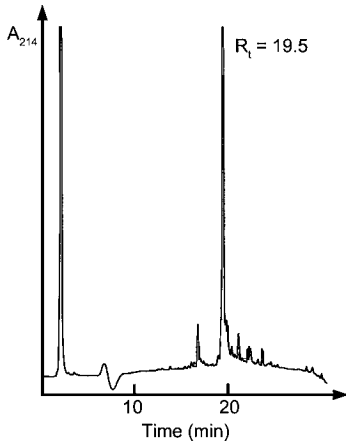


Figure 1. RP-HPLC trace of crude P0(180−199).

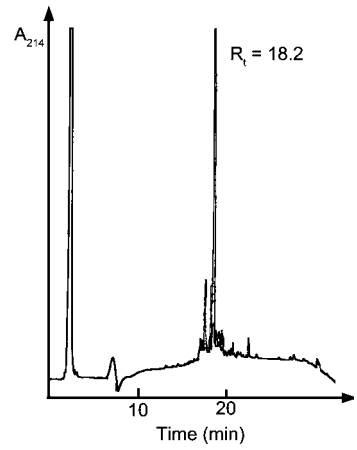


Figure 3. RP-HPLC trace of crude P0(152−171).

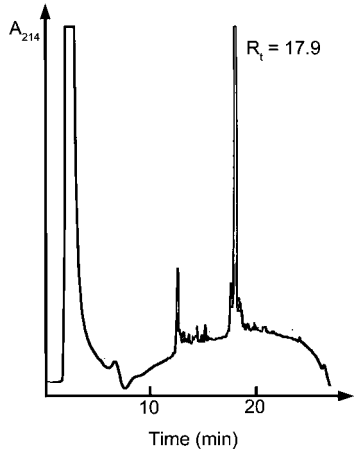


Figure 2. RP-HPLC trace of crude palmitoylated P0(180−199) synthesized according to Scheme 1.

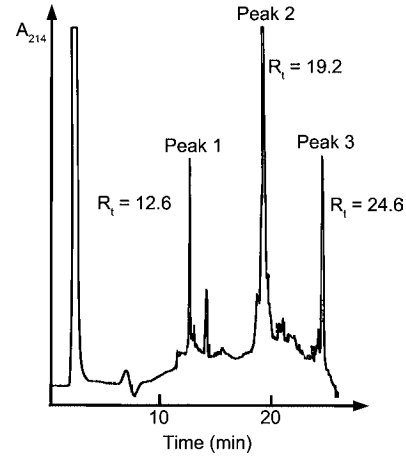


Figure 4. RP-HPLC trace of crude palmitoylated P0(152−171) synthesized according to Scheme 2.

P0(152−171)Cys153 Palm and Non-Palm. On-Resin Palmitoylation with Cys(Mmt)153. The synthesis of peptide P0(152−171)Cys153 was performed manually on a preloaded Wang resin using the Fmoc/tBu strategy with BOP as coupling reagent. Cys153 was coupled as Fmoc-Cys(Mmt)-OH for the on-resin palmitoylation and Boc-Tyr(tBu)-OH was coupled as N-terminal amino acid (Scheme 2).

The non-palm peptide was obtained by cleavage of the peptide−resin with concentrated TFA, and the crude obtained showed a major peak in HPLC (Rt = 18.2) (Figure 3) that was further purified by RP-HPLC and characterized by mass spectrometry (MH^+ = 2436.31 Da).

To obtain the palmitoylated peptide, the Mmt group was removed from the resin-bound peptide with 2% TFA and the Cys thiol group was acylated using activated palmitic acid. After cleavage from the resin, the crude peptide was analyzed by HPLC and showed the presence of three peaks (Figure 4) that were characterized by MALDI-TOF mass spectrometry. Peak 1 (Rt = 12.6 min) showed the same measured mass (MH^+ = 2436.27 Da) as the non-palm peptide obtained previously. Peak 2 (Rt = 19.2 min) and peak 3 (Rt = 24.6 min) were, respectively, identified as monopalmitoylated P0(152−171) (MH^+ = 2674.66 Da) and dipalmitoylated P0(152−171) (MH^+ = 2912.85 Da). The presence of the non-palm peptide (peak 1, 10%) indicates that the Cys(Mmt) deprotection was not complete, but unexpectedly, a dipalmitoylated peptide was obtained, representing 15% of the mixture. We tried to optimize the Cys deprotection by using different percentages of TFA, in order to obtain the monopalmitoylated peptide as the unique compound, but without success (Table 3). We suspected that dipalmitoylation might occur because of a premature deprotection of the

Scheme 2. Solid-Phase Synthesis of Thiopalmitoylated P0(152−171) Using Mmt as the Thiol Protecting Group

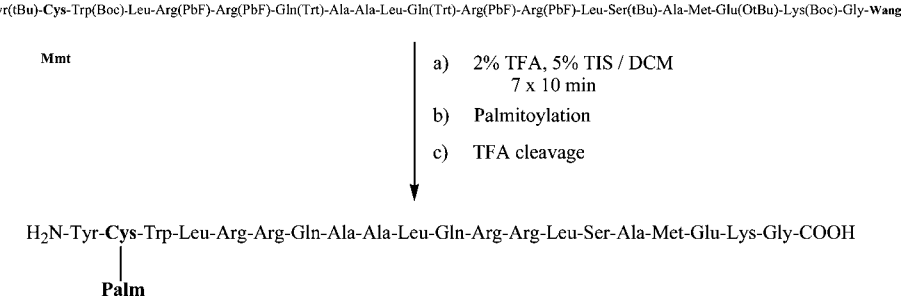


Table 3. Percentage of Non-Palm, Mono-Palm, and Di-Palm P0(152−171) Obtained According to the Percentage of TFA Used for the on-Resin Cys (Mmt) Deprotection

% TFA	% non-palm	% mono-palm	% di-palm
1.5	40	57	3
2	10	75	15
3	0	58	42

Table 4. Sequences of Acetylated Peptides Identified after Trypsin Cleavage of Peak 1 to Peak 4 and Mass Spectrometry Analysis

peptide	percentage	structure
peak 1	51	H_2N−Y**C(StBu)**WLRRQAALQRRLSAMEKG-COOH
peak 2	30	H_2N−Y**C(StBu)**WLRRQAALQRRLSAME**K(Ac)**G-COOH
peak 3	12	**Ac-HN-YC(StBu)**WLRRQAALQRRLSAMEKG-COOH
peak 4	7	**Ac-HN-YC(StBu)**WLRRQAALQRRLSAME**K(Ac)**G-COOH

Boc protecting group either at the N-terminal Tyr or at the Lys170 side chain.

Identification of the Extra Palmitoylation Site in P0(152−171). To identify the extra palmitoylation site in P0(152−171), we initially tested the following strategy: trypsin digestion of palm and di-palm peptides, isolation of the trypsic peptides and identification by mass spectrometry. However, there were two problems with this strategy: (i) the resistance of palmitoylated peptides to trypsin digestion, probably because of their low solubility, and (ii) the sensitivity of the thioester bond to basic pH.

We therefore decided to use the peptide−resin P0(152−171) protected on Cys153 with StBu (vide infra), as this protecting group is stable in TFA, then treat the peptide−resin with 2% TFA as for the deprotection of the Cys(Mmt) protected peptide and finally do the acylation with acetic anhydride in order to obtain acetylated peptides showing better solubility properties than palmitoylated peptides (Scheme 3). After cleavage from the resin, the four different peptides obtained were individually purified by RP-HPLC (Figure 5). Each purified peptide was submitted to trypsin digestion, and the trypsic peptides were individually characterized by mass spectrometry (not shown). From the known cleavage trypsin sites of peptide P0(152−171) and the measured masses of the different trypsic peptides, we could deduce the structures of peptide peak 1 to peak 4 (Table 4). Peak 1, the major peptide (51%), was, as expected, the

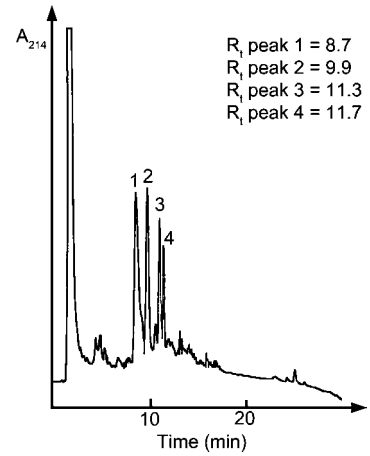
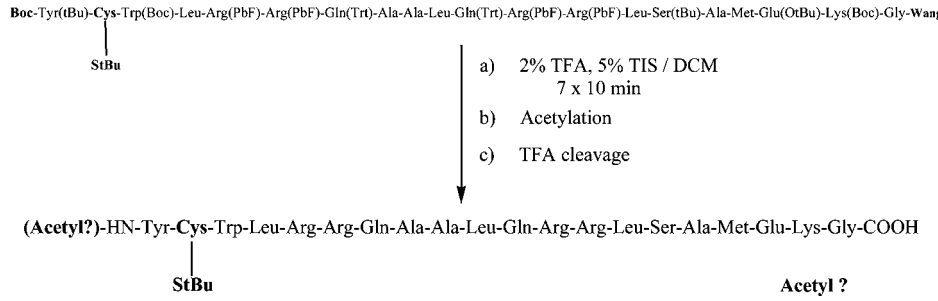


Figure 5. RP-HPLC Trace of Crude Acetylated P0(152−171)-Cys[153](StBu) Obtained According to Scheme 3.

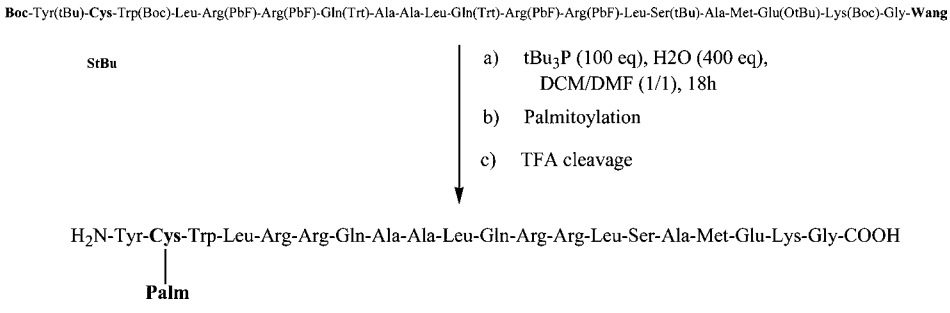
nonacylated one. Peak 2 (30%) was identified as the peptide acetylated at Lys170 resulting from the deprotection of ε-NH-(Boc) and peak 3 (12%) was identified as the peptide acetylated at the N-terminal Tyr152, probably obtained after deprotection of the N-ter Boc protecting group. Finally, peak 4 was identified as the diacylated peptide at Tyr152 and Lys170 resulting from the concomitant deprotection of the Boc group at the N-ter and at the side chain of Lys. From these results, we can conclude that the second palmitoylation obtained during the on-resin palmitoylation of P0(152−171) is probably due to a premature deprotection of the Boc protecting group of the side chain of Lys170 in the presence of 2% TFA and to a lesser extent to the deprotection of the Boc NH_2-terminus protecting group. We cannot exclude that tripalmitoylated P0(152−171) was obtained, but because of its high hydrophobicity, it was probably not eluted in HPLC (Figure 4).

On-Resin Palmitoylation with Cys(StBu)153. The synthesis of peptide P0(152−171)Cys153 was performed manually on a preloaded Wang resin using the Fmoc/tBu strategy with BOP as coupling reagent. Cys153 was coupled as Fmoc-Cys(StBu)-OH for the on-resin palmitoylation, and Boc-Tyr(tBu)-OH was

Scheme 3. Strategy Used to Identify the Extra Palmitoylated Site of Palm P0(152−171) Synthesized According to Scheme 2



Scheme 4. Solid-Phase Synthesis of Thiopalmitoylated P0(152−171) Using StBu as the Thiol Protecting Group



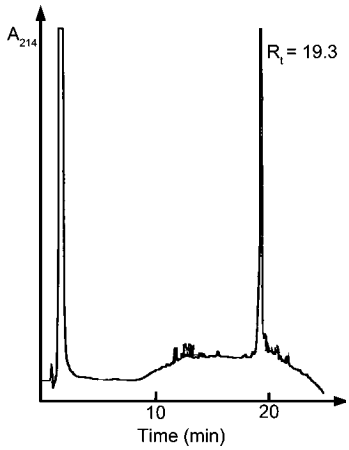


Figure 6. RP-HPLC trace of crude palmitoylated P0(152−171) synthesized according to Scheme 4.

coupled as N-terminal amino acid (Scheme 4). The resin-bound peptide was treated with tributylphosphine (100 equiv in DCM/DMF, 400 equiv H_2O) during 18 h at room temperature. After deprotection, the free Cys thiol was palmitoylated with activated palmitic acid. After cleavage from the resin, the crude peptide was analyzed by HPLC and showed the presence of a single peak (Rt = 19.3 min) (Figure 6) that was purified by preparative RP-HPLC at greater than 95% purity with a yield of purification of 37%. The mass measured by MALDI-TOF mass spectrometry (MH^+ = 2674.59 Da) confirmed its identity as palm P0(152−171).

Circular Dichroism Study. In order to show if palmitoylation has some effect on the secondary structures of P0(152−171) and P0(180−199), we examined the CD spectra of the palm and non-palm peptides in water and in TFE, as TFE is known to stabilize pre-existing structures (*16*).

Table 5. Percentage of α-Helix Content of Non-Palm and Palm P0(152−171) and P0(180−199) Peptides Calculated According to Ellipticity

	α-helix (%)			
% TFE	P0(152−171)	palm P0(152−171)	P0(180−199)	palm P0(180−199)
0	2	1	8	6
10	5	15	8	15
30	39	38	27	19
60	43	47	32	21

The CD spectra analysis of the non-palm and palm P0(152−171) peptides in water showed a broad negative band at 200 nm characteristic of a random coil conformation (Figure 7A). The CD analysis of both peptides showed that increasing amounts of TFE (from 10% to 60%) induced a structuration with one positive band at 190 nm and one negative band at 206 nm. Secondary structural analysis of the spectra showed that the α-helix content of both peptides increased with the percentage of TFE but with no major difference between the palm and non-palm peptides (Table 5). The same observations could be drawn from the analysis of the CD spectra of non-palm and palm P0(180−199) (Figure 7B and Table 5): no major influence of the palmitic chain was noticed on the structuration of the peptide apart from a very slight decrease in helicity at 30% and 60% TFE.

Peptide and Lipopeptide Stability in the Presence of Serum. The aim of this study was to compare the immunogenic and neuritogenic properties of palmitoylated P0 peptides with non-palmitoylated P0 peptides after injection in Lewis rats; we therefore studied and compared their stability in the presence of serum.

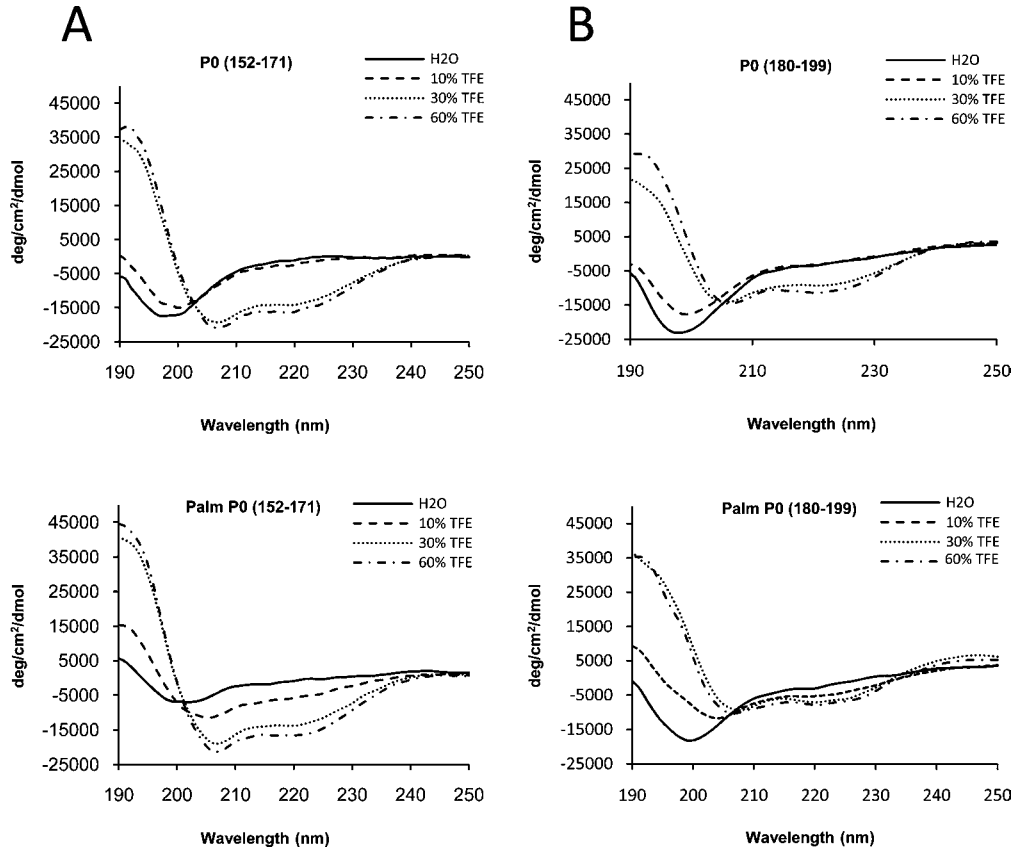


Figure 7. Far-UV circular dichroism (CD) spectra of non-palm and palm P0(152−171) (A) and non-palm and palm P0(180−199) (B) in water and in the presence of various percentages of trifluoroethanol (TFE).

Table 6. Kinetics of Digestion of Peptides and Lipopeptides in the Presence of Serum

	P0(152−171)		P0(180−199)	
time	non-palm	palm	non-palm	palm
0	100	100	100	100
30 min	65	83	61	79
60 min	40	69	40	63
3 h	7	37	0	25
6 h	0	18	0	9
9 h	0	9	0	3

For this purpose, the peptides and lipopeptides were incubated in phosphate buffer in the presence of 10% of fetal calf serum, and the progress of digestion was followed by HPLC. As shown in Table 6, both palmitoylated peptides showed a higher stability than their parent peptide, since most of the non-palm peptide was digested after 3 h, while there was still 37% and 25% of nondigested palm P0(152−171) and palm P0(180−199), respectively.

EAN Induction with P0 Peptides and Lipopeptides. *Comparison of the Neuritogenic Properties of Palm and Non-Palm P0(180−199).* After immunization with P0(180−199), four out of four rats developed EAN, an acute episode of EAN with onset at 12 dpi, a maximum clinical score of 2.9 ± 0.1, and a duration of clinical signs of 15 ± 1 days (Figure 8A). In contrast, the rats injected with palmitoylated P0(180−199) developed a relapsing−remitting type of disease with onset at 13 dpi and a maximum clinical score of 2 ± 0.6 (Figure 8B).

Comparison of the Neuritogenic Properties of Palm and Non-Palm P0(152−171). Only one rat out of four developed neurological deficits after immunization with P0(152−171); it showed an acute type of disease with onset at 17 dpi, a maximum clinical score of 2, and a duration of 20 days (Figure 9A). In contrast, four out of four rats developed neurological deficits after injection of the palmitoylated peptide, with a day of onset ranging from 13 to 22 dpi, and a maximum clinical score of 2.3 ± 1. One rat developed an acute type of disease and another one a more chronic type of disease (Figure 9B). The other two rats in this group were sacrified at the peak of the disease, and therefore, no conclusion could be drawn on the type of disease that they would have developed.

Ab Responses Induced by P0 Peptides and Lipopeptides. Sera of rats injected with the palm and non-palm P0(180−199) and P0(152−171) peptides were collected at days 21, 31, and 62 postinjection and were tested in ELISA against P0(180−199) and P0(152−171), respectively.

Ab Responses Induced by Palm and Non-Palm P0(180−199). Sera from rats immunized with the nonacylated P0(180−199) made a moderate response to that peptide. In contrast, sera of rats immunized with the palm peptide showed a stronger Ab response to P0(180−199) that increased with time (Figure 10A).

Ab Responses Induced by Palm and Non-Palm P0(152−171). Sera from rats immunized with the non-palm peptide made a very poor response to that peptide, while sera of rats immunized with the palm peptide showed a much stronger Ab response, which peaked at 31 dpi and then decreased (Figure 10B).

DISCUSSION

Synthesis. We have successfully synthesized thiopalmitoylated peptides P0(180−199) and P0(152−171) by on-resin acylation using specific cysteine side-chain protecting groups. Our results show that the thiol protecting group had to be adjusted to the peptide sequence: Mmt was efficiently used for

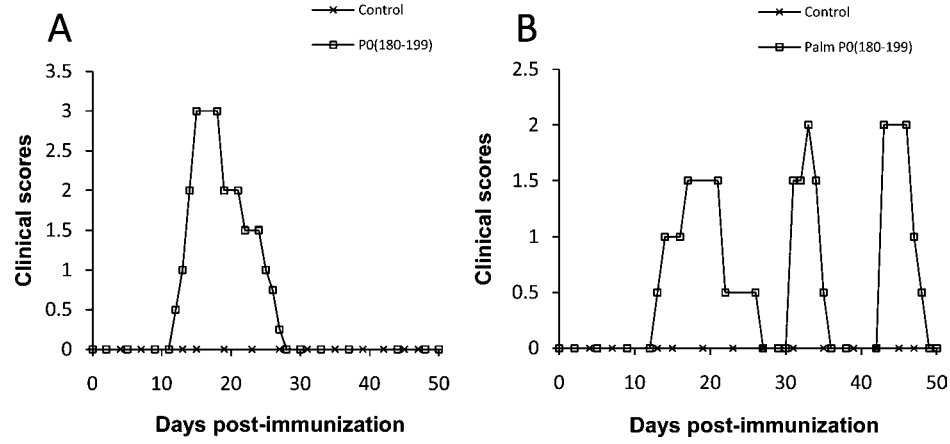


Figure 8. Clinical scores of EAN in P0(180−199) (A) and palm P0(180−199) (B) injected rats.

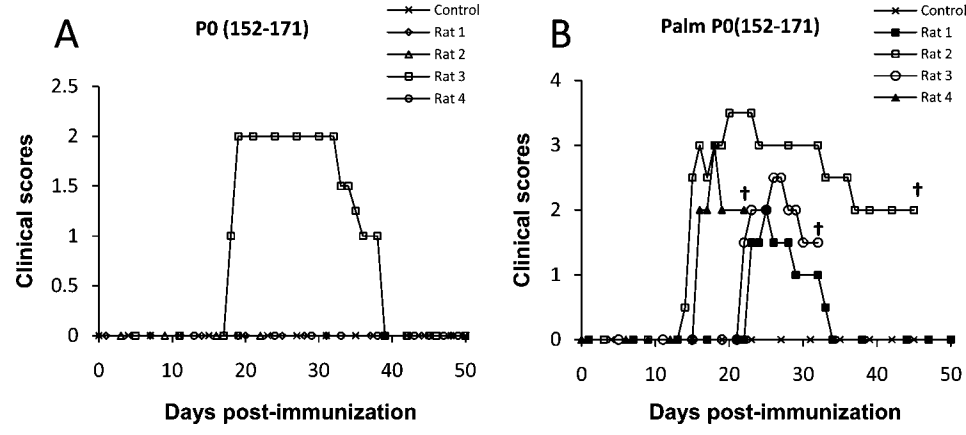


Figure 9. Clinical scores of EAN in P0(152−171) (A) and palm P0(152−171) (B) injected rats. (†) sacrifice.

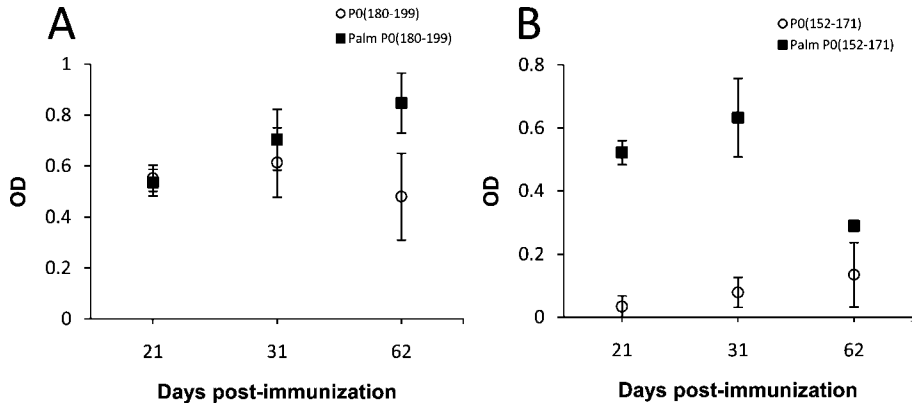


Figure 10. Antibody responses to P0(180−199) induced in rats injected with P0(180−199) or palm P0(180−199) (A) and antibody responses to P0(152−171) induced in rats injected with P0(152−171) or Palm P0(152−171) (B).

P0(180−199) thioacylation, but it was not suitable for thiopalmitoylation of P0(152−171) because of a premature deprotection of the Boc protecting group on the ε-NH_2 Lys in the presence of 2% TFA leading to dipalmitoylation. The deprotection of Lys170 ε-NH(Boc) in the presence of diluted TFA was quite unexpected, as in our previous work we obtained, using the same protocol for on-resin acylation, specific monopalmitoylation of PLP(139−151) using Mmt protecting group for Cys140, even though this peptide possesses two lysines at residues 143 and 150 (*12*). It is interesting to note that P0(180−199) possesses a Lys residue at position 183 and no Boc deprotection was observed in the presence of 2%TFA. From these results, we can conclude that the side deprotection of ε-NH(Boc) of lysine seems to depend on the peptide sequence, but at the moment, we have no rational explanation. We then used the *t*-butylsulfenyl (StBu, labile in the presence of tributylphosphine) protecting group for Cys153, which allowed us to obtain mono-palmitoylated P0(152−171) as the unique compound. Nevertheless, we advise testing Mmt as the thiol protecting group in the first instance, because the non-palm peptide can be obtained from the same peptide−resin without the need of an additional cysteine deprotection step. The purification of lipopeptides by RP-HPLC is generally difficult due to their low solubility and their tendency to aggregate and/or to form micelles, leading to low yield of purification. However, we have succeeded in obtaining palmitoylated P0(180−199) and P0(152−171) peptides at greater than 95% purity with a yield of purification of 30% and 37%, respectively, using the protocol set up in previous studies (*17*).

Immunological Properties. The non-palm and palm P0(180−199) and P0(152−171) were injected in Lewis rats to study the influence of thiopalmitoylation on their immunogenic and neuritogenic properties.

The acute course and profile of EAN induced after injection of non-palm P0(180−199) (Figure 8A) was in complete accordance with the literature (*10*). In contrast, palm P0(180−199) induced a relapsing−remitting type of disease (Figure 8B) indicating that thiopalmitoylation indeed has an important effect on the neuritogenic properties of P0(180−199). In addition, thiopalmitoylation also enhanced its immunogenic properties, since the production of antibodies against P0(180−199) was increased after injection of the palm peptide (Figure 10A), especially at 31 dpi (at the time of the first relapse) and day 62 (the second relapse).

This is the first time that the neuritogenic properties of P0(152−171) are reported; as in the previous studies, this peptide was not described as a potential T-cell epitope for EAN in Lewis rat (*18*). We have shown that only one rat out of four developed acute EAN after injection of P0(152−171) (Figure 9A), and this low incidence may indicate that this peptide is a cryptic epitope of P0, as was described for P0(56−71) (*18*). By contrast, all four rats injected with palm P0(152−171) developed EAN with high clinical scores; however, the clinical course of disease was not homogeneous, as one rat developed an acute course and another one a more chronic course (Figure 9B). P0(152−171) was also very poorly immunogenic and induced only very low amounts Ab; however, its immunogenicity was greatly enhanced by thiopalmitoylation (Figure 10B).

These results show that thiopalmitoylation has a great influence on the neuritogenicity of P0 peptides. It is likely that the increase in neurogenicity and immunogenicity is due to a more efficient uptake of the lipopeptides by antigen presenting cells than the non-palm peptides, leading to induction of a stronger $CD4^+$ T-cell response, as we have shown for palm PLP peptides (*7*). Furthermore, we have reported in this paper that the palm peptides are more stable that the non-palm peptides in the presence of serum (Table 6), and this increase in bioavalability can also be important for the immunological activity of the lipopeptides.

CONCLUSION

With the results obtained with thiopalmitoylated P0(152−171), as occurs naturally in vivo, we provide further support for our hypothesis that the immune response induced by endogenous thiopalmitoylated peptides that are released during myelin breakdown may play a role in the development and chronicity of autoimmune inflammatory demyelinating diseases. Furthermore, the increase of immunogenicity and neuritogenicity observed when P0(180−199) and P0(152−171) are conjugated to palmitic acid via a thioester bond confirms our previous findings that thiopalmitoylation of peptides may provide a simple mean to induce and/or increase MHC class II resricted responses. The next step of our study will be to better characterize the EAN models we have obtained after injection of thiopalmitoylated P0(180−199) and P0(152−171). This is particularly important as, up to now, the most frequently used model for GBS is the EAN model induced by P0(180−199) in Lewis rat, but this really only mimics AIDP. At present, there is no useful animal model for CIDP, the chronic and incurable form of GBS. New animal models for immune-mediated disorders of the PNS will provide a rational basis for studying the mechanisms of pathogenesis and for designing new immunotherapeutic strategies for human autoimmune demyelinating neuropathies.

ACKNOWLEDGMENT

We gratefully acknowledge Dr. J. M. Strub (Laboratoire de Spectrométrie de Masse Bioorganique, IPHC, Strasbourg) for the mass spectrometry analysis, TA Thi Anh Tu for the

assistance in the synthesis of thiopalmitoylated P0(180−199), and Dr. Judith Greer for critical reading of the manuscript.

LITERATURE CITED

(1) Linder, M. E., and Deschenes, R. J. (2007) Palmitoylation: policing protein stability and traffic. *Nat. Rev. Mol. Cell Biol. 8*, 74–84.

(2) Christgau, S., Aanstoot, H. J., Schierbeck, K., Begley, K., Tullin, S., Hejnaes, K., and Baekkeskov, S. (1992) Membrane anchoring of the auroantigen GAD65 to microvesicles in pancreatic β-cells by palmitoylation in the NH2-terminal domain. *J. Cell Biol. 118*, 309–320.

(3) Kang, D., Karbach, D., and Passow, H. (1994) Anion transport function of mouse erythroid band 3 protein (AE1) does not require acylation of cysteine residue 861. *Biochem. Biophys. Acta 1194*, 341–344.

(4) Pedraza, L., Owens, G. C., Green, L. A., and Salzer, J. L. (1990) The myelin-associated glycoproteins: membrane disposition, evidence of a novel disulfide linkage between immunoglobulin-like domains, and posttranslational palmitoylation. *J. Cell Biol. 111*, 2651–2661.

(5) Weimbs, T., and Stoffel, W. (1992) Proteolipid protein (PLP) of CNS myelin: position of free, disulfide-bonded, and fatty acid thioester-linked cysteine residues and implication for the membrane topology of PLP. *Biochemistry 31*, 12289–12296.

(6) Greer, J. M., Denis, B., Sobel, R. A., and Trifilieff, E. (2001) Thiopalmitoylation of myelin proteolipid protein epitopes enhances immunogenicity and encephalitogenicity. *J. Immunol. 166*, 6907–6913.

(7) Pfender, N. A., Grosch, S., Roussel, G., Koch, M., Trifilieff, E., and Greer, J. M. (2008) Route of uptake of palmitoylated encephalitogenic peptides of myelin proteolipid protein by antigen-presenting cells: importance of the type of bond between lipid chain and peptide and relevance to autoimmunity. *J. Immunol. 180*, 1398–1404.

(8) Bizzozero, O. A., Fridal, K., and Pastuszyn, A. (1994) Identification of the palmitoylation site in rat myelin P0 glycoprotein. *J. Neurochem. 62*, 1163–1171.

(9) Hughes, R. AC., and Cornblath, D. R. (2005) Guillain-Barré syndrome. *Lancet 366*, 1653–1666.

(10) Zhu, J., Pelidou, S.-H., Deretzi, G., Levi, M., Mix, E., van der Meide, P., Winblad, B., and Zou, L.-P. (2001) P0 glycoprotein peptides 56−71 and 180−199 dose-dependently induce acute and chronic experimental autoimmune neuritis in Lewis rats associated with epitope spreading. *J. Neuroimmunol. 114*, 99–106.

(11) Meyer zu Hörste, G., Hartung, H.-P., and Kieseier, B. C. (2007) From bench to bedside- experimental rationale for immune-specific therapies in the inflamed peripheral nerve. *Nat. Clin. Pract. Neurol. 3*, 198–211.

(12) Denis, B., and Trifilieff, E. (2000) Synthesis of palmitoyl-thioester T-cell epitopes of myelin proteolipid protein (PLP). Comparison of two thiol protecting groups (StBu and Mmt) for on-resin acylation. *J. Pept. Sci. 6*, 372–377.

(13) Barlos, K., Gatos, D., Chatzi, O., Koutsogianni, S., and Schäfer, W. (1993) Solid phase synthesis using trityl type side chain protecting groups. In *Peptides 1992 (Proceedings of the 22nd European symposium)* (Schneider, C. H., and Eberle, A. N., Eds.) pp 223−224, ESCOM Science, Leiden.

(14) Eritja, R., Ziehler-Martin, J. P., Walker, P. A., Lee, T. D., Legesse, K., Albericio, F., and Kaplan, B. E. (1987) On the use of S-t-butylsulphenyl group for the protection of cysteine in solid-phase peptide synthesis using Fmoc-amino acids. *Tetrahedron 43*, 2675–2680.

(15) Van Iersel, J., Frank, J., and Duine, J. A. (1985) Determination of absoption coefficients of purified proteins by conventional ultraviolet spectrophotometry and chromatography combined with multiwavelength detection. *Anal. Biochem. 151*, 196–204.

(16) Nelson, J. W., and Kallenbach, N. R. (1986) Stabilization of the ribonuclease S-peptide alpha-helix by trifluoroethanol. *Proteins 1*, 211–217.

(17) Pfender, N., Guénin, E., Greer, J. M., and Trifilieff, E. (2003) Solid-phase synthesis of a biotin-labelled thiopalmitoylated myelin proteolipid protein epitope and application in the study of uptake of antigen by macrophages. *Lett. Pept. Sci. 10*, 581–588.

(18) Linington, C., Lassmann, H., Ozawa, K., Kosin, S., and Mongan, L. (1992) Cell adhesion molecules of the immunoglobulin supergene family as tissue-specific autoantigens: induction of experimental allergic neuritis (EAN) by P0 protein-specific T cell lines. *Eur. J. Immunol. 22*, 1813–1817.

BC100039U

Combinatorial Approach to Determine Functional Group Effects on Lipidoid-Mediated siRNA Delivery

Kerry P. Mahon,[†] Kevin T. Love,[†] Kathryn A. Whitehead,[†] June Qin,[‡] Akin Akinc,[‡] Elizaveta Leshchiner,[†] Ignaty Leshchiner,[†] Robert Langer,[†] and Daniel G. Anderson*[,†]

Department of Chemical Engineering and David H. Koch Institute of Integrative Cancer Research, Massachusetts Institute of Technology, 77 Massachusetts Avenue, Cambridge, Massachusetts 02139, and Alnylam Pharmaceuticals, Inc., 300 Third Street, Cambridge, Massachusetts 02142. Received January 20, 2010; Revised Manuscript Received June 22, 2010

The application of RNA interference (RNAi), either in the clinic or in the laboratory, requires safe and effective delivery methods. Here, we develop a combinatorial approach to synthesize a library of delivery vectors based on two lipid-like substrates with known siRNA delivery capabilities. Members of this library have a mixture of lipid-like tails and feature appendages containing hydroxyl, carbamate, ether, or amine functional groups as well as variations in alkyl chain length and branching. Using a luciferase reporter system in HeLa cells, we studied the relationship between lipid chemical modification and delivery performance *in vitro*. The impact of the functional group was shown to vary depending on the overall amine content and tail number of the delivery vector. Additionally, *in vivo* performance was evaluated using a Factor VII knockdown assay. Two library members, each containing ether groups, were found to knock down the target protein at levels comparable to those of the parent delivery vector. These results demonstrate that small chemical changes to the delivery vector impact knockdown efficiency and cell viability both *in vitro* and *in vivo*. The work described here identifies new materials for siRNA delivery and provides new insight into the parameters for optimized chemical makeup of lipid-like siRNA delivery materials.

INTRODUCTION

Over the last thirty years, RNA has been shown to perform a variety of activities within the cell that go beyond its traditional role as a translation template for protein synthesis. In particular, the recent discovery of RNA-mediated regulation of gene expression has spawned widespread interest (*1*). This technology, termed RNA interference (RNAi), is based on the ability of short duplexes of RNA, termed siRNA, to induce the specific cleavage of complementary mRNA, leading to a silencing of gene expression. RNAi has potential both for use as a tool capable of elucidating cellular mechanisms and as a therapeutic for treating disease at the genetic level (*2, 3*).

Despite the opportunities afforded by siRNA, a safe and effective delivery system that can transport the material across the cell membrane for incorporation into the necessary cellular machinery is required for use. Both the size and negative charge of siRNA render active transport across the cell membrane difficult. Furthermore, these RNAs are vulnerable to enzymatic degradation. To circumvent these issues, researchers have made extensive efforts to rationally design chemically modified siRNA (*4, 5*). Covalent attachment of peptides, cholesterol, and aptamers have all been reported to increase cellular uptake (*6*−*11*). Additionally, variants such as substitution at the 2′ position (e.g., 2′-fluoro, 2′-*O*-methyl, 2′-methoxyethyl) and modified phosphate backbone (e.g., phosphorothioate and methylphosphonate) provide for improved efficacy by imparting a greater resistance to nuclease degradation (*12*). While these methods have demonstrated promise *in vivo*, the development of improved delivery methods are required to allow for the fullest application of RNAi in the clinic.

The application of materials previously used for nonviral DNA delivery to siRNA delivery has enabled the rapid development of siRNA for use *in vivo*. For example, both polymer and liposome delivery systems have demonstrated efficacy in animal models (*13*−*15*). However, structural differences between RNA and DNA, as well as differences in their method of action, are likely responsible for the fact that delivery systems for DNA do not always work for siRNA and vice versa (*16*). Therefore, the synthesis of new materials that complex, protect, and deliver siRNA is currently an active area of research. As a result, polymers, polymersomes, dendrimers, lipid-based formulations, and rationally designed systems specific for siRNA delivery have been developed, with varying degrees of success *in vitro* and *in vivo* (*17*−*26*).

Recently, a new approach to the synthesis of lipid-like materials for siRNA delivery vectors using combinatorial methods was reported (*27*). In this study, a library of over 1200 lipid-like materials was generated through the conjugate addition of an amine to an α,β-unsaturated carbonyl and evaluated for siRNA delivery performance. The resulting materials, termed lipidoids, were structurally distinct from other classes of lipid delivery vectors in that they contained multiple protonable amine groups connected to relatively short alkyl chains. In these studies, materials with good *in vitro* and *in vivo* performance were identified, including a lead material 98N12−5 that was shown to be efficacious in primates.

In this study, we build upon the first library of lipidoids to incorporate further diversity into two promising siRNA delivery candidates. These library members feature systematic variation of select side chains with different capacities for hydrogen bonding, hydrophobic interactions, and protonation states,

* To whom correspondence should be addressed. E-mail: dgander@mit.edu.

[†] Massachusetts Institute of Technology.

[‡] Alnylam Pharmaceuticals, Inc.

10.1021/bc100041r © 2010 American Chemical Society
Published on Web 07/16/2010

enabling the exploration of heterogeneously functionalized lipidoids for siRNA delivery.

MATERIALS AND METHODS

Library Synthesis. Lipidoid library members were synthesized by the addition of acrylamides or acrylates to a partially substituted amine-modified core lipidoid. A detailed synthesis of the core lipidoids is found in the Supporting Information. Dodecylacrylamide was purchased from TCI America. Other acrylamides were synthesized as previously described (*27*). Acrylates were purchased from Sigma-Aldrich, Alfa Aesar, and TCI America. Amines were purchased from Sigma-Aldrich. All library reactions were carried out in 2 mL Teflon-lined glass screw-top vials containing a magnetic stir bar. Then, 1.1 equiv of the library acrylate was added to 120 mg of core amine, and the mixture was stirred at 90 °C for 24−48 h. After cooling, the lipidoid mixtures were used without purification for initial siRNA transfection screening. Lead compounds were purified for further testing.

***In Vitro* siRNA Transfection Assay.** To facilitate high throughput screening, all transfections were performed using a multichannel pipet and serial dilutions in a 96-well plate format. HeLa cells stably expressing firefly luciferase and *Renilla* luciferase were seeded at 15,000 cells/well into each well of an opaque white 96-well plate (Corning-Costar) and allowed to attach overnight in growth medium. Growth medium was composed of 90% phenol red-free DMEM, 10% FBS, 100 units/mL penicillin, and 100 mg/mL streptomycin (Invitrogen). Cells were transfected with 50 ng of firefly specific siLuc complexed with lipidoid at lipidoid/siRNA ratios of 2.5:1, 5:1, 10:1, and 15:1 (w/w). Transfections were performed in quadruplicate. Working dilutions of each lipid were prepared in 25-mM sodium acetate buffer (pH 5). Twenty-five microliters of the diluted lipid was added to 25 μL of 2.5 μg/mL siRNA in a well of a 96-well plate. The mixtures were incubated for 20 min to allow for complex formation, and then 30 μL of each of the lipidoid/siRNA solutions was added to 200 μL of fresh growth medium in 96-well polystyrene plates. The growth medium was removed from the cells using a 12-channel aspirating wand (V&P Scientific) after which 150 mL of the DMEM/lipidoid/siRNA solution was immediately added. Cells were allowed to grow for 24 h at 37 °C and 5% CO_2 and were then analyzed for luciferase expression. Control experiments were performed with Lipofectamine 2000, as instructed by the vendor (Invitrogen). Firefly and *Renilla* luciferase expression was analyzed using the Dual-Glo Assay System (Promega). Luminescence was measured using a Victor3 luminometer (Perkin-Elmer). Firefly luminescence was normalized by the internal *Renilla* control luminescence, and treated wells were compared against the untreated control for assessment of knockdown efficacy.

Viability Assessment. Cell viability testing was performed as previously described (*27*). Briefly, HeLa cells were seeded at 15,000 cells/well in a 96-well plate and allowed to adhere overnight. Cells were then transfected with 2.5, 5, 10, or 15 wt/wt ratio of lipidoid to 50 ng of siRNA. After incubation for 24 h, the media were replaced, and CellTiter 96 Aqueous One Solution (Promega) was added. After incubating for one hour, the absorbance at 490 nm was read and viability calculated relative to that of an untransfected control.

***In Vivo* Lipidoid-siRNA Formulation.** Lipidoid-based siRNA formulations comprised lipidoid, cholesterol, polyethylene glycol-lipid (PEG-lipid), and siRNA. Formulations were prepared as described previously (*27*). Stock solutions of lipidoid, cholesterol MW 387 (Sigma-Aldrich), and mPEG2000-Ceramide C16 (Avanti Polar Lipids) MW 2634 were prepared in ethanol and mixed to yield a molar ratio of 42:48:10, respectively. Mixed lipids were added to 200 mM sodium acetate buffer at pH 5 to yield a solution containing 35% ethanol by volume, resulting in the spontaneous formation of empty lipidoid nanoparticles. The resulting nanoparticles were extruded through an 80 nm membrane. siRNA in 35% ethanol and 50 mM sodium acetate at pH 5 was added to the nanoparticles and incubated at 37 °C for 30 min. Ethanol removal and buffer exchange of

Scheme 1. Synthesis of the Lipidoid Library

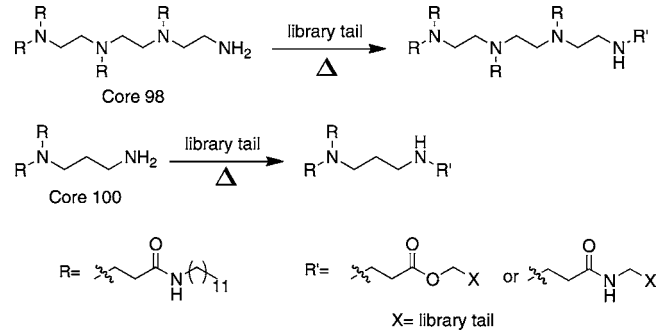
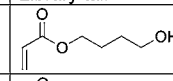
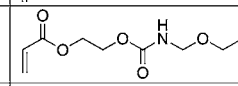
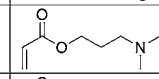
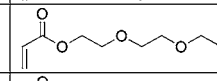
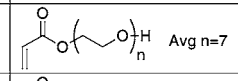
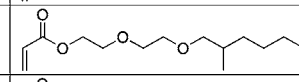
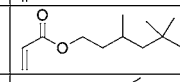
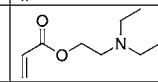
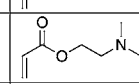
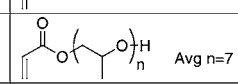
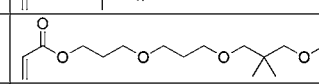
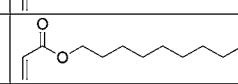
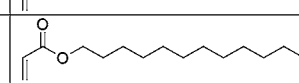
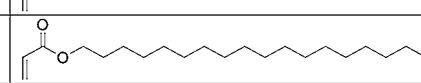
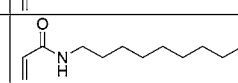
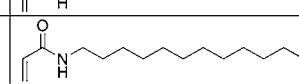
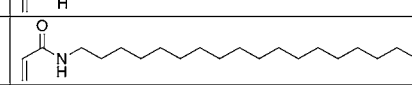


Table 1. Structure of Library Acrylates and Acrylamides

Core 98	Core 100	Library tail
1a	1b	
2a	2b	
3a	3b	
4a	4b	
5a	5b	 Avg n=7
6a	6b	
7a	7b	
8a	8b	
9a	9b	
10a	10b	 Avg n=7
11a	11b	
12a	12b	
13a	13b	
14a	14b	
15a	15b	
16a	16b	
17a	17b	

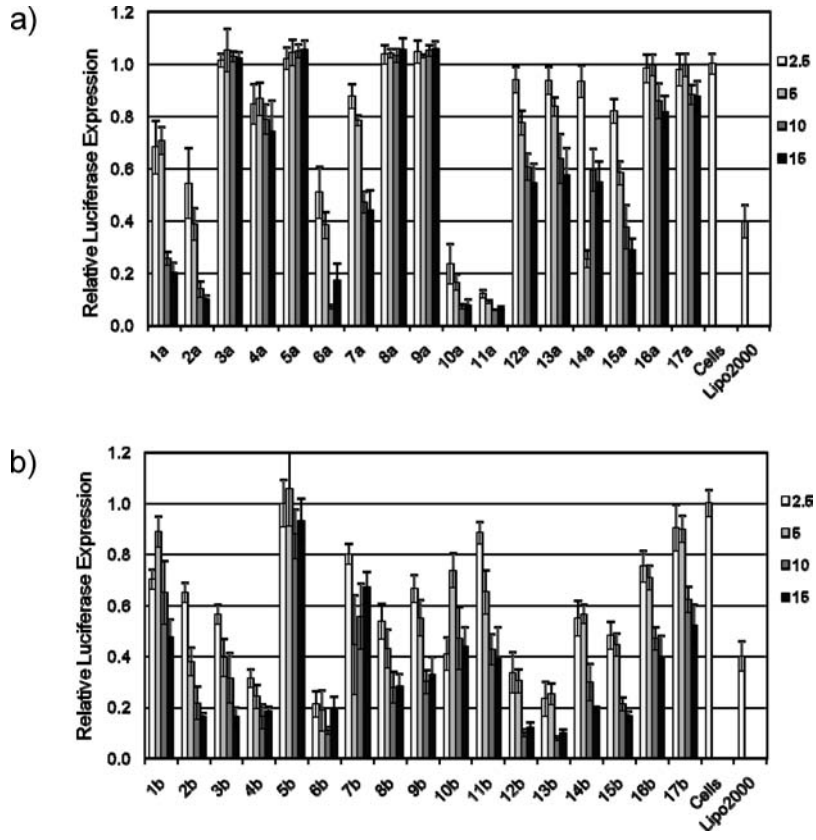


Figure 1. Library screening for siRNA transfection efficiency. HeLa cells stably expressing firefly and *Renilla* luciferase were transfected with 50 ng of firefly specific siRNA complexed at lipidoid/siRNA ratios of 2.5:1, 5:1, 10:1, and 15:1 (w/w). Lipofectamine 2000 was used as instructed by the vendor. Luminescence was measured after 24 h of incubation and the results presented relative to an untransfected control set of cells. (a) Core 98 library. (b) Core 100 library.

siRNA-containing lipidoid nanoparticles were achieved by dialysis against PBS using a 3,500 MWCO membrane. Particle size was determined using a Malvern Zetasizer NanoZS (Malvern). siRNA content and entrapment efficiency were determined using the Quant-iT RiboGreen RNA reagent (Invitrogen).

***In Vivo* Mouse Factor VII Silencing Experiments.** All procedures used in animal studies conducted at MIT were approved by the Institutional Animal Care and Use Committee (IACUC) and were consistent with local, state, and federal regulations as applicable. C57BL/6 mice (Charles River Laboratories) received either saline or siRNA in lipidoid formulations via tail vein injection at a volume of 0.01 mL/g. Seventy-two hours after administration, animals were anesthetized by isofluorane inhalation, and blood was collected into serum separator tubes by retroorbital bleed. Serum levels of Factor VII protein were determined in samples using a chromogenic assay (Biophen FVII, Aniara Corporation) according to the manufacturer's protocols. A standard curve was generated using serum collected from saline-treated animals.

RESULTS

Synthesis of the Heterogeneous Tail Lipidoid Library. The core lipidoid starting materials for this library were synthesized using a three or four step process (Scheme 1 and Supporting Information). Briefly, diethylenetriamine was heated neat at 90 °C with dodecylacrylamide and purified to yield the desired four-tailed isomer. Coupling of 2-(Boc-amino)ethyl bromide followed by deprotection under acidic conditions yielded the amine functionalized library starting material, Core 98. Alternatively, 1,3-diaminopropane was monoprotected with Boc anhydride, heated neat at 90 °C with dodecylacrylamide to add the alkyl tails, and deprotected under acidic conditions to yield the amine functionalized library starting material, Core 100.

Library synthesis was accomplished by reaction of 120 mg of each building block with 1.1 equivalents of the acrylates or acrylamides shown in Table 1. Core 98 reactions yielded compound mixtures that contained mainly the fully substituted (n) and partially substituted ($n - 1$) compounds. Compound mixtures from Core 100 contained a residual starting material in addition to the n and $n - 1$ products. Select lipidoids were purified to isolate the $n - 1$ isomer. The identity of these compounds was confirmed by mass spectrometry (see Supporting Information).

Library Screening for siRNA Delivery. Evaluation of the library for delivering siRNA was performed using a HeLa cell line that is stably transfected with both *Renilla* and firefly luciferase. In this assay, siRNA specific for firefly luciferase is used to measure knockdown, while the *Renilla* luciferase is monitored as a control. Lipofectamine2000, a commonly used commercially available reagent, was also included in the screen. Lipidoids were complexed with the siRNA at weight ratios of 2.5, 5, 10, and 15:1 lipidoid/siRNA. As shown in Figure 1, the knockdown of firefly luciferase was dependent on the ratio of lipidoid used and was affected by the modification with members of the library. In general, the knockdown at a 15:1 weight ratio of lipidoid to siRNA was highest, and the efficiency decreased as the ratio of lipidoid to RNA was decreased. In cases where the knockdown was efficient or where none was observed, the efficiency with the ratios tested was less varied.

While the efficacy of both amine cores were affected by the tail modifications, Core 100 was generally more tolerant of the addition of the functional groups found in the library tails. At the highest ratio of lipidoid/siRNA, 14 of the 17 members of the library showed luciferase knockdown of at least 50%, the most active of which contained ether, carbamate, or amine functionality in the added tail. At the lowest ratio, 9 of the 17

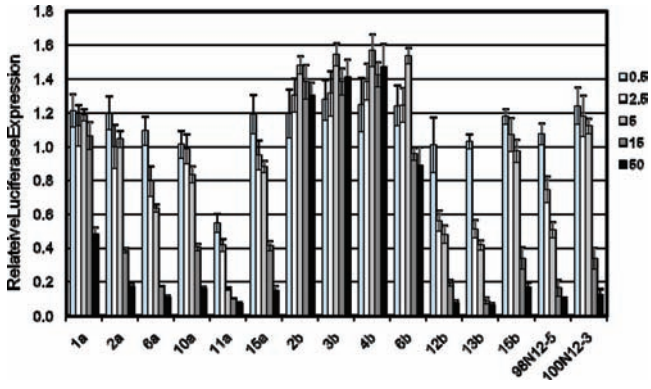


Figure 2. Luciferase knockdown at low doses of siRNA. HeLa cells stably expressing firefly and *Renilla* luciferase were transfected using selected lipidoids at a 15:1 lipidoid/siRNA ratio (w/w) at 0.5, 2.5, 5, 15, and 50 ng of siRNA. Luminescence was measured after 24 h of incubation and the results presented relative to an untransfected control set of cells. Lipidoids were purified to isolate the $n - 1$ isomer prior to transfection.

members showed luciferase knockdown of at least 40%. Only two members, **5b** and **17b**, containing PEG or a long alkyl chain, respectively, were rendered essentially inactive, having less than 10% knockdown at two of the ratios tested.

Fewer derivatives of Core 98 had significant delivery efficiency when compared with that of the number of Core 100 derivatives. Only 4 of the 17 derivatives had luciferase knockdown levels of at least 50% at the 15:1 lipidoid/siRNA ratio and of at least 40% at the 2.5:1 ratio. These active library members contained either a carbamate group or ether functionalities. Core 98 was particularly sensitive to the appendage of other library members. Specifically, **3a**, **5a**, **8a**, **9a**, **16a**, and **17a** showed little ability to deliver siRNA at any lipidoid/siRNA ratio. Interestingly, the ablation of activity due to the addition of a tertiary amine was specific to the Core 98 system, while the addition of PEG or long hydrophobic tails generally disrupted delivery in both Core 98 and Core 100 systems.

Dose−Response of siRNA *in Vitro.* On the basis of the results of our initial screen, we chose 13 of the most promising compound mixtures to purify for further investigation of siRNA delivery efficiency (Figure 2). Two were derivatives obtained through reaction with an acrylamide, while the remaining compounds were all generated via reaction with an acrylate moiety. Earlier screens had identified the most effective compounds as having the $n - 1$ identity. After purification, the identity of the purified compounds was confirmed using mass spectrometry (see Supporting Information).

In this comparison, the purified library members were compared to 98N12-5 and 100N12-3, two members of the original library that were structurally similar to the library members derived from Core 98 and Core 100 but solely contained alkyl tails of uniform length. The majority of the purified set of library compounds, 8 of the 13, had a knockdown of at least 50% using 50 ng of siRNA and at least 60% using 15 ng of siRNA. Decreasing the dose of siRNA to 5 ng led to a significant separation among the library members. Only three members, **11a**, **12b**, and **13b**, retained knockdown efficiency greater than or equal to the parent compound at this level (50% knockdown). Interestingly, **11a** was the most efficient compound for delivering low doses of siRNA in this assay, achieving 50% knockdown using only 0.5 ng of siRNA.

Also of interest is the deleterious effect that purification of the $n - 1$ isomer had on certain compound mixtures. The delivery ability of **1a**, **2b**, **3b**, **4b**, and **6b** were all significantly attenuated after they were removed from the crude mixture. Of these, only **1a** is derived from Core 98, while the other four compounds are derived from Core 100. Only one condition, 50 ng of siRNA with **1a**, showed any luciferase knockdown at all. Activity was completely abolished in all other cases.

Viability after siRNA Delivery with Selected Library Members. Purified library members were evaluated for their effect on cellular viability using an MTS assay (Figure 3). All compounds had at least one weight ratio that gave viability values above 80%, the value also observed using Lipofectamine2000. At a weight ratio of 15:1, **6a**, **10a**, **11a,** and **13b** all had cell viability rates of less than 60%, while the remainder of the purified compounds were at or above 80%.

Factor VII Knockdown *in Vivo.* We further assessed the ability of these selected library members to deliver siRNA *in vivo*. For increased serum stability and enhanced shielding of the payload, lipidoids were formulated with cholesterol and PEG-ceramide prior to complexation with the duplexes. The entrapment efficiency and particle sizes resulting from these formulations varied from 68% to 98% and 45 nm to 138 nm, respectively (see Supporting Information). siRNA directed against the hepatocyte-specific blood-clotting protein Factor VII was administered via tail vein injection. At 72 h post-injection,

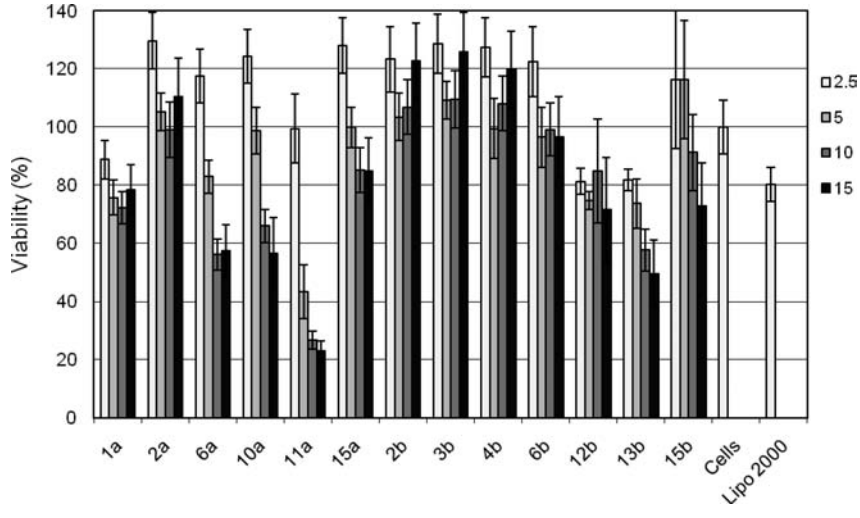


Figure 3. Viability of HeLa cells post-transfection with selected lipidoids. HeLa cells were transfected with 50 ng of siRNA complexed at lipidoid/siRNA ratios of 2.5:1, 5:1, 10:1, and 15:1 (w/w). Lipofectamine 2000 was used as instructed by the vendor. After incubation for 24 h, the media were replaced, and CellTiter viability solution (Promega) was added. The absorbance at 490 nm was read after incubating for 1 h. Values are reported relative to an untransfected set of control cells.

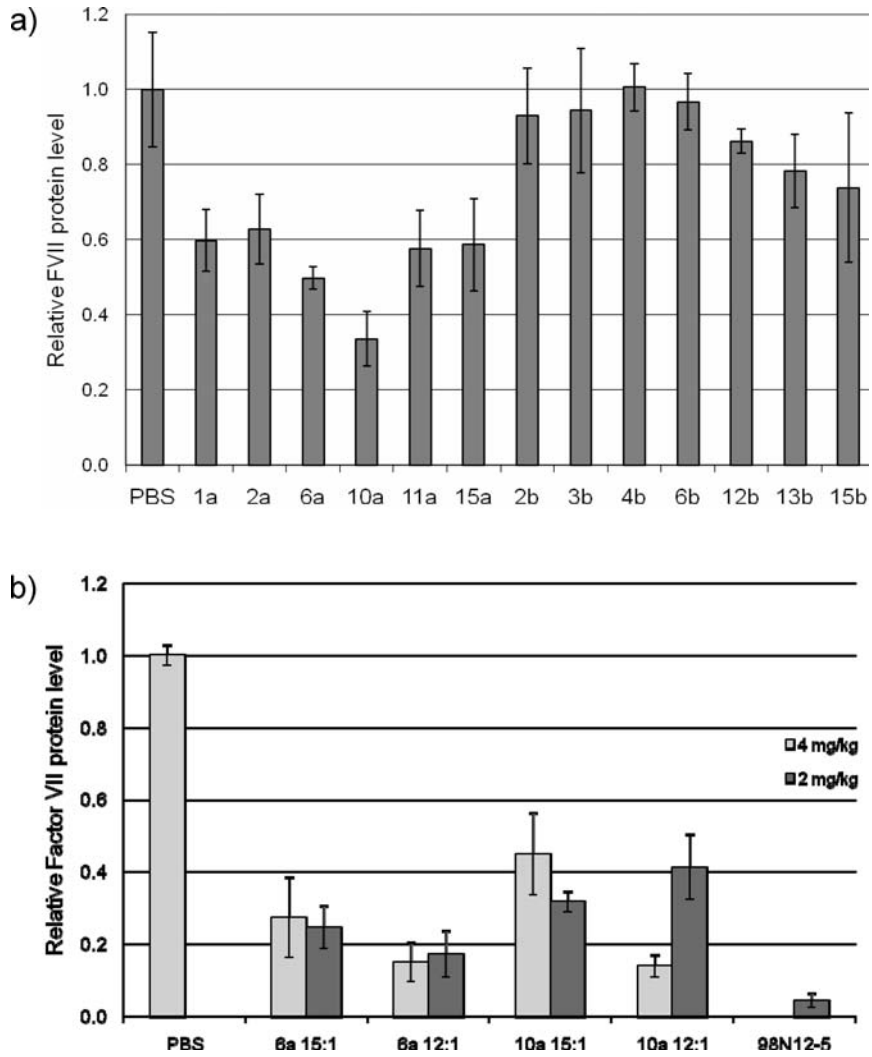


Figure 4. *In vivo* silencing of factor VII in mice. Lipidoids shown to be efficacious in *in vitro* studies were formulated for intravenous delivery of anti-factor VII siRNA to hepatocytes via tail vein injection. (a) Mice were administered a single dose of 2.5 mg/kg siRNA, and blood samples were drawn at 72 h for the detection of factor VII levels in serum. (b) Selected lipidoids are formulated with varied weight ratios of lipiods to siRNA and injected at doses of 4 and/or 2 mg/kg. Factor VII levels in all treated groups are expressed relative to those of PBS injected mice.

mice were bled and assayed for protein levels. Notably, six compounds, **1a**, **2a**, **6a**, **10a**, **11a**, and **15a**, all derivatives of Core 98, were shown to decrease the serum levels of Factor VII by at least 40% when compared to a saline control (Figure 4a). In contrast, none of the Core 100 based compounds had a knockdown efficiency greater than 20%. The two most effective compounds, **6a** and **10a** were screened in this same assay at two different doses of siRNA (Figure 4b). Compound **6a**, when complexed at 12:1 wt/wt at doses of 2 or 4 mg/kg of siRNA resulted in over 80% knockdown of factor VII at 72 h post-injection. Using a higher ratio of 15:1 wt/wt led to a slightly decreased knockdown efficiency. Compound **10a** achieved over 80% knockdown when complexed at 12:1 wt ratio with 4 mg/kg siRNA. Complexes of **10a** at 15:1 wt ratio and a dose of 4 mg/kg or either ratio at 2 mg/kg led to approximately 60% knockdown at 72 h. These compounds compared favorably to the previously identified lead compound 98N12-5, which, while slightly more efficacious, contained no heterogeneity in the tails.

DISCUSSION

The application of siRNA in both laboratory and clinical settings requires safe and effective delivery methods. While a number of materials and methods for siRNA delivery have been investigated, nonviral chemical approaches continue to receive widespread attention due to their relative ease of production and favorable safety profile. To increase the diversity of delivery molecules, the development of alternative lipid-like structures for siRNA delivery has been pursued (*16, 18, 26, 28*−*32*). Here, we systematically investigate the effect of the chemical modification of lipid-like materials.

Most siRNA delivery reagents utilize the overall negative charge of the nucleic acid to facilitate binding and particle formation. Many of these materials feature various degrees of protonable amine functionalities. For example, cationic lipids generally feature one cationic amine, while polymeric vectors such as polylysine and polyethyleneimine (PEI) have multiple amine groups. Previous studies identified the best lipidoid delivery molecules to contain three or four secondary or tertiary amines (*26, 27*). The results here offer further evidence for this optimal number of amines. Compounds **3b**, **8b**, and **9b** all feature three amine functional groups and were among the top performers in the initial library screen. Alternatively, compounds **3a**, **8a**, and **9a**, featuring the same tertiary amine tails conjugated to a tetraamine core, were less efficient. In other polyamine delivery systems, such as PEI, high amine content can lead to cytotoxicity (*21*). In this system, it appears that the increased

amine content serves to disrupt the particle formation and delivery, as little toxicity was observed in those particular molecules.

Other modifications featuring tails of varying degrees of hydrophobicity or hydrogen bonding capacities were generally well tolerated. For example, appendages featuring hydroxyl, ether, and carbamate functional groups predominantly led to increased siRNA delivery efficiency, indicating that these moieties enhanced particle formation for intracellular delivery. Some biophysical characterization of siRNA complexes with nonviral delivery vectors has been reported (*33*−*35*). While electrostatic forces are generally accepted as the driving force behind cationic lipids binding to nucleic acids, entropy, hydrophilic, and hydrophobic forces have been shown to contribute to complex formation (*36*−*38*). The delivery systems described in this work could provide further insight into the contributions of these parameters to siRNA complexation.

Modification of the lipidoid with ligands containing ethylene or propylene glycol units was shown to result in efficient delivery systems *in vivo*. Both polyethylene and polypropylene glycol are commonly used excipients in drug delivery formulations that stabilize particles in serum. Indeed, a recent report indicates successful siRNA delivery to primates using such methods (*10*). In this study, the best performing lipidoids from the *in vitro* screen were also investigated for their ability to deliver siRNA to mice *in vivo* using a Factor VII liver function assay. The range of activity observed *in vivo* indicates that alteration of the lipidoid molecular structure through simple tail modification can affect overall particle characteristics and may have some effect on pharmacokinetic properties and biodistribution. For example, two members of this library containing a combination of alkyl tails and ether groups were particularly well tolerated *in vivo*, indicating that heterogeneous functionalized delivery vectors warrant further investigation. While more in depth studies will have to be conducted to support these ideas, the ability to tune such pharmacodynamic properties may provide a tool to optimize the biodistribution of delivery. Furthermore, the appendage of these stabilizing ligands suggests that other more specific targeting ligands could be utilized with this system to enable localization of siRNA delivery to tumors or specific areas *in vivo*.

CONCLUSIONS

Here, we have demonstrated the utility of combinatorial methods to generate a chemically diverse set of heterogeneously functionalized compounds for siRNA delivery. These compounds are useful as *in vitro* delivery vectors and, importantly, have shown the ability to translate *in vitro* efficacy to *in vivo* utility. Furthermore, the range of activity observed through subtle changes in chemical functionality to the lipidoid provides insight into the relationship between chemical structure and cellular delivery performance.

ACKNOWLEDGMENT

This work was supported by NIH grants EB000244 and CA132091 and a grant from Alnylam.

Supporting Information Available: Detailed synthetic procedures and formulation parameters. This material is available free of charge via the Internet at http://pubs.acs.org.

LITERATURE CITED

(1) Fire, A., Xu, S., Montgomery, M. K., Kostas, S. A., Driver, S. E., and Mello, C. C. (1998) Potent and specific genetic interference by double-stranded RNA in *Caenorhabditis elegans*. *Nature 391*, 806–811.

(2) Shrivastava, N., and Srivastava, A. (2008) RNA interference: an emerging generation of biologicals. *Biotechnol. J. 3*, 339–353.

(3) Pushparaj, P. N., and Melendez, A. J. (2006) Short interfering RNA (siRNA) as a novel therapeutic. *Clin. Exp. Pharmacol. Physiol. 33*, 504–510.

(4) Chiu, Y. L., and Rana, T. M. (2003) siRNA function in RNAi: a chemical modification analysis. *RNA 9*, 1034–1048.

(5) De Paula, D., Bentley, M. V., and Mahato, R. I. (2007) Hydrophobization and bioconjugation for enhanced siRNA delivery and targeting. *RNA 13*, 431–456.

(6) Jeong, J. H., Mok, H., Oh, Y. K., and Park, T. G. (2009) siRNA conjugate delivery systems. *Bioconjugate Chem. 20*, 5–14.

(7) Deshayes, S., Simeoni, F., Morris, M. C., Divita, G., and Heitz, F. (2007) Peptide-mediated delivery of nucleic acids into mammalian cells. *Methods Mol. Biol. 386*, 299–308.

(8) McNamara, J. O., 2nd, Andrechek, E. R., Wang, Y., Viles, K. D., Rempel, R. E., Gilboa, E., Sullenger, B. A., and Giangrande, P. H. (2006) Cell type-specific delivery of siRNAs with aptamer-siRNA chimeras. *Nat. Biotechnol. 24*, 1005–15.

(9) Muratovska, A., and Eccles, M. R. (2004) Conjugate for efficient delivery of short interfering RNA (siRNA) into mammalian cells. *FEBS Lett. 558*, 63–8.

(10) Zimmermann, T. S., Lee, A. C., Akinc, A., Bramlage, B., Bumcrot, D., Fedoruk, M. N., Harborth, J., Heyes, J. A., Jeffs, L. B., John, M., Judge, A. D., Lam, K., McClintock, K., Nechev, L. V., Palmer, L. R., Racie, T., Rohl, I., Seiffert, S., Shanmugam, S., Sood, V., Soutschek, J., Toudjarska, I., Wheat, A. J., Yaworski, E., Zedalis, W., Koteliansky, V., Manoharan, M., Vornlocher, H. P., and MacLachlan, I. (2006) RNAi-mediated gene silencing in non-human primates. *Nature 441*, 111–114.

(11) Wolfrum, C., Shi, S., Jayaprakash, K. N., Jayaraman, M., Wang, G., Pandey, R. K., Rajeev, K. G., Nakayama, T., Charrise, K., Ndungo, E. M., Zimmermann, T., Koteliansky, V., Manoharan, M., and Stoffel, M. (2007) Mechanisms and optimization of in vivo delivery of lipophilic siRNAs. *Nat. Biotechnol. 25*, 1149–1157.

(12) Zhang, H. Y., Du, Q., Wahlestedt, C., and Liang, Z. (2006) RNA Interference with chemically modified siRNA. *Curr Top. Med. Chem. 6*, 893–900.

(13) Grzelinski, M., Urban-Klein, B., Martens, T., Lamszus, K., Bakowsky, U., Hobel, S., Czubayko, F., and Aigner, A. (2006) RNA interference-mediated gene silencing of pleiotrophin through polyethylenimine-complexed small interfering RNAs in vivo exerts antitumoral effects in glioblastoma xenografts. *Hum. Gene Ther. 17*, 751–766.

(14) Lungwitz, U., Breunig, M., Blunk, T., and Gopferich, A. (2005) Polyethylenimine-based non-viral gene delivery systems. *Eur. J. Pharm. Biopharm. 60*, 247–266.

(15) Sato, Y., Murase, K., Kato, J., Kobune, M., Sato, T., Kawano, Y., Takimoto, R., Takada, K., Miyanishi, K., Matsunaga, T., Takayama, T., and Niitsu, Y. (2008) Resolution of liver cirrhosis using vitamin A-coupled liposomes to deliver siRNA against a collagen-specific chaperone. *Nat. Biotechnol. 26*, 431–442.

(16) Gary, D. J., Puri, N., and Won, Y. Y. (2007) Polymer-based siRNA delivery: perspectives on the fundamental and phenomenological distinctions from polymer-based DNA delivery. *J. Controlled Release 121*, 64–73.

(17) Kim, W. J., and Kim, S. W. (2009) Efficient siRNA delivery with non-viral polymeric vehicles. *Pharm. Res. 26*, 657–666.

(18) Kim, Y., Tewari, M., Pajerowski, J. D., Cai, S., Sen, S., Williams, J., Sirsi, S., Lutz, G., and Discher, D. E. (2009) Polymersome delivery of siRNA and antisense oligonucleotides. *J. Controlled Release 134*, 132–140.

(19) Zhou, J., Wu, J., Hafdi, N., Behr, J. P., Erbacher, P., and Peng, L. (2006) PAMAM dendrimers for efficient siRNA delivery and potent gene silencing. *Chem. Commun. (Cambridge, U.K.)* 2362–2364.

(20) Patil, M. L., Zhang, M., Betigeri, S., Taratula, O., He, H., and Minko, T. (2008) Surface-modified and internally cationic

polyamidoamine dendrimers for efficient siRNA delivery. *Bioconjugate Chem. 19*, 1396–1403.
(21) Waite, C. L., Sparks, S. M., Uhrich, K. E., and Roth, C. M. (2009) Acetylation of PAMAM dendrimers for cellular delivery of siRNA. *BMC Biotechnol. 9*, 38.
(22) Rozema, D. B., Lewis, D. L., Wakefield, D. H., Wong, S. C., Klein, J. J., Roesch, P. L., Bertin, S. L., Reppen, T. W., Chu, Q., Blokhin, A. V., Hagstrom, J. E., and Wolff, J. A. (2007) Dynamic polyconjugates for targeted in vivo delivery of siRNA to hepatocytes. *Proc. Natl. Acad. Sci. U.S.A. 104*, 12982–12987.
(23) Wolff, J. A., and Rozema, D. B. (2008) Breaking the bonds: non-viral vectors become chemically dynamic. *Mol. Ther. 16*, 8–15.
(24) Li, W., and Szoka, F. C., Jr. (2007) Lipid-based nanoparticles for nucleic acid delivery. *Pharm. Res. 24*, 438–449.
(25) Tseng, Y. C., Mozumdar, S., and Huang, L. (2009) Lipid-based systemic delivery of siRNA. *Adv. Drug Delivery Rev. 61*, 721–731.
(26) Love, K. T., Mahon, K. P., Levins, C. G., Whitehead, K. A., Querbes, W., Dorkin, J. R., Qin, J., Cantley, W., Qin, L. L., Racie, T., Frank-Kamenetsky, M., Yip, K. N., Alvarez, R., Sah, D. W., de Fougerolles, A., Fitzgerald, K., Koteliansky, V., Akinc, A., Langer, R., and Anderson, D. G. (2010) Lipid-like materials for low-dose, in vivo gene silencing. *Proc. Natl. Acad. Sci. U.S.A. 107*, 1864–1869.
(27) Akinc, A., Zumbuehl, A., Goldberg, M., Leshchiner, E. S., Busini, V., Hossain, N., Bacallado, S. A., Nguyen, D. N., Fuller, J., Alvarez, R., Borodovsky, A., Borland, T., Constien, R., de Fougerolles, A., Dorkin, J. R., Narayanannair Jayaprakash, K., Jayaraman, M., John, M., Koteliansky, V., Manoharan, M., Nechev, L., Qin, J., Racie, T., Raitcheva, D., Rajeev, K. G., Sah, D. W., Soutschek, J., Toudjarska, I., Vornlocher, H. P., Zimmermann, T. S., Langer, R., and Anderson, D. G. (2008) A combinatorial library of lipid-like materials for delivery of RNAi therapeutics. *Nat. Biotechnol. 26*, 561–569.
(28) Baigude, H., McCarroll, J., Yang, C. S., Swain, P. M., and Rana, T. M. (2007) Design and creation of new nanomaterials for therapeutic RNAi. *ACS Chem. Biol. 2*, 237–241.
(29) Ceballos, C., Prata, C. A., Giorgio, S., Garzino, F., Payet, D., Barthelemy, P., Grinstaff, M. W., and Camplo, M. (2009) Cationic nucleoside lipids based on a 3-nitropyrrole universal base for siRNA delivery. *Bioconjugate Chem. 20*, 193–196.
(30) Ghosn, B., Kasturi, S. P., and Roy, K. (2008) Enhancing polysaccharide-mediated delivery of nucleic acids through functionalization with secondary and tertiary amines. *Curr. Top. Med. Chem. 8*, 331–340.
(31) Islam, R. U., Hean, J., van Otterlo, W. A., de Koning, C. B., and Arbuthnot, P. (2009) Efficient nucleic acid transduction with lipoplexes containing novel piperazine- and polyamine-conjugated cholesterol derivatives. *Bioorg. Med. Chem. Lett. 19*, 100–103.
(32) Kim, Y., Tewari, M., Pajerowski, J. D., Cai, S., Sen, S., Williams, J., Sirsi, S., Lutz, G., and Discher, D. E. (2009) Polymersome delivery of siRNA and antisense oligonucleotides. *J. Controlled Release 134*, 132–140.
(33) Bouxsein, N. F., McAllister, C. S., Ewert, K. K., Samuel, C. E., and Safinya, C. R. (2007) Structure and gene silencing activities of monovalent and pentavalent cationic lipid vectors complexed with siRNA. *Biochemistry 46*, 4785–4792.
(34) Grayson, A. C., Doody, A. M., and Putnam, D. (2006) Biophysical and structural characterization of polyethylenimine-mediated siRNA delivery in vitro. *Pharm. Res. 23*, 1868–1876.
(35) Mao, S., Neu, M., Germershaus, O., Merkel, O., Sitterberg, J., Bakowsky, U., and Kissel, T. (2006) Influence of polyethylene glycol chain length on the physicochemical and biological properties of poly(ethylene imine)-graft-poly(ethylene glycol) block copolymer/SiRNA polyplexes. *Bioconjugate Chem 17*, 1209–1218.
(36) Marty, R., N'Soukpoe-Kossi, C. N., Charbonneau, D., Weinert, C. M., Kreplak, L., and Tajmir-Riahi, H. A. (2009) Structural analysis of DNA complexation with cationic lipids. *Nucleic Acids Res. 37*, 849–857.
(37) Pozharski, E., and MacDonald, R. C. (2002) Thermodynamics of cationic lipid-DNA complex formation as studied by isothermal titration calorimetry. *Biophys. J. 83*, 556–565.
(38) Prevette, L. E., Kodger, T. E., Reineke, T. M., and Lynch, M. L. (2007) Deciphering the role of hydrogen bonding in enhancing pDNA-polycation interactions. *Langmuir 23*, 9773–9784.

BC100041R

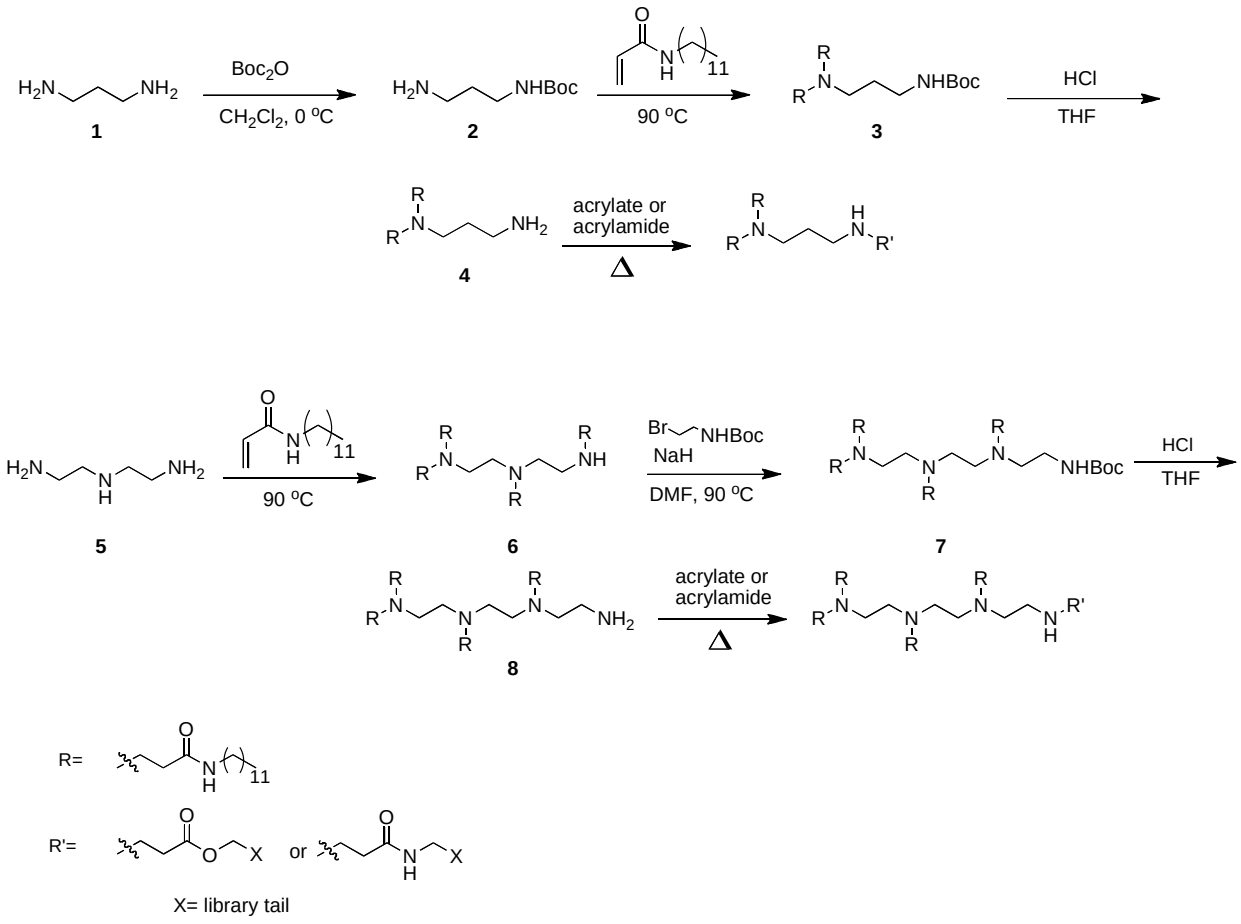
A combinatorial approach to determine functional group effects on lipidoid-mediated siRNA delivery

Kerry P. Mahon[†], Kevin T. Love[†], Kathryn A. Whitehead[†], June Qin[‡], Akin Akinc[‡], Elizaveta Leshchiner[†], Ignaty Leshchiner[†], Robert Langer[†], Daniel G. Anderson[*†]

[†]Department of Chemical Engineering and David H. Koch Institute of Integrative Cancer Research, Massachusetts Institute of Technology, 77 Massachusetts Ave., Cambridge, MA, 02139.[‡]Alnylam Pharmaceuticals, Inc., 300 Third Street, Cambridge, MA 02142

Supporting Information

Scheme 1 Synthesis of amine modified core lipidoids



*Synthesis of **2***

15g of **1 (**1,3-diaminopropane, 74.12g/mol, 243mmol, 1.0 eq.) was added to 150ml of CH_2Cl_2 and the solution was cooled in an ice bath to 4^{O}C. In a separate vessel, 3.9g Di-*tert*-butyl dicarbonate (218.25g/mol, 24.3mmol, 0.1 eq.) was dissolved in 20ml CH_2Cl_2 and added to the amine solution dropwise over one hour. The reaction was allowed to gradually warm to room temperature while stirring overnight. After extraction 5 times with 20ml H_2O, the organic layer

was dried with $MgSO_4$ and concentrated to an oil. 2.6g (83%). MW calc. ($C_8H_{18}N_2O_2$)= 174.13 found 171.15.

^{1}H NMR (300 MHz, $CDCl_3$, δ): 4.95 (s, 1H, N*H*), 3.25-3.13 (m, 2H, NC*H*$_2$), 2.80-2.73 (m, 2H, NC*H*$_2$), 1.55-1.55 (m, 2H, $CH_2CH_2CH_2$), 1.45 (s, CH,(OC*H*$_3$)$_3$).

*Synthesis of **3***

Added 6.05g dodecylacrylamide (239.4g/mol, 19.0mmol, 2.2 eq.) and 2.0g **2** (174.14g.mol, 8.6mmol, 1.0 eq.) to a 20ml scintillation vial equipped with a stirbar. Loosely capped the vial and placed at 90^{O}C for 5 days. Purified using silica gel chromatography with a solvent gradient of 5-30% Ultra (75:22:3 CH_2Cl_2: MeOH: NH_4OH) in CH_2Cl_2 over 120 min. 2.5g (33%).

MW calc.($C_{38}H_{76}N_4O_4$)= 652.58 found 652.57

^{1}H NMR (300 MHz, $CDCl_3$, δ):

6.95–6.85 (m, 2H, N*H*), 4.6 (s, 1H, N*H*), 3.25–3.1 (m, 6H, NC*H*$_2$), 2.70–2.60 (m, 4H, NC*H*$_2$), 2.36-2.31 (m, 2H, NC*H*$_2$)2.29-2.25 (m, 4H, C(O)C*H*$_2$), 1.71 (s, 2H, $NCH_2CH_2CH_2N$), 1.57-1.50 (m, 4H, $NHCH_2CH_2CH_2$), 1.47 (s, 9H, C(O)O(C*H*$_3$)$_3$), 1.26-1.23 (m, 36H, $CH_2CH_2CH_2$), 0.93-0.85 (m, 6H, C*H*$_3$).

*Synthesis of **4***

Dissolved 2.5g **3** (653.03g/mol, 8.1mmol, 1.0 eq.) in 3ml THF. In a separate vessel, added 3.2g 37% HCl (36.46g/mol, 81mmol, 10 eq.) to 1ml THF. Added the HCl solution dropwise to the solution of **2** over 5 min. Stirred rapidly overnight at room temperature. Diluted the reaction mixture in 75ml CH_2Cl_2 and extracted 2x 50 ml H_2O, 1x 50ml brine. Dried the CH_2Cl_2 solution

with $MgSO_4$ and concentrated under vacuum. Purified using silica gel chromatography with a solvent gradient of 20-50% Ultra in CH_2Cl_2 over 80 min. 1.6g (76%)

MW calc.($C_{33}H_{68}N_4O_2$)= 552.53 found 552.54

^{1}H NMR (300 MHz, $CDCl_3$, δ): 6.80-6.75 (m, 2H, N*H*), 3.24-3.13 (m, 4H, NC*H*$_2$), 2.73-2.67 (m, 6H, NC*H*$_2$), 2.51-2.45 (m, 2H, NC*H*$_2$), 2.35-2.29 (m, 4H, C(O)C*H*$_2$), 1.65-1.52 (m, 2H, $NCH_2CH_2CH_2NH_2$), 1.51-1.40 (m, 4H, $NHCH_2CH_2CH_2$), 1.36-1.19 (m, 36H, $CH_2CH_2CH_2$), 0.92-0.83 (m, 6H, C*H*$_3$).

Conjugation to library

Added 120mg **4** (0.21mmol, 1.0 eq.) to a 2ml vial equipped with stir bar. Added 0.24 mmol, 1.1 eq. of the appropriate acrylate/ acrylamide. Placed in a 90^{O}C oven for 18 hrs. (acrylates) or 3 days (acrylamides).

*Synthesis of **6***

Added 515mg **5** (diethylenetriamine, 103.17g/mol, 5.0 mmol, 1.0 eq) and 5.0g dodecylacrylamide (239.4g/mol, 20.9mmol, 4.2eq.) to a 20ml scintillation vial equipped with a stirbar. Set up in duplicate. Loosely capped the vial and placed in an oven at 90^{O}C for 6 days. After cooling, dissolved the material in both vials in 5ml CH_2Cl_2. And purified using silica gel chromatography with a solvent gradient of 10-40% Ultra in CH_2Cl_2 over 40 min. Left with 2.26g (21%) of the desired product.

MW calc.($C_{64}H_{129}N_7O_4$)= 1060.01 found 1060.02

^{1}H NMR (300 MHz, $CDCl_3$, δ): 7.40–7.35 (m, 1H, N*H*), 7.15-7.10 (m, 1H, N*H*), 6.75-6.70 (m, 1H, N*H*), 3.25-3.1 (m, 8H, C(O)CH_2), 2.90-2.25 (m, 24H, NHCH_2, NCH_2), 1.55-1.40 (m, 8H, $NHCH_2CH_2$), 1.40-1.17 (m, 72H, $CH_2CH_2CH_2$), 0.93-0.86 (m, 12H, CH_3).

*Synthesis of **7***

Added 2.2g **6** (1060.1g/mol, 2.1mmol, 1.0 eq) and 1.63g N(Boc)-bromoethylamine (224 g/mol, 7.3mmol, 3.5eq) to a 20ml scintillation vial. Added 3ml DMF and stirbar. Added 292mg NaH.(60% dispersion, 24g/mol, 7.3mmol, 3.5 eq). Loosely capped the vial and placed in a 90^{O}C oven for 2.5 days. Diluted the reaction with 10ml $CHCl_3$ and filtered to remove the solids in the reaction. Further diluted with 100ml $CHCl_3$ and washed 2x 50ml H_2O and 1x50ml brine. Combine aqueous layers and extract with 50 ml $CHCl_3$. Combined the organic layers, dried the solution with $MgSO_4$ and concentrated under vacuum. Purified using silica gel chromatography with a solvent gradient of 10-40% Ultra in CH_2Cl_2 over 60 min. 1.47g (59%).

MW calc.($C_{71}H_{142}N_8O_6$)= 1203.10 found 1203.08

^{1}H NMR (300 MHz, $CDCl_3$, δ): 7.40-7.35 (m, 1H, N*H*), 7.20-7.05 (m, 2H, N*H*), 5.25-5.20 (m, 1H, N*H*), 3.27-3.10 (m, 8H, C(O)CH_2), 2.80-2.25 (m, 28 H, NCH_2CH_2N, NC$H_2$$CH_2$C(O), NHC$H_2$), 1.55-1.40 (m, 17H, $NHCH_2CH_2$, C(O)O(CH_3)$_3$), 1.37-1.20 (m, 72H, $CH_2CH_2CH_2$), 0.95-0.85 (m, 12H, CH_3).

*Synthesis of **8***

Dissolved 1.47g **7** (1203.94g/mol, 1.22mmol, 1.0 eq.) in 2ml THF. In a separate vessel, added 1.2g 37% HCl (36.46g/mol, 12.2mmol, 10 eq.) to 1ml THF. Added the HCl solution dropwise to the solution of **7** over 5 min. Stirred rapidly overnight at room temperature. Brought to pH 10

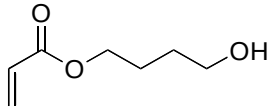
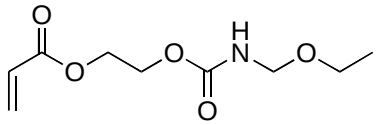
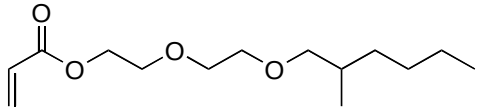
using NH_4OH. Diluted the reaction mixture in 100ml CH_2Cl_2 and extracted 3x 30 ml H_2O, 1x 50ml brine. Combined the aqueous washes and extracted with 60ml CH_2Cl_2. Combined the CH_2Cl_2 solutions, dried the CH_2Cl_2 solution with $MgSO_4$, filtered and concentrated under vacuum. Pruified using silica gel chromatography with a solvent gradient of 10-35% Ultra in CH_2Cl_2 over 40 min. 710mg (53%).

MW calc.($C_{66}H_{134}N_8O_4$)= 1103.05 found 1103.04

^{1}H NMR (300 MHz, $CDCl_3$, δ): 7.60-7.55 (m, 1H, N*H*), 7.40-7.35 (m, 1H, N*H*), 7.25-7.17 (m, 2H, N*H*), 3.25-3.10 (m, 8H, NHCH_2), 2.80-2.60 (m, 10H, NCH_2), 2.55-2.40 (m, 10H, NCH_2), 2.38-2.25 (m, 8H, C(O)CH_2), 1.55-1.45 (m, 8H, $NHCH_2CH_2$), 1.39-1.20 (m, 72H, $CH_2CH_2CH_2$), 0.92-0.83 (m, 12H, CH_3)

Conjugation to library

Added 120mg **8** (0.11mmol, 1.0 eq.) to a 2ml vial equipped with stir bar. Added 0.12 mmol, 1.1 eq. of the appropriate acrylate/ acrylamide. Placed in a 90^{O}C oven for 18 hrs. (acrylates) or 3 days (acrylamides).

Compound	Library Tail	MALDI Analysis
1a		Calc.($C_{73}H_{146}N_8O_7$): 1247.99 Found: 1248.02
2a		Calc.($C_{76}H_{151}N_9O_8$): 1319.07 Found: 1319.12
6a		Calc.($C_{81}H_{162}N_8O_8$): 1376.2 Found: 1376.44

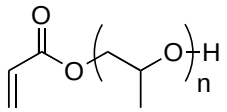
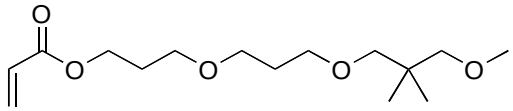
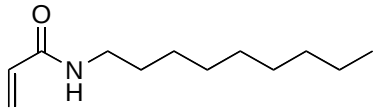
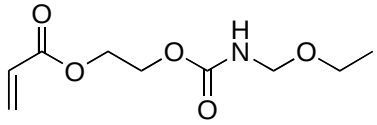
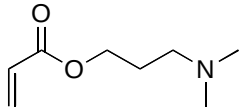
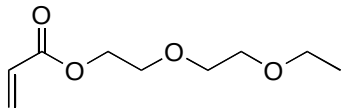
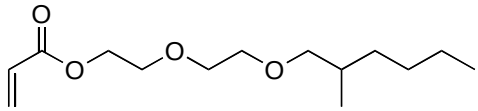
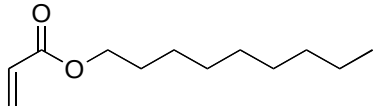
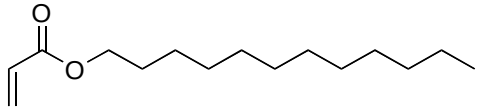
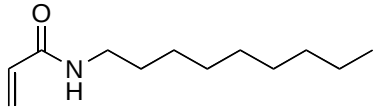
10a		Calc.($C_{90}H_{180}N_8O_{13}$): 1582.44 Found 1584.2
11a		Calc.($C_{81}H_{162}N_8O_9$): 1392.2 Found 1391.96
15a		Calc.($C_{78}H_{157}N_9O_5$): 1301.14 Found 1301.54
2b		Calc.($C_{43}H_{85}N_5O_6$): 768.16 Found: 768.53
3b		Calc.($C_{41}H_{83}N_5O_4$): 710.55 Found: 710.13
4b		Calc.($C_{42}H_{84}N_4O_6$): 741.14 Found: 741.85
6b		Calc.($C_{48}H_{96}N_4O_6$): 825.30 Found 825.65
12b		Calc.($C_{45}H_{90}N_4O_4$): 751.22 Found: 751.61
13b		Calc.($C_{48}H_{96}N_4O_4$): 792.74 Found 792.75
15b		Calc.($C_{45}H_{91}N_5O_3$): 750.24 Found: 750.64

Table S1 Formulation parameters for library testing *in vivo*

	FORMULATION PARAMETERS				CHARACTERIZATION	
COMPOUND	LIPIDOID	CHOLESTEROL	PEG	TOTAL LIPID:SIRNA	SIZE (NM)	ENTRAPMENT (% SIRNA CONTENT)
1a	42	48	10	8	103.5	82
2a	42	48	10	8	48.2	95
6a	42	48	10	8	55.6	96
10a	42	48	10	8	114.1	61
11a	42	48	10	8	45.0	95
15a	42	48	10	8	62.1	95
2b	42	48	10	15	98.7	97
3b	42	48	10	15	138.5	98
4b	42	48	10	15	109.6	86
6b	42	48	10	15	55.4	92
12b	42	48	10	15	85.1	94
13b	42	48	10	15	92.3	91
15b	42	48	10	15	65.1	96

Table S2 Formulation parameters for *in vivo* dose response

	FORMULATION PARAMETERS				CHARACTERIZATION	
COMPOUND	LIPIDOID	CHOLESTEROL	PEG	TOTAL LIPID:SIRNA	SIZE (NM)	ENTRAPMENT (% SIRNA CONTENT)
6a 15:1	42	48	10	15	111.6	95
10a 12:1	42	48	10	12	99.9	96
6a 15:1	42	48	10	15	167.7	95
10a12:1	42	48	10	12	113.7	84

$GABA_C$ Receptor Binding of Quantum-Dot Conjugates of Variable Ligand Valency

Hélène A. Gussin,[†] Ian D. Tomlinson,[||] Niraj J. Muni,[†,‡] Deborah M. Little,[§] Haohua Qian,[†] Sandra J. Rosenthal,[⊥] and David R. Pepperberg*[,†,‡]

Departments of Ophthalmology and Visual Sciences, Bioengineering, Neurology and Rehabilitation, University of Illinois at Chicago, Chicago, Illinois, and Departments of Chemistry, Pharmacology, Physics and Astronomy, and Chemical and Biomolecular Engineering, Vanderbilt University, Nashville, Tennessee. Received January 27, 2010; Revised Manuscript Received June 11, 2010

Highly fluorescent CdSe quantum dots (qdots) can serve as a platform for tethering multiple copies of a receptor-targeted ligand, affording study of how the level of multivalency affects receptor binding. We previously showed that qdots conjugated with long PEG chains terminated by muscimol, a known $GABA_C$ agonist, exhibit specific binding to the surface membrane of $GABA_C$ receptor-expressing *Xenopus* oocytes. The present report addresses the effect of varying the number, i.e., valency, of muscimol- (M-) terminated PEG chains attached to the qdot on binding of the resulting conjugate to $GABA_C$ receptors. M-PEG-qdots of differing muscimol valency were prepared by conjugating AMP-CdSe/ZnS qdots with muscimol-terminated and methylamine-terminated PEG chains in proportions designed to yield varying percentages of muscimol-terminated chains among the total ~150−200 chains bound to the qdot. The investigated valencies represented 0%, ~25%, ~50%, and 100% loading with muscimol (preparations termed M-PEG-qdot0, M-PEG-qdot25, M-PEG-qdot50, and M-PEG-qdot100, respectively. Binding of a given conjugate to surface membranes of $GABA_C$ receptor-expressing oocytes was analyzed by quantitative fluorescence microscopy following defined incubation with ~30 nM of the conjugate. With 5−20 min incubation, the fluorescence signal resulting from incubation with M-PEG-qdot25 exceeded, by ~6-fold, the fluorescence level obtained with M-PEG-qdot preparations that lacked muscimol-terminated chains (M-PEG-qdot0). M-PEG-qdot50 yielded a net signal roughly similar to that of M-PEG-qdot25, and that produced by M-PEG-qdot100 exceeded, by ~30−50%, those for M-PEG-qdot25 and M-PEG-qdot50. The time course of changes in oocyte surface membrane fluorescence resulting from the introduction of and removal of M-PEG-qdots in the medium bathing the oocyte indicated only a modest dependence of both binding and wash-out kinetics on muscimol valency. The results demonstrate a dependence of the binding activity of the M-PEG-qdot conjugates on muscimol valency, presumably reflecting higher $GABA_C$ avidity and/or affinity of the muscimol at high valency, and provide insight on the interactions of membrane receptor proteins with qdot conjugates containing multiple copies of a receptor-targeting ligand.

INTRODUCTION

CdSe/ZnS core−shell nanocrystals (quantum dots; "qdots") are highly fluorescent, photobleach-resistant particles that can be conjugated with biomolecules and used in a wide range of biochemical and biological imaging applications (for recent reviews, see *refs* 1–4). A central feature in the design of qdot conjugates for biological imaging is the attachment to the qdot surface of a ligand that is distally terminated by a small molecular weight compound or by a macromolecule such as an antibody, that promotes interaction of the conjugate with a specific intra- or extracellular site. A variety of surface modification strategies have been developed to enable the conjugation of ligands such as peptides and large proteins, including antibodies, with CdSe-based qdots. For example, Mattoussi et al. (*5*), Goldman et al. (*6*), and Anikeeva et al. (*7*) conjugated proteins to qdots using an electrostatic-based method, involving binding of a chimeric fusion protein to the oppositely charged capped qdots. Other reported modification strategies have included 1-[3-(dimethylamino)propyl]-3-ethylcarbodiimide hydrochloride (EDC) coupling between amino-terminated peptides and carboxylic acid residues on the qdot surface (*8*, *9*), the covalent attachment of proteins through thiol-maleimide conjugation (e.g., antibody conjugates (*10*)), the use of pyridine-capped qdots (*11*), and the conjugation of biotinylated proteins with streptavidin-coated qdots (*12*–*14*).

Relatively few imaging applications of small-molecule qdot conjugates have been investigated, despite the potential of these conjugates to target membrane-bound proteins other than those for which target-specific antibodies or peptides are available. Ligands derived from small molecules may be readily synthesized using conventional synthetic organic techniques enabling the development of a wider array of quantum dot probes that may be useful in studies of fundamental biological processes. For example, Rosenthal et al. (*15*) used qdots functionalized with serotonin to target human and *Drosophila* serotonin transporters (hSERT, dSERT) expressed in HeLa and HEK-293 cells and serotonin- $5HT_3$ receptors expressed in *Xenopus* oocytes.

* Corresponding author. Dr. David R. Pepperberg, Department of Ophthalmology and Visual Sciences, University of Illinois at Chicago, 1855 W. Taylor St., Chicago, IL 60612. Phone: 312-996-4262; Fax: 312-996-7773; E-mail: davipepp@uic.edu.

[†] Department of Ophthalmology and Visual Sciences, University of Illinois at Chicago.

[‡] Department of Bioengineering, University of Illinois at Chicago.

[§] Department of Neurology and Rehabilitation, University of Illinois at Chicago.

[||] Department of Chemistry, Vanderbilt University.

[⊥] Departments of Chemistry, Pharmacology, Physics and Astronomy, and Chemical and Biomolecular Engineering, Vanderbilt University.

10.1021/bc100050s © 2010 American Chemical Society
Published on Web 07/19/2010

GABA receptors are multi-subunit, transmembrane receptor proteins that in vivo respond to the neurotransmitter γ-aminobutyric acid and mediate inhibitory synaptic transmission in the nervous system. One member of this family of receptors, known as the ρ1 $GABA_C$ receptor, is a homopentameric ligand-gated ion channel that exhibits full functionality when expressed in the *Xenopus* oocyte system (*16–19*). In a study of ρ1 $GABA_C$ receptors expressed in *Xenopus* oocytes, Gussin et al. (*20*) found that these receptors exhibit robust binding of a CdSe/ZnS qdot conjugate containing numerous (~150−200) copies of the small molecular weight compound muscimol, a known $GABA_C$ agonist. This structure, here termed M-PEG-qdot, was thus highly multivalent, with many copies of muscimol per qdot available for interaction with the receptor.

The evident binding activity of M-PEG-qdot reported by Gussin et al. (*20*) raises the interesting question as to the extent to which this activity depends on the number of copies of qdot-bound muscimol. The dependence of the reactivity of qdot and other supramolecular conjugates on the valency (i.e., population) of targeting moieties is a topic of substantial interest and one that, to our knowledge, has not been extensively investigated. For example, if multivalency enhanced binding of a qdot conjugate to its target receptor, one might expect an improved ability to dynamically track the receptor. We reasoned that, in addition to its significance for elucidating properties of the $GABA_C$ receptor, determining how differential muscimol loading affects the M-PEG-qdot/$GABA_C$ interaction might prove useful as a model system in studies of multivalency in qdot-based conjugates. Here, we have used quantitative fluorescence imaging of $GABA_C$-expressing *Xenopus* oocytes to investigate how relative muscimol valency affects $GABA_C$ receptor binding of M-PEG-qdot conjugates. Preliminary results have been reported (*21*).

EXPERIMENTAL PROCEDURES

Preparation of Muscimol and Methylamine Capped PEG Ligands. The conjugates used in this study consisted of AMP-coated CdSe/ZnS core−shell nanocrystals with differing ratios of PEG-based ligands covalently attached to the AMP coating. Polydisperse PEG3400 (approximately 77 PEG units) was employed as a linker in these conjugates, as previous studies have shown that long-chain PEGs reduce nonspecific binding of quantum dots to cellular membranes (*22*). The distal ends of these ligands were terminated with either a muscimol (5-aminomethyl 3-hydroxyisoxazole) group linked via an alkyl spacer (*20*) or, as a control, a methylamine group (Figure 1). The muscimol ligand (abbreviated as M-PEG) was synthesized as previously described (*20, 23*), and a modification of this procedure was used to synthesize the methylamine-capped ligand (termed methylamine-PEG) (see Supporting Information).

Preparation of qdot Conjugates. AMP-coated quantum dots with a maximum fluorescence emission of 605 nm were obtained from Invitrogen Corporation (Carlsbad, CA) and used as supplied. All conjugates were synthesized from the same batch of AMP dots to eliminate variability in fluorescence quantum yields. Surface conjugation of the AMP dots with M-PEG and methylamine-PEG ligands was achieved using EDC coupling and was performed as previously described (*20*). The terminating amino group of both ligands served as the point of attachment to the carboxylic acid functionalities of the AMP coating. The conjugation was carried out in borate buffer, pH 8.5 (Polysciences, Inc., Warrington, PA), and involved the following steps. First, 100 μL of a solution containing 8×10^{-7} moles of ligand (M-PEG, methylamine-PEG, or a mixture of M-PEG and methylamine-PEG) dissolved in borate was mixed with a 100 μL solution of AMP-qdots at a concentration of 8 μM (resulting in a ligand: AMP-qdot ratio = 1000:1). After stirring for 10 min, 100 μL of borate containing *N*-hydroxysuccinimide (6×10^{-7} mol) and 100 μL of borate containing EDC (6×10^{-7} mol) were added. The resulting solution was stirred at ambient temperature for 1 h, and each conjugate was then purified via size exclusion chromatography on Sephadex G50 (borate elution). Ligand loading was varied by mixing M-PEG and methylamine-PEG in differing ratios and conjugating the mixture to the AMP-qdot surface. The methylamine-capped and muscimol-capped ligands were assumed to have equal reactivity with the AMP-qdots, since (i) for both ligands, the terminating moiety (muscimol or methylamine) is distant (about 78-PEG units) from the functional group that reacts with the surface of the AMP-qdot, and (ii) the PEG3400 chain is expected to dominate the overall steric bulk of both ligands. Furthermore, as the mass of the PEG3400 chain far exceeds those of the terminating methylamine or muscimol, we assumed a mass of 3400 for both ligands in calculating quantities of the two ligands used in the conjugation. Prior to conjugation to the AMP-qdot surface, the two ligands were mixed in molar ratios (M-PEG: methylamine-PEG) of 1:0, 3:1, 1:1, 1:3, and 0:1. Throughout this paper, preparations resulting from the conjugation of these ratios are termed M-PEG-qdot100, M-PEG-qdot75, M-PEG-qdot50, M-PEG-qdot25, and M-PEG-qdot0, respectively. The ratios of ligands used in this study are described in Table 1 and referred to as "muscimol valency". All conjugates were characterized by UV−visible spectrophotometry using an extinction coefficient of 650 000 M^{-1} cm^{-1} at 598 nm (first absorption feature of the quantum dot) and by gel electrophoresis on 1% agarose as described (*20*). The fluorescent properties of the conjugates at a fixed concentration (7 nM) were determined using an ISS PCI spectrofluorometer (quartz cell, 10 mm path length;

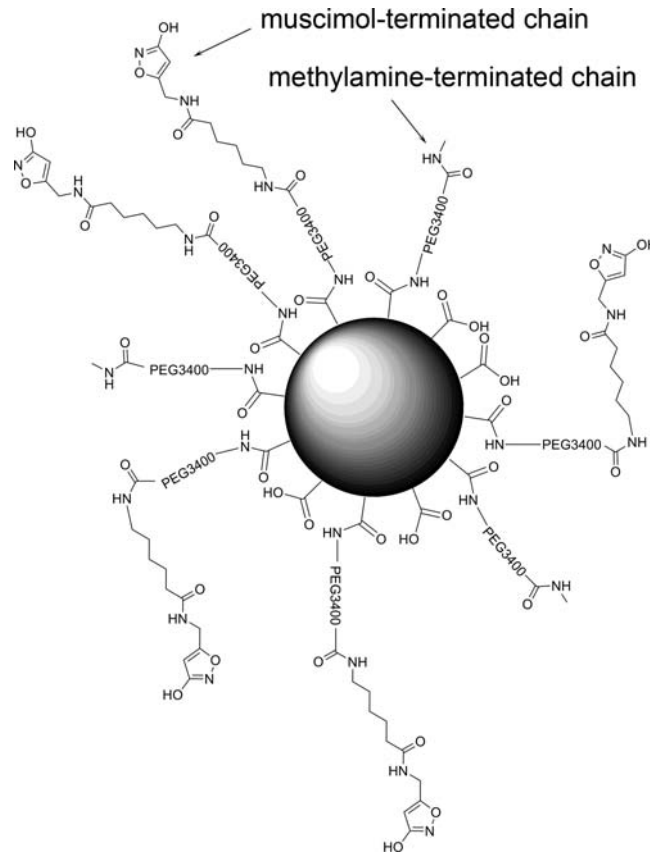


Figure 1. Schematic representation of conjugated qdot structures. The central sphere is the CdSe/ZnS core-shell qdot, functionalized by an AMP coating. Attached to the qdot are long-chain PEG linkers (PEG3400) (~150−200 chains per qdot), each of which is terminated by either muscimol or a methylamine group.

Table 1. Description of the Tested M-PEG-qdot Conjugates[a]

structure designation	respective molar proportion of muscimol- vs methylamine-terminated ligand in the conjugation reaction	approximate number of muscimol moieties per qdot
M-PEG-qdot0	0/100	0
M-PEG-qdot25	25/75	37−50
M-PEG-qdot50	50/50	75−100
M-PEG-qdot75	75/25	100−150
M-PEG-qdot100	100/0	150−200

[a] The quoted approximate number of muscimols tethered to each qdot is based on an assumed equality of the coupling efficiency of muscimol-terminated and methylamine-terminated PEG3400 chains to the AMP-qdots (about 20% (*22*)).

excitation at 400 nm) and compared with properties of an equimolar sample of unconjugated AMP-coated qdots. Figure 1 shows a schematic representation of the resulting conjugates.

Oocyte Preparation and $GABA_C$ Receptor Expression. All animal procedures adhered to institutional policies and to the Statement for the Use of Animals in Ophthalmic and Vision Research adopted by the Association for Research in Vision and Ophthalmology (ARVO). Oocytes were obtained from *Xenopus laevis* toads (*Xenopus* One, Ann Arbor, MI), and human ρ1 $GABA_C$ receptors were expressed in the oocytes through injection of RNA synthesized in vitro (mMessage mMachine, Ambion/Applied Biosystems, Austin, TX) to express the homopentameric human ρ1 $GABA_C$ receptor (*18, 19*). Oocytes that were not injected with RNA, i.e., did not express the $GABA_C$ receptors, were used as controls.

Confocal Microscopy and Image Analysis. Visualization and quantification procedures relevant to the fluorescence analysis of oocytes followed methods similar to those previously described (*20*). Unless otherwise noted, images were obtained in experiments that involved static (i.e., nonperfusing) incubation of the oocyte. Specifically, fluorescence and bright-field images were obtained from oocytes positioned in glass-bottom dishes (MatTek Corp., Ashland, MA) and incubated for defined periods in Ringer solution (100 mM NaCl, 2 mM KCl, 2 mM $CaCl_2$, 1 mM $MgCl_2$, 5 mM HEPES, and 10 mM glucose, pH 7.2−7.4) supplemented with the test components. The bright-field images illustrate the focus of the (opaque) oocyte. Fluorescence was measured using a confocal microscope (Leica model DM-IRE2 with 20× objective; λ excitation = 476 nm; λ emission = 580−620 nm to include the qdot emission peak at λ = 600−605 nm). Microscope settings relevant to excitation illumination and detection of fluorescence emission were established at the beginning of each series of experiments and maintained without change for the entire group of measurements. Experiments on a given day were performed on a single batch of oocytes and employed a single preparation of test solutions. Each fluorescence image was quantitatively analyzed for fluorescence of the oocyte surface membrane and surrounding medium (background) using *MetaMorph* v 7.0r4 software (Universal Imaging Corp., Downingtown, PA), as previously described (*20*). Briefly, the cursor was used to trace the arc-like border of the oocyte as a series of 15−25 straight-line segments that spanned the entire field of view of the border, and included 500−725 pixels (i.e., data points). For determination of background fluorescence (fluorescence of the extracellular medium bathing the oocyte), the multisegment line used to determine the border fluorescence was copied and replicated to cover a representative region in the medium. The intensities of pixels covered by these segmented lines were then obtained. (Figure 2). Net adjusted fluorescence for each halo pixel was calculated as

$$(F_{halo} - F_{background})/SFR \quad (1)$$

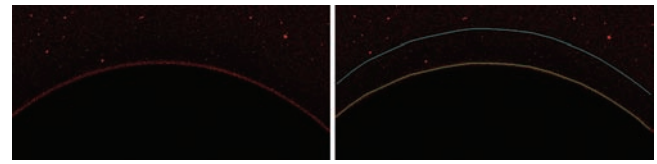


Figure 2. Example of the method used to determine intensities of the fluorescence images obtained by confocal microscopy, using *MetaMorph* v 7.0r4 software. The left-hand panel shows the fluorescence image of an oocyte exhibiting a surface halo. The intensity of the halo was determined as follows. First, the cursor was used to trace the entire arc-like border of the oocyte surface membrane as a series of straight-line segments. The right-hand panel reproduces the image at the left, and the segmented line just described is shown as an overlaid green line. This multisegment line was then copied and replicated to cover a representative region in the surrounding medium (i.e., background). This background multisegment line, shown in blue in the right-hand panel, contained the same number of pixels (data points) as the multisegment green line describing the oocyte border. Intensities of pixels covered by the border and background multisegment lines were then obtained.

where F_{halo} is the raw fluorescence value of the pixel, $F_{background}$ is the median value of raw fluorescence for all measured background pixels, and SFR is the "specific fluorescence ratio" corresponding with each M-PEG-qdot valency (see Results). In some cases, when multiple oocytes were present in the same image, a single determination of background value was used for analysis of all of the oocytes in the image. Because of hard limits on the range of measured values (data could only range from 0 to 255), data from each experiment were submitted to a Kolmogorov−Smirnov test to assess for normal distribution and spread. Testing for normal distribution was performed on all of the reported data; sets of data that passed the test for normal distribution were analyzed using parametric statistics (means, standard errors of means, analysis of variance, and *t*-tests). For data sets that were not normally distributed, nonparametric statistics were used for analysis [median, confidence interval (CI), and chi-square (χ^2)]. For parametric analyses, data were subjected to one- and two-way analysis of variance (ANOVA) for determinations of differential changes in median intensities across images. Posthoc tests of significant ANOVAs were conducted using the Bonferroni correction. For nonparametric data, analysis of histograms of image intensity was conducted, and a set bin-width of 10 units was applied.

Flow Chamber. The kinetics of removal (i.e., wash-out) of M-PEG-qdot preparations from interaction with the oocyte were investigated in experiments that involved superfusion of the oocyte. These experiments employed a customized flow chamber that was compatible with the confocal microscope and maintained the oocyte in a stable position to permit serial image capture (Figure 3). This chamber utilized an oocyte perfusion chamber designed for inverted microscopy (model OPC-4; Bioscience Tools, San Diego, CA). The base of the commercially obtained chamber assembly, which contained a glass bottom at its center and a surrounding well on which the oocyte chamber component was mounted, was reshaped to interface with the confocal microscope's mounting tray positioned above the objective lens. Additionally, safety reservoirs for capturing fluid overflow were added to the base by creating wells around the oocyte chamber; a tunnel designed for an agar bridge in the commercial device was sealed with wax; and the chamber wall near its downstream end was modified to contain a small notch that served to position the oocyte. A gravity-flow perfusion channel system consisting of a seven-channel perfusion manifold (~40 cm tubing length) was used to allow the smooth exchange of test solutions at a flow rate of approximately 0.3 mL/min.

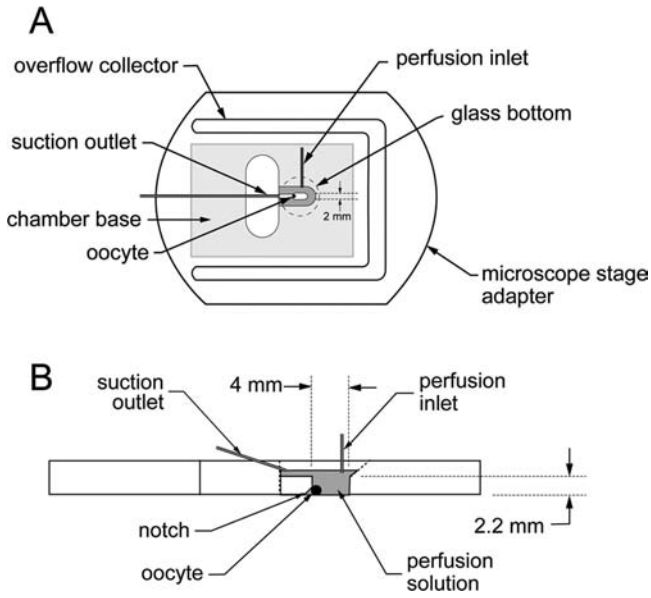


Figure 3. Top view of the base-chamber assembly (A) and of the oocyte flow chamber (B) used to examine wash-out kinetics of qdot conjugates.

The orifice of a vacuum line was positioned at the surface of the fluid in the chamber to minimize rippling.

RESULTS

Electrophoretic and Spectral Properties. Coupling of the PEG ligands (muscimol-terminated and methylamine-terminated) to the surfaces of the AMP-coated quantum dots was assessed by agarose gel electrophoresis. The results, shown in Figure 4A, indicate that the M-PEG-qdot0, M-PEG-qdot25, M-PEG-qdot50, MPEG-qdot75, and M-PEG-qdot100 preparations (lanes 2−6) exhibited fluorescence spots that were elongated by comparison with that due to unconjugated qdots (lane 1). The elongated shape presumably reflected both the heterodispersity of the PEG3400 chain and stochastic variation in loading of a given qdot with methylamine- vs muscimol-terminated chains. Figure 4A results furthermore indicate a progressive decrease in electrophoretic mobility with increased muscimol loading. Such a decrease is generally consistent with previous results obtained with coupling of methylamine-capped PEG2000 ligand to AMP-qdots (*22*). For the present case of muscimol- vs methylamine-terminated chains, the total mass of the PEG3400 chains contained in the conjugate far exceeds the overall mass contribution of either aminohexanoyl muscimol (∼227 Da) or methylamine (∼32 Da). Thus, the presently observed decrease in electrophoretic mobility with increasing muscimol valency cannot be attributed solely to mass differences among the conjugates. Changes in hydrodynamic properties may also influence the observed electrophoretic behavior (see Discussion).

The fluorescence spectra of the investigated batches of M-PEG-qdot100, M-PEG-qdot50, M-PEG-qdot25, and M-PEG-qdot0 were obtained, and the peak fluorescence (at λ ∼602 nm) determined (Figure 4B). Because the spectral properties of the conjugates differed (peak fluorescence intensity in arbitrary units was 34 483.4 for M-PEG-qdot100, 47 971.1 for M-PEG-qdot50, 62 204.9 for M-PEG-qdot25, and 67 257.1 for M-PEG-qdot0), the raw data obtained from fluorescence images were adjusted to reflect the specific fluorescence of each conjugate relative to the M-PEG-qdot100 conjugates. This adjustment involved division of the raw fluorescence values by the specific fluorescence ratio SFR (see eq 1), where the SFR was defined as the ratio of the specific fluorescence of a given M-PEG-qdot divided

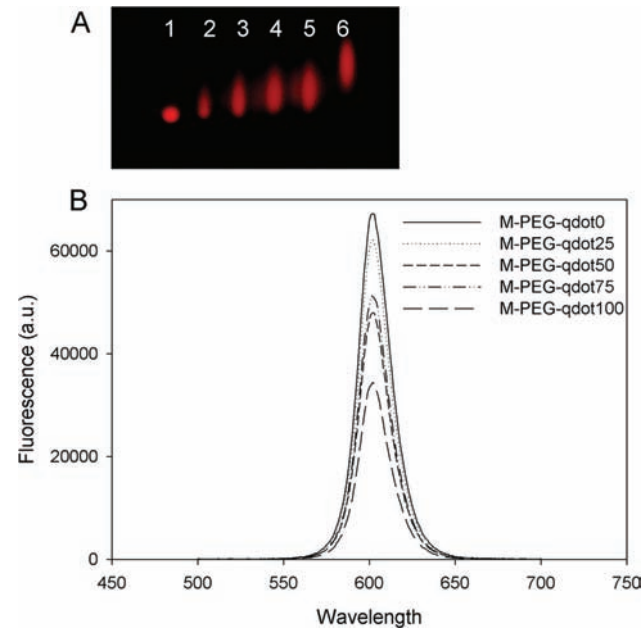


Figure 4. (A) Agarose (1%) gel of the unconjugated qdots and of the qdots conjugated with different ratios of muscimol/nonmuscimol-terminated chains. (1) unconjugated AMP-coated qdots (400 nM); (2) M-PEG-qdot0 (580 nM); (3) M-PEG-qdot25 (530 nM); (4) M-PEG-qdot50 (730 nM); (5) M-PEG-qdot75 (730 nM); and (6) M-PEG-qdot100 (630 nM). (B) Fluorescence spectra of M-PEG-qdot conjugates of different valencies. The concentration of the conjugates used to obtain the spectra was 7 nM for all M-PEG-qdot preparations, and values of fluorescence are plotted relative to those obtained for a 7 nM solution of AMP dots.

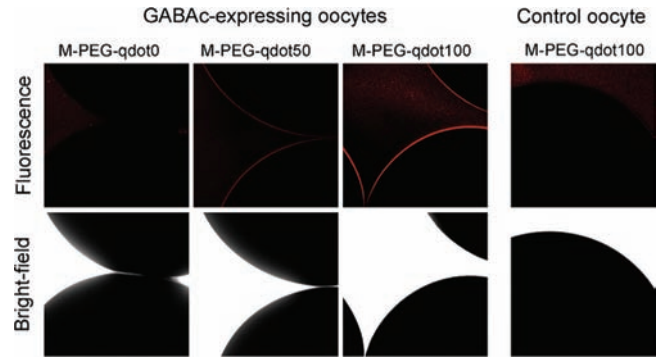


Figure 5. Representative experiments involving 15 min incubation of $GABA_C$-expressing oocytes with 34 nM M-PEG-qdot0, 34 nM M-PEG-qdot50, and 34 nM M-PEG-qdot100. For each condition are shown a fluorescence image (top row) and the corresponding bright-field image of the (opaque) oocyte that illustrates the plane of focus used for fluorescence imaging (bottom row). Representative images obtained from a nonexpressing (control) oocyte incubated for 15 min with M-PEG-qdot100 are shown in the right-hand panel.

by the specific fluorescence of M-PEG-qdot100. The SFR values determined for M-PEG-qdot50, M-PEG-qdot25, and M-PEG-qdot0 were, respectively, 1.3911, 1.8039, and 1.9504.

Oocyte Surface Membrane Binding. *Fluorescence Intensities in Relation to Muscimol Valency.* To investigate the effect of muscimol valency on the binding of the conjugate to the $GABA_C$ receptor, oocytes were incubated with M-PEG-qdot preparations containing differing proportions of muscimol-terminated and methylamine-terminated chains. Figures 5 and 6A show images and histographic data obtained in single representative experiments; results obtained from these and other oocytes are shown in Supporting Information Table S1. Upon completion of a 10−15 min incubation of 30−34 nM of the M-PEG-qdot compounds, as a static bath, with the oocytes,

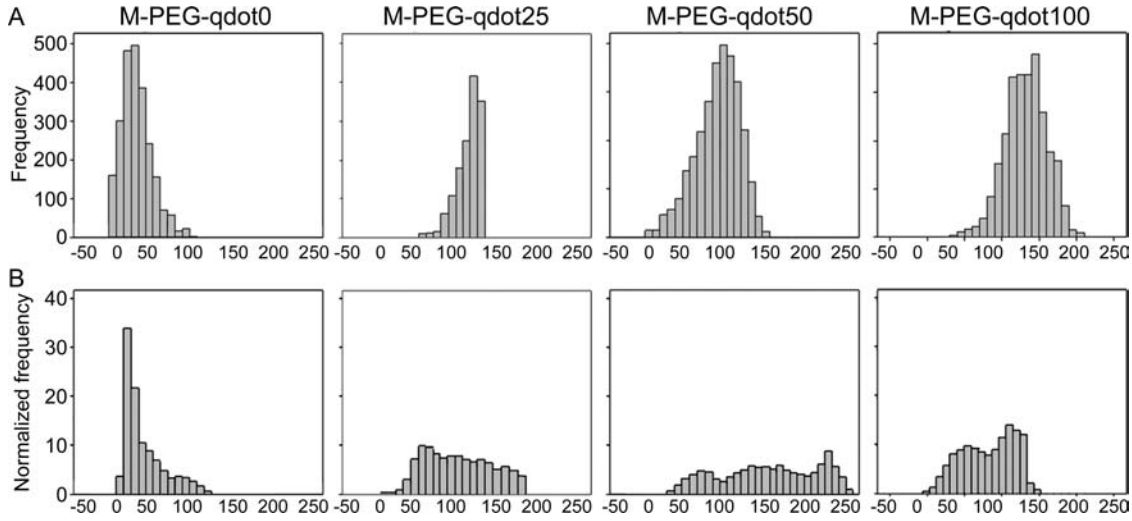


Figure 6. (A) Distributions of net adjusted fluorescence intensity for the border and background regions of representative experiments involving $GABA_C$-expressing oocytes incubated with M-PEG-qdots of different muscimol valencies. Distributions are plotted with fixed bin widths; each bin spans 20 gray scale units. (B) Cumulative normalized frequency of fluorescence intensity, based on total percentage per bin for the adjusted net data.

fluorescence and bright-field images of the oocytes were obtained. Figure 5 shows fluorescence and bright-field images obtained in representative experiments that involved the incubation of ρ1 $GABA_C$-expressing oocytes with M-PEG-qdot0, M-PEG-qdot50, and M-PEG-qdot100 and of nonexpressing (control) oocytes with M-PEG-qdot100. The fluorescence images obtained following incubation with M-PEG-qdot100 and M-PEG-qdot50 with the $GABA_C$-expressing oocytes show marked fluorescence halos at the oocyte surface membrane. By contrast, the nonexpressing control oocyte lacked significant border fluorescence on similar incubation with M-PEG-qdot100. Thus, binding of the M-PEG-qdot conjugate was specific for cells expressing the ρ1 receptor. Fluorescence intensities of the halo and of the surrounding medium (background) were quantified as described above (Experimental Procedures). Fluorescence intensities measured for the ρ1-expressing oocytes shown in Figure 5 are reported in Supporting Information Table S1, lines 17 and 18 for M-PEG-qdot50, and lines 19 and 20 for M-PEG-qdot100. For the nonexpressing oocyte (negative control) incubated with M-PEG-qdot100, fluorescence intensities of the border and background were similar and yielded a null value for net fluorescence (Supporting Information Table S1, line 25), consistent with the absence of a visible surface halo. Incubation of $GABA_C$-expressing oocytes with M-PEG-qdot0, i.e., a compound that lacked muscimol moieties, did not yield a visible halo, as shown on the left-hand side images. Quantitative analyses of these $GABA_C$-expressing oocytes confirmed the absence of significant fluorescence for M-PEG-qdot0 (Supporting Information Table S1, lines 13 and 14).

We examined the distribution of fluorescence intensities to determine whether this distribution is correlated with the valencies of the tested M-PEG-qdot preparations. Figure 6A shows results from a representative a set of experiments involving $GABA_C$-expressing oocytes that included M-PEG-qdot100, -50, and -25. The histograms show net adjusted fluorescence intensity distributions obtained with M-PEG-qdot compounds of different valencies. Within each panel, the illustrated distribution indicates the frequency of pixel value of the border from which the median background value was subtracted and then multiplied by the specific fluorescence ratio. Distributions for the border regions were essentially unimodal, with an exhibited increase in fluorescence with increasing muscimol valency, consistent with the trend in mean fluorescence intensity observed as a rightward shift in distribution with increasing valency. Median values were 17.94 for M-PEG-qdot0, 102.56 for M-PEG-qdot25, 83.39 for M-PEG-qdot50, and 135.00 for M-PEG-qdot100. Additional sets of experimental data were obtained that included M-PEG-qdot75 preparations (not illustrated); these showed similar distribution patterns.

Aggregate Determinations of Binding Extent and Time Course. Data obtained from multiple oocytes ($n = 5$ for each valency, over two different experimental days) were pooled, and the distribution of fluorescence intensity analyzed, for M-PEG-qdot preparations of different valencies. Figure 6B illustrates the aggregate normalized distribution of net adjusted fluorescence. For each valency, fluorescence data were pooled across oocytes and across experiment dates, and the net fluorescence intensity obtained for each data point was adjusted using the specific fluorescence ratio. The intensity determined for each bin (10 fluorescence units) was then normalized to the overall number of observations. Consistent with the pattern observed in Figure 6A, the cumulative distribution for the border regions exhibited a trend toward increased fluorescence with increasing muscimol valency. However, the distribution patterns observed in the aggregate histograms appeared bi- or trimodal, presumably due to differences in fluorescence intensity among the group of oocytes analyzed. For completeness, Supporting Information Table S1, lines 21−24 present both the mean and median aggregate values of fluorescence intensity. The mean and median values indicated a similar trend among preparations of differing valency. That is, net adjusted fluorescence values for the M-PEG-qdot0 preparation are lower than those for the M-PEG-qdot25, M-PEG-qdot50, and M-PEG-qdot100 preparations, and those for the M-PEG-qdot100 preparation are higher than those of the M-PEG-qdot25 and M-PEG-qdot50 preparations. Furthermore, values determined for the M-PEG-qdot25 and M-PEG-qdot50 preparations are close, although the means indicate a higher fluorescence for the M-PEG-qdot50 preparation, while the medians indicate higher fluorescence for the M-PEG-qdot25 preparation.

Figure 7 illustrates overall results obtained from groups of oocytes incubated with the M-PEG-qdot100, -50, -25, and -0 preparations, as described in the preceding paragraph, by considering the relationship between muscimol valency and the fluorescence signal exhibited by the oocyte surface membrane as a function of incubation period. In both panels A and B of the figure, comparisons of aggregate adjusted fluorescence intensities are based on median values (rather than averages)

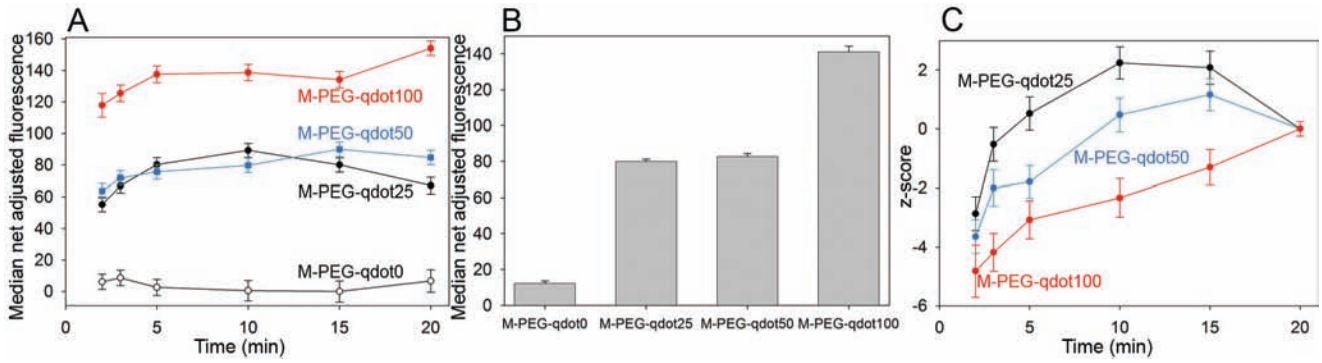


Figure 7. (A) Median net fluorescence intensities obtained with $GABA_C$-expressing oocytes incubated for 2−20 min with M-PEG-qdot100, -50, -25, and -0. Each data point reflects the median fluorescence of $n = 5$ oocytes, measured on two different experiment days, using the same batches of M-PEG-qdot preparations. Values obtained for M-PEG-qdot50, M-PEG-qdot25, and M-PEG-qdot0 were adjusted for the specific fluorescence of the compounds relative to that of M-PEG-qdot100. Error bars indicate a 99% confidence interval (99% CI). (B) Histogram representing median adjusted fluorescence intensities (±99% CI), collapsed across time (between $t = 4$ min and $t = 20$ min), as a function of muscimol valency. (C) Analysis, by *z*-transformation, of the panel A data for binding kinetics of M-PEG-qdot25, M-PEG-50, and M-PEG-qdot100. The illustrated data are median values ±99% CI. See text for further details.

because of the non-normal distribution of pixel data as shown in Figure 6. Figure 7A indicates median adjusted fluorescence data (with error bars corresponding to a 99% confidence interval). These data were submitted to a two-way ANOVA with valency as a between-samples variable and time as a within-samples variable. There was an interaction between valency and time [$F(15, 49272) = 79.94$, $p < 0.0001$]. At all time points, the fluorescence values for M-PEG-qdot100 were higher than those obtained with M-PEG-qdot50 [at $t = 2$ min, $F(1, 3374) = 1646.99$, $p < 0.0001$; at $t = 3$ min, $F(1, 4356) = 1280.90$, $p < 0.0001$; at $t = 5$ min, $F(1, 4351) = 1530.02$, $p < 0.0001$; at $t = 10$ min, $F(1, 4296) = 1125.66$, $p < 0.0001$; at $t = 15$ min, $F(1, 4452) = 764.93$, $p < 0.0001$; and at $t = 20$ min, $F(1, 4480) = 2073.13$, $p < 0.0001$] and with M-PEG-qdot25 [at $t = 2$ min, $F(1, 3388) = 2952.15$, $p < 0.0001$; at $t = 3$ min, $F(1, 4323) = 1749.74$, $p < 0.0001$; at $t = 5$ min, $F(1, 4341) = 1676.36$, $p < 0.0001$; at $t = 10$ min, $F(1, 4444) = 1188.04$, $p < 0.0001$; at $t = 15$ min, $F(1, 4450) = 1205.45$, $p < 0.0001$; and at $t = 20$ min, $F(1, 3833) = 2667.31$, $p < 0.0001$]. For all tested incubation periods, median fluorescence intensity values for M-PEG-qdot0 were significantly lower than those obtained with compounds containing muscimol moieties [$F(3, 8078) = 3195.36$, $p < 0.0001$; Bonferroni paired comparisons for all, $p < 0.0001$]. In particular, at each time point over the period $t = 5-20$ min (i.e., excluding the initial determinations), values of net fluorescence signal obtained with M-PEG-qdot25 exceeded, by ~6-fold, those determined with M-PEG-qdot0. The net fluorescence signals obtained with M-PEG-qdot50 over this same interval were generally similar to those obtained with M-PEG-qdot25, and those obtained with M-PEG-qdot100 exceeded, by ~30−50%, those determined for M-PEG-qdot25 and M-PEG-qdot50.

Figure 7B shows aggregate data collapsed across time-points over the interval of 4−20 min. The median net adjusted fluorescence intensities (±CI) observed across time were 139.88 ± 2.02 for M-PEG-qdot100, 76.82 ± 1.76 for M-PEG-qdot50, 80.78 ± 1.81 for M-PEG-qdot25, and 12.87 ± 2.46, for M-PEG-qdot0 preparations. These data indicate that the median fluorescence intensity, which reflects binding of the M-PEG-qdot preparations to oocytes expressing $\rho 1$ $GABA_C$ receptors, increased with muscimol valency [$F(3, 8610) = 2818.82$, $p < 0.0001$; Bonferroni comparisons between valencies yielded $p < 0.0001$, except for M-PEG-qdot50 compared with M-PEG-qdot25, for which $p = 0.004$]. Moreover, the low level of binding to the $GABA_C$-expressing oocytes exhibited by M-PEG-qdot0, and the low binding to nonexpressing oocytes by the M-PEG-qdot100, provide evidence for low nonspecific binding of the investigated conjugates to oocyte membranes (*22*).

To further examine the relative timing of the approach of the fluorescence signal to near-plateau values with the compounds of different valencies, net fluorescence data obtained in each of the Figure 7A group of experiments were converted to standardized fluorescence values using a *z*-score transformation

$$z = (\chi - \mu)/\sigma \qquad (2)$$

where χ is the net fluorescence value determined at a given time t, μ is the median of the fluorescence data obtained at the final time point ($t_{final} = 20$ min), and σ is the standard deviation of the fluorescence data obtained at t_{final}. This transformation was conducted for each experiment. The transformed data were then averaged across experimental conditions to yield the aggregate results illustrated in the figure. Figure 7C illustrates the resulting *z*-score values determined in the experiments with M-PEG-qdot100, M-PEG-qdot50, and M-PEG-qdot25. (Note here that $z = 0$ corresponds with a net fluorescence equal to the median of the t_{final} data, and $z = -1$ corresponds with a net fluorescence equal to one standard deviation below the median determined at t_{final}.) The *z*-transformed data of Figure 7C demonstrate that there is no significant interaction between valency and time, i.e., binding rates of the M-PEG-qdot conjugates appear not to depend on the valency of the preparations.

Effects of Conjugate Concentration on Time Course of Binding. In an additional series of experiments, we examined the time dependence of binding of differing concentrations of a single muscimol valency (M-PEG-qdot100). In all cases, these experiments involved the measurement of fluorescence intensity at defined times over an approximately 15−20 min period following the initiation of incubation with the M-PEG-qdot conjugate. Figure 8 shows representative images obtained at two fixed times (2 and 15 min) in experiments that involved incubation of the oocyte with 30 nM, 10 nM, and 3 nM of M-PEG-qdot100. These images illustrate the increase in the visible fluorescence intensity of the halo at the oocyte surface membrane. The increase is particularly noticeable when the oocyte was incubated with 30 nM of M-PEG-qdot100. In order to quantify the extent of the rise in intensity, the fluorescence from the images obtained in the experiments described in Figure 8 and in others of similar design was quantified, and the results were analyzed to obtain values of median net fluorescence (median difference in fluorescence of the border halo vs surrounding medium) and 99% confidence intervals (CIs) over the investigated periods of incubation with M-PEG-qdot100 at

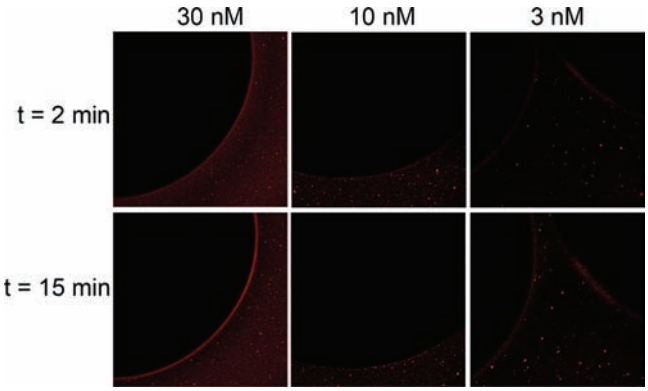


Figure 8. Representative images obtained in binding kinetics experiments with varying concentrations of M- PEG-qdot100 (images obtained at $t = 2$ min and $t = 15$ min).

30 nM, 10 nM, and 3 nM. As illustrated in Figure 9A, the final determination (i.e., the determination at $t = 15$ or $t = 20$ min) varied with M-PEG-qdot100 concentration (78.34 ± 3.82, 27.87 ± 9.22, and 17.64 ± 6.90 for 30 nM, 10 nM, and 3 nM, respectively), and, consistent with previous results (*20*), the data obtained with M-PEG-qdot100 exhibited a median net intensity that, at $t = 5$ min, represented ~75−80% of the near-plateau values determined at $t = 15$−20 min. Values of median net fluorescence obtained with 10 nM of the conjugate, in addition to being considerably smaller than those obtained with the 30 nM concentration, approached a near-plateau level on a relatively long time scale (compare red and green symbols in Figure 9).

The relative timing of the approach of the fluorescence signal to near-plateau values at 30, 10, and 3 nM was further examined by standardizing the raw data obtained in each experiment via a *z*-transformation (cf. eq 2), using the median net fluorescence determined at the final time point (t_{final}) of the incubation as the normalizing value ($t_{final} = 20$ min for 3 and 10 nM, and 15 min for 30 nM). The resulting *z*-transformed data, shown in Figure 9B, indicate that, upon control for the effect of M-PEG-qdot100 concentration, there was relatively little difference in the pattern of data obtained at a given concentration, and the binding kinetics did not significantly depend on concentration, for incubation times of >5 min.

Washout Kinetics. Investigation of the off-kinetics of the M-PEG-qdot preparations of different valencies employed the flow chamber described in the Experimental Procedures section. In these experiments, $GABA_C$-expressing oocytes were incubated for 10 min with a preparation of 30−34 nM M-PEG-qdot (of a given valency). Following this incubation, Ringer solution was passed through the chamber for approximately 5 s to remove excess conjugate, and an image designated $t = 0$ was immediately collected. The flow of a wash-out solution consisting of Ringer or of Ringer supplemented with 1 mM muscimol was then initiated at a rate of 0.3 mL/min, and images were repeatedly collected over a 45−50 min period. Figure 10 shows representative images obtained in wash-out experiments with M-PEG-qdots of differing valencies, at $t = 0$ and $t = 30$ min. The decrease in oocyte surface fluorescence exhibited by the $t = 30$ vs $t = 0$ min image for each of the investigated valences provides evidence for a release of these M-PEG-qdot preparations from the membrane over this 30 min period.

Figure 11 shows *z*-transformed data for the net difference in fluorescence intensity (border minus background) determined in these wash-out experiments with unsupplemented Ringer (panel A) and with 1 mM muscimol (B). For these analyses, the fluorescence value obtained at the conclusion of the initial wash (i.e., at $t = 0$) was used for the *z*-transformation. For each of the valencies examined in the Figure 11A experiments, we specifically compared the normalized values obtained at $t = 10$ min with those obtained at $t = 40$ min and determined that the decrease was significant ($p < 0.0001$) in all cases. However, for all valencies, the observed decline represented an incomplete loss of fluorescence signal, suggesting the occurrence of a persisting component of the M-PEG-qdot binding with the oocytes. Furthermore, the relative extent of decline differed among the tested valencies; the declines in fluorescence determined with M-PEG-qdot25 and M-PEG-qdot75 proceeded more gradually than those determined with M-PEG-qdot50 and M-PEG-qdot100 (using only $t = 10$ and $t = 40$; $p < 0.0001$ for M-PEG-qdot75 vs M-PEG-qdot50 and M-PEG-qdot100; $p < 0.001$ for M-PEG-qdot25 vs M-PEG-qdot50 and M-PEG-qdot100). For each M-PEG-qdot preparation, comparison of untransformed fluorescence intensities obtained at different time points showed a roughly 40−70% decrease in normalized fluorescence intensity over the wash-out period, i.e., a decrease of order similar to that previously reported for M-PEG qdot100 (*20*). A roughly similar pattern of data was observed when 1 mM muscimol was included in the wash-out medium (Figure 11B). Here, the comparison of untransformed fluorescence intensities indicated a roughly 45−80% decrease over the wash-out period, and the decrease occurring over the period $t = 10$ min to $t = 40$ min was significant in all cases ($p < 0.0001$).

DISCUSSION

Using quantitative fluorescence imaging of $GABA_C$-expressing *Xenopus* oocytes, we have compared the $GABA_C$ binding properties of qdot conjugates that differ with respect to their abundance of muscimol, a known $GABA_C$ ligand. The use of these muscimol-containing conjugates of different muscimol valencies extends earlier work that established the $GABA_C$ binding activity of conjugates containing only muscimol-terminated chains (*20*). The main finding of the present study is the dependence of binding on the composition of the linear chain mixture (muscimol-terminated vs methylamine-terminated chains) joined to the qdot. That is, increasing the muscimol valency from M-PEG-qdot25 (approximately 37−50 muscimol/qdot) to M-PEG-qdot100 (approximately 150−200 muscimol/qdot) leads to an increase in fluorescence intensity of the surface of the $GABA_C$-expressing oocyte (Figures 5−7). For example, binding of the M-PEG-qdot100 preparation exceeded, by ~45%, that of the M-PEG-qdot25 preparation, when fluorescence intensity data adjusted for the specific fluorescence of each compound were considered. Accompanying this increase was a shift in the distribution of fluorescence measured with this visualization technique (Figure 6). These findings, which indicate a correlation of receptor binding with the population of qdot-attached ligands, represent, to our knowledge, the first demonstration of differential binding properties of receptor-targeted qdots by variation of the population of an attached receptor ligand.

The precise interplay of differences in avidity vs affinity of the investigated multivalent conjugates remains to be determined. For example, it is possible that higher muscimol valencies, in addition to increasing the avidity of the conjugate, may be associated with a higher binding affinity of a given muscimol moiety within the conjugate. This could reflect differences in the microenvironment of a given muscimol that result from the differing proportions of muscimol- vs methylamine-capped chains. A further point of interest for future investigation is the evident significant increase in binding that occurs over the range 0−25% muscimol loading (Figures 5, 6, 7). Conceivably, the contribution of avidity- vs affinity-dependent processes to changes in binding with increased muscimol valency might differ from the relationship that prevails at higher valencies.

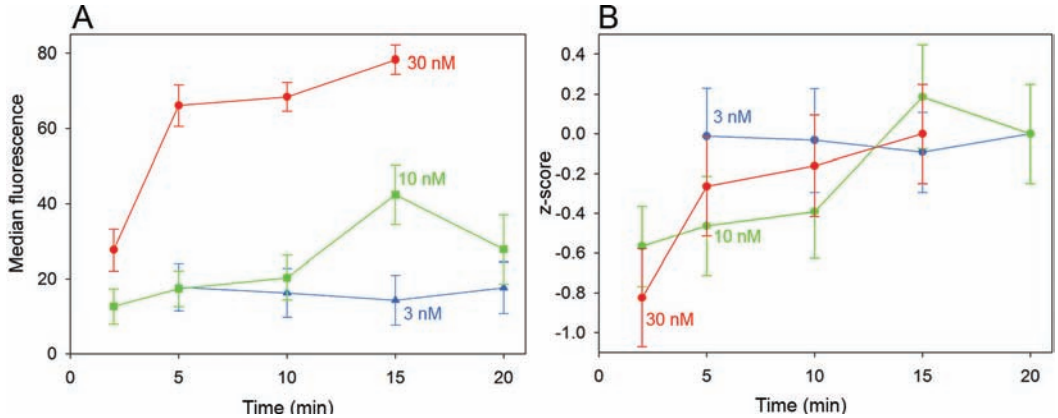


Figure 9. Binding kinetics of M-PEG-qdot100. The illustrated data show non-normalized (A) and normalized (B) values for median net fluorescence intensity. Concentrations of the M-PEG-qdot 100 were 3 nM (blue symbols), 10 nM (green symbols), and 30 nM (red symbols). In each experiment, fluorescence values were measured over a period of 15−20 min following the initiation of incubation with the M-PEG-qdots (time zero). For each concentration, the median net difference in fluorescence intensity obtained at a given time was normalized to the median net intensity obtained at the end of the incubation period, to yield the normalized median fluorescence intensity ±99% CI.

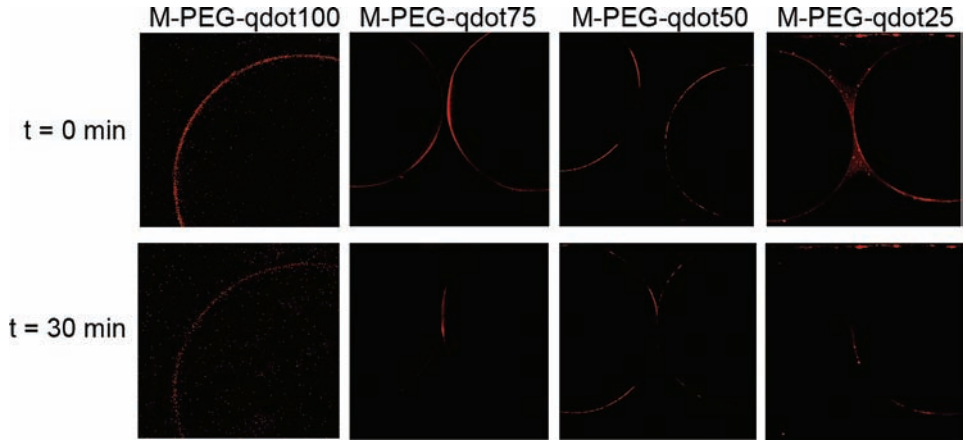


Figure 10. Representative images obtained during wash-out experiments with M-PEG-qdots of different valencies, at $t = 0$ and $t = 30$ min, with a 1 mM muscimol wash-out solution.

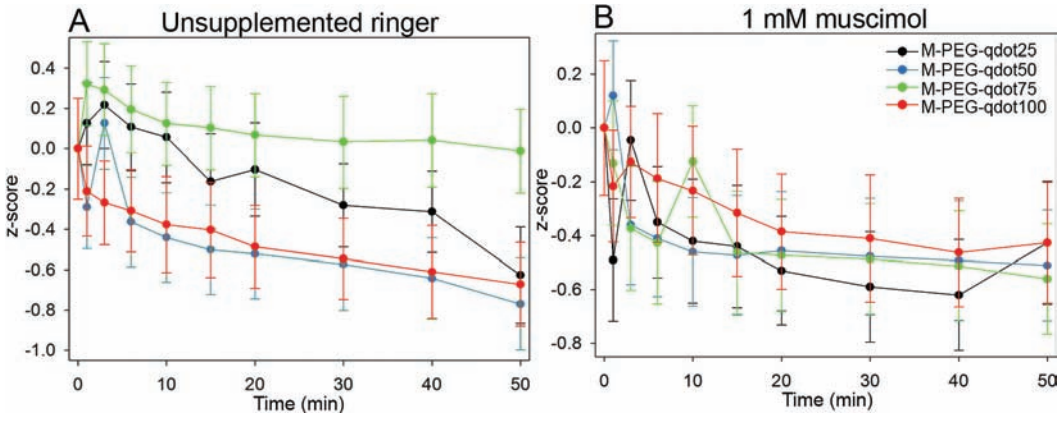


Figure 11. Wash-out of M-PEG-qdots. *z*-Transformed data (median values ±99% CI) obtained with unsupplemented Ringer (A) or Ringer supplemented with 1 mM muscimol (B). In each experiment, presentation of the M-PEG-qdot preparation was immediately followed by a rapid (∼1 s) wash with unsupplemented Ringer (time zero in the experiment) and subsequent incubation with the unsupplemented or muscimol-supplemented perfusing medium.

Electrophoretic analysis of the present qdot conjugates indicated a progressively decreased mobility with increasing muscimol valency (Figure 4A). As noted above (Results), this behavior is unlikely to be due solely to variation in masses of the conjugates. Furthermore, increasing muscimol valency might be expected to increase the net negative charge of the conjugate (due to deprotonation of muscimol under the pH conditions used for electrophoresis). However, an increase in negative charge would be expected, in itself, to increase rather than decrease electrophoretic mobility. Conceivably, the decreased mobility seen with increasing muscimol valency could be due to mechanisms that, as a function of the proportion of muscimol- vs methylamine-terminated chains (including, perhaps, an effect of muscimol deprotonation), alter the hydrodynamic radius of the conjugate. One possibility is that, with increasing proportion of deprotonated muscimol chains, the hydrodynamic radius of

the conjugate might increase as a consequence of electrostatic repulsion among chains. In particular, the relatively large reduction in mobility exhibited by M-PEG-qdot100 vs M-PEG-qdot75 (lanes 5−6 in Figure 4A) could reflect., e.g., a reduced extent of muscimol deprotonation (and thus reduced overall charge) when the conjugate contains only muscimol-terminated chains. Alternatively, the relatively low M-PEG-qdot100 mobility might reflect reduced interchain folding (leading to greater hydrodynamic radius) in the absence of methylamine-terminated chains.

In separate electrophysiology experiments (not illustrated), we tested whether M-PEG-qdot100 elicits an electrophysiological response from $GABA_C$-expressing oocytes and found no detectable response. This absence of activity could reflect an inability of the receptor to transition to its open state following binding of the M-PEG-qdot structure. Alternatively, the M-PEG-qdots may bind to only a small fraction of the receptor population, one sufficient to produce a robust fluorescence signal but insufficient to be measurable electrophysiologically. It is also possible that binding occurs with an occupancy (by a muscimol moiety of the M-PEG-qdot structure) of as little as one of the five ligand binding sites of the pentameric receptor, an event that could lead to a sufficient visualization signal but be insufficient for receptor activation (*16*).

Despite the evident dependence of the normalized M-PEG-qdot binding kinetics on muscimol valency (Figures 5−7), we found no significant dependence of the normalized wash-out kinetics on muscimol valency (Figures 10 and 11). The finding that the off-kinetics do not vary as a function of muscimol valency could reflect an intrinsic similarity across valencies in the mechanism by which a single qdot dissociates from the oocyte surface. Alternatively, it is possible that the observed similarity reflects occurrence of a bulk property of the qdot population that is bound to the oocyte surface at the beginning of the wash-out assay. For example, it is conceivable that, essentially independent of muscimol valency, qdots bound to the oocyte surface at $t = 0$ in the wash-out experiments undergo aggregation and, as a consequence, exhibit a similar retardation of wash-out. However, the clear dependence of binding on valency suggests that such an aggregation effect occurs only upon localization of the M-PEG-qdot structure at the receptor (i.e., receptor binding) and cannot account for the initial muscimol−$GABA_C$ interaction. The wash-out data obtained with presentation of competing muscimol do suggest that the presence of this competing agonist has a modest effect on wash-out kinetics, for at least certain valencies of M-PEG-qdot preparations (Figure 11, M-PEG-qdot75 and M-PEG-qdot25). However, the absence of a wash-out promoting effect among the data collected across all muscimol valencies suggests that wash-out kinetics are governed by multiple factors. These could include, for example, the local density of muscimol (including the effect of variable extension of the PEG-chains, leading to variability in availability of the muscimol) and different mechanisms of removal.

The presence of five potential binding sites for GABA at ρ1 $GABA_C$ receptors (*16*) emphasizes the possibility that the relatively strong binding observed with conjugates of high muscimol valency reflects binding of the conjugate at multiple GABA-binding sites of a given receptor, yielding a polydentate interaction (cf., e.g., ref *24*). An alternative (or perhaps additional) possible mode of interaction relates to the distance potentially spanned by the muscimol-terminated PEG chains of a given M-PEG-qdot. That is, for the present case of muscimol-terminated chains containing PEG3400 (77 ethylene glycol units, on average), and with the PEG chains of a given pair of muscimols in a conformation representing ∼80% full extension (*25*), the maximum distance spanned by the two muscimols would be ∼40 nm, a length considerably greater than the diameter of a given pentameric ρ1 $GABA_C$ receptor, about 8 nm (*26*). Thus, high muscimol valency could favor the binding of a single conjugate to neighboring receptors, and in turn promote an interplay between binding and receptor clustering. Evidence for a close interrelationship between conjugate multivalency and receptor clustering comes from a study by Gestwicki et al. (*27*). These investigators examined the effects of structural parameters such as scaffold shape, size, and density of binding elements of multivalent conjugates on the inhibition and clustering of concanavalin A (Con A). Gestwicki et al. (*27*) found, for example, that structural properties of linear oligomeric ligands favored clustering; and that the shape of a multivalent ligand influenced receptor clustering properties, such as clustering rate, number of receptors in the cluster, and inter-receptor distance. It will be of interest in future studies to examine further the relationship between receptor clustering and the "reach" of (i.e., maximal distance spanned by) multiple targeting ligands conjugated to qdot platforms.

ACKNOWLEDGMENT

The authors thank Ms. Ruth Zelkha for assistance with cell imaging and fluorescence analyses, and Ms. Tiffany Chen, Ms. Feng Feng, Mr. Jerry C. Chang, and Ms. Lisa Birmingham for other technical assistance. Supported by NIH grants EY16094, EY01792, EB003728, EM72048, and MH075791; and by grants from the Daniel F. and Ada L. Rice Foundation (Skokie, IL), Hope for Vision (Washington, DC), the Macular Degeneration Research Program of the American Health Assistance Foundation (Clarksburg, MD), and Research to Prevent Blindness (New York, NY). Some of the present material was contained in a thesis submitted by NJM to the Department of Bioengineering at the University of Illinois at Chicago, in partial fulfillment of the requirements for the PhD degree.

Supporting Information Available: Experimental procedures for preparation of methylamine-capped PEG, and Table S1 indicating fluorescence values determined from 15-min incubation of oocytes with M-PEG-qdot preparations of differing muscimol valency. This material is available free of charge via the Internet at http://pubs.acs.org.

LITERATURE CITED

(1) Medintz, I. L., Uyeda, H. T., Goldman, E. R., and Mattoussi, H. (2005) Quantum dot bioconjugates for imaging, labelling and sensing. *Nat. Mater. 4*, 435–446.

(2) Jaiswal, J. K., and Simon, S. M. (2007) Imaging single events at the cell membrane. *Nat. Chem. Biol. 3*, 92–98.

(3) Willner, I., Basnar, B., and Willner, B. (2007) Nanoparticle-enzyme hybrid systems for nanobiotechnology. *FEBS J. 274*, 302–309.

(4) Biju, V., Itoh, T., Anas, A., Sujith, A., and Ishikawa, M. (2008) Semiconductor quantum dots and metal nanoparticles: syntheses, optical properties, and biological applications. *Anal. Bioanal. Chem. 391*, 2469–2495.

(5) Mattoussi, H., Mauro, J. M., Goldman, E. R., Anderson, G. P., Sundar, V. C., Mikulec, F. V., and Bawendi, M. G. (2000) Self-assembly of CdSe-ZnS quantum dot bioconjugates using an engineered recombinant protein. *J. Am. Chem. Soc. 122*, 12142–12150.

(6) Goldman, E. R., Clapp, A. R., Anderson, G. P., Uyeda, H. T., Mauro, J. M., Medintz, I. L., and Mattoussi, H. (2004) Multiplexed toxin analysis using four colors of quantum dot fluororeagents. *Anal. Chem. 76*, 684–688.

(7) Anikeeva, N., Lebedeva, T., Clapp, A. R., Goldman, E. R., Dustin, M. L., Mattoussi, H., and Sykulev, Y. (2006) Quantum

dot/peptide-MHC biosensors reveal strong CD8-dependent cooperation between self and viral antigens that augment the T cell response. *Proc. Natl. Acad. Sci. U.S.A. 103*, 16846–16851.
(8) Mason, J. N., Farmer, H., Tomlinson, I. D., Schwartz, J. W., Savchenko, V., DeFelice, L. J., Rosenthal, S. J., and Blakely, R. D. (2005) Novel fluorescence-based approaches for the study of biogenic amine transporter localization, activity, and regulation. *J. Neurosci. Methods 143*, 3–25.
(9) Tomlinson, I. D., Mason, J. N., Blakely, R. D., and Rosenthal, S. J. (2005) Peptide-conjugated quantum dots: imaging the angiotensin type 1 receptor in living cells. *Methods Mol. Biol. 303*, 51–60.
(10) Pathak, S., Davidson, M. C., and Silva, G. A. (2007) Characterization of the functional binding properties of antibody conjugated quantum dots. *Nano Lett. 7*, 1839–1845.
(11) Robinson, A., Fang, J. M., Chou, P. T., Liao, K. W., Chu, R. M., and Lee, S. J. (2005) Probing lectin and sperm with carbohydrate-modified quantum dots. *ChemBioChem 6*, 1899–1905.
(12) Dahan, M., Lévi, S., Luccardini, C., Rostaing, P., Riveau, B., and Triller, A. (2003) Diffusion dynamics of glycine receptors revealed by single-quantum dot tracking. *Science 302*, 442–445.
(13) Rajan, S. S., Liu, H. Y., and Vu, T. Q. (2008) Ligand-bound quantum dot probes for studying the molecular scale dynamics of receptor endocytic trafficking in live cells. *ACSNano 2*, 1153–1166.
(14) Orndorff, R. L., Warnement, M. R., Mason, J. N., Blakely, R. D., and Rosenthal, S. J. (2008) Quantum dot *ex vivo* labeling of neuromuscular synapses. *Nano Lett. 8*, 780–785.
(15) Rosenthal, S. J., Tomlinson, I., Adkins, E. M., Schroeter, S., Adams, S., Swafford, L., McBride, J., Wang, Y., DeFelice, L. J., and Blakely, R. D. (2002) Targeting cell surface receptors with ligand-conjugated nanocrystals. *J. Am. Chem. Soc. 124*, 4586–4594.
(16) Amin, J., and Weiss, D. S. (1996) Insights into the activation mechanism of ρ1 GABA receptors obtained by coexpression of wild type and activation-impaired subunits. *Proc. R. Soc. Lond. B 263*, 273–282.
(17) Qian, H., Hyatt, G., Schanzer, A., Hazra, R., Hackam, A. S., Cutting, G. R., and Dowling, J. E. (1997) A comparison of $GABA_C$ and ρ subunit receptors from the white perch retina. *Vis. Neurosci. 14*, 843–851.
(18) Qian, H., Dowling, J. E., and Ripps, H. (1998) Molecular and pharmacological properties of GABA-ρ subunits from white perch retina. *J. Neurobiol. 37*, 305–320.
(19) Vu, T. Q., Chowdhury, S., Muni, N. J., Qian, H., Standaert, R. F., and Pepperberg, D. R. (2005) Activation of membrane receptors by a neurotransmitter conjugate designed for surface attachment. *Biomaterials 26*, 1895–1903.
(20) Gussin, H. A., Tomlinson, I. D., Little, D. M., Warnement, M. R., Qian, H., Rosenthal, S. J., and Pepperberg, D. R. (2006) Binding of muscimol-conjugated quantum-dots to $GABA_C$ receptors. *J. Am. Chem. Soc. 128*, 15701–15713.
(21) Gussin, H. A., Tomlinson, I. D., Little, D. M., Qian, H., Rosenthal, S. J., and Pepperberg, D. R. (2007) Quantum dot conjugates with variable agonist valency: interaction with $GABA_C$ receptors. *Invest. Ophthalmol. Vis. Sci.* 47 ARVO E-Abstract 4590.
(22) Bentzen, E. L., Tomlinson, I. D., Mason, J., Gresch, P., Warnement, M. R., Wright, D., Sanders-Bush, E., Blakely, R., and Rosenthal, S. J. (2005) Surface modification to reduce nonspecific binding of quantum dots in live cell assays. *Bioconjugate Chem. 16*, 1488–1494.
(23) Tomlinson, I. D., Gussin, H. A., Little, D. M., Warnement, M. R., Qian, H., Pepperberg, D. R., and Rosenthal, S. J. (2007) Imaging $GABA_C$ receptors with ligand-conjugated quantum dots. *J. Biomed. Biotechnol. 2007*, 76514.
(24) Krishnamurthy, V. M., Semetey, V., Bracher, P. J., Shen, N., and Whitesides, G. M. (2007) Dependence of effective molarity on linker length for an intramolecular protein-ligand system. *J. Am. Chem. Soc. 129*, 1312–1320.
(25) Bedrov, D., and Smith, G. D. (2003) The role of local conformations in the stretching of a poly(ethylene oxide) chain in solution. *J. Chem. Phys. 118*, 6656–6663.
(26) Adamian, L., Gussin, H. A., Tseng, Y. Y., Muni, N. J., Feng, F., Qian, H., Pepperberg, D. R., and Liang, J. (2009) Structural model of ρ1 $GABA_C$ receptor based on evolutionary analysis: testing of predicted protein-protein interactions involved in receptor assembly and function. *Protein Sci. 18*, 2371–2383.
(27) Gestwicki, J. E., Cairo, C. W., Strong, L. E., Oetjen, K. A., and Kiessling, L. L. (2002) Influencing receptor-ligand binding mechanisms with multivalent ligand architecture. *J. Am. Chem. Soc. 124*, 14922–14933.

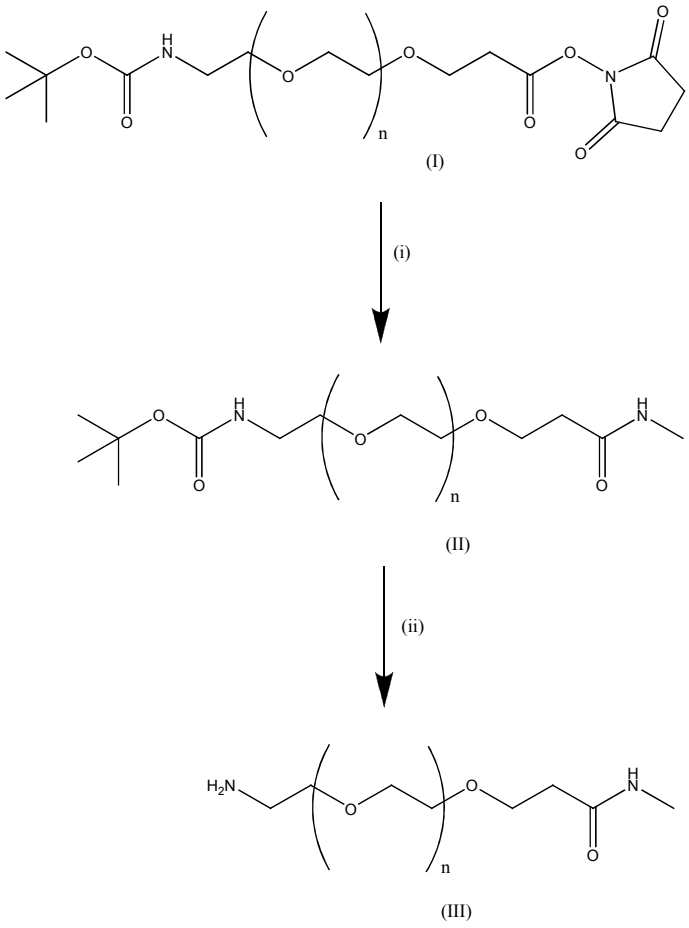
BC100050S

(Gussin et al – MS bc-2010-00050s - Suppl Material - April 28 2010)

SUPPLEMENTAL MATERIAL

Preparation of methylamine-capped PEG

The synthesis of the methylamine terminated PEG is outlined in **scheme 1**. BOC-PEG-NHS (I) was reacted with an excess of methylamine to yield BOC-PEG-methylamine (II). The BOC protecting group was removed by stirring (II) with trifluoroacetic acid to give the methylamine-terminated PEG ligand (III), which was used without further purification.



Scheme 1: (i) CH_3NH_2, methylene chloride, 18 hours, room temperature; (ii) TFA, 1 hour room temperature.

Materials and methods

BOC-PEG3400-NHS (I) was obtained from Laysan Bio Inc. (Arab, Al). Methylamine as a 33% solution dissolved in absolute ethanol and trifluoroacetic acid were obtained from Sigma-Aldrich (St. Louis, MO). All reagents were used as supplied, and the final methylamine-PEG ligand was characterized using MALDI TOF mass spectroscopy (Applied Biosystems Voyager mass spectrometer) equipped with a 337 nm nitrogen laser as previously described (*20*).

Synthesis of BOC protected methylamine intermediate (II). 400mg of BOC-PEG-3400-NHS (I) was placed in a 100ml round bottomed flask equipped with a stirrer. To this, methylene chloride (20 ml) and 33% methylamine dissolved in absolute ethanol (10ml) were added, and the resulting solution was stirred at ambient temperature overnight. The solvent was removed under reduced pressure, and the product was washed with anhydrous diethyl ether (10 x 100ml). The resulting solid was dried for 24 hours under vacuum and used without further purification.

Synthesis of methylamine terminated PEG ligand (III). The BOC protected intermediate (II) was added to trifluoroacetic acid (10ml) and stirred at ambient temperature for 1 hour. The acid was then removed under reduced pressure and the product was washed with anhydrous diethyl ether (10 x 100ml). The resulting material was dried under vacuum for 24 hours to give 300 mg of (III) as a sticky tar that was used without further purification.

Valency		Halo fluorescence (raw)				Background fluorescence (raw)				Net adjusted fluorescence			
		Mean	SD	Median	99% CI	Mean	SD	Median	99% CI	Mean	SD	Median	99% CI
1	0	61	0.85	56	3.34	27	0.33	21	1.28	18	0.58	21	2.25
2	0	65	1.00	58	3.91	25	0.38	20	1.48	20	0.67	23	2.64
3	0	124	1.22	131	4.77	25	0.47	18	1.84	51	0.82	54	3.22
4	25	223	0.79	232	3.08	48	0.30	47	1.18	97	0.53	98	2.08
5	25	190	0.85	198	3.35	51	0.33	49	1.30	77	0.58	78	2.26
6	25	183	0.79	193	3.08	49	0.31	48	1.22	74	0.53	75	2.08
7	50	139	0.78	145	3.05	31	0.30	29	1.17	78	0.53	79	2.06
8	50	165	0.77	176	3.02					96	0.52	98	2.04
9	50	195	0.76	206	2.99					117	0.52	119	2.02
10	100	162	1.15	163	4.52	30	0.38	28	1.48	132	0.78	134	3.05
11	100	152	1.09	150	4.28	32	0.47	30	1.84	120	0.74	122	2.89
12	100	189	0.75	193	2.95	23	0.32	19	1.27	166	0.51	170	1.99
13	0	39	0.88	38	3.43	43	0.34	43	1.32	-2	0.59	-2	2.32
14	0	40	0.95	39	3.74					-2	0.64	-2	2.52
15	25	113	0.80	113	3.15	34	0.31	33	1.21	44	0.54	45	2.13
16	25	164	0.68	159	2.67	31	0.72	30	2.81	74	0.46	74	1.80
17	50	101	0.73	94	2.86	34	0.28	33	1.10	48	0.49	49	1.93
18	50	105	0.77	100	3.02					51	0.52	52	2.04
19	100	237	0.88	241	3.44	35	0.34	33	1.32	202	0.59	204	2.32
20	100	77	0.88	76	3.46					42	0.60	44	2.34
Aggregates													
21	0	60	43.35	44	2.30	31	21.13	29	0.77	14	24.52	15	1.71
22	25	174	61.59	184	1.86	45	17.46	41	0.64	73	32.48	74	1.39
23	50	140	55.41	136	1.83	33	13.45	32	0.86	78	40.39	79	1.36
24	100	167	63.82	171	2.20	29	14.98	28	0.77	136	65.15	139	1.64
Negative control (non-expressing)													
25	100	63.5	25.19	61	8.37	64	20.93	63	2.85	-0.5	25.19	-3	6.40

Table S1. Fluorescence values determined from 15-min incubation of oocytes with M-PEG-qdot preparations of differing muscimol valency. Consecutive rows labeled with identical valency represent data obtained from multiple oocytes. "Net adjusted" data were calculated relative to background values and specific fluorescence factors (see text for further details). Data are organized by experiment day (day 1, rows 1-12; day 2, rows 13-20). Entries for background values that apply to multiple rows represent results obtained from images that contained multiple oocytes.

Targeted Cellular Delivery of Quantum Dots Loaded on and in Biotinylated Liposomes

Valeria Sigot,[†] Donna J. Arndt-Jovin, and Thomas M. Jovin*

Laboratory of Cellular Dynamics, Max Planck Institute for Biophysical Chemistry, 37077 Göttingen, Germany. Received January 27, 2010; Revised Manuscript Received July 13, 2010

We describe the preparation, biophysical characterization, and receptor-mediated cellular internalization of biotinylated lipid particles (BLPs) loaded on the surface and internally with two distinct (colors) of quantum dot (QD) probes. BLPs were formulated with 1.4 and 2.7 mol % PEG−lipids containing either a fusogenic or pH-sensitive lipid to promote bilayer destabilization of endosomal membranes and favor QD cytoplasmic release. The amount of PEG was chosen to provide steric stabilization of the final construct. BLPs were loaded with a red-emitting QD_{655} and surface coated with a green-emitting QD_{525} conjugated to the epidermal growth factor (EGF) ligand in order to target the epidermal growth factor receptor (EGFR). The targeted and QD labeled BLPs showed strong and selective binding to EGFR-expressing tumor cell line and subsequent internalization. The dual-color QD labeling strategy and colocalization analysis allow prolonged live cell imaging of BLPs and loaded cargo independently, using a single excitation wavelength and simultaneous detection of both QDs. The chemistry of bioconjugation for the EGF ligand, the QDs, and the BLPs in a single lipid particle, involves only biotin−streptavidin interaction without requiring further purification from free EGF−QDs preformed complexes. Coupled with an encapsulated drug, the targeted and QD-labeled BLPs could provide imaging and drug delivery in a single multifunctional carrier.

INTRODUCTION

Liposomes that have been sterically stabilized by lipid derivatives of poly(ethylene glycol) (PEG) show persistence in the circulation, increasing the opportunities for specific, ligand- and receptor-mediated targeting into tumor or disease-affected tissues in distal locations of the body (*1, 2*). Unwanted side effects of the PEG-coating include putative inhibition of liposome−cell membrane association and, intracellularly, avoidance of bilayer apposition and membrane fusion required for endosomal escape of the loaded cargo. PEG−lipid dissociation from the liposomes can be facilitated by incorporating fusogenic PEG−lipids with a short acyl chain promoting transfer from the liposome to the bilayer within minutes (*3*). Alternatively, PEG−lipid can be released intracellularly by adding a cleavable, pH-sensitive PEG analogue in which the polymer moiety is cleaved from the liposome surface upon exposure to the acidic environment of certain endosomal compartments (*4*−*8*). An attractive type of unilamellar liposomes, referred to as stable plasmid lipid particles (SPLPs) by Wheeler and co-workers (*9*), are stabilized by PEG−ceramide lipids. They exhibit an average size of 70 nm and up to 70% encapsulation efficiency of plasmid DNA. The transfection competence of the SPLPs has proven superior after replacing PEG-Cer-C20 by the fusogenic ceramide with a shorter acyl chain PEG-Cer-C8 (*10*) or after adding a pH-sensitive PEG−lipid in the SPLP formulation to trigger the intracellular plasmid release (*5, 11*).

Continuous cell imaging has been dramatically improved with the introduction of quantum dots (QDs), colloidal nanocrystals with unique optical properties for long-term and multicolor imaging (*12, 13*). The broad absorption and narrow emission spectra of QDs allow the simultaneous detection of multiple colors of QDs upon illumination with a single light source (*14*). However, QD biocompatibility and potential toxicity remain critical issues for use in humans and thus currently limit their application to in vitro or animal models (*15*).

QDs have to be surface functionalized to act as useful biological probes. Targeting is usually achieved by conjugating a high-affinity ligand or antibody that provides preferential accumulation of the QD−ligand complexes, e.g., in a tumor-bearing organ, in the tumor itself, in individual cancer cells, or in intracellular organelles (*13, 16*). The EGF receptor (EGFR) is an attractive target for drug and gene delivery, since it is overexpressed in a wide variety of human tumors, including brain, lung, liver, and breast cancer (*17*). It has been demonstrated that complexes of streptavidin-conjugated quantum dots (StAv-QDs) with biotinylated ligand EGF are biochemically competent ligands for EGFR (*18*). Protocols for binding biotinylated ligands to commercial streptavidin conjugated QDs have been described (*19, 20*). An important unresolved challenge is to effect the release of monodisperse QDs into the cytoplasm, considering that most of the delivery pathways involve endocytic routes leading to QDs trapped in endosomal compartments. A few reports have shown successful internalization of monodisperse QDs by osmotic lysis of pinosomes (*21, 22*) or microinjection (*23*), although in a nontargeted approach.

The development of tracking techniques combined with QD targeting or loading protocols allows for new strategies to monitor the uptake of drug delivery systems. Recent approaches for QD-labeled lipid-based delivery systems involve the embedding of hydrophobic QDs in lipid bilayers and micelles, or the encapsulation of hydrophilic QDs in liposomes, in order to significantly increase the cellular uptake of these fluorescent QD−lipid complexes ex vivo and in vivo (*24*−*28*). However, several studies have shown that nontargeted QDs micelles

* To whom correspondence should be addressed. E-mail: tjovin@gwdg.de. Phone: 49(0)551-2011381/1382. FAX: 49(0)551-2011467. Laboratory of Cellular Dynamics, Am Fassberg 11, (37077) Göttingen, Germany.

[†] V. Sigot's present address is Centro Binacional Argentina-Italia de Investigaciones en Criobiología Clínica y Aplicada (CAIC). Universidad Nacional de Rosario. Arijón 28 bis (2000) Rosario, Argentina.

10.1021/bc100054c © 2010 American Chemical Society
Published on Web 07/22/2010

undergo unspecific uptake by cells and thus render them unsuitable for many applications (*29*).

Monitoring the behavior of liposomal-based drug delivery systems in living cells is a powerful approach for assessing the route and efficiency of drug delivery as well as the fate of the carrier after releasing the drug. At present, there are only a few published studies on lipid-based delivery systems combining QDs as imaging and targeting probes (*27, 30, 31*). In our study, we explored the simultaneous application of two colors of QDs in a single lipid carrier, one QD as encapsulated cargo and the second as a receptor-targeting probe. We report here the preparation and characterization of biotinylated lipid particles (BLPs), loaded with QD_{655} and surface-modified with preformed complexes of EGF−QD_{525} mediated by biotin−streptavidin linkage. In this study, BLPs containing less than 3 mol % PEG were formulated with either a fusogenic or a pH-sensitive PEG−lipid in order to facilitate PEG transfer and to promote endosomal escape of QD_{655} into the cytoplasm. The EGF-QD_{525}-BLP-QD_{655} were targeted to A431 cells, a human epidermoid carcinoma line overexpressing the EGFR. Live cell imaging with fluorescence confocal microscopy demonstrated the specific binding and internalization of targeted BLPs by simultaneous detection of both QDs.

EXPERIMENTAL PROCEDURES

Chemicals. All reagents were of analytical grade. 1,2-Dioleoyl-*sn*-glycero-3-phosphoethanolamine (DOPE), 1,2-dioleoyloxy-3-trimethylammoniumpropane chloride (DOTAP), 1,2-distearoyl-*sn*-glycero-3-phosphoethanolamine-*N*-[biotinyl-(poly(ethylene glycol)) 2000] ammonium salt (biotin-PEG_{2000}-DSPE), *N*-octanoyl-sphingosine-1-[succinyl (methoxy(poly(ethylene glycol)) 750)] (PEG_{750}-Cer-C8), and 3-*O*-[2′-(ω-monomethoxy(poly(ethylene glycol)) 2000) succinoyl]-1,2-distearoyl-*sn*-glycerol (PEG_{2000}-DSGS) were obtained from Avanti Polar Lipids (Alabaster, USA). Chloroform, ethanol, methanol, isopropanol, and water HPLC quality were purchased from Merck. 1-*O*-*N*-Octyl-β-D-glucopyranoside (OGP), HEPES, NaCl, sucrose, HABA (4-hydroxyazobenzene-2-carboxylic acid), biotin, and biocytin were obtained from Sigma and nonpolar polystyrene adsorbents Bio-Beads SM-2 from BioRad. Biotin-EGF (human recombinant) and streptavidin Alexa Fluor488 (ex. 488 nm/em. 519 nm) were obtained from Invitrogen. Buffer solutions were of analytical grade and filtered through a 0.22-μm-sized membrane. Hepes Buffer Saline (HBS): 150 mM NaCl, 10 mM Na-Hepes, pH 7.2.

Quantum Dots. Quantum dot streptavidin conjugates 525 nm (StAv-QD_{525}), 605 nm (StAv-QD_{605}), and ITK-carboxyl QD_{655} (QD_{655}) with a CdSe core and ZnS shell were obtained from Invitrogen. QD with emission maxima at 655 nm have an ellipsoid core/shell with diameters of 6 nm (minor axis) by 12 nm (major axis). According to the manufacturer and determinations made in a parallel study (*32*), each StAvQD particle contains an average of 6−8 conjugated streptavidins.

Cell Lines and Reagents. A431 (human epidermoid carcinoma) and CHO (Chinese hamster ovary) cell lines were obtained from the American Tissue Culture Collection, and the melanoma cell line WM983A was kindly provided by Prof. Meenhard Herlyn (Wistar Institute, Philadelphia, PA). Dulbecco's Minimal Essential Medium, penicillin, streptomycin, and trypsin were obtained from Gibco. Leibovitz's L15 medium was from Mediatech, Inc. FBS was from PAN, and EDTA, BSA, and glucose were from Sigma. LabTek two-well glass chambers, plastic cell culture dishes, and flasks were purchased from Nunc or Sarstedt.

Preparation of Biotinylated Lipid Particles (BLPs). BLPs were prepared employing the detergent dialysis technique as described by Wheeler et al. (*9*) with modifications. For 1 mL of BLPs formulation, 8.4 μmol DOPE (neutral lipid), 0.6 μmol DOTAP (cationic lipid), and 0.024 μmol biotin−DSPE were mixed in 2 mL glass vials. In individual vials containing this lipid mixture, PEG_{750}-Cer-C8 and PEG_{2000}-DSGS were added to obtain 1.4 and 2.7 mol % PEG and a final concentration of ∼10 μmol lipid/mL. These solutions were dried with a stream of argon and residual chloroform was removed under vacuum overnight.

The resulting lipid film was hydrated in 0.5 mL HBS and 0.2 M OGP detergent with continuous magnetic stirring at 60 °C to favor complete dissolution. After cooling the lipid−detergent mixture to RT, ITK-carboxyl QD_{655} were added in 0.5 mL HBS pH 7.4 at 50 nM final QD_{655} concentration. The mixture was immediately dialyzed against HBS using 10 kDa MWCO dialysis cassettes (Slide-A-Lyzer from Pierce) for 1 h at RT and then dialysis continued in a cold room (∼4 °C) overnight. After two buffer changes of 1 L HBS, residual detergent OGP was removed by adding polystyrene SM2 Biobeads (adsorbent capacity ∼117 mg OGP/g beads), and samples were loaded on top of a sucrose density gradient.

Ultracentrifugation in Sucrose Density Gradient. The sucrose gradient was prepared in 2.5 mL ultraclear thin-walled centrifuge tubes (Beckman) by carefully applying with a tip or syringe 0.6 mL layers of 2.5%, 10%, and 20% (w/v) sucrose in HBS (*10*). The samples recovered from the detergent dialysis were adjusted to 1% (w/v) sucrose and loaded on top of the gradient. Ultracentrifugation was carried out at 160 000 × *g* for 5 h at 10 °C in a TLS-55 swinging bucket rotor and a TL-100 ultracentrifuge (Beckman). The resolved fluorescent bands observed under UV illumination were carefully recovered by manual pipetting and analyzed for QDs encapsulation, particle size, and biotin content.

TEM Analysis. For negative staining of BLPs, a solution containing 1:10 diluted samples was applied to a glow-discharged carbon-coated grid and stained with 1% uranyl acetate. Sample analysis was performed in a Philips 120 kV BioTwin microscope equipped with a 1024 × 1024 pixels GATAN CCD camera.

Particle Size Analysis by Dynamic Light Scattering (DLS). The size of the BLPs was assessed by dynamic light scattering with a NanoZetaSizer particle analyzer (Malvern Instruments, UK) detecting the back-scattered light from a 633 nm laser at a fixed angle of 173°.

Samples were diluted in PBS, previously passed through 0.02 μm pore size filter to eliminate potential interfering impurities, and the measurements were performed at 25 °C. The operating protocol was selected for spherical particles, applying 12 to 15 runs per measurement, which were automatically adjusted according to the concentration of particles in the sample, and three measurements were performed on each sample. The autocorrelation function for size distribution was calculated using the CONTIN mathematical approach for heterodisperse, polydisperse, and multimodal systems.

The mean hydrodynamic diameter obtained represents only an intensity-based average value and does not give any information on the prevailing size distribution. For this reason, the polydispersity index (pdi) is also stated in order to provide information about deviation from a monomodal distribution (pdi ≤ 0.25).

Biotin Quantitation. The biotin content of BLPs was determined on samples recovered after detergent dialysis and ultracentrifugation in sucrose gradient employing a fluorometric assay (*33*). A standard curve was obtained by titrating 50 μL of a solution containing 25 nM StAv-Alexa488 and 125 μM HABA in HBS with biocytin added from an aqueous stock solution to final concentration of 0−200 nM. The fluorescence of standards and samples was measured in a spectrofluorometer

(Varian Cary Eclipse); Alexa Fluor488 dye was excited at 485 nm and the emission spectra were collected between 500 and 700 nm. The fluorescence intensity at the emission maximum (519 nm) was plotted as a function of biocytin concentration, and the data were fitted to a sigmoidal curve to obtain a calibration curve, from which the corresponding values for the unknown samples could be derived. Under the conditions assayed, a ~6-fold increase in fluorescence signal upon complete displacement of HABA was observed with a detection limit of approximately 3 nM biocytin (Supporting Information).

Cell Culture. A431 and CHO cell lines were cultured in Dulbecco's Minimal Essential Medium (D-MEM) supplemented with 10% fetal calf serum (FCS), 50 U/mL of penicillin (Pen), and 50 U/mL of streptomycin (Strep). WM983A cells were grown in three parts DMEM and one part Leibovitz's L15 medium supplemented with 10% heat inactivated (56 °C for 20 min) FCS and Pen−Strep. All cells were grown as a monolayer at 37 °C in a humidified atmosphere containing 5% CO_2. For microscopy experiments, cells were seeded one or two days in advance onto 12-mm-diameter glass coverslips or two-well glass chambers and employed at a 40−50% confluence. For binding experiments, cells were starved in DMEM for 4 h prior to the incubation with EGFR targeted BLPs to reduce signaling induced by growth factors present in the serum.

Labeling and Targeting of BLPs with EGF-QDs Preformed Complexes. According to the manufacturer and confirmed in other studies, the StAv-QDs contain 6−8 streptavidins per QD. Biotin-EGF was coupled to StAv-QD_{525} at a ratio of 4:1 in HBS with 0.5% BSA at final concentration of 50 nM QDs. Solutions were incubated at 15 °C for at least 30 min with gentle agitation before coupling to BLPs.

BLPs with encapsulated QD_{655} were incubated with preformed complexes of EGF-QD_{525} in HBS supplemented with 0.5% BSA. The StAv-QD_{525} concentration was 20 nM, whereas biotin concentrations of BLPs varied from 0.4−0.8 μM depending on the formulation. This mixture was incubated for at least 2 h at 15 °C with continuous shaking and diluted to 1 or 2 nM QD_{525} in Tyrode's buffer for live cell experiments by confocal fluorescence microscopy (see Table S1 in Supporting Information). Separation of EGF-QD-BLPs from EGF-QD complexes by size exclusion chromatography or sucrose gradient (data not shown) led to unacceptable sample loss.

Internalization Studies. A431 cells were seeded onto glass coverslips (2×10^5 cells/mL). At 40−50% confluence, cells were serum starved for 4 h before adding the BLPs. The QD labeled and targeted BLPs (EGF-QD_{525}-BLPs-QD_{655}) were diluted in 200 or 500 μL Tyrode's buffer supplemented with 0.5% BSA and 20 mM glucose and added to cells to obtain final concentrations of 0.5 nM QD525 and 2 nM EGF. Starved cells were precincubated with targeted and nontargeted BLPs at 10 °C, a temperature nonpermissive for endocytosis. Then, cells were warmed and incubated 10 and 60 min at 37 °C. Finally, unbound BLPs were removed and cells rinsed with Tyrode's buffer. Live cell imaging by confocal microscopy was carried out immediately after removing the complexes, for up to 2 h at RT (~20 °C). In another set of experiments, cells were incubated with the BLPs during a 10 min pulse at 37 °C and QDs were chased after 4 and 12 h incubation at 37 °C. When incubation at 37 °C exceeded 1 h after removing the BLPs, Tyrode's buffer was replaced by complete D-MEM.

Competitive Binding Assay. For competitive binding experiments, free EGF (recombinant human) was added to starved A431 cells at a final concentration of 200 ng/mL (33 nM) and cells were incubated for 5 min at 10 °C. EGF-QD_{605}-BLPs-QD_{655} were added to a final concentration of 0.5 nM QD_{605} and 2 nM EGF and incubation resumed for 10 min at 37 °C. Cells were washed with Tyrode's buffer, and confocal microscopy was initiated immediately and performed for 60 min at RT.

Incubation of BLPs with EGFR Negative Cells. EGF-QD_{605}-BLPs-QD_{655} were added to CHO and WM983A cell lines, both devoid of EGF receptor, at a final EGF concentration of 2 nM and incubation proceeded for 5 min at 10 °C, followed by 10 min incubation at 37 °C. Cells were then washed with Tyrode's buffer and images were acquired immediately during 60 min at RT by confocal microscopy.

Simultaneous Tracking of Two Different Colors of QDs. Confocal fluorescence microscopy was performed with a Zeiss 510 confocal laser scanning microscope using a water immersion objective C-Apochromat 63 × 1.2 NA. The simultaneous excitation of QD_{525} and QD_{655} was achieved with the 488 nm laser line, or in some experiments with the 458 nm line to increase the fluorescence intensity. QDs signals were detected simultaneously and collected in separated channels with appropriate filters, in this case, 520/20 BP for QD_{525} and 585 LP for QD_{655}. When QD_{525} was replaced by QD_{605} in preformed complexes with biotin−EGF, the QD_{605} and QD_{655} were detected using 585−615 BP and 650 LP filters, respectively. To eliminate possible crosstalk when using the same excitation wavelength, single color EGF−QD controls were tested for optimization of the gain settings. Confocal planes were acquired with a pinhole set to 1 Airy disk. With the given settings, channel crosstalk was negligible as determined using single-labeled samples.

Z-series were taken at 10.4 μm intervals and deconvoluted using Huygens image processing software (Scientific Volume Imaging, Hilversum, The Netherlands) followed by 3-D reconstruction. For qualitative analysis, images were background-corrected and contrast stretched; fluorescence intensity profile and 3-D reconstruction were performed with the software *Image J* (NIH).

RESULTS

Encapsulation of QDs in Biotinylated Lipid Particles (BLPs). The detergent dialysis technique was explored for the encapsulation of ITK-carboxyl QD_{655}. The PEG−lipid percentages selected for BLP formulation were the lowest that allowed the self-assembly of BLPs without forming aggregates during detergent dialysis. Since we were interested in the cytoplasmic delivery of QD_{655}, the PEG shield should be disrupted in the endosomes. To promote PEG−lipid transfer out of the BLP bilayer and membrane fusion required for endosomal escape, the fusogenic PEG-Ceramide-C8 and pH-sensitive lipid PEG-DSGS were included. Three BLPs formulations were prepared with 1.4% and 2.7% PEG_{750}-Cer-C8 and 1.4% PEG_{2000}-DSGS in combination with 84% DOPE, 6% of the cationic lipid DOTAP, and 0.24% of biotin-DSPE. The QD_{655} were added to the hydrated mixture of lipids and OGP detergent in 10 mM HBS pH 7.4, and the solutions were dialyzed against HBS.

After detergent dialysis a lipid recovery of 58 ± 14% was estimated from the amount of incorporated biotin-DSPE measured by a fluorometric assay (see Supporting Information) in three independent BLPs preparations. To separate and recover QDs loaded BLPs from less dense empty BLP and non-encapsulated QDs, the samples obtained after the detergent dialysis were loaded on top of a discontinuous density gradient of 2.5%, 10%, and 20% sucrose and ultracentrifuged. Three well-defined fluorescent bands were observed (Figure 1A, top right): a bright fluorescent band on top (fraction I), a broader and less intense fluorescent band underneath (fraction II), and a fluorescent pellet (fraction III). Biotin incorporation was detected in fractions I and II but not in the fluorescent pellet, indicating the separation of free and more dense QDs from lipid-containing particles. The presence of QDs in the less dense and brighter band (fraction I) may have resulted from electrostatic

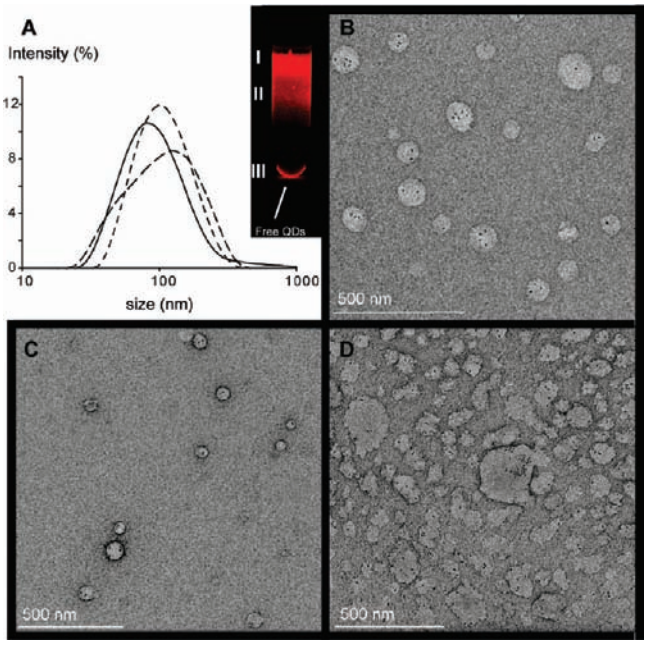


Figure 1. Size characterization of BLP-QD_{655} after purification in sucrose density gradient. (A) (Top right) BLP-QD_{655} recovered in fluorescent fractions II, whereas free QDs appeared mainly in the pellet (fraction III). (Top left) representative size distribution of BLP-QD_{655} measured in fraction II by DLS (- - -) 1.4% PEG_{750}-Cer-C8, (—) 2.7% PEG_{750}-Cer-C8, and (— —) 1.4% PEG_{2000}-DSGS. TEM analysis of QD_{655} encapsulated in BLPs, (B) 1.4% PEG_{750}-Cer-C8, (C) 2.7% PEG_{750}-Cer-C8, (D) 1.4% PEG_{2000}-DSGS. Scale bar 500 nm.

interactions between the carboxylic groups on QD surfaces and the amino groups in free, nonincorporated DOTAP. Because this fraction may have contained empty vesicles (*9*), it was not characterized further.

Size Analysis of QD-Loaded BLPs. The presence of BLPs in fraction II was confirmed by size analysis for all lipid formulations. Figure 1A shows the size distribution of BLP-QD_{655} as determined by DLS. The mean hydrodynamic diameter was 106 nm (pdi = 0.2) for BLPs with 1.4% PEG_{750}-Cer-C8, 91 nm (pdi = 0.4) for BLPs with 2.7% PEG_{750}-Cer-C8, and 122 nm (pdi = 0.4) for BLPs with 1.4% PEG_{2000}DSGS.

Particle analysis by TEM (Figure 1B—D), showed that BLPs formulated with PEG_{750}-ceramides exhibited a spherical shape and revealed the presence of 2 to 5 encapsulated QDs per lipid particle (Figure 1B,C). The diameter of the BLPs varied from 100 to 130 nm, depending on the number of loaded QDs. Empty BLPs, present as a minor fraction, and those containing only one QD were generally smaller than 100 nm. The observed sizes for individual particles were in agreement with the mean hydrodynamic diameters obtained by DLS. Interestingly, the BLPs formulated with 1.4% PEG_{2000}-DSGS appeared amorphous in shape with a more variable number of loaded QDs (Figure 1D) and broader size distribution as compared to BLPs formulated with PEG-Cer-C8.

Cellular Uptake of EGFR Targeted and Two-Color QDs Labeled BLPs. Complexes of streptavidin-conjugated quantum dots (QDs) with biotin-EGF are biochemically competent ligands for erbB1, the EGF receptor (*19*). The first concern to be addressed was whether the internalization BLPs tagged with preformed EGF-QDs complexes could be impaired, as the large size of the lipid carrier (~100 nm) may interfere with the dimerization of the EGFR necessary for the subsequent activation and internalization by endocytosis.

BLPs loaded with QD_{655} were conjugated to preformed complexes of biotin-EGF and StAv-QD_{525} (EGF-QD_{525}). On the basis of previous results in which BLPs were labeled with two

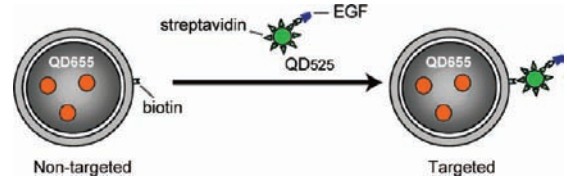


Figure 2. Scheme depicting the targeting and dual color labeling strategy of BLPs with encapsulated QD_{655}. Preformed complexes of EGF-QD_{525} (molar ratio 4:1) are conjugated to biotin molecules on the BLP surface. Specific uptake is evidenced as colocalized dots by confocal fluorescence microscopy. Red fluorescence indicate unspecific binding of nontargeted BLP-QD_{655}. The binding of free unconjugated EGF-QD_{525}, if present, is detected as green dots.

colors of streptavidin—QDs on the surface, we assumed that at least two biotins were available per lipid particle (*34*). In Figure 2, the scheme depicts nontargeted BLPs loaded with QD_{655} (red) and the targeted and two-color labeled BLPs (red—green). With this approach, colocalized red—green dots were expected to indicate specific uptake, whereas the sole detection of red fluorescence would reveal nonspecific binding of nontargeted BLPs-QD_{655}. Additionally, the two-color QD labeling strategy allowed the independent monitoring of the fate of the loaded QD_{655} and also circumvented the problem of purification of targeted BLPs from free EGF-QD_{525} complexes. Any residual free preformed complexes of EGF-QD_{525} competing for the EGFR with the targeted EGF-QD_{525}-BLPs-QD_{655} upon incubation with cells could be identified easily as isolated green dots.

We employed confocal fluorescence microscopy in live cells to distinguish between specific and nonspecific uptake of BLPs by simultaneous tracking the two colors of QDs using a single excitation wavelength (Figure 3). The interaction of targeted and nontargeted BLPs with A431 cells overexpressing the EGFR was evaluated for BLPs formulated with 1.4% and 2.7% PEG_{750}-Cer-C8 and with 1.4% PEG_{2000}-DSGS upon incubation for 1 h at 37 °C. Live cells were monitored for up to 2 h without detectable photobleaching. As shown in Figure 3, both QDs extensively colocalized (yellow spots in overlay) after 1 h at 37 °C and during the 2 h live cell imaging. The BLPs appeared in a characteristic dot-pattern distribution, attributed to the clustering of the lipid particles in endosomal compartments, indicating that the targeted EGF-QD_{525}-BLP-QD_{655} particles were internalized (Figure 3, panels A, B, C, left side). Negligible internalization as evidenced by a faint red fluorescence was detected for nontargeted BLP-QD_{655} for all lipid formulations examined (Figure 3, panels A, B, C, right side). Similar experiments with nontargeted QD_{525} showed negligible binding (data not shown).

Intracellular Distribution of Internalized BLPs and Fate of QD_{655}. The dot pattern distribution was analyzed by *z*-scan with serial confocal slices in representative cells. Targeted BLPs (2.7% PEG_{750}-Cer-C8) were internalized by A431 cells after a 10 min pulse followed by 1 h incubation (chase) at 37 °C (Figure 4A—C). Panel A shows that most of the internalized EGF-QD_{525}-BLP-QD_{655} complexes accumulated in the perinuclear region of the cell, although a large fraction was still visible in small structures underneath the cell membrane (Figure 4B). Close observation of single vesicles (Figure 4D) showed a variable QD fluorescence intensity in the colocalized spots evidenced by the heterogeneous yellow—orange pseudocolor. This finding could be explained by the distribution in the number of encapsulated QDs (1—5) in BLP shown by TEM, and presumably also due to the presence of a variable number of EGF-QD_{525} bound to the multivalent BLPs. In addition, and possibly most important, there could have been fusion of vesicles occurring during endosomal sorting.

In Figure 4E, the fluorescence intensity profile along the line traced in panel D shows the relative contributions of green and

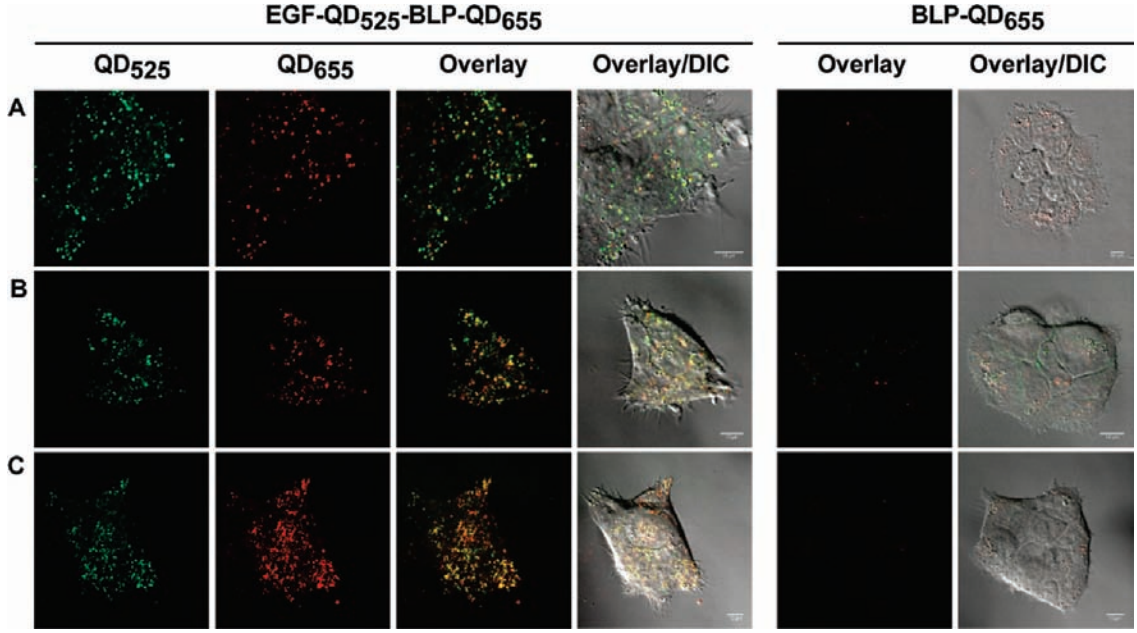


Figure 3. Cellular uptake of targeted EGF-QD_{525}-BLP-QD_{655} and nontargeted BLP-QD_{655}. A431 cells incubated with BLPs for 1 h at 37 °C and monitored by confocal fluorescence microscopy for up to 2 h. Colocalization of QD_{525} and QD_{655} showed targeted BLPs distributed in endosomal compartments (left 12 panels). Nontargeted BLPs shown in right 6 panels. (A) BLPs containing 1.4% PEG_{750}-Cer-C8. (B) BLPs containing 2.7% PEG_{750}-Cer-C8. (C) BLPs containing 1.4% PEG_{2000}-DSGS. Scale bar: 10 μm.

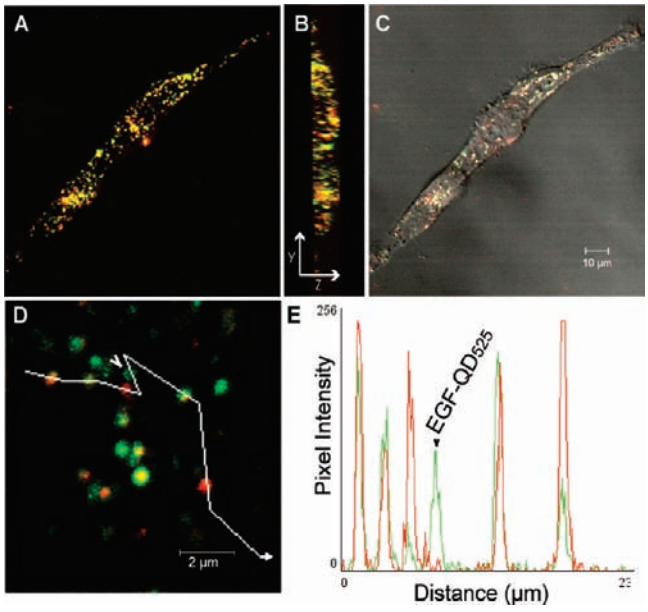


Figure 4. Intracellular fate of EGFR targeted and QDs labeled BLPs. (A) 3-D reconstruction of two A431 cells with internalized BLPs after 10 min pulse incubation and 1 h chase at 37 °C. (B) $y-z$ plane showing colocalized QDs inside cells and underneath the cell membrane. (C) Overlay of image A with DIC image. (D) Line-profile (in white) across six endosomal vesicles. (E) Fluorescence intensity along the line-profile in D revealing different intensity levels for colocalized QDs. Internalized two-color QDs labeled and targeted BLPs containing 2.7% PEG_{750}-Cer-C8. (yellow−orange pseudo color) were distinguished from independently internalized green EGF-QD_{525} complexes (arrowheads in panels D and E).

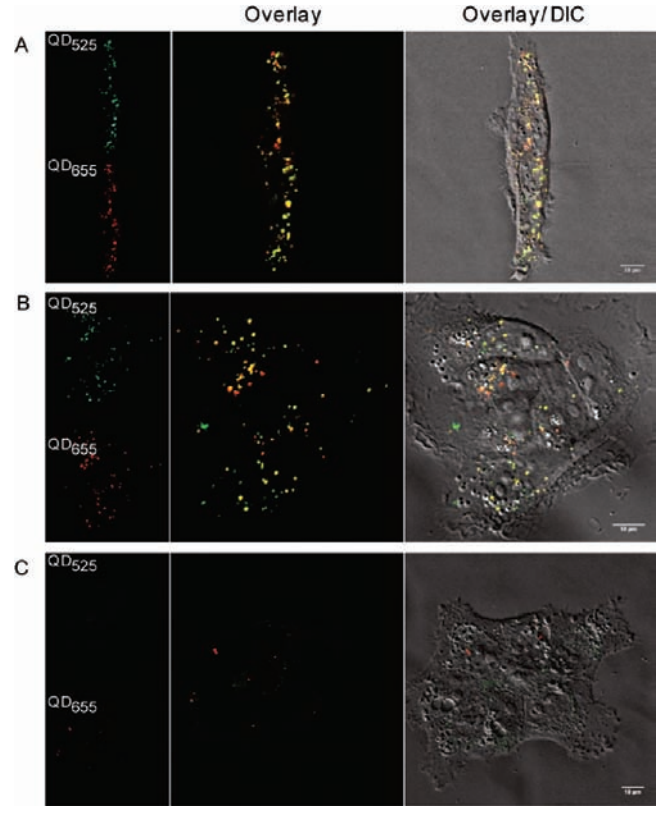


Figure 5. Fate of encapsulated QD_{655} delivered by EGF-QD_{525}-BLP-QD_{655}. After 10 min incubation at 37 °C with A431 cells, unbound EGF-QD_{525}-BLP-QD_{655} were removed and cells imaged by confocal microspcopy after 4 h (A) and 12 h (B), nontargeted BLP-QD_{655} (C). BLP containing 2.7% PEG_{750}-Cer-C8. Scale bar 10 μm.

red QDs to the colocalized loci. The presence of single green dots indicates the binding of free preformed complexes of EGF-QD_{525}. These complexes were expected to be present, as they were not eliminated after conjugation with BLPs.

The BLPs formulated with a pH-sensitive PEGylated lipid or with exchangeable PEG_{750}-CerC8 lipids were expected to fuse more readily with the endosomal membranes, thereby releasing the QDs into the cytoplasm. Consequently, the initial colocalization observed for the dual-labeled EGF-QD_{525}-BLP-QD_{655} was expected to decrease in time. However, as shown in Figure 5, after 4 and 12 h chase of the BLPs at 37 °C dissociation of the two QD signals was not apparent. The dot

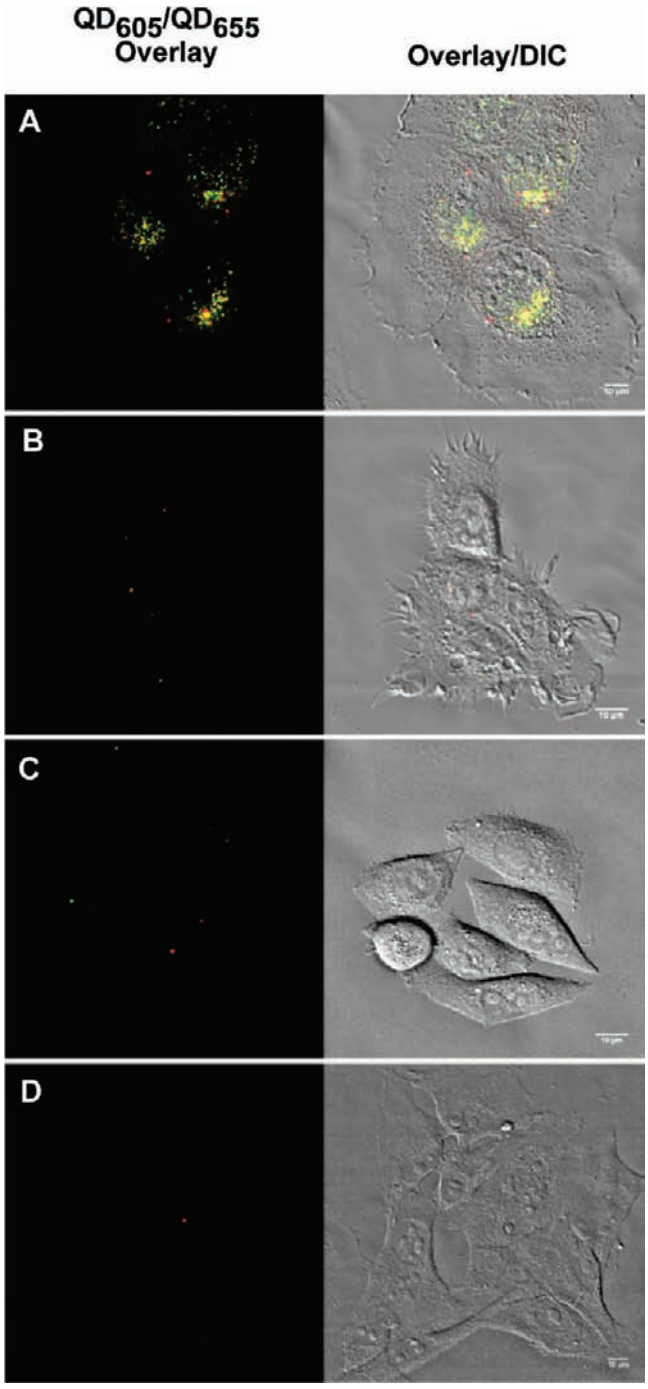


Figure 6. Binding specificity of EGFR targeted BLPs. A431 cells incubated with targeted BLP during a 10 min pulse at 37 °C and chased after 60 min (A) with EGF-QD_{605}-BLP-QD_{655}, (B) coincubated with EGF-QD_{605}-BLP-QD_{655} and a 16-fold molar excess of free competing ligand EGF. (C) CHO cells devoid of EGFR incubated with EGF-QD_{605}-BLP-QD_{655}. (D) WM983A cells devoid of EGFR incubated with EGF-QD_{605}-BLP-QD_{655}. BLP: 2.7% PEG_{750}-Cer-C8. Scale bar 10 μm.

pattern persisted, suggesting that QDs remain trapped in BLPs in endolysosomal compartments.

Specific Binding of EGFR Targeted and QD Labeled BLPs. The specificity of targeting was examined in a competitive binding assay (Figure 6A,B) carried out by incubating the targeted and labeled BLPs with A431 cells in the presence of a 16-fold molar excess of free ligand EGF (panel B). Under these conditions, the absence of colocalized QDs indicated that the binding of the targeted BLPs was substantially diminished as compared to the positive controls performed without competing ligand (panel A). In addition, targeted BLPs were incubated with EGFR-negative cells. Neither CHO cells nor WM983A cells internalized the EGFR targeted BLPs as evidenced by the absence of colocalized dots in Figure 6C,D. Taken together, these results indicate that the enhanced uptake of targeted BLP was due to the specific interaction of the lipid-bound QD-EGF with EGFR and not by macropinocytosis induced by non-lipid-bound QD-EGF.

DISCUSSION

An emerging tool in targeted delivery is the multimodal carrier, in which a therapeutic molecule, an imaging agent, and a targeting entity are assembled in a single nanoparticle for simultaneous imaging and therapy (*25*, *27*, *30*, *35*). In the present work, we developed a QD-labeled and EGFR targeted delivery system mediated by biotinylated lipid particles (BLPs). The originality of our approach lies in the novel encapsulation of QDs in BLPs by a detergent dialysis technique, where the inclusion of as little as 1.4 mol % PEG-lipids allowed the self-assembly of stable BLPs. The sucrose density gradient proved very useful for the separation of QD-loaded BLPs from free QDs (Figure 1A). TEM analysis of the purified fractions showed an average of 2−5 encapsulated QDs in ∼100-nm-sized lipid vesicles (Figure 1B,C,D). This size was in agreement with the mean diameters obtained by DLS for all lipid formulations.

A dual-color labeling strategy with loaded and surface-bound QDs was introduced in order to follow the intracellular localization of the cargo and carrier by colocalization analysis using confocal microscopy. BLP-QD_{655} were surface modified with preformed complexes of EGF-QD_{525} and delivered to A431 cells overexpressing the EGFR. Addition of the biotin−EGF ligand as a preformed complex with StAvQDs instead of direct binding to BLPs was adopted to improve ligand−receptor binding, taking advantage of the multiple streptavidins coating the QDs (6−8 streptavidins according to the manufacturer). The application of these preformed complexes extends the use to any biotinylated ligand. The two-color labeled and targeted EGF-QD_{525}-BLP-QD_{655} were internalized by the A431 cells, whereas nontargeted BLP-QD_{655} showed negligible binding, indicating that uptake of the particles was mediated by the EGFR activation and internalization (Figure 3). The specificity of targeted BLPs for the EGF receptor was supported by a competitive binding assay performed in the presence of 16-fold molar excess of free ligand EGF (Figure 6A,B). Under these conditions, binding to A431 cells was completely abolished. In line with these observations, CHO cells and WM983A melanoma cells that do not express the EGFR showed no binding of the targeted particles (Figure 6C,D).

Upon internalization of EGF-QD_{525}-BLP-QD_{655}, the variations in the relative fluoresecence intensities found for colocalized QDs (Figure 4) were interpreted as the result of an uneven distribution in the number of encapsulated QD_{655} and EGF-QD_{525} complexes conjugated to individual BLP. Additionally, QDs fluorescence intensity variation could be due to endosomal fusion bringing several BLPs together.

We were also interested in the cytoplasmic delivery of the encapsulated QD_{655}. Therefore, BLPs were formulated with 1.4 and 2.7 mol % PEG conjugated to fusogenic or to pH-sensitive lipids in order to destabilize BLPs bilayers and facilitate fusion with endosomes (*8*, *10*, *11*). On the basis of the dual color labeling strategy, the cytoplasmic release of QD_{655} was expected to be evidenced by delocalization of initially colocalized red−green dots However, the dot pattern of colocalized QDs persisted for up to 12 h, regardless of the formulation tested and PEG content. The possible explanations would be that either PEG coating was not completely removed or that QDs aggregated inside the acidic environment of endosomes due to

protonation of carboxyl groups and charge neutralization on QD surfaces. Several approaches have been devised for delivering QDs intracellularly. They include conjugation of QDs to cell penetrating peptides (*36*, *37*) and encapsulation in targeted micelles (*25*) or polymers (*38*). However, QDs remain predominantly trapped in endosomal compartments and only direct microinjection (*23*) into cell cytoplasm and more recently osmotic lysis of pinosomes (*21, 22*) appear as the methods of choice for QD delivery with homogeneous distribution.

The two-color QDs labeling strategy allowed a clear distinction to be made between the targeted and QD_{655}-loaded BLPs (yellow−orange pseudocolors) and the independently internalized green EGF-QD_{525} complexes (Figure 4D,E), avoiding the tedious purification of targeted BLPs from free EGF-QDs complexes. During the continuous live cell imaging for up to 2 h, photobleaching was undetectable, highlighting the photostability of QDs as probes for long-term imaging of dynamic processes.

In the developed lipid carrier, the multivalency of BLPs and StAvQDs serves to increase the number of EGF ligands on the BLP surface. However, variations in size and, as a consequence, the number of biotins in/on individual BLPs influence the controlled and stoichiometric addition of preformed EGF-QD complexes to BLPs. Thus, further refinements of the system are desirable. Nonethless, it is evident that the addition of quantum dots into liposomal carriers, fulfilling a dual role as cargo and surface tag, provides a flexible platform for cell targeting and monitoring receptor-mediated uptake employing any biotinylated ligand attached to StAv-QDs. The expectation is that such targeted lipid-based delivery systems will constitute a new means for the effective cytoplasmic delivery of therapeutic macromolecules.

ACKNOWLEDGMENT

This work was financially supported by the Max Planck Society, the DFG Research Center for Molecular Physiology of the Brain (CMPB) -Excellence Cluster EXC 171 - FZT103 “Microscopy at the Nanometer Range”, and the EU sixth framework (FP6) project FLUOROMAG, LHSB-CT-2006-037465. The authors thank Dr. Dietmar Riedel for conducting the TEM measurements.

Note Added after ASAP Publication: The version of this paper that was published on the Web on July 22, 2010, did not contain all of the author’s corrections. The corrected version was reposted on July 27, 2010.

Supporting Information Available: Fluorometric assay for biotin quantitation and characterization of individual BLPs preparations. This material is available free of charge via the Internet at http://pubs.acs.org.

LITERATURE CITED

(1) Harris, J. M, and Chess, R. B. (2003) Effect of pegylation on pharmaceuticals. *Nat. Rev. Drug Discovery 2*, 214–21.

(2) Woodle, M. C., and Lasic, D. D. (1992) Sterically stabilized liposomes. *Biochim. Biophys. Acta 1113*, 171–99.

(3) Holland, J. W., Hui, C., Cullis, P. R., and Madden, T. D. (1996) Poly(ethylene glycol)-lipid conjugates regulate the calcium-induced fusion of liposomes composed of phosphatidylethanolamine and phosphatidylserine. *Biochemistry 35*, 2618–24.

(4) Kirpotin, D., Hong, K., Mullah, N., Papahadjopoulos, D., and Zalipsky, S. (1996) Liposomes with detachable polymer coating: destabilization and fusion of dioleoylphosphatidylethanolamine vesicles triggered by cleavage of surface-grafted poly(ethylene glycol). *FEBS Lett. 388*, 115–8.

(5) Choi, J. S., MacKay, J. A., and Szoka, F. C., Jr. (2003) Low-pH-sensitive PEG-stabilized plasmid-lipid nanoparticles: preparation and characterization. *Bioconjugate Chem. 14*, 420–9.

(6) Guo, X., MacKay, J. A., and Szoka, F. C., Jr. (2003) Mechanism of pH-triggered collapse of phosphatidylethanolamine liposomes stabilized by an ortho ester polyethyleneglycol lipid. *Biophys. J. 84*, 1784–95.

(7) Guo, X., and Szoka, F. C., Jr. (2001) Steric stabilization of fusogenic liposomes by a low-pH sensitive PEG-diortho ester-lipid conjugate. *Bioconjugate Chem. 12*, 291–300.

(8) Shi, F., Wasungu, L., Nomden, A., Stuart, M. C., Polushkin, E., Engberts, J. B., and Hoekstra, D. (2002) Interference of poly(ethylene glycol)-lipid analogues with cationic-lipid-mediated delivery of oligonucleotides; role of lipid exchangeability and non-lamellar transitions. *Biochem. J. 366*, 333–41.

(9) Wheeler, J. J., Palmer, L., Ossanlou, M., MacLachlan, I., Graham, R. W., Zhang, Y. P., Hope, M. J., Scherrer, P., and Cullis, P. R. (1999) Stabilized plasmid-lipid particles: construction and characterization. *Gene Ther. 6*, 271–81.

(10) Mok, K. W., Lam, A. M., and Cullis, P. R. (1999) Stabilized plasmid-lipid particles: factors influencing plasmid entrapment and transfection properties. *Biochim. Biophys. Acta 1419*, 137–50.

(11) Li, W., Huang, Z., MacKay, J. A., Grube, S., and Szoka, F. C., Jr. (2005) Low-pH-sensitive poly(ethylene glycol) (PEG)-stabilized plasmid nanolipoparticles: effects of PEG chain length, lipid composition and assembly conditions on gene delivery. *J. Gene Med. 7*, 67–79.

(12) Alivisatos, A. P., Gu, W., and Larabell, C. (2005) Quantum dots as cellular probes. *Annu. Rev. Biomed. Eng. 7*, 55–76.

(13) Michalet, X., Pinaud, F. F., Bentolila, L. A., Tsay, J. M., Doose, S., Li, J. J., Sundaresan, G., Wu, A. M., Gambhir, S. S., and Weiss, S. (2005) Quantum dots for live cells, in vivo imaging, and diagnostics. *Science 307*, 538–44.

(14) Smith, A. M., Gao, X., and Nie, S. (2004) Quantum dot nanocrystals for in vivo molecular and cellular imaging. *Photochem. Photobiol. 80*, 377–85.

(15) Kirchner, C., Liedl, T., Kudera, S., Pellegrino, T., Muñoz, J. A., Gaub, H. E., Stolzle, S., Fertig, N., and Parak, W. J. (2005) Cytotoxicity of colloidal CdSe and CdSe/ZnS nanoparticles. *Nano Lett.* 331–338.

(16) Al-Jamal, W. T., and Kostarelos, K. (2007) Liposome-nanoparticle hybrids for multimodal diagnostic and therapeutic applications. *Nanomedicine 2*, 85–98.

(17) Yarden, Y. (2001) The EGFR family and its ligands in human cancer. signalling mechanisms and therapeutic opportunities. *Eur. J. Cancer 37 Suppl 4*, S3–8.

(18) Lidke, D. S., Nagy, P., Heintzmann, R., Arndt-Jovin, D. J., Post, J. N., Grecco, H. E., Jares-Erijman, E. A., and Jovin, T. M. (2004) Quantum dot ligands provide new insights into erbB/HER receptor-mediated signal transduction. *Nat. Biotechnol. 22*, 198–203.

(19) Lidke, D. S., Nagy, P., Jovin, T. M., and Arndt-Jovin, D. J. (2007) Biotin-ligand complexes with streptavidin quantum dots for in vivo cell labeling of membrane receptors. *Methods Mol. Biol. 374*, 69–79.

(20) Sperling, R., Pellegrino, T., Li, J. K., Chang, W. H., and Parak, W. J. (2006) Electrophoretic separation of nanoparticles with a discrete number of functional groups. *Adv. Funct. Mater. 26*, 943–948.

(21) Courty, S., Bouzigues, C., Luccardini, C., Ehrensperger, M. V., Bonneau, S., and Dahan, M. (2006) Tracking individual proteins in living cells using single quantum dot imaging. *Methods Enzymol. 414*, 211–28.

(22) Nelson, R. S., Ali, M. Y., Trybus, K. M., and Warshaw, D. M. (2009) Random walk of processive, quantum dot-labeled myosin va molecules within the actin cortex of COS-7 cells. *Biophys. J. 97*, 509–518.

(23) Derfus, A. M., Chan, W. C. W., and Bhatia, S. N. (2004) Intracellular delivery of quantum dots for live cell labeling and organelle tracking. *Adv. Mater. 16*, 961–966.

(24) Bothun, G. D., Rabideau, A. E., and Stoner, M. A. (2009) Hepatoma cell uptake of cationic multifluorescent quantum dot liposomes. *J. Phys. Chem. B 113*, 7725–8.

(25) Rubinstein, I., Soos, I., and Onyuksel, H. (2008) Intracellular delivery of VIP-grafted sterically stabilized phospholipid mixed nanomicelles in human breast cancer cells. *Chem. Biol. Interact. 171*, 190–4.

(26) Al-Jamal, W. T., Al-Jamal, K. T., Tian, B., Lacerda, L., Bomans, P. H., Frederik, P. M., and Kostarelos, K. (2008) Lipid-quantum dot bilayer vesicles enhance tumor cell uptake and retention in vitro and in vivo. *ACS Nano 2*, 408–18.

(27) Schroeder, J. E., Shweky, I., Shmeeda, H., Banin, U., and Gabizon, A. (2007) Folate-mediated tumor cell uptake of quantum dots entrapped in lipid nanoparticles. *J. Controlled Release 124*, 28–34.

(28) Dubertret, B., Skourides, P., Norris, D. J., Noireaux, V., Brivanlou, A. H., and Libchaber, A. (2002) In vivo imaging of quantum dots encapsulated in phospholipid micelles. *Science 298*, 1759–62.

(29) Maysinger, D., Lovric, J., Eisenberg, A., and Savic, R. (2007) Fate of micelles and quantum dots in cells. *Eur. J. Pharm. Biopharm. 65*, 270–81.

(30) Weng, K. C., Noble, C. O., Papahadjopoulos-Sternberg, B., Chen, F. F., Drummond, D. C., Kirpotin, D. B., Wang, D., Hom, Y. K., Hann, B., and Park, J. W. (2008) Targeted tumor cell internalization and imaging of multifunctional quantum dot-conjugated immunoliposomes in vitro and in vivo. *Nano Lett. 8*, 2851–7.

(31) Sabharwal, N., Holland, E. C., and Vazquez, M. (2009) Live cell labeling of glial progenitor cells using targeted quantum dots. *Ann. Biomed. Eng. 37*, 1967–1973.

(32) Roberti, M. J., Morgan, M., Menendez, G., Pietrasanta, L. I., Jovin, T. M., and Jares-Erijman, E. A. (2009) Quantum dots as ultrasensitive nanoactuators and sensors of amyloid aggregation in live cells. *J. Am. Chem. Soc. 131*, 8102–7.

(33) Batchelor, R. H., Sarkez, A., Cox, W. G., and Johnson, I. (2007) Fluorometric assay for quantitation of biotin covalently attached to proteins and nucleic acids. *Biotechniques 43*, 503–7.

(34) Sigot, V., and Jovin, T. M. (2008) Quantum dots: torch bearers into cells. *Imaging Microsc. 10*, 40–43.

(35) Qi, L., and Gao, X. (2008) Emerging application of quantum dots for drug delivery and therapy. *Expert Opin. Drug Delivery 5*, 263–7.

(36) Lagerholm, B. C. (2007) Peptide-mediated intracellular delivery of quantum dots. *Methods Mol. Biol. 374*, 105–12.

(37) Medintz, I. L., Pons, T., Delehanty, J., Susumu, K., Brunel, F., Dawson, P., and Mattoussi, H. (2008) Intracellular delivery of quantum dot-protein cargos mediated by cell penetrating peptides. *Bioconjugate Chem. 9*, 1785–1795.

(38) Duan, H., and Nie, S. (2007) Cell-penetrating quantum dots based on multivalent and endosome-disrupting surface coatings. *J. Am. Chem. Soc. 129*, 3333–8.

BC100054C

SUPPORTING INFORMATION

TARGETED CELLULAR DELIVERY OF QUANTUM DOTS LOADED BY *in situ* BIOTINYLATED LIPOSOMES

Valeria Sigot [(1)], Donna J. Arndt-Jovin and Thomas M. Jovin*

Laboratory of Cellular Dynamics, Max Planck Institute for Biophysical Chemistry, 37077 Göttingen, Germany

[(*)] To whom correspondence should be addressed.

E-mail: tjovin@gwdg.de

Phone: 49(0)551-2011381/1382 FAX: 49(0)551-2011467

Laboratory of Cellular Dynamics

Am Fassberg 11, (37077) Göttingen, Germany

([1]) V. Sigot's present address is Centro Binacional Argentina-Italia de Investigaciones en Criobiología Clínica y Aplicada (CAIC). Universidad Nacional de Rosario. Arijón 28 bis (2000) Rosario, Argentina.

FLUOROMETRIC ASSAY FOR QUANTITATION OF BIOTIN IN BLPS

The biotin content of BLP was determined on samples recovered after detergent dialysis and ultracentrifugation in sucrose gradient. The fluorometric assay used is based on Foster resonance energy transfer (FRET) (Batchelor *et al.*, 2007), providing high sensitivity to detect nanomolar concentrations of biotin linked to proteins or nucleic acids. In this assay (Figure S1), the Alexa Fluor$_{488}$-streptavidin conjugate (StAv-Alexa$_{488}$) acts as FRET donor and the dye HABA as a quencher, occupying the biotin binding sites of the dye-labeled streptavidin. In the absence of biotin, HABA quenches the fluorescence emission of the Alexa Fluor$_{488}$ dye via FRET. When biotin or a biotinylated molecule is added, HABA is displaced from the biotin binding sites resulting in an increase in the donor fluorescence intensity proportional to the amount of biotin present in the sample.

The standard curve of biocytin, a water-soluble biotin analogue, was obtained by titrating a solution containing 25 nM StAv-Alexa$_{488}$ and 125 µM HABA in HBS. Biocytin was added from an aqueous stock solution to give final concentrations of 0–200 nM in 50 µl samples. Fluorescence of standards and samples was measured in a spectrofluorometer, Alexa Fluor$_{488}$ dye was excited at 485 nm and emission spectra were collected between 500-700 nm.

The fluorescence intensity at the emission maximum (519) nm was plotted as a function of biocytin concentration (nM) and the data were fitted to a sigmoid curve to obtain the corresponding values for the unknown samples (Figure S1 B). In the conditions assayed a ~6-fold increase in fluorescence signal upon complete displacement of HABA was observed with a detection limit of approximately 3 nM biocytin (Figure S1 C).

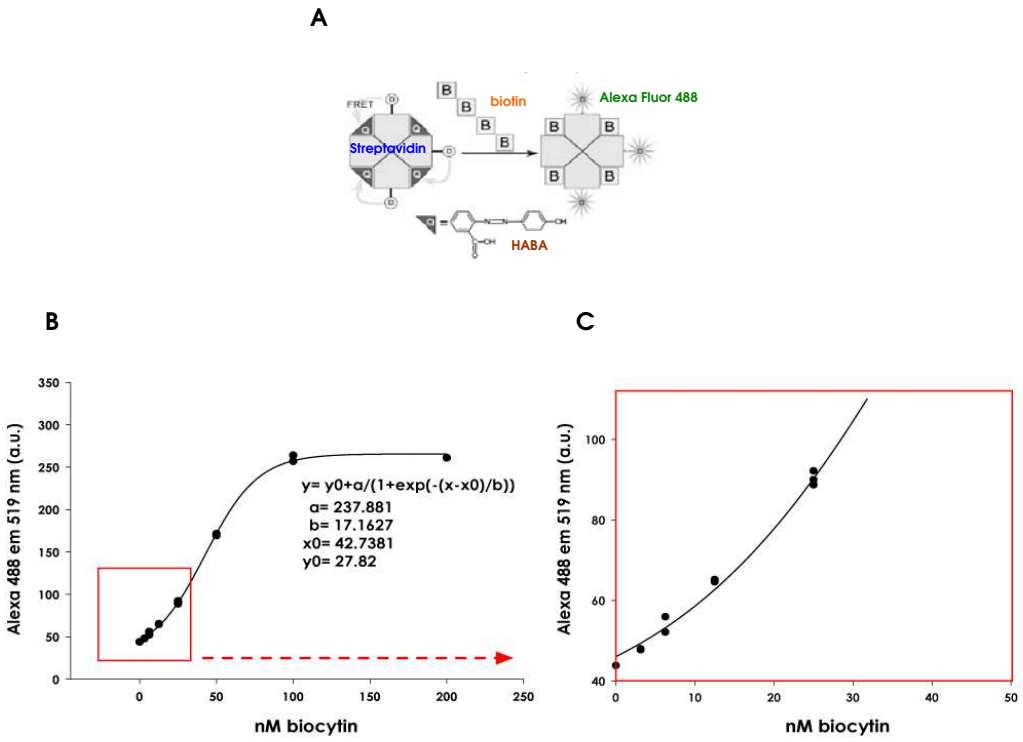


FIGURE S1: FLUOROMETRIC ASSAY FOR BIOTIN QUANTITATION. A. General scheme of the assay adapted from (Batchelor *et al.*, 2007). HABA acts as acceptor of Alexa Fluor$_{488}$ fluorescence while bound to biotin binding sites. When biotin or biocytin is added, HABA is displaced and the fluorescence signal

of Alexa Fluor$_{488}$ increases. **B:** Biocytin standard curve obtained by titrating a solution containing 25 nM StAv-Alexa$_{488}$ and 125 µM HABA in HBS. At least 8 values were obtained to plot the data within a biocytin range of 0-200 nM. Alexa$_{488}$ was excited at 485 nm and emission collected from 500 to 700 nm. The data illustrate a ~6-fold increase in fluorescence signal upon complete displacement of HABA. According to manufacturers, three biotin-binding sites are available per streptavidin molecule corresponding to 75 nM biotin binding sites **C:** The detection limit achieved was approximately 3 nM biocytin.

TABLE S1 Composition and characterization of BLPs formulations

PEG- lipids (%)	***Biotin in purified BLP [a] (nM)***	***Loaded QD_{655} in purified BLP (nM)***	***Biotin/Loaded QD_{655} ratio***	***QD_{525}/QD_{655} ratios in live cell microscopy [b]***
2.7% PEG $_{750}$ CERC8	1280 280	0.2 22	7500 13	36 2
1.4% PEG $_{2000}$ DSGS	600 400	0.8 0.5	750 800	9 31
1.4% PEG $_{750}$ CERC8	600 400	0.2 0.1	3000 3070	36 125

Initial molar ratio of biotin-DSPE to QD_{655} was 480 (24/0.050 nmols in 1 ml formulation).

([a]) Biotin concentration was calculated in BLPs recovered from 10% sucrose fraction.

([b]) QD_{525}/QD_{655} ratios obtained after addition of EGF-QD_{525} complexes to the BLPs in order to achieve working concentrations suitable for confocal microscopy with a final concentration of QD_{525} of 1 or 2 nM and non saturating EGF concentrations with cells. Under this condition, QD_{525} were added to BLP in excess over loaded QD_{655}. Unbound EGF-QD_{525} was not removed and together with variations in QD_{655} loading, as shown by TEM, could explain the observed heterogeneity of Green/Red intensity ratio in confocal microscopy.

Oligopeptide Delivery Carrier for Osteoclast Precursors

Bo Chi,[†] So Jeong Park,[‡] Min Hee Park,[†] Soo Young Lee,*[,‡] and Byeongmoon Jeong*[,†]

Department of Chemistry and Nano Science and Division of Life and Pharmaceutical Sciences, Department of Bioinspired Science, Ewha Womans University, Seoul, Korea. Received February 2, 2010; Revised Manuscript Received June 2, 2010

Dendritic amine and guanidinium group-modified nanoparticles were investigated for the delivery of model peptide drug into primary osteoclast precursor cells (bone marrow macrophages; BMMs). The model peptide drug was encapsulated into the nanoparticle by dropping the drug/carrier dissolved in dimethylsulfoxide/methylene chloride cosolvent into water containing poly(vinyl alcohol) as a stabilizer. Flow cytometry and spectrofluorimetry analysis indicated that the model drug itself was not taken up by the BMMs; however, nanoparticle systems underwent significant cellular uptake. In particular, guanidinium group-modified nanoparticles were taken up more efficiently than amine group-modified ones. Cell viability studies showed that both amine and guanidinium group-modified nanoparticles exhibited no significant cytotoxicity up to 100 μg/mL against the cells.

INTRODUCTION

Cellular communications between osteoblasts and osteoclasts are the basic mechanism of bone homeostasis. Increased activity of osteoclasts relative to osteoblasts leads to diseases such as osteoporosis, periodontitis, and arthritis (*1, 2*). The inhibition of differentiation from precursor cells (bone marrow macrophages; BMMs) into osteoclasts was suggested to be a promising therapeutic treatment for such diseases (*3*). We have been developing oligopeptides that inhibit osteoclast differentiation (*4*). However, they need a carrier system to deliver the drug into the BMMs; otherwise, it cannot enter the cells due to the large size and charge of the drug.

Plasma membrane serves as the protective barrier against extraneous molecules into living cells. To overcome the cell membrane barriers, cell penetrating peptides (CPPs) have been extensively investigated for the plasmid DNA, oligonucleotide, si-RNA, peptide−nucleic acid (PNA), proteins, liposomes, and iron nanoparticles (*5, 6*). TAT, penetratin, model amphipathic peptide (MAP), transportan, vascular endothelial cadherin derived CPP (pVEC), pISL derived from the homeodomain of the rat transcription factor Islet-1, oligoarginine, KETWWETWWTEWSQPKKKRKV (Pep-1), and MANLGYWLLALFVTMWTDVGLCKKRPKP (PrP^c) are typical examples of the CPPs. The structural characteristics of these CPPs are positively charged amino acids such as lysine or arginine in the peptide sequence. In particular, guanidinium moieties are intensively studied by Futaka and Wender, focusing on the dependence of molecular weight of oligoarginine, topological variation into linear and dendritic oligoarginine (*7*−*11*). The optimal number of Arg with 8−9 is critical, because it determines the toxicity, translocation ability of the conjugated drug, and cost of the system (*9, 10*).

In this research, we designed a series of dendritic amine and guanidinium modified molecules, where a hydrophobic stearyl group is connected to the amine or guanidinium groups, and oligophenylalanine is used as a connecting moiety to give structural rigidity to the system (Figure 1). The hydrophobic stearyl group is used to encapsulate the hydrophobic model oligopeptide drug, an FITC conjugated-Ile-Ile-Leu-Ala-Val-Tyr (FITC-IILAVY). Internalization of the model oligopeptide drug into the BMMs was investigated using a series of these nanoparticles carriers.

EXPERIMENTAL PROCEDURES

Materials. FITC-IILAVY was obtained from Peptron (Korea). *N*-Carboxyanhydride of DL-phenylalanine (DL-Phe-NCA) was purchased from M&H laboratories (Korea). α,ε-Di-*tert*-butyloxycarbonyl-L-lysine (α,ε-diboc-Lys) was purchased from Shanghai GL Biochem Ltd. (China). Stearylamine and 1-ethyl-3-(3-dimethyl aminopropyl) carbodiimide (EDC) were purchased from TCI (Japan). *N*-Hydroxysuccinimide (NHS), 4-guanidinobutyric acid (GBA), dimethylsulfoxide (DMSO), paraformaldehyde, and anhydrous *N*,*N*-dimethyl formamide (DMF) were purchased from Sigma (America). Trifluoroacetic acid (TFA) and 4-morpholine ethane sulfonic acid (MES) were purchased from Sigma (America) and used as received.

Synthesis of SF-A1. Stearylamine in anhydrous DMF (5.3 mL, 1.0 M) was added to a DL-Phe-NCA 3.06 g (16.0 mmol) solution dissolved in anhydrous DMF (20 mL), and the reaction was stirred 4 days at 40 °C under N_2 protection (*12*). The mixtures were precipitated in diethyl ether, and the precipitate was washed throughout with diethyl ether. The product was dried in vacuo.

[M-Na+]: 733.7 (calc. 734.0). ^{1}H NMR (CF_3COOD): δ (ppm) stearylamine (CH_3-) = 0.7−1.0; δ stearylamine (-CH_2-) = 1.0−1.5; δ steraylamine (-CH_2NH-) = 3.0−3.1; DL-phenylanine (-CH_2-) = 3.1−3.4; δ DL-phenylanine (−COCH($CH_2C_6H_5$)−) = 4.6−5.0; δ DL-phenylanine (-C_6H_5) = 6.8−7.4.

Synthesis of SF-G1. EDC (0.57 g, 3.0 mmol) and NHS (0.34 g, 3.0 mmol) were added to the GBA (0.43 g, 3.0 mmol) that was dissolved in MES buffer (pH = 5.5, 10 mL). The reaction mixtures were stirred for 4 h. To couple the amino group of the SF-A1 and carboxylic acid group of GBA, SF-A1 (1.51 g, 1.80 mmol) dissolved in DMF (30 mL) was slowly injected to the reaction mixtures at 0 °C (*13*). The reaction was stirred at room temperature for 48 h. The reaction mixtures were precipitated into an excess amount of diethyl ether. The precipitate was filtered and washed with diethyl ether three times. After being dried in vacuo, the product was suspended in 20 mL of deionized water and dialyzed using cellulose

* To whom correspondence should be addressed. B. Jong: Fax 82232772384; Tel 82232773411; E-mail bjeong@ewha.ac.kr. S. Lee: Fax 82232773760; Tel 82232773770; E-mail leesy@ewha.ac.kr.

[†] Department of Chemistry and Nano Science.

[‡] Division of Life and Pharmaceutical Sciences.

10.1021/bc100066k © 2010 American Chemical Society
Published on Web 07/19/2010

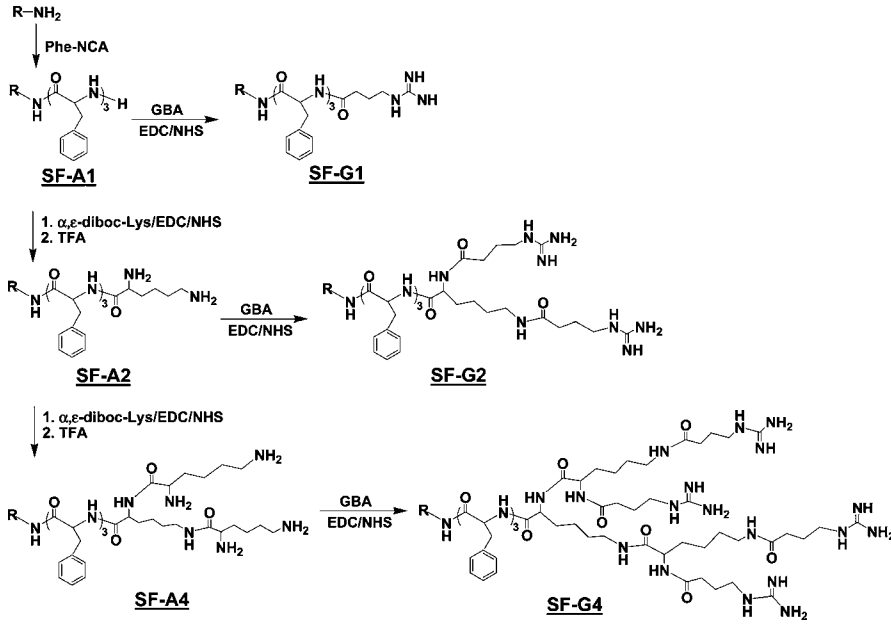


Figure 1. Synthetic scheme of carriers. R is stearyl (C_{17}) group. $n \approx 3$.

membrane (MWCO 500 Da) in deionized water for 24 h. The final product was lyophilized in a powder form.

MALDI-TOF Mass spectra [M-H+]: 839.0 (calc. 839.2). ^{1}H NMR (CF_3COOD): δ (ppm) searylamine (-CH_3-) = 0.7−1.0; δ stearylamine (-CH_2-) = 1.0−1.5; δ GBA (-OC$CH_2CH_2$$CH_2$NH-) = 1.8−2.0; δ stearylamine (-CH_2NH-) = 3.0−3.1; δ DL-phenylanine (-CH_2-) = 3.1−3.4; δ GBA (-CH_2NHC(=NH)NH_2) = 3.3−3.4; δ DL-phenylanine (-COCH($CH_2C_6H_5$)−) = 4.6−5.0; δ DL-phenylanine (-C_6H_5) = 6.8−7.4.

Synthesis of SF-A2. α,ε-Diboc-Lys (2.41 g, 7.0 mmol) was dissolved in MES buffer (pH = 5.5, 10 mL), and then EDC (1.34 g, 7.0 mmol) and NHS (0.81 g, 7.0 mmol) were added to the solution, and the mixture was stirred for 4 h. A solution of SF-A1 (4.00 g, 4.8 mmol) in DMF 30 mL was injected into the mixture at 0 °C. The reaction was stirred at room temperature for 48 h. The protective *t*-butoxycarbonyl groups were removed by TFA. The SF-A1-diboc-lysine (4.34 g, 4.2 mmol) was stirred in a mixed solution of TFA (10 mL) and anhydrous dichloromethane (20 mL) at 0 °C for 3 h. After the solvent was partially evaporated under reduced pressure, an excess amount of diethyl ether was added to precipitate SF-A2. The precipitate was filtered and washed with diethyl ether three times. After being dried in vacuo, the product was dissolved in 20 mL deionized water and dialyzed using cellulose membrane (MWCO 500 Da) in deionized water for 24 h. The final product was collected by lyophilization.

MALDI-TOF Mass spectra [M-H+]: 839.9 (calc. 839.2). ^{1}H NMR (CF_3COOD): δ (ppm) stearylamine (-CH_3-) = 0.7−0.9; δ stearylamine (-CH_2-) = 1.0−1.5; δ lysine (−COCH($CH_2CH_2CH_2CH_2(NH_2)$) = 1.6−1.7; δ lysine (−COCH($CH_2CH_2CH_2CH_2(NH_2)$) = 1.8−2.0; δ lysine (−COCH($CH_2CH_2CH_2CH_2(NH_2)$) = 2.8−3.2; δ stearylamine (-CH_2NH-) = 3.0−3.1; δ DL-phenylanine (-CH_2-) = 3.1−3.4; δ lysine (−COCH($CH_2CH_2CH_2CH_2NH_2$)(NH_2)); and DL-phenylanine (-COCH($CH_2C_6H_5$)−) = 4.6−5.0; δ DL-phenylanine (-C_6H_5) = 6.8−7.4.

Synthesis of SF-G2. GBA (1.30 g, 9.0 mmol) was dissolved in MES buffer (10 mL at pH = 5.5). EDC (1.77 g, 9.0 mmol) and NHS (1.0 g, 9.0 mmol) were added to the solution, and the mixtures were stirred for 4 h at room temperature. SF-A2 (3.15 g, 3.8 mmol) in DMF (30 mL) was injected into the mixture at 0 °C, and the reaction mixtures were stirred at room temperature for 48 h. The reaction mixtures were poured into an excess amount of diethyl ether to precipitate the product. The precipitate was filtered and washed with diethyl ether three times. After the residual solvent was removed in vacuo, the product was redissolved in 20 mL deionized water and dialyzed using cellulose membrane (MWCO 500 Da) in deionized water for 24 h. The final product was collected by lyophilization.

MALDI-TOF Mass spectra [M-H+]: 1094.0 (calc. 1093.5). ^{1}H NMR (CF_3COOD): δ (ppm) stearylamine (-CH_3-) = 0.7−0.9; δ stearylamine (-CH_2-) = 1.0−1.5; δ lysine (−COCH-($CH_2CH_2CH_2CH_2$(NH)−) = 1.6−1.7; δ lysine (−COCH-($CH_2CH_2CH_2CH_2$(NH)−), and GBA (-OC$CH_2CH_2$$CH_2$NH-) = 1.8−2.0; δ stearylamine (-CH_2NH-) = 3.0−3.1; δ lysine (−COCH($CH_2CH_2CH_2CH_2$(NH)−) = 3.0−3.2; δ DL-phenylanine (-CH_2-) = 3.1−3.4; δ GBA (-$CH_2NHC(=NH)NH$-) = 3.3−3.4; δ lysine (−COCH($CH_2CH_2CH_2CH_2NH_2$)(NH-)), and DL-phenylanine (-COCH($CH_2C_6H_5$)−) = 4.7−5.0; δ DL-phenylanine (-C_6H_5) = 7.0−7.4.

Synthesis of SF-A4. α,ε-Diboc-Lys (4.83 g, 14.0 mmol) was dissolved in MES buffer (30 mL, pH = 5.5). EDC (2.70 g, 14.1 mmol) and NHS (1.65 g, 14.0 mmol) were added to the solution, and the mixtures were stirred for 4 h. SF-A2 (3.15 g, 3.8 mmol) dissolved in DMF (30 mL) was injected to the mixture at 0 °C, and the reaction mixtures were stirred at room temperature for 48 h. An excess amount of diethyl ether was added to precipitate the SF-A2-α,ε-diboc-Lys. The precipitate was filtered and washed with diethyl ether three times. After drying the product in vacuo, SF-A2-α,ε-diboc-Lys (5.14 g, 3.4 mmol) was stirred in a mixed solution of TFA (10 mL) and anhydrous dichloromethane (20 mL) at 0 °C for 3 h. After the solvent was partially evaporated under reduced pressure, an excess amount of diethyl ether was added to precipitate the product. The precipitate was filtered and washed with diethyl ether three times. After the residual solvent was removed in vacuo, the product was redissolved in 20 mL deionized water and dialyzed using a cellulose membrane (MWCO 500 Da) in deionized water for 24 h. The final product was collected by lyophilization.

MALDI-TOF Mass spectra [M-Na+]: 1118.0 (calc. 1118.6). ^{1}H NMR (CF_3COOD): δ (ppm) stearylamine (-CH_3-) = 0.7−0.9; δ stearylamine (-CH_2-) = 1.0−1.5; δ lysine (−COCH-($CH_2CH_2CH_2CH_2(NH_2)$) = 1.6−1.7; δ lysine (−COCH-($CH_2CH_2CH_2CH_2(NH_2)$) = 1.8−2.0; δ lysine (−COCH-($CH_2CH_2CH_2CH_2(NH_2)$) = 2.8−3.2; δ stearylamine (-CH_2NH-)

= 3.0−3.1; δ DL-phenylanine (-CH_2-) = 3.1−3.4; δ lysine (−COCH($CH_2CH_2CH_2CH_2NH_2$)(NH_2)); and DL-phenylanine (-COCH($CH_2C_6H_5$)−) = 4.6−5.0; δ DL-phenylanine (-C_6H_5) = 6.8−7.4.

Synthesis of SF-G4. GBA (2.63 g, 18 mmol) was dissolved in MES buffer (pH = 5.5; 10 mL). EDC (3.62 g, 18.9 mmol) and NHS (2.10 g, 18.3 mmol) were added to the solution, and the mixtures were stirred for 4 h. SF-A4 (4.00 g, 3.7 mmol) dissolved in DMF (30 mL) was injected to the mixture at 0 °C, and the reaction mixtures were stirred at room temperature for 48 h. The reaction mixtures were precipitated into an excess amount of diethyl ether. The precipitate was filtered and washed with diethyl ether three times. After the residual solvent was removed in vacuo, the product was redissolved in 20 mL deionized water and dialyzed using cellulose membrane (MWCO 1000 Da) in deionized water for 24 h. The final product was collected by lyophilization.

MALDI-TOF Mass spectra [M-H+]: 1608.6 (calc. 1608.1). ^{1}H NMR (CF_3COOD): δ (ppm) stearylamine (-CH_3-) = 0.7−0.1.0; δ stearylamine (-CH_2-) = 1.0−1.5; δ lysine (−COCH-($CH_2CH_2CH_2CH_2$(NH)−) = 1.6−1.7; δ lysine (−COCH-($CH_2CH_2CH_2CH_2$(NH)−), and GBA (-OC$CH_2CH_2CH_2$NH-) = 1.7−2.0; δ stearylamine (-CH_2NH-) = 3.0−3.1; δ DL-phenylanine (-CH_2-) = 3.1−3.4; δ GBA (-CH_2NHC(=NH)NH-) = 3.3−3.4; δ lysine (−COCH($CH_2CH_2CH_2CH_2NH_2$)(NH-)) = 4.5−4.8; δ DL-phenylanine (-COCH($CH_2C_6H_5$)−) = 4.7−5.0; δ DL-phenylanine (-C_6H_5) = 6.8−7.4.

Preparation of Nanoparticles. FITC-IILAVY loaded nanoparticles were prepared by the emulsion−solvent evaporation technique (*14*). Briefly, the carrier (10 mg) dissolved in methylene chloride (2 mL) was mixed with FITC-IILAVY (100 μg) dissolved in 500 μL DMSO. The mixture was slowly dropped into poly(vinyl alcohol) aqueous solution (50 mL; 1.0% w/v) while stirring at 3200 rpm. The pre-emulsion equilibrated in an ice bath was sonicated for10 min by using a 750 W high-intensity ultrasonic processor (VCX 750, Sonics and Materials Inc., USA) operating at 20 kHz. The organic solvent was then evaporated under gentle agitation (800 rpm) over 12 h at room temperature. The resulting nanoparticles were dialyzed using cellulose membrane (MWCO 3500 Da) in an excess amount of water for 24 h and freeze−dried for 48 h to a powder form.

Particle Size Analysis. Size and size distribution of the drug-loaded nanoparticles were measured by the particle size analyzer (Zetasizer NanoZS2000; Malven Instrument, UK) based on quasi-elastic light scattering. The nanoparticles were resuspended at a 1.0 mg/mL (wt./v) concentration in deionized water. Then, size and size distribution of the nanoparticles were measured at room temperature (n = 3).

Determination of Drug Encapsulation Efficiency and Drug Loading Content. The FITC-IILAVY loaded in the nanoparticles was analyzed by HPLC (Waters LC). Briefly, the drug loaded nanoparticles (1.0 mg) were dissolved in 1.0 mL DMSO. A Waters Nova-Pak C18 (3.9ch150 mm, 4 μm) column and UV/vis detector operating at 220 nm were used to analyze the drug content in the nanoparticle. The flow rate of the mobile phase (acetonitrile/water (50/50 by volume)) was 1.0 mL/min. The drug encapsulation efficiency is defined by the amount of drug encapsulated in the nanoparticle relative to the initial amount of drug. The drug loading content is the ratio of the amount of drug to nanoparticles.

Cell Culture. BMMs were obtained from the femur of 5 week old C57BL/6 mice. BMMs were flushed out of the bone marrow cavity. BMMs were suspended for 3 days in a α-minimal essential medium (α-MEM) (GIBCO-BRL, Grand Island, NY) supplemented with 10% heat-inactivated fetal bovine serum, 100 units/mL penicillin, 100 μg/mL streptomycin (GIBCO), and 30 ng/mL recombinant human macrophage-colony stimulating factor (rhM-CSF) (R&D system, Minneapolis, MN).

Fluorescence Image Assay. BMMs were incubated in α-MEM containing drug-loaded nanoparticles for 4 h. The cells were washed twice with phosphate buffered saline (PBS). Culture dishes were transferred to a Zeiss Axiovert 200 microscope (Carl Zeiss, Oberkochen, Germany) equipped with AXioCam HR.

Fluorescence Activated Cell Sorting (FACS). BMMs were seeded in 6-well plates at a density of 5×10^5 cells per well and incubated for 24 h. BMMs were grown to approximately 60% confluency in 6-well plates and then incubated with nanoparticles for 4 h. After the cells were washed twice with PBS and trypsinized for 3 min, the cells were harvested and washed twice with PBS. The cells were fixed by paraformaldehyde aqueous solution (2.0%) and analyzed by flow cytometry (FACS Calibur: BD Biosciences, San Jose, CA, USA). The excitation wavelength was set at 488 nm.

Cytotoxicity Assay. After treating the BMMs with nanoparticles for indicated time periods (12 h, 24 h, 36 h, and 48 h), they were stained with propidium iodide (Sigma) and then analyzed by a flow cytometer. The excitation wavelength was 488 nm.

RESULTS AND DISCUSSION

Synthesis. In order to enhance the cellular uptake of the oligopeptides model drug into the BMMs, two series of dendritic molecules with amine or guanidinium groups were synthesized as shown in Figure 1. SF-A1 was synthesized by ring-opening polymerization of N-carboxy anhydrides of DL-Phe on the stearylamine. The degree of polymerization was about 3 by ^{1}H NMR spectrum. The SF-A2 was synthesized by the condensation reaction between carboxylic acid of α,ε-dibutyloxycarbonyl-lysine and amino group of SF-A1 by using EDC and NHS as coupling agents. After the deprotection of the butyloxycarbonyl groups of SF-A2 by trifluoroacetic acid (TFA), SF-A2 with dendritic amine groups was prepared. The repetition of the same procedure gave dendritic SF-A4 with four amino groups.

To synthesize the SF-G1 with guanidinium groups, amino group of SF-A1 was coupled with carboxylic acid of 4-guanidinobutyric acid (GBA) using EDC and NHS as coupling agents. SF-G2 and SF-G4 were synthesized from SF-A2 and SF-A4, respectively, by a similar coupling method. ^{1}H NMR, IR analysis, and MALDI-TOF mass spectra confirmed the structure of SF-A1−SF-A4 and SF-G1−SF-G4. In ^{1}H NMR spectra, the methylene peak of the stearyl group at 1.2−1.4 ppm, methylene peak of the lysine group at 1.7−1.8 ppm, and methylene peak of the 4-guanidinobutyric group at 3.2 ppm confirm the progress of the reaction (Supporting Information Figure S1a) (*15, 16*). IR spectra of the SF-G1, SF-G2, and SF-G4 showed stronger peaks at 1649 cm^{-1} and 1555 cm^{-1} corresponding to the stretching vibration of C=N and bending vibration of N−H, respectively (Supporting Information Figure S1b). The wide band at 3400 cm^{-1} corresponds to the stretching vibration of N−H group. The strong peaks at 1649, 1555, and 1380 cm^{-1} suggested that the guanidinylation had been successful (*17*). MALDI-TOF mass spectra confirm the molecular ion peaks for the products as indicated in the experimental section.

Particle Analysis. During preparation of the FITC-IILAVY loaded nanoparticles, the stearyl moieties act as the hydrophobic core of the nanoparticles, whereas the amine groups or guanidinium groups with positive charges are located on the surface of the nanoparticles. The poorly water-soluble FITC-IILAVY was encapsulated into the polymeric nanoparticles due to preferential partitioning of the drug by hydrophobic interactions. The effective hydrodynamic size and zeta potential of FITC-IILAVY loaded nanoparticles were estimated by using a

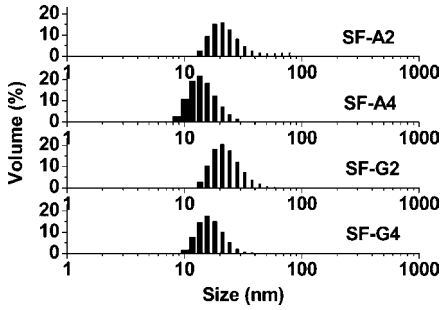


Figure 2. Apparent size of SF-A2, SF-A4, SF-G2, and SF-G4 in water determined by dynamic light scattering study.

Table 1. Zeta-Potential of the Carriers in Water

carrier	SF-A1	SF-A2	SF-A4	SF-G1	SF-G2	SF-G4
ζ potential (mv)	44 ± 3	54 ± 4	55 ± 1	52 ± 1	67 ± 1	85 ± 2

Zetasizer. SF-A1 and SF-G1 formed nanoparticles with a wide range of 40−2000 nm and 50−500 nm, respectively, whereas SF-A2, SF-A4, SF-G2, and SF-G4 formed nanoparticles with a narrow range of 10−45 nm (Figure 2). The encapsulation efficiency of the drug was 17−18% for SF-A2, SF-A4, SF-G2, and SF-G4, resulting in the formation of nanoparticles with a drug loading content of 0.45−0.55%. The drug encapsulated nanoparticles were dialyzed using cellulose membrane (MWCO 3500 Da) in an excess amount of water for 24 h during which some fraction of the drug might be released out of the membrane, thus decreasing the encapsulation efficiency. When the number of amine or guanidinium groups in the carrier increased, size and size distribution of nanoparticles slightly decreased. Zeta potential determines the surface charge of nanoparticles. A high value of zeta potential indicates a high surface charge of the nanoparticles, which leads to strong repellent interactions among the nanopaticles in dispersion and thus can give high stability to the nanoparticle in water. All nanoparticles prepared from SF-A1−SF-A4 and SF-G1−SF-G4 showed positive zeta potential in the range $(44 \pm 3)-(85 \pm 2)$ mV and good stability in water (Table 1). The zeta potentials of the nanoparticles steadily increased as the number of amine groups or guanidinium groups increased. In addition, guanidinium modified carriers showed larger zeta potential than amine modified carriers.

Cellular Uptake. Oligoarginine works as a cell penetrating peptide and the effectiveness of cell penetration of oligoarginine-conjugated protein (GCN 4) increased as the number of arginine repeating units increased (*10*). Our system used the stearyl group and oligophenylalanine as a hydrophobic block, where the drug encapsulated nanoparticles are coated with guanidinium groups by a self-assembly process. The cellular uptake of nanoparticles containing FITC-IILAVY was investigated for SF-G4 and SF-A4 as a function of time. The fluorescence intensity increased with time (1 h, 1.5 h, 2 h, 3 h, 4 h) (Figure 3a). Two points can be emphasized for our system. First, FACS analysis showed that guanidinium groups modified nanoparticles (SF-G4) showed excellent penetration into the BMMs. The oligoarginine with four repeating units (R_4) was reported to be ineffective as CPP (*10*). However, current SF-G4 with four guanidinium groups in a molecule showed excellent translocation ability. This behavior comes from the self-assembly of the SF-G4 with hydrophobic blocks of stearyl-oligophenylalanine and hydrophilic blocks (G_4). On a nanoparticle, the guanidinium groups are located on the surface of the nanoparticle and exhibit a polyarginine-like behavior. Second, guanidinium groups modified nanoparticles (SF-G4) were significantly more effective in

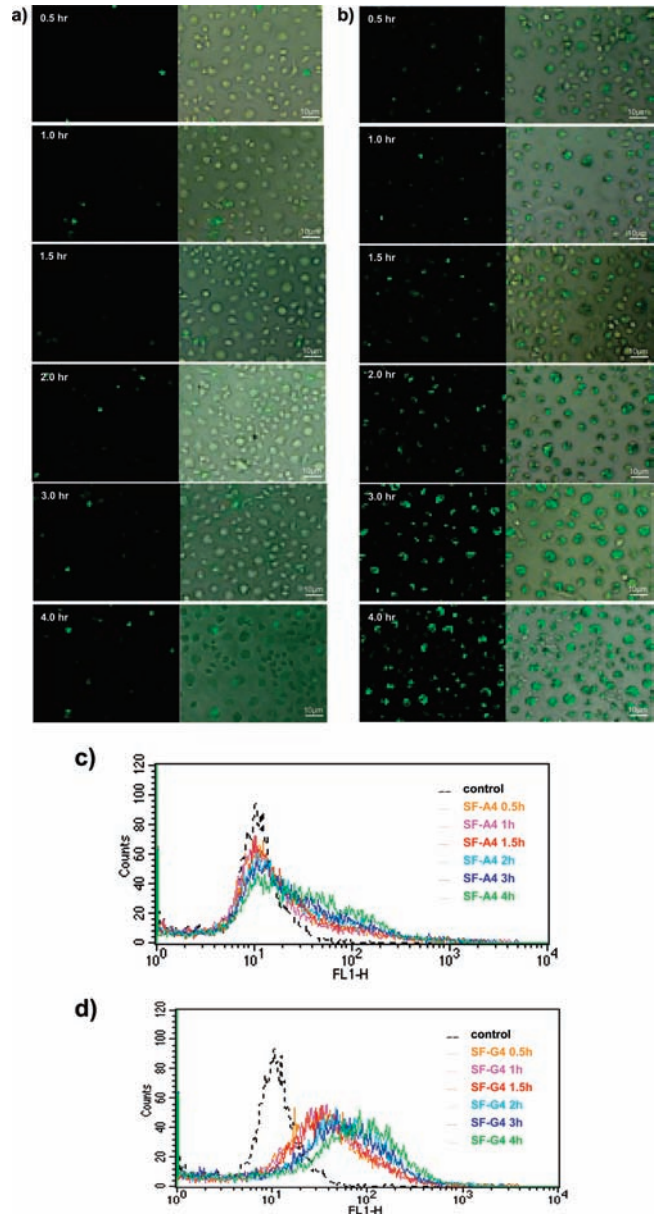


Figure 3. Intracellular delivery of oligopeptides into BMMs. Fluorescence images of internalized oligopeptides by SF-A4 (a) and SF-G4 (b). Both fluorescence images (left) and fluorescence/transmission overlapped images (right) are shown. The scale bars in (a) and (b) are 10 μm. Flow cytometric histograms of internalized oligopeptides by SF-A4 (c) and SF-G4 (d). Control experiment of the model drug is carried out in the absence of carriers.

penetrating into the BMMs than amino group modified nanoparticles (SF-A4). The detailed mechanism of the difference is under investigation. Previous study by Harashima et al. reported that the octaarginine/DNA complex showed higher transfection efficiency than octalysine/DNA complex (*18*). They suggested that the enhanced transfection of octaarginine/DNA complex comes from the different mode of endosomal escape from the late endosome with low pH. In our system, the model neutral oligopeptide drug was encapsulated in the guanidinium group coated nanoparticle. In addition, the enhanced translocation of the nanoparticle is observed more in the guanidinium group coated nanoparticle than the amino group coated nanoparticle. The favorable hydrogen bonding interactions between guanidinium groups with dispersed positive charges and negative residues of the phospholipids present on the cell surface might be responsible for such behavior (*19, 20*). Kinetic study also

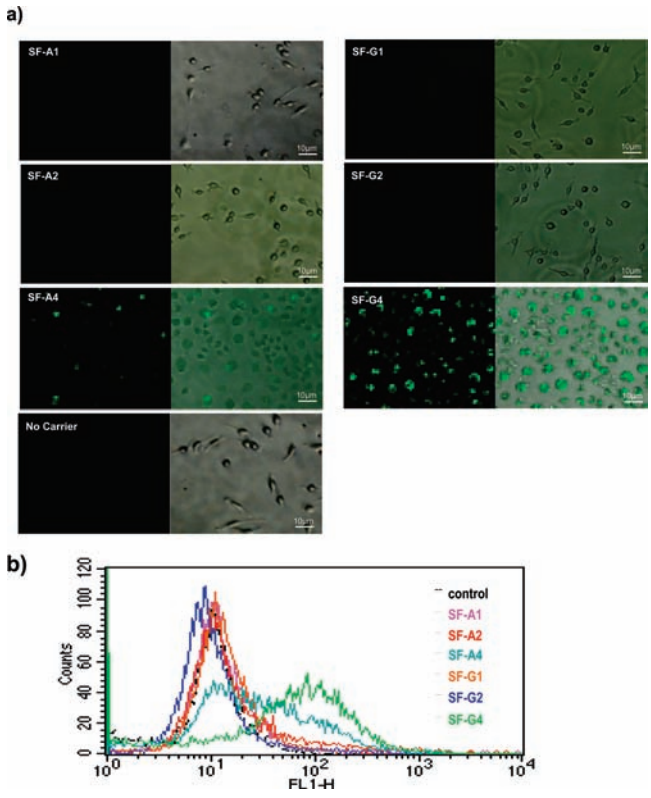


Figure 4. Comparison of carriers for internalization of oligopeptides into BMMs in 4 h. (a) Fluorescence images of internalized oligopeptides by the functionalized carriers. Control experiment of the oligopeptides is carried out in the absence of carriers. The scale bar is 10 μm. Both fluorescence images (left) and fluorescence/transmission overlapped images (right) are shown. (b) Flow cytometric histograms of internalized oligopeptides by the functionalized carriers.

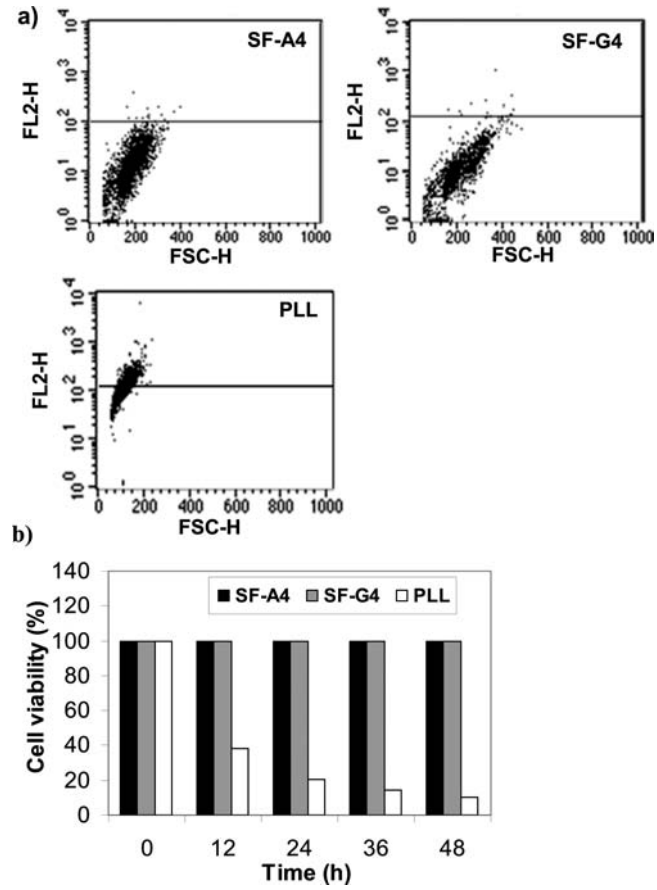


Figure 5. Cytotoxicity of carriers for BMMs. (a) FACS plot of BMMs in 48 h of incubation. (b) Cell viability in the polymer solution (100 μg/mL in culture medium) for 48 h. Poly(L-lysine) (M_w = 15 000−30 000 Da) was used for control.

suggested that 4 h is sufficient for the penetration study of the nanoparticles for comparative purposes with other nanoparticles of SF-A1−SF-A4 and SF-G1−SF-G4.

To compare the penetration of the FITC-IILAVY loaded nanoparticles into the BMMs, BMMs were incubated with nanoparticles for 4 h. Fluorescence image and FACS analysis suggested that the SF-G4 system most efficiently penetrates into the cells (Figure 4). Many variables affect the uptake property of nanoparticles, including adhesion to the cell surface, size, and surface charge of the nanoparticle, and so forth. On the basis of current results, we can speculate that the mechanisms of internalization of nanoparticles through the cell membrane may be endocytosis, where the positive charge of the nanoparticles interacts with the negative charge of the phospholipid membrane. SF-G4 nanoparticles possess higher density of guanidinium group than SF-G1 and SF-G2. The higher uptake of SF-G4 by BMM cells is caused by the high positive charge of the nanoparticles as shown by a large ζ-potential. The fact that SF-G4 showed higher translocation ability than SF-A4 also supports previous suggestion that the guanidinium groups have favorable interactions with negatively charged functional groups in the cell membrane (*19, 20*). The resulting ion pairs have the capability of translocation across the cell membrane.

Cytotoxicity Assay. A drug delivery system should possess biocompatibility or cytocompatibility, as well as a delivery function. HIV-Tat (48−60) was reported to show a 90% cell survival rate at 100 μM for Hela cells and mouse macrophage RAW264.7 (*10, 21*). We investigated the FACS plot of BMMs after incubation for 48 h with SF-A4 and SF-G4 in the polymer solution 100 μg/mL (62 μM for SF-G4 and 91 μM for SF-A4) in culture medium, respectively (Figure 5). PLL (M_w 15 000−30 000) was used as a negative control in this research. SF-A4 and SF-G4 in a concentration of 100 μg/mL did not show cytotoxicity, whereas more than 80% of the BMMs incubated with PLL died.

To conclude, dendritic molecules with amine and guanidinium groups were synthesized and their nanoparticles containing FITC labeled model oligopeptide drug (FITC-IILAVY) were prepared. FACS and spectrofluorimetry analysis showed that (1) the efficiency of intracellular delivery increased by increasing the number of the positive charged groups and (2) the nanoparticles functionalized with dendrtic guanidinium groups demonstrated better ability to cross the BMM membranes than amino groups. The carriers (SF-A4 and SF-G4) did not exhibit any significant cytotoxicity against BMMs. Current research suggests that SF-G4 with hydrophobic block and four hydrophilic guanidinium groups is a promising drug delivery carrier for peptide drug targeting osteoclast precursors.

ACKNOWLEDGMENT

This work was supported by the Midcareer Researcher Program through NRF grant funded by the MEST (2007-0055790/2009-0080447) and Korea Science and Engineering Foundation (KOSEF) National Research Laboratory (NRL) Program grant funded by the Korean government (MEST) (R0A-2008-000-20001-0).

Supporting Information Available: ^{1}H NMR and FTIR of all carriers (SF-A1−SF-A4, SF-G1−SF-G4) are provided. This material is free of charge via the Internet at http://pubs.acs.org.

LITERATURE CITED

(1) Zaidi, M. (2007) Skeletal remodeling in health and disease. *Nat. Med. 13*, 791–801.

(2) Teitelbaum, S. L. (2000) Bone resorption by osteoclast. *Science 289*, 1504–1508.

(3) Greig, I. R., Idris, A. I., Ralston, S. H., and Hof, R. J. V. (2006) Development and characterization of biphenyl sulfonamides as novel inhibitors of bone resorption. *J. Med. Chem. 49*, 7487–7492.

(4) Kim, H., Choi, H. K., Shin, J. H., Kim, K. H., Huh, J. Y., Lee, S. A., Ko, C. Y., Kim, H. S., Shin, H. I., Lee, H. J., Jeong, D., Kim, N., Choi, Y., and Lee, S. Y. (2009) Selective inhibition of RANK blocks osteoclast maturation and function and prevents bone loss in mice. *J. Clin. Invest. 119*, 813–825.

(5) Vladimir, P. T. (2008) Cell-penetrating peptide-modified pharmaceutical nanocarriers for intracellular drug and gene delivery. *Pept. Sci. 90*, 604–610.

(6) Lindgren, M., Hallbrink, M., Prochiantz, A., and Langel, U. (2000) Cell-penetrating peptides. *Trends Pharmacol. Sci. 21*, 99–103.

(7) Futaki, S. (2005) Membrane-permeable arginine-rich peptides and the translocation mechanisms. *Adv. Drug Delivery Rev. 57*, 547–558.

(8) Wender, P. A., Mitchell, D. J., Pattabiraman, K., Pelkey, E. T., Steinman, L., and Rothbard, J. B. (2000) The design, synthesis, and evaluation of molecules that enable or enhance cellular uptake: Peptoid molecular transporters. *Proc. Natl. Acad. Sci. U.S.A. 97*, 13003–13008.

(9) Futaki, S., Goto, S., and Suguira, Y. (2003) Membrane permeability commonly shared among arginine-rich peptides. *J. Mol. Recog. 16*, 260–264.

(10) Futaki, S., Suzuki, T., Ohashi, W., Yagami, T., Tanaka, S., Ueda, K., and Sugiura, Y. (2001) Arginine-rich peptides: An abundant source of membrane-permeable peptides having potential as carriers for intracellular protein delivery. *J. Biol. Chem. 276*, 5836–5840.

(11) Wender, P. A., Galliher, W. C., Goun, E. A., Jones, L. R., and Pillow, T. H. (2008) The design of guanidinium-rich transporters and their internalization mechanisms. *Adv. Drug Delivery Rev. 60*, 452–472.

(12) Jeong, Y., Joo, M. K., Bahk, K. H., Choi, Y. Y., Kim, H. T., Kim, W. K., Lee, H. J., Sohn, Y. S., and Jeong, B. (2009) Enzymatically degradable temperature-sensitive polypeptide as a new in-situ gelling biomaterial. *J. Controlled Release 137*, 25–30.

(13) Montserrat, D. F., Dolors, F. F., Montserrat, M., Victor, S., Hamish, R., Miriam, R., and Fernando, A. (2005) Combinatorial approaches towards the discovery of new tryptase inhibitors. *Bioorg. Med. Chem. Lett. 15*, 1659–1664.

(14) Carolina, G. G., Nicolas, T., Madeleine, B., Amelie, B., and Elias, F. (2007) Encapsulation of dexamethasone into biodegradable polymeric nanoparticles. *Int. J. Pharm. 331*, 153–159.

(15) Martin, A. L., Bernas, L. M., Rutt, B. K., Foster, P. J., and Gillies, E. R. (2008) Enhanced cell uptake of super paramagnetic iron oxide nanoparticles functionalized with dendritic guanidines. *Bioconjugate Chem. 19*, 2375–2384.

(16) Wender, P. A., Kreider, E., Pelkey, E. T., Rothbard, J., and van Deusen, C. L. (2005) Dendrimeric molecular transporters: Synthesis and evaluation of tunable polyguanidino dendrimers that facilitate cellular uptake. *Org. Lett. 7*, 4815–4818.

(17) Wessel, H. P. (1993) Synthesis of 6-guanidino-hexoses and 5-guanidino-pentoses. *J. Carbohydr. Chem. 12*, 1173–1186.

(18) El-Sayed, A., Khalil, I. A., Kogure, K., Futaki, S., and Harashima, H. (2008) Octaarginine-and octalysine-modified nanoparticles have different modes of endosomal escape. *J. Biol. Chem. 283*, 23450–23461.

(19) Rothbard, J. B., Jessop, T. C., Lewis, R. S., Murray, B. A., and Wender, P. A. (2004) Role of membrane potential and hydrogen bonding in the mechanism of translocation of guanidinium-rich peptides into cells. *J. Am. Chem. Soc. 126*, 9506–9507.

(20) Rothbard, J. B., Jessop, T. C., and Wender, P. A. (2005) Adaptive translocation: the role of hydrogen bonding and membrane potential in the uptake of guanidinium-rich transporters into cells. *Adv. Drug Delivery Rev. 57*, 495–504.

(21) Futaki, S., Nakase, I., Suzuki, T., Zhang, Y., and Sugiura, Y. (2002) Translocation of branched-chain arginine peptides through cell membranes: flexibility in the spatial disposition of positive charges in membrane-permeable peptides. *Biochemistry 42*, 7925–7930.

BC100066K

Supporting Information

Oligopeptide delivery carrier for osteoclast precursors

Bo Chi,[†] So Jeong Park,[‡] Min Hee Park,[†] Soo Young Lee,[‡]* and Byeongmoon Jeong[†]*

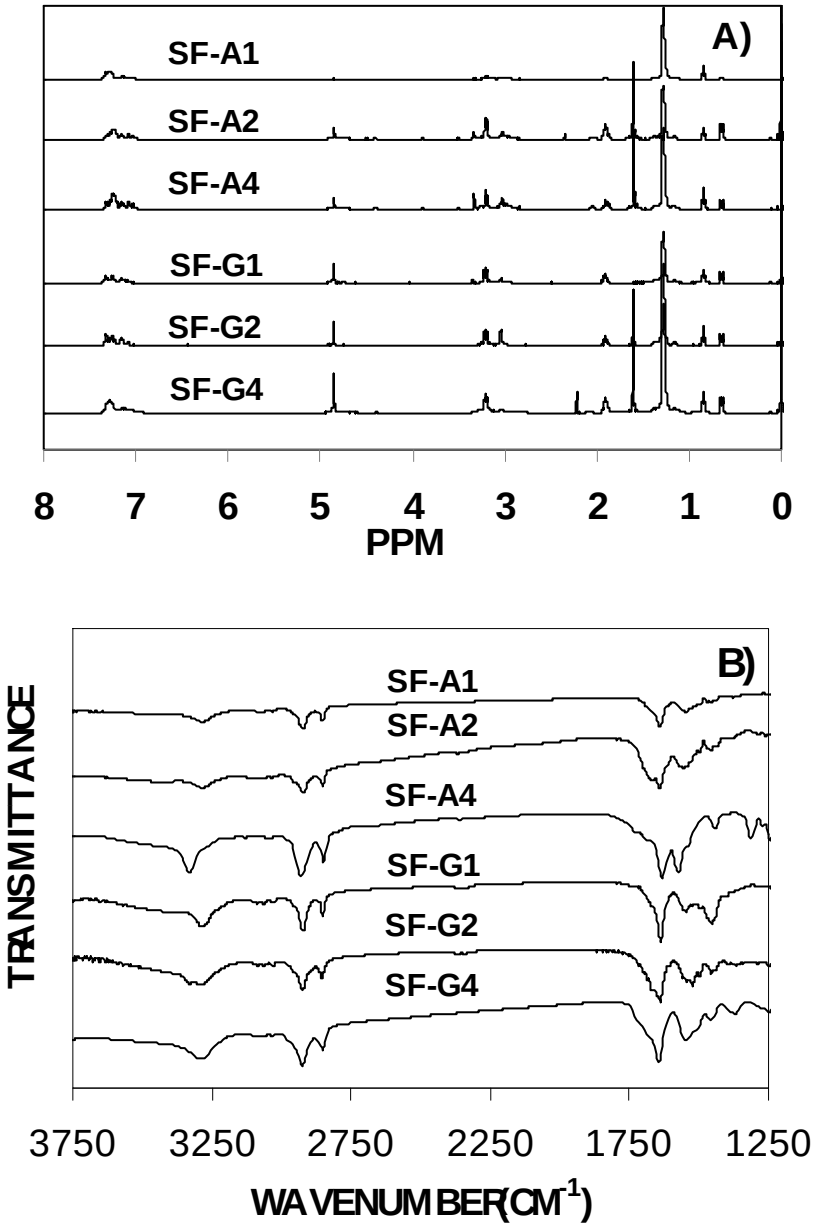


Figure S1. ^{1}H-NMR (CF_3COOD) (a) and IR (b) spectra of the polymers studied.

N-Glycan Targeted Gene Delivery to the Dendritic Cell SIGN Receptor

Kevin Anderson, Christian Fernandez, and Kevin G. Rice*

Divisions of Medicinal and Natural Products Chemistry and Pharmaceutics, College of Pharmacy, University of Iowa, Iowa City, Iowa 52242. Received February 9, 2010

A novel nonviral gene delivery vector composed of a high-mannose N-glycan conjugated to a polyacridine peptide was prepared. The glycopeptide was designed to bind to plasmid DNA by a combination of polyintercalation and ionic binding, and to the DC-SIGN (dendritic cell-specific intracellular adhesion molecule-3 grabbing nonintegrin) receptor expressed on CHO cells by recognition of the high-mannose N-glycan. The glycopeptide conjugate was prepared by purification of a high-mannose N-glycan from affinity fractionated soybean agglutinin (SBA). The SBA was proteolyzed to release the N-glycan which was then modified on its N-terminus with Tyr and a propionate maleimide. A DNA binding polyacridine peptide, Cys-(Acr-Lys)$_4$, was prepared by solid-phase peptide synthesis using Fmoc-Lys(Acr), then conjugated to the maleimide on the N-glycan to produce a glycopeptide. The glycopeptide bound to DNA with high affinity as determined by fluorophore displacement assay and DNA band shift on agarose gel. When bound to Cy5 labeled DNA, the glycopeptide mediated specific uptake in DC-SIGN CHO (+) cells as determined by FACS analysis. In vitro gene transfer studies established that the glycopeptide increased the specificity of gene transfer in DC-SIGN CHO (+) cells 100-fold relative to CHO (−) cells. These studies suggest that a high-mannose N-glycan conjugated to a polyacridine peptide may also facilitate receptor mediated gene delivery in dendritic cells and thereby find utility in the delivery of DNA vaccines.

INTRODUCTION

Dendritic cells (DC) are the primary antigen presenting cells in the immune system and are therefore central to the development of vaccines (*1*). One of the challenges in developing DNA vaccines is the design of vectors that efficiently and selectively target DCs. The DC-SIGN (dendritic cell-specific intracellular adhesion molecule-3 grabbing nonintegrin) receptor is a cell surface endocytosing lectin that is specifically expressed on DCs that binds to glycoprotein N-glycans of the high-mannose or complex type possessing terminal Le^X with a micromolar K_d (*2*−*4*). The receptor is therefore ideally located to facilitate receptor mediated gene delivery to DCs.

Several earlier studies have targeted either immunogenic proteins or plasmid DNA to internalize into DCs via DC-SIGN in an attempt to prime the immune system (*5*−*18*). These studies establish that either encapsulation of DNA into mannosylated liposomes or complexation of DNA with mannosylated-PEI, mannosylated-chitosan, mannan-polylysine, or mannosylated glycolipid results in gene delivery with improved immune response when administered i.m. or i.p. (*10*−*18*). Other studies have determined that high-mannose N-glycans on remodeled glycoproteins are able to target DC-SIGN resulting in uptake into DCs and enhanced immune response (*5*−*8, 19*). While gene delivery to DCs with mannose containing polymers and liposomes has been achieved, no study has yet demonstrated the delivery of DNA to DCs using a natural high-mannose N-glycan.

Reversible binding of an N-glycan to DNA can be accomplished by covalently linking it to a polylysine peptide resulting in cationic polyplex (*20*). However, polylysine peptides of 18 residues or longer are necessary to achieve sufficient affinity to protect DNA, and the resulting electropositive polyplexes bind nonspecifically to numerous proteins in vivo (*21, 22*). To overcome these limitations, we recently demonstrated that short cationic peptides possessing multiple acridines attached to the side chain of Lys residues bind DNA with much higher affinity and protect DNA from metabolism compared to much longer polylysine peptides (*19, 23, 24*).

Functionalized polyacridine peptides, modified with either PEG or a fusogenic peptide, have been shown to mediate gene transfer in vitro or in vivo (*19, 23*). Earlier studies have also demonstrated the efficacy of a polyacridine polymer functionalized with either a nuclear localization signal (NLS) or a neoglycopeptide (*25, 26*). These experiments demonstrate the importance of increasing the DNA binding affinity by increasing the number of acridines. An early report by Ueyama also demonstrated that polyacridine peptides possessing two to five Lys(Acr) residues results in progressively higher affinity for calf thymus DNA (*27*).

To date, there have been no reports of the successful development and use of a polyacridine glycopeptide in gene transfer. Here, we report the purification of a high-mannose N-glycan from soybean agglutinin and its conjugation to a polyacridine peptide. The resulting glycopeptide binds to plasmid DNA with high affinity and mediates targeted uptake and gene expression in DC-SIGN expressing cells in vitro.

MATERIALS AND METHODS

Sepharose CL-4B, D-galactosamine HCl, 6-aminocaproic acid, Boc-tyrosine *N*-hydroxysuccinimide, 9-chloroacridine (97%), Pronase, thiazole orange, phenol, super-DHB diisopropylethylamine, piperidine, triisopropylsilane (TIS), polyethylenimine (PEI), and acetic anhydride were from Sigma-Aldrich (St. Louis, MO). Sephadex G-50 resin was from Amersham Biosciences (Pittsburgh, PA). AG 50W-X2 cation exchange resin was from Bio-Rad (Hercules, CA). 1,1′-carbonyldiimidazole, and *N*-(3-dimethylaminopropyl)-*N*′-ethyl-carbodiimide HCl were Fluka Biochemica products (St. Louis, MO). 3-Maleimidoproprionic acid *N*-hydroxysuccinimide ester was from ABD Bioquest, Inc. (Sunnyvale, CA). NuPAGE Novex Bis-Tris Gels, Dulbecco's Modified Eagle Medium (DMEM), MEM nonessential amino acids, Dulbecco's phosphate buffered saline (DPBS), and fetal

* To whom correspondence should be addressed. kevin-rice@uiowa.edu, tel: 319-335-9903, fax: 319-335-8766.

10.1021/bc1000824 © 2010 American Chemical Society
Published on Web 07/22/2010

bovine serum (FBS) were from Invitrogen (Carlsbad, CA). D_2O was from Cambridge Isotope Laboratories (Cambridge, MA). Untoasted soy flour was obtained from Archer Daniels Midland (Decatur, Illinois). Sodium hydroxide was a Mallinckrodt product through Fisher Scientific (Pittsburgh, PA). Fmoc-Lys-OH was from Novabiochem. Ethidium bromide was from Bio-Rad. Fmoc-Lys(Boc)-Wang resin, Fmoc-Lys(Boc)-OH, Fmoc-Cys(Trt)-OH, *N*-methyl-2-pyrrolidinone (NMP), *O*-benzotriazole-*N*,*N*,*N*′,*N*′-tetramethyl-uronium-hexafluorophosphate (HBTU), and hydroxybenzotriazole hydrate (HOBt) were from Advanced ChemTech (Lexington, KY). *N*′,*N*-dimethylformamide (DMF) was from Amresco (Solon, OH). Human DC-SIGN (+) and DC-SIGN (−) CHO cells were a gift from Drs. Chae Gyu Park and Ralph M. Steinman of the Laboratory of Cellular Immunology and Physiology at The Rockefeller University (*28*). Cy5 *Label*IT was from Mirus Biotechnology (Madison, WI). pGL3 control vector, a 5.3 kb luciferase plasmid containing an SV40 promoter and enhancer, was obtained from the Promega corporation (Madison, WI), amplified in DH5α *E. coli* from Invitrogen, and purified with a Giga kit from Qiagen (Valcencia, CA). D-Luciferin was from Gold Biotechnology (St. Louis, MO), adenosine 5′-triphosphate was from Roche (Indianapolis, IN), and BCA protein assay reagents were Pierce protein research products of Thermo Scientific (Rockford, IL). All reagents and solvents were certified ACS grade, molecular biology grade, or an equivalent.

Preparation of Sepharose *N*-Caproylgalactosamine Affinity Resin. 6-Aminocaproic acid was coupled to activated Sepharose CL-4B as described (*29*). Briefly, a moist cake (50 g) of Sepharose CL-4B was activated with 1,1′-carbonyldiimidazole (CDI) (1.2 g). After a 15 min reaction with CDI, the mixture was washed with 1 L of acetone, then reacted with 14 g of 6-aminocaproic acid in 90 mL of water. The pH of the slurry was adjusted to 10 with 1 M sodium hydroxide and stirred overnight at 4 °C. Ligand coupling proceeded with the addition of 600 mg of galactosamine and 300 mg of CDI followed by reaction for 2 h (*30*). The affinity resin (30 mL) was washed with 90 mL each of 1 M sodium chloride, 1 M sodium chloride in 0.1 M Tris pH 8.6, 1 M sodium chloride in 50 mM sodium formate pH 3.0, 1 M sodium chloride in 0.1 M Tris pH 8.6, water, and PBS.

Purification of Soybean Agglutinin (SBA). Soy flour (10 g) was dissolved in 200 mL of PBS and stirred overnight at 4 °C. The slurry was centrifuged at 9000 × *g* for 15 min, and the supernatant was applied to the affinity column (2.5 × 10 cm). The column was washed with 90 mL PBS until the $Abs_{280\ nm}$ of the effluent was below 0.02 units. The bound SBA was eluted with 90 mL of 0.2 M galactose in PBS (*30*). The SBA was pooled and dialyzed in 12−14 kDa MWCO tubing for 48 h against running water and freeze−dried.

Purification of Man 9 from SBA. Affinity-purified SBA was proteolytically digested to release Man 9 which was then purified following the method of Lis et al. (*31*). Briefly, SBA (600 mg in 8 mL 1 mM hydrochloric acid) was heat denatured at 50 °C for 15 min and digested with 12 mg of Pronase for 48 h at 37 °C. The digest was centrifuged at 4000 × *g* and the supernatant applied to a Sephadex G-50 column (1.5 × 170 cm) eluted with 10 mM acetic acid. The fractions (8.5 mL) were monitored by Abs 280 nm, and an 200 μL aliquot of each fraction was analyzed for carbohydrate by the phenol sulfuric assay (*32*). Carbohydrate containing fractions were pooled, concentrated, and repurified by gel filtration on Sephadex G-50. Man 9 containing fractionations were prepared in 1.5 mL of water then applied to a AG 50W-X2 cation exchange column (1.5 × 50 cm) eluted with 1.2 L of 1 v/v % pyridine/acetic acid, pH 3.2 while detecting carbohydrate by the phenol sulfuric assay. The Man 9 containing fractions eluting a 880 mL were pooled and freeze−dried. The recovery was estimated by phenol sulfuric assay to be 6.7 μmol (45%) based on 18.5 nmol of $Man_9GlcNAc_2Asn = 1\ AU_{490\ nm}$.

The purified Man 9 was analyzed by mass spectroscopy by preparing 2 nmol in 4 μL of 10 mM sodium chloride containing 0.5 mM of super 2,5-DHB. The sample was spotted on the target and analyzed by MALDI-TOF (Biflex III, Bruker) in reflectron mode resulting in the detection of masses of 2019.72 and 2041.66 *m*/*z* corresponding to [M + Na] and [M + 2Na]. Man 9 was analyzed by high-field NMR (600 MHz Varian) by preparing a 1 mM sample in D_2O with acetone as an internal standard. The chemical shift data corresponded with that published previously (*33*).

Synthesis of Cys-(Acr-Lys)$_4$. The nine amino acid peptide, Cys-(Acr-Lys)$_4$, was synthesized using standard Fmoc chemistry with HOBt and HBTU double coupling on a 30 μmol scale with an APEX 396 solid-phase peptide synthesizer using Fmoc-Lys(Acr) prepared as described previously (*34*). The peptide was cleaved from the resin and deprotected with 2 mL of TFA/TIS/H_2O (95:2.5:2.5 v/v/v) for 3 h, followed by precipitation in 40 mL of cold ether. The precipitate was collected by centrifugation at 4000 × *g* for 10 min, and reconstituted in 0.1 v/v % TFA. The peptide was preparatively purified on RP-HPLC by injecting 2 μmol onto a 2 × 25 cm Vydac C18 column eluted at 10 mL per min with 0.1% TFA and a 15−30% acetonitrile gradient over 45 min while detecting at $Abs_{280\ nm}$. The peptide was pooled, concentrated by rotary evaporation, reconstituted in 0.1 v/v % TFA, and then analyzed for purity by RP-HPLC, injecting 5 nmol onto a 0.47 × 25 cm Vydac C18 column eluted at 1 mL/min with 0.1% TFA and a gradient of 15−30% acetonitrile while detecting by positive-mode ESI-MS. The doubly charged ion was detected with an *m*/*z* of 928.7, resulting in an observed mass of 1855.4 *m*/*z* (calc = 1855.5 *m*/*z*). The synthesis resulted in a 17% isolated yield ($\varepsilon_{409\ nm} = 37\ 064\ M^{-1}\ cm^{-1}$) at >95% purity.

Synthesis of a Man 9 Glycopeptide. Man 9 (500 nmol) was prepared in 500 μL of 50 v/v % DMF and 100 mM sodium bicarbonate containing Boc-Tyr-NHS (5 μmol) and reacted for 3 h at RT. The reaction mixture was directly applied to a Sephadex G-25 column (0.5 × 50 cm) eluted with 10 mM acetic acid while detecting $Abs_{280\ nm}$. The Man 9 Tyr-Boc product peak eluting at 50 mL was concentrated by rotary evaporation and reconstituted in water. The product was analyzed for purity by analytical RP-HPLC eluting at 1 mL per min with 0.1% TFA and a 1−30% gradient of acetonitrile over 30 min while detecting by $Abs_{280\ nm}$ and by negative-mode ESI-MS. The doubly charged ion was detected with an *m*/*z* of 1129.4, resulting in a mass of 2260.8 *m*/*z* (calculated 2260.0 *m*/*z*). The Man 9 Tyr-Boc product was >95% pure and the yield ($\varepsilon_{280\ nm} = 1130\ M^{-1}\ cm^{-1}$) was 95%.

To conjugate Man 9 Tyr-Boc to Cys-(Acr-Lys)$_4$, the Boc group was removed from the Tyr and the amine terminus was derivatized with propionate maleimide, prior to reaction with Cys-(Acr-Lys)$_4$. The Boc group was removed by treating Man 9 Tyr-Boc (500 nmol) with 50 μL of 95% TFA for 5 min at RT, followed by freeze−drying to remove TFA. The yield of Man 9 Tyr was quantitative and LC-MS analysis established a mass of 2160.3 *m*/*z* consistent with the anticipated mass (2160.9 *m*/*z*). Man 9 Tyr (500 nmol) was reacted for 1 h with 3-maleimidoproprionic acid NHS ester (5 μmol) in 250 μL of 50 v/v % DMF and 100 mM sodium bicarbonate. The reaction mixture was fractionated on a Sephadex G-25 column (1.5 × 50 cm), eluting with 0.1% acetic acid while detecting $Abs_{280\ nm}$ The product peak (Man 9 Mal), eluting at 35 mL, was pooled and concentrated by rotary evaporation and purified to homogeneity on a semiprep Vydac C18 RP-HPLC column (2 × 25 cm) eluted at 10 mL per min with 0.1% acetic acid and a 30

min acetonitrile gradient (5−15%) resulting in a 23% isolated yield. LC-MS analysis in the negative mode revealed that the Man 9 Mal product produced an ion of 1156.1 *m/z*, resulting in a mass of 2314.2 *m/z*, closely corresponding to the anticipated mass of 2312.1.

To complete the glycopeptide synthesis, Man 9 Mal (500 nmol) was reacted with Cys-(Acr-Lys)$_4$ peptide (600 nmol) in 500 μL of 5 mM Hepes pH 7 for 2 h. The Man 9 glycopeptide product was purified from excess dimeric peptide on analytical RP-HPLC with a 30 min 15−30% acetonitrile gradient in 0.1% TFA. The purity and identity of the Man 9 glycopeptide were verified by analytical RP-HPLC detected by Abs$_{280\ nm}$ and positive-mode ESI-MS. The product peak was >95% pure and produced a triply charged ion detected with an *m/z* of 1390.0 that deconvoluted to an observed mass of 4167.0 *m/z* (calculated 4167.4 *m/z*). The recovery was 102 nmol, resulting in a 23% yield.

Man 9 Glycopeptide DNA Band Shift Assay. pGL3 (1 μg) was combined with 0.05, 0.2, 0.5, and 1 nmol of Man 9 glycopeptide. Each sample was incubated for 30 min before loading onto an agarose gel that was electrophoresed at 80 V for 60 min (*24*). The gel was stained with 0.1 mg per mL of ethidium bromide at 4 °C for 24 h, then photographed while illuminating on a transilluminator.

Thiazole Orange Displacement Assay. A control sample of pGL3 (1 μg) was combined with 40 nM thiazole orange in a total volume of 500 μL of 5 mM Hepes buffer pH 7.4. The Man 9 glycopeptide (0.2, 0.3, 0.4, 1, and 2 nmol) or Cys-(Acr-Lys)$_4$ peptide was added to pGL3 (1 μg) samples containing thiazole orange and incubated for 30 min, followed by measuring the fluorescence intensity at excitation 500 nm and emission 530 nm (*21*). The percent fluorescence intensity relative to control was plotted versus the stoichiometry of glycopeptide or peptide added to DNA to determine the equivalence point.

Glycopeptide DNA Polyplex Binding to DC-SIGN (+) and (−) CHO Cells. pGL3 plasmid (5 μg) was labeled with *Label* IT according to the manufacturer's instructions to prepare Cy5-DNA. The Man 9 glycopeptide (0.5 nmol) was combined with 1 μg Cy5-DNA in 60 μL of water and incubated for 30 min to form a polyplex. DC-SIGN (+) and (−) CHO cells (1 $\times$ 10^6) (*28*) were each plated in triplicate in 35 mm wells and grown in DMEM supplemented with 7% FBS and 1% nonessential amino acids for 24 h. CHO (+) and (−) cells were transfected for 24 h with 1 μg of Cy5-DNA polyplex. The CHO cells were lifted by treatment with 5 mL of 1 mM EDTA in PBS and concentrated by centrifugation by 2000 $\times$ *g*, before diluting to a final volume of 1 mL in PBS. The transfected CHO (+) and (−) cells were analyzed by FACS on a Becton Dickson LSRII with excitation 488 nm and emission 575 nm, and compared to untransfected CHO cells.

In Vitro Transfection with Glycopeptide DNA Polyplexes. DC-SIGN (+) CHO cells (1 $\times$ 10^5) were plated in 6-well plates in triplicate in 1 mL DMEM high glucose supplemented with 7% FBS and 1% MEM nonessential amino acids. After incubation for 24 h at 37 °C in 5% CO_2, the media was removed, and the cells were washed with 1 mL DPBS and replaced with 1 mL DMEM high glucose media supplemented with 2% FBS and 0.3% MEM nonessential amino acids.

Cells were transfected in triplicate for 24 h with pGL3 polyplexes (1 μg DNA and 0.6 nmol of glycopeptide in a total volume of 30 μL). The efficiency of glycopeptide DNA polyplex transfection was compared with PEI−DNA transfection performed by combining 1 μg DNA with 1.2 μg of PEI (N:P of 9) in100 μL of 5 mM Hepes, 270 mM mannitol, pH 7.4. After 24 h, cells were washed with 2 mL of DPBS and lysed with 0.5 mL of lysis buffer (25 mM Tris chloride, 1 mM EDTA, 8 mM magnesium chloride, 1% Triton X-100, pH 7.8) for 10 min at 4 °C. Cell lysates were scraped, transferred to 1.5 mL microcentrifuge tubes, and centrifuged for 10 min at 13 000 *g* (at 4 °C) to pellet cell debris. Lysis buffer (400 μL) and ATP (4.3 μL of a 165 mM solution at pH 7) were combined in a test tube, mixed briefly, and placed in the luminometer. The relative light units were determined with 10 s integration after automatic injection of 100 μL of 0.43 mM D-luciferin. Protein concentrations were measured by a BCA assay with bovine serum albumin as a standard (*35*). The amount of luciferase recovered in each sample was normalized to milligrams of protein and reported as the mean with standard deviation obtained from triplicate transfections.

RESULTS

A strategy was developed to reversibly bind a high-mannose N-glycan to plasmid DNA for the purpose of targeted uptake and expression of a reporter gene in cells expressing the DC-SIGN receptor. While in the present study glycopeptide mediated gene transfer was only tested in a model cell system, the ultimate purpose of this gene delivery system would be to selectively transfect dendritic cells in humans to improve the efficacy of DNA vaccines (*36*).

The polyacridine peptide was designed to reversibly bind to plasmid DNA by a combination of intercalation and ionic interaction as we and others have previously reported (*19, 23, 25, 26, 37*). The solid-phase synthesis of Cys-(Acr-Lys)$_4$ necessitated the large-scale synthesis of Fmoc-Lys(Acr) as an unnatural amino acid. Using this approach, a high-affinity polyacridine peptide containing an N-terminal Cys was obtained in good yield.

The high-mannose N-glycan is a known ligand for DC-SIGN receptor and is the only N-glycan present on SBA (*3, 38*). Because SBA is a galactose-specific lectin, it is readily purified in a single affinity chromatography step. The affinity purification of SBA is essentially the same as first reported by Sharon (*38*), with the exception that the affinity resin was prepared by attaching galactosamine to 6-aminohexanoic acid functionalized Sepharose resin prepared using CDI as reported by Bethel and Ayers (*29*). This approach afforded the scalable preparation of the column resin without the use of cyanogen bromide.

The high-mannose N-glycan on SBA is not easily released by direct treatment with N-glycosidase F. Likewise, affinity purified SBA is very resistant to digestion with trypsin. Consequently, as first described by Sharon, SBA is most efficiently converted to peptides by prolonged Pronase digestion which produces the Man 9 N-glycan possessing a single Asn (*38*). Starting with 10 g of soy flour, the resulting Man 9 N-glycan was purified in good yield (6.7 μmols, 45%) using a combination of gel filtration and cation exchange chromatography as described (*38, 39*). High-field ^{1}H-NMR analysis of the purified Man 9 N-glycan established the presence of nine mannose residues based on the resonance frequency of the anomeric proton for each (*33*). MALDI-TOF analysis was also consistent with the isolation of Man 9 N-glycan containing a single Asn residue.

The conjugation of the Man 9 N-glycan to Cys-(Acr-Lys)$_4$ required functionalization through the Asn residue (Figure 1). To facilitate reaction monitoring by RP-HPLC, the Man 9 N-glycan was first modified by attaching Boc-Tyr to the N-terminus. Analysis of the Man 9 Tyr-Boc obtained from gel filtration chromatography revealed a single peak on analytical RP-HPLC with retention time of 19 min when detected by Abs280 nm (Figure 2A). Removal of the Boc group by treatment with TFA resulted in a shift to an earlier retention time, confirming complete removal of Boc (Figure 2B). The resulting amine terminus on Tyr was then modified with a propionate maleimide to provide a functional group that reacts with the Cys residue on Cys-(Acr-Lys)4. The resulting Man 9 Mal

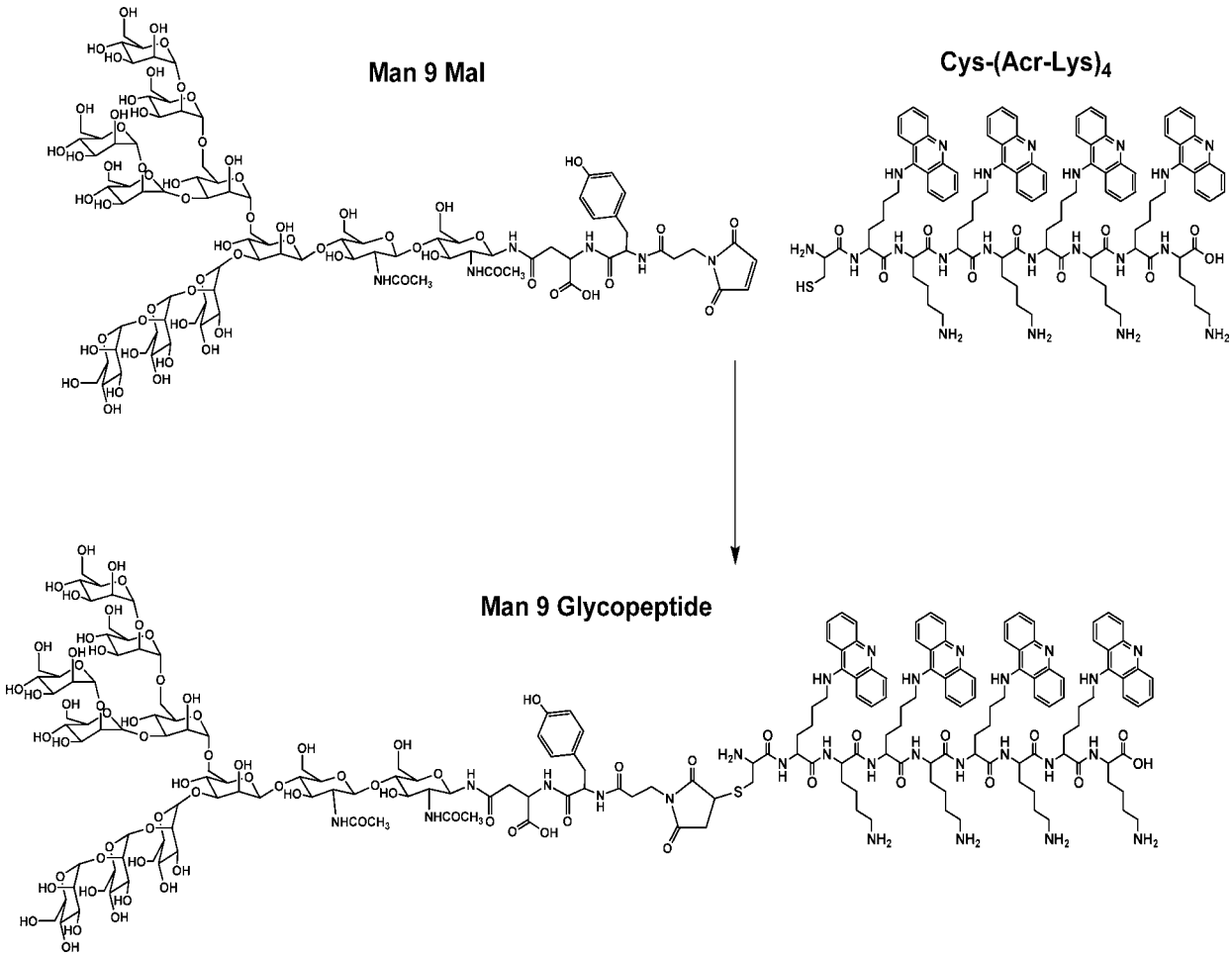


Figure 1. Synthesis of a Man 9 glycopeptide. A high-mannose N-glycan containing a single Asn residue was purified from soybean agglutinin and then functionalized to possess an N-terminal Tyr and propionate maleimide. The resulting Man 9 Mal was reacted with Cys-(Acr-Lys)$_4$, which was prepared by solid-phase peptide synthesis using Fmoc-Lys(Acr). The resulting Man 9 glycopeptide possesses affinity for DC-SIGN and for binding to plasmid DNA through polyintercalation.

N-glycan product was also purified by gel filtration and produced a single product when analyzed on RP-HPLC (Figure 2C). Each N-glycan product described produced ESI-MS consistent with the reported structure.

To complete the synthesis of the Man 9 glycopeptide, the Man 9 Mal was reacted with nearly a stoichiometric amount of Cys-(Acr-Lys)$_4$ (Figure 1). In addition to the desired glycopeptide product, a dimeric peptide product formed. The RP-HPLC analysis of the purified Man 9 glycopeptide established its high purity and produced an ESI-MS consistent with the reported structure (Figure 2D, inset).

To examine the binding of the Man 9 glycopeptide to DNA, an agarose gel electrophoresis band shift assay was used. The electrophoretic migration of DNA was significantly retarded at increasing glycopeptide to DNA stoichiometry such that at 0.4 nmol of glycopeptide per μg of DNA or higher the band shift was complete (Figure 3). In addition, the DNA bands were not visible by incorporating ethidium bromide into the gel prior to electrophoresis. Only poststaining with ethidium bromide following electrophoresis resulted in displacement of the polyacridine containing glycopeptides and the detection of DNA.

An additional analysis of glycopeptide DNA binding affinity utilized a fluorophore displacement assay. Increasing the stoichiometry of Man 9 glycopeptide to DNA resulted in the displacement of thiazole orange from DNA as determined by a decrease in fluorescence intensity. An asymptote in the fluorescence intensity at 0.4 nmol Man 9 glycopeptide per 1 μg DNA established this as the equivalence point for polyplex formation (Figure 4). By comparison, Cys-(Acr-Lys)$_4$ appears to have slightly greater DNA binding affinity. Based on this and the results in Figure 3, a stoichiometry of 0.5 nmol per μg of DNA was used to prepare polyplexes and evaluate cell uptake and in vitro gene transfer.

The uptake of Man 9 glycopeptide Cy5-DNA polyplexes into CHO cells, either with (+) or without (−) stably transfected DC-SIGN receptor, was assayed by FACS analysis (Figure 5). A 24 h 37 °C incubation of Man 9 glycopeptide Cy5-DNA polyplexes with CHO (+) and (−) cells was used to simulate conditions used for in vitro transfection. FACS analysis revealed uptake of Man 9 glycopeptide Cy5-DNA polyplexes in both CHO (+) and (−) cells relative to untreated cells. CHO (−) cells were able to bind Man 9 glycopeptide Cy5-DNA polyplexes nonspecifically through ionic interaction. However, the cell uptake in CHO (+) cells was 10−50-fold higher than CHO (−) cells based on the intensity of fluorescence (Figure 5). The results suggest that DC-SIGN on CHO (+) cells increases the uptake of Man 9 glycopeptide Cy5-DNA polyplexes by receptor mediated endocytosis.

To determine if the increased uptake of Man 9 glycopeptide DNA polyplexes by CHO (+) cells results in increased gene expression, a series of gene transfer experiments were performed in CHO (+) and (−) cells. The results established that PEI-DNA polyplexes were the most efficient in gene transfer but were not selective for (+) or (−) cells (Figure 6). The Cys-(Acr-Lys)$_4$ peptide mediated low-level gene expression in CHO cells but did not demonstrate selectivity. In contrast, Man 9

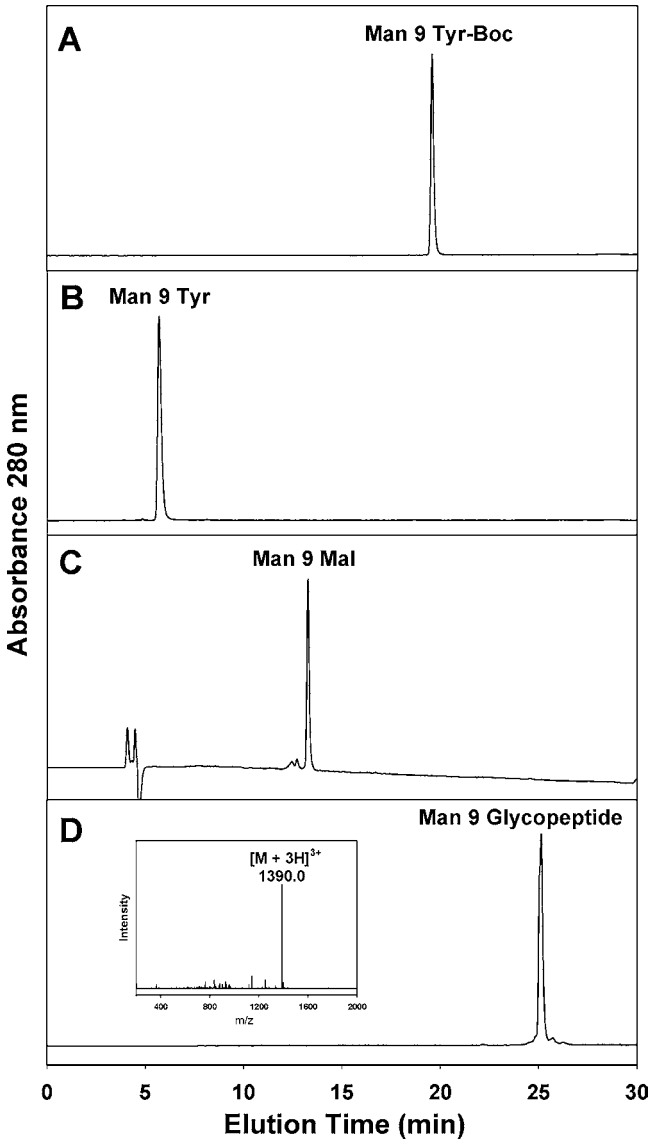


Figure 2. RP-HPLC Analysis of Man 9 derivatives. Man 9 Asn obtained from SBA was N-terminally modified with Boc-Tyr then analyzed for purity by RP-HPLC (panel A). The removal of Boc from Tyr with TFA results in an earlier retention time (panel B). Conjugation of an N-terminal propionate maleimide increased the retention time (panel C) and conjugation of Man 9 Mal with Cys-(Acr-Lys)$_4$ resulted in the formation of Man 9 glycopeptide that rechromatographed as a single peak on RP-HPLC (panel D). The inset in panel D illustrates the ESI-MS analysis of the purified glycopeptide. See figure 1 for structures.

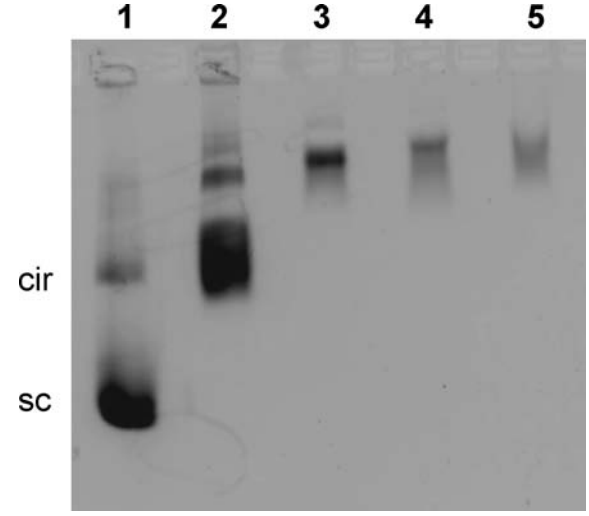


Figure 3. Gycopeptide DNA binding by agarose gel band shift. A DNA band shift assay was performed by adding increasing amounts of glycopeptide to plasmid DNA. Lane 1 represents control plasmid DNA (1 μg), whereas lanes 2−5 are the result of adding 0.2, 0.4, 0.6, and 1 nmol of Man 9 glycopeptide to 1 μg of DNA.

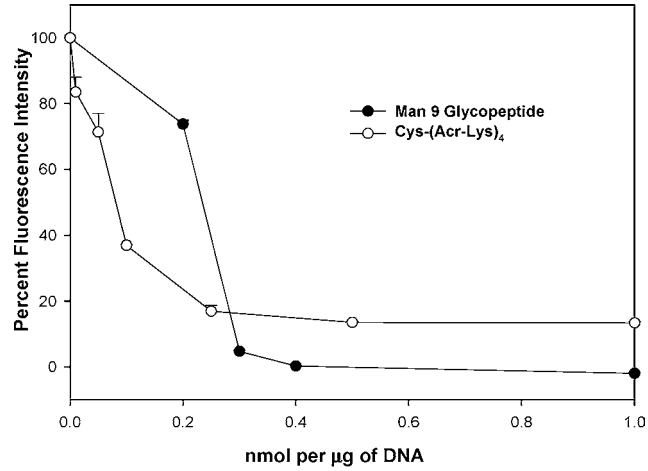


Figure 4. Glycopeptide DNA binding by fluorophore displacement assay. The displacement of a thiazole orange intercalator dye by increasing amounts of Man 9 glycopeptide or Cys-(Acr-Lys)$_4$ results in an asymptote in the fluorescence intensity at 0.2−0.4 nmol per μg of DNA.

glycopeptide DNA polyplexes mediated approximately 100-fold greater gene expression in CHO (+) cells relative to an identical experiment conducted in CHO (−) cells (Figure 6). These results are consistent with the cell uptake studies and support the hypothesis that the DC-SIGN receptor can facilitate receptor-mediated endocytosis of DNA polyplexes.

DISCUSSION

The clinical application of DNA vaccines for the treatment of disease is currently limited by the low efficiency of nonviral delivery systems (*36, 40*). While it will be possible to optimize the DNA vector, it is also necessary to improve the delivery system. A large body of growing evidence suggest that targeting of DNA, as well as adjuvant, to enter dendritic cells leads to an enhanced immune response (*9, 36, 40*). It has been demonstrated that DC-SIGN is an endocytosing, cell surface C-type lectin that can be used to target proteins and DNA into dendritic cells (*9*). Given that the specificity of DC-SIGN is for mannose or Le^X on N-glycans, we explored an approach to reversibly attach a high-mannose N-glycan ligand to plasmid DNA to establish DNA uptake and gene expression in cells expressing DC-SIGN.

To achieve this, a well-known purification of a high-mannose N-glycan from soybean agglutinin was used (*38*). This required the development of a large-scale galactose affinity column by applying a carbodiimide coupling strategy. The purified N-glycan was then systematically modified on the Asn N-terminus to allow coupling to a DNA binding peptide. The conjugation of Boc-Tyr resulted in introduction of a hydrophobic chromophore that could be iodinated. Removal of Boc proceeded in neat TFA to afford the Tyr amine. Modification of the amine with a propionate possessing a maleimide group resulted in a Man 9 Mal that reacted with a thiol on the peptide.

The polyacridine peptide was modeled after similar peptides first reported by Ueyama (*27*). However, a Cys residue was included on the N-terminus to allow specific coupling to Man 9 Mal. This conjugation led to a Man 9 glycopeptide that possessed affinity for DC-SIGN and DNA. The DNA binding

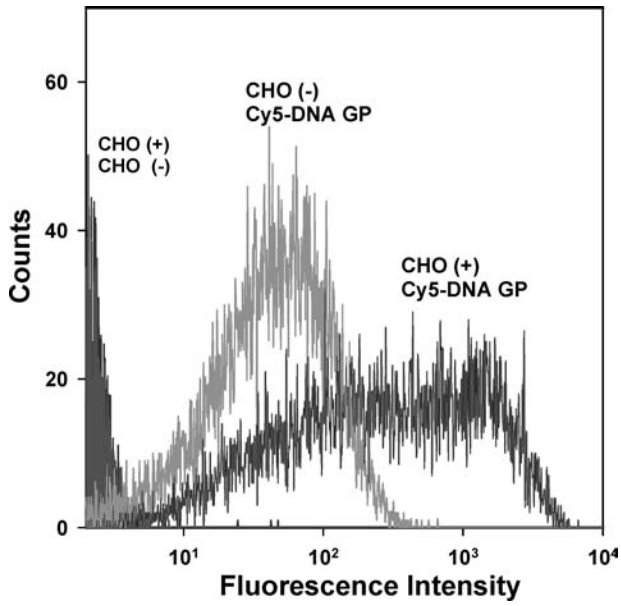


Figure 5. Cy5-DNA glycopeptide polyplex binding to DC-SIGN expressing CHO (+) cells. The results of FACS analysis of Cy5-DNA Man 9 glycopeptide polyplex mediated uptake in DC-SIGN CHO (+) and (−) cells are illustrated. The fluorescence intensity in CHO (+) was nearly 10-fold higher than CHO (−) cells, whereas untreated CHO (+) or (−) cells demonstrated negligible fluorescence intensity.

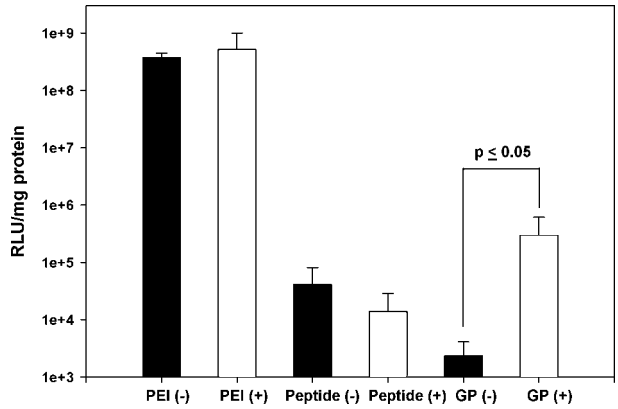


Figure 6. In vitro transfection of CHO (+) and (−) DC-SIGN cells. The result of in vitro transfection of CHO (+) (open bar) and (−) (closed bar) with different gene transfer agents is illustrated. Transfection of CHO (+) and (−) cells with PEI DNA polyplexes (N:P of 9) leads to high level of luciferase expression which is nonselective. Likewise, transfection with Cys-$(Acr\text{-}Lys)_4$ peptide polyplexes results in lower levels of nonselective gene transfer. Alternatively, transfection with Man 9 glycopeptide (GP) polyplexes results in a 100-fold selective gene transfer in CHO (+) cells over CHO (−) cells. Each result is the mean and standard deviation of six independent transfections.

affinity of a polyacridine peptide is related to the number of acridines and the identity of the spacing amino acid (*19*). Two different experiments established that the glycopeptide binds to DNA. A band shift assay and a fluorophore displacement assay both confirmed that the Man 9 glycopeptide binds maximally to DNA at 0.4 nmol per μg of DNA. The binding affinity for the unglycosylated peptide was slightly greater than that of the glycopeptide.

The ability of DC-SIGN to bind to Man 9 glycopeptide DNA polyplexes was established using a CHO cell line stably transfected with the human DC-SIGN receptor. The results of FACS analysis using Cy5-DNA glycopeptide polyplexes confirmed preferential binding to CHO (+) cells compared to CHO (−) cells. It should be noted that Cy5-DNA glycopeptide polyplexes bind weakly to CHO (−) cells perhaps due to the cationic nature of the polyplexes.

The results of FACs analysis compare favorably with those of gene transfer studies. A 100-fold increase in gene transfer was determined when transfecting CHO (+) cells with glycopeptide DNA polyplexes compared to the same transfection of CHO (−) cells. Unglycosylated peptide formed cationic polyplexes that mediated nonspecific gene transfer. While the levels of gene transfer are much lower than that mediated by PEI DNA, the selectivity of Man 9 glycopeptide mediated gene transfer supports the hypothesis that DC-SIGN binds the ligand and transports the DNA polyplex into the cell.

Taken together, this study demonstrates the first application of a high-mannose N-glycan to mediated gene transfer via DC-SIGN, and demonstrates the application of a polyacridine anchor peptide to reversibly bind Man 9 to DNA. These results may be expanded to eventually improve the efficacy of DNA vaccines for use in humans.

ACKNOWLEDGMENT

We gratefully acknowledge the gift of DC-SIGN expressing CHO cells from Drs. Chae Gyu Park and Ralph M. Steinman and also acknowledge support for this work from NIH Grant DK066212 and NIH Fellowship Predoctoral Training Grant Support for KA (T32 GM067795).

LITERATURE CITED

(1) Banchereau, J., and Steinman, R. M. (1998) Dendritic cells and the control of immunity. *Nature 392*, 245–52.

(2) Feinberg, H., Mitchell, D. A., Drickamer, K., and Weis, W. I. (2001) Structural basis for selective recognition of oligosaccharides by DC-SIGN and DC-SIGNR. *Science 294*, 2163–6.

(3) Feinberg, H., Castelli, R., Drickamer, K., Seeberger, P. H., and Weis, W. I. (2007) Multiple modes of binding enhance the affinity of DC-SIGN for high mannose N-linked glycans found on viral glycoproteins. *J. Biol. Chem. 282*, 4202–9.

(4) Guo, Y., Feinberg, H., Conroy, E., Mitchell, D. A., Alvarez, R., Blixt, O., Taylor, M. E., Weis, W. I., and Drickamer, K. (2004) Structural basis for distinct ligand-binding and targeting properties of the receptors DC-SIGN and DC-SIGNR. *Nat. Struct. Mol. Biol. 11*, 591–8.

(5) Singh, S. K., Stephani, J., Schaefer, M., Kalay, H., Garcia-Vallejo, J. J., den Haan, J., Saeland, E., Sparwasser, T., and van Kooyk, Y. (2009) Targeting glycan modified OVA to murine DC-SIGN transgenic dendritic cells enhances MHC class I and II presentation. *Mol. Immunol. 47*, 164–74.

(6) Adams, E. W., Ratner, D. M., Seeberger, P. H., and Hacohen, N. (2008) Carbohydrate-mediated targeting of antigen to dendritic cells leads to enhanced presentation of antigen to T cells. *ChemBioChem 9*, 294–303.

(7) Aarnoudse, C. A., Bax, M., Sanchez-Hernandez, M., Garcia-Vallejo, J. J., and van Kooyk, Y. (2008) Glycan modification of the tumor antigen gp100 targets DC-SIGN to enhance dendritic cell induced antigen presentation to T cells. *Int. J. Cancer 122*, 839–46.

(8) Ramakrishna, V., Treml, J. F., Vitale, L., Connolly, J. E., O'Neill, T., Smith, P. A., Jones, C. L., He, L. Z., Goldstein, J., Wallace, P. K., Keler, T., and Endres, M. J. (2004) Mannose receptor targeting of tumor antigen pmel17 to human dendritic cells directs anti-melanoma T cell responses via multiple HLA molecules. *J. Immunol. 172*, 2845–52.

(9) Nchinda, G., Kuroiwa, J., Oks, M., Trumpfheller, C., Park, C. G., Huang, Y., Hannaman, D., Schlesinger, S. J., Mizenina, O., Nussenzweig, M. C., Uberla, K., and Steinman, R. M. (2008) The efficacy of DNA vaccination is enhanced in mice by targeting the encoded protein to dendritic cells. *J. Clin. Invest. 118*, 1427–36.

(10) Srinivas, R., Karmali, P. P., Pramanik, D., Garu, A., Venkata Mahidhar, Y., Majeti, B. K., Ramakrishna, S., Srinivas, G., and Chaudhuri, A. (2010) Cationic amphiphile with shikimic acid headgroup shows more systemic promise than its mannosyl analogue as DNA vaccine carrier in dendritic cell based genetic immunization. *J. Med. Chem.*

(11) Zhou, X., Liu, B., Yu, X., Zha, X., Zhang, X., Wang, X., Chen, Y., Chen, Y., Chen, Y., Shan, Y., Jin, Y., Wu, Y., Liu, J., Kong, W., and Shen, J. (2007) Enhance immune response to DNA vaccine based on a novel multicomponent supramolecular assembly. *Biomaterials 28*, 4684–92.

(12) Zhou, X., Liu, B., Yu, X., Zha, X., Zhang, X., Chen, Y., Wang, X., Jin, Y., Wu, Y., Chen, Y., Shan, Y., Chen, Y., Liu, J., Kong, W., and Shen, J. (2007) Controlled release of PEI/DNA complexes from mannose-bearing chitosan microspheres as a potent delivery system to enhance immune response to HBV DNA vaccine. *J. Controlled Release 121*, 200–207.

(13) Lu, Y., Kawakami, S., Yamashita, F., and Hashida, M. (2007) Development of an antigen-presenting cell-targeted DNA vaccine against melanoma by mannosylated liposomes. *Biomaterials 28*, 3255–62.

(14) Tang, C. K., Lodding, J., Minigo, G., Pouniotis, D. S., Plebanski, M., Scholzen, A., McKenzie, I. F., Pietersz, G. A., and Apostolopoulos, V. (2007) Mannan-mediated gene delivery for cancer immunotherapy. *Immunology 120*, 325–35.

(15) Hattori, Y., Kawakami, S., Lu, Y., Nakamura, K., Yamashita, F., and Hashida, M. (2006) Enhanced DNA vaccine potency by mannosylated lipoplex after intraperitoneal administration. *J. Gene Med. 8*, 824–34.

(16) Hattori, Y., Kawakami, S., Suzuki, S., Yamashita, F., and Hashida, M. (2004) Enhancement of immune responses by DNA vaccination through targeted gene delivery using mannosylated cationic liposome formulations following intravenous administration in mice. *Biochem. Biophys. Res. Commun. 317*, 992–9.

(17) Hattori, Y., Kawakami, S., Nakamura, K., Yamashita, F., and Hashida, M. (2006) Efficient gene transfer into macrophages and dendritic cells by in vivo gene delivery with mannosylated lipoplex via the intraperitoneal route. *J. Pharmacol. Exp. Ther. 318*, 828–34.

(18) Un, K., Kawakami, S., Suzuki, R., Maruyama, K., Yamashita, F., and Hashida, M. Enhanced transfection efficiency into macrophages and dendritic cells by a combination method using mannosylated lipoplexes and bubble liposomes with ultrasound exposure. *Hum. Gene Ther. 21*, 65−74.

(19) Baumhover, N. J., Anderson, K., Fernandez, C. A., and Rice, K. G. (2010) Synthesis and in vitro testing of new potent polyacridine-melittin gene delivery peptides. *Bioconjugate Chem. 21*, 74–86.

(20) Collard, W. T., Evers, D. L., and McKenzie, D. L. (2000) Synthesis of homogenous glycopeptides and their utility as DNA condensing agents. *Carbohydr. Res. 323*, 176–184.

(21) Wadhwa, M. S., Collard, W. T., Adami, R. C., McKenzie, D. L., and Rice, K. G. (1997) Peptide-mediated gene delivery: influence of peptide structure on gene expression. *Bioconjugate Chem. 8*, 81–8.

(22) Collard, W. T., Yang, Y., Kwok, K. Y., Park, Y., and Rice, K. G. (2000) Biodistribution, metabolism, and in vivo gene expression of low molecular weight glycopeptide polyethylene glycol peptide DNA co-condensates. *J. Pharm. Sci. 89*, 499–512.

(23) Fernandez, C., A., Baumhover, N., J., Anderson, K., and Rice, K. G. (2010) Discovery of metabolically stablized electronegative polyacridine-PEG peptide DNA open polyplexes. *Bioconjugate Chem. 21*, 723–30.

(24) Adami, R. C., Collard, W. T., Gupta, S. A., Kwok, K. Y., Bonadio, J., and Rice, K. G. (1998) Stability of peptide-condensed plasmid DNA formulations. *J. Pharm. Sci. 87*, 678–683.

(25) Shiraishi, T., Hamzavi, R., and Nielsen, P. E. (2005) Targeted Delivery of plasmid DNA into the nucleus of cells via nuclear localization signal peptide conjugated to DNA intercalating bis- and trisacridines. *Bioconjugate Chem. 16*, 1112–1116.

(26) Haensler, J., and Szoka, J. F. C. (1993) Synthesis and characterization of a trigalactosylated bisacridine compound to target DNA to hepatocytes. *Bioconjugate Chem. 4*, 85–93.

(27) Ueyama, H., Takagi, M., Waki, M., and Takenaka, S. (2001) DNA binding behavior of peptides carrying acridinyl units: First example of effective poly-intercalation. *Nucleic Acids Symp. Ser. (Oxford) 1*, 163–164.

(28) Granelli-Piperno, A., Pritsker, A., Pack, M., Shimeliovich, I., Arrighi, J. F., Park, C. G., Trumpfheller, C., Piguet, V., Moran, T. M., and Steinman, R. M. (2005) Dendritic cell specific intercellular adhesion molecule 3-grabbing nonintegrin/CD209 is abundant on macrophages in the normal human lymph node and is not required for dendritic cell stimulation of the mixed leukocyte reaction. *J. Immunol. 7*, 4260–4273.

(29) Bethell, G. S., Ayers, J. S., Hancock, W. S., and Hearn, M. T. (1979) A novel method of activation of cross-linked agarose with 1,1′-carbonyldiimidazole which gives a matrix for affinity chromatography devoid of additional charged groups. *J. Biol. Chem. 254*, 2572–4.

(30) Allen, A. K., and Neuberger, A. (1975) A simple method for the preparation of an affinity absorbent for soybean agglutinin using galactosamine and CH-Sepharose. *FEBS Lett. 50*, 362–4.

(31) Lis, H., and Sharon, N. (1978) Soybean agglutinin--a plant glycoprotein. structure of the carbohydrate unit. *J. Biol. Chem. 253*, 3468–3476.

(32) Dubois, M., Gilles, K., Hamilton, J. K., Rebers, P. A., and Smith, F. (1951) A colorimetric method for the determination of sugars. *Nature 168*, 167.

(33) Dorland, L., van Halbeck, H., Vliegenthart, J. F. G., Lis, H., and Sharon, N. (1981) Primary structure of the carbohydrate chain of soybean agglutinin. a reinvestigation by high resolution 1H NMR spectroscopy. *J. Biol. Chem. 256*, 7708–7711.

(34) Tung, C., Zhu, T., Lackland, H., and Stein, S. (1992) An acridine amino acid derivative for use in Fmoc peptide synthesis. *Pept. Res. 5*, 115–8.

(35) Smith, P. K., Krohn, R. I., Hermanson, G. T., Mallia, A. K., Gartner, F. H., Provenzano, M. D., Fujimoto, E. K., Goeke, N. M., Olson, B. J., and Klenk, D. C. (1985) Measurement of protein using bicinchoninic acid. *Anal. Biochem. 150*, 76–85.

(36) Kutzler, M. A., and Weiner, D. B. (2008) DNA vaccines: ready for prime time? *Nat. Rev. Genet. 9*, 776–88.

(37) Boulanger, C., Di Giorgio, C., and Vierling, P. (2005) Synthesis of acridine-nuclear localization signal (NLS) conjugates and evaluation of their impact on lipoplex and polyplex-based transfection. *Eur. J. Med. Chem. 40*, 1295–306.

(38) Lis, H., Sharon, N., and Katchalski, E. (1966) Soybean hemagglutinin, a plant glycoprotein. I. Isolation of a glycopeptide. *J. Biol. Chem. 241*, 684–689.

(39) Gordon, J. A., Blumberg, S., Lis, H., and Sharon, N. (1972) Purification of soybean agglutinin by affinity chromatography of sepharose-N-e-aminocaproyl-B-D-galactopyranosylamine. *FEBS Lett. 24*, 193–196.

(40) Kutzler, M. A., and Weiner, D. B. (2004) Developing DNA vaccines that call to dendritic cells. *J. Clin. Invest. 114*, 1241–4.

BC1000824

Glycan Encapsulated Gold Nanoparticles Selectively Inhibit Shiga Toxins 1 and 2

Ashish A. Kulkarni,[†] Cynthia Fuller,[‡] Henry Korman,[†] Alison A. Weiss,*[,‡] and Suri S. Iyer*[,†]

UC Chemical and Biosensors group, Department of Chemistry, University of Cincinnati, Cincinnati, Ohio 45221-0172, and Department of Biochemistry, Molecular Genetics, Biochemistry and Microbiology, University of Cincinnati, Cincinnati, Ohio 45267-0524. Received February 24, 2010; Revised Manuscript Received July 7, 2010

Shiga toxins (Stx) released by *Escherichia coli* O157:H7 and *Shigella dysentriae* cause life-threatening conditions that include hemolytic uremic syndrome (HUS), kidney failure, and neurological complications. Cellular entry is mediated by the B-subunit of the AB_5 toxin, which recognizes cell surface glycolipids present in lipid raft-like structures. We developed gold glyconanoparticles that present a multivalent display similar to the cell surface glycolipids to compete for these toxins. These highly soluble glyconanoparticles were nontoxic to the Vero monkey kidney cell line and protected Vero cells from Stx-mediated toxicity in a dose-dependent manner. The inhibition is highly dependent on the structure and density of the glycans; selective inhibition of Stx1 and the more clinically relevant Stx2 was achieved. Interestingly, natural variants of Stx2, Stx2c, and Stx2d possessing minimal amino acid variation in the receptor binding site of the B-subunit or changes in the A-subunit were not neutralized by either the Stx1- or Stx2-specific gold glyconanoparticles. Our results suggest that tailored glyconanoparticles that mimic the natural display of glycans in lipid rafts could serve as potential therapeutics for Stx1 and Stx2. However, a few amino acid changes in emerging Stx2 variants can change receptor specificity, and further research is needed to develop receptor mimics for the emerging variants of Stx2.

INTRODUCTION

Shiga toxin (Stx) is the major pathogenic determinant of several Gram negative bacteria including *Escherichia coli* O157:H7 and *Shigella dysentriae*. Of the estimated 70 000 *E. coli* O157:H7 cases of disease per year in the United States, 10−15% develop hemolytic uremic syndrome (HUS); 3−5% succumb during the acute phase of the disease and an equivalent number suffer brain damage and renal failure (*1*). Treatment of this disease is mostly supportive, as postdiarrheal antibiotic treatment enhances toxin production and progression toward HUS (*2*). Therefore, there is a great need to develop competitive inhibitors as prophylactics or therapeutics for this untreatable disease.

Stx is a member of the AB_5 family of toxins. There are two major antigenic forms, Stx1 and Stx2, of which Stx2 is more potent than Stx1 (*3*). The A-subunit exhibits RNA N-glycosidase catalytic activity and cleaves a single adenine base from the host cell 28S rRNA, rendering the ribosome incapable of protein synthesis, leading to cell death. The B, or binding, subunit is a homopentamer with pentaradial symmetry that binds to globotriaosylceramide (Gb3, Figure 1A) in lipid rafts on the cell surface and ultimately delivers the A-subunit to its cytoplasmic target (*4*). Several designer ligands bearing multiple copies of carbohydrate portion (Pk trisaccharide) of Gb3 to neutralize the action of Stx have been synthesized. Some of these constructs have been demonstrated to possess subnanomolar binding affinities and inhibit the toxins in animal models (*5*−*9*). Unfortunately, phase I human clinical trials using some of these novel compounds were not very promising (*10*). A possible reason could be that Stx1, the less potent toxin, and not the more potent clinically significant variant Stx2, was neutralized by these tailored glycoconjugates. Epidemiological studies indicate that *E. coli* O157:H7 infections that lead to the life-threatening HUS are mainly associated with strains that produce Stx2 and not Stx1 (*11*). Primate and murine models of disease indicate that Stx2 is more potent than Stx1 (*3, 12*). In addition, the two forms of toxin display very different tissue localization preferences 1 h and 24 h postinjection in mice (*3, 13*). These results suggest that, while both Stx1 and Stx2 display a gross affinity for Gb3, they also recognize fine differences in glycan display associated with different organ systems, and these differences in receptor recognition likely influence toxin potency. Despite the differences in potency between the two toxins, development of therapeutics for both variants is ideal because strains of bacteria can produce both toxins. Additionally, since genes for the toxins can be readily exchanged, commensal bacteria can also produce the variants (*14*). Indeed, the CDC recommends testing for the variants and not just *E. coli* O157:H7 (*15*).

Using an ELISA platform, we recently identified novel ligands that bind specifically to Stx2 with high affinity and not to Stx1 (*16*). The major difference between these ligands and Pk trisaccharide is the presence of N-acetyl groups at the 2 position of the galactose moiety. (Figure 1B) (*17*). On the basis of these discoveries, we developed nanoparticles as potential therapies to inhibit both variants.

We used noble metal nanoparticles to obtain a multivalent display as these nanoparticles are increasingly being used for a variety of applications that include cancer imaging (*18, 19*), self-assembled nano/microstructures (*20, 21*), targeted delivery (*22, 23*), and antiadhesives (*24*). Glycan encapsulated gold nanoparticles (GNP) are excellent biomaterials as they offer a multivalent display of glycans similar to the glycocalyx structures covering the surface of cells. Additionally, these materials offer several advantages that include water solubility, ease of preparation, stability, cost, and absence of toxicity (*25*−*27*). GNPs have been used for the detection of lectins (*28*) and toxins (*29, 30*), capture of *E. coli* (*30*), presymptomatic imaging of brain disease (*31*), and

* E-mail: alison.weiss@uc.edu; suri.iyer@uc.edu. Fax: 1 513 556 9239.

[†] UC Chemical and Biosensors group, Department of Chemistry.

[‡] Department of Biochemistry, Molecular Genetics and Microbiology.

10.1021/bc100095w © 2010 American Chemical Society
Published on Web 07/29/2010

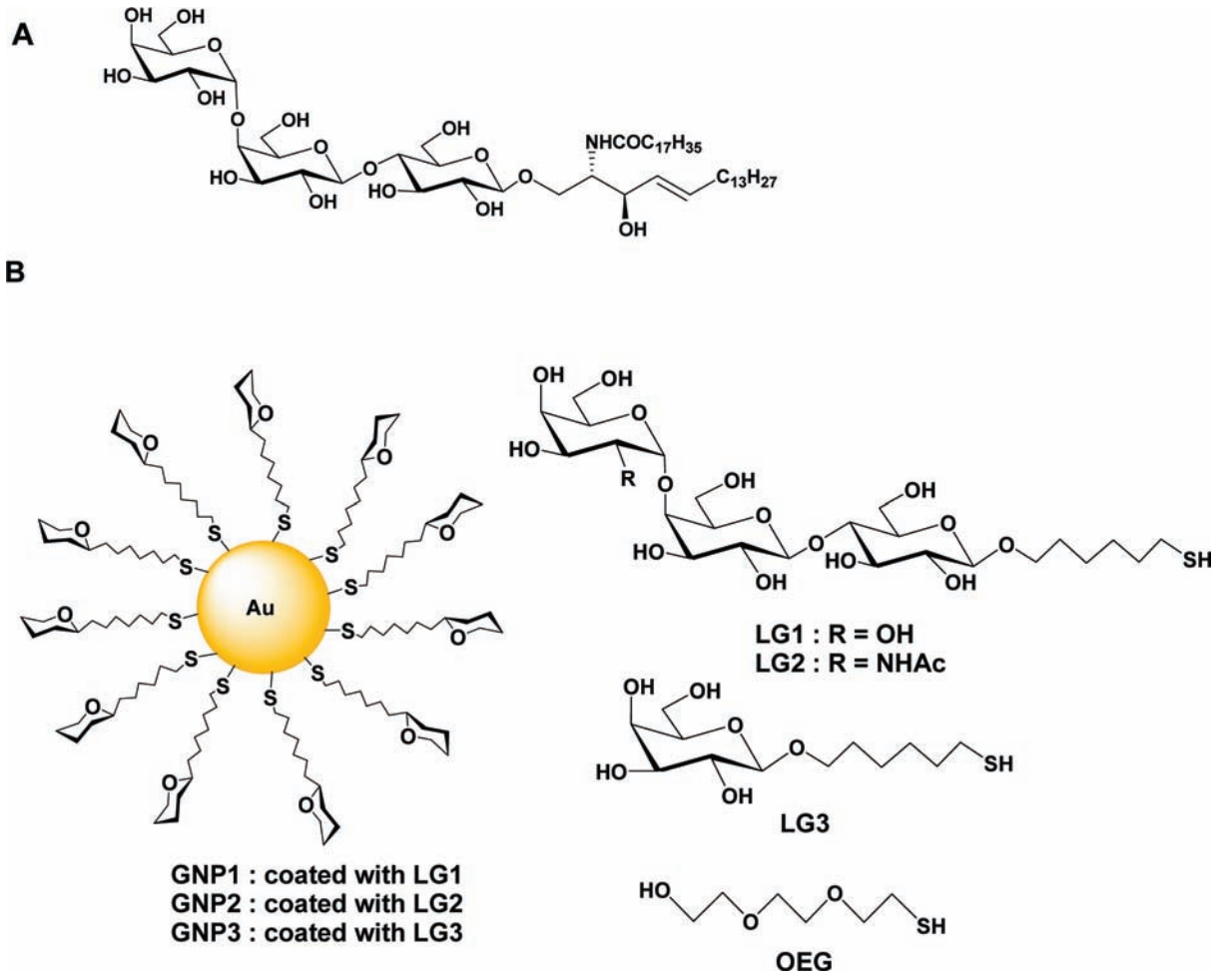


Figure 1. Relevant glycans. (A) Structure of native Gb3. (B) Representation of the gold glyconanoparticle and the structures of the three glycans with linkers terminated in thiol.

the inhibition of melanoma cells to the endothelium (*32*). GNPs have also been used to examine weak glycan−glycan interactions (*33*−*35*). While examples of small molecule encapsulated nanoparticle as antiadhesives to competitively inhibit HIV (*36, 37*), monkey pox (*38*), and hepatitis B viruses (*39*) have been reported, GNPs for the inhibition of toxins and pathogens are limited despite the significant advantages offered by these biomaterials.

In this study, we developed different analogues of Pk trisaccharide, the glycan that exhibits preferential binding to Stx (Figure 1A), and coated them onto gold nanoparticles. Next, we assessed the ability of GNPs coated with Pk trisaccharide analogues to neutralize Stx in a protein synthesis inhibition assay. We found that these GNPs are excellent inhibitors of two variants of Stx. We also found that inhibition is highly dependent on the structure and density of the glycan and, additionally, the structure of the toxin.

EXPERIMENTAL PROCEDURES

Materials. All chemical reagents were of analytical grade, used as supplied without further purification unless indicated. Acetic anhydride and acetyl chloride were distilled under inert atmosphere and stored under argon. 4 Å molecular sieves were stored in an oven (>130 °C) and cooled in vacuo. The acidic ion-exchange resin used was Dowex-50 and Amberlite (H+ form). Analytical thin layer chromatography (TLC) was conducted on silica gel 60-F254 (Merck). Plates were visualized under UV light and/or by treatment with acidic cerium ammonium molybdate followed by heating. Column chromatography was conducted using silica gel (230−400 mesh) from Qualigens. ^{1}H and ^{13}C NMR spectra were recorded on Bruker AMX 400 MHz spectrometer. Chemical shifts are reported in δ (ppm) units using ^{13}C and residual ^{1}H signals from deuterated solvents as references. Spectra were analyzed with Mest−Re-C Lite (Mestrelab Research) and/or XWinPlot (Bruker Biospin). Electrospray ionization mass spectra were recorded on a Micromass Q Tof 2 (Waters), and data were analyzed with *MassLynx 4.0* (Waters) software.

Synthesis of GNPs. The synthesis and complete characterization of the glycans and intermediates are given in the Supporting Information. Using these glycans, GNPs were synthesized using the in situ procedure (*40, 41*). A representative example is described. Briefly, 0.25 mL of a 1% $HAuCl_4$ solution was added to 50 mL of deionized H_2O. Next, **LG1** (2.35 mg, 0.0018 mmol) or **LG2** (2.5 mg, 0.0018 mmol) was added. To this solution, previously cooled $NaBH_4$ solution (0.16 mL, 0.5 mg/mL) was added dropwise with rapid stirring at 0°. The color of the solution changed from light yellow to brown. The resulting brownish solution was stirred for an additional 2 h. The solvent was evaporated in vacuo, and the resulting brownish residue was suspended in 100 mL of CH_3OH and sonicated for 10 min. The resulting slurry was centrifuged at 5000 *g* for 1 h to precipitate the GNPs. The supernatant was removed, and this procedure was repeated three times to remove the excess glycan. The GNPs were dissolved in 1 mL deionized H_2O and lyophilized to yield 1 mg of pure GNPs.

TEM Measurements. The TEM analysis were obtained on a Philips CM20 machine. Briefly, 1 μL of a suspension of the nanoparticle (10 μg dissolved in 1 mL of deionized water) was

placed on a copper grid (200 mesh carbon coated) and the sample was evaporated overnight. A minimum of 50 GNPs were measured to obtain the mean particle diameter and standard deviation (Supporting Information).

Determination of Number of Carbohdyrates Per Nanoparticle. The number of carbohydrates was determined by anthrone−sulfuric acid assay (*41*). Briefly, carbohydrates (1 to 15 μg) were dissolved in 0.5 mL of deionized water. Next, 1 mL of a freshly prepared solution of 0.5% anthrone (w/w) in 95% sulfuric acid was added to 0.5 mL of ice-cold sugar solution. The resulting solution was gently mixed and heated to 100° for 10 min and then allowed to cool to RT. The absorbance was recorded at 620 nm, and the plot of absorbance versus concentration of carbohydrate resulted in a standard curve. Next, different concentrations of the GNPs (100−500 μg) were subjected to the same method. From this concentration, the concentration of sugars in 1 mg of NPs was obtained and the number of carbohydrates per nanoparticle was calculated (Supporting Information).

Protein Inhibition Assay. Vero cells expressing destabilized luciferase (*luc2P* Vero cells) were obtained as follows. The gene for destabilized luciferase, *luc2P*, was excised from pGL4.11[luc2p] (Promega, Madison, WI) with *Hin*dIII and *Xba*I, blunted using Klenow, and cloned into the *Hpa*I site of MigR1 (*42*). HEK GP2−293 retrovirus packaging strain (Clontech, Mountain View, CA) was incubated with 3 μg Luc2p-MigR1 DNA and 1 μg pVSV-G envelope as previously described (*43*). Transfected Vero cells were sorted by flow cytometry; GFP positive cells were propagated and sorted a second time to obtain cells expressing high levels of GFP (*44*). These cells have been deposited with the Biodefense and Emerging Infections Research Resources Repository http://www.beiresources.org/. Crude or purified toxins were diluted in phosphate buffered saline (PBS), followed by half-log serial dilutions; 25 μL aliquots of each dilution were added to white tissue culture-treated, Falcon 96-well microtiter plates (Becton Dickinson, Franklin Lakes, NJ). 100 μL containing 10^4 luciferase-expressing Vero cells was added to the wells, and the plates were incubated for 4 h at 37 °C with 5% CO_2. The cells were washed three times with PBS, 25 μL Superlite Luciferase Substrate (Bioassay Systems, Hayward, CA) was added, and light was measured using the Luminoskan *Ascent* (Thermo Labsystems, Helsinki, Finland). *luc2P* Vero cells incubated without toxin were used as the negative control to determine maximum light production (maximum protein synthesis). The effective dose (ED_{50}; amount of toxin required to achieve a 50% reduction in protein synthesis) was calculated using the two points above and below the midpoint.

Determination of Surface Density of Glycans on Nanoparticle Surface. The distance between glycans was calculated as described previously with slight modifications (*45*). Briefly, the following assumptions were made. (i) The nanoparticles were considered as spheres of 4 nm diameter. (ii) Glycans were assumed to be equally distributed on the nanoparticle surface. (iii) Glycans were assumed to be situated perpendicular to the surface and parallel to each other.

Average surface area of the nanoparticle was determined by using formula $4\pi r^2$, where r is radius of nanoparticle, 2 nm. Since we know the average number of glycans on the nanoparticle surface, we can calculate the average surface density by taking the ratio of the number of glycans over surface density. So, average surface density is 1.3 glycans per nm^2. In order to calculate the distance between two glycans, we assumed that there are an average of 1.3 glycans in 1 nm^2. The average distance between two glycans can be approximated by using the formula $\sqrt{A/n}$, where A is area of the square, which is 1 nm^2, and n is the number of glycans.

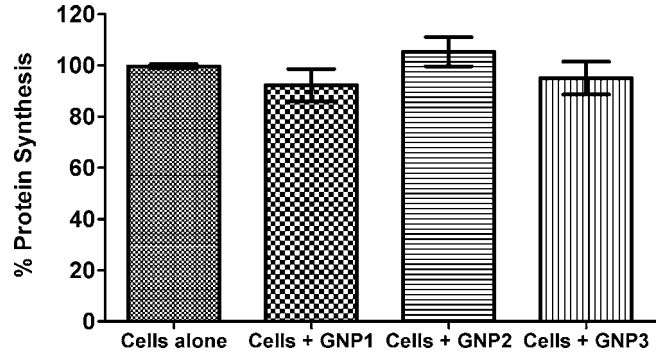


Figure 2. The effect of GNPs in protein synthesis of *luc2P* Vero cells was evaluated by incubating the cells with 10 μg of GNPs or PBS alone. Protein synthesis was unaltered in the presence of GNPs indicating that the GNPs do not perturb protein synthesis in *luc2P* Vero cells.

RESULTS AND DISCUSSION

Synthesis of Gold Glyconanoparticles (GNP). Using our previously published synthetic strategy, we synthesized Pk trisaccharide analogues (Schemes 1 and 2, Supporting Information) with linkers terminated with thiol groups (Figure 1B, LG1 and LG2). Thiolated ligands were used, as they can readily be attached to gold nanoparticles. A thiolated β-galactoside derivative was synthesized as a negative control (Figure 1B, LG3). Next, GNPs were synthesized by previously published method (*40*, *41*) to yield uniform spherical nanoparticles of narrow size distribution (~4 nm). These GNPs were characterized using NMR, UV, IR, and TEM spectroscopies (Supporting Information). The number of glycans conjugated on the nanoparticle surface was determined by using the anthrone method (*41*) (Table 1, Supporting Information). We also synthesized GNPs with different surface densities of glycans by premixing the glycans with a spectator thiolated oligoethylene glycol ligand (OEG, Figure 1) to study the effect of surface density on binding.

Neutralization of Stx Variants Using a Protein Inhibition Assay. Stx inhibits protein synthesis by cleaving the 28S rRNA. We developed a protein inhibition assay (*44*) to quantify the influence of Stx on protein synthesis in the presence and absence of GNPs (Figure 3A). Vero cells were transfected with the MigR1 lentivirus (*42*) containing the cloned *luc2P* gene (destabilized luciferase, from pGL4, Promega, Madison, WI), encoding the gene for luciferase fused to the PEST motif (proline-glutamic acid-serine-threonine), which targets the protein for degradation by the proteosome. This construct allows us to directly measure the rate of protein synthesis by measuring bioluminescence generated by luciferase-mediated oxidation of luciferin. We used this assay as opposed to the MTT assay, because the latter suffers from the problem that it only measures metabolic activity (e.g., due to cell death), not protein synthesis inhibition, and thus only indirectly reflects Shiga toxin activity. The luciferase assay directly indicates toxin-mediated inhibition of protein synthesis. Furthermore, the MTT assay requires 3 days compared to 4 h for the luciferase assay. We evaluated the cytotoxicity of GNPs toward *luc2P* Vero cells by comparing the cells incubated with GNPs to the PBS buffer control. As shown in Figure 2, protein synthesis was unaltered in presence of GNPs, indicating that the GNPs are not cytotoxic to *luc2P* Vero cells.

Next, we studied the ability of the GNPs to neutralize Stx (Figure 3A). Briefly, serial dilutions of Stx ranging from 0.01 to 64 ng were added to the wells of 96-well microtiter plates.

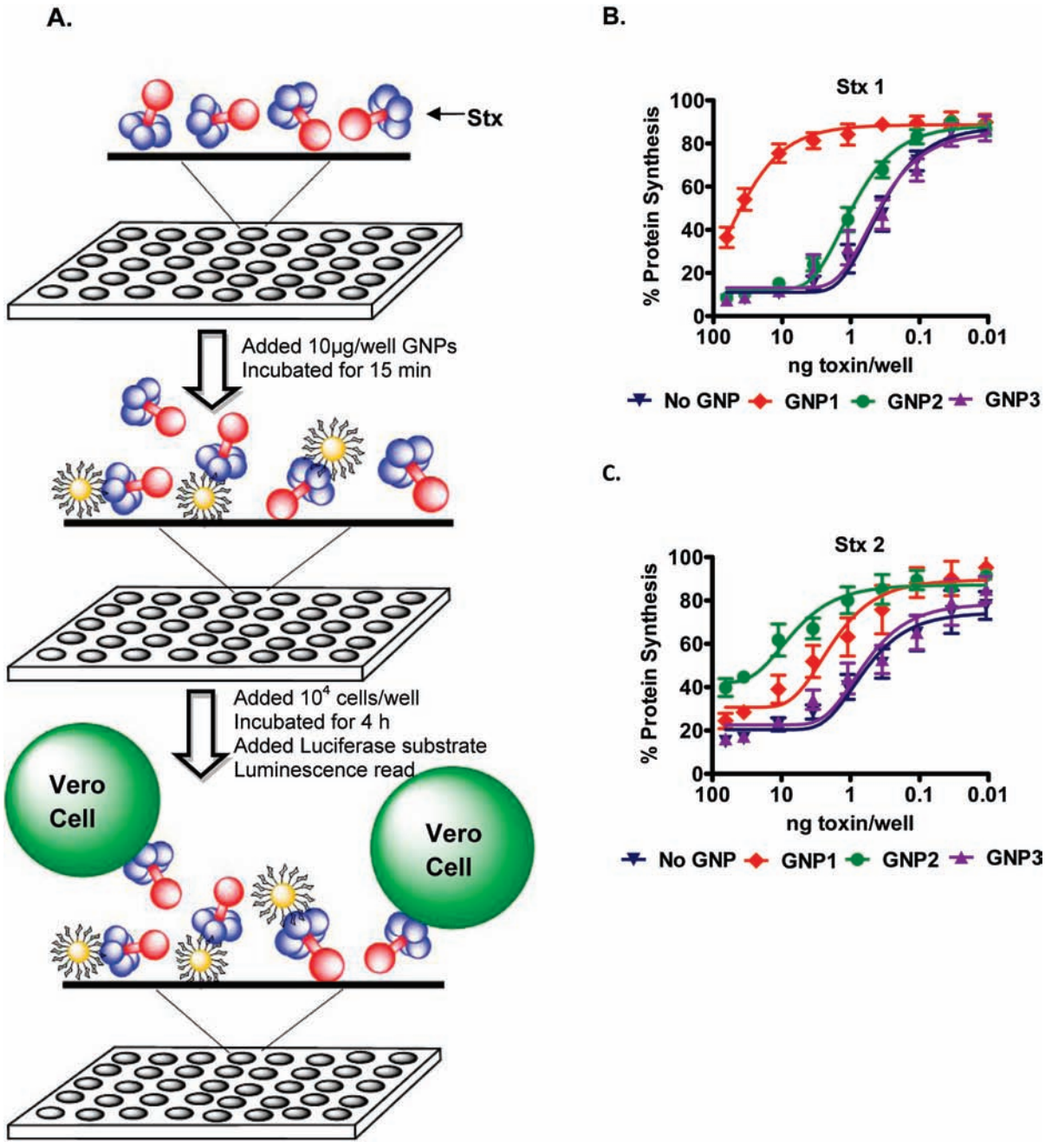


Figure 3. (A) Cartoon presentation of the Vero cell toxin inhibition assay. GNPs were added to wells containing serial dilutions of toxin, followed by addition of 10^4 Vero cells expressing a destabilized form of luciferase, *luc2P*. Plates were incubated at 37 °C for 4 h. Luciferase substrate was added and luminescence was measured on a luminometer. (B) Inhibition of Stx1 using GNPs. (C) Inhibition of Stx2 using GNPs.

GNPs were added at 10 μg/well to the wells and allowed to incubate for 15 min, followed by the addition of 10^4 cells/well. Plates were incubated at 37 °C in 5% CO_2 for 4 h. The cells were washed with PBS, followed by addition of 100 μL/well of SuperLight Luciferase substrate solution (BioAssay Systems; Hayward, CA) containing luciferin, and luminescence was measured using a luminometer (Thermo Labsystems Luminoskan Ascent; Helsinki, Finland) and reported as percentage of maximum signal (% no toxin control). Results for Stx1 are shown in Figure 3B. The blue line indicates the amount of protein synthesis in the presence of different concentrations of Stx1. When we incubated Stx1 with GNP1 (which has Pk saccharide on the nanoparticle surface) prior to addition of cells, we observed significant protection of Vero cells (red line). In contrast, GNP3, β-galactoside coated nanoparticles (violet line), failed to protect the Vero cells from Stx1; while GNP2, which has the N-acetylated version of Pk saccharide on the surface of the nanoparticles (green line), afforded minimal protection, indicating selective inhibition by the GNPs.

Selective neutralization of Stx2 was also observed (Figure 3C). GNP2, the nanoparticle coated with LG2, afforded significant protection of Vero cells from Stx2 (green line), whereas GNP1 exhibited minimal protection of cells from this variant. As in the case of Stx1, β-galactoside coated nanoparticles did not protect cells from Stx2. Preliminary studies using culture supernatant supported previous studies demonstrating that NHAc-Pk GNP2 was not effective at neutralizing Stx1 and Pk GNP1 was not effective at neutralizing Stx2 (Table 1). These studies emphasize the importance of using the appropriate ligand to inhibit the specific variant, as small changes in the structure of the glycan can impact the inhibitory activity significantly.

Table 1. Amount of Toxin Needed to Overcome the Protective Effects of 100 μg/mL of GNPs

	Stx1	Stx2	Stx2c	Stx2d
ED_{50}	0.07 ng/mL	0.6 ng/mL	61 ng/mL	0.5 ng/mL
ED_{50} + GNP1 (fold increase)	25.6 ± 17.3[a] (366)	(5)[b]	118 ± 12 (1.9)	1.3 ± 0.5 (2.6)
ED_{50} + GNP2 (fold increase)	(3)[b]	92 ± 8[a] (153)	111 ± 73 (1.8)	19.3 ± 13.9 (39)

[a] Statistically significant compared to control. [b] Assessed using culture supernatant instead of pure toxin.

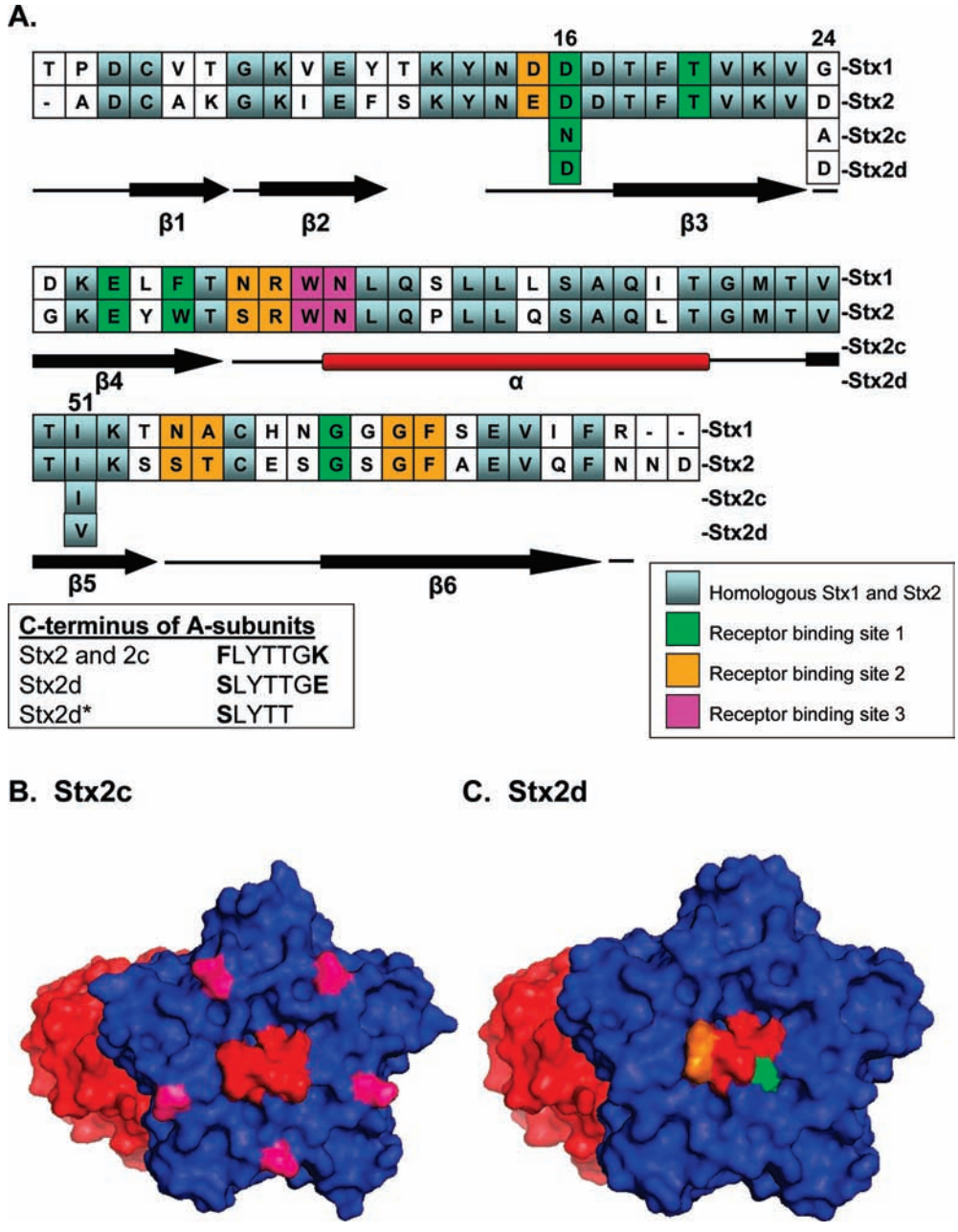


Figure 4. Comparison of the Stx variants. (A) The amino acid sequences of the Stx variants. The numbers correspond to the amino acid coordinates of Stx2B; add 1 to obtain the coordinates for Stx1B. Amino acids involved in the receptor binding sites of Stx1 are indicated; similar receptor binding information is not available for Stx2. The C-terminal amino acids of the A-subunit are indicated in the box. (B,C) Model structures of the Stx2 variants oriented to display the receptor binding sites, generated in PyMol using the published crystal structure of Stx2 (*52*). The enzymatically active A-subunit is shown in red. The binding or B-subunit, a pentamer of five identical subunits, is shown in blue. (B) Stx2c with the amino acid change corresponding to position 16 of the B-subunit (D16N) depicted in pink, and the amino acid change D24A could not be seen in top view, since it is located on the opposite side. (C) Stx2d with the amino acid change corresponding to position 51 of the B-subunit (I51V) is not visible, since it is buried inside, and the amino acid changes of A-subunit corresponding to position 313 (313S) is depicted in green and to position 319 (319E) is depicted in orange.

The ED_{50} (effective dose that produces 50% response) values for purifed Stx1 and Stx2 with the different GNPs (100 μg/mL) are given in Table 1. The ED_{50} of purified Stx1 was 0.07 ng/mL with Vero cells without any inhibitor. When Stx1 was preincubated with GNP1, the ED_{50} value increased to 25.6 ng/mL, demonstrating that 366 times more toxin is needed to inhibit 50% protein synthesis in the presence of GNP1 compared to toxin alone. In the case of Stx2, the ED_{50} of Stx2 was 0.6 ng/mL with Vero cells without any inhibitor. When Stx2 was preincubated with GNP2, an ED_{50} value of 92 ng/mL was obtained, or 153 times more toxin was needed to inhibit 50% protein synthesis in the presence of GNP2 than toxin alone. In

vitro, neutralization with the GNPs occurred at a ratio of about 80 GNPs per Stx2 molecule, or about 5000 glycans per toxin molecule. While we have not investigated neutralization in vivo, in vivo studies using Starfish and Daisy inhibitors observed neutralization at ratios of 1000 to 10 000 inhibitor molecules per toxin molecule (*5, 9*).

Next, we investigated the ability of the GNPs to inhibit emerging variants of Stx2, Stx2c, and Stx2d. The amino acid sequence for these variants is shown in Figure 4A. The B-subunit of Stx2c differs from Stx2 by two amino acids (D16N, D24A), of which position 16 is present in the predicted receptor binding site. These differences lead to a significant drop in the ED_{50} of Stx2c (61 ng/mL) compared to Stx2 (0.6 ng/mL) with cells alone. Since there are five B-subunits in each variant, which binds to a minimum of five glycolipids in a multivalent manner, a single mutation in the receptor binding site would have a 5-fold effect on the ED_{50} (Figure 4A,B). When Stx2c is preincubated with either of the GNPs and exposed to Vero cells, minimal 2-fold protection was observed, which was not statistically significant (Table 1). The lack of neutralization could be due to the inherently decreased toxicity of Stx2c. Alternatively, the amino acid changes could alter the requirements for presentation of the ligand or its density on the nanoparticle, as orientation effects have been demonstrated to influence binding (*46, 47*).

The ED_{50} of Stx2d (0.5 ng/mL) is very similar to that of Stx2 (0.6 ng/mL). However, we observed minimal protection with either GNP. The B-subunit of Stx2d differs from Stx2 by only one amino acid, which is not thought to be in a receptor binding site (I51V, Figure 4A,C). However, the terminal amino acid of the Stx2d A-subunit is different from Stx2 in that the basic amino acid, lysine, has been changed to the acidic amino acid, glutamic acid. The amino acids surrounding the central region of the B-pentamer that forms the pore for the A-subunit serves as a glycan binding site in Stx1. It is unclear if this region also serves as a glycan binding site for Stx2, since the C-terminus of Stx2 extends past the B-pentamer pore, which could occlude a binding site; alternatively, the A-subunit could participate in binding. The different neutralization patterns between Stx2 and Stx2d could be due to the changes in the A terminus. The importance of the C-terminal tail in influencing potency has been established by studies that have shown that a proteolytically processed form of Stx2d (Stx2d*) with the last two amino acids removed is more potent than Stx2d. The activation of Sx2d to the Stx2d* form has been shown to be mediated in vivo by elastase present in mucus secretions (*48*). Overall, these results demonstrate that minor changes in the structure of the toxin can dramatically affect both potency and neutralization by receptor mimics.

Effect of Ligand Density on the Neutralization of Stxs. We were interested in evaluating the effect of differential glycan density on the surface of the GNPs, as several reports indicate that density is an important factor in determining binding affinities (*49, 50*). We premixed the ligand with short oligoethylene glycol spacer terminated in a thiol group (OEG, Figure 1) at different ratios (Glyca/OEG; 100:0 → 25:75) and coated the GNPs similarly. Mean inhibition activity for Stx1 was decreased by 10-fold and for Stx2 was decreased by 3.5-fold for nanoparticles coated at a ratio of 75:25 and 50:50 as compared to the nanoparticles coated at a ratio of 100:0 (Figure 5A,B). However, no inhibition was observed at a ratio of 25:75 (Figure 5A,B). We attribute this decrease to a failure of the toxin to engage multiple glycans. Briefly, for Stx1 there are three proposed binding sites per B-subunit, of which site 2 has been shown to be the most important site (*5, 51*). Stx2 has been proposed to use sites mapping to the corresponding positions. The average distance between the three possible binding sites per B-subunit of Stx2 is ∼1.2 nm. The distance between site1

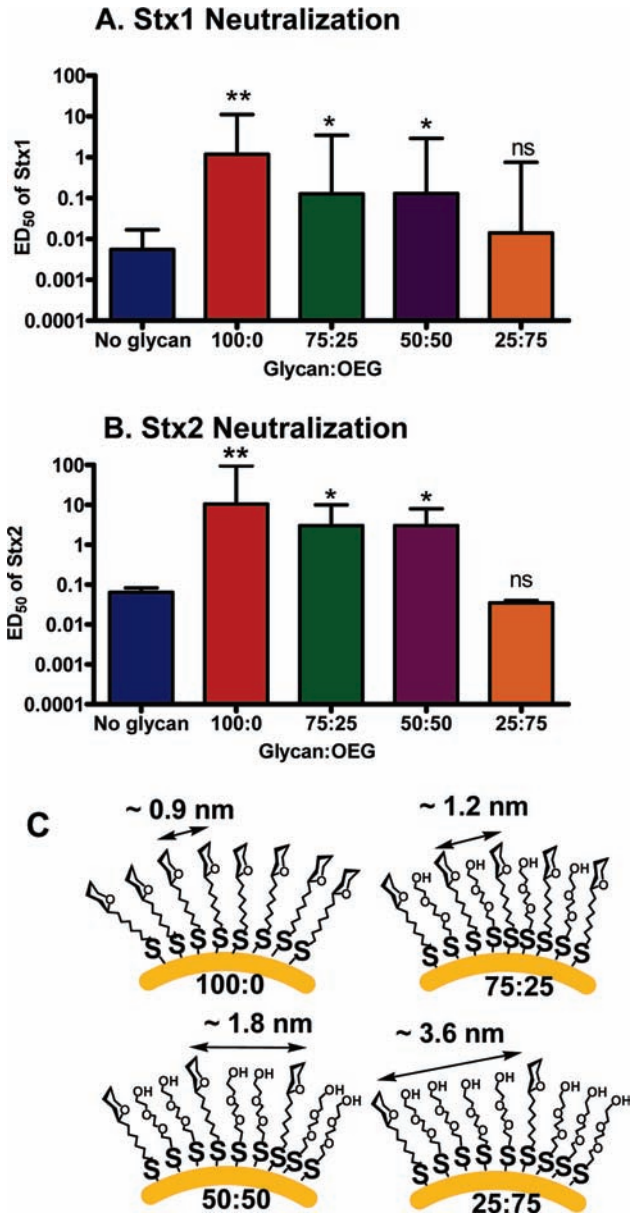


Figure 5. Effect of varying glycan surface density on inhibition activity: (A) Stx 1 in the presence of GNPs of different glycan surface densities. (B) Stx 2 in the presence of GNPs of different glycan surface densities. The data are the average ± standard deviation of three experiments. *: $P < 0.02$; **: $P < 0.002$. ns: not significant. (C) Representation of the gold NP surface with varying density of ligands. Ratio is given as Glycan/OEG.

and site2 is ∼1.3 nm, site1 − site3 is ∼1.6 nm, and site2 − site3 is ∼0.8 nm. The average distance between binding site 2 of 1 B-subunit and the adjacent B-subunit is ∼1.8 nm (Supporting Information). The average distances between adjacent glycans on the nanoparticle surface for 100%, 75%, and 50% coverage were calculated to be ∼0.9, ∼1.2, and ∼1.8 nm, respectively (*45*) (Figure 5C). Thus, there are multiple glycans to engage the binding sites on the B-subunit for these surface densities. When the surface density was decreased to 25%, the average distance is ∼3.6 nm, which is greater than the distance between the binding sites on the toxin. This presumably leads to loss of cooperativity and loss in inhibitory activity.

In summary, we have developed an efficient strategy toward the development of gold glyconanoparticles for the selective inhibition of Stx 1 and 2. These nanoparticles are not toxic to Vero cells and can effectively inhibit Stx variants 1 and 2 from inhibiting protein synthesis in Vero cells. We demonstrate that

the inhibition is highly dependent on the structure and density of the glycans and the structure of the toxin. A single amino acid variation in the receptor binding site of the B-subunit or changes in the A-subunit of the toxin fail to inhibit activity. Our results suggest that tailored glyconanoparticles can serve as potential therapeutics for Stx1 and 2; however, further research is needed to develop strain-specific or broad spectrum therapeutics for emerging variants.

ACKNOWLEDGMENT

We thank NIAID (U01-AI075498 A.A.W. and S.S.I., and R01-064893 to A.A.W.) and NSF (Career CHE-0845005 S.S.I.) for providing financial support.

Supporting Information Available: Detailed procedures of the synthesis of the GNPs and characterization data. Additionally, the TEM pictures and NMR and IR spectra for the GNPs are provided. This material is available free of charge via the Internet at http://pubs.acs.org.

LITERATURE CITED

(1) Siegler, R. L. (2003) Postdiarrheal Shiga toxin-mediated hemolytic uremic syndrome. *JAMA 290*, 1379–81.

(2) Wong, C. S., Jelacic, S., Habeeb, R. L., Watkins, S. L., and Tarr, P. I. (2000) The risk of the hemolytic-uremic syndrome after antibiotic treatment of Escherichia coli O157:H7 infections. *N. Engl. J. Med. 342*, 1930–6.

(3) Rutjes, N. W., Binnington, B. A., Smith, C. R., Maloney, M. D., and Lingwood, C. A. (2002) Differential tissue targeting and pathogenesis of verotoxins 1 and 2 in the mouse animal model. *Kidney Int. 62*, 832–45.

(4) Sandvig, K., and van Deurs, B. (1996) Endocytosis, intracellular transport, and cytotoxic action of Shiga toxin and ricin. *Physiol. Rev. 76*, 949–66.

(5) Kitov, P. I., Sadowska, J. M., Mulvey, G., Armstrong, G. D., Ling, H., Pannu, N. S., Read, R. J., and Bundle, D. R. (2000) Shiga-like toxins are neutralized by tailored multivalent carbohydrate ligands. *Nature 403*, 669–72.

(6) Neri, P., Nagano, S. I., Yokoyama, S., Dohi, H., Kobayashi, K., Miura, T., Inazu, T., Sugiyama, T., Nishida, Y., and Mori, H. (2007) Neutralizing activity of polyvalent Gb3, Gb2 and galacto-trehalose models against Shiga toxins. *Microbiol. Immunol. 51*, 581–92.

(7) Dohi, H., Nishida, Y., Mizuno, M., Shinkai, M., Kobayashi, T., Takeda, T., Uzawa, H., and Kobayashi, K. (1999) Synthesis of an artificial glycoconjugate polymer carrying Pk-antigenic trisaccharide and its potent neutralization activity against Shiga-like toxin. *Bioorg. Med. Chem. 7*, 2053–62.

(8) Kitov, P. I., Mulvey, G. L., Griener, T. P., Lipinski, T., Solomon, D., Paszkiewicz, E., Jacobson, J. M., Sadowska, J. M., Suzuki, M., Yamamura, K., Armstrong, G. D., and Bundle, D. R. (2008) In vivo supramolecular templating enhances the activity of multivalent ligands: a potential therapeutic against the Escherichia coli O157 AB5 toxins. *Proc. Natl. Acad. Sci. U.S.A. 105*, 16837–42.

(9) Griener, T. P., Mulvey, G. L., Marcato, P., and Armstrong, G. D. (2007) Differential binding of Shiga toxin 2 to human and murine neutrophils. *J. Med. Microbiol. 56*, 1423–30.

(10) Trachtman, H., Cnaan, A., Christen, E., Gibbs, K., Zhao, S., Acheson, D. W., Weiss, R., Kaskel, F. J., Spitzer, A., and Hirschman, G. H. (2003) Effect of an oral Shiga toxin-binding agent on diarrhea-associated hemolytic uremic syndrome in children: a randomized controlled trial. *JAMA 290*, 1337–44.

(11) Boerlin, P., McEwen, S. A., Boerlin-Petzold, F., Wilson, J. B., Johnson, R. P., and Gyles, C. L. (1999) Associations between virulence factors of Shiga toxin-producing Escherichia coli and disease in humans. *J. Clin. Microbiol. 37*, 497–503.

(12) Siegler, R. L., Obrig, T. G., Pysher, T. J., Tesh, V. L., Denkers, N. D., and Taylor, F. B. (2003) Response to Shiga toxin 1 and 2 in a baboon model of hemolytic uremic syndrome. *Pediatr. Nephrol. 18*, 92–6.

(13) Armstrong, G. D., Mulvey, G. L., Marcato, P., Griener, T. P., Kahan, M. C., Tennent, G. A., Sabin, C. A., Chart, H., and Pepys, M. B. (2006) Human serum amyloid P component protects against Escherichia coli O157:H7 Shiga toxin 2 in vivo: therapeutic implications for hemolytic-uremic syndrome. *J. Infect. Dis. 193*, 1120–4.

(14) Gamage, S. D., Patton, A. K., Strasser, J. E., Chalk, C. L., and Weiss, A. A. (2006) Commensal bacteria influence Escherichia coli O157:H7 persistence and Shiga toxin production in the mouse intestine. *Infect. Immunol. 74*, 1977–83.

(15) Atkinson, R., Johnson, G., Root, T., Halse, T., Wroblewski, D., Davies, M., Byrd, A., Long, L., Demma, L., Angulo, F., Bopp, C., Gerner-Smidt, P., Strockbine, N., Greene, K., Swaminathan, B., Griffin, P., Schaffzin, J., and Goode, B. (2006) *Morbidity and Mortality Weekly Report* 1042–1045.

(16) Kale, R. R., McGannon, C. M., Fuller-Schaefer, C., Hatch, D. M., Flagler, M. J., Gamage, S. D., Weiss, A. A., and Iyer, S. S. (2008) Differentiation between structurally homologous Shiga 1 and Shiga 2 toxins by using synthetic glycoconjugates. *Angew. Chem., Int. Ed. Engl. 47*, 1265–1268.

(17) Kale, R. R., McGannon, C. M., Fuller-Schaefer, C., Hatch, D. M., Flagler, M. J., Gamage, S. D., Weiss, A. A., and Iyer, S. S. (2008) Differentiation between structurally homologous Shiga 1 and Shiga 2 toxins by using synthetic glycoconjugates. *Angew. Chem., Int. Ed. Engl. 47*, 1265–8.

(18) Mallidi, S., Larson, T., Tam, J., Joshi, P. P., Karpiouk, A., Sokolov, K., and Emelianov, S. (2009) Multiwavelength photoacoustic imaging and plasmon resonance coupling of gold nanoparticles for selective detection of cancer. *Nano Lett.*

(19) Popovtzer, R., Agrawal, A., Kotov, N. A., Popovtzer, A., Balter, J., Carey, T. E., and Kopelman, R. (2008) Targeted gold nanoparticles enable molecular CT imaging of cancer. Nano Lett.

(20) Zhang, J., Wang, J., Xu, X., Zhu, H., Wang, Z., Yang, F., Zhang, B., and Yang, X. (2009) A one-dimensional network from the self-assembly of gold nanoparticles by a necklace-like polyelectrolyte template mediated by metallic ion coordination. *Nanotechnology 20*, 295603.

(21) Toster, J., Iyer, K. S., Burtovyy, R., Burgess, S. S., Luzinov, I. A., and Raston, C. L. (2009) Regiospecific assembly of gold nanoparticles around the pores of diatoms: toward three-dimensional nanoarrays. *J. Am. Chem. Soc. 131*, 8356–7.

(22) Muthu, M. S., and Singh, S. (2009) Targeted nanomedicines: effective treatment modalities for cancer, AIDS and brain disorders. *Nanomedicine 4*, 105–18.

(23) Hwu, J. R., Lin, Y. S., Josephrajan, T., Hsu, M. H., Cheng, F. Y., Yeh, C. S., Su, W. C., and Shieh, D. B. (2009) Targeted Paclitaxel by conjugation to iron oxide and gold nanoparticles. *J. Am. Chem. Soc. 131*, 66–8.

(24) Jain, J., Arora, S., Rajwade, J., Khandelwal, S., and Paknikar, K. M. (2009) Silver nanoparticles in therapeutics: development of an antimicrobial gel formulation for topical use. *Mol. Pharmaceut.*

(25) de La Fuente, J. M., Barrientos, A. G., Rojas, T. C., Rojo, J., Canada, J., Fernandez, A., and Penades, S. (2001) Gold glyconanoparticles as water-soluble polyvalent models to study carbohydrate interactions. *Angew. Chem., Int. Ed. Engl. 40*, 2257–2261.

(26) de la Fuente, J. M., and Penades, S. (2006) Glyconanoparticles: types, synthesis and applications in glycoscience, biomedicine and material science. *Biochim. Biophys. Acta 1760*, 636–51.

(27) Barrientos, A. G., de la Fuente, J. M., Rojas, T. C., Fernandez, A., and Penades, S. (2003) Gold glyconanoparticles: synthetic polyvalent ligands mimicking glycocalyx-like surfaces as tools for glycobiological studies. *Chemistry 9*, 1909–21.

(28) Lin, C. C., Yeh, Y. C., Yang, C. Y., Chen, G. F., Chen, Y. C., Wu, Y. C., and Chen, C. C. (2003) Quantitative analysis of multivalent interactions of carbohydrate-encapsulated gold nanoparticles with concanavalin A. *Chem. Commun. (Camb.)* 2920–1.

(29) Schofield, C. L., Field, R. A., and Russell, D. A. (2007) Glyconanoparticles for the colorimetric detection of cholera toxin. *Anal. Chem. 79*, 1356–61.

(30) El-Boubbou, K., Gruden, C., and Huang, X. (2007) Magnetic glyco-nanoparticles: a unique tool for rapid pathogen detection, decontamination, and strain differentiation. *J. Am. Chem. Soc. 129*, 13392–3.

(31) van Kasteren, S. I., Campbell, S. J., Serres, S., Anthony, D. C., Sibson, N. R., and Davis, B. G. (2009) Glyconanoparticles allow pre-symptomatic in vivo imaging of brain disease. *Proc. Natl. Acad. Sci. U.S.A. 106*, 18–23.

(32) Rojo, J., Diaz, V., de la Fuente, J. M., Segura, I., Barrientos, A. G., Riese, H. H., Bernad, A., and Penades, S. (2004) Gold glyconanoparticles as new tools in antiadhesive therapy. *ChemBioChem 5*, 291–7.

(33) Reynolds, A. J., Haines, A. H., and Russell, D. A. (2006) Gold glyconanoparticles for mimics and measurement of metal ion-mediated carbohydrate-carbohydrate interactions. *Langmuir 22*, 1156–63.

(34) de la Fuente, J. M., and Penades, S. (2004) Understanding carbohydrate-carbohydrate interactions by means of glyconanotechnology. *Glycoconj. J. 21*, 149–63.

(35) de la Fuente, J. M., Eaton, P., Barrientos, A. G., Menendez, M., and Penades, S. (2005) Thermodynamic evidence for Ca2+-mediated self-aggregation of Lewis X gold glyconanoparticles. A model for cell adhesion via carbohydrate-carbohydrate interaction. *J. Am. Chem. Soc. 127*, 6192–7.

(36) Bowman, M. C., Ballard, T. E., Ackerson, C. J., Feldheim, D. L., Margolis, D. M., and Melander, C. (2008) Inhibition of HIV fusion with multivalent gold nanoparticles. *J. Am. Chem. Soc. 130*, 6896–7.

(37) Martinez-Avila, O., Bedoya, L. M., Marradi, M., Clavel, C., Alcami, J., and Penades, S. (2009) Multivalent manno-glyconanoparticles inhibit DC-SIGN-mediated HIV-1 trans-infection of human T cells. *ChemBioChem 10*, 1806–9.

(38) Rogers, J. V., Parkinson, C. V., Choi, Y. W., Speshock, J. L., and Hussain, S. M. (2008) A preliminary assessment of silver nanoparticle inhibition of monkeypox virus plaque formation. *Nanoscale Res. Lett. 3*, 129–133.

(39) Lu, L., Sun, R. W. Y., Chen, R., Hui, C. K., Ho, C. M., Luk, J. M., Lau, G. K. K., and Che, C. M. (2008) Silver nanoparticles inhibit hepatitis B virus replication. *Antiviral Ther. 13*, 253–262.

(40) M. Brust, J. F., Bethell, D., Schiffrin, D. J., and Kiely, C. (1995) Synthesis and reactions of functionalised gold nanoparticles. *J. Chem. Soc.: Chem. Commun.* 1655–1656.

(41) Chien, Y. Y., Jan, M. D., Adak, A. K., Tzeng, H. C., Lin, Y. P., Chen, Y. J., Wang, K. T., Chen, C. T., Chen, C. C., and Lin, C. C. (2008) Globotriose-functionalized gold nanoparticles as multivalent probes for Shiga-like toxin. *ChemBioChem 9*, 1100–9.

(42) Pear, W. S., Miller, J. P., Xu, L., Pui, J. C., Soffer, B., Quackenbush, R. C., Pendergast, A. M., Bronson, R., Aster, J. C., Scott, M. L., and Baltimore, D. (1998) Efficient and rapid induction of a chronic myelogenous leukemia-like myeloproliferative disease in mice receiving P210 bcr/abl-transduced bone marrow. *Blood 92*, 3780–92.

(43) Sherrill, J. D., and Miller, W. E. (2006) G protein-coupled receptor (GPCR) kinase 2 regulates agonist-independent Gq/11 signaling from the mouse cytomegalovirus GPCR M33. *J. Biol. Chem. 281*, 39796–805.

(44) McGannon, C. M., Fuller, C., and Weiss, A. A. (2010) Different classes of antibiotics differentially influence Shiga toxin production *Antimicrob. Agents Chemother*. (in press) doi: 10.1128/AAC.01783-09.

(45) Hill, H. D., Millstone, J. E., Banholzer, M. J., and Mirkin, C. A. (2009) The role radius of curvature plays in thiolated oligonucleotide loading on gold nanoparticles. *ACS Nano 3*, 418–24.

(46) Chandrasekaran, A., Srinivasan, A., Raman, R., Viswanathan, K., Raguram, S., Tumpey, T. M., Sasisekharan, V., and Sasisekharan, R. (2008) Glycan topology determines human adaptation of avian H5N1 virus hemagglutinin. *Nat. Biotechnol. 26*, 107–13.

(47) Lewallen, D. M., Siler, D., and Iyer, S. S. (2009) Factors affecting protein-glycan specificity: effect of spacers and incubation time. *ChemBioChem 10*, 1486–1489.

(48) Kokai-Kun, J. F., Melton-Celsa, A. R., and O'Brien, A. D. (2000) Elastase in intestinal mucus enhances the cytotoxicity of Shiga toxin type 2d. *J. Biol. Chem. 275*, 3713–21.

(49) Dhayal, M., and Ratner, D. M. (2009) XPS and SPR analysis of glycoarray surface density. *Langmuir 25*, 2181–7.

(50) Lewallen, D. M., Siler, D., and Iyer, S. S. (2009) Factors affecting protein-glycan specificity: effect of spacers and incubation time. *ChemBioChem 10*, 1486–9.

(51) Kitov, P. I., Shimizu, H., Homans, S. W., and Bundle, D. R. (2003) Optimization of tether length in nonglycosidically linked bivalent ligands that target sites 2 and 1 of a Shiga-like toxin. *J. Am. Chem. Soc. 125*, 3284–94.

(52) Fraser, M. E., Fujinaga, M., Cherney, M. M., Melton-Celsa, A. R., Twiddy, E. M., O'Brien, A. D., and James, M. N. (2004) Structure of shiga toxin type 2 (Stx2) from Escherichia coli O157:H7. *J. Biol. Chem. 279*, 27511–7.

BC100095W

SUPPORTING INFORMATION

GLYCAN ENCAPSULATED GOLD NANOPARTICLES SELECTIVELY INHIBIT SHIGA TOXINS 1 AND

Ashish A. Kulkarni [†], Cynthia Fuller-Schaefer [‡], Henry Korman [†], Suri S. Iyer [†,*] and Alison A. Weiss[‡,*]

[†] UC Chemical and Biosensors group, Department of Chemistry, University of Cincinnati,

Cincinnati, Ohio. 45221-1072.

[‡] Department of Biochemistry, Molecular Genetics and Microbiology, University of Cincinnati,

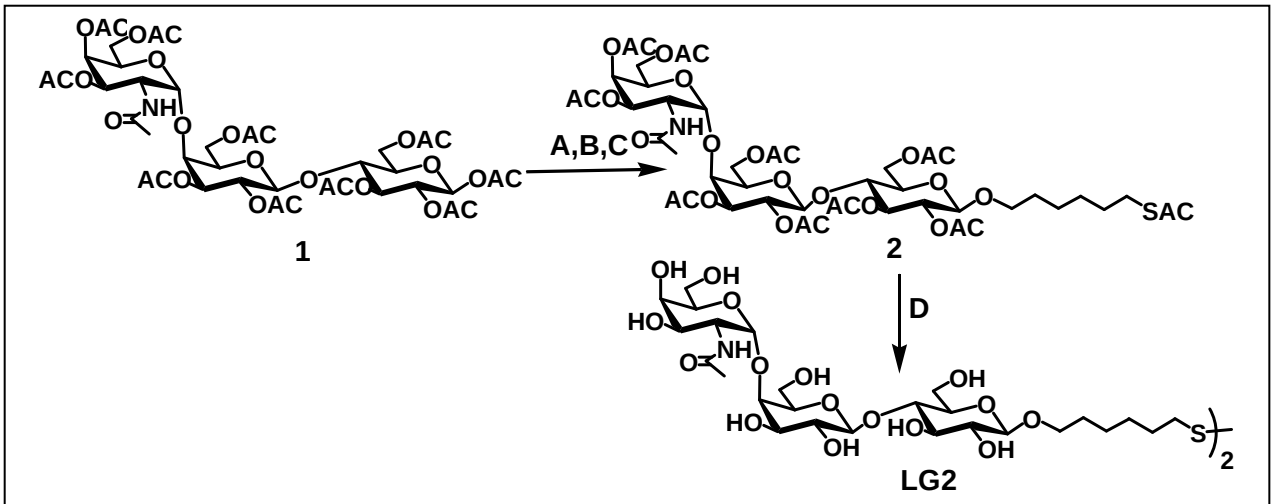
Cincinnati, Ohio. 45267-0524.

TABLE OF CONTENTS

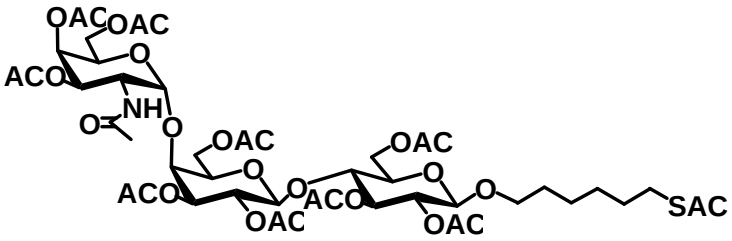
CONTEN	***Page***
General	**S3**
Synthesis of ligands	**S4**
^{1}H, ^{13}C, COSY and HSQC NMR spectra of ligands	**S8**
Figure 1. ^{1}H NMR spectrum of GNP1	**S24**
Figure 2. UV-Vis spectrum of GNP1	**S25**
Figure 3. IR spectra of LG2 and GNP2	**S26**
Figure 4. TEM images of GNPs	**S27**
Figure 5. The plot of concentration of free ligand versus absorbance	**S30**
Figure 6. Inhibition studies of Stx2 with varying concentrations of GNPs	**S31**
Figure 7. Top view presentation of Stx2a pentamer	**S32**
References	**S33**

GENERAL:

All chemical reagents were of analytical grade, used as supplied without further purification unless indicated. Acetic anhydride and acetyl chloride were distilled under an inert atmosphere and stored under argon. 4Å Molecular sieves were stored in an oven (>130 ºC) and cooled *in vacuo*. The acidic ion-exchange resin used was Dowex-50 and Amberlite (H^+ form). Analytical thin layer chromatography (TLC) was conducted on silica gel 60-F254 (Merck). Plates were visualized under UV light, and/or by treatment with acidic cerium ammonium molybdate followed by heating. Column chromatography was conducted using silica gel (230-400 mesh) from Qualigens. ^{1}H and ^{13}C NMR spectra were recorded on Bruker AMX 400MHz spectrometer. Chemical shifts are reported in δ (ppm) units using ^{13}C and residual ^{1}H signals from deuterated solvents as references. Spectra were analyzed with Mest-Re-C Lite (Mestrelab Research) and/or XWinPlot (Bruker Biospin). Electrospray ionization mass spectra were recorded on a Micromass Q Tof 2 (Waters) and data were analyzed with MassLynx 4.0 (Waters) software.



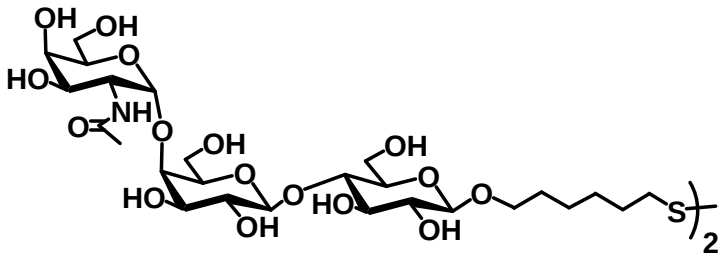
SCHEME 1. *Reagents and conditions:* a) NH_2NH_2.HOAc,THF,rt, 85%; b) K_2CO_3, Cl_3CCN, DCM, rt, 80% ; c) S-acyl-6-mercaptohexanol,TMSOTf, DCM, 0^0C, 75% ; d) NaOMe, MeOH, rt, 16h, 96%



1-Thioacetyl-hexyl (2-N-acetamido 2-deoxy 3,4,6-tri-O-acetyl-α-D-galacto pyranosyl) (1 →4) (2,3,6-tri-O-acetyl-β-D-galactopyranosyl) (1 →4) 2,3,6-tri-O-acetyl-β-D-glucopyranoside.

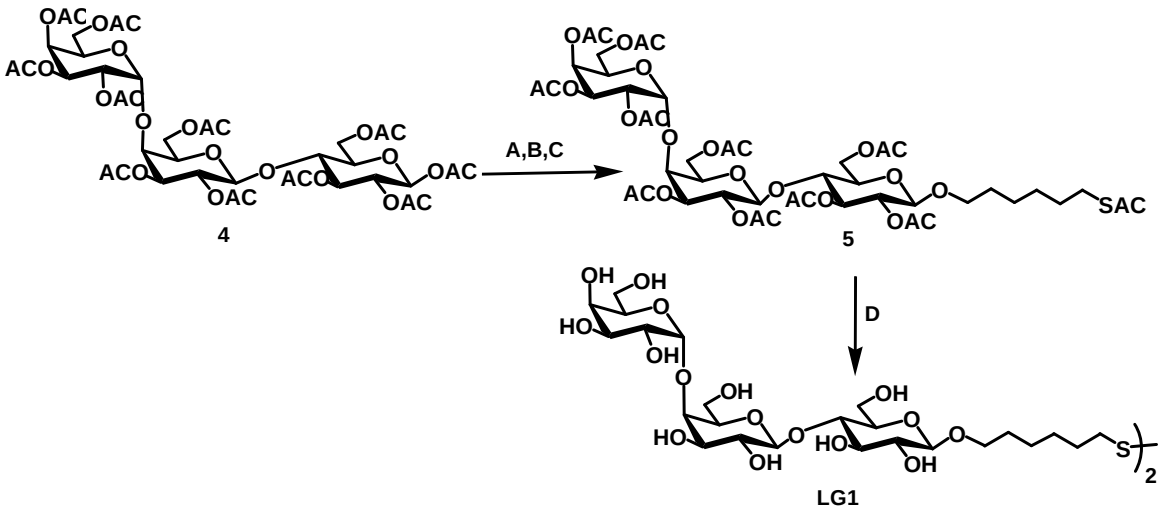
1(*1*) (100 mg, 0.100 mmol) was dissolved in 3 ml of anhydrous THF and NH_2NH_2.HOAc (12 mg, 0.120 mmol) was added to it. The reaction was stirred at rt for 6 h. The reaction mixture was diluted with 5 ml of EtOAc, 5 ml of water was added, and the organic layer was separated and dried in vacuo to give the hemiacetal (80 mg, 85 %), which was directly used in the next step. Anhydrous K_2CO_3 (0.300 g, 2.16 mol) was added to the solution of hemiacetal (80 mg, 0.087 mmol) and trichloroacetonitrile (70 µL, 0.700 mmol) in CH_2Cl_2 (3 ml) at rt. The reaction mixture was stirred at rt for 8 h, washed with water and the organic layer was dried over anhydrous Na_2SO_4, filtered and concentrated in *vacuo*. The residue was purified by column chromatography, eluting with EtOAc, to give the trichloroimidate as a pale yellow solid (75 mg, 80 %). The trichloroimidate (60 mg, 0.056 mmol) and S-(6-Hydroxy-hexyl)thioacetate(*2*) (15 mg, 0.084 mmol) were dissolved in CH_2Cl_2 (2 ml) and cooled to 0 ^{0}C. A 0.22 M solution of TMSOTf in CH_2Cl_2 (65 µl, 0.014 mmol) was added drop

wise and the resulting solution was stirred for 2 h at 0 ^{0}C. The reaction was quenched by triethylamine solution and the solvent was removed in *vacuo.* The crude product was purified by column chromatography, eluting with 8:2 mixture of EtOAc and hexane, to give **2** as white solid (45 mg, 75%). ^{1}H NMR ($CDCl_3$, 400MHz): δ 6.22 (d, 1H, *J* = 8.8 Hz), 5.50 (m, 1H), 5.25-5.20 (m, 2H), 5.14 (dd , 1H, *J* = 8.0, *J* = 10.4), 5.02 (d, 1H, *J* = 3.6), 4.92-4.85 (m, 2H), 4.63-4.38 (m, 6H), 4.16-4.02 (m, 4H), 3.96 (m, 1H), 3.86-3.74 (m, 3H), 3.65-3.60 (m, 1H), 3.50-3.40 (m, 1H), 2.86 (t, 2H, *J* = 7.2), 2.33 (s, 3H), 2.16 (s, 3H), 2.13 (s, 3H), 2.11 (s, 3H), 2.08 (s, 3H), 2.06 (s, 3H), 2.05 (s, 6H), 2.03 (s, 3H), 2.02 (s, 3H). ^{13}C NMR ($CDCl_3$): 195.92, 170.90, 170.69, 170.59, 170.28, 170.20, 170.15, 169.76, 169.57, 169.03, 100.95, 100.41, 99.10, 73.60, 73.03, 72.56, 72.18, 72.10, 72.05, 69.95, 69.41, 67.72, 67.13, 67.03, 62.45, 60.78, 48.62, 30.64, 29.47, 29.24, 28.99, 28.44, 25.35, 23.10, 20.93, 20.69, 20.84, 20.76, 20.72, 20.67, 20.57, 20.53. HRMS Calculated for $[C_{46}H_{67}NO_{26}S+Na]^+$:1104.3570 Found:1104.3284.

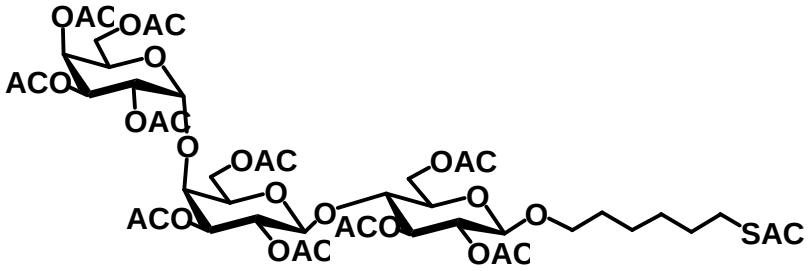


1-Thiohexyl (2-N-acetamido 2-deoxy-α-D-galacto pyranosyl) (1 →4) (β-D-galactopyranosyl) (1 →4)β-D-glucopyranoside.

2 (17 mg, 0.016 mmol) was dissolved in methanol (2 ml) and a solution of NaOMe in MeOH (0.50M, 0.5 ml) was added and the reaction mixture was stirred at rt for 6h. The reaction was neutralized by careful addition of Amberlite-15 H^+ resin and the resin was filtered. The solvent was removed in *vacuo* and the residue was purified by Biogel P-2 gel column chromatography, eluting with methanol, to give the dimerized product **LG2** as a white solid (10 mg, 96%). ^{1}H NMR (CD_3OD, 400MHz): δ 4.88 (bs, 1H), 4.87 (bs, 1H), 4.59 (s, 2H), 4.40-4.33 (m, 4H), 4.26-4.23 (m, 4H), 3.90-3.84(m, 10H), 3.79-3.75 (m, 3H), 3.69-3.65 (m, 6H), 3.61-3.57 (m, 6H), 3.54-3.47 (m, 10H), 3.37-3.34 (m, 2H), 3.22-3.18 (m, 2H), 2.67-2.63 (t, 2H), 2.56-2.53 (t, 2H), 1.98 (s, 6H), 1.67-1.55 (m, 9H), 1.40-1.37 (m, 10H), 1.24 (m, 6H). ^{13}C NMR (CD_3OD): 172.63, 160.08, 103.96, 102.88, 98.94, 79.45, 79.40, 76.43, 75.69, 75.18, 75.05, 73.57, 73.15, 71.11, 70.88, 69.45, 69.01, 68.05, 61.27, 60.57, 59.89, 54.42, 50.31, 38.33, 30.46, 29.61, 29.27, 28.79, 28.26, 27.87, 25.27, 21.39, 21.36. HRMS Calculated for $[2C_{52}H_{92}N_2O_{32}S_2+Na]^+$: 1343.4972. Found: 1343.5111.

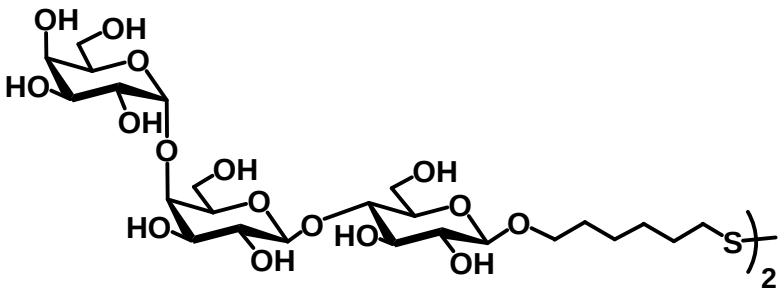


SCHEME 2.*Reagents and conditions:* a) NH_2NH_2.HOAc, THF, rt, 85%; b) K_2CO_3, Cl_3CCN, DCM, rt, 80% ; c) S-acyl-6-mercaptohexanol , TMSOTf, DCM, 0^oC, 85% ; d) NaOMe, MeOH, rt, 16h, 99%

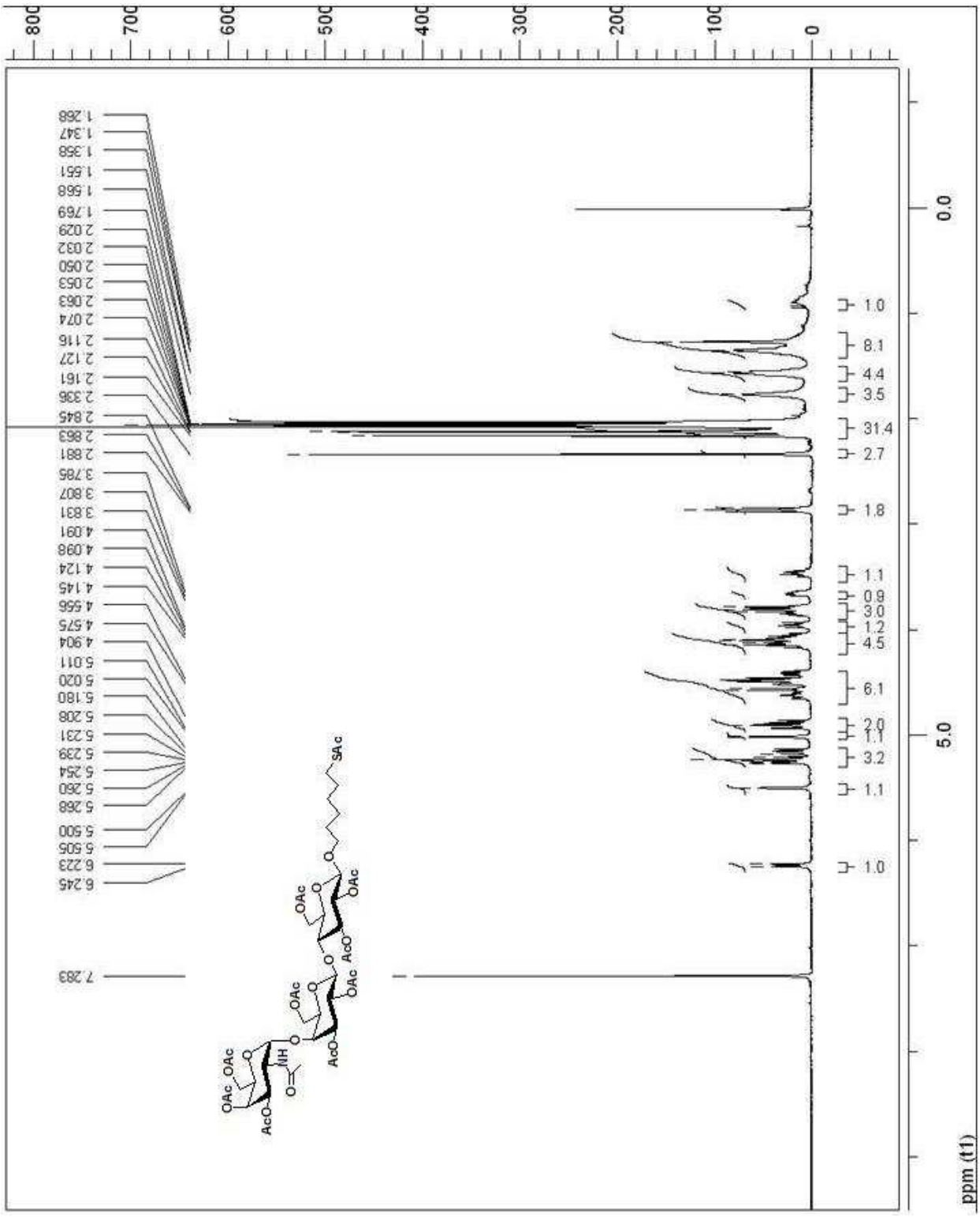


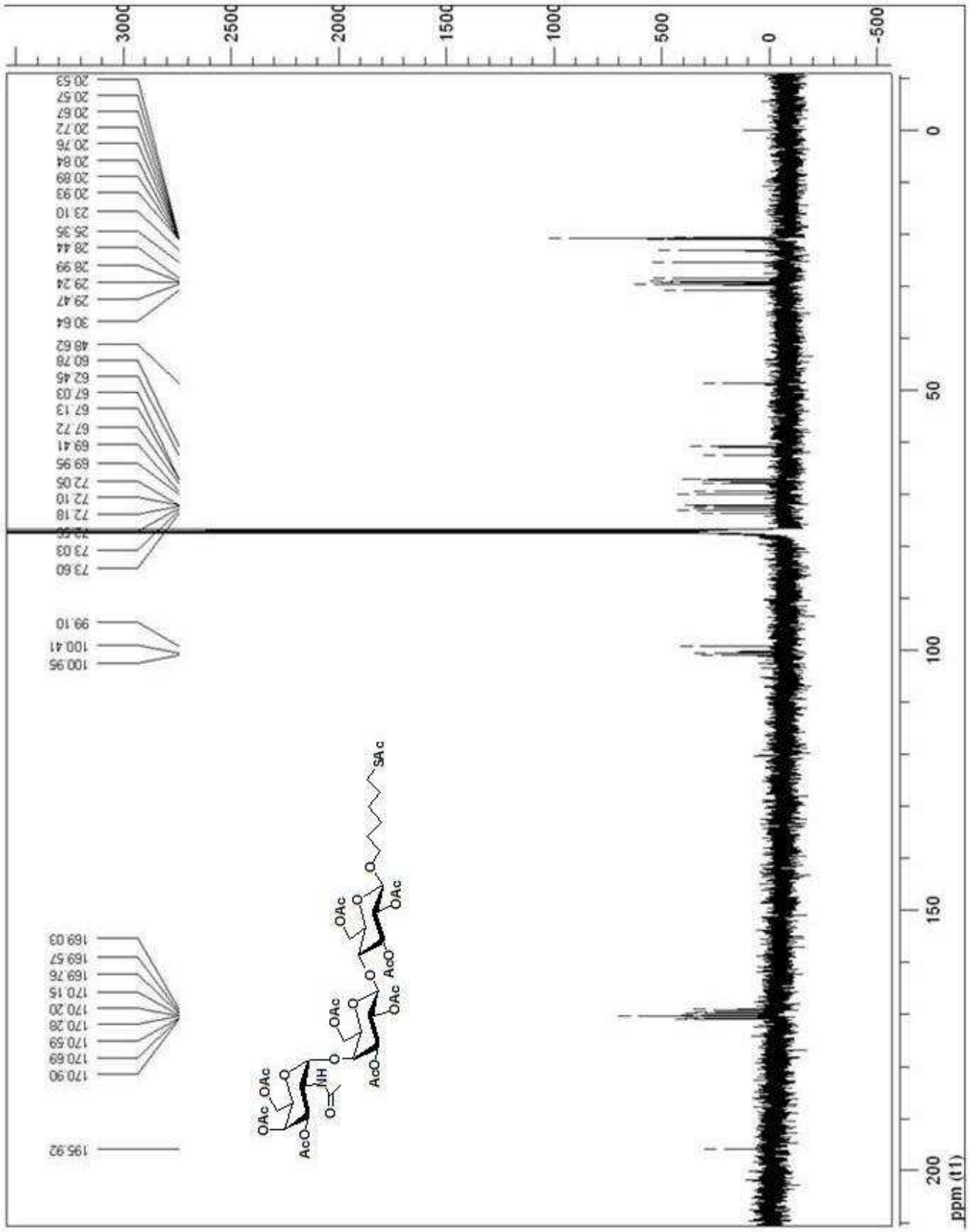
4(*3*) (110 mg, 0.113 mmol) was dissolved in 3 ml of dry THF and NH_2NH_2.HOAc (12.5 mg, 0.136 mmol) was added to it. The reaction was stirred at rt for 6 h. The reaction mixture was diluted with 5 ml of EtOAc and 5 ml of water was added, the organic layer was separated and dried *in vacuo* to give the hemiacetal (89 mg, 85 %), which was directly used in the next step. Anhydrous K_2CO_3 (132 mg, 0.960 mmol) was added to the solution of hemiacetal (89 mg, 0.096 mmol) and trichloroacetonitrile (100 µL, 0.960 mmol) in CH_2Cl_2 (3 ml) at rt. The reaction mixture was stirred at rt for 16 h, washed with water and the organic layer was dried over anhydrous Na_2SO_4, filtered and concentrated *in vacuo*. The residue was purified by column chromatography, eluting with a 1:1 mixture of hexane and EtOAc, to give the trichloroimidate as a pale yellow solid (82 mg, 80 %). The imidate (45 mg, 0.042 mmol) and S-(6-Hydroxy-hexyl)thioacetate(*2*) (11 mg, 0.063 mmol) were dissolved in CH_2Cl_2 (2 ml) and cooled to 0^0C. A 0.22 M solution of TMSOTF in CH_2Cl_2 (42 µl, 0.010 mmol) was added drop wise and the resulting solution was stirred for 2 h at 0^0C. The reaction was quenched by triethylamine solution and the solvent was removed in *vacuo.* The crude product was

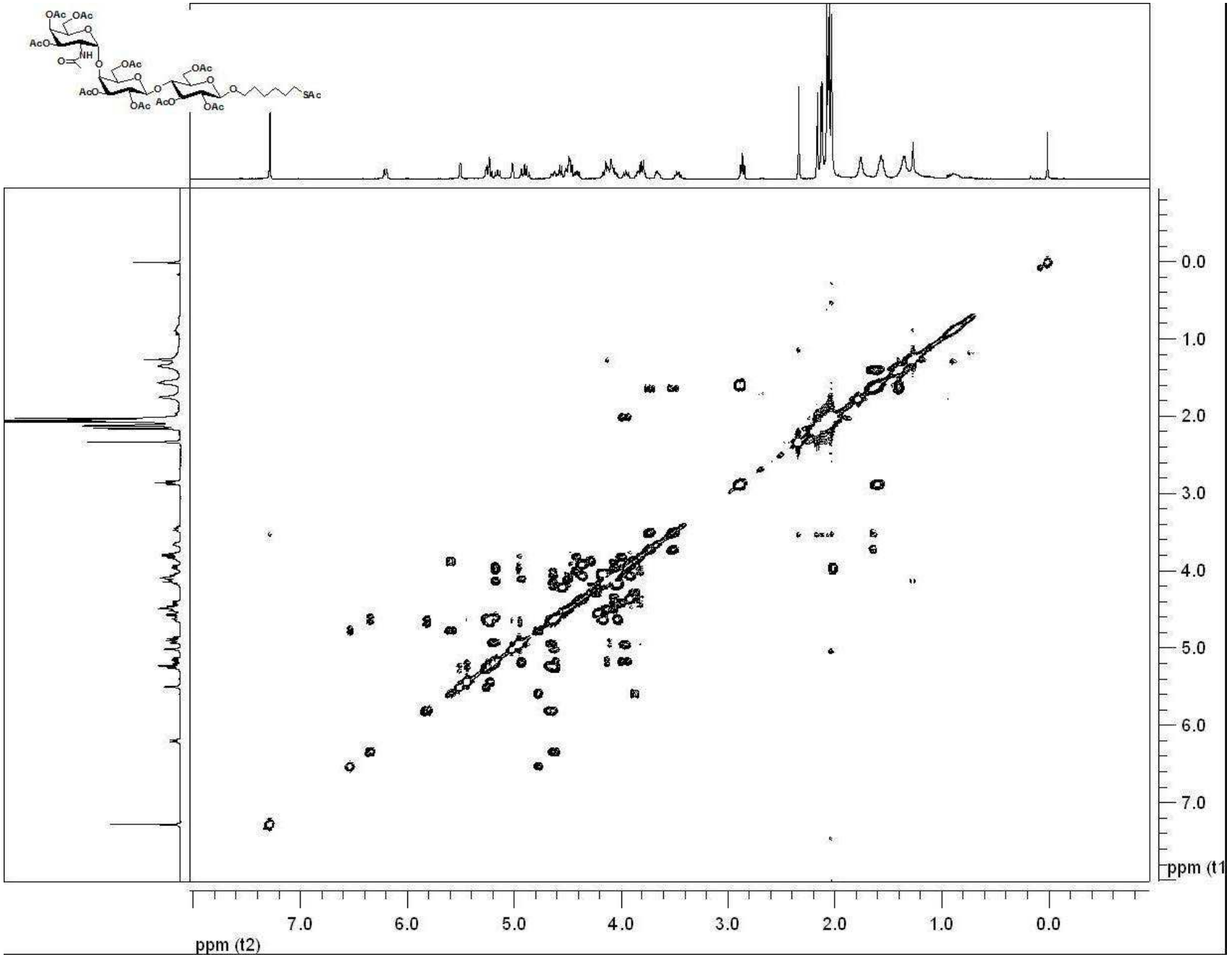
purified by column chromatography, eluting with 7:3 mixture of EtOAc and hexane, to give **5** as white solid (39 mg, 85%). ^{1}H NMR ($CDCl_3$, 400MHz): δ 5.6 (d, 1H, *J* = 2.8Hz), 5.39 (dd, 1H, *J* = 3.2 and 11.2 Hz), 5.23-5.17 (m, 2H), 5.11 (dd, 1H, *J* = 8 and 10.8 Hz), 5.00 (d, 1H, *J* = 3.6 Hz), 4.89 (dd, 1H, *J* = 8.0, 9.2 Hz), 4.74 (dd, 1H, *J* = 2.8 and 10.8 Hz), 4.54 - 4.42 (m, 5H), 4.20 – 4.09 (m, 5H), 4.025 (d, 1H, *J* = 2.4 Hz), 3.85 – 3.77 (m, 3H), 3.65 – 3.62 (m, 1H), 3.47 – 3.45 (m, 1H), 2.9 – 2.84 (m, 4H), 2.33 (d, 4H), 2.14 (s, 3H), 2.13 (s, 3H), 2.1 (s, 3H), 2.09 (s, 3H), 2.08 (s, 6H), 2.07 (s, 3H), 2.06 (s, 3H), 2.04 (s, 3H), 2.00 (s, 3H), 1.61 – 1.55 (m, 4H), 1.41 – 1.27 (m, 4H). ^{13}C NMR ($CDCl_3$): 196.02, 195.93, 170.68, 170.49, 170.45, 170.08, 169.68, 169.53, 168.87, 101.13, 100.54, 99.64, 73.17, 72.85, 72.55, 71.85, 69.95, 69.03, 68.88, 67.94, 67.17, 62.85, 62.27, 62.10, 62.07, 61.37, 61.13, 60.31, 60.09, 60.03, 32.58, 30.65, 29.48, 29.46, 29.25, 29.01, 28.51, 28.44, 25.35, 25.24, 20.95, 20.89, 20.74, 20.69. HRMS Calculated for $[C_{46}H_{66}O_{27}S + Na]^{+}$: 1105.3409; Found: 1105.3167

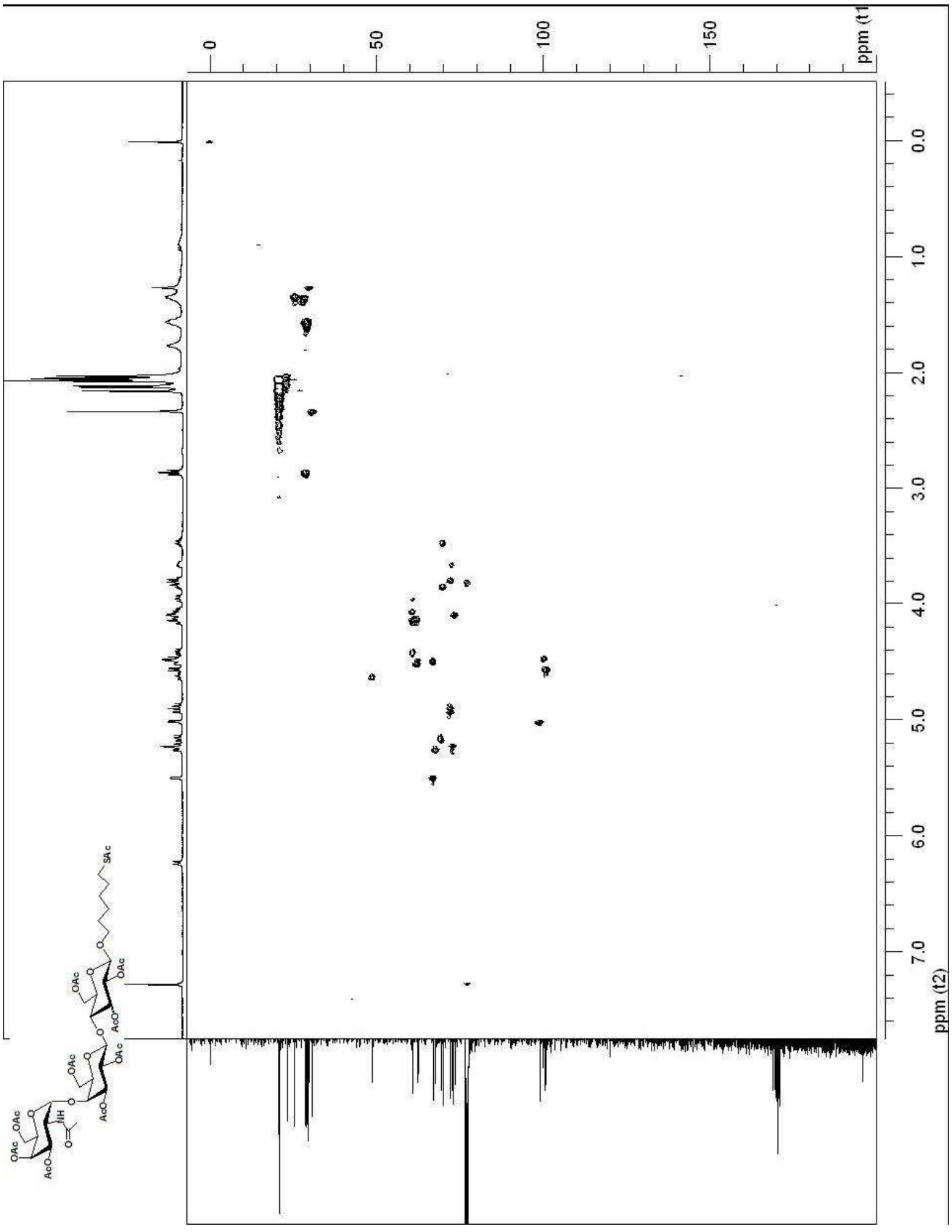


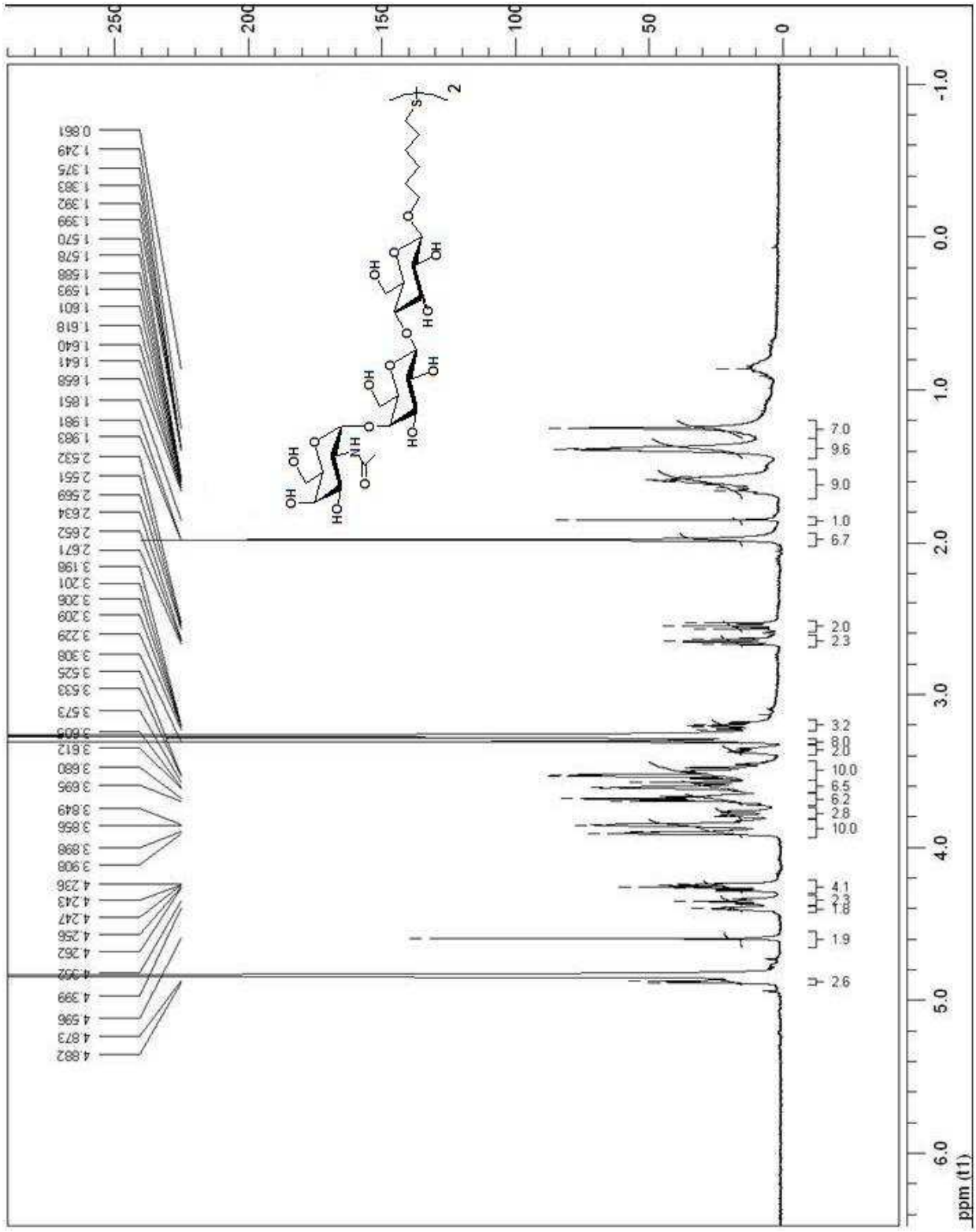
Compound **5** (17 mg, 0.016 mmol) was dissolved in methanol (2 ml) and a solution of NaOMe in methanol (0.5M, 0.5 ml) was added and the reaction mixture was stirred at rt for 6h. The reaction was neutralized by careful addition of Amberlite-15 H^{+} resin and the resin was filtered. The solvent was removed in *vacuo* and the residue was purified by Biogel P-2 gel column chromatography, eluting with methanol, to give dimerized product **LG1** as a white solid (10 mg, 99%). ^{1}H NMR (CD_3OD, 400MHz): δ 4.92 (d, 1H, *J* = 3.6 Hz), 4.6 (bs, 1H), 4.39 – 4.38 (m, 1H), 4.26 -4.23 (m, 2H), 3.95 (bs, 1H), 3.89-3.65 (m, 12H), 3.52-3.48 (m, 6H), 3.32-3.4 (m, 1H), 3.24-3.17 (m, 1H), 2.67 – 2.55 (m, 3H), 1.6-1.46 (m, 6H), 1.45-1.20 (m, 8H). ^{13}C NMR (CD_3OD): 103.97, 102.83, 101.30, 79.67, 79.64, 78.40, 75.13, 75.08, 73.49, 73.28, 71.47, 71.26, 69.89, 69.68, 69.16, 61.50, 61.32, 60.59, 60.07, 38.35, 38.31, 32.13, 30.46, 30.18, 29.65, 29.61, 29.26, 28.79, 28.34, 28.29, 28.26, 27.87, 25.30, 25.27, 25.16. HRMS Calculated for $[2C_{52}H_{92}N_2O_{32}S_2+Na]^{+}$: 1262.4372. Found: 1262.4688.

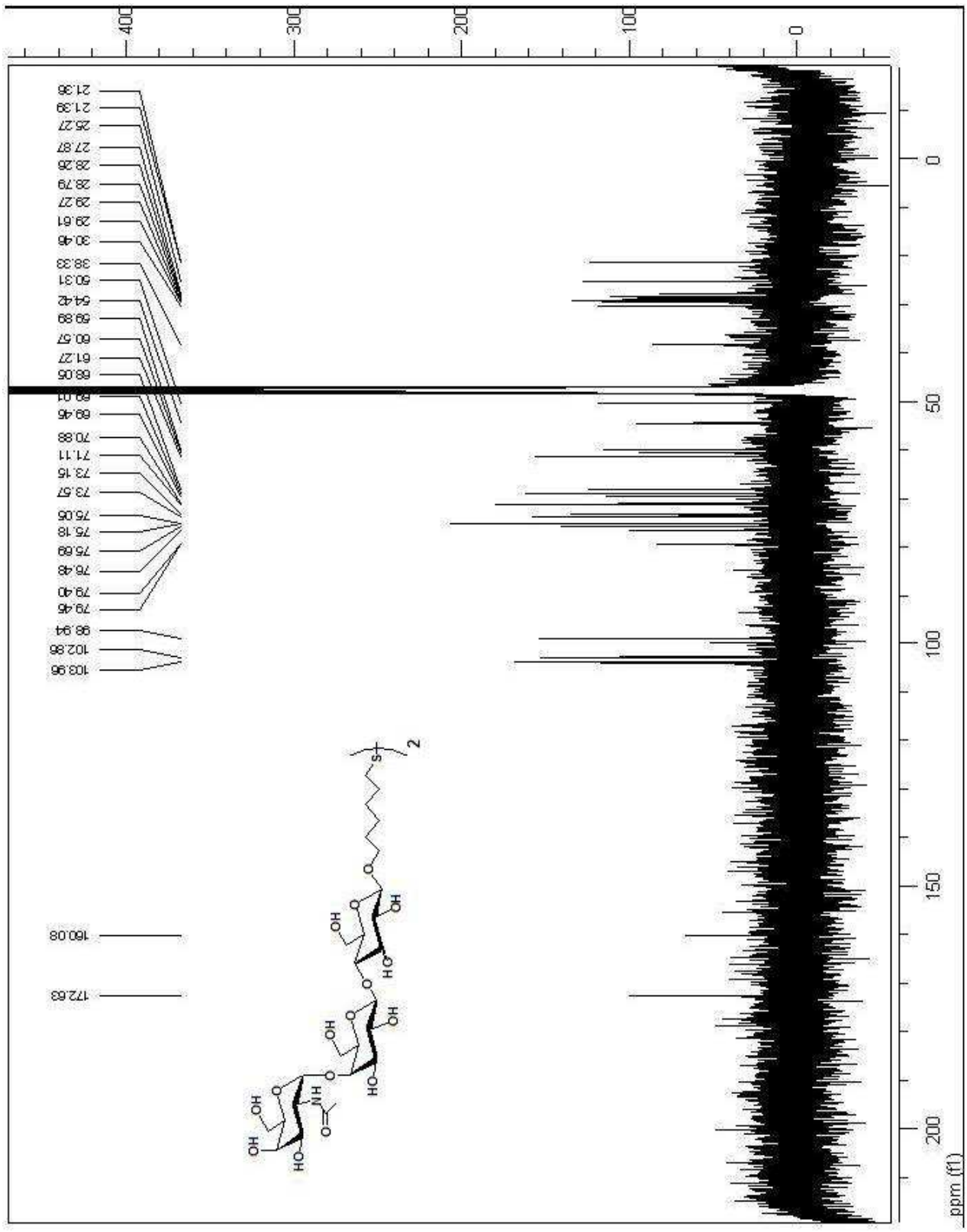

ppm (t1)

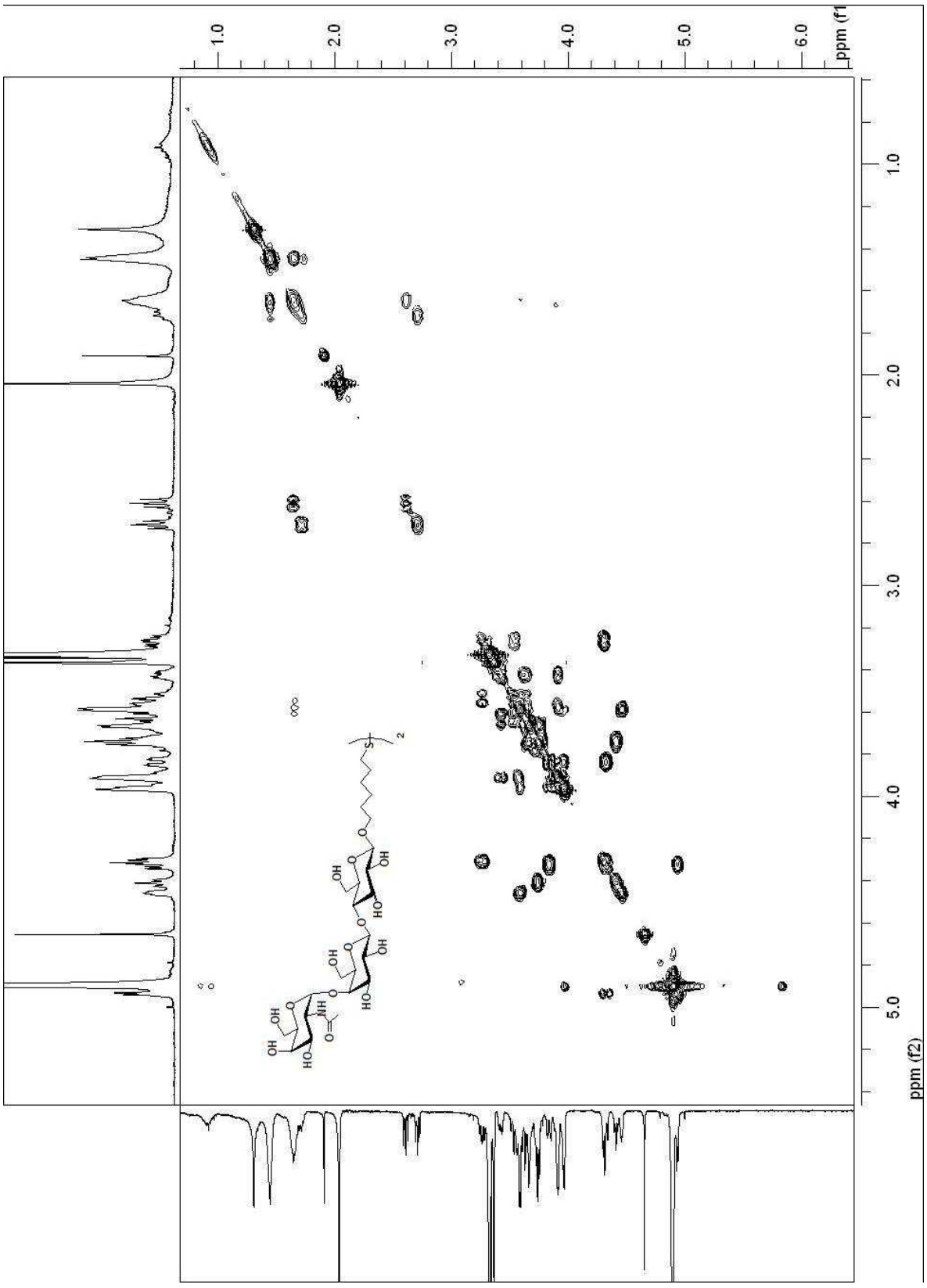

3000
2500
2000
1500
1000
500
0
-500
20.53
20.57
20.67
20.72
20.76
20.84
20.89
20.93
23.10
25.35
28.44
28.99
29.24
29.47
30.64
48.62
60.78
62.45
67.03
67.13
67.72
69.41
69.95
72.05
72.10
72.18
73.03
73.60
99.10
100.41
100.95
169.03
169.57
169.76
170.15
170.20
170.28
170.59
170.69
170.90
195.92
0
50
100
150
200
ppm (t1)

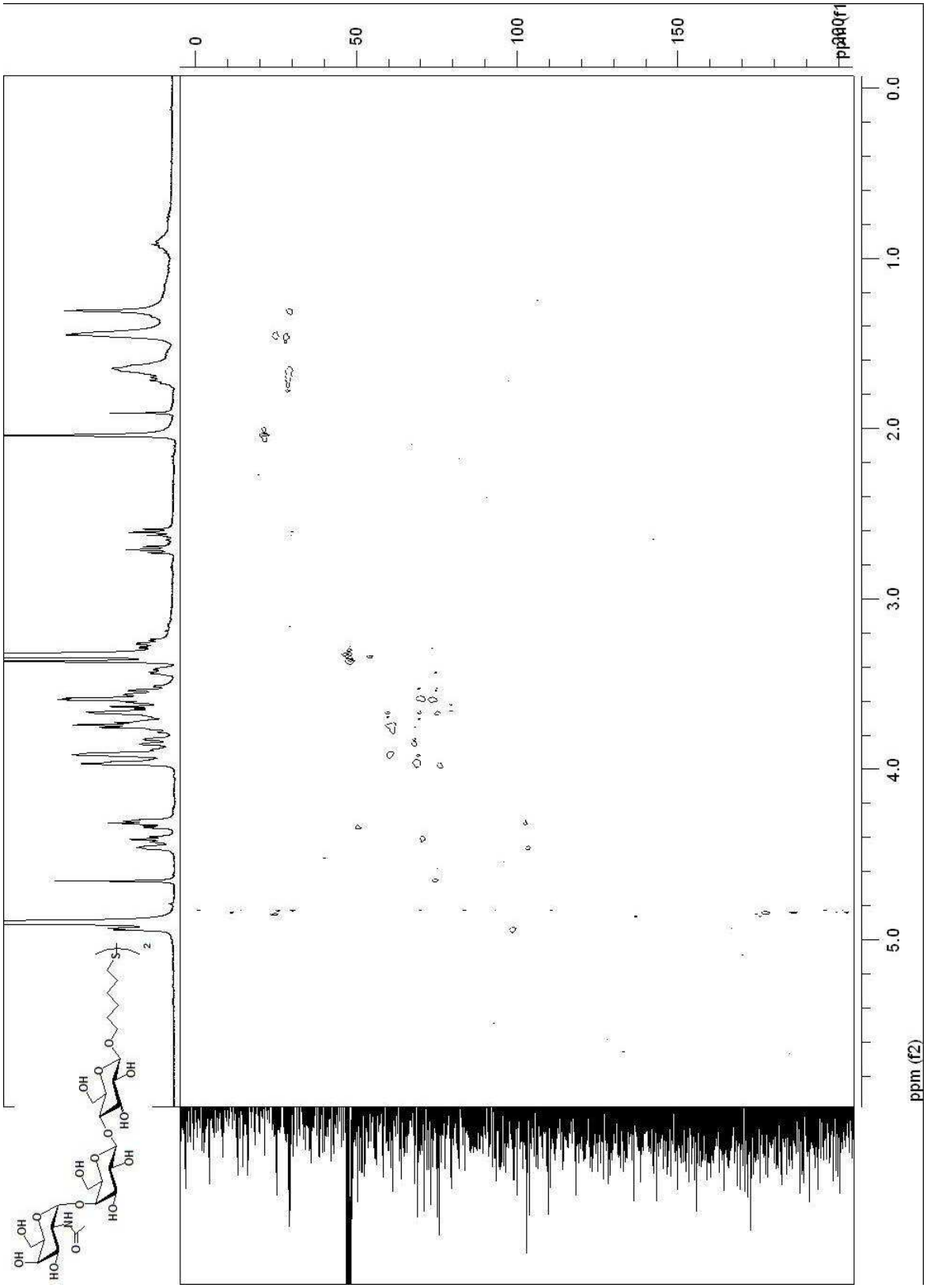

OAc
OAc
AcO
NH
O
OAc
AcO
OAc
AcO
OAc
OAc
SAc
0.0
1.0
2.0
3.0
4.0
5.0
6.0
7.0
ppm (t1
7.0
6.0
5.0
4.0
3.0
2.0
1.0
0.0
ppm (t2)

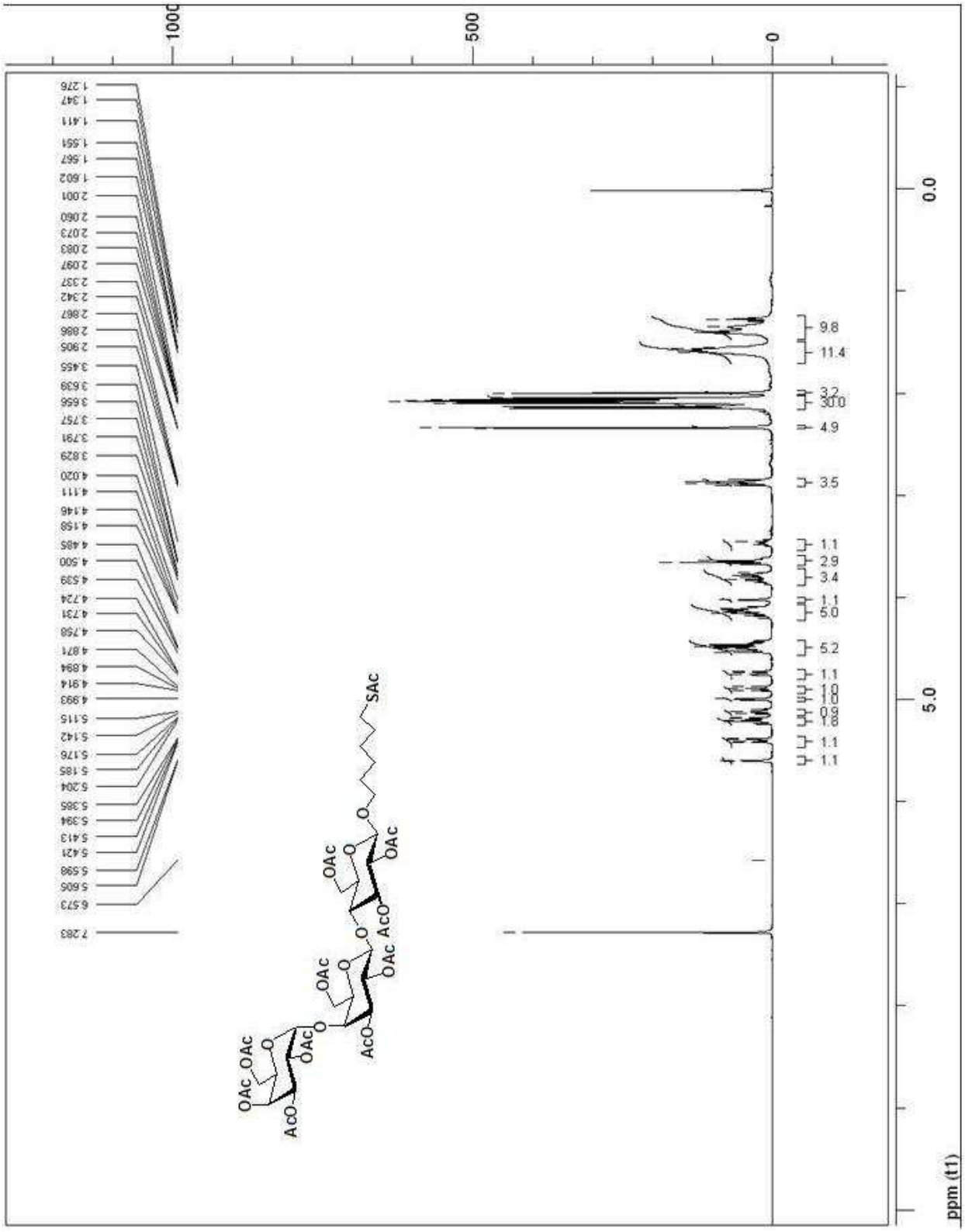

0
50
100
150
ppm (t1
0.0
1.0
2.0
3.0
4.0
5.0
6.0
7.0
ppm (t2)
OAc
AcO
NH
SAc

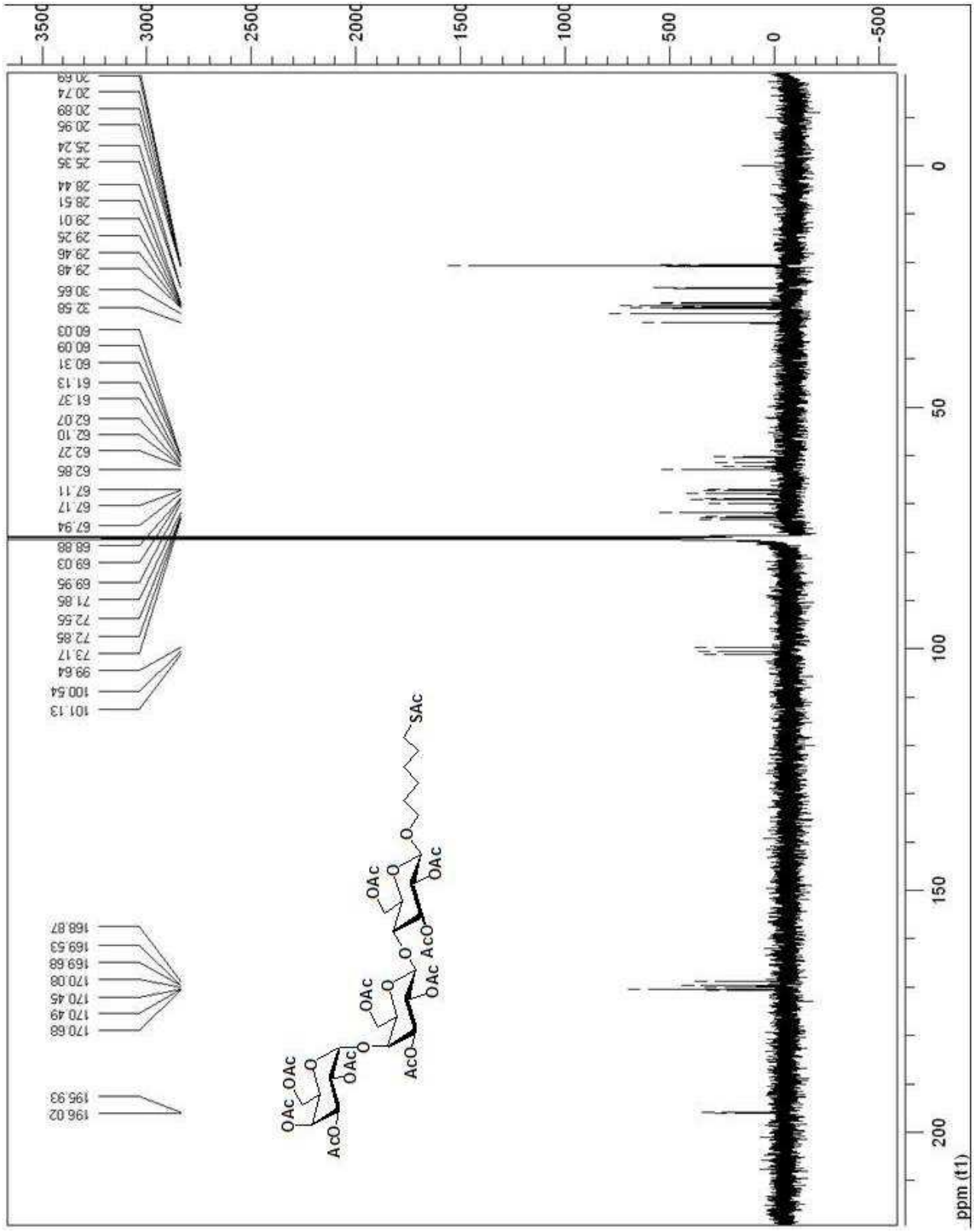

ppm (t1)

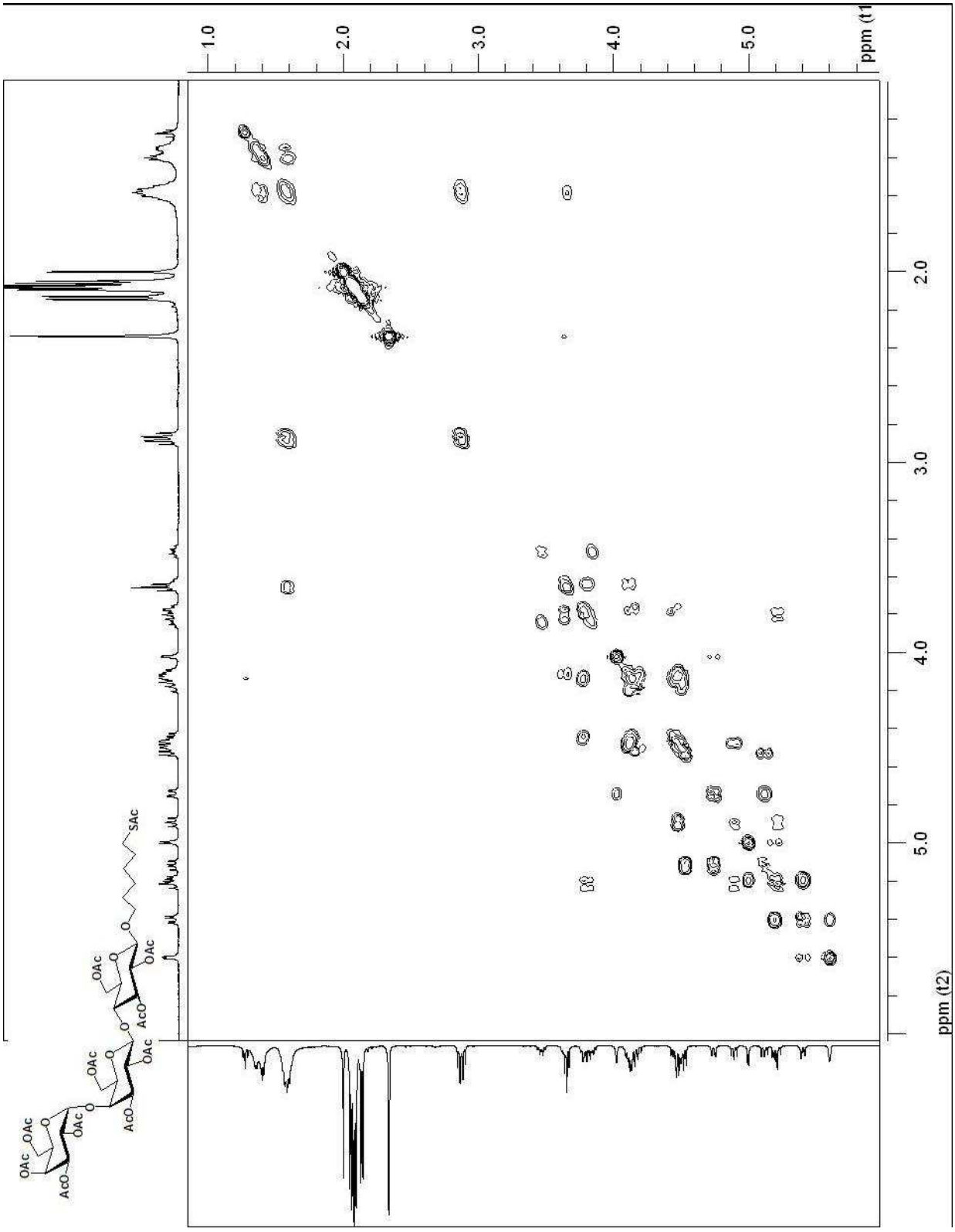

400
300
200
100
0
0
50
100
150
200
ppm (f1)
21.36
21.39
25.27
27.87
28.26
28.79
29.27
29.61
30.46
38.33
60.31
64.42
69.89
60.57
61.27
68.05
69.01
69.46
70.88
71.11
73.15
73.57
75.05
75.18
75.69
76.48
79.40
79.46
98.94
102.86
103.96
172.63
160.08
OH
HO
HN
O
S
2

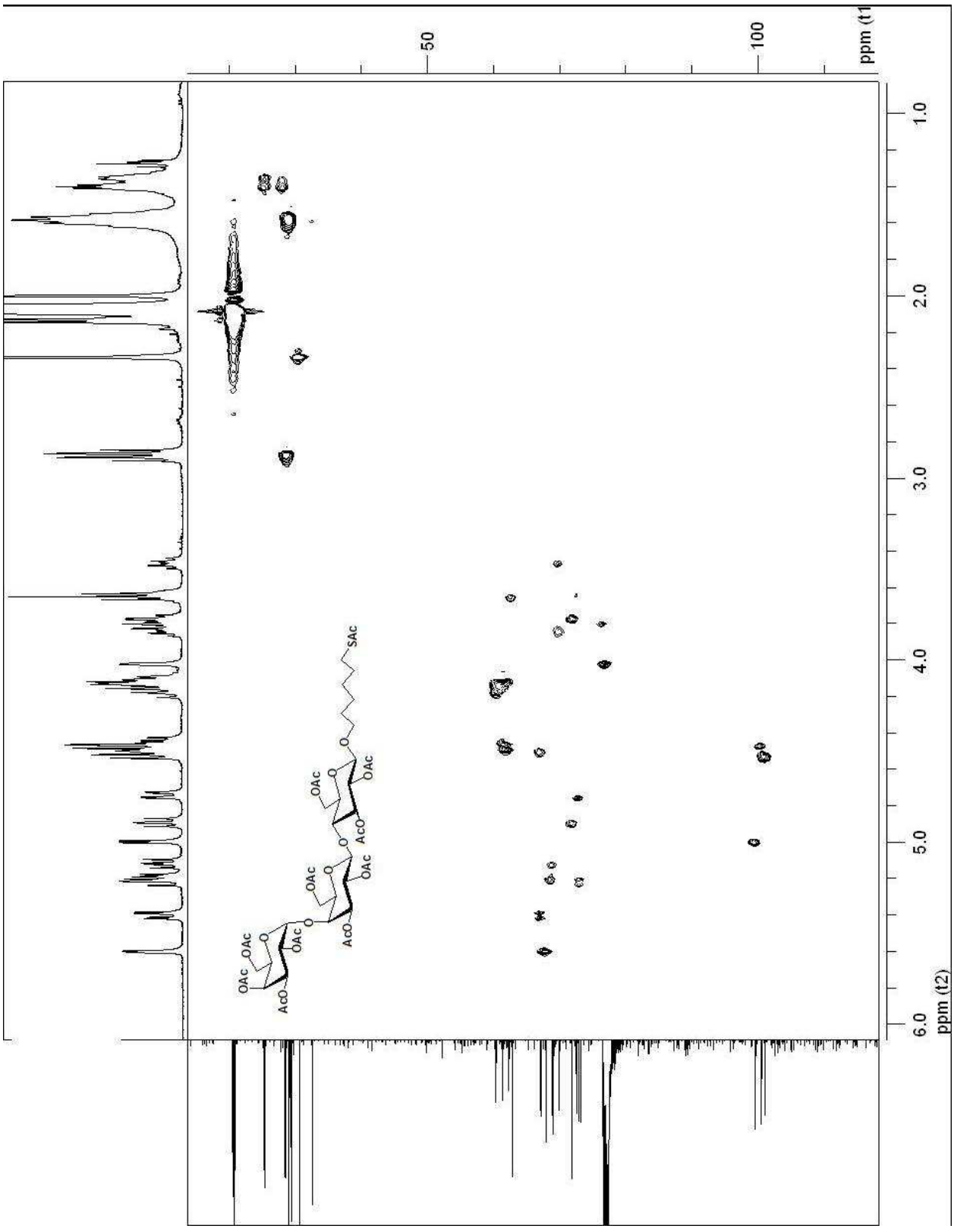

1.0
2.0
3.0
4.0
5.0
6.0
ppm (f1)
1.0
2.0
3.0
4.0
5.0
ppm (f2)

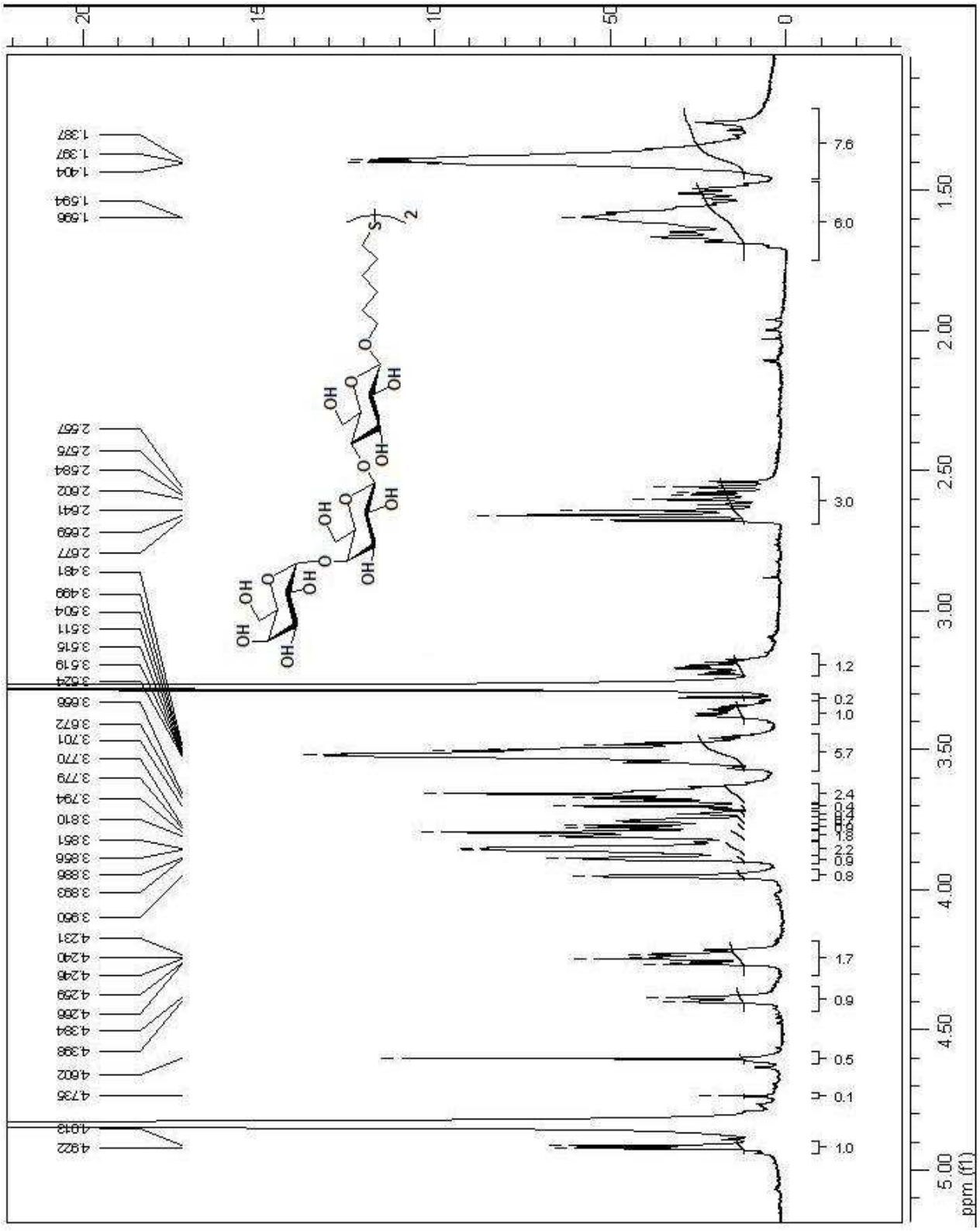

0
50
100
150
ppm(f1)
0.0
1.0
2.0
3.0
4.0
5.0
ppm (f2)

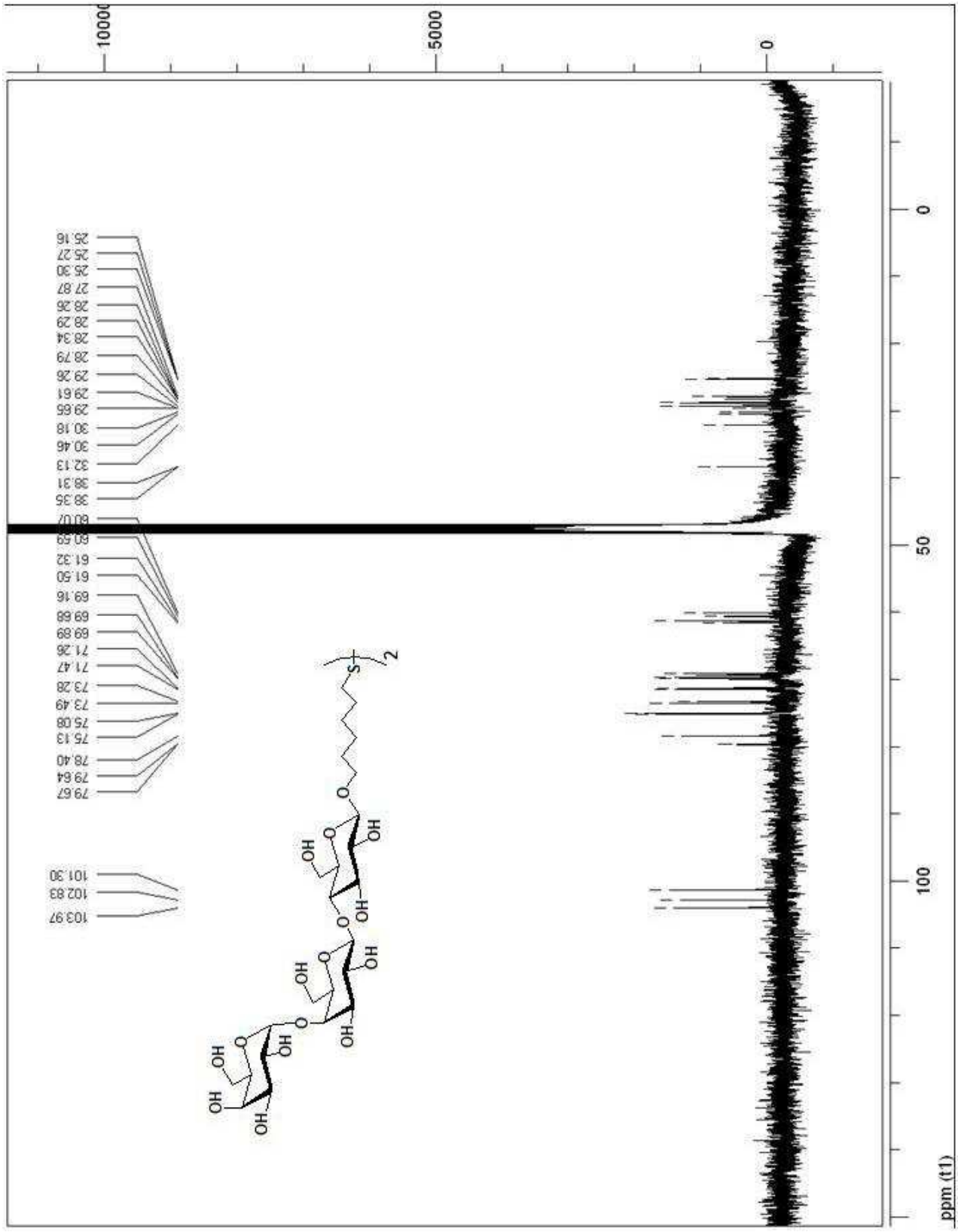

1000
500
0
0.0
5.0
ppm (t1)
9.8
11.4
3.2
30.0
4.9
3.5
1.1
2.9
3.4
1.1
5.0
5.2
1.1
1.0
1.0
0.9
1.8
1.1
1.1
1.276
1.347
1.411
1.551
1.567
1.602
2.001
2.060
2.073
2.083
2.097
2.337
2.342
2.867
2.886
2.905
3.455
3.539
3.656
3.757
3.791
3.829
4.020
4.111
4.146
4.158
4.485
4.500
4.539
4.724
4.731
4.758
4.871
4.894
4.914
4.993
5.115
5.142
5.176
5.185
5.204
5.385
5.394
5.413
5.421
5.598
5.605
6.573
7.283
SAc
OAc
AcO

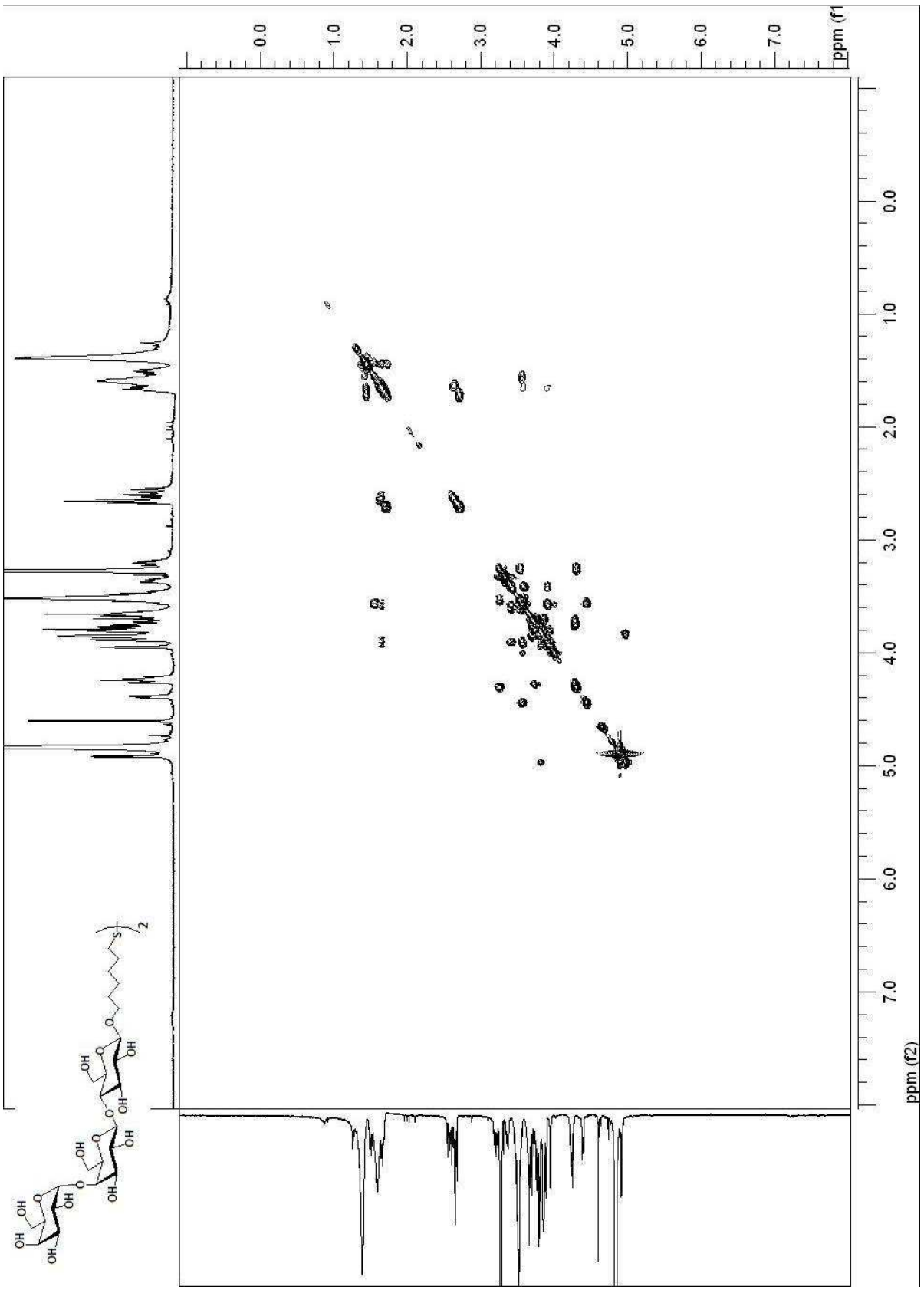

20.69
20.74
20.89
20.96
25.24
25.35
28.44
28.51
29.01
29.25
29.46
29.48
30.65
32.58
60.03
60.09
60.31
61.13
61.37
62.07
62.10
62.27
62.86
67.11
67.17
67.94
68.88
69.03
69.95
71.85
72.55
72.85
73.17
99.64
100.54
101.13
168.87
169.53
169.68
170.08
170.45
170.49
170.68
196.02
196.93
SAc
OAc
AcO
ppm (t1)

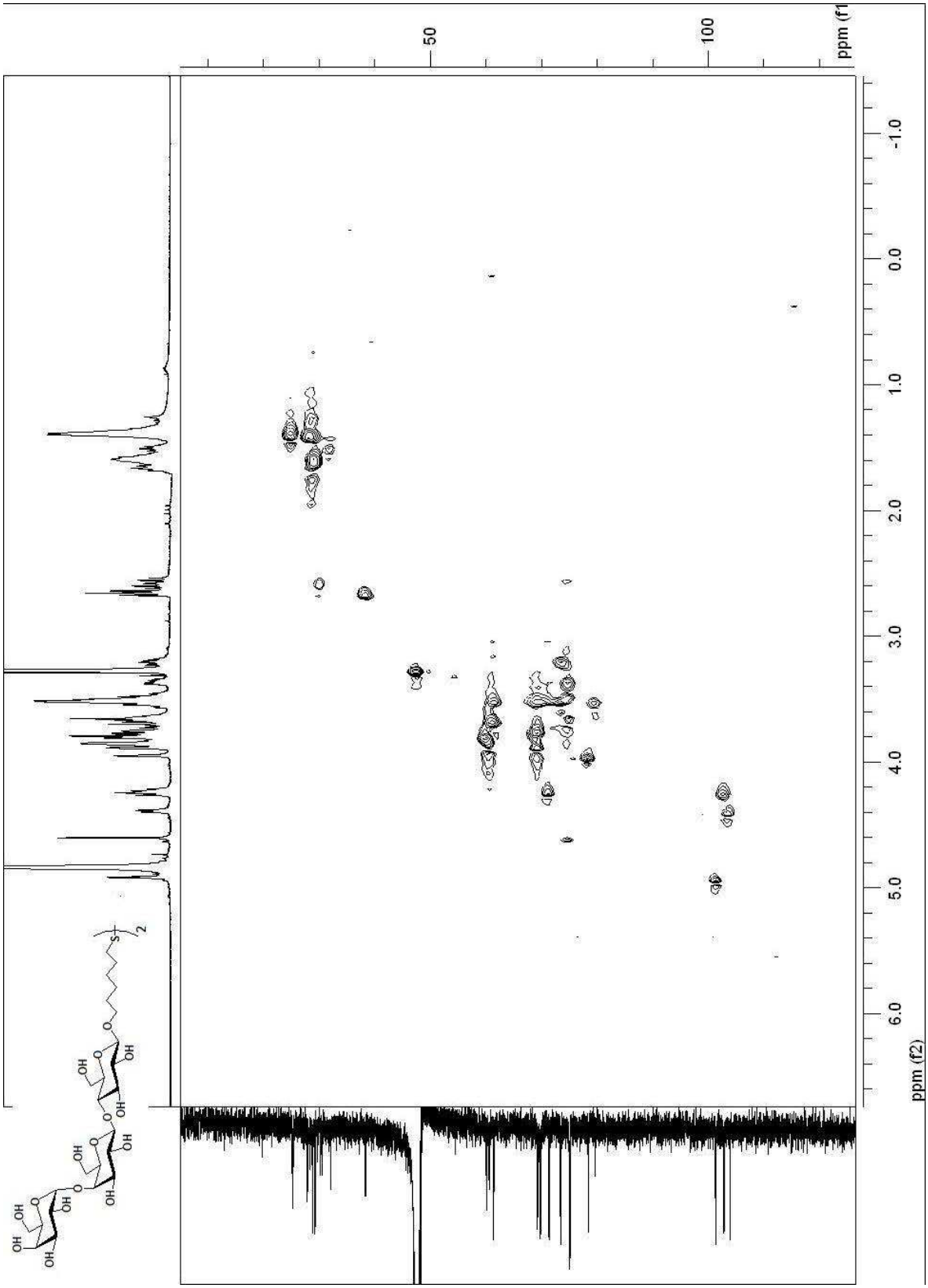

1.0
2.0
3.0
4.0
5.0
ppm (t1
ppm (t2)
OAc
AcO
SAc


50
100
ppm (t1
1.0
2.0
3.0
4.0
5.0
6.0
ppm (t2
SAc
OAc
AcO




10000
5000
0
25.16
25.27
25.30
27.87
28.26
28.29
28.34
28.79
29.26
29.61
29.65
30.18
30.46
32.13
38.31
38.35
60.07
60.59
61.32
61.50
69.16
69.68
69.89
71.26
71.47
73.28
73.49
75.08
75.13
78.40
79.64
79.67
101.30
102.83
103.97
OH
O
S
2
0
50
100
ppm (t1)


0.0
1.0
2.0
3.0
4.0
5.0
6.0
7.0
ppm (f1)
ppm (f2)
OH
O
S
2


50
100
ppm (f1
-1.0
0.0
1.0
2.0
3.0
4.0
5.0
6.0
ppm (f2)
OH
O
S
2

CHARACTERIZATION OF GOLD NPS

The gold NPs were characterized using NMR, UV-VIS and TEM analysis. Typical spectra of gold NPs using different techniques are shown in figures 1-3.

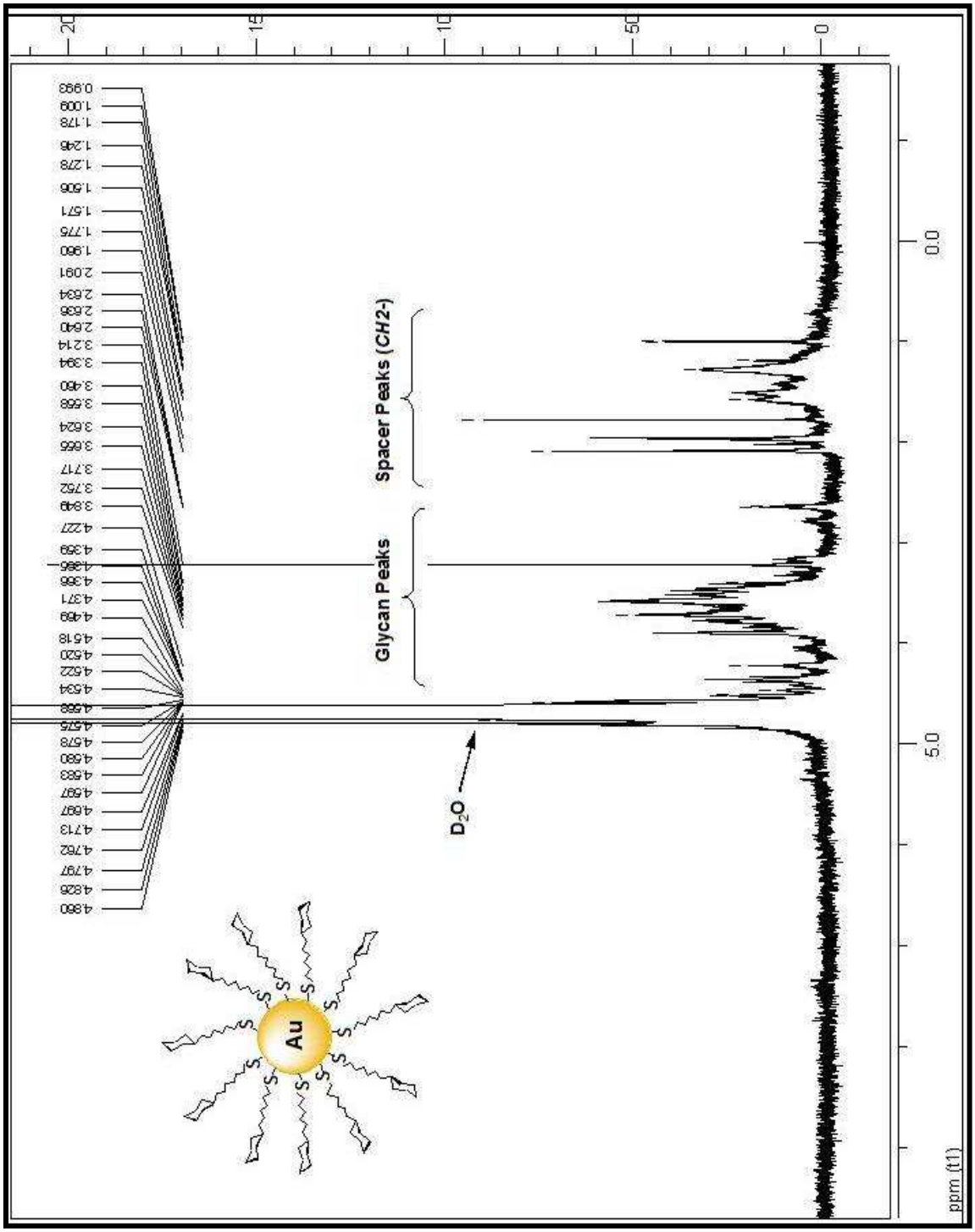


FIGURE .1 ^{1}H NMR spectra of GNP1

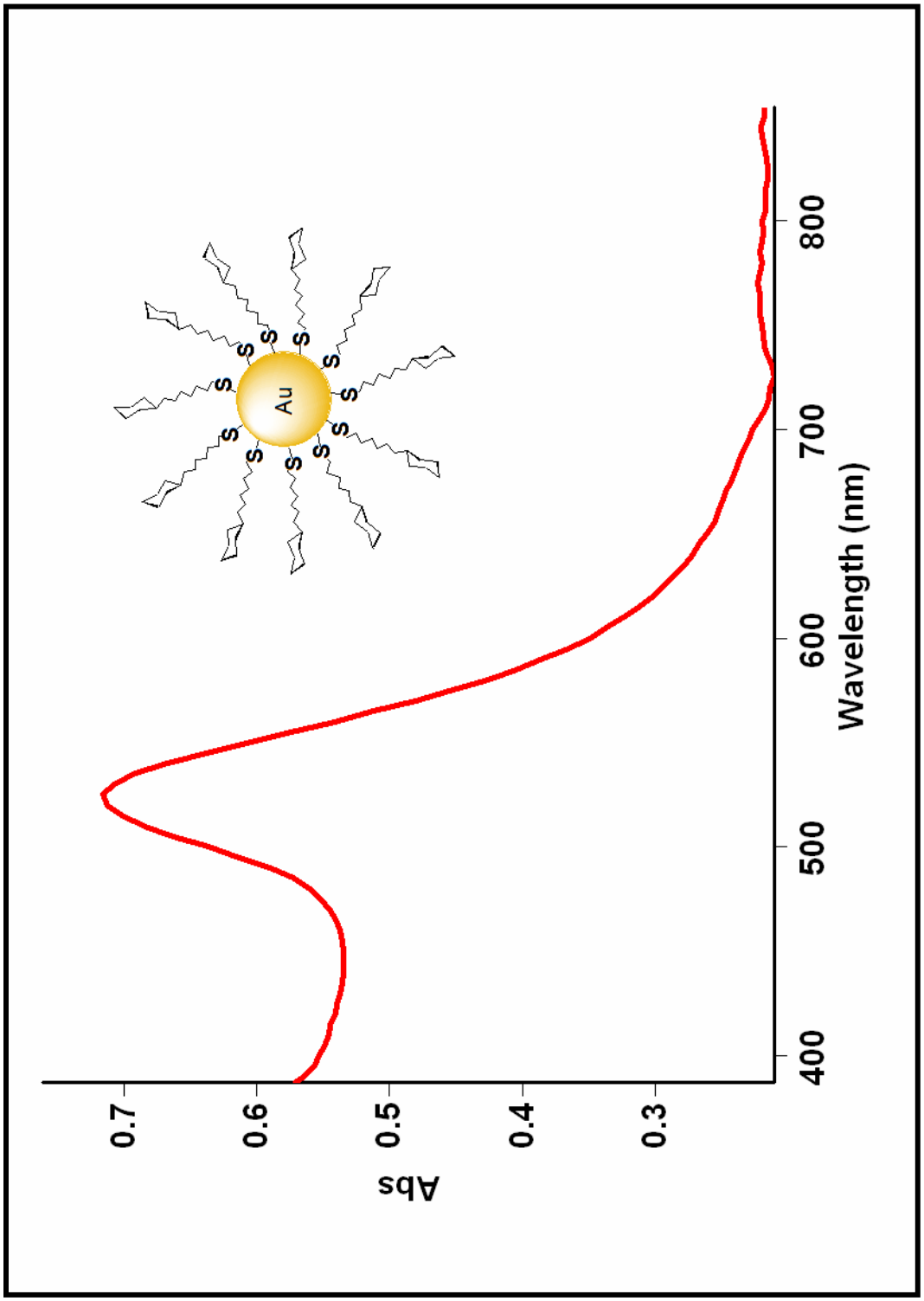
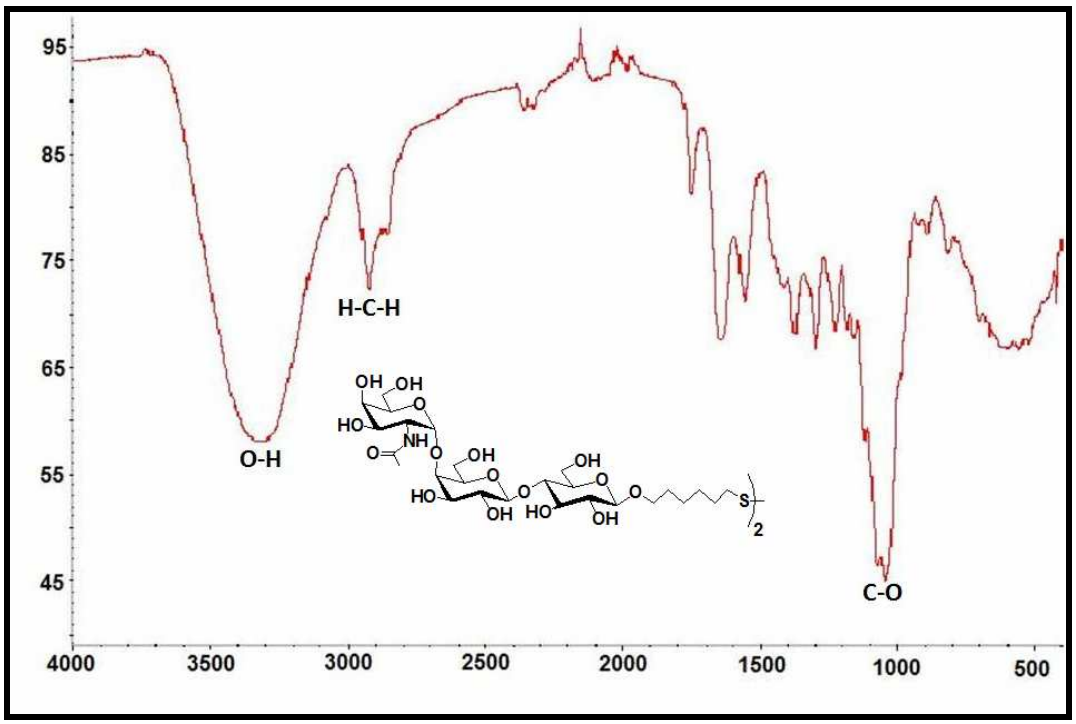


FIGURE 2. UV-VIS spectra of GNP1.The surface plasmon resonance is clearly visible at 515 nm.

A



B

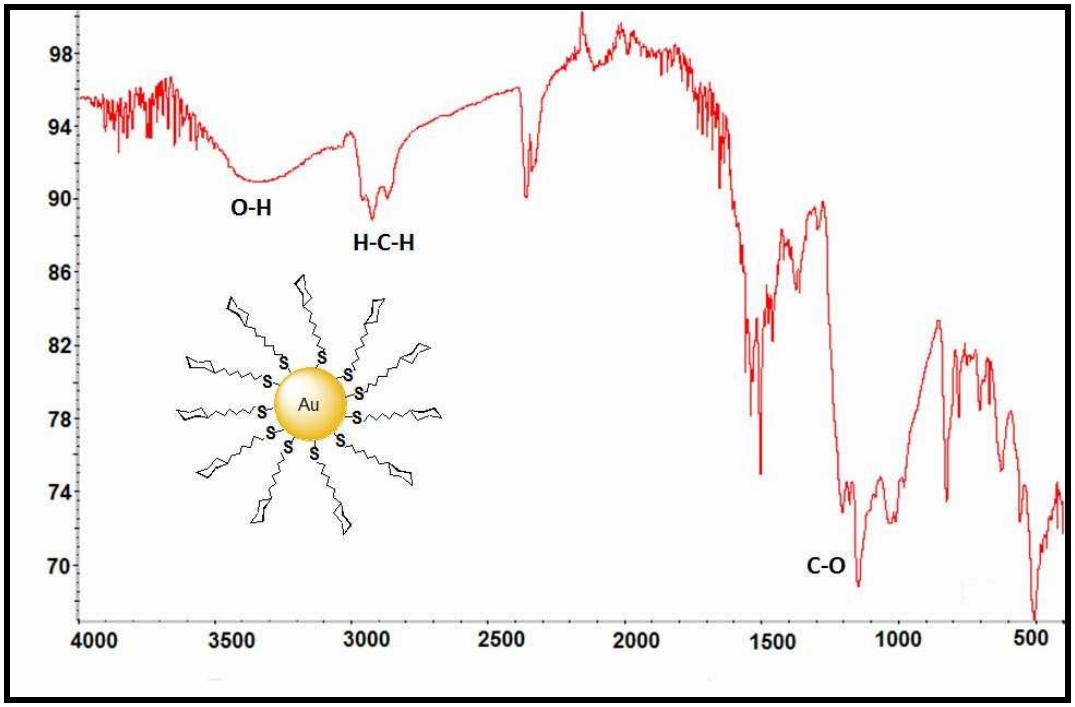
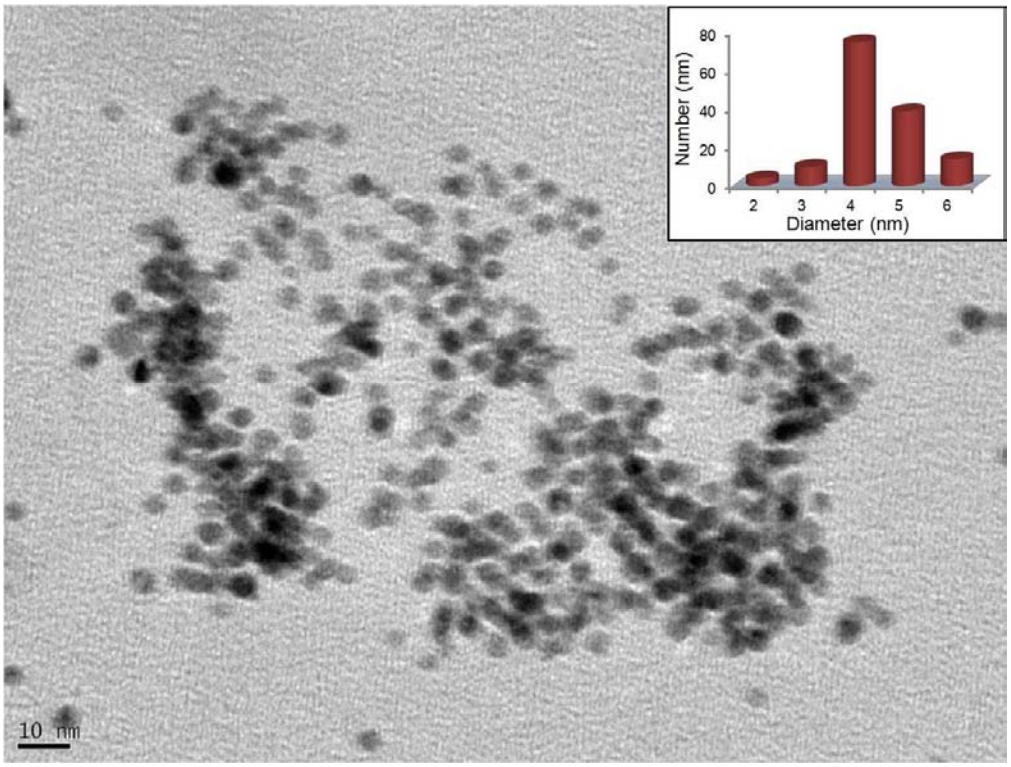
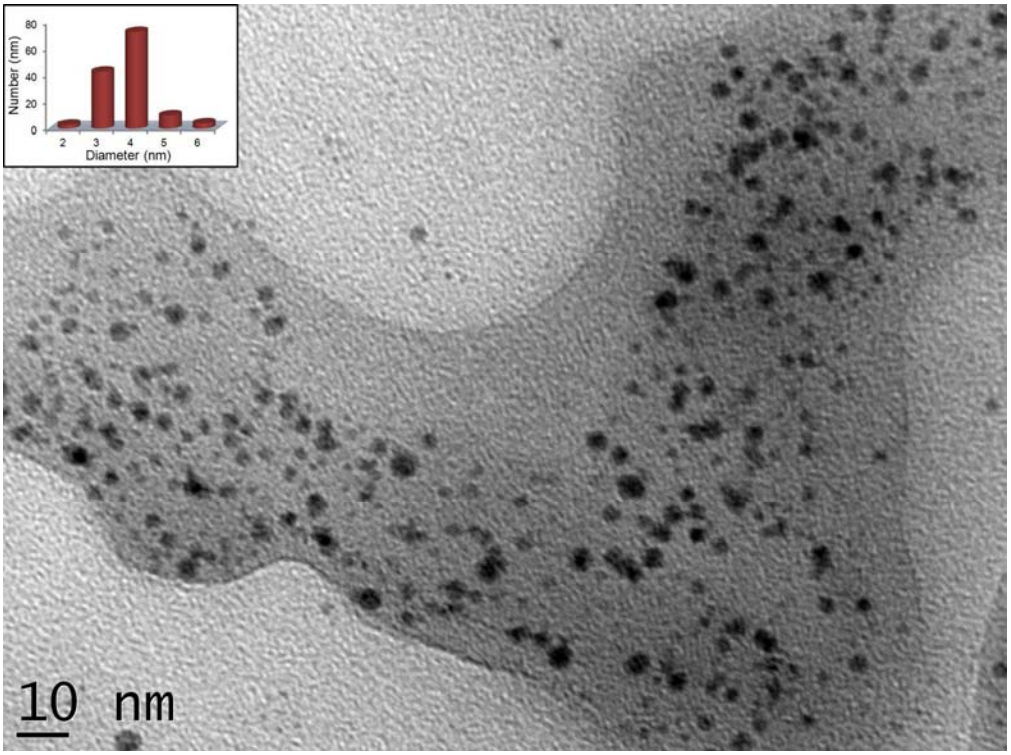


FIGURE 3 (A) IR spectra of LG2, the NHAcGal-Gal-Glu ligand. **(B)** IR spectra of the GNP2.

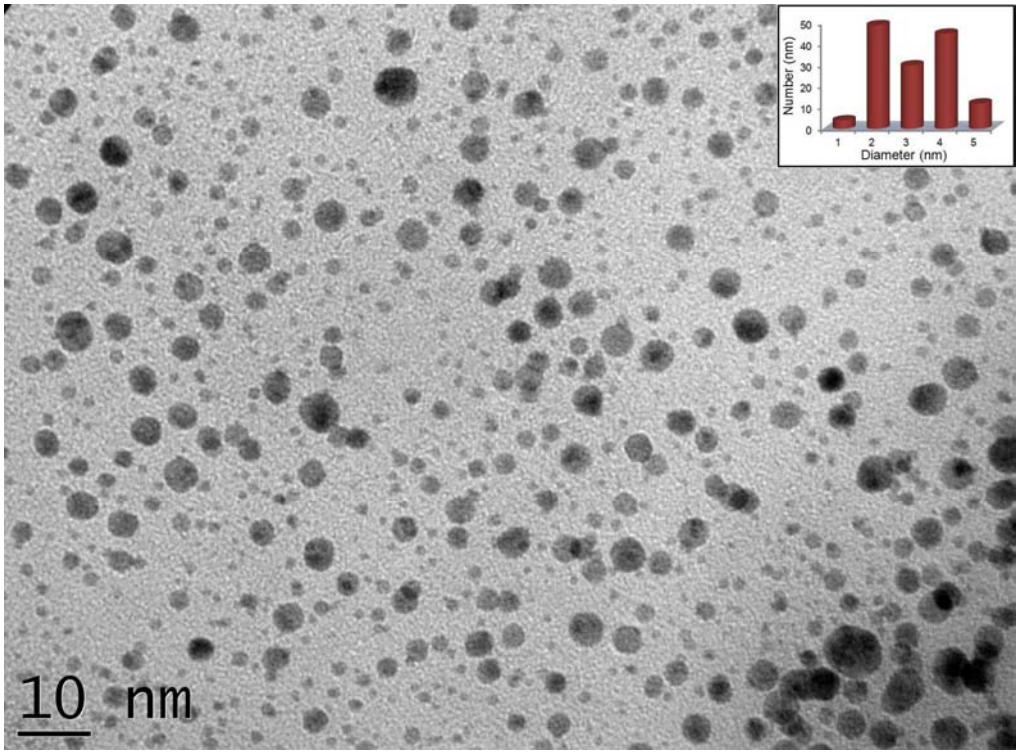
A)


Number (nm)
80
60
40
20
0
2
3
4
5
6
Diameter (nm)
10 nm

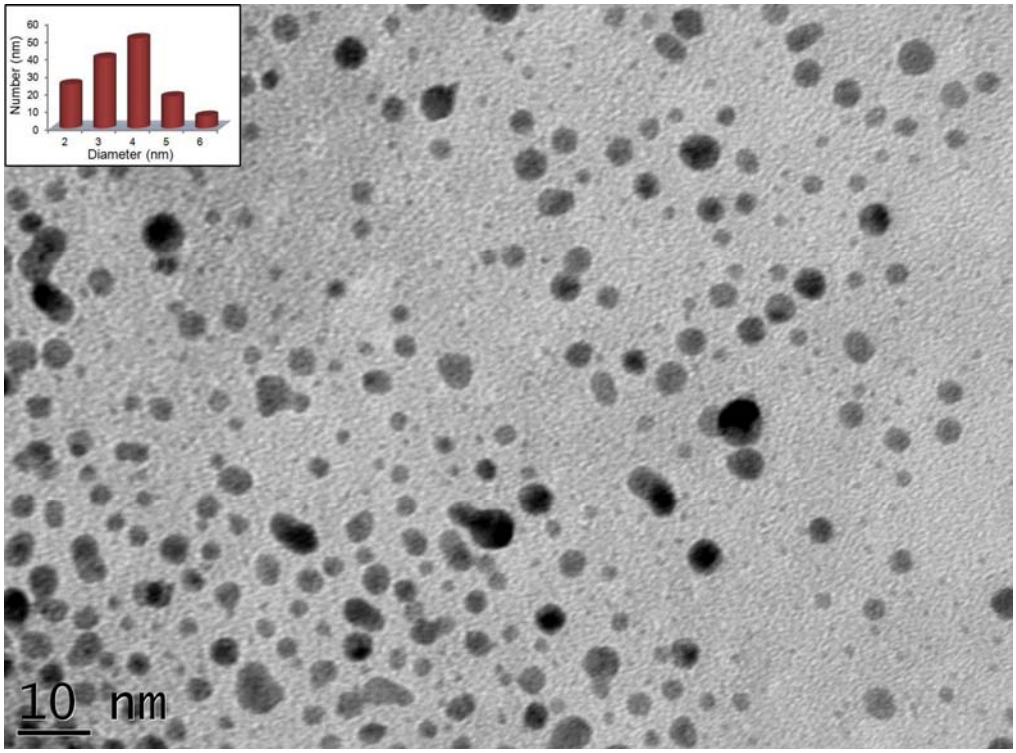
B)


Number (nm)
80
60
40
20
0
2
3
4
5
6
Diameter (nm)
10 nm

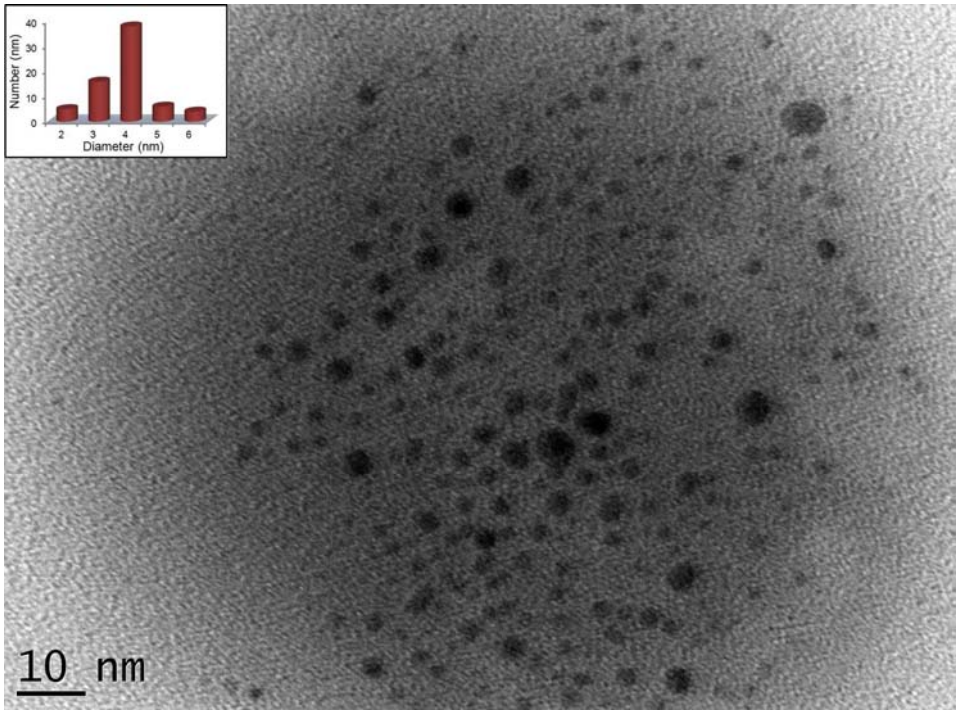
C)


Number (nm)
50
40
30
20
10
0
1
2
3
4
5
Diameter (nm)
10 nm

D)


Number (nm)
60
50
40
30
20
10
0
2
3
4
5
6
Diameter (nm)
10 nm

E)



F)

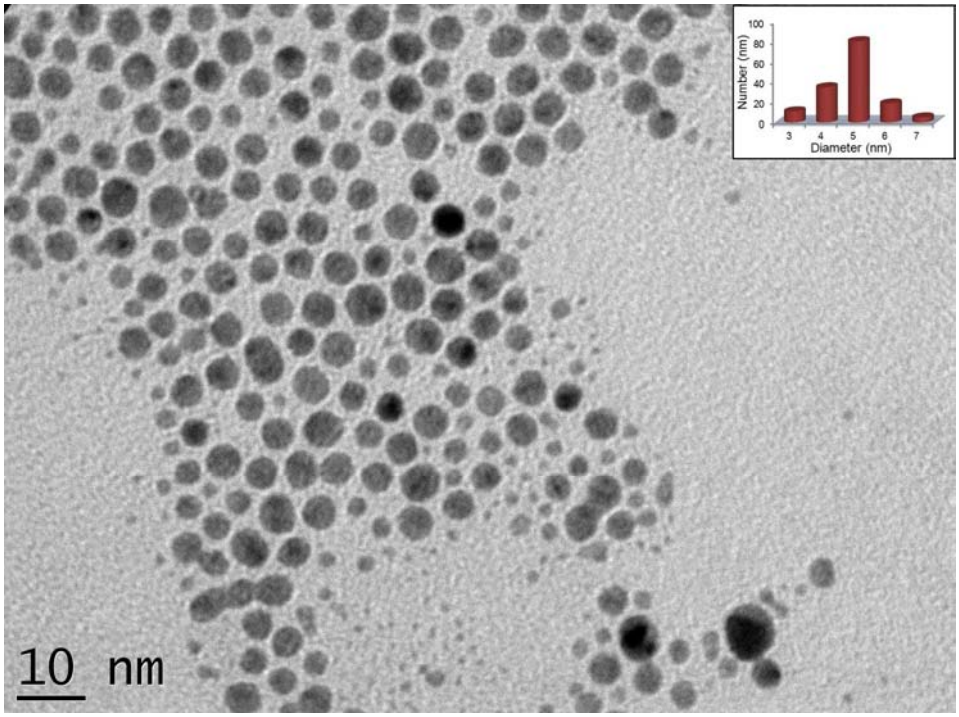


FIGURE 4TEM image of GNP1 **(A)**, GNP2 **(B)**, GNP3 **(C)**, gold NP with LG2:OEG – 75:25 **(D)**, 50:50 **(E)**, 25:75 **(F)**. Inset: The size distribution of the NPs.

DETERMINATION OF NUMBER OF SUGARS PER NANOPARTICLE.

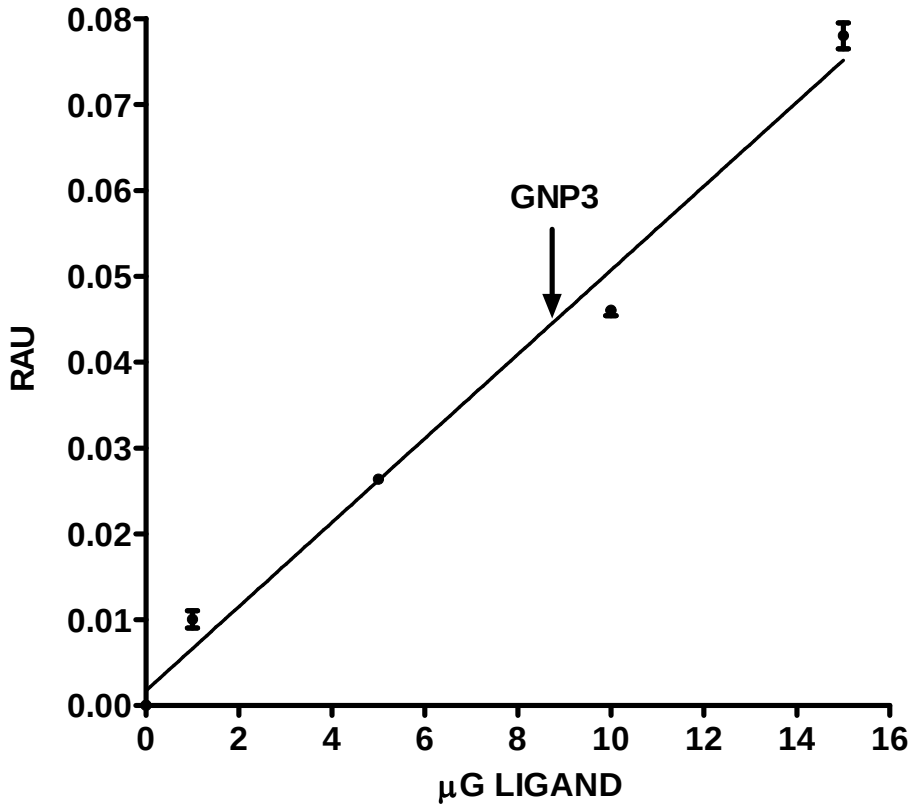
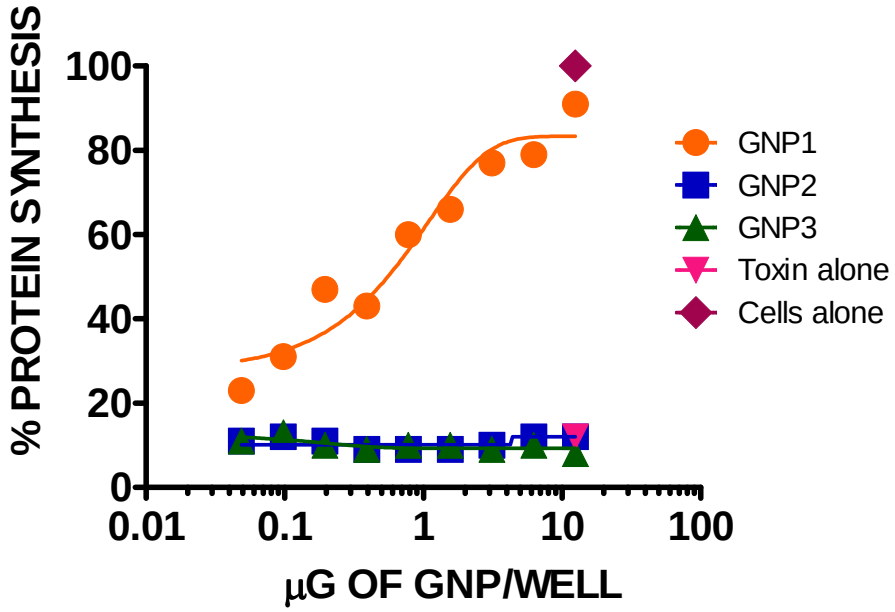


FIGURE .5 The plot of concentration of free ligand versus absorbance.

GNPS	AMOUNT OF SUGAR ON 1 MG OF NPS (µG/MG)	NOS. OF SUGAR PER NPS
GNP1	105	70
GNP2	95	65
GNP3	85	125

TABLE .1 Number of sugars per nanoparticle.

A)



B)

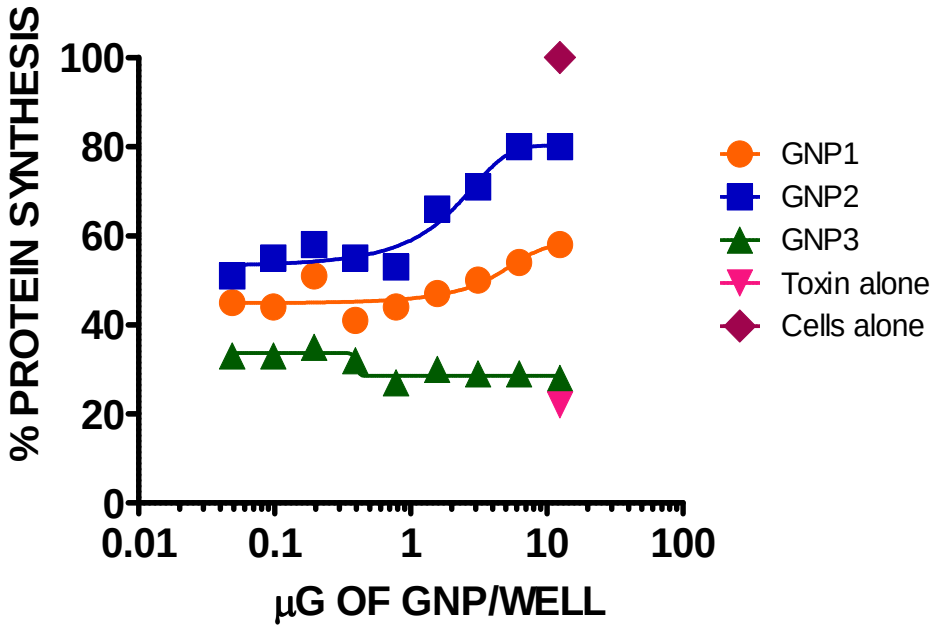


FIGURE 6. (A) Inhibition of 6.4 ng of Stx1 with varying concentrations of GNPs. **(B)** Inhibition of 6.4 ng of Stx 2 with varying concentrations of GNPs

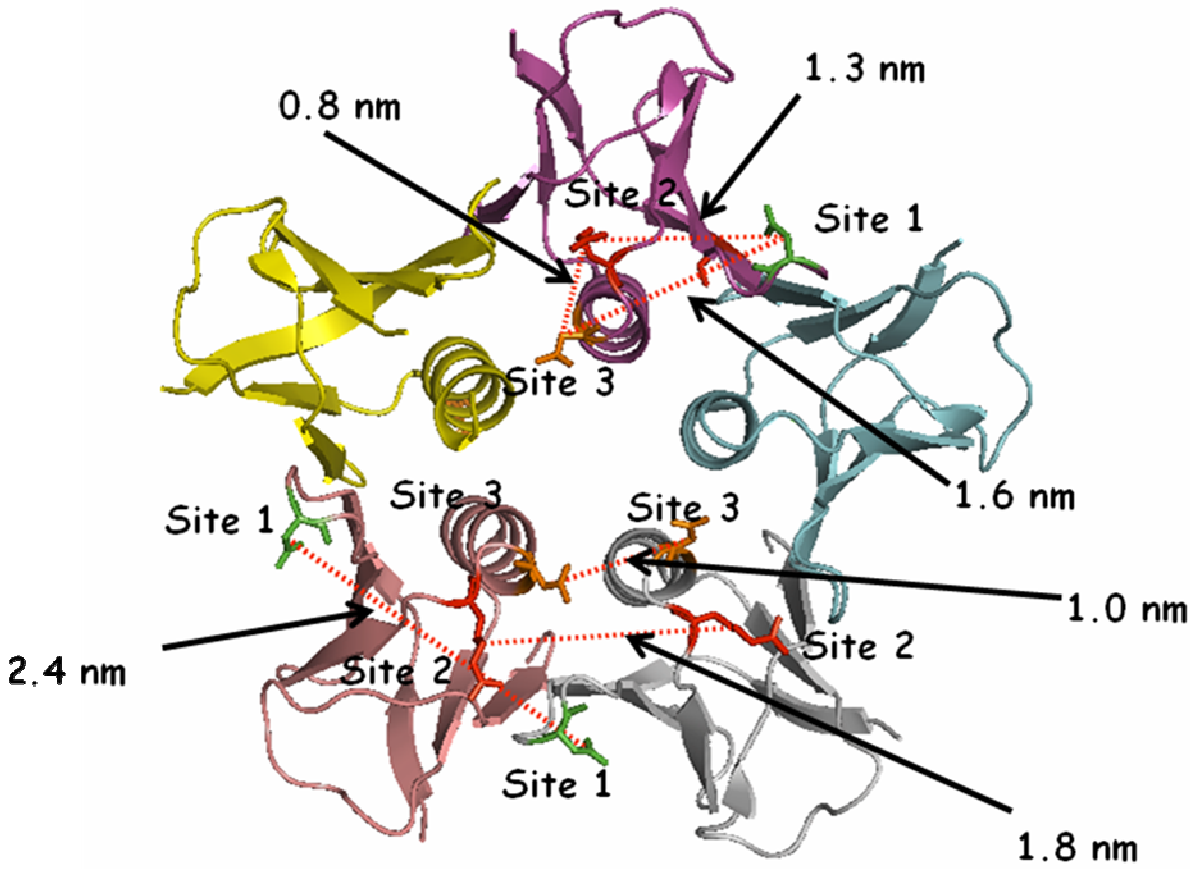


FIGURE 7. Representation of Shiga 2a depicting the distances between the three theoretical binding sites based on studies with Stx1.(*4*) The coordinates were downloaded from NCBI(*5*) and the figure was generated using Pymol®. The distance between site 1 and 2 was calculated to be ~ 1.3 nm, distance between site 2 and 3 was calculated to be 0.8 nm and the distance between site 1 and 3 was calculated to be ~ 1.6 nm. Also the distance between binding sites 2 of adjacent B subunits was calculated to be 1.8 nm.

REFERENCES:

(1) Kale, R. R., McGannon, C. M., Fuller-Schaefer, C., Hatch, D. M., Flagler, M. J., Gamage, S. D., Weiss, A. A., and Iyer, S. S. (2008) Differentiation between Structurally Homologous Shiga 1 and Shiga 2 Toxins by Using Synthetic Glycoconjugates. *Angew Chem Int Ed Engl 47*, 1265-1268.

(2) Wijtmans, M., Rosenthal, S. J., Zwanenburg, B., and Porter, N. A. (2006) Visible light excitation of CdSe nanocrystals triggers the release of coumarin from cinnamate surface ligands. *J Am Chem Soc 128*, 11720-6.

(3) Aly, M. R., Rochaix, P., Amessou, M., Johannes, L., and Florent, J. C. (2006) Synthesis of globo- and isoglobotriosides bearing a cinnamoylphenyl tag as novel electrophilic thiol-specific carbohydrate reagents. *Carbohydr Res 341*, 2026-36.

(4) Ling, H., Boodhoo, A., Hazes, B., Cummings, M. D., Armstrong, G. D., Brunton, J. L., and Read, R. J. (1998) Structure of the shiga-like toxin I B-pentamer complexed with an analogue of its receptor Gb3. *Biochemistry 37*, 1777-88.

(5) Fraser, M. E., Fujinaga, M., Cherney, M. M., Melton-Celsa, A. R., Twiddy, E. M., O'Brien, A. D., and James, M. N. (2004) Structure of shiga toxin type 2 (Stx2) from Escherichia coli O157:H7. *J Biol Chem 279*, 27511-7.

Bis[2-(3-carboxyphenoxy)carbonylethyl]phosphinic Acid (*m*-BCCEP): A Novel Affinity Cross-Linking Reagent for the β-Cleft Modification of Human Hemoglobin

Hongyi Cai,[†] Timothy A. Roach,[†] Margaret Dabek,[†] Karla S. Somerville,[†] Seetharama Acharya,[‡] and Ramachandra S. Hosmane*[,†,§]

Laboratory for Drug Design and Synthesis, Department of Chemistry and Biochemistry, University of Maryland, Baltimore County, 1000 Hilltop Circle, Baltimore, Maryland 21250, and Albert Einstein College of Medicine, Jack and Pearl Resnick Campus, 1300 Morris Park Avenue, Bronx, New York 10461. Received March 3, 2010; Revised Manuscript Received June 18, 2010

The design and synthesis of bis[2-(3-carboxyphenoxy)carbonylethyl]phosphinic acid (*m*-BCCEP, **1**) as a site-directed affinity reagent for cross-linking human hemoglobin have been reported as part of our long-term goal to generate artificial blood for emergency transfusions. Molecular modeling techniques were used to design the reagent, employing crystal coordinates of human hemoglobin A_0 imported from the Protein Data Bank. It was synthesized in four steps commencing from 3-hydroxybenzoic acid. The reagent **1** was converted to its trisodium salt to allow effective cross-linking in an aqueous medium. The reagent **1**, as its trisodium salt, was found to specifically cross-link stroma-free human hemoglobin A_0 in the β-cleft under oxygenated reaction conditions at neutral pH. The SDS-PAGE analyses of the modified hemoglobin pointed to the molecular mass range of 32 kDa as anticipated. The HPLC analyses of the product suggested that the cross-link had formed between the β_1-β_2 subunits. Molecular dynamics simulation studies on the reagent-HbA_0 complex suggested that the predominant amino acid residues involved in the cross-linking are N-terminus Val-1 or Lys-82 on one of the β-subunits and Lys-144 on the other. These predictions were borne out by MALDI-TOF MS analyses data of the peptide fragments obtained from tryptic digestion of the cross-linked product. The data also suggested the presence of a minor cross-link between Val-1 and Lys-82 on the opposing subunits. The oxygen equilibrium measurements of the *m*-BCCEP-modified hemoglobin product at 37 °C showed oxygen affinity (P_{50} = 25.8 Torr) comparable to that of the natural whole blood (P_{50} = 27.0 Torr) and significantly lower than that of stroma-free hemoglobin (P_{50} = 14.19 Torr) assayed under identical conditions. The measured Hill coefficient value of 1.91 of the *m*-BCCEP-modified Hb product points to the reasonable retainment of oxygen-binding cooperativity after the cross-link formation.

INTRODUCTION

Current world events replete with war and terrorism necessitate countless emergency transfusions, resulting in scarcity of blood, especially of rare types (*1*). Even otherwise, limitations on storage stability of whole blood, the necessity for blood-typing and cross-matching before transfusion, and the fear of possible transmission of infectious diseases upon transfusion, not to mention other psychological or religious reasons, reinforce the need to develop a safe and effective blood substitute (*2*−*5*). The latter must be universally acceptable without the requirement for typing or cross-matching, be free of pathogens, be storable for prolonged periods of time, and should allow transfusion at the scene of the accident without having to transport the patient to the nearest hospital (*6*−*10*).

The efforts to replace human blood can be traced back to the early 1900s (*11, 12*). Despite extensive investigations in the past few decades, it still remains a daunting task to discover an optimal blood substitute for emergency transfusion (*7, 13*−*16*). While many approaches have been taken in the past to develop blood substitutes, including plasma expanders (*17*), perfluorocarbon (PFC) suspensions (*18*−*20*), and microencapsulation (*21*−*24*), the one based on cell-free hemoglobins for an oxygen-carrying resuscitation fluid has excellent prospects since (a) hemoglobin solutions are completely metabolizable and are well-tolerated by the body and (b) hemoglobin is fully saturated with oxygen under ambient conditions, has oncotic activity, and exhibits cooperative oxygen binding characteristics (*7, 14, 25*−*30*). Hemoglobin is the iron-containing oxygen-transport protein in the red blood cells (RBCs) of vertebrates (*31*). Nonetheless, approaches employing cell-free hemoglobin are plagued by two major problems, short retention time of hemoglobin in circulation (1−4 h) and high oxygen affinity that causes inadequate oxygen release into tissues. It is highly toxic to the kidney and causes hypertension (*32*). Removal of the RBC membrane stroma resulted in stroma-free hemoglobin (SFHb) that had less renal toxicity in animals (*33*). The phase I clinical trials of SFHb still exhibited renal toxicity, as well as high blood pressure (*34*). Therefore, the use of native Hb was discontinued, and instead, modifications that allow Hb or SFHb function outside the RBCs have been extensively studied (*15*).

When outside the RBCs, Hb tetramer breaks into two $\alpha\beta$ dimers due to the loss of its allosteric effector, 2,3-diphosphoglycerate (DPG) (*35, 36*), which electrostatically holds the two dimers together (see Figure 1). Since $\alpha\beta$ dimer is considerably smaller than the tetramer; it will be easily filtered out of the bloodstream and is consequently cleared by the kidney causing kidney toxicity (*7, 37, 38*). DPG is equipped with multiple negative charges at physiological pH and thus can bind to the positively charged amino acid residues residing on the β-sub-

* To whom the correspondence should be addressed. Tel: 410-455-3717. Fax: 410-455-1148. E-mail: hosmane@umbc.edu.
[†] University of Maryland.
[‡] Albert Einstein College of Medicine.
[§] Recently retired.

10.1021/bc100113y © 2010 American Chemical Society
Published on Web 07/27/2010

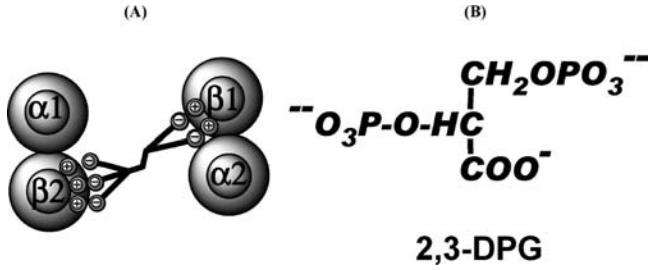
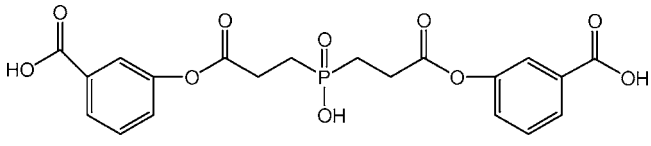


Figure 1. (A) Schematic representation of the tetrameric structure of hemoglobin formed by electrostatic interaction between the anionic charges of 2,3-diphosphoglycerate (2,3-DPG) and the cationic charges of amino acid residues present on the β-subunit of hemoglobin and (B) the molecular structure of 2,3-diphosphoglycerate.

units, forming a stable Hb tetramer with a central cavity called the DPG pocket or β-cleft (*39*). The absence of DPG also leads to high oxygen affinities of Hb, which prevents Hb from unloading sufficient amount of oxygen to tissues (*40*−*42*). Therefore, the current efforts to develop blood substitutes based on cell-free hemoglobin are directed toward (a) tuning its oxygen affinity to afford adequate oxygen delivery from lung to tissues via covalent cross-linking, preferably within the β-cleft, with an appropriate reagent that mimics the hemoglobin's natural allosteric modifier 2,3-diphosphoglycerate (DPG) (*43*), and (b) increasing the steric bulk of the cross-linked hemoglobin through polymerization to allow its retention in circulation for prolonged periods of time (*44*, *45*). The increased size would also prevent its facile sieving through the endothelial lining of blood vessels, where they scavenge nitric oxide (NO), the endothelium-derived relaxation factor (*46*−*50*). The latter is essential for relaxing the muscular walls surrounding the blood vessels, and therefore, its depletion results in elevated arterial pressure (*46*−*50*).

Many laboratories, including ours, have designed and synthesized many intramolecular (interdimer) or intermolecular (intertetramer) cross-linking reagents containing bifunctional or polyfunctional moieties to chemically modify cell-free Hb (*5*, *13*, *51*−*75*). Different degrees of success have been achieved, and a few products have even gone on to clinical trials (*4*, *7*). However, these modified hemoglobins still suffer from one or the other problems, including too high oxygen affinity, too low intravascular retention time, too facile autoxidation of Fe^{2+} to Fe^{3+} in Hb, forming metHb that lacks the capacity to carry oxygen, or other incompatible physiological characteristics (*15*, *76*, *77*). The challenge remains to synthesize an ideal reagent which closely mimics DPG to the extent that it would be specifically attracted to the β-cleft and cause the least conformational change in the native structure of Hb upon subsequent cross-linking and polymerization.

We report here the design, synthesis, and functional studies of bis[2-(3-carboxyphenoxy)-carbonylethyl]phosphinic acid (***m*-BCCEP**, **1**), a novel affinity cross-linking reagent for the



1

Reagent *m*-BCCEP

β-cleft modification of human hemoglobin. Synthesis of this reagent was accomplished in four steps starting from commercially available, inexpensive materials and can easily be scaled up. The reagent as well as its trisodium salt are crystalline solids that are stable at ambient temperature for an indefinite period. Considering that a number of otherwise promising reagents were rejected by industry because of perceived synthetic difficulty, poor yields, lack of prolonged stability, or exorbitant costs of production (*2*, *5*), the observed properties of reagent *m*-BCCEP are indeed promising. We have demonstrated here that its trisodium salt cross-links human hemoglobin under aqueous, physiological conditions. Reverse-phase HPLC in conjunction with SDS-PAGE analyses suggested that the reagent is specific for cross-linking the β chains of hemoglobin.

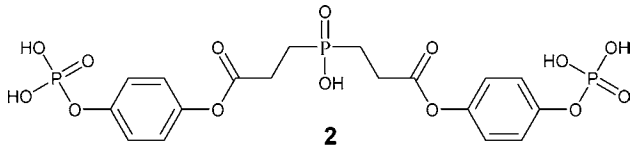
EXPERIMENTAL PROCEDURES

Materials and Methods. IR spectra were obtained on a Thermo Nicolet Avatar 370 FT-IR spectrometer. The NMR spectra were obtained on an Oxford AS 400 (400 MHz) spectrometer. The mass spectra were acquired on either an Esquire 3000 plus ESI mass spectrometer (Bruker Daltonics) or an Autoflex MALDI TOF/TOF MS instrument (Bruker Daltonics).The purity of samples of newly synthesized materials was assessed by a combination of 400 MHz NMR spectroscopy, mass spectrometry, thin layer chromatography, and elemental microanalyses. The latter data were obtained from Atlantic Microlab, Inc., Norcross, Georgia.

Molecular Modeling Studies. Molecular modeling was performed on a Silicon Graphics workstation, using the software Insight/Discover (Accelrys, San Diego, CA, USA). The X-ray coordinates of human Hb (*78*), imported from the Brookhaven National Laboratory, Upton, NY, USA, were employed for molecular modeling studies. It was energy-minimized and docked into the β-cleft (DPG pocket) of hemoglobin, followed by energy minimization of the reagent-Hb complex. All atoms that were 12 Å or farther from the ligand were fixed with a temperature constant of 300 K. No constraints were applied to the remaining residues in and around the ligand site. The complex was minimized to convergence using consecutive steepest descent and conjugate gradient (VAO9A) and Newton−Raphson energy minimization algorithms, with a final total Insight energy of 505.68 kals/mol, average absolute derivative of 0.000 129, standard deviation of absolute derivative of 0.000 114, and rms derivative of 0.000 172. In order to simulate the natural environment even further, a femtosecond molecular dynamics simulation (5000 iterations) at 300 K was performed on the above energy minimized protein−ligand complex by soaking the latter in an aqueous layer of 5 Å thickness all around the complex. There were no morse or cross terms. The distance ranges of the ester carbonyl carbon atoms of the reagent from the appropriate ε-amino nitrogen atoms of lysine residues or the α-amino nitrogen atom of the N-terminus valine were computed from graphs derived from the dynamics trajectories.

Organic Synthesis. Commercial reagents were employed without further purification. Organic reagents and solvents were purchased from Fischer Scientific Co. or Aldrich Chemical Co., and solvents were dried before use.

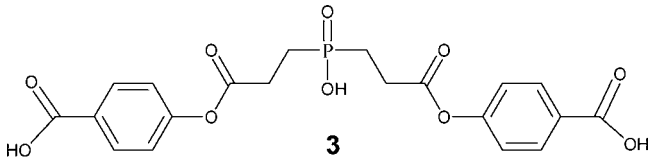
t-Butyl 3-Hydroxybenzoate (2). In a 250 mL round-bottom flask equipped with a magnetic stirrer, 3-hydroxybenzoic acid (4.6 g, 33.3 mmol) was dissolved in anhydrous benzene (200 mL), and the solution was heated to reflux. *N*,*N*′-Dimethylformamide di-*t*-butylacetal (13.54 g, 66.6 mmol) was added dropwise using a dropping funnel. The reaction mixture was allowed to reflux for 90 min or more. The solution was cooled down to room temperature and then washed with saturated aqueous $NaHCO_3$ solution (2 × 300 mL). The organic layer was dried over anhydrous Na_2SO4. Filtration followed by solvent removal under reduced pressure yielded 4.72 g (73%) of pure **2** as a colorless oil. ^1H NMR (DMSO-d_6): δ 9.6 (s, 1H, O**H**), 7.2−6.7 (m, 4H, Ar-**H**), 1.5 (s, 9H, *t*-Bu). Anal. Calcd for $C_{11}H_{14}O_3 \cdot 0.2H_2O$: C, 66.78; H, 7.34. Found: C, 66.80; H, 7.32.



2

Reagent BPPCEP

3-t-Butoxycarbonylphenyl Acrylate (3). To a solution of *t*-butyl 3-hydroxybenzoate (**2**) (4.23 g, 21.8 mmol) in anhydrous THF (120 mL) was added potassium *t*-butoxide (2.53 g, 22.5 mmol). The mixture was allowed to stir for 30 min at 0 °C in an ice bath, after which acryloyl chloride was added (2.15 mL, 26.5 mmol). The reaction mixture was allowed to stir overnight. After filtering the mixture, the THF was removed by rotary evaporation. Then, the mixture was dissolved in ethyl ether (100 mL) and washed with aq. HCl (0.1 N, 3 × 100 mL), followed by distilled water (3 × 100 mL). The organic layer was then dried with Na_2SO_4, filtered, and the filtrate evaporated to give a brownish-yellow oil (4.43 g). This oil was purified by silica gel chromatography, eluting with chloroform to give a yellow oil (**3**) (3.69 g, 68%). ^{1}H NMR ($CDCl_3$): δ 7.9−6.1 (m, 4H,



3

Reagent *p*-BCCEP

Ar-**H**), 6.7−6.6 (d, 1H, CH═C**H**$_2$), 6.4−6.2 (dd, 1H, C**H**═CH$_2$), 6.1−6.0 (d, 1H, CH═C**H**$_2$), 1.6 (s, 9H, *t*-Bu). Anal. Calcd for $C_{14}H_{16}O_4$: C, 67.73; H, 6.50. Found: 67.89; H, 6.51.

Bis[2-(3-t-butoxycarbonyl)phenoxycarbonylethyl]phosphinic Acid (4). To an ice-cold, stirred solution of ammonium phosphinate (0.44 g, 5.25 mmol) in 50 mL dry dichloromethane was added *N,O*-bistrimethylsilylacetamide (3.74 g, 18.4 mmol) and the above acryloyl ester (**3**) (2.61 g, 10.5 mmol) while under argon atmoshere. The reaction mixture was allowed to stir overnight. It was partitioned between CH_2Cl_2 and H_2O, and the organic layer was washed with aq. HCl (0.1 N, 3 × 100 mL). The organic layer was then dried over anhydrous Na_2SO_4, filtered, and the filtrate evaporated to give a brown oil. This oil was purified by silica gel chromatography, eluting with chloroform−methanol mixture (7.5:2.5) to give a brownish-yellow oil (**4**) (2.30 g, 78%). ^{1}H NMR ($CDCl_3$): δ 7.90−7.77 (dd, 2H, Ar-**H**), 7.73−7.62 (m, 2H, Ar-**H**), 7.48−7.34 (m, 2H, Ar-**H**), 7.30−7.18 (d, 2H, Ar-**H**), 3.09−2.82 (m, 4H, C**H**$_2$-PO), 2.38−2.09 (m, 4H, C**H**$_2$-PO), 1.57 (s, 18H, *t*-Bu). Anal. Calcd for $C_{28}H_{35}PO_{10}$ 0.5H_2O: C, 58.84; H, 6.34. Found: C, 58.44; H, 6.54.

Bis[2-(3-carboxyphenoxy)carbonylethyl]phosphinic Acid (1). A solution of (**4**) (563 mg, 1 mmol) in 50 mL of dry dichloromethane was refluxed with 4 mL of trifluoroacetic acid for 3 h. After evaporation of the solvent on a rotavapor, a brownish-yellow residue was obtained, which was washed with diethyl ether to yield 419 mg (93%) white solid compound (**1**). ^{1}H NMR (DMSO-d_6): δ 7.83−7.38 (m, 8H, Ar-**H**), 2.81−2.63 (m, 4H, C**H**$_2$), 2.08−1.85 (m, 4H, C**H**$_2$). ^{13}C NMR (DMSO-d_6): δ 174.10 (ester C═O), 167.85 (acid C═O), 157.92 (O−**C**═C), 132.54 (Ar−C), 130.11 (Ar−C),126.89 (Ar−C), 123.25 (Ar−C), 120.50 (Ar−C), 27.22 (**C**H$_2$C═O), 25.07 (**C**H$_2$P═O); IR (ν_{max}) 3027−2650 (br, CO_2H), 1753 (C═O), 1701 (C═O) cm^{-1}; MS (ESI) *m*/*z* 451 (MH^+). Anal. Calcd for $C_{20}H_{19}PO_{10}$: C, 51.29; H, 4.52. Found: C, 51.26; H, 4.48.

Conversion of Reagent 1 into the Corresponding Trisodium Salt. A glass column (30 cm ×100 cm) was packed with the ion-exchange resin AG 50W-X8 (H^+ form) (Bio-Rad). The resin was converted to its sodium form by equilibration with 1 N NaOH until the PH was basic (pH 14 or more). The column was then thoroughly washed with deionized water until the pH of the eluent was neutral (or equal to the pH of water). Reagent **1** (135 mg, 0.3 mmol) was then dissolved into ethanol (10 mL) and loaded onto the top of the resin, and the column was eluted with 500 mL of deionized water. The combined fractions were frozen using liquid nitrogen and lyophilized for 2 days to yield 118 mg (77%) of a yellowish salt. This salt was used for hemoglobin modification without further purification. ^{1}H NMR (D_2O): δ 7.81−7.26 (m, 8H, Ar-**H**), 2.95−2.87 (m, 4H, C**H**$_2$), 2.11−1.97 (m, 4H, C**H**$_2$).

Reaction of *m*-BCCEP with Hemoglobin. Highly purified stroma-free hemoglobin A (SFHbA) in the oxygenated state was obtained from Walter Reed Army Institute of Research, Washington, DC. A stock solution (2 mM) of human hemoglobin was made by dilution of 2.8 mL concentrated hemoglobin (13.7 g/dL) in the oxygenated state at room temperature with 0.12 mL of 0.1 M phosphate buffer, pH 7.4. Next, into three 2 mL Eppendorf tubes was added 500 μL of the stock (2 mM) Hb solution and 1.16 mL of 0.1 M phosphate buffer, pH 7.4. A 150 mM stock reagent solution of *m*-BCCEP was prepared by dissolving 77.5 mg of *m*-BCCEP (trisodium salt form) into 1 mL of 0.1 M phosphate buffer, pH 7.4, and used immediately in the cross-linking reactions by adding 333 μL to two of the above Eppendorf tubes for a total volume of 2 mL per tube. The final concentration was 25 mM (50-fold excess) for the reagent and 0.5 mM for Hb. The third tube was used for control purposes and was brought to a volume of 2 mL with additional buffer. The reactions were then kept at temperature of 30 °C for 12 h and monitored by reverse-phase HPLC using a C4 column (conditions listed below) every 4 h. After that time, no further modifications were present in the chromatograms, and the solutions were frozen and stored at −81 °C until further analyses could be performed.

HPLC Analysis and Purification of Modified Hemoglobin. The modified and native hemoglobin were analyzed by reverse-phase HPLC using a C4 Vydac 214TP1010 column (10 × 250 mm) with developer A (CH_3CN, 0.1% TFA) and developer B (H_2O, 0.1%TFA). The column was equilibrated with 35% developer A and 65% developer B and a gradient employed to give a final composition of 50% developer A and 50% developer B over a period of 90 min at 3 mL/min while monitoring at λ_{max} 214 nm.

The cross-linking solutions were passed through a Sephadex G-75 column (2.5 × 45 cm) equilibrated with 0.05 M Tris buffer, pH 7.4, 1 M $MgCl_2$, and eluted with the same buffer to denature any un-cross-linked Hb. The fractions were combined and then simultaneously desalted, and the buffer was exchanged (0.05 M Tris, pH 7.4) using Millipore Biomax 50 concentrators. The concentrated Hb was then frozen at −81 °C until further use.

SDS-PAGE Analysis of Modified Hemoglobin. The extent of cross-linking of the hemoglobin was determined by polyacrlamide gel electrophoresis in the presence of sodium dodecyl sulfate (SDS-PAGE). Modified hemoglobin (20 μL) and control hemoglobin (20 μL) were added into 40 μL LB Buffer separately (Laemmli sample buffer/2-mercaptoethanol = 95:5) and heated to boil for 5 min, then loaded 10 μL per well and the gel run (12% polyacrylamide, 0.375 M Tris-HCl, pH 8.8) at 150 V for 35 min. The protein bands on the gel were then stained for 1 h with Coomassie Brilliant Blue dye and then destained using Bio-Rad destain. SDS-PAGE standards were used to compare the molecular weight.

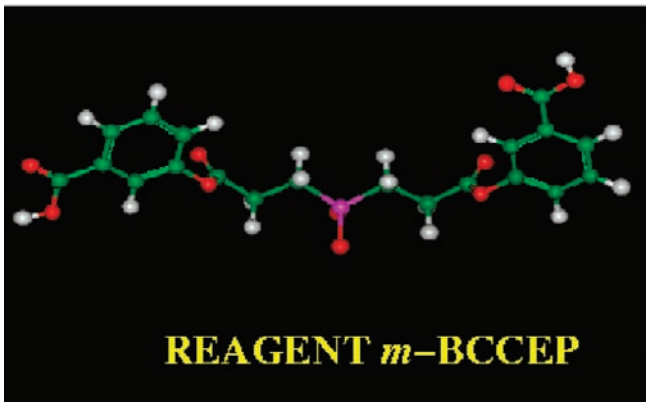


Figure 2. Energy minimized structure of reagent *m*-BCCEP.

Tryptic Digestion Analyses. The native and modified globin chains were purified for tryptic digestion by preparative reverse-phase HPLC using a C4 Vydac 214TP1022 column (22 × 250 mm). The column was equilibrated with 35% developer A (CH_3CN, 0.1% TFA) and 65% developer B (H_2O, 0.1% TFA) and a linear gradient employed to give a final composition of 50% developer A and 50% developer B over a period of 95 min at 13 mL/min while monitoring at λ_{max} 214 nm. The appropriate fractions were then pooled and frozen in a liquid nitrogen bath followed by lyophilization to a powder. The isolated β (1.2 mg) and XL-β chains (1.2 mg) were then dissolved separately into 200 μL buffer (50 mL H_2O, 0.1% SDS, 50 mM Tris-HCl, 5 μM β-mercaptoethanol at pH 8), and 60 μL of TPCK-trypsin (1 μg/ μL) was added (protein/trypsin = 20:1 w/w). Digestion was carried out for 24 h at 37 °C with gentle agitation. Digestion was terminated by freezing the samples and then lyophilizing them to a powder. The digested globin chains were analyzed by reverse-phase HPLC using a C18 Phenomenex column (4.5 × 250 mm, 5 μm, 300 A); the injection was 10 μL, and the column was equilibrated with 5% developer A (CH_3CN, 0.1% TFA) and 95% developer B (H_2O, 0.1%TFA) and a linear gradient employed to give a final composition of 50% developer A and 50% developer B over a period of 120 min at 1 mL/min while monitoring at λ_{max} 214 nm. The fragments obtained were collected from the HPLC column, as they eluted out and lyophilized individually. The fractionated tryptic peptides were then analyzed by matrix-assisted laser desorption/ionization time-of-flight MS (MALDI-TOF).

Mass Spectral Analyses. The fractionated tryptic peptides were analyzed by MALDI-TOF-MS (*79*−*81*), using an Autoflex MALDI-TOF/TOF MS instrument. All experiments were performed using α-cyano-4-hydroxycinnamic acid as the matrix. Matrix (10 mg) was dissolved into 0.5 mL 7:3 H_2O (0.1% TFA): CH_3CN to make a final concentration of matrix as 20 mg/mL. Each lyophilized tryptic fragment was dissolved in 20 μL H_2O, mixed well, and applied 0.5 μL onto a sample well, followed by an equal volume of the above matrix solution. One well is reserved for the matrix alone as a reference. The samples were allowed to dry at room temperature before placing into the spectrometer. Insulin (MW: 5734.51), ACTH (MW: 2465.1989), Angiotensin (MW: 1046.5423) and Insulin Oxidized B chain (MW: 3494.6513) were used to calibrate the machine.

Oxygen Equilibrium (P_{50}) Studies. Oxygen equilibrium curve (OEC) was obtained in the Hemox buffer (pH 7.4) at 37 °C using a Hemox-Analyzer (TCS Scientific Corp., Huntington Valley, PA). The sample was oxygenated with an increasing partial pressure of oxygen and deoxygenated with nitrogen gas. The analyzer detects the oxygen pressure with a Clark oxygen electrode and simultaneously calculates the oxygen saturation of Hb via a dual-wavelength spectropotometry. value for P_{50} (the oxygen pressure where Hb is half-saturated with oxygen) was obtained from the OEC. The Hill coefficient, which represents

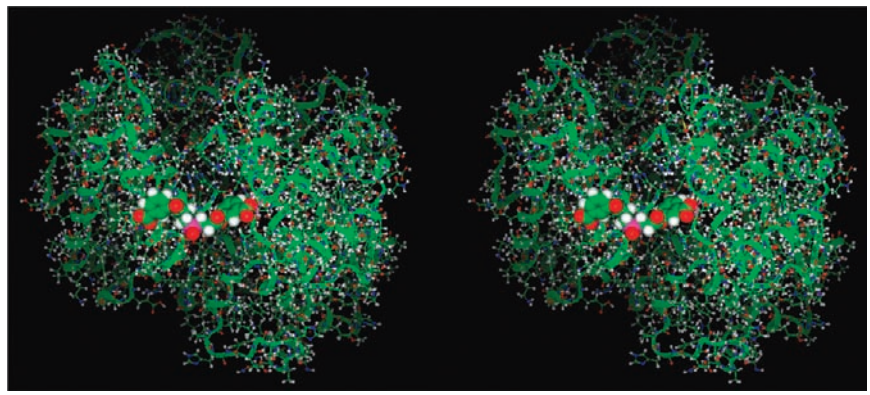


Figure 3. Stereoview of the energy minimized complex of reagent *m*-BCCEP with HbA_0.

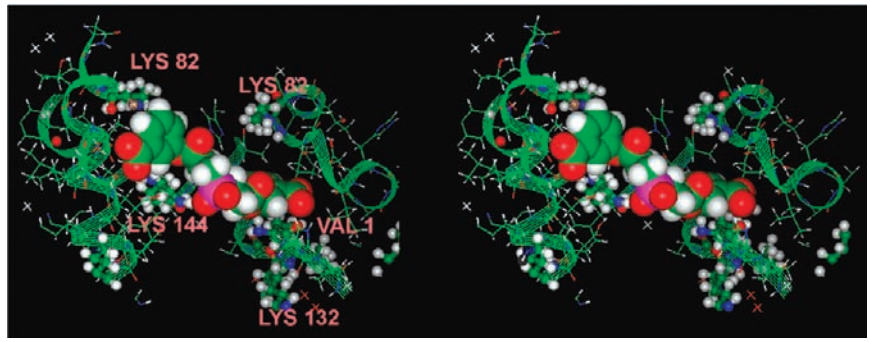


Figure 4. Close-up stereoview of the energy-minimized *m*-BCCEP-HbA_0 complex. Only those amino acid residues of SFHb that lie within a 12 Å radius from the reagent in the β-cleft are shown.

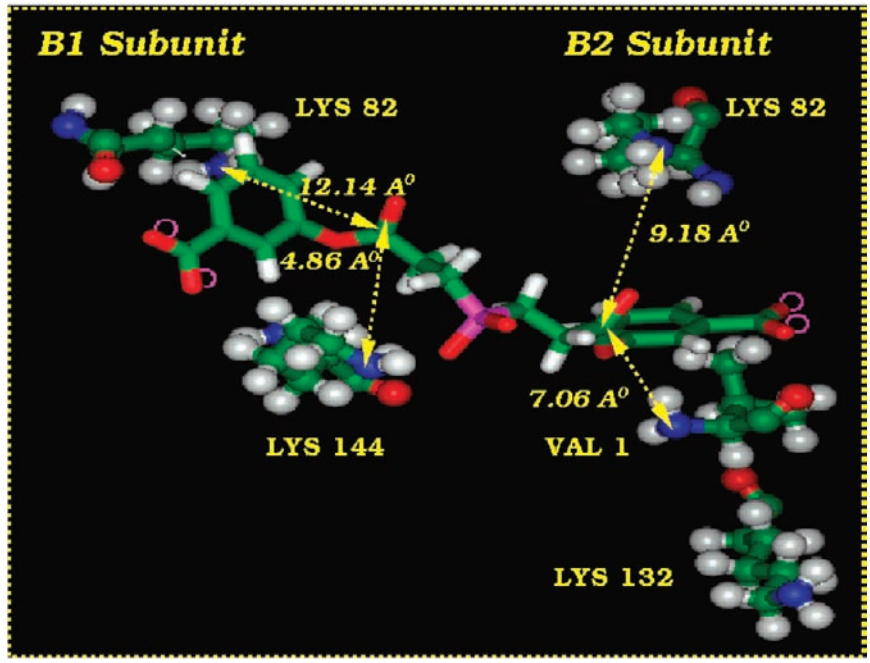


Figure 5. Close-up monoview of the energy-minimized *m*-BCCEP-HbA_0 complex shown in Figure 4, showing the amino acid residues (lysines or α-terminus valine) whose appropriate (ε- or α-) amino groups fall within a ~9 Å distance from the two cross-linking sites of the reagent.

the cooperative effect of the four subunits in Hb molecule, was obtained from the slope of Hill plot (log(Y/(1 − Y) versus log P), where Y is fractional saturation of the Hb with oxygen and P is the oxygen pressure in Torr.

RESULTS AND DISCUSSION

We have recently reported the synthesis and hemoglobin cross-linking studies of a reagent called BPPCEP (**2**) (Bis[2-(4-phosphonooxyphenoxy)carbonylethyl]phosphinic acid) (*59*). The latter contains the same number (five) of anionic charges and the same number (two) of phosphate groups as DPG, but the reagent was so highly reactive that it produced an intractable mixture of products upon hemoglobin cross-linking. Three major products were laboriously isolated from the reaction mixture and fully characterized (*59*). While all three of them were found to be $\beta-\beta$ cross-linked, their oxygen affinities, ranging from 12.5 to 15.5 Torr, were not superior to the oxygen affinity of the stroma-free hemoglobin that was used for cross-linking, which measured 13.1 Torr under identical conditions (*59*). Even worse was their oxygen-binding cooperativity characteristics as measured by the Hill coefficients, which ranged from 0.5 to 0.9 as compared to ~2.5 for HbA_0 (*2, 5*). Interestingly, we had discovered a decade earlier that a carboxylate group in place of a phosphate group as in reagent **3** (bis[2-(4-carboxyphenoxy)-carbonylethyl]phosphinic acid (*p*-BCCEP)), despite possessing only three negative charges under physiological conditions, underwent a much cleaner reaction with hemoglobin, but unfortunately, the yield of the cross-linked product was only 15−20%, thus making it practically unsuitable or unattractive for further development (*57*). Our molecular modeling studies (see below) suggested that the movement of this carboxylate group from the para position to the meta would considerably enhance the interactions of the ligand with the protein, making worthwhile the synthesis and Hb cross-linking studies of the title reagent *m*-BCCEP (**1**). As revealed by the data presented herein, this indeed proved to be the case.

Molecular Modeling Studies. Molecular modeling studies were performed on a Silicon Graphics workstation, using the X-ray coordinates of human HbA_0 (*78*) imported from the Brookhaven National Laboratory, Upton, New York. Although molecular modeling techniques have been used for extensive investigations of allosteric modifications of hemoglobin (*82*−*85*), drug delivery of hemoglobin bioconjugates (*86*) and biophysical characterization of genetic variants (*87*), mutants (*88*), self-association (*89*), and packing (*90*) of hemoglobins, the documented use of molecular modeling for the de novo design of hemoglobin cross-linking reagents is somewhat rare, other than our own earlier reports on the subject (*57, 59, 74*). The initial structural framework for the cross-linking reagent was laid down by assessment of the nature and dimension of the DPG pocket and the identification of the target amino acids on the diagonally opposed β_1 and β_2 subunits for cross-linking, as well as the tether length, geometry, and the electrophilic functional groups required for efficient cross-linking. To this end, the modeling studies were first carried out using DPG itself as the ligand.

The reagent *m*-BCCEP (**1**) was built and energy-minimized employing the molecular modeling software *Insight/Discover* (Accelrys Software, Inc., San Diego, California). The structure of the energy-minimized *m*-BCCEP is shown in Figure 2. The reagent is equipped with two activated ester functionalities to serve as the two cross-linking sites. The two end carboxylate groups and the central phosphinic hydroxyl are anticipated to provide the necessary anionic charges at biological pH for the molecule to be specifically drawn to the β-cleft of hemoglobin. Initial docking and energy minimization studies revealed that five different possibilities existed for the reagent to align itself within the β-cleft: (a) between β_1-Lys-144 and β_2-Val-1, (b) between β_1-Lys-144 and β_2-Lys-82, (c) between β_1-Lys-144 and β_2-Lys-132, (d) between β_1-Lys-82 and β_2-Lys-82, and (e) between β_1-Lys-82 and β_2-Val-1. The energy minimization and molecular dynamics simulation studies performed individually on these five different arrangements of the *m*-BCCEP-Hb complex suggested that the best fit with least energy and maximum reagent−Hb interactions (see below) occurs when *m*-BCCEP is aligned between Lys-144 on the β_1 subunit and midway to N-terminus Val-1 and Lys-82 on the β_2 subunit (intermediate between arrangements a and b described above).

All atoms that were 12 Å or farther from the ligand were fixed with a temperature constant of 300 K. No constraints were applied to the remaining residues in and around the ligand site.

The *m*-BCCEP-Hb complex was then energy minimized to convergence using consecutive steepest descent, conjugate gradient, VAO9A, and Newton energy minimization protocols. A stereoview of the energy minimized *m*-BCCEP-HbA_0 complex is shown in Figure 3, while a close-up view of the same is given in Figure 4. Figure 5 highlights the concerned amino acid residues (lysines or α-terminus valine) whose appropriate (ε- or α-) amino groups fall within an approximate 9 Å distance from the two cross-linking sites of the reagent.

The stereoview in Figure 3 clearly shows that the reagent *m*-BCCEP fits snugly into the β-cleft (DPG pocket) of hemoglobin. The close-up views in Figures 4 and 5 suggest that there are a total of four amino acid residues whose potentially cross-linkable amino groups lie within a ∼9 Å distance from the two activated ester carbonyl groups of the reagent, the anticipated cross-linking sites. Taking into account the sum of the van der Waal's radii of the two concerned atoms involved in cross-linking [(C = 2.0 + N = 1.5) = 3.5 Å total], coupled with the fact that the amino acids lining the periphery of the β-cleft are known to extend as much as 3−5 Å into the cleft to effect cross-links (*91*), the consideration of all amino acids lying within a ∼9.0 Å radius from the reagent sites as potential candidates for cross-linking is reasonable.

A femtosecond molecular dynamics simulation (300 K, 5000 iterations) of the above energy-minimized *m*-BCCEP-Hb complex in the preferred arrangement, soaked with an aqueous layer of 5 Å thickness all around, showed the concerned lysine residues on each β-subunit, lying in close proximity to the cross-linking sites of *m*-BCCEP. The range of distance between the appropriate ester carbonyl of *m*-BCCEP and the ε-amino group of lysine residues or the α-amino group of N-terminus valine, as computed from the graphs derived from dynamics trajectories, indicated that the closest contacts of β_2-Val-1 (4.21 Å), β_2-Lys-82 (5.28 Å), and β_1-Lys-144 (3.51 Å) are all well within the combined van der Waals radii of the two bonding atoms of the concerned amino and carbonyl functions of Hb and *m*-BCCEP, respectively. Thus, the most preferred amino acids to participate in cross-linking by *m*-BCCEP appeared to be Val-1 and Lys-82 on the β_2 subunit and Lys-144 on the β_1 subunit, which correspond to arrangements (a) and (b) described above. While the latter two are the suggested preferred arrangements, our simulation studies did not totally rule out the arrangements (c), (d), and (e) described earlier, which would require the involvement of an additional amino acid on each of the β-chains: Lys-132 on β_2 and Lys-82 on β_1. We did, however, find some experimental evidence, based on MALDI MS analyses of tryptic digests of the cross-linked product (see below), supporting the arrangement (e).

Synthesis of the Reagent *m*-BCCEP (*1*). Synthesis of the target reagent **1** involved four steps that are outlined in Scheme 1. The reaction of 3-hydroxybenzoic acid with *N*,*N*-dimethylformamide di-*t*-butyl acetal gave *t*-butyl 3-hydroxybenzoate (**2**). Condensation of (**2**) with acryloyl chloride in the presence of potassium *t*-butoxide in THF gave 3-*t*-butoxycarbonylphenyl acrylate (**3**). Next, 2 equiv of (**3**) were condensed with ammonium salt of hypophosphorous acid (*59*) with the silylating reagent *N*,*O*-bistrimethylsilylacetamide in anhydrous dichloromethane at 0 °C to produce bis[2-(3-*t*-butoxycarbonyl)phenoxycarbonylethyl]phosphinic acid (**4**). Treatment of the latter with trifluoroacetic acid resulted in removal of the *tert*-butyl protecting group to yield the target bis[2-(3-carboxyphenoxy)-carbonylethyl]phosphinic acid (*m*-BCCEP; **1**). The reagent **1** was converted to its trisodium salt by ion-exchange chromatography over AG 50W-X8 resin (Na^+ form), followed by lyophilization. The crystalline trisodium salt is soluble in water and any aqueous buffers, and was directly used for reacting with hemoglobin.

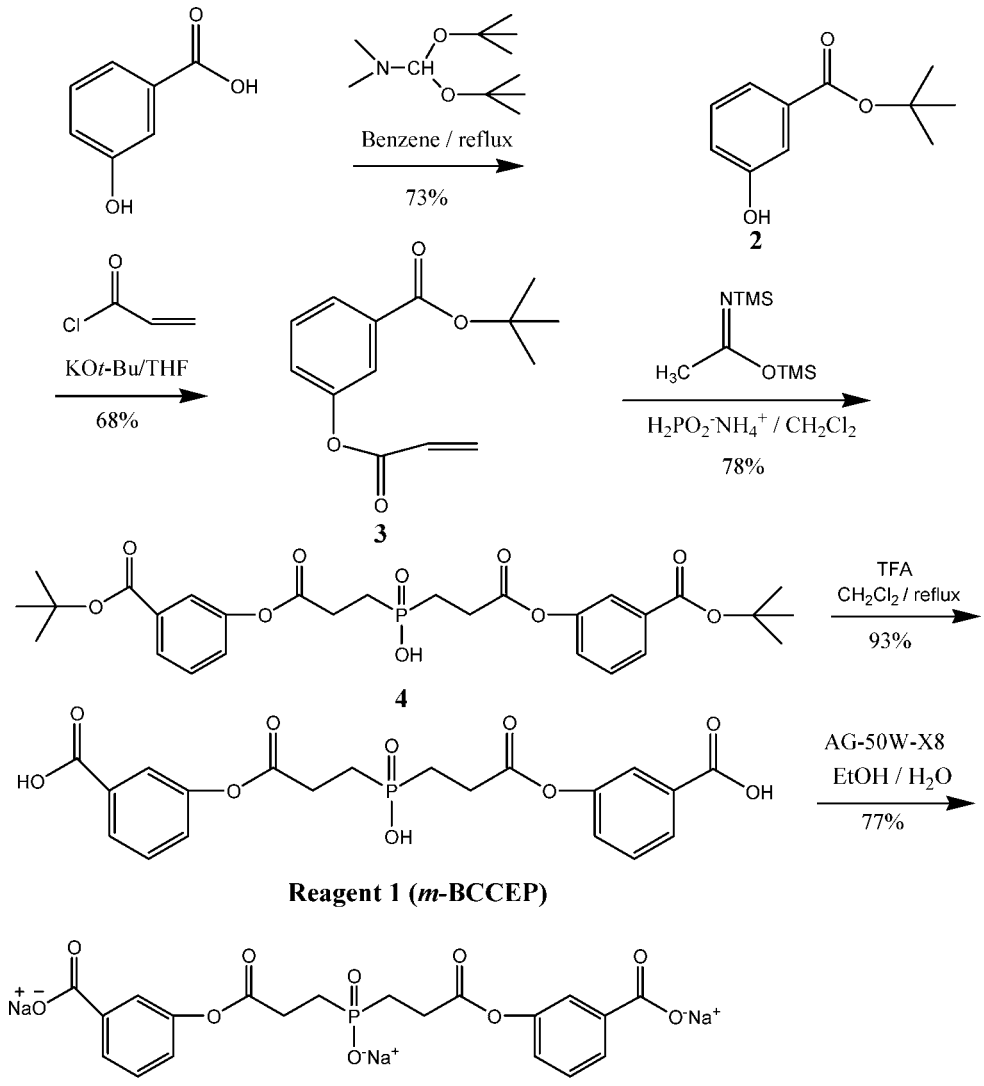
Cross-Linking Reaction of *m*-BCCEP with Hemoglobin. The cross-linking reaction of hemoglobin with the trisodium salt of *m*-BCCEP was carried out under oxygenated conditions in a

Table 1. Comparison of the Observed and Calculated Average Masses of Tryptic Peptides of Human Hb β-Chain[a]

fragment residues	calcd avg mass $[MH]^+$	obsd avg mass $[MH]^+$	tentative structural analysis of tryptic fragment
(1−8)	953.0	953.9	T1
(9−17)	933.0	n.o.[b]	n.o.[b] T2
	1867	1867.8	(T1 + T2) − H_2O
(18−30)	1315.4	1315.1	T3
	1337.4	1337.3	(T3 −1) + Na
(31−40)	1275.5	1277.5	T4
	1298.5	1298.1	(T4 − 1) + Na
(41−59)	2060.3	2060.7	T5
	2082.3	2082.1	(T5 - 1) + Na
(60−61)	246.3	n.a.a.[b]	n.a.a.[b] (T6)
(62−65)	412.5	n.a.a.[b]	n.a.a.[b] (T7)
(66−66)	147.2	n.a.a.[b]	n.a.a.[b] (T8)
(66−82)	1799.1	1799.8	(T8 + T9) − H_2O
	1837.1	1837.8	(T8 + T9 − H_2O − 1) + K
(67−82)	1670.9	1671.7	T9
(83−95)	1422.6	n.o.[b]	n.o.[b] (T10)
(96−104)	1127.2	1128.4	T11
(96−120)−S−S− (105−120)	4569.4	4569.2	(T11 + T12 − H_2O − 1)−S−S−(T12 − 1) + (−1 + Na)
(105−120)	1721.1	n.o.[b]	n.o.[b] (T12)
	1799.1	1799.8	(T12) + (−2 + 2K)
(105−132)	3125.7	3125.9	(T12 + T13 − H_2O) + (−2 + 2Na)
(121−132)	1379.6	1379.6	T13
	1401.6	1401.6	(T13 − 1) + Na
(133−144)	1150.4	1150.1	T14
(133−146)	1510.7	1510.5	(T14 + T15 − H_2O) + (−2 + Na + K)
(145−146)	319.3	n.a.a.[b]	n.a.a.[b] (T15)

[a] The average mass of peptide fragments was calculated using the computer program, *GPMAW* (General Protein Mass Analyzer for Windows), v 2.0, available from Light House Data, Engvej 35, DK-5230, Odense M, Denmark. The following are the calculated masses for the peptide fragments resulting from tryptic digestion of the β-chain of hemoglobin and were employed in all subsequent computations involving these fragments: T1 (1−8), 952.08; T2 (9−17), 932.09; T3 (18−30), 1314.42; T4 (31−40), 1274.53; T5 (41−59), 2059.28; T6 (60−61), 245.33; T7 (62−65), 411.46; T8 (66−66), 146.19; T9 (67−82), 1669.90; T10 (83−95), 1421.59; T11 (96−104), 1126.24; T12 (105−120), 1720.11; T13 (121−132), 1378.55; T14 (133−144), 1149.36; T15 (145−146), 318.34. [b] The following are the abbreviations used in the Table: n.a.a., no assignment attempted; n.o., not observed; T, tryptic peptide.

Scheme 1. Synthesis of the Cross-Linking Reagent *m*-BCCP and Its Trisodium Salt



phosphate buffer (pH 7.4) at 30 °C for 12 h using 2 mM human SFHb stock solution. Various concentrations (5×, 10×, 25×, 50× excess) of *m*-BCCEP (trisodium salt) were analyzed for its cross-linking capabilities. The cross-linking efficiency steadily increased with more cross-linker added and plateaued at 25-fold excess of *m*-BCCEP as determined by sodium dodecyl sulfate−polyacrylamide gel electrophoresis (SDS-PAGE) analyses (Figure 6).

Under extreme denaturing conditions of SDS-PAGE, cross-linked Hb is expected to migrate at nominal molecular weight of 32 kDa, and un-cross-linked Hb migrates at 16 kDa. In Figure 6, lane 1 is the SDS molecular weight markers, lane 2 is SFHb used as control, which showed predominantly a 16 kDa band representing monomeric, unmodified globin chains. Lanes 3 to 6 are the reaction mixtures, which showed strong bands at 32 kDa. Lane 5 (25×) and lane 6 (50×) have the best cross-linking effect, representing a substantial fraction (~40%) of cross-linked Hb. Therefore, the best cross-linking efficiency was obtained with a 0.5 mM SFHb and a 25-fold excess of the reagent.

To determine whether *m*-BCCEP cross-links between the α−α or β−β globin chains, the reaction mixture was analyzed by reverse-phase HPLC using a Vydac C_4 column monitored at λ_{max} 214 nm (see Figure 7). As indicated in Figure 7b, the reagent selectively modified the β globin chains, while the α chains were unaffected when compared to the spectrum of the unreacted SFHb (Figure 7a). This was further confirmed by spiking the reaction mixture with SFHb (Figure 7c), when the unmodified β globin chain intensity increased.

The individual α, β, and the cross-linked β−β chain fractions were further analyzed by MALDI-TOF, which confirmed that

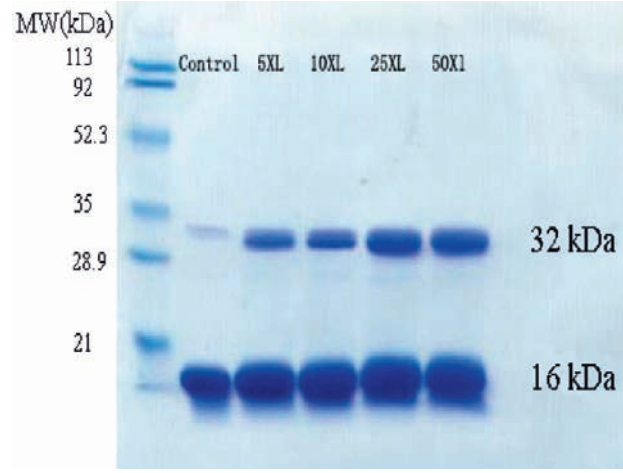


Figure 6. SDS-PAGE analysis for SFHb and *m*-BCCEP-modified Hb.

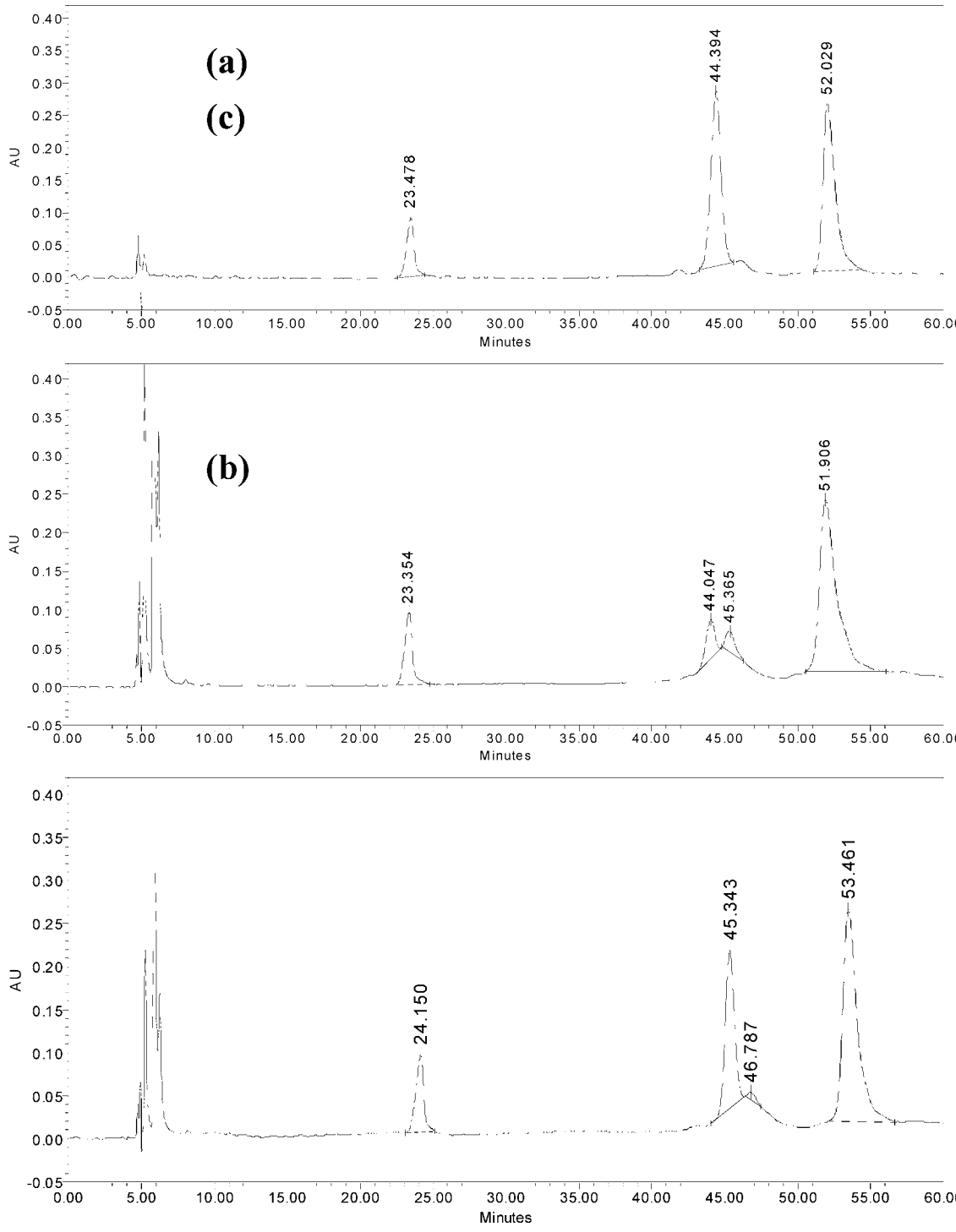


Figure 7. Reverse-phase (C_4) HPLC chromatogram of (a) SFHb, (b) the cross-linked product with the reagent *m*-BCCEP (trisodium salt), and (c) the cross-linked product in (b) spiked with additional SFHb monitored at λ_{max} 214 nm.

the masses of both α and β chains are ~16 kDa, and only the cross-linked $\beta-\beta$ chain has an additional band corresponding to a mass of ~32 kDa.

Tryptic Digestion. To determine the reactive sites of the cross-links, tryptic digestion analyses were carried out. Trypsin cleaves C-terminal lysine and arginine residues. The un-cross-linked β chain and the cross-linked β1-XL-β2 chain were separated by reverse-phase HPLC on a Vydac C_4 column monitored at λ_{max} 214 nm; the collected fractions were concentrated using Millipore Biomax 10 concentrators and then lyophilized into powder. Tryptic digestion was carried out for 24 h at 37 °C with gentle agitation. The digested globin chains were analyzed by reverse-phase HPLC using a C_{18} Phenomenex column. The fragments obtained were collected from the HPLC column (Figure 8) and lyophilized individually. The tryptic digestion of the normal human Hb β-chain (containing 11 lysine and 3 arginine residues) is expected to produce 15 peptides (*57*), (*92*).

MALDI-MS Analyses. The tryptic digestion fragments were analyzed by the matrix-assisted laser desorption/ionization time-of-flight mass spectrometry (MALDI-TOF-MS) (*79*−*81*), using the instrument specified under Materials and Methods above. Listed in Tables 1 and 2 are the observed average masses (MH^+ ions) of predominant peptide fragments of Figure 8a,b, respec-

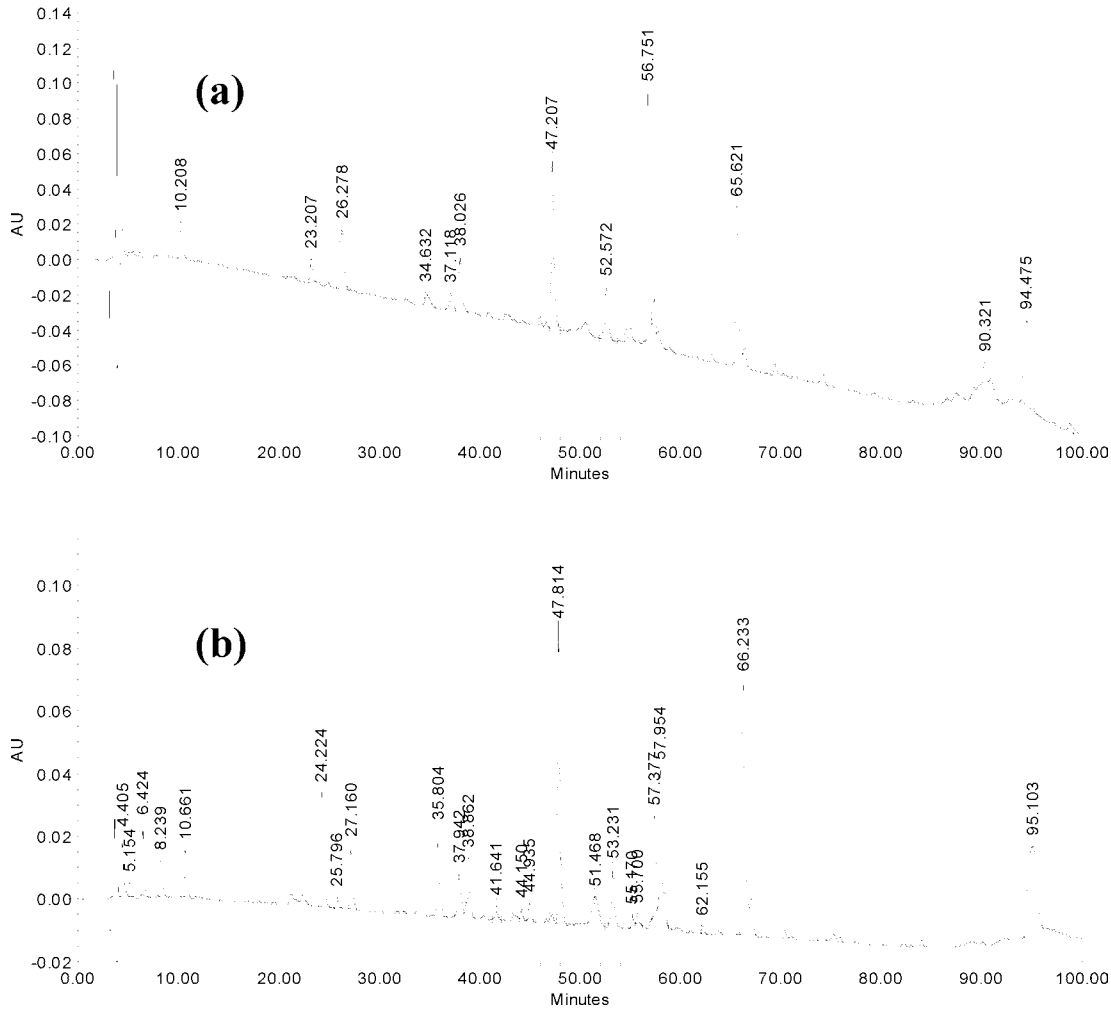


Figure 8. The HPLC profiles of the tryptic digests of (a) pure β chain and (b) cross-linked β1-XL-β2 chain. The peptides were separated on a reverse-phase C_{18} column, using a linear gradient of CH_3CN-H_2O, containing 0.1% CF_3CO_2H.

tively, along with the calculated average masses and tentative structural analyses of each of those fragments. The presence of Na^+ and K^+ ions in a number of the observed fragments is believed to be from the buffer solution used during the cross-linking (*57*). Also listed in both tables are disulfide-linked peptides in the native as well as cross-linked hemoglobins.

The exact sites involved in the cross-linking were determined by identification of ions whose masses were equal to the sum of two tryptic fragments plus an additional mass equal to that of the cross-linking reagent minus the leaving group moieties (in this case, a mass of 176.1 corresponds to the *m*-BCCEP tether). The observed ions listed in Table 2 suggest that there are three intersubunit cross-links in the hemoglobin modified by *m*-BCCEP (Figure 9). They are as follows: (a) β2 Val 1 to β1 Lys 144, supported by ions at *m*/*z* 2466.45, 6462.95; (b) β2 Lys 82 to β1 Lys 144, validated by ions at *m*/*z* 2996.22, 4593.50, and 4781.44; and (c) β2 Val 1 to β1 Lys 82, as corroborated by ions at *m*/*z* 4587.14 and 5535.7. The observed third cross-link in (c) was somewhat unexpected based on our molecular modeling results, which showed that the distance between the carbonyl carbon of the reagent and the ε-amino group of β1-lysine is ~12 Å, a bit farther away for effective cross-linking. However, considering that the described molecular dynamics simulations studies did not completely rule out the possibility of the reagent aligning itself between β1-lysine and β2-valine (arrangement *e* described under Molecular Modeling Studies), this result is not totally surprising. It is also to be noted that since cross-linking is anticipated to block the action of trypsin at the lysine (or arginine) residue involved in the cross-link, all the cross-linked peptide fragments might contain additional peptide units beyond the point of cross-link.

The computation of molecular weight of each cross-linked peptide species is based on (a) adding the molecular weights of the concerned peptides; (b) subtraction of 2 mass units and addition of 176.1 mass units to account for the addition of the reagent tether to two peptides; (c) subtraction of 18 mass units corresponding to a molecule of water for each pair of peptides present; for example, 18 (1 H_2O) or 36 (2 H_2O) mass units would be deducted from a fragment containing 2 or 3 peptide units, respectively; and (d) one mass unit is deducted for each sodium or potassium ion added. As an example, an ion at *m*/*z* 5535.7, representing a cross-link between β1 lysine 1 and β2 lysine 144, is computationally reconciled as follows: [(β1T1 = 952.1) + (β2T8 + β2T9 + β2T10 + β2T11 − $3H_2O$ = 4313.9) + (XL = 176.1) − (peptide amino hydrogens = 2) + (Na + 2K − 3 = 98) + (protonation of the cross-linked peptide during the ionization process = 1) = total *m*/*z* 5535.7]. All other ions listed in Table 2 can be similarly accounted for as shown in the last column of the table.

Some peptide fragments listed in Table 2 also suggest that the peptides contained fragments resulting from *m*-BCCEP-linked single β-chain, due to being hydrolyzed before *m*-BCCEP reaction with another amino group on the other β-chain (*59*).

Oxygen Equilibrium (P_{50}) Studies. The *m*-BCCEP-modified hemoglobin product was analyzed for oxygen affinity (P_{50}) characteristics at 37 °C. For the sake of comparison, P_{50} values

Table 2. Comparison of the Observed and Calculated Average Masses of Tryptic Peptides of Human Hb β-Chain Cross-Linked with the Reagent *m*-BCCEP[a]

fragment residues	calcd avg mass $[M+H]^+$	obsd avg mass $[M+H]^+$	tentative structural analysis of tryptic fragment
(1−8)	953.0	953.46	T1
	975.1	975.50	(T1 − 1) + Na
	1035.0	1035.06	(T1) + (−3 + 2Na + K)
	1051.0	1051.09	(T1) + (−3 + Na + 2K)
	1067.0	1067.04	(T1) + (−3 + 3K)
(1−8) XL (66−104)	5535.1	5535.70	(T1 − 1) XL (T8 + T9 + T10 + T11 − $3H_2O$ − 1) + (−3 + Na + 2K)
(1−8) XL (66−95) + Reagent	4586.9	4587.14	(T1 − 1) XL (T8 + T9 + T10 − $2H_2O$ − 1) + (−1 + R^b) + (−3 + 3Na)
(1−8) XL (133−144)	2466.5	2466.45	(T1 − 1) XL (T14 − 1) + (−5 + 5K)
(1−40) XL (133−146) + Reagent	6463.8	6462.95	(T1 + T2 + T3 + T4 − $3H_2O$ − 1) XL (T14 + 15 − H_2O − 1) + (−1 + R^b) + (−6 + 6K)
(9−17)	933.0	933.17	T2
(18−30)	1315.4	1315.48	T3
(31−40)	1275.5	1275.01	T4
(41−59)	2060.3	2060.15	T5
(60−61)	246.3	n.a.a.[b]	n.a.a.[b] (T6)
(62−65)	412.5	n.a.a.[b]	n.a.a.[b] (T7)
(62−66) XL (133−146)	2164.5	2164.31	(T7 + T8 − H_2O − 1) XL (T14 + T15 − H_2O − 1)
(62−82)	2230.6	2229.70	(T7 + T8 + T9 − $2H_2O$ − 1) + K
	2274.6	2274.76	(T7 + T8 + T9 − $2H_2O$) + (−3 + 2Na + K)
(66−66)	147.2	n.a.a.[b]	n.a.a.[b] (T8)
(66−82)	1837.1	1837.61	(T8 + T9 − H_2O − 1) + K
(66−82) XL (121−144)	4593.2	4593.50	(T8 + T9 − H_2O − 1) XL (T13 + T14 − H_2O − 1) + (−5 + 5Na)
(66−82) XL (121−146)	4783.5	4781.44	(T8 + T9 − H_2O − 1) XL (T13 + T14 + T15 − $2H_2O$ − 1)
(66−95)	3312.7	3312.78	(T8 + T9 + T10 − $2H_2O$) + (−5 + 5Na)
(67−82)	1670.9	n.o.[b]	n.o.[b] (T9)
(67−82) XL (133−144)	2994.4	2996.22	(T9 − 1) XL (T14 − 1)
(83−95)	1422.6	n.o.[b]	n.o.[b] (T10)
	1532.6	1532.59	(T10) + (−5 + 5Na)
(83−104)	2688.8	2689.57	(T10 + T11 − H_2O) + (−5 + 2Na + 3K)
(83−104) + Reagent	2810.9	2810.62	(T10 + T11 − H_2O − 1) + R^b + (−4 + 4Na)
(96−104)	1127.2	n.o.[b]	n.o.[b] (T11)
	1171.2	1171.94	(T11) + (−2 + 2Na)
(105−120)	1721.1	n.o.[b]	n.o.[b] (T12)
	1831.1	1831.31	(T12) + (−5 + 5Na)
(121−132)	1379.6	1379.42	T13
(133−144)	1150.4	n.o.[b]	n.o.[b] (T14)
	1172.4	1172.91	(T14 − 1) + Na
	1194.4	1194.87	(T14) + (−2 + 2Na)
(133−144) + Reagent	1364.5	1364.31	(T14 − 1) + R^b + (−1 + Na)
(133−146)	1450.7	1450.68	T14 + T15 − H_2O
(133−146) + Reagent	1642.8	1642.84	(T14 + T15 − H_2O − 1) + R^b
	1664.8	1664.69	(T14 + T15 − H_2O − 1) + R^b+ (−1 + Na)
(145−146)	319.3	n.a.a.[b]	n.a.a.[b] (T15)

[a] The average mass of peptide fragments was calculated using the computer program, *GPMAW* (General Protein Mass Analyzer for Windows), v 2.0, available from Light House Data, Engvej 35, DK-5230, Odense M, Denmark. The following are the calculated masses for the peptide fragments resulting from tryptic digestion of the β-chain of hemoglobin and were employed in all subsequent computations involving these fragments: T1 (1−8), 952.08; T2 (9−17), 932.09; T3 (18−30), 1314.42; T4 (31−40), 1274.53; T5 (41−59), 2059.28; T6 (60−61), 245.33; T7 (62−65), 411.46; T8 (66−66), 146.19; T9 (67−82), 1669.90; T10 (83−95), 1421.59; T11 (96−104), 1126.24; T12 (105−120), 1720.11; T13 (121−132), 1378.55; T14 (133−144), 1149.36; T15 (145 146), 318.34. [b] The following are the abbreviations used in the Table: n.a.a., no assignment attempted; n.o., not observed; T, tryptic peptide; XL = $C(O)(CH_2)_2P(O)(OH)(CH_2)_2C(O)$ = cross-linked reagent with a mass = 176.1; R = $C(O)(CH_2)_2P(O)(OH)(CH_2)_2CO_2H$ = reagent reacted on only one side, while the other side is hydrolyzed, with a mass of 193.12. Here, reagent is *m*-BCCEP (trisodium salt).

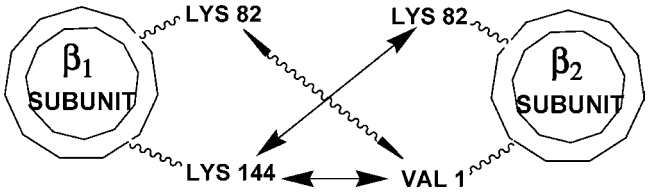


Figure 9. Three intersubunit cross-links present in the *m*-BCCEP modified Hb. The one with a broken arrow is a minor cross-link.

were also measured under the same conditions for the un-cross-linked, stroma-free Hb (SFHb). The graphs of PO_2 vs % Hb saturation for SFHb and the BCCEP-modified Hb are shown in Figure 10. The computed P_{50} value for the modified Hb was 25.8 Torr, in contrast to that of the stroma-free Hb (14.19 Torr). Thus, the *m*-BCCEP-modified Hb showed significantly lowered oxygen affinity as compared with the stroma-free hemoglobin. This was further attested by the observed right-shifting of O_2 equilibrium curve of the cross-linked product relative to that of SFHb. Furthermore, the reasonable retainment of oxygen binding cooperativity after the cross-link formation was suggested by the Hill coefficient *n* (cooperativity of oxygen binding is measured by the Hill coefficient, *n*, which is computed by the Hill equation, $Y = (PO_2)n/[(P_{50})n + (PO_2)_n]$, where *Y* is the fraction of Hb saturated. The value of *n* in whole blood ranges 2.3−2.5), generated from the Hill plots of P_{50} values, which came out to 1.91. This value in whole blood ranges 2.0−2.5 (*93*). However, while the Hill coefficient would be a quantitative indicator of oxygen-binding cooperativity, the computed value from such plots for the *m*-BCCEP-modified Hb is, nonetheless, less meaningful in view of the anticipated and observed multiple cross-linking sites and the consequent heterogeneity of the *m*-BCCEP-modified Hb.

CONCLUSION

The design and synthesis of an efficacious hemoglobin cross-linking reagent, employing modern molecular modeling and organic synthesis techniques, have been reported. The title reagent *m*-BCCEP can be synthesized in four facile, convenient, and good-yielding steps, employing readily available, inexpen-

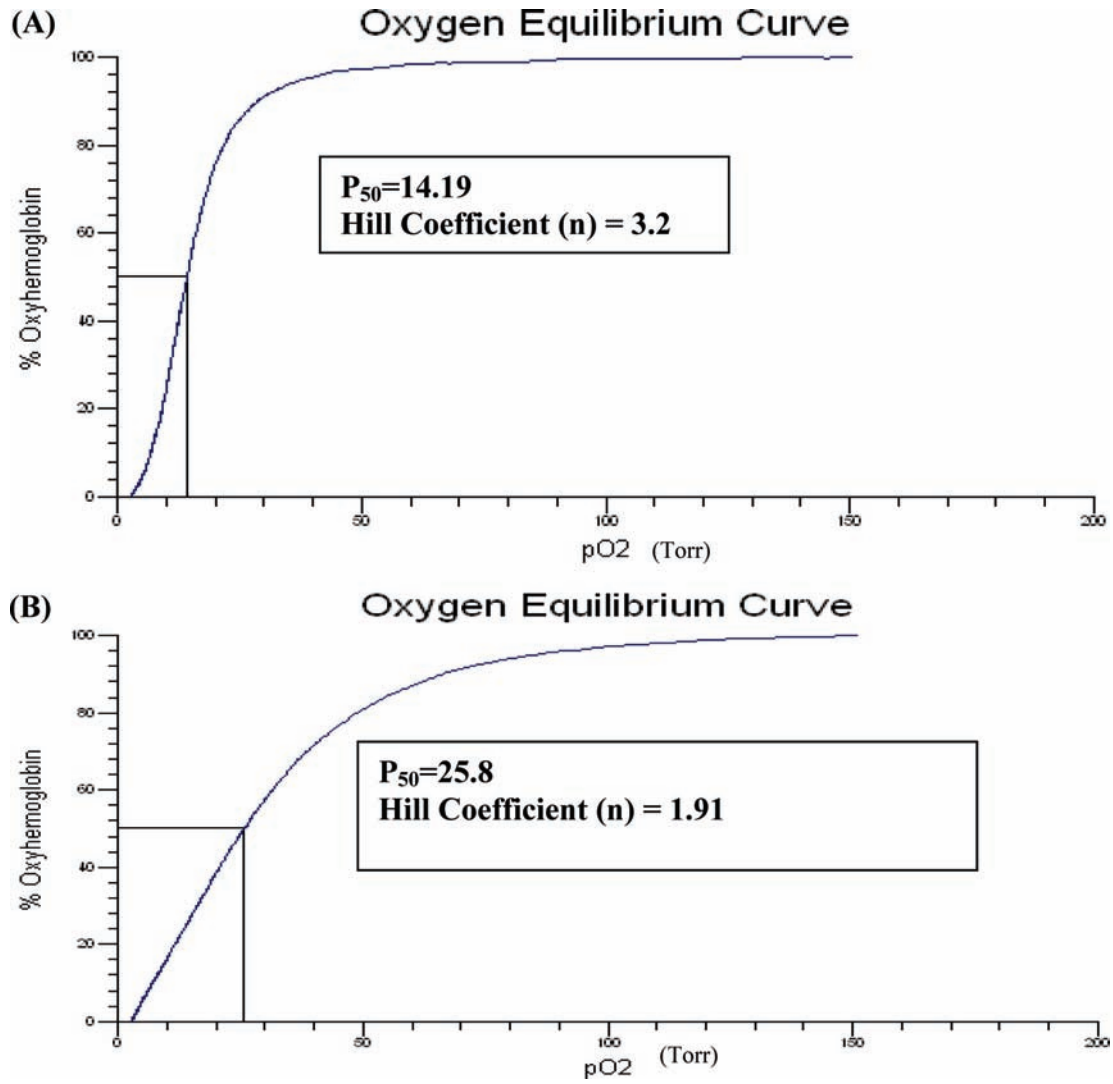


Figure 10. Oxygen equilibrium curves for (a) stroma-free Hb and (b) *m*-BCCEP-modified Hb.

sive starting materials, and can be easily adapted to high-scale production. It has an indefinite shelf life and can be converted into its crystalline trisodium salt that can be employed to cross-link hemoglobin under aqueous biological medium and ambient oxygenated reaction conditions, requiring no special precautions to either preclude oxygen or include carbon monoxide as is the case with many known hemoglobin cross-linking agents. The tryptic digestion and MALDI mass spectral analyses of the modified β-chain fragments suggest that the reagent predominantly forms two cross-links between β1 Lys 144 and either β2 Val 1 or β2 Lys 82, although a minor third cross-link was also found between β1 Lys 82 and β2 Val 1. These results were remarkably consistent with those predicted by molecular modeling studies of the *m*-BCCEP-Hb A_0 complex. The oxygen affinity of the cross-linked product is considerably lower (P_{50} = 25.8 Torr) as desired in comparison with that of stroma-free Hb (P_{50} = 14.2 Torr) and is somewhat comparable to the oxygen affinity of the whole blood (P_{50} = 27 Torr). The cross-linked product also retains some of the oxygen-binding cooperativity characteristics of the native protein, as revealed by its Hill coefficient value (n = 1.91), which is significantly higher than that of the previously reported BPPCEP-modified hemoglobin products, all of which had the n value equal to or less than 1.0 (*59*).

Finally, the field of blood substitutes based on cell-free hemoglobin has a vast and rich history with a wide variety of cross-linking reagents, modified Hb products derived therefrom, and data on their oxygen affinity characteristics, osmotic pressure, vasoconstriction, and other physiological properties, as well as on a few products that have made to the clinical trials. In that context, discovering another Hb-cross-linking reagent with novel characteristics will only be a first step toward an optimal, physiologically feasible, and clinically compatible blood substitute. If history is any indication, even the most ideally modified Hb products are likely to suffer from one or the other historical problems of short circulation times in the bloodstream, inadequate colloidal osmotic pressures (COP), or vasoconstriction due to scavenging of nitric oxide, the endothelium-derived relaxation factor (*46*−*50*). However, these past setbacks should, nonetheless, discourage or halt future scientific efforts to realize an eventually optimal blood substitute that has so much stake in success outcome of almost every major field of modern medicine. To alleviate some of the problems currently encountered in blood substitute field, it may be necessary to increase the steric bulk of the cross-linked hemoglobin through polymerization. This will allow its retention in circulation for prolonged periods of time (*44*, *45*). The increased size would also prevent its facile sieving through the endothelial lining of blood vessels, where they are known to scavenge nitric oxide. Such an effort based on *m*-BCCEP framework and other novel organic reagents is currently in progress in this laboratory.

ACKNOWLEDGMENT

This research was supported by a grant (0755372U) from the American Heart Association. We thank Dr. Victor Macdonald, Chief, Division of Blood Products & Storage, Walter Reed Army Institute of Research, Washington, DC, for generous supply of stroma-free hemoglobin employed in our studies. We are highly grateful to Dr. Fantao Meng of Albert Einstein College of Medicine for assistance in our oxygen equilibrium studies on modified hemoglobins.

LITERATURE CITED

(1) Scholer, M., Frietsch, T., Jambor, C., and Knels, R. (2010) Artificial blood--coming soon or never reaching clinical maturity? *Dtsch. Med. Wochenschr. 135*, 575–581.
(2) Winslow, R. M. (1992) *Hemoglobin-based Red Cell Substitutes*, The Johns Hopkins University Press, Baltimore and London.
(3) Winslow, R. M. (2003) Current status of blood substitute research: towards a new paradigm. *J. Intern. Med. 253*, 508–517.
(4) Winslow, R. M. (2006) Current status of oxygen carriers ('blood substitutes'). *Vox Sang. 91*, 102–10.
(5) Winslow, R. M., Vandegriff, K. D., and Intaglietta, M. (1996) *Blood Substitutes: New Challanges* (Winslow, R. M., Vandegriff, K. D., and Intaglietta, M., Eds) pp 61−63, Birkhauser, Boston.
(6) Alayash, A. I. (2001) Is there a need for blood substitutes in the new millennium and what should we expect in the way of safety and efficacy? A research perspective. *Artif. Cells Blood Substit. Immobil. Biotechnol. 29*, 1–3.
(7) Chang, T. M. (2004) Hemoglobin-based red blood cell substitutes. *Artif. Organs 28*, 789–94.
(8) Jahr, J. S., Nesargi, S. B., Lewis, K., and Johnson, C. (2002) Blood substitutes and oxygen therapeutics: an overview and current status. *Am. J. Ther. 9*, 437–43.
(9) Klein, H. G. (2002) Blood substitutes: how close to a solution? *Oncology (Williston Park) 16*, 147–51.
(10) Squires, J. E. (2002) Artificial blood. *Science 295*, 1002–5.
(11) McCullough, J. J. (1998) *Transfusion Medicine*, pp 91−93, McGraw-Hill, New York.
(12) Rossi, E. C., Simon, T. L., and Moss, G. S. (1991) *Principles of transfusion medicine*, pp 1−11, Williams & Wilkins, Baltimore.
(13) Fronticelli, C., and Koehler, R. C. (2009) Design of recombinant hemoglobins for use in transfusion fluids. *Crit. Care Clin. 25*, 357–371.
(14) Creteur, J., and Vincent, J.-L. (2009) Potential uses of hemoglobin-based oxygen carriers in critical care medicine. *Crit. Care Clin. 25*, 311–324.
(15) Winslow, R. M. (2007) Red cell substitutes. *Semin. Hematol. 44*, 51–9.
(16) Greenburg, A. G. (2009) The ideal blood substitute. *Crit. Care Clin. 25*, 415–424.
(17) Baron, J. F., and Treib, J. (1998) *Volume Replacement*, pp 1−143, Springer, Berlin.
(18) Lowe, K. C. (1998) Fluorocarbon Emulsions as Blood Substitutes, in *Blood Substitutes Present and Future Perspectives* (Tsuchida, E., Ed.) pp 327−338, Elsevier Science S.A., Switzerland.
(19) Riess, J. G. (1993) Overview of Progress in the Fluorocarbon Approach to *in vivo* Oxygen Delivery, in *Blood Substitutes and Oxygen Carriers* (Chang, T. M. S., Ed.) pp 24−43, Marcel Dekker, Inc, New York.
(20) Cohn, C. S., and Cushing, M. M. (2009) Oxygen therapeutics: perfluorocarbons and blood substitute safety. *Crit. Care Clin. 25*, 399–414.
(21) Farmer, M. C, and Gaber, B. P. (1987) Liposome-encapsulated hemoglobin as an artificial oxygen carrying system. *Methods Enzymol. 149*, 184–200.
(22) Rohlfs, R. J., and Vandegriff, K. D. (1996) Non-Phospholipid Liposomes: A Novel Method for the Preparation of Hemoglobin Containing Lipid Vesicles, in *Blood Substitutes: New Challenges* (Winslow, R. M., Vandegriff, K. D., and Intaglietta, M., Eds.) pp163−184, Birkhäuser, Boston.
(23) Rudolph, A. S. (1995) Encapsulation of Hemoglobin in Liposomes, in *Blood Substitutes: Physiological Basis of Efficacy* (Winslow, R. M., Vandegriff, K. D., and Intaglietta, M., Ed.) pp 90−104, Birkhauser, New York.
(24) Chang, T. M. S. (1989) Red Blood Cell Substitutes: Microencapsulated Hemoglobin and Cross-Linked Hemoglobin Including Pyridoxylated Polyhemoglobin & Conjugated Hemoglobin, in *Blood Substitutes* (Chang, T. M. S., and Geyer, R. P., Ed.) pp 11−29, Marcel Dekker, Inc., New York.
(25) Alayash, A. I. (1998) Hemoglobin-based Blood Substitutes and Mechanisms of Toxicity, in *Blood Substitutes Present and Future Perspectives* (Tsuchida, E., Ed.) pp 201−210, Elsevier Sciences S.A., Switzerland.
(26) Alayash, A. I. (1999) Hemoglobin-based blood substitutes: oxygen carriers, pressor agents, or oxidants? *Nat. Biotechnol. 17*, 545–9.
(27) Alayash, A. I. (2000) Hemoglobin-based blood substitutes and the hazards of blood radicals. *Free Radic. Res. 33*, 341–8.
(28) Eastman, A. L., and Minei, J. P. (2009) Comparison of hemoglobin-based oxygen carriers to stored human red blood cells. *Crit. Care Clin. 25*, 303–310.
(29) Napolitano Lena, M. (2009) Hemoglobin-based oxygen carriers: first, second or third generation? Human or bovine? Where are we now? *Critical Care Clinics 25*, 279–301, Table of Contents.
(30) Rudolph, A. S. (1998) Hemoglobin-Based Blood Substitutes, in *Frontiers in Tissue Engineering* (Patrick, C. W., Jr., Mikos, A. G., and McIntyre, L. V., Eds.) pp481−494, Elsevier, New York.
(31) Maton, A., Hopkins, J., McLaughlin, C. W., Johnson, S., Warner, M. Q., LaHart, D., and Wright, J. D. (1993) *Human Biology and Health*, Pearson Prentice Hall, Englewood Cliffs, NJ.
(32) Amberson, W. (1937) Blood substitute. *Biol. Rev.* 12–48.
(33) Rabiner, S. F., Helbert, J. R., Lopas, H., and Friedman, L. H. (1967) Evaluation of a stroma-free hemoglobin solution for use as a plasma expander. *J. Exp. Med. 126*, 1127–42.
(34) Savitsky, J. P., Doczi, J., Black, J., and Arnold, J. D. (1978) A clinical safety trial of stroma-free hemoglobin. *Clin. Pharmacol. Ther. 23*, 73–80.
(35) Horton, H., Moran, L., Ochs, R., Rawn, J., and Scrimgeour, K. (1993) *Principles of Biochemistry*, Neil Patterson, New Jersey.
(36) Astrup, P., and Rorth, M. (1971) *Oxygen Affinity of Hemoglobin and Red Cell Acid Base Status*, Academic Press, New York.
(37) Haney, C. R., Buehler, P. W., and Gulati, A. (2000) Purification and chemical modifications of hemoglobin in developing hemoglobin based oxygen carriers. *Adv. Drug Delivery Rev. 40*, 153–69.
(38) Viele, M. K., Weiskopf, R. B., and Fisher, D. (1997) Recombinant human hemoglobin does not affect renal function in humans: analysis of safety and pharmacokinetics. *Anesthesiology 86*, 848–58.
(39) Arnone, A. (1972) X-ray diffraction of binding of 2,3-diphosphoglycerate to human dexoyhaemoglobin. *Nature 237*, 146–149.
(40) Bakker, J. C., Berbers, G. A., Bleeker, W. K., den Boer, P. J., and Biessels, P. T. (1992) Preparation and characterization of crosslinked and polymerized hemoglobin solutions. *Biomater. Artif. Cells Immobilization Biotechnol. 20*, 233–41.
(41) Gould, S. A., Sehgal, L. R., Sehgal, H. L., and Moss, G. S. (1992) Artificial blood: current status of hemoglobin solutions. *Crit. Care Clin. 8*, 293–309.
(42) Spahn, D. R. (2000) Current status of artificial oxygen carriers. *Adv. Drug Delivery Rev. 40*, 143–51.
(43) Bolin, R., Geyer, R., and Nemo, G. E. (1983) *Advances in Blood Substitute Research*, pp 1−468, Alan R. Liss, Inc., New York.

(44) Jahr, J. S., Moallempour, M., and Lim, J. C. (2008) HBOC-201, hemoglobin glutamer-250 (bovine), Hemopure (Biopure Corporation). *Expert Opin. Biol. Ther. 8*, 1425–1433.

(45) Napolitano, L. M. (2009) Hemoglobin-based oxygen carriers: first, second or third generation? Human or bovine? Where are we now? *Crit. Care Clin. 25*, 279–301.

(46) Allen, B. W., and Piantadosi, C. A. (2006) How do red blood cells cause hypoxic vasodilation? The SNO-hemoglobin paradigm. *Am. J. Physiol. 291*, H1507–H1512.

(47) Angelo, M., Hausladen, A., Singel, D. J., and Stamler, J. S. (2008) Interactions of NO with hemoglobin: from microbes to man. *Methods Enzymol. 436*, 131–168.

(48) Babbar, R., and Agarwal, S. (2005) Nitric oxide-hemoglobin interactions: Role in oxygen uptake and delivery. *Ind. J. Physiol. Pharmacol. 49*, 378–382.

(49) Goedecke, A. (2006) On the impact of NO-globin interactions in the cardiovascular system. *Cardiovasc. Res. 69*, 309–317.

(50) von Dobschuetz, E., Hutter, J., Hoffmann, T., and Messmer, K. (2004) Influence of hemoglobin-based oxygen carriers with different nitric oxide scavenging properties on the pancreatic microcirculation after hemorrhagic shock. *Prog. Appl. Microcirc. 25*, 86–94.

(51) Alleyne, T. A., Wilson, M. T., Antonini, G., Malatesta, F., Vallone, B., Sarti, P., and Brunori, M. (1992) Investigation of the electron-transfer properties of cytochrome c oxidase covalently cross-linked to Fe- or Zn-containing cytochrome c. *Biochem. J. 287*, 951–6.

(52) Hosmane, R. S. (1984) Imidates in organic synthesis: Methyl N-cyanomethylmethanimidate. *Tetrahedron Lett. 25*, 363–6.

(53) Hosmane, R. S., and Bertha, C. (1988) A novel bifunctional reagent: 2,2′-bis(methoxymethylene)-2,2′-sulfonyldiacetonitrile. *Tetrahedron Lett. 29*, 5847–50.

(54) Hosmane, R. S., Bertha, C., Siriwardane, U., and Hosmane, N. (1990) Reagents for bioorganic synthesis. 5. the synthesis of two potential cross-linking reagents: 2,2′-sulfonylbis[3-(benzyamino)-(E,E)-N-(2-oxoethyl)propenamide](SBBOP) and 2,2′-sulfonylbis[3-(benzylamino)-(E,E)-N(-2-chloroethyl)propenamide] (SBBCP). *J. Org. Chem. 55*, 5206–16.

(55) Hosmane, R. S., and Bertha, C. M. (1990) A versatile, highly reactive, cross-linking reagent: 2,2′-sulfonylbis[3-methoxy-(E,E)-2-propenenitrile]. *Biochem. Biophys. Res. Commun. 166*, 567–73.

(56) Hosmane, R. S., Burnett, F., and Albert, M. (1984) Reagents for bioorganic synthesis: preparation, properties, and reactions of ethyl and methyl N-(cyanomethyl)methanimidates. *J. Org. Chem. 49*, 1212–5.

(57) Hosmane, R. S., Peri, S. P., Bhadti, V. S., and Macdonald, V. W. (1998) Bis[2-(4-carboxyphenoxy)carbonylethyl]phosphinic acid (BCCEP): a novel affinity reagent for the beta-cleft modification of human hemoglobin. *Bioorg. Med. Chem. 6*, 767–83.

(58) Mayer, A. N., and Barany, F. (1995) Photoaffinity cross-linking of TaqI restriction endonuclease using an aryl azide linked to the phosphate backbone. *Gene 153*, 1–8.

(59) Roach, T. A., Macdonald, V. W., and Hosmane, R. S. (2004) A novel site-directed affinity reagent for cross-linking human hemoglobin: bis[2-(4-phosphonooxyphenoxy)carbonylethyl]phosphinic acid. *J. Med. Chem. 47*, 5847–59.

(60) Wohlfeil, E. R., and Hudson, R. A. (1991) Synthesis and characterization of a heterobifunctional mercurial cross-linking agent: incorporation into cobratoxin and interaction with the nicotinic acetylcholine receptor. *Biochemistry 30*, 7231–41.

(61) Zhu, Q., and Courtney, R. J. (1994) Chemical cross-linking of virion envelope and tegument proteins of herpes simplex virus type 1. *Virology 204*, 590–9.

(62) Bertha, C. M., Hosmane, S. H., Zhang, H., and Hosmane, N. S. (1994) Reagents for bioorganic synthesis. 6. The design and synthesis of two novel polyfunctional organic reagents for biomacromolecular modification. *J. Biomol. Struct. Dyn. 12*, 413–37.

(63) Chang, T. M. S. (1993) *Blood Substitutes and Oxygen Carriers*, pp 1−871, Marcel Dekker Inc., Montreal.

(64) Chang, T. M. S. (1997) *Blood Substitutes: Principles, Methods, Products and Clinical Trials*, pp 1−142, Vol *1*, Karger Lander Systems.

(65) Crapatureanu, S., Serbanescu, R., Brevitt, S. B., and Kluger, R. (1999) Molecular necklaces. Cross-linking hemoglobin with reagents containing covalently attached ligands. *Bioconjugate Chem. 10*, 1058–67.

(66) Jones, R. T., Head, C. G., Fujita, T. S., Shih, D. T., Wodzinska, J., and Kluger, R. (1993) Modification of human hemoglobin with methyl acyl phosphates derived from dicarboxylic acids. Systematic relationships between cross-linked structure and oxygen-binding properties. *Biochemistry 32*, 215–23.

(67) Jones, R. T., Shih, D. T., Fujita, T. S., Song, Y., Xiao, H., Head, C., and Kluger, R. (1996) A doubly cross-linked human hemoglobin. Effects of cross-links between different subunits. *J. Biol. Chem. 271*, 675–80.

(68) Kluger, R. (1994) 1994 Syntex Award Lecture. Anionic electrophiles, protein modification, and artificial blood. *Can. J. Chem. 72*, 2193–2197.

(69) Kluger, R., Jones, R. T., and Shih, D. T. (1994) Cross-linking hemoglobin by design: lessons from using molecular clamps. *Artif. Cells Blood Substit. Immobil. Biotechnol. 22*, 415–28.

(70) Kluger, R., and Li, X. (1997) Efficient chemical introduction of a disulfide cross-link and conjugation site into human hemoglobin at beta-lysine-82 utilizing a bifunctional aminoacyl phosphate. *Bioconjugate Chem. 8*, 921–6.

(71) Kluger, R., Lock-O'Brien, J., and Teytelboym, A. (1999) Connecting proteins by design. cross-linked bis-hemoglobin. *J. Am. Chem. Soc. 121*, 6780–6785.

(72) Kluger, R., and Stefano, V. D. (2000) Mechanism of site-directed protein cross-linking. protein-directed selectivity in reactions of hemoglobin with aryl trimesates. *J. Org. Chem. 65*, 214–9.

(73) Peri, S. P., Bhadti, V. S., Hosmane, R. S., and Macdonald, V. W. (1997) Bis[2-(4-carboxyphenoxy)carbonylethyl]phosphinic acid (BCCEP): a new reagent for hemoglobin modification. *Artif. Cells Blood Substit. Immobil. Biotechnol. 25*, 511–20.

(74) Peri, S. P., Bhadti, V. S., Somerville-Armstrong, K. S., Liang, R., Macdonald, V. W., and Hosmane, R. S. (1999) Affinity reagents for cross-linking hemoglobin: bis(phenoxycarbonylethyl)phosphinic acid (BPCEP) and bis(3-nitrophenoxycarbonylethyl)phosphinic acid (BNCEP). *Hemoglobin 23*, 1–20.

(75) Ueno, H., Pospischil, M. A., Manning, J. M., and Kluger, R. (1986) Site-specific modification of hemoglobin by methyl acetyl phosphate. *Arch. Biochem. Biophys. 244*, 795–800.

(76) Harrington, J. P., Gonzalez, Y., and Hirsch, R. E. (2000) Redox concerns in the use of acellular hemoglobin-based therapeutic oxygen carriers: the role of plasma components. *Artif. Cells Blood Substit. Immobil. Biotechnol. 28*, 477–92.

(77) Everse, J., and Hsia, N. (1997) The toxicities of native and modified hemoglobins. *Free Radic. Biol. Med. 22*, 1075–99.

(78) Silva, M. M., Rogers, P. H., and Arnone, A. (1992) A third quaternary structure of human hemoglobin A at 1.7A_0. resolution. *J. Biol. Chem. 267*, 17248–17256.

(79) Pimenova, T., Pereira, C. P., Schaer, D. J., and Zenobi, R. (2009) Characterization of high molecular weight multimeric states of human haptoglobin and hemoglobin-based oxygen carriers by high-mass MALDI MS. *J. Sep. Sci. 32*, 1224–1230.

(80) Porubleva, L. V., Rebriiev, A. V., Gromovoy, T. Y., Minia, I. J., and Obolenskaya, M. Y. (2009) MALDI-TOF mass spectrometry in the investigation of high-molecular biological compounds. *Ukrains'kii Biokhimichnii Zhurnal 81*, 46–56.

(81) Vestal, M. L. (2009) Modern MALDI time-of-flight mass spectrometry. *J. Mass Spectrom. 44*, 303–317.

(82) Abraham, D. J., Safo, M. K., Boyiri, T., Danso-Danquah, R. E., Kister, J., and Poyart, C. (1995) How allosteric effectors can bind to the same protein residue and produce opposite shifts in the allosteric equilibrium. *Biochemistry 34*, 15006–20.

(83) Boyiri, T., Safo, M. K., Danso-Danquah, R. E., Kister, J., Poyart, C., and Abraham, D. J. (1995) Bisaldehyde allosteric effectors as molecular ratchets and probes. *Biochemistry 34*, 15021–36.

(84) Randad, R. S., Mahran, M. A., Mehanna, A. S., and Abraham, D. J. (1991) Allosteric modifiers of hemoglobin. 1. Design, synthesis, testing, and structure-allosteric activity relationship of novel hemoglobin oxygen affinity decreasing agents. *J. Med. Chem. 34*, 752–7.

(85) Wireko, F. C., Kellogg, G. E., and Abraham, D. J. (1991) Allosteric modifiers of hemoglobin. 2. Crystallographically determined binding sites and hydrophobic binding/interaction analysis of novel hemoglobin oxygen effectors. *J. Med. Chem. 34*, 758–67.

(86) Trimble, S. P., Marquardt, D., and Anderson, D. C. (1997) Use of designed peptide linkers and recombinant hemoglobin mutants for drug delivery: in vitro release of an angiotensin II analog and kinetic modeling of delivery. *Bioconjugate Chem. 8*, 416–423.

(87) Pechik, I., Ji, X., Fidelis, K., Karavitis, M., Moult, J., Brinigar, W. S., Fronticelli, C., and Gilliland, G. L. (1996) Crystallographic, molecular modeling, and biophysical characterization of the valine$^{\beta 67}$ (E11) -> threonine variant of hemoglobin. *Biochemistry 35*, 1935–45.

(88) Wajcman, H., Kister, J., Prome, D., Blouquit, Y., Prehu, C., Poyart, C., and Galacteros, F. (1995) Interaction of 2 amino acid substitutions within the same beta chain of human hemoglobin: the examples of Hb Corbeil and Hb Villeparisis. *C. R. Acad. Sci. Ser. III 318*, 785–94.

(89) Schaad, O., Vallone, B., and Edelstein, S. J. (1993) Critical residues responsible for self-association differences of hemoglobin $\hat{I}\pm$ and $\hat{I}^2$ chains: Analysis by molecular modeling. *C. R. Acad. Sci. Ser. III 316*, 564–71.

(90) Cretegny, I., and Edelstein, S. J. (1993) Double strand packing in hemoglobin S fibers. *J. Mol. Biol. 230*, 733–8.

(91) Arnone, A., Benesch, R. E., and Benesch, R. (1977) Structure of human deoxyhemoglobin specifically modified with pyridoxal compounds. *J. Mol. Biol. 115*, 627–642.

(92) Yang, T., Horejsh, D. R., Mahan, K. J., Zaluzec, E. J., Watson, T. J., and Gage, D. A. (1996) Mapping cross-linking sites in modified proteins with mass spectrometry: an application to cross-linked hemoglobins. *Anal. Biochem. 242*, 55–63.

(93) Miller, I. F. (1978) Synthetic blood substitutes: where are we and where do we go from here? *CRC Crit. Rev. Bioeng. 3*, 149–179.

BC100113Y

Activation and Alteration of Base Selectivity by Metal Cations in the Functionality-Transfer Reaction for RNA Modification

Kazumitsu Onizuka, Yosuke Taniguchi, and Shigeki Sasaki*

Graduate School of Pharmaceutical Sciences, Kyushu University, 3-1-1 Maidashi, Higashi-ku, Fukuoka 812-8582, Japan, and CREST, Japan Science and Technology Agency, 4-1-8 Motomachi, Kawaguchi, Saitama 332-0012, Japan. Received March 9, 2010; Revised Manuscript Received June 14, 2010

Previously, we reported that the 2-methylidene-1,3-diketone unit of 6-thioguanosine transferred selectively to the amino group of cytosine at pH 7.0 and that its selectivity was changed to the guanine base at pH 9.6. In this study, it was found that the functionality-transfer reaction enhanced selectivity for the guanine base in the presence of divalent transition metal cations such as Ni^{2+} and Co^{2+} at pH 7.4.

INTRODUCTION

A number of oligodeoxynucleotides (ODNs) with an attached chemically reactive accessory molecule have been developed to perform chemical modifications of DNA or RNA in a sequence-specific manner (*1, 2*). In particular, there is increasing demand for methods of the site-specific modifications of RNA because of potential applications as innovative biological tools (*3*−*6*) and therapeutic methods (*7*−*9*).

The accessory molecule needs to be stable, and its reactivity is desired to be induced when it is needed. UV irradiation is frequently used as an exogenous activation signal (*10*−*13*). We have been developing an original strategy for the induction of the reactivity of the accessory molecules by taking advantage of minute environmental changes accompanied by nucleic acid hybridization. The first example was demonstrated by the hybridization-promoted cytosine-selective alkylation using the sulfide derivative of 2-amino-6-vinylpurine nucleoside, in which the stable sulfide precursor was spontaneously activated to the active vinyl species within the complementary duplex having the cytosine base at the target site (*14*−*16*). This strategy was then expanded to nitrosyl group transfer from the sulfur atom of 6-thioguanosine to the amino group of the cytosine base (*17*). Its reactivity was induced in close proximity to the cytosine base in the complementary duplex that affected the nitrosyl transfer to the amino group of the cytosine base. Cytosine deamination following the nitrosyl transfer reaction suggested its potential application as an artificial tool for RNA editing.

For further expansion of this strategy, we developed a functionality-transfer reaction to the amino group of the cytosine base using the ODN incorporating *S*-(2-methylidene-1,3-diketone)-6-thioguanine, and the reaction enabled the site-specific covalent modification of RNAs (Figure 1A and B) (*18*). Interestingly, it was found that the transfer reaction was greatly accelerated toward the guanine base under alkaline conditions and led to a change in base selectivity from rC at pH 7.0 to rG at pH 9.6 (Figure 1C) (*19*). This functionality-transfer reaction has been applied to the site selective transfer of the fluorescent pyrene unit to rG in the RNA substrate (*19*). This method is characteristic in that it might be applied to the modification of large RNA and also in that base selectivity can be controlled by pH change. If the reactivity can be activated by a factor other than pH, this method would find wider utility in chemical modification of natural RNA. The selectivity change was reasonably explained in terms of an increase in the nucleophilicity of the 2-amino group by the enolate formation of the guanine base under alkaline conditions. These considerations led us to hypothesize that transition metal ions such as Ni^{2+}, Co^{2+}, Cu^{2+}, and Zn^{2+}, which are known to coordinate at the N7 position of the guanine base and decrease the p*K*a value of the N1 position (*20*), might enhance the reactivity of rG under neutral conditions. In this article, we report that $Ni^{2+}$and Co^{2+} effectively enhance the reactivity of rG to switch the base selectivity to rG from rC under neutral conditions.

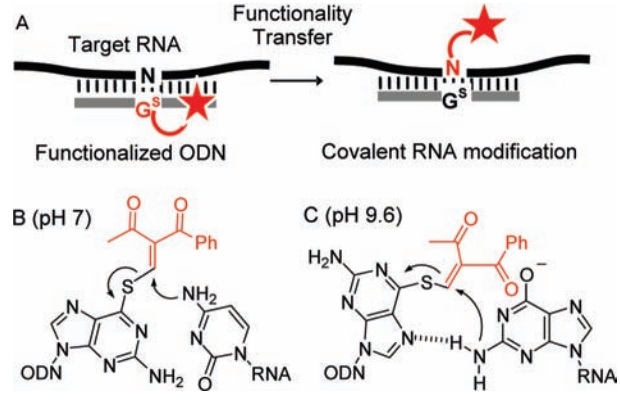


Figure 1. Concept of the functionality-transfer reaction (A) and selective reaction leading to C-modification at pH 7 (B) and G-modification at pH 9.6 (C).

EXPERIMENTAL PROCEDURES

General Methods. All ODNs were synthesized by using an automated DNA synthesizer (Applied Biosystems 394 DNA/RNA synthesizer) at a 1.0 μmol scale. The structures of synthetic ODNs were confirmed by MALDI-TOF MS measurement (Bruker Daltonics Microflex instrument). MALDI-TOF MS results are summarized in Table 2S (Supporting Information). All ORNs were purchased from Gene Design Inc. or Genenet.

Functionality-Transfer Reaction from the Functionalized ODN1F (X = G^S(Me,Ph)) to ORN2 in the Presence of $NiCl_2$ as the General Procedure for the Functionality-Transfer Reaction. ODN**1F** (X = G^S(Me,Ph)) was freshly prepared before the functionality-transfer reaction by mixing ODN**1** and 3-

* Corresponding author. Tel: +81-92-642-6615. Fax: +81-92-642-6786. E-mail: sasaki@phar.kyushu-u.ac.jp.

10.1021/bc100131j © 2010 American Chemical Society
Published on Web 06/29/2010

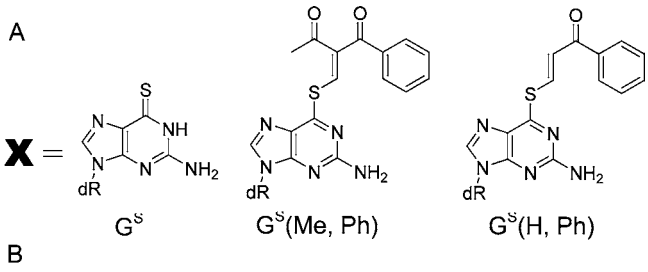


Figure 2. Structure of S-functionalized 6-thioguanosine (A) and the sequences of the ODN probes, the target ORN and ODN (B).

chloromethylene-4-phenylbutane-2,4-dione in carbonate buffer (pH 10). The solution of ODN**1F** (X = G^S(Me,Ph)) and a solution of the target ORN**2** were mixed in MES buffer containing NaCl and $NiCl_2$, and the mixture was kept at 25 °C. The reaction mixture was analyzed by HPLC with UV monitoring at 254 nm or FAM fluorescence at 518 nm with emission at 494 nm. Column, SHISEIDO C18, 4.6 × 250 mm; solvent A, 0.1 M TEAA buffer; B, CH_3CN; B, 10% to 30% /20 min, linear gradient; flow rate, 1.0 mL/min.

UV Melting Temperature Measurements. UV melting temperatures were measured using 1.3 μM of each ODN and ORN strands in MES buffer (pH 7.4) containing 100 mM NaCl and 1 mM MCl_2 with monitoring at 260 nm by a UV−Vis spectrophotometer.

Circular Dichroism Measurements. CD spectra were measured by using 2.5 μM of each ODN and ORN strand in 50 mM MES buffer (pH 7.4) containing 100 mM NaCl and 1 mM MCl_2 at room temperature in a cylindrical quartz cell with a path length of 0.1 cm.

RESULTS AND DISCUSSION

Figure 2 summarizes the structure of the ODN**1** probe incorporating the 6-thioguanosine analogue functionalized with the phenyl-1,3-diketone unit and ORN**2** and ODN**3** as the targets. We first investigated the effect of metal dichloride

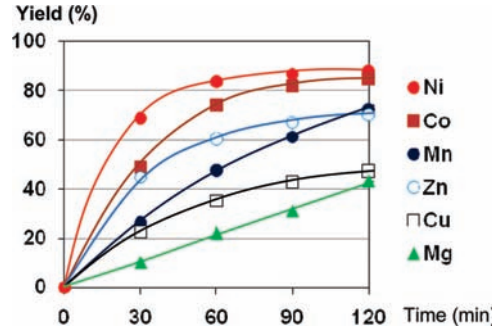


Figure 4. Concentration dependency of the metal cation on the functionality-transfer reaction. The transfer reactions were performed by using 15 μM S-functionalized ODN1F-G^S(Me, Ph) and 10 μM target ORN**2** (G) in 50 mM MES buffer containing 100 mM NaCl in the presence of 0−1 mM MCl_2 at pH 7.4 for 1 h, followed by HPLC with UV monitoring at 254 nm.

on the functionality-transfer reaction to rG of RNA at pH 7.4 using ODN**1F** (X = G^S(Me,Ph)) (Figure 3). The transferred yields at an hour are compared in Figure 3A. A remarkable increase in the reaction yield was observed in the presence of a transition metal cation such as Ni^{2+}, Co^{2+}, Zn^{2+}, or Mn^{2+}. The HPLC profile after 60 min in the presence of Ni^{2+} is shown as an example in Figure 3B representing the formation of the new product together with the decreased ORN**2** and the reproduced ODN**1**. The transferred structure of the new peak eluting at a retention time of 9.6 min was supported by the MALDI-TOF MS measurements (Table 2S (Supporting Information), ORN**2F**). The HPLC analysis of the hydrolysates of the products with bacterial alkaline phosphatase (BAP) and snake venom phosphodiesterase (SVPD) has clearly indicated that the modified rG obtained in the presence of $NiCl_2$ at pH 7.4 is identical to that obtained at pH 9.6 (Figure 9S, Supporting Information), which has been concluded to be the 2-amino modified guanosine in the previous study (*19*).

Alkaline earth metal ions such as Ba^{2+}, Ca^{2+}, and Mg^{2+} slightly promoted the reaction. In contrast, Cu^{2+} and Fe^{2+} did not activate the reaction (Figure 3A). As a result, it turned out that Ni^{2+}, Co^{2+}, Zn^{2+}, and Mn^{2+} were suitable ions to activate the G transfer reaction. According to the Irving−Williams series (*21*), the coordination ability of the metal cations to the nitrogen atom such as N7 of guanosine is in the order of $Zn^{2+} < Cu^{2+} > Ni^{2+} > Co^{2+} > Fe^{2+} > Mn^{2+}$,

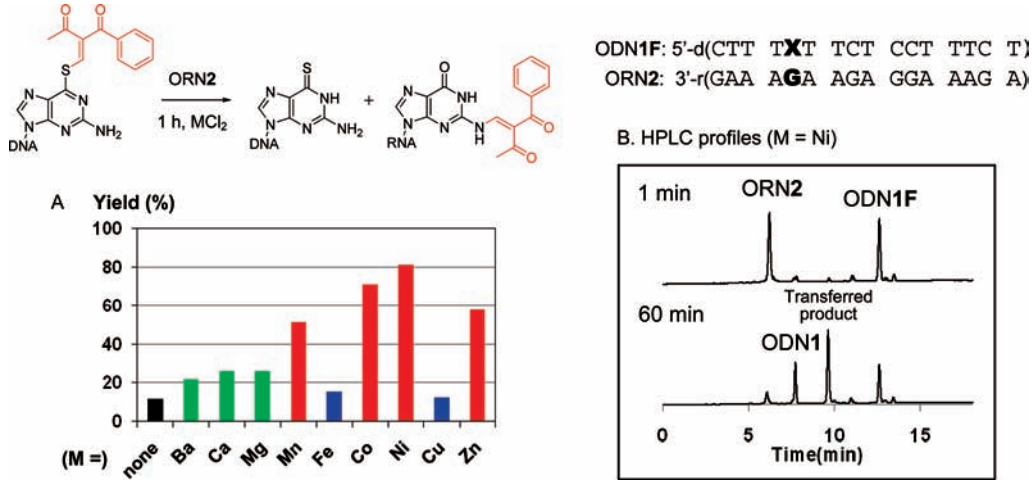


Figure 3. Effect of metal cation on the functionality-transfer reaction (A) and the HPLC profiles on the Ni^{2+}-activated transfer reaction (B). The transfer reactions were performed by using 15 μM S-functionalized ODN1F-G^S(Me, Ph) and 10 μM target ORN**2** (G) in 50 mM MES buffer containing 100 mM NaCl in the presence of 1 mM MCl_2 at pH 7.4 for 1 h, followed by HPLC with UV monitoring at 254 nm.

Table 1. UV Melting Temperatures of the Duplexes Formed with ODN and ORN in the Presence of MCl_2[a]

Metal (M =)	T_m (°C)	ΔT_m (°C)
none	47.8	
Ba	48.9	+1.1
Ca	48.9	+1.1
Mg	49.0	+1.2
Mn	50.0	+2.2
Co	53.5	+5.7
Ni	55.5	+7.7

[a] The T_m values were measured using 1.3 μM S-functionalized ODN**1F**-G^S(H, Ph) and 1.3 μM of the target ORN2 (G) in 50 mM MES buffer (pH 7.4) containing 100 mM NaCl in the presence of 1 mM MCl_2.

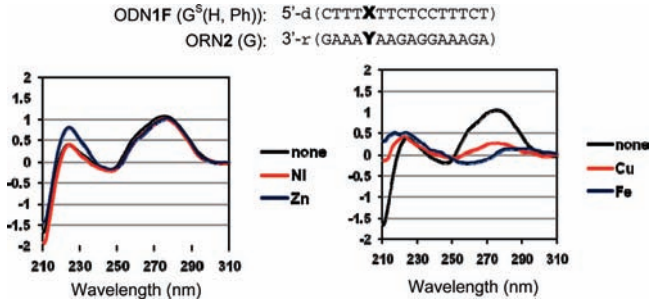


Figure 5. CD spectra in the presence of MCl_2. CD spectra were measured using 2.5 μM duplexes in 50 mM MES buffer (pH 7.4) containing 100 mM NaCl and 1 mM MCl_2.

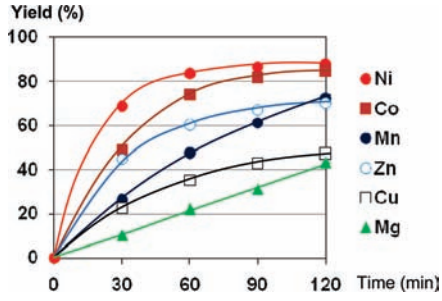


Figure 6. Effect of the metal cation on the transfer reaction rate. The reactions were performed by using 15 μM S-functionalized ODN**1F**-G^S(Me, Ph) and 10 μM target ORN**2** (G) in 50 mM MES buffer containing 100 mM NaCl in the presence of 1 mM MCl_2 or 0.1 mM $CuCl_2$ at pH 7.4, followed by HPLC with UV monitoring at 254 nm.

followed by the alkaline earth metals (Mg^{2+}, Ca^{2+}, and Ba^{2+}). The reaction yields in the presence of these metals followed this order, except for the reaction with Cu^{2+} and Fe^{2+}. One may assume that an excess of these cations induced unfavorable changes in RNA. In order to examine this hypothesis, the concentration dependency of Cu^{2+} or Fe^{2+} was compared with that of Ni^{2+}, Zn^{2+}, or Mg^{2+} (Figure 4). The transfer reaction was remarkably activated with Ni^{2+} at more than 0.05 mM, and its effect reached a plateau at concentrations higher than 0.5 mM. A similar concentration-dependent activation was observed with Zn^{2+}. Activation by Mg^{2+} was small even at 1 mM. However, in the case of Cu^{2+} or Fe^{2+}, the reaction yield was highest at 0.1 mM concentration. To check whether Cu^{2+} and Fe^{2+} decrease the thermal stability of the duplex, T_m values and CD spectra were investigated in the presence of the metal cation at pH 7.4 using ODN**1F** (X = G^S(H,Ph)) containing the nonreactive monoketone unit and the complementary ORN**2** (Y = rG). Clear melting curves were not observed in the presence of 1 mM of Cu^{2+}, Fe^{2+}, and Zn^{2+}. Decomposition of the RNA strand at high temperature in the presence of Zn^{2+} was confirmed by HPLC analysis after T_m measurement (*22*). Mn^{2+}, Co^{2+}, and Ni^{2+} increased the T_m values in the range of 2−8 °C (Table 1). The CD spectra in the presence of 1 mM of Ni^{2+} and Zn^{2+} were similar to those taken in the absence of divalent metal cations, indicating that the duplex was in a conformation between the A and B types (Figure 5). However, Cu^{2+} decreased the intensity of the CD spectra, and the CD spectra in the presence of Fe^{2+} indicated a distortion of the duplex conformation. Therefore, the low reactivity in the presence of Cu^{2+} and Fe^{2+} can be attributable to the induction of unfavorable conformations in the transfer reaction (*23*).

The effect of metal cations on the transfer reaction rate was also investigated with 1 mM of Ni^{2+}, Co^{2+}, Mn^{2+}, Zn^{2+}, and Mg^{2+}, or 0.1 mM of Cu^{2+} (Figure 6). Fe^{2+} was not used because it significantly distorted the duplex conformation as described above. The transfer reaction rate was remarkably high with Ni^{2+} and Co^{2+}, and the yield reached a plateau over 80% within 120 min. The yield of the transferred products was constantly increased even after 120 min in the presence of Mn^{2+} and Mg^{2+}, although the reaction rate was lower than that with Ni^{2+} or Co^{2+}. However, in the case of Zn^{2+} and Cu^{2+}, the yield reached a plateau after 120 min at lower levels. Decomposition of the functional ODN probe in the presence of Zn^{2+} and Cu^{2+} was evidenced by the HPLC analysis, resulting in low yields of the transfer products.

To determine whether metal coordination to N7 plays a role in activation, we next investigated the effect of the nucleobase structure. The transfer reaction proceeded with

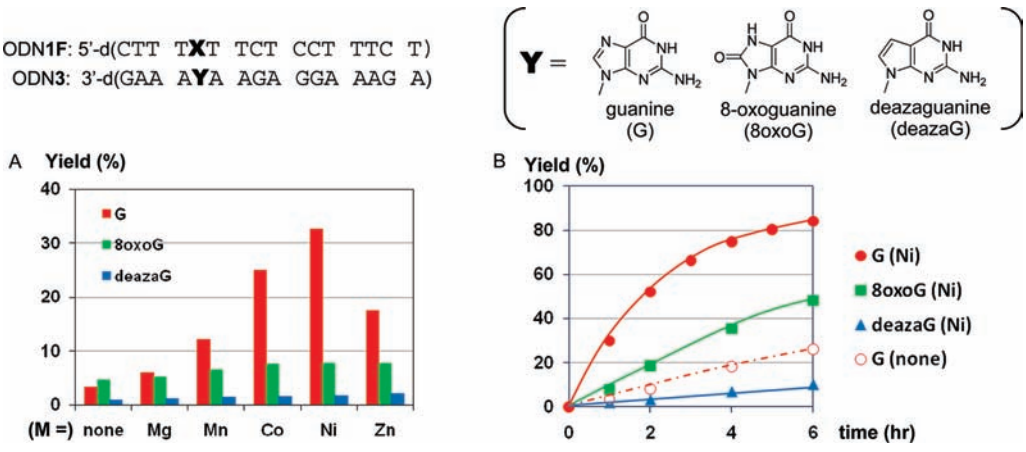


Figure 7. Comparison of the reactivity of the guanine analogues in the presence of the metal cation. The transfer reactions were performed by using 15 μM S-functionalized ODN1F-G^S(Me, Ph) and 10 μM target ODN**3** (Y) in 50 mM MES buffer containing 100 mM NaCl in the presence of 1 mM MCl_2 at pH 7.4 for 1 h (A) or for 0−6 h (B), followed by HPLC with UV monitoring at 254 nm.

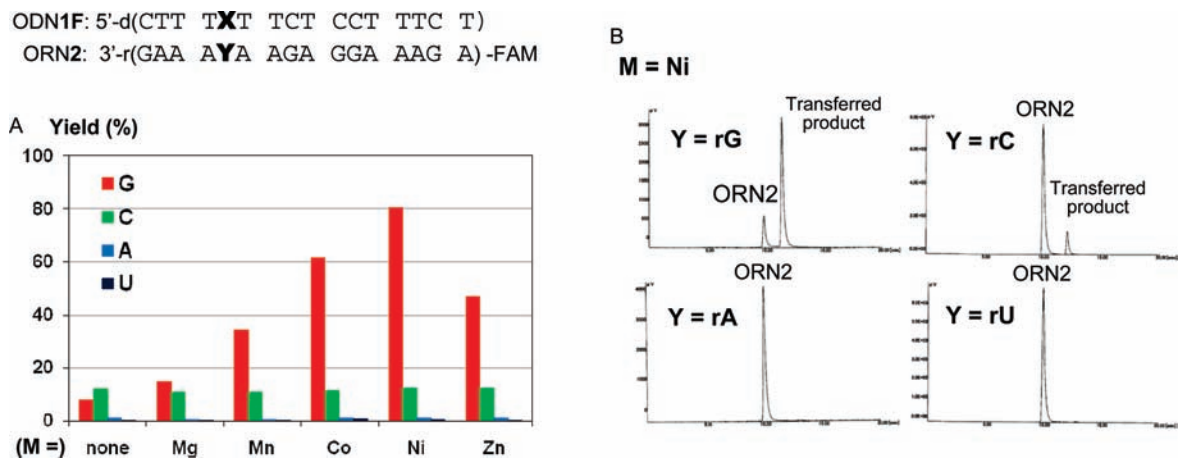


Figure 8. Base selectivity of the transfer reaction in the presence of divalent transition metal cations (A) and the HPLC profiles of the transfer reaction in the presence of $NiCl_2$ (B). The transfer reactions were performed by using 1.5 μM S-functionalized ODN**1**-G^S(Me, Ph) and 1.0 μM target ORN**2** (Y) in 50 mM MES buffer containing 100 mM NaCl in the presence of 1 mM MCl_2 at pH 7.4 for 1 h, followed by HPLC with FAM fluorescence monitoring at 518 nm with emission at 494 nm.

the ODN targets in a similar fashion with the ORN targets with respect to metal cation activation (Figure 10S, Supporting Information) and guanine selectivity (Figure 11S, Supporting Information), although the reaction efficiency was lower than that with RNA substrates. Therefore, the experiments were done with the ODN targets. It was expected that the reaction of 8-oxoguanine (8-oxo-dG) and 7-deazaguanine (7-deazadG) would not be accelerated because of the lack of N7 for coordination with the metal cations. The reactivities of dG, 8-oxo-dG and 7-deaza-dG in the presence or absence of the metal cations are compared in Figure 7. 7-Deaza-dG hardly produced the transferred products either in the presence or the absence of the metal cations. The reactivity of 8-oxo-dG was not affected by the additional metal cations (Figure 7A). In contrast, the transfer reaction to dG was affected in the presence of metal cations, especially by Ni^{2+} and Co^{2+}. These results support the idea that the metal coordination to N7 is a major determinant of the rate of acceleration. All of the transfer reactions to dG, oxodG, and 7-deaza-dG were enhanced under alkaline conditions as previously reported (Figure 12S, Supporting Information) (*19*). Thus, it may be explained, as initially expected, that the enolate becomes favored by metal coordination on N7 of guanine to enhance the reactivity of the 2-amino group of dG under neutral conditions.

The base selectivities at pH 7.4 in the presence of transition metal cations were investigated using the S-functionalized ODN**1F** probe and the complementary ORN**2** (Y = rG, rC, rA, rU) (Figure 8). The HPLC charts of the reaction mixture at 1 h are compared in Figure 8B. In the presence of transition metal cations, especially Ni^{2+} and Co^{2+}, the reaction efficiency with rG was very high compared with that of rC, and no reaction was observed for rA or rU. These results have clearly shown that the functionality-transfer reaction is enhanced selectively for rG by the metal cations to cause selectivity change from rC to rG.

CONCLUSIONS

In conclusion, it has been demonstrated that the functionality-transfer reaction to the guanine base in RNA was greatly and selectively enhanced in the presence of transition metal cations under neutral conditions, resulting in a selectivity change from rC to rG. This method enables the modification of RNA site-selectively with high efficiency under near physiological conditions and is expected to be useful for the study of RNA such as through an application to modify large intact RNA molecules.

ACKNOWLEDGMENT

This work was supported by a Grant-in-Aid for Scientific Research (S) from the Japan Society for the Promotion of Science (JSPS) and CREST from the Japan Science and Technology Agency. We are grateful for the Research Fellowship from the Japan Society for the Promotion of Science (JSPS) for Young Scientists (K.O.).

Supporting Information Available: MALDI-TOF/MS of ODN, ORN, HPLC analysis of the hydrolysates of the modified ORN, comparison of the yield of the transfer reaction in the presence of the metal cations. This material is available free of charge via the Internet at http://pubs.acs.org.

LITERATURE CITED

(1) Sasaki, S., and Nagatsugi, F. (2006) Application of unnatural oligonucleotides to chemical modification of gene expression. *Curr. Opin. Chem. Biol. 10*, 615–621.

(2) Wang, P., Song, Y., Zhang, L., and Zhou, X. (2005) Quinone methide derivatives: important intermediates to DNA alkylating and DNA cross-linking actions. *Curr. Med. Chem. 12*, 2893–2913.

(3) Baum, D. A., and Silverman, S. K. (2007) Deoxyribozyme-catalyzed labeling of RNA. *Angew. Chem., Int. Ed. 46*, 3502–3504.

(4) Yoshimura, Y., Noguchi, Y., and Fujimoto, K. (2007) Highly sequence specific RNA terminal labeling by DNA photoligation. *Org. Biomol. Chem. 5*, 139–142.

(5) Yoshimura, Y., Ohtake, T., Okada, H., and Fujimoto, K. (2009) A new approach for reversible RNA photocrosslinking reaction: application to sequence-specific RNA selection. *ChemBioChem 10*, 1473–1476.

(6) Hattori, K., Hirohama, T., Imoto, S., Kusano, S., and Nagatsugi, F. (2009) Formation of highly selective and efficient interstrand cross-linking to thymine without photo-irradiation. *Chem. Commun.* 6463–6465.

(7) Lee, B. L., Murakami, A., Blake, K. R., Lin, S. B., and Miller, P. S. (1988) Interaction of psoralen-derivatized oligodeoxyribonucleoside methylphosphonates with single-stranded DNA. *Biochemistry 27*, 3197–3203.

(8) Higuchi, M., Kobori, A., Yamayoshi, A., and Murakami, A. (2009) Synthesis of antisense oligonucleotides containing 2′-*O*-psoralenylmethoxyalkyl adenosine for photodynamic regulation of point mutations in RNA. *Bioorg. Med. Chem. 17*, 475–483.

(9) Boudvillain, M., Guérin, M., Dalbiés, R., Saison-Behmoaras, T., and Leng, M. (1997) Transplatin-modified oligo(2′-*O*-methyl ribonucleotide)s: a new tool for selective modulation of gene expression. *Biochemistry 36*, 2925–2931.

(10) Kang, H., and Rokita, S. E. (1996) Site-specific and photo-induced alkylation of DNA by a dimethylanthraquinone-oligodeoxynucleotide conjugate. *Nucleic Acids Res. 24*, 3896–3902.

(11) Buchmuller, K. L., Hill, B. T., Platz, M. S., and Weeks, K. M. (2003) RNA-tethered phenyl azide photocrosslinking via a short-lived indiscriminant electrophile. *J. Am. Chem. Soc. 125*, 10850–10861.

(12) Peng, X. H., Hong, I. S., Li, H., Seidman, M. M., and Greenberg, M. M. (2008) Interstrand cross-link formation in duplex and triplex DNA by modified pyrimidines. *J. Am. Chem. Soc. 130*, 10299–10306.

(13) Qiu, Z., Lu, L., Jian, X., and He, C. (2008) A diazirine-based nucleoside analogue for efficient DNA interstrand photocross-linking. *J. Am. Chem. Soc. 130*, 14398–14399.

(14) Nagatsugi, F., Kawasaki, T., Usui, D., Maeda, M., and Sasaki, S. (1999) Highly efficient and selective cross-linking to cytidine based on a new strategy for auto-activation within a duplex. *J. Am. Chem. Soc. 121*, 6753–6754.

(15) Kawasaki, T., Nagatsugi, F., Ali, Md. M., Maeda, M., Sugiyama, K., Hori, K., and Sasaki, S. (2005) Hybridization-promoted and cytidine-selective activation for cross-linking with the use of 2-amino-6-vinylpurine derivatives. *J. Org. Chem. 70*, 14–23.

(16) Ali, M. M., Oishi, M., Nagatsugi, F., Mori, K., Nagasaki, Y., Kataoka, K., and Sasaki, S. (2006) Intracellular inducible alkylation system that exhibits antisense effects with greater potency and selectivity than the natural oligonucleotide. *Angew. Chem., Int. Ed. 45*, 3136–3140.

(17) Ali, M. M., Alam, M. R., Kawasaki, T., Nakayama, S., Nagatsugi, F., and Sasaki, S. (2004) Sequence- and base-specific delivery of nitric oxide to cytidine and 5-methylcytidine leading to efficient deamination. *J. Am. Chem. Soc. 126*, 8864–8865.

(18) Onizuka, K., Taniguchi, Y., and Sasaki, S. (2009) Site-specific covalent modification of RNA guided by functionality-transfer oligodeoxynucleotides. *Bioconjugate Chem. 20*, 799–803.

(19) Onizuka, K., Taniguchi, Y., and Sasaki, S. (2010) A new usage of functionalized oligodeoxynucleotide probe for site-specific modification of a guanine base within RNA. *Nucleic Acids Res. 38*, 1760–1766.

(20) Sigel, H., Massoud, S. S., and Corfu, N. A. (1994) Comparison of the extent of macrochelate formation in complexes of divalent metal ions with guanosine (GMP^{2-}), Inosine (IMP^{2-}), and Adenosine 5′-Monophosphate (AMP^{2-}). The crucial role of N-7 basicity in metal ion-nucleic base recognition. *J. Am. Chem. Soc. 116*, 2958–2971.

(21) Irving, H., and Williams, R. J. P. (1953) Stability of transition metal complexes. *J. Chem. Soc.* 3192–3210.

(22) Eichhorn, G. L., Tarien, E., and Butzow, J. J. (1971) Interaction of metal ions with nucleic acids and related compounds. XVI. Specific cleavage effects in the depolymerization of ribonucleic acids by zinc(II) Ions. *Biochemistry 10*, 2014–2019.

(23) Eichhorn, G. L. (1962) Metal ions as stabilizers or destabilizers of the deoxyribonucleic acid structure. *Nature 194*, 474–475.

BC100131J

Supporting Information

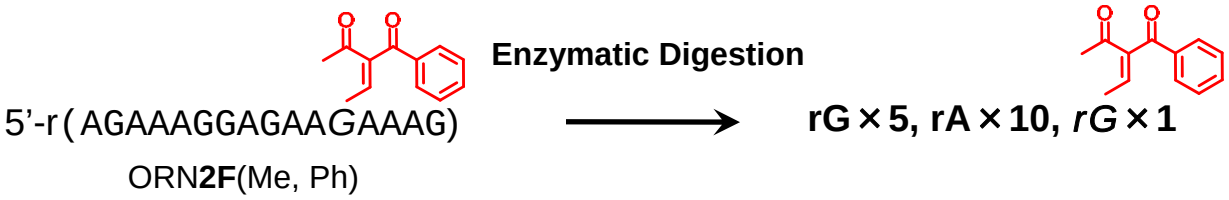
Activation and Alteration of Base Selectivity by Metal Cations in the Functionality-Transfer Reaction for RNA Modification

Kazumitsu Onizuka,Yosuke Taniguchi, Shigeki Sasaki,*

Graduate School of Pharmaceutical Sciences, Kyushu University, 3-1-1 Maidashi, Higashi-ku, Fukuoka 812-8582, Japan, and CREST, Japan Science and Technology Agency.

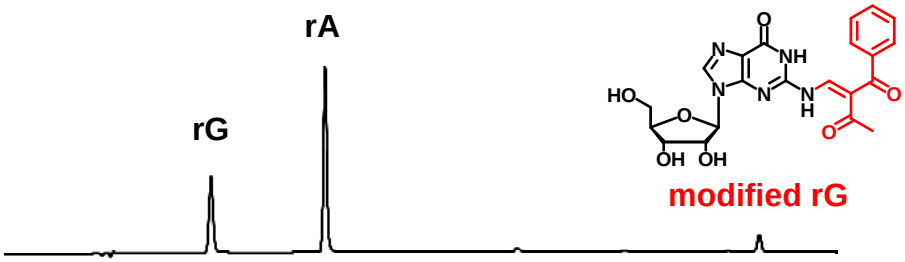
sasaki@phar.kyushu-u.ac.jp

Figure 9S. HPLC analysis of the hydrolysates of the modified ORN2F(Me, Ph). S-2
Figure 10S. Metal cation effects on the reaction with DNA substrate S-3
Figure 11S. Base selectivity with DNA substrates S-4
Figure 12S. Comparison of the reactivity of guanine analogs S-5
Table 2S. MALDI-TOF/MS data of all DNA and RNA S-7



Transfer modified ORN**2F** (10 μM) was hydrolyzed with BAP (30 U/ml) and SVPD (2.0 U/ml) at 37°C for 1h, and the mixture was analyzed by HPLC (Column: SHISEIDO C18, 4.6 x 250 mm; Solvent: A: 50 mM $HCOONH_4$ Buffer, B: CH_3CN, B: 5% to 40% /30 min, linear gradient; Flow rate: 1.0 ml/min; monitored by UV detector at 254 nm).

➢ **Hydrolysate of the Ni^{2+}-activated transfer reaction product**



➢ **Hydrolysate of the transfer reaction product at pH 9.6**

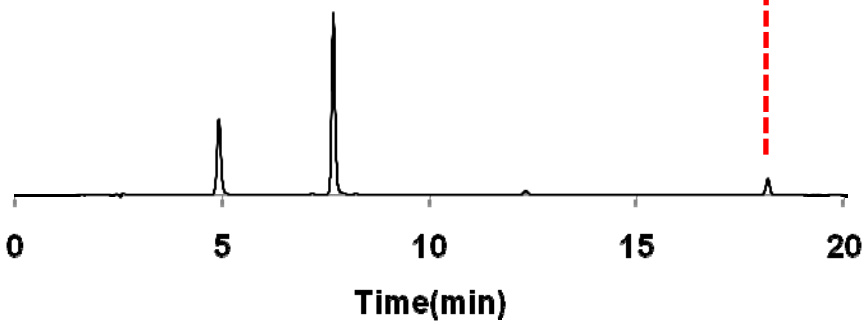


Figure 9S. HPLC analysis of the hydrolysates of the modified ORN2F(Me, Ph). The modified rG was isolated and subjected to ESI-HRMS measurements (calcd for $C_{21}H_{21}N_5O_7$ $(M+Na)^+$: 478.1333, found: 478.1351). Determination of the 2-amino modified structure of the transfer reaction at pH 9.6 has been discussed in the previous study (*19*).

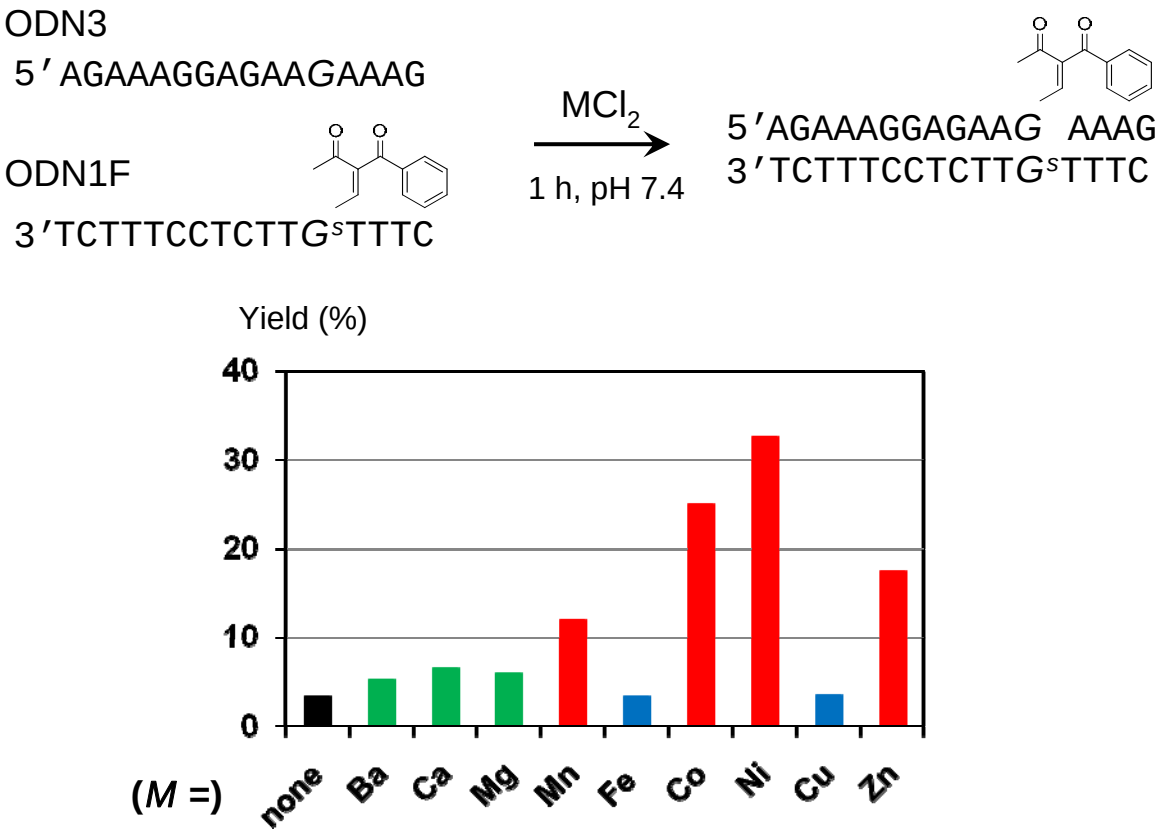


Figure 10S. Metal cation effect on the functionality transfer reaction with DNA substrate. The transfer reactions were performed by using 15 μM of *S*-functionalized ODN1F-G^S(Me, Ph) and 10 μM of the target ODN3 (G) in 50 mM MES buffer containing 100 mM NaCl in the presence of 1 mM MCl_2 at pH 7.4 for 1h, and followed by HPLC.

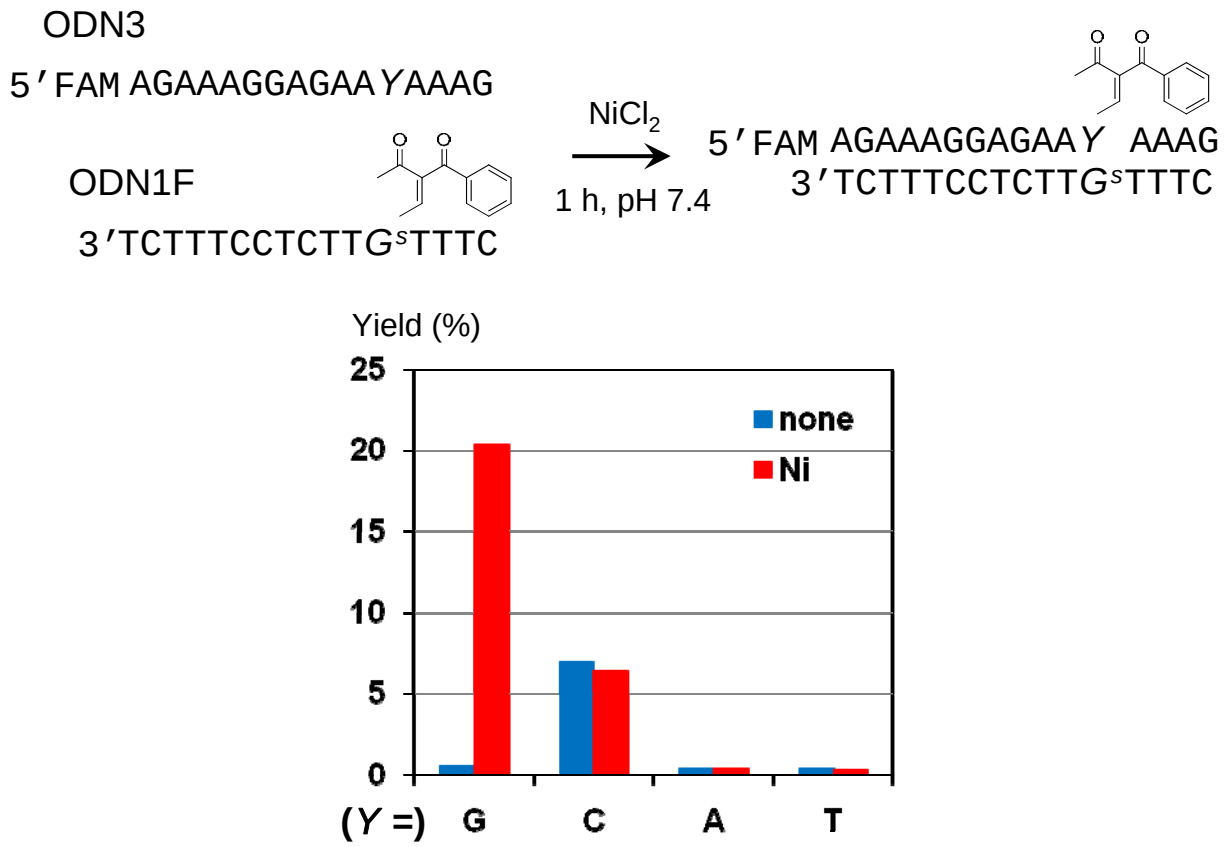


Figure 11S. Base selectivity of transfer reaction with DNA substrates in the presence of $NiCl_2$. The transfer reactions were performed by using 1.5 μM of *S*-functionalized ODN1-G^{S}(Me, Ph) and 1.0 μM of the target ODN3 (Y) in 50 mM MES buffer containing 100 mM NaCl at pH 7.4 for 1h, and followed by HPLC (monitored by monitoring the FAM fluorescence). Blue bars indicate the reaction yield in the absence of $NiCl_2$, and red bars indicate the reaction yield in the presence of 1 mM $NiCl_2$.

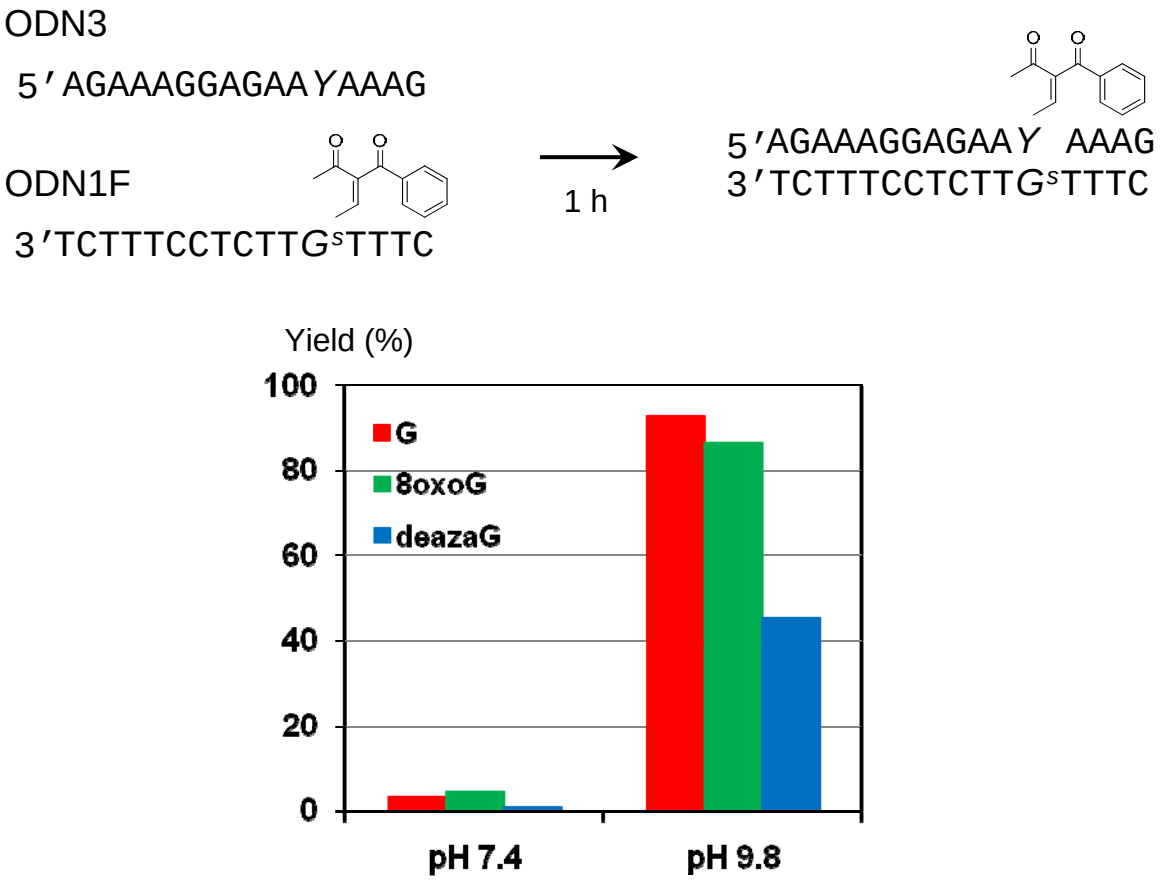


Figure 12S. Comparison of the reactivity of the guanine analogs under alkaline conditions. The transfer reactions were performed by using 15 μM of *S*-functionalized ODN1F-G^{S}(Me, Ph) and 10 μM of the target ODN3 (Y) in 50 mM carbonate buffer containing 100 mM NaCl at pH 9.8 for 1h, and followed by HPLC.

Table 1S. MALDI-TOF/MS Data of all ODN and ORN compounds used in this study.

DNA or RNA	5' Label	X or Y	Calcd ($[M-H]^-$)	Found
ODN**1**		X = G^S	4767.8	4766.5
ODN**1F**		X = G^S(Me, Ph)	4939.7	4939.4
ODN**1F**		X = G^S(H, Ph)	4897.8	4898.8
ORN**2**		Y = rG	5297.8	5297.8
ORN**2**	FAM	Y = rG	5835.9	5835.9
ORN**2**	FAM	Y = rC	5795.9	5795.1
ORN**2**	FAM	Y = rA	5819.9	5819.5
ORN**2**	FAM	Y = rU	5796.9	5796.5
ORN**2F**		Y = rG(Me, Ph)	5469.8	5469.9
ODN**3**	FAM	Y = dG	5579.1	5579.5
ODN**3**	FAM	Y = dC	5539.1	5538.7
ODN**3**	FAM	Y = dA	5563.1	5563.5
ODN**3**	FAM	Y = dT	5554.1	5553.7
ODN**3**		Y = dG	5041.9	5041.6
ODN**3**		Y = 8oxodG	5057.9	5056.8
ODN**3**		Y = deazadG	5040.1	5040.1
ODN**3F**		Y = dG(Me, Ph)	5214.0	5213.6
ODN**3F**		Y = 8oxodG(Me, Ph)	5230.0	5229.9
ODN**3F**		Y = deazadG(Me, Ph)	5212.1	5212.4

Synthesis and Evaluation of Human Serum Albumin-Modified Exendin-4 Conjugate via Heterobifunctional Polyethylene Glycol Linkage with Protracted Hypoglycemic Efficacy

Insoo Kim,[||] Tae Hyung Kim,[‡] Kyungwan Ma,[†] Eun Seong Lee,[§] Dongin Kim,[||] Kyung Taek Oh,[⊥] Don Haeng Lee,[#] Kang Choon Lee,[‡] and Yu Seok Youn*[,†]

College of Pharmacy, Pusan National University, 30 Jangjun-dong, Geumjeong-gu, Busan 609-735, Korea, College of Pharmacy, Sungkyunkwan University, 300 Chonchon-dong, Jangan-gu, Suwon City 440-746, Korea, Division of Biotechnology, The Catholic University of Korea, 43-1 Yeokgok 2-dong, Wonmi-gu, Bucheon-si, Gyeonggi-do 420-743, Korea, The Wallace H. Coulter Department of Biomedical Engineering, Georgia Institute of Technology, 315 Ferst Drive, Atlanta, Georgia 30322, Chung-Ang University, 221 Heukseok dong, Dongjak-gu, Seoul 155-756, Korea, and Department of Internal Medicine, Inha University, 253 Yonghyun-dong Nam-gu, Incheon, 402-751, Korea. Received March 20, 2010; Revised Manuscript Received July 10, 2010

Albumin conjugation is considered to be one of the most effective means of protracting the short *in vivo* lifespans of peptides and proteins. Here, we present a new long-acting antidiabetic exendin-4 conjugate linked with human serum albumin (HSA) via polyethylene glycol (PEG). As a first step toward synthesizing this conjugate, three artificial sulfhydryl groups were introduced in HSA using 2-iminothiolane at pH 8.0. This thiolated HSA was further reacted with the monomer fraction of exendin-4 (6 equiv) conjugated with maleimide-PEG_{5k}-*N*-hydroxysuccinimide (MAL-PEG_{5k}-NHS) for 3 h. Because of the presence of PEG molecules, the resulting conjugate (HSA−PEG−Ex4) was found to have a greater apparent molecular weight and a larger particle size (ca. 195 kDa and 9.48 ± 0.74 nm) than those of HSA-exendin-4 without the PEG linker (HSA−Ex4, ca. 84.3 kDa and 7.77 ± 0.98 nm). Although the receptor binding affinity of HSA−PEG−Ex4 on RIN-m5F cells was significantly lower than that of Ex4, its antihyperglycemic efficacy was slightly higher than that of Ex-4 and HSA−Ex4 in type 2 diabetic db/db mice. Furthermore, HSA−PEG−Ex4 had greater circulating $t_{1/2}$ and AUC_{inf} values than HSA-Ex and native exendin-4 by 2.1- and 10.3-fold, respectively. Accordingly, its hypoglycemic duration was greatly increased to 31.0 h at a dose of 250 nmol/kg vs that of native Ex4 (7.0 h). Results show that the HSA−PEG−Ex4 conjugate produced has distinct advantages over HSA−Ex4 without PEG. We believe that this exendin-4 derivative, which has the merits of albumin conjugation and PEGylation, has considerable potential as a novel type 2 antidiabetic agent.

INTRODUCTION

The therapeutic efficacies of peptides and proteins are restricted by their rapid clearance from the body (*1*), which means that they must be frequently administered to maintain therapeutic levels. Protein-based drugs have circulating half-lives ($t_{1/2}$) of at most a few hours, and especially, the $t_{1/2}$ levels of most peptides range from a few minutes to less than two hours. These short lifespans of therapeutic peptides and proteins are mainly due to renal filtration or proteolysis (*2*, *3*). Exendin-4, a potent glucagon-like peptide-1 (GLP-1) agonist, is no exception in this respect, although it has a much longer $t_{1/2}$ (∼2 h) than GLP-1 (∼2 min) (*4*, *5*), its commercial product, Byetta, must be injected at least twice daily (*6*), which markedly reduces patient compliance. Thus, a strategy is required to extend the therapeutic duration of exendin-4 and maximize its antidiabetic effects, which include appetite suppression and the enhancements of glucose-dependent insulin release and β-cell proliferation (*7*−*9*).

Albumin is an attractive macromolecular carrier due to its biodegradability, nontoxicity, and nonimmunogenicity. Recently, Human serum albumin (HSA) has been used to alter the pharmacokinetic profiles of a number of drugs (*10*) because HSA is long-lived in plasma with an average $t_{1/2}$ of 19 days and seldom undergoes kidney filtration because it is around the same size (∼67 kDa) as glomerulus pores (*11*). Accordingly, the renal clearances of HSA-modified peptides or proteins are much lower, and their *in vivo* lifespans are considerably longer.

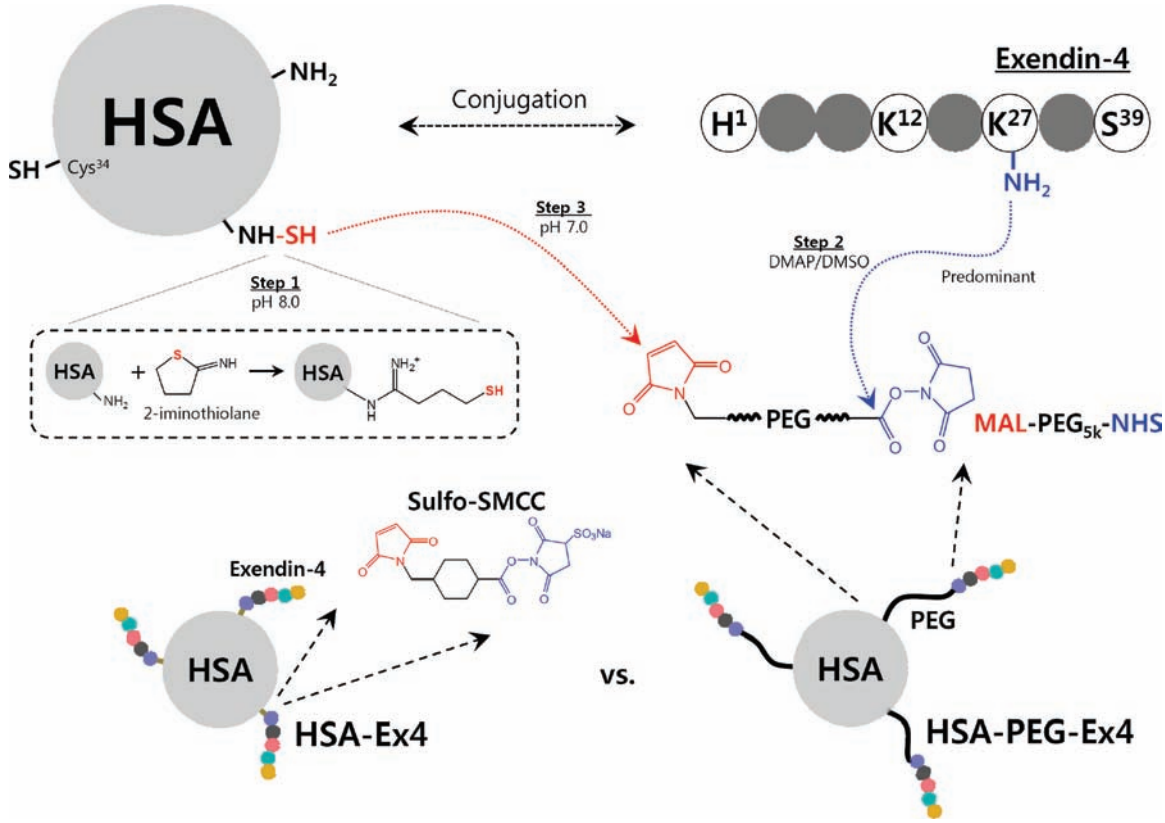
Thus far, three different approaches have been used for binding HSA. The first involves the covalent conjugation of HSA to drugs. This method uses bifunctional spacers to facilitate direct attachment (*2*, *12*, *13*). The second approach involves HSA binding *in vivo* with drugs derivatized with long chain fatty acids (*14*−*16*). Fatty acid acylated drugs bind HSA molecules because HSA possesses five available fatty acid binding sites (*11*). The third approach involves the production of a HSA-fused peptide or protein. This method involves the generation of modified peptides or proteins by fusing the HSA gene to a gene that encodes the active peptide or protein (*17*, *18*). In particular, HSA-based antidiabetic drugs have been reported to have remarkably extended therapeutic durations. Some of these, such as Levemir and Victoza (Novo Nordisk), are already commercially available, and some others, such as CJC-1131/1134 (ConjuChem) and Albiglutide (Human Genome Sciences), are undergoing clinical trials.

In an attempt to produce a long-acting exendin-4 (Ex4) derivative, we devised a new way of conjugating HSA and Ex4.

* Corresponding author. Tel: +82-51-510-2800. Fax: +82-51-513-6754. E-mail: ysyoun@pusan.ac.kr.
[†] Pusan National University.
[‡] Sungkyunkwan University.
[§] The Catholic University of Korea.
[||] Georgia Institute of Technology.
[⊥] Chung-Ang University.
[#] Inha University.

10.1021/bc100143c © 2010 American Chemical Society
Published on Web 07/23/2010

Scheme 1. Syntheses of HSA−Ex4 and HSA−PEG−Ex4



Unlike previously described HSA−peptide conjugates, which involve direct short linking spacers, we linked Ex4 to HSA using a 5 kDa bifunctional PEG with the aim of producing a conjugate with the pharmaceutical merits associated with PEGylation and albumin modification. After establishing the conjugation process, we investigated the receptor-binding and pharmacokinetic characteristics of the HSA−PEG−Ex4 conjugate produced. In addition, its hypoglycemic duration was evaluated in type 2 diabetic db/db mice and compared with that of HSA-conjugated exendin-4 without a PEG linker.

EXPERIMENTAL PROCEDURES

Materials. Exendin-4 (Ex4) and maleimide−polyethylene glycol−*N*-hydroxysuccinimide (MAL−PEG−NHS: M_w 5,000) were purchased from the American Peptide Company (Sunnyvale, CA) and NOF Corporation (Tokyo, Japan), respectively. Sulfo-SMCC (sulfosuccinimidyl 4-(*N*-maleimidomethyl)-cyclohexane-1-carboxylate) and HSA were purchased from Pierce (Rockford, IL) and Sigma-Aldrich (St. Louis, MO), respectively. All other reagents, unless otherwise specified, were obtained from Sigma-Aldrich.

Experimental Animals. Type 2 diabetic C57BL/6 db/db mice (male, 4−5 weeks old) were purchased from Korean Research Institute of Bioscience and Biotechnology (Daejon, Republic of Korea). ICR mice (males, 4−5 weeks old), weighing 16−18 g, were purchased from Hanlim Experimental Animal Laboratory (Seoul). Animals were cared for in accordance with the National Institutes of Health (NIH) Guidelines for the Care and Use of Laboratory Animals (NIH publication 80−23, revised in 1996). Animals were housed in groups of 6−8 under a 12-h light/dark cycle (lights on at 6 a.m.), allowed food and water ad libitum, and acclimatized for 2 weeks. This study was approved by the Ethical Committee on Animal Experimentation at Pusan National University.

Synthesis of HSA-Conjugated Ex4s. HSA-conjugated Ex4 conjugates were prepared by using a modification of a previously described procedure (*19*). First, the primary amines of HSA were thiolated. Briefly, a 100 μL aliquot of 2-iminothiolane (Traut's reagent: 0.06 mg, 0.45 μmol, approximately 3 equiv) was mixed with 2 mL of HSA (10 mg, 0.15 μmol) in 50 mM of sodium carbonate (pH 8.0) and allowed to react for 3 h. The reaction mixture was then dialyzed with 10 mM PBS (pH 7.4) using a dialysis kit (M_w cutoff = 8,000, Gene Bio-Application Ltd., Israel) and stored at a concentration of 0.5 mg/mL at 4 °C until needed. Second, 5 mg of MAL−PEG−NHS (M_w: 5 kDa, 1 μmol) was mixed with 6.3 mg of Ex4 (1.5 μmol) in 0.5 mL of 0.1% dimethylaminopyridine (DMAP)/dimethylsulfoxide (DMSO) at room temperature for 1 h. The buffer media in this mixture was then changed to 10 mM PBS (pH 7.0) by desalting using Sephadex G-25 and concentrated. The final mixture was then applied into a Superdex 200 HR 10/30 column (300 × 10 mm, GE Healthcare Life Sciences, Piscataway, NJ) and eluted with PBS at a flow rate of 0.6 mL/min, and the MAL−PEG−Ex4 monomer fraction was collected. An aliquot (4 mL) of the MAL−PEG−Ex4 monomer (500 μg/mL, 0.48 μmol, exendin-4 equiv) was then quickly transferred to 2 mL of thiolated HSA (2.7 mg/mL, 0.08 μmol) in PBS, and the reaction was allowed to continue at room temperature for 3 h. After an additional chromatography step, the first symmetric fraction of the final HSA−PEG−Ex4 conjugate was collected and stored at 4 °C until needed. Separately, a HSA−Ex4 conjugate (HSA−Ex4) was prepared using the same procedure, but sulfo-SMCC was used instead of MAL−PEG−NHS (Scheme 1). The Ex4 amount in the final conjugates was calculated reversely by determining the unreacted intermediate Ex4 species (sulfo-SMCC-Ex4 or MAL−PEG−Ex4) in the chromatography process, and their concentrations in storage conditions were determined again by using commercial exendin-4 enzyme immunoassay kits (Phoenix Pharmaceuticals, Burlingame, CA).

Characterization of HSA-Conjugated Ex4s. HSA-conjugated Ex4s were characterized by SDS−PAGE, as previously reported (*20*). Briefly, SDS−PAGE was performed in the

Table 1. Pharmacokinetic Parameters and Pharmacological Scores of Ex4, HSA−Ex4, and HSA−PEG−Ex4 in ICR and db/db Mice[a]

PK parameters	Ex4	HSA−Ex4	HSA−PEG−Ex4	pharmacological scores	Ex4	HSA−Ex4	HSA−PEG−Ex4
AUC_{inf} (ng/mL·h)	123.5 ± 31.5	733.3 ± 33.8	1418.7 ± 138.1	HD_{total} (25 nmol/kg)/OGTT (mmol·h/L)	14.2 ± 6.2	19.9 ± 5.3	20.4 ± 0.9
				HD_{total} (25 nmol/kg) (mmol·h/L)	114.9 ± 33.7	187.9 ± 56.2	419.2 ± 117.2
C_{max} (ng/mL)	42.5 ± 8.0	40.2 ± 1.9	40.7 ± 1.7	HD_{total} (250 nmol/kg) (mmol·h/L)	235.0 ± 42.7	374.6 ± 103.4	660.3 ± 145.7
T_{max} (h)	1.0 ± 0.0	1.3 ± 0.5	1.3 ± 0.5	HD_{total} (500 nmol/kg) (mmol·h/L)			1217.9 ± 191.2
Cl/F (mL/h)	8.8 ± 2.7	1.4 ± 0.1	0.7 ± 0.1	hypoglycemic duration (h) (250 nmol/kg)	7.0	15.2	31.0
$t_{1/2}$ (h, β)	2.1 ± 0.5	11.4 ± 2.4	24.2 ± 2.5	hypoglycemic duration (h) (500 nmol/kg)			61.4

[a] Data are means ± SDs. AUC_{inf}, area under the curve from zero to infinity; C_{max}, maximum concentration after intraperitoneal administration; T_{max}, time required to reach C_{max}; Cl/F, systemic clearance from zero time to last time; $t_{1/2}$, half-life in the elimination phase (β).

presence of 0.1% SDS using a 12% slab gel, and electrophoresis was performed using a constant current of 25 mA for 1 h. The gel was soaked in a Coomassie brilliant blue R250 staining solution and then immersed in a destaining solution. Separately, HSA-conjugated Ex4s were subjected to size-exclusion chromatography (SEC) on a Superdex 200 HR 10/30 column and eluted with 10 mM PBS (pH 7.4) at a flow rate of 0.6 mL/min. Chromatograms were recorded at 215 nm. The apparent molecular weights of HSA-conjugated Ex4s were estimated using a calibration curve based on the retention times vs logarithmic molecular weights of globular protein standards. The particle sizes of HSA-conjugated Ex4s in wet conditions were measured by using a Zetasizer Nano-S90 based on dynamic light scattering (DLS) (Malvern Instruments, USA) with a He−Ne Laser beam at a wavelength of 633 nm and a fixed scattering angle of 90°.

Receptor-Binding Affinities of HSA-Conjugated Ex4s to RIN-m5F Cells. The receptor-binding affinities of Ex4 and HSA-conjugated Ex4s were determined using a modification of a previously described method (*21*, *22*). Briefly, RIN-m5F cells (a rat insulinoma cell line, ATCC, Manassas, VA), which express high levels of GLP-1 receptors (GLP-1R), were seeded in 12 well plates at 3×10^5 cells per well, grown for 48 h, washed twice with binding buffer (120 mM NaCl, 1.2 mM $MgSO_4$, 13 mM sodium acetate, 5 mM KCl, 1.2 g/L Tris, 2 g/L bovine serum albumin, and 1.8 g/L glucose, pH 7.6), and treated with unlabeled Ex4 derivatives (final concentration range: 0.001−1000 nM) and 30 pM ^{125}I-exendin-4 (9−39, PerkinElmer, Boston, MA) for 2 h at room temperature. The cells were then washed three times with chilled PBS containing 1 mg/mL of bovine serum albumin and lysed with cell lysis buffer (0.5 N NaOH with 1% SDS) for 15 min, and the radioactive levels in lysates were measured using a γ counter (GMI, Inc., Ramsey, MN).

Radioiodination of HSA-Conjugated Ex4s. Radioiodinated samples were prepared using a modification of the IODO-GEN method, as previously described (*20*, *23*). For native exendin-4, a water-soluble Bolton−Hunter reagent (*N*-sulfosuccinimidyl-3−4-hydroxyphenyl propionate) was utilized to introduce a phenolic moiety to exendin-4 because it does not have tyrosine that is highly reactive with the electrophilic substitution of oxidized iodine. Briefly, a 100 μL aliquot of Bolton−Hunter reagent (0.13 mg/mL, 36 nmol) in 10 mM PBS (pH 7.0) was mixed with 150 μL of exendin-4 (0.5 mg/mL, 18 nmol) at room temperature for 90 min and briefly dialyzed to remove the reagent. Separately, 100 μL of an IODO-GEN (Pierce, Rockford, IL) solution in methylene chloride (0.5 mg/mL) was dispensed into fresh tubes and evaporated under a nitrogen stream. To these tubes were added 50 μL aliquots of either water-soluble Bolton−Hunter reagent-labeled Ex4 or HSA-conjugated Ex4s (approximately 50 μg/mL) and 50 μCi of Na^{125}I (Perkin-Elmer, Boston, MA) diluted with 10 mM PBS (pH 7.4). The reaction was allowed to proceed for 5 min, and then supernatants were loaded into a Sephadex G-25 desalting column (GE Healthcare Life Sciences, Piscataway, NJ) previously equilibrated with 10 mM PBS. ^{125}I-labeled fractions were collected and stored in 10 mM PBS (pH 7.4). Radioactivities were measured by gamma counting (CobraTM Series Auto-Gamma Counting System, Packard Instruments Co., Groningen, The Netherlands). The specific radioactivities of the radioiodinated samples fell in the range $4.8-5.9 \times 10^5$ cpm/μg.

Pharmacokinetics of HSA-Conjugated Ex4s in ICR Mice. The pharmacokinetics of Ex4 and HSA-conjugated Ex4s were evaluated using a modification of a previously described method (*24*−*27*). Radioiodinated samples were administered to ICR mice (~2 μg, ~25 nmol/kg body wt, i.p.). Mice were sacrificed by heart puncture for blood collection at predetermined times, and radioactivities corresponding to 0.2 mL blood samples were determined by gamma counting. These results were then used to calculate the concentration in blood. Pharmacokinetic parameters were calculated by two-compartmental analysis using WinNolin, version 1.1 (Scientific Consulting, Inc., Cary, NC). In particular, AUC_{inf} values were obtained by calculating areas under the curves from zero to infinity time using the trapezoidal rule, and circulating half-lives ($t_{1/2}$) were obtained using the same method (Table 1).

Antihyperglycemic Efficacies of HSA-Conjugated Ex4s in Fasted Type 2 Diabetic db/db Mice. Oral glucose tolerance testing (OGTT) was performed to evaluate the antihyperglycemic efficacies of HSA-conjugated Ex4s after an overnight fast (18 h), as previously described (*24*−*26*, *28*). One hour prior to the first oral glucose challenge (0.2 mL, 1.0 g/kg body wt) (0 h), male db/db mice (n = 4/group, 8−9 weeks old) were administered saline, Ex4, HSA−Ex4, or HSA−PEG−Ex4 (i.p., 25 nmol/kg body wt). A drop of blood was drawn from the tail vein of each animal at 0, 0.25, 0.5, 0.75, 1, 1.5, 2, and 3 h, and blood glucose levels (BGL) were determined using a one-touch blood glucose meter (ACCU-CHEK Sensor, Roche Diagnostics Corp., USA). Antihyperglycemic efficacies were evaluated by calculating total hypoglycemic degrees (HD_{total}; calculated using $AUC_{saline,0-3\ h} - AUC_{test,0-3\ h}$).

Hypoglycemic Efficacies of HSA-Conjugated Ex4s in Nonfasted db/db Mice. Hypoglycemic efficacies of Ex4 and of HSA-conjugated Ex4s were evaluated using a modification of a previously described method (*21*, *22*). Male db/db mice (6−7 weeks old) were used for hypoglycemia testing. Under nonfasting conditions with free access to food and water, the animals received a single i.p. injection of saline, Ex4, or of HSA-conjugated Ex4s (25, 250, 500 nmol/kg body wt). Blood glucose levels (BGL) were monitored using the procedure mentioned above. In addition, a drop of blood was drawn from the tail vein of each animal at different times (0, 0.5, 1, 2, 3, 4, 6, 8, 12, 24, 36, 48, 60, 72, 96, and 120 h), and blood glucose levels (BGL) were determined using a one-touch blood glucose meter (ACCU-CHEK Sensor, Roche Diagnostics, USA). Hypoglycemic efficacies are expressed as HD_{total}, as mentioned above, but the last times measured were different in each group as seen in Figure 6. Furthermore, hypoglycemic durations to maintain a BGL of <8.35 mmol/L (150 mg/dL) were also checked.

Data Analysis. Data are presented as means ± SDs. Statistical significances were determined using One-Way ANOVA, and P values of <0.05 were considered statistically

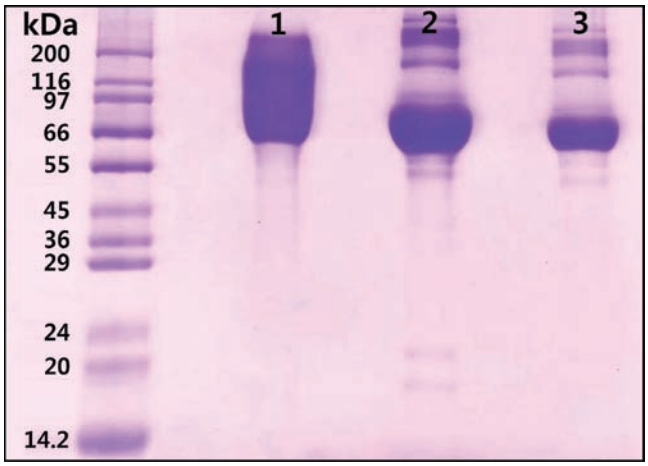


Figure 1. SDS−PAGE analysis (12%) with Coomassie blue staining: (1) molecular weight standard markers, (2) HSA−PEG−Ex4, (3) HSA−Ex4, and (4) HSA.

significant. Pharmacokinetic parameters were calculated by two-compartmental analysis (WinNolin, Scientific Consulting, Inc., Cary, NC).

RESULTS

Characterization of HSA-Conjugated Ex4s. The apparent molecular weights (M_w) of HSA−PEG−Ex4 and HSA−Ex4 were determined by SDS−PAGE. Bands corresponding to HSA−Ex4 and HSA−PEG−Ex4 were at higher positions than that of HSA. Furthermore, HSA−PEG−Ex4 produced a broad band, which was attributed to the linear nature of PEG during electrophoresis, and its M_w was obviously greater than that of HSA (Figure 1). Size-exclusion chromatography showed that the hydrodynamic molecular size (Ms) of HSA−PEG−Ex4 appeared much larger (ca. 195 kDa) than the actual size (ca. 94.6 kDa), whereas HSA and HSA−Ex4 had values similar to their own actual values (~67.0 and 79.4 kDa, respectively). The SEC chromatograms of HSA−PEG−Ex4 and HSA−Ex4 revealed that they were free of impurities and free Ex4 (Figure 2C,D). Separately, the particle sizes of Ex4, HSA, HSA−Ex4, and HSA−PEG−Ex4 in wet conditions were determined to be 3.84 ± 0.18, 6.67 ± 0.57, 7.77 ± 0.98, and 9.48 ± 0.74 nm, respectively. Especially, the particle size of HSA−PEG−Ex4 was significantly greater than those of HSA and HSA−Ex4 ($p < 0.03$) (Figure 2A′−D′).

Receptor Binding of HSA-Conjugated Ex4s. The receptor-binding affinities of Ex4 and of HSA-conjugated Ex4s were examined in RIN-m5F cells, which express high levels of GLP-1 receptors (GLP-1R). Ex4 was found to have high affinity for this receptor, with an IC_{50} of 0.08 ± 0.03 nM, as shown in Figure 3. However, the binding affinities of HSA−Ex4 and HSA−PEG−Ex4 were obviously lower with IC_{50} values of 1.02 ± 0.21 and 1.97 ± 0.17 nM, respectively.

Pharmacokinetics of Ex4 and of HSA-Conjugated Ex4s in ICR Mice. The blood concentration vs time curves of Ex4 and HSA-conjugated Ex4s were investigated after i.p. administrations. As shown in Figure 4, Ex4 was rapidly removed from the circulation with a circulating $t_{1/2}$ of 2.1 ± 0.5 h, whereas HSA-conjugated Ex4s had substantially greater $t_{1/2}$ values. Specifically, the $t_{1/2}$ of HSA−PEG−Ex4 was 24.2 ± 2.5 h, which was 2.1 times greater than that of HSA−Ex4 (11.4 ± 2.4 h), and its AUC_{inf} value (1418.7 ± 138.1 ng·h/mL) was 10.3 times greater than that of Ex4 (118.9 ± 29.9 ng·h/mL). In addition, the systemic clearance (Cl/F) of HSA−PEG−Ex4 (0.7 ± 0.1 mL/h) was 2.0- and 12.6-fold slower than those of HSA−Ex4 and Ex4 (1.4 ± 0.1 and 8.8 ± 2.7 mL/h, respectively).

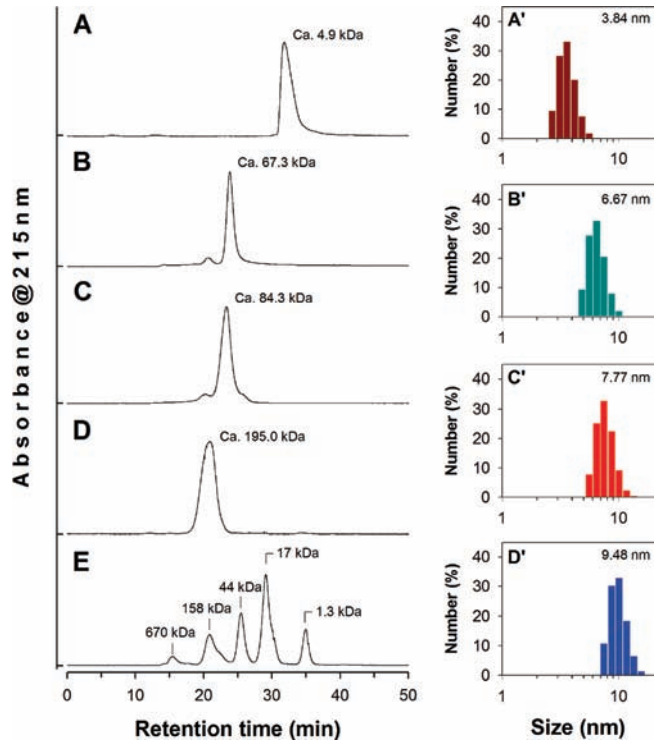


Figure 2. Size-exclusion chromatography of (A) Ex4, (B) HSA, (C) HSA−Ex4, (D) HSA−PEG−Ex4, and of (E) molecular weight standards, and particle size histograms of (A′) Ex4, (B′) HSA, (C′) HSA−Ex4, and (D′) HSA−PEG−Ex4. Data for particle size represent the means ± SDs of at least three determinations, each of which includes three independent measurements.

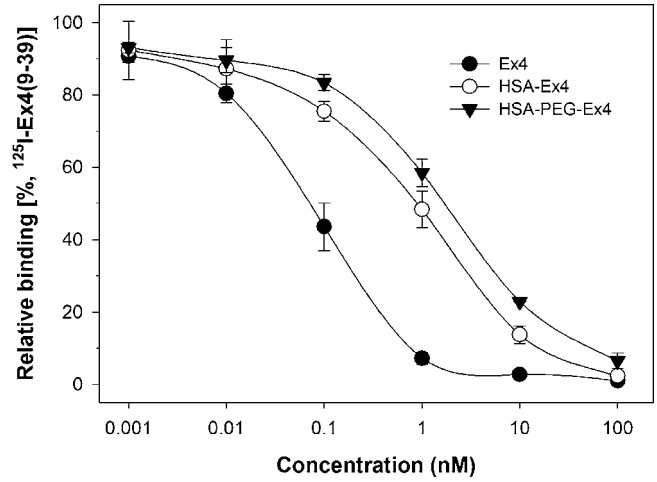


Figure 3. Receptor-binding affinities of HSA−PEG−Ex4 in RIN-m5F cells. Data represent the means ± SDs of five determinations.

Antihyperglycemic Efficacies of HSA-Conjugated Ex4s in Fasted db/db Mice. The antihyperglycemic efficacies of HSA-conjugated Ex4s were examined in fasted type 2 diabetic db/db mice by performing OGTT at 60 min after administering these agents i.p. As shown in Figure 5A, the total hypoglycemic degrees (HD_{total}) of HSA−Ex4 and HSA−PEG−Ex4 were similar (19.9 ± 5.3 vs 20.4 ± 0.9 mmol·h/L), and both were greater than that of Ex4 (14.2 ± 6.2, P = 0.15). However, peak glucose levels were similar for Ex4, HSA−Ex4, and HSA−PEG−Ex4 (13.4 ± 2.2, 14.1 ± 0.6, and 14.1 ± 3.1 mmol/L; $P > 0.3$) at 0.25 h after oral glucose administration. Glucose levels in HSA−Ex4- and HSA−PEG−Ex4-treated mice rapidly stabilized at <8.35 mmol/L at 0.67−0.75 h postglucose admin-

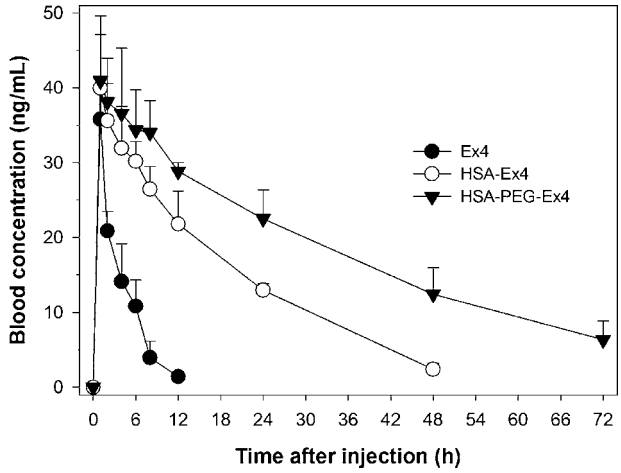


Figure 4. Blood clearance profiles of Ex4, HSA−Ex4, and HSA−PEG−Ex4 in ICR mice after treatment with doses of ∼2 μg (approximately 25 nmol/kg) i.p. Data represent four individual animals and are presented as means ± SDs.

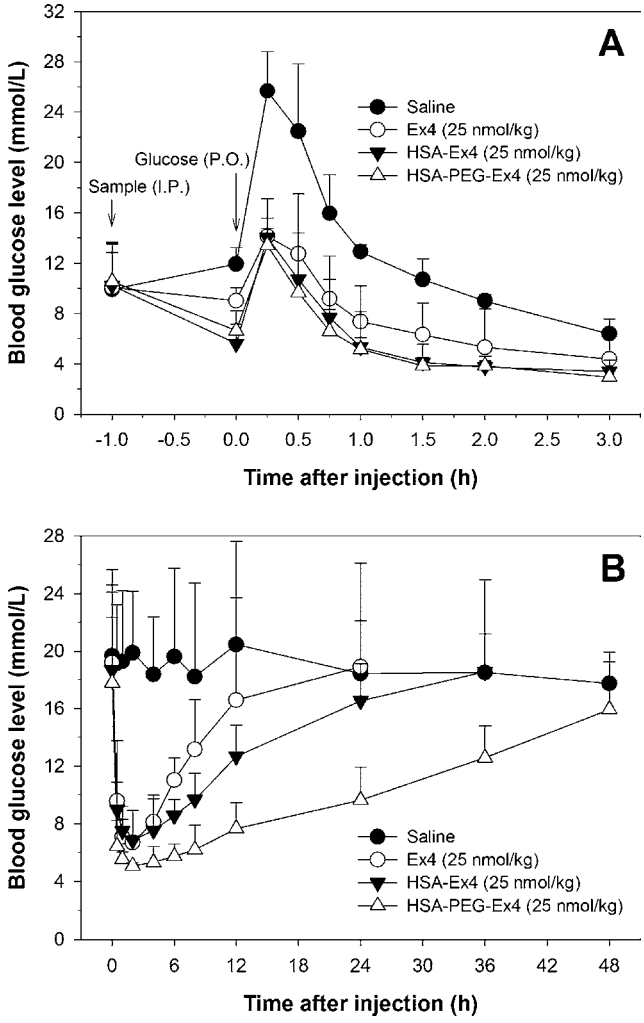


Figure 5. Antihyperglycemic activities of HSA−Ex4 and HSA−PEG−Ex4 as determine by oral glucose tolerance testing in type 2 diabetic db/db mice fasted for 18 h and pretreated with each agent (25 nmol/kg, i.p.) (A). Hypoglycemic efficacies of low dose (25 nmol/kg) Ex4, HSA−Ex4, and HSA−PEG−Ex4 in nonfasted db/db mice (B). Data represent five individual mice and are presented as means ± SDs.

istration, which was slightly faster than that observed in Ex4-treated mice (∼0.8−0.9 h).

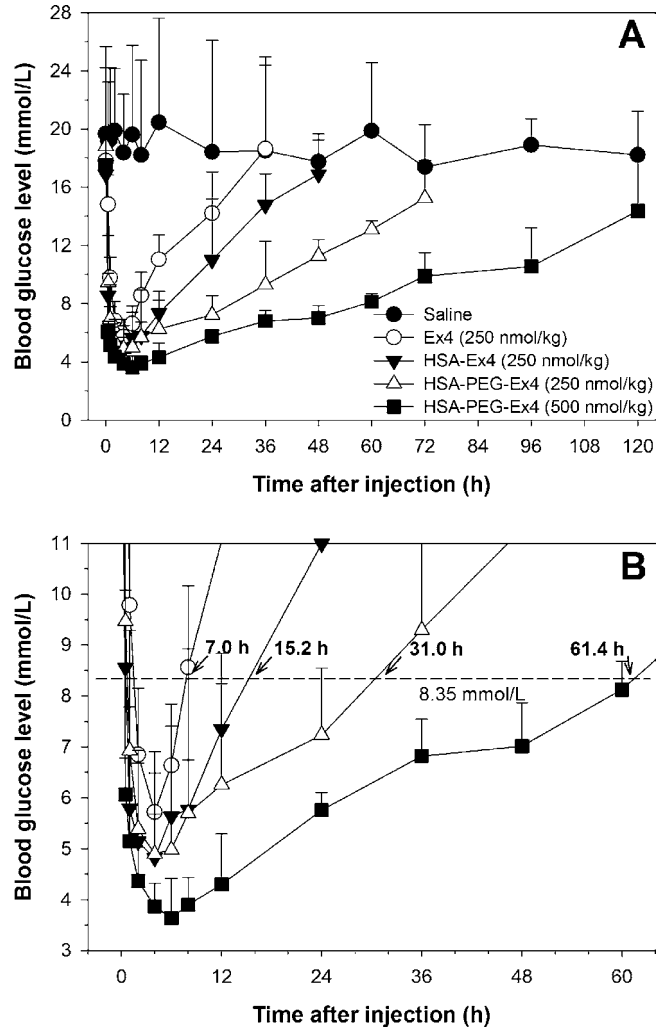


Figure 6. Hypoglycemic efficacies of high dose (250/500 nmol/kg) Ex4, HSA−Ex4, and HSA−PEG−Ex4 in nonfasted db/db mice (A). The focused profile of A (0−62 h, 3−11 mmol/L). Times depict the hypoglycemic duration rebound to 8.35 mmol/L (B). Data represent five individual mice and are presented as means ± SDs.

Hypoglycemic Durations of HSA-Conjugated Ex4s in Nonfasted db/db Mice. The hypoglycemic effects of HSA−Ex4 and HSA−PEG−Ex4 were examined at two doses (25 and 250 nmol/kg, i.p.) in db/db mice. At a dose of 25 nmol/kg, as shown in Figure 5B, the lowest glucose level (5.1 ± 0.2 mmol/L) in HSA−PEG−Ex4-treated mice was slightly, albeit insignificantly, lower than in HSA−Ex4 and Ex4 treated mice (5.5 ± 1.3 and 5.7 ± 0.5 mmol/L) ($P > 0.4$). The HD_{total} value of HSA−PEG−Ex4 (419.2 ± 117.2 mmol·h/L) was 2.3 and 3.7 times greater than those of HSA−Ex4 and Ex4, respectively ($P < 0.007$). Furthermore, the hypoglycemic duration in HSA−PEG−Ex4 mice was much greater, and the time required to rebound to a glucose level of 8.35 mmol/L was ∼16 h as compared with ∼6 and ∼4 h for HSA−Ex4 or Ex4 treated mice, respectively (Figure 6). Furthermore, at 250 nmol/kg, the pharmacological scores of HSA−PEG−Ex4 were much better than those of HSA−Ex4 or Ex4. Its HD_{total} value was 1.8 and 2.8 times greater than those of HSA−Ex4 and Ex4, respectively, and its $t_{\sim 8.35\ mmol/L}$ was 2.0 and 4.4 times greater than those of HSA−Ex4 and Ex4 (31.0 h vs 15.2 and 7.0 h, respectively). In particular, at the highest dose administered (500 nmol/kg), the $t_{\sim 8.35\ mmol/L}$ value of HSA−PEG−Ex4 was 61.4 h, demonstrating

that HSA−PEG−Ex4 stabilized blood glucose levels for 2 days in db/db mice.

DISCUSSION

Albumin attachment to therapeutic peptides/proteins is an attractive means of enhancing their short half-lives in the systemic circulation (*10, 11*). New antidiabetic drug candidates have been produced using albumin-fusion or albumin-conjugation techniques, and in most cases, such as for GLP-1, insulin, and exendin-4, satisfactory extensions of therapeutic duration have been achieved (*12, 13, 17, 29*). However, in all cases, drug components are closely located to large HSA by using small spacers at a drug to HSA molar ratio of 1:1 (*12, 13, 30*). Thus, the overall molecular sizes of HSA−drug conjugates make little difference with HSA itself, and moreover, its receptor binding might be greatly undermined due to the close proximity between the two. In the present study, we used a long PEG spacer to connect HSA and exendin-4, and examined the physicochemical and biological characteristics of the HSA−PEG−Ex4 conjugate produced.

HSA has only one free sulfhydryl group (-SH) on cysteine-34 because its other 34 cysteines are linked together by disulfide bonds. Furthermore, cysteine-34 is located in a hydrophobic crevice that lies 10−12 Å from the surface of HSA, which suggests that its reactivity is limited (*11*). For this reason, ConjuChem Inc. developed peptide maleimide derivatives using a performed conjugate−drug affinity complex (PC-DAC) that show high specific affinity for the cysteine-34 of HSA. Unlike this approach, we attempted to increase the overall conjugation yield by attaching several exendin-4 molecules to one HSA. For this purpose, artificial SH-groups were introduced on the surface of HSA using 2-iminothiolane (3 equiv), which converts amines to sulfhydryls. This thiolation reaction was highly efficient, and thus, almost all 2-iminothiolane molecules were conjugated randomly to the lysine amines of HSA. Furthermore, thiolated HSA was found to be stable at room temperature for one week without forming disulfide bonds (data not shown). However, we used heterobifunctional MAL−PEG_{5k}−NHS, which reacts well with the amines of exendin-4 and the sulfhydryl groups of HSA. By precisely controlling the reaction, we found that the MAL−PEG−Ex4 monomer was produced at a yield of ∼35% and that it was conjugated efficiently with three sulfhydryl groups, showing $a > 93\%$ yield. PEG possessing only a MAL or NHS group is very likely to generate impurities of their own dimers for HSA and Ex4. As initially expected, increasing the number of sulfhydryl groups on HSA increased the reaction rate and resulted in a high reaction yield.

PEGylation provides a practical means of increasing molecular size, protects metabolic and immunogenic sites and thus prolongs plasma half-life and *in vivo* stability, and diminishes immunogenicity. Because of the flexibility of the PEG linker, HSA−PEG−Ex4 was much larger than HSA−Ex4. Furthermore, HSA−PEG−Ex4 has a hydrodynamic molecular size estimated by SEC to be 2.9 and 2.3 times greater than those of native HSA and HSA−Ex4, respectively, and similarly, its actual particle size by DLS was found to be significantly larger than those of HSA−Ex4 and native HSA (>1.7−2.8 nm). Additionally, we designed HSA−PEG−Ex4 to contain three each of Ex4s and connector PEGs because incorporating more than 4−6 Ex4s per HSA resulted in unacceptably large hydrodynamic volume fractions (>approximately 280−340 kDa).

The receptor-binding affinities of peptide drugs after albumin conjugation are often less than 10% of those of parent molecules (*13, 19*), which is largely attributable to the steric hindrance of HSA. Similarly, we found that the receptor-binding affinity of HSA−PEG−Ex4 was only ∼5% of intact Ex4. However, its receptor binding was comparable to that of HSA−Ex4, despite the attachment of three long PEG molecules, which is somewhat surprising because PEGylated drugs usually have markedly lower receptor-binding affinities than native drugs, for example, in a previous study, we found that mono−PEG_{5k}−GLP-1 had only 1% of the binding affinity of GLP-1 (*24*). Bearing in mind the greater size of HSA−PEG−Ex4 as compared with HSA−Ex4, it appears that the flexibility of PEG in HSA−PEG−Ex4 allows Ex4 to better access receptors than Ex4 in HSA−Ex4, in which Ex-4 is directly and thus closely attached to HSA. In contrast to these *in vitro* results, our OGTT results showed that the antihyperglycemic efficacy of HSA−PEG−Ex4 is similar to that of Ex4. Therefore, our findings indicate that HSA−PEG−Ex4 is active enough to activate GLP-1R *in vivo* and that the reduced receptor binding observed *in vitro* is probably due to an inability to maintain binding with GLP-1R rather than a failure to bind and activate GLP-1R.

Because of its substantially larger molecular size, the pharmacokinetic profile of HSA−PEG−Ex4 after i.p. administration was markedly better than that of Ex4 (its AUC was 10-fold greater, and its circulating $t_{1/2}$ was 12-fold greater than those of Ex4). Furthermore, the $t_{1/2}$ of HSA−PEG−Ex4 in the circulation was twice that of HSA−Ex4, probably due to the molecular size increase caused by the attached PEG. It should also be mentioned that HSA and exendin-4 are obvious foreign materials to mice because they have human and reptile origins, respectively. However, PEGylation diminishes immunogenicity, and thus, we suppose the incorporation of PEG protects the HSA−PEG−Ex4 from mice antibodies. The hypoglycemic duration of HSA−PEG−Ex4 in db/db mice was also greatly prolonged vs HSA−Ex4 or native Ex4, regardless of the doses administered. In the present study, a blood glucose level below 8.35 mmol/L (150 mg/dL) was regarded as normal, and the euglycemic duration under that value is considered a practical indication of the potential for antidiabetic treatment. The administration of HSA−PEG−Ex4 sustained normal glycemia for 2 and 4 times longer than native Ex4 or HSA−Ex4, respectively. In addition, drug clearance in humans is known to be much slower than that in rodents, and thus, the antidiabetic duration of HSA−PEG−Ex4 may be substantially greater in humans than the ∼60 h in db/db mice in the present study.

In summary, we describe a new albumin-conjugated exendin-4 derivative, in which these two moieties are connected by a heterobifunctional PEG. Both the albumin and PEG components of HSA−PEG−Ex4 were found to confer therapeutic benefits. The present study also shows that that HSA−PEG−Ex4 has greater molecular size, acceptable GLP-1 receptor-binding affinity, better pharmacokinetics, and a markedly greater hypoglycemic duration than Ex4, specifically due to the incorporation of PEG. We believe that HSA−PEG−Ex4 should be viewed as a potential long-acting treatment for type 2 diabetes.

ACKNOWLEDGMENT

This work was supported by the National Research Foundation of Korea (NRF), by the Korean government (MEST) (no. 2009-0087518), and by a grant from the Ministry of Education, Science and Technology in Korea (2009K001605).

LITERATURE CITED

(1) Caliceti, P., and Veronese, F. M. (2003) Pharmacokinetic and biodistribution properties of poly(ethylene glycol)-protein conjugates. *Adv. Drug Delivery Rev. 55*, 1261–1277.

(2) Yoram, S., Marina, M., Sara, R., Ayala, S., Haim, T., and Mati, F. (2005) Albumin-insulin conjugate releasing insulin slowly under physiological conditions: A new concept for long-acting insulin. *Bioconjugate Chem. 16*, 913–920.

(3) Goodman, L. Gilman, A. G. (1995) *The Pharmacological Basis of Therapeutics*, McGraw-Hill, New York.

(4) Deacon, C. F. (2004) Therapeutic strategies based on glucagon-like peptide 1. *Diabetes. 53*, 2181–2189.

(5) David, P., Carolyn, J., Pam, S., Sonali, N., Liz, R., Ron, G., Kim, C., and Andrew, Y. (2001) Pharmacokinetic actions of exendin-4 in the rat: Comparison with glucagon-like peptide-1. *Drug Dev. Res. 53*, 260–267.

(6) Davidson, M. B., Bate, G., and Kirkpatrick, P. (2005) Exenatide. *Nat. Rev. Drug Discovery 4*, 713–714.

(7) Xu, G., Stoffers, D. A., Habener, J. F., and Bonner-Weir, S. (1999) Exendin-4 stimulates both beta-cell replication and neogenesis, resulting in increased beta-cell mass and improved glucose tolerance in diabetic rats. *Diabetes 48*, 2270–2276.

(8) Szayna, M., Doyle, M. E., Betkey, J. A., Holloway, H. W., Spencer, R. G., Greig, N. H., and Egan, J. M. (2000) Exendin-4 decelerates food intake, weight gain, and fat deposition in Zucker rats. *Endocrinology 141*, 1936–1941.

(9) Edwards, C. M., Stanley, S. A., Davis, R., Brynes, A. E., Frost, G. S., Seal, L. J., Ghatei, M. A., and Bloom, S. R. (2005) Exendin-4 reduces fasting and postprandial glucose and decreases energy intake in healthy volunteers. *Am. J. Physiol. 281*, 155–161.

(10) Chuang, V. T., Kragh-Hansen, U., and Otagiri, M. (2002) Pharmaceutical strategies utilizing recombinant human serum albumin. *Pharm. Res. 19*, 569–577.

(11) Kratz, F. (2008) Albumin as a drug carrier: Design of prodrugs, drug conjugates and nanoparticles. *J. Controlled Release 132*, 171–183.

(12) Kim, J.-G., Baggio, L. L., Bridon, D. P., Castaigne, J.-P., Robitaille, M. F., Jette, L., Benquet, C., and Druker, D. J. (2003) Development and characterization of a glucagon-like peptide 1-albumin conjugate: The ability to activate the glucagon-like peptide 1 receptor in vivo. *Diabetes 52*, 751–759.

(13) Thibaudeau, K., Léger, R., Huang, X., Robitaille, M., Quraishi, O., Soucy, C., Bousquet-Gagnon, N., van Wyk, P., Paradis, V., Castaigne, J.-P., and Bridon, D. (2005) Synthesis and evaluation of insulin-human serum albumin conjugates. *Bioconjugate Chem. 16*, 1000–1008.

(14) Juhl, C. B., Hollingdal, M., Sturis, J., Jakobsen, G., Agersø, H., Veldhuis, J., Pørksen, N., and Schmitz, O. (2002) Bedtime administration of NN2211, a long-acting GLP-1 derivative, substantially reduces fasting and postprandial glycemia in type 2 diabetes. *Diabetes 51*, 424–429.

(15) Kurtzhals, P., Havelund, S., Jonassen, I., and Markussen, J. (1997) Effect of fatty acids and selected drugs on the albumin binding of a long-acting, acylated insulin analogue. *J. Pharm. Sci. 86*, 1365–1368.

(16) Markussen, J., Havelund, S., Kurtzhals, P., Andersen, A. S., Halstrøm, J., Hasselager, E., Larsen, U. D., Ribel, U., Schäffer, L., Vad, K., and Jonassen, I. (1996) Soluble, fatty acid acylated insulins bind to albumin and show protracted action in pigs. *Diabetologia 39*, 281–288.

(17) Baggio, L. L., Huang, Q., Brown, T. J., and Drucker, D. J. (2004) A recombinant human glucagon-like peptide (GLP)-1-albumin protein (albugon) mimics peptidergic activation of GLP-1 receptor-dependent pathways coupled with satiety, gastrointestinal motility, and glucose homeostasis. *Diabetes 53*, 2492–2500.

(18) Subramanian, G. M., Fiscella, M., Lamousé-Smith, A., Zeuzem, S., and McHutchison, J. G. (2007) Albinterferon alpha-2b: a genetic fusion protein for the treatment of chronic hepatitis C. *Nat. Biotechnol. 25*, 1411–1419.

(19) Temming, K., Meyer, D. L., Zabinski, R., Dijkers, E. C., Poelstra, K., Molema, G., and Kok, R. J. (2006) Evaluation of RGD-targeted albumin carriers for specific delivery of auristatin E to tumor blood vessels. *Bioconjugate Chem. 17*, 1385–1394.

(20) Shin, B. S., Kim, C. H., Lee, M. N., Hur, M. W., Lee, K. C., Youn, Y. S., and Yoo, S. D. (2006) Pharmacokinetics of 125I-GST-TatdMt, a recombinant fusion protein possessing potent anti-obesity activity, after intravenous, nasal, oral, and subcutaneous administration. *Regul. Pept. 140*, 74–80.

(21) Chae, S. Y., Jin, C. H., Shin, J. H., Son, S., Kim, T. H., Lee, S., Youn, Y. S., Byun, Y., Lee, M. S., and Lee, K. C. (2010) Biochemical, pharmaceutical and therapeutic properties of long-acting lithocholic acid derivatized exendin-4 analogs. *J. Controlled Release 142*, 206–213.

(22) Jin, C. H., Chae, S. Y., Son, S., Kim, T. H., Um, K. A., Youn, Y. S., Lee, S., and Lee, K. C. (2009) A new orally available glucagon-like peptide-1 receptor agonist, biotinylated exendin-4, displays improved hypoglycemic effects in db/db mice. *J. Controlled Release 133*, 172–177.

(23) Youn, Y. S., Na, D. H., Yoo, S. D., Song, S. C., and Lee, K. C. (2005) Carbohydrate-specifically polyethylene glycol-modified ricin A-chain with improved therapeutic potential. *Int. J. Biochem. Cell Biol. 37*, 1525–1533.

(24) Chae, S. Y., Chun, Y. G., Lee, S., Jin, C. H., Lee, E. S., Lee, K. C., and Youn, Y. S. (2009) Pharmacokinetic and pharmacodynamic evaluation of site-specific PEGylated glucagon-like peptide-1 analogs as flexible postprandial-glucose controllers. *J. Pharm. Sci. 98*, 1556–1567.

(25) Lee, S. H., Lee, S., Youn, Y. S., Na, D. H., Chae, S. Y., Byun, Y., and Lee, K. C. (2005) Synthesis, characterization, and pharmacokinetic studies of PEGylated glucagon-like peptide-1. *Bioconjugate Chem. 6*, 377–382.

(26) Lee, K. C., Chae, S. Y., Kim, T. H., Lee, S., Lee, E. S., and Youn, Y. S. (2009) Intrapulmonary potential of polyethylene glycol-modified glucagon-like peptide-1s as a type 2 anti-diabetic agent. *Regul. Pept. 152*, 101–107.

(27) Youn, Y. S., Jung, J. Y., Oh, S. H., Yoo, S. D., and Lee, K. C. (2006) Improved intestinal delivery of salmon calcitonin by Lys18-amine specific PEGylation: stability, permeability, pharmacokinetic behavior and in vivo hypocalcemic efficacy. *J. Controlled Release 114*, 334–342.

(28) Youn, Y. S., Chae, S. Y., Lee, S., Jeon, J. E., Shin, H. G., and Lee, K. C. (2007) Evaluation of therapeutic potentials of site-specific PEGylated glucagon-like peptide-1 isomers as a type 2 anti-diabetic treatment: Insulinotropic activity, glucose-stabilizing capability, and proteolytic stability. *Biochem. Pharmacol. 73*, 84–93.

(29) Baggio, L. L., Huang, Q., Cao, X., and Drucker, D. J. (2008) An albumin-exendin-4 conjugate engages central and peripheral circuits regulating murine energy and glucose homeostasis. *Gastroenterology 134*, 1137–1147.

(30) Shechter, Y., Mironchik, M., Rubinraut, S., Saul, A., Tsubery, H., and Fridkin, M. (2005) Albumin-insulin conjugate releasing insulin slowly under physiological conditions: a new concept for long-acting insulin. *Bioconjugate Chem. 16*, 913–920.

BC100143C

Oligonucleotide Carbohydrate-Centered Galactosyl Cluster Conjugates Synthesized by Click and Phosphoramidite Chemistries

Gwladys Pourceau,[†] Albert Meyer,[†] Yann Chevolot,[‡] Eliane Souteyrand,[‡] Jean-Jacques Vasseur,[†] and François Morvan*,[†]

Institut des Biomolécules Max Mousseron (IBMM), UMR 5247 CNRS, Université Montpellier 1, Université Montpellier 2, Place Eugène Bataillon, CC1704, 34095 Montpellier Cedex 5, France, and Institut des Nanotechnologies de Lyon (INL), UMR 5270 CNRS Ecole Centrale de Lyon, 36 Avenue Guy de Collongue, 69134 Ecully Cedex, France. Received April 20, 2010; Revised Manuscript Received June 16, 2010

Oligonucleotide glycoconjugates with a mannose or galactose core bearing four galactose residues introduced by phosphoramidite chemistry and copper catalyzed azide alkyne 1,3-dipolar cycloaddition (click chemistry) have been synthesized. A first click reaction allowed the introduction on a solid support of a mannose core on which four pentynyl linkers were introduced using a phosphoramidite derivative. After the elongation of the oligonucleotide, a second click reaction performed either on solid support or in solution allowed the introduction of four galactose azide derivatives. Repeating the phosphoramidite and click chemistries afforded an oligonucleotide glycoconjugate dendrimer bearing 16 galactoses on its periphery.

INTRODUCTION

Carbohydrates are involved in several important biological events such as cell−cell communications, inflammation, or infections by pathogens (*1*−*5*). However, monovalent carbohydrate ligands are generally weakly recognized by carbohydrate-binding protein (lectins) (*6*). To increase affinity and specificity, clusters with the right carbohydrate residues and optimized spatial arrangement are required (*6*−*8*). Since multivalency plays an important functional role in carbohydrate−protein interactions (the so-called cluster effect *6*−*8*), many synthetic multivalent glycomimetics have been designed to interfere effectively with lectins (for recent reviews, see *refs* 9−12). These glycomimetics have been prepared from multiple scaffolds (*13*−*23*) and especially from linear (*9, 12, 24*) and cyclic peptides (*12, 24*−*29*), cyclodextrins (*30*), pentaerythritol (*9, 21, 31*), calix[4]arenes (*18, 32*−*36*), or glycosides (*19, 21, 30, 37*−*43*). This latter kind of glycomimetics, the so-called carbohydrate-centered glycoclusters, have been initially developed by Lindhorst (*37*−*39, 44*). It was reported that their synthesis was mainly hampered by the difficulty in achieving several glycosylation steps with high efficiency since steric hindrance occurs with the progress of the reactions, the last glycosylation step becoming the most difficult one. To overcome this hurdle, we have used a two-step protocol, with first the introduction of an alkyne function by means of the very reactive pentyn-4-yl phosphoramidite derivative **4** (*45*) according to a well established phosphoramidite method (*46*) and second a 1,3-dipolar cycloaddition catalyzed by Cu(I) (click chemistry) between the resulting alkyne and a carbohydrate azide derivative (*47, 48*). Furthermore, the main part of the synthesis was performed on solid support, allowing a rapid, efficient, and automated synthesis.

To further be able to study the affinity of these new glycomimetics for lectins, we conjugated them with an oligonucleotide for immobilization on a DNA chip by DNA directed immobilization (DDI) as previously reported by Niemeyer et al. for proteins (*49*) and by us for glycomimetics (*50*). Indeed, we have recently shown that the resulting glycochip displays high sensitivity and required very minute amounts of material (*50, 51*). It should be noticed that several examples of oligonucleotide glycoconjugates have been reported in the literature (*17, 18, 24, 50, 52*−*63*) to study their interaction with lectins, for cell targeting or cellular uptake.

Herein, we present the synthesis of different mannose- or galactose-centered tetragalactose oligonucleotide conjugates. To evaluate the efficiency and versatility of the synthesis of these conjugates, the carbohydrate-centered tetragalactose cluster was introduced at different positions of the oligonucleotide (i.e., 3′- or 5′-end or inside the sequence). Finally, an oligonucleotide conjugated with a glycodendrimer bearing 16 galactoses on its periphery was obtained repeating the phosphoramidite and click chemistries protocol.

EXPERIMENTAL PROCEDURES

General Procedure for the Synthesis of Oligonucleotide Scaffolds. Oligonucleotides **9**, **10**, **20**, **32**, and **38** were synthesized on a 1 μmol-scale on a DNA synthesizer (ABI 394) by standard phosphoramidite chemistry. For the coupling step, benzylmercaptotetrazole (BMT) was used as the activator (0.3 M in anhydrous CH_3CN), commercially available nucleoside phosphoramidites (0.075 M in anhydrous CH_3CN) were introduced with a 20 s coupling time, and 6-bromohexyl phosphoramidite **8** (0.2 M in anhydrous CH_3CN) and 1-*O*-(4,4′-dimethoxytrityl)-2-propargyloxymethyl-2-methyl-3-*O*-[(2-cyanoethyl)-*N*,*N*-diisopropylphosphoramidite]-1,3-propanediol **31** (0.09 M in anhydrous CH_3CN) were introduced with a 180 s coupling time. The capping step was performed with acetic anhydride using commercial solutions (Cap A/Ac_2O, pyridine, THF 10/10/80 and Cap B/10% *N*-methylimidazole in THF) for 15 s. Oxidation was performed with a commercial solution of iodide (0.1 M I_2, THF/pyridine/water 90/5/5) for 13 s. Detritylation was performed with 2.5% DCA in CH_2Cl_2 for 35 s.

Synthesis of Azide Solid Support 1. See Supporting Information.

* Corresponding author. Tel: +33/467 144 961. Fax: +33/467 042 029. E-mail: morvan@univ-montp2.fr.

[†] Université Montpellier 2.

[‡] UMR 5270 CNRS Ecole Centrale de Lyon.

10.1021/bc1001888 © 2010 American Chemical Society
Published on Web 07/23/2010

Table 1

	click reaction compound	Scale (nmol)	$CuSO_4$ (equiv)	sodium ascorbate (equiv)	**14** (equiv)	**15** (equiv)	solvent volume (H_2O/MeOH 1:1) (μL)
in solution	**12→16**	100	2	10	12	0	250
	25→27						
	35→36						
	13→17	100	6	30	0	12	250
	26→28						
on solid support	**11→19**	~500	4.8	24	0	12	200
	24→30	~250	4.8	24	0	12	200

General Procedure for Cu(I)-Catalyzed 1,3-Dipolar Cycloaddition with 1-*O*-Propargyl Mannose 2. An aqueous solution of 1-*O*-propargyl mannose **2** (*41*) (100 mM, 50 μL), freshly prepared aqueous solutions of $CuSO_4$ (100 mM, 4 μL) and sodium ascorbate (500 mM, 4 μL), water (42 μL) and MeOH (100 μL) were added to 1 μmol of solid support compounds **1** or **20**. The resulting mixture was treated in a sealed tube with a microwave synthesizer at 60 °C for 30 min for azido solid support **1** and 2 × 30 min for 5′-azido-oligonucleotide **20** (premixing time: 30 s). The temperature was monitored with an internal infrared probe. The solution was removed, and CPG beads were washed with H_2O (3 × 2 mL) and MeOH (3 × 2 mL) and dried.

Procedure for Cu(I)-Catalyzed 1,3-Dipolar Cycloaddition with 1-*O*-Propylazide Galactose 33. *Compound 34.* An aqueous solution of 1-*O*-propylazide galactose **33** (*64*) (100 mM, 50 μL), freshly prepared aqueous solutions of $CuSO_4$ (50 mM, 8 μL) and sodium ascorbate (100 mM, 20 μL), phosphate buffer (10 mM, pH 7.3) (40 μL), water (82 μL), and MeOH (200 μL) were added to 1 μmol of the solid-supported alkyne oligonucleotide **32**. The resulting mixture was treated in a sealed tube with a microwave synthesizer at 60 °C for 30 min (premixing time: 30 s). The temperature was monitored with an internal infrared probe. The solution was removed, and CPG beads were washed with H_2O (3 × 2 mL) and CH_3CN (3 × 2 mL) and then dried.

Compound 39. An aqueous solution of 1-*O*-propylazide galactose **33** (100 mM, 120 μL), $CuSO_4$ (100 mM, 20 μL), and sodium ascorbate (100 mM, 100 μL), triethylammonium acetate buffer (TEEAc) (0.1 M, pH 7.7) (30 μL), and water (30 μL) were added to 1 μmol of the solid-supported tetrapentynyl oligonucleotide **38**. The resulting mixture was treated in a sealed tube with a microwave synthesizer at 60 °C for 45 min (premixing time: 30 s), and the beads were washed as described above.

General Procedure for the Elongation on Mannose and Galactose Hydroxyls. Solid-supported mannose derivatives **3** and **21** and galactose derivatives **34** and **39** were treated by phosphoramidite chemistry, on a DNA synthesizer, with pentyn-4-yl phosphoramidite **4** (*45*) or 6-bromohexyl phosphoramidite **8** (*65, 66*) (0.2 M in anhydrous CH_3CN). Only coupling, capping, and oxidation steps were performed. For the coupling step, benzylmercaptotetrazole was used as the activator (0.3 M in anhydrous CH_3CN).

On Compounds 3, 21, and 34. Phosphoramidites (**4** or **8**) were introduced twice (2 × 40 μmol) with a 180 s coupling time, and the capping time was extended to 180 s.

On Compound 39. Solid-supported mannose-centered tetragalactose derivative **39** was treated with pentyn-4-yl phosphoramidite **4** (0.2 M in dry CH_3CN) three times with a 180 s coupling time (3 × 40 μmol) and once with a 10 min coupling time (40 μmol). Each oxidation was performed for 40 s.

General Procedure for Azidation to Afford 11 and 20. The solid-supported oligonucleotides bearing the bromo function (1 μmol) were treated with a solution of TMG-N_3 (31.6 mg, 200 equiv) and NaI (30 mg, 200 equiv) in DMF (1 mL) for 1 h at 65 °C. The beads were washed with DMF (2 × 1 mL), H_2O (3 × 1 mL), and CH_3CN (3 × 1 mL), and dried.

Table 2

click reaction compound	scale (nmol)	Cu nanopowder (mg)	**14** (equiv)	solvent volume (TEEAc/MeOH 1:1) (μL)	heating	times (min)
35→36	100	1	12	250	bath, 70 °C	30
41→42	400	1	48	450	MW, 60 °C	60

General Procedure for the Deprotection of Solid-Supported Oligonucleotides. CPG beads were treated with concentrated aqueous ammonia (1.5 mL) for 15 h at room temperature and for 1 h at 55 °C. The supernatant was withdrawn and evaporated to dryness. The residue was dissolved in water.

General Procedure for Cu(I)-Catalyzed 1,3-Dipolar Cycloaddition with Tetraacetyl-Galactosyl Derivatives 14 and 15. *With Copper Sulfate and Sodium Ascorbate.* To a solid-supported or in-solution oligonucleotide were added tetraacetyl galactosyl derivatives **14** (*16*) or **15** (*41*), freshly prepared aqueous solution of $CuSO_4$ (0.5 equiv/alkyne) and sodium ascorbate (5 equiv/$CuSO_4$), water, and MeOH (Table 1). The tube containing the resulting preparation was sealed and placed in a microwave synthesizer Initiator from Biotage with a 30 s premixing time for 45 min at 70 °C or in a bath at 70 °C for oligonucleotide **35**.

In Solution. After the reaction, solutions were desalted on NAP10 and evaporated. Residues were dissolved in water and purified by reversed-phase preparative HPLC. Pure compounds were treated with concentrated aqueous ammonia (1 mL) for 2 h at room temperature to remove acetyl groups, and evaporated to dryness. Residues were dissolved in water for subsequent analyses.

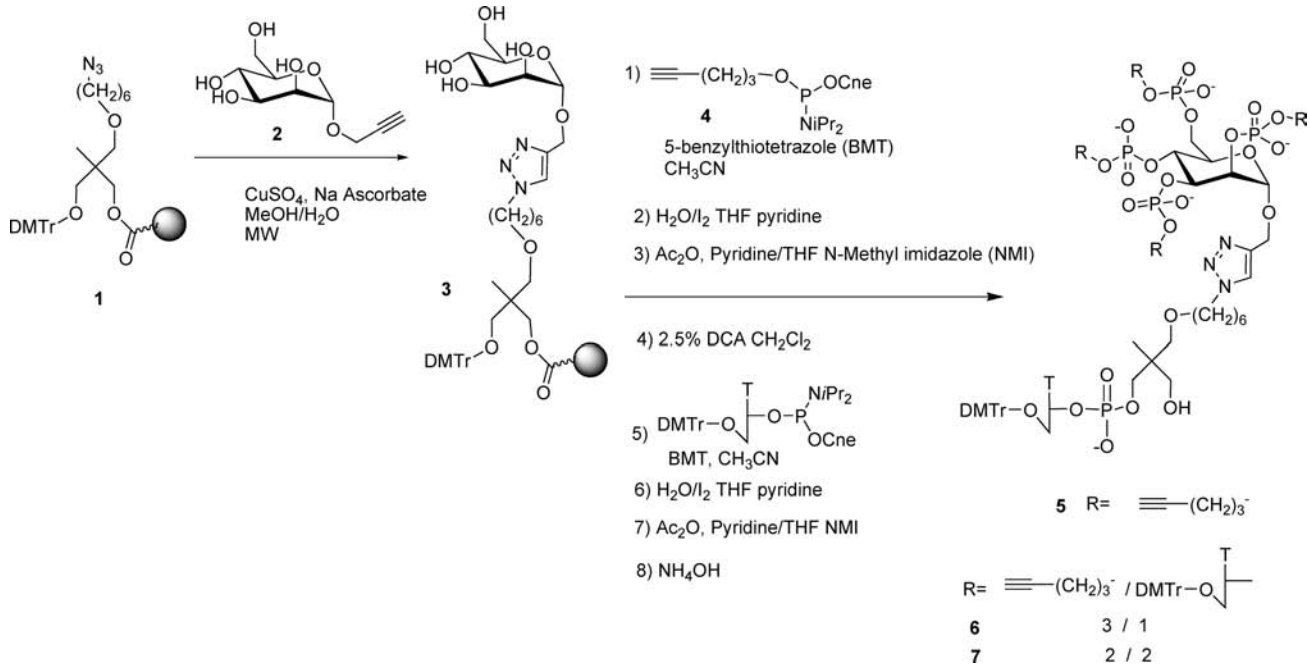
On Solid Support. After the reaction, the solution was removed, and the CPG beads were washed with H_2O (3 × 2 mL) and MeOH (3 × 2 mL) and dried. Deprotection was performed as described above, and the residues were purified by reversed-phase preparative HPLC.

With Copper (0) Nanopowder. Tetraacetyl-galactosyl derivative **14** (3 equiv/alkyne), nanopowder copper, triethylammonium acetate buffer (0.1 M pH 7.7), and MeOH were added to the in-solution oligonucleotides (see Table 2). The tube containing the resulting preparation was sealed and heated in a bath or using a microwave synthesizer.

After the reaction, EDTA (200 μL) was added, and the mixture was filtered off on a membrane (PTFE, 0.45 μm). The solvent was evaporated to dryness. Conjugate **36** was dissolved in water and purified by reversed-phase preparative HPLC, and the pure compound was treated with concentrated aqueous ammonia (1 mL) for 2 h at room temperature affording **37** after evaporation. Conjugate **42** was directly treated with concentrated aqueous ammonia (1 mL) for 1 h at room temperature and evaporated to dryness; the resulting conjugate **43** was finally purified by reversed-phase preparative HPLC.

Analyses and Characterization of Carbohydrate-Centered Galactosylcluster Oligonucleotide Conjugates. The authenticity of each conjugate was confirmed by HPLC and MALDI-TOF MS (see Supporting Information).

Scheme 1. Synthesis of the 3′-[Tetra-(pentynyl phosphodiester)-mannose] Thymidine Conjugate



*Compound **18.*** HPLC RT = 13.8 min, λ_{max} = 263 nm, $\varepsilon_{260\ nm}$ = 124700 L·mol^{-1}·cm^{-1}. MS MALDI-TOF$^-$ *m/z* calcd for $C_{211}H_{311}N_{56}O_{116}P_{16}$ [M − H]$^-$: 5983.615; found, 5983.36, 23 nmol calculated by UV measurement at 260 nm.

*Compound **19** from the Click Reaction in Solution.* HPLC RT = 11.9 min, λ_{max} = 263 nm, $\varepsilon_{260\ nm}$ = 124700 L·mol^{-1}·cm^{-1}. MS MALDI-TOF$^-$ *m/z* calcd for $C_{195}H_{288}N_{56}O_{116}P_{16}$ [M − H]$^-$: 5767.253; found, 5767.37, 13 nmol calculated by UV measurement at 260 nm.

*Compound **19** from the Solid-Supported Click Reaction.* HPLC RT = 12.0 min, λ_{max} = 263 nm, $\varepsilon_{260\ nm}$ = 124700 L·mol^{-1}·cm^{-1}. MS MALDI-TOF$^-$ *m/z* calcd for $C_{195}H_{288}N_{56}O_{116}P_{16}$ [M − H]$^-$: 5767.253; found, 5767.57, 15 nmol calculated by UV measurement at 260 nm.

*Compound **29.*** HPLC RT = 12.9 min, λ_{max} = 263 nm, $\varepsilon_{260\ nm}$ = 124700 L·mol^{-1}·cm^{-1}. MS MALDI-TOF$^-$ *m/z* calcd for $C_{206}H_{301}N_{56}O_{114}P_{16}$ [M − H]$^-$: 5881.483; found, 5882.52, 13 nmol calculated by UV measurement at 260 nm.

*Compound **30** from the Click Reaction in Solution.* HPLC RT = 11.0 min, λ_{max} = 263 nm, $\varepsilon_{260\ nm}$ = 124700 L·mol^{-1}·cm^{-1}. MS MALDI-TOF$^-$ *m/z* calcd for $C_{190}H_{278}N_{56}O_{114}P_{16}$ [M − H]$^-$: 5665.122; found, 5666.64, 5 nmol calculated by UV measurement at 260 nm.

*Compound **30** from the Solid-Supported Click Reaction.* HPLC RT = 11.0 min, λ_{max} = 263 nm, $\varepsilon_{260\ nm}$ = 124700 L·mol^{-1}·cm^{-1}. MS MALDI-TOF$^-$ *m/z* calcd for $C_{190}H_{278}N_{56}O_{114}P_{16}$ [M − H]$^-$: 5665.122; found, 5665.35, 9 nmol calculated by UV measurement at 260 nm.

*Compound **37** from the Click Reaction in Solution with Cu (0).* HPLC RT = 13.4 min, λ_{max} = 263 nm, $\varepsilon_{260\ nm}$ = 124700 L·mol^{-1}·cm^{-1}, MS MALDI-TOF$^-$ *m/z* calcd for $C_{208}H_{305}N_{56}O_{116}P_{16}$ [M − H]$^-$: 5941.598; found, 5941.49, 9 nmol calculated by UV measurement at 260 nm.

*Compound **37** from the Click Reaction in Solution with Cu (II).* HPLC RT = 13.3 min, λ_{max} = 262 nm, $\varepsilon_{260\ nm}$ = 124700 L·mol^{-1}·cm^{-1}. MS MALDI-TOF$^-$ *m/z* calcd for $C_{208}H_{305}N_{56}O_{116}P_{16}$ [M − H]$^-$: 5941.598; found, 5940.67, 15 nmol calculated by UV measurement at 260 nm.

*Compound **43.*** HPLC RT = 14.4 min, λ_{max} = 262 nm, $\varepsilon_{260\ nm}$ = 40300 L·mol^{-1}·cm^{-1}. MS MALDI-TOF$^-$ *m/z* calcd for $C_{419}H_{695}N_{75}O_{214}P_{24}$ [M − H]$^-$: 10949.741; found, 10948.89, 170 nmol calculated by UV measurement at 260 nm.

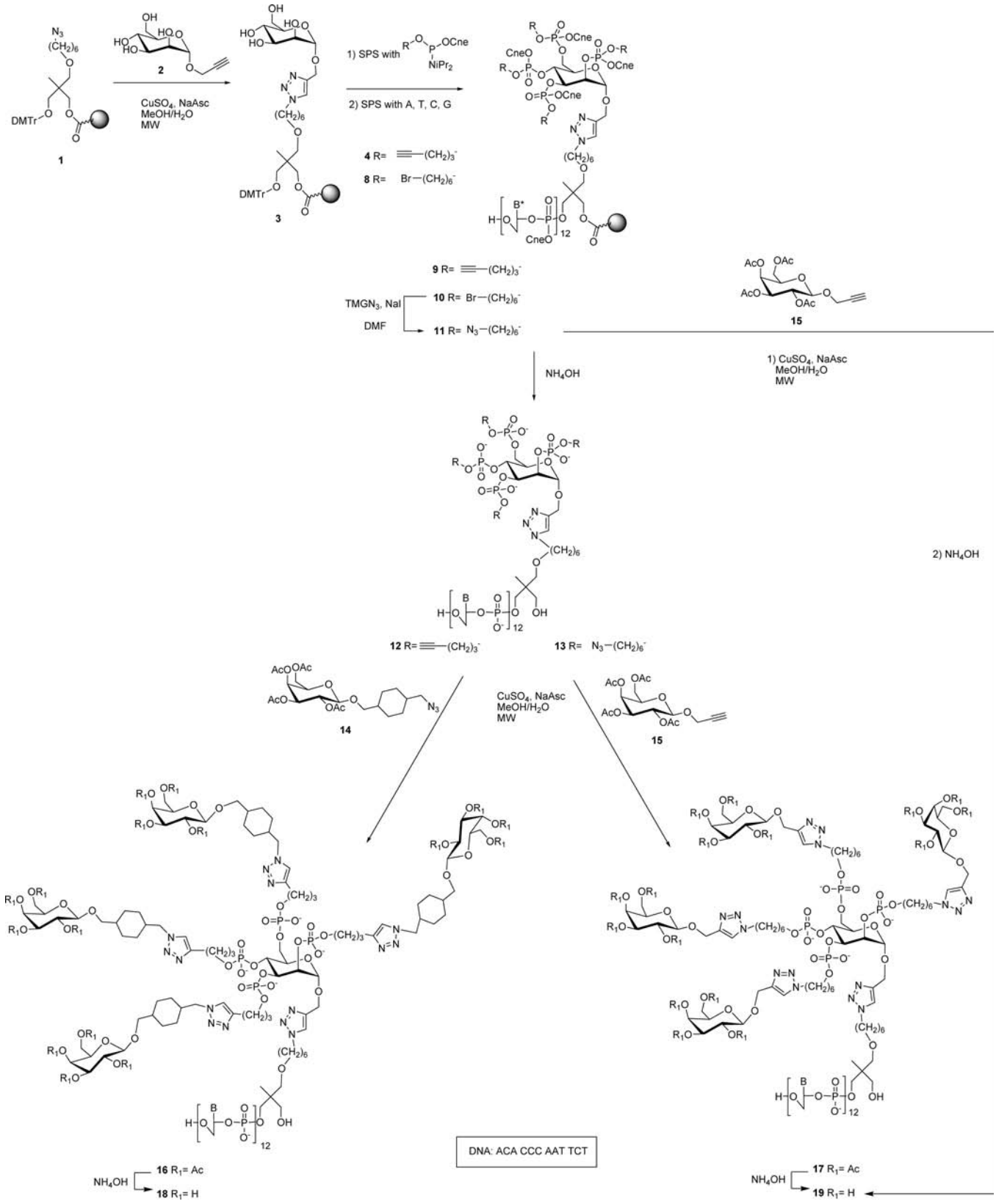
RESULTS AND DISCUSSION

The synthesis of the carbohydrate-centered tetragalactose oligonucleotide conjugates required two 1,3-dipolar cycloadditions click chemistry catalyzed by Cu(I). The first click reaction was used to introduce on a solid support the unprotected mannosyl moiety on which the four hydroxyls were coupled with either pentyn-4-yl or 6-bromohexyl phosphoramidites, required for the second click reaction to introduce at the end four galactose residues on the mannose core of the oligonucleotide conjugate. To obtain different spatial arrangements with different linkers between each galactose moiety, we developed either the possibility to introduce the galactose moieties using an azide or an alkyne derivative. It means that the complementary function alkyne or azide should be introduced on the galactosyl moiety (**15** or **14**, respectively). For that purpose, the alkyne function was introduced using a pentyn-4-yl phosphoramidite **4** (*45*), and the azide function was introduced using a 6-bromohexyl phosphoramidite **8** (*65, 66*), where the bromine atom was further substituted with tetramethylguanidinium azide (TMG N_3) after the elongation of the oligonucleotide.

3′-End Conjugation. For the conjugation at the 3′-end of the oligonucleotide (Scheme 1), we started from a solid support **1** bearing an azide function which was conjugated with 1-*O*-propargyl-α-D-mannopyranose **2** (5 equiv) catalyzed by Cu(I) (0.4 equiv $CuSO_4$, 2 equiv sodium ascorbate) under microwaves (MW) (*59*) at 60 °C for 30 min to give **3** exhibiting a hydroxyl protected with a DMTr group and the four free hydroxyls of mannose.

Then, we studied the coupling reaction of pentynyl phosphoramidite **4** on the four free hydroxyls of the mannose moiety (Scheme 1). This coupling step (2 × 60 s) was performed on a DNA synthesizer using **4** at 0.1 M corresponding to 40 μmol (10 eq/OH) and benzylthiotetrazole (BMT) as the activator. Then, the oxidation of the phosphitetriester linkages was performed using a standard, commercially available solution of iodine and water. Finally, a thymidine was introduced according to a standard elongation cycle (*46*). Some beads of the solid-supported material were withdrawn and treated with ammonia

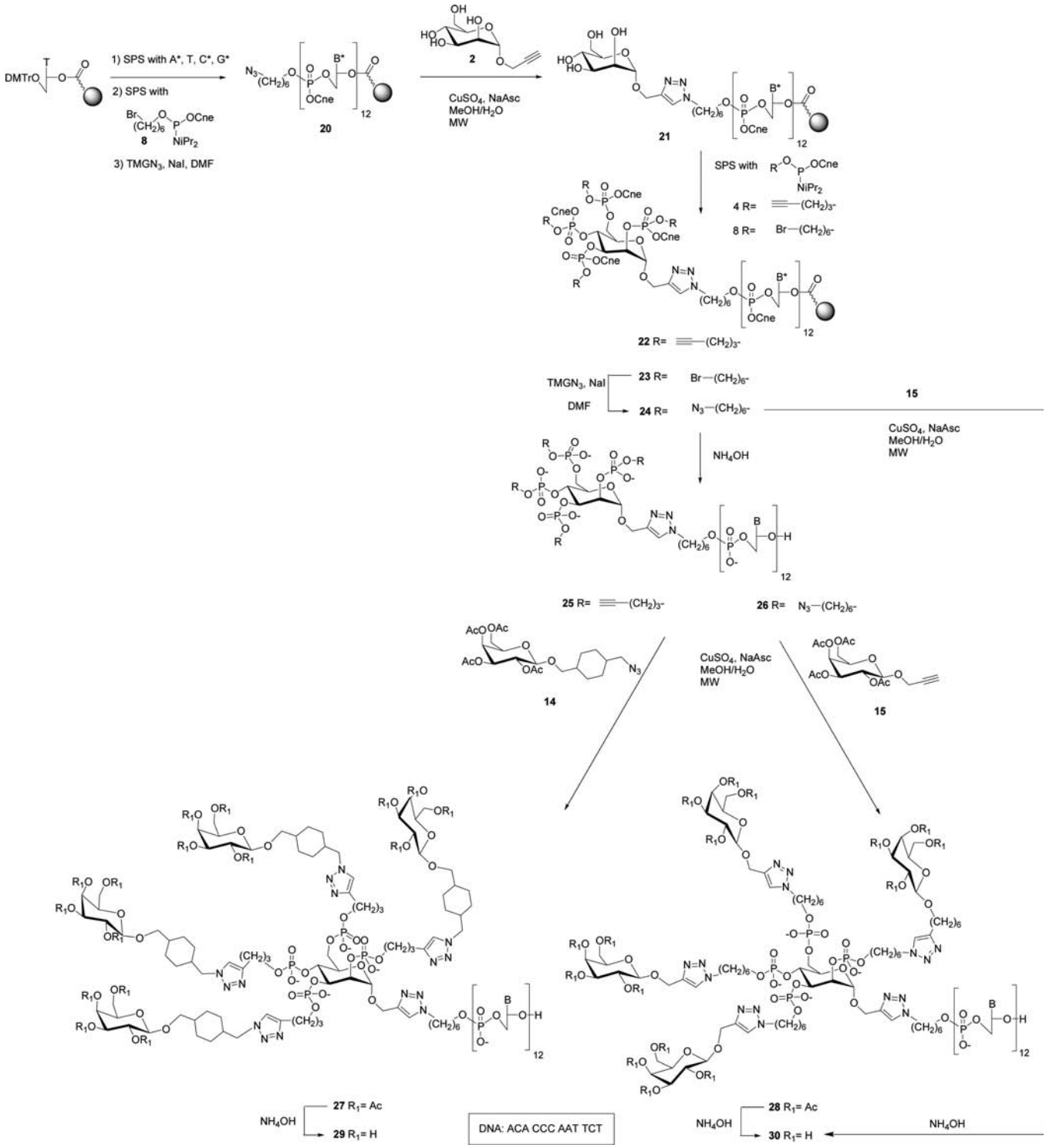
Scheme 2. Synthesis of 3′-(Mannose-Centered Tetragalactose) Oligonucleotide Conjugates[a]



[a] SPS, solid-phase synthesis; (1) phosphoramidite derivative + benzylthiotetrazole; (2) Ac_2O, *N-Me* imidazole, and 2,6-lutidine; (3) 0.1 M I_2 THF/H_2O/pyridine; (4) 2.5% dichloroacetic acid CH_2Cl_2. B* asterisk represents A or C with the benzoyl protecting group, and B represents A, C, or T.

for deprotection and release. HPLC and MALDI-TOF analyses of the mixture showed the presence of the expected compound **5** with the four pentynyl arms ($[M - H]^-$ *m/z* 1653.40) but also two other compounds (**6** and **7**), the first where one pentynyl arm was replaced by one DMTr-thymidine (**6**, $[M - H]^-$ *m/z* 2113.88), and the second where two pentynyl arms were replaced by two DMTr thymidines (**7**, $[M - H]^-$ *m/z* 2574.36). It means that one or two hydroxyls of the mannose reacted

Scheme 3. Synthesis of 5′-(Mannose-Centered Tetragalactose) Oligonucleotide Conjugates[a]



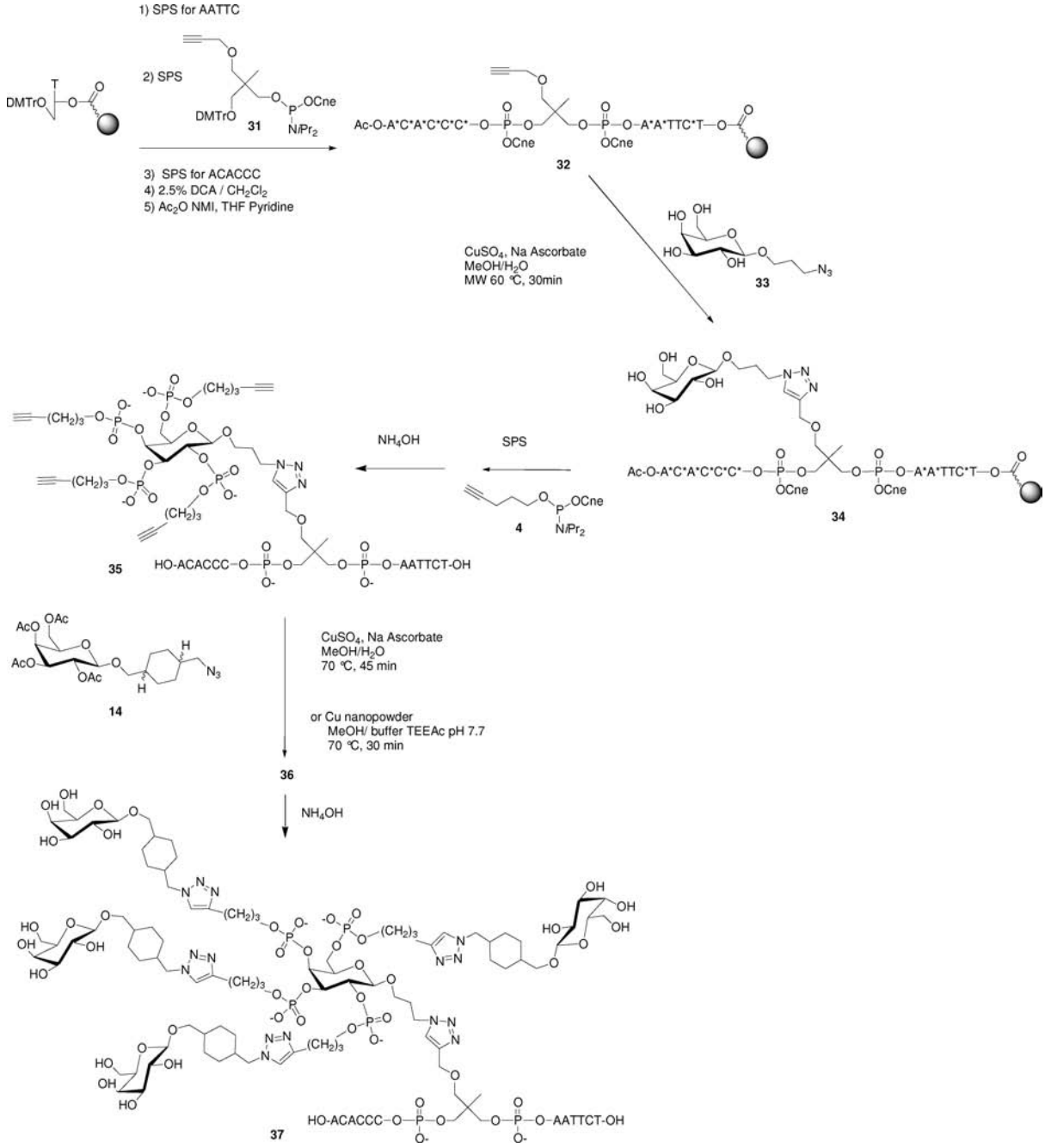
[a] SPS: see the footnote for Scheme 2.

partially with **4** and further reacted with the thymidine phosphoramidite. Interestingly, the ion $[M - H]^-$ at *m*/*z* 850.87 corresponding to the compound DMTr-thymidine with the 3′-azido linker was not observed, suggesting that the click reaction with propargyl mannose **2** was quantitative.

To optimize the coupling of **4** on the mannose moiety, we then used **4** at 0.2 M concentration and applied a double coupling (80 equiv, i.e., 20 equiv/OH) of 180 s each. After the coupling of a thymidine and treatment with ammonia, HPLC and MS analyses showed a full conversion with the exclusive formation of the expected compound **5** bearing the four pentynyl arms.

The optimal conditions for the coupling of phosphoramidite **4** on the mannosyl moiety being set, we then synthesized the oligonucleotide moiety leading to **9**, which was treated with ammonia affording oligonucleotide **12** bearing a 3′-[mannose-centered tetra-(tetrapentynylphosphodiester)] moiety (Scheme 2). The introduction of the four galactoses occurred in a water/methanol (1:1) solution, under Cu(I) catalysis generated *in situ* from $CuSO_4$ reduction with sodium ascorbate, under MW assistance for 30 min at 60 °C using 1-*O*-[[4-(azidomethyl)cyclohexyl]-methyl]-2,3,4,6-tetra-*O*-acetyl-*β*-D-galactopyranoside **14** (*16*). Finally, after the HPLC purification of **16**, its

Scheme 4. Synthesis of an Oligonucleotide Glycoconjugate Exhibiting a Galactose-Centered Tetragalactose Inside the Sequence[a]



[a] SPS: see the footnote for Scheme 2.

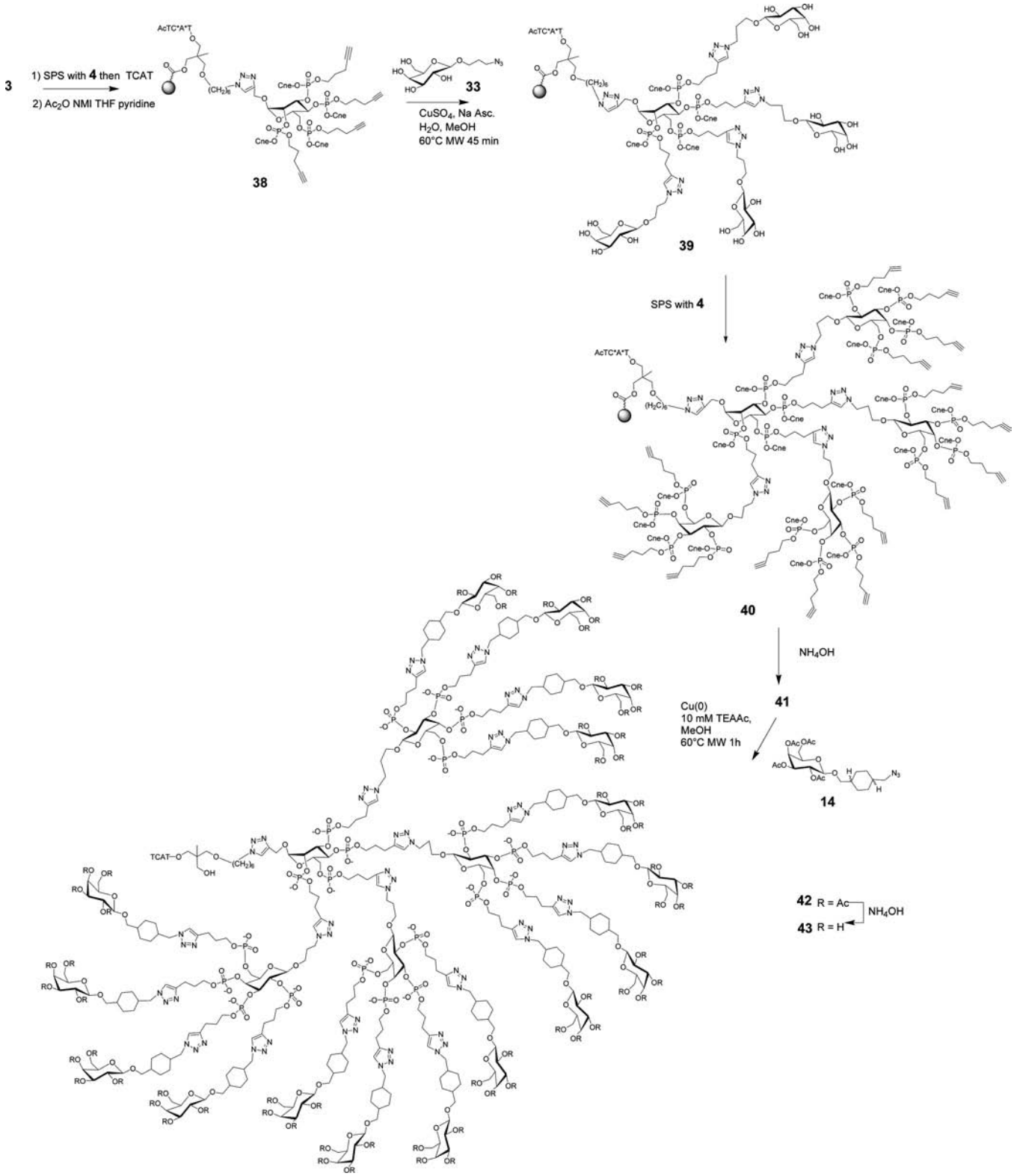
treatment with ammonia for 1 h at room temperature gave the fully deprotected 3′-(mannose-centered tetragalactose) oligonucleotide conjugate **18**.

Starting from **3**, the same protocol was applied using the 6-bromohexyl phosphoramidite **8**, yielding after the elongation of the oligonucleotide, the 3′-[mannose-centered tetra-(6-bromohexylphosphotriester)] oligonucleotide **10** (Scheme 2). This compound was then treated with TMG N_3 in the presence of NaI affording the corresponding 3′-[mannose-centered tetra-(6-azidohexylphosphotriester)] oligonucleotide **11**. In order to have some insights on the efficacy of the click reaction performed on solid support versus in solution, one-half of **11** (∼0.5 μmol) was engaged for an on-solid support click reaction with 1-*O*-propargyl-2,3,4,6-tetra-*O*-acetyl-β-D-galactopyranose **15** (*41*) catalyzed by Cu(I) in water/methanol 1:1 under MW assistance for 1 h at 60 °C. After filtration of the beads and washes, a final ammonia treatment gave the fully deprotected 3′-(mannose-centered tetragalactose) oligonucleotide conjugate **19**.

The second half of **11** was treated with concentrated ammonia affording **13**, which was conjugated in solution with **15** according to the same conditions as those used to synthesize **16**. The resulting acetylated conjugate **17** was purified by HPLC before the hydrolysis of the acetyl groups since the impurities were more easily removed. A final ammonia treatment afforded the expected 3′-(mannose-centered tetragalactose) oligonucleotide conjugate **19**.

5′-End Conjugation. The conjugation of a mannose-centered tetragalactose at the 5′-end of an oligonucleotide proceeded similarly (Scheme 3). The oligonucleotide was synthesized on a DNA synthesizer, and the bromohexyl phosphoramidite **8** was coupled. The bromine atom was substituted with azide using $TMGN_3$ and NaI in DMF affording the solid-supported 5′-

Scheme 5. Second Generation: Synthesis of 3′-Mannose-Centered (Tetragalactose-Centered Hexadecagalactose) Oligonucleotide Conjugate 43[a]



[a] SPS: see the footnote for scheme 2.

azidohexyl oligonucleotide **20**, which was conjugated by click reaction with propargyl mannose **2** catalyzed by Cu(I) under MW at 70 °C (2 × 30 min) to give **21**. The resulting 5′-mannosyl oligonucleotide reacted either with pentynyl or bromohexyl phosphoramidite, affording **22** and **23**, respectively. Bromine atoms of **23** were substituted with azide, leading to **24**. Part of **24** was conjugated by the click reaction with **15** as described above and treated with ammonia for cleavage and deprotection to give the 5′-(mannose-centered tetragalactose) oligonucleotide **30**. The 5′-mannosyl oligonucleotide **22** and the other part of **24** bearing four alkyne functions and four azide functions, respectively, were treated with ammonia, affording **25** and **26**, respectively. They reacted in solution with tetraacetylated galactose azide derivative **14** or propargyl tetraacetylated galactose **15** under Cu(I) catalysis and

MW assistance to form, respectively, the 5′-[mannose-centered tetra(tetraacetylatedgalactose)] oligonucleotide conjugates **27** and **28** exhibiting different linkers between the mannose core and the galactose moiety {4-(phosphodiester-propyl)-1-[(1,4-dimethylcyclohexyl)]-triazole or 1-(phosphodiester-hexyl)-4-(hexyl)-triazole}. After purification by HPLC, the acetyl groups were hydrolyzed by ammonia treatment affording the expected 5′-(mannose-centered tetragalactose) oligonucleotide **29** and **30**, respectively. Here again, we noticed that it was more efficient to purify the conjugates when the acetyl groups are still present since the more lipophilic molecules **29** and **30** are eluted on a HPLC column with a higher retention time than short-mer side products.

Inside Oligonucleotide Conjugation. For the synthesis of the conjugate with the carbohydrate-centered tetragalactose inside the sequence of the oligonucleotide, we proceeded with some small changes in order to minimize the number of steps. Thus, the carbohydrate core was introduced from its azide derivative by reaction with an alkyne function introduced inside the oligonucleotide sequence. The introduction of an alkyne function into the oligonucleotide instead of a bromohexyl group avoided the extra step of the conversion of bromine to azide (Scheme 4).

Starting from a commercially available thymidine solid support, the first part of the oligonucleotide was synthesized, then the alkyne function was introduced using the 1-*O*-(4,4′-dimethoxytrityl)-2-propargyloxymethyl-2-methyl-3-{*O*-[(2-cyanoethyl)-*N*,*N*-diisopropylphosphoramidite]}-1,3-propanediol **31** (*16*), and finally, the second part of the oligonucleotide was elongated, affording the modified oligonucleotide **32** exhibiting propargyl function inside its sequence. Note that the 5′-hydroxyl was capped with Ac_2O to avoid a further reaction with the pentynyl phosphoramidite. The click reaction was performed on solid support using the 1-*O*-(3-azidopropyl)-β-D-galactopyranoside **33** (*64*) under Cu(I) catalysis assisted by MW, affording **34**. The solid-supported oligonucleotide exhibiting the galactose moiety was carefully dried, and the four pentynyl groups were introduced using a DNA synthesizer as described above. In this elongation cycle, the detritylation step was obviously omitted. The expected oligonucleotide **35** with a galactose-centered tetrapentynyldiester moiety was obtained after ammonia treatment. The second click reaction using **14** was performed to synthesize **36** in solution at 70 °C without MW assistance according two protocols: (1) a classic one using $CuSO_4$ and sodium ascorbate in methanol/water and (2) a new one using Cu(0) as the nanopowder (*67*) in methanol/triethylammonium acetate buffer at pH 7.7. Indeed, as previously observed (*16*, *17*, *45*), the click reactions performed in solution can be either done with or without MW assistance with a similar efficiency most of the time when the temperature is similar. Usually, when the click reaction is performed in solution, we observed that more equivalents of copper are required. We assumed that copper could interact with the phosphodiester and the amino function of nucleobases leading to less copper available for catalysis. Furthermore, it is known that the reaction could not proceed at acidic pH since the acidic proton of the alkyne is involved in the mechanism of the catalyzed reaction (*68*). Since oligonucleotides are acidic molecules, we decided to work in a buffer at a pH above 7. Thus, we observed more robust reactions working in the buffer. A phosphate buffer (0.01 M pH 7.3) and a TEAAc buffer (0.01 M pH 7.7) were tried. In both cases, the click reaction was efficient, but the volatile TEAAc buffer was more convenient for workup. After HPLC purification, the acetyl groups were removed by means of ammonia, affording **37**, which was characterized by HPLC and MALTI-TOF MS. Both protocols (i.e., Cu(II) and Cu(0)) gave the same efficiency for the formation of the oligonucleotide glycoconjugate **36** with a similar HPLC profile.

Second Generation: Carbohydrate-Centered Glycodendrimer. Finally, to have some insights on the efficacy of the synthesis of the carbohydrate-centered glycocluster according to this new strategy, we synthesized a dendrimer exhibiting 16 galactoses on its periphery (Scheme 5). Starting from **3**, four pentynyls were introduced on the mannose moiety using phosphoramidite **4**, and a short oligonucleotide TCAT was synthesized with a capping step to protect the 5′-hydroxyl group affording **38**. Then four galactose propylazides **33** were added on the alkyne functions by the click reaction assisted by MW, affording **39**. Pentynyl phosphoramidite **4** was reacted on each of the 16 hydroxyl groups performing an extended coupling (13 min using 160 μmol of **4**, 10 molar equiv/OH) to afford **40** after oxidation. Deprotection with ammonia yielded the fully deprotected TCAT mannose-centered tetra(tetrapentynylphosphodiester galactose) compound **41** in solution. The final click reaction was performed with galactose azide derivative **14** in TEAAc buffer using copper (0) at 60 °C for 60 min under MW yielding **42**, which was directly treated with ammonia affording the fully deprotected oligonucleotide dendrimer **43**, exhibiting 16 galactosyl residues on its periphery. The HPLC profile displays a broad peak due to the presence of cis/trans isomers of the 16 dimethylcyclohexane linkers, and the authenticity of **43** was confirmed by MALDI-TOF MS (see Supporting Information).

CONCLUSIONS

We have designed an efficient and versatile strategy for the synthesis of new carbohydrate-centered glycocluster oligonucleotide conjugates combining click chemistry and phosphoramidite chemistry in a sequential way. Both chemistries are very efficient and yield to quantitative conversion. It is possible to introduce the glycocluster everywhere in the sequence of an oligonucleotide. Finally, a second generation of this glycocluster was performed to synthesize an oligonucleotide conjugated with a carbohydrate-centered glycodendrimer exhibiting 16 galactoses on its periphery. We will apply this strategy to synthesize 5′-fluorescent-3′-carbohydrate-centered galactosyl cluster oligonucleotides bearing different linkers between the galactose moiety and the triazole ring in order to find good inhibitors of the tetrameric lectin PA-IL from *Pseudomonas aeruginosa* (*69*), which recognizes galactose residues (*70*). After the immobilization of the carbohydrate-centered galactosyl cluster oligonucleotide conjugates on a DNA chip by DDI (*50*, *51*), their affinity for PA-IL will be studied. This work is in progress and will be presented elsewhere.

ACKNOWLEDGMENT

This work was financially supported by the CNRS interdisciplinary program “Interface Physique Chimie Biologie: Soutien à la prise de risque”, ANR-08-BLAN-0114-01, Lyon Biopole, and Vaincre la Mucoviscidose. G.P. thanks the CNRS and the Région Languedoc-Roussillon for the award of a research studentship. F.M. is from Inserm.

Supporting Information Available: Protocol to synthesize azide solid support **1** and MALDI-TOF MS and HPLC data of compounds **18**, **19**, **29**, **30**, **37**, **43**. This material is available free of charge via the Internet at http://pubs.acs.org.

LITERATURE CITED

(1) Varki, A. (1993) Biological roles of oligosaccharides: all of the theories are correct. *Glycobiology 3*, 97–130.

(2) Lis, H., and Sharon, N. (1998) Lectins: carbohydrate-specific proteins that mediate cellular recognition. *Chem. Rev. 98*, 637–674.

(3) Bertozzi, C. R., and Kiessling, L. L. (2001) Chemical glycobiology. *Science 291*, 2357–2364.
(4) Seeberger, P. H., and Werz, D. B. (2007) Synthesis and medical applications of oligosaccharides. *Nature 446*, 1046–1051.
(5) Ernst, B., and Magnani, J. L. (2009) From carbohydrate leads to glycomimetic drugs. *Nature Rev. Drug Discovery 8*, 661–677.
(6) Lee, Y. C., and Lee, R. T. (1995) Carbohydrate-protein interactions: basis of glycobiology. *Acc. Chem. Res. 28*, 321–327.
(7) Lee, Y. C., Townsend, R. R., Hardy, M. R., Lonngren, J., Arnarp, J., Haraldsson, M., and Lonn, H. (1983) Binding of synthetic oligosaccharides to the hepatic Gal Galnac lectin-dependence on fine-structural features. *J. Biol. Chem. 258*, 199–202.
(8) Lundquist, J. J., and Toone, E. J. (2002) The cluster glycoside effect. *Chem. Rev. 102*, 555–578.
(9) Morvan, F., Meyer, A., Jochum, A., Sabin, C., Chevolot, Y., Imberty, A., Praly, J. P., Vasseur, J. J., Souteyrand, E., and Vidal, S. (2007) Fucosylated pentaerythrityl phosphodiester oligomers (PePOs): automated synthesis of DNA-based glycoclusters and binding to *Pseudomonas aeruginosa* lectin (PA-IIL). *Bioconjugate Chem. 18*, 1637–1643, and references therein.
(10) Chabre, Y. M., and Roy, R. (2008) Recent trends in glycodendrimer syntheses and applications. *Curr. Top. Med. Chem. 8*, 1237–1285.
(11) Imberty, A., Chabre, Y. M., and Roy, R. (2008) Glycomimetics and glycodendrimers as high affinity microbial antiadhesins. *Chem.—Eur. J. 14*, 7490–7499.
(12) Renaudet, O. (2008) Recent advances on cyclopeptide-based glycoclusters. *Mini-Rev. Org. Chem. 5*, 274–286.
(13) Deguise, I., Lagnoux, D., and Roy, R. (2007) Synthesis of glycodendrimers containing both fucoside and galactoside residues and their binding properties to Pa-IL and PA-IIL lectins from *Pseudomonas aeruginosa*. *New J. Chem. 31*, 1321–1331.
(14) Marotte, K., Eville, C. P., Sabin, C., Pymbock, M. M., Imberty, A., and Roy, R. (2007) Synthesis and binding properties of divalent and trivalent clusters of the Lewis a disaccharide moiety to *Pseudomonas aeruginosa* lectin PA-IIL. *Org. Biomol. Chem. 5*, 2953–2961.
(15) Touaibia, M., and Roy, R. (2008) First synthesis of "majoral-type" glycodendrimers bearing covalently bound alpha-D-mannopyranoside residues onto a hexachlocyclotriphosphazene core. *J. Org. Chem. 73*, 9292–9302.
(16) Pourceau, G., Meyer, A., Vasseur, J. J., and Morvan, F. (2008) Combinatorial and automated synthesis of phosphodiester galactosyl cluster on solid support by click chemistry assisted by microwaves. *J. Org. Chem. 73*, 6014–6017.
(17) Pourceau, G., Meyer, A., Vasseur, J. J., and Morvan, F. (2009) Synthesis of mannose and galactose oligonucleotide conjugates by bi-click chemistry. *J. Org. Chem. 74*, 1218–1222.
(18) Moni, L., Pourceau, G., Zhang, J., Meyer, A., Vidal, S., Souteyrand, E., Dondoni, A., Morvan, F., Chevolot, Y., Vasseur, J. J., and Marra, A. (2009) Design of triazole-tethered glycoclusters exhibiting three different spatial arrangements and comparative study of their affinities towards PA-IL and RCA 120 by using a DNA-based glycoarray. *ChemBioChem 10*, 1369–1378.
(19) Leyden, R., Velasco-Torrijos, T., Andre, S., Gouin, S., Gabius, H.-J., and Murphy, P. V. (2009) Synthesis of bivalent lactosides based on terephthalamide, N,N′-diglucosylterephthalamide, and glycophane scaffolds and assessment of their inhibitory capacity on medically relevant lectins. *J. Org. Chem. 74*, 9010–9026.
(20) Oka, H., Onaga, T., Koyama, T., Guo, C. T., Suzuki, Y., Esumi, Y., Hatano, K., Terunuma, D., and Matsuoka, K. (2009) Syntheses and biological evaluations of carbosilane dendrimers uniformly functionalized with sialyl alpha(2 → 3) lactose moieties as inhibitors for human influenza viruses. *Bioorg. Med. Chem. 17*, 5465–5475.
(21) Perez-Balderas, F., Morales-Sanfrutos, J., Hernandez-Mateo, F., Isac-Garcia, J., and Santoyo-Gonzalez, F. (2009) Click multivalent homogeneous neoglycoconjugates: synthesis and evaluation of their binding affinities. *Eur. J. Org. Chem.* , 2441–2453.
(22) Sakamoto, J. I., Koyama, T., Miyamoto, D., Yingsakmongkon, S., Hidari, K., Jampangern, W., Suzuki, T., Suzuki, Y., Esumi, Y., Nakamura, T., Hatano, K., Terunuma, D., and Matsuoka, K. (2009) Systematic syntheses of influenza neuraminidase inhibitors: a series of carbosilane dendrimers uniformly functionalized with thioglycoside-type sialic acid moieties. *Bioorg. Med. Chem. 17*, 5451–5464.
(23) Schierholt, A., Shaikh, H. A., Schmidt-Lassen, J., and Lindhorst, T. K. (2009) Utilizing Staudinger ligation for the synthesis of glycoamino acid building blocks and other glycomimetics. *Eur. J. Org. Chem.* , 3783–3789.
(24) Singh, Y., Renaudet, O., Defrancq, E., and Dumy, P. (2005) Preparation of a multitopic glycopeptide-oligonucleotide conjugate. *Org. Lett. 7*, 1359–1362.
(25) Virta, P., Karskela, M., and Lonnberg, H. (2006) Orthogonally protected cyclo-beta-tetrapeptides as solid-supported scaffolds for the synthesis of glycoclusters. *J. Org. Chem. 71*, 1989–1999.
(26) Renaudet, O., and Dumy, P. (2004) Chemoselectively template-assembled glycopeptide presenting clustered cancer related T-antigen. *Tetrahedron Lett. 45*, 65–68.
(27) Grigalevicius, S., Chierici, S., Renaudet, O., Lo-Man, R., Deriaud, E., Leclerc, C., and Dumy, P. (2005) Chemoselective assembly and immunological evaluation of multiepitopic glycoconjugates bearing clustered Tn antigen as synthetic anticancer vaccines. *Bioconjugate Chem. 16*, 1149–1159.
(28) Renaudet, O., Boturyn, D., and Dumy, P. (2009) Biomolecular assembly by iterative oxime ligations. *Bioorg. Med. Chem. Lett. 19*, 3880–3883.
(29) Chen, Y. X., Zhao, L., Huang, Z. P., Zhao, Y. F., and Li, Y. M. (2009) Facile synthesis of cyclopeptide-centered multivalent glycoclusters with 'click chemistry' and molecular recognition study by surface plasmon resonance. *Bioorg. Med. Chem. Lett. 19*, 3775–3778.
(30) Ortega-Munoz, M., Morales-Sanfrutos, J., Perez-Balderas, F., Hernandez-Mateo, F., Giron-Gonzalez, M. D., Sevillano-Tripero, N., Salto-Gonzalez, R., and Santoyo-Gonzalez, F. (2007) Click multivalent neoglycoconjugates as synthetic activators in cell adhesion and stimulation of monocyte/machrophage cell lines. *Org. Biomol. Chem. 5*, 2291–2301.
(31) Touaibia, M., Shiao, T. C., Papadopoulos, A., Vaucher, J., Wang, Q. G., Benhamioud, K., and Roy, R. (2007) Tri- and hexavalent mannoside clusters as potential inhibitors of type 1 fimbriated bacteria using pentaerythritol and triazole linkages. *Chem. Commun.* , 380–382.
(32) Baldini, L., Casnati, A., Sansone, F., and Ungaro, R. (2007) Calixarene-based multivalent ligands. *Chem. Soc. Rev. 36*, 254–266.
(33) Andre, S., Sansone, F., Kaltner, H., Casnati, A., Kopitz, J., Gabius, H. J., and Ungaro, R. (2008) Calix[n]arene-based glycoclusters: Bioactivity of thiourea-linked galactose/lactose moieties as inhibitors of binding of medically relevant lectins to a glycoprotein and cell-surface glycoconjugates and selectivity among human adhesion/growth-regulatory galectins. *ChemBioChem 9*, 1649–1661.
(34) Vecchi, A., Melai, B., Marra, A., Chiappe, C., and Dondoni, A. (2008) Microwave-enhanced ionothermal CuAAC for the synthesis of glycoclusters on a calix[4]arene platform. *J. Org. Chem. 73*, 6437–6440.
(35) Cecioni, S., Lalor, R., Blanchard, B., Praly, J. P., Imberty, A., Matthews, S. E., and Vidal, S. (2009) Achieving high affinity towards a bacterial lectin through multivalent topological isomers of calix[4]arene glycoconjugates. *Chem.—Eur. J. 15*, 13232–13240.
(36) Fiore, M., Chambery, A., Marra, A., and Dondoni, A. (2009) Single and dual glycoside clustering around calix[4]arene scaffolds via click thiol-ene coupling and azide-alkyne cycloaddition. *Org. Biomol. Chem. 7*, 3910–3913.
(37) Kieburg, C., Dubber, M., and Lindhorst, T. K. (1997) A new type of carbohydrate clustering: synthesis of a pentavalent glycocluster based on a carbohydrate core. *Synlett* , 1447–1449.
(38) Dubber, M., and Lindhorst, T. K. (2001) Trehalose-based octopus glycosides for the synthesis of carbohydrate-centered

PAMAM dedrimers and thiourea-bridged glycoclusters. *Org. Lett. 3*, 4019–4022.

(39) Lindhorst, T. K. (2002) Artificial multivalent sugar ligands to understand and manipulate carbohydrate-protein interactions. *Host-Guest Chem. 218*, 201–235.

(40) Gao, Y. J., Eguchi, A., Kakehi, K., and Lee, Y. C. (2005) Synthesis and molecular recognition of carbohydrate-centered multivalent glycoclusters by a plant lectin RCA(120). *Bioorg. Med. Chem. 13*, 6151–6157.

(41) Hasegawa, T., Numata, M., Okumura, S., Kimura, T., Sakurai, K., and Shinkai, S. (2007) Carbohydrate-appended curdlans as a new family of glycoclusters with binding properties both for a polynucleotide and lectins. *Org. Biomol. Chem. 5*, 2404–2412.

(42) Gouin, S. G., Vanquelef, E., Fernandez, J. M. G., Mellet, C. O., Dupradeau, F. Y., and Kovensky, J. (2007) Multimannosides based on a carbohydrate scaffold: synthesis, force field development, molecular dynamics studies, and binding affinities for lectin Con A. *J. Org. Chem. 72*, 9032–9045.

(43) Ortega-Munoz, M., Perez-Balderas, F., Morales-Sanfrutos, J., Hernandez-Mateo, F., Isac-Garcia, J., and Santoyo-Gonzalez, F. (2009) Click multivalent heterogeneous neoglycoconjugates: modular synthesis and evaluation of their binding affinities. *Eur. J. Org. Chem.* , 2454–2473.

(44) Kohn, M., Benito, J. M., Mellet, C. O., Lindhorst, T. K., and Fernandez, J. M. G. (2004) Functional evaluation of carbohydrate-centred glycoclusters by enzyme-linked lectin assay: ligands for concanavalin A. *ChemBioChem 5*, 771–777.

(45) Pourceau, G., Meyer, A., Vasseur, J. J., and Morvan, F. (2009) Azide solid support for 3′-conjugation of oligonucleotides and their circularization by click chemistry. *J. Org. Chem. 74*, 6837–6842.

(46) Beaucage, S. L., and Caruthers, M. H. (1981) Deoxynucleoside phosphoramidites: a new class of key intermediates for deoxypolynucleotide synthesis. *Tetrahedron Lett. 22*, 1859–1862.

(47) Rostovtsev, V. V., Green, L. G., Fokin, V. V., and Sharpless, K. B. (2002) A stepwise Huisgen cycloaddition process: copper(I)-catalyzed regioselective "ligation" of azides and terminal alkynes. *Angew. Chem., Int. Ed. 41*, 2596–2599.

(48) Tornoe, C. W., Christensen, C., and Meldal, M. (2002) Peptidotriazoles on solid phase: [1,2,3]-triazoles by regiospecific copper(I)-catalyzed 1,3-dipolar cycloadditions of terminal alkynes to azides. *J. Org. Chem. 67*, 3057–3064.

(49) Wacker, R., and Niemeyer, C. M. (2004) DDI-mu FIA: a readily configurable microarray-fluorescence immunoassay based on DNA-directed immobilization of proteins. *ChemBioChem 5*, 453–459.

(50) Chevolot, Y., Bouillon, C., Vidal, S., Morvan, F., Meyer, A., Cloarec, J. P., Jochum, A., Praly, J. P., Vasseur, J. J., and Souteyrand, E. (2007) DNA-based carbohydrate biochips: A platform for surface glyco-engineering. *Angew. Chem., Int. Ed. 46*, 2398–2402.

(51) Zhang, J., Pourceau, G., Meyer, A., Vidal, S., Praly, J. P., Souteyrand, E., Vasseur, J. J., Morvan, F., and Chevolot, Y. (2009) DNA-directed immobilisation of glycomimetics for glycoarrays application: Comparison with covalent immobilisation, and development of an on-chip IC50 measurement assay. *Biosens. Bioelec. 24*, 2515–2521.

(52) Matsuura, K., Hibino, M., Yamada, Y., and Kobayashi, K. (2001) Construction of glyco-clusters by self-organization of site-specifically glycosylated oligonucleotides and their cooperative amplification of lectin-recognition. *J. Am. Chem. Soc. 123*, 357–358.

(53) Forget, D., Renaudet, O., Defrancq, E., and Dumy, P. (2001) Efficient preparation of carbohydrate-oligonucleotide conjugates (COCs) using oxime bond formation. *Tetrahedron Lett. 42*, 7829–7832.

(54) Dubber, M., and Frechet, J. M. J. (2003) Solid-phase synthesis of multivalent glycoconjugates on a DNA synthesizer. *Bioconjugate Chem. 14*, 239–246.

(55) Katajisto, J., Heinonen, P., and Lonnberg, H. (2004) Solid-phase synthesis of oligonucleotide glycoconjugates bearing three different glycosyl groups: orthogonally protected bis(hydroxymethyl)-N,N′-bis(3-hydroxypropyl)malondiamide phosphoramidite as key building block. *J. Org. Chem. 69*, 7609–7615.

(56) Katajisto, J., Virta, P., and Lonnberg, H. (2004) Solid-phase synthesis of multiantennary oligonucleotide glycoconjugates utilizing on-support oximation. *Bioconjugate Chem. 15*, 890–896.

(57) D'Onofrio, J., de Champdore, M., De Napoli, L., Montesarchio, D., and Di Fabio, G. (2005) Glycomimetics as decorating motifs for oligonucleotides: solid-phase synthesis, stability, and hybridization properties of carbopeptoid-oligonucleotide conjugates. *Bioconjugate Chem. 16*, 1299–1309.

(58) Meyer, A., Bouillon, C., Vidal, S., Vasseur, J. J., and Morvan, F. (2006) A versatile reagent for the synthesis of 5′-phosphorylated, 5′-thiophosphorylated or 5′-phosphoramidate-conjugated oligonucleotides. *Tetrahedron Lett. 47*, 8867–8871.

(59) Bouillon, C., Meyer, A., Vidal, S., Jochum, A., Chevolot, Y., Cloarec, J. P., Praly, J. P., Vasseur, J. J., and Morvan, F. (2006) Microwave assisted "click" chemistry for the synthesis of multiple labeled-carbohydrate oligonucleotides on solid support. *J. Org. Chem. 71*, 4700–4702.

(60) Karskela, M., Virta, P., Malinen, M., Urtti, A., and Lonnberg, H. (2008) Synthesis and cellular uptake of fluorescently labeled multivalent hyaluronan disaccharide conjugates of oligonucleotide phosphorothioates. *Bioconjugate Chem. 19*, 2549–2558.

(61) D'Onofrio, J., Petraccone, L., Martino, L., Di Fabio, G., Iadonisi, A., Balzarini, J., Giancola, C., and Montesarchio, D. (2008) Synthesis, biophysical characterization, and anti-HIV activity of glyco-conjugated G-quadruplex-forming oligonucleotides. *Bioconjugate Chem. 19*, 607–616.

(62) Kiviniemi, A., Virta, P., and Lonnberg, H. (2008) Utilization of intrachain 4′-C-azidomethylthymidine for preparation of oligodeoxyribonucleotide conjugates by click chemistry in solution and on a solid support. *Bioconjugate Chem. 19*, 1726–1734.

(63) Karskela, M., Helkearo, M., Virta, P., and Lonnberg, H. (2010) Synthesis of oligonucleotide glycoconjugates using sequential click and oximation ligations. *Bioconjugate Chem. 21*, 748–755.

(64) Joosten, J. A. F., Loimaranta, V., Appeldoorn, C. C. M., Haataja, S., El Maate, F. A., Liskamp, R. M. J., Finne, J., and Pieters, R. J. (2004) Inhibition of *Streptococcus suis* adhesion by dendritic galabiose compounds at low nanomolar concentration. *J. Med. Chem. 47*, 6499–6508.

(65) Lietard, J., Meyer, A., Vasseur, J. J., and Morvan, F. (2007) An efficient reagent for 5′-azido oligonucleotide synthesis. *Tetrahedron Lett. 48*, 8795–8798.

(66) Lietard, J., Meyer, A., Vasseur, J. J., and Morvan, F. (2008) New strategies for cyclization and bicyclization of oligonucleotides by click chemistry assisted by microwaves. *J. Org. Chem. 73*, 191–200.

(67) Montagnat, O. D., Lessene, G., and Hughes, A. B. (2006) Synthesis of azide-alkyne fragments for 'click' chemical applications formation of oligomers from orthogonally protected trialkylsilyl-propargyl azides and propargyl alcohols. *Tetrahedron Lett. 47*, 6971–6974.

(68) Himo, F., Lovell, T., Hilgraf, R., Rostovtsev, V. V., Noodleman, L., Sharpless, K. B., and Fokin, V. V. (2005) Copper(I)-catalyzed synthesis of azoles. DFT study predicts unprecedented reactivity and intermediates. *J. Am. Chem. Soc. 127*, 210–216.

(69) Cioci, G., Mitchell, E. P., Gautier, C., Wimmerova, M., Sudakevitz, D., Perez, S., Gilboa-Garber, N., and Imberty, A. (2003) Structural basis of calcium and galactose recognition by the lectin PA-IL of Pseudomonas aeruginosa. *FEBS Lett. 555*, 297–301.

(70) Imberty, A., Wimmerova, M., Mitchell, E. P., and Gilboa-Garber, N. (2004) Structures of the lectins from Pseudomonas aeruginosa: insights into the molecular basis for host glycan recognition. *Microbes Infect. 6*, 221–228.

BC1001888

Supporting information

Oligonucleotide Carbohydrate-Centered Galactosyl Cluster Conjugates Synthesized by Click and Phosphoramidite Chemistries

Gwladys Pourceau,† Albert Meyer,† Yann Chevolot,‡ Eliane Souteyrand,‡ Jean-Jacques Vasseur,† and François Morvan†

†Institut des Biomolécules Max Mousseron (IBMM), UMR 5247 CNRS - Université Montpellier 1 - Université Montpellier 2, Place Eugène Bataillon, CC1704, 34095 Montpellier Cedex 5, France, ‡Institut des Nanotechnologies de Lyon (INL), UMR 5270 CNRS Ecole Centrale de Lyon, 36 avenue Guy de Collongue, 69134 Ecully cedex, France

AUTHOR EMAIL ADDRESS: morvan@univ-montp2.fr

Table of contents

General remarks on HPLC analysis, purification and MS characterization S2

Synthesis of (4-CPG-long chain alkyl-carbamoylmethoxy-phenoxy)acetic Acid 2-(4-Azido-butoxymethyl)-3-(4,4'-dimethoxytrityloxymethyl)- 2-methylpropyl Ester 1 ..... S2

^{1}H and ^{13}C NMR spectra of S2 in $CDCl_3$ S4

HPLC profiles and MALDI-TOF spectra of purified oligonucleotide carbohydrate-centered galactosyl clusters S5

General remarks on HPLC analysis, purification and MS characterization

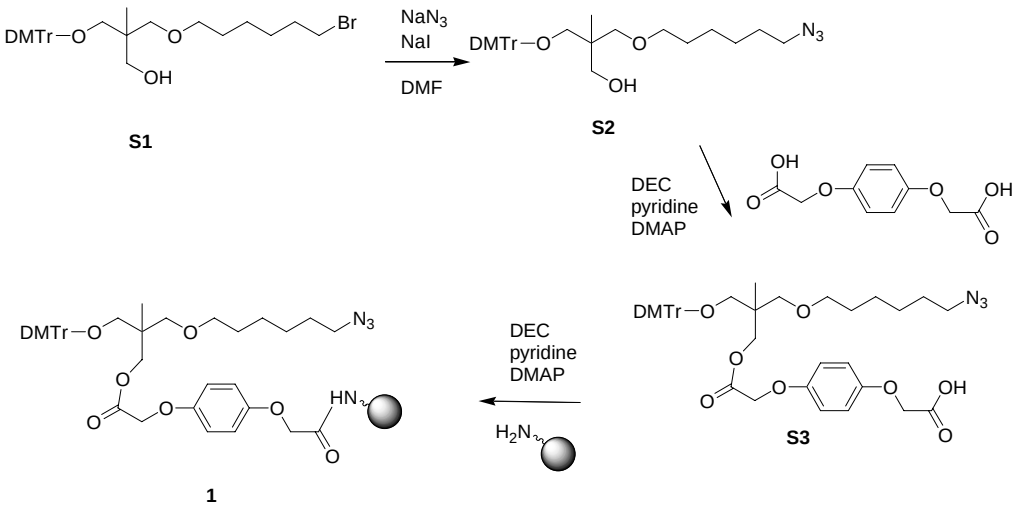
High performance liquid chromatography (HPLC) purifications were performed on a Waters Millipore instrument equipped with a reodyn injector a 600S controller and a Model 996 photodiode array detector. HPLC analyses were performed on a Dionex Ultimate 3000 instrument equipped with a reodyn injector and a photometer DAD 3000.

For analyses, a reverse phase C18 Nucleosil (5 μm) column (150× 4.6 mm; Macherey-Nagel, Germany) was used at a flow rate of 1 mL min^{-1} using a linear gradient of acetonitrile 6% to 24% in 0.05 M aqueous triethylammonium acetate (pH 7) for 20 min.

For purifications, a reverse phase C18 Delta Pak (15 μm) column (7.8× 300 mm; Waters, Japan) was used at a flow rate of 2 mL min^{-1} using a linear gradient of acetonitrile 32% to 44% in 0.05 M aqueous triethylammonium acetate (pH 7) for 15 min for oligonucleotides **16** and **27**, 24% to 40% in 0.05 M aqueous triethylammonium acetate (pH 7) for 15 min for oligonucleotides **17** and **28**, 11% to 18% in 0.05 M aqueous triethylammonium acetate (pH 7) for 15 min for oligonucleotides **19** and **30** and 5 to 40% for 20 min for oligonucleotide **43**.

MALDI-TOF mass spectra were recorded on a Voyager mass spectrometer (Perspective Biosystems, Framingham, MA) equipped with a nitrogen laser. MALDI conditions were: accelerating voltage 24000V; guide wire 0.05% of the accelerating voltage; grid voltage 94% of the accelerating voltage; delay extraction time 500 ns. 1 μL of sample was mixed with 5 μL of a saturated solution of THAP in acetonitrile/water (1:1, v/v) containing 10% of ammonium citrate and few beads of DOWEX 50W-X8 ammonium sulfonic acid resin were added. Then, 1 μL of the mixture was placed on a plate and dried at room temperature and pressure.

Synthesis of (4-CPG-long chain alkyl-carbamoylmethoxy-phenoxy)acetic Acid 2-(4-Azido-butoxymethyl)-3-(4,4'-dimethoxytrityloxymethyl)- 2-methylpropyl Ester 1

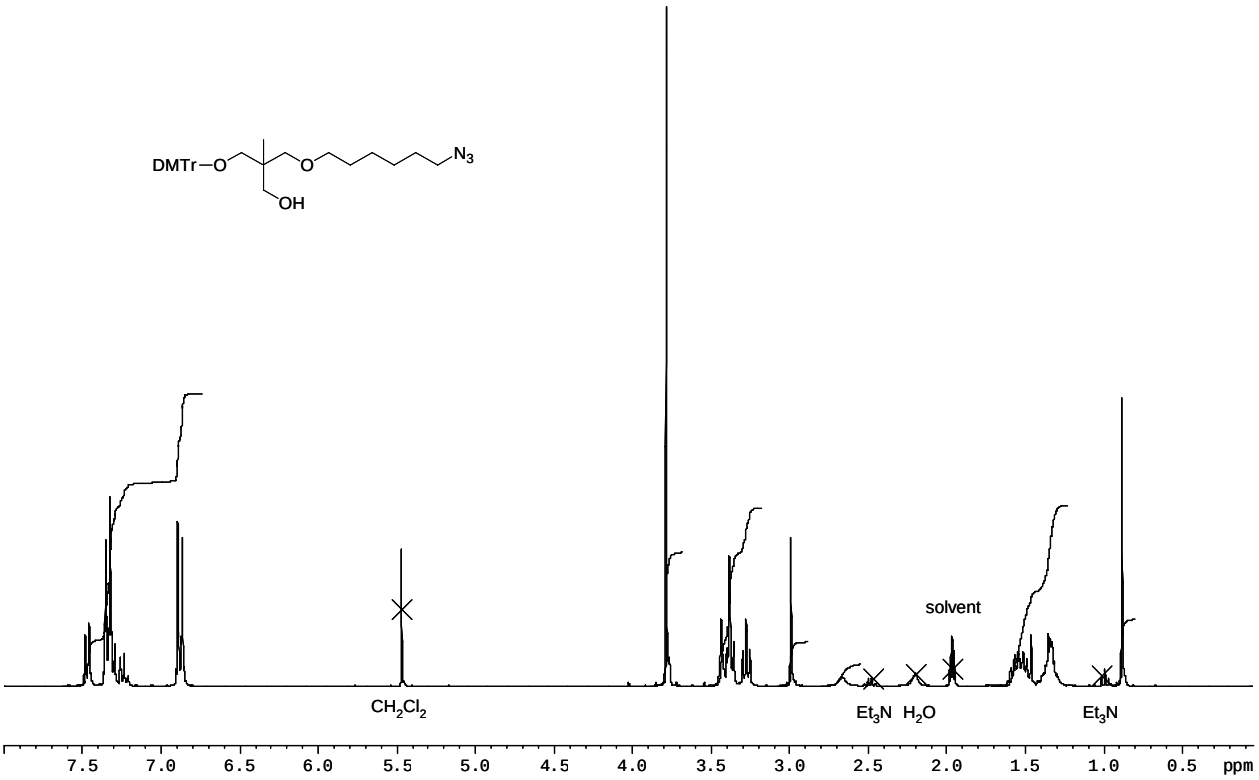


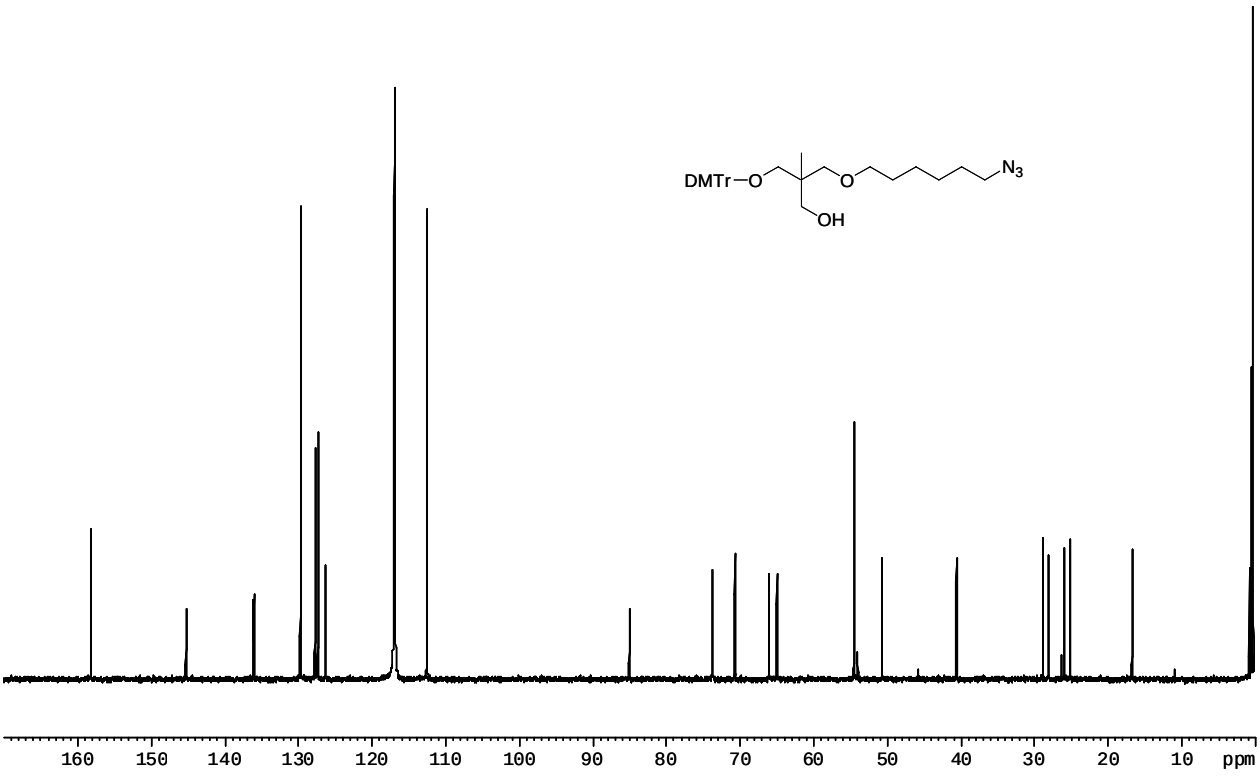
1-*O*-(4,4′-Dimethoxytrityl)-2-(6-azidohexyloxymethyl)-2-methyl-1,3-propanediol S2. 1-*O*-(4,4′-Dimethoxytrityl)-2-(6-bromohexyloxymethyl)-2-methyl-1,3-propanediol S1 (*1*) (1.17 g, 2 mmol) was dried three times by coevaporation with anhydrous acetonitrile and then dissolved in anhydrous acetonitrile (5 mL) before addition of tetramethylguanidinium azide (949 mg, 6 mmol). The reaction was stirred for 3 hr at 50°C, and then diluted with 50 mL of CH_2Cl_2. The organic layer was washed with brine (2 x 70 mL), dried over Na_2SO_4, and evaporated. The crude product was purified by silica gel column chromatography (0 to 30% EtOAc in cyclohexane containing 1 % triethylamine) to afford **S2** (52%) as clear oil. *Rf* : 0.4 (cyclohexane/EtOAc 85:15 v/v). ^{1}H NMR (CD_3CN, 300 MHz): 0.90 (3H, s, -C$\underline{H}_3$), 1.29-1.59 (8H, m, -O-CH$_2$-(C$\underline{H}_2$)$_4$-CH2-N), 2.67 (1H, br s, -O$\underline{H}$), 2.99 (2H, s, DMTr-O-C$\underline{H}_2$-), 3.28 (2H, t, J=6.9 Hz, -C$\underline{H}_2$-N$_3$), 3.36-3.44 (6H, m, -C$\underline{H}_2$-OH,-C$\underline{H}_2$-O-C$\underline{H}_2$-), 3.77 (6H, s, -O-C$\underline{H}_3$), 6.86-7.49 (13H, m, C$\underline{H}_{Ar}$). ^{13}C NMR (CD_3CN, 75 MHz): 16.8, 25.1, 25.9, 28.1, 28.9, 40.6, 50.8, 54.5, 65.0, 66.1, 70.7, 73.8, 85.1, 112.6, 126.3, 127.4, 127.8, 129.8, 136.0, 145.3, 158.2. HRMS ESI (positive mode) *m/z*: calcd for $C_{32}H_{41}N_3O_5Na$ $[M+Na]^+$ 570.2944, found 570.2955.

1-*O*-(4,4′-Dimethoxytrityl)-2-(6-azidohexyloxymethyl)-2-methyl-1,3-propanediol-3-*O*-hydroquinone-*O,O'*-diacetyl CPG S3. Compound **S2** (344 mg, 0.63 mmol) was dissolved in 5 mL dry pyridine with hydroquinone-*O,O'*-diacetic acid (170.5 mg, 0.75 mmol), DMAP (15.4 mg, 0.13 mmol), 1-(3-Dimethylaminopropyl)-3-EthylCarbodiimide DEC (120.2 mg, 0.63 mmol) and stirred at rt overnight. Pyridine was evaporated and the residue was redissolved in CH_2Cl_2 and washed with water (three times). The crude product was purified by silica gel column chromatography (0.5 to 10% MeOH in CH_2Cl_2 containing 1 % pyridine) to afford **S3** (Yield 23%) which was directly anchored on CPG using DMAP (10 mg), DEC (120mg) dry Et_3N (80 µL) in dry pyridine and shacked overnight. After filtration and drying the solid support **1** was capped using Cap A and Cap B solution for 1h. Loading was determined by trityl assay: 61 µmol/g

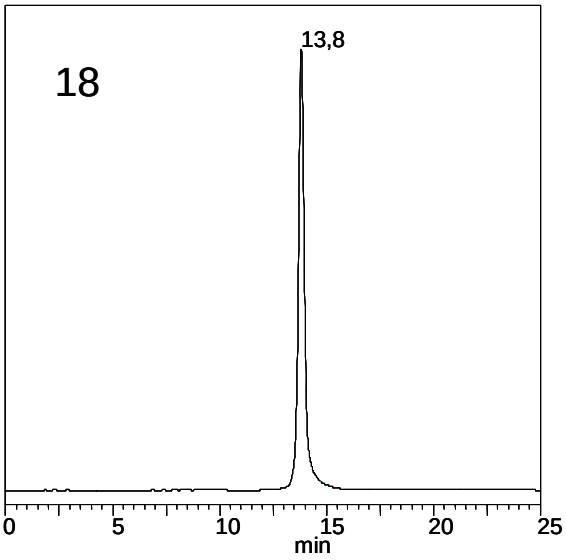
(1) Pourceau, G., Meyer, A., Vasseur, J. J., and Morvan, F. (2009) Synthesis of Mannose and Galactose Oligonucleotide Conjugates by Bi-click chemistry. *J. Org. Chem. 74*, 1218-1222.

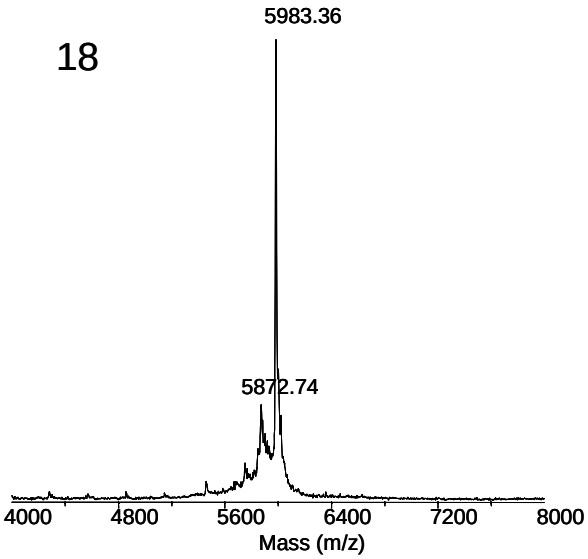
^{1}H and ^{13}C NMR spectra of S2 in $CDCl_3$

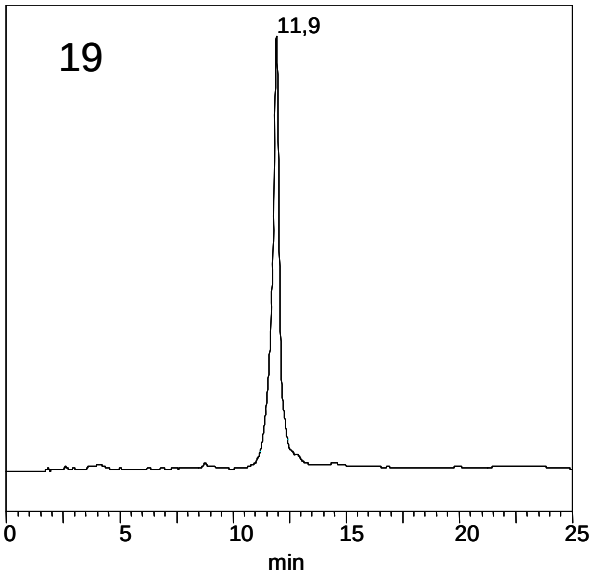




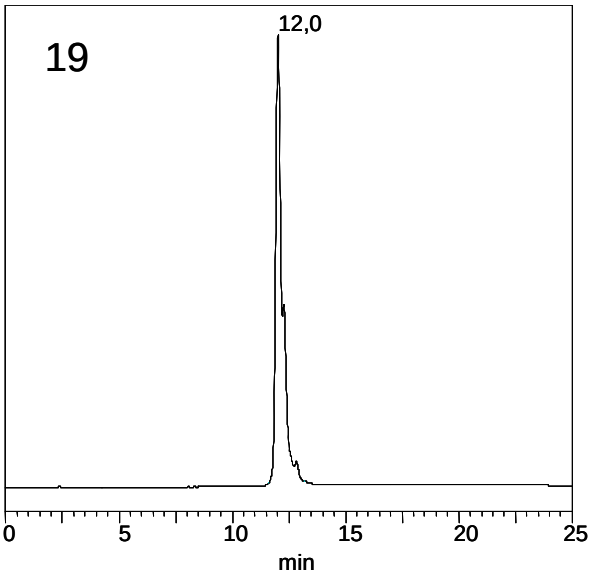
HPLC profiles and MALDI-TOF spectra of purified oligonucleotide carbohydrate-centered galactosyl clusters



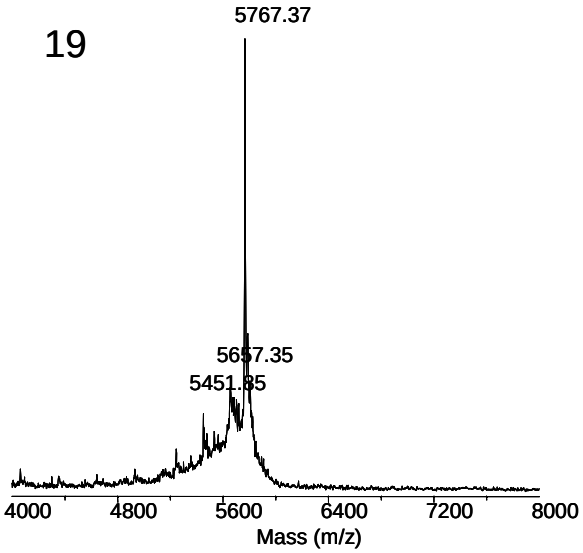




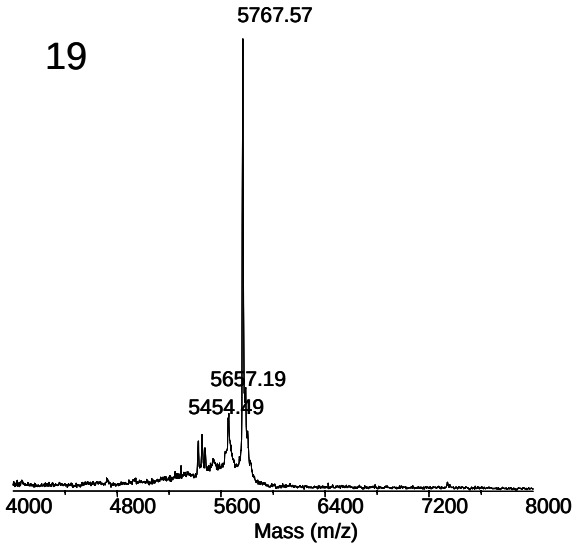
Click performed in solution



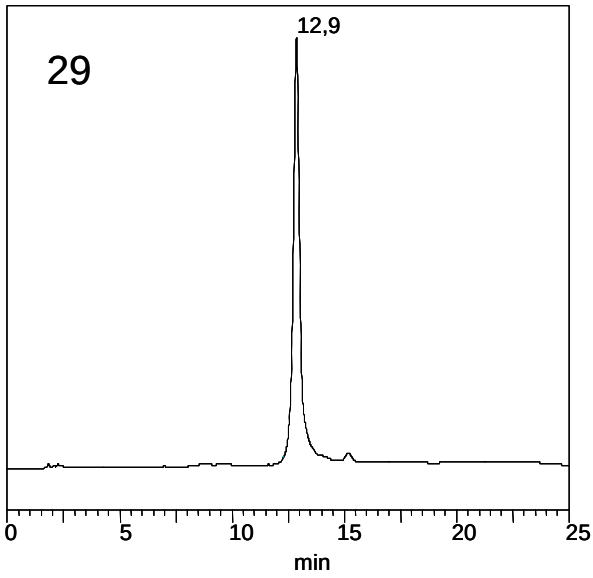
Click performed on solid support

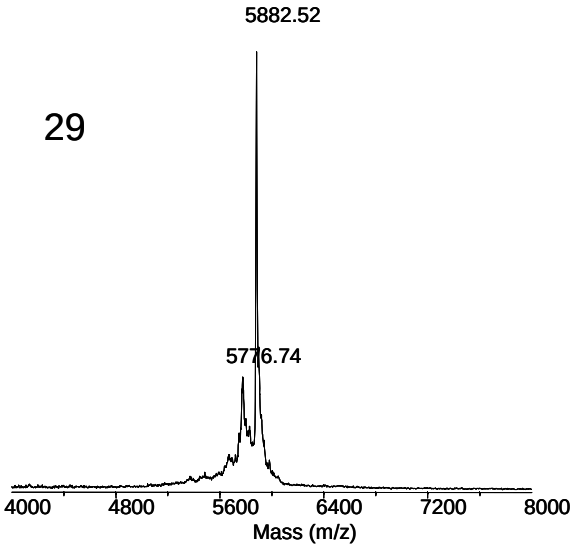


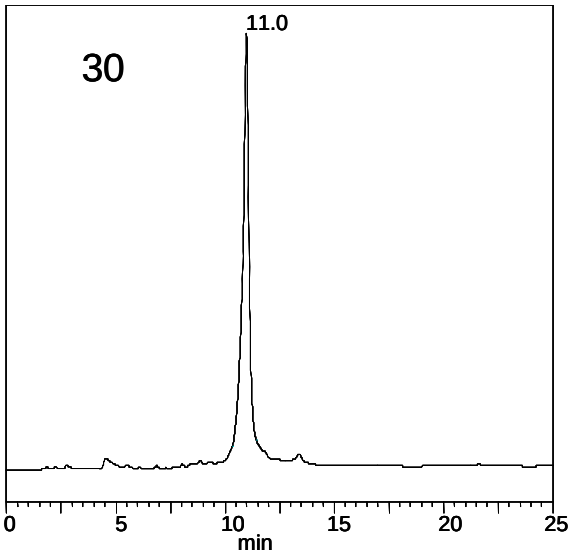
Click performed in solution



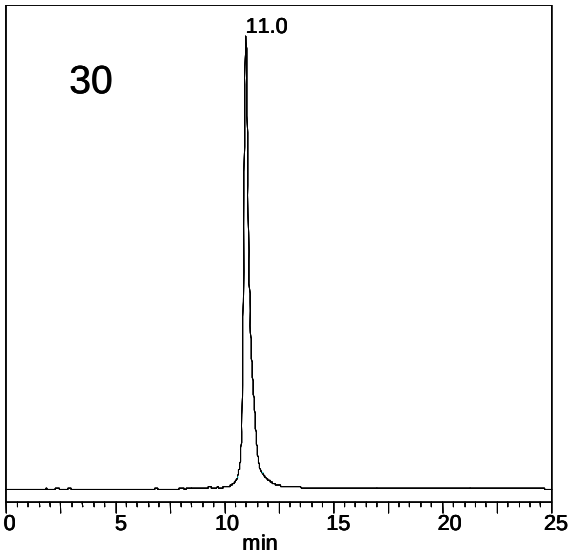
Click performed on solid support



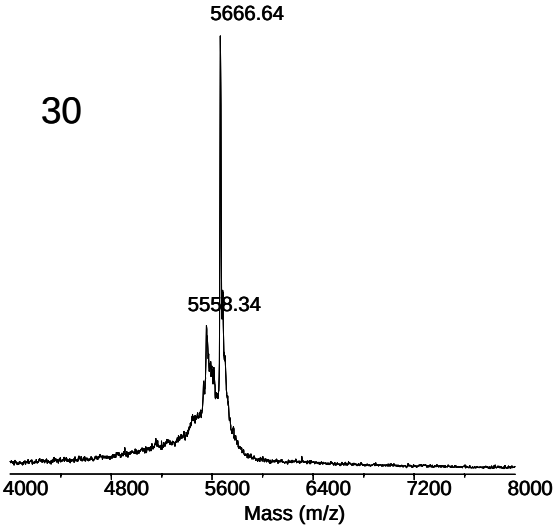




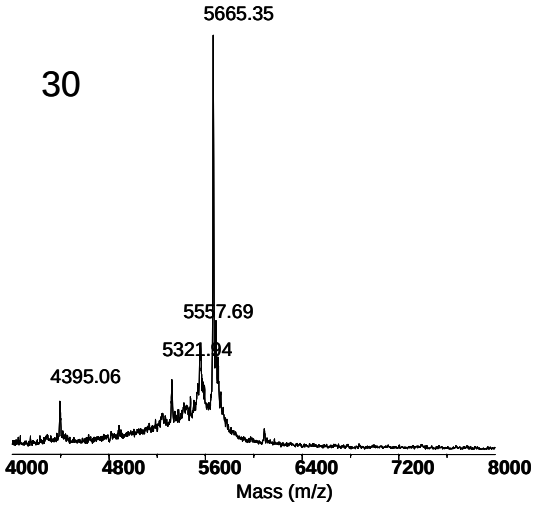
Click performed in solution



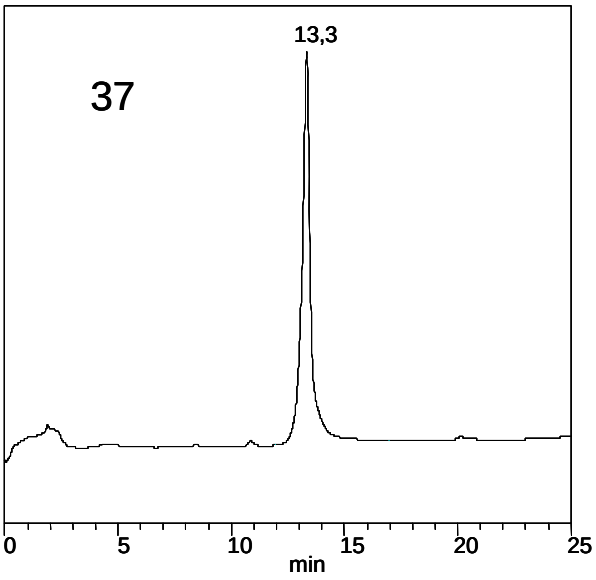
Click performed on solid support

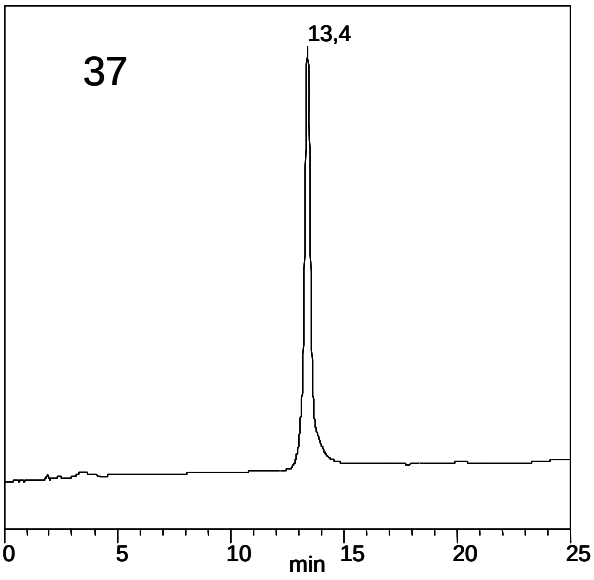


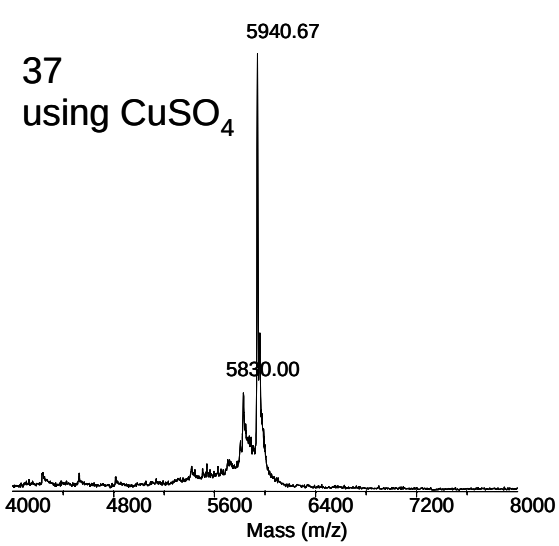
Click performed in solution



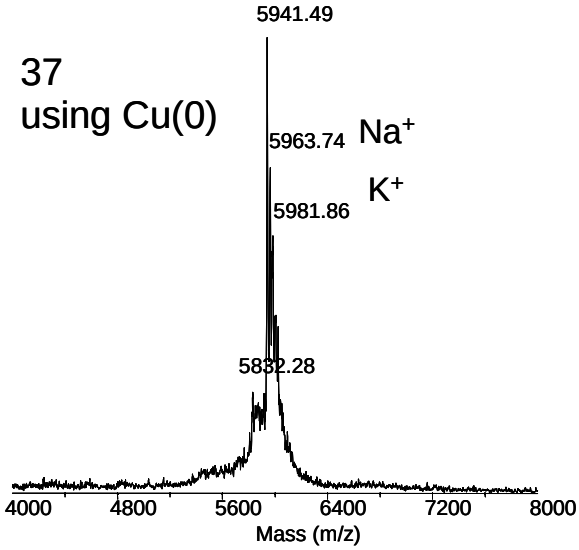
Click performed on solid support



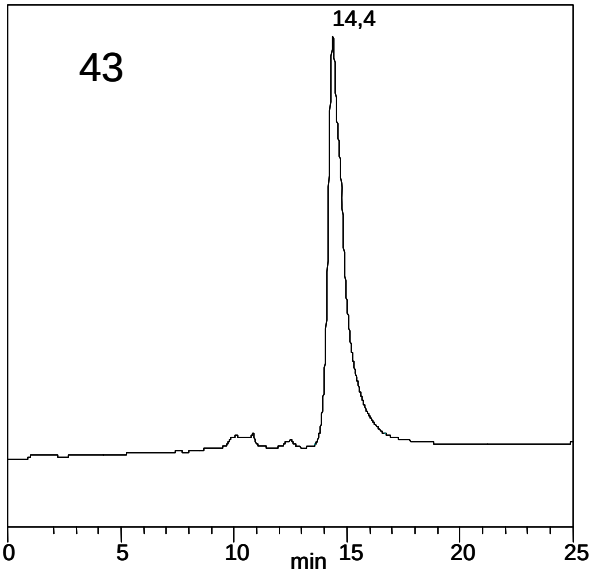


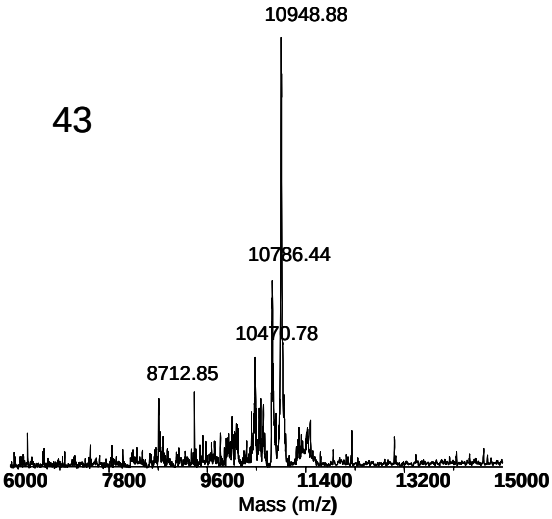


Click performed with $CUSO_4$ Na ascorbate



Click performed with Cu(0)





Effective Stabilization and Delivery of siRNA: Reversible siRNA−Phospholipid Conjugate in Nanosized Mixed Polymeric Micelles

Tiziana Musacchio,[†] Onkar Vaze,[†] Gerard D'Souza,[‡] and Vladimir P. Torchilin*[,†]

Center for Pharmaceutical Biotechnology & Nanomedicine, 360 Huntington Avenue, 312 Mugar Hall, Northeastern University, Boston, Massachusetts 02115, and Pharmaceutical Sciences Department, Massachusetts College of Pharmacy and Health Science, 179 Longwood Avenue, Boston, Massachusetts 20115. Received April 23, 2010; Revised Manuscript Received July 9, 2010

siRNA is a powerful tool to control cellular processes at the post-transcriptional level. However, its therapeutic potential is limited because of low stability in biological fluids and the lack of simple and efficient delivery systems. Chemical modification of siRNA could be used to increase its intracellular delivery, but may affect its specific activity. To overcome these obstacles, we suggest a simple and effective system capable of stabilization, delivery, and subsequent release of free active siRNA within cells. With this in mind, we reversibly modified the double-stranded GFP-siRNA with a phosphothioethanol (PE) portion via the reducible disulfide bond and incorporated the resulting siRNA-S−S-PE conjugate in nanosized PEG-PE micelles. In the mixed siRNA-S−S-PE/PEG-PE micelles obtained, siRNA was well-protected against degradation by nucleases for at least 24 h, and was released easily from these nanoparticles in free form in the presence of glutathione (GSH) at a concentration mimicking the intracellular levels. In GFP-C166 endothelial cells, mixed GFP-siRNA-S−S-PE/PEG-PE micelles down-regulate the GFP production 50-fold more effectively than free siRNA. In addition, siRNA-containing micelles showed none of the cytotoxic side effects typical for siRNA delivery systems that are based on electrostatic association of siRNA with cationic carriers. Thus, a reversible siRNA−phospholipid conjugate formulated into mixed micelles with PEG-PE can be an effective, nontoxic system for stabilization and delivery of siRNA.

INTRODUCTION

Small interfering RNA (siRNA[1]) is a short double-stranded RNA 21 to 23 nucleotides in length (*1*). It behaves like a mediator of the RNA interference phenomenon by silencing specific gene expression by the cleavage of a target mRNA at the post-transcriptional level in the cytoplasm (*2, 3*). siRNA is believed to be a powerful tool for specific gene silencing in gene therapy. However, the real practical use of siRNA for clinical purposes is hindered by its very low stability in biological surroundings and the lack of simple and efficient delivery systems for the siRNA (*4, 5*).

siRNA delivery systems must be properly designed to improve the stability of siRNA upon in vivo administration, deliver siRNA specifically to the targeted tissue site, and facilitate the cellular uptake of siRNA into target cells (*1, 6*). Naked siRNA has low stability when administered intravenously, degrades rapidly, and possesses poor cellular uptake. To address these problems, several kinds of nanosized cationic delivery systems have been studied, which are based on polyelectrolyte complexes resulting from the electrostatic interaction between the negatively charged siRNA and cationic polymers or lipids (*7*). However, cationic agents used to form polyplexes with the siRNA, such as polyethyleneimine, often show strong toxicity which limits their clinical application (*7*). It has also been shown that the direct conjugation of aptamers, lipids, peptides, proteins, or polymers to siRNA can improve its in vivo pharmacokinetics, increase half-life, and increase delivery efficiency (*8–14*). However, chemical modification of siRNA can affect its activity and specificity, and in such conjugates, siRNA still remains open for degradation by nucleases.

In an attempt to build an siRNA delivery system, which thoroughly protects siRNA from degradation in vivo and at the same time is capable of releasing free siRNA when inside cell, we have designed a novel "reversible" siRNA by attaching siRNA (GFP-siRNA was used as an example) to the phospholipid (PE) via a disulfide linkage. When inside the cell, the S−S linkage in such a conjugate will be reduced by the high intracellular glutathione (GSH) and liberate the native siRNA into the cytoplasm. To protect siRNA from the nucleolytic degradation on its route to the target, the siRNA-S−S-PE conjugate was incorporated via its hydrophobic PE moiety, into PEG-PE-based stable polymeric micelles known to demonstrate high stability, prolonged circulation, and good accumulation in pathological areas in vivo (*15*). Such micelles can also be made target-specific (*16*).

Here, we demonstrate that the reversible siRNA-S−S-PE conjugate can be easily incorporated into PEG-PE-based micelles at variable weight ratios, and in such mixed micelles, siRNA is fully protected against nucleases, is liberated from the nanoparticles in the presence of glutathione, and down-regulates GFP production in GFP-expressing C166 endothelial cells. Such properties make siRNA-S−S-PE/PEG-PE nanosized mixed micelles a promising delivery system for siRNA.

EXPERIMENTAL SECTION

Materials. The GFP-siRNA modified with an SPDP group (*N*-succinimidyl 3-(2-pyridyldithio)propionate) at the 3′-end of

* Corresponding author. V. P. Torchilin, PhD, Distinguished Professor Center for Pharmaceutical Biotechnology & Nanomedicine, 360 Huntington Ave, 312 Mugar Hall, Northeastern University, Boston, MA 02115. E-mail: v.torchilin@neu.edu. Tel:+1 617.373.3206. Fax: +1 617 0.373.8886.

[†] Northeastern University.

[‡] Massachusetts College of Pharmacy and Health Science.

[1]Abbreviations: small interfering RNA, siRNA; phosphatidylethanolamine, PE; phosphothioethanol, PE-SH; 1,2-Distearoyl-*sn*-glycero-3-phosphoethanolamine-*N*-[methoxy(poly(ethylene glycol))-2000], PEG-PE; reversible siRNA-PE conjugate, siRNA-S−S-PE; green fluorescent protein, GFP; L-Glutathione, GSH; Dulbecco's modified Eagle medium, DMEM.

10.1021/bc100199c © 2010 American Chemical Society
Published on Web 07/29/2010

its sense strand [sense strand: (from 5′ to 3′) AGCUGAC-CCUGAAGUUCAUTT-SPDP] and the L-glutathione (reduced) were purchased from Invitrogen (Carlsbad, CA) and Sigma-Aldrich (St. Louis, MO), respectively. The 1,2-dipalmitoyl-*sn*-glycero-3-phosphothioethanol (PE-SH, MW 731) and 1,2-distearoyl-*sn*-glycero-3-phosphoethanolamine-*N*-[methoxy(poly(ethylene glycol))-2000] (PEG-PE) were from Avanti Polar Lipids (Alabaster, AL). The d-Salt dextran desalting column was from Pierce (Rockford, IL). Triethylammonium acetate (TEAA) 1 M and chloroform (CH_3Cl) were provided by Sigma-Aldrich (St. Louis, MO) and Fisher Scientific (Fair Lawn, NJ), respectively. The RNase/DNase-free water was obtained from MP Biomedicals (Solon, OH) and the phosphate saline buffer (PBS) 10× solution was from Fisher Scientific (Fair Lawn, NJ). RNase III *E. coli* was provided by Ambion (Austin, TX). The thin layer chromatography (TLC) was supplied by EMD Chemicals Inc. (Gibbstown, NJ). Precast 20% TBE gels, SYBR Gold Nucleic Acid Gel Stain, and Lipofectamine 2000 reagent were from Invitrogen.

Cell Culture. GFP-expressing C166 endothelial cells were grown in DMEM, at 37 °C and 5% CO_2. DMEM and supplements (fetal bovine serum, penicillin, streptomycin, and amphotericin B), Trypan Blue solution and Trypsin were from CellGro (Kansas City, MO).

Methods. *Synthesis of siRNA-S−S-PE Conjugate.* A solution of the SPDP-activated siRNA (20 nmol) in PBS, pH 7.4 (120 μL), was added dropwise to a solution of PE-SH (2 μmol) in DMSO and $CHCl_3$ (total volume of organic solvents 350 μL) The reaction was carried out for 48 h at RT with continuous shaking. The unreacted PE-SH was removed on a desalting column. The collected samples containing the siRNA-conjugate were ultracentrifuged for 1 min at 14.5 × 1000 rpm to further remove mixed solvents and/or PE-SH. The siRNA-S−S-PE conjugate was stored at −20 °C.

Assessment of siRNA-S−S-PE Conjugation after Enzymatic Digestion by Gel Retardation Assay. To confirm the siRNA-S−S-PE conjugate synthesis, we evaluated its stability in presence of *E. coli* Ribonuclease III (a double-stranded RNA specific endoribonuclease that cleaves double-stranded RNA into fragments). It is known that the chemical modification of siRNA is essential to improve nuclease resistance and enhance its stability in biological fluids (*5*). We investigated the stability of the siRNA conjugate compared to its unmodified siRNA precursor by incubation of 4.8 μg siRNA-S−S-PE and siRNA in a final volume of 100 μL. RNase III *E. coli* was added and the samples were incubated at 37 °C. The stability rate of the siRNA conjugate was compared with the native siRNA over a 4 h period. At 30 min and 1, 2, 3, and 4 h, an aliquot of the sample was withdrawn, frozen in dry ice to stop the progression of degradation, and stored at −80 °C until the analysis. Nucleic acid degradation was visualized by gel electrophoresis (20% TBE gel). The analysis was carried out according to the conditions suggested by the provider. The bands were stained with SYBR Gold Nucleic Acid Gel Stain in TBE buffer and visualized with Kodak MI software.

Cleavage of Disulfide Bond by TLC. To verify that the disulfide bond in the siRNA-S−S-PE conjugate is cleavable in reductive conditions, siRNA-S−S-PE (0.5−1 μg) was incubated with 25 μL of a GSH solution (10 mM) in PBS, pH 7.4 (*10*) (the concentration of GSH in the cytosol can reach 10 mM (*17*)). A known amount of the conjugate was lyophilized and then incubated with the GSH solution at 37 °C for 4 h with continuous shaking. The sample was immediately frozen at −80 °C, then lyophilized and finally redissolved in water for analysis by TLC using a mobile phase of $CHCl_3$:MeOH 8:2. After the TCL was dried, it was dipped in Molybdenum Blue dye to highlight the presence of a blue spot corresponding to liberated phospholipid.

Preparation of siRNA-S−S-PE/PEG-PE Mixed Micelles. A thin polymeric film of PEG-PE was prepared from a chloroform solution (*18, 19*). Chloroform was removed by N_2, and the film was further dried under vacuum. An siRNA conjugate in water was added to the PEG-PE film at weight ratios of 1:200, 1:500, and 1:750 in a final total volume of 300 μL, and the system was extensively vortexed to form mixed micelles.

Micelle Properties. Micelle mean size and size distribution were determined by the dynamic light scattering (DLS) using a Zeta Plus Instrument (Brookhaven Instrument Co., Holtsville, NY). Size distribution and morphology of siRNA-containing mixed micelles were also examined using a transmission electron microscopy (TEM). Various samples of PEG-PE and siRNA-S−S-PE/PEG-PE micelles were diluted to a concentration of 1 mg/mL in deionized water. The micelles were stained with 1% uranyl acetate (*20*), placed on a circular copper grid, and examined with a JEOL JEM-1010 electron microscope (JEOL USA, Inc., Peabody, MA).

Zeta potential (ζ) of all micelle formulations (diluted in 1 mM KCl) was measured by zeta phase analysis light scattering (PALS) with an ultrasensitive zeta potential analyzer instrument (Brookhaven Instruments, Holtsville, NY).

siRNA-S−S-PE Conjugate Incorporation into PEG-PE Nanosystem by HPLC. All micelle formulations were analyzed by HPLC (Hitachi, L-7450A) equipped with a UV detector at 260 nm on a XBridge C18 column (Waters, Milford, MA). The analyses were carried out at RT with a mobile phase A composed of 5% acetonitrile in 0.1 M TEAA, pH 7, and mobile phase B of 15% of acetonitrile in 0.1 M TEAA. The analyses were run in a gradient elution from 20% to 58% of B in 15 min with a 1 min/mL flow rate. The same concentrations (1.5 μg/50 μL) of freshly synthesized siRNA-S−S-PE conjugate alone and formulated as different weight ratios of mixed micelles were compared, and the degree of incorporation was evaluated by normalizing the area under the peak of free siRNA-conjugate and the siRNA-conjugate in mixed micelles at the same retention time (t_r ca. 12 min). As a reference, plain PEG-PE micelles were used.

GFP Down-Regulation in C166-GFP Endothelial Cells Estimated by Flow Cytometry. GFP-expressing C166 endothelial cells were grown at 37 °C and 5% CO_2 in DMEM containing 10% FBS in 25 cm^2 flasks until they reached 80% confluence. 35 × 10^4 cells/well were seeded in a twelve-well plate, and after overnight incubation, they were washed once with 1 mL DMEM medium and incubated with freshly made siRNA-PE/PEG_{2K}-PE micelle formulations containing 84 nM siRNA. For comparison, the same concentrations of naked siRNA and siRNA in Lipofectamine were used. Fresh micelle samples were made in 300 μL of DMEM with 10% fetal bovine serum. Untreated cells were used as controls. After 4 h incubation, medium was replaced with 1 mL of fresh DMEM. After 48 h incubation, the cells were washed once with 200 μL of trypsin solution to remove inactivating traces of serum, detached with an additional 200 μL, collected in 15 mL test tubes, and fixed with 1 mL of a 4% paraformaldehyde solution. The samples were kept at 4 °C until the analysis by flow cytometry.

Experiments were realized in triplicate on three separate sample preparations.

Cytotoxicity by Trypan Blue Exclusion. Cell viability after the incubation with siRNA micelle formulations, naked siRNA, and siRNA in Lipofectamine was tested at the same conditions used for the GFP-gene silencing test by the Trypan Blue solution exclusion assay. After incubation with micelles, the cells were washed once with DMEM and once more with 200 μL of trypsin solution. When the cells were detached from the bottom of the

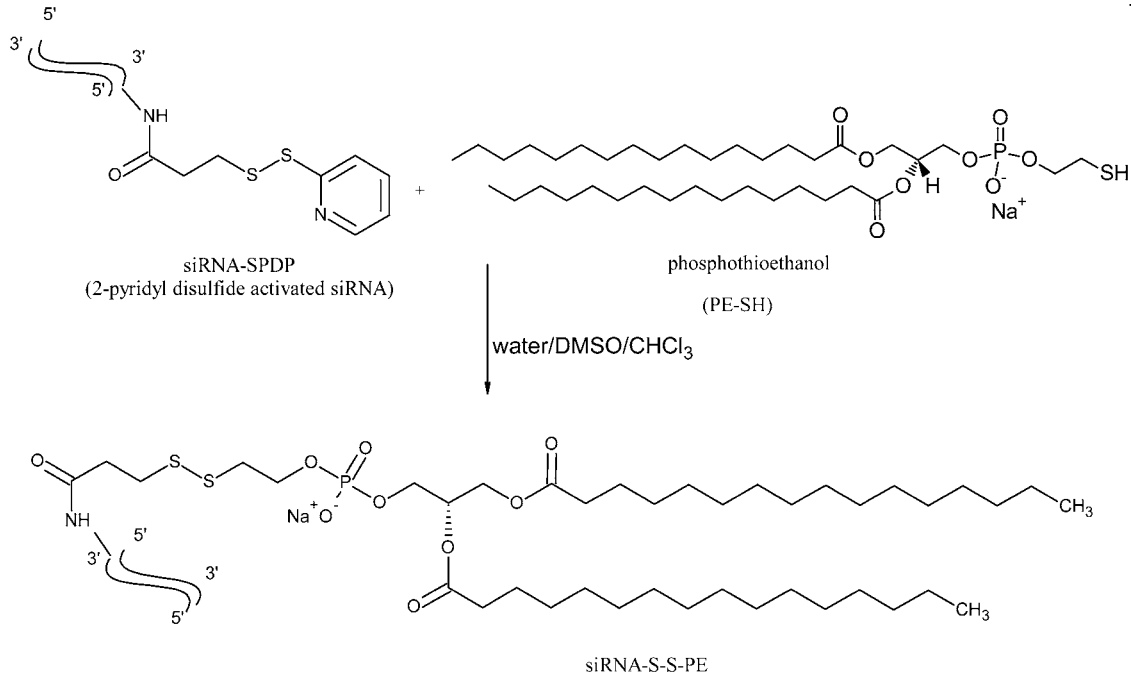


Figure 1. Schematic of siRNA-S−S-PE synthesis.

well, a 5-fold volume excess of complete DMEM was added. They were recovered and counted in Trypan Blue solution on a known dilution cell suspension. Cell viability of each formulation was expressed as a percentage of the total number of treated cells versus the total number of untreated cells. The experiment was done in triplicate on three different sample preparations.

Stability of siRNA-Conjugate in Micelles against Digestion by RNase. After assessing the gene-silencing efficiency of the siRNA-containing formulations, we investigated the efficacy of the PEG-PE polymer shield to further protect the siRNA-conjugate when incorporated in mixed micelles. Freshly prepared siRNA-S−S-PE conjugate was formulated at a 1:750 weight ratio in PEG-PE mixed micelle containing 4.8 μg siRNA-S−S-PE in a final volume of 100 μL. *E. coli* RNase III was added and the sample incubated at 37 °C for up to 24 h. The stability of the siRNA in mixed micelles was observed over a 24 h period. At predetermined time points, an aliquot of the sample was withdrawn, frozen in dry ice to stop the progression of degradation, and stored at −80 °C until the analysis as indicated previously.

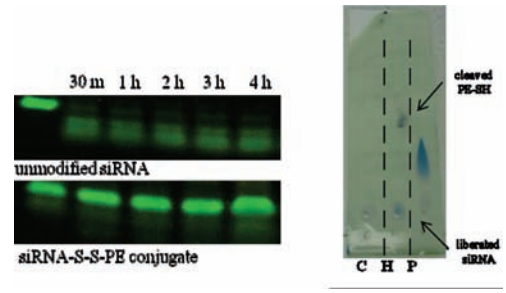


Figure 2. Left panel: siRNA-S−S-PE conjugation assessment by gel retardation assay. The stability rate of siRNA-conjugate was compared to that of the native siRNA over a 4 h enzymatic digestion. The improved nuclease resistance and enhanced stability in such conditions confirms the accomplished chemical modification of siRNA. Right panel: Cleavability of siRNA-S−S-PE conjugate in 10 mM GSH solution by TLC. siRNA-S−S-PE before the hydrolysis (C), siRNA after the hydrolysis of siRNA-conjugate (H), and free phospholipid (P). After dipping the TLC in Molybdenum Blue dye, sample H shows two blue spots: the lower one corresponds to the liberated siRNA and the upper one to free phospholipid.

RESULTS

Assessment of siRNA-S−S-PE Conjugation after Enzymatic Digestion by Gel Retardation Assay. The PE-SH was conjugated to the 3′-end of the modified siRNA sense strand by introducing a disulfide linkage according the schematic in Figure 1.

The characterization of siRNA-S−S-PE was assessed by investigating the stability rate of the conjugate in a RNase solution at 37 °C in comparison with the unmodified precursor. As predicted, the native siRNA showed complete degradation after 30 min incubation. In contrast, the siRNA-S−S-PE conjugate kept its integrity for at least 4 h. This result confirmed that siRNA-S−S-PE conjugation helps maintain the integrity of siRNA to some extent (Figure 2).

siRNA−Conjugate Cleavability in Reducible Conditions. SiRNA-S−S-PE conjugate cleavability was confirmed in a 10 mM GSH solution, mimicking intracellular reductive conditions. Equal amounts of siRNA-S−S-PE conjugate before (C) and after (H) hydrolysis and free PE (P) were run on TLC (Figure 2). Two spots were revealed for the sample H, corresponding to the liberated siRNA (lower spot) and cleaved phospholipid (upper spot). The starting siRNA-conjugate showed no impurities before incubation in the GHS solution. The free PE-SH and the cleaved phospholipid had different retention factors compared to each other due to the different dissolving media used (chloroform for the free PE-SH and buffer for the cleaved one) that can affect the run on the TLC.

Nanosized Mixed Micelles of siRNA-S−S-PE and PEG-PE. Although the chemical modification of the siRNA increases the nuclease resistance, the use of individual molecules of the modified siRNA could hardly allow for its effective delivery and targeting. Since the use of pharmaceutical nanocarriers opens much broader opportunities, we formulated this siRNA-conjugate into mixed micelles with large excess of PEG-PE to design the siRNA delivery system, which could easily be additionally surface-modified with various targeting and/or

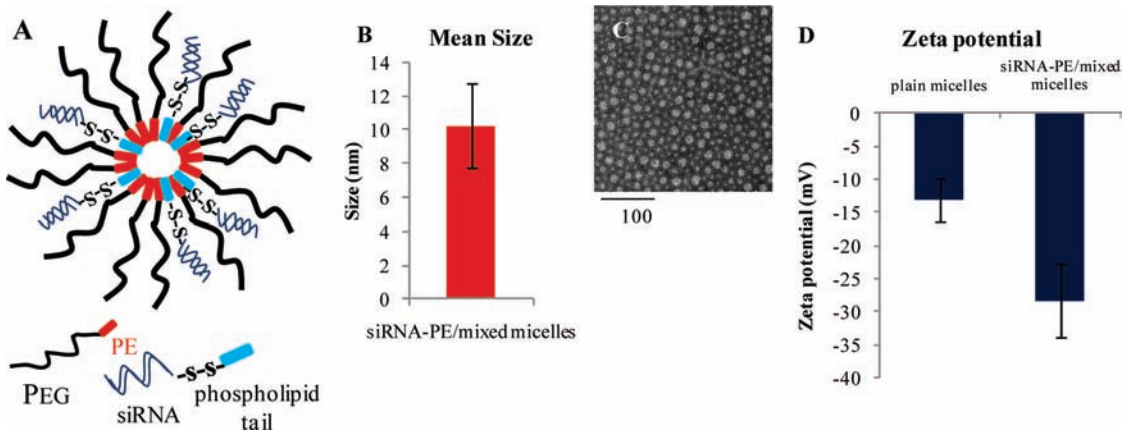


Figure 3. (A) Schematic structure of siRNA-S−S-PE/PEG-PE mixed micelle. (B) Mean size of mixed micelle formulations evaluated by DLS. (C) Morphology and size distribution of 1:750 (w/w) siRNA-PE/PEG-PE micelles by TEM. (D) Mean zeta potential value of siRNA-S−S-PE/PEG-PE mixed micelle formulations and plain PEG-PE micelles.

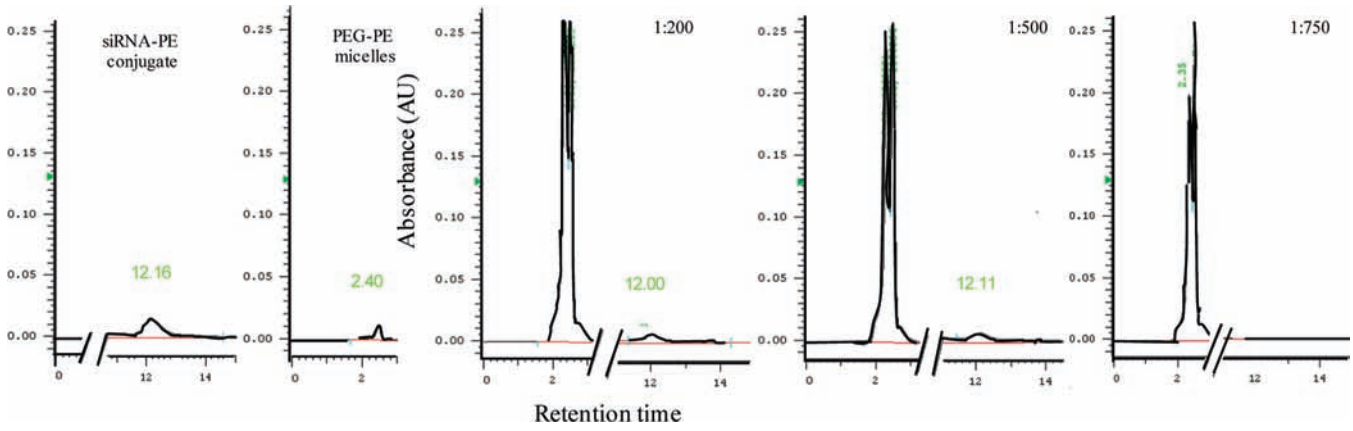


Figure 4. Micelle incorporation of siRNA-S−S-PE conjugate by HPLC. The peak at ca. 2.5 min corresponds to the mixed micelles of siRNA-S−S-PE with PEG-PE; the one at ca. 12 min to free siRNA (not incorporated in micelles). The formulations 1:200 and 1:500 (w/w) allow for siRNA's partial incorporation (62% and 69%, respectively), while at the 1:750 weight ratio, siRNA demonstrated 100% incorporation.

stimuli-sensitive moieties to bring siRNA to and inside selected target cells (*16*).

The siRNA-S−S-PE conjugate incorporates readily into PEG-PE micelles via the PE moiety. The schematic structure of the resulting mixed micelle is shown in Figure 3. Both plain PEG-PE micelles and siRNA-S−S-PE/PEG-PE mixed micelles had a mean size around 10 nm by dynamic light scattering. Transmission electron microscopy (TEM) analysis demonstrated the round shape and confirmed their narrow size distribution. Figure 3 presents the size distribution data for the 1:750 (w/w) siRNA-S−S-PE/PEG-PE micelles (similar results were obtained for 1:200 and 1:500 mixed micelles).

Zeta potential (ζ) measurements of the mixed micelle and plain PEG-PE micelle suspensions diluted with 1 mM KCl demonstrated quite expectedly that the surface charge of siRNA-containing micelles was more negative ($\zeta = -28.3 \pm 5.6$ mV) than that of the plain PEG-PE micelles ($\zeta = -13.2 \pm 3.2$ mV) (Figure 3).

HPLC analysis demonstrated that the peak at ca. 2.5 min corresponded to siRNA-S−S-PE-containing mixed micelles, while the peak at ca. 12 min corresponded to the free siRNA conjugate (Figure 4). Plain PEG-PE micelles injected at the same concentration as mixed micelles showed a small peak at 2.5 min at 260 nm. The increase of the area at this t_r value for mixed micelles was attributed to the presence of the siRNA-S−S-PE conjugate in the PEG-PE micelles. Chromatography also confirmed that, in the formulations with weight ratios of 1:200 and 1:500, siRNA had 62% and 69% incorporation, respectively, while at the 1:750 ratio, quantitative incorporation of siRNA conjugate into the mixed micelles was observed (no free siRNA conjugate peak was seen at 12 min).

GFP-Silencing in GFP-C166 Endothelial Cells. The gene silencing efficiency mediated by the siRNA-conjugate incorporated in PEG-PE micelle formulations was studied with GFP-expressing C166 endothelial cells. As the weight ratio of siRNA-conjugate/PEG-PE increased up to 1:750, the GFP gene expression level decreased. Specifically, the in vitro silencing results (Figures 5 and 6) showed that the weight ratio of siRNA-PE/PEG-PE micelles increased and the GFP down-regulation increased from a mean value of 0.54% for the naked siRNA to of 27.6% for the highest shielding ratio (1:750). This result was comparable to siRNA transfected by Lipofectamine (29.6%, data not shown), but without any induced cell toxicity (see next paragraph). The clearly demonstrated down-regulation of the GFP production confirmed the presence of the active free siRNA inside cells. Thus, while naked siRNA incubated with GFP-C166 cells caused ca. 0.5% decrease in the GFP expression, the same quantity of siRNA in 1:750 mixed micelles resulted in almost 28% gene silencing (Figure 6). The mixed GFP-siRNA-S−S-PE/PEG-PE micelles down-regulated the GFP 50-fold more effectively than free siRNA. Additionally, it clearly appears that the higher the PEG-PE amount, the higher the silencing, meaning that the in vitro shield offered by the 1:750 formulation more efficiently affects the siRNA protection compared to the 1:200 and 1:500 ones, being the most promising formulation for the future in vivo tests.

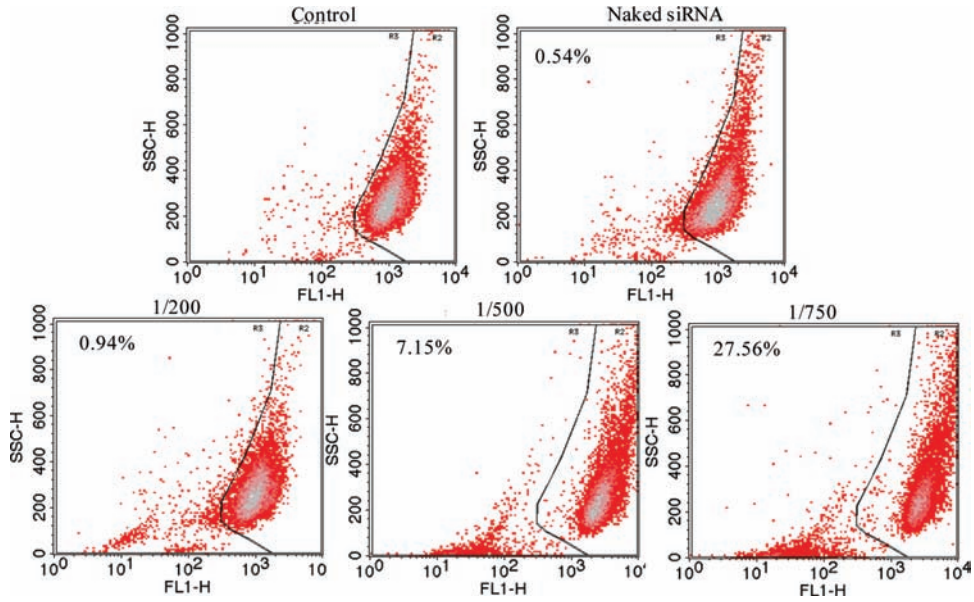


Figure 5. GFP-silencing by flow cytometry. The down-regulation induced by an 84 nM siRNA concentration ranged from 0.54% for the naked siRNA to 27.56% for the 1:750 siRNA-S−S-PE/PEG-PE mixed micelle preparation. The results were collected by analyzing the down-regulation induced in 10×10^3 cells for all samples and control cells.

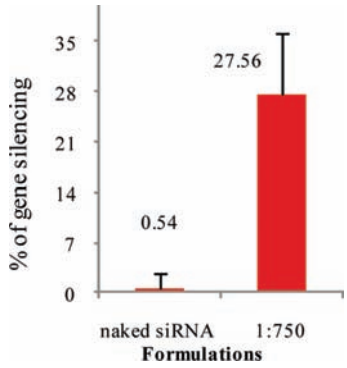


Figure 6. GFP-silencing in GFP-C166 endothelial cells by siRNA-PE/PEG-PE mixed micelles (1:750 w/w ratio). The naked siRNA incubated with GFP-C166 cells caused only ca. 0.5% decrease in the GFP production; the same quantity of siRNA in 1:750 mixed micelles resulted in almost 28% gene silencing demonstrated to induce a 50-fold more effective GFP down-regulation efficiency than free siRNA. The results are represented as mean ± SD collected on three independent experiments.

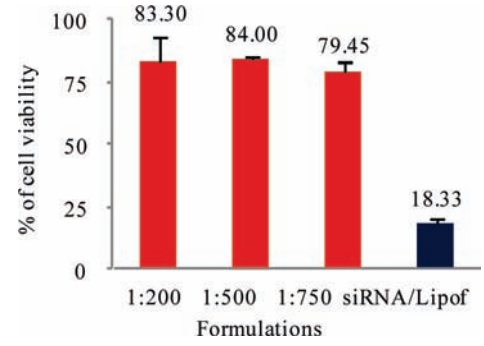


Figure 7. Cell viability by Trypan Blue assay after a 48 h incubation with various siRNA formulations (mean ± S.D., $n = 3$). The viability was close to 100% for all mixed micelle formulations (1:200, 1:500, and 1:750 weight ratios), unlike for cells subjected to the action of siRNA formulated with Lipofectamine (at the same quantity of siRNA), where it was less than 20%.

Cell Viability. The comparison of cytotoxicity of siRNA-S−S-PE/PEG-PE mixed micelles with that of siRNA formulated in the standard transfection reagent, Lipofectamine, which provided a comparable level of target gene silencing, demonstrated that the cell viability by Trypan Blue exclusion was close to 100% for all mixed micelle formulations (1:200, 1:500, and 1:750 weight ratios), whereas the viability of the cells subjected to the action of siRNA formulated with Lipofectamine (at the same quantity of siRNA) was less than 20% (Figure 7). Thus, the micellar formulations lacked the toxic effect associated with the use of such transfecting agents and observed with electrostatic complex-based systems (*7*).

Stability of siRNA-Conjugate in Micelle against Digestion by RNase. To show the increased stability of siRNA contained in PEG-PE nanoparticles against enzymatic degradation versus the siRNA-conjugate itself, siRNA-S−S-PE/PEG-PE mixed micelles were prepared at a 1:750 weight ratio and incubated in the presence of RNase III from *E. coli* for 24 h at 37 °C. We focused only on the 1:750 siRNA-PE/polymer ratio, since it provided the most significant gene silencing effect over the other micelle formulations. The siRNA-S−S-PE conjugate was degraded after a 6 h digestion (Figure 8). There were no degradation products of siRNA-conjugate in PEG-PE micelles after 24 h. The same amount of siRNA-conjugate not exposed to RNase was used as a positive control. This confirmed the

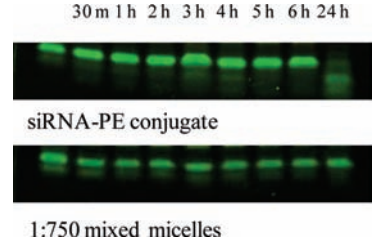


Figure 8. Degradation rate of the siRNA-S−S-PE in mixed micelles with PEG-PE (1:750 w/w). Upper panel: siRNA-conjugate degraded after a 6 h digestion with RNase III. Lower panel: siRNA in mixed micelles remained stable after 24 h.

effectiveness of the PEG-PE polymer in shielding the siRNA compared to the plain conjugate.

DISCUSSION

Efficient siRNA delivery systems for therapeutic applications are greatly needed (*21*). Previous studies utilizing various siRNA delivery systems including micelles and liposomes were based on the use of electrostatic interactions between the siRNA and a carrier (*1*). Here, we used a nanosized micellar siRNA delivery system, into which the siRNA was incorporated after its preliminary "hydrophobization" with a phospholipid. Earlier, this kind of modification was shown to promote better intracellular penetration of siRNA (*1*). In our design, however, the modification of siRNA with phospholipid was only the starting point to the development of a delivery nanosystem. The siRNA−phospholipid conjugate can be considered an amphiphilic copolymer with a hydrophilic (siRNA) and hydrophobic (phospholipid) segment with a structure typical of those polymeric amphiphiles which self-assemble into micelles. Thus, phospholipid-modified siRNA is easily formed into mixed micelles with amphiphiles such as the PEG-PE conjugate, a well-known micelle-forming agent for solubilization and delivery of various poorly soluble drugs (*15*) (see the schematic in Figure 3A).

Since a chemical modification of the siRNA was needed to make possible its subsequent incorporation into PEG-PE nanoparticles, we wanted to be sure that siRNA's specific activity would not be compromised by such a modification and that free siRNA would be liberated from mixed micelles when within cells. With this in mind, we developed a simple chemistry to modify siRNA with a phospholipid (PE) via the reversible -S−S- linkage, which would be easily reduced inside cells by the high intracellular GSH with subsequent liberation of free siRNA from the mixed micelles. We have performed our initial experiments with 10 mM GSH considering cancer cells as a potential target, since in cancer cells, the level of GSH is known to be that high and increases still further in the case of chemotherapy resistance (*22*). However, we can assume that in other cells, because of the generally high intracellular GSH, the hydrolysis of the conjugate still has to proceed at the rate proportional to their intracellular GHS levels.

Thus, we obtained a siRNA-phospholipid conjugate, which can easily be incorporated into polymeric micelles including PEG-PE-based micelles (Figure 3) and degrade in reductive conditions to liberate the native siRNA (Figure 2).

The siRNA-S−S-PE conjugate can readily form mixed micelles with PEG-PE at various weight ratios (1:200, 1:500, 1:750), and in such a polymeric nanosystem, siRNA is fully protected against degradation by nucleases, evidently by steric hindrances created by the PEG moieties against enzymatic attack (Figure 8). In mixed 1:750 micelles, siRNA remained intact for over 24 h in the presence of RNase at a concentration that completely degraded the native siRNA and the siRNA-conjugate.

Small-sized micelles can be taken up by cells via different mechanisms including endocytosis and pinocytosis. However, similar to other described siRNA delivery systems, even in the case of subsequent entrapment in endosomes of siRNA-containing micelles, a certain amount of siRNA still escapes the endosomal compartment and can trigger the cascade of the interfering mechanism, which needs a very small amount of siRNA to be initiated.

The fact that siRNA-S−S-PE/PEG-PE mixed micelles actually liberate free, active siRNA inside cells was clearly confirmed by significant down-regulation of the GFP production in GFP-C166 endothelial cells treated with GFP-siRNA-containing mixed micelles. At the same quantity of siRNA, the micellar nanosystem provided at least a 50-fold more efficient gene silencing than free siRNA (Figures 5 and 6). Additionally, the system is virtually nontoxic for the cells, unlike many other delivery systems based on the use of positively charged carriers (Figure 7). Importantly, such micelles can easily be additionally derivatized with specific ligands (monoclonal antibodies) to make them targeted to certain desired (pathological) tissues or cells, such as cancer cells (*16*) to promote delivery of the siRNA.

To summarize, siRNA-S−S-PE conjugate is an interesting siRNA derivative capable of liberating free, active siRNA under reducing conditions (such as within cells). siRNA-S−S-PE-containing nanosized mixed micelles, such as micelles composed of siRNA-S−S-PE and PEG-PE, may serve as a delivery system for siRNA that provides good protection for siRNA against enzymatic degradation and that lacks nonspecific toxicity toward cells.

ACKNOWLEDGMENT

This study was supported by funds from Samyang R&D Center, Korea.

LITERATURE CITED

(1) De Paula, D., Bentley, M. V., and Mahato, R. I. (2007) Hydrophobization and bioconjugation for enhanced siRNA delivery and targeting. *RNA 13*, 431–56.

(2) Elbashir, S. M., Harborth, J., Lendeckel, W., Yalcin, A., Weber, K., and Tuschl, T. (2001) Duplexes of 21-nucleotide RNAs mediate RNA interference in cultured mammalian cells. *Nature 411*, 494–8.

(3) Hamilton, A. J., and Baulcombe, D. C. (1999) A species of small antisense RNA in posttranscriptional gene silencing in plants. *Science 286*, 950–2.

(4) Jeong, J. H., Kim, S. W., and Park, T. G. (2007) Molecular design of functional polymers for gene therapy. *Prog. Polym. Sci. 32*, 1239–1274.

(5) Jeong, J. H., Mok, H., Oh, Y. K., and Park, T. G. (2009) siRNA conjugate delivery systems. *Bioconjugate Chem. 20*, 5–14.

(6) Dorsett, Y., and Tuschl, T. (2004) siRNAs: applications in functional genomics and potential as therapeutics. *Nat. Rev. Drug Discovery 3*, 318–29.

(7) Gary, D. J., Puri, N., and Won, Y. Y. (2007) Polymer-based siRNA delivery: perspectives on the fundamental and phenomenological distinctions from polymer-based DNA delivery. *J. Controlled Release 121*, 64–73.

(8) Nishina, K., Unno, T., Uno, Y., Kubodera, T., Kanouchi, T., Mizusawa, H., and Yokota, T. (2008) Efficient in vivo delivery of siRNA to the liver by conjugation of alpha-tocopherol. *Mol. Ther. 16*, 734–40.

(9) Chu, T. C., Twu, K. Y., Ellington, A. D., and Levy, M. (2006) Aptamer mediated siRNA delivery. *Nucleic Acids Res. 34*, e73.

(10) Kim, S. H., Jeong, J. H., Lee, S. H., Kim, S. W., and Park, T. G. (2006) PEG conjugated VEGF siRNA for anti-angiogenic gene therapy. *J. Controlled Release 116*, 123–9.

(11) Lorenz, C., Hadwiger, P., John, M., Vornlocher, H. P., and Unverzagt, C. (2004) Steroid and lipid conjugates of siRNAs to enhance cellular uptake and gene silencing in liver cells. *Bioorg. Med. Chem. Lett. 14*, 4975–7.

(12) Moschos, S. A., Jones, S. W., Perry, M. M., Williams, A. E., Erjefalt, J. S., Turner, J. J., Barnes, P. J., Sproat, B. S., Gait, M. J., and Lindsay, M. A. (2007) Lung delivery studies using siRNA conjugated to TAT(48−60) and penetratin reveal peptide induced reduction in gene expression and induction of innate immunity. *Bioconjugate Chem. 18*, 1450–9.

(13) Muratovska, A., and Eccles, M. R. (2004) Conjugate for efficient delivery of short interfering RNA (siRNA) into mammalian cells. *FEBS Lett. 558*, 63–8.

(14) Soutschek, J., Akinc, A., Bramlage, B., Charisse, K., Constien, R., Donoghue, M., Elbashir, S., Geick, A., Hadwiger, P.,

Harborth, J., John, M., Kesavan, V., Lavine, G., Pandey, R. K., Racie, T., Rajeev, K. G., Rohl, I., Toudjarska, I., Wang, G., Wuschko, S., Bumcrot, D., Koteliansky, V., Limmer, S., Manoharan, M., and Vornlocher, H. P. (2004) Therapeutic silencing of an endogenous gene by systemic administration of modified siRNAs. *Nature 432*, 173–8.

(15) Torchilin, V. (2009) Multifunctional and stimuli-sensitive pharmaceutical nanocarriers. *Eur. J. Pharm. Biopharm. 71*, 431–44.

(16) Torchilin, V. P., Lukyanov, A. N., Gao, Z., and Papahadjopoulos-Sternberg, B. (2003) Immunomicelles: targeted pharmaceutical carriers for poorly soluble drugs. *Proc. Natl. Acad. Sci. U.S.A. 100*, 6039–44.

(17) Wang, W., and Ballatori, N. (1998) Endogenous glutathione conjugates: occurrence and biological functions. *Pharmacol. Rev. 50*, 335–56.

(18) Musacchio, T., Laquintana, V., Latrofa, A., Trapani, G., and Torchilin, V. P. (2009) PEG-PE micelles loaded with paclitaxel and surface-modified by a PBR-ligand: synergistic anticancer effect. *Mol. Pharm. 6*, 468–79.

(19) Sawant, R. R., and Torchilin, V. P. (2009) Enhanced cytotoxicity of TATp-bearing paclitaxel-loaded micelles in vitro and in vivo. *Int. J. Pharm. 374*, 114–8.

(20) Tang, N., Du, G., Wang, N., Liu, C., Hang, H., and Liang, W. (2007) Improving penetration in tumors with nanoassemblies of phospholipids and doxorubicin. *J. Natl. Cancer Inst. 99*, 1004–15.

(21) Perkel, J. (2009) RNAi Therapeutics: A Two-Year Update. *Science 326*, 454.

(22) Balendiran, G. K., Dabur, R., and Fraser, D. (2004) The role of glutathione in cancer. *Cell Biochem. Funct. 22*, 343–52.

BC100199C

Properties of Double-Stranded Oligonucleotides Modified with Lipophilic Substituents

Brian M. Laing,[†] Lisa Barrow-Laing,[‡] Maureen Harrington,[§] Eric C. Long,[||] and Donald E. Bergstrom*[,†]

Department of Medicinal Chemistry and Molecular Pharmacology and Bindley Bioscience Center, Purdue University, West Lafayette, Indiana 47907, Department of Microbiology and Immunology, and Department of Biochemistry and Molecular Biology, Indiana University School of Medicine, Indianapolis, Indiana 46202, Department of Chemistry and Chemical Biology, Purdue School of Science, Indiana University−Purdue University Indianapolis (IUPUI), Indianapolis, Indiana 46202. Received April 25, 2010; Revised Manuscript Received June 1, 2010

We have synthesized a series of short, self-complementary oligonucleotide sequences modified at their 5′- and/or 3′- termini with a lipophilic dodecane (C12); these systems serve as models to assess the biophysical properties of double-stranded DNA (dsDNA) equipped with potentially stabilizing lipophilic substituents. Addition of C12 to the 5′-termini of self-complementary 10 nucleotide sequences increased their duplex melting temperatures (T_m) by ∼4−8 °C over their corresponding unmodified sequences. C12 functionalities added to both the 3′- and 5′-termini increased T_m values by ∼10−12 °C. The observed increases in T_m correlated with greater duplex stabilities as determined by the free energy values (ΔG) derived from T_m plots. There is a greater degree of stabilization when C12 is positioned with a C·G base pair at the termini, and the stabilizing effect of lipophilic groups far exceeds the effect seen in adding an additional base pair to both ends of DNA. Stable, short dsDNA sequences are of potential interest in the development of transcription factor decoy oligonucleotides as possible therapeutic agents and/or biological tools. These results suggest that the stability of short dsDNA sequences are improved by lipophilic substituents and can be used as the basis for the design of dsDNAs with improved biological stabilities and function under physiological conditions.

INTRODUCTION

The conjugation of lipophilic groups to oligonucleotides (ONs[1]) is closely linked to their development as antisense-based therapeutics (*1*−*4*). Conjugation of lipophilic groups to the 5′- and/or 3′-termini of ONs have been shown to significantly improve cell uptake and antisense activity (*3*, *5*−*9*) while also providing resistance to nucleases (*10*−*12*). The hybridization properties of ON−lipid conjugates have been studied and reported to result in stabilization (*6*, *13*), destabilization (*5*, *6*), or no effect on duplex stability (*6*, *14*−*16*); however, it is important to note that these studies were done in the context of the antisense ONs and that the effects of strategic placement of the lipophilic moieties on the hybridization of dsDNA were not considered in most cases.

To optimize the type and placement of lipophilic groups on oligonucleotides in order to facilitate cell uptake and intracellular trafficking, it is important to consider how natural biomolecules are tagged by lipophilic groups. Proteins are often conjugated to myristoyl (C14), palmitoyl (C16), farnesyl (C15), and geranylgeranyl (C20) groups (*17*, *18*) that function as anchors for reversible association with cell membranes. Dual lipid modification often occurs on two adjacent amino acids; for example, a terminal glycine may be *N*-acylated with myristic acid and an adjacent cysteine *S*-acylated with palmitic acid. This dual modification appears to facilitate association with lipid rafts (*19*). In order to mimic this cell association behavior, we envisioned the development of dsDNA decoys comprising a single sequence containing self-complementary segments linked by a spacer and terminated at the 3′- and 5′-ends by a myristic acid mimic (Figure 1). The dodecane hydrocarbon chain (C12) was chosen because it almost exactly spans the diameter of the blunt end of a DNA duplex and contains nearly as many methylene groups as myristic acid (11 vs 12, respectively). On self-assembly in aqueous solution, the modified oligonucleotide

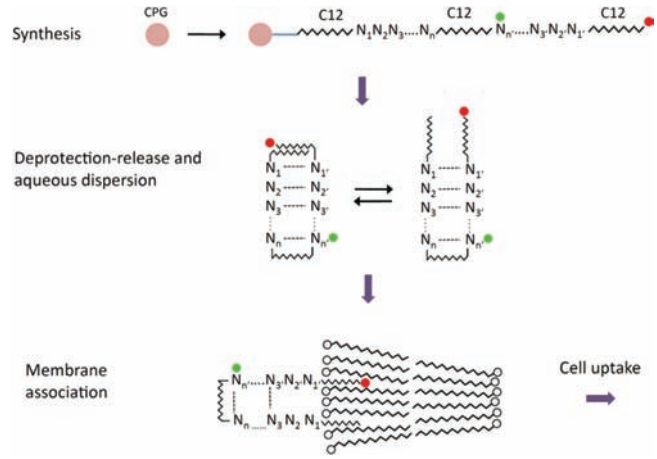


Figure 1. Design of end-capped dsDNA decoy sequences with C12 at the 5′- and 3′-termini for enhanced stability and cell uptake. Fluorescent probes may be attached to either the 5′-end (red circle) or to an internal base (green circle).

* To whom correspondence should be addressed. Department of Medicinal Chemistry and Molecular Pharmacology, Birck Nanotechnology Center, Purdue University, 1205 W. State St., West Lafayette, IN 47907-2057. Tel: (765) 494-6275. Fax: (765) 494-1414. E-mail: bergstrom@purdue.edu.

[†] Purdue University.

[‡] Department of Microbiology and Immunology, Indiana University School of Medicine.

[§] Department of Biochemistry and Molecular Biology, Indiana University School of Medicine.

[||] Indiana University−Purdue University Indianapolis (IUPUI).

[1]Abbreviations: ON, oligonucleotides, dsDNA, double-stranded DNA, T_m, melting temperature.

10.1021/bc100201n © 2010 American Chemical Society
Published on Web 07/30/2010

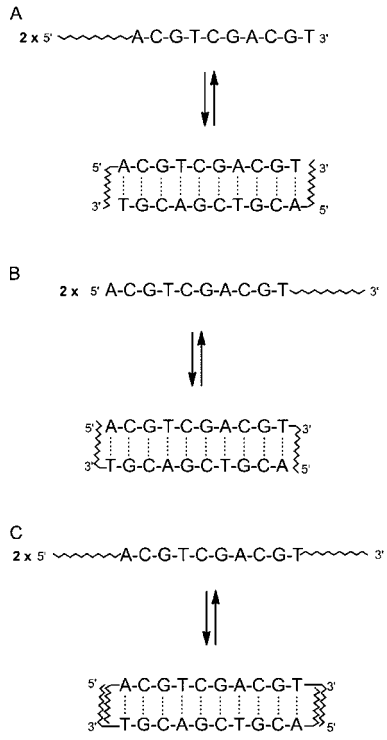


Figure 2. Model system for assessing the biophysical properties of dsDNA conjugated to lipophilic substituents at the 5′- and 3′-termini. (A) Association of self-complementary 10-mer sequence with C12 conjugated to the 5′-terminus. (B) Association of self-complementary 10-mer sequence with C12 conjugated 3′-terminus. (C) Association of self-complementary 10-mer sequence with C12 conjugated to both the 5′- and 3′-termini.

would assemble in such a way that the two terminal C12 groups could fold across the top of the helix. However, the C12 groups could also fold outward to allow the oligonucleotide to anchor into a cell membrane (Figure 1). Membrane integration is a critical step in localization and the eventual uptake of the ON by the cell.

Just as acylation by lipophilic hydrocarbons can stabilize protein secondary structure (*20*), it seemed likely that terminal C12 groups could stabilize DNA secondary structure. In this study, we assessed the effect of terminal lipophilic (C12) groups on the hybridization of double stranded DNA. We used short (10-mer) self-complementary sequences to which we attached a 12-carbon alkyl group to the 5′- and 3′-termini as a model system for assessing the relative effect of lipophilic groups on duplex thermal stability (Figure 2). With this simple model, we were able to obtain thermal melting profiles from which we extracted the melting temperature (T_m) and the thermodynamic parameters ΔH, ΔS, and ΔG. We hypothesized that lipophilic groups attached to the 3′- and 5′-ends of dsONs will self-associate in aqueous solution, thus conferring increased thermal stability. The models utilized in this study are simple alkyl groups in contrast to more lipophilic moieties (e.g., cholesterol) or highly engineered cross-linking molecules used in previous studies (*21*). The results presented here show that there is significant stabilization on addition of simple lipophilic alkyl groups to the termini of dsDNA.

EXPERIMENTAL PROCEDURES

General Information. Reagents for organic synthesis were purchased from Aldrich Chemical Co., Inc. (Milwaukee, WI) and were, unless otherwise stated, used as obtained. Anhydrous solvents were distilled from appropriate drying agents or purchased in Sure-Seal containers. Aminopropyl CPG was purchased from Biosearch Technologies, Inc. (Novato, CA). Standard base monomers, DyLight DY647 phosphoramidite, and reagents for oligonucleotide synthesis were purchased from Glen Research Corp. (Sterling, VA). Thin layer chromatography was performed using Sigma-Aldrich silica gel on glass 60F-254 TLC plates. Purification of compounds by silica gel chromatography was performed using Aldrich 230−400 mesh 60 Å silica gel. Nuclear magnetic resonance spectra were obtained using 300 or 500 MHz Bruker spectrometers. ^{1}H and ^{13}C spectra were referenced to TMS, while ^{31}P spectra were referenced to an 85% phosphoric acid external standard.

C12 Monomer Synthesis. *Dodecyl 2-Cyanoethyl N,N Diisopropylphosphoramidite (**2**).* 1-Dodecanol (0.22 mL, 1 mmol) was dissolved in 10 mL of anhydrous dichloromethane in a dry 25 mL two-necked flask. Diisopropylethylamine (0.63 mL, 3.6 mmol) was added while stirring under argon followed by 2-cyanoethyl *N*,*N*-diisopropylchlorophosphoramidite (0.27 mL, 1.2 mmol). The reaction was allowed to proceed for 1 h at room temperature and then quenched by the addition of four drops of anhydrous methanol and 20 mL of CH_2Cl_2. The reaction mixture was transferred to a dry 125 mL separatory funnel and washed quickly with 5% $NaHCO_3$ (10 mL × 2) and brine (10 mL). The organic layer was dried over anhydrous sodium sulfate and concentrated under reduced pressure. The residue was purified by silica gel flash chromatography (4:1 EtOAc/hexane, 1% Et_3N) to give **2** as a yellow oil (0.34 g, 88%). ^{1}H NMR (300 mHz, $CDCl_3$, δ, ppm): 3.83 (t, 2H, J = 6 Hz), 3.65−3.58 (m, 4H), 2.639 (t, 2H, J = 6 Hz), 1.60 (m, 2H), 1.33−1.20 (m, 18H), 1.19 (dd, 12H), 0.88 (t, 3H, J = 6 Hz). ^{31}P NMR (100.8 MHz, $CDCl_3$, δ, ppm): 148.23 (referenced to external 85% H_3PO_4). HR (ESI)-MS: calculated $(M + H)^+$ 387.3140; found, 387.3137.

*12-(4,4′-Dimethoxytrityloxy)-1-dodecanol (**4**).* Dodecane-1,12-diol (5.0 g, 29.5 mmol) was coevaporated with dry pyridine (3 × 20 mL) and dissolved in dry pyridine (30 mL) with stirring under argon. Dimethoxytrityl chloride (2.0 g, 5.9 mmol) was dissolved in dry pyridine (20 mL) and the solution added dropwise with constant stirring. The reaction was allowed to proceed overnight and quenched with methanol (1 mL). Pyridine was removed under vacuum, the mixture dissolved in dichloromethane (200 mL), and filtered. The filtrate was washed with 5% $NaHCO_3$ (200 mL × 2) followed by brine (100 mL) and dried over anhydrous sodium sulfate. The solution was concentrated under vacuum and the crude product purified by silica gel chromatography (1:1 ether/hexanes, 1% Et_3N). The appropriate fractions were combined, evaporated, and dried in vacuum to give **4** as a pale yellow foam (0.9 g, 30%), R_f 0.18 (1:1 ether/hexanes, 1% Et_3N). ^{1}H NMR (500 MHz, $CDCl_3$, δ, ppm): 7.43 (d, 2H, J = 5 Hz), 7.31−7.33 (m, 4H), 7.27−7.29 (m, 2H), 7.19 (t, 1H, J = 5 Hz), 6.80−6.83 (m, 4H), 3.79 (s, 6H), 3.63(q, 2H, J = 5.5 Hz), 3.02 (t, 2H, J = 6.5 Hz), 1.55−1.61 (m, 4H), 1.21−1.36 (m, 16H). ^{13}C NMR (125.77 MHz, $CDCl_3$, δ, ppm): 158.26, 145.47, 136.79, 130.02, 129.13, 128.21, 127.85, 127.76, 127.66, 126.52, 112.93, 85.59, 65.86, 63.49, 63.09, 55.19, 32.82, 30.09, 29.61, 29.58, 29.53, 29.43, 26.31, 25.74, 15.28. HR (ESI)-MS: calculated $(M + Na)^+$ 527.3137; found, 527.3134.

*12-(4,4′-Dimethoxytrityloxy)dodecyl 2-Cyanoethyl-N,N-diisopropylphosphoramidite (**5**).* C12-DMT (0.66 g, 1.31 mmol) was coevaporated twice with anhydrous CH_2Cl_2 (10 mL) and then dissolved in CH_2Cl_2 (10 mL). DIEA (0.68 mL, 3.92 mmol) was added with stirring under argon followed by the addition of 2-cyanoethyl *N*,*N*-diisopropylchlorophosphoramidite (0.44 mL, 1.96 mmol). The mixture was stirred at room temperature for 2 h and monitored by TLC (1:1 ether/hexane, 1% Et_3N). The reaction was quenched with 4 drops of anhydrous methanol and

the subsequent addition of 20 mL of CH_2Cl_2. The reaction mixture was transferred to a dry 125 mL separatory funnel and washed quickly with 5% $NaHCO_3$ (10 mL × 2) and brine (10 mL). The organic layer was dried over anhydrous sodium sulfate and concentrated under reduced pressure. The residue was purified by silica gel flash chromatography (1:1 ether/hexane, 1% Et_3N). The appropriate fractions were combined, evaporated, and dried in vacuum to give the product as a pale yellow oil (0.73 g, 79%), R_f 0.48 (1:1 ether/hexane 1% Et_3N). ^1H NMR (500 MHz, $CDCl_3$, δ, ppm): 7.43 (d, 2H, $J = 5$ Hz), 7.31−7.33 (m, 4H), 7.27−7.29 (m, 2H), 7.19 (t, 1H, $J = 5$ Hz), 6.80−6.83 (m, 4H), 3.80−3.88 (m, 2H), 3.79 (s, 6H), 3.55−3.65(m, 4H), 3.022 (t, 2H, $J = 6.5$ Hz), 2.63 (t, 2H, $J = 6.5$ Hz), 1.6 (p, 4H, $J = 7$ Hz), 1.55 (s, 1H), 1.21−1.35 (m, 16H), 1.16−1.19 (m, 11 H). ^{13}C NMR (125.77 MHz, $CDCl_3$, δ, ppm): 158.27, 145.48, 136.79, 130.02, 128.21, 127.66, 126.52, 112.93, 99.98, 85.59, 63.82, 63.51, 58.38, 58.23, 55.19, 43.02, 42.92, 31.20, 30.12, 29.62, 29.36, 26.34, 25.95, 24.68, 24.63, 24.58, 24.52, 20.38, 20.32. ^{31}P NMR (202.45 MHz, $CDCl_3$, δ, ppm): 147.81 (referenced to external 85% H_3PO_4). HR (ESI)-MS: calculated $(M + H)^+$, 705.4396; found, 705.4403.

Preparation of C12 CPG. *3-N-(1,3,4-Trimellityl-3,4-anhydride)aminopropyl-CPG (7).* Aminopropyl-CPG (5 g) was placed in a 125 mL Erlenmeyer flask and closed with a stopper. A solution of trimellitic anhydride chloride (1 g) in a mixture of pyridine (10 mL) and methylene chloride (40 mL) was then added. The mixture was placed on a solid phase shaker for 2 h. The CPG was poured in a sintered glass funnel and washed with methylene chloride (3 × 50 mL) and acetonitrile (3 × 50 mL). The support was dried in a vacuum desiccator and tested for the presence of free amino groups with a Kaiser test. The procedure was repeated until the Kaiser test was found to be negative.

1-Dimethoxytrityl-O-dihydroxydodecyl-3-O-(4′- or 5′-trimellityl)-1′-N-trimellityl)aminopropyl-CPG (9). Compound **7** (2 g) was placed in a 125 mL Erlenmeyer flask. 1,12-Dodecanediol (2.6 g) was dissolved in 10 mL of DMF and added to the flask followed by *N*-methylimidazole (0.5 mL). The flask was placed on a solid phase shaker for 18 h. The support was washed and dried as above. Dimethoxytrityl chloride (1 g) in 100 mL of pyridine was added to the flask and placed on a shaker for 16 h. The support was washed and dried as described above. The dimethoxytrityl (DMT) loading, as determined by colorimetric DMT loading assay, was 15 μmol/g.

Molecular Modeling. Molecular modeling analyses were carried out using Sybyl (Tripos) (*35*) installed on a Silicon Graphics IRIS 4D/120GTX workstation. B-DNAs were generated using the biopolymer build module. The straight chain alcohol $C_{12}H_{25}OH$ and the straight chain diol $HOC_{12}H_{24}OH$ were sketched using the sketch molecules tool in Sybyl. The sketched molecules were then minimized using the Kollman force field. Minimization followed the Powell conjugate gradient method for up to 10000 iterations until the gradient change in energy was 0.01 kcal/mol or less. The molecule was solvated with explicit water molecules, and aggregates were defined in the structure such that the minimization would only involve the terminal base pairs adjacent to the hydrophobic groups.

Oligonucleotide Synthesis. Oligonucleotides were synthesized on an Applied Biosystems 392 DNA/RNA synthesizer using standard phosphoramidite chemistry. The syntheses were initiated on columns containing controlled pore glass support loaded with the required 3′ nucleoside phosphoramidite or 3′ C12 for the first base in the synthesis. Syntheses were carried out on a 1 μmole scale, and the standard coupling time (25 s) was used for the standard nucleoside phosphoramidites and an extended coupling time of 300 s (2×) used for the internal C12 phosphoramidites (for cell uptake studies - see Supporting Information), 5′ C12 phosphoramidites, and 5′ -DyLight 647 phosphoramidite. For sequences with fluorescent groups, the ultramild base protected nucleoside phosphoramidite monomers and phenoxyacetyl protected adenine (pac-dA), 4-isopropyl-phenoxyacetyl protected guanine (ipr-pac-dG), and acetyl protected cytosine (ac-dC) were used to facilitate shorter deprotection times with ammonium hydroxide.

Unmodified sequences were synthesized with DMT-on for purification by either reversed phase HPLC or cartridge purification (Glen-Pak or Polypack cartridges, Glen Research, Sterling VA). Both purification methods depend on the hydrophobicity imparted by the DMT group to the oligonucleotide, thus significantly increasing the retention time on a C18 HPLC column or cartridge. C12 modified sequences were synthesized with DMT-off since the C12 modification imparts a similar hydrophobic effect on the oligonucleotides, facilitating easy purification on a C18 reversed phase HPLC column. Some longer double stranded sequences were found to be too hydrophobic for purification on a C18 column and were purified with a less hydrophobic (C4) column (see Supporting Information).

Conditions for RP-HPLC purification were as follows: a Zorbax C18 column (9.4 mm ×250 mm) at a flow rate of 4 mL/min or a Microsorb MV-C4 column (4.6 mm ×250 mm) at a flow rate of 1 mL/min, with a linear gradient from 5% to 50% acetonitrile and an aqueous buffer consisting of 0.1 M triethylammonium acetate, pH 7.0. Elution was monitored by diode array detection at 260 nm. Oligonucleotides were desalted using C18 Sep-pak cartridges (Waters) and analyzed by MALDI-TOF-MS.

Thermal Melting Studies. Absorbance versus temperature profiles (melting and annealing curves) were recorded on a Cary 3 Bio UV−visible spectrophotometer with a 6 × 6 multicell block Peltier temperature controller (Varian, Inc.). Oligonucleotides were dissolved in buffer containing 100 mM NaCl, 10 mM Na_2HPO_4, and 0.1 mM Na_2EDTA, pH 7. Samples were denatured by raising the temperature to 90 °C for 10 min prior to the beginning of an experiment. Melting and annealing experiments were conducted in two stages by starting the experiment at 90 °C, cooling to 5 °C, heating from 5 °C, and ending at 90 °C. Absorbance was measured at 260 nm with a heating/cooling rate of 0.5 °C/min and data collection at 0.2 °C intervals.

Data Analysis. The T_m data obtained were exported to the software application Microcal Origin (OriginLab Corporation, Northampton, MA). Sigmoidal curves were obtained using Boltzmann logged data-fit function, and the melting temperature was obtained by fitting the first derivative of the sigmoidal curve to a Gaussian function to identify the center of the peak, which is the T_m, or melting temperature.

Calculation of Thermodynamic Parameters. Thermodynamic parameters were determined from averages of fits from individual melting curves using the van't Hoff calculation in the Cary WinUV Thermal software (Varian, Inc.). The parameters were derived by van't Hoff analysis for self-complementary sequences where a two state model is assumed for the helix−coil transition using the method described by Puglisi and Tinoco (*36*). The T_m plot (absorbance vs temperature) was converted to an alpha (α) plot (fraction of molecules paired vs temperature) using the equation:

$$\alpha = \frac{A - A_s}{A_d - A_s} \quad (1)$$

where A is the absorbance at given temperature, and A_s and A_d are the absorbance values for the single- and double-stranded states, respectively. The parameter α refers to the fraction of

molecules paired. The upper and lower baselines of the T_m plots were fitted using linear least-squares fits to obtain a good approximation for A_s and A_d. The thermodynamic parameters ΔH, ΔS, and ΔG were determined by generating a van't Hoff plot (ln K vs $1/T$) using values of K calculated at each temperature from the α plot using the following equation:

$$K = \frac{\alpha}{2(1 - \alpha)^2 C_t} \quad (2)$$

where C_t is the total strand concentration. The thermodynamic parameters can be derived directly from the van't Hoff plot in which the slope is $-\Delta H°/R$, and the intercept is $\Delta S°/R$. The free energy change ($\Delta G°$) at any temperature can be determined by using the following relationship:

$$\Delta G° = \Delta H° - T\Delta S° \quad (3)$$

Circular Dichroism Spectroscopy. CD spectra were recorded on a JASCO circular dichroism spectropolarimeter. Oligonucleotide samples were prepared in a buffer containing 100 mM NaCl, 10 mM Na_2HPO_4, and 0.1 mM Na_2EDTA, pH 7. Samples were scanned over the wavelength range of 700 to 225 nm at a rate of 20 nm/min with time constant and bandwidth parameters set at 2 s and 1 nm, respectively. Data were collected at every 0.2 nm increment for each scan, and an average of 3 scans was used to generate each data set. A baseline scan (average of 3 scans) was collected with buffer only prior to each scan, and the baseline was subtracted from the sample scans.

Fluorescence Microscopy. Mouse embryo fibroblasts immortalized with SV-40 large T antigen were seeded into a 24-well plate containing one glass coverslip per well in 1.0 mL of Dulbecco's modified Eagle's media (DMEM) containing 10% fetal bovine serum and supplemented with 1% L-glutamine and 1% penicillin/streptomycin. Cells were incubated overnight in a humidified chamber at 37 °C in an atmosphere containing 5% carbon dioxide. Twenty-four hours after plating, media were aspirated from the wells, and fresh media (0.5 mL) containing the indicated reagents were added and cultures returned to the 37 °C incubator. After the indicated time points, cell monolayers were rinsed three times with 1 mL of phosphate buffered saline (PBS) per well, fixed in methanol, and mounted on glass slides. Fluorescent images were obtained using a Nikon Eclipse microscope.

RESULTS AND DISCUSSION

Design and Synthesis. The design of the ON−lipid conjugates and the choice of the lipophilic alkyl chain lengths examined here were guided by considering (i) the average distance between the 3′-O and 5′-O of a B-DNA duplex (determined to be 16.2 Å (*21*)), (ii) the hydrophobicity of the appending group, and (iii) the ease of synthesis. Molecular models were constructed and demonstrate that an interaction is likely to occur between the terminal C12 alkyl groups and with the terminal base pairs in an energy-minimized conformation (Figure 3, water molecules not displayed for clarity). Modeling of the sequence **10A**, with 5′-C12 and 3′-C12OH modifications (Figure 3A−D), indicated that there are potentially favorable hydrophobic interactions formed between the C12 alkyl chains, which span the distance between the terminal 3′-O and 5′-O and the planar surface of the terminal base pairs. These hydrophobic interactions are expected to shield the terminal hydrogen bonds from solvent water molecules while releasing water molecules in an entropically favorable manner resulting in duplex stabilization.

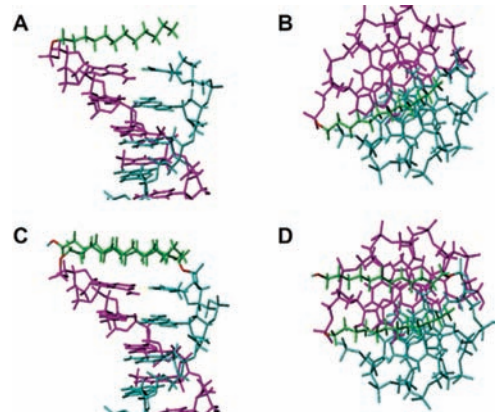


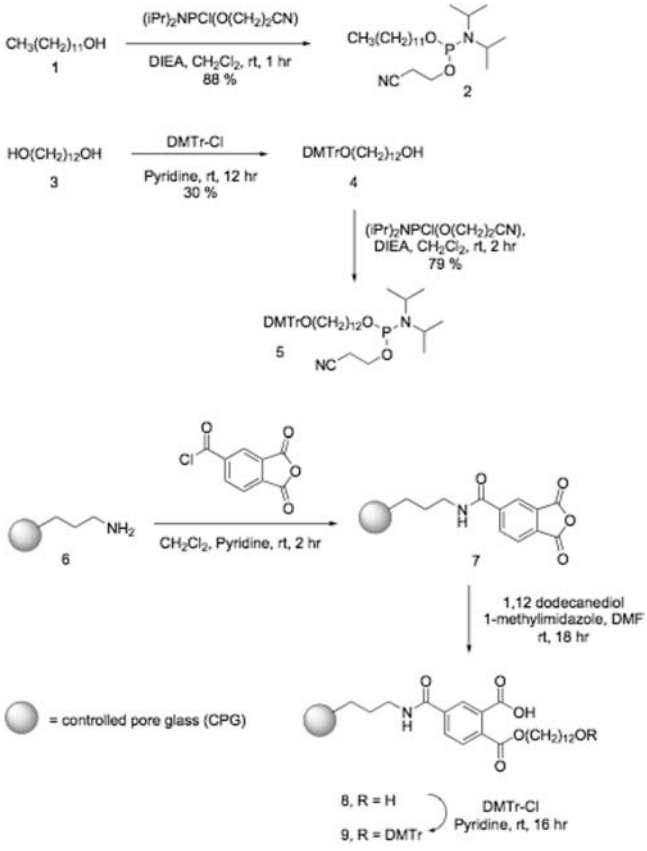
Figure 3. Energy minimized models: (A) 5′-C12 modified **10A**; perspective view perpendicular to the helical axis showing the interaction of 5′-C12 with the terminal base pair. (B) 5′-C12 modified **10A**: perspective view down the helical axis. (C) 5′-C12 and 3′- C12OH modified **10A**: perspective view perpendicular to the helical axis showing the interaction of 5′-C12 and 3′-C12OH with the terminal base pair. (**D**) 5′-C12 and 3′-C12OH modified **10A**: perspective view down the helical axis showing the interaction of 5′-C12 and 3′-C12OH with each other.

The anionic DNA conjugated to a hydrophobic molecule raises the possibility of micelle formation. It is intuitive and also shown experimentally (*22*) that there is a direct correlation between alkyl chain length and the propensity for forming micelles. On the basis of our models, we found the C12 alkyl group to have the optimal length (16.4 Å) for spanning the distance between the terminal base pair and that this length should exhibit a lower propensity for micelle formation in comparison to longer alkyl chains or more hydrophobic groups such as cholesterol. It has been shown that the critical micelle concentrations (CMC) for cholesterol-conjugated 10-mers were greater than 150 μM, and in some cases, no micelles were formed at concentrations less than 1 mM (*10*, *23*). The C12 conjugates used in our studies are less hydrophobic than cholesterol and were studied at a concentration of 10 μM, which is significantly below the reported CMC for cholesterol conjugated 10-mers. Hence, no micelle or liposome formation was anticipated or observed.

The syntheses of C12 modified 10-mer sequences were achieved by solid phase methodologies using standard automated protocols and reagents on an ABI 394 DNA/RNA synthesizer. C12 lipophilic monomers for 5′-end attachment were prepared by synthesis of the phosphoramidite derivative of 1-dodecanol (**2**) for the synthesis of DNA with 5′-C12 modification. The dimethoxytrityl (DMT) phosphoramidite derivative of 1, 12-dodecanediol (**4**) was prepared for the synthesis of DNA with 5′-C12-OH modification after DMTr cleavage and deprotection (Scheme 1). The CPG support bearing the C12 monomer (**9**) was prepared as described (Experimental Procedures) for the 3′-C12-OH modified DNA (Scheme 1).

Thermal Melting Studies. The effects of C12 terminal modifications on duplex DNA stability were assessed by thermal melting (T_m) studies. Self-complementary 10-mer sequences were synthesized bearing C12 on the 5′-and/or 3′-termini. The sequences had 60% GC content with one sequence (**10A**) having an A·T terminal base pair and a second sequence (**10B**) having a C·G terminal base pair in order to compare the effect of hydrophobic group stacking over C·G vs A·T bases. The results show a general trend of increasing T_m value with increasing sequence hydrophobicity as measured by retention on a C18 reversed phase HPLC column (see later sections). C12 or C12-OH added to the 5′-end of sequence **10A** (A·T terminal base pair) increased the T_m value by 4.8 °C over the unmodified

Scheme 1. Preparation of C12 Phosphoramidites and Solid Support for the Synthesis of C12 Modified DNA



sequences, whereas C12 added to both the 3′- and 5′-termini increased the T_m value by 9.8 °C. Addition of C12 to the 3′-end did not exhibit any appreciable effect on T_m value (Figure 4). Similar results were obtained for sequence **10B** (C·G terminal base pair) with an increase of 8.2 and 5.3 °C for 5′-end modification with C12 and C12-OH, respectively. An increase in T_m of 12 °C was observed for C12 added to both 5′- and 3′-ends, and no appreciable difference was observed upon 3′-end modification only (Figure 5).

The thermodynamic parameters (ΔH, ΔS, and ΔG) were extracted from T_m plots as described in Experimental Procedures (Tables 1 and 2). Free energies were calculated at 25 and 37 °C and showed that stabilization of the duplex correlated with

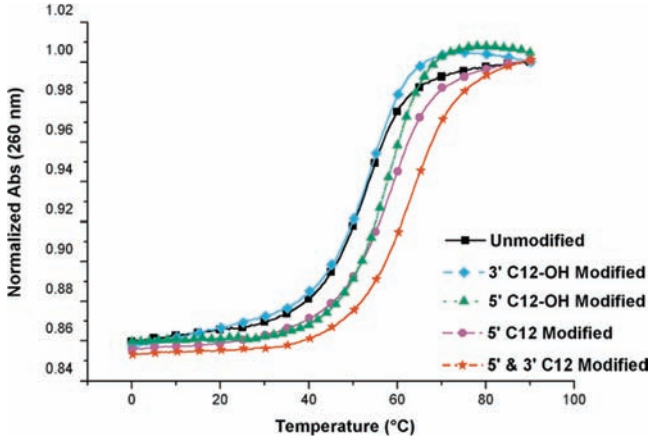


Figure 4. Thermal profile for the self-complementary duplex **10A**: (5′-ACGTCGACGT-3′)$_2$. The thermal profile shows increased T_m values with the addition of C12 substituents: $\Delta T_{m\ (3'C12\text{-}OH)} = +0$ °C, $\Delta T_{m\ (5'C12)} = \Delta T_{m\ (5'C12\text{-}OH)} = +4.8$ °C, and $\Delta T_{m\ (5'+3'\ C12)} = +9.8$ °C.

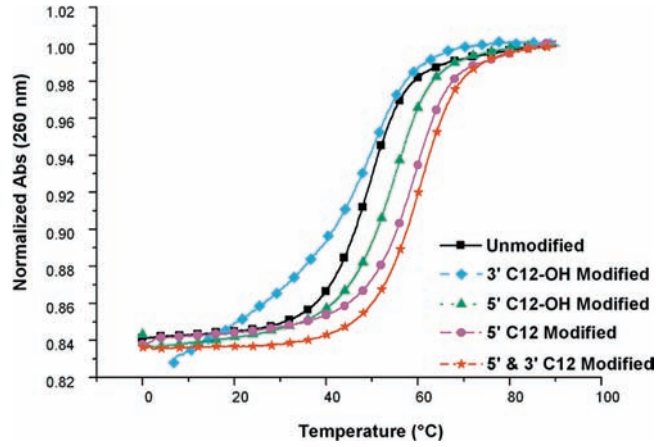


Figure 5. Thermal profile for self-complementary duplex **10B**: (5′-CAGTCGACTG-3′)$_2$. The thermal profile shows increased T_m values with the addition of C12 substituents: $\Delta T_{m\ (3'C12\text{-}OH)} = +0$ °C, $\Delta T_{m\ (5'C12\text{-}OH)} = +5.3$ °C, $\Delta T_{m\ (5'C12)} = +8.2$ °C, and $\Delta T_{m\ (5'\ C12+3'\ C12\text{-}OH)} = +12.3$ °C.

the measured increase in T_m values. The relative stabilities observed also correlated with the order of sequence hydrophobicity as measured by C18 reverse phase HPLC in the order: unmodified < 3′-C12-OH modified < 5′-C12-OH modified ≤ 5′-C12 modified < 5′- and 3′-C12 modified. An exception to the trend occurs with the 3′-C12-OH modified sequences where no increase in T_m or stabilization was observed with the increase in hydrophobicity. This deviation from the trend is apparently not related to the hydroxyl group present at the end of the alkyl chain since the 5′-C12-OH modification confers increased T_m and stabilization to the sequences.

It has been shown previously that hydrophobic, aromatic molecules such as napthalene diimide (*24*, *25*) and *N*,*N*-dimethylstilbene dicarboxamide (*26*, *27*) stabilized DNA duplexes through $\pi-\pi$ stacking interactions with the terminal DNA bases. Our molecular models predict the possibility of CH$-\pi$ interactions between the hydrophobic alkyl groups and the terminal base pairs resulting in stabilization of the duplex and an increase in T_m. A study by Isaksson and Chattopadhyaya (*28*) revealed a correlation between the stacking geometry of dangling terminal bases and duplex stabilization due to shielding of the terminal hydrogen bonds from external water molecules by a single base overhang. In addition to geometry, the degree of stabilization is determined by the size of the overhanging base, the nature of the terminal base pair (A·T, G·C, T·A, or C·G), and the hydrophobicity of the overhanging base. As observed here stabilization afforded by hydrophobic groups is significantly greater than the resulting stability of adding a one base overhang at each end of the sequence or the addition of either a C·G or A·T to both ends of the duplex (Tables 1 and 2). This can be attributed to better shielding of the hydrogen bonds of the terminal base pairs from the solvent due to the hydrophobic nature of the C12 alkyl group. A possible explanation for the lack of stabilization by C12 appended to the 3′-end may be due to the helical and stacking characteristics of the B-DNA (*28*, *29*). The 2′-endo-3′-exo puckering mode of B-DNA translates into helical and stacking characteristics that results in an overhanging moiety (nucleobase or other conjugates) stacking better when attached to the 5′-end than when the same moiety is attached to the 3′-end (*28*, *30*). Finally, stacking of the C12 group over a C·G base pair provides a greater degree of stabilization than stacking over an A·T base pair.

Circular Dichroism. Circular dichroism experiments were performed to determine the effects of our hydrophobic modifications on the structures of the resulting 10-mer DNA duplexes (Figure 6). The results shown in Figure 6 indicate that there is

Table 1. Thermodynamic Data Derived from T_m Curves for Self Complementary Sequence 10A Having an A·T Terminal Base Pair

sequence (5′-3′)	ΔH (kcal/mol)	ΔS (cal/mol/K)	$\Delta G_{(25\ °C)}$ (kcal/mol)	$\Delta G_{(37\ °C)}$ (kcal/mol)	K_d (nM)	T_m[a] (°C)	T_m[b] (°C)
ACG TCG ACG T	−65.2 ± 1.6	−177.4 ± 5.0	−12.4 ± 0.2	−10.2 ± 0.1	58.9	52.7 ± 0.5	52.3 ± 0.5
TAC GTC GAC GT	−50.4 ± 3.7	−131.2 ± 11.1	−11.3 ± 0.4	−9.8 ± 0.5	128	53.4 ± 0.3	53.3 ± 0.2
TAC GTC GAC GTA	−24.3 ± 3.7	−168.3 ± 11.1	−12.7 ± 0.4	−10.7 ± 0.5	28.2	55.9 ± 0.3	54.8 ± 0.2
[C12]-ACG TCG ACG T	−59.7 ± 1.6	−158.2 ± 4.6	−12.5 ± 0.2	−10.7 ± 0.2	29.3	56.8 ± 0.4	57.1 ± 0.3
[C12-OH]-ACG TCG ACG T	−69.1 ± 1.4	−185.7 ± 4.1	−13.7 ± 0.1	−11.5 ± 0.1	8.1	57.5 ± 0.4	57.2 ± 0.4
ACG TCG ACG T-**[C12-OH]**	−68.6 ± 1.1	−187.5 ± 3.5	−12.6 ± 0.4	−10.4 ± 0.4	46.7	52.7 ± 2.0	50.3 ± 1.9
[C12]-ACG TCG ACG T-**[C12-OH]**	−60.2 ± 1.0	−157.1 ± 2.6	−13.3 ± 0.2	−11.5 ± 0.2	8.1	61.2 ± 0.5	62.1 ± 0.3

[a] T_m determined from the α plot. [b] T_m determined by the derivative method. T_m values were measured in 10 mM sodium phosphate buffer (pH 7.2) containing 100 mM NaCl and 0.1 mM EDTA. Data are the average and SD of at least 3 experiments.

Table 2. Thermodynamic Data Derived from T_m Curves for Self Complementary Sequence 10B Having an C·G Terminal Base Pair

sequence (5′ −3′)	ΔH (kcal/mol)	ΔS (cal/mol/K)	$\Delta G_{(25\ °C)}$ (kcal/mol)	$\Delta G_{(37\ °C)}$ (kcal/mol)	K_d (nM)	T_m[a] (°C)	T_m[b] (°C)
CAG TCG ACT G	−72.6 ± 2.2	−201.8 ± 7.9	−12.4 ± 0.7	−10.0 ± 0.7	93.8	48 ± 0.6	48.3 ± 0.5
TCA GTC GAC TG	−83.0 ± 2.0	−235.4 ± 6.1	−12.8 ± 0.2	−10.0 ± 0.2	93.8	47.8 ± 0.1	47.3 ± 0.4
TCA GTC GAC TGA	−67.0 ± 1.1	−183.7 ± 3.2	−12.3 ± 0.1	−10.1 ± 0.1	80.4	51.4 ± 0.2	50.5 ± 0.1
[C12]-CAG TCG ACT G	−71.4 ± 0.9	−193.7 ± 3.1	−13.7 ± 0.4	−11.4 ± 0.5	9.5	55.8 ± 1.0	56.5 ± 0.8
[C12-OH]-CAG TCG ACT G	−68.5 ± 1.3	−186.5 ± 3.9	−12.9 ± 0.1	−10.7 ± 0.1	30.5	54.0 ± 0.0	53.6 ± 0.0
CAG TCG ACT G-**[C12-OH]**	−58.1 ± 0.9	−158 ± 2.0	−11 ± 0.4	−9.1 ± 0.4	365	47.0 ± 0.3	46.2 ± 0.5
[C12]-CAG TCG ACT G-**[C12-OH]**	−70.2 ± 1.1	−187.6 ± 2.3	−14.3 ± 0.5	−12 ± 0.5	3.2	59.7 ± 0.5	60.3 ± 0.5

[a] T_m determined from the α plot. [b] T_m determined by derivative method. T_m values were measured in 10 mM sodium phosphate buffer (pH 7.2) containing 100 mM NaCl and 0.1 mM EDTA. Data are the average and SD of at least 3 experiments.

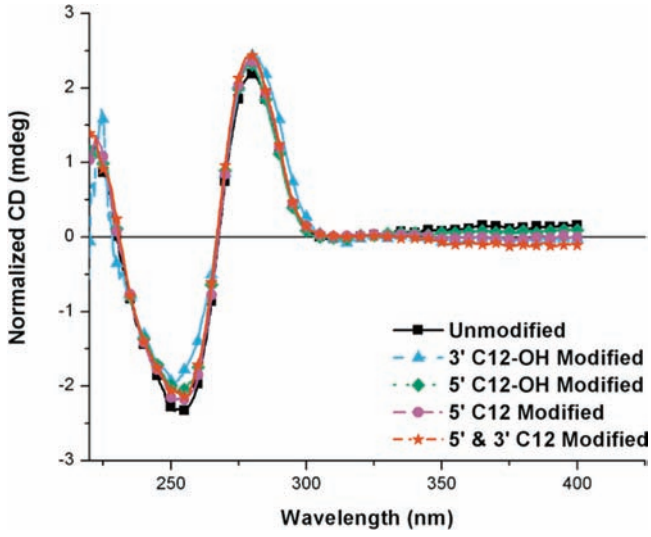


Figure 6. Circular dichroism spectra illustrating that the DNA duplex is unperturbed by the addition of C12 and retains the B-form helical structure.

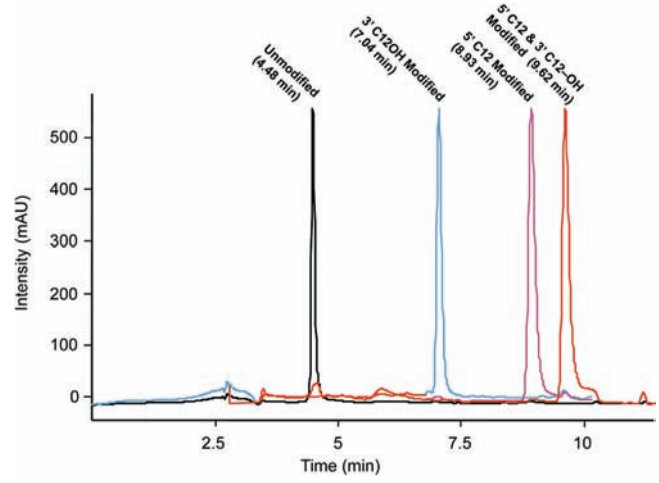


Figure 7. C18 reversed phase HPLC assessment of the relative hydrophobicities of each modified sequence. Hydrophobicity increased with successive additions of C12 to the termini as indicated by the increased retention time on a C18 column.

no deviation from a canonical B-DNA helix, with diagnostic positive signals observed between 265 and 285 nm and a negative signal between 250 and 260 nm. Oligonucleotides bearing modifications that retain a B-DNA duplex structure have the ability to bind proteins and the potential to be used in cocrystallization studies with DNA binding proteins as well as dsDNA transcription factor decoy agents for use as biological tools or therapeutic agents.

HPLC As a Measure of Hydrophobicity. The retention time of C12 modified DNA sequences on a C18 reverse phase HPLC column provides an approximate indication of the relative hydrophobicity of the sequences (Figure 7). The relative hydrophobicity increases in the following order: unmodified (rt: 4.48 min) < 3′-C12-OH modified (rt: 7.04 min) < 5′-C12-OH modified (not shown) < 5′-C12 modified (rt: 8.93 min) < 5′-C12 and 3′-C12-OH modified (9.62 min). The 3′-C12-OH group is less hydrophobic than the 5′-C12-OH, possibly due to the added length and flexibility associated with the 5′-CH_2. These HPLC derived hydrophobicity parameters were used to correlate the relative hydrophobicity of these sequences to the biophysical properties associated with the modifications.

Cell Uptake Studies. The cell uptake of C12-modified dsDNA of the type shown in Figure 1 (having C12 conjugated to both the 3′- and 5′-termini and the opposite termini covalently linked via a C12 end-cap - Supporting Information) was assessed by fluorescence microscopy (Figure 8). Sequences were labeled at the 5′-end with DyLight DY647 fluorescent dye with one sequence (NFκB-Dye) having the C12 end-cap but lacking the 3′- and 5′-C12 modifications as a control. Mouse embryo fibroblast cells were incubated with 0.5 μM and 1 μM fluorescently labeled oligonucleotides for 1, 2, and 4 h time points. The results show a significant increase in cell uptake compared to that of the control sequence at both 0.5 μM and 1 μM oligonucleotide concentrations after 1 h with increased accumulation in the cytoplasm and nucleus as a function of incubation time.

CONCLUSIONS

Much attention has been given to ON−lipid conjugates, particularly cholesterol, for enhancing the cell uptake of antisense oligonucleotides. In the context of double-stranded oligonucleotides, studies on small interfering RNA (siRNA) conjugated to cholesterol, derivatives of lithocholic acid, and

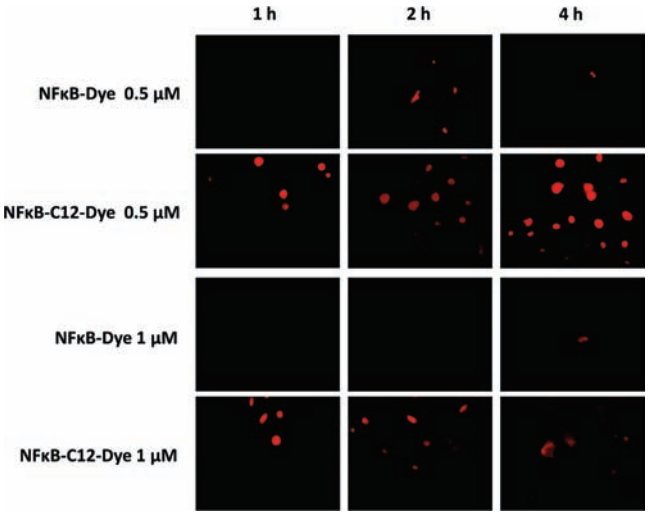


Figure 8. Fluorescence microscopy of mouse embryo fibroblast cells incubated with NFκB decoy oligonucleotide sequences labeled with DyLight DY647. NFκB-Dye: end-capped 16mer dsDNA. NFκB-C12-Dye: end-capped 16-mer dsDNA bearing 5′-C12and 3′-C12-OH of the form described in Figure 1.

derivatives of 12-hydroxy lauric acid at the 5′-end of the sense strands were shown to be taken up into liver cells without the use of transfection reagents (*31*−*33*). This uptake is reported to be mediated by interactions with lipoprotein particles, lipoprotein receptors, and transmembrane proteins that selectively direct the uptake of siRNA into cells of the liver, gut, kidney, and steroidogenic organs (*33*). Indeed, siRNA conjugated to palmitic acid, oleic acid, and cholesterol showed no uptake into human fibrosarcoma cells (HT-1080) without the use of transfection reagents (*34*). In contrast to the more lipophilic groups used in these studies of dsRNA, we see efficient cell uptake of dsDNA with the conjugation of two C12 groups positioned adjacent to each other, mimicking the adjacent post-translational lipidation of proteins in nature that directs proteins to lipid rafts. It can be postulated from these results that, in addition to the relative lipophilicity of the molecules, the positioning of the conjugates relative to each other play a role in enhancing the cell uptake of ON−lipid conjugates. Further study is necessary to confirm the mechanism of cell uptake, which may also be cell type specific.

In this article, we used a simple model to assess the effects of lipophilic groups attached to the termini of double-stranded DNA on the biophysical properties of the duplex, namely, their thermal stabilities. We have found that simple lipophilic alkyl groups attached to the termini of self-complementary sequences increases thermal stability in a manner indicative of (1) the occurrence of CH−π stacking interactions with the terminal base pair, (2) hydrophobic interactions between lipophilic groups on complementary strands of the duplex, and (3) effective shielding of the terminal hydrogen bonds from external water molecules. In comparison to the previous methods employed in stabilizing dsDNA by covalent cross-linking using more complex linker molecules, our current strategy offers a significant advantage in terms of simplicity and ease of synthesis. Taken together, these results may provide the basis for the development of a class of stable dsDNA that can be applied as biological tools or as transcription factor decoy inhibitors with improved stability and cell uptake properties for therapeutic purposes.

ACKNOWLEDGMENT

This work was supported by a grant from the Indiana Elks Foundation, Walther Cancer Institute, and a Purdue Doctoral Fellowship to B.L. We thank Dr. David Thompson for helpful discussions on lipophilic groups suitable for DNA modifications.

Supporting Information Available: ^{1}H, ^{13}C, and ^{31}P NMR spectra, and MALDI-TOF-MS data table for DNA sequences. This material is available free of charge via the Internet at http://pubs.acs.org.

LITERATURE CITED

(1) Gissot, A., Camplo, M., Grinstaff, M. W., and Barthelemy, P. (2008) Nucleoside, nucleotide and oligonucleotide based amphiphiles: a successful marriage of nucleic acids with lipids. *Org. Biomol. Chem. 6*, 1324–1333.

(2) Wilson, C., and Keefe, A. D. (2006) Building oligonucleotide therapeutics using non-natural chemistries. *Curr. Opin. Chem. Biol. 10*, 607–614.

(3) Krieg, A. M., Tonkinson, J., Matson, S., Zhao, Q., Saxon, M., Zhang, L. M., Bhanja, U., Yakubov, L., and Stein, C. A. (1993) Modification of antisense phosphodiester oligodeoxynucleotides by a 5′ cholesteryl moiety increases cellular association and improves efficacy. *Proc. Natl. Acad. Sci. U.S.A. 90*, 1048–1052.

(4) Manoharan, M. (2002) Oligonucleotide conjugates as potential antisense drugs with improved uptake, biodistribution, targeted delivery, and mechanism of action. *Antisense Nucleic Acid Drug Dev. 12*, 103–128.

(5) Letsinger, R. L., Zhang, G. R., Sun, D. K., Ikeuchi, T., and Sarin, P. S. (1989) Cholesteryl-conjugated oligonucleotides: synthesis, properties, and activity as inhibitors of replication of human immunodeficiency virus in cell culture. *Proc. Natl. Acad. Sci. U.S.A. 86*, 6553–6556.

(6) Shea, R. G., Marsters, J. C., and Bischofberger, N. (1990) Synthesis, hybridization properties and antiviral activity of lipid-oligodeoxynucleotide conjugates. *Nucleic Acids Res. 18*, 3777–3783.

(7) Stein, C. A., Pal, R., DeVico, A. L., Hoke, G., Mumbauer, S., Kinstler, O., Sarngadharan, M. G., and Letsinger, R. L. (1991) Mode of action of 5′-linked cholesteryl phosphorothioate oligodeoxynucleotides in inhibiting syncytia formation and infection by HIV-1 and HIV-2 in vitro. *Biochemistry 30*, 2439–2444.

(8) Boutorine, A. S., and Kostina, E. V. (1993) Reversible covalent attachment of cholesterol to oligodeoxyribonucleotides for studies of the mechanisms of their penetration into eucaryotic cells. *Biochimie 75*, 35–41.

(9) Godeau, G., Staedel, C., and Barthelemy, P. (2008) Lipid-conjugated oligonucleotides via “click chemistry” efficiently inhibit hepatitis C virus translation. *J. Med. Chem. 51*, 4374–4376.

(10) Gryaznov, S. M., and Lloyd, D. H. (1993) Modulation of oligonucleotide duplex and triplex stability via hydrophobic interactions. *Nucleic Acids Res. 21*, 5909–15.

(11) Manoharan, M., Tivel, K. L., Condon, T. P., Andrade, L. K., BarberPeoch, I., Inamati, G., Shah, S., Mohan, V., Graham, M. J., Bennett, C. F., Crooke, S. T., and Cook, P. D. (1997) Conjugated Antisense Oligonucleotides. *Nucleosides Nucleotides 16*, 1129−1138.

(12) Otvos, L., Sagi, J., Sagi, G., Szemzo, A., Toth, F. D., and Jeney, A. (1999) Enzymatic hydrolysis and biological activity of oligonucleotides containing 5-substituted pyrimidine bases. *Nucleosides Nucleotides 18*, 1665–1666.

(13) Guzaev, A., and Lonnberg, H. (1999) Solid support synthesis of ester linked hydrophobic conjugates of oligonucleotides. *Tetrahedron 55*, 9101–9116.

(14) Letsinger, R. L., Chaturvedi, S. K., Farooqui, F., and Salunkhe, M. (1993) Use of hydrophobic substituents in controlling self-assembly of oligonucleotides. *J. Am. Chem. Soc. 115*, 7535–7536.

(15) MacKellar, C., Graham, D., Will, D. W., Burgess, S., and Brown, T. (1992) Synthesis and physical properties of anti-HIV antisense oligonucleotides bearing terminal lipophilic groups. *Nucleic Acids Res. 20*, 3411–3417.

(16) Ramzaeva, N., Mittelbach, C., and Seela, F. (1997) 7-deaza-guanine DNA: Oligonucleotides with hydrophobic or cationic side chains. *Helv. Chim. Acta 80*, 1809–1822.
(17) Nadolski, M. J., and Linder, M. E. (2007) Protein lipidation. *FEBS J. 274*, 5202–5210.
(18) Magee, T., and Seabra, M. C. (2005) Fatty acylation and prenylation of proteins: what's hot in fat. *Curr. Opin. Cell Biol. 17*, 190–196.
(19) Zacharias, D. A., Violin, J. D., Newton, A. C., and Tsien, R. Y. (2002) Partitioning of lipid-modified monomeric GFPs into membrane microdomains of live cells. *Science 296*, 913–916.
(20) Poschner, B. C., and Langosch, D. (2009) Stabilization of conformationally dynamic helices by covalently attached acyl chains. *Protein Sci. 18*, 1801–1805.
(21) Ng, P. S., Laing, B. M., Balasundarum, G., Zu, X., Pingle, M. R., Friedman, A., and Bergstrom, D. E. (2010) Synthesis and evaluation of new spacers for use as dsDNA end-caps. *Bioconjugate Chem.* **2010**, DOI: 10.1021/bc100202y.
(22) Ueno, M., Takasawa, Y., Miyashige, H., Tabata, Y., and Meguro, K. (1981) Effects of alkyl chain length on surface and micellar properties of octaethyleneglycol-n alkyl ethers. *Colloid Polym. Sci. 259*, 761–766.
(23) Gosse, C., Boutorine, A., Aujard, I., Chami, M., Kononov, A., Cogne-Laage, E., Allemand, J. F., Li, J., and Jullien, L. (2004) Micelles of lipid-oligonucleotide conjugates: Implications for membrane anchoring and base pairing. *J. Phys. Chem. B 108*, 6485–6497.
(24) Bevers, S., O'De, T. P., and McLaughlin, L. W. (1998) Perylene- and naphthalene-based linkers for duplex and triplex stabilization. *J. Am. Chem. Soc. 120*, 11004–11005.
(25) Bevers, S., Schutte, S., and McLaughlin, L. W. (2000) Naphthalene- and perylene-based linkers for the stabilization of hairpin triplexes. *J. Am. Chem. Soc. 122*, 5905–5915.
(26) Letsinger, R. L., and Wu, T. (1995) Use of a stilbenedicarboxamide bridge in stabilizing, monitoring, and photochemically altering folded conformations of oligonucleotides. *J. Am. Chem. Soc. 117*, 7323–7328.
(27) Lewis, F. D., Wu, Y., and Liu, X. (2002) Synthesis, structure, and photochemistry of exceptionally stable synthetic dna hairpins with stilbene diether linkers. *J. Am. Chem. Soc. 124*, 12165–12173.
(28) Isaksson, J., and Chattopadhyaya, J. (2005) A uniform mechanism correlating dangling-end stabilization and stacking geometry. *Biochemistry 44*, 5390–5401.
(29) Isaksson, J., Acharya, S., Barman, J., Cheruku, P., and Chattopadhyaya, J. (2004) Single-stranded adenine-rich DNA and RNA retain structural characteristics of their respective double-stranded conformations and show directional differences in stacking pattern. *Biochemistry 43*, 15996–6010.
(30) Bommarito, S., Peyret, N., and SantaLucia, J., Jr. (2000) Thermodynamic parameters for DNA sequences with dangling ends. *Nucleic Acids Res. 28*, 1929–1934.
(31) Lorenz, C., Hadwiger, P., John, M., Vornlocher, H.-P., and Unverzagt, C. (2004) Steroid and lipid conjugates of siRNAs to enhance cellular uptake and gene silencing in liver cells. *Bioorg. Med. Chem. Lett. 14*, 4975–4977.
(32) Soutschek, J., Akinc, A., Bramlage, B., Charisse, K., Constien, R., Donoghue, M., Elbashir, S., Geick, A., Hadwiger, P., Harborth, J., John, M., Kesavan, V., Lavine, G., Pandey, R. K., Racie, T., Rajeev, K. G., Rohl, I., Toudjarska, I., Wang, G., Wuschko, S., Bumcrot, D., Koteliansky, V., Limmer, S., Manoharan, M., and Vornlocher, H. P. (2004) Therapeutic silencing of an endogenous gene by systemic administration of modified siRNAs. *Nature 432*, 173–178.
(33) Wolfrum, C., Shi, S., Jayaprakash, K. N., Jayaraman, M., Wang, G., Pandey, R. K., Rajeev, K. G., Nakayama, T., Charrise, K., Ndungo, E. M., Zimmermann, T., Koteliansky, V., Manoharan, M., and Stoffel, M. (2007) Mechanisms and optimization of in vivo delivery of lipophilic siRNAs. *Nat. Biotechnol. 25*, 1149–1157.
(34) Ueno, Y., Kawada, K., Naito, T., Shibata, A., Yoshikawa, K., Kim, H. S., Wataya, Y., and Kitade, Y. (2008) Synthesis and silencing properties of siRNAs possessing lipophilic groups at their 3′-termini. *Bioorg. Med. Chem. 16*, 7698–7704.
(35) Shoji, Y., Akhtar, S., Periasamy, A., Herman, B., and Juliano, R. L. (1991) Mechanism of cellular uptake of modified oligodeoxynucleotides containing methylphosphonate linkages. *Nucleic Acids Res. 19*, 5543–5550.
(36) Puglisi, J. D., and Tinoco, I., Jr. (1989) Absorbance melting curves of RNA. *Methods Enzymol. 180*, 304–325.

BC100201N

SUPPORTING INFORMATION

Properties of Double-Stranded Oligonucleotides Modified with Lipophilic Substituents

Brian M. Laing[†], *Lisa Barrow-Laing*[‡], *Maureen Harrington*[§], *Eric C. Long*[‖] *and Donald E. Bergstrom**[,†]

[†]Department of Medicinal Chemistry and Molecular Pharmacology and Bindley Bioscience Center, Purdue University, West Lafayette, IN 47907, [‡]Department of Microbiology and Immunology and [§]Department of Biochemistry and Molecular Biology, Indiana University School of Medicine, Indianapolis IN 46202, [‖]Department of Chemistry and Chemical Biology, Purdue School of Science, Indiana University-Purdue University Indianapolis (IUPUI), Indianapolis, IN 46202

*Correspondence to: Donald Bergstrom, Department of Medicinal Chemistry and Molecular Pharmacology, Birck Nanotechnology Center, Purdue University, 1205 W State St, West Lafayette, IN 47907-2057. Telephone: (765) 494-6275; Fax: (765) 494-1414; Email: bergstrom@purdue.edu

List of contents:

Table S1: MALDI-TOF-MS analysis of sequences used.

Figure S1: Structure and ^{1}H NMR spectrum of **2**.

Figure S2: Structure and ^{31}P NMR spectrum of **2**.

Figure S3: Structure and ^{1}H NMR spectrum of **4**.

Figure S4: Structure and ^{13}C NMR spectrum of **4**.

Figure S5: Structure and ^{1}H NMR spectrum of **5.**

Figure S6: Structure and ^{13}C NMR spectrum of **5**.

Figure S7: Structure and ^{31}P NMR spectrum of **5**.

Table S1: MALDI-TOF-MS analysis of sequences used.

Sequence (5'-3')	**$(M-H)^-$ Calculated**	**$(M-H)^-$ Observed**
ACG TCG ACG T	3027.0	**3031.0**
CAG TCG ACT G	3027.0	**3025.6**
TAC GTC GAC GT	3331.2	**3329.8**
GCA GTC GAC TG	3356.2	**3358.1**
TAC GTC GAC GT**A**	3645.4	**3644.2**
TCA GTC GAC TG**A**	3646.4	**3646.9**
[C12]-ACG TCG ACG T	3274.6	**3274.8**
[C12]-CAG TCG ACT G	3274.6	**3273.0**
[C12-OH]-ACG TCG ACG T	3291.2	**3293.4**
[C12-OH]-CAG TCG ACT G	3291.2	**3292.5**
ACG TCG ACG T-**[C12-OH]**	3291.3	**3292.5**
CAG TCG ACT G-**[C12-OH]**	3291.3	**3291.5**
[C12]-ACG TCG ACG T-**[C12-OH]**	3537.7	**3537.7**
[C12]-CAG TCG ACT G-**[C12-OH]**	3537.7	**3536.6**
[Dye647]GCA CGA AAG TCC CTA C**[C12**]G TAG GGA CTT TCG TGC	10606.29	**10606.71**
[Dye647]-[C12] GCA CGA AAG TCC CTA C**[C12]**G TAG GGA CTT TCG TGC**[C12-OH]**	11136.37	**11136.37**

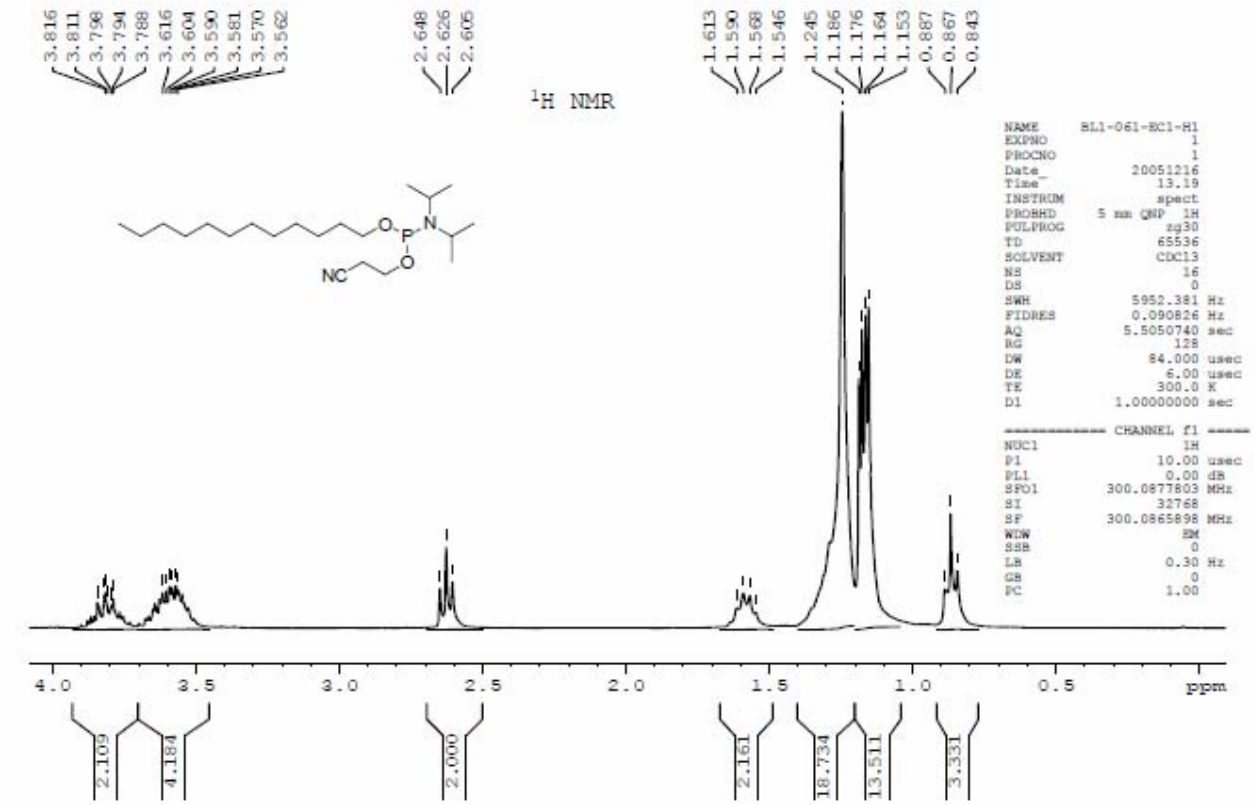


Figure S1: Structure and ^{1}H NMR spectrum of **2**.

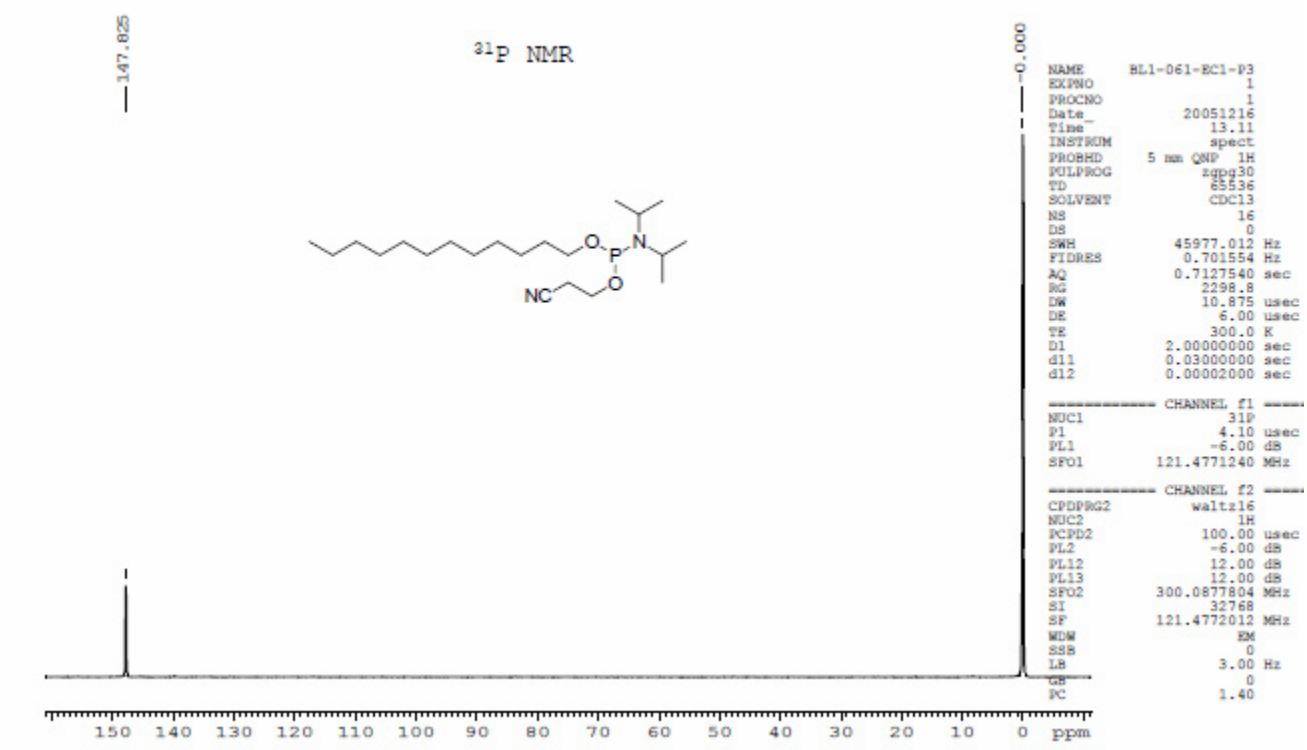


Figure S2: Structure and ^{31}P NMR spectrum of **2**.

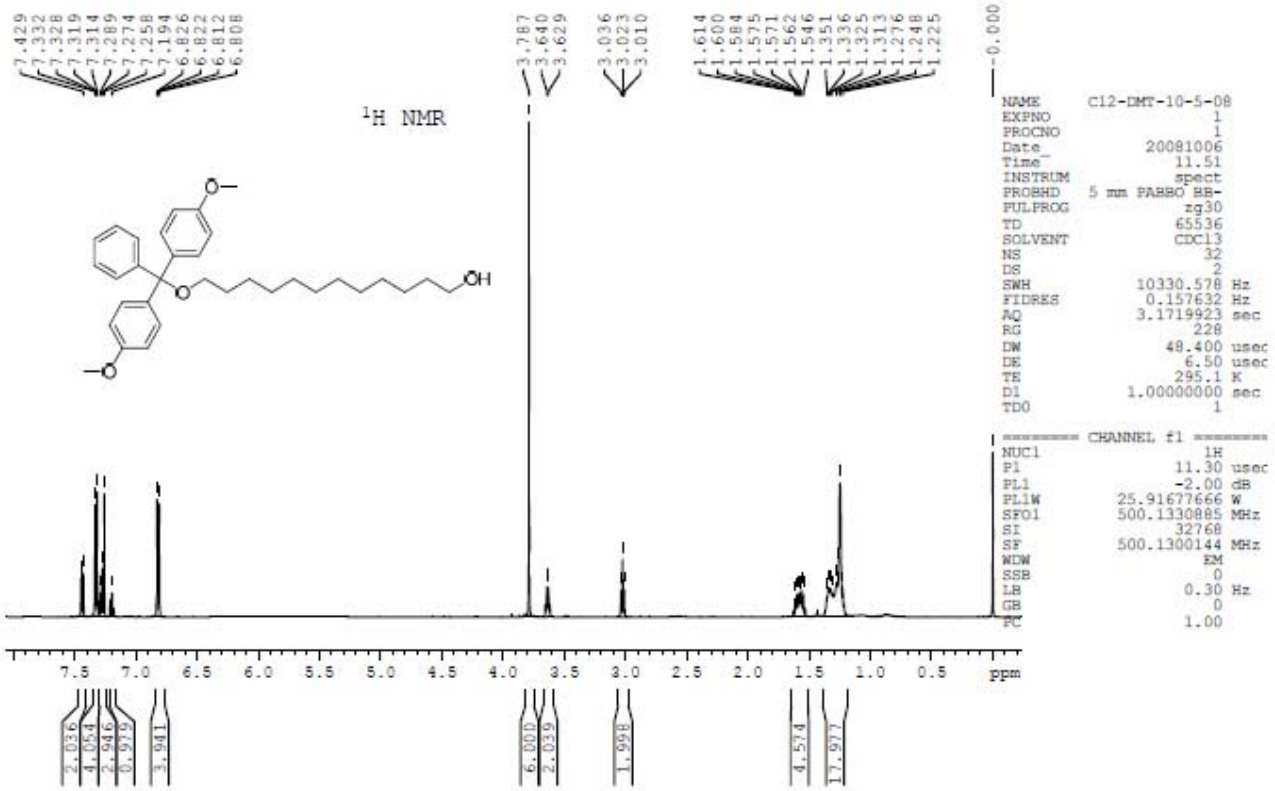


Figure S3: Structure and ^{1}H NMR spectrum of **4**.

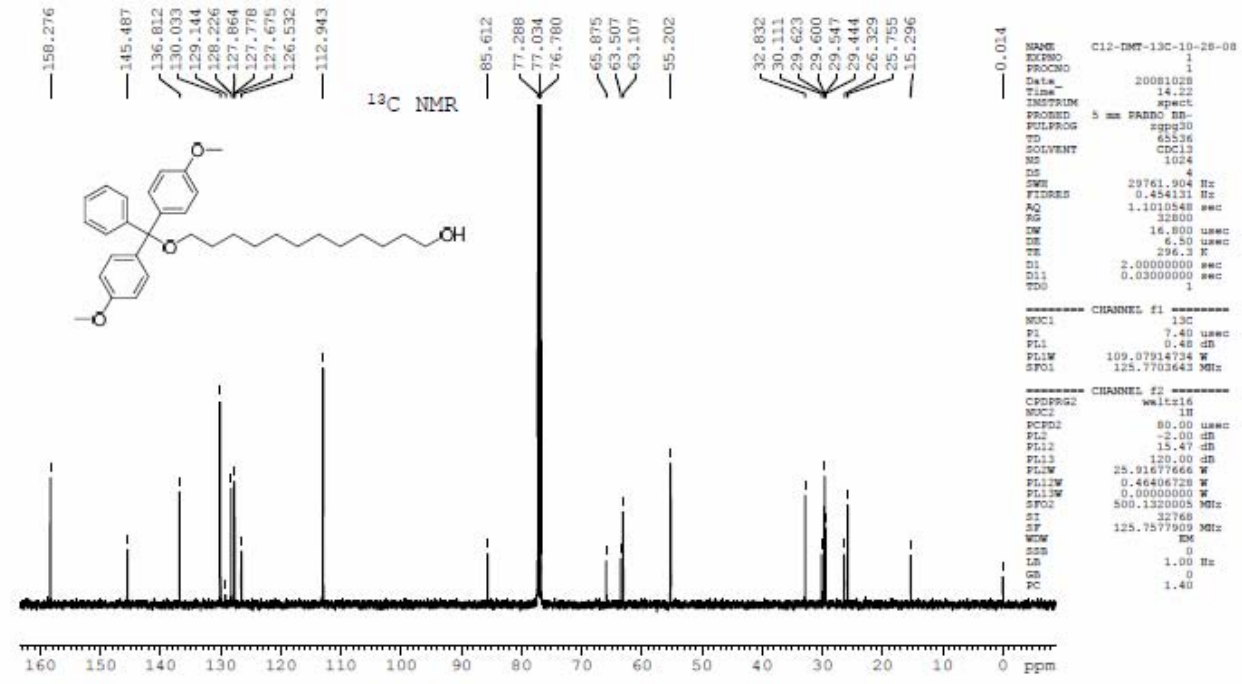


Figure S4: Structure and ^{13}C NMR spectrum of **4**.

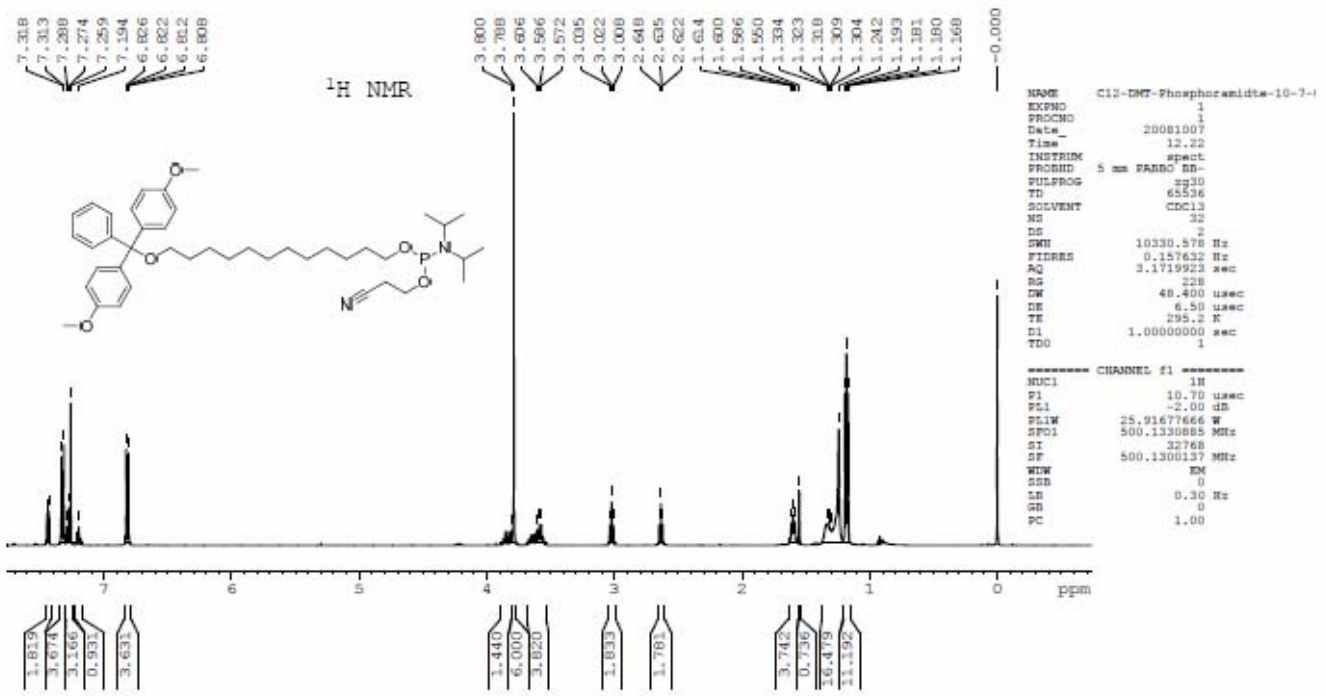


Figure S5: Structure and ^{1}H NMR spectrum of **5.**

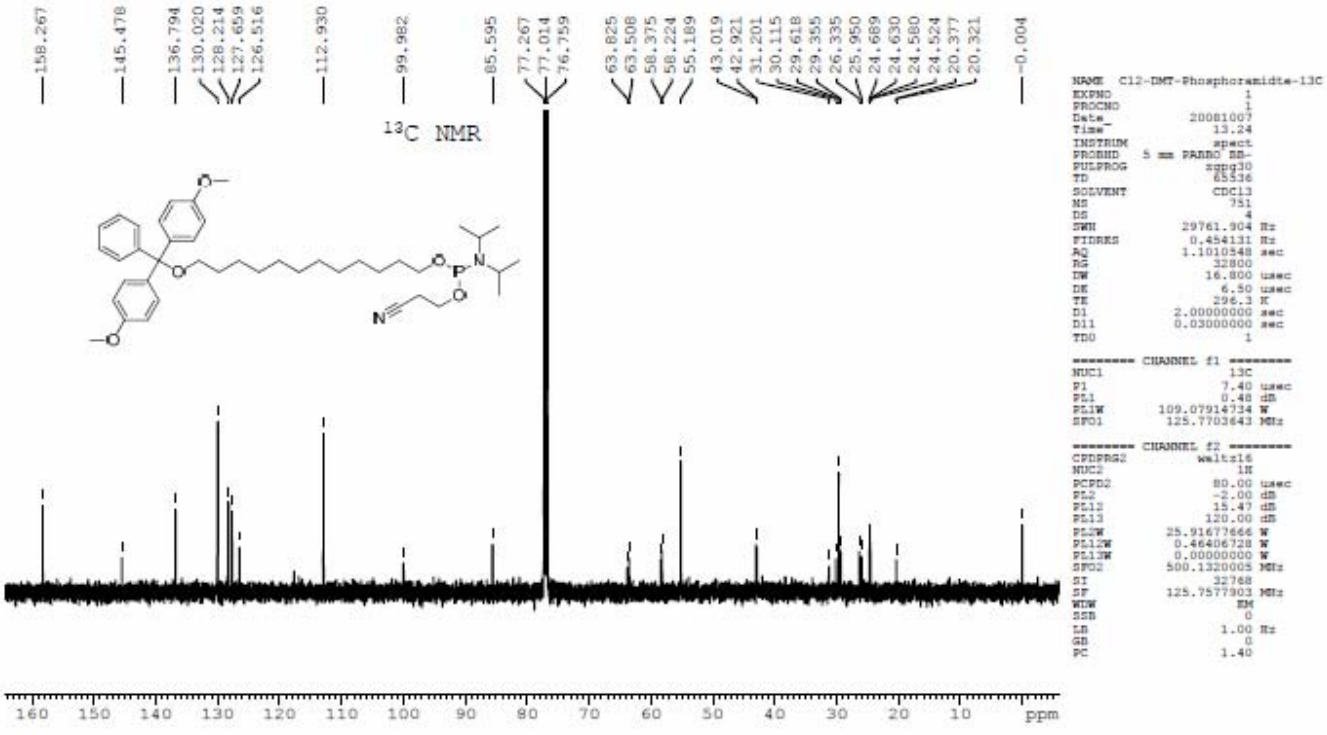


Figure S6: Structure and ^{13}C NMR spectrum of **5**.

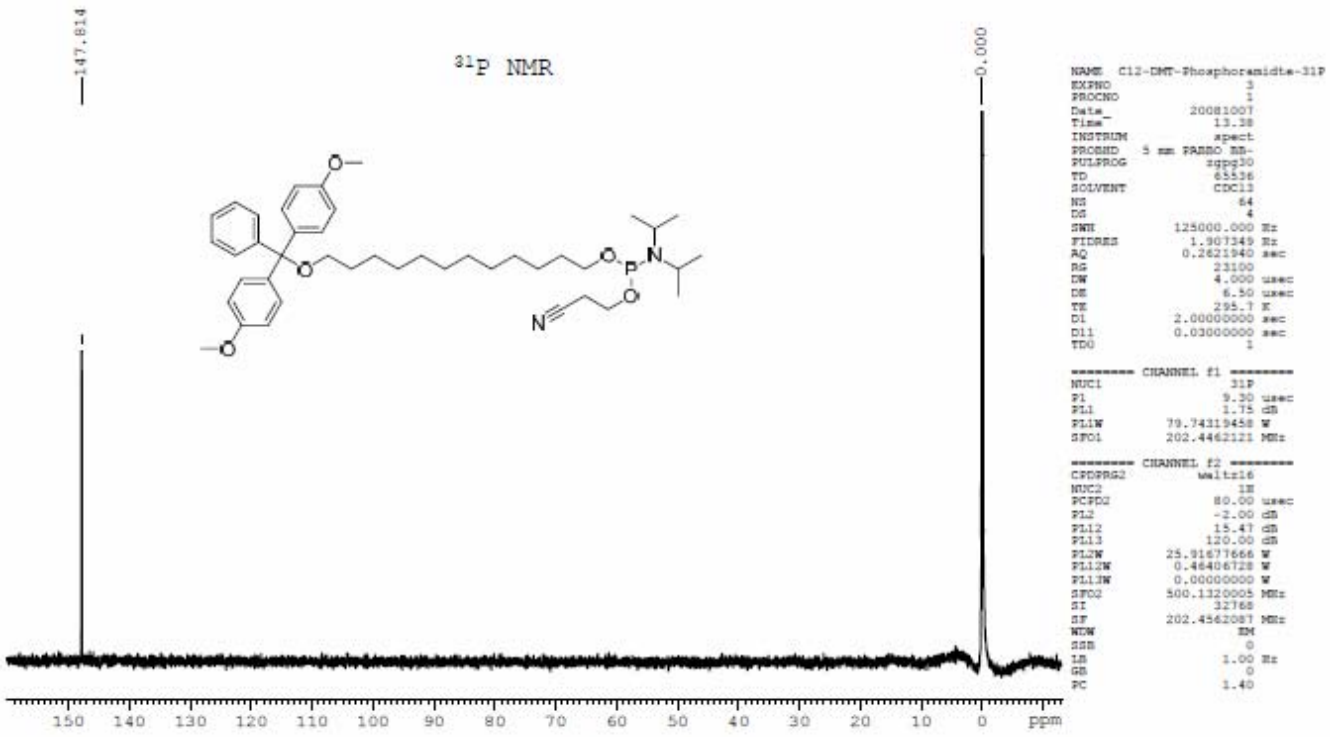


Figure S7: Structure and ^{31}P NMR spectrum of **5**.

Synthesis and Evaluation of New Spacers for Use as dsDNA End-Caps

Pei-Sze Ng,[†] Brian M. Laing,[†,‡] Ganesan Balasundarum,[†] Maneesh Pingle,[†] Alan Friedman,[§] and Donald E. Bergstrom*[,†,‡]

Department of Medicinal Chemistry and Molecular Pharmacology, Department of Biological Sciences, and Bindley Bioscience Center, Purdue University, West Lafayette, Indiana 47907. Received April 25, 2010; Revised Manuscript Received June 18, 2010

A series of aliphatic and aromatic spacer molecules designed to cap the ends of DNA duplexes have been synthesized. The spacers were converted into dimethoxytrityl-protected phosphoramidites as synthons for oligonucleotides synthesis. The effect of the spacers on the stability of short DNA duplexes was assessed by melting temperature studies. End-caps containing amide groups were found to be less stabilizing than the hexaethylene glycol spacer. End-caps containing either a terthiophene or a naphthalene tetracarboxylic acid diimide were found to be significantly more stabilizing. The former showed a preference for stacking above an A•T base pair. Spacers containing only methylene ($-CH_2-$) and amide ($-CONH-$) groups interact weakly with DNA and consequently may be optimal for applications that require minimal influence on DNA structure but require a way to hold the ends of double-stranded DNA together.

INTRODUCTION

Short double-stranded DNA segments are required as components of DNA−protein complexes for crystallographic studies. However, it is often difficult to co-crystallize a protein with an oligonucleotide segment that constitutes the recognition/binding site. Among strategies that merit investigation as potentiators of co-crystallization is the use of short preorganized DNA segments in crystallization experiments. One way to effectively preorganize short oligonucleotides into a duplex structure is to covalently link the two complementary strands (*1*). It is well-established that covalently attached linkers spanning the ends of cDNA strands significantly stabilize the duplex structure (*2*−*10*). This enhanced stabilization could be useful for increasing the preorganization of DNA duplex fragments that are commonly involved in the recognition and binding of enzymes involved in degradation, repair, and synthesis of nucleic acids. We have previously shown that DNA "end-capped" at both ends by non-nucleotide linkers are useful for stabilizing short duplex sequences for studying the DNA footprint of T4 DNA ligase (*11*).

Ideally, the linker should be a molecule that would not alter the duplex in a way that would either hinder binding or prevent readjustment of the structure as dictated by the binding protein. A linker that allows the protein to dictate the crystallization process would be preferable. Although there are a number of well-established linkers, particularly hexaethylene glycol, which is commercially available as a DMTr protected phosphoramidite, the family of stilbene linkers originally developed by Letsinger and co-workers (*8, 9*) and the naphthalene and perylene based linkers reported by McLaughlin and co-workers (*3, 12*), we thought it worthwhile to expand the potential repertoire of linkers. We were concerned that the hexaetheylene glycol spacer was neither sufficiently stabilizing nor useful for crystallographic studies because of its inherent disorder. A disadvantage of the stilbene linkers is that they are photosensitive. In addition, an X-ray structure of a duplex oligonucleotide capped by a stilbene linker has been obtained, and it was found that stilbene has considerable influence on the crystallization because of its tendency to self-associate (*13*) and the perylene-based linkers have been shown to self-associate to form dimerized hairpins (*14*). With these considerations in mind, we designed a set of very simple amide containing spacers, in which the total spacer length was close to the optimal 16−17 Å phosphate-oxygen to phosphate-oxygen distance required to span the ends of a duplex without distortion. The amide groups were expected to confer significantly more rigidity to the spacers than would be expected for hexaethylene glycol. On the basis of X-ray crystallographic studies of DNA polymerases, it is known that amide groups interact with the top face of a duplex base pair (*15, 16*). This interaction appears to involve both a CH−π interaction (acidic α-H positioned in close proximity with the π-orbitals of a nucleobase) and stacking of an amide group and may provide part of the driving force for the conformation switch between the open and closed forms of the DNA polymerase (*16*). In the event that these interactions are significant, and realizing that one could not reasonably design a spacer with sufficiently precise orientation and positioning of the amide groups, we chose to make a series of amide-containing spacers in which the amide positions vary (Figure 1). At the same time, the scope of the study was expanded by including hydrophobic spacers in order to weigh the influence of hydrophobicity on duplex stability in direct comparison to the more hydrophilic amide containing spacers. For these comparative studies, we have adopted a very simple model system, a four base pair stem, for which T_m values fall in a range that can be readily measured, but for which differences in capping ability would be easily differentiated.

EXPERIMENTAL PROCEDURES

General Information. Reagents were purchased from Aldrich Chemical Co., Inc. (Milwaukee, WI) and were used as obtained unless otherwise stated. Anhydrous solvents used for synthesis were purchased in Sure-Seal containers or distilled from appropriate drying reagents. 2-Cyanoethyl tetraisopropylphosphorodiamidite and tetrazole were purchased from ChemGenes

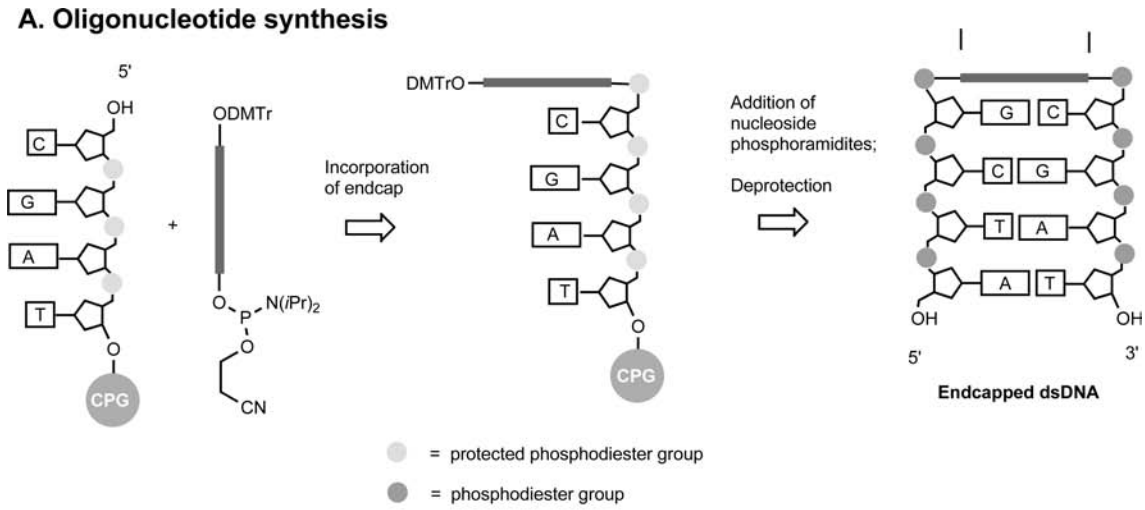
* Correspondence to Donald Bergstrom, Department of Medicinal Chemistry and Molecular Pharmacology, Birck Nanotechnology Center, Purdue University, 1205 W State St, West Lafayette, IN 47907-2057. Telephone: (765) 494-6275; Fax: (765) 494-1414. E-mail: bergstrom@purdue.edu.

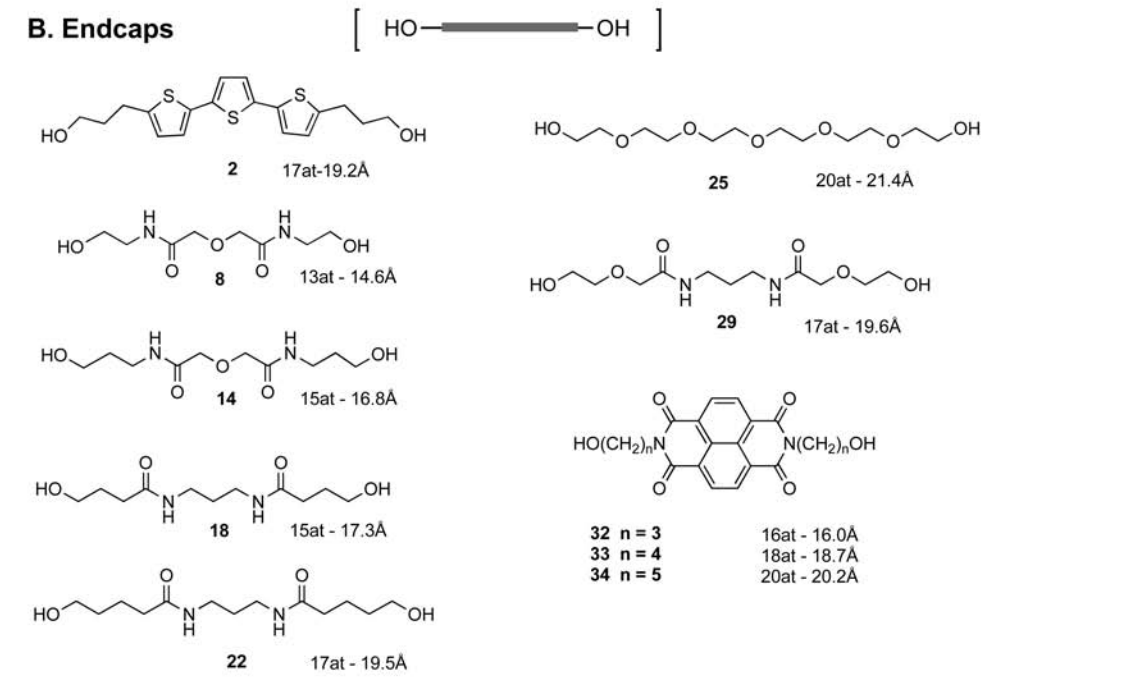
[†] Department of Medicinal Chemistry and Molecular Pharmacology.

[§] Department of Biological Sciences.

[‡] Bindley Bioscience Center.

10.1021/bc100202y © 2010 American Chemical Society
Published on Web 07/16/2010





C. Oligonucleotide sequences

I 5'-GCAT-**X**-ATGC-3'

II 5'-TACG-**X**-CGTA-3'

III 5'-CGAT-**X**-ATCG-3'

IV 5'-GCTA-**X**-TAGC-3'

V 5'-ATGC-**X**-GCAT-3'

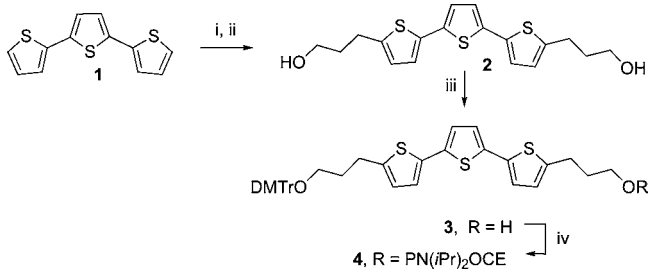
X = **2, 8, 14, 18, 22, 25, 29, 32, 33, 34,** TTTT

Figure 1. Structure of end-capped DNA sequences. (A) Synthetic scheme for the incorporation of end-caps into oligonucleotides sequences. (B) Structures of end-caps used in this study. (C) Tetramer oligonucleotides sequences.

Corporation (Waltham, MA). Standard phosphoramidite monomers and other reagents for oligonucleotide synthesis were purchased from Glen Research Corp. (Sterling, VA). Thin-layer chromatography (TLC) was performed using Sigma-Aldrich TLC plates, silica gel on aluminum 60F-254 plates. Purification of compounds by silica gel chromatography was performed using Aldrich 230−400 mesh, 60 Å silica gel. Nuclear magnetic resonance spectra were obtained using 250, 300, or 500 MHz Bruker spectrometers. ^{1}H and ^{13}C spectra were referenced to TMS, while ^{31}P spectra were referenced to an 85% phosphoric acid external standard.

Oligonucleotides (Figure 1) were synthesized on an Applied Biosystems 392 DNA/RNA synthesizer using standard phosphoramidite chemistry. Oligonucleotides were either purified by 20% polyacrylamide gel (PAGE, 60 cm × 40 cm × 0.15 cm) (trityl off) with 7 M urea in 1× Tris-borate-EDTA (TBE) buffer at a constant power of 60 W or by HPLC (trityl on) on a Varian C18 Dynamax-100 60 Å column (7.9 mm × 250 mm) at a flow rate of 4 mL/min. Mobile phase A was 0.1 M triethylammonium acetate (pH 7.0)/5% acetonitrile and mobile phase B was 90% acetonitrile. The solvent program was a gradient starting at 100% A and linearly increasing to 45% B in 60 min. For analytical HPLC, a Varian Microsorb-MV-100 Å (4.6 mm × 250 mm) column at a flow rate of 1 mL/min was used. The diode array detector was set at 260 nm. The oligonucleotides were desalted by 2-propanol precipitation or

Scheme 1. Synthetic Pathway for the Preparation of the Phosphoramidite Derivative of End-Cap 2[a]



[a] Reagents and conditions: (i) BuLi, −78°C; (ii) BF_3 - Et_2O, oxetane; (iii) DMTrCl, pyridine; (iv) 2-cyanoethyl-*N*,*N*-diisopropyl-chlorophosphoramidite, diisopropylethylamine.

by elution using CH_3CN/H_2O (1:1) from C18 Sep-pak cartridges (Waters). The oligonucleotides were characterized by MALDI-TOF MS (Supporting Information Table S4).

Spacer Synthesis. The synthetic transformations are summarized in Schemes 1−4.

*2-(tert-Butyldimethylsilyloxy)ethylamine (***6***).* To a solution of ethanolamine (**5**) (7.24 mL, 120 mmol, 1 equiv) in anhydrous CH_2Cl_2 (100 mL) at 0 °C were added anhydrous triethylamine (18.5 mL, 132 mmol, 1.1 equiv), *tert*-butyldimethylsilyl chloride (20.10 g, 132 mmol, 1.1 equiv), and a catalytic amount of 4-(*N*,*N*-dimethylamino)pyridine (DMAP) (0.5 g). The reaction mixture was stirred under argon overnight. The reaction was quenched with water (50 mL) and the layers separated. The organic layer was washed with water, brine, dried (Na_2SO_4), filtered, and concentrated in vacuo to give colorless oil (17.96 g, 86%). ^{1}H NMR (250 MHz, $CDCl_3$, δ, ppm): 3.63 (t, 2H, J = 5.5 Hz), 2.78 (t, 2H, J = 6 Hz), 0.81 (s, 9H), 0.06 (s, 6H). ^{13}C NMR (75 MHz, $CDCl_3$, δ, ppm): 65.16, 44.27, 25.90, 18.30, −5.33. HRMS (EI, M-CH_3^+): calcd. for $C_7H_{18}NOSi$ 160.1158; act. 160.1165.

*N,N′-Bis[2-(tert-butyldimethylsilyloxyethyl]-2,2′-oxidiacetamide (***7***).* To a solution of **6** (16.26 g, 93 mmol, 2.2 equiv) in anhydrous CH_2Cl_2 (40 mL) at 0 °C was added anhydrous triethylamine (17.8 mL, 127 mmol, 3 equiv), and diglycolyl chloride (5 mL, 42.5 mmol, 1 equiv) was added dropwise with a syringe. The reaction mixture was stirred under argon overnight. The reaction was quenched with water (40 mL) and the layers separated. The organic layer was washed with 5% acetic acid (2 × 40 mL), 5% aqueous $NaHCO_3$ (2 × 40 mL), and brine, and dried (Na_2SO_4) and concentrated in vacuo to give a brown oil (14.75 g, 78%). ^{1}H NMR (250 MHz, $CDCl_3$, δ, ppm): 4.07, (s, 4H), 3.71 (t, 4H, J = 5.6 Hz), 3.41−3.48 (t, 4H, J = 5.6 Hz), 0.090 (s, 18H), 0.076 (s, 9H). ^{13}C NMR (75 MHz, $CDCl_3$, δ, ppm): 168.14, 71.16, 61.58, 40.99, 25.78, 18.19, −5.42. HRMS (EI, M+H^+): calcd. for $C_{20}H_{45}N_2O_5Si_2$ 449.2867; act. 449.2849.

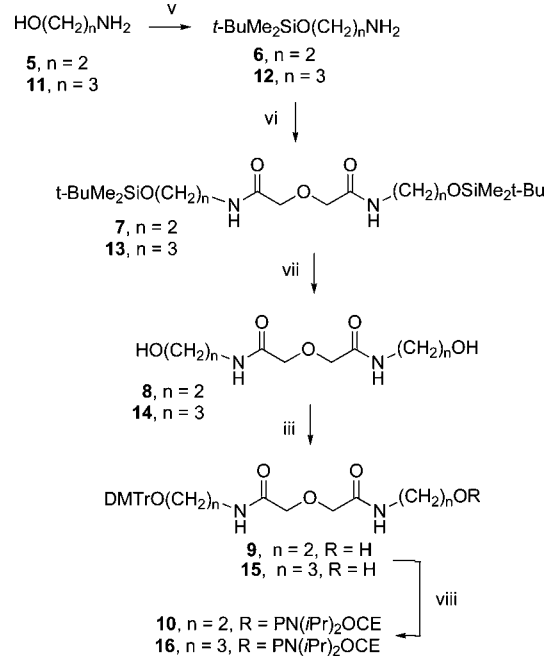
*N,N′-Bis(2-hydroxyethyl)-2,2′-oxidiacetamide (***8***; Scheme 2).* To a solution of **7** (14.06 g, 31.3 mmol) in 95% ethanol (15 mL) was added 2.9% w/w of conc. HCl in 95% ethanol (15 mL). The reaction mixture was stirred under argon for 15 min and solvent removed in vacuo to give an orange solid. The orange solid was dissolved in methanol (20 mL), washed with hexane (3 × 30 mL), dried (Na_2SO_4), and concentrated in vacuo to give an orange solid (6.47 g, 94%). ^{1}H NMR (250 MHz, $CDCl_3$, δ, ppm): 4.06 (s, 4H), 3.63 (t, 4H, J = 5.8 Hz), 3.34−3.39 (m, 4H). ^{13}C NMR (75 MHz, $CDCl_3$, δ, ppm): 172.00, 71.42, 61.44, 42.58. HRMS (EI, M−OH^+): calcd. for $C_8H_{15}N_2O_4$ 203.1032; act. 203.1034.

*N-[2-(4, 4′-Dimethoxytrityl)oxyethyl]-N′-(2-hydroxyethyl)-2,2′-oxidiacetamide (***9***).* To a solution of **8** (2.00 g, 90.8 mmol, 1 equiv) in anhydrous pyridine (35 mL) at 0 °C was added 4,4′-dimethoxytrityl chloride (3.23 g, 90.8 mmol, 1 equiv). The reaction mixture was stirred under argon overnight. Upon completion as judged by TLC, pyridine was removed in vacuo. The crude brown product was dissolved in CH_2Cl_2 (40 mL), washed with aqueous 5% $NaHCO_3$ and brine, and dried (Na_2SO_4). CH_2Cl_2 was removed in vacuo and the crude product purified by flash chromatography (silica gel, 0−5% CH_3OH/1% Et_3N/CH_2Cl_2) to give a brown foam (1.67 g, 35.2%). ^{1}H NMR (250 MHz, CD_2Cl_2, δ, ppm): 6.82−7.46 (m, 13H), 4.03 (s, 2H), 4.01 (s, 2H), 3.78 (s, 6H), 3.59 (m, 2H), 3.48 (m, 2H), 3.33 (m, 2H), 3.20 (m, 2H). ^{13}C NMR (75 MHz, CD_2Cl_2, δ, ppm): 169.81, 168.93, 158.98, 145.32, 136.31, 130.32, 128.34, 128.21, 127.22, 113.52, 86.53, 71.44, 62.52, 62.02, 55.61, 42.23, 39.54. HRMS (ESI, M+H^+): calcd. for $C_{29}H_{35}N_2O_7$ 523.2444; act. 523.2445.

*N-[3-O-(2-cyanoethyl-N,N-diisopropylphosphoramidite)ethyl]-N′-[2-(4,4′-dimethoxytrityl)oxyethyl]-2,2′-oxidiacetamide (***10***).* To a solution of **9** (211.2 mg, 0.404 mmol, 1 equiv) in anhydrous CH_2Cl_2 (5 mL) were added anhydrous diisopropylethylamine (0.25 mL, 1.45 mmol, 3.6 equiv) and 2-cyanoethyldiisopropyl chlorophosphoramidite (0.49 mL, 0.485 mmol, 1.2 equiv). The reaction was stirred for two hours at room temperature under argon. When the reaction was completed as judged by TLC, the reaction mixture was washed with aqueous 5% $NaHCO_3$ and water and dried (Na_2SO_4). The crude product was further purified by flash chromatography (silica gel, 5:4:1 hexane/CH_2Cl_2/Et_3N) to give a yellow oil (106.7 mg, 53.5%). ^{31}P NMR (100.8 MHz, CD_2Cl_2, δ, ppm): 148.3 (referenced to external 85% H_3PO_4).

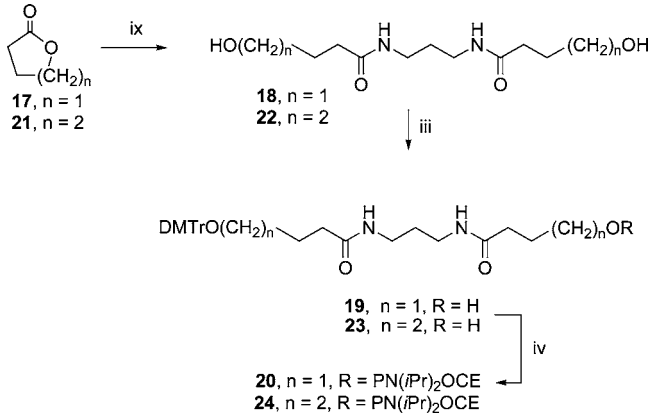
*N,N′-Bis-(4-hydroxybutanoyl)-1,3-propanediamine (***18***; Scheme 3).* 1,3-Diaminopropane (2.0 mL, 24 mmol), δ-butyrolactone (**17**) (6.2 mL, 80 mmol), and DMAP (40 mg, 0.32 mmol) in methanol (30 mL) were kept under reflux for overnight. The solvent was removed by rotary evaporation, and CH_2Cl_2 (50 mL) was added to the residue with stirring on low heat to break up the white-colored solid. The solid was filtered and mixed with CH_2Cl_2 (50 mL) and again stirred at low heat and filtered.

Scheme 2. Synthetic Pathway for the Preparation of the Phosphoramidite Derivatives of End-Caps 8 and 14[a]



[a] Reagents and conditions: (iii) DMTrCl, pyridine; (v) *t*$BuMe_2SiCl$, *N*,*N*-dimethylaminopyridine (DMAP), Et_3N; (vi) diglycolyl chloride, Et_3N; (vii) HCl, EtOH; (viii) 2-cyanoethyl-*N*,*N*,*N*′,*N*′-tetraisopropylphosphorodiamidite, tetrazole.

Scheme 3. Synthetic Pathway for the Preparation of the Phosphoramidite Derivatives of End-Caps 18 and 22[a]



[a] Reagents and conditions: (iii) DMTrCl, pyridine; (iv) 2-cyanoethyl-*N*,*N*-diisopropyl-chlorophosphoramidite, diisopropylethylamine; (ix) 1,3-diaminopropane, DMAP, methanol.

This procedure was repeated once more, and the final white solid was dried under vacuum (4.6 g, 80%). ^{1}H NMR (250 MHz, DMSO-d_6, δ, ppm) 1.43−1.65 (m, 6H), 2.07 (t, J = 9 Hz, 4H), 2.99 (t, J= 6 Hz, 2H), 3.01 (t, J = 6 Hz, 2H), 3.34 (t, J =6 Hz, 4H), 4.48 (s, 2H), 7.76 (t, J = 6 Hz, 2H); ^{13}C NMR (75 MHz, $CDCl_3$, δ, ppm) 29.01, 29.65, 32.52, 36.62, 60.67, 172.52. HRMS (ESI, M + H$^+$) calcd. for $C_{11}H_{22}N_2O_4$ 247.1657, found 247.1657.

*N-{4-[4,4′-(Dimethoxytrityl)oxy]butanoyl}-N′-4-hydroxybutanoyl-1,3-propanediamine (***19***).* Diol **18** (2.46 g, 10 mmol) was co-evaporated with dry pyridine (3 × 20 mL) and dissolved in dry pyridine (30 mL), and after cooling to 0 °C in an ice bath, 4,4′-dimethoxytrityl chloride (4.4 g, 13 mmol) in CH_2Cl_2 (20 mL) was added dropwise slowly. The flask was removed from ice, and the reaction mixture was stirred overnight, quenched with methanol (1 mL), diluted with CH_2Cl_2 (200 mL), washed with 5% $NaHCO_3$ (2 × 200 mL) and brine (100 mL), and dried over anhydrous sodium sulfate. The solution was concentrated in vacuo, and the crude product was purified by silica gel chromatography in a gradient of methanol (0 to 5%) in $CHCl_3$ containing 0.5% Et_3N. The appropriate fractions were combined, evaporated, and dried in vacuo to give compound **19** as pale yellow foam (2.9 g, 53%), R_f 0.50 ($CHCl_3$−MeOH 9:1 v/v). ^{1}H NMR (250 MHz, $CDCl_3$, δ, ppm) 1.49−1.53 (m, 2H), 1.81−1.94 (m, 4H), 2.31 (t, J = 6 Hz, 2H), 2.33 (t, J = 6 Hz, 2H), 3.08−3.20 (m, 6H), 3.63 (t, J = 6 Hz, 2H), 3.76 (s, 6H), 6.82 (d, J = 12.3, 4H), 7.18−7.32 (m, 7H), 7.39 (d, J = 9.0 Hz, 2H); ^{13}C NMR (62.5 MHz, $CDCl_3$, δ, ppm) 26.04, 28.18, 29.42, 33.70, 33.83, 35.75, 35.81, 55.11, 61.96, 62.32, 85.83, 112.96, 126.62, 127.68, 127.99, 129.86, 136.17, 144.94, 158.28, 173.76, 173.95. HRMS (ESI, M + Na$^+$) calcd. for $C_{32}H_{40}N_2O_6$ 571.2784; act. 571.2785.

*N-[4-O-(2-cyanoethyl-N,N-diisopropylphophoramidite)butanoyl]-N′-{4-[4,4′-(dimethoxytrityl)oxy]butanoyl}-1,3-propanediamine (***20***).* The mono-DMT-derivative **19** (0.55 g, 1 mmol) was co-evaporated with 10% dry pyridine in CH_2Cl_2 (3 × 10 mL), and DIEA (0.63 mL, 3.6 mmol) was added with stirring under nitrogen followed by the addition of 2-cyanoethyl diisopropylchlorophosphoramidite (0.27 mL, 1.2 mmol). The reaction was performed at room temperature for two hours with TLC monitoring. After reaction completion, the mixture was quenched with 4 drops of anhydrous methanol, and CH_2Cl_2 (20 mL) was added. The methylene chloride solution was washed once with 5% $NaHCO_3$ (20 mL), once with brine (10 mL), and then dried over anhydrous sodium sulfate. The solution was concentrated in vacuo, and the crude product was purified by silica gel chromatography in a gradient of methanol (0% to 5%) in CH_2Cl_2 containing 0.5% Et_3N. The appropriate fractions were combined, evaporated, and dried under vacuum to give phosphoramidite **20** as pale yellow product (0.4 g, 54%), R_f 0.90 (CH_2C_2−MeOH 9:1 v/v); HRMS (ESI, M+H$^+$) calcd. for $C_{41}H_{57}N_4O_7P$ 749.4043, found 749.4050; ^{31}P NMR (100.8 MHz, $CDCl_3$, ppm) δ 165.0 (referenced to external 0.0485 M triphenylphosphate in $CDCl_3$).

*N,N′-Bis-(5-hydroxypentanoyl)-1,3-propanediamine (***22***).* 1,3-Diaminopropane (1.7 mL, 20 mmol), δ-valerolactone (7.5 mL, 80 mmol), and DMAP (40 mg, 0.32 mmol) in methanol (30 mL) were refluxed overnight. The solvent was removed by rotary evaporation, and CH_2Cl_2 (50 mL) was added to the residue with stirring on low heat to break up the white-colored solid. The solid was filtered and mixed with CH_2Cl_2 (50 mL) and again stirred at low heat and filtered. This procedure was repeated once more, and the final white solid was dried under vacuum (4.65 g, 85%). ^{1}H NMR (250 MHz, DMSO-d_6, δ, ppm) 1.31−1.54 (m, 10 H), 2.03 (t, J = 9 Hz, 4H), 2.99 (t, J = 6 Hz, 2H), 3.01 (t, J = 6 Hz, 2H), 3.33−3.38 (m, 4H), 4.35 (s, 2H), 7.74 (t, J = 3 Hz, 2H); ^{13}C NMR (75 MHz, DMSO-d_6, δ, ppm) 22.30, 29.75, 32.42, 35.63, 36.60, 60.79, 172.45. HRMS (ESI, M+H$^+$) calcd. for $C_{13}H_{26}N_2O_4$ 275.1970, act. 275.1972.

*N-{5-[4,4′-(Dimethoxytrityl)oxy]pentanoyl}-N′-(5-hydroxypentanoyl]-1,3-propanediamine (***23***).* Diol **22** (2.75 g, 10 mmol) was co-evaporated with dry pyridine (3 × 20 mL) and then dissolved in dry pyridine (30 mL), and after cooling to 0 °C in an ice bath, 4,4′-dimethoxytrityl chloride (4.4 g, 13 mmol) in CH_2Cl_2 (20 mL) was added dropwise slowly. The flask was removed from ice, and the reaction mixture was stirred overnight, quenched with methanol (1 mL), diluted with CH_2Cl_2 (200 mL), washed with 5% $NaHCO_3$ (2 × 200 mL) and brine (100 mL), and dried over anhydrous sodium sulfate. The solution was concentrated in vacuo, and the crude product was purified by silica gel chromatography in a gradient of methanol (0% to 5%) in $CHCl_3$ containing 0.5% Et_3N. The appropriate fractions were combined, evaporated, and dried in vacuum to give compound **23** as pale yellow foam (2.65 g, 46%), R_f 0.5 ($CHCl_3$−MeOH 9:1 v/v); ^{1}H NMR (250 MHz, $CDCl_3$, δ, ppm) 1.54−1.72 (m, 10H), 2.12−2.24 (m, 4H), 3.06 (t, J = 6 Hz, 2H), 3.19 (t, J = 6 Hz, 2H), 3.21 (t, J = 6 Hz, 2H), 3.58 (t, J = 6 Hz, 2H), 3.75 (s, 6H), 6.81 (d, J = 6 Hz, 4H), 7.17−7.32 (m, 7H), 7.40−7.43 (m, 2H); ^{13}C NMR (75 MHz, $CDCl_3$, δ, ppm) 22.01, 22.75, 29.61, 29.63, 31.98, 35.80, 35.89, 36.10, 36.47, 55.18, 61.78, 62.93, 76.75, 77.18, 77.60, 85.77, 112.99, 126.62, 127.71, 128.13, 129.98, 136.49, 145.23, 158.30, 173.92, 173.98. HRMS (ESI, M+Na$^+$) calcd. for $C_{34}H_{44}N_2O_6$ 599.3097, found 599.3106.

*N-[5-O-(2-Cyanoethyl-N,N-diisopropylphosphoramidite)pentanoyl]-N′-{5-[4,4′-(dimethoxytrityl)oxy]pentanoyl}-1,3-propanediamine (***24***).* The mono-DMT-derivative **23** (0.4 g, 0.7 mmol) was co-evaporated with 10% dry pyridine in CH_2Cl_2 (3 × 10 mL), and DIEA (0.43 mL, 2.5 mmol) was added with stirring under nitrogen followed by the addition of 2-cyanoethyl diisopropylchlorophosphoramidite (0.19 mL, 0.84 mmol). The reaction was performed at room temperature for two hours with TLC monitoring. After reaction completion, the mixture was quenched with 4 drops of anhydrous methanol, CH_2Cl_2 (20 mL) was added, and the mixture was washed with 5% $NaHCO_3$ (2 × 20 mL) and brine (10 mL) and dried over anhydrous sodium sulfate. The solution was concentrated in vacuo, and the crude product was purified by silica gel chromatography in a gradient of methanol (0% to 5%) in CH_2Cl_2 containing 0.5% Et_3N. The appropriate fractions were combined, evaporated, and dried in vacuum to give phosphoramidite **24** as pale yellow product (0.3 g, 55%), R_f 0.92 (CH_2Cl_2−MeOH 9:1 v/v); HRMS (ESI, M+Na$^+$) calcd. for $C_{43}H_{61}N_4O_7P$ 799.4175, found 799.4169;

^{31}P NMR (100.8 MHz, $CDCl_3$, δ, ppm) 164.5 (referenced to external 0.0485 M triphenylpohosphate in $CDCl_3$).

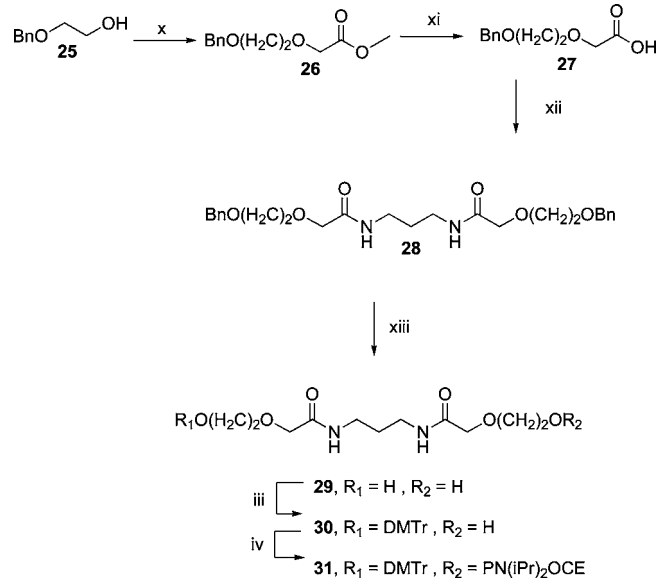
*Methyl 2-(2-(Benzyloxy)ethoxy)acetate (***26***).* 2-Benzyloxyethanol (**25**) (9.96 mL, 70 mmol) was added to a suspension of NaH (3.4 g, 84 mmol) in anhydrous THF (100 mL) under argon. The mixture was stirred for 1 h at r.t., then cooled to 0 °C. Methyl bromoacetate (7.72 mL, 84 mmol) was added slowly, and the mixture was allowed to react at room temperature for 16 h. The reaction was quenched with H_2O (30 mL) and the product extracted with ethyl acetate (5 × 50 mL). The ethyl acetate fractions were combined and washed successively with H_2O (3 × 100 mL) and brine (3 × 100 mL). The organic fraction was dried over anhyd $MgSO_4$ and concentrated in vacuo. The crude product was purified by silica gel chromatography (ethyl acetate−hexanes 1:4). The appropriate fractions were combined, evaporated, and dried under vacuum to give **26** (13.2 g, 84%) as yellow oil. R_f 0.67 (ethyl acetate−hexanes 1:1 v/v). ^{1}H NMR (300 MHz, $CDCl_3$, ppm): 7.28 (m, 5H), 4.56 (s, 2H), 4.18 (s, 2H), 3.80−3.68 (m, 7H). ^{13}C NMR (75 MHz, $CDCl_3$,, ppm): 170.8, 138.1, 128.3, 127.7, 73.2, 71, 69.5, 68.7. HRMS (EI, M^+) calcd for $C_{12}H_{16}O_4$ 224.1049, act. 224.1045.

*2-(2-(Benzyloxy)ethoxy)acetic Acid (***27***).* **26** (7 g, 29.38 mmol) was dissolved in 20 mL methanol and heated to ∼35 °C with stirring. KOH (4.95 g, 88.13 mmol) was added. The mixture was stirred with TLC monitoring (1:1 ethyl acetate/hexanes) for 1 h. The reaction was quenched by adding 80 mL H_2O. The unreacted ester was extracted with ether (2 × 50 mL). The aqueous portion was acidified to pH 2 with 6 N HCl, then extracted with ether (3 × 50 mL); the ether layers were combined, dried over Na_2SO_4, and dried under vacuum to yield **27** (5.83 g 95%) as a clear oil. ^{1}H NMR (300 MHz, DMSO-d_6, ppm): 12.62 (s, 1H), 7.33 (m, 5H), 4.48 (s, 2H), 4.04 (s, 2H), 3.55−3.65 (m, 4H). ^{13}C NMR (75 MHz, DMSO-d_6, δ, ppm): 171.73, 138.48, 128.26, 127.56, 127.43, 72.07, 71.74, 69.89, 67.16, 60.31. HRMS (ESI, M + H^+) calcd. for $C_{11}H_{15}O_4$ 211.0970, act. 211.0971.

*N,N′-Bis-(2-(2-benzyloxyethoxy)ethanoyl)-1,3-propanediamine (***28***).* **27** (2.13 g, 10.12 mmol) was dissolved in dry DMF (10 mL) under argon. TBTU (3.25 g, 10.12 mmol) and *N*-methylmorpholine (1.02 g, 10.12 mmol) were added and the mixture stirred for 15 min. 1,3-Diaminopropane (0.28 mL, 4.05 mmol) was dissolved in dry DMF (5 mL) and added slowly. The mixture was stirred overnight at room temperature. DMF was evaporated under reduced pressure, and the residue was dissolved in ethyl acetate (100 mL), and washed with 5% $NaHCO_3$ (75 mL × 2), 10% $CuSO_4$ (75 mL × 2), and brine (75 mL). The organic layer was dried over anhyd magnesium sulfate and concentrated under vacuum. The crude product was purified by silica gel chromatography (0−5% MeOH/ethyl acetate). The appropriate fractions were combined, evaporated, and dried under vacuum to yield **28** (0.92 g, 50%) as a light brown oil, R_f 0.68 (10% MeOH/ethyl acetate 9:1 v/v). ^{1}H NMR (300 MHz, DMSO-d_6,, ppm): 7.71 (t, J = 7 Hz, 2H), 7.30 (m, 10H), 4.49 (s, 4H), 3.86 (s, 4H), 3.61 (m, 8H), 3.03 (q, 4H, J = 7 Hz), 1.44 (t, 2H, J = 7 Hz). ^{13}C NMR (75 MHz, DMSO-d_6, ppm): 169.17, 138.33, 128.23, 127.52, 72.11, 70.23, 70.01, 68.95, 35.50, 29.38. HRMS (ESI, M + H^+) calcd. for $C_{25}H_{35}N_2O_6$ 459.2495, act. 459.2502.

*N,N′-Bis-(2-(2-hydroxyethoxy)ethanoyl)-1,3-propanediamine (***29***; Scheme 4).* **28** (2.73 mg, 5.9 mmol) was dissolved in 40 mL EtOH. Pd/C (10 wt %, 800 mg) was added, and the mixture was treated with H_2 gas (55 psi) on a Parr apparatus for 12 H. The mixture was filtered over Celite on a sintered glass funnel, evaporated, and dried in vacuum to give compound **29** as a white solid (1.548 g, 94%). ^{1}H NMR (300 MHz, DMSO-d_6, ppm): 7.91 (s, 2H), 4.84 (s, 2H), 3.92 (s, 4H), 3.48 (m, 8H), 3.12 (m, 4H), 1.562 (m, 2H). ^{13}C NMR (75 MHz, DMSO-d_6, ppm): 169.53, 72.91, 69.99, 60.13, 35.71, 29.44. HRMS (ESI, M + Na^+) calcd. for $C_{11}H_{22}N_2NaO_6$ 301.1376, act. 301.1372.

Scheme 4. Synthetic Pathway for the Preparation of the Phosphoramidite Derivative of End-Cap 29[a]



[a] Reagents and conditions: (iii) DMTrCl, pyridine; (iv) 2-cyanoethyl-*N*,*N*-diisopropyl-chlorophosphoramidite, diisopropylethylamine; (x) methyl bromoactetate, NaH, THF reflux, r.t.; (xi) MeOH, KOH, 35 °C; (xii) 1,3-diaminopropane, TBTU, r.t.; (xiii) H_2, Pd/C.

*N-(2-(2-(4,4′-Dimethoxytrityloxy)ethoxy)ethanoyl)-N′-(2-(2-hydroxyethoxy)ethanoyl)-1,3-propanediamine (***30***).* Diol **29** (0.56 g, 2 mmol) was co-evaporated with dry pyridine (3 × 10 mL), dissolved in dry pyridine (15 mL), and after cooling to 0 °C, 4,4′-dimethoxytrityl chloride (0.81 g, 2.4 mmol) in CH_2Cl_2 was added dropwise slowly. The flask was removed from the ice and the reaction mixture stirred overnight, quenched with methanol (0.5 mL), and diluted with CH_2Cl_2 (50 mL). The mixture was washed with 5% $NaHCO_3$ (50 mL × 2) and brine (50 mL) and dried over anhydrous sodium sulfate. The solution was concentrated in vacuo, and the crude product was purified by silica gel chromatography (0−5% MeOH/CH_2Cl_2 containing 1% Et_3N). The appropriate fractions were combined, evaporated, and dried in vacuum to give **30** as a yellow foam (0.12 g, 10%), R_f 0.60 (8% MeOH/CH_2Cl_2). ^{1}H NMR (500 MHz, DMSO-d_6, ppm): 7.85 (t, 1H, J = 6 Hz), 7.74 (t, 1H, J = 6 Hz), 7.38−7.39 (m, 2H), 7.31 (t, 2H, J = 7.5 Hz), 7.22−7.26 (m, 5H), 6.89 (d, 4H, J = 9 Hz), 4.76 (t, 1H, J = 5 Hz), 3.91 (s, 2H), 3.85 (s, 2H), 3.73 (s, 6H), 3.63 (t, 2H, J = 5 Hz), 3.53 (t, 2H, J = 5 Hz), 3.47 (t, 2H, J = 5 Hz), 3.08−3.14 (m, 6H), 1.54 (p, 2H, J = 6.5 Hz). ^{13}C NMR (125.76 MHz, DMSO-d_6, ppm): 29.37, 35.52, 35.61, 54.96, 59.99, 62.55, 69.92, 70.15, 70.22, 72.78, 85.45, 112.70, 113.11, 123.79, 126.57, 127.63, 127.71, 128.82, 129.57, 135.64, 135.99, 144.82, 149.52, 158.01, 169.07, 169.22. HRMS (ESI, M+Na^+) calcd. for $C_{32}H_{40}N_2NaO_8$ 603.2682, act. 603.2680.

*N-(2-(2-O-(2-Cyanoethyl-N,N-diisopropylphosphoramidite)-ethoxy)ethanoyl)-N′-(2-(2-(4,4′-dimethoxytrityloxy)ethoxy)ethanoyl)-1,3-propanediamine (***31***).* **30** (0.11 g, 0.19 mmol) was co-evaporated with 10% anhydrous pyridine in CH_2Cl_2 (2 × 10 mL), then dissolved in anhydrous CH_2Cl_2 (10 mL). DIEA (0.1 mL, 0.76 mmol) was added with stirring under argon followed by the addition of 2-cyanoethyl diisopropylchlorophosphoramidite (0.11 mL, 0.47 mmol). The mixture was stirred at room temperature for 2 h with TLC monitoring (10% MeOH/ethyl acetate, 1% Et_3N). The reaction was quenched with 4 drops anhydrous methanol and 20 mL CH_2Cl_2 was added. The reaction mixture was transferred to a dry 125 mL separatory funnel and

washed quickly with 5% $NaHCO_3$ (10 mL × 2) and brine (10 mL). The organic layer was dried over anhydrous sodium sulfate and concentrated under reduced pressure. The residue was purified by silica gel flash chromatography (0−5% MeOH/ethyl acetate, 1% Et_3N). The appropriate fractions were combined, evaporated, and dried in vacuum to give product as a pale yellow oil (0.12 g, 81%). ^{31}P NMR (202.46 MHz, DMSO-d_6, ppm): 148.68 (referenced to external 85% H_3PO_4).

Spacers **2**, **14**, **32**, **33**, *and* **34.** The synthetic procedures for these spacers have been published (*10*).

Thermal Melting Measurements. Absorbance vs temperature (melting and annealing curves) profiles of the oligonucleotides were determined in Teflon-capped 1 cm path length quartz cells under a nitrogen atmosphere using a Cary 3 Bio UV−visible spectrophotometer with a 6 × 6 multicell block Peltier and a temperature controller. Oligonucleotides were dissolved in 1.0 M NaCl, 10 mM Na_2HPO_4, 0.1 mM Na_2EDTA, pH 7 degassed buffer, and were prepared in three concentrations: 1 μM, 5 μM, and 15 μM. Samples were covered with a layer of silicone oil and denatured by raising the temperature to 85 °C for 10 min prior to an experiment. Melting and annealing experiments were conducted in two stages by starting the experiment at 85 °C and cooling to 5 °C and heating from 5 °C and ending at 85 °C. Absorbance was measured at 260 nm and the heating rate/cooling rate as 0.3 °C/min with data collection at 0.2 °C intervals. The absorbance vs temperature data obtained on the Cary 3 spectrometer were exported in ASCII format to the software application Microcal *Origin*. The data were normalized to produce relative absorbance values, and sigmoidal curves were obtained using Boltzmann logged data-fit function. First derivative of the melting curve was obtained from the above sigmoidal curve and then fitted with a Gaussian function to identify the center of the peak, which is T_m or the melting temperature.

RESULTS AND DISCUSSION

Spacer Design. A series of four spacers, each containing two amide groups (shown as the parent diols **8**, **14**, **18**, and **22** in Figure 1B), was designed based on three criteria. First, the spacers in fully extended conformations had terminal oxygen atoms separated by 14.6 to 17.3 Å. The distances were chosen to lie within the middle of the range observed in crystal and NMR structures between the terminal 3′-O and 5′-O of B-DNA duplexes. We checked these distances by downloading a series of PDB format files of B-DNA NMR and X-ray structures from the Protein Data Bank of the Research Collaboratory for Structural Bioinformatics (RCSB). These were displayed in the molecular modeling program Sybyl (Tripos Inc.), wherein the distance between the terminal 3′-O and 5′-O of 17 B-DNA molecules was found to vary between 13.8 and 18.8 Å. The average distance between the 3′-O and 5′-O of a B-DNA duplex is 16.2 Å. The number of atoms (shortest direct path of connectivity) and the distance between the terminal oxygen atoms is shown for each spacer in Figure 1. This distance provides a rough guide for design; the actual distance would be expected to vary in order for the end-cap to accommodate the geometry of the terminal base pair. Second, the series of spacers provides variation in the placement of the carboxamide groups over the top of the terminal bases. Direct contact appears to exist between the glycine carboxamide group and the template base in the closed form of Taq DNA polymerase (*15*, *16*), but there are too many variables to allow us to design a spacer that would provide exactly the observed contact geometry. Third, the linkers and their DMT protected monophosphoramidites were easy and inexpensive to synthesize and could be incorporated into synthetic oligonucleotides on automated synthesizers with conventional reagents and conditions.

For comparison to previously studied end-caps, this study included hexaethylene glycol (**25**), the napthalenetetracarboxylate dimides **26**−**28**, and a tetrathymidine loop. In addition, we prepared the terthiophene spacer **2**, which provided an opportunity to study and compare an exceptionally hydrophobic end-cap. Several research groups had reported that hydrophobic, aromatic molecules such as naphthalene diimides **32**−**34** (*3*, *12*, *17*), *N*,*N*-dimethylstilbene dicarboxamide (*8*), trimethoxystilbenes (*18*), and stilbene ether (*9*) stabilized DNA duplexes through stacking interactions with the DNA bases. We expected that end-cap **2**, with a terthiophene core, would also have significant stacking interactions with the base pairs in a DNA duplex. The hydrophilic end-caps **8**, **14**, **18**, and **22** more closely resemble the hexaethylene glycol linker (**25**) in hydrophilicity.

The strategy for synthesis of each of the spacers as a symmetrical diol is illustrated in Schemes 1−4. Diol **2** could be obtained in good yield by reaction of the dilithium salt of terthiophene with 2 equiv of oxetane (*10*). Diols **8** and **14** were obtained by reaction of the *O*-*t*-butyldimethylsilyl ethers of ethanolamine and propanolamine with diglcolyl chloride, followed by removal of the silyl protecting group with ethanolic HCl. Details for the synthesis of diol **14** have been reported (*10*). Diols **18** and **22** were obtained more directly by the reaction of either γ-butyrolactone or δ-valerolactone with 1,3-propanediamine. Diol **29** was obtained by reaction of methyl bromoacetate with 2-benzyloxyethanol to form the benzyl protected methyl ester (**26**), which is converted to the carboxylic acid derivative for coupling with 1,3-propanediamine to form the benzyl protected diol **28**. Deprotection by catalytic hydrogenation with Pd/C catalyst gives diol **29** in good yield. The synthesis of diols **32**−**34** followed the procedure described by Pingle et al. (*10*) Each diol is symmetrical and could be synthesized as a mono-DMTr derivative by reaction with 1 equiv of DMTr chloride. Yields are generally in the 35−50% range, which, although low, was not limiting because of the ease with which one can produce large amounts of the diols. Separation of the monotritylated products from starting material and bistritylated side product by silica gel chromatorgraphy was facile in each case. The tritylated spacers were easily transformed into the corresponding phosphoramidites by conventional protocols and the 4,4′-dimethoxytrityl protected phosphoramidite derivatives incorporated into the oligonucleotide on an automated DNA synthesizer in good yield as illustated in Figure 1A. The sequences synthesized for this study are included in Tables 2 and 3.

Thermal Melting Studies. Thermal melting studies were carried out on four-base-pair duplexes containing the nucleosides dA, T, dG, and dC and end-caps **14** and **18** (Table 2) and **2**, **8**, **22**, **25**, **29**, **32**, **33**, and **34** (Table 3). The thermal melting profile of all end-capped DNA duplexes at varied concentrations (1−15 μM) was a sigmoidal curve indicative of the formation of a hairpin and a concentration independent, unimolecular process. If the oligonucleotides were dimerizing rather than forming hairpin stuctures, one would expect to see an increase in T_m values with an increase in concentration. In order to determine the end-cap preferences for specific base pairs, we examined one sequence, **IV**, in which the end-caps were stacked over an A•T base-pair and a second sequence, **V**, in which the end-caps were stacked over a C•G base-pair. With two of the end-caps, **14** and **18**, we included additional sequences in which the end-caps were placed over T•A (**I** and **III**) and G•C base pairs (**II**).

The T_m values of the control sequences i−v (Table 1, no end-caps) were not determined. These sequences contain only two C•G (G•C) base pairs and consequently would be expected to melt well below room temperature. Complementary 4-mers containing all C•G (G•C) base pairs have been reported to have

Table 1. Calculated Free Energy of Change for Association of Complementary Unmodified Tetramers[a]

DNA sequences (5′→3′)	$-\Delta G$ (kcal/mol)
i. GCAT/ATGC	3.59
ii. TACG/CGTA	3.16
iii. CGAT/ATCG	3.37
iv. GCTA/TAGC	3.12
v. ATGC/GCAT	3.54

[a] All DNA sequences are written in the 5′→3′ direction. The free energy factor for end effects was added only for the end opposite that covalently linked by end-caps (see oligonucleotides **I**−**V**.

Table 2. T_m Values of Oligonucleotides I−V Containing 14 and 18[a]

	end-cap T_m values (°C)	
oligonucleotide	**14**	**18**
I GCATXATGC	48	53
II TACGXCGTA	45	50
III CGATXATCG	44	48
IV GCTAXTAGC	41	44
V ATGCXGCAT	51	56

[a] All DNA sequences are written in 5′→3′ direction. X: end-cap.

T_m values ranging from 16.7 to 27.8 °C. For comparison of relative stability, we have tabulated the predicted free energies of association for complementary sequences i−v (Table 1), based on the unified parameters reported by SantaLucia (*19*). For purposes of comparison, the free energy contribution from the end effect was included only for the corresponding uncapped end (compare to sequences in Table 2). From the calculated free energies of association, we might predict the relative order of the T_m values of the DNA duplexes of Table 1 to be i ≥ v > iii > ii ≥ iv. Deviation from this order in the corresponding end-cap containing oligonucleotides would indicate base-specific association effects with the end-cap.

The T_m values observed for sequences **I**−**V** containing end-caps **14** or **18** (Table 2) do not completely correlate with the predicted trend of the T_m values of unmodified DNA duplexes based on the calculated ΔG values in Table 1. The most stable duplex is **V**, in which the end-caps are positioned over a C•G base pair. Oligonucleotide **I** would be predicted to be slightly more stable based on the calculated free energies for association. Furthermore, the T_m values for oligonucleotide **II** containing either end-cap **14** or **18** are higher than the T_m values for oligonucleotide **III**, which is contrary to prediction. These results suggest that there is a greater stabilization effect when the end-caps are adjacent to either a G•C or a C•G base pair. This observation is concordant with results reported by Benight and co-workers (*20*) from a study on hairpin DNA oligonucleotides. Stems with C•G base pairs closing the loop show greater stability than stems in which the loop closing base pair is A•T.

Because of the number of different end-caps, we wished to investigate, other end-caps were incorporated only into sequences **IV** and **V**. This was sufficient to probe differences between the end-caps for stabilization of closing A•T versus C•G base pairs. As can be seen from the data, all of the end-caps stabilize the four-base-pair duplex, but the differences in stabilization are significant. Among the diamide aliphatic linkers, the degree of stabilization is related to the length. The shortest linker (**8**) is least stabilizing with T_m values for **IV** and **V** at 39 and 42 °C, while the longest (**22**) is most stabilizing, with T_m values for **IV** and **V** at 46 and 56 °C. Although **14**, **18**, and **22**, when fully extended, are all longer than the average distance of 16.2 Å observed for the 3′-O to 5′-O span between duplex ends in B-DNA, if the carbon−carbon bonds adjacent to these oxygens are in a gauche conformation rather than an anti-periplanar conformation, the lengths shorten by 1.6 to 2.9 Å. For example, linkers **14** and **18**, which are both near the optimum length at 16.8 and 17.3 Å, respectively, both show

Table 3. T_m Values of Oligonucleotides IV and V Containing 2, 8, 22, 29, 32−34, and TTTT[a]

	end-cap T_m values (°C)								
oligonucleotide	**2**	**8**	**22**	**25**	**29**	**32**	**33**	**34**	**TTTT**
IV	66	39	46	50	48	62	53	60	39
V	62	42	56	61	56	75	66	74	58

[a] All DNA sequences are written in 5′→3′ direction. X: end-cap.

distances of 14.5 Å in a minimized structure in which the two terminal C−C bonds are gauche. Linker **8** (14.6 Å fully extended) spans only 11.4 Å in a minimized gauche conformation, while the longest linker, **22**, which is 19.5 Å fully extended, falls to 17.9 Å. The X-ray crystal structure for bis(2-hydroxyethyl)-stilbene-4,4′-diether linker capping a six-base-pair stem (*13*) clearly shows that the terminal -OCH_2CH_2O- exist in the gauche form. In modeling studies of the bridged duplexes, the 3′-O to 5′-O distances were found to be 11.3, 14.7, 17.1, and 19.9 Å, for **8**, **14**, **18**, and **22**, respectively. These models are interesting because each linker shows its own particular pattern of conformational preferences, but the gauche form is noticeably absent from the carbon bonds adjacent to the phosphodiester group. In each of the structures, the 3′-endo (characteristic of B-DNA) conformation is maintained in all deoxyribose residues including those linked to the end-cap.

Comparison to the hexaethylene glycol end-cap (**25**) is instructive. This spacer is far longer (21.4 Å) but contains -OCH_2CH_2O- bonds for which the gauche conformation is favorable. The corresponding T_m values for oligonucleotides **IV** and **V** are higher (50 and 61 °C) than for any of the amide containing end-caps. As a consequence, it is not possible to say whether or not the amide groups provide any degree of stabilization through direct interactions with the face of the terminal base pair. It may be that the penalty for adopting higher energy conformations in order to fit between the 3′-O and 5′-O base pairs negates any advantage of amide−heterocycle interactions. Finally, we modified linker **22** by replacing two carbon atoms by oxygen atoms to create an analogue in which the two terminals now contain the -OCH_2CH_2O- group (linker **29**). Presumably, this analogue, like **25** could more readily adopt a gauche conformation. In fact, the resulting T_m values (Table 3) were almost identical to those measured for compound **22**. It is possible that the increased flexibility was compromised by too short of a spacer distance with both terminal -OCH_2CH_2O- groups in a gauche conformation.

Stabilization by end-caps is greatest when aromatic residues capable of stacking interactions are included as part of the structure (*3, 8, 13*). For comparison, we have included two types of aromatic moiety containing end-caps in these studies. The naphthalene tetracarboxylic acid diimide linker was studied previously by Bevers et al. (*3*); however, they used a -$OCH_2CH_2OCH_2CH_2$- spacer between the phosphodiester groups and the imide nitrogen atoms, whereas we used -$(CH_2)_3$-, -$(CH_2)_4$-, and -$(CH_2)_5$- spacers (**32**, **33**, and **34**, respectively) in our studies. Both Bevers et al. with the naphthalendicarboxamide linkers and Lewis and co-workers (*9*) in the case of the stilbene linkers included -OCH_2CH_2O- spacers as part of the structure. Interestingly, the lack of this spacer in our linkers does not appear to have compromised stability in all cases. One of these linkers (**34**) is nearly identical to the Bevers et al. linker. The difference is that we used $OCH_2CH_2CH_2CH_2CH_2$- in place of -$OCH_2CH_2OCH_2CH_2$-. Also, we measured T_m values in much shorter oligonucleotides sequences (ATGC-**34**-GCAT, $T_m = 74°$ and GCTA-**34**-TAGC, $T_m = 60°$ versus TCTTTTCTT-Y-AGAAAAGAA, $T_m = 72°$). Despite the shorter oligonucleotides, we obtained a higher T_m value when the naphthalene tetracarboxylate diimide was stacked over the C•G base pair. Our observed T_m value is significantly lower when the naph-

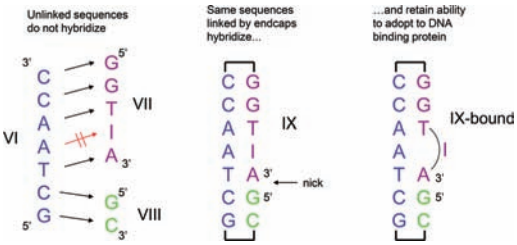


Figure 2. Oligonucleotides VII and VIII do not form a stable hybrid duplex with oligonucleotide VI. Combination of the same nucleotide sequences with end-cap **18** linking VIII and VII to VI gives duplex IX, which can be cocrystallized with Endo V to give the structure shown in Figure 3.

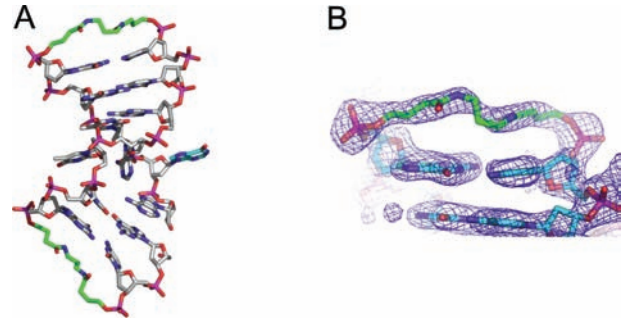


Figure 3. Structure of oligonucleotide IX bound to Endo V (protein not shown). (A) Complete structure. (B) Details of end-cap **18**.

thalene was stacked over the A•T base pair. In the Bevers sequence, the naphthalene is adjacent to a T•A base pair. It is likely that the Bevers linker would have caused a similar increase in stabilization when placed over a G•C or C•G base pair. Nevertheless, based on our high T_m values it does not appear likely that the absence of an -OCH_2CH_2O-spacer in our linker significantly compromised the stability. Furthermore, the C3 spacer (in linker **32**), which would presumably be far too short based on our earlier analysis (16.0 Å fully extended), is the most stabilizing.

The hydrophobic terthiophene end-cap **2** stabilized oligonucleotide **IV** (T_m = 66 °C) to a greater extent than oligonucleotide **V** (T_m = 62 °C). This difference is particulary profound because nonbridged duplex **V** is considerably more stable than duplex **IV** (Table 1). This presumably results from the greater hydrophobicity of the A•T base pair versus the C•G base pair.

CONCLUSIONS

This study confirms that end-caps containing conjugated aromatic π-systems, capable of base stacking, stabilize a short oligonucleotide duplex significantly more than end-caps containing other types of functionality. Moreover, we have now demonstrated that a highly hydrophobic end-cap (**2**) enhances the stability of a duplex to a greater extent when positioned over an A•T base pair than when stacked over a C•G base pair. The more hydrophilic naphthalene tetracarboxylate diimide stabilizes a duplex to a much greater extent when stacked over a C•G base pair.

The significantly greater stabilization of the four-base-pair stems from a hexaethylene glycol in comparison to the four diamide containing aliphatic end-caps included in this study suggests that greater spacer flexibility may allow the terminal base pair to achieve optimal conformation. Our results further support the contribution of π-stacking interactions in duplex stabilization by end-caps, as well as the importance of spacer structure linking the aromatic residue to the oligonucleotides phosphodiester groups.

An important goal of this research was to find spacers that would not alter the duplex in a way that would either hinder binding or prevent readjustment of the structure as dictated by a protein binding to the dsDNA. On the basis of the T_m studies and taking into account spacer length, spacer **18** was incorporated into sequence IX (Figure 2). The spacer made it possible to create a single sequence (IX) that would take the place of three separate oligonucleotides (GCTAACC (VI), GGTIA (VII), and GC (VIII) required for the co-crystallization of the enzyme Endo V with its substrate, a nicked DNA. Sequences VII and VIII do not hybridize to the heptamer VI, because VIII is too short (dimer) and VII contains an inosine mismatch. However, as illustrated in Figure 3, the sequence is able to assume a duplex structure that in the presence of Endo V can flip out the inosine nucleotide. Details of the Endo V structure and its interaction with sequence IX will be reported in a separate manuscript.

ACKNOWLEDGMENT

This work was supported by NASA under award NCC 2-1363, a grant from the National Institutes of Health (1R21EB006308), the National Science Foundation (0554990), the Indiana Elks Foundation, and Walther Cancer Institute. Assistance from the National Cancer Institute Grant (P30 CA23168) awarded to Purdue University is also gratefully acknowledged. A Purdue Doctoral Fellowship provided support for Brian Laing.

Supporting Information Available: ^1H, ^{13}C, and ^{31}P NMR spectra of synthesized compounds; oligonucleotide MALDI-TOFMS characterization data. This material is available free of charge via the Internet at http://pubs.acs.org.

LITERATURE CITED

(1) Kool, E. T. (1997) Preorganization of DNA: design principles for improving nucleic acid recognition by synthetic oligonucleotides. *Chem. Rev. 97*, 1473–1488.

(2) Altmann, S., Labhardt, A. M., Bur, D., Lehmann, C., Bannwarth, W., Wüthrich, K., and Leupin, W. (1995) NMR studies of DNA duplexes singly cross-linked by different synthetic linkers. *Nucleic Acids Res. 23*, 4827–4835.

(3) Bevers, S., O'Dea, T. P., and McLaughlin, L. W. (1998) Perylene- and naphthalene-based linkers for duplex and triplex stabilization. *J. Am. Chem. Soc. 120*, 11004–11005.

(4) Doktycz, M. J., Paner, T. M., and Benight, A. S. (1993) Studies of DNA dumbbells. IV. Preparation and melting of a DNA dumbbell with the 16 base-pair sequence 5′-GTATCCCTCTG-GATAC-3′ linked on the ends by dodecyl chains. *Biopolymers 33*, 1765–1777.

(5) Durand, M., Chevrie, K., Chassignol, M., Thuong, N. T., and Maurizot, J. C. (1990) Circular dichroism studies of an oligonucleotide containing a hairpin loop made of a hexaethylene glycol chain: conformation and stability. *Nucleic Acids Res. 18*, 6353–6359.

(6) Gao, H., Chidambaram, N., Chen, B. C., Pelham, D. E., Patel, R., Yang, M., Zhou, L., Cook, A., and Cohen, J. S. (1994) Double-stranded cyclic oligonucleotides with non-nucleotide bridges. *Bioconjugate Chem. 5*, 445–453.

(7) Glick, G. D. (1998) Design, synthesis, and analysis of conformationally constrained nucleic acids. *Biopolymers (Nucleic Acid Sciences) 48*, 83–96.

(8) Letsinger, R. L., and Wu, T. F. (1995) Use of a stilbenedicarboxamide bridge in stabilizing, monitoring, and photochemically altering folded conformations of oligonucleotides. *J. Am. Chem. Soc. 117*, 7323–7328.

(9) Lewis, F. D., Wu, Y., and Liu, X. (2002) Synthesis, structure, and photochemistry of exceptionally stable synthetic DNA hairpins with stilbene diether linkers. *J. Am. Chem. Soc. 124*, 12165–12173.

(10) Pingle, M. R., Ng, P. S., Xu, X., and Bergstrom, D. E. (2003) Synthesis of endcap dimethoxytrityl phosphoramidites for end-capped oligonucleotides. In *Current Protocol in Nucleic Acid Chemistry, Chapter 5*, Unit 5.6.

(11) Ng, P. S., and Bergstrom, D. E. (2004) Protein-DNA footprinting by endcapped duplex oligodeoxyribonucleotides. *Nucleic Acids Res. 32*, e107.

(12) Bevers, S., Schutte, S., and McLaughlin, L. W. (2000) Naphthalene-perylene-based linkers for the stabilizattion of hairpin triplexs. *J. Am. Chem. Soc. 122*, 5905–5915.

(13) Egli, M., Tereshko, V., Mushudov, G. N., Sanishivili, R., Liu, X. Y., and Lewis, F. D. (2003) Face-to-face and edge-to-face pi-pi interactions in a synthetic DNA hairpin with a stilbenediether linker. *J. Am. Chem. Soc. 125*, 10842–10849.

(14) Hariharan, M., Zheng, Y., Long, H., Zeidan, T. A., Schatz, G. C., Vura-Weis, J., Wasielewski, M. R., Zuo, X., Tiede, D. M., and Lewis, F. D. (2009) Hydrophobic dimerization and thermal dissociation of perylenediimide-linked DNA hairpins. *J. Am. Chem. Soc. 131*, 5920–5929.

(15) Li, Y., and Waksman, G. (2001) Crystal structures of a ddATP-, ddTTP-, ddCTP, and ddGTP- trapped ternary complex of Klentaq1: insights into nucleotide incorporation and selectivity. *Protein Sci. 10*, 1225–1233.

(16) Paul, N., Nashine, V. C., Hoops, G., Zhang, P., Zhou, J., Bergstrom, D. E., and Davisson, V. J. (2003) DNA polymerase template interactions probed by degenerate isosteric nucleobase analogs. *Chem. Biol. 10*, 815–825.

(17) Ng, P. S., Pingle, M. R., Balasundarum, G., Friedman, A., Zu, X., and Bergstrom, D. E. (2003) Endcaps for stabilizing short DNA duplexes. *Nucleosides Nucleotides Nucleic Acids, 22*, 1635–1637.

(18) Tuma, J., Paulini, R., Rojas Stutz, J. A., and Richert, C. (2004) How much pi stacking do DNA termini seek? solution structure of a self-complementary DNA hexamer with trimethoxystilbenes capping the terminal base pairs. *Biochemistry 43*, 15680–15687.

(19) SantaLucia, J. (1998) A unified view of polymer, dumbbell, and oligonucleotide DNA nearest-neighbor thermodynamics, *Proc. Natl. Acad. Sci. U.S.A. 95*, 1460−1465.

(20) Vallone, P. M., Paner, T. M., Hilario, J., Lane, M. J., Faldasz, B. D., and Benight, A. S. (1999) Melting studies of short DNA hairpins: influence of loop sequence and adjoining base pair identity on hairpin thermodynamic stability. *Biopolymers 50*, 425–442.

BC100202Y

SUPPORTING INFORMATION

Synthesis and evaluation of new spacers for use as dsDNA endcaps

Pei-Sze Ng,[†] *Brian M. Laing,*[†,‡] *Ganesan Balasundarum,*[†] *Maneesh Pingle,*[†] *Alan Friedman,*[§] *and Donald E. Bergstrom*[*,†,‡]

[†]Department of Medicinal Chemistry and Molecular Pharmacology, [§]Department of Biological Sciences, and [‡]Bindley Bioscience Center, Purdue University, West Lafayette, IN 47907

*Correspondence to: Donald Bergstrom, Department of Medicinal Chemistry and Molecular Pharmacology, Birck Nanotechnology Center, Purdue University, 1205 W State St, West Lafayette, IN 47907-2057. Telephone: (765) 494-6275; Fax: (765) 494-1414; Email: bergstrom@purdue.edu

List of contents:

Table S4 Oligonucleotide MALDI-TOFMS data

Figure S1: ^{1}H NMR spectrum of 2-(*tert*-Butyldimethylsilyloxy)ethylamine (**6**).

Figure S2: ^{13}C NMR spectrum of 2-(*tert*-Butyldimethylsilyloxy)ethylamine (**6**).

Figure S3: ^{1}H NMR spectrum of *N*,*N*'-Bis[2-(*tert*-butyldimethylsilyloxyethyl]-2,2'-oxydiacetamide (**7**)

Figure S4: ^{13}C NMR spectrum of *N*,*N*'-Bis[2-(*tert*-butyldimethylsilyloxyethyl]-2,2'-oxydiacetamide (**7**)

Figure S5: ^{1}H NMR spectrum of *N*,*N*'-Bis(2-hydroxyethyl)-2,2'-oxydiacetamide (**8**)

Figure S6: ^{13}C NMR spectrum of *N*,*N*'-Bis(2-hydroxyethyl)-2,2'-oxydiacetamide (**8**)

Figure S7: ^{1}H NMR spectrum of *N*-[2-(4, 4'-dimethoxytrityl)oxyethyl]-*N*'-(2-hydroxyethyl)-2,2'-oxydiacetamide (**9**)

Figure S8: ^{13}C NMR spectrum of *N*-[2-(4, 4'-dimethoxytrityl)oxyethyl]-*N*'-(2-hydroxyethyl)-2,2'-oxydiacetamide (**9**)

Figure S9: ^{1}H NMR spectrum of *N*-[3-O-(2-cyanoethyl-*N*,*N*-diisopropylphosphoramidite)ethyl]-*N*'-[2-(4,4' –dimethoxytrityl)oxyethyl]-2,2'-oxydiacetamide (**10**)

Figure S10: ^{31}P NMR spectrum of *N*-[3-O-(2-cyanoethyl-*N*,*N*-diisopropylphosphoramidite)ethyl]-*N*'-[2-(4,4' –dimethoxytrityl)oxyethyl]-2,2'-oxydiacetamide (**10**)

Figure S11: ^{1}H NMR spectrum of *N*, *N*'-Bis-(4-hydroxybutanoyl)-1,3-propanediamine (**18**)

Figure S12: ^{13}C NMR spectrum of *N*, *N*'-Bis-(4-hydroxybutanoyl)-1,3-propanediamine (**18**)

Figure S13: ^{1}H NMR spectrum of *N*-{4-[4,4'-(Dimethoxytrityl)oxy]butanoyl}-*N*'-4-hydroxybutanoyl-1,3-propanediamine (**19**)

Figure S14: ^{13}C NMR spectrum of *N*-{4-[4,4'-(Dimethoxytrityl)oxy]butanoyl}-*N*'-4-hydroxybutanoyl-1,3-propanediamine (**19**)

Figure S15: ^{1}H NMR spectrum of *N*-[4-O-(2-cyanoethyl-*N*,*N*-diisopropylphophoramidite)butanoyl]-*N*'-{4-[4,4'-(dimethoxytrityl)oxy]butanoyl}-1,3-propanediamine (**20**)

Figure S16: ^{1}H NMR spectrum of *N*, *N*'-Bis-(5-hydroxypentanoyl)-1,3-propanediamine (**22**)

Figure S17: ^{13}C NMR spectrum of *N*, *N*'-Bis-(5-hydroxypentanoyl)-1,3-propanediamine (**22**)

Figure S18: ^{1}H NMR spectrum of *N*-{5-[4,4'-(Dimethoxytrityl)oxy]pentanoyl}-*N*'-(5-hydroxypentanoyl]-1,3-propanediamine (**23**)

Figure S19: ^{13}C NMR spectrum of *N*-{5-[4,4'-(Dimethoxytrityl)oxy]pentanoyl}-*N*'-(5-hydroxypentanoyl]-1,3-propanediamine (**23**)

Figure S20: ^{1}HNMR spectrum of Methyl 2-(2-(benzyloxy)ethoxy)acetate (**26**)

Figure S21: ^{13}C NMR spectrum of Methyl 2-(2-(benzyloxy)ethoxy)acetate (**26**)

Figure S22: ^{1}H NMR spectrum of 2-(2-(Benzyloxy)ethoxy)acetic acid (**27**)

Figure S23: ^{13}C NMR spectrum of 2-(2-(Benzyloxy)ethoxy)acetic acid (**27**)

Figure S24: ^{1}H NMR spectrum of *N*, *N*'-Bis-(2-(2-benzyloxyethoxy)ethanoyl)-1,3-propanediamine (**28**)

Figure S25: ^{13}C NMR spectrum of *N*, *N*'-Bis-(2-(2-benzyloxyethoxy)ethanoyl)-1,3-propanediamine (**28**)

Figure S26: ^{1}H NMR spectrum of *N*, *N*'-Bis-(2-(2-hydroxyethoxy)ethanoyl)-1,3-propanediamine (**29**)

Figure S27: ^{13}C NMR spectrum of *N*, *N*'-Bis-(2-(2-hydroxyethoxy)ethanoyl)-1,3-propanediamine (**29**)

Figure S28: ^{1}H NMR spectrum of *N*-(2-(2-(4, 4'-dimethoxytrityloxy)ethoxy)ethanoyl)-*N*'-(2-(2-hydroxyethoxy)ethanoyl)-1,3-propanediamine (**30**)

Figure S29: ^{13}C NMR spectrum of *N*-(2-(2-(4, 4'-dimethoxytrityloxy)ethoxy)ethanoyl)-*N*'-(2-(2-hydroxyethoxy)ethanoyl)-1,3-propanediamine (**30**)

Figure S30: ^{1}H NMR spectrum of *N*-(2-(2-O-(2-cyanoethyl-*N*, *N*-diisopropylphosphoramidite)ethoxy)ethanoyl)-*N*'-(2-(2-(4, 4'-dimethoxytrityloxy)ethoxy)ethanoyl)-1,3-propanediamine (**31**)

Figure S31: ^{31}P NMR spectrum of *N*-(2-(2-O-(2-cyanoethyl-*N*, *N*-diisopropylphosphoramidite)ethoxy)ethanoyl)-*N*'-(2-(2-(4, 4'-dimethoxytrityloxy)ethoxy)ethanoyl)-1,3-propanediamine (**31**)

Table S4 Oligonucleotide MALDI-TOFMS data

Oligonucleotide	$(M+H)^+$ Calculated	$(M+H)^+$ Observed	Comments
GCTA-**8**-TAGC	2693.9	2693.4	
ATGC-**8**-GCAT	2693.9	2693.2	
GCAT-**14**-ATGC	2717.9	2717.3	Confirmed by enzymatic sequencing*
TACG-**14**-CGTA	2717.9	2715.3	Confirmed by enzymatic sequencing
CGAT-**14**-ATCG	2717.9	2717.5	
GCTA-**14**-TAGC	2717.9	2715.9	Confirmed by enzymatic sequencing
ATGC-**14**-GCAT	2717.9	2715.4	Confirmed by

			enzymatic sequencing
GCAT-**18**-ATGC	2716.9	2719.6	
TACG-**18**-CGTA	2716.9	2712,2	
CGAT-**18**-ATCG	2716.9	2714.0	
GCTA-**18**-TAGC	2716.9	2713.9	
ATGC-**18**-GCAT	2716.9	2714.7	
GCTA-**22**-TAGC	2744.9	2743.5	
ATGC-**22**-GCAT	2744.9	2748.0	
GCTA-**29**-TAGC	2748.9	2750.6	
ATGC-**29**-GCAT	2748.9	2750.6	

*Enzymatic sequencing involved exonuclease digestion from the 3'-end in combination with MALDI

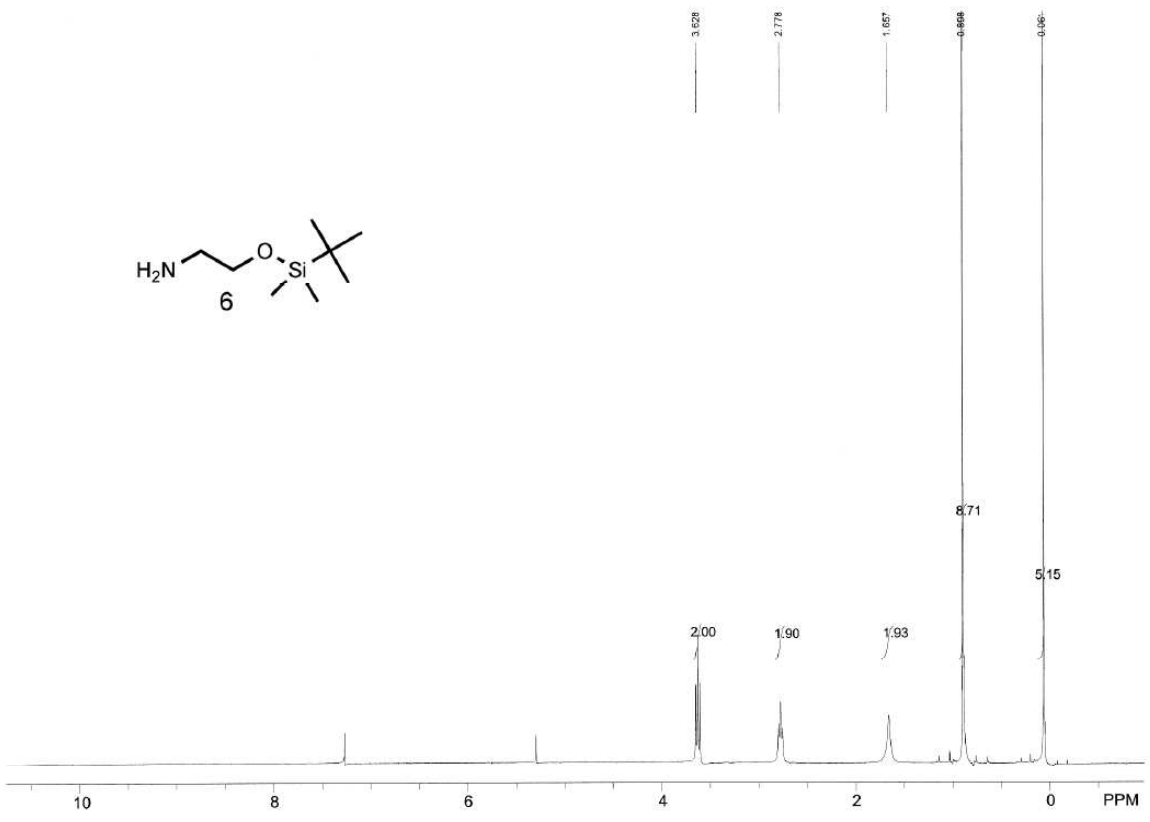


Figure S1: ^{1}H NMR spectrum of 2-(*tert*-Butyldimethylsilyloxy)ethylamine (**6**)

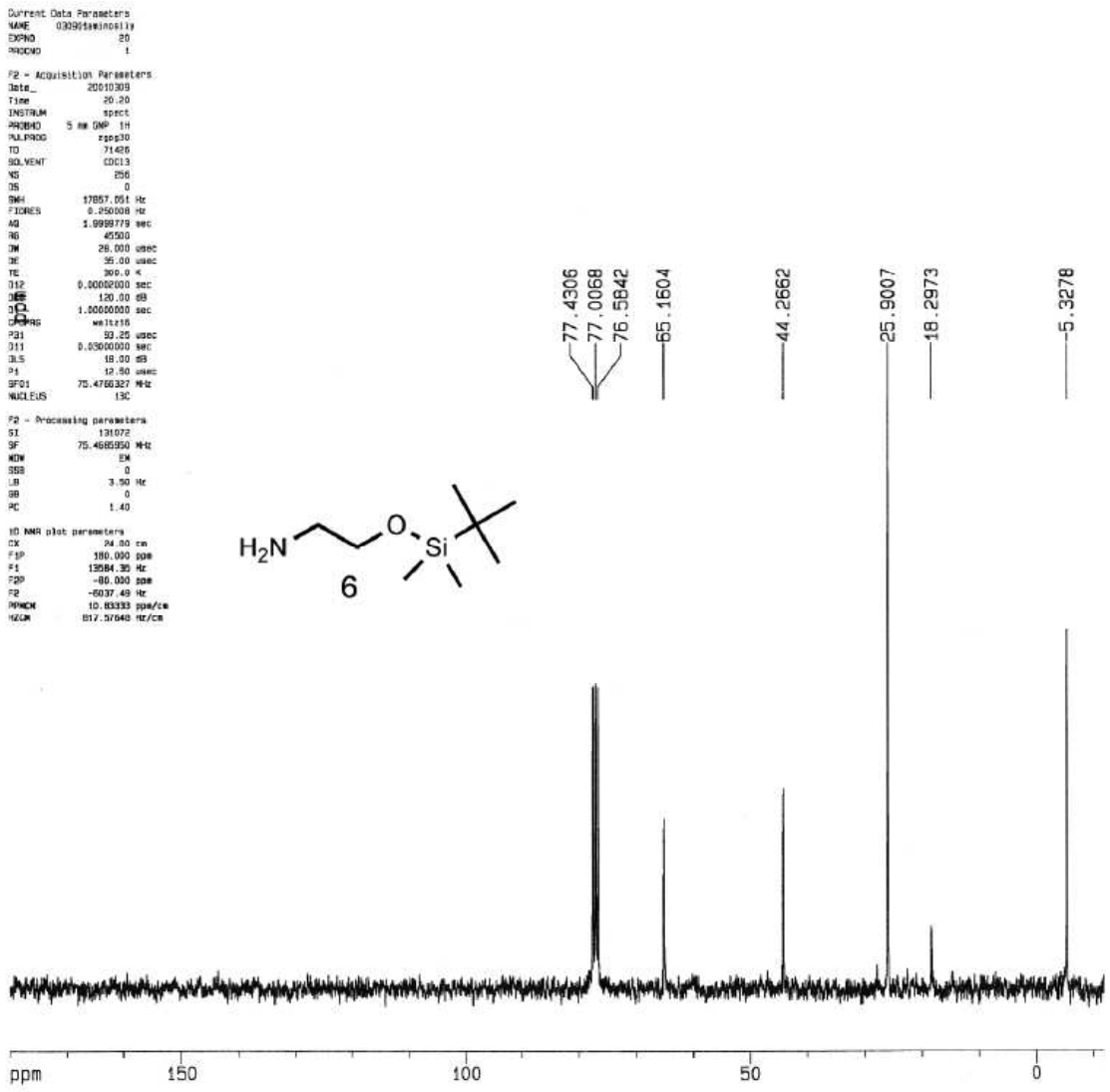


Figure S2: ^{13}C NMR spectrum of 2-(*tert*-Butyldimethylsilyloxy)ethylamine (**6**)

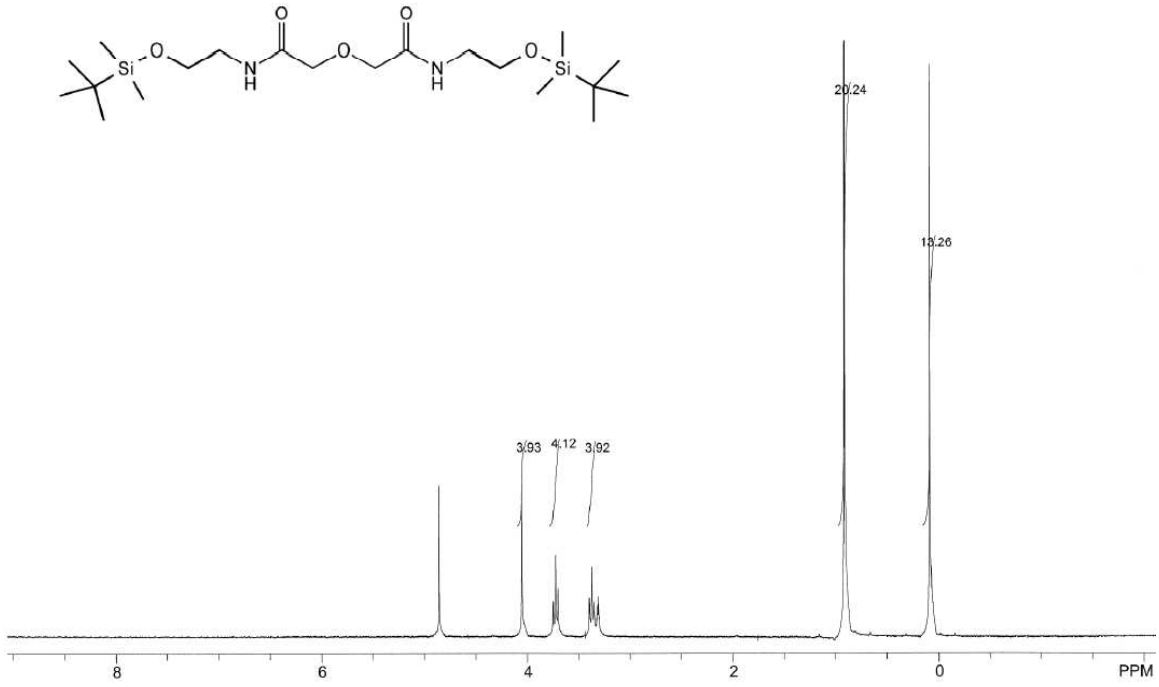


Figure S3: ^{1}H NMR spectrum of *N*,*N*'-Bis[2-(*tert*-butyldimethylsilyloxyethyl]-2,2'-oxydiacetamide (**7**)

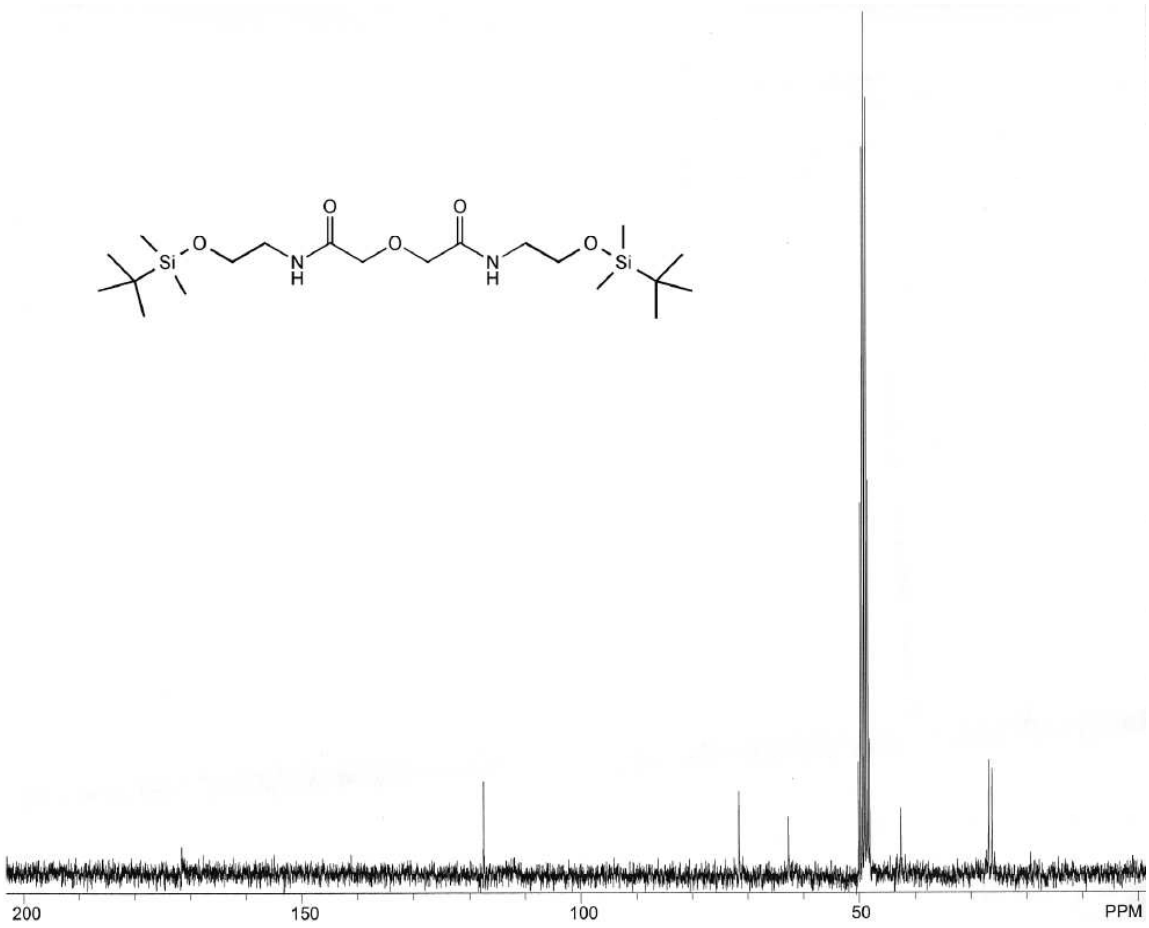


Figure S4: ^{13}C NMR spectrum of *N*,*N*'-Bis[2-(*tert*-butyldimethylsilyloxyethyl]-2,2'-oxydiacetamide (**7**)

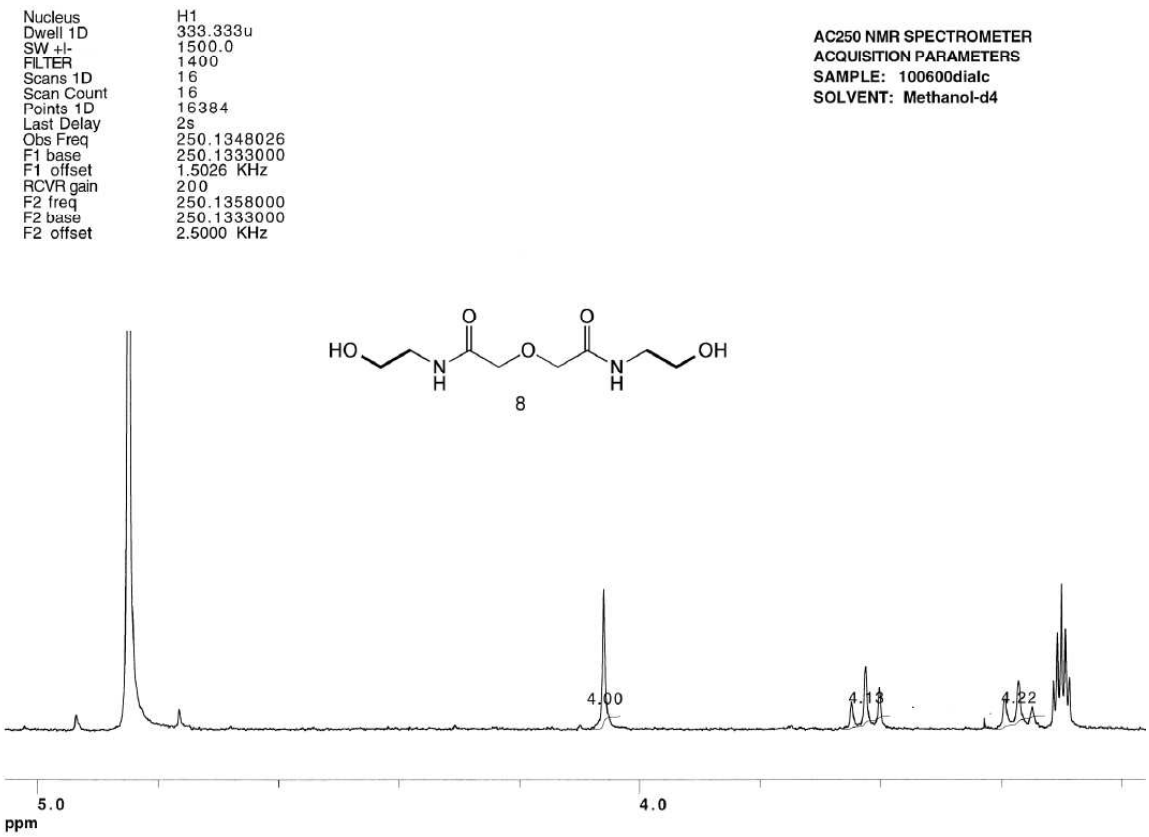


Figure S5: ^{1}H NMR spectrum of *N*,*N*'-Bis(2-hydroxyethyl)-2,2'-oxydiacetamide (**8**)

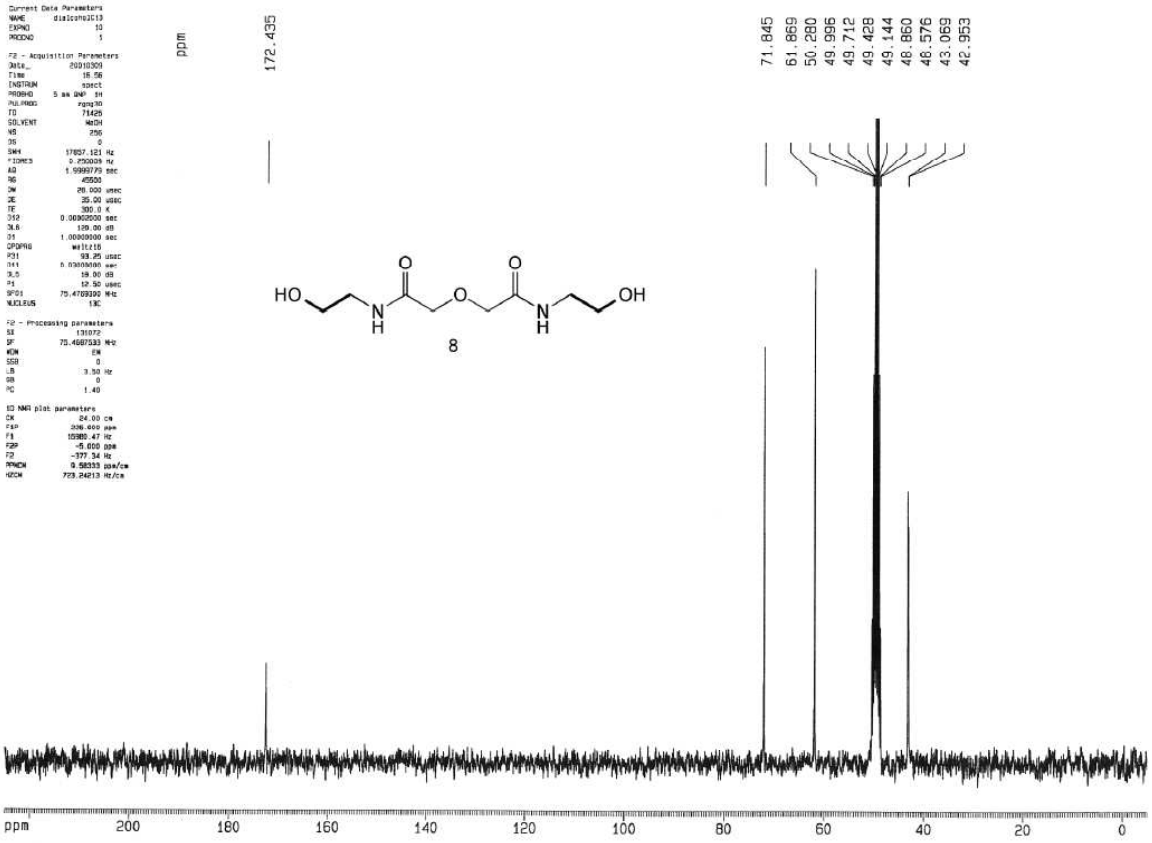


Figure S6: ^{13}C NMR spectrum of *N*,*N*'-Bis(2-hydroxyethyl)-2,2'-oxydiacetamide (**8**)

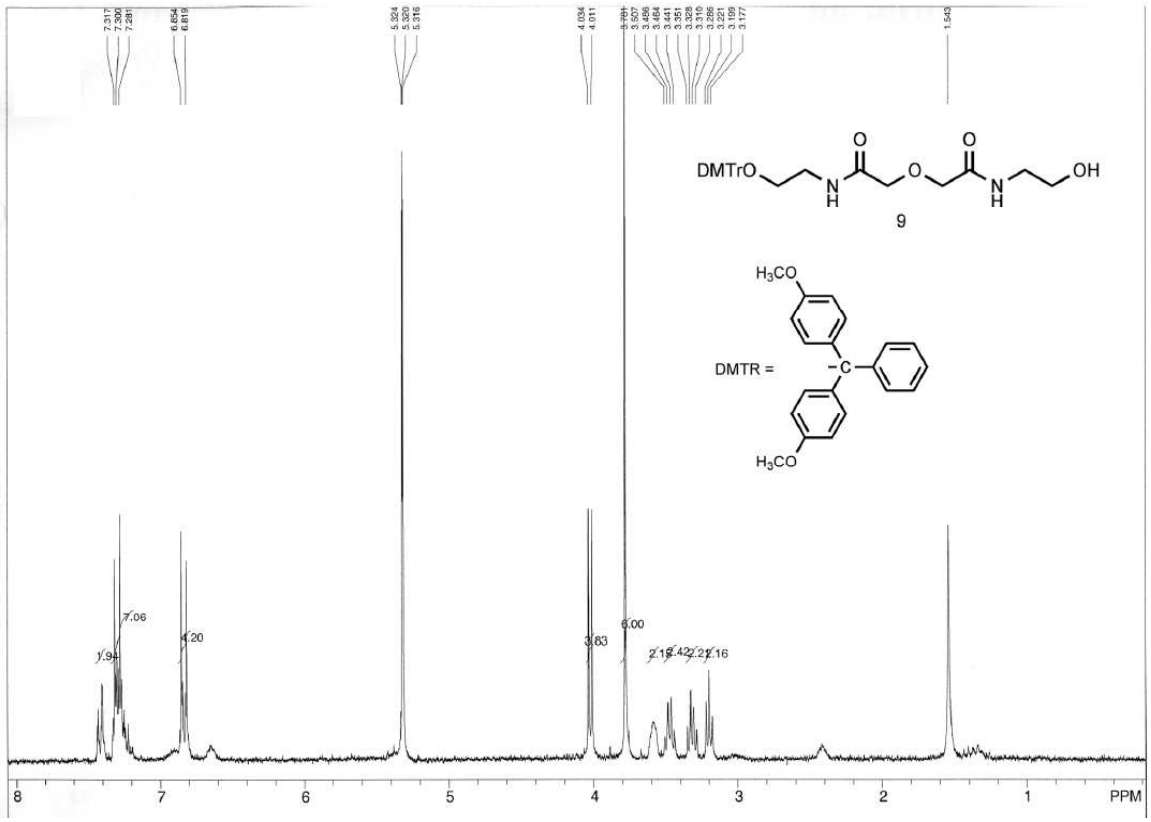


Figure S7: ^{1}H NMR spectrum of *N*-[2-(4, 4'-dimethoxytrityl)oxyethyl]-*N*'-(2-hydroxyethyl)-2,2'-oxydiacetamide (**9**)

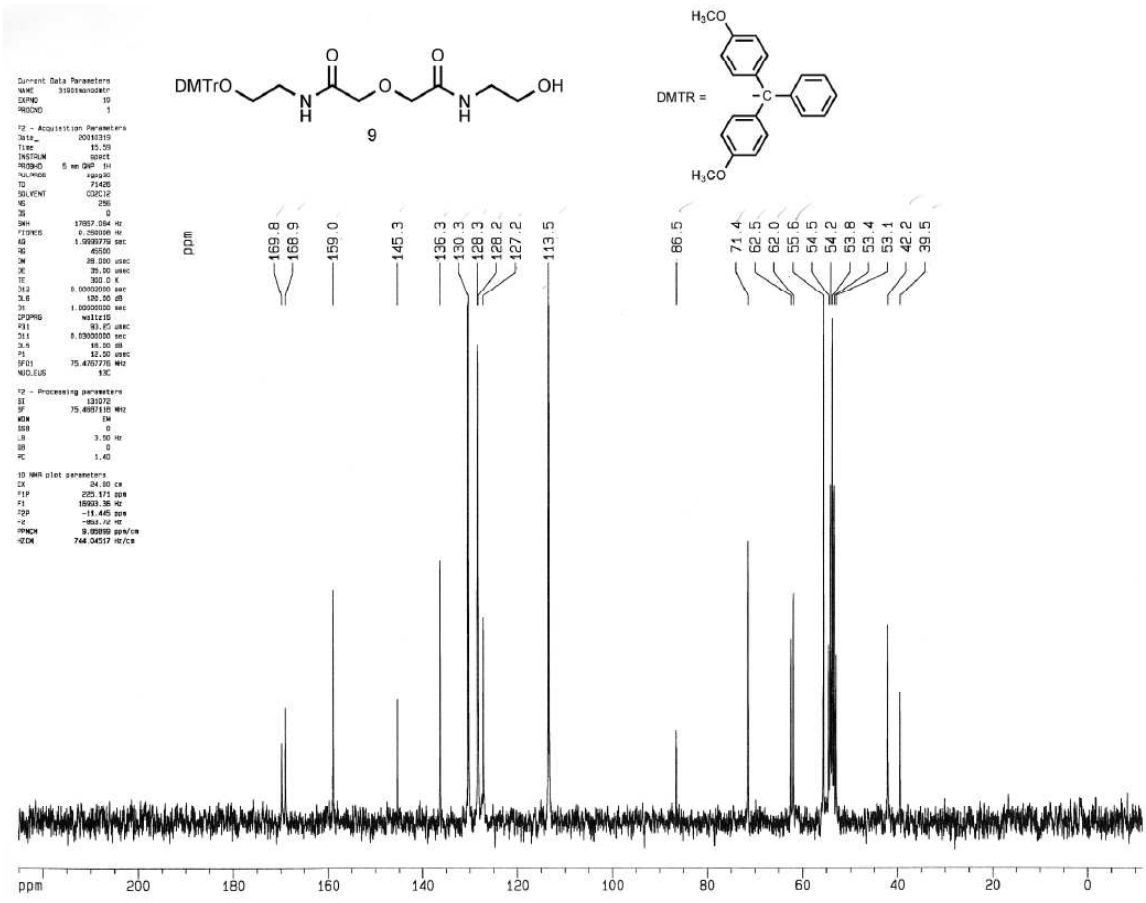


Figure S8: ^{13}C NMR spectrum of *N*-[2-(4, 4'-dimethoxytrityl)oxyethyl]-*N*'-(2-hydroxyethyl)-2,2'-oxydiacetamide (**9**)

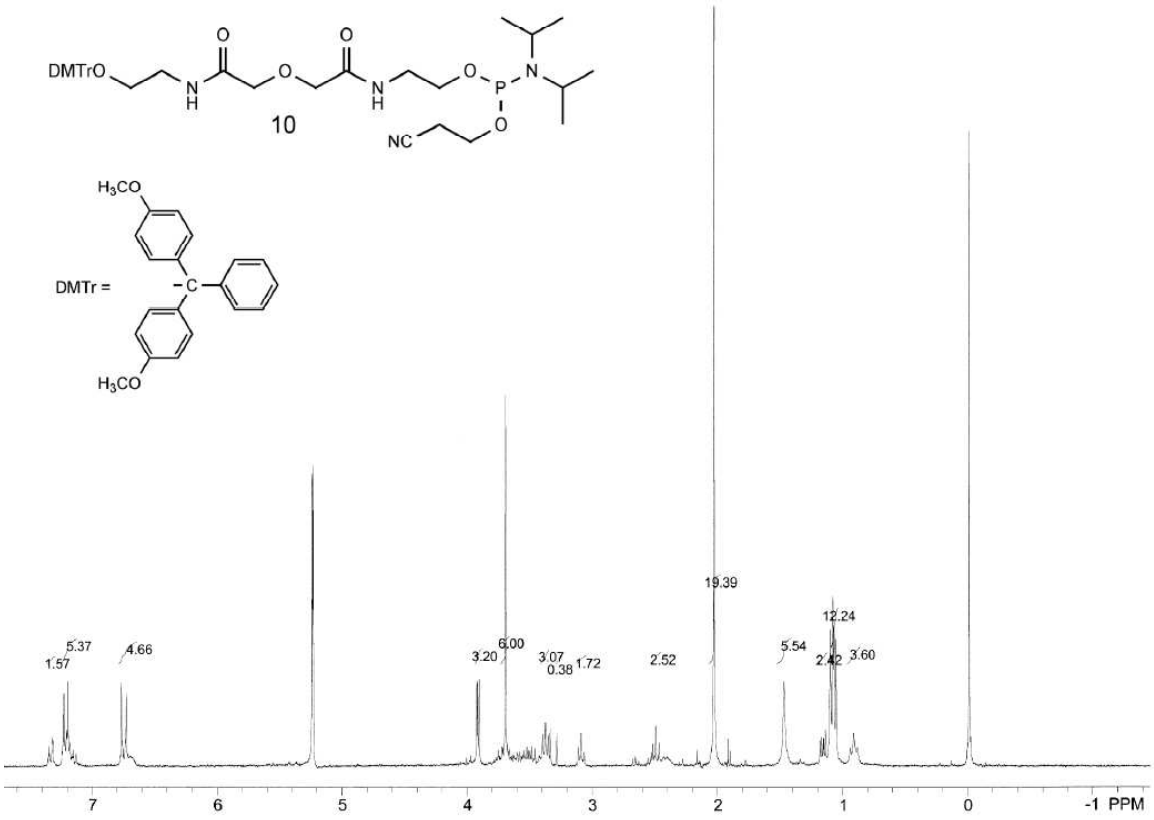


Figure S9: ^{1}H NMR spectrum of *N*-[3-O-(2-cyanoethyl-*N*,*N*-diisopropylphosphoramidite)ethyl]-*N*'-[2-(4,4' –dimethoxytrityl)oxyethyl]-2,2'-oxydiacetamide (**10**)

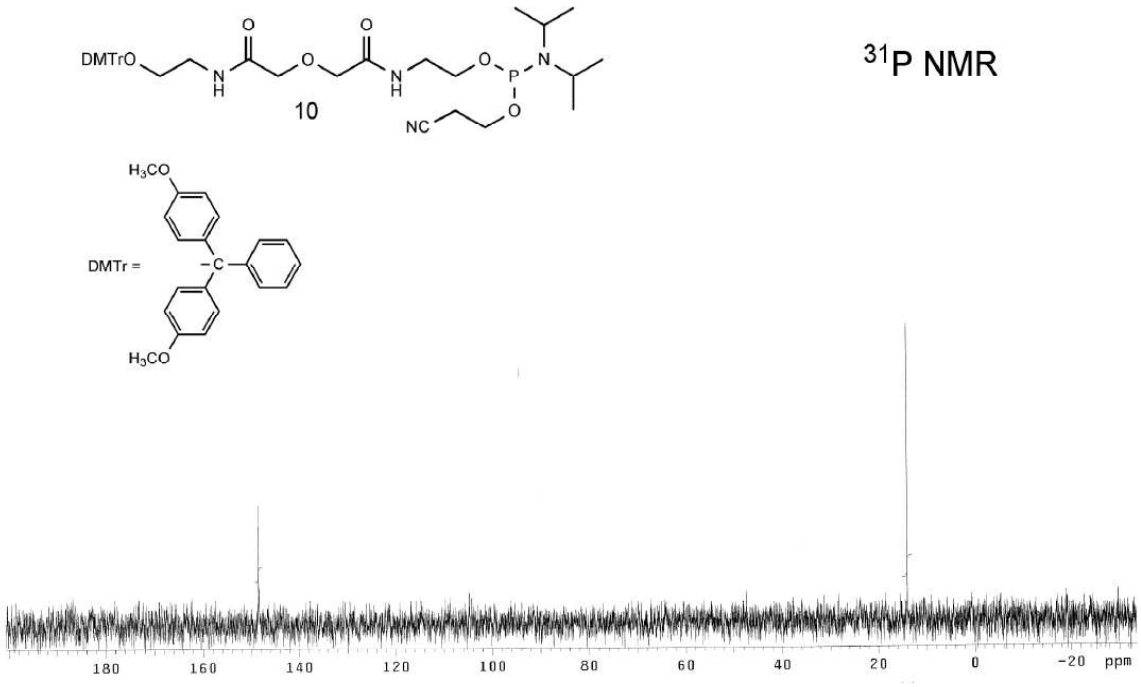


Figure S10: ^{31}P NMR spectrum of *N*-[3-O-(2-cyanoethyl-*N*,*N*-diisopropylphosphoramidite)ethyl]-*N*'-[2-(4,4' –dimethoxytrityl)oxyethyl]-2,2'-oxydiacetamide (**10**)

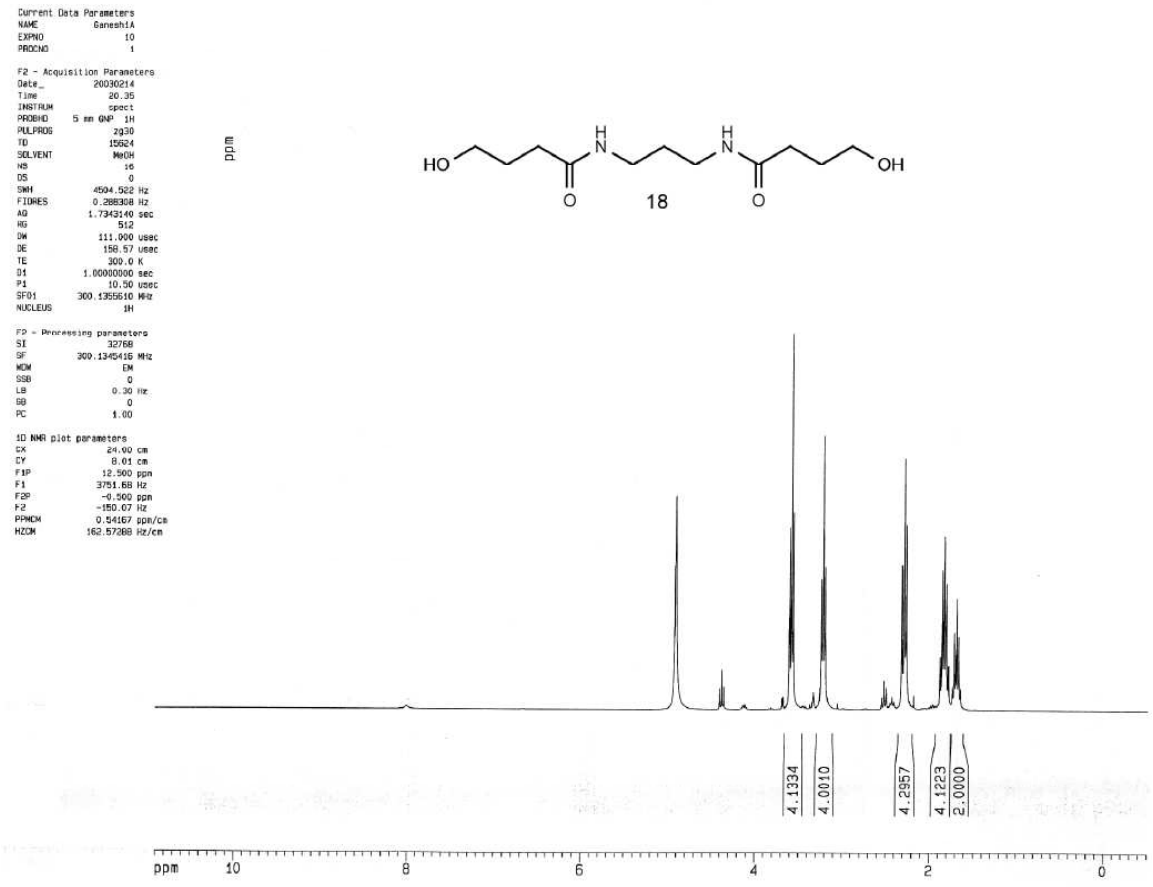


Figure S11: ^{1}H NMR spectrum of *N*, *N*'-Bis-(4-hydroxybutanoyl)-1,3-propanediamine (**18**)

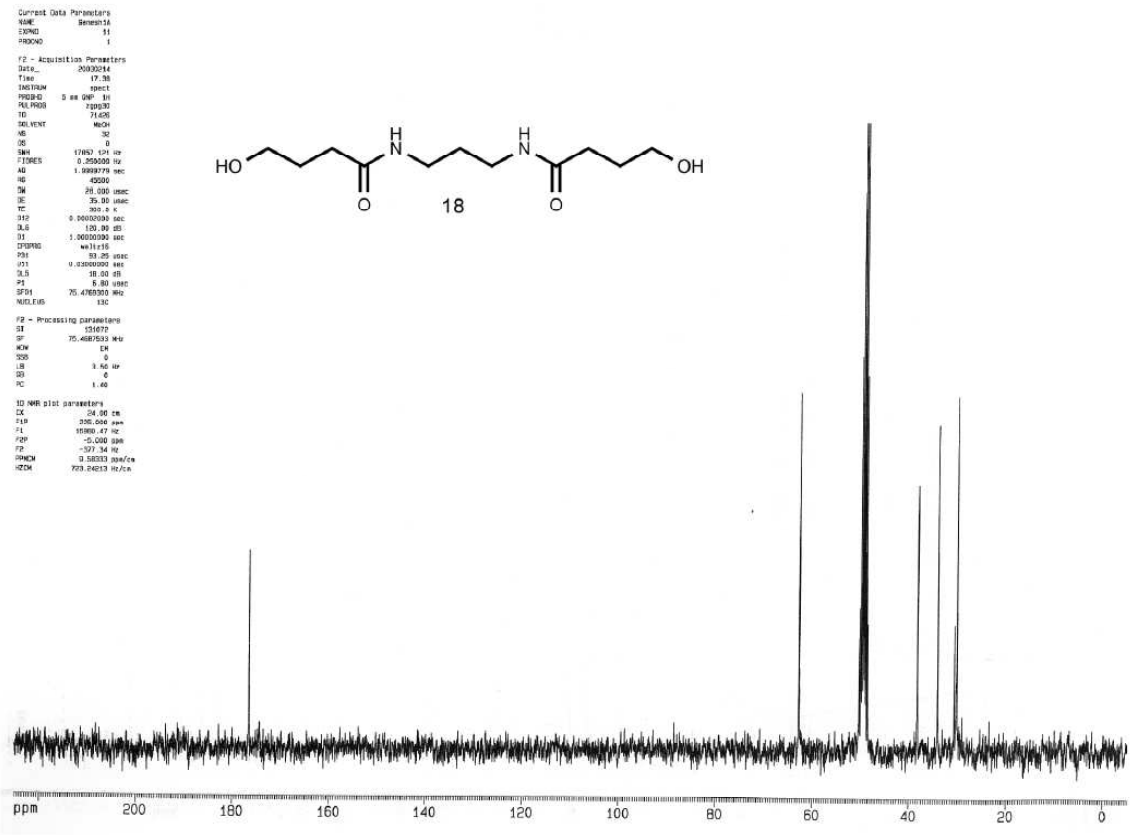


Figure S12: ^{13}C NMR spectrum of *N*, *N*'-Bis-(4-hydroxybutanoyl)-1,3-propanediamine (**18**)

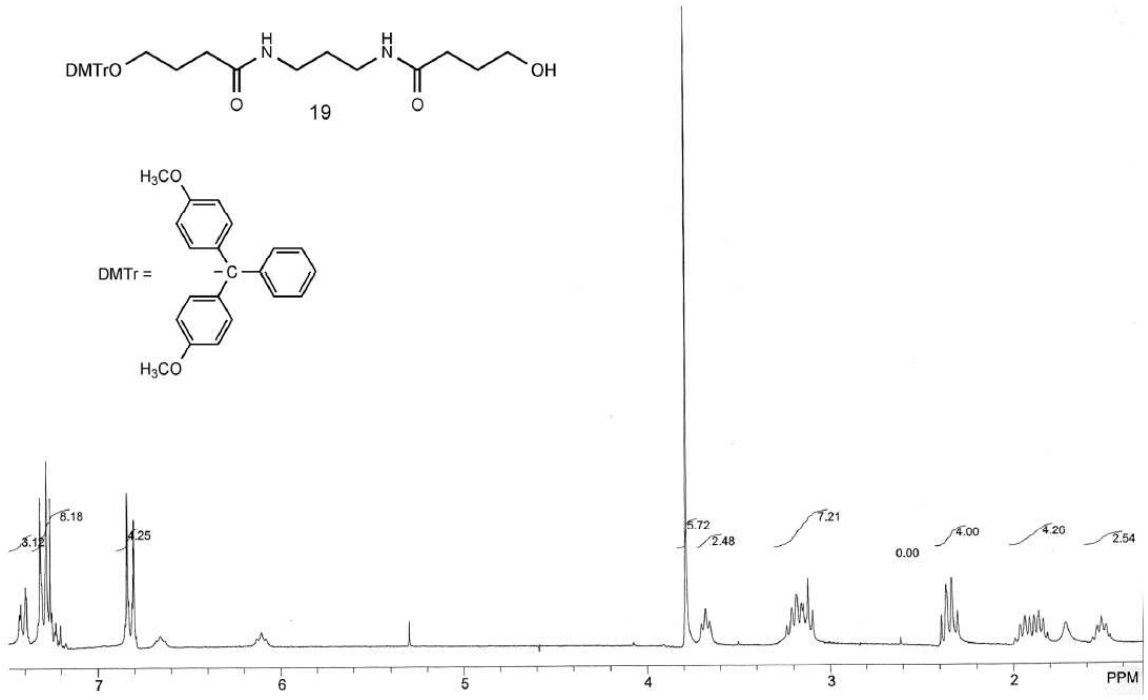


Figure S13: ^{1}H NMR spectrum of *N*-{4-[4,4'-(Dimethoxytrityl)oxy]butanoyl}-*N*'-4-hydroxybutanoyl-1,3-propanediamine (**19**)

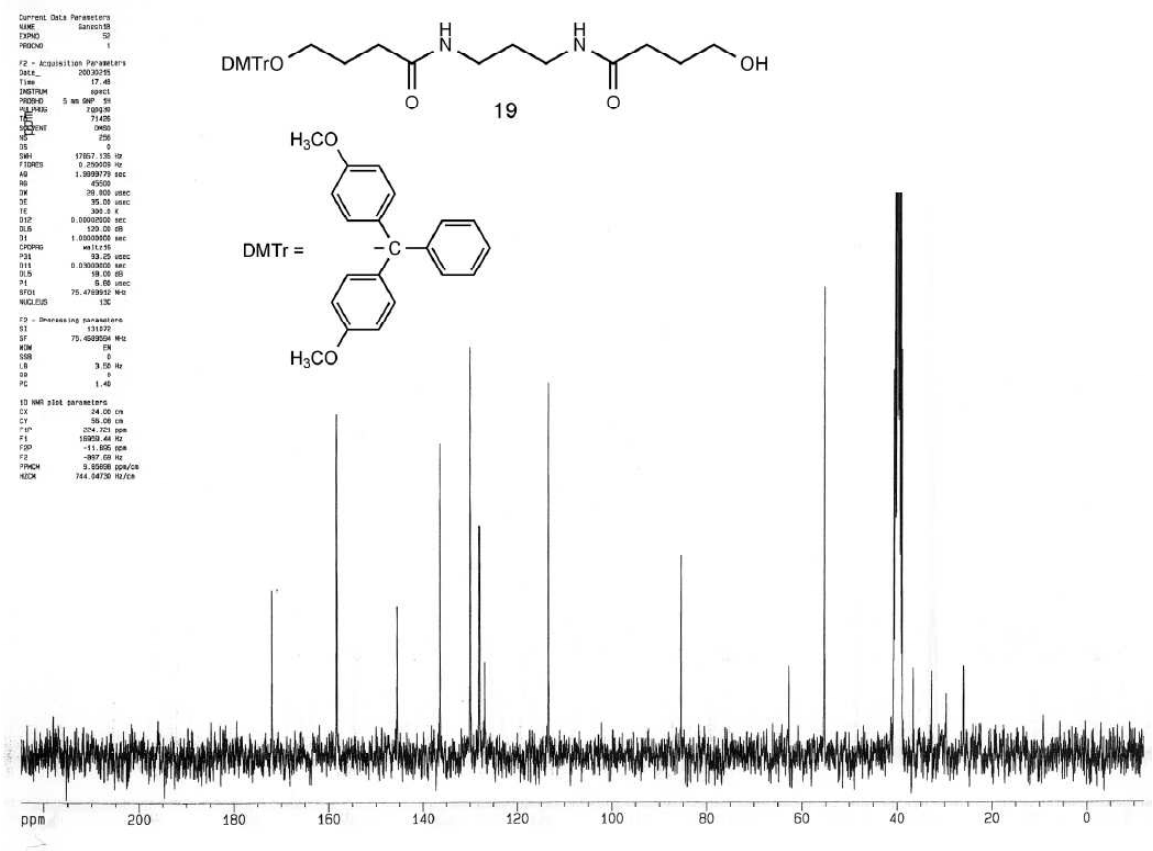


Figure S14: ^{13}C NMR spectrum of *N*-{4-[4,4'-(Dimethoxytrityl)oxy]butanoyl}-*N*'-4-hydroxybutanoyl-1,3-propanediamine (**19**)

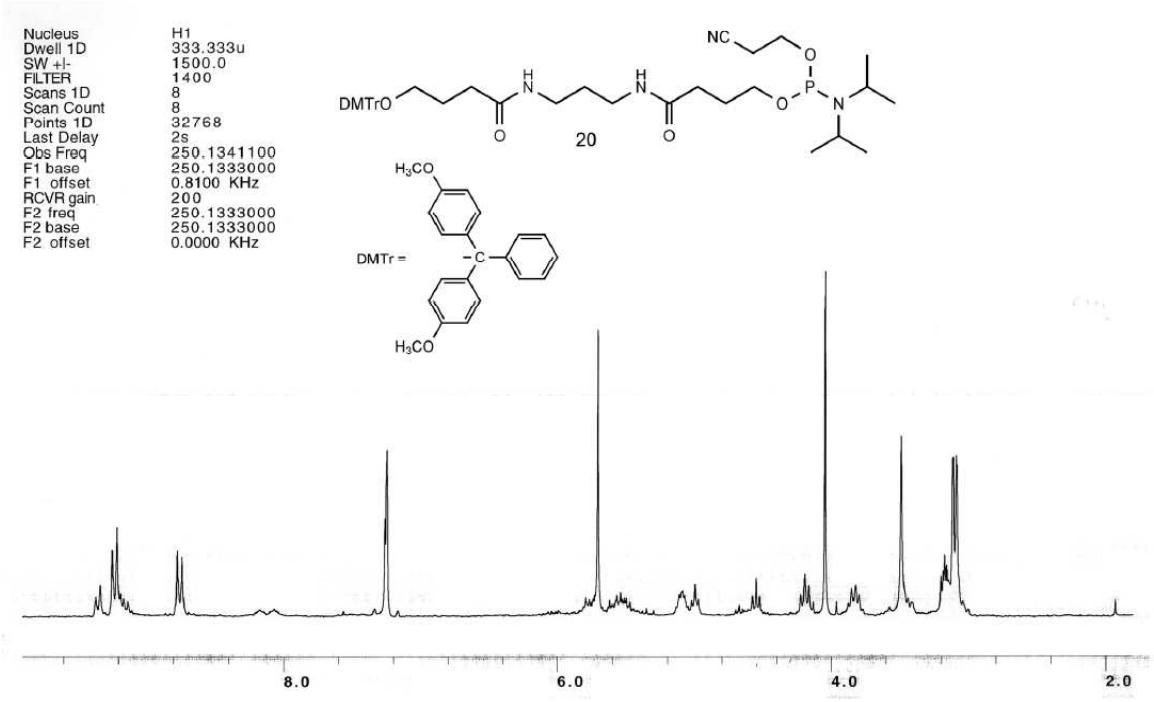


Figure S15: ^{1}H NMR spectrum of *N*-[4-O-(2-cyanoethyl-*N*,*N*-diisopropylphophoramidite)butanoyl]-*N*'-{4-[4,4'-(dimethoxytrityl)oxy]butanoyl}-1,3-propanediamine (**20**)

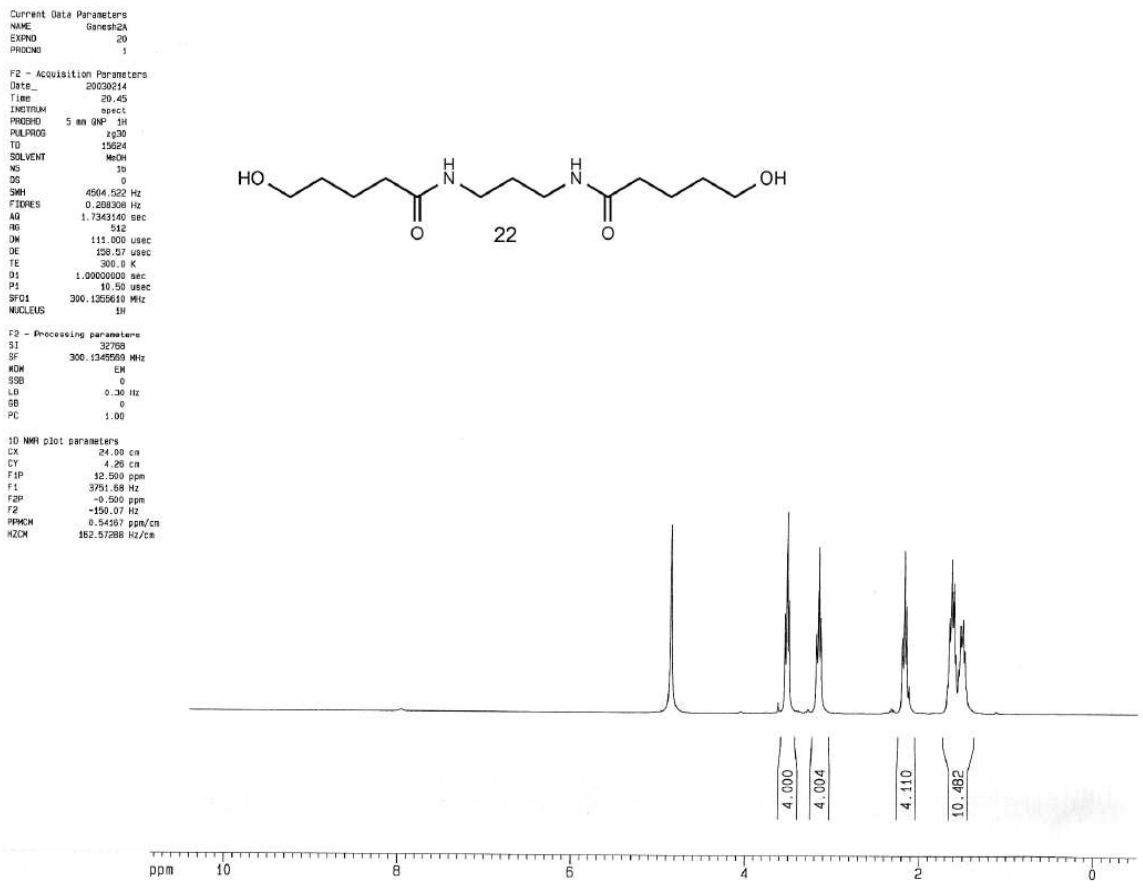


Figure S16: ^{1}H NMR spectrum of *N*, *N*'-Bis-(5-hydroxypentanoyl)-1,3-propanediamine (**22**)

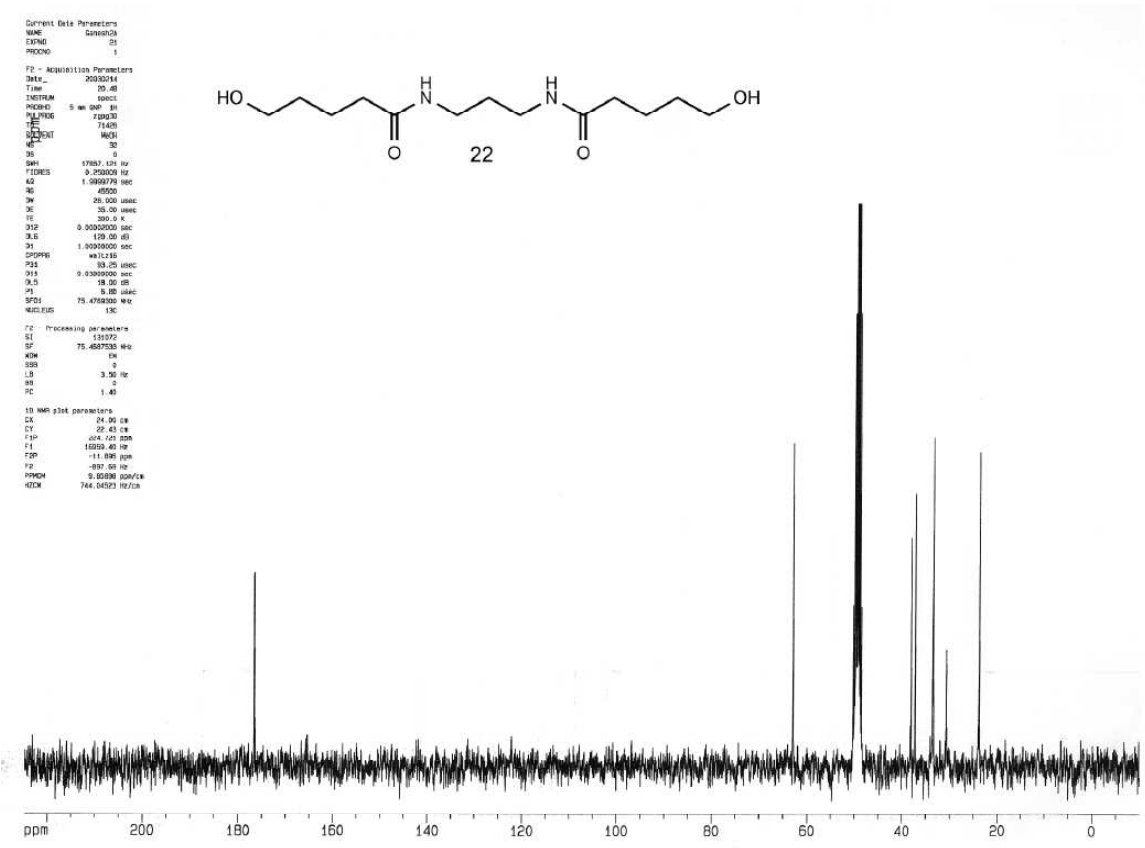


Figure S17: ^{13}C NMR spectrum of *N*, *N*'-Bis-(5-hydroxypentanoyl)-1,3-propanediamine (**22**)

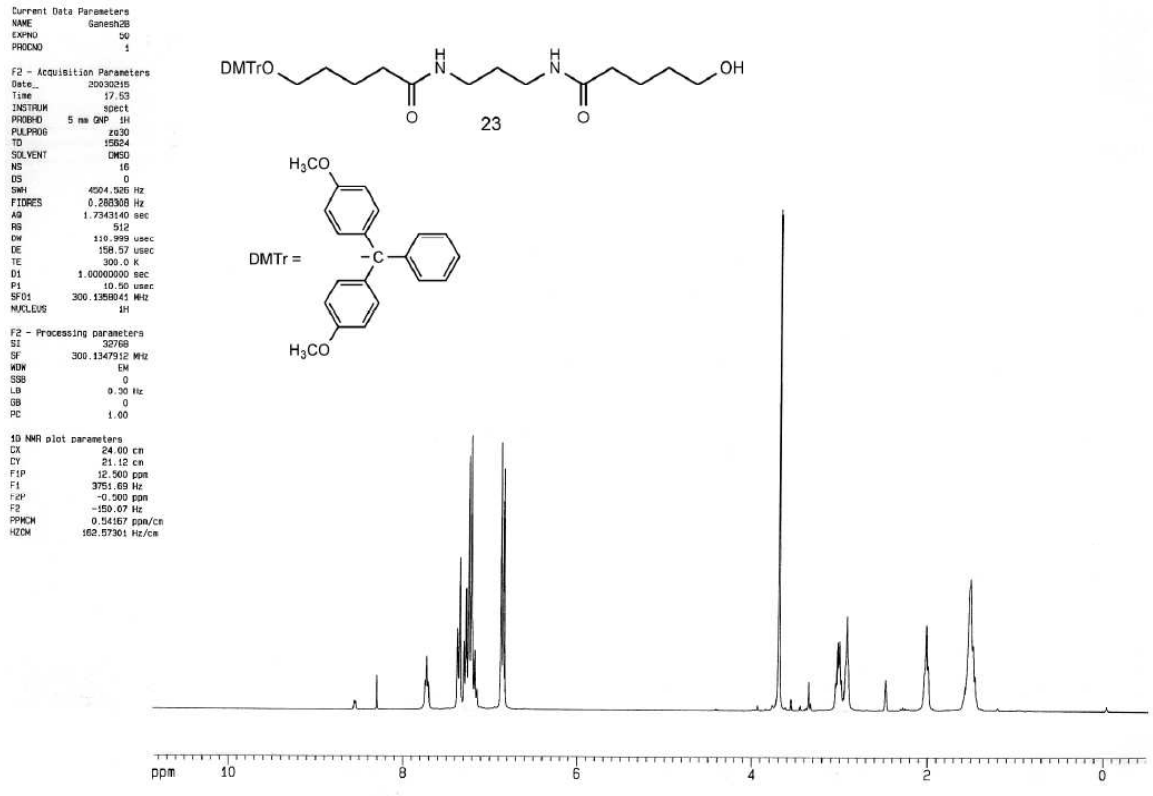


Figure S18: ^{1}H NMR spectrum of *N*-{5-[4,4'-(Dimethoxytrityl)oxy]pentanoyl}-*N*'-(5-hydroxypentanoyl]-1,3-propanediamine (**23**)

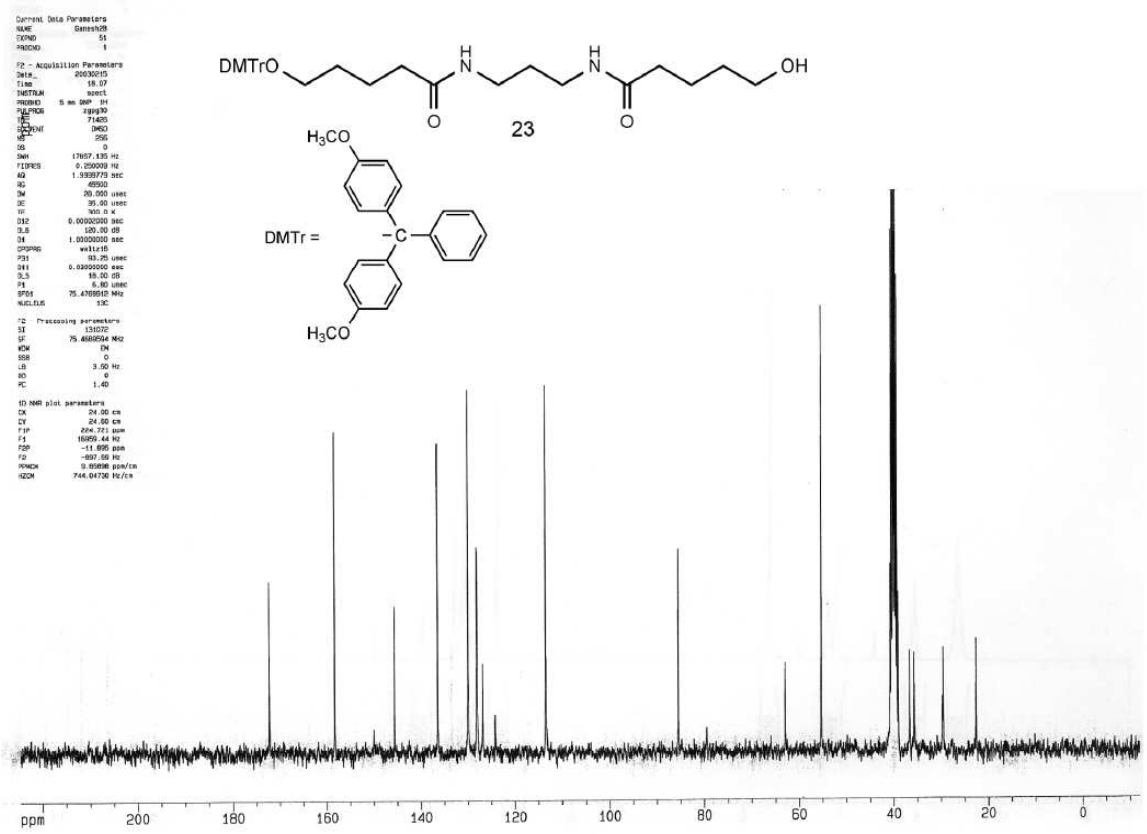


Figure S19: ^{13}C NMR spectrum of *N*-{5-[4,4'-(Dimethoxytrityl)oxy]pentanoyl}-*N*'-(5-hydroxypentanoyl]-1,3-propanediamine (**23**)

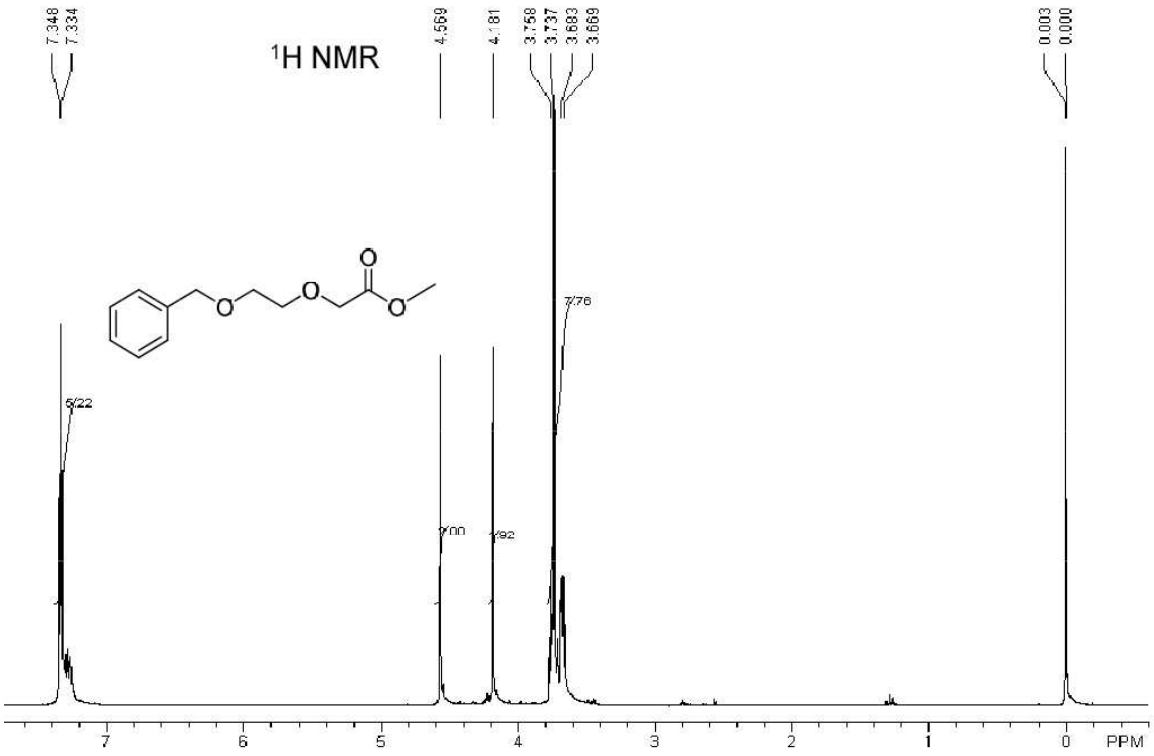


Figure S20: ^{1}HNMR spectrum of Methyl 2-(2-(benzyloxy)ethoxy)acetate (**26**)

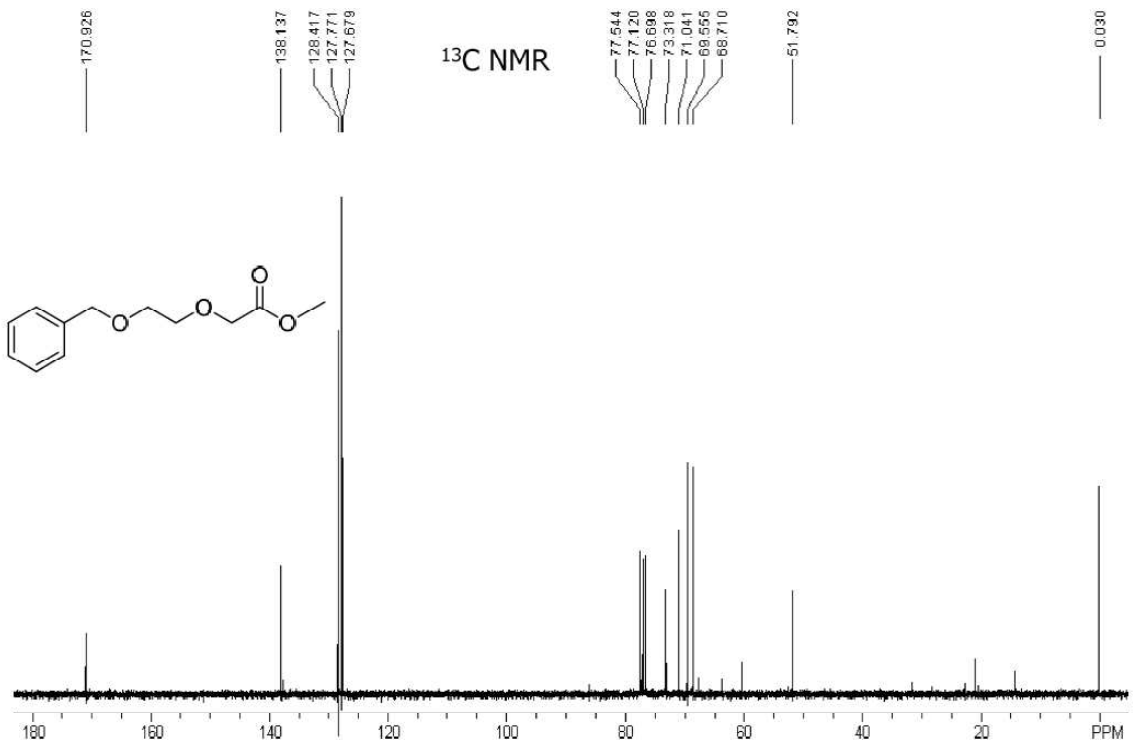


Figure S21: ^{13}C NMR spectrum of Methyl 2-(2-(benzyloxy)ethoxy)acetate (**26**)

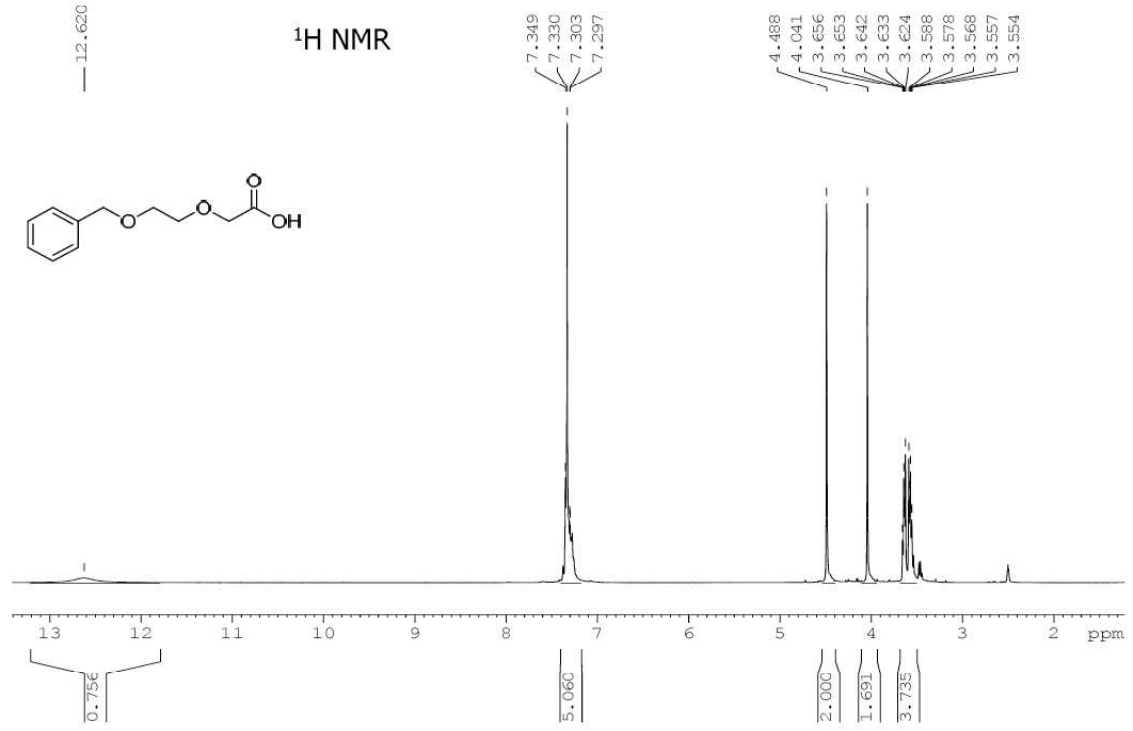


Figure S22: ^{1}H NMR spectrum of 2-(2-(Benzyloxy)ethoxy)acetic acid (**27**)

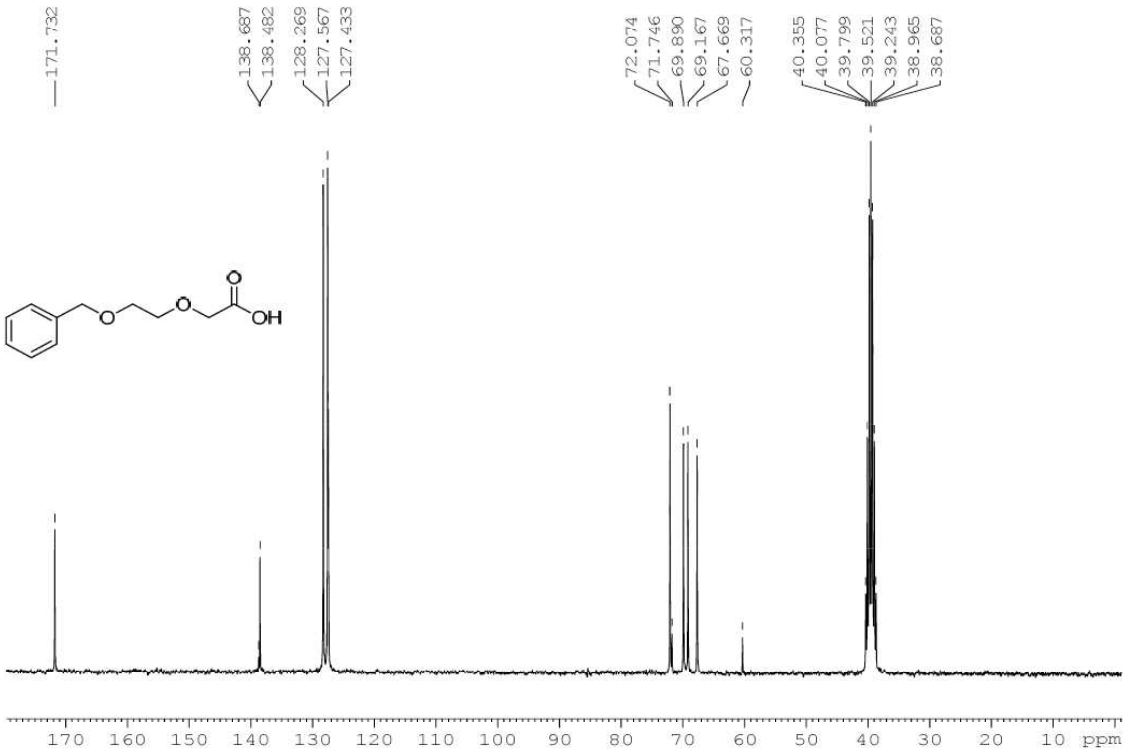


Figure S23: ^{13}C NMR spectrum of 2-(2-(Benzyloxy)ethoxy)acetic acid (**27**)

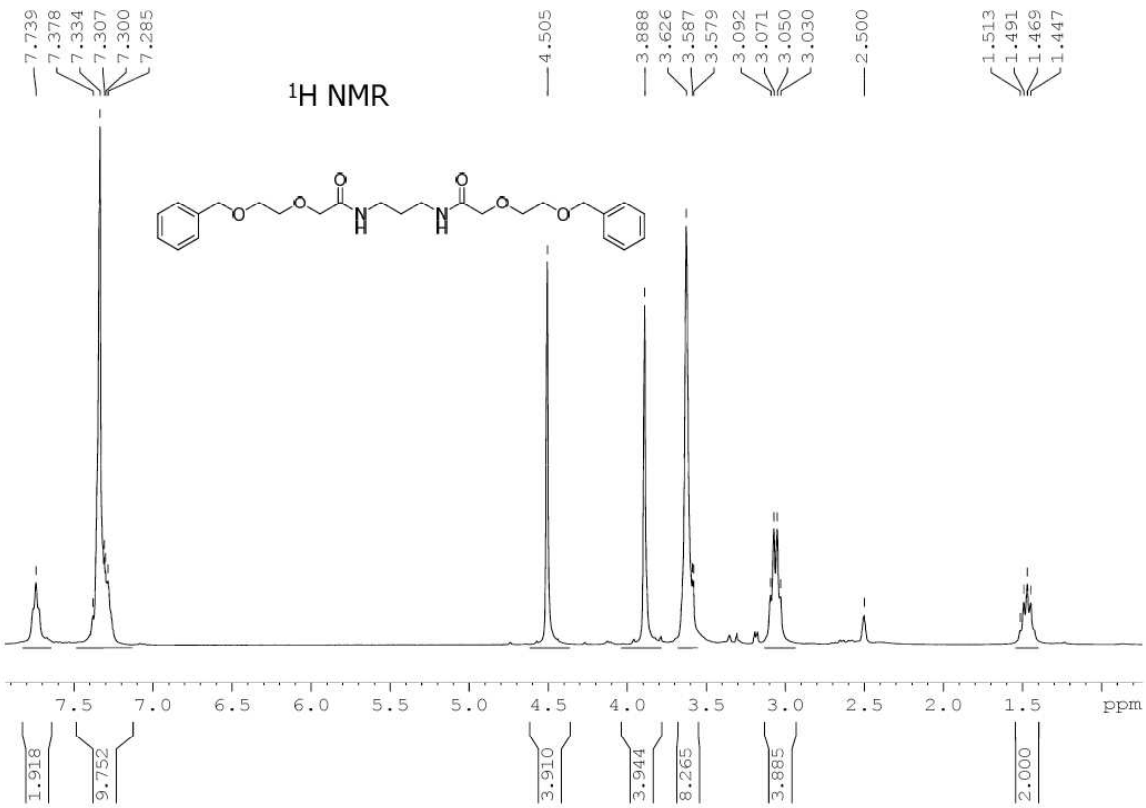


Figure S24: ^{1}H NMR spectrum of *N*, *N'*-Bis-(2-(2-benzyloxyethoxy)ethanoyl)-1,3-propanediamine (**28**)

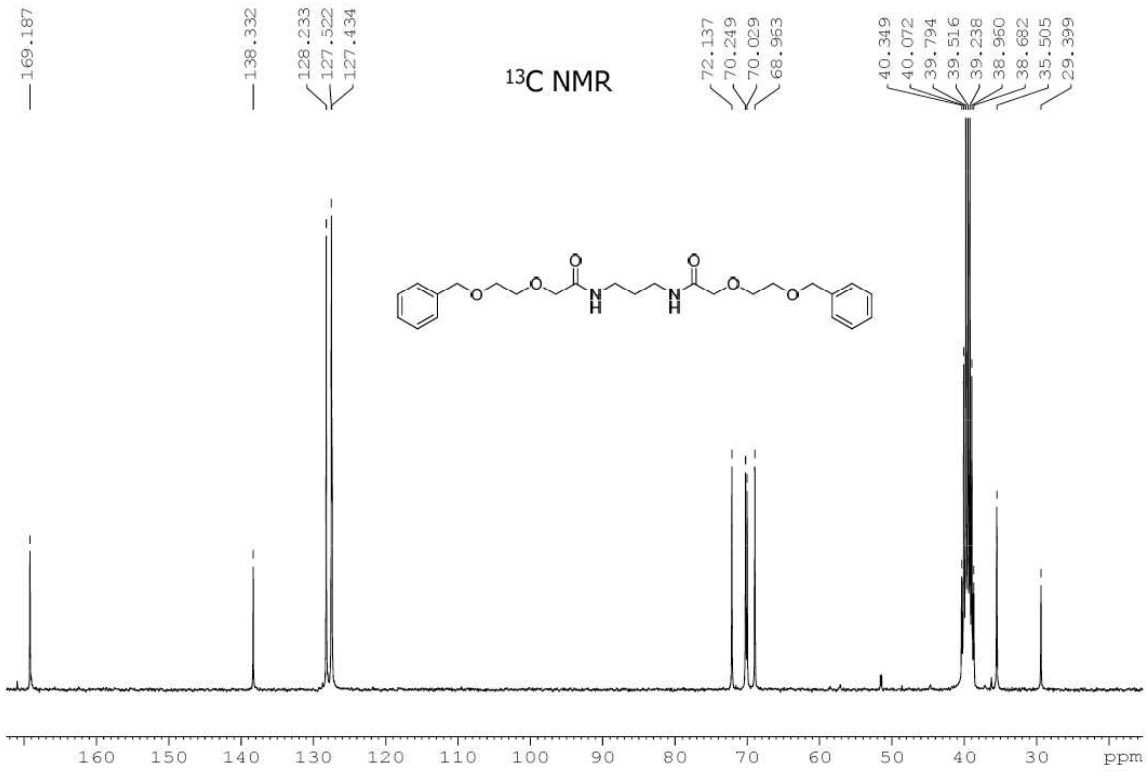


Figure S25: ^{13}C NMR spectrum of *N*, *N*'-Bis-(2-(2-benzyloxyethoxy)ethanoyl)-1,3-propanediamine (**28**)

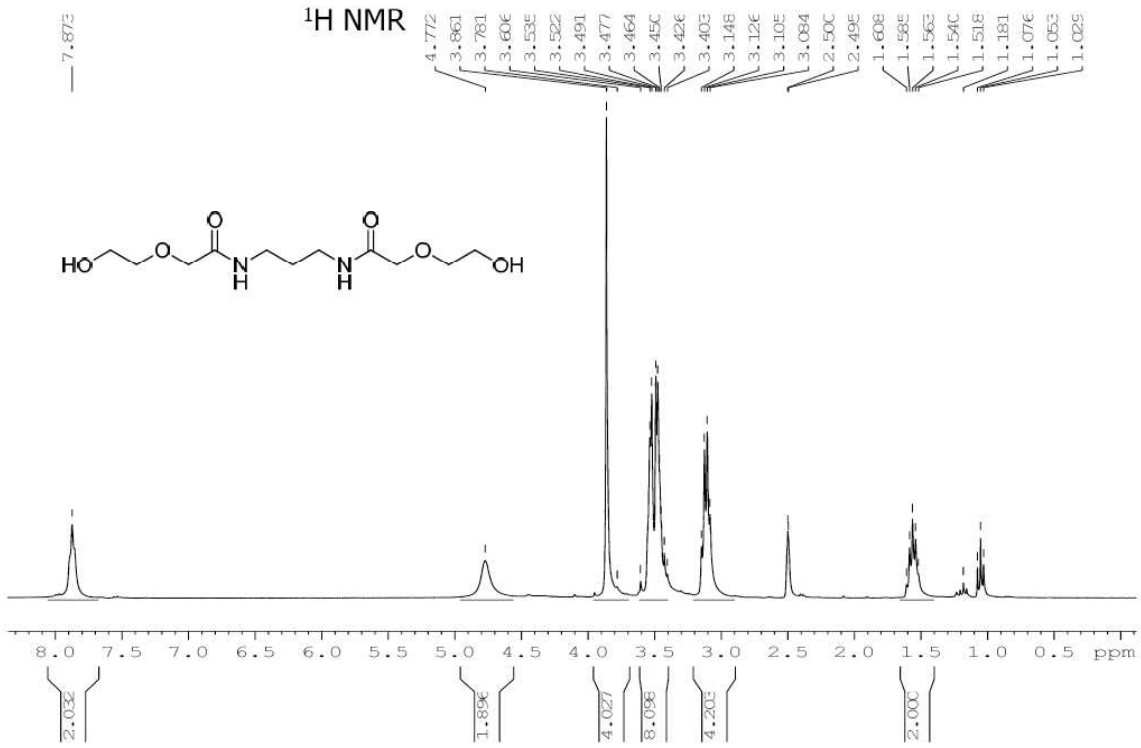


Figure S26: ^{1}H NMR spectrum of *N*, *N*'-Bis-(2-(2-hydroxyethoxy)ethanoyl)-1,3-propanediamine (**29**)

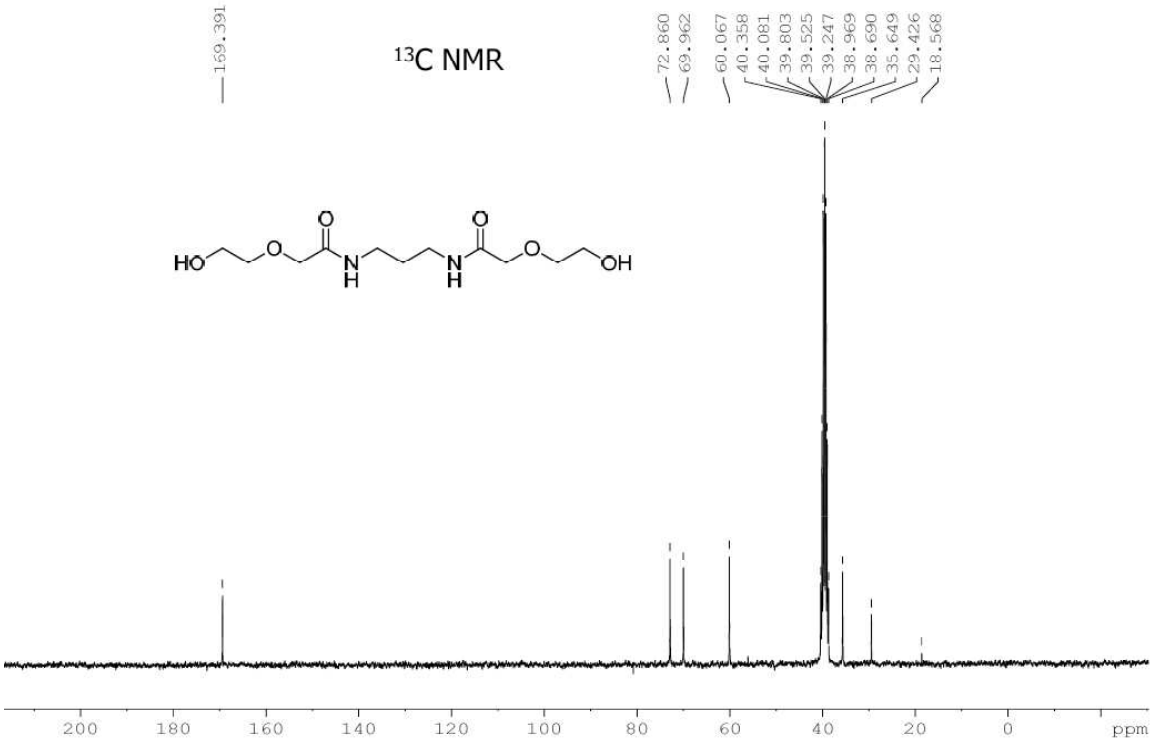


Figure S27: ^{13}C NMR spectrum of *N*, *N*'-Bis-(2-(2-hydroxyethoxy)ethanoyl)-1,3-propanediamine (**29**)

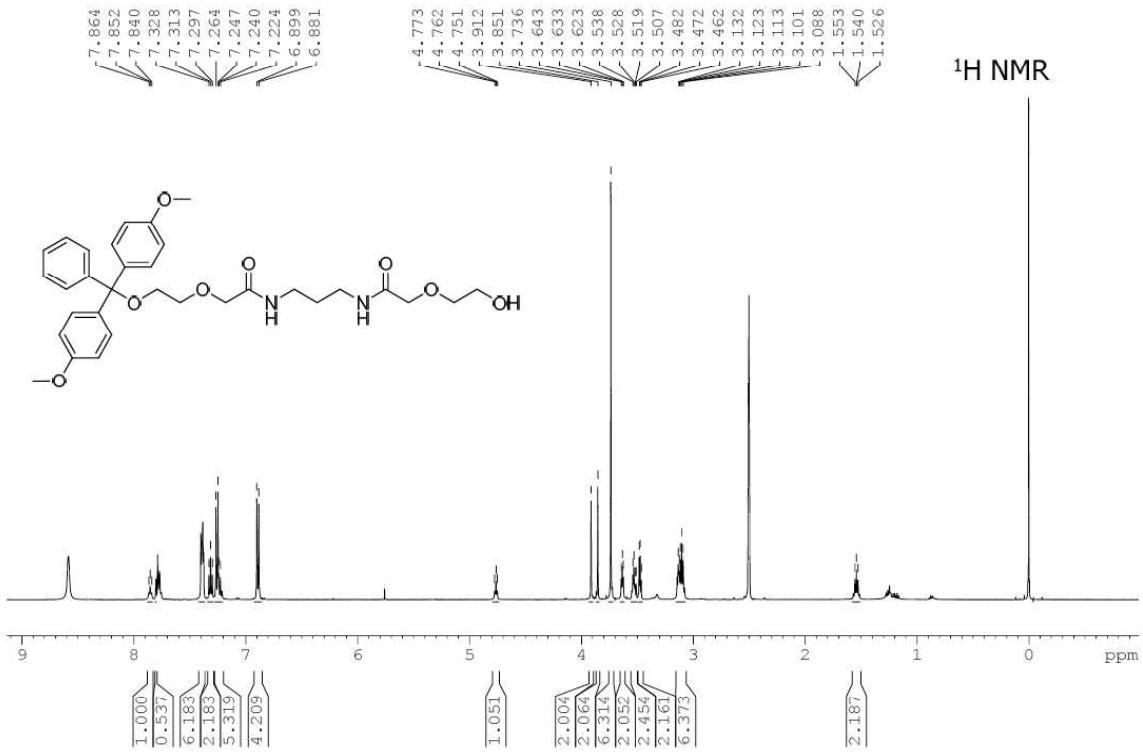


Figure S28: ^{1}H NMR spectrum of *N*-(2-(2-(4, 4'-dimethoxytrityloxy)ethoxy)ethanoyl)-*N*'-(2-(2-hydroxyethoxy)ethanoyl)-1,3-propanediamine (**30**)

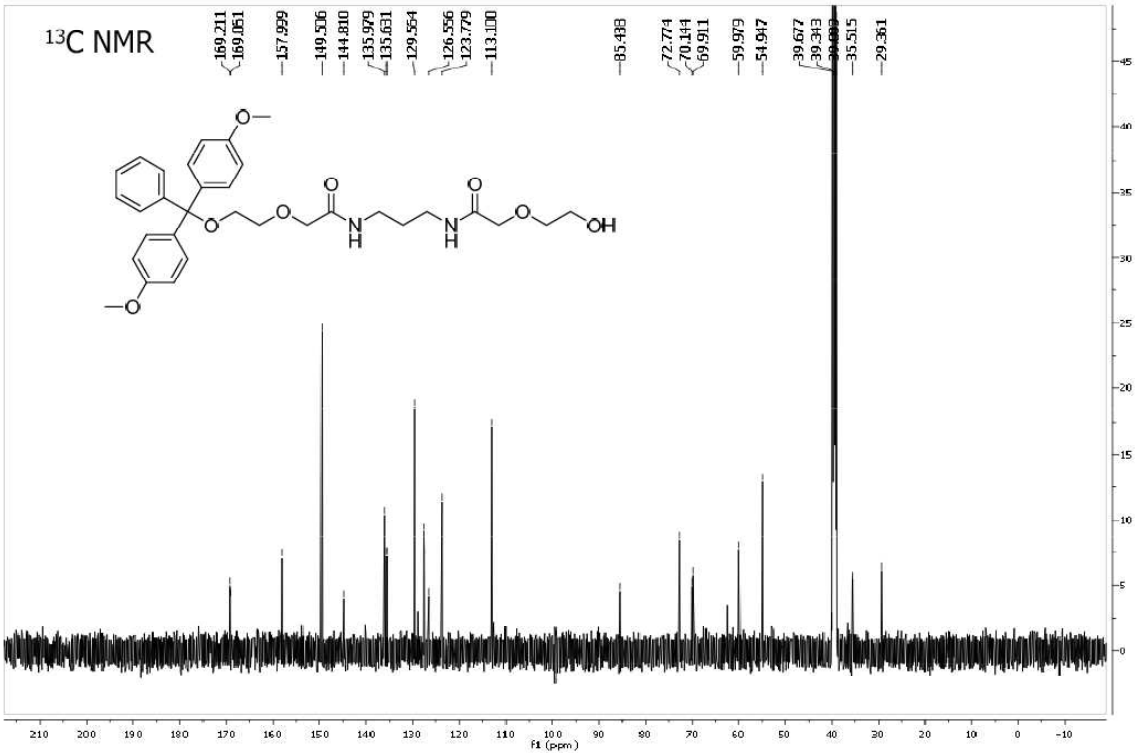


Figure S29: ^{13}C NMR spectrum of *N*-(2-(2-(4, 4'-dimethoxytrityloxy)ethoxy)ethanoyl)-*N*'-(2-(2-hydroxyethoxy)ethanoyl)-1,3-propanediamine (**30**)

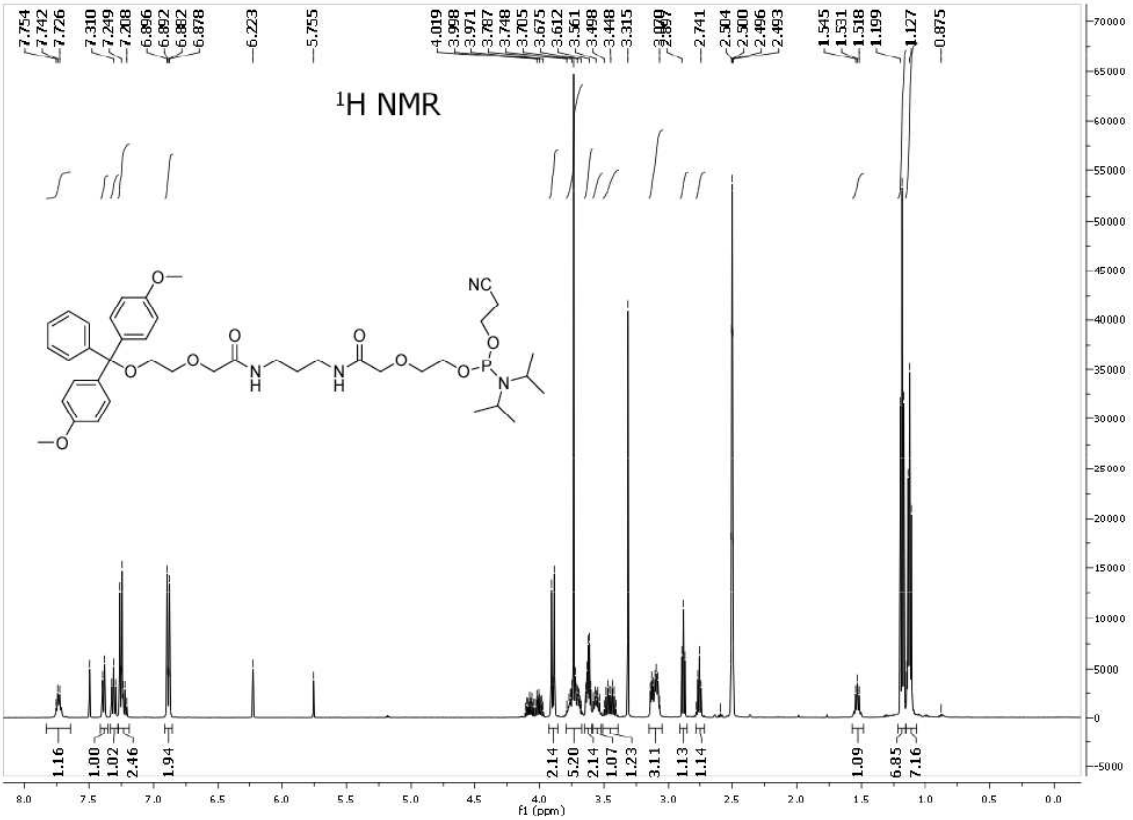


Figure S30: ^{1}H NMR spectrum of *N*-(2-(2-O-(2-cyanoethyl-*N*, *N*-diisopropylphosphoramidite)ethoxy)ethanoyl)-*N*'-(2-(2-(4, 4'-dimethoxytrityloxy)ethoxy)ethanoyl)-1,3-propanediamine (**31**)

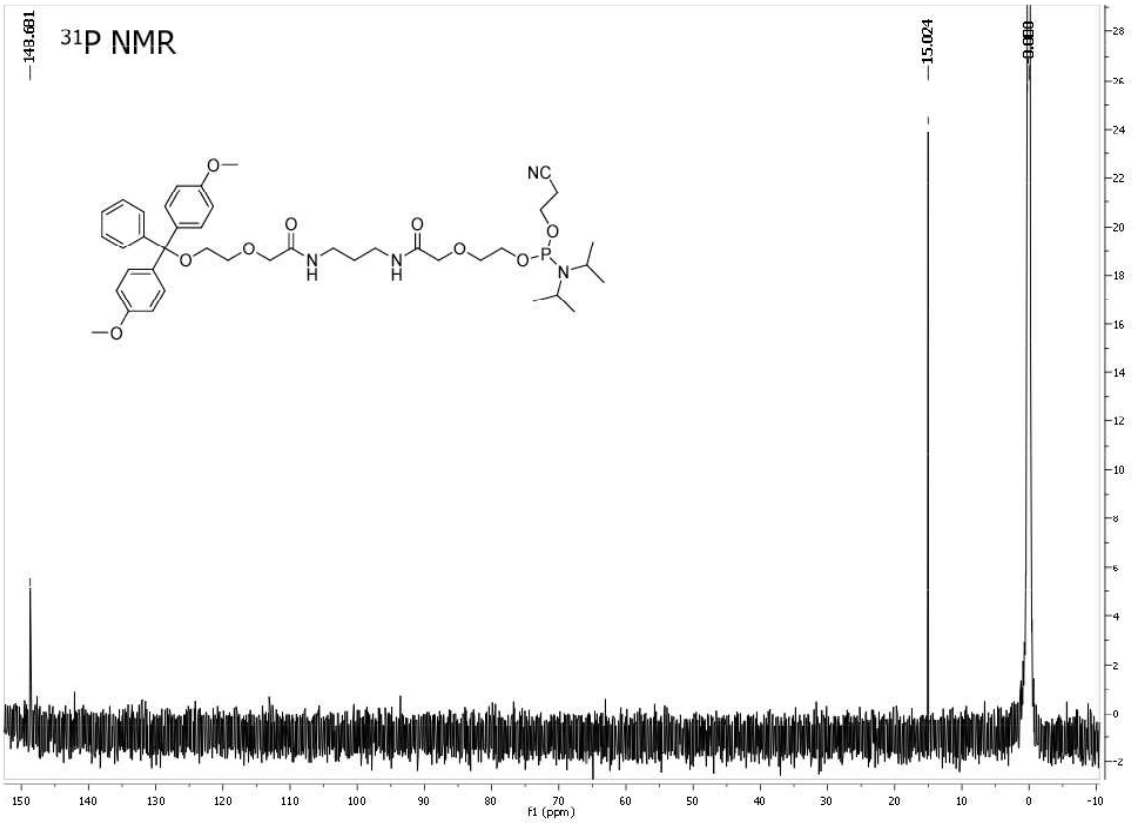


Figure S31: ^{31}P NMR spectrum of *N*-(2-(2-O-(2-cyanoethyl-*N*, *N*-diisopropylphosphoramidite)ethoxy)ethanoyl)-*N*'-(2-(2-(4, 4'-dimethoxytrityloxy)ethoxy)ethanoyl)-1,3-propanediamine (**31**)

Characterization of a Recombinant Form of Annexin VI for Detection of Apoptosis

Christina Smith,[†] Ranjana Mehta,[†] Donald F. Gibson,[†] Zoia Levashova,[‡] Francis G. Blankenberg,[‡] and Jonathan F. Tait*,[†]

Department of Laboratory Medicine, University of Washington, Seattle, Washington 98195-7110, and Department of Radiology, Stanford University, Palo Alto, California 94305. Received May 23, 2010; Revised Manuscript Received July 13, 2010

We developed a recombinant form of human annexin VI called annexin VI-601 (M_r 76,224) with the N-terminal extension of Ala-Gly-Gly-Cys-Gly-His to allow ready attachment of fluorescent or radioactive labels. The protein was produced by expression in *E. coli* and was purified by calcium-dependent membrane binding, anion-exchange chromatography, and heparin−Sepharose affinity chromatography. The protein could be readily labeled with iodoacetamidofluorescein and with ^{99m}Tc. The protein bound with high affinity to PS-containing phospholipid vesicles and to erythrocytes with exposed phosphatidylserine. Fluorescent annexin VI-601 readily detected apoptosis of Jurkat cells by flow cytometry at much lower calcium concentrations than those required for equivalent detection by annexin V. In vivo administration of radiolabeled protein showed that blood clearance was much slower than annexin V. In conclusion, annexin VI may have advantages over annexin V in certain situations for both in vitro and in vivo detection of apoptosis and therapeutic targeting of PS due to its lower calcium requirement for membrane binding and its higher molecular weight.

INTRODUCTION

Detection of apoptosis is a key experimental technique in many fields, and numerous methods have been developed for this purpose (*1*). One commonly used method relies on detection of phosphatidylserine (PS)[1] exposure at the extracellular face of the plasma membrane, which is an early event in apoptosis (*2*). PS exposure is most commonly detected with annexin V, a calcium-dependent PS-binding protein (*3, 4*). More recently, other proteins have been used, including synaptotagmin I (*5*) and lactadherin (*6*−*8*). While these agents provide a wide choice for various applications, there are several areas for potential improvements. One would be a protein with higher molecular weight than existing proteins, which should result in prolonged blood clearance time. A second potential advantage would be a protein with a lower calcium requirement for binding than annexin V. Of the protein-based agents developed to date, only lactadherin has this property.

Annexin VI (or annexin A6) is a member of the annexin protein family (*9*). While it shares the basic biochemical and structural properties of the other members of the family, it is unique among all members of the family in having eight rather than four of the canonical 70-amino-acid repeating units that are the hallmark of the primary structure of annexins (Figure 1). This means that it has about twice the molecular mass of other annexins (ca. 76 000 vs 36 000 Da). It binds to anionic phospholipids in the same manner as other annexins and has an apparent PS binding affinity as high as or higher than annexin V (*10*).

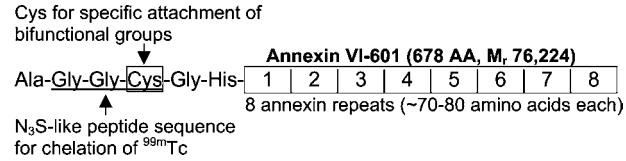


Figure 1. Schematic structure of Annexin VI-601 The protein is a recombinant construct that consists of amino acids 2−673 of natural human annexin VI plus an added N-terminal extension of six amino acids that provides a high-affinity site for Tc labeling (*11*). "601" is an arbitrary number used to uniquely identify the recombinant protein construct.

The goal of this project was to develop a recombinant form of human annexin VI suitable for detection of exposed PS via fluorescence or nuclear medicine techniques via labeling with sulfhydryl-reactive reagents or technetium-99m. To accomplish this, we used an approach that we previously developed for annexin V (*11, 12*): the sequence Ala-Gly-Gly-Cys-Gly-His was attached to the N-terminus of the natural protein sequence. This peptide sequence forms a high-affinity N_3S-like Tc chelation site and was previously shown to increase Tc radiolabeling yield from 4% (for wild-type annexin V) to 90% (after addition of the N-terminal peptide) (*11*). The cysteine residue in this sequence is also readily accessible to bifunctional alkylating agents, as it is not part of an endogenous disulfide bridge in the native protein structure. We show that the resulting recombinant protein, annexin VI-601, can be readily produced in *E. coli* and binds with high affinity to phospholipid vesicles and apoptotic cells with exposed PS.

EXPERIMENTAL PROCEDURES

Construction of pJ601 Plasmid. The starting material was the plasmid pCMV6-XL5 (OriGene, Rockville, MD) encoding human annexin VI, transcript variant 1 (amino acid sequence available from the NCBI RefSeq collection under accession

* Corresponding author. Dr. Jonathan Tait, Department of Laboratory Medicine, University of Washington, Box 357110, Seattle, WA 98195-7110. Telephone: (206)598-6131, Fax: (206)598-6189, E-mail: tait@u.washington.edu.

[†] University of Washington.

[‡] Stanford University.

[1]Abbreviations: C_7−PC, diheptanoyl-phosphatidylcholine; EC_{50}, calcium concentration causing 50% of maximum protein−membrane binding; FRET, fluorescence resonance energy transfer; IAF, 5′-iodoacetamidofluorescein; PC, phosphatidylcholine; PS, phosphatidylserine; R-PE, rhodamine-labeled phosphatidylethanolamine; pK_d, negative logarithm of equilibrium dissociation constant K_d; SD, standard deviation.

10.1021/bc100239k © 2010 American Chemical Society
Published on Web 07/30/2010

#NP_001146.2). PCR primers were designed to amplify amino acids 2−673 of the protein-coding region, to add the desired N-terminal extension (MAGGCGH) and to delete the initiator methionine present in the wild-type sequence. Amplification for 30 cycles was performed with *Pfu* DNA polymerase, and then 3′dA overhangs were added with 3 cycles of PCR with *Taq* DNA polymerase. This PCR product was purified by gel electrophoresis and ligated into the protein expression vector pETBlue-1 Acceptor Vector (Novagen, Madison, WI). The ligation mixture was transformed into Nova Blue *E. coli* (Novagen) and plated onto L broth agar plus carbenicillin, X-gal, and IPTG. Several white colonies were picked for culture, plasmid was isolated, the presence of the desired insert in the proper orientation was verified with restriction mapping, and the presence of the correct sequence throughout the insert was verified by automated sequencing in the institutional core sequencing facility. The resulting plasmid was designated "pJ601" and was transformed into Tuner (DE3) pLacI *E. coli* (Novagen) cells for protein expression.

Expression and Purification of Annexin VI-601. Bacterial host cells containing the expression plasmid were grown overnight at 37 °C with shaking in T broth with carbenicillin (50 μg/mL) and chloramphenicol (34 μg/mL) to an OD_{600} of about 9.0. The cells were harvested by centrifugation, lysed by sonication in ice-cold buffer (50 mM Tris pH 7.2, 10 mM calcium chloride), centrifuged, and the supernatant discarded. The recombinant protein was released from the pelleted membranes by resuspension in 50 mM Tris pH 7.2, 20 mM EDTA, and the membrane fragments were removed by centrifugation. The supernatant was treated with Benzonase nuclease to digest DNA and RNA and dialyzed extensively against 20 mM Tris-HCl pH 8.0. The protein was purified by anion-exchange chromatography with the same buffer plus 1 mM betamercaptoethanol on a MonoQ HR5/5 column (GE Healthcare), with peak elution occurring at 0.25 M NaCl. After dialysis into 20 mM HEPES-Na, pH 7.4, 100 mM NaCl, the annexin VI-601 was further purified via calcium-dependent affinity chromatography on a HiTrap heparin−Sepharose column (GE Healthcare). The column was equilibrated with buffer composed of 20 mM Tris-HCl, pH 8.0, 0.5 mM $CaCl_2$, 0.02% Tween-20, and 1.0 mM DTT. The protein in 20 mM Tris-HCl, pH 8.0, was supplemented with 0.5 mM $CaCl_2$, 0.02% Tween-20, and 1 mM DTT and applied to the column. The column was washed with the equilibration buffer, then washed with the same buffer with 1 mM EDTA substituted for the $CaCl_2$. The annexin VI-601 was eluted with buffer containing 20 mM Tris-HCl, pH 8.0, 2.0 M NaCl, 1 mM EDTA, and 1.0 mM DTT. The final product was dialyzed against 10 mM HEPES-Na pH 7.4, 140 mM NaCl, concentrated with a Centriplus 30 spin column (Amicon), and quantitated by absorption at 280 nm (extinction coefficient of 0.6 mL/mg.cm). Purity and identity were verified by SDS−polyacrylamide gel electrophoresis and electrospray mass spectrometry on a Micromass Quattro II tandem quadrupole mass spectrometer (Micromass Ltd., Manchester, U.K.) in the Mass Spectrometry Center (Department of Medicinal Chemistry, University of Washington).

Fluorescence Labeling of Annexin VI-601. Annexin VI-601, 2 mg in 10 mM HEPES-Na, pH 7.4, 140 mM NaCl, was reduced with 1.0 mM DTT at 37 °C for 15 min. The DTT was removed with a NAP-25 column (GE Healthcare) with elution into 3.5 mL deoxygenated 20 mM HEPES pH 7.4, 100 mM NaCl buffer. The addition of 2.6 μL of IAF (10 mM in dimethylformamide) to the protein (0.57 mg/mL) gave a final concentration of 7.4 μM for both protein and IAF. The reaction was incubated for 2 h at room temperature, protected from light. The IAF-labeled protein was dialyzed against 20 mM Tris-HCl, pH 8.0, at 4 °C protected from light. Final purification was by anion-exchange chromatography on a MonoQ HR5/5 column in 20 mM Tris-HCl, pH 8.0 buffer, with fluorescent protein eluting between 0.34 and 0.38 M NaCl. The labeled protein was quantitated by colorimetric protein assay (Pierce BCA reagent), and incorporation of fluorescent dye was determined by reading absorbance at 492 nm ($\varepsilon_{492} = 67\,500\ M^{-1}\ cm^{-1}$).

Phospholipid Vesicle Binding Affinity Assay. We used a fluorescence quenching assay to measure the binding of IAF-annexin VI-601 to phospholipid vesicles labeled with rhodamine as previously described (*13*). Unilamellar phospholipid vesicles were prepared with 25% PS (1-palmitoyl-2-oleoyl), 2% rhodamine-labeled phosphatidylethanolamine, 20% 1,2-diheptanoyl-phosphatidylcholine, and 53% 1-palmitoyl-2-oleoyl phosphatidylcholine (Avanti Polar Lipids, Alabaster, AL) in a buffer containing 50 mM HEPES-Na, pH 7.4, 3 mM NaN_3, and 100 mM NaCl. Assays were performed in the same buffer plus 100 μg/mL ovalbumin. Reactions usually contained 1.5 nM IAF-annexin VI-601, 30 μM phospholipid vesicles, and 0−350 μM calcium chloride. After a 10 min incubation at 25 °C in the dark, fluorescence intensity was measured and fluorescence quenching calculated relative to the fluorescence intensity seen in the absence of calcium. Data were analyzed as described (*13*) to determine the binding parameters of EC_{50}, slope, and affinity (pK_d).

Phospholipid Vesicle Binding Stoichiometry Assay. The stoichiometry of phospholipid binding to annexin VI-601 molecules was determined with a modification of the vesicle binding assay. Reactions were performed with a large excess of calcium to ensure that all added phospholipid would be bound to protein until saturation was reached. IAF-annexin VI-601 (2.5 nM) was added to assay buffer containing 2 mM calcium chloride and a range from 0 to 2000 nM of phospholipid vesicles. After 10 min at 25 °C in the dark, fluorescence intensity was measured and the fluorescence quenching calculated relative to the fluorescence intensity seen in the absence of phospholipid. The stoichiometry was calculated from the maximum fluorescent quenching at saturation divided by the slope of the linear part of the titration curve.

RBC Binding Affinity Assay for Labeled Proteins. The bioactivity of labeled forms of annexin VI was also determined by quantitative calcium titration assay with erythrocytes with exposed PS as the cell substrate with both fluorescent (*13*) and radioactive forms of annexin (*12*). Briefly, labeled protein was added at 1 nM final concentration to a solution containing 1×10^8 RBC in a buffer of 50 mM HEPES pH 7.4, 100 mM NaCl, 3 mM NaN_3, 1 mg/mL BSA, and calcium chloride ranging from 0 to 5 mM. After an 8 min incubation at room temperature, cells were centrifuged, the supernatant removed, and the cells resuspended in fresh buffer at the same calcium concentration. After this wash step, the annexin bound to the RBC was released by addition of 5 mM EDTA and then quantitated as appropriate by fluorometry or gamma spectrometry. Calcium titration curves were analyzed as described above for phospholipid vesicles.

Flow Cytometry. Jurkat T-leukemia cells were treated with UV light to induce apoptosis as previously described (*14*). Flow cytometry assays were set up with treated or untreated Jurkat cells at 2.5×10^6 cells/mL with 30 nM IAF-annexin VI-601 in a buffer consisting of 10 mM HEPES-Na, pH 7.4, 130 mM NaCl, 4 mM KCl, 0.9 mM $MgCl_2$, 0.8 mM NaH_2PO_4, 5 mM glucose, 1.0 mg/mL BSA, and $CaCl_2$ varying from 0 to 2.0 mM. After incubation in the dark at 25 °C for 6 min, cells were analyzed on a flow cytometer with a 488 nm laser. The cells were delineated with forward and side-scatter gating; IAF was read in channel FL1. Cells grown and treated under these experimental conditions had a negligible (<2%) fraction of necrotic cells; thus, a marker for necrosis (such as propidium iodide) was not routinely included in the flow cytometry assays.

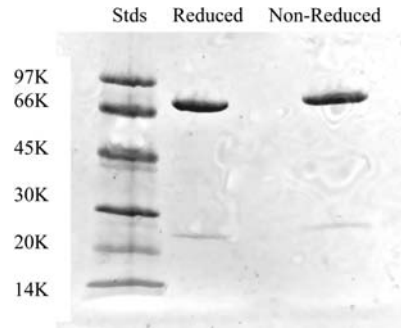


Figure 2. SDS−polyacrylamide gel analysis of purified recombinant annexin VI-601. The protein has the expected molecular weight and is present almost entirely in monomeric form (note similar gel pattern in the presence and absence of the reducing agent β-mercaptoethanol).

Labeling with ^{99m}Tc on Endogenous Chelation Site. Annexin VI-601 was labeled with ^{99m}Tc as previously described for annexin V-128 (*12*). The protein was diluted with phosphate buffered saline (PBS) pH 7.4 to 3.0 mg/mL and reduced under argon with 1 mM DTT for 15 min at 37 °C. The DTT was then removed with a Sephadex G-25 column under anaerobic conditions and the protein recovered at 1.0 mg/mL in 20 mM trisodium citrate pH 5.4, 100 mM NaCl buffer, under argon. The labeling reaction was set up, adding the following reagents in sequence: ~100 μL $^{99m}TcO_4$ (5 mCi) in deoxygenated 0.9% NaCl, 5 μL tin reagent (0.124 mg glucoheptonate sodium salt, 3.2 μg $SnCl_2 \cdot 2H_20$, 3.2 μg gentisic acid sodium salt) and 50 μL (50 μg) protein; the reaction was incubated for 60 min at 37 °C under argon. The percent incorporation was determined by ITLC, the protein purified by gel filtration in PBS on a Sephadex G25 column, and the annexin VI-601 was diluted into assay buffer as needed.

Blood Clearance in Vivo. Adult Balb/c mice were injected via tail vein with a single dose of 100 μCi (1 μg), and blood samples were taken in duplicate at 1, 5, 10, 15, 30, 60, 120, 180, and 300 min after injection.

RESULTS

Annexin VI-601 Can Be Readily Produced by Expression in *E. coli.* We designed an annexin VI construct that can be labeled readily with fluorophores or Tc (Figure 1). The expression vector (plasmid pJ601) was constructed, sequence-verified, transformed into *E. coli*, and a protein product of the expected size (76 kDa) was produced (Figure 2). After sonication, calcium-dependent membrane binding, nuclease treatment, cation-exchange chromatography, and heparin−Sepharose affinity chromatography, a total of about 10 mg of annexin VI was produced per liter of starting culture at a purity of about 97−98% by SDS-PAGE analysis. The measured molecular mass of the protein construct by electrospray mass spectrometry was 76 250 ± 30, consistent with the calculated mass of 76 224.

IAF-Annexin VI-601 has High Affinity for Phospholipid Vesicles and Erythrocytes with Exposed PS. To verify that the protein has high binding affinity, the protein was labeled with IAF and binding to PS-containing phospholipid vesicles was measured. Binding measurements performed with limiting calcium and excess phospholipid (low-occupancy conditions) allow measurement of binding affinity and cooperativity with respect to calcium (*13*, *15*). A representative curve is shown in Figure 3A, which shows the highly cooperative binding previously observed for annexin V (*13*). Assays were also performed under conditions where phospholipid is the limiting component to determine the stoichiometry of phospholipid binding (Figure 3B). The mean stoichiometry was 184 ± 31 (mean ± SD, 7 determinations) phospholipid per mole annexin VI, compared

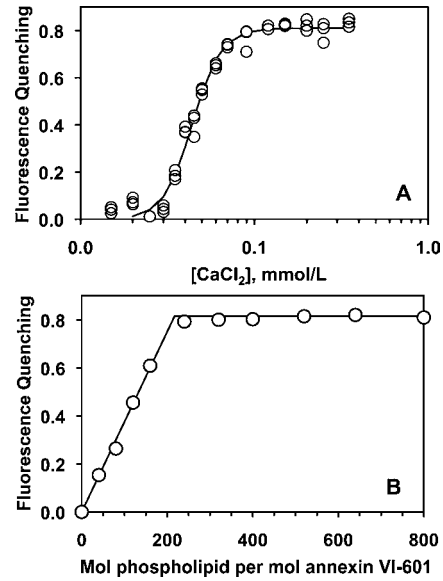


Figure 3. Binding of IAF-annexin V-601 to phospholipid vesicles (A) Calcium titration at low membrane occupancy to determine affinity of binding. Vesicles containing 25% PS (30 μM total phospholipid) were incubated with IAF-annexin VI-601 (1.5 nM) and the indicated concentrations of calcium. Binding was measured via fluorescence quenching as described in the Experimental Procedures. The line represents the fitted function used to determine the binding parameters EC_{50}, slope, and pK_d. (B) Stoichiometry of phospholipid binding. IAF-annexin VI-601 (2.5 nM) was incubated with phospholipid vesicles (0 to 2000 nM) in the presence of 2 mM $CaCl_2$. Fluorescence quenching was calculated relative to the fluorescence of free protein in the absence of phospholipid. The maximum amount of phospholipid required to bind all the available annexin VI-601 was determined from the point at which fluorescence quenching first reached a maximum (intersection point of two lines in figure).

to a value of 102 for annexin V (*13*). Since annexin VI is about twice the size of annexin V, this is consistent with the expected value if nearly all of the protein binds to the vesicle surface in a single layer of protein. (The stoichiometries given are based on total phospholipid added to the reaction; the actual number of phospholipid molecules covered by the protein would be about half this value, allowing for the phospholipid molecules on the inner face of the membrane bilayer that are inaccessible to the protein.) We also measured binding to RBC with calcium titration assays at low occupancy (Figure 4A), which also showed high-affinity binding, with binding saturating at a calcium concentration of about 0.6 mM. Binding parameters for both vesicle assay and RBC assay are summarized in Table 1. The overall picture is similar to annexin V in that binding to vesicles with 25% PS has a lower EC_{50} and higher pK_d value than binding to cell membranes (*13*, *16*, *17*).

IAF-Annexin VI Detects Apoptosis in Vitro. To verify that annexin VI-601 could detect apoptosis, we tested it on Jurkat T leukemia cells (Figure 5). PS-positive cells are well-separated from PS-negative cells, in the same manner as typically seen with annexin V (*14*). In view of the lower calcium requirements for binding to vesicles and erythrocytes determined above, we also determined whether assays could be successfully performed at low calcium concentrations. Titration with calcium (Figure 5C) showed that cells became annexin-positive at much lower calcium concentrations for annexin VI-601 compared to annexin V. Thus, annexin VI can be used successfully to detect apoptotic cells at calcium concentrations as low as 0.3 mM.

^{99m}Tc-Annexin VI-601 Can Be Readily Prepared and Has Prolonged Blood Clearance Compared with Annexin V. The protein was directly labeled with ^{99m}Tc on its endogenous N_3S-like N-terminal peptide chelation site and tested for

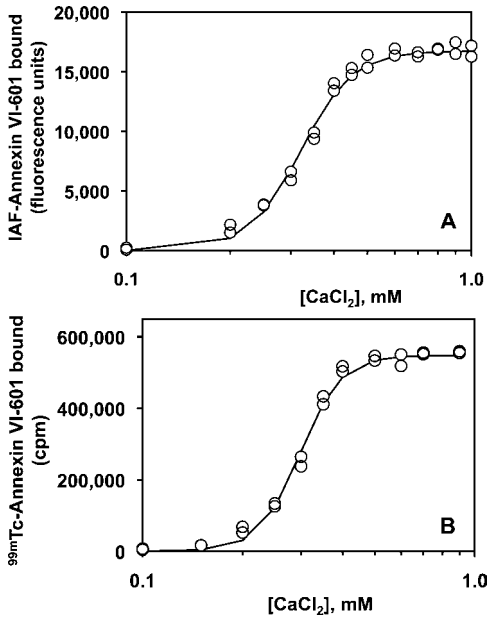


Figure 4. Binding of annexin VI-601 to RBC with exposed PS. (A) IAF-annexin VI-601. IAF-annexin VI-601 (1 nM) was incubated with RBC and varying concentrations of calcium, and the amount of bound protein was determined as described in the Experimental Procedures. (B) ^{99m}Tc-Annexin VI-601 was radiolabeled with ^{99m}Tc via direct chelation to its endogenous peptide chelation site. Binding to RBC was determined by calcium titration as in panel A.

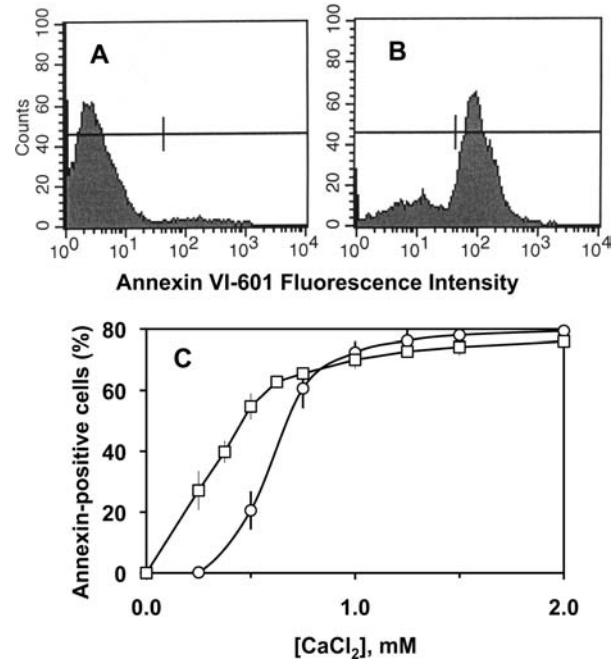


Figure 5. Detection of apoptosis by flow cytometry with IAF-annexin VI-601. (A,B) Apoptosis was induced in Jurkat T-leukemia cells with ultraviolet light. After 3.5 h, untreated control cells (A, left panel) or UV-treated cells (B, right panel) were incubated with 30 nM IAF-annexin VI-601 and 1.25 mM $CaCl_2$ as described in Experimental Procedures. Cells were assayed by flow cytometry, with fluorescein detected in the FL1 channel. The gates in the figure were used to determine the percentage of annexin-positive cells in each panel. Necrotic cells make a negligible contribution to the overall population of annexin-positive cells (see Experimental Procedures). (C) Apoptotic cells were assayed with IAF-annexin VI-601 (squares) or IAF-annexin V-117 (circles) with the indicated concentration of $CaCl_2$. The percentage of annexin-positive cells was determined with the gates as shown in panel B.

bioactivity in the calcium titration assay with erythrocytes with exposed PS (Figure 4B, Table 1). The results were essentially the same as those obtained with IAF-labeled protein, indicating that technetium labeling did not adversely affect bioactivity, although there was somewhat greater variability in affinity between preparations, as indicated by the wider SD in Table 1.

Blood clearance of ^{99m}Tc-annexin VI-601 was measured in mice (Figure 6). Clearance was much slower than for ^{99m}Tc-annexin V-128 labeled and injected in the same manner. Thus, the higher molecular weight of annexin VI (76 kDa) led to reduction in blood clearance compared to annexin V (36 kDa), most likely due to a dramatic reduction in glomerular filtration rate for the larger protein.

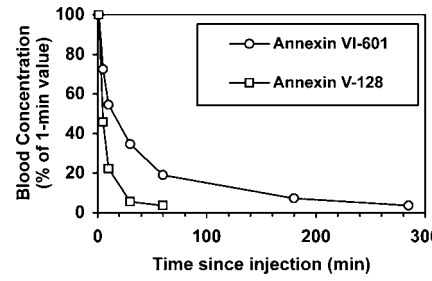


Figure 6. Blood clearance of ^{99m}Tc-Annexin VI-601. ^{99m}Tc-annexin VI-601 (100 μCi, 90 μCi/μg) was injected intravenously via tail vein into Balb/c mice ($n = 3$ per time point). At the indicated time points, blood samples were taken, radioactivity and mass were measured, and values of %ID/g blood were calculated. Data are normalized to the value at the initial 1 min time point. Shown for comparison is the blood clearance curve of ^{99m}Tc-annexin V-128 labeled in the same manner via direct chelation to its endogenous chelation site (reproduced from Figure 5 in Tait et al. (*12*)).

DISCUSSION

We have developed a recombinant form of human annexin VI that can be produced in high yield and is readily labeled with both fluorescent and radioactive labels. The labeled protein has the expected high affinity for PS in both phospholipid vesicles and erythrocytes. It also efficiently detects apoptosis of Jurkat T leukemia cells by flow cytometry. In comparison with annexin V, annexin VI binds to Jurkat cells at lower calcium concentrations (circa 0.3 mM versus 1.25 mM). This property may make annexin VI useful for in vitro assays of apoptosis when it is desired to keep calcium concentrations at subphysiological levels. In vivo, physiological ionized calcium is normally between about 1.15 and 1.3 mmol/L in whole blood, which at face value appears to be adequate to support binding of annexin V. However, the binding affinity of annexin V is a very steep function of calcium concentration in this range (*13*), so it is possible that uptake of annexin V is in fact limited by calcium concentration in tissues under some pathological

Table 1. Binding Parameters for Phospholipid Vesicles and Cells[a]

substrate	ligand	EC_{50} (mM)	slope	pK_d	number of assays
Phospholipid vesicles, 25% PS	IAF-annexin VI-601	0.043 ± 0.006	5.8 ± 0.9	32.5 ± 4.1	15
Erythrocytes with exposed PS	IAF-annexin VI-601	0.321 ± 0.040	5.2 ± 0.5	24.8 ± 1.5	10
Erythrocytes with exposed PS	^{99m}Tc-annexin VI-601	0.240 ± 0.048	5.0 ± 1.5	24.7 ± 5.8	9

[a] Measurements were made as described under Experimental Procedures. Values given are mean ± SD. The EC_{50} value is the calcium concentration at which annexin binding is half maximal in quantitative calcium titration assays (cf. Figures 3 and 4 and ref *13*).

circumstances where ionized calcium drops below the physiologic range. In support of this view, mutations in annexin V that decrease binding affinity only modestly cause a disproportionately large decrease in uptake in apoptotic tissues in vivo (*12*). Thus, annexin VI may have improved binding to apoptotic cells under some circumstances in vivo.

In vivo, the blood clearance of labeled annexin VI-601 is considerably slower than annexin V, as would be predicted based on the higher molecular weight. Although the rapid blood clearance of annexin V is an advantage when imaging must be performed soon after injection (such as in detection of cardiac ischemia (*18*)), slower blood clearance may paradoxically improve imaging results in some other clinical applications. For example, it has been very difficult to establish the optimal time for injection of annexin V for imaging the clinical response to cancer chemotherapy because of the biphasic time course of annexin V uptake in this application (*19, 20*). A longer blood residence time would allow a more flexible injection protocol, while still allowing adequate blood pool clearance when imaging is performed 24 or 48 h after injection. It is also possible that the prolonged blood residence time will increase permeation into poorly perfused tumors that may show limited uptake during the brief blood residence time of annexin V.

In addition to their diagnostic uses, PS-binding proteins may have therapeutic uses in several areas, and the prolonged blood residence time of annexin VI may be particularly useful in this type of application. Annexins function as anticoagulants, and annexin V has shown in vivo anticoagulant efficacy in several animal models (*21, 22*). Annexin VI may be more advantageous because of its longer blood residence time, which will presumably result in a greater duration of anticoagulation compared to annexin V. Another interesting recent application is prevention of reperfusion injury in organ transplantation: an annexin V dimer helps prevent hepatic ischemia-reperfusion injury in a mouse model (*23*); this has potential applications to liver surgery and transplantation in humans, and perhaps to other organ systems subject to ischemia−reperfusion injury. Overall, annexin VI-601 is promising as a new approach to detection and targeting of exposed PS in circumstances where a higher molecular weight and slower blood clearance would be beneficial.

ACKNOWLEDGMENT

This research was supported by USPHS CA-102348 and EB-000898.

LITERATURE CITED

(1) Tait, J. F. (2008) Imaging of apoptosis. *J. Nucl. Med. 49*, 1573–1576.

(2) Fadok, V. A., Voelker, D. R., Campbell, P. A., Cohen, J. J., Bratton, D. L., and Henson, P. M. (1992) Exposure of phosphatidylserine on the surface of apoptotic lymphocytes triggers specific recognition and removal by macrophages. *J. Immunol. 148*, 2207–2216.

(3) Martin, S. J., Reutelingsperger, C. P., McGahon, A. J., Rader, J. A., van Schie, R. C., LaFace, D. M., and Green, D. R. (1995) Early redistribution of plasma membrane phosphatidylserine is a general feature of apoptosis regardless of the initiating stimulus: inhibition by overexpression of Bcl-2 and Abl. *J. Exp. Med. 182*, 1545–1556.

(4) Blankenberg, F. G., Katsikis, P. D., Tait, J. F., Davis, R. E., Naumovski, L., Ohtsuki, K., Kopiwoda, S., Abrams, M. J., Darkes, M., Robbins, R. C., Maecker, H. T., and Strauss, H. W. (1998) In vivo detection and imaging of phosphatidylserine expression during programmed cell death. *Proc. Natl. Acad. Sci. U.S.A. 95*, 6349–6354.

(5) Jung, H. I., Kettunen, M. I., Davletov, B., and Brindle, K. M. (2004) Detection of apoptosis using the C2A domain of synaptotagmin I. *Bioconjugate Chem. 15*, 983–987.

(6) Dasgupta, S. K., Guchhait, P., and Thiagarajan, P. (2006) Lactadherin binding and phosphatidylserine expression on cell surface-comparison with annexin A5. *Transl. Res. 148*, 19–25.

(7) Hanayama, R., Tanaka, M., Miwa, K., Shinohara, A., Iwamatsu, A., and Nagata, S. (2002) Identification of a factor that links apoptotic cells to phagocytes. *Nature 417*, 182–187.

(8) Shi, J., Shi, Y., Waehrens, L. N., Rasmussen, J. T., Heegaard, C. W., and Gilbert, G. E. (2006) Lactadherin detects early phosphatidylserine exposure on immortalized leukemia cells undergoing programmed cell death. *Cytometry A 69*, 1193–1201.

(9) Moss, S. E., and Morgan, R. O. (2004) The annexins. *Genome Biol. 5*, 219.

(10) Raynal, P., and Pollard, H. B. (1994) Annexins: the problem of assessing the biological role for a gene family of multifunctional calcium- and phospholipid-binding proteins. *Biochim. Biophys. Acta 1197*, 63–93.

(11) Tait, J. F., Brown, D. S., Gibson, D. F., Blankenberg, F. G., and Strauss, H. W. (2000) Development and characterization of annexin V mutants with endogenous chelation sites for (99m)Tc. *Bioconjugate Chem. 11*, 918–925.

(12) Tait, J. F., Smith, C., and Blankenberg, F. G. (2005) Structural requirements for in vivo detection of cell death with 99mTc-annexin V. *J. Nucl. Med. 46*, 807–815.

(13) Tait, J. F., Gibson, D. F., and Smith, C. (2004) Measurement of the affinity and cooperativity of annexin V-membrane binding under conditions of low membrane occupancy. *Anal. Biochem. 329*, 112–119.

(14) Smith, C., Gibson, D. F., and Tait, J. F. (2009) Transmembrane voltage regulates binding of annexin V and lactadherin to cells with exposed phosphatidylserine. *BMC Biochem. 10*, 5.

(15) Bazzi, M. D., and Nelsestuen, G. L. (1991) Highly sequential binding of protein kinase C and related proteins to membranes. *Biochemistry 30*, 7970–7977.

(16) Jin, M., Smith, C., Hsieh, H. Y., Gibson, D. F., and Tait, J. F. (2004) Essential role of B-helix calcium binding sites in annexin V-membrane binding. *J. Biol. Chem. 279*, 40351–40357.

(17) Jeppesen, B., Smith, C., Gibson, D. F., and Tait, J. F. (2008) Entropic and enthalpic contributions to annexin V-membrane binding. *J. Biol. Chem. 283*, 6126–6135.

(18) Boersma, H. H., Kietselaer, B. L., Stolk, L. M., Bennaghmouch, A., Hofstra, L., Narula, J., Heidendal, G. A., and Reutelingsperger, C. P. (2005) Past, present, and future of annexin A5: from protein discovery to clinical applications. *J. Nucl. Med. 46*, 2035–2050.

(19) Blankenberg, F. (2002) To scan or not to scan, it is a question of timing: technetium-99m-annexin V radionuclide imaging assessment of treatment efficacy after one course of chemotherapy. *Clin. Cancer Res. 8*, 2757–2758.

(20) Mandl, S. J., Mari, C., Edinger, M., Negrin, R. S., Tait, J. F., Contag, C. H., and Blankenberg, F. G. (2004) Multi-modality imaging identifies key times for annexin V imaging as an early predictor of therapeutic outcome. *Mol. Imaging 3*, 1–8.

(21) Tait, J. F. (1996) Clinical application of annexins, In *Annexins: Molecular Structure to Cellular Function* (Seaton, B. A., Ed.), pp 213−220, R. G. Landes Company, Austin, TX.

(22) Thiagarajan, P., and Benedict, C. R. (1997) Inhibition of arterial thrombosis by recombinant annexin V in a rabbit carotid artery injury model. *Circulation 96*, 2339–2347.

(23) Teoh, N. C., Ito, Y., Field, J., Bethea, N. W., Amr, D., McCuskey, M. K., McCuskey, R. S., Farrell, G. C., and Allison, A. C. (2007) Diannexin, a novel annexin V homodimer, provides prolonged protection against hepatic ischemia-reperfusion injury in mice. *Gastroenterology 133*, 632–646.

BC100239K

PEG-Attached PAMAM Dendrimers Encapsulating Gold Nanoparticles: Growing Gold Nanoparticles in the Dendrimers for Improvement of Their Photothermal Properties

Yasuhito Umeda,[†] Chie Kojima,[‡] Atsushi Harada,[†] Hiromichi Horinaka,[§] and Kenji Kono*[,†]

Department of Applied Chemistry, Graduate School of Engineering, Nanoscience and Nanotechnology Research Center, Research Organization for the 21st Century, and Department of Physics and Electronics, Graduate School of Engineering, Osaka Prefecture University, Osaka 599-8531, Japan. Received March 17, 2010; Revised Manuscript Received June 15, 2010

Recently, we demonstrated that loading of $HAuCl_4$ in poly(ethylene glycol) (PEG)-attached poly(amidoamine) (PAMAM) G4 dendrimers and subsequent reduction with $NaBH_4$ yield dendrimers encapsulating gold nanoparticles (Au NPs), which have photoinduced heat-generating properties. This study was undertaken to enhance photothermal properties of the Au NP-incorporated PEG-attached dendrimers by growing Au NPs in the dendrimers. Repeated loading of $HAuCl_4$ in the PEG-attached dendrimers and subsequent reduction with $NaBH_4$ enhanced the surface plasmon resonance, indicating that Au NPs were grown in the PEG-attached dendrimers using that procedure. Transmission electron microscopy (TEM) analysis revealed that the size of Au NPs formed in the dendrimers increased with the number of repetitions of $HAuCl_4$ loading and subsequent reduction in the dendrimers, although the size distribution of the Au NPs remained narrow. The photoinduced-heat generation capability of the Au NPs-encapsulating dendrimers increased as the Au NPs grew. These dendrimers with Au NPs exhibited strong cytotoxicity against HeLa cells under visible light irradiation. The result demonstrates that PEG-attached dendrimers encapsulating the grown Au NPs might be useful as devices for target-specific therapy when used with light irradiation.

INTRODUCTION

Gold nanoparticles (Au NPs) are used in widely various fields including chemistry, physics, and biology (*1*). Especially, the application of Au NPs in biomedical fields is attractive because of their heat-generating properties under visible light irradiation, which is useful for the detection and treatment of tumors (*1*−*4*). This unique physical property of Au NPs was derived from the excitation of surface plasmons by light, designated as surface plasmon resonance (SPR), and subsequent conversion to heat (*5*). Although spherical Au NPs show an SPR of around 530 nm, their SPR can be modified by controlling their shape and architecture, as shown in the case of Au nanorods or nanoshells, which exhibit SPR in the infrared region (*4, 5*). Therefore, this thermo-optical property of Au NPs might lead to a new type of therapeutic nanodevice that detects tumor tissues precisely and treats them effectively when used along with photoirradiation (*3*−*7*).

To achieve an efficient therapeutic effect with Au NPs, a biocompatible surface should be given to them to increase colloidal stability in the body and efficacy of their accumulation at the target tumor tissues. For this purpose, attempts have been made to use particulate carrier systems such as liposomes and polymer micelles, which retain Au NPs in their interiors or surfaces (*8*−*16*). Among these carrier systems, dendrimers are attractive because of their well-defined structure and a globular shape (*17*−*21*). Especially, dendrimers with biocompatible surfaces are highly attractive as Au NP carriers (*22*−*24*).

For previous studies, we developed poly(amidoamine) (PAMAM) dendrimers having biocompatible poly(ethylene glycol) (PEG) grafts at every chain end (*25*). Results showed that these PEG-attached PAMAM dendrimers are excellent candidates as Au NP carriers (*22*). In fact, Au NPs were held in the PEG-attached dendrimers, where they generated heat upon irradiation of visible light, suggesting that these Au-NP-loaded dendrimers with biocompatible surfaces might be useful for photothermal therapy.

We prepared PEG-attached PAMAM dendrimers encapsulating Au-NPs by mixing $HAuCl_4$ with PEG-attached PAMAM G4 dendrimers and by subsequent reduction of $AuCl_4^-$ bound to tertiary amines of the dendrimer interiors using a reducing agent $NaBH_4$ (*22*). After the reduction, the tertiary amines of the dendrimer interiors become available again for $AuCl_4^-$ binding. Consequently, additional reduction of $AuCl_4^-$ can be conducted: repetition of mixing of $HAuCl_4$ with the PEG-attached dendrimers and subsequent reduction of $AuCl_4^-$ are expected to engender further growth of Au NPs in the dendrimers.

To obtain efficient therapeutic effects with the Au-NP-loaded dendrimers, it is necessary to deliver a sufficiently large amount of Au NPs to the diseased tissues to attack them strongly with light-induced heat. In this study, we attempted to obtain Au-NP-containing PEG-attached dendrimers that exhibit strong photoinduced heat-generating properties through repeated growth of Au-NPs in the interiors of PEG-attached dendrimers (Scheme 1). High capabilities of PEG-attached dendrimers loaded with grown Au NPs to generate heat and to attack cells were observed.

EXPERIMENTAL SECTION

Materials. $HAu(III)Cl_4$ and $NaBH_4$ were purchased from Wako Pure Chemical (Osaka, Japan) and Kishida Chemical (Osaka,

* To whom correspondence should be addressed. Department of Applied Chemistry, Graduate School of Engineering, Osaka Prefecture University, 1-1 Gakuen-cho, Naka-ku, Sakai, Osaka 599-8531, Japan. Tel: +81 72 254 9330. Fax: +81 72 254 9330. E-mail: kono@chem.osakafu-u.ac.jp.

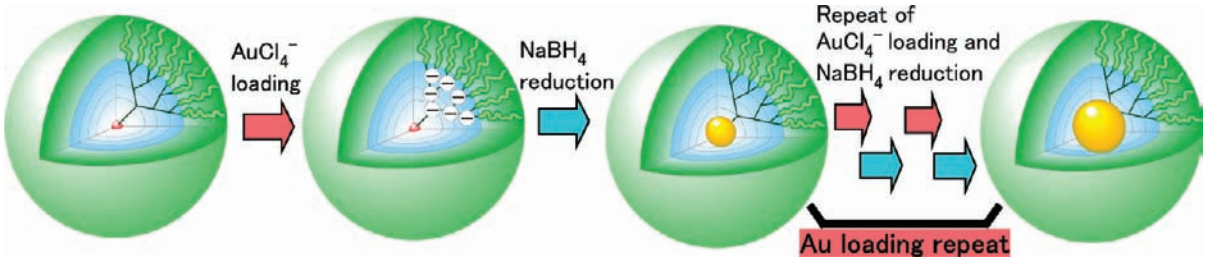
[†] Department of Applied Chemistry.

[‡] Nanoscience and Nanotechnology Research Center.

[§] Department of Physics and Electronics.

10.1021/bc1001399 © 2010 American Chemical Society
Published on Web 07/28/2010

Scheme 1. Preparation Procedure of PEG-Attached PAMAM G4 Dendrimers Encapsulating Grown Au NPs



Japan), respectively. Ethylenediamine core PAMAM G4 dendrimer, polyethylene glycol monomethyl ether (molecular weight: 2k Da), and propidium iodide (PI) were obtained from Sigma-Aldrich Japan (Tokyo, Japan). Polyethylene glycol-attached dendrimer was synthesized using the PAMAM G4 dendrimer and polyethylene glycol monomethyl ether according to our previous report (*25*). Opti-MEM without phenol red was obtained from Invitrogen (Carlsbad, USA). Calcein-acetoxymethyl ester (calcein-AM) was from Nacalai Tesque (Kyoto, Japan).

PEG-Attached Dendrimer Encapsulating Au-NPs. PEG-attached dendrimers encapsulating Au-NPs were prepared according to our previous paper (*22*). Also, Au-NPs were grown in the dendrimers by repetition of loading of $AuCl_4^-$ in the dendrimer interiors and subsequent reduction of $AuCl_4^-$ with $NaBH_4$ (Scheme 1). An aqueous solution of PEG-modified dendrimer (2.1 μM, 100 mL) and 55 equiv of $HAuCl_4$ (2 mM, 5.85 mL) in water were mixed. The mixed solution was reduced by adding a 5-fold molar excess of $NaBH_4$ (150 mM) dissolved in 0.3 M NaOH (389.4 μL) along with vigorous stirring for 1 h. The obtained solution of the Au-NP-loaded dendrimer (40 mL) was acidified with 0.3 M HCl (88 μL) and stirred for 1 h under N_2 atmosphere to decompose residual $NaBH_4$. An aliquot (88 μL) of 0.3 M NaOH and an aqueous $HAuCl_4$ solution (2 mM, 2.17 mL) were added to the Au-loaded dendrimer solution. Then, $NaBH_4$ (150 mM) dissolved in 0.3 M NaOH (145 μL) was added to the Au-loaded dendrimer solution and stirred for 30 min. This procedure was repeated 0−10 times to grow Au-NPs in the PEG-attached dendrimers.

Characterization. Absorption spectra ranging from 400 to 800 nm were measured with a Jasco Model V-560 spectrophotometer. Transmission electron microscopy (TEM) analysis was performed using a JEOL2000 with carbon-coated copper grids.

Photoirradiation Experiment. The solution (3 mL) of Au-NP-loaded dendrimers of a given concentration of dendrimer (0.35 μM) or Au atom (55 μM) was irradiated by Nd:YVO4 LASER (JUNO1000, $\lambda = 532$ nm) at 12 W/cm^2. The sample temperature was monitored by SK-1250MC (SATO KEIRYOKI MFG. Co., Ltd.) immersed in the solution of the cell. The initial temperature of the solution before light irradiation was 24 °C.

Photocytotocixity. HeLa cells (2×10^5 cells) were cultured in Dulbecco's modified Eagle's medium (DMEM) with 10% fetal bovine serum (FBS) for 1 day in 35-mm dishes and were washed with phosphate-buffered saline (PBS; 8 mM Na_2HPO_4, 2 mM KH_2PO_4, 137 mM NaCl, 3 mM KCl, 0.9 mM $CaCl_2$, and 0.5 mM $MgCl_2$). The Au-NP-loaded dendrimers dissolved in the phenol red-free Opti-MEM were added to the HeLa cells and incubated at 37 °C for 6 h. Then, the cells were washed with PBS and immersed in fresh Opti-MEM without the Au-NP-loaded dendrimers (2 mL). The cells around the central region of the dish with 3 mm diameter were irradiated with light ($\lambda = 532$ nm) using Nd:YVO4 SHG LASER (JUNO10000) at ca. 12 W/cm^2 for 15 min and further incubated for 3 h at 37 °C. The staining solution was prepared by adding 10 μL of calcein-AM in DMSO solution (1 mg/mL) and 15 μL of aqueous PI solution (1 mg/mL) to 15 mL of PBS. The staining solution (2 mL) was added to the cells and incubated for 30 min at 37 °C. Then, the cells were washed with PBS and observed with fluorescence microscopes (IMT-2, Olympus and BX51WI, Olympus).

RESULTS AND DISCUSSION

In a previous study (*22*), we have shown that the loading of 55 equiv of tetrachloroauric acid to the PEG-attached PAMAM G4 dendrimer and the subsequent reduction with $NaBH_4$ generate homogeneous Au-NPs of ca. 2 nm in the dendrimer because $AuCl_4^-$ ions were bound to tertiary amines of the dendrimer interior before their reduction (*13*, *15*, *22*). The Au NPs encapsulated in the dendrimers exhibited heat generation under visible light irradiation and therefore suggest the feasibility of the PEG-attached dendrimers as a delivery vehicle of Au NPs for photothermal therapy (*22*). Their capability of generating heat under light irradiation derives from Au NPs of the dendrimer interior. Therefore, it is expected that increased Au loading into the dendrimer will improve their performance. Considering that tertiary amines of the dendrimer interior might become vacant after the reduction, these groups could again be available for binding to $AuCl_4^-$. Toward the development of Au NPs-based therapeutic devices with precisely controlled sizes, we increased Au loading by repeating both the addition of $AuCl_4^-$ ions in the dendrimer interior and their subsequent reduction (Scheme 1).

Figure 1A shows the change occurring in the absorption spectra of the PEG-attached dendrimers after repeated reduction of Au ions in the dendrimer interior. Absorbance of PEG-attached dendrimers was negligible at wavelengths greater than 500 nm. However, the dendrimers displayed absorption centered at 530 nm after the reduction of Au ions; that absorption is derived from SPR of Au NPs (*4*, *26*). In addition, absorbance of the Au NPs-loaded dendrimers around 530 nm increased concomitantly with repetitions of the Au ion loading and reduction procedure, indicating that the amount of the loaded Au atoms in the dendrimers increased by repeating the reduction procedure (Figure 1B).

To estimate influence of the repeated Au loading on the efficiency of SPR of the Au NPs forming in the dendrimer interior, we compared UV−vis spectra at the same Au atom concentration among the Au-NP-loaded dendrimers (Figure 1C and D). Apparently, absorbance around 530 nm increased concomitantly with increasing time of the Au ion loading and reduction repeats, although these dendrimer solutions contained the same concentration of Au atoms (110 μM). This might be explained by the increasing ratio of Au atoms in the particle surface contributing SPR with their increasing particle size. The result indicates that SPR-derived photothermal properties of Au NPs formed in the PEG-attached dendrimers can be improved by growing them by repeating the Au-loaded process.

We observed that absorption spectra derived from SPR for the PEG-attached dendrimers encapsulating the grown Au NPs hardly changed for more than 14 days, indicating that the PEG-attached dendrimers can provide high colloidal stability to well-grown Au NPs even through 10 repetitions of the

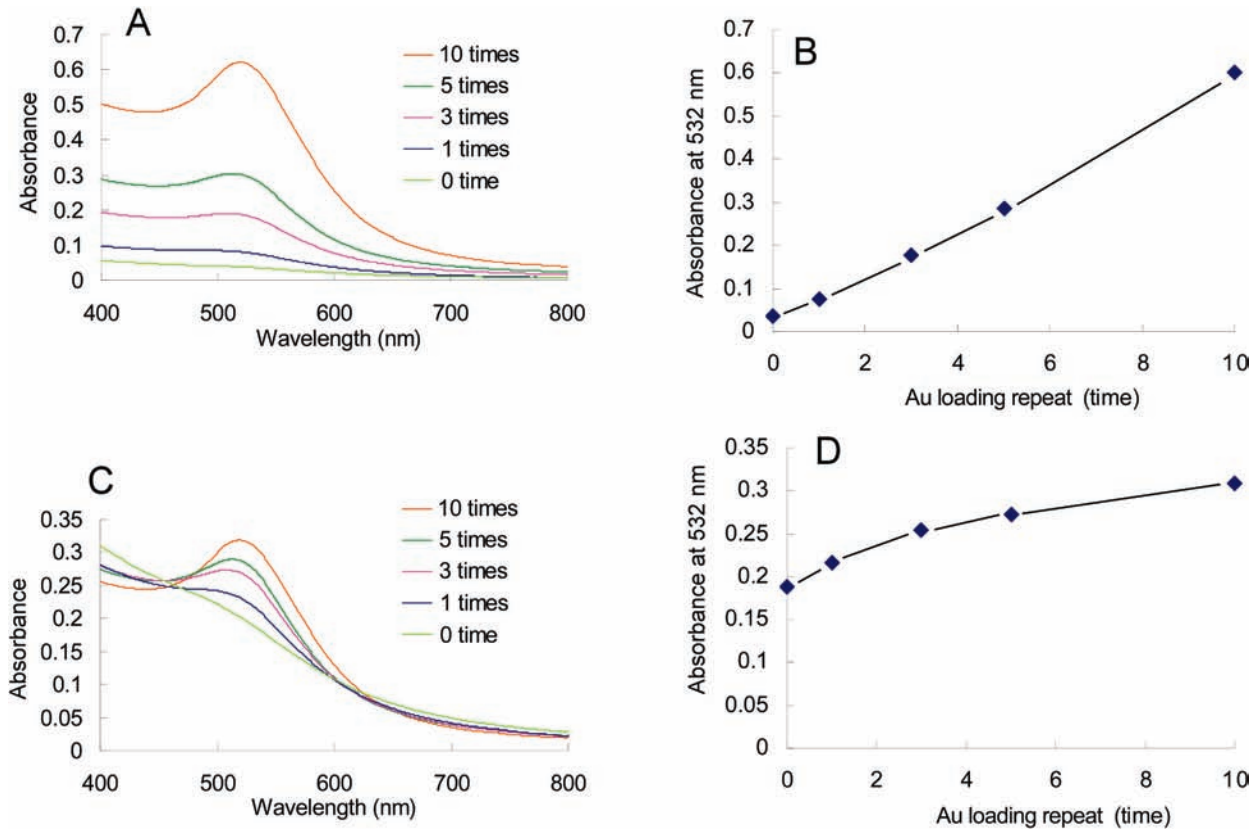


Figure 1. UV−vis spectra of ungrown and grown Au-NPs through varying times of Au loading repeat. UV−vis spectra were measured at the same dendrimer concentration (0.35 μM) (A,B) or at the same Au atom concentration (110 μM) (C,D). The absorption spectra (A,C) and the increase in absorbance at 532 nm after varying times of Au loading repeats (B,D) are shown.

Au ion loading and reduction procedure (see Supporting Information, Figure S1).

The growth of Au NPs in the dendrimers through repeated Au ion loadings and reduction procedures was examined further using TEM (Figure 2). An earlier study demonstrated that the homogeneous Au NPs with an average diameter of 2.0 nm can be formed in the PEG-attached PAMAM G4 dendrimers after Au ion loading and subsequent reduction (*22*). Figures 2A−C show TEM images and size distributions of the Au NPs formed in the PEG-attached dendrimers through 1, 3, and 5 repetitions of the Au loading procedure. The Au NPs with quite a narrow size distribution were observed, although their sizes apparently increase with repeated Au ion loading and reduction.

To further investigate the growing process of gold nanoparticles in the dendrimers, TEM images of higher magnification were also given in Figure 2D and E. The Au NPs prepared through one Au loading repeat exhibit mostly spherical shapes with a diameter of around 2−3 nm, indicating that particles were grown as a single particle in the dendrimer (Figure 2D). Similarly, a large fraction of Au NPs retain the spherical shape with a diameter of around 3 nm after growing through 5 Au loading repeats, suggesting that these particles might be grown as a single particle in the dendrimer (Figure 2E). In addition, there are few particles exhibiting irregular shapes, most of which seem to be formed by joining two spherical particles. On the basis of the observation with TEM, it is likely that most Au NPs might be grown as a single particle in the dendrimer, although joining of the particles may also occasionally take place during their growth. Furthermore, in the TEM image of the dendrimers encapsulating well-grown Au NPs, we still observe relatively small Au NPs having a particle size similar to that of ungrown Au NPs in addition to large particles (Figure 2D and E). This fact may suggest the existence of newly generated Au NPs during each Au-loading process.

The relationship between the number average diameter of the Au NPs formed in the dendrimers and the repetition time of the Au ion loading and reduction procedure is presented in Figure 2F. Apparently, the Au NP size in the dendrimers increases concomitantly with the number of repetitions, indicating that the Au NPs grow by repeating the Au ion loading and subsequent reduction. Even after 10 repetitions of the Au growth procedure, the sizes of Au NPs are less than or about equal to the size of the PAMAM G4 dendrimer, which is estimated as 4−5 nm (*27*), and much smaller than the PEG-attached PAMAM G4 dendrimer of ca. 15 nm (*25*, *28*, *29*). These results imply that Au NPs were grown in the PAMAM dendrimer moiety and that they are effectively covered with PEG chains grafted onto the chain ends of the dendrimer, which might provide high colloidal stability to the grown Au NPs.

Next, we examined the influence of Au growth on the heat-generating capability of the Au-NP-loaded PEG-attached dendrimers. Figure 3A depicts the effects of light irradiation (λ = 532 nm) on temperatures of aqueous solutions of the PEG-attached dendrimers encapsulating Au NPs grown through varying numbers of Au-ion-reduction repetitions at the same dendrimer concentration. Indeed, temperatures of the solutions of Au-loaded PEG-attached dendrimers increased with time; moreover, the dendrimer solutions having more grown Au-NPs exhibited a greater increase in temperature. The increase in temperature for solutions of these Au NP-loaded dendrimers after 1 min of light irradiation against the number of repetitions of the Au reduction process is shown in Figure 3B. The ΔT of the dendrimer solutions increased concomitantly with the increasing growth time of Au-NPs, demonstrating that the photoinduced heat-generating ability of Au NPs loaded in the PEG-attached dendrimers was greatly elevated by growing them in the dendrimer interior.

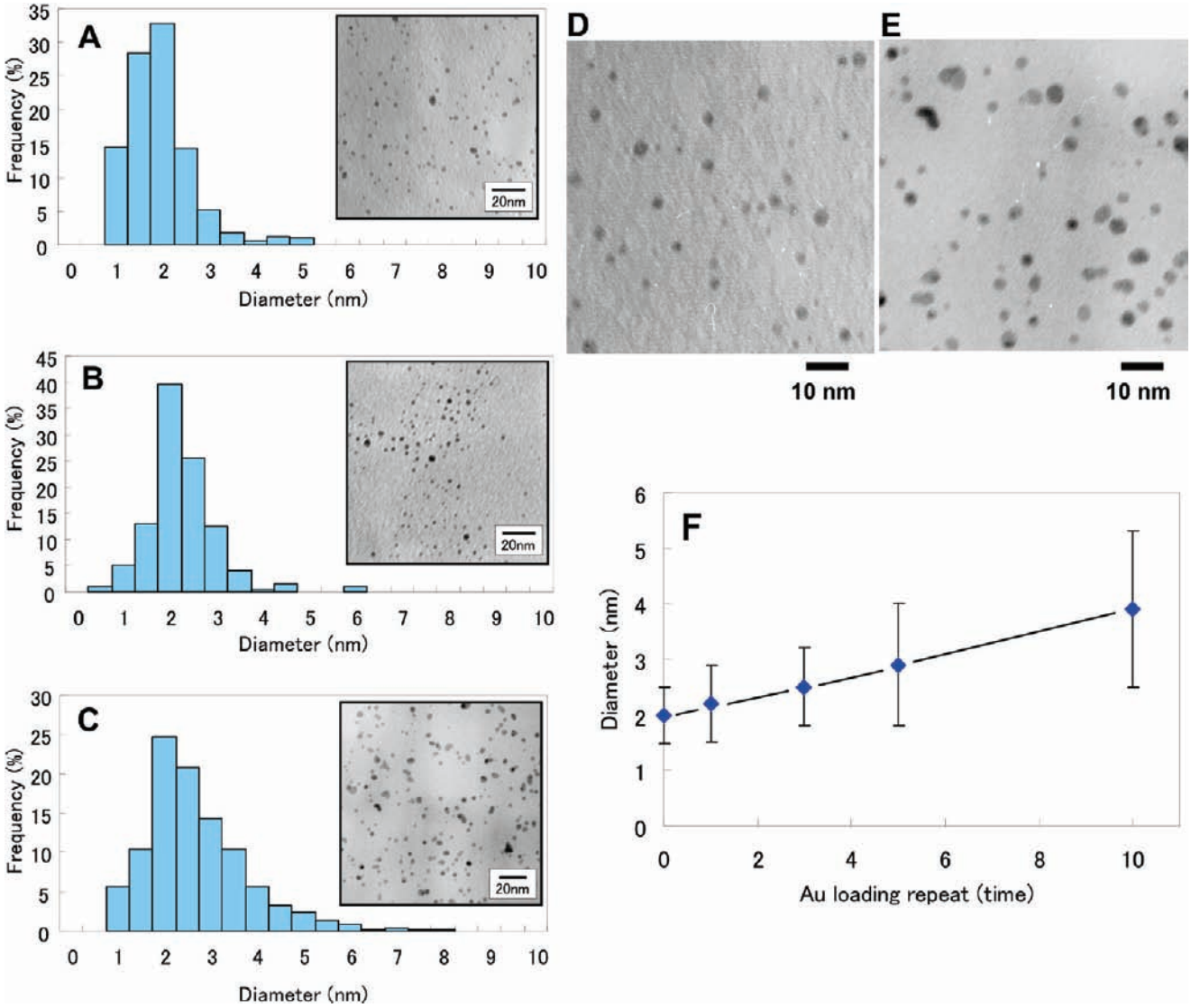


Figure 2. TEM analysis of PEG-attached dendrimers encapsulating Au NPs grown through once (A), 3 times (B), and 5 times (C) of Au loading repeats. Size distributions and TEM images of Au-NPs formed in the dendrimers are shown. TEM images (D) and (E) are views at high magnification of parts of TEM images A and C, respectively. (F) Mean diameter and standard deviation for the Au NPs were plotted against the time of Au loading repeats.

We also examined the photoinduced temperature increase for these Au-NP-loaded dendrimers at the same Au atom concentration to estimate how the repeated Au-loading into the dendrimer affects the photothermal properties of the Au NPs. The result is also shown in Figure 3B. Although these solutions contain the same number of Au atoms, the dendrimer encapsulating more grown Au NPs showed a greater temperature increase. Compared to the Au-NP-loaded dendrimers prepared using the single Au reduction process, those with Au NPs grown through five repetitions of the Au-ion loading and reduction procedure exhibited 1.5-fold higher ability to generate heat upon light irradiation, which might derive from the more efficient SPR of well-grown Au NPs (Figure 2C). These results demonstrate the importance of growing Au NPs to produce PEG-attached dendrimers having Au NPs, which exhibit high photoinduced heat-generating ability.

Finally, we examined the effect of the Au NP growth on photoinduced cytotoxic activity of the Au NPs-loaded dendrimers. We used dendrimers having Au-NPs grown through five repetitions of the Au-ion-loading and reduction procedure and compared their performance to that of the Au-NP dendrimers without that procedure. For estimation of the photoinduced cytotoxicity of these dendrimers, HeLa cells were treated with these Au-NP-loaded dendrimers for 6 h and washed with PBS. Then, green light ($\lambda = 532$ nm) was irradiated to the cells to the 3-mm-diameter area for 15 min using a Nd:YVO4 laser. After the irradiation, the live and dead cells were stained, respectively, with calcein-AM (green) and PI (red) (*30*). Figure 4A portrays the calcein fluorescence of the cells treated with the PEG-attached dendrimers encapsulating ungrown Au NPs. Calcein fluorescence was observed from almost all cells, indicating that these cells were alive after photoirradiation. Figure 4B and C, respectively, present calcein fluorescence and PI fluorescence of the cells around the center region of the photoirradiated area portrayed in Figure 4A. Only the cells in a limited area of 0.1 mm diameter were killed by light irradiation. In contrast, the same light irradiation induced cellular damage in a much larger area for cells treated with PEG-attached dendrimers encapsulating well-grown Au NPs (Figure 4D). Figure 4E and F depict calcein fluorescence and PI fluorescence of the cells, respectively, around the center region of the photoirradiated area portrayed in Figure 4D. No calcein fluorescence or intensive PI fluorescence was observed in either Figure 4E or F, indicating that the cells in the 1.5-mm-diameter irradiated region had been killed completely. Indeed, results verified that the PEG-attached

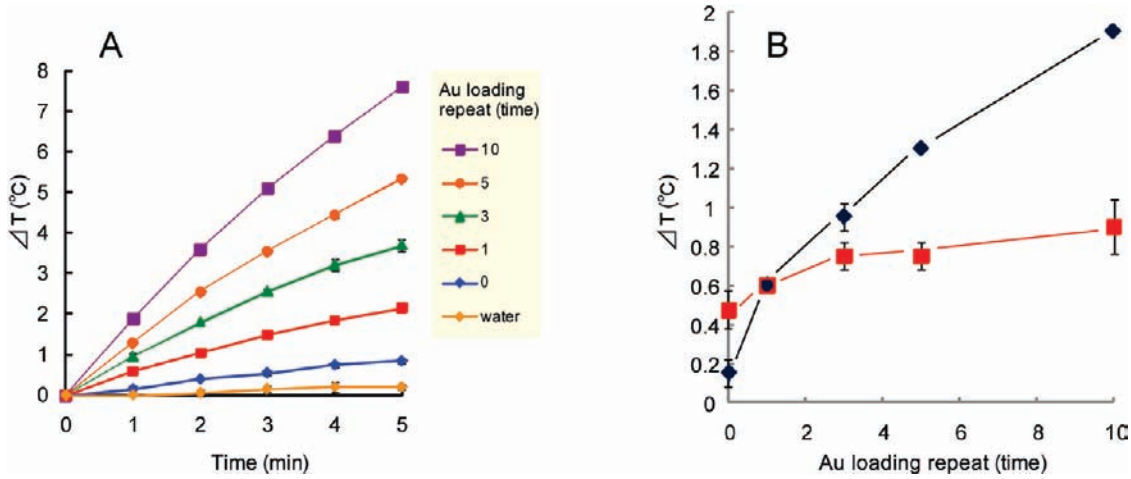


Figure 3. (A) Time-dependent temperature increase of aqueous solutions of PEG-attached dendrimers encapsulating ungrown or grown Au NPs through varying times of Au loading repeats under photoirradiation (λ = 532 nm) at 12 W/cm^2. Concentration of the PEG-attached dendrimer was 0.35 μM. Initial temperature of the solutions was 24 °C. (B) Temperature increase in aqueous solutions of PEG-attached dendrimers encapsulating ungrown or grown Au NPs through varying times of Au loading repeats. Temperature increases of the Au-NPs-loaded dendrimer solutions after 1 min of photoirradiation were measured at the same dendrimer concentration (0.35 μM) (dark blue curve with diamonds) or at the same Au atom concentration (55 μM) (red curve with squares). Data were plotted against the time of Au loading repeats for the growth of Au NPs in the dendrimer interior.

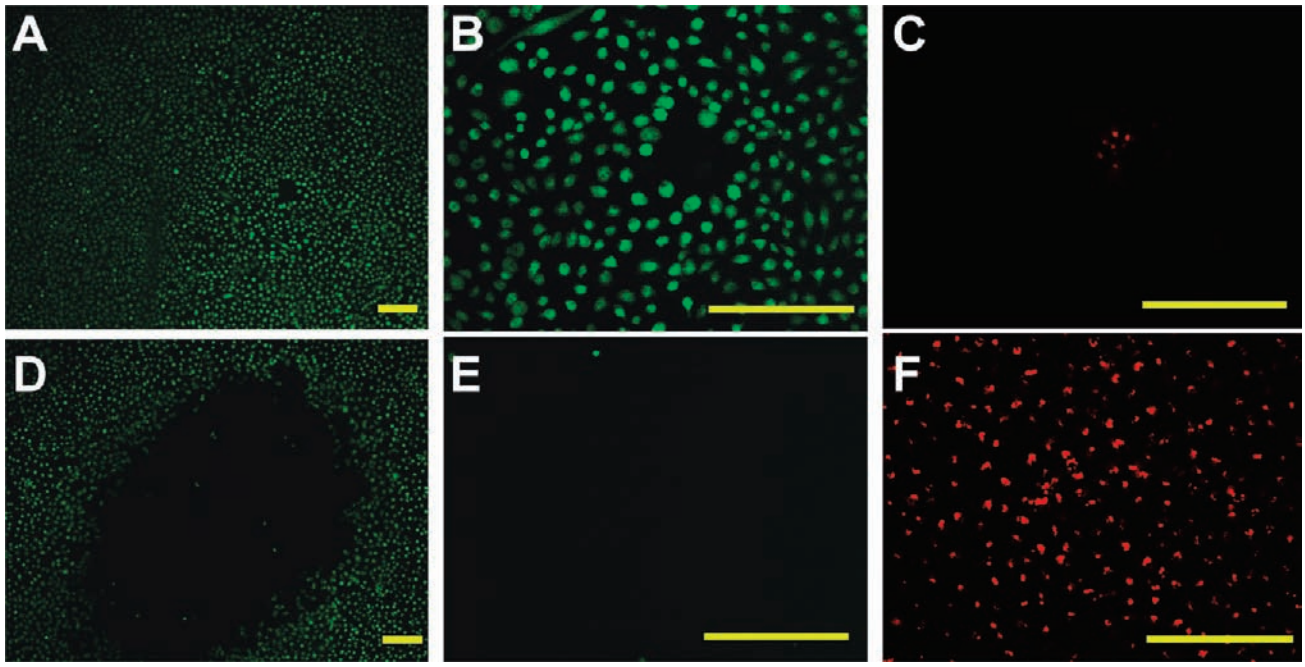


Figure 4. Photoinduced cytotoxicity of the PEG-attached dendrimers encapsulating ungrown (A−C) or grown Au NPs (D−F) through Au loading repeat 5 times. Alive and dead cells were stained with Calcein-AM (A,B,D,E) and PI (C,F). Images B and C are the same region around the center of the photoirradiated area shown in A. Images E and F are the same region around the center of the photoirradiated area shown in D. Scale bars indicate 200 μm. [Au] = 600 μM. Concentrations of PEG-dendrimers were 10.8 μM (A−C) and 1.8 μM (D−F).

dendrimers encapsulating ungrown Au NPs at the same PEG-attached dendrimers (1.8 μM) did not induce cellular death under the same photoirradiation as that detected by their staining with calcein-AM and PI (see Supporting Information, Figure S2). These results demonstrate the importance of growing Au NPs in the PEG-attached dendrimers for the delivery of sufficient amounts of Au NPs with high photo-induced heat-generating ability to induce strong cellular damage under light irradiation.

In conclusion, results show that Au-NPs formed in the PEG-attached PAMAM dendrimers can be grown in a highly controlled manner by repeating the loading of Au ions into the dendrimer interiors and through subsequent reduction with $NaBH_4$. The size of Au NPs increased while retaining their narrow size distribution by repeating the Au-loading and reduction procedure. The Au NPs exhibited SPR more efficiently, with increased heat-generating ability with their growth. In fact, we observed that the PEG-attached dendrimers encapsulating well-grown Au NPs exhibited strong cytotoxic activity under irradiation of light, although they showed only slight cytotoxic effects as long as the light was not irradiated. Considering features of the PEG-attached dendrimers, such as their highly controllable molecular size, biocompatible surface, capability of encapsulation of Au NPs, and regulated growth of Au NPs in their interiors, the PEG-attached dendrimers might be regarded as ideal vehicles of Au NPs for Au-based photothermal therapy and imaging.

ACKNOWLEDGMENT

This work was supported by Grants-in-aid from the Ministry of Education, Culture, Sports, Science, and Technology of Japan (MEXT).

Supporting Information Available: Time-dependent UV-Vis spectra of PEG-attached dendrimers encapsulating Au-NPs through varying times of the Au loading repeat and photoinduced cytotoxicity of the PEG-attached dendrimers encapsulating un-grown Au NPs. This material is available free of charge via the Internet at http://pubs.acs.org.

LITERATURE CITED

(1) Daniel, M.-C., and Astruc, D. (2004) Gold Nanoparticles: assembly, supramolecular chemistry, quantum-size-related properties, and applications toward biology, catalysis, and nanotechnology. *Chem. Rev. 104*, 293–346.

(2) Sonvico, F., Dubernet, C., Colombo, P., and Couvreur, P. (2005) Metallic colloid nanotechnology, applications in diagnosis and therapeutics. *Curr. Pharm. Des. 11*, 2091–2105.

(3) Jain, P. K., El-Sayed, I. H., and El-Sayed, M. A. (2007) Au nanoparticles target cancer. *Nano Today 2*, 18–29.

(4) Hu, M., Chen, J., Li, Z. Y., Au, L., Hartland, G. V., Li, X., Marquez, M., and Xia, Y. (2006) Gold nanostructures: engineering their plasmonic properties for biomedical applications. *Chem. Soc. Rev. 35*, 1084–1094.

(5) Govorov, A. O., and Richardson, H. H. (2007) Generating heat with metal nanoparticles. *Nanotoday 2*, 30–38.

(6) Pissuwan, D., Valenzuela, S. M., and Cortie, M. B. (2006) Therapeutic possibilities of plasmonically heated gold nanoparticles. *Trends Biotechnol. 24*, 62–67.

(7) Jain, P. K., Lee, K. S., El-Sayed, I. H., and El-Sayed, M. A. (2006) Calculated absorption and scattering properties of gold nanoparticles of different size, shape, and composition: applications in biological imaging and biomedicine. *J. Phys. Chem. B 110*, 7238–7248.

(8) Paasonen, L., Laaksonen, T., Johans, C., Yliperttula, M., Kontturi, K., and Urtti, A. (2007) Gold nanoparticles enable selective light-induced contents release from liposomes. *J. Controlled Release 122*, 86–93.

(9) Kojima, C., Hirano, Y., Yuba, E., Harada, A., and Kono, K. (2008) Preparation and characterization of complexes of liposomes with gold nanoparticles. *Colloids Surf., B 66*, 246–252.

(10) Park, S. H., Oh, S. G., Mun, J. Y., and Han, S. S. (2006) Loading of gold nanoparticles inside the DPPC bilayers of liposome and their effects on membrane fluidities. *Colloids Surf., B 48*, 112–118.

(11) Chen, S., Guo, C., Hu, G. H., Wang, J., Ma, J. H., Liang, X. F., Zheng, L., and Liu, H. Z. (2006) Effect of hydrophobicity inside PEO-PPO-PEO block copolymer micelles on the stabilization of gold nanoparticles: experiments. *Langmuir 22*, 9704–9711.

(12) Carrot, G., Valmalette, J. C., Plummer, C. J. G., Scholz, S. M., Dutta, J., Hofmann, H., and Hilborn, J. G. (1998) Gold nanoparticle synthesis in graft copolymer micelles. *Colloid Polym. Sci. 276*, 853–859.

(13) Crooks, R. M., Lemon, B. I., Sun, L., Yeung, L. K., and Zhao, M. (2001) Dendrimer-encapsulated metals and semiconductors: synthesis, characterization, and applications. *Top. Curr. Chem. 212*, 81–135.

(14) Balogh, L., Valluzzi, R., Hagnauer, G. L., Laverdure, K. S., Gido, S. P., and Tomalia, D. A. (1999) Formation of silver and gold dendrimer nanocomposites. *J. Nanoparticle Res. 3*, 353–368.

(15) Grohn, F., Bauer, B. J., Akpalu, Y. A., Jackson, E. J., and Amis, E. (2000) Dendrimer templates for the formation of gold nanoclusters. *Macromolecules 33*, 6042–6050.

(16) Esumi, K., Kameo, A., Suzuki, A., and Torigoe, K. (2001) Preparation of gold nanoparticles in formamide and N, N-dimethylformamide in the presence of poly(amidoamine) dendrimers with surface methyl ester groups. *Colloids Surf., A 189*, 155–161.

(17) Tomalia, D. A. (2005) Birth of a new macromolecular architecture: dendrimers as quantized building blocks for nanoscale synthetic polymer chemistry. *Prog. Polym. Sci. 30*, 294–324.

(18) Lee, C. C., MacKay, J. A., Frechet, J. M. J., and Szoka, F. C. (2005) Designing dendrimers for biological applications. *Nat. Biotechnol. 12*, 1517–1526.

(19) Medina, S. H., and El-Sayed, M. E. H. (2009) Dendrimers as carriers for delivery of chemotherapeutic agents. *Chem. Rev. 109*, 3141–3157.

(20) Wolinsky, J. B., and Grinstaff, M. W. (2008) Therapeutic and diagnostic applications of dendrimers for cancer treatment. *Adv. Drug Delivery Rev. 60*, 1037–1055.

(21) Tekade, R. K., Kumar, P. V., and Jain, N. K. (2009) Dendrimers in oncology: an expanding horizon. *Chem. Rev. 109*, 49–87.

(22) Haba, Y., Kojima, C., Harada, A., Ura, T., Horinaka, H., and Kono, K. (2007) Preparation of poly(ethylene glycol)-modified poly(amidoamine) dendrimers encapsulating gold nanoparticles and their heat-generating ability. *Langmuir 23*, 5243–5246.

(23) Hedden, R. C., Bauer, B. J., Smith, A. P., Grohn, F., and Amis, E. (2002) Templating of inorganic nanoparticles by PAMAM/PEG dendrimer-star polymers. *Polymer 43*, 5473–5481.

(24) Boisselier, E., Diallo, A. K., Salmon, L., Ruiz, J., and Astruc, D. (2008) Gold nanoparticles synthesis and stabilization via new "clicked" polyethyleneglycol dendrimers. *Chem. Commun.* 4819–4821.

(25) Kojima, C., Kono, K., Maruyama, K., and Takagishi, T. (2000) Synthesis of polyamidoamine dendrimers having polyethylene glycol grafts and their ability to encapsulate anticancer drugs. *Bioconjugate Chem. 11*, 910–917.

(26) Sarathy, K. V., Raina, G., Yadav, R. T., Kulkarni, G. U., and Rao, C. N. R. (1997) Thiol-derivatized nanocrystalline arrays of gold, silver, and platinum. *J. Phys. Chem. B 101*, 9876–9880.

(27) Uppuluri, S., Keinath, S. E., Tomalia, D. A., and Dvornic, P. R. (1998) Rheology of dendrimers. I. Newtonian flow behavior of medium and highly concentrated solutions of polyamidoamine (PAMAM) dendrimers in ethylenediamine (EDA) solvent. *Macromolecules 31*, 4498–4510.

(28) Kono, K., Fukui, T., Takagishi, T., Sakurai, S., and Kojima, C. (2008) Preparation of poly(ethylene glycol)-modified poly(amidoamine) dendrimers with a shell of hydrophobic amino acid residues and their function as a nanocontainer. *Polymer 49*, 2832–2838.

(29) Lee, H., and Larson, R. G. (2009) Molecular dynamics study of the structure and interparticle interactions of polyethylene glycol-conjugated PAMAM dendrimers. *J. Phys. Chem. B 113*, 13202–13207.

(30) Barth, E. E., Hallworth, R., and Nichols, M. G. (2005) A comparison of the sensitivity of photodamage assays in rat basophilic leukemia cells. *Photochem. Photobiol. 81*, 556–562.

BC1001399

Supporting Information

PEG-attached PAMAM dendrimers encapsulating gold nanoparticles: growing gold nanoparticles in the dendrimers for improvement of their photothermal properties

Yasuhito Umeda[1], Chie Kojima[2], Atsushi Harada[1], Hiromichi Horinaka[3], Kenji Kono[1]*

[1]Department of Applied Chemistry, Graduate School of Engineering, Osaka Prefecture University

[2]Nanoscience and Nanotechnology Research center, Research Institutes for the Twenty First Century, Osaka Prefecture University

[3]Department of Physics and Electronics, Graduate School of Engineering, Osaka Prefecture University

E-mail: kono@chem.osakafu-u.ac.jp.

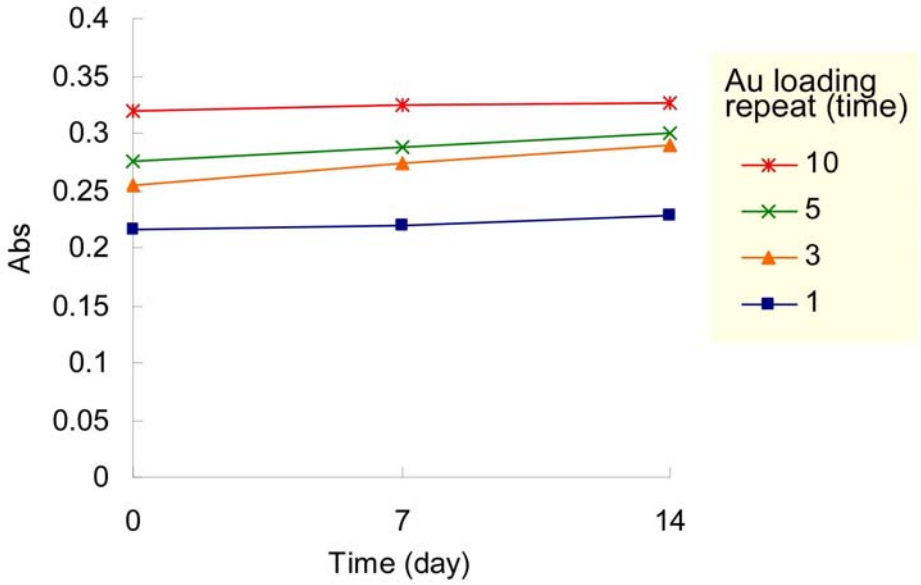


Fig. S1. Time-dependent UV-Vis spectra of PEG-attached dendrimers encapsulating Au-NPs through varying times of Au loading repeat. [Au] = 110 μM.

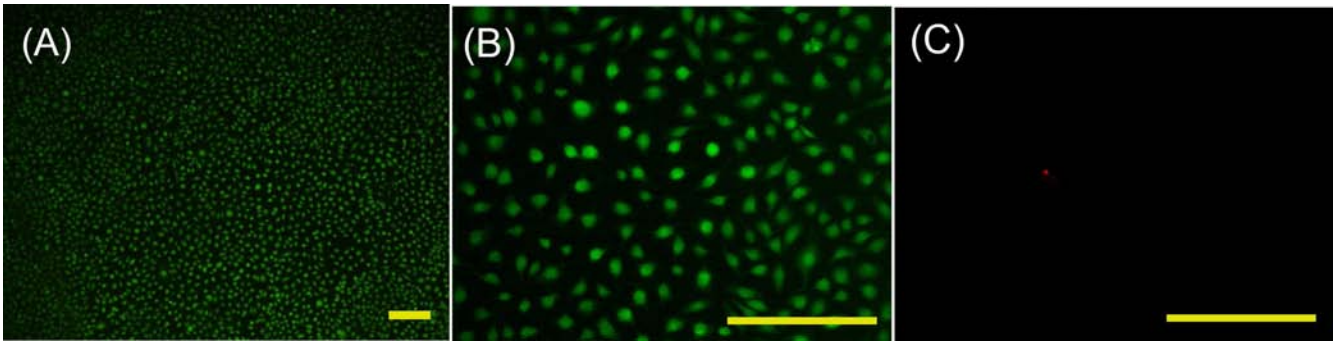


Fig. S2. Photo-induced cytotoxicity of the PEG-attached dendrimers encapsulating un-grown Au NPs. Alive and dead cells were stained with Calcein-AM (A,B) and PI (C). Images (B) and (C) are the same region around the center of the photo-irradiated area shown in (A). Scale bars indicate 200 μm. Concentrations of PEG-dendrimers and Au atom were 1.8 μM and 100 μM, respectively.

Comparison of ^{18}F PET and ^{99m}Tc SPECT Imaging in Phantoms and in Tumored Mice

Dengfeng Cheng, Yi Wang, Xinrong Liu, P. Hendrik Pretorius, Minmin Liang, Mary Rusckowski, and Donald J. Hnatowich*

Division of Nuclear Medicine, Department of Radiology, University of Massachusetts Medical School, Worcester, Massachusetts 01655. Received March 25, 2010; Revised Manuscript Received July 1, 2010

Our objective was to compare the performance of a micro-single photon emission computed tomography (micro-SPECT) with that of a micro-positron emission tomography (microPET) in a Her2+ tumored mice using an anti-Her2 nanoparticle radiolabeled with ^{99m}Tc and ^{18}F. Camera performance was first compared using phantoms; then a tumored mouse administered the ^{99m}Tc-nanoparticle was imaged on a Bioscan NanoSPECT/CT, while another tumored mouse received the identical nanoparticle, labeled now with ^{18}F, and was imaged on a Philips Mosaic HP PET camera. The nanoparticle was radiolabeled with ^{99m}Tc via MAG_3 chelation and with ^{18}F via SFB as an intermediate. Phantom imaging showed that the resolution of the SPECT camera was clearly superior, but even with 4 heads and multipinhole collimators, detection sensitivity was 15-fold lower. Radiolabeling of the nanoparticle by chelation with ^{99m}Tc was considerably easier and safer than manual covalent attachment of ^{18}F. Both cameras provided accurate quantitation of radioactivity over a broad range. In conclusion, when deciding between ^{99m}Tc vs ^{18}F, an advantage rests with the chelation of ^{99m}Tc over covalent attachment of ^{18}F, achieved manually or otherwise, but with these small animal cameras, this choice also results in trading lower sensitivity for higher resolution.

INTRODUCTION

While the nuclear imaging modality of choice in the clinic is often positron emission tomography (PET) rather than single photon emission computed tomography (SPECT) in part because of superior sensitivity, resolution, and quantitative ability, it is unclear whether the same advantages apply to small animal imaging (*1–6*). This investigation was conducted primarily to compare the relative spatial resolution and detection sensitivity for ^{99m}Tc on a NanoSPECT/CT camera (Bioscan Inc., Washington D.C., USA) with ^{18}F on a Mosaic HP PET (Philips Medical Systems, Inc., Cleveland, Ohio, USA). Several reports have appeared comparing radioactivity quantitation, imaging sensitivity, and specificity of clinical SPECT and PET cameras in the diagnosis and monitoring of cancers and other disease states in patients (*7–10*). The number of comparison studies of SPECT and PET imaging of small animals using the same agent with different radiolabels is at present limited to ^{123}I and ^{124}I labeled metaiodobenzylguanidine (MIBG) for reporter gene imaging (*11, 12*).

As a model radiopharmaceutical for this comparison, a delivery nanoparticle under development in this laboratory was used in which the biotinylated phosphodiamidate morpholino (MORF) oligomer (*13*), after radiolabeling with ^{99m}Tc or ^{18}F, was linked to the biotinylated Trastuzumab (Herceptin) antiHer2 antibody via streptavidin as shown in Scheme 1. While the radiolabeling of the nanoparticle and its biodistribution was not an objective of this investigation, and although the MORF nanoparticle has been repeatedly and successfully radiolabeled with ^{99m}Tc via MAG_3 for antisense imaging (*14*), this technical note also describes the first labeling of an amine-derivitized MORF with ^{18}F. Following the construction of each Trastuzumab nanoparticle by the addition of the biotinylated labeled MORF, both ^{99m}Tc and ^{18}F were administered to a mouse bearing Her2+ SUM190 tumor xenografts and the animals imaged using the appropriate camera.

* Corresponding author: Tel: 774-442-4256. Fax: 508-856-6363. E-mail: Donald.Hnatowich@umassmed.edu.

MATERIALS AND METHODS

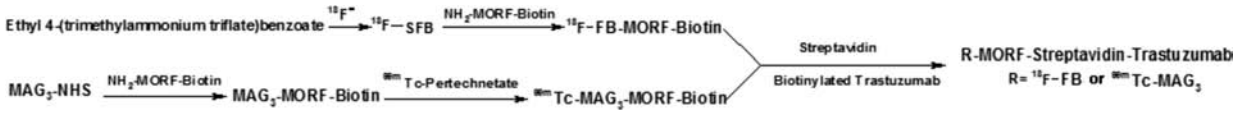
General Experimental Methods. A phosphodiamidate morpholino (MORF) oligomer with the base sequence 5′-GCGTGCCTCCTCACTGGC was purchased with a biotin group on the 3′ equivalent end via a 6-aminohexanoic acid linker and a primary amine on the 5′ equivalent end (Gene Tools, Philomath, OR, USA). The *S*-acetyl NHS-MAG_3 was synthesized in house and its structure confirmed by proton nuclear magnetic resonance and mass spectroscopy (*15*). The anti-Her2 Trastuzumab (Herceptin) was obtained from Genentech Inc. (South San Francisco, CA, USA) as the clinical product. The Sulfo-NHS-LC-Biotin was purchased from Pierce (Rockford, IL, USA) and used to biotinylate the Trastuzumab antibody. Streptavidin was purchased from Sigma (St. Louis, MO, USA). Standard chemicals were obtained from various suppliers and used without purification. The ^{99m}Tc pertechnetate was eluted from a ^{99} Mo-^{99m}Tc radionuclide generator (Bristol-Myers Squibb Medical Imaging Inc., North Billerica, MA, USA). The ^{18}F-fluoride was obtained on a QMA ion exchanging cartridge from PET-NET Solutions Inc. (Woburn, MA, USA). The human breast cancer cell line SUM190 was purchased from Asterand Company (Detroit, MI, USA). Ethyl 4-(trimethylammonium)benzoate trifluoromethanesulfonate was synthesized in house following published procedures (*16*), and the structure confirmed by ^{1}H NMR (300 MHz, D_2O): d 1.18−1.23 (3H, t), 3.51 (9H, s), 4.20−4.27 (2H, q), 7.77−7.80 (2H, m), 8.04−8.07 (2H, m).

Preparation of *N*-Succinimidyl-4-[^{18}F] Fluorobenzoate. The amine-derivitized MORF was radiolabeled with ^{18}F via *N*-succinimidyl-4-[^{18}F] fluorobenzoate (^{18}F-SFB) as the intermediate, selected because of its high radiochemical yield and in vivo stability (*17*). The synthesis of ^{18}F-SFB was achieved according to Cheng et al. (*16*).

The ^{18}F-fluoride was eluted from the QMA ion exchanging cartridge using 1.5 mL of a mixed solution of Kryptofix 2.2.2 (1−2 mg) in 0.5 mL of CH_3CN and K_2CO_3 (10−12 mg) in 1 mL of H_2O. Of this, 0.5 mL (7.4×10^3 MBq) was injected into a 5 mL V-vial and the solution dried azeotropically by adding

10.1021/bc1001467 © 2010 American Chemical Society
Published on Web 08/03/2010

Scheme 1. Preparation Scheme for ^{99m}Tc and ^{18}F Labeling Streptavidin Nanoparticles



0.5 mL of CH_3CN and evaporating at 90 °C under a stream of N_2. Repeating the process two more times was necessary to obtain an anhydrous product. Ethyl 4-(trimethylammonium)-benzoate trifluoromethane sulfonate, 10 mg in 200 μL of anhydrous CH_3CN was added to the vial containing the dried Kryptofix 2.2.2/K^+ complex of [^{18}F]F^- and the solution heated at 90 °C for 5 min. The ethyl ester was then hydrolyzed by adding 0.5 mL of 1 M NaOH and heating at 90 °C for 5 min, before neutralizing with 0.8 mL of 1 M HCl. The neutral solution was diluted with 2 mL of H_2O and loaded onto an activated C18 Sep-Pak cartridge (Waters, Milford, MA, USA). The Sep-Pak cartridge was washed with 2 mL of 0.1 M HCl to remove unlabeled ^{18}F, and the 4-[^{18}F]fluorobenzoic acid (^{18}F-FBA) was then eluted with 2 mL of CH_3CN. The HPLC analysis, performed on a Vydac 218TP C18 5 μm column (Grace, Deerfield, IL, USA) using 1:1 0.08% TFA in CH_3CN and 0.1% TFA in H_2O as eluant at 1 mL/min, showed the radiochemical purity of ^{18}F-FBA to be over 98%.

To synthesize the active ester, ^{18}F-SFB, tetrapropylammonium hydroxide (15 μL, 1 M in H_2O), and *O*-(*N*-succinimidyl) *N*,*N*,*N*′,*N*′-tetramethyluronium tetrafluoroborate (TSTU, 10 mg) (Sigma-Aldrich) were added to the vial containing ^{18}F-FBA in CH_3CN and the vial sealed and heated at 90 °C for 5 min. Acidification was instantaneous following the addition of 3 mL of 5% HOAc followed by 6 mL of H_2O. The mixture was loaded onto another activated C18 Sep-Pak cartridge. After washing with 10 mL of CH_3CN/H_2O (1:7, v/v), about 1.85×10^3 MBq of purified ^{18}F-SFB was eluted with 2 mL of CH_2Cl_2. The product was identified by comparison to a stable SFB sample by HPLC as described above and was also shown to be over 99% radiochemically pure including radioactivity recovery.

Preparation of the ^{18}F Labeled MORF Nanoparticle. The amine derivative MORF oligomer (50 μg in 50 μL of 0.3 M HEPES, pH 8.0) was added to the preparation vial containing 370 MBq ^{18}F-SFB in 20 μL of CH_3CN and incubated at room temperature for 40 min with vigorous vortexing. The reaction solution containing ^{18}F-MORF was transferred slowly but with vigorous mixing to a 0.5 mL nonstick microfuge tube with 235 μg of streptavidin in 100 μL of normal saline. Because only about half the MORF obtained from the manufacturer was biotinylated, the MORF was added to the streptavidin at a 2-fold molar excess. The mixture was incubated at room temperature for 30 min. The Trastuzumab antibody was biotinylated as previously described and added at a 1:1 molar ratio to the MORF/streptavidin (*13*). After incubation at room temperature for an additional 30 min, the mixture was purified on an open G75 column with 0.1 M PBS as the eluant. The fractions with peak radioactivity were combined.

Preparation of the ^{99m}Tc Labeled MORF Nanoparticle. The amine-derivitized MORF was conjugated with NHS-MAG_3 as previously described (*18*). Because the preferred procedure for radiolabeling the MAG_3-MORF with ^{99m}Tc involves heating at temperatures that could potentially denature streptavidin, the MORF was again radiolabeled before adding to streptavidin. The radiolabeling of the MAG_3-MORF was achieved by adding about 407 MBq (120 μL) of ^{99m}Tc-pertechnetate generator eluant into a combined solution consisting of about 14 μg of MORF in 26 μL of 0.25 M NH_4OAc, 60 μL of 100 mg/mL Na_2tartrate·$2H_2O$ in pH 9.2 labeling buffer (0.5 M NH_4HCO_3, 0.25 M NH_4OAc, and 0.175 M NH_3·H_2O), and 15 μL of fresh 10 μg/μL $SnCl_2$ dissolved in pH 8.7 labeling buffer. The final pH was about 8.5. After vortexing, the mixture was incubated at room temperature for 30 min followed by incubation at 95 °C for 22 min. Purification was achieved by C18 Sep-Pak chromatography in which the first elution with 0.2 M NH_4OAc removes the radiolabeled pertechnetate and tartrate, and the second elution with 40% CH_3CN removes radiolabeled MORF, while radiolabeled colloids are retained on the cartridge.

To prepare the nanoparticle, streptavidin (12.9 μL in PBS, 64.5 μg) was added to 50 μL of PBS in a 0.5 mL nonstick microfuge tube. After vortexing, the ^{99m}Tc labeled MORF solution was slowly added at a 2:1 molar ratio (again at a molar excess to compensate for approximately half the MORF that was received without a biotin group attached) with continuous stirring. After the addition, the solution was incubated at room temperature for 30 min followed by purification on an open G75 column. Fractions of 0.5 mL each were collected. To a combined fraction containing 4 μg of streptavidin, 10 μg of biotinylated Trastuzumab was added at a molar ratio of 1: 1, and, after incubation at room temperature for an additional 30 min, the product was drawn into a 1 mL U-100 Insulin Syringe for injection.

SPECT/CT and PET/CT Phantom Imaging. In any SPECT tomographic imaging approach, the distance of the object to be imaged from each pinhole, the diameter of the pinholes, the number of pinholes, the location of each pinhole, and the number of projections all play important roles in determining detection sensitivity. In the case of the Mosaic HP PET animal camera, the detection sensitivity also depends upon the position of the object since sensitivity is maximum in the center of the FOV and decreases linearly down to zero at the edge of the FOV as more coincidences are lost when one or both of the annihilation photons escape.

Regarding resolution in SPECT imaging, the specifications of the multipinhole apertures, the intrinsic resolution of the crystal, the magnification employed in an imaging setup, and the reconstruction settings combine to determine the reconstructed resolution. In the case of microPET imaging, in addition to the positron range that varies among PET imaging radionuclides, the reconstructed resolution depends on factors such as crystal pitch, noncollinearity of the annihilation photons caused by residual momentum of the positron, depth of interaction effects, and the reconstruction methodology and settings (*19*).

Before proceeding to animals, resolution and detection sensitivities were compared using phantoms. To compare sensitivity, a 3 mL plastic syringe containing 18.5 MBq of ^{99m}Tc-pertechnetate in 2.5 mL of H_2O was inserted into a Lucite calibration phantom (Bioscan) with an inner and outer diameter of 1 and 2 cm, and the phantom was placed in the mouse bed of the NanoSPECT/CT camera. Images with a pixel size of 1 mm were recorded over 360° in 256 × 256 matrices with an acquisition time of 60 s per projection, resulting in a total of 24 projections per head over 30 min. The identical phantom was used to measure the PET sensitivity but with the syringe now containing 90 MBq of ^{18}F in 2.5 mL of H_2O. The ^{18}F phantom was put in the center of the field of view (FOV) of the Mosaic camera and an emission-only acquisition was obtained at a 120 mm scan length. The total scanning time was 5 min. Images of coincidence counts with a pixel size of 1 mm were recorded in 128 × 128 matrices.

Because of the expected differences in resolution between the cameras, two phantoms (Data Spectrum Corp., Hillsborough,

North Carolina, USA) of different sizes were required. The smaller phantom used with ^{99m}Tc was provided by Bioscan and was a similar but smaller version of the Jaszczak mini hot spot phantom, with hot rods of 1.2 to 1.7 mm. The larger phantom used with ^{18}F was the Deluxe Mini Jaszczak phantom with hot rods of 1.2 to 4.8 mm. In each case, the imaging protocols were similar to those described for the sensitivity measurements. The SPECT acquisition was obtained with 52 MBq of ^{99m}Tc in 24 min, while the PET acquisition was obtained with 12 MBq of ^{18}F in 5 min. Using a dose calibrator (Capintec Inc., NJ, USA) and a NaI(Tl) well counter, both calibrated for counts per minute per microcurie for both radionuclides as the standard of accuracy, we determined radioactivity quantitation on both cameras with five individual measurements for identical polyethylene tubes 12 mm wide and 75 mm long containing from 0.74 to 9.25 MBq of ^{99m}Tc or 0.37 to 12.21 MBq of ^{18}F.

SPECT/CT and PET/CT Animal Imaging. All animal studies were performed with approval of the UMMS Institutional Animal Care and Use Committee. Two mice (30−40 g, NIH Swiss, Taconic Farms, Germantown, NY, USA) bearing SUM190 (Her2+) tumors in one thigh were used when tumor size was just below 1 cm in any dimension.

One animal was injected intravenously with 0.4 μg of ^{99m}Tc-MORF (13 MBq in 100 μL) as the MORF/Trastuzumab nanoparticle, and tomographic imaging was performed at 3 and 9 h post-administration. A CT acquisition was performed before each SPECT acquisition, at standard frame resolution, 45 kVp tube voltage, and 500 ms of exposure time. About 4 min was required for each CT acquisition. The SPECT image parameters were again 1 mm/pixel, 256 × 256 frame size, and 60 s per projection with 24 projections. Data were acquired in a step-and-shoot mode with the bed also stepping to include the whole body. Acquisition time was approximately 30 min. During imaging, we lightly anesthetized the animal with 1.8% isoflurane in 1.5 L/min O_2. The CT and SPECT reconstruction was performed using InVivoScope 1.37 software (Bioscan). The CT reconstruction was at standard resolution, and SPECT acquisitions were reconstructed with a voxel size of 0.4 mm using the ordered subsets expectation maximization (OSEM) iterative reconstruction algorithm with 4 subsets and 6 iterations. During reconstruction, we selected high noise suppression with filtering to achieve smooth and more artifact-free images. Finally, the SPECT/CT fusion image was obtained using the automatic fusion feature of the software. Region-of-Interest (ROI) analysis was also obtained using InVivoScope 1.37 software. The volume of interest (VOI) was obtained in the form of a cylinder, by first circling the ROI from the transverse profile, then selecting the length of the ROI from the maximum intensity projection.

Another tumored mouse was injected intravenously with 0.4 μg of ^{18}F-MORF (0.22 MBq in 100 μL) as the identical MORF/Trastuzumab nanoparticle, and PET imaging was performed at 2 and 6 h post-administration with 30 min acquisition time. The animal was lightly anesthetized during imaging as before. The PET images were reconstructed without photon attenuation correction using the PETView program (Philips) with the fully 3D iterative reconstruction algorithm, giving a pixel size of 1 mm. Region-of-interest (ROI) analysis was performed digitally using the Syntegra, version 2.0j, program (Philips). VOI was obtained from drawing the ROI in the slices of transverse profile, then interpolating the selected contours. After each PET acquisition, the mouse, immobilized on the Minerva bed (Bioscan), was transferred to the NanoSPECT/CT camera for the CT acquisition, and reconstruction was performed as before. The PET image DICOM files were transferred to the NanoSPECT/CT reconstruction workstation to provide the PET/CT fusion image.

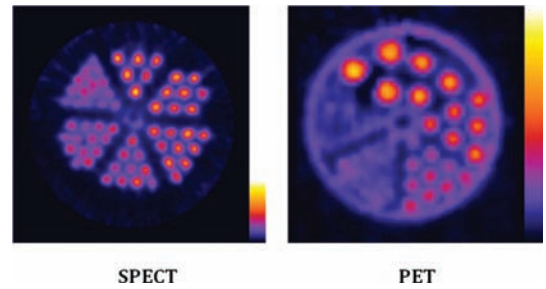


Figure 1. Tomographic image of a ^{99m}TC phantom with hot rods of 1.2 mm to 1.7 mm obtained on the NanoSPECT/CT small animal imaging camera (left panel) and a tomographic image of another ^{18}F phantom with hot rods of 1.2 mm to 4.8 mm obtained on the Mosaic HP PET (right panel) small animal imaging camera.

RESULTS

Radiolabeling. The synthesis of ^{18}F-MORF and the preparation of the MORF/Trastuzumab nanoparticle required about 4 h with a final yield of 0.55 MBq labeled to 1 μg of MORF (i.e., 0.55 MBq/μg) and in a nanoparticle with 9.5 μg of streptavidin and 19 μg of Trastuzumab contained in 0.3 mL of PBS.

The labeling of ^{99m}Tc-MORF and the preparation of the MORF/Trastuzumab nanoparticle was accomplished in 2 h with 13 MBq labeled to 0.4 μg of MORF (i.e., 33 MBq/μg) and in a nanoparticle with 4 μg of streptavidin and 10 μg of Trastuzumab contained in 0.1 mL of PBS. The radiochemical purity by size exclusion HPLC of both nanoparticles was over 99% as shown by a single peak and a radioactivity recovery of 100% in both cases.

SPECT and PET Phantom Imaging. The resolution obtainable by SPECT imaging of ^{99m}Tc on the NanoSPECT/CT camera and by PET imaging of ^{18}F on the Mosaic HP PET camera are illustrated in Figure 1. By recognizing the smallest visible size of hot rods in phantoms, the tomograms provide a value of 1.2 mm for the resolution of the SPECT image and a value of 2.4 mm for the resolution of the PET image.

While the spatial resolution of the NanoSPECT/CT camera was superior to that of the Mosaic HP PET camera, the opposite was true for sensitivity. Under the conditions of this study, 2.47 × 10^8 counts were obtained in 5 min with 90 MBq of ^{18}F to provide a sensitivity for the Mosaic HP PET camera of 9189 cps/MBq. By comparison, 9.88 × 10^6 counts were obtained in 30 min with 18 MBq of ^{99m}Tc and therefore a sensitivity of 622 cps/MBq for the NanoSPECT/CT camera, a difference of about a factor of 15. However, in considering this comparison, it is important to appreciate that while the entire phantom was within the field of view at all times during acquisition on the Mosaic HP PET camera, this was not the case during acquisition on the NanoSPECT/CT camera. Because of the motion of both the gantry and the bed during acquisition, the SPECT sensitivity varies with the position of the phantom. This is illustrated in Figure 2 in which the average counting rate from the four heads is presented individually for each of the 24 projections. From the 10th to 20th projection, the whole phantom was in the field of view, where the four detectors can see the total radioactivity of the phantom, resulting in maximum sensitivity for these projections.

Figure 3 shows the agreement in radioactivity quantitation between well counting and PET (top panel) and SPECT (bottom panel) imaging. In both cases, the linear regression analysis generated a coefficient of determination (R^2) of over 0.99.

SPECT and PET Animal Imaging. The SPECT/CT fused images of the anterior (left panels) and left lateral (middle

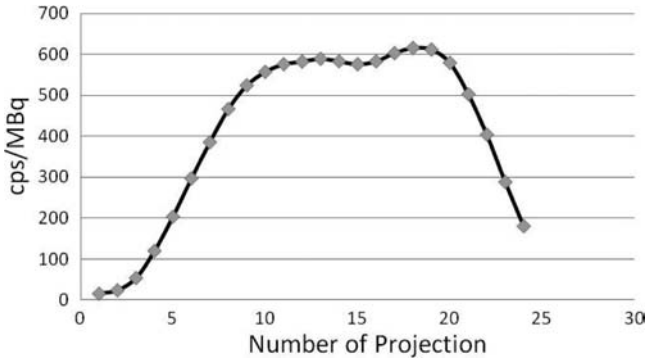


Figure 2. Detection sensitivity in cps/MBq vs projection number showing variation due to the motion of both the gantry and the animal bed during imaging on the NanoSPECT/CT camera.

panels), are presented as maximum intensity projections in Figure 4 from the 3 h (top row) and 9 h (bottom row) post-injection acquisitions of one mouse. Maximum intensity projections (MIP) are defined by the manufacturer as those generated by all slices from all projections. The corresponding PET/CT fused images, also of the anterior (left panels) and left lateral (middle panels), are presented in Figure 5 from the 2 h (top row) and 6 h (bottom row) post-injection acquisitions of another mouse. All acquisitions required about 30 min.

Along with each image in both cases are presented tomographic slices through the tumored thigh at the same level in both animals (right panels). Tumor accumulation in the left thigh is prominent in all images. Comparison of the early and late SPECT images provide evidence of rapid blood clearance, especially from the heart and carotid arteries, and slower clearance from the liver, kidneys, and especially the tumor. The pharmacokinetic behavior of the MORF/Trastuzumab two component nanoparticle is consistent with that previously reported for this ^{99m}Tc labeled nanoparticle (*14*). Comparison of the early and late PET images provides evidence of rapid blood clearance, especially from the heart and carotid arteries, and possibly slower clearance from the liver and especially the tumor, although animal-to-animal differences cannot be excluded.

The percent of injected dosage in the whole body, kidneys, liver, and in the tumor were estimated by quantitating the SPECT and PET acquisitions at both time points for each animal. Other organs were not included in this quantitation measurements either because of low accumulations or because of interference.

The results are presented in the histograms of Figure 6 (SPECT) and Figure 7 (PET). A comparison of the quantitation results show that the decay corrected whole body ^{99m}Tc radioactivity decreased from 8.66 MBq (66% ID) to 7.28 MBq (56% ID) from 3 to 9 h while the ^{18}F radioactivity decreased from 0.16 MBq (71% ID) to 0.15 MBq (66% ID) from 2 to 6 h. The results also show similar radioactivity accumulations at both time points in the tumor; however, the heart and liver show much higher radioactivity accumulations of ^{18}F. Surprisingly, the kidney accumulations are obviously much lower in the mouse receiving the ^{18}F agent.

DISCUSSION

The superior sensitivity and excellent resolution of clinical PET compared to those of clinical SPECT cameras have advanced the field of nuclear medicine, and the increasing availability of commercial PET clinical cameras provides opportunities to exploit new radiopharmaceuticals labeled with PET radionuclides for oncologic, cardiac, neurologic imaging, etc. (*3*). However, the large difference in subject size between human patients and small animals requires different physics for the optimization of the performance of the cameras. We

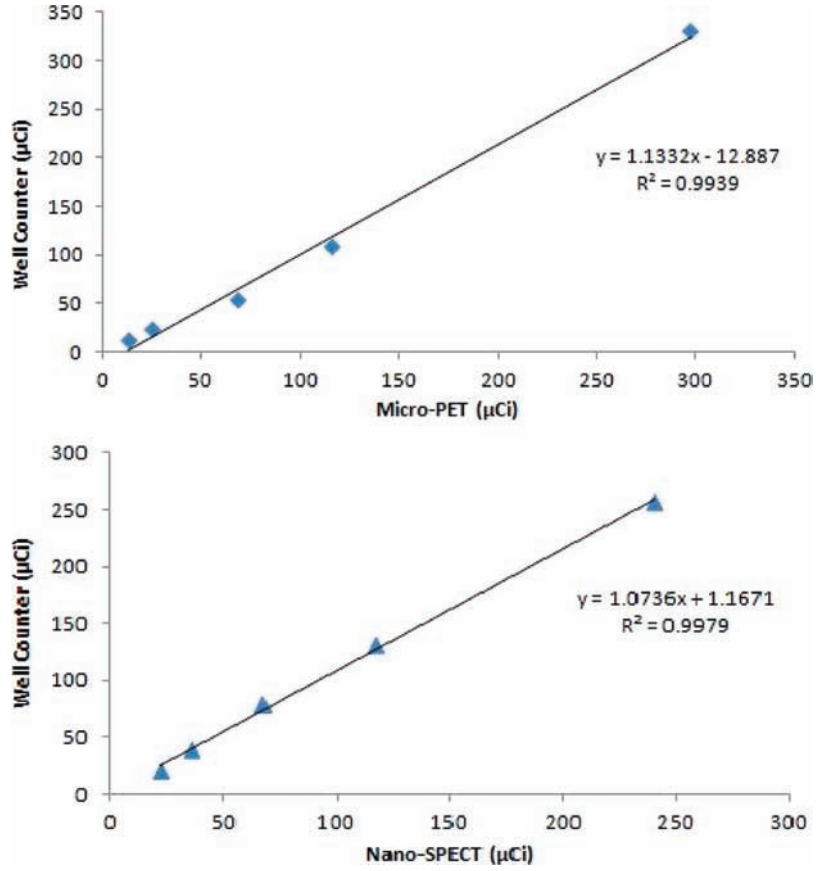


Figure 3. Radioactivity quantitation comparison between well counting and PET (top panel) and SPECT (bottom panel) imaging. The solid line connecting data points was drawn by a linear regression analysis.

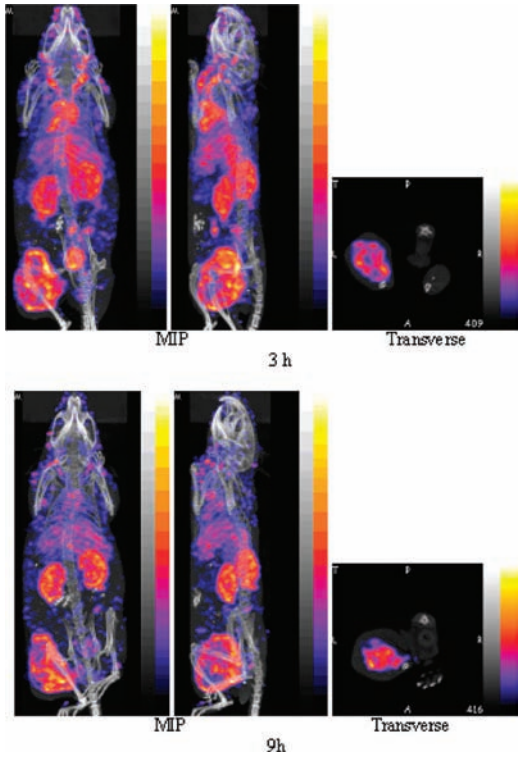


Figure 4. SPECT and fused CT projections obtained by imaging one mouse bearing a SUM190 tumor in the left thigh at 3 h (top row) and again at 9 h (bottom row) post-injection of 100 μL (13 MBq) of a ^{99m}Tc labeled nanoparticle with each acquisition requiring 30 min. Each row presents an anterior (left panel) and left lateral projection (middle panel), both maximum intensity projections (MIP), and a transverse slice (right panel) of the acquisition centered on the tumor.

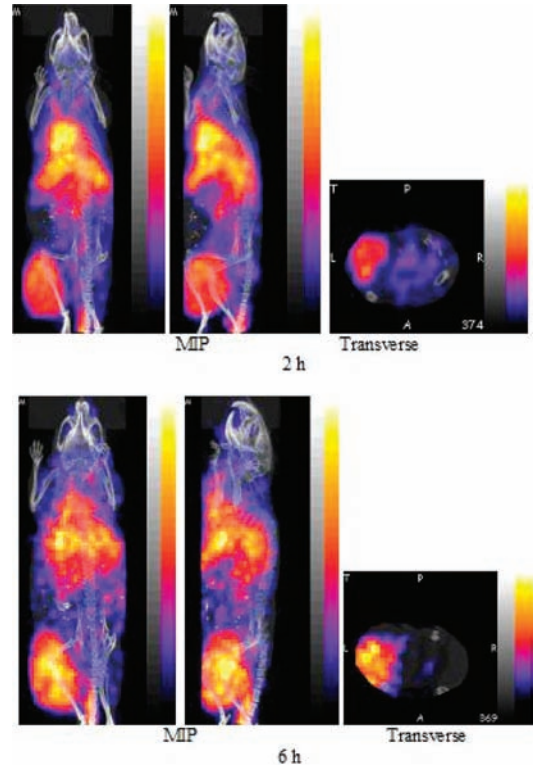


Figure 5. PET and fused CT projections obtained by imaging one mouse bearing a SUM190 tumor in the left thigh 2 h (top row) and again at 6 h (bottom row) post-injection of 100 μL (0.22 MBq) of ^{18}F labeled nanoparticle with each acquisition requiring 30 min. Each presents an anterior (left panel) and left lateral projection (middle panel), both maximum intensity projections (MIP), and a transverse slice (right panel) of the acquisition centered on the tumor.

therefore asked whether the advantages of PET over SPECT tomographic imaging in the clinic extend to the imaging of small animals such as tumored mice. Although not the object of this investigation, because of differences in camera performance, we also asked whether labeling our delivery nanoparticle with ^{18}F would offer advantages over labeling with ^{99m}Tc. Because of the large size of the nanoparticle, the pharmacokinetics was expected to be largely radiolabel independent.

Apart from camera performance, there clearly are advantages to radiolabeling with ^{99m}Tc, usually the preferred SPECT radionuclide, compared to radiolabeling with ^{18}F, often the preferred PET radionuclide (*20–22*). For those radiopharmaceuticals not commercially available and therefore requiring in-house preparation, radiolabeling by chelation with ^{99m}Tc will in all cases require less time and effort and less personnel exposure than radiolabeling with ^{18}F. The use of a remote ^{18}F automated synthesis apparatus would significantly increase the efficiency of the synthesis and decrease personal exposure, but the effort would still not approach the simplicity of chelation labeling as shown in this research in the labeling of the MORF oligomer with ^{99m}Tc and ^{18}F.

To our knowledge, this investigation is the first to compare the Bioscan NanoSPECT/CT and Philips Mosaic HP PET cameras by imaging mice administered the same agent but with different radiolabels. We recognize that arriving at a meaningful comparison between PET and SPECT imaging is complicated by the distinctly different detection physics involved. Regarding camera performance, whereas clinical PET cameras are reported to provide superior spatial resolution compared to that by SPECT cameras at least in the case of PET radionuclides such as ^{18}F with relatively low maximum beta energies, the opposite was found to be the case for the small animal cameras of this investigation. A comparison of the PET and SPECT phantom

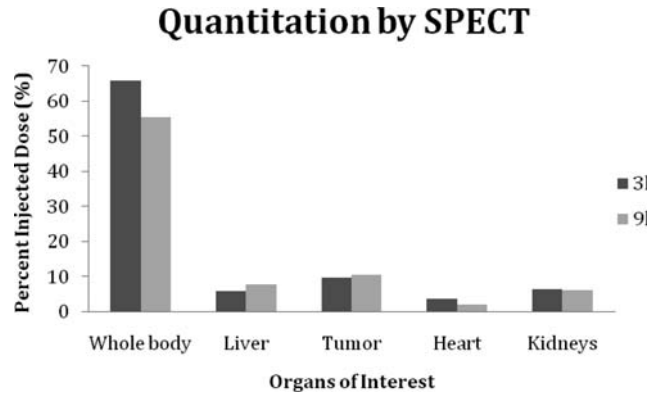


Figure 6. Percent injected dose (% ID) in the whole body, tumor, and three normal organs at 3 and 9 h post-administration of the ^{99m}Tc-MORF/Trastuzumab nanoparticle to a tumored mouse. Radioactivity quantitation was accomplished by using InVivoScope software.

images in Figure 1 clearly shows the latter to provide superior spatial resolution. The NanoSPECT is a conventional gamma camera configured as a small animal imaging system using, in this case, four multipinhole aperture plates each with 9 pinholes of 1.4 mm (Aperture 1, Bioscan) rather than the conventional parallel hole or fan-beam collimators. The superior spatial resolution is also evident in a comparison of the whole body images shown in Figures 4 and 5. However, in agreement with the experiences with clinical cameras, the higher detection sensitivity of PET cameras extended to small animal cameras. Under the conditions of this study, two sources positioned in identical geometry in both cameras provided approximately 15-fold higher counts in the Mosaic HP PET camera compared to that in the NanoSPECT/CT camera. Accordingly, the images

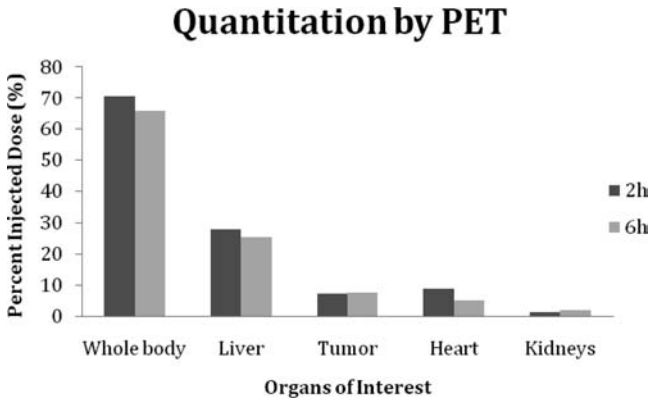


Figure 7. Percent injected dose (% ID) in the whole body, tumor, and three normal organs at 2 and 6 h post-administration of the ^{18}F-MORF/Trastuzumab nanoparticle to a tumored mouse. Radioactivity quantitation was accomplished by using the Syntegra, version 2.0j, program.

of Figures 4 and 5 were obtained in animals injected with 13 MBq of ^{99m}Tc and only 0.22 MBq of ^{18}F requiring 30 min for both SPECT and PET acquisitions.

Since this investigation was more concerned with comparing camera performance than with comparing the pharmacokinetics of the two radiolabeled nanoparticles, only two tumored mice were imaged, relying upon the results of the phantoms studies to compare resolution, sensitivity, and accuracy. Accordingly, the animal results are subject to uncertainties related to animal-to-animal variations. This may explain the small but important differences observed in the pharmacokinetics of the two nanoparticles. While tumor accumulations were identically high due to the targeting of the Her2+ SUM190 xenografts by the antiHer2 antibody within each nanoparticle, accumulations of ^{18}F were higher in the blood (heart) and liver at both time points. These differences were unexpected since the large size of the nanoparticle was expected to mask small differences in chemical properties related to the different labeling methods.

CONCLUSIONS

Radiolabeling of the MORF oligomer within the nanoparticle by chelation with ^{99m}Tc was considerably more efficient than radiolabeling with ^{18}F via the manual synthesis with ^{18}F-SFB. Thus when deciding between ^{99m}Tc versus ^{18}F as the radiolabel for the nanoparticle (and other similar biomolecules) for imaging on the NanoSPECT/CT and Mosaic HP PET small animal imaging cameras, an advantage rests with the chelation of over the covalent attachment of ^{18}F, however, the choice of ^{99m}Tc trades lower sensitivity for higher resolution.

ACKNOWLEDGMENT

We are grateful to Dr. Jack Hoppin (Bioscan Inc., Washington D.C.) for his valuable comments. This research was supported in part by the National Institutes of Health (S10 RR023066).

LITERATURE CITED

(1) Culver, J., Akers, W., and Achilefu, S. (2008) Multimodality molecular imaging with combined optical and SPECT/PET modalities. *J. Nucl. Med. 49*, 169–172.

(2) Herschman, H. R. (2003) Micro-PET imaging and small animal models of disease. *Curr. Opin. Immunol. 15*, 378–384.

(3) Seo, Y. (2008) Quantification of SPECT and PET for drug development. *Curr. Radiopharm. 1*, 17–21.

(4) Liang, H., Yang, Y., Yang, K., Boone, J. M., and Cherry, S. R. (2007) A microPET/CT system for in vivo small animal imaging. *Phys. Med. Biol. 52*, 3881–3894.

(5) Lundqvist, H., and Tolmachev, V. (2002) Targeting peptides and positron emission tomography. *Biopolymers (Pept. Sci.) 66*, 381–392.

(6) Chatziioannou, A. F. (2005) Instrumentation for molecular imaging in preclinical research Micro-PET and Micro-SPECT. *Proc. Am. Thorac. Soc. 2*, 533–536.

(7) Eshuis, A., Jager, P. L., Maguire, R. P., Jonkman, S., Dierckx, R. A., and Leenders, K. L. (2009) Direct comparison of FP-CIT SPECT and F-DOPA PET in patients with Parkinson's disease and healthy controls. *Eur. J. Nucl. Med. Mol. Imaging 36*, 454–462.

(8) Vlasenko, A., Petit-Taboué, M., Bouvard, G., Morello, R., and Derlon, J. (1996) Comparative quantitation of cerebral blood volume: SPECT versus PET. *J. Nucl. Med. 38*, 919–924.

(9) Bremner, J. D., Baldwin, R., Horti, A., Staib, L. H., Ng, C. K., Tan, P. Z., Zea-Ponce, Y., Zoghbi, S., Seibyl, J. P., Soufer, R., Charney, D. S., and Innis, R. B. (1999) Quantitation of benzodiazepine receptor binding with PET [^{11}C]iomazenil and SPECT [^{123}I]iomazenil: preliminary results of a direct comparison in healthy human subjects. *Psychiatry Res. 91*, 79–91.

(10) Even-Sapir, E., Metser, U., Mishani, E., Lievshitz, G., Lerman, H., and Leibovitch, I. (2006) The detection of bone metastases in patients with high-risk prostate cancer: ^{99m}Tc-MDP planar bone scintigraphy, single- and multi-field-of-view SPECT, ^{18}F-fluoride PET, and ^{18}F-fluoride PET/CT. *J. Nucl. Med. 47*, 287–297.

(11) Doubrovin, M. M., Doubrovina, E. S., Zanzonico, P., Sadelain, M., Larson, S. M., and O'Reilly, R. J. (2007) In vivo imaging and quantitation of adoptively transferred human antigen-specific T cells transduced to express a human norepinephrine transporter. *Gene. Cancer Res. 67*, 11959–69.

(12) Moroz, M. A., Serganova, I., Zanzonico, P., Ageyeva, L., Beresten, T., Dyomina, E., Burnazi, E., Finn, R. D., Doubrovin, M., and Blasberg, R. G. (2007) Imaging hNET reporter gene expression with ^{124}I-MIBG. *J. Nucl. Med. 48*, 827–836.

(13) Liu, X., Wang, Y., Nakamura, K., Kubo, A., and Hnatowich, D. J. (2008) Cell studies of a three-component antisense MORF/tat/Herceptin nanoparticle designed for improved tumor delivery. *Cancer Gene Ther. 15*, 126–132.

(14) Wang, Y., Liu, X., Chen, L., Rusckowski, M., and Hnatowich, D. J. (2009) Tumor delivery of antisense oligomer using trastuzumab within a streptavidin nanoparticle. *Eur. J. Nucl. Med. Mol. Imaging 36*, 1977–1986.

(15) Wang, Y., Liu, X., and Hnatowich, D. J. (2007) An improved synthesis of NHS-MAG3 for conjugation and radiolabeling of biomolecules with ^{99m}Tc at room temperature. *Nat. Protoc. 2*, 972–978.

(16) Cheng, D., Yin, D., Zhang, L., Wang, M., Li, G., and Wang, Y. (2007) Preparation of the novel fluorine-18-labeled VIP analog for PET imaging studies using two different synthesis methods. *J. Fluorine Chem. 128*, 196–201.

(17) Wester, H. J., Hamacher, K., and Stöcklin, G. (1996) A comparative study of N.C.A.: Fluorine-18 labeling of protein via acylation and photochemical conjugation. *Nucl. Med. Biol. 23*, 365–372.

(18) Wang, Y., Nakamura, K., Liu, X., Kitamura, N., Kubo, A., and Hnatowich, D. J. (2007) Simplified preparation via streptavidin of antisense oligomers/carriers nanoparticles showing improved cellular delivery in culture. *Bioconjugate Chem. 18*, 1338–1343.

(19) Levin, C. S., and Hoffman, E. J. (1999) Calculation of positron range and its effect on the fundamental limit of positron emission tomography system resolution. *Phys. Med. Biol. 44*, 781–799.

(20) Stöcklin, G. L. (1998) Is there a future for clinical fluorine-18 radiopharmaceuticals (excluding FDG)? *Eur. J. Nucl. Med. 25*, 1612–1616.

(21) Okarvi, S. M. (2001) Recent progress in fluorine-18 radiopharmaceuticals. *Eur. J. Nucl. Med. 28*, 929–938.

(22) Cai, L., Lu, S., and Pike, V. W. (2008) Chemistry with [^{18}F]fluoride ion. *Eur. J. Org. Chem. 17*, 2853–2873.

BC1001467

Drug Discovery with DNA-Encoded Chemical Libraries

Fabian Buller,[†] Luca Mannocci,[‡] Jörg Scheuermann,[†] and Dario Neri*[,†]

Institute of Pharmaceutical Sciences, Department of Chemistry and Applied Biosciences, and Philochem AG, ETH Zurich, Wolfgang-Pauli-Strasse 10, CH-8093 Zurich, Switzerland. Received March 24, 2010; Revised Manuscript Received June 14, 2010

DNA-encoded chemical libraries represent a novel avenue for the facile discovery of small molecule ligands against target proteins of biological or pharmaceutical importance. Library members consist of small molecules covalently attached to unique DNA fragments that serve as amplifiable identification barcodes. This encoding allows the in vitro selection of ligands at subpicomolar concentrations from large library populations by affinity capture on a target protein of interest, in analogy to established technologies for the selection of binding polypeptides (e.g., antibodies). Different library formats have been explored by various groups, allowing the construction of chemical libraries comprising up to millions of DNA-encoded compounds. Libraries before and after selection have been characterized by PCR amplification of the DNA codes and subsequent relative quantification of library members using high-throughput sequencing. The most enriched compounds have then been further analyzed in biological assays, in the presence or in the absence of linked DNA. This article reviews experimental strategies used for the construction of DNA-encoded chemical libraries, revealing how selection, decoding, and hit validation technologies have been used for drug discovery programs.

INTRODUCTION

The isolation of specific ligands to target proteins of interest is a key step for the development of pharmaceutical agents or biochemical probes. Technologies which facilitate ligand discovery may substantially contribute to a better understanding of biological processes and to drug discovery. The facile identification of specific binders to target proteins have been accomplished by selection of large polypeptide repertoires (e.g., antibody libraries) (*1*−*3*), but these reagents are typically not suited for interfering with intracellular biochemical processes. The discovery of low molecular weight ligands is usually more cumbersome (*4*, *5*).

Conventional technologies for the discovery of small molecule ligands against a target protein of choice often feature the use of collections of chemical compounds ("compound libraries"), which are individually screened (i.e., one molecule at a time), based on enzymatic activity of the target protein or by displacement of labeled ligands. Such a high-throughput screening (HTS) approach for 10 000−1 000 000 compounds is complex and expensive in terms of library synthesis, management, logistics, and screening (*6*). The HTS of compound libraries does not always result in hits of acceptable quality and is hardly accessible to academic laboratories. The use of structural information in "virtual screening" may reduce the number of compounds that need to be evaluated (*7*, *8*). Alternatively, a fragment-based approach may be used for the identification of multidentate ligands with suitable binding affinity and pharmacological properties (*5*, *9*−*11*).

Phage display technology (Figure 1A) (*1*, *2*) has revolutionized the way binding polypeptides (e.g., antibodies) are isolated from a large library. Billions of polypeptides, displayed on the surface of the filamentous phage, exploit a physical linkage between their potential binding properties ("phenotype") and the corresponding genetic information contained inside the phage ("genotype"). Libraries have been panned on target antigens immobilized on solid support, and washing cycles allow the isolation of binding molecules (*3*). Following similar logic, ribosome display (Figure 1B) (*12*, *13*) allows the association of mRNA, coding for a polypeptide, together with its translation product. Phage display, ribosome display, and conceptually similar technologies (peptides on plasmid; yeast display, puromycin display, covalent DNA display) (*14*−*18*) allow the amplification of the genetic information of selected binders after affinity capture, e.g., through bacterial amplification (phage display). As these technologies rely on transcription and translation, they are only compatible with the display and selection of polypeptides and cannot directly be used for the display and selection of small organic molecules.

The concept of linking genotype and phenotype for selection purposes can be translated into the world of small organic molecules by encoding them with unique DNA fragments that serve as amplifiable identification bar codes (*19*−*21*) (Figure 1C,D). In analogy to polypeptide-based display technologies, DNA-encoded small molecules can be panned against a target protein of interest. Washing cycles allow the enrichment of specific binding moieties, whose DNA codes are subsequently amplified by PCR (Figure 2) (*20*, *21*). Brenner and Lerner first proposed the concept of DNA-encoded chemical libraries in 1992, suggesting the alternated synthesis of peptides and oligonucleotides on the same solid support (Figure 1C) (*19*). Since then, several strategies for the synthesis of DNA-encoded chemical libraries have been developed, including the direct linkage of small molecules to their encoding DNA tag (Figure 1D) (*22*−*32*). Furthermore, the concept of DNA encoding has been recently extended to peptide nucleic acids (Figure 1E) (*33*). In this review, we focus on small molecule DNA-encoded chemical libraries and their use for drug discovery.

Single Pharmacophore DNA-Encoded Chemical Libraries. DNA-encoding represents an attractive avenue for the synthesis of large combinatorial libraries, as the DNA tag itself can facilitate library construction via different strategies (Figures 3 and 4) (*25*−*27*, *30*, *31*, *34*). The simplest format for a DNA-encoded chemical library is the covalent attachment of individual compounds to unique DNA fragments. If a single organic

* Correspondence to Dario Neri, Tel: (+41)-44-6337401, e-mail: neri@pharma.ethz.ch.

[†] Institute of Pharmaceutical Sciences, Department of Chemistry and Applied Biosciences.

[‡] Philochem AG.

10.1021/bc1001483 © 2010 American Chemical Society
Published on Web 08/03/2010

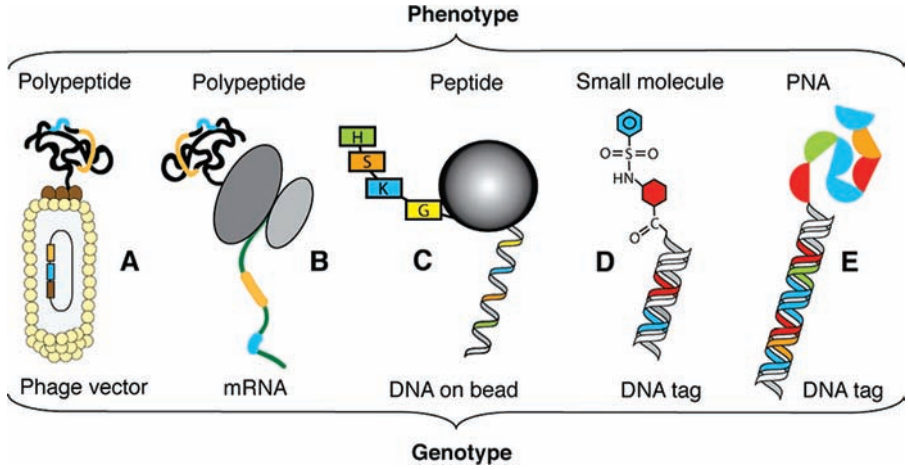


Figure 1. Libraries of binding entities ("phenotype") linked to their encoded information ("genotype"). Phage display libraries (A) consist of polypeptides displayed on the surface of filamentous phage, carrying the polypeptide sequence information in the phage genome. In ribosome display libraries (B), mRNA is linked to the ribosome and the corresponding polypeptide. (C) Peptide sequences immobilized on a bead have been encoded with short DNA fragments that serve as amplifiable identification barcodes of the peptides. DNA-encoded small molecule libraries consist of compounds covalently attached to coding DNA fragments (D). Peptide nucleic acids (PNA) can be covalently attached to DNA tags (E) using DNA-templated synthesis.

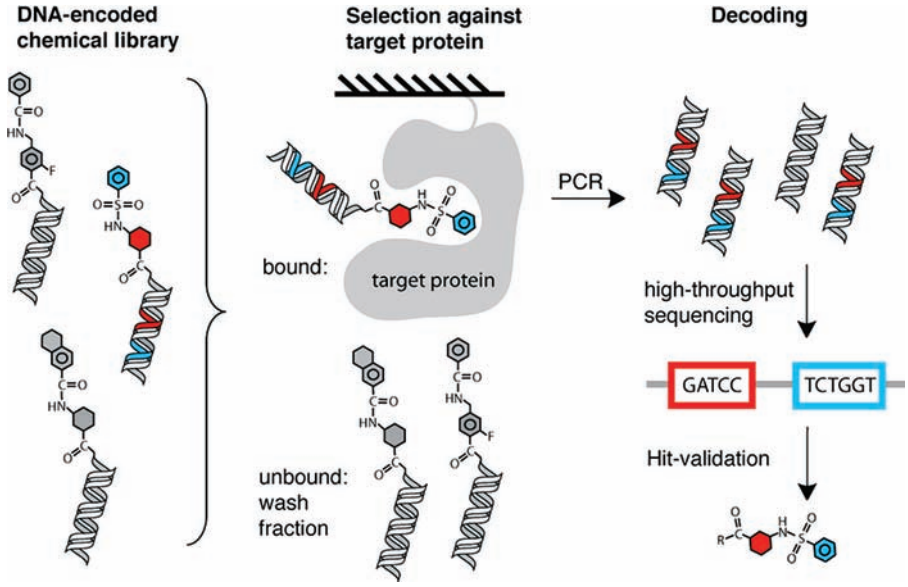


Figure 2. Affinity-based selections using DNA-encoded chemical libraries. A typical selection process with DNA-encoded chemical libraries is based on the following steps: (i) incubation of the library with a target protein of choice immobilized on a solid support, (ii) removal of nonbinders by washing cycles of the solid support, (iii) PCR amplification of the DNA codes corresponding to the retained library members, (iv) assessment of the relative quantification of library codes after selection using high-throughput sequencing, and (v) resynthesis of identified compounds in the absence of a DNA tag for biological or biochemical assays.

molecule is displayed on each DNA fragment, the corresponding library can be termed "single pharmacophore library" (Figure 3A−D) (*25*, *27*, *30*, *31*, *34*). By contrast, "dual pharmacophore libraries" feature the display of pairs of chemical structures at the two extremities of complementary DNA strands (Figure 3E) (*28*). Single pharmacophore libraries can be further classified by their library synthesis in (i) libraries being based on a split-and-pool combinatorial assembly of building blocks and encoding DNA fragments (Figures 3A,B and 4A) (*25*, *30*, *34*) and (ii) libraries for which a DNA-templated synthesis was used in the construction step (Figures 3C,D and 4B) (*26*, *27*, *31*).

Split-and-pool synthesis approaches have proven to be versatile tools for the construction of DNA-encoded chemical libraries (*25*, *30*, *34*). A convenient experimental strategy is illustrated in Figure 4A, which features the following sequential steps: (i) conjugation of a first set of chemical compounds representing building block 1 to distinct amino-modified synthetic oligonucleotides; (ii) pooling of the first reactions, followed by a splitting step into separate reaction vessels corresponding to the reactions for the incorporation of a second building block; (iii) chemical coupling of the second building block; (iv) encoding of the second building block (e.g., by hybridization of partially complementary oligonucleotides followed by Klenow fragment-mediated DNA polymerization); (v) pooling of the encoded reactions to yield a DNA-encoded chemical library. These steps have been iterated, for the construction of libraries containing three or more sets of building blocks and three or more coding regions, yielding library sizes between 10^5 and 10^9 encoded small molecules (*25*). For certain applications, it may be convenient to covalently link the two DNA strands in single-pharmacophore encoded chemical libraries and use the linker for the display of organic molecules (Figure 3B) (*25*).

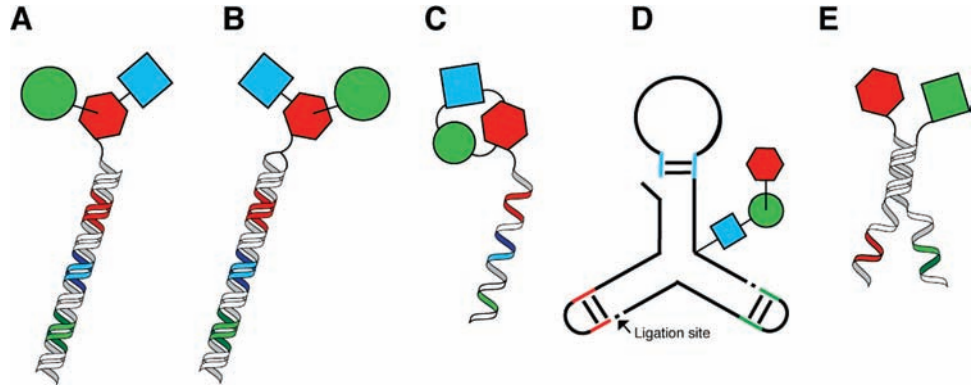


Figure 3. DNA-encoded library formats. "Single pharmacophore DNA-encoded chemical libraries" (A−D) display a single chemical compound on one DNA strand, in contrast to "dual pharmacophore DNA-encoded chemical libraries" (E) which feature the display of pairs of chemical structures at the two extremities of complementary DNA strands. Different chemical synthesis strategies have been considered for the construction of single pharmacophore libraries, including the simple attachment of small molecules to one DNA strand (A) (e.g., to a 5′-amino-modified oligonucleotide with a C12 linker), using a linker which connects both DNA strands (i.e., two short DNA strands were cross-linked by poly(ethylene glycol) spacers and a 2-(4-aminobutyl)propane-1,3-diol group; additionally, an amino-modified tetraoxopentadecanoic acid linker was used as a spacer between the DNA and the small molecule (*25*)) (B) or using DNA templated synthesis (C,D) to construct macrocyclic structures (C) or linear structures with the help of a triple hairpin structure (D).

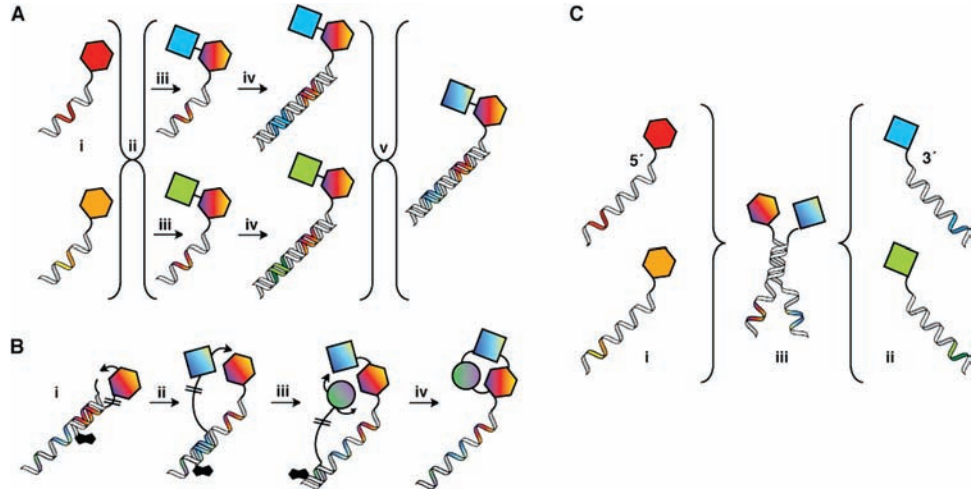


Figure 4. Synthesis schemes of DNA-encoded chemical libraries. (A) Split-and-pool synthesis of DNA-encoded chemical libraries is based on alternated synthesis and encoding steps: (i) conjugation of a first set of chemical compounds representing building block 1 to distinct amino-modified synthetic oligonucleotides; (ii) pooling of the reactions, followed by a splitting step into separate reaction vessels corresponding to the reactions for the incorporation of a second building block; (iii) chemical coupling of the second building block; (iv) encoding of the second building block (e.g., by hybridization of partially complementary oligonucleotides followed by Klenow fragment-mediated DNA polymerization); (v) pooling of the encoded reactions to yield a DNA-encoded chemical library. (B) Single pharmacophore DNA-encoded chemical library can be constructed using DNA-templated synthesis, in which individual chemical moieties are linked to a short single-stranded biotinylated DNA-fragment serving as a "donor strand". Upon hybridization to the template DNA strand, the chemical moiety is transferred to the template strand by covalent bond formation, followed by cleavage and avidin-assisted donor strand removal (i−iv). Macrocyclic structures could be obtained in the last reaction step (iv). (C) Dual-pharmacophore chemical libraries can be self-assembled out of two complementary sublibraries, in which each DNA strand displays a small molecule (iii). The first sublibrary contains chemical entities attached at the 5′-extremity of distinct single-stranded oligonucleotides (i), whereas the second sublibrary displays chemical moieties at the 3′-extremity of unique oligonucleotides (ii), containing a hybridization domain for the first sublibrary.

In general, the construction of DNA-encoded chemical libraries by split-and-pool synthesis is facilitated by the ability to perform chemical reactions at high yields and with good purities, using synthetic methodologies which work well in water and preserve the integrity of DNA (*30*, *34*). The DNA tag itself can facilitate library construction via a split-and-pool route, as chemical reactions can be performed with a large excess of small molecule reagents relative to the oligonucleotide, and as DNA can facilitate purification, e.g., by precipitation of the DNA conjugate or by immobilization on positively charged resin (*30*, *34*, *35*). Libraries have been constructed using amide bond forming reactions (*30*), chloride substitutions on cyanuric chloride with amines (*25*), or Diels−Alder cycoaddition reactions (*34*), while other reactions could also be considered.

While DNA-encoded chemical libraries have been used for the de novo isolation of binders against a target protein of choice, lead compounds are often further modified in order to improve their performance for drug discovery applications[1]. The "affinity maturation" of lead structures can efficiently be performed using single pharmacophore DNA-encoded chemical libraries, incorporating the lead structure during DNA-encoded library synthesis[1]. In this context, we recently described the synthesis of a benzamidine-based single pharmacophore library, which allowed the affinity maturation of benzamidine toward serine proteases and the

[1]Mannocci et al. Isolation of potent and specific trypsin inhibitors from a DNA-encoded chemical library, *Bioconjugate Chem.* In press.

Table 1

library	size	format[a]	target protein	selection results
Halpin & Harbury, 2004 (*59*)	1 mio	DNA routing	anti-enkephalin mAb	proof-of-principle
Gartner et al. 2004 (*26*)	65	C	carbonic anhydrase (CA)	proof-of-principle
Melkko et al. 2004 (*28*)	138	E	streptavidin, CA	proof-of-principle
Melkko et al. 2007 (*24*)	550	E	trypsin	98 nM (based on lead structure)
Wrenn et al. 2007 (*60*)	100 mio	DNA routing	N-CrkSH3	16 μM (focused library)
Dumelin et al. 2008 (*22*)	550	E	HSA	3.2 μM (de novo)[b]
Scheuermann et al. 2008 (*29*)	550	E	MMP-3	9.9 μM (de novo)[b]
Mannocci et al. 2008 (*30*)	4000	A (2)	streptavidin	0.35 μM (de novo)[c]
Mannocci et al. 2008 (*30*)	4000	A (2)	polyIgG	chromatography resin
Melkko et al. 2010 (*39*)	4000	A (2)	Bcl-xL	0.93 μM (de novo)[c]
Tse et al. 2008 (*27*)	13824	C	not reported	
Clark et al. 2009 (*25*)	ca. 7 mio	B (3)	p38 MAP kinase	$\leq$2nM (based on lead structure)[b]
Clark et al. 2009 (*25*)	ca. 7 mio	B (3)	Aurora A kinase	0.27$-$6.3 μM (de novo)[b]
Clark et al. 2009 (*25*)	ca. 800 mio	B (4)	p38 MAP kinase	0.25 μM (de novo)[b,d]
Hansen et al. 2009 (*31*)	100	D	Anti-enkephalin mAb	proof-of-principle
Buller et al. 2009 (*32*)	4000	A (2)	TNF	20 μM (de novo)[c]
Buller et al. 2009 (*32*)	4000	A (2)	Bcl-xL	10 μM (de novo)[c]
Mannocci et al.[1]	8000	A (2)	trypsin	3 nM (based on lead structure)[b]
Buller et al.[2]	1 mio	A (3)	CAIX	<0.6 μM (based on lead structure)[b]

[a] DNA-encoded library format corresponding to Figure 3; the number in brackets indicates the number of building blocks and coding regions used for single pharmacophore library construction. [b] IC_{50} measurements. [c] K_d measurements by fluorescence polarization. [d] Possible hydrolysis or ethanolysis products with $\leq$7 nM potency have been reported (*25*).

identification of nanomolar binders against trypsin as a model target[1] (Table 1).

Liu and co-workers pioneered an alternative way for the construction of a DNA-encoded chemical library, which makes use of complementary oligonucleotide derivatives in order to facilitate chemical reactions ("DNA-templated synthesis") (*26, 27, 36*) (Figures 3C and 4B). The DNA sequence itself is used as a genetic code for the organic chemistry steps, performed on the same DNA strand. Individual chemical moieties are linked to a short single-stranded biotinylated DNA fragment serving as a "donor strand". Upon hybridization to the template DNA strand, the chemical moiety is transferred to the template strand by covalent bond formation, followed by cleavage and avidin-assisted donor strand removal. DNA-templated chemical reactions may be accelerated by hybridization-induced proximity of the two reactants (*26, 27, 36*).

In contrast to single and dual pharmacophore DNA-encoded chemical libraries, the concept of DNA-templated synthesis may be compatible with the execution of multiple rounds of selection and amplification, in analogy to rounds of panning in phage and ribosome display technologies (*26*). The library format allows the chemical resynthesis of the enriched library members after PCR amplification (Figures 3C and 4B), thus enabling an iterative amplification of preferential binders. The synthesis of a templated DNA-encoded library of 13 000 small molecule macrocycles using amide bond formations has been described (*27*), but its use for in vitro selection has not been reported yet.

Another DNA-templated library synthesis variant makes use of DNA three-way junctions, i.e., chemical building blocks associated with hairpin loop structures. These DNA fragments are hybridized and ligated, enabling the chemical reactions between the building blocks (Figure 3D), followed by a subsequent cleavage step (*31*). The DNA junctions themselves may facilitate DNA-templated chemical reactions due to a close proximity of the reaction centers. Hansen and co-workers used a 100-membered library in a proof-of-principle experiment, performing two rounds of in vitro selection on an immobilized antibody target, which led to the preferential isolation of an enkephalin peptide used as positive control (*31*).

DNA-Encoded Self-Assembling Libraries. Dual-pharmacophore chemical libraries can be constructed by the combinatorial self-assembly of two complementary sublibraries, in which each DNA strand displays a small molecule (Figures 3E and 4C) (*22*$-$*24, 28, 29, 37*). The first sublibrary contains chemical entities attached at the 5′-extremity of distinct single-stranded DNA-fragments, whereas the second sublibrary displays chemical moieties at the 3′-extremity of unique DNA fragments, containing a hybridization domain for the first sublibrary (Figure 4C) (*24, 28, 29*). Both sublibraries can be synthesized by the individual covalent coupling of chemical entities to modified DNA fragments (e.g., the coupling of a reactive moiety to amino-modified DNA fragment) (Figure 4C) (*23, 28*). The sublibraries can be HPLC-purified to homogeneity after conjugation with a small molecule, ensuring an extremely high library quality. Additionally, large combinatorial libraries can be assembled by hybridization of two relatively small sublibraries. The display of two neighboring chemical entities may enable the simultaneous binding of two compounds to adjacent non-overlapping binding sites on a target protein (*37*). Subsequently, these individual binding entities have to be linked and assembled into a single organic molecule, in full analogy to fragment-based drug discovery approaches (*5, 24, 29*).

Selection Strategies. DNA-encoded chemical libraries can be selected by affinity capture on virtually any target protein of interest (Figure 2) (*20, 21, 38*), in analogy to antibody phage display technology. The library is incubated at low concentration (pM to fM concentration of individual library members) with the target protein. Upon separation of the "bound" and "unbound" fractions, the "bound" library members are PCR-amplified (Figure 2). The resulting amplicon mixture must then be deconvoluted, by quantifying the relative concentration of all library members (e.g., by high-throughput sequencing) (*25, 30, 32*). Subsequently, identified "hits" have been characterized biologically or biochemically, in the presence or absence of linked DNA (*25, 30, 32*).

Selections (i.e., the separation of bound and unbound library members) can be performed using various technologies, which may depend in part on features of the target protein of interest and on selection goals (*38*). Typically, libraries dissolved in 10$-$100 μL have been panned on immobilized protein. Antigens immobilized via CNBr-activated sepharose resin (*29, 30, 32, 39*) and His-tagged proteins on metal affinity chromatography resin (IMAC) have been considered (*25*). Alternatively, DNA-encoded chemical libraries can be incubated in solution with a

[2] Buller, F., and Neri D. Unpublished results.

biotinylated interaction partner, followed by the subsequent capture of the binding fraction on streptavidin-coated resin or magnetic beads (*30*). As for antibody phage display technology, selection stringency has been optimized varying the concentration of the target protein (e.g., the coating density on the resin) or the number of washing steps (*24*)[1]. Blocking agents have been used during the selection to prevent unspecific binding, including nonrelated DNA (e.g., herring sperm DNA) and bovine serum albumin (*25, 29, 30, 32, 39*). In principle, alternative selection technologies could also be explored, in which binding DNA conjugates are displaced by known ligands, in order to direct library selections toward a distinct pocket of the protein. As for polypeptide display methodologies, selections can in principle be directed toward an epitope of choice on the target protein of interest by the use of a competitor or by performing parallel panning reactions on a set of closely related proteins (*40*).

Decoding. After binders are selected from a DNA-encoded chemical library, their DNA code can be amplified by PCR. Binding molecules have been identified by comparing the relative frequency of each DNA code in the library before and after selection pressure (*30, 32*). Amplicon mixtures from the first DNA-encoded chemical libraries have been decoded by subcloning and sequencing of individual colonies or, alternatively, by hybridization of fluorescent DNA-amplicons to DNA microarrays (*23*). These technologies have proven to be versatile tools to decode small DNA-encoded chemical libraries, but are not applicable for the decoding of amplicon mixtures with thousands to millions of different DNA codes. We and others have recently described the application of Roche's 454 high-throughput sequencing technology for the decoding of DNA-encoded chemical libraries (*25, 30−32, 39*). The technology relies on emulsion PCR and subsequent pyrosequencing of DNA-coated beads in high-density picoliter reactors (picotiter plate) and allows sequencing of >1 million sequence tags per picotiter plate (*41*). Sequence counts of individual library members can be plotted for all possible code combinations in the library. A sequence enrichment profile, resulting from a single pharmacophore DNA-encoded chemical library with 4000 compounds, is depicted in Figure 5A. The enriched code combinations are highlighted in blue (*32*). Figure 5B shows a pseudo four-dimensional plot of a sequence enrichment profile of a million compound library, generated using three sets of building blocks[2]. The three codes are presented on the axis *x*, *y*, and *z*, while the dot size correlates with the sequence counts. A compound class sharing the same first and second building block is highlighted in blue.

High-throughput sequencing using 454-technology only requires the introduction of the instrument-specific adaptor sites during the PCR after selection (*41*). The specific adaptor sites are necessary for bead-immobilization of a single DNA template molecule. Beads are subsequently decorated with clones of the template DNA molecule using emulsion PCR. The separation of the beads after PCR in wells of a picotiter plate allows pyrosequencing in each well (*41, 42*). The 454 technology offers the advantage of sequencing different selection experiments in the same sequencing experiment by either (i) physically dividing the picotiter plate into up to 16 fragments or (ii) encoding different samples with a DNA bartag, introduced by PCR. Until now, in-house programs are used to count code combinations found in the amplicon mixture, which can then be plotted versus the code combinations (*30, 32*).

The statistical analysis of sequence-based decoding experiments is invaluable for the quantitative assessment of the significance of enrichment results. We have reported that the sequence distribution of libraries prior to selection can be conveniently described by a negative binomial density function

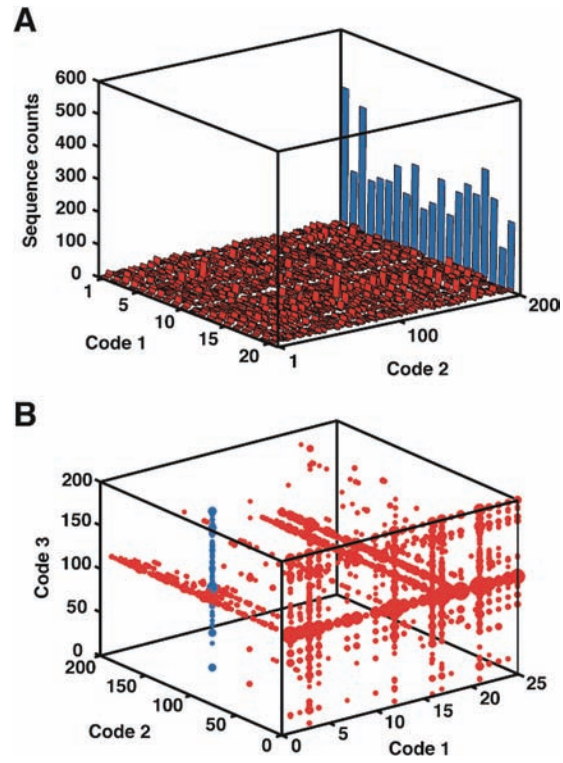


Figure 5. Sequence count profiles after selection, obtained by high-throughput sequencing. (A) Sequence counts of a single pharmacophore library with two building blocks (i.e., two coding regions) were analyzed after selection against a target protein using high-throughput sequencing. Only code combinations with code 2 = 200 are enriched in the selection experiment and highlighted in blue. (B) Selection results of a three building block library (i.e., three coding regions) are plotted in a pseudo four-dimensional plot. The three codes are presented on the axis *x*, *y*, and *z*, while the dot size correlates with the sequence counts. A compound class sharing the same first and second building block is highlighted in blue.

(Figure 6A). Quantile−Quantile plots are particularly useful to monitor the agreement between theoretical and experimental distribution of code frequencies (Figure 6A), as well as to identify preferentially enriched compounds after selection (Figure 6B). *p*-values have been calculated to describe the significance of enrichment results (*32*).

Alternative sequencing technologies based on the Illumina/Solexa platform or the SOLiD platform can be implemented for the deconvolution of amplicon mixtures from DNA-encoded chemical libraries (*42−45*). These technologies differ in terms of read-length, read-quality, and the total amount of sequences. For example, Illumina technology generates about 20 Gigabases (GB) of sequence information in a single sequencing experiment with a current read-length of up to 100 bp, while the SOLiD technology generates 15−30 GB of 50 bp reads (*42−45*). We have recently confirmed the applicability of Illumina sequencing for DNA-encoded chemical library decoding (*46*), while no results on the SOLiD system have been reported up to now. In the future, emerging technologies based on single-molecule sequencing may prove to be useful for the decoding of very large DNA-encoded chemical libraries (*42*).

Hit Validation. After selection of binding molecules from a DNA-encoded chemical library, preferential binders are typically resynthesized without DNA tag in order to confirm protein interaction and to determine affinity constants (*30, 32, 39*). Good correlations of the sequencing counts after the selection experiment and the final affinity of the compound without DNA tag have been reported (*39*). However, large DNA-encoded libraries may identify hundreds of enriched compounds, making con-

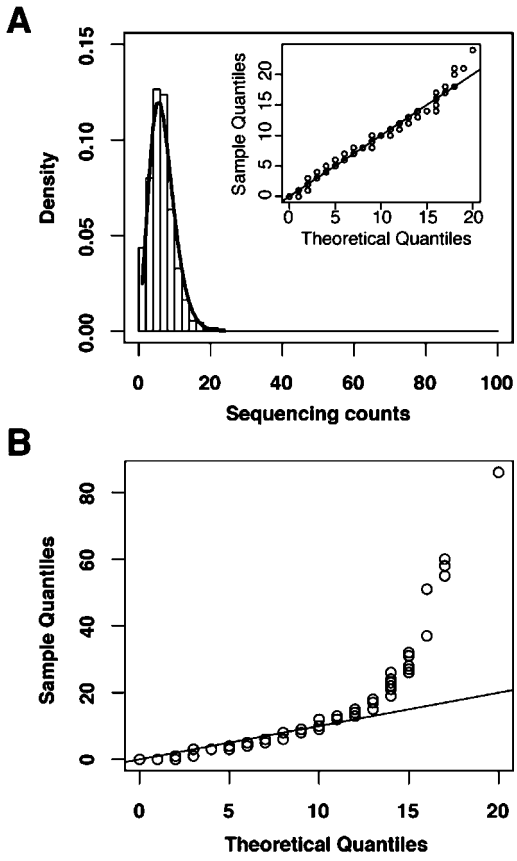


Figure 6. Statistical analysis of high-throughput sequencing results from DNA-encoded chemical libraries. (A) Histogram of the sequence counts obtained from high-throughput sequencing of a DNA-encoded chemical library before selection. The solid curve is the negative binomial density function used for the fitting procedure. For each experimental sequence count, the corresponding quantile (the fraction of counts below a given value, e.g., $q_{0.5}$ = average sequence count, 50% of the sequences are below this value) is compared to the same quantile derived from the fitted negative binomial density function. The resulting quantile−quantile plot (insert) is a graphical technique for comparing the experimental sequence count distribution with the fitted distribution. Prior to selection pressure, no significant deviations from the diagonal are observed, indicating good model fit (insert). (B) Sequence distribution after affinity-based selection is compared to the fitted negative binomial density function as in (A). Deviations from the diagonal reveal enriched candidate compounds.

ventional hit-validation processes (e.g., affinity or inhibition measurements, fluorescence polarization measurements of fluorescein-conjugated compounds) more cumbersome. In this case, additional selections with an increased selection pressure might define the number of hits to validate (*24*). Alternatively, the affinity or potency of the DNA-conjugated compounds can be determined directly on DNA. The advantage of DNA-based hit-validation relies on the fact that (i) synthesis procedures of library construction can be used also for individual molecules; (ii) the DNA-tag can facilitate purification (e.g., DNA precipitation) and quality control (e.g., ESI-MS); (iii) the DNA tag can be used for quantification (e.g., absorbance measurements, fluorescence measurements with intercalating dyes, quantitative PCR), for detection, and/or for immobilization purposes (Figure 7). The solution-based hit-validation of DNA-conjugated compounds in biological assays (Figure 7A) has been applied whenever assay conditions can be found which allow the presence of a short DNA tag, e.g., inhibition or competition assays. Affinity measurements by polyacrylamide electromobility shift assays have been reported (Figure 7B) (*23*) and require minimal quantities of DNA-conjugated compounds. Alternatively, the retention time of radiolabeled DNA conjugates on affinity resin has been measured in order to rank hit-compounds after selection (Figure 7C) (*23*). In analogy to the hit-validation of polypeptide display technologies, the target protein can also be immobilized on a solid support (e.g., ELISA plate, BIAcore chip), and the DNA-tag can be used for detection (Figure 7D) (*47*). In principle, the reverse setup with an immobilized DNA conjugate and an interacting protein in solution could also be considered (Figure 7E). The use of DNA-encoded hits for validation purposes is particularly convenient in the case of dual-pharmacohore libraries, as the individual sublibrary members are stored in separate tubes and can be reassembled at will. However, the subsequent incorporation of two binding moieties into a single organic molecule requires some synthetic work and, possibly, medicinal chemistry efforts (*24, 29*).

Drug Discovery by DNA-Encoded Chemical Libraries. For some DNA-encoded chemical library formats (Figure 3), only proof-of-principle selection experiments with positive controls have been reported so far (Table 1). Recently, de novo discovery efforts have been reported by GlaxoSmithKline and by our group in collaboration with Philochem (*30, 32, 39*), even though Ensemble Discovery (library format C), Nuevolution, and Vipergen (library format D) are also developing DNA-encoded chemical libraries for pharmaceutical applications.

DNA-encoded libraries have led to the discovery of a general class of portable albumin binders based on 4-(*p*-iodophenyl)-butyric acid structures (*22*), which has been used to improve pharmacokinetic properties of small organic molecules (*48*) and of tumor-targeting antibodies, leading to enhanced tumor uptake (*49*). The compound was also conjugated to contrast agents (e.g., fluorescein or gadolinium complexes for MRI applications), improving their in vivo imaging performance (*22*).

Selections with seven million DNA-encoded compounds (single pharmacophore library with three building blocks) were performed against Aurora A kinase, and novel structures with submicromolar potency were discovered and further characterized (Table 1) (*25*). Additionally, a single pharmacophore library with four building blocks containing 800 million members was panned against p38 MAP kinase, and compounds with 0.25 μM potency were discovered using 454-sequencing (Table 1) (*25*).

DNA-encoded chemical libraries are a novel tool for the discovery of protein−protein interaction inhibitors, as large libraries of compounds can be screened in affinity-based selections. Bcl-xL, a promising target protein for cancer therapy (*50*−*52*), was chosen for library selections using a two building block library of 4000 compounds, and a compound with 0.93 μM affinity was discovered (Table 1). The molecule was able to compete with a Bak-derived BH3 peptide, an antagonist of Bcl-xL function (*39*). We have recently described a selection against tumor necrosis factor (TNF), and a 4000 compound library based on Diels−Alder cycloaddition reactions yielded ligands with micromolar affinity to TNF (Table 1) (*32*). The best compound showed complete inhibition of TNF-mediated killing of L-M fibroblast in vitro (*32*). Recently, we used Diels−Alder cycloaddtions to construct a library containing one million compounds, based on three sets of building blocks which were combinatorially assembled for library synthesis. From this compound collection, submicromolar inhibitors specific to carbonic anhydrase IX, a tumor associated antigen, were isolated.[2]

Furthermore, DNA-encoded chemical libraries were used as a tool to convert known lead structures into novel derivatives with potency in the single-digit nanomolar concentration range (Table 1). The observation that high-affinity kinase inhibitors (*25*) and protease inhibitors (*24*)[1] can efficiently be isolated from DNA-encoded chemical libraries confirms the potential of this technology for the targeting of pharmaceutically relevant

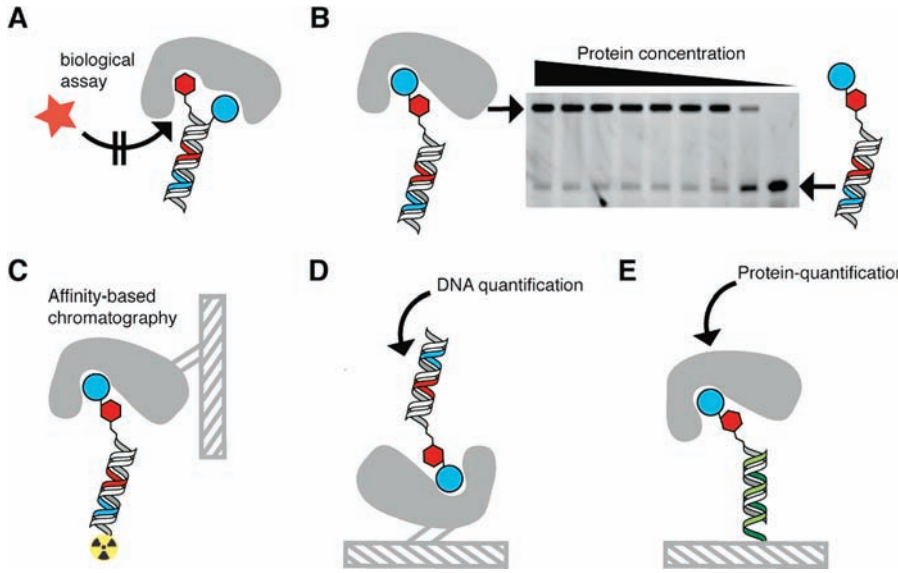


Figure 7. Hit-validation strategies using DNA-conjugated small molecules. (A) Scheme for the measurement of a reporter assay (e.g., inhibition assay, competition assay) with a small molecule conjugated to a DNA tag and a protein of interest. (B) Affinity-measurement of a DNA-conjugated small molecule with a protein in an electromobility shift assay: Complex formation between the protein and the DNA-conjugated ligand leads to band shift in a polyacrylamide gel electrophoresis compared to the free DNA-conjugated ligand. (C) Affinity chromatography of radiolabeled DNA−small molecule conjugates allows ranking of binding structures according to their retention time on the resin during washing cycles. (D) In analogy to the hit-validation of polypeptide display technologies, the target protein can be immobilized on a solid support and the DNA-tag used for quantification (e.g., using PCR, biotin−streptavidin interaction, or surface plasmon resonance measurements). (E) The reverse setup consists of DNA-conjugate immobilization and protein quantification (e.g., using antibodies, biotin−streptavidin interaction, or surface plasmon resonance measurements).

proteins. Such affinity maturation strategies may be an alternative, and potentially more rapid, compared to conventional medicinal chemistry technologies for the modification of lead structures.

DISCUSSION

DNA-encoding facilitates the combinatorial assembly of thousands to millions of small molecules, enabling the identification of ligands after affinity capture on immobilized protein targets. This experimental strategy expands to the realm of organic chemistry selection and amplification technologies which have previously been extensively used for the discovery of binding polypeptides. Several strategies have been implemented for the construction of DNA-encoded chemical libraries, which differ in compound structure (e.g., small compounds, macrocyclic structures, bidentate ligands), library size (i.e., number of building blocks used for library construction), and encoding/decoding technologies (Figure 3). Large collections of small molecule−DNA conjugates have already allowed the de novo discovery of ligands to protein classes of pharmaceutical interest (Table 1).

Affinity-based screening technologies offer an alternative for ligand discovery compared to conventional screening methods using individual molecules and reporter assays (*38*). Since mixtures of DNA-tagged compounds can be panned simultaneously, very large libraries can be synthesized and used for ligand discovery. Indeed, already now DNA-encoded chemistry allows the construction of libraries larger than those available at leading pharmaceutical companies and high-throughput screening facilities. The simple capture of small molecules on a target protein immobilized on a solid support enables (i) the screening of molecules without development of a functional assay, (ii) the investigation of multiple forms of closely related macromolecules (e.g., a protein in its active or inactive form) and (iii) selection procedures using low amounts of target protein (i.e., few milligrams). As no biological or biochemical assays are directly needed in affinity selections, many artifacts commonly observed in high-throughput screening (e.g., compound aggregation, fluorescence absorption or quenching) are eliminated. On the other hand, affinity screening does not deliver a functional readout after selection and requires biochemical or cellular validation of compound hits. The affinity screening of small molecule mixtures (e.g., the separation of molecules capable of protein interaction by gel filtration) has proven practical for drug discovery purposes (*53*), as hydrophobic pockets on target proteins appear to be preferential binding sites for affinity selection strategies. In the absence of DNA tags, however, the conventional affinity-screening of compounds in mixtures is usually limited to a few hundred structures that can be simultaneously analyzed, due to insufficient compound solubility or detection sensitivity (e.g., MS-spectrometric, crystallographic, or NMR detection) (*53*−*55*). The affinity-based selection of DNA-encoded compounds circumvents these limitations, as the DNA code can be PCR-amplified, and selections can be performed at subpicomolar concentrations of individual library members. The relative frequency of DNA codes of individual compounds can be quantified before and after selection using high-throughput sequencing technologies. Selections are best performed on pure proteins. However, it would be conceivable to perform selections on complex mixtures of antigens (e.g., transfected and nontransfected cells), provided that intelligent avenues are found to block nucleolytic activities which may damage DNA and hinder library recovery and decoding.

The number of library members of DNA-encoded single pharmacophore libraries depends mainly on the number of building blocks incorporated during library synthesis, i.e., the number of split-and-pool steps used for library construction. In general, smaller libraries contain compounds of lower molecular weight (Figure 8A), which may feature drug-like properties (e.g., Lipinski rule of 5) (*56*, *57*) and may thus be suitable for the inhibition of intracellular proteins. The use of multiple building blocks enables the construction and screening of libraries of unprecedented size, thus dramatically increasing compound

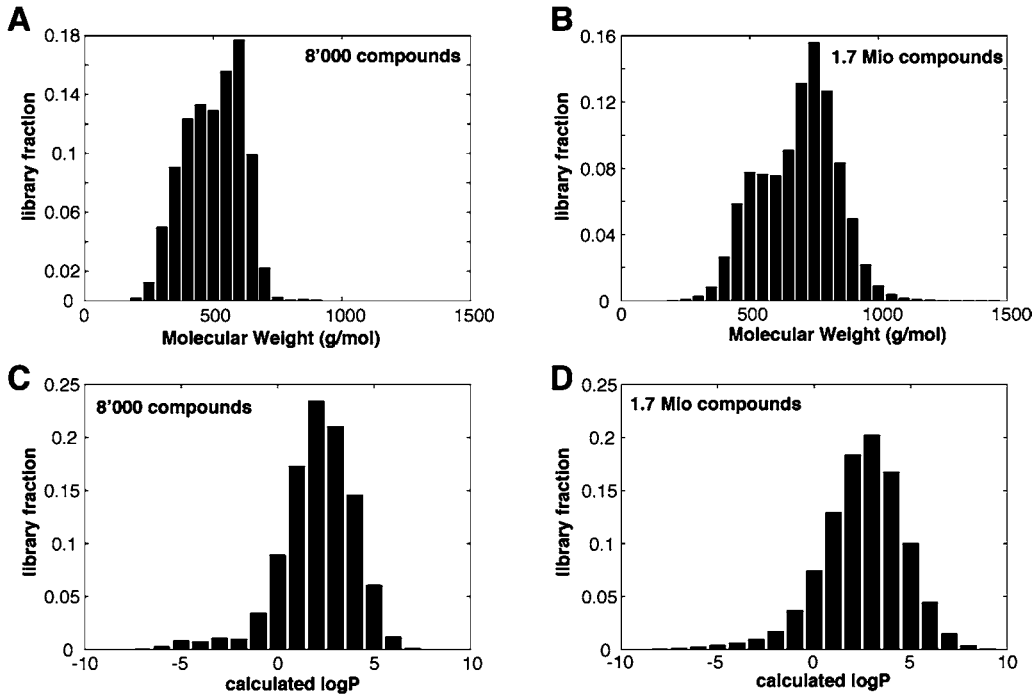


Figure 8. Comparison of the molecular weight and the calculated logP of library compounds in single pharmacophore libraries based on two or three building blocks. 8000 molecules resulting from two DNA-encoded chemical libraries based on a two building block synthesis strategy were assembled "in silico" from their building blocks without DNA tag (i.e., the ethylamide derivatives) (*61*) and their molecular weight (A) and logP (C) was calculated and plotted as histograms. In analogy, compounds from two DNA-encoded chemical libraries based on a three building block synthesis (in total, ca. 1.7 million compounds) were assembled "in silico" and their molecular weight (B) and logP (D) calculated. "Instant JChem" was used for structure database management, search, and prediction (*Instant JChem 5.3.1*, 2010, ChemAxon; http://www.chemaxon.com).

diversity. This library size is gained at the expense of growing molecular weight (MW typically >400, Figure 8B) and decreasing library quality due to incomplete reactions. As an illustration, we calculated the partition coefficient (*C* logP, an important parameter for the estimation of absorption, distribution, metabolism, and excretion properties (ADME)), for all members (in the absence of the DNA tag) of DNA-encoded chemical libraries constructed using two or three sets of building blocks. Similar *C* logP distributions were observed (Figure 8c,d), with most compounds exhibiting a *C* logP < 5, in good agreement with typical solubility and permeability requirements in drug discovery (*57*). Initial promising results have been reported for the targeting of "difficult" protein epitopes (e.g., protein−protein interaction; Bcl-xL, TNF) with such libraries (*32, 39*). Additional research will be needed, in order to reveal whether these challenging structures can be targeted with molecules displaying acceptable pharmaceutical properties (*58*).

In contrast to DNA-encoded single pharmacophore libraries, the dual display of distinct chemical moieties based on the assembly of two complementary oligonucleotides represents a novel route to discover small molecule ligands. A simultaneous binding of two ligands is facilitated by the hybridized DNA strands, which can lead to a chelate effect of the ligand pair during binding interaction (*37*). Dual pharmacophore libraries might therefore be particularly useful for the targeting of proteins with neighboring pockets or clefts. The direct linking of two ligands without the attachment to relatively flexible DNA strands may further allow increase of binding affinity, similar to fragment-based ligand discovery approaches, but requires medicinal chemistry efforts. Large dual pharmacophore libraries can be constructed with high quality (i.e., HPLC purification of single-stranded library members) and their application to drug discovery is part of our current research.

DNA-encoded chemical libraries are particularly attractive for the affinity maturation of known lead structures. Upon introduction of a lead structure during DNA-encoded library synthesis, compounds with single-digit nanomolar potency against target proteins of interest were isolated (Table 1). Furthermore, parallel selection experiments with protein classes of pharmaceutical relevance (e.g., proteases or kinases) may allow one to derive selectivity information from decoding results.

Many different implementations of DNA-encoded chemical libraries for ligand discovery are currently investigated in Academia as well as in the Pharmaceutical Industry. Approaches differ in terms of library design and chemical nature of the displayed molecules, offering complementary strategies for ligand discovery. In summary, while still in its infancy, DNA-encoded chemical library technology has credibly shown its potential to construct and screen very large compound collections and is already well-poised to assist drug discovery and development programs.

ACKNOWLEDGMENT

Financial support from the Gebert-Rüf Foundation (Grant No. GRS-076/06), the Kommission für Technologie und Innovation (KTI Grant No. 8868.1 PFDS-LS), the ETH Zürich and Philochem AG is gratefully acknowledged. We would like to thank Dr. J.-P. Gapian-Bianké, Dr. G. Casi, M. Leimbacher, and M. Steiner for helpful discussions.

LITERATURE CITED

(1) Smith, G. P. (1985) Filamentous fusion phage: novel expression vectors that display cloned antigens on the virion surface. *Science 228*, 1315–7.
(2) McCafferty, J., Griffiths, A. D., Winter, G., and Chiswell, D. J. (1990) Phage antibodies: filamentous phage displaying antibody variable domains. *Nature 348*, 552–4.
(3) Winter, G., Griffiths, A. D., Hawkins, R. E., and Hoogenboom, H. R. (1994) Making antibodies by phage display technology. *Annu. Rev. Immunol. 12*, 433–55.
(4) Drews, J. (2000) Drug discovery: a historical perspective. *Science 287*, 1960–4.

(5) Hajduk, P. J., and Greer, J. (2007) A decade of fragment-based drug design: strategic advances and lessons learned. *Nat. Rev. Drug Discovery 6*, 211–9.
(6) Mayr, L. M., and Bojanic, D. (2009) Novel trends in high-throughput screening. *Curr. Opin. Pharmacol. 9*, 580–8.
(7) Kitchen, D. B., Decornez, H., Furr, J. R., and Bajorath, J. (2004) Docking and scoring in virtual screening for drug discovery: methods and applications. *Nat. Rev. Drug Discovery 3*, 935–49.
(8) Bajorath, J. (2002) Integration of virtual and high-throughput screening. *Nat. Rev. Drug Discovery 1*, 882–94.
(9) Schreiber, S. L. (2000) Target-oriented and diversity-oriented organic synthesis in drug discovery. *Science 287*, 1964–9.
(10) Pellecchia, M., Bertini, I., Cowburn, D., Dalvit, C., Giralt, E., Jahnke, W., James, T. L., Homans, S. W., Kessler, H., Luchinat, C., Meyer, B., Oschkinat, H., Peng, J., Schwalbe, H., and Siegal, G. (2008) Perspectives on NMR in drug discovery: a technique comes of age. *Nat. Rev. Drug Discovery 7*, 738–45.
(11) Rees, D. C., Congreve, M., Murray, C. W., and Carr, R. (2004) Fragment-based lead discovery. *Nat. Rev. Drug Discovery 3*, 660–72.
(12) Mattheakis, L. C., Bhatt, R. R., and Dower, W. J. (1994) An in vitro polysome display system for identifying ligands from very large peptide libraries. *Proc. Natl. Acad. Sci. U.S.A. 91*, 9022–6.
(13) Hanes, J., and Pluckthun, A. (1997) In vitro selection and evolution of functional proteins by using ribosome display. *Proc. Natl. Acad. Sci. U.S.A. 94*, 4937–42.
(14) Heinis, C., Rutherford, T., Freund, S., and Winter, G. (2009) Phage-encoded combinatorial chemical libraries based on bicyclic peptides. *Nat. Chem. Biol. 5*, 502–7.
(15) Roberts, R. W. (1999) Totally in vitro protein selection using mRNA-protein fusions and ribosome display. *Curr. Opin. Chem. Biol. 3*, 268–73.
(16) Boder, E. T., and Wittrup, K. D. (1997) Yeast surface display for screening combinatorial polypeptide libraries. *Nat. Biotechnol. 15*, 553–7.
(17) Bertschinger, J., and Neri, D. (2004) Covalent DNA display as a novel tool for directed evolution of proteins in vitro. *Protein Eng. Des. Sel. 17*, 699–707.
(18) Cull, M. G., Miller, J. F., and Schatz, P. J. (1992) Screening for receptor ligands using large libraries of peptides linked to the C terminus of the lac repressor. *Proc. Natl. Acad. Sci. U.S.A. 89*, 1865–9.
(19) Brenner, S., and Lerner, R. A. (1992) Encoded combinatorial chemistry. *Proc. Natl. Acad. Sci. U.S.A. 89*, 5381–3.
(20) Melkko, S., Dumelin, C. E., Scheuermann, J., and Neri, D. (2007) Lead discovery by DNA-encoded chemical libraries. *Drug Discovery Today 12*, 465–71.
(21) Scheuermann, J., Dumelin, C. E., Melkko, S., and Neri, D. (2006) DNA-encoded chemical libraries. *J. Biotechnol. 126*, 568–81.
(22) Dumelin, C. E., Trussel, S., Buller, F., Trachsel, E., Bootz, F., Zhang, Y., Mannocci, L., Beck, S. C., Drumea-Mirancea, M., Seeliger, M. W., Baltes, C., Muggler, T., Kranz, F., Rudin, M., Melkko, S., Scheuermann, J., and Neri, D. (2008) A portable albumin binder from a DNA-encoded chemical library. *Angew. Chem., Int. Ed. Engl. 47*, 3196–201.
(23) Dumelin, C. E., Scheuermann, J., Melkko, S., and Neri, D. (2006) Selection of streptavidin binders from a DNA-encoded chemical library. *Bioconjugate Chem. 17*, 366–70.
(24) Melkko, S., Zhang, Y., Dumelin, C. E., Scheuermann, J., and Neri, D. (2007) Isolation of high-affinity trypsin inhibitors from a DNA-encoded chemical library. *Angew. Chem., Int. Ed. Engl. 46*, 4671–4.
(25) Clark, M. A., Acharya, R. A., Arico-Muendel, C. C., Belyanskaya, S. L., Benjamin, D. R., Carlson, N. R., Centrella, P. A., Chiu, C. H., Creaser, S. P., Cuozzo, J. W., Davie, C. P., Ding, Y., Franklin, G. J., Franzen, K. D., Gefter, M. L., Hale, S. P., Hansen, N. J., Israel, D. I., Jiang, J., Kavarana, M. J., Kelley, M. S., Kollmann, C. S., Li, F., Lind, K., Mataruse, S., Medeiros, P. F., Messer, J. A., Myers, P., O'Keefe, H., Oliff, M. C., Rise, C. E., Satz, A. L., Skinner, S. R., Svendsen, J. L., Tang, L., van Vloten, K., Wagner, R. W., Yao, G., Zhao, B., and Morgan, B. A. (2009) Design, synthesis and selection of DNA-encoded small-molecule libraries. *Nat. Chem. Biol. 5*, 647–54.
(26) Gartner, Z. J., Tse, B. N., Grubina, R., Doyon, J. B., Snyder, T. M., and Liu, D. R. (2004) DNA-templated organic synthesis and selection of a library of macrocycles. *Science 305*, 1601–5.
(27) Tse, B. N., Snyder, T. M., Shen, Y., and Liu, D. R. (2008) Translation of DNA into a library of 13,000 synthetic small-molecule macrocycles suitable for in vitro selection. *J. Am. Chem. Soc. 130*, 15611–26.
(28) Melkko, S., Scheuermann, J., Dumelin, C. E., and Neri, D. (2004) Encoded self-assembling chemical libraries. *Nat. Biotechnol. 22*, 568–74.
(29) Scheuermann, J., Dumelin, C. E., Melkko, S., Zhang, Y., Mannocci, L., Jaggi, M., Sobek, J., and Neri, D. (2008) DNA-encoded chemical libraries for the discovery of MMP-3 inhibitors. *Bioconjugate Chem. 19*, 778–85.
(30) Mannocci, L., Zhang, Y., Scheuermann, J., Leimbacher, M., De Bellis, G., Rizzi, E., Dumelin, C., Melkko, S., and Neri, D. (2008) High-throughput sequencing allows the identification of binding molecules isolated from DNA-encoded chemical libraries. *Proc. Natl. Acad. Sci. U.S.A. 105*, 17670–5.
(31) Hansen, M. H., Blakskjaer, P., Petersen, L. K., Hansen, T. H., Hojfeldt, J. W., Gothelf, K. V., and Hansen, N. J. (2009) A yoctoliter-scale DNA reactor for small-molecule evolution. *J. Am. Chem. Soc. 131*, 1322–7.
(32) Buller, F., Zhang, Y., Scheuermann, J., Schafer, J., Buhlmann, P., and Neri, D. (2009) Discovery of TNF inhibitors from a DNA-encoded chemical library based on diels-alder cycloaddition. *Chem. Biol. 16*, 1075–86.
(33) Brudno, Y., Birnbaum, M. E., Kleiner, R. E., and Liu, D. R. (2010) An in vitro translation, selection and amplification system for peptide nucleic acids. *Nat. Chem. Biol. 6*, 148–55.
(34) Buller, F., Mannocci, L., Zhang, Y., Dumelin, C. E., Scheuermann, J., and Neri, D. (2008) Design and synthesis of a novel DNA-encoded chemical library using Diels-Alder cycloadditions. *Bioorg. Med. Chem. Lett. 18*, 5926–31.
(35) Halpin, D. R., Lee, J. A., Wrenn, S. J., and Harbury, P. B. (2004) DNA display III. Solid-phase organic synthesis on unprotected DNA. *PLoS Biol. 2*, E175.
(36) Li, X., and Liu, D. R. (2004) DNA-templated organic synthesis: nature's strategy for controlling chemical reactivity applied to synthetic molecules. *Angew. Chem., Int. Ed. Engl. 43*, 4848–70.
(37) Melkko, S., Dumelin, C. E., Scheuermann, J., and Neri, D. (2006) On the magnitude of the chelate effect for the recognition of proteins by pharmacophores scaffolded by self-assembling oligonucleotides. *Chem. Biol. 13*, 225–31.
(38) Makara, G. M., and Athanasopoulos, J. (2005) Improving success rates for lead generation using affinity binding technologies. *Curr. Opin. Biotechnol. 16*, 666–73.
(39) Melkko, S., Mannocci, L., Dumelin, C. E., Villa, A., Sommavilla, R., Zhang, Y., Grutter, M. G., Keller, N., Jermutus, L., Jackson, R. H., Scheuermann, J., and Neri, D. (2010) Isolation of a small-molecule inhibitor of the antiapoptotic protein Bcl-xL from a DNA-encoded chemical library. *ChemMedChem 5*, 584–90.
(40) Hoogenboom, H. R. (2005) Selecting and screening recombinant antibody libraries. *Nat. Biotechnol. 23*, 1105–16.
(41) Margulies, M., Egholm, M., Altman, W. E., Attiya, S., Bader, J. S., Bemben, L. A., Berka, J., Braverman, M. S., Chen, Y. J., Chen, Z., Dewell, S. B., Du, L., Fierro, J. M., Gomes, X. V., Godwin, B. C., He, W., Helgesen, S., Ho, C. H., Irzyk, G. P., Jando, S. C., Alenquer, M. L., Jarvie, T. P., Jirage, K. B., Kim, J. B., Knight, J. R., Lanza, J. R., Leamon, J. H., Lefkowitz, S. M., Lei, M., Li, J., Lohman, K. L., Lu, H., Makhijani, V. B., McDade, K. E., McKenna, M. P., Myers, E. W., Nickerson, E., Nobile, J. R., Plant, R., Puc, B. P., Ronan, M. T., Roth, G. T., Sarkis, G. J., Simons, J. F., Simpson, J. W., Srinivasan, M., Tartaro,

K. R., Tomasz, A., Vogt, K. A., Volkmer, G. A., Wang, S. H., Wang, Y., Weiner, M. P., Yu, P., Begley, R. F., and Rothberg, J. M. (2005) Genome sequencing in microfabricated high-density picolitre reactors. *Nature 437*, 376–80.

(42) Pettersson, E., Lundeberg, J., and Ahmadian, A. (2009) Generations of sequencing technologies. *Genomics 93*, 105–11.

(43) Fox, S., Filichkin, S., and Mockler, T. C. (2009) Applications of ultra-high-throughput sequencing. *Methods Mol. Biol. 553*, 79–108.

(44) Morozova, O., and Marra, M. A. (2008) Applications of next-generation sequencing technologies in functional genomics. *Genomics 92*, 255–64.

(45) Schuster, S. C. (2008) Next-generation sequencing transforms today's biology. *Nat. Methods 5*, 16–8.

(46) Buller, F., Steiner, M., Scheuermann, J., Mannocci, L., Nissen, I., Kohler, M., Beisel, C., and Neri, D. (2010) High-throughput sequencing for the identification of binding molecules from DNA-encoded chemical libraries. *Bioorg. Med. Chem. Lett.* doi: 10.1016/j.bmcl.2010.05.053.

(47) Winzor, D. J. (2004) Determination of binding constants by affinity chromatography. *J. Chromatogr., A 1037*, 351–67.

(48) Ahlskog, J. K., Dumelin, C. E., Trussel, S., Marlind, J., and Neri, D. (2009) In vivo targeting of tumor-associated carbonic anhydrases using acetazolamide derivatives. *Bioorg. Med. Chem. Lett. 19*, 4851–6.

(49) Trussel, S., Dumelin, C., Frey, K., Villa, A., Buller, F., and Neri, D. (2009) New strategy for the extension of the serum half-life of antibody fragments. *Bioconjugate Chem. 20*, 2286–92.

(50) Degterev, A., Lugovskoy, A., Cardone, M., Mulley, B., Wagner, G., Mitchison, T., and Yuan, J. (2001) Identification of small-molecule inhibitors of interaction between the BH3 domain and Bcl-xL. *Nat. Cell Biol. 3*, 173–82.

(51) Tse, C., Shoemaker, A. R., Adickes, J., Anderson, M. G., Chen, J., Jin, S., Johnson, E. F., Marsh, K. C., Mitten, M. J., Nimmer, P., Roberts, L., Tahir, S. K., Xiao, Y., Yang, X., Zhang, H., Fesik, S., Rosenberg, S. H., and Elmore, S. W. (2008) ABT-263: a potent and orally bioavailable Bcl-2 family inhibitor. *Cancer Res. 68*, 3421–8.

(52) Marzo, I., and Naval, J. (2008) Bcl-2 family members as molecular targets in cancer therapy. *Biochem. Pharmacol. 76*, 939–46.

(53) Muckenschnabel, I., Falchetto, R., Mayr, L. M., and Filipuzzi, I. (2004) SpeedScreen: label-free liquid chromatography-mass spectrometry-based high-throughput screening for the discovery of orphan protein ligands. *Anal. Biochem. 324*, 241–9.

(54) Blundell, T. L., Jhoti, H., and Abell, C. (2002) High-throughput crystallography for lead discovery in drug design. *Nat. Rev. Drug Discovery 1*, 45–54.

(55) Shuker, S. B., Hajduk, P. J., Meadows, R. P., and Fesik, S. W. (1996) Discovering high-affinity ligands for proteins: SAR by NMR. *Science 274*, 1531–4.

(56) Lipinski, C. A. (2000) Drug-like properties and the causes of poor solubility and poor permeability. *J. Pharmacol. Toxicol. Methods 44*, 235–49.

(57) Lipinski, C. A., Lombardo, F., Dominy, B. W., and Feeney, P. J. (2001) Experimental and computational approaches to estimate solubility and permeability in drug discovery and development settings. *Adv. Drug Delivery Rev. 46*, 3–26.

(58) Wells, J. A., and McClendon, C. L. (2007) Reaching for high-hanging fruit in drug discovery at protein-protein interfaces. *Nature 450*, 1001–9.

(59) Halpin, D. R., and Harbury, P. B. (2004) DNA display II. Genetic manipulation of combinatorial chemistry libraries for small-molecule evolution. *PLoS Biol. 2*, 1022–30.

(60) Wrenn, S. J., Weisinger, R. M., Halpin, D. R., and Harbury, P. B. (2007) Synthetic ligands discovered by in vitro selection. *J. Am. Chem. Soc. 129*, 13137–43.

(61) Schüller, A., Schneider, G., and Byvatov, E. (2003) SMILIB: Rapid assembly of combinatorial libraries in SMILES notation. *QSAR Comb. Sci. 22*, 719–21.

BC1001483

Design and Assembly of New Nonviral RNAi Delivery Agents by Microwave-Assisted Quaternization (MAQ) of Tertiary Amines

Animesh Ghosh,[†] Koushik Mukherjee,[†] Xinpeng Jiang,[‡] Ying Zhou,[‡] Joshua McCarroll,[||,†] James Qu,[†] Pamela M. Swain,[†] Huricha Baigude,[‡] and Tariq M. Rana*[,†,‡]

Department of Biochemistry and Molecular Pharmacology, University of Massachusetts Medical School, Worcester, Massachusetts 01605, and Program for RNA Biology, Sanford-Burnham Medical Research Institute, 10901 North Torrey Pines Road, La Jolla, California 92037. Received November 2, 2009; Revised Manuscript Received June 17, 2010

RNA interference (RNAi) is a gene-silencing phenomenon whereby double-stranded RNA (dsRNA) triggers the sequence-specific degradation of homologous mRNA. RNAi has been quickly and widely applied to discover gene functions and holds great potential to provide a new class of therapeutic agents. However, new chemistry and delivery approaches are greatly needed to silence disease-causing genes without toxic effects. We reasoned that conjugation of the cholesterol moiety to cationic lipids would enhance RNAi efficiencies and lower the toxic effects of lipid-mediated RNAi delivery. Here, we report the first design and synthesis of new cholesterol-conjugated cationic lipids for RNAi delivery using microwave-assisted quaternization (MAQ) of tertiary amines. This strategy can be employed to develop new classes of nonviral gene delivery agents under safe and fast reaction conditions.

RNA interference (RNAi), a gene-silencing phenomenon whereby double-stranded RNA (dsRNA) triggers the sequence-specific degradation of homologous mRNA (*1*). RNAi has been quickly and widely applied to discover gene functions and holds great potential to provide a new class of therapeutic agents (*2*). During RNAi, long dsRNA is processed by Dicer into short-interfering RNAs (siRNAs) and incorporated into the RNA-induced silencing complex (RISC) (*3*), a multiturnover enzyme complex that cleaves the target mRNA (*4*). Endogenously produced small RNAs, called miRNAs, inhibits translation by binding imperfectly matched sequences in the 3′ untranslated region (3′UTR) of target mRNA (*5, 6*). The RNAi machinery can also be programmed in cells by introducing duplexes of siRNAs (*7, 8*) that are assembled into siRISC containing Dicer, Argonautes, and other proteins (reviewed in ref *4*). Therefore, new siRNA-based therapeutic agents could be designed to lower concentrations of specific disease-causing gene products.

The potential advantage of RNAi in medical applications is that it may provide a cure for diseases that cannot be treated by conventional small molecular medicines. By introducing siRNA to the cell, specific genes can be silenced, resulting in either decreased translational product of the silenced gene or increased protein levels of a gene that is downregulated by the silenced sequence. However, *in vivo* delivery of siRNA has been a challenge due to the instability of siRNA in blood (in the case of systemic delivery), its relatively large molecular size, and its highly negative charge. Recent advances in understanding the rules for chemically modifying siRNA sequences without compromising their gene-silencing efficiency (*9*−*11*) have allowed the design and synthesis of therapeutically effective siRNA molecules that can silence target genes *in vivo* (*12, 13*). Furthermore, siRNAs have recently been delivered *in vivo* to successfully inhibit various gene functions. This delivery has been facilitated by conjugating cholesterol to siRNA (*13*) or to oligonucleotide inhibitors of miRNA (*14*), by forming stable nucleic acid−lipid particles (SNALP) of siRNA (*12, 15*), and by assembling lipid-siRNA complexes (*16, 17*). In addition, a protamine−antibody fusion protein has been used to deliver siRNAs to HIV-infected cells (*18*). Recently, the design and creation of interfering nanoparticles (iNOPs) as new systemic gene-silencing agents has been reported (*19*). iNOPs have two subunits: (i) a well-defined functionalized lipid nanoparticle as a delivery agent and (ii) a chemically modified siRNA for sustained silencing *in vivo*. iNOPs containing only 1−5 mg kg^{-1} siRNA were injected into mice, resulting in the following: an endogenous gene for apolipoprotein B (apoB) was silenced in liver, plasma levels of apoB decreased, and total plasma cholesterol was lowered. iNOP treatment was nontoxic and did not induce an immune response (*19*).

Despite this progress, new chemistry and delivery approaches are greatly needed to silence disease-causing genes without toxic effects. We reasoned that conjugation of the cholesterol moiety to cationic lipids would enhance RNAi efficiencies and lower the toxic effects of lipid-mediated RNAi delivery. Cationic vectors have been extensively employed to deliver nucleic acids in cells and in animals (reviewed in ref *20*). Chemistry of quaternization of cationic lipids is quite challenging and requires chemically harsh and potentially hazardous conditions (*21, 22*). Microwave-assisted organic synthesis reactions have been an important tool in combinatorial approaches to generate a variety of compounds (*23, 24*). Substantial reductions in reaction times and improved yields can be achieved for a wide selection of organic reactions (*25, 26*). Here, we report the design and synthesis of new cholesterol-conjugated cationic lipids for RNAi delivery using microwave-assisted quaternization (MAQ) of tertiary amines. This strategy can be employed to develop new classes of nonviral gene delivery agents under safe and fast reaction conditions.

Lipids **4**−**6** were designed to improve RNAi delivery and to reduce related toxic effects on cells (Figure 1). The key difference in molecular structure is that one lipid chain of the commercially available transfection reagents (**1**−**3**) has been replaced by cholesteryl hemisuccinate moiety in lipids **4**−**6**. Scheme 1 outlines the synthetic procedure for lipids **1** and **2**.

* To whom correspondence should be addressed: trana@sanfordburnham.org.

[†] University of Massachusetts Medical School.

[‡] Sanford-Burnham Medical Research Institute.

[||] Present address: Children's Cancer Institute Australia for Medical Research, Randwick, NSW 2031, Australia.

10.1021/bc900482r © 2010 American Chemical Society
Published on Web 08/19/2010

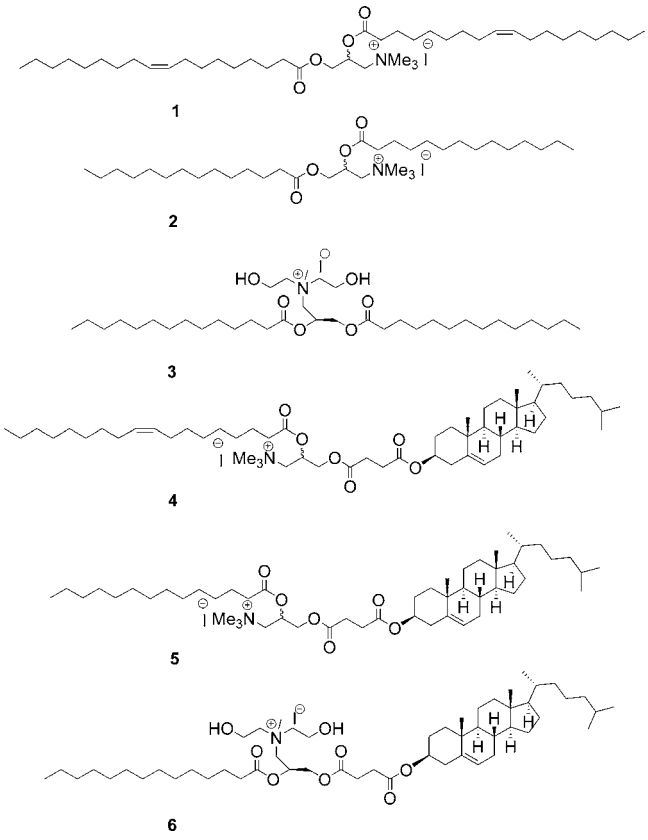
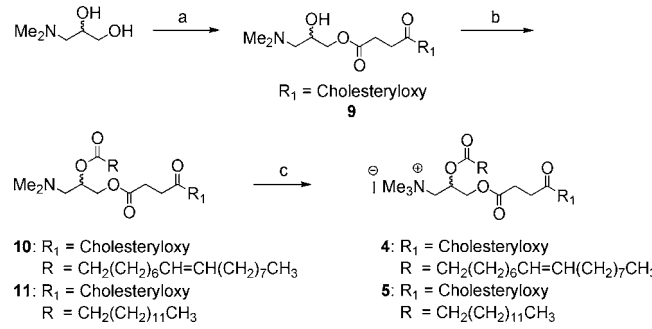


Figure 1. Structures of commercially available cationic lipids (**1**−**3**) and cholesterol-conjugated cationic lipids (**4**−**6**) are shown. Commonly used names of commercially available lipids are as follows: 1, DOTAP; 2, DMTAP; and 3, Transfast. Cholesterol conjugated lipids are denoted as the following: **4**, Dotap_chol; **5**, Dmtap_chol; and **6**, Transfast_chol.

The hydroxyl groups of the starting material 3-(dimethylamino)-1,2-propanediol were acylated with RCOCl using pyridine as base following a reported procedure (*21*). The mixture of intermediate tertiary amine (**7** or **8**) and MeI in $CHCl_3$-DMSO (1:1) solution was subjected to 150 W microwave irradiation at 70 °C for 1 h to give the target lipids **1** and **2** in very high yield. Microwave-assisted quaternization of tertiary amines required the lesser quantity of reagent (MeI) and shortened the reaction period giving very high yield. To the best of our knowledge from the literature, this is the first report on microwave-irradiated quaternization (MAQ) of tertiary amine for the synthesis of cationic lipids. The synthesis strategy for cholesterol-based cationic lipids is shown in Scheme 2. The primary hydroxyl group of the starting material 3-(dimethylamino)-1,2-propanediol was selectively coupled with cholesteryl hemisuccinate using DCC as coupling reagent to give **9** in 34% yield. The free hydroxyl group of the intermediate **9** was acylated with RCOCl using pyridine as base to give tertiary amine intermediates **10** and **11**. The tertiary amine intermediates thus obtained were subjected to microwave-assisted quaternization as described above to give

Scheme 2. Synthesis of Lipids 4 and 5



Reagents and conditions: (a) cholesteryl hemisuccinate, DCC, 0 °C, 5 min, then rt, 6 h, 34%; (b) RCOCl, pyridine, DMAP, CH_2Cl_2, 6 h, 87%; (c) microwave irradiation, 150 W, 70 °C, $CHCl_3$−DMSO (1:1), 1 h, 90%.

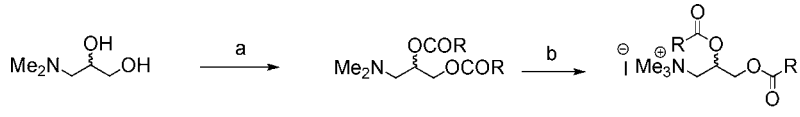
the cholesterol-based cationic lipids **4** and **5** as a diastereomeric mixture in very high yield.

The synthesis of lipid **3** was carried out following the reported procedure (*22*), except the microwave-assisted quaternization of tertiary amine in the final step (Scheme 3). The synthesis strategy for lipid **6** is shown in Scheme 4. The free hydroxyl group of the intermediate **13** was acylated with myristoyl chloride using Et_3N as base in the presence of a catalytic amount of DMAP to give **17**. Trityl deprotection of **17** was achieved by treating with 85% HCO_2H at room temperature to give the intermediate **18**. The hydroxyl group of **18** was coupled with the free carboxyl group of cholesteryl hemisuccinate in DMF solution using DCC as coupling agent to give **19** (79%), which was next treated with $Bu_4NF \cdot 3H_2O$ to give the desilylated intermediate **20**. Quaternization of the tertiary amine **20** was performed under 150 W microwave irradiation at 80 °C for 3.5 h to give the cholesterol-based cationic lipid **6** in 33% yield.

To determine whether the new lipids (*4*−*6*), Dotap_cholesterol, Dmtap_cholesterol or Transfast_cholesterol, could deliver active siRNA to its target and silence apo B mRNA in FL83B cells, we complexed siRNA using these lipids and analyzed gene silencing in cells by quantitative RT-PCR. Unmodified apo B siRNA complexed to the above lipids was able to silence apo B mRNA expression (∼70%) for both Dotap_cholesterol and Dmtap_cholesterol, while Transfast_cholesterol was able to silence Apo B mRNA levels by 80% in FL83B cells when compared to controls (Figure 2A-C). Notably, the level of apo B mRNA silencing using Dotap_chol, Dmtap_chol, or Transfast_chol as an RNA transporter was similar to that of cells when siRNA was delivered by commonly used transfection agents such as Lipofectamine 2000 (*19*).

We next analyzed the toxicity profiles of these lipid−RNA complexes. We confirmed that the observed reduction in apo B mRNA levels in FL83B cells was not due to cell toxicity of the lipids complexed to the siRNA by using a modified MTS

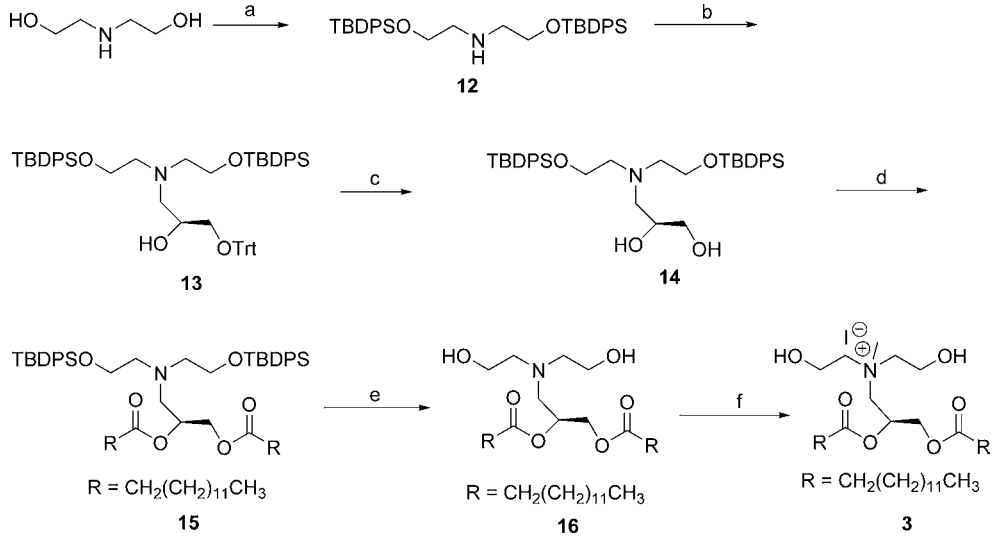
Scheme 1. Synthesis of Lipids 1 and 2



7: R = $CH_2(CH_2)_6CH{=}CH(CH_2)_7CH_3$ **1**: R = $CH_2(CH_2)_6CH{=}CH(CH_2)_7CH_3$
8: R = $CH_2(CH_2)_{11}CH_3$ **2**: R = $CH_2(CH_2)_{11}CH_3$

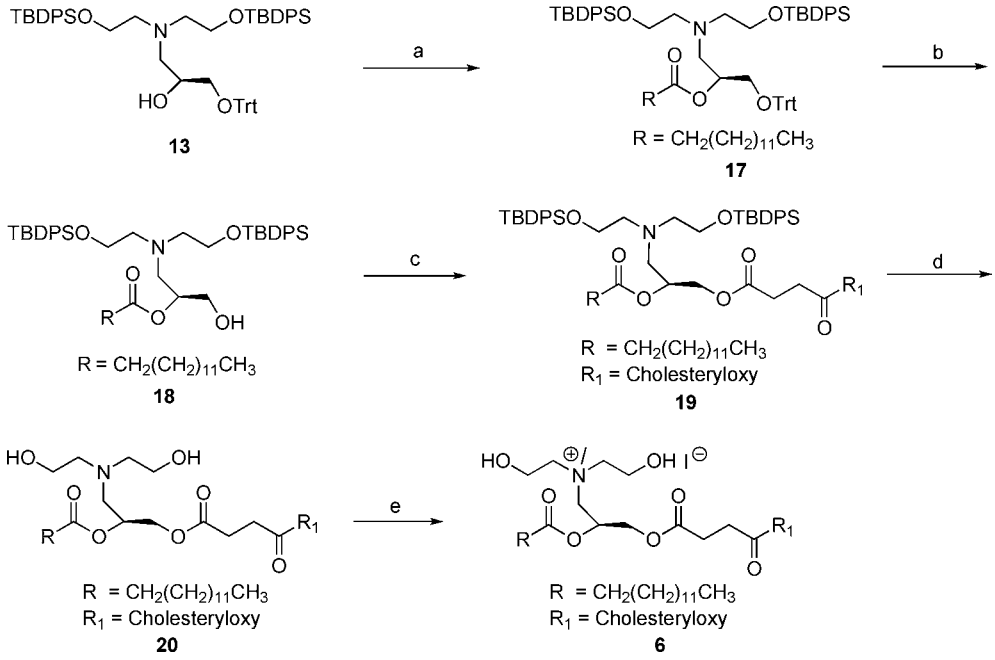
Reagents and conditions: (a) RCOCl, pyridine, DMAP, CH_2Cl_2, 6 h; (b) microwave irradiation, 150 W, 70 °C, 1 h, 90%.

Scheme 3. Synthesis of Lipid 3



Reagents: (a) Et_3N, DMAP, TBDPSCl, CH_2Cl_2, 0 °C to rt, 20 h, 90%; (b) $LiClO_4$, (*R*)-(+)-Trityl glycidyl ether, EtOH, 28 h, 65 °C, 93%; (c) 85% HCO_2H, Et_2O, rt, 20 h, 67%; (d) Et_3N, DMAP, $CH_3(CH_2)_{12}COCl$, 0 °C to rt, 5 h, 47%; (e) $Bu_4NF \cdot 3H_2O$, THF, 5.5 h, 0 °C to rt, 72%; (f) MeI, microwave irradiation (150 W, 80 °C, 3.5 h), 81%.

Scheme 4. Synthesis of Lipid 6



Reagents: (a) Et_3N, DMAP, $CH_3(CH_2)_{12}COCl$, CH_2Cl_2, 0 °C to rt, 24 h, 81%; (b) 85% HCO_2H, Et_2O, 20 h, rt, 64%; (c) cholesteryl hemisuccinate, DCC, DMF, rt, 6 h, 79%; (d) $Bu_4NF \cdot 3H_2O$, THF, 0 °C to rt, overnight, 69%; (e) MeI, microwave irradiation (150 W, 80 °C, 3.5 h), 33%.

cell toxicity assay (Figure 2D-F). Taken together, these results show that new cholesterol-conjugated lipids are nontoxic and can deliver siRNA for efficient gene silencing.

EXPERIMENTAL PROCEDURES

General Methods. ^1H NMR and ^{13}C NMR spectra were recorded at 400 and 100 MHz, respectively. ESI-MS were recorded with Microwmass ZQ. All the reagents were purchased from commercial sources. When required, reactions were carried out under argon atmosphere with standard techniques for the exclusion of air and moisture. All solvents were dried before use. TLC was performed using fluorescent $60F_{254}$ coated plates.

(±)-N,N-Dimethyl-N-[2,3-bis(9-(Z)-octadecanoyloxy)-propyl]-amine (7). To a solution of 3-(dimethylamino)-1,2-propandiol (0.2 mL, 1.68 mmol), pyridine (0.55 mL, 6.72 mmol), and DMAP (20 mg, 0.17 mmol), in CH_2Cl_2 (10 mL) at 0 °C was added dropwise oleoyl chloride (1.38 mL, 4.2 mmol). The reaction mixture was allowed to warm up slowly to room temperature. It was stirred for 6 h at room temperature, diluted with CH_2Cl_2 (50 mL), washed sequentially with 5% aqueous sodium bicarbonate (15 mL), water (15 mL), and saturated aqueous NaCl (15 mL). The organic layer was dried (Na_2SO_4), filtered, and concentrated *in vacuo*. Purification by column chromatography (silica gel, elution with 0.2% MeOH in $CHCl_3$) furnished compound **7** (0.782 g, 72%) as an oily liquid.^1H NMR ($CDCl_3$): δ 5.47−5.32 (m, 4H), 5.28−5.18 (m, 1H), 4.40 (dd, J = 11.8, 3.0 Hz, 1H), 4.13 (dd, J = 12.0, 6.8 Hz, 1H), 2.56−2.42 (m, 2H), 2.35 (dt, J = 7.6, 2.8 Hz, 4H), 2.30 (s, 6H), 2.12−1.97 (m, 8H), 1.71−1.58 (m, 4H), 1.44−1.23 (m, 40H), 0.92 (t, J = 7.0 Hz, 6H).

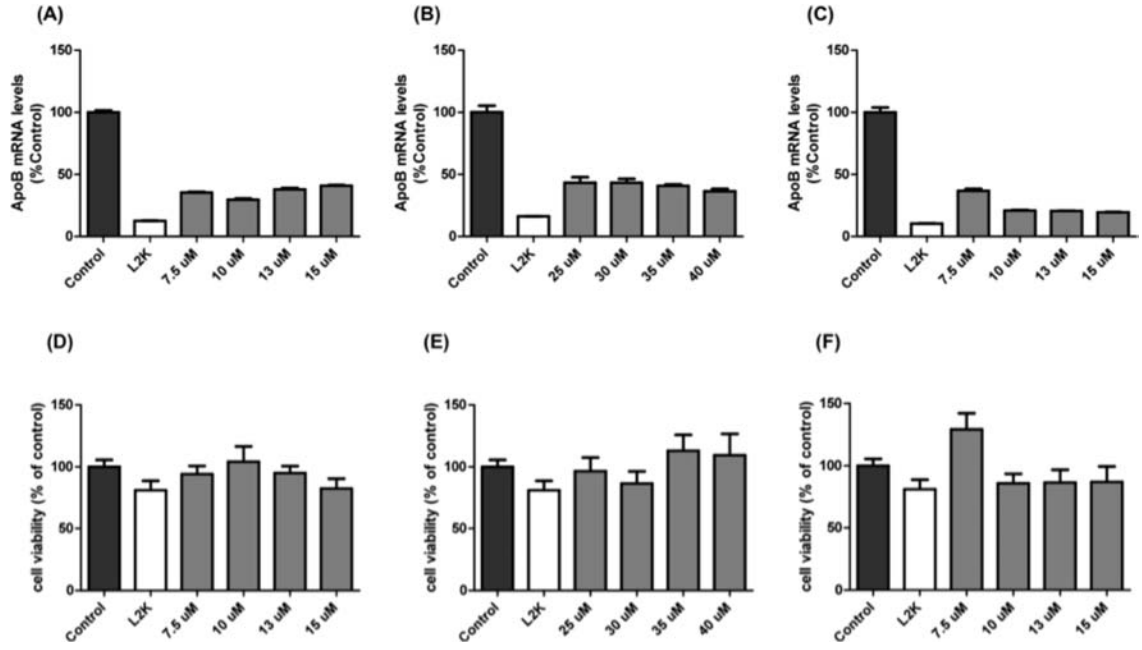


Figure 2. *In vitro* silencing of apo B by RNAi delivered by cholesterol modified lipids. Representative graphs show apo B mRNA levels in FL83B cells treated with different concentrations of lipids (A, Dotap_chol; B, Dmtap_chol; C, Transfast_chol) and corresponding cell viability after 24 h of siRNA−lipid treatments (D, Dotap_chol; E, Dmtap_chol; F, Transfast_chol). Apo B mRNA levels are expressed as a percentage of control transfection. Each value was derived from the mean ± SEM of duplicate cultures and is representative of at least two separate experiments. Cell toxicity levels are expressed as a percentage of control transfection. Each value was derived from the mean ± SEM of duplicate cultures and is representative of at least two separate experiments.

*(±)-N,N-Dimethyl-N-[2,3-bis(tetradecanoyloxy)-propyl]amine (**8**).* ^{1}H NMR ($CDCl_3$): δ 5.24−5.15 (m, 1H), 4.35 (dd, J = 12.0, 3.2 Hz, 1H), 4.08 (dd, J = 11.6, 6.0 Hz, 1H), 2.52−2.38 (m, 2H), 2.30 (dt, J = 7.2, 3.6 Hz, 4H), 2.61 (s, 6H), 1.67−1.53 (m, 4H), 1.36−1.17 (m, 40H), 0.87 (t, J = 6.4 Hz, 6H).

*(±)-N,N,N-Trimethyl-N-[2,3-bis(9(Z)-octadecanoyloxy)-propyl]-ammonium Iodide (**1**).* A solution of **7** (190 mg, 0.29 mmol) and methyl iodide (0.022 mL, 0.35 mmol) in $CHCl_3$ (1 mL) and DMSO (1 mL) was taken in a 10 mL microwave vial covered with a plastic cap. The reaction mixture was subjected to 150 W microwave irradiation at 70 °C for 1 h. The reaction mixture was concentrated to dryness under high vacuum. Purification of this crude product by column chromatography (silica gel, elution with 8% MeOH in $CHCl_3$) furnished **1** (208 mg, 90%) as a white solid.^{1}H NMR ($CDCl_3$): δ 5.64−5.56 (m, 1H), 5.39−5.28 (m, 4H), 4.58−4.47 (m, 2H), 4.14 (dd, J = 12.0, 5.6 Hz, 1H), 3.86 (dd, J = 14.4, 8.8 Hz, 1H), 3.53 (s, 9H), 2.35 (t, J = 2.6 Hz, 4H), 2.07−1.92 (m, 8H), 1.69−1.53 (m, 4H), 1.39−1.18 (m, 40H), 0.87 (t, J = 7.2 Hz, 6H); ^{13}C NMR ($CDCl_3$) δ 173.42, 172.96, 130.30, 130.26, 129.91, 128.85, 66.44, 65.88, 63.08, 55.02, 34.41, 34.19, 32.13, 29.99, 29.97, 29.93, 29.76, 29.55, 29.48, 29.40, 29.39, 29.33, 29.31, 29.29, 27.45, 27.42, 27.39, 24.97, 24.84, 22.91, 14.36; MS (ESI) *m/z* calculated: 663.1 $[M+H]^+$, found: 663.3 $[M+H]^+$.

*(±)-N,N,N-Trimethyl-N-[2,3-bis(tetradecanoyloxy)-propyl]ammonium Iodide (**2**).* ^{1}H NMR ($CDCl_3$): δ 5.59−5.51 (m, 1H), 4.45 (dd, J = 12.0, 3.6 Hz, 1H), 4.18 (d, J = 14.0 Hz, 1H), 4.07 (dd, J = 12.0, 5.6 Hz, 1H), 3.76 (dd, J = 14.8, 8.8 Hz, 1H) 3.35 (s, 9H), 2.31 (dt, J = 13.6, 2.0 Hz, 4H), 1.63−1.51 (m, 4H), 1.33−1.14 (m, 40H), 0.84 (t, J = 7.2 Hz, 6H); ^{13}C NMR ($CDCl_3$) δ 173.63, 173.11, 66.54, 65.83, 63.21, 54.84, 34.35, 34.10, 32.10, 29.86, 29.83, 29.80, 29.68, 29.64, 29.54, 29.49, 29.42, 29.29, 29.26, 24.91, 24.80, 22.87, 14.27; MS (ESI) *m/z* calculated: 554.9 $[M+H]^+$, found: 555.1 $[M+H]^+$.

*N,N-Dimethyl-N-[2-hydroxy,3-succinyloxy(4-cholesteryloxy)-propyl]amine (**9**).* To an ice-cooled solution of cholesteryl hemisuccinate (4.09 g, 8.42 mmol) in DMF (35 mL), 3-(dimethylamino)-1,2-propandiol (1.0 mL, 8.42 mmol) followed by *N,N′*-dicyclohexylcarbodiimide (3.47 g, 16.84 mmol) was added. After 5 min, the ice bath was removed and the reaction mixture was stirred for an additional 6 h at room temperature. The resulting precipitation of dicyclohexylurea was removed by filtration. The filtrate was transferred to a 100 mL round-bottom flask and concentrated to dryness under vacuum. The pasty mass was dissolved in $CHCl_3$ (200 mL) and washed with H_2O (30 mL), saturated aqueous NaCl (30 mL), dried (Na_2SO_4), and concentrated *in vacuo*. Purification by column chromatography (silica gel, elution with 5% MeOH in $CHCl_3$) furnished **9** (1.68 g, 34%) as wax. ^{1}H NMR ($CDCl_3$): δ 5.36 (d, J = 4.0 Hz, 1H), 4.67−4.56 (m, 1H), 4.19 (dd, J = 11.6, 3.6 Hz, 1H), 4.04 (dd, J = 11.6, 6.0 Hz, 1H), 3.97−3.89 (m, 1H), 2.70−2.56 (m, 4H), 2.44 (t, J = 10.0 Hz, 1H), 2.36−2.23 (m, 9H), 2.05−1.75 (m, 5H), 1.66−0.80 (m, 33H), 0.67 (s, 3H).

*N,N-Dimethyl-N-[2-(9(Z)-octadecanoyloxy),3-succinyloxy(4-cholesteryloxy)-propyl]amine (**10**).* To a solution of **9** (178 mg, 0.3 mmol), pyridine (0.036 mL, 0.45 mmol), and DMAP (6 mg, 0.04 mmol) in CH_2Cl_2 (4 mL) at 0 °C was added dropwise oleoyl chloride (0.12 mL, 0.36 mmol). The reaction mixture was allowed to warm up slowly to room temperature. It was stirred for 6 h at room temperature, diluted with CH_2Cl_2 (20 mL), and washed sequentially with 5% aqueous sodium bicarbonate (10 mL), water (10 mL), and saturated aqueous NaCl (10 mL). The organic layer was dried (Na_2SO_4), filtered, and concentrated *in vacuo*. Purification by column chromatography (silica gel, elution with 0.2% MeOH in $CHCl_3$) furnished **10** (0.222 g, 87%) as a wax. ^{1}H NMR ($CDCl_3$): δ 5.39−5.28 (m, 3H), 5.23−5.14 (m, 1H), 4.66−4.55 (m, 1H), 4.40−4.34 (m, 1H), 4.11 (dd, J = 12.0, 6.4 Hz, 1H), 2.66−2.54 (m, 4H), 2.51−2.38 (m, 2H), 2.35−2.27 (m, 4H), 2.25 (s, 6H), 2.07−1.76 (m, 9H), 1.69−0.80 (m, 58H), 0.67 (s, 3H).

*N,N-Dimethyl-N-[2-(tetradecanoyloxy),3-succinyloxy(4-cholesteryloxy)-propyl]amine (**11**).* ^{1}H NMR ($CDCl_3$): δ 5.36 (d, J = 4.8 Hz, 1H), 5.22−5.14 (m, 1H), 4.66−4.56 (m, 1H), 4.37 (dd, J = 12.0, 3.2 Hz, 1H), 4.11 (dd, J = 11.6, 6.0 Hz, 1H),

2.67−2.54 (m, 4H), 2.43(dt, J = 14.0, 7.2 Hz, 2H), 2.35−2.27 (m, 4H), 2.25 (s, 6H), 2.03−1.90 (m, 2H), 1.89−1.66 (m, 3H), 1.68−0.82 (m, 58H), 0.67 (s, 3H).

*N,N,N-Trimethyl-N-[2-(9(Z)-octadecanoyloxy),3-succinyloxy(4-cholesteryloxy)-propyl]ammonium Iodide (**4**).* A solution of **10** (175 mg, 0.2 mmol) and methyl iodide (0.0152 mL, 0.246 mmol) in $CHCl_3$ (1 mL) and DMSO (1 mL) was taken in a 10 mL microwave vial covered with a plastic cap. The reaction mixture was subjected to 150 W microwave irradiation at 70 °C for 1 h. The reaction mixture was concentrated to dryness under high vacuum. Purification of this crude product by column chromatography (silica gel, elution with 8% MeOH in $CHCl_3$) furnished **4** (183 mg, 90%) as a yellowish solid. ^{1}H NMR ($CDCl_3$): δ 5.62−5.54 (m, 1H), 5.39−5.27 (m, 3H), 4.60−4.52 (m, 1H), 4.48 (dd, J = 12.0, 4.0 Hz, 1H), 4.39 (d, J = 13.2 Hz, 1H), 4.22 (dd, J = 12.0, 4.4 Hz, 1H), 3.96 (dd, J = 14.4, 9.2 Hz, 1H), 3.53 (s, 9H), 2.71−2.57 (m, 4H), 2.36 (dt, J = 7.2, 3.6 Hz, 2H), 2.33−2.22 (m, 2H), 2.08−1.75 (m, 9H), 1.66−0.82 (m, 58H), 0.66 (s, 3H); ^{13}C NMR ($CDCl_3$) δ 172.89, 172.23, 172.13, 139.68, 130.28, 129.88, 123.11, 74.87, 66.17, 65.89, 62.77, 56.87, 56.34, 54.95, 50.13, 42.52, 39.90, 39.72, 38.32, 38.29, 37.12, 36.81, 36.39, 36.02, 34.38, 32.13, 32.11, 32.05, 29.99, 29.96, 29.77, 29.55, 29.42, 29.36, 29.30, 28.45, 28.23, 27.98, 27.46, 27.42, 24.80, 24.50, 24.07, 23.05, 22.91, 22.78, 21.24, 19.52, 18.93, 14.37, 12.07; MS (ESI) *m/z* calculated: 867.4 $[M+H]^+$, found: 867.6 $[M+H]^+$.

*N,N,N-Trimethyl-N-[2-(tetradecanoyloxy),3-succinyloxy(4-cholesteryloxy)-propyl]ammonium Iodide (**5**).* ^{1}H NMR ($CDCl_3$): δ 5.62−5.52 (m, 1H), 5.37−5.29 (m, 1H), 4.60−4.50 (m, 1H), 4.48 (dd, J = 12.4, 4.4 Hz, 1H), 4.41 (d, J = 13.6 Hz, 1H), 4.21 (dd, J = 12.4, 4.8 Hz, 1H), 3.96 (dd, J = 16.0, 9.2 Hz, 1H), 3.52 (s, 9H), 2.70−2.56 (m, 4H), 2.35 (dt, J = 7.6, 3.6 Hz, 2H), 2.32−2.22 (m, 2H), 2.04−1.75 (m, 5H), 1.64−0.78 (m, 58H), 0.65 (s, 3H); ^{13}C NMR ($CDCl_3$) δ 172.93, 172.22, 172.07, 139.69, 123.07, 74.82, 66.12, 65.92, 62.89, 56.87, 56.34, 54.96, 50.14, 42.51, 39.90, 39.71, 38.30, 38.28, 37.12, 36.80, 36.39, 36.01, 34.40, 32.16, 32.09, 32.04, 29.96, 29.93, 29.91, 29.76, 29.61, 29.53, 29.35, 29.28, 28.45, 28.23, 27.98, 27.96, 24.81, 24.50, 24.07, 23.05, 22.93, 22.78, 21.23, 19.52, 18.92, 14.37, 12.06; MS (ESI) *m/z* calculated: 813.3 $[M+H]^+$, found: 813.5 $[M+H]^+$.

*N,N-[Bis(2-tert-butyldiphenylsilyloxyethyl)]amine (**12**).* To a solution of diethanol amine (1.0 mL, 10.42 mmol), Et_3N (3.56 mL, 25.52 mmol), and DMAP (127 mg, 1.04 mmol) in CH_2Cl_2 at 0 °C was added *tert*-butyldiphenylchlorosilane (6.75 mL, 26.05 mmol) dropwise. The reaction mixture was allowed to warm to room temperature slowly. It was stirred for 20 h at room temperature, diluted with CH_2Cl_2 (50 mL), and washed sequentially with 5% $NaHCO_3$ (30 mL), water (30 mL), and saturated aqueous NaCl (30 mL). The organic layer was dried (Na_2SO_4), filtered, and concentrated *in vacuo*. Purification by column chromatography (silica gel, elution with 2% methanol in $CHCl_3$) furnished **12** (5.45 g, 90%) as an oily liquid. ^{1}H NMR ($CDCl_3$): δ 7.74−7.67 (m, 8H), 7.48−7.34 (m, 12H), 3.81 (t, J = 5.2 Hz, 4H), 2.81 (t, J = 5.2 Hz, 4H), 1.065 (s, 18H).

*3-[N,N-Bis(2-tert-butyldiphenylsilyloxyethyl)amino]-1-(triphenylmethoxy)-2-propanol (**13**).* To a solution of **12** (4.52 g, 7.78 mmol) and lithium perchlorate (2.27 g, 21.34 mmol) in ethanol (30 mL) was added (*R*)-(+)-trityl glycidyl ether (2.95 g, 9.33 mmol) at room temperature. The reaction mixture was stirred at 65 °C for 28 h, cooled to room temperature, diluted with CH_2Cl_2 (100 mL), and washed with 5% $NaHCO_3$ (40 mL) followed by saturated aqueous NaCl (40 mL). The organic layer was dried (Na_2SO_4), filtered, and concentrated *in vacuo*. Purification by column chromatography (silica gel, elution with 0.5% methanol in $CHCl_3$) furnished **13** (6.48 g, 93%) as an oily liquid. ^{1}H NMR ($CDCl_3$): δ 7.64−7.12 (m, 35H), 3.83−3.62 (m, 5H), 3.16−3.08 (m, 2H), 3.01 (dd, J = 10.0, 5.2 Hz, 2H), 2.90−2.78 (m, 4H), 0.98 (s, 18H).

*3-[N,N-Bis(2-tert-butyldiphenylsilyloxyethyl)amino]-1,2-propanol (**14**).* To a solution of **13** (2.0 g, 2.23 mmol) in diethyl ether (3 mL) was added 85% formic acid (8.2 mL) at room temperature. The reaction mixture was stirred for 20 h and cooled at 0 °C, and solid $NaHCO_3$ was added in portions to neutralize the acidic solution. It was then diluted with diethyl ether (80 mL) and washed with water (25 mL), followed by saturated aqueous NaCl (25 mL). The organic layer was dried (Na_2SO_4), filtered, and concentrated *in vacuo*. Purification by column chromatography (silica gel, elution with 4% MeOH in $CHCl_3$) furnished **14** (0.97 g, 67%) as an oily liquid.^{1}H NMR ($CDCl_3$): δ 7.70−7.61 (m, 8H), 7.49−7.31 (m, 12H), 3.73−3.55 (m, 6H), 4.397 (dd, J = 11.6, 4.4 Hz, 1H), 2.78−2.54 (m, 5H), 2.57 (d, J = 6.8 Hz, 1H) 1.02 (s, 18H).

*3-[N,N-Bis(2-tert-butyldiphenylsilyloxyethyl)amino]-1,2-bis(tetradecanoyloxy)propane (**15**).* To a solution of **14** (0.65 g, 0.99 mmol), Et_3N (0.35 mL, 2.48 mmol), and DMAP (12 mg, 0.1 mmol) in CH_2Cl_2 (5 mL) at 0 °C was added dropwise myristoyl chloride (0.65 mL, 2.43 mmol). The reaction mixture was allowed to warm up slowly to room temperature. It was stirred for 5 h at room temperature, diluted with CH_2Cl_2 (50 mL), and washed sequentially with 5% aqueous sodium bicarbonate (15 mL), water (15 mL), and saturated aqueous NaCl (15 mL). The organic layer was dried (Na_2SO_4), filtered, and concentrated *in vacuo*. Purification by column chromatography (silica gel, elution with 2.5% EtOAc in hexane) furnished **15** (0.50 g, 47%) as an oily liquid. ^{1}H NMR ($CDCl_3$): δ 7.67−7.23 (m, 20H), 5.04−4.95 (m, 1H), 4.25 (dd, J = 12.0, 2.8 Hz, 1H), 4.03 (dd, J = 11.6, 5.6 Hz, 1H), 3.61 (t, J = 8.0 Hz, 4H), 2.75−2.58 (m, 6H), 2.24−2.33 (m, 4H), 1.60−1.50 (m, 4H), 1.35−1.18 (m, 40H), 1.01 (s, 18H), 0.87 (t, J = 6.4 Hz, 6H).

*3-[N,N-Bis(2-hydroxyethyl)amino]-1,2-bis(tetradecanoyloxy)propane (**16**).* Tetrabutylammonium fluoride trihydrate (0.50 g, 1.60 mmol) was added to an ice-cooled solution of **15** (0.43 g, 0.40 mmol) in THF (3 mL) under N_2 atmosphere. The reaction mixture was allowed to warm up to room temperature. It was stirred overnight at room temperature, diluted with CH_2Cl_2 (30 mL), and washed sequentially with 5% $NaHCO_3$ (10 mL), water (10 mL), and saturated aqueous NaCl (10 mL). The organic layer was dried (Na_2SO_4), filtered, and concentrated *in vacuo*. Purification by column chromatography (silica gel, elution with 2% methanol in $CHCl_3$) furnished **16** (172 mg, 72%) as a wax. ^{1}H NMR ($CDCl_3$): δ 5.24−5.14 (m, 1H), 4.35 (dd, J = 12.0, 3.2 Hz, 1H), 4.10 (dd, J = 12.4, 6.4 Hz, 1H), 3.60 (t, J = 5.2 Hz, 4H), 2.77−2.66 (m, 6H), 2.38−2.26 (m, 4H), 1.66−1.54 (m, 4H), 1.36−1.18 (m, 40H), 0.87 (t, J = 6.0 Hz, 6H).

*N,N-[Bis(2-hydroxyethyl)]-N-methyl-N[2,3-bis(tetradecanoyloxy)-propyl]ammonium Iodide (**3**).* A mixture of **16** (122 mg, 0.2 mmol) and methyl iodide (1.5 mL) was taken in a 10 mL microwave vial covered with a plastic cap. The reaction mixture was then subjected to 150 W microwave irradiation at 80 °C for 3.5 h. The reaction mixture was concentrated to dryness under high vacuum. Purification of this crude product by column chromatography (silica gel, elution with 8% MeOH in $CHCl_3$) furnished **3** (120 mg, 81%) as a yellowish solid. ^{1}H NMR ($CDCl_3$): δ 5.73−5.64 (m, 1H), 4.47 (dd, J = 12.0, 3.6 Hz, 1H), 4.32−3.74 (m, 11H), 3.37 (s, 3H), 2.42−2.30 (m, 4H), 1.66−1.53 (m, 4H), 1.37−1.18 (m, 40H), 0.87 (t, J = 6.8 Hz, 6H); ^{13}C NMR ($CDCl_3$) δ 173.60, 173.10, 65.84, 65.72, 65.18, 64.48, 63.54, 56.08, 56.03, 51.51, 34.52, 34.25, 32.16, 29.95, 29.91, 29.78, 29.75, 29.61, 29.54, 29.38, 29.34, 24.99, 24.91, 22.93, 14.37; MS (ESI) *m/z* calculated: 615.0 $[M+H]^+$, found: 615.2 $[M+H]^+$.

*3-[N,N-Bis(2-tert-butyldiphenylsilyloxyethyl)amino]-1-(triphenylmethoxy)-2-(tetradecanoyloxy)propane (**17**).* To a solution of **13** (1.60 g, 1.78 mmol), Et_3N (0.50 mL, 3.56 mmol), and DMAP

(22 mg, 0.178 mmol) in CH_2Cl_2 (12 mL) at 0 °C was added dropwise myristoyl chloride (0.53 mL, 1.96 mmol). The reaction mixture was allowed to warm up slowly to room temperature. It was stirred for 24 h at room temperature, diluted with CH_2Cl_2 (50 mL), and washed sequentially with 5% aqueous sodium bicarbonate (15 mL), water (15 mL), and saturated aqueous NaCl (15 mL). The organic layer was dried (Na_2SO_4), filtered, and concentrated *in vacuo*. Purification by column chromatography (silica gel, elution with 0.2% MeOH in $CHCl_3$) furnished **17** (1.60 g, 81%) as an oily liquid. ^{1}H NMR ($CDCl_3$): δ 7.34−7.05 (m, 35H), 5.05−4.96 (m, 1H), 3.53−3.42 (m, 4H), 3.08 (dd, J = 10.0, 3.2 Hz, 1H), 2.99 (dd, J = 10.0, 6.0 Hz, 1H), 2.68−2.54 (m, 6H), 2.25 (t, J = 8.0 Hz, 2H), 1.64−1.55 (m, 2H), 1.35−1.14 (m, 20H), 0.98 (s, 18H), 0.88 (t, J = 6.8 Hz, 3H).

*3-[N,N-Bis(2-tert-butyldiphenylsilyloxyethyl)amino]-2-(tetradecanoyloxy)-1-propanol (**18**).* To a solution of **17** (1.55 g, 1.40 mmol) in diethyl ether (2 mL) was added 85% formic acid (5.2 mL) at room temperature. The reaction mixture was stirred for 20 h at room temperature and cooled at 0 °C, and solid $NaHCO_3$ was added in portions to neutralize the acidic solution. The reaction mixture was then diluted with diethyl ether (70 mL) and washed with water (20 mL) and saturated aqueous NaCl (20 mL). The organic layer was dried (Na_2SO_4), filtered, and concentrated *in vacuo*. Purification by column chromatography (silica gel, elution with 1% MeOH in $CHCl_3$) furnished **18** (0.77 g, 64%) as an oily liquid. ^{1}H NMR ($CDCl_3$): δ 7.65−7.24 (m, 20H), 4.08 (dd, J = 11.2, 3.6 Hz, 1H), 3.95 (dd, J = 11.2, 5.6 Hz, 1H), 3.84−3.56 (m, 5H), 2.83−2.58 (m, 6H), 2.31 (t, J = 8.0 Hz, 2H), 1.68−1.50 (m, 2H), 1.36−1.16 (m, 20H), 1.02 (s, 18H), 0.88 (t, J = 7.0 Hz, 3H).

*3-[N,N-Bis(2-tert-butyldiphenylsilyloxyethyl)amino]-2-(tetradecanoyloxy)-1-[succinyloxy(4-cholesteryloxy)]propane (**19**).* To an ice-cooled solution of **18** (0.52 g, 0.60 mmol) and cholesteryl hemisuccinate (0.44 g, 0.90 mmol) in DMF (5 mL) was added *N,N′*-dicyclohexylcarbodiimide (0.31 g, 1.5 mmol). After 5 min, the ice bath was removed, and the reaction mixture was stirred for 6 h at room temperature. The resulting precipitation of dicyclohexylurea was removed by filtration. The filtrate was diluted with dichloromethane (30 mL) and washed with H_2O (10 mL), saturated aqueous NaCl (10 mL), and dried (Na_2SO_4) and concentrated *in vacuo*. Purification by column chromatography (silica gel, elution with 5% MeOH in $CHCl_3$) furnished **19** (0.632 g, 79%) as wax. ^{1}H NMR ($CDCl_3$): δ 7.68−7.28 (m, 20H), 5.40−5.31 (m, 1H), 5.04−4.93 (m, 1H), 4.65−4.51 (m, 1H), 4.26 (dd, J = 11.6, 2.4 Hz, 1H), 4.03 (dd, J = 12.0, 6.0 Hz, 1H), 3.61 (t, J = 6.0 Hz, 4H), 2.75−2.42 (m, 10H), 2.31 (d, J = 7.2 Hz, 2H), 2.18 (t, J = 7.6 Hz, 2H), 2.08−1.75 (m, 5H), 1.64−0.78 (m, 76H), 0.67 (s, 3H).

*3-[N,N-Bis(2-hydroxyethyl)amino]-2-(tetradecanoyloxy)-1-[succinyloxy(4-cholesteryloxy)]propane (**20**).* Tetrabutylammonium fluoride trihydrate (0.49 g, 1.55 mmol) was added to an ice-cooled solution of **19** (0.52 g, 0.39 mmol) in THF (3 mL) under N_2 atmosphere. The reaction mixture was allowed to warm up to room temperature. It was stirred at room temperature for 5.5 h, then diluted with CH_2Cl_2 (20 mL) and washed with water (10 mL) followed by saturated aqueous NaCl (10 mL). The organic layer was dried, filtered, and concentrated *in vacuo*. Purification by column chromatography (silica gel, elution with 2% methanol in $CHCl_3$) furnished **20** (231 mg, 69%) as a wax. ^{1}H NMR ($CDCl_3$): δ 5.40−5.33 (m, 1H), 5.27−5.18 (m, 1H), 4.66−4.54 (m, 1H), 4.30 (dd, J = 12.0, 3.6 Hz, 1H), 4.08 (dd, J = 12.0, 5.6 Hz, 1H), 3.68−3.50 (m, 4H), 2.90 (brs, 2H), 2.81−2.48 (m, 10H), 2.42−2.22 (m, 4H), 2.04−1.75 (m, 5H), 1.70−0.77 (m, 58H), 0.66 (s, 3H).

*N,N-[Bis(2-hydroxyethyl)]-N-methyl-N-[2-(tetradecanoyloxy)-1-[succinyloxy(4-cholesteryloxy)]ammonium Iodide (**6**).* A mixture of **20** (167 mg, 0.19 mmol) and methyl iodide (2 mL) was taken in a 10 mL microwave vial covered with a plastic cap. The reaction mixture was then subjected to 150 W microwave irradiation at 80 °C for 3.5 h. The reaction mixture was concentrated to dryness under high vacuum. Purification of this crude product by column chromatography (silica gel, elution with 8% MeOH in $CHCl_3$) furnished **6** (62 mg, 33%) as yellowish solid. ^{1}H NMR ($CDCl_3$): δ 5.77−5.70 (m, 1H), 5.36 (d, J = 5.2 Hz, 1H), 4.60−4.50 (m, 1H), 4.47 (dd, J = 12.0, 3.6 Hz, 1H), 4.33−3.67 (m, 11H), 3.40 (s, 3H), 2.82−2.47 (m, 4H), 2.35 (t, J = 7.6 Hz 2H), 2.31−2.22 (m, 2H), 2.06−1.92 (m, 2H), 1.90−1.76 (m, 3H), 1.64−0.82 (m, 58H), 0.67 (s, 3H); ^{13}C NMR ($CDCl_3$) δ 173.64, 172.30, 172.05, 139.54, 123.20, 75.19, 66.28, 65.77, 65.48, 64.30, 63.33, 56.88, 56.34, 56.18, 56.12, 51.47, 50.15, 42.53, 39.93, 39.73, 38.25, 37.10, 36.80, 36.40, 36.02, 34.22, 32.17, 32.12, 32.06, 29.96, 29.92, 29.79, 29.61, 29.59, 29.36, 29.26, 28.45, 28.24, 27.98, 24.97, 24.51, 24.07, 23.05, 22.93, 22.79, 21.24, 19.51, 18.93, 14.37, 12.08; MS (ESI) *m/z* calculated: 873.3 $[M+H]^+$, found: 873.6 $[M+H]^+$.

Preparations of siRNA. All siRNAs used in these studies were chemically synthesized by Dharmacon (USA) and received as desalted, deprotected oligonucleotides. Duplexes were annealed by standard procedures as described previously (*10, 11*).

***In Vitro* RNAi Activity with Chol-Lipids.** FL83B (mouse hepatocytes) cells were maintained at 37 °C with 5% CO_2 in F12 khangians modified culture medium (ATCC, USA) supplemented with 10% fetal bovine serum (FBS), 100 U/mL penicillin, and 100 μg/mL streptomycin. Cells were regularly passaged and plated in 96-well and 6-well culture plates 16 h prior to transfection at 70% confluency. Lipids were suspended in a HEPES buffered saline and different concentrations of poly(ethylene glycol) methyl ether (Mn ∼2000, Sigma) were added to lipid suspensions, followed by sonicating for 8 min at 25 °C. The molar ratios of lipids to PEG were as follows: Dotap_chol:PEG, 4:1; Dmtap_chol:PEG, 3:1; Transfect_chol: PEG, 5:2. Complexes of 100nM unmodified apo B siRNA (sense 5′-GUCAUCACACUGAAUACCAAU-3′, antisense 5′-AUUGGUAUUCAGUGUGAUGACAC-3′) and different concentrations of Dotap_cholesterol, Dmtap_cholesterol, or Transfast_cholesterol were prepared by incubation for 20 min at room temperature in Opti-MEM culture medium (Invitrogen). Cells were transfected with 1 mL of the complex per well for 6 h at 37 °C. Medium was removed after 6 h and replaced with full-growth medium without antibiotics and incubated for an additional 24 h. Cell viability was assessed using a CellTiter 96 AQ_{ueous} One Solution cell proliferation assay according to the manufacturer's instructions (Promega, USA). Total RNA was extracted using RNeasy minispin columns and DNase I treated before quanatation (Qiagen, USA). cDNA was prepared by random priming using Superscript II reverse transcriptase (Invitrogen, USA). Real-time quantitative PCR (qPCR) was performed using SYBR Green (Qiagen USA). ApoB mRNA levels were assessed using the following primers: apo B, forward 5′-TTCCAGCCATGGGCAACTTTACCT-3′ and reverse apo B 5′-TACTGCAGGGCGTCAGTGACAAAT-3′. apo B mRNA levels were then normalized against the housekeeping gene GAPDH: forward 5′-ATCAAGAAGGTGGTGAAGCAGGCA-3′ and reverse 5′-TGGAAGAGTGGGAGTTGCTGTTGA-3′.

ACKNOWLEDGMENT

We thank Craig Mello, Greg Hannon, and members of the Rana lab for helpful discussions and critical reading of the manuscript. This work was supported in part by grants from the NIH to T.M.R.

LITERATURE CITED

(1) Fire, A., Xu, S., Montgomery, M. K., Kostas, S. A., Driver, S. E., and Mello, C. C. (1998) Potent and specific genetic interference by double-stranded RNA in Caenorhabditis elegans. *Nature 391*, 806–11.

(2) Hannon, G. J., and Rossi, J. J. (2004) Unlocking the potential of the human genome with RNA interference. *Nature 431*, 371–8.

(3) Hammond, S. M., Bernstein, E., Beach, D., and Hannon, G. J. (2000) An RNA-directed nuclease mediates post-transcriptional gene silencing in Drosophila cells. *Nature 404*, 293–6.

(4) Rana, T. M. (2007) Illuminating the silence: understanding the structure and function of small RNAs. *Nat. Rev. Mol. Cell Biol. 8*, 23–36.

(5) Chu, C. Y., and Rana, T. M. (2006) Translation repression in human cells by microRNA-induced gene silencing requires RCK/p54. *PLoS Biol. 4*, e210.

(6) Chu, C. Y., and Rana, T. M. (2007) Small RNAs: regulators and guardians of the genome. *J. Cell. Physiol. 213*, 412–9.

(7) Caplen, N. J., Parrish, S., Imani, F., Fire, A., and Morgan, R. A. (2001) Specific inhibition of gene expression by small double-stranded RNAs in invertebrate and vertebrate systems. *Proc. Natl. Acad. Sci. U.S.A. 98*, 9742–7.

(8) Elbashir, S. M., Harborth, J., Lendeckel, W., Yalcin, A., Weber, K., and Tuschl, T. (2001) Duplexes of 21-nucleotide RNAs mediate RNA interference in cultured mammalian cells. *Nature 411*, 494–8.

(9) Amarzguioui, M., Holen, T., Babaie, E., and Prydz, H. (2003) Tolerance for mutations and chemical modifications in a siRNA. *Nucleic Acids Res. 31*, 589–95.

(10) Chiu, Y. L., and Rana, T. M. (2003) siRNA function in RNAi: a chemical modification analysis. *RNA 9*, 1034–48.

(11) Chiu, Y. L., and Rana, T. M. (2002) RNAi in human cells: basic structural and functional features of small interfering RNA. *Mol. Cell 10*, 549–61.

(12) Morrissey, D. V., Lockridge, J. A., Shaw, L., Blanchard, K., Jensen, K., Breen, W., Hartsough, K., Machemer, L., Radka, S., Jadhav, V., Vaish, N., Zinnen, S., Vargeese, C., Bowman, K., Shaffer, C. S., Jeffs, L. B., Judge, A., MacLachlan, I., and Polisky, B. (2005) Potent and persistent in vivo anti-HBV activity of chemically modified siRNAs. *Nat. Biotechnol. 23*, 1002–7.

(13) Soutschek, J., Akinc, A., Bramlage, B., Charisse, K., Constien, R., Donoghue, M., Elbashir, S., Geick, A., Hadwiger, P., Harborth, J., John, M., Kesavan, V., Lavine, G., Pandey, R. K., Racie, T., Rajeev, K. G., Rohl, I., Toudjarska, I., Wang, G., Wuschko, S., Bumcrot, D., Koteliansky, V., Limmer, S., Manoharan, M., and Vornlocher, H. P. (2004) Therapeutic silencing of an endogenous gene by systemic administration of modified siRNAs. *Nature 432*, 173–8.

(14) Krutzfeldt, J., Rajewsky, N., Braich, R., Rajeev, K. G., Tuschl, T., Manoharan, M., and Stoffel, M. (2005) Silencing of microRNAs in vivo with 'antagomirs'. *Nature 438*, 685–9.

(15) Zimmermann, T. S., Lee, A. C., Akinc, A., Bramlage, B., Bumcrot, D., Fedoruk, M. N., Harborth, J., Heyes, J. A., Jeffs, L. B., John, M., Judge, A. D., Lam, K., McClintock, K., Nechev, L. V., Palmer, L. R., Racie, T., Rohl, I., Seiffert, S., Shanmugam, S., Sood, V., Soutschek, J., Toudjarska, I., Wheat, A. J., Yaworski, E., Zedalis, W., Koteliansky, V., Manoharan, M., Vornlocher, H. P., and MacLachlan, I. (2006) RNAi-mediated gene silencing in non-human primates. *Nature 441*, 111–4.

(16) Palliser, D., Chowdhury, D., Wang, Q. Y., Lee, S. J., Bronson, R. T., Knipe, D. M., and Lieberman, J. (2006) An siRNA-based microbicide protects mice from lethal herpes simplex virus 2 infection. *Nature 439*, 89–94.

(17) Santel, A., Aleku, M., Keil, O., Endruschat, J., Esche, V., Fisch, G., Dames, S., Loffler, K., Fechtner, M., Arnold, W., Giese, K., Klippel, A., Kaufmann, J. (2006) A novel siRNA-lipoplex technology for RNA interference in the mouse vascular endothelium. *Gene Ther.*

(18) Song, E., Zhu, P., Lee, S. K., Chowdhury, D., Kussman, S., Dykxhoorn, D. M., Feng, Y., Palliser, D., Weiner, D. B., Shankar, P., Marasco, W. A., and Lieberman, J. (2005) Antibody mediated in vivo delivery of small interfering RNAs via cell-surface receptors. *Nat. Biotechnol. 23*, 709–17.

(19) Baigude, H., McCarroll, J., Yang, C. S., Swain, P. M., and Rana, T. M. (2007) Design and creation of new nanomaterials for therapeutic RNAi. *ACS Chem. Biol. 2*, 237–41.

(20) Morille, M., Passirani, C., Vonarbourg, A., Clavreul, A., and Benoit, J. P. (2008) Progress in developing cationic vectors for non-viral systemic gene therapy against cancer. *Biomaterials 29*, 3477–96.

(21) Bennett, M. J., Aberle, A. M., Balasubramaniam, R. P., Malone, J. G., Malone, R. W., and Nantz, M. H. (1997) Cationic lipid-mediated gene delivery to murine lung: correlation of lipid hydration with in vivo transfection activity. *J. Med. Chem. 40*, 4069–78.

(22) Nantz, M. H., Bennett, M. J., and Balasubramaniam, R. P. (1999), The Regents of the University of California, Oakland, CA, USA.

(23) Lee, H. K., Cao, H., and Rana, T. M. (2005) Design, microwave-assisted synthesis, and photophysical properties of small molecule organic antennas for luminescence resonance energy transfer. *J. Comb. Chem. 7*, 279–84.

(24) Lee, H. K., and Rana, T. M. (2004) Microwave-assisted parallel synthesis of a 4,6-diamino-2,2-dimethyl-1,2-dihydro-1-phenyl-s-triazine library. *J. Comb. Chem. 6*, 504–8.

(25) Diaz-Ortiz, A., and del la Hoz, A. (2007) Microwave assisted high throughput synthesis. *Comb. Chem. High Throughput Screen. 10*, 733–4.

(26) Roberts, B. A., and Strauss, C. R. (2005) Toward rapid, "green", predictable microwave-assisted synthesis. *Acc. Chem. Res. 38*, 653–61.

BC900482R

Physicochemical Stability of the Antibody−Drug Conjugate Trastuzumab-DM1: Changes due to Modification and Conjugation Processes

Aditya A. Wakankar,*,† Maria B. Feeney,‡ Javier Rivera,† Yan Chen,|| Michael Kim,|| Vikas K. Sharma,§ and Y. John Wang†

Late Stage Pharmaceutical and Processing Development, Early Stage Pharmaceutical Development, and Protein and Analytical Chemistry, Genentech Inc., 1 DNA Way, South San Francisco, California 94080, and Department of Pharmaceutical Chemistry, The University of Kansas, 2095 Constant Avenue, Lawrence, Kansas 66047. Received October 5, 2009; Revised Manuscript Received July 19, 2010

In the manufacture of the antibody-drug conjugate Trastuzumab-DM1 (T-DM1), the lysine residues on the antibody trastuzumab (Tmab) are modified to form the intermediate Tmab-MCC (T-MCC) and then conjugated with the drug DM1. Our goal is to understand the effects of modification and conjugation steps on the physicochemical stability of the antibody. The structural stability of Tmab relative to its modified and conjugated forms was assessed, employing thermally induced stress conditions to formulations containing Tmab, T-MCC, and T-DM1. DSC, SEC, CE-SDS, and LC-MS were used to study the stability of Tmab, T-MCC, and T-DM1 to thermal stress. The DSC thermograms show a decrease in melting temperature for the CH2 transition, in the order Tmab > T-MCC > T-DM1. As per SEC analysis, a significant increase in level of aggregation was detected in T-MCC (∼32%) and T-DM1 (∼5%) after 14 days at 40 °C. Tmab did not show significant aggregate formation. CE-SDS and LC-MS data demonstrate that the aggregation in the case of T-MCC is largely covalent and involves mechanisms other than formation of intermolecular disulfide cross-links. The aggregation observed for T-MCC was significantly inhibited upon addition of amino acids with nucleophilic side chains containing thiol (Cys) and hydroxyl moieties (Ser, Tyr). The covalent aggregation observed for T-MCC and the ability of nucleophilic amino acids, particularly Cys, to inhibit it indicate that the maleimide moiety in the MCC linker may react to form intermolecular covalent cross-links between T-MCC molecules, possibly through a Michael addition mechanism. In addition, DSC results demonstrate that the conjugation of the drug moiety DM1 to Tmab results in destabilization of the CH2 domain of the antibody.

INTRODUCTION

Antibody-drug conjugates, or immunoconjugates, are a class of chemotherapeutic agents that harness the site specificity of monoclonal antibodies to achieve targeted delivery of cytotoxic drug moieties (*1, 2*). On the basis of the targeted delivery of these cytotoxins, these antibody−drug conjugates selectively eliminate the cancer cells that express the surface antigen (*3*−*6*).

Antibody−maytansine conjugates are a subclass of these immunoconjugates that provide for selective delivery of the cytotoxin maytansine to the tumor cells. Maytansines, first isolated from the East African shrub *Maytenus serrata* by Kupchan and co-workers, are members of the ansamycin group of natural products (*7, 8*). DM1, a semisynthetic ansamacrolide derived from the naturally occurring compound maytansine, exhibits its cytotoxicity by inhibiting microtubule polymerization, thereby blocking cell division (*9, 10*). Several antibody-maytansinoid conjugates involving the maytansine derivative, DM1, have been evaluated in clinical trials. Examples of these include bivatuzumab mertansine (*7*), huN901-DM1, BB-10901, MLN-DM1 (*3, 7*), and DM1-huJ591 (*11, 12*), which are evaluated in clinical trials to treat different forms of cancers, including small-cell lung cancer and prostate cancer.

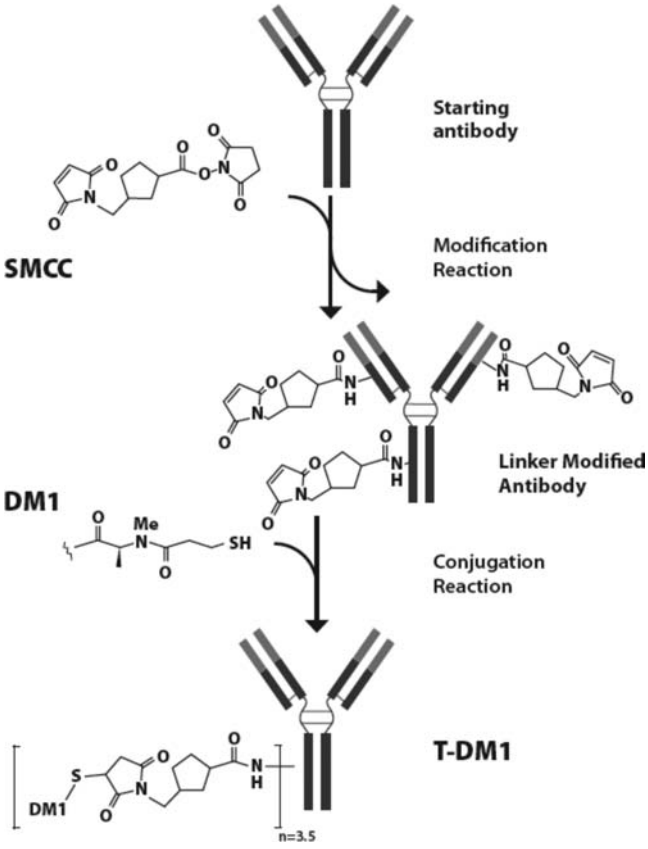
Trastuzumab-DM1, or T-DM1, consists of the therapeutic anti-HER2 monoclonal antibody trastuzumab (Herceptin) covalently linked to DM1 via a linker moiety to achieve targeted delivery of the cytotoxic agent to tumor cells overexpressing HER2 (*3, 10, 13, 14*). This antibody-drug conjugate is currently being evaluated in clinical trials for treatment of HER2 refractory metastatic breast cancer (*13, 15*).

Scheme 1 illustrates the synthesis involved in the manufacture of the antibody-drug conjugate T-DM1. The manufacture of T-DM1 consists of a two-step process in which the lysine residues on the antibody trastuzumab (Tmab) are first modified using the linker species SMCC to form the intermediate Tmab-MCC (T-MCC). In the second step, T-MCC is reacted with the drug DM1 to obtain the antibody-drug conjugate T-DM1. This conjugation scheme results in a heterogeneous distribution having an average of ∼3.5 DM1 molecules per molecule of the antibody Tmab (*16*). The heterogeneity of T-DM1 arises due to the potential number of lysines (total ∼88) on Tmab that could be linked to DM1, as well as the variability in the particular sites of conjugation. Previous studies with antibody-drug conjugates have provided insight into the distribution, load, and location of conjugation sites on these antibodies (*9, 12, 17*−*19*). However, the effect of these modification and conjugation reactions on the physicochemical stability of the antibody has not been addressed. As shown in the synthetic scheme for T-DM1, the manufacturing process results in neutralization of the surface charge on the lysine residues that are modified and conjugated, as well as addition of a hydrophobic DM1 moiety to the surface of the antibody molecule. We hypothesize that the addition of

* wakankar.aditya@gene.com.
† Late Stage Pharmaceutical and Processing Development, Genentech Inc.
‡ The University of Kansas.
§ Early Stage Pharmaceutical Development, Genentech Inc.
|| Protein and Analytical Chemistry, Genentech Inc.

10.1021/bc900434c © 2010 American Chemical Society
Published on Web 08/10/2010

Scheme 1. Process Flow for Production of T-DM1 from Tmab, via the Key Intermediate T-MCC



the linker and drug moieties during processing, as well as the hydrophobicity of the drug DM1 itself, could lead to structural changes on the antibody molecule that affect its physicochemical properties. In our studies, we employed thermal stress using a differential scanning calorimetry (DSC) temperature scan to assess the changes in structural stability of Tmab due to modification and conjugation reactions. The thermal stability of Tmab has been investigated previously using DSC (*20*). In this study, the stability of Tmab (an IgG1) and its modified (T-MCC) and conjugated forms (T-DM1) to thermally induced stress was analyzed using DSC, SEC, CE-SDS, and LC-MS. This information could be important for selecting appropriate processing, storage, and handling conditions for critical intermediates during manufacture of antibody-drug conjugates such as T-DM1.

MATERIALS AND METHODS

Materials. Trastuzumab (Tmab), a humanized IgG1 monoclonal antibody, was manufactured at Genentech, South San Francisco. The modified (T-MCC) and conjugated (T-DM1) forms of Tmab were obtained from an early developmental manufacturing run. The amino acids used in the blocking studies had their N-termini capped as an N-acetyl derivative. The amino acids used were obtained from different sources: cysteine and serine from Sigma Aldrich (St. Louis, MO), histidine from VWR (West Chester, PA), and lysine and tyrosine from Fisher Scientific. (Pittsburgh, PA).

Formulation Preparation. Tmab, T-MCC, and T-DM1 solutions were dialyzed into 10 mM sodium succinate buffer (pH 5) and then concentrated using tangential flow filtration (TFF). After measuring the protein concentration of this TFF pool by UV absorption, 10 mM sodium succinate buffer (pH 5) was added to adjust to a target protein concentration of 24 mg/mL. To five parts of this solution was added one part of a conditioning buffer, containing 10 mM sodium succinate, 36% (w/v) trehalose dihydrate, and 0.12% (v/v) polysorbate 20 (pH 5). The final formulation thus consists of 20 mg/mL antibody in 10 mM sodium succinate buffer (pH 5), containing 6% w/v trehalose dihydrate and 0.02% w/v polysorbate 20. The final formulation was filtered through a 0.2 μm filter prior to using it for our stability investigations.

Accelerated Stability Studies. The formulations were prepared as aliquots of either 200 or 60 μL per vial, depending on the study, in 3 mL Foma Vitrum glass vials, covered with 13 mm Daikyo D777−1 Fluoro Tec coated stoppers, and then sealed with Parafilm to prevent evaporation of solution during incubation. The glass vials and rubber stoppers were autoclaved prior to use. Duplicate vials were prepared for each sample time point and then placed in an incubator room held at 40 °C. The vials were sampled at each predetermined time point and then stored frozen at −70 °C prior to analyses.

Formulation with Selected Amino Acids. Using a stock solution of amino acids in deionized water, each amino acid was added to a formulation to achieve an amino acid concentration of 3 mM in the final protein formulations. This concentration corresponds to a 5-fold molar excess of the amino acid over the linker moiety, MCC. The concentration of the linker moiety was calculated based on the average antibody/linker ratio of 4.5, determined using LC-MS analysis (internal document) of the development lot. In separate sample sets, N-Ac-Cys was tested using a 2-fold molar excess of this amino acid, and N−Ac−Ser was tested using a 20-fold molar excess over the linker moiety. Accelerated stability studies of the formulation samples spiked with amino acids were conducted as described under the section "accelerated stability studies".

Differential Scanning Calorimetry (DSC). Thermal analysis of Tmab, T-MCC, and T-DM1 was performed using high-throughput VP Capillary DSC (MicroCal; Northampton, MA). Formulations of Tmab, T-MCC, and T-DM1 were diluted to give a final protein concentration of 1 mg/mL by adding 475 μL formulation buffer to 25 μL of sample in a 96-well plate, alternating with wells containing 500 μL formulation buffer. The instrument scanned each sample−buffer pair over the temperature range 15−95 °C at a rate of 1 °C/min. In the case of experiments to evaluate the reversibility of the melting transitions, samples were scanned twice at the rate of 1 °C/min in the temperature range 15−70 °C. Data analysis was performed using *Origin* software (OriginLab; Northampton, MA).

Size-Exclusion Chromatography (SEC). TSKgel G3000SW$_{XL}$ 7.8 × 300 mm size-exclusion column from Tosoh Biosciences (So. San Francisco, CA) was connected to an Agilent 1100 series HPLC system (Agilent, Santa Clara, CA). The mobile phase consisted of 0.2 M potassium phosphate buffer (pH 6.8), 0.2 M potassium chloride, and 15% isopropyl alcohol and was pumped at a flow rate of 0.5 mL/min. 5 μL of sample volume was injected for analysis. The column was maintained at 25 °C using a built-in thermostat. Detection was performed by monitoring UV absorbance at 280 nm.

On-Chip Capillary Gel Electrophoresis (Nonreduced Conditions). Agilent 2100 Bioanalyzer and Agilent Protein 230 Kit were purchased from Agilent. Formulations of Tmab, T-MCC, and T-DM1 were diluted with water to a final protein concentration of 1 mg/mL. Gel−dye solution, destaining solution, sample buffer, and ladder kit reagents were prepared as per the protocol (internal document). To 24 μL of sample buffer was added 4 μL of sample and 2 μL of denaturing solution. Samples and ladder were heated to 70 °C for 5 min in a temperature-controlled water bath, then cooled and diluted with 60 μL water. The chip was primed as instructed by the manufacturer, and 6 μL of each sample was loaded onto a well

on the chip. The chip was placed into the Bioanalyzer, and electrophoresis with fluorescence detection was performed using the manufacturer's preprogrammed assay parameters in the software. Peaks were manually integrated, and relative peak areas were used to calculate percentages for aggregate, monomer, and fragment.

On-Chip Capillary Gel Electrophoresis (Reduced Conditions). The on-chip capillary gel electrophoresis was conducted using the same instrument as described in the protocol above. The sample preparation involved addition of 4 μL of sample (protein concentration 1 mg/mL), 2 μL of denaturing solution, and 4 μL of β-mercaptoethanol (BME) to 20 μL of 0.5% SDS solution. The sample treatment, priming, and analysis was identical to that described in the previous section.

LC/MS Analysis of Deglycosylated and Reduced T-MCC Samples. A PE-Sciex QSTAR Pulsar mass spectrometer (Applied Biosystems, Foster City, CA) was used for protein-mass measurement. Samples were analyzed in positive ion mode. The capillary and cone voltages were optimized for maximum sensitivity. The optimized instrument conditions included applying an electrospray voltage of 5200 V, a first and second declustering potential (DP) of 60 V (DP1) and 15 V (DP2), and a focusing potential of 200 V. MS data were acquired and deconvoluted using *Analyst QS 1.1* software. The mass spectrometer was calibrated using an aqueous solution containing 2 mg/mL NaI, 0.05 mg/mL CsI, and 30% acetonitrile for acquiring mass ranges of 650 to 2000 *m*/*z* for protein mass measurement.

Deglycosylation was performed by incubating 200 μg of T-MCC samples with 2 μL of PNGase F (New England Biolabs, Ipswich, MA) at 37 °C overnight. Deglycosylated T-MCC samples were reduced with 20 mg/mL tris(2-carboxy-ethyl) phosphine (TCEP) at 37 °C for 60 min. Approximately 15 μg reduced, deglycosylated sample was loaded onto a PLRP-S 2.1 × 150 mm, reverse-phase HPLC column (Varian Inc., Palo Alto, CA) equilibrated at 78 °C and coupled with QSTAR mass spectrometer. The column was eluted with a flow rate of 0.25 mL/min using a gradient of acetonitrile in water as follows: 15% acetonitrile in water for 3 min, then 15−47% acetonitrile in 37 min, 47−95% in 0.5 min, equilibration at 95% for 2 min, and back to 15% acetonitrile in 0.5 min and equilibration at 15% for 7.5 min. The HPLC flow was diverted to waste during the first 4.5 min of the gradient to avoid salt interference.

RESULTS

DSC Analysis. The thermal stability of Tmab, T-MCC, and T-DM1 was assessed using DSC (Figure 1). Tmab and its modified and conjugated forms were analyzed in solutions containing the same formulation components with the antibody concentration at 1 mg/mL. The DSC thermograms for these three molecules show two major transitions. The second DSC transition did show differences in melting temperatures (t_m) for the three forms investigated. A slight decrease (~0.8 °C) in t_m was observed following modification and conjugation of Tmab, giving the following order for t_m values: Tmab > T-MCC > T-DM1. The first transition showed a significantly greater difference in the thermal stability of Tmab and its modified and conjugated forms. The first transition for Tmab occurred at 68.2 °C, whereas the same transition for T-MCC and T-DM1 occurred at 66.2 and 63.8 °C, respectively.

The reversibility of the first transition was also evaluated for Tmab and its modified and conjugated forms. This calorimetric reversibility typically indicates that the transition from the native to the unfolded state is reversible and that the unfolded state does not undergo any subsequent reactions such as aggregation. The implication of reversibility in DSC is that the unfolded state will return to the native state upon cooling (*20*). For testing

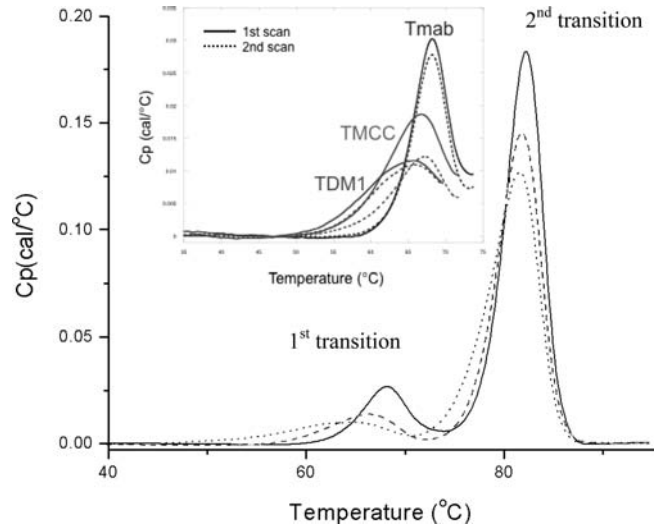


Figure 1. Comparison of the DSC thermograms of Tmab, T-MCC, and T-DM1 ([antibody] = 1 mg/mL) in 10 mM sodium succinate, 6% w/v trehalose dihydrate, and 0.02% w/v polysorbate 20. Inset in the figure depicts reversibility of the first (CH2) transition for Tmab, T-MCC, and T-DM1.

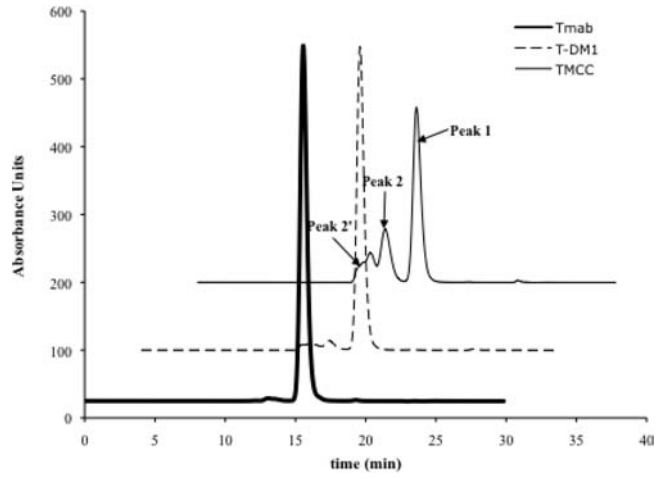


Figure 2. SEC chromatograms showing elution profiles of Tmab, T-MCC, and T-DM1 after 7 days of storage at 40 °C. Each individual SEC elution profile shows the main peak (Peak 1), the dimer peak (Peak 2), and the high molecular weight aggregate peak (Peak 2′).

reversibility, the samples were rescanned following the initial sample scan in temperature range ~15−70 °C. The trace of the DSC thermograms of the initial sample scan and the subsequent rescan were assessed for superimposability, as shown in the inset on Figure 1. On the basis of our results, the first DSC transition for Tmab and T-DM1 was reversible. However, in the case of T-MCC, the first transition was observed to be partially reversible.

Effect of Modification and Conjugation on Aggregation Behavior. *SEC Analysis.* The aggregation behavior of Tmab and its modified (T-MCC) and conjugated (T-DM1) forms was assessed using size exclusion chromatography (SEC). The changes in the SEC profile following storage for 7 days at 40 °C are shown in Figure 2. Each chromatographic profile shows monomer species (Peak 1), dimer species (Peak 2), and higher-molecular-weight aggregate species (Peak 2′). No significant level of fragmentation was detected under conditions of the assay.

The aggregation kinetics for Tmab, T-MCC, and T-DM1 were followed for up to 70 days at 40 °C using the SEC assay (Figure 3). T-MCC showed an increase of up to ~40% aggregate

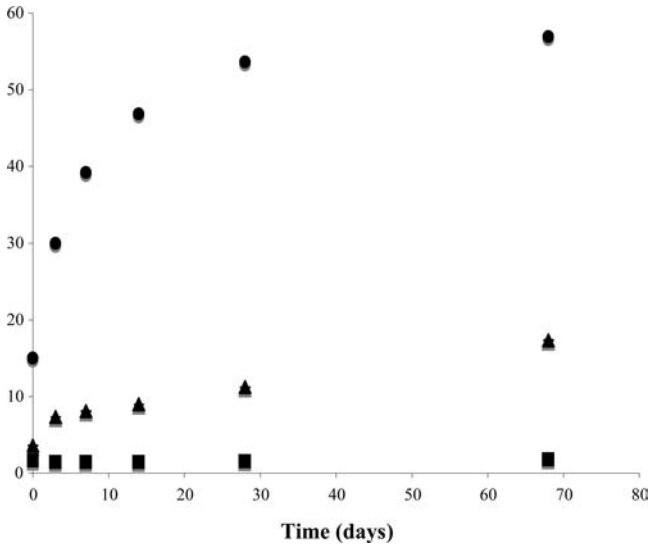


Figure 3. Time course displaying the formation of the aggregates, as per SEC analysis, in T-MCC (●), T-DM1 (▲), and Tmab (■) samples incubated at 40 °C over ∼70 day time period.

formation at the end of the 70day incubation period, whereas Tmab and T-DM1 showed ∼0% and ∼11% increase, respectively. Also, the aggregation kinetics for T-MCC exhibited a biphasic increase: a fast initial aggregation rate followed by a much slower rate of aggregation. The majority of the aggregate formation occurred during the first 14 days of storage at 40 °C.

On-Chip Nonreduced and Reduced CE-SDS Analysis. The aggregate formation in Tmab, T-MCC, and T-DM1 samples after storage at 40 °C for 14 days was further analyzed using nonreduced and reduced CE-SDS. The nonreduced CE-SDS profile of T-MCC showed the presence of covalent aggregates corresponding to molecular weights of 260, 330, and 390 kDa (Figure 4a). The nonreduced CE-SDS profile of T-DM1 upon incubation was similar to T-MCC. However, the total peak area contribution from the covalent aggregates in T-DM1 was ∼3% compared to ∼39% observed in the case of T-MCC. Aggregates were not detected in Tmab sample incubated at 40 °C (data not shown).

To assess whether the covalent aggregation observed in T-MCC was due to formation of interchain disulfides, on-chip CE-SDS was performed under reducing conditions. As shown in Figure 4b, the reduced CE-SDS profile of T-MCC shows two main peaks corresponding to the heavy chain (molecular weight ∼60 kDa) and light chain (molecular weight ∼20 kDa). These peaks were the only two peaks observed in the reduced CE-SDS profile of Tmab (data not shown). However, in case of T-MCC in addition to these two main peaks, several other peaks corresponding to molecular weights of ∼85, 120, 140, and 160 kDa were observed. On the basis of the calculated molecular weights, these additional peaks corresponded to fractions such as HL, HH, HHL, and HHLL. These peaks contributed to ∼45% of the total peak area. The detection of these peaks suggests that, in the case of T-MCC, the formation of interchain cross-links involves mechanisms other than disulfide bond formation. The reduced CE-SDS profile of T-DM1 sample was similar to T-MCC; however, the peaks corresponding to interchain cross-links contributed to less than 10% of the total peak area (data not shown).

The reduced T-MCC samples were also analyzed using LC-MS. The most intense ions in the deconvoluted mass spectra of the reduced T-MCC samples correspond to light chain and heavy chain related fragments as expected (data not shown). As shown in Figure 5, minor species with *m*/*z* of 72 822 and 73 041 Da were also observed. The theoretical and experimental molecular weights for cross-linked species comprising light chain and heavy chain linked through one and two MCC linkers are shown in Table 1. Our results show agreement between the experimental molecular weights and the theoretical molecular weights.

The total extents of aggregation, both covalent and noncovalent, for Tmab, T-MCC, and T-DM1 were compared after 14 days of storage at 40 °C using results obtained from SEC and nonreduced CE-SDS analysis (Figure 6). For T-MCC, a majority of the aggregation observed was covalent in nature. However, for T-DM1, the majority of the aggregation observed was noncovalent in nature (Figure 6). No significant level of aggregation, either covalent or noncovalent, was observed for Tmab under the conditions of incubation. A comparison of the results for T-DM1 with T-MCC demonstrates that the extent

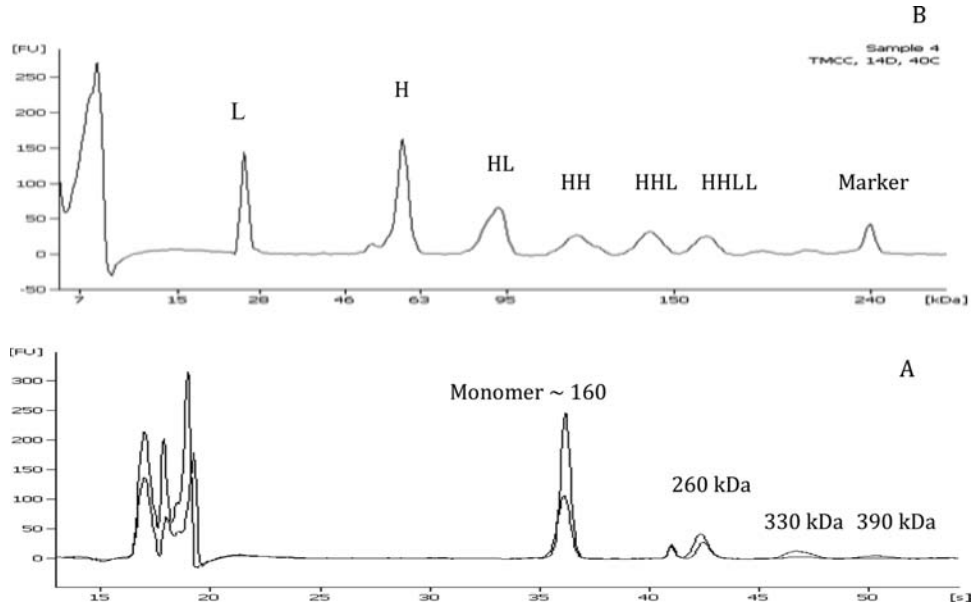


Figure 4. Electropherograms showing the elution profile of T-MCC upon incubation for up to 14 days at 40 °C. Panel A is the elution profile of T-MCC (0 and 14 days) analyzed using on-chip CE-SDS under nonreduced conditions, whereas Panel B is the elution profile of T-MCC analyzed by on-chip CE-SDS under reduced conditions. The labels on Panel B correspond to the heavy chain (H) and light chain (L) moieties and also the combinations of these H and L moieties that were observed.

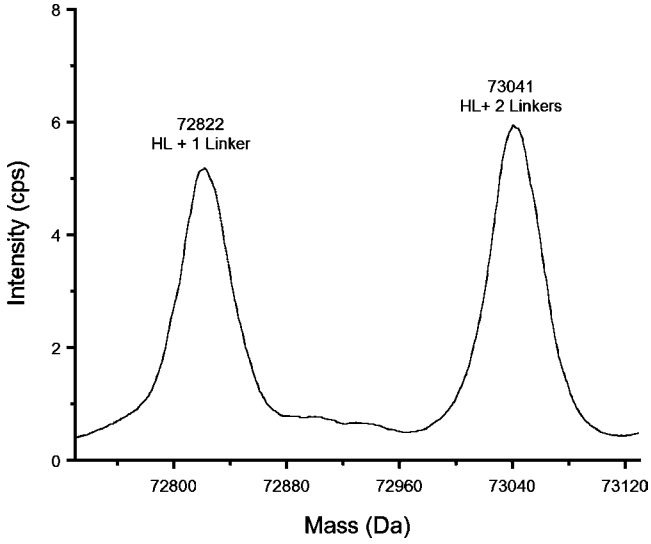


Figure 5. Deconvoluted mass graph of T-MCC showing cross-linked heavy chain−light chain (HL) with one linker and two linkers.

Table 1. Masses of Reduced Fragments, Heavy Chain (H) and Light Chain (L), and Cross-Linked Heavy Chain−Light Chain (HL) Observed from LC-MS along with Their Respective Theoretical Masses

	L	H	HL+1 Linker	HL+2 Linkers
theoretical	23443	49157	72819	73038
experimental	23443	49156	72822	73041

of aggregation is substantially inhibited when T-MCC is conjugated with the drug DM1 (Figure 6).

Effect of Blocking Agents on Aggregation of T-MCC. On the basis of this result, it was hypothesized that maleimide species in T-MCC could be responsible for covalent aggregation. Our goal was to assess whether the aggregation behavior of T-MCC could be inhibited using agents that react with the free maleimidyl species. N-acetyl derivatives of amino acids such as Cys, Lys, His, Ser, and Thr, each with nucleophilic side-chains, were added to the formulation of T-MCC to investigate their ability to react with the maleimide moiety of the T-MCC species. Tmab has very low levels of free Cys residues ~0.2 mol/mol of Tmab (internal document), as these residues are involved in formation of both inter- and intrachain disulfide linkages. On the other hand, nucleophilic residues such as Lys, His, Ser, and Thr are abundant in Tmab and could also potentially interact with the maleimide moiety of the linker.

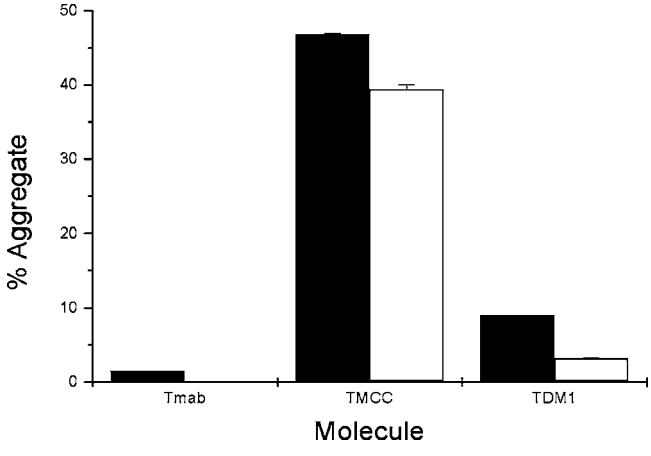


Figure 6. Comparison of the aggregate formation in formulation samples of Tmab, T-MCC, and T-DM1 incubated for 14 days in 40 °C based on SEC (black bars) and nonreduced CE-SDS data (white bars).

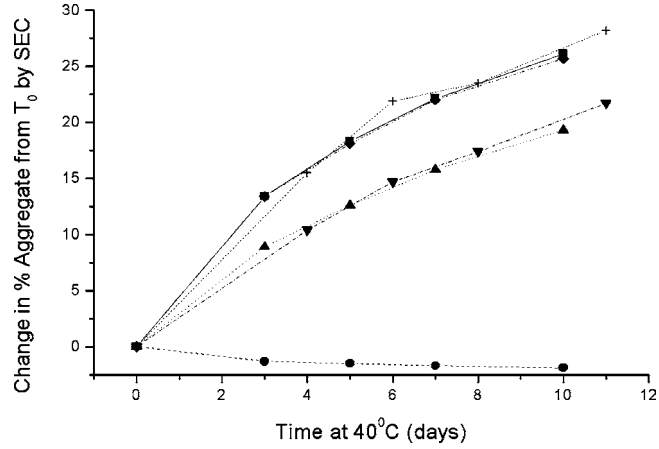


Figure 7. Effect of addition of N-acetylated amino acids Cys (●), Ser (▲), Tyr (▼), Lys (◆), and His (+) on aggregate formation observed in the control (■) formulation. The control formulation consisted of 20 mg/mL T-MCC, 10 mM succinate (pH 5.0), 6% w/v trehalose dihydrate, and 0.02% w/v polysorbate 20. The concentration of the N-acetyl amino acids was maintained at 3 mM, and the different formulation samples were incubated at 40 °C for up to 11 days.

T-MCC and its formulations with the different amino acid residues were incubated for a period of ~11 days at 40 °C. The samples were then assessed using SEC analysis. Our results shown in Figure 7 demonstrate ~25% increase in aggregation in the control sample of T-MCC, with no amino acids added, following storage for up to 10 days at 40 °C. No significant level of aggregate formation was detected in formulations containing 3 mM Cys as an additive. Also, formulations containing 3 mM Ser or Tyr greatly reduced the extent of aggregation observed relative to the control. The total amount of aggregation observed for T-MCC in the presence of 3 mM His and Lys was comparable to the control.

To determine if lower amounts of Cys could result in a similar inhibitory effect on T-MCC aggregation, a formulation containing a 2-fold excess of Cys over the MCC moiety in T-MCC was prepared. This formulation was stored at 40 °C and the stability assessed over a 10 day period. On the basis of our results, the inhibitory effect on T-MCC was comparable in formulations containing a 2-fold and a 5-fold molar excess of Cys. Also, formulations containing a 20-fold molar excess of Ser showed one-third the amount of aggregation observed in solutions containing a 5-fold excess (data not shown).

To further confirm the results obtained using SEC analysis, the T-MCC formulation samples containing no added amino acid (control), Cys, Ser, and Tyr incubated at 40 °C for ~11 days were reduced and analyzed using LC-MS assay (Figure 8). Figure 8 shows the relative peak areas of the cross-linked HL species for the control and samples containing the different amino acid additives. Both the addition of Ser and Tyr leads to reduction in the HL peak area, whereas no HL species was observed in incubated samples containing Cys.

DISCUSSION

In the manufacturing scheme for T-DM1, the lysine residues on the antibody Tmab are first modified via reaction with SMCC to obtain the intermediate T-MCC (Scheme 1). This intermediate consists of lysine residues on the antibody covalently bonded to the linker moiety MCC through an amide bond. In the subsequent conjugation reaction, the free thiol of the drug moiety DM1 reacts with the maleimide of the intermediate T-MCC via a Michael addition mechanism to produce the antibody-drug conjugate T-DM1. This process, a modification of the surface lysine residues, results in neutralization of the positive charge

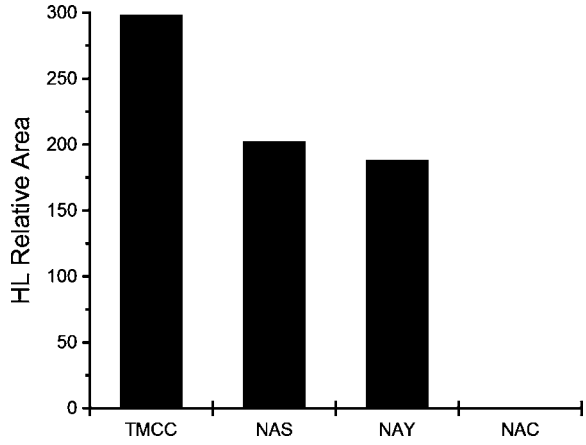


Figure 8. Differences in levels of cross-linked species present in thermally stressed samples of T-MCC and T-MCC treated with N-acetylated amino acids Ser (NAS), Tyr (NAY), and Cys (NAC). Relative levels of cross-linking were quantified from deconvoluted mass spectra.

on these residues as well as addition of a large (molecular weight ~959 Da) hydrophobic moiety on the antibody surface. The conjugated antibody T-DM1 that results from this processing is a heterogeneous species, with regard to both the number of lysine residues that are conjugated as well as the location of these conjugation sites. The average drug to antibody ratio of T-DM1 is 3.5 having anywhere from 1 to 7 lysine residues modified. Our studies assess the impact of these modification and conjugation reactions on the physicochemical attributes of the antibody.

To assess the structural stability of Tmab and its modified and conjugated forms, the three antibody forms were subjected to temperature-induced unfolding using DSC. The DSC profile for Tmab, the parent antibody, shows two transitions: the first transition at 68.2 °C and the second transition at 82.2 °C (Figure 1). Using DSC, Ionescu et al. studied the temperature-induced unfolding of three humanized IgG1 molecules and their Fab and Fc fragments (*20*). Their studies also included an investigation of the effect of variable domains present in IgG1s on the structural stability of the antibody. On the basis of the measured enthalpy of unfolding, it was proposed that, if the variable domain sequences in the IgG1 do not affect the thermal stability of the Fab fragment, then the first transition in the DSC thermogram represents the melting of the conserved heavy chain 2 (CH2) domain and the second transition represents melting of the CH3 domain and the Fab fragment. Tmab was one of three IgG1s investigated in their research study, and it was demonstrated that the first transition, which has a lower experimental enthalpy, represents the unfolding of the CH2 domain, while the second transition, with a higher experimental enthalpy, represents melting of the CH3 domain and the Fab region. Our results for Tmab were consistent with their observations. The DSC profiles of T-MCC and T-DM1, similar to Tmab, also showed two transitions (Figure 1). A comparison of the DSC profiles of the three antibody forms showed a decrease in t_m for both the first and second transitions following modification and conjugation processes with the following order: Tmab > T-MCC > T-DM1. The decrease in t_m observed for the first transition of Tmab following modification and conjugation processes was ~4.4 °C, whereas the decrease in t_m observed for the second transition was only ~0.8 °C. Also, the CH2 domain unfolding was observed to be a partially reversible transition in case of T-MCC. These results suggest that the modification and conjugation of Tmab has a significantly greater impact on the thermal stability of the CH2 domain than on the rest of the antibody.

Comparison to huN901-DM1, another humanized IgG1 antibody-maytansinoid conjugate that utilizes a similar linker chemistry to covalently attach the drug species DM1 to lysine residues on the antibody surface, provides some insight to the results presented here for T-DM1. The structural characterization of huN901-DM1 was performed by Wang et al. using mass spectrometry (*9*). Their studies identified 40 different conjugation sites on the IgG1 antibody, out of a total of 86 lysine residues that could possibly be covalently attached to the DM1 species. A majority of these conjugation sites were observed to be in the constant heavy chain and light chain regions of the antibody. Their investigations demonstrated that the drug molecules can distribute over ~47% of the available lysine residues, with the abundance of drug molecules at each particular site being relatively low. Out of the 40 conjugation sites that were identified, 12 were identified in the CH2 domain. The X-ray crystal structure of the CH2 domain of an IgG1 molecule (PDB ID: 1L6X) structure reveals that the Lys residues in the CH2 domain of the IgG1 show a high degree of solvent accessibility (structure not shown). The atomic displacement parameter, the *B* values, for the Lys side chains were computed based on the X-ray crystal structure of the IgG1. The *B* values were used to determine the local flexibilities of the lysine side chains. The values for the lysine side chain residues indicate that these lysine residues located in the CH2 domain are associated with more flexible regions of the IgG1 molecule (*9*). Both the surface accessibility and the flexibility are factors that could lead to greater reactivity of the CH2 Lys residues. The decrease in the structural stability observed, as per DSC, for the CH2 domain of Tmab after modification and conjugation could be attributed to the density of Lys residues present in the CH2 region as well as their propensity to react with the linker and drug species.

To further assess the biophysical stability of Tmab, T-MCC, and T-DM1, the three antibody forms were incubated at a stress condition of 40 °C over approximately 70 days (Figure 3). The major degradants identified following temperature stress at 40 °C using SEC were the dimer species and some higher-molecular-weight aggregate species (Figure 2). With regard to formation of these degradants, the following order of stability to temperature stress was observed among the three antibody forms investigated: Tmab > T-DM1 > T-MCC.

Recall that the structural stability predicted as per DSC was as follows: Tmab > T-MCC > T-DM1. Thus, the order of susceptibility of the three antibody forms to aggregate formation is not consistent with the order of thermal stability predicted as per DSC. Also, the aggregation behavior of T-MCC demonstrated a biphasic profile with a faster aggregation rate observed during the initial time period of 14 days (Figure 3), followed by a much slower aggregation rate upon prolonged storage. The unique aggregation behavior observed for T-MCC may be indicative of mechanisms other than the typical hydrophobic interactions that play a role in its degradation.

To further investigate the aggregation phenomenon observed in T-MCC, formulation samples subjected to temperature stress at 40 °C were analyzed using on-chip CE-SDS under nonreduced and reduced conditions (Figure 4a,b), as were samples of Tmab and T-DM1 exposed to the same thermal stress (electropherograms not shown). Under nonreduced conditions, several peaks corresponding to covalent aggregates were observed in the electrophoretic profile of T-MCC (Figure 4a). The observed molecular weights of these aggregates suggest presence of a covalent dimer species (molecular weight ~330 kDa), as well as some other aggregates involving monomer and dimer species. A comparison of the aggregate levels in SEC and nonreduced CE-SDS indicated that covalent aggregation contributed to ~84% of the total aggregation in the case of

T-MCC and ~30% of the total aggregation observed in the case of T-DM1 (Figure 6).

The free thiol content of Tmab is fairly low, experimentally determined to be ~0.2 mol/mol of antibody (internal document). As a result, the extent of aggregation observed cannot be explained solely on the basis of formation of intermolecular disulfide cross-links. However, the processing of Tmab to T-MCC could probably generate free thiols within the antibody via potential reduction of Cys residues.

To investigate the mechanism of covalent aggregation in case of T-MCC, on-chip CE-SDS was performed under reducing conditions. As shown in Figure 4b, for T-MCC a number of peaks in addition to those corresponding to heavy chain and light chain were observed. On the basis of the calculated molecular weights, these additional peaks corresponded to species such as HL, HH, HHL, and HHLL. If the covalent aggregates were primarily mediated through disulfide bonds, then the predominant species in the reduced CE-SDS is expected to be the H-chain and the L-Chain. The presence of various cross-linked species (HL, HH, HHL, and HHLL) suggests that other forms of covalent interactions are involved. Furthermore, it is possible that the cross-linking could be either intramolecular (i.e., within an antibody molecule) or intermolecular (i.e., involving different antibody molecules). It was noted that during incubation the percent increase in covalent aggregates for T-MCC, measured as per nonreduced CE-SDS assay, was comparable to the percent increase in cross-linked species, determined as per reduced CE-SDS assay (data not shown). This suggests that the formation of covalent aggregates in T-MCC samples results predominantly from formation of intermolecular nondisulfide mediated covalent cross-linking between the different H and L chains.

Mass spectrometric analysis of reduced T-MCC samples was performed to confirm the presence of the cross-linked species observed in the reduced CE-SDS assay. The most intense ions in the deconvoluted mass spectra of the reduced T-MCC samples correspond to light chain and heavy chain related fragments with minor species observed at *m*/*z* of 72 822 and 73 041 Da (Figure 5). The molecular weights of these species are in agreement with cross-linking between light chain and heavy chain through one and two MCC linkers, respectively (Table 1). However, other interchain cross-linked species such as HH, HHL, and HHLL were not observed. This is possibly the result of factors including poor ionization efficiency and poor transmission of higher mass ions through the mass spectrometer.

A comparison of the aggregation behavior of T-MCC and T-DM1 shows that T-DM1 has an increased stability to aggregation compared to T-MCC. As mentioned earlier, the aggregation of T-MCC is predominantly covalent in nature. The chemical difference between T-MCC and T-DM1 is the presence of free maleimide moieties on the T-MCC surface. T-DM1 is the product of the conjugation reaction, during which the thiol group of DM1 undergoes nucleophilic Michael addition to the double bond of the maleimidyl moiety of T-MCC. Other nucleophilic groups, such as amino groups and hydroxyl groups that are present abundantly on amino acid side chains of Tmab, can also react with the maleimide moiety of T-MCC to form interchain cross-links.

To investigate whether the formation of these intermolecular cross-links between nucleophilic amino acid side chains of T-MCC and its maleimide moiety was responsible for the covalent aggregation observed, the N-acetylated amino acids Cys, Lys, His, Ser, and Tyr were added to T-MCC formulations at concentration of 3 mM. After ~11 days under thermal stress conditions at 40 °C, SEC results (Figure 7) demonstrate that the aggregation observed for T-MCC was inhibited completely following addition of 3 mM Cys to the formulation. At 1.2 mM concentration of Cys, this represents a 2-fold molar excess over free maleimide moieties; a similar effect on inhibition of T-MCC aggregation was observed. Addition of amino acids Ser and Tyr also resulted in a significant (~8%) decrease in aggregation. In the case of Ser, it was noted that this inhibitory effect was concentration-dependent with a 4-fold increase in Ser concentration leading to 3-fold increase in inhibition. The inhibitory effect of Cys, Ser, and Tyr was also confirmed using LC-MS analysis of the reduced T-MCC formulation samples containing the different amino acids. Figure 8 shows the relative response of the cross-linked HL species in these samples. It was observed that reaction of T-MCC with Cys resulted in a very stable product where little to no cross-linked species were present after ~11 days under thermal stress conditions at 40 °C. Samples stressed in the presence of Ser and Tyr amino acids showed lower amounts of the cross-linked HL species compared with the control. This inhibition in the cross-linked HL species could be due to nucleophilic addition of Cys, Ser, and Tyr amino acids to the maleimide moiety that is present on T-MCC. This reaction would block formation of both intermolecular and intramolecular cross-links between the different heavy chain and light chains.

In conclusion, the modification and conjugation processes involved in synthesis of the antibody−drug conjugate T-DM1 destabilize the CH2 domain of the antibody. Wang et al. demonstrated that the lysine residues in this domain, due to their greater flexibility and solvent accessibility, are more susceptible to conjugation with the drug species DM1 than are those in other parts of the molecule (*9*). The increased susceptibility of the CH2 Lys residues to conjugation leads to disruption in the structural stability of this domain. In addition, T-MCC, an intermediate in the processing of T-DM1, is highly susceptible to covalent aggregation. This covalent aggregation could be due to formation of intermolecular cross-links involving the maleimidyl moiety and the side chains of nucleophilic amino acid such as Cys, Ser, or Tyr. The conjugation of the drug DM1 to T-MCC greatly increases the stability of the molecule to aggregation behavior.

ACKNOWLEDGMENT

The authors thank Drs. Oscar Salas-Solano and Fred Jacobson for their technical support and advice. We also thank Dr. Charlie Eigenbrot for providing us the X-ray crystal structure information on the IgG1 CH2 domain.

LITERATURE CITED

(1) Chari, R. V. (1998) Targeted delivery of chemotherapeutics: tumor-activated prodrug therapy. *Adv. Drug Delivery Rev. 31*, 89–104.

(2) Chari, R. V. (2008) Targeted cancer therapy: conferring specificity to cytotoxic drugs. *Acc. Chem. Res. 41*, 98–107.

(3) Erickson, H. K., Park, P. U., Widdison, W. C., Kovtun, Y. V., Garrett, L. M., Hoffman, K., Lutz, R. J., Goldmacher, V. S., and Blattler, W. A. (2006) Antibody-maytansinoid conjugates are activated in targeted cancer cells by lysosomal degradation and linker-dependent intracellular processing. *Cancer Res. 66*, 4426–4433.

(4) Payne, G. (2003) Progress in immunoconjugate cancer therapeutics. *Cancer Cell 3*, 207–212.

(5) Wu, A. M., and Senter, P. D. (2005) Arming antibodies: prospects and challenges for immunoconjugates. *Nat. Biotechnol. 23*, 1137–1146.

(6) Lambert, J. M. (2005) Drug-conjugated monoclonal antibodies for the treatment of cancer. *Curr. Opin. Pharmacol. 5*, 543–549.

(7) Cassady, J. M., Chan, K. K., Floss, H. G., and Leistner, E. (2004) Recent developments in the maytansinoid antitumor agents. *Chem. Pharm. Bull. (Tokyo) 52*, 1–26.

(8) Kupchan, S. M., Komoda, Y., Court, W. A., Thomas, G. J., Smith, R. M., Karim, A., Gilmore, C. J., Haltiwanger, R. C., and Bryan, R. F. (1972) Maytansine, a novel antileukemic ansa macrolide from Maytenus ovatus. *J. Am. Chem. Soc. 94*, 1354–1356.

(9) Wang, L., Amphlett, G., Blattler, W. A., Lambert, J. M., and Zhang, W. (2005) Structural characterization of the maytansinoid-monoclonal antibody immunoconjugate, huN901-DM1, by mass spectrometry. *Protein Sci. 14*, 2436–2446.

(10) Ranson, M., and Sliwkowski, M. X. (2002) Perspectives on anti-HER monoclonal antibodies. *Oncology 63* (Suppl 1), 17–24.

(11) Ross, S., Spencer, S. D., Holcomb, I., Tan, C., Hongo, J., Devaux, B., Rangell, L., Keller, G. A., Schow, P., Steeves, R. M., Lutz, R. J., Frantz, G., Hillan, K., Peale, F., Tobin, P., Eberhard, D., Rubin, M. A., Lasky, L. A., and Koeppen, H. (2002) Prostate stem cell antigen as therapy target: tissue expression and in vivo efficacy of an immunoconjugate. *Cancer Res. 62*, 2546–2553.

(12) Lu, S. X., Takach, E. J., Solomon, M., Zhu, Q., Law, S. J., and Hsieh, F. Y. (2005) Mass spectral analyses of labile DOTA-NHS and heterogeneity determination of DOTA or DM1 conjugated anti-PSMA antibody for prostate cancer therapy. *J. Pharm. Sci. 94*, 788–797.

(13) Beeram, M., Krop, I., Modi, S., Tolcher, A., Rabbee, N., Girish, S., Tibbitts, J., Holden, S., Lutzker, S., and Burris, H. (2007) A phase I study of trastuzumab-MCC-DM1(T-DM1), a first-in-class HER2 antibody-drug conjugate (ADC), in patients (pts) with HER2+ metastatic breast cancer (BC). *J. Clin. Oncol., ASCO Annual Meeting Proceedings 25*.

(14) Lewis-Phillips, G. D., Li, G., Dugger, D. L., Crocker, L. M., Parsons, K. L., Mai, E., Blattler, W. A., Lambert, J. M., Chari, R. V., Lutz, R. J., Wong, W. L., Jacobson, F. S., Koeppen, H., Schwall, R. H., Kenkare-Mitra, S. R., Spencer, S. D., and Sliwkowski, M. X. (2008) Targeting HER2-positive breast cancer with trastuzumab-DM1, an antibody-cytotoxic drug conjugate. *Cancer Res. 68*, 9280–9290.

(15) Morris, P. G., and Fornier, M. N. (2009) Novel anti-tubulin cytotoxic agents for breast cancer. *Exp. Rev. Anticancer Ther. 9*, 175–185.

(16) Jacobson, F., Wang, Y., Wakankar, A., Rivera, J., Lee, C., Bechtel, C., and Chen, Y. (2009) Characterization and comparability of Trastuzumab-DM1, *WCBP 2009 Abstracts P-127-M*.

(17) Adamczyk, M., Gebler, J., Shreder, K., and Wu, J. (2000) Region-selective labeling of antibodies as determined by electrospray ionization-mass spectrometry (ESI-MS). *Bioconjugate Chem. 11*, 557–563.

(18) Siegel, M. M., Tabei, K., Kunz, A., Hollander, I. J., Hamann, R. R., Bell, D. H., Berkenkamp, S., and Hillenkamp, F. (1997) Calicheamicin derivatives conjugated to monoclonal antibodies: determination of loading values and distributions by infrared and UV matrix-assisted laser desorption/ionization mass spectrometry and electrospray ionization mass spectrometry. *Anal. Chem. 69*, 2716–2726.

(19) Lazar, A. C., Wang, L., Blattler, W. A., Amphlett, G., Lambert, J. M., and Zhang, W. (2005) Analysis of the composition of immunoconjugates using size-exclusion chromatography coupled to mass spectrometry. *Rapid Commun. Mass Spectrom. 19*, 1806–1814.

(20) Ionescu, R. M., Vlasak, J., Price, C., and Kirchmeier, M. (2008) Contribution of variable domains to the stability of humanized IgG1 monoclonal antibodies. *J. Pharm. Sci. 97*, 1414–1426.

BC900434C

Cholic Acid-Modified Dendritic Multimolecular Micelles and Enhancement of Anticancer Drug Therapeutic Efficacy

Kun Zhang,[†] Yongjian Wang,*[,‡] Ao Yu,[§] Yue Zhang,[‡] Hao Tang,[§] and X. X. Zhu*[,†,#]

Key Laboratory of Functional Polymer Materials (Ministry of Education), Institute of Polymer Chemistry; Key Laboratory of Bioactive Materials (Ministry of Education), College of Life Sciences; and Central Laboratory, College of Chemistry, Nankai University, Tianjin 300071, China and Département de chimie, Université de Montréal, C.P. 6128, Succursale Centre-ville, Montréal, Quebec H3C 3J7, Canada. Received November 8, 2009; Revised Manuscript Received July 15, 2010

To improve the efficacy and bioacceptability of polyamidoamine (PAMAM) in potential biomedical applications, the PAMAM dendrimers (first generation) were partially modified with cholic acid. ^{1}H NMR studies and acid−base titration show that two cholic acid molecules are linked to one PAMAM. The modified PAMAM dendrimers self-assemble to form dendritic multimolecular micelles in aqueous solutions, with a diameter of 120 nm measured by dynamic light scattering. These micelles can encapsulate hydrophobic drug molecules in aqueous media and exhibit pH sensitivity. The in vitro results demonstrate that the anticancer activity of camptothecin is significantly enhanced at low drug dose after being encapsulated by these micelles in the presence of serum. Therefore, the dendritic multimolecular micelles based on low generation dendrimers may have potential applications in the delivery of drugs.

INTRODUCTION

Dendrimers, which are monodisperse macromolecules with well-defined highly branched architecture, have attracted much attention in drug delivery (*1*−*4*), gene therapy (*5*−*7*), MRI contrast enhancement (*8, 9*), liquid crystalline materials (*10, 11*), electronics (*12*−*14*), and catalysis (*15, 16*). Their unique architecture makes them capable of encapsulating, complexing, or conjugating various molecules as unimolecular micelles (*17*). However, dendrimers as unimolecules are small in size. For example, the hydrodynamic diameters of G0-G7 polyamidoamine (PAMAM) dendrimers with an ethylenediamine core are in the range 1.4−8.8 nm (*18*) and G1-G5 poly(propylene imine) dendrimers are in the range 0.6−2.0 nm (*19*). Thus, they accumulate less in tumoral tissues than micelles, because the usual size of pharmaceutical carriers with the enhanced permeation and retention (EPR) effect is between 10 and 100 nm (*20*). On the other hand, the regulatory hurdles of high generation dendrimers with good quality and purity are difficult to overcome. The self-assembly of dendrimers into larger and more complex forms may resolve these problems and lead to a wider range of potential applications. Fahmy and co-workers showed that the self-assembly of partial fluorinated G3 PAMAM into larger, dense nanoparticulates enabled the detection of their site-specific accumulation in vivo by ^{19}F magnetic resonance imaging (*21*). Thayumanavan and co-workers used facially amphiphilic dendrons (G1−G3) which exhibited environmentally dependent aggregation to selectively extract peptides from aqueous solutions and found that the organization of the dendrons themselves was crucial for the binding event (*22, 23*). Therefore, the aggregation may improve the properties of dendrimers, especially low generation ones. However, reports on dendritic multimolecular micelles for drug delivery have been rare to date.

Dendritic multimolecular micelles can be obtained by amphiphilic dendrimers with self-assembling properties (*22, 24*). The end groups of dendrimers can be modified to vary the property of the dendrimers and improve their performance. PAMAM dendrimers, which are commercially available and have been widely studied in biomedical fields (*4*), may form multimolecular micelles once they are hydrophobically modified on their terminal groups (*21, 25*−*27*). The residual surface groups can be further modified into other functional groups to serve for imaging, targeted release, and drug anchors (*28*−*30*). Furthermore, the positive charges of the remaining unmodified surface groups improve drug therapeutic efficiency by enhancing intracellular delivery (*31*).

Cholic acid is a facially amphiphilic natural compound and has been used to construct supramolecular systems (*32*−*35*). It has pharmacological potential to act as an adjuvant of liver-specific drugs and absorption enhancers (*36, 37*). In this work, we prepared dendrimer-based multimolecular micelles by the self-assembly of the first generation PAMAM (G1 PAMAM) dendrimers partially modified with cholic acid and investigated its aggregation behavior and application on improving drug efficacy, where camptothecin (CPT) was used as a hydrophobic anticancer drug model.

EXPERIMENTAL PROCEDURES

Materials and General Characterization. G1 PAMAM with an ethylenediamine core, cholic acid, pyrene, Oil Red O, and 3-(4,5-dimethyl-2-thiazolyl)-2,5-diphenyl-2*H*-tetrazolium bromide (MTT) were purchased from Sigma-Aldrich (USA). CPT was purchased from Mianyang Dongfangyuan Biotechnology Co., Ltd. (Sichuan, China). *N*-Hydroxysuccinimide and dicyclohexyl carbodiimide (DCC) were obtained from Shanghai Medpep Co., Ltd. (Shanghai, China). Methanol-d_4 was provided by J&K Chemical, Ltd. (Beijing, China). Methanol, acetonitrile, and tetrahydrofuran (THF) were supplied from Kermel Chemical Reagent Co., Ltd. (Tianjin, China), and distilled prior to use following standard procedures. Dulbecco's modified Eagle's medium (DMEM) was purchased from Gibco (Grand Island, USA). Fetal bovine serum (FBS) and penicillin−streptomycin

* Corresponding author. Y. Wang: Tel./Fax: +86 22 23501393, yongjian_wang@nankai.edu.cn. X. X. Zhu: Tel.: +1 514 340 5172; Fax: +1 514 340 5290, julian.zhu@umontreal.ca.

[†] Key Laboratory of Functional Polymer Materials, Nankai University.

[‡] Key Laboratory of Bioactive Materials, Nankai University.

[§] Central Laboratory, Nankai University.

[#] Université de Montréal.

10.1021/bc900490u © 2010 American Chemical Society
Published on Web 08/18/2010

were from Us-bio (Tianjin, China). Unless otherwise noted, all chemicals were used without further purification. ^{1}H and ^{13}C NMR spectra were all recorded on a Varian Mercury 300 NMR spectrometer (^{1}H, 300 MHz; ^{13}C, 75 MHz). Mass spectrum was obtained on a Bruker Biflex III MALDI-TOF spectrometer.

Synthesis of *N*-Succinimidyl Ester of Cholic Acid (CA-NHS). This compound was synthesized by reacting cholic acid with *N*-hydroxysuccinimide in dry THF and acetonitrile with DCC according to a procedure published previously (*38*). The crude product was purified by column chromatography (petroleum ether/acetone = 1/1.5). Yield: 62.6%; mp: 119−120 °C.

Synthesis of PAMAM1-CA$_2$. CA-NHS (0.3727 g, 0.738 mmol) and G1 PAMAM (0.5269 g, 0.369 mmol) were mixed in methanol (15 mL) and stirred at room temperature for 48 h. The product was purified by dialysis (MWCO 2000) against methanol. After dialysis, methanol was evaporated under reduced pressure, and the residue was dried in vacuo to afford a white powder. The yield was 0.73 g (89.6%). ^{1}H NMR (300 MHz, CD_3OD) δ: 0.70 (s, 6H, 18-H), 0.91 (s, 6H, 19-H), 1.03 (d, 6H, 21-H), 2.37 (s, 24H, CH_2CO), 2.48 (s, 4H, the core CH_2N), 2.57 (s, 8H, CH_2N), 2.79 (s, 24H, NCH_2), 3.60 (m, 2H, 3β-H), 3.79 (s, 2H, 12β-H), 3.95 (s, 2H, 7β-H). ^{13}C NMR (75 MHz, CD_3OD) δ: 11.97, 16.75, 22.12, 23.15, 26.76, 27.66, 28.12, 28.52, 30.11, 32.16, 33.65, 34.76, 35.38, 35.85, 37.49, 38.95, 39.88, 40.85, 41.67, 41.90, 42.04, 46.33, 46.82, 47.91, 48.76, 50.02, 67.82, 71.69, 72.79, 174.01, 174.94, 175.43. MALDI-TOF: *m/z* calcd for $C_{110}H_{204}N_{26}O_{20}$ $[M+H]^+$ 2211.585, $[M+Na]^+$ 2233.567, found $[M+H]^+$ 2211.586, $[M+Na]^+$ 2233.563.

Acid−Base Titration. The titration experiments were performed using a Metrohm model 809 Titrando apparatus (Metrohm, Herisau, Switzerland) controlled by *Metrohm Tiamo 1.2* software at room temperature. Approximately 150 mg of G1 PAMAM or PAMAM1-CA$_2$ was dissolved in 50 mL of 0.1 M NaCl solution. These solutions were titrated by aqueous hydrochloric acid to a pH value around 2.0, followed by back-titration to pH 11.0 using 0.0935 M NaOH. The number of primary amines was determined from the back-titration data.

Preparation of PAMAM1-CA$_2$ Micelles. PAMAM1-CA$_2$ was dispersed evenly in citrate buffer (0.1 M, pH 5.0), phosphate buffer (0.1 M, pH 5.5, 6.8, 7.4), or borate buffer (0.1 M, pH 9.0) after sonication for 2 min. Then, the mixture was equilibrated by shaking at 65 °C for 3 h.

Preparation of CPT-Loaded Micelles. A measured volume of a CPT chloroform solution was added to a vial and the solvent was then evaporated. Ten milliliters of PAMAM1-CA$_2$ solution were then added to this vial and dispersed evenly by sonication for 2 min. The mixture was equilibrated at 65 °C for 3 h. After cooling, the solutions were filtered via 0.22 μm filter. The concentration of CPT in the solution was determined by UV−vis spectrometry (Varian Cary 100 BIO, America) (369 nm).

Dye Solubilization. A series of PAMAM1-CA$_2$ solutions with different pH values (5.0, 7.4, and 9.0) were added to the vials containing an excess amount of Oil Red O and were equilibrated at 65 °C for 3 h. After cooling, the solutions were filtered to remove the residual dye. Absorbance data were recorded on a UV−vis spectrophotometer at 518 nm.

Fluorescence Spectroscopy. The pyrene fluorescence emission spectra were recorded with a Varian Cary Eclipse fluorescence spectrophotometer. A given amount of pyrene stock solution in acetone was placed in empty vials, and the solvent was then evaporated. Five milliliter aliquots of PAMAM1-CA$_2$ aqueous solutions of various concentrations were then added to these vials. The final pyrene concentration was 6×10^{-7} M. The mixtures were equilibrated to form PAMAM1-CA$_2$ micelles. The fluorescence emission spectra of pyrene were recorded at an excitation wavelength of 339 nm, and the scanning wavelength range was from 360 to 460 nm.

Transmission Electronic Microscopy (TEM) and Dynamic Light Scattering (DLS). The sample for TEM was prepared at room temperature by placing a drop of PAMAM1-CA$_2$ solution on 300 mesh carbon-coated copper grids. The excess fluid was blotted off using filter paper, and then the sample was dried in vacuo. Microscopy was done on a FEI Tecnai G2 20 S-TWIN transmission electron microscope equipped with Gatan 794 CCD camera. The DLS measurement was done with a Malvern Nano ZS instrument with a 633 nm 4 mW He−Ne laser. The sample (2 g/L) was measured at 25 °C and at a backscatter angle of 173°.

Cytotoxicity Study. Mouse embryonic fibroblast cells (NIH 3T3) and human hepatocellular liver carcinoma cells (HepG2) were cultured in DMEM containing 10% (v/v) FBS and 0.5% (w/v) penicillin−streptomycin, at 37 °C in a humidified 5% CO_2/95% air atmosphere.

Cells were seeded in 96-well plates at a density of 1×10^4 cells/well and allowed to adhere for 24 h. The culture medium was replaced by fresh DMEM containing various drug and dendrimer samples (CPT, PAMAM1-CA$_2$ and CPT encapsulated in G1 PAMAM or PAMAM1-CA$_2$), and the mixture was further incubated for 24 h. Fresh culture medium without drug or dendrimer was used as control. Each sample was replicated in five wells. The cells were then washed twice with phosphate buffer, and the fresh culture medium was added. Ten microliters of MTT solution (5 g/L in phosphate buffer) were added to each well and the cells were incubated further for 4 h at 37 °C. After the media were removed, the cells were washed with phosphate buffer and dissolved in DMSO. The optical density (OD) was measured at 570 nm with a Multiskan Ascent plate reader (Thermo Labsystems, Helsinki, Finland). Cell viability (%) = $(OD_{sample}/OD_{control}) \times 100\%$, where $OD_{control}$ and OD_{sample} were obtained in the absence or presence of drug and dendrimer samples, respectively. The inhibition of cell growth was calculated from: Inhibition (%) = 100% − cell viability (%).

RESULTS AND DISCUSSION

Characterization of the Dendrimers. The G1 PAMAM dendrimers used in this study are based on an ethylenediamine core and possess 8 amino groups on the surface. Cholic acid-functionalized PAMAM was synthesized by reacting the primary amine groups of G1 PAMAM with CA-NHS under mild conditions (Scheme 1). The modified PAMAM (PAMAM1-CA$_2$) has 2 cholic acid groups per PAMAM molecule as characterized by ^{1}H NMR and acid−base titration (Table 1). The product reserves most of the terminal amino groups maintaining its solubility in aqueous solutions (with a saturation concentration of ca. 8 g/L in 0.1 M phosphate buffer).

Aggregation Properties. The formation of micelles was evidenced by dye solubilization (*39*) with Oil Red O, a diazo dye with a strong hydrophobic character. Large amounts of Oil Red O were added to the vials containing PAMAM1-CA$_2$ solutions of various concentrations. The mixtures were equilibrated by shaking at 65 °C for 3 h and cooling to room temperature. Red solutions were obtained after filtering the mixtures to remove residual insoluble dye (Figure 1). The UV−vis absorption results of the filtrates showed that Oil Red O was transferred into the hydrophobic environment of the micelles formed.

The encapsulation of the guest molecules by the micelles is pH-dependent since Oil Red O has a lower solubility in acidic media (pH 5.0) than in neutral or basic media (pH 7.4−9.0) (Figure 1). This may be ascribed to the conformation change of PAMAM along with pH (*40*).

Scheme 1

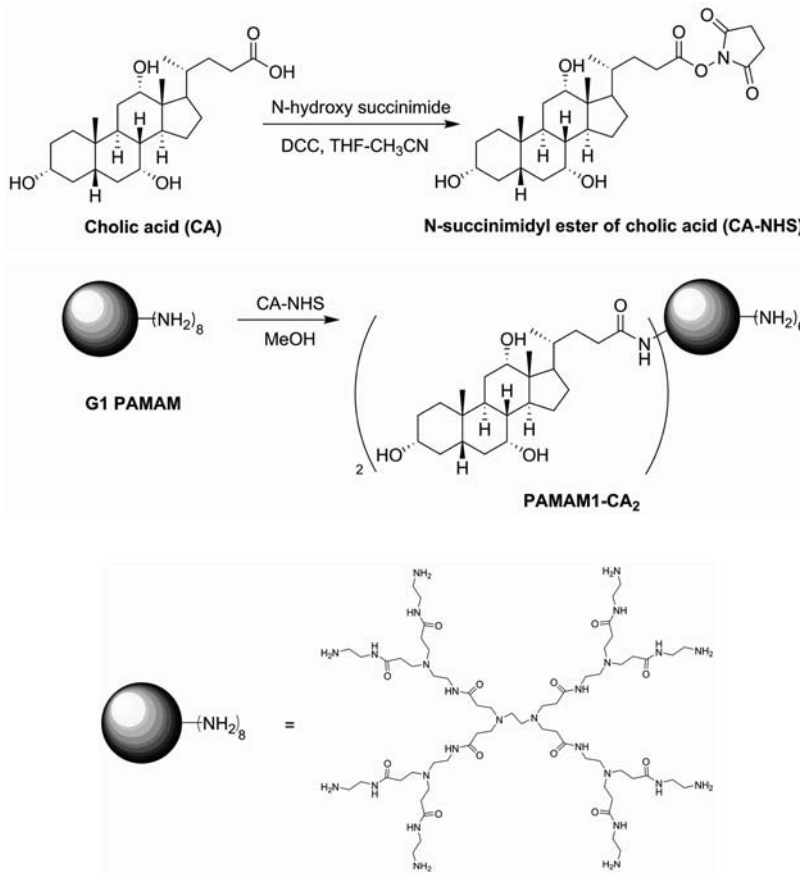


Table 1. Numbers of Terminal Amino Groups and Cholic Acid Groups

sample	number of terminal amino groups measured by titration	number of cholic acid groups	
		titration[a]	^{1}H NMR[b]
G1 PAMAM	7.53	-	-
PAMAM1-CA_2	5.36	2.17	1.96

[a] Number of cholic acid groups = Number of terminal amino groups of G1 PAMAM − Number of terminal amino groups of PAMAM1-CA_2. [b] Obtained from ^{1}H NMR.

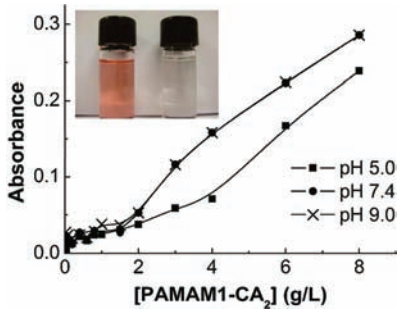


Figure 1. Oil Red O solubilization (absorbance at 518 nm) as a function of PAMAM1-CA_2 concentration at different pH values, showing that the dye solubilization by PAMAM1-CA_2 is pH-dependent. The insert shows the solubilization of Oil Red O in phosphate buffer at pH 7.4 with PAMAM1-CA_2 (left) and G1 PAMAM (right).

The formation of micelles in aqueous solution was further verified by a fluorescence technique with pyrene as a hydrophobic probe (*41*). In the emission spectra, the fluorescence intensity of pyrene in water was very low since pyrene is sparingly soluble in water. However, its intensity in PAMAM1-CA_2 solutions increased with increasing PAMAM1-CA_2 concentration above a certain level, since more pyrene molecules entered the hydrophobic environment upon the aggregation of PAMAM1-CA_2. From the plot of fluorescence intensity ratio (I_3/I_1) versus PAMAM1-CA_2 concentration (Figure 2), it can be observed that the I_3/I_1 value was almost constant at low PAMAM1-CA_2 concentrations followed by an abrupt increase at a certain PAMAM1-CA_2 concentration, indicating the transfer of pyrene into the hydrophobic environment of the micelles formed. The critical micelle concentration (CMC) of PAMAM1-CA_2 in an aqueous solution is thus defined by the intersection of the two linear segments of the curve. The CMC value was estimated to be ca. 80 mg/L (3.6×10^{-5} M), a value between the CMC of block polymers (10^{-6}−10^{-7} M) and that of small molecule surfactants (10^{-3}−10^{-4} M). These results indicate that the micelles are stable in aqueous solutions.

The aggregated PAMAM1-CA_2 showed spherical nanoparticles, and the mean diameter was in the range 50−70 nm with

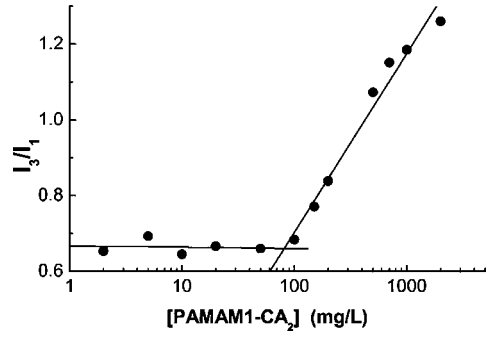


Figure 2. Ratio of vibronic bands (I_3/I_1) in the pyrene fluorescence emission spectra as a function of PAMAM1-CA_2 concentration (concentration of pyrene was 6×10^{-7} M in phosphate buffer at pH 7.4.), showing that the CMC of PAMAM1-CA_2 is 80 mg/L.

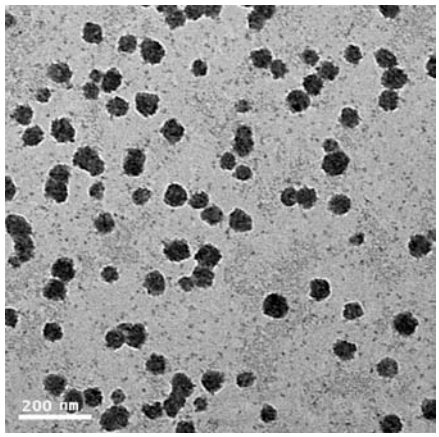


Figure 3. TEM image of the PAMAM1-CA_2 micelles (100 mg/L in phosphate buffer, pH 7.4), showing that the average size of the micelles is in the range 50−70 nm.

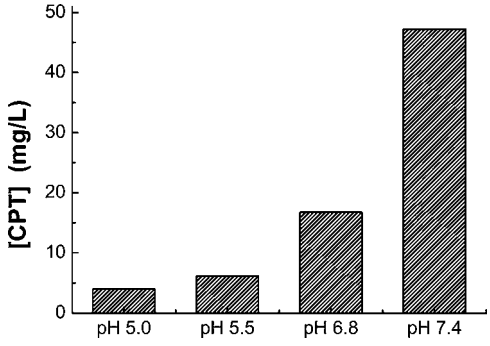


Figure 4. The solubility of CPT in phosphate buffer solutions with PAMAM1-CA_2 micelles, showing the pH-dependence of the drug encapsulation.

a narrow size distribution observed from the TEM images (Figure 3), while the diameter of PAMAM1-CA_2 in aqueous solution was about 120 nm which was measured by DLS. The dimension of PAMAM1-CA_2 molecules should be approximately 4 nm, based on the diameter of G1 PAMAM and the length of the cholic acid molecule (about 2.2 nm (*42*) and 1.5 nm, respectively). Therefore, PAMAM1-CA_2 forms multimolecular aggregates in aqueous solutions. According to the literature (*20*), the usual size of a pharmaceutical micelle is between 10 and 100 nm, and its CMC value is expected to be in the low millimolar region. Thus, the PAMAM1-CA_2 micelle may be used as a drug carrier.

Drug Encapsulation Property. On the basis of the fact that the encapsulation of Oil Red O by the micelles is pH-dependent, we further examined the influences of medium pH values on the solubility property of CPT. Four pH values (5.0, 5.5, 6.8, and 7.4) of dissolution media were utilized. As shown in Figure 4, pH values of medium notably affected CPT solubility. When pH decreased from 7.4 to 5.0, the solubility of CPT was much decreased. With this pH-sensitivity, PAMAM1-CA_2 may be used for the controlled release of encapsulated drugs by a pH trigger in physiological environments of tumor tissues or intracellular endosome and lysosome where there is a significant drop in the pH value. Therefore, these micelles may act as smart drug-releasing devices responding to pH change and targeting tumor tissues.

Cytotoxicity Studies. The cytotoxicity of the dendrimers was done with a methylthiazoletetrazolium method in NIH 3T3 and HepG2. The IC_{50} value, a concentration at which 50% cells are killed, of PAMAM1-CA_2 was ca. 117 mg/L for NIH 3T3, while that of the molecular umbrella analogues (with a similar molecular weight) and polyethyleneimine (with a molecular weight of 25 kDa) are 4 mg/L (*43*) and 6 mg/L (*44*), respectively. The results indicate that the dendrimer-based multimolecular micelles have a lower cytotoxicity.

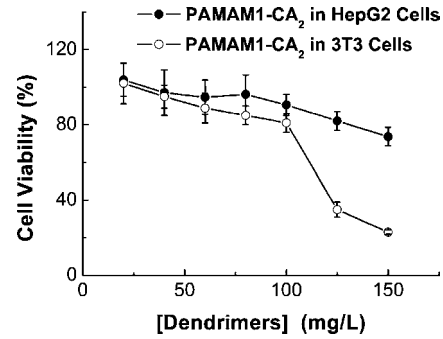


Figure 5. Cytotoxicity assay with 3T3 and HepG2 cells (10^4 cells/well) after incubation with dendrimers at 37 °C for 24 h, showing that PAMAM1-CA_2 is not cytotoxic (>80% cell viability) below a concentration of 100 mg/L for NIH 3T3 and 125 mg/L for HepG2, respectively.

As indicated in Figure 5, PAMAM1-CA_2 was not cytotoxic (>80% cell viability) below a concentration of 100 mg/L for NIH 3T3 and 125 mg/L for HepG2, respectively. On the basis of these data, the investigation of anticancer activity of the micelles was carried out in a dendrimer concentration of 100 mg/L. Under this condition, the micelles are not cytotoxic and the enhancement of drug therapeutic efficacy should be attributed to the contribution of the micelles encapsulated with the drug.

Inhibition of Tumor Cell Growth. To investigate the enhancement of therapeutic efficacy by the micelles, the inhibition of tumor cell (HepG2) growth was evaluated. HepG2 cells (10^4 cells/well) were exposed to an equivalent concentration (4.5 mg/L, 13 μM) of free CPT or CPT encapsulated in G1 PAMAM or the micelles (PAMAM1-CA_2 concentration at 100 mg/L) in the presence of serum for 24 h, and the cell growth inhibition was determined using the methylthiazoletetrazolium assay. The inhibition was significantly enhanced in the case of CPT encapsulated in PAMAM1-CA_2 (enhancement of 46.4% over free CPT), while it had no apparent increase in the case of CPT encapsulated in G1 PAMAM (only 1.3% enhancement over free CPT) (Figure 6A). These data reveal that the cholic acid-modified dendrimers (PAMAM1-CA_2) can improve the drug efficacy at the same drug dose of free CPT while the non-modified dendrimers (G1 PAMAM) cannot. We further investigated the effect of PAMAM1-CA_2 concentration on drug efficacy. The results show that the cell growth inhibition is close to that by free CPT when the PAMAM1-CA_2 concentration is lower than its CMC (80 mg/L), but inhibition increases sharply to over 90% at a higher concentration (above CMC, Figure 6B). These results indicate that the individual PAMAM1-CA_2 molecules cannot improve the drug efficacy but its micellar aggregates can. Also, the improvement by these dendrimer-based multimolecular micelles does not require a high drug dose. This micellar drug delivery system can effectively avoid the problems of drug accumulation in other tissues and the effects on metabolism which are caused by higher drug doses in the clinical use of drug delivery systems of polymeric micelles or nanoparticles.

To examine the effect of dendritic multimolecular micelles on drug efficacy, we further investigated the cytotoxicity of CPT-encapsulated PAMAM1-CA_2 micelles against tumor cells at several CPT doses (Figure 7). The PAMAM1-CA_2 concentration was fixed at 100 mg/L at which the micelles are noncytotoxic. In comparison with free CPT, the CPT-encapsulated PAMAM1-CA_2 micelles induced a significant cytotoxic effect

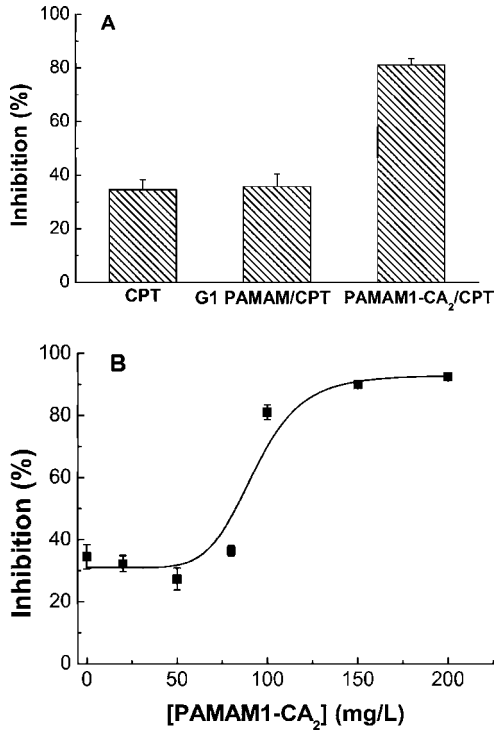


Figure 6. Comparative tumor cell growth inhibition profiles of free CPT and CPT encapsulated in G1 PAMAM (G1 PAMAM/CPT) and PAMAM1-CA_2 (PAMAM1-CA_2/CPT) in HepG2 cells (A) and the effect of PAMAM1-CA_2 concentration on the tumor cell growth inhibition (B). The amount of CPT is 4.5 mg/L in every experiment. HepG2 cells were incubated for 24 h. Dulbecco's modified Eagle's medium (DMEM) was chosen as a control. The cytotoxicity was measured by the methylthiazoletetrazolium assay. Data are shown as mean ± SD ($n = 5$). The results showed that the drug efficacy was significantly enhanced in the case of CPT encapsulated in micelles. PAMAM1-CA_2 had no cytotoxicity under the experimental conditions.

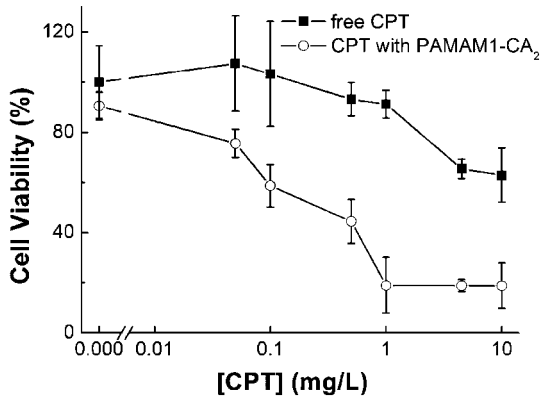


Figure 7. Cytotoxicity assay with HepG2 cells (10^4 cells/well) after incubation with free CPT and CPT encapsulated in PAMAM1-CA_2 micelles (100 mg/L) at 37 °C for 24 h, showing that the dendritic multimolecular micelles can improve drug efficacy.

to the tumor cells, even at relatively low drug concentration. Therefore, the results indicate that the dendritic multimolecular micelles can improve drug efficacy without increasing the chemotherapeutic drug dose.

It is necessary for CPT to be transported into the cells before it takes pharmacological effect. Since the CPT molecules go through the plasma membrane by passive diffusion, a high dose is needed to increase the therapeutic efficacy. Micelles may be internalized by cells mainly through an efficient endocytic process (*45*, *46*). In addition, the positive charges of the amines on the micelle surface may improve the cellular uptake of micelles, including the drugs which encapsulated in the micelles. Hence, the micelles would greatly enhance the cellular uptake efficiency of the drug so that it is much more potent than the free drug, even at a low drug dose. Although the PAMAM dendrimers themselves also have amines on the surface, they scarcely have the capacities to interact with CPT. Therefore, the unmodified PAMAM cannot enhance the cellular uptake of CPT efficiently.

CONCLUSION

Multimolecular micelles were obtained in aqueous media by the self-assembly of G1 PAMAM dendrimers partially modified with cholic acid. In comparison with the dendrimer alone, the modified dendrimers can significantly enhance the anticancer activity of camptothecin after its encapsulation in the micelles under low dose in the presence of serum. The new micelles may improve drug efficiency without increasing the drug dose. These multimolecular micelles based on low generation dendrimers may have important clinical relevance for cancer therapy. Issues regarding the stability of the micelles in biological media and the optimization of the system remain to be investigated.

ACKNOWLEDGMENT

The financial support from the National Natural Science Foundation of China (Grant no. 20574039), Tianjin Natural Science Foundation (Grant no. 07JCYBJC02700), and the Canada Research Chair Program is acknowledged. X.X.Z. thanks Fonds Barré for travelling support during his sabbatical leave in Nankai University.

LITERATURE CITED

(1) Medina, S. H., and El-Sayed, M. E. H. (2009) Dendrimers as carriers for delivery of chemotherapeutic agents. *Chem. Rev. 109*, 3141–3157.
(2) Tekade, R. K., Kumar, P. V., and Jain, N. K. (2009) Dendrimers in oncology: an expanding horizon. *Chem. Rev. 109*, 49–87.
(3) Boas, U., and Heegaard, P. M. H. (2004) Dendrimers in drug research. *Chem. Soc. Rev. 33*, 43–63.
(4) Esfand, R., and Tomalia, D. A. (2001) Poly(amidoamine) (PAMAM) dendrimers: from biomimicry to drug delivery and biomedical applications. *Drug Discovery Today 6*, 427–436.
(5) Wang, Y., Kong, W., Song, Y., Duan, Y., Wang, L., Steinhoff, G., Kong, D., and Yu, Y. (2009) Polyamidoamine dendrimers with a modified pentaerythritol core having high efficiency and low cytotoxicity as gene carriers. *Biomacromolecules 10*, 617–622.
(6) de Jong, G., Telenius, A., Vanderbyl, S., Meitz, A., and Drayer, J. (2001) Efficient in-vitro transfer of a 60-Mb mammalian artificial chromosome into murine and hamster cells using cationic lipids and dendrimers. *Chromosome Res. 9*, 475–485.
(7) Eichman, J. D., Bielinska, A. U., Kukowska-Latallo, J. F., and Baker, J. R. (2000) The use of PAMAM dendrimers in the efficient transfer of genetic material into cells. *Pharm. Sci. Technol. Today 3*, 232–245.
(8) Konda, S. D., Wang, S., Brechbiel, M., and Wiener, E. C. (2002) Biodistribution of a 153Gd-folate dendrimer, generation = 4, in mice with folate-receptor positive and negative ovarian tumor xenografts. *Invest. Radiol. 37*, 199–204.
(9) Kobayashi, H., Kawamoto, S., Jo, S. K., Bryant, H. L., Brechbiel, M. W., and Star, R. A. (2003) Macromolecular MRI contrast agents with small dendrimers: pharmacokinetic differences between sizes and cores. *Bioconjugate Chem. 14*, 388–394.

(10) Balagurusamy, V. S. K., Ungar, G., Percec, V., and Johansson, G. (1997) Rational design of the first spherical supramolecular dendrimers self-organized in a novel thermotropic cubic liquid-crystalline phase and the determination of their shape by X-ray analysis. *J. Am. Chem. Soc. 119*, 1539–1555.
(11) Goran, U., Virgil, P., Marian, N. H., Gary, J., and James, A. H. (2000) Heat-shrinking spherical and columnar supramolecular dendrimers: their interconversion and dependence of their shape on molecular taper angle. *Chem.—Eur. J. 6*, 1258–1266.
(12) Pitois, C., Hult, A., and Lindgren, M. (2005) Lanthanide-cored fluorinated dendrimer complexes: synthesis and luminescence characterization. *J. Lumin. 111*, 265–283.
(13) D'Ambruoso, G. D., and McGrath, D. V. (2008) Energy harvesting in synthetic dendrimer materials, *Advances in Polymer Science. Vol. 214: Photoresponsive Polymers II*, (Marder, S. R., and Lee, K.-S., Eds.) pp 87−147, Chapter 2, Springer-Verlag Berlin, Berlin.
(14) Archut, A., Azzellini, G. C., Balzani, V., De Cola, L., and Vogtle, F. (1998) Toward photoswitchable dendritic hosts. Interaction between azobenzene-functionalized dendrimers and eosin. *J. Am. Chem. Soc. 120*, 12187–12191.
(15) Kollner, C., Pugin, B., and Togni, A. (1998) Dendrimers containing chiral ferrocenyl diphosphine ligands for asymmetric catalysis. *J. Am. Chem. Soc. 120*, 10274–10275.
(16) Twyman, L. J., King, A. S. H., and Martin, I. K. (2002) Catalysis inside dendrimers. *Chem. Soc. Rev. 31*, 69–82.
(17) D'Emanuele, A., and Attwood, D. (2005) Dendrimer-drug interactions. *Adv. Drug Delivery Rev. 57*, 2147–2162.
(18) Tomalia, D. A., Naylor, A. M., and Goddard, W. A. (1990) Starburst dendrimers: molecular-level control of size, shape, surface chemistry, topology, and flexibility from atoms to macroscopic matter. *Angew. Chem., Int. Ed. Engl. 29*, 138–175.
(19) Scherrenberg, R., Coussens, B., van Vliet, P., Edouard, G., Brackman, J., de Brabander, E., and Mortensen, K. (1998) The molecular characteristics of poly(propyleneimine) dendrimers as studied with small-angle neutron scattering, viscosimetry, and molecular dynamics. *Macromolecules 31*, 456–461.
(20) Gullotti, E., and Yeo, Y. (2009) Extracellularly activated nanocarriers: a new paradigm of tumor targeted drug delivery. *Mol. Pharmaceutics 6*, 1041–1051.
(21) Criscione, J. M., Le, B. L., Stern, E., Brennan, M., Rahner, C., Papademetris, X., and Fahmy, T. M. (2009) Self-assembly of pH-responsive fluorinated dendrimer-based particulates for drug delivery and noninvasive imaging. *Biomaterials 30*, 3946–3955.
(22) Vutukuri, D. R., Basu, S., and Thayumanavan, S. (2004) Dendrimers with both polar and apolar nanocontainer characteristics. *J. Am. Chem. Soc. 126*, 15636–15637.
(23) Gomez-Escudero, A., Azagarsamy, M. A., Theddu, N., Vachet, R. W., and Thayumanavan, S. (2008) Selective peptide binding using facially amphiphilic dendrimers. *J. Am. Chem. Soc. 130*, 11156–11163.
(24) Radowski, M. R., Shukla, A., von Berlepsch, H., Bottcher, C., Pickaert, G., Rehage, H., and Haag, R. (2007) Supramolecular aggregates of dendritic multishell architectures as universal nanocarriers. *Angew. Chem., Int. Ed. 46*, 1265–1269.
(25) Zhang, D. H., Hamilton, P. D., Kao, J. L. F., Venkataraman, S., Wooley, K. L., and Ravi, N. (2007) Formation of nanogel aggregates by an amphiphilic cholesteryl-poly(amidoamine) dendrimer in aqueous media. *J. Polym. Sci., Part A: Polym. Chem. 45*, 2569–2575.
(26) Wang, B. B., Zhang, X., Jia, X. R., Li, Z. C., Ji, Y., Yang, L., and Wei, Y. (2004) Fluorescence and aggregation behavior of poly(amidoamine) dendrimers peripherally modified with aromatic chromophores: the effect of dendritic architectures. *J. Am. Chem. Soc. 126*, 15180–15194.
(27) Zhao, Y., Song, Y., Jiang, W., Zhang, B., Li, Y., Sha, K., Wang, S., Chen, L., Ma, L., and Wang, J. (2008) Synthesis of a novel star polymer consisting of a dendritic polyamidoamine core and polystyrene arms and its self-assembly to form large multimolecular micelles. *J. Appl. Polym. Sci. 109*, 1039–1047.
(28) Yang, W., Cheng, Y., Xu, T., Wang, X., and Wen, L.-p. (2009) Targeting cancer cells with biotin-dendrimer conjugates. *Eur. J. Med. Chem. 44*, 862–868.
(29) Majoros, I. J., Myc, A., Thomas, T., Mehta, C. B., and Baker, J. R. (2006) PAMAM dendrimer-based multifunctional conjugate for cancer therapy: synthesis, characterization, and functionality. *Biomacromolecules 7*, 572–579.
(30) Boswell, C. A., Eck, P. K., Regino, C. A. S., Bernardo, M., Wong, K. J., Milenic, D. E., Choyke, P. L., and Brechbiel, M. W. (2008) Synthesis, characterization, and biological evaluation of integrin $\alpha v\beta 3$-targeted PAMAM dendrimers. *Mol. Pharmaceutics 5*, 527–539.
(31) Hafez, I. M., Maurer, N., and Cullis, P. R. (2001) On the mechanism whereby cationic lipids promote intracellular delivery of polynucleic acids. *Gene Ther. 8*, 1188–1196.
(32) Gautrot, J. E., and Zhu, X. X. (2006) Biodegradable polymers based on bile acids and potential biomedical applications. *J. Biomater. Sci., Polym. Ed. 17*, 1123–1139.
(33) Luo, J., Chen, Y., and Zhu, X. X. (2009) Invertible amphiphilic molecular pockets made of cholic acid. *Langmuir 25*, 10913–10917.
(34) Zhang, J., Luo, J., Zhu, X. X., Junk, M. J. N., and Hinderberger, D. (2010) Molecular pockets derived from cholic acid as chemosensors for metal ions. *Langmuir 26*, 2958–2962.
(35) Li, Y., Li, G. T., Wang, X. Y., Lin, C. X., Zhang, Y. H., and Ju, Y. (2008) Poly(p-phenylene ethynylene)s with facially amphiphilic pendant groups: solvatochromism and supramolecular assemblies. *Chem.—Eur. J. 14*, 10331–10339.
(36) Mukhopadhyay, S., and Maitra, U. (2004) Chemistry and biology of bile acids. *Curr. Sci. 87*, 1666–1683.
(37) Enhsen, A., Kramer, W., and Wess, G. (1998) Bile acids in drug discovery. *Drug Discovery Today 3*, 409–418.
(38) Hazra, B. G., Pore, V. S., Dey, S. K., Datta, S., Darokar, M. P., Saikia, D., Khanuja, S. P. S., and Thakur, A. P. (2004) Bile acid amides derived from chiral amino alcohols: novel antimicrobials and antifungals. *Bioorg. Med. Chem. Lett. 14*, 773–777.
(39) Han, S. O., Mahato, R. I., and Kim, S. W. (2001) Water-soluble lipopolymer for gene delivery. *Bioconjugate Chem. 12*, 337–345.
(40) Chen, W., Tomalia, D. A., and Thomas, J. L. (2000) Unusual pH-dependent polarity changes in PAMAM dendrimers: evidence for pH-responsive conformational changes. *Macromolecules 33*, 9169–9172.
(41) Gouin, S., and Zhu, X. X. (1998) Fluorescence and NMR studies of the effect of a bile acid dimer on the micellization of bile salts. *Langmuir 14*, 4025–4029.
(42) Lin, W., Galletto, P., and Borkovec, M. (2004) Charging and aggregation of latex particles by oppositely charged dendrimers. *Langmuir 20*, 7465–7473.
(43) DeLong, R. K., Yoo, H., Alahari, S. K., Fisher, M., Short, S. M., Kang, S. H., Kole, R., Janout, V., Regan, S. L., and Juliano, R. L. (1999) Novel cationic amphiphiles as delivery agents for antisense oligonucleotides. *Nucleic Acids Res. 27*, 3334–3341.
(44) Shuai, X. T., Merdan, T., Unger, F., and Kissel, T. (2005) Supramolecular gene delivery vectors showing enhanced transgene expression and good biocompatibility. *Bioconjugate Chem. 16*, 322–329.
(45) Prokop, A., and Davidson, J. M. (2008) Nanovehicular intracellular delivery systems. *J. Pharm. Sci. 97*, 3518–3590.
(46) Fan, L., Li, F., Zhang, H., Wang, Y., Cheng, C., Li, X., Gu, C.-h., Yang, Q., Wu, H., and Zhang, S. (2010) Co-delivery of PDTC and doxorubicin by multifunctional micellar nanoparticles to achieve active targeted drug delivery and overcome multidrug resistance. *Biomaterials 31*, 5634–5642.

BC900490U

Efficient Gene Transfection Using Novel Cationic Polymers Poly(hydroxyalkylene imines)

Lolita Zaliauskiene,[†,‡] Ula Bernadisiute,[†,§] Ausvydas Vareikis,[§] Ricardas Makuska,[§] Ieva Volungeviciene,[‡] Agne Petuskaite,[‡] Laurynas Riauba,[‡] Arunas Lagunavicius,[‡] and Sarunas Zigmantas*[,‡]

Thermo Fisher Scientific (formely Fermentas), Graiciuno 8, LT-02241 Vilnius, Lithuania, and Department of Polymer Chemistry, Vilnius University, Naugarduko 24, LT-03225 Vilnius, Lithuania. Received December 4, 2009; Revised Manuscript Received June 4, 2010

A series of novel cationic polymers poly(hydroxyalkylene imines) were synthesized and tested for their ability to transfect cells *in vitro* and *in vivo*. Poly(hydroxyalkylene imines), in particular, poly(2-hydroxypropylene imine) (pHP), poly(2-hydroxypropylene imine ethylene imine) (pHPE), and poly(hydroxypropylene imine propylene imine) (pHPP) were synthesized by polycondensation reaction from 1,3-diamino-2-propanol and the appropriate dibromide. Electron microscopic examination demonstrated that the resulting polymers condensed DNA into toroid shape complexes of 100−150 nm in size. Transfection studies showed that all three polymers were able to deliver genetic material into the cell, with pHP being superior to pHPP and pHPE. pHP acted as an efficient gene delivery agent in a variety of different cell lines and outcompeted most of the widely used polymer or lipid based transfection reagents. Intravenous administration of pHP-DNA polyplexes in mice followed by the reporter gene analysis showed that the reagent was suitable for *in vivo* applications. In summary, the results indicate that pHP is a new efficient reagent for gene delivery *in vitro* and *in vivo*.

INTRODUCTION

Gene delivery has become a valuable research instrument and a potential means of treating many human diseases such as immunodeficiency, cystic fibrosis, Parkinson's disease, or cancer. However, efficient and safe DNA transfer still remains a considerable challenge in gene therapy (*1*). Initial studies concentrated on virus-mediated gene delivery (*2*). Although viral vectors are effective gene carriers, they still have several major disadvantages. Viruses have to be chemically or physically inactivated in order to eliminate their pathogenic properties, and the risk of reversion back to virulence is difficult to estimate. The main drawback of using viruses *in vivo* is their immunogenicity to animals and humans. Viral systems are expensive, difficult to use, and complicated to handle. Moreover, the virus envelope has a definitive volume and therefore can deliver limited-sized DNA (*3*). Nonviral gene delivery systems can overcome most of the obstacles associated with viral vectors. The main advantage of nonviral transfection reagents is that they elicit lower immune response and are easier to handle. Most nonviral gene delivery systems are synthetic materials and can be classified into three major groups: cationic lipids, dendrimers, and cationic polymers.

Recently, a lot of attention has been given to the cationic polymers (*4–6*). Polycations are able to condense DNA into small particles and initiate cellular uptake via endocytosis. The best-known cationic polymers are poly(L-lysine) (PLL), polyethylene imine (PEI), and poly(β-amino ester)s. Polylysine is one of the first cationic polymers that was used as a transfection reagent (*7*). Due to polypeptide structure, PLL has a biodegradable nature, and this property is essential for the use *in vivo*. However, PLL exhibits moderate to high toxicity, suffers from immunogenicity because of the peptide backbone, and has relatively low transfection efficiency. In addition, PLL complexes with DNA undergo nonspecific binding to cell membrane, limiting PLL application to certain cell lines. The pK_a value of lysine ε-amino groups is about 10, and therefore, at physiological pH all these amines are protonated. Although positively charged PLL can compact DNA and efficiently transfer it into the cell, due to PLL amino groups full protonation, PLL−DNA complexes cannot work as a proton sponge, cannot facilitate endoosmolysys, and, therefore, cannot rapidly escape from the endosomes (*8*).

Polyethyleneimine is the most intensively studied cationic polymer to date. Behr's group was the first to show that PEI can be an efficient transfection agent (*9*). PEI can be obtained in branched or linear forms, and both forms can be used for transfection *in vitro* and *in vivo*. Linear PEI was reported to be a less toxic, more efficient, and faster acting transfection agent than branched PEI. This can be explained by the fact that linear PEI-DNA complexes are less condensed and can dissociate more efficiently than branched PEI-DNA complexes when inside the cell. PEI is slightly toxic to the cells because of its nonbiodegradable nature. Studies showed that PEI transfection efficiency is molecular weight dependent. The optimal molecular weight for linear PEI is in the range from 5 kDa to 25 kDa (*10*). Linear PEIs longer than 25 kDa show similar transfection activities but are more toxic. Linear PEIs shorter than 5 kDa, on the other hand, are less toxic but also less efficient. The linear PEI is extensively applied *in vivo*. It was used for local gene delivery to various anatomical sites of experimental animals, as well as introduced systemically. Experiments showed that linear PEI polyplexes with DNA are superior to cationic liposomes for gene delivery by intravenous and intratracheal administration (*11, 12*).

More recently, Robert Langer, Daniel Anderson, and co-workers reported synthesis and evaluation of the library of poly(β-amino

* Corresponding author. Sarunas Zigmantas, Thermo Fisher Scientific (formely Fermentas), Graiciuno 8, LT-02241 Vilnius, Lithuania. E-mail: sarunas.zigmantas@thermofisher.com. Tel.: +3705294231. Fax.: +37052602142.

† Lolita Zaliauskiene and Ula Bernadisiute contributed equally to this work and should be treated as joint first authors.

‡ Thermo Fisher Scientific (formely Fermentas).

§ Vilnius University.

10.1021/bc900535k © 2010 American Chemical Society
Published on Web 08/09/2010

ester)s as gene delivery vectors (*13–15*). The key advantage of poly(β-amino ester)s is their ability to degrade to monomeric units inside the cell within a few hours with no negative effect on cell viability. It was shown that the transfection activity of poly(β-amino ester)s depends on molecular weight, end group, and polymer/DNA ratio. The best results were obtained using polymers capped with primary diamines (*14, 15*).

Lately, the development of transfection reagents has mainly focused on optimization of already developed transfection reagents rather than finding new classes of materials. The scope of our study was to find an easy approach to the formation of polycationic polymers bearing imine groups, a fundamental unit in transfection reagents. In this paper, we present poly(hydroxyalkylene imines), a new family of cationic polymers that can be obtained by polycondensation reaction. We demonstrate that this approach allows easy manipulation of monomers in order to generate polymers with the desired features. We hope that this study will open a new window into the development of efficient and innovative gene carriers.

EXPERIMENTAL PROCEDURES

Materials. 1,3-Diamino-2-propanol (98%) and 1,2-dibromoethane (98%) were obtained from Fluka. 1,3-Dibromopropane (99%) and 1,3-dibromo-2-propanol (95%) were purchased from Aldrich. Dubelcco's Modified Eagle's Medium (DMEM), Trypsin-EDTA, and L-glutamine were purchased from Sigma Aldrich. Fetal bovine serum (FBS) was purchased from Biochrom AG. HeLa cells were purchased from HPACC (Salisbury, UK).

Synthesis of Poly(2-hydroxypropylene imine) (pHP). In a three-neck 50 mL round-bottom reaction flask fitted with a stirrer, a dropping funnel, and a thermometer, 1,3-diamino-2-propanol (1.5 g, 16.6 mmol) was dissolved in methanol (3 mL). The resulting solution was preheated to 50 °C, and 1,3-dibromo-2-propanol (3.63 g, 16.6 mmol) was added with vigorous stirring. The reaction mixture was stirred for 48 h at 50 °C. Upon completion, the viscous product of polycondensation was diluted with distilled water (10 mL) and dialyzed against water for 5 days using SERVA Membra-Cel dialysis tubing MWCO 4 kDa. The dialyzed solution was concentrated using a rotating evaporator until reduced to ca. 25% of the starting volume and then freeze−dried to give 0.78 g of pHP (yield 32%).

Synthesis of Poly(2-hydroxypropylene imine ethylene imine) (pHPE) and Poly(2-hydroxypropylene imine propylene imine) (pHPP). Synthesis of pHPE and pHPP was done by polycondensation of 1,3-diamino-2-propanol with 1,2-dibromoethane and 1,3-dibromopropane, respectively. The procedure for synthesis of pHP was applied using double amount (33.3 mmol) of the reactants and 4 mL of methanol. The dialyzed solution of each polymer was concentrated to a viscous bulk using rotating evaporator, and the obtained product was dried in a vacuum oven to give 0.81 g of pHPE and 1.2 g of pHPP (yields 21% and 28%, respectively).

Spectroscopic Measurements. The infrared absorption spectra were recorded with a Perkin Elmer Spectrum BX spectrometer under dry air at 20 °C by the KBr pellet method. The ^{1}H NMR and (^{1}H−^{1}H) COSY spectra were acquired on Unity Inova Varian spectrometer 300 MHz at 29 °C. The polymer samples were dissolved in D_2O. In order to prepare the samples with fully deprotonized imine groups, pH of the solutions in D_2O was adjusted to 12−13 by adding few drops of 40% NaOD in D_2O. Chemical shifts were referenced to the signal of water (4.68 ppm for neutral and 4.74 ppm for alkaline solutions, respectively). The XPS spectra were obtained by using Mg K_α ($h\gamma = 1253.6$ eV) radiation at an average of 10 scans with step size 0.05 eV. All data were corrected by a linear shift such that the peak maximum of the C 1s binding energy of adventitious carbon corresponded to 284.6 eV. The samples for XPS were prepared in two ways as follows.

A. A polyimine (0.05 g) was dissolved in 1.5 mL of water. The surface of a sital plate (1 × 1 cm^2) was carefully cleaned with ethanol, then a drop of the sample solution was spread over the plate, and the plate was dried. The same procedure was repeated three times, generating three layers of the polymer.

B. In order to prepare a deprotonized sample, polyimine (0.3 g) was dissolved in 5 mL of distilled water, and 1 M NaOH aqueous solution was added dropwise until pH ≈ 12. The solution was dialyzed against water for 2 days using SERVA Membra-Cel dialysis tubing MWCO 4 kDa. Three layers of the polymer were prepared as described in section A.

Size Exclusion Chromatography. Molecular weight and molecular weight distribution (MWD) of pHP, pHPE, and pHPP were determined by size exclusion chromatography (SEC) using a Viscotek TDA302-GPC2 triple detection system with LALS/RALS, viscosity, and RI detection. General chromatography conditions: two columns ViscoGEL GMPW×l (mixed bead), eluent water, eluent flow rate 0.7 mL/min, temperature 35 °C. Prior to injection, all aqueous sample solutions were filtered using 0.45 μm Nylon filter.

Potentiometric Titration. Potentiometric titration was carried out at room temperature using Eutech instruments pH 6000 pH-meter and a microburet of 2 mL capacity. A poly(hydroxyalkylene imine) (0.1 g) was dissolved in 10 mL of 0.1 M aqueous NaCl, and two equal parts of the solution were titrated with 0.1 M HCl/0.1 M NaCl and 0.1 M NaOH/0.1 M NaCl.

DNA−Cationic Polymer Complexes. Complexes were prepared as follows: DNA (1 μg) was diluted in 100 μL of 0.15 M NaCl; cationic polymers were deposited on the wall of the same Eppendorf tube and vortexed immediately for few seconds to ensure an even distribution of the material. The final concentration of the cationic polymers in the reaction mixture (based on N residues) was 0.15 mM for pHP, 0.2 mM for pHPP, and 2.14 mM for pHPE, which corresponded to N/P ratios of 5, 6.6, and 75, respectively. ExGen 500 (Fermentas, Lithuania) was used at N/P ratio of 6 yielding 0.17 mM polymer concentration in the reaction mixture. The complexes were allowed to form for 15−20 min at room temperature. For *in vivo* experiments, 50 μg of plasmid DNA was diluted in 400 μL of 5% sterile glucose solution; the final concentration of pHP in the reaction mixture was 1.5 mM; the complexes were allowed to form for 15 min.

Particle Size Measurements. Particles were measured using dynamic light scattering device Malvern Zetasizer NanoS. Experimental data were analyzed using Malvern *DTS* v 5.10 software package. The size of polymer particles prior to complex formation with DNA was estimated in 2.5 M NaCl solution at 30 mM polymer concentration. DNA−polymer complexes were prepared as described for *in vitro* experiments; the measurements were performed immediately (without waiting 15 min).

Electron Microscopy. Carbon film covered grids were purchased from Agar Scientific Ltd. (Essex, England). A 10 μL drop of preformed polyplexes was loaded onto the grid and allowed to sediment for 5 min. The excess liquid was removed with blotting paper, and the complexes were stained with 10 μL of an aqueous uranylacetate solution (1%, w/w). Following 5 min of incubation, the excess liquid was removed with blotting paper and samples were analyzed at 80 kV with a digital Morgagni 268 transmission electron microscope (Eindhoven, Netherlands).

Fluorescent Labeling of Plasmid DNA. DNA was labeled using FluoroULS labeling kit (Fermentas, Lithuania). The kit is based on the Universal Labeling System (ULS) which uses a special platinum compound. The Pt-compound has two free binding sites, one of which is used to bind a marker group,

thus forming a marker/platinum complex (here, FluoroULS reagent). The other binding site could be used to link the complex to the purines of DNA, RNA, PNA, or chromosomes. FluoroULS reagent (1 unit) was mixed with 1 μg of plasmid DNA; the volume of the reaction was adjusted to 20 μL using the kit-provided Labeling solution. The reaction was carried out for 30 min at 85 °C and stopped following the addition of Stop solution (5 μL). Labeled DNA was purified on Illustra Microspin G-25 columns (GE Healthcare) to remove unreacted reagents and prepared for transfection as described earlier, using 1 μg of DNA/sample.

Transfection. For *in vitro* transfections, one day before the experiment, HeLa cells were seeded in a 24-well tissue culture plate at the density of 5×10^4 cells per well in the total volume of 1 mL DMEM culture medium supplemented with 10% FBS. The cells were incubated at 37 °C in a CO_2 incubator until they reached 70−80% confluency (usually within 24 h). Preformed DNA−polymer complexes were added to the cells in a dropwise manner. The transfection efficiency was tested 48 h later by flow cytometry using Guava Technologies EasyCyte Plus system and Guava CytoSoft 5.2 cell acquisition/analysis software (Guava Technologies, CA).

Cellular Uptake of DNA−Polymer Complexes. Uptake was analyzed using fluorescein-labeled DNA. The cells were incubated with each polyplex solution for 3 h at 37 °C in a CO_2 incubator. At the end of incubation, unbound complexes were removed by thorough washing with PBS, the cells were trypsinized, washed with PBS again, centrifuged, and resuspended in FACS buffer (1×PBS/2% FBS/0.1% Na azide) for fluorescence analysis on a Guava EasyCyte Plus system.

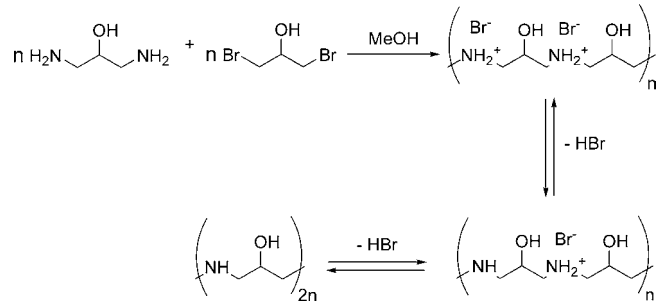
Polymer Toxicity. Toxicity was estimated using ViaCount assay (Millipore), which distinguishes viable and nonviable cells based on the differential permeability of DNA-binding dyes in the ViaCount Reagent. The fluorescence of each dye is resolved operationally to allow the quantitative assessment of both viable and nonviable cells present in a suspension. The polymers were diluted in 100 μL 0.15 M NaCl and added to 1 mL of HeLa cell cultures so that final concentration of polymers was 5−7.5−10−15−20−25−30−40−50 μM (concentrations were calculated based on N residues; stock solution of LPEI (ExGen 500) − 5.47 mM, pHP − 7.5 mM). The cells were tested 48 h later by flow cytometry. For that, the cells were trypsinized, centrifuged, and resuspended in 100 μL of FACS buffer; 15 μL of each cell suspension was mixed with 135 μL of Guava ViaCount reagent, incubated for 5 min in the dark, and analyzed by flow cytometry.

For *in vivo* transfections, preformed polyplexes were injected via the lateral tail vein into the Balb/c mice. The transfection efficiency (luciferase expression) was tested 24 h later. Mice were sacrificed; different organs were homogenized in a mammalian cell lysis solution (Fermentas, Lithuania). Samples were prepared using SuperLight Luciferase Reporter Gene Assay kit (BioAssay Systems), luminescence was measured on a Synergy 2 multimode microplate reader (BioTek Instruments, Inc.). Protein concentration of each sample was estimated using Bradford assay; relative luminescence units (RLU) were recalculated for 1 mg of protein.

Cytokine Level Analysis. Blood was collected at 0, 1, 3, 6, and 24 h after transfection. Samples were incubated for 30 min at 37 °C, overnight at 4 °C, and centrifuged at 1400 × *g* for 5 min to collect the supernatants. Serum was diluted 100× for TNF-α, IL-6, and IFN-γ analysis, 50× for IL-12 analysis, and 10× for IL-1β analysis. Cytokine concentrations were determined using ELISA kits from eBioscience (San Diego, CA).

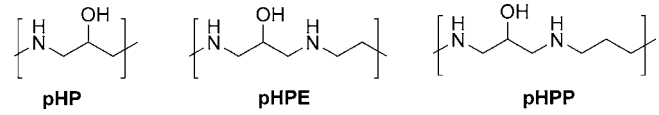
Confocal Microscopy. Leica SP5 confocal microscope system was used to image triple gene expression in HeLa cells. HeLa cells were grown in a 24 well glass-bottom plate (MatTec Corporation). Equal amounts (0.7 μg each) of pMTC plasmids expressing synthetic genes for eGFP, eCFPnuc, and DsRmem under CMV promoter were combined in 100 μL of 0.15 M NaCl solution. The complexes with pHP were prepared as described earlier. The cells were imaged live following 48 h of incubation. Imaging was performed on a Leica TCS SP5 system (Leica Microsystems, Exton, PA) using Leica DMI 6000 inverted microscope 63× objective. Argon and helium−neon lasers were used to excite CFP, GFP, and DsRed (458, 488, and 568 nm laser lines, respectively). Samples were imaged by sequential scanning. Optical sections (0.5 μm each) through the *z*-axis were generated; flattened maximum projections of image stacks were prepared using Leica application suite (LAS AF) confocal imaging software (Leica).

Scheme 1. Polycondensation of 1,3-Dibromo-2-propanol with 1,3-Diamino-2-propanol[a]



[a] The reaction product poly(2-hydroxypropylene imine) is presented by several structures reflecting different degrees of protonization.

Scheme 2. Structures of pHP, pHPE, and pHPP (unprotonized form)



RESULTS AND DISCUSSION

Synthesis and Properties of Poly(hydroxyalkylene imines). Poly(hydroxyalkylene imines) were prepared by polycondensation of 1,3-diamino-2-propanol with 3 different dibromides: 1,2-dibromoethane, 1,3-dibromopropane, and 1,3-dibromo-2-propanol (Scheme 1). Although the resulting poly(hydroxyalkylene imines) have similar structures (Scheme 2), pHP is likely the most hydrophilic polymer in the series, while pHPP is the most hydrophobic. Moreover, pHPE slightly differs from two other poly(hydroxyalkylene imines) by higher density of NH groups which could affect complexing properties. All novel cationic polymers bearing a hydroxyl group in repeating units, in contrast to linear poly(ethylene imine), are soluble not only in acidic, but also in neutral and slightly alkaline water.

The structure of poly(hydroxyalkylene imines) was confirmed by FT-IR, ^{1}H NMR, and XPS spectroscopy. FT-IR absorption band at 1624−1637 cm^{-1} is specific for protonized imine groups NH^+_2. The absorption band at 3369−3401 cm^{-1} evidence the presence of NH^+_2 and OH groups. Strong absorption band at 1066−1070 cm^{-1} was consistent with hydroxyl groups. Absorption band at 1452−1458 cm^{-1} was attributed to deformation mode of CH_2 groups. ^{1}H NMR spectra of poly(hydroxyalkylene imines) recorded in D_2O and alkaline D_2O (pH 12−13) were rather different (Figure 1). Imine groups of poly(hydroxyalkylene imines) were partially protonized in D_2O, giving broad signals of methylene and methyne protons. In alkaline solutions, proton signals were shifted toward higher field and became relatively narrow and well-resolved. For instance, the spectrum

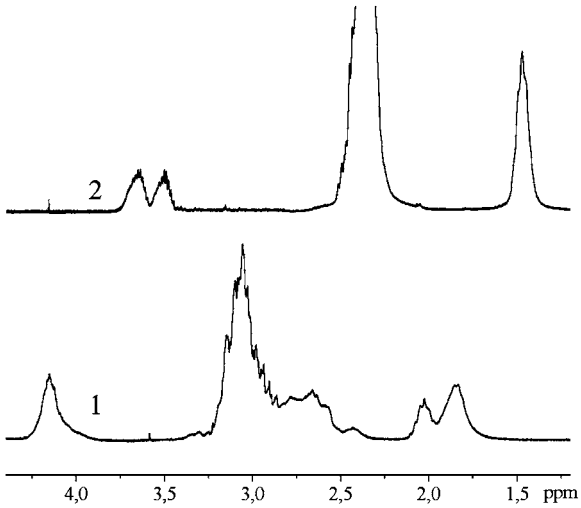


Figure 1. ^{1}H NMR spectra of pHPP in D_2O (1) and D_2O containing NaOD, pH 13 (2).

of pHPP (Figure 1) contained the signals at 1.47 ppm (−CH_2-$\underline{CH_2}$-CH_2−), 2.36 ppm (−NH-$\underline{CH_2}$-CH_2-$\underline{CH_2}$-NH-$\underline{CH_2}$-CH(OH)-$\underline{CH_2}$-), and a double peak at 3.50 and 3.64 ppm (−CH_2-$\underline{CH}$(OH)-CH_2−). (^{1}H−^{1}H) COSY experiments confirmed that both signals at 3.50 ppm and 3.64 ppm were associated with the signal at 2.36 ppm. The spectra of pHPE and pHP were similar to that of pHPP presented in Figure 1, but they did not contain the signal at around 1.5 ppm. The ratio of the integrals of the signals corresponding to the protons in various groups was in good agreement with the presumptive structure of the polymers. The only uncertainty was the splitting of the signal attributed to (−$\underline{CH}$(OH)−) protons in alkaline media into two well-resolved components. This phenomenon was characteristic for all three polymers. There are two possible, and not mutually exclusive, explanations of the two peaks attributed to the methyne protons. Since synthesis joins multiple prochiral 1,3-diamino-2-propanol molecules into a single covalent chain, formation of mixtures of diastereomers is inevitable. Peaks at 3.50 and 3.64 ppm may represent signals from −CH(OH)− groups in different chiral surroundings, found in different diastereomers of polymeric molecules. Alternatively, conformational isomerism also provides a plausible explanation. It is reported (*16*) that 1,3-diamino-2-propanol, the main monomer used for the synthesis of poly(hydroxyalkylene imines), exists as a mixture of conformers. Possibly, hindered rotation of the main chain in polymer molecules produces two relatively stable conformers in which methyne groups experience different environments, thereby giving rise to two peaks in NMR spectra. More work is needed to investigate these two possibilities, which is beyond the scope of the present study.

In order to obtain information about possible branching of poly(hydroxyalkylene imines) and degree of protonation of imine groups in upper layers of their films, XPS spectra were recorded and analyzed. Wide-scan XPS spectra of these polymers showed four main peaks at about 67, 285, 400, and 533 eV associated with bromine, carbon, nitrogen, and oxygen species, respectively. Deprotonization of poly(hydroxyalkylene imines) resulted in disappearance of the signal attributed to bromine. C 1s core-level spectra of the polymers were deconvoluted into two peak components associated with carbon atoms bonded to carbon (284.6 eV) and to nitrogen or oxygen (285.7 eV).

N 1s core-level XPS spectra (Figure 2) contained two components at about 398.4 and 400.7 eV, the first of which was apparently associated with imine groups (═NH), while the second was with their protonated form (═NH_2^+). No component

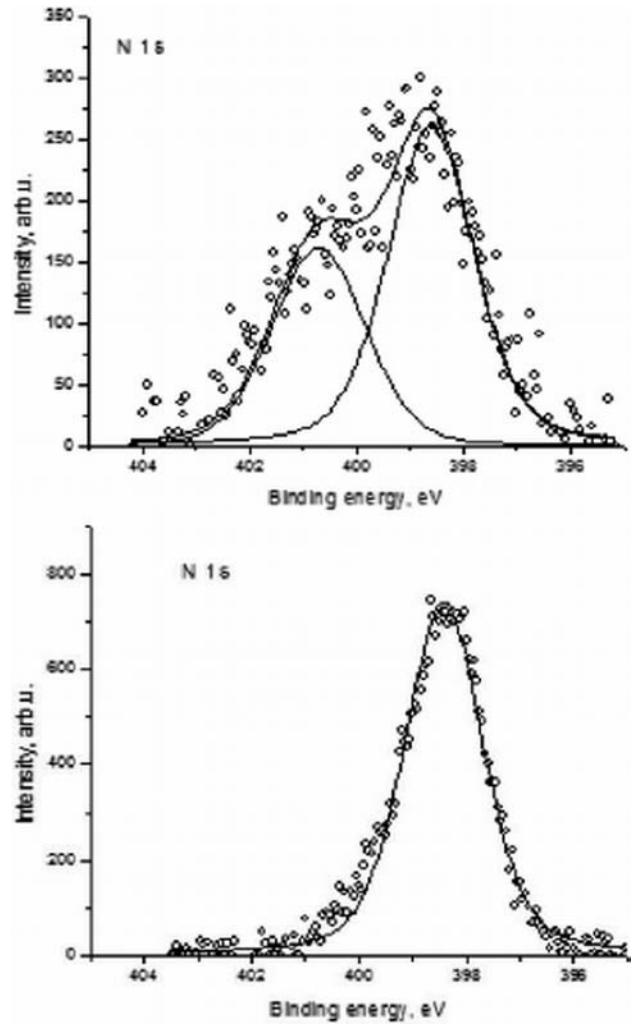


Figure 2. XPS N 1s spectra of pHPE in protonized (upper) and unprotonized (right) forms.

attributable to the presence of tertiary amine (═N−), which could prove branching of macromolecules of the novel polymers, was detected. It should be noted, however, that the component of N 1s core-level XPS spectrum associated with tertiary amine (═N−) could be located at almost the same position as that of (═NH) (*17*, *18*). The degree of protonization of imine groups acquired by comparing integrals of the components attributed to protonated and unprotonated forms of imine groups was ca. 25−30% and was in good agreement with the ratio of bromine to nitrogen determined from the same XPS spectra.

SEC measurement showed that molecular weight distribution of the poly(hydroxyalkylene imines) was large (Figure 3). Obviously, the products of polycondensation of dibromoalkanes with 1,3-diamino-2-propanol are oligomers and polymers with molecular weight ranging from less than 2 kDa to over 100 kDa. The fraction of macromolecules with the lowest molecular weight (up to 2 kDa) was effectively cut by dialysis. The fraction of macromolecules with high molecular weight (>100 kDa) was very small (less that 1%) or even absent (for pHPE). Weight average molecular weight M_w of the polymers slightly depended on the structure of dibromoalkanes used and ranged from 8 to 20 kDa. Table 1 summarizes various parameters characterizing poly(hydroxyalkylene imines). Besides large polydispersity indices, these polymers are characterized by low intrinsic viscosity and small hydrodynamic radius suggesting that macromolecular structures are tightly packed.

The use of SEC with triple detection allowed us to obtain some additional information related to conformation and

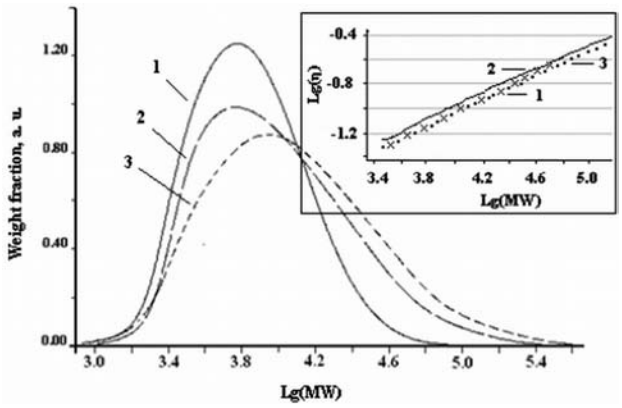


Figure 3. Molecular weight distribution of pHPE (1), pHP (2), and pHPP (3). Inset: data of SEC with refractive index, light scattering, and viscosity detection presented in the coordinates of Mark−Houvink equation.

Table 1. Parameters Characterizing Poly(hydroxyalkylene imines)[a]

polymer	M_w, kDa	M_w/M_n	IV, dL/g	R_h, nm	$K\cdot10^3$	α	pK_α	*n*
pHPE	7.87	1.67	0.088	2.11	1.10	0.500	7.93	2.18
pHP	14.5	2.48	0.126	2.78	1.17	0.495	7.78	2.27
pHPP	20.1	2.98	0.128	3.10	1.15	0.495	7.98	2.37

[a] M_w, weight-average molecular weight; M_w/M_n, polydispersity index; IV, intrinsic viscosity; R_h, hydrodynamic radius; *K* and α, constants of Mark−Houwink equation; pK_α, a negative logarithm of the ionization constant; *n*, slope value of the dependence in the coordinates of Henderson−Hasselbalch equation.

branching of the novel polymers. The data from viscosity and light scattering detectors are presented as double-logarithmic plots of intrinsic viscosity against MW in the coordinates of the Mark−Houwink equation (see inset, Figure 3). The Mark−Houwink plot reflects structural changes in a polymer, such as polymer branching and chain rigidity (*19*, *20*). Linear polymers result in a linear Mark−Houwink plot from which the slope is calculated and information about the coiling properties is derived. For branched polymers, downward curvature is observed which is related to the increasing number of side chains toward the high molecular weight region and, as a consequence, higher density of macromolecular coils, resulting in relatively lower intrinsic viscosity. The double-logarithmic plots of intrinsic viscosity against MW are linear for poly(hydroxyalkylene imines) (see inset, Figure 3) suggesting linearity of the novel polymers. Nevertheless, a certain reservation should be made by low values of Mark−Houwink exponent α which is equal or very close to 0.5 (Table 1). It is known that Mark−Houwink constant α typically varies between 0.5 and 0.2 for branched polymers depending on the degree of branching (*21*), while the value 0.5 is characteristic for linear polymers in Θ solvents.

Potentiometric titration of poly(hydroxyalkylene imines) in 0.1 M NaCl solution gave titration curves with two inflections (Figure 4). The difference between these two inflections allowed one to calculate the concentration of imine groups, as well as the actual concentration of a poly(hydroxyalkylene imine). Determination of actual concentration of imine groups is relevant, since novel cationic polymers are very hydroscopic and almost immediately adsorb a considerable amount of water. Analysis of the potentiometric titration data revealed that the adsorbed water constituted up to 45% of the sample weight.

From the data of potentiometric titration presented in the form of the Henderson−Hasselbalch equation (Figure 4), pK_α values of the poly(hydroxyalkylene imines) were evaluated (Table 1). pK_α values of the novel cationic polymers are close to each other and are consistent with pK_α values of other polyimines (*22*, *23*).

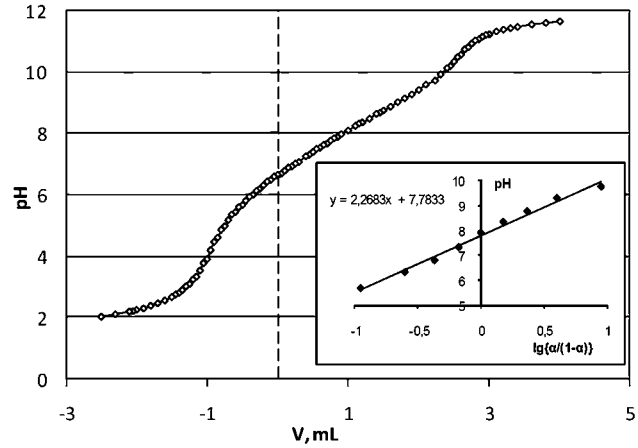


Figure 4. Potentiometric titration curve of pHP. Inset: data of the potentiometric titration, presented in the coordinates of the Henderson−Hasselbalch equation.

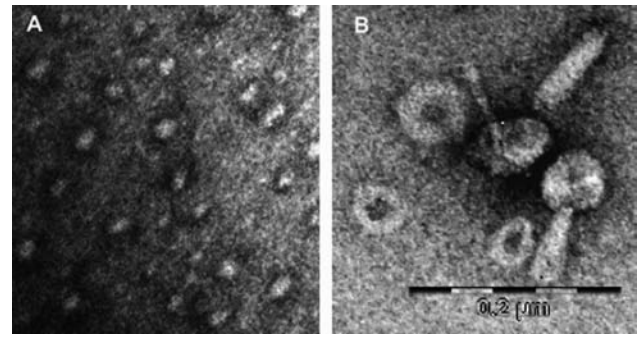


Figure 5. Transmission electron micrographs of pHP: (A) uncomplexed polymer, (B) DNA−polymer complexes. The magnification is the same for both images. The scale bar in B is 200 nm.

Surprisingly high slope values in the coordinates of the Henderson−Hasselbalch equation (*n*) suggests that ionization of imine groups of these polymers is seriously affected by neighboring already protonized imine groups.

Characterization of DNA/Polymer Complexes. For cationic polymers to function as gene delivery vectors, they should be able to condense DNA into nanosized particles. The ability of poly(hydroxyalkylene imines) to form complexes (polyplexes) with DNA was examined using electron microscopy and dynamic light scattering (DLS). All three polymers were composed of small particles with diameters ranging from 9 to 20 nm. Transmission electron microscope representative image of pHP is shown in Figure 5A. Similar polymer particle sizes, 6−16 nm, were observed using dynamic light scattering measurements. In the presence of DNA, polymers formed 100−150 nm toroidal complexes and rod-like particles (Figure 5B). DLS experiments supported the data of electron microscopy; formation of particles with 80−100 nm *Z*-average size was observed immediately after addition of polymers to the DNA solution. However, within 2 h of incubation, complexes with pHPE aggregated, and the size of particles increased up to 600 nm, while the size of pHPP and pHP polyplexes increased only slightly from 80 to 100 nm and 115 to 150 nm, respectively. Analysis of DNA−polymer complex formation, size, and morphology has been used as a model system to study and optimize artificial gene delivery (*24*). Condensation of DNA into nanoparticles has been demonstrated to begin with the formation of rods (predominating form) and toroids and shift to a more thermodynamically stable toroid form within 20 min (*24*). However, it has also been proposed that toroids and rods are isoenergetic, exist at equilibrium (*25*), and continuously

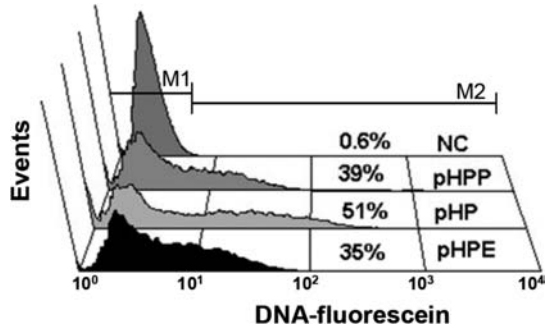


Figure 6. Uptake of DNA−polymer complexes by HeLa cells. The cells were incubated with DNA−fluorescein free (negative control) or in the complex with pHPE, pHP, or pHPP for 3 h. The uptake of fluorescent nanoparticles was analyzed by flow cytometry. M1 outlines the fluorescein-negative cells; M2 shows fluorescein-positive fraction of cell population.

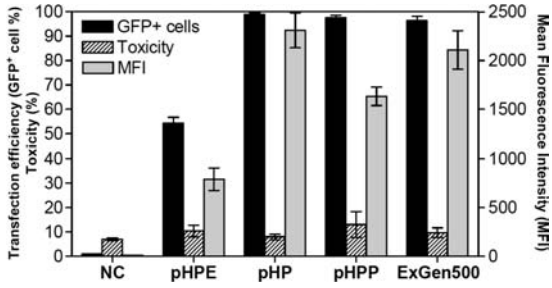


Figure 7. Transfection analysis of poly(hydroxyalkylene imine) compacted DNA nanoparticles. HeLa cells were transfected with eGFP encoding vector using pHPE, pHP, or pHPP. LPEI (ExGen500) was used as a positive control. Transfection efficiency was analyzed 48 h later using Guava EasyCyte Plus flow cytometry system (graph shows mean values ± SD from 3 separate experiments).

convert from one shape to another (*26*). In our experiments, when complexes were allowed to form for 5 min, we observed similar number of rods and toroids (data not shown). Following a longer incubation period (15 min), the toroid population became increasingly dominant, and no major changes in the ratio of these two shapes were observed upon the further increase of incubation time up to 1 h. This suggested that toroids were in fact a more stable form of polyplexes.

The size of polymeric gene delivery complexes is known to dramatically affect the transfection efficacy (*6, 27, 28*). For the top-performing vectors, particle sizes were usually smaller than 150 nm. Endocytosis has been established as the main mechanism of internalization for nonviral vectors. The size of endocytic vesicles, depending on the means of entry, ranges from 50 to 150 nm (for caveolae and clathrin mediated endocytosis, respectively) and can be up to 5 μm (for macropinocytosis) (*29*). In our experiments, the size of DNA-pHP and DNA-pHPP complexes stayed within 90−150 nm and did not change for at least 3 h suggesting that these complexes would have no size restrictions to efficient endocytosis. The DNA-pHPE complexes, on the other hand, were observed to continuously grow in size and reach 600 nm by 3 h. The endocytosis of larger complexes may be more problematic but still feasible, since they can be accommodated into macropinosomes. Overall, our results allowed us to expect that all three poly(hydroxyalkylene imines), but more likely pHPP and pHP, could act as efficient gene delivery vectors.

***In Vitro* Transfection.** To follow the uptake and intracellular transport of DNA−polymer complexes by flow cytometry and fluorescent microscopy, the plasmid DNA was labeled with fluorescein and complexed with poly(hydroxyalkylene imines) as described in the Expermental Procedures. Internalization of

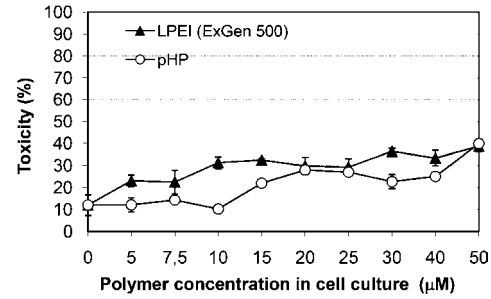


Figure 8. LPEI and pHP induced cellular toxicity comparison. HeLa cells were treated with increasing concentrations of LPEI (ExGen500) or pHP (final concentrations in cell culture are indicated on *x*-axis). Cells were analyzed 48 h later; apoptotic and dead cells were stained using Guava ViaCount reagent and analyzed by flow cytometry (graph shows mean values ± SD, $n = 3$).

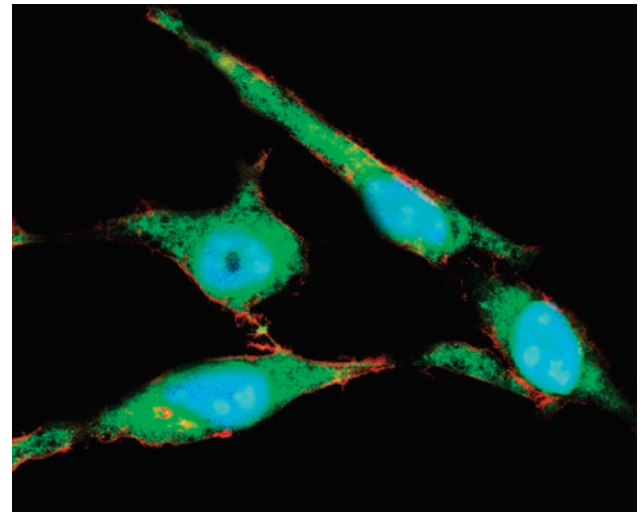


Figure 9. Multiple gene cotransfection using pHP. Three different plasmids encoding eGFP, eCFPnuc, and DsRmem proteins under the CMV promoters were mixed in equal ratios (0.7 μg each) and transfected into HeLa cells using pHP. Gene expression was analyzed 48 h later using Leica confocal microscope. Three gene expressions within single cells are shown: DsRmem (membrane localization), eGFP (cytosolic), and eCFPnuc (nuclear localization).

DNA−polymer complexes was visualized and confirmed by laser confocal microscope (data not shown), but the actual percent of transfected cells was assessed by flow cytometry. When HeLa cells were incubated for 3 h with fluorescein-labeled DNA alone, no fluorescence (0.6%) was registered using FACS analysis. However, when DNA was compacted by cationic polymers, the increase in fluorescent cell numbers (35% to 51%) was observed with all three polymers (Figure 6), suggesting that internalization of complexes took place; the greatest effect was seen exclusively with pHP (51% positive cells).

The transfection efficiency of cationic polymers pHP, pHPP, and pHPE was tested on a variety of cell lines (HeLa cell results are shown) using enhanced green fluorescent protein (eGFP) expressing vector and evaluated by FACS using three criteria: the percent of green fluorescent protein (GFP) positive cells (transfection efficiency), the percent of dead cells (toxicity), and the mean fluorescence intensity (MFI). Relative cellular viability was estimated based on the side and forward scatter (SSC, FSC) profiles; dead cells were gated away and presented as a percent of polymer-induced cellular toxicity. Nontreated cells were used as a negative control. To better assess the potential of newly synthesized polymers, the LPEI (ExGen500) was included in the experiments as the positive control.

Table 2. Different Cell Line Transfection Data

Cell Line	full cell line name	transfection efficiency (%) pHP	LPEI
	Adherent Cell Cultures		
Cos-7	African green monkey kidney cells	100	100
Hela	Cervix adenocarcinoma cells	98	80
Hek293	Human embryonic kidney cells	94	78
B50	Rat nervous tissue neuronal cells	67	34
Calu1	Human lung epidermoid carcinoma cells	43	17
Raw264	Mouse leukemic monocyte-macrophage cells	78	48
Wehi 164	Mouse induced fibrosarcoma cell line	75	77
Mdck	Madin Darby Canine Kidney cells	98	93
Hep2c	Human larynx carcinoma cells	90	91
Hepg2	Human hepatocellular carcinoma cell line	55	4
L929	Mouse connective tissue fibroblast cells	62	50
Colo	Human colon adenocarcinoma cells	26	40
	Suspension Cell Cultures		
Raji	Human Burkitt's lymphoma cells	0.2	0.2
Jurkat	Human leukemic T cells	8	5
Sp2/Ag14	Mouse myeloma cells	22	24
HeLa S3	Human cervix carcinoma (suspension) cells	46	30

The results showed that with pHPE the transfection efficiency reached only 55%, while with pHP and pHPP, the transfection efficiency at an optimal polymer concentration was about 98%. Cellular toxicity levels were 10−13% for all transfections and 8% for untransfected controls. The pHP and pHPP polymers transfected HeLa cells as well as LPEI (Figure 7). Biophysical properties of the particles examined earlier were found to correlate with transfection data: the polymers with more compact particle architecture (pHP and pHPP) transfected the cells with higher efficiency than polymers forming larger particles with DNA. The number of transfected cells and the mean fluorescence intensity increased in the sequence pHPE < pHPP < pHP, with the decreasing content of NH groups with respect to molecular weight of the repeating units.

Considering that pHP yielded the best results in transfection studies (mainly due to the MFI levels), we further analyzed it more extensively; the following experiments were performed: cell toxicity analysis, multiple gene cotransfections, transfections with different cell lines (adherent and suspension), and comparison with other transfection reagents available in the market.

To evaluate the polymer induced cellular toxicity, the cells were treated with increasing amounts of pHP or LPEI polymers, ranging from 5 to 50 μM final concentrations (based on nitrogen residues) in cell cultures. The condition of cells following 48 h of incubation was assessed by flow cytometry using cell-permeant DNA staining compounds (Guava ViaCount reagent). The percent of dead cells in untreated controls was 10−12% and increased steadily with rising concentrations of polycations in the culture (Figure 8). The levels of both polymer-induced toxicities were very similar along the entire series of samples, although slightly higher for LPEI. The recommended polymer concentration to accomplish maximal transfection efficiency is 16 μM for ExGen 500 and 13 μM for pHP. The viability of cells was not significantly compromised at these particular polymer concentrations. In any transfection-mediated cell function assays, it is essential to minimize the cytotoxicity of DNA/vector complexes. In our study, we demonstrate that pHP facilitated slightly lower levels of cytotoxicity compared to LPEI but a similar level of transgene expression.

Reporter genes have been commonly used in cotransfection experiments with specific gene of interest (GOI). The expression of GOI could be identified, assessed, or normalized based on the expression of the reporter gene (*30*). Rather than using single gene transfer to impact isolated events, multiple gene transfer by cotransfection may facilitate simultaneous modulation of concurrent cellular events. Here, we tested pHP in double−triple reporter gene (eGFP, eCFP, and DsRed) transfers. The transfection results were visualized by confocal microscopy; gene transfer efficiencies were determined by FACS analysis. To identify three reporter genes within one cell by microscope, each gene was synthesized with different targeting signal: eGFP (no tag), cytoplasmic expression; eCFP, nuclear localization signal (*31*); DsRed, membrane localization signal (*32*). The result of triple transfection is shown in Figure 9. Each reporter was expressed in 85−97% of cells (single transfection); 72−78% of cells expressed two genes (double transfection), assessed by FACS analysis (data not shown); 60% of cells expressed all three genes (triple transfections), estimated by fluorescence microscopy.

The results of different cell line transfections are summarized in Table 2. The comparisons were done with widely used LPEI (ExGen500 *in vitro* transfection reagent). The results showed

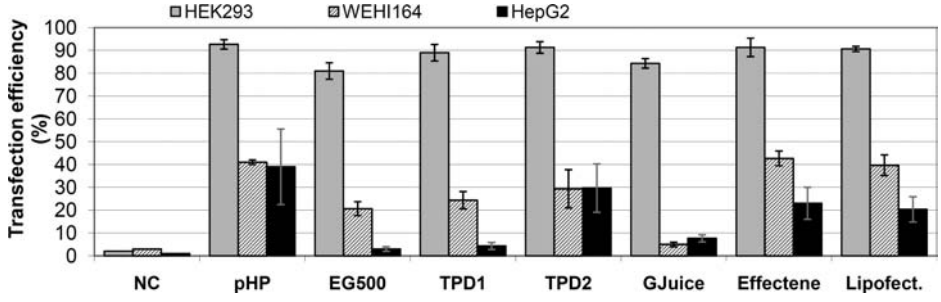


Figure 10. pHP transfection efficiency compared with other commercial transfection reagents. HEK293, WEHI164, and HepG2 cells were transfected with eGFP expressing vector using different transfection reagents: ExGen 500 (EG500), TransPass D1 (TPD1), TransPass D2 (TPD2), GeneJuice (GJuice), Effectene, and Lipofectamine. Gene expression was analyzed 48 h later. Graph shows mean values ± SD (n = 3).

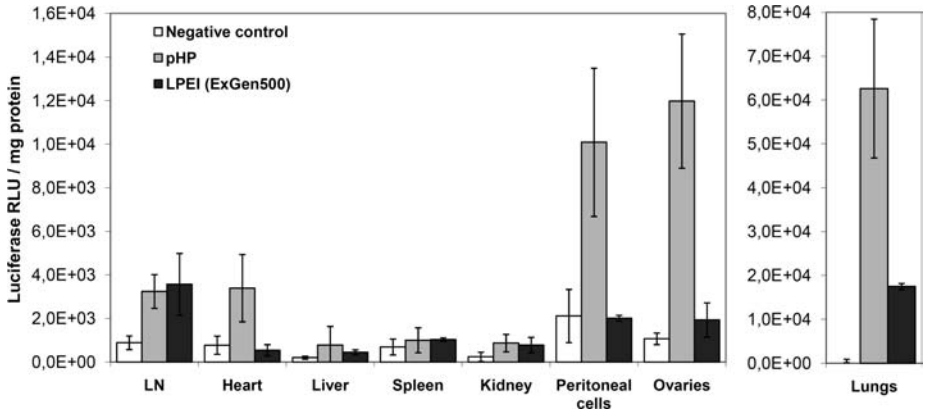


Figure 11. Luciferase expression in different organs following systemic administration of pHP−DNA complexes. Balb/c mice were injected intravenously with 50 μg of firefly luciferase encoding vector in complex with pHP or LPEI. Reporter gene was analyzed 24 h later. Each value represents the mean ± SD ($n = 3$ for each group).

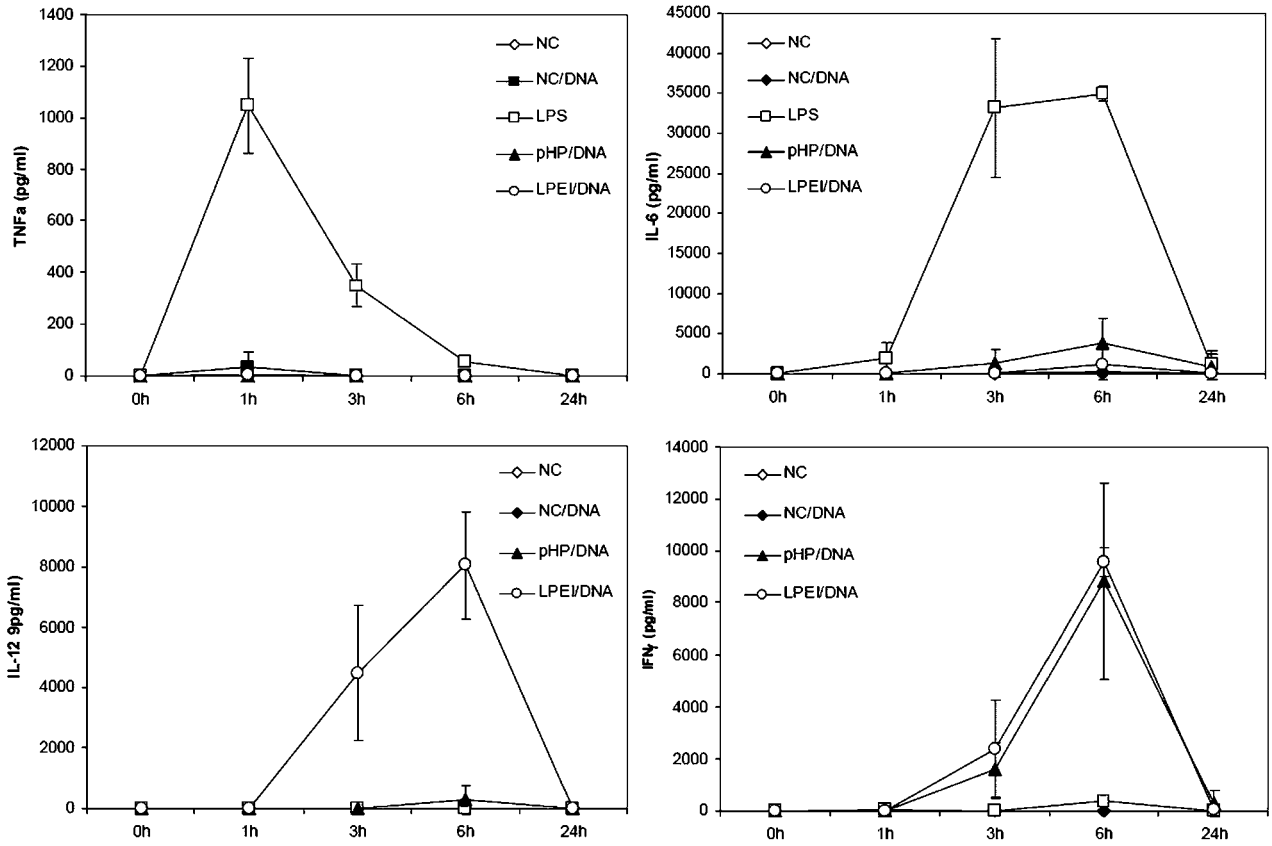


Figure 12. Pro-inflammatory cytokine (TNF-α, IL-6, IL-12, IFN-γ) levels in serum after intravenous administration of pHP complexes. Luciferase encoding vector (50 μg) alone or in complex with pHP or LPEI (in 400 μL of 5% glucose) was injected via the lateral tail vein into the BALB/c mice. Blood samples were collected at different time points; serum cytokine levels were determined by ELISA. Each value represents the mean ± SD ($n = 3$ for controls, $n = 4$ for pHP and LPEI).

that highly efficient transfections were taking place in the majority of analyzed adherent cell cultures. Suspension cell transfections, however, were significantly lower (Jurkat and Raji cells − below 10%). HeLa S3 and Sp2/Ag14 suspension cells are loosely adherent and, therefore, may have different surface architecture (more like adherent cells), which enables them to internalize cationic polymer complexes and consequently yield 46% and 22% transfection efficiencies, respectively. LPEI, a thoroughly investigated cationic polymer (*33, 34*) has been shown to enter the cell via the heparan sulfate proteoglycans (HSPG) abundantly expressed on the surface of adherent cells (*35*). Since poly(hydroxyalkylene imines) are positively charged cationic polymers, we predict that they internalize using the similar mechanism as LPEI (*36*) and, therefore, are not efficiently delivered into the suspension cells, normally low on HSPG expression (*37*). The actual mechanism of pHP mediated gene transfer has still to be elucidated.

Having compared pHP to LPEI, we further examined it against other commercially available and commonly used transfection reagents (TransPass, GeneJuice, Effectene, and Lipofectamine). Results in Figure 10 show that HEK293 cells were readily transfected with all reagents tested. The differences started to show, when WEHI164 and HepG2 cell lines were used in the same experiment. First of all, lower transfection efficiencies were observed with all reagents, but furthermore, GeneJuice turned out to be inefficient in WEHI164 cell

transfection (same experimental condition as with HEK293). With HepG2 cells, only pHP-mediated reporter gene expression was around 40%; slightly lower transfection was achieved with TransPassD2 (30%), and Lipofectamine and Effectene were even less effective (20−23% for both). Overall, the transfection data suggest that pHP is able to deliver genetic material into a variety of different cell lines and acts comparably (or better) to the most popular transfection reagents in the market.

***In Vivo* Gene Delivery.** Reporter gene transfection experiments *in vivo* were performed to extend the *in vitro* studies on the use of pHP as a gene delivery vehicle. The comparisons were done with LPEI (ExGen500 *in vivo* transfection reagent) using firefly luciferase expression as a reporter system. The control reagent in our experiments performed inconsistently. The results using pHP, on the other hand, always demonstrated the highest reporter gene expression levels in the lungs (intravenous transfection), less in the ovaries, heart and spleen, and peritoneal cells (Figure 11). The size of the polyplexes has been considered a critical parameter for *in vivo* application. Larger particles could cause problems due to physical exclusions in the capillaries and tissues (*38*). Small particles that are stable in serum are typically preferred. The LPEI polyplex size in glucose had been reported to be about 40−50 nm (*11*). DLS measurements showed that the size of DNA−pHP complexes formed in 5% glucose did not significantly differ from the size of complexes formed in 0.15 M NaCl solution being 90 and 115 nm, respectively (data not shown), which suggests that 90 nm particle size is sufficient to pass the endothelial barrier. In most tissues, the endothelial barrier is tight, and only organs and tissues with an irregular fenestration, such as the liver, spleen, bone marrow, and certain tumors, have endothelia with large meshes, which allow extravasation of molecules up to 0.1−1 μm (*39*). Surprisingly, in our experiments, little reporter gene expression was seen in the spleen or liver. Although the lung capillaries possess tight endothelia (*39*), reporter gene expression following i.v. application was higher than in other organs. Dull et al. demonstrated cationic peptides facilitating lung endothelial heparan sulfate cross-linking as a result inducing cytoskeletal reorganization and subsequent barrier dysfunction (*40*). Other studies have shown polyplexes rapidly crossing the endothelial barrier (*41*), but the mechanism was not elucidated.

A critical aspect of any gene delivery *in vivo* is the immune system reaction to the introduced nanocomplexes. Having determined that pHP can convey the genetic material into tissues, we next examined the pro-inflammatory cytokine (TNF-α, IL-6, IL-12, IFN-γ, and IL-1β) levels in serum 0−1−3−6−24 h after intravenous administration of the polyplexes. LPS, known to initiate an acute inflammatory response (*42*), was used as a positive control, while 5% glucose solution with or without DNA was used as a negative control. Strong TNF-α and IL-6 responses were observed after LPS injection, but not after pHP or LPEI-mediated transfections (Figure 12). Transient IFN-γ level increase at 6 h after injection was seen with both pHP and LPEI; however, no cytokine was detected 24 h after transfection. The IL-1β amount in serum was very low (less than 50 pg/mL) under all experimental conditions (not shown). Interestingly, LPEI-mediated short IL-12 cytokine level increased in serum (3−6 h after transfection), which was not observed when pHP was used as a delivery agent. LPEI−DNA polyplexes were previously shown to induce transient IL-12 production, the levels of which were considered to be negligible since they were significantly lower than that generated by lipoplex injections (*43–46*). Taken together, our data show that no major inflammation is induced after intravenous administration of pHP−DNA complexes.

CONCLUSIONS

In this work, we present a facile synthesis of poly(hydroxyalkylene imines) using the polycondensation reaction. Three novel cationic polymers pHP (poly(2-hydroxypropylene imine)), pHPE (poly(2-hydroxy-propylene imine ethylene imine)), and pHPP poly(2-hydroxypropylene imine propylene imine) were synthesized by reaction of dibromoalkanes with 1,3-diamino-2-propanol. The resultant poly(hydroxyalkylene imines) were linear polymers with very compact structure of macromolecular coils, soluble in acidic, neutral, and slightly alkaline aqueous solutions. All synthesized polymers formed toroidal complexes with DNA with average size of 100 nm that is optimal for endocytosis. Indeed, all poly(2-hydroxypropylene imines) appeared to be suitable for gene delivery studies, with pHP being superior over pHPE and pHPP. Further examination of pHP showed that this polymer has no significant effect on tested cell viability and is a very efficient gene delivery agent, often more effective than commercially available transfection reagents like Exgen500, Lipofectamine, Effectene, and others. Cotransfection experiments showed that pHP can successfully deliver 2−3 different plasmids simultaneously without the significant loss of triple transgene expression efficiency in a single cell. *In vivo* experiments demonstrated that pHP could be adapted to animal studies as well; high transgene expression in the lungs and no major inflammation were induced after pHP-mediated DNA delivery.

Altogether, these studies introduce a straightforward route for generation of polyimine polymers bearing various functional groups as a prospective set of nonviral gene delivery vectors for specific applications *in vitro* and *in vivo*.

ACKNOWLEDGMENT

We would like to thank Dr. Staniulis (Insitute of Biochemistry, Vilnius) for the assistance with TEM imaging; Prof. V. Kirveliene (Vilnius Univesity, Dept. Chair of Biochemistry and Biophysics) for giving us the access to the confocal microscope facility. We thank Prof. A. Zvirbliene (Institute of Biotechnology, Vilnius) for providing us different cell lines used in transfection experiments.

LITERATURE CITED

(1) Mintzer, M. A., and Simanek, E. E. (2009) Nonviral vectors for gene delivery. *Chem. Rev. 10*, 259–302.
(2) Anderson, W. F. (1998) Human gene therapy. *Nature 392*, 25–30.
(3) Verma, I. M., and Somia, N. (1997) Gene therapy - promises, problems and prospects. *Nature 389*, 239–242.
(4) Pack, D. W., Hoffman, A. S., Pun, S., and Stayton, P. S. (2005) Design and development of polymers for gene delivery. *Nat. Rev. Drug Discovery 4*, 581–593.
(5) Wagner, E., and Kloeckner, J. (2006) Gene delivery using polymer therapeutics. *Adv. Polym. Sci. 192*, 135–173.
(6) Thomas, M., and Klibanov, A. M. (2003) Non-viral gene therapy: polycation-mediated DNA delivery. *Appl. Microbiol. Biotechnol. 62*, 27–34.
(7) Lemmli, U. K. (1975) Characterization of DNA condensates induced by poly(ethylene oxide) and polylysine. *Proc. Natl. Acad. Sci. U.S.A. 72*, 4288–4292.
(8) Akinc, A., and Langer, R. (2002) Measuring the pH environment of DNA delivered using nonviral vectors: Implications for lysosomal trafficking. *Biotechnol. Bioeng. 78*, 503–508.
(9) Boussif, O., Lezoualc'h, F., Zanta, M. A., Mergny, M. D., Scherman, D., Demeneix, B., and Behr, J.-P. (1995) A versatile vector for gene and oligonucleotide transfer into cells in culture

and in vivo: polyethylenimine. *Proc. Natl. Acad. Sci. U.S.A. 92*, 7297–7301.
(10) Neu, M., Fischer, D., and Kissel, T. (2005) Recent advances in rational gene transfer vector design based on poly(ethylene imine) and its derivatives. *J. Gene Med. 7*, 992–1009.
(11) Bragonzi, A., Boletta, A., Biffi, A., Muggia, A., Sersale, G., Cheng, S. H., Bordignon, C., Assael, B. M., and Conese, M. (1999) Comparison between cationic polymers and lipids in mediating systemic gene delivery to the lungs. *Gene Ther. 6*, 1995–2004.
(12) Ferrari, S., Moro, E., Pettenazzo, A., Behr, J. P., Zacchello, F., and Scarpa, M. (1997) ExGen 500 is an efficient vector for gene delivery to lung epithelial cells in vitro and in vivo. *Gene Ther. 4*, 1100–1106.
(13) Lynn, D. M., and Langer, R. (2000) Degradable poly(β-amino esters): synthesis, characterization, and self-assembly with plasmid DNA. *J. Am. Chem. Soc. 122*, 10761–10768.
(14) Zugates, G. T., Tedford, N. C., Zumbuehl, A., Jhunjhunwala, S., Kang, C. S., Griffith, L. G., Lauffenburger, D. A., Langer, R., and Anderson, D. G. (2007) Gene delivery properties of end-modified poly(β-amino ester)s. *Bioconjugate Chem. 18*, 1887–1896.
(15) Green, J. J., Langer, R., and Anderson, D. G. (2008) A combinatorial polymer library approach yields insight into nonviral gene delivery. *Acc. Chem. Res. 4*, 749–759.
(16) Cheng, X. J. M., Heller, J. P., Petterson, K. A., and Roberts, J. D. (2002) Effect of pH on the rotational conformations of 1,3-diamino-2-hydroxypropane. *Magn. Reson. Chem. 40*, 666–671.
(17) Keen, I., Broota, P., Rintoul, L., Fredericks, P., Trau, M., and Grondahl, L. (2006) Introducing amine functionalities on a poly(3-hydroxybutyrate-*co*-3-hydroxyvalerate) surface: Comparing the use of ammonia plasma treatment and ethylenediamine aminolysis. *Biomacromolecules 7*, 427–434.
(18) Liao, J.-D., Lin, S.-P., and Wu, Y.-T. (2005) Dual properties of the deacetylated sites in chitosan for molecular immobilization and biofunctional effects. *Biomacromolecules 6*, 392–399.
(19) Bahary, W. S., and Hogan, M. P. (1996) Assessment of branching in polymers by size exclusion chromatography with light scattering, viscosity, and refractive index detection. *Int. J. Polym. Anal. Charact. 2*, 121–133.
(20) Kharchenko, S. B., Kannan, R. M., Cernohous, J. J., and Venkataramani, S. (2003) Role of architecture on the conformation, rheology, and orientation behavior of linear, star, and hyperbranched polymer melts. 1. Synthesis and molecular characterization. *Macromolecules 36*, 399–406.
(21) Muthukrishnan, S., Drechsler, M., Mori, H., and Müller, A. H. E. (2005) Glycopolymers with branched architectures: Sugar balls and sugar sticks. *Polym. Prepr. (Am. Chem. Soc., Div. Polym. Chem.) 46*, 247–248.
(22) Shepherd, E. J., and Kitchner, J. A. (1956) The ionization of ethyleneimine and polyethyleneimine. *J. Chem. Soc.* 2448–2453.
(23) Han, J., Kim, S. K., Cho, T.-S., Lee, J.-C., and Joung, H. S. (2004) Polyplex formation of calf thymus DNA with branched and linear polyethyleneimine. *Macromol. Res. 12*, 501–506.
(24) Vilfan, I. D., Conwell, C. C., Sarkar, T., and Hud, N. V. (2006) Time study of DNA condensate morphology: implications regarding the nucleation, growth, and equilibrium populations of toroids and rods. *Biochemistry 45*, 8174–8183.
(25) Bloomfield, V. A. (1991) Condensation of DNA by multivalent cations: Considerations on mechanism. *Biopolymers 31*, 1471–1481.
(26) Hud, N. V., and Vilfan, I. D. (2005) Toroidal DNA condensates: unraveling the fine structure and the role of nucleation in determining size. *Annu. Rev. Biophys. Biomol. Struct. 34*, 295–318.
(27) Anderson, D. G., Akinc, A., Hossain, N., and Langer, R. (2005) Structure/property studies of polymeric gene delivery using a library of poly(beta-amino esters). *Mol. Ther. 11*, 426–434.
(28) Ogris, M., Steinlein, P., Kursa, M., Mechtler, K., Kircheis, R., and Wagner, E. (1998) The size of DNA/transferrin-PEI complexes is an important factor for gene expression in cultured cells. *Gene Ther. 5*, 1425–1433.
(29) Khalil, I. A., Kogure, K., Akita, H., and Harashima, H. (2006) Uptake pathways and subsequent intracellular trafficking in nonviral gene delivery. *Pharmacol. Rev. 58*, 32–45.
(30) Vesuna, F., Winnard, P., Jr., and Raman, V. (2005) Enhanced green fluorescent protein as an alternative control reporter to Renilla luciferase. *Anal. Biochem. 342*, 345–347.
(31) Yoneda, Y. (1997) How proteins are transported from cytoplasm to the nucleus. *J. Biochem. 121*, 811–817.
(32) Liu, Y., Fisher, D. A., and Storm, D. R. (1994) Intracellular sorting of Neuromodulin (GAP-34) mutants modified in the membrane targeting domain. *J. Neurosci. 14*, 5807–5817.
(33) Bieber, T., Meissner, W., Kostin, S., Niemann, A., and Elsasser, H. P. (2002) Intracellular route and transcriptional competence of polyethylenimine-DNA complexes. *J. Controlled Release 82*, 441–454.
(34) Breunig, M., Lungwitz, U., Liebl, R., Fontanari, C., Klar, J., Blunk, T., and Goepferich, A. (2005) Gene delivery with low molecular weight linear polyethylenimines. *J. Gene Med. 7*, 1287–1298.
(35) Bernfield, M., Kokenyesi, R., Kato, M., Hinkes, M. T., Spring, J., Gallo, R. L., and Lose, E. J. (1992) Biology of the syndecans: a family of transmembrane heparin sulfate proteoglycans. *Annu. Rev. Cell Biol. 8*, 365–393.
(36) Kopatz, I., Remy, J. S., and Behr, J. P. (2004) A model for non-viral gene delivery: through syndecan adhesion molecules and powered by actin. *J. Gene Med. 6*, 769–776.
(37) Mislick, K. A., and Baldeschwieler, J. D. (1996) Evidence for the role of proteoglycans in cation-mediated gene transfer. *Proc. Natl. Acad. Sci. U.S.A. 93*, 12349–12354.
(38) Greene, J. J., Shi, J., Chiu, E., Leshchiner, E. S., Langer, R., and Anderson, D. G. (2006) Biodegradable polymeric vectors for gene delivery to human endothelial cells. *Bioconjugate Chem. 17*, 11622–1169.
(39) Merdan, T., Kopecek, J., and Kissel, T. (2002) Prospects for cationic polymers in gene and oligonucleotide therapy against cancer. *Adv. Drug Delivery Rev. 54*, 715–758.
(40) Dull, R. O., Dinavahi, R., Schwartz, L., Humphries, D. E., Berry, D., Sasisekharan, R., and Garcia, J. G. N. (2003) Lung endothelial heparan sulfates mediate cationic peptide-induced barrier dysfunction: a new role for the glycocalyx. *Am. J. Physiol. Lung Cell. Mol. Physiol. 285*, 986–995.
(41) Zou, S. M., Erbacher, P., Remy, J. S., and Behr, J. P. (2000) Systemic linear polyethylenimine (L-PEI)-mediated gene delivery in the mouse. *J. Gene Med. 2*, 128–134.
(42) Pulendran, B., Kumar, P., Cutler, C. W., Mohamadzadeh, M., Van Dyke, T., and Banchereau, J. (2001) Lipopolysaccharides from distinct pathogens induce different classes of immune responses in vivo. *J. Immunol. 167*, 5067–5076.
(43) Bonnet, M. E., Erbacher, P., and Bolcato-Bellemin, A. L. (2008) Systemic delivery of DNA or siRNA mediated by linear polyethylenimine (L-PEI) does not induce an inflammatory response. *Pharm. Res. 25*, 2972–2982.
(44) Kawakami, S., Ito, Y., Charoensit, P., Yamashita, F., and Hashida, M. (2006) Evaluation of proinflammatory cytokine production induced by linear and branched polyethylenimine/plasmid DNA complexes in mice. *J. Pharmacol. Exp. Ther. 317*, 1382–1390.
(45) Tousignant, J. D., Gates, A. L., Ingram, L. A., Johnson, C. L., Nietupski, J. B., Cheng, S. H., Eastman, S. J., and Scheule, R. K. (2000) Comprehensive analysis of the acute toxicities induced by systemic administration of cationic lipid:plasmid DNA complexes in mice. *Hum. Gene Ther. 11*, 2493–2513.
(46) Li, S., Wu, S. P., Whitmore, M., Loeffert, E. J., Wang, L., Watkins, S. C., Pitt, B. R., and Huang, L. (1999) Effect of immune response on gene transfer to the lung via systemic administration of cationic lipidic vectors. *Am. J. Physiol. 276*, 796–804.

BC900535K

Matrix Metalloproteinase 9 Targeting Peptides: Syntheses, ^{68}Ga-labeling, and Preliminary Evaluation in a Rat Melanoma Xenograft Model

Tiina Ujula,[†] Merja Huttunen,[‡] Pauliina Luoto,[†] Hannu Peräkylä,[‡] Ilkka Simpura,[‡] Ian Wilson,[§] Mathias Bergman,[‡] and Anne Roivainen*[,†,||]

Turku PET Centre, University of Turku and Turku University Hospital, Turku, Finland, Karyon-CTT Ltd., Helsinki, Finland, Turku Imanet, GE Healthcare Medical Diagnostics, Turku, Finland, and Turku Center for Disease Modeling, University of Turku, Turku, Finland.
Received February 1, 2010; Revised Manuscript Received April 14, 2010

Biopanning of tumor cells was used in order to identify matrix metalloproteinase 9 (MMP-9) targeting peptides. The tumor cell targeting peptide (TCTP-1) and two modified versions thereof were evaluated as imaging agents for positron emission tomography (PET) using a rat melanoma xenograft model. For the PET imaging purposes, the 3 peptides were 1,4,7,10-tetraazacyclo-dodecane-*N*′,*N*″,*N*‴,*N*⁗-tetraacetic acid (DOTA) conjugated and labeled with Gallium-68 (^{68}Ga) and preliminarily evaluated: (1) cyclic ^{68}Ga-DOTA-TCTP-1 with cystine bridge, (2) cyclic ^{68}Ga-DOTA-lactam-TCTP-1 with a lactam bridge, and (3) linear ^{68}Ga-DOTA-lin-TCTP-1. The whole-body distribution kinetics and tumor targeting of the intravenously administered ^{68}Ga-DOTA-peptides were evaluated *in vivo* by PET and *ex vivo* by measuring the radioactivity of excised tissues. In addition, the *in vivo* stability of the radiolabeled peptides in rat plasma, tumor tissue, and urine was studied. All ^{68}Ga-DOTA-peptides were cleared via the liver and kidneys, and approximately 44% of injected radioactivity was excreted in urine during 120 min after injection. *Ex vivo* biodistribution studies showed a tumor-to-muscle ratio of 5.5 ± 1.3 (mean ± SD) for ^{68}Ga-DOTA-TCTP-1, 3.2 ± 0.2 for ^{68}Ga-DOTA-lactam-TCTP-1, and 3.2 ± 0.6 for ^{68}Ga-DOTA-lin-TCTP-1 at 120 min after injection. The ^{68}Ga-DOTA-lactam-TCTP-1 peptide appeared to be the most stable *in vivo*. The fraction of intact ^{68}Ga-DOTA-lactam-TCTP-1 in tumor was 59 ± 4.2% at 120 min after injection. The stability was moderate for ^{68}Ga-DOTA-TCTP-1 and poor for ^{68}Ga-DOTA-lin-TCTP-1. The possibility of imaging tumors that overexpress MMP-9, such as melanoma, by using radiolabeled TCTP peptides in PET imaging makes these peptides highly attractive for diagnostic and therapeutic applications. However, further modifications to improve the stability and affinity of the peptides are needed.

INTRODUCTION

Matrix metalloproteinases (MMPs) play a major role in tissue modeling and remodeling in normal physiology and pathophysiology by being capable of degrading extracellular matrix (ECM) proteins. For example, MMPs are associated with morphogenesis, wound healing, and tissue resorption (*1*). Cancerous growth of tumors into surrounding structures and tumor spread require degradation of the surrounding ECM. Twenty-three variants of MMPs have been identified and divided into subtypes (*2*).

MMP-9, also known as gelatinase B, belongs to a MMP family of zinc-dependent proteolytic enzymes (*3*). Normal tissue expression of MMP-9 is low and mainly found in keratinocytes, neutrophils, and eosinophils (*4*). Overexpression of MMP-9 has been associated with tumorigenesis in many malignancies (*5*). A large range of solid tumors overexpress/activate MMP-9, particularly during the processes of invasion and metastization (*6*). In these processes, MMP-9 degrades the gelatin of the ECM and thus promotes tumor cell migration and invasion into blood vessels and surrounding tissues. Importantly, endothelial cells of the tumor blood vessels also express MMP-9 as part of their growth process in tumors (*7*−*9*).

MMP-9 is synthesized as an inactive pro-enzyme and transported in specialized, kinesin-associated vesicles to the cell surface, where it stays associated with the cell membrane or becomes secreted (*6, 10, 11*). The proteinase then becomes activated on the cell surface or pericellularly via its own activity, by other MMPs or by serine proteases. MMP-9 can also be activated by the dissociation of complex partners or inhibitors (e.g., tissue inhibitors of metalloproteinases, TIMPs) (*12*−*14*).

MMP-9 is of clinical relevance in sarcomas, carcinomas, gliomas, malignant melanomas, and lymphomas (*2, 15, 16*), as well as in brain metastases (*17*). Elevated serum levels of MMP-9 are associated with rapid tumor progression in melanoma patients (*18*). Since MMP-9 has been implicated in tumor growth, invasion, and angiogenesis, it may be a suitable target for developing new imaging agents. Indeed, it has been reported that ^{11}C-labeled MMP inhibitors could be useful when imaging breast cancer (*19*). The ^{68}Ga-DOTA-peptides targeting MMP-9 could be useful in the diagnostic imaging of not only cancer but also inflammatory and degenerative diseases with an elevated MMP-9 level, such as atherosclerosis, heart failure, restenosis, amyotrophic lateral sclerosis, cerebrovascular disease, Alzheimer's disease, neuroinflammatory disease, and chronic obstructive pulmonary disease (*20*−*26*).

The objective of this proof-of-concept study was to determine whether the original peptide, discovered through biopanning (phage display) (*27*) of living cells of a malignantly transformed human cell line (*28*), and its modified versions are suitable vectors for the development of new radiopharmaceuticals for tumor imaging. The tumor cell targeting peptide (TCTP-1), functioning as ligand for MMP-9 (*29*−*31*), and two modified

* To whom correspondence should be addressed. Turku PET Centre, Turku University Hospital, Kiinamyllynkatu 4-8, FI-20521 Turku, Finland. Phone: +358-2-3132862. Fax: +358-2-2318191. E-mail: anne.roivainen@utu.fi.

[†] Turku PET Centre.

[‡] Karyon-CTT Ltd.

[§] GE Healthcare Medical Diagnostics.

[||] Turku Center for Disease Modeling.

10.1021/bc1000643 © 2010 American Chemical Society
Published on Web 08/26/2010

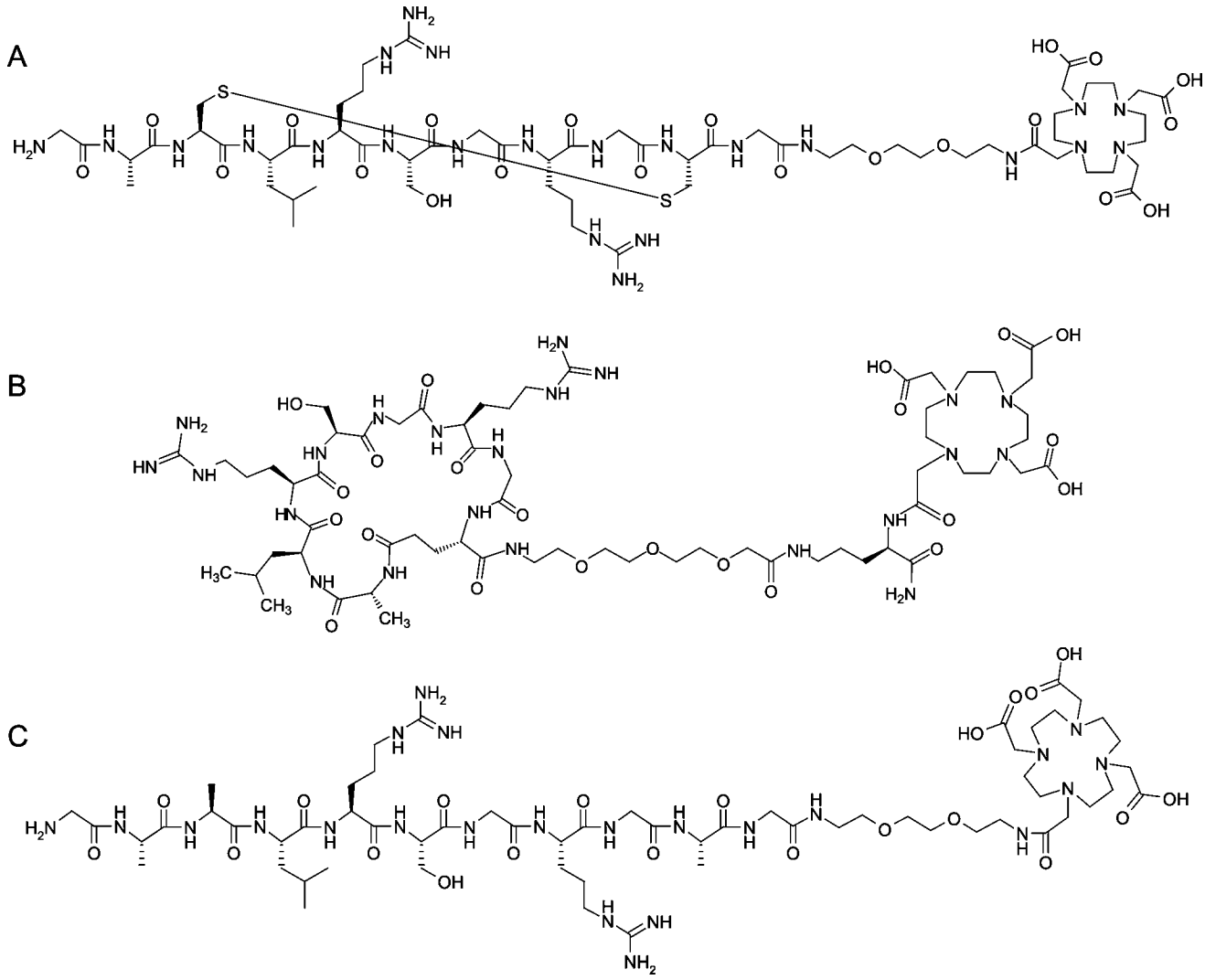


Figure 1. Structures of (A) DOTA-TCTP-1 (Cys3-10; H-Gly-Ala-Cys-Leu-Arg-Ser-Gly-Arg-Gly-Cys-Gly-PEG(3)-DOTA), (B) DOTA-lactam-TCTP-1 [Glu^{8}-Ala^{1} 5.8−2.1 lactam; D-Ala-Leu-Arg-Ser-Gly-Arg-Gly-Glu-(11-amino-3,6,9-trioxaundecanoyl)-δ-D-Orn(2-N-DOTA)-NH_2], and (C) DOTA-lin-TCTP-1 (Gly-Ala-Ala-Leu-Arg-Ser-Gly-Arg-Gly-Ala-Gly-PEG(3)-NH-DOTA). DOTA denotes 1,4,7,10-tetraazacyclo-dodecane-1,4,7,10-tetraacetic acid short of one hydroxyl due to coupling. PEG(3) denotes 3,6-dioxaoctane-1,8-diamine. D-Orn denotes (*S*)-2,5-diaminopentanoic acid.

versions thereof were evaluated as imaging agents for positron emission tomography (PET). The syntheses, ^{68}Ga-labeling, and preliminary evaluation using a rat melanoma xenograft model are reported here.

EXPERIMENTAL PROCEDURES

Synthesis of DOTA-TCTP-1 Peptide. Chelating agent 1,4,7,10-tetraazacyclo-dodecane-*N*′,*N*″,*N*‴,*N*⁗-tetraacetic acid (DOTA) was purchased from Macrocyclics, Dallas, TX, USA. The TCTP-1 peptide [Dde-Gly-Ala-Cys(*tert*-butyl)-Leu-Arg-Ser-Gly-Arg-Gly-Cys(*t*-Bu)-Gly-PEG(3)-DOTA(*t*-Bu)] (Figure 1A) was synthesized using a fully automated peptide synthesizer (ABI 433A, Applied Biosystems, Foster City, CA) with a slow-moc single couple. The synthesizer was loaded with *O*-bis-(aminoethyl)ethylene glycol trityl resin (568 mg of 0.44 mmol/g resin, 0.25 mmol) and aminoacid cartridges (1 mmol) that were previously activated with 2-(1*H*-benzotriazole-1-yl)-1,1,3,3-tetramethyluronium hexafluorophosphate (HBTU). The protected TCTP peptide was purified using preparative high performance liquid chromatography (Prep-HPLC; column: Phenomenex Luna 5 μm C18 (2) 250 × 50 mm; detection, 214 nm; electrospray ionization (ESI)-MS positive mode). H_2O/0.1% trifluoroacetic acid (TFA) (A) and CH_3CN/0.1% TFA (B) were used as solvents. The flow rate was 50 mL/min, and the gradient was 10−60% B over 60 min. The yield was analyzed using liquid chromatography with mass spectrometry detection (LC-MS; column: Phenomenex Luna 3 μm C18 (2) 50 × 2 mm; detection, 214 nm). The solvents described above were used. The flow rate was 0.3 mL/min and the gradient 10−60% B over 10 min. The expected MH+ was 1997.2, and the found *m*/*z* was 1996.9.

1-(4,4-Dimethyl-2,6-dioxocyclohex-1-ylidene)-ethyl (Dde) groups were removed from the TCTP peptide. The peptide was treated with 2% hydrazine monohydrate/*N*,*N*-dimethylformamide (DMF) (50 mL) for 60 min. The solvents were evaporated in vacuum, diethyl ether was added to the residue, and the precipitate was washed with diethyl ether and air-dried. The yield was analyzed with LC-MS as described above. The expected MH+ was 1833.1, and the found *m*/*z* was 1832.9.

Thereafter, *t*-Bu groups were removed from DOTA in the TCTP peptide. The peptide was treated with 5% H_2O/TFA (50 mL) for 3 h and 30 min. The solvents were evaporated in vacuum, diethyl ether was added to the residue, and the precipitate was washed with diethyl ether and air-dried. The yield was analyzed as described above. The expected MH+ was 1664.9, and the found *m*/*z* was 1664.9.

After the removal of *t*-Bu groups, the TCTP peptide was cyclized. The TCTP peptide was treated with 5% dimethyl sulfoxide/TFA (50 mL) for 50 min. The solvents were evaporated in vacuum, diethyl ether was added to the residue, and the precipitate was washed with diethyl ether and air-dried. The yield was analyzed with LC-MS as described above. The gradient was 0−30% B over 10 min. The expected MH + was 1550.8. The yield was purified by prep-HPLC (column, Phenomenex Luna 5 μm C18 (2) 250 × 21.20 mm; detection, 214 nm). The flow rate was 10 mL/min and the gradient 0−30% B over 40 min. The purified cyclized TCTP peptide was analyzed with LC-MS. The expected MH+ was 1550.8 and the found *m*/*z* was 1550.7.

Purification with prep-HPLC gave a t_R of 24.8 min and a yield of 18 mg. The t_R detected with LC-MS was 6.88 min, and the *m*/*z* found was 1550.8 (expected MH + 1550.8).

Synthesis of DOTA-lactam-TCTP-1 Peptide. A manual peptide synthesis protocol for DOTA-lactam-TCTP-1 [Glu^8-Ala^1 5.8−2.1 lactam; D-Ala-Leu-Arg-Ser-Gly-Arg-Gly-Glu-(11-amino-3,6,9-trioxaundecanoyl)-δ-D-Orn(2-N-DOTA)-NH_2] (Figure 1B) synthesis was developed and optimized. The synthesis was performed on solid support (SPPS), and each synthesis cycle included the following steps: (1) removal of the NH_2-terminal protective group, (2) activation of the coupled amino acid/linker/DOTA, (3) coupling reaction, and (4) capping with acetic anhydride. Careful washings with dichloromethane and DMF were performed between the various steps of the synthesis cycles. DOTA was coupled to the N-terminus of D-ornithine (o), and the peptide was synthesized from the side branch of D-ornithine. The peptide was cyclized using on-resin macrolactamization, after which the product was released from the resin. A linear tetraethyleneglycol [TEG, $NH_2(CH_2CH_2O)$•COOH] linker was used.

Purification was performed by prep-HPLC (column, DiscoveryBIO Wide Pore 10 μm C18 150 × 21.2 mm; detection, 218 nm). The same solvents were used as previously. The flow rate was 13.48 mL/min and gradient 0−30% over 30 min. T_R was 16 min, and the yield was 24 mg. Purity was >92%. The product was analyzed with positive MALDI-TOF mass spectrum. The M + 1 ion of the product was predominant. The calculated MW (isotopic) was 1514.79. The observed signals were 1515.83 M + 1, 1537.82 M + Na, and 1553.78 M + K.

Synthesis of DOTA-lin-TCTP-1 Peptide. The synthesis of the linear control peptide, DOTA-lin-TCTP-1 [Gly-Ala-Ala-Leu-Arg-Ser-Gly-Arg-Gly-Ala-Gly-PEG(3)-NH-DOTA] (Figure 1C), was performed on a fully automatic Peptide Synthesizer with a slow-moc single couple. *O*-Bis-(aminoethyl)ethylene glycol trityl resin (568 mg) (0.44 mmol/g; scale = 0.25 mmol) and 1 mmol aminoacid cartridges activated with HBTU were used.

Cleavage from the resin was performed by treating the product with a solution of 2.5% thiocresol, 2.5% triisopropylsilane (TIS), and 2.5% H_2O in TFA (10 mL) for 3 h. The mixture was filtered off in a small flask and concentrated with a rotary evaporator. The residue was added to ether, collected by centrifugation, and washed three times with ether. The yield was analyzed with LC-MS but with a different gradient than the one used for cyclic DOTA-TCTP-1. The gradient was 10−50% B over 10 min and the flow rate 0.3 mL/min. The expected and found MH+ was 1324.6.

Prep-HPLC was used for purification. The product (200 mg) was dissolved in 5.5 mL of 30% acetonitrile in H_2O with 0.1% TFA and filtered. The solution was divided in two and purified by prep-HPLC (column, Phenomenex Luna 5 μm C18 (2) 250 × 21.20 mm; detection, 214 nm). The gradient was 20−50% B and the flow rate 10 mL/min for 40 min. A peak at 22 min was collected manually and freeze-dried.

The peptide was then conjugated with DOTA-tris(*t*-Bu)-COOH. Pure peptide (0.01 mmol) (13.3 mg) was dissolved in 0.5 mL of DMF, and a mixture of 0.02 mmol DOTA-tris(*t*-Bu)-COOH (11.5 mg), 0.04 mmol *N*-methylmorpholine (NMM) (4.4 μL), and 0.02 mmol *O*-(7-azabenzotriazol-1-yl)-*N*,*N*,*N*′,*N*′-tetramethyluronium hexafluorophosphate (HATU) (7.6 mg) was added in 0.5 mL of DMF; pH 6. The solution was shaken overnight. The yield was analyzed with LC-MS but with a different gradient from the one used previously (20−50% B over 10 min). The solution was evaporated in vacuum, and the residue was precipitated in ether, collected by centrifugation, and washed three times with ether.

For the removal of *t*-Bu groups, the crude substance was dissolved in 4.75 mL of TFA with 2.5% TIS and 2.5% H_2O. After 2 h, the solution was evaporated in vacuum, and the residue was precipitated in ether, collected by centrifugation, and washed three times with ether. The analysis was performed with LC-MS.

Fmoc groups were removed by dissolving 0.01 mmol of the crude product described above in DMF (2 mL) and adding 0.1 mmol 1-octanethiole (17.4 μL) and 0.015 mmol 1,8-diazabicyclo[5,4,0]undec-7-ene (DBU) (2.3 μL) to the solution. After 1 h and 30 min, there was no starting material left. The analysis was performed by LC-MS using a gradient of 0−30% B over 10 min and the ESI-MS negative mode. The expected and found MH+ were 1487.0.

The solution was evaporated under vacuum, and the residue was precipitated in ether, collected by centrifugation, and washed three times with ether. Purification was performed by prep-HPLC using a gradient of 0−20% B over 40 min. T_R was 28.2 min and the yield 33 mg. The analysis was performed with LC-MS using a gradient of 0−20% B over 10 min. T_R was 7.86 min, and the *m*/*z* found was 1488.8, as expected.

Radiolabeling. ^{68}Ga was obtained in the form of $^{68}GaCl_3$ from a ^{68}Ge/^{68}Ga generator (Cyclotron Co., Obninsk, Russia) by elution with 0.1 M HCl. The ^{68}Ge/^{68}Ga generator consisted of ^{68}Ge ($T_{1/2}$ = 271 days) attached to an inorganic matrix, titanium dioxide (TiO_2), with 1850 MBq (50 mCi) of nominal radioactivity. The elution of the ^{68}Ge/^{68}Ga generator was monitored online with a positron sensitive photodiode detector (Hamamatsu S5591, Hamamatsu Photonics K.K. Solid State Division, Japan), and the radioactive elution peak was collected manually on the basis of changes in the voltage values of the detector. The radiolabeling of DOTA-peptides was performed as follows: $^{68}GaCl_3$ (500 μL), sodium acetate (219 μmol), and DOTA-peptide (30 nmol) were mixed and incubated at 95 °C for 25 min. Each peptide (DOTA-TCTP-1, DOTA-lactam-TCTP-1, and DOTA-lin-TCTP-1) was radiolabeled under the same conditions and with the same reaction proportions. TCTP-1 without the DOTA chelator was used as a negative labeling control. The radiochemical purity was determined by radio-HPLC with reversed-phase column (μBondapak 10 μm C18, 7.8 × 300 mm, pore size 125 Å; Waters Corporation, Milford, MA, USA). The radio-HPLC system consisted of LaChrom instruments (Hitachi; Merck Darmstadt, Germany), including pump L7100, UV detector L-7400, and interface D-7000; an online radioisotope detector (Radiomatic 150 TR, Flow Scintillation Analyzer; Packard, Meriden, CT, USA); and a computerized data acquisition system. The quantity of ^{68}Ga-radioactivity retained on the column was controlled. The HPLC conditions were the following: flow rate, 6 mL/min; λ = 215 nm; A = 50 mM phosphoric acid; B = 50 mM ammonium acetate/acetonitrile 1:1; C = 50 mM ammonium acetate; and A/B/C gradients, 0−3 min 0/15/85, 3−4 min 0/30/70, 4−5 min 0/60/40, 5−9 min 0/70/30, and 9−13 min 100/0/0 for all radiolabeled peptides.

***In Vitro* Tests.** The log *D* value of ^{68}Ga-DOTA-TCTP-1 was determined using the following procedure: Approximately 5 kBq

of ^{68}Ga-DOTA-TCTP-1 in 500 μL of phosphate buffered saline (PBS) at pH 7.4 was added to 500 μL of 1-octanol reperfused with PBS in an Eppendorf tube. After being vortexed for 3 min, the mixture was centrifuged at 12,000*g* for 6 min, and 100-μL aliquots of both layers were counted in a gamma counter (1480 Wizard 3″ Gamma Counter; EG & G Wallac, Turku, Finland). The test was repeated eight times.

To examine the *in vitro* stability, approximately 13 MBq (400 μL) of the ^{68}Ga-DOTA-peptide and 2 mL of physiological saline or human plasma were mixed and incubated at 37 °C for 4 h. During the incubation, 200-μL samples were taken at different time points. In the case of plasma samples, proteins were precipitated with 280 μL of acetonitrile (5:7, v/v), and the supernatant obtained after centrifugation (3,900*g* for 5 min at RT) was analyzed by radio-HPLC as described above. Saline incubation samples were analyzed as such with radio-HPLC. The test was repeated three times for each radiolabeled peptide.

To determine plasma protein binding, approximately 13 MBq (400 μL) of ^{68}Ga-DOTA-TCTP-1 was mixed with human plasma and incubated at 37 °C for 30 min. Subsequently, plasma proteins were precipitated with acetonitrile as described above. The radioactivity in the protein precipitate and supernatant was measured. Four parallel analyses were performed.

Melanoma Xenografts in Rats. C8161T/M1 cells were derived from the human cutaneous malignant melanoma cell line C8161 (*32*) by growing the cells as lung metastatic tumors in mice. The C8161T/M1 cell line represents a highly invasive subpopulation of the original cell line, isolated from a lung metastatic tumor (Karyon-CTT Ltd., Helsinki, Finland). This cell line was grown in DMEM supplemented with fetal calf serum, 2 mM L-glutamine, 100 U/mL penicillin, and streptomycin (100 μg/mL), and then injected ($1-10 \times 10^6$ cells/rat) subcutaneously (s.c.) into the necks of 51 athymic male Hsd: RH-rnu/rnu rats (Harlan, The Netherlands) at the age of 6 weeks. For the determination of MMP-9 expression levels by zymography as described below, the xenografts were examined after different growth times (1−4 weeks).

The rats were kept in the Central Animal Laboratory of the University of Turku in filter-top cages and allowed food and water ad libitum. All animal studies were approved by the Laboratory Animal Care and Use Committee of the University of Turku.

***In Vivo* Stability of ^{68}Ga-DOTA-Peptides.** *In vivo* stability was tested in 18 athymic rats (9 healthy and 9 tumor-bearing) anesthetized with isoflurane inhalation (Isofluran Baxter, Baxter Oy, Helsinki, Finland) and i.v. administered with 32 ± 14 MBq of the ^{68}Ga-DOTA-peptide (^{68}Ga-DOTA-TCTP-1 ($n = 9$), ^{68}Ga-DOTA-lactam-TCTP-1 ($n = 6$), or ^{68}Ga-DOTA-lin-TCTP-1 ($n = 3$)). Plasma, urine, and tumor samples were taken up to 2 h post-injection (p.i.). Tumor samples were homogenized (Ultra-Turrax T8 homogenizer; IKA Werke GmbH & Co. KG, Staufen, Germany) in ice-cold 1.5 mL of acetonitrile (v/v 5:7), centrifuged at 3,900*g* for 5 min at 4 °C, and filtered through 0.45 μm Acrodisc syringe filter (Waters Corporation, Milford, MA, USA). For all tissue samples, plasma proteins were precipitated with acetonitrile (v/v 5:7), and supernatants were analyzed with radio-HPLC, as described above.

To determine the percentage of extraction, rat blood and tumor samples were collected without prior ^{68}Ga-DOTA-peptide injection. To these control samples, ^{68}Ga-DOTA-peptide was added, and samples were processed in a way similar to that used with the other samples.

***In Vivo* PET Imaging.** To visualize and quantify the whole-body distribution kinetics of ^{68}Ga-DOTA-peptides, dynamic PET imaging was performed on rats with tumors that had grown for 1 week ($n = 8$), and 2 weeks ($n = 4$). The rats were sedated with s.c injection of 0.5 mg of fluanisone and 0.01 mg of fentanyl citrate (Hypnorm, Janssen Pharmaceutica, Beerse, Belgium). Anesthesia was induced with a mixture of 0.3 mg of midazolam (Midazolam Hameln 5 mg/mL, Hameln Pharmaceuticals GmbH, Hameln, Germany) and 0.67 mg of fluanisone plus 0.013 mg of fentanyl citrate via an intramuscular injection. The rats were kept on a warm pallet during the imaging procedure.

PET studies were performed with a HRRT camera (CPS Innovations, Knoxville, TN, USA). For attenuation correction, all PET studies started with a 6-min transmission scan using a single-photon transmission point source. Following the transmission, a tracer was intravenously (i.v.) injected as a bolus via a tail vein. The mean ± SD injected radioactivity was 19 ± 3.0 MBq for ^{68}Ga-DOTA-TCTP-1 ($n = 6$), 18 ± 0.5 MBq for ^{68}Ga-DOTA-lactam- TCTP-1 ($n = 3$), and 18 ± 0.9 MBq for ^{68}Ga-DOTA-lin-TCTP-1 ($n = 3$). This dose contained all of the peptide used for labeling, i.e., 30 nmol (approximately 40−50 μg, depending on the peptide in question). The dynamic imaging started at the time of injection. The acquisition times were as follows: 6×10 s, 4×60 s, and 23×300 s, with the total duration being 120 min. Data acquired in a list mode were iteratively reconstructed with the ordered subsets expectation maximization 3D algorithm. Spatial resolution in a reconstructed image is 2.5−3.5 mm.

Quantitative analysis was performed by drawing a circular region of interest (ROI) in the tumor, heart, kidney, liver, lung, muscle, and urinary bladder areas. The average radioactivity concentration in the ROI (kBq/mL) was used for further analyses. The uptake levels of ^{68}Ga-DOTA-TCTP-1, ^{68}Ga-DOTA-lactam-TCTP-1, and ^{68}Ga-DOTA-lin-TCTP-1 were reported as standardized uptake values (SUV (g/mL)), which were calculated as the radioactivity of the ROI (kBq/mL) divided by the relative injected radioactivity expressed per animal body weight (kBq/g). Biokinetic curves, representing the radioactivity concentration in the organ of interest versus time after injection, were determined accordingly.

***Ex Vivo* Measurements.** Immediately after PET imaging or without prior PET recording, the animals were terminated, and samples of tumor, blood, lung, liver, and muscle were excised, weighed, and measured for radioactivity in a gamma counter (1480 Wizard 3″, EG&G Wallac, Turku, Finland), which was cross-calibrated with a dose calibrator (VDC-202, Veenstra Instruments, Joure, The Netherlands) and the PET camera. Tracer uptakes were determined as a percentage of the injected dose per gram of tissue (% ID/g), standardized uptake value (SUV), tumor-to-blood, tumor-to-muscle, tumor-to-lung, and tumor-to-liver ratios. For biodistribution studies, 19 ± 3.0 MBq for ^{68}Ga-DOTA-TCTP-1 ($n = 2$), 18 ± 0.9 MBq for ^{68}Ga-DOTA-lactam-TCTP-1 ($n = 3$), and 18 ± 0.5 MBq for ^{68}Ga-DOTA-lin-TCTP-1 ($n = 3$) was injected per rat. To further study the effect of tumor growth on the tracer uptake, the original and most promising peptide, ^{68}Ga-DOTA-TCTP-1 (15 ± 2.6 MBq per rat, $n = 27$), was selected. Accumulation of ^{68}Ga-DOTA-TCTP-1 was studied at 2, 3, or 4 weeks after tumor inoculation. Three different time points of circulation were used: 2, 30, and 60 min.

Zymography. In a preliminary study, in order to get an idea of the MMP-9 expression levels in the rat model, zymography was run on rat samples ($n = 39$). Rat tumor samples were weighed and homogenized in a lysis buffer (10 mM Tris-HCl at pH 7.4, 10 mM NaCl, 3 mM $MgCl_2$, and 1% Triton X-100). The protein concentrations of lysates were determined using the Bradford method. Equal amounts of proteins were loaded on zymogram gels (Bio-Rad). Samples were separated at 30 mA for 15 min and 15 mA for 2 h. The gel was incubated in a renaturation buffer (0.25% Triton X-100) for 1 h and in a development buffer (5 mM Tris-HCl at pH 7.4, 20 mM NaCl,

0.5 mM $CaCl_2$, and 0.002% Triton X-100) at +37 °C overnight. The gel was stained with PageBlue Protein Staining Solution (Fermentas, Helsinki, Finland) for 1 h and destained in milli-Q H_2O. Recombinant human MMP-9 (R&D Systems, MN, USA) was used as a positive control. For the quantification of MMP-9, digital images of the gels were scanned and analyzed using the ImageJ software (National Institute of Mental Health, Bethesda, MD, USA).

MMP-9 Immunohistochemistry of Melanoma Xenografts. To confirm the expression of MMP-9 in tumor tissue, melanoma tumors of different stages of growth were dissected from rats and fixed in 10% paraformaldehyde. The samples were embedded in paraffin and sectioned with a microtome in 5 or 7 μm sections, and placed on slides. The slides were deparaffinized and stained with anti-MMP-9 antibody (C-20, Santa Cruz Biotechnology, Inc., Santa Cruz, CA, USA). The primary antibody was detected with biotinylated secondary antibody (Biotinylated antigoat IgG, Vector Laboratories, Burlingame, CA, USA). The signal was amplified using TSA Biotin System (PerkinElmer, Boston, MA, USA). The presence of MMP-9 was revealed by the stain from 3,3′-diaminobenzidine (Vector Laboratories, Inc.).

RESULTS

Radiolabeling. The radiochemical yield and radiochemical purity of ^{68}Ga-DOTA-peptides were >95% throughout the study. The specific radioactivity of ^{68}Ga-DOTA-TCTP-1, ^{68}Ga-DOTA-lactam-TCTP-1, and ^{68}Ga-DOTA-lin-TCTP-1 were 2.0 ± 0.8, 3.3 ± 0.8, and 1.5 ± 0.6 MBq/nmol (mean ± SEM), respectively. Figure 2A shows the HPLC chromatograms of the radiolabeled peptides. The retention times for ^{68}Ga-DOTA, ^{68}Ga-DOTA-TCTP-1, and ^{68}Ga were 2.86 ± 0.06 min, 8.12 ± 0.22 min, and 11.34 ± 0.33 min, respectively. The retention times for ^{68}Ga-DOTA-lactam-TCTP-1 and ^{68}Ga-DOTA-lin-TCTP-1 were 7.32 ± 0.55 min and 7.91 ± 0.40 min, respectively. Incubation of TCTP-1 peptide without the DOTA chelator with the ^{68}Ga-labeling mixture revealed no ^{68}Ga binding to the peptide.

***In Vitro* Tests.** The log *D* value of ^{68}Ga-DOTA-TCTP-1 was −3.6 ± 0.8, indicating very high hydrophilicity. All three ^{68}Ga-DOTA-peptides remained stable in the physiological saline at RT for >4 h (data not shown). In human plasma, the TCTP-1 peptide cyclized via a lactam bridge was more stable than the cystine bridged compound. No degradation of ^{68}Ga-DOTA-lactam-TCTP-1 was seen after 4 h of incubation in human plasma, whereas the half-lives of ^{68}Ga-DOTA-TCTP-1 and ^{68}Ga-DOTA-lin-TCTP-1 were approximately 2.5 and 1 h, respectively.

To estimate the bioavailability of ^{68}Ga-DOTA-TCTP-1 in blood circulation, the plasma protein binding was determined *in vitro*. Approximately 35 ± 1.2% of the compound was complexed with plasma proteins.

***In Vivo* Stability.** The ^{68}Ga-DOTA-lactam-TCTP-1 was the most stable *in vivo*, whereas ^{68}Ga-DOTA-lin-TCTP-1 degraded very rapidly (Table 1). The ^{68}Ga-DOTA-TCTP-1 showed moderate stability *in vivo* (Table 1 and Figure 2B). The tumor stability was quite low at 120 min p.i., and additional analysis at 15 min p.i. revealed 45 ± 1.2% of the intact radiolabeled peptide (Table 1 and Figure 2C). The fraction of intact ^{68}Ga-DOTA-lactam-TCTP-1 in tumor tissue was 59 ± 4.2% at 120 min p.i. In comparison, the fractions in plasma and urine were 23 ± 6.2% and 97 ± 2.6% at the same time point p.i., respectively. Because the plasma stability of ^{68}Ga-DOTA-lin-TCTP-1 was very low, it was not studied for tumor stability.

Extraction efficiency of ^{68}Ga-radioactivity from blood and tumor homogenates (control samples) was between 65% and 80%.

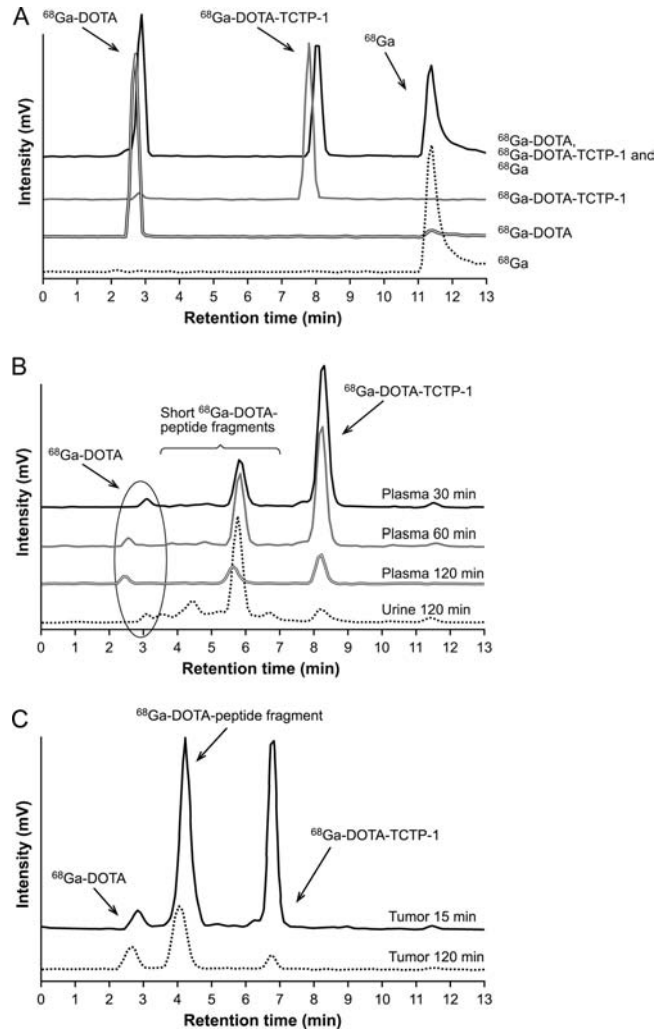


Figure 2. Representative radio high-performance liquid chromatography (radio-HPLC) chromatograms of (A) authentic standards, i.e., ^{68}Ga, ^{68}Ga-DOTA, and intact ^{68}Ga-DOTA-TCTP-1, and their mixture, (B) rat plasma and urine, and (C) tumor tissue homogenates of rat melanoma xenografts obtained 2 h after intravenous injection of ^{68}Ga-DOTA-TCTP-1. For HPLC, the stationary phase was C18, and the mobile phase consisted of a gradient of ammonium acetate, acetonitrile, and phosphoric acid (for details, see Experimental Procedures, Radiolabeling).

Table 1. Amount (%) of Intact ^{68}Ga-DOTA-Peptides in Rat Plasma, Tumor, and Urine at Various Time Points after Intravenous Injection, as Analyzed by Radio-HPLC[a]

	plasma		tumor		urine
tracer	15 min	120 min	15 min	120 min	120 min
^{68}Ga-DOTA-TCTP-1	71 ± 4.2	35 ± 18	45 ± 1.2	9.5 ± 2.6	5.3 ± 3.3
^{68}Ga-DOTA-lactam-TCTP-1	91 ± 2.0	23 ± 6.2		59 ± 4.2	97 ± 2.6
^{68}Ga-DOTA-lin-TCTP-1	0.2 ± 0.4[b]				

[a] The results are expressed as mean ± SD (n = 3). [b] Because of the very low plasma stability of ^{68}Ga-DOTA-lin-TCTP-1, no further analyses were performed.

***In Vivo* PET Imaging.** Representative PET images of the average radioactivity concentration at 10−55 min p.i. of ^{68}Ga-DOTA-TCTP-1 are presented in Figure 3A. Tumors were clearly visualized by ^{68}Ga-DOTA-TCTP-1 and ^{68}Ga-DOTA-lactam-TCTP-1. In addition, radioactivity uptake in the heart, liver, kidney, and urinary bladder was seen. The ^{68}Ga-DOTA-lin-TCTP-1 peptide showed an overall background and strong liver signal.

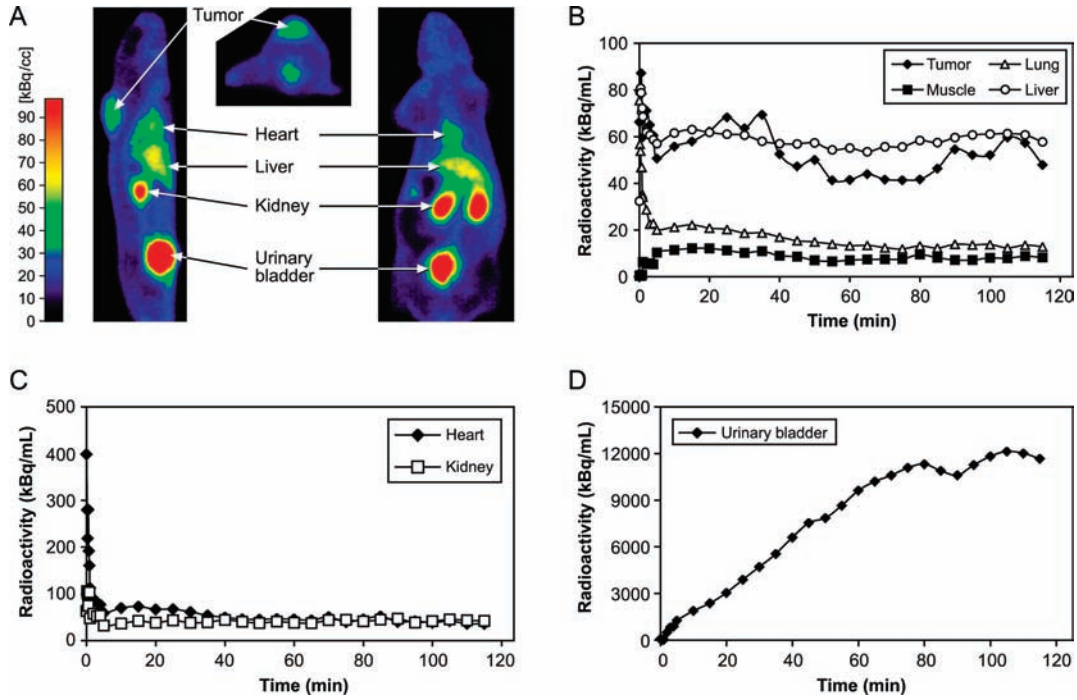


Figure 3. (A) Representative sagittal, transaxial, and coronal PET images of ^{68}Ga-DOTA-TCTP-1 distribution. An athymic rat (weight 284 g) with a 1-week-old subcutaneous human melanoma xenograft was intravenously injected with 30 MBq of ^{68}Ga-DOTA-TCTP-1. PET images represent summations of data collected 10−55 min after injection. Radioactivity uptake in the tumor, heart, liver, kidney, and urinary bladder is clearly visible. Corresponding time-activity curves for (B) tumor, muscle, lung and liver, (C) heart and kidney, and (D) urinary bladder.

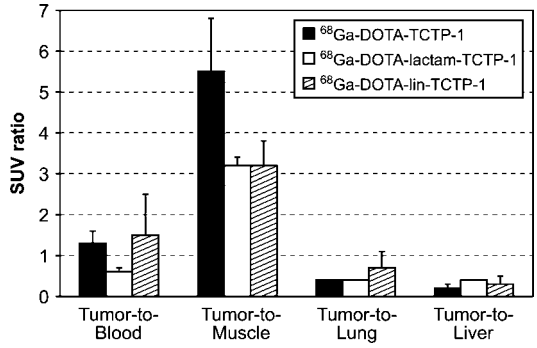


Figure 4. *Ex vivo* measurements of radioactivity in tissues after intravenous injection of ^{68}Ga-DOTA-peptides in tumor-bearing rats. Results are presented as SUV ratios (mean ± SD) measured at 120 min after intravenous injection of ^{68}Ga-DOTA-TCTP-1 ($n = 2$), ^{68}Ga-DOTA-lactam-TCTP-1 ($n = 3$), and ^{68}Ga-DOTA-lin-TCTP-1 ($n = 3$).

The biokinetic curves of ^{68}Ga-DOTA-TCTP-1 for the main organs and tumors are presented in Figure 3B−D. As regards all of the studied peptides, most of the i.v. administered radioactivity was excreted rapidly through the kidneys to the urinary bladder. All three peptide conjugates were rapidly taken up by the tumors but with slightly different kinetics. ^{68}Ga-DOTA-TCTP-1 was secreted the most slowly to urine. ^{68}Ga-DOTA-lactam-TCTP-1 showed slower uptake and longer retention in the tumor. ^{68}Ga-DOTA-lin-TCTP-1 showed the highest heart uptake as compared with the other radiolabeled peptides studied. The heart SUV of ^{68}Ga-DOTA-lin-TCTP-1 reached a plateau at 50 min p.i. and was about 1.0.

***Ex Vivo* Measurements.** The *ex vivo* results presented as tumor-to-control tissue ratios are summarized in Figure 4. ^{68}Ga-DOTA-TCTP-1 had the highest tumor-to-muscle ratio of 5.5 ± 1.3. The corresponding values for ^{68}Ga-DOTA-lactam-TCTP-1 and ^{68}Ga-DOTA-lin-TCTP-1 were 3.2 ± 0.2 and 3.2 ± 0.6, respectively. ^{68}Ga-DOTA-TCTP-1 had tumor-to-blood ratio 1.2 ± 0.3. With regard to the tumor-to-lung and tumor-to-liver ratios, there was not much difference between the three tested compounds.

Effect of tumor growth on the ^{68}Ga-DOTA-TCTP-1 uptake are presented in Tables 2 and 3. The highest tumor-to-muscle and tumor-to-blood ratios were measured at 60 min p.i. in tumors that had developed for three weeks ($n = 2-4$ at each time point). The greatest target-to-background ratio of 4.8 ± 0.4 was observed when comparing tumor to muscle at 60 min p.i.

The tumor SUV values after ^{68}Ga-DOTA-TCTP-1 administration were 0.4 ± 0.1, 0.3 ± 0.1, and 0.2 ± 0.04 at 2 min, and 30 and 60 min p.i. ($n = 9$ at each time point), respectively. The values are averages over all of the rats with tumors of different growth times.

A weak correlation between MMP-9 levels and the biodistribution results was seen. The correlation coefficient between MMP-9 level and tumor-to-muscle ratio was 0.33.

MMP-9 Immunohistochemistry of Melanoma Xenografts. MMP-9 was clearly detected at 2 and 6 weeks after inoculation of the C8161T/M1 cells, and the signal was located both in the endothelium layer of the blood vessels and in the ECM (Figure 5).

Zymography. The MMP-9 expression in rat xenografts, which had grown for three weeks, was on average 0.5 ng/mg tumor tissue (Table 4).

DISCUSSION

Synthetic peptides binding to MMP-9 may be useful for the purpose of diagnosing certain cancers by means of *in vivo* imaging. In this study, we used biopanning of tumor cells in order to identify MMP-9 targeting peptides. The peptide designated TCTP-1 and two modified versions thereof were evaluated as imaging agents for PET using a rat melanoma xenograft model. For the PET imaging purposes, the peptides were DOTA conjugated and labeled with ^{68}Ga. Our results revealed that the best visualization of tumor xenografts was

Table 2. *Ex Vivo* Biodistribution of Intravenously Administered ^{68}Ga-DOTA-TCTP-1 in Tumor-Bearing Rats Expressed as %ID/g

	Time after tumor inoculation								
	2 weeks			3 weeks			4 weeks		
organ	2 min[a]	30 min	60 min	2 min	30 min	60 min	2 min	30 min	60 min
blood	1.1 ± 0.4	0.3 ± 0.1	0.2 ± 0.01	1.1 ± 0.4[b]	0.4 ± 0.03	0.2 ± 0.03	0.7 ± 0.4[c]	0.3 ± 0.1	0.3 ± 0.1
liver	0.4 ± 0.2	0.3 ± 0.2	0.3 ± 0.1	0.8 ± 0.6[b]	0.4 ± 0.04	0.4 ± 0.1	0.4 ± 0.2[c]	0.4 ± 0.2	0.6 ± 0.1
lung	1.3 ± 0.9	0.6 ± 0.5	0.4 ± 0.1	1.3 ± 0.9[b]	0.6 ± 0.1	0.6 ± 0.2	0.7 ± 0.5[c]	0.3 ± 0.2	0.4 ± 0.1
muscle	0.1 ± 0.03	0.1 ± 0.03	0.03 ± 0.001	0.2 ± 0.1[b]	0.1 ± 0.01	0.04 ± 0.01	0.1 ± 0.1[c]	0.1 ± 0.02	0.1 ± 0.02
tumor	0.2 ± 0.1	0.2 ± 0.1	0.1 ± 0.02	0.2 ± 0.1[b]	0.2 ± 0.05	0.2 ± 0.03	0.1 ± 0.06[c]	0.2 ± 0.1	0.2 ± 0.1

[a] Time after intravenous injection. [b] The results are expressed as mean ± SD ($n = 3$ except $n = 4$). [c] The results are expressed as mean ± SD ($n = 3$ except $n = 2$).

Table 3. *Ex Vivo* Biodistribution (Tumor-to-Background Ratio) of Intravenously Administered ^{68}Ga-DOTA-TCTP-1 in Tumor-Bearing Rats at Different Time Points after Tumor Inoculation 2−60 min Post-Injection

time after tumor inoculation	tumor-to-blood			tumor-to-liver			tumor-to-lung			tumor-to-muscle		
(weeks)	2 min[a]	30 min	60 min	2 min	30 min	60 min	2 min	30 min.	60 min.	2 min	30 min	60 min
2	0.2 ± 0.1	0.5 ± 0.1	0.7 ± 0.1	0.6 ± 0.3	0.9 ± 0.8	0.4 ± 0.1	0.2 ± 0.1	0.5 ± 0.3	0.3 ± 0.1	1.3 ± 0.6	3.3 ± 0.7	4.0 ± 0.5
3	0.2 ± 0.04[b]	0.6 ± 0.1	0.9 ± 0.03	0.3 ± 0.1[b]	0.6 ± 0.1	0.5 ± 0.2	0.2 ± 0.1[b]	0.4 ± 0.1	0.3 ± 0.03	1.2 ± 0.4[b]	3.7 ± 0.9	4.8 ± 0.4
4	0.2 ± 0.1[c]	0.5 ± 0.1	0.6 ± 0.04	0.3 ± 0.1[c]	0.7 ± 0.4	0.3 ± 0.1	0.1 ± 0.1[c]	0.6 ± 0.2	0.5 ± 0.1	1.1 ± 0.1[c]	3.4 ± 0.6	3.4 ± 0.9

Results are expressed as mean ±SD ($n = 3$). [a] Time after intravenous injection. [b] $n = 4$. [c] $n = 2$.

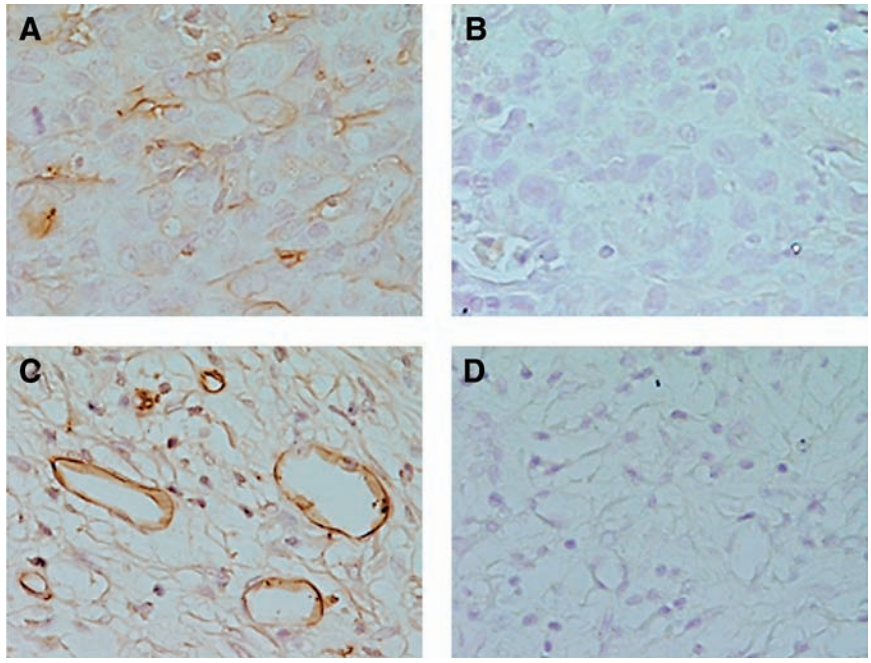


Figure 5. Immunohistological detection of MMP-9 in melanoma xenografts grown subcutaneously in athymic rats. Examples of anti-MMP-9 stainings are shown for paraffin sections of tumors inoculated (A) 2 weeks and (C) 6 weeks earlier. Cell nuclei are counterstained with hematoxylin. The MMP-9 signal is located both in the endothelial layer of the blood vessels and in the extracellular matrix of the tumor cells. B and D are the corresponding control stainings without the primary antibody.

Table 4. Quantity of MMP-9 in Melanoma Xenografts in Rats, as Determined by Zymography of Tumor Lysates[a]

	time after tumor inoculation (weeks)			
	1 ($n = 3$)	2 ($n = 13$)	3 ($n = 13$)	4 ($n = 10$)
MMP-9	3 ± 1	138 ± 140	525 ± 642	315 ± 264

[a] The results are expressed as ng/g of tumor tissue (mean ± SD).

obtained with the parental cyclic peptide, ^{68}Ga-DOTA-TCTP-1. Replacement of the cystine bridge by a lactam bridge in the cyclization of the DOTA-TCTP-1 peptide increased the stability drastically, suggesting that the key properties of this targeting agent can be easily modified. The fact that the lactam derivative of TCTP-1 showed slightly lower tumor accumulation indicates, however, that further studies are needed to optimize the pharmacokinetics of the compound. In general, this proof-of-principle study demonstrates that the methods described here are feasible to identifying, modifying, and optimizing novel imaging agents.

Animal Model. An *in vivo* model was established by implanting MMP-9 expressing human melanoma C8161T/M1 cells into athymic rats and by allowing the cells to form s.c. tumors. This particular cell line was chosen because previous studies had shown that the C8161T/M1 cells readily form s.c. tumors in rodents and because the MMP-9 expression level of the cell line is significant. Human melanoma xenografts in rats showed increased levels of MMP-9 during the tumor growth. Gelatin gel zymography was used to demonstrate MMP-9 activity in xenografts. This method allows for the detection of both latent (pro-MMP-9, 92 kDa) and active (72 kDa) forms of MMPs.

Characteristics of Peptides Studied. The synthesis of DOTA-peptides was straightforward, and the peptides were water-soluble. ^{68}Ga-DOTA-TCTP-1 had as low a log *D*, as was measured with our assay. The DOTA-conjugated TCTP-peptides were selectively and efficiently labeled with ^{68}Ga without any need for further purification. The specific radioactivity varied according to the age of the ^{68}Ge/^{68}Ga-generator from 0.4 to 7.0 MBq/nmol during the course of this study.

All three tested ^{68}Ga-DOTA-peptides were highly stable in physiological saline *in vitro*. Replacement of the cystine bridge by a lactam bridge increased the stability drastically, as expected (*33*). ^{68}Ga-DOTA-TCTP-1 showed moderate stability, but the lactam derivative of TCTP-1 showed no degradation after 4 h. The linear peptide was degraded very rapidly by proteolytic enzymes, it had a half-life of approximately 1 h, and released a large portion of shorter ^{68}Ga-DOTA-peptide fragments from the peptide structure. The lactam-bridged compound had the best *in vivo* stability in rats, as well, while both the cystine-bridged and linear TCTP-1 variants were moderately or highly labile *in vivo* in rats. The degradation products included most probably a ^{68}Ga-DOTA chelator, short ^{68}Ga-DOTA-peptide fragments, and a small amount ($\leq$3%) of ^{68}Ga (Figure 2). Although a peak with retention time similar to that of authentic ^{68}Ga-DOTA was observed, it most probably represents ^{68}Ga-DOTA attached to one to three amino acids, as DOTA itself is not recognized by enzymes. Identification of the degradation sites might aid in the construction of more stable peptides. Since Ga binds to proteins such as transferrin, ferritin, and lactoferrin present in plasma and tissues, it is possible that the Ga peak seen in radio-HPLC is a consequence of sample handling *in vitro*.

Of ^{68}Ga-DOTA-TCTP-1, 35% was found complexed with plasma proteins. This can be considered quite an acceptable situation, leaving most of the compound free to interact with the desired target, while still keeping a pool of molecules potentially protected from degradation.

Of the studied peptides, ^{68}Ga-DOTA-TCTP-1 showed the highest tumor uptake by PET imaging of melanoma rats. Dynamic analyses of the ^{68}Ga-DOTA-TCTP-1 PET imaging data showed a prolonged presence in the tumors during the 2 h imaging period (Figure 3B). The best tumor-to-muscle ratio was the *ex vivo* value of 5.5 $\pm$ 1.3 at 2 h p.i. for ^{68}Ga-DOTA-TCTP-1 (Figure 4). The corresponding ratios for ^{68}Ga-DOTA-lactam-TCTP-1 and ^{68}Ga-DOTA-lin-TCTP-1 at the same time point were 3.2 $\pm$ 0.2 and 3.2 $\pm$ 0.6, respectively (Figure 4).

The tumor accumulation of the test compounds and the control compound, ^{68}Ga-DOTA-lin-TCTP-1, was roughly at the same level, but the control showed high background signals throughout the body. The biokinetics showed that ^{68}Ga-DOTA-TCTP-1 had maximal tumor uptake (SUV of 0.6) immediately after injection, and it slowly decreased during 2 h of imaging. ^{68}Ga-DOTA-lactam-TCTP-1 showed a maximal tumor SUV of 0.4 at a slightly later time point (at 10 min p.i.) than other ^{68}Ga-DOTA-peptides, and it showed a slightly slower wash-out from tumors than ^{68}Ga-DOTA-TCTP-1 did. Some extent of tumor uptake may be due to blood flow. Comparative studies with a perfusion marker and ^{68}Ga-DOTA-TCTP-1 peptide are warranted and should clarify this concern.

All ^{68}Ga-DOTA-peptides showed fairly equal kidney uptake, and they were cleared via the kidneys and the liver, thus showing slightly different kinetics. ^{68}Ga-DOTA-lin-TCTP-1 had the highest and ^{68}Ga-DOTA-lactam-TCTP-1 the lowest liver uptake.

A closer examination of tumor accumulation by means of radio-HPLC of tumor homogenates revealed the origin of radioactivity. ^{68}Ga-DOTA-TCTP-1 had moderate *in vivo* stability, showing a half-life <15 min in tumor tissue (Table 1). Therefore, it is logical that after ^{68}Ga-DOTA-TCTP-1 had reached the maximal tumor SUV in PET, the tumor SUV started decreasing due to degradation of the radiolabeled peptide. Because ^{68}Ga-DOTA-lactam-TCTP-1 had the best tumor stability of 59 $\pm$ 4.2% at 120 min p.i., its wash-out from tumor sites was slower than that of the other tested radiolabeled peptides. However, despite the strong increase in stability achieved through replacing the cystine bridge by a lactam bridge, tumor targeting of ^{68}Ga-DOTA-lactam-TCTP-1 was slightly reduced, compared with the cystine variant, as shown both by PET and the *ex vivo* biodistribution analyses. Since the *in vivo* stability of ^{68}Ga-DOTA-lin-TCTP-1 was poor, it makes sense that a strong background signal was detected.

Previous Studies by Others. Imaging MMP-9 expression in tumors using PET and single photon emission computed tomography (SPECT) has previously been studied by others. Several synthetic compounds have been radiolabeled with carbon-11 (^{11}C), fluorine-18 (^{18}F), copper-64 (^{64}Cu), indium-111 (^{111}In), iodine-123 (^{123}I), or technetium-99 m ($^{99\,m}$Tc), and preliminarily evaluated in various experimental tumor models (*19, 34*−*40*). Yet, none of these compounds has proven its *in vivo* tumor imaging potential and has not proceeded any further. The most intensively studied compound is a peptide called CTT, which was discovered by Koivunen and co-workers (*28*). This MMP-2/MMP-9 inhibitor has been radiolabeled and preclinically evaluated by four distinct groups, i.e., Sprague et al. (*36*), Hanaoka et al. (*37*), Kuhnast et al. (*39*), and Medina et al. (*40*). However, selective binding to MMP-2/MMP-9 was not demonstrated, and all modifications of this peptide exhibited poor *in vivo* stability resulting in low tumor uptake. Our results are quite similar; although the *in vitro* properties of ^{68}Ga-DOTA-TCTP-1 peptides seemed promising, the *in vivo* tumor accumulation of the tested radiolabeled peptides remained quite low.

Possible Limitations. It is possible that the melanoma xenografts in rats did not produce a sufficient quantity of MMP-9 to facilitate fully optimal targeting of the tested ^{68}Ga-DOTA-peptides. However, the relatively weak tumor accumulation by the studied ^{68}Ga-DOTA-peptides might also be due to the type of MMP-9 expressed. In rat xenografts, the melanoma cells produce *human* MMP-9, and the growing tumor blood vessels produce *rat* MMP-9. These proteins differ slightly in their sequence, which is enough for them to be differently detected by various antibodies. These differences may further affect the ^{68}Ga-DOTA-peptide binding to MMP-9. A more detailed characterization of the tumor xenografts with respect to their MMP-9 expression (Western Blot, RNA content) might have been useful. In this study, ^{68}Ga-DOTA-peptides were shown to bind at least to human MMP-9, expressed by human melanoma tumors. Another fact, which may also affect the accumulation of ^{68}Ga-DOTA-peptides, is that the tumors showed a collapsed morphology with a hollow and necrotic center, especially at the later stages. The MMP-9 expression of the melanoma tumors in the rats showed only a weak correlation with the ^{68}Ga-DOTA-TCTP-1 accumulation in tumor tissue.

The state or conformation of the MMP-9 molecules may vary during the growth process of the melanomas. Since MMP-9 is a very dynamic protein with the capability of associating with a number of cell surface and ECM proteins, it is possible that the accumulation of ^{68}Ga-DOTA-TCTP-1 is facilitated at some stages of tumorigenesis and hindered at others. Since no dose finding study was performed within the scope of the present work, it is possible that the animals received too large a dose. Consequently, tumor accumulation may have been masked by the strong background signal from the blood.

The injected dose of peptide (40−50 μg, 30 nmol) was quite high in this study, and it has possibly caused oversaturation. In general, the specific radioactivity of ^{68}Ga-DOTA-peptides

decreases together with the age of generator, and the parent nuclide ^{68}Ge decays. During these studies, the generator was already quite old (>1 year). It would be expected that an increase in specific radioactivity would be achievable with a newer generator. Usually, the average amount of i.v. injected ^{68}Ga-DOTA-peptides for PET imaging of rats has been 19 μg (range 0.5−40 μg). However, in order to estimate the possible oversaturation effect of a compound it is more important to compare injected moles rather than mass.

We did not perform any blocking studies *in vivo* with ^{68}Ga-DOTA-peptides. Blocking studies would have been helpful in order to further elucidate the specificity of the peptides. The purpose of this study was to preliminarily evaluate three different TCTP-peptide modifications for PET imaging purposes, i.e., to clarify their whole-body distribution kinetics and tumor visualization properties. However, the properties (including specificity) of TCTP-peptides have been analyzed at Karyon-CTT Ltd., Helsinki, Finland to quite a large extent, e.g., that the *in vivo* tumor accumulation of Eu-DTPA-TCTP-1 peptide is blocked by an injection of anti-MMP-9 antibody into mice (*33, 41*).

Conclusions. This proof-of-concept study showed that MMP-9 targeting peptides can be identified by panning of biological structures in or on living cells. The identified peptide and two of its modifications were easy to synthesize, they were hydrophilic, and they allowed for efficient labeling with ^{68}Ga. The cyclic forms showed acceptable plasma stability and plasma protein binding properties. While ^{68}Ga-DOTA-TCTP-1 was able to delineate tumors by PET, further studies are needed to elucidate the value of this peptide as an imaging agent targeting MMP-9 *in vivo*.

ACKNOWLEDGMENT

We thank the members of the Angiomouse consortium and the staff of Karyon Ltd. for all their contributions. We also thank Professor Seppo Pyrhönen for providing patient samples and Satu Salomäki and Henri Sipilä for assistance in ^{68}Ga-labeling and radio-HPLC-analyses. This study was partially funded by Turku Imanet, GE Healthcare Medical Diagnostics, Turku Finland, and Karyon-CTT Ltd., Helsinki, Finland. T.U. is a Ph.D. student supported by the National Drug Discovery Graduate School, the Cancer Foundation of Southwestern Finland, the Finnish Society of Nuclear Medicine, and the Instrumentarium Foundation. The study was conducted within the Finnish Centre of Excellence in Molecular Imaging in Cardiovascular and Metabolic Research supported by Academy of Finland, University of Turku, Turku University Hospital, and Åbo Akademi University.

LITERATURE CITED

(1) Benbow, U., and Brinckerhoff, C. E. (1997) The AP-1 site and MMP gene regulation: what is the fuss about? *Matrix. Biol. 15*, 519–526.

(2) Vihinen, P., Ala-aho, R., and Kähäri, V. M. (2005) Matrix metalloproteinases as therapeutic targets in cancer. *Curr. Cancer Drug Targets 5*, 203–220.

(3) Johansson, N., Ahonen, M., and Kähäri, V. M. (2000) Matrix metalloproteinases in tumor invasion. *Cell. Mol. Life Sci. 57*, 5–15.

(4) Ståhle-Bäckdahl, M., and Parks, W. C. (1993) 92kD gelatinase is actively expressed by eosinophils and stored by neutrophils in squamous cell carcinoma. *Am. J. Pathol. 42*, 995–1000.

(5) Bloomston, M., Zervos, E. E., and Rosemurgy, A. S. (2002) Matrix metalloproteinases and their role in pancreatic cancer: A review of preclinical studies and clinical trials. *Ann. Surg. Oncol. 9*, 668–674.

(6) Sternlicht, M. D., and Werb, Z. (2001) How matrix metalloproteinases regulate cell behaviour. *Annu. Rev. Cell Dev. Biol. 17*, 463–516.

(7) Phillips, P. G., and Birnby, L. M. (2004) Nitric oxide modulates caveolin-1 and matrix metalloproteinase-9 expression and distribution at the endothelial cell/tumour cell surface. *Am. J. Physiol. Lung Mol. Physiol. 286*, 1055–1065.

(8) Del Bufalo, D., Trisciuoglio, D., Scarsella, M., D'Amati, G., Candiloro, A., Iervolino, A., Leonetti, C., and Zupi, G. (2004) Lonidamine causes inhibition of angiogenesis-related endothelial cell functions. *Neoplasia 6*, 513–522.

(9) Wikström, S. A., Keski-Oja, J., and Alitalo, K. (2003) Matrix reloaded to circulation hits the tumor target. *Cancer Cell 3*, 513–514.

(10) Hofman, U. B., Westphal, J. R., Waas, E. T., Becker, J. C., Ruiter, D. J., and Van Muijen, G. N. (2000) Coexpression of integrin alpha(v)beta(3) and matrix metalloproteinase-2 (MMP2) coincides with MMP2 activation: correlation with melanoma progression. *J. Invest. Dermatol. 115*, 625–632.

(11) Schnaeker, E. M., Ossig, R., Ludwig, T., Dreier, R., Oberleithner, H., Wilhelmi, M., and Schneider, S. W. (2004) Microtubule-dependent matrix metalloproteinase-2/matrix metalloproteinase-9 exocytosis: prerequisite in human melanoma cell invasion. *Cancer Res. 64*, 8924–8931.

(12) Sato, H., Takino, T., Okada, Y., Cao, J., Shinagawa, A., Yamamoto, E., and Seiki, M. (1994) A matrix metalloproteinase expressed on the surface of invasive tumour cells. *Nature 370*, 61–65.

(13) Brooks, P. C., Stromblad, S., Sanders, L. C., von Schalscha, T. L., Aimes, R. T., Stetler-Stevenson, W. G., Quigley, J. P., and Cheresh, D. A. (1996) Localization of matrix metalloproteinase MMP-2 to the surface of invasive cells by interaction with integrin alpha v beta 3. *Cell 85*, 683–693.

(14) Deryugina, E. I., Ratnikov, B., Monosov, E., Postnova, T. I., DiScipio, R., Smith, J. W., and Strongin, A. Y. (2001) MT1-MMP initiates activation of pro-MMP-2 and integrin alphavbeta3 promotes maturation of MMP-2 in breast carcinoma cells. *Exp. Cell Res. 263*, 209–223.

(15) Raithatha, S. A., Muzik, H., Rewcastle, N. B., Johnston, R. N., Edwards, D. R., and Forsyth, P. A. (2000) Localization of gelatinase-A and gelatinase-B mRNA and protein in human gliomas. *Neuro-Oncology (Durham, NC, U. S.) 2*, 145–150.

(16) Sakata, K., Satoh, M., Someya, M., Asanuma, H., Nagakura, H., Oouchi, A., Nakata, K., Kogawa, K., Koito, K., Hareyama, M., and Himi, T. (2004) Expression of matrix metalloproteinase 9 is a prognostic factor in patients with non-Hodgkin lymphoma. *Cancer 100*, 356–365.

(17) Spinale, F. G. (2002) Matrix metalloproteinases: regulation and dysregulation in the failing heart. *Circ. Res. 90*, 520–530.

(18) Nikkola, J., Vihinen, P., Vuoristo, M. S., Kellokumpu-Lehtinen, P., Kähäri, V. M., and Pyrhönen, S. (2005) High serum levels of matrix metalloproteinase-9 and matrix metalloproteinase-1 are associated with rapid progression in patients with metastatic melanoma. *Clin. Cancer Res. 11*, 5158–5166.

(19) Zheng, Q. H., Fei, X., Liu, X., Wang, J. Q., Bin Sun, H., Mock, B. H., Lee Stone, K., Martinez, T. D., Miller, K. D., Sledge, G. W., and Hutchins, G. D. (2002) Synthesis and preliminary biological evaluation of MMP inhibitor radiotracers [^{11}C]methyl-halo-CGS 27023A analogs, new potential PET breast cancer imaging agents. *Nucl. Med. Biol. 29*, 761–770.

(20) Robertson, L., Grip, L., Mattsson Hultén, L., Hulthe, J., and Wiklund, O. (2007) Release of protein as well as activity of MMP-9 from unstable atherosclerotic plaques during percutaneous coronary intervention. *J. Intern. Med. 262*, 659–667.

(21) Whittager, M., Floyd, C. D., Brown, P., and Gearing, A. J. H. (1999) Design and therapeutic application of matrix metalloproteinase inhibitors. *Chem. Rev. 99*, 2735–2776.

(22) Lim, G. P., Backstrom, J. R., Cullen, M. J., Miller, C. A., Atkinson, R. D., and Tökés, Z. A. (1996) Matrix metalloproteinases in the neocortex and spinal cord of amyotrophic lateral sclerosis patients. *J. Neurochem. 67*, 251–259.

(23) Lukes, A., Mun-Bryce, S., Lukes, M., and Rosenberg, G. A. (1999) Extracellular matrix degradation by metalloproteinases and central nervous system disease. *Mol. Neurobiol. 19*, 267–284.

(24) Backstrom, J. R., Miller, C. A., and Tökés, Z. A. (1992) Characterization of neutral proteinases from Alzheimer-affected and control brain specimens: identification of calcium-dependent metalloproteinases from the hippocampus. *J. Neurochem. 58*, 983–992.

(25) Mun-Bryce, S., Lukes, A., Wallace, J., Lukes-Marx, M., and Rosenberg, G. A. (2002) Stromelysin-1 and gelatinase A are upregulated before TNF-alpha in LPS-stimulated neuroinflammation. *Brain Res. 933*, 42–49.

(26) Segura-Valdez, L., Pardo, A., Gaxiola, M., Uhal, B. D., Becerril, C., and Selman, M. (2000) Upregulation of gelatinases A and B, collagenases 1 and 2, and increased parenchymal cell death in COPD. *Chest 117*, 684–694.

(27) Smith, G. (1985) Filamentous fusion phage: Novel expression vectors that display cloned antigens on the virion surface. *Science 228*, 1315–1317.

(28) Koivunen, E., Arap, W., Valtanen, H., Rainisalo, A., Medina, O. P., Heikkilä, P., Kantor, C., Gahmberg, C. G., Salo, T., Konttinen, Y. T., Sorsa, T., Ruoslahti, E., and Pasqualini, R. (1999) Tumor targeting with a selective gelatinase inhibitor. *Nat. Biotechnol. 17*, 768–774.

(29) Koivunen, E., Wang, B., Dickinson, C. D., and Ruoslahti, E. (1994) Peptides in cell adhesion research. *Methods Enzymol. 245*, 346–369.

(30) Auvinen, M., Paasinen, A., Andersson, L. C., and Hölttä, E. (1992) Ornithine decarboxylase activity is critical for cell transformation. *Nature 360*, 355–358.

(31) Auvinen, M., Laine, A., Paasinen-Sohns, A., Kangas, A., Kangas, L., Saksela, O., Andersson, L. C., and Hölttä, E. (1997) Human ornithine decarboxylase-overproducing NIH3T3 cells induce rapidly growing, highly vascularized tumors in nude mice. *Cancer Res. 57*, 3016–3025.

(32) Welch, D. R., Bisi, J. E., Miller, B. E., Conaway, D., Seftor, E. A., Yohem, K. H., Gilmore, L. B., Seftor, R. E., Nakajima, M., and Hendrix, M. J. (1991) Characterization of a highly invasive and spontaneously metastatic human malignant melanoma cell line. *Int. J. Cancer 47*, 227–237.

(33) Peräkylä, H., Huttunen, M., Karisalmi, E. K., Bergman, M., and Elo, H. (2007) Peptide Conjugates, U.S. Patent App Pub US 0231258, WO/2007/113386.

(34) Zheng, Q. H., Fei, X., Liu, X., Wang, J. Q., Stone, K. L., Martinez, T. D., Gay, D. J., Baity, W. L., Miller, K. D., Sledge, G. W., and Hutchins, G. D. (2004) Comparative studies of potential cancer biomarkers carbon-11 labeled MMP inhibitors (S)-2-(4′-[11C]methoxybiphenyl-4-sulfonylamino)-3-methylbutyric acid and N-hydroxy-(R)-2-[[(4′-[11C]methoxyphenyl)sulfonyl]benzylamino]-3-methylbutanamide. *Nucl. Med. Biol. 31*, 77–85.

(35) Wagner, S., Breyholz, H. J., Höltke, C., Faust, A., Schober, O., Schäfers, M., and Kopka, K. (2009) A new 18F-labelled derivative of the MMP inhibitor CGS 27023A for PET: radiosynthesis and initial small-animal PET studies. *Appl. Radiat. Isot. 67*, 606–610.

(36) Sprague, J. E., Li, W. P., Liang, K., Achilefu, S., and Anderson, C. J. (2006) In vitro and in vivo investigation of matrix metalloproteinase expression in metastatic tumor models. *Nucl. Med. Biol. 33*, 227–237.

(37) Hanaoka, H., Mukai, T., Habashita, S., Asano, D., Ogawa, K., Kuroda, Y., Akizawa, H., Iida, Y., Endo, K., Saga, T., and Saji, H. (2007) Chemical design of a radiolabeled gelatinase inhibitor peptide for the imaging of gelatinase activity in tumors. *Nucl. Med. Biol. 34*, 503–510.

(38) Oltenfreiter, R., Staelens, L., Lejeune, A., Dumont, F., Frankenne, F., Foidart, J. M., and Slegers, G. (2004) New radioiodinated carboxylic and hydroxamic matrix metalloproteinase inhibitor tracers as potential tumor imaging agents. *Nucl. Med. Biol. 31*, 459–468.

(39) Kuhnast, B., Bodenstein, C., Haubner, R., Wester, H. J., Senekowitsch-Schmidtke, R., Schwaiger, M., and Weber, W. A. (2004) Targeting of gelatinase activity with a radiolabeled cyclic HWGF peptide. *Nucl. Med. Biol. 31*, 337–344.

(40) Medina, O. P., Kairemo, K., Valtanen, H., Kangasniemi, A., Kaukinen, S., Ahonen, I., Permi, P., Annila, A., Sneck, M., Holopainen, J. M., Karonen, S. L., Kinnunen, P. K., and Koivunen, E. (2005) Radionuclide imaging of tumor xenografts in mice using a gelatinase-targeting peptide. *Anticancer Res. 25*, 33–42.

(41) Koivistoinen, A., Taube, S., Huttunen, M., Sihvo, E., Peräkylä, H., Salo, J., and Bergman, M. G. (2006) Novel cancer targeting peptides for non-neuroendocrine tumour imaging. *Eur. J. Nucl. Med. Mol. Imaging 33*, S265.

BC1000643

Synthesis and Properties of Oligonucleotides Carrying Isoquinoline Imidazo[1,2-*a*]azine Fluorescent Units

Sónia Pérez-Rentero,[†] Nicola Kielland,[‡] Montserrat Terrazas,[†] Rodolfo Lavilla,*[,‡,§] and Ramon Eritja*[,†]

Institute for Research in Biomedicine, IQAC−CSIC, CIBER-BBN Networking Centre on Bioengineering, Biomaterials and Nanomedicine, Baldiri Reixac 10, 08028 Barcelona, Spain, Institute for Research in Biomedicine, Laboratory of Organic Chemistry, Faculty of Pharmacy, University of Barcelona, Baldiri Reixac 10−12, 08028 Barcelona, Spain, and Laboratory of Organic Chemistry, Faculty of Pharmacy, University of Barcelona, Avda Joan XXIII s/n, 08028 Barcelona, Spain. Received February 18, 2010; Revised Manuscript Received June 28, 2010

Oligonucleotides carrying novel fluorescent compounds with a dipolar isoquinoline imidazo[1,2-*a*]azine core were prepared. Analysis of the melting curves demonstrates that DNA duplexes carrying these fluorescent labels at their ends have a slight increase in DNA duplex stability. The UV absorption and fluorescent properties of the oligonucleotide conjugates were analyzed. The fluorescent label is sensitive to duplex formation, as cooperative melting curves are also observed at 366 nm and fluorescence has a large increase upon denaturation. Cell uptake studies allow observation of these fluorescently labeled oligonucleotides internalized into HeLa cells.

INTRODUCTION

There is a considerable interest in the development of new dyes and the introduction of these into biomolecules such as peptides, proteins, and nucleic acids (*1*). Furthermore, the development of new methodologies for the selective and straightforward modification of biomolecules is having an increasing impact on biopharmaceuticals. When fluorescent molecules are attached to biomolecules that are not fluorescent, the resulting new entity acquires the fluorescent properties. Thus, fluorescent labels allow sensitive and selective detection of a specific component of complex biomolecular assemblies. Fluorescence-labeled oligonucleotides have large numbers of applications in several fields, such as biotechnology (*2*), cell biology (*3*), molecular biology (*4*), and biophysics (*5*). Therefore, the development of new fluorescent labels for oligonucleotides is of particular relevance (*6, 7*).

Recently, we described the synthesis of a new class of fluorescent mesoionic acid fluorides using a multicomponent strategy. The reaction involves the participation of an azine, an isocyanide, and a fluorinated anhydride and yields dipolar derivatives with an isoquinoline imidazo[1,2-*a*]azine core (see Scheme 1) (*8*). These compounds are fluorescent, and when trifluoroacetic anhydride is used, they contain a reactive acid fluoride group that can be used to introduce the fluorescent label, by means of amide formation, into biomolecules that carry amino groups. The modular character of this multicomponent reaction (MCR) (*9*) allows the convergent synthesis of a large variety of structural analogs in a single step. Thus, both the fluorescent and biological properties of the dye can be optimized for specific applications. In this respect, the present study determines the features of the conjugation of these stable dipolar acyl fluorides with oligonucleotides, a fruitful strategy often used in peptide synthesis (*10*), which to our knowledge is unprecedented in the oligonucleotide field.

Here, we report the conjugation of mesoionic acid fluorides **1a** and **1b** with oligonucleotides carrying alkyl amino groups (Scheme 2) and demonstrate that fluorescence-labeled oligonucleotides can be prepared in good yields directly from the reaction of amino-oligonucleotides and mesoionic acid fluorides in aqueous media. Dipoles **1a** and **1b**, bearing, respectively, cyclohexyl and benzyl groups as substituents at the imidazole nitrogen, were selected from a set of described analogues for the following reasons. First, they can be synthesized on a multigram scale with a simple methodology and are well characterized (X-ray, NMR, and spectroscopy); in addition, their substituents at the imidazole nitrogen (cyclohexyl and benzyl) featuring relevant differences in terms of shape, volume, polarity, and conformational behavior may confer to the corresponding bioconjugates distinct properties. Furthermore, both residues are chemically stable, unlikely to suffer degradation in physiological media, and, from an exploratory point of view, easy to replace by a wide number of analogues.

Our results indicate that the novel fluorescent oligonucleotides show potentially interesting properties for denaturation monitoring procedures as well as for cellular uptake studies.

EXPERIMENTAL PROCEDURES

The phosphoramidites and ancillary reagents used during oligonucleotide synthesis were from Applied Biosystems (PE Biosystems Hispania S.A., Spain) and Link Technologies Ltd. (Scotland). The rest of the chemicals were purchased from Aldrich, Sigma, or Fluka (Sigma-Aldrich Química S.A., Spain). 1-Cyclohexyl-3-(fluorocarbonyl)-2-oxo-2,3-dihydro-1*H*-imidazo-[2,1-*a*]isoquinolin-4-ium-3-ide (**1a**), 1-benzyl-3-(fluorocarbonyl)-2-oxo-2,3-dihydro-1*H*-imidazo[2,1-*a*]isoquinolin-4-ium-3-ide (**1b**), 1-cyclohexyl-3-(4-methoxybenzylcarbamoyl)-2-oxo-2,3-dihydro-1*H*-imidazo[2,1-*a*]isoquinolin-4-ium-3-ide (**1c**), and 1-cyclohexyl-3-(methoxycarbonyl)-2-oxo-2,3-dihydro-1*H*-imidazo[2,1-*a*]isoquinolin-4-ium-3-ide (**1d**) were prepared following literature procedures (*8*) (Scheme 1).

Synthesis of Oligonucleotides. Oligonucleotide sequences A, 5′-CCAATTGG-3′; B, 5′-TTCCGGAA-3′; and C, 5′-CTCTCGCACCCATCTCTCTCCTTCT-3′ were prepared on an automatic Applied Biosystems 3400 DNA synthesizer on 0.2− or 1−μmol scale using commercially available chemicals. The

* To whom correspondence should be addressed. Phone 34-934039942. E-mail recgma@cid.csic.es; rlavilla@pcb.ub.es.

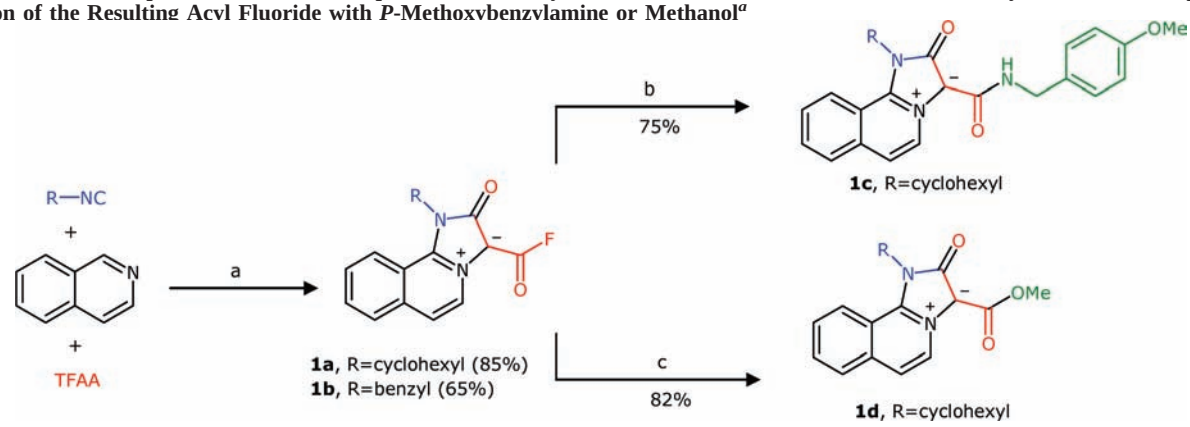
[†] CIBER-BBN Networking Centre on Bioengineering, Biomaterials and Nanomedicine.

[‡] Institute for Research in Biomedicine, University of Barcelona.

[§] Laboratory of Organic Chemistry, University of Barcelona.

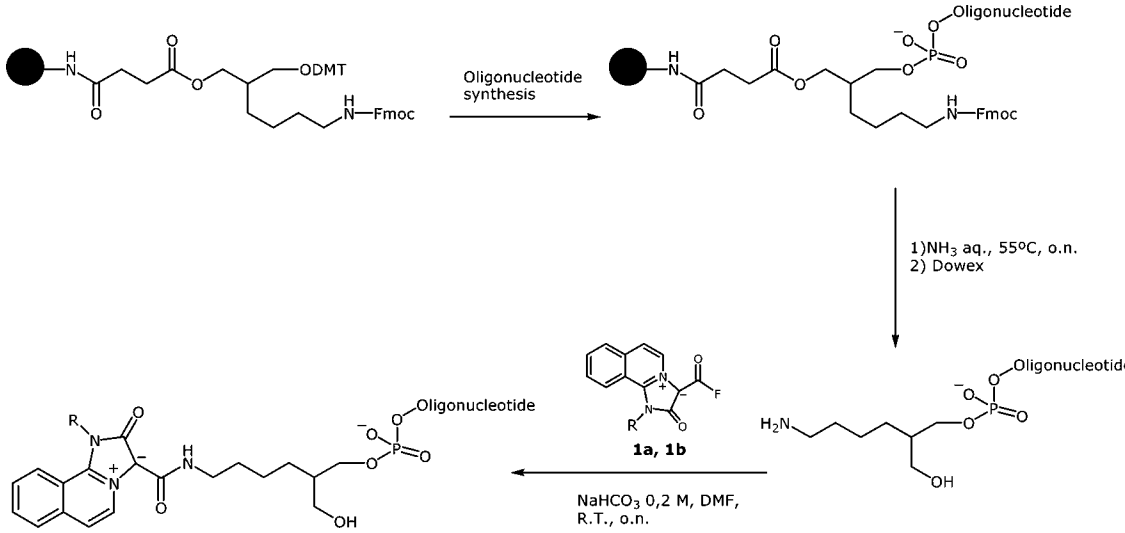
10.1021/bc1000966 © 2010 American Chemical Society
Published on Web 08/05/2010

Scheme 1. Three-Component Reaction of Isoquinoline and Isocyanides in the Presence of Trifluoroacetic Anhydride and Subsequent Reaction of the Resulting Acyl Fluoride with *P*-Methoxybenzylamine or Methanol[a]



[a] Reagents and conditions: (a) CH_2Cl_2, 14 h, r.t.; (b) *p*-methoxybenzylamine, TEA, CH_2Cl_2 anh., r.t., overnight; (c) MeOH, TEA, reflux.

Scheme 2. Synthesis of Oligonucleotides Carrying a Derivative of Isoquinoline at the 3′-End



sequences were prepared with and without the amino group at the 3′-end. The synthesis was carried out using the standard phosphite triester methodology and a controlled-pore-glass support carrying the 2-(*N*-{[(9*H*-fluoren-9-yl)methoxy]carbonyl}-4-aminobutyl)propane-1,3-diol linker (*11*) (Scheme 2) or in regular low-volume (LV200) polystyrene supports. The benzoyl (Bz) group was used to protect the amino group of dC and dA, and the isobutyryl (ibu) group to protect dG. Coupling yields were >95%. The last DMT group was removed at the end of the synthesis. The oligonucleotide was deprotected and cleaved from the support by treatment with aqueous concentrated ammonia for 12 h at 55 °C. Under these conditions, all protecting groups, including Fmoc, were removed to yield unprotected 3′-amino-oligonucleotide. The mixture was filtered, and the ammonia solution was concentrated to dryness. The residue was passed through a Dowex 50 × 4 (Na^+ form) column to exchange ammonium ions for Na^+ ions. The solution was analyzed by HPLC and used directly in the dye conjugation. Analytical HPLC solutions: Solvent A, 5% acetonitrile (MeCN) in 100 mM triethylammonium acetate (pH = 7); and solvent B, 70% MeCN in 100 mM triethylammonium acetate (pH = 7). Column: X-Bridge OST C18 (2.5 μm, 4.6 × 50 mm). Flow rate: 1 mL/min. Conditions for the analysis of octamers: 10 min linear gradient from 0−30% B at 60 °C; for the analysis of 25mer: 4 min linear gradient from 0−12% B, then 6 min linear gradient from 12−50% B at 60 °C. The desired oligonucleotides eluted at 2.5−3.5 min. Alternatively, oligonucleotides were purified by HPLC (see below).

Octamer sequence A (200 nmol scale): 33% yield (5 OD_{260}) t_R = 2.6 min. Octamer sequence A 3′-NH_2 (1 μmol scale): 47% yield (36 OD_{260}), t_R = 2.6 min. MALDI-TOF MS *m/z* (negative mode, THAP-CA, $[M-H]^-$) expected for $C_{85}H_{106}N_{31}O_{50}P_8$ 2617.8, found 2618.7. Octamer sequence B (200 nmol scale): 39% yield (6 OD_{260}) t_R = 3.2 min. Octamer sequence B 3′-NH_2 (1 μmol scale): 54% yield (42 OD_{260}), t_R = 3.2 min. MALDI-TOF MS *m/z* (negative mode, THAP-CA, $[M-H]^-$) calculated for $C_{85}H_{106}N_{31}O_{50}P_8$ 2617.8, found 2617.9. 25mer sequence C 3′-NH_2 (1 μmol scale): 58% yield 118 OD_{260}, t_R = 4.0 min. MALDI-TOF MS *m/z* (negative mode, THAP-CA, $[M-H]^-$) expected for $C_{244}H_{301}N_{73}O_{159}P_{25}$ 7600, found 7603.6.

General Protocol for Conjugation. The amino-oligonucleotides were reacted with 1-cyclohexyl-3-(fluorocarbonyl)-2-oxo-2,3-dihydro-1*H*-imidazo[2,1-*a*]isoquinolin-4-ium-3-ide (**1a**) or 1-benzyl-3-(fluorocarbonyl)-2-oxo-2,3-dihydro-1*H*-imidazo[2,1-*a*]isoquinolin-4-ium-3-ide (**1b**) or with fluorescein isothiocyanate (**FITC**) (Isomer I, Sigma) as follows. Oligonucleotides (7 O.D.) were dissolved with 250 μL of an aqueous solution of 0.2 M $NaHCO_3$ (pH = 9). Then, 10 equiv of a solution of compound **1a** or **1b** or **FITC** in 0.25 mL of *N*,*N*-dimethylformamide (DMF) were added and the mixture was left to react for 8 h at room temperature. Then, 100 μL of an aqueous solution of 0.2 M $NaHCO_3$ (pH = 9) and an additional 10 equiv of compound **1a** or **1b** in 100 μL of DMF were added and the mixture was left overnight at room temperature. The mixtures were concentrated to dryness, and the residues were dissolved in 1 mL of H_2O. The solutions were purified by Sephadex G-25 (NAP-10

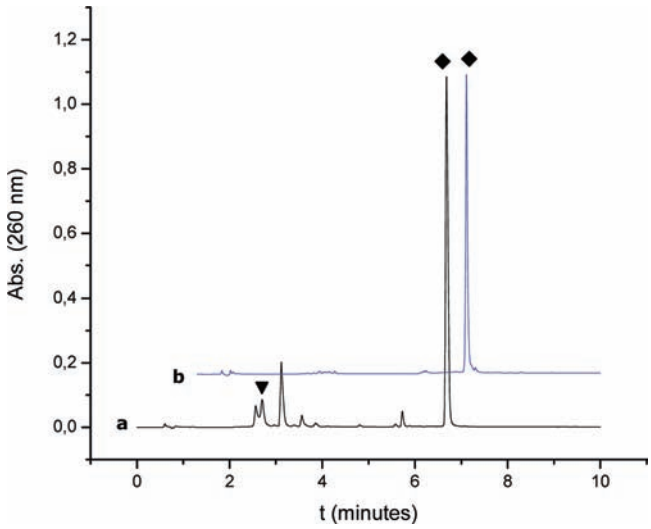


Figure 1. HPLC profiles of (a) the mixture obtained after the reaction with compound **1a** and amino-oligonucleotide sequence A to yield compound **2** (conversion 91%) and (b) purified compound **2**. HPLC conditions: 4 min linear gradient from 0−12% B, then 6 min linear gradient from 12−50% B at 60 °C. The desired oligonucleotide (compound **2**) eluted at 8.7 min (▼ stands for amino-oligonucleotide sequence A and ◆ stands for oligomer 2).

columns). The fractions containing oligonucleotides were analyzed by HPLC as described above (Figure 1). Octamer **5** and 25mer **6** were used in the next step without further purification. Octamers **2**−**4** were purified by HPLC on a Nucleosil 120C18 (10 μm, 200 × 10 mm) column. Flow rate: 3 mL/min. Conditions: 10 min linear gradient from 0−30% B, then a 10 min linear gradient from 30−100% B. The resulting products were desalted with Sephadex G-25 (NAP-5 Column). The coupling efficiency was determined by HPLC analyses (octamer **2** 91%, octamer **3** 91%, octamer **4** 94%, 25mer **6** 85%, octamer **5** (**FITC**) 94%. HPLC solutions as described above. Column: X-Bridge OST C18 (2.5 μm, 4.6 × 50 mm). Flow rate: 1 mL/min. Conditions: 4 min linear gradient from 0−12% B, then a 1 min linear gradient from 12−40% B, then 5 min linear gradient from 40−45% B at 60 °C. The purified oligomers were analyzed by MS (MALDI-TOF) and UV−vis (Table 1).

Octamer **2**: 39% yield (2.7 OD_{260}), t_R = 6.7 min, λ = 260 and 347 nm, MALDI-TOF MS *m*/*z* negative mode, THAP-CA, $[M-H]^-$ calculated for $C_{103}H_{122}N_{33}O_{52}P_8$ 2910.1, found 2911.8.

Octamer **3**: 54% yield (3.8 OD_{260}), t_R = 6.7 min, λ = 260 and 346 nm, MALDI-TOF MS *m*/*z* negative mode, THAP-CA, $[M-H]^-$ calculated for $C_{103}H_{122}N_{33}O_{25}P_8$ 2910.1, found 2906.8.

Octamer **4**: 26% yield (1.8 OD_{260}), t_R = 6.4 min, λ = 260 and 345 nm, MALDI-TOF MS *m*/*z* negative mode, THAP-CA, $[M-H]^-$ calculated for $C_{104}H_{118}N_{33}O_{52}P_8$ 2918.3, found 2914.9.

Octamer **5**: 84% yield (5.9 OD_{260}), t_R = 5.8 min, λ = 260 and 493 nm, MALDI-TOF MS *m*/*z* negative mode, THAP-CA, $[M-H]^-$ calculated for $C_{106}H_{128}N_{32}O_{55}P_8S$ 3008.9, found 3004.0.

25mer **6** (from 30 OD_{260}): 71% yield (21.3 OD_{260}), t_R = 8.3 min (4 min linear gradient 0−12% B, then 6 min linear gradient 12−50% B, at 60 °C), λ = 268 and 348 nm; MALDI-TOF MS *m*/*z* negative mode, THAP-CA, $[M-H]^-$ expected 7892.3, found 7870.2.

Melting Experiments. Melting experiments were performed in duplicate at concentrations ranging 1.5−14 μM of duplex. Solutions of each oligonucleotide were mixed in a solution containing 1 M NaCl and 100 mM sodium phosphate buffer pH = 7. The DNA concentrations were determined by UV-absorbance measurements (260 nm) at 80 °C, using the ε_{260} values calculated by the nearest-neighbor method for the DNA coil state. For octamer **5**, the ε_{260} value was calculated by the nearest-neighbor method as well and adding the contribution of fluorescein (the extinction coefficient of fluorescein (measured as FITC) at 260 nm is around 13.7 mM^{-1} cm^{-1}). Samples were heated at 90 °C for 5 min, allowed to cool slowly to room temperature to induce annealing, and then kept overnight in a refrigerator (4 °C).

Melting curves were recorded by heating the samples with a temperature controller from 15 to 80 °C at a constant rate of 1 °C/min and monitoring the absorbance at 260 nm. During the experiment, when the temperature was below 25 °C, argon was flushed to prevent water condensation on cuvettes. Absorption spectra and melting experiments (absorbance vs temperature) were recorded in 1 cm path-length cells. Melting curves were analyzed by computer-fitting the denaturation data, using *Meltwin 3.5* software. Melting temperatures (T_m) decreased with the concentration *c*, as expected for a bimolecular reaction (*12*). The plot of $1/T_m$ vs ln *c* was linear, giving a slope and a *y*-intercept, from which ΔH, ΔS, and ΔG were obtained (Table 2).

Fluorescence Analysis. Fluorescence spectra were measured in solutions containing 1 M NaCl and 100 mM sodium phosphate buffer (pH = 7) at a concentration of 2.3 μM. Excitation was set at 345 nm for octamers **2**−**4** and 493 nm for octamer **5**. Fluorescence spectra were measured before (F_D) and after (F_{RC}) duplex denaturation to yield relative fluorescence intensity (F_{RC}/F_D)). Results are shown in Figure 2 and Table 4.

Flow Cytometry Experiments. HT-29 cells were incubated for 8 h with dipole **1c** at concentrations of 2 μM, 5 μM, 10 μM, 20 μM, and 40 μM in a low glucose DMEM (Biological Industries) medium in the absence of phenol red. A blank control was also prepared. The supernatant was separated and placed in falcon tubes. The cells were treated with trypsin and placed in the corresponding falcon tubes. Each tube was centrifuged for 4 min at 2000 rpm. The supernatant was removed and PBS (500 μL) was added to each tube. The samples were treated with a propidium iodide solution (5 μL of a 1 μg/mL solution) and analyzed with a Cell Lab Quanta SC cytometer (Beckman Coulter).

Confocal Microscopy Experiments. HT-29 cells were incubated with dipole **1c** and **1d** (20 μM) for 2 h in a DMEM medium without phenol red. The living cells were treated with the plasmatic membrane marker WGA (Texas Red-x)-D (excitation at 595 nm, emission 615 nm). After 15 min, the cells were analyzed in vivo with a Leica TCS SP2 confocal microscope (excitation at 350 nm, emission between 400 and 500 nm). In these experiments, a blank control with the cells in the absence of dipole **1c** or its conjugate was analyzed. The intensity of the laser was adjusted in order to prevent detection of autofluorescent processes. Products **1c** and **1d** were detected in the cytoplasmatic region and they formed well-defined aggregates (see Supporting Information). Using the same procedure, HeLa cells were incubated with **1c** and oligonucleotide **6** (20 μM) for 4 h. While **1c** showed the same result as in the previous experiment, no fluorescence was detected using oligonucleotide **6**. In the presence of Lipofectamine 2000, oligonucleotide **6** penetrated the cytoplasmatic region.

RESULTS AND DISCUSSION

Synthesis and Thermodynamic Properties of Fluorescence Labeled Oligonucleotides. Small ligands can be incorporated into synthetic oligonucleotides at specific sites by preparing oligonucleotides carrying aliphatic amino groups and performing a conjugation reaction with the carboxylic derivatives of the ligands (*11*, *13*, *14*). This strategy was used to incorporate the acyl fluorides derivatives **1a** and **1b** into oligonucleotides (Scheme 2). Oligonucleotide sequences (Table 1) carrying an amino group at the 3′-end were assembled using a controlled

Table 1. Mass Spectra and UV Maxima of Fluorescent Oligonucleotides Prepared in This Study

#	sequence (5′−3′)	MS (expected)	MS (found)	UV_{max}, nm
2	CCAATTGG-NHCO-**1a**	2910.1	2911.8	260, 347
3	TTCCGGAA- NHCO-**1a**	2910.1	2906.8	260, 346
4	CCAATTGG-NHCO-**1b**	2918.3	2914.9	260, 345
5	TTCCGGAA-NHCO-**FITC**	3008.9	3004.4	260, 493
6	CTCTCGCACCCATCTCTCTCCTTCT NHCO-**1a**	7892.3	7870.2	267, 348

Table 2. Thermodynamic Parameters for Duplex-to-Random-Coil Transitions[a]

#	Duplex	T_m [°C][b]	ΔH [kcal/mol]	ΔS [kcal/mol.K]	ΔG [kcal/mol]	$\Delta\Delta G$[c][kcal/mol]
	$^{5'}$CCAATTGG$^{3'}$	33.3	−119.5	−340.5	−18.0	0
2	$^{5'}$CCAATGG-**1a**$^{3'}$	41.1	−116.8	−322.5	−20.6	1.3
4	$^{5'}$CCAATGG-**1b**$^{3'}$	34.0	−103.7	−288.3	−17.7	−0.15
	$^{5'}$TTCCGGAA$^{3'}$	31.8	−107.5	−303.0	−17.2	0
3	$^{5'}$TTCCGGAA-**1a**$^{3'}$	44.2	−107.0	−287.8	−21.2	2

[a] (1 M NaCl and 100 mM sodium phosphate buffer at pH = 7). ΔG is calculated at 25 °C, with the assumption that ΔH and ΔS do not depend on temperature; analysis was carried out with melting temperatures obtained from denaturation curves. [b] T_m calculated at 4 μM duplex concentration. [c] ΔG (modified octamer) − ΔG (unmodified octamer)/2 fluorescent molecules.

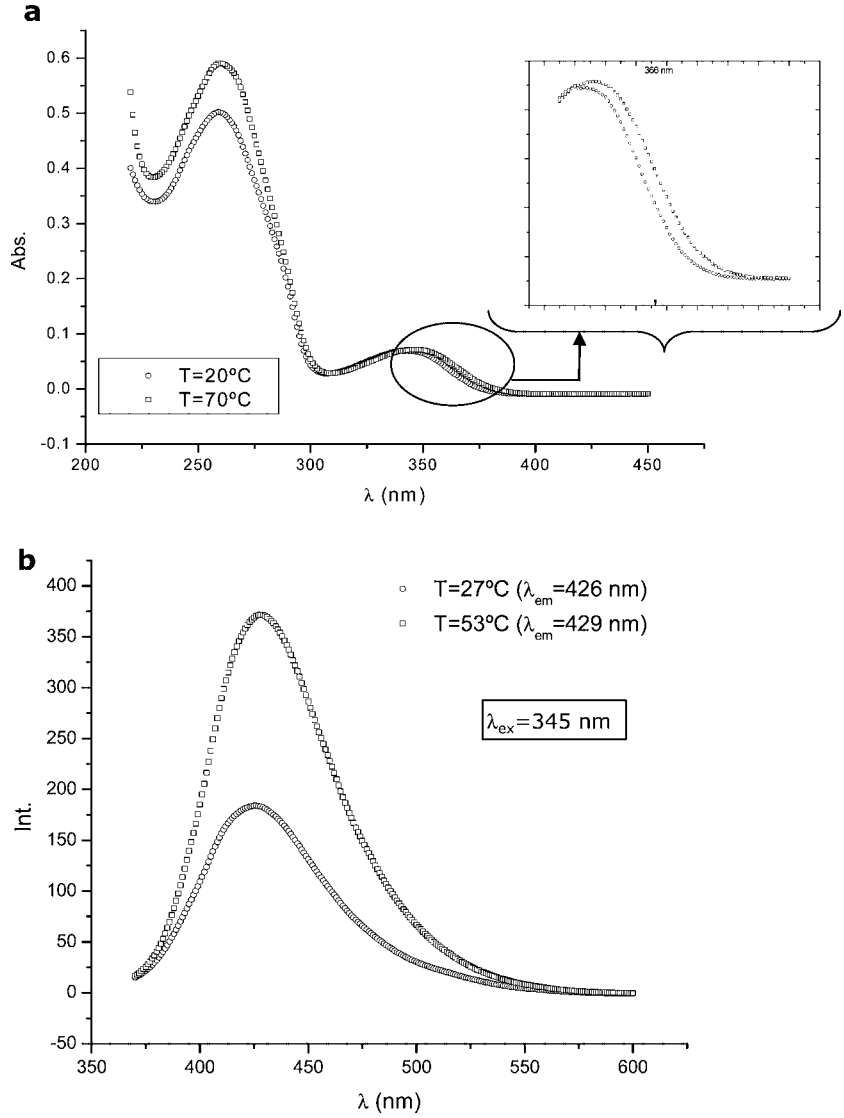


Figure 2. (a) UV and (b) fluorescence spectra of oligonucleotide **2**.

pore glass support carrying the 2-(*N*-{[(9*H*-fluoren-9-yl)methoxy]-carbonyl}-4-aminobutyl)propane-1,3-diol linker (*11*) and following standard protocols. The resulting oligonucleotides were used in the reaction with acyl fluorides (Scheme 1).

Amino-oligonucleotides were reacted with an excess of acyl fluorides **1a** and **1b** in aqueous dimethylformamide (DMF) mixtures at pH 9 and room temperature. In these mild conditions, the desired fluorescent oligonucleotides **2**−**4** and **6** were produced in good yields as shown by the presence of new products with higher retention time, which were characterized by mass spectrometry and UV spectra (Figure 1 and Table 1). In addition, we have prepared the fluoresceine-labeled octamer **5** by reaction of the appropriate amino-octamer with fluoresceine isothiocyanate (**FITC**).

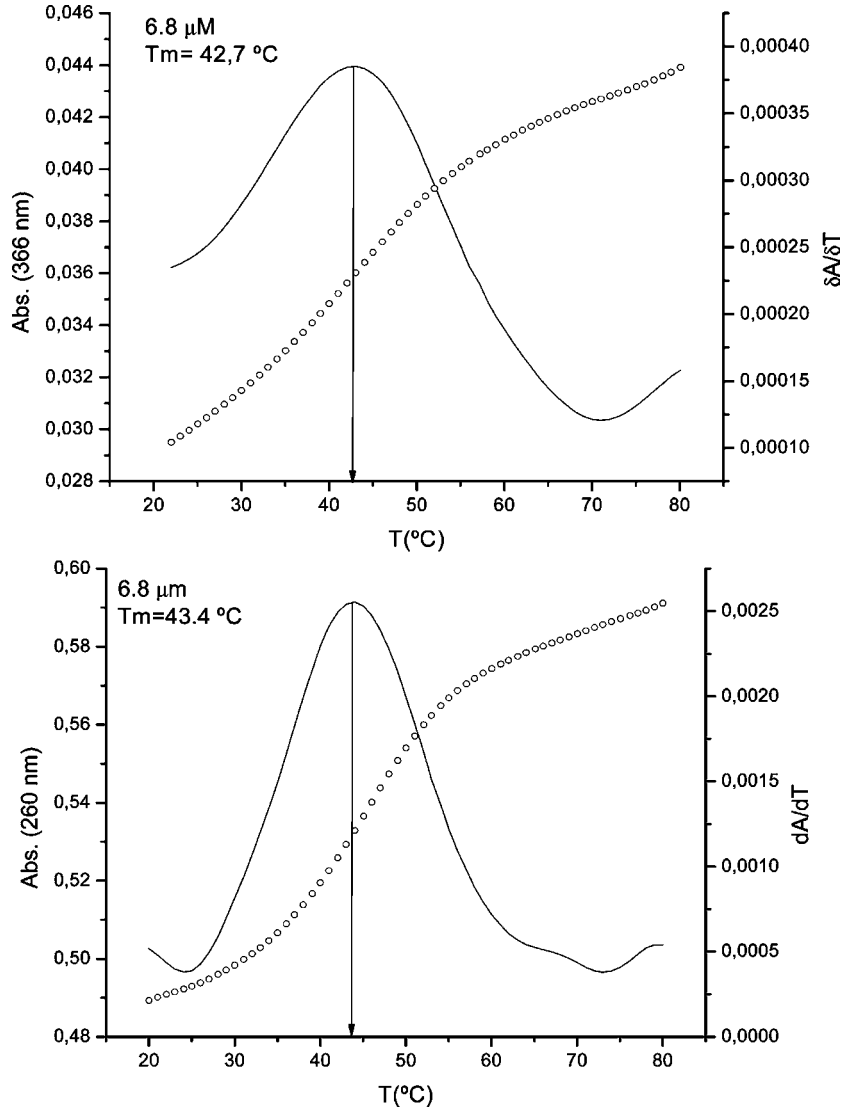


Figure 3. Melting curves of self-complementary oligonucleotide **2** measured at 260 and 366 nm.

The hybridization properties of the oligonucleotides carrying the isoquinoline imidazo[1,2-*a*]azine group were measured spectrophotometrically on the self-complementary octamer duplexes **2**−**4**. Unmodified octamers were included for comparison purposes (Table 2). The duplex formed by sequence **A**, which carried two molecules of compound **1a** (octamer **2**), melted at 41.1 °C (Δ*G* 20.6 kcal/mol), while the unmodified duplex melted at 33.3 °C (Δ*G* 18.0 kcal/mol). This observation implies an increase in duplex stability of 3.8 °C (ΔΔ*G* 1.3 kcal/mol) per fluorescent molecule. In contrast, the duplex formed by sequence **A**, carrying two molecules of compound **1b** (octamer **4**), melted at 34 °C (Δ*G* 17.7 kcal/mol), thereby indicating a small destabilization of the duplex. This effect should reflect the previously mentioned differences between the substituents on the imidazole nitrogen of the dipoles, presumably arising from the distinct interactions at the conformational level of the cyclohexyl and benzyl groups with the oligonucleotide backbone. The stabilizing properties of compound **1a** were slightly increased in octamer **3** (ΔΔ*G* 2.0 kcal/mol), thereby indicating that the stabilizing properties of this compound are not dependent on the DNA sequence at the end as octamer **3** has A.T base pairs, while octamer **2** has G.C base pairs.

Preliminary conformational studies of the linkers containing cyclohexyl or benzyl substituents by means of computer-based molecular modeling (Spartan'04 and Hyperchem'08; molecular mechanics conformational search and geometry optimization) suggest that, in the lower energy conformations, the isoquinoline imidazo[1,2-*a*]azine core containing a cyclohexyl substituent stacks over the terminal guanine nucleobase, at a distance of approximately 3 to 4 Å, whereas the isoquinoline imidazo[1,2-*a*]-azine core containing a benzyl substituent does not interact significantly with the terminal guanine (see Supporting Information Figure S1). These studies were carried out by keeping frozen the duplex of DNA and by allowing the linker to move freely during the calculations. In order to explore the rotational freedom of the cyclohexyl or benzyl-fluorescent isoquinoline imidazo[1,2-*a*]azine in more detail and to determine the dynamic behavior of the conjugates, molecular dynamics simulations and NMR studies on these modified duplexes would be necessary. A comprehensive study is currently under way in our laboratory.

UV spectra of the modified oligonucleotides **2**−**4** at 20 °C (duplex) and 70 °C obtained in a solution containing 1 M NaCl and 100 mM sodium phosphate buffer of pH = 7 at a concentration of 6.8 μM are shown in Figure 2a. The maximum caused by the isoquinoline derivative shows a slight shift depending on the temperature. The hyperchromism in the absorption spectra at 70 °C and the bathochromical shift indicated that the molecule attached to the oligonucleotide is sensitive to the presence of a duplex or a random coil form. The UV spectra indicated a change in hyperchromicity between 340 and 380 nm, the difference being maximum around 366 nm, and so melting curves were recorded at 366 nm. Melting

Table 3. Melting Temperatures of Modified and Unmodified Duplex at Different λ

#	oligonucleotide	Abs. (260 nm, 70 °C)	T_m (°C) (260 nm)	T_m (°C) (λ)[a]
2	5′CCAATGG-**1a**3′	0.59	43.2	42.9
3	5′TTCCGGAA-**1a**3′	0.48	45.9	35.4
4	5′CCAATGG-**1b**3′	0.61	37.2	36.8
5	5′ TTCCGGAA-**FITC**3′	0.63	44.2	44.8

[a] Melting experiments performed at 366 nm for **2** and **4**, 364 nm for **3**, and 493 nm for **5**.

Table 4. Fluorescence Spectral Data for the Modified Oligonucleotides before and after Duplex Denaturation

	temperature (°C)	emission maximum (nm)	fluorescence intensity (I)	F_{RC}/F_D	ΔI (%)
2	27	426	184	2.02	+102
	53	429	371		
3	24	427	322	1.74	+74
	51	430	560		
4	17	418	312	1.34	+34
	39	423	418		
5	20	522	117	0.82	−18
	60	520	96		

curves were recorded simultaneously at 260 and 366 nm for comparison purposes (Figure 3). Melting temperatures at these two wavelengths were similar, although at 366 nm, the duplex showed a lower T_m (see, for example, compound **2** T_m: 42.9 °C at 366 nm and 43.2 °C at 260 nm; Table 3). This indicates that base pair dissociation observed at the end of the oligonucleotide (measured at 366 nm where the fluorescent tag is located) happens at a slightly lower temperature of the global melting of the duplex (measured at 260 nm). A similar behavior has been described for fluorescent compounds attached in the middle a DNA duplex (*15, 16*). The fluoresceine octamer **5** had a melting temperature of the same range than octamers carrying the isoquinoline imidazo[1,2-*a*]azine core with the cyclohexyl group (**1a**) **2** and **3** (Table 3). Surprisingly, at 493 nm it had a slightly higher melting temperature (T_m 44.8 °C at 493 nm, T_m 44.2 °C at 260 nm).

Next, we studied the effects of duplex denaturation in fluorescence. Fluorescent spectra of self-complementary duplex **2** in 1 M NaCl and 100 mM sodium phosphate buffer pH = 7 at a concentration of 2.3 μM at different temperatures were recorded. Figure 2b shows the fluorescent spectra at 27 and 53 °C. Excitation was set at 345 nm. Absorption maxima of oligonucleotides **2**−**4** at high and low temperatures are summarized in Table 4. A strong increase in fluorescence was observed upon duplex denaturation. These results and the slight increase in T_m indicates that the fluorescent label interacts with the DNA duplex most probably as an end-cap and the complex has a lower florescence. Upon duplex denaturation, the fluorescent label changes the environment duplicating the fluorescence emission. These effects were more intense in octamers carrying compound **1a** (oligonucleotides **2** and **3**) than those carrying compound **1b** (oligonucleotide **4**). This effect may be a consequence of the conformational preference of the isoquinoline imidazo[1,2-*a*]azine core containing a cyclohexyl substituent to stack over the terminal nucleobase described above. The fluoresceine octamer **5** does not increase the fluorescence upon heating, but on the contrary, a clear decrease on the fluorescence properties is observed (Table 4).

In summary, dipolar isoquinoline derivatives **1a**−**b** readily prepared by MCR are efficient and inexpensive reagents for introducing of fluorescent labels into synthetic oligonucleotides. Reagent **1a** is particularly useful as it produces fluorescence-labeled oligonucleotides that are sensitive to hybridization and have duplex-stabilizing properties. Next, we studied the capacity of fluorescence-labeled oligonucleotides to monitor cellular uptake.

Cell Uptake Experiments. A 25mer oligonucleotide sequence with an amino group at the 3′-end (Table 1) was also prepared. This sequence corresponds to an antisense oligonucleotide known as GEM91 (*17*), which is complementary to the initiation codon of gag gene of HIV-1 RNA. Reaction of 3′-amino GEM91 with **1a** yielded the expected fluorescence-labeled oligonucleotide (**6**) in excellent yields (85% conversion judged by HPLC, 71% isolated yield). The resulting product was used in the transfection assays without further purification.

We first performed flow cytometry experiments with the model isoquinoline compound **1c** in order to assess the potential toxicity of the dye. HT-29 cells were incubated for 8 h with dipole **1c** and analyzed by flow cytometry. The percentage of living or dead cells remained almost constant at all concentrations of **1c** and was very similar to the control value (see Supporting Information). These results support the notion that this compound has a low toxicity profile.

We then performed confocal microscopy experiments to analyze the distribution of the compound **1c** inside the cells. Compound **1c** was detected in the cytoplasmatic region and formed well-defined aggregates (see Supporting Information). The analogous methyl ester dipole **1d** (*8*) was analyzed under the same conditions and showed a similar distribution pattern (see Supporting Information).

We then performed further confocal microscopy experiments to optimize the conditions in order to evaluate the capacity of conjugate **6** to penetrate HeLa cells in the presence (or absence) of Lipofectamine 2000. When cells were incubated with conjugate **6** (20 μM) for 4 h, no fluorescence was detected, whereas the same product in the presence of Lipofectamine 2000 penetrated the cytoplasmatic region. Longer incubation times (22 h) with conjugate **6** (20 μM) in the presence of Lipofectamine 2000 induced strong cell toxicity and no living cells were found. This result may reflect the toxicity of Lipofectamine under these conditions.

CONCLUSIONS

Here, we describe the use of unexpensive reagents in the synthesis of oligonucleotides carrying highly sensitive fluorophores. The acid fluoride derivative of the fluorophore required for the preparation of the fluorescent-labeled oligonucleotides was synthesized in high yield in a one-pot reaction using an efficient MCR which has been described previously (*8*). The acyl fluorides reacted efficiently in aqueous buffers at pH 9 with amino-oligonucleotides to yield the desired conjugates. The resulting oligonucleotides show intense fluorescent properties in presence of ions, have slightly improved hybridization properties, and are sensitive to denaturation. Flow cytometry and confocal microscopy experiments showed a low toxicity profile and good cell membrane permeability, respectively, for dyes **1c** and **1d**. Oligonucleotide **6** had the capacity to penetrate cells in the presence of Lipofectamine 2000 transfection reagent.

ACKNOWLEDGMENT

This study was supported by the "Dirección General de Investigación Científica y Técnica" (grant BFU2007-63287, CTQ2010-20541 and CTQ2009-07758), and the Generalitat de Catalunya (2009/SGR/208). N. K. thanks the DGICYT for Ph.D. fellowship.

Supporting Information Available: Structure of the most energetically stable conformations of **1a** and **1b** conjugates by molecular mechanics (MM) conformational searches and geometry optimization. Flow cytometry experiments with dipolar

amide **1c**. Confocal microscopy images from cell uptake experiments. Mass spectrometry, HPLC analysis, and melting curves of purified oligonucleotides. This material is available free of charge via the Internet at http://pubs.acs.org.

LITERATURE CITED

(1) Mayer, A., and Neuenhofer, S. (1994) Luminescent labels - more than just an alternative to radioisotopes? *Angew. Chem., Int. Ed. 33*, 1044–1072.

(2) Gait, M. J. (1991) DNA/RNA synthesis and labeling. *Curr. Opin. Biotechnol. 2*, 61–68.

(3) Wang, K., Tang, Z., Yang, C. J., Kim, Y., Fang, X., Li, W., Wu, Y., Medley, C. D., Cao, Z., Li, J., Colon, P., Lin, H., and Tan, W. (2009) Molecular engineering of DNA: Molecular Beacons. *Angew. Chem., Int. Ed. 48*, 856–870.

(4) Schubert, F., Cech, D., Reinhardt, R., and Wiesner, P. (1992) Fluorescent labelling of sequencing primers for automated oligonucleotide synthesis. *DNA Seq. 2*, 273–279.

(5) Lilley, D. W., and Wilson, T. J. (2000) Fluorescence resonance energy transfer as a structural tool for nucleic acids. *Curr. Opin. Mol. Biol. 4*, 507–517.

(6) Cuppoletti, A., Cho, Y., Park, J. S., Strässler, C., and Kool, E. T. (2005) Oligomeric fluorescent labels for DNA. *Bioconjugate Chem. 16*, 528–534.

(7) Singh, S., and Singh, R. K. (2007) Synthesis and fluorescence studies of some new fluorophores and their effect on hybridization of oligodeoxyribonucleotides. *J. Fluoresc. 17*, 139–148.

(8) Arévalo, M. J., Kielland, N., Masdeu, C., Miguel, M., Isambert, N., and Lavilla, R. (2009) Multicomponent access to functionalized mesoionic structures based on TFAA activation of isocyanides: Novel domino reactions. *Eur. J. Org. Chem.* 617–625.

(9) Zhu, J., and Bienaymé, H. (2005) in *Multicomponent Reactions*, Wiley-VCH, Weinheim.

(10) Carpino, L. A., Beyermann, M., Wenschuh, H., and Bienert, M. (1996) Peptide synthesis via amino acid halides. *Acc. Chem. Res. 29*, 268–274.

(11) Nelson, P. S., Kent, M., and Muthini, S. (1992) Oligonucleotide labeling methods. 3. Direct labeling of oligonucleotides employing a novel, non-nucleosidic, 2-aminobutyl-1,3-propanediol backbone. *Nucleic Acids Res. 20*, 6253–6259.

(12) Mergny, J. L., and Lacroix, L. (2003) Analysis of thermal melting curves. *Oligonucleotides 13*, 515–537.

(13) Connolly, B. A. (1987) The synthesis of oligonucleotides containing a primary amino group at the 5′-terminus. *Nucleic Acids Res. 15*, 3131–3139.

(14) Davies, M. J., Shah, A., and Bruce, I. J. (2000) Synthesis of fluorescently labelled oligonucleotides and nucleic acids. *Chem. Soc. Rev. 29*, 97–107.

(15) Eritja, R., Kaplan, B. E., Mhaskar, D., Sowers, L. C., Petruska, J., and Goodman, M. F. (1986) Synthesis and properties of defined DNA oligomers containing base mispairs involving 2-aminopurine. *Nucleic Acids Res. 14*, 5869–5884.

(16) Ramzaeva, N., Rosemeyer, H., Leonard, P., Mühlegger, K., Bergmann, F., von der Eltz, H., and Seela, F. (2000) Oligonucleotides functionalized by fluoresceine and rhodamine dyes: Michael addition of methyl acrylate to 2′-deoxypseudouridine. *Helv. Chim. Acta 83*, 1108–1126.

(17) Lisziewicz, J., Sun, D., Weichold, F. F., Thierry, A. R., Lusso, P., Tang, J., Gallo, R. C., and Agrawal, S. (1994) Antisense oligodeoxynucleotide phosphorothioate complementary to gag mRNA blocks replication of human immunodeficiency virus type 1 in human peripheral blood cells. *Proc. Natl. Acad. Sci. U.S.A. 91*, 7942–7946.

BC1000966

Synthesis and properties of oligonucleotides carrying isoquinoline imidazo[1,2-a]azine fluorescent units.

Sónia Pérez-Rentero[‡], *Nicola Kielland*[§], *Montserrat Terrazas*[‡], *Rodolfo Lavilla*,[*,§,†] *and Ramon Eritja*[*,‡]

[‡]Institute for Research in Biomedicine, IQAC-CSIC, CIBER-BBN Networking Centre on Bioenginnering, Biomaterials and Nanomedicine. Baldiri Reixac 10, 08028 Barcelona, Spain.

[§]Institute for Research in Biomedicine, Barcelona Science Park, Baldiri Reixac 10, 08028 Barcelona, Spain.

[†]Laboratory of Organic Chemistry, Faculty of Pharmacy. University of Barcelona. Avda. Diagonal sn, 08028 Barcelona, Spain.

SUPPORTING INFORMATION:

Page 2. Figure S1. Structure of the most energetically stable conformations of **1a** and **1b** conjugates by molecular mechanics (MM) conformational searches and geometry optimization
Page 3: Figure S2. Flow cytometry experimental data.
Page 4-5: Confocal microscopy images. Figures S3-S7.

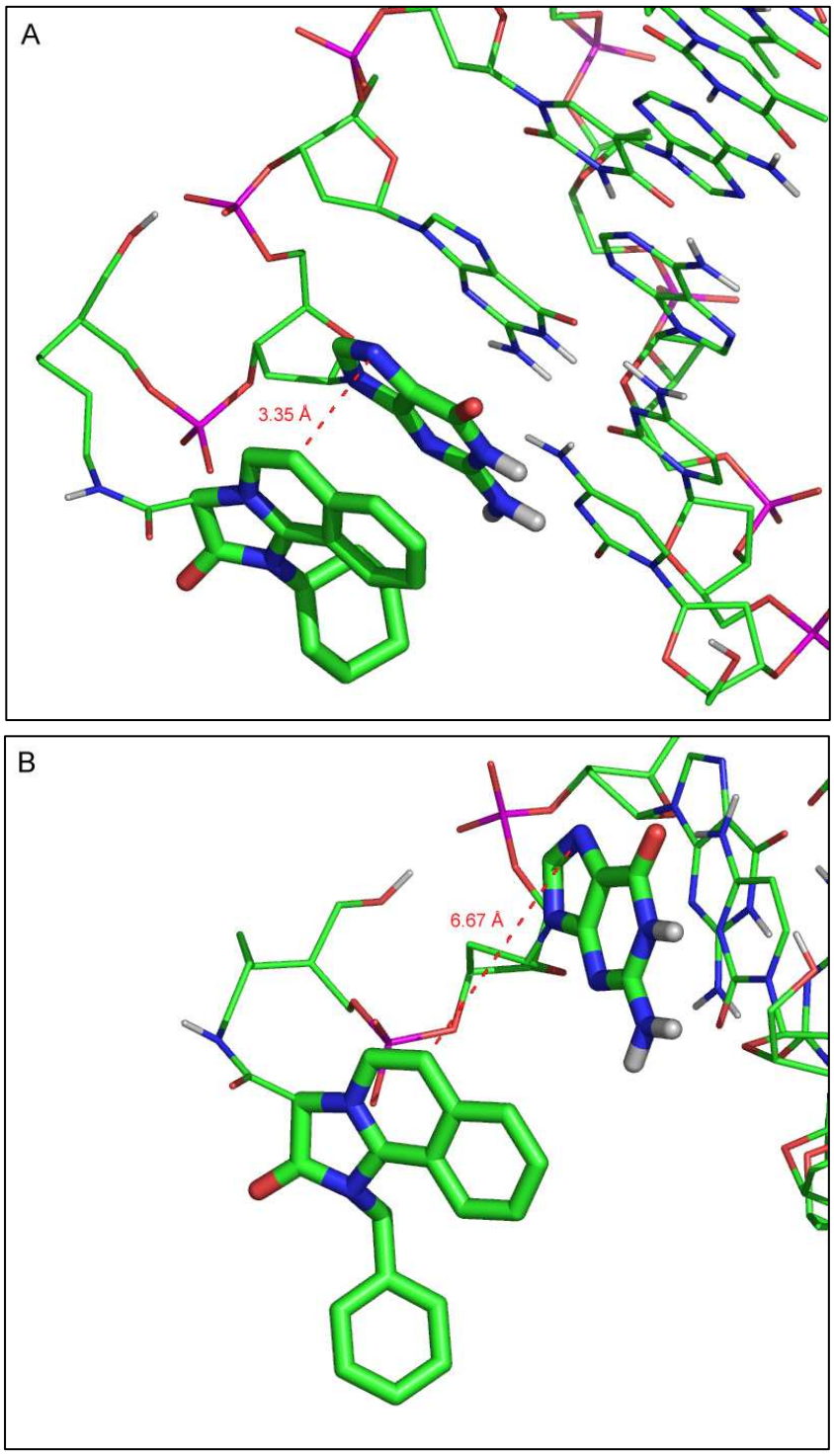


Figure S1. Most energetically stable conformations of **1a** and **1b** conjugates (panels A and B, respectively). The terminal guanine nucleobase and the triazine core are shown as thick lines. Distances between guanine and the isoquinoline imidazo[1,2-a]azine core are indicated. The figures were prepared with PyMOL (http://pymol.sourceforge.net/). Molecular mechanics (MM) conformational searches and geometry optimization of the most energetically stable conformers were carried out with the Amber force field by using the softwares Spartan'04 from Wavefunction and HyperChem'08 and by using water as a solvent. The duplex of DNA was kept frozen and the linker was allowed to move freely during the calculations.

Flow cytometry experimental data:

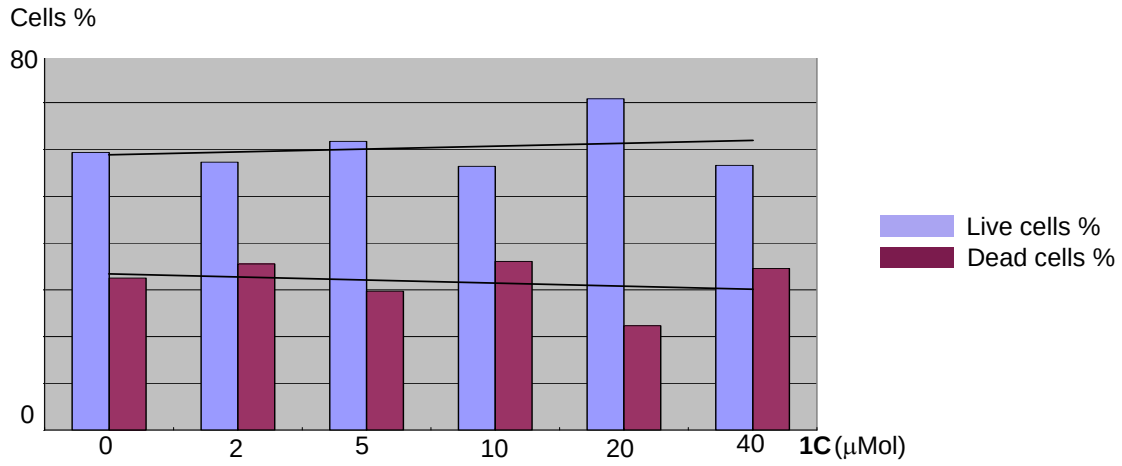


Figure S2: Evaluation of the cytotoxicity profile of **1c** by flow cytometry on HT-29 cells. Incubation time 8h.

Confocal microscopy images:

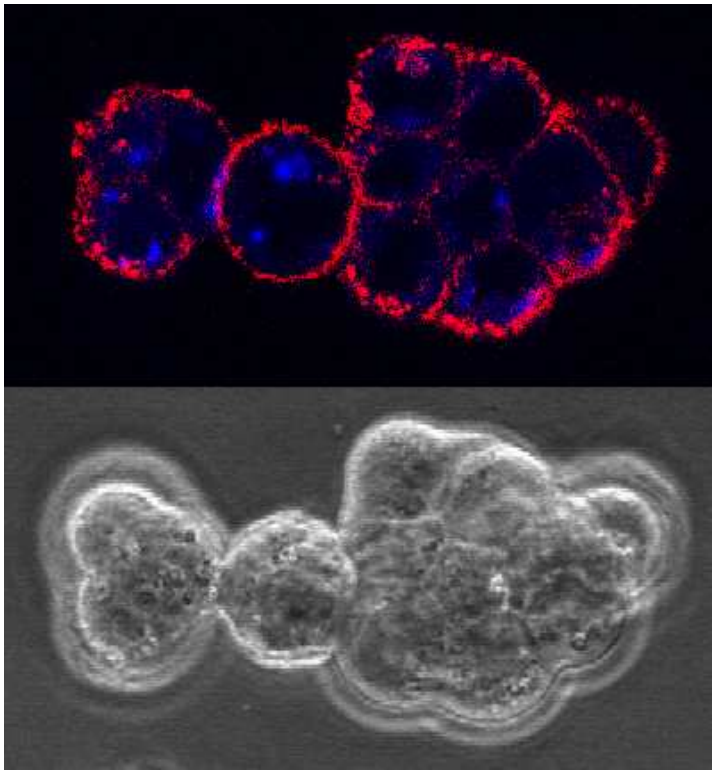


Figure S3: **1c** [20 μM] in HT-29 cells (2h incubation)

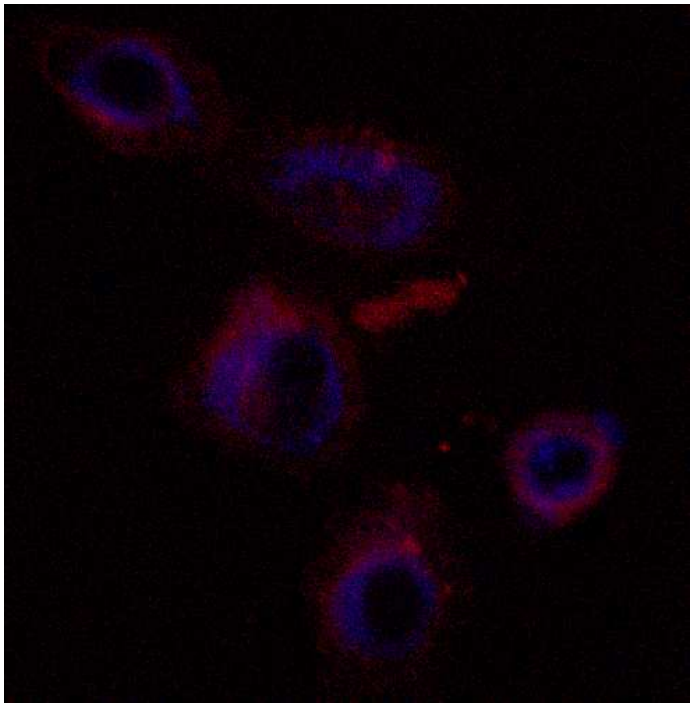


Figure S4.: **1c** [20 μM] in Hela cells (4h incubation)

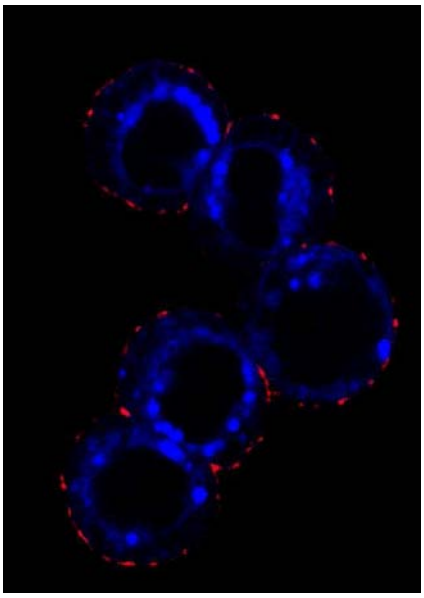


Figure S5: **1d** [20 μM] in HT-29 cells (2h incubation)

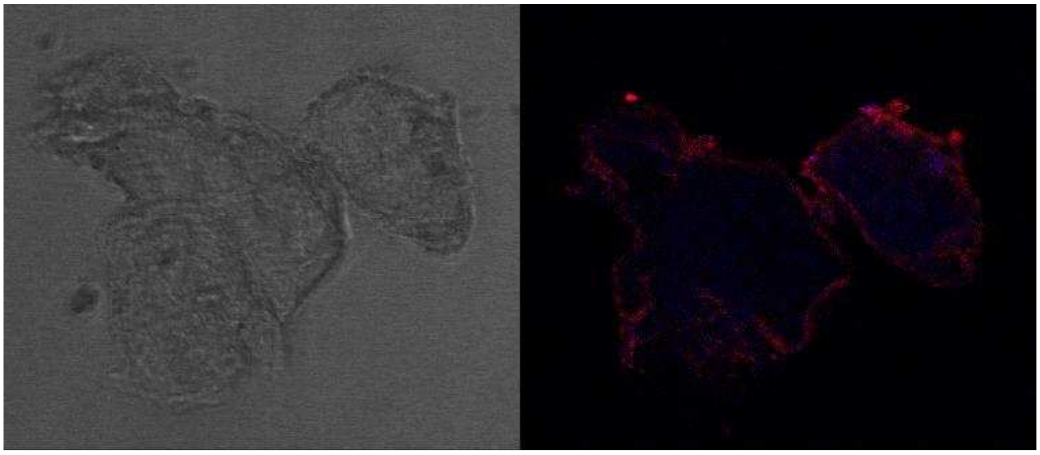


Figure S6.: Oligonucleotide **6** [20 μM] with Lipofectamine in Hela cells (4h incubation)

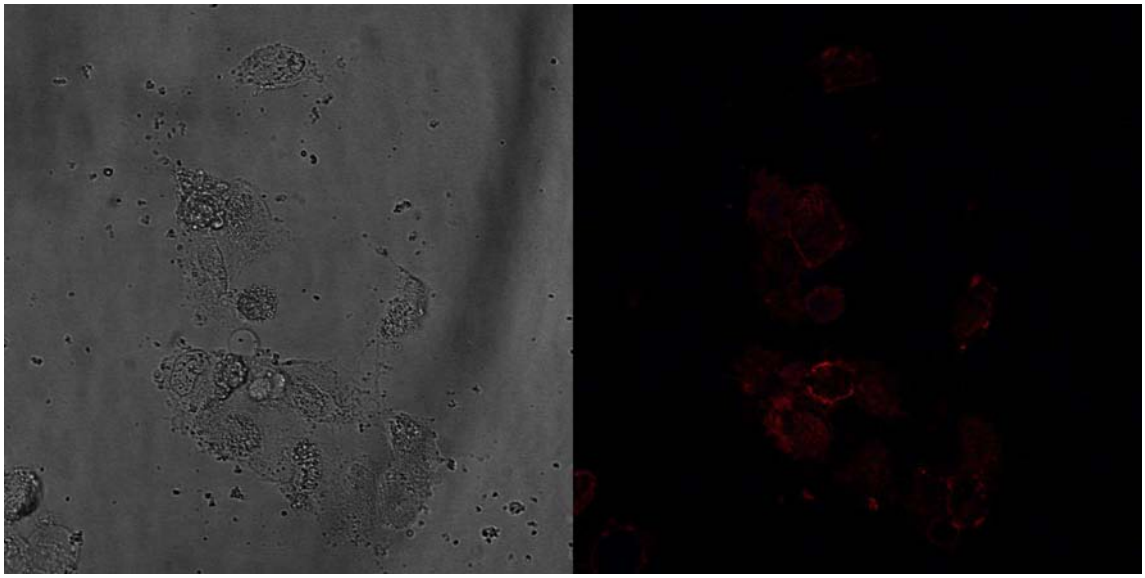


Figure S7. Oligonucleotide **6** [20 mM] with Lipofectamine in Hela cells (22 h incubation).

Azide−Alkyne "Click" Conjugation of 8-Aza-7-deazaadenine-DNA: Synthesis, Duplex Stability, and Fluorogenic Dye Labeling

Frank Seela* and Suresh S. Pujari

Laboratory of Bioorganic Chemistry and Chemical Biology, Center for Nanotechnology, Heisenbergstraβe 11, 48149 Münster, Germany, and Laboratorium für Organische and Bioorganische Chemie, Institut für Chemie, Universität Osnabrück, Barbarastraβe 7, 49069 Osnabrück, Germany. Received February 19, 2010; Revised Manuscript Received May 31, 2010

The internal dye labeling of DNA by the Huisgen-Meldal-Sharpless "click" reaction is described. Fluorogenic 9-azidomethyl anthracene **2** and 3-azido-7-hydroxycoumarin **3** were employed in the postsynthetic functionalization of oligonucleotides incorporating octa-(1,7)-diynyl-8-aza-7-deaza-2′-deoxyadenosine **1**. Nucleoside **1** was prepared by Sonogashira cross coupling from the corresponding 7-iodo compound, converted into the corresponding phosphoramidite, and oligonucleotides were synthesized. To evaluate the influence of ligands on the oligonucleotide duplex stability, benzyl azide **4** (nonpolar), and 2′,3′-dideoxy azidothymidine **5** (AZT) (polar) were introduced along with the fluorogenic dyes **2** and **3**. DNA duplexes with octa-1,7-diynyl side chains (i.e., containing **1**) are more stable than oligonucleotides containing 8-aza-7-deaza-2′-deoxyadenosine, unveiling that this side chain has steric freedom. A single conjugation by an anthracene residue led to a 9 °C T_m increase of duplex melting. Contrary to 7-deazaadenine dye conjugates, the 8-aza-7-deazaadenine conjugates show virtually no fluorescence quenching, thereby developing almost as strong fluorescence as side chain click derivatives (**32** and **33**) in the absence of 8-aza-7-deazaadenine moiety. Duplexes containing the 8-aza-7-deazaadenine dye conjugate show increased fluorescence over single-stranded DNA. Mismatches with dA, dG, and dC develop reduced fluorescence compared to the fully matched base pair. Molecular dynamics simulations revealed that the bulky dye molecules are accommodated well in duplex DNA.

INTRODUCTION

The visualization of biomolecules provides information about the quantity, localization, and transport in vivo or in vitro (*1*−*3*). Fluorescence spectroscopy is widely used for this purpose, as it is one of the most sensitive spectroscopic techniques (*4*−*6*). As canonical DNA is virtually nonfluorescent, fluorescent or fluorogenic reporter groups are attached to the DNA to enhance its detectibility. Fluorogenic dyes with azido groups can be activated to highly fluorescent molecules by the Cu (I)-catalyzed Huisgen-Meldal-Sharpless azide−alkyne cycloaddition (CuAAC), where the azido group becomes part of a triazole system. Those molecules are used to impart the fluorescence to the nonfluorescent species via a conjugation process (*7*).

The postmodification of DNA by the Cu(I) catalyzed Huisgen 1,3-dipolar cycloaddition reaction (CuAAC) led to consequential improvements in both rate and regioselectivity for introducing reporter molecules in nucleic acids (*8*−*11*). These contributions from Meldal (*12*) and Sharpless (*13*) have changed the perspective of cycloaddition chemistry over the past years. In the quest for near-perfect chemical reactions, the Huisgen-Meldal-Sharpless "click" reaction has emerged as an ideal bioorthogonal protocol for the preparation of rich chemical diversity. As a bioconjugation tool, this concept is extended to life sciences, especially to chemical biology (*14*−*19*) where DNAs or proteins are functionalized for imaging purposes or detection (*20, 21*).

By employing the CuAAC reaction, dye conjugation is performed most efficiently when the ligand is introduced in the major groove of DNA. So, space-demanding molecules do not affect the overall DNA structure. Consequently, pyrimidine nucleobases have been modified at position-5 (*22*−*25*). In purines, the situation is more complex. In principle, the 8-position of adenine or guanine as well as the 6-amino group of adenine can be selected for this purpose (*26*−*28*). (Purine numbering is used throughout the manuscript). However, conjugation at the 8-position interferes with the ribose moiety sterically. So, it is advantageous to use 7-deazapurines in place of purines. They can be efficiently functionalized at that position (*29*) and do not disturb the duplex structure. Our laboratory has had many contributions to this matter over the years (*30*−*32*). Unfortunately, 7-deazapurine pyrrolo[2,3-*d*]pyrimidines can quench the fluorescence of dyes by charge transfer processes (*14, 33*−*37*). This results from the low oxidation potential of pyrrolo[2,3-*d*]pyrimidine nucleosides (*38*), in particular, of 7-deaza-2′-deoxyguanosine and 7-deaza-2′-deoxyadenosine.

Pyrazolo[3,4-*d*]pyrimidines like pyrrolo[2,3-*d*]pyrimidines are ideal shape mimics of purines. They are considered to be much more inert against oxidation thereby leading to a brighter fluorescence of dye molecules covalently linked to DNA (*39*−*43*). Different from purines, and similar to pyrrolo[2,3-*d*]pyrimidines, they can be functionalized at position-7. Consequently, reporter groups of moderate size will be accommodated well in the major groove of B-DNA employing the CuAAC reaction (*14, 18, 19, 37*).

In this manuscript, we report on the synthesis of 8-aza-7-deaza-7-(octa-1,7-diynyl)-2′-deoxyadenosine (**1**). The molecule was converted into the corresponding phosphoramidite **11**, which is further employed in solid-phase oligonucleotide synthesis. The effect of single substitutions as well as of multiple incorporations on the base pairing is evaluated. The ligation with fluorogenic dyes such as 9-azido methyl anthracene **2** (*44*−*46*) or 3-azidocoumarin **3** (*47, 48*) via "click" reaction is studied; benzyl azide **4** and 3′-azido-2′,3′-dideoxythymidine **5** (*49*) were selected to monitor the behavior of less space-demanding residues (Figure 1). The photophysical properties of 8-aza-7-deazapurine conjugates are investigated on the

* Prof. Dr. Frank Seela. Phone: +49(0)251 53406 500. Fax: +49(0)251 53406 857. E-mail: Frank.Seela@uni-osnabrueck.de; Seela@uni-muenster.de. Homepage: www.seela.net.

10.1021/bc100090y © 2010 American Chemical Society
Published on Web 08/03/2010

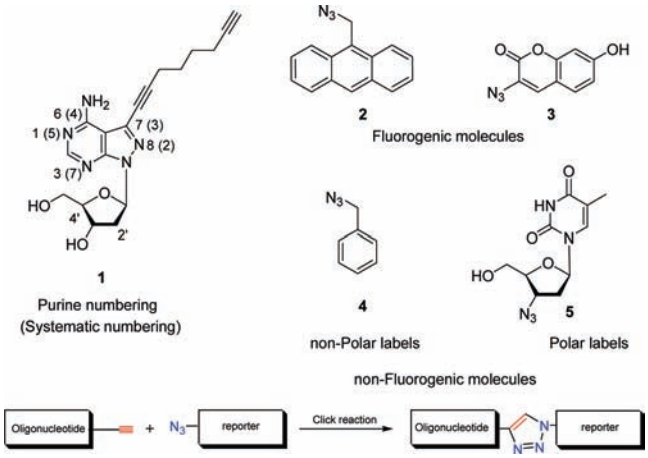


Figure 1. Copper(I)-catalyzed azide−alkyne cycloaddition. Purine numbering; systematic numbering is shown in parentheses.

monomer level, as well as in single-stranded and duplex DNA, and the duplex stability is determined after introducing ligands by "click" conjugation.

EXPERIMENTAL PROCEDURES

General Methods and Materials. All chemicals were purchased from Acros, Fluka, or Sigma-Aldrich (Sigma-Aldrich Chemie GmbH, Deisenhofen, Germany). Solvents were of laboratory grade. Flash column chromatography (FC): silica gel 60 (VWR, Germany) at 0.4 bar; UV spectra: U-3200 spectrometer (Hitachi, Tokyo, Japan). Reversed-phase HPLC was carried out on a 250 × 4 mm RP-18 column (Merck) with a Merck-Hitachi HPLC pump (model L-7100) connected with a variable wavelength monitor (model L-7400). NMR spectra: Avance-DPX-300 spectrometer (Bruker, Rheinstetten, Germany), at 300 MHz for ^{1}H and 75.48 MHz for ^{13}C; δ in ppm relative to Me_4Si as internal standard or external 85% H_3PO_4 for ^{31}P. For NMR spectra recorded in DMSO, the chemical shift of the solvent peak was set to 2.50 ppm for ^{1}H NMR and 39.50 ppm for ^{13}C NMR. MALDI-TOF mass spectra were recorded with Applied Biosystems Voyager DE PRO spectrometer with 3-hydroxypicolinic acid (3-HPA) as a matrix. Elemental analyses were performed by Mikroanalytisches Laboratorium Beller (Göttingen, Germany). The melting temperature curves were measured with a Cary-100 Bio UV−vis spectrophotometer (Varian, Australia) equipped with a Cary thermo-electrical controller. The temperature was measured continuously in the reference cell with a Pt-100 resistor. Fluorescence spectra were recorded in the wavelength range 300−600 nm using the fluorescence spectrophotometer F-2500 (Hitachi, Tokyo, Japan). For solubility reasons, all the 1,2,3-triazole conjugates were dissolved in 0.5 mL DMSO and then diluted with 99.5 mL of methanol. All measurements were performed with identical concentration (9.8×10^{-6} mol/L).

For the synthetic procedure of compound **32**, see the Supporting Information.

1-[2-Deoxy-3,5-di-*O*-(*p*-toluoyl)-β-D-erythropentofuranosyl]-3-(octa-1,7-diynyl)-4-methoxy-1*H*-pyrazolo[3,4-*d*]pyrimidine (7a). A solution of 1-[2-deoxy-3,5-di-*O*-(*p*-toluoyl)-β-D-erythropentofuranosyl]-3-iodo-4-methoxy-1*H*-pyrazolo[3,4-*d*]pyrimidine (**6a**) (*29*) (0.5 g, 0.79 mmol) in dry DMF (7.5 mL) was treated with CuI (0.032 g, 0.16 mmol), $Pd(PPh_3)_4$ (0.096 g, 0.08 mmol), dry Et_3N (0.169 g, 230 μL, 1.67 mmol), and 10 equiv of octa-1,7-diyne (1.03 mL, 7.95 mmol). The reaction mixture which slowly turns to black was stirred under inert atmosphere for 12 h (TLC monitoring). The combined filtrate was evaporated and the oily residue was adsorbed on silica gel and subjected to FC (silica gel, column 15 × 3 cm, eluted with petroleum ether/EtOAc 95:5 → 90:10) affording one main zone. Evaporation of the solvent gave **7a** (0.40 g, 83%) as a yellowish foam. TLC (silica gel, petroleum ether/EtOAC 7.5:2.5). R_f 0.7. UV λ_{max} (MeOH)/nm 275 (ε/dm^3 mol^{-1} cm^{-1} 8300). Anal. ($C_{35}H_{34}N_4O_6$) C, H, N. ^{1}H NMR [DMSO (d_6), 300 MHz]: δ 1.69 (s, 4H, 2 × CH_2), 2.25−2.26 (m, 2H, CH_2), 2.37, 2.39 (2s, 6H, 2 × CH_3), 2.58 (s, 2H, CH_2), 2.79−2.81 (m, 2H, C2′-H$_\beta$, C≡CH), 4.11 (s, 3H, OCH_3), 4.44−4.57 (m, 3H, C5′-H, C4′-H), 5.79−5.84 (m, 1H, C3′-H), 6.81−6.85 (t, J = 6.3 Hz, 1H, C1′-H), 7.28−7.36 (m, 4H, Ar−H), 7.87−7.94 (m, 4H, Ar−H), 8.63 (s, 1H, C2−H).

1-[2-Deoxy-β-D-erythropentofuranosyl]-3-(octa-1,7-diynyl)-4-methoxy-1*H*-pyrazolo[3,4-*d*]pyrimidine (7b). As described above for **7a**, with **6b** (0.196 g, 0.5 mmol) in dry DMF (4 mL), CuI (0.019 g, 0.10 mmol), $Pd(PPh_3)_4$ (0.057 g, 0.05 mmol), dry Et_3N (0.01 g, 13 μL, 0.1 mmol), and 10 equiv of octa-1,7-diyne (0.81 mL, 5.02 mmol). FC (silica gel, column 15 × 3 cm, eluted with CH_2Cl_2/MeOH 95:5 → 90:10) affording one main zone. Evaporation of the solvent gave **7b** (0.11 g, 60%) as a colorless solid. TLC (silica gel, CH_2Cl_2/MeOH 9:1). R_f 0.5. UV λ_{max} (MeOH)/nm 233 (ε/dm^3 mol^{-1} cm^{-1} 18 300), 281 (7700). Anal. ($C_{19}H_{22}N_4O_4$) C, H, N. ^{1}H NMR [DMSO (d_6), 300 MHz]: δ 1.67 (s, 4H, 2 × CH_2), 2.25−2.33 (m, 3H, CH_2, C2′-H$_\alpha$), 2.56 (s, 2H, CH_2), 2.77−2.82 (m, 2H, C2′-H$_\beta$, C≡CH), 3.31−3.55 (m, 2H, C5′-H), 3.79−3.85 (m, 1H, C4′-H), 4.11 (s, 3H, OCH_3), 4.42−4.45 (m, 1H, C3′-H), 4.70−4.74 (t, J = 5.7 Hz, 1H, C5′−OH), 5.31−5.32 (d, J = 4.3 Hz, 1H, C3′−OH), 6.61−6.65 (t, J = 6.6 Hz, 1H, C1′-H), 8.63 (s, 1H, C2−H).

1-[2-Deoxy-β-D-erythropentofuranosyl]-3-iodo-1*H*-pyrazolo[3,4-*d*]pyrimidin-4-amine (8). Compound **6a** (*29*) (0.45 g, 0.71 mmol) was stirred at 100 °C for 6 h with a saturated NH_3/MeOH solution (200 cm^3) in an autoclave. The solution was evaporated to dryness and the residue was subjected to FC (column 15 × 3 cm). Evaporation of the solvent afforded compound **8** (0.25 g, 90%) as colorless solid. TLC (silica gel, CH_2Cl_2/MeOH 9:1). R_f 0.6. UV λ_{max} (MeOH)/nm 241 (ε/dm^3 mol^{-1} cm^{-1} 7900), 262 (7300), and 284 (8900). Anal. ($C_{10}H_{12}IN_5O_3$) C, H, N. ^{1}H NMR [DMSO (d_6), 300 MHz]: δ 2.19−2.27 (m, 1H, C2′-H$_\alpha$), 2.72−2.80 (m, 1H, C2′-H$_\beta$), 3.46−3.54 (m, 2H, C5′-H), 3.77−3.82 (m, 1H, C4′-H), 4.38−4.44 (m, 1H, C3′-H), 4.76−4.81 (t, J = 6.0 Hz, 1H, C5′−OH), 5.28−5.29 (d, J = 4.5 Hz, 1H, C3′−OH), 6.47−6.51 (t, J = 6.6 Hz, 1H, C1′-H), 8.22 (s, 1H, C2−H).

1-[2-Deoxy-β-D-erythropentofuranosyl]-3-(octa-1,7-diynyl)-1*H*-pyrazolo[3,4-*d*]pyrimidin-4-amine (1). As described above for **7a**, with **8** (0.398 g, 1.05 mmol) in dry DMF (6 mL), CuI (0.040 g, 0.21 mmol), $Pd(PPh_3)_4$ (0.121 g, 0.10 mmol), dry Et_3N (0.218 g, 2.11 mmol, 0.3 mL), and 8 equiv of octa-1,7-diyne (1.08 mL, 8.4 mmol). FC (silica gel, column 15 × 3 cm, eluted with CH_2Cl_2/MeOH 95:5 → 90:10) afforded one main zone. Evaporation of the solvent gave **1** (0.28 g, 75%) as a colorless foam. TLC (silica gel, CH_2Cl_2/MeOH 9:1). R_f 0.5. UV λ_{max} (MeOH)/nm 249 (ε/dm^3 mol^{-1} cm^{-1} 11 000), 286 (11 300). Anal. ($C_{18}H_{21}N_5O_3$) C, H, N. ^{1}H NMR [DMSO (d_6), 300 MHz]: δ 1.54−1.74 (m, 4H, 2 × CH_2), 2.20−2.27 (m, 3H, CH_2, C2′-H$_\alpha$), 2.55−2.60 (t, J = 6.9 Hz, 2H, CH_2), 2.72−2.81 (m, 2H, C2′-H$_\beta$, C≡CH), 3.27−3.54 (m, 2H, C5′-H), 3.77−3.82 (m, 1H, C4′-H), 4.39−4.42 (m, 1H, C3′-H), 4.75−4.79 (t, J = 6.0 Hz, 1H, C5′−OH), 5.26−5.27 (d, J = 4.5 Hz, 1H, C3′−OH), 6.50−6.54 (t, J = 6.6 Hz, 1H, C1′-H), 8.22 (s, 1H, C2−H).

1-[2-Deoxy-β-D-erythropentofuranosyl]-3-(octa-1,7-diynyl)-4-{[(*N*,*N*-dimethylamino)methylidene)]amino}-1*H*-pyrazolo[3,4-*d*]pyrimidine (9). To a solution of **1** (0.36 g, 0.88 mmol) in MeOH (40 mL) was added *N*,*N*-dimethylformamide dimethyl acetal (3.02 g, 3.36 mL, 25.3 mmol) and the reaction mixture was stirred at rt for 30 min. Then, solvent was evaporated and

residue was subjected to FC (silica gel, column 10 × 4 cm, eluted with CH_2Cl_2/MeOH 97:3 → 90:10). Evaporation of the main zone afforded compound **9** (0.33 g, 79%) as a colorless foam. TLC (CH_2Cl_2/MeOH 9:1). R_f 0.6. UV λ_{max} (MeOH)/nm 322 (ε/dm^3 mol^{-1} cm^{-1} 24 400). Anal. ($C_{21}H_{26}N_6O_3$) C, H, N. ^{1}H NMR [DMSO (d_6), 300 MHz]: δ 1.62−1.67 (m, 4H, 2 × CH_2), 2.21−2.24 (m, 3H, CH_2, C2′-H$_\alpha$), 2.48−2.55 (m, 2H, CH_2), 2.77−2.81 (m, 2H, C2′-H$_\beta$, C≡CH), 3.19, 3.22 (2s, 6H, 2 × CH_3), 3.47−3.52 (m, 1H, C5′-H), 3.79−3.81 (d, J = 3.6 Hz, 1H, C4′-H), 4.41 (s, 1H, C3′-H), 4.77−4.81 (m, 1H, C5′−OH), 5.25−5.26 (d, J = 4.2 Hz, 1H, C3′−OH), 6.55−6.59 (t, J = 6.3 Hz, 1H, C1′-H), 8.43 (s, 1H, C2−H), 8.90 (s, 1H, N═CH).

1-[2-Deoxy-5-*O*-(4,4′-dimethoxytrityl)-β-D-erythropentofuranosyl]-4-{[(*N*,*N*-dimethylamino)methylidene]amino}-3-(octa-1,7-diynyl)-1*H*-pyrazolo[3,4-*d*]pyrimidine (10). Compound **9** (0.59 g, 1.44 mmol) was dried by repeated coevaporation with dry pyridine (3 × 5 mL). The residue was dissolved in dry pyridine and stirred with 4,4′-dimethoxytrityl chloride (0.58 g, 1.72 mmol) at rt for 6 h. After completion of the reaction (monitored by TLC), methanol (6 mL) was added to the reaction mixture, and stirring was continued for another half an hour. The reaction mixture was evaporated to dryness under reduced pressure and the remaining residue was dissolved in dichloromethane (50 mL) and washed with 5% aq $NaHCO_3$ solution (2 × 250 mL) and water (80 mL). The organic layer was dried over Na_2SO_4, the solvent was evaporated under reduced pressure, and the residue was subjected to FC (silica gel, column 10 × 4 cm, eluted with CH_2Cl_2/acetone 95:5 → 90:10). Evaporation of the main zone afforded **10** (0.72 g, 70%) as a colorless foam. TLC (silica gel, CH_2Cl_2/MeOH 9:1). R_f 0.7. UV λ_{max} (MeOH)/nm 225 (ε/dm^3 mol^{-1} cm^{-1} 41 800), 320 (24 900). Anal. ($C_{42}H_{44}N_6O_5$) C, H, N. ^{1}H NMR [DMSO (d_6), 300 MHz]: δ 1.58−1.69 (m, 4H, 2 × CH_2), 2.17−2.22 (m, 2H, CH_2), 2.28−2.32 (m, 1H, CH), 2.49−2.54 (m, 2H, CH_2), 2.77−2.88 (m, 2H, C≡CH, C2′-H$_\beta$), 3.00−3.09 (m, 2H, C5′-H), 3.19−3.22 (s, 6H, 2 × CH_3), 3.69 (s, 6H, 2 × OCH_3), 3.90−3.93 (m, 1H, C4′-H), 4.51−4.52 (m, 1H, C3′-H), 5.30−5.32 (d, J = 4.8 Hz, 1H, C3′−OH), 6.58−6.62 (m, 1H, C1′-H), 6.70−6.77 (m, 4H, Ar−H), 7.14−7.21 (m, 7H, Ar−H), 7.29−7.31 (m, 2H, Ar−H), 8.46 (s, 1H, C2−H), 8.90 (s, 1H, N═CH).

1-[2-Deoxy-5-*O*-(4,4′-dimethoxytrityl)-β-D-erythropentofuranosyl]-4-{[(*N*,*N*-dimethylamino)methylidene]amino}-3-(octa-1,7-diynyl)-1*H*-pyrazolo[3,4-*d*]pyrimidin-3′-(2-cyanoethyl)-*N*,*N*-diisopropylphosphoramidite (11). A solution of **10** (0.12 g, 0.16 mmol) in dry CH_2Cl_2 (10 mL) was stirred with (i-Pr)$_2$NEt (57 μL, 0.33 mmol) at rt. Then, 2-cyanoethyl diisopropylphosphoramidochloridite (75 μL, 0.33 mmol) was added, and the reaction mixture was stirred for 30 min. After completion of the reaction (monitored by TLC), the reaction mixture was diluted with CH_2Cl_2 (30 mL) and was poured into 5% $NaHCO_3$ solution (30 mL) and extracted with CH_2Cl_2 (3 × 30 mL). The combined organic phases were dried over Na_2SO_4, and the solvent was evaporated. The residual foam was applied to FC (silica gel, column 8 × 3 cm, eluted with CH_2Cl_2/acetone 100:0 → 95:5). Evaporation of the main zone afforded **11** (0.11 g, 74%) as a colorless foam. TLC (silica gel, CH_2Cl_2/acetone 9:1). R_f 0.7. ^{31}P NMR ($CDCl_3$, 121 MHz): 148.26, 148.39.

4-Amino-1-[2-deoxy-β-D-erythropentofuranosyl]-3-[(methylanthracene-1′,2′,3′-triazol-4′-yl)hexylidyne]-1*H*-pyrazolo[3,4-*d*]pyrimidine (12). To a solution of **1** (0.15 g, 0.42 mmol) and anthracene azide **2** (0.12 g, 0.50 mmol) in THF/H_2O/t-BuOH, (3:1:1; 5 mL) was added sodium ascorbate (419 μL, 0.41 mmol) of a freshly prepared 1 M solution in water, followed by the addition of copper(II) sulfate pentahydrate 7.5% in water (362 μL, 0.10 mmol). The emulsion was stirred for 12 h at rt, and the solution was evaporated and applied to FC (silica gel, column 10 × 3 cm, CH_2Cl_2/MeOH 88:12). From the main zone, compound **12** (0.21 g, 85%) was isolated as a yellowish foam. TLC (silica gel, CH_2Cl_2/MeOH 8:2). R_f 0.5. UV λ_{max} (MeOH)/nm 348 (ε/dm^3 mol^{-1} cm^{-1} 5600), 365 (7600), 386 (6900). Anal. ($C_{33}H_{32}N_8O_3$) C, H, N. ^{1}H NMR [DMSO (d_6), 300 MHz]: δ 1.13−1.19 (m, 2H, CH_2), 1.55−1.65 (m, 4H, 2 × CH_2), 2.19−2.27 (m, 1H, C2′-H$_\alpha$), 2.48−2.54 (m, 2H, CH_2), 2.73−2.78 (m, 1H, C2′-H$_\beta$), 3.79−3.84 (m, 1H, C4′-H), 4.40 (br s, 1H, C3′-H), 4.81 (br s, 1H, C5′−OH), 5.29−5.34 (m, 1H, C3′−OH), 6.50−6.54 (m, 1H, C1′-H), 6.58 (s, 2H, CH_2), 7.53−7.66 (m, 4H, Ar−H), 7.71 (s, 1H, triazole-H), 8.13 (s, 1H, Ar−H), 8.16 (s, 1H, Ar−H), 8.22 (s, 1H, C2−H), 8.56 (s, 1H, Ar−H), 8.60 (s, 1H, Ar−H), 8.72 (s, 1H, Ar−H). ESI-TOF: [M + Na]$^+$ calcd 611.66. Found 611.20.

4-Amino-1-[2-deoxy-β-D-erythropentofuranosyl]-3-[(7-hydroxycoumarin-1′,2′,3′-triazol-4′-yl)hexylidyne]-1*H*-pyrazolo[3,4-*d*]pyrimidine (13). As described above for **12**. A solution of **1** (0.100 g, 0.28 mmol) and 3-azido-7-hydroxy-coumarin **3** (0.068 g, 0.43 mmol) in THF/H_2O/t-BuOH (3:1:1, 4 mL), sodium ascorbate (280 μL, 0.28 mmol), copper(II) sulfate pentahydrate 7.5% in water (242 μL, 0.07 mmol). FC (silica gel, column 10 × 3 cm, CH_2Cl_2/MeOH 88:12) afforded **13** (0.135 g, 86%) as a yellowish solid. TLC (silica gel, CH_2Cl_2/MeOH 8:2). R_f 0.6. UV λ_{max} (MeOH)/nm 287 (ε/dm^3 mol^{-1} cm^{-1} 15 200), 346 (19 500). ^{1}H NMR [DMSO (d_6), 300 MHz]: δ 1.65−1.80 (m, 4H, 2 × CH_2), 2.17−2.25 (m, 1H, C2′-H$_\alpha$), 2.58−2.63 (m, 2H, CH_2), 2.73−2.79 (m, 3H, C2′-H$_\beta$, CH_2), 3.47−3.52 (m, 2H, C5′-H), 3.76−3.79 (m, 1H, C4′-H), 4.39 (br s, 1H, C3′-H), 4.78 (br s, 1H, C5′−OH), 5.27 (br s, 1H, C3′−OH), 6.48−6.53 (t, J = 6.3 Hz, 1H, C1′-H), 6.83 (s, 1H, C7″-H), 6.87−6.91 (d, J = 3.0 Hz, 1H, C9″-H), 7.70−7.73 (d, J = 8.7 Hz, 1H, triazole-H), 8.21 (s, 1H, C6″-H), 8.33 (s, 1H, C2−H), 8.55 (s, 1H, C4″-H). ESI-TOF: [M + Na]$^+$ calcd 581.55. Found 581.18.

4-Amino-1-[2-deoxy-β-D-erythropentofuranosyl]-3-{[(1,2,3,4-tetrahydro-5-methyl-2,4-dioxopyrimidin-1-yl)furan-3-yl]-(1,2,3-triazol-4′-yl)hexylidyne}-1*H*-pyrazolo[3,4-*d*]pyrimidine (14). As described above for **12**. A solution of **1** (0.05 g, 0.14 mmol) and AZT **5** (0.045 g, 0.16 mmol) in THF/H_2O/t-BuOH, (3:1:1, 3 mL), sodium ascorbate (150 μL, 0.15 mmol), copper(II) sulfate pentahydrate 7.5% in water (130 μL, 0.03 mmol). FC (silica gel, column 10 × 3 cm, CH_2Cl_2/MeOH 80:20) afforded **14** (0.071 g, 81%) as a colorless solid. TLC (silica gel, CH_2Cl_2/MeOH 7:3). R_f 0.2. UV λ_{max} (MeOH)/nm 269 (ε/dm^3 mol^{-1} cm^{-1} 17 900). Anal. ($C_{28}H_{34}N_{10}O_7$) C, H, N. ^{1}H NMR [DMSO (d_6), 300 MHz]: δ 1.66−1.76 (m, 4H, CH_2), 1.80 (s, 3H, CH_3), 2.08 (s, 3H, CH_3), 2.13−2.44 (m, 1H, C2′-H$_\alpha$), 2.57−2.62 (m, 3H, CH_2, C2′-H$_\beta$), 2.66−2.80 (m, 4H, CH_2), 3.47−3.52 (m, 2H, C5′-H), 3.57−3.67 (m, 2H, C5′-H), 3.70−3.82 (m, 2H, C4′-H), 4.18−4.19 (m, 1H, C3′-H), 4.39−4.42 (m, 1H, C3′-H), 4.72−4.77 (m, 1H, 3′−OH), 5.27−5.31 (m, 2H, 5′−OH), 6.38−6.42 (t, J = 6.6 Hz, 1H, C1′-H), 6.49−6.54 (t, J = 6.3 Hz, 1H, C1′-H), 7.81 (s, 1H, triazole-H), 8.06 (s, 1H, C2−H), 8.22 (s, 1H, C2−H), 11.36 (s, 1H, NH). ESI-TOF: [M + Na]$^+$ calcd 645.63. Found 645.25.

4-Amino-1-[2-deoxy-β-D-erythropentofuranosyl]-3-[(benzyl-1′,2′,3′-triazol-4′-yl)hexylidyne]-1*H*-pyrazolo[3,4-*d*]pyrimidine (15). As described above for **12**. A solution of **1** (0.100 g, 0.28 mmol) and benzyl azide **4** (0.045 g, 0.33 mmol) in THF/H_2O/t-BuOH, (3:1:1, 5 mL), sodium ascorbate (280 μL, 0.28 mmol), copper(II) sulfate pentahydrate 7.5% in water (242 μL, 0.07 mmol). FC (silica gel, column 10 × 3 cm, CH_2Cl_2/MeOH 90:10) afforded **15** (0.124 g, 90%) as a colorless solid. TLC (silica gel, CH_2Cl_2/MeOH 8:2). R_f 0.5. UV λ_{max} (MeOH)/nm 249 (ε/dm^3 mol^{-1} cm^{-1} 10 500), 287 (10 100). Anal. ($C_{25}H_{28}N_8O_3$) C, H, N. ^{1}H NMR [DMSO (d_6), 300 MHz]: δ 1.60−1.73 (m, 4H, 2 × CH_2), 2.22−2.25 (m, 1H, C2′-H$_\alpha$),

2.55−2.60 (t, J = 6.9 Hz, 2H, CH_2), 2.64−2.68 (t, J = 7.2 Hz, 2H, CH_2), 2.71−2.80 (m, 1H, C2′-H_β), 3.47 (s, 1H, C5′-H), 3.78−3.82 (m, 1H, C4′-H), 4.40 (br s, 1H, C3′-H), 4.78 (br s, 1H, C5′−OH), 5.28 (br s, 1H, C3′−OH), 5.54 (s, 2H, CH_2), 6.50−6.54 (t, J = 6.3 Hz, 1H, C1′-H), 7.26−7.35 (m, 4H, Ar−H), 7.91 (s, 1H, triazole-H), 8.22 (s, 1H, C2−H). ESI-TOF: $[M + H]^+$ calcd 489.54. Found 489.23.

4-Amino-7-[2-deoxy-β-D-erythropentofuranosyl]-5-[(methylanthracen-1′,2′,3′-triazol-4′-yl)hexylidyne]-7*H*-pyrrolo[2,3-*d*]pyrimidine (16). As described above for **12**. A solution of 1-(2-deoxy-β-D-erythropentofuranosyl)-5-(octa-1,7-diynyl)-1*H*-pyrrolo[2,3-*d*]pyrimidin-4-amine (*14*) (0.100 g, 0.28 mmol) and anthracence azide **2** (0.079 g, 0.33 mmol) in THF/H_2O/*t*-BuOH, (3:1:1, 4 mL), sodium ascorbate (280 μL, 0.28 mmol), copper(II) sulfate pentahydrate 7.5% in water (242 μL, 0.073 mmol). FC (silica gel, column 10 × 3 cm, CH_2Cl_2/MeOH 88:12) afforded **16** (0.13 g, 78%) as a yellowish solid. TLC (silica gel, CH_2Cl_2/MeOH 8:2). R_f 0.5. UV λ_{max} (MeOH)/nm 279 (ε/dm^3 mol^{-1} cm^{-1} 17 400), 348 (8300), 366 (12 300), 386 (11 300). Anal. ($C_{34}H_{33}N_7O_3$) C, H, N. ^{1}H NMR [DMSO (d_6), 300 MHz]: δ 1.48−1.65 (m, 4H, 2 × CH_2), 2.17−2.20 (m, 1H, C2′-H_α), 2.40−2.45 (m, 2H, CH_2), 2.49−2.56 (m, 3H, C2′-H_β, CH_2), 3.52−3.55 (m, 2H, C5′-H), 3.80−3.84 (m, 1H, C4′-H), 4.33 (s, 1H, C3′-H), 5.08 (br s, 1H, C5′−OH), 5.27 (br s, 1H, C3′−OH), 6.44−6.49 (m, 3H, CH_2, C1′-H), 6.58 (s, 2H, Ar−H, C8−H), 7.52−7.65 (m, 4H, Ar−H), 7.70 (s, 1H, triazole-H), 8.13 (s, 1H, Ar−H), 8.16 (s, 1H, Ar−H), 8.57 (s, 1H, C2−H), 8.59 (s, 1H, Ar−H), 8.71 (s, 1H, Ar−H), 8.70 (s, 1H, Ar−H). ESI-TOF: $[M + Na]^+$ calcd 610.67. Found 611.25.

Synthesis, Purification, and Characterization of Oligonucleotides 17−26. The syntheses of oligonucleotides were performed on a DNA synthesizer, model 392−08 (Applied Biosystems, Weiterstadt, Germany), at 1 μmol scale using the phosphoramidite **11** following the synthesis protocol for 3′-*O*-(2-cyanoethyl)phosphoramidites. After cleavage from the solid support, the oligonucleotides were deprotected in 25% aqueous ammonia solution for 16 h at 60 °C. The purification of the "trityl-on" oligonucleotides was carried out on reversed-phase HPLC using the following gradient system at 260 nm: (A = MeCN, B = 0.1 M (Et_3NH)OAc (pH 7.0)/MeCN, 95:5): 0−3 min 10−15% A in B, 3−15 min 15 −50% A in B, and 15−20 min 50−10% A in B; flow rate 1.0 mL/min. The purified "trityl-on" oligonucleotides were treated with 2.5% $CHCl_2COOH$/CH_2Cl_2 for 5 min at 0 °C to remove the 4,4′-dimethoxytrityl residues. The detritylated oligomers were purified again by reversed-phase HPLC (gradient: 0−20 min 0−20% A in B; 20−25 min, 20% A in B, 25−30 min 20−0% A in B, flow rate 1.0 mL/min). The oligonucleotides were desalted on column (RP-18) using water for elution of salt, while the oligonucleotides were eluted with H_2O/MeOH (2:3). The oligonucleotides were lyophilized on a Speed-Vac evaporator to yield colorless solids which were frozen at −24 °C. The enzymatic hydrolysis of oligonucleotide **19** was performed using snake-venom phosphodiesterase (EC 3.1.15.1, *Crotallus adamanteus*) and alkaline phosphatase (EC 3.1.3.1, *Escherichia coli* from Roche Diagnostics GmbH, Germany) in 0.1 M Tris HCl buffer (pH 8.5) at 37 °C, which was analyzed by reversed-phase HPLC (RP-18) showing the peaks of the modified and unmodified nucleosides. The extinction coefficients ε_{260} of the nucleosides: dA 15400, dG 11700, dT 8800, dC 7300, and **1** 8500. The molecular masses of oligonucleotides **17−30** were determined by MALDI-TOF mass spectrometry in the linear negative mode (Supporting Information).

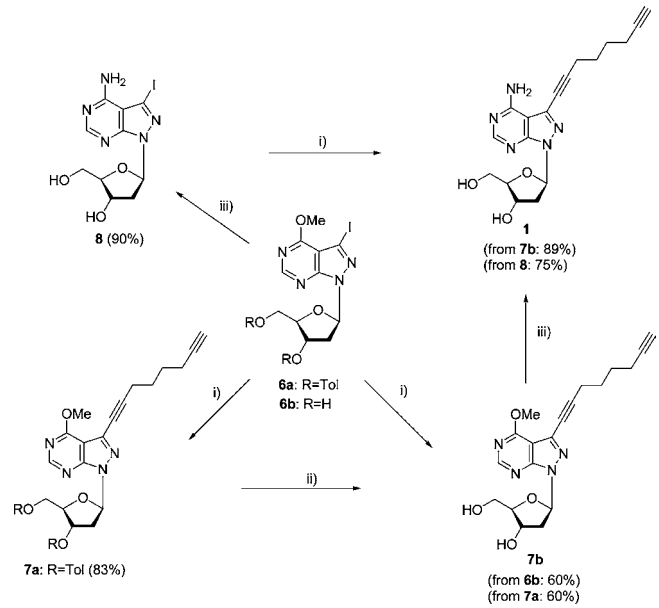
Click Conjugation of Oligonucleotide 19 with Azides 2−5 to Yield Oligonucleotide Conjugates 27−30. To the single-stranded oligonucleotide **19** (5 A_{260} units), a 1:1 $CuSO_4$−TBTA ligand complex (50 μL of a 20 mM stock solution in *t*-BuOH/H_2O 1:9), tris(carboxyethyl)phosphine (TCEP; 50 μL of a 20 mM stock solution in water), respective azide (50 μL of a 20 mM stock solution in dioxane/H_2O 1:1), sodium bicarbonate (50 μL of a 20 mM aq solution), and 35 μL DMSO were added and stirred at room temperature for 12 h. The reaction mixture was concentrated in a speed vac and dissolved in 0.5 mL bidistilled water and centrifuged for 20 min at 14 000 rpm. The supernatant solution was collected and further purified by reversed-phase HPLC. Oligonucleotides **28−30** were purified by the following gradient [0−20 min 0−20% A in B; 20−25 min 20% A in B, 25−30 min 20−0% A in B, flow rate 1.0 mL/min] to give the "click" product. The oligonucleotide **27** was purified by reversed-phase HPLC using following gradient system [A = MeCN, B = 0.1 M (Et_3NH)OAc (pH 7.0)/MeCN, 95: 5): 0−3 min 10−15% A in B, 3−15 min 15 −50% A in B, and 15−20 min 50−10% A in B; flow rate 1.0 mL/min]. The molecular masses of oligonucleotides **27−30** were determined by MALDI-TOF mass spectrometry in the linear negative mode (Supporting Information).

RESULTS AND DISCUSSION

Synthesis and Characterization of Monomers. The synthesis and behavior of oligonucleotides incorporating 7-deaza-7-(octa-1,7-diynyl)-2′-deoxyadenosine (*14*) was reported by our laboratory. Now, oligonucleotides containing 8-aza-7-deaza-7-(octa-1,7-diynyl)-2′-deoxyadenosine **1** were synthesized. For the synthesis of nucleoside **1**, two alternative routes were employed: (a) Sonogashira cross coupling was performed on the sugar-protected 6-methoxy nucleoside **6a** (*29*) with octa-1,7-diyne to yield **7a** in 83%. This was deprotected with sodium methoxide in methanol to give **7b** (60%) (*29*). Amination in saturated methanolic ammonia (steel vessel, 100 °C) resulted in **1** in 89%. (b) Deprotection of the methoxy compound **6a** in methanolic ammonia to **6b** under simultaneous amination gave **8** (90%). Sonogashira cross coupling on **8** with octa-1,7-diyne gave **1** in 75% yield (Scheme 1). The 6-methoxy compound **6a** is a ubiquitous precursor for a series of 6-substituted nucleosides.

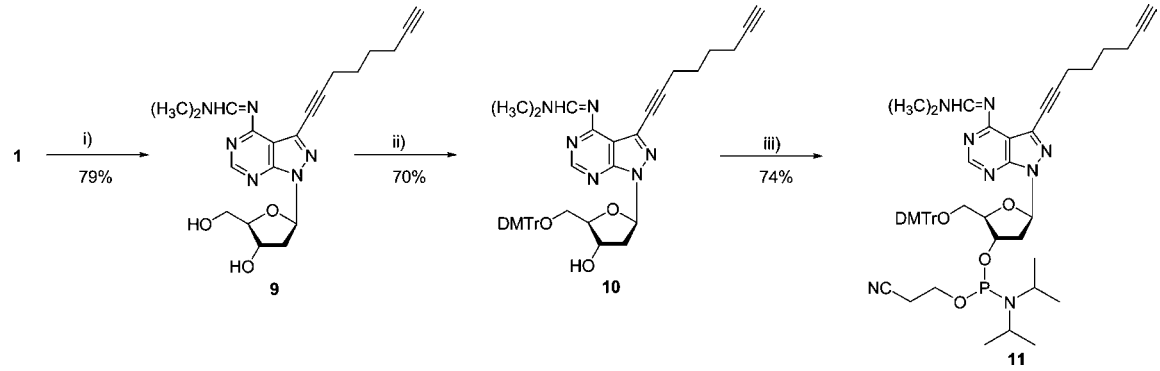
Next, the phosphoramidite building block **11** was prepared from the alkynylated nucleoside **1** (Scheme 2). Amino group protection was performed on **1** with the *N*,*N*-dimethylaminomethylidene group to afford the intermediate **9** in 79% yield. This

Scheme 1. Synthesis of Nucleoside 1 and Related Derivatives[a]



[a] (i) Octa-1,7-diyne, [$Pd^0[P(Ph_3)_4]$], CuI, DMF, Et_3N, rt, 12 h; (ii) NaOMe/MeOH, rt, 8 h (*29*); (iii) NH_3/MeOH, autoclave 100 °C, 6 h.

Scheme 2. Synthesis of Phosphoramidite Building Block 11[a]



[a] (i) *N,N*-Dimethylformamide dimethylacetal, MeOH, rt, 30 min; (ii) 4,4′-dimethoxytriphenylmethyl chloride, anhydrous pyridine, rt, 6 h; (iii) 2-cyanoethyl-*N,N* diisopropylchlorophosphoramidite, anhydrous CH_2Cl_2, $(i\text{-Pr})_2EtN$, rt, 30 min.

Table 1. ^{13}C NMR Chemical Shifts of the 8-Aza-7-deaza-2′-deoxyadenosine Derivatives[a]

	C(2)[b] C(6)[c]	C(4)[b] C(7a)[c]	C(5)[b] C(3a)[c]	C(6)[b] C(4)[c]	C(7)[b] C(3)[c]	C≡C	CH_2	CH_3/N=CH	C(1′)	C(2′)	C(3′)	C(4′)	C(5′)
1	156.6	153.6	100.8	157.8	127.2	96.4	27.3	--	84.0	37.9	70.9	87.7	62.3
						84.3	26.7						
						72.2	18.4						
						71.4	17.2						
7a	156.2	154.9	103.3	163.5	127.8	95.2	27.0	54.6	84.2	35.3	74.6	81.6	63.8
						84.3	26.8	21.2					
						72.5	18.2						
						71.4	17.3						
7b	156.0	154.7	103.2	163.5	127.4	95.1	27.1	54.5	84.4	37.9	70.9	87.8	62.3
						86.9	26.8						
						72.6	18.2						
						71.4	17.3						
8	156.2	153.9	103.4	157.6	91.2	--	--	--	83.9	37.8	70.9	87.6	62.3
9	155.8	154.4	107.7	162.2	128.9	93.8	27.3	34.7	83.9	37.9	70.9	87.7	62.3
						84.2	27.0	40.7					
						73.6	18.3	157.7					
						71.4	17.2						
10	155.8	154.5	107.8	162.2	128.9	93.6	27.3	34.7	83.7	38.0	70.5	85.3	64.1
						84.2	27.1	40.7					
						73.8	18.4	157.9					
						71.4	17.3						

[a] Measured in DMSO(d_6) at 298 K. All ^{13}C chemical shifts were unambiguously assigned by gated-decoupled $^1H-^{13}C$ NMR spectra. For $^1H-^{13}C$ coupling constants, see Table S1, Supporting Information. [b] Purine numbering. [c] Systematic numbering.

protected nucleoside was converted to the respective 5′-*O*-DMT-derivative under standard reaction conditions, to yield **10** in 70%, and further phosphitylation gave the corresponding phosphoramidite **11** in 74% (Scheme 2).

All the synthesized compounds were characterized by either elemental analyses or molecular mass, ^1H and ^{13}C NMR, as well as $^1H-^{13}C$ NMR gated decoupled spectra (for $^1H-^{13}C$ NMR coupling constants, see Supporting Information). The ^{13}C NMR chemical shifts are listed in Table 1. Terminal triple bonds are not affected by the Pd-assisted Sonogashira cross coupling by the competitive reactions like allene formation, as the table indicates four signals of methylene carbons (27.3, 26.7, 18.4, and 17.2 ppm) and four signals for the triple bond carbons (**1**: 71.4, 72.2, 84.3, 96.4 ppm; Table 1) and even confirmed by inverted signals of distortionless enhancement by polarization transfer (DEPT-135) spectra.

Synthesis, Characterization, and Duplex Stability of Oligonucleotides Containing Nucleoside 1. To evaluate the potential of the base modification on the duplex stability and fluorescence behavior, oligonucleotides were prepared by solid-phase synthesis using the phosphoramidite **11** as building block. The synthesis was performed in a 1 μmol scale. The coupling yields were always higher than 95%. Deprotection of the oligonucleotides was performed in 25% aqueous NH_3 at 60 °C for 16 h. The oligonucleotides were purified by both "trityl on" and "trityl off" modus by reversed-phase HPLC. (For details, see Experimental Procedures.) The base composition of the oligonucleotides was determined by tandem enzymatic hydrolysis with snake-venom phosphodiesterase followed by alkaline phosphatase in 0.1 M Tris-HCl buffer (pH 8.5) at 37 °C (Supporting Information). Molecular masses were determined by MALDI-TOF mass spectrometry, which were found in agreement with calculated values.

Earlier, we reported on the influence of substituents on the duplex stability and base pairing properties of 5-substituted pyrimidines and 7-substituted-7-deazapurines containing alkynyl side chains (*14*, *50*). It was inferred that nucleosides having halogen and propynyl side chains attached to the 7-position of pyrrolo[2,3-*d*]pyrimidines or pyrazolo[3,4-*d*]pyrimidines are accommodated well in the major groove of DNA, thus rendering thermal stability to the duplexes (*51*−*54*). Further studies showed that 7-alkynyl chains of length three to six carbon atoms and one triple bond led to stabilization of DNA duplex while longer chains show a negative effect on the stability because of the increased hydrophobic character, which arises due to the alkynyl chain (*51*−*54*). On the other hand, we demonstrated that long chain linkers with terminal triple bonds such as octa-1,7-diynyl or propargyl ether show a positive influence on the duplex stability similar to that of a propynyl residue (*14*, *50*).

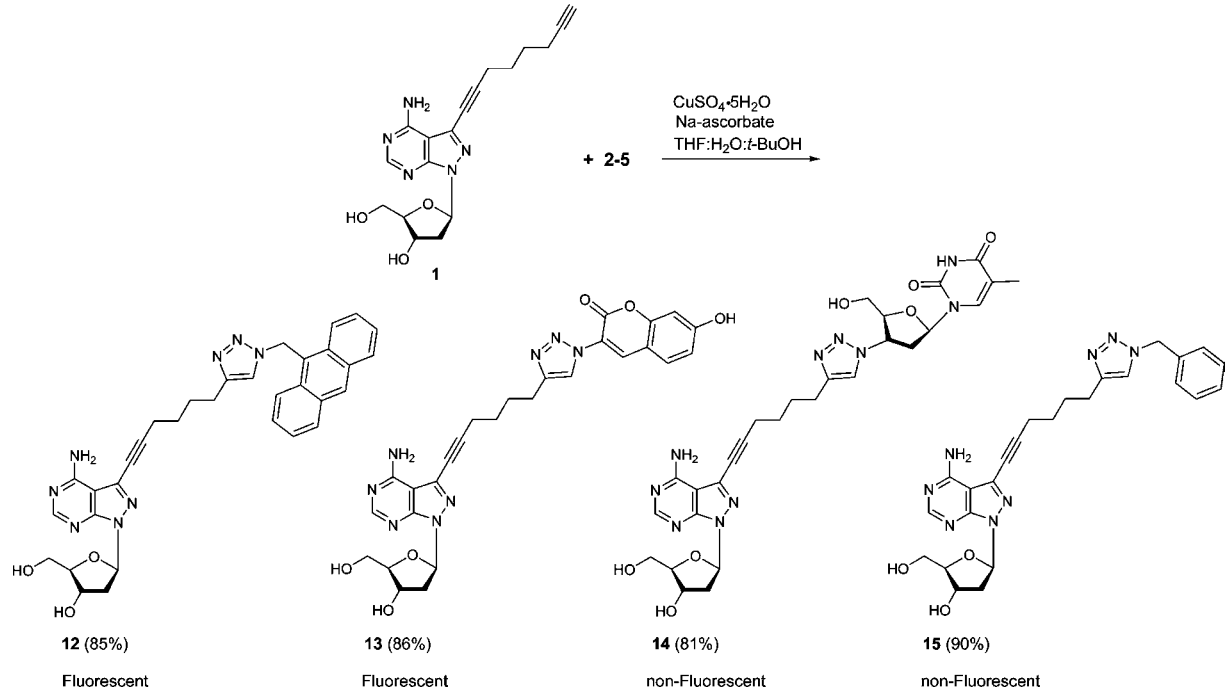
Now, the duplex stability of oligonucleotides is studied to determine the influence of modification by nucleoside **1** as surrogate of 2′-deoxyadenosine. The oligonucleotide duplex 5′-

Table 2. T_m Values and Thermodynamic Data of Oligonucleotide Duplexes Containing Nucleoside 1

duplexes	T_m [a] [°C]	ΔT_m [b] [°C]	ΔH° [c] [kcal/mol]	ΔS° [cal/(mol K)]	ΔG°_{310} [kcal/mol]
5′-d(TAG GTC AAT ACT) (**17**)					
3′-d(ATC CAG TTA TGA) (**18**)	50	--	−89	−249	−11.6
5′-d(TAG GTC **1**AT ACT) (**19**)					
3′-d(ATC CAG TTA TGA) (**18**)	51	+1	−83	−231	−11.6
5′-d(TAG GTC **11**T ACT) (**20**)					
3′-d(ATC CAG TTA TGA) (**18**)	54	+4	−84	−232	−12.3
5′-d(T**1**G GTC **11**T **1**CT) (**21**)					
3′-d(ATC CAG TTA TGA) (**18**)	56	+6	−92	−256	−13.2
5′-d(TAG GTC AAT ACT) (**17**)					
3′-d(ATC CAG TTA TG**1**) (**22**)	52	+2	−85	−238	−11.8
5′-d(TAG GTC AAT ACT) (**17**)					
3′-d(ATC C**1**G TT**1** TGA) (**23**)	53	+3	−93	−259	−12.2
5′-d(TAG GTC **1**AT ACT) (**19**)					
3′-d(ATC CAG TTA TG**1**) (**22**)	51	+1	−84	−233	−11.7
5′-d(TAG GTC **1**AT ACT) (**19**)					
3′-d(ATC C**1**G TT**1** TGA) (**23**)	55	+5	−89	−245	−12.9
5′-d(TAG GTC **11**T ACT) (**20**)					
3′-d(ATC CAG TTA TG**1**) (**22**)	54	+4	−80	−218	−12.3
5′-d(TAG GTC **11**T ACT) (**20**)					
3′-d(ATC C**1**G TT**1** TGA) (**23**)	59	+9	−86	−234	−13.6
5′-d(T**1**G GTC **11**T **1**CT) (**21**)					
3′-d(ATC CAG TTA TG**1**) (**22**)	57	+7	−95	−261	−13.8
5′-d(T**1**G GTC **11**T **1**CT) (**21**)					
3′-d(ATC C**1**G TT**1** TGA) (**23**)	60	+10	−109	−301	−15.5

[a] Measured at 260 nm in 1 M NaCl, 100 mM $MgCl_2$, and 60 mM Na-cacodylate (pH 7.0) with 5 μM + 5 μM single-strand concentration. [b] Refers to the contribution of the modified residues. [c] Thermodynamic values were calculated with the program *MeltWin* 3.0 and are with 10% deviation.

Scheme 3. Synthesis of Nucleoside "Click" Conjugates 12−15



d(TAG GTC AAT ACT) (**17**)·3′-d(ATC CAG TTA TGA) (**18**) is chosen as reference duplex. This standard duplex is further modified at various positions with alkynyl nucleoside **1**. One of the dA residues was replaced at the peripheral position with the alkynyl-modified residue and melting studies have been performed. As is shown in Table 2, this resulted in about 2 °C increase in T_m value per modification (**17**·**22**), whereas incorporation at the central position resulted 1 °C increase (**19**·**18**). Further, the measurements were performed with multiple incorporations at different positions with different numbers. When one strand is modified with two residues keeping the complementary strand unchanged (duplexes **17**·**23** and **20**·**18**), a 3 and 4 °C increase in T_m per modification is observed, respectively. These encouraging results tempted us to modify one strand completely keeping its complementary strand unchanged. T_m measurement result of duplex **21**·**18** showed 6 °C T_m increase. Of note, furthermore modifications (total six modifications in a duplex) were performed resulting in oligonucleotide duplex **21**·**23**, which gave a T_m value 10 °C higher than the unmodified duplex.

"Click" Reaction Performed on 8-Aza-7-deaza-2′-deoxyadenosine Derivative 1 and Properties of Nucleoside Conjugates. The efficacy of the "click" reaction on nucleoside **1** was studied with the two nonfluorescent molecules benzyl azide **4** (nonpolar) and AZT **5** (polar). Then, the cycloaddition was performed also with the fluorogenic dyes 9-azidomethyl anthracene **2** and 3-azido-7-hydroxycoumarin **3** (Scheme 3). We were successfully able to "click" all four azides (**2**−**5**) to nucleoside **1** (to get click conjugates**12**−**15**). The reactions were performed in the presence of $CuSO_4 \cdot 5H_2O$ using sodium

Table 3. ^{13}C NMR Chemical Shifts of the Nucleoside Conjugates[a]

compd	C(2)[b] C(6)[c]	C(4)[b] C(7a)[c]	C(5)[b] C(3a)[c]	C(6)[b] C(4)[c]	C(7)[b] C(3)[c]	C≡C	triazole	ligand CH_2/CH_3
12	156.7	153.6	100.8	157.8	127.3	96.6, 72.1	146.6, 124.0	54.9
13	156.6[d]	156.3[d]	102.1	157.7	127.3	96.5, 72.2	146.8, 122.9	--
14	156.1	153.1	100.3	157.2	126.8	96.0, 71.6	146.4, 120.9	11.7
15	156.7	153.6	100.8	157.8	127.3	96.5, 72.2	146.9, 122.1	52.7
16	152.6	149.0	95.6	157.6	127.1	92.4, 73.7	146.6, 124.1	54.9

compd	C1′	C2′	C3′	C4′	C5′	side chain CH_2/CH_3
12	84.0	37.9	71.0	87.7	62.4	28.3, 27.2, 24.3, 18.6
13	84.0	37.9	70.9	87.7	62.3	28.2, 27.2, 24.3, 18.7
14	83.9	37.3	71.6	87.2	61.8	27.7, 26.7, 24.0, 18.2
15	84.0	37.9	71.0	87.7	62.4	28.4, 27.3, 24.5, 18.7
16	83.1	38.7	71.0	87.5	61.9	28.3, 27.8, 24.4, 18.6

[a] Measured in DMSO-d_6 at 298 K. ^{13}C chemical shifts were unambiguously assigned by gated-decoupled ^{1}H−^{13}C NMR spectra if not otherwise stated. For ^{1}H−^{13}C coupling constants, see Table S2, Supporting Information. [b] Purine numbering. [c] Systematic numbering. [d] Tentative.

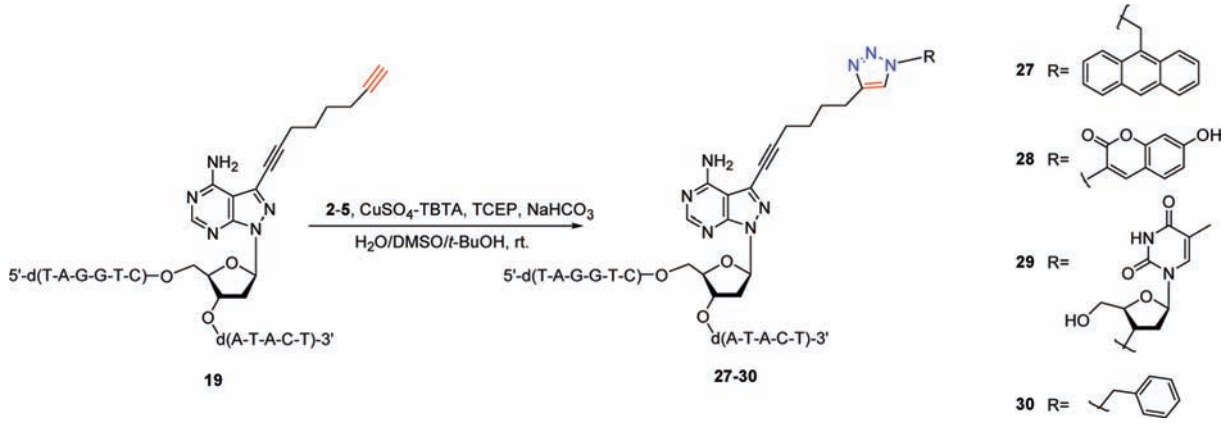
ascorbate as a reducing agent in the aqueous media of *t*-BuOH/THF (1:3) at room temperature. The purification of polar residue conjugated nucleosides and oligonucleotides is somewhat difficult as is the case with residues **3** and **5**. As expected, the nucleoside conjugate **14**, which becomes more polar after conjugation through triazole formation, migrates faster than the nucleoside **1** itself (Supporting Information). The more hydrophobic benzyl residue increases the lipophilicity of the conjugate **15** making it more nonpolar. Therefore, it moves more slowly than nucleoside **1**. The HPLC profiles of the conjugates were taken as a reference for the oligonucleotide separation after click reaction.

The "click" conjugates were characterized by ^{1}H and ^{13}C NMR, as well as ^{1}H−^{13}C NMR gated decoupled spectra (for ^{1}H−^{13}C NMR coupling constants, see Supporting Information). Appearance of two new signals at (i) δ = 146.6 and 124.0 ppm (**12**), (ii) δ = 146.8 and 122.9 ppm (**13**), (iii) δ = 146.4 and 120.9 ppm (**14**), and (iv) 146.9 and 122.1 ppm (**15**) (Table 3) and absence of terminal C≡C carbon atom signals in ^{13}C NMR confirms formation of the triazole system where steric hindrance offers no space for bis-functionlization of the second C≡C. The ^{13}C NMR chemical shifts of the side chain for the functionalized dye conjugates are listed in Table 3.

The 7-alkynyl side chain has a decisive influence on the UV−vis spectra of 8-aza-7-deaza-2′-deoxyadenosine (**34**). Already, the nonfunctionalized 8-aza-7-deaza-2′-deoxyadenosine shows a rather different spectrum (Supporting Information) compared to that of 2′-deoxyadenosine (one main maximum at 261 nm); the octadiynyl side chain of derivative **1** induces further changes which are due to the triple bond of the side chain being in conjugation with the heterocyclic moiety. Significant changes occur in the case of click conjugates. Already, the adducts with AZT (**14**) and benzylazide (**15**) change the UV spectra significantly due to the addition of the UV-active ligands and the generation of the 1,2,3-triazole system (Supporting Information). When 3-azidocoumarin **3** or 9-azidomethyl anthracene **2** are clicked to compound **1**, additional UV absorbance emerge in the 300−400 nm region (Supporting Information). For the quantification of the modified oligonucleotides by UV spectroscopy, the extinction coefficients of conjugates were determined at the UV maxima. For spectra and extinction coefficient values, see Supporting Information.

"Click" Reactions Performed on Oligonucleotides Containing Nucleoside 1 and Photophysical Properties of Dye Conjugates. Next, the "click" reaction was performed on oligonucleotide **19** to prove the feasibility of the reaction in a more crowded situation like in DNA (Scheme 4). The reaction was performed at room temperature in aqueous solution of DMSO and *t*-BuOH to yield postsynthetically labeled ODNs. For this, at first the Cu:TBTA ligand complex was prepared by mixing the components in a 1:1 ratio in H_2O/*t*-BuOH (9:1). Then, the alkyne containing oligonucleotide was added. Thereafter, other components like azide, TCEP, and $NaHCO_3$ were added and the reaction mixture was stirred at rt for 12 h. Afterward, the reaction mixture was dried and dissolved in 0.5 mL of water and centrifuged (14 000 rpm) to remove the inorganic salts and insoluble materials. Purification by RP-HPLC led to the modified ODNs. The polytriazole ligand, TBTA, is used to stabilize Cu(I), in the presence of TCEP as a reducing agent. Excess and/or uncomplexed copper led to the strand breaks of the oligonucleotide chain. Hence, it is necessary to add copper and azide in the specified amount. It appears that the click reaction proceeds at different velocities with respect to the particular azide. Nevertheless, kinetic experiments have not been performed. Usually, the click reactions were carried out with 5 A_{260} units of oligonucleotide. For details, see the Experimental Procedures section.

Scheme 4. "Click" Conjugates 27−30 Formed by the Cycloaddition of Oligonucleotide 19 with Azides 2−5



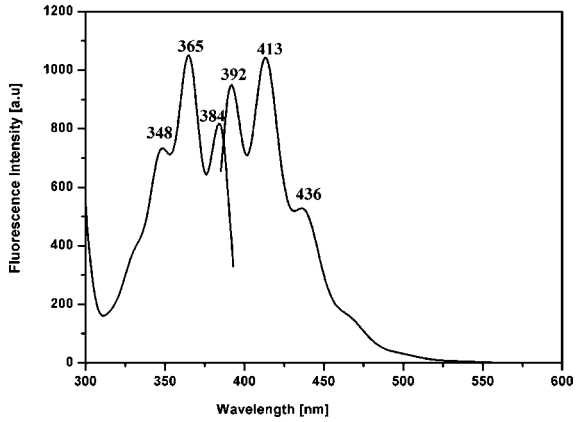


Figure 2. Excitation and emission spectra of the nucleoside anthracene conjugate **12** measured in methanol.

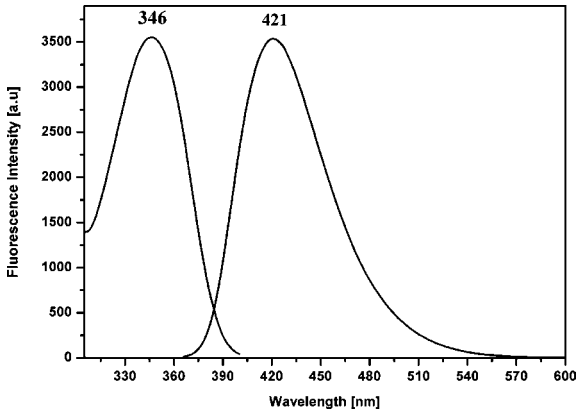


Figure 3. Excitation and emission spectra of the nucleoside coumarin conjugate **13** measured in methanol.

Photoexcitable dyes such as anthracene or coumarin suffer from fluorescence quenching, when conjugated to nucleobases such as purines or 7-deazapurines. The quenching causes problems in the in situ fluorescence hydridization (FISH). The quenching is often unwanted, e.g., in DNA-sequencing with fluorescence dye-labeled terminators or on biochips. However, intramolecular fluorescence quenching is used in dye-labeled molecular beacons. Apart from environmental effects (salt, solvent, etc.), quenching occurs by fluorescence resonance energy transfer (FRET) or charge separation between the dye and a DNA base. In order to evaluate the influence of the 8-aza-7-deazaadenine base, the fluorescence properties of nucleoside conjugates **12** and **13** were investigated and compared. The measurements were performed in methanol (Figures 2 and 3). For solubility reasons, dye conjugates were dissolved in 0.5 mL of DMSO and then diluted with 99.5 mL methanol. In all experiments, the concentration of the nucleoside dye conjugates was identical (0.98 μmol). Conjugate **12** shows the main excitation maximum at 365 nm with an emission maximum at 413 nm (Figure 2). However, nucleoside dye conjugate **13** shows an excitation maximum at 346 nm and emission maximum at 421 nm (Figure 3). While the Stokes shift of the anthracene conjugate is only 48 nm, it amounts to 75 nm in the coumarin conjugate.

To evaluate quenching of the 8-aza-7-deazaadenine moiety within the monomeric anthracene conjugate **12**, fluorescence data of the anthracene conjugate were compared with that of the abasic alkyne side chain conjugate **32**. Similar experiments were performed on the 8-aza-7-deazaadenine coumarin conjugate **13** and the abasic coumarin alkyne derivative **33**. It was anticipated that the octyne side chain conjugated with triazole

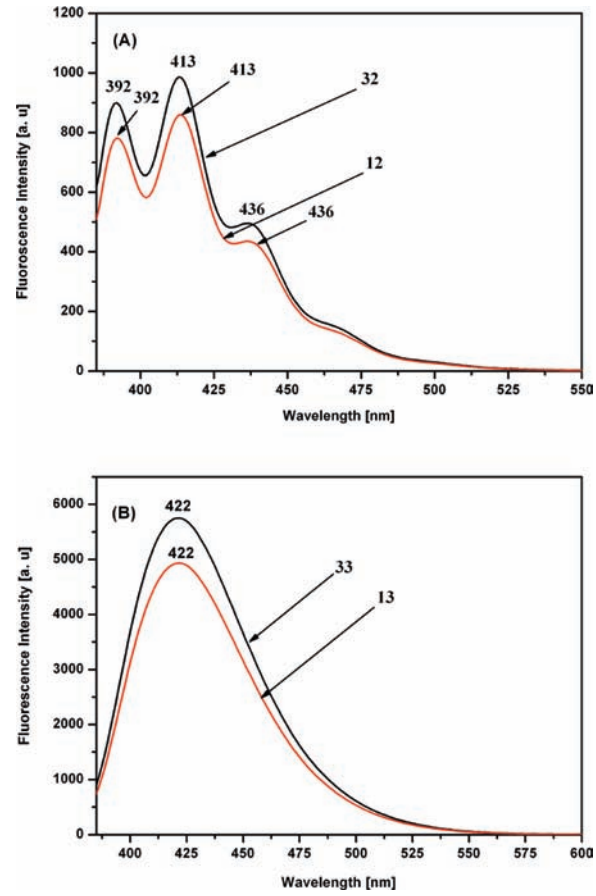
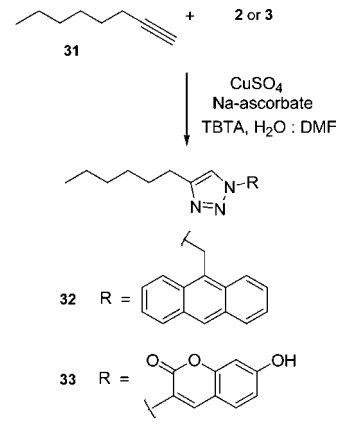


Figure 4. (A) Fluorescence emission spectra of the nucleoside conjugate **12** and the octyne conjugate **32**. (B) Fluorescence emission spectra of the nucleoside conjugate **13** and octyne conjugate **33**. For measurements, identical molar concentrations of the triazole conjugates were used. Spectra were measured in methanol.

Scheme 5. Synthesis of Abasic Click Conjugates



moiety should have no significant influence on the fluorescence of the dye. After clicking the azido dye **2** to the octyne **31**, the formed conjugate was purified by FC and compound **32** was isolated in 91% yield. As shown in Figure 4A,B, both nucleoside conjugates **12** and **13** do not develop significant fluorescence quenching when compared with corresponding abasic octyne derivatives **32** and **33**. So, 8-aza-7-deazaadenine virtually do not quench the fluorescence within the coumarin or anthracene conjugates.

Further, the fluorescence quenching behavior of pyrazolo[3,4-*d*]pyrimidine vs pyrrolo[2,3-*d*]pyrimidine is compared. To evaluate quenching of the 7-deaza-2′-deoxyadenosine within the

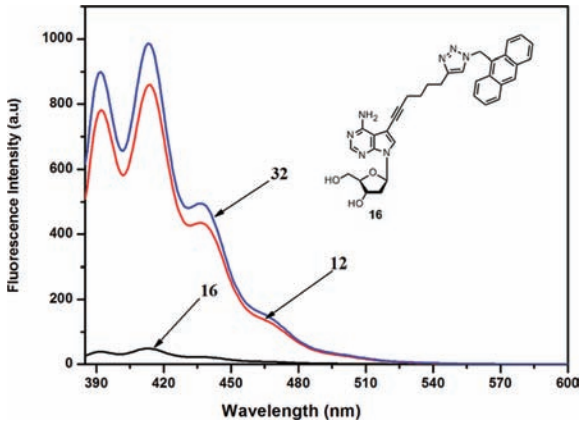


Figure 5. Comparison of fluorescence of anthracene click conjugates **12**, **32**, and **16**. Measurements were performed at identical molar concentration (0.98 μM) in methanol.

anthracene conjugate **16**, the octa-1,7-diynyl nucleoside derivative was functionalized with anthracene azide **2** in a similar way as 8-aza-7-deaza-2′-deoxyadenosine derivative **1**, yielding the conjugate **16** in 78%. When compared, the fluorescence intensity is reduced by around 95%, to that of the pyrazolo[3,4-*d*]pyrimidine conjugate **12** or the abasic anthracene derivative **32** (Figure 5). As in other cases (*14*, *33*, *36*, *37*), quenching within the 7-deazaadenine conjugate **16** is attributed to a charge transfer between the nucleobase and the dye. This results from the low oxidation potentials of 7-deazapurine-2′-deoxyribonucleosides compared to purines. The oxidation potentials against the standard calomel electrode (SCE) decrease in the following order dA (1.39 V) > c^7A_d (1.15 V) > dG (1.07 V) > c^7G (0.74 V) (*38*). The oxidation potential is further influenced by nearest-neighbor bases in single-stranded DNA, by base pairing in duplex DNA and by modification of the base moiety with side chains as in compound **1**. During charge separation, the nucleobase (NB) can be oxidized forming the radical cation, and a dye yields a radical anion ($DYE^{\bullet-} - NB^{\bullet+}$) (*35*, *55*−*57*). Depending on the redox potential of the nucleobase and the dye molecule, the process can be reversed leading to the formation of a dye radical cation and a nucleobase anion ($DYE^{\bullet+} - NB^{\bullet-}$) (*35*, *55*−*57*). Consequently, DNA bases and base surrogates can act in either way according to their redox potentials. The experiments described above clearly evidence that contrary to the 7-deazaadenine moiety—which is attributed to the low oxidation potential of pyrrolo[2,3-*d*]pyrimidine—the 8-aza-7-deazaadenine moiety of the 8-aza-7-deazaadenine conjugate is not able to quench the fluorescence of the dye significantly, most likely due to its higher oxidation potential.

Next, fluorescence measurements were performed on major groove functionalized oligonucleotides. The fluorescence spectra of single-stranded (ss) oligonucleotide 5′-d(TAG GTC **13**AT ACT) (**28**) bearing the coumarin dye shows an excitation maximum at 398 nm and an emission at 478 nm (Figure 6A). The corresponding anthracene conjugate 5′-d(TAG GTC **12**AT ACT) (**27**) shows a strong fluorescence with emission maximum at 424 nm and excitation maximum at 371 nm (Figure 6C). Upon hybridization with the unmodified complementary strand,

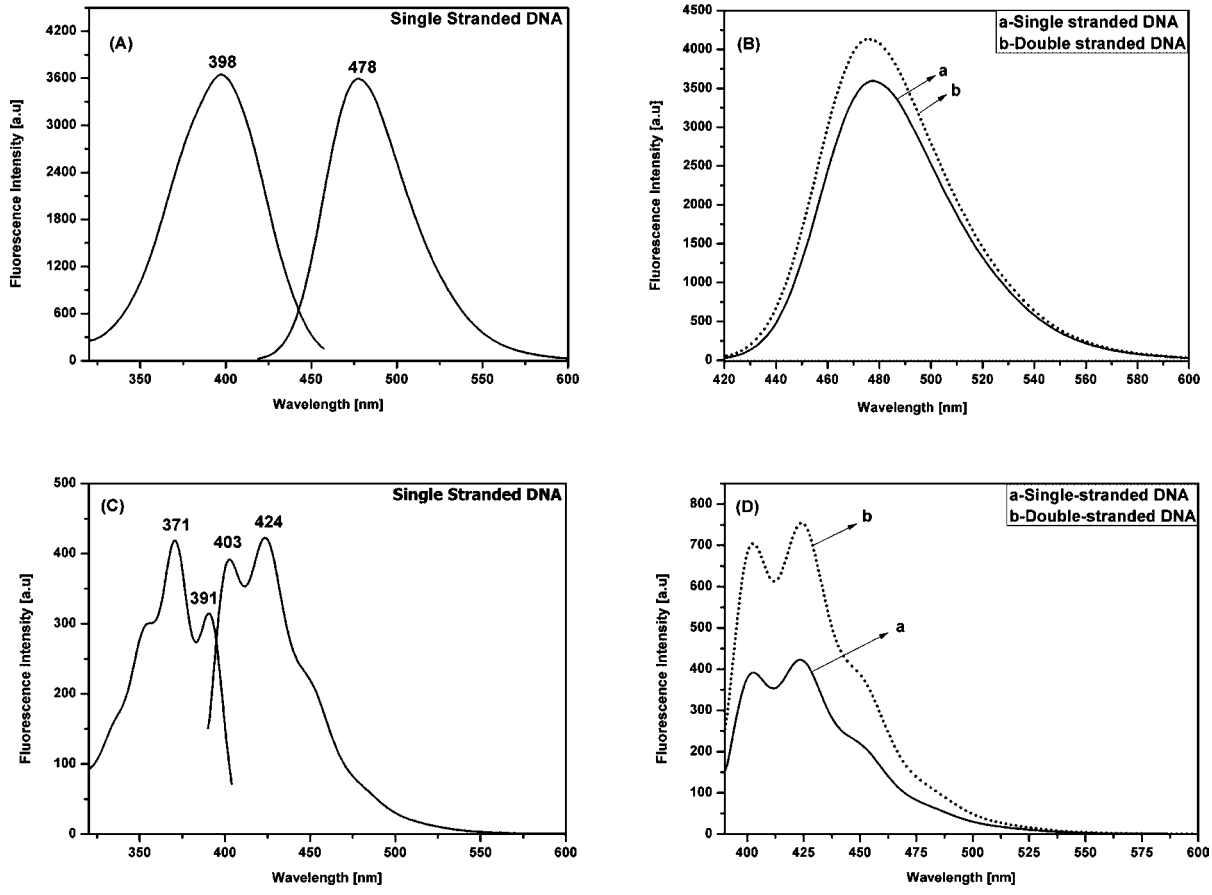


Figure 6. (A) Excitation and emission spectra of the single-stranded oligonucleotide coumarin conjugate **28** (2 μM single-strand concentration). (B) Comparison of the fluorescence emission spectra of the single-stranded oligonucleotide **28** and the duplex **28·18** (2 μM + 2 μM single-strand concentration) when excited at 398 nm. (C) Excitation and emission spectra of the single-stranded oligonucleotide anthracene conjugate **27** (2 μM single-strand concentration). (D) Comparison of the fluorescence emission spectra of the single-stranded oligonucleotide **27** and the duplex **27·18** (2 μM + 2 μM single-strand concentration) when excited at 371 nm. Spectra were measured in 1 M NaCl, 100 mM $MgCl_2$, 60 mM Na-cacodylate buffer at pH = 8.5.

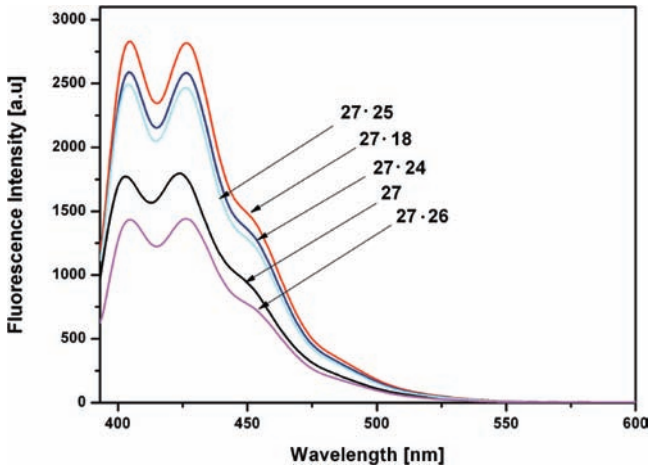


Figure 7. Fluorescence spectra of oligonucleotide duplexes **27·18**, **27·25**, **27·24**, and **27·26** containing the anthracene conjugate **12** and single-stranded oligonucleotide **27**. For oligonucleotide sequences, see Table 4. Measurements were performed in 1 M NaCl, 100 mM $MgCl_2$, and 60 mM Na-cacodylate (pH 7.0) with 5 μM + 5 μM single-strand concentration.

the duplexes 5′-d(TAG GTC **12**AT ACT) (**27**)·3′-d(ATC CAG TTA TGA) (**18**) and 5′-d(TAG GTC **13**AT ACT) (**28**)·3′-d(ATC CAG TTA TGA) (**18**) were formed, where in both cases the dye residue is located at the center of ODN. In case of duplex **27·18**, fluorescence intensity is significantly increased by almost a factor of 2 (ss vs ds) from single strand to duplex (Figure 6D), whereas only a small fluorescence increase is observed during duplex formation of the oligonucleotide coumarin conjugate (ODNs ss **28** and ds **28·18**, viz., 3590 vs 4130 fluorescence intensity; Figure 6B), which is contrary to that of the related pyrrolo[2,3-*d*]pyrimidine oligonucleotide coumarin conjugates (*14*, *18*).

The strong fluorescence increase upon duplex formation observed for the oligonucleotide anthracene conjugate prompted us to evaluate the potential of fluorescence change for single-base mismatch discrimination. A set of the single-stranded oligonucleotides **24**−**26** was synthesized and hybridized with a complementary strand containing anthracene conjugate **12** generating a duplex with fully matched base pairs and three duplexes with mismatches at the center of the oligonucleotide duplex. As mentioned earlier, the fluorescence intensity of the fully matched duplex (**27·18**) is the highest, while that with the **12**-dC mismatch (**27·26**) is the lowest. The **12**-dA and **12**-dG mismatches (**27·24** and **27·25**) show similar fluorescence intensity (Figure 7). From this, we can conclude that an anthracene "click" conjugate linked to fully matched base pairs can be distinguished from a mismatch situation. However, as observed in many other cases, it is difficult to differentiate among the various mismatched base pairs. We anticipate that the anthracene moiety interacts with distant base pairs one or two positions away from the site of the mismatch, a situation which does not lead to extreme changes of the dye fluorescence.

Furthermore, the stabilities of the fully matched and mismatched duplexes were measured and compared. The anthracene residue leads to a tremendous increase in stability (ΔT_m 9 °C per modification) in fully matched and mismatched duplexes (Table 4). The fully matched duplex **27·18** displays the highest melting temperature (59 °C) and also displays the maximum fluorescence intensity compared to the counterpart mismatched duplexes. The duplexes with mismatches are significantly less stable (ΔT_m −11 to −15 °C). The duplex with the mismatched base dC gives the lowest T_m value (43 °C), which also exhibits the lowest fluorescence intensity among the mismatched duplexes. Nevertheless, duplexes with mismatches bearing anthracene are almost as stable as the unmodified duplex **17·18**. To shed more light into this matter, the mismatch discrimination was studied in the unmodified duplexes. Almost similar T_m decreases (−12 to 16 °C) are observed as for the duplexes containing the anthracene conjugate but with a value always approximately 9 °C lower than those of the modified ones (Table 4). This implies that the anthracene moiety is always interacting with the same base pair, most likely one or two positions away from the mismatch site. To model this situation, energy minimization calculations using Amber MM+ force field (*Hyperchem 7.0/8.0*; Hypercube Inc., Gainesville, FL, USA, 2001) were performed on the 12-mer duplexes **27·18**, **28·18**, and **29·18**, taking B-type DNA in account.

Table 4. T_m Values and Thermodynamic Data of Oligonucleotide Duplexes Containing Mismatches

duplexes	T_m[a] [°C]	ΔT_m[b] [°C]	$\Delta H°$[c] [kcal/mol]	$\Delta S°$ [cal/(mol K)]	$\Delta G°_{310}$ [kcal/mol]
5′-d(TAG GTC **12**AT ACT) (**27**)					
3′-d(ATC CAG **T**TA TGA) (**18**)	59	0	−85	−230	−13.7
5′-d(TAG GTC **12**AT ACT) (**27**)					
3′-d(ATC CAG **A**TA TGA) (**24**)	44	−15	−69	−193	−9.6
5′-d(TAG GTC **12**AT ACT) (**27**)					
3′-d(ATC CAG **G**TA TGA) (**25**)	47	−12	−74	−206	−10.2
5′-d(TAG GTC **12**AT ACT) (**27**)					
3′-d(ATC CAG **C**TA TGA) (**26**)	43	−16	−70	−196	−9.4
5′-d(TAG GTC **A**AT ACT) (**17**)					
3′-d(ATC CAG **T**TA TGA) (**18**)	50	0	−89	−249	−11.6
5′-d(TAG GTC **A**AT ACT) (**17**)					
3′-d(ATC CAG **A**TA TGA) (**24**)	38	−12	−63	−178	−8.2
5′-d(TAG GTC **A**AT ACT) (**17**)					
3′-d(ATC CAG **G**TA TGA) (**25**)	39	−11	−68	−193	−8.3
5′-d(TAG GTC **A**AT ACT) (**17**)					
3′-d(ATC CAG **C**TA TGA) (**26**)	35	−15	−73	−212	−7.6

[a] Measured at 260 nm in 1 M NaCl, 100 mM $MgCl_2$, and 60 mM Na-cacodylate (pH 7.0) with 5 μM + 5 μM single-strand concentration. [b] Refers to the contribution of the modified residues. [c] Thermodynamic values were calculated with the program *MeltWin 3.0* and are with 10% deviation.

Table 5. T_m Values and Thermodynamic Data of Oligonucleotide Duplexes Containing Nucleosides 12−15

duplexes	T_m[a] [°C]	ΔT_m[b] [°C]	$\Delta H°$[c] [kcal/mol]	$\Delta S°$ [cal/(mol K)]	$\Delta G°_{310}$ [kcal/mol]
5′-d(TAG GTC AAT ACT) (**17**)					
3′-d(ATC CAG TTA TGA) (**18**)	50	--	−89	−249	−11.6
5′-d(TAG GTC **12**AT ACT) (**27**)					
3′-d(ATC CAG TTA TGA) (**18**)	59	+9	−85	−230	−13.7
5′-d(TAG GTC **13**AT ACT) (**28**)					
3′-d(ATC CAG TTA TGA) (**18**)	50	0	−82	−229	−11.2
5′-d(TAG GTC **14**AT ACT) (**29**)					
3′-d(ATC CAG TTA TGA) (**18**)	51	+1	−94	−275	−12.0
5′-d(TAG GTC **15**AT ACT) (**30**)					
3′-d(ATC CAG TTA TGA) (**18**)	51	+1	−82	−226	−12.4

[a] Measured at 260 nm in 1 M NaCl, 100 mM $MgCl_2$, and 60 mM Na-cacodylate (pH 7.0) with 5 μM + 5 μM single-strand concentration. [b] Refers to the contribution of the modified residues. [c] Thermodynamic values were calculated with the program *MeltWin 3.0* and are with 10% deviation.

Duplex Stability of Oligonucleotide Conjugates and Molecular Dynamics Calculations. Next, stability of the duplexes formed with complementary strands by "click" functionalized oligonucleotides was investigated. For this, T_m measurements were performed. As shown in Table 5, the coumarin dye conjugate **13** exerts no significant influence on the stability of duplex **28·18**, while the AZT and benzyl conjugates slightly stabilize the DNA duplex. A T_m value increase of 1 °C in both cases was observed, indicating positive interactions between these residues within duplex DNA. A significant stabilization (+9 °C) is observed in duplex **27·18** bearing an anthracenyl side chain. We think that the anthracene residue intercalates to proximal DNA bases (*58*). The strong

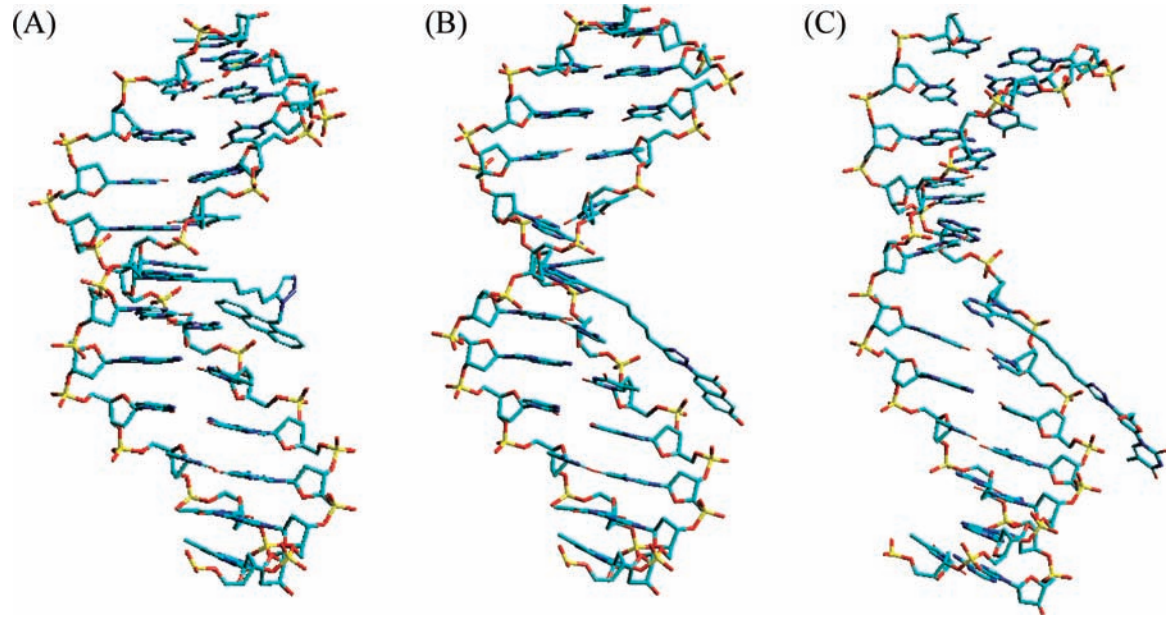


Figure 8. Molecular dynamics (MD) simulation models of oligonucleotide duplexes. The models were constructed using *Hyperchem 8.0* and energy minimized using AMBER calculations. (A) Oligonucleotide duplex **27·18** with an octa-1,7-diynyl side chain modified with anthracene azide. (B) Duplex **28·18** with an octadiynyl side chain modified with coumarin azide. (C) Duplex **29 ·18** with an octadiynyl chain modified with AZT. For a better view, structure (C) was rotated counter-clockwise.

hydrophobic interaction arising due to anthracene π-system, as a major binding mode with the DNA bases, results in an intercalated anthracene probe (*59*). The contribution of methylene groups present in the octa-1,7-diyinyl side chain toward free energy is substantial (*60*). Combined effect of these factors stabilizes the DNA helix (duplex **27·18**) to a significant extent with concomitant increase in melting temperature (+9 °C) compared to duplex **17·18**.

Next, energy minimization calculations were performed. According to Figure 8, back-folding of the side chain and possible π-stacking of the anthracene residue is supported by energy minimization. We do not see the intercalation of the anthracene residue with the mentioned program, while the polar, negatively charged coumarin fluorophore protrudes into the more polar environment. Both bulky residues are accommodated well in the B-DNA duplex.

CONCLUSIONS

Oligonucleotides incorporating octa-(1,7)-diynyl-8-aza-7-deaza-2′-deoxyadenosine **1** were prepared and further functionalized by azide−alkyne Huisgen-Meldal-Sharpless cycloaddition ("click" reaction), on both nucleoside and oligonucleotide level. The nonfluorescent fluorogenic reporter groups led to the formation of highly fluorescent dye conjugates after click reaction. The anthracene dye conjugate, which acts as a strong DNA binding ligand, pronounces the stability of a DNA duplex by 9 °C by a single modification. This results from anticipated intercalation of the dye and the hydrophobic interaction of the side chain. The 8-aza-7-deaza-2′-deoxyadenosine dye conjugates **12** and **13** show almost no fluorescence quenching, whereas the fluorescence is strongly quenched in the case of the 7-deazaadenine counterpart **16**. Quenching was also studied with the 1-octyne click conjugates taking both fluorogenic and polar as well as nonpolar dyes **2** and **3**. The fluorescence of single-stranded dye conjugates is increased upon duplex formation. A fully matched duplex shows a higher fluorescence than those with mismatches formed with dA, dG, and dC located opposite compound **1**, which also shows the highest T_m value. Thus, the 8-aza-7-deaza-2′-deoxyadenosine is an ideal shape mimic of 2′-deoxyadenosine, allowing functionalization at the 7-position without disturbing the DNA helix structure, which was supported by molecular dynamics simulations. It generates virtually no fluorescence quenching by charge transfer as observed for 7-deazaadenine conjugates.

ACKNOWLEDGMENT

We would like to thank Dr. V. R. Sirivolu, Dr. P. Chittepu, and Dr. P. Leonard for helpful discussions and support. We also thank Dr. S. Budow and Mr. D. Jiang for measuring the NMR spectra, Dr. T. Koch from Roche Diagnostics GmbH, Penzberg, Germany, for the measurement of the MALDI spectra, and Mr. Nhat Quang Tran for the oligonucleotide syntheses. Financial support by the Roche Diagnostics GmbH and ChemBiotech, Muenster, Germany, is highly appreciated.

Supporting Information Available: $^{1}H-^{13}C$ NMR coupling constants, extinction coefficients, HPLC profiles, MALDI-TOF masses and purification profiles of the oligonucleotides, melting profiles, ^{1}H and ^{13}C NMR spectra of the nucleoside derivatives and click conjugates. This material is available free of charge via the Internet at http://pubs.acs.org.

LITERATURE CITED

(1) Kobayashi, H., Ogawa, M., Alford, R., Choyke, P. L., and Urano, Y. (2010) New strategies for fluorescent probe design in medical diagnostic imaging. *Chem. Rev.* DOI: 10.1021/cr900263j.

(2) Hrdlicka, P. J., Babu, B. R., Sørensen, M. D., Harrit, N., and Wengel, J. (2005) Multilabeled pyrene-functionalized 2′-amino-LNA probes for nucleic acid detection in homogeneous fluorescence assays. *J. Am. Chem. Soc. 127*, 13293–13299.

(3) Astakhova, I. V., Korshun, V. A., Jahn, K., Kjems, J., and Wengel, J. (2008) Perylene attached to 2′-amino-LNA: Synthesis, incorporation into oligonucleotides, and remarkable fluorescence properties *in vitro* and in cell culture. *Bioconjugate Chem. 19*, 1995–2007.

(4) Marti, A. A., Jockusch, S., Stevens, N., Ju, J., and Turro, N. J. (2007) Fluorescent hybridization probes for sensitive and selective DNA and RNA detection. *Acc. Chem. Res. 40*, 402–409.

(5) Hakala, H., and Lönnberg, H. (1997) Time-resolved fluorescence detection of oligonucleotide hybridization on a single microparticle: Covalent immobilization of oligonucleotides and quantitation of a model system. *Bioconjugate Chem. 8*, 232–237.

(6) Cuppoletti, A., Cho, Y., Park, J.-S., Strässler, C., and Kool, E. T. (2005) Oligomeric fluorescent labels for DNA. *Bioconjugate Chem. 16*, 528–534.

(7) Droumaguet, C. L., Wang, C., and Wang, Q. (2010) Fluorogenic click reaction. *Chem. Soc. Rev.* DOI: 10.1039/b901975h.

(8) Best, M. D. (2009) Click chemistry and bioorthogonal reactions: Unprecedented selectivity in the labeling of biological molecules. *Biochemistry 48*, 6571–6584.

(9) Huisgen, R. (1989) Kinetics and reaction mechanisms: Selected examples from the experience of forty years. *Pure Appl. Chem. 61*, 613–628.

(10) Huisgen, R., Szeimies, G., and Moebius, L. (1967) Kinetik der Additionen organischer Azide an CC-Mehrfachbindungen. *Chem. Ber. 100*, 2494–2507.

(11) Meldal, M., and Tornøe, C. W. (2008) Cu-catalyzed azide-alkyne cycloaddition. *Chem. Rev. 108*, 2952–3015.

(12) Tornøe, C. W., Christensen, C., and Meldal, M. (2002) Peptidotriazoles on solid phase: [1,2,3]-Triazoles by regiospecific copper(I)-catalyzed 1,3- dipolar cycloadditions of terminal alkynes to azides. *J. Org. Chem. 67*, 3057–3064.

(13) Rostovtsev, V. V., Green, L. G., Fokin, V. V., and Sharpless, K. B. (2002) A stepwise Huisgen cycloaddition process: Copper (I)-catalyzed regioselective "ligation" of azides and terminal alkynes. *Angew. Chem., Int. Ed. 41*, 2596–2599.

(14) Seela, F., Sirivolu, V. R., and Chittepu, P. (2008) Modification of DNA with octadiynyl side chains: Synthesis, base pairing, and formation of fluorescent coumarin dye conjugates of four nucleobases by the alkyne-azide "click" reaction. *Bioconjugate Chem. 19*, 211–224.

(15) Gramlich, P. M. E., Wirges, C. T., Manetto, A., and Carell, T. (2008) Postsynthetic DNA modification through the copper-catalyzed azide-alkyne cycloaddition reaction. *Angew. Chem., Int. Ed. 47*, 8350–8358.

(16) Kocalka, P., El-Sagheer, A. H., and Brown, T. (2008) Rapid and efficient DNA strand cross-linking by click chemistry. *ChemBioChem 9*, 1280–1285.

(17) Hotha, S., and Kashyap, S. (2006) "Click chemistry" inspired synthesis of *pseudo*-oligosaccharides and amino acid glycoconjugates. *J. Org. Chem. 71*, 364–367.

(18) Seela, F., Xiong, H., Leonard, P., and Budow, S. (2009) 8-Aza-7-deazaguanine nucleosides and oligonucleotides with octadiynyl side chains: Synthesis, functionalization by the azide-alkyne 'click' reaction and nucleobase specific fluorescence quenching of coumarin dye conjugates. *Org. Biomol. Chem. 7*, 1374–1387.

(19) Sirivolu, V. R., Chittepu, P., and Seela, F. (2008) DNA with branched internal side chains: Synthesis of 5-tripropargylamine-dU and conjugation by an azide-alkyne double click reaction. *ChemBioChem 9*, 2305–2316.

(20) Agnew, B., Buck, S., Nyberg, T., Bradford, J., Clarke, S., and Gee, K. (2008) Click chemistry for labeling and detection of biomolecules. Molecular probes for biomedical applications II; 21−22 January 2008, San Jose, CA, USA; 6867, 1−686708−10.

(21) Baskin, J. M., Prescher, J. A., Laughlin, S. T., Agard, N. J., Chang, P. V., Miller, I. A., Lo, A., Codelli, J. A., and Bertozzi, C. R. (2007) Copper-free click chemistry for dynamic in vivo imaging. *Proc. Natl. Acad. Sci. U.S.A. 104*, 16793–16797.

(22) Froehler, B. C., Wadwani, S., Terhorst, T. J., and Gerrard, S. R. (1992) Oligodeoxynucleotides containing C-5 propyne analogs of 2′-deoxyuridine and 2′-deoxycytidine. *Tetrahedron Lett. 33*, 5307–5310.

(23) Graham, D., Parkinson, J. A., and Brown, T. (1998) DNA duplexes stabilized by modified monomer residues: Synthesis and stability. *J. Chem. Soc., Perkin Trans. 1*, 1131–1138.

(24) Sági, J., Szemzö, A., Ébinger, K., Szabolcs, A., Sági, G., Ruff, É., and Ötvös, L. (1993) Base-modified oligodeoxynucleotides. I: Effect of 5-alkyl, 5-(1-alkenyl) and 5-(1-alkynyl) substitution of the pyrimidines on duplex stability and hydrophobicity. *Tetrahedron Lett. 34*, 2191–2194.

(25) Kottysch, T., Ahlborn, C., Brotzel, F., and Richert, C. (2004) Stabilizing or destabilizing oligodeoxynucleotide duplexes containing single 2′-deoxyuridine residues with 5-alkynyl substituents. *Chem.—Eur. J. 10*, 4017–4028.

(26) Seela, F., Zulauf, M., and Debelak, H. (2000) Base-pairing properties of 8-aza-7-deazaadenine linked via the 8-position to the DNA backbone. *Helv. Chim. Acta 83*, 1437–1453.

(27) Seela, F., and Debelak, H. (2001) 8-Aza-7-deazaadenine and 7-deazaguanine: Synthesis and properties of nucleosides and oligonucleotides with nucleobases linked at position-8. *Nucleosides, Nucleotides Nucleic Acids 20*, 577–585.

(28) Seela, F., Zulauf, M., Sauer, M., and Deimel, M. (2000) 7-Substituted 7-deaza-2′-deoxyadenosines and 8-aza-7-deaza-2′-deoxyadenosines: Fluorescence of DNA base analogues induced by the 7-alkynyl side chain. *Helv. Chim. Acta 83*, 910–927.

(29) Seela, F., and Zulauf, M. (1998) Synthesis of 7-alkynylated 8-aza-7-deaza-2′-deoxy adenosines via the Pd-catalysed cross-coupling reaction. *J. Chem. Soc., Perkin Trans. 1*, 3233–3239.

(30) He, J., and Seela, F. (2002) 8-Aza-7-deazapurine-pyrimidine base pairs: The contribution of 2- and 7-substituents to the stability of duplex DNA. *Tetrahedron 58*, 4535–4542.

(31) He, J., and Seela, F. (2002) Propynyl groups in duplex DNA: Stability of base pairs incorporating 7-substituted 8-aza-7-deazapurines or 5-substituted pyrimidines. *Nucleic Acids Res. 30*, 5485–5496.

(32) Seela, F., Jawalekar, A. M., Sun, L., and Leonard, P. (2005) Oligonucleotides containing pyrazolo[3,4-d]pyrimidines: 8-Aza-7-deazaadenines with bulky substituents in the 2- or 7-position. *Nucleosides, Nucleotides Nucleic Acids 24*, 1485–1505.

(33) Wagenknecht, H.-A. (2006) *Charge Transfer in DNA.* Published by Wiley-VCH Verlag GmbH & Co. DOI: 10.1002/3527606629.

(34) Latimer, L. J. P., and Lee, J. S. (1991) Ethidium Bromide does not fluoresce when intercalated adjacent to 7-deazaguanine in duplex DNA. *J. Biol. Chem. 266*, 13849–13851.

(35) Li, H., Peng, X., and Seela, F. (2004) Fluorescence quenching of parallel-stranded DNA bound ethidium bromide: The effect of 7-deaza-2′-deoxyisoguanosine and 7-halogenated derivatives. *Bioorg. Med. Chem. Lett. 14*, 6031–6034.

(36) Genereux, J. C., and Barton, J. K. (2010) Mechanisms for DNA charge transport. *Chem. Rev.* DOI:10.1021/cr900228f.

(37) Seela, F., and Ingale, S. A. (2010) "Double Click" reaction on 7-deazaguanine DNA: Synthesis and excimer fluorescence of nucleosides and oligonucleotides with branched side chains decorated with proximal pyrenes. *J. Org. Chem. 75*, 284–295.

(38) Seidel, C. A. M., Schulz, A., and Sauer, M. H. M. (1996) Nucleobase-specific quenching of fluorescent dyes. 1. Nucleobase one-electron redox potentials and their correlation with static and dynamic quenching efficiencies. *J. Phys. Chem. 100*, 5541–5553.

(39) Cosyn, L., Palaniappan, K. K., Kim, S.-K., Duong, H. T., Gao, Z.-G., Jacobson, K. A., and Van Calenbergh, S. (2006) 2-Triazole-substituted adenosines: A new class of selective A_3 adenosine receptor agonists, partial agonists, and antagonists. *J. Med. Chem. 49*, 7373–7383.

(40) Gierlich, J., Burley, G. A., Gramlich, P. M. E., Hammond, D. M., and Carell, T. (2006) Click chemistry as a reliable method for the high-density postsynthetic functionalization of alkyne-modified DNA. *Org. Lett. 17*, 3639–3642.

(41) Seo, T. S., Li, Z., Ruparel, H., and Ju, J. (2003) Click chemistry to construct fluorescent oligonucleotides for DNA sequencing. *J. Org. Chem. 68*, 609–612.

(42) Hainke, S., and Seitz, O. (2009) Binaphthyl-DNA: Stacking and fluorescence of a nonplanar aromatic base surrogate in DNA. *Angew. Chem., Int. Ed. 48*, 8250–8253.

(43) Dose, C., and Seitz, O. (2008) Single nucleotide specific detection of DNA by native chemical ligation of fluorescence labeled PNA-probes. *Bioorg. Med. Chem. 16*, 65–77.

(44) Chang, K.-C., Su, I.-H., Senthilvelan, A., and Chung, W.-S. (2007) Triazole-modified calix[4]crown as a novel fluorescent on-off switchable chemosensor. *Org. Lett. 9*, 3363–3366.

(45) Stack, D. E., Hill, A. L., Diffendaffer, C. B., and Burns, N. M. (2002) Synthesis of a new fluorescent probe specific for catechols. *Org. Lett. 4*, 4487–4490.

(46) Xie, F., Sivakumar, K., Zeng, Q., Bruckman, M. A., Hodges, B., and Wang, Q. (2008) A fluorogenic 'click' reaction of azidoanthracene derivatives. *Tetrahedron 64*, 2906–2914.

(47) Sivakumar, K., Xie, F., Cash, B. M., Long, S., Barnhill, H. N., and Wang, Q. (2004) A fluorogenic 1,3-dipolar cycloaddition reaction of 3-azidocoumarins and acetylenes. *Org. Lett. 6*, 4603–4606.

(48) Franzini, R. M., and Kool, E. T. (2008) 7-Azidomethoxycoumarins as profluorophores for templated nucleic acid detection. *ChemBioChem 9*, 2981–2988.

(49) Seela, F., and Sirivolu, V. R. (2007) Nucleosides and oligonucleotides with diynyl side chains: The Huisgen-Sharpless cycloaddition "click"reaction" performed on DNA and their constitutents. *Nucleosides, Nucleotides Nucleic Acids 26*, 597–601.

(50) Seela, F., and Zulauf, M. (1999) Oligonucleotides containing 7-deazaadenines: The influence of the 7-substituent chain length and charge on the duplex stability. *Helv. Chim. Acta 82*, 1878–1898.

(51) Becher, G., He, J., and Seela, F. (2001) Major-groove-halogenated DNA: The effects of bromo and iodo substituents replacing H-C(7) of 8-aza-7-deazapurine-2,6-diamine or H-C(5) of uracil residues. *Helv. Chim. Acta 84*, 1048–1065.

(52) Seela, F., and Becher, G. (1999) Oligonucleotides containing pyrazolo[3,4-d]pyrimidines: The influence of 7-substituted 8-aza-7-deaza-2′-deoxyguanosines on the duplex structure and stability. *Helv. Chim. Acta 82*, 1640–1655.

(53) Seela, F., and Becher, G. (2001) Pyrazolo[3,4-d]pyrimidine nucleic acids: Adjustment of dA-dT to dG-dC base pair stability. *Nucleic Acids Res. 29*, 2069–2078.

(54) Seela, F., and Shaikh, K. I. (2005) Oligonucleotides containing 7-propynyl-7-deazaguanine: Synthesis and base pair stability. *Tetrahedron 61*, 2675–2681.

(55) Wagenknecht, H.-A. (2006) DNA as functional π-system: Electron transfer in synthetically modified oligonucleotides. *Functional Organic Materials - Synthesis, strategies, and applications* (Bunz, U. F., and Müller, T. T. J., Eds) pp 441−464, Wiley-VCH, Weinheim, Germany.

(56) Wagenknecht, H.-A. (2006) Electron transfer processes in DNA: Mechanisms, biological relevance and applications in DNA analytics. *Nat. Prod. Rep. 23*, 973–1006.

(57) Wagenknecht, H.-A. (2003) Reductive electron transfer and excess electron migration in DNA. *Angew. Chem., Int. Ed. 42*, 2454–2460.

(58) Wilson, W. D., Wang, Y.-H., Kusuma, S., Chandrasekaran, S., Yang, N. C., and Boykin, D. W. (1985) Binding strength and specificity in DNA interactions: The design of A•T specific intercalators. *J. Am. Chem. Soc. 107*, 4989–4995.

(59) Kumar, C. V., and Asuncion, E. H. (1993) DNA binding studies and site selective fluorescence sensitization of an anthryl probe. *J. Am. Chem. Soc. 115*, 8547–8553.

(60) Duff, M. R., Jr., Mudhivarthi, V. K., and Kumar, C. V. (2009) Rational design of anthracene-based DNA binders. *J. Phys. Chem. B 113*, 1710–1721.

BC100090Y

Supporting Information

Azide-Alkyne "Click" Conjugation of 8-Aza-7-deazaadenine-DNA: Synthesis, Duplex Stability and Fluorogenic Dye Labelling

Frank Seela* and Suresh S. Pujari

Laboratory of Bioorganic Chemistry and Chemical Biology, Center for Nanotechnology, Heisenbergstraße 11, 48149 Münster, Germany and Laboratorium für Organische and Bioorganische Chemie, Institut für Chemie, Universität Osnabrück, Barbarastraße 7, 49069 Osnabrück, Germany.

Telephone: +49 (0)251-53406-500; Fax: +49 (0)251-53406-857

E-mail: Frank.Seela@uni-osnabrueck.de; Seela@uni-muenster.de

Web: www.seela.net

Table of Contents:

Synthetic procedure for 1-Anthracen-9-ylmethyl-4-hexyl-1*H*-[1,2,3]triazole (32)……..4

Table S1. Coupling constants for 8-aza-7-deaza-2'-deoxyadenosine derivatives……..5

Table S2. Coupling constants for 8-aza-7-deaza-2'-deoxyadenosine click conjugates……..6

Table S3. Molecular Masses of Selected Oligonucleotides……7

Figure S4. UV/Vis spectrum of 8-aza-7-deaza-2'-deoxyadenosine and click conjugates…...8

Table S5. UV Maxima and Extinction Coefficients……9

Table S6. Elemental analysis of the nucleoside derivatives and click conjugates……10

Figure S7. HPLC profiles of the click conjugates……..…11

Figure S8. Purification profiles of the oligonucleotides……12

Figure S9. Melting profiles of the duplexes…..……..13

Figure S10. ^{1}H-NMR spectrum of compound **7a**……..…….14

Figure S11. ^{13}C-NMR spectrum of compound **7a**……..……15

Figure S12. ^{1}H-NMR spectrum of compound **7b**……16

Figure S13. ^{13}C-NMR spectrum of compound **7b** ……..17

Figure S14. ^{1}H-NMR spectrum of compound **1**……..18

Figure S15. ^{13}C-NMR spectrum of compound **1**…….....19

Figure S16. ^{1}H-NMR spectrum of compound **9** ……20

Figure S17. ^{13}C-NMR spectrum of compound **9**…….21

Figure S18. ^{1}H-NMR spectrum of compound **10** ……22

Figure S19. ^{13}C-NMR spectrum of compound **10**……23

Figure S20. ^{1}H-NMR spectrum of compound **12** ……....24

Figure S21. ^{13}C-NMR spectrum of compound **12**……....25

Figure S22. ^{1}H-NMR spectrum of compound **13** ……....26

Figure S23. ^{13}C-NMR spectrum of compound **13**……....27

Figure S24. ^{1}H-NMR spectrum of compound **14** ……....28

Figure S25. ^{13}C-NMR spectrum of compound **14**……....29

Figure S26. ^{1}H-NMR spectrum of compound **15**.... .....……30

Figure S27. ^{13}C-NMR spectrum of compound **15**……31

Figure S28. ^{1}H-NMR spectrum of compound **16** ……32

Figure S29. ^{13}C-NMR spectrum of compound **16**……33

Figure S30. ^{1}H-NMR spectrum of compound **32**…….34

Figure S31. ^{13}C-NMR spectrum of compound **32**……35

Synthetic procedure for 1-Anthracen-9-ylmethyl-4-hexyl-1*H*-[1,2,3]triazole (32).

Compound **32** was synthesized as reported in the literature with anthracene azide **2** (0.069 g, 0.30 mmol) and 1-octyne **31** (0.033 g, 0.30 mmol) suspended in a 3:1 mixture (v/v) of DMF and water (24 mL). Copper sulfate (0.007 g, 0.04 mmol), sodium ascorbate (0.014 g, 0.09 mmol) and tris[(N-benzyltriazolyl)methyl]amine (TBTA) ligand (0.008 g, 0.01 mmol). Yield (0.094 g, 91%) as a pale yellow solid. TLC (silica gel, EtOAc/petroleum ether 8:2). R_f 0.3. UV λ_{max}(MeOH)/nm 347 (ε/dm^3 mol^{-1} cm^{-1} 6900), 365 (10600), 386 (9900). Anal. ($C_{23}H_{25}N_3$) C, H, N. ^{1}H-NMR [$CDCl_3$, 300 MHz]: δ 0.76-0.79 (m, 3H, CH_3), 1.18 (s, 6H, 3 x CH_2), 1.45-1.48 (m, 2H, CH_2), 1.60 (s, 1H, CH_2), 2.49-2.54 (t, J = 7.8 Hz, 2H, CH_2), 6.50 (s, 2H, CH_2), 6.82 (s, 1H, triazole-H), 7.50-7.63 (m, 4H, Ar-H), 8.07-8.09 (d, J = 8.1 Hz, 2H, Ar-H), 8.30-8.33 (d, J = 8.7 Hz, 2H, Ar-H), 8.58 (s, 1H, Ar-H). ESI-TOF: $[M + H]^+$ calcd 344.46. Found 344.21.

Table S1. ^{1}H-^{13}C-coupling constants of 8-aza-7-deaza-2'-deoxyadenosine derivatives. [a,b]

			J (Hz)		
^{1}H-^{13}C-Coupling Constants	**7a**	**7b**	**1**	**9**	**10**
^{1}J(C6, H-C6)	206.3	206.5	200.1	200.4	198.0
^{3}J(C4, H-C6)	10.9	10.8	10.5	10.4	10.3
^{2}J(C7'', H-C8'')	4.2	4.1	4.1	4.2	4.1
^{1}J(C8'', H-C8'')	247.5	248.1	248.3	244.1[c]	244.0[c]
^{1}J(C1', H-C1')	169.8	166.2	164.5	165.7	166.0
^{1}J(C3', H-C3')	157.6	150.3	151.3	150.9	149.9
^{1}J(C4', H-C4')	152.2	148.6	149.2	148.1	146.7
^{1}J(C5', H-C5')	150.2	138.7	139.9	139.8	143.6
^{1}J(N=C, H-N)	--	--	--	179.6	180.4

[a] Measured in DMSO-d_6 at 298 K. [b] Systematic numbering. [c] Tentative.

Table S2. ^{1}H-^{13}C-coupling constants of 8-aza-7-deaza-2'-deoxyadenosine click conjugates.[a,b]

	J (Hz)				
^{1}H-^{13}C-Coupling Constants	**12**	**13**	**14**	**15**	**16**
^{1}J(C6, H-C6)	200.1	199.5	200.1	199.9	--
^{3}J(C4, H-C6)	11.0	11.0	10.3	11.2	--
^{1}J(C1', H-C1')	167.8	166.0	161.2	166.0	165.5
^{1}J(C3', H-C3')	154.6	148.1	147.6	149.2	151.2
^{1}J(C4', H-C4')	147.6	146.9	147.2	147.4	147.5
^{1}J(C5', H-C5')	140.1	138.7	141.4	140.4	139.5

[a] Measured in DMSO-d_6 at 298 K. [b] Systematic numbering.

The ^{13}C-NMR chemical shifts were assigned using ^{1}H-^{13}C-NMR gated decoupled and DEPT spectra and coupling constants of the sugar moiety of new compounds are in accordance with the literature values (*1*).

Reference

(1) Seela, F., and Bussmann, W. (1985) Assignment of ^{13}C chemical shifts of α-D-ribonucleoside sugar carbons by ^{1}J (CH) coupling constants. *Nucleosides & Nuceotides 3*, 391-394.

Table S3. Molecular Masses [M-1]$^-$ of Selected Oligonucleotides Determined by MALDI-TOF Mass Spectrometry.

Oligonucleotides	Mol Wt (calcd)	[M-1]$^-$ (found)
5'-d(TAG GTC **1**AT ACT)-3' (**19**)	3748.56	3747.11
5'-d(TAG GTC **11**T ACT)-3' (**20**)	3852.71	3851.67
5'-d(T**1**G GTC **11**T **1**CT)-3' (**21**)	4060.01	4059.60
3'-d(ATC CAG TTA TG**1**)-5' (**22**)	3748.56	3747.52
3'-d(ATC C**1**G TT**1** TGA)-5' (**23**)	3852.71	3851.47
5'-d(TAG GTC **12**AT ACT)-3' (**27**)	3981.83	3980.84
5'-d(TAG GTC **13**AT ACT)-3' (**28**)	3951.71	3950.33
5'-d(TAG GTC **14**AT ACT)-3' (**29**)	4015.80	4014.89
5'-d(TAG GTC **15**AT ACT)-3' (**30**)	3881.71	3880.67

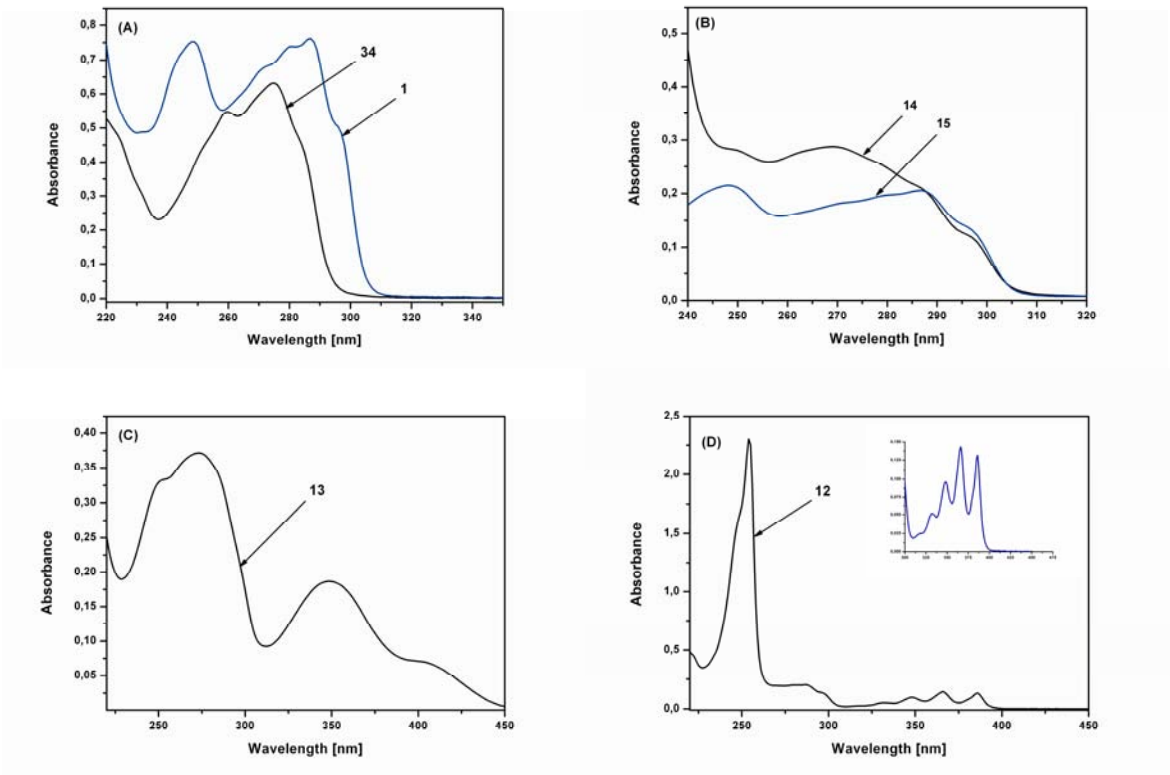
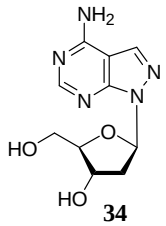


Figure S4. (A) UV/Vis spectra of 8-aza-7-deaza-2'-deoxyadenosine (**34**) and octa-1,7-diynyl derivative **1**. (B) UV/Vis spectra of nucleoside conjugate **14** and **15**. (C) UV/Vis spectra of coumarin nucleoside conjugate **13**. (D) UV/Vis spectra of anthracene nucleoside conjugate **12**. Spectra were measured in methanol.

Table S5. UV Maxima and Extinction Coefficients of Compound 1 and Its Derivatives[a].

Comp	λ_{max}/(nm)	(ε)	Comp	λ_{max}/(nm)	(ε)
7a	275	8300	**14**	269	17900
7b	233	18200	**15**	249	10500
	281	7700		287	10100
1	249	11000	**16**	279	17400
	287	11300		386	11300
9	322	24400	**32**	347	6900
10	320	24900		386	9900
12	348	5600	**34**	260	9500
	386	6900		275	10900
13	287	15200			
	346	19500			

[a] Measured in methanol. λ_{max}-wavelength, ε –extinction coefficient. Compound **23** is non functionalized 8-aza-7-deaza-2'-deoxyadenosine.

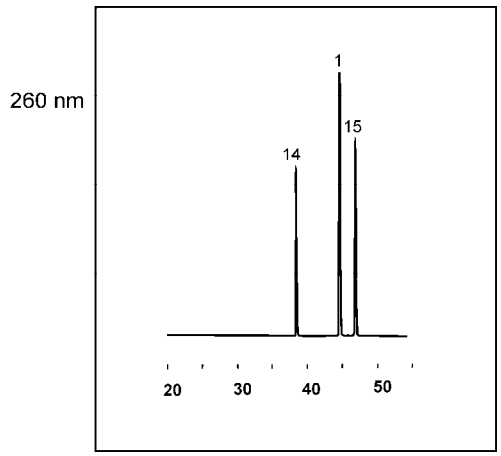


34

Table S6. Elemental Analysis of the Nucleoside Derivatives and Click Conjugates.

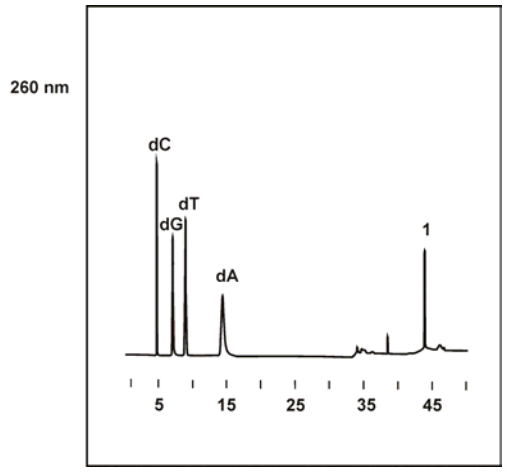
Compound	Calculated			Found		
	C	H	N	C	H	N
1	60.83	5.96	19.71	60.72	5.88	19.58
7a	69.29	5.65	9.24	69.27	5.99	9.51
7b	61.61	5.99	15.13	61.67	5.85	15.06
8	31.85	3.21	18.57	31.67	3.20	18.70
9	61.45	6.38	20.47	61.25	6.22	20.34
10	70.77	6.22	11.79	70.79	6.12	11.66
12	67.33	5.48	19.04	67.13	5.44	18.82
14	54.01	5.50	22.50	53.94	5.34	22.29
15	61.46	5.78	22.94	61.19	5.65	22.71
16	69.49	5.66	16.68	68.98	5.48	16.87

(A)



t_R [min]

(B)



t_R [min]

Figure S7. (A) Artificial mixture of nucleoside conjugates **14**, **15** and nucleoside **1**. (B) The enzymatic digest profile of oligonucleotide 5'-d(TAG GTC **1**AT ACT) (**19**) with snake venom phosphodiesterase and alkaline phosphatase in 1 mL of 0.1 M Tris-HCl buffer (pH 8.5) at 37 °C. Gradient: 0-20 min 100% B, 20-30 min 20-80% A in B; 30-40 min 30-70%, 40-50 min 40-60%, flow rate 0.7 mL/min. The following solvent systems were used: MeCN (A) and 0.1 M (Et_3NH)OAc (pH 7.0)/MeCN, 95:5) (B).

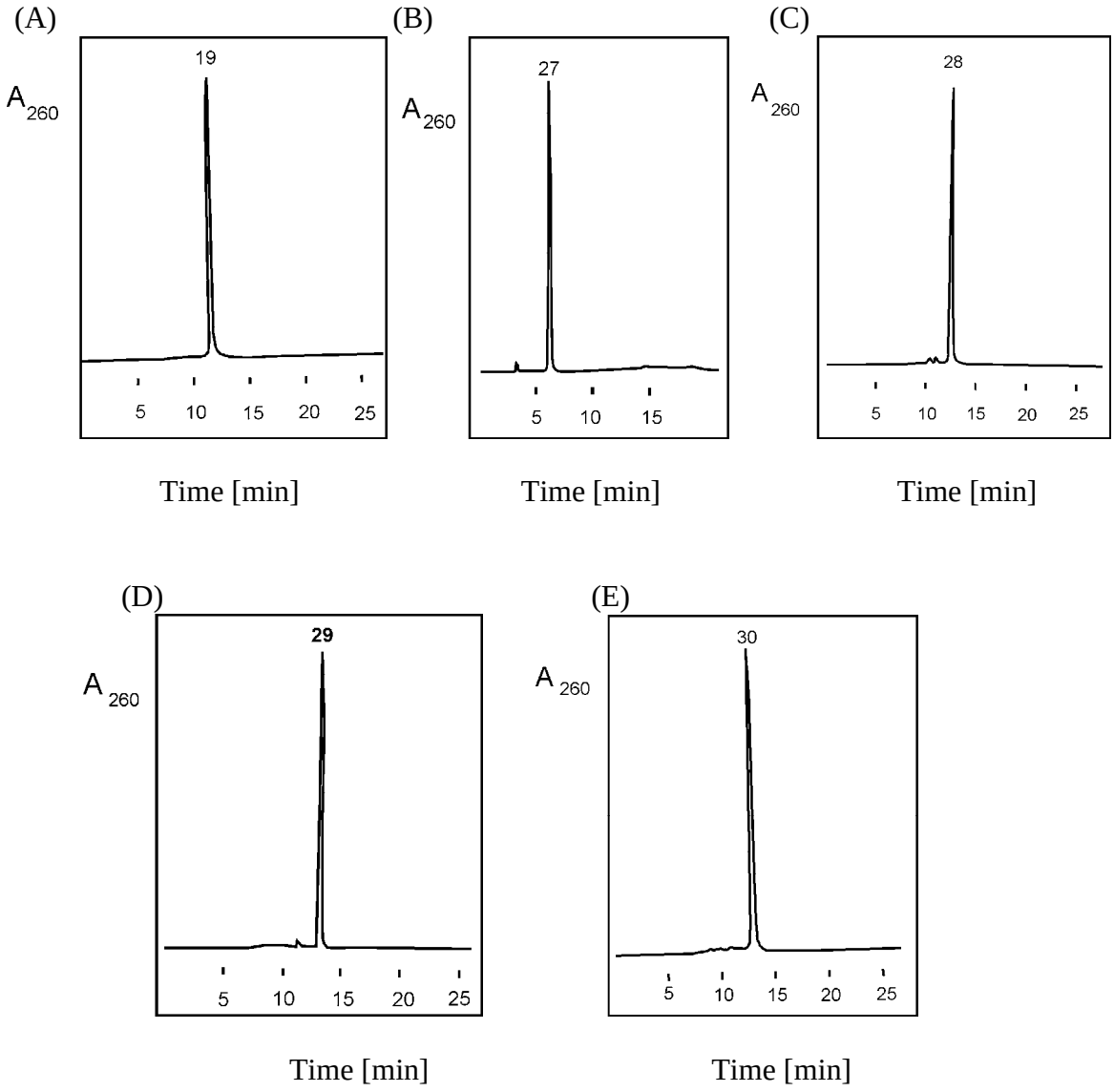


Figure S8. HPLC (RP-18) profiles determined at 260 nm of single-stranded oligonucleotide conjugates. (A) 5'-d(TAG GTC **1**AT ACT) (**19**), (B) 5'-d(TAG GTC **12**AT ACT) (**27**), (C) 5'-d(TAG GTC **13**AT ACT) (**28**), (D) 5'-d(TAG GTC **14**AT ACT) (**29**), (E) 5'-d(TAG GTC **15**AT ACT) (**30**). For elution the following system was used: MeCN (A) and 0.1 M (Et_3NH)OAc (pH 7.0) (B). Gradient: 0-20 min 0-20% A in B; 20-25 min, 20% A in B, 25-30 min 20-0% A in B, flow rate 1.0 mL/min. For oligonucleotide **19**, the following gradient was used: 0-3 min 10-15% A in B, 3-15 min 15 -50% A in B, and 15-20 min 50-10% A in B; flow rate 1.0 mL/min.

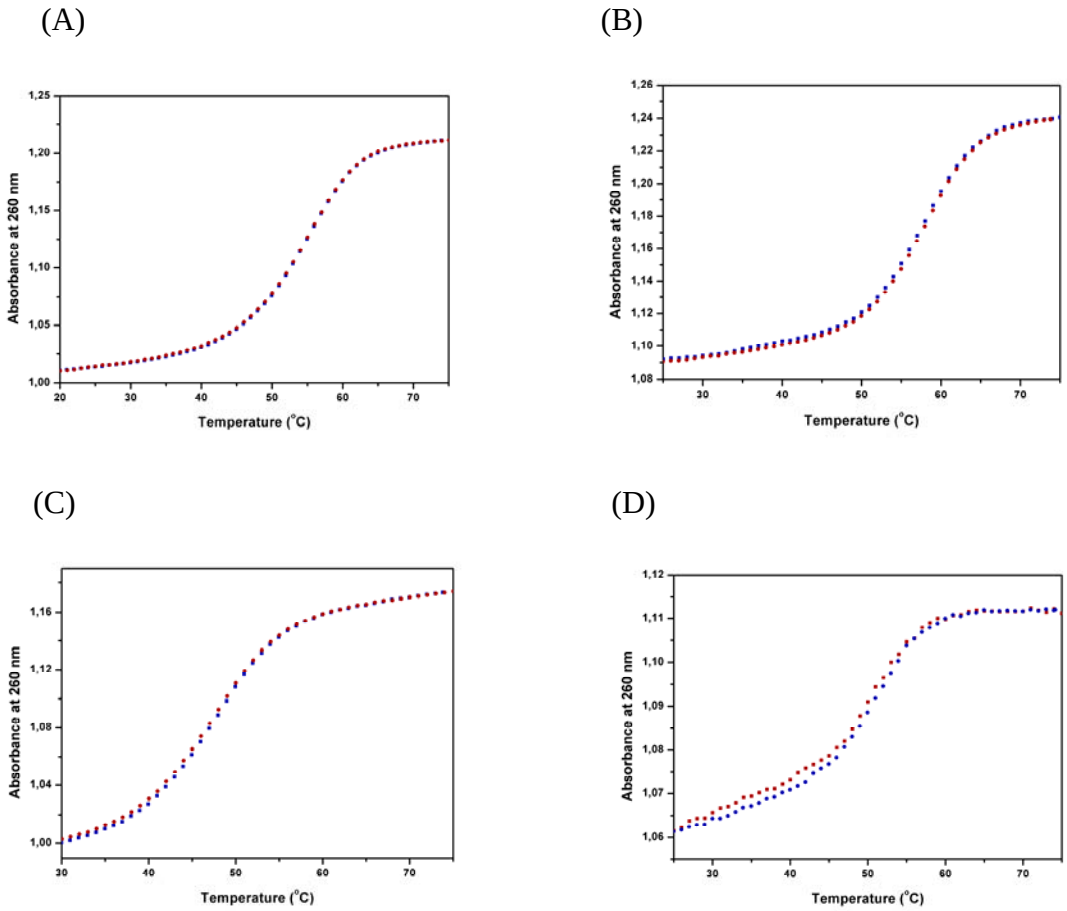


Figure S9. The melting profiles of the duplexes (A) **21 • 22**, (B) **20 • 22**, (C) **27 • 25** and (D) **29 • 18**. The curves indicated in red are heating profiles while the blue curves represents cooling profiles in all the graphs.

Figure S10. ^{1}H-NMR spectrum of toluoyl protected 4-methoxy-octa-(1,7)-diynyl-8-aza-7-deaza-2'-deoxyadenosine (7a)

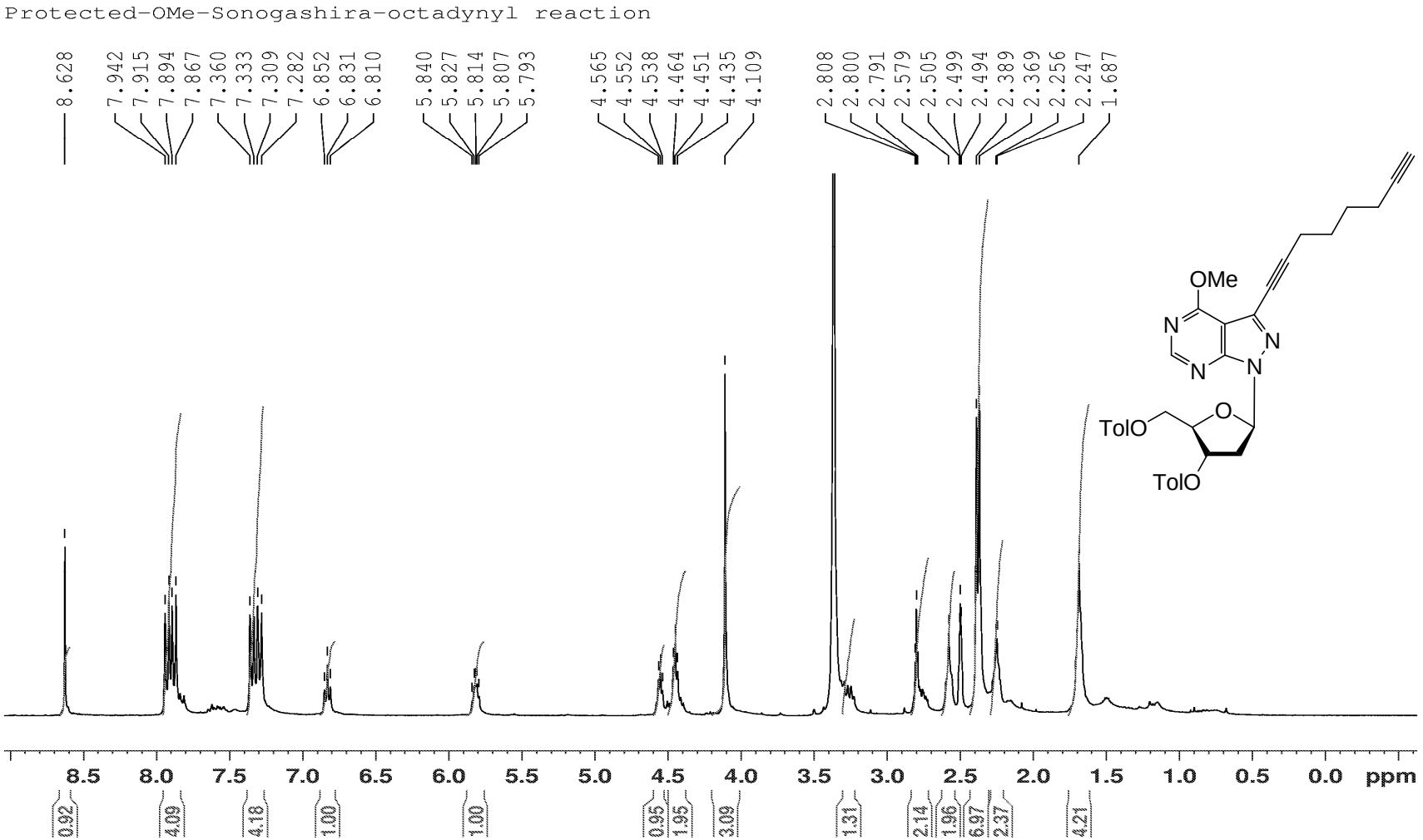


Figure S11. ^{13}C-NMR spectrum of toluoyl protected 4-methoxy-octa-(1,7)-diynyl-8-aza-7-deaza-2'-deoxyadenosine (7a)

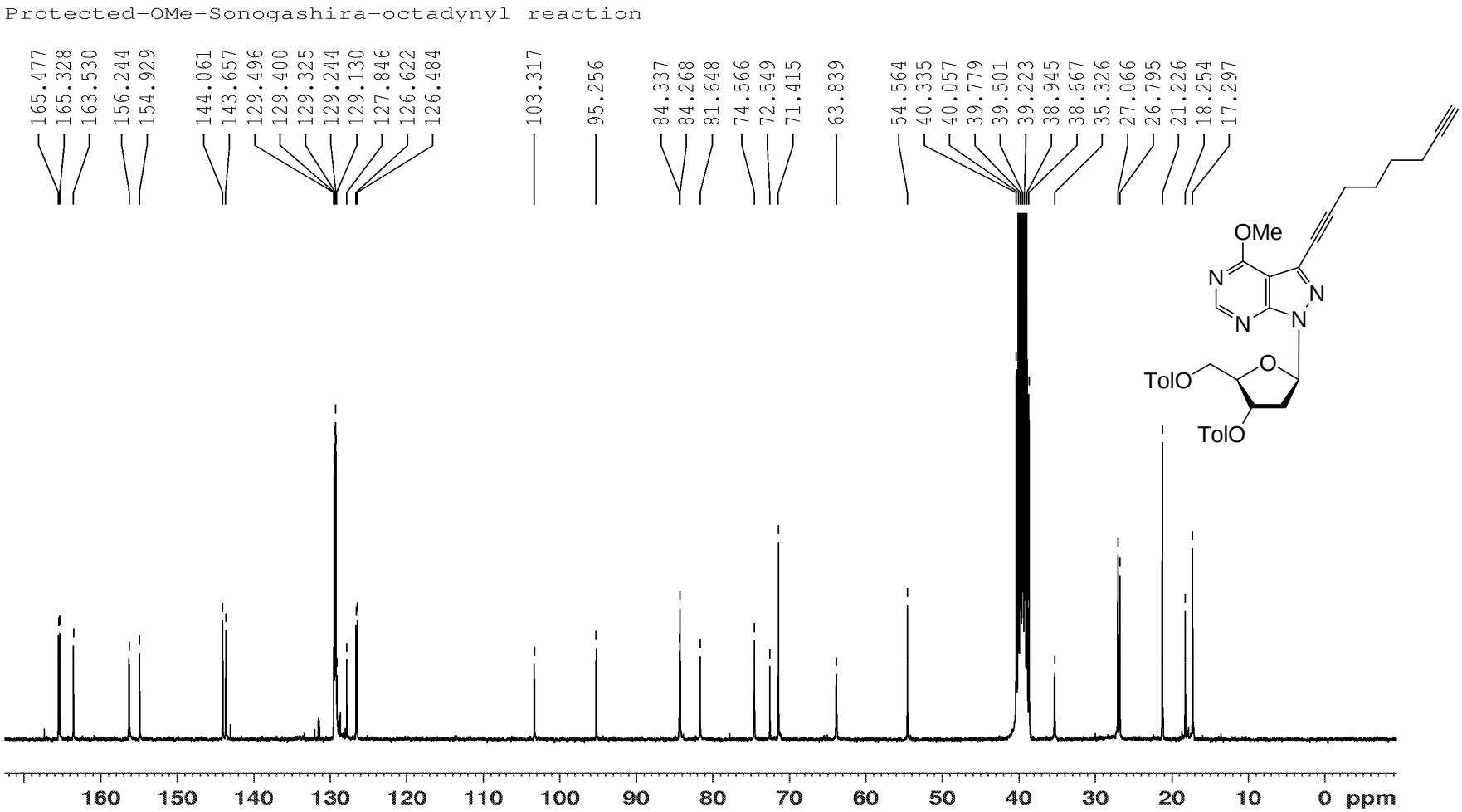


Figure S12. ^{1}H-NMR spectrum of 4-methoxy-octa-(1,7)-diynyl-8-aza-7-deaza-2'-deoxyadenosine (7b)

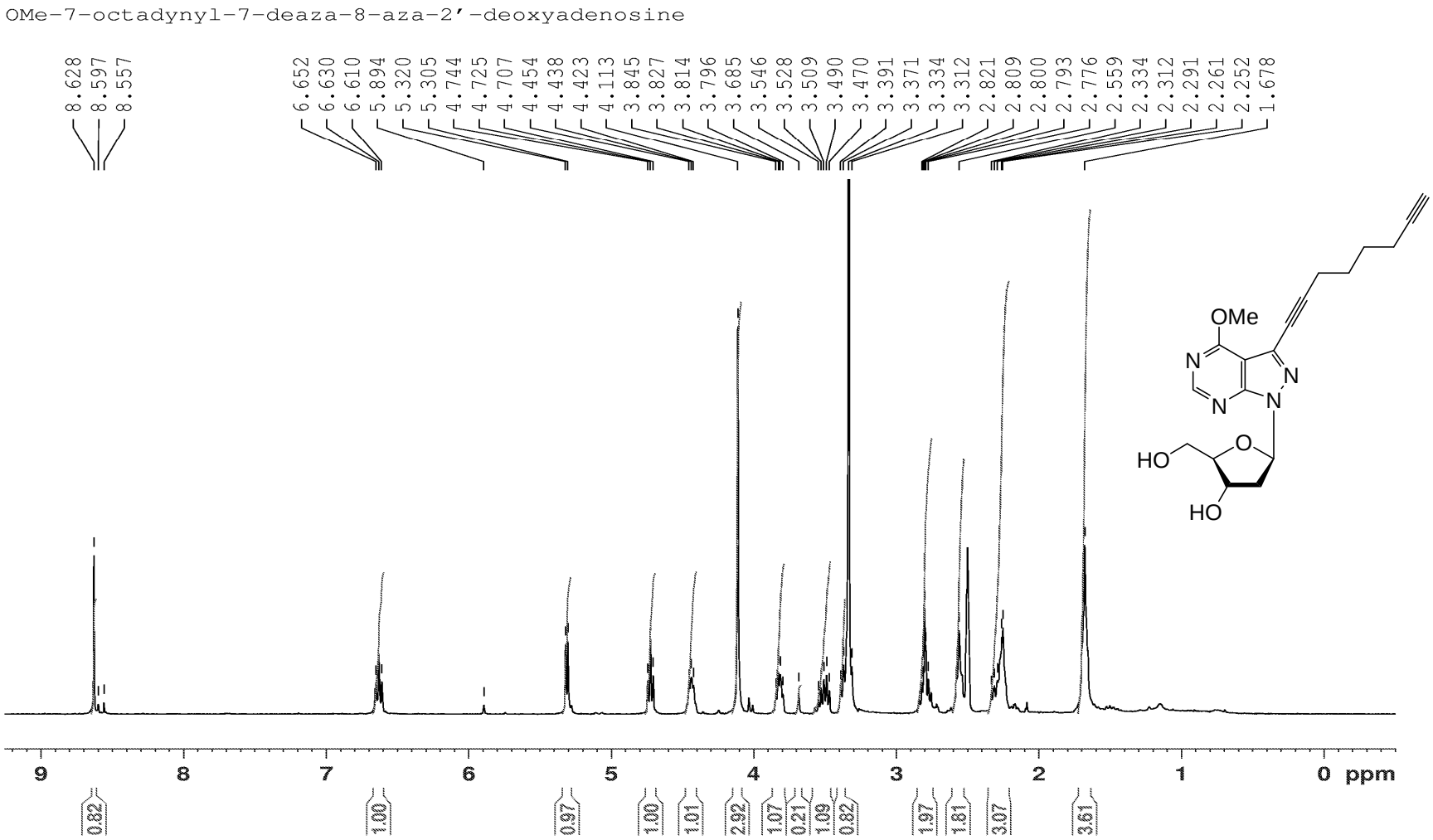


Figure S13. ^{13}C-NMR spectrum of 4-methoxy-octa-(1,7)-diynyl-8-aza-7-deaza-2'-deoxyadenosine (7b)

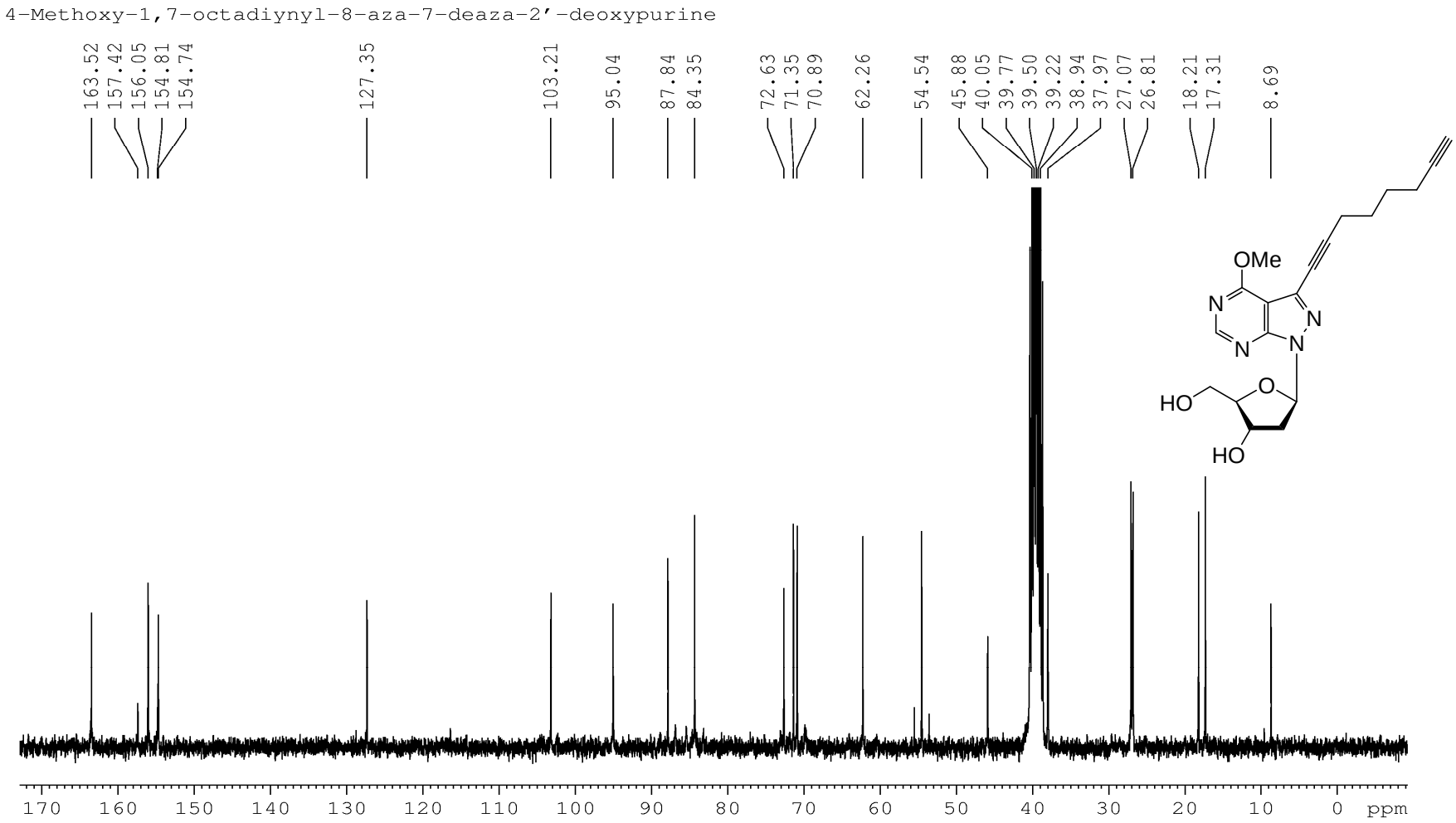


Figure S14. ^{1}H-NMR spectrum of 7-octa-(1,7)-diynyl-8-aza-7-deaza-2'-deoxyadenosine (1)

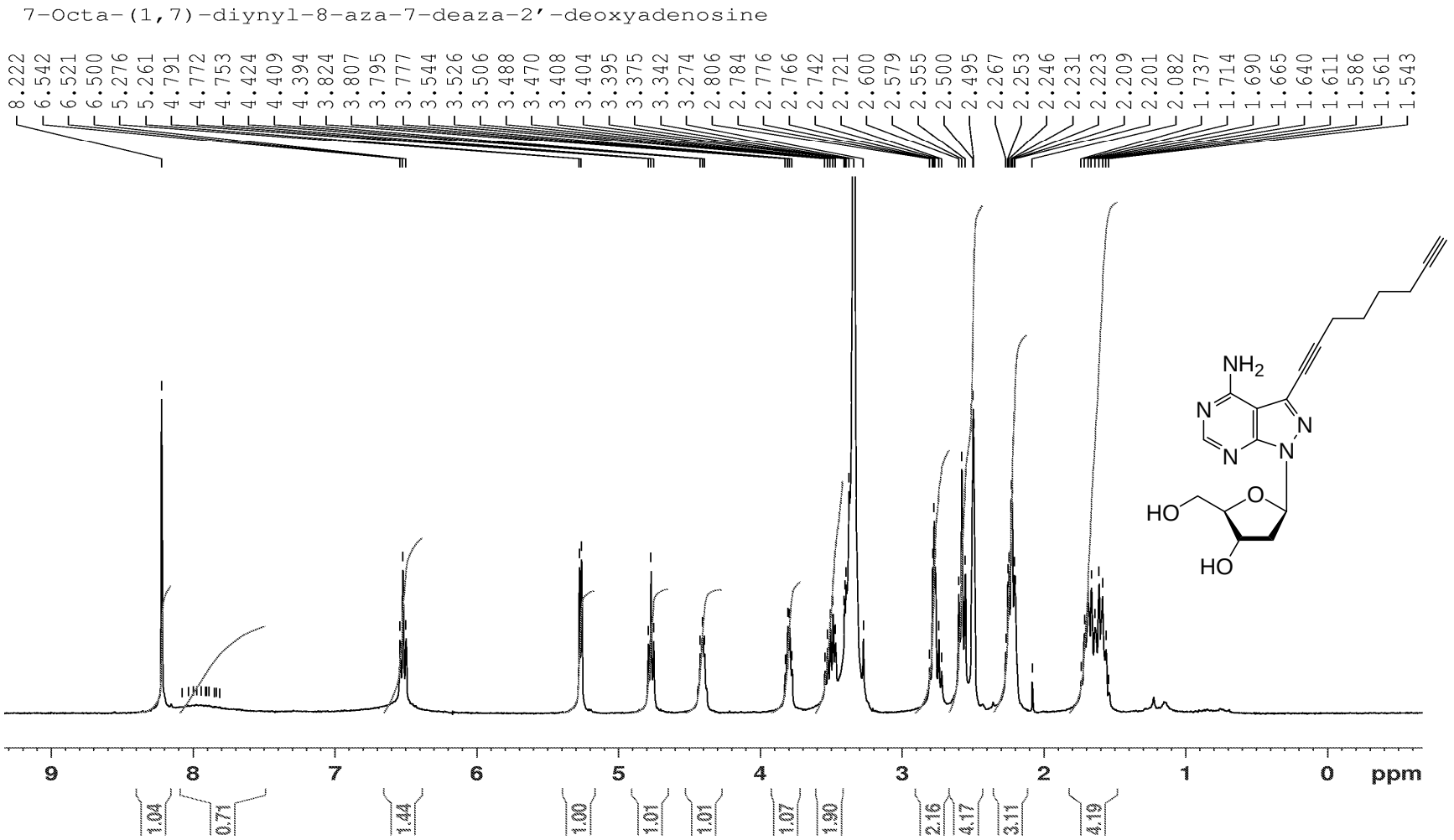


Figure S15. ^{13}C-NMR spectrum of 7-octa-(1,7)-diynyl-8-aza-7-deaza-2'-deoxyadenosine (1)

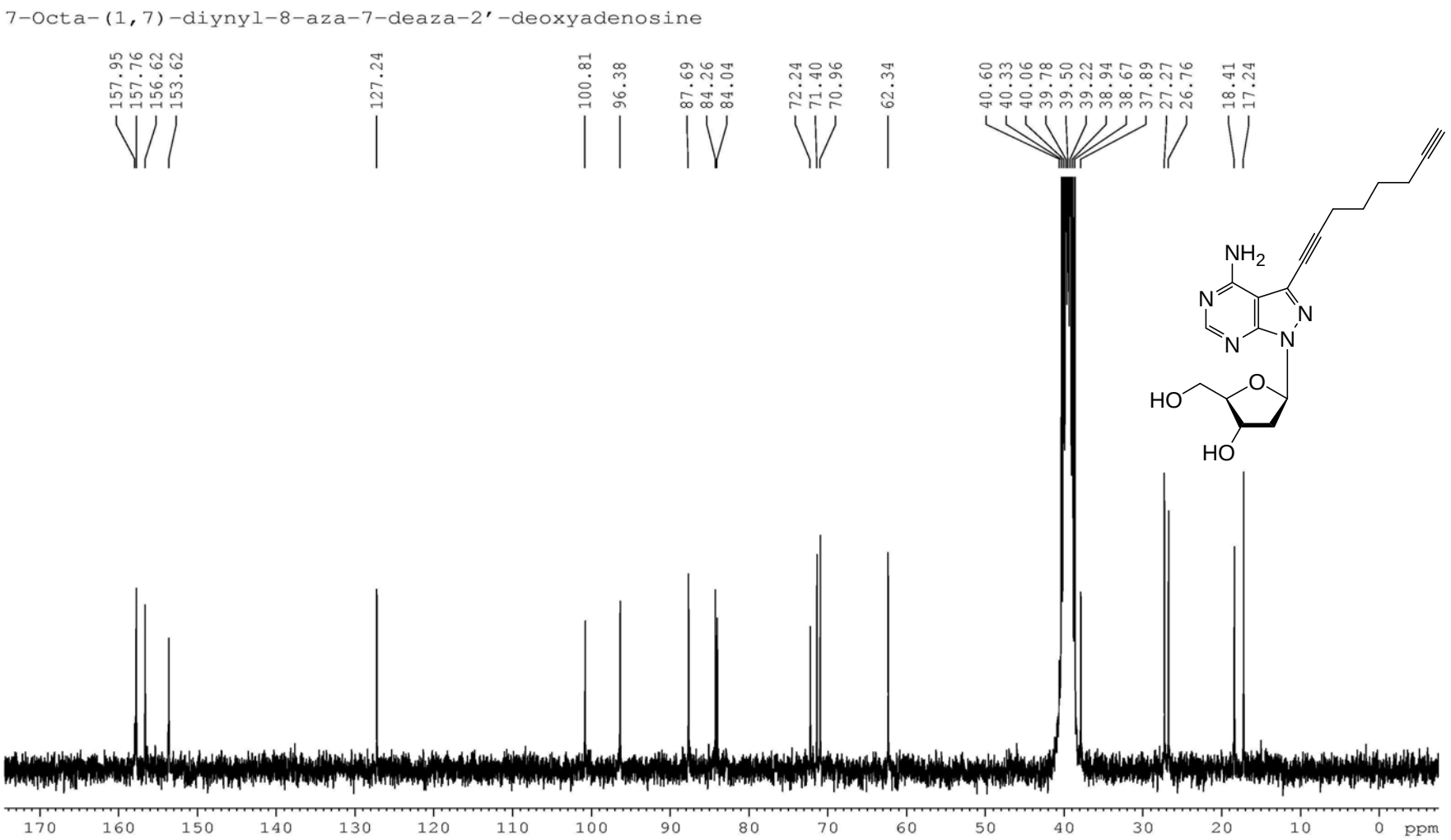


Figure S16. ^{1}H-NMR spectrum of formamidine protected 7-octa-(1,7)-diynyl-8-aza-7-deaza-2'-deoxyadenosine (9)

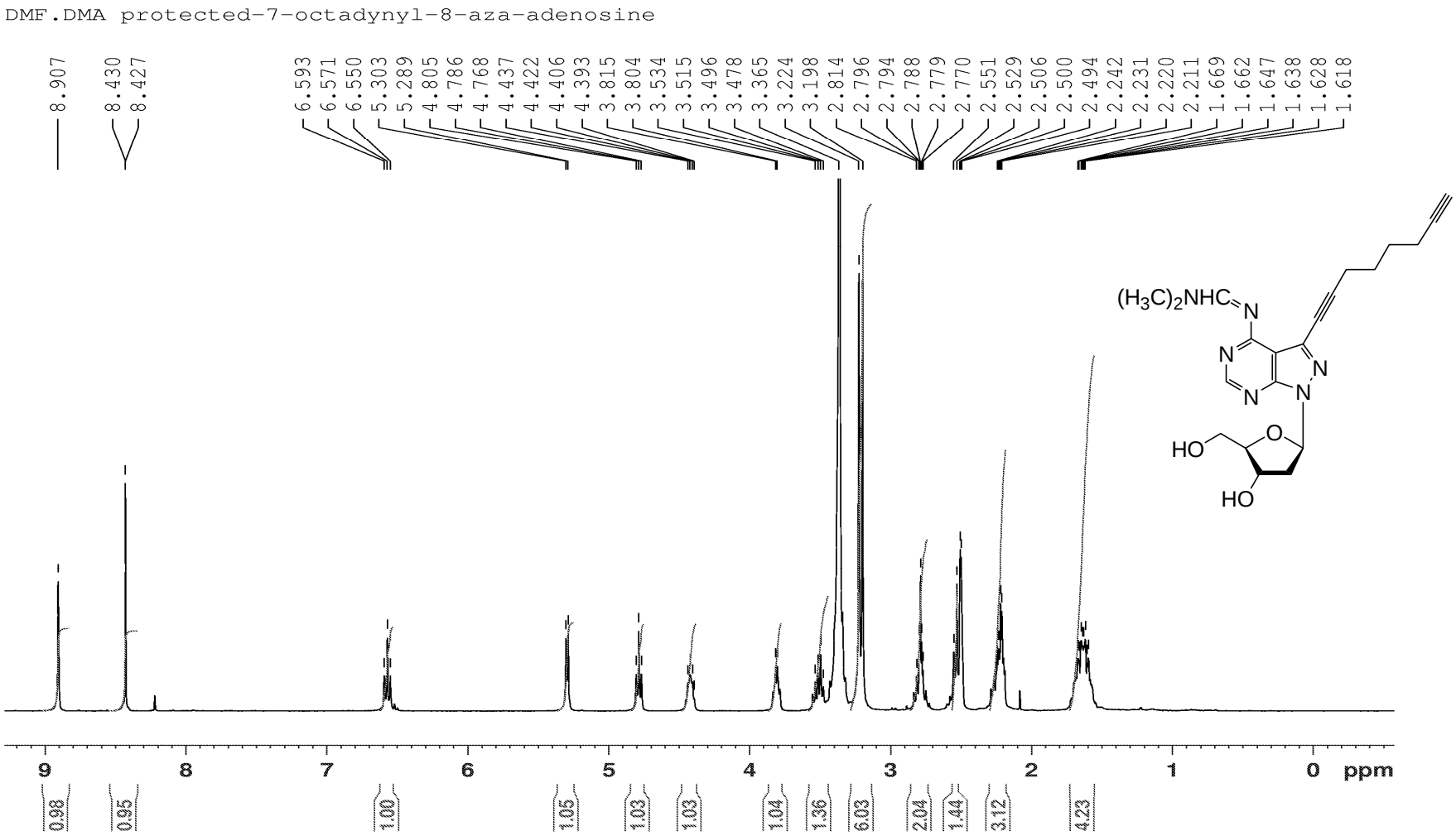


Figure S17. ^{13}C-NMR spectrum of formamidine protected 7-octa-(1,7)-diynyl-8-aza-7-deaza-2'-deoxyadenosine (9)

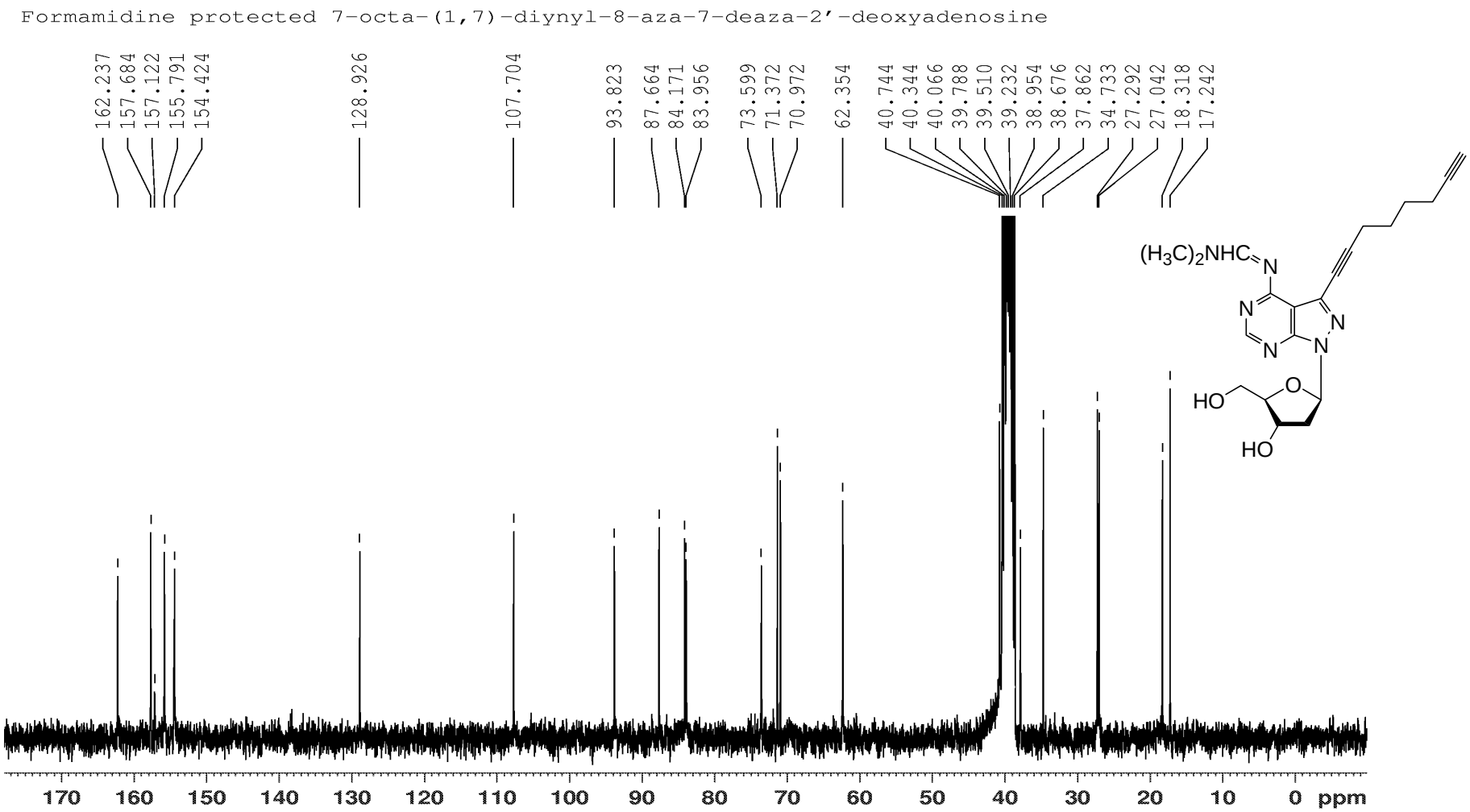


Figure S18. ^{1}H-NMR spectrum of 5'-*O*-DMT-formamidine protected-7-octa-(1,7)-diynyl-8-aza-7-deaza-2'-deoxyadenosine (10)

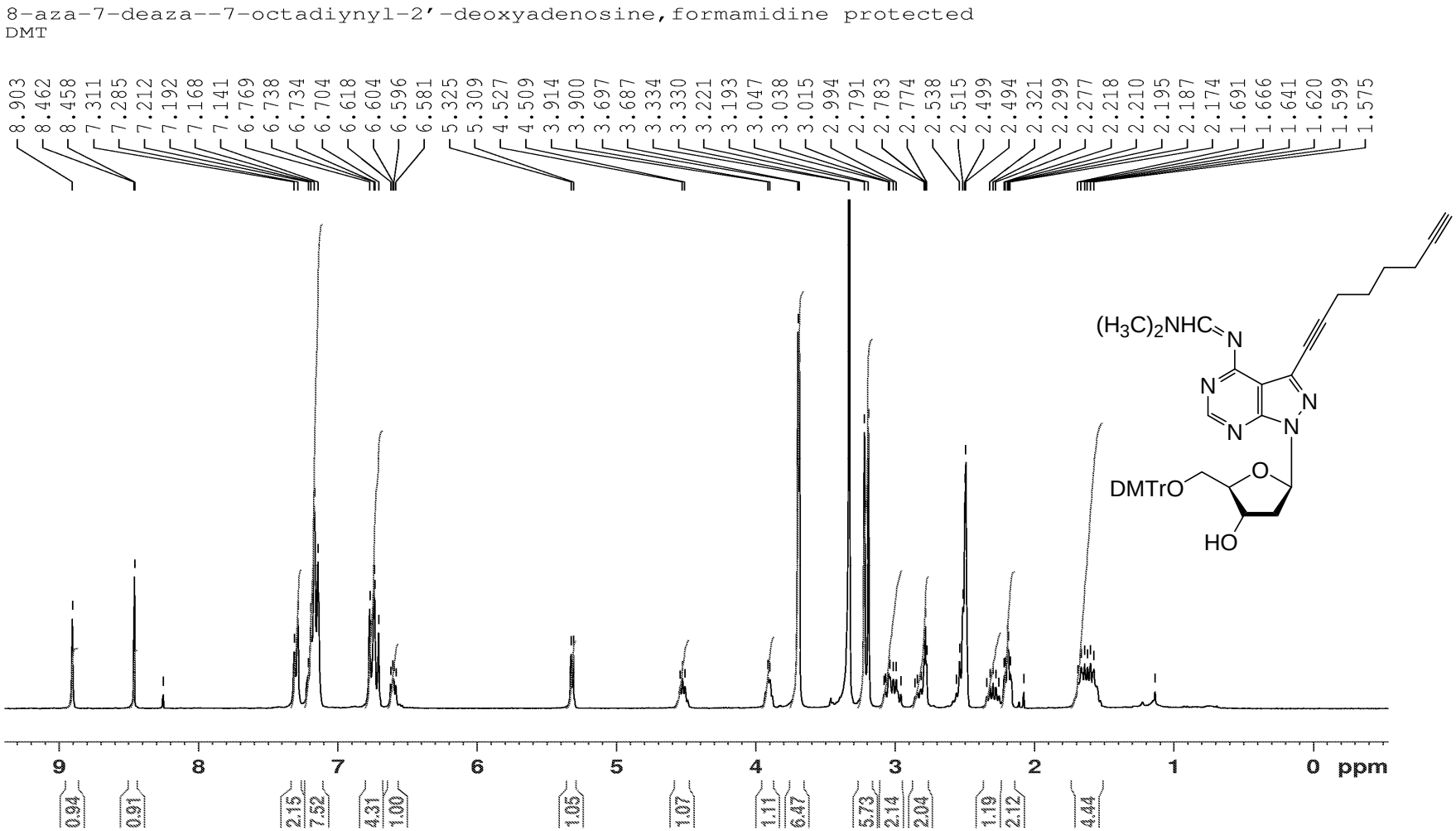


Figure S19. ^{13}C-NMR spectrum of 5'-*O*-DMT-formamidine protected-7-octa-(1,7)-diynyl-8-aza-7-deaza-2'-deoxyadenosine (10)

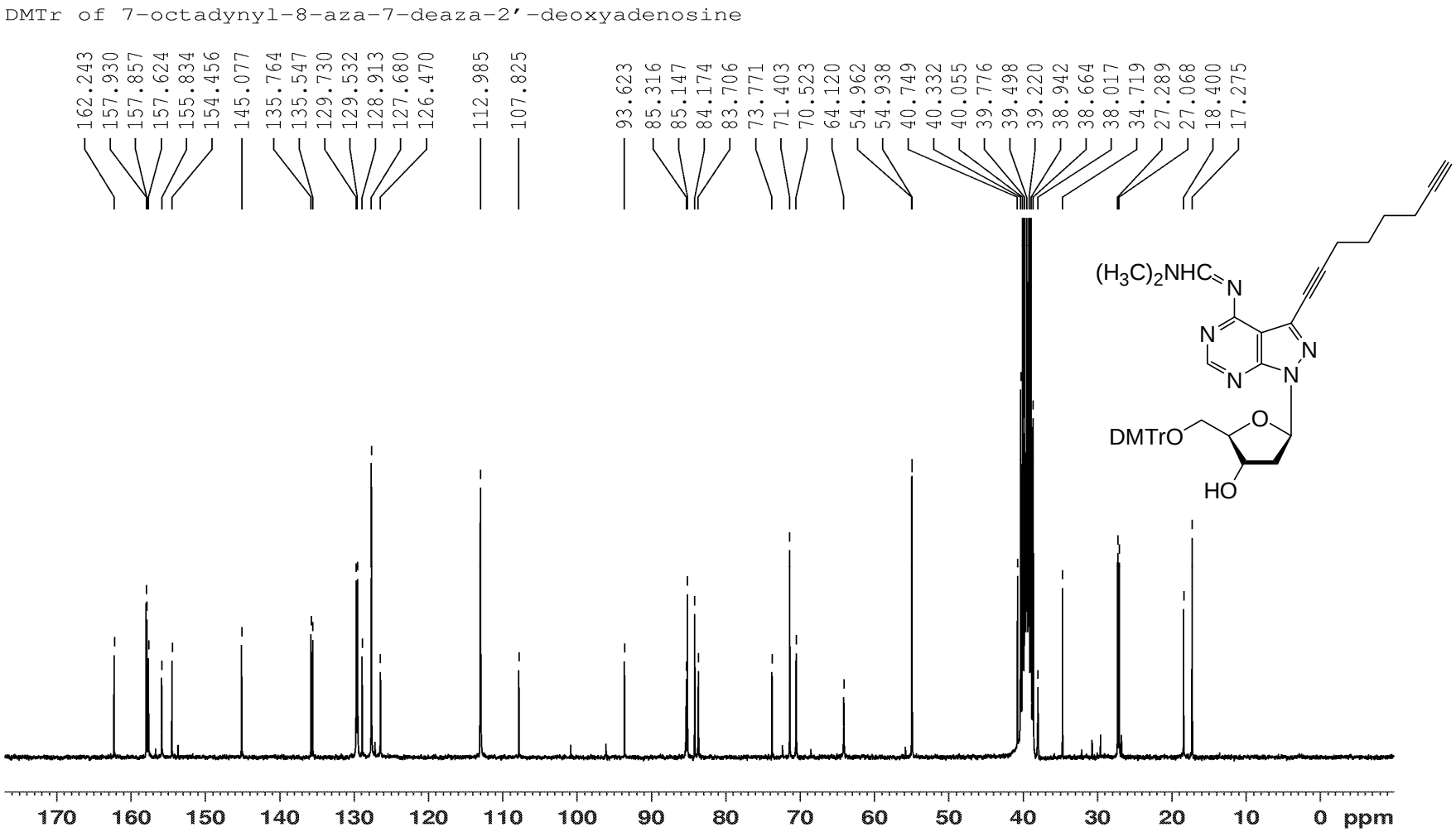


Figure S20. ^{1}H-NMR spectrum of click product of anthracene azide and 7-octa-(1,7)-diynyl-8-aza-7-deaza-2'-deoxyadenosine (12)

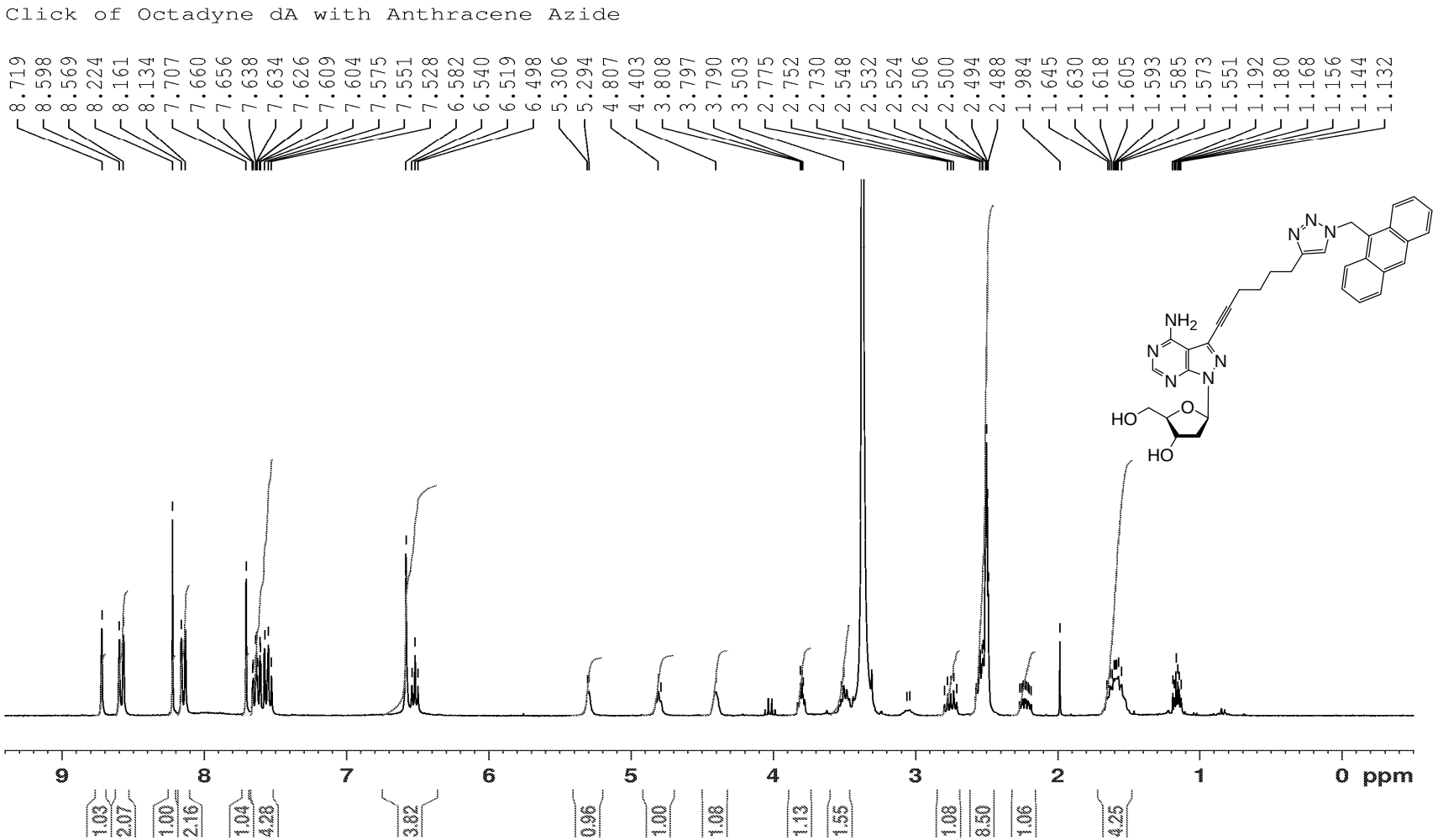


Figure S21. ^{13}C-NMR spectrum of click product of anthracene azide and 7-octa-(1,7)-diynyl-8-aza-7-deaza-2'-deoxyadenosine (12)

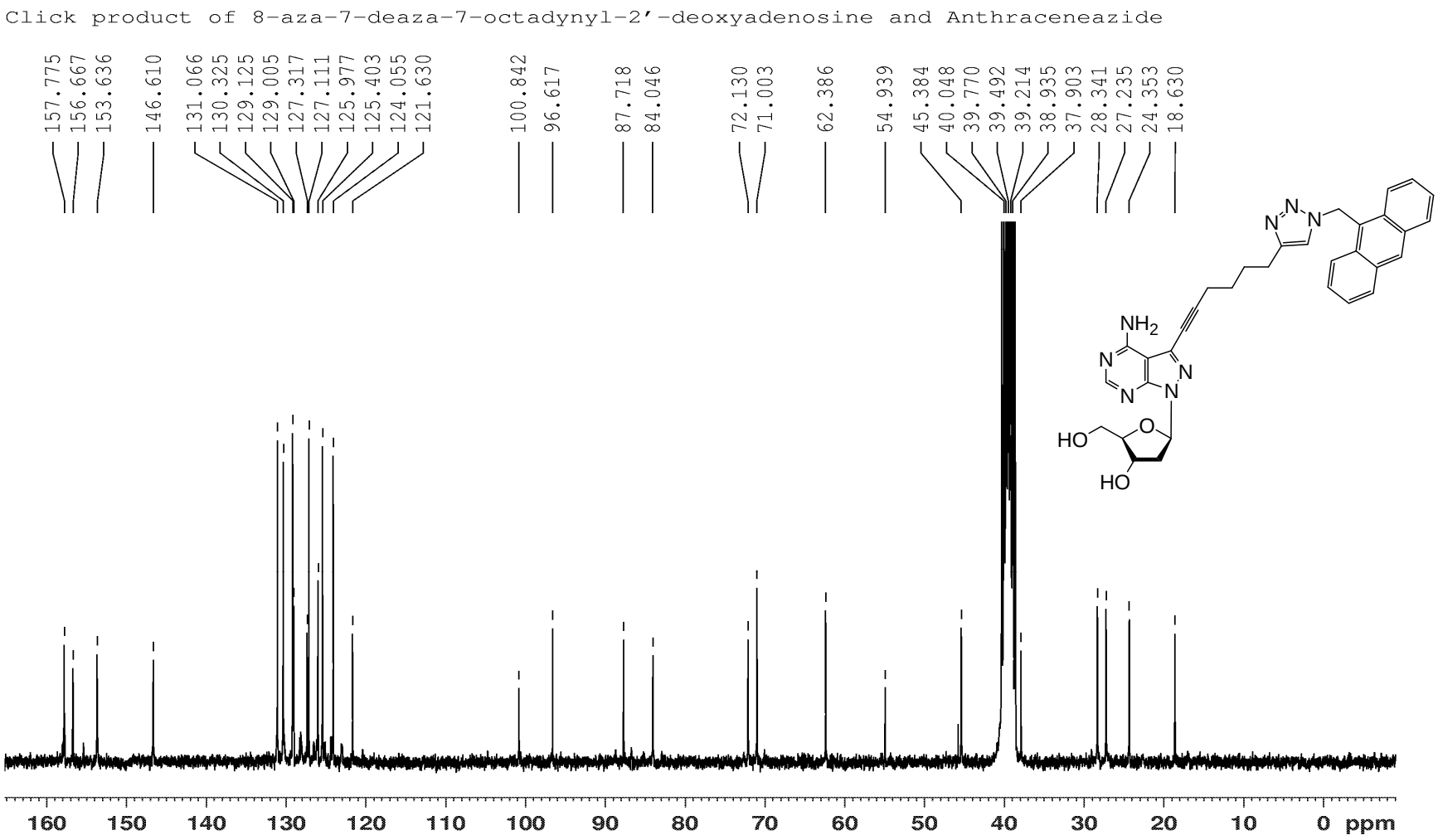


Figure S22. ^{1}H-NMR spectrum of click product of coumarin azide and 7-octa-(1,7)-diynyl-8-aza-7-deaza-2'-deoxyadenosine (13)

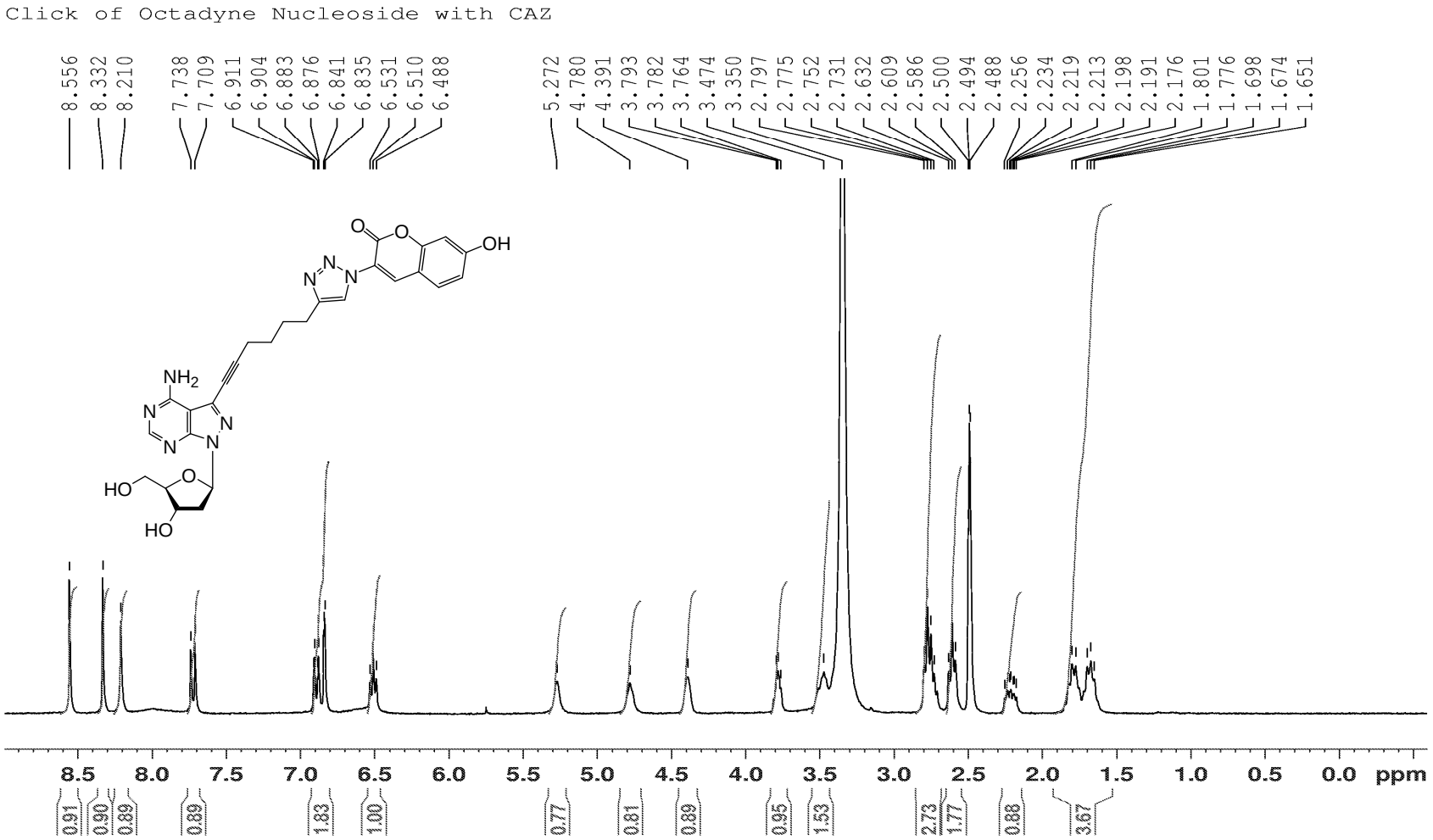


Figure S23. ^{13}C-NMR spectrum of click product of coumarin azide and 7-octa-(1,7)-diynyl-8-aza-7-deaza-2'-deoxyadenosine (13)

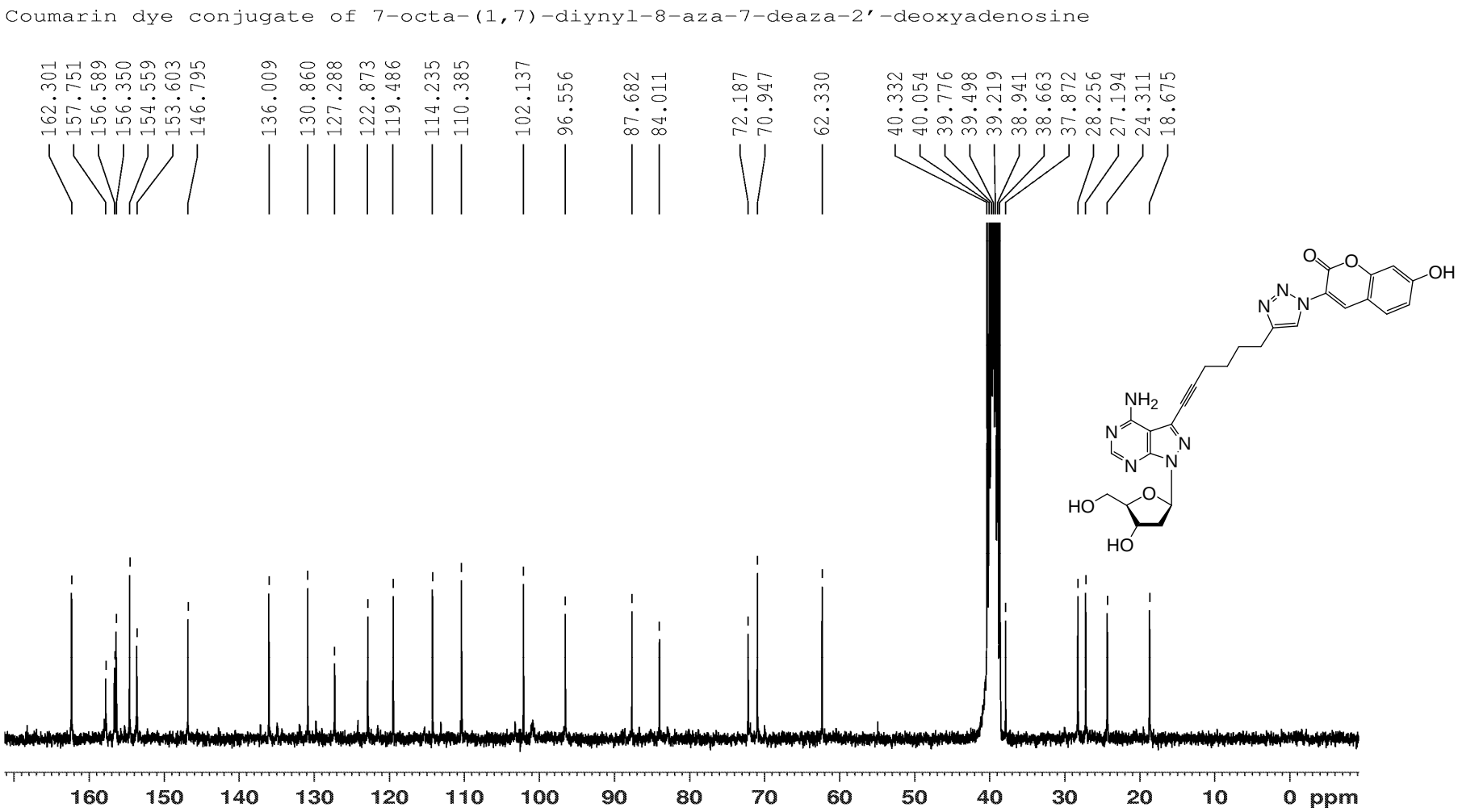


Figure S24. ^{1}H-NMR spectrum of click product of AZT and 7-octa-(1,7)-diynyl-8-aza-7-deaza-2'-deoxyadenosine (14)

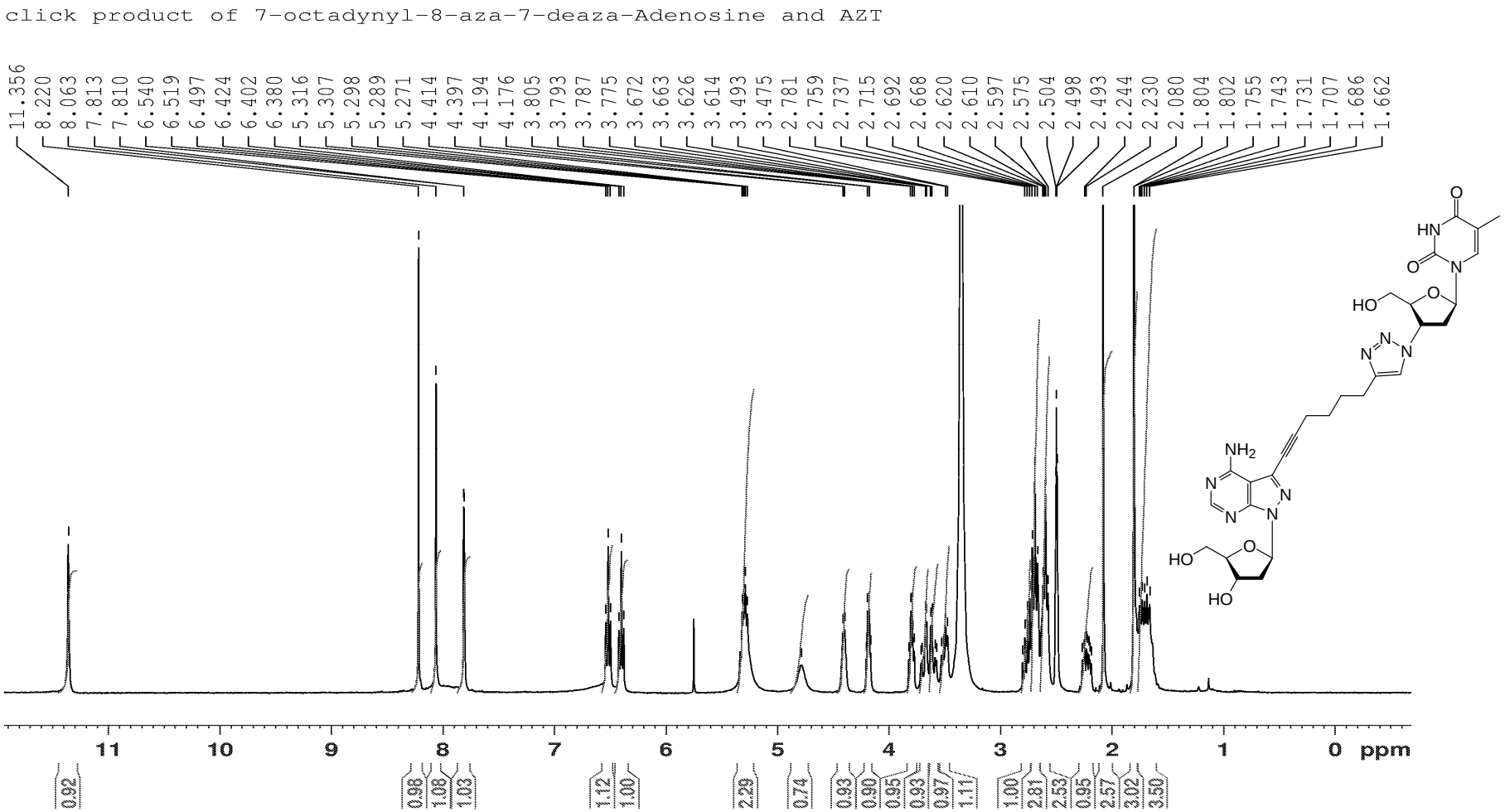


Figure S25. ^{13}C-NMR spectrum of click product of AZT and 7-octa-(1,7)-diynyl-8-aza-7-deaza-2'-deoxyadenosine (14)

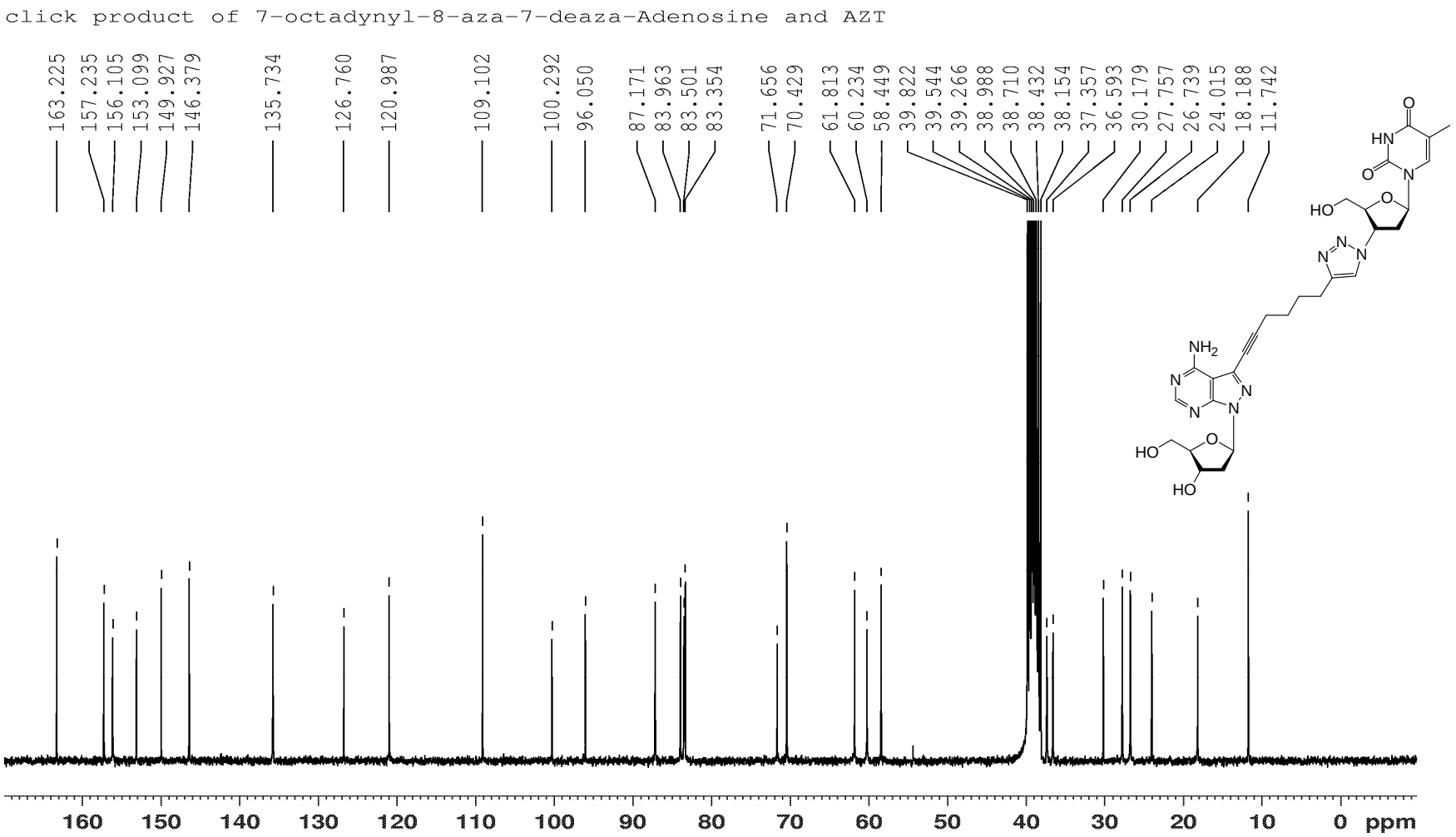


Figure S26. ^{1}H-NMR spectrum of click product of benzyl azide and 7-octa-(1,7)-diynyl-8-aza-7-deaza-2'-deoxyadenosine (15)

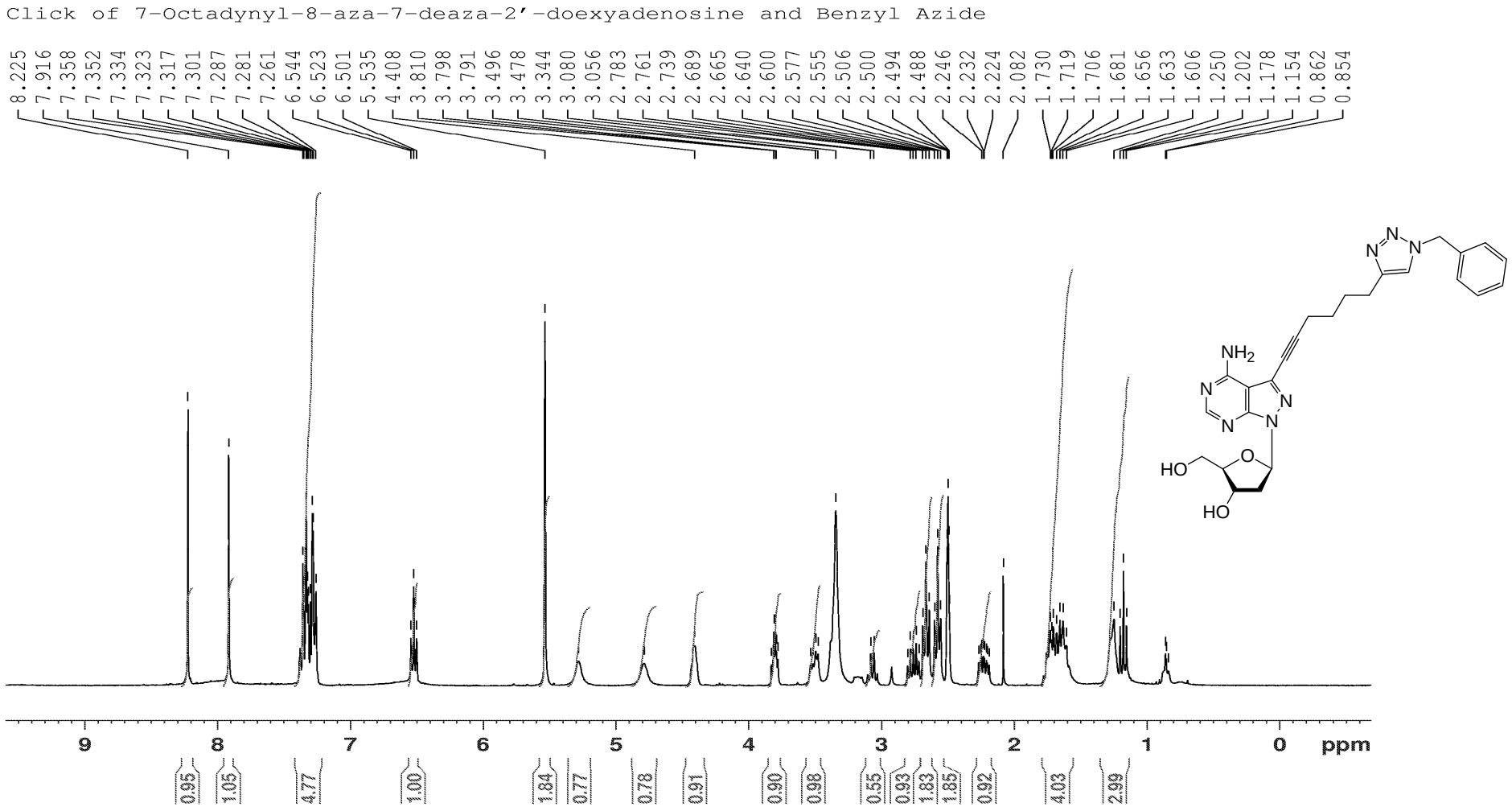


Figure S27. ^{13}C-NMR spectrum of click product of benzyl azide and 7-octa-(1,7)-diynyl-8-aza-7-deaza-2'-deoxyadenosine (15)

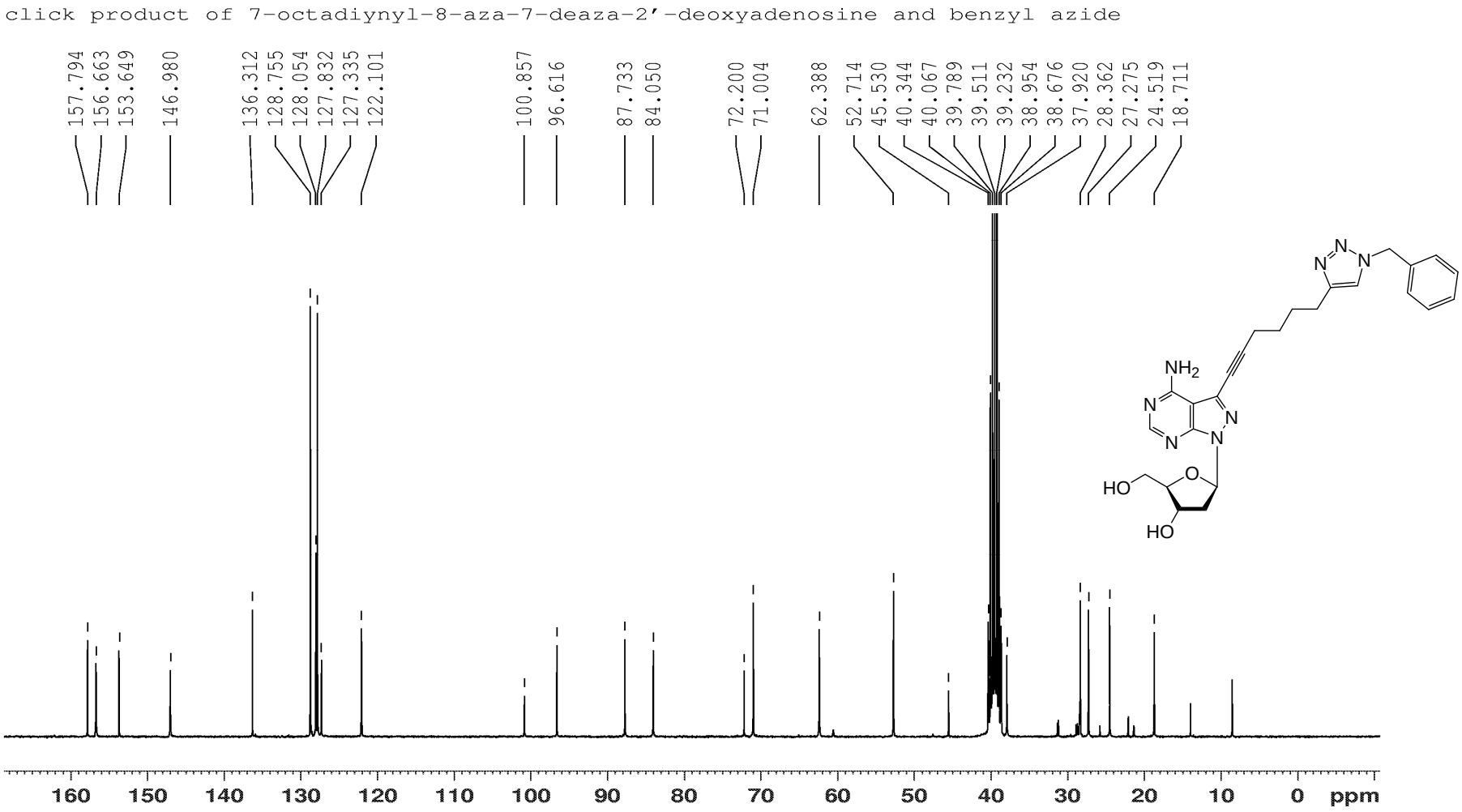


Figure S28. ^{1}H-NMR spectrum of click product of anthracene azide and 7-octa-(1,7)-diynyl-7-deaza-2'-deoxyadenosine (16)

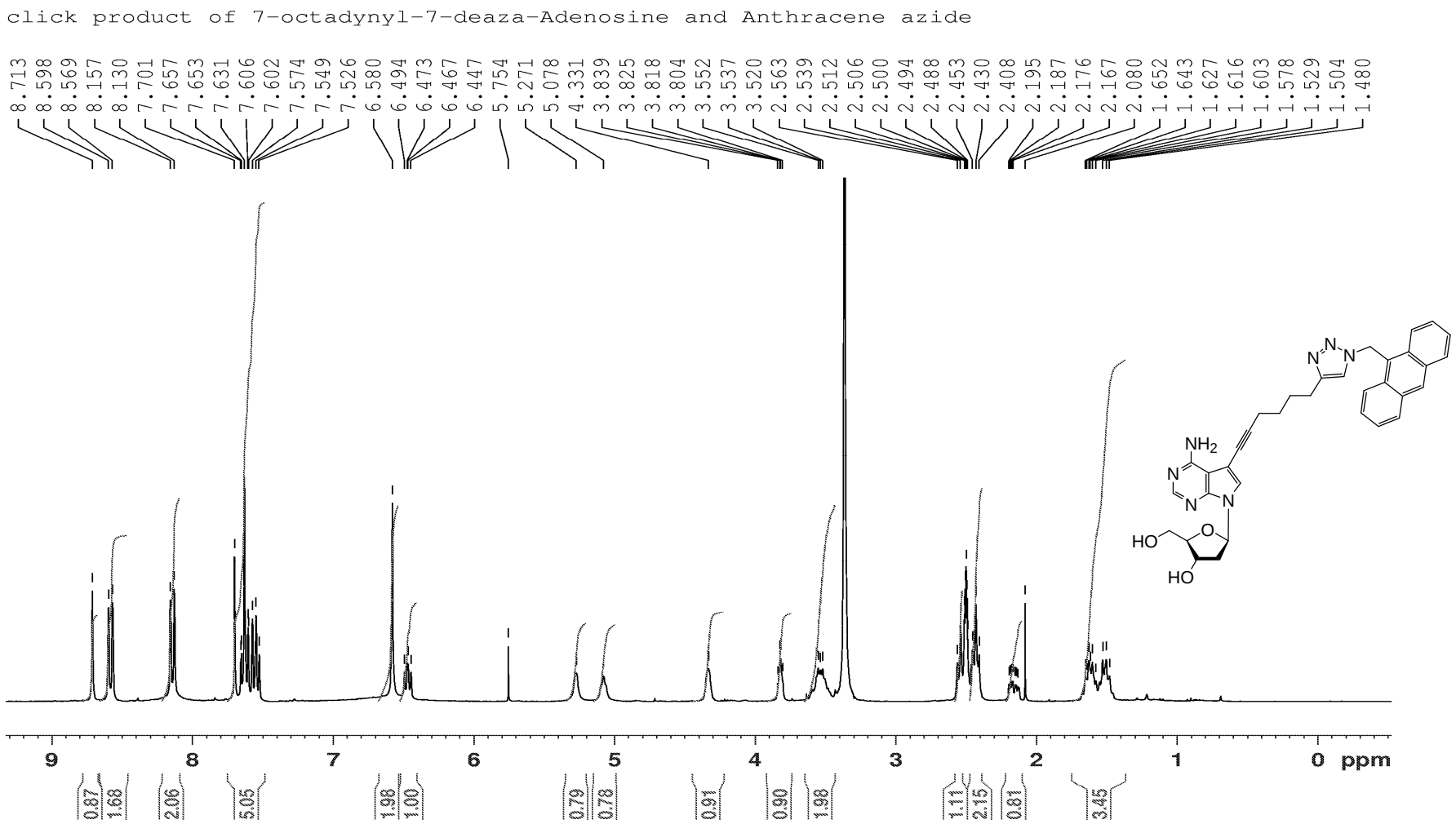


Figure S29. ^{13}C-NMR spectrum of click product of anthracene azide and 7-octa-(1,7)-diynyl-7-deaza-2'-deoxyadenosine (16)

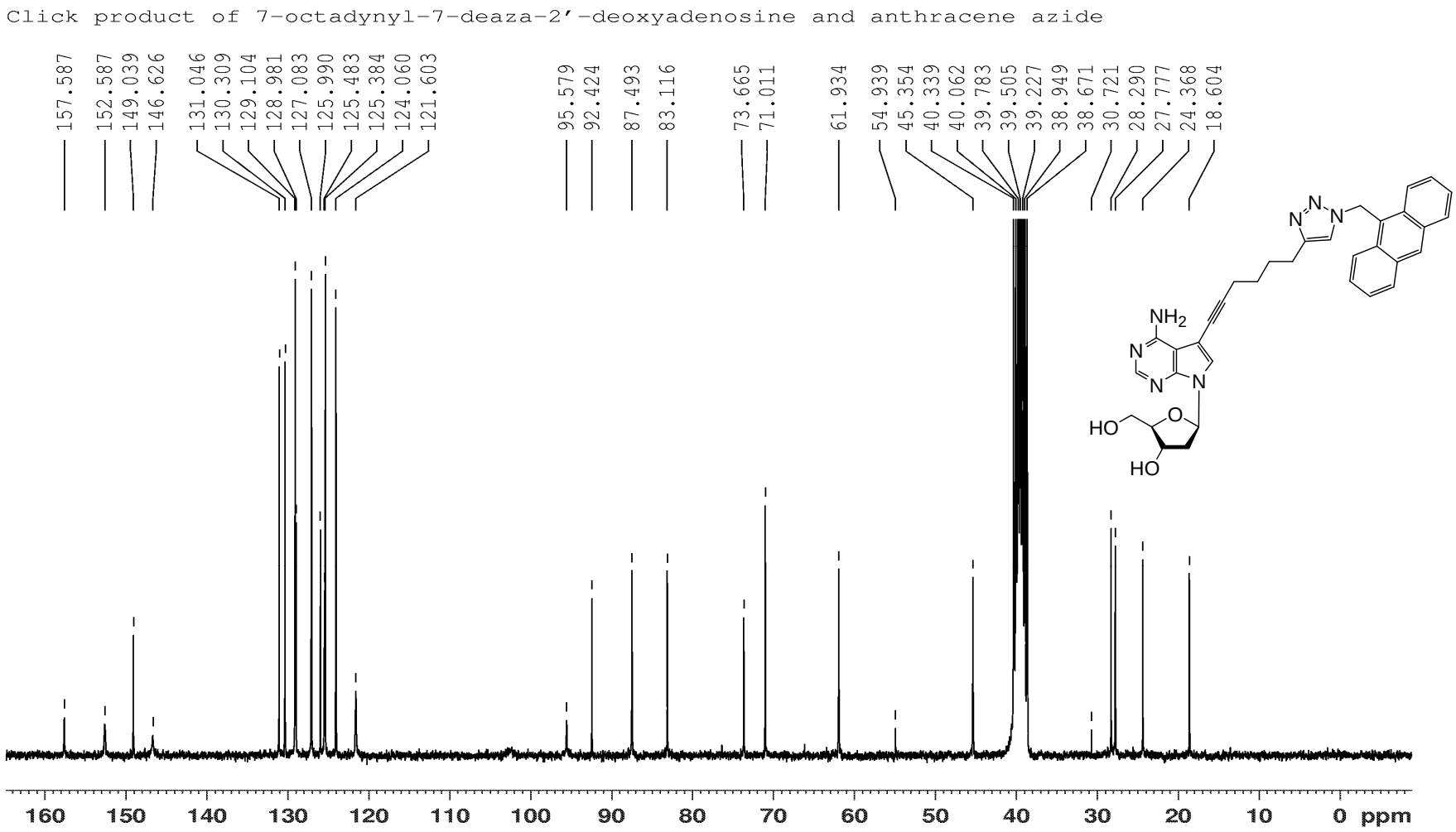


Figure S30. ^{1}H-NMR spectrum of 1-anthracen-9-ylmethyl-4-hexyl-1*H*-[1,2,3]triazole (32)

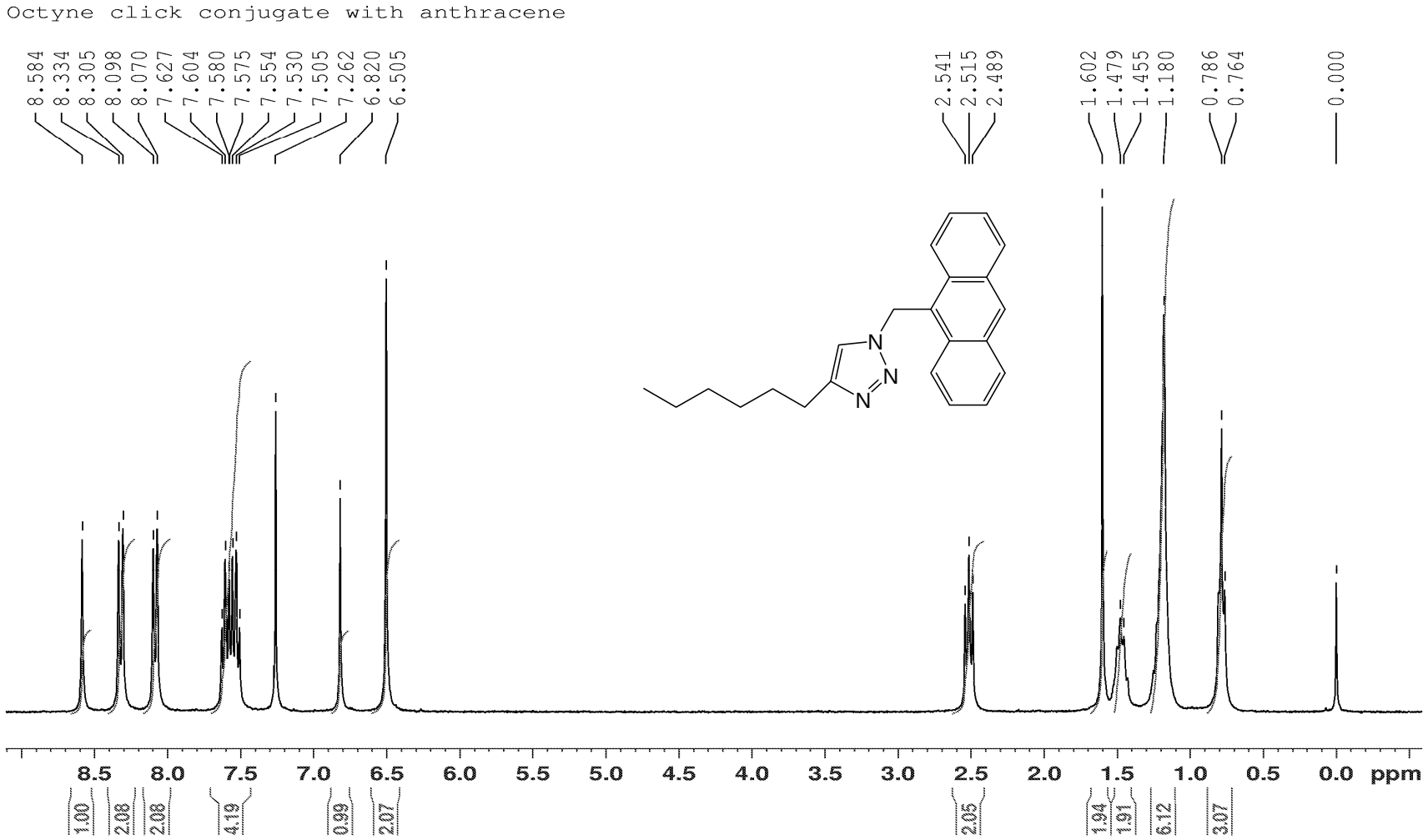
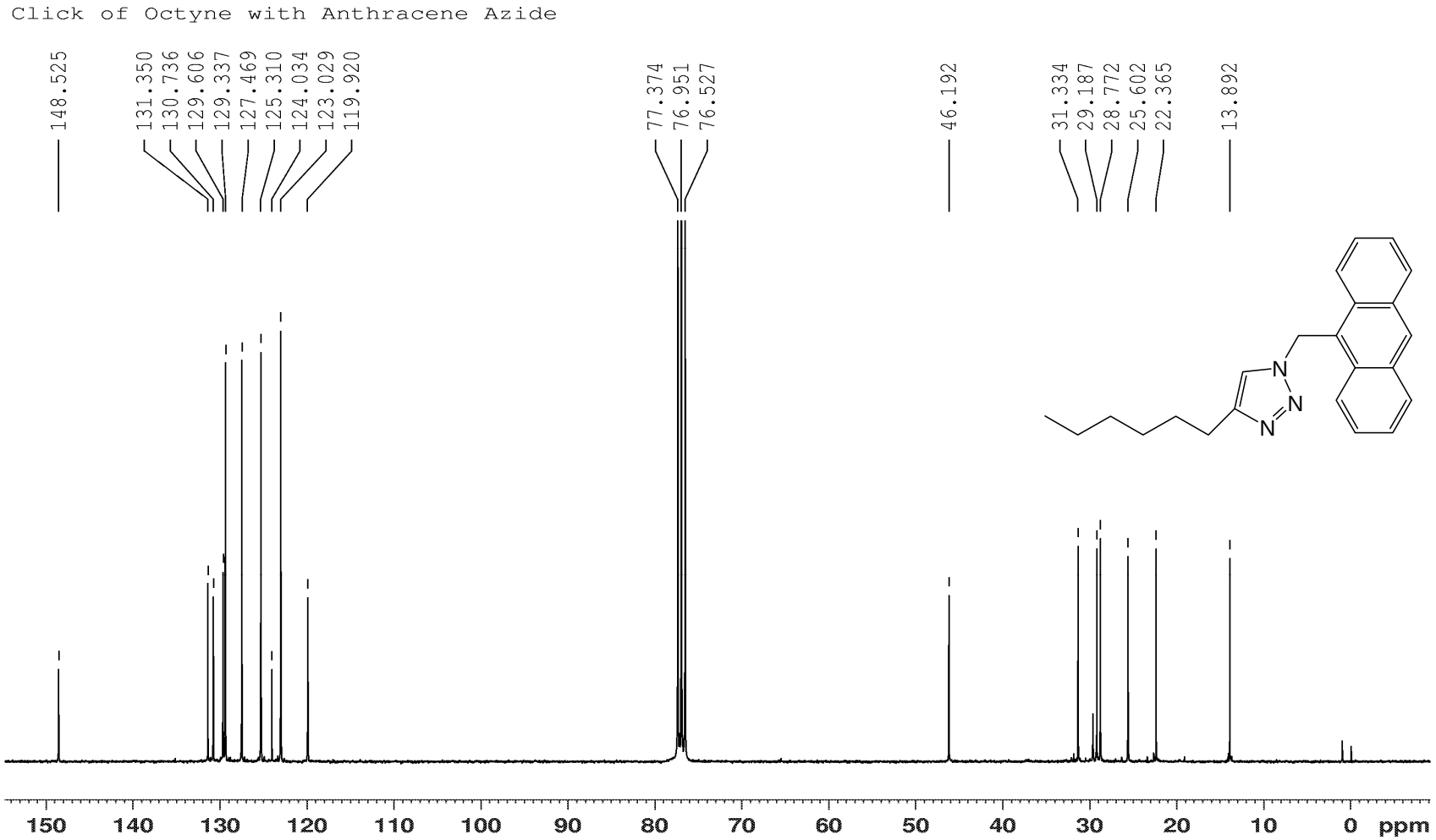


Figure S31. ^{13}C-NMR spectrum of 1-anthracen-9-ylmethyl-4-hexyl-1*H*-[1,2,3]triazole (32)



Versatile Phosphoramidation Reactions for Nucleic Acid Conjugations with Peptides, Proteins, Chromophores, and Biotin Derivatives

Tzu-Pin Wang,*[,†] Yi-Jang Chiou,[†] Yi Chen,[†] Eng-Chi Wang,[†] Long-Chih Hwang,[†] Bing-Hung Chen,[‡] Yen-Hsu Chen,[§] and Chun-Han Ko[||] Department of Medicinal and Applied Chemistry, Department of Biotechnology, Graduate Institute of Medicine, and Department of Internal Medicine, Kaohsiung Medical University, Kaohsiung, 80708, Taiwan, and School of Forestry and Resource Conservation, National Taiwan University, Taipei, 10617, Taiwan Received March 25, 2010; Revised Manuscript Received July 9, 2010

Chemical conjugations of nucleic acids with macromolecules or small molecules are common approaches to study nucleic acids in chemistry and biology and to exploit nucleic acids for medical applications. The conjugation of nucleic acids such as oligonucleotides with peptides is especially useful to circumvent cell delivery and specificity problems of oligonucleotides as therapeutic agents. However, current approaches are limited and inefficient in their ability to afford peptide−oligonucleotide conjugates (POCs). Here, we report an effective and reproducible approach to prepare POCs and other nucleic acid conjugates based on a newly developed nucleic acid phosphoramidation method. The development of a new nucleic acid phosphoramidation reaction was achieved by our successful synthesis of a novel amine-containing biotin derivative used to systematically optimize the reactions. The improved phosphoramidation reactions dramatically increased yields of nucleic acid−biotin conjugates up to 80% after 3 h reaction. Any nucleic acids with a terminal phosphate group are suitable reactants in phosphoramidation reactions to conjugate with amine-containing molecules such as biotin and fluorescein derivatives, proteins, and, most importantly, peptides to enable the synthesis of POCs for therapeutic applications. Polymerase chain reactions (PCRs) to study incorporation of biotin or fluorescein-tagged DNA primers into the reaction products demonstrated that appropriate controls of nucleic acid phosphoramidation reactions incur minimum adverse effects on inherited base-pairing characteristics of nucleotides in nucleic acids. The phosphoramidation approach preserves the integrity of hybridization specificity in nucleic acids when preparing POCs. By retaining integrity of the nucleic acids, their effectiveness as therapeutic reagents for gene silencing, gene therapy, and RNA interference is ensured. The potential for POC use was demonstrated by two-step phosphoramidation reactions to successfully synthesize nucleic acid−tetraglycine conjugates. In addition, phosphoramidation reactions provided a facile approach to prepare nucleic acid−BSA conjugates with good yields. In summary, the new approach to phosphoramidation reactions offers a universal method to prepare POCs and other nucleic acid conjugates with high yields in aqueous solutions. The methods can be easily adapted to typical chemistry or biology laboratory setups which will expedite the applications of POCs for basic research and medicine.

INTRODUCTION

Covalent modifications of nucleic acids have been used to explore the diverse functions of nucleic acids and to characterize their intrinsic biochemical properties in biological systems. Continuous development of covalent conjugation methods for nucleic acids further facilitates applications of nucleic acids as research tools for chemical and biomedical studies, improves potency, and promotes specificity of nucleic acids as therapeutic reagents in medicine. For example, the combination of covalently modified nucleic acids and in vitro selection methods has contributed to the discovery of novel catalytic nucleic acids such as ribozymes (catalytic RNA) able to perform the Diels−Alder cycloaddition (*1*), the Michael addition (*2*), the aldol condensation (*3*), NAD^+-dependent alcohol dehydrogenation (*4*), and NADH-dependent aldehyde hydrogenation (*5*). Conjugation of fluorophores with nucleic acids has provided sensitive detection methods to study tertiary structure transitions relevant to RNA folding (*6*−*9*) and ribozyme catalysis (*7*, *10*, *11*), genomics (*12*, *13*), and DNA microarray preparation (*14*). Finally, oligonucleotides conjugated with peptides to afford peptide−oligonucleotide conjugates (POCs) hold promise as an effective therapeutic reagent to treat viral infections and genetic diseases (*15*−*17*). Applications of POCs in basic and clinical research have produced nucleic acids with improved biological stability (*18*), cellular uptake efficiency (*18*, *19*), and in vivo cell-specific targeting (*20*).

Preparation of POCs is essential for therapeutic applications of nucleic acids such as oligonucleotides. The direct use of oligonucleotides in medicine generally falls short of disease treatment expectations due to poor cell specificity and uptake of nucleic acids, and inaccessibility of nucleic acids to cell nuclei (*15*−*17*). The conjugation of oligonucleotides with peptides is thus the most common approach to circumvent cell delivery and specificity problems of oligonucleotides (*15*−*17*). However, methods currently available to prepare POCs are inefficient and inconvenient for typical research laboratories. The difficulties experienced when preparing desired effective POCs restrict the broad applications of POCs in achieving their much-needed medical applications.

POCs are generally prepared by post solid-phase synthesis to couple peptides with oligonucleotides (fragment coupling

* Corresponding author. E-mail: tzupinw@cc.kmu.edu.tw. Contact address: Department of Medicinal and Applied Chemistry, Kaohsiung Medical University, Kaohsiung, 80708, Taiwan, Tel: +886-07-312-1101, ext. 2756, Fax: +886-07-312-5339.

[†] Department of Medicinal and Applied Chemistry, Kaohsiung Medical University.

[‡] Department of Biotechnology, Kaohsiung Medical University.

[§] Graduate Institute of Medicine and Department of Internal Medicine, Kaohsiung Medical University.

[||] National Taiwan University.

10.1021/bc1001505 © 2010 American Chemical Society
Published on Web 08/06/2010

strategy) or stepwise solid-phase synthesis (online solid-phase synthesis) (*15*−*17*). POC preparation is generally more feasible using fragment coupling strategy to avoid chemical intolerance between peptides and oligonucleotides during standard solid-phase synthesis (*15, 16*). The generic fragment coupling strategy separately synthesizes peptides and oligonucleotides by standard solid-phase synthesis protocols, and then, both are covalently linked together post solid-phase synthesis. There are limited reactions available for POC formation because peptides primarily use unstable phosphodiester linkages when conjugating to 5′- or 3′-termini or ester linkages when linking to 2′-positions of riboses in oligonucleotides (*17*). Diverse and stable chemical linkages between peptides and oligonucleotides can be attained only if nonconventional nucleotides are used during solid-phase synthesis of oligonucleotides in order to introduce additional functionalities. The need to incorporate nonconventional nucleotides into oligonucleotides increases the cost of oligonucleotide solid-phase synthesis and deters current use of POCs. The development of a facile approach to use hydroxyl or phosphate groups in standard oligonucleotides to afford stable POCs with high purity and yields is highly desirable.

An ideal method to prepare POCs is nucleic acid phosphoramidation which offers the advantage of providing a stable phosphoramidate bond for conjugations between peptides and oligonucleotides. Stability of the phosphoramidate linkage has long been recognized and extensively used to acquire POCs by solid-phase synthesis (*17*). The methodology and applications of nucleic acid phosphoramidation in aqueous solutions were previously studied by Orgel's lab (*21*). They exploited 1-ethyl-3-[3-dimethylaminopropyl]carbodiimide (EDC) activation to transiently generate reactive phosphorimidazolide intermediates of nucleotides, followed by the coupling reaction with a nucleophile at rt for 24 h to result in oligonucleotide conjugates with maximum yields of 50% (*21*). The concept of phosphoramidation reactions for nucleic acid conjugations is analogous to the effective amidation reaction achieved by the intermediate step to form isolatable reactive *N*-hydroxysuccinimide (NHS) esters of carboxylic acids (*22*). The aqueous-phase phosphoramidation reaction, however, has received little attention and failed to gain popularity as a standard method for nucleic acid conjugation. Failure to gain support was likely due to cumbersome and time-consuming procedures and low yields. A later report of an aqueous-phase phosphoramidation method claimed to have quantitative yields of reactions between RNA and ethylenediamine after 4−8 h of incubation (*23*). However, further exploration of more extensive applications of phosphoramidation for nucleic acid conjugations was not conducted.

An effective and efficient aqueous-phase nucleic acid phosphoramidation method became important during our studies of RNA conjugations and ribozyme catalysis. We thus synthesized a new biotin derivative (**11**) to systematically optimize the nucleic acid phosphoramidation methods of Chu et al. (*21*) with the goal to improve effectiveness and efficiency. The synthesis of **11** was successfully accomplished with an excellent overall yield of 38.7%. The afforded **11** has a biotin tag and a primary amine which can be used to optimize phosphoramidation reactions with nucleic acids. The new aqueous-phase phosphoramidation method provided up to 80% yield for **11**−nucleic acid conjugates after 3 h of reaction. The method was able to complete conversions for 1,6-hexanediamine-nucleic acid conjugates after only 10−20 min of reaction. The phosphoramidation reaction between a model peptide tetraglycine (**12**) and nucleic acids was also successful in producing the desired POCs. The integrity of hybridization characteristics of nucleic acids after phosphoramidation reactions was demonstrated by polymerase chain reactions (PCRs) in which almost all the phosphoramidation-prepared DNA−**11** conjugate primers were integrated into PCR products. The phosphoramidation reactions were also applied to effective preparation of nucleic acid−BSA conjugates. The hallmark of the nucleic acid phosphoramidation reactions is that they offer a facile and universal approach to prepare POCs with no restrictions on compositions of either nucleic acids or peptides and without compromising base-pairing preference in nucleotides. The new aqueous-phase phosphoramidation reaction will provide an advantageous method for nucleic acid conjugate preparation and expedite medical applications of POCs as therapeutic reagents for gene silencing, gene therapy, and RNA interference (*15*−*17, 24*).

MATERIALS AND METHODS

All reagents were purchased from commercial sources (Sigma-Aldrich, Acros, Alfa Aesar, Mallinckrodt Baker, and Merck KGaA) except where noted and were further purified if necessary. Both disuccinimidyl suberate (DSS) and disuccinimidyl glutarate (DSG) for oligonucleotide−peptide conjugates were synthesized according to published methods (*25*). The procedures modified from those of Boger et al. (*26*) were used to synthesize H_2N-Gly-Gly-Gly-Gly-OH (tetraglycine; **12**). ^1H and ^{13}C NMR spectra were recorded using either a Varian 200 or 400 MHz spectrometer (Varian, Inc., Palo Alto, CA, USA) at Kaohsiung Medical University, Taiwan. NMR samples were prepared in CD_3OD, DMSO-d_6, or $CDCl_3$, and the chemical shifts of ^1H signals were given in parts per million downfield from TMS. ^{13}C signals were given in parts per million based on the internal standard of each deuteriated solvent. ESI high-resolution mass spectra were acquired from Department of Chemistry, National Sun Yat-Sen University, Taiwan, on a Bruker APEX II Fourier-transfer mass spectrometry (FT-MS; Bruker Daltonics Inc., Taiwan). Nucleic acid conjugates were analyzed by urea polyacrylamide gel electrophoresis (PAGE) or streptavidin (SAv) gel shift assay in urea PAGE, visualized, and quantified by an Amersham Typhoon phosphoimager (GE Healthcare Bio-Sciences AB, Uppsala, Sweden).

Synthesis of the Biotin Derivative (11). *5-(2-Oxo-hexahydro-thieno[3,4-d]imidazol-4-yl)-pentanoic Acid 2,5-Dioxo-pyrrolidin-1-yl Ester* (**2**). The method for synthesis of **2** was modified from that of Bayer and Wilchek (*27*). In brief, biotin (**1**; 0.31 g, 1.26 mmol) was completely dissolved in DMF (9 mL) with gentle warming. After cooling the **1** solution to room temperature without reprecipitation, it was added to *N*,*N*′-dicyclohexylcarbodiimide (DCC; 0.26 g, 1.28 mmol) and pyridine (0.10 mL, 1.26 mmol) while stirring for 5 min at room temperature, followed by the addition of *N*-hydroxysuccinimide (NHS; 0.19 g, 1.65 mmol) with continuous stirring for 24 h. The reaction product was filtered and concentrated under reduced pressure. The obtained solid was redissolved in 2-propanol (50 mL) with gentle heating, cooled down to room temperature, and reprecipitated at 4 °C overnight. The product was scraped out of the glassware, washed with cold 2-propanol, and air-dried to give **2** as white solid (0.36 g; 82.4%). ^1H NMR (400 MHz) (DMSO) δ: 6.46 (s, 1H, CONH), 6.39 (s, 1H, CONH), 4.31 (t, 1H, CHN), 4.16 (t, 1H, CHN), 3.12 (dd, 1H, CHS), 2.83 (s, 4H, CH_2 of NHS), 2.71 (d, 1H, C*H*HS), 2.69 (t, 2H, CH_2CO), 2.59 (d, 1H, C*H*HS), 1.43−1.68 (m, 6H). ^{13}C NMR (100.67 MHz) (DMSO) δ: 170.42, 162.85, 61.01, 59.28, 55.33, 30.08, 27.91, 27.68, 25.51. HRMS (ESI) calculated for $C_{14}H_{19}N_3O_5S$, $[M+Na]^+$ 364.0943 (calcd.), 364.0940 (found).

6-[5-(2-Oxo-hexahydro-thieno[3,4-d]imidazol-4-yl)-pentanoylamino]-hexanoic Acid (**3**). 5-(2-Oxo-hexahydro-thieno[3,4-*d*]imidazol-4-yl)-pentanoic acid 2,5-dioxo-pyrrolidin-1-yl ester (**2**; 0.35 g, 1.03 mmol) was completely dissolved in DMF (3 mL) with gentle warming (*28*). After cooling the **2** solution to room temperature without reprecipitation, it was mixed with a solution of ε-aminocaproic acid (0.18 g, 1.37 mmol) in sodium bicarbon-

ate buffer (0.1 M, pH 8.0; 4 mL) while stirring. After 4 h at room temperature, the reaction mixture was acidified by HCl solution (1 N) to assist in the formation of white precipitate. The white solid was washed with cold HCl solution, dried over ether, and air-dried to afford **3** (0.30 g; 80.5%). ^{1}H NMR (400 MHz) (DMSO) δ: 7.78 (s, 1H, CONH), 6.46 (s, 1H, CONH), 6.38 (s, 1H, CONH), 4.32 (t, 1H, CHN), 4.14 (t, 1H, CHN), 3.11 (dd, 1H, CHS), 3.02 (t, 2H, C*H*$_2$NH), 2.84 (d, 1H, C*H*HS), 2.59 (d, 1H, C*H*HS), 2.18 (t, 2H, C*H*$_2$COOH), 2.05 (t, 2H, CH_2CO), 1.23−1.68 (m, 12H). ^{13}C NMR (100.67 MHz) (DMSO) δ: 174.45, 171.79, 162.70, 61.03, 59.18, 55.43, 35.21, 33.60, 28.90, 28.02, 25.97, 25.33, 24.22. HRMS (ESI) calculated for $C_{16}H_{27}N_3O_4S$, $[M+Na]^+$ 380.1620 (calcd.), 380.1617 (found).

*6-[5-(2-Oxo-hexahydro-thieno[3,4-d]imidazol-4-yl)-pentanoylamino]-hexanoic Acid 2,5-Dioxo-pyrrolidin-1-yl Ester (***4***).* Synthesis of **4** with high purity was achieved following the method of Wilchek and Bayer with critical changes in workup procedures (*28*). 6-[5-(2-Oxo-hexahydro-thieno[3,4-*d*]imidazol-4-yl)-pentanoylamino]-hexanoic acid (**3**; 0.31 g, 0.87 mmol) was completely dissolved in DMF (20 mL) with gentle warming. After cooling the **3** solution to room temperature without reprecipitation, DCC (0.34 g, 1.65 mmol) and pyridine (0.07 mL, 0.83 mmol) were added to the solution while stirring for 5 min, followed by the addition of NHS (0.16 g, 1.46 mmol) with continuous stirring for 18 h. The reaction product was filtered and concentrated under reduced pressure. The remaining solid was redissolved in 2-propanol (40 mL) with gentle heating, cooled down to room temperature, and reprecipitated at 4 °C overnight. The product was scraped out of the glassware, washed with cold 2-propanol, and air-dried to obtain **4** (0.22 g; 56.8%) as a white solid. ^{1}H NMR (400 MHz) (DMSO) δ: 7.77 (s, 1H, CONH), 6.45 (s, 1H, CONH), 6.38 (s, 1H, CONH), 4.31 (t, 1H, CHN), 4.15 (t, 1H, CHN), 3.11 (dd, 1H, CHS), 3.03 (t, 2H, C*H*$_2$NH), 2.83 (s, 4H, CH_2 of NHS), 2.79 (d, 1H, C*H*HS), 2.67 (t, 2H, C*H*$_2$COOH), 2.60 (d, 1H, C*H*HS), 2.06 (t, 2H, CH_2CO), 1.04−1.75 (m, 12H). ^{13}C NMR (100.67 MHz) (DMSO) δ: 171.90, 170.36, 169.03, 162.79, 61.13, 59.27, 55.53, 38.14, 35.32, 30.24, 28.74, 28.32, 28.14, 25.54, 25.41, 24.05. HRMS (ESI) calculated for $C_{20}H_{30}N_4O_6S$, $[M+Na]^+$ 477.1784 (calcd.), 477.1784 (found).

*(6-Amino-hexyl)-carbamic Acid tert-Butyl Ester (***5***).* 1,6-Hexanediamine (1.0 g, 8.61 mmol) was completely dissolved in dichloromethane (DCM; 7 mL) (*29*). The solution was chilled to 0 °C, followed by the addition of di-*tert*-butyl dicarbonate (0.63 g, 2.87 mmol) with stirring. The reaction was allowed to proceed at room temperature overnight. The acquired reaction product was diluted with chloroform (7.5 mL), extracted with 5% Na_2CO_3 twice, and its organic phase concentrated under reduced pressure. The obtained solid was dissolved in 1 N HCl and extracted with ether twice. The pH of the acquired aqueous phase was adjusted to 10 with NaOH and extracted with ethyl acetate (EA) five times. The final organic phase was dried over $MgSO_4$ and concentrated under reduced pressure to give oil-like **5** (0.25 g; 39.8%). ^{1}H NMR (400 MHz) ($CDCl_3$) δ: 4.54 (s, 1H, CONH), 3.11 (t, 2H, C*H*$_2$NH), 2.68 (t, 2H, C*H*$_2$NH$_2$), 1.40−1.50 (s, 9H, CH_3; m, 4H, CH_2), 1.25−1.37 (m, 4H, CH_2). ^{13}C NMR (100.67 MHz) (DMSO) δ: 77.00, 41.98, 33.55, 29.95, 28.33, 26.48. HRMS (ESI) calculated for $C_{11}H_{24}N_2O_2$, $[M+H]^+$ 217.1916 (calcd.), 217.1917 (found).

*(6-{6-[5-(2-Oxo-hexahydro-thieno[3,4-d]imidazol-4-yl)-pentanoylamino]-hexanoylamino}-hexyl)-carbamic Acid tert-Butyl Ester (***6***).* 6-[5-(2-Oxo-hexahydro-thieno[3,4-*d*]imidazol-4-yl)-pentanoylamino]-hexanoic acid 2,5-dioxo-pyrrolidin-1-yl ester (**4**; 0.39 g, 0.86 mmol) was completely dissolved in DMF (15 mL) with gentle warming. After cooling the solution to room temperature without reprecipitation, it was mixed with triethylamine (Et_3N; 0.52 g, 5.15 mmol) followed by the addition of **5** (0.25 g, 1.14 mmol) in DMF (3 mL) dropwise while stirring. After overnight reaction at room temperature, the mixture was filtered, evaporated in vacuo, and loaded to a silica column for further purification. The products were separated by eluting with mobile phases of 5−20% MeOH in DCM to afford **6** (0.45 g; 93.8%) as a yellowish solid. ^{1}H NMR (400 MHz) (CD_3OD) δ: 4.53 (t, 1H, CHN), 4.34 (t, 1H, CHN), 3.25 (dd, 1H, CHS), 3.20 (t, 2H, C*H*$_2$NH), 3.08 (t, 2H, C*H*$_2$NH), 2.96 (d, 1H, C*H*HS), 2.73 (d, 1H, C*H*HS), 2.22 (t, 4H, CH_2CO), 1.38−1.80 (m, 29H). ^{13}C NMR (100.67 MHz) (DMSO) δ: 176.02, 175.97, 166.05, 158.50, 79.50, 63.39, 61.63, 57.01, 41.24, 41.04, 40.24, 36.99, 36.82, 30.90, 30.35, 30.13, 29.78, 29.49, 28.80, 27.56, 26.92, 26.74. HRMS (ESI) calculated for $C_{27}H_{49}N_5O_5S$, $[M+Na]^+$ 578.3352 (calcd.), 578.3349 (found).

*6-[5-(2-Oxo-hexahydro-thieno[3,4-d]imidazol-4-yl)-pentanoylamino]-hexanoic Acid (6-amino-hexyl)-amide, TFA Salt (***7***).* (6-{6-[5-(2-Oxo-hexahydro-thieno[3,4-*d*]imidazol-4-yl)-pentanoylamino]-hexanoylamino}-hexyl)-carbamic acid *tert*-butyl ester (**6**; 0.23 g, 0.39 mmol) was dissolved in trifluoroacetic acid (TFA) and stirred at room temperature for 45 min. The product was concentrated under reduced pressure, washed by ether, and again concentrated under reduced pressure to obtain oil-like **7** (0.22 g; 100%) as TFA salts. ^{1}H NMR (400 MHz) (CD_3OD) δ: 4.58 (t, 1H, CHN), 4.35 (t, 1H, CHN), 3.25 (dd, 1H, CHS), 3.21 (t, 4H, C*H*$_2$NH), 2.96 (d, 1H, C*H*HS), 2.95 (t, 2H, CH_2NH^{3+}), 2.75 (d, 1H, C*H*HS), 1.22−1.80 (m, 20H). ^{13}C NMR (100.67 MHz) (DMSO) δ: 176.67, 166.14, 63.38, 61.63, 57.03, 41.05, 40.64, 40.19, 40.01, 36.98, 36.81, 30.17, 29.78, 29.50, 28.50, 27.53, 27.33, 26.96, 26.72, 26.27. HRMS (ESI) calculated for $C_{22}H_{41}N_5O_3S$, $[M+H]^+$ 456.3008 (calcd.), 456.3009 (found).

*Carbamoylmethyl-carbamic Acid tert-Butyl Ester (***8a***).* Glycine (0.45 g, 6.05 mmol) was dissolved in 6 mL of dioxane/water mixture (dioxane:water = 4:2) with stirring, followed by the addition of 1 N NaOH (2 mL). The acquired glycine solution was immersed in an ice−water bath and mixed with di-*tert*-butyl dicarbonate (1.38 g, 6.31 mmol) dropwise while stirring to initiate the reaction. The reaction was allowed to proceed at room temperature overnight. The reaction was diluted with water (2 mL) and EA (10 mL), extracted with 1 N HCl twice, and extracted with water twice. The final organic phase was dried over $MgSO_4$ and evaporated under reduced pressure to give oil-like **8a** (0.94 g; 90%). ^{1}H NMR (400 MHz) ($CDCl_3$) δ: 5.42 (s, 1H, CONH), 3.91 (d, 2H, CH_2CO), 1.44 (s, 9H, CCH_3). ^{13}C NMR (100.67 MHz) ($CDCl_3$) δ: 177.0, 156.0, 79.6, 35.8, 34.3, 28.2.

*tert-Butoxycarbonylamino-acetic Acid 2,5-Dioxo-pyrrolidin-1-yl Ester (***8b***).* Carbamoylmethyl-carbamic acid *tert*-butyl ester (**8a**; 0.61 g, 3.48 mmol) and NHS (0.61 g, 5.34 mmol) were dissolved in THF (7 mL), followed by dropwise addition of DCC (1.42 g, 6.9 mmol) in THF (7 mL) with stirring (*30*). After overnight reaction at room temperature, the mixture was quenched by the addition of three drops of glacial acetic acid, stirred for 1 h, and filtered to remove suspension. The acquired filtrate was concentrated under reduced pressure, resuspended in 2-propanol (25 mL) while stirring for 1 h, and filtered to separate the suspension from its filtrate. The remaining solid was washed by 2-propanol and dried to afford white-colored **8b** (0.62 g; 68.8%). ^{1}H NMR (400 MHz) ($CDCl_3$) δ: 5.00 (s, 1H, CONH), 4.27 (d, 2H, CH_2CO), 2.85 (s, 4H, CNOC*H*$_2$CH$_2$), 1.43 (s, 9H, CCH_3). ^{13}C NMR (100.67 MHz) ($CDCl_3$) δ: 168.6 (CONH), 77.0 (CH_2N), 40.2 (CH_2CO), 37.4 (CH_2CO), 25.5 (CH_3CO).

*[(6-{6-[5-(2-Oxo-hexahydro-thieno[3,4-d]imidazol-4-yl)-pentanoylamino]-hexanoylamino}-hexylcarbamoyl)-methyl]-carbamic Acid tert-Butyl Ester (***9***).* *tert*-Butoxycarbonylamino-acetic acid 2,5-dioxo-pyrrolidin-1-yl ester (**8b**; 0.18 g, 0.69 mmol) dissolved in DMF (5 mL) was added slowly to a DMF solution (3 mL)

containing 6-[5-(2-oxo-hexahydro-thieno[3,4-*d*]imidazol-4-yl)-pentanoylamino]-hexanoic acid (6-amino-hexyl)-amide (**7**; 0.16 g, 0.27 mmol) and Et_3N (0.1 mL, 0.72 mmol) while stirring at room temperature. The reaction was stopped after 3 h by evaporating DMF in vacuo, and the remaining residue was redissolved in a limited volume of a DCM/MeOH (19:1) solution and loaded to a preequilibrated silica column. The products were separated by eluting with mobile phases of 1−6.67% MeOH in DCM to afford **9** (0.10 g; 62.2%) as a yellow solid. ^{1}H NMR (400 MHz) (CD_3OD) δ: 4.30 dd, 1H, CHN), 4.15 (dd, 1H, CHN), 3.94 (d, 2H, CH_2CO), 3.32 (quin, 4H, C*H*$_2$NH), 2.99 (q, 2H, CH_2N), 2.92 (d, 1H, C*H*HS), 2.75 (d, 1H, CH*H*S), 2.20 (t, 4H, CH_2CO), 1.44−1.88 (m, 29H). ^{13}C NMR (100.67 MHz) (CD_3OD) δ: 175.9 (CO), 63.7 (CHN), 61.6 (CHN), 56.9 (CHS), 49.0 (CH_2N), 41.0 (CH_2CO), 40.2 (CH_2N), 36.9 (CH_2S), 30.1 (CH_2CO), 28.6 (CH_3CO), 26.7 (CH_2CH_2). HRMS (ESI) calculated for $C_{29}H_{52}N_6O_6S$, $[M+Na]^+$ 635.3567 (calcd.), 635.3564 (found).

*6-[5-(2-Oxo-hexahydro-thieno[3,4-d]imidazol-4-yl)-pentanoylamino]-hexanoic Acid [6-(2-Amino-acetylamino)-hexyl]-amide, TFA Salt (***10***).* [(6-{6-[5-(2-Oxo-hexahydro-thieno[3,4-*d*]imidazol-4-yl)-pentanoylamino]-hexanoylamino}-hexylcarbamoyl)-methyl]-carbamic acid *tert*-butyl ester (**9**; 0.38 mg, 0.62 mmol) was dissolved in TFA (3 mL) and stirred for 45 min. The product was evaporated under reduced pressure, washed by chloroform, and again concentrated under reduced pressure to remove chloroform and to obtain brown oil-like **10** (0.32 g, 100%). ^{1}H NMR (400 MHz) (CD_3OD) δ: 4.50 (dd, 1H, CHN), 4.30 (dd, 1H, CHN), 3.64 (s, 2H, CH_2CO), 3.13−3.23 (m, 4H, C*H*$_2$NH), 2.99 (q, 2H, CH_2N), 2.93 (dd, 1H, C*H*HS), 2.72 (d, 1H, CH*H*S), 2.20 (t, 4H, CH_2CO), 1.29−1.88 (m, 20H). ^{13}C NMR (100.67 MHz) (CD_3OD) δ: 175.9 (CO), 63.7 (CHN), 61.6 (CHN), 56.9 (CHS), 49.0 (CH_2N), 41.0 (CH_2CO), 40.2 (CH_2N), 36.9 (CH_2S), 30.1 (CH_2CO), 26.7 (CH_2CH_2). HRMS (ESI) calculated for $C_{24}H_{44}N_6O_4S$, $[M+H]^+$ 513.3223 (calcd.), 513.3226 (found).

*6-[5-(2-Oxo-hexahydro-thieno[3,4-d]imidazol-4-yl)-pentanoylamino]-hexanoic Acid [6-(2-Amino-acetylamino)-hexyl]-amide (***11***).* The TFA salt of 6-[5-(2-oxo-hexahydro-thieno[3,4-*d*]imidazol-4-yl)-pentanoylamino]-hexanoic acid [6-(2-amino-acetylamino)-hexyl]-amide, TFA salt (**10**; 0.52 g, 0.88 mmol) was dissolved in 5 mL of DCM/MeOH mixture (DCM:MeOH = 1:1) and mixed with 10 equiv of Amberlyst A-21 (1.1 mg, 8.8 mmol) while shaking for 30 min (*31*). After filtering to remove Amberlyst A-21, the filtrate of the reaction products was concentrated under reduced pressure to afford yellow oil-like **11** (0.42 mg, 93.8%). ^{1}H NMR (400 MHz) (CD_3OD) δ: 4.49 (dd, 1H, CHN), 4.30 (dd, 1H, CHN), 3.32 (s, 2H, CH_2CO), 3.14−3.29 (m, 4H, CH_2N), 2.99 (q, 2H, CH_2N), 2.86 (s, 1H, CHS), 2.72 (d, 1H, CHS), 2.20 (q, 4H, CH_2CO), 1.29−1.88 (m, 20H). ^{13}C NMR (100.67 MHz) (CD_3OD) δ: 175.9 (CO), 63.7 (CHN), 61.6 (CHN), 56.9 (CHS), 49.0 (CH_2N), 41.0 (CH_2CO), 40.2 (CH_2N), 36.9 (CH_2S), 30.1 (CH_2CO), 26.7 (CH_2CH_2). HRMS (ESI) calculated for $C_{24}H_{44}N_6O_4S$, $[M+H]^+$ 513.3223 (calcd.), 513.3226 (found).

Nucleic Acid Preparation. Single-stranded DNA (the 5′ primer, 5′-AACACGCATATGTAATACGACTCACTATAGGGATCGTCAGTGCATTGAG-3′; the 3′ primer, 5′-TACCCCTTGGGGATACCACC-3′) was purchased from Purigo Biotech, Inc., Taiwan, and purified by PAGE. Both the 5′ and 3′ primers were used in a standard PCR reaction to amplify the double-stranded TW17 DNA (119 bp; 5′-GGTAACACGCATATGTAATACGACTCACTATAGGGATCGTCAGTGCATTGAGAATGTCAGTGTCTTGCGCTGGGTTCGAGCGGTCCGTGGTGCTGGCCCGGTGGTATCCCCAAGGGGTA-3′) from a plasmid derived from the pGEM-T vector (Promega, Madison, WI, USA; Wang et al., unpublished results). PCR products were extracted by phenol−chloroform solutions, precipitated in the presence of ethanol, and redissolved in 50 mM KCl. The GMP-primed TW17 RNA (87-mer; 5′-GGGAUCGUCAGUGCAUUGAGAAGUGCAGUGUCUUGCGCUGGGUUCGAGCGGUCCGUGGUGCUGGCCCGGUGGUAUCCCCAAGGGGUA-3′) was transcribed from the PCR-amplified double-stranded TW17 DNA carrying T7 promoter sequences under the T7 RNA polymerase runoff reaction in the presence of 6.25 mM each of ATP, CTP, GTP, and UTP, 10 mM GMP (guanosine monophosphate) and with or without 5 μCi [α-^{32}P]UTP (Izotop, Hungary). The GMP-primed TW17 RNA transcript was separated by 8% urea PAGE (220 V, 120 min) followed by ethanol precipitation. Acquired nucleic acids were quantified by their absorption at A_{260}.

Nucleic Acid Radiolabeling. The TW17 RNA was body-labeled with ^{32}P during T7 RNA polymerase runoff transcription stated previously. The double-stranded and single-stranded DNA molecules were ^{32}P-labeled at their 5′-ends with the procedures following the manufacture's instruction (Promega, Madison, WI, USA) and briefly described below. The double-stranded or single-stranded DNA (200 pmol) was dissolved in 20 μL of DEPC (diethyl dicarbonate) water, followed by the addition of 10× reaction buffer (3 μL), alkaline phosphatase (3 U), and DEPC water (4 μL). The reaction was stopped after 2 h at 37 °C, and the reaction product was purified by phenol/chloroform and chloroform extractions, followed by ethanol precipitation. The 5′-OH nucleic acids were redissolved in 7 μL of DEPC water, mixed with 10× reaction buffer (1 μL), [γ-^{32}P]ATP (Izotop, Hungary) and T4 polynucleotide kinase (10 U; Promega, Madison, WI, USA), and reacted 2 h at 37 °C. ^{32}P-labeled double-stranded DNA was purified by phenol/chloroform and chloroform extractions, followed by ethanol precipitation. Single-stranded DNA with ^{32}P-labeled 5′-end was purified by 20% urea PAGE.

Nucleic Acid Phosphoramidation Reactions. *One-Step Phosphoramidation Reactions.* The standard one-step phosphoramidation reaction for RNA was carried out by dissolving the GMP-primed TW17 RNA (92 pmol) and EDC (6.52 μmol) in 20 μL urea−imidazole buffer (8 M urea, 0.1 M imidazole, pH 6.0) and activating at rt for 90 min, followed by the addition of 7.5 μL urea−EPPS buffer (8 M urea, 100 mM EPPS, 2 mM EDTA, pH 8.0) and 5 μL of **11** (187.2 mM in DMF) to react at 41 °C for 3 h. The double-stranded TW17 DNA was also conjugated with **11** according to the same phosphoramidation reaction stated above. For single-stranded DNA (the 3′-primer DNA) the phosphoramidation reaction was modified by dissolving single-stranded DNA (92 pmol) and EDC (6.52 μmol) in 20 μL imidazole buffer (0.1 M imidazole, pH 6.0) and activating at rt for 90 min, followed by the addition of 7.5 μL EPPS buffer (100 mM EPPS, 2 mM EDTA, pH 8.0) and 5 μL of **11** (187.2 mM in DMF) with subsequent reactions at 41 °C for 3 h. No urea was used here to ensure higher reaction yields. All resulting nucleic acid−substrate conjugates were purified twice by ethanol precipitation, and their reaction yields were analyzed by SAv gel shift assay (8% urea PAGE for the TW17 DNA and RNA, and 20%/8% biphasic urea PAGE for single-stranded DNA), visualized, and quantified by an Amersham Typhoon phosphoimager.

Two-Step Phosphoramidation Reactions. The standard two-step phosphoramidation reaction for RNA was carried out by dissolving the GMP-primed TW17 RNA (92 pmol) and EDC (6.52 μmol) in 20 μL urea−imidazole buffer (8 M urea, 0.1 M imidazole, pH 6.0) and activating at rt for 90 min. The resulting 5′-phosphorimidazolide was purified by ethanol precipitation, redissolved in 27.5 μL of urea−EPPS buffer (8 M urea, 100 mM EPPS, 2 mM EDTA, pH 7.5), and added to 5 μL of **11** (187.2 mM in DMF) under reaction temperature at 41 °C for 3 h. For the single-stranded 3′-primer DNA, the two-step

phosphoramidation reaction was modified by dissolving single-stranded DNA (92 pmol) and EDC (6.52 μmol) in 20 μL imidazole buffer (0.1 M imidazole, pH 6.0) and activating at rt for 90 min. Again, the resulting 5′-phosphorimidazolides were also purified by ethanol precipitation, redissolved in 27.5 μL of EPPS buffer (100 mM EPPS, 2 mM EDTA, pH 7.5), and added to 5 μL of **11** (187.2 mM in DMF) to react at 41 °C for 3 h. The double-stranded TW17 DNA was also conjugated with **11** according to the same two-step phosphoramidation reaction for the single-stranded DNA. It is noted that urea was not used in two-step phosphoramidation reactions for the doubled-stranded and single-stranded DNA molecules to attain higher reaction yields. All acquired nucleic acid−**11** conjugates were purified twice by ethanol precipitation, and their reaction yields were analyzed by SAv gel shift assay in the same urea PAGE described for one-step phosphoramidation reaction analysis, visualized, and quantified by an Amersham Typhoon phosphoimager.

Nucleic Acid-1,6-Hexanediamine Conjugate Preparation. The phosphoramidation reaction between the TW17 RNA and 1,6-hexanediamine followed the standard one-step phosphoramidation method stated above but with **11** replaced by 1,6-hexanediamine. The phosphoramidation reaction between DNA and 1,6-hexanediamine was carried out by the standard one-step phosphoramidation method with the following modifications: (1) **11** replaced by 1,6-hexanediamine, (2) EDC activation time shortened to 15 min, (3) nucleophilic coupling reaction time shortened to 10 min for both the double-stranded TW17 DNA and the single-stranded 3′ primer DNA. The afforded nucleic acid−1,6-hexanediamine conjugates were purified twice by ethanol precipitation, and the reaction yields were analyzed by 8% (the TW17 DNA and RNA) or 20% (the 3′-primer DNA) urea PAGE, visualized, and quantified by an Amersham Typhoon phosphoimager.

Single-Stranded 3′-Primer DNA−Fluorescein Conjugate Preparation. The single-stranded 3′-primer DNA−fluorescein conjugate was prepared from its corresponding single-stranded 3′-primer DNA−1,6-hexanediamine conjugate described previously. In a typical reaction for the preparation of single-stranded DNA−fluorescein conjugates, the single-stranded 3′-primer DNA−1,6-hexanediamine conjugate was redissolved in 20 μL sodium carbonate buffer (0.1 M, pH 9.0) to give a final concentration of 2 μM (*32*). Under a darkened laboratory setup, fluorescein isothiocyanate (FITC, Acros) was weighted and dissolved in dry DMSO for a final concentration of 1 mg/mL (2.57 μM). In the same darkened laboratory, 20 μL of the FITC solution was slowly added to the singled-stranded 3′-primer DNA−1,6-hexanediamine conjugate solution while gentle mixing. The reaction was allowed to proceed for 8 h at 4 °C in the dark. The afforded single-stranded DNA−fluorescein conjugate was purified twice by ethanol precipitation.

PCR Reactions to Determine DNA Amplification Efficiency for the Biotin-Labeled 3′-Primer DNA or to Demonstrate Formation of the 3′-Primer DNA−Fluorescein Conjugate. Standard PCR procedures were applied to determine DNA amplification efficiency using the **11**-modified 3′-primer DNA under the condition that the normal 3′-primer (100 μM, 0.75 μL) was substituted with a mixture of the normal 3′-primer (100 μM, 0.15 μL) and ^{32}P-labeled and **11**-modified 3′-primer (1.9 μM, 10 μL). After 15 cycles of the PCR reaction, the product was purified by a standard phenol−chloroform extraction procedure, analyzed by biphasic urea PAGE (top gels of 6% acrylamide and bottom gels of 20% acrylamide), and visualized through an Amersham Typhoon phosphoimager. For the fluorescein-labeled 3′-primer DNA, its formation was studied by the same PCR reaction except that ^{32}P-labeled and **11**-modified 3′-primer was substituted with nonradiolabeled fluorescein-modified 3′-primer (1.9 μM, 10 μL). The PCR reaction product was also purified by a standard phenol−chloroform extraction procedure, analyzed by urea PAGE, and visualized under an Amersham Typhoon phosphoimager using an excitation wavelength of 488 nm and an emission filter set at 525 nm.

Preparation of Nucleic Acid−Tetraglycine (*12*) Conjugates by Phosphoramidation Reactions. The phosphoramidation reaction between nucleic acids and tetraglycine **12** followed the standard two-step phosphoramidation method stated above with **11** substituted with **12**. The afforded nucleic acid−tetraglycine conjugates were purified twice by ethanol precipitation, and the reaction yields were analyzed by high-resolution 8% urea PAGE for the TW17 RNA−**12** and the TW17 DNA−**12** conjugates or high-resolution 20% urea PAGE for the 3′-primer DNA−**12** conjugate. All electrophorized samples were visualized and quantified by an Amersham Typhoon phosphoimager.

Nucleic Acid−BSA (Bovine Serum Albumin) Conjugate Preparation. The standard procedures for preparation of nucleic acid−BSA conjugates were modified from those of Jablonski et al. (*33*). Oligonucleotide−1,6-hexanediamine conjugates were dissolved in 10 μL of EDTA−bicarbonate buffer (0.1 M sodium bicarbonate, 2 mM EDTA, pH 8.25) to give a concentration of 0.02 mM. Nucleic acid−1,6-hexanediamine conjugate solutions were then reacted with 20 μL of DSS or DSG solutions (182 mM in DMSO) for 5 min at rt in the dark. Reaction products were immediately purified twice by ethanol precipitation to avoid hydrolysis of the remaining succinimidyl esters. The afforded nucleic acid conjugates were again redissolved in 30 μL of BSA (10 mg/mL) in sodium phosphate buffer (0.1 M, pH 7.5) to give a molar ratio of BSA to nucleic acid conjugates of 2. The reaction was allowed to proceed for 2−16 h at rt, and the reaction product was purified twice by ethanol precipitation. Yields of nucleic acid−BSA conjugates were also determined by urea PAGE analysis and visualized through an Amersham Typhoon phosphoimager.

RESULTS

Synthesis of the Biotin Derivative (11) and Coupling to the TW17 RNA for Optimization of Phosphoramidation Reactions. The synthesis of **11** started from biotin (**1**) which was activated by carbodiimide to give its NHS ester (**2**), followed by coupling **2** with 4-aminocaproic acid to produce **3** which was again activated by carbodiimide to afford the corresponding NHS ester **4** (Scheme 1). We initially observed that the yield for **4** was always higher than 100%, an indication of ineffective product purification despite following the method of Wilchek and Bayer (*28*). We thus changed the workup procedures by reprecipitating the product in 2-propanol to acquire a fairly clean **4** (56.8%) as confirmed by ^{1}H and ^{13}C NMR and HRMS (ESI). Compound **4** was then reacted with previously synthesized **5** to afford **6** (93.8%), followed by TFA Boc-deprotection (**7**) and amidation with previously synthesized **8b** to give **9** (86.4%). The final product **11** (93.8%) was almost quantitatively obtained after TFA deprotection of **9** and TFA removal of **10**, as confirmed by ^{1}H and ^{13}C NMR and HRMS (ESI).

Successful synthesis of **11** paved the way for the optimization of aqueous-phase nucleic acid phosphoramidation reactions. As noted previously, aqueous-phase nucleic acid phosphoramidation reactions exploit EDC to activate 5′-terminal phosphate groups in nucleic acids and to transiently form reactive phosphorimidazolide intermediates of nucleic acids (Supporting Information Scheme S1). Phosphorimidazolide intermediates of nucleic acids can be purified or used directly to couple with amine-containing nucleophiles to result in desired nucleic acid conjugates. We believed that a key factor affecting final yields for phosphoramidation-prepared nucleic acid conjugates would rely on

Scheme 1. Synthesis of the Biotin Derivative 11 for Optimization of Nucleic Acid Phosphoramidation Reactions

providing a reasonable high concentration of phosphorimidazolide intermediates for nucleophilic attack by **11**. We thus refined phosphoramidation reactions to provide a steady supply of phosphorimidazolide intermediates to **11** during the course of the reactions. Refinements included systematic modifications of reaction conditions such as reactant and EDC concentrations, activation time, reaction time with nucleophile **11**, reaction temperature, pH, and surfactant effects. Both one-step and two-step phosphoramidation reactions were studied with the ultimate goal of improving reaction efficiency and effectiveness.

The optimized one-step phosphoramidation reaction provided an excellent yield of 79% for conjugation of the TW17 RNA with **11** after 3 h reactions (Figure 1A). Further improvement in the phosphoramidation reaction yield was not achieved, probably reflecting the lability of phosphorimidazolide intermediates and inaccessibility of phosphorimidazolide intermediates to **11**. A constant reaction temperature is essential for attaining high phosphoramidation reaction yields. The choice of 41 °C as a reaction temperature balances an enhanced reaction rate and prevention of phosphorimidazolide hydrolysis and RNA hydrolysis at higher temperatures. Maintenance of denaturing conditions by 6.77 M urea during the phosphoramidation reaction plays a pivotal role in achieving higher yields by preventing formation of RNA secondary structures. A very small portion of the GMP-primed TW17 RNA suffered from degradation during the reaction, an amount too insignificant to decrease overall reaction efficiency and yield.

Chu et al. also performed a two-step nucleic acid phosphoramidation method attained by purification of phosphorimidazolide intermediates of DNA which were subsequently reacted with nucleophiles to afford DNA phosphoramidation conjugates (*21*). We therefore also exploited the two-step phosphoramidation method for the TW17 RNA conjugation with **11** to study its effectiveness in preventing RNA degradation observed during the one-step phosphoramidation reaction. Yields of the two-step phosphoramidation reactions for the TW17 RNA−**11** conjugate preparation were consistent with expectations of lower

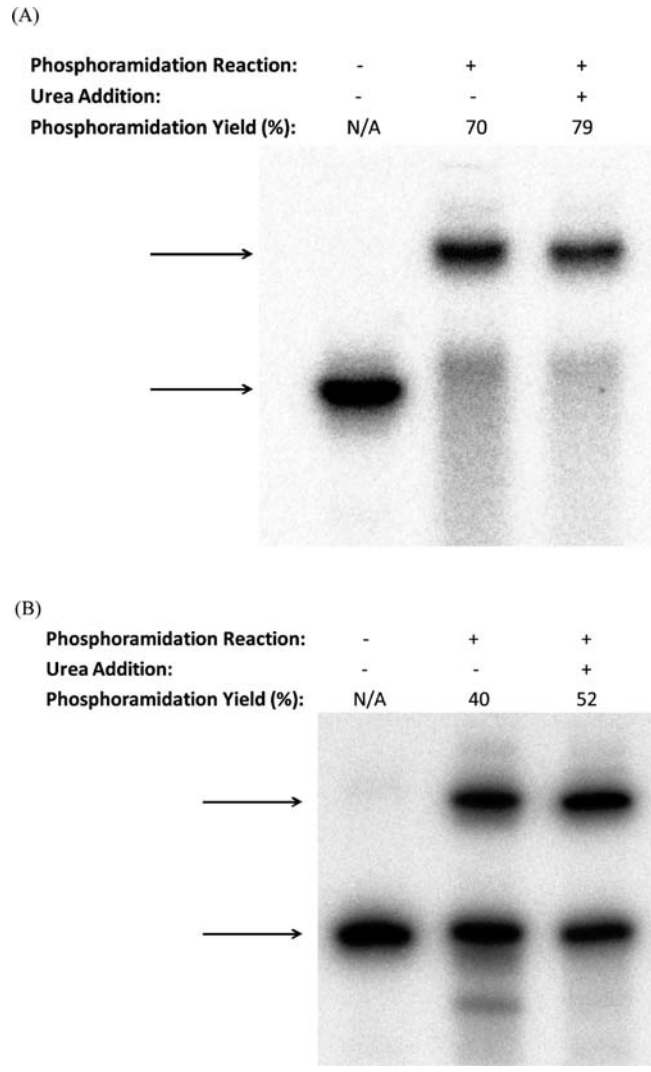


Figure 1. Phosphoramidation reactions of the ^{32}P-labeled GMP-primed TW17 RNA with **11**. (A) Results from the one-step phosphoramidation reaction were analyzed by streptavidin (SAv) gel shift assay in 8% urea PAGE and visualized by autoradiogram. (B) Results from the two-step phosphoramidation reaction were again analyzed by SAv gel shift assay in 8% urea PAGE and autoradiogram. The samples in each figure, starting from the left, are the TW17 RNA without the phosphoramidation reaction, the TW17 RNA conjugated with **11** by the phosphoramidation reaction without the addition of 6.77 M urea, and the TW17 RNA conjugated with **11** by the phosphoramidation reaction in the presence of 6.77 M urea, respectively. In both figures, the top arrow indicates the location of the TW17 RNA−**11** conjugate; the bottom arrow represents migration of the GMP-primed TW17 RNA.

yields than the one-step phosphoramidation reactions (52% in the presence of 6.77 M urea and 40% without 6.77 M urea; Figure 1B). Lower yields for two-step phosphoramidation reactions are attributed to phosphorimidazolide intermediate hydrolysis during its workup step. Both two-step phosphoramidation reactions, with or without 6.77 M urea, still provided reasonably good yields for the TW17 RNA−**11** conjugates, comparable to those prepared by the one-step phosphoramidation reactions. Two-step phosphoramidation reactions can be an advantageous approach to conjugate carbodiimide-sensitive nucleophiles with nucleic acids (vide infra). However, similar to the one-step reactions, RNA degradation was also observed. RNA degradation was thus not caused by prolonged carbodiimide activation but rather by the nucleophile attack step or by a higher reaction temperature at 41 °C.

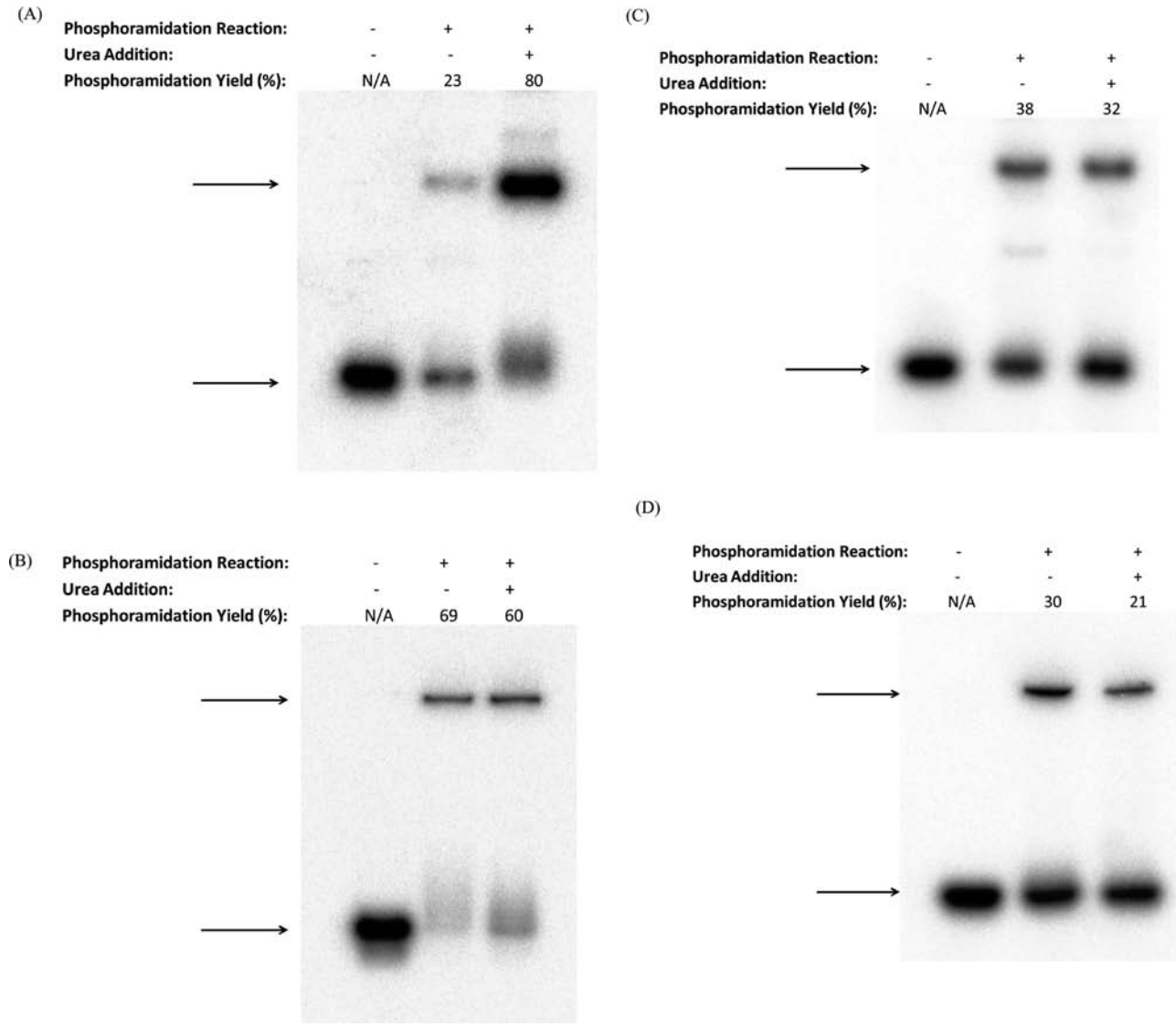


Figure 2. Phosphoramidation reactions of the ^{32}P-labeled DNA with **11**. Results from one-step phosphoramidation reactions were analyzed by SAv gel shift assays in (A) 8% urea PAGE for the double-stranded DNA (the TW17 DNA) conjugations or (B) 20% urea PAGE for the single-stranded DNA (the 3′-primer) conjugations, and visualized by autoradiogram. Results from two-step phosphoramidation reactions were again analyzed by SAv gel shift assays in (C) 8% urea PAGE for the double-stranded DNA (the TW17 DNA) conjugations or (D) 20% urea PAGE for the single-stranded DNA (the 3′-primer) conjugations, and also visualized by autoradiogram. The samples in each figure, starting from the left, are the DNA without the phosphoramidation reaction, the DNA conjugated with **11** by a phosphoramidation reaction without the addition of 6.77 M urea, and the DNA conjugated with **11** by a phosphoramidation reaction in the presence of 6.77 M urea, respectively. Also in each figure, the top arrow indicates the location of the DNA−**11** conjugate; the bottom arrow represents migration of the DNA without phosphoramidation reactions.

Preparation of Phosphoramidated DNA−11 Conjugates. One-step and two-step phosphoramidation reactions were carried out to prepare DNA−**11** conjugates and study universal applications of the phosphoramidation reaction protocol developed for the TW17 RNA−**11** conjugate. The one-step phosphoramidation reactions for the conjugations of either the single-stranded 3′-primer or the double-stranded TW17 DNA with **11** in the presence of 6.77 M urea offered a yield of 80% for the TW17 DNA−**11** conjugate and 60% for the 3′-primer DNA−**11** conjugate (Figure 2A,B). These yields were comparable to the 79% yield for the TW17 RNA−**11** conjugate. The addition of 6.77 M urea significantly improved the yields for the TW17 DNA−**11** conjugates from 23%, without urea, to 80% in the presence of urea. These yields parallel the positive effect of urea during the phosphoramidation reactions to prepare the TW17 RNA−**11** conjugates and are consistent with the proposed function of urea to disassemble secondary structures in nucleic acids and increase the availability of terminal phosphate groups for phosphoramidation reactions. The positive effect of urea on phosphoramidation reaction yields was, however, not observed upon preparation of the 3′-primer DNA−**11** conjugates. Slight deterioration of the phosphoramidation reaction yield for the 3′-primer DNA−**11** conjugates was observed in the presence of urea. This finding indicates very limited secondary structure formation in a relatively small 3′-primer DNA and adverse effects of urea on single-stranded DNA phosphoramidation reactions. In contrast to results of the TW17 RNA phosphoramidation reactions, DNA degradation was not observed during the one-step DNA phosphoramidation reactions.

The two-step phosphoramidation reactions for conjugation of either the 3′-primer or the TW17 DNA with **11** again provided yields lower than those for the one-step reactions (Figure 2C,D). Interestingly, both phosphoramidation reactions performed better in the absence of 6.77 M urea in which the yield for the TW17 DNA−**11** conjugate was 38% and that for the 3′-primer DNA−**11** conjugate was 30%. The inhibitory effect of urea on phosphoramidation reactions was clearly more prominent than its beneficial effect on denaturation of nucleic acids to disrupt

their secondary structures in the two-step DNA phosphoramidation reaction. DNA degradation during the two-step DNA phosphoramidation reaction was not observed. Overall, we demonstrated the feasibility of using two phosphoramidation reaction formats to prepare the DNA−**11** conjugates and the stability of DNA during phosphoramidation reactions.

Preparation of Nucleic Acid-1,6-Hexanediamine Conjugates. The success in using **11** to develop effective nucleic acid phosphoramidation methods encouraged us the further applications of the phosphoramidation reaction to the preparation of nucleic acid−1,6-hexanediamine conjugates. These conjugates can serve as key intermediates for covalently linking chromophores or oligopeptides to nucleic acids. One-step phosphoramidation reactions were chosen to attain higher phosphoramidation yields for nucleic acid−1,6-hexanediamine conjugates. We were encouraged by observing quantitative production of the TW17 RNA−1,6-hexanediamine conjugates according to the same phosphoramidation reaction for the TW17 RNA−**11** conjugate (Figure 3A). Quantitative formation of the TW17 DNA−1,6-hexanediamine or the 3′-primer DNA−1,6-hexanediamine conjugates was also attained even under the conditions of reduced times for EDC activation (15 min) and for 1,6-hexanediamine coupling (10 min for both DNA molecules) in the phosphoramidation reactions (Figure 3B,C). Unexpectedly, multiple conjugations of 1,6-hexanediamine to either the TW17 DNA or the 3′-primer DNA were very significant, but the conjugates were never observed to produce TW17 RNA−1,6-hexanediamine conjugates. Substitutions of 1,6-hexanediamine with ethylenediamine significantly decreased phosphoramidation reaction yields for all nucleic acid conjugates (Wang et al., unpublished results). These results imply that the pK_a, lipophilicity and diamine characteristics of 1,6-hexadiamine play an essential role in accomplishing higher yields and multiple conjugations in nucleic acid phosphoramidation reactions.

Preparation of the 3′-Primer DNA−Fluorescein Conjugate. The quantitative 1,6-hexanediamine−3′ primer DNA conjugates were applied to conjugations with FITC through covalent thiourea linkages between newly acquired primary amines in the 5′-termini of nucleic acids and FITC. Conventional high-resolution urea PAGE methods to determine yields for the 3′-primer DNA conjugate preparation could not be used due to multiple conjugations of the 3′-primer DNA with 1,6-hexanediamine (Figure 3C). Instead of obtaining quantitative measurements, we pursued qualitative data to demonstrate formation of the 3′-primer DNA−fluorescein conjugates by applying the fluorescein-tagged 3′-primer DNA to PCR amplification. Formation of the 3′-primer DNA−fluorescein conjugates was clearly shown in the results of PCR amplification. The fluorescence signals from either the PCR products or the fluorescein-tagged 3′-primer DNA were vividly observed (Supporting Information Figure S1). The signals corresponding to the PCR products were less than 30% of the total fluorescein signal, a sharp contrast to quantitative yields for the 3′-primer DNA−1,6-hexanediamine conjugate preparation. Nevertheless, the PCR results supported formation of the covalently linked 3′-primer DNA−fluorescein conjugates.

Characteristics of Hybridization Specificity in Nucleic Acids after Phosphoramidation Reactions. The effectiveness of POCs as therapeutic reagents strongly depends on intact hybridization specificity in nucleic acids after preparation. Thus, assurance of the integrity of hybridization specificity in nucleic acids after phosphoramidation reactions is essential to POC preparation reactions. Retention of hybridization specificity in the 3′-primer DNA after phosphoramidation and followup coupling reactions was ambiguous according to our qualitative studies of the 3′-primer DNA−fluorescein conjugate preparation (Supporting Information Figure S1). The low PCR product yield

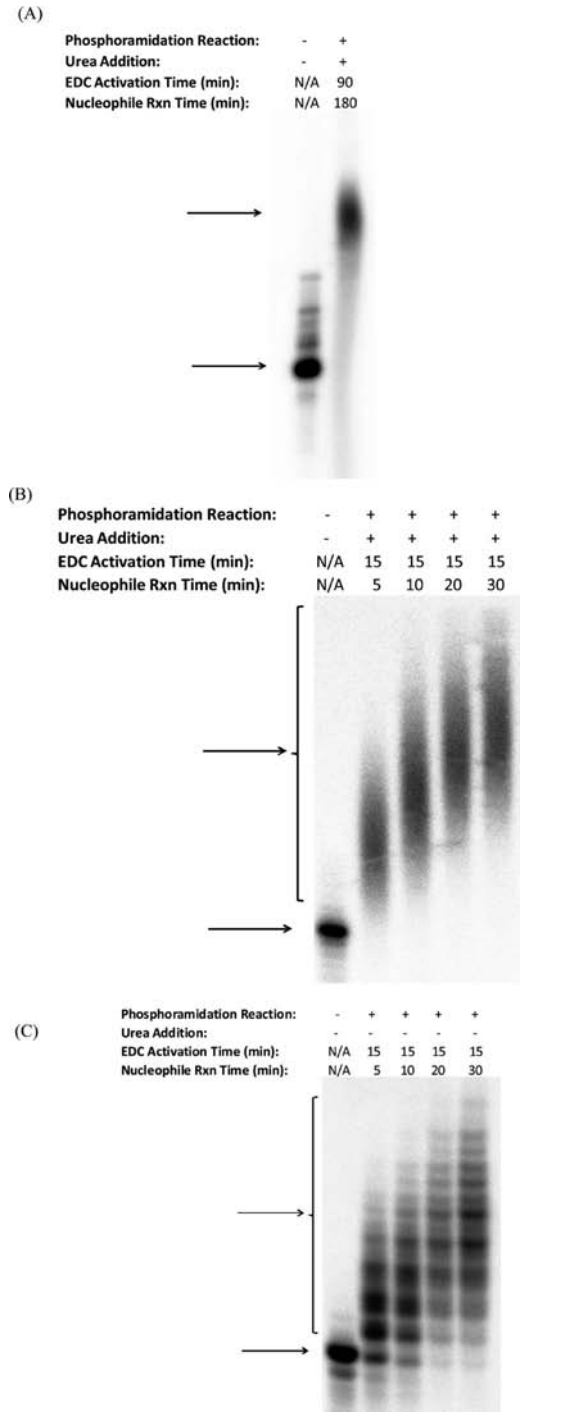


Figure 3. Phosphoramidation reactions of the ^{32}P-labeled DNA or RNA with 1,6-hexanediamine. Products from each one-step phosphoramidation reaction were analyzed by (A) 8% urea PAGE for the GMP-primed TW17 RNA conjugations, (B) 8% urea PAGE for the doubled-stranded TW17 DNA conjugations, or (C) 20% high-resolution urea PAGE for the single-stranded 3′-primer DNA conjugations, and visualized by autoradiogram. The samples in Figure 3A, starting from the left, are the RNA without phosphoramidation reactions, and formation of the RNA−1,6-hexanediamine conjugate by the phosphoramidation reaction with 60 min EDC activation and 180 min coupling reactions of with 1,6-hexanediamine in the presence of 6.77 M urea, respectively. The samples in Figure 3B,C, starting from the left, are DNA without phosphoramidation reactions, and formation of DNA−1,6-hexanediamine conjugates by the phosphoramidation reactions with 15 min EDC activation and 5, 10, 20, and 30 min coupling reactions of 1,6-hexanediamine in the presence of 6.77 M urea, respectively. Also in each figure, the top arrow indicates location(s) of nucleic acid−1,6-hexanediamine conjugate(s); the bottom arrow represents migration of the nucleic acid without phosphoramidation reactions.

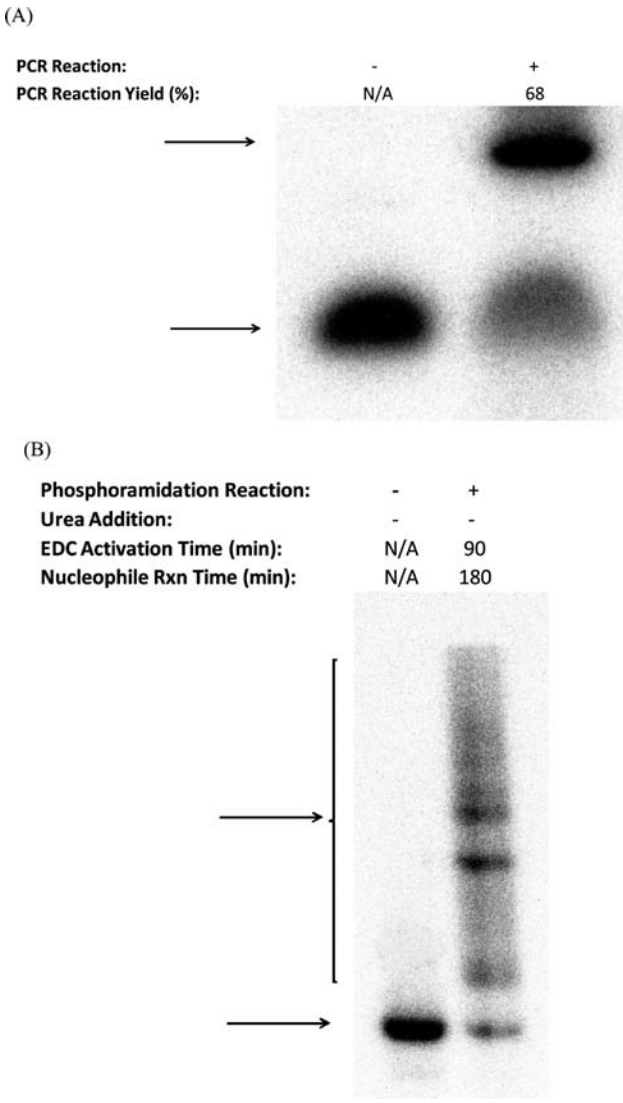


Figure 4. Demonstration of intact hybridization characteristics and minor multiple conjugations for the 3′-primer DNA after the phosphoramidation reaction with **11**. (A) The one-step phosphoramidation-prepared 3′-primer DNA−**11** conjugate (19 pmol) was mixed into the nonlabeled 3′-primer DNA (15 pmol) and used for PCR reactions. The samples of the 3′-primer DNA−**11** conjugates before (the left sample) and after (the right sample) a PCR reaction were analyzed by a biphasic urea PAGE with the top gel of 6% acrylamide and the bottom gel of 20% acrylamide to attain good resolutions. The top arrow indicates the location of the 119-mer DNA PCR products; the bottom arrow represents migration of the 3′-primer DNA−**11** conjugate. (B) The same samples in Figure 2B were analyzed by a 20% urea PAGE without the addition of SAv and visualized by autoradiogram.

could not be attributed to the poor coupling efficiency of FITC with the 3′-primer DNA−1,6-hexanediamine conjugates or to changes in hybridization specificity of the 3′-primer DNA−fluorescein conjugate. We thus applied the 3′-primer DNA−**11** conjugate, with a known product yield (Figure 2B), to PCR reactions to clearly demonstrate intact hybridization specificity. Results from the PCR reaction indicated that 68% of the radiolabeled 3′-primer DNA was incorporated into the PCR DNA product (Figure 4A). As the yield for the 3′-primer DNA−**11** conjugate preparation, in the absence of 6.77 M urea, was 69% (Figure 2B), we concluded that all of the phosphoramidation-prepared 3′-primer DNA−**11** conjugates had effectively hybridized with the provided DNA template to produce the desired DNA product. The impressive PCR amplification efficiency of the 3′-primer DNA−**11** conjugate is in sharp contrast to the poor PCR amplification efficiency of the 3′-primer DNA−fluorescein conjugate. Since the discrepancy in PCR product yields was not likely caused by differences between biotin and fluorescence moieties in nucleic acid conjugates, we questioned whether changes of PCR amplification efficiency could be attributed to the extent of multiple conjugations from phosphoramidation reactions. Consistent with predictions, the phosphoramidation reaction between the 3′-primer DNA and **11** entailed fewer extents of multiple conjugations, likely a key factor in sustaining hybridization specificity in nucleic acids (Figure 4B). Nucleic acid phosphoramidation reactions under appropriate controls provide an outstanding method to efficiently and effectively prepare nucleic acid conjugates, including POCs, without loss of hybridization specificity in nucleic acids moieties.

Preparation of Nucleic Acid−Tetraglycine (12) Conjugates. Understanding the basic chemistry for nucleic acid phosphoramidation provided essential information to develop appropriate and simple protocols for POC preparation. Our results initially implied that one-step phosphoramidation reactions were superior in preparing POCs because of their better reaction yields (Figures 1 and 2). Phosphoramidation reactions of DNA with 1,6-hexanediamine, however, revealed that the one-step approach was too reactive to produce multiple conjugations in DNA molecules and had adverse effects on hybridization specificity (Supporting Information Figure S1). In addition, generic one-step nucleic acid phosphoramidation reactions have restrictions on nucleophile carbodiimide-sensitive functionalities, which demands the use of carboxyl-protected peptides to participate in one-step nucleic acid phosphoramidation reactions for POC preparation. The need to modify peptides for one-step nucleic acid phosphoramidation reactions can impair the intrinsic binding affinity to their natural counterpart receptors on cell membranes (increase of K_d) to prohibit effective POC uptake by cells. Furthermore, peptide modifications can transform peptides into ligands of undesirable receptors on nontargeted cell membranes to incur side effects or lethal complications in clinical applications. It is a delicate balance between producing POCs with high yields and developing POCs for effective medical treatments with minimum adverse effects.

We anticipated that the combination of two-step nucleic acid phosphoramidation reactions and natural peptides free from any chemical modifications could be harnessed to afford POCs devoid of the drawbacks of using modified peptides. To test the concept, we synthesized tetraglycine (**12**) as a model peptide (*26*) and allowed it to react with nucleic acids by two-step phosphoramidation reactions. Consistent with the previous studies of nucleic acid conjugations with **11** by two-step phosphoramidation reactions, the acquired nucleic acid−**12** conjugates after 3 h of coupling reactions with nucleophile **12** had the following yields: the TW17 RNA−**12** conjugate of 44%, the TW17 DNA−**12** conjugate of 39%, and the 3′-primer DNA−**12** conjugate of 27% (Figure 5). The molecular mass difference between two DNA strands in the double-stranded TW17 DNA, which is over 500 Da, contributes to the observation of a dual DNA signal before and after the phosphoramidation reaction (Figure 5B; calculated molecular mass: the positive strand of the TW17 DNA, 36 963.8 g/mol; the negative strand of the TW17 DNA, 36 448.6 g/mol). The product yields are comparable to the two-step phosphoramidation reactions for nucleic acid−**11** conjugate preparation. Extending the reaction time for **12** to overnight (16 h) improved DNA−**12** conjugate yields, but not for the TW17 RNA−**12** conjugate. A lower yield for the TW17 RNA−**12** conjugate after the overnight coupling reaction could be attributed to instability of RNA during a prolonged coupling period. However, 3 h of reactions with peptide nucleophiles in two-step nucleic acid phosphoramidation

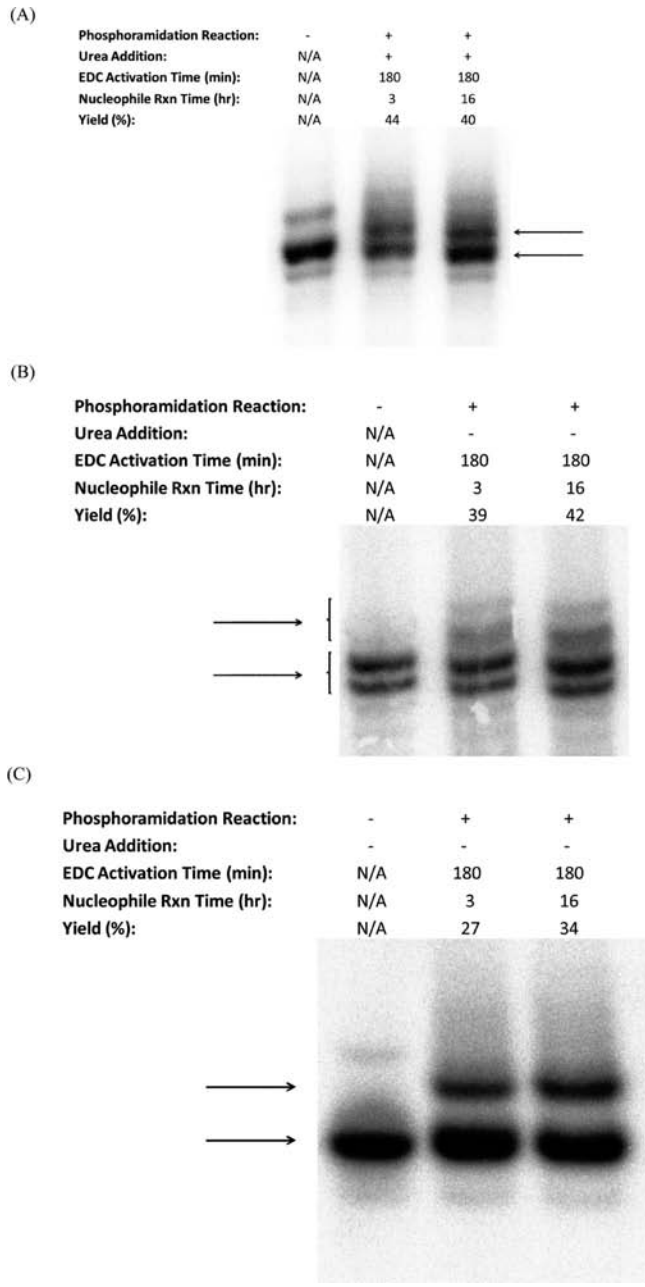


Figure 5. Phosphoramidation reactions of the ^{32}P-labeled DNA or RNA with tetraglycine (**12**) to prepare nucleic acid−tetraglycine conjugates. Products from each two-step phosphoramidation reaction were analyzed by (A) 8% high-resolution urea PAGE for the GMP-primed TW17 RNA conjugations, (B) 8% high-resolution urea PAGE for the doubled-stranded TW17 DNA conjugations, or (C) 20% high-resolution urea PAGE for the single-stranded 3′-primer DNA conjugations, and visualized by autoradiogram. The samples in each figure, starting from the left, are the nucleic acid without phosphoramidation reactions, the nucleic acid conjugated with **12** by phosphoramidation reactions without the addition of 6.77 M urea, and the nucleic acid conjugated with **12** by phosphoramidation reactions in the presence of 6.77 M urea, respectively. Also in each figure, the top arrow indicates the location of the nucleic acid−**12** conjugate; the bottom arrow represents migration of the original nucleic acid.

is enough to prepare suitable amounts of POCs. No multiple conjugations were observed in any nucleic acid−**12** conjugates, implying the integrity of hybridization specificity in nucleic acid moieties. These results clearly validate the two-step phosphoramidation reaction to prepare appropriate POCs for medical applications.

Phosphoramidation Reactions for Preparation of Nucleic Acid−BSA Conjugates. We further explored the use of phosphoramidation reactions to develop a generic approach for the preparation of nucleic acid−protein conjugates. Starting with the previously prepared nucleic acid−1,6-hexanediamine conjugates (Figure 3), they were first reacted with either DSS or DSG to effectively convert -NH_2 to the NHS ester of a carboxylic acid in 5′-termini of the nucleic acids (*33*). Activated acyl group characters of NHS esters allowed easy formation of new amide linkages between nucleic acids and proteins such as BSA to acquire nucleic acid−protein conjugates. Incorporation of 3 M NaCl in coupling reactions was proposed to be indispensible to diminish electric repulsions between nucleic acids and proteins to attain higher yields for nucleic acid−protein conjugates (*33*). Therefore, we performed the coupling reactions in the presence or absence of 3 M NaCl to ascertain any benefit.

The yields for the TW17 RNA−BSA conjugates were only 8% using DSS linkers and 22% using DSG linkers after 2 h reactions in the absence of 3 M NaCl (Figure 6A). Extension of the reaction time from 2 to 16 h, however, improved the yields for the TW17 RNA−BSA conjugates to 44% using DSS linkers and 34% using DSG linkers. Despite neutral pH reaction conditions (pH = 7.4), RNA suffered severe degradation for both DSS and DSG linker conjugates after prolonged coupling reactions. Preparation of the TW17 RNA−BSA conjugates after 2 h reactions in the presence of 3 M NaCl offered reasonable good yields by both DSS and DSG linkers and was comparable to the overnight (16 h) coupling reactions in the absence of 3 M NaCl (Figure 6B). Unexpectedly, extending the reaction time to 16 h was not necessary to improve reaction yields. The loss of the TW17 RNA−BSA conjugates during overnight reactions was observable; RNA degradation was again prevalent and more intensive during the longer reaction time. Overall, additions of 3 M NaCl when preparing the TW17 RNA−BSA conjugates, although not significantly increasing the conjugate yields, reduced the coupling time from 16 to 2 h, which is critical in preventing RNA degradation during POCs preparation.

Similar coupling yields were never obtained for the preparation of the TW17 DNA−BSA conjugates. Yields were less than 20% when using DSS or DSG linkers in the absence of 3 M NaCl (Supporting Information Figure S2A). No improvements in yields for the coupling reactions between BSA and the TW17 DNA derivatives were observed when the reaction times were increased from 2 to 16 h or for reactions carried out in the presence of 3 M NaCl (Supporting Information Figure S2B). Such results defy the beneficial effects of prolonged reaction times and the use of 3 M NaCl to enhance the formation of DNA−alkaline phosphatase conjugates (*33*). The studies of nucleic acid−BSA conjugate preparations underscore the fundamental difference between DNA and RNA toward phosphoramidation reactions which significantly effect yields of nucleic acid−BSA conjugates. Yields for all phosphoramidation reactions are provided in Table 1.

DISCUSSION

We have successfully synthesized a new amine-containing biotin derivative **11** suitable for conjugation with biomolecules such as proteins or nucleic acids for versatile applications. We harnessed the amine functionality and the biotin moiety in **11** to develop the phosphoramidation reactions for preparation of nucleic acid−**11** conjugates with excellent yields and efficiency, but without compromising hybridization specificity of nucleic acids. Both two-step and one-step phosphoramidation reactions were studied, and as expected, one-step phosphoramidation reactions always performed better than two-step formats, which can be attributed to phosphorimidazolide intermediate lability in aqueous solutions. A one-step phosphoramidation reaction

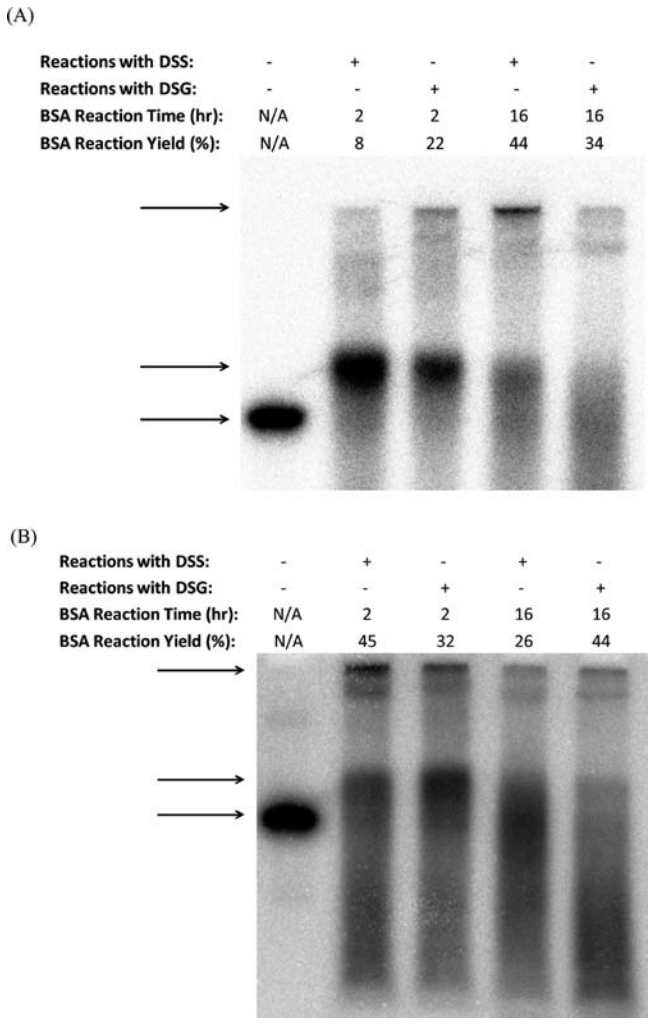


Figure 6. Preparation of the TW17 RNA−BSA conjugates. The ^{32}P-labeled GMP-primed TW17 RNA was conjugated with 1,6-hexanediamine using the one-step phosphoramidation reaction stated previously, followed by reactions with DSS or DSG and finally coupled with BSA (A) in the absence of 3 M NaCl or (B) in the presence of 3 M NaCl. The samples in both (A) and (B) were analyzed by 8% urea PAGE and visualized by autoradiogram. The samples in each figure, starting from the left, are the TW17 RNA without any modification reactions and formation of the TW17 RNA−BSA conjugates by using the DSS linker with 2 h coupling reactions, the DSG linker with 2 h coupling reactions, the DSS linker with 16 h coupling reactions, and the DSG linker with 16 h coupling reactions, respectively. The top arrow indicates the location of the TW17 RNA−BSA conjugate; the middle arrow stands for the migration of the TW17 RNA conjugates before coupling with BSA; the bottom arrow represents migration of the original GMP-primed TW17 RNA before phosphoramidation reactions.

is recommended when higher conjugation yields are a priority. Two-step phosphoramidation reactions, in spite of lower reaction yields, can be an advantageous approach. Two-step formats circumvent the problems of nucleophiles when containing a carbodiimide-sensitive functionality and the intricate phenomena of multiple conjugations, which deteriorate hybridization specificity in nucleic acids.

The outstanding properties of phosphoramidation reactions demonstrate their potential to afford diverse POCs not limited by sequences of peptides and nucleic acids or by properties of nucleic acids as DNA or RNA. We demonstrated the universal applications of this approach by effectively conjugating the model peptide tetraglycine (**12**) to RNA, single-stranded DNA, or doubled-stranded DNA with reasonably good yields. The facile procedures of two-step phosphoramidation reactions will alleviate difficulties in preparing POCs in typical biomedical research laboratories and will enable POCs to be used for important therapeutic and scientific applications such as gene therapy, gene silencing, or RNA interference (*24*) (Scheme 2).

Besides the facile approach and suitable yields, the hallmark of two-step phosphoramidation reactions for POC preparation is the general requirements of peptides and nucleic acids involved in reactions. Essentially, any nucleic acids with 5′-phosphate groups and any peptides with no previous modification are suitable reactants in phosphoramidation reactions to prepare desired POCs. A prerequisite of 5′-phosphate groups in nucleic acids ensures that any nucleic acid, ranging from DNA to RNA and natural to artificial nucleotides, will participate in phosphoramidation reactions. Natural or synthetic peptides with no protection groups can follow two-step phosphoramidation reactions to conjugate with nucleic acids to afford POCs. There is no need to protect carbodiimide-sensitivity functionality in peptides prior to coupling reactions. Peptides with any compositions of amino acid residues and no previous modifications can participate in phosphoramidation reactions to obtain POCs. Furthermore, two-step phosphoramidation reactions can be the only method to acquire POCs when the introduction of protection group(s) to peptides severely deteriorates binding affinities between modified peptides and their receptors to inhibit effective uptake of POCs into cells (vide infra). However, two-step phosphoramidation reactions have disadvantages in a lower coupling efficiency than the one-step approach. The disadvantage was demonstrated by the two-step phosphoramidation reactions between **11** and nucleic acids (Figures 1 and 2). We are exploring additional approaches to enhance the half-life of phosphorimidazolide intermediates during two-step phosphoramidation reactions to improve POC yields.

One-step nucleic acid phosphoramidation reactions with higher product yields remain an effective approach to acquire POCs under selected circumstances. As previously noted, the validity of one-step phosphoramidation reactions for POC preparation is warranted only if we can demonstrate that structure-modified peptides preserve the same levels of binding affinity and specificity to their intrinsic receptors. It is thus essential to determining the difference in dissociation constants K_d between protected and unprotected peptides when adsorbed to specific protein receptors before one-step phosphoramidation-prepared POCs can be exploited for in vivo applications and biomedical studies. The assurance of the integrity of hybridization specificity for nucleic acid moieties in one-step phosphoramidation-prepared POCs is especially important. The findings presented on one-step phosphoramidation reactions indicate that these reactions are very reactive to attain higher product yields and multiple conjugations, especially in cases of DNA (Figure 3). Significant multiple conjugations by one-step phosphoramidation reactions were particularly problematic to DNA in which extents of multiple conjugations paralleled a loss of hybridization specificity in DNA (Figure 4 and Supporting Information Figure S1). In essence, one-step nucleic acid phosphoramidation reactions require appropriate controls of the reaction conditions to obtain high product yields and minimize multiple conjugations to retain integrity of hybridization specificity in nucleic acids.

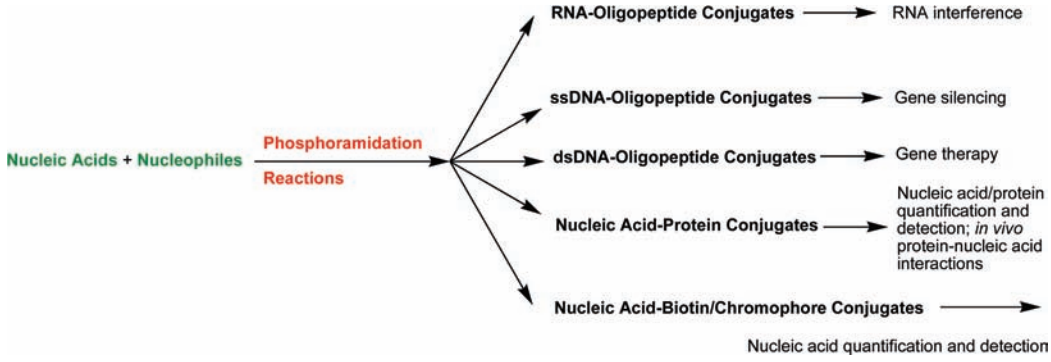
The cause of multiple conjugations in nucleic acids during phosphoramidation reactions can be traced back to the structures of nucleic acids and nucleophiles. The findings presented indicate that DNA molecules have a far greater tendency to experience multiple conjugations during phosphoramidation reactions than RNA. The difference between DNA and RNA is the presence of 2′-hydroxyl group in RNA and an extra methyl group in thymine of DNA when compared to uracil in RNA. 2′-Hydroxyl groups in RNA have no reason to be activated by EDC and react with nucleophiles to contribute multiple conjuga-

Table 1. Yields for Nucleic Acid Conjugates Directly or Indirectly Prepared from Phosphoramidation Reactions in Current Studies

nucleophiles	TW17 RNA	TW17 DNA	3′ primer
11 (one-step phosphoramidation)	70%[a], 79%[b]	23%[a], 80%[b]	69%[a], 60%[b]
11 (two-step phosphoramidation)	40%[a], 52%[b]	38%[a], 32%[b]	30%[a], 21%[b]
12 (two-step phosphoramidation)	44%[c], 40%[d]	39%[c], 42%[d]	27%[c], 34%[d]
1,6-hexanediamine (one-step phosphoramidation)	100%	100%	100%[e]
BSA (one-step phosphoramidation)[f]	8%[g], 44%[h], 45%[i], 26%[j]	5%[g], 5%[h], 2%[i], 4%[j]	N/A[k]
BSA (one-step phosphoramidation)[l]	22%[g], 34%[h], 32%[i], 44%[j]	10%[g], 12%[h], 5%[i], 7%[j]	N/A[k]

[a] In the absence of 6.77 M urea. [b] In the presence of 6.77 M urea. [c] For a 3 h phosphoramidation reaction. [d] For a 16 h phosphoramidation reaction. [e] Under the conditions of 15 min EDC activation and 20 min 1,6-hexanediamine coupling reactions. [f] Using DSS as the linker. [g] For a 2 h coupling reaction with BSA in the absence of 3 M NaCl. [h] For a 16 h coupling reaction with BSA in the absence of 3 M NaCl. [i] For a 2 h coupling reaction with BSA in the presence of 3 M NaCl. [j] For a 16 h coupling reaction with BSA in the presence of 3 M NaCl. [k] Not analyzed. [l] Using DSG as the linker.

Scheme 2. Versatile Applications of Nucleic Acid Phosphoramidation Reactions in Science and Medicine[a]



[a] dsDNA, double-stranded DNA; ssDNA, single-stranded DNA.

tions. It is likely that the presence of the thymine base is one reason to confer multiple conjugations in DNA during phosphoramidation reactions. The ability of the extra methyl group in uracil to transform thymine in DNA into a relatively good electrophile in phosphoramidation reactions remains unanswered. The other factor to bestow multiple conjugations in nucleic acids during phosphoramidation reactions is the pK_a of the amine moieties in nucleophiles and the structures of nucleophiles, particularly their lipophilicity and NH_2 functionality contents. According to the results from nucleic acid phosphoramidation reactions with **11**, **12**, ethylenediamine, and 1,6-hexanediamine, the increase of amine pK_a, lipophilicity or NH_2 contents in nucleophiles promotes multiple conjugations in nucleic acids. We thus observed the vigorous activity of 1,6-hexanediamine in phosphoramidation reactions to produce multiple conjugations in nucleic acids (Figure 3). Appropriate designs of nucleophile lipophilicity and NH_2 contents can afford high yields of nucleic acid conjugates while avoiding multiple conjugations in nucleic acids during one-step phosphoramidation reactions.

The problem of multiple conjugations in nucleic acids during phosphoramidation reactions is the negative effect on nucleic acid hybridization specificity manifested by the single-stranded DNA−fluorescein conjugate studies. The decline of nucleic acid hybridization specificity is intimately related to the extent of multiple conjugations in nucleic acid, especially modifications which damage the base-pairing property of thymine. The extents of multiple conjugations may also be a determinant to contribute to lower yields of nucleic acid−BSA conjugates (Figure 6 and Supporting Information Figure S2). These results contradict our earlier assumption that more conjugations in nucleic acids would provide more reactive groups to aid in covalently linking BSA to nucleic acids and thereby increasing yields of nucleic acid−BSA conjugates. In contrast, the extent of multiple conjugations in phosphoramidation-prepared nucleic acid conjugates had the opposite effect on yields of nucleic acid−BSA conjugates (Figure 6 and Supporting Information Figure S2). The TW17 RNA−1,6-hexanediamine conjugates with a minor multiple conjugations offered better coupling efficiency with BSA compared to the same coupling reactions using DNA−1,6-hexanediamine conjugates with more extensive multiple conjugations. The actual cause of higher extents of multiple conjugations in DNA to render low yields of DNA−BSA conjugates is under investigation currently. However, results from these nucleic acid−BSA conjugate preparations suggest that two-step phosphoramidation reaction schemes are a desirable approach to acquire DNA−protein conjugates with better yields.

The controversial role of high concentration of urea in nucleic acid phosphoramidation reaction was intriguing. Urea of 6.77 M was introduced to nucleic acid phosphoramidation reactions to disrupt secondary structures in nucleic acids and to expose 5′-phosphate groups for phosphoramidation reactions. Urea in high concentrations is a common approach in biochemical research to denature nucleic acids because of its typical inertness toward chemical reactions. We thus expected to have higher yields for nucleic acid phosphoramidation reactions in the presence of 6.67 M urea, yet only RNA molecules had better phosphoramidation reaction yields with additions of 6.77 M urea. Furthermore, high concentrations of urea had definite negative effects on two-step DNA phosphoramidation reactions (Figures 1B and 2C,D). The unexpected results can be explained by the ambient nucleophile characteristics in urea (*34*−*36*). The current results suggested that urea plays a dual role in nucleic acid phosphoramidation reactions: one as a surfactant to denature nucleic acids, and the other as a nucleophile to divert phosphoramidation reactions and to reduce product yields. The observed product yield from nucleic acid phosphoramidation reactions is the competition between two counteracting activities. The greater adverse effect of urea in DNA phosphoramidation reactions can be attributed to the presence of a more reactive thymine base in DNA which reacts with urea to decrease product yields. The negative effect of urea in two-step DNA phosphoramidation reactions is further ascribed to the hydrolysis of phosphorimidazolide intermediates of nucleic acids during the workup procedures. We conclude that high concentrations of urea will have beneficial

effects only when applied to RNA phosphoramidation reactions. The substitution of urea with more inert surfactants to increase one-step and two-step nucleic acid phosphoramidation reaction product yields is being undertaken.

In summary, we successfully synthesized a new biotin derivative **11** which was exploited to develop facile one-step and two-step nucleic acid phosphoramidation reactions with excellent yields. One-step phosphoramidation reactions offered better yields of nucleic acid conjugates than two-step phosphoramidation approaches. One-step phosphoramidation reactions were, however, more reactive than two-step phosphoramidation reactions and resulted in multiple conjugations accompanied by deterioration of hybridization specificity in nucleic acids. Multiple conjugations in phosphoramidation-prepared nucleic acid conjugates were most apparent in DNA and nucleophiles contained multiple NH_2 functional groups. Understanding the basic chemistry underlying phosphoramidation reactions allowed an effective application of the reactions to nucleic acid−biotin and nucleic acid−protein conjugate preparations for biomolecule detection and biomedical research (Scheme 2). Most importantly, the phosphoramidation approach provides versatile POCs without scarifying hybridization specificity in nucleic acids. Facile phosphoramidation reactions to achieve effective POC preparation can facilitate therapeutic applications of POCs and fulfill the goals of using POCs for RNA interference, gene silencing, and gene therapy in science and medicine.

ACKNOWLEDGMENT

We thank Dr. Susan Fetzer for critical reading of the manuscript. This work was supported with grants from the National Science Council of Taiwan (96-2113-M-037-004-MY2 and 98-2113-M-037-002-) awarded to T.-P. W.

Supporting Information Available: Full details of a reaction scheme, NMR and MS spectra for compounds **2**−**11**, and supporting figures referenced in the text. This material is available free of charge via the Internet at http://pubs.acs.org.

LITERATURE CITED

(1) Seelig, B., and Jaschke, A. (1999) A small catalytic RNA motif with Diels-Alderase activity. *Chem. Biol. 6*, 167–176.
(2) Sengle, G., Eisenfuhr, A., Arora, P. S., Nowick, J. S., and Famulok, M. (2001) Novel RNA catalysts for the Michael reaction. *Chem. Biol. 8*, 459–473.
(3) Fusz, S., Eisenfuhr, A., Srivatsan, S. G., Heckel, A., and Famulok, M. (2005) A ribozyme for the aldol reaction. *Chem. Biol. 12*, 941–950.
(4) Tsukiji, S., Pattnaik, S. B., and Suga, H. (2003) An alcohol dehydrogenase ribozyme. *Nat. Struct. Biol. 10*, 713–717.
(5) Tsukiji, S., Pattnaik, S. B., and Suga, H. (2004) Reduction of an aldehyde by a NADH/Zn2+-dependent redox active ribozyme. *J. Am. Chem. Soc. 126*, 5044–5045.
(6) Pereira, M. J. B., Nikolova, E. N., Hiley, S. L., Jaikaran, D., Collins, R. A., and Walter, N. G. (2008) Single VS ribozyme molecules reveal dynamic and hierarchical folding toward catalysis. *J. Mol. Biol. 382*, 496–509.
(7) Boots, J. L., Canny, M. D., Azimi, E., and Pardi, A. (2008) Metal ion specificities for folding and cleavage activity in the Schistosoma hammerhead ribozyme. *RNA 14*, 2212–2222.
(8) Mortimer, S. A., and Weeks, K. M. (2009) C2′-endo nucleotides as molecular timers suggested by the folding of an RNA domain. *Proc. Natl. Acad. Sci. U.S.A. 106*, 15622–15627.
(9) Shi, X., Mollova, E. T., Pljevaljci, G., Millar, D. P., and Herschlag, D. (2009) Probing the dynamics of the P1 helix within the Tetrahymena group I intron. *J. Am. Chem. Soc. 131*, 9571–9578.
(10) Ikawa, Y., Moriyama, S., and Furuta, H. (2008) Facile syntheses of BODIPY derivatives for fluorescent labeling of the 3′ and 5′ ends of RNAs. *Anal. Biochem. 378*, 166–170.
(11) Tinsley, R. A., Furchak, J. R. W., and Walter, N. G. (2007) Trans-acting glmS catalytic riboswitch: locked and loaded. *RNA 13*, 468–477.
(12) Smith, L. M., Sanders, J. Z., Kaiser, R. J., Hughes, P., Dodd, C., Connell, C. R., Heiner, C., Kent, S. B. H., and Hood, L. E. (1986) Fluorescence detection in automated DNA sequence analysis. *Nature 321*, 674–679.
(13) Prober, J., Trainor, G., Dam, R., Hobbs, F., Robertson, C., Zagursky, R., Cocuzza, A., Jensen, M., and Baumeister, K. (1987) A system for rapid DNA sequencing with fluorescent chain-terminating dideoxynucleotides. *Science 238*, 336–341.
(14) Niemeyer, C. M., and Blohm, D. (1999) DNA Microarrays. *Angew. Chem., Int. Ed. 38*, 2865–2869.
(15) Lu, K., Duan, Q.-P., Ma, L., and Zhao, D.-X. (2010) Chemical strategies for the synthesis of peptide-oligonucleotide conjugates. *Bioconjugate Chem. 21*, 187–202.
(16) Eritja, R. (2007) Solid-phase synthesis of modified oligonucleotides. *Int. J. Pept. Res. Ther. 13*, 53–68.
(17) Zatsepin, T. S., Turner, J. J., Oretskaya, T. S., and Gait, M. J. (2005) Conjugates of oligonucleotides and analogues with cell penetrating peptides as gene silencing agents. *Curr. Pharm. Des. 11*, 3639–3654.
(18) Fraley, A. W., Pons, B., Dalkara, D., Nullans, G., Behr, J.-P., and Zuber, G. (2006) Cationic oligonucleotide-peptide conjugates with aggregating properties enter efficiently into cells while maintaining hybridization properties and enzymatic recognition. *J. Am. Chem. Soc. 128*, 10763–10771.
(19) Rogers, F. A., Manoharan, M., Rabinovitch, P., Ward, D. C., and Glazer, P. M. (2004) Peptide conjugates for chromosomal gene targeting by triplex-forming oligonucleotides. *Nucleic Acids Res. 32*, 6595–6604.
(20) Kwok, K. Y., Park, Y., Yang, Y., Mckenzie, D. L., Liu, Y., and Rice, K. G. (2003) In vivo gene transfer using sulfhydryl cross-linked PEG-peptide/glycopeptide DNA co-condensates. *J. Pharm. Sci. 92*, 1174–1185.
(21) Chu, B. C., Wahl, G. M., and Orgel, L. E. (1983) Derivatization of unprotected polynucleotides. *Nucleic Acids Res. 11*, 6513–6529.
(22) Anderson, G. W., Zimmerman, J. E., and Callahan, F. M. (1964) The use of esters of N-hydroxysuccinimide in peptide synthesis. *J. Am. Chem. Soc. 86* 1839–1842.
(23) Qin, P. Z., and Pyle, A. M. (1999) Site-specific labeling of RNA with fluorophores and other structural probes. *Methods 18*, 60–70.
(24) Achenbach, T. V., Brunner, B., and Heermeier, K. (2003) Oligonucleotide-based knockdown technologies: antisense versus RNA interference. *ChemBioChem 4*, 928–935.
(25) Berg, T. A., v, d., Feringa, B. L., and Roelfes, G. (2007) Double strand DNA cleavage with a binuclear iron complex. *Chem. Commun.* 180–182.
(26) Boger, D. L., Zhou, J., Winter, B., and Kitos, P. A. (1995) Key analogs of the tetrapeptide subunit of RA-VII and deoxybouvardin. *Bioorg. Med. Chem. 3*, 1579–1593.
(27) Bayer, E., and Wilchek, M. (1974) Insolubilized biotin for the purification of avidin. *Methods Enzymol. 34*, 265–267.
(28) Wilchek, M., and Bayer, E. A. (1990) Biotin-containing reagents. *Methods Enzymol. 184*, 123–138.
(29) Callahan, J. F., Ashton-Shue, D., Bryan, H. G., Bryan, W. M., Heckman, G. D., Kinter, L. B., McDonald, J. E., Moore, M. L., Schmidt, D. B., Silvestri, J. S., et al. (1989) Structure-activity relationships of novel vasopressin antagonists containing C-terminal diaminoalkanes and (aminoalkyl)guanidines. *J. Med. Chem. 32*, 391–396.
(30) Laurent, S., Botteman, F., Vander Elst, L., and Muller, R. N. (2004) Relaxivity and transmetallation stability of new benzyl-substituted derivatives of gadoliniumDTPA complexes. *Helv. Chim. Acta 87*, 1077–1089.

(31) Srinivasan, N., Yurek-George, A., and Ganesan, A. (2005) Rapid deprotection of N-Boc amines by TFA combined with freebase generation using basic ion-exchange resins. *Mol. Divers. 9*, 291–293.

(32) Hermanson, G. T. (1996) *Bioconjugate techniques*, Academic Press, San Diego, pp 670−671.

(33) Jablonski, E., Moomaw, E. W., Tullis, R. H., and Ruth, J. L. (1986) Preparation of oligodeoxynucleotide-alkaline phosphatase conjugates and their use hybridization probes. *Nucleic Acids Res. 14*, 6115–6128.

(34) Bar, G. L. J., Lloyd-Jones, G. C., and Booker-Milburn, K. I. (2005) Pd(II)-catalyzed intermolecular 1,2-diamination of conjugated dienes. *J. Am. Chem. Soc. 127*, 7308–7309.

(35) Kluger, R., and Adawadkar, P. D. (1976) A reaction proceeding through intramolecular phosphorylation of a urea. A chemical mechanism for enzymic carboxylation of biotin involving cleavage of adenosine 5′-triphosphate. *J. Am. Chem. Soc. 98*, 3741–3742.

(36) Tamaru, Y., Hojo, M., Higashimura, H., and Yoshida, Z. (1988) Urea as the most reactive and versatile nitrogen nucleophile for the palladium(2+)-catalyzed cyclization of unsaturated amines. *J. Am. Chem. Soc. 110*, 3994–4002.

BC1001505

Supporting Information

Versatile phosphoramidation reactions for nucleic acid conjugations with peptides, proteins, chromophores and biotin derivatives

Tzu-Pin Wang[*, †], Yi-Jang Chiou[†], Yi Chen[†], Eng-Chi Wang[†], Long-Chih Hwang[†], Bing-Hung Chen[‡], Yen-Hsu Chen[§], and Chun-Han Ko[‖]

Running title: Nucleic acid phosphoramidation and applications

*Corresponding author: tzupinw@cc.kmu.edu.tw

*Contact address: Department of Medicinal and Applied Chemistry, Kaohsiung Medical University, Kaohsiung, 80708, Taiwan

Tel: +886-07-312-1101, ext. 2756, Fax: +886-07-312-5339

Scheme S1. The reaction scheme for phosphoramidation reactions to prepare nucleic acid-**11** conjugates.

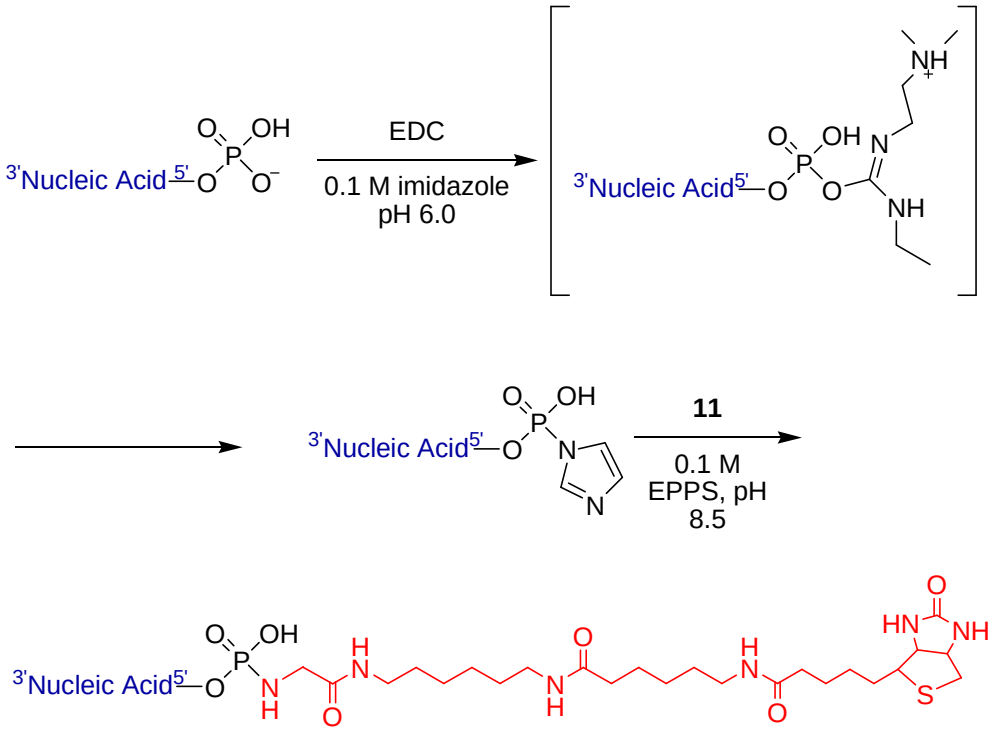
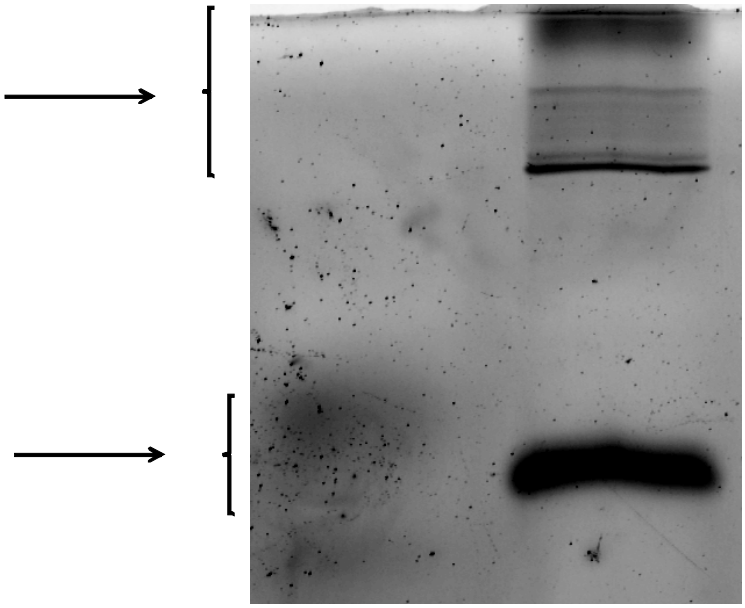


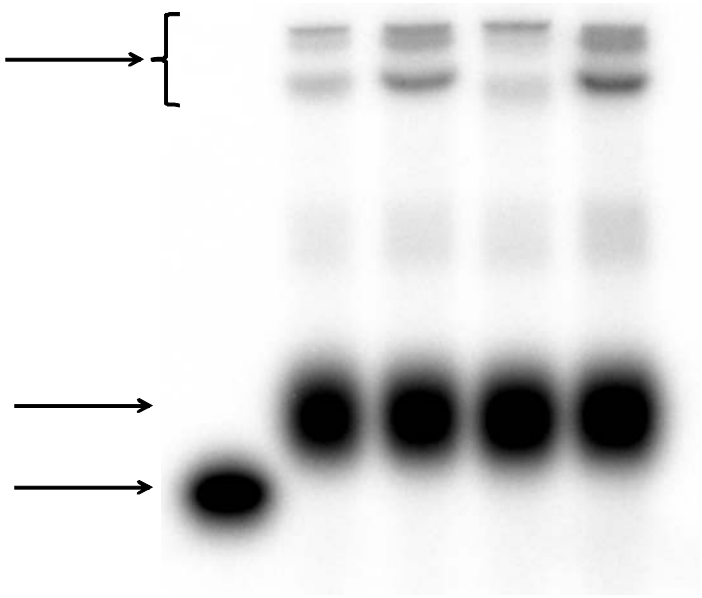
Figure S1. Formation of the 3'-primer DNA-fluorescein conjugate demonstrated by PCR amplification and urea PAGE analysis. Both nonradio-labeled samples were analyzed by biphasic urea PAGE (the top gel of 6% acrylamide and the bottom gel of 20% acrylamide) and visualized by an Amersham Typhoon phosphoimager.



PCR Reaction:	-	+
PCR Reaction Yield (%):	N/A	30

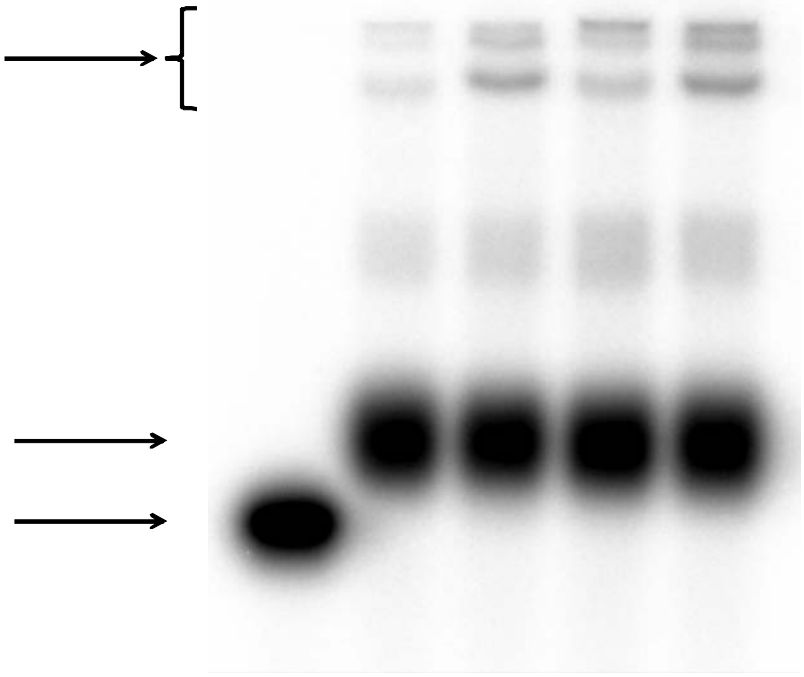
Figure S2. Applications of phosphormaidation reactions to preparation of the double-stranded TW17 DNA-BSA conjugates (A) in the absence of 3 M NaCl and (B) in the presence of 3 M NaCl. All ^{32}P-labeled samples were analyzed by 8% urea PAGE and visualized by an Amersham Typhoon phosphoimager.

(A)



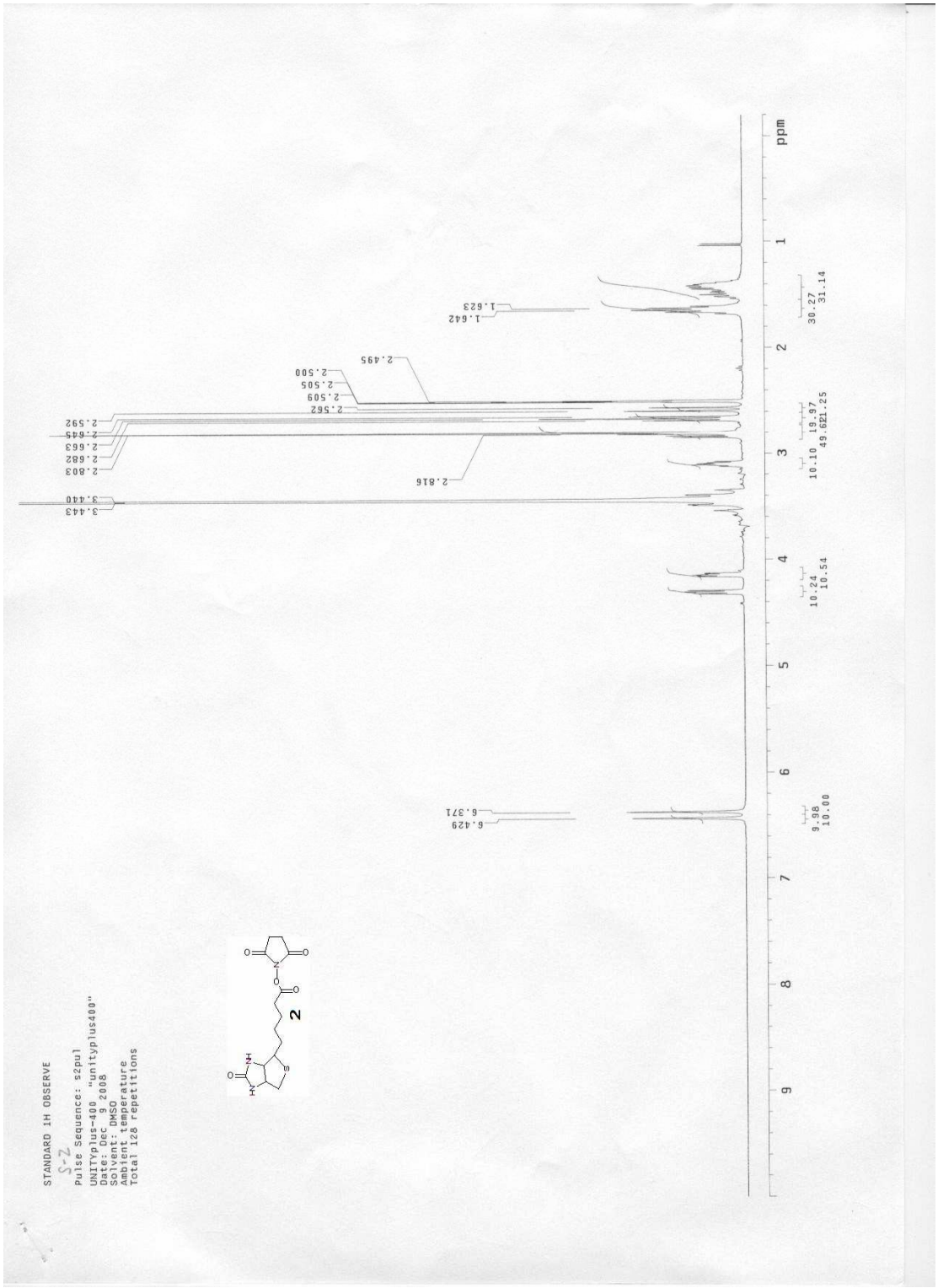
Reactions with DSS:	-	+	-	+	-
Reactions with DSG:	-	-	+	-	+
BSA Reaction Time (hr):	N/A	2	2	16	16
BSA Reaction Yield (%):	N/A	5	10	5	12

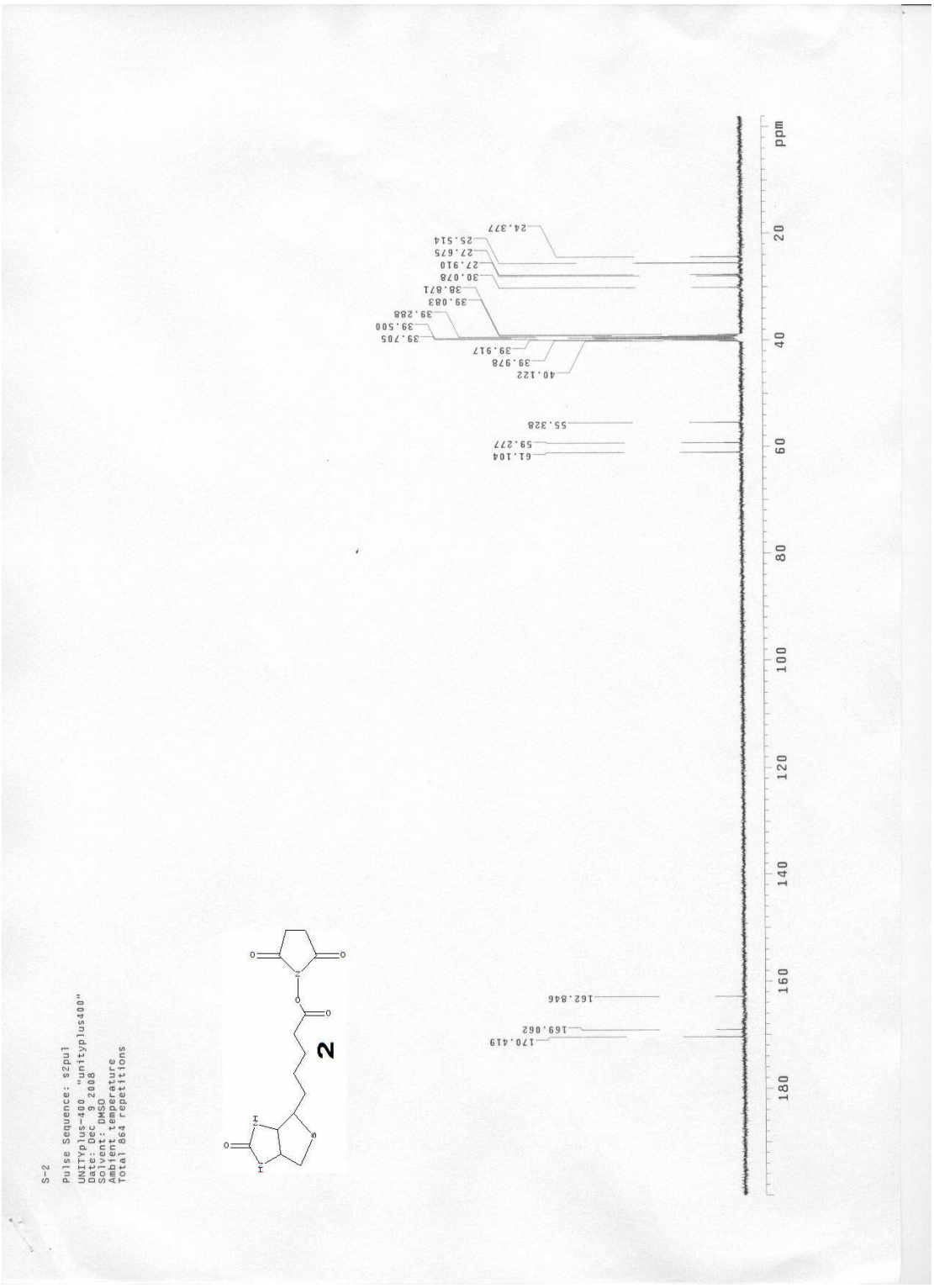
(B)



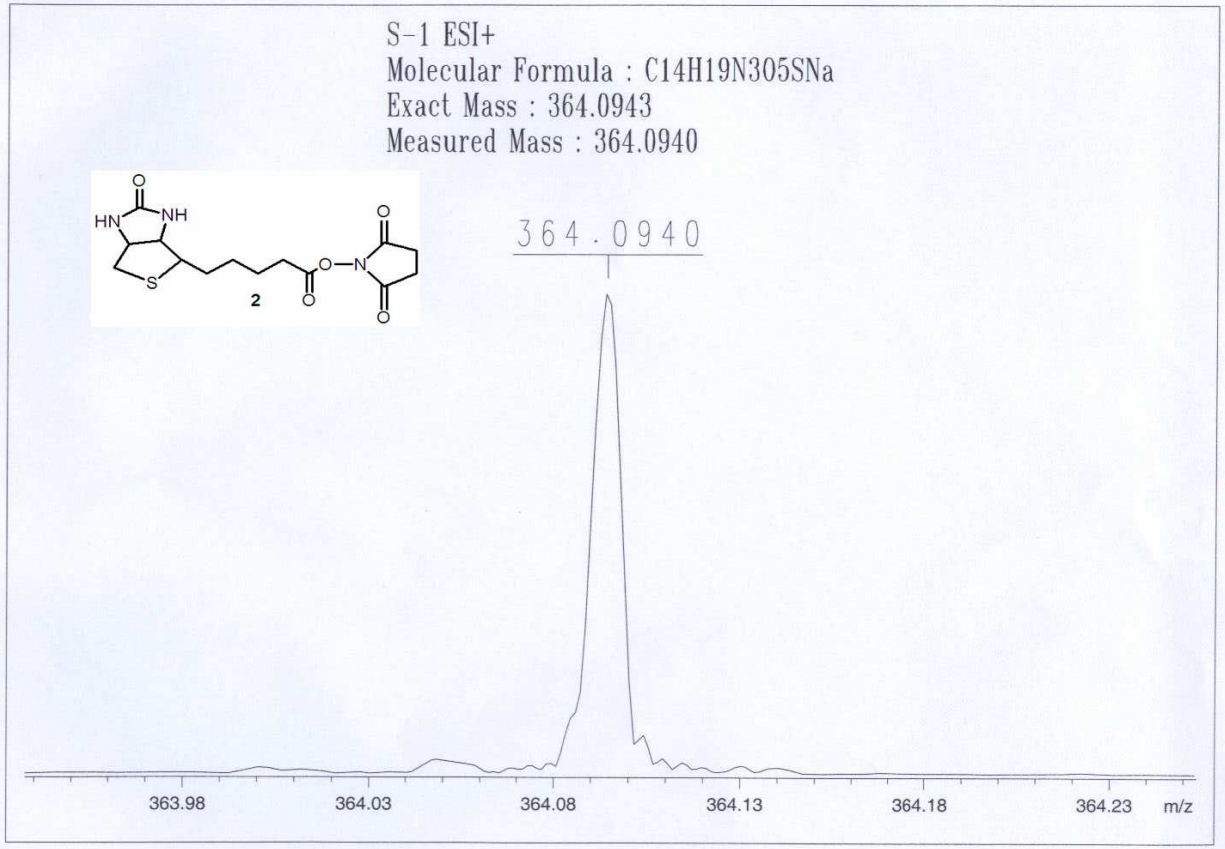
Reactions with DSS:	-	+	-	+	-
Reactions with DSG:	-	-	+	-	+
BSA Reaction Time (hr):	N/A	2	2	16	16
BSA Reaction Yield (%):	N/A	2	5	4	7

NMR and MS spectra for Compounds 2-11

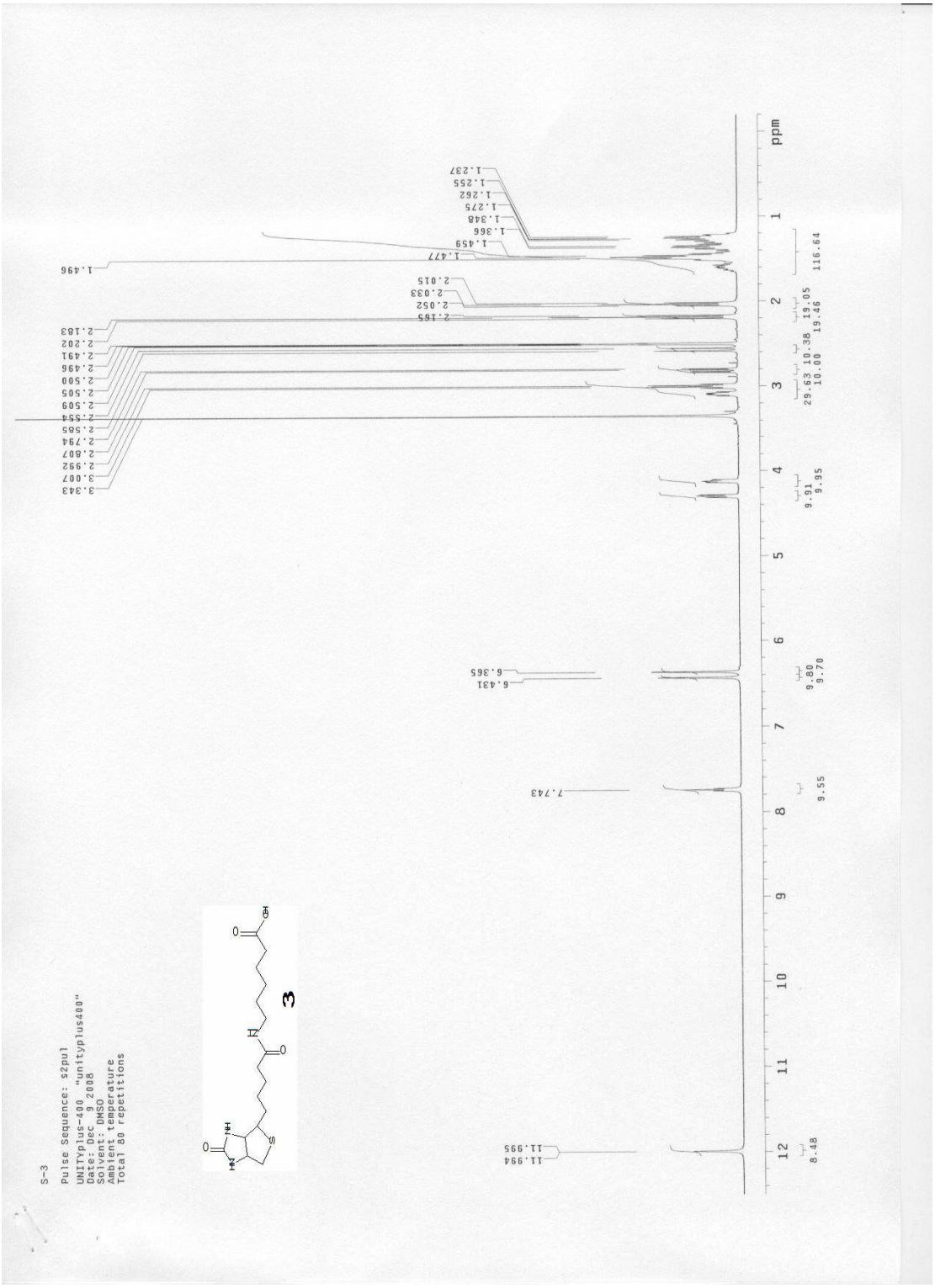


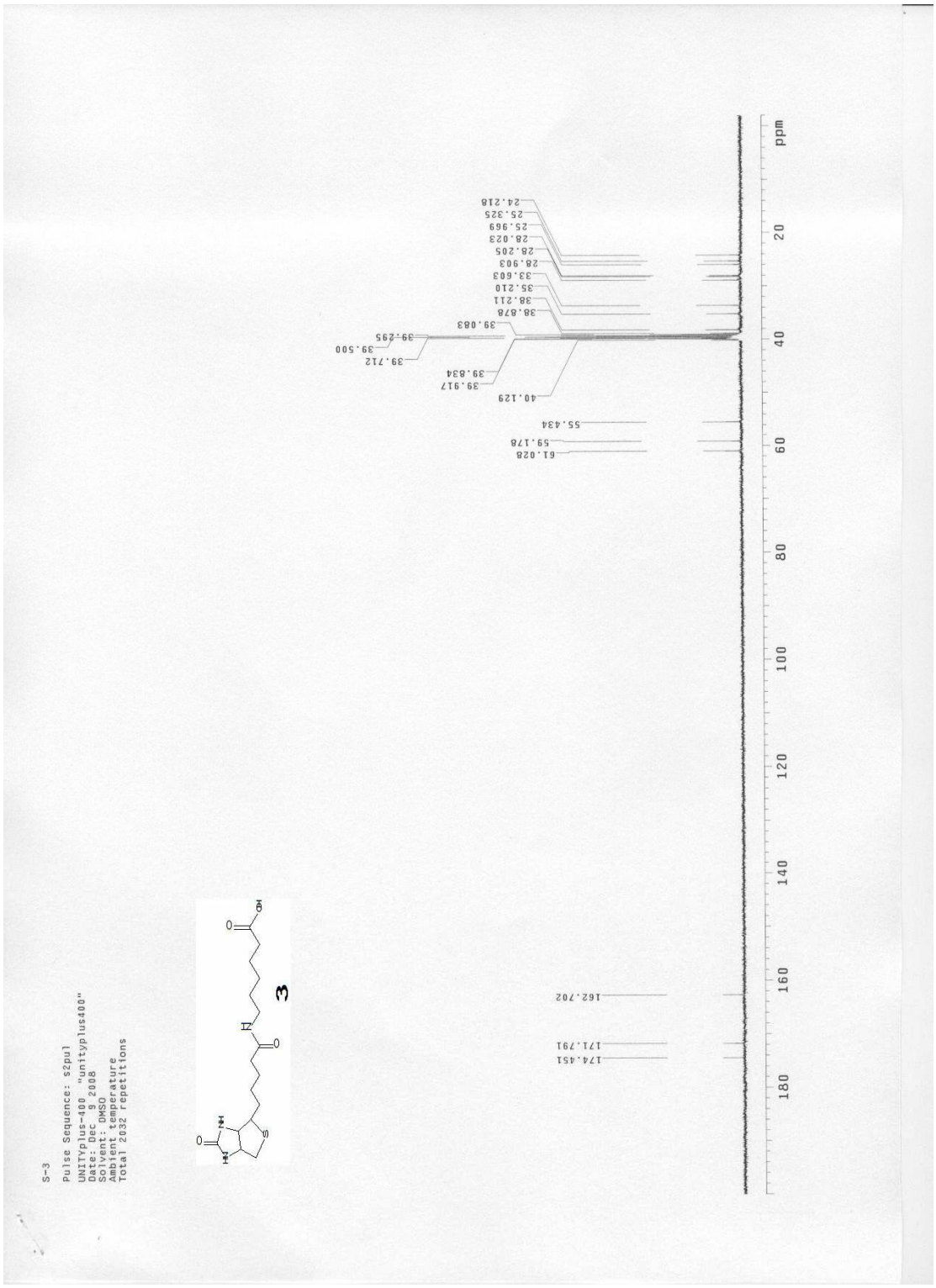

S-2
Pulse Sequence: s2pul
UNITYplus-400 "unityplus400"
Date: Dec 9 2008
Solvent: DMSO
Ambient temperature
Total 864 repetitions
2
170.419
169.062
162.846
61.104
59.277
55.328
40.122
39.978
39.917
39.705
39.500
39.288
39.083
38.871
30.078
27.910
27.675
25.514
24.377
ppm
180
160
140
120
100
80
60
40
20

S-1 ESI+
Molecular Formula : C14H19N3O5SNa
Exact Mass : 364.0943
Measured Mass : 364.0940

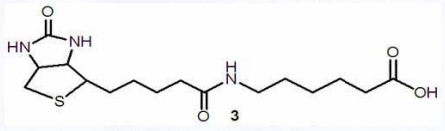


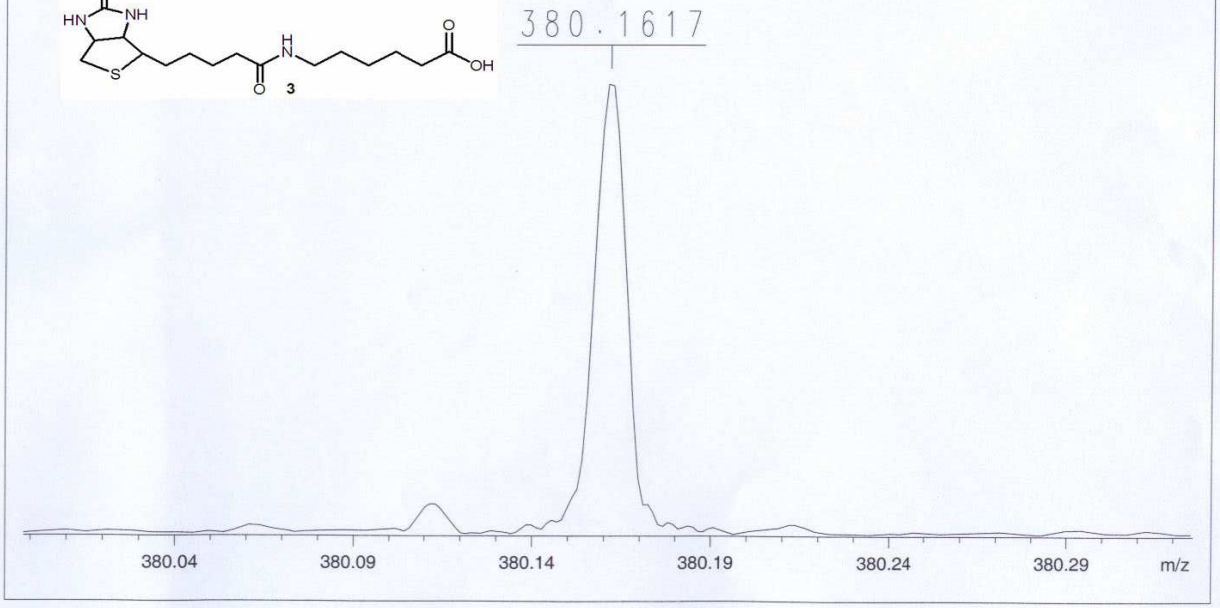
/d=/Data/yu/S1/1/pdata/1 Administrator Thu Sep 11 13:41:52 2008


S-3
Pulse Sequence: s2pul
UNITYplus-400 "unityplus400"
Date: Dec 9 2008
Solvent: DMSO
Ambient temperature
Total 80 repetitions
3
ppm

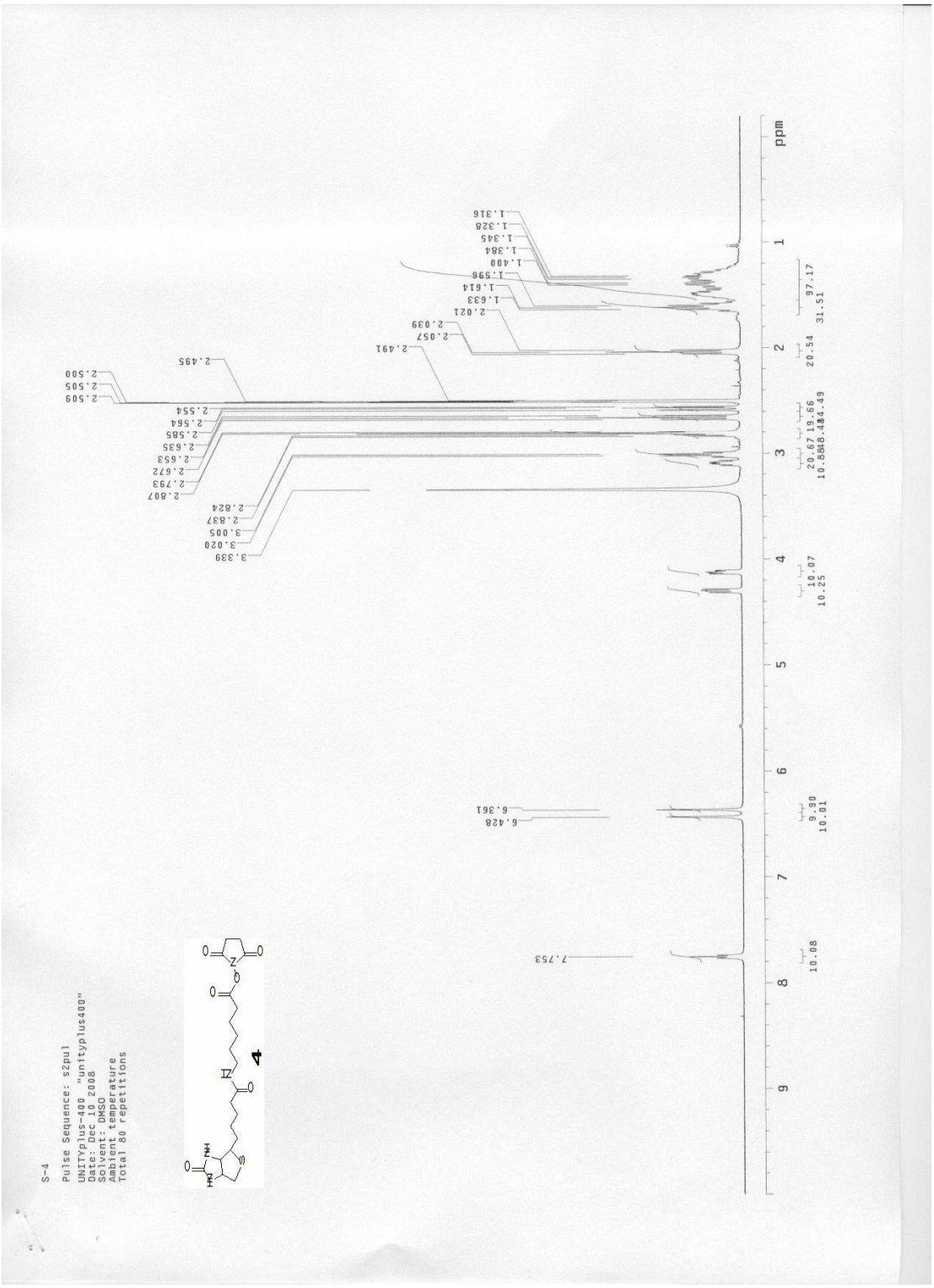

S-3
Pulse Sequence: s2pul
UNITYplus-400 "unityplus400"
Date: Dec 9 2008
Solvent: DMSO
Ambient temperature
Total 2032 repetitions
3
174.451
171.791
162.702
55.434
61.028
59.178
40.129
39.917
39.834
39.712
39.500
39.295
39.083
38.878
38.211
35.210
33.603
28.903
28.205
28.023
25.969
25.325
24.218
ppm

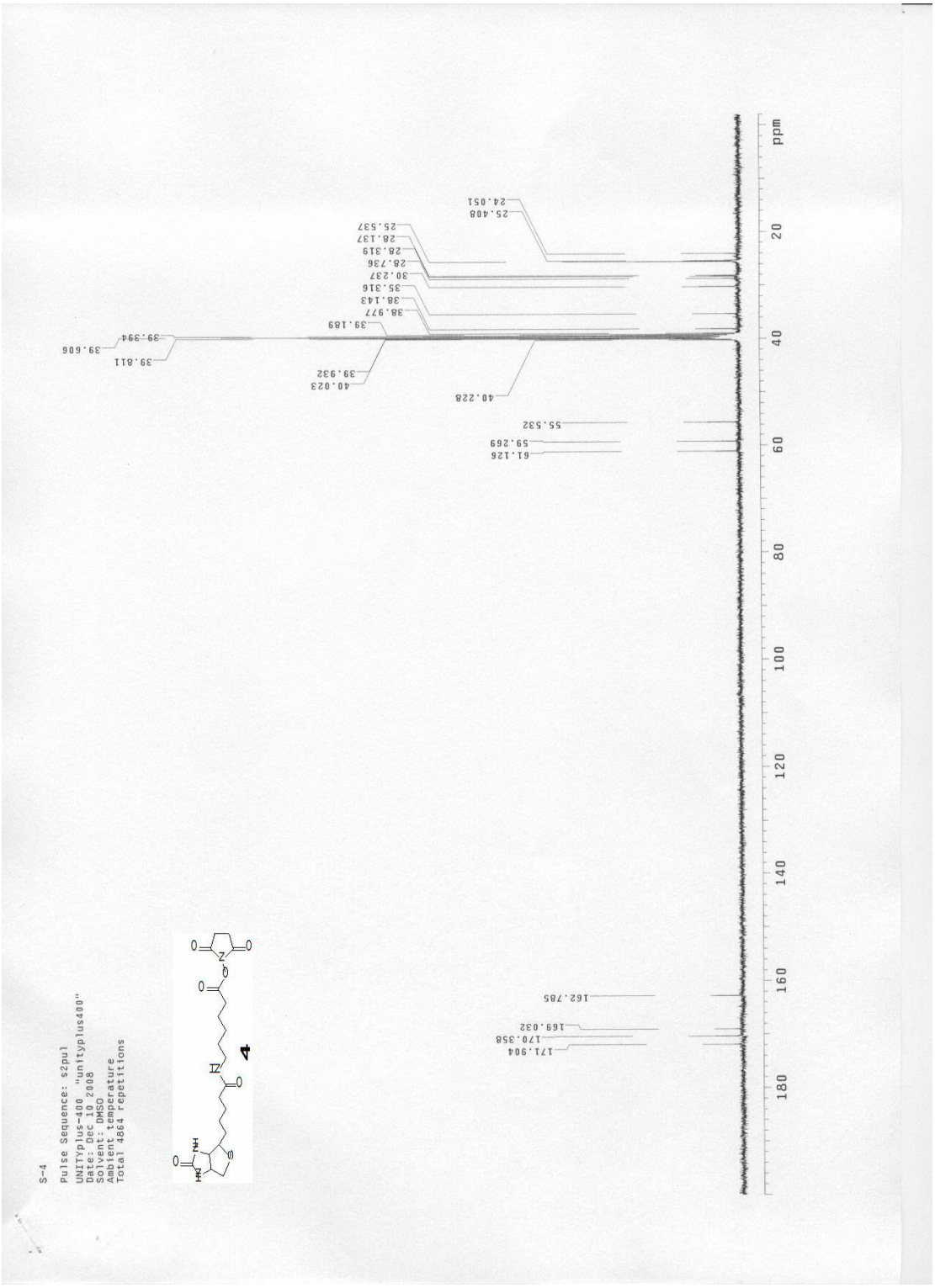
S-6 ESI+
Molecular Formula : C16H27N3O4SNa
Exact Mass : 380.1620
Measured Mass : 380.1617

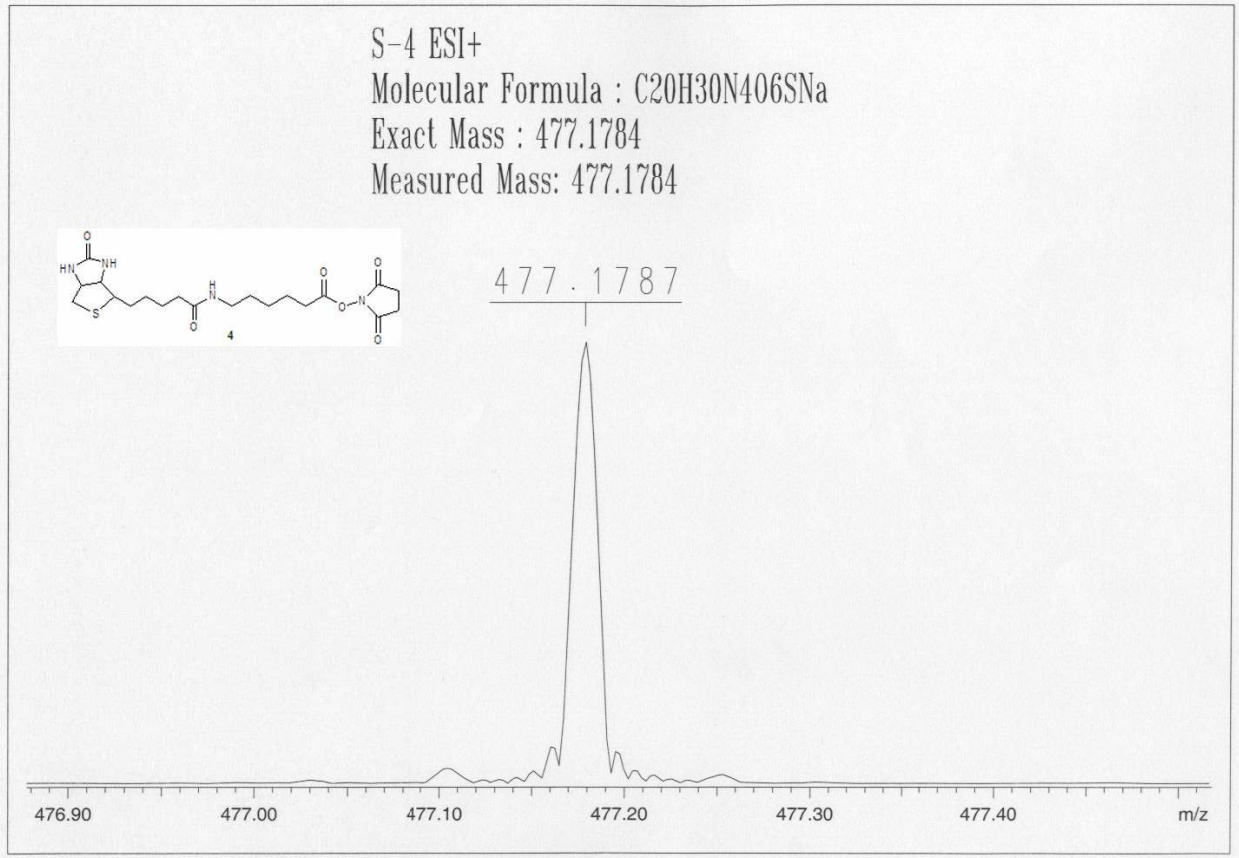


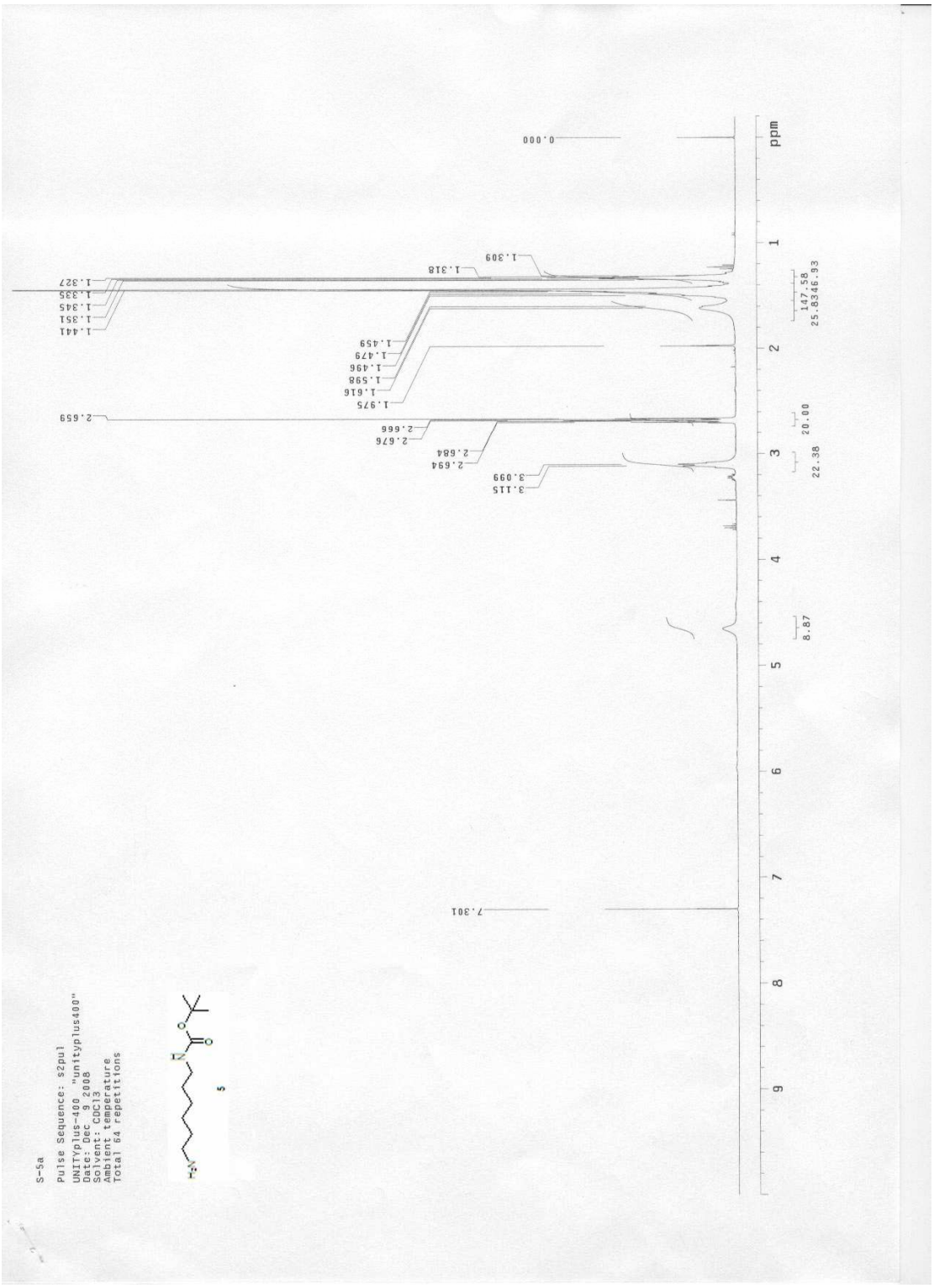


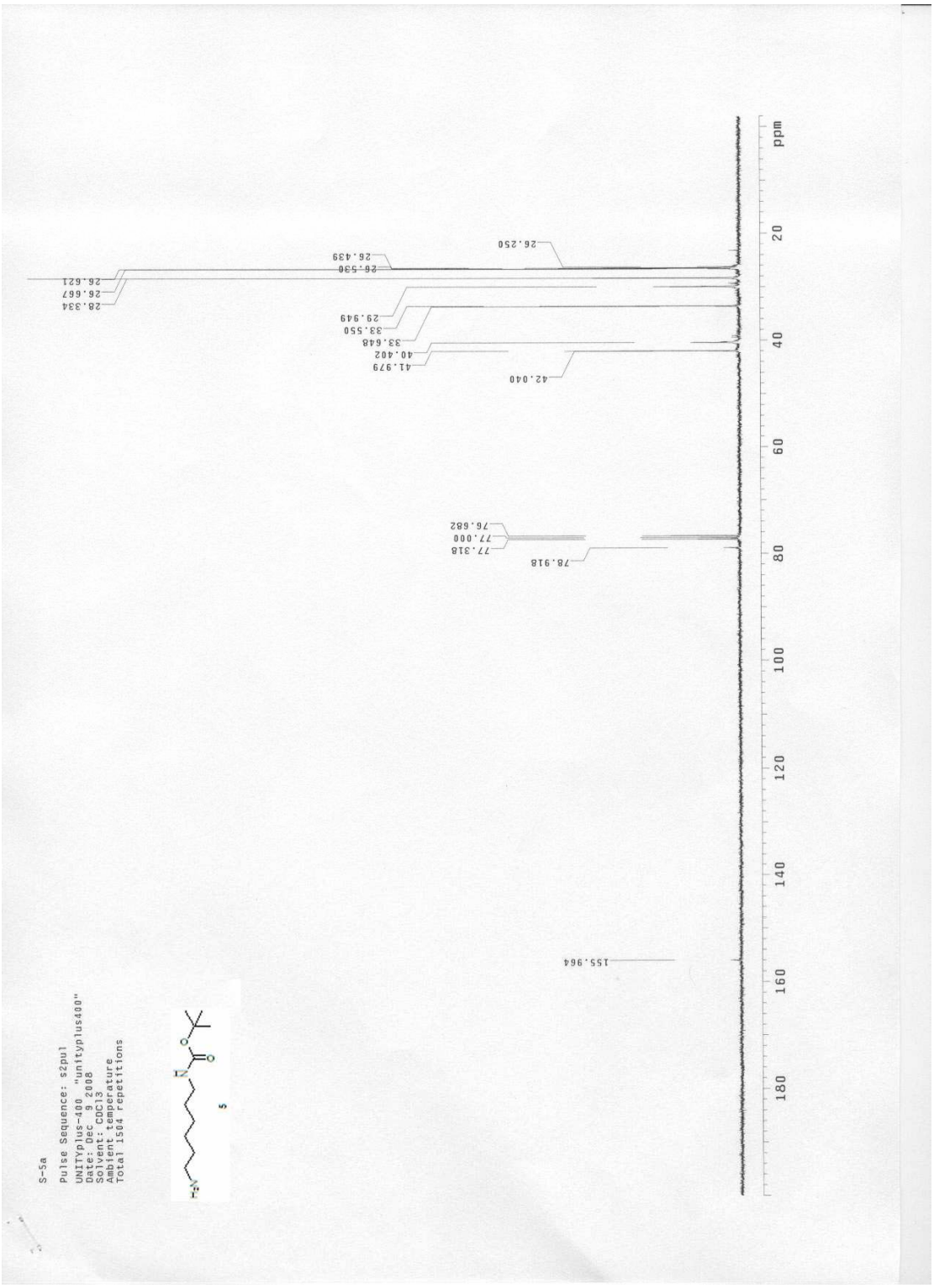
/d=/Data/yu/S6/3/pdata/1 Administrator Thu Sep 11 14:55:09 2008

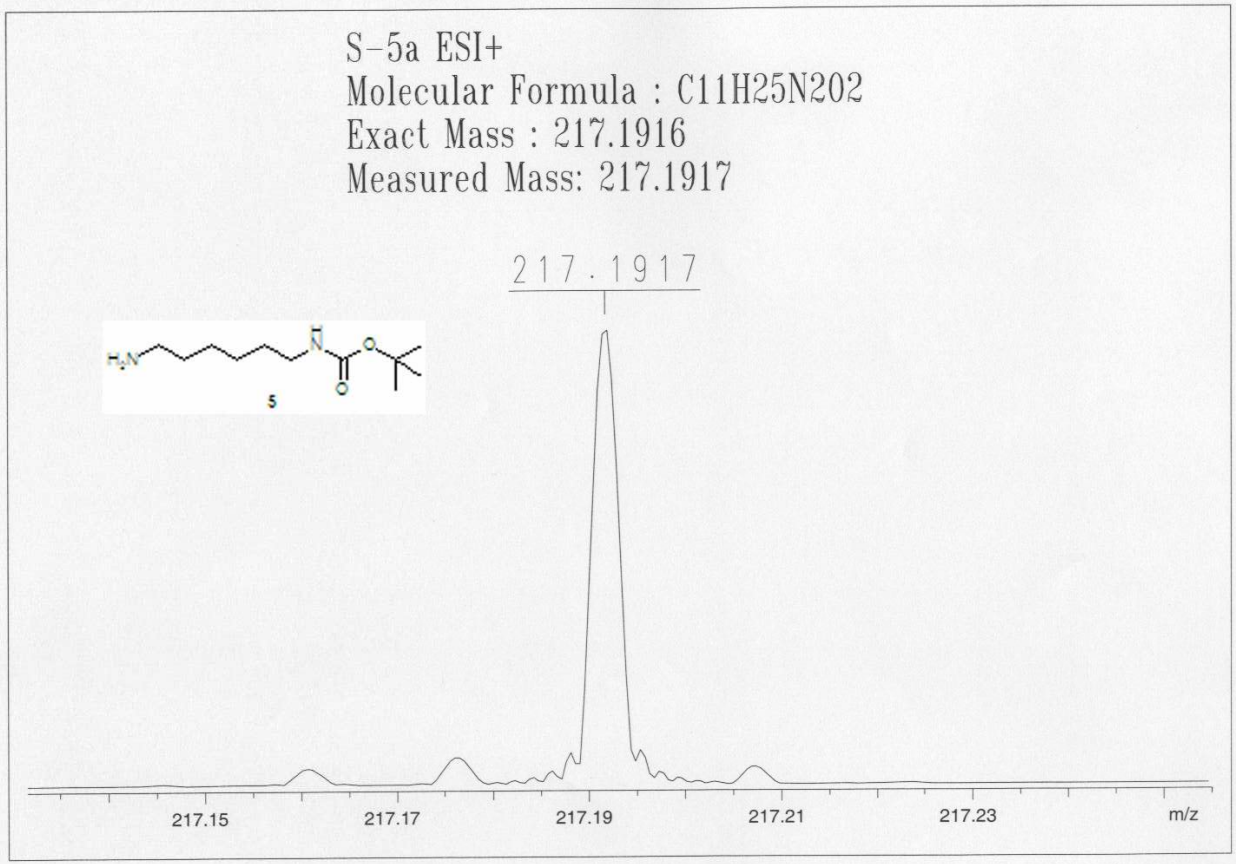

S-4
Pulse Sequence: s2pul
UNITYplus-400 "unityplus400"
Date: Dec 10 2008
Solvent: DMSO
Ambient temperature
Total 80 repetitions
4
ppm
7.753
6.428
6.361
3.339
3.020
3.005
2.837
2.824
2.807
2.793
2.672
2.653
2.635
2.585
2.564
2.554
2.509
2.505
2.500
2.495
2.491
2.057
2.039
2.021
1.633
1.614
1.596
1.400
1.384
1.345
1.328
1.316

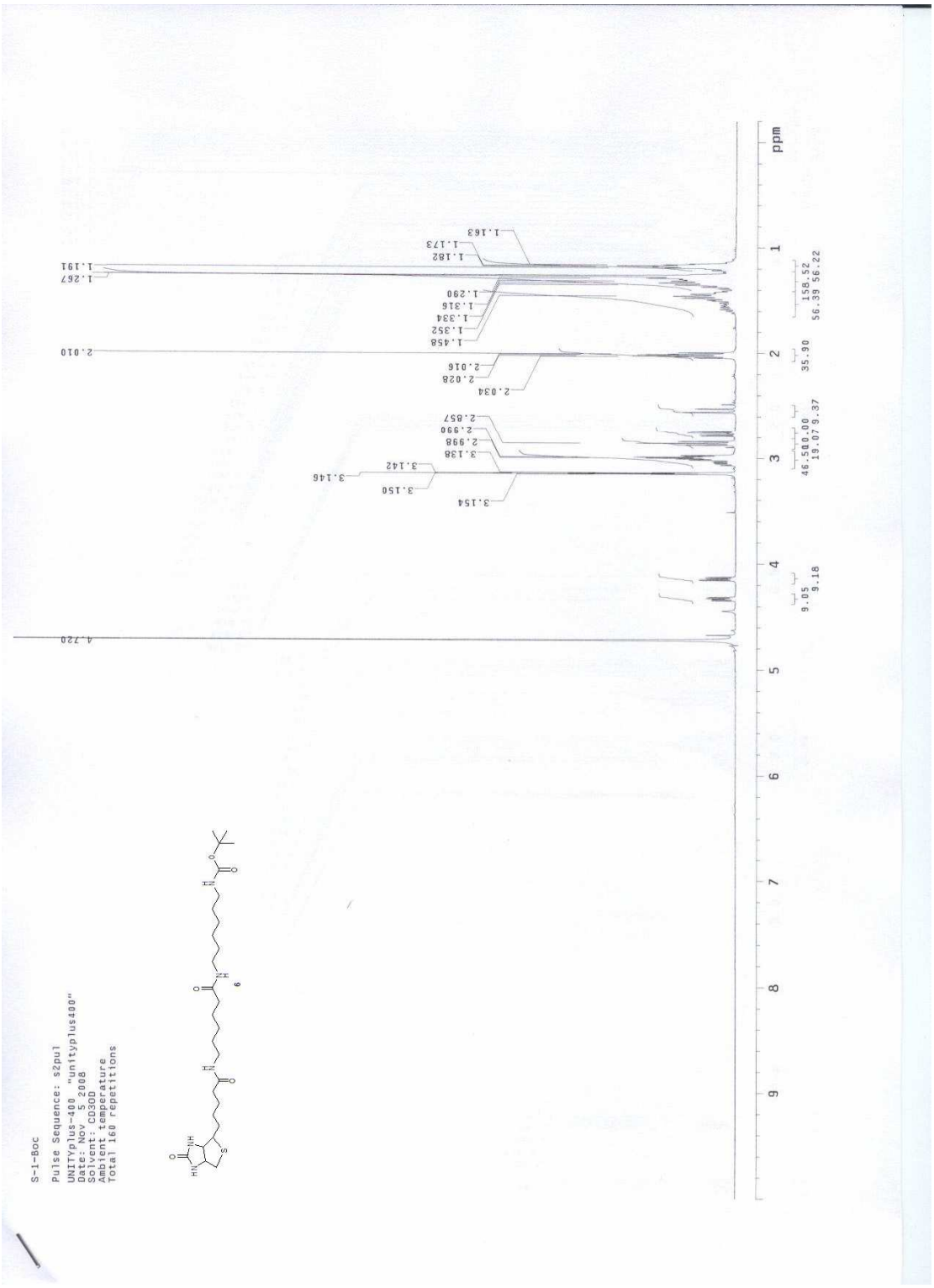

S-4
Pulse Sequence: s2pul
UNITYplus-400 "unityplus400"
Date: Dec 10 2008
Solvent: DMSO
Ambient temperature
Total 4864 repetitions
4
ppm
20
40
60
80
100
120
140
160
180
24.051
25.408
25.537
28.137
28.319
28.736
30.237
35.316
38.143
38.977
39.189
39.394
39.606
39.811
40.023
39.932
40.228
55.532
59.269
61.126
162.785
169.032
170.358
171.904

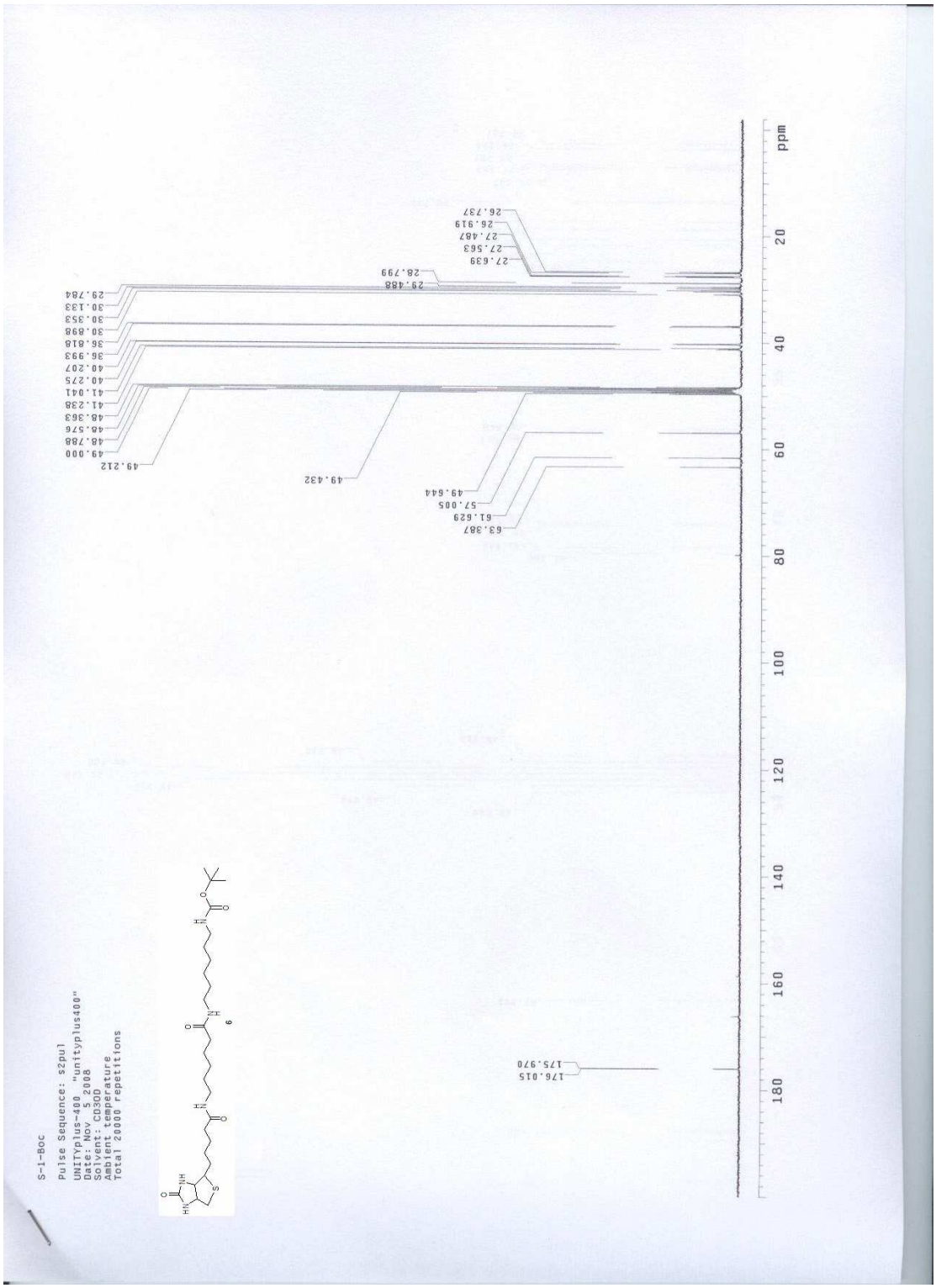

S-4 ESI+
Molecular Formula : C20H30N406SNa
Exact Mass : 477.1784
Measured Mass: 477.1784
477.1787
476.90
477.00
477.10
477.20
477.30
477.40
m/z
/d=/Data/yu/s4/11/pdata/1 Administrator Mon Dec 1 16:17:28 2008

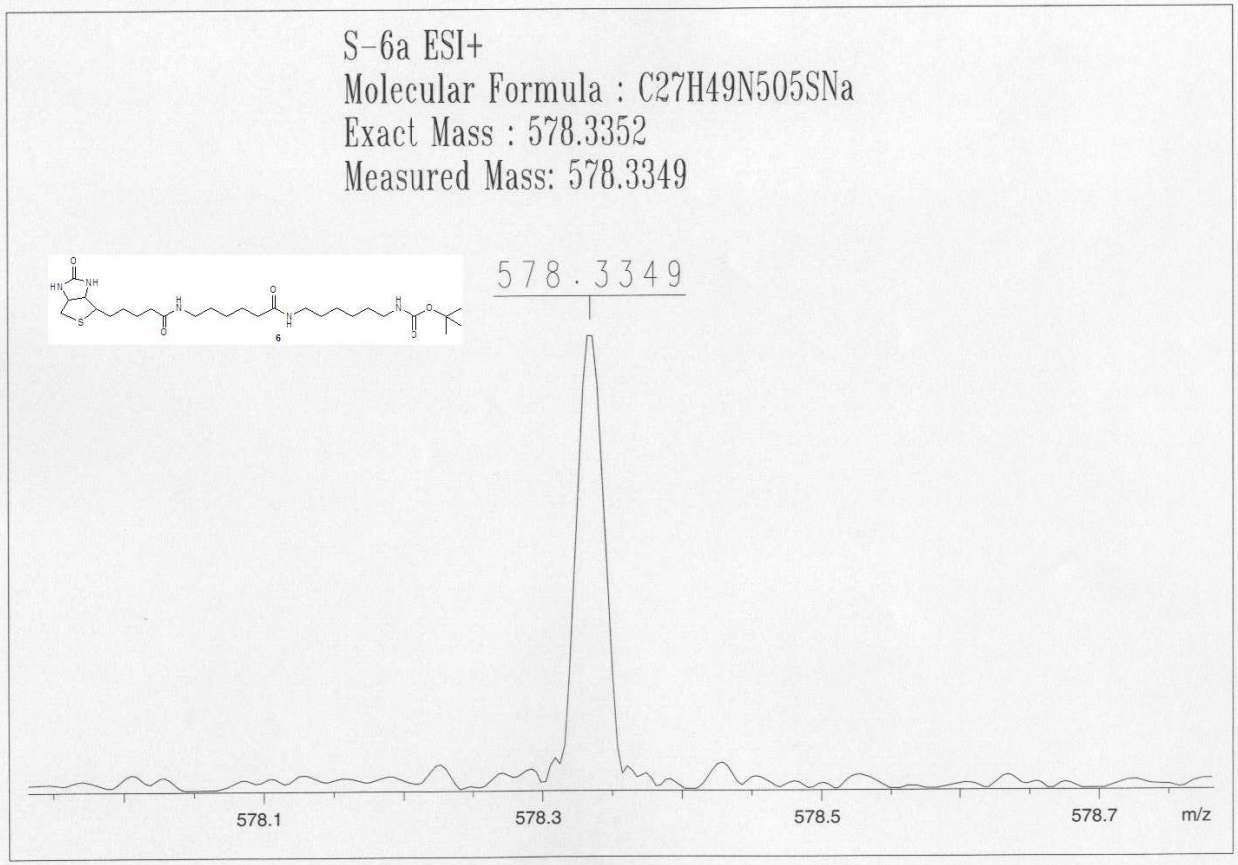

S-5a
Pulse Sequence: s2pul
UNITYplus-400 "unityplus400"
Date: Dec 9 2008
Solvent: CDCl3
Ambient temperature
Total 64 repetitions
5
ppm
0.000
1.309
1.318
1.327
1.335
1.345
1.351
1.441
1.459
1.479
1.496
1.598
1.616
1.975
2.659
2.666
2.676
2.684
2.694
3.099
3.115
7.301
147.58
25.8346.93
20.00
22.38
8.87

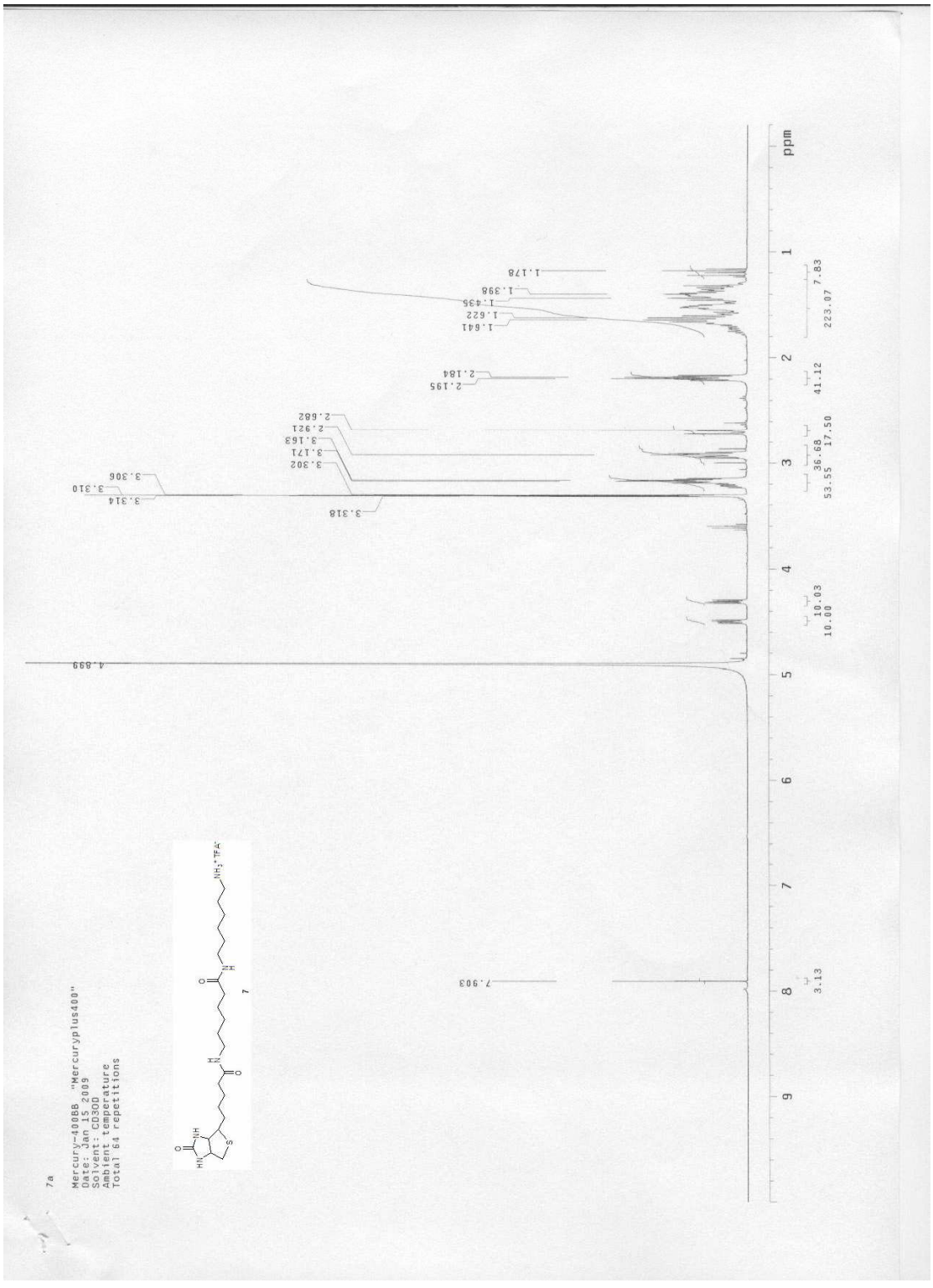

S-5a
Pulse Sequence: s2pul
UNITYplus-400 "unityplus400"
Date: Dec 9 2008
Solvent: CDCl3
Ambient temperature
Total 1504 repetitions
155.964
78.918
77.318
77.000
76.682
42.040
41.979
40.402
33.648
33.550
29.949
28.334
26.667
26.621
26.530
26.439
26.250
ppm

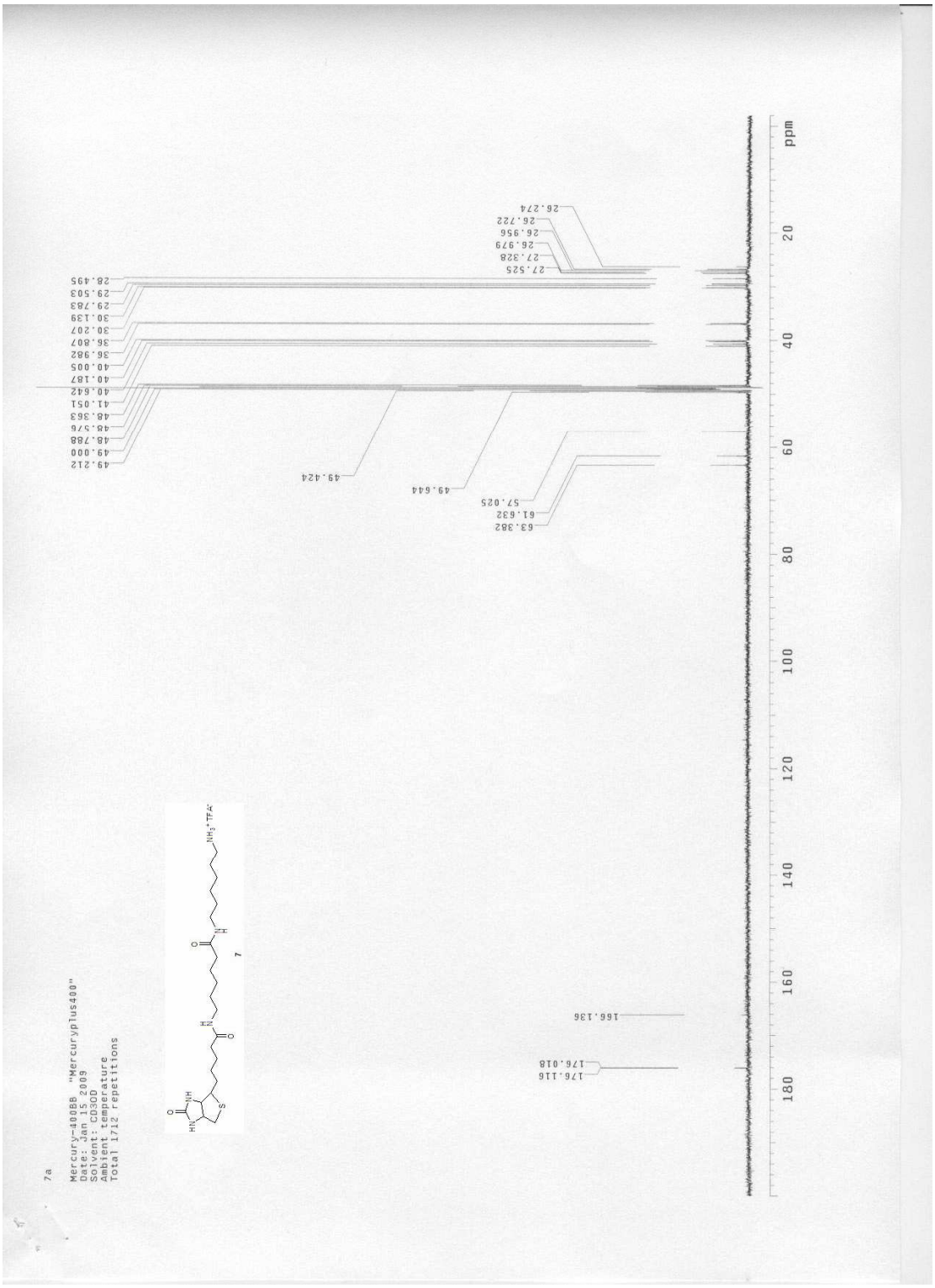

S-5a ESI+
Molecular Formula : C11H25N2O2
Exact Mass : 217.1916
Measured Mass: 217.1917
217.1917
5
217.15
217.17
217.19
217.21
217.23
m/z
/d=/Data/yu/S5A/2/pdata/1 Administrator Mon Dec 1 15:54:10 2008

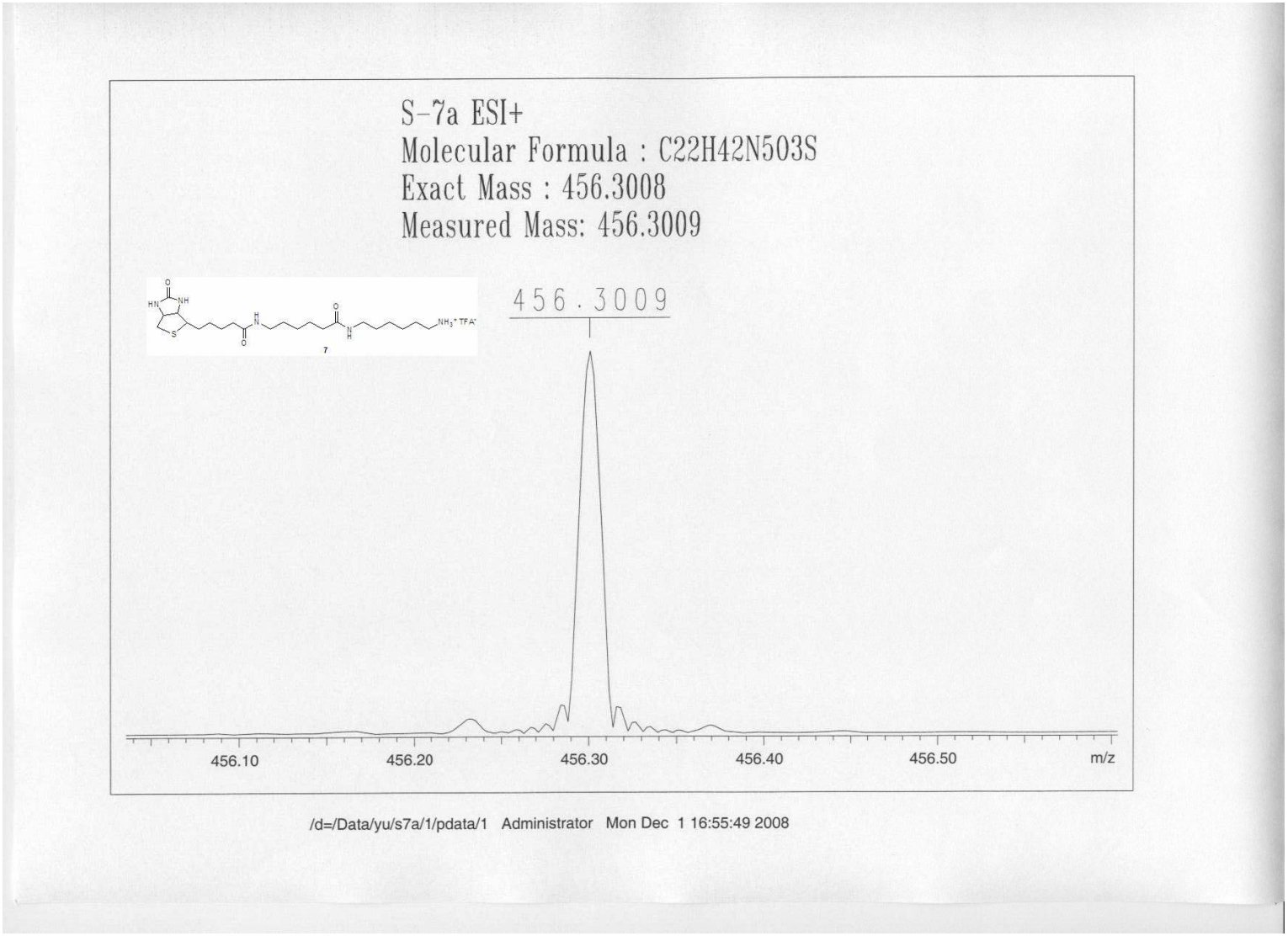

S-1-Boc
Pulse Sequence: s2pul
UNITYplus-400 "unityplus400"
Date: Nov 5 2008
Solvent: CD3OD
Ambient temperature
Total 160 repetitions
ppm
1.163
1.173
1.182
1.191
1.267
1.290
1.316
1.334
1.352
1.458
2.010
2.016
2.028
2.034
2.857
2.990
2.998
3.138
3.142
3.146
3.150
3.154
4.720
158.52
56.39 56.22
35.90
46.540.00
19.07 9.37
9.05
9.18

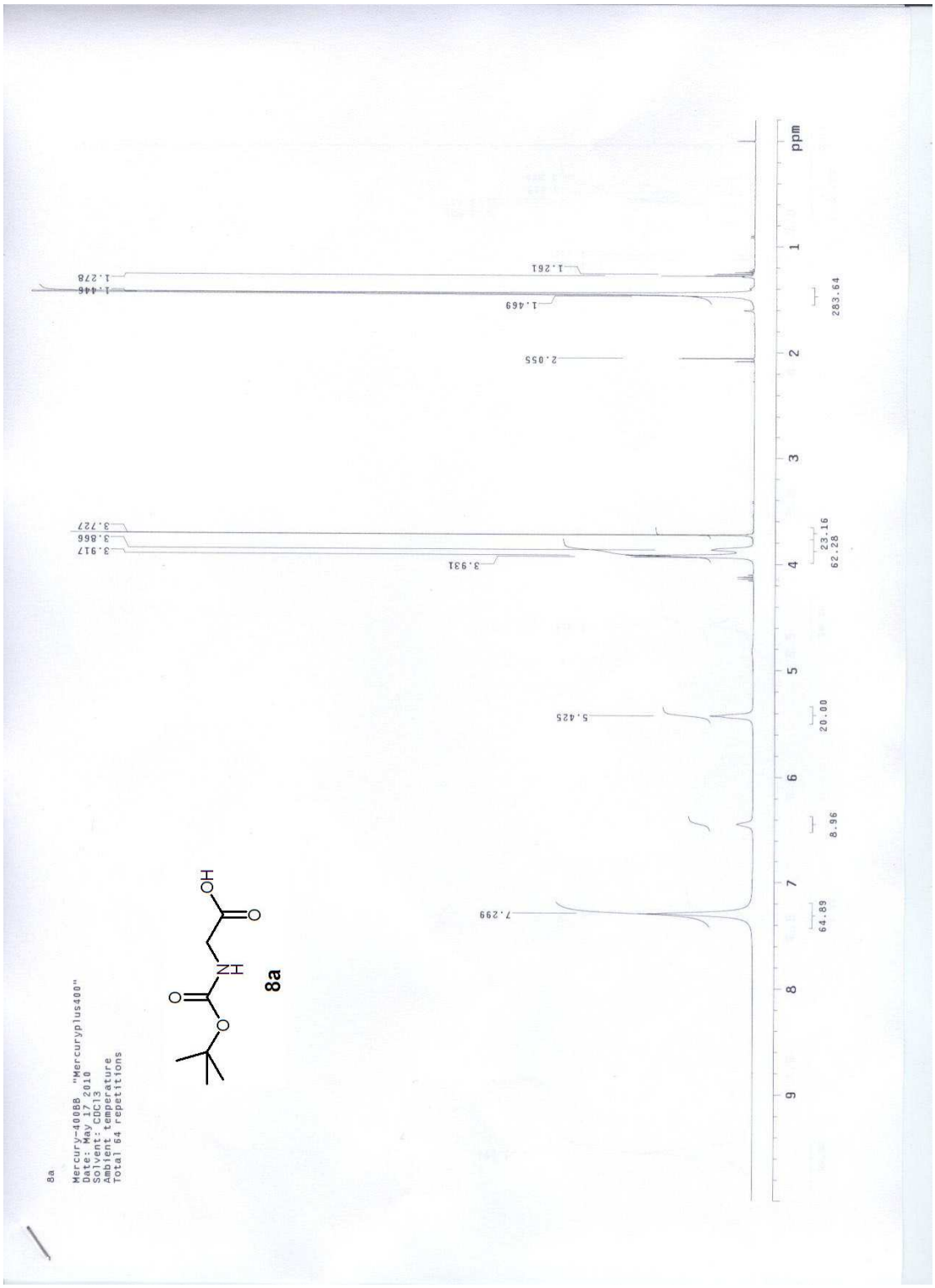

S-1-Boc
Pulse Sequence: s2pul
UNITYplus-400 "unityplus400"
Date: Nov 5 2008
Solvent: CD3OD
Ambient temperature
Total 20000 repetitions
ppm
20
40
60
80
100
120
140
160
180
175.970
176.015
63.387
61.629
57.005
49.644
49.432
49.212
49.000
48.788
48.576
48.363
41.238
41.041
40.275
40.207
36.993
36.818
30.898
30.353
30.133
29.784
29.488
28.799
27.639
27.563
27.487
26.919
26.737

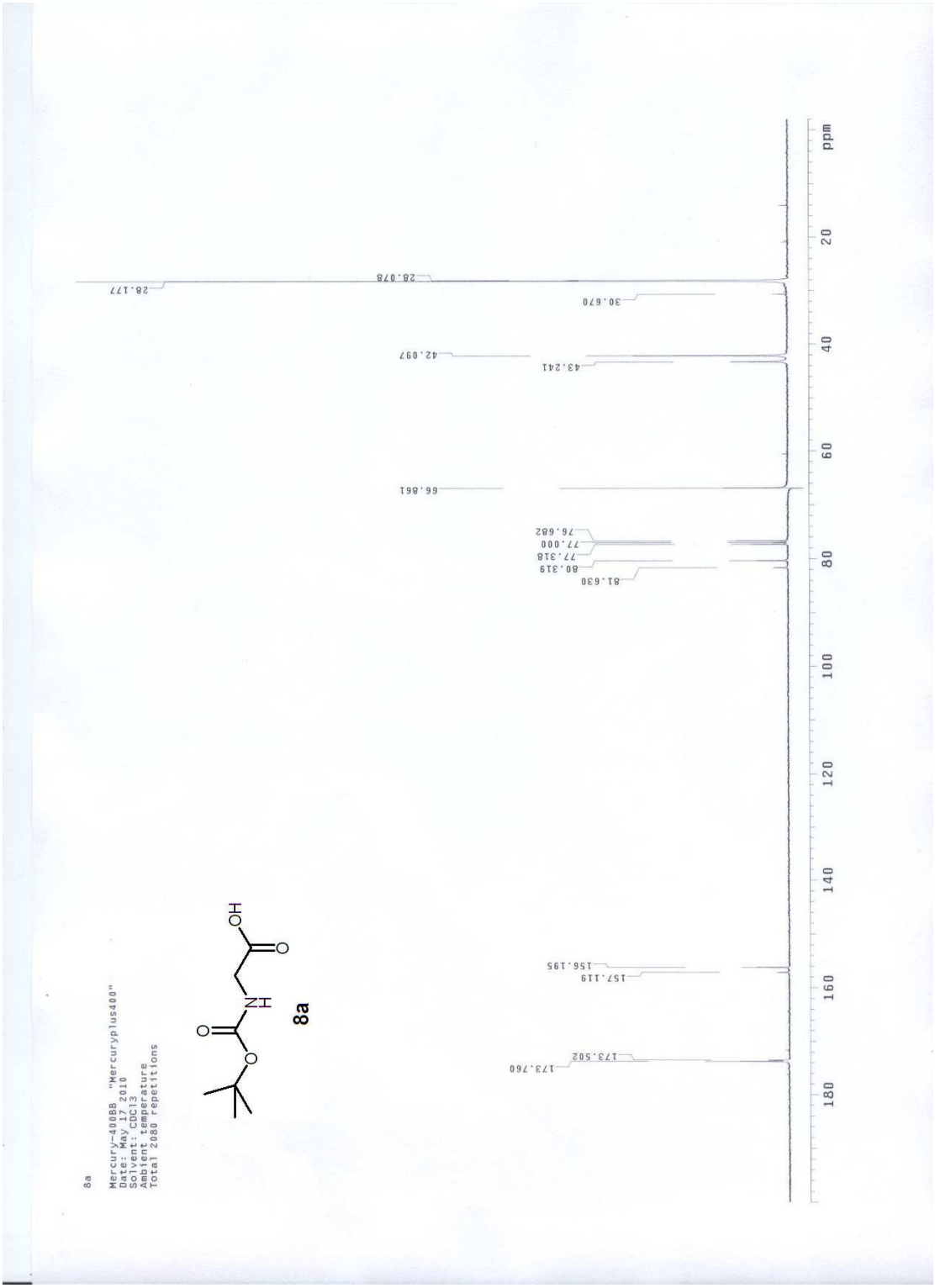

S-6a ESI+
Molecular Formula : C27H49N5O5SNa
Exact Mass : 578.3352
Measured Mass: 578.3349
578.3349
578.1
578.3
578.5
578.7
m/z
/d=/Data/yu/S6A/3/pdata/1 Administrator Mon Dec 1 16:07:00 2008

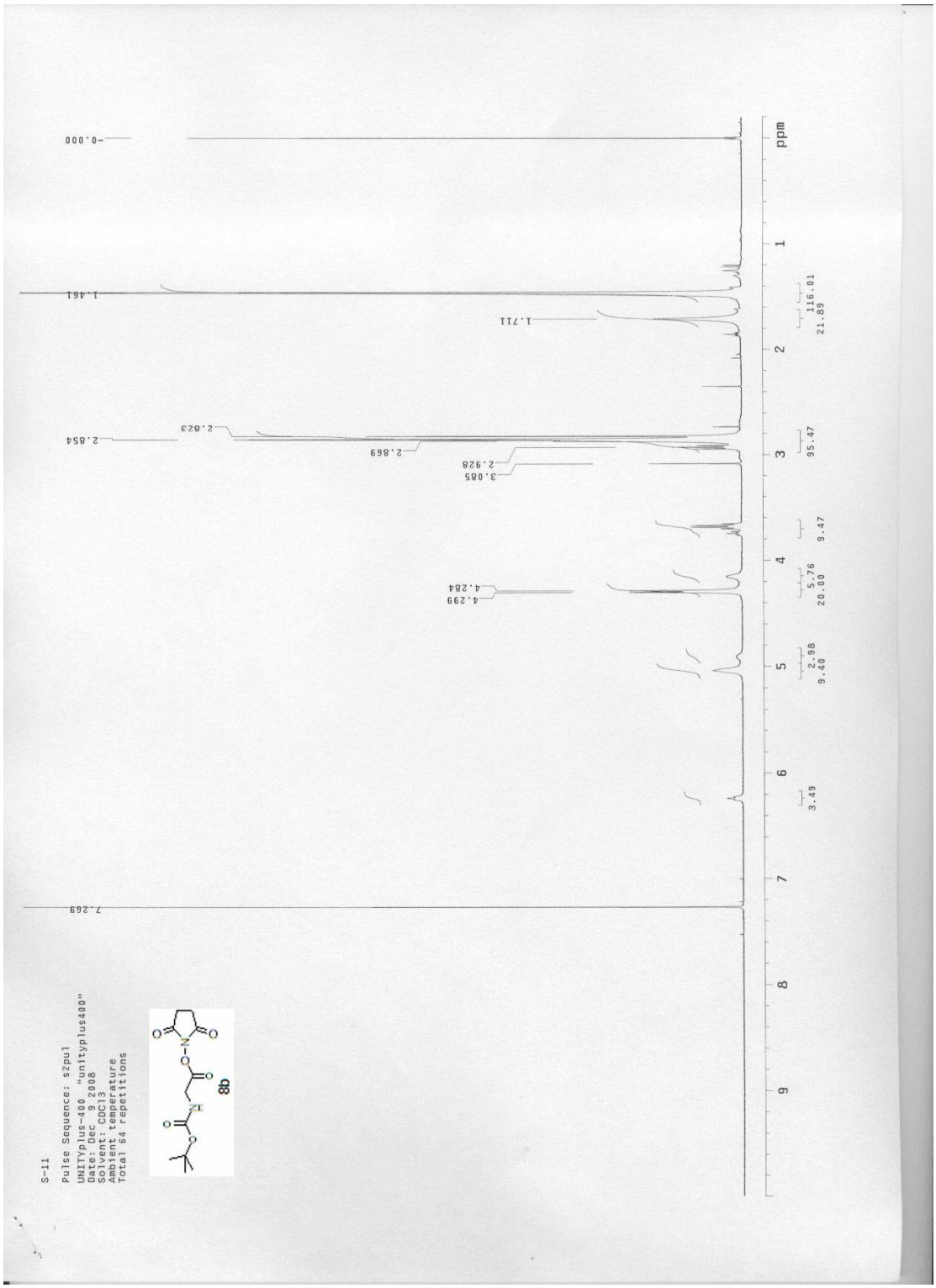

7a
Mercury-400BB "Mercuryplus400"
Date: Jan 15 2009
Solvent: CD3OD
Ambient temperature
Total 64 repetitions
4.899
3.314
3.310
3.306
3.318
3.302
3.171
3.163
2.921
2.682
2.195
2.184
1.641
1.622
1.435
1.398
1.178
7.903
ppm
10.03
10.00
36.68
53.55
17.50
41.12
223.07
7.83
3.13
NH3+TFA-
7

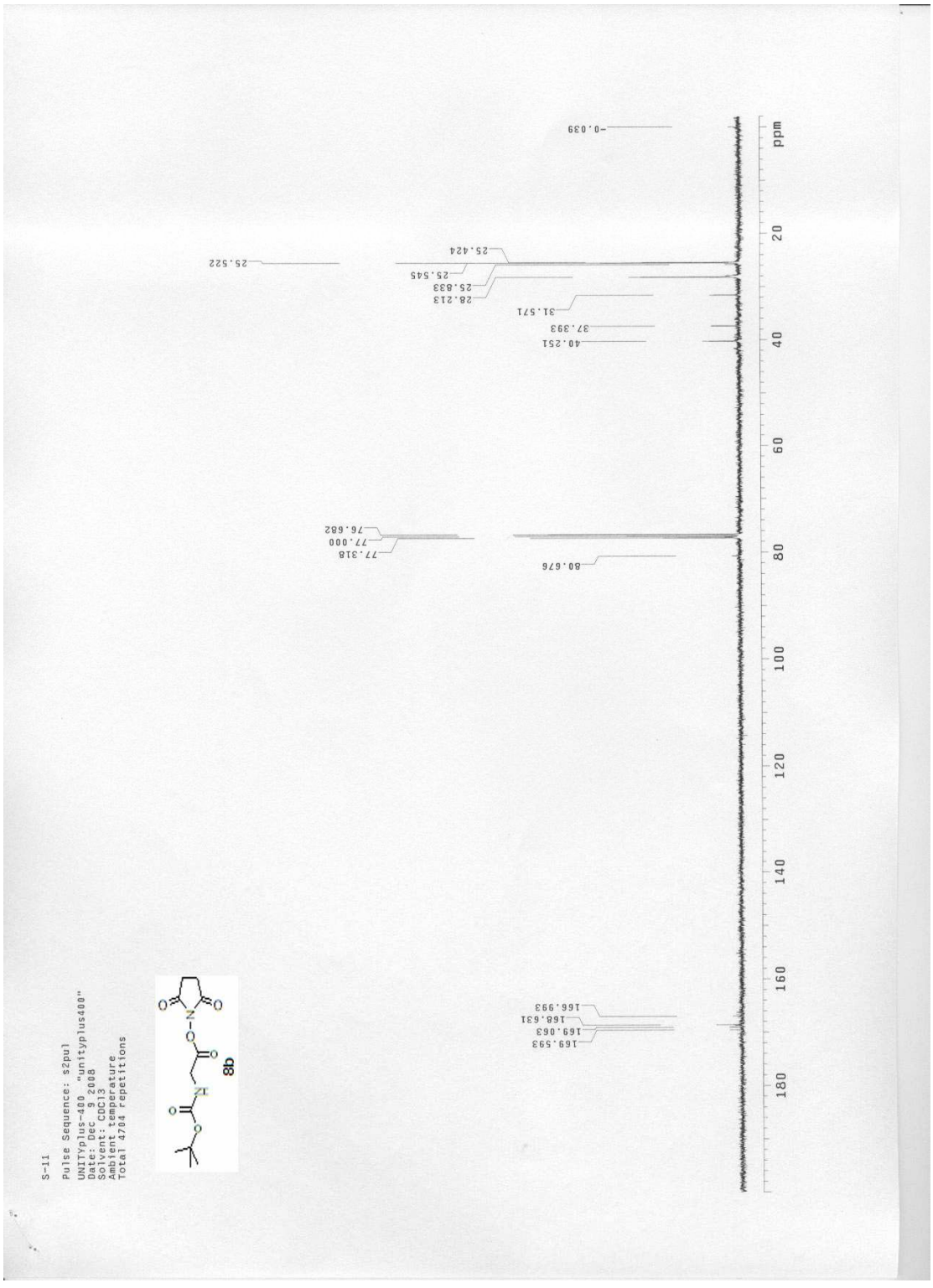

7a
Mercury-400BB "Mercury plus 400"
Date: Jan 5 2009
Solvent: CD3OD
Ambient temperature
Total 1712 repetitions
7
ppm
20
40
60
80
100
120
140
160
180
26.274
26.722
26.956
26.979
27.328
27.525
28.495
29.503
29.783
30.139
30.207
36.807
36.982
40.005
40.187
40.642
41.051
48.363
48.576
48.788
49.000
49.212
49.424
49.644
57.025
61.632
63.382
166.136
176.018
176.116

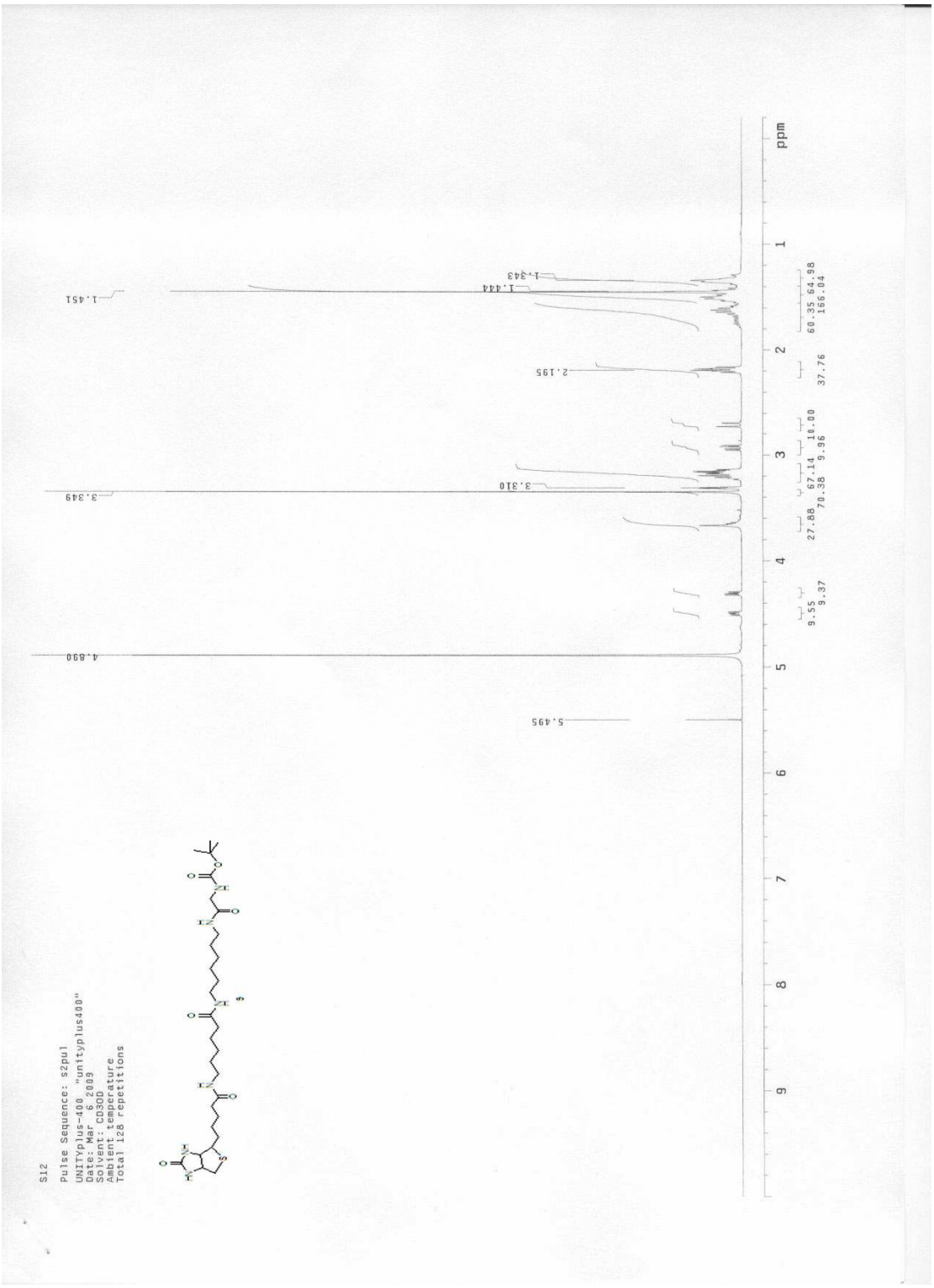

S-7a ESI+
Molecular Formula : C22H42N5O3S
Exact Mass : 456.3008
Measured Mass: 456.3009
456.3009
456.10
456.20
456.30
456.40
456.50
m/z
/d=/Data/yu/s7a/1/pdata/1 Administrator Mon Dec 1 16:55:49 2008

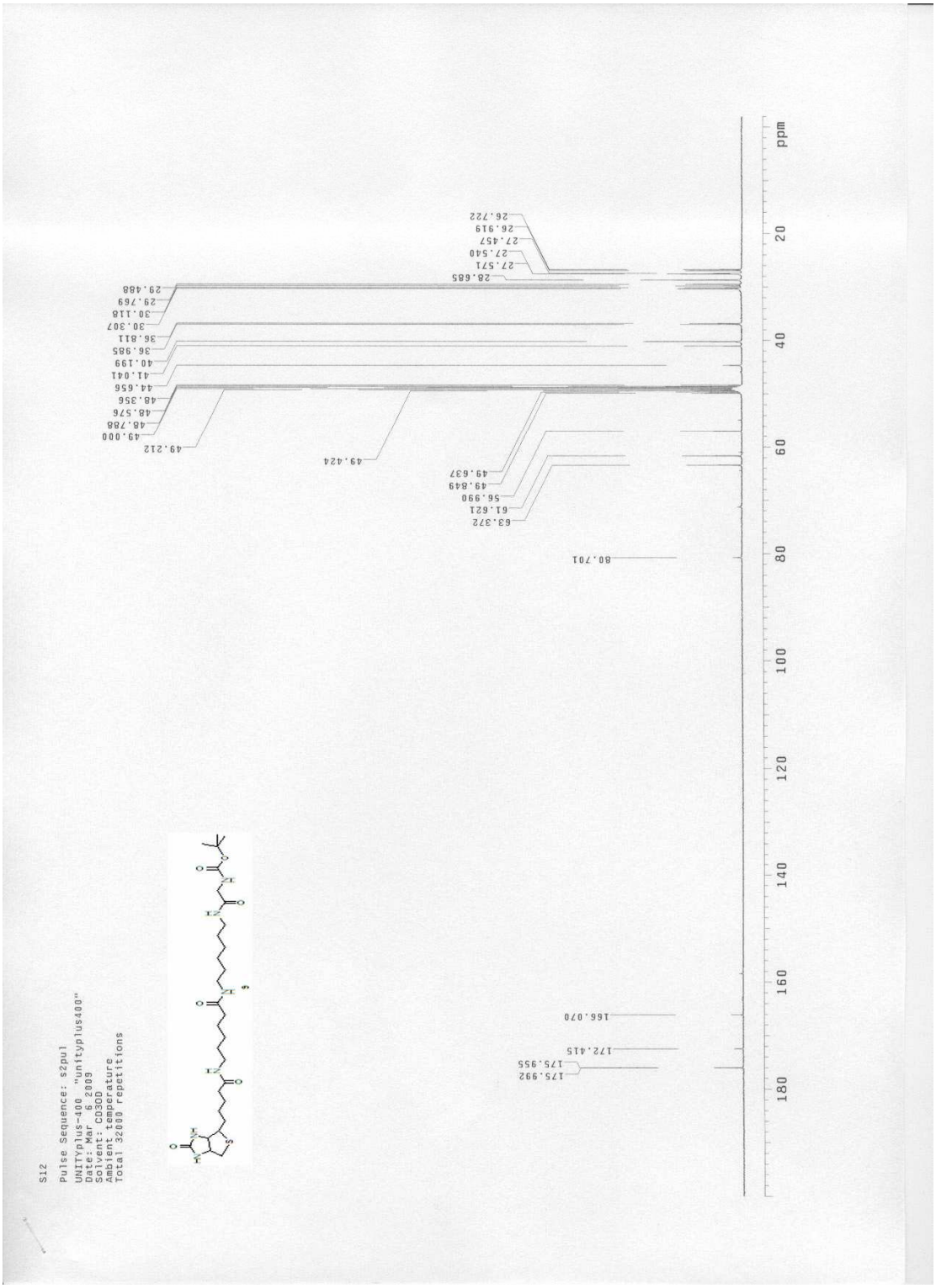

8a
Mercury-400BB "Mercuryplus400"
Date: May 17 2010
Solvent: CDCl3
Ambient temperature
Total 64 repetitions
8a
ppm
7.299
5.425
3.931
3.917
3.866
3.727
2.055
1.469
1.446
1.278
1.261
64.89
8.96
20.00
23.16
62.28
283.64

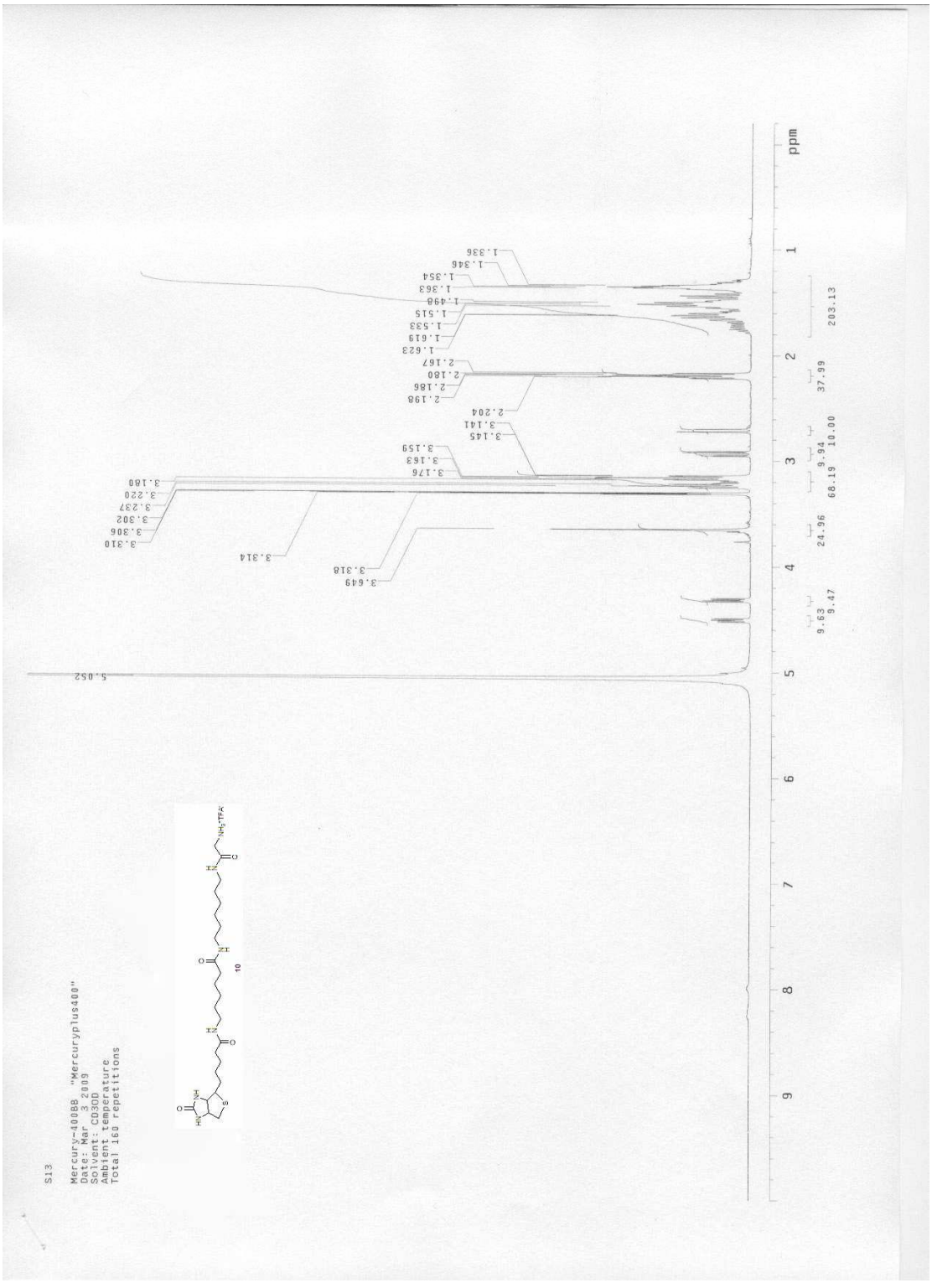

8a
Mercury-400BB "Mercuryplus400"
Date: May 17 2010
Solvent: CDCl3
Ambient temperature
Total 2080 repetitions
8a
ppm
20
40
60
80
100
120
140
160
180
28.177
28.078
30.670
42.097
43.241
66.861
76.682
77.000
77.318
80.319
81.630
156.195
157.119
173.502
173.760

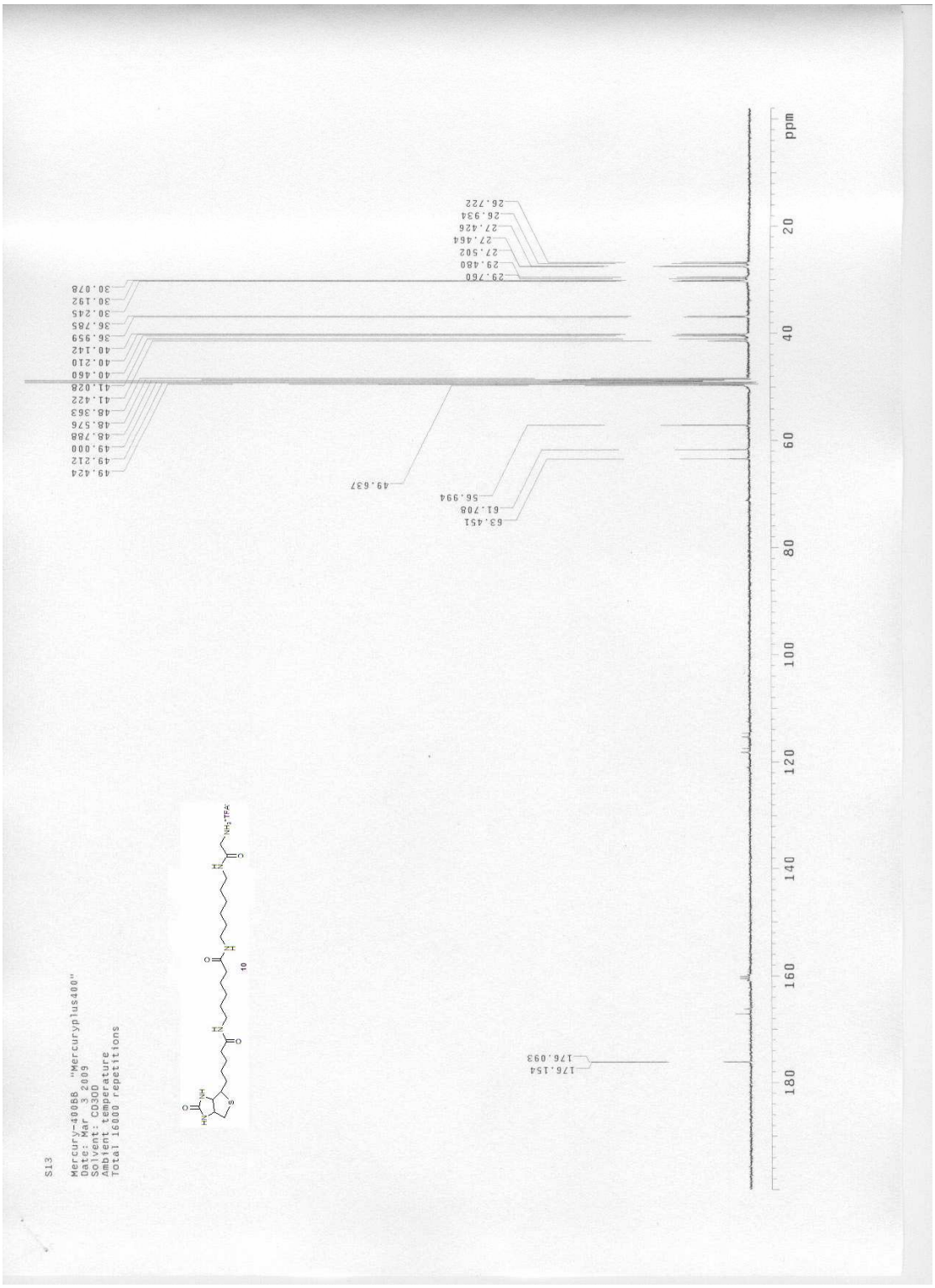

S-11
Pulse Sequence: s2pul
UNITYplus-400 "unityplus400"
Date: Dec 9 2008
Solvent: CDCl3
Ambient temperature
Total 64 repetitions
8b
7.269
1.461
2.854
2.823
2.869
2.928
3.085
4.284
4.299
1.711
0.000
ppm
1
2
3
4
5
6
7
8
9
116.01
21.89
95.47
5.76
20.00
9.47
2.98
9.40
3.49

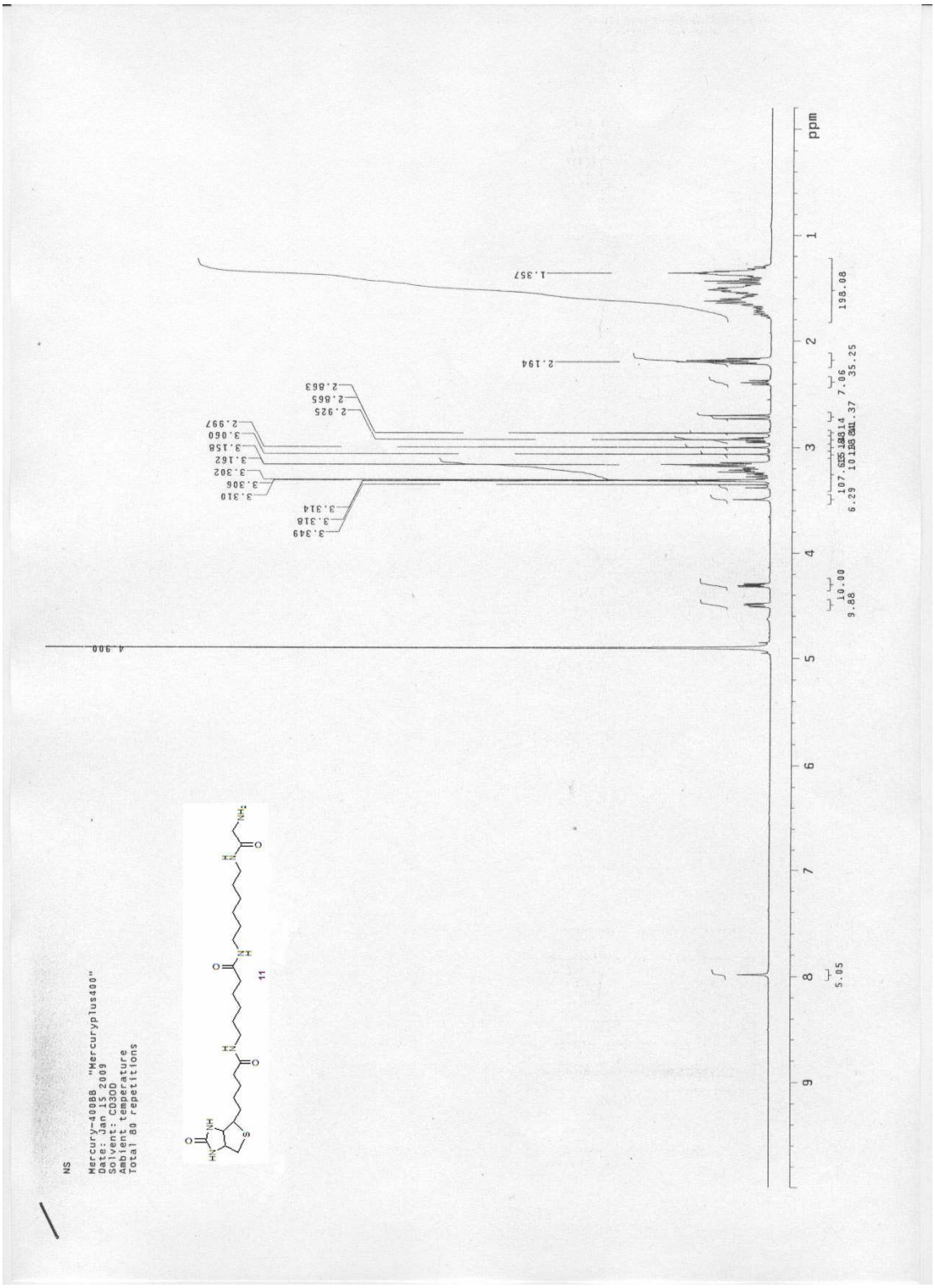

S-11
Pulse Sequence: s2pul
UNITYplus-400 "unityplus400"
Date: Dec 9 2008
Solvent: CDCl3
Ambient temperature
Total 4704 repetitions
8b
-0.039
25.522
25.424
25.545
25.833
28.213
31.571
37.393
40.251
76.682
77.000
77.318
80.676
166.993
168.631
169.063
169.593
ppm
20
40
60
80
100
120
140
160
180

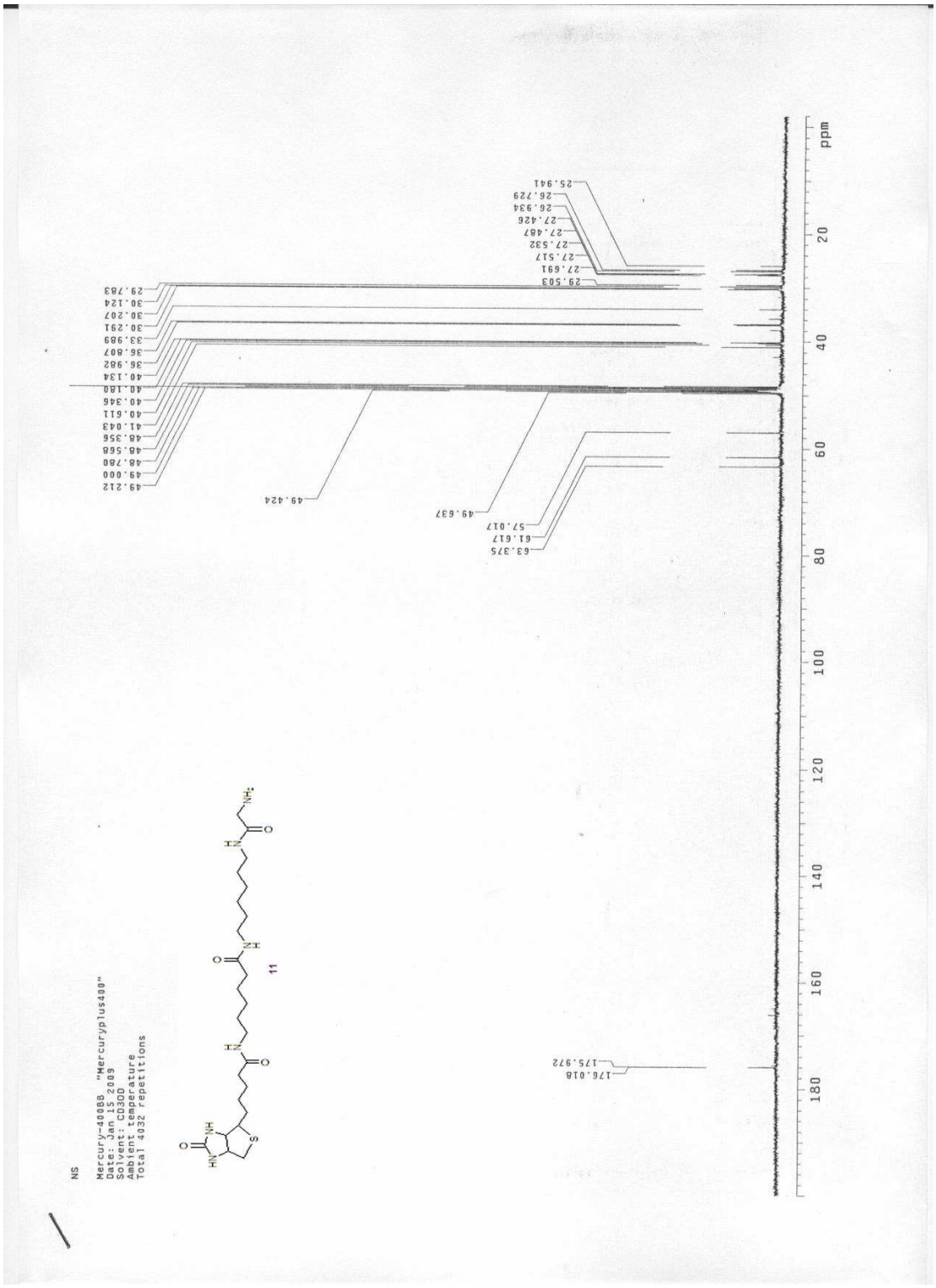

S12
Pulse Sequence: s2pul
UNITYplus-400 "unityplus400"
Date: Mar 6 2009
Solvent: CD3OD
Ambient temperature
Total 128 repetitions
4.890
3.349
1.451
5.495
3.310
2.195
1.444
1.343
ppm

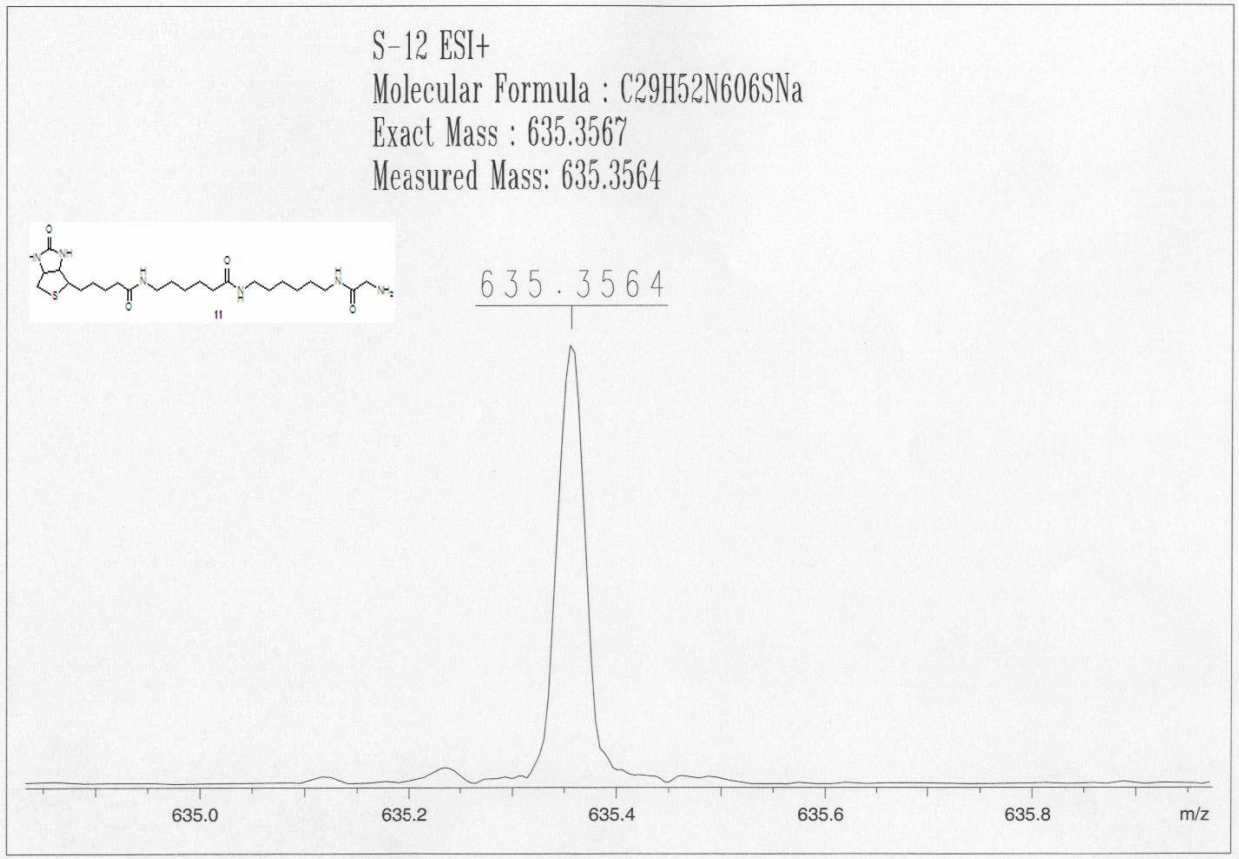

S12
Pulse Sequence: s2pul
UNITYplus-400 "unityplus400"
Date: Mar 6 2009
Solvent: CD3OD
Ambient temperature
Total 32000 repetitions
ppm
20
40
60
80
100
120
140
160
180
26.722
26.919
27.457
27.540
27.571
28.685
29.488
29.769
30.118
30.307
36.811
36.985
40.199
41.041
44.656
48.356
48.576
48.788
49.000
49.212
49.424
49.637
49.849
56.990
61.621
63.372
80.701
166.070
172.415
175.955
175.992


S13
Mercury-400BB "Mercuryplus400"
Date: Mar 3 2009
Solvent: CD3OD
Ambient temperature
Total 160 repetitions
5.052
3.649
3.318
3.314
3.310
3.306
3.302
3.237
3.220
3.180
3.176
3.163
3.159
3.145
3.141
2.204
2.198
2.186
2.180
2.167
1.623
1.619
1.533
1.515
1.498
1.363
1.354
1.346
1.336
ppm
9.63
9.47
24.96
68.19
9.94
10.00
37.99
203.13


S13
Mercury-400BB "Mercuryplus400"
Date: Mar 3 2009
Solvent: CD3OD
Ambient temperature
Total 16000 repetitions
ppm
20
40
60
80
100
120
140
160
180
176.154
176.093
63.451
61.708
56.994
49.637
49.424
49.212
49.000
48.788
48.576
48.363
41.422
41.028
40.460
40.210
40.142
36.959
36.785
30.245
30.192
30.078
29.760
29.480
27.502
27.464
27.426
26.934
26.722


NS
Mercury-400BB "Mercuryplus400"
Date: Jan 15 2009
Solvent: CD3OD
Ambient temperature
Total 80 repetitions
11
4.300
3.349
3.318
3.314
3.310
3.306
3.302
3.162
3.158
3.060
2.997
2.925
2.865
2.863
2.194
1.357
ppm


NS
Mercury-400BB "Mercuryplus400"
Date: Jan 15 2009
Solvent: CD3OD
Ambient temperature
Total 4032 repetitions
11
ppm
20
40
60
80
100
120
140
160
180
25.941
26.729
26.934
27.426
27.487
27.532
27.517
27.691
29.503
29.783
30.124
30.207
30.291
33.989
36.807
36.982
40.134
40.180
40.346
40.611
41.043
48.356
48.568
48.780
49.000
49.212
49.424
49.637
57.017
61.617
63.375
175.972
176.018


S-12 ESI+
Molecular Formula : C29H52N6O6SNa
Exact Mass : 635.3567
Measured Mass: 635.3564
635.3564
635.0
635.2
635.4
635.6
635.8
m/z
/d=/Data/yu/s12/11/pdata/1 Administrator Mon Dec 1 16:27:58 2008

Liposomal Formulation of Amphiphilic Fullerene Antioxidants

Zhiguo Zhou,* Robert P. Lenk, Anthony Dellinger, Stephen R. Wilson, Robert Sadler, and Christopher L. Kepley

Luna nanoWorks, a division of Luna Innovations Incorporated, 521 Bridge Street, Danville, Virginia 24541. Received April 5, 2010; Revised Manuscript Received June 28, 2010

Novel amphiphilic fullerene[70] derivatives that are rationally designed to intercalate in lipid bilayers are reported, as well as its vesicular formulation with surprisingly high loading capacity up to 65% by weight. The amphiphilic C_{70} bisadduct forms uniform and dimensionally stable liposomes with auxiliary natural phospholipids as demonstrated by buoyant density test, particle size distribution, and ^{31}P NMR. The antioxidant property of fullerenes is retained in the bipolarly functionalized C_{70} derivative, amphiphilic liposomal malonylfullerene[70] (ALM), as well as in its liposomal formulations, as shown by both electron paramagnetic resonance (EPR) studies and in vitro reactive oxygen species (ROS) inhibition experiments. The liposomally formulated ALM efficiently quenched hydroxyl radicals and superoxide radicals. In addition, the fullerene liposome inhibited radical-induced lipid peroxidation and maintained the integrity of the lipid bilayer structure. This new class of liposomally formulated, amphipathic fullerene compounds represents a novel drug delivery system for fullerenes and provides a promising pathway to treat oxidative stress-related diseases.

INTRODUCTION

Fullerenes and their derivatives have been proposed as free radical scavengers (*1*), and a number of investigations have studied fullerene (C_{60}) derivatives as potential free radical antioxidant therapeutics (*2*−*5*). Fullerenes (both pristine and derivatized fullerenes) have a tendency toward aggregation in aqueous environments making them unsuitable for therapeutic applications. For example, formulation techniques for preparing fullerene-based therapeutic candidates include host−guest complexation with cyclodextrins and calixerenes, surfactant solubilization with Tween-20 and polyvinylpyrrolidone (PVP), and so forth. These preparations have their respective limitations in terms of uniformity of formulation, loading capacity, aggregation, and partition coefficient (*5*). Derivatization of fullerenes by directly adding moieties to the carbon cage has been used as a strategy to produce useful drug candidates. Such fullerene compounds including polyhydroxylated C_{60} (fullerenol) (*6*, *7*), polysulfonated C_{60} (*8*), and carboxylated fullerenes (*9*, *10*) have been shown to block free radical damages in several oxidative stress-related diseases including ischemia/reperfusion injury, inflammatory apoptosis, and neurogenerative diseases. However, aggregation in aqueous media to form particles with a broad range of diameter distributions is a general problem for many of those compounds (*11*). Polyderivatized fullerenes are often a mixture of many compounds, poorly characterized and not suitable for pharmaceutical development. In addition, it has been shown that cytotoxicity of fullerenes is related to the degree of cage derivatization, water solubility, aggregation, and particle size (*11*). An alternative approach in which fullerenes are encapsulated in bilayer vesicles such as liposomes has been proposed to overcome these limitations. Bensasson described the preparation of vesicles by incorporating C_{60} into L-α-phophatidyl choline purified from egg yolk (Egg-PC) (*12*). However, the authors reported that only 3% or less C_{60} was incorporated in Egg-PC liposomes and the preparation was not uniformly reproducible. Incorporation of C_{60} into L-α-phophatidyl ethanolamine (PE) was limited to 7% (*13*). Fullerene liposomes have also been prepared by transferring fullerenes from their water-soluble host−guest complexes (C_{60}•γ-CD and C_{70}•γ-CD) to lipid membranes for photodynamic therapy (PDT) (*14*, *15*). The limited number of reports on liposomal fullerene formulations were all intended to use underivatized fullerenes that are not lipophilic, rather aromatic, and structurally incompatible with natural phospholipids; therefore, the fullerene contents were low and their dimensional stabilities were problematic. Further, the loading capacity of lipophilic drugs physically entrapped in the liposome bilayer is limited because of the membrane destabilization effect. Thus, it is necessary to develop new drug delivery strategies that can efficiently deliver fullerenes for therapeutic applications.

Given the low contents of pristine fullerenes in liposomal formulations, we hypothesized that incorporating amphiphilic fullerenes in vesicles would greatly increase their ability to be intercalated within the lipid bilayers. Herein, we report the design and synthesis of this new class of amphiphilic fullerenes, their liposome formulation and biological activities as radical scavengers. A key to obtaining a uniform vesicular preparation with high fullerene content and dimensional stability is to incorporate amphiphilic fullerene derivatives which mimic the structure of natural phospholipids. Hirsch has reported amphiphilic C_{60} derivatives in which multiple aliphatic hydrocarbons were attached at various sites on the fullerene cage (*16*, *17*). However, these "buckysomes" do not assemble into stable bilayers readily, and the addition of multiple groups could significantly damage their bioactivity.

Figure 1 illustrates the design strategy in which the amphiphilic fullerenes and phospholipids are hypothesized to coassemble and form bilayer vesicles. As shown below, this method leads to highly increased loading capacity of fullerenes. The amphiphilic fullerene compounds do not form bilayer vesicles by themselves, but require membrane-forming lipids with lipid-to-fullerene molar ratio greater than 1:1 in order to produce uniform and dimensionally stable vesicles. We have also discovered that the oval structure of C_{70} molecule (as opposed to the spherical C_{60}) provides a novel structural platform to prepare this new type of amphiphilic fullerenes. C_{70} has two reactive poles and a relatively inert equatorial region, and this

* Corresponding author. Zhiguo Zhou, Luna nanoWorks, a division of Luna Innovations Incorporated, 521 Bridge Street, Danville, VA 24541. E-Mail: zhouz@lunainnovations.com; Phone: 434-483-4234; Fax: 434-483-4195.

10.1021/bc1001664 © 2010 American Chemical Society
Published on Web 07/15/2010

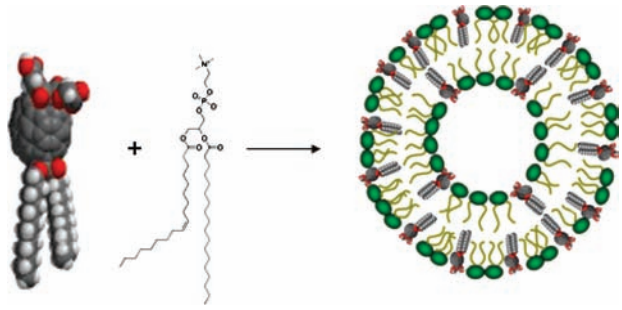


Figure 1. Vesicle formation of amphiphilic fullerenes with auxiliary phospholipids.

allows for sequentially attaching lipophilic and hydrophilic groups at the two poles, respectively (*18*). The large underivatized zone around the C_{70} belt has very high radical reactivity due to the significant orbital overlap of its lowest unoccupied molecular orbital (LUMO) and highest occupied molecular orbital (HOMO) that is expected for sites of maximum radical reactivity (*19*−*21*). The fullerene-enriched liposome provides a novel formulation approach that not only enhances the fullerene delivery efficiency, but also maintain their antioxidative properties.

MATERIALS AND METHODS

Synthesis of C_{70} Monoadduct 2. To a stirred solution of C_{70} (84.0 mg, 0.1 mmol), didodeceylmalonate **1** (44.0 mg, 0.1 mmol) prepared using literature procedure (*22*), and iodine (25.4 mg, 0.1 mmol) in 60 mL of dry toluene was added dropwise a solution of DBU (38.0 mg, 0.25 mmol) in 5 mL of dry toluene under nitrogen at room temperature. Upon completion of addition, the reaction mixture was stirred for an additional 3 h. The reaction mixture was then washed with brine and dried over anhydrous $MgSO_4$. The raw mixture was subjected to flash chromatography on silica gel. Unreacted C_{70} was removed by eluting the column with a mixture of toluene and hexanes (60/40, v/v), and then, the eluant was changed to toluene/hexanes (90/10, v/v) to give the product **2** (108 mg, 85%). The undesirable bisadducts were eluted from the column with DCM. MALDI-MS: 1278.4, ^{1}H NMR ($CDCl_3$): δ 0.79 (6H, t), 1.20 (32H, m), 1.38 (4H, m), 1.75 (4H, m), 4.37 (4H, t); ^{13}C NMR ($CDCl_3$) δ 14.5, 22.3, 25.8, 28.7, 29.1, 29.2, 29.3, 29.8 (3×), 31.9, 37.2, 67.0, 130.7, 130.8, 130.9, 132.8, 133.6, 137.0, 140.7, 141.6, 142.2, 142.8, 143.0, 143.5, 143.8, 143.9, 144.9, 145.9, 146.0, 146.5, 147.0, 147.3, 147.5, 147.6, 148.4, 148.5, 148.6, 148.8, 149.1, 149.3, 149.4, 150.6, 150.8, 151.2, 151.3, 151.4, 155.1, 163.5.

Synthesis of Di(*tert*-butylglycolate)malonate 3. To a stirred solution of malonic acid (1.04 g, 10 mmol) in 60 mL 1,4-dioxane was added 2.78 mL of TEA (2.02 g, 20 mmol). The mixture was stirred for 15 min before *tert*-butyl bromoacetate (4.68 g, 24 mmol) was added dropwise. The resulting mixture was vigorously stirred for 2−3 days until the reaction was complete as monitored by TLC. The precipitates were then filtered and the filtrate was washed twice with brine, dried over $MgSO_4$, and rotavaped in vacuo to give the pure di(*tert*-butylglycolate)-malonate **3** as a colorless oil (2.92 g, 88%). ^{1}H NMR ($CDCl_3$): δ ppm 1.39 (18H, s), 3.51 (2H, s), 4.49 (4H, s); ^{13}C NMR ($CDCl_3$) δ ppm 28.5, 40.2, 61.4, 82.3, 165.5, 167.3.

Synthesis of ALM. To a stirred solution of monoadduct **2** (127.8 mg, 0.1 mmol), di(*tert*-butylglycolate)malonate **3** (33.2 mg, 0.1 mmol), and iodine (25.4 mg, 0.1 mmol) in 60 mL of dry toluene was dropwise added a solution of DBU (35.0 mg, 0.22 mmol) in 5 mL of dry toluene under nitrogen at room temperature. The resulting reaction mixture was stirred for 6 h. The reaction mixture was washed with brine and then dried over anhydrous $MgSO_4$. The raw mixture was subjected to flash chromatography on silica gel. Unreacted monoadduct was removed by eluting the column with toluene, and then the eluant was changed to DCM to give the product (121 mg, 75%). MALDI-MS: 1608.2. ^{1}H NMR ($CDCl_3$): δ 0.75 (6H, m), 1.19 (32H, m), 1.38 (4H, m), 1.43 (18H, s), 1.71 (4H, m), 4.39 (4H, m), 4.75 (4H, m). The product diester (80.0 mg) was dissolved in a mixture of 30 mL DCM and 9 mL TFA, and stirred for 2 h. The solvent was evaporated and dried under vacuum to quantitatively yield pure ALM. MALDI-MS: 1498.2 (see MALDI-MS spectra in Supporting Information), ^{1}H NMR (DMSO): δ 0.79 (6H, m), 1.21 (32H, m), 1.39 (4H, m), 1.74 (4H, m), 4.40 (4H, m), 4.78 (4H, m).

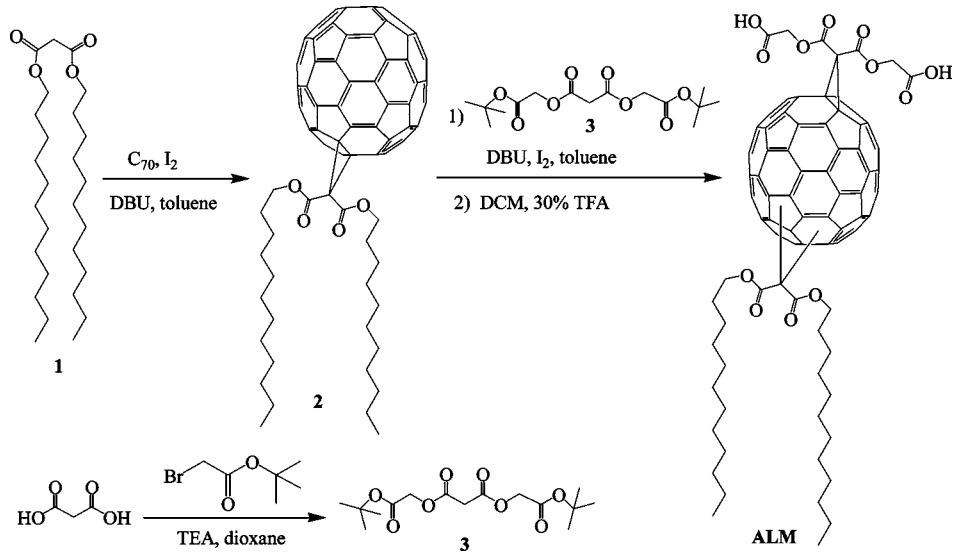
Liposome Preparation. Two parts (by weight) of egg-PC or other lipids such as DMPC and DSPC were added to one part amphipathic ALM in diethyl ether (1 mg/mL). The addition of lipids enhanced the solubility of ALM, although ALM itself has reasonable solubility in diethyl ether. The mixture was sonicated for 2 min before filtration via 0.2 μm filter. To the filtrate, an aqueous buffered solution (PBS, phosphate buffered saline, pH = 7.4) was added, and the two-phase mixture was sonicated in a bath sonicator while purging with nitrogen to produce oligolamellar vesicles. Those oligolamellar vesicles were extruded with nucleopore membranes of 0.4, 0.2, and 0.1 μm, twice each pore size. The final ALM concentration in liposome suspensions was determined by UV−vis spectroscopy with a standard curve after extracting it to organic solvents. Size distribution of extruded liposomes was measured by dynamic light scattering (DLS) with Zetasizer nano S90.

Inhibition of Lipid Peroxidation. Dye-encapsulated liposomes were prepared by adding a buffered solution of the dye HPTS (20 mM, pH = 6.6) to an ether solution of egg-PC lipids (1 mg/mL) with or without ALM (1% by weight), purging nitrogen to remove ether in a bath ultrasonicator at room temperature, and extruding the crude liposomes with 400, 200, and 100 nm nuclear-pore membranes twice each. Dye-encapsulated liposome materials were separated from free dyes by SEC (size exclusion chromatography) on a Sephadex G-50 column with a buffered solution (pH = 7.8) (*23, 24*). The final dye concentration was 0.2 mM as determined by its UV−vis absorption. The absorption spectrum of the purified dye-encapsulated liposome samples were taken before and after the addition of Fenton reagents, and the final concentrations of H_2O_2 and $FeSO_4$ are 1 mM and 0.05 mM, respectively. Each scan was recorded at 30 min, 1 h, 2 h, 4 h, 8 h, 16 h, 24 h, 32 h, and 48 h after the radical initiation. The absorbance ratio ($A_{450\ nm}/A_{405\ nm}$) and absorbance difference ($A_{450\ nm} - A_{405\ nm}$) were plotted as a function of reaction time.

EPR Experiments. EPR studies on radical quenching (hydroxyl radicals and superoxide radicals) were performed as described (*25*). Compound ALM was dissolved in dry DMSO at 1.0 mg/mL (0.67 mM), and DMSO was run as a vesicle control. Hydroxyl radicals were generated using standard concentrations of Fe^{2+}/H_2O_2 through Fenton reactions. Superoxide radical anions $O_2\cdot^-$ were generated through xanthine oxidase metabolism of hypoxanthine (HX/XO). EPR signals were acquired after 20 min incubation of ALM with radical-generating systems.

Cellular ROS Inhibition. U937 monocyte cells obtained from ATCC (Manassas, VA) were cultured in RPMI-1640 media supplemented with 10% FBS (fetal bovine serum). Cells were pretreated with ALM liposome or control liposome or untreated overnight in a 37 °C incubator with 6% CO_2, washed, and resuspended in RPMI medium containing 5 μM DCFH-DA (2′,7′-dichlorodihydrofluorescein diacetate) at 37 °C for 30 min. After incubation, the cells were washed (to remove any excess DCFH-DA) and activated with 10 μg/mL LPS (li-

Scheme 1. Synthesis of Amphiphilic Fullerene C_{70} ALM (the ALM Structure Represents Three Isomers)



popolysaccharide). Activation-induced changes in mean fluorescence were measured in real time using a Perkin-Elmer LS55 Spectrofluorometer with excitation at 502 nm and emission at 523 nm for 15 min. The data are presented as fluorescence intensity of the 523 nm emission over time. All experiments were performed in triplicate. The ROS inhibition was defined as the percentage of the loss of DCF fluorescence when treated with liposome samples relative to the fluorescence intensity of untreated ones. Separate experiments were performed to ensure that the liposomal fullerenes do not interfere with the indicator dye in terms of the intensity of fluorescent signals.

RESULTS AND DISCUSSION

Synthesis. Scheme 1 shows the synthesis of amphiphilic C_{70} compound ALM. The hydrophilic and hydrophobic groups are introduced to C_{70} through two-step cyclopropanation reactions of respective malonates under typical Bingel-Hirsch conditions in high yield (*26, 27*). Di(*tert*-butylglycolate)malonate **3** was prepared from malonic acid and *tert*-butylbromoacetate in the presence of TEA (triethylamine) in 1,4-dioxane at room temperature for 2−3 days. After solvents were evaporated, two-phase extraction (water and chloroform) yielded pure compound **3** in 85% yield. C_{70} monoadduct **2** was synthesized in 80% yield by reacting C_{70} and didodecylmalonate **1** and purified with silica gel column. Compound **2** then underwent the second cyclopropanation reaction with malonate **3** to produce the protected precursor of ALM, which was subsequently treated with 30% TFA (trifluoroacetic acid) in DCM to deprotect the *tert*-butyl esters and produce the amphiphilic compound ALM (*22*). Both ALM and its *tert*-butyl ester precursor were fully characterized by NMR, MALDI-MS, FT-IR, and UV−vis absorption spectroscopy. In addition, we have demonstrated that the three regioisomers of the C_{70} bisadduct ALM could be separated by reverse-phase HPLC (0.1% TFA in ethanol, C6-phenyl column; Supporting Information Figure S1), and the structure of each of the three peaks in the HPLC chromatogram was assigned based on their polarity and distinct UV−vis absorption in the range 350−600 nm (*18*). This general synthetic approach can be used to prepare a variety of amphiphilic C_{70} compounds, simply by replacing its glycolic acid residues with other polar groups.

Liposome Preparation. ALM was first formulated in liposomes with egg-PC (L-α-phosphatidylcholine) by the reverse-phase method, and the resulting suspension was extruded to obtain small vesicles (*28, 29*). ^{31}P NMR spectroscopy confirmed the formation of bilayer liposomes and ^{31}P spectrum of ALM-PC liposome (1 mg/mL ALM) shows a very sharp signal at 2.55 ppm, with a half line-width of 2.8 Hz, which is comparable to the corresponding values of liposomes made of only egg-PC (Supporting Information Figure S2) (*30*). The particle sizes of extruded (with 0.1 μm polycarbonate nucleopore membrane) liposomes were confirmed by DLS with an average diameter of 100 ± 20 nm (*31*). Intriguingly, the fullerene liposomes were dimensionally very stable. The amphipathic fullerene did not separate from the phospholipids during and after nucleopore extrusion. This was confirmed by buoyant density separation test under conditions (high-speed centrifugation at 18 000 *g* for 30 min.) where fullerenes not stably incorporated in bilayer membranes would separate from lipid vesicles and precipitate to the bottom of the 40% sucrose cushion. All fullerenes were found to stay on the top of sucrose solution after centrifugation, indicating that they remained tightly associated with lipids (Supporting Information Figure S3). The tight association between ALM and PC lipids was further confirmed by the observed coelution of ALM and egg-PC on a size exclusion column. The fact that ALM only did not form liposome and it needs the assistance of regular lipids to coassemble into liposomes also demonstrates the successful incorporation of ALM molecule in the bilayer structure formed by the auxiliary lipids (Supporting Information Figure S4). In fact, the ALM−liposome is stable for at least one year without noticeable precipitation or aggregation. The chemical stability of the fullerene compound in liposome formulations was also monitored by MALDI-MS, UV−vis, and HPLC after extracting fullerenes into organic solvents from aliquots of liposome samples, showing no decomposition or other structural changes. Next, we examined the ratio of fullerenes to lipids in the course of forming stable liposome and found that fullerene-to-lipid molar ratio could be as high as 1:1 (or mass ratio of roughly 2:1 or 65% fullerenes). In typical preparations, the fullerene concentration is 1.0 mg/mL liposome in phosphate buffered saline. ALM was also demonstrated to form liposomes in a similar fashion with other lipids such as 1,2-dimyristoyl-*sn*-glycero-3-phosphocholine) (DMPC) and (1,2-distearoyl-*sn*-glycero-3-phosphocholine) (DSPC).

EPR Studies. Electron paramagnetic resonance (EPR) studies were conducted as described by Ali et al (*25*) to confirm that bipolarly functionalized C_{70} compounds were still capable of efficiently scavenging oxygen radicals (hydroxyl and superoxide radicals). Representative EPR spectra (Figure 2, insert) show

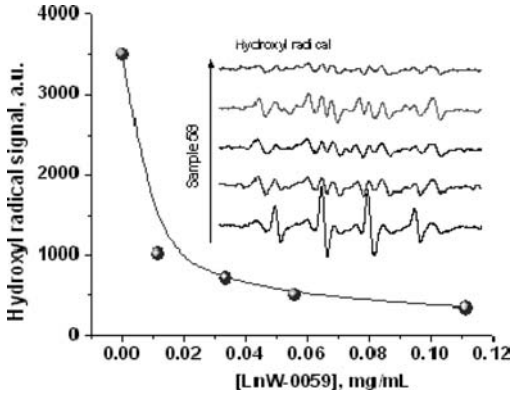


Figure 2. Hydroxyl radical quenching by ALM at four different concentrations. Insert shows EPR spectra of hydroxyl radicals generated via the Fenton reaction, with (top 4 curves) or without (bottom curve) the addition of a DMSO solution of ALM (LnW-0059) at 0.01 mg/mL, 0.03 mg/mL, 0.05 mg/mL, and 0.11 mg/mL. All observed signals were mixtures of DMPO−OH + DMPO−Me (Fenton products). (The DMPO-Me signal is attributable to radical reactions with DMSO).

typical HO· signals, as well as their quenching by ALM at four different concentrations. Figure 2 also shows the dose−response curve of hydroxyl radical-quenching by ALM solution in DMSO. As expected, ALM is a highly potent scavenger for hydroxyl radicals, significantly reducing HO· 4-fold at 10 μg/mL (6.7 μM). ALM also effectively quenched superoxide radicals to a slightly lesser extent. It is noteworthy to point out that ALM, due to its amphipathic nature, forms micelles in the assay media, and its antioxidative efficacy might be partially masked due to its limited access and interaction with free radicals generated in the media.

Protection of Lipid Peroxidation. When lipid molecules, especially unsaturated lipids in cell membrane, are exposed to radicals such as hydroxyl radicals, highly reactive lipid species (lipid alkyl radicals and lipid peroxy radicals) are formed and the resulting lipid peroxidation can eventually cause membrane leakage and cellular dysfunction (*32*). Fullerenes formulated in liposome vesicles are particularly attractive for inhibiting lipid peroxidation. The protection effects of ALM liposome on hydroxyl radical-induced lipid peroxidation were therefore evaluated. The hydroxyl radicals were generated by the Fenton reaction as described above. A pH-sensitive dye 8-hydroxyl-pyrene-1,3,6-trisulfonic acid trisodium salt (HPTS) was encapsulated in the internal aqueous compartment of ALM−liposome and control liposome (without ALM) with a lower pH of 6.6 (*23, 24*). The outer bulk aqueous phase has a higher pH of 7.9. Upon membrane leakage caused by lipid peroxidation, the dye absorption ratio $A_{455\ nm}/A_{405\ nm}$ increases due to the rising pH, and a higher ratio $A_{455\ nm}/A_{405\ nm}$ indicates a greater extent of membrane leakage and lipid peroxidation. Fullerenes have strong absorption in the range 400−450 nm; thus, the ALM content was kept very low at 1% to clearly monitor the spectral changes of the dye. In order to explicitly demonstrate the protection effects, both absorbance ratio ($A_{455\ nm}/A_{405\ nm}$) and absorbance difference ($A_{455\ nm} - A_{405\ nm}$) were plotted as a function of time ($t = 0$ when HO· generation reaction was initiated) (Figure 3). The membrane leakage in the control liposome was dramatic, but it was minimal in the ALM−liposome sample. Additional control experiments were also conducted, and the $A_{455\ nm}/A_{405\ nm}$ of HPTS was monitored in ALM−liposome or control liposome samples in the absence of the Fenton reagents. No noticeable changes in the absorption spectra of HPTS were observed for both samples, excluding the possibility that the control liposome is inherently leakier than the ALM-encapsulated liposome. These results clearly demonstrate the

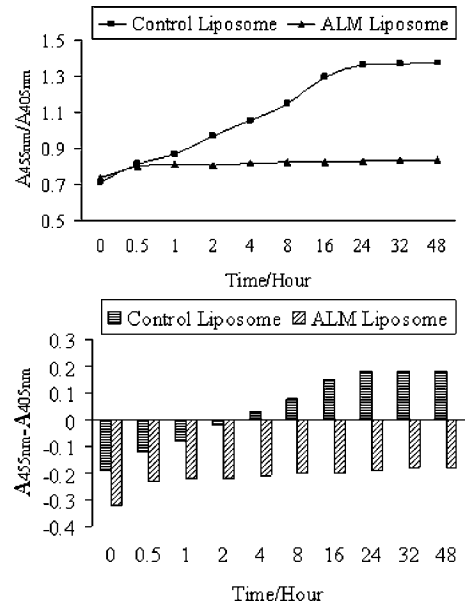


Figure 3. Absorbance ratio ($A_{455\ nm}/A_{405\ nm}$, top) and absorbance difference ($A_{455\ nm} - A_{405\ nm}$, bottom) of HPTS as a function of reaction time from when the Fenton reagents were added to the liposome samples. 1% fullerene was contained in ALM liposome. (1.0 mM H_2O_2 and 0.05 mM Fe^{2+} ions of final concentrations).

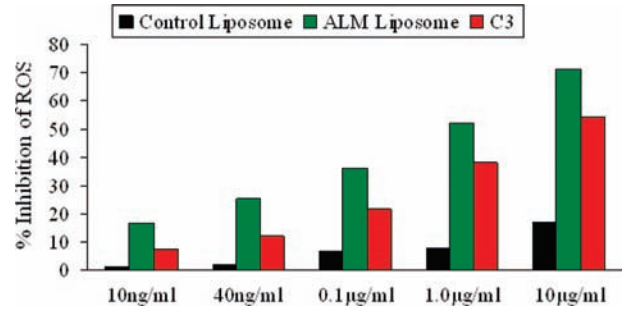


Figure 4. Inhibition of ROS in U937 monocytes by liposomes. For each concentration, the same volume of control liposome was used as the control. The fluorescence intensity was recorded and used as the measure to quantify ROS inhibition.

strong protection effects of ALM liposome against radical-induced peroxidation and membrane leakage.

In Vitro ROS Inhibition and Cytotoxicity. ALM liposome was also evaluated for its capability to quench extra cellular reactive oxygen species (ROS) release triggered by lipopolysaccharide (LPS) (*33, 34*). The monocyte cell line U937 used in this study is clinically relevant to atherosclerosis. The generation of foam cells from activated monocytes involves ROS overproduction and is a key inflammatory process in atherosclerotic plaque buildup (*35*). U937 monocytes, before LPS activation, were treated with a cell-permeable fluorogenic probe 2′,7′-dichlorodihydrofluorescein diacetate (DCFH-DA) (*36*). Following LPS activation, DCFH-DA underwent cellular hydrolysis and oxidation by ROS to generate the highly fluorescent 2′,7′-dichlorofluorescein (DCF). As shown in Figure 4, ALM liposome inhibited cellular ROS release, while the control liposome (without ALM) did not. More than 80% ROS release was inhibited when the cells were treated with 6 μM ALM liposome samples, and even at 6 nM, the inhibition was over 20%. This suggests that the liposome formulation efficiently delivered amphiphilic fullerenes into cells and effectively exerted its anti-ROS efficacy. The liposomal ALM was also compared with a well-studied water-soluble C_{60} derivative-C_3 (six carboxyl groups—three malonic acids directly attached to a C_{60} cage) in

this assay (*9*). As shown in Figure 4, ALM was 40−70% more potent than C_3 in scavenging cellular ROS when compared at equal molar concentrations. This could be explained by the difference in their dipole moments, structural dimension, and the resultant ability to intercalate in lipid bilayer and permeate cell membranes. Amphiphilic fullerene ALM has higher lipid/aqueous partition coefficient than C_3 in favor of cellular membrane permeation in addition to the potential endocytotic uptake of ALM liposome.

Finally, the cytotoxicity of the ALM liposome was examined. A number of factors including chemical structure, surface modification, water solubility, aggregation, particle size, and preparation procedures appear to have impacts on fullerene toxicity and behavior in biological systems (*11*, *37*). In general, well-characterized fullerene derivatives with high solubility in buffer have little or no toxicities. We evaluated the cytotoxicity of ALM liposome with U937 monocytes, and ALM was found not cytotoxic to U937 cells when incubated with up to 67 μM (0.1 mg/mL) of ALM for 6 days. The cell viabilities were comparable for ALM-treated, vitamin E-treated, and untreated cells at all concentrations (Supporting Information Figure S5).

CONCLUSIONS

We have presented a novel fullerene delivery approach via liposomes enriched with amphiphilic C_{70} bisadducts that were designed to structurally mimic cellular membrane lipids. The choice of C_{70} along with its inherent bipolar bisaddition pattern represents a novel pathway to design amphiphilic fullerene compounds compatible for vesicular incorporation. The strong association between reported fullerenes and auxiliary lipids allow them to form dimensionally stable liposomes with as high as 65% (by weight) fullerene. By mimicking the structure of naturally occurring lipid molecules, this design overcomes several limitations in previously reported formulations including (1) low fullerene content of 3%−7% due to their use of underivatized C_{60} (*12*, *13*) or lipophilically functionalized C_{60} (*38*), structures of which are not dimensionally compatible with the polar head/lipophilic double-tail structure of lipids; and (2) damaged antioxidative bioactivity due to the multiple additions of six groups to C_{60} in an octahedral pattern where the spherical π-electron conjugation is interrupted leading to interconnected biphenyls (*16*, *39*). As a drug delivery vehicle, the high fullerene loading capacity is very important, and it is advantageous especially for in vivo studies such as the delivery of fullerene to its intended region of action at sufficient concentrations with lower dose volumes. The vesicularly formulated fullerene ALM has been demonstrated as potent radical scavengers in three separate ROS-related experiment settings. In summary, this present approach provides a new way to deliver fullerenes to sites where their antioxidant properties can be exploited and provides a platform for synthesizing new fullerene-based therapeutics that not only retain their biological activity, but can also be delivered via liposome carriers.

ACKNOWLEDGMENT

This work was partially supported by NIH Grants 1R01GM083274-01 and 1R43HL087578-01A1 (CLK). We thank Dr. Anthony Ribeiro at Duke NMR Center for assistance in acquiring the ^{31}P NMR spectrum.

Supporting Information Available: Additional information as described in the text and mass spectra. This material is available free of charge via the Internet at http://pubs.acs.org.

LITERATURE CITED

(1) Krustic, P. J., Wasserman, E., Keizer, P. N., Morton, J. R., and Preston, K. F. (1991) Radical reactions of C_{60}. *Science 254*, 1183–1185.

(2) Partha, R., and Conyers, J. L. (2009) Biomedical applications of functionalized fullerene-based nanomaterials. *Int. J. Nanomed. 4*, 261–275.

(3) Bosi, S., Da Ros, T., Spalluto, G., and Prato, M. (2003) Fullerene derivatives: an attractive tool for biological applications. *Eur. J. Med. Chem. 38*, 913–923.

(4) Nakamura, E., and Isobe, H. (2003) Functionalized fullerenes in water. The first 10 years of their chemistry, biology, and nanoscience. *Acc. Chem. Res. 36*, 807–815.

(5) Jensen, A. W., Wilson, S. R., and Schuster, D. I. (1996) Biological applications of fullerenes. *Bioorg. Med. Chem. 4*, 767–779.

(6) Tsai, M. C., Chen, Y. H., and Chiang, L. Y. (1997) Polyhydroxylated C_{60}, fullerenol, a novel free-radical trapper, prevented hydrogen peroxide- and cumene hydroperoxide-elicited changes in rat hippocampus in-vitro. *J. Pharm. Pharmacol. 49*, 438–445.

(7) Husebo, L. O., Sitharaman, B., Furukawa, K., Kato, T., and Wilson, L. J. (2004) Fullerenols revisited as stable radical anions. *J. Am. Chem. Soc. 126*, 12055–12064.

(8) Huang, S. S., Tsai, S. K., Chih, C. L., Chiang, L. Y., Hsieh, H. M., Teng, C. M., and Tsai, M. C. (2001) Neuroprotective effect of hexasulfobutylated C_{60} on rats subjected to focal cerebral ischemia. *Free Radic. Biol. Med. 30*, 643–649.

(9) Dugan, L. L., Turetsky, D. M., Du, C., Lobner, D., Wheeler, M., Almli, C. R., Shen, C. K.-F., Luh, T.-Y., Choi, D. W., and Lin, T.-S. (1997) Carboxyfullerenes as neuroprotective agents. *Proc. Natl. Acad. Sci. U.S.A. 94*, 9434–9439.

(10) Brettreich, M., and Hirsch, A. (1998) A highly water-soluble dendro[60]fullerene. *Tetrahedron Lett. 39*, 2731–2734.

(11) Johnston, H. J., Hutchison, G. R., Christensen, F. M., Aschberger, K., and Stone, V. (2010) The biological mechanisms and physicochemical characteristics Responsible for driving fullerene toxicity. *Toxicol. Sci. 114*, 162–182.

(12) Bensasson, R. V., Bienvenue, E., Dellinger, M., Leach, S., and Seta, P. J. (1994) C_{60} in model biological systems. A visible-UV absorption study of solvent-dependent parameters and solute aggregation. *J. Phys. Chem. 98*, 3492–3496.

(13) Hungerbuhler, H., Guldi, D. M., and Asmus, K. D. (1993) Incorporation of C_{60} into artificial lipid membranes. *J. Am. Chem. Soc. 115*, 3386–3390.

(14) Ikeda, A., Doi, Y., Hashizume, M., Kikuchi, J., and Konishi, T. (2007) An extremely effective DNA photocleavage utilizing functionalized liposomes with a fullerene-enriched lipid bilayer. *J. Am. Chem. Soc. 129*, 4140–4141.

(15) Kato, S., Kikuchi, R., Aoshima, H., Saitoh, Y., and Miwa, N. (2010) Defensive effects of fullerene-C_{60}/liposome complex against UVA-induced intracellular reactive oxygen species generation and cell death in human skin keratinocytes HaCaT, associated with intracellular uptake and extracellular excretion of fullerene-C_{60}. *J. Photochem. Photobiol. B 98*, 144–151.

(16) Brettreich, M., Burghardt, S., Bottcher, C., Bayerl, T., Bayerl, S., and Hirsch, A. (2000) Globular amphiphiles: Membrane-forming hexaadducts of C_{60}. *Angew. Chem., Int. Ed. 39*, 1845–1848.

(17) Maierhofer, A. P., Brettreich, M., Burghardt, S., Vostrowsky, O., Hirsch, A., Langridge, S., and Bayerl, T. M. (2000) Structure and electrostatic interaction properties of monolayers of amphiphilic molecules derived from C_{60}-fullerenes: A film balance, neutron, and infrared reflection study. *Langmuir 16*, 8884–8891.

(18) Herrmann, A., Rüttimann, M., Thilgen, C., and Diederich, A. (1995) Multiple Cyclopropanations of C_{70}. Synthesis and characterization of bis-, tris-, and tetrakis-adducts and chiroptical properties of bis-adducts with chiral addends, including a recommendation for the configurational description of fullerene derivatives with a chiral addition pattern. *Helv. Chim. Acta 78*, 1673–1704.

(19) Gan, L., Huang, S., Zhang, X., Zhang, A., Cheng, B., Cheng, H., Li, X., and Shang, G. (2002) Fullerenes as a tert-butylperoxy radical trap, metal catalyzed reaction of tert-butyl hydroperoxide with fullerenes, and formation of the first fullerene mixed peroxides. *J. Am. Chem. Soc. 124*, 13384–13385.

(20) Birkett, P. R., Avent, A. G., Darwish, A. D., Kroto, H. W., Taylor, R., and Walton, D. R. M. (1995) Formation and characterization of $C_{70}Cl_{10}$. *J. Chem. Soc., Chem. Commun.* 683–684.

(21) Scuseria, G. E. (1991) The equilibrium structure of C_{70}. An ab initio Hartree-Fock study. *Chem. Phys. Lett. 180*, 451–469.

(22) Zhou, Z., Schuster, D. I., and Wilson, S. R. (2003) Selective syntheses of novel polyether fullerene multiple adducts. *J. Org. Chem. 68*, 7612–7617.

(23) Kano, K., and Fendler, J. H. (1978) Pyranine as a sensitive pH probe for liposome interiors and surfaces. pH gradients across phospholipid vesicles. *Biochim. Biophys. Acta 509*, 289–296.

(24) Wang, C., Tai, L. A., Lee, D. D., Kanakamma, P. P., Shen, C., K. F., Luh, T. Y., Cheng, C. H., and Hwang, K. C. (1999) C_{60} and water-soluble fullerene derivatives as antioxidants against radical-initiated lipid peroxidation. *J. Med. Chem. 42*, 4614–4620.

(25) Ali, S. S., Hardt, J. I., Quick, K. L., Kim-Han, J. S., Erlamger, B. F., Huang, T. T., Epstein, C. J., and Dugan, L. L. (2004) A biologically effective fullerene C_{60} derivative with superoxide dismutase mimetic properties. *Free Radic. Biol. Med. 37*, 1191–1202.

(26) Bingel, C. (1993) Cyclopropylation of fullerenes. *Chem. Ber. 126*, 1957–1958.

(27) Zhou, Z., and Wilson, S. R. (2005) Tether-directed multiple functionalization of fullerene[60]. *Curr. Org. Chem. 9*, 789–811.

(28) Pidgeon, C., McNeely, S., Schmidt, T., and Johnson, J. E. (1987) Multilayered vesicles prepared by reverse-phase evaporation: liposome structure and optimum solute entrapment. *Biochemistry 26*, 17–29.

(29) Gruner, S. M., Lenk, R. P., Janoff, A. S., and Ostro, M. J. (1985) Novel multilayered lipid vesicles: comparison of physical characteristics of multilamellar liposomes and stable plurilamellar vesicles. *Biochemistry 24*, 2833–2842.

(30) Berden, J. A., Cullis, P. R., Hoult, D. I., McLaughlin, A. C., Radda, G. K., and Richards, R. E. (1974) Frequency dependence of 31P NMR linewidths in sonicated phospholipid vesicles: effects of chemical shift anisotropy. *FEBS Lett. 46*, 55–58.

(31) Winterhalter, M., and Lasic, D. D. (1993) Liposome stability and formation: experimental parameters and theories on the size distribution. *Chem. Phys. Lipids 64*, 35–43.

(32) Niki, E. (2009) Lipid peroxidation: physiological levels and dual biological effects. *Free Radic. Biol. Med. 47*, 469–484.

(33) Stocker, R., and Keaney, J. F. (2004) Role of oxidative modifications in atherosclerosis. *Physiol. Rev. 84*, 1381–1478.

(34) Aviram, M. (1999) Macrophage foam cell formation during early atherogenesis is determined by the balance between prooxidants and antioxidants in arterial cells and blood lipoproteins. *Antioxid. Redox. Signal. 1*, 585–594.

(35) Schwartz, C. J., Kelley, J. L., Nerem, R. M., Sprague, E. A., Rozek, M. M., Valente, A. J., Edwards, E. H., Prasad, A. R., Kerbacher, J. J., and Logan, S. A. (1989) Pathophysiology of the atherogenic process. *Am. J. Cardiol. 64*, 23G–30G.

(36) Rosenkranz, A. R., Schmaldienst, S., Stuhlmeier, K. M., Chen, W., Knapp, W., and Zlabinger, G. J. (1992) A microplate assay for the detection of oxidative products using 2′,7′-dichlorofluorescin-diacetate. *J. Immunol. Methods 156*, 39–45.

(37) Kolosnjaj, J., Szwarc, H., and Moussa, F. (2007) Toxicity studies of fullerenes and derivatives. *Adv. Exp. Med. Biol. 620*, 168–180.

(38) Lens, M., Medenica, L., and Citernesi, U. (2008) Antioxidative capacity of C-60 (buckminsterfullerene) and newly synthesized fulleropyrrolidine derivatives encapsulated in liposomes. *Biotechnol. Appl. Biochem. 51*, 135–140.

(39) Partha, R., Lackey, M., Hirsch, A., Casscells, S. W., and Conyers, J. L. (2007) Self assembly of amphiphilic C60 fullerene derivatives into nanoscale supramolecular structures. *J. Nanobiotechnol. 5:6*, 1–11.

BC1001664

Liposomal Formulation of Amphiphilic Fullerene Antioxidants

Zhiguo Zhou,* Robert P. Lenk, Anthony Dellinger, Stephen R. Wilson, Robert Sadler and Christopher L. Kepley

Luna nanoWorks, a division of Luna Innovations Incorporated, 521 Bridge Street, Danville VA 24541

E-Mail: zhouz@lunainnovations.com; Phone: 434-483-4234; Fax: 434-483-4195.

General Experimental Procedures:
All reaction solvents and other reagents were commercially available, and used without further purification. HPLC grade ethanol was used for HPLC and TFA was filtered with 0.2μm before mixed with ethanol. C_{70} was purchased from BuckyUSA Inc. Compounds were purified by flash column chromatography or HPLC and characterized by NMR (300 MHz) and MALDI-TOF mass spectrometry. EPR studies were conducted in a contractor lab at UCSD by Dr. Laura L. Dugan.

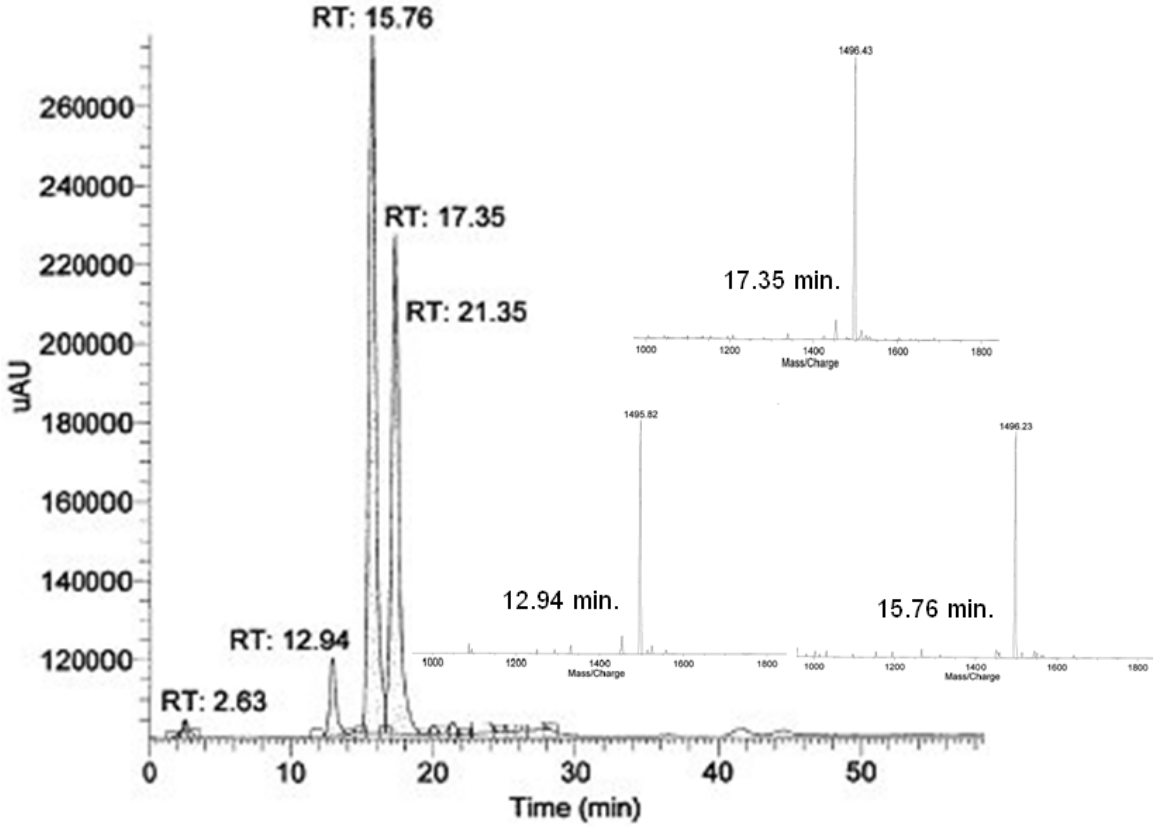


FIGURE S1: HPLC of ALM (C6-Phenyl column, 0.1% TFA-trifluoroacetic acid in ethanol). Three major bisadduct isomers were eluted at 12.94 min, 15.76 min., and 17.35 min. The minor peaks around 26-29 min. and 42-45 min. correspond to the mono ethyl ester and diethyl esters of ALM formed in the analytical process as confirmed by MALDI-MS (TFA catalyzed ester formation between COOH of ALM and ethanol when the fractions were concentrated). Insets show the MALDI-Mass spectra of the three ALM isomers at 1495.82, 1496.23 and 1496.43 respectively (calculated MW of ALM: 1496). HPLC grade ethanol was used and TFA was filtered with 0.2μm before mixed with ethanol. HPLC conditions: Gemini 3μ C6-Phenyl 110A column (4.6 mm x 150 mm) with 0.5% TFA in ethanol as the mobile phase. See MALDI-MS spectrum of ALM prior to HPLC separation in FIGURE S6.

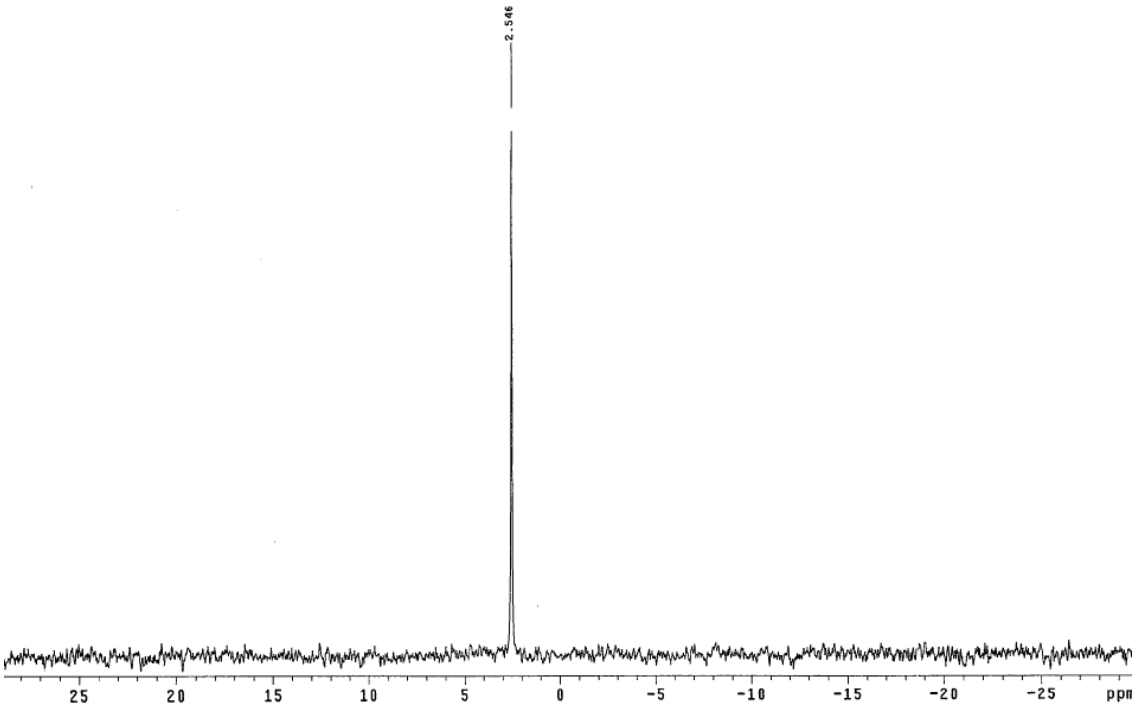


FIGURE S2: ^{31}P NMR of ALM-PC liposome in D_2O showing a very sharp signal at 2.55 ppm with a very small half-width $W_{1/2}$ of 2.8 Hz, which is comparable to that for liposomes made of phophatidylcholine only, indicating that ALM is structurally compatible with lipids and its presence does not interfere with the assembly of lipid molecules. The ALM content in the liposome sample is 50% by weight (1:1 molar ratio of ALM to lipids).

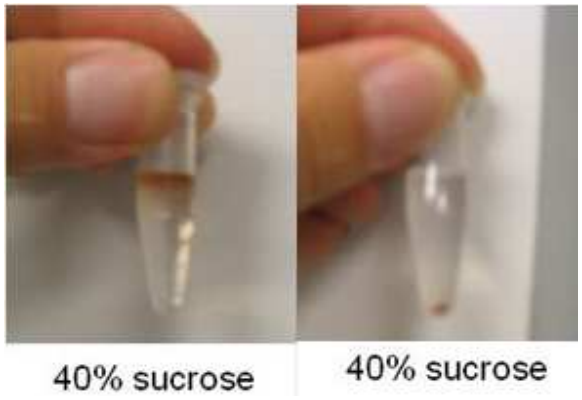


FIGURE S3: Buoyant density test under high-speed centrifugation at 18,000 G for 30 min. Left: ALM liposome sample (1:1 egg-PC to ALM), where fullerenes (brownish) stably associated in lipid bilayers stayed on the top of 40% sucrose cushion. Right: fullerene ALM itself didn't form stable liposomes and precipitated to the bottom of the sucrose solution.



FIGURE S4: Left - ALM liposome samples made of egg-PC and ALM at 1:1 weight ratio, at 4 different concentrations. Right – comparison of preparations made of 1:1 ALM/egg-PC and ALM only at 1mg/mL, showing that ALM only didn't form vesicles at 1mg/mL with most materials precipitated to the bottom of the vial 3 days after its preparation. Only 15-20% ALM self-assembled into vesicles in the absence of egg-PC, demonstrating the necessity of regular lipids to promote the formation of high-loading and high-content ALM-PC liposome. It also demonstrated the incorporation of ALM into the lipid bilayer.

Cytotoxicity: The effects of ALM liposome on U937 monocyte cell viability was examined at different concentrations in parallel with Vitamin E, a natural antioxidant. As seen in Figure S5, cells incubated with Vitamin C or ALM did not have toxic effects on the viability of serum-starved cells. No significant differences in cell viability were observed using up to 67 μM ALM (100 μg/mL) compared to control cells at days 3 and 6. The cell viability was evaluated with well established MTT assay.

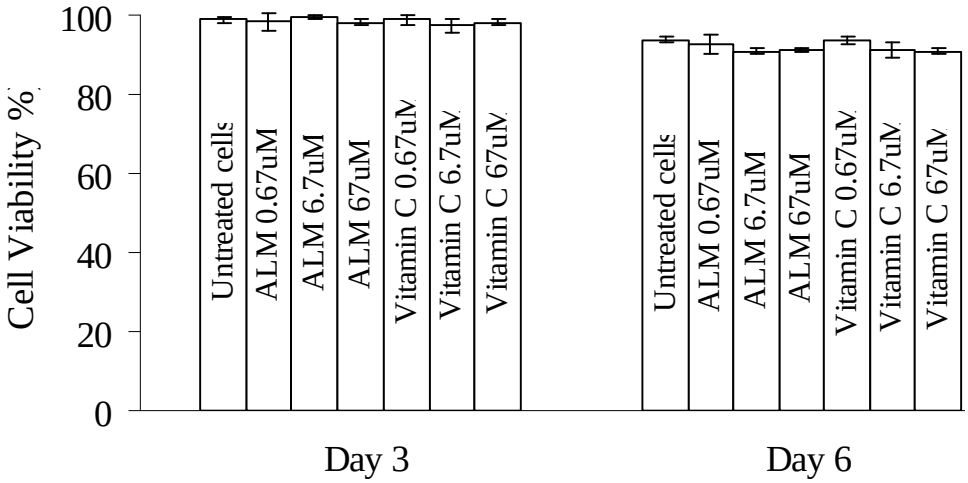


FIGURE S5: Toxic effects of ALM liposome and natural antioxidant Vitamin C on cell viability shown with error bars. Serum-starved U937 monocyte cells were treated with indicated concentrations of ALM or Vitamin C, or untreated through 6 days.

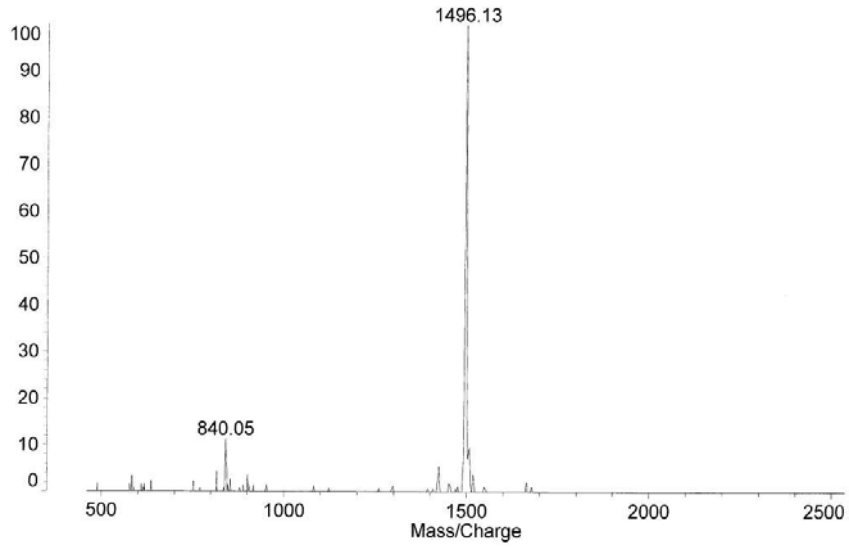


FIGURE S6: MALDI-MS spectrum of ALM prior to HPLC separation showing the molecular ion peak of ALM at 1496.13 and C_{70} fragment at 840.05 formed under laser desorption/ionization conditions (Calculated MW of ALM: 1496).

Cellular Internalization Kinetics of (Luciferin-)Cell-Penetrating Peptide Conjugates

Emelía Eiríksdóttir,[§,†] Imre Mäger,*[,§,†,‡] Taavi Lehto,[‡] Samir El Andaloussi,[¶,†,‡] and Ülo Langel[†,‡]

Department of Neurochemistry, The Arrhenius Laboratories for Natural Sciences, Stockholm University, SE-106 91 Stockholm, Sweden, and University of Tartu, Institute of Technology, Tartu, Estonia. Received April 9, 2010; Revised Manuscript Received June 22, 2010

Cell-penetrating peptides (CPPs) belong to a class of delivery vectors that have been extensively used for the cellular delivery of various, otherwise impermeable, macromolecules. However, results on the cellular internalization efficacy of CPPs obtained from various laboratories are sometimes challenging to compare because of differences in the experimental setups. Here, for the first time, the cellular uptake kinetics of eight well-established CPPs is compared in HeLa pLuc 705 cells using a recently published releasable luciferin assay. Using this assay, the kinetic behavior of cytosolic entry of these luciferin−CPP conjugates are registered in real time. Our data reveal that the uptake rate of CPPs reaches its maximum either in seconds or in tens of minutes, depending on the CPP used. Tat and higher concentrations of MAP and TP10 display fast internalization profiles that resemble the kinetic profile of membrane-permeable free luciferin. The uptake of the other peptides, *p*Vec, penetratin, M918, and EB1, is much slower and is consistent with the reported observations of endocytosis being the predominant internalization mechanism. Additionally, to some extent, the latter CPPs can be clustered into subgroups which are based on time points when the most pronounced uptake rates are observed. This may indicate once more involvement of various (concentration dependent) mechanisms in the uptake of CPPs. In summary, the variances in the internalization profiles for the CPPs demonstrate the importance of measuring kinetics instead of only relying on simple end-point studies, and with the luciferin−CPP assay, more lucid information can be retrieved when studying the internalization mechanisms of CPPs.

INTRODUCTION

Ever since the first cell-penetrating peptides (CPPs)[1]were introduced in mid-1990s (*1, 2*), research on these cargo delivery vehicles has been highly active. The origin of CPPs is manifold, ranging from protein-derived sequences (*3, 4*) with some having inherent biological activity (*5*−*7*) to fully artificial peptides, which are designed based on physical and chemical properties required for specific interactions with cargo molecules and/or cell-membrane components (*8*−*10*). Also, several successful attempts have been made to modify well-established CPPs in order to increase their potency (*11*−*16*). These polycationic and/or amphipathic peptides have shown great promise in cargo delivery, both in vivo and in vitro (*17*−*20*). However, it is important to keep in mind that CPPs might have disparate translocation capabilities and their potency often depends on the type of a cargo molecule used and whether the cargo is attached to the CPP using covalent or noncovalent strategy.

There are several methods available to assess the delivery efficacy of CPPs that are mostly based on the use of fluorescent labels or functional assays, which generate readouts that arise from a biological response. Each method has its advantages and limitations. While fluorometric assays are relatively fast and straightforward to implement, these methods might not provide biologically relevant information because the readout might be biased by fluorescence originating from membrane-bound and/or endosomally entrapped CPP-cargo constructs, which are not biologically available (*21*). Therefore, in order to avoid misleading results by overestimation of internalization efficacy, it is more relevant to take advantage of biological assays, such as the splice correction assay (*22*). However, the readout depends on whether the cargo molecule is delivered into the correct cellular compartment, e.g., the nucleus in case of the splice correction assay. This might, on the other hand, not reflect the delivery efficacy into other parts of a cell, such as the cytoplasm, which is also of great interest from a pharmacological point of view (when, for example, RNAi effects are studied).

Both the high background in fluorescence assays and the lack of biological readout call for novel assays to measure the delivery efficacy of CPPs. A releasable luciferin-transporter system (Figure 1) is a recently published assay, which allows real-time analysis of cellular uptake and cytosolic release of the transporter molecule (*23*). This assay relies on the luciferin−luciferase reaction which is known for its high

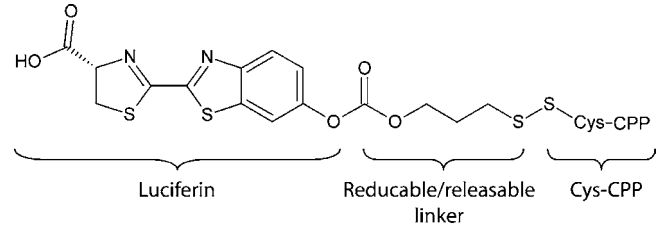


Figure 1. Structure of the luciferin−CPPs. The luciferin−CPP conjugates are composed of luciferin, a reducable/releasable linker, and a cysteine-containing CPP, as previously described (*23*).

* Corresponding author. Tel.: +372 737 4871; fax: +372 737 4900; E-mail address: imre.mager@ut.ee.

§ These authors contributed equally to this work.

† Stockholm University.

‡ University of Tartu.

¶ Present address: Department of Laboratory Medicine, Karolinska Institute, 141 86, Stockholm, Sweden.

[1]Abbreviations: CPP, cell-penetrating peptide; TP10, Transportan 10; MAP, model amphipathic peptide; HKRg, HEPES-buffered Krebs Ringer containing 1 mg/mL glucose; PBSg, phosphate buffered saline containing 1 mg/mL glucose; LDH, lactate dehydrogenase.

10.1021/bc100174y © 2010 American Chemical Society
Published on Web 08/04/2010

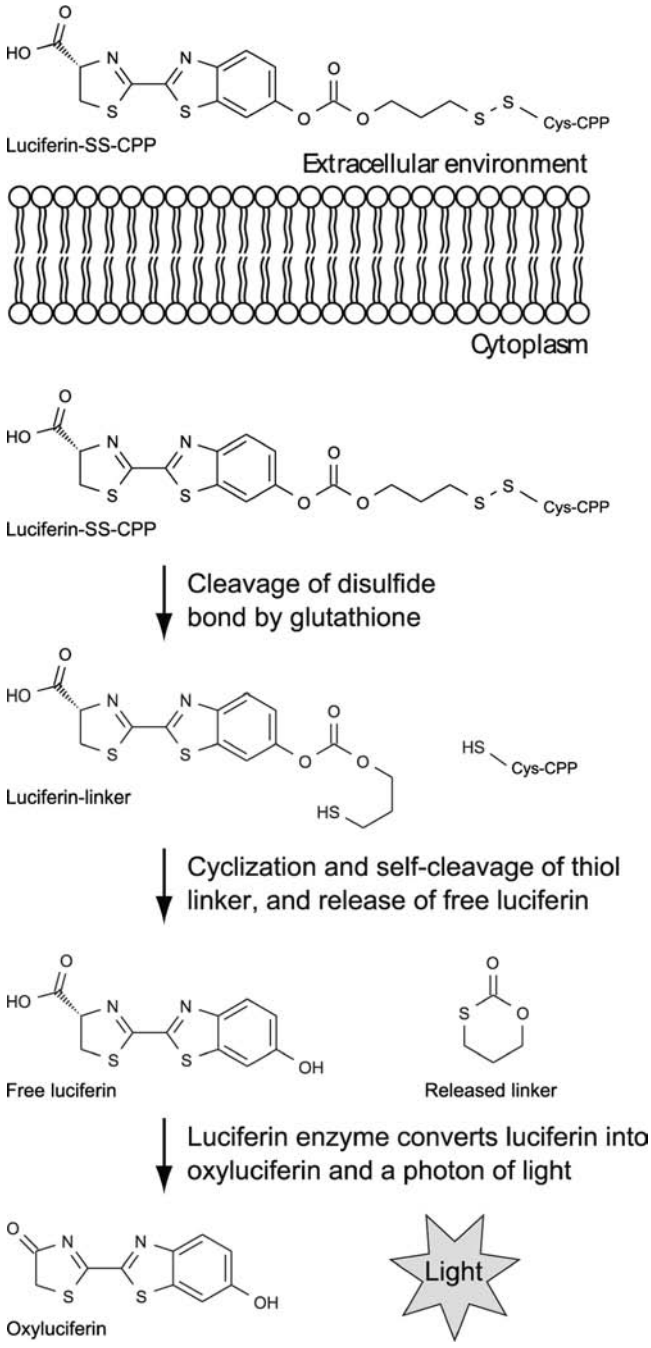


Figure 2. Scheme of the cellular fate of the luciferin−CPP conjugates. Upon cytosolic entry via an endocytic or direct pathway, (1) the disulfide bridge is reduced by cytosolic glutathione, (2) the linker between the luciferin and the CPP undergoes cyclization and free luciferin is released, (3) the luciferase enzyme converts the luciferin to oxyluciferin and a photon, and (4) the photon is detected by a luminometer.

quantum yield and minimal background (*24*). In short, after the cytosolic entry, the disulfide bond between the luciferin and the transporter (a CPP in our study) is reduced, free luciferin is released, and in turn, it is converted by luciferase into oxyluciferin and a photon (Figure 2). The produced light thereby reflects the amount of the corresponding CPP from the luciferin−CPP conjugate. This approach has previously been used to quantify polyarginine uptake and cargo release in luciferase expressing transgenic mice by whole body imaging technique (*25*).

In order to correctly assess and compare uptake efficacy of CPP-cargo constructs with in vitro model systems, it is important to monitor the kinetics of the uptake process since the total uptake depends on the treatment duration. Furthermore, inhibition of a certain internalization pathway in a mechanistic study might in some cases only change the kinetics but not the total uptake or vice versa (*26*). Therefore, one time point for the readout does not reveal all aspects of a certain peptide carrier.

Here, the releasable luciferin−CPP conjugate system is used for the first time to compare the cargo delivery efficacy of eight CPPs into cells: the protein derived peptides penetratin (*1*), EB1 (*27*), Tat (*2*), M918 (*28*), *p*Vec (*29*), and TP10 (*30*) (with cargo attached to the N-terminus or to Lys^7), and a designed peptide MAP (*31*). We demonstrate that this assay is sensitive enough to efficiently detect differences of the CPPs in terms of their uptake kinetics. We also show how the CPPs under this study could be clustered into subgroups regarding to their uptake kinetics profile and kinetic parameters.

EXPERIMENTAL PROCEDURES

Peptide Synthesis. The peptides (Table 1) were synthesized in a stepwise manner on an automated peptide synthesizer (Applied Biosystems model 433A, USA) by *tert*-butoxycarbonyl (*t*-Boc) chemistry. *t*-Boc amino acids (Neosystem, France; Iris Biotech, Germany; Bachem AG, Switzerland) were coupled as hydroxybenzotriazole (HOBt) esters (Iris Biotech, Germany) in the presence of *N*,*N*′-dicyclohexylcarbodiimide (DCC; Iris Biotech, Germany) and *N*,*N*′-diisopropylethylamine (DIEA; Iris Biotech, Germany) on 4-methylbenzhydrylamine resin (Iris Biotech, Germany) to generate C-terminally amidated peptides.

Manual coupling of the Cys residue to the ε-amino group on Lys^7 of TP10 was carried out with HOBt, 2-(1*H*-benzotriazole-1-yl)-1,1,3,3-tetramethylaminium tetrafluoroborate (TBTU) and DIEA activation.

Peptides containing His(Dnp) or Trp(For) were deprotected with 20% thiophenol in *N*,*N*′-dimethylformamide (DMF) for 1 h or 20% piperidine in DMF for 1 h, respectively, and all peptides were then cleaved from the resin under anhydrous hydrogen fluoride/*p*-cresol/*p*-thiocresol (90/5/5) for 1 h at 4 °C and collected with ether precipitation. Finally, the peptides were purified by semipreparative reverse-phase HPLC column (DiscoveryBIO Wide Pore C-18, Supelco, Sigma-Aldrich, Sweden), and their purity was analyzed by RP-HPLC analytical column (Discovery C-18, Supelco). The correct molecular weight was verified by MALDI-TOF (Perkin-Elmer prOTOF 2000, Perkin-Elmer, Sweden) mass spectrometry.

Synthesis of Luciferin−CPP Conjugates. Luciferin linker was synthesized as previously reported (see Scheme 1 in ref *32*). Luciferin linker and Cys−CPPs were mixed in 1:1 molar ratio at 0.88 mM concentration in DMF/acetic acid buffer (pH 5, 50 mM) for 1 h under nitrogen. Luciferin−CPP conjugates (Figure 1) were purified by semipreparative RP-HPLC column, and their purity (>99%) was analyzed by RP-HPLC analytical column. The correct molecular weight was verfied by MALDI-TOF mass spectrometry (Table 1).

Cell Culture. HeLa pLuc 705 cells, kindly provided by Ryszard Kole, were grown in DMEM (Dulbecco's modified Eagle's medium) with glutamax, supplemented with 0.1 mM nonessential amino acids, 1.0 mM sodium pyruvate, 10% FBS (fetal bovine serum), 100 U/mL penicillin, and 100 mg/mL streptomycin (hereafter referred to as complete medium). Cells were grown at 37 °C in a humidified 5% CO_2 incubator. All cell culture media and supplements were purchased from Invitrogen, Sweden.

Uptake Kinetics. 10^6 cells were seeded onto a 6 cm cell culture dish 96 h prior to experiments. 48 h prior to experiments, the cells were transfected with 4 μg luciferase encoding pGL3 plasmid (Promega, Sweden) using 10 μL Lipofectamine 2000 (Invitrogen, Sweden) in 6 mL complete medium for 4 h. The

Table 1. Sequences of the Used Cell-Penetratin Peptides (CPPs) with Physicochemical Characteristics[a]

CPP	Cys-CPP sequence	ref	number of Lys	number of Arg	calcd [M+H$^+$]	exp [M+H$^+$]	$\langle H\rangle^b$	$\langle \mu\rangle^c$
MAP	C-KLALKLALKALKAALKLA-amide	*31*	5	0	2375.32	2375.32	0.99	0.16
TP10	C-AGYLLGKINLKALAALAKKIL-amide	*30*	4	0	2680.42	2680.42	0.93	0.07
TP10(Cys)	AGYLLGK(C)[d]INLKALAALAKKIL-amide	*30*	4	0	2680.42	2680.43	0.93	0.07
EB1	C-LIRLWSHLIHIWFQNRRLKWKKK-amide	*27*	4	3	3597.86	3597.88	−0.63	0.04
Penetratin	C-RQIKIWFQNRRMKWKK-amide	*1*	4	3	2745.32	2745.29	−1.73	0.01
*p*Vec	C-LLIILRRRIRKQAHAHSK-amide	*29*	2	4	2707.42	2707.42	−0.44	0.08
Tat	C-GRKKRRQRRRPPQ-amide	*2*	2	6	2217.08	2217.07	−3.49	0.04
M918	C-MVTVLFRRLRIRRASGPPRVRV-amide	*28*	0	7	3133.62	3133.61	−0.05	0.01

[a] Luciferin is conjugated to the N-terminal cysteine residue, unless stated otherwise. Amino acids with a positive charge at physiological pH are underlined. [b] Mean hydrophathy (GRAVY score) was calculated using WinPep with Kyle and Doolittle scale (*73*). [c] Mean amphipathy moment was calculated using WinPep (calculations assume α-helical conformation of the peptides). [d] Luciferin was coupled to the cysteine at the ε-amino group on Lys[7].

transfection medium was replaced with complete medium and the cells grown for further 20 h. 9×10^3 cells were seeded in a white 96-well clear-bottom plate (Greiner Bio-One, Germany) 24 h prior to luciferin−CPP treatment.

On the day of the experiment, the cells were washed once with 100 μL cell culture media or HEPES-buffered Krebs Ringer buffer containing 1 mg/mL glucose (HKRg), which was then replaced with various concentrations of 120 μL luciferin-CPP solution in complete medium or HKRg, respectively. All experiments were carried out at RT (25 °C) for either 2 h (in complete medium) or 1 h (in HKRg) in atmospheric CO_2. Luminescence was measured by GLOMAX 96 microplate luminometer (Promega, Sweden) where data points were recorded in 93 s time interval.

In order to exclude overestimation of peptide cytosolic delivery and overrule possibilities of false-positive signals due to extracellular cleavage of the conjugates by potential leak of glutathione, we monitored changes in extracellular free thiol concentration. The cells were seeded into 96-well tissue culture plates one day prior experiment, as described above. On the day of the experiment, the cells were washed with phosphate buffered saline (PBS) and incubated with 5 μM luciferin−CPP conjugates in a solution of 250 μM Ellman's reagent (5,5′-dithiobis-(2-nitrobenzoic acid) or DTNB) in PBS supplemented with 1 mg/mL glucose (PBSg). Ellman's reagent reacts with free thiols, releasing the yellow dianion 2-nitro-5-thiobenzoate (TNB^{2-}). By monitoring absorption at 412 nm (the absorption peak of TNB^{2-}), change in the free thiol concentration in the extracellular media can be determined. The absorption was measured over time in triplicate using a Tecan Sunrise microplate absorbance reader (Tecan Group Ltd., Switzerland). As a positive control, we measured the absorbance of lysed cells which were incubated in a solution of luciferin−CPP and Ellman's reagent.

Lactate Dehydrogenase (LDH) Leakage. Membrane integrity was measured using the Promega CytoTox-ONE assay (Promega, USA). 9×10^3 cells were seeded in a clear 96-well plate (Greiner Bio-One, Germany) 24 h prior to treatment. Cells were washed twice with 120 μL complete medium prior to 35 min or 2 h incubation with 120 μL luciferin−CPP conjugates at four different concentrations (1, 2.5, 5, and 10 μM) in complete medium at RT (25 °C). Finally, 80 μL of extracellular medium was transferred to a black 96-well plate (Labdesign, Sweden) containing 80 μL of CytoTox-ONE reagent, incubated for 10 min at RT, and fluorescence measured at 560/590 nm. LDH release from cells lysed with 0.2% Triton X-100 in HKRg was defined as 100% leakage and LDH release from untreated cells as 0% leakage.

Statistical Analysis. All data were processed in *GraphPad Prism* v 5 for Windows (GraphPad Software Inc., USA) with results displayed as mean ± SEM. The uptake measurements in complete medium are three independent experiments performed in triplicate while the uptake experiments in HKRg were carried out twice in triplicate. The cytotoxicity measurements include two independent experiments performed in triplicate.

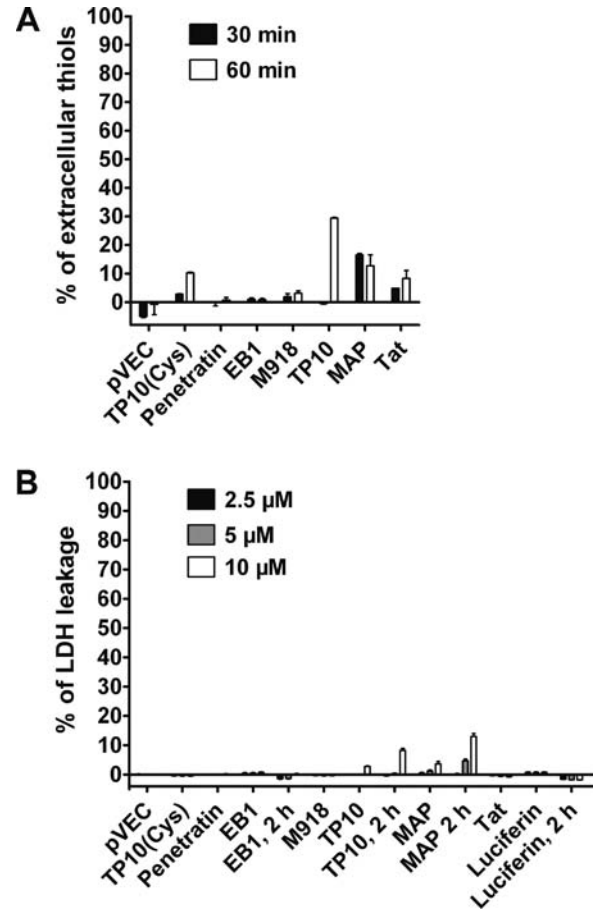


Figure 3. (A) An increase in extracellular free thiol content after 30−60 min treatment with 5 μM CPP in PBSg buffer. (B) Cellular toxicity. LDH leakage was measured after 35 min or 2 h treatment with 2.5−10 μM CPP in complete medium. LDH release from cells lysed with 0.2% Triton X-100 in HKRg was defined as 100% leakage, and LDH release from untreated cells as 0%. The values display the means of two independent experiments performed in HeLa pLuc 705 cells in triplicates (mean ± SEM, $n = 2$).

Data Fitting and Comparison of Uptake Kinetics Parameters. The uptake kinetics raw data of replicate samples were averaged for each experiment, and a modified logistic model was used to fit the averaged data. The fitting procedure was carried out in *Prism 5* (GraphPad Software Inc., USA) according to the formula

$$S(t) = \frac{P_2 + P_5 \cdot t}{1 + \exp[-P_4 \cdot (t - P_3)]} + P_1 \quad (1)$$

where $S(t)$is the signal intensity at time t, P_1 approximates the baseline signal intensity, P_2 approximates the amplitude of the plateau above the baseline, P_3 (s) correlates with the time point at which maximal change of the signal occurs, P_4 (s^{-1}) correlates with the maximum slope of the signal, and P_5 (s^{-1}) describes the terminal slope of the uptake curve (*33*). Thereafter, the maximum slope (maximum first derivate) of the uptake curve and the time at which the maximum slope occurs (i.e., the inflection point of a sigmoidal curve) were determined from the fitted curve for each experiment. Finally, average of these parameters along with standard error of mean (SEM) were calculated.

RESULTS

Uptake Measurements in Complete Medium; Exponential Kinetic Profiles versus Sigmoidal. Here, we have used the luminescence of the samples in each time point to produce kinetic curves of the uptake that correlate with turnover of the luciferin−luciferase reaction in these data points (in units of RLU per second). By calculating the area under the kinetic curve (Figure 4), the total emitted light from the luciferin−luciferase reaction, and thereby the total cytosolic release of luciferin-CPP, could be evaluated. This integration can be carried out for any chosen time point from a single experiment, and we have chosen 15, 30, and 60 min time points (Figure 5B−D) since the majority of CPP end point uptake studies are within this incubation time range. In addition, we determined the total uptake level after 2 h incubation (Figure 5A) because the luminescence for most CPPs used in this study was still increasing after 1 h.

Judging by the kinetic profiles of the peptides, it is apparent that they can be divided into two categories. Tat and free luciferin displayed a fast cytosolic entry with a decaying exponential profile (Figure 4A) while EB1, TP10(Cys), M918, penetratin, and *p*Vec showed a slower cytosolic entry with a sigmoidal profile (Figure 4B), which reached a maximal uptake rate after different time periods. MAP and TP10 fall into both categories depending on their concentrations; 10 μM TP10 and 10 μM and 5 μM MAP (Figure 4A) aligned with Tat, while other concentrations showed the same pattern as TP10(Cys) (i.e., "slow" uptake pattern). The uptake kinetic curves for the peptides in the fast uptake group look roughly the same. The internalization took place very rapidly; the uptake rate reached a maximum in a matter of seconds (Tat, 10 μM MAP) up to few minutes (TP10, 5 μM MAP) and decayed rapidly. On the other hand, the peptides following a sigmoidal or slow uptake pattern can be further subdivided. The kinetic curves for EB1, TP10(Cys), and M918 are similar in shape with higher maximum uptake and faster internalization (steeper initial slope) than *p*Vec and penetratin. Another way of categorizing the peptides can be according to the time of their initial internalization (i.e., cytosolic entry). EB1 and penetratin started to internalize immediately after their application to the cells. On the other hand, the first sign of internalization of *p*Vec, M918, and TP10(Cys) was after 15 min. Furthermore, EB1 was the only peptide from the sigmoidal group that exhibited a deviation or a certain phase change within its kinetic curves; the maximal uptake rate for the 10 μM peptide occurred roughly 30 min earlier than at the lower concentrations (data not shown).

Even though the peptides show heterogeneous total uptake (Figure 5A−D), the concentration dependence of uptake is quite similar but not linearly dependent on the concentration, although higher peptide concentrations naturally gave higher uptake. Interestingly, the total uptake of the peptides that display the sigmoidal uptake profile exceeded the total uptake of the peptides with the fast uptake profile if given enough time, e.g., 2 h (Figure 5A); however, care must be taken when interpreting these results since an unknown signal portion may have been left unregistered for the fast profile compounds due to short lag period between addition of the peptides and registration of the very first data point. In addition, the uptake rate of the slow internalization group remains high even after 2 h incubation (Figure 4B). This indicates that differences in total uptake of these two groups are strongly time dependent.

EB1 is an analogue of penetratin, designed to have α-helical structure upon protonation at low pH, i.e., in endosomal compartments, and to promote endosomal escape. It is intriguing that, in 30 min, the uptake for EB1 indeed started to exceed that of penetratin (Figure 5C), and this difference increased over time. The kinetic profiles for these two peptides differ (Figure 4B)—EB1 reached its maximal internalization rate faster and to a higher extent. This indicates that the rationale behind its endosomolytic design is indeed effective and that EB1 escapes the endosomes better than penetratin, which is in line with earlier hypotheses and previously published results (*27*).

TP10 showed a considerably higher uptake in the beginning of the incubation, but TP10(Cys) reached the uptake level of TP10 in 1 h and exceeded it by more than 2-fold after 2 h treatment. The only difference between the sequences of TP10 and TP10(Cys) is the localization of the cysteine residue, which is at the N-terminus in TP10 and on the side chain of Lys^7 in TP10(Cys). TP10(Cys) is the milder peptide of the two in the

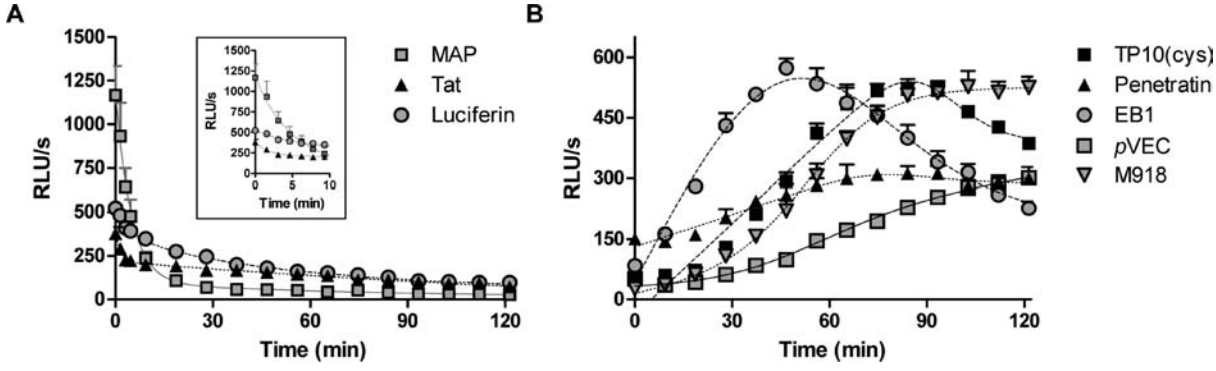


Figure 4. Internalization kinetics profiles of the CPPs. (A) Fast internalization profiles for 10 μM luciferin, Tat, and MAP in complete medium. The internalization profile for TP10 was omitted for clarity because it is analogous to the internalization profile for MAP. The inset describes the first 10 min of the uptake. (B) Slow internalization profiles for 10 μM EB1, TP10(Cys), M918, penetratin, and *p*Vec in complete medium. The values display the means of three independent experiments performed in HeLa pLuc 705 cells in triplicates (mean ± SEM, $n = 3$). The number of displayed data points is reduced for clarity.

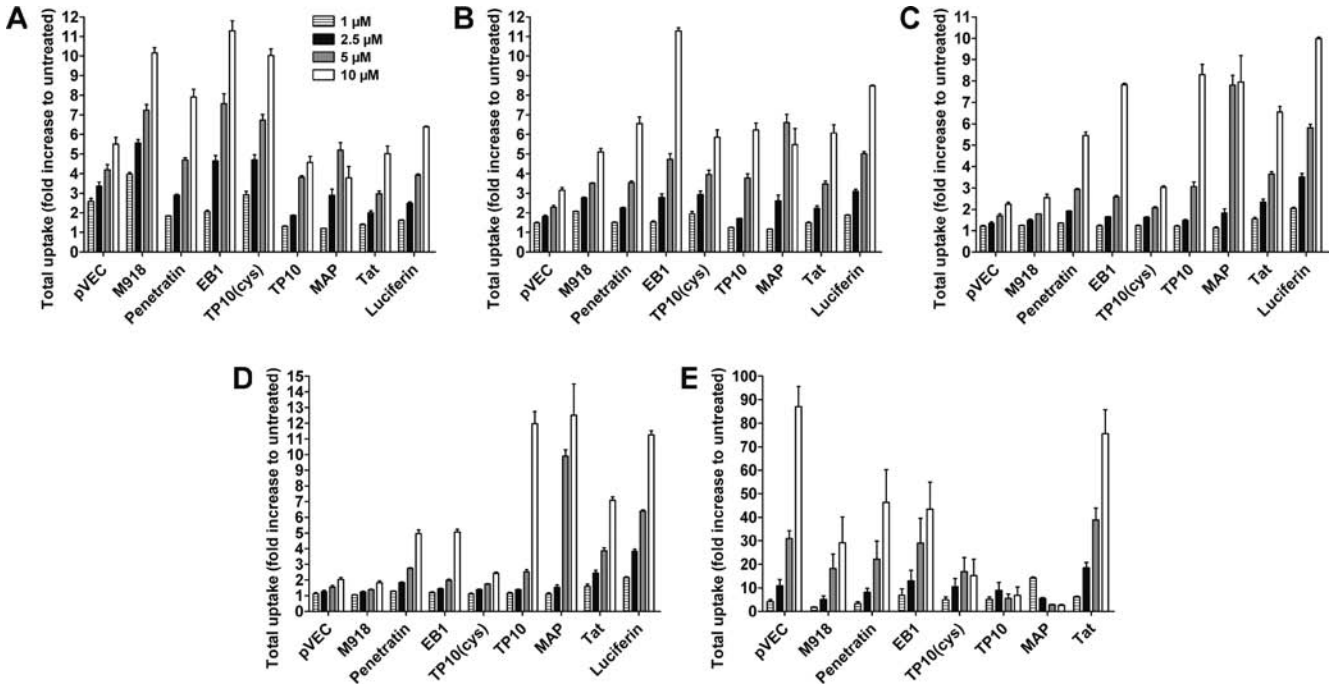


Figure 5. Total cellular internalization of the CPPs. (A) Total cellular internalization of 1−10 μM luciferin−CPPs after 2 h incubation in complete medium. (B) 1 h incubation in complete medium. (C) 30 min incubation in complete medium. (D) 15 min incubation in complete medium. (E) 1 h incubation in HKRg buffer. All graphs are presented as fold increase compared to untreated cells. The values display the means of (A−D) three independent experiments performed in HeLa pLuc 705 cells in triplicates (mean ± SEM, $n = 3$), (E) two independent experiments performed in HeLa pLuc 705 cells in triplicates (mean ± SEM, $n = 2$).

sense that it provokes no membrane disturbance and has been reported to show higher uptake than TP10 (*34*).

To verify that the uptake values we observed were not a consequence of extracellular cleavage of the conjugates or glutathione outflow from the cells, we monitored changes in extracellular free thiol content using Ellman's reagent while incubating the cells with luciferin−CPP conjugates in PBSg buffer. Virtually no change in thiol concentration could be seen, except for TP10 and MAP between 0.5 and 1 h incubation, and also to some extent for Tat and TP10(Cys) peptide (Figure 3A). When incubating the cells with various concentrations of Ellman's reagent without adding the peptide conjugates, it was apparent that its cleavage rate was significantly slower than the uptake rate of CPP conjugates. This was true even when using Ellman's reagent at a concentration which was much higher than the determined K_m value of the Ellman's reagent cleavage reaction, i.e., when this reaction was ongoing at maximal rate (data not shown).

Peptide Toxicity by Lactate Dehydrogenase (LDH) Leakage Assay. Cellular leakage of large M_w LDH has been shown to correlate with the leakage of deoxyglucosephosphate (a small molecule) (*35*). LDH leakage could therefore be used to predict leakage of a small, intracellular molecule like glutathione into the extracellular environment. This is an important factor in the releasable luciferin−CPP assay used herein, because extracellular glutathione could cause a reduction of extracellular luciferin−CPP conjugates. Released free luciferin would consequently enter cells, and the internalization efficacy of the corresponding CPP could be overestimated. Therefore, to exclude artifacts from a leaky membrane, the level of membrane disturbance or toxicity provoked by luciferin and the luciferin−CPP conjugates in complete medium was measured by the LDH leakage assay (Figure 3B).

None of the peptide concentrations used herein (1−10 μM) compromised the membrane integrity after 35 min incubation. Changes in the cell morphology after 2 h incubation were only noticeable for MAP (5 and 10 μM), TP10 (10 μM), and EB1 (10 μM), as judged by microscopy (data not shown). MAP and TP10 triggered a mild LDH leakage (13.0% and 8.2%, respectively) after 2 h incubation; however, EB1 can be considered nontoxic. Our results are thus in good agreement with previously published data (*34*, *35*).

Uptake Measurements in Media versus Buffer. Uptake measurements can be carried out in different incubation solutions, e.g., in complete or serum free cell growth media, or in various buffers such as HKR and PBS.

Cellular uptake measurements using buffer as an incubation media do not closely represent physiological conditions. Buffer systems have nevertheless been applied in the past (*23*, *36*, *37*), which prompted us to compare our results carried out in complete media with those in HKRg buffer. As expected, the kinetic profiles for all of the peptides, except MAP and TP10, were different from the experiments carried out in media (data not shown). No peptide displayed a sigmoidal slow uptake profile; instead, a steady increase in the luminescence along with time was detected for *p*Vec, M918, and EB1 (1−5 μM). Furthermore, Tat, TP10(Cys), penetratin, TP10, and 10 μM EB1 exhibited a dip followed by a steady increase, similar to penetratin when the uptake experiments were carried out in complete medium.

The level of uptake was markedly higher for the buffer experiments where the most pronounced increases were 28- and 12-fold for 10 μM *p*Vec and Tat, respectively (Figure 5B and E). The several-fold lower uptake for most of the CPPs in complete media can be explained by the presence of serum proteases and the affinity of CPPs toward negatively charged serum proteins.

Data Fitting and Comparison of Uptake Kinetics Parameters. A modified logistic function according to eq 1 was fitted to the raw luminescence data of replicate samples measured during independent experiments. Only the peptides that belong to the slow-uptake group could be fitted using this model, i.e., Tat, and higher concentrations of TP10 and MAP conjugates were left out from this analysis. The goodness of fit was

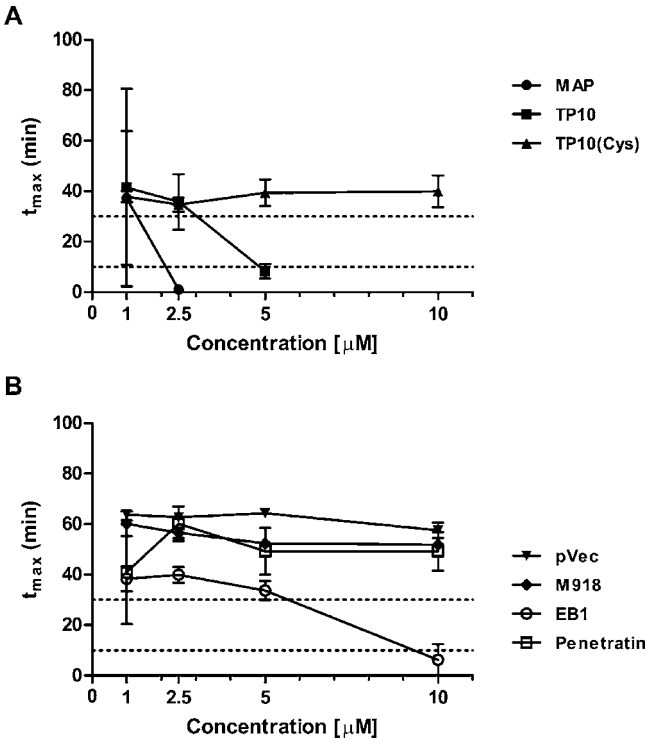


Figure 6. Data fitting and comparison of uptake kinetic parameters. The raw luminescence data of replicate samples measured during independent experiments were fitted to a modified logistic function according to eq 1, and inflection point of the sigmoidal curve (t_{max}) was calculated for (A) MAP, TP10, and TP10(Cys); and for (B) *p*Vec, M918, EB1, and penetratin. The values display the means of three independent experiments performed in HeLa pLuc 705 cells in triplicates (mean ± SEM, $n = 3$).

quantified by the R^2 parameter which was typically in the range 0.92−0.99. Thereafter, from the fitted curve we calculated the following kinetic parameters for three independent experiments: maximum slope, in other words the maximum uptake rate of the signal (a_{max}), and the time at which the maximum slope occurs, i.e., the inflection point of the sigmoidal curve (t_{max}).

Generally, the a_{max} for all the CPPs increases linearly with increasing concentration. The change is most pronounced for EB1 peptide, exceeding at least two times the dependence between a_{max} and concentration for all the other tested peptides; and interestingly, the a_{max} for penetratin and *p*Vec does not significantly depend on the peptide concentration at all (data not shown).

When analyzing the time where the maximum slope of uptake (i.e., the maximal rate of uptake) occurs and how this depends on peptide concentration, we observed that the data points are clustered into two subareas. The maximal rate of uptake took place after 30−60 min incubation for most of the CPPs, but 10 μM EB1, 5 μM TP10, and 2.5 μM MAP displayed a maximal rate already after 1−10 min incubation despite that these peptides belong to the "slow" uptake group at these concentrations (Figure 6A,B).

DISCUSSION

Comparison of the uptake potency of new and old CPPs is a flourishing and important research field. Several assays have been used for this purpose that rely on different readouts from distinct cellular compartments (*38*). This sometimes gives disparate results, which can be difficult to interpret and compare, especially if the whole study is not carried out within the same research group and with same experimental conditions.

This is the first time a comparative uptake study on several CPPs is carried out with the releasable luciferin assay (*23*). We measured cytosolic cargo delivery kinetics of eight disulfide conjugated luciferin−CPP constructs (Table 1), where luciferin and the CPP are separated by a linker (Figure 1). The readout is produced by the processes described in Figure 2. We measured the rate of the CPP internalization by registering luminescence versus time and calculated cumulative uptake (total uptake) by integrating the kinetic curve for specific time-points.

Free luciferin is capable of entering cells without any transport vector (*39*) with much faster and distinct kinetic profile than luciferin−transporter conjugates (*23*). Most CPPs, on the other hand, do not possess direct membrane translocation properties. Instead, various endocytic processes have been found to be involved in peptide-mediated cargo delivery. Nevertheless, several reports have concluded that direct translocation cannot be ruled out for unconjugated CPPs. For example, translocation of free Tat peptide has been reported to be independent of endocytosis, since the peptide frequently internalizes at low temperature and into genetically modified cells lacking certain endocytic pathways (*40*). MPG and Pep are two other peptides that also translocate cells via direct penetration mechanisms, even when conjugated to cargos (*8, 15*). Additionally, based on microscopy observations and flow cytometry experiments, there seems to be a certain concentration threshold above which the direct translocation could be favored (*41, 42*). This is consistent with our results where we observe similar kinetic profiles in the uptake of membrane permeable free luciferin and luciferin−Tat conjugate in complete media. However, numerous other studies have shown involvement of endosomal pathways for Tat (*21, 43, 44*) with an uptake profile that does not resemble our "fast" uptake curve (*45*).

We also observe free luciferin-like "fast" uptake profile for 10 μM luciferin−TP10 and 5−10 μM luciferin−MAP. While both TP10 and MAP have been reported to be taken up by endocytosis (*21, 37*), the behavior of TP10 in our case does not reflect that. It raises a question whether it can partially be explained by the minor cytotoxic effects observed in the LDH assay after 2 h incubation and also with specific TP10 membrane interactions (*46*). However, minor leakage-induced glutathione outflow should not have a significant impact on the extracellular cleavage of the conjugates, since the volume of incubation media compared to volume of a cell is very large. Additionally, our direct measurement of glutathione outflow after treatment with TP10 indicated no effect after 30 min when the incubation was carried out in PBSg buffer. Hence, we hypothesize that the amount of internalized peptide can be overestimated only if the conjugates leak into the cell. It has been observed in the past that TP10, depending on the cargo molecule, induces different levels of LDH leakage from HeLa cells (*34*). Additionally, under certain circumstances this peptide forms transient pores in large unilamellar vesicles (LUVs) and promotes calcein leakage from these vesicles (*46*). However, when small membrane disturbances (lower concentrations in our case) are experienced, the main translocation mechanism is still endocytosis (*46*).

In the case of MAP peptide, the free luciferin-like uptake behavior is somewhat more complicated to interpret, and care must be taken when analyzing the results. We observe slight toxicity of luciferin−MAP treated cells, although previous results have shown high toxic effects of MAP peptide, which have been attributed to its high amphipaticity (*35*). However, the toxicity was negligible in the first 0.5 h incubation, while we still observed an increase in extracellular thiol content in this time frame which was not present after 15 min, as measured in PBSg buffer. It is therefore unlikely that membrane disturbance and/or extracellular glutathione explain the exponential profiles that both peptides, TP10 and MAP, displayed at these concentrations, because that fast uptake process started instantly after the peptide treatment. On the other hand, it has previously

been shown (*41*, *42*, *47*) that the mechanism of cellular entry sometimes changes from endocytic to direct translocation with increasing CPP concentration, which could also be the key factor here. In contrast, it has also been observed that MAP is highly endocytosed into cells, specifically into the nuclei (*48*), although MAP remains a quite inefficient peptide in some nuclear delivery assays (*21*). This controversy might be explained, to some extent, by calcium inflow triggered membrane repair response (MRR) which may mask membranolytic effects of this peptide (*49*). The MRR could lead to less observed LDH leakage while allowing high and fast direct uptake of MAP peptide.

None of the other peptides (EB1, penetratin, M918, *p*Vec, TP10(Cys), 1−5 μM TP10, and 1−2.5 μM MAP) that we tested follow free luciferin-like fast uptake. However, the uptake profile of penetratin displayed a characteristic dip in the first minutes of incubation, which indicates that a small portion of this CPP enters the cytosol quickly. This is consistent with previously published results that state that direct translocation for this peptide cannot account for its efficient uptake (*50*). These results emphasize the importance of endocytosis in this process (*50*).

The peptides which fall into the "slow" internalization category display similar uptake characteristics. In most cases, the recorded luminescence flux slowly increased in time, but after a certain time point, it reached a plateau and started to decrease. This indicates that the internalization rate reaches a characteristic point where the increase in uptake starts to decrease (i.e., the uptake rate starts to approach a certain equilibrium) and that the luciferin−luciferase reaction occurs more rapidly than the uptake of luciferin−CPP constructs. On the other hand, when interpreting these results it is important to remember that side products of the luciferin−luciferase reaction, namely, oxyluciferin and dehydroluciferyl adenylate, can influence the readout, since these compounds may inhibit the reaction to some extent (*51*).

The key factor of the releasable luciferin assay is a cytosolic release of luciferin from the carrier molecule. It seems to be a common belief that a disulfide bond is suitable when cytosolic delivery is studied, because it is supposed to be cleaved only in the cytoplasm due to high concentration of glutathione (*52*). However, there are some discrepancies in the literature. The disulfide bridge approach has been extensively used in many studies in the field (*21*, *53*−*56*) despite some concerns that disulfide bonds may be reduced partially on the cell membrane of some cells and in vesicular compartments by protein disulfide isomerase or gamma-interferon-inducible lysosomal thiol reductase (*57*). It has been shown that the main reduction, nevertheless, takes place in the cytoplasm (*58*). Then again, a recent publication claims that the reduction occurs extracellularly and is dependent on the peptide sequence (*59*), which means that the reduction potency may have to be established for each peptide. Despite all these controversies, we did not observe any increase in extracellular sulfhydryl content (i.e., disulfide bond cleavage or glutathione outflow) in the extracellular environment in a relevant time frame, except in the case of TP10(Cys) after 1 h (Figure 3A). MAP and Tat undeniably showed some increase in extracellular sulfhydryl content after 30 min (Figure 3A), which was not observed after 15 min incubation (data not shown). However, due to technical reasons this experiment was carried out in PBSg buffer and not in complete media as the uptake experiments, and it is known that the peptides could be considerably more toxic in buffers than in cell growth media. Also, the Ellman's reagent cleavage rate by cells in complete media was much slower than the uptake rate of the CPP conjugates (data not shown).

Our uptake results (Figure 5A) are in accordance with previous results from the splice correction assay with TP10(Cys), M918, and penetratin, showing high cytosolic entry while *p*Vec, Tat, and MAP fall into the low efficacy group (*21*). *p*Vec has been shown to display excellent uptake according to fluorometric methods but fails to induce oligonucleotide-mediated splice correction, indicating that *p*Vec remains entrapped in endosomal vesicles. Here, we find that *p*Vec matches Tat, MAP, and TP10 in cytosolic entry after 2 h treatment. However, it should be noted that the uptake of peptides belonging to the fast exponential internalization group may be somewhat underestimated due to approximately 30 s lag between adding the peptide to cells and starting the measurement, during which large signals may be left unregistered.

The advantage of using the luciferin-releasable linker−CPP method over the splice correction assay is that the results of the former assay can be obtained faster, and more importantly, information about kinetic behavior can also be obtained. A caveat with the assay is possible artifacts emanating from potential premature reduction of the disulfide bridge in the luciferin−CPP conjugate. However, we observe the same trend in uptake as with the splice correction assay, and thus, extracellular reduction does not appear to be a problem here. In fact, while extracellular reduction of luciferin−CPP conjugate would generate a high readout, corresponding CPP−PNA reduction would give a low readout, because free PNA does not enter cells. Reduction of the conjugates should therefore give opposite results, which is not the case. Furthermore, when establishing the releasable luciferin−transporter assay, Jones et al. verified that the main portion of the measured CPP internalization was due to uptake of the luciferin−CPP conjugate and subsequent release of the luciferin rather than direct translocation of luciferin after extracellular reduction of some portion of the luciferin−CPP conjugate (*23*).

Due to serum proteases or negatively charged serum proteins, CPPs are likely degraded or retained in extracellular environment to some extent in the presence of serum (*60*−*62*). CPPs are also susceptible to extracellular degradation in buffer, probably caused by membrane-bound proteases (*37*). However, owing to the relevance of serum in in vivo studies, we measured the uptake of CPPs in complete media containing 10% serum and compared it to the uptake in HKRg buffer. The differences in results were apparent; the peptides showed higher internalization in buffer than in media with up to 28-fold difference. Also, the CPPs that showed the best characteristics in terms of uptake rate and total uptake when incubating the conjugates in complete media were not necessarily the best cargo carriers when the incubations were carried out in HKRg.

It has been widely noted that peptides that are more positively charged and/or have higher amphipathic moments often display more cell-penetrating capabilities than others. However, there is no obvious correlation between the peptide uptake (30 min, 60 min, or 120 min) or LDH leakage with their hydropathy score or amphipathic moments according to our measurements (data not shown). Nevertheless, the two peptides with the highest above-mentioned parameters, MAP and TP10, were the only ones showing significant LDH leakage.

As mentioned before, only one time-point measurement may not reflect the overall properties of a certain carrier molecule. In order to draw conclusions from the kinetic behavior of our conjugates, a modified logistic function according to eq 1 was fitted to the raw luminescence data for the slow uptake profiles. Next, we calculated the average values and SEM of the maximum slope of the signal (a_{max}) and the time at which the maximum slope occurred (t_{max}), i.e., the inflection point of sigmoidal uptake curves, which is often compared with half-life of uptake in the literature.

The a_{max} differs among CPPs, but the value is generally higher at higher peptide concentrations. However, we did not observe any drastic changes in a_{max}, and tested CPPs could not be

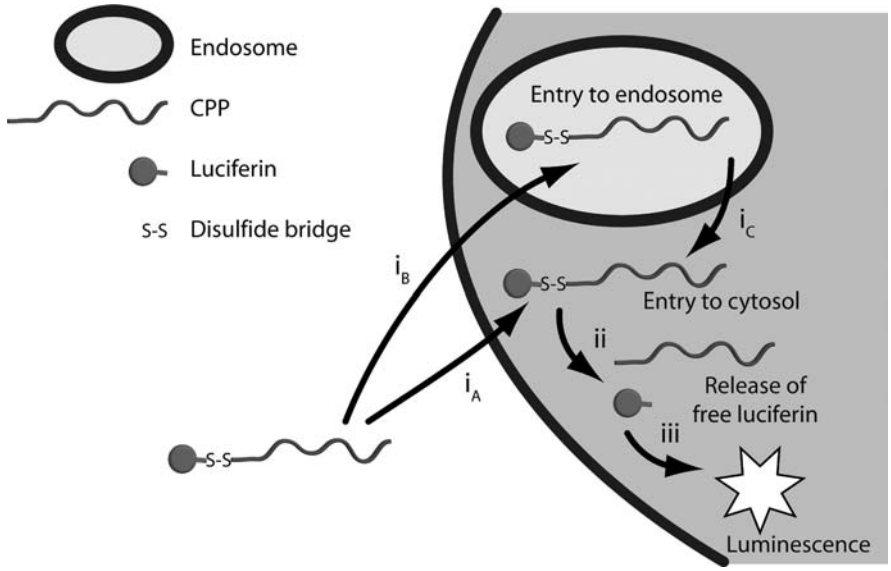


Figure 7. Hypothetical entry routes of luciferin−CPP conjugates according to their internalization kinetics. The conjugates belonging to the "fast" internalization group (Tat, TP10*, MAP*) cross the cell membrane rapidly (i_A), while representatives of the "slow" kinetics group (*p*Vec, penetratin, EB1, M918, TP10(Cys), TP10*, MAP*) go through endocytosis (i_B) and reach the cytosol after endosomal escape (i_C) followed by the release of free luciferin (ii) and production of light (iii). The data reveal that CPPs marked with * (see text) differ in their endosomal escape rate and ability to move between the "fast" and the "slow" internalization groups according to their concentration.

grouped into subpopulations based on this parameter. The only exception was perhaps EB1, which displayed the most pronounced dependence between a_{max} and concentration, exceeding at least 2-fold the other CPPs we tested. This may indicate the presence of a certain peptide concentration threshold level above which endosomal escape of the conjugate is initiated more rapidly.

The time at which a_{max} is found (t_{max}) differs among CPPs as well. According to our model, t_{max} for higher concentrations of EB1, TP10, and MAP conjugates is very short, less than 10 min, whereas in the case of the other tested CPPs, the t_{max} is in the range 30−60 min and it remains at similar levels for all concentrations. Interestingly, for lower concentrations of EB1, TP10, and MAP conjugate the t_{max} increased to comparable levels with the other CPP conjugates (Figure 6A,B). This indicates that the delay in uptake increases significantly, which in turn might show that at lower concentrations the mode of uptake for these peptides could be different or there could be a phase change in the endosomal escape rate.

The t_{max} value can be compared with presented half-life of uptake from the literature. For example, 1 μM penetratin in a work which addressed cytosolic delivery of CPPs into Bowes cells using a quenched fluorescence assay had a half-life of uptake of ∼60 min (*45*). In the same work, the half-lives of Tat, transportan, and MAP were approximately 30, 10 and 7 min, respectively (*45*). This is in line with earlier works where the half-life of radioactively labeled transportan was found to be around 10 min (*4, 63*), and this is analogous to our results except in the case of the Tat−luciferin conjugate. In addition, sigmoidal uptake curves were not observed in the above-mentioned studies, which may reflect involvement of more processes in our case (such as linker cyclization and enzymatic conversion of free luciferin), different cell lines and incubation conditions. Interestingly, 1 μM NBD-labeled penetratin internalized in a similar time frame into K562 cells, but the signal could have arisen largely from a portion of conjugates trapped in endosomes due to experimental setup (*64*). In opposition to this, penetratin has been observed to have rapid uptake in the first 15 min, and the authors discuss involvement of a direct penetration mechanism in addition to endocytosis (*65*); but a penetratin analogue entered CHO cells with a half-life of approximately 30 min, as assessed from an uptake kinetics graph measured by mass spectrometry, while the entry into GAG-deficient CHO cells occurred slightly more rapidly but yet to a remarkably lower extent (*66*). It must be noted that the authors find the internalization of naked penetratin to be a multimechanism process with a clear temperature-independent component which was more pronounced at lower concentrations in the case of GAG-deficient cells, which does not completely agree with our results and hypotheses.

Kinetics of unconjugated 5 μM penetratin, Tat, polyarginine, and transportan have been compared in A549, HeLa, and CHO cells in another study from 2005, but unfortunately, the authors do not provide any numerical data regarding kinetics, and the comparisons can only be made on a qualitative basis (*67*). However, it is apparent that in different cell lines the kinetics, and also the total uptake, is different. For instance, in their case the half-life of uptake appears to be 1−2 h for penetratin, 0.5−1 h for Tat, and ∼0.5 h for polyarginine and transportan (*67*). Additionally, the authors emphasize involvement of various endocytic pathways in the internalization process; however, the internalization kinetics seems to depend also on the presence/absence of a peptide cargo (*67*), which should be considered when comparing our data.

FACS analysis with 10 μM Tat showed similar internalization kinetics as endocytosis markers in another study, both at physiological temperature and at +4 °C. The uptake had not reached a plateau after 60 min, and the half-life of uptake could not be estimated (*68*). However, the uptake of Tat was saturated after 90 min incubation in another experiment where it took place quickly, allowing internalization of half of the final peptides in less than 10 min (*69*). This adds more controversy to uptake kinetics studies of this peptide in light of our results where we observe evidence of direct penetration of this peptide.

The kinetic curves of free and plasmid complexed Tat peptide have been also compared. In a work conducted on CHO cells, the authors observed different kinetic profiles for free and plasmid-complexed Tat peptide (*70*). While the uptake of free Tat peptide resembled a first-order process with a half-life about 15 min, as assessed from the figures, the uptake of plasmid complexes increased linearly with time. In addition, more interestingly, unlike in the case of Tat−plasmid complexes, the

uptake of free Tat peptide did not depend on sodium azide, an inhibitor of ATP-dependent cellular transport (*70*) which supports our data of this peptide belonging to the "fast" internalization group. When Tat peptide was used to deliver a cargo peptide into cytosol, it was shown to enter cells following a sigmoidal uptake curve with the maximal rate of uptake occurring approximately at 30 min starting from the incubation (*52*). To demonstrate the role of a cargo peptide to the uptake kinetics even more, the existing well-established peptides were modified with short penetration accelerating sequence (Pas), and the uptake curve, approximately linear in time, was changed to a first-order like curve with an approximate half-life of 15 min for polyarginine in full media (*71*). This work, as all the other mentioned kinetics studies, emphasizes quite strongly how important the experimental conditions are when comparing different measurement results. Just as the cell lines (e.g., suspension cells vs adherent cells) used in the discussed experiments could change the results, different cargoes play an important role here too. Therefore, when comparing the uptake kinetics of CPPs this should be especially strongly kept in mind.

In summary, our results demonstrate that in complete media there are two types of uptake kinetic profiles for the CPPs tested herein: either an early uptake that reached maximum within minutes or a later type of uptake with maximum rate that varied from 30 to 60 min. Tat, luciferin, 10 μM TP10, and 5−10 μM MAP belong to the fast uptake group. The rest of the peptides (EB1, penetratin, M918, *p*Vec, TP10(Cys), 1−5 μM TP10, and 1−2.5 μM MAP) fall into the slower uptake category. We hypothesize that, since free luciferin can cross plasma membranes directly without being endocytosed, the CPPs whose uptake profiles are similar to the profile of free luciferin (i.e., the fast uptake group) are also capable of crossing cell membranes directly. CPPs with the slow uptake profile, on the other hand, are presumably exploiting endocytic routes when entering cells (Figure 7). The clustering and behavior of luciferin−CPP conjugates fall in line with a CPP structural versatility and polymorphism study except for the Tat peptide (*72*). Precisely which endocytic routes are exploited will be tested in a follow-up study, and the work is ongoing regarding this matter. The peptide conjugates whose kinetic parameters a_{max} and t_{max} differ to large extent at various concentrations might display dual uptake modes as opposed to other CPPs. This is not surprising for the higher concentration conjugates of TP10 and MAP, which shift from the fast internalization group into the slow internalization group when their concentration is decreased, but for the EB1 conjugate, this finding is very interesting. It seems that indeed there might be a group of CPPs whose mode of uptake could depend significantly on their concentration and that a phase change of uptake might explain deviating results found in the literature.

In conclusion, we find that, when comparing CPPs in terms of their uptake and internalization mechanisms, kinetic data provide a valuable additional tool to conventional end-point measurements with various biological assays. Our data also indicate that this luciferin−CPP system as a (semi)biological assay is a promising tool for studying uptake mechanisms of CPPs more thoroughly, since it is capable of shedding more light onto CPP subgroups which could remain hidden if kinetic data of conventional biological readout assays are discarded.

ACKNOWLEDGMENT

The work presented in this article was supported by Swedish Research Council (VR-NT); by SSF (Sweden−Japan); by Center for Biomembrane Research, Stockholm; by Knut and Alice Wallenberg's Foundation; by the EU trough the European Regional Development Fund through the Center of Excellence in Chemical Biology, Estonia; by the targeted financing SF0180027s08 from the Estonian Government; by the DoRa Program of The European Social Fund; and by Archimedes Foundation. Conflicts of interest: none.

LITERATURE CITED

(1) Derossi, D., Joliot, A. H., Chassaing, G., and Prochiantz, A. (1994) The third helix of the Antennapedia homeodomain translocates through biological membranes. *J. Biol. Chem. 269*, 10444–50.

(2) Vivés, E., Brodin, P., and Lebleu, B. (1997) A truncated HIV-1 Tat protein basic domain rapidly translocates through the plasma membrane and accumulates in the cell nucleus. *J. Biol. Chem. 272*, 16010–7.

(3) Elliott, G., and O'Hare, P. (1997) Intercellular trafficking and protein delivery by a herpesvirus structural protein. *Cell 88*, 223–33.

(4) Pooga, M., Hällbrink, M., Zorko, M., and Langel, Ü. (1998) Cell penetration by transportan. *FASEB J. 12*, 67–77.

(5) Lee, H. S., Park, C. B., Kim, J. M., Jang, S. A., Park, I. Y., Kim, M. S., Cho, J. H., and Kim, S. C. (2008) Mechanism of anticancer activity of buforin IIb, a histone H2A-derived peptide. *Cancer Lett. 271*, 47–55.

(6) Park, C. B., Yi, K. S., Matsuzaki, K., Kim, M. S., and Kim, S. C. (2000) Structure-activity analysis of buforin II, a histone H2A-derived antimicrobial peptide: the proline hinge is responsible for the cell-penetrating ability of buforin II. *Proc. Natl. Acad. Sci. U.S.A. 97*, 8245–50.

(7) Zania, P., Gourni, D., Aplin, A. C., Nicosia, R. F., Flordellis, C. S., Maragoudakis, M. E., and Tsopanoglou, N. E. (2009) Parstatin, the cleaved peptide on proteinase-activated receptor 1 activation, is a potent inhibitor of angiogenesis. *J. Pharmacol. Exp. Therapeut. 328*, 378–389.

(8) Crombez, L., Aldrian-Herrada, G., Konate, K., Nguyen, Q. N., McMaster, G. K., Brasseur, R., Heitz, F., and Divita, G. (2009) A new potent secondary amphipathic cell-penetrating peptide for siRNA delivery into mammalian cells. *Mol. Ther. 17*, 95–103.

(9) Ivanova, G. D., Arzumanov, A., Abes, R., Yin, H., Wood, M. J. A., Lebleu, B., and Gait, M. J. (2008) Improved cell-penetrating peptide−PNA conjugates for splicing redirection in HeLa cells and exon skipping in mdx mouse muscle. *Nucleic Acids Res. 36*, 6418–6428.

(10) Morris, M. C., Depollier, J., Mery, J., Heitz, F., and Divita, G. (2001) A peptide carrier for the delivery of biologically active proteins into mammalian cells. *Nat. Biotechnol. 19*, 1173–1176.

(11) Futaki, S., Ohashi, W., Suzuki, T., Niwa, M., Tanaka, S., Ueda, K., Harashima, H., and Sugiura, Y. (2001) Stearylated arginine-rich peptides: A new class of transfection systems. *Bioconjugate Chem. 12*, 1005–1011.

(12) Mäe, M., El Andaloussi, S., Lundin, P., Oskolkov, N., Johansson, H. J., Guterstam, P., and Langel, Ü. (2009) A stearylated CPP for delivery of splice correcting oligonucleotides using a non-covalent co-incubation strategy. *J. Controlled Release 134*, 221–227.

(13) Nakamura, Y., Kogure, K., Futaki, S., and Harashima, H. (2007) Octaarginine-modified multifunctional envelope-type nano device for siRNA. *J. Controlled Release 119*, 360–367.

(14) Rothbard, J. B., Kreider, E., Vandeusen, C. L., Wright, L., Wylie, B. L., and Wender, P. A. (2002) Arginine-rich molecular transporters for drug delivery: Role of backbone spacing in cellular uptake. *J. Med. Chem. 45*, 3612–3618.

(15) Simeoni, F., Morris, M. C., Heitz, F., and Divita, G. (2003) Insight into the mechanism of the peptide-based gene delivery system MPG: implications for delivery of siRNA into mammalian cells. *Nucleic Acids Res. 31*, 2717–2724.

(16) Tonges, L., Lingor, P., Egle, R., Dietz, G. P. H., Fahr, A., and Bahr, M. (2006) Stearylated octaarginine and artificial virus-like particles for transfection of siRNA into primary rat neurons. *RNA 12*, 1431–1438.

(17) Abes, R., Arzumanov, A., Moulton, H., Abes, S., Ivanova, G., Gait, M. J., Iversen, P., and Lebleu, B. (2008) Arginine-rich

cell penetrating peptides: Design, structure-activity, and applications to alter pre-mRNA splicing by steric-block oligonucleotides. *J. Pept. Sci. 14*, 455–460.
(18) Chen, B., Liu, Q. L., Zhang, Y. L., Xu, L., and Fang, X. H. (2008) Transmembrane delivery of the cell-penetrating peptide conjugated semiconductor quantum dots. *Langmuir 24*, 11866–11871.
(19) Järver, P., Langel, K., El Andaloussi, S., and Langel, Ü. (2007) Applications of cell-penetrating peptides in regulation of gene expression. *Biochem. Soc. Trans. 35*, 770–774.
(20) Kersemans, V., Kersemans, K., and Cornelissen, B. (2008) Cell penetrating peptides for in vivo molecular imaging applications. *Curr. Pharm. Des. 14*, 2415–2427.
(21) Lundin, P., Johansson, H., Guterstam, P., Holm, T., Hansen, M., Langel, U., and El Andaloussi, S. (2008) Distinct uptake routes of cell-penetrating peptide conjugates. *Bioconjugate Chem. 19*, 2535–42.
(22) Kang, S. H., Cho, M. J., and Kole, R. (1998) Up-regulation of luciferase gene expression with antisense oligonucleotides: Implications and applications in functional assay developments. *Biochemistry 37*, 6235–6239.
(23) Jones, L. R., Goun, E. A., Shinde, R., Rothbard, J. B., Contag, C. H., and Wender, P. A. (2006) Releasable luciferin-transporter conjugates: tools for the real-time analysis of cellular uptake and release. *J. Am. Chem. Soc. 128*, 6526–7.
(24) Seliger, H. H., and Mc, E. W. (1960) Spectral emission and quantum yield of firefly bioluminescence. *Arch. Biochem. Biophys. 88*, 136–41.
(25) Wender, P. A., Goun, E. A., Jones, L. R., Pillow, T. H., Rothbard, J. B., Shinde, R., and Contag, C. H. (2007) Real-time analysis of uptake and bioactivatable cleavage of luciferin-transporter conjugates in transgenic reporter mice. *Proc. Natl. Acad. Sci. U.S.A. 104*, 10340–5.
(26) Mäger, I., Eiríksdóttir, E., Langel, K., El Andaloussi, S., and Langel, Ü. (2010) Assessing the uptake kinetics and internalization mechanisms of cell-penetrating peptides using a quenched fluorescence assay. *Biochim. Biophys. Acta 1798*, 338−343.
(27) Lundberg, P., El Andaloussi, S., Sütlü, T., Johansson, H., and Langel, Ü. (2007) Delivery of short interfering RNA using endosomolytic cell-penetrating peptides. *FASEB J. 21*, 2664–2671.
(28) El Andaloussi, S., Johansson, H. J., Holm, T., and Langel, Ü. (2007) A novel cell-penetrating peptide, M918, for efficient delivery of proteins and peptide nucleic acids. *Mol. Ther. 15*, 1820–1826.
(29) Elmquist, A., Lindgren, M., Bartfai, T., and Langel, Ü. (2001) VE-cadherin-derived cell-penetrating peptide, pVEC, with carrier functions. *Exp. Cell Res. 269*, 237–244.
(30) Soomets, U., Lindgren, M., Gallet, X., Hällbrink, M., Elmquist, A., Balaspiri, L., Zorko, M., Pooga, M., Brasseur, R., and Langel, Ü. (2000) Deletion analogues of transportan. *Biochim. Biophys. Acta 1467*, 165–176.
(31) Oehlke, J., Scheller, A., Wiesner, B., Krause, E., Beyermann, M., Klauschenz, E., Melzig, M., and Bienert, M. (1998) Cellular uptake of an alpha-helical amphipathic model peptide with the potential to deliver polar compounds into the cell interior non-endocytically. *Biochim. Biophys. Acta 1414*, 127–139.
(32) Eiríksdóttir, E., Langel, Ü., and Rosenthal-Aizman, K. (2009) An improved synthesis of releasable luciferin-CPP conjugates. *Tetrahedron Lett. 50*, 4731–4733.
(33) Moate, P. J., Dougherty, L., Schnall, M. D., Landis, R. J., and Boston, R. C. (2004) A modified logistic model to describe gadolinium kinetics in breast tumors. *Magn. Reson. Imaging 22*, 467–473.
(34) El Andaloussi, S., Järver, P., Johansson, H. J., and Langel, Ü. (2007) Cargo-dependent cytotoxicity and delivery efficacy of cell-penetrating peptides: a comparative study. *Biochem. J. 407*, 285–292.
(35) Saar, K., Lindgren, M., Hansen, M., Eiríksdóttir, E., Jiang, Y., Rosenthal-Aizman, K., Sassian, M., and Langel, Ü. (2005) Cell-penetrating peptides: a comparative membrane toxicity study. *Anal. Biochem. 345*, 55–65.
(36) Myrberg, H., Lindgren, M., and Langel, Ü. (2007) Protein delivery by the cell-penetrating peptide YTA2. *Bioconjugate Chem. 18*, 170–174.
(37) Palm, C., Jayamanne, M., Kjellander, M., and Hällbrink, M. (2007) Peptide degradation is a critical determinant for cell-penetrating peptide uptake. *Biochim. Biophys. Acta 1768*, 1769–1776.
(38) Henriques, S. T., Melo, M. N., and Castanho, M. (2007) How to address CPP and AMP translocation? Methods to detect and quantify peptide internalization in vitro and in vivo (Review). *Mol. Membr. Biol. 24*, 173–U2.
(39) Craig, F. F., Simmonds, A. C., Watmore, D., McCapra, F., and White, M. R. (1991) Membrane-permeable luciferin esters for assay of firefly luciferase in live intact cells. *Biochem. J. 276* (Pt 3), 637–41.
(40) Ter-Avetisyan, G., Tunnemann, G., Nowak, D., Nitschke, M., Herrmann, A., Drab, M., and Cardoso, M. C. (2009) Cell entry of arginine-rich peptides is independent of endocytosis. *J. Biol. Chem. 284*, 3370–8.
(41) Duchardt, F., Fotin-Mleczek, M., Schwarz, H., Fischer, R., and Brock, R. (2007) A comprehensive model for the cellular uptake of cationic cell-penetrating peptides. *Traffic 8*, 848–866.
(42) Futaki, S., Nakase, I., Tadokoro, A., Takeuchi, T., and Jones, A. T. (2007) Arginine-rich peptides and their internalization mechanisms. *Biochem. Soc. Trans. 35*, 784–7.
(43) Richard, J. P., Melikov, K., Brooks, H., Prevot, P., Lebleu, B., and Chernomordik, L. V. (2005) Cellular uptake of unconjugated TAT peptide involves clathrin-dependent endocytosis and heparan sulfate receptors. *J. Biol. Chem. 280*, 15300–6.
(44) Wadia, J. S., Stan, R. V., and Dowdy, S. F. (2004) Transducible TAT-HA fusogenic peptide enhances escape of TAT-fusion proteins after lipid raft macropinocytosis. *Nat. Med. 10*, 310–5.
(45) Hällbrink, M., Florén, A., Elmquist, A., Pooga, M., Bartfai, T., and Langel, Ü. (2001) Cargo delivery kinetics of cell-penetrating peptides. *Biochim. Biophys. Acta 1515*, 101–109.
(46) Barany-Wallje, E., Gaur, J., Lundberg, P., Langel, Ü., and Gräslund, A. (2007) Differential membrane perturbation caused by the cell penetrating peptide Tp10 depending on attached cargo. *FEBS Lett. 581*, 2389–93.
(47) Fretz, M. M., Penning, N. A., Al-Taei, S., Futaki, S., Takeuchi, T., Nakase, I., Storm, G., and Jones, A. T. (2007) Temperature-, concentration- and cholesterol-dependent translocation of L- and D-octa-arginine across the plasma and nuclear membrane of CD34(+) leukaemia cells. *Biochem. J. 403*, 335–342.
(48) Zaro, J. L., Vekich, J. E., Tran, T., and Shen, W. C. (2009) Nuclear localization of cell-penetrating peptides is dependent on endocytosis rather than cytosolic delivery in CHO cells. *Mol. Pharm*.
(49) Palm-Apergi, C., Lorents, A., Padari, K., Pooga, M., and Hällbrink, M. (2009) The membrane repair response masks membrane disturbances caused by cell-penetrating peptide uptake. *FASEB J. 23*, 214–23.
(50) Barany-Wallje, E., Keller, S., Serowy, S., Geibel, S., Pohl, P., Bienert, M., and Dathe, M. (2005) A critical reassessment of penetratin translocation across lipid membranes. *Biophys. J. 89*, 2513–2521.
(51) Ribeiro, C., and Esteves da Silva, J. C. (2008) Kinetics of inhibition of firefly luciferase by oxyluciferin and dehydroluciferyl-adenylate. *Photochem. Photobiol. Sci. 7*, 1085–90.
(52) Cheung, J. C., Kim Chiaw, P., Deber, C. M., and Bear, C. E. (2009) A novel method for monitoring the cytosolic delivery of peptide cargo. *J. Controlled Release 137*, 2−7.
(53) Barnes, M. P., and Shen, W. C. (2009) Disulfide and thioether linked cytochrome c-oligoarginine conjugates in HeLa cells. *Int. J. Pharm. 369*, 79–84.
(54) El Andaloussi, S., Guterstam, P., and Langel, Ü. (2007) Assessing the delivery efficacy and internalization route of cell-penetrating peptides. *Nat. Protoc. 2*, 2043–7.
(55) Patel, L. N., Wang, J., Kim, K. J., Borok, Z., Crandall, E. D., and Shen, W. C. (2009) Conjugation with cationic cell-penetrat-

ing peptide increases pulmonary absorption of insulin. *Mol. Pharm. 6*, 492–503.
(56) Turner, J. J., Jones, S., Fabani, M. M., Ivanova, G., Arzumanov, A. A., and Gait, M. J. (2007) RNA targeting with peptide conjugates of oligonucleotides, siRNA and PNA. *Blood Cells Mol. Dis. 38*, 1–7.
(57) Saito, G., Swanson, J. A., and Lee, K. D. (2003) Drug delivery strategy utilizing conjugation via reversible disulfide linkages: role and site of cellular reducing activities. *Adv. Drug Delivery Rev. 55*, 199–215.
(58) Shen, W. C., Ryser, H. J., and LaManna, L. (1985) Disulfide spacer between methotrexate and poly(D-lysine). A probe for exploring the reductive process in endocytosis. *J. Biol. Chem. 260*, 10905–8.
(59) Aubry, S., Burlina, F., Dupont, E., Delaroche, D., Joliot, A., Lavielle, S., Chassaing, G., and Sagan, S. (2009) Cell-surface thiols affect cell entry of disulfide-conjugated peptides. *FASEB J. 23*, 2956–2967.
(60) Adessi, C., and Soto, C. (2002) Converting a peptide into a drug: Strategies to improve stability and bioavailability. *Curr. Med. Chem. 9*, 963–978.
(61) El Andaloussi, S., Johansson, H. J., Lundberg, P., and Langel, Ü. (2006) Induction of splice correction by cell-penetrating peptide nucleic acids. *J. Gene Med. 8*, 1262–1273.
(62) Kosuge, M., Takeuchi, T., Nakase, I., Jones, A. T., and Futaki, S. (2008) Cellular internalization and distribution of arginine-rich peptides as a function of extracellular peptide concentration, serum, and plasma membrane associated proteoglycans. *Bioconjugate Chem. 19*, 656–664.
(63) Lindgren, M., Gallet, X., Soomets, U., Hällbrink, M., Bråkenhielm, E., Pooga, M., Brasseur, R., and Langel, Ü. (2000) Translocation properties of novel cell penetrating transportan and penetratin analogues. *Bioconjugate Chem. 11*, 619–26.
(64) Drin, G., Cottin, S., Blanc, E., Rees, A. R., and Temsamani, J. (2003) Studies on the internalization mechanism of cationic cell-penetrating peptides. *J. Biol. Chem. 278*, 31192–201.
(65) Letoha, T., Gaal, S., Somlai, C., Czajlik, A., Perczel, A., and Penke, B. (2003) Membrane translocation of penetratin and its derivatives in different cell lines. *J. Mol. Recognit. 16*, 272–9.
(66) Jiao, C. Y., Delaroche, D., Burlina, F., Alves, I. D., Chassaing, G., and Sagan, S. (2009) Translocation and endocytosis for cell-penetrating peptide internalization. *J. Biol. Chem. 284*, 33957–65.
(67) Jones, S. W., Christison, R., Bundell, K., Voyce, C. J., Brockbank, S. M., Newham, P., and Lindsay, M. A. (2005) Characterisation of cell-penetrating peptide-mediated peptide delivery. *Br. J. Pharmacol. 145*, 1093–102.
(68) Richard, J. P., Melikov, K., Vives, E., Ramos, C., Verbeure, B., Gait, M. J., Chernomordik, L. V., and Lebleu, B. (2003) Cell-penetrating peptides. A reevaluation of the mechanism of cellular uptake. *J. Biol. Chem. 278*, 585–90.
(69) Suzuki, T., Futaki, S., Niwa, M., Tanaka, S., Ueda, K., and Sugiura, Y. (2002) Possible existence of common internalization mechanisms among arginine-rich peptides. *J. Biol. Chem. 277*, 2437–43.
(70) Ignatovich, I. A., Dizhe, E. B., Pavlotskaya, A. V., Akifiev, B. N., Burov, S. V., Orlov, S. V., and Perevozchikov, A. P. (2003) Complexes of plasmid DNA with basic domain 47−57 of the HIV-1 Tat protein are transferred to mammalian cells by endocytosis-mediated pathways. *J. Biol. Chem. 278*, 42625–36.
(71) Takayama, K., Nakase, I., Michiue, H., Takeuchi, T., Tomizawa, K., Matsui, H., and Futaki, S. (2009) Enhanced intracellular delivery using arginine-rich peptides by the addition of penetration accelerating sequences (Pas). *J. Controlled Release 138*, 128–33.
(72) Eiríksdóttir, E., Konate, K., Langel, Ü., Divita, G., and Deshayes, S. Secondary structure of cell-penetrating peptides controls membrane interaction and insertion. *Biochim. Biophys. Acta 1798*, 1119−1128.
(73) Hennig, L. (1999) WinGene/WinPep: User-friendly software for the analysis of amino acid sequences. *Biotechniques 26*, 1170–1172.

BC100174Y

Biocompatible Silica Nanoparticles−Insulin Conjugates for Mesenchymal Stem Cell Adipogenic Differentiation

Dan Liu,[†,§] Xiaoxiao He,[*,†,§] Kemin Wang,[*,‡,§] Chunmei He,[†,§] Hui Shi,[‡,§] and Lixin Jian[‡,§]

Institute of Biology, State Key Laboratory of Chemo/Biosensing and Chemometrics, College of Chemistry and Chemical Engineering, Hunan University, Changsha 410082, China, and Key Laboratory for Bio-Nanotechnology and Molecule Engineering, Hunan Province, Changsha 410082, China. Received April 24, 2010; Revised Manuscript Received July 5, 2010

There is increasing interest in developing bioconjugated carriers for the cellular delivery of bioactive molecules to stem cells, since they can allow modulation of stem cell differentiation. The present study reported biocompatible silica nanoparticle−insulin conjugates for rat mesenchymal stem cell (RMSC) adipogenic differentiation in vitro. A systematic study was first carried out on the biocompatibility of the SiNPs with RMSCs. The cell viability assay was performed to screen the SiNP concentration for creating little cytotoxicity on RMSCs. Furthermore, transmission electron microscopy (TEM) and adipogenesis and osteogenesis assays revealed that the pure SiNPs had no effect on cellular ultrastructures, adipogenic differentiation, and osteogenic differentiation. Under the optimized SiNP concentration with little cytotoxicity on RMSC and no effects on the RMSC phenotype, SiNP−insulin conjugates were prepared and used for RMSC adipogenic differentiation. Results showed that RMSCs had the ability to differentiate into adipocytes when cultured in the presence of insulin-conjugated SiNPs. This work demonstrated that the biological activity of insulin conjugated to the SiNPs was not affected and the SiNPs could be used as biocompatibile carriers of insulin for RMSC adipogenic differentiation, which would help to expand the new potential application of SiNPs in stem cell research.

INTRODUCTION

Ongoing advances in the directed differentiation in vitro of stem cells have offered great prospects for medical research and opened new avenues for therapy in many human disorders (*1*−*3*). Until now, various strategies have been developed and employed to direct and control stem cell differentiation in vitro, including development of defined culture milieu (*4*), use of extracellular matrix (*5*, *6*), co-culturing with fully differentiated somatic cell types (*7*, *8*), up-regulating the expression of connexin proteins to enhance the gap junction formation and intercellular coupling (*9*), and directing stem cell differentiation through genetic modulation (*10*). Among the strategies to achieve controlled differentiation of stem cells into well-defined lineages in vitro, bioactive molecules such as cytokines, growth factors, and small chemicals as defined culture conditions have been widely used to promote stem cell differentiation in vitro (*11*). Especially for the adult stem cells, differentiation cannot appear spontaneously in the absence of cytokines and growth factors.

For stem cell differentiation in vitro using bioactive molecules as defined culture conditions, the differentiation efficiency would usually be affected not only by the internal factors such as genetic, developmental potential of stem cells, but also by the characteristics of exogenous bioactive molecules, such as their biological activity (*12*), solubility (*13*), and cell toxicity (*14*). Although endogenous bioactive molecules could be produced with recombinant DNA constructs through genetic manipulation and have successfully induced the transfected stem cell differentiation in vitro, the risk of mutagenesis and/or oncogenesis of recombinant DNA and the viral-based vectors is still unpredictable (*15*). Therefore, the development of novel strategies to deliver exogenous bioactive molecules to the stem cells is still regarded as a hot issue for stem cell differentiation in vitro.

Recently, the wide spectrum of nanotechnologies holds great promise for the study of stem cell biology and the development of new approaches to stem cell research (*16*). The potential applications of nanotechnologies in stem cell research include magnetic nanoparticles for stem cell isolation and sorting (*17*), the fluorescent nanoparticle labeling method for stem cell labeling and stem cell in vivo tracking (*18*), engineering nanometer-scale materials for proliferation and differentiation of stem cells (*19*, *20*), and nanomaterial-based carriers for the intra/extracellular delivery of genes, drugs, and bioactive molecules for stem cell differentiation (*21*−*23*). For intra/extracellular delivery of bioactive molecules to stem cells, the use of nanomaterial-based carriers is expected to maintain the biological activity and stability of bioactive molecules and likely extend the duration of exposure of cells to the bioactive molecules (*24*). In the case of nanomaterial-based carriers for bioactive molecules to stem cells, most efforts are focused on the development of polymeric nanoparticles. For example, a novel dexamethasone-loaded carboxymethylchitosan/poly(amidoamine) dendrimer (Dex-loaded CMCht/PAMAM) nanoparticle has been designed and combined with either ceramic or polymeric scaffolds to induce the differentiation of rat bone marrow stromal cells in vitro, and it has demonstrated that Dex-loaded CMCht/PAMAM dendrimer nanoparticles could be used as intracellular nanocarriers of biological agents to modulate the early osteogenic differentiation of rat bone marrow stromal cells in vitro (*22*). The biocompatible and biodegradable

* Corresponding authors. Kemin Wang, State Key Laboratory of Chemo/Biosensing and Chemometrics, College of Chemistry & Chemical Engineering, Hunan University, No. 1 Lushan South Road, Changsha, Hunan, 410082, PR China. Tel.: +86-731-88821566; Fax: +86-731-88821566, E-mail: kmwang@hnu.cn. Xiaoxiao He, Institute of Biology, Hunan University, No. 1 Lushan South Road, Changsha, Hunan, 410082, PR China. Tel.: +86-731-88823073; Fax: +86-731-88823780; E-mail: xiaoxiaohe@hnu.cn.

† Institute of Biology, Hunan University.

‡ State Key Laboratory of Chemo/Biosensing and Chemometrics, College of Chemistry and Chemical Engineering, Hunan University.

§ Key Laboratory for Bio-Nanotechnology and Molecule Engineering.

10.1021/bc100177v © 2010 American Chemical Society
Published on Web 08/24/2010

poly(lactide-*co*-glycolide) (PLGA) particles with different sizes have also been used as a model system to design growth-factor-releasing systems for controlling the differentiation of human embryonic stem cells (hESCs) into the vascular lineage (*23*).

By comparing with polymer nanoparticles, silica nanoparticles (SiNPs) are of interest for their biocompatibility and their mechanical properties. Because of their unique characteristics, SiNPs have been widely studied in a range of areas including chemistry, engineering, and biomedicine, especially the application of functionalized SiNPs for cancer diagnostics and therapy (*25, 26*). Recently, they are also emerging as an idea agent for efficient stem cell labeling and tracking (*27, 28*). To our knowledge, SiNPs have not previously been used as carriers of bioactive molecules for stem cell differentiation in vitro. In the present study, the SiNP-based carriers of insulin for Sprague−Dawley (SD) rat mesenchymal stem cell (RMSC) adipogenic differentiation have been reported. The cell viability assay of RMSCs in the presence of pure SiNPs was first performed using the MTT assay and morphology test to screen the SiNP concentration needed to create little cytotoxicity in the RMSCs. After further confirmation that the pure SiNPs in the concentration needed to create little cytotoxicity had no effect on cellular ultrastructures, adipogenic differentiation, and osteogenic differentiation, the SiNPs were then selected as carriers to be conjugated with insulin, one of the important growth factor supplements for RMSC adipogenic differentiation. In vitro cell studies were carried out in order to evaluate the adipogenic efficacy of adipogenic induction media containing SiNP−insulin conjugates in the control experiments. The results showed that the biological activity of insulin conjugated to the SiNPs was not affected and the SiNP−insulin conjugates could be used for RMSC adipogenic differentiation, which would help to expand the new potential application of SiNPs in stem cell research.

EXPERIMENTAL PROCEDURES

Materials. Tris(2,2-bipyridyl)dichlororuthenium(II) hexahydrate (Rubpy), Triton X-100, and aspartic acid were purchased from Sigma-Aldrich. Insulin was supplied by Invitrogen. *N*-(*p*-Maleimidophenyl)isocyanate (PMPI) was obtained from Thermo. 3-(4,5-Dimethylthiazol-2-yl)-2,5-diphenyl tetrazolium bromide (MTT) was supplied by Amersco. Oil red-O and Alizarin red were purchased from Dingguo Biotech. Sprague−Dawley rat mesenchymal stem cells (SD RMSCs), trypsin-EDTA, and phosphate-buffered saline (PBS, pH 7.2−7.4) were purchased from Cyagen biosciences. LG-DMEM growth medium consisting of low-glucose Dulbecco's modified Eagle's medium (LG-DMEM), 10% fetal bovine serum (FBS), 100 mg/mL streptomycin, 100 U/mL penicillin, and 2 mM glutamine; adipogenic induction media containing LG-DMEM growth medium and other supplements (5×10^{-4} M 3-isobutyl-1-methyl-xanthine, 1×10^{-4} M indomethacin, 1×10^{-6} M dexamethasone, 0.01 mg/mL insulin); adipogenic maintenance media consisting of LG-DMEM growth medium and 0.01 mg/mL insulin; osteogenic media containing LG-DMEM growth medium and other supplements (0.8 mM ascorbate, 0.01 M β-glycerophosphate, 1×10^{-7} M dexamethasone) were also supplied by Cyagen Biosciences. Other chemicals if not specified were all commercially available and used as received. All aqueous solutions were prepared exclusively with 18 MΩ deionized water (Barnstead Thermolyne Nanopure, Garner, NC).

Preparation of SiNPs and FSiNPs. Silica nanoparticles (SiNPs) and Rubpy dye-doped silica nanoparticles (FSiNPs) were synthesized using the water-in-oil (W/O) microemulsion method as reported before (*29*). Briefly, a solution containing cyclohexane, Triton X-100, and *n*-hexanol (with volume ratio 4:1:1) was mixed with adequate water and stirred for 5 min (for FSiNPs, followed by the addition of Rubpy dye solutions as the core material). In the presence of tetraethylorthosilicate (TEOS), polymerization reaction was initiated by adding concentrated NH_4OH. The reaction was allowed to continue for 24 h. Then, the nanoparticles were isolated by acetone and washed with ethanol and water several times to remove surfactant molecules.

Culture of RMSCs in Vitro. RMSCs were seeded at a density of 4×10^3 cells/cm^2 in the T25 or T75 flasks and cultured in the LG-DMEM growth medium, containing 10% FBS, 100 mg/mL streptomycin, 100 U/mL penicillin, and 2 mM glutamine. Cultures were maintained at 37 °C in a humidified incubator with 5% CO_2. The cells were then dissociated with trypsin−EDTA solution and subcultured at a 1:3 ratio when they were grown to 80−90% confluence.

Cell Viability and Proliferation Assay. The effect of pure SiNP concentration on RMSC viability and proliferation was first examined using MTT reduction and morphology testing. For cell viability and proliferation experiment using MTT assay, the RMSCs were grown in 96-well plates at an initial density of 4×10^3 cells/well and cultured in 200 μL LG-DMEM growth medium for 24 h. Then, the cells were exposed to the pure SiNPs with final concentrations of 0.05, 0.1, 0.2, 0.3, 0.4, 0.5, 1, and 2 mg/mL, respectively. After the cells were cultured in the media containing pure SiNPs with different concentrations for a further 24, 48, and 72 h, 20 μL of MTT (5 mg/mL in PBS) was added to each well and incubated with the cells at 37 °C for 4 h. Thereafter, the medium was removed and 150 μL of dimethyl sulfoxide (DMSO) was added and incubated for 10 min. After all crystals were dissolved, the optical density of each well was measured at 570 nm using a microplate reader (Bio-Rad ELISA reader, Hercules, CA). The RMSCs untreated with SiNPs were provided as the normal control group, and the LG-DMEM growth media in wells were prepared as the blank control group. The cell viability was calculated according to the following Formula 1.

$$\text{Formula 1:}\quad \text{Cell viability \%} = (A_{\text{SiNPs}} - A_{\text{blank control}})/(A_{\text{normal control}} - A_{\text{blank control}}) \times 100\%$$

In addition, the effects of pure SiNP concentration on the morphology of RMSCs were also investigated. Briefly, the cells were cultured in a monolayer for 24 h and fed with LG-DMEM growth medium containing pure SiNPs with different final concentrations as mentioned above for a further 72 h. Then, the media was removed, and the cells were washed twice with PBS and observed under the microscope.

Determination of Cellular Uptake of Pure SiNPs by RMSCs and the Effect of SiNPs on Cellular Ultrastructure. To determine the uptake of SiNPs by RMSCs, the well-grown cells were incubated with 0.1 mg/mL of Rubpy-doped SiNPs (FSiNPs) suspension in LG-DMEM growth medium at 37 °C for 24, 48, and 72 h. Treated cells were then washed three times with cold PBS to remove excess FSiNPs. Then, the cells were resuspended with PBS and further stained using DAPI as a nuclear counter-stain. The fluorescent dye incorporated in FSiNPs served as a marker to determine their cellular uptake and analyzed by laser scanning confocal microscopy.

Transmission electron microscopy (TEM) was subsequently performed to investigate if the uptaken SiNPs had an effect on cellular ultrastructures. The well-grown cells were incubated with 0.1 mg/mL SiNPs suspension in LG-DMEM growth medium at 37 °C for 72 h. Treated cells were then washed with PBS to get rid of excess unbound nanoparticles. Afterward, the trypsinized cells were fixed in 2.5% glutaraldehyde for 2 h, washed with PBS, and postfixed with 2% osmium tetroxide for 1 h. Then, the cells were dehydrated through a graded series of acetone, embedded in Araldite resin, and sectioned with an

Scheme 1. Schematic Drawings of Insulin Conjugation onto the SiNPs

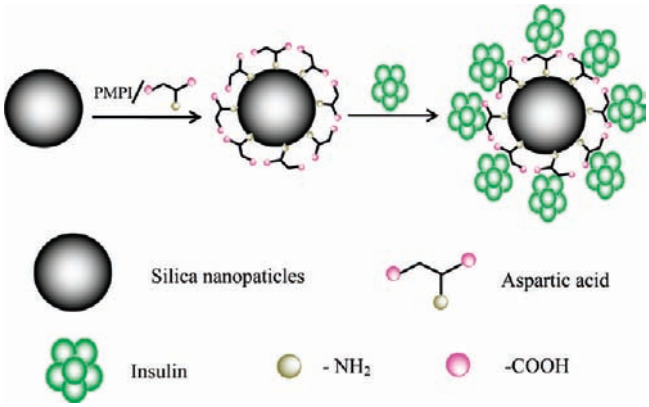


Table 1. Adipogenic Differentiation Treatment of RMSCs with Different Induction Media and Different Maintenance Media

no.	1	2	3	4
Step 1 Induction Media				
complete adipogenic differentiation medium	+	−	−	−
adipogenic differentiation medium without of insulin	−	+	+	+
pure SiNPs	−	−	−	+
SiNP−insulin conjugates	−	+	−	−
Step 2 Maintenance Media				
insulin/LG-DMEM	+	−	−	−
LG-DMEM	−	+	+	+
Pure SiNPs	−	−	−	+
SiNP−insulin conjugates	−	+	−	−

ultramicrotome. The prepared ultrathin sections (70 nm) were imaged with transmission electron microscopy (JEM-1230) at an accelerating voltage of 80 kV. The RMSCs untreated with SiNPs were also prepared for the control experiments.

Determination of the Effect of Pure SiNPs on RMSC Phenotype. Mesenchymal stem cells are multipotent stem cells which can differentiate into a variety of cell types in vitro or in vivo, including osteoblasts, adipocytes, chondrocytes, myocytes, and endotheliums (*30*). In order to demonstrate the effect of pure SiNPs on RMSC phenotype, adipogenesis and osteogenesis assays were conducted in the presence of pure SiNPs. The effects of pure SiNPs on adipogenic differentiation were performed as follows. RMSCs were seeded onto six-well tissue culture plates in LG-DMEM growth medium at 2×10^4 cells/cm^2. The cells grown in culture plates were then incubated with 0.1 mg/mL pure SiNPs for 24 h and maintained in LG-DMEM growth medium until post-confluence. Then, the LG-DMEM growth medium with SiNPs was replaced with LG-DMEM growth medium. The pure SiNP-incubated RMSCs were subjected to four cycles of adipogenic induction/maintenance media. Each cycle consisted of incubation with the induction media for 3 days, followed by 1 day incubation with maintenance media. After induction, oil red-O staining was performed to investigate the presence of lipid-containing vacuoles. Briefly, the induced RMSCs were washed with PBS and fixed in a PBS solution containing 4% paraformaldehyde for 30 min, then washed with PBS twice and stained with oil red-O for 20 min. To further quantify the lipid vacuole content, the oil red O was extracted using 100% isopropanol, and absorbance was measured at a wavelength of 490 nm.

To evaluate the effect of pure SiNPs on osteogenesis differentiation, RMSCs were plated in six-well tissue culture plates at 3×10^3 cells/cm^2 and exposed to 0.1 mg/mL pure SiNPs for 24 h. After the treatment, the pure SiNP incubated RMSCs were subjected to osteogenic differentiation. The osteogenic differentiation medium was replaced every three days, and induction was continued for a four-week period. After four weeks of osteogenic differentiation, RMSCs were rinsed with PBS, fixed for 30 min in 4% paraformaldehyde, and stained in Alizarin red solution for 7 min. For quantization by calcium assay, cells stained with Alizarin red were destained with 10% cetylpyridinium chloride (CPC10%) and the absorbance of destaining solution was measured at a wavelength of 562 nm. The amount of calcium was calculated according to a standard curve of Alizarin red.

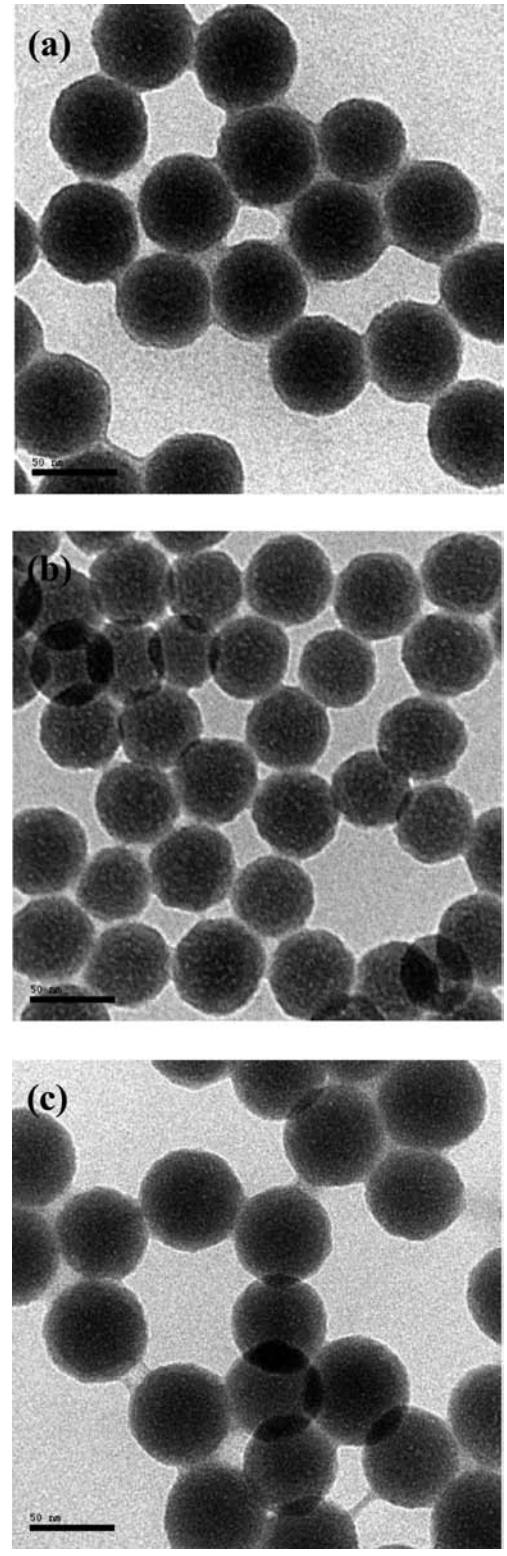


Figure 1. Transmission electron microscopy images of SiNPs (a), FSiNPs (b), and SiNP−insulin conjugates (c).

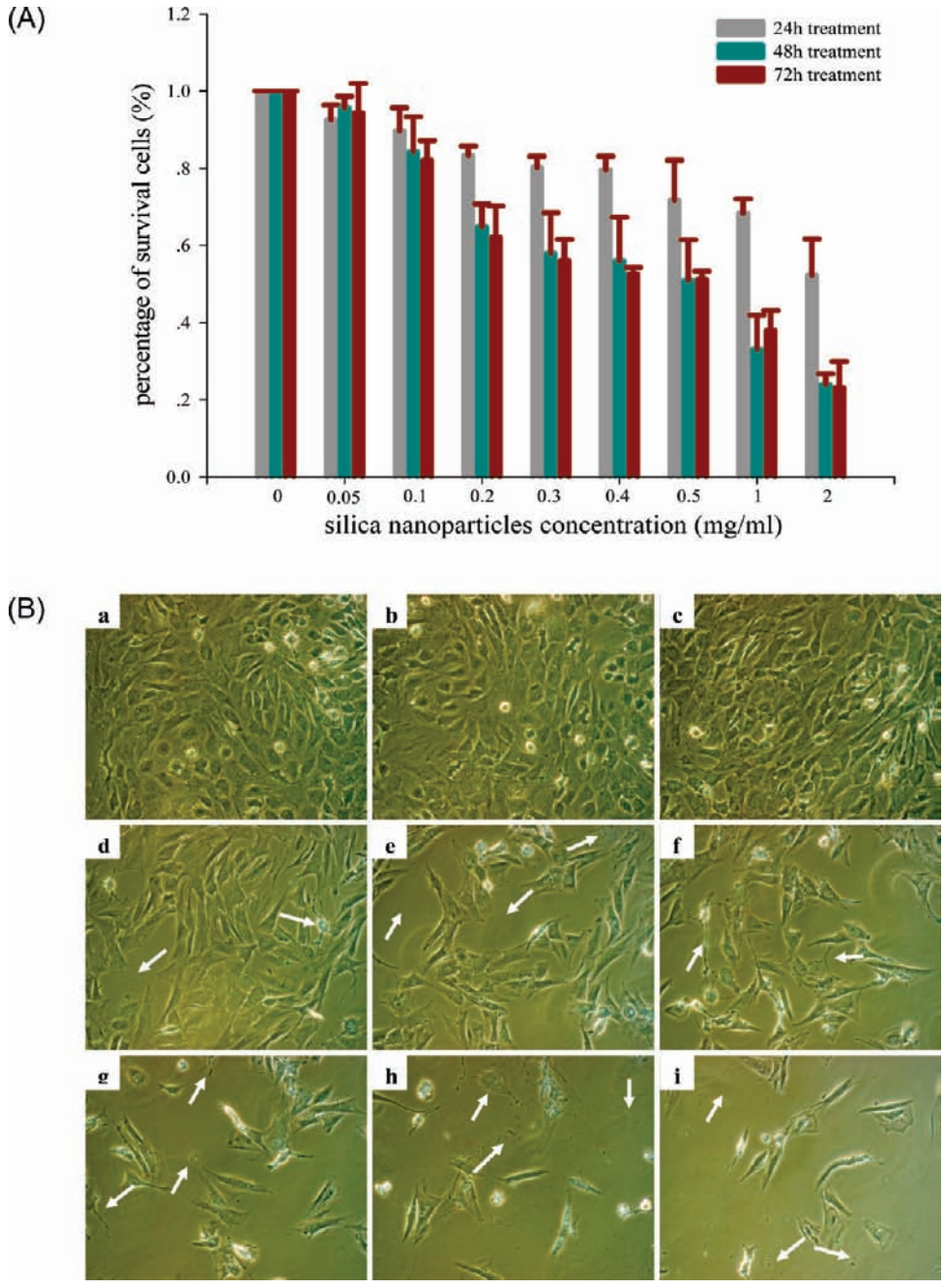


Figure 2. (A) RMSC viability in the presence of pure SiNPs of different concentrations from 0 to 2 mg/mL after the treatment at 24, 48, and 72 h, respectively. (B) Cell morphology of RMSCs treated with pure SiNPs at last concentration of (a) 0, (b) 0.05, (c) 0.1, (d) 0.2, (e) 0.3, (f) 0.4, (g) 0.5, (h) 1, and (i) 2 mg/mL, respectively, for 72 h.

Preparation and Characterization of SiNP−Insulin Conjugates. Under the optimized SiNP concentration with little cytotoxicity on the RMSC and no effect on the RMSC phenotype, SiNPs as biocompatible carriers of insulin for RMSC adipogenic differentiation were investigated. Insulin was conjugated to the surface of SiNPs via hydrogen bonds with aspartic acid-modified SiNPs, as shown in Scheme 1. First, the SiNPs were modified with aspartic acid through conjugation of the hydroxyl group of SiNPs to the amino group of aspartic acid by using PMPI heterobifunctional cross-linking. The SiNPs (20 mg) washed with ethanol were suspended in 2 mL of dimethyl sulfoxide (DMSO). A solution containing 2.1846 mg of PMPI in 150 μL of DMSO was then added to the SiNP suspension and incubated with gentle shaking for 1 h at 37 °C. The PMPI activated SiNPs were washed and resuspended in 2 mL $NaHCO_3$ solution (pH 8.3). 2 mL of 5 mg/mL aspartic acid was added to 1 mL of 10 mg/mL PMPI activated SiNPs and reacted for 12 h at 4 °C. Then, the mixture of aspartic acid modified SiNPs and aspartic acid was then thoroughly washed to remove uncoordinated aspartic acid. After the SiNPs were modified with aspartic acid, 875 μL of 4 mg/mL insulin was added to the solutions of aspartic acid-capped SiNPs and incubated for 16 h at 4 °C. Following repetitive washing of SiNP−insulin conjugates and removal of unconjugated insulin by centrifugation, the SiNP−insulin conjugates were redispersed in PBS for future usage. The unconjugated insulin presented in the supernatant was determined using the Bradford method. The amount of conjugated insulin was calculated as Formula 2 (*31*), where q was the amount of insulin conjugated onto a unit mass of SiNPs (mg/mg). W_{ti}, W_{si}, and W_{SiNPs} represented the total amount of insulin added, the amount of insulin in supernatant after conjugation, and the mass of SiNPs, respectively. To determine

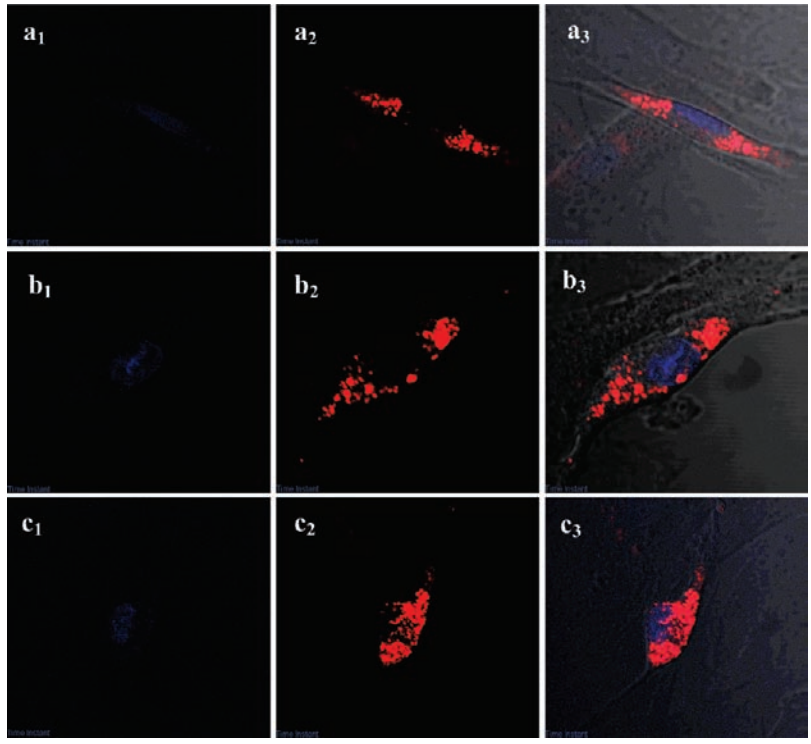


Figure 3. Confocal fluorescence images of RMSCs after treatment with 0.1 mg/mL FSiNPs for (a) 24 h, (b) 48 h, and (c) 72 h, respectively. (a_1), (b_1), and (c_1) represented the blue fluorescence imaging of RMSCs from DAPI stained nuclear imaging; (a_2), (b_2), and (c_2) represented the red fluorescence imaging of RMSCs from FSiNPs; (a_3), (b_3), and (c_3) represented the merger of blue fluorescence imaging and red fluorescence imaging of RMSCs.

if the insulin was conjugated to the SiNPs, the insulin reacted SiNPs were characterized by Fourier transform infrared (FTIR) spectroscopy analysis.

$$\text{Formula 2:} \quad q = \frac{W_{ti}(\text{mg}) - W_{si}(\text{mg})}{W_{SiNP}(\text{mg})}$$

Assessment of RMSC Adipogenic Differentiation with SiNP−Insulin Conjugates. RMSCs were seeded onto six-well tissue culture plates in LG-DMEM growth medium at the density of 2×10^4 cells/cm^2 and cultured to 100% confluence. To assess the adipogenic differentiation of RMSCs treated with SiNP−insulin conjugates, the cells were exposed to four rounds of adipogenic induction with different induction media for three days, with a resting period of one day in different maintenance media, respectively, as shown in Table 1. After treatment by adipogenic induction, the qualitative and quantitative analysis for RMSC adipogenesis was studied as mentioned above. All experiments were carried out more than three times.

RESULTS AND DISCUSSION

Characterization of SiNPs. The SiNPs, FSiNPs and insulin-conjugated SiNPs were first characterized by transmission electron microscopy (JEM-1230). The morphological analysis showed that all of them were well-dispersed spherical nanoparticles and uniform in size (Figure 1a,b,c). The diameters of SiNPs, FSiNPs, and insulin-conjugated SiNPs were 58.7 ± 1.1 nm, 52.6 ± 1.2 nm, and 60.4 ± 1.4 nm, respectively. The insulin-conjugated SiNPs were obtained through the covalent modification of insulin on the surface of SiNPs. The TEM imaging results indicated that the sizes of insulin-conjugated SiNPs were a little larger than that before modification, possibly due to the conjugation of insulin. Additionally, the size distribution of SiNPs before and after bioconjugation has also been determined by dynamic light scattering (DLS) assay using a Malvern Zetasizer (Zetasizer NanoZS). The results showed that the hydrodynamic diameter of SiNPs before bioconjugation was about 141 nm. When the SiNPs were conjugated with insulin, the size of the insulin-conjugated SiNPs was little changed, with diameter of about 153 nm (Supporting Information Figure S1), which was consistent with the size change trends characterized by TEM imaging. While the mean diameters of SiNPs before and after bioconjugation determined by DLS were both larger than those determined by TEM, the reason for this is that the DLS values of nanoparticles in aqueous solution are always larger than solid-state diameters in a monolayer by TEM, as reported in the literature (*32*).

Effect of Pure SiNPs with Different Concentration on Cell Viability and Proliferation. Our previous biocompatibility studies of SiNPs with cancer cells and normal cells have shown that the bioeffects of SiNPs on cancer cells and normal cells were both concentration-dependent. The cytotoxicity increased with increasing SiNP concentration (*33*). Therefore, the effect of SiNP concentration on the metabolic activity of RMSCs, a parameter commonly used to reflect cytotoxicity, was first assessed before using SiNPs as carriers of insulin for RMSC adipogenic differentiation. As shown in Figure 2A, addition of SiNPs to the cell culture medium with last concentration of 0.05 mg/mL did not affect the metabolic activity of RMSC cells after exposure for 24, 48, or 72 h. Although the cell survival rate decreased as the concentration of SiNPs increased to 0.1 mg/mL, the survival rate of the cells after exposure for SiNPs of 24, 48, and 72 h remained 90 ± 6%, 84 ± 9%, and 82 ± 5%, respectively. Moreover, the difference in effects observed for the cells treated with either 0.05 mg/mL or 0.1 mg/mL SiNPs was not more than 10% in the three time points. The results indicated that addition of SiNPs to the cell culture medium with last concentrations of 0.05 mg/mL and 0.1 mg/mL did not affect the metabolic activity and proliferation of RMSCs. As the concentration of SiNPs increased, the cell survival rate de-

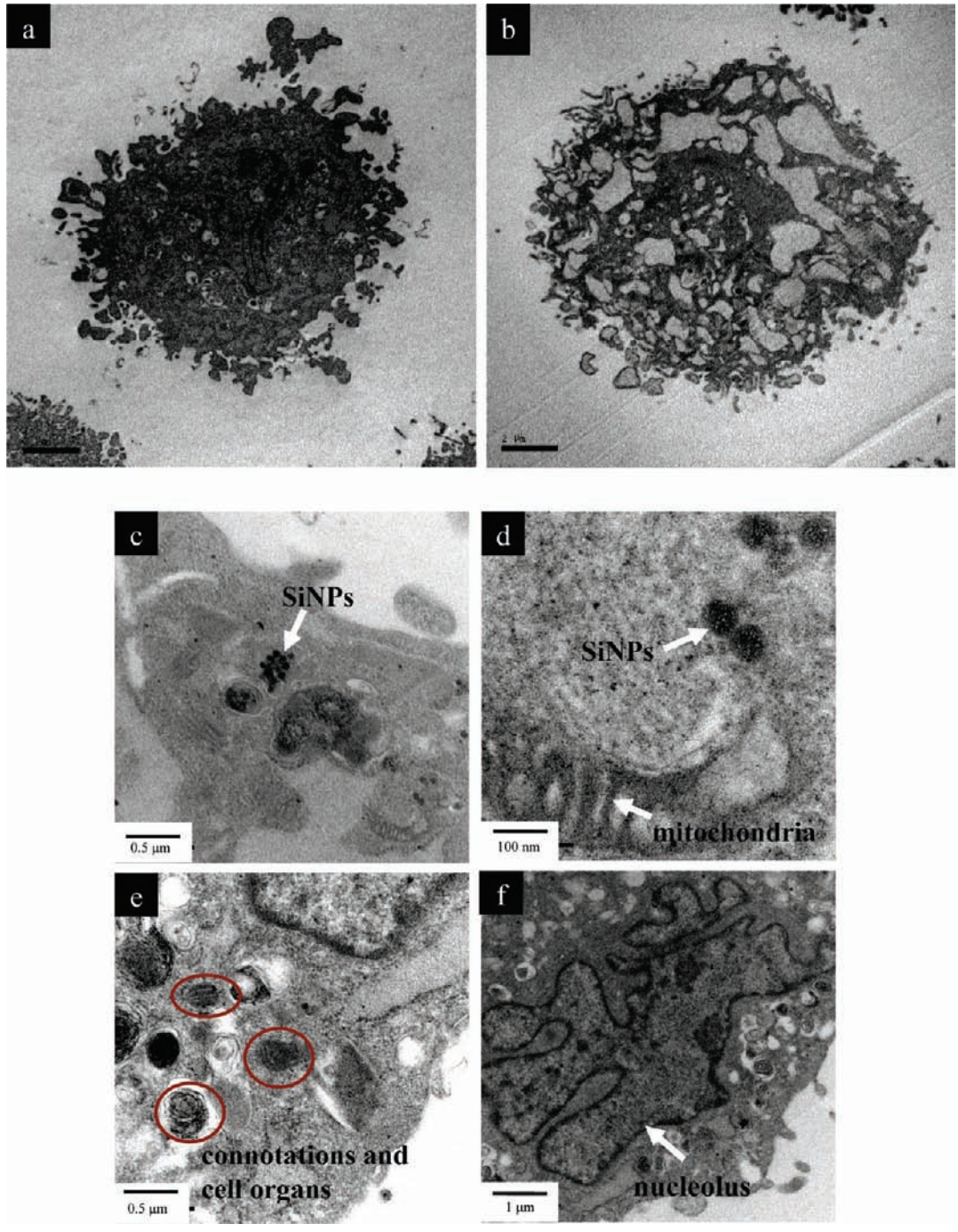


Figure 4. Transmission electron microscopy images of (a) RMSCs without treatment of SiNPs, (b) RMSCs after treatment with 0.1 mg/mL SiNPs for 72 h, (c) SiNPs, (d) SiNPs and mitochondria cytoplasm, (e) connotations similar to glycogen and cell organs, and (f) cell nucleolus.

creased. If the last concentration of SiNPs was not higher than 0.1 mg/mL, the survival rate of the cells after exposure for 24 h remained around 80%. However, the treatment with SiNPs for either 48 or 72 h significantly decreased the metabolic activity of RMSCs at concentrations starting from 0.1 mg/mL. When SiNP concentration was increased to 2 mg/mL, the treatment of RMSCs at 24, 48, or 72 h caused a reduction in metabolic activity to 52 ± 9%, 24 ± 3%, and 23 ± 7%, respectively. These data indicated that the effect of SiNPs on RMSC viability and proliferation was concentration-dependent. With the increase of SiNP concentration, cytotoxicity increased gradually. The SiNPs were biocompatible with RMSCs if the treatment concentration of SiNPs was not more than 0.1 mg/mL.

The morphological changes and cell confluence of treated RMSCs with different concentrations of SiNPs for 72 h were also observed under an inverted phase-contrast microscope. After 72 h exposure to SiNPs with last concentration of either 0.05 or 0.1 mg/mL, the microscopic evaluation of RMSCs showed no major changes in cell morphology and cell confluence as compared to unexposed RMSCs (Figure 2B, a−c). Most cells showed a fibroblast-like morphology, growing in a spindle shape and polygon shape. They displayed eddy current array after 90−100% confluence. However, proliferation of RMSCs has been shown to be inhibited when the RMSCs were treated with high concentrations of nanoparticles starting from 0.1 mg/mL. When SiNP concentration was increased to 2 mg/mL, there was only about 70% confluence (Figure 2B, d). With further increase of SiNPs concentration, the confluence of cells that were involved in fusion was less than 50%, and the cells appeared to retract and showed a greater tendency to die. The

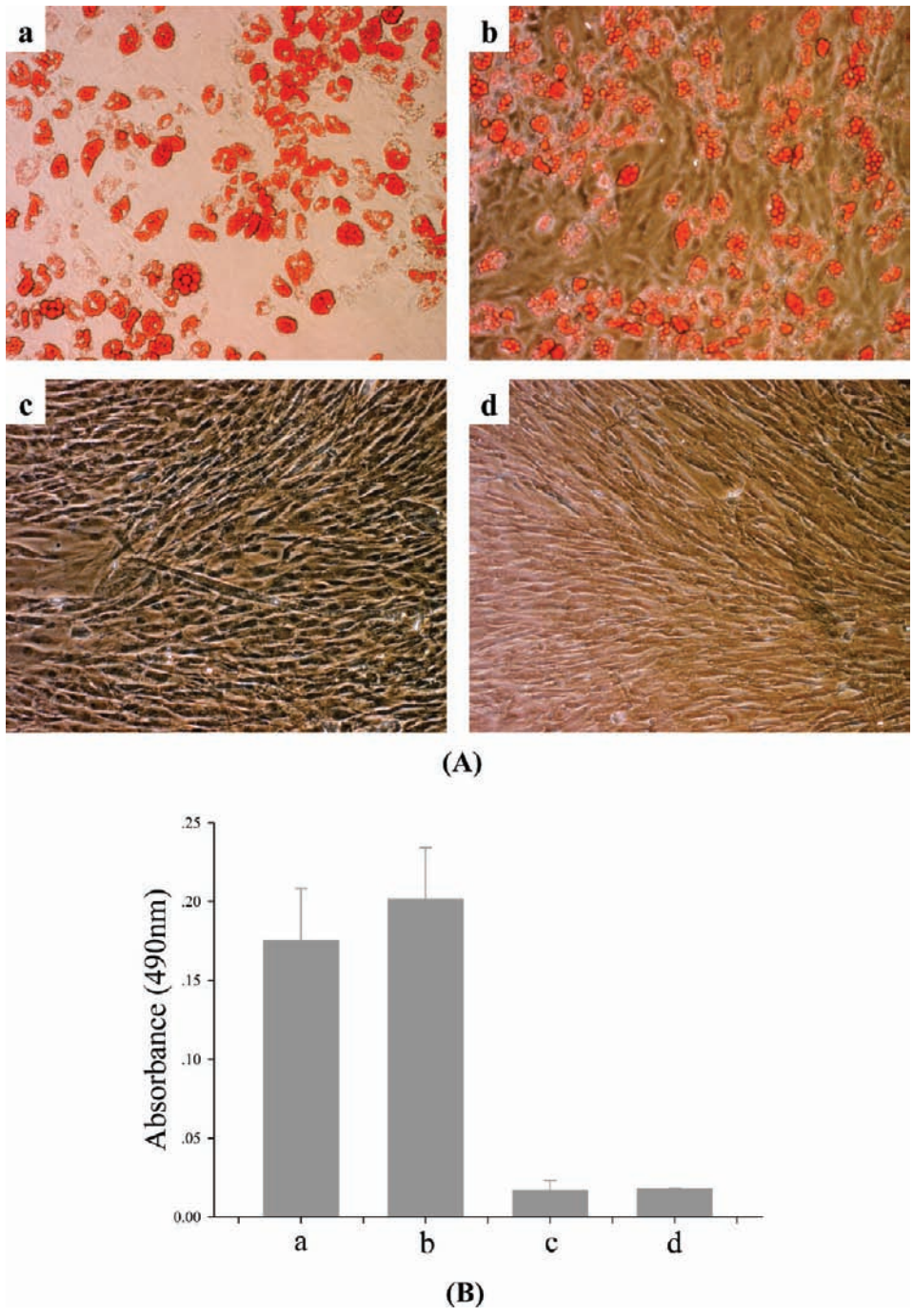


Figure 5. Effect of 0.1 mg/mL SiNPs on adipogenic differentiation of RMSCs. (A) Imaging of oil red-O stained lipid vacuoles of RMSCs. (B) Absorbance intensity of oil red-O stained RMSCs. (a), (b), (c), and (d) represented adipogenic differentiation medium induced SiNP pretreated RMSCs, adipogenic differentiation medium induced RMSCs, RMSCs without adipogenic differentiation medium, and SiNP pretreated RMSCs without adipogenic differentiation medium, respectively.

cell toxicity increased obviously. Cell morphology had a clear retraction and the trace of the dead cells separated from the dishes could be easily observed, as shown by the arrow marks in Figure 2B, e−i. The morphological analysis results also confirmed that the effect of SiNPs on RMSC viability and proliferation was concentration-dependent.

After screening the SiNP concentration creating little cytotoxicity on the RMSCs, further experiments were confirmed to investigate if the pure SiNPs with concentration of 0.1 mg/mL had any effect on the cellular ultrastructure, adipogenic differentiation, and osteogenic differentiation.

Cellular Uptake of SiNPs and Effect of Uptaken SiNPs on Cellular Ultrastructures. Using confocal laser scanning microscopy, the cellular uptake of SiNPs by RMSCs was determined by the incorporated Rubpy fluorescence dye. Merged images of the red fluorescence from FSiNPs and the blue fluorescence from DAPI stained nuclei indicated that FSiNPs could be effectively taken up by the RMSCs and mainly occupied the cytoplasm after the RMSCs were treated with 0.1 mg/mL FSiNPs for 24, 48, and 72 h, respectively (Figure 3). The RMSCs still maintained good shape and growth conditions after uptake of a large number of particles.

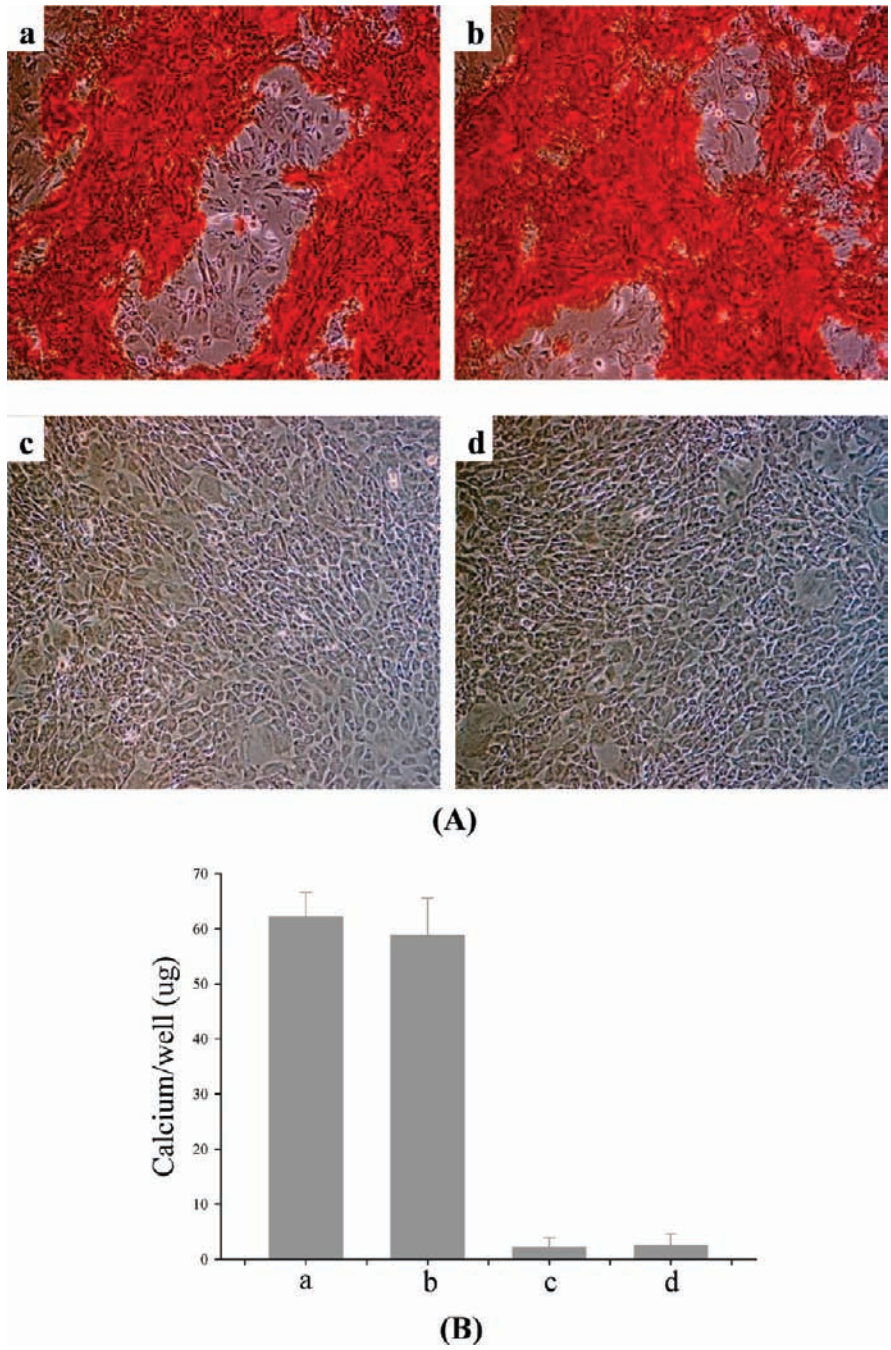


Figure 6. Effect of 0.1 mg/mL SiNPs on osteogenic differentiation of RMSCs. (A) Imaging of Alizarin red stained RMSCs. (B) Amount of calcium mineralization. (a), (b), (c), and (d) represented osteogenic differentiation medium induced SiNP pretreated RMSCs, osteogenic differentiation medium induced RMSCs, RMSCs without osteogenic differentiation medium, and SiNP pretreated RMSCs without osteogenic differentiation medium, respectively.

In order to further confirm the uptake of SiNPs by RMSCs and investigate the effect of uptaken SiNPs on cellular ultrastructures, TEM analyses of RMSCs treated with 0.1 mg/mL of SiNPs for 72 h were performed (Figure 4a,b). From the whole-cell images taken, the structures of RMSC cells treated with SiNPs were preserved by comparison with the control group without treatment with SiNPs. The uptaken SiNPs were obviously distributed in the cells and still retained the well-dispersed spherical and uniformity in size after their internalization into cells (Figure 4c,d). The cristae and matrix of the mitochondria were clearly seen (Figure 4d), and the connotations similar to glycogen and cell organs were distributed richly in the SiNP-treated RMSCs (Figure 4e). The nucleolus remained intact with nuclear bags, excrescences, and nucleolus (Figure 4f). As we know, the RMSCs are multipotent stem cells that can differentiate into a variety of cell types in vivo and in vitro. The rich cell organs are the necessary structural and functional units of RMSCs, and the connotations similar to glycogen can provide the energy for differentiation. These cell ultrastructure image results indicated that the treated RMSCs stayed in a relatively active period with normal cell function.

Effect of Pure SiNPs on the Adipogenesis and Osteogenesis of RMSCs. The effect of SiNPs on the ability of RMSCs to differentiate into adipocytes and osteocytes was subsequently examined. For differentiation into adipocytes, RMSCs were seeded onto six-well tissue culture plates in growth medium at 2×10^4 cells/cm^2 and exposed to 0.1 mg/mL SiNPs for 24 h. Then, RMSCs were subjected to adipogenic differentiation

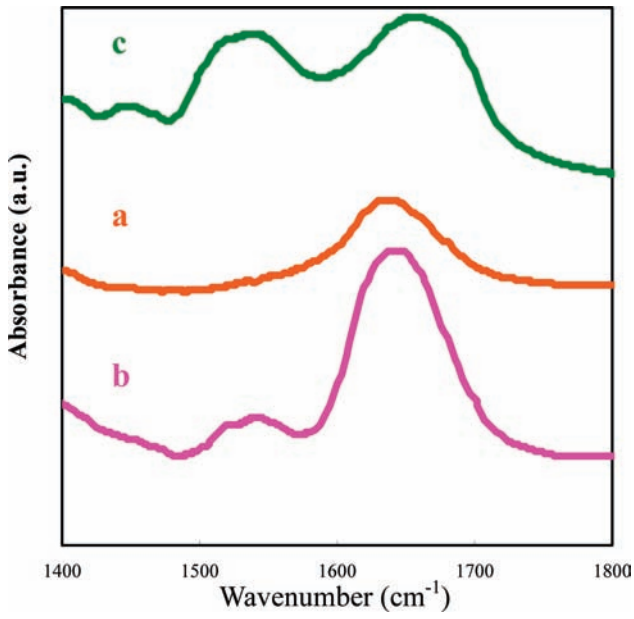


Figure 7. Fourier transform infrared (FTIR) spectroscopy measurements of (a) pure SiNPs, (b)SiNP−insulin conjugates, and (c) insulin.

medium for 18 days. Meanwhile, three control groups were designed, including the RMSC adipogenic induction without pretreatment of SiNPs, the RMSCs cultured in the absence of adipogenic stimulants, and the SiNP pretreated RMSCs cultured in the absence of adipogenic stimulants. The intracellular lipid accumulation was determined by examination with light microscopy and absorbance measurement at 490 nm after Oil red-O staining. As shown in Figure 5A, the total amount of accumulated lipids in the SiNP pretreated RMSCs was close to the untreated RMSC group following the 18 days of adipogenic stimulation in the presence of adipogenic stimulants. The absorbance values lacked any significant difference between SiNP-treated RMSCs and untreated RMSCs during adipogenic differentiation (Figure 5B). However, both the RMSCs and SiNP pretreated RMSCs had no lipid vacuoles if they were not induced by adipogenic stimulants. These results revealed that the presence of pure SiNPs did not interfere with adipogenic differentiation of RMSCs.

For differentiation into osteocytes, RMSCs were seeded onto six-well tissue culture plates in growth medium at 3×10^3 cells/cm^2 and exposed to 0.1 mg/mL SiNPs for 24 h. Then, RMSCs were subjected to osteogenic differentiation medium for 30 days. Three control groups were also designed, which included the RMSC osteogenic induction without pretreatment with SiNPs, the RMSCs cultured in the absence of osteogenic differentiation medium, and the SiNP pretreated RMSCs cultured in the absence of osteogenic differentiation medium. Alizarin red staining showed that the RMSCs had good biological characteristics of osteocytes in the presence of SiNP treated RMSCs similar to untreated cells following the 30 days of osteogenic stimulation (Figure 6), and both the RMSCs and SiNP pretreated RMSCs were not stained because they were not subjected to osteogenic differentiation medium. The amount of calcium mineralization by the calcium assay results also lacked significant difference between SiNP treated RMSCs and untreated RMSCs following 30 days of osteogenic stimulation, suggesting that the presence of SiNPs had no effect on osteogenic differentiation of RMSCs.

Characterization of SiNP−Insulin Conjugates Using Fourier Transform Infrared (FTIR) Spectroscopy. FTIR spectroscopy was used to determine if the insulin was conjugated to the SiNPs. FTIR spectra of pure SiNPs and pure insulin as control group were also recorded. As shown in Figure 7, a comparison of spectra with that recorded from the pure SiNP samples (curve a) revealed the presence of prominent resonance at 1630 cm^{-1}, which was ascribed to the physically adsorbed water, probably in the micropores (*34*). The determination of spectra with that recorded from insulin-conjugated SiNPs samples (curve b) showed the presence of prominent resonance at 1540 cm^{-1}. This absorption band absent in FTIR spectra recorded from the SiNPs samples was identified as the amide II vibrational mode, suggesting that insulin was indeed conjugated to the SiNPs. Insulin is a very important biologically active protein composed of 51 amino acids. Each insulin protein had strong absorption bands at 1540 cm^{-1} and 1640 cm^{-1} (curve c), which were identified as the amide I and II vibrational modes, respectively. The position of these two bands was important to the biological activity of insulin protein. The absorption band at 1640 cm^{-1} (amide I) recorded from the insulin-conjugated SiNP samples should be overlap the spectra of SiNPs and insulin. The amount of conjugated insulin on the SiNPs was 0.3437 mg/mg calculated from Formula 2.

Effect of Insulin-Conjugated SiNPs on the Adipogenic Differentiation of RMSCs. To induce the RMSC adipogenic differentiation in vitro using defined culture milieu, the adipogenic differentiation medium should be complete. Insulin is one of the important supplements of adipogenic induction and adipogenic maintenance media. In the present study, the insulin-conjugated SiNPs for RMSC adipogenic differentiation have been investigated. After culturing in a different culture medium for a period of 18 days, oil red-O staining of the lipid vacuoles of RMSCs was carried out. As shown in Figure 8A, the RMSCs had plenty of lipid vacuoles after induction with complete adipogenic differentiation medium, which indicated the adipogenic differentiation of RMSCs in vitro. When the insulin in the complete adipogenic differentiation medium and maintenance media were both replaced with equal-quantity insulin conjugated SiNPs, the RMSCs also had plenty of lipid vacuoles. However, very few lipid vacuoles were observed for the RMSCs exposed to the adipogenic medium absent of insulin or the adipogenic medium without insulin but with 0.1 mg/mL pure SiNPs. Figure 8B showed the quantitative investigation of oil red-O staining for lipid vacuoles of RMSCs cultured in a different culture medium for the period of 18 days. There were no significant differences in the absorbance values for the RMSCs exposed to the complete adipogenic differentiation medium and the insulin conjugated SiNP adipogenic differentiation medium after 18 d of culturing. Low absorbance values were observed for the RMSCs exposed to the adipogenic medium without insulin but with 0.1 mg/mL pure SiNPs. These results obviously demonstrated that insulin is necessary for the adipogenic differentiation of RMSCs in vitro. The adipogenic differentiation medium without insulin could not induce the adipogenic differentiation of RMSCs even though pure SiNPs had been added. When the insulin was conjugated to SiNPs, the biological activity of insulin as a supplement of the adipogenic differentiation medium was still retained.

As we all know, the successful release of biomolecules from the nanoparticles is critical for nanoparticle-based carriers to meet specific needs. The release of the conjugated biomolecules from the nanoparticles is related to many factors, including the materials of the nanoparticles, the interaction of nanoparticles with biomolecules, and so on. In this work, the nature of interaction between insulin and SiNPs carriers would be expected to play a major role in the release of insulin. As described above, insulin was linked to the aspartic acid−SiNP surface coating via much weaker hydrogen bonding. In this case, the release of insulin is more facile and faster in the biological system as reported previously (*35*). Therefore, the release of

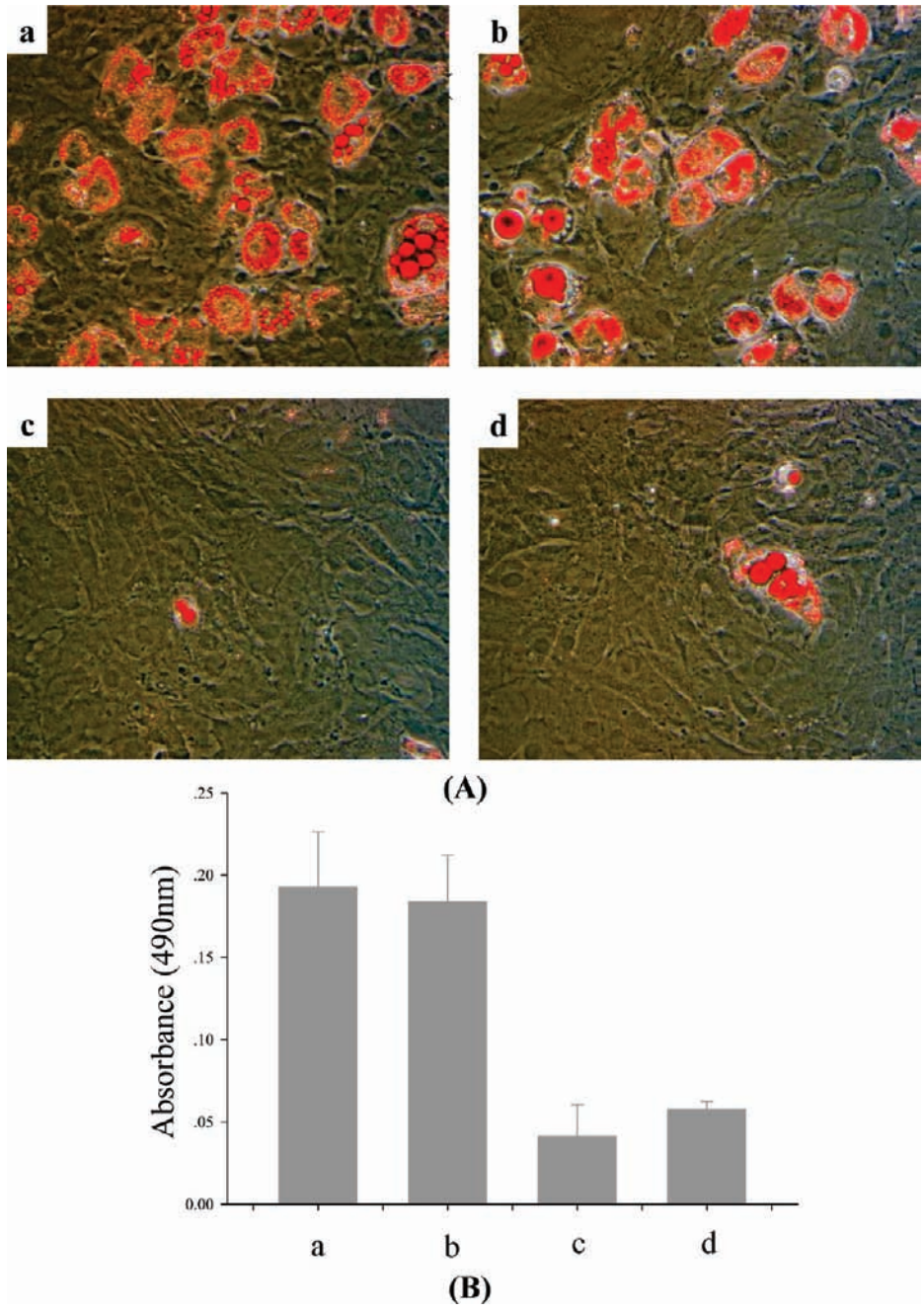


Figure 8. Imaging (A) and absorbance intensity (B) of oil red-O stained RMSCs after induction with different culture medium (a) complete adipogenic differentiation medium and insulin/LG-DMEM maintenance media; (b) adipogenic differentiation medium and maintenance media containing SiNP−insulin conjugates; (c) adipogenic differentiation medium and maintenance media without insulin; and (d) adipogenic differentiation medium and maintenance media without insulin but with 0.1 mg/mL SiNPs.

insulin from SiNP conjugates would be possible after uptake by the RMSCs. Then, the potential release characteristic made the SiNPs able to be used successfully as biocompatibile carriers of insulin for RMSC adipogenic differentiation.

The aforementioned cell viability assay of SiNPs with RMSCs and the in vitro cell studies of insulin-conjugated SiNPs on the adipogenic differentiation of RMSCs have clearly demonstrated that SiNPs could be used as biocompatible carriers of insulin for RMSCs adipogenic differentiation. The SiNP-based carriers are expected to keep the biomolecules' activity and stability. It is conceivable that this novel nanocarrier for the intracellular and controlled delivery of bioactive molecules can likely be an excellent candidate for modulation of the cellular functions in a more effective manner ex vivo and maintenance of the cellular phenotype in vivo upon reimplantation. If substituting the insulin to suit other biomolecules, it is believed that the SiNP based carrier holds great potential application in other stem cell directed differentiation in vitro and in vivo.

CONCLUSION

In this work, we demonstrated the biocompatible silica nanoparticle−insulin conjugates for RMSC adipogenic differentiation. The biocompatibility of the SiNPs with RMSCs was first investigated, namely, for cell viability, proliferation, cellular uptake, cellular ultrastructures, adipogenic differentiation, and osteogenic differentiation. Results showed that the SiNPs with concentration creating little cytotoxicity on the RMSCs could be well uptaken by RMSCs and would not affect the cellular ultrastructures, RMSC adipogenic differentiation, and osteogenic differentiation. Further experiments demonstrated

that insulin could be conjugated to the SiNPs and retain its biological activity for induction of the adipogenic differentiation of RMSCs in combination with other supplements. Therefore, SiNPs could be used as biocompatible intracellular nanocarriers of biological agents able to modulate the behavior of stem cells.

ACKNOWLEDGMENT

This work was partially supported by Program for Innovative Research Team of Hunan National Science Foundation (10JJ7002), Program for New Century Excellent Talents in University (NCET-06-0697) and National Science Foundation of P.R.China (90606003, 20775021).

Supporting Information Available: Characterization of SiNPs and SiNP−insulin conjugates by dynamic light scattering (DLS). This material is available free of charge via the Internet at http://pubs.acs.org.

LITERATURE CITED

(1) Gardner, R. L. (2007) Stem cells and regenerative medicine: principles, prospects and problems. *C. R. Biol. 330*, 465–473.
(2) Zur Nieden, N. I., Kempka, G., and Ahr, H. J. (2007) In vitro differentiation of embryonic stem cells into mineralized osteoblasts. *Differentiation 71*, 18–27.
(3) Wernig, M., Meissner, A., Foreman, R., Brambrink, T., Ku, M., Hochedlinger, K., Bernstein, B. E., and Jaenisch, R. (2007) In vitro reprogramming of fibroblasts into a pluripotent ES-cell-like state. *Nature 448*, 318–324.
(4) Chevallier, N., Anagnostou, F., Zilber, S., Bodivit, G., Maurin, S., Barrault, A., Bierling, P., Hernigou, P., Layrolle, P., and Rouard, H. (2010) Osteoblastic differentiation of human mesenchymal stem cells with platelet lysate. *Biomaterials 31*, 270–278.
(5) Chaubey, A., and Burg, K. J. L. (2008) Extracellular matrix components as modulators of adult stem cell differentiation in an adipose system. *J. Bioact. Compatible Polym. 23*, 20–37.
(6) Evans, N. D., Gentleman, E., Chen, X., Roberts, C. J., Polak, J. M., and Stevens, M. M. (2010) Extracellular matrix-mediated osteogenic differentiation of murine embryonic stem cells. *Biomaterials 31*, 3244–3252.
(7) Qiu, C., Hanson, E., Olivier, E., Inada, M., Kaufman, D. S., Gupta, S., and Bouhassira, E. E. (2005) Differentiation of human embryonic stem cells into hematopoietic cells by coculture with human fetal liver cells recapitulates the globin switch that occurs early in development. *Exp. Hematol. 33*, 1450–1458.
(8) Gai, H., Nguyen, D. M., Moon, Y. J., Aguila, J. R., Fink, L. M., Ward, D. C., and Ma, Y. (2010) Generation of murine hepatic lineage cells from induced pluripotent stem cells. *Differentiation 79*, 171–181.
(9) Chang, J.-C., Hsu, S.-H., and Su, H.-L. (2009) The regulation of the gap junction of human mesenchymal stem cells through the internalization of quantum dots. *Biomaterials 30*, 1937–1946.
(10) Klöpper, J., Lindenmaier, W., Fiedler, U., Mehlhorn, A., Stark, G. B., and Finkenzeller, G. (2008) High efficient adenoviral-mediated VEGF and Ang-1 gene delivery into osteogenically differentiated human mesenchymal stem cells. *Microvasc. Res. 75*, 83–90.
(11) Heng, B. C., Haider, H. K., Sim, E. K.-W., Cao, T., and Ng, S. C. (2004) Strategies for directing the differentiation of stem cells into the cardiomyogenic lineage in vitro. *Cardiovasc. Res. 62*, 34–42.
(12) Ashman, L. K. (1999) The biology of stem cell factor and its receptor C-kit. *Int. J. Biochem. Cell Biol. 31*, 1037–1051.
(13) Kawakami, K., Oda, N., Miyoshi, K., Funaki, T., and Ida, Y. (2006) Solubilization behavior of a poorly soluble drug under combined use of surfactants and cosolvents. *Eur. J. Pharm. Sci. 28*, 7–14.
(14) Stahn, C., Löwenberg, M., Hommes, D. W., and Buttgereit, F. (2007) Molecular mechanisms of glucocorticoid action and selective glucocorticoid receptor agonists. *Mol. Cell. Endocrinol. 275*, 71–78.
(15) Rovira, M., Jané-valbuena, J., Marchand, M., Savatier, P., Real, F. X., and Skoudy, A. (2007) Viral-mediated coexpression of Pdx1 and p48 regulates exocrine pancreatic differentiation in mouse ES cells. *Cloning Stem Cells 9*, 327–338.
(16) Ferreira, L., Karp, J. M., Nobre, L., and Langer, R. (2008) New opportunities: The use of nanotechnologies to manipulate and track stem cells. *Cell Stem Cell 3*, 136–146.
(17) Jing, Y., Moore, L. R., Williams, P. S., Chalmers, J. J., Farag, S. S., Bolwell, B., and Zborowski, M. (2007) Blood progenitor cell separation from clinical leukapheresis product by magnetic nanoparticle binding and magnetophoresis. *Biotechnol. Bioeng. 96*, 1139–54.
(18) Lei, Y., Tang, H. Y., Yao, L. D., Yu, R. C., Feng, M. F., and Zou, B. S. (2008) Applications of mesenchymal stem cells labeled with Tat peptide conjugated quantum dots to cell tracking in mouse body. *Bioconjugate Chem. 19*, 421–427.
(19) Lee, J. B., Jeong, S. M., Kim, K. J., Cho, D. H., Kwon, I. K., Yoon, I. C., Choi, K., Suh, J.-K. F., Park, J. H., Park, Y. D., Chung, J. H., Choi, K. K., Kim, G. T., Choi, G. W., and Choi, Y. S. (2009) Osteogenic differentiation of human adipose-derived stem cells (hADSCs) on a dexamethasone eluting nanofiber scaffolds. *J. Tissue Eng. Regen. Med. 6*, 371–379.
(20) Curran, J. M., Chen, R., Stokes, R., Irvine, E., Graham, D., Gubbins, E., Delaney, D., Amro, N., Sanedrin, R., Jamil, H., and Hunt, J. A. (2010) Nanoscale definition of substrate materials to direct human adult stem cells towards tissue specific populations. *J. Mater. Sci. Mater. Med. 21*, 1021–1029.
(21) Santos, J. L., Oramas, E., Pêgo, A. P., Granja, P. L., and Tomás, H. (2009) Osteogenic differentiation of mesenchymal stem cells using PAMAM dendrimers as gene delivery vectors. *J. Controlled Release 134*, 141–148.
(22) Oliveira, J. M., Sousa, R. A., Kotobuki, N., Tadokoro, M., Hirose, M., Mano, J. F., Reis, R. L., and Ohgushi, H. (2009) The osteogenic differentiation of rat bone marrow stromal cells cultured with dexamethasone-loaded carboxymethylchitosan/poly(amidoamine) dendrimer nanoparticles. *Biomaterials 30*, 804–813.
(23) Ferreira, L., Squier, T., Park, H., Choe, H., Kohane, D. S., and Langer, R. (2008) Human embryoid bodies containing nano- and microparticulate delivery vehicles. *Adv. Mater. 20*, 2285–2291.
(24) Edelman, E. R., Nugent, M. A., and Karnovsky, M. J. (1993) Perivascular and intravenous administration of basic fibroblast growth factor: Vascular and solid organ deposition. *Proc. Natl. Acad. Sci. U.S.A. 90*, 1513–1517.
(25) Choi, J., Burns, A. A., Williams, R. M., Zhou, Z., Flesken-Nikitin, A., Zipfel, W. R., Wiesner, U., and Nikitin, A. Y. (2007) Core-shell silica nanoparticles as fluorescent labels for nanomedicine. *J. Biomed. Opt. 12*, 064007.
(26) Lee, J. E., Lee, N., Kim, H., Kim, J., Choi, S. H., Kim, J. H., Kim, T., Song, I. C., Park, S. P., Moon, W. K., and Hyeon, T. (2010) Uniform mesoporous dye-doped Silica nanoparticles decorated with multiple magnetite nanocrystals for simultaneous enhanced magnetic resonance imaging, fluorescence imaging, and drug delivery. *J. Am. Chem. Soc. 132*, 552–557.
(27) Huang, D.-M., Hung, Y., Ko, B.-S., Hsu, S.-C., Chen, W.-H., Chien, C.-L., Tsai, C.-P., Kuo, C.-T., Kang, J.-C., Yang, C.-S., Mou, C.-Y., and Chen, Y.-C. (2005) Highly efficient cellular labeling of mesoporous nanoparticles in human mesenchymal stem cells: implication for stem cell tracking. *FASEB J. 19*, 2014–2016.
(28) Lu, C.-W., Hung, Y., Hsiao, J.-K., Yao, M., Chung, T.-H., Lin, Y.-S., Wu, S.-H., Hsu, S.-C., Liu, H.-M., Mou, C.-Y., Yang, C.-S., Huang, D.-M., and Chen, Y.-C. (2007) Bifunctional magnetic silica nanoparticles for highly efficient human stem cell labeling. *Nano Lett. 7*, 149–154.
(29) He, X. X., Wang, K. M., Tan, W. H., Li, J., Yang, X. H., Huang, S. S., Li, D., and Xiao, D. (2002) Photostable luminescent nanoparticles as biological label for cell recognition of system

lupus erythematosus patients. *J. Nanosci. Nanotechnol. 2*, 317–320.

(30) Barry, F. P., and Murphy, J. M. (2004) Mesenchymal stem cells: clinical applications and biological characterization. *Int. J. Biochem. Cell Biol. 36*, 568–584.

(31) Yavuz, H., and Denizli, A. (2005) Immunoadsorption of cholesterol on Protein A oriented beads. *Macromol. Biosci. 5*, 39–48.

(32) Büscher, K., Helm, C. A., Gross, C., Glöckl, G., Romanus, E., and Weitschies, W. (2004) Nanoparticle composition of a ferrofluid and its effects on the magnetic properties. *Langmuir 20*, 2435–2444.

(33) He, X. X., Wu, X., Wang, K. M., Shi, B. H., and Hai, L. (2009) Methylene blue-encapsulated phosphonate-terminated silica nanoparticles: A bifunctional carrier for simultaneous in vivo imaging and photodynamic therapy. *Biomaterials 30*, 5601–5609.

(34) Li, L. Y., Wang, J. G., Sun, P. C., Liu, X. H., Ding, D. T., and Chen, T. H. (2008) Microporous silica hollow nanospheres templated by anionic polypeptide. *Acta Phys. Chim. Sin. 24*, 359–63.

(35) Joshi, H. M., Bhumkar, D. R., Joshi, K., Pokharkar, V., and Sastry, M. (2006) Gold nanoparticles as carriers for efficient transmucosal insulin delivery. *Langmuir 22*, 300–305.

BC100177V

Supplement materials for

Biocompatible Silica Nanoparticles-Insulin Conjugates for Mesenchymal Stem Cells Adipogenic Differentiation

Authors:

Dan Liu[1,3], Xiaoxiao He[1,3*], Kemin Wang[2,3*], Chunmei He[1,3], Hui Shi[2,3], Lixin Jian[2,3]

[1]Institute of Biology

Hunan University

Changsha 410082, China.

[2]State Key Laboratory of Chemo/Biosensing and Chemometrics

College of Chemistry & Chemical Engineering

Hunan University

Changsha 410082, China.

[3]Key Laboratory for Bio-Nanotechnology and Molecule Engineering

Hunan Province

Changsha 410082, China.

*corresponding author: Kemin Wang, State Key Laboratory of Chemo/Biosensing and Chemometrics,College of Chemistry & Chemical Engineering, Hunan University, No. 1 Lushan South Road, Changsha, Hunan, 410082, PR China. Tel.: +86-731-88821566; Fax: +86-731-88821566, E-mail: kmwang@hnu.cn; Xiaoxiao He, Institute of Biology, Hunan University, No. 1 Lushan South Road, Changsha, Hunan, 410082, PR China. Tel.: +86-731-88823073; Fax: +86-731-88823780; E-mail: xiaoxiaohe@hnu.cn.

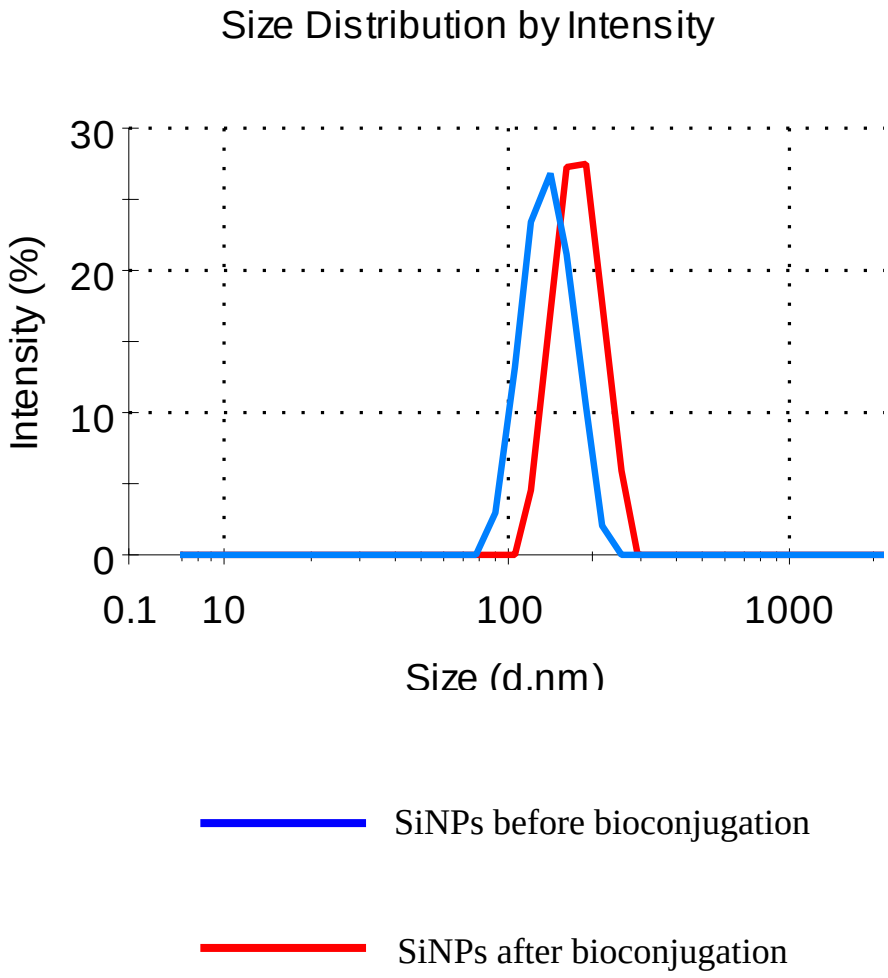


Figure S1. Characterization of SiNPs and SiNPs-insulin conjugates by dynamic light scattering (DLS).

Simple Solid-Phase Synthesis and Biological Properties of Carbohydrate−Oligonucleotide Conjugates Modified at the 3′-Terminus

Yutaka Ikeda,[†] Daisuke Kubota,[‡] and Yukio Nagasaki*

Grauate School of Pure and Applied Science, Tsukuba Research Center for Interdisciplinary Materials Science (TIMS), Center for Tsukuba Advanced Reserch Aliance (TARA), International Center for Materials Nanoarchitectonics Satellite (MANA), and National Institute for Materials Science (NIMS), University of Tsukuba, CREST, Japan Science and Technology Agency (JST), and Master's School of Medical Sciences, Graduate School of Comprehensive Human Science. Received April 28, 2010; Revised Manuscript Received June 30, 2010

A novel synthesis method for oligonucleotides possessing a functional moiety at the 3′-terminus was established based on solid-phase synthesis. In order to install the functional group at the 3′-terminus of the oligonucleotide, a solid support possessing the functional group was prepared. A carbohydrate was employed in this study for the functionalization of the oligonucleotide. To prepare a glycosylated solid support, a novel glycosyl acceptor (**2**) was synthesized using 4,4-dihydroxymethyl-cyclopenta-1-ene as the starting compound. The glycosylation reaction proceeded smoothly (yield = 95%) to yield the suitable glycosylated compound (**3**). After **8** was immobilized on the solid support, it was subjected to solid-phase oligonucleotide synthesis by the standard phosphoramidite coupling method. An oligonucleotide possessing a sugar moiety at the 3′-terminus was obtained after the products were deprotected and cleaved from the solid support. The stability of the carbohydrate-modified oligonucleotide was greatly increased even in the serum buffer, indicating that the sugar moiety at the 3′-position improved the resistance against enzymatic degradation. This technique was also applied to RNA synthesis. Galactose-ended siRNA was prepared and was confirmed to possess enough ability, at a concentration of 10 nM, to regulate the expression of the target gene.

INTRODUCTION

Oligonucleotide-based drugs such as antisense, aptamer, and siRNA drugs have attracted considerable attention as promising therapeutic agents in the treatment of human diseases (*1*, *2*). Especially, siRNA is considered to be a new class of drug because it can suppress the expression of the target gene even at low concentrations (*3*). Several oligonucleotide drugs are now being evaluated in clinical trials; however, at present, only two drugs, Macugen and Vitramune, have been approved by the U.S. Food and Drug Administration. This reflects the present difficulty of exploiting therapeutic oligonucleotides. Several issues must be overcome in the development of drugs based on oligonucleotides, including the instability of oligonucleotides against enzymatic degradation and the requirement that the drug delivery system should be efficient and safe.

To increase the stability of oligonucleotide drugs, various chemical modifications of oligonucleotides have been attempted. Such chemical modifications must be designed so that they do not inhibit the activity of the oligonucleotide (*4*). For example, in the case of siRNA, the modifications should not interfere with the recognition of siRNA by the RNA-induced silencing complex (RISC), which mediates the destruction of the target RNA in RNAi, and should also not interfere with subsequent reactions, including the degradation of the target mRNA.

In general, the activity of oligonucleotide drugs strongly depends on their modification sites in the sequence. For example, when the 3′-terminus of siRNA is modified with a rigid nucleic acid, called a "locked nucleic acid (LNA)", in an overhang fashion, the gene-silencing efficiency is retained at almost the original level regardless of whether the modification is made in one or both of the strands. However, the function of siRNA is substantially impaired by modification with LNA at the 5′-terminus of the antisense strand (*5*). Terminal modification of the oligonucleotide with a biologically functional molecule is very useful, because this type of modification can be anticipated not only to increase the stability of the oligonucleotide, but also to incorporate the additional biological function into the oligonucleotide drug. For example, Soutschek et al. have reported that the modification of the 3′-terminus of the sense strand in siRNA with cholesterol improves its pharmacokinetic properties *in vivo*, probably due to the enhancement of the binding of the cholesterol-ended siRNA (chol-siRNA) to serum albumin (*6*). Even 24 h after the injection of the conjugate into mice, significant levels of chol-siRNA were detected in the liver, heart, kidney, adipose tissue, and lung (*6*).

Cationic cell-penetrating peptides (CPPs), such as the HIV-derived Tat peptides and the Antennapedia peptide, are known to be taken up by eukaryotic cells, and are therefore one important candidate as ligands to deliver a variety of molecules into cells by conjugation (*7*). Because CPPs possess a positive charge, the design of the conjugates must be carefully considered. When an anionic oligonucleotide is conjugated with a cationic CPP, for example, electrostatic aggregation cannot be avoided; this lowers the cell-penetrating ability and subsequently decreases the delivery efficiency of the conjugate (*8*). Uncharged antisense oligonucleotides, such as peptide nucleic acids (PNAs) (*9*) and phosphorodiamidate morpholino oligomers (PMOs) (*10*), must be employed instead.

Another candidate for conjugation with oligonucleoptides is carbohydrates. Carbohydrates are ubiquitous in living systems and are present either as free carbohydrates or as glycoconjugates, such as glycoproteins or glycolipids. They play roles in

* yukio@nagalabo.jp.

[†] Grauate School of Pure and Applied Science,TIMS, and TARA, University of Tsukuba, and CREST, JST.

[‡] Grauate School of Pure and Applied Science, and TIMS, University of Tsukuba.

10.1021/bc100205v © 2010 American Chemical Society
Published on Web 08/12/2010

bacterial and viral adhesion, tumor cell metastasis, the regulation of hormone and enzyme activities, and so forth (*11*). For example, various membrane lectins mediate the sugar-ligand-assisted endocytosis of complexes followed by complex dissociation in the acidic environment of the endosomes (*12*). Lectins also play an important role in delivering conjugates to the right cellular compartment, such as the cytosol or the nucleus. Since most carbohydrates are electrically neutral, the undesirable interactions mentioned above can be avoided through covalent conjugation with different types of biomolecules. Thus, these biological activities and the chemical properties of carbohydrates are useful in the development of functional conjugates for drug delivery systems.

To date, several groups have reported the development of methods to modify oligonucleotides with carbohydrates (*13*). Conjugation of a reactive carbohydrate with an oligonucleotide in solution is one of the major methods of modification (*14*). For mass production, however, it is obvious that conjugation on a solid phase during the synthesis of the oligonucleotide is much more advantageous than conjugation in solution. One of the most evident ways to incorporate a carbohydrate residue into an oligonucleotide on a solid phase is to synthesize a phosphoramidite derivative. If sugar-conjugated phosphoramidite derivatives are newly prepared, the carbohydrate can be introduced not only at the 5′-terminus, but at any site in the oligonucleotide sequence (*15*, *16*).

Few studies have been carried out on the modification of the 3′-terminus of the oligonucleotide, due to the rather complicated modification reaction at this terminus. Adinolfi et al. have reported the installation of a carbohydrate at the 3′-terminus of an oligonucleotide (*16*). They used a protected carbohydrate on a solid phase and synthesized the oligonucleotide from the C6 position of the carbohydrate. To our knowledge, only Maier's group has developed the glycosylated solid support for the synthesis of sugar-conjugated oligonucleotides, in which the C1 position of the carbohydrate is linked to the 3′ terminus of the oligonucleotide. They prepared an oligonucleotide possessing a carbohydrate at the 3′-terminus by using ε-aminocapronic acid as a bifunctional linker. They prepared 1-β-aminocarbohydrate, followed by condensation with protected ε-aminocapronic acid (*17*). Recently, they developed another method (*18*) of conjugation based on the method previously reported by Reed et al. (*19*). In their method, however, the carbohydrate has to be converted to aminocarbohydrate before the condensation reaction with the bifunctional linker, resulting in a complicated reaction scheme for the preparation of the glycosylated solid support. Accordingly, we tried to establish an alternative method of modifying the oligonucleotide at the 3′-terminus with the C1 position of the carbohydrate.

In this report, we describe our novel, simple, solid-phase synthesis method of fabricating carbohydrate−oligonucleotide conjugates modified at the 3′-terminus of the oligonucleotide. We created a novel glycosylated solid support for efficient 3′-terminus modification. In our method, a protected carbohydrate is directly conjugated by the glycosylation reaction, without any transformation. The modified oligonucleotide is much more stable against enzymatic degradation. We also evaluated the effect of the modification on the activity of siRNA. The gene-silencing activities of the modified siRNAs were well retained after the conjugation.

EXPERIMENTAL PROCEDURES

Synthesis. *(1-(Benzyloxymethyl)cyclopent-3-enyl)methanol (**2**).* Compound **1** was synthesized according to a previously reported method (*20*). Compound **1** (300 mg, 2.3 mmol) was dissolved in 6 mL of *N*,*N*-dimethylformamide (DMF). To the solution, NaH (140 mg, 2.3 mmol) in DMF (2 mL) was added. After stirring at room temperature for 1 h, benzyl bromide (306 μL, 2.6 mmol) was added and stirred at room temperature for 12 h. The reaction mixture was extracted with ethyl acetate and saturated ammonium chloride. The organic solvent was washed with brine, dried over $MgSO_4$, and concentrated. Purification on a silica gel column with hexane−ethyl acetate gave compound **2** (440 mg, 86%). ^{1}H NMR ($CDCl_3$, 270 MHz) δ 7.42−7.27 (5H, m), 5.63 (2H, s), 4.56 (2H, s), 3.64 (2H, d, J = 5.8), 3.55 (2H, s), 2.34−2.17 (4H, m). ESI TOF/MS *m*/*z*: $[M+Na]^+$ 241.1769.

*(1-(Benzyloxymethyl)cyclopent-3-enyl)methyl 2,3,4,6-tetra-O-acetyl-β-D-galactopyranoside (**3**).* Compound **2** (100 mg, 0.46 mmol) and 1,2,3,4,6-penta-*O*-acetyl-D-galactose (179 mg,0.46 mmol) were co-evaporated 3 times with dry toluene and dissolved in 4 mL of CH_2Cl_2. To the solution, boron trifluoride diethyl etherate (84.9 μL, 0.69 mmol) was added. After stirring at room temperature for 12 h, the reaction was quenched with aqueous $NaHCO_3$. The reaction mixture was extracted with ethyl acetate. The organic solvent was washed with brine, dried over $MgSO_4$, and concentrated. Purification on a silica gel column with hexane−ethyl acetate gave compound **3** (240 mg, 95%). ^{1}H NMR ($CDCl_3$, 500 MHz) δ 7.38−7.27 (5H, m), 5.58 (2H, s), 5.38 (1H, dd, J = 2.4, 3.5), 5.21 (1H, dd, J = 8.0, 10.5), 5.00 (1H, dd, J = 10.5, 3.5), 4.53 (2H, d, J = 2.9), 4.44 (1H, d, J = 8.0), 4.15 (2H, m), 3.89 (1H, dd, J = 6.83, 2.4), 3.85 (1H, d, J = 9.3), 3.50 (1H, J = 9.3), 3.40 (1H, d, 8.7), 3.34 (1H, d, 8.7), 2.22 (2H, d, 11.7), 2.17 (3H, s), 2.14 (2H, d, 11.7), 2.06 (3H, s), 2.05 (3H, s), 2.00 (3H, s). ESI TOF/MS *m*/*z*: $[M+Na]^+$ 571.2296.

*(1-(Benzyloxymethyl)-3,4-dihydroxycyclopentyl)methyl 2,3,4,6-tetra-O-acetyl-β-D-galactopyranoside (**4**).* Compound **3** (240 mg, 0.44 mmol) was dissolved in acetone/H_2O/acetonitrile (1:1:1, v/v/v). To the solution, 4-methylmorpholine *N*-oxide (103 mg, 0.87 mmol) and osmium oxide-immobilized catalyst I (Wako) (3 mg) were added. After stirring at room temperature for 12 h, the reaction mixture was extracted with ethyl acetate and brine. The organic solvent was dried over $MgSO_4$ and concentrated. Purification on a silica gel column with hexane−ethyl acetate gave compound **4** in diastereomers (170 mg, 67%). ^{1}H NMR ($CDCl_3$, 500 MHz) δ 7.37−7.32 (5H, m), 5.38 (1H, d, J = 2.9), 5.21 and 5.17 (1H, dd, J = 7.4, 10.5 and J = 7.9, 10.5), 5.01 (1H, dd, J = 3.6, 10.5), 4.58 (1H, d, J = 6.05), 4.48 (1H, d, 6.05), 4.47 and 4.39 (1H, d, J = 7.4 and J = 7.9), 4.17 (1H, dd, J = 4.8, 11.2), 4.12 (1H, dd, J = 4.4, 11.2), 4.00 (1H, m), 3.94 (1H, m), 3.86 (1H, m), 3.71 and 3.24 (1H, d, J = 9.0 and 8.8), 3.44 and 3.22 (1H, d, J = 9.0 and 8.8), 3.36 and 3.22 (1H, d, J = 8.4 and 9.1), 3.30 and 3.20 (1H, d, J = 8.4, 9.1), 3.00 and 2.98 (1H, d, J = 9.1), 2.48 and 2.44 (1H, d, J = 7.7), 2.17 (3H, s), 2.04 (3H, s), 2.03 (3H, s), 1.99 (3H, s), 1.88 (1H, dd, J = 6.4, 13.8), 1.81 (1H, dd, J = 9.1, 13.8), 1.76 (1H, dd, J = 7.7, 13.5), 1.70 (1H, dd, J = 5.2, 13.5). ESI TOF/MS *m*/*z*: $[M+Na]^+$ 605.6320.

*(3-Acetoxy-1-(benzyloxymethyl)-4-hydroxycyclopentyl)methyl 2,3,4,6-tetra-O-acetyl-β-D-galactopyranoside (**5**).* Compound **4** (470 mg, 0.82 mmol) was dissolved in 8.2 mL of toluene. To the solution, acetic anhydride (114 μL, 1.2 mmol) was added. After stirring at room temperature for 12 h, the reaction mixture was extracted with aqueous 1 N HCl and ethyl acetate. The organic solvent was washed with aqueous $NaHCO_3$ and brine, dried over $MgSO_4$, and concentrated. Purification on a silica gel column with hexane−ethyl acetate gave compound **5** (292 mg, 57%) in diastereomers. ^{1}H NMR ($CDCl_3$, 500 MHz) δ 7.37−7.22 (5H, m), 5.38 (d, J = 2.8), 5.19 (1H, dd, J = 7.8, 10.5), 4.99 (1H, dd, J = 2.8, 10.5), 4.55 (1H, d, J = 4.6), 4.5 (1H, d, J = 4.6), 4.42 (1H, d, J = 7.8), 4.22 (1H, m), 4.18 (1H, m), 3.88 (1H, m), 3.76 and 3.37 (1H, d, J = 9.0 and 8.4), 3.46 and 3.33 (1H, d, J = 9.0 and 8.4), 3.35 and 3.29 (1H, d, J =

10.3 and 8.8), 3.13 and 3.23 (10.3 and 8.8), 2.83 (1H, d, J = 7.7), 2.16 (3H, s), 2.10 (3H, s), 2.05 (3H, s), 2.01 (3H, s), 1.98 (3H, s), 1.93 (1H, m), 1.81 (1H, m), 1.72 (1H, m), 1.65 (1H, m). ESI TOF/MS *m*/*z*: $[M+Na]^+$ 647.7208.

*(3-Acetoxy-4-hydroxy-1-(hydroxymethyl)cyclopentyl)methyl 2,3,4,6-tetra-O-acetyl-β-D-galactopyranoside (***6***).* A stirred mixture of compound **5** (600 mg, 0.96 mmol) and palladium on carbon (Pd/C) (488 mg) in methanol (13 mL) was hydrogenated at ambient pressure (balloon) and temperature for 24 h. The mixture was filtered through Celite. The solvent was evaporated, and the residue was chromatographed on silica gel with hexane−ethyl acetate to give compound **6** in diastereomers. This material was used in the next step without further purification.

*(3-acetoxy-1-O-(4,4′-dimethoxytrityl)methyl-4-hydroxy)cyclopentyl)methyl 2,3,4,6-tetra-O-acetyl-β-D-galactopyranoside (***7***).* Compound **6** (200 mg, 0.37 mmol) was dissolved in 3 mL of pyridine. To the solution, 4,4′-dimethoxytrityl chloride (140 mg, 0.41 mmol) was added. After stirring at room temperature for 12 h, the reaction mixture was extracted with aqueous $NaHCO_3$ and ethyl acetate. The organic solvent was washed with brine, dried over MgSO4, and concentrated. Purification on a silica gel column with hexane−ethyl acetate gave compound **7** (250 mg, 70% from **5**) in diastereomers. ^{1}H NMR ($CDCl_3$, 500 MHz) δ 7.42−7.22 (5H, m), 6.85−6.82 (4H, m), 5.39 (1H, d, J = 3.6), 5.19 (1H, dd, J = 7.9, 10.5), 4.99 (1H, dd, J = 3.6, 10.5), 4.46 (1H, d, J = 7.9), 4.19 (1H, m), 4.15 (1H, m), 4.13 (1H, m), 4.11 (1H, m), 4.00 and 3.90 (1H, d, J = 9.0 and 9.1), 3.47 and 3.37 (1H, d, J = 9.0 and 9.1), 3.13 and 3.05 (1H, d, J = 9.0 and 8.6), 3.00 and 2.84 (1H, d, J = 9.0 and 8.6), 2.16 (3H, s), 2.12 (3H, s), 2.01 (3H, s), 1.98 (3H, s), 1.93 (3H, s), 1.89 (1H, m), 1.82 (1H, m), 1.74 (1H, m), 1.65 (1H, m). ESI TOF/MS *m*/*z*: $[M+Na]^+$ 859.3449.

Synthesis of the Solid Support. Compound **7** (70 mg, 0.083 mmol) was dissolved in 2 mL of CH_2Cl_2. To the solution, 4-(dimethylamino)pyridine (26 mg, 0.21 mmol) and succinic anhydride (33 mg, 0.33 mmol) were added. After stirring at room temperature for 12 h, the reaction mixture was extracted with 10% citric acid and ethyl acetate. The organic solvent was washed with brine, dried over MgSO4, and concentrated. Purification on a silica gel column with hexane−ethyl acetate gave compound **8** (77 mg, 98%) in diastereomers.

An LCAA CPG resin (915 mg) was suspended in CH_2Cl_2 (5 mL). To the solution, compound **8** (30 mg, 32 μmol) and *N*,*N*′-dicyclohexylcarbodiimide (20 mg, 97 μmol) were added. After stirring at room temperature for 24 h, the resin was filtered and washed with CH_2Cl_2 and acetonitrile. A capping solution (pyridine−acetic anhydride, 9;1, v/v) was added to the resin and stirred at room temperature for 12 h. The resin was washed with CH_2Cl_2 and acetonitrile and dried *in vacuo*. The amount of compound **8** loaded onto the solid support was calculated to be 11 μmol/g, based on the calculation of the dimethoxytrityl cation released by the use of a solution of 60% $HClO_4$−EtOH (3:2, v/v).

Oligonucleotide Synthesis. Oligonucleotides were synthesized on a Nihon Techno Service NTS H-8 DNA/RNA synthesizer. Deprotection of the bases and phosphates was performed in concentrated NH_4OH/EtOH (3:1, v/v) at 55 °C for 5 h. In the case of RNA synthesis, the 2′-TBDMS groups were removed by triethylamine trihydrofluoride at room temperature for 24 h. The deprotected DNA and RNA were purified with a Sep-Pak C18 cartridge, followed by denaturing 20% polyacrylamide gel electrophoresis to afford DNAs and RNAs. These oligonucleotides were analyzed by matrix-assisted laser desorption/ionization time-of-flight mass spectrometry (MALDI-TOF/MS).

Serum Stability Assay. The serum stability of the oligonucleotides was evaluated by treatment with medium containing 10% serum at 37 °C. The modified oligonucleotides, which were labeled with fluorescence at the 5′-end of the strand and galactose at the 3′-end of the strand, and the control oligonucleotide, which was labeled with fluorescence at the 5′-end of the strand, were assayed for serum stability. Each oligonucleotide (400 pmol) was incubated with medium (100 μL) containing 10% of serum at 37 °C for the indicated time. After the incubation, the solution was diluted with formamide (100 μL) and heated at 100 °C for 2 min to quench the degradation. The samples were subjected to polyacrylamide gel electrophoresis and visualized by fluorescence scanning on a Typhoon 9400 (GE Healthcare).

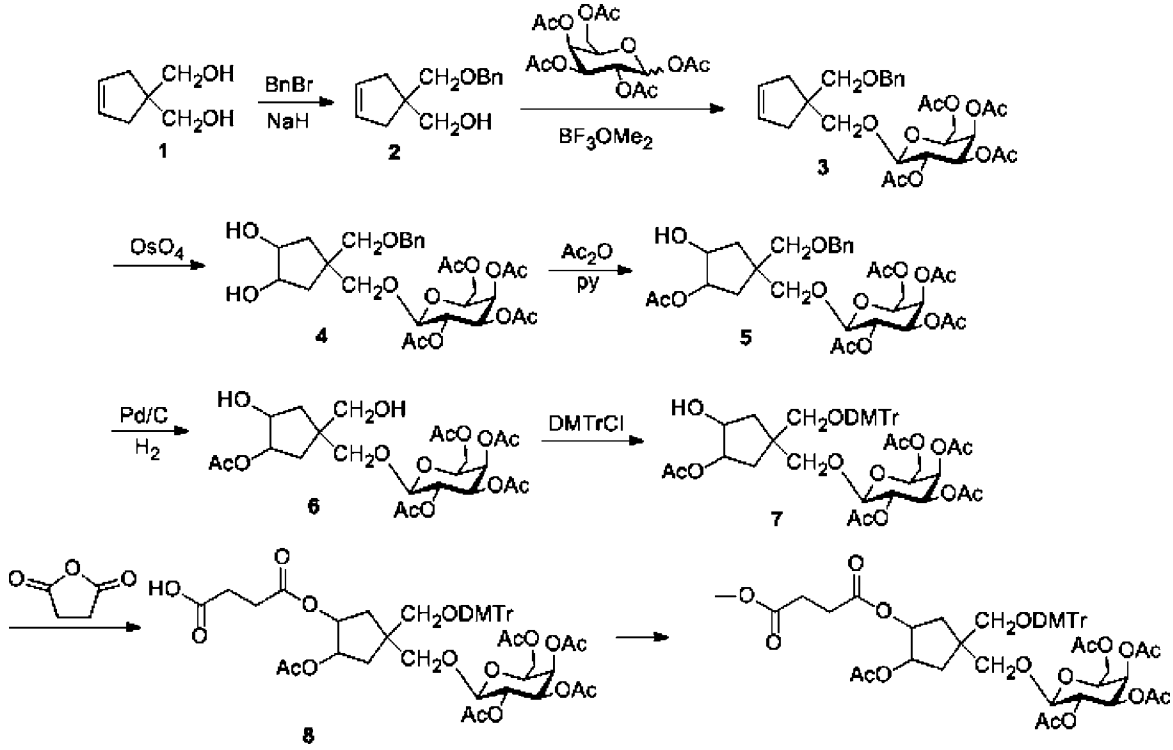
Transfection of siRNA for Surviving and Quantification of Survivin mRNA. HeLa cells were cultured in Dulbecco's modified Eagle's medium (Sigma-Aldrich, St. Louis, Mo) supplemented with 10% heat-inactivated fetal bovine serum and grown at 37 °C in a humidified atmosphere of 5% CO_2. 1×10^4 HeLa cells were cultured in 96-well culture plates in 100 μL of DMEM supplemented with 10% FBS, and incubated for 24 h. The indicated amounts of siRNA were transfected by Lipofectamine 2000 (Invitrogen) according to manufacturer's protocol. siRNA was mixed with 24 μL of OPTI-MEM. 0.5 μL of Lipofectamine 2000 was diluted in 24.5 μL of OPTI-MEM. After 5 min of incubation, they were combined and incubated for 20 min at room temperature. This solution was added to the cells, and the cells were incubated for an additional 48 h.

The amounts of survivin mRNA were determined by quantitative RT-PCR on a Thermal Cycler Dice Real Time System (TP-800) (TaKaRa). Isolation of the total RNA was performed using a CellAmp Direct RNA Prep Kit for One-Step RT-PCR (TaKaRa). Synthesis of cDNA and quantitative RT-PCR were performed using a One-Step SYBR PrimeScript RT-PCR Kit II (TaKaRa). The gene-specific primers used in the quantitative PCR were as follows: survivin forward primer, 5′-AGAACTG-GCCCTTCTTGGAGG-3′; survivin reverse primer, 5′-CTTTT-TATGTTCCTCTATGGGGTC-3′; GAPDH forward primer, GGTGGTCTCCTCTGACTTCAACA-3′; and GAPDH reverse primer, 5′-GTTGCTGTAGCCAAATTCGTTGT-3′. The relative quantification of gene expression was performed as described in the above-mentioned user's manual, using GAPDH as an internal standard.

RESULTS

In order to synthesize an oligonucleotide possessing a carbohydrate the at 3′-terminus, solid-phase synthesis was employed in this study. The synthesis procedure is summarized in Scheme 1. Compound **1** was synthesized as previously reported (*20*). Before the glycosylation reaction, we protected one of the hydroxyl groups of compound **1** with benzyl bromide, because the electron-donating benzyl group is known to increase the reactivity in the glycosylation reaction. Acetylated galactose was introduced by the glycosylation reaction via boron trifluoride methyl etherate as a Lewis acid. The yield of this glycosylation reaction was 95%. After the oxidation of compound **3** with osmium oxide, one of the hydroxyl groups on the cyclopentane was protected by acetyl chloride to afford compound **5**. The deprotection of the benzyl group of compound **5** was carried out with Pd/C, followed by protection with DMTr-Cl. Finally, compound **8** was immobilized onto the controlled pore glass (CPG). Carbohydrate−oligonucleotide conjugates were synthesized by a DNA/RNA synthesizer using the glycosylated CPG as the matrix. After the solid-phase synthesis, the obtained oligomer was deprotected and cleaved from the solid support with concentrated NH_4OH/EtOH (3:1, v/v) at 55 °C for 5 h to obtain carbohydrate-ended oligoDNA. In the case of glycosyl-ended oligoRNA, protected RNAs were incubated with triethylamine trihydrofluoride at room temperature for 24 h. The

Scheme 1[a]



[a] Reagents and conditions: (a) benzyl bromide, NaH, DMF, rt; (b) pentaacetyl-D-galactose, boron trifluoride methyl etherate, CH_2Cl_2, rt; (c) OsO_4, 4-methylmorpholine *N*-oxide, H_2O/acetonitrile/acetone (1:1:1, v/v), rt; (d) Ac_2O, pyridine, rt; (f) H_2, Pd/C, rt; (g) DMTrCl, pyridine, rt; (h) succinic anhydride, DMAP, CH_2Cl_2, rt; (i) LCAA-CPG, DCC, CH_2Cl_2, rt.

Table 1. Synthesized Galactose−Oligonucleotide Conjugates

name	sequence	calcd.	found
DNA1	Fluorescein-(dT)20-galactose	7011.4	7012.1
RNA1	GGACCACCGCAUCUCUACAdTdT-galactose	6992.3	6996
TNA2	UGUAGAGAUGCGGUGGUCCdTdT-galactose	7145.5	7151.8

deprotected DNA and RNA thus obtained were purified with a Sep-Pak C18 cartridge, followed by denaturing 20% polyacrylamide gel electrophoresis to afford sugar-ended oligomers. These oligomers were analyzed by matrix-assisted laser desorption/ionization time-of-flight mass spectrometry (MALDI-TOF/MS). Table 1 shows the sequences and the results of the MALDI-TOF-MS analysis of the synthesized oligonucleotide conjugates.

The serum stability of the oligonucleotide−carbohydrate conjugates was then investigated. The oligonucleotide which was modified with galactose at the 3′-terminus and the control oligonucleotide without galactose at the 3′-terminus were incubated with medium containing 10% of serum at 37 °C. Both oligonucleotides possessed a fluorescence probe at the 5′-terminus. After the incubation, the samples were subjected to polyacrylamide gel electrophoresis and visualized by fluorescence scanning. As shown in Figure 1, the oligonucleotide without 3′-galactose showed a degradation band, while that with 3′-galactose showed no change in molecular mass, indicating the serum stability of the oligonucleotide conjugated with galactose at the 3′-terminus. It was confirmed that ca. 80% of the incubated 3′-galactose-ended oligonucleotide remained after 180 min of incubation. It was also surprising that more than 40% of the oligonucleotide remained even after 24 h of incubation, as shown in Figure 1b.

In order to obtain further information on the modification of the oligonucleotide with the carbohydrate at the 3′-terminus, the activities of carbohydrate-modified siRNAs were investigated. For this objective, four samples were prepared, which are listed in Table 2. siRNA-targeting survivin, which is a member of the apoptosis inhibitor family (*21*), was transfected into HeLa cells with Lipofectamine 2000. After incubation for 48 h, the amount of survivin mRNA was analyzed by quantitative RT PCR. Figure 2 shows the silencing activities of the siRNAs conjugated with galactose. siRNA2, which was conjugated with galactose at the 3′-terminus of sense strand, did not show any significant change in activity at a concentration of 10 nM, as compared to the unmodified siRNA (siRNA1). Although the modification at the 3′-terminus of the antisense strand (siRNA3) reduced the silencing activity of siRNA to some extent, siRNA3 maintained its ability to reduce the amount of mRNA to 20% at 10 nM. It is worth noting that, even in the case of siRNA4, which was modified at the 3′-terminus of both strands, the amount of mRNA was reduced to 20%, i.e., almost the same level as that of siRNA3.

DISCUSSION

A safe and efficient system of delivering oligonucleotides is in great demand for the development of oligonucleotide-based therapy. However, research in this area suffers from the instability of oligonucleotides *in vivo* and the inefficient and nonselective cellular uptake of oligonucleotide drugs. To overcome these problems, we focused on glycoconjugates in our present study, because of the biologically important properties of carbohydrates. To date, various methods of delivering plasmid DNA or oligonucleotides into cells via molecules modified with a carbohydrate, such as glycosylated polyamine and glycosylated streptavidin, have been described (*22*). In these systems, the glycosylated molecules can form complexes with DNA via noncovalent interactions. In contrast to noncovalent formation, covalent oligonucleotide−carbohydrate conjugates have several advantages, e.g., the structural homogeneity of the product and the low toxicity of the components of the conjugate

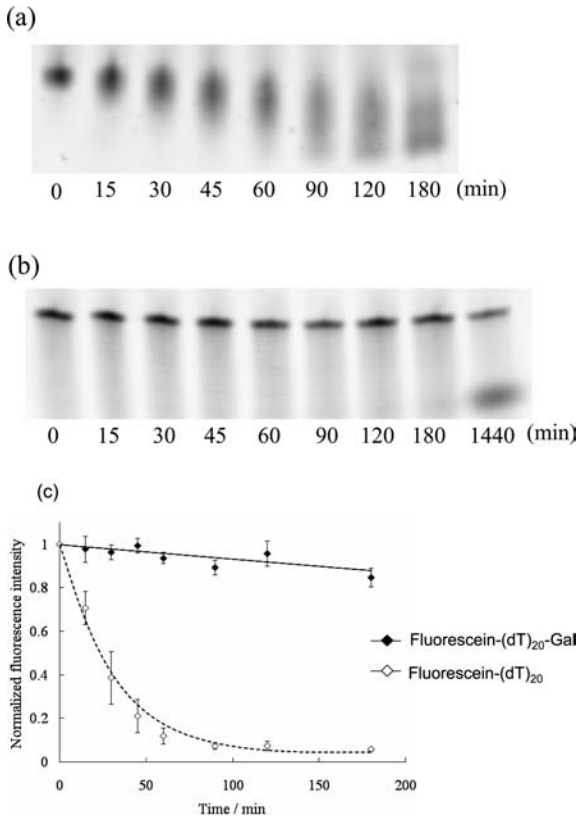


Figure 1. Comparison of the serum stabilities of the oligonucleotides. Each oligonucleotide, which was modified or not modified with galactose, was incubated in 10% serum at 37 °C for the durations indicated. All oligonucleotides were labeled with fluorescein at the 5′-end. The oligonucleotides, not conjugated with galactose (a) or conjugated with galactose (b), were subjected to polyacrylamide gel electrophoresis and visualized by fluorescence scanning. (c) Time-course of the degradation of the oligonucleotides. This result indicates that 3′-end modification with galactose improved the serum stability of the oligonucleotides.

Table 2. Sequences of the Oligonucleotides and siRNAs Used in This Study

siRNA	ON	sequence
siRNA1	ON1	5′-GGACCACCGCAUCUCUACAdTdT-3′
	ON3	3′-dTdTCCUGGUGGCGUAGAGAUGU
siRNA2	ON1	5′-GGACCACCGCAUCUCUACAdTdT-3′
	ON4	3′-**Gal**-dTdTCCUGGUGGCGUAGAGAUGU
siRNA3	ON2	5′-GGACCACCGCAUCUCUACAdTdT-**Gal**3′
	ON3	3′-dTdTCCUGGUGGCGUAGAGAUGU
siRNA4	ON2	5′-GGACCACCGCAUCUCUACAdTdT-**Gal**3′
	ON4	3′-**Gal**-dTdTCCUGGUGGCGUAGAGAUGU

compared to those of polycationic compounds such as poly(L-lysine), which is toxic at concentrations above 100 μM.

In this study, we developed an easy solid-phase synthesis method of producing carbohydrate−oligonucleotide conjugate modified at the 3′ terminus. In the synthesis scheme, the glycosylation reaction is the key reaction. Especially, when an expensive carbohydrate such as a rare sugar is used for the conjugation, the high yield of glycosylation reaction is desirable. In general, the yield of the glycosylation reaction is dependent on the protecting groups on the glycosyl donor and the glycosyl acceptor. Electron-withdrawing groups, such as the acetyl or the benzoyl group, have been found to decrease the reactivity of the donor/acceptor, and electron-donating groups, such as the benzyl group, have been found to increase the reactivity of the donor/acceptor. In our case, compound **2**, which is a glycosyl acceptor, contained a benzyl group, resulting in a good yield of the glycosylation reaction. In contrast to a previous study in

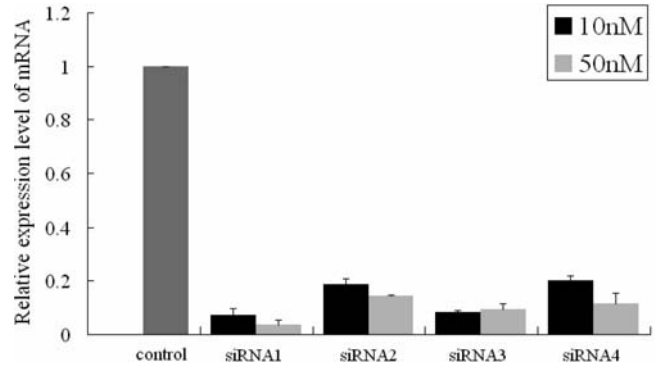


Figure 2. Survivin mRNA level in HeLa cells. HeLa cells were transfected with siRNA1, siRNA2, siRNA3, and siRNA4 at the indicated concentrations. After incubation for 48 h, the amount of survivin mRNA was measured by quantitative RT-PCR. The relative amount of survivin mRNA from the HeLa cells without any treatment was employed as a control.

which a carbohydrate was conjugated by condensation via a bifunctional linker, our approach is based on the general method of carbohydrate synthesis. Accordingly, compound **2**, which is a good glycosyl acceptor, can be easily conjugated with other glycosyl donors that have been well studied and synthesized in the field of oligosaccharide synthesis (*23*).

In an effort to increase the stability of oligonucleotides against enzymatic degradation, several chemical modifications resulting in the formation of compounds, such as phosphorothioate oligonucleotides and 2′-*O*-methyl oligonucleotide, have been reported. These modifications stabilize the oligonucleotides; however, in some cases, the modified oligonucleotides have been found to be toxic. For example, the application of phosphorothioate oligonucleotide to the central nervous system produces irritation and toxicity (*24*). In our system, oligonucleotides can be stabilized to a remarkable degree by modifying them only at the 3′-terminus. In the case of oligodeoxynucleotides, degradation usually starts to occur at the 3′-terminus of the strand. Accordingly, protection at the 3′-terminus of the strand is very important for the stabilization of the oligonucleotides (*25*). This method can be applied to oligodeoxynucleotide-based drugs, such as antisense, decoy DNA, and aptamer drugs.

We also evaluated the activities of RNA interference of carbohydrate−oligonucleotide conjugates. In some cases, the position of the modification affects the activity of the oligonucleotide drugs. For example, Kitade et al. have conjugated several lipophilic molecules at the 3′-terminus of either the sense or the antisense stand of siRNA and evaluated the activities of siRNA (*26*). In the case of modification at the 3′-terminus of the antisense strand, the activity of siRNA was slightly reduced, especially in the case of modification with cholesterol, and the silencing activity was substantially impaired (*26*). These results indicate that the properties of the compounds conjugated with oligonucleotides and the site of conjugation are important factors for efficient gene silencing. The modified siRNA in this study maintained its ability to reduce the amount of target mRNA to 20% at 10 nM, even in the case of modification at the 3′-terminus of both the sense and the antisense strands of siRNA. This indicates that two ligands can be introduced at the 3′-termini of the sense and antisense strands. Although only galactose was employed for conjugation with the end of siRNA in this work, it is anticipated from the obtained data that two kinds of ligands can be introduced, one at each end of siRNA. For example, cholesterol and a carbohydrate might be introduced at the 3′-terminus of the sense and antisense strands of siRNA, respectively, without great impairment of the siRNA activity.

In conclusion, a novel method of modifying oligonucleotides at the 3′-terminus was developed based on solid-phase synthesis.

In this study, a carbohydrate was conjugated at the 3′-terminus of an oligonucleotide on a novel glycosylated solid support. The stability of the oligonucleotide increased greatly upon carbohydrate modification. The activity of the modified siRNA, in which galactose was conjugated at the 3′-terminus, was found to possess sufficient ability to regulate the gene expression of the target gene. The novel modification method described in this report can be applied not just to carbohydrate modification, but to any modification of oligonucleotides. Studies thereon are currently being undertaken.

LITERATURE CITED

(1) Moschos, S. A., Spinks, K., Williams, A. E., and Lindsay, M. A. (2008) Targeting the lung using siRNA and antisense based oligonucleotides. *Curr. Pharm. 14*, 3620–3627.

(2) Que-Gewirth, N. S., and Sullenger, B. A. (2007) Gene therapy progress and prospects: RNA aptamers. *Gene Ther. 14*, 283–291.

(3) Castanotto, D., and Rossi, J. J. (2009) The promises and pitfalls of RNA-interference-based therapeutics. *Nature 457*, 426–433.

(4) Juliano, R., Bauman, J., Kang, H., and Ming, X. (2009) Biological barriers to therapy with antisense and siRNA oligonucleotides. *Mol. Pharm. 6*, 686–695.

(5) Elmén, J., Thonberg, H., Ljungberg, K., Frieden, M., Westergaard, M., Xu, Y., Wahren, B., Liang, Z., Ørum, H., Koch, T., and Wahlestedt, C. (2005) Locked nucleic acid (LNA) mediated improvements in siRNA stability and functionality. *Nucleic Acids Res. 33*, 439–447.

(6) Soutschek, J., Akinc, A., Bramlage, B., Charisse, K., Constien, R., Donoghue, M., Elbashir, S., Geick, A., Hadwiger, P., Harborth, J., John, M., Kesavan, V., Lavine, G., Pandey, R. K., Racie, T., Rajeev, K. G., Röhl, I., Toudjarska, I., Wang, G., Wuschko, S., Bumcrot, D., Koteliansky, V., Limmer, S., Manoharan, M., and Vornlocher, H. P. (2004) Therapeutic silencing of an endogenous gene by systemic administration of modified siRNAs. *Nature 432*, 173–178.

(7) Fonseca, S. B., Pereria, M. P., and Kelley, S. O. (2009) Recent advances in the use of cell-penetrating peptides for medical and biological applications. *Adv. Drug Delivery Rev. 61*, 953–964.

(8) Meade, B. R., and Dowdy, S. F. (2007) Exogenous siRNA delivery using peptide transduction domains/cell penetrating peptides. *Adv. Drug Delivery Rev. 59*, −40.

(9) Koppelhus, U., Shiraishi, T., Zachar, V., Pankratova, S., and Nielsen, P. E. (2008) Improved cellular activity of antisense peptide nucleic acids by conjugation to a cationic peptide-lipid (CatLip) domain. *Bioconjugate Chem. 19*, 1526–1534.

(10) Amantana, A., Moulton, H. M., Cate, M. L., Reddy, M. T., Whitehead, T., Hassinger, J. N., Youngblood, D. S., and Iversen, P. L. (2007) Pharmacokinetics, biodistribution, stability and toxicity of a cell-penetrating peptide-morpholino oligomer conjugate. *Bioconjugate Chem. 18*, 1325–1331.

(11) Taylor, M. E., and Drickamer, K. (2003) *Introduction to glycobiology*, Oxford University Press, United Kingdom.

(12) Vasta, G. R. (2009) Roles of galectins in infection. *Nat. Rev. Microbiol. 7*, 424–438.

(13) Zatsepin, T. S., and Oretskaya, T. S. (2004) Synthesis and applications of oligonucleotide-carbohydrate conjugates. *Chem. Biodivers. 1*, 1401–1417.

(14) Oishi, M., Nagasaki, Y., Itaka, K., Nishiyama, N., and Kataoka, K. (2005) Lactosylated poly(ethylene glycol)-siRNA conjugate through acid-labile beta-thiopropionate linkage to construct pH-sensitive polyion complex micelles achieving enhanced gene silencing in hepatoma cells. *J. Am. Chem. Soc. 127*, 1624–1625.

(15) Sheppard, T. L., Wong, C. H., and Joyce, G. F. (2000) Nucleoglycoconjugates: design and synthesis of a new class of DNA-carbohydrate conjugates. *Angew. Chem., Int. Ed. Engl. 39*, 3660–3663.

(16) Adinolfi, M., Napoli, L. D., Fabio, G. D., Iadonisi, A., Montesarchio, D., and Piccialli, G. (2002) Solid phase synthesis of oligonucleotides tethered to oligo-glucose phosphate tails. *Tetrahedron 58*, 6697–6704.

(17) Maier, M. A., Yannopoulos, C. G., Mohamed, N., Roland, A., Fritz, H., Mohan, V., Just, G., and Manoharan, M. (2003) Synthesis of antisense oligonucleotides conjugated to a multivalent carbohydrate cluster for cellular targeting. *Bioconjugate Chem. 14*, 18–29.

(18) Manoharan, M., Rajeev, K. G., Narayanannair, J. K., and Maier, M. U. S. Patent Appl. US 2009/0239814 A1.

(19) Reed, M. W., Adams, A. D., Nelson, J. S., and Meyer, R. B., Jr. (1991) Acridine- and cholesterol-derivatized solid supports for improved synthesis of 3′-modified oligonucleotides. *Bioconjugate Chem. 2*, 217–225.

(20) Kang, J. H., Chung, H. E., Kim, S. Y., Kim, Y., Lee, J., Lewin, N. E., Pearce, L., Blumberg, P. M., and Marquez, V. E. (2003) Conformationally constrained analogues of diacylglycerol (DAG). Effect on protein kinase C (PK-C) binding by the isosteric replacement of Sn-1 and Sn-2 esters in DAG-lactones. *Bioorg. Med. Chem. 11*, 2529–2539.

(21) Ryan, B. M., O'Donovan, N., and Duffy, M. J. (2009) Survivin: a new target for anti-cancer therapy. *Cancer Treat. Rev. 35*, 553–562.

(22) Lemarchand, C., Gref, R., and Couvreur, P. (2004) Polysaccharide-decorated nanoparticles. *Eur. J. Pharm. Biopharm. 58*, 327–341.

(23) Khan, S. H., and O'Neill, R. A. (1996) *Modern methods in carbohydrate synthesis*, Harwood Academic Publishers, United States.

(24) Peng Ho, S., Livanov, V., Zhang, W., Li, J., and Lesher, T. (1998) Mdificatin of phosphorothiate oligonucleotides yields potent analogs with mininmal toxicity for antisensene experiments in the CNS. *Brain Re. Ml. Brain Res. 62*, 1–11.

(25) Gamper, H. B., Reed, M. W., Cox, T., Virosco, J. S., Adams, A. D., Gall, A. A., Scholler, J. K., and Meyer, R. B., Jr. (1993) Facile preparation of nuclease resistant 3′ modified oligodeoxynucleotides. *Nucleic Acids Res. 21*, 145–150.

(26) Ueno, Y., Kawada, K., Naito, T., Shibata, A., Yoshikawa, K., Kim, H. S., Wataya, Y., and Kitade, Y. (2008) Synthesis and silencing properties of siRNAs possessing lipophilic groups at their 3′-termini. *Bioorg. Med. Chem. 16*, 7698–7704.

BC100205V

Antitumor Activity of Ribonuclease Multimers Created by Site-Specific Covalent Tethering

Thomas J. Rutkoski,[†,‡] John A. Kink,[§] Laura E. Strong,[§] Christine I. Schilling,[||] and Ronald T. Raines*[,†,#]

Departments of Biochemistry and Chemistry, University of Wisconsin-Madison, Madison, Wisconsin 53706, Quintessence Biosciences, Inc., 505 South Rosa Road, Madison, Wisconsin 53719, and Institut für Organische Chemie, Universität Karlsruhe (TH), Fritz-Haber Weg 6, D-76131 Karlsruhe, Germany. Received June 28, 2010; Revised Manuscript Received July 21, 2010

Site-specific cross-linking can generate homogeneous multimeric proteins of defined valency. Pancreatic-type ribonucleases are an especially attractive target, as their natural dimers can enter mammalian cells, evade the cytosolic ribonuclease inhibitor (RI), and exert their toxic ribonucleolytic activity. Here, we report on the use of eight distinct thiol-reactive cross-linking reagents to produce dimeric and trimeric conjugates of four pancreatic-type ribonucleases. Both the site of conjugation and, to a lesser extent, the propinquity of the monomers within the conjugate modulate affinity for RI, and hence cytotoxicity. Still, the cytotoxicity of the multimers is confounded *in vitro* by their increased hydrodynamic radius, which attenuates cytosolic entry. A monomeric RI-evasive variant of bovine pancreatic ribonuclease (RNase A) inhibits the growth of human prostate and lung tumors in mice. An RI-evasive trimeric conjugate inhibits tumor growth at a lower dose and with less frequent administration than does the monomer. This effect is attributable to an enhanced persistence of the trimers in circulation. On a molecular basis, the trimer is ~300-fold more efficacious and as well tolerated as erlotinib, which is in clinical use for the treatment of lung cancer. These data encourage the development of mammalian ribonucleases for the treatment of human cancers.

INTRODUCTION

Bovine seminal ribonuclease (BS-RNase[1]) and several amphibian ribonucleases, including ranpirnase (Onconase; ONC), exhibit innate antitumoral activity (*1*−*3*). ONC has demonstrated responses in patients with breast, non-small cell lung, and esophageal cancer, and unresectable malignant mesothelioma (*4*−*6*). Although these two homologues of bovine pancreatic ribonuclease (RNase A (*7*)) differ dramatically in both primary and quaternary structure (*8*, *9*), they both evade inhibition by ribonuclease inhibitor (RI (*10*)), a protein that resides in the cytosol of mammalian cells. BS-RNase is a natural dimer that evades RI by steric repulsion (*11*); whereas ONC is a small monomer whose truncated surface loops cannot interact intimately with RI (*12*). The ability to retain ribonucleolytic activity in the presence of RI is a primary determinant of the cytotoxicity of BS-RNase, ONC, and engineered ribonucleases (*13*).

Prior to the discovery of BS-RNase (*14*), lyophilization of solutions of RNase A from aqueous acetic acid was found to yield dimers and higher order oligomers of RNase A (*15*). These oligomers of RNase A—as large as nonameric (*16*)—formed by domain swapping of the N- or C-termini, or both (*17*), and displayed antitumoral activity concomitant with their degree of oligomerization: tetramers > trimers > dimers (*18*). Tandem dimers of RNase A are likewise toxic to cancer cells (*19*).

In contrast to domain-swapping, covalent cross-linking does not allow for monomer dissociation (*20*, *21*). Dimers of RNase A formed by cross-linking with amine-reactive imido esters, inhibit tumor cell proliferation *in vitro* (*22*), exhibit antitumoral activity in mice (*23*, *24*), and have enhanced persistence in the circulation of rats (*25*). Cross-linked trimers of RNase A generated with a dimethyl suberimidate linker displayed higher toxicity towads a cervical carcinoma cell line than did cross-linked dimers (*26*).

Lysine is a common residue. RNase A contains 10 lysine residues, as well as an N-terminal amino group. Accordingly, a disadvantage of using amine-reactive reagents to cross-link RNase A is the heterogeneity of the ensuing products. Moreover, the amino group in the side-chain of Lys41 has a low pK_a of ~8.8 (*27*) and is thus especially reactive. Its modification can reduce catalytic proficiency by 10^5-fold (*28*) and obviate cytotoxicity (*29*).

Previously, we used dibromobimane (**1**) (Figure 1) to prepare a BS-RNase dimer by forming thioether bonds at a particular cysteine residue (*31*). We found this dimer to be toxic to cancer cells *in vitro*, but did not determine its affinity for RI. Guided by the structure of the RI·RNase A complex (Figure 2), Youle and co-workers generated homogeneous homodimeric conjugates of both human pancreatic ribonuclease (RNase 1) and

* Corresponding author at Department of Biochemistry, University of Wisconsin-Madison, 433 Babcock Drive, Madison, WI 53706-1544. Tel: 608-262-8588. Fax: 608-262-3453. E-mail: rtraines@wisc.edu.

[†] Department of Biochemistry, University of Wisconsin-Madison.

[‡] Current address: Deciphera Pharmaceuticals, LLC, 643 Massachusetts Street, Suite 200, Lawrence, KS 66044.

[§] Quintessence Biosciences, Inc.

[||] Institut für Organische Chemie.

[#] Department of Chemistry, University of Wisconsin-Madison.

[1] Abbreviations: BSA, bovine serum albumin; BS-RNase, bovine seminal ribonuclease; DMF, dimethylformamide; DPBS, Dulbecco's phosphate-buffered saline; DTNB, 5,5′-dithiobis(2-nitrobenzoic acid); DTT, dithiothreitol; EDTA, ethylenediamine tetraacetic acid; 6-FAM, 6-carboxyfluorescein; FBS, fetal bovine serum; GSH, reduced glutathione; GSSG, oxidized glutathione; i.p., intraperitoneal; MALDI-TOF, matrix-assisted laser desorption ionization-time-of-flight; MOPS, 4-morpholinepropanesulfonic acid; NEM, *N*-ethylmaleimide; NTB, 2-nitro-5-thiobenzoic acid; ONC, ranpirnase or Onconase (a registered trademark of Tamir Biotechnology); p.o., per os or by mouth; qd, *quaque die* or once daily; RI, ribonuclease inhibitor; RNase A, bovine pancreatic ribonuclease; PAGE, poly(acrylamide) gel electrophoresis; SDS, sodium dodecyl sulfate; 6-TAMRA, 6-carboxytetramethylrhodamine; TGI, tumor growth inhibition; Tris, tris(hydroxymethyl)-aminomethane; *Z*, net molecular charge: arginine + lysine - aspartate - glutamate - pyroglutamate.

10.1021/bc100292x © 2010 American Chemical Society
Published on Web 08/12/2010

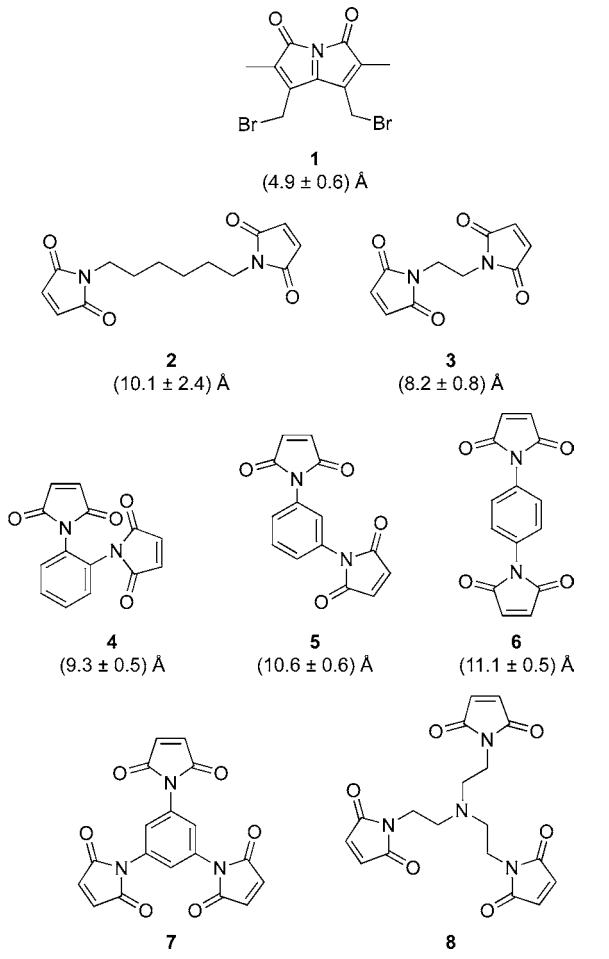


Figure 1. Structures of thiol-reactive linkers used to tether ribonucleases into dimers and trimers. The distances are between sulfur atoms in dimeric conjugates as calculated with stochastic molecular dynamics simulations (*30*).

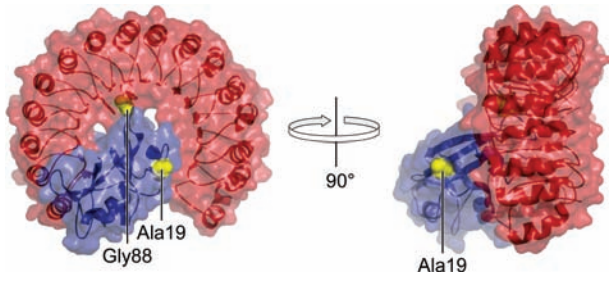


Figure 2. Structure of the porcine RI·RNase A complex showing the location of residues 19 and 88 (yellow), which were replaced with cysteine in variants of RNase A (blue). The image was created with the program PyMOL (DeLano Scientific, South San Francisco, CA) using protein data bank entry 1dfj (*32*).

human eosinophil-derived neurotoxin (RNase 2) by installing a cysteine at a residue that contacts RI and reacting its thiol with 1,6-bis(maleimido)hexane (**2**) (Figure 1) (*33*). The resulting conjugates were less sensitive to inhibition by RI and were cytotoxic. The thiol-reactive linker used by Youle and coworkers was, however, long and flexible, inserting 12 atoms and 9 rotatable bonds between the sulfur atoms of the nascent cysteine residues. We reasoned that greater RI-evasion, and thus greater cytotoxicity, could be achieved by using linkers that introduced fewer degrees of freedom between the ribonuclease moieties. In addition, we were inspired by the increased cytotoxicity of RNase A trimers, formed by noncovalent, domain-swapping (*18*), or nonspecific cross-linking (*26*).

Here, we describe the semisynthesis and characterization of 13 dimeric and trimeric ribonuclease conjugates, derived from cross-linkers **1**−**8** and RNase A, BS-RNase, RNase 1, and ONC. We show that the choice of cross-linker as well as the site and valency of cross-linking affect the toxic activity toward cancer cells. The results have important implications for the development of ribonucleases as cancer chemotherapeutic agents.

MATERIALS AND METHODS

Materials. *Protein Production and Characterization. E. coli* BL21(DE3) cells, and pET22b(+) and pET27b(+) plasmids were from Novagen (Madison, WI). K-562 (derived from a continuous human chronic myelogenous leukemia line), DU 145 (human prostate carcinoma), and A549 (human non-small cell lung carcinoma) cells were from the American Type Culture Collection (ATCC; Manassas, VA). Cell culture medium, Dulbecco's phosphate-buffered saline (DPBS), antibiotics, trypsin, and fetal bovine serum (FBS) were from Invitrogen (Carlsbad, CA). [*methyl*-^{3}H]Thymidine (6.7 Ci/mmol) was from PerkinElmer (Boston, MA). Oligonucleotides for site-directed mutagenesis and sequencing, and the ribonuclease substrates, 6-FAM-dArUdAdA-6-TAMRA and 6-FAM-dArUdGdA-6-TAMRA, were from Integrated DNA Technologies (Coralville, IA).

1,6-Bis(maleimido)hexane (**2**), 1,2-bis(maleimido)ethane (**3**), tris(*N*-maleimidoethyl)amine (**8**), and *N*-ethylmaleimide were from Thermo Fisher Scientific (Rockford, IL). 1,2-Bis(maleimido)-benzene (**4**), 1,3-bis(maleimido)benzene (**5**), and 1,4-bis(maleimido)benzene (**6**) were from Sigma-Aldrich. Dibromobimane (**1**) was from Molecular Probes (Eugene, OR).

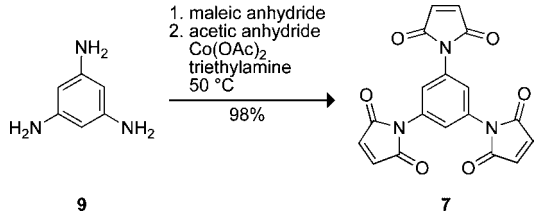
FPLC HiLoad 26/60 Superdex G75 and G200 gel-filtration columns, HiTrap Desalting, SP, and Q columns were from GE Healthcare (Uppsala, Sweden). Gel-filtration standards, SDS-PAGE molecular-weight standards, and precast gels for poly(acrylamide) gel electrophoresis were from BioRad (Hercules, CA). Flat-bottom, black polystyrene (PS), Costar assay plates (96-well) with nonbinding surface (NBS) were from Corning Life Sciences (Acton, MA). Molecular biology-grade bovine serum albumin (BSA) was obtained as a 20 mg/mL solution from Sigma-Aldrich (St. Louis, MO). Fluorometric enzymatic activity measurements were made using 4.5 mL methacrylate cuvettes from VWR (West Chester, PA). All other chemicals used were of commercial reagent grade or better, and were used without further purification.

Chemical Synthesis. DMF was drawn from a Baker CYCLETAINER solvent delivery system. All other reagents were from Sigma-Aldrich or Fisher Scientific (Hanover Park, IL) and used without further purification. Thin-layer chromatography was performed using aluminum-backed plates coated with silica gel containing F_{254} phosphor and visualized by UV illumination or staining with I_2, ceric ammonium molybdate, or phosphomolybdic acid. NMR spectra were obtained with a Bruker DMX-400 Avance spectrometer at the National Magnetic Resonance Facility at Madison (NMRFAM).

Xenograft Studies. Erlotinib hydrochloride (Tarceva) was from Genentech (South San Francisco, CA); docetaxel and cisplatin were from Sigma-Aldrich. Homozygous (*nu*/*nu*) male Balb/c (−/−) mice were from Harlan Sprague−Dawley (Indianapolis, IN).

Instrumentation. [*methyl*-^{3}H]Thymidine incorporation into K-562 and A549 genomic DNA was quantitated by scintillation counting using a Microbeta TriLux liquid scintillation and luminescence counter (PerkinElmer, Wellesley, MA). The molecular mass of ribonuclease variants and multimeric conjugates was confirmed by MALDI-TOF mass spectrometry using 3,5-dimethoxy-4-hydroxycinnamic acid as a matrix and a Voyager-DE-PRO Biospectrometry Workstation (Applied Bio-

Scheme 1



systems, Foster City, CA) in the Biophysics Instrumentation Facility at the University of Wisconsin-Madison. Cuvette-scale fluorescence measurements were made with a QuantaMaster1 photon-counting fluorometer equipped with sample stirring (Photon Technology International, South Brunswick, NJ). Fluorescence-based activity inhibition assays, competition binding assays performed in 96-well plate format, and cell-viability assays utilizing CellTiter-Blue were read with an EnVison 2100 microplate reader (Perkin-Elmer, Waltham, MA) in the Keck Center for Chemical Genomics at the University of Wisconsin-Madison. Thermal denaturation data were acquired using a Cary 400 Bio double-beam spectrophotometer equipped with a Cary temperature controller (Varian, Palo Alto, CA) in the Biophysics Instrumentation Facility.

Synthesis of 1,3,5-Tris(maleimido)benzene (7). Linker **7** was designed to be a trimeric version of phenylene linkers **4**−**6** and to be more compact than known linker 1,3,5-tris(*N*-maleimidomethyl)benzene (*34*). Linker **7** was synthesized by the reaction shown in Scheme 1. First, 1,3,5-triaminobenzene (**9**) was synthesized by hydrogenation of fluoroglucinol trioxime with Raney nickel, as described previously (*35*). Then, maleic anhydride (271 mg, 2.76 mmol) was dissolved in DMF (0.6 mL) under Ar(g). Compound **9** (98 mg, 0.78 mmol) in DMF (0.5 mL) was added dropwise, giving rise to a white precipitate. Acetic anhydride (0.7 mL, 7.41 mmol), a catalytic amount of $Co(OAc)_2$, and triethylamine (40 μL, 0.29 mmol) were added, and the resulting brown solution was stirred for 20 h at 50 °C, protected from light. The reaction mixture was poured into ice water, and the resulting dark brown precipitate was collected by filtration. The solid was washed with water and Et_2O, and dried under high vacuum ($\leq$1 mmHg). Linker **7** was isolated as a dark brown powder and used without further purification (286 mg, 98% yield). ^{1}H NMR (400 MHz, DMSO-d_6) δ (ppm): 7.43 (s, 3H), 7.21 (s, 6H). ^{13}C NMR (100 MHz, DMSO-d_6) δ (ppm): 169.50, 134.82, 132.26, 124.12.

Design of Cysteine-Containing Ribonuclease Variants. *RNase A.* We sought to test the hypothesis that greater evasion of RI would be attainable by tethering multiple ribonuclease monomers intimately via a residue within the RI-ribonuclease interface (*36*). In RNase A, residue 88 was chosen for conjugation (Figure 2), as single amino-acid substitutions there were known to be highly destabilizing to the RI·RNase A complex (*37*,*38*). Residue 88 is a glycine, and its substitution with cysteine does not alter the net charge of the protein. Multimers of G88C were made with linkers **1**−**8** (Figure 1). Residue 19 of RNase A was chosen as a representative site outside of the RI-RNase A interface (Figure 2). Small molecules had been attached there without any detectable reduction in affinity for RI (*39, 40*). A trimer of A19C was made with linker **8**. Trimeric conjugates were also prepared with D38R/R39D/N67R/G88C RNase A, which is a variant of RI-evasive D38R/R39D/N67R/G88R RNase A (*38*), using linker **8**.

BS-Rnase. BS-RNase And RNase A have high sequence identity (83%) and structural similarity (*41*). Accordingly, amino-acid substitutions in BS-RNase analogous to those that enabled RNase A to evade RI were also effective in endowing monomeric (that is, C31A/C32A) variants of BS-RNase with the ability to evade RI (*42*). Accordingly, we reasoned that tethering at residue 88 with linker **8** would enable BS-RNase to evade RI.

RNase 1. Although no single amino-acid substitution in the β4-β5 loop of RNase 1 has been shown to be as effective as the G88R substitution in RNase A in effecting RI-evasion, the importance of this loop in mediating contacts with RI is well established (*43*−*45*). Youle and co-workers demonstrated the utility of the G89C substitution to create RNase 1 dimers that evade RI (*33*). We choose that same substitution and made trimers using linker **8**.

ONC. Linker **8** was used to tether ONC via residue 72 in its β4−β5 loop, which is truncated relative to that in mammalian homologues (*9*). The ensuing (S72C ONC)$_3$−**8** trimer, like the D38R/R39D/N67R/G88C RNase A trimer, was composed of RI-evasive monomers and thus revealed the effect of molecular size, apart from RI evasion, on cytotoxicity.

Production of Ribonucleases and RI. cDNA encoding ribonuclease variants was generated by Quickchange site-directed mutagenesis (Stratagene, La Jolla, CA) using plasmid pBXR (RNase A) (*46*), pSR1 (BS-RNase) (*47*), pHP-RNase (RNase 1) (*44*), pONC (ONC) (*37*), or pET27b(+) containing cDNA encoding D38R/R39D/N67R/G88R RNase A (*38*). Plasmid pHP-RNase was modified to install the missing codon for the C-terminal threonine residue (Thr128), which establishes native RNase 1 (*48*). RNase A, RNase 1, ONC, and G88R RNase A were produced as described previously (*37, 38, 44*). Free cysteine-containing variants of RNase A (A19C, G88C, and D38R/R39D/N67R/G88C), BS-RNase (C31A/C32A/G88C), RNase 1 (G89C), and ONC (S72C), were prepared in a similar manner, but with several alterations. The protein solution containing dissolved inclusion bodies was diluted by 10-fold with a thoroughly degassed solution of acetic acid (20 mM), subjected to centrifugation to remove precipitate, and dialyzed overnight against aqueous acetic acid (20 mM) that had been purged with N_2(g) or Ar(g). Ribonucleases were allowed to refold for $\geq$3 days at 4 °C following slow dilution into 0.10 M Tris−HCl buffer at pH 8.0, containing NaCl (0.10 M), L-arginine (0.5 M), ethylenediamine tetraacetic acid (EDTA; 10 mM), reduced glutathione (GSH; 1.0 mM), and oxidized glutathione (GSSG; 0.2 mM). For free-cysteine containing variants of RNase 1, the concentrations of GSH and GSSG used were 3.0 mM and 0.6 mM, respectively. The refolding solution was purged with N_2(g) or Ar(g) prior to the addition of denatured protein to prevent the oxidation of the free cysteines. Following purification by gel-filtration chromatography, the free thiol groups of the unpaired cysteine residues were protected from inadvertent air oxidation by reaction with 5,5′-dithiobis(2-nitrobenzoic acid) (DTNB) as described previously (*28*). The resulting NTB-protected ribonucleases were applied to a HiTrap SP cation-exchange column, eluted with a linear gradient of NaCl (0.15−0.40 M) in 50 mM NaOAc buffer at pH 5.0, and stored at 4 °C until subsequent modification with thiol-reactive compounds. Protein concentration (excluding NTB-protected ribonucleases) was determined either by using a bicinchoninic acid-based kit (Thermo Fisher Scientific) (*49*) and measuring absorbance at 570 nm in a 96-well plate using an ELx800 microplate reader (Bio-Tek Instruments, Winooski, VT) or by UV spectroscopy using an extinction coefficient of $\varepsilon_{278} = 0.72$ $(mg/mL)^{-1}$ cm^{-1} for RNase A and its variants (*50*), $\varepsilon_{278} = 0.465$ $(mg/mL)^{-1}$ cm^{-1} for C31A/C32A/G88C BS-RNase (*51*), $\varepsilon_{280} = 0.53$ $(mg/mL)^{-1}$ cm^{-1} for RNase 1 and its variants (*44*), and $\varepsilon_{280} = 0.87$ $(mg/mL)^{-1}$ cm^{-1} for ONC and its variants (*37*).

Human RI was produced and purified as described previously (*38, 45, 52*) and stored in DPBS containing dithiothreitol (DTT; 10 mM). Freshly prepared RI was assumed to be 100% active

(i.e., fully reduced) for up to one month following purification and was not used beyond this time without repurification.

After their purification, ribonucleases and RI migrated as single bands during SDS-PAGE (e.g., Supporting Information Figure S1). The identity and integrity of purified ribonuclease variants was confirmed by MALDI-TOF mass spectrometry.

Semisynthesis of Ribonuclease Dimers and Trimers. The pH of the solution containing NTB-protected ribonucleases in HiTrap SP elution buffer was adjusted from 5.0 to ~8.0 by the addition of either 10× DPBS (to 10% v/v) or 1.0 M Tris−HCl buffer at pH 8.0 (to 8−10% v/v). Deprotection by the addition of DTT (5−10 equiv) resulted in the generation of the yellow 2-nitro-5-thiobenzoate anion (*53*). Ribonucleases were separated from small molecules using a HiTrap desalting column that had been equilibrated with DPBS containing EDTA (1 mM).

Semisynthetic Dimers. Stock solutions (20−100 mM) of cross-linkers **3**−**6** and **1** were prepared in DMF, and 0.6 equiv was added to a solution containing a deprotected ribonuclease (50−250 μM). This substoichiometric amount of linker was found to produce the desired dimeric (or trimeric) conjugates in high yield, as reported previously for the dimerization of C31S BS-RNase (*54*). A 0.6−5.0-fold molar excess of linker favored the production of a bis(maleimide)-derivatized ribonuclease monomer; a >10-fold molar excess of linker resulted in the undesirable nonspecific modification of the ε-amino group of lysine residues, despite the maleimido group being $>10^3$-fold more reactive with thiols than amines at pH 7 (*55*). Conjugation reaction mixtures were protected from light, and reactions were allowed to proceed at room temperature for 2 h or overnight at 4 °C. Reactions were terminated by the addition of DTT (5 equiv versus ribonuclease). The resulting crude reaction mixture was applied to a HiLoad 26/60 G75 Superdex gel-filtration column and eluted with 50 mM NaOAc buffer at pH 5.0 containing NaCl (0.10 M) and NaN_3 (0.05% w/v). Fractions were analyzed by SDS-PAGE to distinguish monomeric and multimeric species, and then combined to yield the final desired conjugate at ≥95% homogeneity. Typical yields for the production of homodimers and homotrimers were 70% and 50%, respectively. Semisynthetic variants were dialyzed exhaustively against DPBS prior to further biochemical characterization.

Semisynthetic Trimers. Trimeric ribonuclease conjugates were synthesized in the manner described above for dimeric conjugates, except that the tris(maleimide)-containing linkers in DMF were added to DPBS containing ribonucleases (50−250 μM) at 0.4 mol equiv (**8**) or 2.0 mol equiv (**7**).

Modification of Ribonucleases with *N*-Ethylmaleimide. To enable comparisons of G88C RNase A and G89C RNase 1 to the wild-type enzymes, these variants were modified with *N*-ethylmaleimide (NEM) under conditions similar to those used for the semisynthesis of dimers and trimers, except that NEM (5 equiv from a 100 mM stock solution in DMF) was added to the deprotected protein that had been desalted into DPBS. The reaction mixture was protected from light, and the reaction was allowed to proceed overnight at 4 °C and then quenched by the addition of DTT (final concentration of 1 mM). The reaction mixture was then diluted 10-fold with NaOAc buffer (50 mM) at pH 5.0, applied to a HiTrap SP cation-exchange column, and eluted with a linear gradient of NaCl (0−0.4 M). The masses of the resulting ribonuclease−NEM conjugates were confirmed by MALDI-TOF mass spectrometry.

Biochemical Characterization of Ribonuclease Dimers and Trimers. The succinimidyl thioether formed by conjugation of a thiol and maleimide is susceptible to a low rate of spontaneous hydrolysis (*56*). The products are isomeric succinamic acid thioethers that bear an additional carboxylate group, which could obfuscate our analyses. Accordingly, ribonuclease conjugates were used within 3 months of their semisynthesis.

Ribonucleolytic Activity. The enzymatic activity of ribonucleases was determined by assaying their ability to catalyze the cleavage of the hypersensitive fluorogenic substrate 6-FAM-dArUdAdA-6-TAMRA (20 nM) (λ_{ex} = 493 nm; λ_{em} = 515 nm) (*57*). Assays were carried out at ambient temperature in DPBS (2.0 mL) containing BSA (0.1 mg/mL) to prevent the nonspecific binding of ribonuclease to the cuvette. Values of k_{cat}/K_M were obtained with the equation

$$k_{cat}/K_m = \left(\frac{\Delta I/\Delta t}{I_{max} - I_0}\right)/[E] \quad (1)$$

where $\Delta I/\Delta t$ is the initial reaction velocity for cleavage of 6-FAM-dArUdAdA-6-TAMRA upon addition of ribonuclease (E) to the cuvette, and I_0 and I_{max} are, respectively, the fluorescence intensities prior to enzyme addition and following the complete cleavage of substrate by addition of excess RNase A. Activity values for ONC and its conjugates were determined likewise using the substrate 6-FAM-dArUdGdA-6-TAMRA (50 nM) (*58*).

Binding by RI. The affinity of ribonucleases for RI was determined directly by using a fluorescence-based competition assay, as described previously (*52*). For the unlabeled competing multimeric ribonuclease conjugates, the molar concentration used was that of the constituent active sites and not that of the entire conjugate.

Inhibition of Ribonucleolytic Activity by RI. 2-fold serial dilutions of RI (2 μM to 1 pM) were prepared in 10 mM MOPS buffer at pH 7.1 containing NaCl (0.138 M), BSA (0.1 mg/mL), and DTT (5 mM) using Eppendorf Protein LoBind tubes. These RI-containing serial dilutions were delivered (50 μL/well) to a 96-well plate. Ribonucleases and their conjugates were diluted in the same buffer and added to the RI-containing wells (50 μL/well; typical final working concentration: 15 pM active site). Plates were incubated for at least 30 min at ambient temperature prior to the addition of fluorogenic substrate (6-FAM-dArUdAdA-6-TAMRA; final concentration: 50 nM) to initiate the assay. The plate was shaken briefly (30 s), and the fluorescence intensity was measured at 30 s intervals for 5 min on a microplate reader using a FITC filter set (excitation at 485 nm with a 14 nm bandwidth; emission at 535 nm with a 25 nm bandwidth; dichroic mirror cutoff at 505 nm). An identical quantity of 6-FAM-dArUdAdA-6-TAMRA was cleaved with an excess amount of ribonuclease (>10 nM), and the final fluorescence was measured to ensure that <10% of the total substrate was degraded over the course of the activity assays. Additionally, an aliquot of the untreated substrate was assayed at the end of the experiment to confirm that it had not degraded appreciably during the course of the experiment, which would be indicative of ribonuclease contamination. Initial slope values were obtained from the data points by linear regression. Relative activities were determined by comparison to a control containing no RI. Relative activity plots were fitted by nonlinear regression to a sigmoidal variable-slope curve using the equation

$$y = F_B + \frac{F_T - F_B}{1 + 10^{(\log(K_i) - \log[RI])h}} \quad (2)$$

In eq 2, h is the slope of the curve, and F_T and F_B correspond to the maximum relative activities at both low and high concentrations of RI, respectively.

Gel-Filtration Analysis. Ribonucleases (1 mL of a 1 mg/mL solution in gel-filtration buffer) were applied to a HiLoad 26/60 Superdex G200 gel-filtration column and eluted with NaOAc buffer (50 mM) at pH 5.0 containing NaCl (0.10 M) and NaN_3 (0.05% w/v) at a flow rate of 4 mL/min. Gel-filtration standards were prepared and separated by chromatography using the same column.

Conformational Stability. The conformational stability of dimers and trimers of RNase A was determined by measuring their T_m value, which is the temperature at the midpoint of the transition between the folded and unfolded states. Protein was dialyzed exhaustively against DPBS and diluted to a concentration of ~25 μM in DPBS. Assays were performed by slow incremental heating (0.15 °C/min from 25−80 °C) and monitoring of the absorbance at 287 nm, which decreases upon RNase A denaturation (*59*, *60*). Data were collected and analyzed with the program THERMAL from Varian Analytical Instruments (Walnut Creek, CA), which fitted the data to a two-state process and enabled the determination of the value of T_m (*61*).

Inhibition of Tumor Cell Proliferation *in Vitro.* Pancreatic-type ribonucleases can inhibit tumor cell proliferation by evoking apoptosis (*62*). This cytotoxic activity was assessed by measuring the effect of ribonucleases on the incorporation of [*methyl*-^{3}H]thymidine into the nascent DNA of K-562 cells, as described previously (*37*). Cells were grown in Roswell Park Memorial Institute 1640 medium (Mediatech, Herndon, VA). Cell-proliferation assays were performed at least three times in triplicate. Each data point represents the mean (±SE) of three or more experimental values. Values of IC_{50}, which is the concentration of ribonucleases that decreases cell proliferation to 50%, were calculated by fitting the data using nonlinear regression to a sigmoidal dose−response curve (eq 3).

$$y = \frac{100\%}{1 + 10^{(\log(IC_{50}) - \log[\text{ribonuclease}])h}} \quad (3)$$

In eq 3, y is the DNA synthesis following a 4 h [*methyl*-^{3}H]thymidine pulse, and h is the slope of the curve.

Inhibition of Tumor Cell Proliferation *in Vivo.* Trimeric ribonucleases were tested for their ability to suppress the growth of human tumors implanted into the flanks of nude mice. DU 145 cells (prostate cancer) and A549 cells (non-small cell lung cancer) were selected for both their ability to proliferate in mice and their low rate of spontaneous regression. Moreover, each line represents a clinically relevant target that is used often in the testing of new chemotherapeutic agents.

DU 145 cells were grown in Dulbecco's modified Eagle's medium (ATCC) containing FBS (10% v/v); A549 cells were grown in F12K medium (ATCC) containing FBS (10% v/v). Cells were implanted into the right rear flank of 5−6 week old male homozygous (*nu*/*nu*) nude mice. Tumors were allowed to grow to a volume of ≥75 mm^3 before the initiation of treatment. All the test compounds were diluted in vehicle (DPBS), and one set of animals was treated with vehicle alone on the dosing schedule with greatest frequency. All treatments were administered either by intraperitoneal injection (i.p.) or orally with a gavage needle (p.o.); the volume of administered solution was based upon the body weight of the animal (10 μL/g). Treatment with all agents was ongoing throughout the entire experiment.

(G88C RNase A)$_3$−**8** was used to treat the DU 145 and A549 xenograft models. Mice in the A549 xenograft model were each implanted with 4×10^6 cells; treatment was administered at a dose of 25 mg/kg (i.p., 1 × wk). Mice in the DU 145 xenograft model each received 3×10^6 cells; again, treatment was administered at a dose of 25 mg/kg (i.p., 1 × wk). Mice in the A549 xenograft model were also treated with (G89C RNase 1)$_3$−**8** at doses of 7.5 and 75 mg/kg (i.p., 1 × wk).

Mice treated with trimeric RNase A or RNase 1 were compared with mice treated with monomeric K7A/D38R/R39D/G88R RNase A at doses of 5, 15, and 45 mg/kg (i.p., qd ×5) and 75 mg/kg (i.p., 1 × wk), and monomeric ONC at a dose of 5 mg/kg (i.p., 1 × wk), as well as the approved chemotherapeutic agents docetaxel (15 mg/kg; i.p., 1 × wk), cisplatin (6 mg/kg; i.p., 1 × wk), and erlotinib (100 mg/kg; p.o., 2 × wk).

Tumor size was measured twice weekly using calipers, and tumor volume (mm^3) was estimated by using the formula for a spheroid (eq 4)

$$\text{volume} = \frac{l \times w^2}{2} \quad (4)$$

The percent tumor growth inhibition (% TGI) was calculated with eq 5

$$\%\text{TGI} = \left(1 - \left(\frac{(\text{volume}_{\text{final}} - \text{volume}_{\text{initial}})_{\text{treated}}}{(\text{volume}_{\text{final}} - \text{volume}_{\text{initial}})_{\text{control}}}\right)\right) \times 100 \quad (5)$$

RESULTS

Conformational Stability. To maintain its biological activity, a ribonuclease must maintain its native tertiary structure (*63*). To assess whether the covalent tethering of ribonucleases into dimers or trimers compromises their conformational stability, we determined the T_m values of G88C RNase A−NEM, (G88C RNase A)$_2$−**3** and (G88C RNase A)$_3$−**8** (Table 1). All three had T_m values nearly indistinguishable from that of RNase A (Supporting Information Figure S2; Table 1). Thus, multimerization did not appear to be deleterious to the conformational stability of these conjugates. No evidence of cooperative unfolding was observed for dimeric or trimeric conjugates.

Ribonucleolytic Activity. Site-specific covalent tethering of mammalian ribonucleases had a negligible effect on their ribonucleolytic activity (Table 1). Most multimeric conjugates as well as G88C RNase A−NEM exhibited k_{cat}/K_M values (per active site) that were within error of that of RNase A. Exceptions were (G88C RNase A)$_2$−**1**, (G88C RNase A)$_2$−**2**, and trimeric conjugates of G88C RNase A prepared with either of the homotrifunctional linkers (**7** or **8**), which displayed ~2-fold increased activity per active site toward the 6-FAM-dArUdAdA-6-TAMRA substrate. The S72C ONC trimer displayed the largest change in activity upon trimerization, as its k_{cat}/K_M value per active site was nearly 7-fold higher than that of ONC.

Affinity for Ribonuclease Inhibitor. Dimeric and trimeric ribonuclease conjugates could conceivably be bound by more than one RI molecule. In addition, the initial binding of one RI molecule to the conjugate is likely to influence the likelihood of subsequent binding events or preclude subsequent RI-binding entirely. The fluorescence-based competition assay used herein did not report on the stoichiometry of RI-binding or determine microscopic values of K_d. Hence, only values of apparent K_d (K_d') are reported for the various conjugates.

The K_d = 1.8 nM obtained for G88R RNase A (Table 1) was in gratifying agreement with values obtained previously (*38*, *52*). G88C RNase A−NEM exhibited a nearly equivalent affinity for RI, having a K_d = 1.4 nM. Among the dimeric conjugates, (G88C RNase A)$_2$−**4** had the lowest affinity for RI, with K_d' = 18 nM. With the exception of (G88C RNase A)$_2$−**2** (K_d' = 2.6 nM), the remaining dimeric conjugates of G88C RNase A all had similar affinity for RI, with K_d' = 8.2−14 nM. Each trimeric conjugate of G88C RNase A displayed a significantly different affinity for RI. Those prepared with the novel tris(maleimide) linker **7** were substantially more evasive than those prepared with **8**, with K_d' = 39 and 17 nM, respectively. In general, trimeric conjugates of G88C RNase A had a lower affinity for RI than did dimers of G88C RNase A. (BS-RNase)$_3$−**8** trimeric conjugates were the most RI-evasive of the conjugates assayed, having K_d' = 84 nM. Trimers of A19C RNase A, which are tethered outside of the RI interface, possessed an affinity for RI that was sufficiently high to preclude quantitation in our assay (K_d' < 1.4 nM).

Table 1. *In Vitro* Attributes of Ribonucleases and Their Conjugates

ribonuclease	T_m[a] (°C)	k_{cat}/K_M[b] (10^6 $M^{-1}s^{-1}$)	K_d'[c] (nM)	IC_{50}[d] (μM)	IC_{50}[e] (μM)	Z
RNase A	64	6.4 ± 0.3	4.4×10^{-5}[f]	>25	>25	+4
G88R RNase A	63	8.2 ± 0.2	1.8 ± 0.3	3.3 ± 0.1	3.4	+5
G88C RNase A−NEM	64	6.8 ± 0.1	1.4 ± 0.4	28 ± 2	28	+4
(G88C RNase A)$_2$−**1**	ND[j]	12 ± 1	8.2 ± 0.2	22 ± 3	44	+8
(G88C RNase A)$_2$−**2**	ND	11 ± 1	2.6 ± 0.2	25 ± 1	50	+8
(G88C RNase A)$_2$−**3**	64	6.6 ± 0.6	9.6 ± 0.4	11 ± 1	21	+8
(G88C RNase A)$_2$−**4**	ND	7.4 ± 0.5	18 ± 2	10 ± 1	20	+8
(G88C RNase A)$_2$−**5**	ND	8.6 ± 0.1	8.6 ± 1.6	14 ± 1	27	+8
(G88C RNase A)$_2$−**6**	ND	5.5 ± 0.03	14 ± 3	27 ± 2	55	+8
(G88C RNase A)$_3$−**7**	ND	12 ± 1	39 ± 3	16 ± 1	48	+12
(G88C RNase A)$_3$−**8**	64	16 ± 0.4	17 ± 1	8.6 ± 0.5	27	+13
(A19C RNase A)$_3$−**8**	ND	7.5 ± 0.4	<1.4	>25	>25	+13
(D38R/R39D/N67R/G88C RNase A)$_3$−**8**	ND	8.4 ± 0.3	ND	1.0 ± 0.1	3.3	+16
(C31A/C32A/G88C BS-RNase)$_3$−**8**	ND	5.8 ± 0.3	84 ± 12	0.78 ± 0.05	2.1	+28
RNase 1	58	29 ± 1	2.9×10^{-7}[g]	>25	>25	+6
(G89C RNase 1)$_3$−**8**	ND	16 ± 3	<1.4	1.5 ± 0.1	4.6	+19
ONC	90[h]	0.0018 ± 0.00005	>150[i]	0.22 ± 0.01	0.22	+5
(S72C ONC)$_3$−**8**	ND	0.012 ± 0.0005	ND	0.79 ± 0.05	2.8	+16

[a] Values T_m (±2 °C) in 1 × DPBS and determined by UV spectroscopy. [b] Per active-site values of k_{cat}/K_M (±SE) for catalysis of 6-FAM-dArU(dA)$_2$-6-TAMRA cleavage in 1 × DPBS containing BSA (0.1 mg/mL) at (20 ± 2) °C. 6-FAM-dArUdGdA-6-TAMRA was the substrate for ONC and (S72C ONC)$_3$−**8**. [c] Per active-site values of K_d' (±SE) for the complex with RI at (20 ± 2) °C. [d] Per molecule values of IC_{50} (±SE) for incorporation of [*methyl*-^{3}H]thymidine into the DNA of K-562 cells exposed to a ribonuclease and calculated with eq 3. [e] Per active-site values of IC_{50} calculated by multiplying the IC_{50} value by the number of monomers in the conjugate. [f] From ref *64*. [g] From ref *45*. [h] From ref *37* and determined by circular dichroism spectroscopy. [i] Value of K_i from ref *12*. [j] ND, not determined.

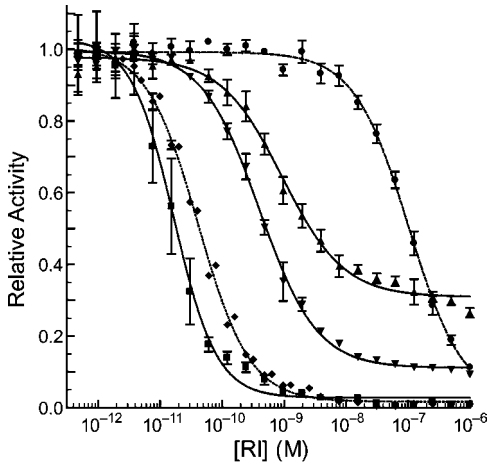


Figure 3. Relative enzymatic activity of ribonucleases after preincubation with increasing concentrations of RI. Data points are the mean (±SE) from three separate experiments, and were fitted with eq 2. G88R RNase A (◆), K31A/D38R/R39D/N67R/G88R RNase A (•), (G88C RNase A)$_2$−**3** (▼), (G88C RNase A)$_3$−**8** (▲), and (A19C RNase A)$_3$−**8** (■).

A novel assay was developed to determine the stoichiometry of RI-binding. The ability of the ribonuclease conjugates to cleave a fluorogenic substrate following preincubation with varying concentrations of RI was assayed. Apparent K_i' values were obtained by applying eq 2 to the data in Figure 3.

The G88R and K31A/D38R/R39D/N67R/G88R variants of RNase A had $K_i' = 41.4$ pM and 103 nM, respectively. (G88C RNase A)$_3$−**8** exhibited $K_i' = 0.94$ nM, which is 23-fold higher than that of G88R RNase A. Near physiological concentrations of RI, the fractional activity of the trimeric conjugate reached a plateau at ∼0.31. This value is consistent with one of the three active sites in the trimer remaining inaccessible to micromolar concentrations of RI. (G88C RNase A)$_3$−**7** behaved in a nearly identical manner to (G88C RNase A)$_3$−**8** (data not shown). Conversely, (A19C RNase A)$_3$−**8**, which differs from (G88C RNase A)$_3$−**8** only in that it is restrictively tethered through a residue outside of the interface with RI, is inhibited tightly and completely by RI with $K_i' = 17$ pM. This value is close to the concentration of enzymic active sites present in the assay solution (15 pM), and thus merely represents an upper limit for the K_i' value (*65*).

(G88C RNase A)$_2$−**3** was more readily inhibited by RI than was (G88C RNase A)$_3$−**8**, with $K_i' = 0.40$ nM. Interestingly, the fractional activity of this dimer also reached a plateau at micromolar concentrations of RI, though the significance of its relative activity (∼0.11) is obvious. Nonetheless, we conclude that trimers in the cytosol would retain a larger amount of unfettered ribonuclease activity than would dimers.

Cytotoxicity *in Vitro.* The toxicity of each ribonuclease was measured toward the K-562 human leukemia cell line. IC_{50} values are given in Table 1 on both a conjugate and an active-site basis, and were derived by applying eq 3 to the data in Figure 4. The results and fitted curves in Figure 4 are based upon the concentration of the entire conjugate, not just the active sites, and those will be the IC_{50} values discussed herein unless indicated otherwise. ONC and G88R RNase A displayed IC_{50} values similar to those reported previously (*37*, *38*). (A19C RNase)$_3$−**8** exhibited no cytotoxic activity, even at concentrations of 20 μM (Figure 4A). This lack of cytotoxicity is consistent with its preserved sensitivity to RI and underscores the importance of constraining the ribonucleases by tethering within the RI−RNase A interface. G88C RNase A−NEM (IC_{50} = 28 μM; Figure 4A) was nearly 10-fold less cytotoxic than G88R RNase A. This substantial decrease in cytotoxic activity was surprising because of their nearly identical affinities for RI. (G88C RNase A)$_2$−**3** (IC_{50} = 11 μM) was 3-fold less toxic to K-562 cells than was G88R RNase A (Figure 4A) despite its substantially greater resistance to inhibition by RI *in vitro* (Figure 3).

The differential effects on cytotoxicity of linking two molecules of G88C RNase A ortho, meta, or para to each other about a phenyl ring is shown in Figure 4B. Surprisingly, the relatively subtle chemical differences led to detectable and reproducible differences in cytotoxicity. The IC_{50} values exhibited by (G88C RNase A)$_2$−**4**, (G88C RNase A)$_2$−**5**, and (G88C RNase A)$_2$−**6** were 10, 14, and 27 μM, respectively, consistent with our hypothesis that more restrictive tethering endows greater cytotoxicity.

Three homologous mammalian ribonucleases, RNase A, RNase 1, and BS-RNase, were tethered with linker **8** through analogous residues within their β4−β5 surface loop. The resulting trimers were tested for their ability to inhibit the

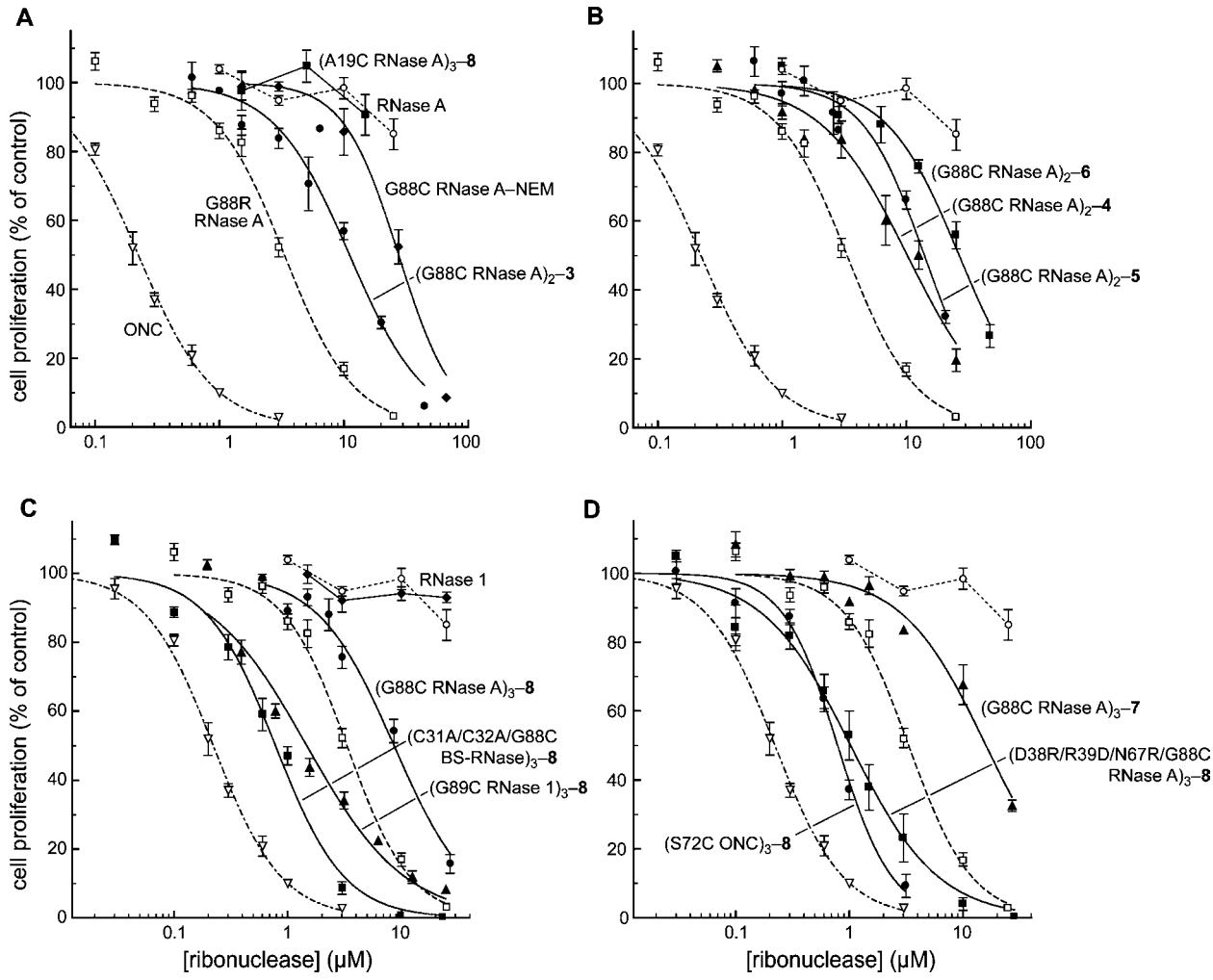


Figure 4. Effect of ribonucleases on the proliferation of K-562 cells. The incorporation of [*methyl*-^{3}H]thymidine into cellular DNA was used to monitor the proliferation of K-562 cells in the presence of ribonucleases. Data points are the mean (±SE) from at least three separate experiments carried out in triplicate, and were fitted with eq 3. Values of IC_{50} are listed in Table 1. For dimeric and trimeric conjugates, the concentration is of the molecule, not the constitutive active sites. Each panel depicts a different theme; data for RNase A (○), G88R RNase A (□), and ONC (▽) are repeated for comparison. (A) Tethering within or outside of the RI−ribonuclease interface. (B) Analogous dimeric conjugates made with bis(maleimido)benzene linkers **4**−**6**. (C) Analogous trimeric conjugates of RNase A ($Z = +13$), RNase 1 ($Z = +19$), and BS-RNase ($Z = +28$). (D) Trimeric conjugates of evasive monomers or made with linker **7**.

proliferation of K-562 cells (Figure 4C). As reported previously (*44*), RNase 1 had no effect on the proliferation of K-562 cells. Per conjugate molecule, the (G88C RNase A)$_3$−**8** conjugate ($IC_{50} = 8.6$ μM) was more cytotoxic than any of the dimeric conjugates of RNase A linked through the same residue. (G89C RNase 1)$_3$−**8** ($IC_{50} = 1.5$ μM) and (C31A/C32A/G88C BS-RNase)$_3$−**8** ($IC_{50} = 0.78$ μM) were even more cytotoxic than the analogous RNase A trimer.

ONC and D38R/R39D/N67R/G88R RNase A are monomeric ribonucleases that are highly cytotoxic ($IC_{50} = 0.27$ and 0.19 μM, respectively) because they are insensitive to RI (*38*). The cytotoxic activities of trimeric conjugates of these two ribonucleases are shown in Figure 4D. Both (S72C ONC)$_3$−**8** ($IC_{50} = 0.79$ μM) and (D38R/R39D/N67R/G88C RNase A)$_3$−**8** ($IC_{50} = 1.0$ μM) are less cytotoxic than their monomers. On a per active-site basis, the cytotoxic activity of ONC and D38R/R39D/N67R/G88R RNase A is reduced by 10- and 17-fold, respectively, upon trimer formation.

Xenograft Mouse Studies. DU 145 prostate carcinoma cells are known to be sensitive to RI-evasive variants of RNase A (*38*). To establish an effective dose and administration schedule, mice bearing DU 145 prostate carcinoma tumors were treated with K7A/D38R/R39D/G88R RNase A and ONC. A dose of 15 mg/kg (i.p., qd × 5) was identified as being optimal for eliciting the maximum inhibition of tumor growth (TGI = 83%; Figure 5A) while displaying minimal off-target effects as monitored by change in body weight (Figure 5A inset). Indeed, this dose of K7A/D38R/R39D/G88R RNase A inhibits the growth of DU 145 tumors in mice as well as the effective dose of ONC (5 mg/kg; i.p., 1 × wk) (Figure 5B). Although the mice treated with the RNase A variant received 15-fold more ribonuclease (by mass) on a weekly basis than did those treated with ONC, the mammalian ribonuclease seems to be better tolerated, as indicated by the large decrease in body weight of the animals in the ONC treatment group during the course of the experiment (Figure 5B inset).

The importance of frequent administration of K7A/D38R/R39D/G88R RNase A to achieve maximal tumor growth inhibition is shown in Figure 5C. These mice received 75 mg/kg (1 × wk) instead of the previous 15 mg/kg (qd ×5). Although equivalent on a mass/week basis, once-weekly administration of K7A/D38R/R39D/G88R RNase A was dramatically less effective at inhibiting tumor growth (TGI = 15% versus 83%).

Next, mice were treated with a trimeric ribonuclease: (G88C RNase A)$_3$−**8**. A dose of 25 mg/kg (1 × wk) of (G88C RNase A)$_3$−**8**, which is a third of the ribonuclease by mass that was used in the experiments depicted in Figure 5C, was administered to mice bearing DU 145 tumors. This dose led to a dramatic

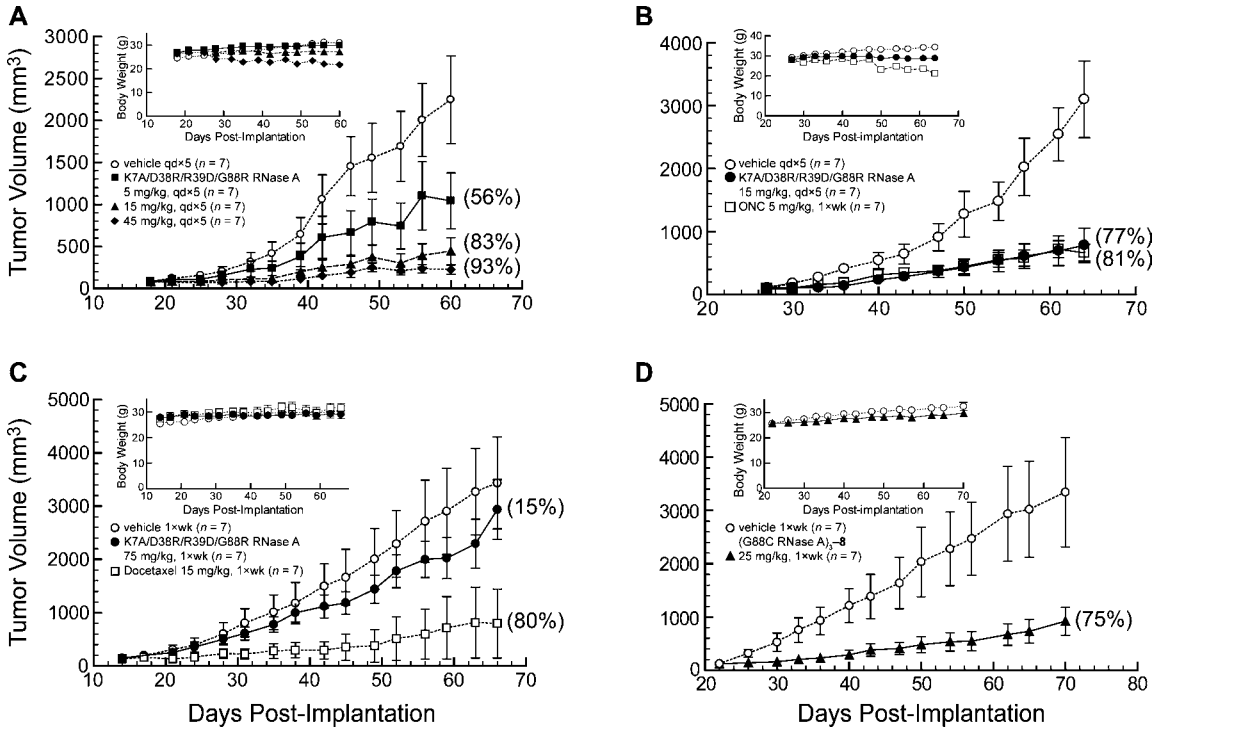


Figure 5. Effect of K7A/D38R/R39D/G88R RNase A and (G88C RNase A)$_3$-**8** on the tumor volume and body weight (insets) of Balb c(−/−) mice in xenograft models bearing human DU 145 prostate tumors. Data points are the mean (±SE) for *n* mice; % TGI values in parentheses were calculated with eq 5. Vehicle control (○; $n = 7$). (A) K7A/D38R/R39D/G88R RNase A (■, 5 mg/kg; ▲, 15 mg/kg; ◆, 45 mg/kg; i.p., qd ×5; $n = 7$). (B) K7A/D38R/R39D/G88R RNase A (•, 15 mg/kg; i.p., qd ×5; $n = 7$), ONC (□, 5 mg/kg; i.p., 1 × wk; $n = 7$). (C) K7A/D38R/R39D/G88R RNase A (•, 75 mg/kg; i.p., 1 × wk; $n = 7$) and docetaxel (□, 15 mg/kg; i.p., 1 × wk, $n = 7$, though 4 mice died during the course of the experiment such that $n = 6$ on day 28, $n = 5$ on day 35, $n = 4$ on day 49, and $n = 3$ on day 63). (D) (G88C RNase A)$_3$−**8** (▲, 25 mg/kg; i.p., 1 × wk, $n = 7$).

inhibition of tumor growth (TGI = 75%; Figure 5D), despite the infrequent administration.

Xenograft studies were continued with A549 lung adenocarcinoma cells, which are less sensitive than DU 145 cells to RI-evasive variants of RNase A (*38*). A dose of 25 mg/kg (1 × wk) of (G88C RNase A)$_3$−**8** inhibited the growth of these tumors substantially (TGI = 68%; Figure 6A). Photographs of mice from the vehicle and treatment groups upon completion of the experiment show the large reduction in the size of the tumors in treated animals (Figure 6B).

The human conjugate, (G89C RNase 1)$_3$−**8**, was also administered to mice bearing A549 tumors. Although a dose of 7.5 mg/kg (1 × wk) inhibited tumor growth only slightly (TGI = 30%) (Figure 6C), a 10-fold higher dose of 75 mg/kg (1 × wk) inhibited the growth of these tumors at a high level (TGI = 79%) that was indistinguishable from that of a 100 mg/kg (2 × wk) dose of erlotinib hydrochloride. This tyrosine kinase inhibitor was approved in 2004 for the treatment of non-small cell lung cancer (*66*). It is noteworthy that a single molecule of the human ribonuclease conjugate achieved the same efficacy as ∼300 molecules of erlotinib.

Hydrodynamic Radius. The hydrodynamic radius of RNase A conjugates was assessed by gel-filtration chromatography. As expected, the radii decreased in the order trimer > dimers > monomers (Figure 7), suggesting that trimers persist longest in plasma circulation.

DISCUSSION

Thiol-reactive cross-linking reagents have found broad utility in a wide range of applications (*55*, *67*, *68*). For example, these reagents have been used as "molecular rulers" to probe the structure of large macromolecular complexes (*69*−*74*). Inspired by dimeric linkers **4**−**6**, we synthesized the novel trimeric linker **7** (Scheme 1), expecting its phenyl scaffold to afford an even more constrained linkage than tren linker **8**.

Preservation of Ribonucleolytic Activity. The enzymatic activity of RNase A is known to diminish upon nonspecific cross-linking with diimido esters (*21*). In contrast, site-specific tethering did not have a deleterious effect on the catalytic activity of any of the ribonucleases herein (Table 1). Indeed, (S72C ONC)$_3$−**8** exhibited increased activity. The low catalytic activity of ONC is thought to originate in its low affinity for substrate (*58*). The increased charge density could accelerate the rate of substrate association.

Linkage Position. Site-specific tethering can allow or disallow a biomolecular interaction. We prepared two trimeric conjugates of RNase A, (A19C RNase A)$_3$−**8** and (G88C RNase A)$_3$−**8**, that differ only at their site of linkage (Figure 2). Residue 19 lies within the α1−α2 loop of RNase A. Tethering three ribonuclease moieties there can readily accommodate the binding of three molecules of RI with high affinity ($K_i' \leq 17$ pM; Figure 3). This preservation of sensitivity to RI is corroborated by the results of the competition binding assay ($K_d' \leq 1.4$ nM; Table 1). In marked contrast, one active site of (G88C RNase A)$_3$−**8** remains free to degrade cellular RNA in the presence of micromolar RI (Figure 3). This evasion of RI endows (G88C RNase A)$_3$−**8** with toxicity for K-562 cells (Figure 4). This result is consistent with the report of Yamada and co-workers, who spliced human basic fibroblast growth factor (bFGF) into human pancreatic ribonuclease (RNase 1) as a separate domain through insertional fusion (*75*). RI-evasion, and thus efficacy as an immunotoxin, was greater when the bFGF graft was between residues 89 and 90, as opposed to residues 19 and 20, which are structurally analogous to the linkage positions explored in this work (H. Tada, personal communication).

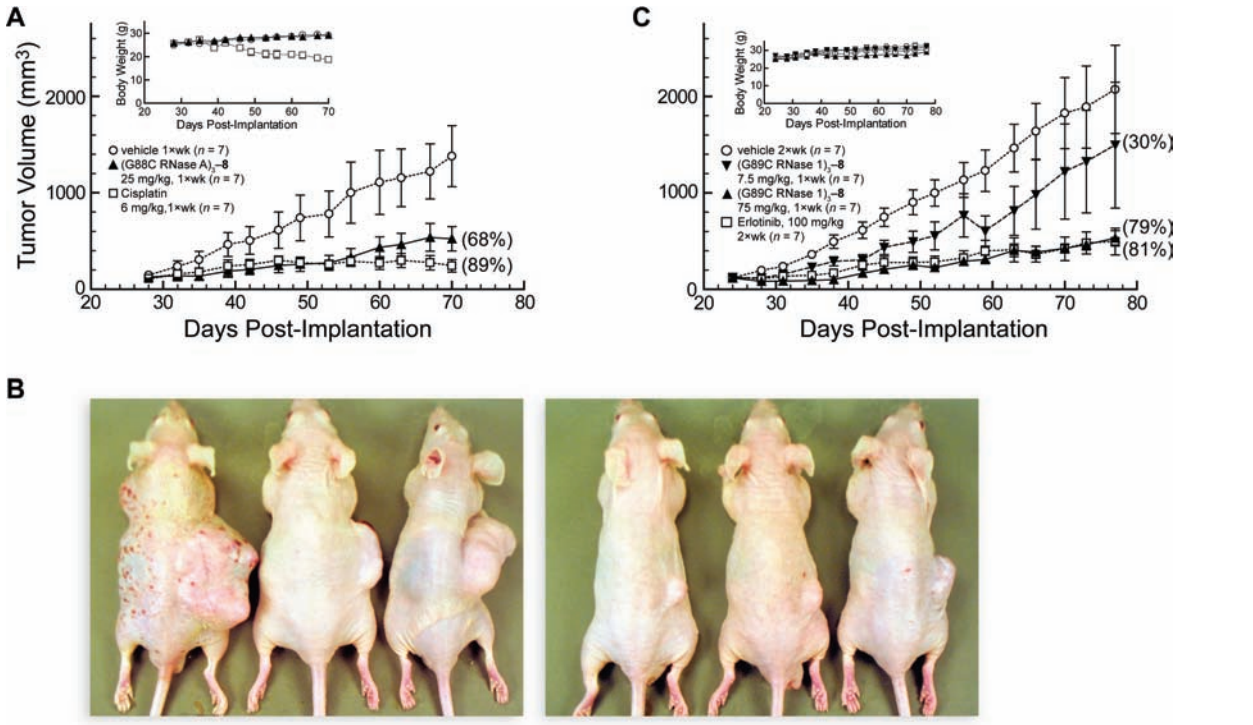


Figure 6. Effect of trimeric ribonuclease conjugates on tumor volume and body weight (insets) of Balb c(−/−) mice in xenograft models bearing human A549 lung tumors. Data points are the mean (±SE) for *n* mice; % TGI values in parentheses were calculated with eq 5. Vehicle control (○; $n = 7$). (A) (G88C RNase A)$_3$−**8** (▲, 25 mg/kg; i.p., 1 × wk, $n = 7$) and cisplatin (□, 6 mg/kg; i.p., 1 × wk, $n = 7$). (B) Photographs of representative mice treated with vehicle (left) or (G88C RNase A)$_3$−**8** (right) on day 70 of the experiment in panel A. (C) (G89C RNase 1)$_3$−**8** (▼, 7.5 mg/kg; ▲, 75 mg/kg; i.p., 1 × wk, $n = 7$) and erlotinib (□, 100 mg/kg; p.o., 2 × wk, $n = 7$).

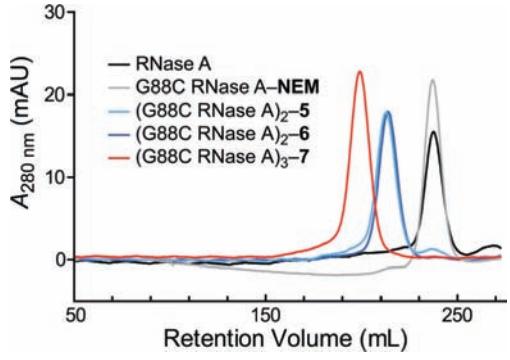


Figure 7. Elution profile of monomeric, dimeric, and trimeric ribonucleases from gel-filtration chromatography.

Linker Conformation. A motivation of our work was to characterize ribonuclease multimers that were tethered more restrictively than those prepared with linker **2**. All of the bifunctional reagents tested yielded dimeric ribonuclease conjugates that were indeed more RI-evasive than (G88C RNase A)$_2$−**2** (Table 1). Moreover, all but one of the reagents (**6**) yielded ribonuclease dimers that were more effective at inhibiting the proliferation of K-562 cells than was (G88C RNase A)$_2$−**2**. The novel linker **7** likewise yielded more RI-evasive trimers (∼2-fold) than those prepared with its more flexible congener, **8**. Surprisingly, the greater ability of (G88C RNase A)$_3$−**7** to evade RI did not translate into greater cytotoxicity. The amino group of linker **8** is likely to be protonated at physiological pH values, giving this trimeric conjugate a net charge of +13 compared to +12 for (G88C RNase A)$_3$−**7**. The cationicity of ribonucleases has been correlated with their efficiency of internalization and therefore cytotoxicity (*76*−*79*), and could contribute to the greater than expected cytotoxicity of (G88C RNase A)$_3$−**8** relative to (G88C RNase A)$_3$−**7**.

Net Molecular Charge and Cytotoxicity. RNase A ($Z = +4$), RNase 1 ($Z = +6$), and BS-RNase ($Z = +9$) are highly cationic proteins with >80% amino acid sequence identity and comparable ribonucleolytic activity, yet (G88C RNase A)$_3$−**8**, (G89C RNase 1)$_3$−**8**, and (C31A/C32A/G88C BS-RNase)$_3$−**8** possess significantly different net charges: $Z = +13$, +19, and +28, respectively. A correlation of net charge with cytotoxicity (*76*−*79*) is apparent in the trimeric ribonuclease conjugates, which have IC_{50} values of 8.6, 1.5, and 0.78 μM, respectively (Table 1; Figure 4C).

Molecular Size and Cytotoxicity. The hydrodynamic radius of the ribonuclease conjugates changes in a predictable manner (Figure 7). Previously, we showed that the quaternary structure of BS-RNase was a liability to its cytotoxic activity, as monomeric variants of BS-RNase that evade RI are more cytotoxic than are dimers of the same variants (*42*). Likewise, trimerization of D38R/R39D/N67R/G88R RNase A and ONC, which evade RI as monomers, reduces their cytotoxicity by 10- and 17-fold, respectively (Table 1). What is the basis for this decrease? The cellular uptake of fluorescent latex beads of discrete size was found to correlate inversely with size (*80*). Although these beads were 50−500 nm in diameter and thus larger than our conjugates, our data suggest that the correlation between cellular uptake and molecular size extends to smaller entities as well.

Molecular Size and Circulation. The glomerular capillary wall acts as a molecular sieve, removing small proteins (e.g., proteohormones) from plasma circulation but retaining large ones (e.g., albumin and IgG antibodies). In both mice and rats, the half-life of intravenously administered monomeric ribonucleases is 2−5 min (*23*, *25*, *81*), which is similar to the glomerular filtration rate (*81*, *82*). For a particular molecule, this rate is determined largely by molecular size; only when molecular size approaches that of the filtration pore do other attributes, such as molecular charge, have an appreciable

influence (*83*−*85*). Given the small size of monomeric ribonucleases (Figure 7), their rapid clearance is not surprising (*86*, *87*). Dimeric ribonucleases exhibit a longer half-life in circulating plasma (*23*, *25*, *81*). Trimeric ribonuclease conjugates such as (G88C RNase A)$_3$−**8** are likely to persist even longer, as they are similar in size to albumin. Such greater plasma retention could contribute to the superior ability of trimeric ribonuclease conjugates to reduce tumor growth *in vivo* (Figures 5 and 6).

CONCLUSIONS

Using eight different thiol-reactive homobifunctional linkers (six dimeric and two trimeric), we have demonstrated that the cytotoxic activity of ribonuclease multimers correlates with how well they evade RI. Importantly, the catalytic activity and conformational stability are preserved in tethered ribonucleases. Finally, trimeric conjugates of G88C RNase A and G89C RNase 1 prepared with linker **8** were as effective as highly evasive monomeric variants of RNase A at inhibiting tumor growth in tumor-bearing mouse models, but could be administered less frequently and at a lower dose. Thus, this work demonstrates the potential of nonreducible, covalent conjugates of mammalian ribonucleases as human cancer therapeutics.

ACKNOWLEDGMENT

This work was supported by grant R01 CA073808 (NIH). We are grateful to L. D. Lavis for advice on the synthesis of linker **7**, G. A. Ellis for the production and purification of RI, and J. Kalia, B. D. Smith, R. J. Johnson, G. A. Ellis, L. D. Lavis, and R. F. Turcotte for contributive discussions. T.J.R. was supported by Biotechnology Training Grant 08349 (NIH) and a William R. & Dorothy E. Sullivan Wisconsin Distinguished Graduate Fellowship. The Biophysics Instrumentation Facility was established with grants BIR-9512577 (NSF) and S10 RR13790 (NIH). The Keck Center for Chemical Genomics was established with a grant from the W.M. Keck Foundation. NMRFAM was supported by grant P41 RR02301 (NIH).

Supporting Information Available: Figures S1 and S2. This material is available free of charge via the Internet at http://pubs.acs.org.

LITERATURE CITED

(1) Benito, A., Ribó, M., and Vilanova, M. (2005) On the track of antitumour ribonucleases. *Mol. Biosyst. 1*, 294–302.

(2) Arnold, U., and Ulbrich-Hofmann, R. (2006) Natural and engineered ribonucleases as potential cancer therapeutics. *Biotechnol. Lett. 28*, 1615–1622.

(3) Arnold, U. (2008) Aspects of the cytotoxic action of ribonucleases. *Curr. Pharm. Biotechnol. 9*, 1615–1622.

(4) Costanzi, J., Sidransky, D., Navon, A., and Goldsweig, H. (2005) Ribonucleases as a novel pro-apoptotic anticancer strategy: review of the preclinical and clinical data for ranpirnase. *Cancer Invest. 23*, 643–650.

(5) Pavlakis, N., and Vogelzang, N. J. (2006) Ranpirnase-an antitumour ribonuclease: Its potential role in malignant mesothelioma. *Expert Opin. Biol. Ther. 6*, 391–399.

(6) Lee, J. E., and Raines, R. T. (2008) Ribonucleases as novel chemotherapeutics: The ranpirnase example. *BioDrugs 22*, 53–58.

(7) Raines, R. T. (1998) Ribonuclease A. *Chem. Rev. 98*, 1045–1065.

(8) Capasso, S., Giordano, F., Mattia, C. A., Mazzarella, L., and Zagari, A. (1983) Refinement of the structure of bovine seminal ribonuclease. *Biopolymers 22*, 327–332.

(9) Mosimann, S. C., Ardelt, W., and James, M. N. G. (1994) Refined 1.7 Å X-ray crystallographic structure of P-30 protein, an amphibian ribonuclease with anti-tumor activity. *J. Mol. Biol. 236*, 1141–1153.

(10) Dickson, K. A., Haigis, M. C., and Raines, R. T. (2005) Ribonuclease inhibitor: Structure and function. *Prog. Nucleic Acid Res. Mol. Biol. 80*, 349–374.

(11) Murthy, B. S., and Sirdeshmukh, R. (1992) Sensitivity of monomeric and dimeric forms of bovine seminal ribonuclease to human placental ribonuclease inhibitor. *Biochem. J. 281*, 343–348.

(12) Turcotte, R. F., and Raines, R. T. (2008) Interaction of onconase with the human ribonuclease inhibitor protein. *Biochem. Biophys. Res. Commun. 377*, 512–514.

(13) Rutkoski, T. J., and Raines, R. T. (2008) Evasion of ribonuclease inhibitor as a determinant of ribonuclease cytotoxicity. *Curr. Pharm. Biotechnol. 9*, 185–199.

(14) D'Alessio, G., Parente, A., Guida, C., and Leone, E. (1972) Dimeric structure of seminal ribonuclease. *FEBS Lett. 27*, 285–288.

(15) Crestfield, A. M., Stein, W. H., and Moore, S. (1962) On the aggregation of bovine pancreatic ribonuclease. *Arch. Biochem. Biophys. Suppl. 1*, 217–222.

(16) Gotte, G., Laurents, D. V., and Libonati, M. (2006) Three-dimensional domain-swapped oligomers of ribonuclease A: Identification of a fifth tetramer, pentamers and hexamers, and detection of trace heptameric, octameric and nonameric species. *Biochim. Biophys. Acta 1764*, 44–54.

(17) Libonati, M., and Gotte, G. (2004) Oligomerization of bovine ribonuclease A: Structural and functional features of its multimers. *Biochem. J. 380*, 311–327.

(18) Libonati, M. (2004) Biological actions of the oligomers of ribonuclease A. *Cell. Mol. Life Sci. 61*, 2431–2436.

(19) Leich, F., Koditz, J., Ulbrich-Hofman, R., and Arnold, U. (2006) Tandemization endows bovine pancreatic ribonuclease with cytotoxic activity. *J. Mol. Biol. 358*, 1305–1313.

(20) Hartman, F. C., and Wold, F. (1967) Cross-linking of bovine pancreatic ribonuclease A with dimethyl adipimidate. *Biochemistry 6*, 2439–2448.

(21) Wang, D., Wilson, G., and Moore, S. (1976) Preparation of cross-linked dimers of pancreatic ribonuclease. *Biochemistry 15*, 660–665.

(22) Bartholeyns, J., and Baudhuin, P. (1976) Inhibition of tumor cell proliferation by dimerized ribonuclease. *Proc. Natl. Acad. Sci. U.S.A. 73*, 573–576.

(23) Tarnowski, G. S., Kassel, R. L., Mountain, I. M., Blackburn, P., Wilson, G., and Wang, D. (1976) Comparison of antitumor activities of pancreatic ribonuclease and its cross-linked dimer. *Cancer Res. 36*, 4074–4078.

(24) Bartholeyns, J., and Zenebergh, A. (1979) In vitro and in vivo antitumor effect of dimerized ribonuclease A. *Eur. J. Cancer 15*, 85–91.

(25) Bartholeyns, J., and Moore, S. (1974) Pancreatic ribonuclease: Enzymic and physiological properties of a cross-linked dimer. *Science 186*, 444–455.

(26) Gotte, G., Testolin, L., Costanzo, C., Sorrentino, S., Armato, U., and Libonati, M. (1997) Cross-linked trimers of bovine ribonuclease A: Activity on double-stranded RNA and antitumor action. *FEBS Lett. 415*, 308–312.

(27) Murdock, A. L., Grist, K. L., and Hirs, C. H. W. (1966) On the dinitrophenylation of bovine pancreatic ribonuclease A. Kinetics of the reaction in water and 8 M urea. *Arch. Biochem. Biophys. 114*, 375–390.

(28) Messmore, J. M., Fuchs, D. N., and Raines, R. T. (1995) Ribonuclease A: Revealing structure-function relationships with semisynthesis. *J. Am. Chem. Soc. 117*, 8057–8060.

(29) Bretscher, L. E., Abel, R. L., and Raines, R. T. (2000) A ribonuclease A variant with low catalytic activity but high cytotoxicity. *J. Biol. Chem. 275*, 9893–9896.

(30) Green, N. S., Reisler, E., and Houk, K. N. (2001) Quantitative evaluation of the lengths of homobifunctional protein cross-

linking reagents used as molecular rulers. *Protein Sci. 10*, 1293–1304.
(31) Kim, J.-S., Souček, J., Matoušek, J., and Raines, R. T. (1995) Mechanism of ribonuclease cytotoxicity. *J. Biol. Chem. 270*, 31097–31102.
(32) Kobe, B., and Deisenhofer, J. (1995) A structural basis of the interactions between leucine-rich repeats and protein ligands. *Nature 374*, 183–186.
(33) Suzuki, M., Saxena, S. K., Boix, E., Prill, R. J., Vasandani, V. M., Ladner, J. E., Sung, C., and Youle, R. J. (1999) Engineering receptor-mediated cytotoxicity into human ribonucleases by steric blockage of inhibitor interaction. *Nat. Biotechnol. 17*, 265–270.
(34) Farha, O. K., Julius, R. L., and Hawthorne, M. F. (2006) Synthesis of a homotrifunctional conjugation reagent based on maledimide chemistry. *Tetrahedron Lett. 47*, 2619–2622.
(35) Arai, I., Sei, Y., and Maramatsu, I. (1981) Preparation of 1,3,5-triaminobenzene by reduction of phloroglucinol trioxime. *J. Org. Chem. 46*, 4597–4599.
(36) Kobe, B., and Deisenhofer, J. (1996) Mechanism of ribonuclease inhibition by ribonuclease inhibitor protein based on the crystal structure of its complex with ribonuclease A. *J. Mol. Biol. 264*, 1028–1043.
(37) Leland, P. A., Schultz, L. W., Kim, B.-M., and Raines, R. T. (1998) Ribonuclease A variants with potent cytotoxic activity. *Proc. Natl. Acad. Sci. U.S.A. 98*, 10407–10412.
(38) Rutkoski, T. J., Kurten, E. L., Mitchell, J. C., and Raines, R. T. (2005) Disruption of shape-complementarity markers to create cytotoxic variants of ribonuclease A. *J. Mol. Biol. 354*, 41–54.
(39) Kothandaraman, S., Hebert, M. C., Raines, R. T., and Nibert, M. L. (1998) No role for pepstatin-A-sensitive acidic proteinases in reovirus infections of L or MDCK cells. *Virology 251*, 264–272.
(40) Abel, R. L., Haigis, M. C., Park, C., and Raines, R. T. (2002) Fluorescence assay for the binding of ribonuclease A to the ribonuclease inhibitor protein. *Anal. Biochem. 306*, 100–107.
(41) Sica, F., Di Fiore, A., Zagari, A., and Mazzarella, L. (2003) The unswapped chain of bovine seminal ribonuclease: Crystal structure of the free and liganded monomeric derivative. *Proteins 52*, 263–271.
(42) Lee, J. E., and Raines, R. T. (2005) Cytotoxicity of bovine seminal ribonuclease: Monomer versus dimer. *Biochemistry 44*, 15760–15767.
(43) Gaur, D., Swaminathan, S., and Batra, J. K. (2001) Interaction of human pancreatic ribonuclease with human ribonuclease inhibitor. Generation of inhibitor-resistant cytotoxic variants. *J. Biol. Chem. 276*, 24978–24984.
(44) Leland, P. A., Staniszewski, K. E., Kim, B.-M., and Raines, R. T. (2001) Endowing human pancreatic ribonuclease with toxicity for cancer cells. *J. Biol. Chem. 276*, 43095–43102.
(45) Johnson, R. J., McCoy, J. G., Bingman, C. A., Phillips, G. N., Jr., and Raines, R. T. (2007) Inhibition of human pancreatic ribonuclease by the human ribonuclease inhibitor protein. *J. Mol. Biol. 368*, 434–449.
(46) delCardayré, S. B., Ribó, M., Yokel, E. M., Quirk, D. J., Rutter, W. J., and Raines, R. T. (1995) Engineering ribonuclease A: Production, purification, and characterization of wild-type enzyme and mutants at Gln11. *Protein Eng. 8*, 261–273.
(47) Kim, J.-S., and Raines, R. T. (1993) Bovine seminal ribonuclease produced from a synthetic gene. *J. Biol. Chem. 268*, 17392–17396.
(48) Seno, M., Futami, J., Kosaka, M., Seno, S., and Yamada, H. (1994) Nucleotide sequence encoding human pancreatic ribonuclease. *Biochim. Biophys. Acta 1218*, 466–468.
(49) Smith, P. K., Krohn, R. I., Hermanson, G. T., Mallia, A. K., Gartner, F. H., Provenzano, M. D., Fujimoto, E. K., Goeke, N. M., Olson, B. J., and Klenk, D. C. (1985) Measurement of protein using bicinchoninic acid. *Anal. Biochem. 150*, 76–85.
(50) Sela, M., Anfinsen, C. B., and Harrington, W. F. (1957) The correlation of ribonuclease activity with specific aspects of tertiary structure. *Biochim. Biophys. Acta 26*, 502–512.
(51) D'Alessio, G., Floridi, A., De Prisco, R., Pignero, A., and Leone, E. (1972) Bull semen ribonucleases 1. Purification and physico-chemical properties of the major component. *Eur. J. Biochem. 26*, 153–161.
(52) Lavis, L. D., Rutkoski, T. J., and Raines, R. T. (2007) Tuning the pK_a of fluorescein to optimize binding assays. *Anal. Chem. 79*, 6775–6782.
(53) Ellman, G. L. (1958) A colorimetric method for determining low concentrations of mercaptans. *Arch. Biochem. Biophys. 74*, 443–450.
(54) Kim, J.-S., and Raines, R. T. (1995) Dibromobimane as a fluorescent crosslinking reagent. *Anal. Biochem. 225*, 174–176.
(55) Ji, T. H. (1983) Bifunctional reagents. *Methods Enzymol. 91*, 580–609.
(56) Kalia, J., and Raines, R. T. (2007) Catalysis of imido group hydrolysis in a maleimide conjugate. *Bioorg. Med. Chem. Lett. 17*, 6286–6289.
(57) Kelemen, B. R., Klink, T. A., Behlke, M. A., Eubanks, S. R., Leland, P. A., and Raines, R. T. (1999) Hypersensitive substrate for ribonucleases. *Nucleic Acids Res. 27*, 3696–3701.
(58) Lee, J. E., and Raines, R. T. (2003) Contribution of active-site residues to the function of onconase, a ribonuclease with antitumoral activity. *Biochemistry 42*, 11443–11450.
(59) Hermans, J., Jr., and Scheraga, H. A. (1961) Structural studies of ribonuclease. V. Reversible change of configuration. *J. Am. Chem. Soc. 83*, 3283–3292.
(60) Eberhardt, E. S., Wittmayer, P. K., Templer, B. M., and Raines, R. T. (1996) Contribution of a tyrosine side chain to ribonuclease A catalysis and stability. *Protein Sci. 5*, 1697–1703.
(61) Pace, C. N., Hebert, E. J., Shaw, K. L., Schell, D., Both, V., Krajcikova, D., Sevcik, J., Wilson, K. S., Dauter, Z., Hartley, R. W., and Grimsley, G. R. (1998) Conformational stability and thermodynamics of folding of ribonucleases Sa, Sa2 and Sa3. *J. Mol. Biol. 279*, 271–286.
(62) Haigis, M. C., Kurten, E. L., and Raines, R. T. (2003) Ribonuclease inhibitor as an intracellular sentry. *Nucleic Acids Res. 31*, 1024–1032.
(63) Klink, T. A., and Raines, R. T. (2000) Conformational stability is a determinant of ribonuclease A cytotoxicity. *J. Biol. Chem. 275*, 17463–17467.
(64) Lee, F. S., Shapiro, R., and Vallee, B. L. (1989) Tight-binding inhibition of angiogenin and ribonuclease A by placental ribonuclease inhibitor. *Biochemistry 28*, 225–230.
(65) Henderson, P. J. F. (1972) A linear equation that describes the steady-state kinetics of enzymes and subcellular particles interacting with tightly bound inhibitors. *Biochem. J. 127*, 321–333.
(66) Cohen, M. H., Johnson, J. R., Chen, Y. F., Sridhara, R., and Pazdur, R. (2005) FDA drug approval summary: Erlotinib (Tarceva®) tablets. *Oncologist 10*, 461–466.
(67) Hermanson, G. T. (2008) *Bioconjugate Techniques*, 2nd ed., Academic Press, San Diego, CA.
(68) Kalia, J., and Raines, R. T. (2010) Advances in bioconjugation. *Curr. Org. Chem. 14*, 138–147.
(69) Fasold, H., Klappenberger, J., Meyer, C., and Remold, H. (1971) Bifunctional reagents for the crosslinking of proteins. *Angew. Chem., Int. Ed. 10*, 795–801.
(70) Chang, F. N., and Flaks, J. G. (1972) The specific cross-linking of two proteins from the *Escherichia coli* 30 S ribosomal subunit. *J. Mol. Biol. 68*, 177–180.
(71) Peters, K., and Richards, F. M. (1977) Chemical cross-linking: Reagents and problems in studies of membrane structure. *Annu. Rev. Biochem. 46*, 523–551.
(72) Swaney, J. B. (1986) Use of cross-linking reagents to study lipoprotein structure. *Methods Enzymol. 128*, 613–626.
(73) Rappsilber, J., Siniossoglou, S., Hurt, E. C., and Mann, M. (2000) A generic strategy to analyze the spatial organization of multi-protein complexes by cross-linking and mass spectrometry. *Anal. Chem. 72*, 267–275.
(74) Kwaw, I., Sun, J., and Kaback, H. R. (2000) Thiol cross-linking of cytoplasmic loops in the lactose permease of *Escherichia coli*. *Biochemistry 39*, 3134–3140.

(75) Tada, H., Onizuka, M., Muraki, K., Masuzawa, W., Futami, J., Kosaka, M., Seno, M., and Yamada, H. (2004) Insertional-fusion of basic fibroblast growth factor endowed ribonuclease 1 with enhanced cytotoxicity by steric blockade of inhibitor interaction. *FEBS Lett. 568*, 39–43.

(76) Futami, J., Maeda, T., Kitazoe, M., Nukui, E., Tada, H., Seno, M., Kosaka, M., and Yamada, H. (2001) Preparation of potent cytotoxic ribonucleases by cationization: Enhanced cellular uptake and decreased interaction with ribonuclease inhibitor by chemical modification of carboxyl groups. *Biochemistry 26*, 7518–7524.

(77) Fuchs, S. M., Rutkoski, T. J., Kung, V. M., Groeschl, R. T., and Raines, R. T. (2007) Increasing the potency of a cytotoxin with an arginine graft. *Protein Eng. Des. Sel. 20*, 505–509.

(78) Johnson, R. J., Chao, T.-Y., Lavis, L. D., and Raines, R. T. (2007) Cytotoxic ribonucleases: The dichotomy of coulombic forces. *Biochemistry 46*, 10308–10316.

(79) Turcotte, R. F., Lavis, L. D., and Raines, R. T. (2009) Onconase cytotoxicity relies on the distribution of its positive charge. *FEBS J. 276*, 3846–3857.

(80) Rejman, J., Oberle, V., Zuhorn, I. S., and Hoekstra, D. (2004) Size-dependent internalization of particles via the pathways of clathrin- and caveolae-mediated endocytosis. *Biochem. J. 377*, 159–169.

(81) Vasandani, V. M., Wu, Y.-N., Mikulski, S. M., Youle, R. J., and Sung, C. (1996) Molecular determinants in the plasma clearance and tissue distribution of ribonucleases of the ribonuclease A superfamily. *Cancer Res. 56*, 4180–4186.

(82) Lázníček, M., Schiavon, O., Caliceti, P., and Veronese, F. M. (1993) Pharmacokinetics and distribution of ribonuclease and its monomethoxypoly(ethylene glycol) derivatives in rats. *Pharmacol. Res. 28*, 153–161.

(83) Maddox, D. A., Deen, W. M., and Brenner, B. M. (1992) Glomerular filtration, in *Renal Physiology* (Windhager, E. E. , Ed.), pp 545−638, *Vol 1*, Oxford University Press, New York.

(84) Venturoli, D., and Rippe, B. (2005) Ficoll and dextran vs. globular proteins as probes for testing glomerular permselectivity: Effects of molecular size, shape, charge, and deformability. *Am. J. Physiol. Renal Physiol. 288*, F605–613.

(85) Alpern, R. J., and Hebert, S. C., Eds. (2007) *Seldin and Geibisch's The Kidney: Physiology and Pathophysiology*, 4th ed., Academic Press, New York.

(86) Maack, T. (1975) Renal handling of low molecular weight proteins. *Am. J. Med. 58*, 57–64.

(87) Maack, T., Johnson, V., Kau, S. T., Figueiredo, J., and Sigulem, D. (1979) Renal filtration, transport, and metabolism of low-molecular-weight proteins: A review. *Kidney Int. 16*, 251–270.

BC100292X

Antitumor Activity of Ribonuclease Multimers Created by Site-Specific Covalent Tethering

Thomas J. Rutkoski, John A. Kink, Laura E. Strong, Christine I. Schilling, and Ronald T. Raines*

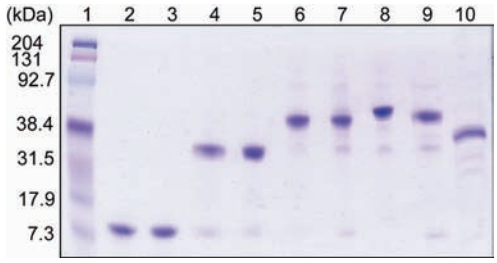


Figure S1. SDS–PAGE (12% w/v acrylamide; Tris–HCl) analysis of ribonuclease monomers and multimeric conjugates (2 μg each). Lane 1: Pre-stained molecular weight markers. Lane 2: G88R RNase A. Lane 3: G88C RNase A–**NEM**. Lanes 4: (G88C RNase A)$_2$–**3**. Lane 5: (G88C RNase A)$_2$–**4**. Lane 6: (G88C RNase A)$_3$–**7**. Lane 7: (G88C RNase A)$_3$–**8**. Lane 8: (G89C RNase 1)$_3$–**8**. Lane 9: (G88C BS-RNase)$_3$–**8**. Lane 10: (S72C ONC)$_3$–**8**. Molecular weights are for myosin (204 kDa), β-galactosidase (131), bovine serum albumin (92.7), carbonic anhydrase (38.4), soybean trypsin inhibitor (31.5), lysozyme (17.9), and aprotinin (7.3). The gel was stained with Coomassie Brilliant Blue R-250.

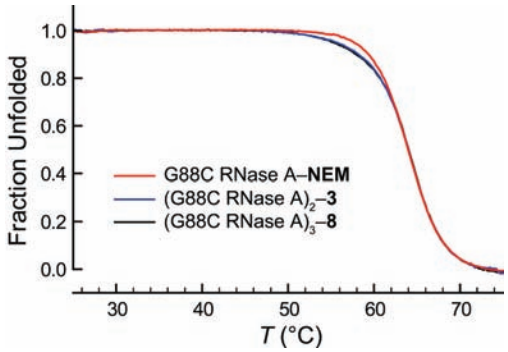


Figure S2. Thermal denaturation curves for G88C RNase A–**NEM** (red), (G88C RNase A)$_2$–**3** (blue), and (G88C RNase A)$_3$–**8** (black).

New Protocol for Oligonucleotide Microarray Fabrication using SU-8-Coated Glass Microslides

D. Sethi,[§] A. Kumar,[§] R. P. Gandhi,[†] P. Kumar,[§] and K. C. Gupta*[,‡,§]

Indian Institute of Toxicology Research (CSIR), Mahatma Gandhi Marg, Lucknow-226001, India, and Institute of Genomics and Integrative Biology (CSIR), Mall Road, Delhi University Campus, Delhi-110007, India. Received June 9, 2010; Revised Manuscript Received July 19, 2010

Microarray technology has become an important tool for detection and analysis of nucleic acid targets. Immobilization of modified and unmodified oligonucleotides on epoxy-functionalized glass surfaces is often used in microarray fabrication. Here, we demonstrate a protocol that employs coating of SU-8 (glycidyl ether of bisphenol A) onto glass microslides to obtain high density of epoxy functions for efficient immobilization of aminoalkyl-, thiophosphoryl-, and phosphorylated oligonucleotides with uniform spot morphology. The resulting microarrays exhibited high immobilization (∼65%) and hybridization efficiency (30−36%) and were sufficiently stable over a range of temperature and pH conditions. The prominent feature of the protocol is that spots can be visualized distinctly at 0.05 μM probe (a 20-mer oligonucleotide) concentration. The constructed microarrays were subsequently used for detection of base mismatches and bacterial diseases (meningitis and typhoid).

INTRODUCTION

Over the past few decades, oligonucleotide-based arrays have emerged as a promising and convenient tool for high-throughput experimentation in disease diagnosis, mapping, and gene expression analysis, as these offer distinct advantages in terms of requirement of a very small amount of biological probes (nanomoles and picomoles) (*1*−*6*).

Direct syntheses (in situ) of oligonucleotides on the chip surface following conventional or photolithographic methods and immobilization of presynthesized oligonucleotides on selected substrates (the deposition method) are two predominant methods for fabrication of oligonucleotide microarrays (*6*−*21*). The in situ synthesis protocol, which allows the preparation of high-density oligonucleotide microarrays, suffers from certain drawbacks (*6*−*8, 17*). The deposition method, on the other hand, offers flexibility, in the sense that a variety of biomolecules can be immobilized on a surface of choice but is limited to generation of low-to-medium-density arrays.

The choice of substrate and the chemistry employed for attachment of oligonucleotides are key factors that govern the quality and efficacy of constructed microarray significantly, especially in cases of low probe and target concentrations. A number of solid surfaces have been proposed for the fabrication of biochips (*20*−*34*). Of these, glass and PMMA appear attractive because these supports can easily be derivatized generating reactive functional groups such as aminoalkyl, mercaptoalkyl, carboxyl, aldehyde, and so forth on the surface. However, glass, an inexpensive material, proffers some advantages, as it reveals low intrinsic fluorescence and has a relatively homogeneous chemical surface. Recently, in order to realize the full potential of biochip technology for disease diagnosis, limitation of sensitivity has been a major concern. A general drawback of glass slides is the low functional group density due to its nonporous nature, which limits the number of reactive groups that can participate in the binding of oligonucleotides, resulting in poor surface coverage with the probes. Therefore, to develop such biochips, highly functionalized matrices having high immobilization capacity with good accessibility to target molecules are required. For this purpose, a vast variety of reagents and polymers have been used for coating to obtain highly functionalized glass surfaces (*30*−*34*). In one of the approaches, Preininger et al. (*31*) reported high-capacity ARChip epoxy as the reactive chip obtained after coating the glass microslide with 1% epoxy resin for immobilization of modified oligonucleotides with higher immobilization and hybridization efficiency; however, poor reproducibility of the coating process and enhanced background signals limited its commercial feasibility. Likewise, other methodologies, which were developed, required multistep processing (*32*−*34*). Recently, the epoxy-based photoresist, SU-8, a biocompatible, rigid, inexpensive, thermally, and chemically stable and transparent-to-light above 360 nm (*25, 26, 35*−*37*), has been employed as a structural material in microfabricated devices such as probes for scanning probe microscopy, waveguides, optical-based devices, and a large variety of lab-on-a-chip applications. Besides, an attempt has also been made to develop SU-8 surfaces for immobilization of DNA and proteins (*36, 37*).

Here, we demonstrate a process of biochip fabrication by directly immobilizing modified oligonucleotides (aminoalkyl-, thiophosphoryl-, and phosphorylated oligomers) onto SU-8 coated high-density glass microslides. This protocol provides higher signal reproducibility with superior spot morphology and homogeneity. The optimal thickness of the SU-8 layer required for immobilization and threshold concentration of oligomer required for visualization and thermal and pH stability of constructed microarrays were evaluated in a detailed study before validating these biochips for detection of base mismatches and of bacterial diseases such as meningitis and typhoid.

EXPERIMENTAL PROCEDURES

General. Virgin glass microslides (75 × 22 mm^2), *N*-methylimidazole (NMI), and 3-glycidyloxypropyltrimethoxysilane (GOPTS) were obtained from Sigma-Aldrich Chemical Co., St Louis, MO. SU-8 2002 was purchased from MicroChem

* E-mail: kcgupta@iitr.res.in; kcgupta@igib.res.in; Tel.: +91 522 2621856.

[†] INSA Honorary Scientist.

[‡] Indian Institute of Toxicology Research.

[§] Institute of Genomics and Integrative Biology.

10.1021/bc100262n © 2010 American Chemical Society
Published on Web 08/16/2010

Table 1. Synthesis of Oligonucleotides, Deprotection Conditions, and Yields

Sample number	Oligomer sequence	Deprotection conditions[a]	Yields O.D. at A_{260}
1	TET-d(CTT CTT TTT CCT GTT ACC GT)-O- (PO_3^{2-}/ PSO_2^{2-}/ PO_2^{-}-$O(CH_2)_2$-O-$(CH_2)_2$-NH_2)	Aq. NH_4OH, 55 °C, 16 h	20.5−22.4
2	d(CTT CTT TTT CCT GTT ACC GT)-O- (PO_3^{2-}/PSO_2^{2-}/ PO_2^{-}-$O(CH_2)_2$-O-$(CH_2)_2$-NH_2)	-Do-	22.1−24.5
3	TET-d(ACG GTA ACA GGA AAA AGA AG)	-Do-	22.1
4	d(CTT CTT TTT ACT GTT ACC GT)-O- (PO_3^{2-}/PSO_2^{2-}/ PO_2^{-}-$O(CH_2)_2$-O-$(CH_2)_2$-NH_2)	-Do-	24.1−24.8
5	d(TTT TTT TTT TTT TTT TTT TT)-OPO_3^{2-}	-Do-	23.7
6	TET-d(ACC GGT GGA TGT GGC TTC CTT G)	-Do-	21.2
7	TET-d(TGG TCT GCA GCA CCT TTT GAA C)	-Do-	20.5
8	d(ACC GGT GGA TGT GGC TTC CTT GTT TT)-OPO_3^{2-}	-Do-	24.2
9	TET-d(GCT GCG GTA GGT GGT TCA A)	-Do-	21.2
10	TET-d(TTG TCG CGG ATT TGC AAC TA)	-Do-	20.6
11	d(ACG TGT CAG CTG CAC ATT CGT TTT T)-OPO_3^{2-}	-Do-	23.8

[a] In the case of thiophosphorylated oligomers, aq. NH_4OH containing 50 mM DTT was used.

Corp., Newton, MA. Absolute ethanol was procured from Tedia Company Inc., Fairfield. 4,5,6,7-Tetrachlorofluorescein (TET) phosphoramidite was obtained from Applied Biosystems Inc., Foster City, CA. All other reagents used were of analytical grade and used as received from commercial source, unless specified.

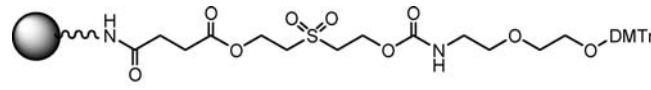
Instrumentation. ScanArray Gx Plus Microarray Scanner (Perkin Elmer), Speed vac concentrator (Hetovac VR-1), and Lambda Bio 20 spectrophotometer (Perkin-Elmer) were used. Spin-coating of microslides with SU-8 was carried out on Deltaspin (*38*)(Delta Scientific, Delhi, India).

Reagents and Buffers. Reaction buffer: 100 mM *N*-methylimidazole (NMI) was prepared by dissolving 80 μL in 10 mL of Milli-Q water (containing 10% DMSO). Capping buffer: 0.1 M Tris buffer containing 50 mM ethanolamine, pH 8.0. Washing buffer: 125 mM SSC buffer containing 750 mM sodium chloride, pH 7.0. Hybridization buffer: 125 mM SSC buffer containing 1 M sodium chloride, pH 7.0.

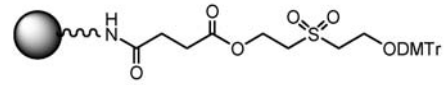
Cleaning, Silanization, and SU-8 Coating of Glass Slides. The glass slides were cleaned and silanized following the reported protocol (*15*). After washing and drying, the slides were stored under inert atmosphere. SU-8 2000 photoresist was coated with thickness of 2, 2.5, and 3 μm by spin-coating onto a glass microchip according to manufacturer's protocol (*38*). After spinning, the excess solvent was evaporated in a soft bake at 65 °C for 1 min and at 95 °C for 2 min. The microslides were stored under inert atmosphere.

Oligonucleotide Synthesis and Purification. In the present study, oligonucleotide sequences (Table 1) were assembled on Pharmacia Gene Assembler Plus at 0.2 μmol scale following the standard phosphoramidite chemistry. 3′-Modified oligonucleotides were synthesized on the engineered polymer supports (**I** and **II**). For 5′-labeled oligonucleotides, synthesis was carried out following the conventional protocol and the last coupling was performed with the TET-phosphoramidite reagent in a manner analogous to the normal nucleoside phosphoramidite coupling. Post-synthesis work-up and purification were carried out following the reported protocol (*14*).

Determination of Optimal Thickness Required for Immobilization. In order to arrive at optimal thickness of coated SU-8 photoresist (2, 2.5, 3 μm) onto glass microslides required for efficient immobilization of oligomers, attachment of probe was carried out following the reported protocol (*15*). Briefly, a labeled oligomer, TET-d(CTT CTT TTT CCT GTT ACC GT)-OPO_3^{2-}, was dissolved in the reaction buffer and spotted (0.5 μL) onto SU-8 coated glass slides at a concentration of 0.1 μM using a pipettmen followed by incubation at 45 °C for 2 h. Then, the microslide was washed with 1 × SSC buffer (2 × 50 mL) followed by Milli-Q water (2 × 50 mL), and dried under vacuum. Subsequently, the spots on the microslide were visualized under a laser scanner and quantified.



I : Support for synthesis of 3'-aminoalkylated oligonucleotides



II : Support for synthesis of 3'-phosphoryl- and thiophosphorylated oligonucleotides

Evaluation of Chip Surface for Immobilization. To evaluate the homogeneity of the SU-8 coated microslide surface, the following experiment was performed. An oligomer sequence, TET-d(CTT CTT TTT CCT GTT ACC GT)-OPO_3^{2-} (0.1 μM), dissolved in the reaction buffer, was spotted manually on a coated glass microslide at different locations all over the slide and kept at 45 °C for 2 h. The slide was processed and visualized, as described above.

Determination of Threshold Concentration Required for Visualization. In an attempt to arrive at the threshold concentration of oligonucleotides required for fluorescence detection, a TET-labeled oligomer, TET-d(CTT CTT TTT CCT GTT ACC GT)-OPO_3^{2-} diluted (1, 0.5, 0.1, 0.05, 0.025, and 0.01 μM) in the reaction buffer, was spotted (0.5 μL) onto an SU-8 coated glass microslide and kept at 45 °C for 2 h. After the reaction, the slide was washed with 1 × SSC buffer (3 × 25 mL) and Milli-Q water (2 × 25 mL). The slide was dried and scanned under a laser scanner. The immobilization efficiencies were determined using the standard curve.

Immobilization of thiophosphoryl- and aminoalkylated oligonucleotides was also performed in a similar way. Subsequently, the slides were washed, dried, and visualized under a laser scanner.

Thermal and pH Stability. In order to evaluate the thermal stability of immobilization, a microarray was constructed by spotting a TET-labeled oligomer sequence, TET-d(CTT CTT TTT CCT GTT ACC GT)-OPO_2^{-}-O-$(CH_2)_2$-O-$(CH_2)_2$-NH_2 (0.1 μM), as mentioned above. After the usual washings, the constructed microarray was subjected to PCR-like conditions for 0 and 20 cycles in 1 × SSC buffer (pH 7). The microarray was first subjected to 94 °C for 30 s (denaturation step), followed by cooling to 54 °C for 30 s (annealing step), and then heating to 72 °C for 30 s (chain extension step). After thermocycling, the slide was washed, dried, and visualized under laser scanner. Likewise, thermal stability of immobilization of thiophosphoryl- and phosphorylated oligonucleotides was assessed.

The pH stability of the constructed microarray was evaluated by spotting the SU-8 coated microslides, as described above, and then subjecting them to washings with 1 × SSC buffer of different pH (7, 8, and 9). After usual washings and drying, the microslides were scanned under a laser scanner. The stability of the microarrays constructed using thiophosphoryl- and phosphorylated oligonucleotides was examined.

Hybridization Studies. In order to study the accessibility of attached probe sequence to target sequence, d(CTT CTT TTT CCT GTT ACC GT)-OPO_3^{2-}, dissolved in the reaction buffer, was spotted onto SU-8 coated glass microslide at 0.5 μM and kept at 45 °C for 2 h. Then, the spotted slide was washed with the capping buffer (3 × 50 mL) followed by Milli-Q water (2 × 50 mL) and dried. Subsequently, the spots on the microslide were hybridized with a complementary labeled oligomer. Briefly, in a glass Petri dish, the spotted glass slide was kept on a wet blotting paper, and the complementary oligomer, TET-d(ACG GTA ACA GGA AAA AGA AG) (40 μM dissolved in 40 μL of hybridization buffer), was spread on the spotted area. The area was covered with a coverslip and the slide kept at 60 °C for 5 min, and later at ambient temperature for 2 h and at 10 °C for another 2 h. The coverslip was removed, and the slide was washed with the washing buffer (3 × 50 mL). After washings with the hybridization buffer (3 × 50 mL), the microslide was dried and subjected to laser scanning followed by quantification.

Later, hybridization assays were performed on glass slides immobilized with aminoalkyl- and thiophosphoryl-oligomers.

Base-Mismatch Detection. The specificity of the system was demonstrated by immobilizing modified oligomers on SU-8 coated glass microslides. Three oligonucleotides, viz., d(CTT CTT TTT CCT GTT ACC GT)-OPO_3^{2-}, d(CTT CTT TTT **A**CT GTT ACC GT)-OPO_3^{2-}, and d(TTT TTT TTT TTTTTT TTT TT)-OPO_3^{2-} (perfect match, single mismatch, and noncomplementary probes, respectively), were spotted on a coated glass microslide at 0.5 μM and kept at 45 °C for 2 h. Subsequently, the microslide was washed, dried, and the spots hybridized with a complementary labeled TET-d(ACG GTA ACA GGA AAA AGA AG), as described above. Similar studies were carried out using aminoalkyl- and thiophosphorylated oligomer immobilized glass slides.

Detection of Bacterial Diseases. *Bacterial Typhoid. PCR-Amplification.* The PCR reaction was performed in 25 μL PCR Eppendorf tubes containing 0.25 mM dNTPs (of each dATP, dCTP, dGTP, and dTTP), forward primer [TET-d(ACC GGT GGA TGT GGC TTC CTT G)], and reverse primer [TET-d(TGG TCT GCA GCA CCT TTT GAA C)] (0.4 μM of each), genomic DNA (50 ng/reaction), Taq polymerase (0.75 units), and Milli-Q water. All PCR reactions were performed on an MJ Research thermocycler using the following profile: (1) 5 min at 95 °C (initial denaturation step); (2) 35 cycles of 60 s min at 95 °C (denaturation step), 40 s at 61.6 °C (annealing step), 2 min at 72 °C (extension step); (3) 7 min at 72 °C (final extension step); hold temperature 4 °C. The labeled PCR-amplifications, 503 bp fragment of *tyv* gene (*Salmonella typhi*), were analyzed by agarose gel electrophoresis, and detection was performed by ethidium bromide (10 μg/mL) in standard TAE buffer, pH 8.

Bacterial Meningitis. PCR Amplification. In a similar fashion, PCR reaction was performed to obtain 111 bp fragment of *ctrA* gene (*Neisseria meningitides*, serogroup A) except by taking forward primer TET-d(GCT GCG GTA GGT GGT TCA A), and reverse primer TET-d(TTG TCG CGG ATT TGC AAC TA) using the following conditions: (1) 5 min at 95 °C (initial denaturation step); (2) 35 cycles of 50 s at 95 °C (denaturation step), 40 s at 58 °C (annealing step), 1 min at 72 °C (extension step); (3) 7 min 72 °C (final extension step); hold temperature 4 °C.

Immobilization of Probes and Detection of Diseases. Two oligonucleotide probes, d(ACC GGT GGA TGT GGC TTC CTT GTT TT)-OPO_3^{2-} (complementary to *tyv* gene) and d(ACG TGT CAG CTG CAC ATT CGT TTT T)-OPO_3^{2-} (complementary to *ctrA* gene) were immobilized on two SU-8 coated glass microslides. PCR amplicons of two diseases were hot-denatured (5 min, 95 °C), cooled on ice (10 min), and used for the hybridization assay. One of the microslides was hybridized with PCR amplicons corresponding to *ctrA* gene, and the other one was exposed to amplicons corresponding to *tyv* gene. After usual washings, the slides were visualized under a laser scanner.

Signal Evaluation and Quantification. Microarrays were scanned on a ScanArray Gx Plus Microarray Scanner fitted with a Cy3 optical filter at 20 μm resolution. PMT and laser power were set to 55% and 65%, respectively. Spot intensities were quantified and graphs were plotted in MS *Excel*.

For quantification of immobilized oligonucleotides, a TET-labeled oligonucleotide sequence, TET-d(ACG GTA ACA GGA AAA AGA AG), was diluted from 0.5 to 0.005 μM concentration and spotted on a virgin microslide. After drying, the slide was scanned and spots were quantified. A standard calibration curve was plotted between fluorescence intensity (A.U.) and concentration (μM).

For each experimental condition tested on the microarrays, the experiment was repeated 2−3 times. Immobilization and hybridization data presented are the average of these repetitions, and the error bars represent the percentage error (±2−4%) observed on this average.

RESULTS AND DISCUSSION

Since the advent of microarray technology, glass has remained a substrate of choice and several chemistries have been proposed for attachment of oligonucleotides onto it. However, low density of silanol groups often results in poor surface coverage with the probes, which ultimately affects the sensitivity of the constructed microarrays. In order to address this problem, attempts have been made to improve the sensitivity of an array by increasing the surface density of the functional groups (high-capacity biochips) to anchor oligomer probes. Recently, glass microslides coated with functional group-rich polymers (chitosan, polyethylenimine, acrylic acid-*co*-acrylamide, SU-8, etc.) have gained attention as substrates for the fabrication of microarrays. Of the polymers employed for coating of slides, SU-8 has garnered greater attention as a possible material for a variety of biomedical applications. Nucleic acids can be immobilized onto SU-8 coated surfaces by covalent linkages or by noncovalent hydrophobic interactions. Covalent attachment of probes is a preferred approach, as it results in higher stability of the constructed microarrays. The presence of epoxy functionalities on the surfaces, coated with SU-8 photoresist, allows attachment of oligonucleotides with different nucleophilic/electrophilic functionalities. By taking advantage of above-mentioned points, a rapid and clean protocol has been developed for direct immobilization of oligonucleotides bearing different functional groups onto SU-8 coated glass microslides.

Determination of Optimal Thickness Required for Immobilization. In order to study the effect of thickness of SU-8 photoresist on immobilization of oligomers, the attachment of a probe was carried out at different thickness (2, 2.5, and 3 μm). After usual washings and drying, the spots on the microslide were visualized under a laser scanner and quantified. The results obtained with a layer of thickness 2.5 μm (Figure 1) were found to be appropriate for immobilization, as it showed the highest immobilization efficiency. Therefore, in subsequent

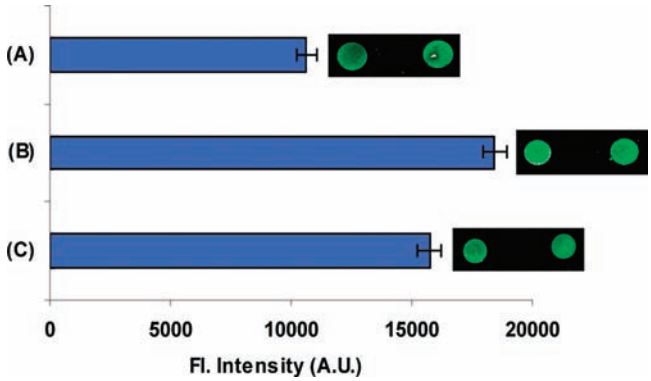


Figure 1. Fluorescence intensity data and pictorial representation of immobilization of TET-labeled oligonucleotide at (A) 2 μm, (B) 2.5 μm, and (C) 3 μm.

experiments, glass microslides coated with SU-8 (2.5 μm thickness) were employed.

Evaluation of Chip Surface for Immobilization. Homogeneity of the surface is one of the important factors for obtaining good-quality microarrays based on fluorescence detection. In the present study, the uniformity of epoxy functionalities on the surface of SU-8 coated microslides was evaluated by spotting an oligomer sequence at different locations all over the slide. After usual washings and drying, the slide was visualized under a laser scanner and the fluorescence intensity of spots was found to be in the range of ~18,000−18,500 A.U., which showed that the density of epoxy-functionalities on the coated glass surface was present almost uniformly throughout.

Determination of Threshold Concentration Required for Visualization. In order to optimize the threshold concentration of oligonucleotides required for fluorescence detection, a labeled oligomer, diluted (1, 0.5, 0.1, 0.05, 0.025, and 0.01 μM) was spotted onto an SU-8 coated glass microslide and incubated at 45 °C for 2 h. After usual washings and drying, the slide was scanned under a laser scanner, and the pictorial view of the slide is depicted in Figure 2A. Immobilization of thiophosphoryl- and aminoalkylated oligonucleotides was performed in a similar way (Figure 2B,C). The immobilization efficiency against each concentration was determined with the help of a standard curve (Figure 3). From these results, it was observed that immobilization efficiency increased when increasing the concentration of spotted oligonucleotides, and the fluorescent intensity of spots reached saturation at a concentration corresponding to 1 μM. The threshold concentration to visualize spots was found to be 0.05 μM; however, to construct a good-quality biochip for hybridization assays, a concentration of 0.5 μM was selected, as the highest immobilization efficiency was attained at this concentration.

Thermal and pH Stability. The thermal stability of constructed microarrays was evaluated by immobilizing a TET-labeled oligomer sequence (0.1 μM), as mentioned above, followed by subjecting it to 0 and 20 cycles of PCR-like conditions in 1 × SSC buffer (pH 7). The percentage reduction in fluorescence intensity was observed to be ~6.2% for aminoalkyl-, ~8.5% for thiophosphoryl-, and ~7.9% for phosphorylated oligomers after 20 cycles (Figure 4A), indicating that constructed microarrays were sufficiently stable to be used in biological research. The stability of constructed microarrays was also analyzed at different pH values (7, 8, and 9). The results indicated that the constructed microarrays were sufficiently stable in SSC buffer of different pH. The decrease in fluorescence intensity was ~3.7% and ~5.6% for aminoalkyl-, ~7.0% and ~11.8% for thiophosphoryl-, and ~4.6% and ~8.3% for phosphorylated oligomers at pH 8 and 9, respectively, as compared to fluorescence intensity at pH 7 for the immobilized oligomers (Figure 4B).

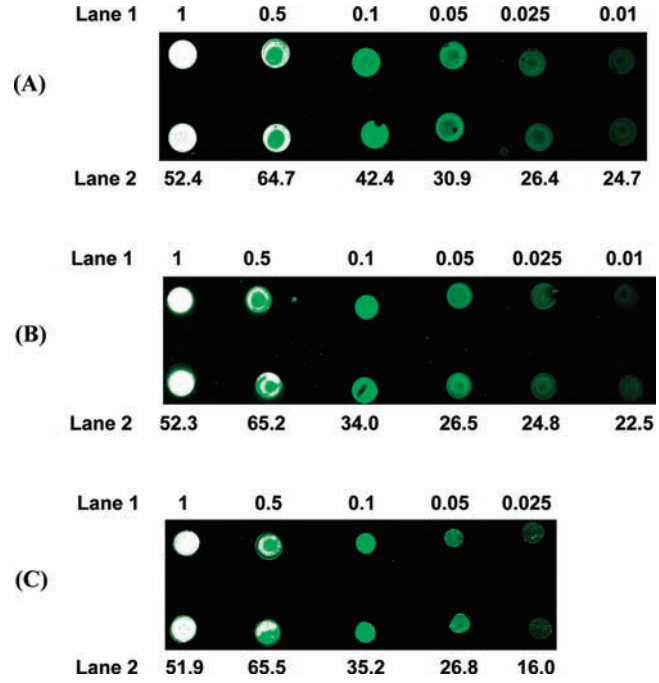


Figure 2. Threshold concentration of (A) phosphoryl-, (B) thiophosphoryl-, and (C) aminoalkylated oligonucleotides required for fluorescence visualization. Lane 1: Probe concentration (μM). Lane 2: Immobilization efficiency (%).

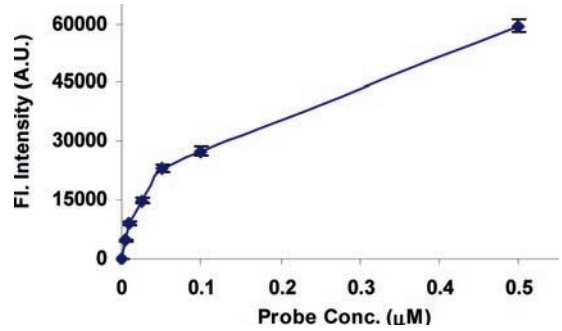


Figure 3. Correlation sketch between concentration of immobilized probe (μM), TET-d(ACG GTA ACA GGA AAA AGA AG), and fluorescence intensity (A.U).

Hybridization Studies. The applicability of the projected strategy was evaluated by performing hybridization assay of slides fabricated via immobilization of phosphoryl-, thiophosphoryl-, and aminoalkylated oligomers onto the SU-8 coated glass slides at 0.5 μM concentration. After incubation at 45 °C for 2 h, the slides were subjected to treatment with the capping buffer to block residual epoxy functions on the slide surface (*15*). Subsequently, the spots on the microslide were hybridized with complementary labeled oligomers. After washings with the hybridization buffer, the slides were scanned and fluorescent spots on the microslides were quantified. The projected strategy resulted in high hybridization efficiencies (~33.4% for aminoalkyl-, ~30.5% for thiophosphoryl-, and 35.7% for phosphorylated oligonucleotides).

Detection of Base Mismatches. The specificity of the system was demonstrated by immobilizing modified oligomers on SU-8 coated glass microslides. Three oligonucleotides, viz., d(CTT CTT TTT CCT GTT ACC GT)-OPO_2-$O(CH_2)_2O(CH_2)_2NH_2$, d(CTT CTT TTT **A**CT GTT ACC GT)-OPO_2-$O(CH_2)_2$-$O(CH_2)_2NH_2$, and d(TTT TTT TTT TTTTTT TTT TT)-OPO_2-$O(CH_2)_2O(CH_2)_2NH_2$ (perfect match, single mismatch, and

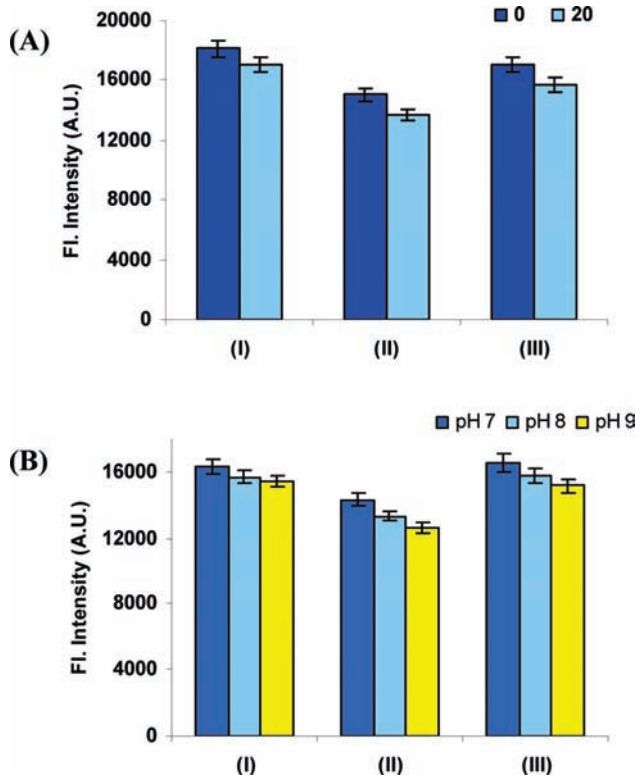


Figure 4. (A) Graphical representation showing thermal stability of immobilized (I) aminoalkyl-, (II) thiophosphoryl-, and (III) phosphorylated probes {TET-d(CTT CTT TTT CCT GTT ACC GT)—X} after 0 and 20 cycles of PCR-like conditions; (B) pH stability of the (I) aminoalkyl-, (II) thiophosphoryl-, and (III) phosphorylated probes immobilized onto SU-8 coated glass microslides ($n = 3$).

noncomplementary probes, respectively), were spotted on a glass microslide and incubated at 45 °C for 2 h. After treatment with the capping buffer followed by washings, the microslide was washed, dried, and hybridized with a complementary labeled oligomer, TET-d(ACG GTA ACA GGA AAA AGA AG), as described above. Figure 5A (I) clearly shows the base mismatches. The results revealed that the highest fluorescence intensity was obtained in the case of a perfect match and this decreased for single-mismatch, while the noncomplementary oligonucleotide did not exhibit significant signal intensity after hybridization, thus suggesting specificity of the hybridization in this case. Similar studies were carried out using thiophosphoryl- and phosphorylated oligomers, as shown in Figures 5A (II) and (III). The quantification data are depicted in Figure 5B.

Detection of Bacterial Diseases. In order to develop biochips for diagnosis of the bacterial infections, two microarrays were constructed on SU-8 coated glass microslides using a unique probe sequence of the *tyv* and *ctrA* genes, as described under Experimental Procedures. The spots on the first microslide were subjected to hybridization with the labeled PCR amplicons corresponding to the *ctrA* gene. After washings and drying, the slide was visualized under a laser scanner. Figure 6A shows the pictorial view of the slide. Spots of probe sequence specific to *ctrA* gene of bacteria (*N. meningitidis*) showed fluorescence, while the spots pertaining to *tyv* gene did not fluoresce at all. Spots on the second microslide were hybridized with PCR amplicons corresponding to *tyv* gene. Figure 6B depicts that spots of probe sequence specific to *tyv* gene exhibited fluorescence, while the spots pertaining to *ctrA* gene did not fluoresce at all. The experiment signifies the

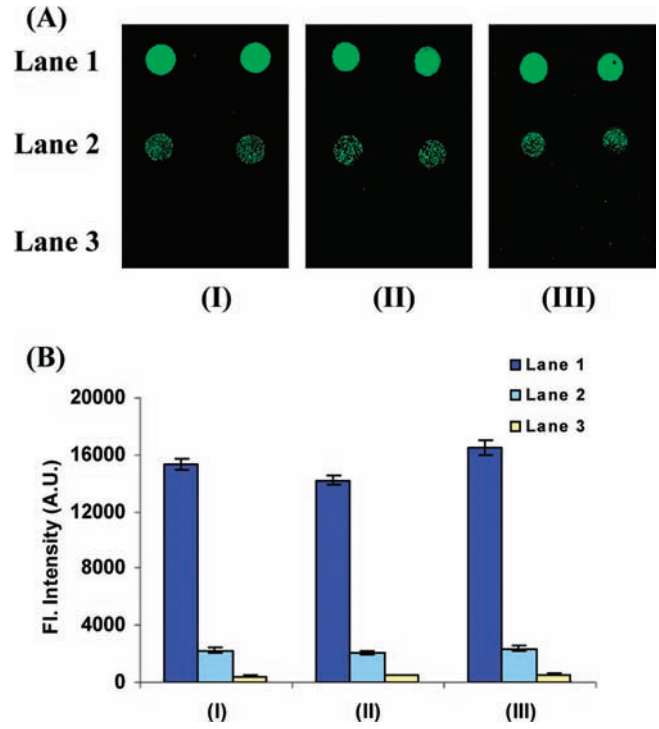


Figure 5. (A) Detection of base mismatches using (I) aminoalkyl-, (II) thiophosphoryl-, and (III) phosphorylated probes. (B) Quantitative data of the fluorescence intensity of the spots.

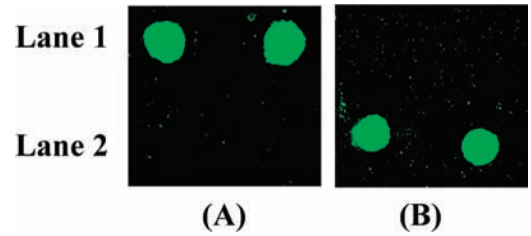


Figure 6. Detection of bacterial (A) meningitis and (B) typhoid. Lane 1: *ctrA* probe sequence {d(ACG TGT CAG CTG CAC ATT CGT TTT T)-OPO_3^{2-}}. Lane 2: *tyv* probe sequence {d(ACC GGT GGA TGT GGC TTC CTT GTT TT)-OPO_3^{2-}) were immobilized on SU-8 coated glass microslides.

specificity of the system to prepare biochips for the detection of bacterial meningitis and typhoid.

CONCLUSIONS

A versatile high-density epoxy-coated (SU-8) glass substrate has been developed for the construction of microarrays. Highlighting features of the projected strategy are as follows: covalent tethering of modified oligonucleotides with high immobilization and hybridization efficiency; stability of the immobilized probes toward a wide range of temperature and pH conditions; visualization of immobilized probes at the concentration of 0.05 μM (sensitivity almost 20—100 times); and ability to detect base mismatches and diagnose bacterial diseases. It is anticipated that the protocol will provide individuals, particularly end users, easy access to oligonucleotide microarrays for various routine biological studies.

ACKNOWLEDGMENT

Authors are thankful to Drs. S. Gupta and S. Khare, NICD, Delhi, India, for processing of patient samples. D.S. thanks the University Grants Commission, New Delhi, India, for the award of a Senior Research Fellowship.

LITERATURE CITED

(1) Grant, S. F., and Hakonarson, H. (2008) Microarray technology and applications in the area of genome-wide association. *Clin. Chem. 54*, 1116–1124.

(2) Miller, M. B., and Tang, Y. W. (2009) Basic concepts of microarrays and potential applications in clinical microbiology. *Clin. Microbiol. Rev. 22*, 611–633.

(3) Chen, X., Jorgenson, E., and Cheung, S. T. (2009) New tools for functional genome analysis. *Drug Discovery Today 14*, 754–760.

(4) Shen, Y., and Wu, B.-L. (2009) Microarray-based genomic DNA profiling technologies in clinical molecular diagnosis. *Clin. Chem. 55*, 659–669.

(5) Stangegaard, M., Wang, Z., Kutter, J. P., Dufva, M., and Wolff, A. (2006) Whole genome expression profiling using DNA microarray for determining biocompatibility of polymeric surfaces. *Mol. Biosyst. 2*, 421–428.

(6) Seliger, H., Hinz, M., and Happ, E. (2003) Arrays of immobilized oligonucleotides-Contributions to nucleic acids technology. *Curr. Pharm. Biotechnol. 4*, 379–395.

(7) Sethi, D., Gandhi, R. P., Kumar, P., and Gupta, K. C. (2009) Chemical strategies for immobilization of oligonucleotides. *Biotechnol. J. 4*, 1513–1529.

(8) Vaijayanthi, B., Kumar, P., Ghosh, P. K., and Gupta, K. C. (2003) Recent advances in oligonucleotide synthesis and their applications. *Ind. J. Biochem. Biophys. 40*, 377–391.

(9) Lane, S. M., Monot, J., Petit, M., Tellier, C., Bujoli, B., and Talham, D. R. (2008) Poly(dG) spacers lead to increased surface coverage of DNA probes: An XPS study of oligonucleotide binding to zirconium phosphonate modified surfaces. *Langmuir 24*, 7394–7299.

(10) Misra, A., and Shahid, M. (2009) Immobilization of self-quenched DNA hairpin probe with a heterobifunctional reagent on a glass surface for sensitive detection of oligonucleotides. *Bioorg. Med. Chem. 17*, 5826–5833.

(11) Wu, O., Ma, W., Zhu, L., Guo, Q., Zhang, B., Kulageri, S. M., and Zheng, W. (2008) Oligo-Microarray based on oligonucleotide immobilization on glass surface modified with activated acrylic acid-co-acrylamide copolymer. *J. Biomed. Mater. Res., Part B: Appl. Biomater. 87*, 67–72.

(12) Mahajan, S., Kumar, P., and Gupta, K. C. (2006) Oligonucleotide microarrays: Immobilization of phosphorylated oligonucleotides on epoxylated surface. *Bioconjugate Chem. 17*, 1184–1189.

(13) Lockett, M. R., Phillips, M. F., Jarecki, J. L., Peelen, D., and Smith, L. M. (2008) A tetrafluorophenylactivated ester self-assembled monolayer for the immobilization of amine-modified oligonucleotides. *Langmuir 24*, 69–75.

(14) Sethi, D., Patnaik, S., Kumar, A., Gandhi, R. P., Gupta, K. C., and Kumar, P. (2009) Polymer supported synthesis of aminooxy-alkylated oligonucleotides, and some applications in the fabrication of microarrays. *Bioorg. Med. Chem. 17*, 5442–5450.

(15) Mahajan, J., Sethi, D., Seth, S., Kumar, A., Kumar, P., and Gupta, K. C. Construction of oligonucleotide microarrays (biochips) via thioether linkage for the detection of bacterial meningitis. *Bioconjugate Chem. 20*, 1703–1710.

(16) Sethi, D., Kumar, A., Gupta, K. C., and Kumar, P. (2008) A facile method for the construction of oligonucleotide microarrays. *Bioconjugate Chem. 19*, 2136–2143.

(17) Beaucage, S. L. (2001) Strategies in the preparation of DNA oligonucleotide arrays for diagnostic applications. *Curr. Med. Chem. 8*, 1213–1244.

(18) Dufva, M. (2005) Fabrication of high quality microarrays. *Biomol. Eng. 22*, 173–184.

(19) Fuentes, M., Mateo, C., Garcia, L., Tercero, J. C., Guisan, J. M., and Fernandez-Lafuente, R. (2004) Directed covalent immobilization of aminated DNA probes on aminated plates. *Biomacromolecules 5*, 883–888.

(20) Afanassiev, V., Hanemann, V., and Wolfl, S. (2000) Preparation of DNA and protein micro arrays on glass slides coated with an agarose film. *Nucleic Acids Res. 28*, e66.

(21) Diaz-Quijada, G. A., and Wayner, D. D. M. (2004) A simple approach to micropatterning and surface modification of poly-(dimethylsiloxane). *Langmuir 20*, 9607–9611.

(22) Benters, R., Niemeyer, C. M., Drutschmann, D., Blohm, D., and Wöhrle, D. (2002) DNA microarrays with PAMAM dendritic linker systems. *Nucleic Acids Res. 30*, e10.

(23) Cha, T.-W., Boiadjiev, V., Lozano, J., Yang, H., and Zhu, X.-Y. *Anal. Biochem. 311*, 27–32.

(24) Consolandi, C., Severgnini, M., Castiglioni, B., Bordoni, R., Frosini, A., Battaglia, C., Bernardi, L. R., and De Bellis, G. (2006) A structured chitosan-based platform for biomolecule attachment to solid surfaces: Application to DNA microarray preparation. *Bioconjugate Chem. 17*, 371–377.

(25) Deepu, A., Sai, V. V., and Mukherji, S. (2009) Simple surface modification techniques for immobilization of biomolecules on SU-8. *J. Mater. Sci. Mater. Med. 20*, S25–S28.

(26) Erkan, Y., Czolkos, I., Jesorka, A., Wilhelmsson, L. M., and Orar, O. (2007) Direct immobilization of cholesteryl-TEG-modified oligonucleotides onto hydrophobic SU-8 surfaces. *Langmuir 23*, 5259–5263.

(27) Fontanel, M. L., Bazin, H., and Teoule, R. (1993) End attachment of phenol-oligonucleotide conjugates to diazotized cellulose. *Bioconjugate Chem. 4*, 380–385.

(28) Lie, L. H., Patole, S. N., Pike, A. R., Ryder, L. C., Connolly, B. A., Ward, A. D., Tuite, E. M., Houlton, A., and Horrocks, B. R. (2004) Immobilisation and synthesis of DNA on Si(111), nanocrystalline porous silicon and silicon nanoparticles. *Faraday Discuss. 125*, 235–249.

(29) Okutucu, B., and Telefoncu, A. (2004) Covalent attachment of oligonucleotides to cellulose acetate membranes. *Artif. Cells Blood Substit. Immobil. Biotechnol. 32*, 599–608.

(30) Fixe, F., Dufva, M., Telleman, P., and Christensen, C. B. V. (2004) One-step immobilization of aminated and thiolated DNA onto poly(methylmethacrylate) (PMMA) substrates. *Lab Chip 4*, 191–195.

(31) Preininger, C., Sauer, U., Dayteg, J., and Pichler, R. (2005) Optimizing processing parameters for signal enhancement of oligonucleotide and protein arrays on ARChip epoxy. *Bioelectrochemistry 67*, 155–162.

(32) Hong, B. J., Sunkara, V., and Park, J. W. (2005) DNA microarrays on nanoscale-controlled surface. *Nucleic Acids Res. 33*, e106.

(33) Lim, S. B., Kim, K.-W., Lee, C.-W., Kim, H.-S., Lee, C.-S., and Oh, M.-K. (2008) Improved DNA chip with poly(amidoamine) dendrimer peripherally modified with biotin and avidin. *Biotechnol. Bioprocess Eng. 13*, 683–689.

(34) Benters, R., Niemeyer, C. M., Drutschmann, D., Blohm, D., and Wohrle, D. (2002) DNA microarrays with PAMAM dendritic linker systems. *Nucleic Acids Res. 30*, e10.

(35) Abgrall, P., Conedera, V., Camon, H., Gue, A. M., and Nguyen, N. T. (2007) SU-8 as a structural material for labs-on-chips and microelectromechanical systems. *Electrophoresis 28*, 4539–4551.

(36) Joshi, M., Kal, N., Lal, R., Ramgopal, R. V., and Mukherji, S. (2007) A novel dry method for surface modification of SU-8 for immobilization of biomolecules in Bio-MEMS. *Biosens. Bioelectron. 22*, 2429–2435.

(37) Marie, R., Schmid, S., Johansson, A., Ejsing, L., Nordstrom, M., Hafliger, D., Christensen, C. B., Boisen, A., and Dufva, M. (2006) Immobilization of DNA to polymerized SU-8 photoresist. *Biosens. Bioelectron. 21*, 1327–1332.

(38) *Delta Scientific Equipments Pvt. Ltd. Manual*, Delhi, India (2007).

BC100262N

Multimodal Tumor-Targeting Peptides Functionalized with Both a Radio- and a Fluorescent Label

Joeri Kuil,[†] Aldrik H. Velders,[‡] and Fijs W. B. van Leeuwen*[,†]

Division of Diagnostic Oncology, The Netherlands Cancer Institute, Antoni van Leeuwenhoek Hospital, 1066 CX Amsterdam, The Netherlands, Supramolecular Chemistry and Technology, MESA + Institute for Nanotechnology, University of Twente, PO Box 217, 7500 AE, Enschede, The Netherlands. Received June 17, 2010; Revised Manuscript Received August 4, 2010

The use of monolabeled tumor-targeting peptides for molecular imaging is widespread. However, it is often desirable to use the same compound for different clinical applications, e.g., combined pre- and intraoperative tumor detection. On the basis of their detection sensitivity, the combination of radioactivity and fluorescence is probably the most valuable in multimodal molecular imaging. In this review, we compare multimodal peptide derivatives and discuss the influence of the diagnostic labels on receptor affinity and biodistribution. On the basis of the described constructs, we propose improvements for the design of future multimodal tumor-targeting peptide derivatives.

INTRODUCTION

For molecular imaging several modalities are in use, of which two important ones are radionuclide-based and fluorescence-based imaging (*1*). To overcome the individual limitations of these modalities, taking advantage of their individual strengths, they can be combined in so-called multimodal imaging approaches (*2, 3*). For each imaging modality, different molecular labels (also referred to as diagnostic functionalizations) are required. To link the different applications, it is desirable to use one-and-the-same imaging agent (*4*−*6*), functionalized with multiple diagnostic labels. A potential application for such multimodal compounds could be an integrated use of preoperative diagnostics and surgical planning (radioactivity-based), with intraoperative surgical image guidance (fluorescence-based) to the predefined lesion location (Figure 1).

For preoperative imaging and surgical planning, radionuclide-based imaging technologies, such as single photon emission computed tomography (SPECT) (*1*) and positron emission tomography (PET) (*7*), are commonly used. Both modalities have a sensitivity in the nanomolar range (*8*), but suffer from limited spatial resolution. The total body penetration of the γ-radiation enables whole-body scans in 3D and allows for quantitative analysis of the tracer pharmacokinetics and distribution. To generate anatomical detail, these modalities are often used in combination with computed tomography (CT).

Fluorescence-based molecular imaging becomes increasingly important, mainly due to the development of highly sensitive cameras and the very high spatial resolution that can be achieved with fluorescence imaging (*9, 10*). However, fluorescent signals have a limited tissue penetration making quantitative biodistribution analysis difficult. Despite this potential shortcoming, 'superficial' detection during surgical interventions, so-called fluorescence image guidance is a very promising application for fluorescence imaging (*11*). Indeed, various fluorescent compounds have already been suggested for such (intraoperative) imaging applications (*12*−*15*).

Peptides have been extensively used in receptor-targeted imaging (*16*−*19*) and can be considered intermediate-sized targeting compounds that are somewhat larger than small organic compounds but significantly smaller than antibodies. In peptides, an attachment point for relatively large diagnostic labels can be introduced away from the pharmacophore. This is less feasible for small organic compounds, which cannot easily be functionalized without loss of affinity (*19*). In addition, the biodistribution of peptides is in general better than that of antibodies, because peptides are much smaller than antibodies.

Next to radiolabeled peptides (*19*), fluorescently and multimodal functionalized peptides have also been studied. In this review, we focus on the latter. For peptide-based receptor imaging, multiple targets are known (*19*), of which some have been targeted with multimodal peptides, viz., the somatostatin receptor, the gastrin releasing peptide receptor, the interleukin-11 receptor α, and $\alpha_v\beta_3$ integrin. For these targets, we here discuss multimodal peptides functionalized with a combination of radio- and fluorescent labels, grouped by the receptor target. To establish the influence of the labels on receptor binding and biodistribution of these peptides, the unlabeled and monolabeled peptides are included for comparison.

SOMATOSTATIN ANALOGUES

Somatostatin receptors (especially subtype 2, sst_2) can be upregulated in, e.g., neuroendocrine tumors (*20*), and targeting of this receptor for diagnostic purposes has been extensively studied. Particularly, (derivatives of) the truncated somatostatin cyclic analogues octreotide (D-Phe-cyclo(Cys-Phe-D-Trp-Lys-Thr-Cys)-Threol, **1**) and octreotate (D-Phe-cyclo(Cys-Phe-D-Trp-Lys-Thr-Cys)-Thr-OH, **2**) have been used in the clinic for tumor visualization and therapy (Figure 2) (*20*). These two peptides possess low-nanomolar affinity for sst_2 and have higher plasma half-lives than the native ligand somatostatin, i.e., 1.5 h versus a few minutes, respectively (*21*−*23*).

For radioiodination, the second phenylalanine (Phe^3) in octreotide is generally replaced by a tyrosine (Figure 2). The iodine labeled peptide [^{123}I-Tyr^3]octreotide, **3**, has low-nanomolar affinity for its receptor: the dissociation constant (K_D) = 0.7−5.9 nM for cells obtained from clinical tumors (*24, 25*). In addition, it has reasonably good in vivo properties (Table 1) (*26*). Two major drawbacks of this radioiodinated octreotide are the in vivo instability of iodinated tyrosine (*27*) and the rapid clearance via the liver; i.e., after 24 h, tumor accumulation

* Corresponding author. E-mail: fw.v.leeuwen@nki.nl.
[†] The Netherlands Cancer Institute.
[‡] University of Twente.

10.1021/bc100276j © 2010 American Chemical Society
Published on Web 09/02/2010

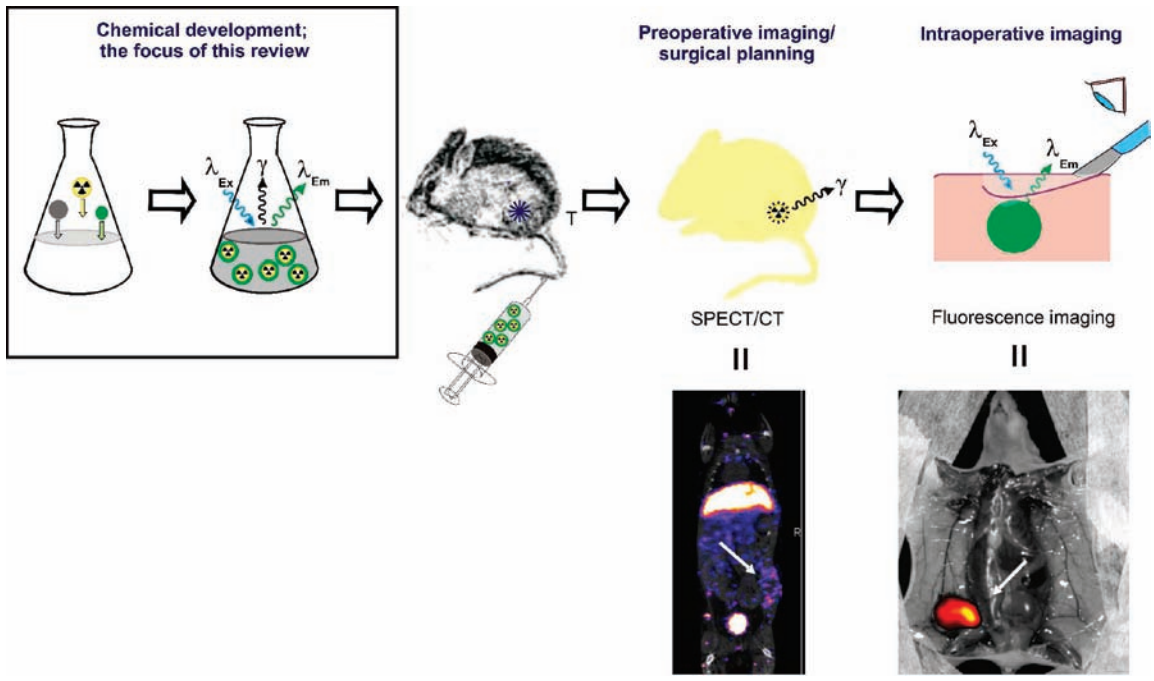


Figure 1. Schematic overview of the development and potential use of multimodal tumor-targeting peptides. The preoperative SPECT/CT example shows a tumor-bearing mouse, whereby the tumor was visualized with an indium-labeled peptide (In-DTPA-Ac-TZ14011) (*79*) that binds to the CXCR4 receptor (*80*). In the fluorescence surgical guidance image, the tumor was visualized with the same Ac-TZ14011 peptide labeled with the CyTE-777 near-infrared label (*80, 81*). A multimodal version of Ac-TZ14011 would allow both SPECT/CT and fluorescence imaging with the same compound.

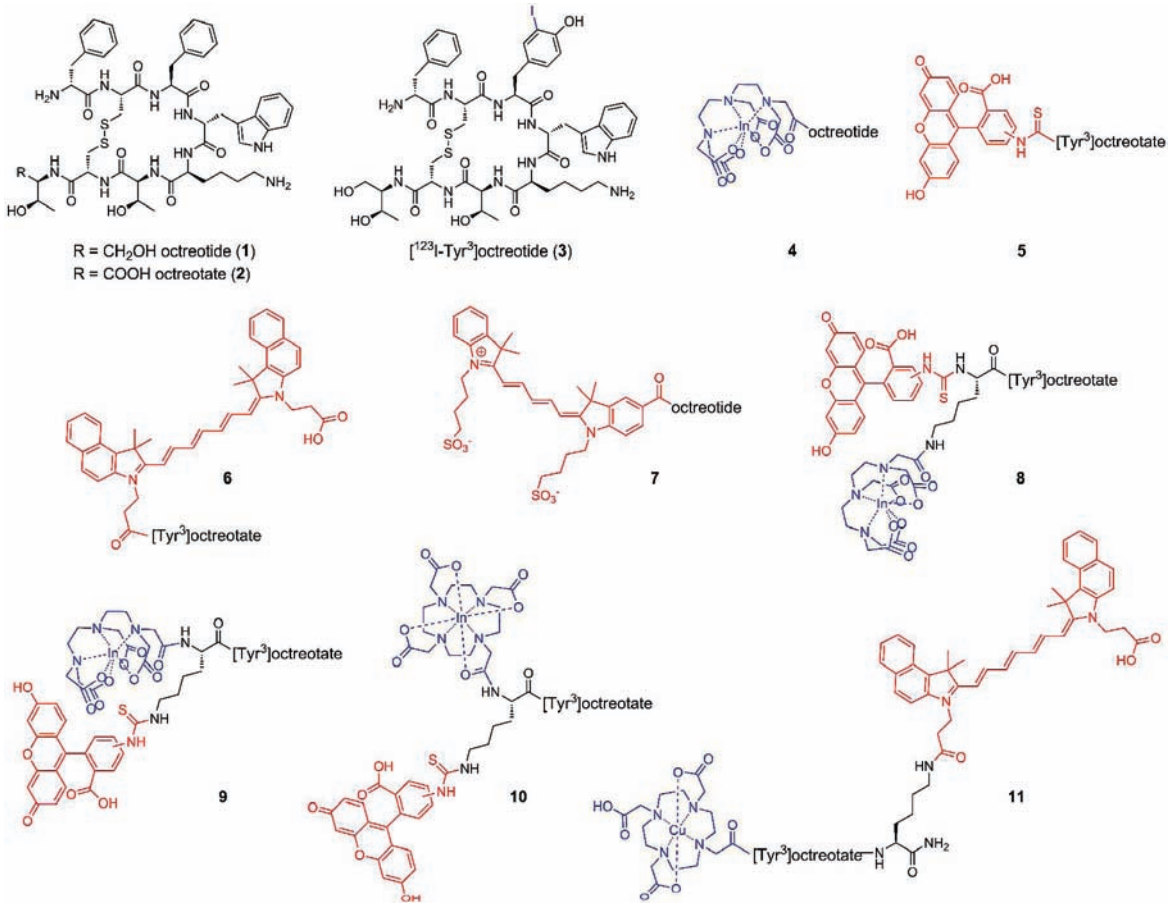


Figure 2. Somatostatin receptor targeting peptides **1**−**11**. In all compounds, the labels were attached to the N-terminus of the peptide, and in compound **11**, the dye was attached to the C-terminus. For compounds **5** and **8**−**10**, it was not specified which FITC isomer (or isomeric mixture) was used, and therefore, FITC is depicted without specification of isomer. The radiolabels are represented in blue and the fluorescent dyes in red.

Table 1. Receptor Affinity, Biodistribution, and Imaging Data of the Somatostatin Analogues

somatostatin analogue	IC_{50} (nM)	K_D (nM)	%ID/g[a]	tumor-to-muscle ratio[a,b]	imaging modality	ref
1	0.4 ± 0.07	-	n/a[c]	n/a	n/a	*23*
2	0.6 ± 0.10	-	n/a	n/a	n/a	*23*
3	1.8−24.7	0.7−5.9	5.53 ± 1.06 (1 h)	21.3 (1 h)	radioactivity	*26*
4	22 ± 3.6	-	1.5 ± 0.4 (24 h)	150 (24 h)	radioactivity	*22*
5	9.9 ± 2.1	-	−	-	fluorescence	*23*
6	4.6 ± 0.7	-	−	-	fluorescence	*23*
7	-	-	0.28 (24 h)	7.0 (24 h)	fluorescence	*29*
8	71.3	-	−	-	−	*23*
9	10.3 ± 1.8	-	−	-	−	*23*
10	10.3 ± 2.1	-	−	-	−	*23*
11	45.9 ± 7.2	11.5 ± 1.8	0.287 ± 0.046 (1 h)	1.5 (24 h)	fluorescence	*30*

[a] Measurement time post injection between parentheses. [b] Tumor-to-muscle ratios are based on radioactivity data, except for **11**, which is based on fluorescence. [c] Not applicable.

could no longer be detected (*25, 28*). Both these problems can be overcome by using a chelate-based DTPA label (labeled with ^{111}In for SPECT): this complex is stable and yields an improved biodistribution profile with reduced liver uptake (*25*). Since attachment of a hydrophilic glucose unit also improved the tumor accumulation, this improvement in the biodistribution is most likely induced by the hydrophilic nature of DTPA (*26*). Both octreotide and octreotate have been N-terminally functionalized with a chelating DTPA or DOTA moiety, and both display a low-nanomolar affinity for the somatostatin receptor subtype sst2 (Table 1) (*22*). The ^{111}In-labeled [DTPA^0]octreotide **4** (Figure 2) is widely applied in the clinic (OctreoScan) and can be considered a clinical standard (*20*).

Next to radiolabeling, somatostatin analogues have also been functionalized with various fluorescent dyes. [Tyr^3]octreotate has, for example, been N-terminally labeled with fluorescein isothiocyanate (FITC) (**5**) and a carbocyanine near-infrared (NIR) dye (**6**) (Figure 2) (*23*). Although both labels reduced the receptor affinity by approximately a factor of 10 compared to the unlabeled peptide (Table 1), the octreotates **5** and **6** could be used to visualize tumors in vivo. Another interesting derivative is the (NIR) dye−octreotate construct **7** (Figure 2) (*29*). This compound has been used to visualize subdermal tumors in mice. To determine the biodistribution, Becker et al. labeled compound **7** with ^{125}I, by radioiodination on the aromatic rings of the dye using a similar synthetic procedure as used for tyrosine labeling (*29*). Analysis 24 h postinjection confirmed that the tumor uptake of **7** was specific (Table 1).

Achilefu et al. prepared octreotate peptides **8**−**10** labeled with both FITC and a DOTA or DTPA chelate (Figure 2 and Table 1) (*23*). The octreotate peptide **8** possesses an IC_{50} (50% inhibitory concentration) value of 71.3 nM for the somatostatin receptor. Surprisingly, changing the position of the labels improved the receptor affinity by almost a factor of 7, with peptides **9** and **10** both having an IC_{50} value of 10.3 nM. The affinity of the unfunctionalized octreotate for the somatostatin receptor is, however, significantly higher under these conditions, i.e., IC_{50} = 0.6 nM. In other words, the multimodal label does interfere with receptor binding, but the affinities of **9** and **10** are still reasonably good and comparable with the monolabeled peptides **5** and **6**. The biodistribution profile of the multimodal compounds **8**−**10** was unfortunately not examined in vivo.

As a follow-up study, Edwards et al. prepared octreotate **11**, which was N- and C-terminal functionalized with DOTA and the NIR dye cypate, respectively (Figure 2) (*30*). This DOTA−peptide construct was labeled with ^{64}Cu to enable PET studies. Compound **11** with and without copper in the chelate had K_D values of 11.5 nM and 2.03 nM, respectively. This indicates that even the binding of a metal ion can significantly alter the receptor affinity. The unfunctionalized octreotate possessed a K_D value of 0.427 nM under the same conditions. Compound **11** mainly accumulated in the liver and kidneys, and the uptake in the tumor was not significantly higher than in healthy tissue. The poor in vivo behavior of the multimodal octreotate **11** appeared to be caused by a lack of internalization into tumor cells (*30*).

BOMBESIN ANALOGUES

By binding to the gastrin releasing peptide receptor (GRPR), the gastrin-releasing peptide and bombesin-like peptides can act as growth factors in many types of cancer, including prostate and (small cell) lung cancer (*19, 31*). Radiolabeled bombesin analogues have preclinically proven their potential in GRPR-targeted tumor imaging (*32, 33*). Native bombesin consists of 14 amino acid residues, while the last eight residues are most important for binding (*34, 35*). This octapeptide, Gln-Trp-Ala-Val-Gly-His-Leu-Met (**12** in Figure 3), is used in the multimodal bombesin peptides and is defined as bombesin(7−14) is this review.

Similar to octreotide, bombesin analogues have also been radioiodinated, e.g., [^{125}I-D-Tyr^6,βAla^{11},Phe^{13},Nle^{14}]bombesin-(6−14) (**13**) (*35, 36*). For SPECT and PET imaging, various chelate-containing bombesin peptides have been described (*37*−*39*). Direct N-terminal labeling of bombesin(7−14) with ^{111}In-DOTA (**14**) decreased the affinity from low-nanomolar (**13**) to 110.6 nM (Table 2 and Figure 3) (*34*). However, when a β-alanine (**15a**), 1-aminopentanoic acid (**15b**), or 1-aminooctanoic acid (**15c**) spacer was inserted between the chelate and the peptide, the affinity was restored to the low-nanomolar range (IC_{50} = 2.1, 1.7, and 0.6 nM, respectively). An even longer 11-aminoundecanoic acid spacer (**15d**), however, again reduced the affinity (i.e., IC_{50} = 64.0 nM) (*34*). The tumor uptake of ^{111}In-DOTA-1-aminooctanoic acid-Gln-Trp-Ala-Val-Gly-His-Leu-Met (**15c**) was reasonable in PC 3 tumor-bearing SCID mice (*34*). Another study with bombesin(7−14) peptide **15c** by Garrison et al. confirmed this tumor specificity (*37*).

Bombesin(7−14) has also been fluorescently labeled with Alexa Fluor 680 attached to the N-terminus (*40*). In this compound (**16**), three glycine residues were placed between bombesin(7−14) and the dye, which is approximately as long as the 1-aminooctanoic acid spacer in **15c** (Figure 3). The peptide **16** had an IC_{50} value of 7.7 nM and showed tumor specific uptake in vivo, although this was not quantified (Table 2).

Bombesin analogues have also been dual-labeled with FITC and DTPA or DOTA (compounds **17**−**19** in Figure 3) (*23*). For the introduction of the two labels, an extra lysine residue was N-terminally introduced. The attachment of a DTPA chelate to the N-terminus decreased the affinity more than 10-fold. Intriguingly, no negative influence of the DTPA label was observed when DTPA was coupled to the side chain of the N-terminal lysine residue. The same trend was observed for dual-labeled peptides: compound **17**, with DTPA attached to the N-terminus and FITC to the side chain of lysine, had a lower

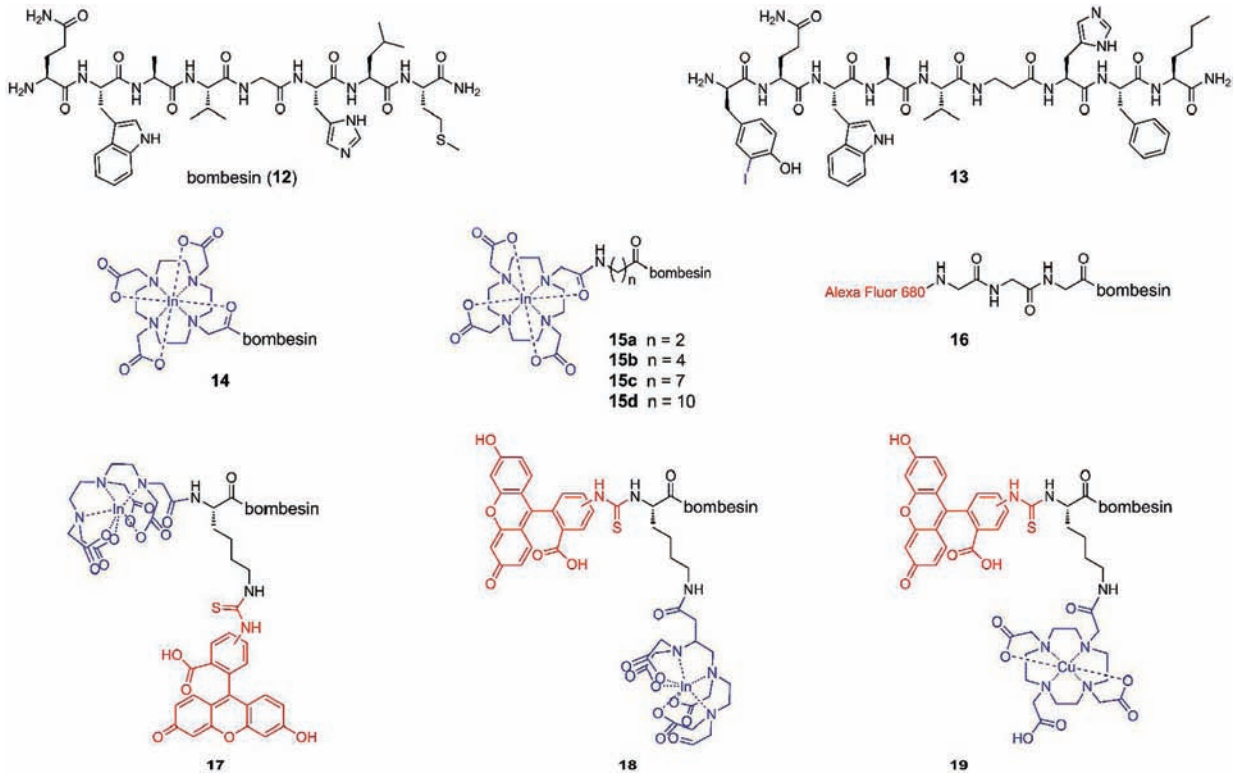


Figure 3. Bombesin derivatives **12**−**19**. In all compounds, the labels were attached to the N-terminus of bombesin(7−14). For compounds **17**−**19**, it was not specified which FITC isomer (or isomeric mixture) was used, and therefore, FITC is depicted without specification of isomer. The radiolabels are represented in blue and the fluorescent dyes in red.

Table 2. Receptor Affinity, Biodistribution, and Imaging Data of the Bombesin Derivatives

bombesin derivative	IC_{50} (nM)	K_D (nM)	%ID/g[a]	tumor-to-muscle ratio[a]	imaging modality	ref
12	28.3 ± 3.7	-	n/a[b]	n/a	n/a	*23*
13	0.72−1.1	-	−	-	−	*35*
14	110.6 ± 32.3	-	−	-	−	*34*
15a	2.1 ± 0.3	-	−	-	−	*34*
15b	1.7 ± 0.4	-	−	-	−	*34*
15c	0.6 ± 0.1	-	1.56 ± 0.45 (24 h)	31.2 (24 h)	radioactivity	*34*, *37*
15d	64.0 ± 11.2	-	−	-	−	*34*
16	7.7 ± 1.4	-	−	-	fluorescence	*40*
17	276	-	−	-	−	*23*
18	20 ± 11.7	-	−	-	−	*23*
19	15 ± 9	-	−	-	−	*23*

[a] Measurement time post injection between parentheses. [b] Not applicable.

binding affinity (Table 2). Switching the position of the dye and chelate substantially improved the receptor affinity (IC_{50} = 20 nM and 15 nM for compounds **18** and **19**, respectively) when compared to the 276 nM of **17**. The use of either DTPA or DOTA as a chelate for bombesin(7−14) did not have a significant influence on the binding affinity. A result similar to that was described for octreotate (see above and Tables 1 and 2). Unfortunately, none of these multimodal bombesin(7−14) peptides were studied in vivo.

IL-11 ANALOGUE

The 21 kDa cytokine Interleukin-11 (IL-11) and its receptor (IL-11Rα) have been related to breast cancer and breast cancer related bone metastasis (*41*, *42*). By means of phage display, the cyclic nonapeptide cyclo(Cys-Gly-Arg-Arg-Ala-Gly-Gly-Ser-Cys) was identified as a selective IL-11Rα ligand, but no affinity constant has been provided (*43*, *44*). Wang et al. dual-labeled the cyclic peptide ligand **20** with the NIR dye IR-783 and a DTPA chelate (Figure 4) (*45*). They showed that the multimodal construct could label cells that possessed the IL-11Rα receptor, and preliminary in vivo results demonstrated

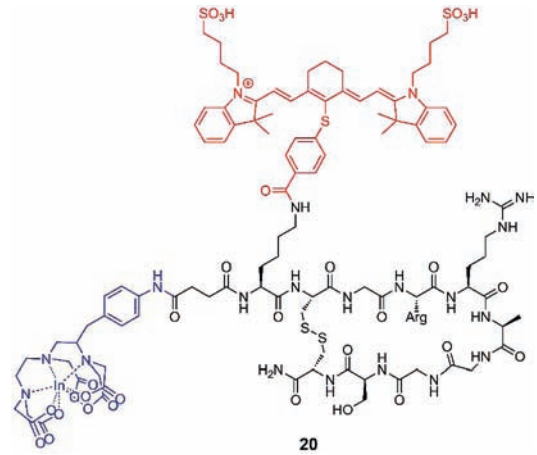


Figure 4. Multimodal labeled IL-11Rα receptor ligand **20**. The radiolabels are represented in blue and the fluorescent dyes in red.

that the construct has tumor targeting abilities. Accumulation in the kidneys was rather high, but no quantitative biodistribution

data were presented. Unfortunately, no radioactive nor fluorescent monolabeled peptidic Il-11Rα ligands have been reported. The lack of such reference compounds makes it difficult to establish the influence of the multimodal labels on the targeting properties.

RGD PEPTIDES

Since tumor growth depends on sufficient blood supply, tumor cells stimulate the formation of new blood vessels via angiogenesis. $\alpha_v\beta_3$ Integrin is a biomarker that is generally overexpressed during (tumor-induced) angiogenesis (*46*). Several extracellular matrix proteins, e.g., vitronectin, fibrinogen, and laminin, can bind to $\alpha_v\beta_3$ by means of the Arg-Gly-Asp (RGD) sequence, present in these proteins (*47*). On the basis of this RGD sequence, the cyclic pentapeptide cyclo(Arg-Gly-Asp-D-Phe-Val) **21** was designed, which has an IC_{50} in the high-nanomolar range (100−4000 nM; Figure 5 and Table 3) (*48*).

The D-phenylalanine residue of RGD was substituted for D-tyrosine to allow radioiodination (^{125}I) for SPECT analysis (*49, 50*). The radioiodinated peptide cyclo(Arg-Gly-Asp-^{125}I-D-Tyr-Val) ([^{125}Tyr^4]RGD, **23**) had a similar binding affinity for $\alpha_v\beta_3$ as cyclo(Arg-Gly-Asp-D-Phe-Val) **21** and cyclo(Arg-Gly-Asp-D-Tyr-Val) **22** (Figure 5 and Table 3), indicating that substitution for tyrosine and subsequent iodination is well-tolerated. Others, however, found that substitution of phenylalanine (**21**) for tyrosine (**22**) slightly reduced the affinity, i.e., IC_{50} = 65 and 144 nM, respectively (*51*).

For the attachment of a chelate and/or a dye to the RGD peptide, the valine residue is commonly substituted for a lysine (compound **24** in Figure 5), which again does not seem to affect the binding affinity (Table 3) (*52*). A representative example of such a construct is ^{111}In-DOTA-Glu-cyclo(Arg-Gly-Asp-D-Phe-Lys) **25**, which has a dissociation constant in the low-nanomolar range (K_D = 8.92 nM, IC_{50} = 236 nM) (*53*). The uptake was 2.70%ID/g with a tumor-to-muscle ratio of 14.2 (Table 3) and **25** was rapidly cleared (*54*).

Dye-labeled cyclic RGD peptides have also been widely studied and are exemplified by compound **26** (Figure 5 and Table 3) (*55*). This construct, which is labeled with the commercial available cyanine dye Cy5.5, has an IC_{50} value of 42.9 nM. The uptake in tumor bearing mice was approximately 6%ID/g 24 h after injection, the tumor-to-blood ratio was 10, and the tumor-to-muscle ratio 5. These numbers were obtained by measuring the fluorescence in dissected organs. However, the tumor-to-normal tissue ratio in living mice was 2.22 according to a fluorescence whole-body scan. The considerable difference between the numbers obtained with the two fluorescence approaches demonstrates that quantitative biodistribution analysis using fluorescence is less reliable than radioactivity-based (quantitative) biodistribution analysis.

Garanger et al. introduced the concept of a reactive multimodal label, which can be used to label any peptide or protein (*56*). They reasoned that such a label would decrease the chance of interference with receptor binding compared to the use of two separate labels. As an example, they labeled RGD with a label consisting of an NBD fluorescent dye and a DTPA chelate, resulting in compound **27** (Figure 5) (*57*). The receptor binding and targeting ability of **27** was quantified using SPECT and (fluorescence) immunohistochemistry.

Cyclic RGD has also been functionalized with a combination of NIR dye IRDye800 and ^{111}In-DTPA, yielding compound **28** (Figure 5) (*58, 59*). The IC_{50} value (3.86 μM) of this multimodal RGD derivative was similar to cyclic RGD itself under the same conditions. This indicates that the multimodal labels did not interfere with receptor binding of RGD (Table 3). Furthermore, biodistribution studies demonstrated that **28** had a tumor uptake of 1.41%ID/g at 24 h with a tumor-to-muscle ratio of 5.0. Unfortunately, the tumor uptake was accompanied by a higher degree of nonspecific uptake as compared to peptide **28** without the IRDye800 label. This suggests that the addition of IRDye800 enhances nonspecific background uptake (*59*).

Recently, Edwards et al. published a similar construct as **28**: cyclic RGD labeled with a cypate dye and ^{111}In-DOTA (compound **29** in Figure 5) (*60*). They confirmed that the dual introduction of a chelate and a cypate dye does not reduce the binding affinity for $\alpha_v\beta_3$ (IC_{50} = 0.046 nM, K_D = 0.029 nM) compared to [Tyr^4]RGD (**22**) (Table 3). The high affinity found for **29**, however, differs from other data, e.g., those obtained with **28**. This discrepancy can be a result of the smaller hill coefficient (slope) of the inhibition curve. The tumor uptake of this agent was 7.59%ID/g at 24 h and 2.48%ID/g at 72 h. The tumor-to-muscle ratio was 6.36 according to radioactivity data (24 h post injection) and the fluorescence intensity in the individial organs revealed a similar distribution trend. These data seem very promising, although it is difficult to compare **29** with other (multimodal) agents, e.g., compounds **27** and **28**, as different control samples were used.

Yet another multimodal RGD peptide **30** possesses a cypate dye and desferrioxamine (DFO) as a chelate (Figure 5) (*61*). DFO is an iron chelator that also binds ^{67}Ga/^{68}Ga, which can be used as isotope for PET imaging. The IC_{50} value of **30** is 180 nM, which is slightly lower than that of RGD itself under the same conditions (Table 3). The multimodal peptide was rapidly internalized into cells within 1 h after incubation. Unfortunately, no in vivo experiments were conducted.

Besides the relatively small multimodal RGD peptides mentioned above, larger peptide structures have also been synthesized. The 33 residue-containing RGD peptide "knottin" was engineered by means of yeast surface display and directed evolution (*62*). The IC_{50} value of this knottin peptide was 19 nM in a cell binding assay, and N-terminal labeling with Cy5.5 and a DOTA chelate (**31**) did not have a large effect on the binding affinity (Figure 5 and Table 3) (*63*). The addition of a Cy5.5 dye increased the in vivo tumor retention and kidney uptake compared to the DOTA functionalized derivative. The biodistribution of **31** was assessed with PET using a ^{64}Cu radiolabel. The tumor uptake was 4.57%ID/g, and the tumor-to-muscle ratio was approximately 12, both determined 24 h post injection (Table 3).

The PAMAM dendrimer PAMAM-(Alexa594)$_{0.75}$-(Gd-DTPA)$_{23}$-(^{111}In-DTPA)$_{0-4}$-(cyclo(Arg-Gly-Asp-D-Phe-Lys))$_2$ **32** has been used for NIR fluorescence and radioactivity-based imaging in combination with magnetic resonance (MR) imaging (Figure 5) (*64*). This compound contains a third-generation PAMAM ethylenediamine core dendrimer, consisting of 32 end groups. Because MR imaging requires large quantities of contrast agents, 28 end groups were functionalized with DTPA, of which 23 were labeled with paramagnetic gadolinium (Gd). The remaining four DTPA chelates were partly labeled with ^{111}In (i.e., 0−4 labeled DTPA chelates per dendrimer), and on average, 0.75 end groups in each dendrimer were functionalized with the Alexa594 dye. Only two end groups were functionalized with RGD peptides to bind $\alpha_v\beta_3$ expressing cells in vitro. The binding affinity was not determined in this study, which makes comparison with other RGD constructs difficult. Moreover, in vivo studies failed to demonstrate tumor uptake of the dendrimer and almost all of the injected compound accumulated in the kidneys, liver, and spleen. This indicates two possible design flaws: (i) not enough RGD peptides are present in dendrimer **32** and (ii) the macromolecular PAMAM-dendrimer scaffold has a negative influence on the biodistribution and thus the targeting ability of the RGD-peptides.

RGD-tagged quantum dots (QDs) have been functionalized with DOTA chelates (DOTA-QD-RGD, **33**) to enable PET

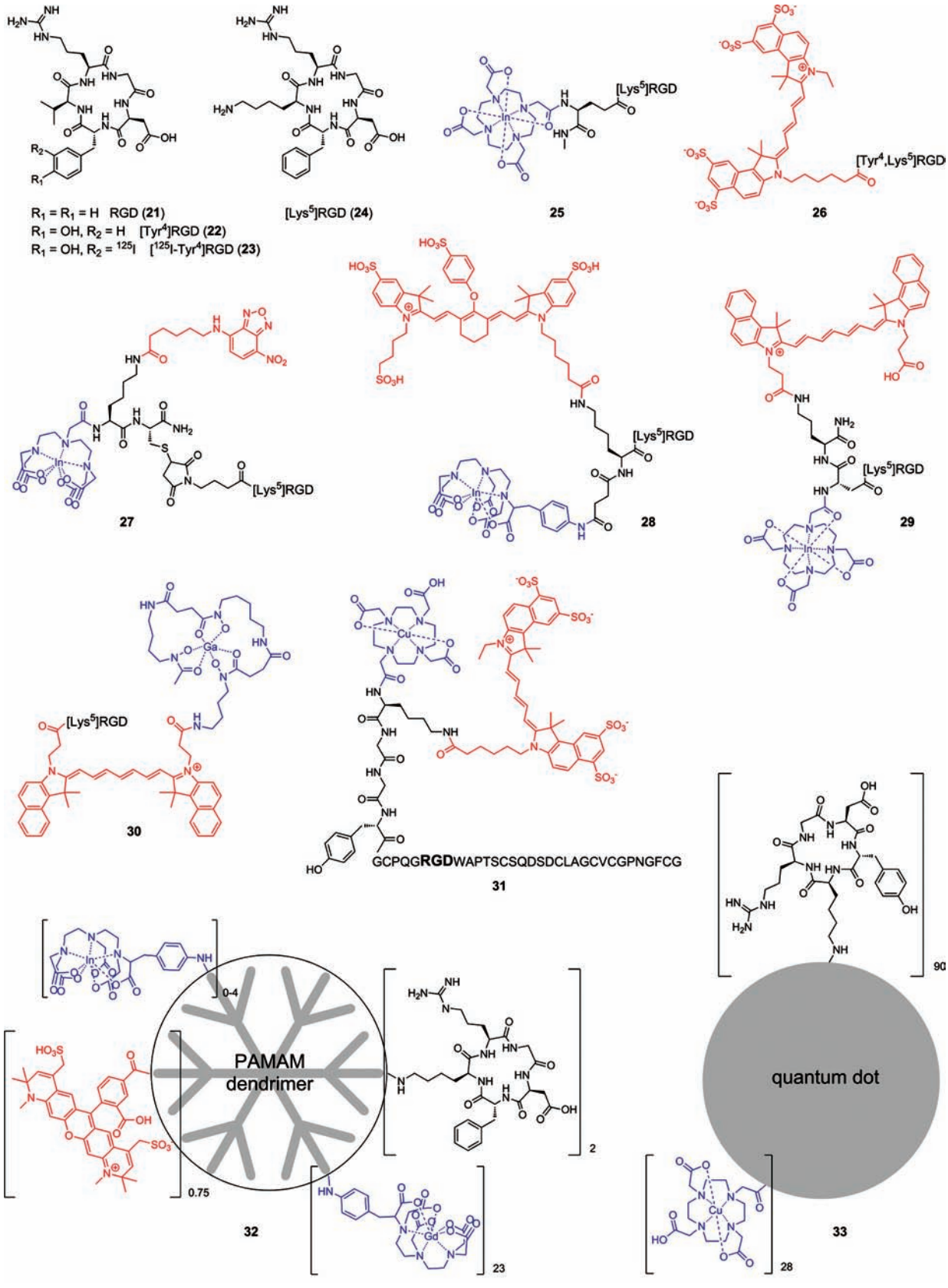


Figure 5. Representation of RGD-peptide based imaging constructs **21**−**33**. In all compounds, except **23** and **31**, the labels were attached to the side chain of the lysine residue. For clarity reasons, the large PAMAM-dendrimer and QD scaffold have been schematically represented in a relatively smaller size. The radiolabels are represented in blue and the fluorescent dyes in red.

studies using ^{64}Cu (Figure 5) (*65*). These QDs had approximately 90 RGD peptides and 28 DOTA chelates per particle and subsequently yielded a 60-fold higher affinity for $\alpha_v\beta_3$ than [Tyr^4,Lys^5]RGD (Table 3). The relatively large QDs, however, in vivo gave a high degree of nonspecific liver uptake (40−55%). Despite this, RGD tagged ^{64}Cu-DOTA-QD-RGD **33** gave significantly more tumor uptake (4.3%ID/g after 25 h) compared to a nontargeted control ^{64}Cu-DOTA-QD (less than

Table 3. Receptor Affinity, Biodistribution, and Imaging Data of the RGD Derivatives

RGD derivative	IC_{50} (nM)	K_D (nM)	%ID/g[a]	tumor-to-muscle ratio[a,b]	imaging modality	ref
21	100−4000	-	n/a[c]	n/a	n/a	*48*
22	similar to **21**	-	n/a	n/a	n/a	*49*
23	similar to **21**	-	0.77 ± 0.10 (2 h)	4.5 (2 h)	radioactivity	*49, 51*
24	similar to **21**	-	−	-	−	*52*
25	236	8.92	2.70 ± 0.29 (2 h)	14.2 (2 h)	radioactivity	*53, 54, 78*
26	42.9 ± 1.2	-	6 (24 h)	5 (24 h)	fluorescence	*55*
27	-	-	−	-	radioactivity	*57*
28	3860 ± 360	-	1.41 ± 0.49 (24 h)	5.0 (24 h)	radioactivity, fluorescence	*58, 59*
29	0.046 ± 0.023	0.029 ± 0.016	7.59 ± 0.45 (24 h)	6.36 ± 0.04 (24 h) 3.41 ± 0.21 (24 h)	radioactivity, fluorescence	*60*
30	180	-	−	-	−	*61*
31	30 ± 7	-	4.57 ± 0.70 (24 h)	12 (24 h)[d] 12.5 (24 h)[d]	radioactivity, fluorescence	*63*
32	-	-	1.25 ± 0.51 (2 h)	3.30 ± 0.03 (2 h)[e]	-	*64*
33	3.88	-	4.3 ± 0.5 (25 h)	4.1 ± 1.1 (5 h)	radioactivity	*65*

[a] Measurement time post injection between parentheses. [b] Tumor-to-muscle ratios are based on radioactivity data, except for 5 (**26**), 3.41 ± 0.21 (**29**), and 12.5 (**31**), which are based on fluorescence. [c] Not applicable. [d] Tumor-to-background tissue ratio. [e] Tumor-to-blood ratio.

1%ID/g after 25 h; Table 3). Tissue staining showed a good overlap between CD31 antibody staining of blood vessels and **33** staining, indicating that the vast majority of injected QD **33** did not extravasate from the angiogenic blood vessels. This result is similar to that found for the PAMAM dendrimer **32** (see above) (*64*).

COMPARISON OF THE MULTIMODAL TUMOR-TARGETING PEPTIDES

The use of multiple diagnostic functionalizations in one imaging agent enables tumor detection with different techniques. As stated in the Introduction, we think that a promising application of such compounds would be the combined use for preoperative and intraoperative imaging (Figure 1). In our opinion, the combined use of radioactive and fluorescent labels is the best option for this application. Such an application, however, has also been suggested for the combination of MR and optical imaging (*66*−*68*).

Of the four different types of tumor-targeting peptides discussed in this review, RGD has been studied the most in combination with multimodal labels. As all the different peptides target receptors on the cell surface, there is no clear reason why the RGD peptide is more suitable for multimodal functionalization than the others. Most likely, this apparent focus on RGD is caused by the wide applicability of angiogenesis imaging.

In addition to the four different tumor-targeting peptides described in this review, this multimodal technology can in theory also be expanded to peptides that target different tumor-specific receptors, e.g., the cholescystokinin-B, the vasoactive intestinal peptide receptor, the melanocortin-1 receptor, the neurotensin receptor, the neuropeptide Y receptor, the gonadotropin releasing hormone receptor, the glucagon-like peptide-1 receptor, and the chemokine receptor 4 (*19*). Furthermore, the multimodal concept has already been applied in non-receptor-targeted peptides, namely, in a caspase-3 substrate and Tat peptides (*69*−*71*).

A challenge in designing multimodal peptides is to retain the receptor affinity and the biodistribution of the original receptor-targeting peptide. Comparing reported multimodal peptides, as has been done in this paper, can facilitate the design of future multimodal peptide-derivatives. Unfortunately, comparison of the different multimodal peptide-derivatives is difficult due to lack of complete data sets for all the individual peptides. An IC_{50} value has been reported for most peptides (Tables 1−3), but as IC_{50} values are dependent on experimental settings (e.g., the concentration of competing ligand), it is difficult to compare the data from different studies. A more adequate comparison of the binding affinity found in different experiments can be made based on association or dissociation constants (K_A/K_D). Nevertheless, these can still differ for cell types. Unfortunately, only a limited number of K_D values have been reported (Tables 1−3). Furthermore, the amount of actual in vivo studies is limited (Tables 1−3) (*5*), which hinders the analysis of the effect that the multimodal labels have on the biodistribution and the tumor targeting efficacy of the different peptides. All together, this suggests that a standardization of the experiments, including receptor affinity data and in vivo data, is desirable. For future compounds, if possible, we propose a combined report of IC_{50}, K_D, in vivo distribution profile, as well as the tumor accumulation.

Despite the difficulties in comparing the multimodal peptides, some general observations can be made regarding (i) the position of the labels, (ii) the type of labels, and (iii) the size relation between the targeting moiety and the label. These points are discussed below.

Position of the Labels. The binding affinity of peptides is reduced when a diagnostic label is placed close to the pharmacophore. The bombesin(7−14) peptide **14**, for example, has a chelate directly attached to the peptide, resulting in a decrease in the peptide's binding affinity. When a 1-octanoic acid spacer was placed between the peptide and the chelate (peptide **15c**), the binding affinity was regained. This effect also appears to be valid for other peptides. Therefore, by choosing the attachment point strategically, far away from the pharmacophore, and by incorporation of the appropriate spacer between the peptide and the labels, multimodal labels should have a minimal effect on the receptor binding affinity.

When the diagnostic labels are placed relatively close to the pharmacophore, seemingly minor changes can already result in large differences in the receptor affinity. This is exemplified in octreotate and bombesin derivatives. Both peptide derivatives have been N-terminally functionalized with a lysine residue. On this lysine, one label was attached to the side chain and one to the N-terminus. For octreotate, the chelate had to be attached to the N-terminus and the FITC dye to the side chain, as reversed attachment significantly reduced the receptor affinity (compounds **8**−**10** in Figure 2 and Table 1). Intriguingly, the opposite trend was observed for bombesin(7−14) with respect to the positions of the dye and the chelate (compounds **17**−**19** in Figure 3 and Table 2). It is not directly clear what causes this discrepancy between the two peptides.

Type of Labels. The choice of dye mainly depends on the spectral properties and the sensitivity of the detection modality used. Besides having different spectral properties, organic dyes can also be structurally and chemically very different (Figures 2−5), something that has an influence on the distribution of the peptide (*72*). Changing a visual dye to a NIR dye to improve its value in deep tissue imaging (*29, 73*) will most likely result in an altered biodistribution of the peptide conjugate. Hence, application dictated that dye variations have to be individually studied for their receptor affinity and distribution prior to use.

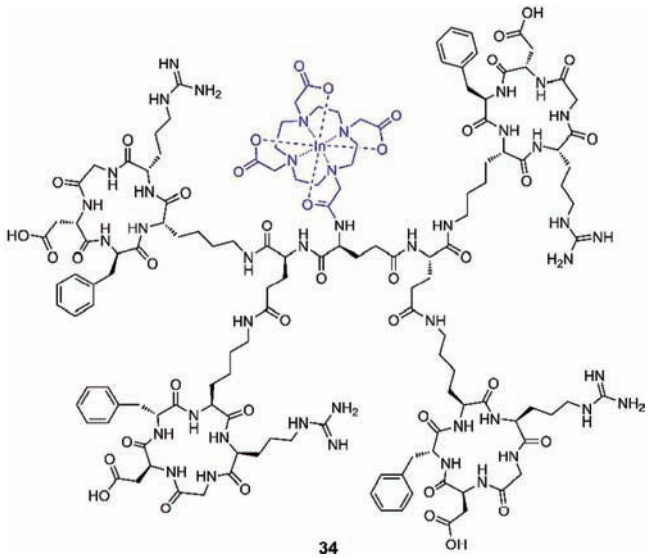


Figure 6. Tetravalent RGD-functionalized dendrimer **34** with an ^{111}In-DOTA chelate (*54*). The radiolabel is represented in blue.

The attachment of a radiolabel to a peptide should have a minimal (negative) influence on its properties. Here, addition of a single radioactive atom to the peptide via, e.g., direct iodination (^{123}I and ^{125}I for SPECT or ^{124}I for PET) will have the smallest influence on the distribution. The most important drawback of iodination is rapid deiodination of mono- and diiodotyrosine by hepatic deiodases (*27*). Because of this instability, most multimodal peptides contain stable but relatively large chelate−metal complexes, e.g., DTPA or DOTA with ^{111}In, ^{64}Cu, or ^{68}Ga. A disadvantage of the predominantly used DTPA and DOTA, however, is that they have a larger influence on the receptor affinity than iodination.

A multimodal label consisting of a dye, a chelate, and, optionally, a spacer is generally as large as the peptide to be labeled (Figures 2−5). Clearly, this can influence the biodistribution and nonspecific uptake. The only reported small multimodal peptide with good in vivo properties is RGD peptide **29**. However, for the structurally related compound **28** it was found that the dye caused nonspecific tissue uptake compared to the monolabeled derivative, while the extent of such an effect has not been investigated for **29**.

Size of the Peptides with Respect to the Labels. One approach to reduce the negative influence of the labels on the biodistribution is to use larger peptides. This strategy was successful for "knottin" peptide **31**; both the binding affinity for its receptor and the tumor specific biodistribution were not greatly affected by the diagnostic labels. However, it is unclear whether this approach can be employed more widely, since **31** is the only example in the literature. Furthermore, larger peptides tend to be less metabolically stable and can be immunogenic (*74*).

Possible Improvements in the Structural Design of Multimodal Peptide Derivatives. Enhancing the ratio of peptide/label in the molecule via multimerization is expected to reduce the negative influence of the diagnostic labels. This strategy has already been successfully applied for monolabeled peptides (*54*, *75*−*77*); e.g., a tetravalent RGD peptide-functionalized dendrimer (**34**) with a DOTA chelate conjugated to the core of the dendrimer (Figure 6) (*54*). This tetravalent construct has approximately six times more affinity for $\alpha_v\beta_3$ integrin than the monovalent peptide (IC_{50} = 19.6 and 120 nM, respectively). Moreover, the tetravalent dendrimer had a significantly better biodistribution than the monovalent peptide. This illustrates the value of enhancing the peptide/label ratio by means of multimerization. Surprisingly, such a multivalent, multimodal derivative has not been reported yet. It is important to note, however, that the above data indicate that structures which are too large have a negative influence on the biodistribution, viz., PAMAM dendrimer **32** and quantum dot **33** cannot extravasate into a tumor.

"Shielding" of the diagnostic labels caused by multimerization (Figure 6) is a promising side effect, which may help reduce the influence of the labels. Such dendritic structures allow placement of the multimodal label in the core, while the targeting moieties are placed on the extremities. This design most likely reduces the interactions between the multimodal labels and the biological environment. Therefore, a multimodal core functionalized with multiple peptides has, in our opinion, the highest chance for success and is currently under investigation in our group.

CONCLUSIONS

Targeted multimodal peptides have the potential to be used in various diagnostic applications. For example, multimodal peptides can be employed in an integrated approach for combined pre- and intraoperative imaging of tumor tissue. The receptor affinity and the biodistribution of most reported multimodal peptides are not as good as those found for the unlabeled and/or monolabeled peptides. However, this partial loss of affinity and targeting ability is compensated by the fact that multimodal peptides allow for use in novel diagnostic applications such as the combined pre- and intraoperative imaging paradigm. Furthermore, the use of multimodal labels in multimeric peptide structures may reduce the negative influence of a multimodal label. In such an increasingly optimized structural design, multimodal labeled peptides based on radioactivity and fluorescence should reveal their full potential.

ACKNOWLEDGMENT

This research is supported, in part, by the Technology Foundation, applied, science division of NWO, and the technology program of the Ministry of Economic Affairs (Grant No. STW BGT 7528 Veni; FvL), a KWF-translational research award (Grant No. PGF 2009-4344; FvL), and within the framework of CTMM, the Centre for Translational Molecular Medicine (http://www.ctmm.nl), project Breast CARE (grant 030-104; JK).

LITERATURE CITED

(1) Mather, S. (2009) Molecular imaging with bioconjugates in mouse models of cancer. *Bioconjugate Chem. 20*, 631–643.
(2) Culver, J., Akers, W., and Achilefu, S. (2008) Multimodality molecular imaging with combined optical and SPECT/PET modalities. *J. Nucl. Med. 49*, 169–172.
(3) Lee, S., and Chen, X. (2009) Dual-modality probes for in vivo molecular imaging. *Mol. Imaging 8*, 87–100.
(4) Jennings, L. E., and Long, N. J. (2009) Two is better than one"-probes for dual-modality molecular imaging. *Chem. Commun.* 3511–3524.
(5) Louie, A. (2010) Multimodality imaging probes: design and challenges. *Chem. Rev. 110*, 3146–3195.
(6) Zhang, Z., Liang, K., Bloch, S., Berezin, M., and Achilefu, S. (2005) Monomolecular multimodal fluorescence-radioisotope imaging agents. *Bioconjugate Chem. 16*, 1232–1239.
(7) Ametamey, S. M., Honer, M., and Schubiger, P. A. (2008) Molecular imaging with PET. *Chem. Rev. 108*, 1501–1516.
(8) Meikle, S. R., Kench, P., Kassiou, M., and Banati, R. B. (2005) Small animal SPECT and its place in the matrix of molecular imaging technologies. *Phys. Med. Biol. 50*, R45–61.

(9) Tung, C. H. (2004) Fluorescent peptide probes for in vivo diagnostic imaging. *Biopolymers 76*, 391–403.
(10) Rao, J., Dragulescu-Andrasi, A., and Yao, H. (2007) Fluorescence imaging in vivo: recent advances. *Curr. Opin. Biotechnol. 18*, 17–25.
(11) Cassidy, P. J., and Radda, G. K. (2005) Molecular imaging perspectives. *J. R. Soc. Interface 2*, 133–144.
(12) Troyan, S. L., Kianzad, V., Gibbs-Strauss, S. L., Gioux, S., Matsui, A., Oketokoun, R., Ngo, L., Khamene, A., Azar, F., and Frangioni, J. V. (2009) The FLARE intraoperative near-infrared fluorescence imaging system: a first-in-human clinical trial in breast cancer sentinel lymph node mapping. *Ann. Surg. Oncol. 16*, 2943–2952.
(13) Frangioni, J. V. (2003) In vivo near-infrared fluorescence imaging. *Curr. Opin. Chem. Biol. 7*, 626–634.
(14) Chin, P. T. K., Buckle, T., Aguirre de Miguel, A., Meskers, S. C. J., Janssen, R. A. J., and van Leeuwen, F. W. B. (2010) Dual emissive quantum dots for multispectral intraoperative fluorescence imaging. *Biomaterials 31*, 6823−6832.
(15) Kobayashi, H., Ogawa, M., Alford, R., Choyke, P. L., and Urano, Y. (2010) New strategies for fluorescent probe design in medical diagnostic imaging. *Chem. Rev. 110*, 2620–2640.
(16) Tweedle, M. F. (2009) Peptide-targeted diagnostics and radiotherapeutics. *Acc. Chem. Res. 42*, 958–968.
(17) Lee, S., Xie, J., and Chen, X. (2010) Peptides and peptide hormones for molecular imaging and disease diagnosis. *Chem. Rev. 110*, 3087–3111.
(18) Reubi, J. C. (2003) Peptide receptors as molecular targets for cancer diagnosis and therapy. *Endocr. Rev. 24*, 389–427.
(19) Schottelius, M., and Wester, H. J. (2009) Molecular imaging targeting peptide receptors. *Methods 48*, 161–177.
(20) Weckbecker, G., Lewis, I., Albert, R., Schmid, H. A., Hoyer, D., and Bruns, C. (2003) Opportunities in somatostatin research: biological, chemical and therapeutic aspects. *Nat. Rev. Drug Discovery 2*, 999–1017.
(21) Werle, M., and Bernkop-Schnurch, A. (2006) Strategies to improve plasma half life time of peptide and protein drugs. *Amino Acids 30*, 351–367.
(22) Reubi, J. C., Schar, J. C., Waser, B., Wenger, S., Heppeler, A., Schmitt, J. S., and Macke, H. R. (2000) Affinity profiles for human somatostatin receptor subtypes SST1-SST5 of somatostatin radiotracers selected for scintigraphic and radiotherapeutic use. *Eur. J. Nucl. Med. 27*, 273–282.
(23) Achilefu, S., Jimenez, H. N., Dorshow, R. B., Bugaj, J. E., Webb, E. G., Wilhelm, R. R., Rajagopalan, R., Johler, J., and Erion, J. L. (2002) Synthesis, in vitro receptor binding, and in vivo evaluation of fluorescein and carbocyanine peptide-based optical contrast agents. *J. Med. Chem. 45*, 2003–2015.
(24) Virgolini, I., Angelberger, P., Li, S., Yang, Q., Kurtaran, A., Raderer, M., Neuhold, N., Kaserer, K., Leimer, M., Peck-Radosavljevic, M., Scheithauer, W., Niederle, B., Eichler, H. G., and Valent, P. (1996) In vitro and in vivo studies of three radiolabelled somatostatin analogues: 123I-octreotide (OCT), 123I-Tyr-3-OCT and 111In-DTPA-D-Phe-1-OCT. *Eur. J. Nucl. Med. 23*, 1388–1399.
(25) Krenning, E. P., Bakker, W. H., Kooij, P. P., Breeman, W. A., Oei, H. Y., de Jong, M., Reubi, J. C., Visser, T. J., Bruns, C., Kwekkeboom, D. J., et al. (1992) Somatostatin receptor scintigraphy with indium-111-DTPA-D-Phe-1-octreotide in man: metabolism, dosimetry and comparison with iodine-123-Tyr-3-octreotide. *J. Nucl. Med. 33*, 652–658.
(26) Schottelius, M., Wester, H. J., Reubi, J. C., Senekowitsch-Schmidtke, R., and Schwaiger, M. (2002) Improvement of pharmacokinetics of radioiodinated Tyr(3)-octreotide by conjugation with carbohydrates. *Bioconjugate Chem. 13*, 1021–1030.
(27) Behr, T. M., Gotthardt, M., Becker, W., and Behe, M. (2002) Radioiodination of monoclonal antibodies, proteins and peptides for diagnosis and therapy. A review of standardized, reliable and safe procedures for clinical grade levels kBq to GBq in the Gottingen/Marburg experience. *Nuklearmed. 41*, 71–79.
(28) Bakker, W. H., Krenning, E. P., Breeman, W. A., Koper, J. W., Kooij, P. P., Reubi, J. C., Klijn, J. G., Visser, T. J., Docter, R., and Lamberts, S. W. (1990) Receptor scintigraphy with a radioiodinated somatostatin analogue: radiolabeling, purification, biologic activity, and in vivo application in animals. *J. Nucl. Med. 31*, 1501–1509.
(29) Becker, A., Hessenius, C., Licha, K., Ebert, B., Sukowski, U., Semmler, W., Wiedenmann, B., and Grotzinger, C. (2001) Receptor-targeted optical imaging of tumors with near-infrared fluorescent ligands. *Nat. Biotechnol. 19*, 327–331.
(30) Edwards, W. B., Xu, B., Akers, W., Cheney, P. P., Liang, K., Rogers, B. E., Anderson, C. J., and Achilefu, S. (2008) Agonist-antagonist dilemma in molecular imaging: evaluation of a monomolecular multimodal imaging agent for the somatostatin receptor. *Bioconjugate Chem. 19*, 192–200.
(31) Cornelio, D. B., Roesler, R., and Schwartsmann, G. (2007) Gastrin-releasing peptide receptor as a molecular target in experimental anticancer therapy. *Ann. Oncol. 18*, 1457–1466.
(32) Gonzalez, N., Moody, T. W., Igarashi, H., Ito, T., and Jensen, R. T. (2008) Bombesin-related peptides and their receptors: recent advances in their role in physiology and disease states. *Curr. Opin. Endocrinol. Diabetes Obes. 15*, 58–64.
(33) Schroeder, R. P., van Weerden, W. M., Bangma, C., Krenning, E. P., and de Jong, M. (2009) Peptide receptor imaging of prostate cancer with radiolabelled bombesin analogues. *Methods 48*, 200–204.
(34) Hoffman, T. J., Gali, H., Smith, C. J., Sieckman, G. L., Hayes, D. L., Owen, N. K., and Volkert, W. A. (2003) Novel series of 111In-labeled bombesin analogs as potential radiopharmaceuticals for specific targeting of gastrin-releasing peptide receptors expressed on human prostate cancer cells. *J. Nucl. Med. 44*, 823–831.
(35) Nock, B. A., Nikolopoulou, A., Galanis, A., Cordopatis, P., Waser, B., Reubi, J. C., and Maina, T. (2005) Potent bombesin-like peptides for GRP-receptor targeting of tumors with 99mTc: a preclinical study. *J. Med. Chem. 48*, 100–110.
(36) Mantey, S. A., Weber, H. C., Sainz, E., Akeson, M., Ryan, R. R., Pradhan, T. K., Searles, R. P., Spindel, E. R., Battey, J. F., Coy, D. H., and Jensen, R. T. (1997) Discovery of a high affinity radioligand for the human orphan receptor, bombesin receptor subtype 3, which demonstrates that it has a unique pharmacology compared with other mammalian bombesin receptors. *J. Biol. Chem. 272*, 26062–26071.
(37) Garrison, J. C., Rold, T. L., Sieckman, G. L., Naz, F., Sublett, S. V., Figueroa, S. D., Volkert, W. A., and Hoffman, T. J. (2008) Evaluation of the pharmacokinetic effects of various linking group using the 111In-DOTA-X-BBN(7−14)NH_2 structural paradigm in a prostate cancer model. *Bioconjugate Chem. 19*, 1803–1812.
(38) Mansi, R., Wang, X., Forrer, F., Kneifel, S., Tamma, M. L., Waser, B., Cescato, R., Reubi, J. C., and Maecke, H. R. (2009) Evaluation of a 1,4,7,10-tetraazacyclododecane-1,4,7,10-tetraacetic acid-conjugated bombesin-based radioantagonist for the labeling with single-photon emission computed tomography, positron emission tomography, and therapeutic radionuclides. *Clin. Cancer Res. 15*, 5240–5249.
(39) Prasanphanich, A. F., Retzloff, L., Lane, S. R., Nanda, P. K., Sieckman, G. L., Rold, T. L., Ma, L., Figueroa, S. D., Sublett, S. V., Hoffman, T. J., and Smith, C. J. (2009) In vitro and in vivo analysis of [(64)Cu-NO2A-8-Aoc-BBN(7−14)NH(2)]: a site-directed radiopharmaceutical for positron-emission tomography imaging of T-47D human breast cancer tumors. *Nucl. Med. Biol. 36*, 171–181.
(40) Ma, L., Yu, P., Veerendra, B., Rold, T. L., Retzloff, L., Prasanphanich, A., Sieckman, G., Hoffman, T. J., Volkert, W. A., and Smith, C. J. (2007) In vitro and in vivo evaluation of Alexa Fluor 680-bombesin(7-14)NH_2 peptide conjugate, a high-affinity fluorescent probe with high selectivity for the gastrin-releasing peptide receptor. *Mol. Imaging 6*, 171–180.

(41) Kang, Y., He, W., Tulley, S., Gupta, G. P., Serganova, I., Chen, C. R., Manova-Todorova, K., Blasberg, R., Gerald, W. L., and Massague, J. (2005) Breast cancer bone metastasis mediated by the Smad tumor suppressor pathway. *Proc. Natl. Acad. Sci. U.S.A. 102*, 13909–13914.

(42) Lewis, V. O., Ozawa, M. G., Deavers, M. T., Wang, G., Shintani, T., Arap, W., and Pasqualini, R. (2009) The interleukin-11 receptor alpha as a candidate ligand-directed target in osteosarcoma: consistent data from cell lines, orthotopic models, and human tumor samples. *Cancer Res. 69*, 1995–1999.

(43) Zurita, A. J., Troncoso, P., Cardo-Vila, M., Logothetis, C. J., Pasqualini, R., and Arap, W. (2004) Combinatorial screenings in patients: the interleukin-11 receptor alpha as a candidate target in the progression of human prostate cancer. *Cancer Res. 64*, 435–439.

(44) Arap, W., Kolonin, M. G., Trepel, M., Lahdenranta, J., Cardo-Vila, M., Giordano, R. J., Mintz, P. J., Ardelt, P. U., Yao, V. J., Vidal, C. I., Chen, L., Flamm, A., Valtanen, H., Weavind, L. M., Hicks, M. E., Pollock, R. E., Botz, G. H., Bucana, C. D., Koivunen, E., Cahill, D., Troncoso, P., Baggerly, K. A., Pentz, R. D., Do, K. A., Logothetis, C. J., and Pasqualini, R. (2002) Steps toward mapping the human vasculature by phage display. *Nat. Med. 8*, 121–127.

(45) Wang, W., Ke, S., Kwon, S., Yallampalli, S., Cameron, A. G., Adams, K. E., Mawad, M. E., and Sevick-Muraca, E. M. (2007) A new optical and nuclear dual-labeled imaging agent targeting interleukin 11 receptor alpha-chain. *Bioconjugate Chem. 18*, 397–402.

(46) Avraamides, C. J., Garmy-Susini, B., and Varner, J. A. (2008) Integrins in angiogenesis and lymphangiogenesis. *Nat. Rev. Cancer 8*, 604–617.

(47) Plow, E. F., Haas, T. A., Zhang, L., Loftus, J., and Smith, J. W. (2000) Ligand binding to integrins. *J. Biol. Chem. 275*, 21785–21788.

(48) Gurrath, M., Muller, G., Kessler, H., Aumailley, M., and Timpl, R. (1992) Conformation/activity studies of rationally designed potent anti-adhesive RGD peptides. *Eur. J. Biochem. 210*, 911–921.

(49) Haubner, R., Wester, H. J., Reuning, U., Senekowitsch-Schmidtke, R., Diefenbach, B., Kessler, H., Stocklin, G., and Schwaiger, M. (1999) Radiolabeled alpha(v)beta3 integrin antagonists: a new class of tracers for tumor targeting. *J. Nucl. Med. 40*, 1061–1071.

(50) Lee, K. H., Jung, K. H., Song, S. H., Kim, D. H., Lee, B. C., Sung, H. J., Han, Y. M., Choe, Y. S., Chi, D. Y., and Kim, B. T. (2005) Radiolabeled RGD uptake and α_v integrin expression is enhanced in ischemic murine hindlimbs. *J. Nucl. Med. 46*, 472–478.

(51) Kuijpers, B. H., Groothuys, S., Soede, A. C., Laverman, P., Boerman, O. C., van Delft, F. L., and Rutjes, F. P. (2007) Preparation and evaluation of glycosylated arginine-glycine-aspartate (RGD) derivatives for integrin targeting. *Bioconjugate Chem. 18*, 1847–1854.

(52) Haubner, R., Gratias, R., Diefenbach, B., Goodman, S. L., Jonczyk, A., and Kessler, H. (1996) Structural and functional aspects of RGD-containing cyclic pentapeptides as highly potent and selective integrin $\alpha_3\beta_v$ antagonists. *J. Am. Chem. Soc. 118*, 7461–7472.

(53) Dijkgraaf, I., Kruijtzer, J. A., Frielink, C., Soede, A. C., Hilbers, H. W., Oyen, W. J., Corstens, F. H., Liskamp, R. M., and Boerman, O. C. (2006) Synthesis and biological evaluation of potent $\alpha_v\beta_3$-integrin receptor antagonists. *Nucl. Med. Biol. 33*, 953–961.

(54) Dijkgraaf, I., Kruijtzer, J. A., Liu, S., Soede, A. C., Oyen, W. J., Corstens, F. H., Liskamp, R. M., and Boerman, O. C. (2007) Improved targeting of the $\alpha_v\beta_3$ integrin by multimerisation of RGD peptides. *Eur. J. Nucl. Med. Mol. Imaging 34*, 267–273.

(55) Cheng, Z., Wu, Y., Xiong, Z., Gambhir, S. S., and Chen, X. (2005) Near-infrared fluorescent RGD peptides for optical imaging of integrin $\alpha_v\beta_3$ expression in living mice. *Bioconjugate Chem. 16*, 1433–1441.

(56) Garanger, E., Blois, J., Hilderbrand, S. A., Shao, F., and Josephson, L. (2010) Divergent oriented synthesis for the design of reagents for protein conjugation. *J. Comb. Chem. 12*, 57–64.

(57) Garanger, E., Aikawa, E., Reynolds, F., Weissleder, R., and Josephson, L. (2008) Simplified syntheses of complex multifunctional nanomaterials. *Chem. Commun.* 4792–4794.

(58) Houston, J. P., Ke, S., Wang, W., Li, C., and Sevick-Muraca, E. M. (2005) Quality analysis of in vivo near-infrared fluorescence and conventional gamma images acquired using a dual-labeled tumor-targeting probe. *J. Biomed. Opt. 10*, 054010.

(59) Li, C., Wang, W., Wu, Q., Ke, S., Houston, J., Sevick-Muraca, E., Dong, L., Chow, D., Charnsangavej, C., and Gelovani, J. G. (2006) Dual optical and nuclear imaging in human melanoma xenografts using a single targeted imaging probe. *Nucl. Med. Biol. 33*, 349–358.

(60) Edwards, W. B., Akers, W. J., Ye, Y., Cheney, P. P., Bloch, S., Xu, B., Laforest, R., and Achilefu, S. (2009) Multimodal imaging of integrin receptor-positive tumors by bioluminescence, fluorescence, gamma scintigraphy, and single-photon emission computed tomography using a cyclic RGD peptide labeled with a near-infrared fluorescent dye and a radionuclide. *Mol. Imaging 8*, 101–110.

(61) Ye, Y., Bloch, S., Xu, B., and Achilefu, S. (2008) Novel near-infrared fluorescent integrin-targeted DFO analogue. *Bioconjugate Chem. 19*, 225–234.

(62) Kimura, R. H., Levin, A. M., Cochran, F. V., and Cochran, J. R. (2009) Engineered cystine knot peptides that bind alphavbeta3, alphavbeta5, and alpha5beta1 integrins with low-nanomolar affinity. *Proteins 77*, 359–369.

(63) Kimura, R. H., Miao, Z., Cheng, Z., Gambhir, S. S., and Cochran, J. R. (2010) A dual-labeled knottin peptide for PET and near-infrared fluorescence imaging of integrin expression in living subjects. *Bioconjugate Chem. 21*, 436–444.

(64) Boswell, C. A., Eck, P. K., Regino, C. A., Bernardo, M., Wong, K. J., Milenic, D. E., Choyke, P. L., and Brechbiel, M. W. (2008) Synthesis, characterization, and biological evaluation of integrin alphavbeta3-targeted PAMAM dendrimers. *Mol. Pharm. 5*, 527–539.

(65) Cai, W., Chen, K., Li, Z. B., Gambhir, S. S., and Chen, X. (2007) Dual-function probe for PET and near-infrared fluorescence imaging of tumor vasculature. *J. Nucl. Med. 48*, 1862–1870.

(66) Kircher, M. F., Mahmood, U., King, R. S., Weissleder, R., and Josephson, L. (2003) A multimodal nanoparticle for preoperative magnetic resonance imaging and intraoperative optical brain tumor delineation. *Cancer Res. 63*, 8122–8125.

(67) Veiseh, O., Sun, C., Gunn, J., Kohler, N., Gabikian, P., Lee, D., Bhattarai, N., Ellenbogen, R., Sze, R., Hallahan, A., Olson, J., and Zhang, M. (2005) Optical and MRI multifunctional nanoprobe for targeting gliomas. *Nano Lett. 5*, 1003–1008.

(68) Uzgiris, E. E., Sood, A., Bove, K., Grimmond, B., Lee, D., and Lomnes, S. (2006) A multimodal contrast agent for preoperative MR Imaging and intraoperative tumor margin delineation. *Technol. Cancer Res. Treat. 5*, 301–309.

(69) Lee, H., Akers, W. J., Cheney, P. P., Edwards, W. B., Liang, K., Culver, J. P., and Achilefu, S. (2009) Complementary optical and nuclear imaging of caspase-3 activity using combined activatable and radio-labeled multimodality molecular probe. *J. Biomed. Opt. 14*, 040507.

(70) Bullok, K. E., Dyszlewski, M., Prior, J. L., Pica, C. M., Sharma, V., and Piwnica-Worms, D. (2002) Characterization of novel histidine-tagged Tat-peptide complexes dual-labeled with (99m)Tc-tricarbonyl and fluorescein for scintigraphy and fluorescence microscopy. *Bioconjugate Chem. 13*, 1226–1237.

(71) Lewin, M., Carlesso, N., Tung, C. H., Tang, X. W., Cory, D., Scadden, D. T., and Weissleder, R. (2000) Tat peptide-derivatized magnetic nanoparticles allow in vivo tracking and recovery of progenitor cells. *Nat. Biotechnol. 18*, 410–414.

(72) Berkers, C. R., van Leeuwen, F. W. B., Groothuis, T. A., Peperzak, V., van Tilburg, E. W., Borst, J., Neefjes, J. J., and Ovaa, H. (2007) Profiling proteasome activity in tissue with fluorescent probes. *Mol. Pharm. 4*, 739–748.

(73) Licha, K., Hessenius, C., Becker, A., Henklein, P., Bauer, M., Wisniewski, S., Wiedenmann, B., and Semmler, W. (2001) Synthesis, characterization, and biological properties of cyanine-labeled somatostatin analogues as receptor-targeted fluorescent probes. *Bioconjugate Chem. 12*, 44–50.

(74) Purcell, A. W., McCluskey, J., and Rossjohn, J. (2007) More than one reason to rethink the use of peptides in vaccine design. *Nat. Rev. Drug Discovery 6*, 404–414.

(75) McNerny, D. Q., Kukowska-Latallo, J. F., Mullen, D. G., Wallace, J. M., Desai, A. M., Shukla, R., Huang, B. H., Holl, M. M. B., and Baker, J. R. (2009) RGD dendron bodies; synthetic avidity agents with defined and potentially interchangeable effector sites that can substitute for antibodies. *Bioconjugate Chem 20*, 1853–1859.

(76) Almutairi, A., Rossin, R., Shokeen, M., Hagooly, A., Ananth, A., Capoccia, B., Guillaudeu, S., Abendschein, D., Anderson, C. J., Welch, M. J., and Frechet, J. M. (2009) Biodegradable dendritic positron-emitting nanoprobes for the noninvasive imaging of angiogenesis. *Proc. Natl. Acad. Sci. U.S.A. 106*, 685–690.

(77) Liu, S. (2009) Radiolabeled cyclic RGD peptides as integrin alpha(v)beta(3)-targeted radiotracers: maximizing binding affinity via bivalency. *Bioconjugate Chem. 20*, 2199–2213.

(78) Chen, X., Park, R., Tohme, M., Shahinian, A. H., Bading, J. R., and Conti, P. S. (2004) MicroPET and autoradiographic imaging of breast cancer alpha v-integrin expression using 18F- and ^{64}Cu-labeled RGD peptide. *Bioconjugate Chem. 15*, 41–49.

(79) Hanaoka, H., Mukai, T., Tamamura, H., Mori, T., Ishino, S., Ogawa, K., Iida, Y., Doi, R., Fujii, N., and Saji, H. (2006) Development of a 111In-labeled peptide derivative targeting a chemokine receptor, CXCR4, for imaging tumors. *Nucl. Med. Biol. 33*, 489–494.

(80) Buckle, T., van den Berg, N. S., Kuil, J., Oishi, S., Fujii, N., and van Leeuwen, F. W. B. (2010) Unpublished data.

(81) Hilderbrand, S. A., Kelly, K. A., Weissleder, R., and Tung, C. H. (2005) Monofunctional near-infrared fluorochromes for imaging applications. *Bioconjugate Chem. 16*, 1275–1281.

BC100276J

A Novel Approach to Oral Delivery of Insulin by Conjugating with Low Molecular Weight Chitosan

Eunhye Lee, Jinju Lee, and Sangyong Jon*

School of Life Sciences, Gwangju Institute of Science and Technology, 261 Cheomdangwagi-ro, Gwangju 500-712, Republic of Korea. Received February 16, 2010; Revised Manuscript Received August 9, 2010

A new oral delivery system for insulin was developed aiming to improve bioavailability based on a conjugate between insulin and low molecular weight chitosan (LMWC) of narrow molecular weight distribution. The conjugate was synthesized from the reaction between site-specifically modified insulin at the lysine residue of the B-chain and sulfhydryl-modified LMWC. To investigate the effect of MWs of LMWC on oral bioavailability of insulin, various LMWCs (3, 6, 9, and 13k average MW) with narrow MW distribution were used to synthesize LMWC−insulin conjugates. The content of insulin in the LMWC−insulin conjugates was calculated by UV spectrophotometer: 62%, 44%, 38%, and 29% for 3, 6, 9, and 13 kDa LMWC, respectively. The biological activity of insulin in LMWC(6k)−insulin conjugate in vivo was 43 ± 0.7%. LMWC−insulin conjugates after oral administration to diabetic rat models could control blood glucose levels effectively for several hours. Of those conjugates, LMWC(9k)-insulin exhibited the highest pharmacodynamic bioavailability of 3.7 ± 0.3% relative to that of subcutaneously (s.c.) injected insulin (100%).

INTRODUCTION

Progress in biotechnology has enabled the large-scale production of therapeutic proteins, including insulin, calcitonin, antibodies, and growth hormones. Most of these therapeutic proteins continue to be administered parenterally because their bioavailability is poor when delivered via an oral route, resulting in poor patient compliance. Thus, convenient and effective delivery of such peptide and protein drugs to the body via nonparenteral routes remains a major challenge.

Among the most often used therapeutic peptides and proteins currently is insulin. Conventional insulin therapy requires multiple subcutaneous injections and is the mainstay for diabetic patients. However, this standard treatment regimen is associated with a number of problems, including imprecise hyperglycemic control, physiological stress, pain, inconvenience, infection, inability to handle protein, fat deposition at the injection sites, and the need to load injections (*1*−*4*). In recent years, there has been considerable interest on the part of the pharmaceutical industry in developing systems for nonparenteral insulin delivery, including oral, nasal, buccal, pulmonary, transdermal, rectal, and ocular delivery systems (*5*, *6*). Because oral delivery is expected to result in enhanced patient compliance as well as improved clinical outcomes, many attempts have been made to develop oral insulin delivery systems (*2*). However, formidable barriers in the gastrointestinal (GI) tract, including acidic environments in the stomach, enzymatic degradation by proteases, and tightly bound intestinal epithelial cells (enterocytes) result in poor bioavailability for oral insulin delivery (*2*, *7*). A few recent successes in oral insulin delivery have been achieved using insulin covalently modified with carriers, including polyethylene glycol, bile acid, and fatty acids. These modified insulins have shown improved physicochemical properties in terms of solubility, stability, circulation half-life, and permeability (*8*−*11*).

Chitosan has been widely used as a functional biopolymer, for example, in the food and pharmaceutical field, because it is biocompatible, biodegradable, and relatively nontoxic. Of particular interest has been the oral delivery of protein drugs using chitosan, presumably because it is highly mucoadhesive and capable of opening tight junctions of intestinal epithelium to facilitate paracellular transport (*12*−*15*). Recently, a low molecular weight chitosan (LMWC) form has demonstrated even more favorable characteristics, such as improved water solubility, lower toxicity, and a narrower molecular weight distribution compared with the conventional high molecular weight chitosan (*16*).

Previously, we reported the development of a new oral delivery system for sparingly water-soluble taxane drugs such as paclitaxel and docetaxel by conjugating them to LMWC; notably, these LMWC-taxane conjugates showed the following: (i) enhanced water solubility; (ii) increased stability in the GI tract; and (iii) remarkable bioavailability of the parent taxane drugs (*17*, *18*) after oral administration.

These previous successes indicate that the analogous covalent modification (conjugation) of insulin with LMWC would be expected to increase the retention time of the conjugate in the GI tract due to the mucoadhesive property of LMWC and subsequently may facilitate uptake of the conjugate via the paracellular pathway, resulting in improved oral bioavailability. In this study, we report the design and synthesis of LMWC−insulin conjugates and assessment of their in vivo efficacy to examine the feasibility of the conjugate system as a novel oral delivery platform of peptide and protein drugs.

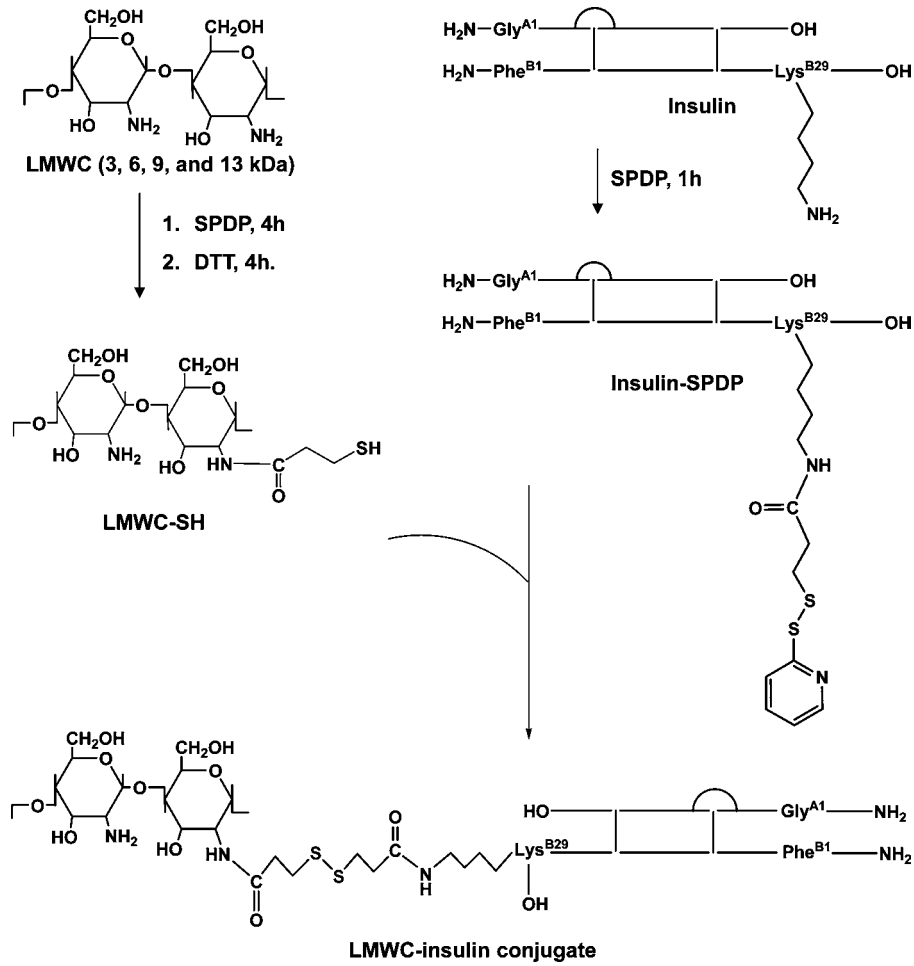
RESULTS AND DISCUSSION

Design and Synthesis of LMWC−Insulin Conjugates. Disulfide linkage is applicable to a protein conjugation strategy, since free protein easily released from protein conjugate in the plasma (*19*). In addition, sulfhydryl containing materials were shown to improve the permeation of proteins from the GI tract (*20*). The mechanism responsible for this permeation enhancing effect is based on the sulfhydryl groups which inhibit protein involved in the closing process of tight junctions, via a GSH-

* To whom correspondence should be addressed. Phone: + 82 62 715 2504. Fax: + 82 62 715 2484. E-mail: syjon@gist.ac.kr.

10.1021/bc100093v © 2010 American Chemical Society
Published on Web 09/17/2010

Scheme 1. Synthesis of LMWC−Insulin Conjugates



mediated mechanism (*20*). With these in mind, we designed an insulin linkage to LMWC through a disulfide bond (Scheme 1). Four different MWs of LMWC (3, 6, 9, and 13k) were used to conjugate with insulin to examine the effect of MW on oral bioavailability of insulin. In the first step, both insulin and LMWC were modified with a heterobifunctional cross-linker, *N*-succinimidyl-3-(2-pyridyldithio)-propionate (SPDP). We designed a strategy in which the primary amine group of lysine at the B^{29} position of insulin was reacted with SPDP to introduce disulfide bonds. In the second step, LMWC-SPDP was reduced by dithiothreitol (DTT) to afford LMWC-SH bearing a free sulfhydryl group. In the final step, the SPDP-modified insulin reacted with the free sulfhydryl group of LMWC-SH to afford the LMWC−insulin conjugates containing a disulfide linkage.

Characterization of LMWC−Insulin Conjugates. The SPDP-modified insulin was purified by a high-pressure liquid chromatogram (HPLC) on a C18 column by gradient elution; under the conditions used, insulin−SPDP was eluted with a retention time of about 15 min, whereas free insulin eluted approximately at 13 min (Supporting Information Figure S1). MALDI-TOF mass spectroscopic analysis revealed that SPDP was monosubstituted at insulin (predicted conjugate MW 6005). We examined whether SPDP was conjugated to the amine group of B^{29}-Lys of insulin. Because the pK_a value and the reactivity of the primary amine group at B^{29}-Lys (>10) of insulin are greater than those of the two N-termini (8.4 for A^1-Gly and 7.1 for B^1-Phe, respectively), insulin could be selectively modified at the B^{29}-Lys site under basic conditions (*8, 9, 21*). Arrows in Figure 1A indicate the amide bonds in the insulin and the insulin−SPDP conjugates that are expected to be cut by trypsin. Two possible cleavage sites for native insulin are available: one between B^{22}-Arg and B^{23}-Gly and the other between B^{29}-Lys and B^{30}-Thr. In the case of the insulin−SPDP, the site between B^{29}-Lys and B^{30}-Thr is not accessible, because the side chain of lysine is blocked by the SPDP modification. After trypsin treatment, cleavage fragments from insulin and the insulin−SPDP were analyzed by HPLC. For insulin, the retention times of the major fragment (A1−21 B1−22) and minor fragment (B23−29) were 12.2 and 9.8 min, respectively (Figure 1B). The two fragment peptides were characterized by HPLC and MALDI-TOF analyses (Figure 1C). As expected, peaks corresponding to both A1−21 B1−22 and B23−30−SPDP were identified in the mass spectrum. The major fragment (A1−21 B1−22) from the insulin−SPDP was identical to that from insulin, showing the same retention time and mass. In contrast, the minor fragment (B23−30) from the insulin−SPDP had a different retention time (12.2 → 17.5 min) and mass spectrum (858.1 → 1158.1) corresponding to the expected mass of the B23−30 fragment bearing SPDP. These results indicate that SPDP was attached to the ε-amine group of B^{29}-Lys and not to the N-terminus of the A- or B-chain.

SPDP-modified LMWC (3, 6, 9, 13k) were characterized by ^{1}H NMR analysis, which revealed that approximately ∼2 molecules of SPDP were attached to each LMWC (Supporting Information Figure S2; a typical ^{1}H NMR spectrum of SPDP-modified 6k LMWC).

Conjugation reactions between insulin−SPDP and a 2-fold molar excess of the thiolated-LMWC were conducted at ambient temperature, and the resulting conjugates were purified by reverse-phase preparative HPLC. The insulin content of the LMWC−insulin conjugates were calculated by UV spectrophotometer measurements at 275 nm, which showed that the

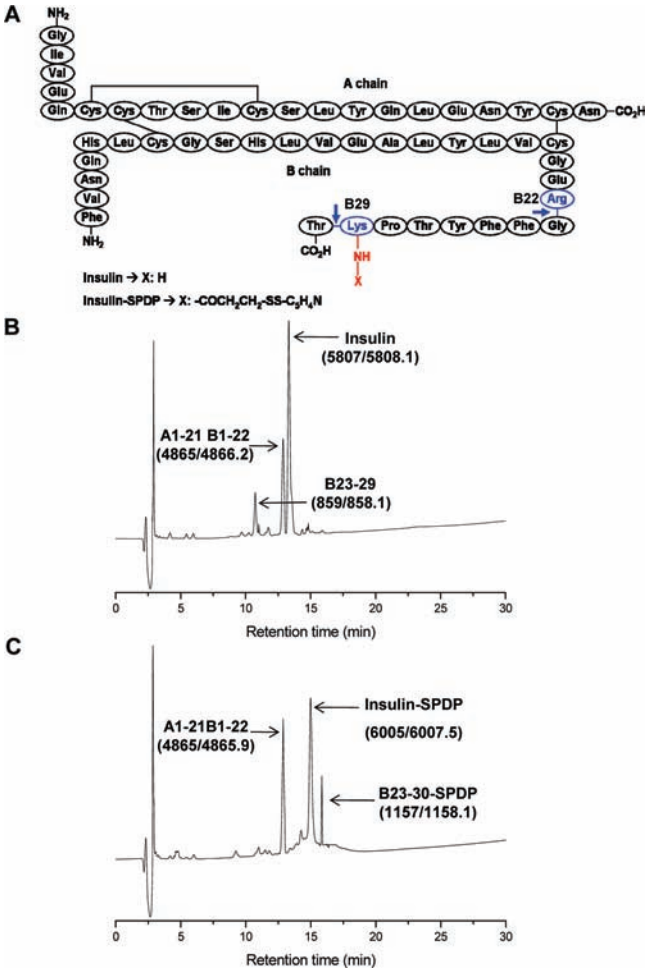


Figure 1. (A) Primary structure of insulin and insulin−SPDP (arrows indicate sites of trypsin cleavage). HPLC spectra of (B) insulin and (C) insulin−SPDP conjugate after trypsin cleavage (theoretical MW/measured MW).

conjugates contained approximately 62%, 44%, 38%, and 29% (w/w) insulin for 3, 6, 9, and 13k of LMWC (data not shown).

In Vivo Evaluation of Diabetic Rats. LMWC−insulin conjugates could not be analyzed by enzyme-linked immunosorbent assays (ELISA) (data not shown). This result may indicate that the conjugate form did not bind to the insulin receptor and insulin was not released from the conjugate under the ELISA experimental conditions (*8*). We therefore evaluated the biological activity of LMWC−insulin conjugates using diabetic Sprague−Dawley (SD) rats. Figure 2 shows blood glucose levels following intravenous injection of native insulin or LMWC(6k)−insulin conjugate. Insulin and LMWC(6k)−insulin conjugate reduced glucose levels by 56.7% and 44.9%, respectively. From this result, the calculated relative bioactivity of LMWC−insulin conjugate was about 43 ± 0.7% relative to that of native insulin, suggesting that the SPDP-modified insulin is released from the conjugate via cleavage of the disulfide bond under physiological conditions (*8*).

To evaluate the oral bioavailability of LMWC−insulin conjugates, we administered the LMWC−insulin conjugates orally to diabetic rats and monitored blood glucose levels at various time points. As shown in Figure 3, native insulin (50 IU/kg) and LMWC alone (2.23 mg/kg) did not change blood glucose levels after oral administration. In contrast, LMWC−insulin conjugates (50 IU/kg) reduced blood glucose levels in proportion to the molecular weight of the conjugated LMWC. We speculate that this molecular weight dependency may be attributed to the

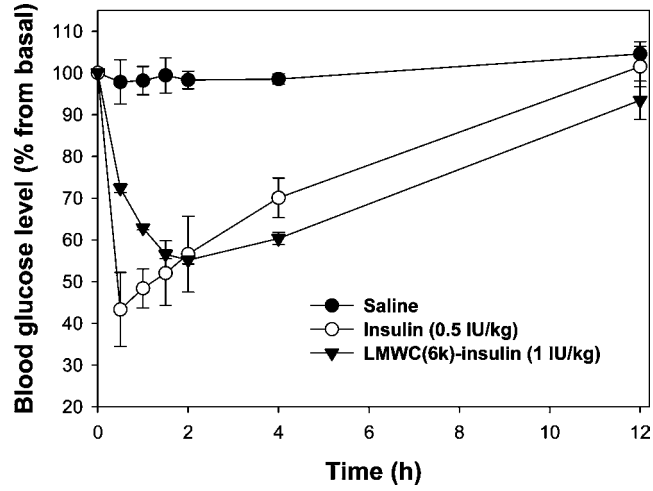


Figure 2. Change in blood glucose levels after intravenous injection of insulin (0.5 IU/kg) or LMWC(6k)−insulin conjugate (1 IU/kg). Results are means ± SEs.

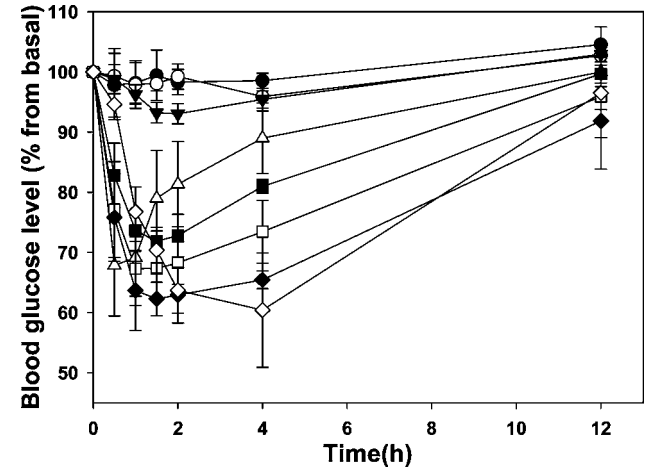


Figure 3. Effect of a single oral administration of insulin or LMWC−insulin conjugates on blood glucose levels in STZ-rats. STZ-rats received saline (●), 2.23 mg/kg LMWC (○), orally administered 50 IU/kg Zn^{2+} insulin (▼), subcutaneous injected 0.5 IU/kg Zn^{2+} insulin (△), or 50 IU/kg LMWC−insulin conjugates; 3k (■), 6k (□), 9k (◆), and 13k (◇). Results are means ± SEs.

discrepancy in the ability to open the tight junction of intestinal epithelial cells and the mucoadhesiveness of each LMWC (*16*).

The relative pharmacodynamic bioavailability (PDBA) of the conjugate was calculated from the area under the curve (AUC) in the graph of blood glucose levels (Table 1). The PDBA values for 3, 6, and 9k LMWC−insulin conjugates were 1.9 ± 0.3%, 2.7 ± 0.4%, and 3.7 ± 0.3%, respectively, relative to subcutaneously injected native insulin (100%). This range of bioavailability values is higher than that of the previously reported oral delivery system formulated with chitosan−enzyme inhibitor conjugates and uptake enhancers (*22*). This high bioavailability may be attributed to the ability of LMWC to act as a mucoadhesive polymer and to open tight junctions of intestinal epithelial layers. It is anticipated that LMWC−insulin conjugate may also be able to escape hepatic enzymatic degradation once absorbed in blood, as demonstrated in our previous reports on oral delivery of taxanes in the form of LMWC conjugates (*17, 18*).

Interestingly, although the LMWC(13k)−insulin did not follow the MW-dependent pattern of LMWC forms, it did show a more sustained release profile than other LMWC conjugates. This effect might be caused by altered physical properties, such as decreased solubility and increased viscosity. This interpreta-

Table 1. Relative Pharmacodynamic Bioavailability of LMWC−Insulin Conjugates after Oral Administration in Streptozotocin-Induced Type I Diabetes in SD Rats

	LMWC−insulin conjugates			
	3k LMWC	6k LMWC	9k LMWC	13k LMWC
insulin contents (%)	62	44	38	29
bioavailability (%) (s.c.:100%)	1.9 ± 0.3	2.7 ± 0.4	3.7 ± 0.3	3.3 ± 0.3

tion is consistent with previous observations that the lower molecular weight forms of LMWC (<10 kDa) have greater water solubility and lower viscosity than higher molecular weight forms (>10 kDa).

In conclusion, the reported work illustrates a novel insulin oral delivery by conjugating with mucoadhesive, cationic biopolymer, and LMWC. LMWC−insulin conjugates were synthesized by site-specific modification of insulin using a heterobifunctional cross-linker. The in vivo biological activity test demonstrated that LMWC(6k)−insulin retains about half of insulin activity. Additionally, the relative pharmacodynamic bioavailability of orally administered LMWC−insulin conjugates in diabetic rat models indicated that the intestinal absorption of insulin was significantly enhanced. Taken together, the LMWC−insulin conjugate system offers a promising strategy to achieve high oral bioavailability of insulin and the strategy may be applied to oral delivery of other peptide or protein drugs. Additional studies are currently underway to optimize the conjugate system.

ACKNOWLEDGMENT

This work was supported by the Converging Research Center Program through the National Research Foundation of Korea (NRF) funded by the Ministry of Education, Science and Technology (grant number: 2009-0093628).

Supporting Information Available: Experimental procedures for the synthesis, characterization, and in vivo hyperglycemic effects of LMWC−insulin conjugates. This material is available free of charge via the Internet at http://pubs.acs.org.

LITERATURE CITED

(1) Binder, C., Lauritzen, T., Faber, O., and Pramming, S. (1984) Insulin pharmacokinetics. *Diabetes Care 7*, 188–199.

(2) Carino, G. P., and Mathiowitz, E. (1999) Oral insulin delivery. *Adv. Drug Delivery Rev. 35*, 249–257.

(3) Zambanini, A., Newson, R. B., Maisey, M., and Feher, M. D. (1999) Injection related anxiety in insulin-related diabetes. *Diabetes Res. Clin. Pract. 46*, 239–46.

(4) Kennedy, F. P. (1991) Recent developments in insulin delivery techniques Current status and future potential. *Drugs 42*, 213–227.

(5) Owens, D. R. (2002) New horizons-alternative routes for insulin therapy. *Nat. Rev. Drug Discovery 1*, 529–540.

(6) Cheng, J., Teply, B. A., Jeong, S. Y., Yim, C. H., Ho, D., Sherifi, I., Jon, S., Farokhzad, O. C., Khademhosseini, A., and Langer, R. S. (2006) Magnetically responsive polymeric microparticles for oral delivery of protein drugs. *Pharm. Res. 23*, 557–564.

(7) Goldberg, M., and Gomez-Orellana, I. (2003) Challenges for the oral delivery of macromolecules. *Nat. Rev. Drug Discovery 2*, 289–295.

(8) Hinds, K., Koh, J. J., Joss, L., Liu, F., Baudys, M., and Kim, S. W. (2000) Synthesis and characterization of poly(ethylene glycol)-insulin conjugate. *Bioconjugate Chem. 11*, 195–201.

(9) Lee, S., Kim, K., Kumar, T. S., Lee, J., Kim, S. K., Lee, D. Y., Lee, Y. K., and Byun, Y. (2005) Synthesis and biological properties of insulin-deoxycholic acid chemical conjugates. *Bioconjugate Chem. 16*, 615–620.

(10) Mi, F. L., Wu, Y. Y., Lin, Y. H., Sonaje, K., Ho, Y. C., Chen, C. T., Juang, J. H., and Sung, H. W. (2008) Oral delivery of peptide drugs using nanoparticles self-assembled by poly(γ-glutamic acid) and a chitosan derivative functionalized by trimethylation. *Bioconjugate Chem. 19*, 1248–1255.

(11) Rekha, M. R., and Sharma, C. P. (2009) Synthesis and evaluation of lauryl succinyl chitosan particles towards oral insulin delivery and absorption. *J. Controlled Release 135*, 144–151.

(12) Illum, L. (1998) Chitosan and its use as a pharmaceutical excipient. *Pharm. Res. 15*, 1326–1331.

(13) Thanou, M., Verhoef, J. C., and Junginger, H. E. (2001) Chitosan and its derivatives as intestinal absorption enhancers. *Adv. Drug Delivery Rev. 50*, S91–101.

(14) Senel, S., and McClure, S. J. (2004) Potential applications of chitosan in veterinary medicine. *Adv. Drug Delivery Rev. 56*, 1467–1480.

(15) Kean, T., and Thanou, M. (2010) Biodegradation, biodistribution and toxicity of chitosan. *Adv. Drug Delivery Rev. 62*, 3–11.

(16) Chae, S. Y., Jang, M. K., and Nah, J. W. (2005) Influence of molecular weight on oral absorption of water soluble chitosans. *J. Controlled Release 102*, 383–394.

(17) Lee, E., Lee, J., Lee, I. H., Yu, M., Kim, H., Chae, S. Y., and Jon, S. (2008) Conjugated chitosan as a novel platform for oral delivery of paclitaxel. *J. Med. Chem. 51*, 6442–6449.

(18) Lee, E., Kim, H., Lee, I. H., and Jon, S. (2009) In vivo antitumor effects of chitosan-conjugated docetaxel after oral administration. *J. Controlled Release 140*, 79–85.

(19) Melton, R. G., and Sherwood, R. F. (1996) Antibody-enzyme conjugates for cancer therapy. *J. Natl. Cancer Inst. 88*, 153–165.

(20) Bernkop-Schnürch, A., Kast, C. E., and Guggi, D. (2003) Permeation enhancing polymers in oral delivery of hydrophilic macromolecules: thiomer/GSH systems. *J. Controlled Release 93*, 95–103.

(21) Myers, S. R., Yakubu-Madus, F. E., Johnson, W. T., Baker, J. E., Cusick, T. S., Williams, V. K., Tinsley, F. C., Kriauciunas, A., Manetta, J., and Chen, V. J. (1997) Acylation of human insulin with palmitic acid extends the time action of human insulin in diabetic dogs. *Diabetes 46*, 637–642.

(22) Krauland, A. H., Guggi, D., and Bernkop-Schnürch, A. (2004) Oral insulin delivery: the potential of thiolated chitosan-insulin tablets on non-diabetic rats. *J. Controlled Release 24*, 547–555.

BC100093V

Supporting Information for:

A Novel Approach to Oral Delivery of Insulin by Conjugating with Low Molecular Weight Chitosan

Eunhye Lee, Jinju Lee, and Sangyong Jon*

EXPERIMENTAL PROCEDURES

Materials. Human crystalline zinc insulin (Zn^{2+} insulin) was purchased from Serologicals® Corporation (Norcross, GA, USA). Low molecular weight chitosan (LMWC) was from KITTOLIFE (Seoul, Korea) and was further purified by ultrafiltration to obtain different MWs of LMWC. N-succinimidyl 3-(2-pyridyldithio)-propionate (SPDP) and dithiothreitol (DTT, Cleland's reagent) were from Pierce (Rockford, IL, USA). All other solvents and reagents were of reagent-grade and were used as received from Sigma Chemical (St. Louis, MO, USA). All animals were obtained from Orient Bio Inc. (Seoul, Korea) and were handled in accordance with the guidelines of the Animal Care and Use Committee, Gwangju Institute of Science and Technology.

Synthesis of insulin (B^{29})-SPDP conjugates. Insulin was reacted with SPDP to introduce disulfide bonds at the primary amine group of lysine at the B^{29} position of insulin. Insulin (100 mg) was dissolved in 8 mL of 10 mM HCl, and the pH of the insulin solution was raised to 10 by addition of 1 N NaOH; 16 mg of SPDP dissolved in 500 μL of dimethyl formamide (DMF) was then added. The pH of the reaction solution was maintained between 9.7 and 10.3 during the reaction. After 1 h, the reaction solution was diluted with deionized water, and the pH was adjusted to 7 with 1 N HCl. Insulin-SPDP was purified by preparative reverse-phase

HPLC (Shimadzu, Tokyo, Japan) using a Shim-pack Prep-ODS column (20 x 250 mm). The mobile phase consisted of 0.1% TFA in water and acetonitrile. Insulin-SPDP was eluted through mobile phase with a linear gradient of 35% to 70% acetonitrile for 35 min at a flow rate of 8 mL/min, and was detected at a wavelength of 280 nm

Synthesis of LMWC-SPDP. LMWC (100 mg) with an average MW of 3, 6, 9, or 13k was dissolved in 6 mL of PBS, and 16 mg of SPDP was dissolved in 500 μL DMF. The mixtures were stirred for 2 h at room temperature and then poured into cold acetone (60 mL); the resulting precipitate was dried in a vacuum. The purified LMWC-SPDP was dissolved in PBS buffer (pH 7.4), and then 25 mM DTT was added. After 4 h, the DTT-reduced LMWC-SPDP (thiol-modified LMWC; LMWC-SH) solution was purified using a precipitation method. Finally, LMWC-SH was obtained as a brown powder, and the conjugates were characterized using ^{1}H NMR (400 MHz, Jeol, Tokyo, Japan).

Synthesis of LMWC-insulin conjugates. Insulin-SPDP (50 mg) was dissolved in 100 mM HCl and diluted with sodium citrate buffer (pH 4). A two-fold molar excess of LMWC-SH was dissolved in sodium citrate buffer (pH 4) and then added to the insulin solution. After stirring the reaction mixture for 5 h at 4ºC, LMWC-insulin conjugate was purified by preparative reverse-phase HPLC using a Shim-pack Prep-ODS column (20 x 250 mm). The mobile phase consisted of 0.1% TFA in water and acetonitrile. LMWC-insulin conjugate was eluted in mobile phase with a linear gradient of 10% to 40% acetonitrile for 30 min at a flow rate of 5 mL/min, and was detected at a wavelength of 280 nm.

Characterization of SPDP-modified insulin. The location of the SPDP attachment site was confirmed using a trypsin cleavage method. Insulin and insulin-SPDP conjugate were dissolved in 100 mM HCl and diluted in PBS (pH 7.4) to a concentration of 5 μg/mL. Trypsin (50 μL of a 1-mg/mL solution) was added, and the reaction was allowed to incubate

for 2 h at 37ºC. The enzyme reaction was quenched by adding an equal volume of a 0.1% TFA solution. The digestion fragments were then analyzed by HPLC and MALDI-TOF.

Evaluation of biological activity *in vivo*. Insulin-LMWC conjugates were tested for their ability to reduce blood glucose levels in diabetic SD rats. Diabetes was induced by a single intraperitoneal injection of 60 mg/kg streptozotocin in citrate buffer (pH 4.5). Rats were considered to be diabetic when base line glucose levels exceeded 2.5 mg/mL. One week after attaining a diabetic state, rats were administered insulin (0.33 IU/kg, 17.7 μg/kg) or insulin-LMWC conjugate (0.66 IU/kg, 35.3 μg/kg; equivalent insulin/kg) intravenously. Blood samples for the analysis of blood glucose levels were taken from the tail veins and analyzed immediately using a blood glucose monitoring system (Glucocard II, Arkray, Kyoto, Japan). Results are presented as percent reduction from the basal levels. The biological activity of the conjugate was calculated from the area under the curve (AUC) in the graph of blood glucose levels (Figure 2). Intravenously injected native insulin was regarded as 100% biological activity and the % biological activity of the conjugate by using the following eqaution:

$$\% \text{ biological activity of the conjugate} = (AUC_{conjugate} / AUC_{insulin}) \times 100$$

***In vivo* hypoglycemic effect of orally administered LMWC-insulin conjugates**. After fasting overnight, diabetic SD rats were orally administered one of four kinds of insulin-LMWC conjugate (3, 6, 9, or 13k) at a dose of 1.77 mg/kg. Three control groups were included: diabetic control (saline), insulin control (same dose of native insulin as contained in insulin-LMWC conjugate), and LMWC control (same dose of LMWC as contained in insulin-LMWC conjugate). The bioavailability of insulin formulations was calculated relative to subcutaneously administered 17.7 μg/kg insulin solutions. Fasting glucose levels and glucose levels at different times after oral administration were determined from blood samples collected from the tail vein, as described above.

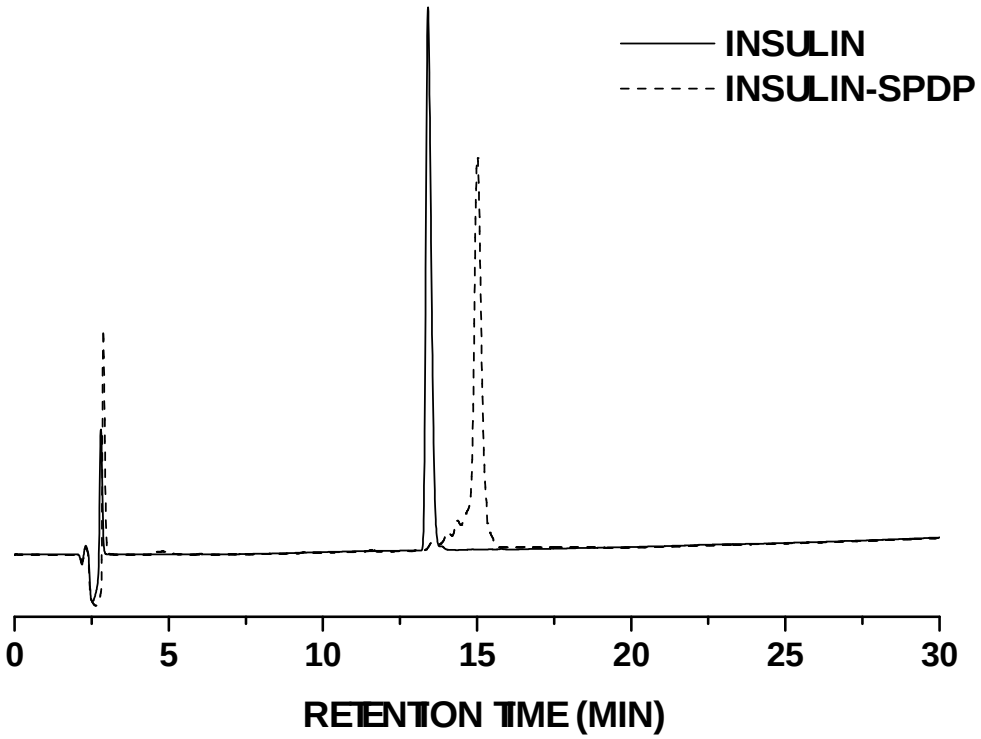


Figure S1. HPLC spectra of insulin and insulin-SPDP conjugate

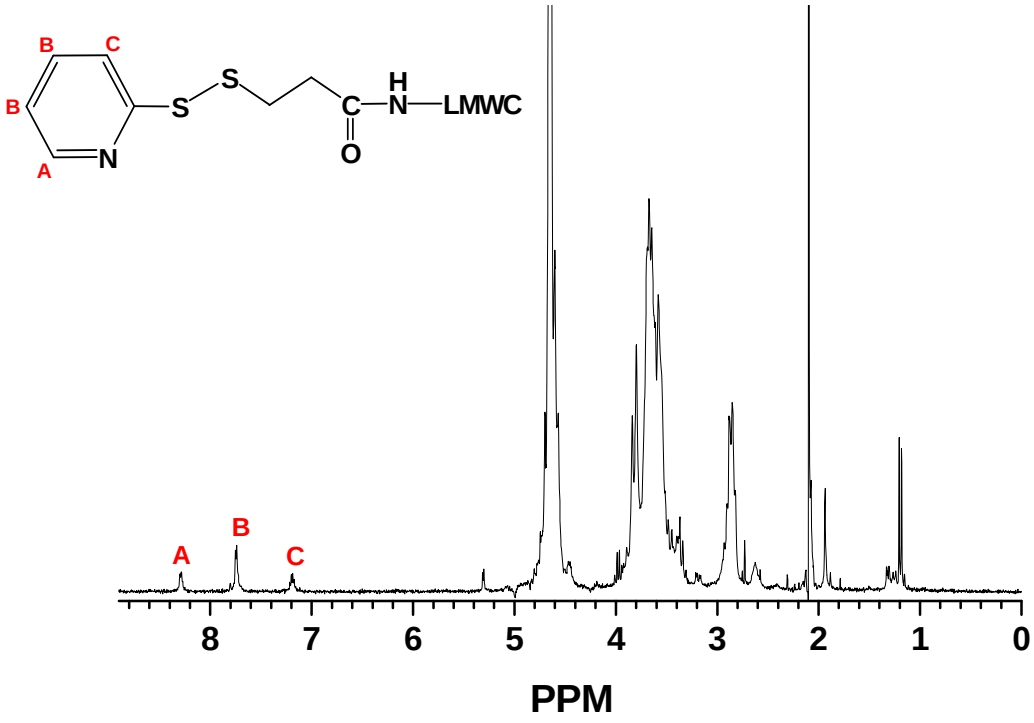


Figure S2. A ^{1}H NMR spectrum of LMWC(6k)-SPDP in D_2O

Design and Synthesis of Phospholipase C and A_2-Activatable Near-Infrared Fluorescent Smart Probes

Anatoliy V. Popov,*[,†] Theresa M. Mawn,[†] Soungkyoo Kim,[†] Gang Zheng,[†,‡] and E. James Delikatny[†]

University of Pennsylvania, Department of Radiology, Philadelphia Pennsylvania 19104, United States, and University of Toronto, Department of Medical Biophysics, Toronto, Ontario, M5G 1L7, Canada. Received June 14, 2010; Revised Manuscript Received September 20, 2010

The primary focus of this work was to develop activatable probes suitable for in vivo detection of phospholipase activity. Phospholipases (PLs) are ubiquitous enzymes that perform a number of critical regulatory functions. They catalyze phospholipid breakdown and are categorized as A_1, A_2 (PLA_2), C (PLC), and D (PLD) based on their site of action. Here, we report the design, synthesis, and characterization of self-quenching reporter probes that release fluorescent moieties upon cleavage with PLA_2 or PLC. A series of phospholipids were synthesized bearing the NIR fluorophore pyropheophorbide *a* (Pyro) at the *sn*-2 position. Fluorescence quenching was achieved by attachment of either a positively charged black hole quencher-3 (BHQ-3) to the phospholipid headgroup or another neutral Pyro moiety at the *sn*-1 position. The specificity to different phospholipases was modulated by insertion of spacers (C_6, C_{12}) between Pyro and the lipid backbone. The specificity of the quenched fluorescent phospholipids was assayed on a plate reader against a number of phospholipases and compared with two commercial probes bearing the visible fluorophore BODIPY. While PyroC_6-PyroC_6-PtdCho revealed significant background fluorescence, and a 10% fluorescence increase under the action of PLA_2, Pyro-PtdEtn-BHQ demonstrated high selective sensitivity to PLC, particularly to the PC-PLC isoform, and its sensitivity to PLA_2 was negligible due to steric hindrance at the *sn*-2 position. In contrast, the C_{12}-spacered PyroC_{12}-PtdEtn-BHQ demonstrated a remarkable selectivity for PLA_2 and the best relative PLA_2/PLC sensitivity, significantly outperforming previously known probes. These results open an avenue for future in vivo experiments and for new probes to detect PL activity.

Phospholipases (PLs) are ubiquitous enzymes that perform a number of critical regulatory functions. They catalyze phospholipid breakdown and are categorized as A_1, A_2 (PLA_2), C (PLC), and D (PLD) based on their site of action (*1*, *2*) (Figure 1).

Since PLA_2 is elevated in a number of diseases (e.g., prostate and breast cancer, rheumatoid arthritis, etc.) (*3*−*5*), we have chosen to develop probes that distinguish PLA_2 from other PLs. In addition, since increased PLC is detected in melanoma and ovarian and breast cancers and PLC has been implicated in maintaining the high levels of phosphocholine (PC) and phosphoethanolamine (PE) characteristic of many human tumors (*6*−*10*), we are also developing probes to specifically detect the actions of this enzyme.

The primary focus of this work is to develop methods to investigate the expression and activity of PLs in vivo in mammals. The above diseases can be detected, monitored, and, in some cases, treated using soft tissue penetrating near-infrared (NIR) light (*11*, *12*). As a result, we are employing optical imaging using NIR fluorophores (NIRF).

Our approach is to design self-quenching reporter probes that release fluorescent moieties only upon cleavage with PLA_2 or PLC. The structures of these smart probes are depicted in Figure 2. The hypothesis is that a bulky porphyrin moiety attached at the *sn*-2 position without a spacer would sterically hinder PLA_2 activity while leaving open the PLC cleavage site, whereas incorporation of spacers of different length will make the C−O bond at the *sn*-2-position accessible for PLA_2-mediated hydrolysis. We have chosen Pyropheophorbide *a* (Pyro, **1**, λ_{abs} = 675 nm, λ_{em} = 725 nm) (*13*, *14*) as an NIRF. For quenchers,

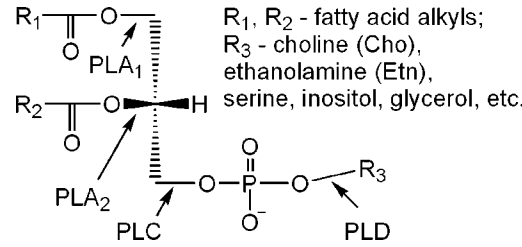


Figure 1. Phospholipase-mediated cleavage sites.

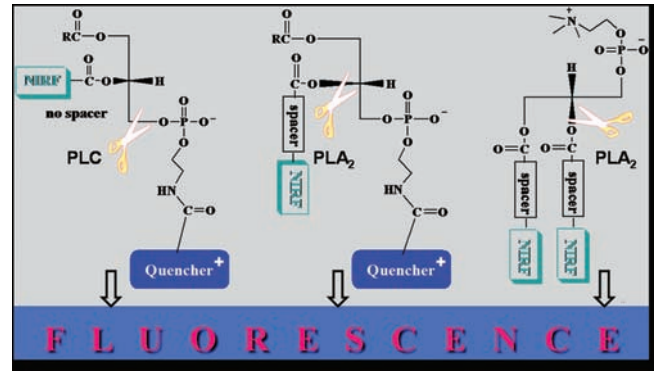


Figure 2. Design of NIRF-bearing PLC- and PLA_2 cleavable self-quenched phospholipids.

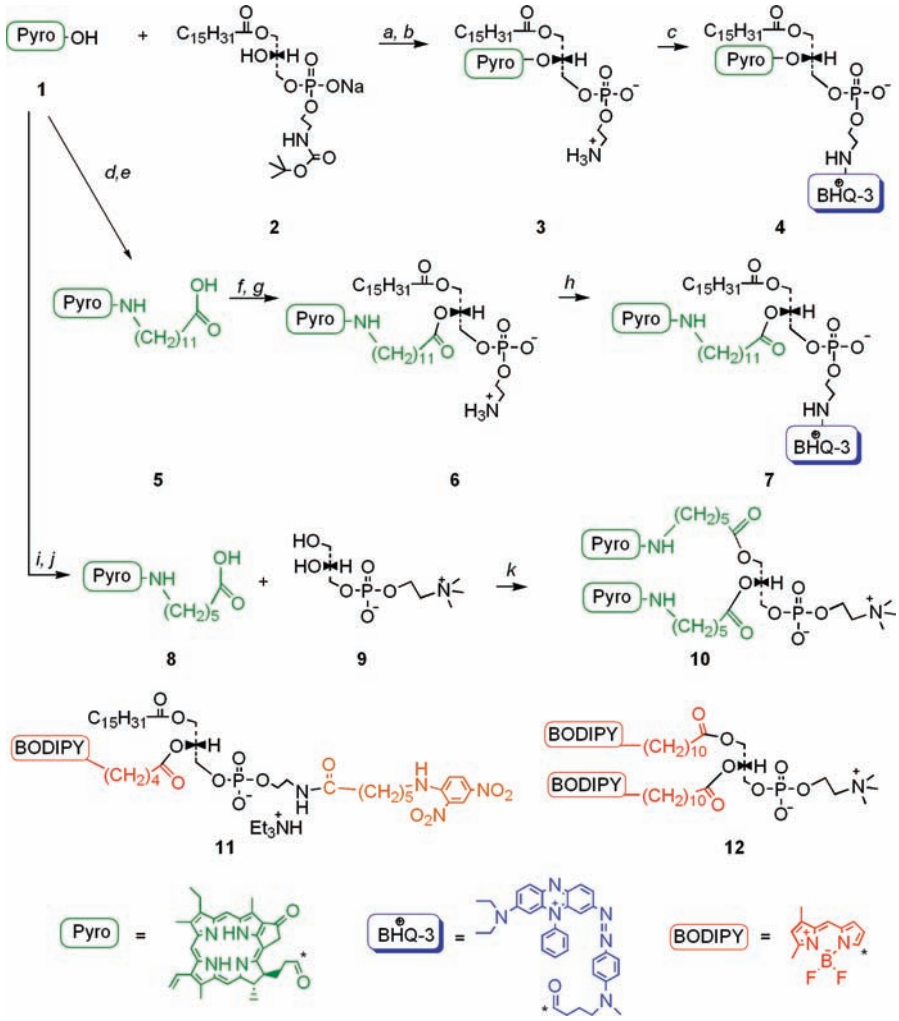
* Corresponding author. University of Pennsylvania, Department of Radiology, 231 South 34th St., Chemistry Wing 1958, R285, Philadelphia, PA 19104, USA. Tel. 1-215-746-8761, Fax 1-215-746-8764, E-mail: avpopov@mail.med.upenn.edu.

† University of Pennsylvania.

‡ University of Toronto.

10.1021/bc100271v © 2010 American Chemical Society
Published on Web 09/30/2010

Scheme 1. Synthesis of Pyro-PtdEtn-BHQ (4), PyroC_{12}-PtdEtn-BHQ (7), and PyroC_6-PyroC_6-PtdCho (10) and Structures for Comparison of Commercially Available Self-Quenched PLA_2-Sensitive Green Fluorescent Phospholipid Probes PED-6 (11) and B7701 (12)[a]



[a] Reagents, conditions (all reactions were performed under Ar in dark) and isolated yields (relative to starting NIRF **1**, one arrow indicates one-pot reaction): (a) EDC, DMAP, DCM, rt, 72 h; (b) TFA, DCM, 0 °C, 4 h, 20%; (c) BHQ-3^+-SU PF_6-, TEA, DCM, rt, 12 h, 15%; (d) NHS, EDC, DMAP, DCM, rt, 3 h; (e) $H_2N(CH_2)_{11}CO_2H$, TEA, DCM, rt, 72 h, 85%; (f) **2**, EDC, DMAP, DCM, rt, 72 h; (g) TFA, DCM, 0 °C, 4 h, 15%; (h) BHQ-3^+-SU PF_6-, TEA, DCM, rt 12 h, 10%; (i) NHS, EDC, DMAP, DCM, rt, 3 h; (j) $H_2N(CH_2)_5CO_2H$, TEA, DCM, rt, 72 h, 75%; (k) EDC, DMAP, DCM, 40 °C, 85 h, 8%. *Attachment sites for fluorophores/quencher.

we employ either the positively charged black hole quencher-3 (BHQ-3) (*13*, *14*) attached to the headgroup of the phospholipid or another neutral Pyro moiety at the *sn*-1 position.

Scheme 1 demonstrates the synthesis of three self-quenched Pyro-bearing probes **4**, **7**, and **10**. NIRF acid **1** was coupled with *N*-BOC *Lyso*-phosphatidylethanolamine (*Lyso*-PtdEtn, **2**) under basic conditions in order to conserve the steric configuration at the *sn*-2 site and avoid racemization (*15*, *16*). Next, TFA-mediated BOC-deprotection resulted in the permanently fluorescent Pyro-PtdEtn (**3**). In the final step, BHQ-3 was attached to the amino group of lipid **3** resulting in a self-quenching Pyro-PtdEtn-BHQ (**4**). To incorporate spacers, we have synthesized PyroC_{12}- (**5**) and PyroC_6- (**8**) acids. Acid **5** was used as described above with acid **1** for production of the permanent lipid fluorophore PyroC_{12}-PtdEtn (**6**), which was then converted into its self-quenched derivative (**7**). Two molecules of acid **8** were conjugated with *sn*-glycero-3-phosphocholine (**9**) to give rise to PyroC_6-PyroC_6-PtdCho (**10**) where self-quenching is achieved by interactions between the two NIRFs.

Farber et al. had demonstrated that PLA_2 activity can be detected by visual fluorescence in transparent zebra fish larvae (*17*, *18*). These and other probes are now available commercially (Scheme 1, compounds **11**, **12**). The sensitivity of those phospholipids **11** and **12** to PLs other than PLA_2 was not tested at that time. As seen from Scheme 1, compounds **4**, **7**, and **11** have a fluorophore attached at the *sn*-2 position and a quencher bound to the nitrogen atom of the PE head. Compounds **10** and **12** exploit self-quenching of two of the same fluorophores attached to the *sn*-1 and *sn*-2 positions.

We have tested our three self-quenched probes **4**, **7**, and **10**, as well as commercial probes **11** and **12**, as substrates for different phospholipases. The results are presented in Figure 3. Probe **4** revealed high selective sensitivity to PLC, particularly to the PC-PLC isoform (Figure 3a), while sensitivity to other tested phospholipases including PLA_2 is negligible. NIRF compounds **10** and **7** were tested as potential PLA_2-sensitive probes in comparison with their visible counterparts **12** and **11**, respectively. PtdCho **10** revealed significant background fluorescence (Figure 3b), because both substituents at *sn*-1 and *sn*-2 positions are self-fluorescent and their quenching efficiency is not high. Only a modest (10%) fluorescence increase was detected under the action of PLA_2, similar to those observed for the visible analogue **12** (Figure 3f). In contrast, the C_{12}-spacered PtdEtn **7** demonstrated a remarkable selectivity for PLA_2 (Figure 3c) and the best relative PLA_2/PLC sensitivity, significantly outperforming the magnitude of the best previously

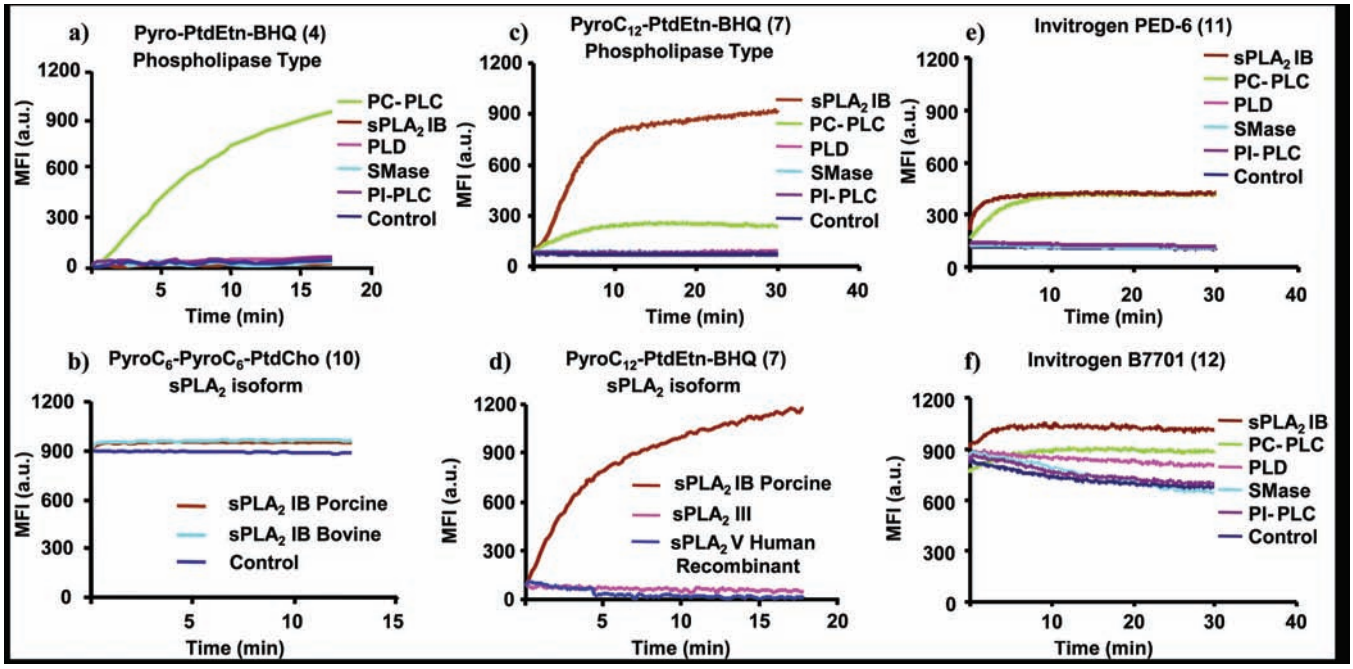


Figure 3. Sensitivity of self-quenched fluorescent probes to different phospholipase isoforms as measured by fluorescence release on a plate reader (see Supporting Information).

known probe **11** (Figure 3e). Moreover, this construct exhibited significant PLA_2 isoform specificity with Porcine $sPLA_2$ IB demonstrating the highest activity (Figure 3d).

PC-PLC was able to cleave Pyro-PtdEtn-BHQ **4** and PED-6 **11** even though relatively bulky quencher moieties were attached to the headgroup. PC-PLC, in contrast to its name, has a relatively broad range of headgroup specificities. It has been shown to be effective at hydrolyzing phospholipids other than PtdCho, including PtdEtn and PtdSer with relative specificities of 10:7:1 (*19*−*22*). $PyroC_{12}$-PtdEtn-BHQ **7** and PED-6 **11**, on the other hand, were both effectively cleaved by porcine $sPLA_2$ IB. For $sPLA_2$s, cleavage specificities are primarily due to differences in binding to the vesicle surface. $sPLA_2$s, including $sPLA_2$ IB bind tightly and act preferentially on anionic phospholipid vesicles (PtdGro, PtdEtn, and PtdSer) compared to charge-neutral PtdCho vesicles. The isoforms of $sPLA_2$ III and V employed, on the other hand, will hydrolyze both anionic phospholipids and PtdCho (*23*−*26*). Their inactivity to $PyroC_{12}$-PtdEtn-BHQ **7** may be a result of the bulky BHQ headgroup, but variations in chain length may also play a role as discussed below. SMase and PI-PLC are highly headgroup specific to their substrates (*27*−*30*). Table 1 in the Supporting Information contains additional information on the enzymes employed here and their substrate specificities.

Our results showed that increasing the chain length in the *sn*-2 position conferred increased sensitivity to $sPLA_2$ IB but decreased sensitivity to PC-PLC. Although fatty acid composition is relatively unimportant in determining $sPLA_2$ specificity (*24*), the presence of bulky substituents in the *sn*-1 position will lessen the enzymatic activity due to steric hindrance (*31*). It has also been shown that $sPLA_2$ activity is dependent on the *sn*-2 fatty acid chain length, which must be 7 carbons or greater, with optimal activity obtained with chain lengths between 16 and 21 carbons (*32*−*34*). The chain length requirements are not as important for PC-PLC, which contains a shallow cleft for phospholipid docking (*32*−*35*).

The phospholipase-sensitive probes described here are highly lipophilic, and we have employed egg-yolk PtdCho vesicles to solubilize them (see Supporting Information). For in vivo experiments, similar techniques will be required using either micelles or liposomes for delivery. Liposomal formulations for drug delivery are well-established (*36*), and more lipophilic molecules are often processed and excreted through the liver and stool.

In conclusion, we have designed, synthesized, and tested for the first time near-infrared self-quenched phospholipid probes that reveal high sensitivity to PLC and PLA_2. These results open an avenue for in vivo experiments with mammals and for the development of sensitive new probes to detect PL activity.

ACKNOWLEDGMENT

Financial support was provided by the NIH (grants R01-CA114347 (EJD), R01-CA129176 (EJD), and U24-CA083105 Penn Small Animal Imaging Resource), and DoD (W81XWH-08-1-0716 (AVP)).

Supporting Information Available: Experimental procedures and characterization. This material is available free of charge via the Internet at http://pubs.acs.org.

LITERATURE CITED

(1) Hanahan, D. J. (1997) *A Guide to Phospholipid Chemistry*, Oxford University Press, New York.

(2) Wilton, D. C. (2008) Phospholipases, in *Biochemistry of Lipids, Lipoproteins and Membranes*, 5th ed. (Vance, D. E., and Vance, J. E., Eds.) pp 305−329, Elsevier Science.

(3) Stefanski, E., Pruzanski, W., Sternby, B., and Vadas, P. (1986) Purification of a soluble phospholipase A_2 from synovial fluid in rheumatoid arthritis. *J. Biochem. 100*, 1297–1303.

(4) Sved, P., Scott, K. F., McLeod, D., King, N. J. C., Singh, J., Tsatralis, T., Nikolov, B., Boulas, J., Nallan, L., Gelb, M. H., Sajinovic, M., Graham, G. G., Russell, P. J., and Dong, Q. (2004) Oncogenic action of secreted phospholipase A_2 in prostate cancer. *Cancer Res. 64*, 6934–6940.

(5) Yamashita, S.-i., Ogawa, M., Sakamoto, K., Abe, T., Arakawa, H., and Yamashita, J.-i. (1994) Elevation of serum group II phospholipase A_2 levels in patients with advanced cancer. *Clin. Chim. Acta 228*, 91–99.

(6) Degani, H., DeJordy, J. O., and Salomon, Y. (1991) Stimulation of cAMP and phosphomonoester production by melanotropin in melanoma cells: phosphorus-31 NMR studies. *Proc. Natl. Acad. Sci. U.S.A. 88*, 1506–1510.

(7) Iorio, E., Ricci, A., Bagnoli, M., Pisanu, M. E., Castellano, G., Di Vito, M., Venturini, E., Glunde, K., Bhujwalla, Z. M., Mezzanzanica, D., Canevari, S., and Podo, F. (2010) Activation of phosphatidylcholine cycle enzymes in human epithelial ovarian cancer cells. *Cancer Res. 70*, 2126–2135.

(8) Paris, L., Cecchetti, S., Spadaro, F., Abalsamo, L., Lugini, L., Pisanu, M. E., Iorio, E., Natali, P. G., Ramoni, C., Podo, F. (2010) Inhibition of phosphatidylcholine-specific phospholipase C downregulates HER2 overexpression on plasma membrane of breast cancer cells. *Breast Cancer Res.* [Online early access] DOI: 10.1186/bcr2575. Published Online: May 12, 2010.

(9) Soderquist, A. M., Todderud, G., and Carpenter, G. (1992) Elevated membrane association of phospholipase C-gamma 1 in MDA-468 mammary tumor cells. *Cancer Res. 52*, 4526–4529.

(10) Spadaro, F., Ramoni, C., Mezzanzanica, D., Miotti, S., Alberti, P., Cecchetti, S., Iorio, E., Dolo, V., Canevari, S., and Podo, F. (2008) Phosphatidylcholine-specific phospholipase C activation in epithelial ovarian cancer cells. *Cancer Res. 68*, 6541–6549.

(11) Mahmood, U., and Weissleder, R. (2003) Near-infrared optical imaging of proteases in cancer. *Mol. Cancer Ther. 2*, 489–496.

(12) Ntziachristos, V., Bremer, C., and Weissleder, R. (2003) Fluorescence imaging with near-infrared light: new technological advances that enable in vivo molecular imaging. *Eur. Radiol. 13*, 195–208.

(13) Lo, P.-C., Chen, J., Stefflova, K., Warren Michael, S., Navab, R., Bandarchi, B., Mullins, S., Tsao, M., Cheng Jonathan, D., and Zheng, G. (2009) Photodynamic molecular beacon triggered by fibroblast activation protein on cancer-associated fibroblasts for diagnosis and treatment of epithelial cancers. *J. Med. Chem. 52*, 358–368.

(14) Stefflova, K., Chen, J., Li, H., and Zheng, G. (2006) Targeted photodynamic therapy agent with a built-in apoptosis sensor for in vivo near-infrared imaging of tumor apoptosis triggered by its photosensitization in situ. *Mol Imaging 5*, 520–532.

(15) Lindberg, J., Ekeroth, J., and Konradsson, P. (2002) Efficient synthesis of phospholipids from glycidyl phosphates. *J. Org. Chem. 67*, 194–199.

(16) Rosseto, R., Bibak, N., DeOcampo, R., Shah, T., Gabrielian, A., and Hajdu, J. (2007) A new synthesis of lysophosphatidylcholines and related derivatives. Use of p-toluenesulfonate for hydroxyl group protection. *J. Org. Chem. 72*, 1691–1698.

(17) Farber, S. A., Pack, M., Ho, S.-Y., Johnson, L. D., Wagner, D. S., Dosch, R., Mullins, M. C., Hendrickson, H. S., Hendrickson, E. K., and Halpern, M. E. (2001) Genetic analysis of digestive physiology using fluorescent phospholipid reporters. *Science (Washington, DC, U. S.) 292*, 1385–1388.

(18) Hendrickson, H. S., Hendrickson, E. K., Johnson, I. D., and Farber, S. A. (1999) Intramolecularly quenched BODIPY-labeled phospholipid analogs in phospholipase A_2 and platelet-activating factor acetylhydrolase assays and in vivo fluorescence imaging. *Anal. Biochem. 276*, 27–35.

(19) Antikainen, N. M., Hergenrother, P. J., Harris, M. M., Corbett, W., and Martin, S. F. (2003) Altering substrate specificity of phosphatidylcholine-preferring phospholipase C of bacillus cereus by random mutagenesis of the headgroup binding site. *Biochemistry 42*, 1603–1610.

(20) Benfield, A. P., Goodey, N. M., Phillips, L. T., and Martin, S. F. (2007) Structural studies examining the substrate specificity profiles of PC-PLC_{Bc} protein variants. *Arch. Biochem. Biophys. 460*, 41–47.

(21) Hergenrother, P. J., and Martin, S. F. (1997) Determination of the kinetic parameters for phospholipase C (Bacillus cereus) on different phospholipid substrates using a chromogenic assay based on the quantitation of inorganic phosphate. *Anal. Biochem. 251*, 45–49.

(22) Hergenrother, P. J., and Martin, S. F. (2001) Phosphatidylcholine-preferring phospholipase C from B. cereus. function, structure, and mechanism. *Top. Curr. Chem. 211*, 131–167.

(23) Kudo, I., and Murakami, M. (2002) Phospholipase A_2 enzymes. *Prostaglandins Other Lipid Mediators 68−69*, 3–58.

(24) Murakami, M., and Kudo, I. (2001) Diversity and regulatory functions of mammalian secretory phospholipase A_2s. *Adv. Immunol. 77*, 163–194.

(25) Murakami, M., and Kudo, I. (2002) Lipid signaling. Phospholipase A_2. *J. Biochem. 131*, 285–292.

(26) Kinkaid, A., and Wilton, D. C. (1991) Comparison of the catalytic properties of phospholipase A_2 from pancreas and venom using a continuous fluorescence displacement assay. *Biochem. J. 278*, 843–848.

(27) Berg, O. G., Yu, B.-Z., Apitz-Castro, R. J., and Jain, M. K. (2004) Phosphatidylinositol-specific phospholipase C forms different complexes with monodisperse and micellar phosphatidylcholine. *Biochemistry 43*, 2080–2090.

(28) Ikezawa, H., Yamanegi, M., Taguchi, R., Miyashita, T., and Ohyabu, T. (1976) Studies on phosphatidylinositol phosphodiesterase (phospholipase C type) of Bacillus cereus. I. Purification, properties and phosphatase-releasing activity. *Biochim. Biophys. Acta, Lipids Lipid Metab. 450*, 154–164.

(29) Ryan, M., Liu, T., Dahlquist, F. W., and Griffith, O. H. (2001) A catalytic diad involved in substrate-assisted catalysis: NMR study of hydrogen bonding and dynamics at the active site of phosphatidylinositol-specific phospholipase C. *Biochemistry 40*, 9743–9750.

(30) Tomita, M., Sawada, H., Taguchi, R., and Ikezawa, H. (1987) The action of sphingomyelinase from Bacillus cereus on ATP-depleted bovine erythrocyte membranes and different lipid composition of liposomes. *Arch. Biochem. Biophys. 255*, 127–135.

(31) Linderoth, L., Peters, G. H., Jorgensen, K., Madsen, R., and Andresen, T. L. (2007) Synthesis of sn-1 functionalized phospholipids as substrates for secretory phospholipase A_2. *Chem. Phys. Lipids 146*, 54–66.

(32) Caramelo, J. J., Florin-Christensen, J., Florin-Christensen, M., and Delfino, J. M. (2000) Mapping the catalytic pocket of phospholipases A_2 and C using a novel set of phosphatidylcholines. *Biochem. J. 346*, 679–690.

(33) Lewis, K. A., Bian, J., Sweeney, A., and Roberts, M. F. (1990) Asymmetric short-chain phosphatidylcholines: defining chain binding constraints in phospholipases. *Biochemistry 29*, 9962–9970.

(34) Soltys, C. E., Bian, J., and Roberts, M. F. (1993) Polymerizable phosphatidylcholines: Importance of phospholipid motions for optimum phospholipase A_2 and C activity. *Biochemistry 32*, 9545–9552.

(35) El-Sayed, M. Y., DeBose, C. D., Coury, L. A., and Roberts, M. F. (1985) Sensitivity of phospholipase C (Bacillus cereus) activity to phosphatidylcholine structural modifications. *Biochim. Biophys. Acta, Lipids Lipid Metab. 837*, 325–335.

(36) Torchilin, V. P., Weissig, V. (2003) *Liposomes, Second Edition: A Practical Approach*, Oxford University Press, New York.

BC100271V

Supporting Information

Design and Synthesis of Phospholipase C and A_2-Activatable Near Infrared Fluorescent Smart Probes

Anatoliy V. Popov,*[,†] Theresa M. Mawn,[†] Soungkyoo Kim,[†] Gang Zheng,[†,‡] and E. James Delikatny[†]

[†]*University of Pennsylvania, Department of Radiology, Philadelphia PA, 19104, USA*

[‡]*University of Toronto, Department of Medical Biophysics, Toronto ON, M5G 1L7, Canada*

*E-mail: avpopov@mail.med.upenn.edu

Table of Contents

List of abbreviations	S2
General Information	S4
Synthesis	S6
^{1}H NMR Spectra	S14
Enzyme mediated cleavage	S21
References	S21

List of abbreviations

BHQ-3 carboxylic acid – black hole quencher-3, 3-diethylamino-5-phenylphenazium-7-diazobenzene-4''-(*N*-methyl)-*N*-butyric acid

BHQ-3^{+}-SU PF_6^{-} – succinimidyl ester of BHQ-3 carboxylic acid, hexafluorophosphate

BOC – *tert*-butoxycarbonyl

Cho – choline

DCM – dichloromethane, CH_2Cl_2

DMAP – 4-dimethylaminopyridine

EDC – 1-ethyl-3-(3-dimethylaminopropyl) carbodiimide, hydrochloride salt

Etn – ethanolamine

$H_2N(CH_2)_{11}CO_2H$ – λ-aminolauric acid

$H_2N(CH_2)_5CO_2H$ – ε-aminocaproic acid

Invitrogen PED6 – *N*-((6-(2,4-dinitrophenyl)amino)hexanoyl)-2-(4,4-difluoro-5,7-dimethyl-4-bora-3a,4a-diaza-*s*-indacene-3-pentanoyl)-1-hexadecanoyl-*sn*-glycero-3-phosphoethanolamine, triethylammonium salt

Invitrogen B77101 – 1,2-bis-(4,4-difluoro-5,7-dimethyl-4-bora-3a,4a-diaza-*s*-indacene-3-undecanoyl)-*sn*-glycero-3-phosphocholine

MALDI-TOF – Matrix Assisted Laser Desorption/Ionization Time-of-Flight Mass Spectrometry

N-BOC *Lyso* PtdEtn – 1-palmytoyl-*sn*-glycero-3-phosphoethanolamine-*N*-(*tert*-butoxycarbonyl) (sodium salt)

NHS – *N*-hydroxysuccinimide

NIR – near infrared

NIRF – near infrared fluorophore

PC – phosphocholine

PC-PLC – phosphatidylcholine-specific phospholipase C

PC-PLD – phosphatidylcholine-specific phospholipase D

PE – phosphoethanolamine

PI-PLC – phosphatidylinositol-specific phospholipase C

PL – phospholipase

PLs – phospholipases

PtdCho – phosphatidylcholine

PtdEtn – phosphatidylethanolamine

PtdGro – phosphatidylglycerol

PtdIns – phosphatidylinositol

PtdSer – phosphatidylserine

Pyro – pyropheophorbide *a*

Pyro-SU – succinimidyl ester of pyropheophorbide *a*

PyroC_{12} acid – λ-Pyropheophorbideamidolauric acid or 17^3-deoxy-17^3-(α-carbhydroxyundecylene-λ- amino)pyropheophorbide *a*

PyroC_{12}-PtdEtn – 1-palmitoyl-2-(λ-pyropheophorbideamidolauroyl)-*sn*-glycero-3-phosphoethanolamine

PyroC_{12}-PtdEtn-BHQ – 1-palmitoyl-2-(λ-pyropheophorbideamidolauroyl)-*sn*-glycero-3-phosphoethanolamide of BHQ-3 carboxylic acid

PyroC_6 acid – ε-Pyropheophorbideamidocaproic acid or 17^3-deoxy-17^3-(α-carbhydroxypentylene-ε-amino)pyropheophorbide *a*

PyroC_6-PyroC_6-PtdCho – 1,2-bis(ε-pyropheophorbideamidocaproyl)-*sn*-glycero-3-phosphocholine

Pyro-PtdEtn – 1-palmitoyl-2-pyropheophorbide-*sn*-glycero-3-phosphoethanolamine

Pyro-PtdEtn-BHQ – 1-palmitoyl-2-pyropheophorbide-*sn*-glycero-3-phosphoethanolamide of BHQ-3 carboxylic acid

SMase – sphingomyelinase

sPLA_2 – secretory phospholipase A_2

TEA, Et_3N – triethylamine

TFA – trifluoroacetic acid

TLC – thin layer chromatography

I. General Information

Dry solvents were purchased from ACROS Organics. Regular solvents and Celite were purchased from Fisher Scientific. *Spirulina Pacifica* algae (the starting material for Pyropheophorbide *a*) was purchased from Cyanotech Corporation, Kailua-Kona, HI, USA. *N*-BOC *Lyso* PtdEtn (N-Boc16:0 Lyso PE) was purchased from Avanti Polar Lipids, Inc., Alabaster, AL, USA. BHQ-3 carboxylic acid succinimidyl ester hexafluorophosphate was purchased from Bioresearch Technologies, Novato, CA, USA. Other reagents/reactants were purchased from Sigma-Aldrich and used without further purification. Silica Gel Standard Grade (230x450 mesh) was purchased from Sorbent Technologies, Atlanta, GA, USA. Thin Layer Chromatography Plates, Partsil® PK6F, Silica Gel 60 Å, 20x20 cm, were purchased from Whatman, washed with EtAc-MeOH (60:40, v/v) and baked at 150 °C overnight before use. All chemical reactions with pyropheophorbide *a* and its derivatives were carried out in the dark under dry Ar. ^{1}H NMR spectra were recorded using a Bruker DMX 360 MHz spectrometer. MALDI-TOF mass-spectra were recorded with an Applied Biosystems Voyager DE Mass Spectrometer using a positive mode ionization and CHCA (α-Cyano-4-hydroxycinnamic Acid) or HABA (2-(4-hydroxyphenylazo)benzoic acid) matrix. Time-dependent release of fluorescence was measured using a SpectraMax M5 fluorescent plate reader.

Table 1. Phospholipases

PL	Company	Catalog №	CAS №	Source	E.C. №	Enzyme Specificity
PLD	Sigma	P0065	9001-87-0	*Streptomyces chromofuscus*	3.1.4.4	Hydrolyzes the phosphate bonds of phospholipids, lysophospholipids and sphingomyelin to give the corresponding phosphatidic acid [a] . Prefers PtdCho and PtdEtn to PtdSer, PtdIns or PtdGro (*1*).
SMase	Sigma	S7651	9031-54-3	*Bacillus cereus*	3.1.4.12	Highly specific. Generates ceramide from sphingomyelin. Activity enhanced by the presence of PtdEtn or cholesterol and inhibited by PtdCho (*2*).
PI-PLC	Sigma	P5542	37288-19-0	*Bacillus cereus*	4.6.1.13	Highly specific. Cleaves PtdIns and phosphorylated derivatives (*3*). Does not cleave PtdCho, PtdEtn or Sphingomyelin (*4, 5*).
$sPLA_2$ IB porcine	Sigma	P6534	9001-84-7	Porcine pancreas	3.1.1.4	Acts preferentially on anionic (PtdGro, PtdEtn and PtdSer) compared to charge-neutral PtdCho phospholipid vesicles (*6-9*).
$sPLA_2$ IB bovine	Sigma	P8913	9001-84-7	Bovine pancreas	3.1.1.4	See above
$sPLA_2$ III	Cayman Chemical	60500	9001-84-7	Bee venom	3.1.1.4	Preferred substrates are PtdCho, PtdEtn and their plasmalogen analogues. PtdIns and PtdSer are also hydrolyzed ([a] and (*10*)).
$sPLA_2$ V [b]	Cayman Chemical	10009563	9001-84-7	Human recombinant	3.1.1.4	Hydrolyzes both anionic phospholipids and PtdCho (*11-13*).

[a] manufacturer's product information

[b] Accession № NP_000920 (provided by Cayman Chemical)

Phospholipases were dissolved in Tris buffer (50 mM Tris-HCl, pH 7.4) and stored in aliquots at -20 °C.

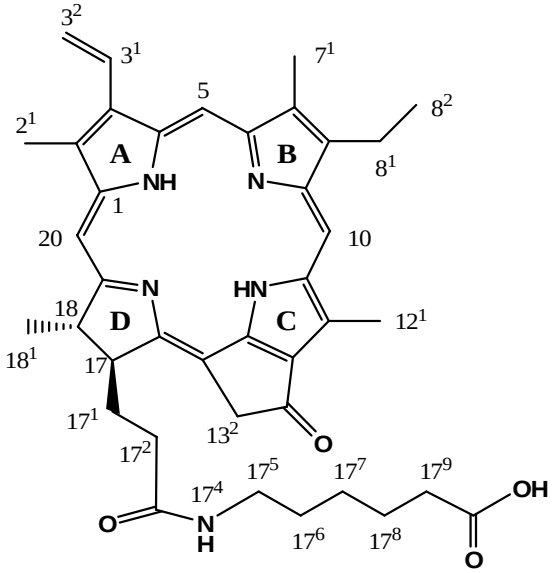
II. Synthesis

Pyropheophorbide *a* (**1**) was prepared from *Spirulina Pacifica* algae according to procedure (*14*).

General procedure for synthesis of *N*-Pyropheophorbide substituted ω-amino acids (PyroC$_6$ and PyroC$_{12}$ acids)

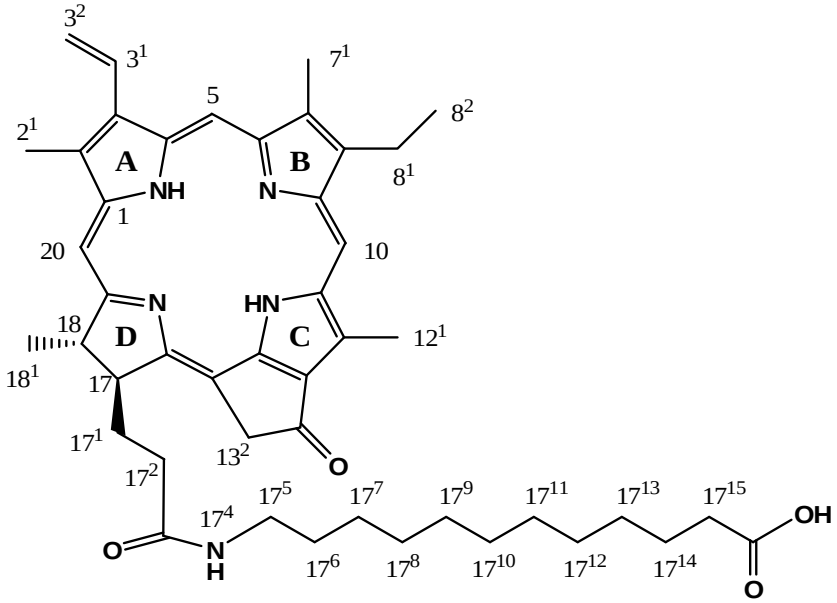
A 500 mL round bottom flask was charged with pyropheophorbide acid (**1**) (0.38 mmol), NHS (0.38 mmol), EDC (0.38 mmol), DMAP (23.3 mg. 0.19 mmol) and 200 ml of dry DCM. The reaction mixture was stirred in dark under Ar for 3 h until Pyropheophorbide acid was converted completely into its succinimidyl ester (TLC $CHCl_3$/MeOH = 5/1, v/v). Then $H_2N(CH_2)_nCO_2H$ (n = 5, 11, 0.38 mmol) and dry pyridine (25 ml) were added. The second reaction was carried out for 48 h until complete conversion of Pyro-SU. The solvents were then evaporated; the solid residue was dissolved in 100 ml of DCM, rinsed twice with 2% HCl, then water. The product was isolated by column chromatography on silica gel using (DCM-ethyl acetate (0-100%), then ethyl acetate-MeOH (0-40%)). Isolated yields are 75-85%.

ε-Pyropheophorbideamidocaproic acid or 17^3-deoxy-17^3-(α-carbhydroxypentylene-ε-amino)pyropheophorbide *a*, PyroC$_6$ acid (8)



Yield 185 mg, 75%. ^{1}H NMR (360 MHz, $CDCl_3$, CD_3OD δ ppm): 9.14, 9.02 and 8.38 (each s, 1H, 5-*H*, 10-*H* and 20-*H*); 7.74 (dd, J=11.5 Hz, J=17.6 Hz, 1H, 3^1-C*H*=CH_2); 6.09 (d, J=17.6 Hz, 1H, *trans*-3^2-CH=CH*H*); 5.99 (d, J=11.5 Hz, 1H, *cis*-3^2-CH=C*H*H); 5.03 (AB, A=5.11, B=4.96, J_{AB}=20.2 Hz, 2H, 13^2-CH_2); 4.32 (q, J=8.1 Hz, 1H, 18-*H*); 4.12 (dm, 8.7 Hz, 1H, 17-*H*); 3.45-3.32 m 5H, 3.27-3.12 m 5H and 2.94 s 3H (2^1-CH_3, 12^1-CH_3, 7^1-CH_3, 8^1-CH_2, 17^5-CH_2); 2.61-2.39 m 2H and 2.31-2.08 m 4H (17^2-CH_2, 17^9-CH_2, 17^1-CH_2); 1.77-1.40 m 10H (18^1-CH_3, 8^2-CH_3, 17^6-CH_2, 17^8-CH_2); 1-36-1.21 (m, 2H, 17^7-CH_2). MALDI-TOF, *m/z*: $(M+Na)^+$ 670.41, calculated for $C_{39}H_{45}N_5NaO_4$ 670.34.

λ-Pyropheophorbideamidolauric acid or 17^3-deoxy-17^3-(α-carbhydroxyundecylene-λ-amino)pyropheophorbide *a*, PyroC_{12} acid (5)

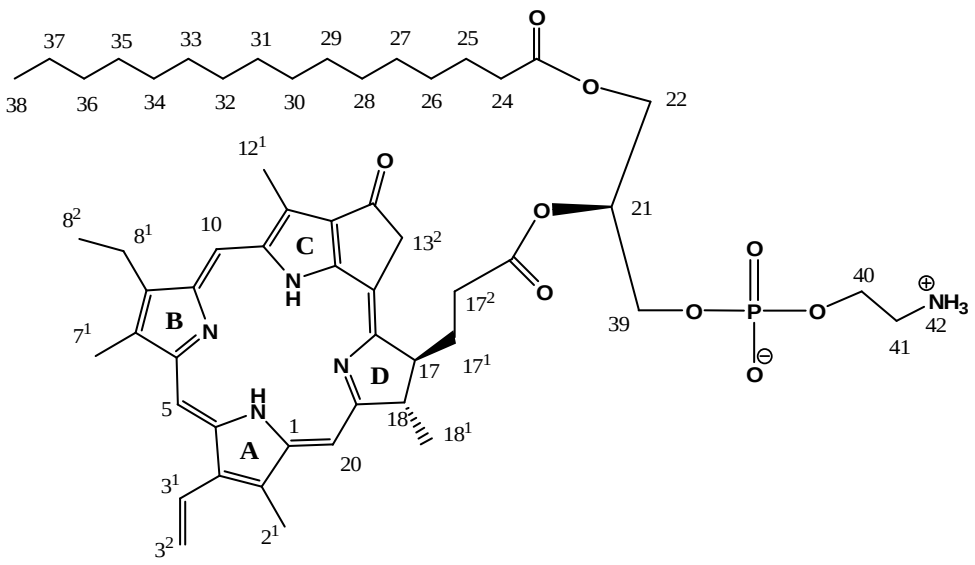


Yield 236 mg, 85%. ^{1}H NMR (360 MHz, $CDCl_3$, CD_3OD δ ppm): 9.17, 9.06 and 8.41 (each s, 1H, 5-*H*, 10-*H* and 20-*H*); 7.77 (dd, J=11.5 Hz, J=17.6 Hz, 1H, 3^1-C*H*=CH_2); 6.11 (d, J=17.6 Hz, 1H, *trans*-3^2-CH=CH*H*); 6.02 (d, J=11.5 Hz, 1H, *cis*-3^2-CH=C*H*H); 5.06 (AB, A=5.14, B=4.99, J_{AB}=20.2 Hz, 2H, 13^2-CH_2); 4.36 (q, J=8.1 Hz, 1H, 18-*H*); 4.15 (dm, 8.7 Hz, 1H, 17-*H*); 3.51-3.35 m 5H, 3.30-3.14 m 5H and 2.98 s 3H (2^1-CH_3, 12^1-CH_3, 7^1-CH_3, 8^1-CH_2, 17^5-CH_2); 2.67-2.41 m 2H and 2.35-2.08 m 4H (17^2-CH_2, 17^{15}-CH_2, 17^1-CH_2); 1.79-1.46 m 10H (18^1-CH_3, 8^2-CH_3, 17^6-CH_2, 17^{14}-CH_2); 1.44-1.12 (m, 14H, 17^7-17^{13} 7xCH_2). MALDI-TOF, *m/z*: $(M+Na)^+$ 754.51, calculated for $C_{45}H_{57}N_5NaO_4$ 754.43.

General procedure for synthesis of 2-pyropheophorbide *a* (with and without C_{12} spacer) substituted 1-palmitoyl-*sn*-glycero-3-phosphoethanolamines

A 200 mL dry flask was charged with *N*-BOC *Lyso* PtdEtn (0.087 mmol), a Pyro-containing acid (0.087 mmol), EDC (0.130 mmol), DMAP (0.043 mmol) and DCM (70 mL). The conversion of Pyro-acid was monitored by TLC ($CHCl_3$/MeOH = 4/2). After 72 h the reaction mixture was diluted with hexanes (30 mL) and passed through a small column with Celite to eliminate non-soluble by-products. After evaporation of solvents, the solid was dissolved in a small amount of DCM and moved into a dry 100 mL flask. After solvent evaporation the residue was dried under high vacuum overnight. Then dry DCM (25 mL) was added, the flask was cooled until -20 °C and TFA (5 mL) was added. The BOC-deprotection reaction was carried out at 0 °C 4 h. Following that, dry toluene (20 mL) was added (to avoid TFA concentrating under evaporation) and volatiles were removed under vacuum. The solid residue was treated with 5% solution of Et_3N in DCM (30 mL) to neutralize traces of TFA. After liquids evaporation the residue was dried under high vacuum overnight. This residue was then dissolved in dry DCM and put onto 6 preparative TLC plates. Preparative TLC (20% MeOH in $CHCl_3$) resulted in the Pyro-PtdEtn derivative as a dark green amorphous solid.

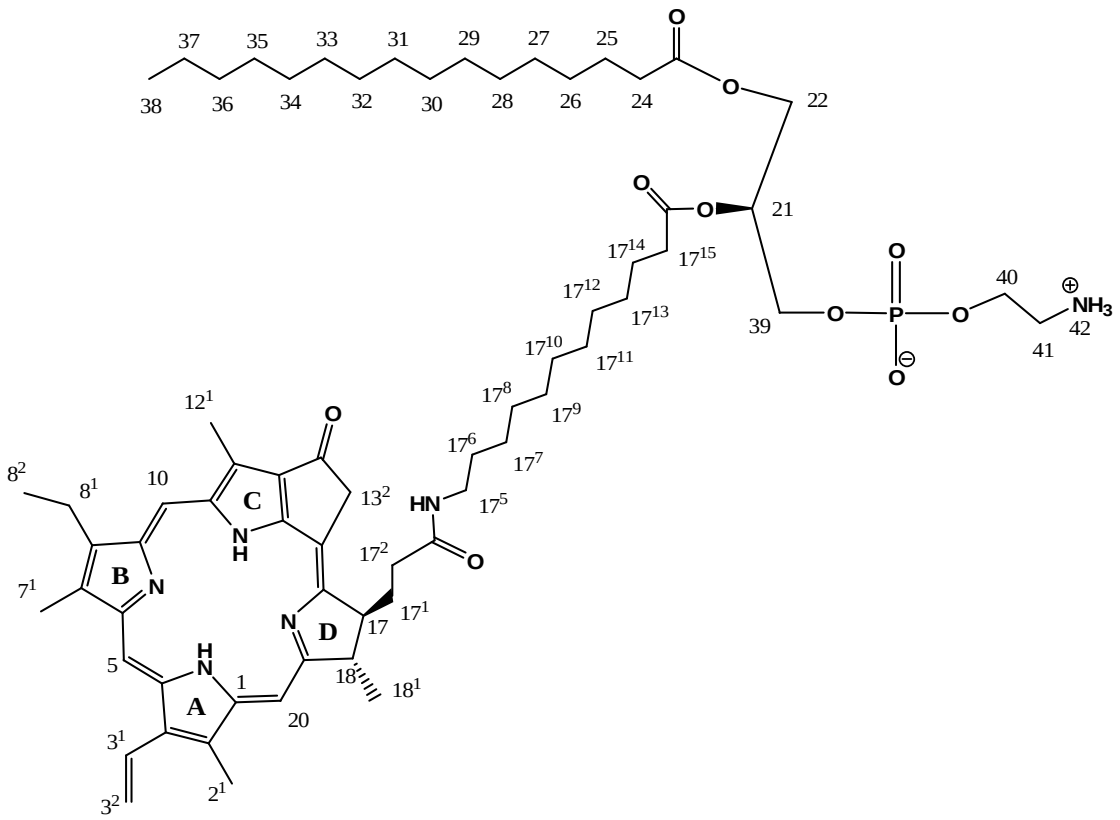
1-palmitoyl-2-pyropheophorbide-*sn*-glycero-3-phosphoethanolamine, Pyro-PtdEtn (3)



Yield 17 mg, 20%. R_f = 0.40 ($CHCl_3$/CH_3OH = 4/1, v/v). ^{1}H NMR (360 MHz, $CDCl_3$/CD_3OD, δ ppm): 9.37, 9.28 and 8.50 (each s, 1H, 5-*H*, 10-*H* and 20-*H*); 7.93 (dd, J=11.5 Hz, J=17.6 Hz, 1H, 3^1-C*H*=CH_2); 6.24 (d, J=17.6 Hz, 1H, *trans*-3^2-CH=CH*H*); 6.13 (d, J=11.5 Hz, 1H, *cis*-3^2-

CH=C*H*H); 5.40-5.01 m 3H (21-*H*, 13^2-CH_2); 4.45 m 2H and 4.32-3.94 m 6H (18-H, 17-H, 22-CH_2, 39-CH_2, 40-CH_2); 3.71-3.51 m 5H, 3.47-3.29 m 5H and 3.18 s 3H (2^1-CH_3, 12^1-CH_3, 7^1-CH_3, 8^1-CH_2, 41-CH_2); 3.12-2.53 m 2H and 2.41-2.14 m 4H (17^2-CH_2, 24-CH_2, 17^1-CH_2); 1.85-1.56 m 8H and 1.45-1.14 m 24H (18^1-CH_3, 8^2-CH_3, 25-37 13xCH_2); 1.05-0.87 (m, 3H, 38-CH_3). MALDI-TOF, *m/z*: $(M+Na)^+$ 992.69, calculated for $C_{54}H_{76}N_5NaO_9P$ 992.53.

1-palmitoyl-2-(λ-pyropheophorbideamidolauroyl)-*sn*-glycero-3-phosphoethanolamine, PyroC$_{12}$-PtdEtn (6)



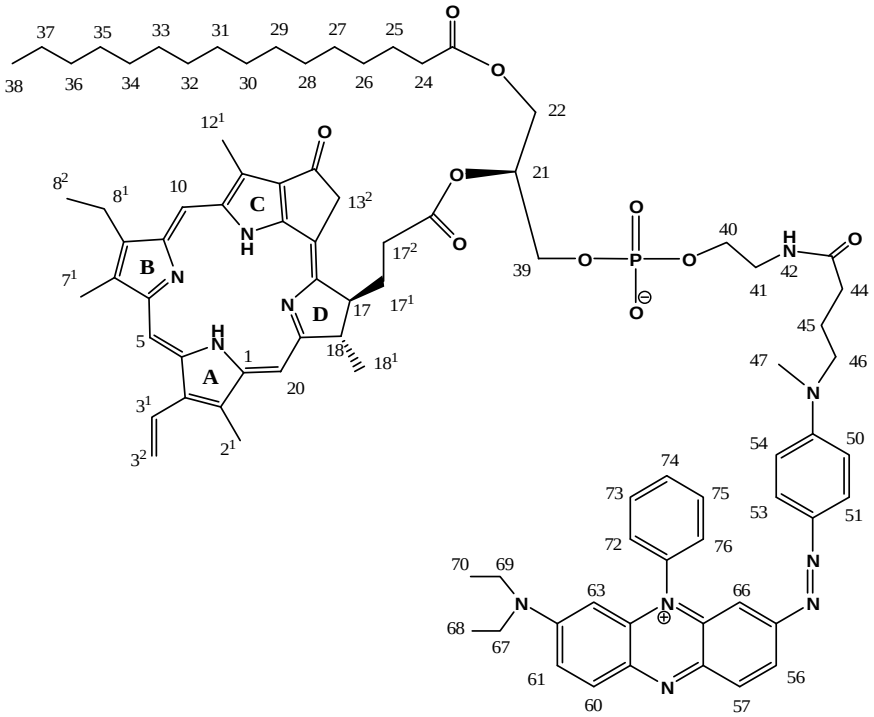
Yield 18 mg, 18%. R_f = 0.25 ($CHCl_3/CH_3OH$ = 4/1, v/v). ^{1}H NMR (360 MHz, $CDCl_3/CD_3OD$, CD_2Cl_2, δ ppm): 9.18, 9.07 and 8.42 (each s, 1H, 5-*H*, 10-*H* and 20-*H*); 7.79 (dd, J=11.5 Hz, J=17.6 Hz, 1H, 3^1-C*H*=CH_2); 6.13 (d, J=17.6 Hz, 1H, *trans*-3^2-CH=CH*H*); 6.04 (d, J=11.5 Hz, 1H, *cis*-3^2-CH=C*H*H); 5.18-4.93 m 3H (21-*H*, 13^2-CH_2, overlapped partially with CD_2Cl_2); 4.60-3.96 m 8H (18-*H*, 17-*H*, 22-CH_2, 39-CH_2, 40-CH_2); 3.55-2.91 m, m and s 15H, (2^1-CH_3, 12^1-CH_3, 7^1-CH_3, 8^1-CH_2, 17^5-CH_2, 41-CH_2); 2.64-2.11 m 8H (17^2-CH_2, 24-CH_2, 17^1-CH_2, 17^{15}-

CH_2); 1.85-1.14 m 50H (18^1-CH_3, 8^2-CH_3, 25-37 and 17^6-17^{14} 22xCH_2); 1.06-0.90 (m, 3H, 38-CH_3). MALDI-TOF, *m/z*: $(M+Na)^+$ 1189.86, calculated for $C_{66}H_{99}N_6NaO_{10}P$ 1189.71.

General procedure for synthesis of Pyro-PtdEtn-BHQ and PyroC_{12}-PtdEtn-BHQ

A 100 mL flask was loaded with a Pyro-containing PtdEtn (**3** or **6**) (0.013 mmol), BHQ-3$^+$-SU PF_6^- (0.013 mmol) and 50 mL of dry DCM. After dissolution 1 drop of Et_3N was added. The reaction was carried out for 4 h. Volatiles were removed in a rotary evaporator and the residue was dried under high vacuum overnight. The residue was dissolved in $CHCl_3$ and put onto 4 preparative TLC plates. Thin layer preparative chromatography gave in result the final product as a dark sea-green amorphous solid.

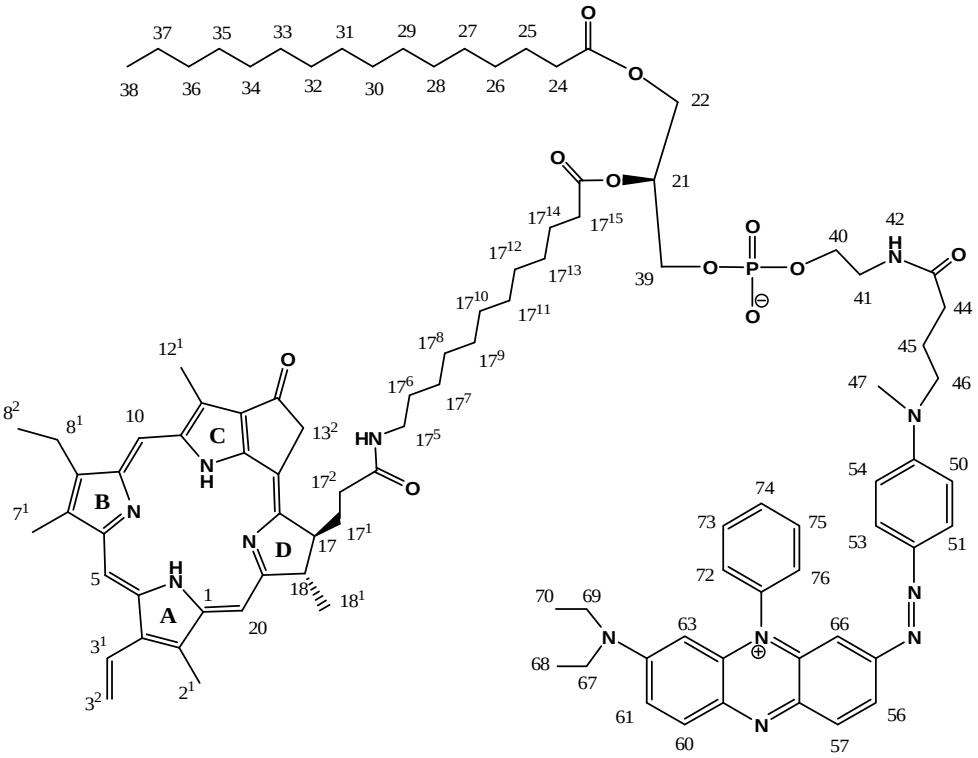
1-palmitoyl-2-pyropheophorbide-*sn*-glycero-3-phosphoethanolamide of BHQ-3 carboxylic acid, Pyro-PtdEtn-BHQ (4)



Yield 14.5 mg, 75%. R_f = 0.6 ($CHCl_3$/CH_3OH = 5/1, v/v). ^{1}H NMR (360 MHz, $CDCl_3$, CD_3OD, δ ppm): 9.39, 9.29 and 8.54 (each s, 1H, 5-*H*, 10-*H* and 20-*H*); 8.09-6.46 m 16H (50-*H*, 51-*H*, 53-*H*, 54-*H*, 56-*H*, 57-*H*, 60-*H*, 61-*H*, 63-*H*, 72-76 5x*H*, 3^1-C*H*=CH_2, overlapped partially with $CDCl_3$); 6.26 (d, J=17.6 Hz, 1H, *trans*-3^2-CH=CH*H*); 6.15 (d, J=11.5 Hz, 1H, *cis*-3^2-CH=C*H*H); 5.33-5.05 m 3H (21-*H*, 13^2-CH_2); 4.51-3.89 (m, 8H, 18-*H*, 17-*H*, 22-CH_2, 39-CH_2, 40-CH_2);

3.70-3.08 m 19H and 2.90 s 3H (2^1-C*H*$_3$, 12^1-C*H*$_3$, 7^1-C*H*$_3$, 47-C*H*$_3$ 8^1-C*H*$_2$, 41-C*H*$_2$, 46-C*H*$_2$, 67-C*H*$_2$, 69-C*H*$_2$); 2.74-2.14 (m, 8H, 17^2-C*H*$_2$, 24-C*H*$_2$, 17^1-C*H*$_2$, 44-C*H*$_2$); 1.96-1.10 (m, 40H, 18^1-C*H*$_3$, 8^2-C*H*$_3$, 68-C*H*$_3$, 70-C*H*$_3$, 25-37 and 46- 14xC*H*$_2$); 1.04-0.86 (m, 3H, 38-C*H*$_3$). MALDI-TOF, *m/z*: $(M+Na)^+$ 1520.93, calculated for $C_{87}H_{108}N_{11}NaO_{10}P$ 1520.79.

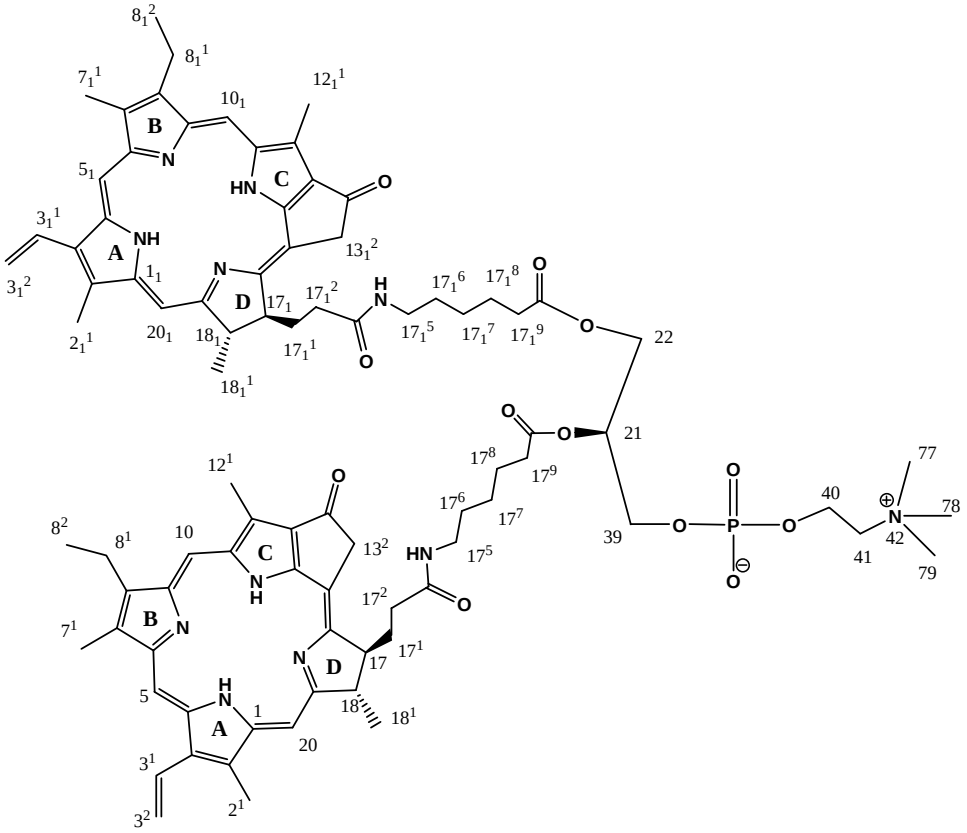
1-palmitoyl-2-(λ-pyropheophorbideamidolauroyl)-*sn*-glycero-3-phosphoethanolamide of BHQ-3 carboxylic acid, PyroC$_{12}$-PtdEtn-BHQ (7)



Yield 12.5 mg, 57%. R_f = 0.3 ($CHCl_3$/CH_3OH = 5/1, v/v). ^{1}H NMR (360 MHz, $CDCl_3$,CD_3OD, CD_2Cl_2, δ ppm): 9.19, 9.09 and 8.44 (each s, 1H, 5-*H*, 10-*H* and 20-*H*); 8.06-6.52 m 16H (50-*H*, 51-*H*, 53-*H*, 54-*H*, 56-*H*, 57-*H*, 60-*H*, 61-*H*, 63-*H*, 72-76 5x*H*, 3^1-C*H*=CH_2, overlapped partially with $CDCl_3$); 6.14 (d, J=17.6 Hz, 1H, *trans*-3^2-CH=CH*H*); 6.05 (d, J=11.5 Hz, 1H, *cis*-3^2-CH=C*H*H); 5.24-4.93 m 3H (21-*H*, 13^2-C*H*$_2$, overlapped partially with CD_2Cl_2); 4.65-3.94 (m, 8H, 18-*H*, 17-*H*, 22-C*H*$_2$, 39-C*H*$_2$, 40-C*H*$_2$); 3.59-3.13 m 18H, 2.98 s 3H and 2.90 s 3H (2^1-C*H*$_3$, 12^1-C*H*$_3$, 7^1-C*H*$_3$, 47-C*H*$_3$, 8^1-C*H*$_2$, 17^5-C*H*$_2$, 41-C*H*$_2$, 46-C*H*$_2$, 67-C*H*$_2$, 69-C*H*$_2$); 2.64-2.10 (m, 10H, 17^2-C*H*$_2$, 24-C*H*$_2$, 17^1-C*H*$_2$, 17^{15}-C*H*$_2$, 44-C*H*$_2$); 1.93-1.08 (m, 58H, 18^1-C*H*$_3$, 8^2-C*H*$_3$, 68-

CH_3, 70-CH_3, 25-37, 46- and 17^6-17^{14} 23xCH_2); 1.05-0.95 (m, 3H, 38-CH_3). MALDI-TOF, *m/z*: $(M+Na)^+$ 1718.14, calculated for $C_{99}H_{131}N_{12}NaO_{11}P$ 1717.97.

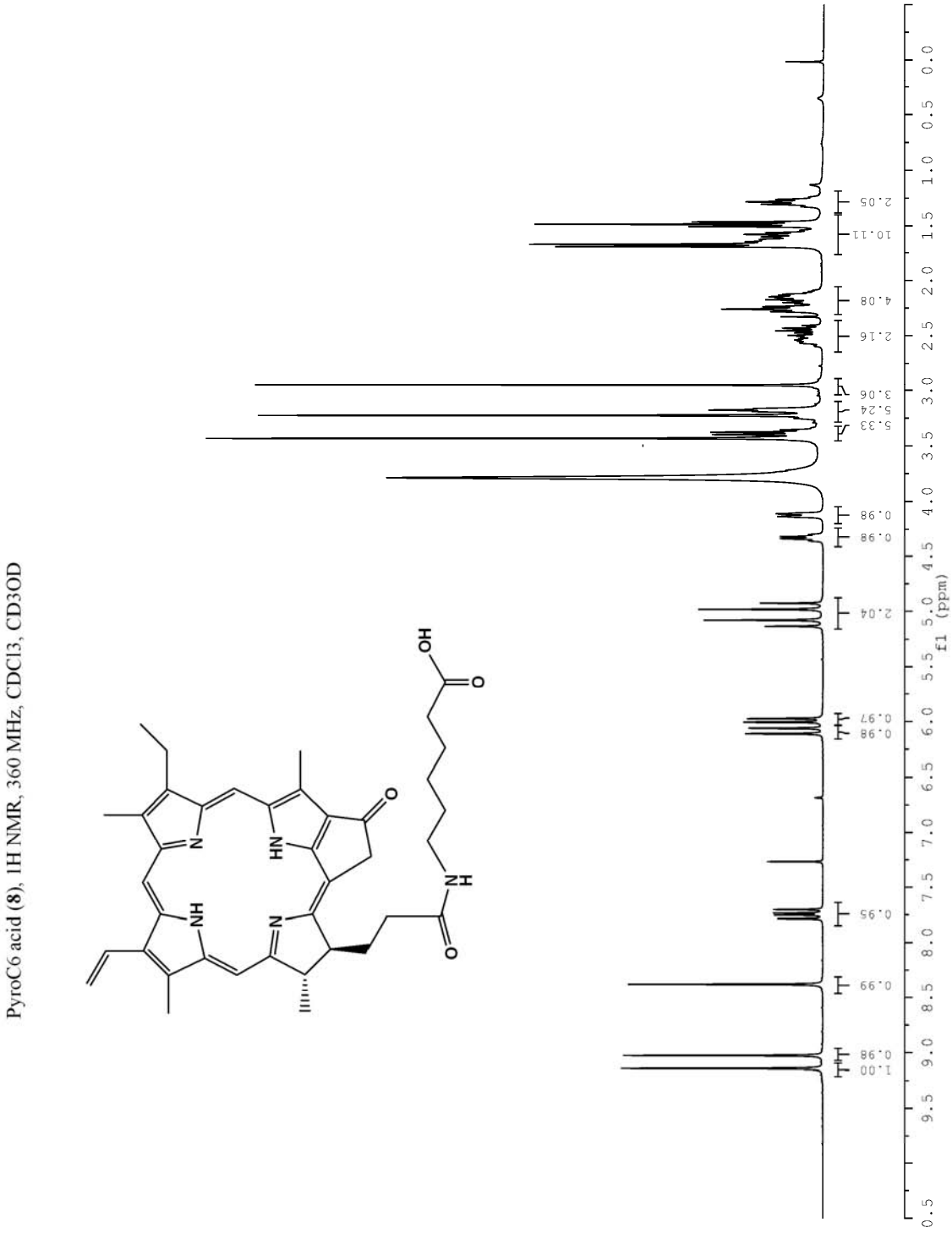
Synthesis of 1,2-bis(ε-pyropheophorbideamidocaproyl)-*sn*-glycero-3-phosphocholine, PyroC$_6$-PyroC$_6$-PtdCho (10)



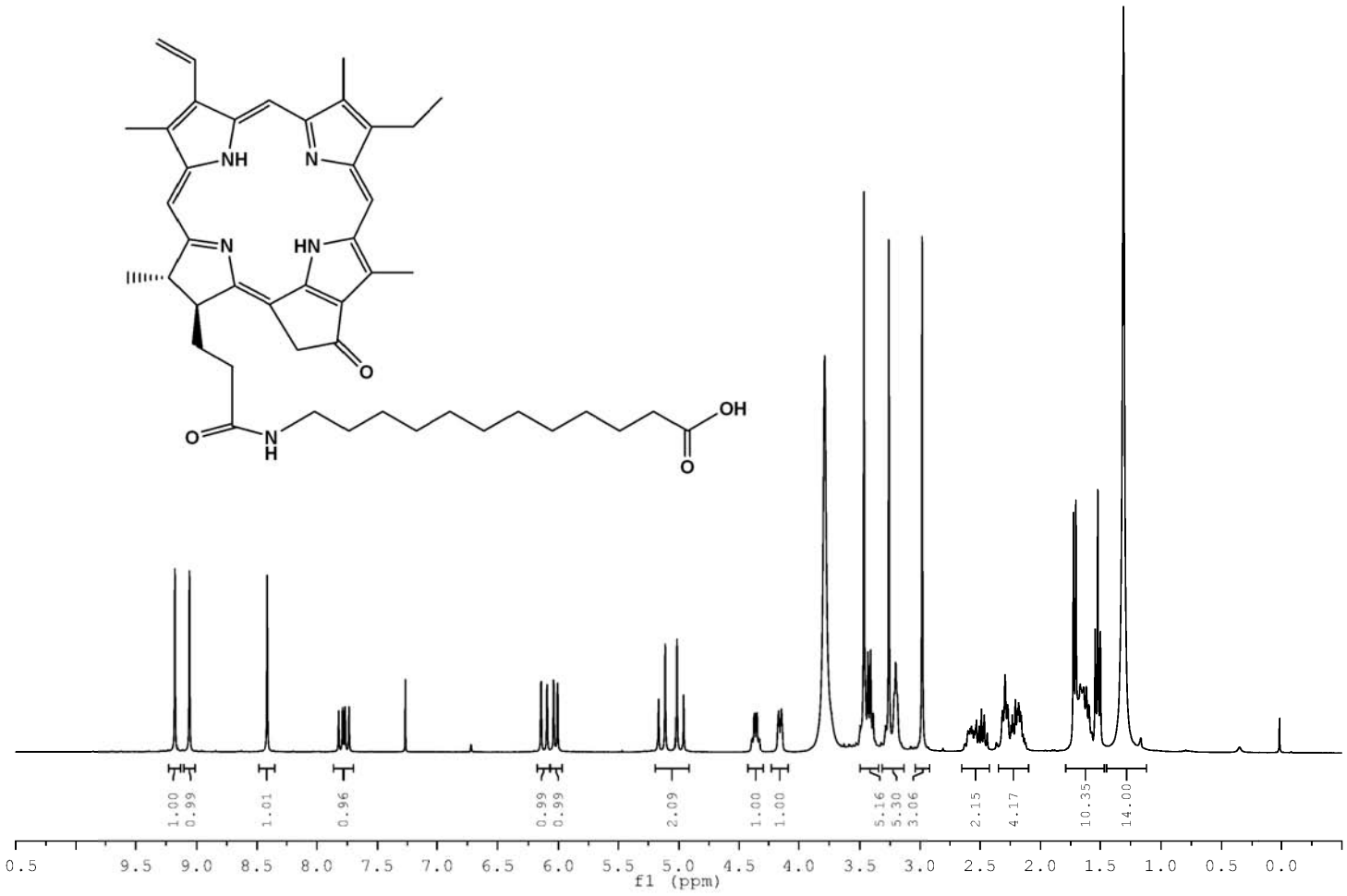
A 100 mL flask was loaded with *sn*-glycero-3-phosphocholine (**9**) (0.026 mmol), ε-Pyropheophorbideamidocaproic acid (**8**) (0.077 mmol), and 50 mL dry MeOH. The mixture was stirred 1h at rt. Then methanol was evaporated under low pressure and the resulting film was dried under high vacuum overnight. Next, EDC (0.077 mmol), DMAP (0.077 mmol) and dry DCM (50 mL) were added to the flask. The reaction mixture was stirred in dark under Ar at 40 °C for 85 h. After that the solution was rinsed with 0.5N HCl, and dried over Na_2SO_4. After solvent evaporation the mixture was dissolved in DCM and put onto three preparative TLC plates. Preparative TLC with $CHCl_3$/MeOH (3/1, v/v) resulted in a mixture of mono- and disubstituted *sn*-glycero-3-phosphocholines (R_f=0.1-0.2). The latter was separated a second time on TLC plates with $CHCl_3$/MeOH/H_2O (2/1/1, v/v/v). The target product (R_f=0.35,

$CHCl_3$/MeOH/H_2O = 2/1/1, v/v/v) was isolated with the yield of 11% (4.3 mg) as an amorphous dark green solid. ^{1}H NMR (360 MHz, $CDCl_3$, CD_3OD, CD_2Cl_2, δ ppm): 9.36, 9.27, 9.16, 9.04, 8.49, and 8.40 (each s, 1H, 5-*H*, 10-*H*, 20-*H*, 5_1-*H*, 10_1-*H* and 20_1-*H*); 7.99-7.70 (m, 2H, 3^1-*H* and $3_1{}^1$-*H*), 6.30-5.98 (m, 4H, 3^2-C*H*$_2$ and $3_1{}^2$-C*H*$_2$), 5.33-4.93 (m, 5H, 21-*H*, 13^2-C*H*$_2$ and $13_1{}^2$-C*H*$_2$, overlapped partially with CD_2Cl_2); 4.52-3.90 (m, 10H, 18-*H*, 17-*H*, 18_1-*H*, 17_1-*H*, 22-C*H*$_2$, 39-C*H*$_2$, 40-C*H*$_2$); 3.67-2.93 (m, 37H, 2^1-C*H*$_3$, $2_1{}^1$-C*H*$_3$, 12^1-C*H*$_3$, $12_1{}^1$-C*H*$_3$, 7^1-C*H*$_3$, $7_1{}^1$-C*H*$_3$, 77-C*H*$_3$, 78-C*H*$_3$, 79-C*H*$_3$, 8^1-C*H*$_2$, $8_1{}^1$-C*H*$_2$, 17^5-C*H*$_2$, $17_1{}^5$-C*H*$_2$, 41-C*H*$_2$, overlapped partially with CD_3OD); 2.71-2.10 (m, 12H, 17^2-C*H*$_2$, 17^9-C*H*$_2$, 17^1-C*H*$_2$, $17_1{}^2$-C*H*$_2$, $17_1{}^9$-C*H*$_2$, $17_1{}^1$-C*H*$_2$); 1.83-1.46 (m, 20H, 18^1-C*H*$_3$, 8^2-C*H*$_3$, 17^6-C*H*$_2$, 17^8-C*H*$_2$, $18_1{}^1$-C*H*$_3$, $8_1{}^2$-C*H*$_3$, $17_1{}^6$-C*H*$_2$, $17_1{}^8$-C*H*$_2$); 1.36-1.20 (m, 4H, 17^7-C*H*$_2$, $17_1{}^7$-C*H*$_2$). MALDI-TOF, *m/z*: $(M+Na)^+$ 1538.92, calculated for $C_{86}H_{106}N_{11}NaO_{12}P$ 1538.77.

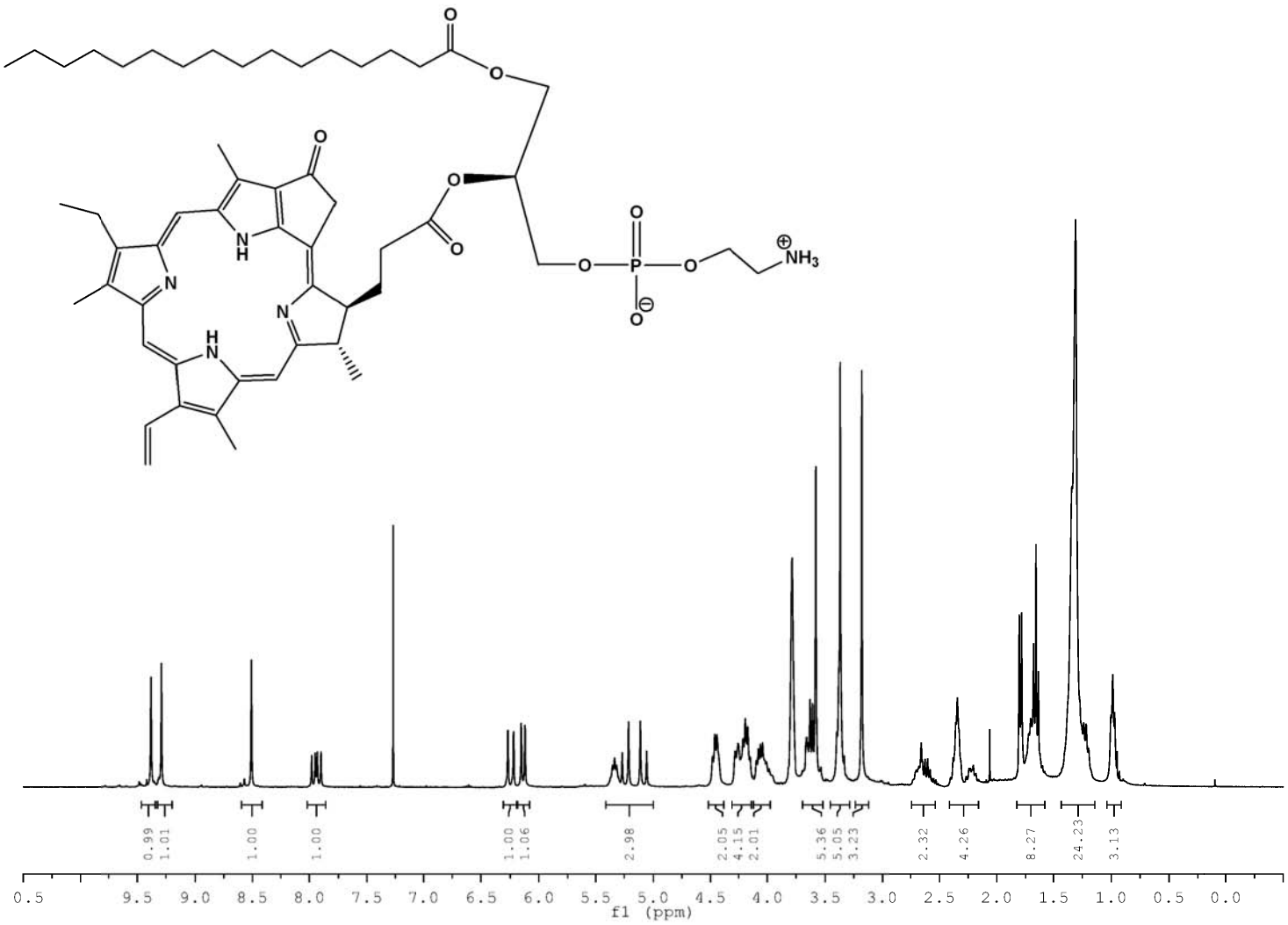
III. ^{1}H NMR Spectra



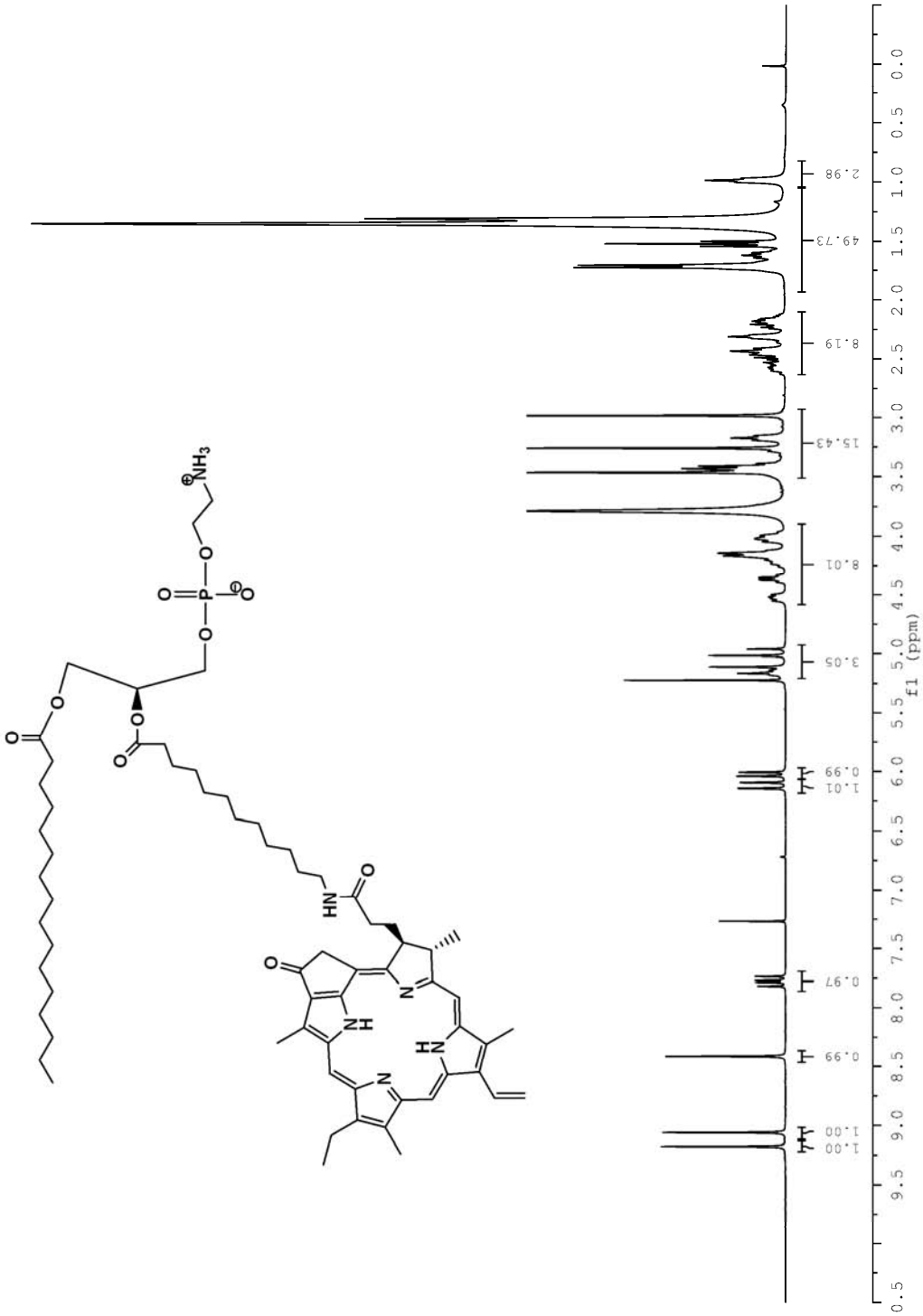
PyroC12 acid (**5**), 1H NMR, 360 MHz, CDCl3, CD3OD



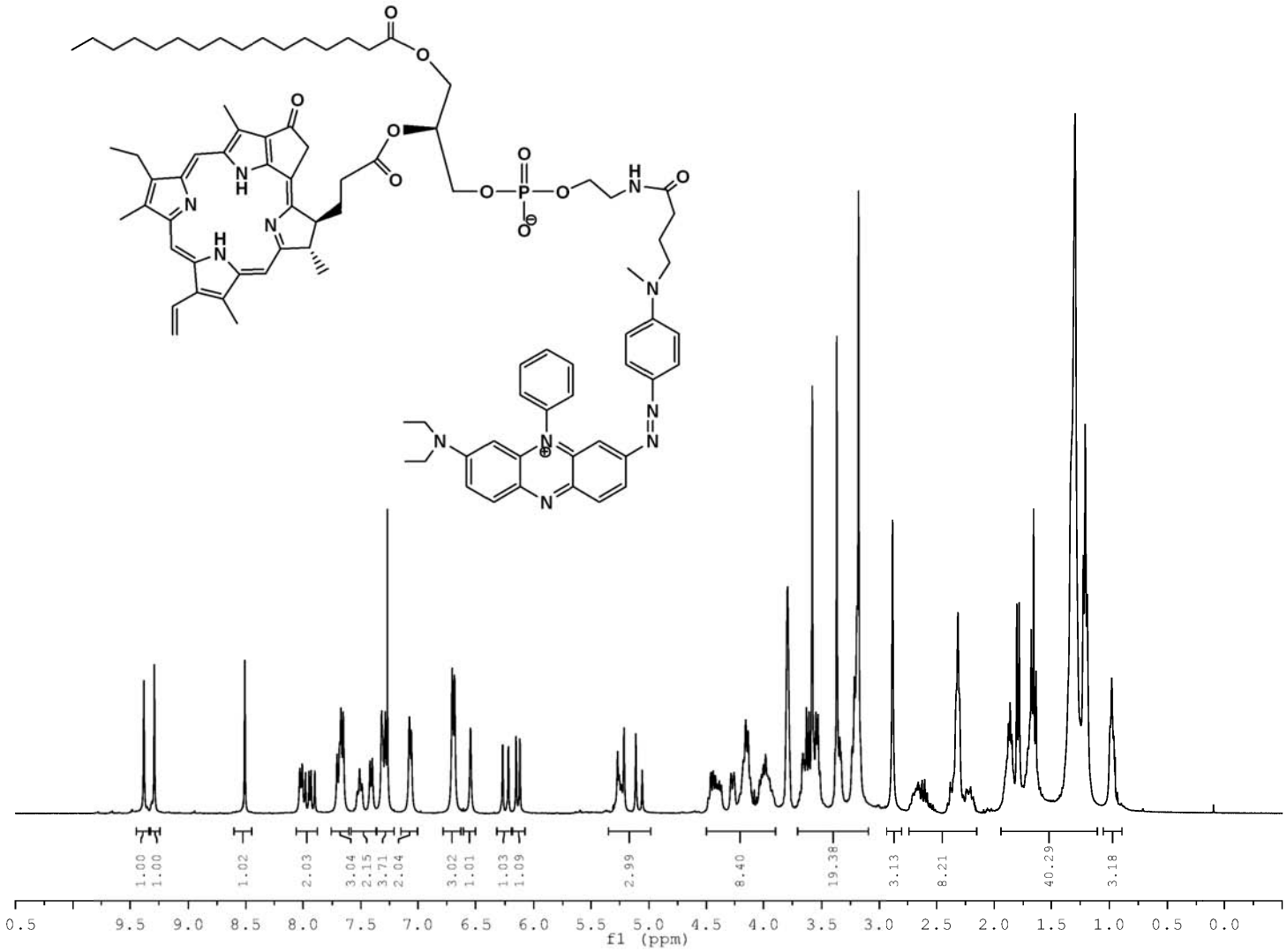
Pyro-PtdEtn (**3**), 1H NMR, 360 MHz, CDCl3, CD3OD



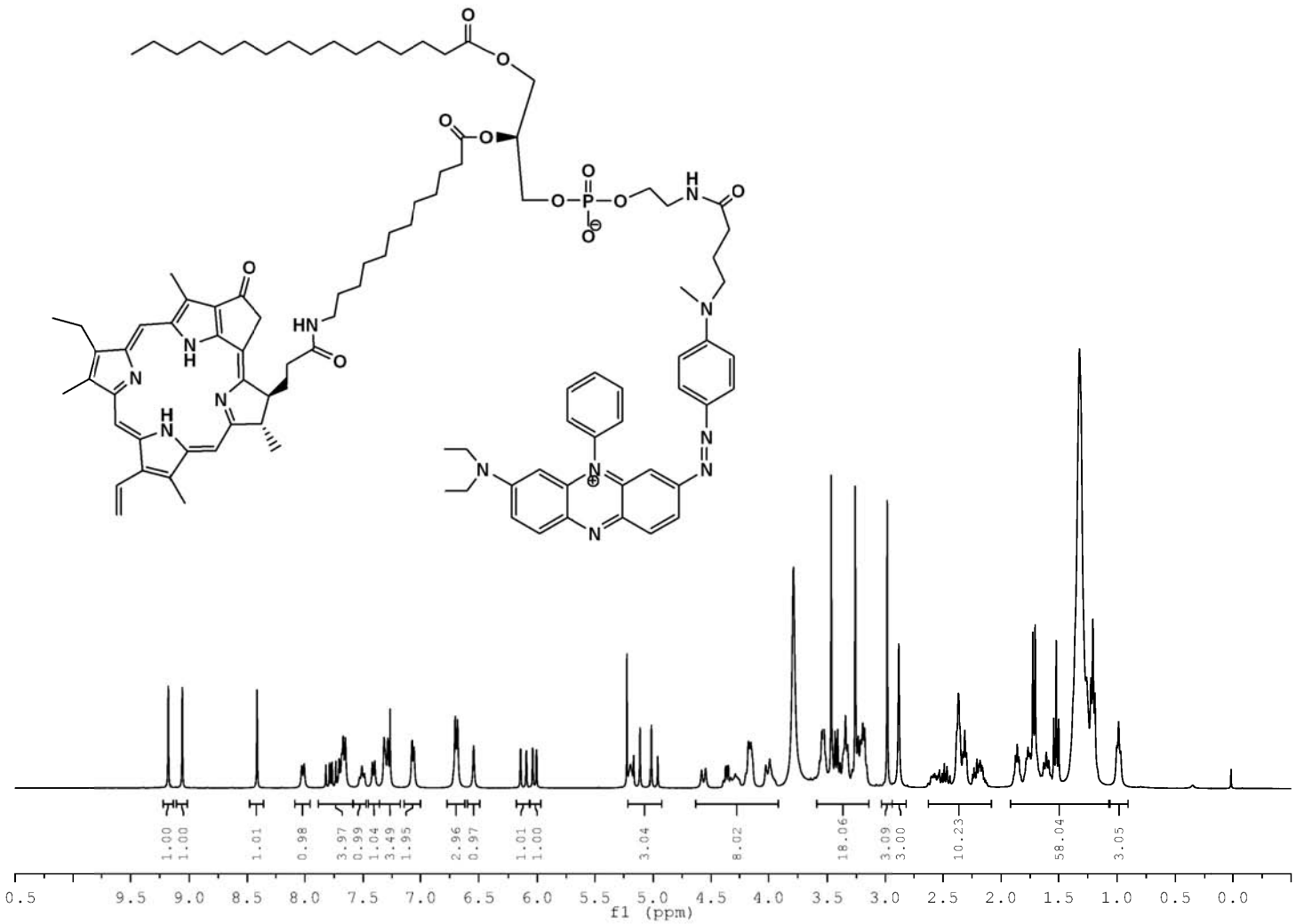
Pyro12-PtdEtn (**6**), 1H NMR, 360 MHz, CDCl3, CD3OD, CD2Cl2



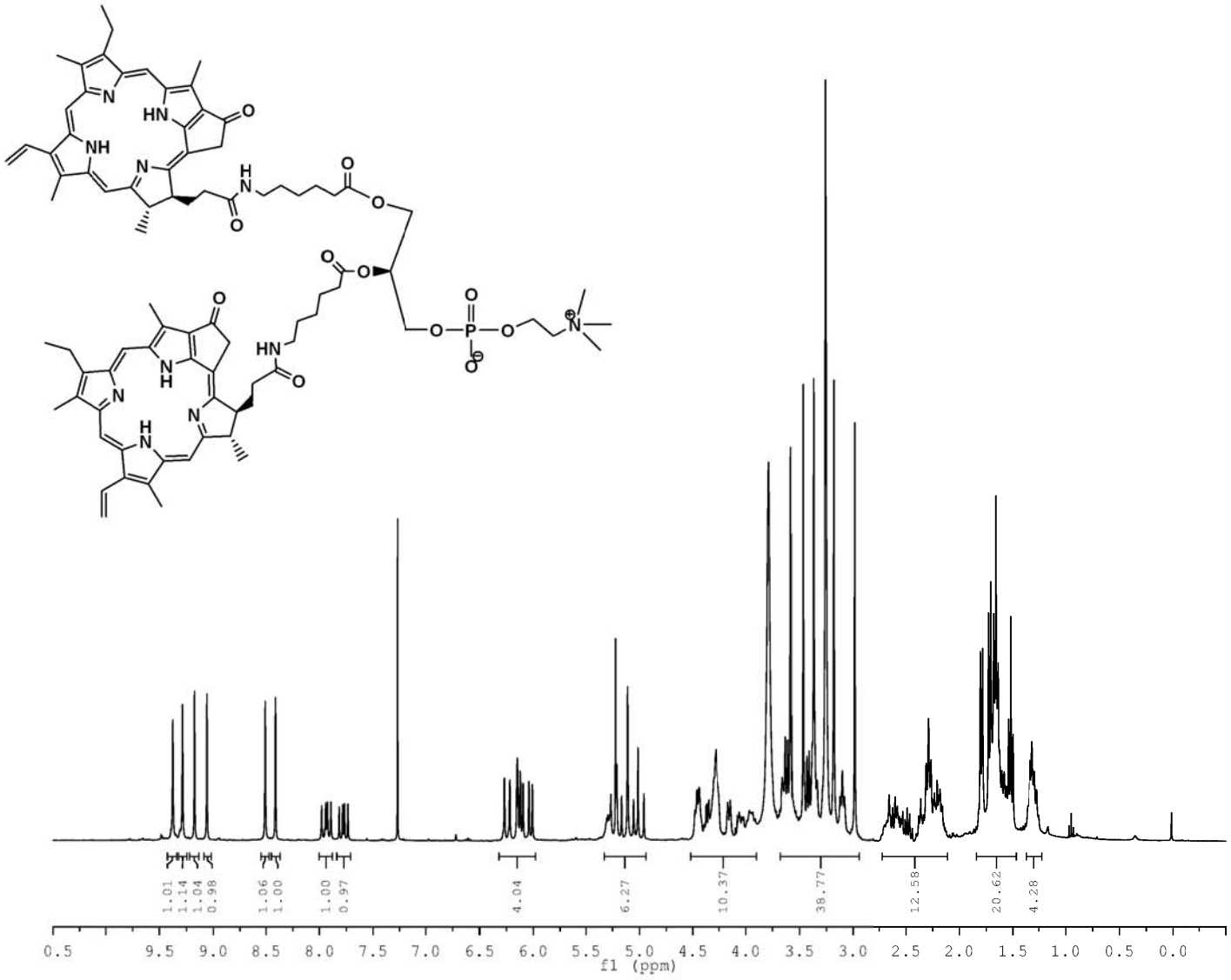
Pyro-PtdEtn-BHQ (**4**), 1H NMR, 360 MHz, CDCl3, CD3OD



Pyro12-PtdEtn-BHQ (7), 1H NMR, 360 MHz, CDCl3, CD3OD, CD2Cl2



PyroC6-PyroC6-PtdCho (**10**), 1H NMR, 360 MHz, CDCl3, CD3OD, CD2Cl2



IV. Enzyme mediated probe cleavage

The specificity of each probe to a series of phospholipases was determined by measuring fluorescence release in an *in vitro* assay. Probes were prepared in egg-phosphatidylcholine vesicle by adding fluorophores to a measured amount of egg-PtdCho in chloroform. Probe concentration was determined using the Beer-Lambert law by measuring optical density at 418 nm and using an extinction coefficient of 110,000 $M^{-1}cm^{-1}$. Chloroform was removed by evaporation, and the resulting film was resuspended in 50 mM Tris-HCl, pH 7.4, sonicated and vortexed until optically clear. The final concentration was 1 μM self-quenched phospholipid probe in 50 μM egg-yolk-PtdCho vesicles (i.e. mole fraction of 0.02). Lipid dispersions were aliquotted into 96-well plates at volumes of 100 μL. Reaction mixtures were incubated for 10 minutes at 37°C and reactions were started by addition of 10U of enzyme. The time-dependent release of fluorescence was measured using a Molecular Devices SpectraMax M5 fluorescent plate reader (λ_{Ex} 418 nm, λ_{Em} 675 nm for the Pyro-derivatives, λ_{Ex} 488 nm, λ_{Em} 530 nm for the BODIPY- derivatives).

V. References

(1) Yang, H., and Roberts, M. F. (2003) Phosphohydrolase and transphosphatidylation reactions of two Streptomyces phospholipase D enzymes: Covalent versus noncovalent catalysis. *Protein Sci. 12,* 2087-2098.

(2) Tomita, M., Sawada, H., Taguchi, R., and Ikezawa, H. (1987) The action of sphingomyelinase from Bacillus cereus on ATP-depleted bovine erythrocyte membranes and different lipid composition of liposomes. *Arch. Biochem. Biophys. 255,* 127-135.

(3) Ryan, M., Liu, T., Dahlquist, F. W., and Griffith, O. H. (2001) A Catalytic Diad Involved in Substrate-Assisted Catalysis: NMR Study of Hydrogen Bonding and Dynamics at the Active Site of Phosphatidylinositol-Specific Phospholipase C. *Biochemistry 40*, 9743-9750.

(4) Berg, O. G., Yu, B.-Z., Apitz-Castro, R. J., and Jain, M. K. (2004) Phosphatidylinositol-Specific Phospholipase C Forms Different Complexes with Monodisperse and Micellar Phosphatidylcholine. *Biochemistry 43,* 2080-2090.

(5) Ikezawa, H., Yamanegi, M., Taguchi, R., Miyashita, T., and Ohyabu, T. (1976) Studies on phosphatidylinositol phosphodiesterase (phospholipase C type) of Bacillus cereus. I. Purification, properties and phosphatase-releasing activity. *Biochim. Biophys. Acta, Lipids Lipid Metab. 450,* 154-164.

(6) Antikainen, N. M., Hergenrother, P. J., Harris, M. M., Corbett, W., and Martin, S. F. (2003) Altering Substrate Specificity of Phosphatidylcholine-Preferring Phospholipase C of Bacillus cereus by Random Mutagenesis of the Headgroup Binding Site. *Biochemistry 42*, 1603-1610.

(7) Benfield, A. P., Goodey, N. M., Phillips, L. T., and Martin, S. F. (2007) Structural studies examining the substrate specificity profiles of PC-PLCBc protein variants. *Arch. Biochem. Biophys. 460*, 41-47.
(8) Hergenrother, P. J., and Martin, S. F. (1997) Determination of the kinetic parameters for phospholipase C (Bacillus cereus) on different phospholipid substrates using a chromogenic assay based on the quantitation of inorganic phosphate. *Anal Biochem 251*, 45-49.
(9) Hergenrother, P. J., and Martin, S. F. (2001) Phosphatidylcholine-preferring phospholipase C from B. cereus. function, structure, and mechanism. *Top. Curr. Chem. 211*, 131-167.
(10) Kinkaid, A., and Wilton, D. C. (1991) Comparison of the catalytic properties of phospholipase A2 from pancreas and venom using a continuous fluorescence displacement assay. *Biochem. J. 278*, 843-848.
(11) Kudo, I., and Murakami, M. (2002) Phospholipase A2 enzymes. *Prostaglandins Other Lipid Mediators 68-69*, 3-58.
(12) Murakami, M., and Kudo, I. (2001) Diversity and regulatory functions of mammalian secretory phospholipase A2s. *Adv. Immunol. 77*, 163-194.
(13) Murakami, M., and Kudo, I. (2002) Lipid signaling. Phospholipase A2. *J. Biochem. 131*, 285-292.
(14) Zheng, G., Li, H., Zhang, M., Lund-Katz, S., Chance, B., and Glickson, J. D. (2002) Low-density lipoprotein reconstituted by pyropheophorbide cholesteryl oleate as target-specific photosensitizer. *Bioconjug Chem 13*, 392-396.

Optimization of the N-Lost Drugs Melphalan and Bendamustine: Synthesis and Cytotoxicity of a New Set of Dendrimer−Drug Conjugates as Tumor Therapeutic Agents

Ana Maria Scutaru,[†] Maxi Wenzel,[†] Heike Scheffler,[†] Gerhard Wolber,[†] and Ronald Gust*[,†,‡]

Institute für Pharmazie, Freie Universität Berlin, Königin Luise Str. 2 + 4, 14195 Berlin, Germany, and Institut für Pharmazie, Universität Innsbruck, Innrain 52, A-6020 Innsbruck, Austria. Received October 15, 2009; Revised Manuscript Received July 19, 2010

Bendamustine and melphalan are very promising alkylating drugs with applicability in the treatment of various tumoral diseases, e.g., chronic lymphocytic leukemia (CLL) or breast cancer. However, numerous adverse effects limited their use. Therefore, 1,3,5-tris(3-aminopropyl)benzene (**G0**) and its **G1** analogue 3,5-bis(3-aminopropyl)-*N*-(3-{3,5-bis[3-{3,5-bis(3-aminopropyl)benzoylamino}propyl]phenyl}propyl)benzamide were selected to design cytostatic drug−dendrimer conjugates to achieve tumor cell accumulation by endocytosis as already demonstrated for platinum complexes. The dendrimers act as carriers and an *N*-(2-hydroxyethyl)maleimide spacer between drug and carrier should guarantee a selective release of the cytostatics in the tumor cells. The resulting cytotoxicity was determined in vitro using the human MCF-7 and MDA-MB-231 breast cancer cell lines. It was demonstrated that melphalan caused cytotoxic effects depending on its free amino group (Boc protection strongly decreased the activity) but independent of a derivation of the carboxylic group (dendrimers and spacer binding). Esterification of bendamustine with the *N*-(2-hydroxyethyl)maleimide spacer strongly increased the hydrolytic stability of the N-lost moiety, so antiproliferative effects were yet observed in vitro.

INTRODUCTION

Designing miscellaneous dendritic structures containing both a drug and a targeting residue has played a very important role in drug development during the past years (*1*−*4*). The main objective has been to diminish the side effects induced through drug therapy. Accumulation of these conjugates in the tumor tissue is explained by the EPR (enhanced permeability and retention) effect, the property by which macromolecules build up in the tumor due to the special properties of the cells (e.g., poor lymphatic drainage) (*5, 6*). Current studies by Baker et al. showed remarkable results and proved the selective uptake of PAMAM dendrimer-based multifunctional conjugates in the tumor tissues (*7*−*9*).

Bendamustine is a drug with high potency in the treatment of several tumoral diseases. It was first synthesized by Ozegowski et al. and has been in clinical use since 1985 (*10*). The molecule consists of three structural elements: a mechlorethanamine group, a benzimidazole core, and a butyric acid chain. It was proposed that the latter (together with the protonated heterocycle) mediates water solubility and the benzimidazole moiety should lead to tumor cell accumulation by purine base transporters.

Bendamustine belongs to the class of nitrogen mustard agents like chlorambucil, melphalan, and cyclophosphamide and should induce cell death, possibly through apoptosis. Recent clinical trials have illustrated remarkable results in the treatment of chronic lymphocytic leukemia (CLL), and thus, in March 2008, bendamustine was also approved in the USA for the treatment of CLL (*11*). Additionally, bendamustine has a promising future in the treatment of breast cancer (*12*). The mechanism of action is thought to include both alkylating agent properties (comparable to melphalan) and purine antimetabolite characteristics.

Melphalan is a typical alkylating agent and contains two functional groups: the amino acid phenylalanine (drug targeting by using amino acid transporter of tumor cells) and the N-Lost moiety (cross-link of DNA strands). It is used in the treatment of cancer and other diseases, including ovarian cancer, malignant melanoma, multiple myeloma (bone-marrow cancer), breast cancer, and chronic myelogenous leukemia.

Both bendamustine and melphalan are very effective antitumor drugs, without having the proposed tumor selectivity. Therefore, we decided to use them in our approach to increase the selectivity for malignant cells following the concept of Kratz et al. They synthesized in 1998 a protein-conjugate with chlorambucil capable of releasing the drug in breast cancer (MCF-7) and leukemia (MOLT4) cells. Chlorambucil was attached through an ester or amide bond to a maleimide spacer, which is able to bind selectively to thiol groups of human serum albumin (HSA) (*13, 14*). HSA is a handy protein in pure form, is nontoxic and biodegradable, and is essentially assimilated by the tumor cells (*15, 16*). The resulting drug−HSA conjugates should accumulate in the tumors due to the EPR effect and then release the drug in the cells (drug targeting). The in vitro cell tests illustrated a relationship between the linker and the efficacy of the conjugates, and in vivo studies demonstrated the possibility of administering a conjugate with a lower IC_{50} value than chlorambucil in a higher dose to mice.

These positive results induced us to bind melphalan and bendamustine directly or through a cleavable maleimide spacer to the dendrimers **G0** and **G1** (see Figure 1) synthesized in a former SAR study (*17*). In vitro antitumor activity studies on MCF-7 and MDA-MB-231 cell lines showed for **G0** and **G1** no cytotoxic effects (see Supporting Information), making them suitable as carriers.

Initially, three different spacers were considered for the assembling of the conjugates (Figure 1). Due to the instability of the hydrazone linkers under the given reaction conditions,

* Corresponding author. Phone: +43 512 507 5245; Telefax: +43 512 507 2940; E-mail: ronald.gust@uibk.ac.at.
[†] Freie Universität Berlin.
[‡] Universität Innsbruck.

10.1021/bc900453f © 2010 American Chemical Society
Published on Web 09/17/2010

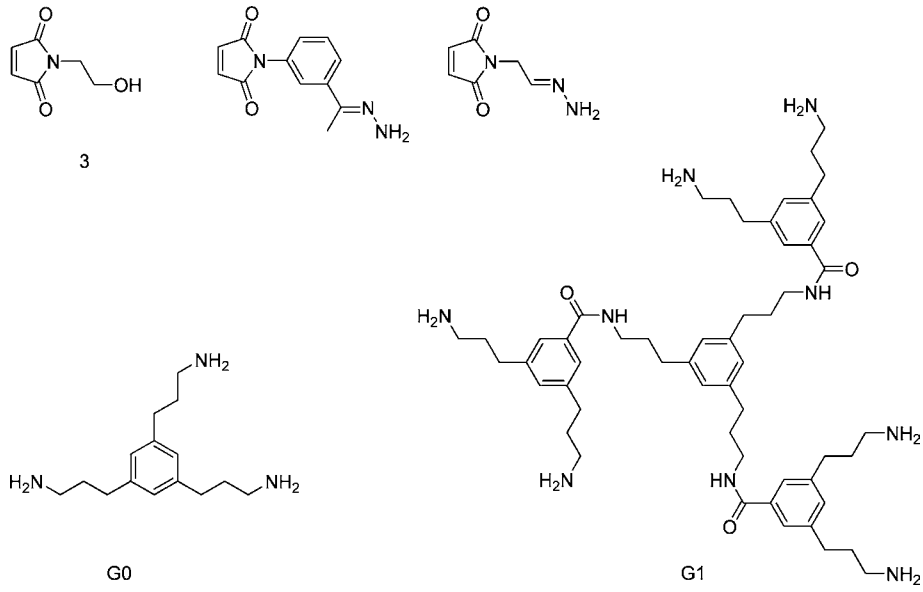


Figure 1. Structures of the considered spacers and dendrimers.

the synthesis was first limited to the use of *N*-(2-hydroxyethyl)maleimide **3**.

EXPERIMENTAL SECTION

General. ^{1}H and ^{13}C NMR spectra were taken on a Bruker Avance/DPX 400 MHz with TMS as internal standard. Melting points (uncorrected) were measured with a Büchi Melting Point B-545. All column chromatography purifications were done using silica gel 60 (0.063−0.1 mm, Merck). TLC was performed on silica gel 60 GF_{254} plates (Merck). Elemental analysis was carried out on a Vario EL (Hanau). EI spectra were recorded on a Thermo-Fisions VG Auto Spec (70 eV). The FAB spectra were measured on a CH-5, Varian MAT, Bremen. The ESI-TOF spectra were measured on an Agilent 6210 ESI-TOF, Agilent Technologies, Santa Clara, CA, USA. Solvent flow rate was adjusted to 4 μL/min, with spray voltage set to 4 kV. Drying gas flow rate was set to 15 psi (1 bar). All other parameters were adjusted for a maximum abundance of the relative $[M+H]^+$.

Synthesis. The following compounds were prepared according to literature procedures: **G0** (*17*), **G1** (*17*), *N-tert*-butoxycarbonyl-4-[bis(2-chloroethyl)amino]-L-phenylalanine (*2*) (*18*). Bendamustine hydrochloride was a gift from the company Bendalis. Melphalan hydrochloride was synthesized as described by Bergel (*19*). All other starting materials were purchased from commercial sources and used without purification. Solvents were dried under standard conditions.

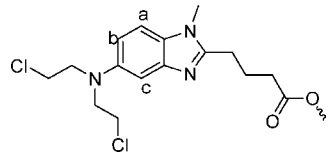
*O-{N-tert-Butoxycarbonyl-4-[bis(2-chloroethyl)amino]-L-phenylalanyl}-2-hydroxyethylmaleimide (**4**).* [1]MelBoc **2** (330 mg, 0.81 mmol), DMAP (tip of a spatula), and *N*-(2-hydroxyethyl)-maleimide **3** (441 mg, 3.1 mmol) were dissolved in 30 mL of dry dichloromethane at room temperature. DCC (176.5 mg, 0.85 mmol), dissolved in 25 mL of dry dichloromethane, was added dropwise to this solution within 1 h, and the solution stirred for additional 20 h. The solution was filtered and evaporated in vacuo. The red residue was chromatographed on a silica gel column (hexane/ethyl acetate 2:1) to afford the desired product (137 mg, 32%) as yellow solid: $R_f = 0.3$ (hexane/ethyl acetate 2:1); mp 101 °C; ^{1}H NMR (400 MHz, $CDCl_3$) $\delta = 1.29$ (s, 9H, CH_3), 2.62 (m, 1H, CH_2Ar), 2.74 (dd, ^3J(H,H) = 4.46 Hz, 9.44 Hz, 1H, CH_2Ar), 3.62 (t, ^3J(H,H) = 5.28 Hz, 2H, $CH_{2\ maleimide}$), 3.66 (s, 8H, CH_2CH_2Cl), 4.09 (m, 2H, CH_2O), 4.22 (m, 1H, CH), 6.63 (d, ^3J(H,H) = 8.52 Hz, 2H, Ar*H*), 7.02 (d, 2H+2H, Ar*H*+$H_{maleimide}$), 7.17 (d, ^3J(H,H) = 8.01 Hz, 1H, NH); ^{13}C NMR ($CDCl_3$) δ = 28.31 (CH_3), 36.64 (CH_2Ar), 36.98 ($CH_2N_{maleimide}$), 40.46 ($CH_2NAr+CH_2Cl$), 54.49 (CH), 62.11 (CH_2O), 79.84 ($C(CH_3)_3$), 112.09 ($C_{aromatic}$), 124.8 (C), 130.56 ($C_{aromatic}$), 134.25 ($CH_{maleimide}$), 145.04 ($C_{aromatic}$), 155.07 (COOBoc), 170.29 ($CO_{maleimide}$), 171.75 (COO); MS (EI, 80 eV, 300 °C) *m*/*z* (%) 527.2 (5.93) [M^+-1], 404.1 (0.36) [$M-C_6H_6NO_2]^+$, 230.3 (100) $C_{15}H_{14}NCl_2$; Anal. ($C_{24}H_{31}Cl_2N_3O_6$) C, H, N.

*O-{4-[Bis(2-chloroethyl)amino]-L-phenylalanyl}-2-hydroxyethylmaleimide Hydrochloride (**5**).* MelBoc-spacer **4** (350 mg, 0.66 mmol) was dissolved in 6 mL of THF. To this solution, 250 μL of hydrochloric acid (w = 25%) was added and the mixture was stirred for 20 h at room temperature. The solvent was removed under reduced pressure. The remaining oil was dissolved in methanol, and the product was precipitated with diethyl ether, filtered, and dried, to afford 245 mg (80%) as a colorless solid: mp 130 °C; ^{1}H NMR (400 MHz, CD_3OD) δ = 3.00 (dd, ^3J(H,H) = 7.89 Hz, 14.59 Hz, 1H, CH_2Ar), 3.14 (dd, ^3J(H,H) = 5.22 Hz, 14.60 Hz, 1H, CH_2Ar), 3.69 (m, 4H, CH_2Cl), 3.78 (m, 4H+2H, CH_2CH_2Cl+C$H_{2\ maleimide}$), 4.18 (m, 1H, CH), 4.38 (m, 1H, CH), 6.77 (d, ^3J(H,H) = 8.81 Hz, 2H, Ar*H*), 6.86 (s, 2H, $H_{maleimide}$), 7.11 (d, ^3J(H,H) = 8.75 Hz, 2H, Ar*H*); ^{13}C NMR (CD_3OD) δ = 37.55 ($CH_2N_{maleimide}$), 39.67 (CH_2Ar), 41.07 (CH_2N), 42.6 (CH_2Cl), 53.7 (CH), 60.14 (CH_2O), 119.5 ($C_{aromatic}$), 132.50 ($C_{aromatic}$), 132.54 ($C_{aromatic}$), 132.7 ($C_{aromatic}$), 135.43 ($CH_{maleimide}$), 135.68 ($C_{aromatic}$), 170.33 ($CO_{maleimide}$), 172.3 (COO); MS (ESI) calcd. for $C_{19}H_{24}N_3O_4Cl_2^+$ 428.1138, found 428.1152; Anal. ($C_{19}H_{25}Cl_3N_3O_4\cdot$HCl) C, H, N.

*O-{4-[6-Bis(2-chloroethyl)amino-3-methylbenzimidazoyl(2)]-butanoyl}-2-hydroxyethylmaleimide (**7**).* Bendamustine free base **6** (2 g, 5.6 mmol), DMAP (35 mg, 0.26 mmol), and *N*-(2-hydroxyethyl)maleimide **3** (2.36 g, 16.7 mmol) were dissolved in 250 mL of dry dichloromethane at room temperature. DCC (1.27 g, 6.16 mmol), dissolved in 100 mL of dry dichloromethane, was added dropwise to this solution within 1 h and the solution stirred for additional 24 h. The solution was filtered and evaporated in vacuo. The residue was chromatographed on

[1]Abbreviations: Mel, Melphalan; DMAP, 4-dimethylaminopyridine; DCC, *N*,*N*-dicyclohexylcarbodiimide; DIPEA, *N*-ethyl-diisopropylamine; Benda, Bendamustine; TFA, trifluoroacetic acid; TBTU, *O*-(1*H*-benzotriazol-1-yl)-*N*,*N*,*N*′,*N*′-tetramethyluronium tetrafluoroborate; HOBT, hydroxybenzotriazole hydrate; EDC, *N*-(3-dimethylaminopropyl)-*N*′-ethylcarbodiimide hydrochloride.

Chart 1. Supporting Scheme for NMR Data of Compound 7



a silica gel column (dichloromethane/methanol 20:1, dichloromethane/acetone 3:1) to afford the desired product (1.89 g, 70.1%) as yellow solid: $R_f = 0.4$ (dichloromethane/acetone 3:1); mp 115 °C; ^{1}H NMR (400 MHz, DMSO) δ = 1.95 (quin, ^3J(H,H) = 7.31 Hz, 2H, CH_2), 2.39 (t, ^3J(H,H) = 7.27 Hz, 2H, CH_2CO), 2.79 (t, ^3J(H,H) = 7.37 Hz, 2H, $CH_2CO_{benzimidazole}$), 3.64 (m, 4H+2H, CH_2CH_2Cl+CH_2O), 3.70 (s, 4H+3H, CH_2CH_2Cl+$NCH_{3\ benzimidazole}$), 4.14 (t, ^3J(H,H) = 5.32 Hz, 2H, $CH_{2\ maleimide}$), 6.77 (dd, ^3J(H,H) = 2.21 Hz, 8.8 Hz, 1H, CH b), 6.91 (d, ^3J(H,H) = 2.08 Hz, 1H, CH c), 7.02 (s, 2H, $H_{maleimide}$), 7.31 (d, ^3J(H,H) = 8.77 Hz, 1H, CH a) (Chart 1); ^{13}C NMR ($CDCl_3$) δ = 25.0 (CH_2), 26.4 (CH_2), 33.0 (NCH_3), 33.9 (CH_2), 36.9 (CH_2), 40.8 (CH_2CH_2Cl), 61.4 (CH_2N), 103.5 ($C_{aromatic}$), 109.6 ($C_{aromatic}$), 110.6 ($C_{aromatic}$), 129.8 ($C_{aromatic}$), 134.6 ($C_{maleimide}$), 143.8 ($C_{aromatic}$), 154.7 ($C_{benzimidazole}$), 170.4 ($CO_{maleimide}$), 172.9 (CO); MS (EI, 80 eV, 300 °C) *m/z* (%) 479.8 (32.78) [M^+-1], 431.0 (95.45) [M-CH_2Cl]$^+$, 321.9 (100) $C_{16}H_{20}ClN_3O_2$; Anal. ($C_{22}H_{26}Cl_2N_4O_4$) C, H, N.

*1,3,5-Tris{N-[(2-(2,5-dioxopyrrolidin-1-yl)ethyl-3-(4-(bis(2-chloroethyl)amino)phenyl)-2-(tert-butoxycarbonylamino)propanoate)-1-yl]propylamino}benzene (***8***).* MelBoc-spacer **4** (620 mg, 1.17 mmol) was dissolved in 20 mL of chloroform. To this solution was added dropwise a mixture of **G0**·3HCl (125 mg, 0.35 mmol) and DIPEA (137 mg, 1.05 mmol, 186 μL) dissolved in 2 mL of dry methanol. The reaction mixture was refluxed for 72 h and was continuously monitored by TLC. The solution was then washed once with sodium hydrogen carbonate solution and once with brine. The organic layer was dried over magnesium sulfate and the solvent evaporated in vacuo. The residue was purified by column chromatography (silica gel, dichloromethane/methanol 20:1) to afford the desired product (192 mg, 30%) as a white solid: $R_f = 0.2$ (dichloromethane/methanol 20:1); mp 230 °C; ^{1}H NMR (400 MHz, $CDCl_3$) δ = 1.40 (s, 27H, **1** CH_2), 1.79 (quin, ^3J(H,H) = 7.29 Hz, 6H, **2** CH_2), 2.35 (s, 3H, **1** NH), 2.49 (m, 3H, **3** CH_2), 2.61 (m, 3H+6H, **3**+**4** CH_2), 2.71 (m, 3H, **5** CH_2), 2.88−3.03 (m, 3H+6H, **5**+**6** CH_2), 3.59 (t, ^3J(H,H) = 6.30 Hz, 12H, **7** CH_2), 3.68 (t, ^3J(H,H) = 6.57 Hz, 12H, **8** CH_2), 3.75 (m, 3H+6H, **9** CH_2), 4.33 (m, 3H, **10** CH_2), 4.45 (m, 3H, **10** CH_2), 4.94 (t, ^3J(H,H) = 7.56 Hz, 3H, **11** CH), 6.59 (d, ^3J(H,H) = 8.52 Hz, 12H, **12** CH), 6.82 (s, 3H, **13** CH), 7.00 (d, ^3J(H,H) = 7.08 Hz, **14** CH); ^{13}C NMR (CD_3OD) δ = 26.79 (**2** CH_2), 28.79 (CH_3), 32.31 (**3** CH_2), 34.80 (**4**+**5** CH_2), 38.64 (**9** CH_2), 41.73 (**7**+**8** CH_2), 48.2 (**6** CH_2), 54.49 (**9**+**11** CH_2), 62.42 (**10** CH_2), 80.6 (C), 113.41 (**12** CH), 127.02 ($C_{aromatic}$), 129.26 (**14** CH), 129.97 ($C_{aromatic}$), 131.59 (**13** CH), 146.63 ($C_{aromatic}$), 159.90 (CONH), 172.9 (COO), 173.76 ($CO_{maleimide}$), 176.95 ($CO_{maleimide}$); MS (ESI) calcd. for $C_{87}H_{121}N_{12}O_{18}Cl_6$ 1835.7034, found 1835.6977; Anal. ($C_{87}H_{121}N_{12}O_{18}Cl_6$) C, H, N.

*1,3,5-Tris{N-[(2-(2,5-dioxopyrrolidin-1-yl)ethyl-3-(4-(bis(2-chloroethyl)amino)phenyl)-2-aminopropanoate)-1-yl]propylamino}benzene trishydrochloride (***9***).* The G0 dendrimer **8** (280 mg, 0.15 mmol)) was dissolved in 10 mL of THF. To this solution, 173 μL of hydrochloric acid (w = 25%) was added and the mixture was stirred at room temperature. After monitoring the reaction by TLC, 400 μL of hydrochloric acid (25%) was added. After 72 h, the solvent was removed under reduced pressure to afford the deprotected product as a brown solid (240 mg, 95%) after lyophilization from water: mp 255 °C; ^{1}H NMR (400 MHz, CD_3OD) δ = 2.12 (m, 6H, **1** CH_2), 2.76 (m, 6H, **2** CH_2), 3.06−3.12 (m, 6H, **3** CH_2), 3.18−3.26 (m, 6H+6H, **4**+**5** CH_2), 3.68 (m, 12H+6H, **6**+**9** CH_2), 3.82 (m, 12H, **8** CH_2), 4.29 (m, 3H, **7** CH), 4.42 (m, 3H, **11** CH_2), 4.52 (m, 3H, **11** CH_2), 4.61 (m, 3H, **10** CH), 6.89 (d, ^3J(H,H) = 8.37 Hz, 6H, **12** CH), 7.07 (s, 3H, **13** CH), 7.23 (d, ^3J(H,H) = 8.37 Hz, 6H, **14** CH) (Chart 2); ^{13}C NMR (CD_3OD) δ = 28.84 (**1** CH_2), 33.52 (**3** CH_2), 34.22 (**2** CH_2), 36.45 (**9** CH_2), 39.08 (**5** CH_2), 41.12 (**8** CH_2), 41.19 (**6** CH_2), 47.42 (**4** CH_2), 55.21 (**10** CH), 59.29 (**7** CH), 63.83 (**11** CH_2), 115.32 (**12** CH), 127.97 ($C_{aromatic}$), 131.95 ($C_{aromatic}$+**14** CH), 132.02 ($C_{aromatic}$), 145.95 ($C_{aromatic}$), 169.91 (COO), 171.34 ($CO_{maleimide}$), 173.80 ($CO_{maleimide}$); MS (ESI): calcd. for $C_{72}H_{97}N_{12}O_{12}Cl_6$ 1535.5445, found 1535.5312.

Chart 2. Supporting Scheme for NMR Data of Compound 9

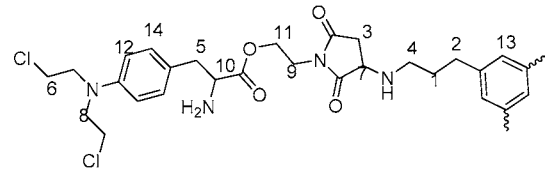
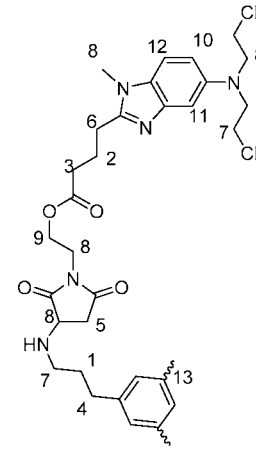


Chart 3. Supporting Scheme for NMR Data of Compound 10



*1,3,5-Tris{N-[(2-(2,5-dioxopyrrolidin-1-yl)ethyl-4-(5-(bis(2-chloroethyl)amino)-1-methyl-1H-benzo[d]imidazol-2-yl)butanoate)-1-yl]propylamino}benzene (***10***).* Benda-spacer **7** (470 mg, 0.97 mmol) was dissolved in 20 mL of chloroform. To this solution, a mixture of **G0**·3HCl (77.8 mg, 0.216 mmol) and 116 μL of DIPEA dissolved in 2 mL of dry methanol was added dropwise. The reaction mixture was refluxed for 72 h, being continuously monitored by TLC. The reaction mixture was then washed once with sodium hydrogen carbonate solution and once with brine. The organic layer was dried over magnesium sulfate and the solvent was evaporated in vacuo. The residue was purified by column chromatography (silica gel, chloroform/methanol 20:1) to afford the desired product (290 mg, 79%) as an ochre solid: $R_f = 0.44$ (dichloromethane/methanol 10:1); ^{1}H NMR (400 MHz, $CDCl_3$) δ = 1.79 (quin, ^3J(H,H) = 7.22 Hz, 6H, **1** CH_2), 2.17 (m, 6H, **2** CH_2), 2.48 (m, 6H, **3** CH_2), 2.60 (m, 6H+3H, **4**+**5**CH_2), 2.69−2.75 (m, 3H, **5** CH_2), 2.93 (m, 6H, **6** CH_2), 3.64 (m, 12H+6H, **7** CH_2), 3.71−3.79 (m, 12H+3H+6H+9H, **8** CH_2), 4.23 (m, 6H, **9** CH_2), 6.79 (dd, ^3J(H,H) = 2.17 Hz, 8.75 Hz, 3H, **10** CH), 6.83 (s, 3H, **13** CH), 7.08 (d, ^3J(H,H) = 1.96 Hz, 3H, **11** CH), 7.19 (d, ^3J(H,H) = 8.76 Hz, 3H, **13** CH) (Chart 3); ^{13}C NMR ($CDCl_3$) δ = 22.2 (**2** CH_2), 26.3 (**6** CH_2), 29.4 (**1** CH_2), 31.9 (**8** CH_2), 32.9 (**3** CH_2), 33.1 (**5** CH_2), 33.3 (**4** CH_2), 37.8 (**8** CH_2), 40.86 (**7**+**8** CH_2), 47.1 (**7** CH_2), 54.6 (**8** CH_2), 60.8 (**9** CH_2), 102.6 ($C_{aromatic}$), 110.0 ($C_{aromatic}$), 110.9 ($C_{aromatic}$), 126.1 ($C_{aromatic}$), 129.1 ($C_{aromatic}$), 141.8 ($C_{aromatic}$), 142.9

Chart 4. Supporting Scheme for NMR Data of Compound 11

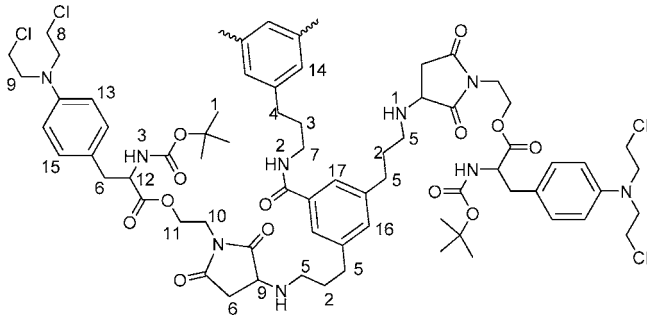
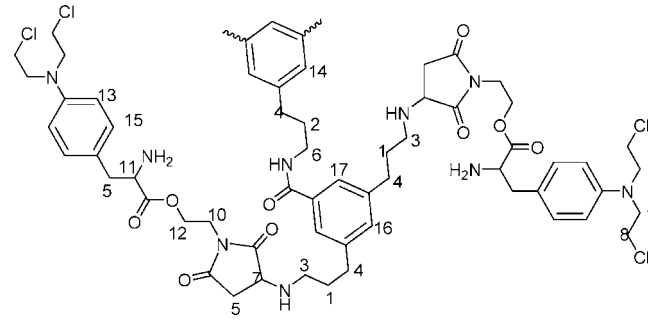


Chart 5. Supporting Scheme for NMR Data of Compound 12



($C_{aromatic}$), 154.2 ($C_{benzimidazole}$), 173.02 (CO), 175.06 (CO), 177.6 (CO); MS (ESI): calcd. for $C_{81}H_{106}N_{15}O_{12}Cl_6$ 1692.6258, found 1692.6193; $C_{81}H_{106}N_{15}O_{12}Cl_6^{2+}$ 846.8165, found 846.8170.

*1,3,5-Tris{3,5-bis-[N-[(2-(2,5-dioxopyrrolidin-1-yl)ethyl-3-(4-(bis(2-chloroethyl)amino)phenyl)-2-(tert-butoxycarbonylamino)-propanoate)-1-yl]propylamino]-N-propylbenzamide}benzene (***11***).* To a solution of MelBoc-spacer **4** (700 mg, 1.32 mmol) in 50 mL of chloroform was added dropwise a solution of **G1**·CF_3COOH (320 mg, 0.2 mmol) and DIPEA (156 mg, 0.12 mmol, 115 μL) in dry methanol. The reaction mixture was refluxed for 70 h. After complete reaction (TLC), the solution was washed once with sodium hydrogen carbonate solution and once with brine. The organic layer was dried over magnesium sulfate; the solvent was evaporated in vacuo and the residue purified through column chromatography (silica gel, dichloromethane/methanol 20:1 and chloroform/methanol 10:1) to afford the compound as a yellow oil (200 mg, 24.5%): R_f = 0.26 (chloroform/methanol 10:1); ^{1}H NMR (400 MHz, $CDCl_3$) δ = 1.32 (s, 54H, **1** CH_2), 1.71 (m, 12H, **2** CH_2), 1.86 (m, 6H, **3** CH_2), 2.40 (m, 6H, **4** CH_2), 2.56 (m, 24H, **5** CH_2), 2.80−2.95 (m, 12H+12H, **6** CH_2), 3.35 (m, 6H, **7** CH_2), 3.52 (m, 24H, **8** CH_2), 3.61 (m, 24H+6H, **9** CH_2), 3.68 (m, 12H, **10** CH_2), 4.09−4.18 (m, 6H, **11** CH_2), 4.27 (m, 6H, **11** CH_2), 4.36 (m, 6H, **12** CH), 4.93 (m, 6H, **1** NH), 6.52 (d, ^3J(H,H) = 8.03 Hz, 12H, **13** CH), 6.74 (s, 3H, **2** NH), 6.82 (s, 3H, **14** CH), 6.92 (d, ^3J(H,H) = 7.38 Hz, 12H, **15** CH), 7.04 (s, 6H, **3** NH), 7.06 (s, 3H, **16** CH), 7.33 (s, 6H, **17** CH) (Chart 4); ^{13}C NMR (CD_3OD) δ = 29.22 (CH_3+**2**+**3** CH_2), 31.16 ($CH_{2\ maleimide}$+CH_2Ar+CH_2Ar), 39.9 (**10** CH_2+Ar$CH_{2\ melphalan}$), 42.17 (CH_2NHCO+*C*H_2*C*H_2Cl), 44.23 ($CH_2NH_{maleimide}$), 54.86 (**12** CH), 56.28 ($CH_{maleimide}$+**11** CH_2), 81.07 (C), 113.82 (**13** CH), 126.69 ($C_{aromatic}$), 131.92 ($C_{aromatic}$), 132.28 ($C_{aromatic}$), 140.13 ($C_{aromatic}$), 143.95 ($C_{aromatic}$), 150.3 ($C_{aromatic}$), 158.15 (NH-*C*OO), 174.21 (CO), 175.25 ($CO_{maleimide}$); MS (ESI) calcd. for $C_{198}H_{269}N_{27}O_{39}Cl_{12}^{2+}$ 2037.307, found 2037.3243.

*1,3,5-Tris{3,5-bis-[N-[(2-(2,5-dioxopyrrolidin-1-yl)ethyl-3-(4-(bis(2-chloroethyl)amino)phenyl)-2-aminopropanoate)-1-yl]-propylamino]-N-propylbenzamide}benzene Hexatrifluoroacetate (***12***).* The G1 dendrimer **11** (180 mg, 0.044 mmol) was dissolved in 10 mL of dichloromethane and treated with 2.8 mL of TFA (w = 95%). The mixture was stirred for 24 h at room temperature and continuously monitored by TLC. The solvent was then evaporated in vacuo to afford the deprotected dendrimer as brown oil (170 mg, 93%): ^{1}H NMR (CD_3OD) δ = 1.92 (m, 12H, **1** CH_2), 2.09 (s, br, 12H, **2** CH_2), 2.65 (m, 12H, **3** CH_2), 2.77 (m, 18H, **4** CH_2), 2.99−3.05 (m, 6H+12H, **5** CH_2), 3.21 (m, 6H+6H, **5** CH_2+**6** CH_2), 3.40 (m, 6H, **7** CH_2), 3.67 (m, 24H, **8** CH_2), 3.74 (m, 24H, **9** CH_2), 3.84 (m, 12H, **10** CH_2), 4.19 (m, 6H, **11** CH), 4.37 (m, 12H, **12** CH_2), 6.76 (d, ^3J(H,H) = 8.13 Hz, 12H, **13** CH_2), 6.93 (s, 3H, **14** CH_2), 7.14 (d, ^3J(H,H) = 8.19 Hz, 12H, **15** CH_2), 7.32 (s, 3H, **16** CH_2), 7.55 (s, 6H, **17** CH_2) (Chart 5); ^{13}C NMR (CD_3OD) δ = 27.77 (**1**+**2** CH_2), 28.84 (**4** CH_2), 31.17 (**4** CH_2), 33.31 (**5** CH_2), 36.29 (**5** CH_2), 36.44 (**10** CH_2), 39.01 (**6** CH_2), 41.67 (**9** CH_2), 47.6 (**3** CH_2), 54.32 (**8** CH_2), 55.52 (**11** CH), 63.85 (**7**+**12** CH_2), 113.85 (**13** CH), 118.45 ($C_{aromatic}$), 121.22 ($C_{aromatic}$), 126.47 ($C_{aromatic}$), 128.85 ($C_{aromatic}$), 131.7 (**16** CH), 142.54 ($C_{aromatic}$), 143.29 ($C_{aromatic}$), 147.55 ($C_{aromatic}$), 160.34 (CO), 160.70 (CO), 170.11 (CO), 174.64 (CO); MS (ESI) calcd. for $C_{168}H_{219}N_{27}O_{27}Cl_{12}Na_2^{2+}$ 1760.1307, found 1760.1456.

*1,3,5-Tris[3-(4-(bis(2-chloroethyl)amino)phenyl)-2-(tert-butoxycarbonylamino)-N-propylpropionamide]benzene (***13***).* A solution of **2** (910 mg, 2.5 mmol) in a mixture of dry dichloromethane/DMF (14:1/v:v) was cooled to −20 °C. A solution of TBTU (740 mg, 2.35 mmol) in dry DMF was added slowly and the reaction mixture was allowed to warm to room temperature. The reaction mixture was stirred at room temperature for additional 30 min, cooled to −20 °C again, followed by the dropwise addition of DIPEA (1040 μL, 6 mmol) and a solution of **G0**·3HCl (179.39 mg, 0.5 mmol) in dry methanol. The mixture was allowed to warm to room temperature and was stirred for additional 20 h. After complete reaction (TLC), the mixture was washed twice with sodium hydrogen carbonate solution, then once with brine, and then dried over magnesium sulfate. The solvent was removed under reduced pressure and column chromatography (silica gel, dichloromethane/methanol 20:1) afforded the desired product (400 mg, 0.28 mmol, 57%) as a brown oil: R_f = 0.36 (dichloromethane/methanol 24:1); ^{1}H NMR (400 MHz, $CDCl_3$) δ = 1.36 (s, 27H, CH_3), 1.7 (quin, ^3J(H,H) = 6.892 Hz, 6H, CH_2), 2.55 (t, ^3J(H,H) = 6.9 Hz, 6H, CH_2Ar), 2.68 (dd, ^2J(H,H) = 13.46 Hz, 3H, $CH_2Ar_{melphalan}$), 2.83 (dd, ^2J(H,H) = 13.46 Hz, 3H, $CH_2Ar_{melphalan}$), 3.1 (m, 6H, CH_2N), 3.71 (s, 24H, C*H*$_2$C*H*$_2$Cl), 4.08 (m, 3H, C*H*$CH_2Ar_{melphalan}$), 6.68 (d, ^3J(H,H) = 8.168 Hz, 6H, Ar*H*$_{melphalan}$), 6.82 (d, ^3J(H,H) = 8.45 Hz, 3H, N*H*-Boc), 6.86 (s, 3H, G0-Ar*H*), 7.12 (d, ^3J(H,H) = 8.19 Hz, 6H, Ar*H*$_{melphalan}$), 7.9 (s, br, 3H, NH); ^{13}C NMR ($CDCl_3$) δ = 28.3 (CH_2), 30.5 (Ar*C*H_2), 37.6 ($NHCH_2$), 40.4 (*C*H_2*C*H_2Cl), 54.5 ($CHNH_2$), 79.8 (*C*-$(CH_3)_3$), 112.1 ($C_{aromatic}$), 124.9 ($C_{aromatic}$), 126.4 ($C_{aromatic}$), 130.6 ($C_{aromatic}$), 144.9 ($C_{aromatic}$), 155.7 ($C_{aromatic}$), 171.6 (CO); MS (ESI) calcd. for $C_{69}H_{99}N_9O_9Cl_6Na^+$ 1432.5572, found 1432.5566.

*1,3,5-Tris[3-(4-(bis(2-chloroethyl)amino)phenyl)-2-amino-N-propylpropionamide]benzene Tristrifluoroacetate (***14***).* A solution of **13** (590 mg, 0.42 mmol) in 10 mL of TFA (w = 95%) was stirred for 4 h at room temperature. After complete reaction (TLC), the solvent was repeatedly removed in vacuo to afford the deprotected dendrimer (580 mg, 0.39 mmol, 95%) as brown solid: mp 150 °C; ^{1}H NMR (400 MHz, CD_3OD) δ = 1.63 (quin, ^3J(H,H) = 7.09 Hz, 6H, CH_2), 2.44 (t, ^3J(H,H) = 7.28 Hz, 6H, CH_2Ar), 2.84 (dd, ^2J(H,H) = 12.85 Hz, 3H, C*H*$_2Ar_{melphalan}$), 2.91 (dd, ^2J(H,H) = 12.84 Hz, 3H, C*H*$_2Ar_{melphalan}$), 3.02 (m, 3H, CH_2N), 3.15 (m, 3H, CH_2N), 3.65 (s, 24H, C*H*$_2$C*H*$_2$Cl), 3.83 (m, 1H, C*H*$CH_2Ar_{melphalan}$), 6.69 (d, ^3J(H,H) = 8.58 Hz, 6H, Ar*H*$_{melphalan}$), 6.8 (s, 3H, G0-Ar*H*), 7.05 (d, ^3J(H,H) = 8.43 Hz, 6H, Ar*H*$_{melphalan}$), 8.1 (s, br, 6H, NH_2), 8.4 (t, ^3J(H,H) = 5.24 Hz, 3H, NH); ^{13}C NMR (CD_3OD) δ = 31.9 (CH_2), 34.0 (Ar*C*H_2), 40.2 ($NHCH_2$), 41.6 (*C*H_2*C*H_2Cl), 56.0 ($CHNH_2$), 113.6 ($C_{aromatic}$), 123.8 ($C_{aromatic}$), 127.3 ($C_{aromatic}$), 131.7 ($C_{aromatic}$),

Chart 6. Supporting Scheme for NMR Data of Compound 15

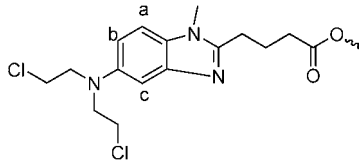
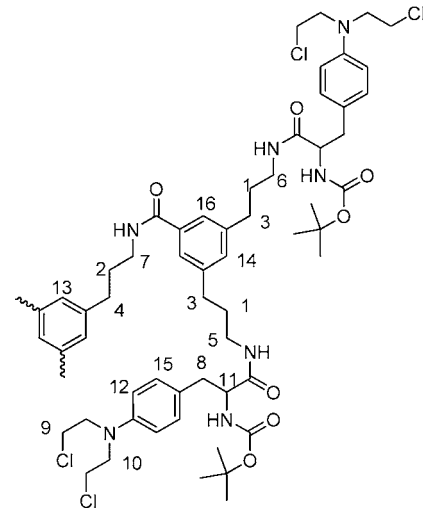


Chart 7. Supporting Scheme for NMR Data of Compound 16



143.0 ($C_{aromatic}$), 147.2 ($C_{aromatic}$), 169.6 (CO); MS (ESI); Anal. ($C_{60}H_{78}Cl_6N_9O_9F_9$) C, H, N.

*1,3,5-Tris[4-(5-(bis(2-chloroethyl)amino)-1-methyl-1H-benzo[d]imidazol-2-yl)-N-propylbutyramide]benzene (***15***).* A solution of bendamustine free base **6** (430 mg, 1.2 mmol) in a mixture of dry dichloromethane/DMF (7 mL/2 mL) was cooled to −20 °C. A solution of TBTU (352 mg, 1.128 mmol) in dry DMF was added slowly, and the reaction mixture was allowed to warm to room temperature. The reaction mixture was stirred at room temperature for additional 30 min and cooled to −20 °C again, followed by the dropwise addition of DIPEA (502 μL, 2.88 mmol) and a solution of **G0**·3HCl (85.4 mg, 0.24 mmol) in dry methanol. The mixture stirred was allowed to warm to room temperature and was stirred for additional 20 h. After complete reaction (TLC), the mixture was washed twice with sodium hydrogen carbonate solution, then once with brine, and dried over magnesium sulfate. The solvent was removed under reduced pressure, and column chromatography (silica gel, chloroform/methanol 20:1) afforded the desired product (130 mg, 1.02 mmol, 42%) as a brown oil: R_f = 0.5 (chloroform/methanol 10:1); ^{1}H NMR (400 MHz, $CDCl_3$) δ = 1.71 (quin, ^3J(H,H) = 6.91 Hz, 6H, CH_2), 2.05 (quin, ^3J(H,H) = 6.85 Hz, 6H, CH_2 bendamustine), 2.23 (t, ^3J(H,H) = 6.66 Hz, 6H, $CH_2CO_{bendamustine}$), 2.48 (t, ^3J(H,H) = 7.01 Hz, 6H, CH_2ArG0), 2.85 (t, ^3J(H,H) = 7.08 Hz, 6H, CH_2 benzimidazole), 3.08 (m, 6H, CH_2N), 3.50−3.67 (m, 24H, CH_2CH_2Cl), 3.50−3.67 (m, 9H, NCH_3 bendamustine), 6.71 (dd, ^3J(H,H) = 2.30 Hz, 8.86 Hz, 3H, CH b), 6.73 (s, 3H, ArHG0), 6.93 (d, ^3J(H,H) = 2.09 Hz, 3H, CH c), 7.1 (d, ^3J(H,H) = 8.8 Hz, 3H, CH a) (Chart 6); ^{13}C NMR (CD_3OD) δ = 26.0 (CH_2 benzimidazole), 27.29 (CH_2CH_2CO), 29.33 (CH_2), 31.91 (CH_3), 32.76 (CH_2Ar), 38.69 (CH_2CO), 40.02 ($CH_2NHCO+CH_2N$), 42.1 (CH_2Cl), 104.1 (CH c), 112.92 (CH a+b), 125.85 ($C_{aromatic}NCH_3+C_{aromatic}$), 131.2 ($C_{aromatic}NC+C_{aromatic}$), 146.2 ($C_{aromatic}+CNCH_3$), 163.91 (CO); MS (ESI) calcd. for $C_{63}H_{84}N_{12}O_3Cl_6Na^+$ 1291.4800, found 1291.4634.

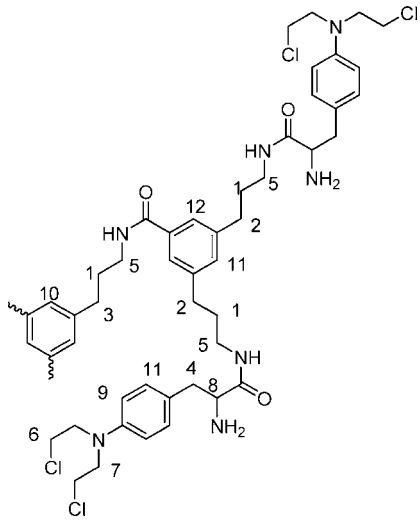
*1,3,5-Tris{3,5-bis-[3-(4-(bis(2-chloroethyl)amino)phenyl)-2-(tert-butoxycarbonylamino)-N-propylpropionamide]-N-propylbenzamide}benzene (***16***).* MelBoc **2** (472 mg, 1.16 mmol) was dissolved in 15 mL of dry dichloromethane, HOBT (165 mg, 1.22 mmol) was added, and the solution was stirred for 30 min at room temperature. Afterward, the orange mixture was cooled to −20 °C, EDC (245.3 mg, 1.28 mmol) was added, and the mixture was subsequently stirred for additional 2 h. During that time, the reaction mixture was allowed to warm up to room temperature. After complete reaction (TLC), the mixture was cooled to −30 °C. **G1**·CF_3COOH (440 mg, 0.3 mmol) dissolved in 10 mL of dry methanol and DIPEA (1.22 mL, 7 mmol) were added dropwise slowly. The solution was stirred for additional 16 h and during that time allowed to warm up to room temperature. After complete reaction, the solution was washed twice with sodium hydrogen carbonate solution and once with brine. The organic layer was dried over magnesium sulfate, the solvent was removed in vacuo, and the crude product was purified by column chromatography (silica gel, dichloromethane/methanol 20:1) to afford the **G1** dendrimer (30 mg, 3.1%) as a brown oil: R_f = 0.33 (dichloromethane/methanol 10:1); ^{1}H NMR (400 MHz, $CDCl_3$) δ = 1.37 (s, 54H, CH_3), 1.66 (m, 18H, **1** CH_2), 1.97 (m, 6H, **2** CH_2), 2.43 (m, 12H, **3** CH_2), 2.66 (m, 6H, **4** CH_2), 2.93 (m, 6H+6H, **5**+**8** CH_2), 3.08 (m, 6H+6H, **6**+**8** CH_2), 3.41 (m, 6H, **7** CH_2), 3.53 (m, 24H, **9** CH_2), 3.64 (m, 24H, **10** CH_2), 4.32 (m, br, 6H, **11** CH), 6.55 (d, ^3J(H,H) = 8.14 Hz, 12H, **12** CH), 6.92 (s, 3H, **13** CH), 6.98 (s, 3H, **14** CH), 7.06 (d, ^3J(H,H) = 8.28 Hz, 12H, **15** CH), 7.32 (s, 6H, **16** CH) (Chart 7); ^{13}C NMR (CD_3OD) δ = 27.33 (CH_3), 30.34 (**1** CH_2), 30.85 (**2** CH_2), 32.38 (**3** CH_2), 32.98 (**4** CH_2), 36.63 (**8** CH_2), 38.48 (**5**+**6** CH_2), 38.67 (**7** CH_2), 40.16 (**9**+**10** CH_2), 54.12 (**11** CH), 79.3 (C), 113.69 (**12** CH), 123.38 ($C_{aromatic}$), 124.77 ($C_{aromatic}$), 128.65 ($C_{aromatic}$), 130.09 ($C_{aromatic}$), 131.62 ($C_{aromatic}$), 134.54 ($C_{aromatic}$), 135.82 ($C_{aromatic}$), 141.83 ($C_{aromatic}$), 156.2 (NHCOO), 167.75 (NHCO), 167.92 (NH*C*OCH); MS (ESI) calcd. for $C_{162}H_{225}N_{21}O_{21}Cl_{12}^{+2}$ 1615.1781, found 1615.1794.

*1,3,5-Tris{3,5-bis-[3-(4-(bis(2-chloroethyl)amino)phenyl)-2-amino-N-propylpropionamide]-N-propylbenzamide}benzene Hexahydrochloride (***17***).* The **G1** dendrimer **16** (100 mg, 0.031 mmol) was dissolved in 5 mL of THF. To this solution, hydrochloric acid (w = 25%) was added dropwise and the mixture stirred for 3 days at room temperature. The reaction was continuously monitored by TLC. The solvent was then removed under reduced pressure to afford the deprotected product as a brown oil (85 mg, 96%) after lyophilization from water: ^{1}H NMR (400 MHz, CD_3OD) δ = 1.75 (m, 18H, **1** CH_2), 2.49 (m, 12H, **2** CH_2), 2.65 (m, 6H, **3** CH_2), 3.02 (m, 12H+18H, **4**+**5** CH_2), 3.54 (s, br, 24H, **6** CH_2), 3.65 (s, br, 24H, **7** CH_2), 3.8 (s, 6H, **8** CH), 6.75 (m, 12H, **9** CH), 6.89 (s, 3H, **10** CH), 7.15 (m, 12H+3H, **11** CH), 7.44 (s, 6H, **12** CH) (Chart 8); ^{13}C NMR (CD_3OD) δ = 27.78 (**1** CH_2), 35.12 (**2**+**3** CH_2), 40.21 (**4**+**5**+**7** CH_2), 42.32 (**6** CH_2), 53.00 (**8** CH), 112.50 (**9** CH), 127.70 (**10**+**12** CH), 128.66 (**11** CH), 129.16 ($C_{aromatic}$), 130.45 (**11** CH), 131.45 ($C_{aromatic}$), 134.53 ($C_{aromatic}$), 140.4 ($C_{aromatic}$), 146.2 ($C_{aromatic}$), 165.87 (CO), 170.2 (CO); MS (ESI) calcd. for $C_{132}H_{177}N_{21}O_9Cl_{12}Na_2^{+2}$ 1333.005, found 1333.0546.

HPLC Analytic Procedure. The stability of the compounds was determined in aqueous solution at a concentration of 1 mg/mL. Degradation was followed by HPLC analytic using a Kontron HPLC system: HPLC-pump 420; HPLC-autosampler 460; UV-Detector 430; Kontron Data System Kroma 2000. An RP 18 column (250 × 6 × 4 mm Nucleosil 100−5 C18 (Macherey-Nagel)) was used. The solutions were held at 37 °C, and every hour, 20 μL was injected onto the column and isocratically analyzed using a methanol/H_2SO_4 (0.001 N, 20 mmol Na_2SO_4) mixture (50:50). A wavelength of λ = 254 nm was selected for UV-detection.

The stability in PBS (pH 5 and 7.4) was measured at a concentration of 0.1 mg/mL. For protein binding, 40 mg/mL HSA and 0.1 mg/mL compound were incubated at 37 °C. The

Chart 8. Supporting Scheme for NMR Data of Compound 17



protein was separated by ethanolic precipitation. After centrifugation, the supernatant was evaluated for drug content.

Conformational Analysis for Molecular Extent Prediction. Conformational analysis was performed using the program *OMEGA* (*20*) from OpenEye Scientific Software (www.eyesopen.com). The maximum possible number of conformations was set to 10 000, and the MMFF94 force field was used for conformational search and subsequent energy minimization with a dielectric constant of 80 simulating a water environment. For all other parameters, default values were kept. This setup resulted in 918 conformations for **12** and 6005 for **10**. Subsequently, all conformations were converted and analyzed using a custom routine implemented in the LigandScout framework (*21, 22*) for determining the maximum extent of each conformation.

Biological Methods. *Cell Culture.* The human MCF-7 and MDA-MB-231 breast cancer cell lines were obtained from the American Type Culture Collection (ATCC). The MCF-7 breast cancer cell line originated from a 69-year-old Caucasian woman and is a well-characterized estrogen receptor (ER) positive control cell line (cells are positive for cytoplasmic estrogen receptors). The human cell line MDA-MB-231 is a prototype for the study of hormone-independent breast cancer. Cell line banking and quality control were performed according to the seed stock concept reviewed by Hay (*23*). Both cell lines were maintained in L-glutamine and sodium pyruvate containing DMEM High Glucose (4.5 g/L) supplemented with 5% fetal calf serum (FCS, Gibco) using 25 cm^2 culture flasks in a humidified atmosphere (5% CO_2) at 37 °C. The cell lines were passaged weekly after treatment with trypsin (0.05%)/ethylenediaminetetraacetic acid (EDTA, 0.02%, Boehringer). Mycoplasma contamination was regularly monitored, and only mycoplasma-free cultures were used.

In Vitro Chemosensitivity Assays. Briefly, 100 μL of a cell suspension of 7500 cells mL^{-1} culture medium were plated into each well of a 96-well microtiter plate and incubated at 37 °C for 3 days in a humidified atmosphere (5% CO_2). By adding an adequate volume of a stock solution of the appropriate compound (solvent: H_2O, DMF, DMSO, MeOH) to the medium, the desired test concentration was obtained. After the proper incubation time, the medium was removed and the cells were fixed with a glutardialdehyde solution and stored under phosphate buffered saline (PBS) at 4 °C. Cell biomass was determined by a crystal violet staining technique described previously (*24, 25*). The efficiency of the compounds is expressed as corrected $\%T/C_{corr}$ values according to the following equations:

$$\text{cytostatic effect: } \%T/C_{corr} = [(T - C_0)/(C - C_0)] \times 100 \quad (1)$$

$$\text{cytocidal effect: } \%\tau = [(T - C_0)/C_0] \times 100 \quad (2)$$

in which T (test) and C (control) are the optical density values at 578 nm of the crystal violet extract of the cells in the wells (that is, the chromatin-bound crystal violet extracted with 70% ethanol), and C_0 is the density of the cell extract immediately before treatment. A microplate reader at 590 nm (Flashscan Analytik Jena AG) was used for the automatic estimation of the optical density of the crystal violet extract in the wells. The calculated $\%T/C$ values can be interpreted as follows:

$T/C > 80\%$ no antiproliferative effect

$80\% > T/C > 20\%$ antiproliferative effect

$20\% > T/C > 0\%$ cytostatic effect

$\tau = T/C < 0\%$ cytocidal effect

RESULTS

Synthesis. The synthesis first implicated the building of the drug−spacer derivatives which were then attached to the dendrimers.

Melphalan hydrochloride was Boc-protected in a first step and then reacted in a second step with *N*-(2-hydroxyethyl)maleimide using a Steglich reaction to give the ester **4** which was purified by column chromatography. Treatment of **4** with aqueous HCl yielded **5** as a colorless solid (Scheme 1).

Bendamustine hydrochloride was initially transformed to the free base **6** (*26*) and then converted to **7** through a similar approach as described for **4**.

The binding of the drug−spacer to the dendrimers was achieved in the last step of the synthetic route. Due to their nucleophilic properties, the terminal amine groups of the dendrimers were able to bind the maleimide residue. For this purpose, the reactants were dissolved in chloroform and heated to reflux. Cleavage of the Boc groups in melphalan derivatives was performed with 25% HCl. The analytically pure products were obtained after column chromatography. Schemes 2 and 3 depict the synthesis of the **G0** generation dendrimers conjugates **9** and **10**.

The melphalan-spacer **4** was bound to the **G1** dendrimer via the same synthetic route (see Scheme 4).

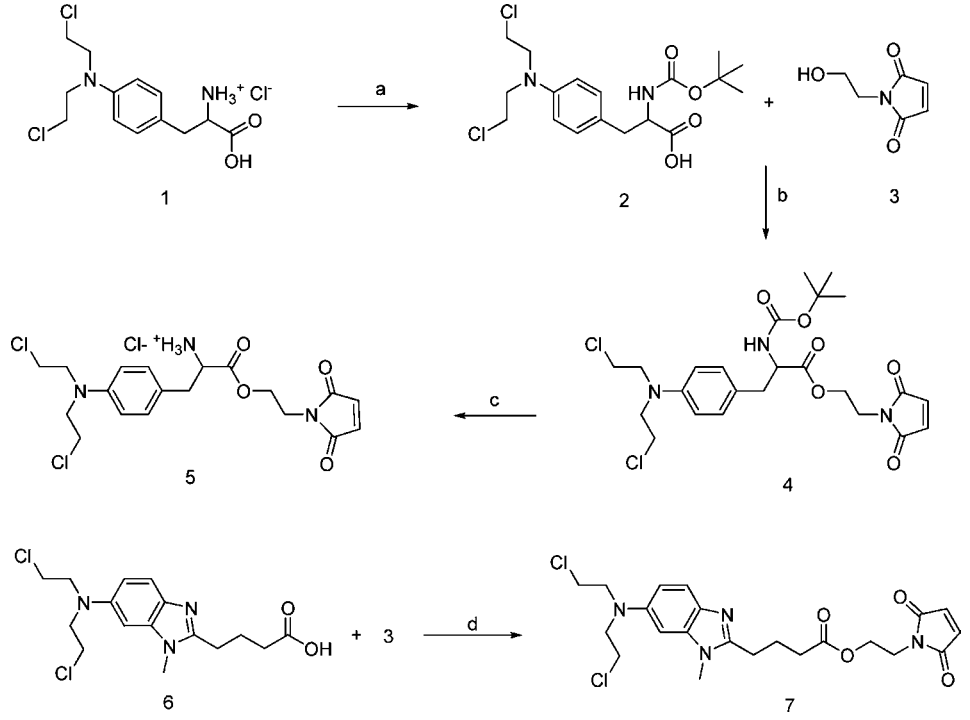
In order to evaluate the significance of the spacer **3** for the mode of action, the cytostatics were also directly bound to the dendrimer by formation of an amide bond using the standard peptide coupling reactions (*27*−*29*) (Schemes 5 and 6).

For this reaction, it is necessary to activate the carboxyl group of melphalan and bendamustine with peptide coupling agents, which led to the formation of reactive anhydrides or ester intermediates (for the mechanism of the reaction and the methods used, see ref *17*). The syntheses of **G0** dendrimer−drug conjugates were then carried out as depicted in Scheme 5 using TBTU as coupling agent.

Structural Characterization. All products and those compounds used in biological tests were characterized by their fully assigned ^1H and ^{13}C NMR spectra and molecular ion peaks in the mass spectra. Their purity was proven by high-resolution ESI-TOF mass spectrometry. All deprotected dendrimers were fully soluble in water and in buffered cell culture media as judged by visual examination.

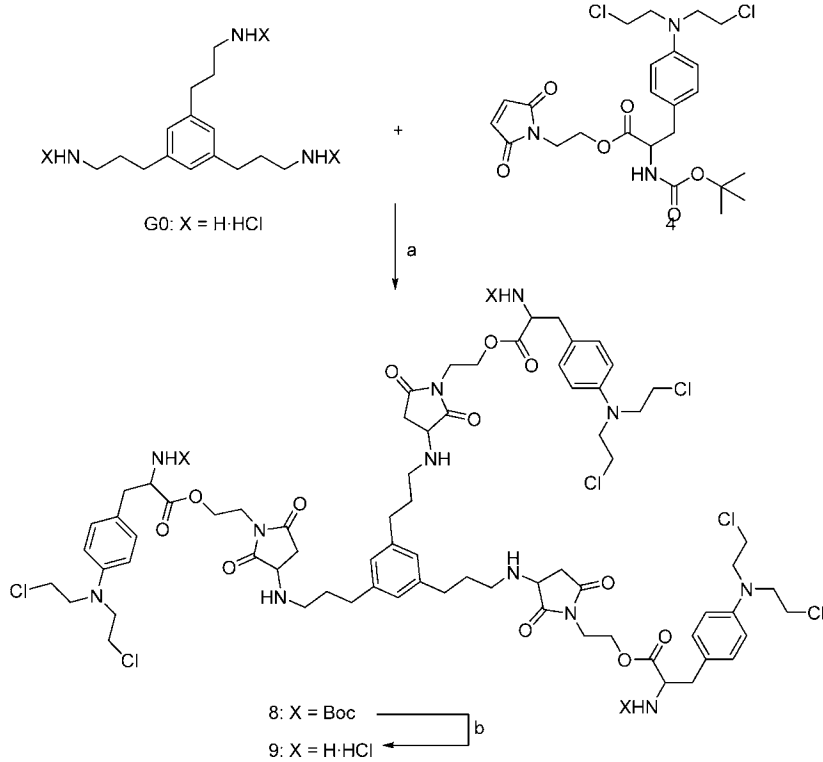
Computational Molecule Size Estimation for Assessing Enhanced Permeation and Retention. In order to estimate the molecule size in solution, the maximum extent of the

Scheme 1. Synthesis of the Drug−Spacer[a]



[a] Reagents and conditions: (a) Boc_2O, TEA, methanol, RT, 1 h; (b) DCC, DMAP, CH_2Cl_2, RT, 24 h; (c) aqueous HCl, THF, RT, 24 h; (d) DCC, DMAP, CH_2Cl_2, RT, 20 h.

Scheme 2. Synthesis of the Mel-spacer-G0 Conjugates[a]

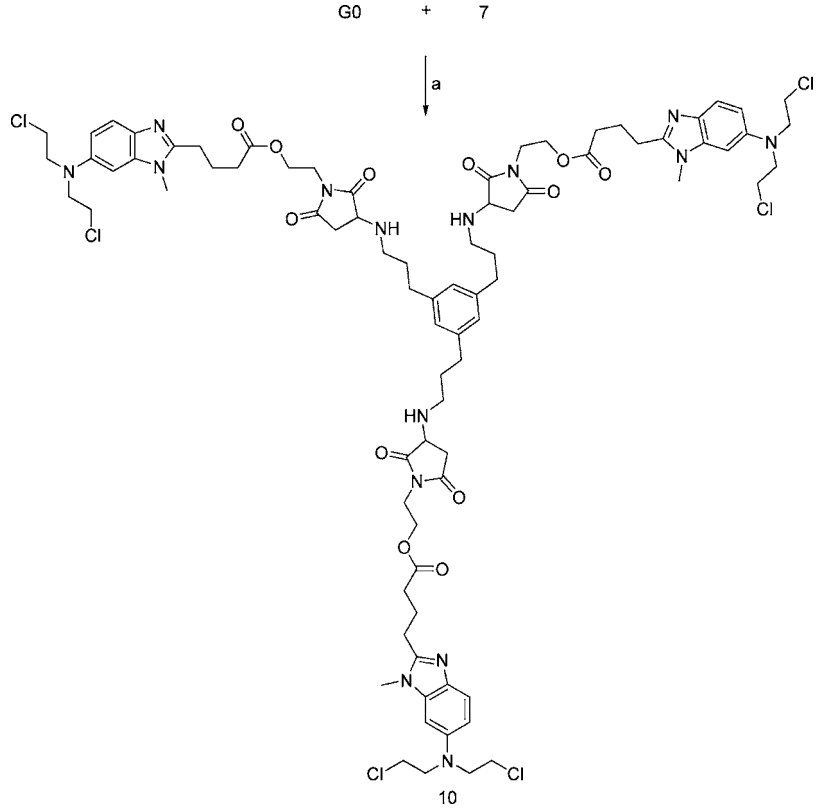


[a] Reagents and conditions: (a) chloroform, DIPEA, reflux, 72 h; (b) aqueous HCl, THF, RT.

compounds was calculated by performing an exhaustive conformational analysis using the software *OMEGA* and the cheminformatics framework of the software package *LigandScout* (*21*, *22*). Figure 2 shows representative conformations of **10** and **12**, respectively, while Figure S1 (see Supporting Information) shows a histogram of the maximum extent distributions over the calculated three-dimensional conformational space for the two compounds. The relative extent frequencies reach their maxima near the average values of about 31 Å for compound **12** and at about 38 Å for **10** (Table S1, see Supporting Information).

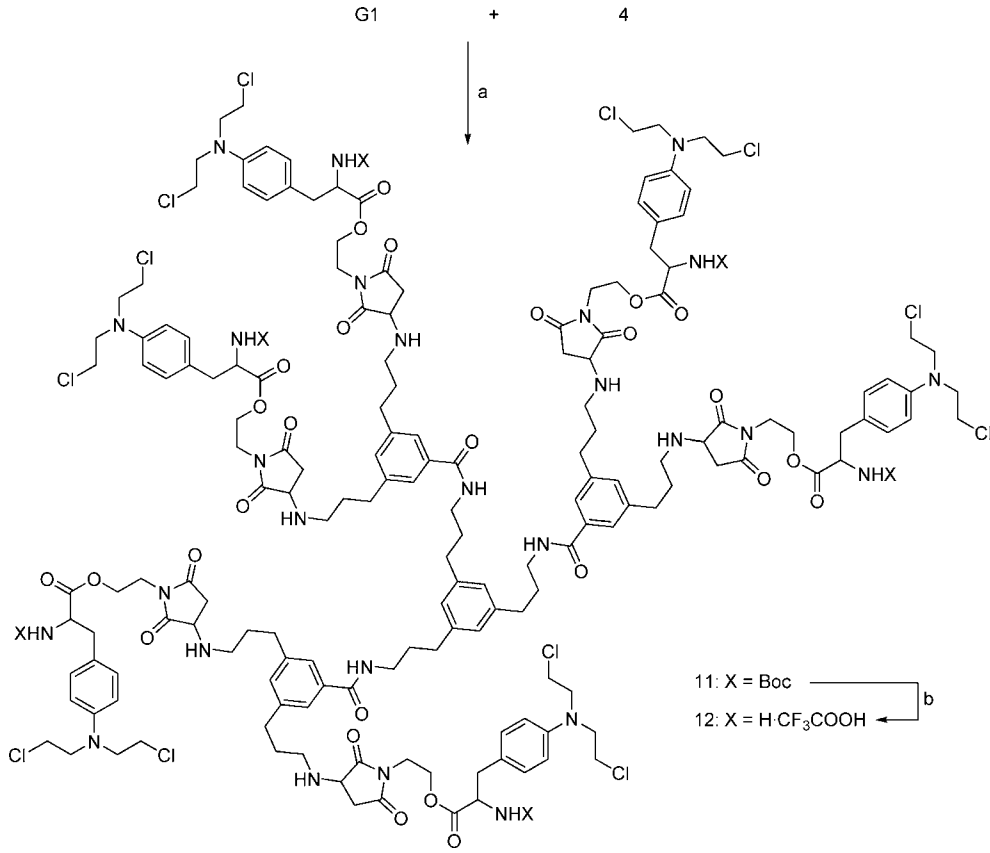
Antitumor Activity. The antiproliferative activity of the synthesized drug−dendrimer conjugates was determined in time-dependent cytotoxicity tests on the human MCF-7 and MDA-

Scheme 3. Synthesis of the Benda-spacer-G0 Conjugates[a]



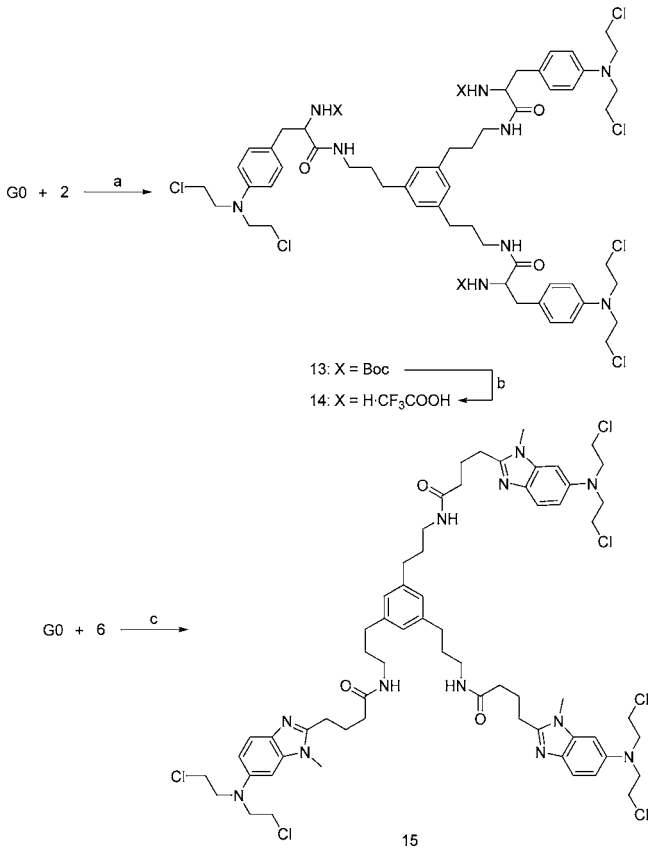
[a] Reagents and conditions: (a) DIPEA, chloroform, reflux, 72 h.

Scheme 4. Synthesis of the Mel-spacer-G1 Conjugates[a]



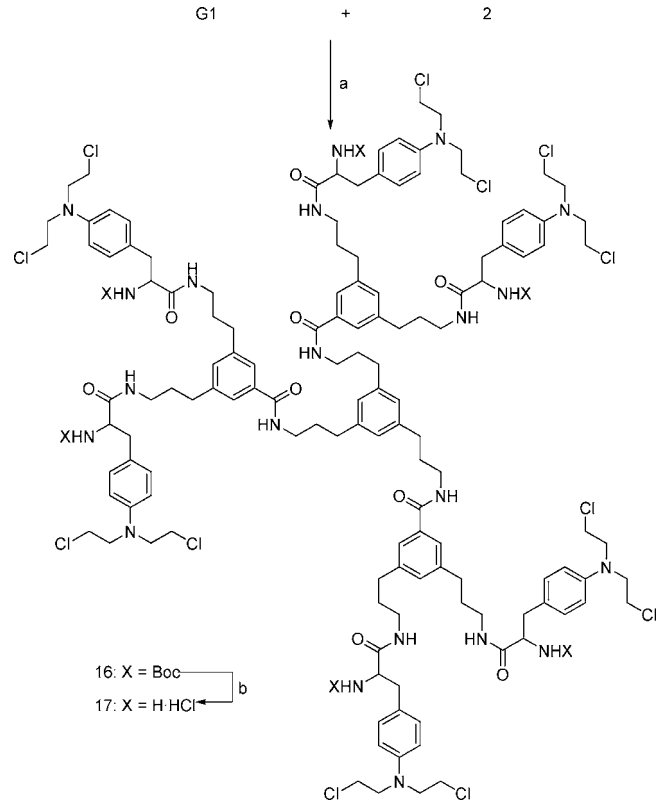
[a] Reagents and conditions: (a) chloroform, DIPEA, reflux, 70 h; (b) aqueous HCl, THF, RT.

Scheme 5. Synthesis of the Drug−G0 Conjugates[a]



[a] Reagents and conditions: (a) CH_2Cl_2, DMF, −20°C, TBTU/30 min, **G0**, DIPEA, methanol, RT, 20 h; (b) TFA (95%), RT, 4 h; (c) CH_2Cl_2, DMF, −20°C, TBTU/30 min, **G0**, DIPEA, methanol, RT, 20 h.

Scheme 6. Synthesis of the Mel−G1 Conjugates[a]



[a] Reagents and conditions: (a) EDC, HOBt, CH_2Cl_2, −20°C/1 h, RT/2 h, **G1**, DIPEA, −30°C/1 h, RT/16 h; (b) aqueous HCl, THF, RT, 3 h.

MB-231 breast cancer cell lines. From the graphs, antiproliferative and cytostatic effects (80% > T/C_{corr} > 0%), as well as cytocidal effects ($\tau = T/C_{corr} < 0\%$), can be deduced.

Cisplatin (DDP) was used as positive control. It influenced the cell growth in a concentration-dependent manner and caused almost 100% growth inhibition at both cell lines at a concentration of 5 μM. The two basic dendrimers **G0** and **G1** were previously tested at concentrations of 1, 5, and 10 μM (*17*, *30*). **G0** was completely inactive, while the **G1** dendrimer marginally reduced cell proliferation at 10 μM ($T/C_{corr} = 60\%$).

It should be mentioned that the cytotoxic properties of the tested compounds were similar at the MCF-7 and MDA-MB-231 cell lines (except where noted; MDA-MB-231 graphs, see Supporting Information).

Melphalan hydrochloride **1** exhibited cytotoxic properties at 10 μM (Figure 3A). Boc protection led to the inactive compound **2** (data not shown) whose activity increased by esterification with the maleimide **3**. The resulting compound **4** showed cytocidal characteristics at concentrations of 5 and 10 μM after an incubation time of 48 h (Figure 3B).

Cleavage of the Boc group increased the cytotoxicity further. The maleimide ester **5** was cytostatic at the lowest concentration used ($T/C_{corr} \approx 0\%$; conc. 1 μM), however, not before the end of the test (incubation time 144 h, see Figure 3C). The comparison of the time response curves in Figure 3A and C clearly documented an ∼10-fold higher activity of **5** compared to that of Melphalan **1**.

Binding of **4** to **G0** (→ **8**) decreased the activity at the MCF-7 cell line (compare Figures 3B and 4A) but marginally enhanced the antiproliferative effects at the MDA-MB-231 compared to the MCF-7 cell line. The activity of the **G0**-bound compound

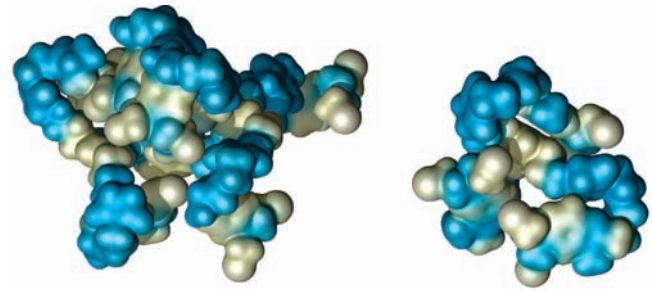


Figure 2. Representative examples of minimized 3D conformations for compounds **12** (left, extent: 38.3 Å) and **10** (right, extent: 30.6 Å). Both molecules are shown as their Van-der-Waals surfaces colored by hydrophobicity (blue: hydrophilic, gray: hydrophobic).

5 (→ **9**) remained nearly unchanged (compare Figures 3C and 4B). Only at 1 μM was a somewhat lower growth inhibition observed.

The increased generation of the dendrimer reduced the cytotoxicity of the Boc-protected compound further. Compound **11** showed only weak activity ($T/C_{corr} \approx 40\%$) even at the highest concentration used (10 μM). In contrast, the activity of **5**, **9**, and **12** is nearly independent of the presence of a dendrimer and its generation (compare Figures 3C, 4B, and 5B).

The same trend was determined for bendamustine (*6*), its maleimide derivative (*7*), and its **G0** conjugate (*10*). Bendamustine was inactive at the MCF-7 and the MDA-MB-231 cell lines (Figure 6A and Supporting Information). Esterification with the maleimide **3** (→ **7**, Figure 6B) increased the antiproliferative effects (cytostatic effects ($T/C_{corr} = 0\%$) at 5 μM and cytocidal effects ($T/C_{corr} < 0\%$) at 10 μM). Binding to **G0** (→ **10**) reduced the activity slightly (compare Figures 6B and 7A).

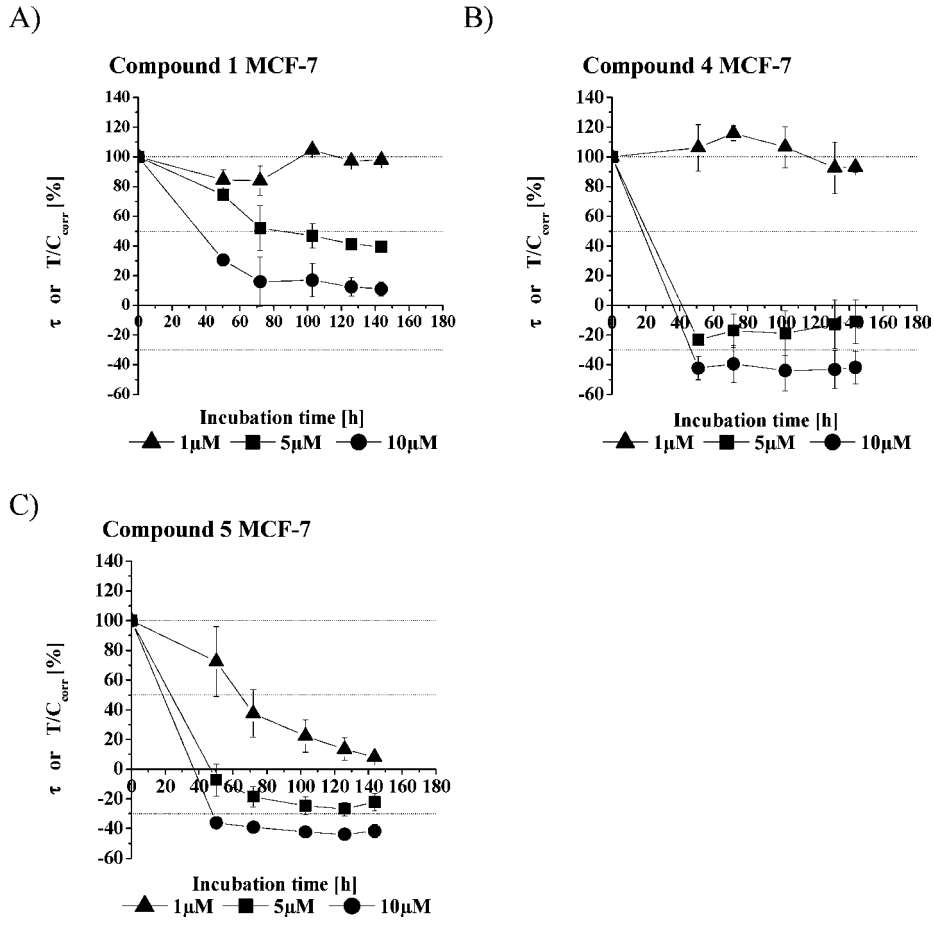


Figure 3. In vitro cytotoxicity ($\tau = T/C_{corr} < 0\%$): (A) Mel, (B) MelBoc-spacer **4**, and (C) Mel-spacer **5**. For detailed information on the investigation of the T/C_{corr} [%] and τ[%] values, see Experimental Section.

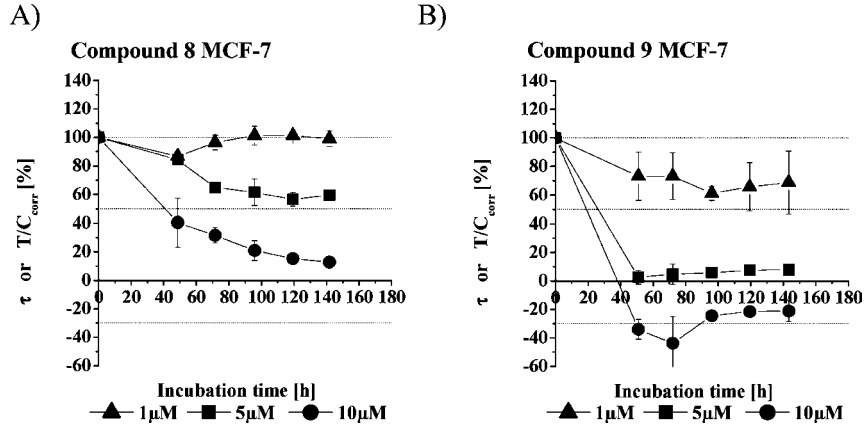


Figure 4. In vitro cytotoxicity ($\tau = T/C_{corr} < 0\%$): (A) MelBoc-spacer-**G0 8**, (B) Mel-spacer-**G0 9**.

In order to estimate the significance of the maleimide spacer for the cytotoxicity of bendamustine, the drugs were directly bound to the dendrimers via an amide bond. This binding led to a complete inactive compound (→ **15**, see Figure 7B). This means that in vitro cytotoxicity of bendamustine needs binding to a maleimide spacer.

In contrast to this, the amide binding of melphalan to **G0** only slightly reduced the activity. The MelBoc-spacer-**G0** derivative **8** reached the $T/C_{corr} = 50\%$ at 5 μM, its congener without spacer **13** (MelBoc-G0) at 10 μM. The cleavage of the Boc groups resulted in the compounds **9** and **14**, which showed similar antiproliferative effects at the low concentration of 1 μM. At 5 and 10 μM, **14** distinctly reached cytocidal effects (see Figure 8B).

If dendrimers with higher generation were used, the effects were independent of the presence of a maleimide spacer (compare Figure 5 with Figure 9).

Investigations into the Hydrolysis of Bendamustine and Melphalan. Bendamustine belongs to the class of alkylating agents of the N-Lost type. Binding to the DNA occurs by attachment to guanine bases. In aqueous solution, the drug underwent hydrolysis into the hydroxyl (**HP1**, Figure 10) or dihydroxyl species (**HP2**, Figure 10). This aquation is accompanied by an inactivation of the drug.

In order to investigate the stability of bendamustine in aqueous solution, it was incubated in water for 24 h at 37 °C and the degradation was followed by HPLC analysis (RP 18; methanol/H_2SO_4 (0.001 N, Na_2SO_4 (20 mM)) and UV-detection

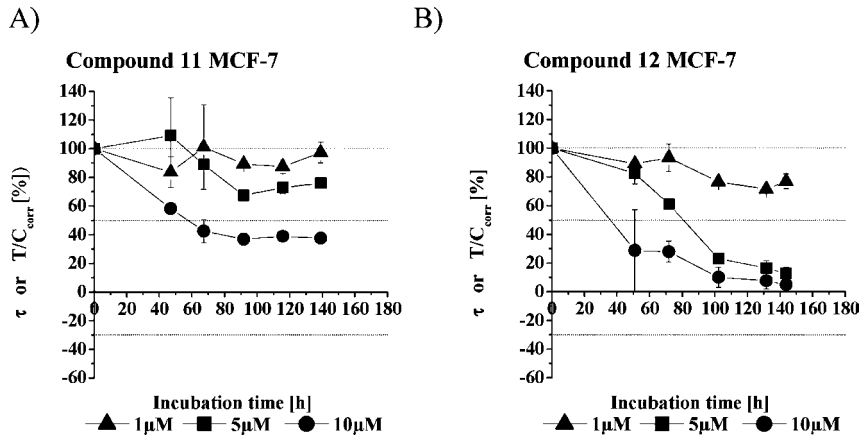


Figure 5. In vitro cytotoxicity ($\tau = T/C_{corr} < 0\%$): (A) MelBoc-spacer-**G1 11**, (B) Mel-spacer-**G1 12**.

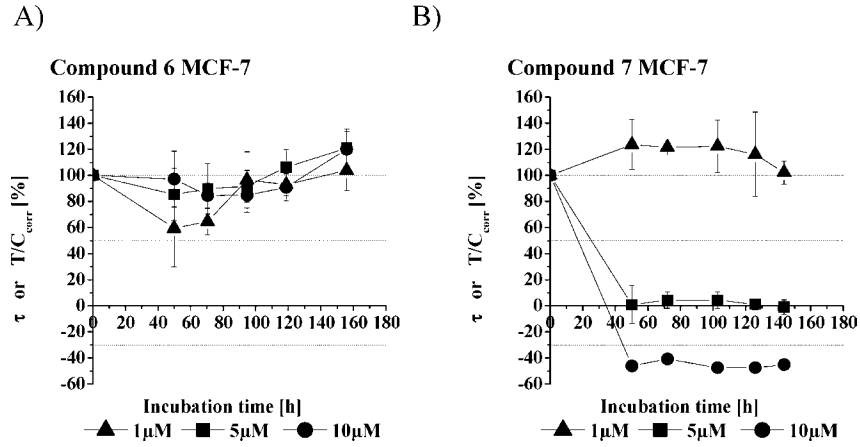


Figure 6. In vitro cytotoxicity ($\tau = T/C_{corr} < 0\%$): (A) Benda **6**; (B) Benda-spacer **7**.

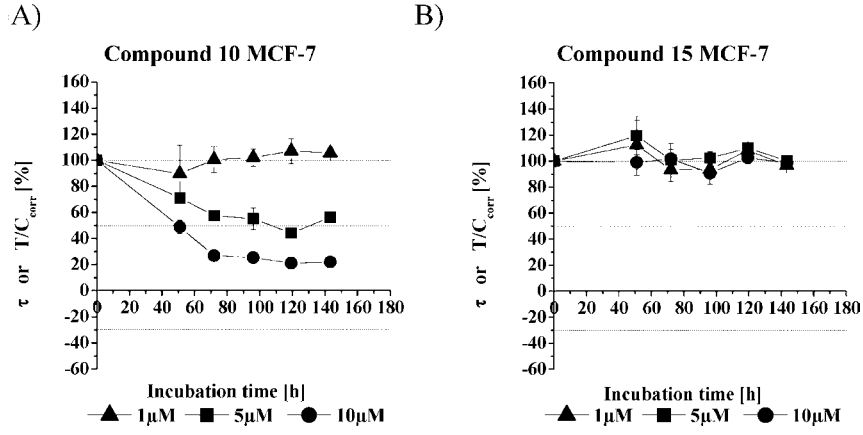


Figure 7. In vitro cytotoxicity ($\tau = T/C_{corr} < 0\%$): (A) Benda-spacer-**G0 10**; (B) Benda-**G0 15**.

(254 nm). During the first 2 h, 55.6% of bendamustine hydrolyzed to **HP1** (36.8%) and **HP2** (18.8%). After 8 h, amounts of 81.6% of **HP2**, 14.7% of **HP1**, and only 3.7% of bendamustine were detected. Incubation of 24 h led to a complete hydrolysis into **HP2**.

Melphalan was distinctly less stable. An amount of 88.1% hydrolyzed after 2 h to the monohydroxyl (24.7%) and dihydroxyl (63.5%) species, while after 8 h, only the dihydroxyl species was present.

The bendamustine-maleimide derivative **7** was tested under the same conditions. A representative of a chromatogram is depicted in Figure 11.

The maleimide residue mediated **7** high hydrophobicity resulting in an increased retention time of RT = 57.3 min (bendamustine RT = 25.7 min). It is visible that two reactions took place: (1) cleavage of the ester bond in **7** resulting in bendamustine **6** and the maleimide **3**; (2) hydrolysis of **7** to the hydroxyl and dihydroxyl compounds **7-OH** and **7-diOH**. Bendamustine itself hydrolyzed to **HP1** and **HP2** (see Figure 10).

After 8 h, 14% (sum of **6**, **HP1**, and **HP2**) of bendamustine was set free. Aquation products of **7** were detected at RT = 14.6 min (**7-OH**; 38%) and RT = 5.28 min (**7-diOH**; 7.5%). Unchanged **7** amounted to 39.5%. It is obvious that the esterification of

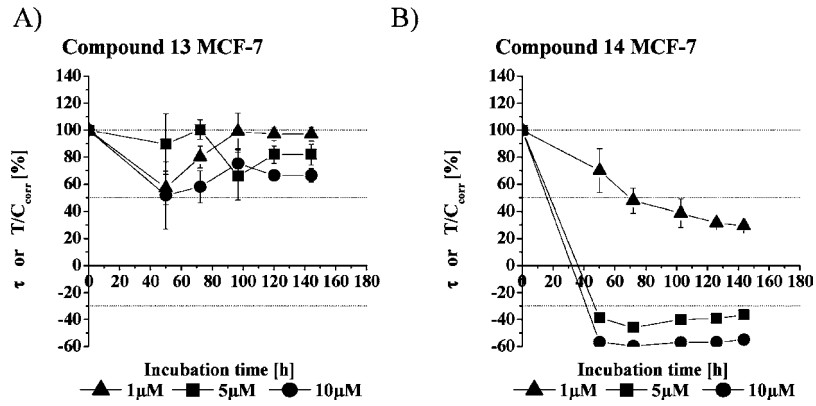


Figure 8. In vitro cytotoxicity ($\tau = T/C_{corr} < 0\%$): (A) MelBoc-**G0 13**, (B) Mel-**G0 14**.

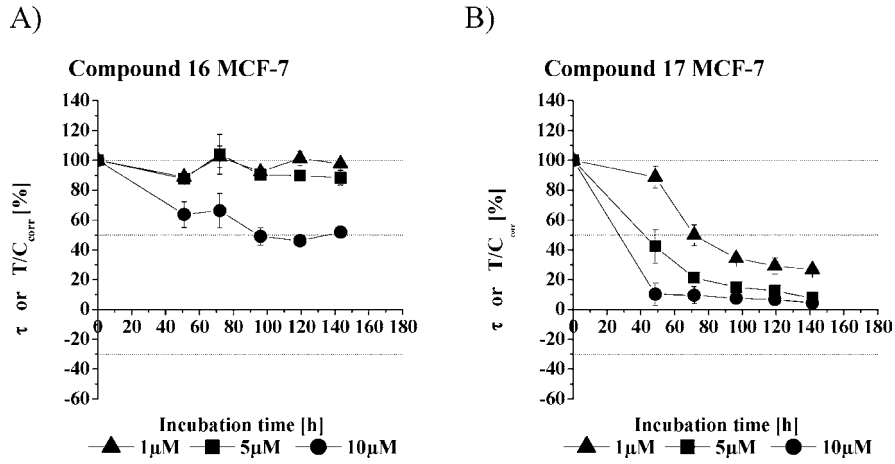


Figure 9. In vitro cytotoxicity ($\tau = T/C_{corr} < 0\%$): (A) MelBoc-**G1 16**, (B) Mel-**G1 17**.

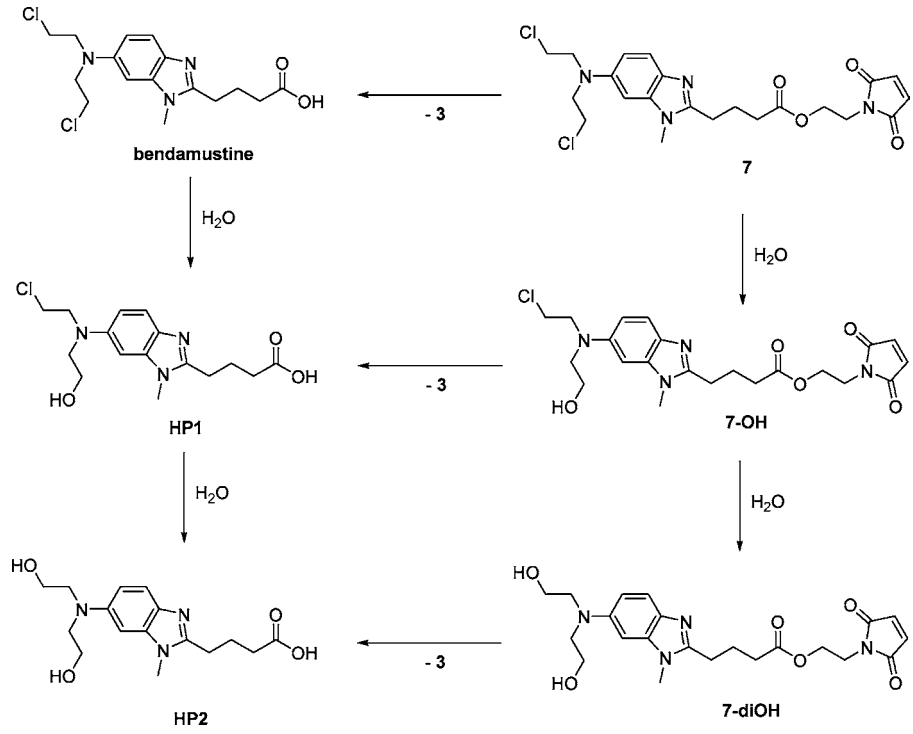


Figure 10. Hydrolysis of **7** at 37 °C in water.

bendamustine increased the stability in aqueous solution, but bendamustine was released over 36 h and held a level up to 7%. **HP1** and **HP2** are not only the hydrolysis products of bendamustine, but also the degradation products of **7-OH** and **7-diOH**.

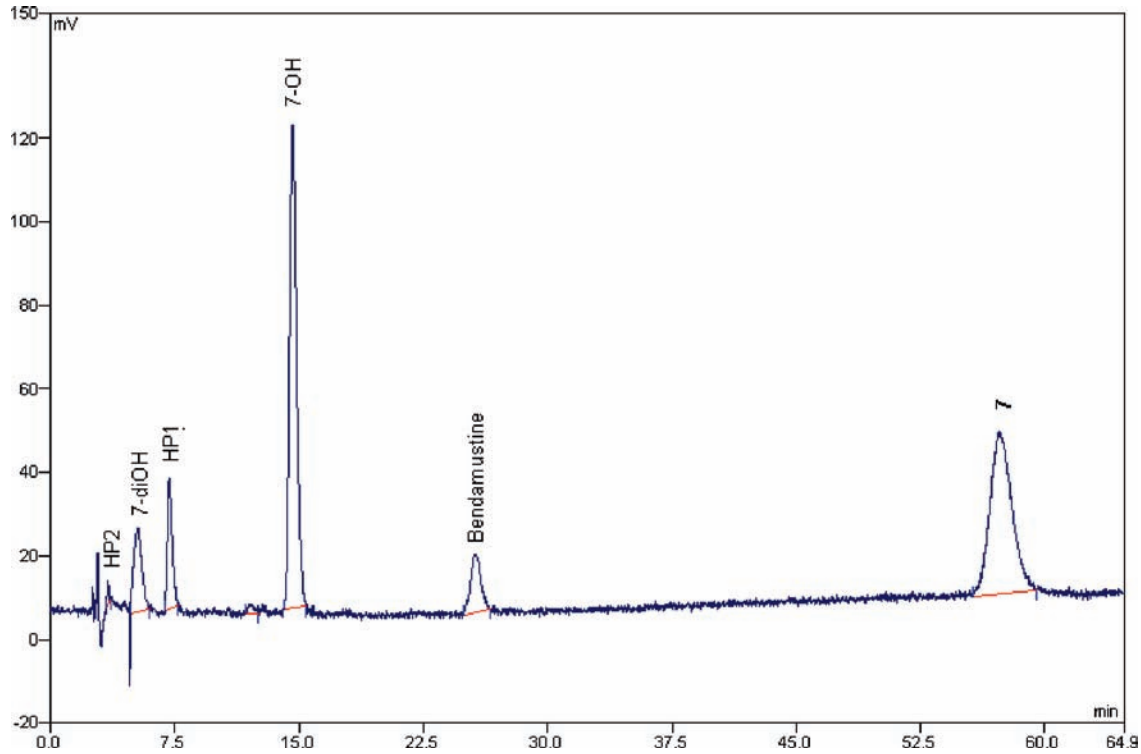


Figure 11. Chromatogram of **7** after incubation in water at 37 °C for 8 h.

The same modification done with melphalan did not increase the stability. The maleimide derivative **5** degraded ($t_{1/2}$ = 37 min) comparable to melphalan ($t_{1/2}$ = 30 min). It should be mentioned that **5** showed the same degradation profile as **7**.

In order to model blood circulation (buffer pH 7.4) and intracellular/endosomal environment (buffer pH 5), the same hydrolysis experiments were performed with bendamustine and **7** in PBS at relevant pH.

Bendamustine showed pH-sensitive degradation. It was completely hydrolyzed to **HP2** during 2 h at pH 7.4, while at pH 5, after 4 h only 50% and after 24 h 92% of bendamustine degraded. Compound **7** showed distinctly increased stability. The half-life in PBS was 8.5 h at pH 5 and 10 h at pH 7.4.

The hydrolysis rates at pH 5 and pH 7.4 were not as different as observed for bendamustine. The half-lives was 120 and 98 min, respectively. Interestingly, after derivation to **5**, a complete degradation (100%) occurred at pH 7.4 and a slightly increased stability at pH 5 ($t_{1/2}$ = 154 min).

HSA solution (40 mg/mL) was used to study protein binding. Ethanolic precipitation indicated protein binding of bendamustine. After incubation for 2 h, 50% were protein-bound and 6% hydrolyzed to **HP1** and **HP2**, respectively. In contrast, during the same incubation time only 25% of **7** were HSA-bound and 18% hydrolyzed to **7-OH**.

Melphalan was strongly HSA-bound. After 2 h, 14.3% of hydroxyl derivatives and 18.9% of melphalan could be detected. The amount of 66.8% was bound to the protein. A still faster interaction with HSA was found for **5**. No drug was identified in the chromatograms after 30 min.

DISCUSSION

The preliminary in vitro tests on MCF-7 and MDA-MB-231 breast cancer cells confirmed the existing literature data about the antitumor activity of melphalan hydrochloride (*1*). It reduced the concentration-dependent growth of MCF-7 and MDA-MB-231 breast cancer cells. At 10 μM, cytostatic effects ($T/C_{corr} \approx$ 0%) were determined (Figure 3), which depended on the presence of a free amino group. The Boc-protected melphalan derivative **2** was inactive. Interestingly, the esterification with *N*-(2-hydroxyethyl)maleimide **3** strongly increased the activity. The melphalan-Boc-protected spacer analogue **4** was proven to exhibit cytocidal effects on both cell lines. As expected, the deprotection leading to compound **5** increased the influence on the cells. Already, at a concentration of 1 μM cytostatic effects were achieved.

A possible explanation could be the binding of the spacer derivative to human serum albumin (HSA) present in the cell culture media. In some previous work, Kratz et al. synthesized such conjugates of the nitrogen mustard chlorambucil (*14*). They also demonstrated an HSA binding of the spacer derivative in situ after iv administration. Due to the considerable uptake of the macromolecule-bound drug in tumor cells, this concept has a promising future as a drug carrier system (*31*).

This mode of action can principally be realized for maleimide derivatives **4**, **5**, and **7**. HSA binding was confirmed on the examples of **5** and **7**. Fast binding also occurred with bendamustine and melphalan. After 2 h of incubation, more than 50% were bound.

Besides HSA or transferrin as carrier molecules (*32*−*34*), some synthetic polymers were designed to bind drugs for selective accumulation in tumors and tumor cells (*35*, *36*). In previous studies (*17*), we used the 1,3,5-tris(3-aminopropyl)benzene (**G0**) and its **G1** analogue 3,5-bis(3-aminopropyl)-*N*-(3-{3,5-bis[3-{3,5-bis(3-aminopropyl)benzoylamino}-propyl]phenyl}propyl)benzamide for the transport of drugs into MCF-7 and MDA-MB-231 cells. The concept was very successful in the case of platinum(II) complexes (*30*).

Already, in the 1990s covalent conjugation of melphalan to macromolecular carriers was described (*37*). It was, e.g., linked to *N*-(2-hydroxypropyl)methacrylamide (HPMA) copolymers via enzymatically cleavable peptide side chains. In 2008, Shukla et al. published poly(ethylene glycol) conjugates of melphalan demonstrating enhanced dose-dependent in vitro cytotoxicity (*38*).

Therefore, we decided to bind melphalan to **G0** or **G1** dendrimers via the maleimide spacer (**8**, **9** and **11**, **12**) or directly

via an amide bond (**13**, **14** and **16**, **17**) to evaluate their cytotoxic potency in vitro. The BOC-protected conjugates **8**, **11**, **13**, and **16** were only marginally active at MCF-7 and MDA-MB-231 cells. Only the drug-spacer-**G0** conjugate **8** showed low cytostatic properties at the highest concentration. The **G1**-conjugates with free NH_2 groups (**12** and **17**) only slightly differ in their activity. They showed cytostatic properties at 5 and 10 μM.

These results indicated a relatively high stability of the conjugates. We assume that melphalan interacted after transport into the tumor cells in free form and also dendrimer-bound with the DNA via the N-lost group. The resulting cross-links led to cell death. Bendamustine belongs to the same class of antitumor agents. However, its cytotoxic behavior in free form, maleimide bound, or as dendrimer conjugate differs from that of melphalan.

Melphalan and bendamustine are sensitive to hydrolysis in water and were degraded at 37 °C to the bis(hydroxyethyl)amino compounds over 24 h. The results of Chang et al. demonstrated for melphalan a retarded hydrolysis in the presence of bovine serum albumin or human plasma proteins (*39*). In a Roswell Park Memorial Institute Medium containing 10% fetal bovine serum, the half-life of melphalan at 37 °C was 1.13 ± 0.10 h and was only slightly higher compared to that in pure water (*40*). In our experiments, besides strong HSA binding a reduced amount of hydrolysis was detected, too.

Bendamustine showed a half-life of about 100 min in pure water and increased stability in physiological NaCl solution (*41*). This correlates very well with the hydrolysis of melphalan (*39*). However, the attempt failed to stabilize the aqueous solution of bendamustine by HSA. A drug amount of 50% was HSA-bound during an incubation time of 2 h and an amount of 12% was hydrolyzed. In PBS buffer at pH = 7.4, fast hydrolysis took place. After 2 h, only **HP2** was present. Therefore, we assume that under cell culture conditions not enough active drug was present to reduce the growth of MCF-7 and MDA-MB-231 cells.

The mode of action of bendamustine is discussed in very contradictory terms. However, it is still accepted that DNA-alkylation is the main cause of cell death in vivo. Preclinical data demonstrate that bendamustine induces rapid, sustained single- and double-strand DNA damage, which results in apoptosis, or programmed cell death, in the tumor. It also induces mitotic checkpoint inhibition, which results in nonapoptotic cell death (*42*−*44*).

Such a mode of action requires an intact N-lost moiety. The dihydroxybendamustine derivative **HP2** is inactive in cell culture experiments. The participation of the partially hydrolyzed **HP1** to the antiproliferative effects is still unknown. This assumption is confirmed by the fact that in in vitro assays bendamustine is inactive (*45*) (see also Figure 6A). If it were possible to prevent hydrolysis in aqueous solution, antiproliferative properties should be observed. The stability is enhanced in alcoholic solution (unpublished results) which is not usable in in vitro conditions. However, in this SAR study it was at first demonstrated that esterification of the carboxylic group increased the water stability.

The maleimide moiety of compound **7** is attached to bendamustine by a hydroxyethyl chain. The resulting ester was incubated at 37 °C in water and the degradation was followed by HPLC.

After 8 h of incubation, degradation to bendamustine followed by hydrolysis to **HP1** was observed. Furthermore, besides intact **7**, its monohydroxyl derivative **7-OH** was determined, too. Interestingly, the stability of **7** in PBS was higher than that of bendamustine and independent of the pH. The half-life of **7** at pH 7.4 was 10 h, and guaranteed higher amounts of active compounds resulting in increased antiproliferative effects in cell culture experiments.

The binding of **7** to **G0** through the maleimide spacer slightly reduced the activity from cytocidal to cytostatic. In contrast, the direct binding of bendamustine to **G0** via an amide bond terminated the cytotoxic effects. The higher stability of the amide bond prevents a release of bendamustine from the molecule. Therefore, it is very likely that it was not **10** itself causing cell death but the hydrolytically cleaved bendamustine **6**. This contrasts with the results obtained with melphalan, which was active in free as well as dendrimer bound via the spacer and the amide bond.

Our concept to increase the activity of melphalan and bendamustine by an adequate carrier (dendrimer) was successful. Through the binding to the dendrimer via spacer, not only can it be assumed that the new bendamustine derivatives accumulated in the tumor cells probably through endocytosis, but it can be also presumed that the hydrolysis of bendamustine is suppressed.

The investigations pointed, on one hand, to a participation of the butyric acid in the hydrolytic processes; on the other hand, Pencheva et al. achieved for bendamustine immobilized onto polyphosphoester a higher stability by the formation of molecular associates (*46*). If this were true, the stability of bendamustine should increase using polymers such as poly(ethylene glycol)s. In our lab, however, we cannot find increased stability with PEG 400/water mixtures.

Hopwood and Stock demonstrated that macromolecules with lipophilic moieties are capable of diminishing the hydrolysis of drugs (*47*). Albumin proved to be the most efficient at protecting the anticancer agents. This may also be true for the bendamustine maleimide derivative **7**. However, the binding mode at HSA is yet unknown.

CONCLUSIONS

A new set of dendrimer and dendrimer−spacer conjugates of melphalan and bendamustine have been successfully synthesized. The antiproliferative activity of these compounds and their maleimide precursors has been determined against MCF-7 and MDA-MB-231 cell lines. No selectivity for one of the cell lines was detected. The cytotoxicity of melphalan depended on a free amino group and was independent of the kind of bond to the spacer or the dendrimer.

The antiproliferative activity of bendamustine was strongly increased due to reduced hydrolytic processes after esterification with the *N*-(2-hydroxyethyl)maleimide. An amide bond to 1,3,5-tris(3-aminopropyl)benzene terminated the activity. Therefore, it is very likely that the cell death promoting effects were caused after transport into the tumor cells and release of the intact drug from the core molecule **G0**.

In a following study, we will investigate the hydrolysis reactions and the release of bendamustine from dendrimers of higher generation. Furthermore, we will evaluate the binding mode at the carboxylic acid necessary for increased activity.

ACKNOWLEDGMENT

The presented study was supported by grants Gu285/4-1, Gu285/5-1, and Gu285/5-2 from the Deutsche Forschungsgemeinschaft.

Supporting Information Available: Elemental analyses of the new compounds, their results (cytotoxicity tests) on the MDA-MB-231 cell line, the cytotoxicity of **G0** and **G1** on the MCF-7 cell line, a histogram of the maximum extent distributions over the calculated three-dimensional conformational space for **10** and **12** and median, average and maximum values for molecule sizes of **10** and **12**. This material is available free of charge via the Internet at http://pubs.acs.org.

LITERATURE CITED

(1) Gillies, E. R., and Frechet, J. M. J. (2005) Dendrimers and dendritic polymers in drug delivery. *Drug Discovery Today 10*, 35–43.

(2) Wolinsky, J. B., and Grinstaff, M. W. (2008) Therapeutic and diagnostic applications of dendrimers for cancer treatment. *Adv. Drug Delivery Rev. 60*, 1037–1055.

(3) D'Emanuele, A., and Attwood, D. (2005) Dendrimer-drug interactions. *Adv. Drug Delivery Rev. 57*, 2147–2162.

(4) Caminade, A. M., Laurent, R., and Majoral, J. P. (2005) Characterization of dendrimers. *Adv. Drug Delivery Rev. 57*, 2130–2146.

(5) Takakura, Y., Mahato, R. I., and Hashida, M. (1998) Extravasation of macromolecules. *Adv. Drug Delivery Rev. 34*, 93–108.

(6) Noguchi, Y., Wu, J., Duncan, R., Strohalm, J., Ulbrich, K., Akaike, T., and Maeda, H. (1998) Early phase tumor accumulation of macromolecules: A great difference in clearance rate between tumor and normal tissues. *Jpn. J. Cancer Res. 89*, 307–314.

(7) Majoros, I. J., Myc, A., Thomas, T., Mehta, C. B., and Baker, J. R. (2006) PAMAM dendrimer-based multifunctional conjugate for cancer therapy: Synthesis, characterization, and functionality. *Biomacromolecules 7*, 572–579.

(8) Choi, Y., Thomas, T., Kotlyar, A., Islam, M. T., and Baker, J. R. (2005) Synthesis and functional evaluation of DNA-assembled polyamidoamine dendrimer clusters for cancer cell-specific targeting. *Chem. Biol. 12*, 35–43.

(9) Thomas, T. P., Majoros, I. J., Kotlyar, A., Kukowska-Latallo, J. F., Bielinska, A., Myc, A., and Baker, J. R. (2005) Targeting and inhibition of cell growth by an engineered dendritic nanodevice. *J. Med. Chem. 48*, 3729–3735.

(10) Ozegowski, W., and Krebs, D. (1963) Amino acid antagonists. III. ω-[Bis-(β-chloroethyl)amino-2-benzimidazolyl]propionic and -butyric acids as potential cytostats. *J. Prakt. Chemie 20*, 178–186.

(11) Keating, M. J., Bach, C., Yasothan, U., and Kirkpatrick, P. (2008) Bendamustine. *Nat. Rev. Drug Discovery 7*, 473–474.

(12) Eichbaum, M. H. R., Schuetz, F., Khbeis, T., Lauschner, I., Foerster, F., Sohn, C., and Schneeweiss, A. (2007) Weekly administration of bendamustine as salvage therapy in metastatic breast cancer: Final results of a phase II study. *Anti-Cancer Drugs 18*, 963–968.

(13) Kratz, F., Beyer, U., Roth, T., Schutte, M. T., Unold, A., Fiebig, H. H., and Unger, C. (1998) Albumin conjugates of the anticancer drug chlorambucil: Synthesis, characterization, and in vitro efficacy. *Arch. Pharm. 331*, 47–53.

(14) Beyer, U., Roth, T., Schumacher, P., Maier, G., Unold, A., Frahm, A. W., Fiebig, H. H., Unger, C., and Kratz, F. (1998) Synthesis and in vitro efficacy of transferrin conjugates of the anticancer drug chlorambucil. *J. Med. Chem. 41*, 2701–2708.

(15) Matsumura, Y., and Maeda, H. (1986) A new concept for macromolecular therapeutics in cancer-chemotherapy - mechanism of tumoritropic accumulation of proteins and the antitumor agent smancs. *Cancer Res. 46*, 6387–6392.

(16) Sinn, H., Schrenk, H. H., Friedrich, E. A., Schilling, U., and Maier-Borst, W. (1990) Design of compounds having an enhanced tumor uptake, using serum-albumin as a carrier. Part 1. *Int. J. Rad. Appl. Instrum. B 17*, 819–827.

(17) Fuchs, S., Kapp, T., Otto, H., Schöneberg, T., Franke, P., Gust, R., and Schlüter, A. D. (2004) A surface-modified dendrimer set for potential application as drug delivery vehicles: Synthesis, in vitro toxicity, and intracellular localization. *Chem.—Eur. J. 10*, 1167–1192.

(18) Giraud, I., Rapp, M., Maurizis, J. C., and Madelmont, J. C. (2002) Synthesis and in vitro evaluation of quaternary ammonium derivatives of chlorambucil and melphalan, anticancer drugs designed for the chemotherapy of chondrosarcoma. *J. Med. Chem. 45*, 2116–2119.

(19) Bergel, F., and Stock, J. A. (1954) Cyto-active amino-acid and peptide derivatives.1. Substituted phenylalanines. *J. Chem. Soc.* 2409–2417.

(20) Hawkins, P. C., Skillman, A. G., Warren, G. L., Ellingson, B. A., and Stahl, M. T. (2010) Conformer generation with OMEGA: Algorithm and validation using high quality structures from the Protein Databank and Cambridge Structural Database. *J. Chem. Inf. Model. 50*, 572–84.

(21) Wolber, G., and Langer, T. (2005) LigandScout: 3D pharmacophores derived from protein-bound ligands and their use as virtual screening filters. *J. Chem. Inf. Model. 45*, 160–169.

(22) Wolber, G., Dornhofer, A. A., and Langer, T. (2006) Efficient overlay of small organic molecules using 3D pharmacophores. *J. Comput.-Aided Mol. Des. 20*, 773–788.

(23) Hay, R. J. (1988) The seed stock concept and quality-control for cell-lines. *Anal. Biochem. 171*, 225–237.

(24) Bernhardt, G., Reile, H., Birnböck, H., Spruss, T., and Schönenberger, H. (1992) Standardized kinetic microassay to quantify differential chemosensitivity on the basis of proliferative activity. *J. Cancer Res. Clin. Oncol. 118*, 35–43.

(25) Reile, H., Birnbock, H., Bernhardt, G., Spruss, T., and Schönenberger, H. (1990) Computerized determination of growth kinetic curves and doubling times from cells in microculture. *Anal. Biochem. 187*, 262–267.

(26) Werner, W., Letsch, G., and Ihn, W. (1987) Hydrolysis products of the cancerostatic drug cytostasan (Bendamustin). *Pharmazie 42*, 272–273.

(27) Klausner, Y. S., and Bodansky, M. (1972) Coupling reagents in peptide synthesis. *Synthesis* 453–463.

(28) Sheehan, J. C., and Ledis, S. L. (1973) Total synthesis of a monocyclic peptide lactone antibiotic, Etamycin. *J. Am. Chem. Soc. 95*, 875–879.

(29) Sheehan, J. C., Preston, J., and Cruicksh., P. A. (1965) A rapid synthesis of oligopeptides derivates without isolation of intermediates. *J. Am. Chem. Soc. 87*, 2492–2493.

(30) Kapp, T., Dullin, A., and Gust, R. (2010) Platinum(II)-dendrimer conjugates: synthesis and investigations on cytotoxicity, cellular distribution, platinum release, DNA, and protein binding. *Bioconjugate Chem. 21*, 328–337.

(31) Testa, U., Pelosi, E., and Peschle, C. (1993) The transferrin receptor. *Crit. Rev. Oncogen. 4*, 241–276.

(32) Tajmir-Riahi, H. A. (2007) An overview of drug binding to human serum albumin: Protein folding and unfolding. *Sci. Iran. 14*, 87–95.

(33) Zhou, Q. J., Bi, Y. J., Xiang, J. F., Tang, Y. L., Yang, Q. F., and Xu, G. Z. (2008) Investigation on a potential targeting drug delivery system consisting of folate, mitoxantrone and human serum albumin. *Chin. J. Chem. 26*, 1385–1389.

(34) Wagner, E., Cotten, M., Mechtler, K., Kirlappos, H., and Birnstiel, M. L. (1991) DNA-binding transferrin conjugates as functional gene-delivery agents - synthesis by linkage of polylysine or ethidium homodimer to the transferrin carbohydrate moiety. *Bioconjugate Chem. 2*, 226–231.

(35) Khandare, J., and Minko, T. (2006) Polymer-drug conjugates: Progress in polymeric prodrugs. *Prog. Polym. Sci. 31*, 359–397.

(36) Khandare, J. J., Chandna, P., Wang, Y., Pozharov, V. P., and Minko, T. (2006) Novel polymeric prodrug with multivalent components for cancer therapy. *J. Pharmacol. Exp. Ther. 317*, 929–937.

(37) Duncan, R., Hume, I. C., Yardley, H. J., Flanagan, P. A., Ulbrich, K., Subr, V., and Strohalm, J. (1991) Macromolecular prodrugs for use in targeted cancer chemotherapy: Melphalan covalently coupled to N-(2-hydroxypropyl)methacrylamide copolymers. *J. Controlled Release 16*, 121–36.

(38) Shukla, G., Tiwari, A. K., Kumar, N., Sinha, D., Mishra, P., Chandra, H., and Mishra, A. K. (2008) Polyethylene glycol conjugates of methotrexate and melphalan: Synthesis, radiolabeling and biologic studies. *Cancer Biother. Radiopharm. 23*, 571–580.

(39) Chang, S. Y., Alberts, D. S., Farquhar, D., Melnick, L. R., Walson, P. D., and Salmon, S. E. (1978) Hydrolysis and protein-binding of melphalan. *J. Pharm. Sci. 67*, 682–684.

(40) Bosanquet, A. G. (1985) Stability of melphalan solutions during preparation and storage. *J. Pharm. Sci. 74*, 348–351.

(41) Gust, R., and Krauser, R. (1997) Investigations on the stability of bendamustine, a cytostatic agent of the nitrogen mustard type. Part 1. Synthesis, isolation, and characterization of reference substances. *Monatsh. Chem. 128*, 291–299.

(42) Kalaycio, M. (2009) Bendamustine. A new look at an old drug. *Cancer 115*, 473–479.

(43) Plosker, G. L., and Carter, N. J. (2008) Bendamustine. A review of its use in the management of indolent non-Hodgkin lymphoma. *Drugs 68*, 2645–2660.

(44) Leoni, L. M., Bailey, B., Reifert, J., Bendall, H. H., Zeller, R. W., Corbeil, J., Elliott, G., and Niemeyer, C. C. (2008) Bendamustine (Treanda) displays a distinct pattern of cytotoxicity and unique mechanistic features compared with other alkylating agents. *Clin. Cancer Res. 14*, 309–317.

(45) Konstantinov, S. M., Kostovski, A., Topashka-Ancheva, M., Genova, M., and Berger, M. R. (2002) Cytotoxic efficacy of bendamustine in human leukemia and breast cancer cell lines. *J. Cancer Res. Clin. Oncol. 128*, 271–278.

(46) Pencheva, I., Bogomilova, A., Koseva, N., Obreshkova, D., and Troev, K. (2008) HPLC study on the stability of bendamustine hydrochloride immobilized onto polyphosphoesters. *J. Pharm. Biomed. Anal. 48*, 1143–1150.

(47) Hopwood, W. J., and Stock, J. A. (1971) The effect of macromolecules upon rates of hydrolysis of aromatic nitrogen mustard derivatives. *Chem. Biol. Interact. 4*, 31–39.

BC900453F

Supporting information

Optimization of the N-Lost Drugs Melphalan and Bendamustine: Synthesis and Cytotoxicity of a New Set of Dendrimer-Drug Conjugates as Tumor Therapeutic Agents

Ana Maria Scutaru[a], Maxi Wenzel[a], Heike Scheffler[a], Gerhard Wolber[a], Ronald Gust[a,b,]*

[a] Institut für Pharmazie, Freie Universität Berlin, Königin Luise Str. 2+4, 14195 Berlin, Germany

[b] Institut für Pharmazie, Universität Innsbruck, Innrain 52, A-6020 Innsbruck, Austria

*Corresponding author. Phone: : +43 512 507 5245; Telefax: +43 512 507 2940;
E-mail: ronald.gust@uibk.ac.at.

Content

Elemental analyses of new compounds

Table S1: Median, average and maximum values for molecule sizes of **10** and **12**.

Figure S1: Distribution of maximum molecule extent (Å) in 3D conformational space for **10** and **12**.

Figure S2: *In vitro* cytotoxicity of relevant compounds on the MDA-MB-231 cell line

Figure S3: *In vitro* cytotoxicity of G0 and G1 on the MCF-7 cell line

Elemental analyses of new compounds:

O-{N-tert-Butoxycarbonyl-4-[bis(2-chloroethyl)amino]-L-phenylalanyl}-2-hydroxyethyl-maleimide (4): Anal. ($C_{24}H_{31}Cl_2N_3O_6$) C: calcd, 54.55; found 54.81, H: calcd, 5.91; found 6.37, N: calcd, 7.95; found, 7.98.

O-{4-[Bis(2-chloroethyl)amino]-L-phenylalanyl}-2-hydroxyethylmaleimide hydrochloride (5): Anal. ($C_{19}H_{25}Cl_3N_3O_4 \cdot HCl$) C: calcd, 45.44; found 45.81, H: calcd, 5.22; found 5.33, N: calcd, 8.37; found, 8.79.

O-{4-[6-Bis(2-chloroethyl)amino-3-methylbenzimidazoyl(2)]butanoyl}-2-hydroxy-ethylmaleimide (7): Anal. ($C_{22}H_{26}Cl_2N_4O_4$) C: calcd, 54.98; found 54.88, H: calcd, 5.44; found 5.84, N: calcd, 11.64; found, 11.13.

1,3,5-Tris{N-[(2-(2,5-dioxopyrrolidin-1-yl)ethyl-3-(4-(bis(2-chloroethyl)amino)phenyl)-2-(tertbutoxycarbonylamino)propanoate)-1-yl]propylamino}benzene (8): Anal. ($C_{87}H_{121}N_{12}O_{18}Cl_6$) C: calcd, 56.95; found 57.11, H: calcd, 6.59; found 6.65, N: calcd, 9.16; found, 8.99.

1,3,5-Tris[3-(4-(bis(2-chloroethyl)amino)phenyl)-2-amino-N-propylpropionamide]-benzene tristrifluoroacetate (14): Anal. ($C_{60}H_{78}Cl_6N_9O_9F_9$) C: calcd, 49.60; found 49.68, H: calcd, 5.41; found 5.51, N: calcd, 8.68; found, 8.95.

Table S1. Median, average and maximum values for molecule sizes of **10** and **12**.

	12	**10**
Average	38.30 Å	31.00 Å
Median	37.89 Å	30.63 Å
Minimum	33.53 Å	23.08 Å
Maximum	48.67 Å	46.67 Å

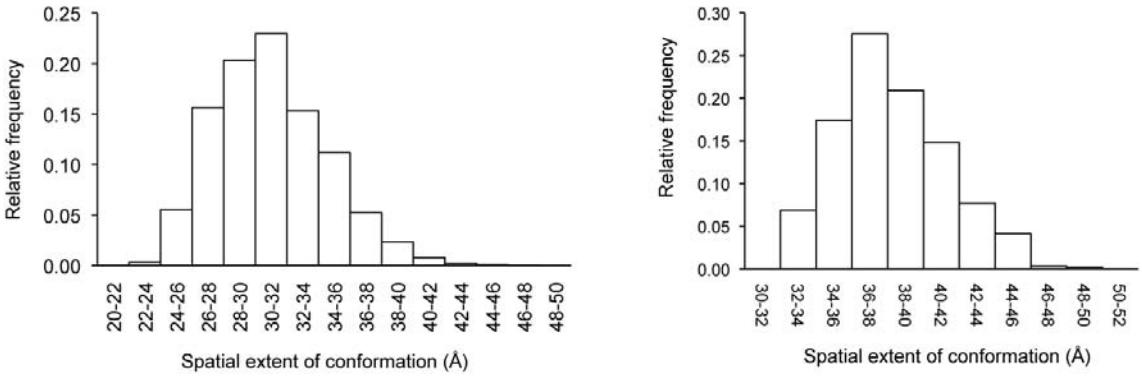
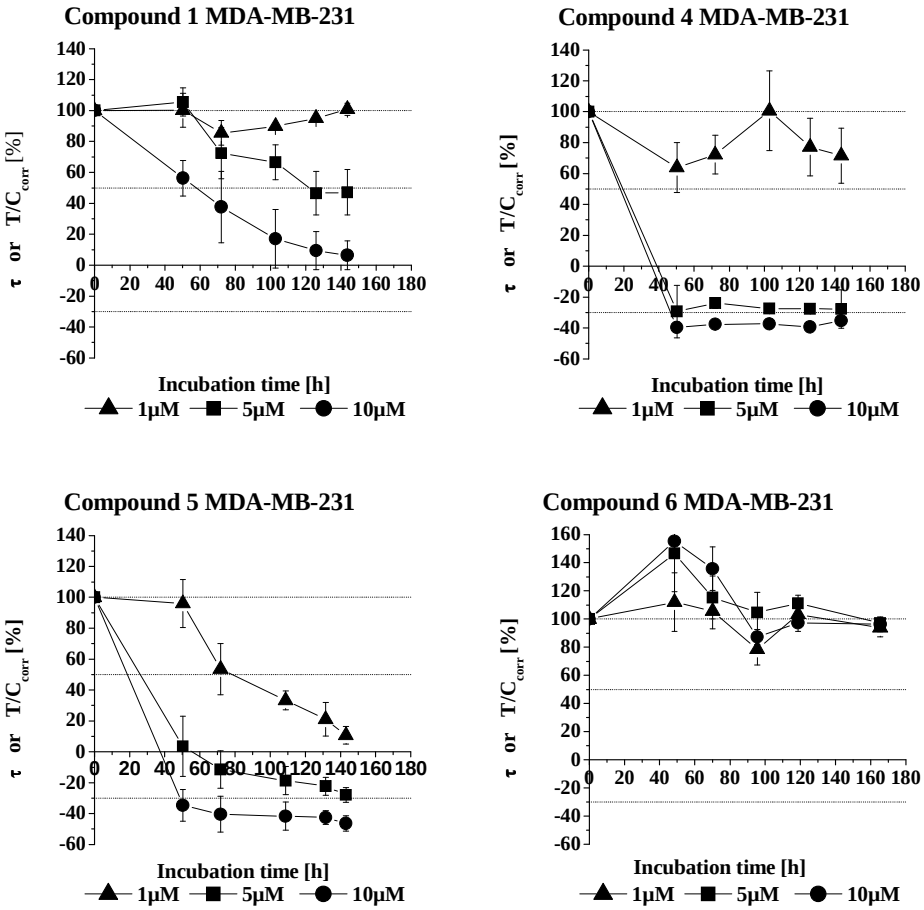
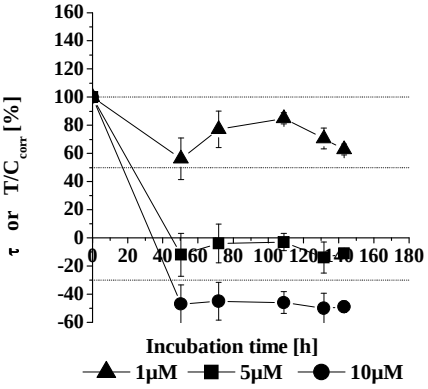


Figure S1. Distribution of maximum molecule extent (Å) in 3D conformational space for **10** (left) and **12** (right).

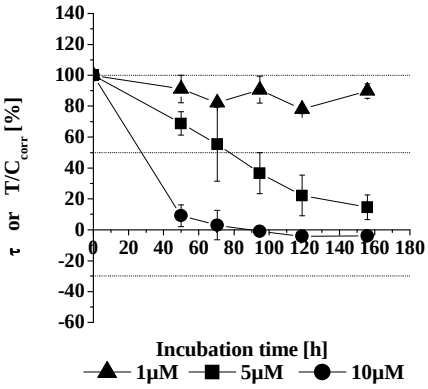
Figure S2: *In vitro* cytotoxicity of the relevant compounds on the MDA-MB-231 cell line



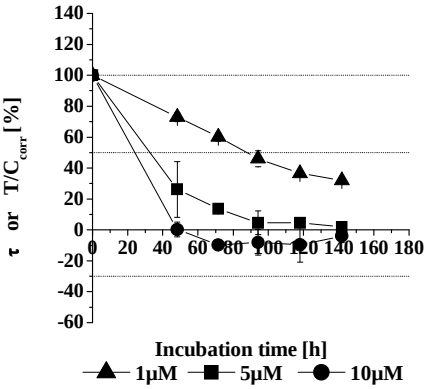
Compound 7 MDA-MB-231



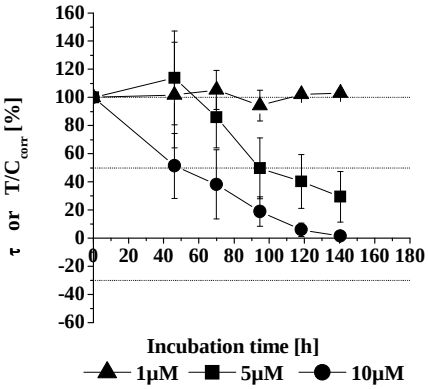
Compound 8 MDA-MB-231



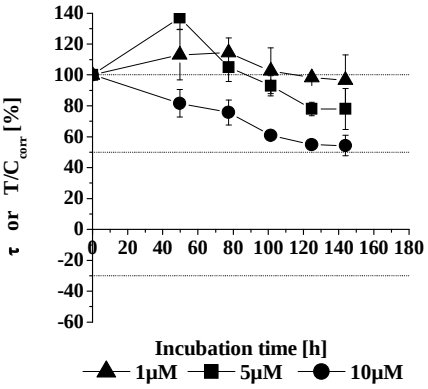
Compound 9 MDA-MB-231



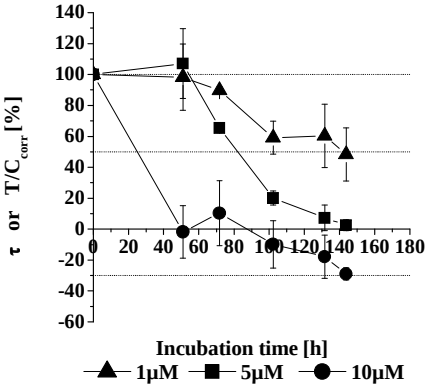
Compound 10 MDA-MB-231



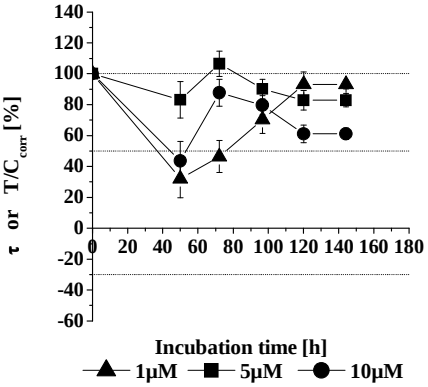
Compound 11 MDA-MB-231



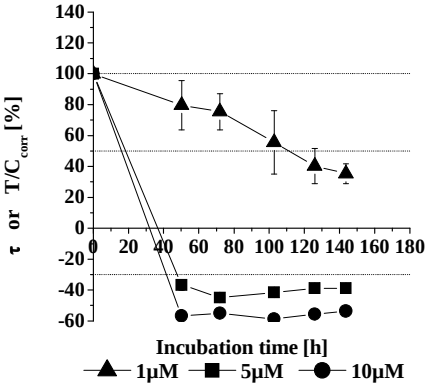
Compound 12 MDA-MB-231



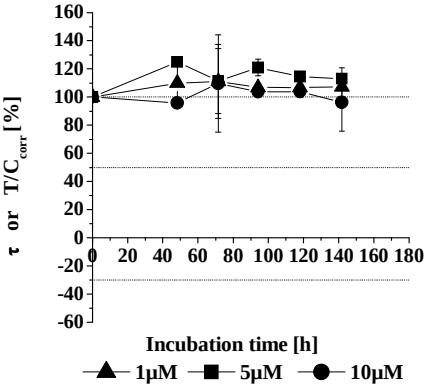
Compound 13 MDA-MB-231



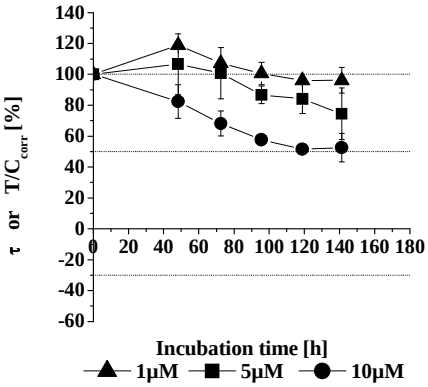
Compound 14 MDA-MB-231



Compound 15 MDA-MB-231



Compound 16 MDA-MB-231



Compound 17 MDA-MB-231

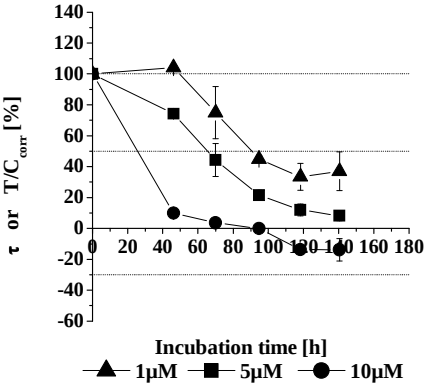
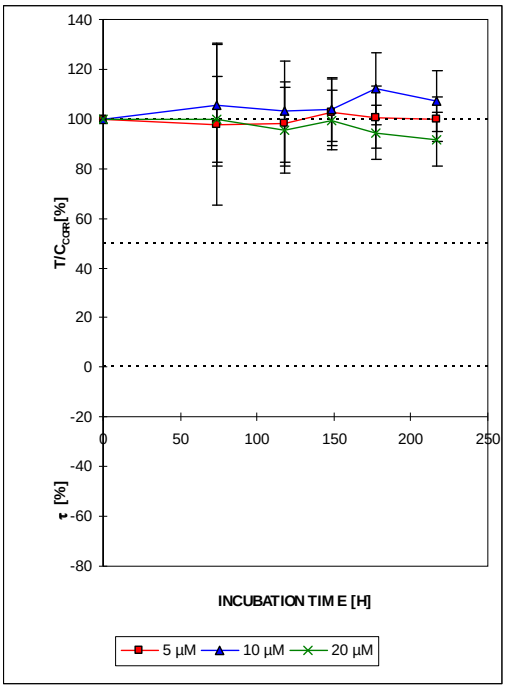
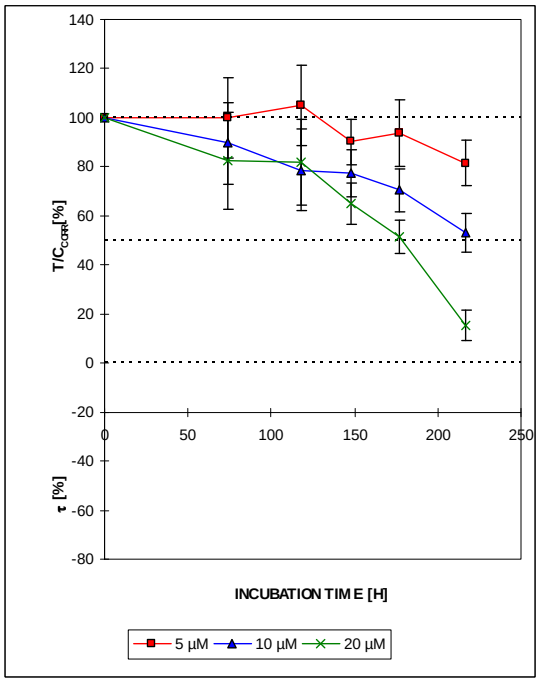


Figure S3: *In vitro* cytotoxicity of G0 and G1 on the MCF-7 cell line (from ref 17)





Dendritic Polyglycerols with Oligoamine Shells Show Low Toxicity and High siRNA Transfection Efficiency in Vitro

Wiebke Fischer,[†] Marcelo Calderón,[†] Andrea Schulz,[†] Ioanna Andreou,[‡] Martin Weber,[‡] and Rainer Haag*,[†]

Institut für Chemie und Biochemie, Freie Universität Berlin, Takustrasse 3, D-14195 Berlin, and QIAGEN GmbH, Corporate Research, QIAGEN Strasse 1, D-40724 Hilden. Received October 19, 2009; Revised Manuscript Received June 18, 2010

RNA interference provides great opportunities for treating diseases from genetic disorders, infection, and cancer. The successful application of small interference RNA (siRNA) in cells with high transfection efficiency and low cytotoxicity is, however, a major challenge in gene-mediated therapy. Several pH-responsive core shell architectures have been designed that contain a nitrogen shell motif and a polyglycerol core, which has been prepared by a two-step protocol involving the activation of primary and secondary hydroxyl groups by phenyl chloroformate and amine substitution. Each polymer was analyzed by particle size and ζ potential measurements, whereas the respective polyplex formation was determined by ethidium bromide displacement assay, atomic force microscopy (AFM), and surface charge analysis. The in vitro gene silencing properties of the different polymers were evaluated by using a human epithelial carcinoma cell (HeLaS3) line with different proteins (Lamin, CDC2, MAPK2). Polyplexes yielded similar knockdown efficiencies as HiPerFect controls, with comparably low cytotoxicity. Therefore, these efficient and highly biocompatible dendritic polyamines are promising candidates for siRNA delivery in vivo.

INTRODUCTION

Since its discovery, siRNA has been widely used to identify gene functions and has great potential for providing a new class of therapeutics (*1*). The major drawbacks are that such highly polar anionic molecules are unstable in biological fluids and display poor cellular penetration (*2*). Successful application of RNA interference in mammalian cells requires an efficient transfection agent to complex the siRNA and to provide a suitable level of siRNA in the cytosol (*3*−*5*).

In principle, two basic carrier systems, viral and nonviral transfection agents for the delivery of oligonucleotides in target cell, are under development (*6*−*8*). Viral gene therapy has a high efficacy but is plagued by serious safety risks, production and manufacturing challenges, and other limitations like cargo space (*6*). In contrast, nonviral gene delivery systems, while addressing these challenges, remain less effective (*9, 10*). Discovery and use of potent but nontoxic carriers is the key to unlocking the potential of nonviral gene delivery (*11*).

A large variety of cationic compounds were shown to be able to efficiently deliver nucleic acids into the cell. The electrostatic interaction between the negative phosphates backbones of the DNA/RNA strand with agents that carry multiple positively charged groups is the principle which is used in nonviral gene delivery methods (*3, 4, 9, 12, 13*). Cationic lipids and cationic polymers are the best studied compounds for this purpose (*14, 15*).

The interaction between a single protonated amine and the phosphate backbone of DNA is relatively weak and competes with salt binding under biological conditions. Therefore, polyamines are used to achieve DNA binding (*16*) with a higher gene transfer efficiency. From the structural point of view, polyamines used for gene transfection widely vary in their structures, which range from linear (*17*−*22*), branched (*3, 17, 21*), and hyperbranched (*23, 24*) to dendrimers (*25*−*28*). The controlled nanostructured shape, narrow molecular weight distribution, and regular and highly branched three-dimensional architecture make the dendritic polymeric scaffold an ideal candidate for biomedical applications (*29*). The general drawbacks of any perfect dendrimer are the tedious multistep preparation of higher generations and the steric hindrance and site−site interactions at the outer functional shell (*30, 31*). As an alternative, hyperbranched polymers proved to be equally efficient, because of their facile synthesis, easy purification, and straightforward scale-up. In addition, dendritic architectures with 50−70% branching seem to represent an optimal scaffold for gene delivery (*25, 30*). They also overcome such limitations as low loading capacities, solubility, and chemical stability.

Hyperbranched polyglycerol is one example of a polymer that can be obtained on a kilogram scale by an one-step ring-opening polymerization of glycidol with narrow molecular weight distribution (MWD) and with molecular weights from 1 up to 800 kDa (*32*−*34*). The easy accessibility of PGs with various sizes and degrees of branching, their chemical stability, the large number of functional groups, and their biocompatibility profile in vitro and in vivo render them ideal candidates for different biomedical applications (*30, 35*).

Several amine-functionalized PGs have been reported as potential gene vectors. In comparison to other dendritic structures, these scaffolds have the added advantage of being open and flexible, which is a prerequisite for gene interaction. Due to the polyether structure, the toxicity remains in a considerably low range. Kizhakkedathu et al. presented a complete study of blood compatibility and DNA binding of PG decorated with PEG chains and tris(2-aminoethyl)amine (*36*). The scaffolds with different degrees of amine quaternization showed insignificant effects on hemolysis, erythrocyte aggregation, complement activation, platelet activation, and coagulation. In comparison to standard cationic polymers like PEI, much lower cytotoxicity of the PG derivatives was observed. In DNA binding, a high affinity in the nanomolar range was found at low levels of quaternization, comparable to the binding affinities of cationic multivalent dendrimers with their much lower

* Correspondence should be addressed to haag@chemie.fu-berlin.de; tel.: +49-30-838-52633; fax: +49-30-838-53357.
[†] Freie Universität Berlin.
[‡] QIAGEN GmbH.

10.1021/bc900459n © 2010 American Chemical Society
Published on Web 09/21/2010

biocompatibility (*36*). In a different approach, hyperbranched PG was partially functionalized with quaternary and tertiary ammonium groups with different loading degrees (*23*). All the polymers showed interaction with DNA and formed neutral polyplexes. These quarternized polymers showed transfection efficiency comparable to that of PEI but with significantly lower cytotoxicity in mammalian cells.

The particularly safe profile of the above-described polyglycerol-based systems motivated us to prepare responsive scaffolds derived from hyperbranched PG bearing biodegradable carbamate linkers (*37*−*40*). Herein, we report the synthesis of a family of novel core−shell architectures with different shell lengths and nitrogen contents. In addition, we explored the use of hyperbranched polyglycerolamine, with primary amines in the convenient 1,2-disposition (*3*). The effects on the siRNA complexation, cytotoxicity, and transfection efficiency were systematically evaluated regarding the optimal shell length, nitrogen content, and amine disposition within the polyglycerol-based scaffolds.

EXPERIMENTAL PROCEDURES

Materials and Methods. DNA (Lamin A/C) was purchased from Qiagen and used for physicochemical studies. The sequence is as follows: (5′-CTGGACTTCCAGAAGAACATT-3′). For the knockdown experiments in cell cultures and physicochemical studies, a siRNA-duplex was obtained from Qiagen. The sequence is as follows: r(CUGGACUUCCAGAA-GAACA)d(TT). For the de-esterification experiments, Lipozyme and Novozyme (CALB L) were used, which were obtained as a gift from Novozymes A/s, Copenhagen, Denmark.

The details of the dendritic polyamine synthesis and their chemical characterization are presented in the Supporting Information.

Biodegradability Experiments. Enzyme-mediated cleavage of the aminated shells was performed with a general de-esterification method using Lipozyme and Novozyme (*41, 42*).

Ten milligrams of the dendritic polyamines were dissolved in PBS buffer (phosphate buffered saline, 10 mM, pH 7.4, 3 mL); a few drops of *n*-butanol were added, and finally, the enzyme (200 wt % of wrt dendritic polyamine carbamate) was added to the solution. The reaction mixture was stirred at 40 °C for 48 h; after completion of reaction, the enzyme was filtered off. The solvent was then removed under reduced pressure, and the residue was isolated and checked by IR chromatography.

Dynamic Light Scattering (DLS). Mean hydrodynamic diameters of the various polyamines were conducted using a NanoDLS particle sizer (Brookhaven Instruments Corp.) at 25 °C. The instrument employed an automatic, variable power laser at a wavelength of 638 nm, with the detector angle at 90°. The polyamines were measured in aqueous phosphate buffered saline solution (PBS-Buffer) at a pH of 7.4.

Surface Charge Measurements. Zeta potential measurements were carried out on a Zetasizer Nano ZS analyzer with integrated 4 mW He−Ne laser, $\lambda = 633$ nm (Malvern Instruments Ltd., U.K.). To elucidate the surface charge of the polyamines, siRNA, and polyplexes, zeta potentials were measured in aqueous phosphate buffer of pH 7.4. Dendrimer and siRNA solutions were freshly prepared by dissolving an appropriate amount of dry compound (1 mg/mL) in 0.01 M of buffer solution. After mixing and incubation for 15 min, the sample solutions were then stirred thoroughly to ensure proper mixing and dissolution. Zeta potential was measured by applying an electric field across the sample solutions using the technique of laser Doppler anemometry. All measurements were carried out at 25 °C using folded capillary cells (DTS 1060) in three replicate measurements.

Ethidium Bromide Displacement Assay. The experimental procedure to carry out the ethidium bromide (EtBr) displacement assay was based on a previously reported study (*43, 44*). Fluorescence spectroscopy measurements were performed in a JASCO FP-6500 spectrofluorometer. Excitation of the sample was done with 546 nm excitation light, and emission was measured from 560 to 700 nm. 1000 mL buffer was prepared containing 0.476 mg (2 mmol) of HEPES, 3.722 mg (10 μmol) EDTA, and 0.5492 g (9.4 mmol) NaCl, and the pH was adjusted to 7.2. 0.1242 mg of ethidium bromide was dissolved in 50 mL buffer to provide 1.26 μM concentration. In order to prepare 100 mL, 5 μM solution of DNA, 0.07625 mg of each strand of DNA was measured in an accurate scale. For preparation of double helix, incubation was done by keeping strands at 90 °C for 1 min, then 2 h in 37 °C. DNA was provided from Operon Biotechnologies GmbH. Mother solutions (1000 μM based in nitrogen content) for each tested polyamine were prepared in buffer solution. Solutions containing DNA and ethidium bromide in buffer were first incubated at room temperature for 15 min to ensure interaction between DNA and ethidium bromide. The fluorescence of plasmid DNA solution with EtBr was set at 100%. Consequently, an appropriate quantity of the corresponding polyamine was added in order to reach the desired N/P ratio followed by further incubation for 30 min after each addition. Controlled experiments were also conducted, which only contained ethidium bromide and the polyamines treated in the same manner. Results were normalized against the controlled experiments and expressed as a percent reduction of the relative fluorescence intensity. As control experiments, no indication of polyplex formation between the parent hyperbranched polyglycerol and DNA was observed.

Atomic Force Microscopy (AFM). Polyamines were imaged by atomic force microcopy (AFM) using a MultiMode IIIa scanning probe microscope with Extender Module (Digital Instruments, Inc., Santa Barbara, CA) in the dynamical modus. Backside reflective coated cantilevers were used with a typical resonance frequency in the range 140−185 kHz and a spring constant of 17−40 N/m; a width of 30 ± 5 μm, a length of 250 $\pm$ 10 μm, and a thickness of 7 ± 1 μm (Nascatec, Stuttgart). The height images were captured in the trace direction and the phase image in the retrace direction. A solution of 20 μL siRNA ($0.5-1.0 \times 10^{-5}$ M) was placed on the surface of freshly cleaved mica, which is covered with 20 μL of 10 mM of a sodium chloride solution and the spin-coating method was used with 5000 rpm, 20 min (Spin Coater SCV, J. Reinmuth, Merkkleeberg). The pure polymers were prepared with 5 μL (0.5×10^{-5} M) on freshly cleaved mica. After 10 s, the solution was blotted.

Transfection Efficacy. HeLaS3 cells were seeded in a 24 well plate at a density of 60 000 cells/well 24 h before the experiment in growth medium. Cells are completely diluted in 500 μL DMEM and cultured at 37 °C. The appropriate amount of siRNA (25 nM, 50 nM, 100 nM) was diluted in DMEM, and then, 3 or 6 μL of transfecting agent (lyophilized samples were diluted in H_2O at a concentration of 1 mg/mL, storage at 4 °C) was added and diluted in DMEM to a final volume of 100 μL. The medium was mixed and incubated at room temperature for 10 min to allow transfection-complex formation. The transfection complexes were added dropwise onto the cells. The cells were incubated at 37 °C until silencing analysis.

The silencing efficacy was analyzed on a transcription level (RNA Prep and Duplex RT-PCR, using GAPDH for normalization). Results were compared to transfections performed with lipid-based transfection reagent (HiPerFect) (*45, 46*).

RNA Preparation. For RNA isolation, cells were lysed with 350 μL RLT-Lysis buffer, and RNA was purified using RNeasy96 plates according to the standard RNeasy 96 protocol

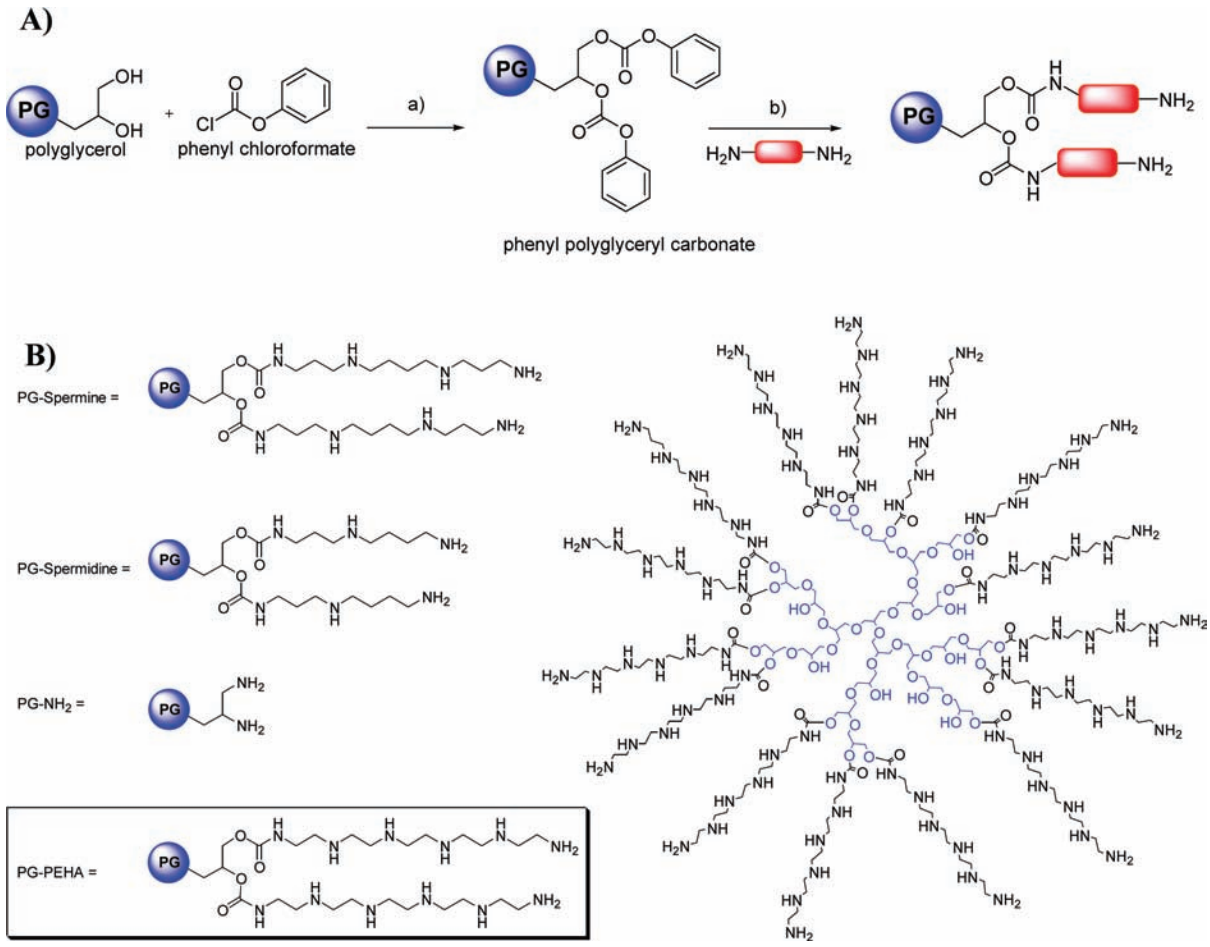


Figure 1. (A) Two-step synthesis of core−shell architectures with nitrogen-containing shell motifs. Reagents and conditions: (a) 0 °C → RT, 16 h, dry pyridine, (b) 10 equiv of amine, 0.01 equiv of DMAP, 0 °C, reflux, dry pyridine. (B) Abbreviation of the depicted structures of polyglyceryl spermine carbamate (PG-spermine), polyglycerol spermidine carbamate (PG-spermidine), polyglycerol amine (PG-NH_2), and polyglycerol pentaethylenhexamine (PG-PEHA) and the full structure of PG-PEHA (the depicted structure is a small idealized fragment of the actual polymer).

"for isolation of total RNA from animal cells using the spin technology" (QIAGEN GmbH, Germany).

Quantitative Reverse Transcribed Real-Time PCR (qRT PCR). Silencing was quantified using one-step duplex quantitative RT-PCR. 200 ng total-RNA was used for simultaneous amplification of the tested target sequence and the housekeeping gene GAPDH, which was used for normalization. For the amplification, gene-specific primer pairs and TaqMan probes were used. For reverse transcription and amplification, the RNA sample was performed using the QuantiTect Probe RT-PCR Kit (QIAGEN GmbH, Germany) and analyzed in the DNA Engine Opticon2 (MJR, USA). Reverse transcription was performed at 50 °C for 30 min, followed by a polymerase activation step (15 min at 95 °C), and amplification (40 reaction cycles; 15 s 94 °C to 60 s 60 °C). Sample amplification was run in 4 replicates, and each transfection was run in duplicate, giving a mean out of 8 values. For additional information on the quantification of the relative expression of the silenced targets, see Supporting Information.

In Vitro Cytotoxicity. Cytotoxicity was determined by LDH measurement in the supernatant of the treated cells (using the Roche Cytotoxicity Detection Kit (LDH) according to the instruction manual of the product, cat. no. 1644793). Results were compared to transfections performed with lipid-based transfection reagent (HiPerFect). Results obtained with respect to "no treatment" are a negative control representing the normal rate of cytotoxicity observed in a cell culture due to the usual biological processes such as apoptosis. "High control" refers to a positive control. Twenty-four hours after transfection of the cells, 40 μL of a 10% (w/v) Triton X-100 solution was added to the medium of nontransfected cells. After incubation at 37 °C for 1 h, the supernatant was removed and centrifuged. 100 μL of the resulting supernatant was then subjected to the cytotoxicity assay. The high control probe was diluted 1:2 and measured in parallel in order to ensure that a measurable signal will be obtained. This is a standard QC experiment that was performed to qualify whether the transfection efficiency results were due to the silencing efficiency or cell damage.

RESULTS

General Procedure of the Synthesis of Polyglycerol Amines. The synthesis of various dendritic polyamine carbamates is shown in Figure 1A. The first step yielded a quantitative formation of phenyl chloroformate, which turned out to be a useful electrophilic PG derivate (*47*). The second step involves the conjugation of the more reactive phenyl polyglyceryl carbonate with various natural and synthetic oligoamines (spermidine, spermine, and pentaethylenhexaamine) to form the biodegradable carbamate bond. Enzyme-mediated cleavage of the carbamate bonds was confirmed by disappearance of the carbonyl signal in the IR spectrum at 1697 cm^{-1} after incubation with Novozyme and Lipozyme.

Hyperbranched polyglycerol with high amine loading (PG-NH_2, 97% aminated) was synthesized as reported previously (Supporting Information) (*47*).

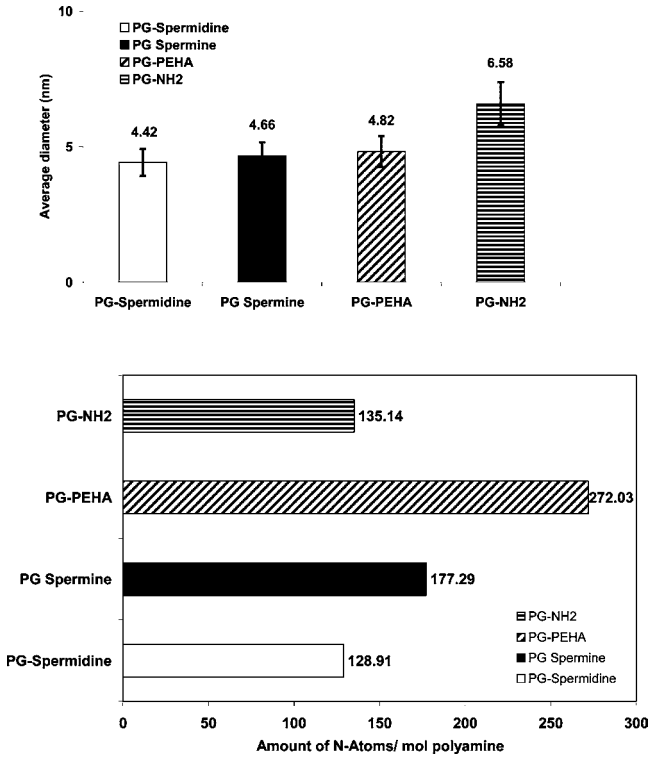


Figure 2. (a) Average diameter (nm) of the polyamines assessed by DLS measurements and (b) amount of N-atoms/mol of dendritic polyamine.

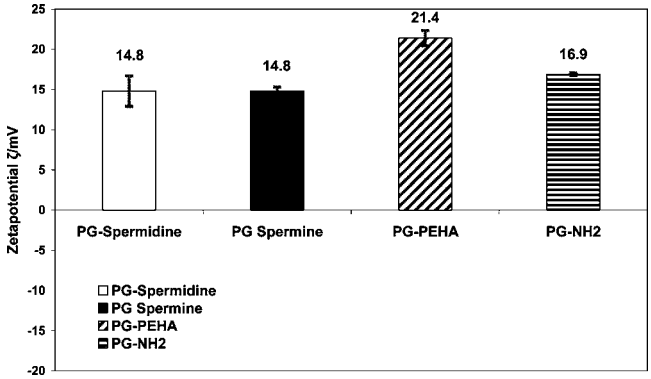


Figure 3. Zeta potential values of dendritic polyamines (pH 7.4).

Analysis of Particle Size and Surface Charge. Dynamic light scattering (DLS) was employed to determine the size of each polyamine. The measured sizes for the polyamines are shown in Figure 2A. The obtained values, which ranged from 4.4 to 6.6 nm, represent the average value of three runs. Sizes obtained for the siRNA and the polyplexes are shown in the Supporting Information in Table S1. Interestingly, the size of the polyplexes were in the range 100−300 nm in diameter.

To explore the surface charge of the different polyglycerolamines, siRNA, and polyplexes in physiological conditions, zeta potential values were measured in buffered aqueous solution at pH 7.4. Average results from the zeta potential measurements for the polyamines are illustrated in Figure 3, while the results for the siRNA and polyplexes are shown in Supporting Information Table S1. At physiological conditions, all the polyamines are highly positively charged, which is a prerequisite for complexing negatively charged genetic material. siRNA, on the other hand, proved to be highly negatively charged (−17.3 mV) at pH 7.4. As expected, the highly negatively charged surface of siRNA was neutralized after mixing with the

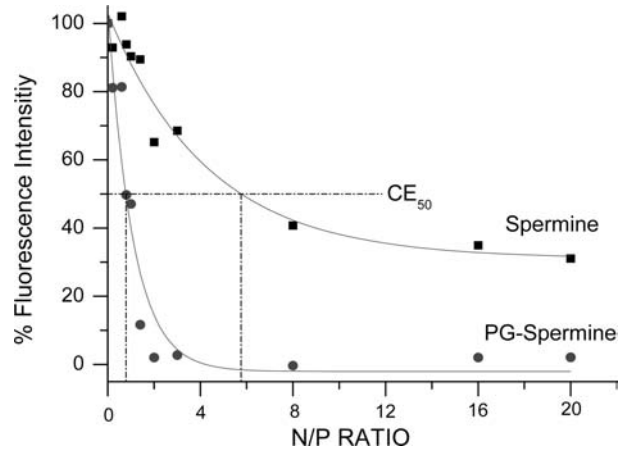


Figure 4. Titration curve for spermine and PG-Spermine.

polyamines at pH 7.4, yielding polyplexes with slightly negative or positive charges.

Ethidium Bromide Displacement Assay. With the attempt to verify multivalent interactions between the dendritic polyamines and low molecular weight gene fragments, binding affinities of the polyamines were evaluated using an ethidium bromide displacement assay (*43*, *44*) and compared with their monomeric counterparts. The intercalation of the ethidium bromide within the DNA double helix causes an enhancement in its fluorescence. Addition of polyamines caused a competition between EtBr and polyamine for intercalation in DNA which could be monitored with a decrease in fluorescent intensity. Twenty-one base pairs of DNA were compared as a model compound of the short siRNA sequences to evaluate the gene binding affinities of the different dendritic polyamines.

Comparative results for the fluorescence tritrations for spermine and its dendritic counterpart (PG-Spermine) are shown in Figure 4. Similar results were obtained for spermidine, pentaethylenhexamine, PG-Spermidine, PG-PEHA, and PG-NH_2.

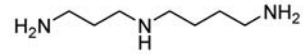
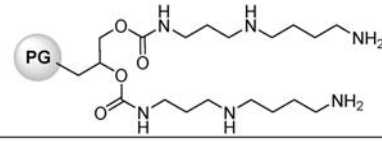
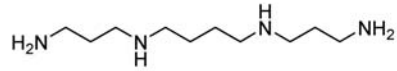
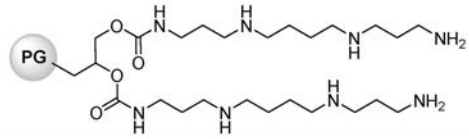
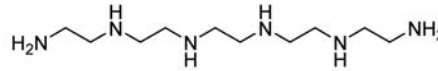
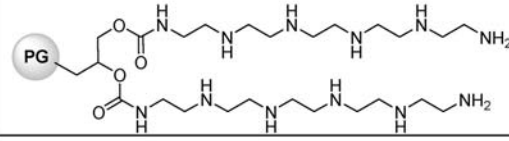
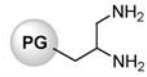
For a better comparison, the data which are presented in terms of CE_{50} indicate a nitrogen to phosphorus ratio (N/P) which caused a 50% of decrease in fluorescence intensity with respect to the ethidium bromide intercalated within the DNA double helix. The CE_{50} values for all the polyamines analyzed are presented in Table 1.

Atomic Force Microscopy. The morphology of the polyplexes was determined by atomic force microscopy (AFM). Figure 5 illustrates the condensation of siRNA by PG-PEHA and PG-NH_2. AFM images for siRNA, the dendritic polyamines, and the polyplexes formed with PG-Spermine and PG-Spermidine are shown in the Supporting Information.

SiRNA Transfection Efficiency. The ability of the dendritic polyamine to deliver siRNA to the cytosol was evaluated through the expression silencing of lamin, CDC2, and MAPK2 in the HeLaS3 cell line. A series of experiments using different siRNA concentrations (25, 50, and 100 nM) and different amounts of transfection agents (3 and 6 μL of 1 mg/mL polyamine solution) were conducted to compare the expression silencing of lamin, CDC2, and MAPK2 (shown in Supporting Information). The results were compared to the control transfection reagent HiPerFect which is the in vitro benchmark transfection reagent from Qiagen. PG-PEHA and PG-NH_2 were found to be highly efficient and thus very well suited for transfection of HeLaS3 cells; the results using 100 nM siRNA solution and 6 μL of polyamine solutions are summarized in Figure 6.

In Vitro Cytotoxicity. Cytotoxicity and quality of the cell cultures were determined by the enzymatic measuring of lactato dehydrogenasa (LDH) amounts in the supernatant of the cell

Table 1. CE_{50} Values for All Analyzed Polyamines

Sample name	Structure	CE_{50} (N/P)
Spermidine		15
PG-Spermidine		0.6
Spermine		5.8
PG-Spermine		0.8
PEHA		14.4
PG-PEHA		1.6
$PG\text{-}NH_2$		0.1

cultures. LDH is a stable enzyme, that is present in all cell types and rapidly released into the cell culture medium upon damage of the plasma membrane. Supernatant of cell treated with two different concentrations of Tween 20 was used as high control. Since PG-PEHA and $PG\text{-}NH_2$ were found to be efficient for transfection into HeLaS3 cell lines, they were tested for their cytotoxicity behavior. In both cases, almost no cytotoxicity was observed after administering 3 μL transfection agents (Figure 8). The toxicity, however, showed a slight increment upon increasing doses of transfection agents as could be seen from experiments using 6 μL of the respective transfection agents (for further details, see Supporting Information).

DISCUSSION

The synthesis of hyperbranched polyglycerol (PG) based core−shell architectures with nitrogen-containing shells allows easy control of the transfection/toxicity ratio by tuning the surface chemistry (*36*). Two kinds of architectures were explored: the first with aminated shells connected to the polyglycerol through a carbamate bond (Figure 7) and a second

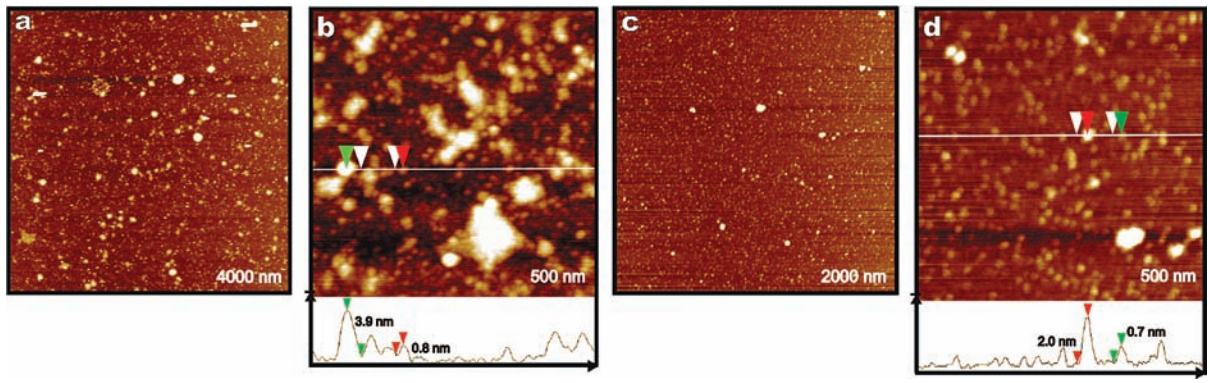


Figure 5. Typical atomic force microscope images of siRNA-polymer polyplexes. (a,b) (siRNA/PG-PEHA) and (c,d) (siRNA/$PG\text{-}NH_2$). The height differences on the surface are indicated by the color code (lighter regions indicate higher heights).

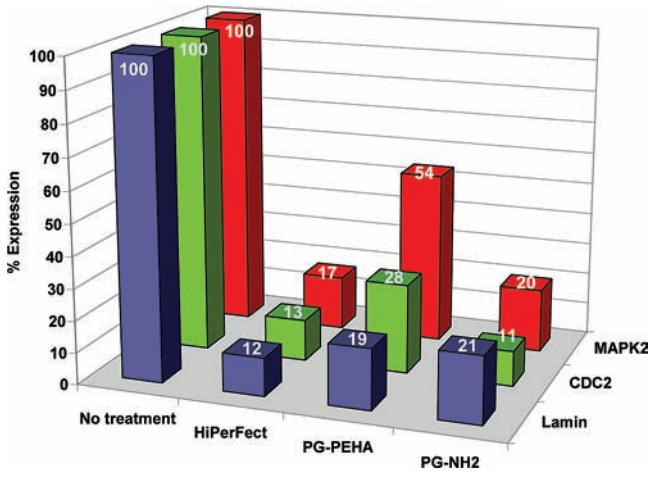


Figure 6. Transfection efficiencies of PG-PEHA and PG-NH_2 compared with HiPerFect in HeLaS3 cells. siRNAs directed against Lamin, CDC2, and MAPK2 were used. The expression of the protein without any treatment was set at 100%.

with primary amine groups spread all around the polyglycerol structure (PG-NH_2, see Supporting Information). Because the above-mentioned enzyme-mediated cleavage experiment proved the biodegradability of the carbamate bond, the cleavage of the shell in the intracellular compartments should lead to the reduction of gene affinity and its consequent intracellular release (*47*, *48*). PG-NH_2 has promising properties as a gene carrier, because it has a high charge profile with a relatively low cytotoxicity and an optimal charge/pH ratio as far as the proton sponge effect is concerned (*49*−*51*).

The synthetic approach for the preparation of the core/shell architectures was carried out according to Figure 1A. Hyperbranched polyglycerols of average molecular weight of 5 kDa reacted with excess phenyl chloroformate to yield a phenyl polyglycerol carbonate, which was then reacted with various polyamines, either naturally occurring (spermidine and spermine) or their hexaminated synthetic analogue (pentaethylenhexamine). Hyperbranched polyglycerol with high amine loading (PG-NH_2, 97% aminated) was synthesized as previously reported (*47*). Here, a three-step protocol was followed, consisting of a conversion of OH groups into mesyl (Ms) groups, transformation of Ms groups into azide (N_3) functionalities, and finally reduction of the N_3 groups to primary amine (NH_2) groups using thiphenyphosphine as reducing agent (scheme showed in Supporting Information).

Analysis of the physicochemical properties of the obtained scaffolds showed a nanosized character with diameters ranging from 4 to 7 nm. In a previous study, it was found that this size range allowed cell internalization (*49*). The study of the surface charge clearly showed that all the synthesized polyamines are highly positively charged at physiological conditions, which is a prerequisite for efficient transfection (*51*). In order to study the influence of nitrogen atoms in the shell and transfection efficiency, the size and zeta potential of each polyamine and polyplex were examined. Figure 2 shows the average sizes of each polyamine. PG-spermidine, PG-spermine, and PG-PEHA are based on PG 5 kDa core, whereas PG-NH_2 is based on a 10 kDa core. It is therefore not surprising that PG-NH_2 formed the largest particles. In the row of PG-spermidine, PG-spermine, and PG-PEHA, a specific correlation could be observed, namely, that the length of the amine increased the particle size. The zeta potential was between +14.8 mV and +21.4 mV. The average results are shown in Figure 3. Interestingly enough, we obtained the same zeta potential, even though each arm of PG-spermidine had one nitrogen less than PG-spermine. PG-PEHA showed the highest zeta potential, but with 6 nitrogens per arm, it also possessed the most nitrogens in this family. For these three PG-amino carbamates, the particle size and the charge increased

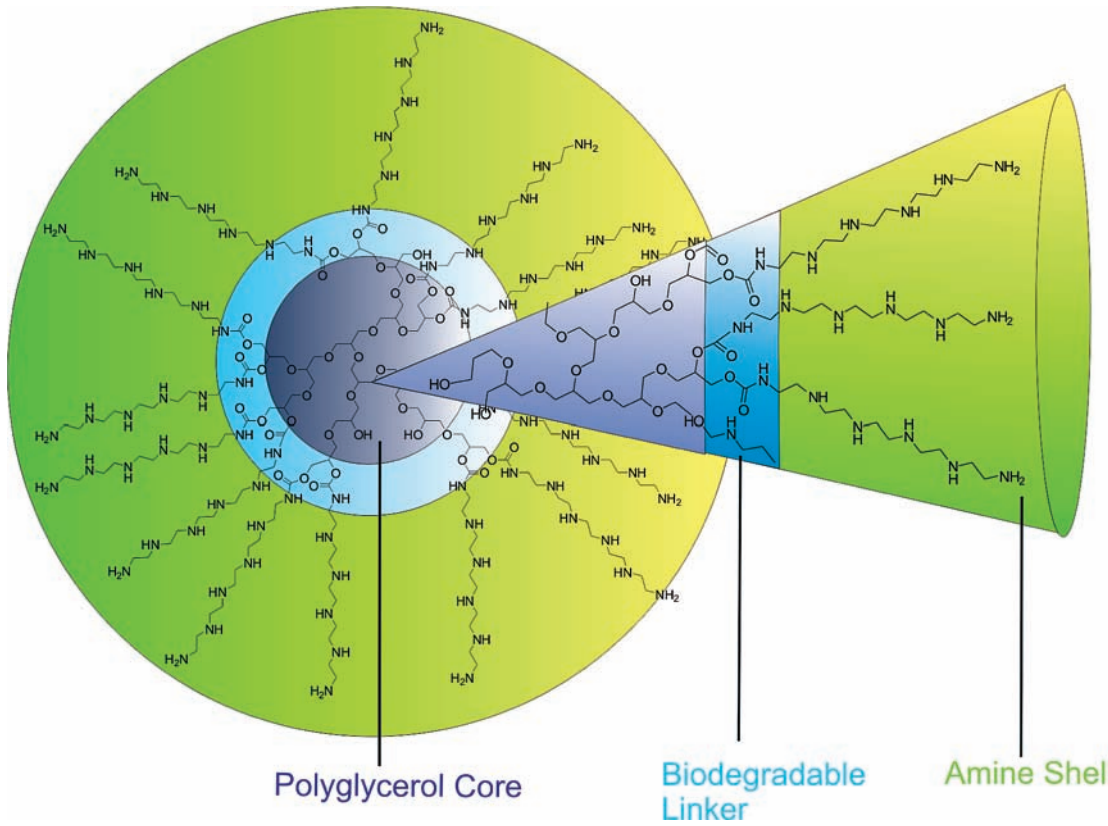


Figure 7. The core−shell architecture based on PG bearing an amine-shell connected through a biodegradable linker. The represented structure shows only a small idealized fragment of the core−shell architecture.

with the length of the amine shell, but this was not true for PG-NH_2. Even though PG-NH_2 formed the largest molecule, the zeta potential became less positive than PG-PEHA. This might be due to different pK_a values. Itaka et al. reported the unique properties of siRNA nanocarriers, which possessed two primary amines in 1,2-orientation with different pK_a values. These carriers were able to interact with the siRNA and, due to their buffering capacity, also exhibited remarkable gene knockdown (*3*).

The extent of the affinity between a nanocarrier and genetic material is crucial for the prediction of whether the polyplex will be stable in physiological conditions or not. An easy and reproducible method to characterize the binding affinity as well as the multivalency effects for gene delivery is the so-called ethidium bromide displacement assay. Here, competitive binding between EtBr and different polyamines allows a comparative analysis based on a fluorescence assay. Figure 4 compares the binding affinity of spermine and its corresponding dendritic analogue. Spermine binds to DNA with moderate strength, which is evident by the low effect over the fluorescence of EtBr. The dendritic system, on the other hand, showed significantly enhanced DNA binding because it displaced ethidium bromide effectively. In Table 1, the CE_{50} values obtained for all the analyzed compounds are summarized. Comparison of the CE_{50} values (the charge excess which causes a 50% decrease in the fluorescence intensity of EtBr) afforded similar conclusions for the spermine systems. In the case of the spermidine system, the monomeric analogue showed a low affinity for DNA (CE_{50} = 15). The dendritic analogue, on the other hand, again showed a better affinity profile (CE_{50} = 0.6). Equivalent results were observed for the PEHA (CE_{50} = 14.4) and its multivalent counterpart (CE_{50} = 1.6). Interestingly, the system with simple conversion of the hydroxyl groups from polyglycerol to amine groups had the strongest binding to DNA among the analyzed systems. The low CE_{50} value (CE_{50} = 0.1), as well as the complete exclusion of the intercalating agent, which reached 0% of fluorescence, is evidence of the strong affinity for DNA. These results showed that the hyperbranched structure of the dendritic polyamines causes specific advantages such as enhancement of the weak binding because of multivalent interactions on the dendritic surface. The high affinity provided by the multivalent arrangement makes these polyamines suitable for gene complexation and intracellular delivery.

Atomic force microscopy confirmed siRNA condensation by the dendritic polyamines and the formation of polyplexes. As shown in Figure 5, the morphology of siRNA (see also Supporting Information) changed from fibers shaped to more globular aggregates after incubation with the dendritic polyamines PG-PEHA and PG-NH_2. Equivalent results are presented in the Supporting Information for the PG-Spermine and PG-Spermidine systems. As expected, the particle size of the polyplexes decreases accordingly with higher polyamine/siRNA ratios in the complex.

The neutralization of siRNA (−17.3 mV) following mixture with the highly positive polyamines was confirmed by ζ-potential measurements. As expected, the highly negatively charged surface of siRNA was neutralized after mixing with the polyamines at pH 7.4, yielding polyplexes with slightly negative or positive charges (ranging from −0.65 to +10.73 mV). These findings showed that strong binding occurred between siRNA molecules and the dendrimers with amine groups, which indicates that an electrostatic complex is formed between the positively charged amine groups at the dendrimer and the negatively charged phosphate groups of siRNA. Interestingly, the size of the polyplexes was in the range 100−300 nm in diameter.

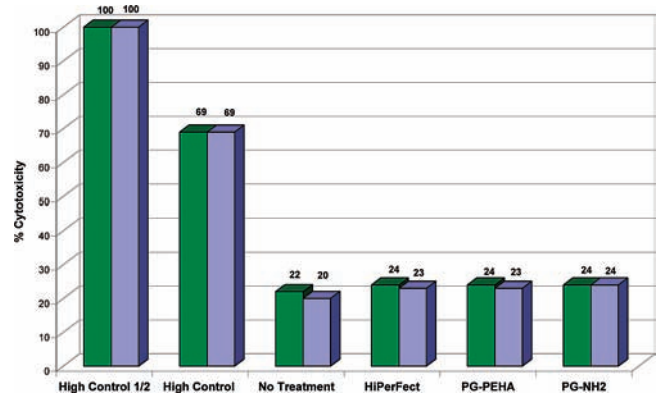


Figure 8. Cytotoxicity profile of the dendritic polyamines (3 μL of 1 mg/mL polyamine solution) against HeLa S3 cell lines.

To determine the in vitro activity of the core shell architectures, the knockdown efficiency of siRNA-polyplexes was studied in cell cultures and compared to HiPerFect. Both PG-PEHA and PG-NH_2 were found to be particularly efficient transfection vectors causing significant silencing. Transfection experiments were performed in HeLaS3 cells with siRNAs directed against different mRNAs and leading to expression reduction of the following proteins: Lamin, CDC2, and MAPK2. Detailed results are shown in Figure 6. The first column shows the expression of the protein without any treatment (control experiment). The following columns show the results of each transfection reagent in the following row: HiPerFect, PG-PEHA, and PG-NH_2. Both PG-PEHA and PG-NH_2 showed efficient silencing of Lamin, and only 19−21% of residual expression level was observed. Knockdown efficiency was in the same range as with HiPerFect. In the case of CDC2 (second row), efficient silencing was possible with PG-PEHA and PG-NH_2, although the extent of silencing was lower than that found with Lamin expression; 11% for PG-NH_2 and 28% for PG-PEHA of residual expression level in comparison to 13% for HiPerFect. In the last row, the results of MAPK2 knockdown experiments are shown. MAPK 2 could be silenced with HiPerFect. Silencing was strong with PG-NH_2 (20% of the usual expression). With PG-PEHA, residual expression level was 54%.

Due to their high surface charge under physiological conditions, the nanocarriers were also tested for cytotoxicity, which provided information about the condition of the cells and the quality of the RNAi experiment. Figure 8 shows that PG-PEHA and PG-NH_2 have similar cytotoxic effects to the standard transfectant Hyperfect, and since they are only 3−4% higher than the nontreated controls, it can be considered as low cytotoxic (*45*, *46*). These results allow us to demonstrate that the core−shell polyamine scaffolds are well-suited for further in vivo studies.

CONCLUSIONS

Herein, we reported on the synthesis and properties of responsive core−shell architectures based on polyglycerol with a star-like oligoamine shell. In contrast to polyethylenimine (PEI) and other known polyamines used as carriers in gene delivery, these novel compounds carry charges at physiological pH on their surface or shell, whereas the core is composed of a highly biocompatible noncharged aliphatic polyether. We proved that it is possible, by fine-tuning the nitrogen-containing shell, to modulate the properties of the nanocarriers toward a better transfection/toxicity ratio in vitro. We could demonstrate that PG-PEHA, which has the highest amount of amines per arm, shows the best balance between transfection and toxicity of all the biodegradable systems. Surprisingly, PG-NH_2 shows the best transfection/toxicity ratio, which may be due to the

favorable primary amines in 1,2-orientation that are mainly responsible for a high degree of DNA/siRNA binding. Because of their high biocompatibility, these nanocarriers are therefore potential candidates for in vivo applications and are currently under investigation.

ACKNOWLEDGMENT

R.H. is thankful to the German Ministry of Science (BMBF) for financial support by NanoFuture Award. Furthermore, Dr. Pamela Winchester is thanked for proofreading and Mr. Diego Galliari for graphical support in the preparation of this manuscript.

Supporting Information Available: Experimental procedures, AFM images from the dendritic polyamines and their polyplexes, and in vitro cytotoxicity results. This material is available free of charge via the Internet at http://pubs.acs.org.

LITERATURE CITED

(1) Fire, A., Xu, S., Montgomery, M. K., Kostas, S. A., Driver, S. E., and Mello, C. C. (1998) Potent and specific genetic interference by double-stranded RNA in Caenorhabditis elegans. *Nature 391*, 806–11.

(2) Oishi, M., Nagasaki, Y., Itaka, K., Nishiyama, N., and Kataoka, K. (2005) Lactosylated poly(ethylene glycol)-siRNA conjugate through acid-labile beta-thiopropionate linkage to construct pH-sensitive polyion complex micelles achieving enhanced gene silencing in hepatoma cells. *J. Am. Chem. Soc. 127*, 1624–5.

(3) Itaka, K., Kanayama, N., Nishiyama, N., Jang, W. D., Yamasaki, Y., Nakamura, K., Kawaguchi, H., and Kataoka, K. (2004) Supramolecular nanocarrier of siRNA from PEG-based block catiomer carrying diamine side chain with distinctive pKa directed to enhance intracellular gene silencing. *J. Am. Chem. Soc. 126*, 13612–3.

(4) Minakuchi, Y., Takeshita, F., Kosaka, N., Sasaki, H., Yamamoto, Y., Kouno, M., Honma, K., Nagahara, S., Hanai, K., Sano, A., Kato, T., Terada, M., and Ochiya, T. (2004) Atelocollagen-mediated synthetic small interfering RNA delivery for effective gene silencing in vitro and in vivo. *Nucleic Acids Res. 32*, e109.

(5) Spagnou, S., Miller, A. D., and Keller, M. (2004) Lipidic carriers of siRNA: Differences in the formulation, cellular uptake, and delivery with plasmid DNA. *Biochem. J. 43*, 13348–13356.

(6) Luo, D., and Saltzman, W. M. (2000) Synthetic DNA delivery systems. *Nat. Biotechnol. 18*, 33–7.

(7) Verma, I. M., and Somia, N. (1997) Gene therapy -- promises, problems and prospects. *Nature 389*, 239–42.

(8) Li, S., and Huang, L. (2000) Nonviral gene therapy -- promises and challenges. *Gene Ther. 7*, 31–4.

(9) Pack, D. W., Hoffman, A. S., Pun, S., and Stayton, P. S. (2005) Design and development of polymers for gene delivery. *Nat. Rev. Drug Discovery 4*, 581–593.

(10) Green, J. J., Zugates, G. T., Tedford, N. C., Huang, Y.-H., Griffith, L. G., Lauffenburger, D. A., Sawicki, J. A., Langer, R., and Anderson, D. G. (2007) Combinatorial modification of degradable polymers enables transfection of human cells comparable to adenovirus. *Adv. Mater. 19*, 2836–2842.

(11) Christensen, L. V., Chang, C. W., Kim, W. J., Kim, S. W., Zhong, Z., Lin, C., Engbersen, J. F., and Feijen, J. (2006) Reducible poly(amido ethylenimine)s designed for triggered intracellular gene delivery. *Bioconjugate Chem. 17*, 1233–40.

(12) Khalil, I. A., Kogure, K., Akita, H., and Harashima, H. (2006) Uptake pathways and subsequent intracellular trafficking in nonviral gene delivery. *Pharmacol. Rev. 58*, 32–45.

(13) Carmichael, G. G. (2002) Medicine: silencing viruses with RNA. *Nature 418*, 379–80.

(14) Karmali, P. P., and Chaudhuri, A. (2007) Cationic liposomes as non-viral carriers of gene medicines: resolved issues, open questions, and future promises. *Med. Res. Rev. 27*, 696–722.

(15) Martin, B., Sainlos, M., Aissaoui, A., Oudrhiri, N., Hauchecorne, M., Vigneron, J. P., Lehn, J. M., and Lehn, P. (2005) The design of cationic lipids for gene delivery. *Curr. Pharm. Des. 11*, 375–94.

(16) Vijayanathan, V., Thomas, T., Shirahata, A., and Thomas, T. J. (2001) DNA condensation by polyamines: a laser light scattering study of structural effects. *Biochemistry 40*, 13644–51.

(17) Dunlap, D. D., Maggi, A., Soria, M. R., and Monaco, L. (1997) Nanoscopic structure of DNA condensed for gene delivery. *Nucleic Acids Res. 25*, 3095–101.

(18) Brissault, B., Kichler, A., Guis, C., Leborgne, C., Danos, O., and Cheradame, H. (2003) Synthesis of linear polyethylenimine derivatives for DNA transfection. *Bioconjugate Chem. 14*, 581–7.

(19) Kichler, A., Leborgne, C., Coeytaux, E., and Danos, O. (2001) Polyethylenimine-mediated gene delivery: a mechanistic study. *J. Gene Med. 3*, 135–44.

(20) Boussif, O., Lezoualc'h, F., Zanta, M. A., Mergny, M. D., Scherman, D., Demeneix, B., and Behr, J. P. (1995) A versatile vector for gene and oligonucleotide transfer into cells in culture and in vivo: polyethylenimine. *Proc. Natl. Acad. Sci. U.S.A. 92*, 7297–301.

(21) Wightman, L., Kircheis, R., Rossler, V., Carotta, S., Ruzicka, R., Kursa, M., and Wagner, E. (2001) Different behavior of branched and linear polyethylenimine for gene delivery in vitro and in vivo. *J. Gene Med. 3*, 362–72.

(22) Kabanov, A. V., and Kabanov, V. A. (1995) DNA complexes with polycations for the delivery of genetic material into cells. *Bioconjugate Chem. 6*, 7–20.

(23) Tziveleka, L. A., Psarra, A. M., Tsiourvas, D., and Paleos, C. M. (2008) Synthesis and evaluation of functional hyperbranched polyether polyols as prospected gene carriers. *Int. J. Pharm. 356*, 314–24.

(24) Luger, K., Mader, A. W., Richmond, R. K., Sargent, D. F., and Richmond, T. J. (1997) Crystal structure of the nucleosome core particle at 2.8 A resolution. *Nature 389*, 251–60.

(25) Krämer, M., Stumbé, J. F., Grimm, G., Kaufmann, B., Krüger, U., Weber, M., and Haag, R. (2004) Dendritic polyamines: simple access to new materials with defined treelike structures for application in nonviral gene delivery. *ChemBioChem 5*, 1081–7.

(26) Lee, J. H., Lim, Y. B., Choi, J. S., Lee, Y., Kim, T. I., Kim, H. J., Yoon, J. K., Kim, K., and Park, J. S. (2003) Polyplexes assembled with internally quaternized PAMAM-OH dendrimer and plasmid DNA have a neutral surface and gene delivery potency. *Bioconjugate Chem. 14*, 1214–21.

(27) Luo, D., Haverstick, K., Belcheva, N., Han, E., and Saltzman, W. M. (2002) Poly(ethylene glycol)-conjugated PAMAM dendrimer for biocompatible, high-efficiency DNA delivery. *Macromolecules 35*, 3456–3462.

(28) Zhou, J., Wu, J., Hafdi, N., Behr, J. P., Erbacher, P., and Peng, L. (2006) PAMAM dendrimers for efficient siRNA delivery and potent gene silencing. *Chem. Commun. (Camb.)* 2362–4.

(29) Service, R. F. (1995) Dendrimers: dream molecules approach real applications. *Science 267*, 458–459.

(30) Haag, R. (2001) Dendrimers and hyperbranched polymers as high-loading supports for organic synthesis. *Chemistry 7*, 327–35.

(31) Roller, S., Siegers, C., and Haag, R. (2004) Dendritic polyglycerol as a high-loading support for parallel multistep synthesis of GABA lactam analogues. *Tetrahedron 60*, 8711–8720.

(32) Sunder, A., Hanselmann, R., Frey, H., and Mülhaupt, R. (1999) Controlled synthesis of hyperbranched polyglycerols by ring-opening multibranching polymerization. *Macromolecules 32*, 4240–4246.

(33) Vandenberg, E. J. (1985) Polymerization of glycidol and its derivatives: a new rearrangement polymerization. *J. Polym. Sci.: Polym. Chem. 23*, 915–949.

(34) Kainthan, R. K., Muliwan, E. B., Hatzikiriakos, S. G., and Brooks, D. E. (2006) Synthesis, characterization, and viscoelastic properties of high molecular weight hyperbranched polyglycerols. *Macromolecules 39*, 7707–7718.

(35) Calderón, M., Quadir, M. A., Sharma, S. K., and Haag, R. (2010) Dendritic polyglycerols for biomedical applications. *Adv. Mater. 22*, 190–218.

(36) Kainthan, R. K., Gnanamani, M., Ganguli, M., Ghosh, T., Brooks, D. E., Maiti, S., and Kizhakkedathu, J. N. (2006) Blood compatibility of novel water soluble hyperbranched polyglycerol-based multivalent cationic polymers and their interaction with DNA. *Biomaterials 27*, 5377–90.

(37) Gillies, E. R., Dy, E., Fréchet, J. M. J., and Szoka, F. C. (2005) Biological evaluation of polyester dendrimer: poly(ethylene oxide) "bow-tie" hybrids with tunable molecular weight and architecture. *Mol. Pharmaceutics 2*, 129–138.

(38) Almutairi, A., Guillaudeu, S. J., Berezin, M. Y., Achilefu, S., and Fréchet, J. M. J. (2007) Biodegradable pH-sensing dendritic nanoprobes for near-infrared fluorescence lifetime and intensity imaging. *J. Am. Chem. Soc. 130*, 444–445.

(39) Welsh, D. J., Jones, S. P., and Smith, D. K. (2009) On-off" multivalent recognition: degradable dendrons for temporary high-affinity DNA binding. *Angew. Chem. 121*, 4107–4111.

(40) Calderón, M., Quadir, M. A., Strumia, M., Haag, R. (2010) Functional dendritic polymer architectures as stimuli responsive nanocarriers, *Biochimie. 92*, 1242−1251.

(41) Bashir, N. B., Phythian, S. J., Reason, A. J., and Roberts, S. M. (1995) Enzymatic esterification and de-esterification of carbohydrates: synthesis of a naturally occurring rhamnopyranoside of p-hydroxybenzaldehyde and a systematic investigation of lipase-catalysed acylation of selected arylpyranosides. *J. Chem. Soc., Perkin Trans. 1*, 2203–2222.

(42) Mora-Pale, J. M., Pérez-Munguía, S., González-Mejía, J. C., Dordick, J. S., and Bárzana, E. (2007) The lipase-catalyzed hydrolysis of lutein diesters in non-aqueous media is favored at extremely low water activities. *Biotechnol. Bioeng. 98*, 535–542.

(43) Cain, B. F., Baguley, B. C., and Denny, W. A. (1978) Potenial antitumor agents. 28. Deoxyribonucleic acid polyintercalating agents. *J. Med. Chem. 21*, 658–68.

(44) Kostiainen, M. A., Smith, D. K., and Ikkala, O. (2007) Optically triggered release of DNA from multivalent dendrons by degrading and charge-switching multivalency. *Angew. Chem. 119*, 7744–7748.

(45) N'Diaye, M., Le Ferrec, E., Lagadic-Gossmann, D., Corre, S., Gilot, D., Lecureur, V., Monteiro, P., Rauch, C., Galibert, M. D., and Fardel, O. (2006) Aryl hydrocarbon receptor- and calcium-dependent induction of the chemokine CCL1 by the environmental contaminant benzo[a]pyrene. *J. Biol. Chem. 281*, 19906–15.

(46) Carralot, J. P., Kim, T. K., Lenseigne, B., Boese, A. S., Sommer, P., Genovesio, A., and Brodin, P. (2009) Automated high-throughput siRNA transfection in raw 264.7 macrophages: a case study for optimization procedure. *J. Biomol. Screen. 14*, 151–60.

(47) Roller, S., Zhou, H., and Haag, R. (2005) High-loading polyglycerol supported reagents for Mitsunobu- and acylation-reactions and other useful polyglycerol derivatives. *Mol. Divers. 9*, 305–16.

(48) Haag, R. (2004) Supramolecular drug-delivery systems based on polymeric core-shell architectures. *Angew. Chem., Int. Ed. Engl. 43*, 278–82.

(49) Khandare, J., Mohr, A., Calderon, M., Welker, P., and Licha, K., Haag, R. Structure-biocompatibility relationship of dendritic polyglycerol derivatives. *Biomaterials. 31*, 4268−4277.

(50) Ofek, P., Fischer, W., Calderón, M., Haag, R., and Satchi-Fainaro, R. (2010) *In vivo* delivery of small interfering RNA to tumors and their vasculature by novel dendritic nanocarriers. *FASEB J. 24*, 3122−3134.

(51) Fischer, W., Calderón, M., and Haag, R. (2010) Hyperbranched Polyamines for Transfection, in *Nucleic Acid Transfection (Top Curr Chem)*; pp 35, Springer-Verlag Berlin, Heidelberg, 10.1007/128_2010_64.

(52) Zelphati, O., and Szoka, F. C., Jr. (1996) Mechanism of oligonucleotide release from cationic liposomes. *Proc. Natl. Acad. Sci. U.S.A. 93*, 11493–11498.

BC900459N

SUPPORTING INFORMATION

for

Dendritic polyglycerols with oligoamine shells show low toxicity and high siRNA transfection efficiency in vitro

Wiebke Fischer,[†] Marcelo Calderón,[†] Andrea Schulz,[†] Ioanna Andreou,[‡] Martin Weber,[‡] and Rainer Haag[†*]

[†] Institut für Chemie und Biochemie, Freie Universität Berlin, Takustrasse 3, D-14195 Berlin

[‡] QIAGEN GmbH, Corporate Research, QIAGEN Strasse 1, D-40724 Hilden

*Correspondence should be addressed to haag@chemie.fu-berlin.de; tel.: +49-30-838-52633; fax: +49-30-838-53357

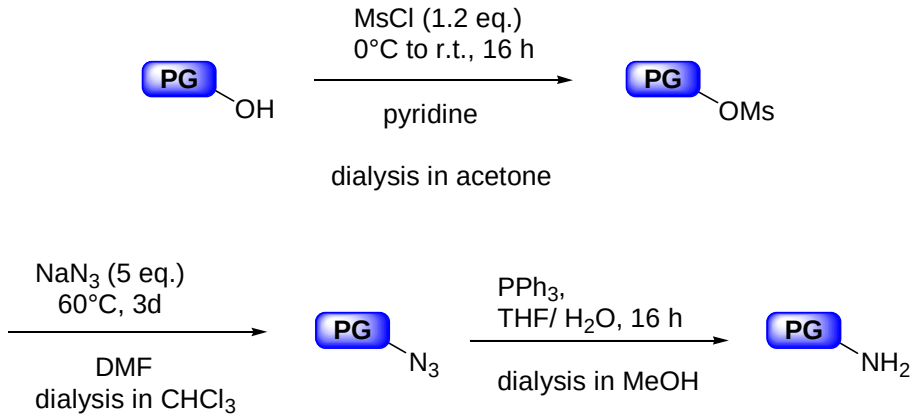
Materials and Methods. All solvents were purified by conventional methods prior to use. HPLC gradient solvents, as well as deuterated solvents, and all reagents were used as purchased from commercial suppliers without any prior purification. All reactions which involved air or water sensitive compounds were carried out in dried flasks under an argon atmosphere. Water of Millipore quality (resistivity ~18 MΩ·cm^{-1}, pH = 5.6 ± 0.2) was used in all experiments and for preparation of all samples.

Hyperbranched polyglycerols (dPGs) with various molecular weights (5 and 10 kDa) and functionalities were prepared according to our previously published procedures [1, 2]. Several studies have demonstrated the biocompatibility of dendritic PGs, and its potential safe profile for in vitro and in vivo applications. In preliminary cell culture experiments, hyperbranched PG with a molecular weight of 5 kDa showed absolutely no toxicity at cellular level.[3] Brooks et al. reported several studies including a comprehensive analysis of PGs in a broad MW distribution and with different compositions [4-6]. Both linear and hyperbranched PGs were reported to have a similar or even better biocompatibility profile than PEG with MW ranging from 4.2 kDa to 670 kDa. In vivo studies conducted on mice revealed no sign of toxicity after i.v. injection of the dose up to 1 g/kg. For a period of 28 days no sign of weight disturbances

or untoward effects were observed. Although the biocompatibility of polymers in general is a function of molecular weight, no MW dependant toxicity was found up to 540 kDa for dendritic PG architectures.

^{1}H and ^{13}C NMR spectra were recorded on a Bruker AC 250 (250 MHz; 125 MHz), on a Jeol ECX-400 400 MHz spectrometer or on an AMX 500 (500 MHz) instrument at room temperature. Chemical shifts δ are given in parts per million (ppm) according to the literature [7].

Synthesis of polyglycerolamine. PG-NH_2 of average molecular weight 10 kDa with quantitative conversion of the OH-groups to NH_2 (~97 %) was achieved according to published procedures [1]. ^{1}H-NMR (300 MHz, CD_3OD): δ = 4.01–3.21 (PG), 3.31−2.40 (functionalized PG-groups); ^{13}C-NMR (75 MHz, CD_3OD): δ = 83.0–65.5 (PG), 55.5–43.6 (functionalized PG-groups); IR (KBr): ν = 3354, 2874, 2362, 2338, 2103, 1576, 1473, 1338, 1104, 820, 668 cm^{-1}.



Scheme S1. Synthesis of polyglycerol amine PG-NH_2

Synthesis of phenyl polyglyceryl carbonate (carbonic acid phenylpolyglyceryl ester) (Scheme 1). [1] This reaction was performed under an inert gas atmosphere and exclusion of water. Phenyl chloroformate (19.6 ml, 24.4 g, 156 mmol, 1.2 equivalents (eq.)) was added to absolute (abs.) pyridine (100 ml) in a three necked 500-ml flask with drop funnel, thermometer, and magnetic stirrer while stirring at 0 °C. On addition a white precipitate formed.

Subsequently, a solution of polyglycerol (average molecular weight 5 kDa, 10.0 g, 135 mmol OH-groups) in abs. pyridine (80 ml) was added at 0 °C. The mixture was stirred in the thawing ice bath for 16 h. Then H_2O and $CHCl_3$ were added until the solid was dissolved. The phases were separated and the organic layer was extracted three times with $CHCl_3$. The

combined organic layers were dried over $MgSO_4$, concentrated in vacuo, and dialysed in $CHCl_3$ to give a brown honey-like product. ^{1}H-NMR (500 MHz, $CDCl_3$): δ= 7.61–6.87 (Ar-H), 5.32−4.92 (functionalized secondary PG-groups), 4.76−4.10 (functionalized primary PG-groups), 4.05−3.06 (PG), 1.73 (PG-starter), 0.86 (PG-starter); ^{13}C-NMR (125 MHz, $CDCl_3$): δ = 153.5 (1-C), 151.1 (2-C), 129.6 (4-C/6-C), 126.2 (5-C), 121.1 (3-C/7-C); IR (KBr): ν = 3125–2750, 1761, 1592, 1494, 1458, 1237, 1072, 1023, 913, 775, 727, 688 cm^{-1}.

Synthesis of polyglyceryl amino carbamate (Scheme 1). [1] A solution of phenyl polyglyceryl carbonate (1 eq.) in p.a. pyridine was dropped over 2 h at 0 °C into an emulsion of the desired amine (10 eq.) and 4-(dimethylamino)-pyridine (DMAP; 0.01 eq.) in pyridine. The mixture was refluxed for 16 h and concentrated in vacuo after cooling. After removal of pyridine residues in high vacuum, the raw product was dialyzed in methanol (MeOH) to give a brown honey-like product. The structures of the obtained polyamines were confirmed by the proton NMR characterization and by FT-IR. ^{1}H-NMR (PG-Spermidine, 250 MHz, CD_3OD): *δ* = 4.40–3.03 (PG), 1.41 (PG-starter); 1.55- 1.67 (-(CH_2)-NH_2)-, 2.61- 2.65 (-(CH_2)-NH)- , 3.09- 3.35 (-(CH_2)-NH)-, 4.01- 4.45 (CH_2-CH_2-NH-O-CO; ^{13}C-NMR (75 MHz, D_2O): *δ* = 159.4 (CO), 81.2–59.4 (PG); ^{1}H-NMR (PG-Spermine, 250 MHz, CD_3OD): *δ* = 3.96–3.41 (PG), 1.41 (PG-starter); 1.80- 1.41(-(CH_2)-(CH_2)-NH_2)-, 2.75- 2.30 (-(CH_2)-NH)-, 4.41- 3.97 (CH_2-CH_2-NH-O-CO; ^{13}C-NMR (75 MHz, D_2O): *δ* = 159.4 (CO), 81.2–59.4 (PG); ^{1}H-NMR (PG-PEHA, 250 MHz, CD_3OD): δ =4.40–3.03 (PG), 1.41 (PG-starter), 0.89 (PG-starter); 13CNMR (75 MHz, D_2O): δ = 159.4 (CO), 81.2–59.4 (PG) 40.2- 50.0 (PEHA); IR (KBr): ν = 3328, 2876, 2361, 1721, 1630, 1514, 1461, 1278, 1180, 1077 cm^{-1}.

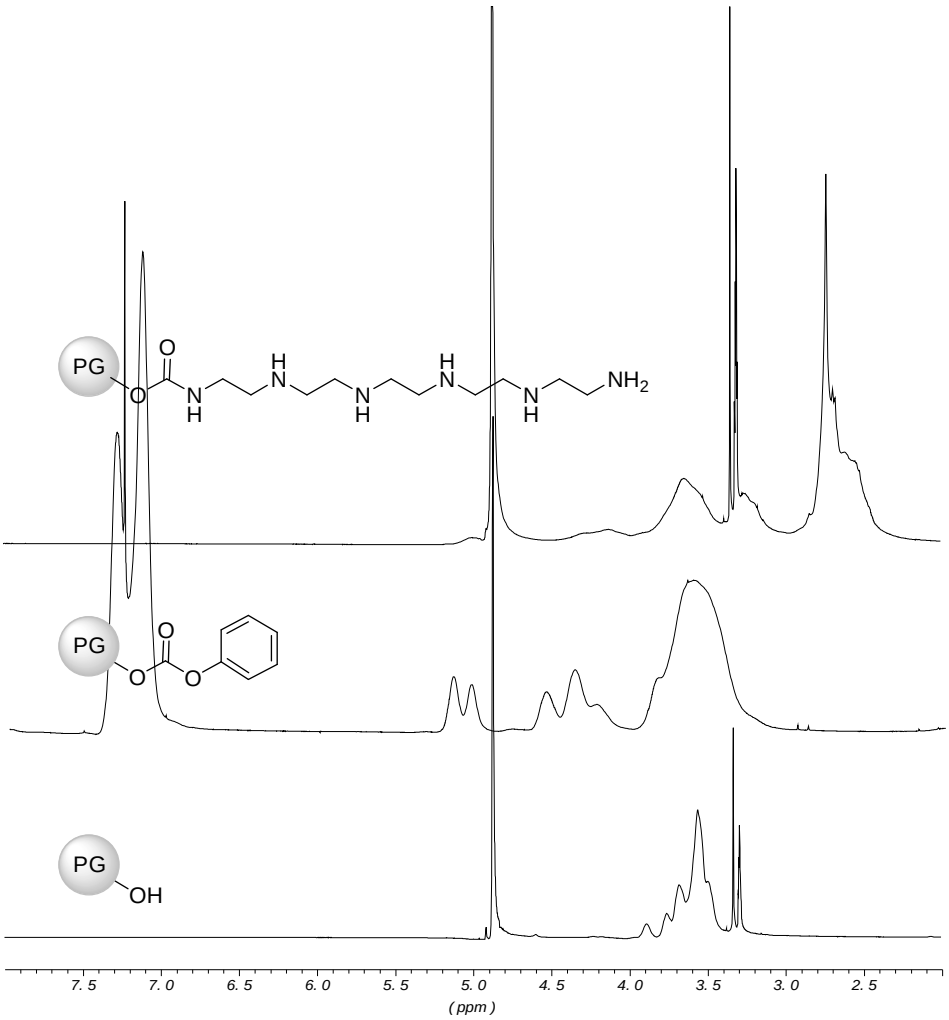


Figure S1. ^{1}H-NMR analysis of the two step synthesis of core-shell architectures with nitrogen-containing shell motifs.

Table S1. Z potential and diameter values for siRNA and polyplexes.

Sample name	**Z potential (mV)**[a]	**Diameter polyplex (nm)**[b]
siRNA	-17.28	----
PG-Spermidine / siRNA	+3.76	296.9
PG-Spermine / siRNA	+10.73	332.4
PG-PEHA / siRNA	-2.20	200.7
PG-NH_2 / siRNA	-0.65	128.4

[a] mV with I = 0.01, ±0.2 and polymer concentration 1 mg ml^{-1}. [b] Mean diameter determined by DLS in PBS solution pH 7.4.

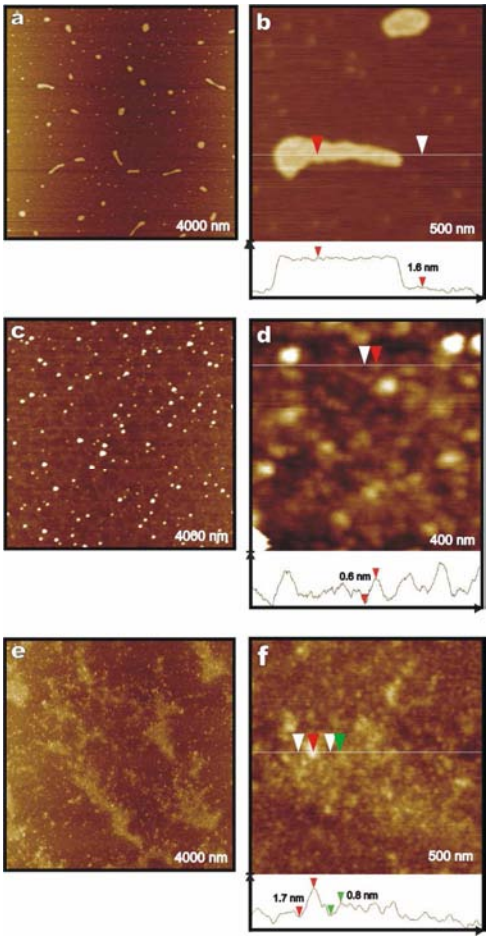


Figure S2. Atomic force microscope images of siRNA (a,b), PG-PEHA (c, d), and PG-NH_2 (e, f). The height differences on the surface are indicated by the color code: lighter regions indicate higher heights.

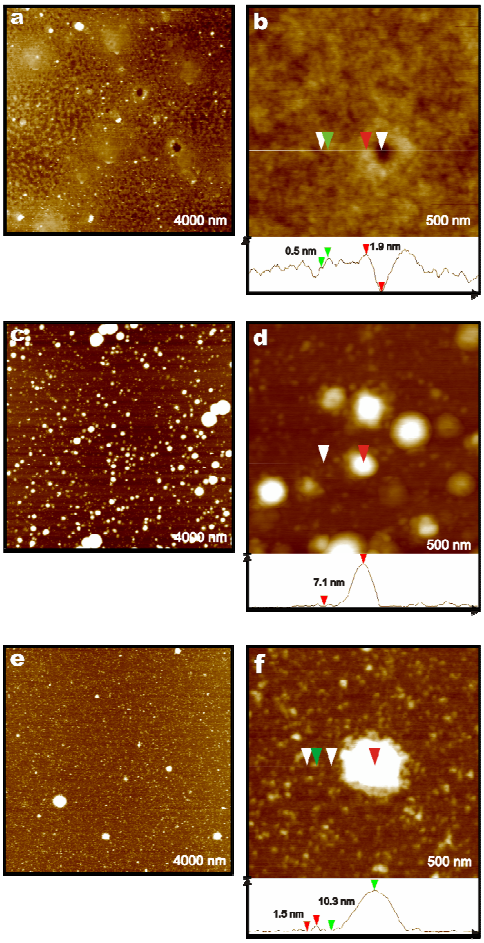


Figure S3. Atomic force microscope images of PG-Spermine (a,b), siRNA/PG-Spermine 1:1 (c, d), and siRNA/PG-Spermine 1:2 (e, f). The height differences on the surface are indicated by the color code: lighter regions indicate higher heights.

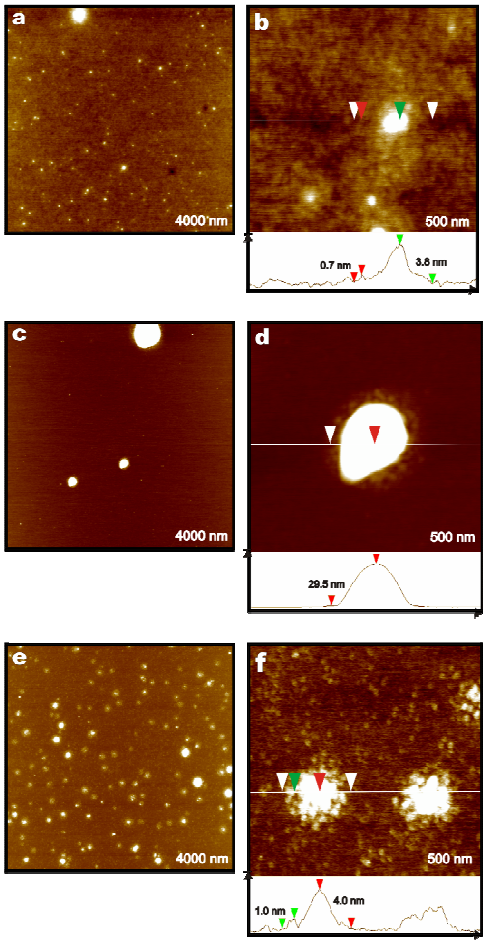


Figure S4. Atomic force microscope images of PG-Spermidine (a,b), siRNA/PG-Spermidine 1:1 (c, d), and siRNA/PG-Spermidine 1:2 (e, f). The height differences on the surface are indicated by the color code: lighter regions indicate higher heights.

Quantification of the relative expression of silenced targets.

In general, the relative expression of the given target gene in treated cells is compared to the relative expression of the target gene in control samples (untreated cells). For the quantification of the silencing effect the relative expression of the target gene was normalized to the expression of a reference gene, that is a constitutive expressed gene, a so called house keeping gene, represented by GAPDH (glyceraldehydes-3-phosphate-dehydrogenase). Moreover, the silencing effect was determined by comparing the expression of the target-gene related to the house keeping gene expression for both; samples, which were silenced by RNAi and control samples without treatment. The use of the duplex amplification and the described strategy of normalization reduces the variation of the expression results, which may occur because of variations in the living cell number or in the RNA purification or RT efficiency. These variations will affect to the same degree the tested target gene and the house keeping

gene, so that the relative expression will represent real differences between the compared samples. One advantage of our method is also that there is no need for accurate OD quantification of the isolated RNA and the appropriate dilution prior to reaction setup.
The evaluation of silencing, is based on the determination of the quotient of cts (reference gene in the treated sample divided by the reference gene in the untreated sample). This quotient represents the factor of variation of the house keeping gene between two samples. The multiplication of this quotient with the target-ct of the treated sample is resulting in the normalized target-ct. The difference (Δct) between the target-ct of the untreated sample and the normalized target-ct of the treated sample represents a numerical value of the difference in relative target gene expression between both samples. The relative expression (RE) in percent of the target gene of the treated sample compared to the target of the untreated is given by the formula [$RE = 2^{\Delta ct} \times 100$]. (see attached RNAi paper for comparisons and further details)
GFP-siRNA is a standard siRNA control which was used as a negative control in cells that do not express the GFP protein. This GFP-siRNA is active and able to enter the RISC and the RNAi machinery. This siRNA is a very suitable negative control for comparing the putative side effects of polyplexes (transfection agents/ siRNA complex), and many independent studies have been performed.[8]

In vitro cytotoxicity results.

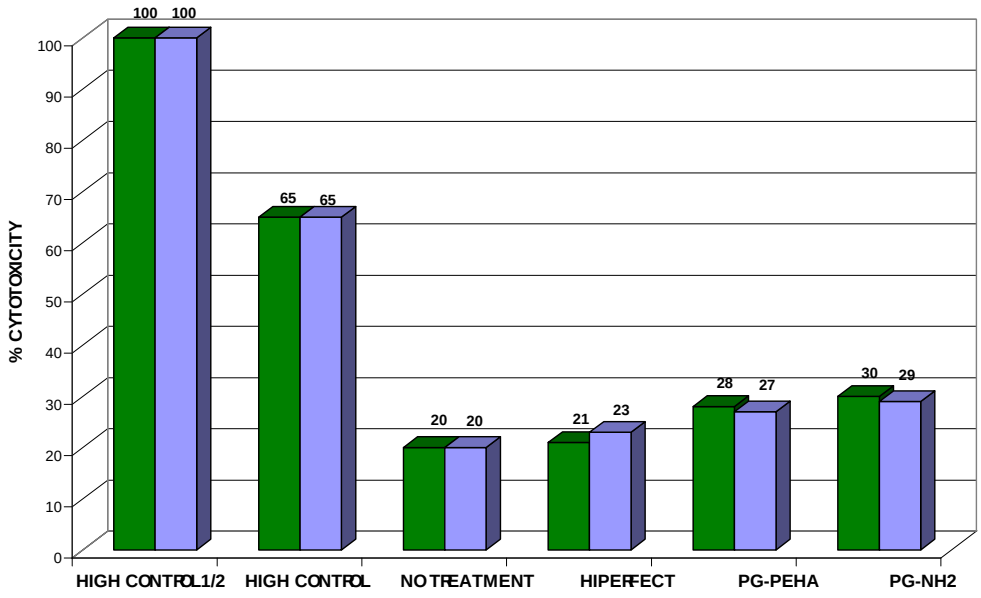


Figure S5. Cytotoxicity profile of the dendritic polyamines (6 µl of 1 mg/ml polyamine solution) against HeLa S3 cell lines.

[1] S. Roller, H. Zhou, R. Haag, *Mol Divers* **2005**, *9*, 305.
[2] H. Turk, R. Haag, S. Alban, *Bioconjug Chem* **2004**, *15*, 162.
[3] H. Frey, R. Haag, *J. Biotechnol.* **2002**, *90*, 257.
[4] R. K. Kainthan, D. E. Brooks, *Biomaterials* **2007**, *28*, 4779.
[5] R. K. Kainthan, S. R. Hester, E. Levin, D. V. Devine, D. E. Brooks, *Biomaterials* **2007**, *28*, 4581.
[6] R. K. Kainthan, J. Janzen, E. Levin, D. V. Devine, D. E. Brooks, *Biomacromolecules* **2006**, *7*, 703.
[7] H. M. M. Hesse, B. Zeeh, *Spektroskopische Methoden in der organischen Chemie*, 7 ed., Thieme Georg Verlag, **2005**.
[8] S. M. Elbashir, J. Harborth, W. Lendeckel, A. Yalcin, K. Weber, Thomas Tuschl, *Nature* **2001**, *411*, 494-498.

Mixtures of Poly(triethylenetetramine/cystamine bisacrylamide) and Poly(triethylenetetramine/cystamine bisacrylamide)-*g*-poly(ethylene glycol) for Improved Gene Delivery

Jonathan H. Brumbach,[†] Chao Lin,[‡] James Yockman,[†] Won Jong Kim,[§] Katherine S. Blevins,[†] Johan F. J. Engbersen,[‡] Jan Feijen,[‡] and Sung Wan Kim*,[†]

Department of Pharmaceutics and Pharmaceutical Chemistry, University of Utah, 20 South 2030 East, Salt Lake City, Utah 84112-5820, Department of Polymer Chemistry and Biomaterials, University of Twente, P.O. Box 217, 7500 AE Enschede, The Netherlands, and Department of Chemistry, BK21 program, Polymer Research Institute, Pohang University of Science and Technology, San 31, Hyoja-dong, Pohang 790−784, Korea. Received November 25, 2009; Revised Manuscript Received July 21, 2010

Branched disulfide-containing poly(amido ethyleneimines) (SS-PAEIs) are biodegradable polymeric gene carrier analogues of the well-studied, nondegradable, and often toxic branched polyethylenimines (bPEIs), but with distinct advantages for cellular transgene delivery. Clinical success of polycationic gene carriers is hampered by obscure design and formulation requirements. This present work reports synthetic and formulation properties for a graft copolymer of poly(ethylene glycol) (PEG) and a branched SS-PAEI, poly(triethylentetramine/cystaminebisacrylamide) (p(TETA/CBA)). Several laboratories have previously demonstrated the advantages of PEG conjugation to gene carriers, but have also shown that PEG conjugation may perturb plasmid DNA (pDNA) condensation, thereby interfering with nanoparticle formation. With this foundation, our studies sought to mix various amounts of p(TETA/CBA) and p(TETA/CBA)-g-PEG2k to alter the relative amount of PEG in each formulation used for polyplex formation. The influence of different PEG/polycation amounts in the formulations on polymer/nucleic acid nanoparticle (polyplex) size, surface charge, morphology, serum stability and transgene delivery was studied. Polyplex formulations were prepared using p(TETA/CBA)-g-PEG2k, p(TETA/CBA), and mixtures of the two species at 10/90 and 50/50 volumetric mixture ratios (wt/wt %), respectively. As expected, increasing the amount of PEG in the formulation adversely affects polyplex formation. However, optimal polymer mixtures could be identified using this facile approach to further clarify design and formulation requirements necessary to understand and optimize carrier stability and biological activity. This work demonstrates the feasibility to easily overcome typical problems observed when polycations are modified and thus avoids the need to synthesize multiple copolymers to identify optimal gene carrier candidates. This approach may be applied to other polycation−PEG preparations to alter polyplex characteristics for optimal stability and biological activity.

INTRODUCTION

Gene therapy is a feasible alternative to conventional therapies that simply manage symptoms of diseases and lack an effective treatment. However, gene therapy's clinical success is impaired by uncertain design and formulation requirements for safe and efficient nucleic acid delivery to cells. Recent research advancements have improved carrier safety and efficacy through carrier chemical modification to alter surface charge and/or tissue specificity using poly(ethylene glycol) (PEG) and/or cell-specific targeting ligands (*1*). Polymeric nonviral gene carriers have distinct advantages, because if designed prudently, they are nonimmunogenic and are easily modified to exhibit multifunctional properties (*2*). Nonviral polycations are also relatively cost-effective, easy to produce industrially, and can carry relatively large amounts of therapeutic nucleic acid (*3, 4*).

Many structurally different polymers and copolymers consisting of linear, branched, or dendritic architectures have been tested for their efficacy and suitability for in vitro and in vivo gene delivery. Polyethylenimine gene carriers (PEIs) have been most rigorously studied and are a standard for polycationic gene carriers, because they easily condense DNA into nucleic acid/polycation nanoparticles (polyplexes) that protect nucleic acid from serum nuclease degradation, as well as exhibit relatively high transgene delivery and expression in many cell types in vitro and in vivo. Unfortunately, PEIs often exhibit cellular toxicity due to intracellular accumulation of nondegradable polycations (*3, 5*). Increased PEI molecular weight and branching, which influence polycation charge density, correlate not only with increased transgene expression, but also with cellular toxicity. Conversely, low molecular weight PEIs show reduced cellular toxicity that correlates with reduced transgene expression (*6, 7*). As predicted, the design of degradable polycationic gene carriers such as the reducible disulfide-containing poly(amidoamine) (SS-PAA) and poly(amido ethylenimines) (SS-PAEI), as well as hydrolyzable poly(*β*-amino ester) families, have demonstrated comparable or improved cellular gene delivery and less cell toxicity when compared to PEIs (*8*−*10*). Reducible SS-PAEIs are synthetic analogues of the PEI family but have the aforementioned advantages of improved biological activity and compatibility (*11*). A recent abstract by Martello et al. showed that hyperbranched SS-PAAs can condense plasmid DNA (pDNA) into polyplexes with sizes similar to bPEI25 kDa, encouraging further functional studies (*12*).

Often, cationic polyplexes interact with net negatively charged proteins found in serum, leading to particle aggregation and reduced efficacy in vitro and in vivo (*13*−*15*). In order to

* Corresponding author. Prof. Sung Wan Kim, Department of Pharmaceutics and Pharmaceutical Chemistry, University of Utah, 20 S. 2030 E. Salt Lake City, UT 84112-5820, USA. Tel: 01 801 581 6801, Fax: +01 801 581 7848, E-mail: sw.kim@pharm.utah.edu.

[†] University of Utah.

[‡] University of Twente.

[§] Pohang University of Science and Technology.

10.1021/bc900522x © 2010 American Chemical Society
Published on Web 09/30/2010

overcome this hurdle, poly(ethylene glycol) (PEG) conjugation to polycations has been employed, and studies have shown that PEGylation often improves carrier function in the presence of serum. However, previous studies have also clearly shown that increasing targeting ligand and/or PEG conjugation to PEIs, especially to low molecular weight (LMW) PEI of ~5 kDa, adversely affects polyplex formation and carrier function (*16, 17*).

In order to better design and formulate hyperbranched SS-PAEIs and their corresponding graft PEG copolymers, several SS-PAEI polycationic gene carriers are synthesized and the influence of varying the relative PEG/polycation amounts on polyplex formation, size, surface charge, morphology, serum stability, and ultimately biological activity are studied. Polyplex formulations were prepared using a known SS-PAEI grafted PEG, p(TETA/CBA)5k-g-PEG2k, or by mixing the two species at 10/90 and 50/50 volumetric ratios, respectively. Altering the formulation mixture was employed to identify a suitable strategy to easily alter the gene carrier's physiochemical properties and identify a suitable formulation with synthetic ease to enhance carrier efficacy.

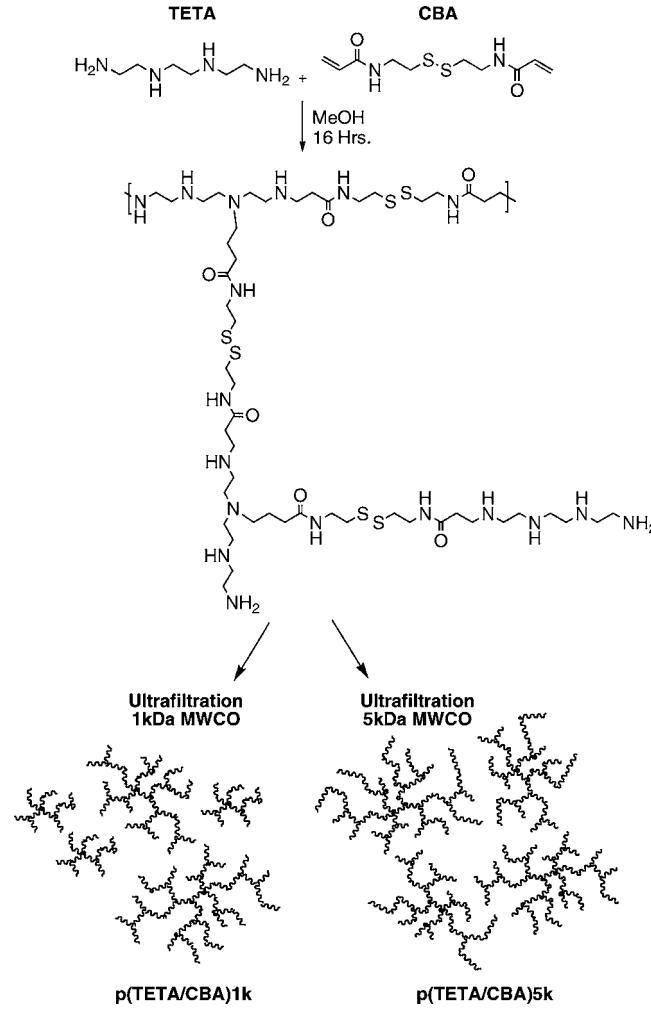
EXPERIMENTAL PROCEDURES

Materials. Triethylenetetramine (TETA), tris(2-carboxyethyl)phosphine) (TCEP), *N*-ethylemaleimide (NEM), hyperbranched polyethylenimine (bPEI, *M*w 25 000 (bPEI25 kDa)), and HPLC-grade methanol were purchased from Sigma-Aldrich (St. Louis, MO). *N*′,*N*′-Cystamine bisacrylamide (CBA) was purchased from Polysciences, Inc. (Warrington, PA). Ultrafiltration devices and regenerated cellulose membranes (1 kDa and 5 kDa) were supplied by Millipore Corporation (Billerico, MA). The reporter gene plasmid, pCMVLuc, was designed previously by insertion of luciferase cDNA into a pCI plasmid (Promega, Madison, WI) driven by the pCMV promoter and was purified using Maxiprep (Invitrogen, Carlsbad, CA) protocols. Dulbecco's Modified Eagle's Medium (DMEM), penicillin−streptomycin, trypsin-like enzyme (TrypLE Express), and Dulbecco's phosphate buffered saline were purchased from Gibco BRL (Carlsbad, CA). EBM-2 with EGM-2 singlequots was purchased from Lonza. Fetal bovine serum (FBS) was purchased from Hyclone Laboratories (Logan, UT).

p(TETA/CBA) Synthesis. Synthesis of p(TETA/CBA) was performed with minor adaptation of the previously described method at 50 °C (*11*). The polymerization reaction was split in half after the pH was adjusted to 7.0 and purified by ultrafiltration using a 1 kDa or 5 kDa MWCO regenerated cellulose membrane. The polycations were subsequently lyophilized (Scheme 1). Composition of the polymer was monitored using ^{1}H NMR (400 MHz, D_2O). p(TETA/CBA) δ 2.61 ($COCH_2CH_2NH$, 4H), 2.72 ($NHCH_2CH_2S-S$, 4H), 2.90−3.21 ($COCH_2CH_2NHCH_2CH_2$, 16H), 3.41 ($NHCH_2CH_2S-S$, 4H).

p(TETA/CBA)5k-g-2k Synthesis. Methoxy PEG2k was dried using anhydrous toluene and subsequently precipitated in anhydrous ice-cold ether. The white precipitate was collected and dried in vacuo. The mPEG2k was then activated using *p*-nitrophenyl chloroformate in DCM as solvent and reacted on ice overnight while stirring. The activated PEG product was collected by precipitation in anhydrous ice-cold ether and dried in vacuo. Following NMR analysis to assess the degree of PEG activation, p(TETA/CBA)5k and equal molar active PEG2k were dissolved in anhydrous pyridine/DMSO as solvent, and the poly(ethylene glycol)−carbonate solution was added dropwise to the dissolved p(TETA/CBA)5k. The reaction was stirred at room temperature, and the release of *p*-nitrophenolate was monitored optically at 400 nm using UV−vis. When the reaction was complete at approximately 16 h, the sample was purified by ultrafiltration (5 kDa MWCO) before being lyophilized. The composition of p(TETA/CBA)-g-PEG2k copolymer conjugates

Scheme 1. Synthesis and Schematics for p(TETA/CBA) Fractions



was monitored using ^{1}H NMR (400 MHz, D_2O). p(TETA/CBA)5k-g-PEG2k δ 2.61 ($COCH_2CH_2NH$, 4H), 2.72 ($NHCH_2CH_2S-S$, 4H), 2.90−3.21 ($COCH_2CH_2NHCH_2CH_2$, 16H), 3.41 ($NHCH_2CH_2S-S$, 4H), 3.45−3.7 (CH_2CH_2O, 4H).

Polymer Characteristics. Relative molecular weight analysis for p(TETA/CBA)1k, p(TETA/CBA)5k, and p(TETA/CBA)5k-PEG2k was performed using AKTA/FPLC (Amersham Pharmacia Biotech Inc.). A SuperdexPeptide column HR 10/30 was used to analyze p(TETA/CBA)1k (2 mg/mL). The calibration curve was prepared using poly(hydroxy propyl methacrylamide) (poly(HMPA) standards ranging from 2 kDa to 10 kDa. p(TETA/CBA)5k and p(TETA/CBA)5k-g-PEG2k were analyzed using a Superose 6 10/300 GL column and poly(HMPA) standards ranging from 40 kDa to 150 kDa. For calibration and analysis, a 0.3 M NaOAc, pH 4.4, with 30% (v/v) acetonitrile eluent buffer was used after it was filtered through a 0.2 μm filter (Nylon, Alltech) and degassed. The flow rate was set to 0.4 mL/min.

Polyplex Formation. In all cases, polyplex was formed with a known amount of pDNA and a corresponding and desired amount of polymer. The two solutions were combined, lightly vortexed, and allowed to equilibrate for 30 min. When the 10% and 50% polyplex mixtures were formed, a known amount of pDNA was brought up in solution, and a corresponding and desired concentration of p(TETA/CBA) and p(TETA/CBA)5k-g-PEG2k were prepared. The polymer solutions were mixed prior to polyplex formation at either 10% p(TETA/CBA)5k-g-PEG2k/90% p(TETA/CBA) by volume or 50% p(TETA/

CBA)5k-g-PEG2k/50% p(TETA/CBA). The mixtures were then added to the pDNA solution and prepared as mentioned above.

Polycation Branching. The relative degree of branching was determined as previously described by the reduction and protection of disulfide bonds using tris(2-carboxyethyl)phosphine hydrochloride (TCEP) and *N*-ethylmaleimide (NEM), respectively (*5*). MALDI-TOF analysis was performed on the NEM conjugated polymer repeat units using a Voyager-DE STR Biospectrometry Workstation (PerSeptive Biosystems) in positive-ion mode with delayed extraction. Spectra were externally calibrated using a peptide standard mixture spanning a nominal mass range from 325 to 2465 Da.

Acid−Base Titrations. The buffering capacity of each polycation was determined using a previously established method (*11*). In brief, 6 mg polymer was dissolved in 30 mL NaCl solution (0.1 M) and initially titrated to pH 10 with 0.1 M NaOH. The pH was subsequently lowered with the addition of 0.1 M HCl. Because the absolute molecular weight is not known for these polymers, titration values were determined in micromoles of HCl required to lower the pH of the polycation solution from 7.4 to 5.1. Branched PEI25 kDa was used as a reference control.

Light Scattering and ζ-Potential Measurements. The surface charge and polymer/pDNA particle (polyplex) diameters were measured at 25 °C using a Zetasizer 2000 instrument (DTS5001 cell) and a dynamic light scattering (DLS) unit on a Malvern 4700 system, respectively. Polyplexes were prepared by adding equal volume polymer solution (200 μL) at increasing concentrations in HEPES buffer (20 mM, pH 7.4, 5% glucose) to a desired concentration of 8 μg pDNA in HEPES buffer (200 μL). Polyplexes were allowed to equilibrate for 30 min and were subsequently diluted in filtered milliQ water to a final 2 mL volume.

Transmission Electron Microscopy (TEM). Polyplex was prepared in HEPES buffer (20 mM, pH 7.4, 5% glucose) at 0.05 μg/μL and 5 μL was deposited on TEM copper grid plates to dry. Residual buffer salt was removed by carefully rinsing each grid with filtered, deionized water thrice. The samples were then stained with filtered phosphotungstenic acid (PTA) for 1 min before washing again with filtered deionized water. Images were visualized using a Technai T12 scope (EFM) at 80 kV. Magnification ranging from 20 000 to 200 000× was utilized, and the micrograph images were taken at 110 000×. Particle sizes were analyzed using *ImageJ* software.

Polyplex Stability in 90% Fresh Rabbit Serum. Polyplex stability and resulting pDNA stability against nuclease activity in serum was evaluated using 500 ng free pDNA as a control and 500 ng pDNA complexed with polymer mixtures preformed in HEPES buffer. Polyplex formation was carried out by combining equal-volume solutions of p(DNA) and polymer mixtures using a polymer/pDNA at N/P 50 (24 w/w) and allowed to equilibrate for 30 min. Preformed polyplex was then diluted in 90% fresh rabbit serum and incubated at 37 °C over time. Twenty-five microliter aliquots (125 ng pDNA) were taken at each time point and 10 μL stop buffer (250 mM NaCl, 25 mM EDTA, 2% SDS) was added to each. The samples were frozen at −70 °C until further analysis. Once the samples were thawed, they were incubated overnight at 60 °C to completely dissociate polycation from the pDNA, and 2 μL of 50 mM DTT was added to each sample and incubated at 37 °C for an additional 30 min to ensure complete decomplexation. Lastly, the samples were loaded onto a 2% agarose gel stained with ethidium bromide (EtBr) and subjected to electrophoresis at 96 V for 30 min in TAE (40 mM Tris-acetate, 1 mM EDTA) buffer. The gel image was viewed using *GelDoc* software ($n = 2$).

Cell Culture. Mouse pancreatic islet endothelial cells (SVR) and colon adenocarcinoma cells (CT-26) (ATCC) were cultured in DMEM containing 10% FBS and 1% penicillin−streptomycin at 37 °C in a humidified incubator with an atmosphere containing 5% (v/v) CO_2. Human umbilical vein endothelial cells (HUVEC) (Invitrogen) were cultured in EBM-2 media with EGM-2 singlequots at 37 °C in a humidified incubator with an atmosphere containing 5% (v/v) CO_2.

In Vitro Transgene Expression. Luciferase reporter gene expression in cell culture was performed using each polymer and pCMVLuc plasmid DNA. Cells were plated in 24-well plates containing 0.5 mL media. Once the cells were approximately 70% confluent, polyplexes were prepared using 0.5 μg pDNA at N/P 50 (24 w/w) in HEPES buffer. Polyplexes were allowed to equilibrate for 30 min, and the cells were transfected in the presence of serum by adding 20 μL polyplex (0.5 μg pDNA) to each well for 4 h before replacing with fresh culture media. The cells remained in the incubator for a total of 48 h before they were washed with 1 mL PBS and treated with cell culture lysis buffer (Promega). Luciferase quantification was performed using a Luciferase assay system (Promega) on a luminometer from Dynex Technologies, Inc. (Chantilly, VA). The amount of protein in the cell lysate was determined using a standard curve of bovine serum albumin (Sigma) and a BCA protein assay kit (Pierce) ($n = 6$).

Cell Viability Assay. Cells were plated in 24-well plates and gene transfections were carried out when the cells were approximately 70% confluent. Polyplexes were prepared as they were for the luciferase reporter gene assay. Respective cell cultures were transfected in the presence of serum with the addition of 20 μL equilibrated polyplex in HEPES buffer solution (0.5 μg pDNA) to each well. Cells were left to incubate for a total of 18 h before analyzing cell viability using an MTT assay (Sigma). Percent cell viability was determined relative to untreated cells ($n = 6$).

RESULTS

Synthesis and Characterization. *p(TETA/CBA).* Polymerization of p(TETA/CBA) occurs via Michael-type addition of the amines present in the TETA monomer to the acrylamide group of the CBA (monomer). Because four reactive amine groups exist within the TETA monomer, highly branched products can be obtained during synthesis and differentially purified (Scheme 1). In the present study, polymerization reactions were carried out at different temperatures in 100% MeOH and monitored by ^{1}H NMR. Synthesis temperature was shown to correlate with the degree of branching in each sample (data not shown). Eliminating oligomer polycations from the sample by using a 5 kDa MWCO ultrafiltration membrane reduced the sample polydispersity index (PDI), as expected, which further correlates with the relative molecular weight of the sample as determined using AKTA/FPLC. Commercial bPEI25k was also analyzed as an external control for comparison. Because the M_n and M_w values for bPEI25 kDa determined using AKTA/FPLC were lower than reported by the commercial provider, extrapolations need to be made to estimate p(TETA/CBA) molecular weight. Moreover, p(TETA/CBA)5k has a similar buffering capacity to the sample obtained using the original purification approach (1 kDa MWCO) (Table 1).

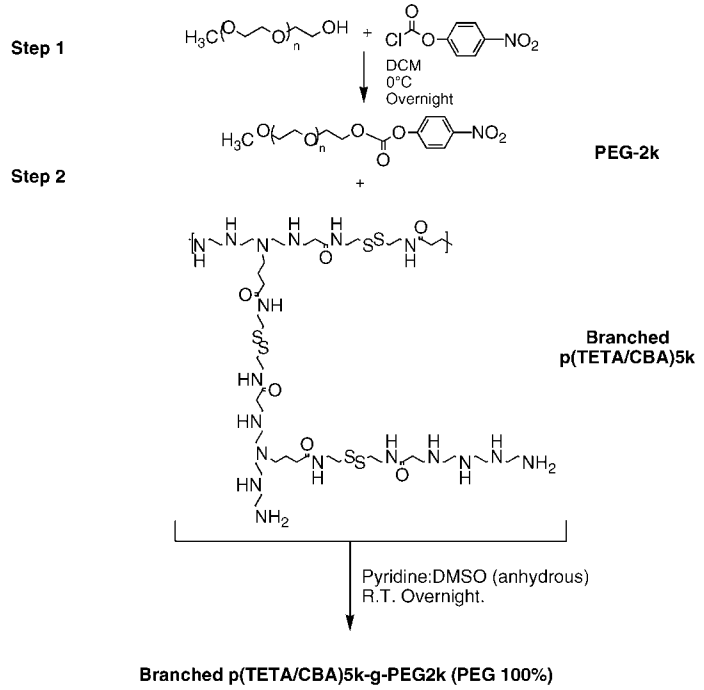
Mixture Formulations to Alter the Relative Amount of PEG for Polyplex Formation. PEGylation may often improve polycationic carrier function in the presence of serum both in vitro and in vivo, which is largely due to its ability to reduce polyplex surface charge and maintain a steric barrier against protein adsorption (*23*). Particles with a surface charge close to neutral tend to aggregate in solution due to their reduced ionic repulsive forces influenced by the isoelectric point, molecular weight, and pH of the solution (*24*). Therefore, we sought to synthesize a p(TETA/CBA)5k-PEGylated product that could be

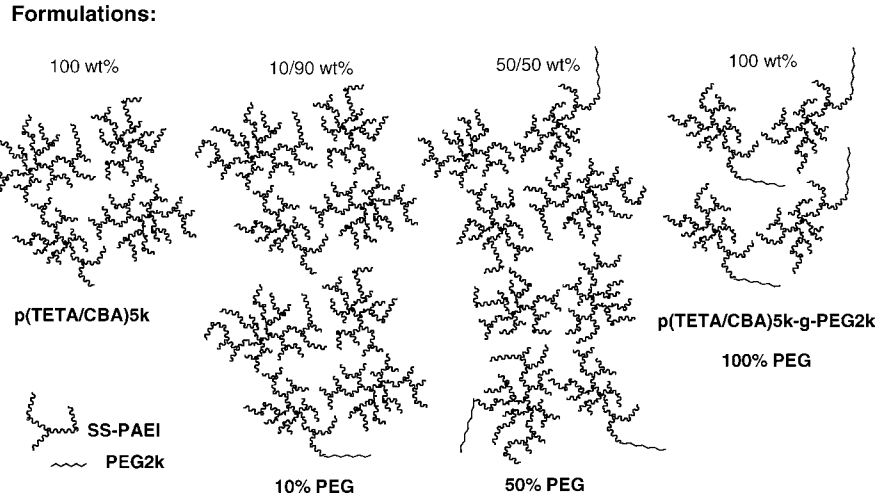
Table 1. Polymer and Copolymer Characteristics

sample	M_n (kDa)[a]	M_w (kDa)[a]	PDI (M_w/M_n)	titration[b] (μmol HCl)	degree[c] branching
p(TETA/CBA)1k	4.2	8.2	1.95	25.2	0.68
p(TETA/CBA)5k	5.8	8.85	1.53	27.6	0.91
p(TETA/CBA)5k-g-PEG2k	8.9	10.6	1.19	22.3	--
bPEI 25 kDa	16.4	21.0	1.28	32	--

[a] Number average molecular weight (M_n), weight average molecular weight (M_w), and polydispersity (M_w/M_n) determined using FPLC. [b] Polymer fraction buffer capacity titrations determined by the mol of HCl required to shift pH from 7.4 to 5.1 in 0.1 M aqueous NaCl. [c] Degree branching was determined by reduction of disulfide bonds with TCEP followed by protection of free sulfhydryls with NEM and analyzed by MALDI-TOF.

Scheme 2. p(TETA/CBA)5k-g-PEG2k Synthesis and Illustrations of Evaluated Formulations





mixed in conjunction with p(TETA/CBA)5k, if necessary, to easily control the amount of PEG used in the formulations in order to examine the effects on particle characteristics and functionality with a nontoxic branched polycation as a model system (Scheme 2). PEG conjugation to the polycation was monitored by following the release of *p*-nitrophenolate at 400 nm with a UV−vis spectrophotometer. Reactions were complete by 16 h. NMR analysis and comparison of peak AUC suggested approximately 0.96/1 mol PEG/(TETA/CBA)5k and is in good agreement with the AKTA/FPLC analysis (Table 1).

Influence of p(TETA/CBA) PDI and Molecular Weight on Biological Activity. As mentioned previously, LMW PEI exhibits limited pDNA condensation at low N/P ratios and is often perturbed by PEG conjugation. Thus, reducing the PDI of p(TETA/CBA) by eliminating destabilizing oligomers and increasing the average molecular weight without perturbing carrier performance are preferred (*17*). As seen in Figure 1, a reduced p(TETA/CBA) PDI and correlating molecular weight increase have no adverse effects on carrier performance. It performs similarly to the original polycation, p(TETA/CBA)1k.

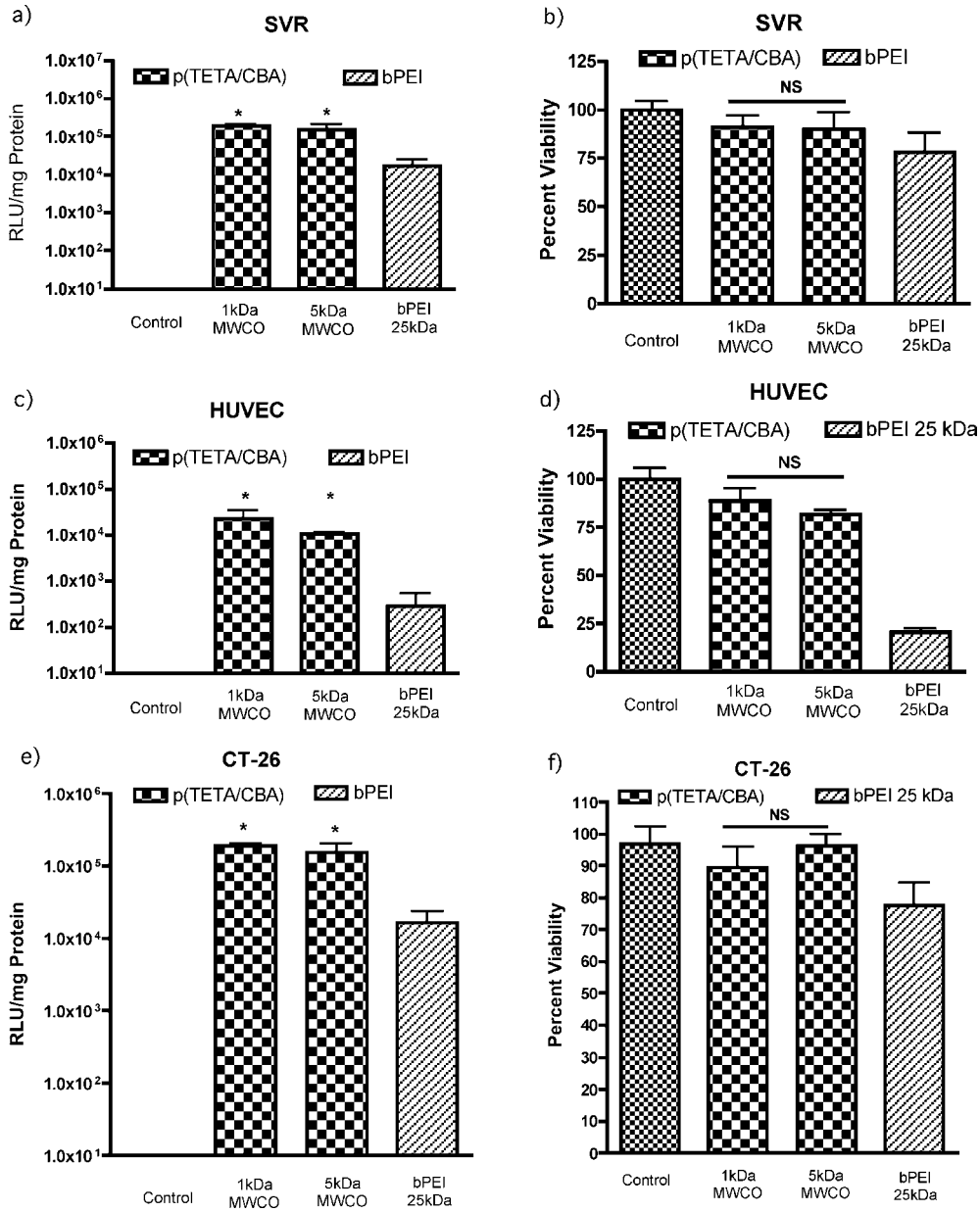


Figure 1. Transfection efficiency (a,c,e) and cell viability (b,d,f) in SVR, HUVEC, and CT-26 cells, in the presence of 10% serum for different p(TETA/CBA) molecular weight analogues compared to the positive control bPEI 25 kDa. pCMVLuc was used as the reporter gene. Commercial bPEI 25 kDA and p(TETA/CBA) polyplexes were prepared at N/P 10 (1.3 w/w) and N/P 50 (24 w/w), respectively (*$p < 0.05$, $n = 6$).

More importantly, p(TETA/CBA)5k is significantly less toxic in primary HUVEC endothelial cells than bPEI 25kDA, as well as providing greater luciferase transgene expression in HUVEC and SVR endothelial cells, as well as the colon adenocarcinoma cell line, CT-26. The toxicity of bPEI25 kDa is likely due to the intracellular accumulation of high molecular weight polycationic species (*3*). Three cell lines were used because trends seen in multiple cell lines confirms that any trends seen in gene transfection are justifiable, and second, the endothelial cells (SVR and HUVEC) as well as adenocarcinoma cells (CT-26) comprising the tumor microenvironment in many malignant tumors that are best treated with systemic administration of therapeutic gene. The PEGylation of polycations is most often employed for systemic delivery of gene and drug carriers. Therefore, we tested the biological activity of our gene carriers using both endothelial cells often exposed during systemic administration to examine potential activity and the adenocarcinoma cell line (CT-26) that is used in our lab for a mouse tumor model when testing therapeutic gene activity in vivo. Often, polycationic species can interact with and disrupt cell membrane function, and/or they can interact with intracellular proteins and nucleic acids, thereby perturbing intracellular and nuclear processes such as cellular trafficking and gene transcription and translation (*18, 19*). The bioreducible polycation, p(TETA/CBA), likely mitigates these intracellular interactions, as it degrades to small molecular weight species intracellularly, thereby limiting toxicity in the primary endothelial cell line, irrespective of its relative molecular weight (*20*). The enhanced transgene expression observed using p(TETA/CBA) is also likely explained by this phenomenon and its ability to more easily release pDNA (*6, 9*).

Serum Effects on p(TETA/CBA). Serum-containing media and serum encountered when polyplex is administered in vivo often reduce polycationic performance through particle destabilization and nuclease degradation of therapeutic gene or uptake by the reticular endothelial system in vivo. The data presented in Figure 2 is consistent with previously published findings where transgene expression is reduced in the presence of serum

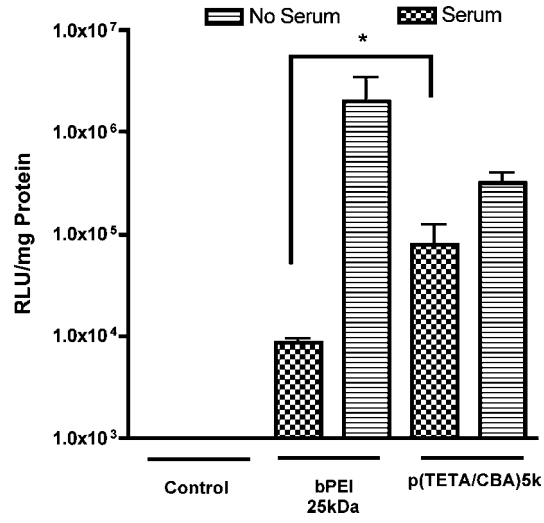


Figure 2. Comparison of p(TETA/CBA)5k/pCMVLuc transfection efficiency in the presence and absence of 10% serum in culture media. Transfection efficiency was evaluated by luciferase trangene expression in CT-26 cells. p(TETA/CBA) at N/P 50 (w/w 24) exhibits greater reporter transgene expression than bPEI 25 kDa N/P 10 (w/w 1.3) in serum-containing media but is still perturbed compared to its performance in the absence of serum ($*p < 0.05$, $n = 6$).

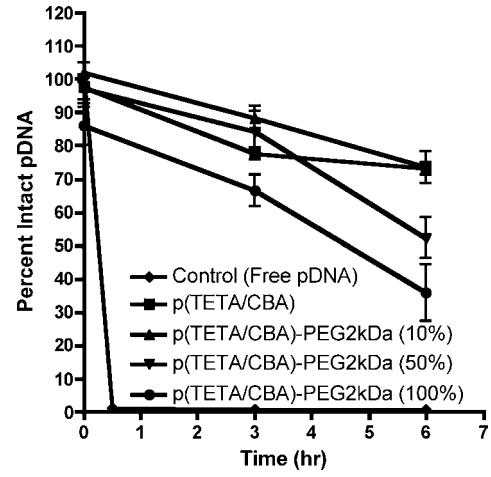


Figure 4. Polyplex stability in 90% rabbit serum at 37 °C for p(TETA/CBA)5k, poly(TETA/CBA)5k-g-PEG2k, 10/90 (10% PEG) and 50/50 (50% PEG) wt/wt % formulations for p(TETA/CBA)5k-g-PEG2k and p(TETA/CBA)5k, respectively. 500 ng pCMVLuc was complexed with each formulation N/P 50 (w/w 24). The relative percent of intact pDNA over time was determined by band pixel intensity using *GelDoc* software. Increasing the PEG wt % in the polyplex formulations inversely correlates with pDNA protection ($n = 2$).

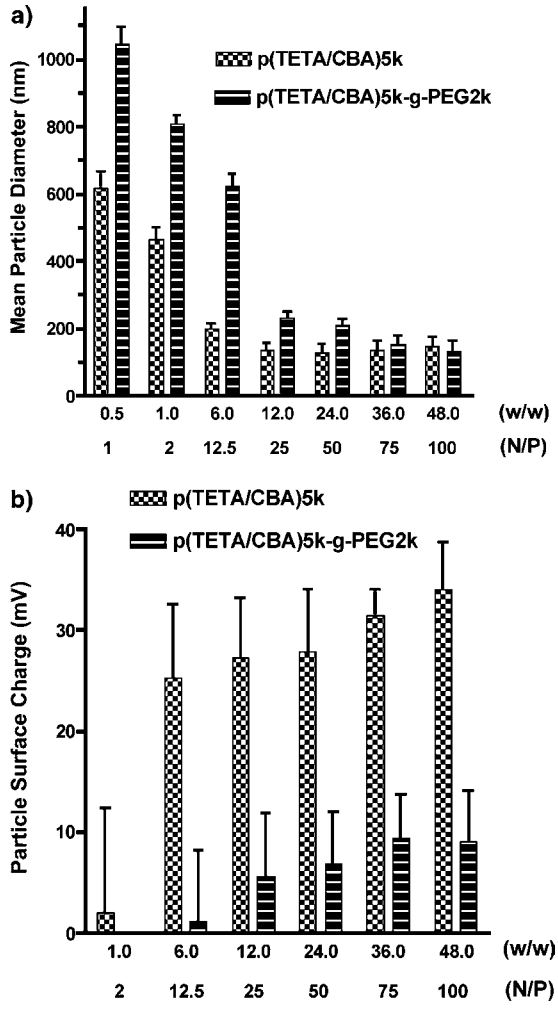


Figure 3. Physiochemical characteristics of p(TETA/CBA)5k and p(TETA/CBA)5k-g-PEG2k/pCMVLuc polyplexes. (a) Particle size and (b) ζ-potential measurements of each respective gene carrier at increasing polymer concentrations using a known amount of pDNA. PEG2k conjugation to p(TETA/CBA) reduces polyplex surface charge, but interferes with pDNA condensation.

compared to nonserum conditions. In addition, the biological activity of p(TETA/CBA) on colon adenocarcinoma cells (CT-26) in serum-containing media is significantly better than that with bPEI25 kDa (Figure 2). Evaluation of serum effects on gene transfection was performed solely on CT-26 cells because the data presented in Figure 1 showed similar trends to the other two cell lines. In combination, these results demonstrate the advantages of p(TETA/CBA)5k over bPEI25 kDa and suggest the need to PEGylate p(TETA/CBA)5k for improved gene delivery in the presence of serum.

Polyplex Characterization. The ability of p(TETA/CBA)5k and p(TETA/CBA)5k-g-PEG2k to form condensed polyplexes was investigated by particle size analysis and ζ-potential measurements. Indeed, nanosized particles below or near 100 nm in diameter were formed for both potential gene carriers. As expected, PEG conjugation interfered with polyplex formation at preferred, low polymer concentrations (Figure 3a). PEG conjugation sufficiently decreased polyplex surface charge. However, higher polymer concentrations are required in this case in order to condense p(DNA) into 200 nm polyplexes (Figure 3b).

PEG Effects on Polyplex Characteristics. Our findings coincide with previous studies that used PEGylated polyethyleneimine gene carriers (*17*) and show that PEGylation of the p(TETA/CBA) polycation perturbs nucleic acid condensation and polyplex size. To overcome this problem and validate the possibility of premixing polymer/PEG−copolymer solutions in order to control the relative PEG/polycation amounts, as well as identify an ideal formulation that maintains homogeneous and stable polyplex with reduced surface charge, polyplexes were prepared using p(TETA/CBA)5k-g-PEG2k, p(TETA/CBA)5k, and mixtures of the two molecular entities at 10/90 and 50/50 volumetric ratios, respectively, at a summed polycation/pDNA N/P = 50 (24 w/w). Mixtures are schematically represented in Scheme 2.

Serum Stability. In order to test the influence of increasing PEG content on polyplex stability and pDNA protection against serum nuclease activity, polyplexes were formed and, following a 30 min equilibration time, were added to fresh rabbit serum to a final serum concentration equal to 90% at 37 °C. Aliquots were electrophoresed on an agarose gel to visualize intact

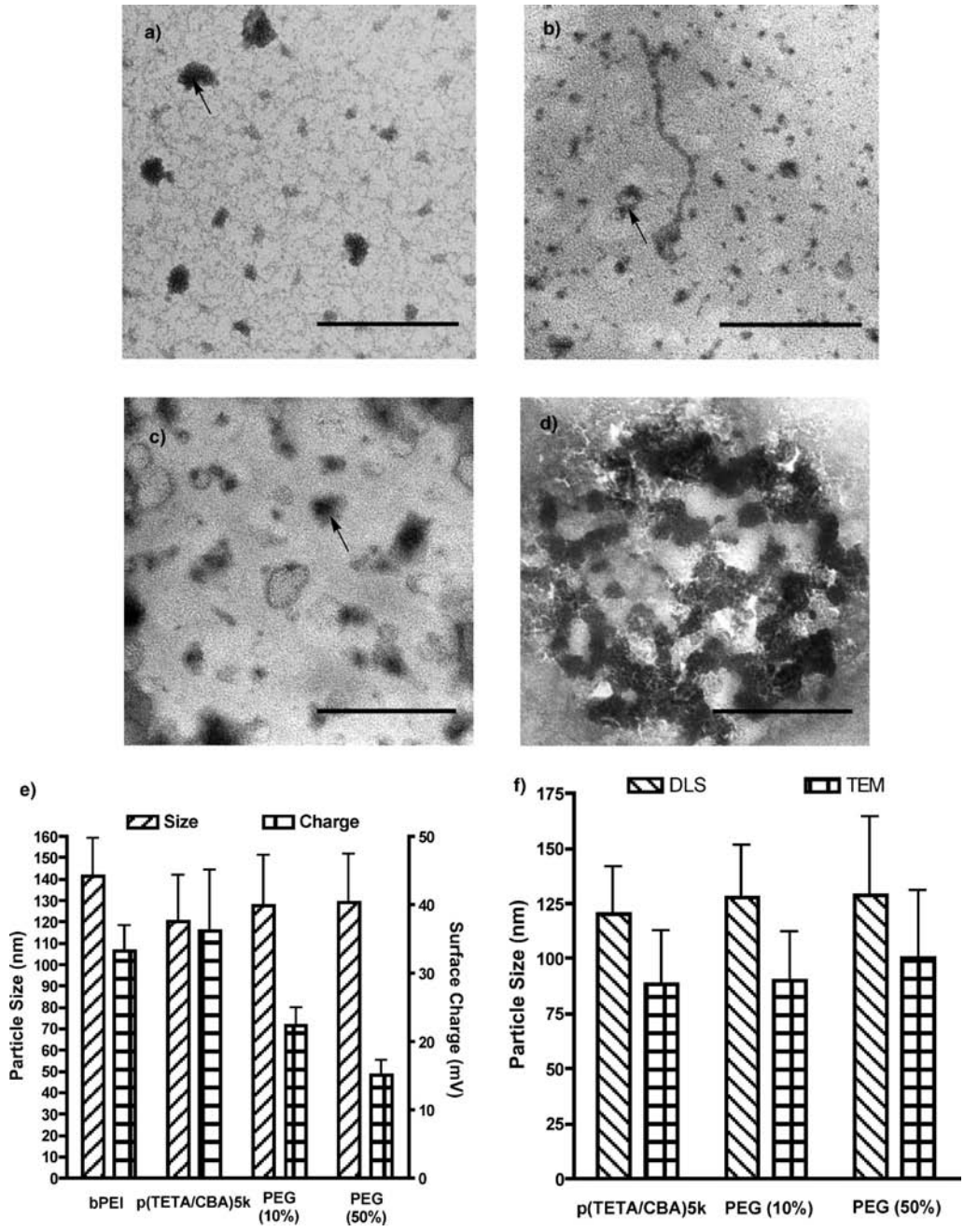


Figure 5. Polyplex formulations visualized with TEM (a−d) and studied using DLS (e) at 24 w/w. (a) p(TETA/CBA)5k; (b) 10% PEG; (c) 50% PEG; (d) p(TETA/CBA)5k-g-PEG2k. Scale bars equal 200 nm. (e) Particle size and ζ-potential of polyplex formulations. (f) Comparison of polyplex size using TEM and DLS.

pCMVLuc at each time point and further compared to untreated control at zero hours. Figure 4 shows that p(TETA/CBA)5k and 10% p(TETA/CBA)5k-g-PEG2k protect pDNA from nuclease degradation nearly 80% or more at 6 h. Increasing p(TETA/CBA)5k-g-PEG2k to 50% or 100% reduces particle stability and offers less pDNA protection where approximately 60% and 40% pDNA are preserved, respectively, at 6 h incubation time.

Polyplex Analysis. For formulation ease and improved carrier function, stable polyplex was formed using different amounts of PEG. Formulations should display unimodal polyplex size and surface charge with uniform morphology. Polyplex size for each formulation was visualized using TEM (Figure 5a−d) and their size and distribution were compared to measurements provided by dynamic light scattering (DLS). The arrows contained in Figure 5a−d show a relevant particle, and the particle size was analyzed using *ImageJ* software. The values between TEM and DLS are in close agreement with each other. The TEM particle sizes are smaller than those determined using DLS because the polyplexes examined using TEM are in a dehydrated state, whereas polyplexes analyzed by DLS are in aqueous buffer and are thus hydrated, lending to a larger particle size. Figure 5a−d reveals morphological changes and less compact polyplex with translucent outer shells as the amount of PEG in the formulation increases. These translucent outer shells are thought to be from increasing the amount of PEG. p(TETA/CBA)5k-g-PEG2k exhibited aggregation as seen in (Figure 5d). This aggregation was also noted when analyzed using DLS and adversely influenced the data. Therefore, this formulation is excluded from the analysis and not shown in Figure 5e. p(TETA/CBA)5k, 10% and 50% PEG formulations generate sub-150 nm polyplexes in solution, and the amount of

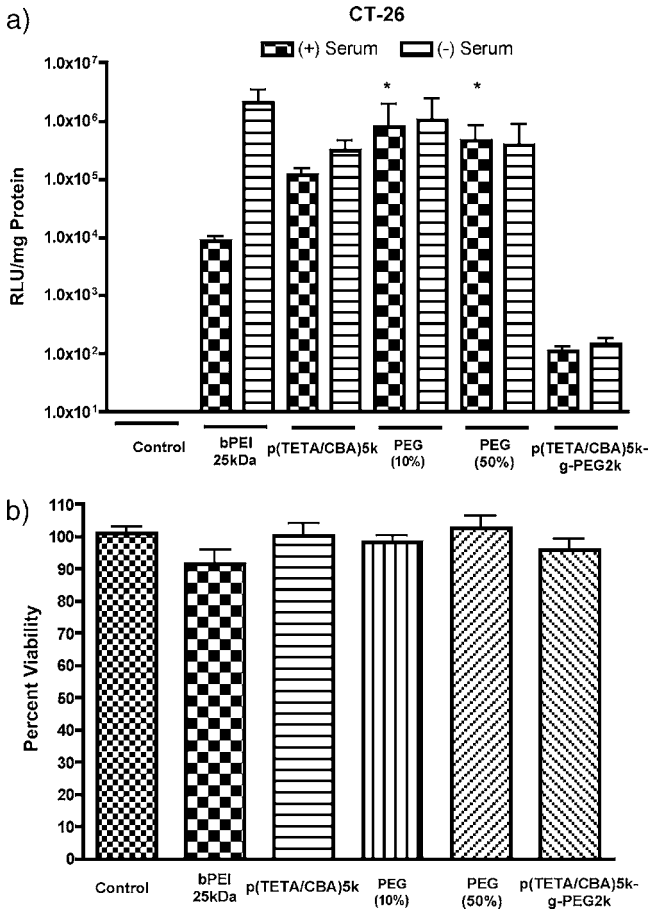


Figure 6. (a) Transfection efficiency of p(TETA/CBA)5k, 10/90%, 50/50%, and 0/100% p(TETA/CBA)5k/p(TETA/CBA)5k-g-PEG2kpolyplex formulations with CMVLuc in the presence and absence of serum. The 10% and 50% PEG formulations are significantly better gene carriers than bPEI 25 kDa and p(TETA/CBA) in the presence of serum. However, these two formulations are not significantly different from each other. (b) Cell viability with analogous polyplex formulations in serum-containing media ($p < 0.05$, $n = 6$).

PEG inversely correlates with polyplex surface charge as expected (Figure 5e).

PEG Formulations on Carrier Function and in Vitro Biological Activity. To investigate the potential advantages of PEG-copolymer formulations for gene delivery in the presence of serum, a luciferase transgene assay was performed using colon adenocarcinoma cells (CT-26). The 10% and 50% PEG formulations have significantly better ($p < 0.05$; $n = 6$) transgene expression than bPEI 25 kDa and p(TETA/CBA) in the presence of serum (Figure 6a). However, these PEG formulations are not significantly different from each other. Moreover, these formulated polyplexes are nontoxic to these cells (Figure 6b).

DISCUSSION

Clinical advancements of polycationic gene carriers is hampered by uncertain design and formulation requirements. In the present work, we show that a graft copolymer of poly(ethylene glycol) (PEG), and a branched SS-PAEI can be synthesized and used in formulation mixtures to alter the relative amount of PEG, thereby altering the physiochemical characteristics of the gene carrier in order to easily study the design and formulation requirements to improve gene carrier function. Knowing that PEG conjugation can interfere with polyplex formation and carrier function, this work demonstrates the feasibility to easily overcome these issues by preparation of homogeneous polyplexes that alter the relative amount of PEG using a mixture of un-PEGylated p(TETA/CBA) and the PEGylated counterpart, p(TETA/CBA)5k-g-PEG2k, to evaluate and identify products that are functionally viable. More importantly, this approach may be applied to other polycation-PEG preparations to easily alter polyplex characteristics to optimize polyplex stability and biological activity in vitro. Further studies need to be performed to understand the feasibility of using this approach for in vivo screening and evaluation of gene carriers.

When synthesizing p(TETA/CBA)5k-g-PEG2k, reducing the PDI of p(TETA/CBA) by removing polycationic oligomers with a limited ability to properly condense pDNA is preferred, given that PEG conjugation may interfere with polyplex formation as it is. Therefore, in order to reduce the PDI of p(TETA/CBA) following the Michael-addition of the bisacrylamide group with TETA, ultrafiltration was performed using a higher molecular weight cutoff membrane (5 kDa) than was used previously (*11*). As expected, this approach was effective in reducing the polycation's PDI and correlates with a relative increase in molecular weight. Prior research has shown that increasing the molecular weight and branching profile of polyethyleneimines correlates not only with increased transgene expression, but also with cellular toxicity. Therefore, the present study investigated this putative effect with regard to p(TETA/CBA) and found no significant influence on its biological activity in primary and immortalized cell lines (*6*, *7*). These results are explained by the gene carrier's ability to exploit the intracellular redox potential and avoid disruption of intracellular function through relatively high molecular weight polycationic species (*21*).

While p(TETA/CBA) demonstrated significantly better transgene expression than bPEI 25 kDa in serum-containing media, p(TETA/CBA) delivery capacity was noticeably lower when compared to its activity in the absence of serum. Therefore, to reduce p(TETA/CBA)/pDNA polyplex interactions with serum proteins and thus improve carrier function in the presence of serum, poly(ethylene glycol) was conjugated to p(TETA/CBA)5k at an equimolar ratio and confirmed by ^{1}H NMR spectroscopy following purification. The corresponding relative molecular weight was also in agreement with what is expected for equimolar conjugation when analyzed using AKTA/FPLC. Conjugating PEG2k to p(TETA/CBA)5k reduced polyplex surface charge, however, adversely affected nucleic acid condensation. This result coincides with prior findings by our lab and others (*16*, *22*). Because poly(ethylene glycol) and/or ligand conjugation for cell-specific gene delivery commonly mitigates nucleic acid condensation, synthesis of multiple copolymeric gene carriers is required to ascertain optimal ratios for maximal carrier performance. In an attempt to overcome this problem and avoid the need to synthesize multiple carriers for screening, this study investigated the feasibility of altering and optimizing PEG/polycation amounts by formulating mixtures of a polycation and its corresponding PEGylated counterpart. Polyplex stability in serum was evaluated in this study for p(TETA/CBA)5k-g-PEG2k alone, p(TETA/CBA)5k alone, and 10/90 or 50/50 volumetric mixtures of p(TETA/CBA)5k-g-PEG2k/p(TETA/CBA)5k, respectively. Polyplex formed using p(TETA/CBA) and 10/90% sufficiently protects up to 70% of the pDNA from serum nuclease degradation over 6 h. Increasing the p(TETA/CBA)5k-g-PEG2k amount to 50% and 100% reduced the relative pDNA protection in serum, which correlates with the capability of each formulation to condense pDNA into nanosized polyplex determined using DLS and TEM. One potential concern is that if polyplex is formed at a unified 50 N/P (24 w/w) the N/P ratios could be significantly different between p(TETA/CBA) alone and the mixtures. However, NMR results demonstrate that there is approximately 1 PEG chain per TETA/CBA molecule. If a 50 N/P (24 w/w) is used for formulations, there are approximately 1.2% of the amines

PEGylated in the 100% p(TETA/CBA)(5k)-g-PEG(k) formulation, ~0.6% for the 50% formulation, ~0.12% for the 10% formulation, and 0% for p(TETA/CBA)(5k). This being the case, the difference in N/P ratios between the formulations is insignificant. Moreover, the 10% formulation that demonstrated significantly better transgene expression than p(TETA/CBA)(5k) in the presence of serum has only 0.12% less amines for use in formulating polyplex.

Luciferase transgene expression and cell viability was investigated in cell culture using the aforementioned formulations to evaluate their bioactivity. As expected, PEG was able to improve gene delivery in serum-containing media compared to p(TETA/CBA) alone. However, this improvement was observed only at specific PEG ratios. These results provide evidence that PEG/polycation ratios can be easily altered in order to easily evaluate and optimize PEG ratios for improved gene carrier function. In doing so, one can avoid synthesis of multiple bioreducible copolymers with different physiochemical characteristics currently employed for gene carrier optimization.

CONCLUSIONS

In the present study, we developed a novel gene carrier composed of an efficient and nontoxic bioreducible polycation in conjunction with its PEGylated counterpart to improve carrier performance in the presence of serum. In addition, we provide a feasible and facile approach to tailor polycationic-PEG copolymer formulations to alter the relative amount of PEG in several formulations in order to obtain optimal physiochemical properties for ideal gene carrier function. By doing so, synthesis of multiple candidate copolymers for gene delivery is avoided when designing a gene carrier with preferred physiochemical properties, which may also be employed for facile in vivo evaluation.

ACKNOWLEDGMENT

This work was supported by NIH grant CA107070. We thank Jindrich Kopecek's group for their assistance with AKTA/FPLC analysis (Department of Pharmaceutics, University of Utah), as well as the University of Utah Core Facilities for assistance with Maldi-TOF analysis and TEM imaging.

LITERATURE CITED

(1) Saito, G., Swanson, J. A., and Lee, K. D. (2003) Drug delivery strategy utilizing conjugation via reversible disulfide linkages: role and site of cellular reducing activities. *Adv. Drug Delivery Rev. 55*, 199–215.

(2) Christiano, R. J., and Roth, J. A. (1995) Molecular conjugates: a targeted gene delivery vector for molecular medicine. *J. Mol. Med. 73*, 479.

(3) Merdan, T., Kopecek, J., and Kissel, T. (2002) Prospects for cationic polymers in gene and oligonucleotide therapy against cancer. *Adv. Drug Delivery Rev. 54*, 715–758.

(4) Lee, M., and Kim, S. W. (2004) Polyethylene glycol-conjugated copolymers for plasmid DNA delivery. *Pharm. News 9*, 597.

(5) Boussif, O., Lezoualc'h, F., Zanta, M. A., Mergny, M. D., Scherman, D., Demeneix, B., and Behr, J. (1995) A versatile vector for gene and oligonucleotide transfer into cells in culture and in vivo: polyethylenimine. *Proc. Natl. Acad. Sci. 92*, 7297–7301.

(6) Banerjee, P., Reichardt, W., Weissleder, R., and Bogdanov, A. (2004) Novel hyperbranched dendron for gene transfer in vitro and in vivo. *Bioconjugate Chem. 15*, 960–968.

(7) Fischer, D., Bieber, T., Li, Y., Elsasser, H. P., and Kissel, T. (1999) A novel non-viral vector for DNA delivery based on low molecular weight, branched polyethylenimine: effect of molecular weight on transfection efficiency and cytotoxicity. *Pharm. Res. 16*, 1273–1279.

(8) Luten, J., Van Nostrum, C. F., De Smedt, S. C., and Hennink, W. E. (2008) Biodegradable polymers as non-viral carriers for plasmid DNA delivery. *J. Controlled Release 126*, 97–110.

(9) Lin, C., Zhong, Z., Lok, M. C., Jiang, X., Hennink, W. E., Feijen, J., and Engbersen, J. F. J. (2007) Novel bioreducible poly(amido amine)s for highly efficient gene delivery. *Bioconjugate Chem. 18*, 138–145.

(10) Anderson, D. G., Lynn, D. M., and Langer, R. (2003) Semiautomated synthesis and screening of a large library of degradable cationic polymers for gene delivery. *Angew. Chem., Int. Ed. Engl. 42*, 3153–3158.

(11) Christensen, L. V., Chang, C. W., Kim, W. J., Kim, S. W., Zhong, Z., Lin, C., Engbersen, J. F., and Feijen, J. (2006) Reducible poly(amido ethylenimine) designed for triggered intracellular gene delivery. *Bioconjugate Chem. 17*, 1233–1240.

(12) Martello, F., Engbersen, J. F. J., and Ferruti, P. (2008) *J. Controlled Release 132*, e1−e18.

(13) Plank, C., Mechtler, K., Jr., and Wagner, E. (1996) Activation of the complement system by synthetic DNA complexes: potential barrier for intravenous gene delivery. *Hum. Gene Ther. 7*, 1437–1446.

(14) Wagner, E., Plank, C., Zatloukal, K., Cotten, M., and Birnstiel, M L. (1992) Influenza virus hemagglutinin HA-2 N-terminal fusogenic peptides augment gene transfer by transferrin-polylysine-DNA complexes: toward a synthetic virus-like gene-transfer vehicle. *Proc. Natl. Acad. Sci. U.S.A. 89*, 7934–7938.

(15) Verbaan, F. J., Oussoren, C., Van Dam, I. M., Takakura, Y., Hashida, M. D., Crommelin, J. A., Hennink, W. E., and Storm, G. (2001) The fate of poly(2-dimethyl amino ethyl)methacrylate-based polypolylysine as a synthetic vector for gene transfer into plexes after intravenous administration. *Int. J. Pharm. 214*, 99–101.

(16) Suh, W., Han, S., Yu, L., and Kim, S. W. (2002) An angiogenic, endothelial-cell-targeted polymeric gene carrier. *Mol. Ther. 6*, 664–672.

(17) Merkel, O. M., Germershaus, O., Wada, C. K., Tarcha, P. J., Merdan, T., and Kissel, T. (2009) Integrin $\alpha_v\beta_3$ targeted gene delivery using RGD peptidomimetic conjugates with copolymers of PEGylated poly(ethylene imine). *Bioconjugate Chem. 20*, 1270–1280.

(18) Burckhardt, B. C., and Thelen, P. (1995) Effect of primary, secondary and tertiary amines on membrane potential and intracellular pH in Xenopus laevis oocytes. *Pflugers Arch. 429*, 306–312.

(19) Wang, H., Wang, Y., and Yan, H. (2006) Binding of sodium dodecyl sulfate with linear and branched polyethyleneimines in aqueous solution at different pH values. *Langmuir 22*, 1526–1533.

(20) Godbey, W. T., Wu, K. K., and Mikos, A. G. (2001) Poly(ethylenimine)-mediated gene delivery affects endothelial cell function and viability. *Biomaterials 22*, 471–480.

(21) Lin, C., Zhong, Z., Lok, M. C., Jiang, X., Hennink, W. E., Feijen, J., and Engbersen, J. F. J. (2006) Linear poly(amido amine)s with secondary and tertiary amino groups and variable amounts of disulfide linkages: Synthesis and in vitro gene transfer properties. *J. Controlled Release 116*, 130–137.

(22) Kunath, K., Merdan, T., Hegener, O., Häberlein, H., and Kissel, T. (2003) Integrin targeting using RGD-PEI conjugates for *in vitro* gene transfer. *J. Gene Med. 5*, 588–599.

(23) Pasche, S., Voros, J., Griesser, H. J., Spencer, N. D., and Textor, M. (2005) Effects of ionic strength and surface charge on protein adsorption at PEGylated surfaces. *J. Phys. Chem. B 109*, 17545–17552.

(24) Ga, Q., Wang, T., Cochrane, C., and McCarron, P. (2005) Modulation of surface charge, particle size and morphological properties. *Colloids Surf., B 44*, 65–73.

BC900522X

Site-Specific PEGylation of Bone Morphogenetic Protein-2 Cysteine Analogues

Junli Hu,* Viswanadham Duppatla, Stefan Harth, Werner Schmitz, and Walter Sebald

Physiological Chemistry II, Biocenter, University of Würzburg, Am Hubland, 97074 Würzburg, Germany. Received December 21, 2009; Revised Manuscript Received September 4, 2010

Three cysteine analogues of bone morphogenetic protein (BMP)-2, BMP2A2C, BMP2N56C, and BMP2E96C, were generated in order to enable the attachment of SH-reactive poly(ethylene glycol) (PEG) at specific sites. Three different approaches (Ap) were used for SH-specific PEGylation: (Ap1) reaction of glutathione activated proteins with thiol PEG; (Ap2) reaction of DTT reduced proteins with orthopyridyl disulfide PEG; (Ap3) reaction of DTT reduced proteins with maleimide PEG. Non-, mono-, and di-PEGylated BMP-2 analogues could be separated by RP-HPLC. Trypsin digestion of PEGylated proteins and Trypsin and GluC double-digestion of *N*-ethylmaleimide-labeled proteins confirmed that the modifications were site-specific. Surface plasmon resonance analysis of type I and type II receptor binding of the PEGylated BMP-2 analogues revealed that all three PEGylation approaches were equivalent. PEGylation at positions 2 and 96 caused a similar decrease in receptor affinity. PEGylation at position 56 resulted in a larger decrease in affinity for both types of receptors. Mono-PEGylated BMP-2 analogues exhibited intermediate affinities in comparison with unmodified and di-PEGylated proteins. However, the biological activity of the PEGylated BMP-2 analogues as measured in alkaline phosphatase assay was higher than BMP-2 wild-type for the PEGylated BMP2A2C, slightly reduced for the BMP2N56C, and strongly reduced for the BMP2E96C. These results taken together indicate that specific attachment of PEG at engineered sites of BMP-2 is possible and that the attachment site is critical for biological activity. Furthermore, the biological activity of PEGylated BMP-2 analogues in cell culture seems to be determined not only by receptor affinity, but also by other factors such as protein solubility and stability. It is also discussed that the attached PEG interferes with the binding of BMP-2 to modulator proteins, co-receptors, or heparinic sites of proteoglycans in the extracellular matrix.

INTRODUCTION

Bone morphogenetic protein-2 (BMP-2 or BMP2WT), as a member of the large transforming growth factor-β (TGF-β) superfamily of multifunctional cytokines, can induce ectopic bone and cartilage formation in adult vertebrates (*1, 2*) and plays important roles in early embryonal development in animals (*3*). It has received intense interest during the past decade due to its therapeutic use in regenerative medicine. BMP-2 is applied together with a carrier during surgery (*4*). Its poor solubility under physiological conditions, the presence of a heparin-binding site, and a short circulation half-life promote a desirable localized action of BMP-2 for indications in spinal fusion, repair of nonunion fractures, and sinus lift augmentation (*5, 6*).

In the organism, the biological activity and solubility of several BMPs[1]seem to be modulated by post-translational modifications. In BMP-2, BMP-6, BMP-7, and several other BMPs, an invariant asparagine side chain corresponding to Asn 56 of mature BMP-2 becomes N-glycosylated (*7*−*9*). BMP-6 and BMP-7 contain two additional N-glycosylation sites near the N-terminus. It was therefore challenging to explore in a proof-of-principle study with BMP-2 whether BMP proteins can be chemically modified at specific sites and how far a chemical modification influences the solubility and the biological activity of the BMP protein.

Poly(ethylene glycol) (PEG) is biocompatible and readily soluble in water. PEGs are available with low polymer dispersity index (less than 1.02) and as derivatives carrying functional groups for chemical modification at different reactive sites. Protein PEGylation has been a very successful approach to slow down ultrafiltration in the kidney, to alter tissue distribution, and to reduce phagocytosis, proteolysis, and immunogenicity (*10, 11*). During the past two decades, several PEGylated protein products like Adagen, Oncaspar, PEG-Intron, Pegasys, Neulasta, and Somavert have been approved for human use. Many others are undergoing clinical evaluation (*10*).

Most chemical strategies of PEGylation were based on the nucleophilic or electrophilic reaction between PEG derivatives and the reactive groups of amino acid residues, e.g., amino group from lysine and N-terminus, thiol group from cysteine, or hydroxyl group from serine (*12*). Due to the polyfunctional nature of proteins, such nonselective strategies often lead to a mixture of chemically different entities, which may complicate the prediction of the pharmaceutical behavior of the protein. Therefore, site-specific PEGylation is highly desirable. Different routes were developed for this purpose. Kinstler et al. described a method that specifically PEGylates N-terminal amino group relying on the difference in pK_a of α-amino group of N-terminus and the ε-amino group of lysine residues (*13*). Mutagenesis has

* Correspondence to Junli Hu. Current address: School of Dentistry, University of California, Los Angeles, Advanced Prosthodontics, 10833 Le Conte Avenue, Room 23-032 CHS, Los Angeles, CA 90095-166815. Tel: 1-323-470-0638, E-mail: junlihu100@yahoo.com.

[1]Abbreviations: BMP, bone morphogenetic protein; BMP2A2C, bone morphogenetic protein-2 analogue with mutation from Ala to Cys at position 2; BMP2N56C, bone morphogenetic protein-2 analogue with mutation from Asn to Cys at position 56; BMP2E96C, bone morphogenetic protein-2 analogue with mutation from Glu to Cys at position 96; PEG, poly(ethylene glycol); Ap, approach; DTT, dithiothreitol; PEGylation, conjugation with poly(ethylene glycol); ALP, alkaline phosphatase; TGF, transforming growth factor; PEG-SH, thiol poly-(ethylene glycol); PEG-MA, maleimide poly(ethylene glycol); PEG-OPSS, orthopyridyl disulfide poly(ethylene glycol); PMSF, phenylmethylsulfonyl fluoride; HAc, acetic acid; Tris, tris(hydroxymethyl) aminomethane; HCl, hydrogen chloride; NaCl, sodium chloride; PBS, phosphate buffered saline; NEM: *N*-ethylmaleimide; cam: acetamidation by iodoacetamide; Rmax: maximal binding to receptor.

10.1021/bc9005706 © 2010 American Chemical Society
Published on Web 10/01/2010

been used to make single-site attachment possible (*14*). PEGylation at the thiol group of cysteines not involved in disulfide bridges is one of the most specific methods because cysteines are rarely present in proteins or normally form disulfide bridges, and mutagenesis technique provides a convenient way to generate single cysteine for PEGylation. Interferon-α2 (*15*), cyanovirin-N (*16*), and granulocyte colony-stimulating factor (*17*) were site-specifically PEGylated either as wild-type protein or as cysteine analogue.

The wild type of BMP-2 forms a disulfide-bonded homodimer in its native state. Each of the BMP-2 monomers has seven cysteines. Six of them form three intramolecular disulfides (Cys 43/Cys 111, Cys 47/Cys 113, and Cys 14/Cys 79), constituting a cysteine knot, which is a common feature of all members of the TGF-β superfamily (*18*). The cysteine knot is crucial for the conformation and thus for the activity of the BMP-2. One cysteine (Cys 78) forms an intermolecular disulfide with the other monomer, constituting the dimer (*19*). It contains no free cysteine side chains. There are a few examples of PEGylation at amino groups of BMP-2 and the related TGF-β1 and TGF-β2 for their applications in tissue engineering. PEGylation was employed to immobilize the protein on scaffolds and thus to improve local bone regeneration (*20*), to lengthen local fibroblastic response (*21*), or to increase muscle matrix production (*22*). The large number of amino groups (7−9 lysines and one N-terminus in each monomer) made the PEGylation heterogenic. Unfortunately, no detailed biochemical data on the PEGylated proteins were reported.

BMP-2 homodimer formed by two hand-like monomers contains two wrist epitopes for type I receptor binding and two knuckle epitopes for type II receptor binding (*23*). The crystal structure of ternary complexes consisting of BMP-2 and the ectodomains of type I and type II receptors has been reported (*24*). During the present study, BMP-2 cysteine analogues were generated by site-directed mutagenesis at amino acid positions Ala 2, Asn 56, and Glu 96 differing in their distances to the binding epitopes for the receptors. Three approaches for SH-specific PEGylation were compared with respect to site-specificity, as well as yield and solubility of the modified analogues. The biological activities of the PEGylated BMP-2 cysteine analogues were analyzed and compared in detail applying receptor interaction and cell-based assays.

EXPERIMENTAL PROCEDURES

Chemicals. Thiol PEG (PEG-SH, M_n = 4503 Da, Sunbright ME-050SH) and maleimide PEG (PEG-MA, M_n = 5426 Da, Sunbright ME-050MA) were purchased from NOF Inc. (Kyoto, Japan). Functional PEG was dissolved in analytical-grade dimethylsulfoxide (DMSO, Sigma, St. Louis, MO, USA) and stored at −20 °C. 2,2′-dithio dipyridine and *p*-nitrophenyl phosphate were purchased from Sigma (St. Louis, MO, USA). Dithiothreitol (DTT), buffer chemicals, and SDS-polyacrylamide gel electrophoresis (SDS-PAGE) chemicals were purchased from Carl Roth (Karlsruhe, Germany). Phenylmethylsulfonyl fluoride (PMSF) and Trypsin (sequencing grade) were purchased from Merck (Darmstadt, Germany). *N*-Ethylmaleimide (NEM) was purchased from Thermo Scientific (Dreieich, Germany). RapiGest was supplied by Waters (Massachusetts, USA); Endoproteinase GluC was purchased from New England Biolabs (Frankfurt am Main, Germany).

Cloning DNA Sequences Encoding BMP-2 Cysteine Analogues. DNAs encoding BMP-2 cysteine analogues at the position of Ala 2, Asn 56, or Glu 96 (BMP2A2C, BMP2N56C, BMP2E96C) were amplified by means of the polymerase chain reaction (PCR) method using primers BMP2A2C5′(CCATGGCTCAATGCAAACACAAACAG) and BMP2A2C3′ (CTGTTTGTGTTTGCATTGAGCCATGG) for BMP2A2C, BMP2N56C5′ (GCTGATCATCTGTGCTCCACTAATCAT) and BMP2N56C3′ (ATGATTAGTGGAGCACAGATGATCAGC) for BMP2N56C and BMP2E96C5′ (GTACCTTGACGAGAATTGCAAGGTTG) and BMP2E96C3′ (CAACCTTGCAATTCTCGTCAAGGTAC) for BMP2E96C. Plasmid vector QKA BMP-2, which has a BMP-2 cDNA insert corresponding to residues 283−396 of the mature protein plus an N-terminal Met-Ala extension, was used as a template. The PCR products were digested with NcoI and *Bam*HI and cloned into digested plasmid vector, creating plasmids QKA BMP2A2C, QKA BMP2N56C, and QKA BMP2E96C. The plasmids encoding the cysteine analogues were transformed into the *E. coli* host MM294. Correct DNA sequences of all cysteine analogues were confirmed by DNA sequence analysis.

Expression and Purification of BMP-2 Cysteine Analogues. The wild type of recombinant human BMP-2 (BMP2WT) was expressed and purified as described previously (*25*). Heparin sepharose chromatography was applied as an additional final purification step (*26*). During refolding of the proteins, 2 mM oxidized and 1 mM reduced glutathione were added.

The plasmids encoding the BMP-2 cysteine analogues were transformed to BLR(DE)3 *E. coli* host strains, and expressed and purified by the same procedure as those for BMP2WT.

Electrospray Ionization Mass Spectrometry Analysis (ESI-MS). ESI-MS was performed using an APEX-II FT-ICR (Bruker Daltonic GmbH, Bremen) equipped with a 7.4 T magnet and an Apollo ESI ion source in positive mode. Desalted proteins were dissolved in methanol/H_2O/HAc (49.5/49.5/1) at the concentration range 1−5 μM. Sample was injected using a Hamilton syringe at a speed of 2 μL/min with a capillary voltage of 100 mV. Detection range was typically set to 300−3000 *m/z* in preliminary measurements. The detection range was optimized to the signal-containing area afterward. 256 scans were added at a resolution of 256 K.

DTT Reduction of Glutathione Oxidized BMP-2 Cysteine Analogues. Glutathione oxidized BMP-2 cysteine analogues (noted as BMP2A2C/N56C/E96C^{ox}) were incubated at 1 mg/mL in 0.1 mM DTT, 4 M urea, 50 mM Tris, pH 8 for 2 h at room temperature and then submitted to reversed-phase HPLC (RP-HPLC) to remove DTT and buffer salts. The reduced proteins were designated as BMP2A2C/N56C/E96C^{re} in the following text.

Preparation of Orthopyridyl Disulfide PEG (PEG-OPSS). PEG-OPSS was prepared according to Woghiren et al. (*27*) with minor modifications. Briefly, 284 mg PEG-SH and 245 mg 2,2′-dithio dipyridine were dissolved in 1.5 mL methanol, and then 0.17 mL 0.4 M Tris, 1.2 M NaCl, pH 10, was added. The mixture was then shaken at 1400 rpm and 50 °C for 1 h. Methanol was evaporated under a stream of nitrogen. The activated PEG was extracted twice with 1 mL 100 mM HAc. The combined supernatants containing the activated PEG were loaded on a size exclusion chromatography column (Bio-Gel $P\bar{6}$ DG Desalting Gel, Bio-Rad, Hercules, CA, USA) and eluted with 100 mM HAc. The pooled peak fractions were freeze−dried and stored at −80 °C.

PEGylation at Analytical Scale. BMP-2 cysteine analogues (1 mg/mL) and different amount of activated PEG (molar ratio of PEG to protein between 1:1 and 100:1) were incubated in 0.1 mL of 4 M urea, 50 mM Tris, pH 8, containing 10% (v/v) DMSO. The PEGylation mixtures were shaken at room temperature at 700 rpm for 2−48 h.

PEGylation at Preparative Scale. Three different approaches (Ap1−3) were used to PEGylate protein at a preparative scale as listed in Table 1.

BMP-2 cysteine analogues (1 mg/mL) and 30-fold excess PEG-SH (Ap1) or 3-fold excess PEG-OPSS (Ap2) or PEG-MA (Ap3) reacted in 4 M urea, 50 mM Tris, pH 8, containing

Table 1. Three Approaches Used for PEGylation of BMP-2 Cysteine Analogues

approach	protein	PEG	product
Ap1	BMP2A2C/N56C/E96C^{ox}	PEG-SH	mono/diPEG-SS-BMP2A2C/N56C/E96C^{ox}
Ap2	BMP2A2C/N56C/E96C^{re}	PEG-OPSS	mono/diPEG-SS-BMP2A2C/N56C/E96C^{re}
Ap3	BMP2A2C/N56C/E96C^{re}	PEG-MA	mono/diPEG-SMA-BMP2A2C/N56C/E96C^{re}

10% (v/v) DMSO. The PEGylation mixtures were shaken at room temperature at 700 rpm for 48 h (Ap1) or 2 h (Ap2 and 3). The PEGylation mixtures were then submitted to RP-HPLC for separation.

SDS-Polyacrylamide Gel Electrophoresis (SDS-PAGE). SDS-PAGE was performed using a 12% polyacrylamide gel as described previously (*28*). Protein solutions were diluted 2- to 5-fold with nonreducing sample buffer. The gels were stained with Coomassie Blue.

Trypsin Digestion. PEGylated BMP-2 cysteine analogues (0.1 mg) dissolved in 70 μL 1 mM HCl were mixed with 10 μL 0.1 mg/mL Trypsin solution in 1 mM HCl. A 20 μL solution of 2.5 M Tris and 250 mM NaCl, pH 8.5, was then added, and the whole mixtures were kept at 37 °C for 4 h. PMSF of 1 mM was added to stop the reaction before sample preparations for SDS-PAGE.

Reduction and NEM-Labeling of BMP-2 Cysteine Analogues. Proteins were reduced with DTT as described above. For the E96C analogues, however, the DTT concentration was increased from 0.1 mM to 0.3 mM. MS analysis established that all proteins were devoid of glutathione and contained the expected seven disulfide bridges. After RP-HPLC, the proteins were freeze−dried and stored at −20 °C.

The reduced protein was dissolved in 4 M urea, 50 mM Tris, pH 8, at 1 mg/mL and incubated with a 3-fold molar excess of NEM for 2 h at room temperature. The mixture was submitted to RP-HPLC (see below). The protein was eluted as a main peak with a small shoulder. Protein fractions were combined, freeze−dried, dissolved in water, and stored at −20 °C.

Double-Digestion of NEM-Labeled BMP-2 Proteins with Trypsin and GluC. The NEM-labeled BMP-2 protein (3.5 μg in 10 μL H_2O) was mixed with RapiGest, reduced with DTT, reacted with an excess of iodoacetamide, and finally digested with Trypsin and Endoproteinase GluC as specified by the suppliers. The complete solution was then taken to dryness. The residue dissolved in 30 μL of 1% trifluoroacetic acid was applied to a C18-ZipTip (Millipore, Germany), and peptides were eluted in 50 μL methanol/H_2O/HAc (49.5/49.5/1 v/v/v). The whole eluted peptide fraction was subjected to mass spectrometry.

RP-HPLC. RP-HPLCs on a Grace Vydac 214TP54 C4 column (250 × 4.6 mm) were performed on a liquid chromatography system equipped with a Merck Hitachi L-6200A intelligent pump, a Merck Hitachi L-4000 UV detector, and a Gilson FC203B fraction collector.

DTT reduced BMP-2 cysteine analogues were eluted with a linear gradient of 0.1% trifluoroacetic acid (Buffer A) and acetonitrile (Buffer B). (0% to 100% buffer B in 50 min). PEGylation mixtures of BMP-2 cysteine analogues were separated by applying the following protocol: 0% to 30% buffer B in 10 min, 30% to 50% B in 40 min, and 50% to 100% B in 10 min.

Solubility Analysis in Phosphate Buffered Saline (PBS). The UV spectra of PEGylated BMP-2 in PBS (150 mM NaCl, 10 mM sodium phosphate salt, pH 7.4) were recorded with a UV−vis spectrophotometer (Cary 50 BIO, Varian). Unmodified BMP-2 was used as the control. Stock aqueous solutions containing 4 μM of free and PEGylated BMP-2 cysteine analogues were diluted with the same volume of double concentrated PBS, mixed thoroughly, and kept at room temperature for 2 h. The spectra of the solution were recorded between 250 and 320 nm.

Biosensor Interaction Analysis. Biosensor experiments were carried out on a BIAcore 2000 system (Pharmacia Biosensor) at 25 °C at a flow rate of 10 μL/min in running buffer (10 mM 4-(2-hydroxyethyl)-1-piperazine ethanesulfonic acid, pH 7.4, 500 mM NaCl, 3.4 mM ethylenediaminetetraacetic acid, 0.005% surfactant polyoxyethylene sorbitan P20) with a data collection rate of 2.5/s. A CM5 biosensor chip was first coated with streptavidin in all four flow cells, and subsequently the biotinylated ectodomains of BMP receptor IA (BMPR-IA) or Activin receptor IIB (ActR-IIB) was immobilized on the streptavidin matrix in flow cells 2 and 3 (*29*).

C2C12 Alkaline Phosphatase Assay. Alkaline phosphatase (ALP) activity was determined in serum-starved mouse C2C12 cells. The promyoblast C2C12 cells (ATCC-CRL1772) in Eagle's minimal essential medium containing 10% fetal calf serum were incubated at 1×10^5 cells/mL in 100 μL aliquots in a 96-well plate for 24 h at 37 °C and 5% carbon dioxide. Afterward, the medium was substituted with 100 μL fresh medium containing 2% fetal calf serum containing various concentrations of the BMP proteins. After a further cultivation for three days, cells were lysed in 100 μL lysis buffer (0.1 M glycine, 1% nonyl phenoxylpolyethoxylethanol, 1 mM magnesium chloride, 1 mM zinc chloride, pH 9.6) and alkaline phosphatase activity was determined in 100 μL aliquots of the cleared lysate using 100 μL 0.3 mM *p*-nitrophenylphosphate in the color buffer (0.1 M glycine, 1% nonyl phenoxylpolyethoxylethanol, 1 mM magnesium chloride, 1 mM zinc chloride, pH 9.6) as substrate. Absorbance at 405 nm was recorded after incubation of 50 min.

RESULTS AND DISCUSSION

BMP-2 Cysteine Analogues. All three analogues could be prepared, but with lower yields (6.8, 5.2, 3.5 mg/L culture medium for BMP2A2C, BMP2N56C, BMP2E96C, respectively) than BMP2WT (46 mg/L). Mass spectrometry of the purified BMP-2 analogues reveals that BMP2A2C^{ox} and BMP2E96C^{ox} have molecular weights 610 Da larger than those expected for the cysteine proteins (Figure 1A−C). This increase in size corresponds to two glutathione groups minus four hydrogen atoms. Two species of BMP2N56C^{ox} were identified by mass spectrometry, whose molecular weights were in accordance with a mono- and diglutathione derivative. The glutathione becomes attached most likely by a disulfide bond during the refolding step of the recombinant BMP proteins. As redox couple, oxidized glutathione and reduced glutathione were present in the refolding reaction to provide the appropriate redox potential that allows formation and reshuffling of disulfides bonds (see Experimental Procedures). The attached glutathione might have served as a protecting group during protein purification. On the other hand, the attached glutathione could be used as activating group allowing the reaction with SH-activated PEG for PEGylation.

The attached glutathione could be removed by treatment of BMP2A2C and BMP2N56C with DTT of very low concentration (0.1 mM) when the dimer is still stable but the attached glutathione will be removed. Figure 1D−F shows the mass spectra of the proteins after DTT treatment. For BMP2A2C and BMP2N56C, both glutathione groups in dimer were removed successfully by DTT treatment, but for BMP2E96C, DTT treatment could remove the glutathione only partially. This resulted in a mixture of fully glutathione-oxidized, half oxidized,

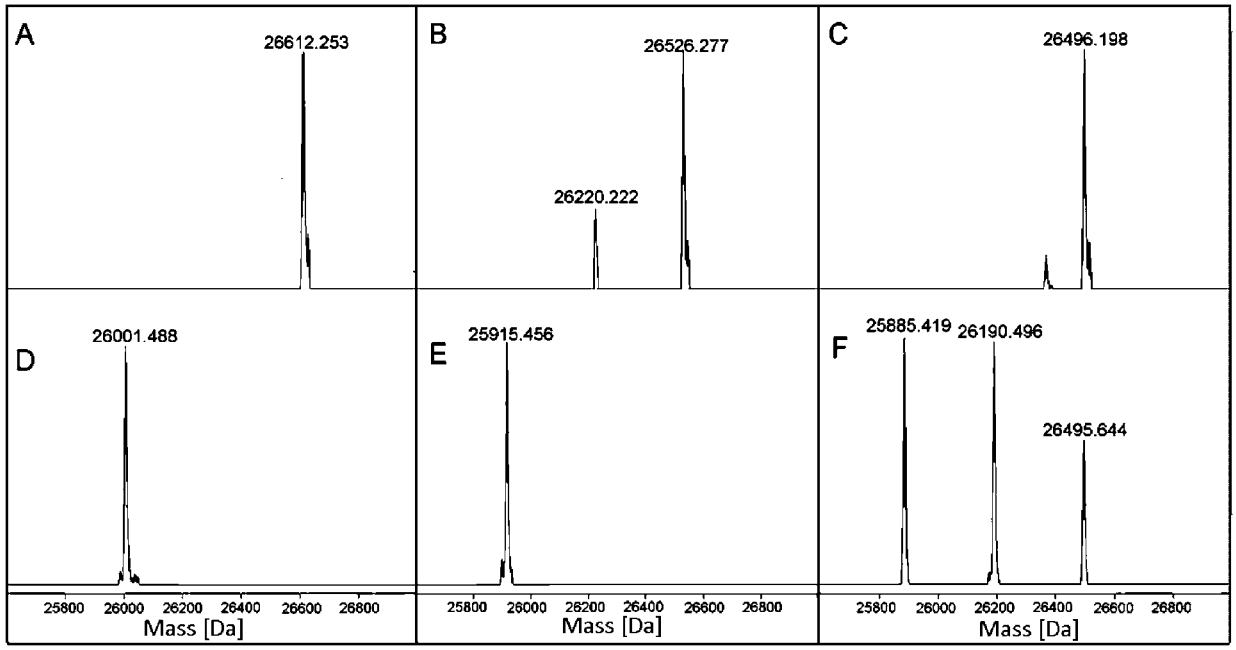


Figure 1. Mass spectra of BMP-2 cysteine analogues before (A, B, C) and after (D, E, F) DTT reduction. A, D: BMP2A2C. B, E: BMP2N56C. C, F: BMP2E96C. The analysis of these proteins by SDS-PAGEs is shown in Figure 2.

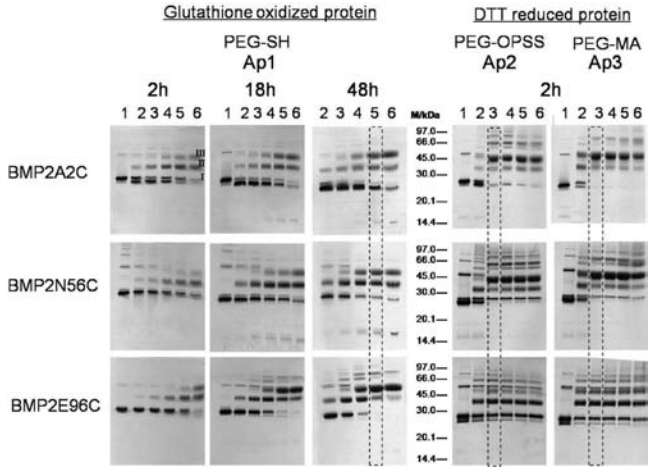


Figure 2. SDS-PAGE analysis of PEGylation mixtures obtained by Ap1, Ap2, and Ap3 listed in Table 1. Lane 1 always corresponds to BMP-2 cysteine analogues before PEGylation; lanes 2−6 correspond to PEGylation products obtained at a molar PEG excess of 1, 3, 10, 30, and 100, respectively. The conditions marked by dashed rectangles were used for PEGylations at preparative scale. Bands I, II, and III correspond to free, mono-, and di-PEGylated proteins, respectively.

and fully reduced BMP2E96C at the ratio of about 2:2:1. The only partial reduction observed in several experiments is difficult to explain, since Cys 96 of each monomer is supposed to be exposed on the protein surface (*24*). At 0.3 mM DTT, however, the attached glutathione groups also of BMP2E96C were completely removed (see below).

Optimizing the Conditions for PEGylation of BMP-2 Cysteine Analogues. Figure 2 presents SDS-PAGE analysis of whole PEGylation products obtained at different PEG/protein molar ratios by three different approaches (Table 1): Ap1, PEG-SH reacted with the glutathione oxidized proteins; Ap2, PEG-OPSS reacted with the reduced proteins; Ap3, PEG-MA also reacted with the reduced proteins. Methods Ap1 and Ap2 generate disulfide bonds between protein and PEG. Method Ap3 involving a reaction between maleimide and thiol group results in a nonreducible single bond connecting protein and PEG.

In order to obtain high PEGylation levels of the glutathione-oxidized proteins with Ap1, 30- to 100-fold molar excess of PEG-SH and a 48 h reaction time had to be applied. The major products were mono- or di-PEGylated proteins, migrating as the first and second upper bands (bands II and III in Figure 2, respectively). A few proteins with higher molecular weights were observed which might represent multimers or multi-PEGylated proteins. When lower molar excess of PEG-SH was applied, the amount of mono- and di-PEGylated protein always increased with the reaction time. At higher PEG-SH input (30- to 100-fold excess), the yield of di-PEGylated protein increased with the reaction time, while the yield of mono-PEGylated proteins decreased at later time points (18 to 48 h), probably due to the conversion of the mono- to the di-PEGylated form.

In contrast, the DTT reduced proteins were more reactive than the oxidized proteins, but also less stable. For BMP2A2C^{re} and BMP2N56C^{re}, already a 3-fold molar excess of PEG-OPSS or PEG-MA yielded the di-PEGylated proteins as major products. This suggests that both SH groups of the dimer exhibited the same reactivity. For BMP2E96C^{re}, the mono-PEGylated form dominated, probably because only one of the SH groups was free in most protein dimers (see above).

Several proteins of higher molecular weight appeared in the SDS-PAGE. These are most pronounced with Ap2 and somewhat less so with Ap3. At least some of them likely represent multimers generated by oxidative disulfide formation between two or more BMP-2 proteins, since bands with the same mobility are seen after SDS-PAGE of the non-PEGylated protein or of the protein incubated at low molar excess of the activated PEG. Remarkably, multimers are least abundant with the analogue A2C. This is possibly related to the observation that the N-terminal cysteines can form an intramolecular disulfide bond (data not shown). The strong multimer formation with Ap2 possibly results from a disulfide exchange with PEG-OPSS especially at low molar excess of this disulfide activated PEG. It has also to be considered that the rate of PEGylation might differ among the three analogues and that disulfide formation as a side reaction can therefore proceed for different time periods. One of the additional bands obtained with Ap3 might correspond to a tri-PEGylated BMP-2 protein most likely

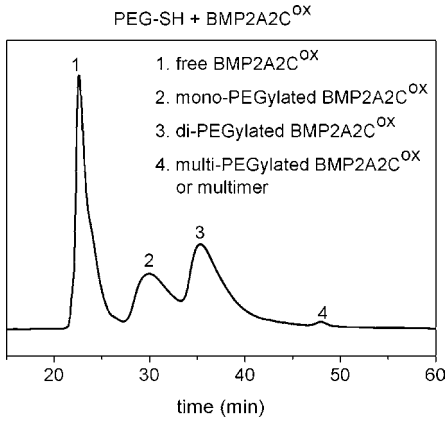


Figure 3. Representative RP-HPLC chromatogram for the separation of PEGylated BMP2A2C after labeling by Ap1. Peaks 1−3 correspond to free BMP2A2C^{ox}, mono-, and di-PEGylated BMP2A2C^{ox}, respectively. Peak 4 corresponds to multi-PEGylated BMP2A2C^{ox} or multimers of the BMP2A2C.

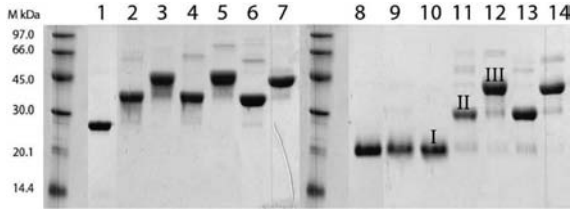


Figure 4. SDS-PAGE analysis of PEGylated BMP-2 cysteine analogues conjugated with maleimide PEG (Ap3) (lanes 2−7) and their Trypsin digests (lanes 9−14). Lane 2, monoPEG-SMA-BMP2A2C^{re}; 3, diPEG-SMA-BMP2A2C^{re}; 4, monoPEG-SMA-BMP2N56C^{re}; 5, diPEG-SMA-BMP2N56C^{re}; 6, monoPEG-SMA-BMP2E96C^{re}; 7, diPEG-SMA-BMP2E96C^{re}. Lanes 9−14 correspond to the Trypsin digests of 2−7, respectively. BMP2WT (lane 1) and its Trypsin digests (lane 8) were served as references. Band I corresponds to the large BMP-2 fragment with cleaved-off N-terminal part. Bands II and III correspond to the large fragment containing one and two PEG chains, respectively.

generated by unspecific MA-PEGylation at amino groups (see the fifth section).

Preparative PEGylation and RP-HPLC. For preparative PEGylation of glutathione oxidized proteins, we chose a PEG/protein molar ratio of 30 and a reaction time of 48 h. These conditions are marked as the left dashed rectangle in Figure 2. For preparative PEGylation of DTT reduced proteins, we chose a PEG/protein molar ratio of 3 (see middle and right dashed rectangles in Figure 2). Figure 3 shows a representative RP-HPLC chromatograph for the separation of free, mono-, and di-PEGylated BMP-2 cysteine analogues. Lanes 2−7 in Figure 4 show the SDS-PAGEs of PEGylated proteins (Ap3 only) after RP-HPLC purification. All the isolated PEGylated proteins exhibit a purity of more than 90%.

Trypsin Digestion of PEGylated Proteins. BMP2WT can be cleaved by Trypsin between Lys 8, Arg 9, and Lys 11 at the N-terminal part (Figure 4, lanes 8−14, Figure 5). The cleavage sites are inferred from the mass of the three larger cleavage products which are 23231.735, 23471.860, and 23627.891 Da, respectively. Therefore, band I in Figure 4 corresponds to the BMP-2 fragment missing the N-terminal part. The mono- and di-PEGylated BMP2A2C from all preparations were digested to a protein migrating as the digested BMP2WT, clearly indicating that PEG was attached at the cleaved N-terminal end; this means at Cys 2, suggesting that PEGylations at Cys 2 were site-specific.

In contrast, mono- and di-PEGylated BMP2N56C or BMP2E96C from all preparations retained the attached PEG in the large BMP fragment after Trypsin cleavage. This is indicated by the migration of the fragments with one or two additional PEGs in bands II and III, respectively. Limited trypsin digestion of PEG-modified BMP-2 cysteine mutants and subsequent SDS-PAGE analysis showed that PEGylation occurred with the A2C protein in the N-terminal peptide whereas with N56C and E96C in the cystine-knot domain (Figure 4). There exists only one single cysteine in the N-terminal peptide of the A2C analogue which can be responsible for the cysteine-specific PEGylation detected in this peptide. The cysteine knot domain, however, contains the introduced cysteine residues and, in addition, the seven

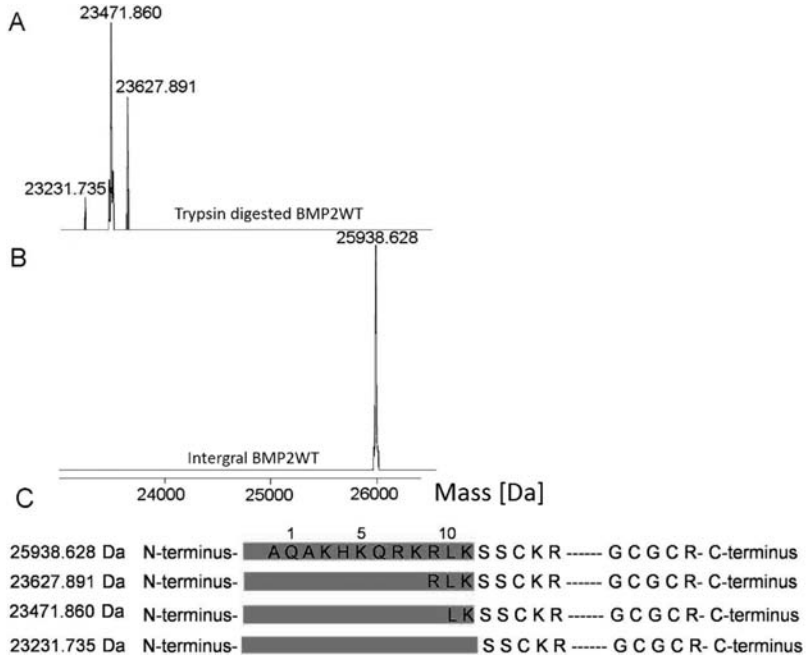


Figure 5. Mass spectra of (A) the large Trypsin fragments of BMP2WT, in comparison with (B) undigested BMP2WT. (C) Proposed N-terminal sequences of the fragments that have been aligned with mature BMP2WT sequence. The clustered basic amino acids in the N-terminal segment represent a heparin-binding epitope (*25*).

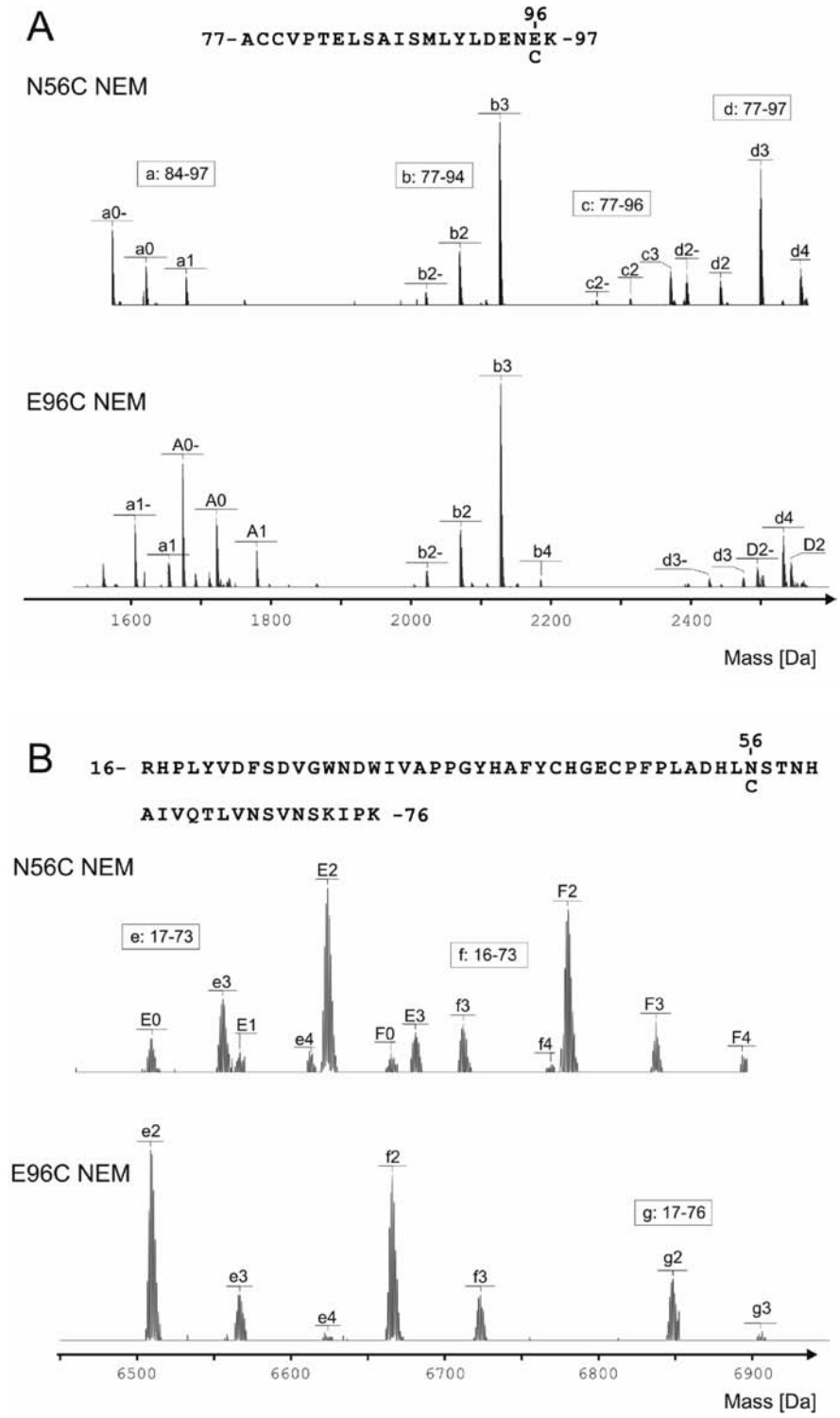


Figure 6. Mass spectra of peptides generated by double-digestion of NEM-labeled BMP2N56C and BMP2E96C with Trypsin/GluC. The deconvoluted spectra represent different mass regions of the same record for each of the analogues. The designation of the peptides and their molecular weights, intensities, and assignments are listed in Supporting Information Tables S-2A and S-2B. (A) Peptides a/A, b, c, and d/D represent BMP-2 sequences from amino acid 77 to 97 as indicated by the boxed position ranges. (B) Peptides e/E, f/F, and g represent BMP-2 sequences from amino acids 16 to 76 as indicated by the boxed position ranges. Peptides labeled with NEM are assigned by capital letters A, D (E96C NEM), and E, F (N56C NEM). Multiple forms of a peptide can be generated by partial elimination of methylmercaptan (MeSH) from Met containing peptides (*32*), and/or from acetamidation of mercapto- and/or amino-groups by iodoacetamide (cam) (*31*). Peptides formed after elimination of MeSH are designated by "-". The number of acetamide modified residues of a peptide is designated as a suffix to the characterizing letter of the peptide. All peptides containing intramolecular SS-bridges prior to reduction become labeled with two cams after reduction and iodacetamide treatment (b2, c2, d2, D2, e2, E2, f2, F2, and g2).

cysteines of BMP-2 which represent potential PEGylation sites in the case of protein misfolding and/or partial reduction. The specificity of PEGylation at N56C and E96C thus cannot be confirmed only by these results. However, the nonlabeling of the A2C analogue in the cysteine knot domain strongly suggests that in the di-PEGylated analogues N56C and E96C the label has been attached to the introduced cysteine residues as analyzed in detail in the following section.

NEM-Labeling of BMP-2 Cysteine Analogues Is Specific for the Introduced Cysteine Residue. In order to define the specificity of labeling in more detail, the N56C and E96C analogues were further analyzed by mass spectrometry.

Initial trials with maleimide-di-PEGylated proteins showed that positive identification of PEGylated peptides by mass spectrometry was not possible, since the MA-PEG contained multiple species differing by one ethoxy group. This heterogeneity is not apparent at the lower resolution of SDS-PAGE analysis. Therefore, labeling was performed with NEM (see Experimental Procedures) representing only the reactive N-ethylmaleimide group without the PEG side chain. NEM is a classical SH-reagent. Side reactions with amino groups have been observed, however, in particular, if the reaction is performed at pH values higher than 7.5 (*30*). MS analysis identified the di-NEM derivatives as major reaction product of all cysteine analogues (see Supporting Information Figure S-1, Table S-1). Smaller amounts of tri-NEM- and spurious amounts of tetra-NEM-derivatives could be also observed.

The whole reaction products were submitted to a double-digestion with Trypsin and GluC. The expected diagnostic peptides after complete or partial digestion were identified by MS covering sequence positions 16 to 76 (annotated "e, f, and g" in Figure 6B), including Cys 56 in the N56C analogue, as well as sequence positions 77 to 97 (annotated "a, b, c, and d" in Figure 6A), including the Cys 96 of the E96C analogue. NEM labeling was detected only in peptides F (16−73) and E (17−73) of BMP2N56C (Figure 6A) and in peptides A (84−97) and D (77−97) of BMP2E96C (Figure 6B). Virtually no NEM labeling could be identified either in the corresponding non-mutated peptides from both analogues (Figure 6; compare peptides labeled with capital letters or with small letters) or in the corresponding non-mutated peptides from the BMP2A2C analogue (data not shown). These results show that NEM labeling is found as expected only in peptides containing the introduced cysteine residues of N56C and E96C analogues. They furthermore strongly suggest that unspecific labeling has not occurred at positions of the native cysteine residues forming the cysteine knot and the covalent homodimer of BMP-2. Because the reactivities of NEM and MA-PEG are comparable, we conclude that in the PEGylated analogues SH-specific labeling also occurs only at the positions of the introduced cysteine residues.

Remarkably, the occurrence of tri-NEM labeled proteins (Supporting Information Figure S-1) is not reflected by detectable amounts of additional NEM-labeled peptides. Possibly, this NEM label is unspecifically attached to amino groups (see above) and distributed randomly over several side chains. This labeling might be therefore below the detection limit. Most peptides had been modified by cam during sample preparation as expected by the presence of cysteines in the native BMP-2 proteins. In addition, a small amount of unspecific, i.e., non-SH labeling, by cam, was observed as described previously (*31*). Some triple-cam peptides from the N56C protein indicate that the NEM-labeling was not complete. Actually, a small amount of free N56C protein was seen after MS analysis of the complete protein (Supporting Information Figure S-1).

It was not attempted in the present experiments to separate the different NEM-labeled BMP-2 proteins. However, the di-MA-PEGylated species described above (Figure 4) were separated from non-, mono-, and multi-PEGylated proteins (Figure 3). This will further ensure the selectivity of labeling at the introduced cysteine residues.

Solubility. BMP2WT is poorly soluble under physiological conditions. Its solubility limit in PBS is around 200 nM. In the organism, this might prevent systemic activity of BMP-2. In order to see whether PEGylation improves solubility in PBS, the spectral properties of 2 μM BMP2WT, analogues, and their

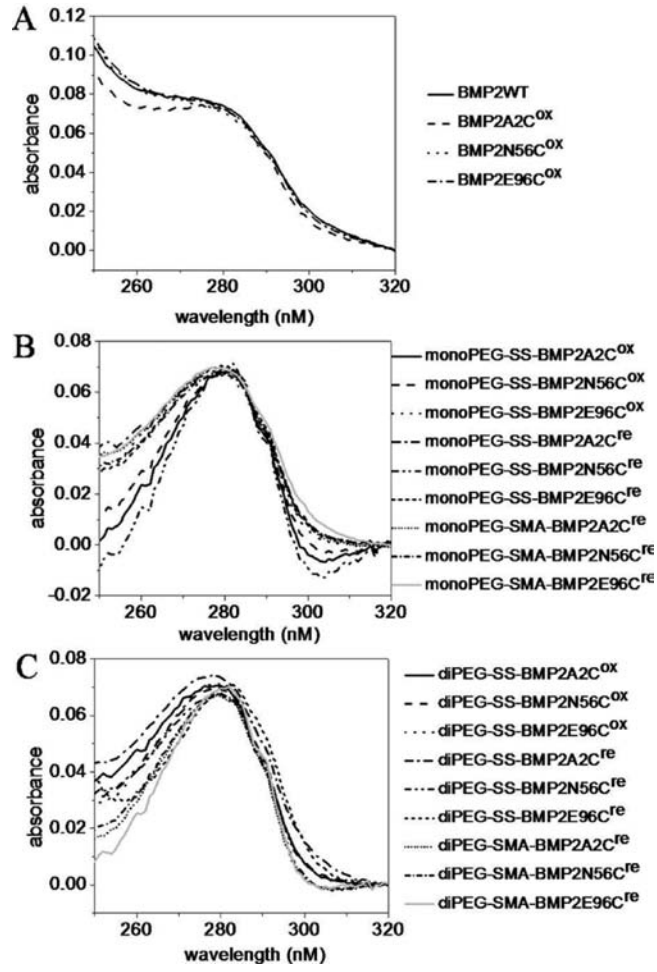


Figure 7. Spectra of 2 μM solutions of free BMP-2 analogues (A) and mono- (B), as well as di- (C), PEGylated BMP-2 analogues in PBS.

PEGylated derivatives were determined, as shown in Figure 7. The spectra of BMP2WT and its cysteine analogues (glutathione oxidized proteins) (Figure 7A) showed a continuous increase of absorption from 320 to 250 nm, which is typically observed due to the light scattering when protein aggregates are present (*33*). In contrast, the spectra of PEGylated BMP-2 cysteine analogues (Figure 7B,C), no matter whether for mono-PEGylated or di-PEGylated ones, showed low extinction at 320 nm and low intercept at 250 nm, signifying a more molecularly dispersed BMP-2 protein solution. This indicates that indeed the attached PEG enhances the solubility of BMP-2 under physiological pH and ionic strength at least up to 2 μM concentrations.

Biosensor Interaction Analysis. The mono- and di-PEGylated BMP-2 analogues were analyzed for receptor binding by surface plasmon resonance. Immobilized ectodomains of receptors ActR-IIB and BMPR-IA were perfused with BMP-2 proteins at concentrations from 20 to 100 nM. Figure 8 shows representative sensorgrams recorded for the binding of 60 nM PEGylated proteins in comparison with 60 nM unmodified wild-type BMP-2. A semiquantitative evaluation is presented in Figure 9. A calculation of the exact kinetic and equilibrium constants was not attempted in the present study, since BMP-2 is a dimeric protein and neither the association nor the dissociation phase could be fitted on the basis of a 1:1 interaction model. Depending on the concentration of the ligand and on the occupancy of the immobilized receptor protein, both 1:1 and 2:1 interactions can occur (*34*, *35*).

For the un-PEGylated BMP-2 analogues in oxidized form, approximate dissociation constants and rate constants are

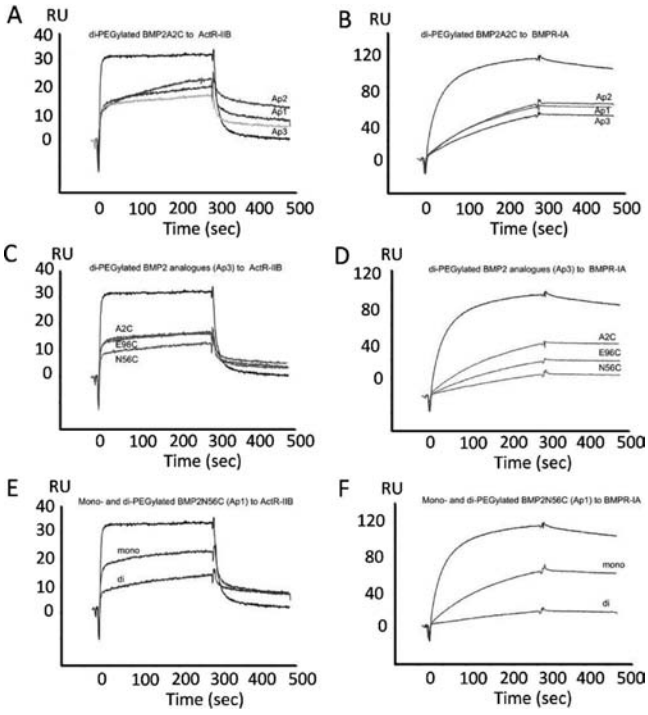


Figure 8. Representative sensorgrams for the binding of 60 nM PEGylated BMP-2 analogues in comparison with 60 nM unmodified BMP2WT (top curve of each figure). The sensorgrams during the first 300 s represent association with the receptor, and those after 300 s represent dissociation. Steep curves indicate fast association or dissociation rate.

compiled in Supporting Information Table S-3. Together with the sensorgrams in Supporting Information Figure S-2, these data show that the A2C and E96C analogues interact with the receptor proteins similar to BMP-2 wild-type. The affinity of BMP2N56C, however, is reduced about 5-fold with BMPR-IA and less than 2-fold with ActR-IIB. The crystal structure of the ternary complex consisting of BMP-2 and the ectodomains of BMPR-IA and ActR-IIB (*36*) indicate that the side chains at all three position are freely accessible. However, Asn 56 in BMP-2 is very close to the interface with BMPR-IA and ActR-IIB, so that the glutathione attached to the oxidized protein might somewhat interfere with receptor binding.

The three different PEGylation approaches yielded modified BMP-2 analogues with similar receptor binding properties as shown for the di-PEGylated BMP2A2C proteins at 60 nM concentrations in Figure 8A,B. Equilibrium binding to ActR-IIB was reduced to the same extent (Figure 9). During the interaction with the BMPR-IA receptor, all three PEGylation approaches yielded modified BMP-2 analogues with a strongly reduced association rate and a small reduction in the dissociation rate. This indicates that the highly specific chemistry based on SH/SS exchange (Ap1, Ap2) yields similar results as the NEM-based modification (Ap3).

The mono-PEGylated BMP-2 analogues exhibited intermediate affinities compared to unmodified and di-PEGylated proteins for both receptors throughout (Figure 8E,F and Figure 9). The intermediate affinity likely results from the parallel receptor interaction of the un-PEGylated and the modified monomer in the dimeric BMP-2 analogues.

A comparison of the effect of PEGylation at positions 2, 56, and 96 is presented in Figure 8C and D. Only PEGylation by the maleimide PEG is shown. Di-PEGylation of BMP2A2C caused the smallest effect for the interaction with both receptors. The di-PEGylated BMP2E96C bound as the modified BMP2A2C protein to ActR-IIB and with somewhat lower affinity to the BMPR-IA receptor. The binding of di-PEGylated BMP2N56C was affected to the largest extent with both receptors compared to the other two analogues. An evaluation of the apparent rate and equilibrium constants is presented in Supporting Information Table S-3.

The differences in the results of the biosensor interaction analysis observed with the three BMP-2 analogues PEGylated at the positions 2, 56, and 96 could indicate that PEGylation specificity varies among the three analogues. However, such differences in PEGylation specificity if existing at all should be small, since NEM modification yielded similar results with all three analogues (Supporting Information Figure S-1, Table S-1). As discussed at the end of the second section, differences in multimer formation after PEGylation of the three analogues (Ap2) can be explained by an intramolecular disulfide formation in A2C and an intermolecular disulfide formation in N56C and E96C. We therefore suggest that the differences in receptor interaction likely reflect the location of the side chains at positions 2, 56, and 96 in relation to the receptor binding epitopes. The PEGylation sites at position 56 (green) and 96 (blue) are shown in Figure 10 according to the reported crystal structure data (*37*). The N-terminal residues 1 to 10 including position 2 (magenta) appear to be flexible, since they are not determined by X-ray analysis. For maleimide PEG ($M_n = 5426$ Da) taken as an example, the mean-squared end-to-end distance is calculated to be 6.4 nm (*38*). The circle area with radius of 6.4 nm around the PEGylation site is therefore regarded as the maximal area reached by PEG (olive, attached to Cys 56). Obviously, an attached PEG coil could move freely on the whole

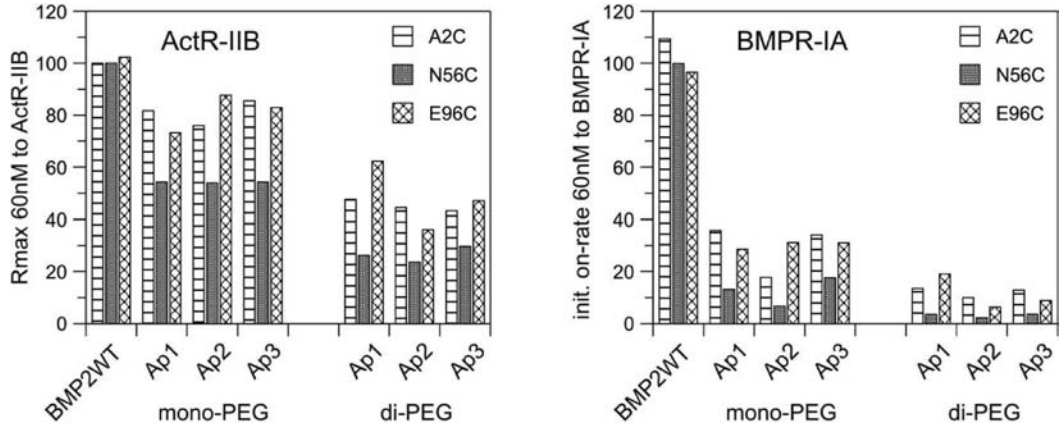


Figure 9. Comparison of the receptor binding of BMP-2 cysteine analogues after mono- and di-PEGylation by Ap1, Ap2, and Ap3. Sensorgrams of BMP-2 proteins at 60 nM concentrations (see Figure 8) were evaluated for maximal binding (Rmax) to ActR-IIB and for the initial on-rate for the binding to BMPR-IA. Values determined for unmodified BMP2WT were taken as 100.

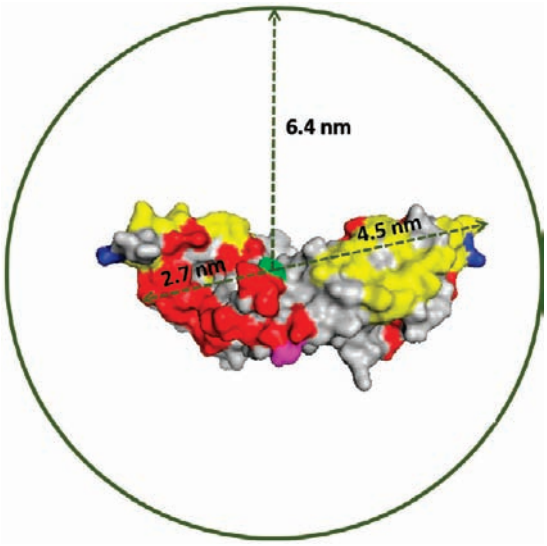


Figure 10. Surface model of BMP-2 proteins with the PEGylation sites at position 56 (green) and 96 (blue). The N-terminal residues including position 2 (magenta) are flexible and not determined by X-ray analysis. The binding sites for ActR-IIB (yellow) and BMPR-IA (red) are marked, as well as a calculated maximal area reached by maleimide PEG (M_n = 5426 Da, olive circle) attached to Cys 56.

BMPR-IA (red) and ActR-IIB (yellow) binding epitopes. However, the statistical probability that it blocks the epitopes might be affected by the distance and orientation between the attachment site and the binding epitopes.

The flexible N-terminal ends emanate from the middle of the dimeric BMP-2 protein (colored magenta in Figure 10). Therefore, Cys 2 appears to be far away from all receptor binding epitopes. Remarkably, the receptor binding properties of the PEGylated BMP2E96C proteins are similar to those of PEGylated BMP2A2C, in particular, for interaction with ActR-IIB. The association rate for the BMPR-IA receptor seems to be affected to a slightly higher extent with this analogue. Cys 96 is located at the tip of finger 2 of the BMP-2 monomers outside but juxtaposed to the receptor binding epitopes. Cys 56 is located between the binding epitopes for ActR-IIB and BMPR-IA. It is therefore not surprising that the affinities for both receptors are reduced to a larger extent than that of the two other modified analogues. However, despite the close proximity to these epitopes a considerable affinity is still retained in the PEGylated BMP2N56C proteins. Remarkably, when Asn 56 of natural BMP-2 is glycosylated the receptor binding affinity is similar to that in the unglycosylated form. In BMP-6, glycosylation of the corresponding Asn side chain is even required for binding of the receptor ActR-IA, but not of receptors BMPR-IA and IB (*9*).

The PEGylation affects the interaction with BMPR-IA to a higher extent than that with ActR-IIB. In particular, the association rate with BMPR-IA is strongly reduced for modified N56C and somewhat less so for the other two analogues. The initial on rates are reduced to 5−15% compared to the wild-type at 60 nM concentration of the di-PEGylated proteins. The particularly strong effect of BMP-2 PEGylation on the association rate with the BMPR-IA receptor might be caused by a direct association of the PEG with the binding epitope. The crystal structure of BMP-2 (*19*) and other BMP-like proteins (*39*) showed a bound low-molecular-weight compound (methylpentanediol, dioxan) in the BMPR-IA binding epitope. Possibly, the PEG also interacts weakly with such a site. Furthermore, the BMP-2 epitope shows a pronounced disorder-to-order transition during complex formation with BMPR-IA (*40*). The attached PEG might interfere with this transition. Both processes

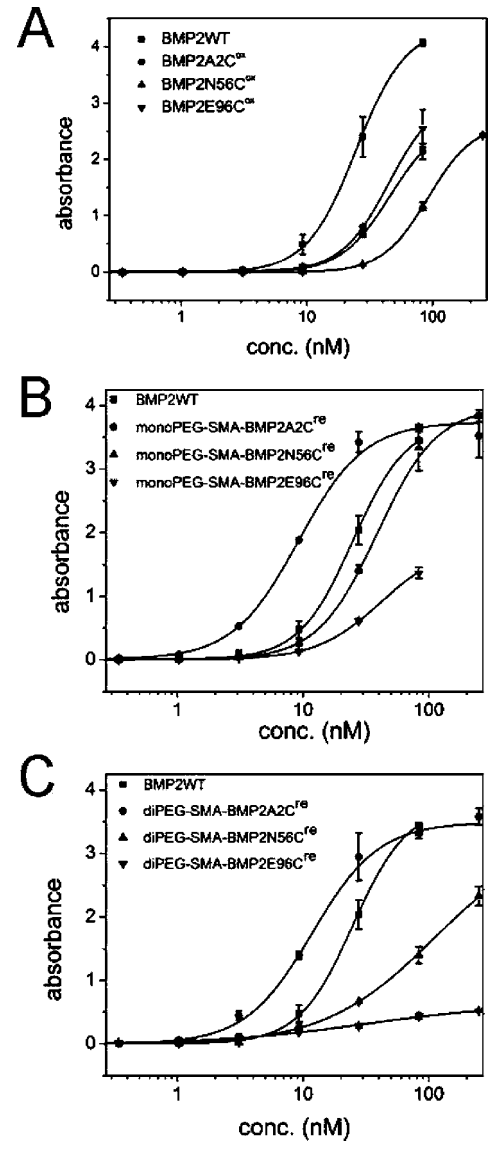


Figure 11. Biological activity of site-specific PEGylated BMP-2 analogues. Dose-dependent induction of alkaline phosphatase in C2C12 cells was determined for (A) BMP2WT and non-PEGylated cysteine analogues, (B) mono-PEGylated, and (C) di-PEGylated BMP-2 analogues. Maleimide PEG was conjugated with the free SH group of the reduced BMP-2 analogues (Ap3). BMP2WT analyzed in parallel served as a reference.

would lower the availability of the free epitope and thus retard association with the receptor.

Bioactivity Evaluated by Alkaline Phosphatase Cell Assay. The effects of PEGylation on the biological activity of the BMP-2 cysteine analogues were analyzed in C2C12 cells using BMP2WT and the non-PEGylated analogues as a reference. This assay measures the BMP-2 dependent induction of alkaline phosphatase during a 3-day time period. As discussed above, methods Ap1 and 2 yield disulfide-bonded protein−PEG conjugates, while method Ap3 generates a nonreducible bond between protein and PEG. Because the stability of disulfide-bound PEG during this long culture time is unknown, only thiol-maleimide-conjugated BMP-2 proteins were employed. Representative dose−response curves are shown in Figure 11.

The non-PEGylated BMP-2 cysteine analogues exhibited 2- to 3-fold lower activity than BMP2WT. The dose−response curve was similar for the A2C and E96C analogues. The N56C analogue was the least active. This is comparable to the relative

activities found in the receptor interaction SPR assay (Supporting Information Figure S-2).

Remarkably, mono- as well as di-PEGylation at Cys 2 yielded BMP-2 proteins with higher biological activity than the wild-type, indicating that the PEGylation at this site improved the bioactivity of proteins. The N-terminal sequence of BMP-2 contains a heparin binding site, which reduces the specific activity of BMP-2 in cellular assays probably by interacting with heparinic sites in the extracellular matrix (*25*). It is tempting to speculate that the attached PEG shields the heparin binding site. This would prevent a competitive interaction with the extracellular matrix and thus improve the bioactivity of the PEGylated A2C analogues.

Mono-PEGylation at Cys 56 increased and di-PEGylation at Cys 56 decreased the activity compared to the non-PEGylated analogue, suggesting that PEGylation at this site can inhibit and/or enhance bioactivity. The increased solubility of the PEGylated analogue might enhance activity, but the attached PEG could also interact with the receptor binding site and thereby partially inhibit activity as discussed in the seventh section.

It was unexpected that the Cys 96 analogue exhibited reduced activity after mono-PEGylation and a strongly reduced activity after di-PEGylation when compared with the non-PEGylated analogue. This differs clearly from the results of the receptor interaction SPR assay where the PEGylated E96C analogue showed affinities for type I and type II receptors similar to that of the PEGylated A2C analogue (Figure 9). This strongly suggests that PEGylation at Cys 96 has a special effect differing from the effects on receptor interaction or solubility. It is possible, and this remains to be established, that the interaction with modulator proteins or co-receptors, as repulsive guidance molecule-a or betaglycan (*41, 42*), are affected differently by PEGylation of BMP2A2C and BMP2E96C.

ACKNOWLEDGMENT

We thank Christian Söder for excellent technical assistance and Dr. Joachim Nickel for helpful discussions and suggestion.

Supporting Information Available: Additional data associated with this article. Figure S-1 shows mass spectra of NEM-labeled BMP-2 cysteine analogues. Table S-1 shows evaluation of mass spectra of NEM modified BMP-2 cysteine analogues. Table S-2A and S-2B show peptides identified by mass spectrometry after double-digestion of NEM-labeled BMP2N56C and BMP2E96C with Trypsin and GluC. Figure S-2 shows representative sensorgrams for the interaction of 60 nM BMP-2 cysteine analogues in comparison with 60 nM BMP2WT. Table S-3 shows Apparent Rate Constants k_{on}, k_{off}, K_D (k_{off}/k_{on}), and K_{Deq}, of the binding of BMP-2 proteins and PEGylated proteins by Ap3 to ActR-IIB and BMPR-IA. This material is available free of charge via the Internet at http://pubs.acs.org.

LITERATURE CITED

(1) Reddi, A. H. (1997) Bone morphogenetic proteins: an unconventional approach to isolation of first mammalian morphogens. *Cytokine Growth Factor Rev. 8*, 11–20.

(2) Reddi, A. H. (1998) Role of morphogenetic proteins in skeletal tissue engineering and regeneration. *Nat. Biotechnol. 16*, 247–151.

(3) Hogan, B. L. (1996) Bone morphogenetic proteins in development. *Curr. Opin. Genet. Dev. 6*, 432–438.

(4) Seeherman, H., and Wozney, J. M. (2005) Delivery of bone morphogenetic proteins for orthopedic tissue regeneration. *Cytokine Growth Factor Rev. 16*, 329–345.

(5) Robinson, Y., Heyde, C. E., Tschoke, S. K., Mont, M. A., Seyler, T. M., and Ulrich, S. D. (2008) Evidence supporting the use of bone morphogenetic proteins for spinal fusion surgery. *Expert Rev. Med. Devices 5*, 75–84.

(6) Kwong, F. N., and Harris, M. B. (2008) Recent developments in the biology of fracture repair. *J. Am. Acad. Orthop. Surg. 16*, 619–625.

(7) Israel, D. I., Nove, J., Kerns, K. M., Moutsatsos, I. K., and Kaufman, R. J. (1992) Expression and characterization of bone morphogenetic protein-2 in Chinese hamster ovary cells. *Growth Factors 7*, 139–150.

(8) Griffith, D. L., Keck, P. C., Sampath, T. K., Rueger, D. C., and Carlson, W. D. (1996) Three-dimensional structure of recombinant human osteogenic protein 1: structural paradigm for the transforming growth factor beta superfamily. *Proc. Natl. Acad. Sci. U.S.A. 93*, 878–883.

(9) Saremba, S., Nickel, J., Seher, A., Kotzsch, A., Sebald, W., and Müller, T. D. (2008) Type I receptor binding of bone morphogenetic protein 6 is dependent on N-glycosylation of the ligand. *FEBS J. 275*, 172–183.

(10) Veronese, M. F., and Pasut, G. (2005) PEGylation, a successful approach to drug delivery. *Drug Discovery Today 10*, 1451–1458.

(11) Caliceti, P., and Veronese, M. F. (2003) Pharmacokinetic and biodistribution properties of poly(ethylene glycol)-protein conjugates. *Adv. Drug Delivery Rev. 55*, 1261–1277.

(12) Roberts, M. J., Bentley, M. D., and Harris, J. M. (2002) Chemistry for peptide and protein PEGylation. *Adv. Drug Delivery Rev. 54*, 459–476.

(13) Kinstler, O., Molineux, G., Treuheit, M., Ladd, D., and Gegg, C. (2002) Mono-N-terminal poly(ethylene glycol)-protein conjugates. *Adv. Drug Delivery Rev. 54*, 477–485.

(14) Long, D. L., Doherty, D. H., Eisenberg, S. P., Smith, D. J., Rosendahl, M. S., Christensen, K. R., Edwards, D. P., Chlipala, E. A., and Cox, G. N. (2006) Design of homogeneous, monopegylated erythropoietin analogs with preserved in vitro bioactivity. *Exp. Hematol. 34*, 697–704.

(15) Rosendahl, S. M., Doherty, H. D., Smith, J. D., Carlson, J. S., Chlipala, A. E., and Cox, G. N. (2009) A long-acting, highly potent Interferon α−2 conjugate created using site-specific pegylation. *Bioconjugate Chem. 16*, 200–207.

(16) Zappe, H., Snell, M. E., and Bossard, M. J. (2008) PEGylation of cyanovirin-N, an entry inhibitor of HIV. *Adv. Drug Delivery Rev. 60*, 79–87.

(17) Veronese, M. F., Mero, A., Caboi, F., Sergi, M., Marongiu, C., and Pasut, G. (2007) Site-specific Pegylation of G-CSF by reversible denaturation. *Bioconjugate Chem. 18*, 1824–1830.

(18) Rider, C. C., and Mulloy, B. (2010) Bone morphogenetic protein and growth differentiation factor cytokine families and their protein antagonists. *Biochem. J. 429*, 1–12.

(19) Scheufler, C., Sebald, W., and Hülsmeyer, M. (1999) Crystal structure of human bone morphogenetic protein-2 at 2.7 Å Resolution. *J. Mol. Biol. 287*, 103–115.

(20) Bentz, H., Schroeder, J. A., and Estridge, T. D. (1998) Improved local delivery of TGF-β2 by binding to injectable fibrillar collagen via difunctional polyethylene glycol. *J. Biomed. Mater. Res. 39*, 539–548.

(21) Liu, H. W., Chen, C. H., Tsai, C. L., Lin, I. H., and Hsiue, G. H. (2007) Heterobifunctional poly(ethylene glycol)-tethered bone morphogenetic protein-2-stimulated bone marrow mesenchymal stromal cell differentiation and osteogenesis. *Tissue Eng. 13*, 1113–1124.

(22) Brebda, K., Mann, R., Schmedlen, H., and West, J. L. (2001) Tethered-TGF-β increases extracellular matrix production of vascular smooth muscle cells. *Biomaterials 22*, 439–444.

(23) Sebald, W., Nickel, J., Zhang, J., and Müller, T. D. (2004) Molecular recognition in bone morphogenetic protein (BMP)/receptor interaction. *Biol. Chem. 385*, 697–710.

(24) Allendorph, G. P., Vale, W. W., and Choe, S. (2006) Structure of the ternary signaling complex of a TGF-β superfamily member. *Proc. Natl. Acad. Sci. U.S.A. 103*, 7643–7648.

(25) Ruppert, R., Hoffmann, E., and Sebald, W. (1996) Human bone morphogenetic protein 2 contains a heparin-binding site which modifies its biological activity. *Eur. J. Biochem. 237*, 295–302.

(26) Groppe, J., Rumpel, K., Economides, A. N., Stahl, N., Sebald, W., and Affolter, M. (1998) Biochemical and biophysical characterization of refolded Drosophila DPP, a homolog of bone morphogenetic protein 2 and 4. *J. Biol. Chem. 273*, 29052–29065.

(27) Woghiren, C., Sharma, B., and Stein, S. (1993) Protected thiol-polyethylene glycol: A new activated polymer for reversible protein modification. *Bioconjugate Chem. 4*, 314–318.

(28) Laemmli, U. K. (1970) Cleavage of structural proteins during the sssembly of the head of bacteriophage T4. *Nature 227*, 680–685.

(29) Kirsch, T., Nickel, J., and Sebald, W. (2000) BMP-2 antagonists emerge from alterations in the low-affinity binding epitope for receptor BMPR-II. *EMBO J. 19*, 3314–3324.

(30) Riordan, J. F., and Vallee, B. L. (1972) Reactions with N-ethylmaleimide and p-mercuribenzoate. *Methods Enzymol. 25*, 449–456.

(31) Yang, Z., and Attygalle, A. B. (2007) LC/MS characterization of undesired products formed during iodoacetamide derivatization of sulfhydryl groups of peptides. *J. Mass Spectrom. 42*, 233–243.

(32) Jones, M. D., Merewether, L. A., Clogston, C. L., and Lu, H. S. (1994) Peptide map analysis of recombinant human granulocyte colony stimulating factor: elimination of methionine modification and nonspecific cleavages. *Anal. Biochem. 216*, 135–146.

(33) Pellaud, J., Schote, U., Arvinte, T., and Seelig, J. (1999) Conformation and self-association of human recombinant transforming growth factor-b3 in aqueous solutions. *J. Biol. Chem. 274*, 7699–7704.

(34) Kubetzko, S., Balic, E., Waibel, R., Zangemeister-Wittke, U., and Plückthun, A. (2006) PEGylation and multimerization of the anti-p185^{HER-2} single chain Fv fragment 4D5: effects on tumor targeting. *J. Biol. Chem. 281*, 35186–35201.

(35) Heinecke, K., Seher, A., Schmitz, W., Müller, T. D., Sebald, W., and Nickel, J. (2009) Receptor oligomerization and beyond: a case study in bone morphogenetic proteins. *BMC Biol. 7*, 59.

(36) Weber, D., Kotzsch, A., Nickel, J., Harsh, S., Seher, A., Müller, U., Sebald, W., and Müller, T. D. (2007) A silent H-bond can be mutationally activated for high-affinity interaction of BMP-2 and activin type IIB receptor. *BMC Struct. Biol. 7*, 6.

(37) Keller, S., Nickel, J., Zhang, J. L., Sebald, W., and Müller, T. D. (2004) Molecular recognition of BMP-2 and BMP receptor IA. *Nat. Struct. Biol. 11*, 481–488.

(38) Knoll, D., and Hermans, J. (1983) Polymer-protein interactions: comparison of experiment and excluded volume theory. *J. Biol. Chem. 258*, 5710–5715.

(39) Mittl, P. R. E., Priestle, J. P., Cox, D. A., Mcmaster, G., Cerletti, N., and Grütter, M. G. (1996) The crystal structure of TGF-β3 and comparison to TGF-β2: Implications for receptor binding. *Protein Sci. 5*, 1261–1271.

(40) Klages, J., Kotzsch, A., Coles, M., Sebald, W., Nickel, J., Müller, T., and Kessler, H. (2008) The solution structure of BMPR-IA reveals a local disorder-to-order transition upon BMP-2 binding. *Biochemistry 47*, 11930–11939.

(41) Wiater, E., and Vale, W. (2003) Inhibin is an antagonist of bone morphogenetic protein signaling. *J. Biol. Chem. 278*, 7934–7941.

(42) Xia, Y., Yu, P. B., Sidis, Y., Beppu, H., Bloch, K. D., Schneyer, A. L., and Lin, H. Y. (2007) Repulsive guidance molecule RGMa alters utilization of bone morphogenetic protein (BMP) type II receptors by BMP2 and BMP4. *J. Biol. Chem. 282*, 18129–8140.

BC9005706

Supporting Information

Site-Specific PEGylation of Bone Morphogenetic Protein-2 Cysteine Analogues

Junli Hu,* Viswanadham Duppattla, Stefan Harth, Werner Schmitz, Walter Sebald

Physiological Chemistry II, Biocenter, University of Würzburg, Am Hubland, 97074 Würzburg, Germany

The Supporting Information (SI) herein contains the following content:

Figure S-1. Mass spectra of NEM-labeled BMP-2 cysteine analogues. Proteins were reduced and reacted with NEM as detailed under Experimental Procedures. The whole reaction mixture was submitted to HPLC and the peak fractions analyzed by mass spectrometry. The spectra were evaluated as compiled in Supporting Information Table S-1.

Table S-1. Evaluation of mass spectra (see Supporting Information Figure S-1) of NEM modified BMP-2 cysteine analogues.

Table S-2A. Peptides identified by mass spectrometry (see Figure 6) after double-digestion of NEM-labeled BMP2N56C with Trypsin and GluC.

Table S-2B. Peptides identified by mass spectrometry (see Figure 6) after double-digestion of NEM-labeled BMP2E96C with Trypsin and GluC.

Figure S-2. Representative sensorgrams for the interaction of 60 nM BMP-2 cysteine analogues (green traces) in comparison with 60 nM BMP2WT (blue trace).

Table S-3. Apparent Rate Constants k_{on}, k_{off}, K_D (k_{off}/k_{on}), and K_{Deq}, of the binding of BMP-2 proteins and PEGylated proteins by Ap3 to ActR-IIB and BMPR-IA.

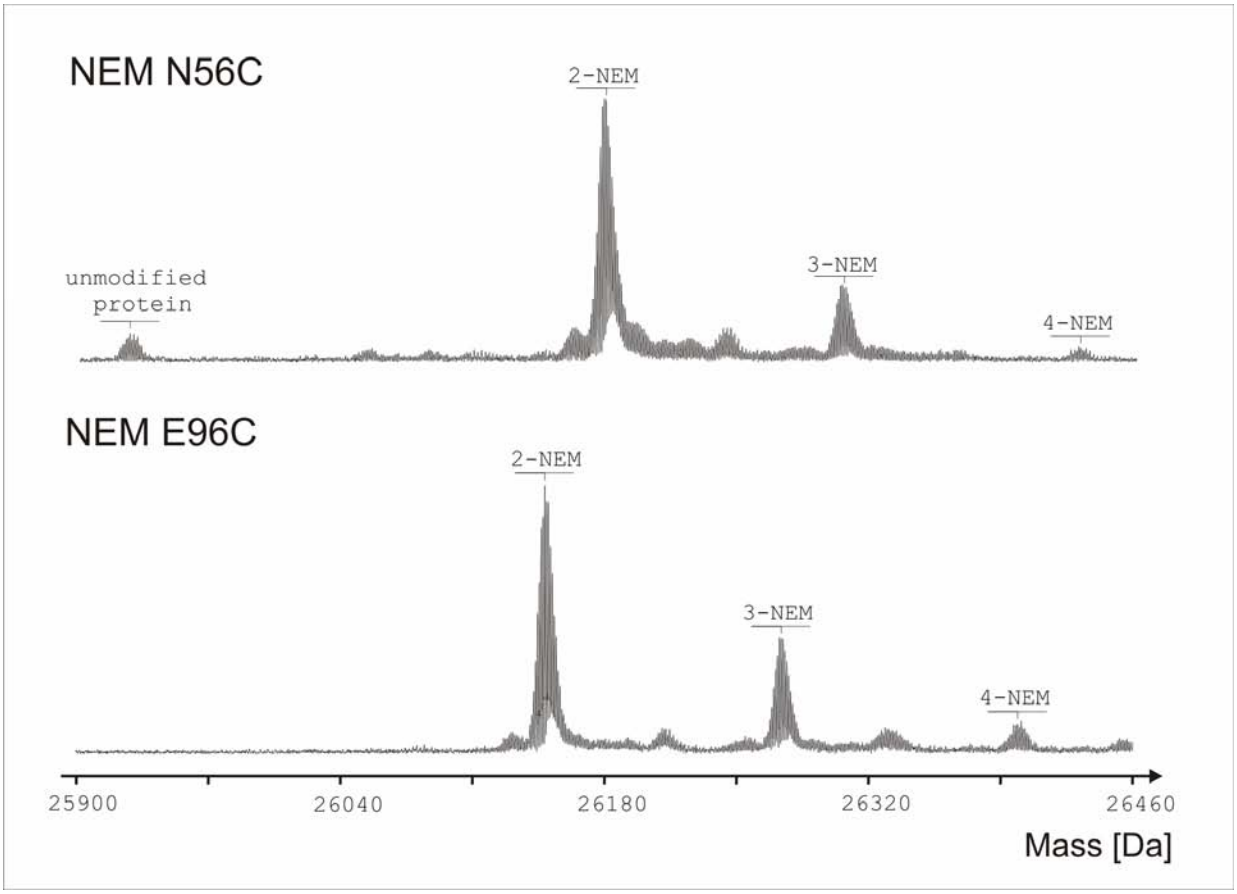


Figure S-1. Mass spectra of NEM-labeled BMP-2 cysteine analogues. Proteins were reduced and reacted with NEM as detailed under Experimental Procedures. The whole reaction mixture was submitted to HPLC and the peak fractions were analyzed by mass spectrometry. The spectra were evaluated as compiled in Supporting Information Table S-1.

Table S-1. Evaluation of mass spectra (see Supporting Information Figure S-1) of NEM modified BMP-2

	observed		modification	calculated	
	Mw (Da)	intensity		Mw (Da)	error (ppm)
NEM A2C	26251.49	11.90	2NEM	26252.73	47.07
	26377.70	2.81	3NEM	26377.78	2.76
NEM N56C	25913.65	0.63	unmodified	25913.61	-1.54
	26165.73	5.80	2NEM	26166.72	37.78
	26291.80	1.72	3NEM	26191.77	-1.30
	26416.85	0.33	4NEM	26416.81	-1.33
NEM E96C	26135.48	5.92	2NEM	26135.72	9.24
	26260.58	2.53	3NEM	26260.76	7.03
	26385.71	0.66	4NEM	26385.81	3.78

cysteine analogues.

Table S-2A. Peptides identified by mass spectrometry (see Figure 6) after double-digestion of NEM-labeled BMP2N56C with Trypsin and GluC.

designation	observed		assignment peptide/modification			calculated	
	Mw (Da)	intensity	from aa[a]	to aa	modification	Mw (Da)	error (ppm)
a0-	1577.81	34.54	84	97	-MeSH	1577.81	3.80
a0	1625.83	17.90	84	97	unmodified	1625.81	15.38
a1	1682.85	12.84	84	97	cam	1682.83	9.83
b2-	2024.96	6.04	77	94	-MeSH, 2cam	2024.94	10.37
b2	2072.96	24.59	77	94	2cam	2072.95	8.68
b3	2130.00	83.42	77	94	3cam	2129.97	13.87
c2-	2268.05	2.33	77	96	-MeSH, 2cam	2268.03	8.38
c2	2316.06	3.33	77	96	2cam	2316.03	12.95
c3	2373.08	15.58	77	96	3cam	2373.05	10.34
d2-	2396.14	14.67	77	97	-MeSH, 2cam	2396.12	7.51
d2	2444.14	11.12	77	97	2cam	2444.13	7.36
d3	2501.16	62.19	77	97	3cam	2501.17	-0.98
d4	2558.19	16.85	77	97	4cam	2558.19	1.20
E0	6510.15	0.62	17	73	NEM	6510.06	13.98
e3	6556.15	1.36	17	73	3cam	6556.15	0.00
E1	6567.19	0.37	17	73	cam, NEM	6567.08	15.68
e4	6613.20	0.30	17	73	4cam	6613.17	3.78
E2	6624.20	3.44	17	73	2cam, NEM	6624.08	18.42
F0	6665.15	3.04	16	73	NEM	6665.27	-16.80
E3	6681.21	0.74	17	73	3cam, NEM	6681.10	16.25
f3	6712.26	0.90	16	73	3cam	6712.18	12.70
f4	6769.22	0.90	16	73	4cam	6769.20	3.25
F2	6780.27	3.04	16	73	2cam, NEM	6780.21	9.29
F3	6837.29	0.93	16	73	3cam, NEM	6837.29	-0.07
F4	6893.33	0.32	16	73	4cam, NEM	6893.30	4.06
E0	6510.15	0.62	17	73	NEM	6510.06	13.98
e3	6556.15	1.36	17	73	3cam	6556.15	0.00

[a] amino acid

Table S-2B. Peptides identified by mass spectrometry (see Figure 6) after double-digestion of NEM-labeled BMP2E96C with Trypsin and GluC.

designation	observed		assignment peptide/modification			calculated	
	Mw (Da)	intensity	from aa	to aa	modification	Mw (Da)	error (ppm)
a1-	1608.80	36.73	84	97	-MeSH, cam	1608.79	3.11
a1	1656.81	13.90	84	97	cam	1656.80	4.83
A0-	1676.83	72.09	84	97	-MeSH, NEM	1676.82	6.56
A0	1724.84	40.11	84	97	NEM	1724.82	9.86
A1	1781.86	21.28	84	97	cam, NEM	1781.89	-17.40
b2-	2024.96	9.15	77	94	-MeSH, 2cam	2024.94	7.90
b2	2072.96	33.25	77	94	2cam	2072.95	6.27
b3	2129.99	117.58	77	94	3cam	2129.97	10.11
b4	2187.02	4.59	77	94	4cam	2186.99	16.04
d3-	2427.13	5.20	77	97	-MeSH, 3cam	2427.11	8.65
d3	2475.13	5.39	77	97	3cam	2475.11	5.66
D2-	2495.15	11.43	77	97	-MeSH, 2cam, NEM	2495.14	4.41
d4	2532.14	29.56	77	97	4cam	2532.14	3.37
D2	2543.15	14.63	77	97	2cam, NEM	2543.14	5.51
D3	2600.18	70.28	77	97	3cam, NEM	2600.16	5.89
D4	2657.21	10.66	77	97	4cam, NEM	2657.18	11.24
e2	6509.14	45.34	17	73	2cam	6509.08	9.22
e3	6567.19	10.88	17	73	3cam	6567.09	14.42
e4	6624.18	1.82	17	73	4cam	6624.11	9.21
f2	6666.23	39.44	16	73	2cam	6666.19	5.85
f3	6723.26	10.86	16	73	3cam	6723.21	6.92
g2	6848.38	14.59	17	76	2cam	6848.32	7.74
g3	6905.34	2.05	17	76	3cam	6905.34	0.12

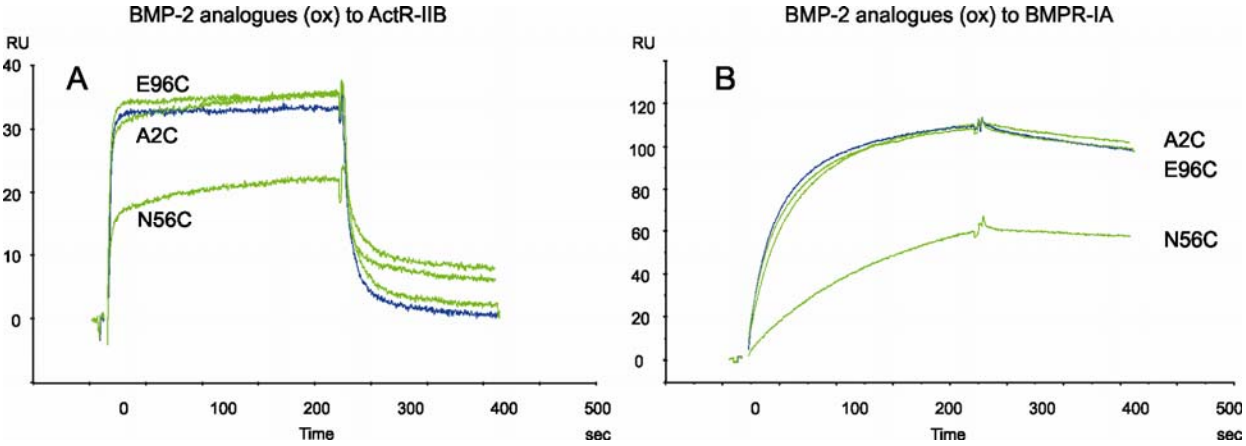


Figure S-2. Representative sensorgrams for the interaction of 60 nM BMP-2 cysteine analogues (green traces) in comparison with 60 nM BMP2WT (blue trace).

Table S-3. Apparent Rate Constants k_{on}, k_{off}, K_D (k_{off}/k_{on}), and K_{Deq}, of the binding of BMP-2 proteins and PEGylated proteins by Ap3 to ActR-IIB and BMPR-IA[a].

receptor	protein	app.[b] k_{off} (10^{-4} s^{-1})	app. k_{on} (10^4 M^{-1} s^{-1})	app. K_D (k_{off}/k_{on}) (nM)	Rmax at 60nM (RU)	app. K_{Deq} (nM)	init. on-rate at 60nM ($dRUs^{-1}$)
ActR-IIB	BMP2WT	820	580	14	33	24 to 33[c]	
	BMP2A2C^{ox}	610	420	14	35	33	
	BMP2N56C^{ox}	720	410	17	21	33	
	BMP2E96C^{ox}	850	590	14	34	22	
	diPEG-SMA-BMP2A2C^{re}				17	68	
	diPEG-SMA-BMP2N56C^{re}		ne[d]		13	190	
	diPEG-SMA-BMP2E96C^{re}				18	69	
BMPR-IA	BMP2WT	7.6	59	1.3			2.6
	BMP2A2C^{ox}	6.4	37	1.7			1.9
	BMP2N56C^{ox}	5.8	8.8	6.6			0.4
	BMP2E96C^{ox}	7.3	55	1.3			2.1
	diPEG-SMA-BMP2A2C^{re}	2.1	9.5	2.2			0.3
	diPEG-SMA-BMP2N56C^{re}	2.5	2.8	8.8			0.1
	diPEG-SMA-BMP2E96C^{re}	2.7	6.2	3.6			0.2

[a] SPR measurements were done at 25 ^oC(see Experimental Procedures).

[b] For all the values only the apparent (app.) constants were calculated on the basis of a 1:1 interaction model. It was not taken into account that one dimeric BMP proteins can interact with two or one receptor.

[c] From different experiments.

[d] Not evaluated

Microwave-Mediated Synthesis of Labeled Nucleotides with Utility in the Synthesis of DNA Probes

Mark Lefever, Jerome W. Kosmeder II, Michael Farrell, and Christopher Bieniarz

Ventana Medical Systems, Inc., a member of the Roche Group, 1920 East Innovation Park Drive, Tucson, Arizona 85755.
Received January 7, 2010; Revised Manuscript Received July 22, 2010

A novel method of linking haptens to deoxycytidine 5′-triphosphate via microwave-mediated bisulfate-catalyzed transamination with hydrazine has been developed. This method enables the tethering of small molecule haptens to dCTP via a discrete polyethylene glycol (PEG) spacer, yielding N^4-aminodeoxycytidine 5′-triphosphate−dPEG−haptens. This synthetic approach employs microwave-catalyzed hydrazinolysis that enables the attachment of spacers via hydrazine linkages. The microwave-mediated introduction of this hydrazine handle provides a significant improvement in yield over those of published thermal methods. The microwave reaction was shown to be scalable, and the final product was amenable to labeling with a wide variety of haptens. The resulting nucleotide triphosphates, N^4-aminodeoxycytidine 5′-triphosphate−dPEG−haptens, can serve as unique substrates for the enzyme-mediated labeling of DNA probes. The efficacy of incorporation of one such novel nucleotide, N^4-aminodeoxycytidine 5′-triphosphate−dPEG$_4$−DNP, has been demonstrated in nick translation labeling of HER2 and HPV probes. The labeled probes have been shown to be effective in visualizing their target genes in tissue.

INTRODUCTION

Chemically modified nucleic acids are used as probes in hybridization assays, e.g., Southern blots, Northern blots, dot blots, and in situ hybridization (ISH), to detect RNA transcripts, gene amplification, and translocations in cells, in microarray assays, and in surface attachment chemistries and to generate various kinds of bioconjugates (*1*−*3*). Recently, the use of ISH assays both by fluorescent in situ hybridization detection (FISH) and by enzymatic signal deposition for brightfield detection via silver in situ hybridization (SISH) and chromogenic in situ hybridization (CISH) has found important clinical applications (*4, 5, 6, 7*). The amplification of the human epidermal growth factor 2 (*HER2)* gene in breast and stomach cancers has been shown to identify patients who can benefit from Herceptin treatment (*8, 9*). The amplification status of other genes is being used increasingly to assist in diagnosis and to profile tumors as the practice of personalized medicine progresses (*10*). Detection of viral genomes in cells by ISH has many potential clinical applications [e.g., human papilloma virus (HPV) in cervical cancer] (*11, 12*).

For the generation of chemically modified nucleic acids, uridine and cytidine are the most frequently used bases (*13*). Enzymatic methods are frequently used to make probes by incorporating modified nucleotide triphosphates to produce a nucleic acid containing a label or reactive residue to which a label, e.g., a hapten or fluorophore, can be subsequently coupled.

The bisulfite-mediated displacement of the C4 amino group of cytosine, first reported in 1970 by Shapiro and Weisgras (*21*), has become a widely reported method for the introduction of bifunctional nucleophilic handles onto cytosine residues (*14*−*22*). These newly introduced nucleophilic handles can then serve as reaction centers for the introduction of reporter groups derivatized with appropriate electrophilic handles. Reporter groups that have been employed include immunoreactive groups, photochemical cross-linking agents, fluorescent tags, alkylating agents, and catalytically active metal chelates (*14*−*22*). The bisulfite-catalyzed transamination of cytosine involves a number of discrete steps: addition of bisulfite across the 5−6 double bond of cytosine, transamination via attack of the nitrogen nucleophile and release of ammonia, and base-catalyzed elimination of bisulfite to regenerate the double bond (*20*).

In initial attempts to obtain cytosine derivatives tagged with nucleophilic handles, the procedure described by Negishi was employed (*23*). Although the detailed procedure was strictly followed, the reaction produced more hydrolysis than product. The initial failure led to the exploration of alternative conditions employing microwave technology. This choice was based on a number of studies indicating that microwaves are capable of accelerating a wide range of thermally driven reactions, including additions, cycloadditions, condensations, substitutions, rearrangements, organometallic reactions, and a host of others (*24*−*29*). The application of microwave energy results in a very rapid transfer of energy to the reactant molecules enabling the activation energy to be reached quickly (*30, 31*). Consequently, thermodynamic products are produced more rapidly, often avoiding the generation of unwanted side products that occur with traditional thermal methods. The commercial microwave synthesizers that are available allow for precise control of energy and offer the option of simultaneous cooling. The ability to maintain strict control of reaction conditions has proven to be indispensible in achieving reproducibility. Failure to provide sufficient microwave energy led to incomplete reactions, whereas overheating led to product decomposition.

Herein is described the microwave-mediated synthesis of N^4-amino-dCTP and its use in labeling DNA. The assembly of these reagents involved the tethering of various moieties to N^4-amino-dCTP via discrete water-soluble polyethylene glycol (PEG) linkers. The resulting haptenylated nucleotide triphosphates can serve as unique substrates for the enzyme-mediated labeling of DNA probes via nick translation and/or random priming (*32*−*35*). One such novel nucleotide, N^4-aminodeoxycytidine 5′-triphosphate−(dPEG$_4$-2,4-dinitrophenylamino)(N^4-amino-dCTP-PEG$_4$-DNP) was used to label DNA for use as a probe.

EXPERIMENTAL PROCEDURES

Materials. Deoxycytidine 5′-triphosphate, hydrazine monohydrate, sodium bisulfite, *N*-hydroxysuccinimide, 1-fluoro-2,4-

10.1021/bc100013b © 2010 American Chemical Society
Published on Web 09/02/2010

dinitrobenzene, and all organic solvents were commercial products of Sigma Aldrich. Discrete dPEG amino acids were products of Quanta Biodesign Ltd. (Powell, OH). Concentrated HCl from VWR was utilized to make pH adjustments.

Microwave and Thermal Hydrazinolysis. We prepared reaction solutions by combining sodium bisulfite (203 mg, 2.85 mmol) and hydrazine monohydrate (1.0 mL, 20.6 mmol), cooling the mixture on an ice bath, and adjusting the pH to 7.2 with the careful addition of concentrated HCl (1.48 mL). In this premade hydrazine/bisulfite solution was dissolved deoxycytidine 5′-triphosphate (300 mg, 0.587 mmol). The pH was adjusted to 7.2 with additional hydrazine hydrate, and the solution was transferred to a 10 mL glass microwave tube. The tubes were either heated in a CEM Discover microwave reactor at 55 °C (5 W max), with cooling, for times ranging from 1 to 60 min or placed in a 55 °C water bath for the appropriate length of time. Aliquots (20 μL) were withdrawn at intervals and diluted with 100 μL of methanol, and the extent of the reaction was determined by immediate HPLC analysis. Analysis was performed on a Waters BioAlliance HPLC system fitted with a 2996 photodiode array detector and a XBridge 5 μm, C18(2), 100A, 150 mm × 4.6 mm column (10 μL injection per run). The column was eluted with 125 mM triethylammonium carbonate and 1−4% ACN over 10 min at pH 8.5 and a flow rate of 1 mL/min.

***N*^{4}-Aminodeoxycytidine 5′-Triphosphate Purification.** Reaction mixtures were fractionated by HPLC utilizing a Waters Delta 600 HPLC system fitted with a 2996 photodiode array detector and a Waters Sunfire Prep 10 μ, C18(2), 100A, 250 mm × 50 mm column (350 μL of reaction mixture per run). The column was eluted with 125 mM triethylammonium carbonate and 1−4% acetonitrile (ACN) over 20 min at pH 8.5 and a flow rate of 20 mL/min. The *N*^{4}-amino-dCTP fraction eluted at 30−32 min with a λ_{max} of 275 nm. The *N*^{4}-amino-dCTP fraction was lyophilized three times from deionized (DI) water to ensure removal of all residual triethylammonium carbonate and then stored at −80 °C until it was used. To obtain the sodium salt, cation exchange was performed on a 50 mL column packed with Sp Sephadex C-25 equilibrated with 0.2 N NaOH and washed with water until the pH of the eluant buffer was 7.0. The lyophilized triethylammonium salt was taken up in 1 mL (4 × 0.250 mL) of water, loaded on the cation exchange column, and eluted with water. The UV−vis spectra of the collected fractions were recorded on an Agilent 8453 UV−vis spectrophotometer, and the *N*^{4}-amino-dCTP-containing fraction were pooled and lyophilized to give the sodium salt of *N*^{4}-amino-dCTP as a white crystalline solid (284 mg, 85%): ^{1}H NMR (600 MHz, D_2O) δ 2.22 (m, 1 H), 2.31 (m, 1 H), 3.99 (m, 1 H), 4.10 (m, 2 H), 4.53 (d, J = 2.7 Hz, 1 H), 5.96 (br s, 1 H), 6.23 (m, 1 H), 7.74 (s, 1 H); ^{13}C NMR (63 MHz, D_2O) δ 42.42, 68.19 (d, J = 5.5 Hz, 1 C), 73.53, 88.81 (d, J = 9.1 Hz, 1 C), 89.32, 98.51, 146.42, 153.68, 163.84; ^{31}P NMR (121 MHz, D_2O) δ −8.01 (d, J = 48 Hz, 1 P), 10.22 (d, J = 50 Hz, 1 P), −21.56 (t, J = 45 Hz, 1 P); ESI-MS *m*/*z* 481.0 (M − H); ESI-HRMS calcd for $C_9H_{17}N_4O_{13}P_3$ (M − H) 480.9927, found 480.9943.

Synthesis of 3-[2-(2-{2-[2-(2,4-Dinitrophenylamino)ethoxy]-ethoxy}ethoxy)ethoxy]propanoic Acid (2). To a solution of 3-[2-(2-{2-[2-(2-aminoethoxy)ethoxy]ethoxy}ethoxy)ethoxy]-propanoic acid (0.5 g, 1.89 mmol) and Na_2CO_3 (0.317 g, 3.77 mmol) in 5 mL of water was added 1-fluoro-2,4-dinitrobenzene (227 mL, 1.89 mmol), and the solution was irradiated in a CEM Discovery microwave synthesizer set at 80 °C (30 W maximum), with cooling for 30 min. After cooling, the solution was acidified with 0.25 M HCl and extracted three times with 20 mL of ethyl acetate. Concentration of the combined organic fractions under vacuum provided a thick yellow oil that was purified utilizing an Isco CombiFlash automated chromatography unit fitted with a 40 g silica gel column (MeOH/DCM, 0 to 20% MeOH over 25 min), affording the aniline as a yellow oil (748 mg, 92%): ^{1}H NMR (250 MHz, $CDCl_3$) δ 2.58 (t, J = 6.0 Hz, 2 H), 3.57−3.84 (m, 18 H), 6.94 (d, J = 9.5 Hz, 1 H), 8.25 (dd, J = 9.5, 2.6 Hz, 1 H), 8.81 (br s, 1 H), 9.12 (d, J = 2.7 Hz, 1 H); ^{13}C NMR (126 MHz, CD_3OD) δ 36.0, 44.2, 67.9, 70.0, 71.5, 71.6, 71.71, 71.72, 71.74, 71.77, 116.2, 124.8, 131.1, 131.6, 137.1, 150.0, 175.4; ESI-MS *m*/*z* 430 (M − H); TOF-HRMS calcd for $C_{17}H_{24}N_3O_{10}$ (M − H) 430.1462, found 430.1441.

Synthesis of 3-[2-(2-{2-[2-(2,4-Dinitrophenylamino)ethoxy]-ethoxy}ethoxy)ethoxy]propanate-*N*-hydoxysuccinimide Ester (3). The acid **1** (748 mg, 1.73 mmol) was dissolved in 1.9 mL of anhydrous dichloromethane (DCM); 1.0 M dicyclohexylcarbodiimide (DCC) in DCM (1.92 mL, 1.92 mmol) and *N*-hydroxysuccinimide (NHS) (221 mg, 1.92 mmol) were added. The solution was blanketed with dry argon and shaken at ambient temperature for 16 h. After the solvent had been removed in vacuo, the residue was taken up in dry DCM and the urea byproduct was removed by filtration. Purification was performed by silica gel chromatography utilizing an Isco CombiFlash automated chromatography unit fitted with a 40 g silica gel column (2-propanol/DCM, 0 to 20% 2-propanol over 25 min) and afforded the active ester as a thick yellow oil (561 mg, 61%): ^{1}H NMR (600 MHz, $CDCl_3$) δ 9.05 (d, J = 2.6, 1 H), 8.75 (s, 1 H), 8.20 (dd, J = 9.5, 2.6 Hz, 1 H), 6.94 (d, J = 9.5 Hz, 1 H), 3.87−3.75 (m, 5 H), 3.71−3.55 (m, 16 H), 2.84 (t, J = 6.4 Hz, 3 H), 2.80 (dd, J = 19.3, 7.8 Hz, 4 H), 1.99 (s, 1 H); ^{13}C NMR (63 MHz, $CDCl_3$) δ 25.27, 31.79, 42.96, 65.36, 68.27, 70.10, 70.27, 70.32, 70.38, 114.09, 123.85, 129.89, 130.04, 135.58, 148.19, 166.48, 168.90; ESI-MS *m*/*z* 529 (M + H); ESI-HRMS calcd for $C_{21}H_{28}N_4O_{12}$ (M + NH_4) 546.20475, found 546.20655.

Synthesis of *N*^{4}-Aminodeoxycytidine 5′-Triphosphate−dPEG$_4$−DNP (4). Active ester **3** (124 mg, 0.234 mmol) in 2 mL of dry dimethyl sulfoxide (DMSO) was added to a solution of *N*^{4}-aminodeoxycytidine 5′-triphosphate triethylammonium salt (173 mg, 0.195 mmol) in 1.5 mL of anhydrous DMSO. The solution was blanketed with dry argon and vortexed until all solids had dissolved. After being stirred for 16 h at room temperature, the reaction mixture was fractionated by HPLC utilizing a Waters Delta 600 HPLC system fitted with a model 2996 photodiode array detector and a Sunfire Prep 10 μ, C18(2), 100A, 250 mm × 50 mm column. Elution with 125 mM triethylammonium carbonate and 5−50% ACN over 60 min at pH 8.5 and a flow rate of 20 mL/min provided the triethylammonium salt of *N*^{4}-amino-dCTP−dPEG$_4$−DNP. Cation exchange was performed on a 50 mL column packed with Sp Sephadex C-25 equilibrated with 0.2 N NaOH and washed with water until the pH of the eluent buffer was 7.0. The lyophilized triethylammonium salt was taken up in 1 mL (4 × 0.250 mL) of DI water loaded on top of the cation exchange column and eluted with water. The UV−vis spectra of the collected fractions were recorded on an Agilent 8453 UV−vis spectrophotometer, and the *N*^{4}-amino-dCTP−dPEG$_4$−DNP fractions were pooled and lyophilized to give 145 mg of the tetrasodium salt of *N*^{4}-amino-dCTP−dPEG$_4$−DNP as a yellow crystalline solid: ^{1}H NMR (250 MHz, D_2O) δ 2.27 (m, 1 H), 2.36 (br m, 1 H), 2.63 (t, J = 4.8 Hz, 2 H), 3.85−3.63 (m, 18 H), 4.18 (d, J = 4 Hz, 3 H), 4.58 (br s, 1 H), 6.19 (br s, 2 H), 7.15 (d, J = 8 Hz), 7.94 (br s, 1 H), 8.27 (d, J = 8.3 Hz, 1 H), 9.04 (s, 1 H); ^{13}C NMR (126 MHz, D_2O) δ 34.4, 39.8, 42.8, 65.47, 65.51, 66.62, 68.82, 69.94, 70.02, 70.06, 70.10, 70.72, 71.94, 85.98, 86.37, 92.7, 115.4, 124.9, 130.3, 130.8, 135.7, 141.7, 143.6, 149.3, 173.2, 173.6; ^{31}P NMR (121 MHz, D_2O) δ −8.39 (d, J = 41 Hz, 1 P), 10.58 (d, J = 48 Hz, 1 P), −22.00 (t, J = 48 Hz, 1 P); ESI-MS

m/*z* 984.1 (M + H); FAB-HRMS calcd for $C_{26}H_{37}N_7Na_4O_{22}P_3$ (M + H) 984.0795, found 984.0790.

Labeling DNA with DNP−PEG$_4$−dCTP. Double-stranded DNA was labeled with DNP−dPEG$_4$−dCTP by nick translation (*34*). No unmodified dCTP was added to the nick translation reaction mixture. The reaction was stopped when the size of the DNA was reduced to ∼300 bp as judged by agarose gel electrophoresis. The resulting DNA was purified by column chromatography (Qiagen) and precipitation by 2-propanol. The extent of labeling was estimated from optical absorption measurements at 260 and 365 nm. Typically, from ∼1 to 5% of the nucleotides in the resulting DNA was labeled with DNP.

Tissue Staining. The BenchMark XT automated slide processing system (Ventana Medical Systems, Inc., Tucson, AZ) was used for to assess performance of the in situ hybridization assay for *HER2* and HPV DNA targets.

Pretreatments. Automated deparaffinization, pretreatment, hybridization, stringency wash, signal detection, and counterstaining were performed on the BenchMark XT system. Formalin-fixed paraffin-embedded tissue sections on glass slides were baked at 65 °C for 20 min prior to the deparaffinization step with EZ Prep (Ventana) at 75 °C for 16 min. Deparaffinized tissue sections were exposed to a combination of heat treatment with reaction buffer [Tris-based solution (pH 7.6), Ventana] and ISH Protease 2 or ISH Protease 3 (Ventana) to unmask DNA targets.

Hybridization and Signal Development. For *HER2* gene detection, the INFORM *HER2* DNA Probe (Ventana) was applied to the glass slide and the probe and sample DNA were codenatured by incubation at 95 °C for 10 min. Then, the hybridization step was conducted at 52 °C for 2 h. After three stringency wash steps were performed at 72 °C with 2× SCC (Ventana), tissue sections were incubated with monoclonal rabbit anti-DNP antibody (Ventana) for 20 min and then with HRP-conjugated anti-rabbit antibody for 16 min at 37 °C. The peroxidase catalyzed silver deposition was developed using the ultraView SISH Detection Kit (Ventana) (*36*). *HER2* probe slides were counterstained with Hematoxylin II (Ventana) for 4 or 8 min and Bluing Reagent (Ventana) for 4 min.

For the HPV assays, the DNP-labeled HPV probe was detected using the Ventana ISH iView Blue Plus detection kit on the BenchMark XT system.

RESULTS

Synthesis. A novel methodology involving the bisulfite-mediated, microwave-promoted hydrazinolysis of cytosine was utilized to efficiently produce nucleotide conjugates suitable for the labeling of DNA via nick translation. The synthesis of one such conjugate, N^4-amino-dCTP−dPEG$_4$−DNP, is outlined in Scheme 1. A number of microwave-mediated transamination reactions of deoxycytosine triphosphate (dCTP) with bidentate nitrogen nucleophiles were explored. Of these, the reaction with hydrazine to produce N^4-aminodeoxycytidine 5′-triphosphate (N^4-amino-dCTP) proved to be the highest yielding and most reproducible. To obtain optimal results, strict control of reaction parameters, including applied microwave power, pH, and temperature, had to be maintained. On a 300 mg scale, under optimal microwave conditions, the hydrazinolysis of cytosine proceeded nearly quantitatively within 30 min. The corresponding thermal reaction produced a <20% yield of the hydrazinolysis product after heating for 1 h. The microwave reaction was shown to be scalable to 3.5 g, and the final product was amenable to labeling with a wide variety of molecules such as haptens or fluorophores.

Early attempts to purify N^4-aminodeoxycytidine 5′-triphosphate under acidic HPLC conditions described in the literature led to extensive product degradation (*23*). To circumvent this issue, ion pair chromatography was explored. Under the appropriate ion pair conditions, N^4-amino-dCTP was easily fractionated with negligible degradation.

The synthesis of the electrophilic species, DNP−dPEG$_4$−NHS, also benefited from the use of microwave conditions. Under aqueous microwave conditions, DNP−dPEG$_4$−CO_2H was obtained in >90% yield after irradiation for only 30 min. The corresponding reaction in organic solvent in the absence of microwave irradiation never afforded a >60% yield and required several hours to complete. The synthesis of DNP−dPEG$_4$−NHS was accomplished by conversion of the acid intermediate to the NHS ester via treatment with NHS and DCC in DCM overnight. The crude NHS ester obtained following the removal of the urea byproduct was sufficiently stable to allow for purification on the silica gel.

Overnight reaction of the nucleotide (**1**) and the NHS ester (**3**) in anhydrous DMSO proceeded smoothly to give the final nucleotide conjugate that was efficiently purified by ion pair chromatography. Ion exchange provided the sodium salt of N^4-amino-dCTP−dPEG$_4$−DNP that was used in the labeling of DNA.

DNA Labeling with DNP−dPEG$_4$−dCTP and Tissue Staining. Double-stranded *HER2* and HPV DNA were labeled with DNP−dPEG$_4$−dCTP by nick translation using *Escherichia coli* DNA polymerase I. The resulting probes were typically labeled at 1−5% of the nucleotide residues. The probes were used to visualize gene amplification of *HER2* DNA in *HER*+ breast cancer and to detect human papilloma virus DNA in cervical tumors. In situ hybridization assays for *HER2* and HPV DNA signals utilizing the BenchMark XT automated slide processing system (Ventana) were effective in visualizing the *HER2* and HPV DNA targets in tissue. HPV was visualized utilizing a chromogenic ISH protocol, whereas *HER2* was visualized via SISH (Figure 1). The observed signals were strong and easily discernible with little or no background (Figure 2).

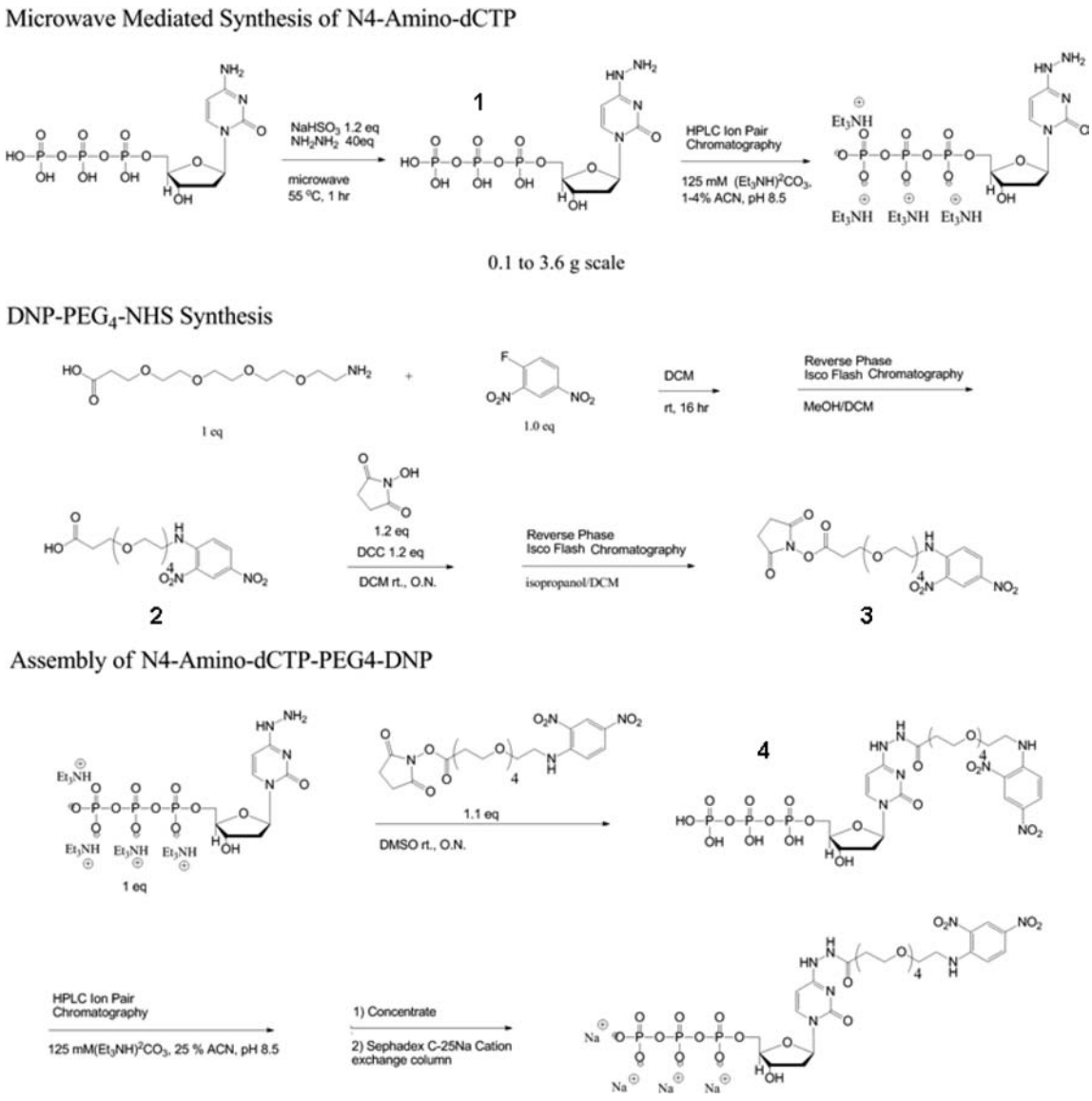
DISCUSSION

Efforts to efficiently produce nucleotide conjugates suitable for the labeling of double-stranded DNA via nick translation have led to a novel methodology involving the bisulfite-mediated, microwave-promoted hydrazinolysis of cytosine at the C4 position. By utilizing microwave acceleration, the hydrazine moiety was effectively installed while side reactions were prevented and phosphate hydrolysis was minimized. HPLC analysis of thermally promoted and microwave-promoted reactions indicated that microwave energy accelerates the hydrazinolysis reaction with no effect on the rate of phosphate hydrolysis. This observation allowed the optimization of 4-amino-dCTP formation by employing the minimum effective reaction time. The reaction was shown to be scalable within the capacity limits of the microwave synthesizer. As the scale was increased, slightly longer microwave reaction times were required to affect complete hydrazinolysis. As such, larger scale reactions produced slightly lower yields.

There are several examples of nucleotides that have been synthetically modified to contain nucleophilic handles (*37, 38*). To the best of our knowledge, the methodology that we reported here represents a particularly efficient route for producing such nucleotides.

The utility of 4-amino-dCTP as a reagent for the assembly of hapten-labeled nucleotides that can be incorporated into DNA via nick translation has been demonstrated via the synthesis of DNP−dPEG$_4$−dCTP. Nick translation of double-stranded *HER2* and HPV DNA in the prescence of DNP−dPEG$_4$−4-amino-dCTP consistently produced probes labeled at 3−4% of the nucleotide residues. Visualization of *HER2* and HPV DNA targets in tissue via in situ hybridization utilizing the BenchMark

Scheme 1. Synthesis of N^4-Amino-dCTP−PEG_4−DNP



XT automated slide processing system (Ventana) consistently provided strong and easily discernible signals with little or no background.

As the percent of labeled nucleotide incorporation increases for a given probe, effects on the DNA melting temperature and hybridization specificity became evident. These phenomena are

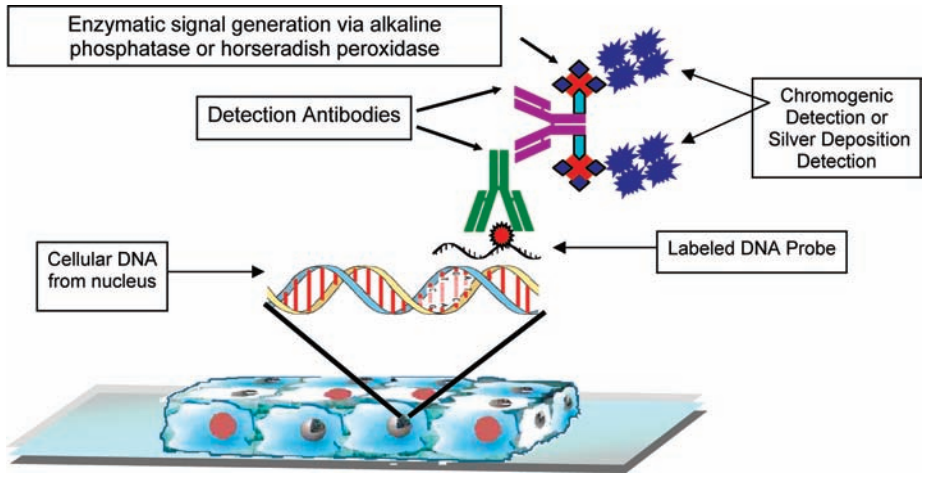


Figure 1. Alkaline phosphatase (AP)-mediated chromogenic detection (SISH) and horseradish peroxidase (HRP)-mediated silver deposition detection (SISH) (*5*).

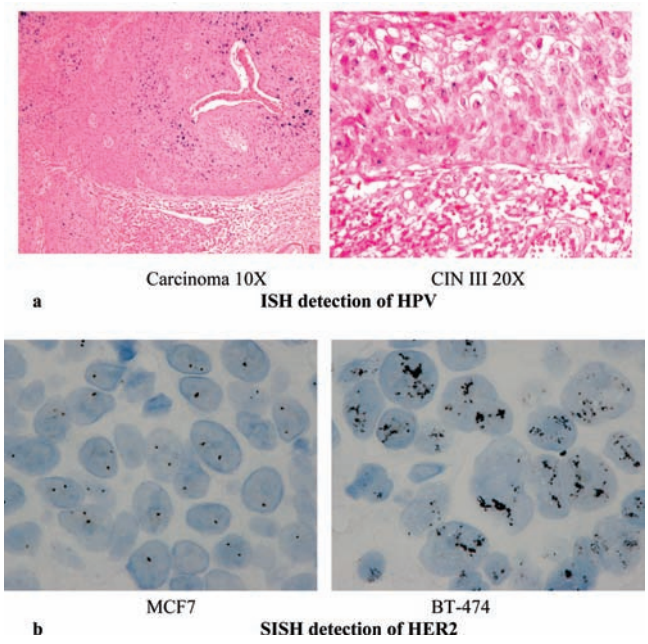


Figure 2. (a) Detection of HPV DNA in cervical cancer tissues by in situ hybridization with a DNP-labeled HPV DNA probe cocktail followed by immunohistochemical detection of the probe with a rabbit anti-DNP monoclonal antibody followed by an alkaline phosphatase-conjugated goat anti-rabbit antibody and Ventana's *I*View$_{Blue}$ Plus Detection kit. The blue nuclear signal indicates the presence of *HPV* DNA. (b) Detection of *HER2* genes in breast cancer cell lines. In situ hybridization with a DNP-labeled *HER2* DNA probe was followed by reaction with a rabbit anti-DNP monoclonal antibody that was detected by a peroxidase-conjugated goat anti-rabbit antibody. Peroxidase-catalyzed silver deposition generated the black spots representing the *HER2* genes (Ventana's *INFORM HER2* SISH assay). MCF-7 cells contain the normal two copies of the gene. In BT474 cells, the *HER2* gene is amplified as indicated by the many spots in each nucleus.

likely a result of the weakened ability of labeled nucleotides to form stable hydrogen bonds with complementary bases and may also be a function of hydrophobic hapten−hapten interactions, particularly at higher hapten loadings. At ∼7% incorporation of labeled nucleotides, the probe performance suffers as shown by the increased background. If fluorescent derivatives are used, then quenching also becomes significant at high labeling levels.

We have found the optimal level of labeled nucleotide incorporation as it relates to the quality of ISH or SISH signals to be in the range of 3−5% of the total nucleotides. The labeling level is typically controlled by adding a proportion of the natural nonlabeled nucleotide to the labeling reaction. The conditions for producing desirable labeling levels are diverse and depend on the particular nucleotide derivative (spacer composition and length, size, and chemical composition of the label being introduced) and the enzyme used for incorporation of the derivative. Many natural enzymes and mutated derivatives of natural enzymes are now in use, especially for PCR-related methods and in DNA sequencing reactions. We used the described derivative to label DNA by nick translation to show that a compound made by this method behaves as expected in DNA labeling and that the resulting probe functions in hybridization assays.

We intend to utilize this methodology to assemble a wide variety of hapten−dPEG−amino-dCTP derivatives to be used in the construction of a diverse array of DNA probes. The construction of such a probe library has the potential to facilitate the simultaneous visualization of multiple DNA targets within an individual patient sample. This last objective is of critical importance in the fast developing area of individualized medicine and diagnostics, which seeks to do away with the cancer paradigms of "trial and error" and "one drug fits all", replacing them with targeted therapies tailored for the specific genomic profiles of an individual patient's disease. This has become possible because of the recent advent of multiplexed light microscopy-based in situ hybridization methods, which allow for the visualization of individual copies of genes and amplification states. The use of *HER2* as a prognostic and predictive biomarker for the determination of breast cancer patient eligibility for Herceptin (Genentech) treatment exemplifies this emerging approach to personalized cancer diagnosis and therapy.

ACKNOWLEDGMENT

We thank Dr. Lidija Pestic-Dragovich for biological tissue staining data and many discussions and Mr. Philip Miller for continuing support of this work. Ventana, BenchMark, INFORM, and UltraView are trademarks of Roche. All other trademarks are property of their respective owners.

Supporting Information Available: Characterization of synthesized small molecules, including ^{1}H NMR, ^{13}C NMR, ^{31}P NMR, and HRMS data. This material is available free of charge via the Internet at http://pubs.acs.org.

LITERATURE CITED

(1) Mansfield, E. S., Worley, J. M., McKenzie, S. E., Surrey, S., Rappaport, E., and Fortina, P. (1995) Nucleic acid detection using non-radioactive labeling methods. *Mol. Cell. Probes 9* (3), 145–156.
(2) Niemeyer, C. M. (2001) Semi-synthetic nucleic acid-protein conjugates: Applications in life sciences and nanobiotechnology. *Rev. Mol. Biotechnol. 82* (1), 47–66.
(3) Koehler, A. N. (2009) Microarrays in chemical biology. *Wiley Encyclopedia of Chemical Biology*, Vol. 3, pp 134−143, Wiley, New York.
(4) Halling, K. C., and Kipp, B. R. (2007) Fluorescence in situ hybridization in diagnostic cytology. *Hum. Pathol. 38* (8), 1137–1144.
(5) Ross, J. S. (2009) Breast cancer biomarkers and HER2 testing after 10 years of anti-HER2 therapy. *Drug News Perspect. 22* (2), 93–106.
(6) Bieniarz, C., Kernag, C. A., Kosmeder, J. W., Rogers, P., and Wong, J. (2009) Enzyme-catalyzed metal deposition for the enhanced in situ detection of immunohistochemical epitopes and nucleic acid sequences. U.S. Patent 7,632,652 B2.
(7) Hainfeld, J. F. (2008) Test methods using enzymatic deposition and alteration of metals. U.S. Patent 7,364,872 B1.
(8) Lee-Hoeflich, S., and Stern, H. (2008) Gene expression markers of tumor resistance to treatment by HER2 inhibitors. PCT Int. Appl., pp 96.
(9) Van Cutsem, E., Kang, Y., Chung, H., Shen, L., Sawaki, A., Lordick, F., Hill, J., Lehle, M., Feyereislova, A., and Bang, Y. (2009) Efficacy results from the ToGA trial: A phase III study of trastuzumab added to standard chemotherapy (CT) in first-line human epidermal growth factor receptor 2 (HER2)-positive advanced gastric cancer (GC). *Journal of Clinical Oncology, ASCO Annual Meeting Proceedings (Post-Meeting Edition)*, 27, 18S (June 20 Supplement), LBA4509.
(10) Ross, J. S., Slodkowska, E. A., Symmans, W. F., Pusztai, L., Ravdin, P. M., and Hortobagyi, G. N. (2009) The HER-2 receptor and breast cancer: Ten years of targeted anti-HER-2 therapy and personalized medicine. *Oncologist 14* (4), 320–368.
(11) Finan, J. E., and Zhao, R. Y. (2007) From molecular diagnostics to personalized testing. *Pharmacogenomics 8* (1), 85–99.

(12) Evans, M. F., and Cooper, K. (2004) Human papillomavirus integration: Detection by in situ hybridization and potential clinical application. *J. Pathol. 202* (1), 1–4.

(13) Beaucage, S. L., and Iyer, R. P. (1992) Advances in the Synthesis of Oligonucleotides by the Phosphoramidite Approach. *Tetrahedron 48* (12), 2223–2311.

(14) Shapiro, R., Servis, R., and Welcher, M. (1970) Reactions of uracil and cytosine derivatives with sodium bisulfite. A specific deamination method. *J. Am. Chem. Soc. 92*, 422–424.

(15) Draper, D. E., and Gold, L. (1980) A Method for Linking Fluorescent Labels to Polynucleotides: Application to Studies of Ribosome-Ribonucleic Acid Interactions. *Biochemistry 19*, 1774–1781.

(16) Viscidi, R. P., Connelly, C. J., and Yolken, R. H. (1986) Novel Chemical Method for the Preparation of Nucleic Acids for Nonisotopic Hybridization. *J. Clin. Microbiol. 23*, 311–317.

(17) Turchinskii, M. F., Ainbinder, E. I., and Sverdlov, E. D. (1988) Multiple Hybridization in Genome Analysis. I. Reaction of Diamines and Bisulfite with Cytosine for Introduction of Nonradioactive labels into DNA. *Mol. Biol. (Moscow) 22*, 1229–1235.

(18) Karpyshev, N. N., Bondarenko, T. Y., Vtorushina, I. A., and Kipriyanov, S. M. (1991) Introduction of Aminoalkyl Functions into Synthesized Oligodeoxyribonucleotides via Transamination of Cytosine Residues. *Bioorg. Khim. 17*, 809–812.

(19) Avignolo, C., Roner, R., Cai, S., and Bignone, F. A. (1991) Biotinylation of Denatured Double-stranded DNA after Transamination of Cytidines: Molecular Biology Applications. *J. Biochem. Biophys. Methods 23*, 193–202.

(20) Avignolo, C., Pizzorno, G., Cai, S., and Bignone, F. A. (1991) HPLC Analysis of DNA upon Cytidine Transamination at 100 °C. *J. Biochem. Biophys. Methods 23*, 202–205.

(21) Shapiro, R., and Weisgras, J. M. (1970) Bisulfite-catalyzed Transamination of Cytosine and Cytidine. *Biochem. Biophys. Res. Commun. 40*, 839–843.

(22) Molander, J., Hurskainen, P., Hovinen, J., Lahti, M., and Lonnberg, H. (1993) Bisulfite Ion-Catalyzed Transamination of Cytosine Residues with α,ω-Alkanediamines: The Effect of Chain Length on the Reaction Kinetics. *Bioconjugate Chem. 4*, 362–365.

(23) Negishi, K., Harada, C., Ohara, Y., Oochara, K., Nitta, N., and Hayatsu, H. (1983) N4-Aminocytidine, a nucleoside analog that has exceptionally high mutagenic activity. *Nucleic Acids Res. 11*, 5223–5233.

(24) Romanov, N. N., Gravis, A. G., Leshcheva, I. F., and Bundel, Y. G. (1998) 1,2-Asymmetric Induction in Nucleophilic Michael Addition Reactions of Amines Under Microwave Irradiation. *Mendeleev Commun. 35*, 147–148.

(25) Lu, Y. F., and Fallis, A. G. (1995) A Cycloaddition Approach to Tricyclic Taxoid Skeletons. *Can. J. Chem. 73*, 2239–2252.

(26) Mitra, A. K., De, A., and Karchaudhuri, N. (1999) Solvent-Free Microwave Enhanced Knoevenagel Condensation of Ethyl Cyanoacetate with Aldehydes. *Synth. Commun. 29*, 2731–2739.

(27) Jaisinghani, H. G., and Khadilkar, B. M. (1997) Rapid and efficient synthesis of 1-arylpiperazines under microwave irradiation. *Tetrahedron Lett. 38*, 6875–6876.

(28) Bosch, A. I., de la Cruz, P., Diez-Barra, E., Loupy, A., and Langa, F. (1995) Microwave Assisted Beckmann Rearrangement of Ketoximes in Dry Media. *Synlett 12*, 1259–1260.

(29) Alterman, M., Andersson, H. O., Garg, N., Ahlsen, G., Lovgren, S., Cleasson, B., Danielsson, U. H., Kvarnstrom, I., Vrang, L., Unge, T., Samuelsson, B., and Halberg, A. (1999) Design and Fast Synthesis of C-Terminal Duplicated Potent C_2-Symmetric P1/P1′-Modified HIV-1 Protease Inhibitors. *J. Med. Chem. 42*, 3835–3844.

(30) Perreux, L., and Loupy, A. (2001) A Tentative Rationalization of Microwave Effects in Organic Synthesis According to the Reaction Medium, and Mechanistic Considerations. *Tetrahedron 57*, 9199–9223.

(31) Lidstrom, P., Tierney, J., Wathey, B., and Westman, J. (2001) Microwave Assisted Organic Synthesis: A Review. *Tetrahedron 57*, 9225–9283.

(32) Pinkel, D., Segraves, R., Sudar, D., Clark, S., Poole, I., Kowbel, D., Collins, C., Kuo, W., Chen, C., Zhai, Y., Dairkee, S. H., Ljung, B., Gray, J. W., and Albertson, D. G. (1998) High-resolution analysis of DNA copy number variation using comparative genomic hybridization to microarrays. *Nat. Genet. 20*, 207–211.

(33) Pollack, J. R., Sorlie, T., Perou, C. M., Rees, C. A., Jeffrey, S. S., Lonning, P. E., Tibshirani, R., Botstein, D., Borresen-Dale, A., and Brown, P. O. (2002) Microarray analysis reveals a major direct role of DNA copy number alteration in the transcriptional program of human breast tumors. *Proc. Natl. Acad. Sci. U.S.A. 99*, 12963–12968.

(34) Pollack, J. R., Perou, T., Alizadeh, A. A., Eisen, M. B., Pergamenschikov, A., Williams, C. F., Jeffrey, S. S., Botstein, D., and Brown, P. O. (1999) Genome-wide analysis of DNA copy-number changes using cDNA microarrays. *Nat. Genet. 23*, 41–46.

(35) Rigby, P., Dieckmann, M., Rhodes, C., and Berg, P. (1977) Labeling deoxyribonucleic acid to high specific activity *in vitro* by nick translation with DNA polymerase I. *J. Mol. Biol. 113* (1), 237–251.

(36) Tubbs, R. R., Pettay, J., Skacel, M., Downs-Kelly, E., Powell, R. D., Hicks, D. G., and Hainfeld, J. F. (2005) Gold- and silver-facilitated metallographic in situ hybridization procedures for detection of *HER2* gene amplification. *Mol. Morphol. Hum. Tissues*, 101–106.

(37) Langer, P. R., Waldrop, A. A., and Ward, D. C. (1981) Enzymatic synthesis of biotin-labeled polynucleotides: Novel nucleic acid affinity probes. *Proc. Natl. Acad. Sci. U.S.A. 78*, 6633–6637.

(38) Mishra, N. C., Khorshidi, H. S., Gan, Y., Szweda, P., and George, J. (1997) Modified nucleotides for nucleic acid labeling. U.S. Patent 5,684,142.

BC100013B

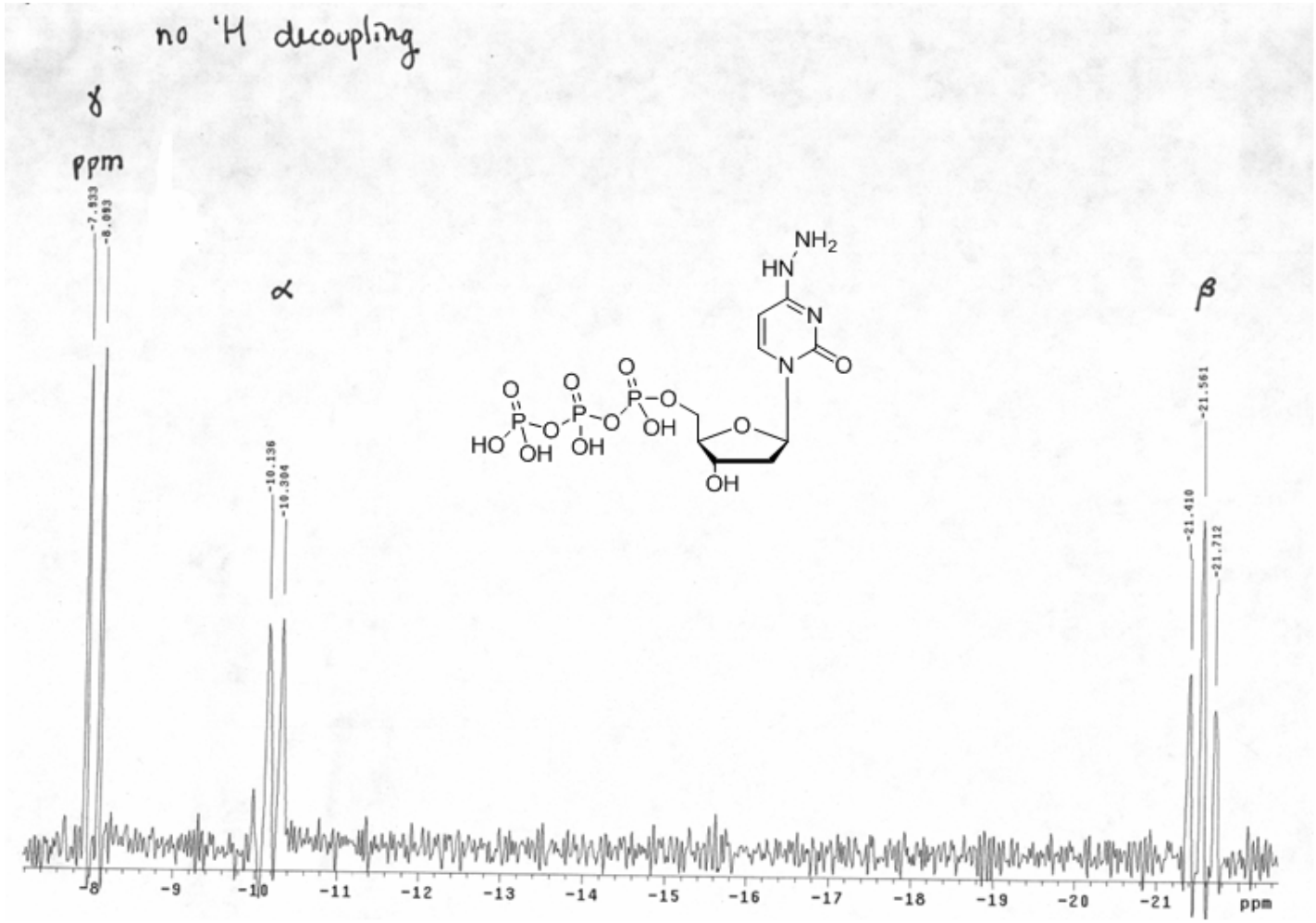
Supporting Information

Mark Lefever, Jerome W. Kosmeder 2nd, Michael Farrell, and Christopher Bieniarz

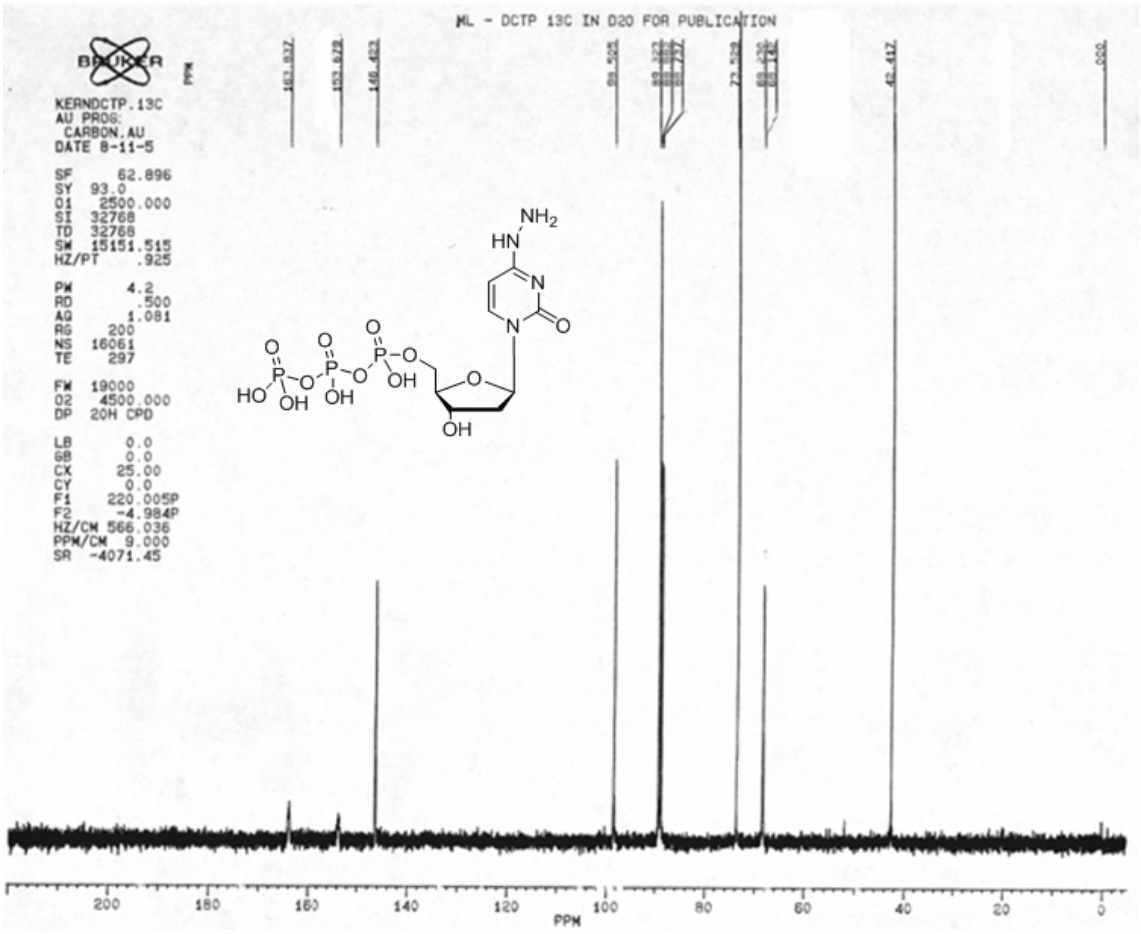
Microwave-Mediated Synthesis of Labeled Nucleotides with Utility in the Synthesis of DNA Probes

Table of Contents

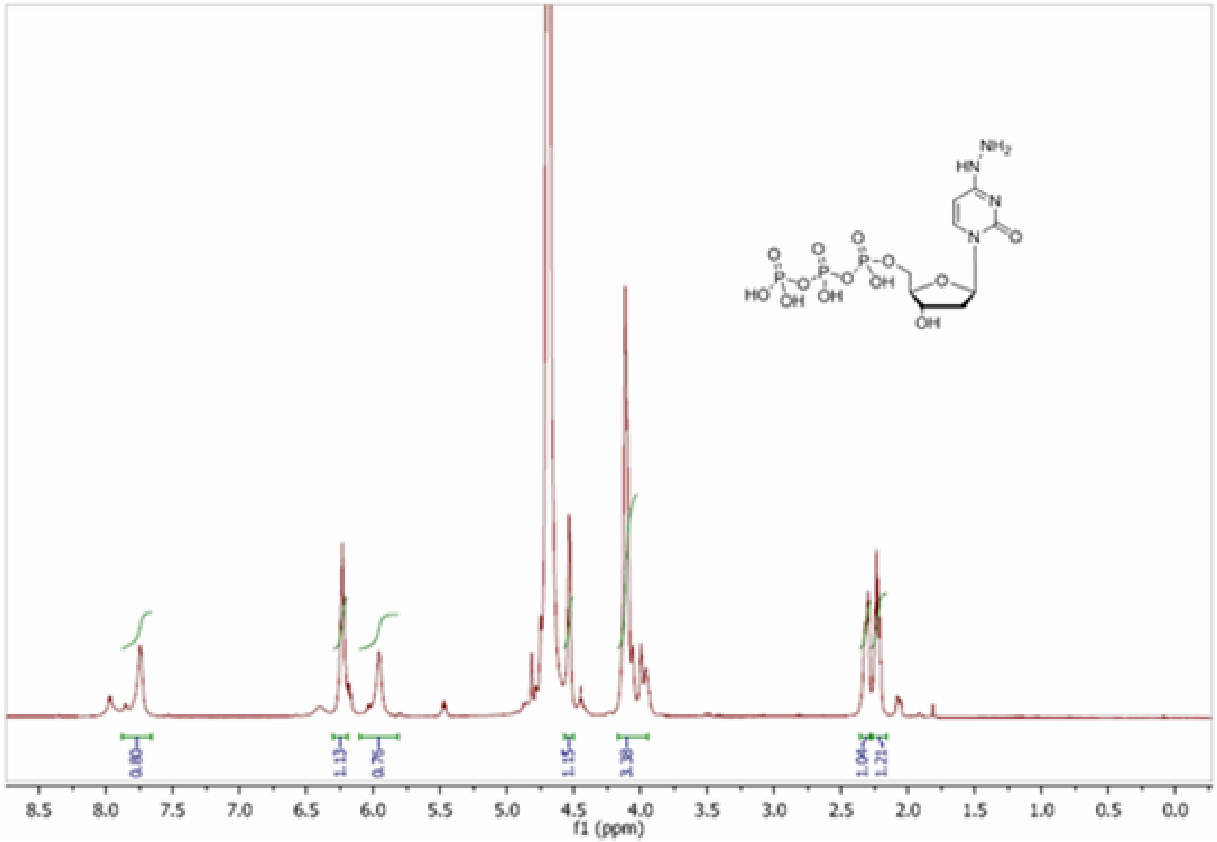
N[4]-amino-deoxycytidine 5'-triphosphate ^{31}P NMR……..……..…...2
N[4]-amino-deoxycytidine 5'-triphosphate ^{13}C NMR…….……...3
N[4]-amino-deoxycytidine 5'-triphosphate ^{1}H NMR…….…..…..4
N[4]-amino-deoxycytidine 5'-triphosphate HRMS…….…….....5
3(2(2(2(2(2,4 dinitrophenylamino)ethoxy)ethoxy)ethoxy)ethoxy) propanoic acid HRMS.....6
3(2(2(2(2(2,4 dinitrophenylamino)ethoxy)ethoxy)ethoxy)ethoxy) propanoic acid ^{13}C NMR…….....…….....7
3(2(2(2(2(2,4 dinitrophenylamino)ethoxy)ethoxy)ethoxy)ethoxy) propanoic acid ^{1}H NMR…….……...…8
3(2(2(2(2(2,4dinitrophenylamino)ethoxy)ethoxy)ethoxy)ethoxy) propanate-N-hydoxysuccinimide ester ^{1}H NMR…….....9
3(2(2(2(2(2,4dinitrophenylamino)ethoxy)ethoxy)ethoxy)ethoxy) propanate-N-hydoxysuccinimide ester ^{13}C NMR…….....10
3(2(2(2(2(2,4dinitrophenylamino)ethoxy)ethoxy)ethoxy)ethoxy) propanate-N-hydoxysuccinimide ester HRMS.....11
N[4]-amino-deoxycytidine 5'-triphosphate-dPEG$_4$™-DNP ^{1}H NMR.....12
N[4]-amino-deoxycytidine 5'-triphosphate-dPEG$_4$™-DNP ^{13}C NMR.....13
N[4]-amino-deoxycytidine 5'-triphosphate-dPEG$_4$™-DNP ^{31}P NMR.....14
N[4]-amino-deoxycytidine 5'-triphosphate-dPEG$_4$™-DNP HRMS.....15



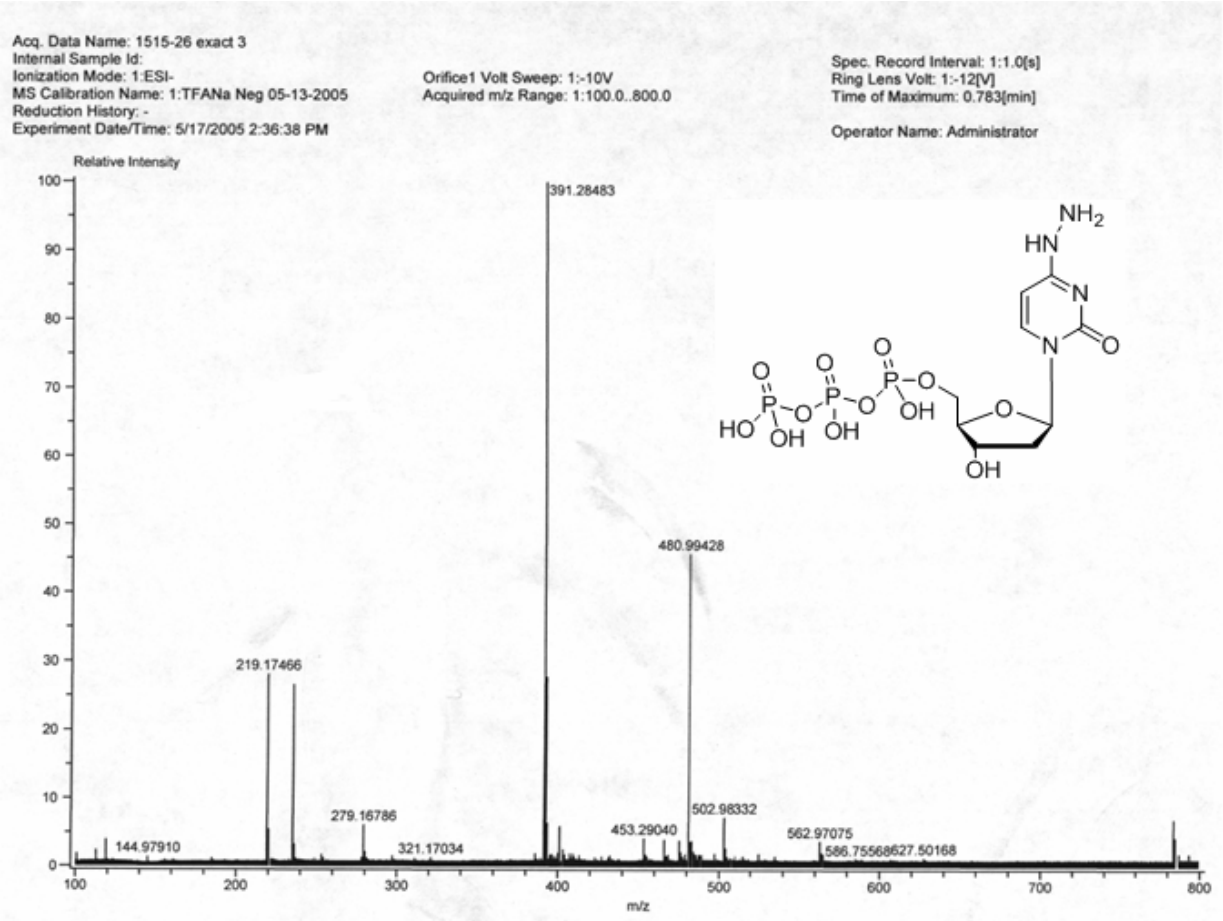
N^4-amino-deoxycytidine 5'-triphosphate ^{31}P NMR



N^4-amino-deoxycytidine 5'-triphosphate ^{13}C NMR



***N*[4]-amino-deoxycytidine 5'-triphosphate ^{1}H NMR**



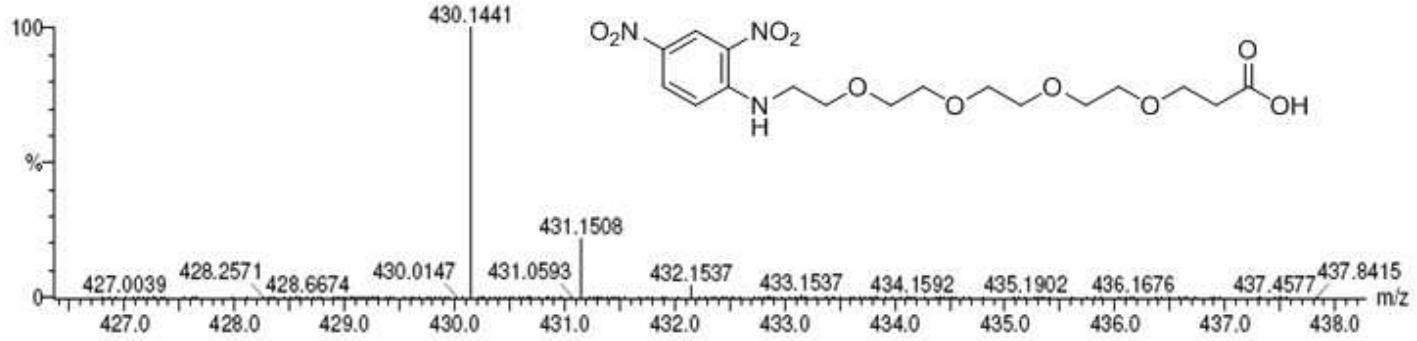
N^4-amino-deoxycytidine 5'-triphosphate HRMS

Elemental Composition Report Page 1

Single Mass Analysis
Tolerance = 5.0 PPM / DBE: min = -1.5, max = 100.0
Element prediction: Off
Number of isotope peaks used for i-FIT = 3

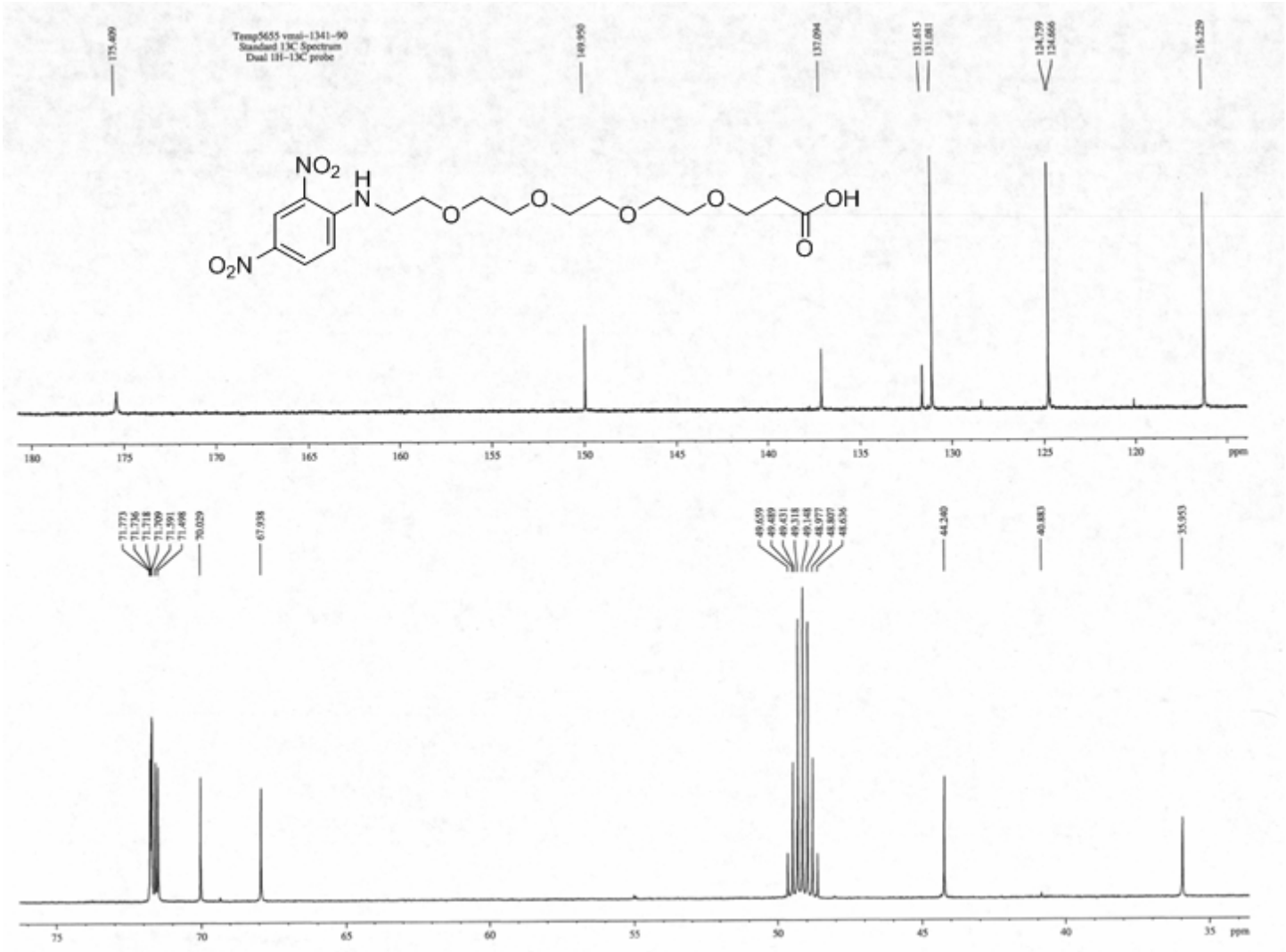
Monoisotopic Mass, Even Electron Ions
1342 formula(e) evaluated with 7 results within limits (up to 20 best isotopic matches for each mass)
Elements Used:
C: 0-50 H: 0-100 N: 0-20 O: 0-50

1:10 dilution of ML sample Collision Energy = 5.0 Pusher Freq = 11494 10-Nov-2009 14:15:00
DNP-PEG4-Acid - Sample 1 - LeuEnk LM - Neg 369 (1.943) AM (Cen,4, 80.00, Ar,16000.0,554.26,0.70,LS 10); Sm (SG, 1x3.00); Cm (361:370)

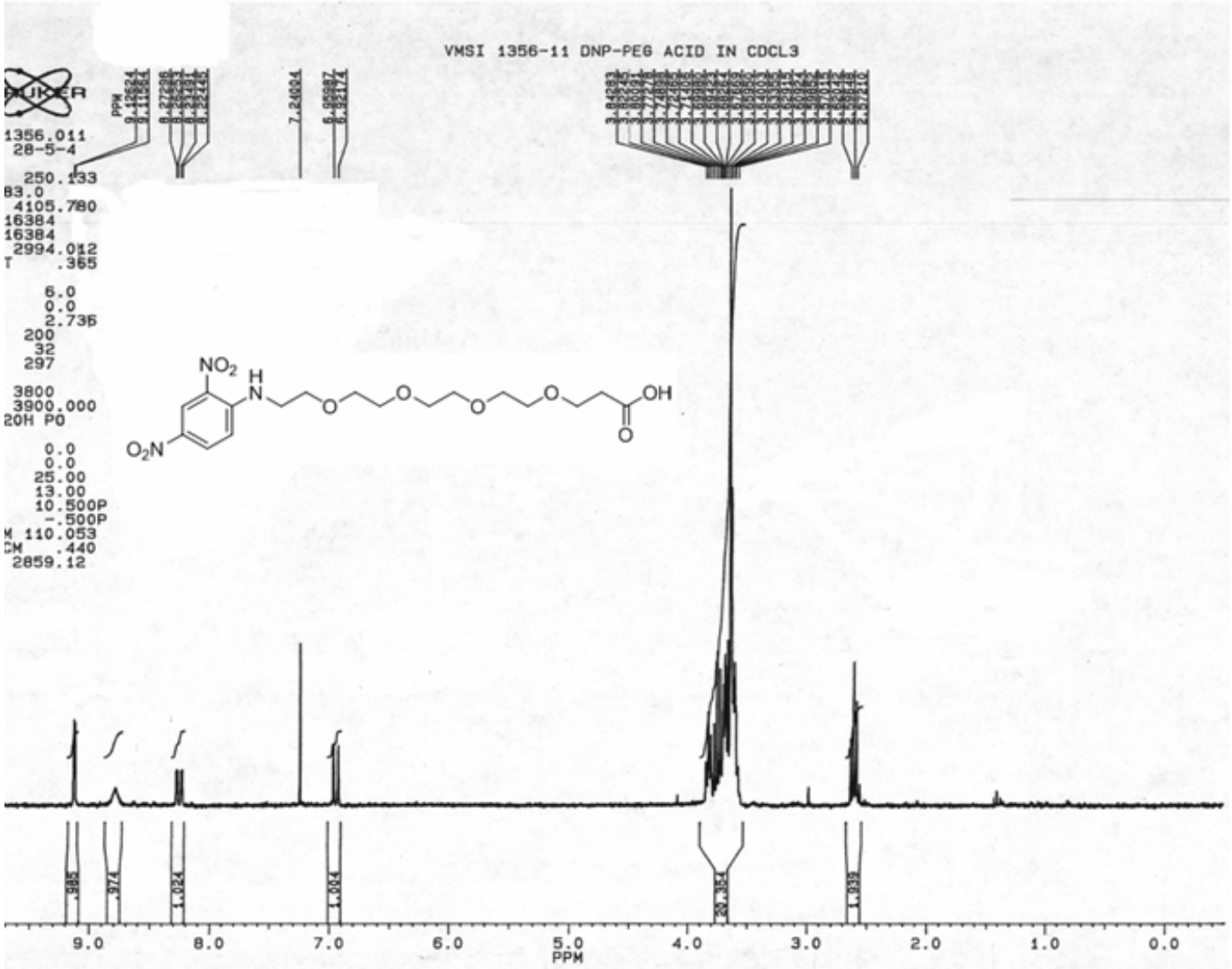


Minimum:				-1.5			
Maximum:		5.0	5.0	100.0			
Mass	Calc. Mass	mDa	PPM	DBE	i-FIT	i-FIT (Norm)	Formula
430.1441	430.1462	-2.1	-4.9	7.5	309.2	0.0	C17 H24 N3 O10

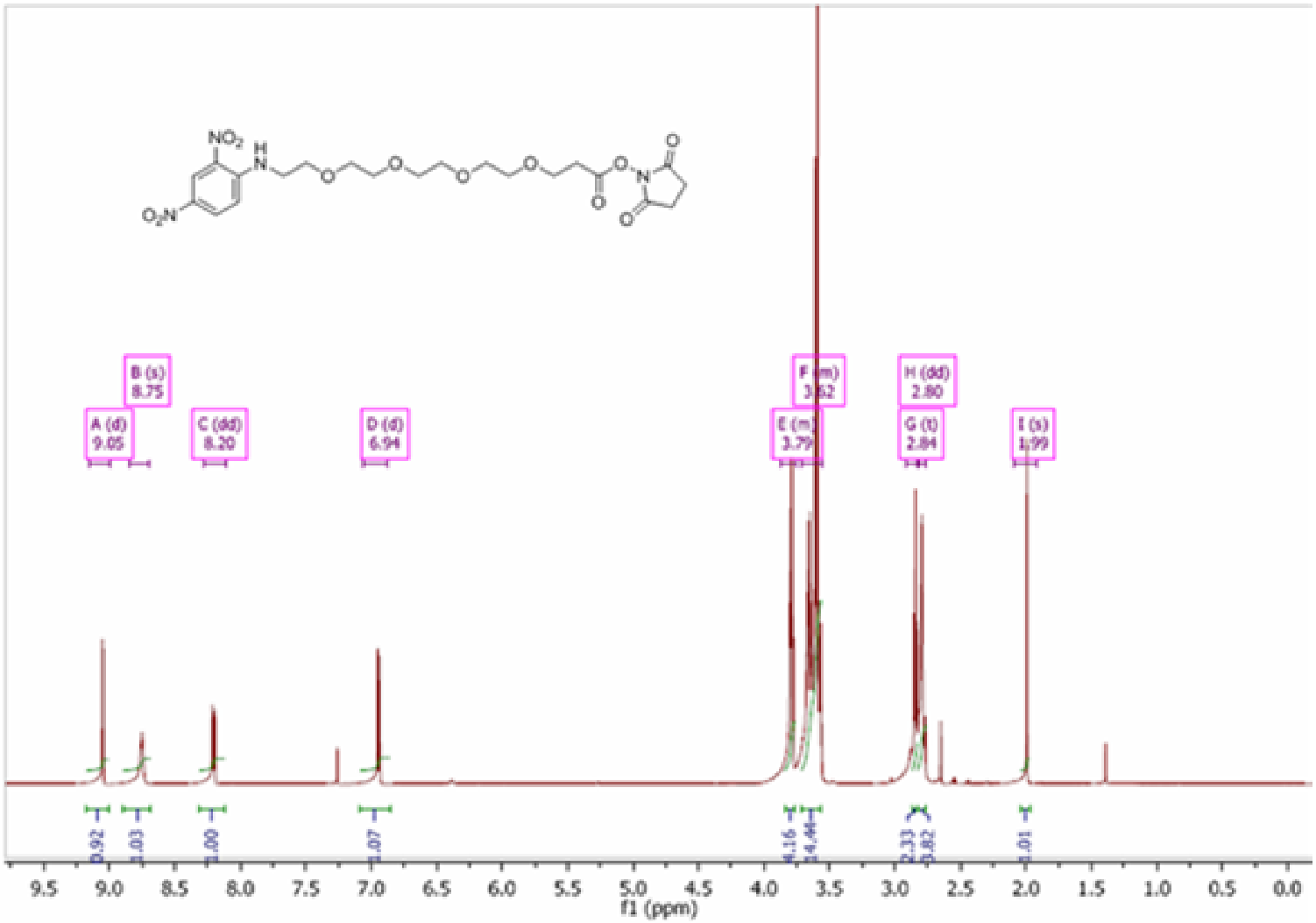
3(2(2(2(2(2,4 dinitrophenylamino)ethoxy)ethoxy)ethoxy)ethoxy) propanoic acid HRMS



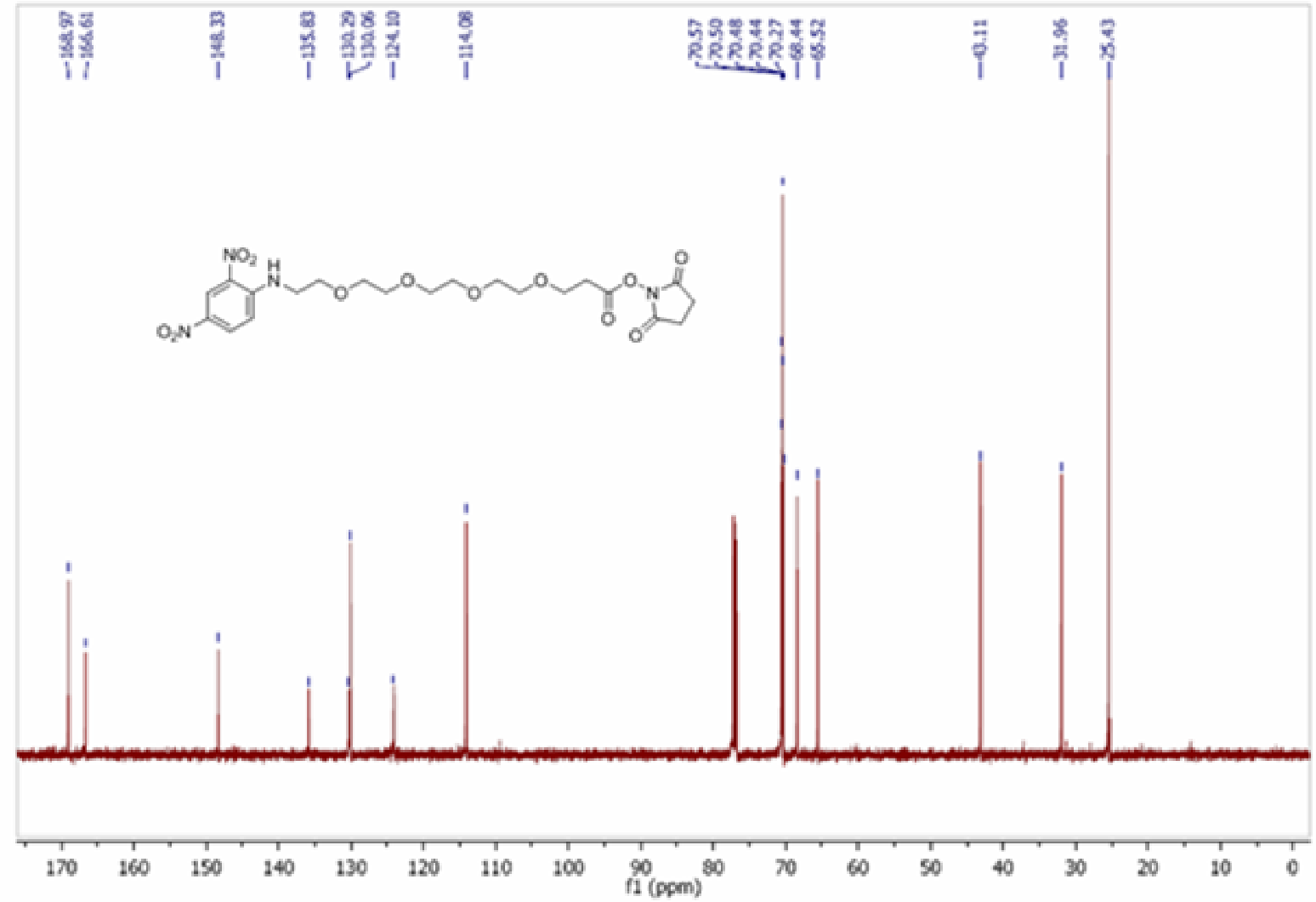
3(2(2(2(2(2,4 dinitrophenylamino)ethoxy)ethoxy)ethoxy)ethoxy) propanoic acid ^{13}C NMR



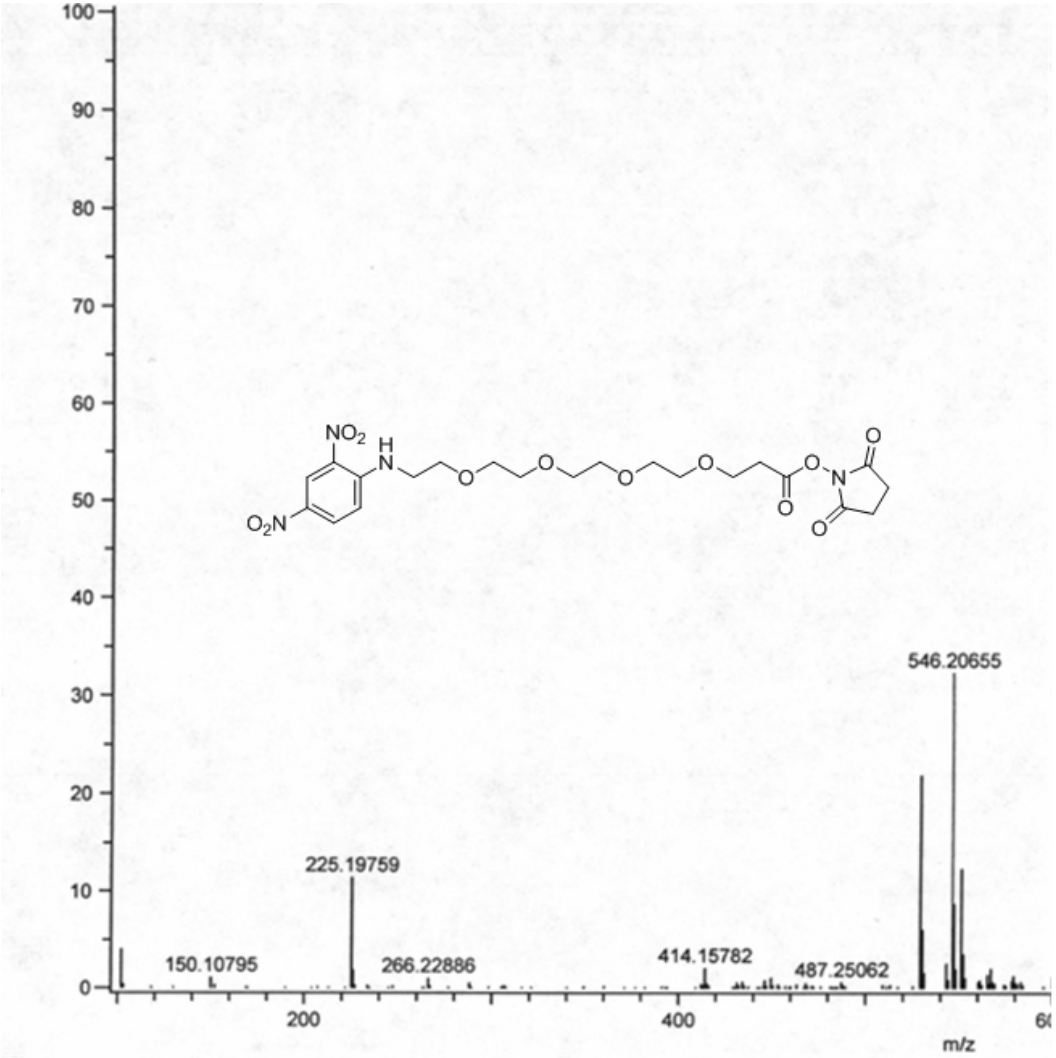
3(2(2(2(2(2,4 dinitrophenylamino)ethoxy)ethoxy)ethoxy)ethoxy) propanoic acid ^{1}H NMR



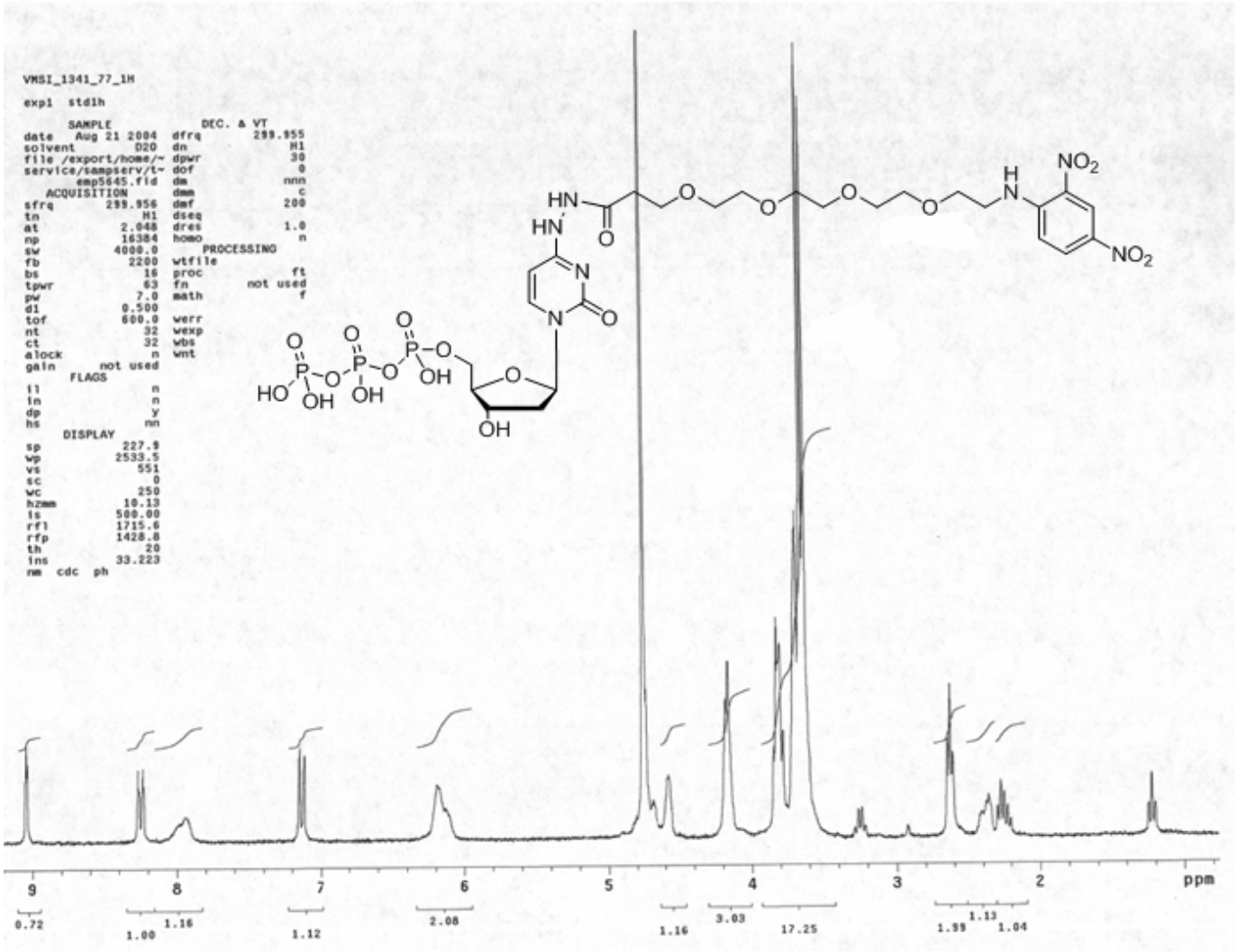
3(2(2(2(2(2,4dinitrophenylamino)ethoxy)ethoxy)ethoxy)ethoxy)propanate-N-hydoxysuccinimide ester ^{1}H NMR



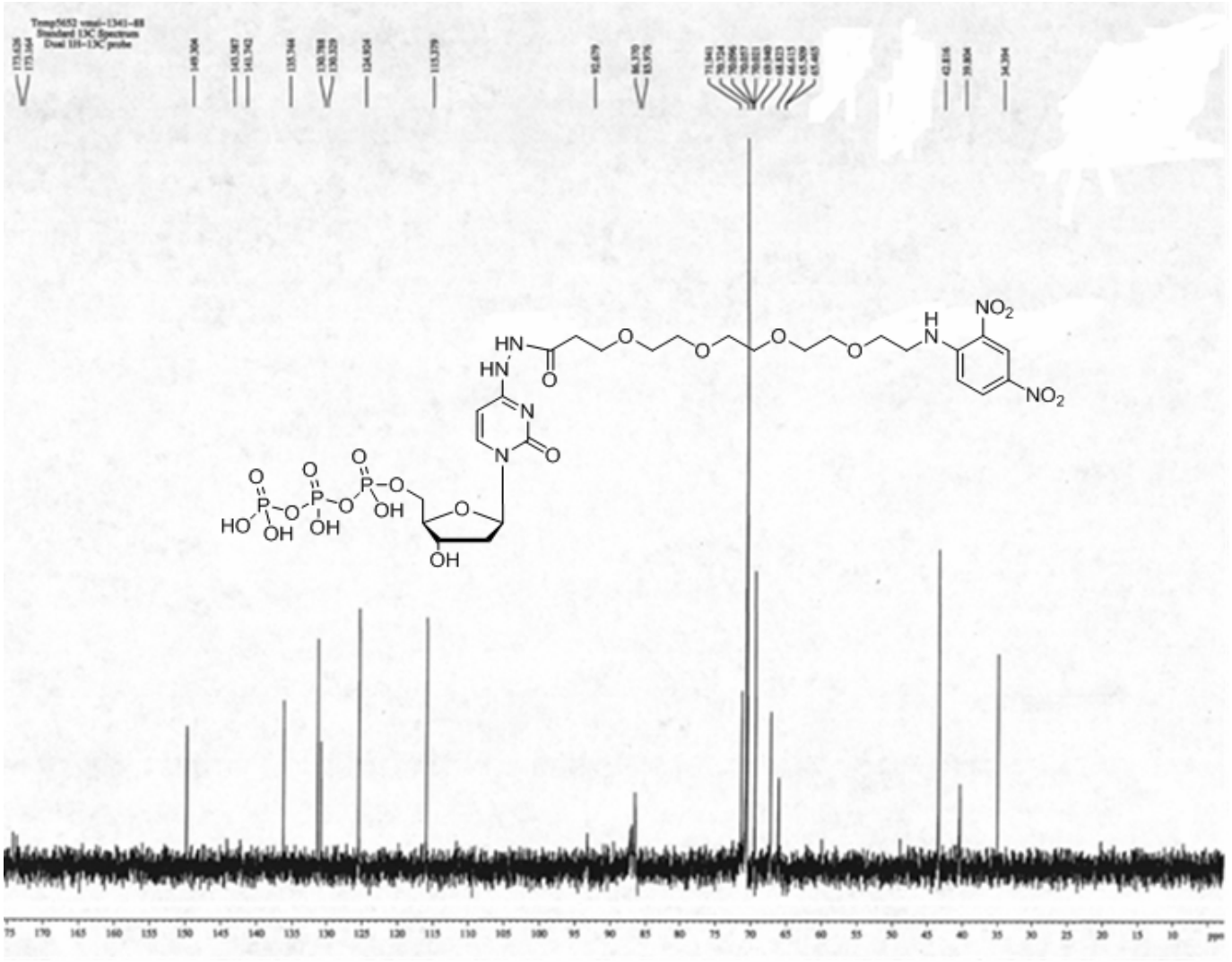
3(2(2(2(2(2,4dinitrophenylamino)ethoxy)ethoxy)ethoxy)ethoxy)propanate-N-hydoxysuccinimide ester ^{13}C NMR



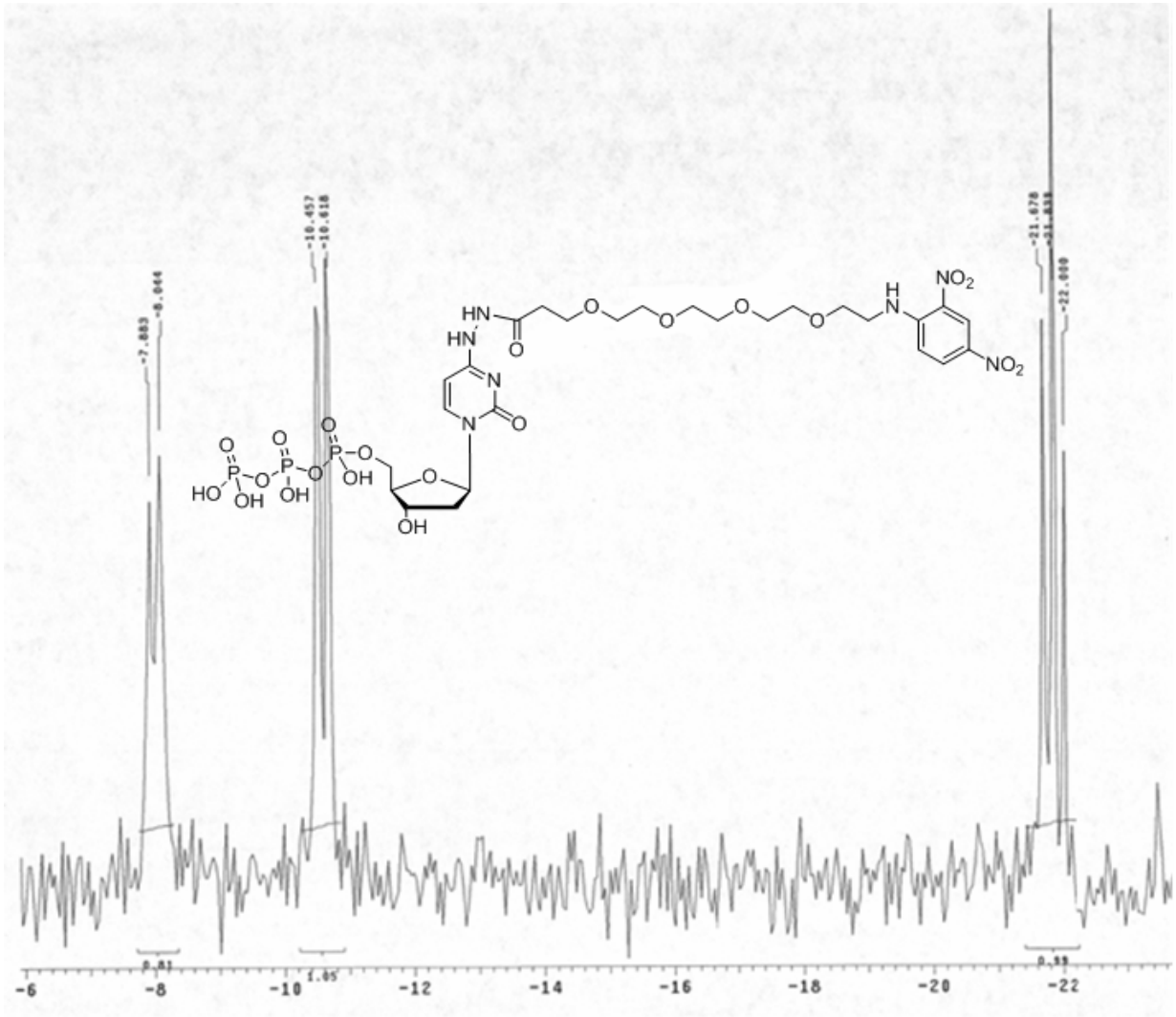
3(2(2(2(2(2,4dinitrophenylamino)ethoxy)ethoxy)ethoxy)ethoxy)propanate-N-hydoxysuccinimide ester HRMS

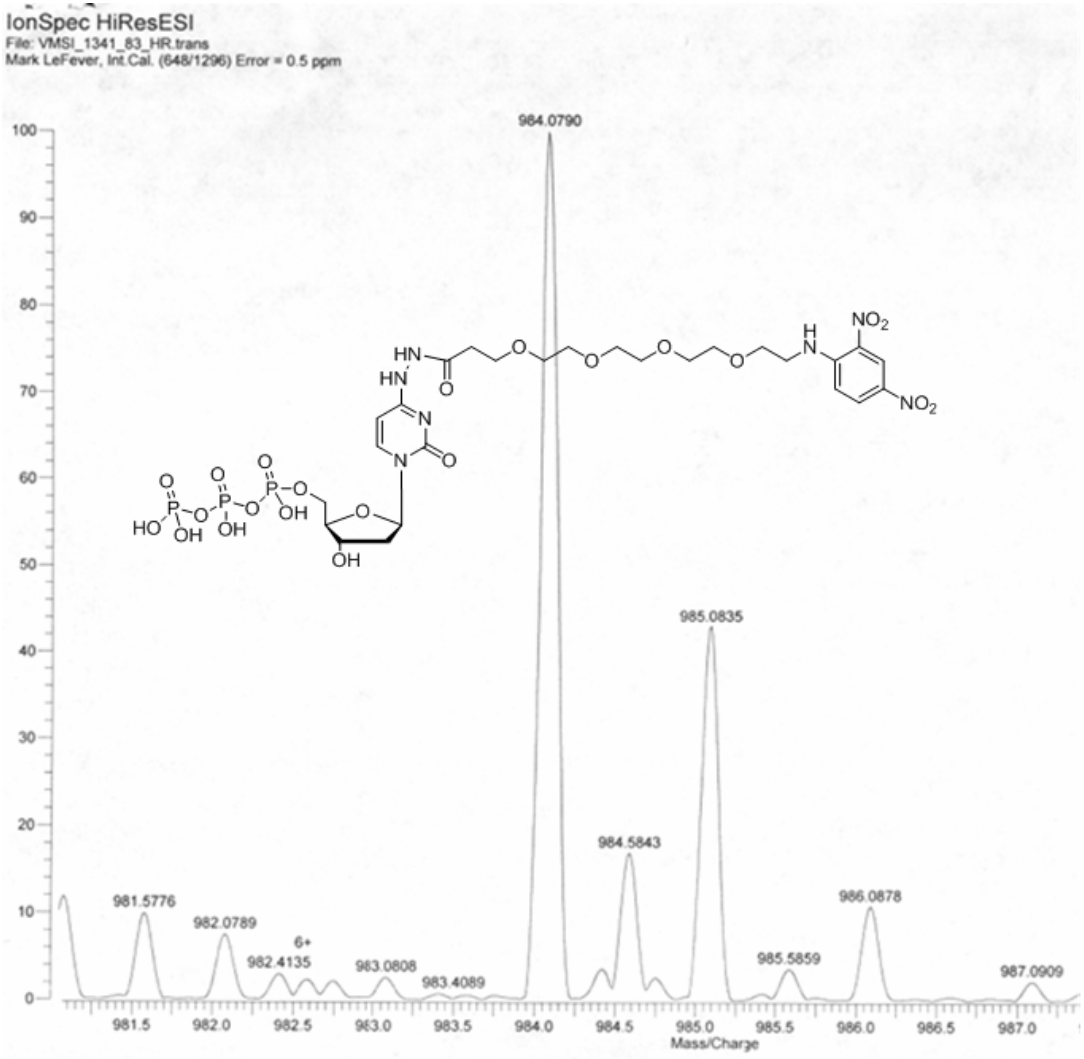


***N*[4]-amino-deoxycytidine 5'-triphosphate-dPEG$_4$[TM]-DNP [1]H NMR**



N^4-amino-deoxycytidine 5'-triphosphate-dPEG$_4$™-DNP ^{13}C NMR


-7.883
-8.044
-10.457
-10.618
-21.678
-21.839
-22.000
HN
HN
O
N
N
O
O
O



N^4-amino-deoxycytidine 5'-triphosphate-dPEG$_4^{TM}$-DNP HRMS

Comparison of Hydrazone Heterobifunctional Cross-Linking Agents for Reversible Conjugation of Thiol-Containing Chemistry

R. James Christie, Diana J. Anderson, and David W. Grainger*

Department of Chemistry, Colorado State University, Fort Collins, Colorado 80523-1872. Received January 26, 2010; Revised Manuscript Received June 12, 2010

Reversible covalent conjugation chemistries that allow site- and condition-specific coupling and uncoupling reactions are attractive components in nanotechnologies, bioconjugation methods, imaging, and drug delivery systems. Here, we compare three heterobifunctional cross-linkers, containing both thiol- and amine-reactive chemistries, to form pH-labile hydrazones with hydrazide derivatives of the known and often published water-soluble polymer, poly[*N*-(2-hydroxypropyl methacrylamide)] (pHPMA), while subsequently coupling thiol-containing molecules to the cross-linker via maleimide addition. Two novel cross-linkers were prepared from the popular heterobifunctional cross-linking agent, succinimidyl-4-(*N*-maleimidomethyl) cyclohexane-1-carboxylate (SMCC), modified to contain either terminal aldehyde groups (i.e., 1-(*N*-3-propanal)-4-(*N*-maleimidomethyl) cyclohexane carboxamide, PMCA) or methylketone groups (i.e., 1-(*N*-3-butanone)-4-(*N*-maleimidomethyl) cyclohexane carboxamide, BMCA). A third cross-linking agent was the commercially available *N*-4-acetylphenyl maleimide (APM). PMCA and BMCA exhibited excellent reactivity toward hydrazide-derivatized pHPMA with essentially complete hydrazone conjugation to polymer reactive sites, while APM coupled only ∼60% of available reactive sites on the polymer despite a 3-fold molar excess relative to polymer hydrazide groups. All polymer hydrazone conjugates bearing these bifunctional agents were then further reacted with thiol-modified tetramethylrhodamine dye, confirming cross-linker maleimide reactivity after initial hydrazone polymer conjugation. Incubation of dye-labeled polymer conjugates in phosphate buffered saline at 37 °C showed that hydrazone coupling resulting from APM exhibited the greatest difference in stability between pH 7.4 and 5.0, with hydrolysis and dye release increased at pH 5.0 over a 24 h incubation period. Polymer conjugates bearing hydrazones formed from cross-linker BMCA exhibited intermediate stability with hydrolysis much greater at pH 5.0 at early time points, but hydrolysis at pH 7.4 was significant after 5 h. Hydrazones formed with the PMCA cross-linker showed no difference in release rates at pH 7.4 and 5.0.

INTRODUCTION

Recent developments in nanomaterials, biotechnology, and advanced drug delivery and imaging systems have prompted innovation of new molecular building blocks and methods to attach components together to achieve advanced materials with specific functionality. For polymer-based therapeutics, in particular, the benefits of conjugating drugs to water-soluble polymers are well-known and include the following: increased circulation half-life, reduced nonspecific activity, enhanced targeting ability, and physiological solubility (*1*). While these benefits provide strong incentives for use of polymers and new particle carriers in drug delivery, methods to chemically couple therapeutic and imaging agents to such carriers have been frequently inflexible and performance limiting. Yet, control and versatility of the chemistry used to couple molecules together is crucial to their function and purpose. Most therapeutic agents are best released from carriers at the desired physiological site of drug activity to be most effective, while retaining stability in circulation until the construct reaches its therapeutic target. Many cleverly designed coupling agents and cross-linkers have therefore been developed for stable covalent attachment under one set of conditions (i.e., normal circulation) and reversible uncoupling chemistries under other sets of conditions (*2*−*4*). That these chemistries reside in a single coupling agent that responds reliably to desired stimuli (e.g., local pH, thermal or optical gradients, enzymes, electrochemical or redox inputs) to couple and uncouple connected cargo is a challenging goal.

Strategies for site-specific nanoparticle- or polymer-based agent delivery often exploit biochemical conditions intrinsic to cell internalization and processing pathways to specifically release drug into the cellular cytoplasm (*5*). Polymer and nanoparticle constructs internalized into cells by endocytosis are transported to lysosomes—membrane-encapsulated cytoplasmic organelles more acidic (pH ∼5.0) than normal physiological conditions, and containing a host of specific enzymes (*6*). Therapeutic agents with activity beyond the lysosomal compartment (i.e., most drugs) must achieve lysosomal release at sufficient dosing in order to exert their desired activity. For these reasons, polymer− and nanoparticle−drug conjugation chemistry is often designed to degrade once inside the cell via cleavage by lysosome-specific enzymes, as well as by nonspecific pH-dependent and organelle-specific mechanisms. The Gly-Phe-Lys-Gly (GFLG) peptide sequence has been shown to degrade specifically by the lysosome enzyme, cathepsin B, and is a distinguishing component in the poly[*N*-(2-hydroxypropyl) methacrylamide] (pHPMA) copolymer−doxorubicin (DOX) anticancer drug PK1, currently in clinical trials (*7*−*11*). Other degradable peptide spacers such as the dipeptides valine-citrulline, asparagine-D-lysine, and methionine-D-lysine have been used to produce antibody−drug conjugates where the drug is released by proteolysis of the peptide linker (*12, 13*). Nonspecific pH-driven hydrolytic degradation and agent de-

* Corresponding author. D. W. Grainger. Current address: Department of Pharmaceutics and Pharmaceutical Chemistry, College of Pharmacy, Health Sciences Campus, University of Utah, Salt Lake City, UT 84112 USA; Email: david.grainger@utah.edu. Phone: +1 801.581.3715; Fax: +1 801 0.581.3674.

10.1021/bc100049c © 2010 American Chemical Society
Published on Web 08/09/2010

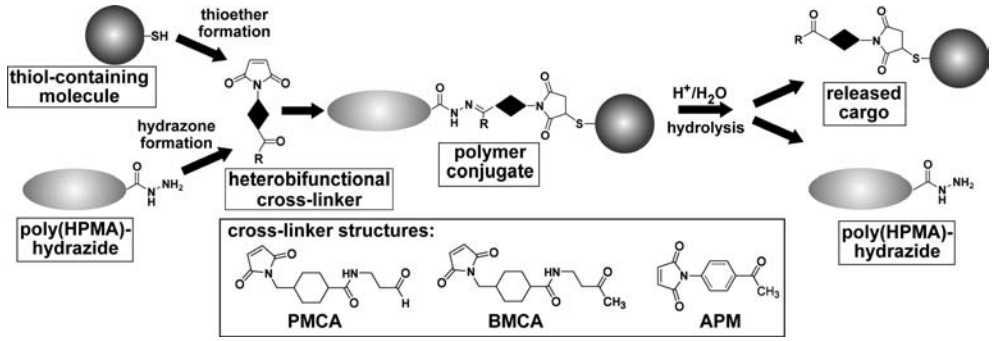


Figure 1. Design strategy for reversible coupling of thiols to pHPMA and cross-linker structures.

coupling have been demonstrated for a variety of coupling chemistries including hydrazone, acetal, carbamate, and *cis*-aconityl moieties (*14*−*17*).

More specifically, hydrazone bonds have been successfully used to generate a variety of pH-sensitive conjugates of the anticancer drug doxorubicin with various polymers, particles, micelles, and antibodies by reaction with hydrazide-derivatized carriers and cross-linkers with the 13-keto position of this drug (*15*, *16*, *18*−*24*). Hydrazone bonds are formed by condensation of hydrazides with aldehydes or ketones after elimination of the carbonyl oxygen as water, resulting in a metastable imine bond. This reaction can be performed under aqueous conditions with careful control of pH and reaction stoichiometry but is most often performed under organic conditions with an acid catalyst such as acetic acid or trifluoroacetic acid to facilitate dehydration and formation of the hydrazone bond (*19*, *25*, *26*). While certain types of hydrazone linkages are known to be stable at pH 7.4 and degrade at low pH (i.e., <5.0), chemistries adjacent to both hydrazide and ketone functionality greatly affect pH and hydrolytic stability. Hence, specific substituents have been used to achieve different bond cleavage rates and pH sensitivities (*15*, *16*). This chemistry can also be tailored to present other functional groups useful for other conjugation strategies.

This work evaluates three heterobifunctional cross-linkers designed to couple thiol-containing molecules to hydrazone-derivatized pHPMA drug carriers enjoying a long history of use (*9*, *10*, *27*). Thiol-based drug conjugation to polymer-linked hydrazones is not widely studied. Efficiency of cross-linker coupling to reactive sites on the polymer backbone, and their subsequent stability at pH 7.4 and 5.0 were investigated. While both polymer and cross-linker can be designed to provide the hydrazide functionality, we placed this functional group on the polymer carrier as previously described (*19*, *20*). Crosslinkers that facilitate reversible coupling of thiol-containing molecules to pHPMA contain ketone or aldehyde functional groups on one terminus for reaction with pHPMA hydrazide, and a maleimide functionality at the other terminus to react with sulfhydryl groups on the target adduct via a 1,4-Michael addition reaction (*19*, *20*). This thiol coupling strategy is advantageous for coupling unmodified proteins/peptides lacking aldehyde/ketone functionality, or other thiol-containing molecules, to known hydrazide-derivatized pHPMA water-soluble carriers, or analogous chemistry. Two heterobifunctional cross-linkers investigated, 1-(*N*-3-propanal)-4-(*N*-maleimidomethyl) cyclohexane carboxamide (PMCA), and 1-(*N*-3-butanone)-4-(*N*-maleimidomethyl) cyclohexane carboxamide (BMCA) were prepared from the popular commercial cross-linker succinimidyl-4-(*N*-maleimidomethyl) cyclohexane-1-carboxylate (SMCC), while the third was a commercially available benzene derivative, *N*-4-acetylphenyl maleimide. Illustration of the reversible coupling/release strategy and cross-linking chemistry structures involving hydrazone−thiol coupling are shown in Figure 1.

MATERIALS AND METHODS

General Procedures and Materials. All solvents were ACS-certified grade purchased from Fisher Scientific (Fair Lawn, USA) and used without further purification unless otherwise noted. Trinitrobenzene sulfonic acid (5% w/v solution in methanol) (TNBSA), cystamine hydrochloride (98%), diisopropylethylamine (DIPEA), ethyl carbazate (97%), *N*-hydroxysuccinamide (NHS) (98%), 4-(aminomethyl)cyclohexane carboxylic acid (97%), maleic anhydride (98+%), acetic anhydride, dicyclohexanecarbodiimide (DCC) (99%), hydrazine monohydrate (98%), 3-amino-1-propanol (99+%), triethyl amine (99.5%), oxalyl chloride (99+%), and glacial acetic acid were all purchased from Aldrich (St. Louis, USA). *N*-4-(Acetylphenyl) maleimide (APM) (98+%) was purchased from Lancaster Synthesis (Pelham, USA). 4-Amino-2-butanol (98%) was purchased from Acros Organics (Geel, Belgium). Reducing gel with immobilized tris(2-carboxyethyl) phosphine hydrochloride (TCEP) was purchased from Pierce (Rockford, USA). Spectra/Por 1, 6−8 kDa molecular weight cutoff dialysis tubing was obtained from Spectrum Laboratories, Inc. (Rancho Dominguez, USA). Sephadex G-25 and LH-20 size exclusion chromatography gel were purchased from Amersham Biosciences (Uppsala, Sweden). Dimethyl sulfoxide-d_6 containing 0.05% w/v tetramethylsilane was purchased from Cambridge Isotope Laboratories, Inc. (Andover, MA). 5(6)-Tetramethylrhodamine-succinimidyl ester (TAMRA-NHS) was obtained from AnaSpec (San Jose, USA). Poly(HPMA) molecular weight standards were a gift from Prof. P. Kopeckova, Univ. Utah, USA. Water was Millipore-filtered ASTM Type I quality. All NMR spectra were recorded on a Magnex Scientific Inova 400 MHz instrument in DMSO-d_6 containing 5% w/v tetramethylsilane as an internal standard. Absorbance measurements were obtained on a Varian Carey 500 Scan instrument.

4-(*N*-Maleimidomethyl)cyclohexane Carboxylic Acid (MCCA) (1). 4-(Aminomethyl)cyclohexane carboxylic acid (40.71 g, 0.26 mol, 1 equiv) was dissolved in dimethyl acetamide (DMAc, 100 mL). A solution of maleic anhydride (25.20 g, 0.26 mol, 1 equiv) was prepared in DMAc (50 mL), then added to the 4-(aminomethyl)cyclohexane carboxylic acid solution dropwise while stirring. The reaction vessel was purged with nitrogen, capped, and stirred for 24 h at room temperature. After 24 h, sodium acetate (5.00 g, 0.06 mol, 0.24 equiv) and acetic anhydride (43 mL, 0.455 mol, 1.75 equiv) were added and the reaction was continued for an additional 24 h. After 24 h, the reaction was heated to 65 °C and stirred for 5 h, then concentrated to ∼125 mL under vacuum and poured into 1 L cold water while stirring. The light-brown precipitate was collected by filtration and dried under vacuum. The aqueous portion was extracted twice with methylene chloride (500 mL), and product was isolated after evaporation of solvent. Both solid portions were combined and dissolved in methylene chloride (500 mL), then silica gel (5 g) was added to the solution and

the suspension was stirred for 30 min. The resulting colorless solution was filtered and solid product was obtained by evaporation of solvent under vacuum. Crude product was further purified by crystallization from ethyl acetate to yield a white solid. Yield: 14.70 g, 24%. ^{1}H NMR, δ ppm: 0.926 (dd, 2H), 1.22 (dd, 2H), 1.517 (m, 1H), 1.6165 (d, 2H), 1.869 (d, 2H), 2.109 (m, 1H), 3.2355 (d, 2H), 7.012 (s, 2H), 12.010 (s, 1H). ^{13}C NMR, δ ppm: 27.932, 29.112, 36.013, 42.105, 42.861, 134.273, 171.549, 176.497. MS calcd $[M + H]^+$ ($C_{12}H_{15}NO_4$): 238.107. Found: (FAB) 238.108.

1-(*N*-3-Propanol)-4-(*N*-maleimidomethyl)cyclohexane Carboxamide (2). Cross-linker precursor MCAA (3.00 g, 1.0 equiv, 13 mmol) was dissolved in methylene chloride (75 mL), purged with nitrogen, capped, and cooled to −15 °C. A suspension of NHS was prepared (1.45 g, 1.0 equiv, 13 mmol) in methylene chloride (25 mL), then cooled to −15 °C. Next, a solution of DCC was prepared (2.87 g, 1.1 equiv, 14 mmol) in methylene chloride (25 mL) and cooled to −15 °C. The DCC solution was added to the solution of MCAA, followed by addition of the NHS suspension. The reaction flask was purged with nitrogen, stirred at −15 °C for 24 h, and then filtered to remove dicyclohexylurea (DCU). The filtrate was retained and 3-amino-1-propanol (1.98 mL, 1.9 equiv, 25 mmol) was added dropwise. The reaction was purged with nitrogen, capped, and stirred at room temperature for 3 h. After 3 h, the reaction mixture was filtered to remove liberated NHS, and the filtrate was concentrated to ∼2/3 original volume under vacuum, cooled to −20 °C, and then refiltered. The resulting filtrate volume was doubled by addition of diethyl ether to form a precipitate, which was isolated by filtration. The solid product was further purified by silica gel chromatography (10 × 40 cm, 90/10 methylene chloride/methanol mobile phase) and isolated by evaporation of solvent under vacuum. Yield: 1.91 g, 51.6%, white solid. ^{1}H NMR, δ ppm: 0.886 (dd, 2H), 1.265 (dd, 2H), 1.508 (q, 3H), 1.618 (d, 2H), 1.682 (d, 2H), 1.998 (m, 1H), 2.5 (solvent overlap), 3.047 (q, 2H), 3.234 (d, 2H), 3.372 (q, 2H), 4.399 (t, 1H), 7.013 (s, 2H), 7.652 (t, 1H). ^{13}C NMR, δ ppm: 28.488, 29.349, 32.386, 35.423, 36.060, 42.980, 43.704, 58.307, 134.277, 171.188, 174.825. MS calcd $[M + H]^+$ ($C_{15}H_{22}N_2O_4$): 295.1657. Found: (FAB) 295.1654.

1-(*N*-3-Butanol)-4-(*N*-maleimidomethyl)cyclohexane Carboxamide (3). This product was obtained by an analogous procedure used to synthesize compound **2** (vida infra) with the only difference being the use of 4-amino-2-butanol (1.65 mL, 1.1 equiv, 17.3 mmol) in methylene chloride (30 mL) as the amidation reagent. Yield: 2.88 g, 60%, white powder. ^{1}H NMR, δ ppm: 0.887 (dd, 2H), 1.036 (d, 3H), 1.267 (dd, 2H), 1.521 (m, 1H), 1.620 (d, 2H), 1.686 (d, 2H), 1.998, (m, 1H), 3.065 (q, 2H), 3.240 (d, 2H), 3.585 (septet, 1H), 4.443 (d, 1H), 7.018 (s, 2H), 7.645 (t, 1H). ^{13}C NMR, δ ppm: 23.509, 28.459, 29.334, 35.489, 36.046, 38.719, 42.966, 43.694, 63.628, 134.267, 171.168, 174.776. MS calcd $[M + H]^+$ ($C_{16}H_{24}N_2O_4$): 309.1814. Found (FAB) 309.1819.

1-(*N*-3-propanal)-4-(*N*-maleimidomethyl)cyclohexane Carboxamide, PMCA (4). PMCA was prepared using the Swern procedure for oxidation of alcohols to aldehydes (*28*). The alcohol **2** (500 mg, 1.0 equiv, 1.72 mmol) was dissolved in freshly distilled methylene chloride (20 mL) and cooled to −80 °C. An activated dimethyl sulfoxide (DMSO) solution was prepared by combining DMSO (295 μL, 2.4 equiv, 4.13 mmol) and oxalyl chloride (950 μL of 2.0 M solution in methylene chloride, 1.1 equiv, 1.9 mmol) in methylene chloride (1.5 mL) at −80 °C. The alcohol solution was slowly added to the activated DMSO solution over 5 min. The reaction was allowed to proceed for 15 min at −80 °C, followed by addition of triethylamine (1.2 mL, 5.0 equiv, 8.5 mmol). The reaction was equilibrated to room temperature, and then water (15 mL) was added and the mixture was stirred for 10 min. The organic layer was separated, and the aqueous portion was re-extracted with 2 × 10 mL methylene chloride, and then all organic portions were combined. The organic portion was washed with 1 M HCl, dilute $NaHCO_3$, and H_2O, and then dried with Na_2SO_4. Product was isolated after removal of Na_2SO_4 and evaporation of solvent. Yield: 0.350 g, 66%, white powder. ^{1}H NMR, δ ppm: 0.878 (dd, 2H), 1.232 (dd, 2H), 1.507 (m, 1H), 1.636 (m, 2H), 1.976 (m, 1H), 2.502, (solvent overlap) 3.23 (d, 2H), 3.284 (q, 2H), 7.011 (s, 1H), 7.796 (t, 1H), 9.604 (t, 1H). ^{13}C NMR, δ ppm: 28.378, 29.286, 32.393, 36.037, 42.957, 43.265, 43.566, 134.274, 171.185, 174.958, 202.195. MS calcd $[M + H]^+$ ($C_{15}H_{20}N_2O_4$): 293.1501. Found (FAB) 293.1507.

1-(*N*-3-Butanone)-4-(*N*-maleimidomethyl)cyclohexane Carboxamide, BMCA (5). BMCA was prepared using the same Swern procedure described above to prepare PMCA, except starting with **3** (2.00 g, 1.0 equiv, 6.5 mmol) as the alcohol to be oxidized. Yield: 1.34 g, 68%, white powder. ^{1}H NMR, δ ppm: 0.875 (q, 2H), 1.243 (q, 2H), 1.511 (m, 1H), 1.511 (m, 1H), 1.638 (m, 4H), 1.975 (m, 1H), 2.070 (s, 3H), 2.545 (t, 2H), 3.180 (q, 2H), 3.228 (d, 2H), 7.011 (s, 2H), 7.677 (t, 1H). ^{13}C NMR, δ ppm: 28.407, 29.305, 29.752, 33.626, 36.043, 42.620, 42.962, 43.548, 134.273, 171.179, 174.796, 207.179. MS calcd $[M + H]^+$ ($C_{16}H_{22}N_2O_4$): 307.1657. Found (FAB): 307.1657.

Thiol-Containing Tetramethylrhodamine (6). Thiolated tetramethylrhodamine was prepared by reaction of TAMRA-NHS with cystamine hydrochloride activated with diisopropylethylamine (DIPEA) to form the TAMRA disulfide dimer (ssTAMRA) as previously described (*29*). Briefly, cystamine hydrochloride (9.6 mg, 0.9 equiv amines, 0.043 mmol) was activated in dimethylformamide (DMF, 2.5 mL) containing DIPEA (30 μL, 1.8 equiv, 0.17 mmol). This solution was added to TAMRA-NHS (50.0 mg, 1.0 equiv, 0.095 mmol) in DMF (1.5 mL) and stirred at room temperature in the dark for 30 min followed by addition of DIPEA (15 μL, 0.086 mmol, 1.0 equiv) and reaction for an additional hour. Product was precipitated by addition of 50 mL cold diethyl ether, washed five times, and dried under vacuum overnight. Further purification was achieved by repeat precipitation from methanol into cold ether. Yield: 24.81 mg, 54%, dark red solid. MS calcd $[M+H]^+$ ($C_{54}H_{52}N_6O_8S_2$): 977.3366. Found (FAB): 977.3348.

Poly[*N*-(2-hydroxypropyl)methacrylamide], pHPMA (7). PHPMA was synthesized to contain 5 mol % reactive nitrophenol ester terminated, nondegradable glycylglycine side chains using previously described procedures (*30*−*32*). *N*-(2-Hydroxypropyl)methacrylamide (HPMA) and methacryloyl glycylglycine nitrophenol ester (MAGGONP) monomers were prepared in house and confirmed with NMR and mass spectrometry. A detailed procedure for monomer synthesis and subsequent polymerization is provided as Supporting Information. The number of active esters in the resulting copolymer was estimated to be 2.55×10^{-4} mol/g polymer (3.8 mol %) by measuring the absorbance of released *p*-nitrophenolate anion at 400 nm ($\varepsilon = 1.74 \times 10^4$ M^{-1} cm^{-1}) following hydrolysis of ester bonds in 0.05 M sodium hydroxide for 3 h at 37 °C. No increase in absorbance after the 3 h incubation period was observed, showing complete cleavage of *p*-nitrophenol esters. Copolymer molecular weight was estimated to be 18 200 Da by size exclusion chromatography using a HP1050A HPLC equipped with a HP1047A refractive index detector and BioSil 125 column calibrated with pHPMA samples of known molecular weights. Samples were eluted at 0.5 mL/min with 0.1 M sodium phosphate, 0.05 M NaCl, pH 7.4.

Hydrazide Derivatized pHPMA (8). pHPMA copolymer was further modified to contain hydrazide-terminated side chains by reaction of *p*-nitrophenol ester-terminated MAGGONP side

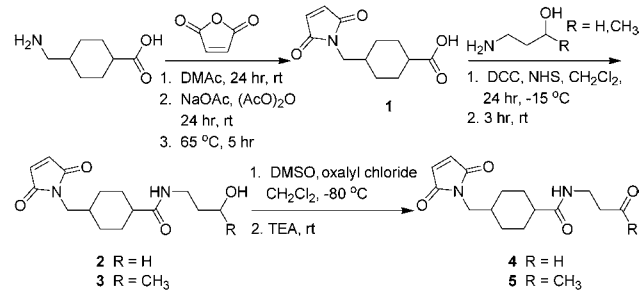
chains with excess hydrazine monohydrate using methods previously described (*19*, *20*). Briefly, *p*-nitrophenol activated pHPMA (2.0 g, 1.0 equiv, 0.51 mmol active ester) was dissolved in methanol (25 mL). The pHPMA solution was added dropwise to a solution of hydrazine monohydrate (267 μL, 10.8 equiv, 5.5 mmol) in methanol (25 mL). The reaction was purged with nitrogen, capped, and stirred for 3 h at room temperature. The reaction solution turned dark yellow indicating reaction of active ester groups and release of *p*-nitrophenol. After complete reaction, the reaction mixture was dripped into cold water (50 mL) and low molecular weight byproducts were removed by dialysis against water (SpectraPore, 6−8 kDa molecular weight cutoff, 2 days). Polymer product was isolated by lyophilization. Yield: 0.120 g, 60%, white powder. Hydrazide content: 2.63×10^{-4} mol/g, 100.5% conversion.

Analysis of pHPMA Hydrazide Content. Hydrazide content was estimated using a modified trinitrobenzene sulfonic acid (TNBSA) assay and methacryloyl glycylglycine hydrazide (MAGGH) standards (see Supporting Information for details regarding synthesis of MAGGH standards). For each pHPMA hydrazide content analysis, stock solutions of 0.1% w/v TNBSA and $\sim 2 \times 10^{-4}$ M MAGGH were prepared in 0.1 M $NaHCO_3$, pH 8.5. The MAGGH solution was further diluted with 0.1 M $NaHCO_3$ to generate standards in the range $\sim(0.3-2) \times 10^{-4}$ M. Next, hydrazide derivatized pHPMA solutions in 0.1 M $NaHCO_3$ were prepared at concentrations of 0.2−0.4 mg/mL for samples prior to cross-linker reactions and 1−2 mg/mL for cross-linker reacted samples. TNBSA stock solution (0.5 mL) was combined with MAGGH standard or pHPMA solutions (1.0 mL) and incubated for 1.5 h at 37 °C. After incubation, sample absorbance was measured at 505 nm and hydrazide content was estimated from the MAGGH standard curve.

Reaction of Hydrazide-Derivatized pHPMA with Cross-Linkers (10, 11, 12). Hydrazide-derivatized pHPMA (**8**, 0.20 g, 1.0 equiv, 52 μmol hydrazide) was dissolved in 50/50 methylene chloride/methanol (2 mL), and 100 mg Na_2SO_4 was added. Cross-linker solutions (PMCA, **4**, 46.0 mg; BMCA, **5**, 48.0 mg; APM, **9**, 34.0 mg, 3.1 equiv, 160 μmol) were prepared in 50/50 methylene chloride/methanol (2 mL) and then added dropwise to the pHPMA solution at room temperature. After complete addition, acetic acid (5 μL of 34% v/v solution in methylene chloride, 0.6 equiv, 30 μmol) was added, and the reaction was stirred under nitrogen at room temperature for 24 h. The reaction was terminated by precipitation of pHPMA product into ether. Product was further purified by size exclusion chromatography (Sephadex LH-20, 1 × 15 cm, methanol mobile phase). Typical yields: pHPMA-PMCA **10**, 116 mg 59%; pHPMA-BMCA **11**, 122 mg, 61%; pHPMA-APM **12**, 126 mg, 63%; all as white powders. Hydrazide content postconjugation was determined using a TNBSA assay, as described above. Cross-linker content was determined by optical absorbance measurement at λ_{max} and using the molar extinction coefficients of corresponding ethyl carbazate cross-linker hydrazone derivatives: **10**, 297 nm, $\varepsilon = 5.5 \times 10^2$ M^{-1} cm^{-1}; **11**, 299 nm, $\varepsilon = 5.7 \times 10^2$ M^{-1} cm^{-1}; **12**, 288 nm, $\varepsilon = 1.9 \times 10^4$ M^{-1} cm^{-1} (see Supporting Information). Polymer cross-linker-bearing conjugates were analyzed by ^1H NMR to confirm maleimide presence on the polymer backbone.

Coupling Thiolated TAMRA to Maleimide Activated pHPMA (13, 14, 15). Dimeric TAMRA disulfide **6** was reduced using TCEP-immobilized gel immediately prior to reaction with cross-linker-derivatized pHPMA. TAMRA disulfide dimer (17.46 mg, 0.036 mmol, 1 equiv) was dissolved in 1 mL DMSO and added dropwise into an immobilized TCEP gel suspension (5 mL gel, ~1.1 equiv, ~0.04 mmol TCEP) in 12 mL phosphate buffer (0.1 M sodium phosphate, 0.05 M NaCl, 2.5 mM EDTA, pH 7.0). The reduction reaction was allowed to proceed for 1.25 h, followed by removal of TCEP gel by centrifugation. The gel material was washed with 6 mL buffer (pH 7.0, 2.5 mM EDTA), centrifuged, and the supernatant retained and combined with the first fraction.

Scheme 1. Thiol-Reactive Crosslinker Synthesis



Reduced TAMRA solution (3 mL,~1.1 equiv,~5.9 μmol) was added separately to pHPMA cross-linker conjugates **10**, **11**, and **12** (20.0 mg in 2 mL sodium phosphate, 0.05 M NaCl, 2.5 mM EDTA, pH 7.0, ~1 equiv, ~5.3 μmol). Reaction mixtures were degassed, purged with nitrogen, capped, and stirred at room temperature in the dark for 3 h. The coupling procedure was terminated by separation of unreacted TAMRA thiol after passage through an SEC column (Sephadex, G-25, 2 × 20 cm, H_2O mobile phase). The polymer conjugate fraction was collected as the first red band eluting from the column and lyophilized. Typical yields of TAMRA conjugated pHPMA: 15.3−19.5 mg, 76−96%. TAMRA conjugation efficiency to maleimide groups was determined by absorbance measurements at 554 nm using $\varepsilon = 6.4 \times 10^4$ M^{-1} cm^{-1}. TAMRA content (μmol/g polymer): **13** = 105.2, **14** = 47.8, **15** = 25.9.

Determination of Decoupling Hydrolysis Rates for Cross-Linkers on Conjugates 13−15. Release of free TAMRA dye from pHPMA was monitored at pH 5.0 (0.1 M sodium acetate buffer) and pH 7.4 (0.1 M sodium phosphate buffer). TAMRA-conjugated pHPMA samples (1.5−2.5 mg) were dissolved in the appropriate buffer (8.5 mL) and incubated at 37 °C in the dark while stirring. At various time points, 750 μL of polymer solution was withdrawn and free TAMRA was separated from polymer using a Sephadex G-25 SEC column (1 × 13 cm, H_2O mobile phase). The two resulting bands were collected and water was evaporated using a speed-vac. The samples were then dissolved in 500 μL water and the percentage of free TAMRA was determined by the ratio of absorbance at 554 nm that of the two fractions. For pHPMA conjugate **15**, TAMRA release was also determined after acidification (pH 3.0) of a sample incubated for 72 h at pH 7.4 (0.1 M phosphate buffer). All release experiments comprised 4 individual samples and data was analyzed using Microsoft *Excel*.

RESULTS AND DISCUSSION

Cross-Linker Design and Synthesis. Although several heterobifunctional cross-linkers are commercially available that form hydrazone bonds and also contain thiol-coupling reactivity, most are synthesized to contain hydrazide groups that react with synthetic ketone-containing drugs such as doxorubicin or oxidized sugar moieties present on biomolecules. We know of only one commercially available cross-linker that contains both ketone and maleimide functionality (APM), since hydrazide groups are not a common target for reaction with biomolecules or synthetic drugs. However, synthetic polymers, particles, surfaces, and so forth can easily be prepared with hydrazide functionality for reversible conjugation of thiolated molecules using the cross-linkers described in this work.

Synthesis of the aldehyde or methyl ketone SMCC-based heterobifunctional cross-linkers is shown in Scheme 1. The

Table 1. Summary of pHPMA−Cross-Linker Coupling Reactions[a]

polymer conjugate	cross-linker	cross-linker content[b] (μmol/g)	conversion[b] (%)	remaining hydrazide[c] (μmol/g)	conversion[c] (%)
13	PMCA	373.0 ± 21.2	141.8 ± 8.1	19.5 ± 0.1	92.6 ± 4.3
14	BMCA	248.9 ± 8.1	94.6 ± 3.1	18.6 ± 0.1	92.9 ± 5.6
15	APM	166.7 ± 14.5	69.8 ± 6.1	90.9 ± 0.1	62.0 ± 1.9

[a] $n = 4$ for all measurements. [b] Determined by cross-linker optical absorbance. [c] Determined by TNBSA assay.

cyclohexyl SMCC core was chosen as it is known to produce a stable maleimide functional group. Maleimide groups are subject to degradation by hydrolysis and the increased hydrophobicity and lack of a conjugated aromatic system in the cyclohexyl spacer may reduce the hydrolysis rate (*2, 33*). Early attempts to synthesize these cross-linkers involved direct modification of commercially available SMCC, but synthesis of SMCC precursors in-house allowed inexpensive scale-up. Synthesis of the corresponding alcohols of SMCC was performed in a one-pot reaction after activation of carboxylic acid with NHS using well-known carbodiimide chemistry (*2*). Direct coupling of 4-amino-2-butanol and 3-amino-1-propanol to 4-(*N*-maleimidomethyl)cyclohexane carboxylic acid (**1**) following DCC activation without NHS led to a mixture of products, presumably due to addition of alcohol groups to the highly reactive DCC-activated carboxylic acid. The choice of methylene chloride as the solvent aided in product purification due to the limited solubility of NHS byproduct, which precipitated from solution and was easily removed by filtration after concentration and cooling the reaction mixture. Residual NHS was removed by aqueous extraction for cross-linker precursor **3**, but this purification strategy for **2** resulted in reduced yields due to higher water solubility. Chromatographic purification of **2** resulted in markedly increased yields.

Oxidation of alcohol groups in cross-linker precursors **2** and **3** was readily achieved using the mild oxidation conditions of the Swern procedure to yield the corresponding aldehyde- and methylketone-containing reactive cross-linkers. No side reactions were observed with other functional groups in the molecule. Other attempts to oxidize the alcohol functional groups using pyridinium chlorochromate resulted in oxidation of alcohol groups, but removal of chromium salt byproduct was difficult, resulting in low yields (data not shown).

Cross-Linker Coupling to pHPMA. Synthesis of hydrazide-derivatized pHPMA (**8**) was easily achieved by reaction of active *p*-nitrophenol esters on pendant side chains with hydrazine monohydrate as previously described (*19, 20*). This construct has been previously utilized to couple doxorubicin via a hydrazone bond to allow pH-dependent release (*19, 20*). The number of reactive sites in pHPMA was controlled by monomer feed ratios in the free radical-initiated polymerization reaction to produce pHPMA, with reactive sites kept fairly low so as to not alter the polymer solubility after cross-linker conjugation. Formation of hydrazone bonds has been reported for doxorubicin conjugates with pHPMA and poly(ethylene glycol) in polar protic conditions with methanol used as the solvent and acetic acid as the catalyst (*19, 20*). Since the hydrophobic cross-linkers used in this study were only minimally soluble in methanol, and the more hydrophilic pHPMA was only minimally soluble in solvents ideal for cross-linker solvation, a mixed solvent system was used. The best methanol-based solvent system for optimal cross-linker/polymer solubility was found to be 50/50 methanol/methylene chloride. PHPMA−cross-linker reactions showing conjugation efficiency are summarized in Table 1. With the reactive sites on the polymer controlled by monomer feed ratio, an excess of cross-linker was used to maximize conjugation to the polymer.

Reaction of cross-linkers PMCA (**4**) and BMCA (**5**) resulted in complete conversion of hydrazide groups to hydrazone conjugates as determined directly by cross-linker absorbance and indirectly by determination of remaining hydrazide groups using TNBSA measurements. Optical absorption measurements of the pHPMA−PMCA cross-linker product **10** showed the highest coupling efficiency, indicative of the higher reactivity of aldehyde functional groups. Although more than stoichiometric conversion was observed for the aldehyde cross-linker, the excess coupling was small compared to the total polymer units in the pHPMA carrier, indicating that polymer units lacking the hydrazide functionality were generally unreactive toward the aldehyde. The amount of hydrazide containing monomer units in pHPMA was ~4 mol %; thus, the ~140% coupling of the aldehyde cross-linker observed under these reaction conditions corresponds to modification of only ~2% of the polymer side chains in an unintended fashion. One possible explanation for the higher coupling rate observed for the aldehyde cross-linker is the formation of acetals with the alcohol groups contained in pHPMA side chains or mixed acetals formed by reaction with pHPMA and MeOH, as the reaction conditions used for hydrazone formation are similar to those used for acetal formation (i.e., acid catalyst and dehydrating agent). The methylketone group of **5** reacted with pHPMA hydrazide groups in a stoichiometric fashion, with absorbance and remaining hydrazide content in good agreement for conjugate **11**. This demonstrates that the less reactive methyl ketone functionality resulted in more readily controlled conjugation. The resonance stabilized APM cross-linker **9** was less reactive and did not stoichiometrically react with hydrazide-containing pHPMA **8** to produce conjugate **12**. Only 60−70% conjugation was observed in the cross-linker-derivatized product **12**, with cross-linker absorbance and remaining hydrazide measurement in good agreement. A similar result was observed in the analogous reaction of APM with ethyl carbazate (see Supporting Information). ^{1}H NMR analysis of the cross-linker polymer conjugates **10**−**12** also revealed a convenient analytical signal to confirm conjugation due to the sharp maleimide peak at 7.0−7.2 ppm, shown in Figure 2.

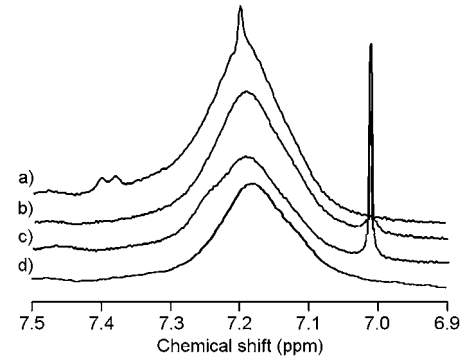
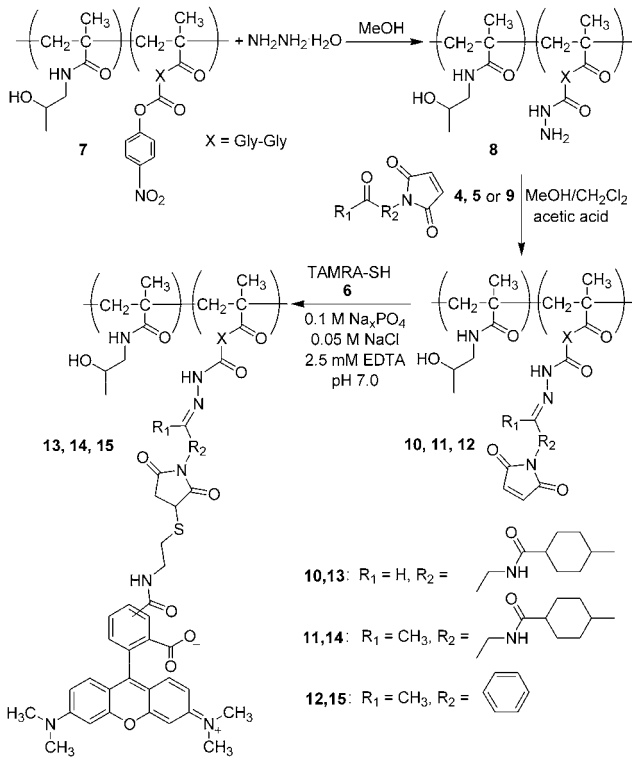


Figure 2. ^{1}H NMR spectra of pHPMA conjugates showing the pHPMA amide peak (broad) and cross-linker maleimide peak (sharp). Spectra recorded at 400 MHz, 25 °C in DMSO-d_6. (a) pHPMA−APM conjugate **12**, (b) pHPMA−BMCA conjugate **11**, (c) pHPMA−PMCA conjugate **10**, (d) pHPMA−hydrazide **8**.

For conjugates **10** and **11**, the maleimide peak appeared in an unobscured region of the ^{1}H NMR spectrum allowing easy detection. Additionally, formation of conjugate **10** was confirmed by the disappearance of the aldehyde peak present in

Scheme 2. Synthesis of pHPMA Conjugates



unreacted cross-linker **4** at 9.6 ppm. Although the maleimide signal overlapped with the polymer backbone signal for conjugate **12** containing APM, it was still visible protruding above the broad amide peak. Additionally, the ability of each cross-linker to form hydrazone linkages was modeled with the hydrazide-containing small molecule ethyl carbazate, with confirmation of hydrazone formation more analytically straightforward than with a small percentage of reactive sites in a polymer conjugate (see Supporting Information). For PMCA and BMCA, rapid, stoichiometric conversion to hydrazone product was obtained, with only a simple purification procedure needed to isolate pure hydrazone product. However, reaction of APM with ethyl carbazate resulted in formation of several products, and purification required a separation procedure for isolation, which resulted in a lower overall yield.

Attachment of Thiolated TAMRA to pHPMA and Subsequent Release. Synthesis of the pHPMA cross-linker TAMRA conjugates **13**−**15** is shown in Scheme 2. Thiol-modified TAMRA (**6**) was used as a model cargo compound to react with maleimide groups resulting from cross-linker conjugation to pHPMA. This model system was convenient, as TAMRA is fairly water-soluble, readily detected by simple absorbance measurements, and released dye is sufficiently smaller in size to allow rapid separation from the polymer-bound fraction using size exclusion chromatography. Reduction of the TAMRA disulfide **6** was performed with TCEP-immobilized gel, allowing easy separation of reducing agent. Free TCEP, DTT, or combinations of both resulted in lower conjugation of TAMRA to the polymer (data not shown). Although free TCEP is generally believed to be unreactive toward maleimide functional groups, similar observations regarding interference with maleimide coupling have been reported (*34, 35*). Reaction times of TAMRA with cross-linker-derivatized pHPMA were kept short (3 h) in this study, as degradation rates of the hydrazones were unknown. TAMRA conjugation was not efficient under these conditions, with couplings relative to cross-linker content of ∼20% observed for all pHPMA−cross-linker conjugates. Maleimide coupling efficiency for all cross-linkers

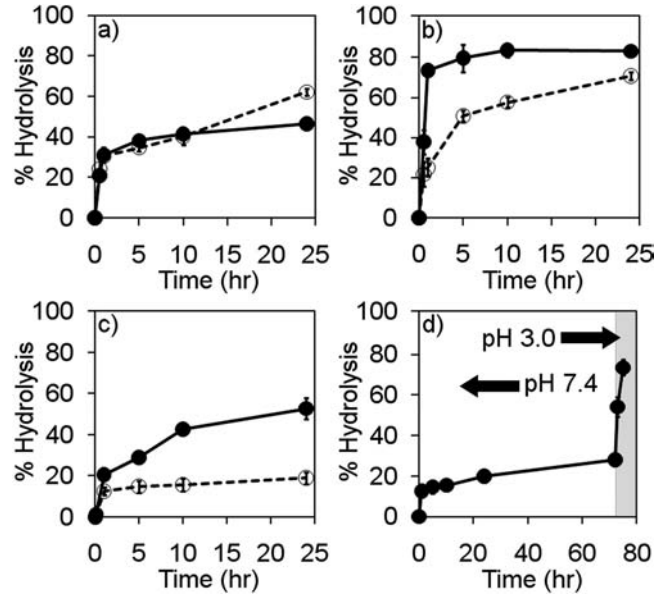


Figure 3. Hydrolysis rates for pHPMA-cross-linker-TAMRA conjugates. Graphs a−c represent hydrolysis at pH 7.4 (dashed) and pH 5.0 (solid): (a) pHPMA-PMCA-TAMRA conjugate **13**, (b) pHPMA-BMCA-TAMRA conjugate **14**, (c) pHPMA-APM-TAMRA conjugate **15**. (d) Hydrolysis of pHPMA-APM-TAMRA conjugate **15** upon acidification following 75 h incubation at pH 7.4. Each data point represents the average of 4 samples ± the standard deviation.

may increase with longer reaction times until hydrazone degradation and release from the polymer competes with thiol conjugation.

Release of conjugated TAMRA from the polymer backbone at physiologically relevant temperature and pH [pH 7.4 (circulation) and pH 5.0 (lysosomes), 37 °C] was influenced by cross-linker structure as shown in Figure 3a−c. The conditions used to observe hydrazone degradation are not physiological, only a simple approximation, as the addition of other physiologically relevant components such as serum interfere with the ability to separate released TAMRA dye from the macromolecular component of the mixture by size exclusion chromatography: TAMRA can associate with high molecular weight serum components in more complex milieu via nonspecific interactions. Ideally, for systemic administration of a drug delivery system, the hydrolytic stability of the hydrazone bond between the carrier and therapeutic agent should be stable at systemic pH (∼7.4) for the same period of time that it takes for the carrier to reach its site of activity. However, if the carrier is rapidly cleared from circulation, and the therapeutic target is also the site of rapid accumulation (i.e., kidney or liver tissue), the hydrazone does not necessarily need to exhibit extended stability at systemic pH. For carriers targeting cancer tissue by the EPR effect, the hydrazone used for preparation of the conjugate should exhibit minimal hydrolysis at pH 7.4, as accumulation into cancer tissue by the EPR effect requires a carrier with extended circulation (*36*). In this regard, the stability of the hydrazone used to couple the therapeutic agent to the carrier depends on the properties of the carrier used.

Polymer conjugates **13** and **14** containing aliphatic acyl hydrazone bonds were relatively unstable at physiological pH, with more than 30% of conjugated TAMRA released after 5 h. Release for conjugate **13** prepared with the aldehyde-containing PMCA cross-linker showed no difference between pH 7.4 and 5.0, with a maximum of 40−60% release observed after only a few hours, with little increase after 24 h. Hydrolysis of conjugate **13** rapidly plateaued at a value less than that for complete hydrolysis, which may be attributed to the reversible nature of the hydrazone bond and the closed system used to study the

release profile which could result in the highly reactive aldehyde-containing PMCA cross-linker reaching equilibrium between the aldehyde and hydrazone forms at this concentration and temperature. Alternatively, the additional PMCA attached to the polymer (~140% conjugation to pHPMA was observed) could be interfering with the observation of hydrazone bond hydrolysis, assuming that the additional conjugation resulted in a hydrolytically unstable bond (i.e., acetal). Polymer conjugate **14** formed with the BMCA cross-linker showed a marked difference in hydrazone degradation at early time points, with more than 75% of cargo released after only 2 h at pH 5.0 while only 25% of TAMRA was released at pH 7.4 in the same time frame. This difference in initial pH stability for BMCA containing conjugate **14** compared to the hydrazone formed with PMCA in conjugate **13** is likely due to increased electron donation ability of a methyl group relative to a hydrogen, which would facilitate protonation of the imine nitrogen but also sterically hinder the imine carbon electrophile toward nucleophilic attack by water. This property may be useful for targeting or delivery devices that can efficiently reach a target site of lower pH without prolonged residence in the off-target environment, with rapid release of cargo at the site of lower pH.

The desired difference in stability of polymer conjugates at pH 7.4 and 5.0 was most pronounced for the pHPMA−APM containing conjugate **15**. Polymer conjugate **15** containing the resonance-stabilized hydrazone was most stable at pH 7.4 with less than 30% of degradation occurring after 24 h, while degradation at pH 5.0 steadily increased during the same time period (Figure 3c). Increased degradation rate of conjugate **15** upon acidification after extended incubation at pH 7.4 is shown in Figure 3d; hydrolysis increased immediately upon lowering the pH. This result shows that polymer-bound payload is likely to be released within target cells in vivo following extended circulation, cellular internalization, and trafficking to acidic subcellular organelles (lysosomes).

Hydrazones investigated in this work showed the following trend for increased difference in stability at pH 7.4 and 5.0 based on the functional groups attached to the imine carbon: phenyl, CH_3 > alkyl, CH_3 > alkyl, H. A similar trend has also been observed for other hydrazone systems recently reviewed elsewhere (*15*). This trend is directly related to cross-linker reactivity toward polymer hydrazide groups, with highly reactive carbonyl groups forming hydrazone bonds with decreased pH-dependent hydrolysis. The acyl hydrazide functionality utilized on the pHPMA component of the hydrazone forming system was not varied, but the acyl hydrazide was convenient to prepare by simple aminolysis of active esters by hydrazine and also likely aided in the stability of the resulting hydrazones at pH 7.4. A recent detailed study of hydrazone stability showed that an acyl hydrazone had a first-order rate constant for hydrolysis a few hundred-fold lower relative to an alkyl hydrazone at pH 7.0 (*37*).

The pH-dependent release mechanism for hydrazone hydrolysis involves (1) protonation of the imine nitrogen, (2) nucleophilic attack of a water molecule at the imine carbon, (3) formation of a tetrahedral carbinolamine intermediate, and (4) decomposition of the carbinolamine and cleavage of the C−N bond (*15, 17, 37, 38*). The rate at which this hydrolysis occurs is influenced by substituents adjacent to the hydrazone. In general, cross-linker electron-donating groups can facilitate pH-dependent hydrolysis by encouraging protonation of the imine nitrogen, which activates the imine carbon toward nucleophilic attack from water, as the nitrogen can then accept a pair of electrons from the imine bond to form the tetrahedral carbinolamine intermediate. Electron withdrawing groups decrease pH sensitivity by decreasing electron density of the imine carbon making it more susceptible to nucleophilic attack by water (*15, 37, 39, 40*). Aromatic groups in π-bond conjugation with hydrazones have also been shown to increase their stability, due to resonance stabilization, as was observed in our results (*41*). The desired stability for controlled pH-dependent hydrolysis is dependent on a delicate balance of groups adjacent to the carbonyl and hydrazide reaction partners used to form the hydrazone.

Modification of the carbonyl portion of cross-linkers described here may result in increased stability at pH 7.4 and hydrolysis rate at pH 5.0, while retaining excellent hydrazide reactivity. For example, glyoxylyl aldehydes prepared from N-terminal serine-modified amino acids have been recently used to form pH-sensitive hydrazones with acyl hydrazides (*42*). These findings suggest that further optimization of the SMCC-based cross-linker chemistries described here could be achieved by incorporation of different chemistries on carbon atoms adjacent to the reactive ketone functionality.

CONCLUSIONS

This work demonstrates the feasibility of forming thiol-reactive pHPMA conjugates with varying coupling and decoupling stability controlled by different chemical substitution patterns in analogous heterobifunctional cross-linker chemistries. Currently, the APM cross-linker is likely the best choice for long-circulation in vivo application due to the high stability at pH 7.4, with desired increased degradation occurring in acidic conditions analogous to the lysosome environment within cells. However, although APM shows the desired release properties for a long circulating conjugate, this cross-linker has the inherent disadvantage of lower hydrazide reactivity. BMCA is attractive for use in rapid release of cargo at a target site where extended stability is not desired (i.e., conjugates that rapidly accumulate at their site of activity or those that need to be rapidly cleared after use, i.e., gadolinium imaging agents). Alternatively, modifications of chemistry contained in the hydrazide part of synthetic constructs could result in conjugates with more stable hydrazone linkages formed with PMCA and BMCA.

The utility of these thiol-reactive cross-linkers may be further extended to produce nondegradable conjugates. In this case, addition of a hydrazone reducing agent such as sodium cyanoborohydride would result in a stable amide bond. Thus, the excellent hydrazide and maleimide reactivity of PMCA and BMCA would be attractive. Additionally, hydrazide reactivity is different from amine reactivity due to the lower pK_a of hydrazides. Nonreversible conjugation of the cross-linkers described here to hydrazides in the presence of primary amines could be achieved by control of reaction pH and the use of a hydrazone reducing agent.

In summary, the thiol-reactive cross-linkers described in this work could prove to be useful new tools for preparation of bioconjugates with specific coupling/decoupling properties. Hydrazide functionality is readily incorporated into synthetic systems, while thiol functionality is readily contained in biological components targeted for conjugation and subsequent release. These cross-linkers could be used for conjugation and subsequent triggered release as described here, for nonreversible conjugation by simply changing the reaction conditions, or serve as a starting point for design of more advanced cross-linkers with specific performance features.

ACKNOWLEDGMENT

We thank Andrew Higginbotham and Dr. Mark Kerr for helpful discussion regarding organic procedures. Partial support from NIH grant EB000894 is gratefully acknowledged.

Supporting Information Available: Experimental details regarding pHPMA synthesis, synthesis of methacryloyl glycylglycine TNBSA assay standards, reaction of cross-linkers

with ethyl carbazate, and spectral properties of hydrazones formed with cross-linkers and ethyl carbazate are described. This material is available free of charge via the Internet at http://pubs.acs.org.

LITERATURE CITED

(1) Monfardini, C., and Veronese, F. M. (1998) Stabilization of substances in circulation. *Bioconjugate Chem. 9*, 418–50.

(2) Hermanson, G. T. (1996) *Bioconjugate techniques*, Academic Press, San Diego.

(3) Brinkley, M. (1992) A brief survey of methods for preparing protein conjugates with dyes, haptens, and cross-linking reagents. *Bioconjugate Chem 3*, 2–13.

(4) Mattson, G., Conklin, E., Desai, S., Nielander, G., Savage, M. D., and Morgensen, S. (1993) A practical approach to crosslinking. *Mol. Biol. Rep. 17*, 167–83.

(5) Asokan, A., and Cho, M. J. (2002) Exploitation of intracellular pH gradients in the cellular delivery of macromolecules. *J. Pharm. Sci. 91*, 903–13.

(6) Wattiaux, R., Laurent, N., Wattiaux-De Coninck, S., and Jadot, M. (2000) Endosomes, lysosomes: their implication in gene transfer. *Adv. Drug Delivery Rev. 41*, 201–8.

(7) Satchi, R., Connors, T. A., and Duncan, R. (2001) PDEPT: polymer-directed enzyme prodrug therapy. I. HPMA copolymer-cathepsin B and PK1 as a model combination. *Br. J. Cancer 85*, 1070–6.

(8) Duncan, R., Gac-Breton, S., Keane, R., Musila, R., Sat, Y. N., Satchi, R., and Searle, F. (2001) Polymer-drug conjugates, PDEPT and PELT: basic principles for design and transfer from the laboratory to clinic. *J. Controlled Release 74*, 135–46.

(9) Kopecek, J., Kopeckova, P., Minko, T., Lu, Z. R., and Peterson, C. M. (2001) Water soluble polymers in tumor targeted delivery. *J. Controlled Release 74*, 147–158.

(10) Putnam, D., and Kopecek, J. (1995) Polymer conjugates with anticancer activity. *Biopolymers II 122*, 55–123.

(11) Seymour, L., Ferry, D., Kerr, D., Rea, D., Whitlock, M., Poyner, R., Boivin, C., Hesslewood, S., Twelves, C., Blackie, R., Schatzlein, A., Jodrell, D., Bissett, D., Calvert, H., Lind, M., Robbins, A., Burtles, S., Duncan, R., and Cassidy, J. (2009) Phase II studies of polymer-doxorubicin (PK1, FCE28068) in the treatment of breast, lung and colorectal cancer. *Int. J. Oncol. 34*, 1629–1636.

(12) Doronina, S., Toki, B., Torgov, M., Mendelsohn, B., Cerveny, C., Chace, D., DeBlanc, R., Gearing, R., Bovee, T., Siegall, C., Francisco, J., Wahl, A., Meyer, D., and Senter, P. (2003) Development of potent monoclonal antibody auristatin conjugates for cancer therapy. *Nat. Biotechnol.* 778–784.

(13) Doronina, S., Bovee, T., Meyer, D., Miyamoto, J., Anderson, M., Morris-Tilden, C., and Senter, P. (2008) Novel peptide linkers for highly potent antibody-auristatin conjugate. *Bioconjugate Chem. 19*, 1960–1963.

(14) Gillies, E. R., Goodwin, A. P., and Frechet, J. M. J. (2004) Acetals as pH-sensitive linkages for drug delivery. *Bioconjugate Chem. 15*, 1254–1263.

(15) West, K. R., and Otto, S. (2005) Reversible covalent chemistry in drug delivery. *Curr. Drug Discovery Technol. 2*, 123–60.

(16) Kratz, F., Beyer, U., and Schutte, M. T. (1999) Drug-polymer conjugates containing acid-cleavable bonds. *Crit. Rev. Ther. Drug 16*, 245–288.

(17) D'Souza, A. J., and Topp, E. M. (2004) Release from polymeric prodrugs: linkages and their degradation. *J. Pharm. Sci. 93*, 1962–79.

(18) Flenniken, M. L., Liepold, L. O., Crowley, B. E., Willits, D. A., Young, M. J., and Douglas, T. (2005) Selective attachment and release of a chemotherapeutic agent from the interior of a protein cage architecture. *Chem. Commun.* 447–449.

(19) Etrych, T., Chytil, P., Jelinkova, M., Rihova, B., and Ulbrich, K. (2002) Synthesis of HPMA copolymers containing doxorubicin bound via a hydrazone linkage. Effect of spacer on drug release and in vitro cytotoxicity. *Macromol. Biosci. 2*, 43–52.

(20) Etrych, T., Jelinkova, M., Rihova, B., and Ulbrich, K. (2001) New HPMA copolymers containing doxorubicin bound via pH-sensitive linkage: synthesis and preliminary in vitro and in vivo biological properties. *J. Controlled Release 73*, 89–102.

(21) King, H. D., Dubowchik, G. M., Mastalerz, H., Willner, D., Hofstead, S. J., Firestone, R. A., Lasch, S. J., and Trail, P. A. (2002) Monoclonal antibody conjugates of doxorubicin prepared with branched peptide linkers: inhibition of aggregation by methoxytriethyleneglycol chains. *J. Med. Chem. 45*, 4336–43.

(22) Bae, Y., Fukushima, S., Harada, A., and Kataoka, K. (2003) Design of environment-sensitive supramolecular assemblies for intracellular drug delivery: Polymeric micelles that are responsive to intracellular pH change. *Angew. Chem., Int. Ed. 42*, 4640–4643.

(23) Rodrigues, P. C. A., Beyer, U., Schumacher, P., Roth, T., Fiebig, H. H., Unger, C., Messori, L., Orioli, P., Paper, D. H., Mulhaupt, R., and Kratz, F. (1999) Acid-sensitive polyethylene glycol conjugates of doxorubicin: Preparation, in vitro efficacy and intracellular distribution. *Bioorg. Med. Chem. 7*, 2517–2524.

(24) Padilla De Jesus, O. L., Ihre, H. R., Gagne, L., Frechet, J. M., and Szoka, F. C., Jr. (2002) Polyester dendritic systems for drug delivery applications: in vitro and in vivo evaluation. *Bioconjugate Chem. 13*, 453–61.

(25) King, T. P., Zhao, S. W., and Lam, T. (1986) Preparation of protein conjugates via intermolecular hydrazone linkage. *Biochemistry 25*, 5774–5779.

(26) Kaneko, T., Willner, D., Monkovic, I., Knipe, J. O., Braslawsky, G. R., Greenfield, R. S., and Vyas, D. M. (1991) New hydrazone derivatives of adriamycin and their immunoconjugates - a correlation between acid stability and cytotoxicity. *Bioconjugate Chem. 2*, 133–141.

(27) Kopecek, J., Kopeckova, P., Minko, T., and Lu, Z. (2000) HPMA copolymer-anticancer drug conjugates: design, activity, and mechanism of action. *Eur. J. Pharm. Biopharm. 50*, 61–81.

(28) Omura, K., and Swern, D. (1978) Oxidation of alcohols by activated dimethyl-sulfoxide - preparative, steric and mechanistic study. *Tetrahedron 34*, 1651–1660.

(29) Christie, R., Tadiello, C., Chamberlain, L., and Grainger, D. (2009) Optical properties and application of a reactive and bioreducible thiol-containing tetramethylrhodamine dimer. *Bioconjugate Chem. 20*, 476–480.

(30) Kopecek, J. (1977) Reactive copolymers of N-(2-hydroxypropyl)methacrylamide with N-methacryloylated derivatives of L-leucine and L-phenylalanine. 1. Preparation, characterization, and reactions with diamines. *Macromol. Chem. Phys. 178*, 2169–2183.

(31) Drobnik, J., Kopecek, J., Labsky, J., Rejmanova, P., Exner, J., Saudek, V., and Kalal, J. (1976) Enzymatic cleavage of side-chains of synthetic water-soluble polymers. *Macrom. Chem. Phys. 177*, 2833–2848.

(32) Ulbrich, K., Subr, V., Strohalm, J., Plocova, D., Jelinkova, M., and Rihova, B. (2000) Polymeric drugs based on conjugates of synthetic and natural macromolecules I. Synthesis and physicochemical characterisation. *J. Controlled Release 64*, 63–79.

(33) Ishikawa, E., Imagawa, M., Hashida, S., Yoshitake, S., Hamaguchi, Y., and Ueno, T. (1983) Enzyme-labelling of antibodies and their fragments for enzyme-immunoassay and immunohistochemical staining. *J. Immunoassay* 209–327.

(34) Getz, E. B., Xiao, M., Chakrabarty, T., Cooke, R., and Selvin, P. R. (1999) A comparison between the sulfhydryl reductants tris(2-carboxyethyl)phosphine and dithiothreitol for use in protein biochemistry. *Anal. Biochem. 273*, 73–80.

(35) Shafer, D. E., Inman, J. K., and Lees, A. (2000) Reaction of tris(2-carboxyethyl)phosphine (TCEP) with maleimide and alpha-haloacyl groups: Anomalous elution of TCEP by gel filtration. *Anal. Biochem. 282*, 161–164.

(36) Maeda, H., Wu, J., Sawa, T., Matsumura, Y., and Hori, K. (2000) Tumor vascular permeability and the EPR effect in macromolecular therapeutics: a review. *J. Controlled Release 65*, 271–284.

(37) Kalia, J., and Raines, R. (2008) Hydrolytic stability of hydrazones and oximes. *Angew. Chem., Int. Ed. 47*, 7523–7526.
(38) Cordes, E. H., and Jencks, W. P. (1963) Mechanism of hydrolysis of Schiff bases derived from aliphatic amines. *J. Am. Chem. Soc. 85*, 2843–2848.
(39) Harnsberger, H. F., Cochran, E. L., and Szmant, H. H. (1955) The basicity of hydrazones. *J. Am. Chem. Soc. 77*, 5048–5050.
(40) Nguyen, R., and Huc, I. (2003) Optimizing the reversibility of hydrazone formation for dynamic combinatorial chemistry. *Chem. Commun.* 942–943.
(41) Kale, A., and Torchilin, V. (2007) Design, synthesis, and characterization of pH-sensitive PEG-PE conjugates for stimuli-sensitive pharmaceutical nanocarriers: The effect of substitutes at the hydrazone linkage on the pH stability of PEG-PE conjugates. *Bioconjugate Chem. 18*, 363–370.
(42) Galande, A. K., Weissleder, R., and Tung, C. H. (2006) Fluorescence probe with a pH-sensitive trigger. *Bioconjugate Chem. 17*, 255–257.

BC100049C

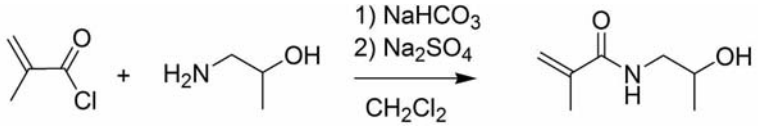
SUPPORTING INFORMATION

1. Synthesis of pHPMA monomers
   1.1. HPMA monomer: *N*-2-hydroxypropyl methacrylamide (HPMA)
   1.2. Active ester-containing monomer:methacryloyl glycylglycine 4-nitrophenyl ester (MAGGONP)
2. Synthesis of pHPMA copolymer
3. Synthesis of methacryloyl glycylglycine hydrazide (MAGGH)
4. Reaction of heterobifunctional crosslinkers with model hydrazide ethyl carbazate
   4.1. PMCA
   4.2. BMCA
   4.3. APM
5. Spectral properties of hydrazones formed with crosslinkers and ethyl carbazate

1. Synthesis of pHPMA.

1.1. HPMA monomer: N-2-hydroxypropyl methacrylamide.

N-(2-hydroxypropyl) methacrylamide (HPMA) was synthesized by reaction of DL-1-amino-2-propanol with methacryloyl chloride as shown in Scheme S1. 1-amino-2-propanol (24.3 mL, 0.311 mol, 1 eq) and sodium bicarbonate (33.6 g, 0.40 mol, 1.3 eq) was added to CH_2Cl_2 (85 mL) and the suspension was purged with N_2, capped, and placed in an ice bath. A second solution containing methacryloyl chloride (29.5 mL, 0.304 mol, 0.98 eq) in CH_2Cl_2 (40 mL) was prepared and cooled to –20 ^oC. Next, the methacryloyl chloride solution was slowly added to the 1-amino-2-propanol solution under N_2 with vigorous stirring. After complete addition the reaction was stirred for 15 min at 25 ^oC, and anhydrous Na_2SO_4 (10 g) was added. The solution was manually stirred for an additional 10 minutes and the solution was filtered through paper. Solids were washed twice with 20 mL CH_2Cl_2 and the filtrates were combined. The combined filtrates were concentrated under vacuum to ~ 50% of the original volume then placed in a –20 ^oC freezer overnight. HPMA crystals were collected by filtration and washed with cold acetone. Product was purified by repeated crystallization from acetone. Typical yield: ~15.0 g, 30%, semi-transparent white crystals. ^1H NMR, δ ppm: 1.008 (d, 3H), 1.848 (s, 3H), 3.041 (t, 2H), 3.678 (m, 1H), 4.693 (s, 1H), 5.483 (d, 2H), 7.820 (s, 1H). Mp = 72 ^oC (sharp).

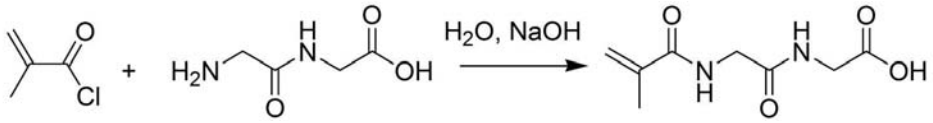


Scheme S1. Synthesis of *N*-2-hydroxypropyl methacrylamide monomer (HPMA).

Reference: Ulbrich K, Subr V, Strohalm J, Plocova D, Jelinkova M, Rihova B. (2000) Polymeric drugs based on conjugates of synthetic and natural macromolecules I. Synthesis and physico-chemical characterisation. J. Controlled Release *64(1-3)*, 63-79.

1.2. Active ester-containing monomer:methacryloyl glycylglycine 4-nitrophenyl ester (MAGGONP).

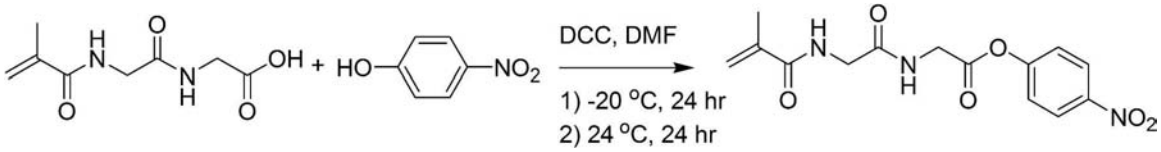
N-methacryloyl glycylglycine 4-nitrophenyl ester (MAGGONP) synthesis began with preparation of methacryloyl glycylglycine (MAGG) using the Schotten-Baumann procedure in aqueous alkaline medium as shown in Scheme S2. Glycylglycine (10 g, 76 mmol, 1 eq) was dissolved in 0.5 M NaOH (15.1 mL, 76 mmol, 1 eq) over 30 minutes then cooled to 0 ^{o}C. Methacryloyl chloride (7.5 mL, 77 mmol, 1eq) and 5.0 M NaOH (15.1 mL, 76 mmol, 1 eq) were added drop wise and simultaneously to the glycylglycine solution while stirring at 0 ^{o}C. After complete addition, the reaction was stirred for an additional hour at room temperature, then concentrated HCl was added until a dense white precipitate formed. Solids were collected by filtration and washed with cold water until the filtrate was neutral. Crude solid product was dried under vacuum and further purified by repeat crystallization from 50/50 (v/v) ethanol/water. Typical yield: ~5.0 g, 30%, small white crystals. ^{1}H NMR: (400 MHz, DMSO-d_6) δ ppm: 1.876 (s, 3H), 3.766 (d, 4H), 5.561 (d, 2H), 8.132 (t, 1H), 8.190 (t, 1H), 12.594 (s, 1H). Mp = 175-205 ^{o}C.



Scheme S2. Synthesis of methacryloyl glycylglycine (MAGG).

Methacryloyl glycylglycine (MAGG) was esterified with 4-nitrophenol using carbodiimide chemistry to yield methacryloyl glycylglycine 4-nitrophenyl ester (MAGGONP) as shown in Scheme S3. MAGG (5.23 g, 26.1 mmol, 1 eq) was dissolved in dry dimethyl formamide (DMF, 50 mL) and cooled to –15 ^{o}C. 4-nitrophenol (4.0 g, 28.71 mmol, 1.1 eq) and dicyclohexylcarbodiimide (DCC) (5.39 g, 26.1 mmol, 1.0 eq) were each dissolved in DMF (26 mL) in separate flasks and cooled to –15 ^{o}C. After all solutions were cooled, the 4-nitrophenol and DCC solutions were added drop wise to the MAGG solution sequentially while stirring. The reaction was stirred for 4 hr at –15 ^{o}C followed by 24 hr at –20 ^{o}C. Upon complete reaction, dicyclohexyl urea (DCU) byproduct was removed by filtration. The filtrate was collected and allowed to sit at room temperature for 24 hrs under N_2 and then cooled to –20 ^{o}C. The solution was again filtered to remove DCU crystals. The filtrate was retained and 100 mL cold water was added. This mixture was placed on ice for 1 hr. The pale-yellow solids were collected by filtration and dried under vacuum. Hot 50/50 water/ethanol was added to the dried solids until ~ 80% dissolved. The solution was boiled for an additional 10 minutes then filtered. Small, pale-yellow, fish-scale crystals formed slowly in the filtrate over a 3 hr

period at room temperature. Solids were collected by filtration and dried under vacuum. Typical yield ~ 2.0 g, 22%, yellow crystals. ^{1}H NMR, δ ppm: 1.884 (s, 3H), 3.809 (d, 2H), 4.176 (d, 2H), 5.577 (d, 2H), 7.435 (m,2H), 8.267 (t, 1H), 8.326 (m, 2H), 8.479 (t, 1H). Mp = 143-160 ^{o}C.

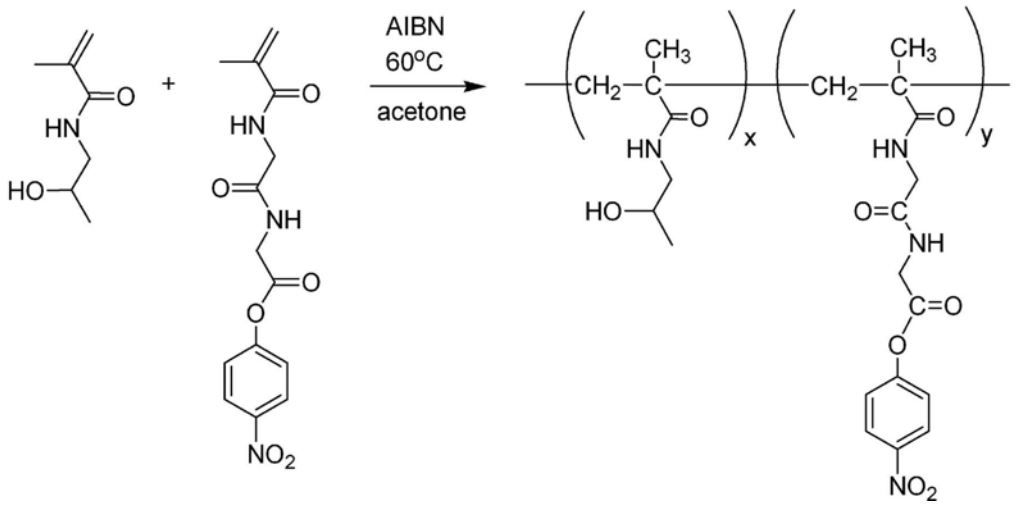


Scheme S3. Synthesis of methacryloyl glycylglycine 4-nitrophenyl ester (MAGGONP).

Reference: Kopecek J. (1977) Reactive Copolymers of N-(2-Hydroxypropyl) Methacrylamide with N-Methacryloylated Derivatives of L-Leucine and L-Phenylalanine .1. Preparation, Characterization, and Reactions with Diamines. Makromol. Chem. Macromol. Chem. Phys. *178(8)*, 2169-83.

2. Synthesis of pHPMA copolymer.

HPMA copolymer was prepared by free radical initiated polymerization as previously described using 12.5% (w/v) monomer and 0.6% initiator (AIBN) in freshly distilled acetone. Reactive side chain content in the polymer product was controlled by feed ratio of MAGGONP. The following is a typical procedure to produce an HPMA copolymer with 95 mole% HPMA units and 5 mole% MAGGONP units. HPMA monomer (3.35 g, 23.4 mmol, 1 eq), MAGGONP (0.40 g, 1.2 mmol, 0.05 eq), and AIBN (0.18 g, 1.1 mmol, 0.05 eq) were added to acetone (26 mL) in a Chemglass 50 mL pressure flask containing a magnetic stir bar. The solution was degassed by sonication under N_2 flow for 5 minutes and then capped. This solution was stirred until all solids dissolved (~ 30 minutes) and placed in a hot water bath and stirred at 60^{o}C for 24 hrs. After complete reaction, solids were collected by filtration, washed with cold acetone, and dried under vacuum. Solids were further purified by repeat precipitation from 90/10 CH_2Cl_2/MeOH (v/v) into a 10-fold excess of cold acetone. Typical yield: ~ 2.2 g, 56%, cream colored powder.

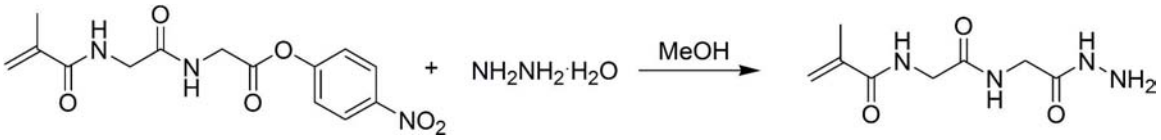


Scheme S4. Free radical initiated copolymerization of *N*-2-hydroxypropyl methacrylamide and methacryloyl glycylglycine nitrophenyl ester.

Reference: Kopecek J. (1977) Reactive Copolymers of N-(2-Hydroxypropyl)Methacrylamide with N-Methacryloylated Derivatives of L-Leucine and L-Phenylalanine. 1. Preparation, Characterization, and Reactions with Diamines. Makromol. Chem. Macromol. Chem. Phys. *178(8)*, 2169-83.

3. Synthesis of methacryloyl glycylglycine hydrazide (MAGGH).

Methacryloyl glycylglycine hydrazide (MAGGH) was synthesized to serve as a control compound in the TNBSA assay for quantification of pHPMA hydrazide functional groups. MAGGH was synthesized by reaction of MAGGONP with hydrazine monohydrate as follows: MAGGONP (750 mg, 1.0 equiv, 2.3 mmol) was dissolved in methanol (90 mL), then dripped into a solution of hydrazine monohydrate (567 µL, 5.0 equiv, 11.7 mmol) and stirred for 5 hr at room temperature under nitrogen. Solvent was removed under vacuum to yield crude solids that were then dissolved in 90/10 methylene chloride/methanol (40 mL), filtered, and loaded onto a silica gel column (2.5 x 17.5 cm) equilibrated with 90/10 methylene chloride/methanol. After the sample was loaded onto the column, the elution solvent was changed to methanol and MAGGH eluted after the visible yellow p-nitrophenol band. Yield: 0.156 g, 31%, white powder. ^{1}H NMR, δ ppm: 1.836 (s, 1H), 3.619 (d, 2H), 3.712 (d, 2H), 4.165 (d, 2H), 5.341 (d, 1H), 5.698 (d, 1H), 8.048 (t, 1H), 8.131 (t, 1H), 8.907 (s, 1H). ^{13}C NMR, δ ppm: 18.479, 40.779, 42.402, 119.752, 139.356, 167.597, 168.011, 169.204. MS calcd $[M+H]^+$ ($C_8H_{14}N_4O_3$): 215.1144. Found (FAB): 215.1147.



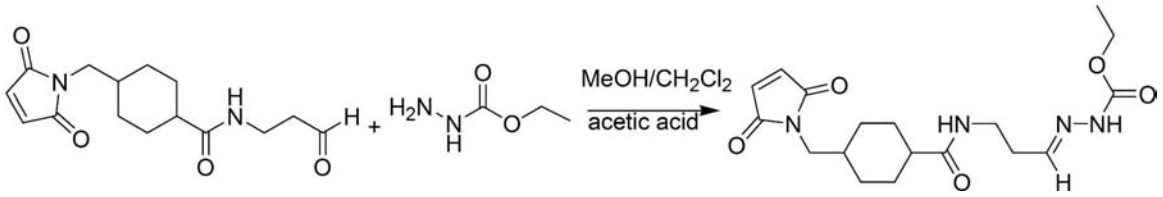
Scheme S5. Synthesis of methacryloyl glycylglycine hydrazide (MAGGH).

4. Reaction of heterobifunctional crosslinkers with model hydrazide ethyl carbazate.

The ability of each crosslinker to form hydrazone linkages was modeled with the hydrazide-containing small molecule ethyl carbazate, with confirmation of hydrazone formation being more analytically straightforward than with a small percentage of reactive sites in a polymer conjugate. For PMCA and BMCA, rapid, stoichiometric conversion to hydrazone product was obtained, with only a simple purification procedure needed to isolate pure hydrazone product. However, reaction of APM with ethyl carbazate resulted in formation of several products and purification required a separation procedure for isolation, which resulted in a lower overall yield. Although extensive analysis of reaction by-products was not performed, one by-product of the APM reaction with ethyl carbazate did show loss of maleimide functionality by ^{1}H NMR analysis.

4.1. PMCA.

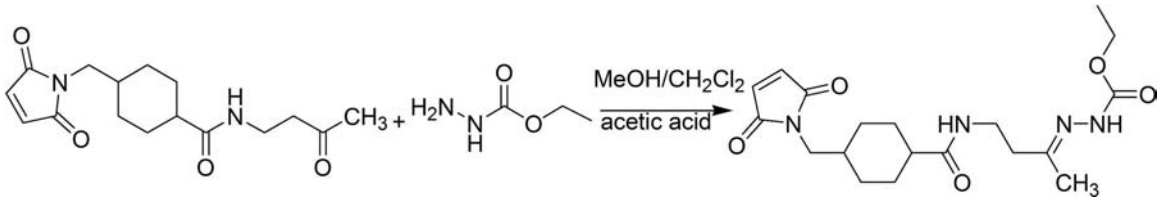
PMCA (100 mg, 0.342 mmol, 1.0 eq) was dissolved in 50/50 methylene chloride/methanol (2mL), followed by addition of Na_2SO_4 (100 mg, 0.70 mmol, 2.5 eq). Ethyl carbazate (35.6 mg, 0.342 mmol, 1.0 eq) was dissolved in 2 mL 50/50 methylene chloride/methanol (2 mL) and added to the PMCA solution drop wise. After 30 minutes acetic acid (5.0 μL, 0.087 mmol, 0.25 eq) was added and the reaction was stirred for 12 hrs under nitrogen and periodically monitored by TLC. After 12 hrs, the reaction mixture was filtered through a 0.2 μm filter, then washed with 0.1 M $NaHCO_3$. The organic layer was retained, dried with Na_2SO_4 and product was obtained after evaporation of solvent. Yield: 116.2 mg, 89.8%, white powder. ^{1}H NMR, δ ppm: 0.882 (q, 3H), 1.175 (t, 3H), 1.243 (q, 3H), 1.506 (m, 1H), 1.603 (d, 2H), 1.679 (2, 2H), 1.980 (m, 1H), 2.251 (q, 2H), 3.153 (q, 2H), 3.232 (d, 2H), 4.059 (q, CH2), 7.014 (s, 2H), 7.214 (s, 1H), 7.760 (t, 1H), 10.681 (s, 1H). 13C NMR, δ ppm: 14.516, 28.422, 29.336, 32.341, 35.698, 36.095, 42.984, 43.724, 60.021, 134.298, 145.493, 153.287, 171.211, 174.839. MS calcd $[M+H]^+$ ($C_{18}H_{26}N_4O_5$): 379.1981, found (FAB): 379.1976. Product was further analyzed by UV-Vis spectroscopy and a molar extinction coefficient was calculated using dilutions in methanol.



Scheme S6. Reaction of PMCA with ethyl carbazate.

4.2 BMCA.

BMCA (100 mg, 0.326 mmol, 1.0 eq) was dissolved in 50/50 methylene chloride/methanol (2 mL), followed by addition of Na_2SO_4 (100 mg, 0.70 mmol, 2.2 eq). Ethyl carbazate (33.9 mg, 0.326 mmol, 1.0 eq) was dissolved in 50/50 methylene chloride/methanol (2 mL) and added to the BMCA solution drop wise through a septum. After 30 minutes acetic acid (5.0 uL, 0.087 mmol, 0.27 eq) was added and the reaction was allowed to proceed for 12 hrs. After 12 hrs the reaction mixture was filtered through a 0.2 μm filter, then washed with 0.1 M $NaHCO_3$. The organic layer was retained, dried with Na_2SO_4, and product was obtained after evaporation of solvent. Yield: 116.1 mg, 91.0%, white solid. ^{1}H NMR, δ ppm: 0.873 (q, 2H), 1.193 (t, 3H), 1.232 (m, 2H), 1.501 (m, 1H), 1.595 (d, 2H), 1.673 (d, 2H), 1.777 (s, 3H), 1.963 (m, 1H), 2.250 (t, 2H), 3.190 (q, 2H), 3.228 (d, 2H), 4.083 (q, 2H), 7.015 (s, 2H), 7.669 (t, 1H), 9.653 (s, 1H). ^{13}C NMR δ ppm: 14.565, 15.917, 28.408, 29.345, 33.292, 36.080, 36.623, 42.980, 43.757, 60.245, 134.290, 154.058, 156.534, 171.194, 174.704. MS calcd $[M+H]^+$ ($C_{19}H_{28}N_4O_5$): 393.2137, found (FAB): 393.2135. Product was further analyzed by UV-Vis spectroscopy and a molar extinction coefficient was calculated using dilutions in methanol.

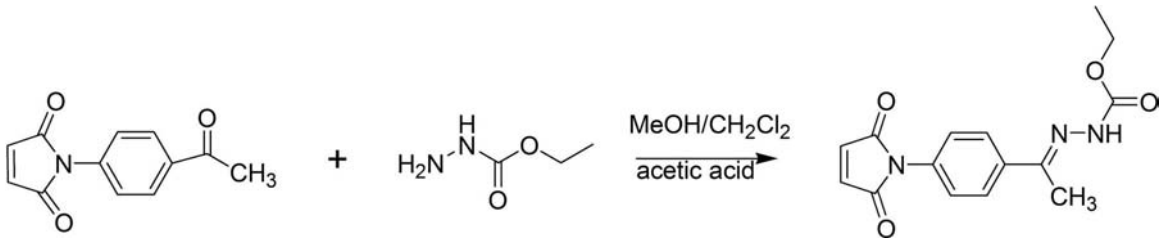


Scheme S7. Reaction of BMCA with ethyl carbazate.

4.3. APM.

APM (400.0 mg, 1.86 mmol, 1.0 eq) was dissolved in 50/50 methylene chloride/methanol (2 mL), followed by addition of Na_2SO_4 (528 mg, 3.72 mmol, 2.2 eq). Ethyl carbazate (176.0 mg, 1.69 mmol, 0.91 eq) was dissolved in 50/50 methylene chloride/methanol (2 mL) and added to the APM solution drop wise with stirring. After 30 minutes acetic acid (5.0 μL, 0.174 mmol, 0.1 eq) was added and the reaction was continued for 12 hrs at room temperature. After 12 hrs the reaction mixture was filtered through a 0.2 μm filter and washed with 0.1M $NaHCO_3$. The organic layer was retained, dried with Na_2SO_4, and crude

product was obtained after evaporation of solvent. Product was further purified by silica gel chromatography (50/50 methylene chloride/ethyl acetate mobile phase). Yield: 0.150 g, 27%, yellow solid. ^{1}H NMR, δ ppm: 1.262 (d, 3H), 2.234 (s, 3H), 4.177 (q, 2H), 7.197 (s, 2H), 7.368 (m, 2H), 7.827 (m, 2H), 10.173 (s, 1H). ^{13}C NMR, δ ppm: 13.782,14.545, 60.509, 126.246, 126.356, 131.830, 134.676, 137.458, 147.997, 154.097,169.744. MS calcd $[M+H]^+$ ($C_{15}H_{15}N_3O_4$): 302.1140, found (FAB): 302.1137. Product was further analyzed by UV-Vis spectroscopy, and the molar extinction coefficient was calculated using dilutions in methanol.



Scheme S8. Reaction of APM with ethyl carbazate.

5. Spectral properties of hydrazones formed with crosslinkers and ethyl carbazate.

The spectroscopic properties of hydrazones formed from crosslinker reaction with ethyl carbazate are summarized in Table S1.

Table S1. Spectral properties of crosslinkers and corresponding hydrazones formed with ethyl carbazate

crosslinker	λ_{max} (nm)	λ_{max} of hydrazone (nm)	ε ($M^{-1}cm^{-1}$) of hydrazone
PMCA	299	297	5.53×10^2
BMCA	297	299	5.66×10^2
APM	268	288	1.90×10^4

Spectral properties of PMCA and BMCA crosslinkers before and after hydrazone formation were nearly identical, preventing analysis of hydrazone formation or degradation by simple absorbance measurements. The absorbance of PMCA and BMCA at 297 nm is due to the maleimide functional group, while the more intense and red-shifted APM absorbance results from the conjugated π system. The relatively high molar extinction coefficient of APM provides a convenient analytical tool for determination of the degree of conjugation, even at low concentrations.

Neutrophil Targeting Heterobivalent SPECT Imaging Probe: cFLFLF-PEG-TKPPR-^{99m}Tc

Yi Zhang,[†] Li Xiao,[†,‡] Mahendra D. Chordia,[‡] Landon W. Locke,[†] Mark B. Williams,[†] Stuart S. Berr,[†] and Dongfeng Pan*[,†]

Research Division of the Department of Radiology and Department of Chemistry, University of Virginia, Charlottesville, Virginia 22908. Received February 3, 2010; Revised Manuscript Received May 31, 2010

A new heterobivalent peptide ligand specifically targeting polymorphonuclear leukocytes (PMNs) with favorable pharmacological parameters to monitor sites of inflammation for imaging is designed. The detailed synthesis, characterization, and pharmacological evaluation of the ligands are reported here. Two separate peptide binding ligands for formyl peptide and tuftsin receptors were chosen to link together based on the high expression levels of the two receptors on activated PMNs The heterobivalency and pegylated links were incorporated in the structural design to improve the sensitivity of the detection and to improve the bioavailability along with blood clearance profile, respectively. Two chemical constructs, cFLFLF-$(PEG)_n$-TKPPR-^{99m}Tc ($n = 4$, 12), were evaluated in vitro with human PMNs for binding affinity and bioavailability. As a result, cFLFLF-$(PEG)_{12}$-TKPPR-^{99m}Tc was found to have more favorable pharmacological properties and was therefore used for further in vivo studies. Preliminary in vivo assessment of the agent was performed using single gamma emission computed tomography (SPECT) imaging of a mouse model of ear inflammation. The results of these studies indicate cFLFLF-$(PEG)_{12}$-TKPPR-^{99m}Tc may be a desirable imaging agent for binding to PMNs to identify sites of inflammation by SPECT.

INTRODUCTION

High-quality nuclear imaging can be a useful diagnostic and prognostic tool for detecting sites of inflammation. This should aid in designing therapies to control pathological conditions. However, the ability to detect and characterize inflammation has been elusive so far (*1*). One of the hallmarks of inflammation is migration and activation of leukocytes. Current leukocyte imaging techniques include ex vivo white blood cell labeling with ^{67}Ga citrate, ^{111}In, or ^{99m}Tc containing complexes and reinjection of the labeled cells back into patients. Although the utility of this method is proven, the process is laborious and involves handling of blood products, thereby increasing the risk of contamination. Tracking neutrophils by intravenous administration of highly specific radiolabeled binding probes would circumvent these limitations. As a result, numerous chemotactic peptides, such as fMLF and its analogues have been investigated as potential neutrophil imaging probes (*2, 3*). However, exhibition of undesired biological side effects and/or poor pharmacokinetic parameters have limited their clinical utility.

We have recently reported a novel PET imaging agent, cFLFLF-PEG-^{64}Cu (PEG = 3.4 kDa), which binds to the formyl peptide receptor (FPR) without prompting neutrophil activation and, in addition, has favorable pharmacokinetic characteristics such as increased hydrophilicity to minimize nonspecific liver uptake (*4, 5*). However, the high cost of PET imaging and the limited supply of the cyclotron-produced ^{64}Cu isotope may restrict its widespread application in research and clinics. A ^{99m}Tc version of the probe for single gamma emission computed tomography (SPECT) imaging of neutrophils provides an attractive alternative because of the wider availability and lower cost of ^{99m}Tc. In addition, to further enhance the detection sensitivity, binding affinity, and specificity of the ligand toward neutrophils, we designed a heterobivalent peptide, cFLFLF-PEG-TKPPR-^{99m}Tc, that simultaneously targets the FPR and tuftsin receptor. Heterobivalent ligands have demonstrated higher affinity than monovalent and symmetrical bivalent binders (homodimer) (*6, 7*).

Because of inclusion of the polar TKPPR sequence in the present heterobivalent ligand design, the size of PEG linker was reduced in comparison with the larger PEG linker reported earlier in cFLFLF-PEG-^{64}Cu (PEG = 3.4 kDa) in order to maintain roughly the same water solubility. Thus, the two binding peptide sequences were linked through either a bifunctional PEG_4 or PEG_{12} moiety. An additional lysine residue was incorporated in the construct as a handle for the HYNIC group and its coordination to radiometal (Scheme 1). We wish to report here the detailed synthetic method, the observed pharmacokinetic parameters for these new probes, and a preliminary demonstration of its application to SPECT imaging of inflammation in vivo.

EXPERIMENTAL PROCEDURES

Materials and Methods. All chemicals obtained commercially were of analytical grade and used without further purification. Na^{99m}TcO$_4$ was obtained from Cardinal Health, Inc. (Charlottesville, VA). 6-Boc-hydrazinonicotinic acid (6-Boc-HYNIC acid) was obtained from SoluLink (San Diego, CA). Fmoc-Arg-PS resin was purchased from Applied Biosystems (Foster City, CA). Fmoc-amino acids were purchase from Anaspec Inc. (Fermont, CA). N-Fmoc-amino-dPEG$^{TM}_4$ acid and N-Fmoc-amino-dPEG$^{TM}_{12}$ acid were purchased from Quanta Biodesign, Ltd. (Powell, OH). *N*-Hydroxysulfosuccinimide (Sulfo-NHS) and 1-ethyl-3-[3-(dimethylamino)-propyl]carbodiimide (EDC) were purchased from Pierce (Rockford, IL). All other chemical reagents and solvents were obtained from Sigma-

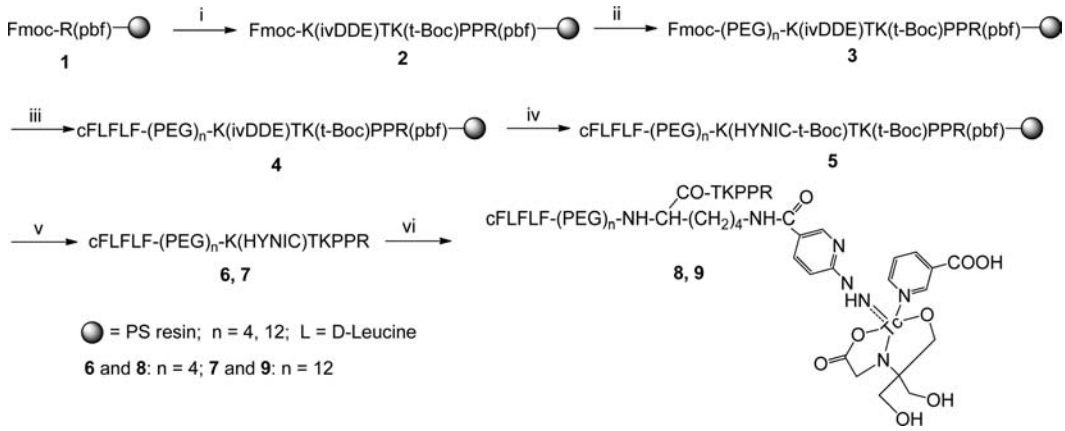
* Corresponding author. Room 263, Snyder Building, 480 Ray C. Hunt Drive, Fontaine Research Park, Charlottesville, VA 22908. E-mail: dp3r@virginia.edu; Tel: (434) 243-2893; Fax: (434) 924-9435.

[†] Research Division of the Department of Radiology.

[‡] Department of Chemistry.

10.1021/bc100063a © 2010 American Chemical Society
Published on Web 09/15/2010

Scheme 1[a]



[a] Reagent and conditions: (i) standard solid phase Fmoc chemistry; (ii) (1) piperidine, (2)Fmoc-(PEG)*n*-COOH, HBTU, DIEA; (iii) standard solid phase Fmoc chemistry; (iv) (1) 2% hydrazine, (2) 6-Boc-HYNIC acid, HBTU, DIEA; (v) TFA (95%); (vi) $^{99m}TcO_4^-$, $SnCl_2$, tricine, nicotinic acid, pH 5.2.

Aldrich. For purification of peptide precursors and ^{99m}Tc labeled products, semipreparative reversed-phase high-performance liquid chromatography (RP-HPLC) was performed with an Apollo C18 reversed-phase column (5 μ, 250 $\times$ 10 mm) on a Varian system with ABI Spectroflow 783 UV detector and Bioscan NaI solid scintillation flow count radio-HPLC detector. The mobile phase was changed from 60% Solvent A (0.1% TFA in water) and 40% Solvent B (0.1% TFA in 80% aqueous acetonitrile) to 100% Solvent B at 30 min at a flow rate 3 mL/min. MALDI-TOF mass spectroscopy analysis was performed on samples of peptide products at the W. M. Keck Biomedical Mass Spectrometry Laboratory at the University of Virginia (UVa) and the data obtained on a Bruker Daltonics system (Billerica, MA). Peptides were synthesized manually by standard solid-phase method, following a conventional Fmoc strategy using 2-(1*H*-benzotriazole-1-yl)-1,1,3,3-tetramethyluronium hexafluorophosphate (HBTU) as the coupling agent. Lysine was used as handle to incorporate HYNIC to the peptide. High-performance liquid chromatographic (HPLC) analysis of the nonradiolabeled compounds was performed on a Varian Prostar system equipped with a ProStar 335 HPLC diode array detector. HPLC solvents were purchased from Fisher Scientific (Pittsburgh, PA) and used without further purification. Typical yields of the crude peptides were 80−85%.

Human tumor necrosis factor-α (TNF-α) was procured from Peprotech, and fMLF was purchased from Sigma. Aliquots of both samples were taken (TNF-α, 10 U/mL, and fMLF, 10 mM) and stored at −20 °C. For every assay, the solutions were thawed to ambient temperature and freshly diluted with hepatic arterial (HA) buffer before use. Multiscreen high-throughput screening (HTS) with glass fiber filter (FC) 96-well plates, type C, with 1.2 mm glass filters were purchased from Millipore. Filtration from 96- well plates was performed under vacuum on a Brandel filtration device. The membranes from each well were collected by punching with the Millipore Multiscreen punching instrument. The radioactivity from ^{99m}Tc-bound ligand was measured with Minaxi (Packard), Autogamma 5000 series (Packard), or Wallac 1420Wizard (Perkin-Elmer) γ-counters. Radioactivity was measured for 1 min per sample and was not corrected for decay.

Human neutrophils were prepared from normal heparinized (10 U/mL) venous blood by a one-step Ficoll-Hypaque separation procedure (*8, 9*), yielding approximately 98% neutrophils; greater than 95% viable as determined with trypan blue containing less than 50 pg/mL of endotoxin. After separation, neutrophils were washed with Hank's balanced salt solution with heparin (10 U/mL) 3 times. After the third wash, neutrophils were resuspended in HA buffer, which was Hank's balanced salt solution supplemented with 0.1% human albumin (Bayer Healthcare). Neutrophil experiments were completed in HA buffer.

Female FVB mice, 5 months old, were purchased from the National Cancer Institute (Frederick, MD). Mice were housed in a controlled environment (12 h light/12 h dark photoperiod, 22 ± 1 °C, 60 ± 10% relative humidity), and were provided free access to autoclaved pellet food and tap water. All procedures were in accordance with current National Institutes of Health (NIH) guidelines and were approved by the University of Virginia Animal Care and Use Committee (ACUC).

SPECT/CT imaging was performed with a microSPECT/CT scanner designed and built at UVa under NIH funding (*10*). The scanner uses an open-barrel type gantry consisting of two 38 in steel wheels connected by aluminum profile pieces. CT and SPECT scanning are performed sequentially, and the animal is translated axially from one subsystem to another between two fixed locations along a 1-in-diameter carbon fiber half-cylinder that is located at the gantry axis of rotation. Reproducibility of animal table location permits consistent and simple fusion of CT and SPECT images using stored offset parameters. The scanner can be operated with two different types of X-ray detectors: CCD-based for high spatial resolution (modulation transfer function in the reconstructed CT image of 0.1 at a spatial frequency of 14.7 mm^{-1} when used with an 8 μm X-ray source) or CMOS-based for fast readout (2 frames per second). Microfocus X-ray sources with focal spot sizes ranging between 8 and 50 μm are available. SPECT scanning can be performed using up to four gamma cameras (10 cm $\times$ 10 cm fields of view) simultaneously. Respiratory and cardiac gating are available for both CT and SPECT scanning. CT projection images are preprocessed for detector sensitivity uniformity correction and dark count subtraction using a custom-written IDL program and then are reconstructed with a Feldkamp three-dimensional filtered backprojection algorithm (COBRA, Exxim, Inc., Pleasanton, CA). SPECT data are acquired using a custom-written interface using Kmax (Sparrow Corp., Port Orange, FL) software and reconstructed using a custom-written maximum-likelihood expectation-maximization algorithm (*11*).

Synthesis of cFLFLF-PEG$_n$-K(HYNIC)TKPPR 6 and 7. (Scheme 1). Fmoc-Arg-PS resin **1** (150 mg, 0.21 mmol/g) was loaded to a peptide synthesis vessel, suspended in DMF (2 mL), and shaken at 600 rpm for 5 min and drained. Fmoc was removed by adding 2 mL of 20% piperidine−DMF solution to the synthesis vessel. The vessel was shaken on a vibrator (Labnet Shaker 20, Woodbridge, NJ) for 5 min, and the solution was

drained. The same deprotection step was repeated once again by shaking for 20 min. The deprotected resin was washed six times each with 2 mL of DMF. The resin was then coupled to the Fmoc-protected amino acid by successively adding 4 molar excess of the Fmoc-protected amino acid (0.84 mmol) in DMF (0.1 M), 4 equiv of HBTU in DMF (0.1 M), and 8-fold excess of DIEA (1.68 mmol). The reaction vessel was shaken for 90 min. The reaction solution was drained off, and the resin was washed with 3 × 2 mL of DMF. The peptide resin was subsequently capped by adding 10-fold molar excess of acetic anhydride (0.5 mL) and DIEA and shaking at 600 rpm for 30 min. After draining off the solution, the resin was washed with 6 × 2 mL of DMF and was then ready for the next cycle of coupling. To obtain the resin-bound peptide sequence **4**, the amino acids and special residues were coupled in the following order: Fmoc-Pro, Fmoc-Pro, Fmoc-Lys(*t*-Boc), Fmoc-Thr(t-Bu), Fmoc-Lys(ivDDE), *N*-Fmoc-amino-dPEG$^{TM}_4$ acid or N-Fmoc-amino-dPEG$^{TM}_{12}$ acid, Fmoc-Phe, Fmoc-(D)Leu, Fmoc-Phe, Fmoc-(D)Leu, Fmoc-Phe, and Trans-cinnamic acid. The ivDDE protecting group of **4** was removed to free the ω-NH_2 of the lysine by treatment with 2% hydrazine in DMF for 60 min. After draining, the peptide resin was repeatedly washed with DMF (2 mL) six times. To conjugate the chelating HYNIC moiety at the ω-NH_2 of the lysine, a solution of 4 molar excess of 6-Boc-HYNIC acid, 4 equiv of HBTU, and 8 equiv of DIEA in 1.6 mL of DMF was added into the reaction vessel. The vessel was shaken for 90 min, the solution was drained off, and the resin was washed with DMF (2 mL) three times. The peptide cFLFLF-PEG$_n$-K(HYNIC)TKPPR **6** or **7** was cleaved from the resin support using a 95% TFA. The crude products were purified with the HPLC conditions described above. The molecular weights of the purified precursors were verified by MALDI-TOF mass spectroscopy.

cFLFLF-PEG$_n$-TKPPR-^{99m}Tc 8 or 9. To a 1.5 mL vial was consecutively added 100 μg of cFLFLF-PEG$_n$-K(HYNIC)TKPPR **6** or **7** in 200 μL of citrate buffer (10 mM, pH 5.2), 200 μL of tricine solution (30 mg/mL in 10 mM citrate buffer, pH 5.2), 100 μL of nicotinic acid solution (10 mg/mL in 10 mM citrate buffer, pH 5.2), 37 MBq of $^{99m}TcO_4^-$ solution (370 MBq/mL in saline), and 25 μL of $SnCl_2$ solution (1.0 mg/mL in 0.1 N HCl). The reaction mixture was stirred by shaking and heated at 60 °C for 15 min. After being cooled to room temperature for 10 min, the reaction mixture was purified by the same HPLC conditions mentioned above. The observed retention times of cFLFLF-PEG$_4$-TKPPR-^{99m}Tc **8** and cFLFLF-PEG$_{12}$-THPPK-^{99m}Tc **9** were 17.8 and 16.8 min, respectively.

Partition Coefficient. Freshly HPLC purified cFLFLF-PEG$_n$-KTKPPR-^{99m}Tc **8** or **9** (~350 kBq) in 500 μL of water was mixed with 500 μL of octanol in an Eppendorf microcentrifuge tube. The tube was sonicated 10 min and then centrifuged at 4000 rpm 5 min (Fisher Scientific Marathon Micro-A). Aliquots (100 μL) of octanol and aqueous layers were carefully separated and radioactivity of samples counted. Log *P* is derived as the log of the ratio of radioactivity in octanol to radioactivity in water. The measurement was repeated in triplicate and data presented are the average of three measurements.

Neutrophil Binding. Freshly isolated human neutrophils (4 × 10^6 cells/mL) were treated with TNF-α (10 U/mL, Peprotech) twenty minutes prior to binding studies and transferred to a 96 well plate (Multiscreen HTS FC by Millipore, Billerica, MA. 1.2 μm glass filter type C, 50.0 μL, ~2.0 × 10^5 cells/well). Saturation assays were carried out using eight different concentrations of cFLFLF-PEG$_{12}$-TKPPR-^{99m}Tc ranging from 1.0 μM to 0.01 nm incubated at 25 °C for 90 min. Neutrophils were incubated with the excess radioligand at 25 °C for 90 min to obtain total binding. Following incubation, the plates were filtered rapidly under vacuum using a Brandel filtration device (Brandel Inc., Gaithersburg, MD), washed three times with cold Tris-Mg buffer (−5 °C, 10 mM, 150 μL each time/well) to remove the unbound radioligand, and dried under vacuum. The plates were then wiped with Kimwipes EX-L at room temperature, and membranes from each well were collected by Millipore multiscreen punching instrument (Billerica, MA). The bounded radioactivity remaining on the membranes was measured in a gamma counter. Specific binding was calculated as the difference between total binding and nonspecific binding at the highest concentration. Nonradioactive peptide (cFLFLF-PEG$_{12}$-TKPPR) was used in excess (100 μM) to determine nonspecific binding. Saturation experiment data (K_d and B_{max} values) were obtained by computer analysis using *Prism 4.0* (GraphPad).

Blood Clearance. Blood kinetics of cFLFLF-PEG$_{12}$-TKPPR-^{99m}Tc was studied in 3 control (non-inflamed) mice. Approximately 50 μL samples of blood from the contralateral tail vein were collected in capillary tubes at 15, 30, 45, 60, 120, and 180, and 360 min after tracer injection (0.37−0.74 MBq). The capillary tubes were placed in a vial that was weighed beforehand and afterward. Activity in each blood sample was measured in a radioisotope-calibrated well counter (CRC-15W, Capintec, Inc., NJ), decay-corrected back to the time of tracer injection, normalized for injected dose and animal body weight, and expressed as %ID/g of blood.

Serum Stability of cFLFLF-PEG$_{12}$-TKPPR-^{99m}Tc. Fifty microcuries of the cFLFLF-PEG$_{12}$-TKPPR-^{99m}Tc was added in to 100 μL of fetal bovine serum (Invitrogen, Grand Island, NY). After incubation at 37 °C for 1, 3, and 6 h, aliquots of the mixture were filtered through a 0.2 μM microspin filter. The filtrates were analyzed by reverse-phase HPLC with a Bioscan Flow Count Radio-HPLC detector. All of the newly formed γ-peaks besides the original cFLFLF-PEG$_{12}$-TKPPR-^{99m}Tc peak would be considered as degraded products.

Biodistribution. Body distribution of radioactivity was determined in control ($n = 3$) mice at 3 and 18 h after injection of the tracer. After a single blood sample had been taken from the tail vein, mice were euthanized by deep halothane anesthesia. The organs and tissues (ear, heart, lungs, muscle, bone, liver, kidney, spleen, small intestine, and stomach) were collected, rinsed with PBS, wiped with filter paper, and weighed in a preweighed vial. The radioactivity of each sample was measured in a γ-well counter and decay-corrected back to the time of tracer injection. Biodistribution values are expressed as a percentage of the injected dose (%ID) and normalized by body and organ/tissue mass.

Mouse Ear Inflammation Model. A female FVB mouse, 5 month old, with left ear inflammatory lesion was used to preliminarily assess the ability of the cFLFLF-PEG$_{12}$-TKPPR-^{99m}Tc to detect inflammation as a result of neutrophil migration and accumulation. The animal model is similar to that described by Gross et al. (*12*). Topical application of PMA (2.5 μg in 20 μL DMSO) onto the left earlobe induces acute dermatitis, manifested by local swelling, erythema, and infiltration of neutrophils (*13, 14*). The right ear served as control and received only DMSO (vehicle). The SPECT/CT imaging was correlated with myeloperoxidase (MPO) activity determined by noninvasive bioluminal-bioluminescence imaging (*12*).

Luminal-Bioluminescence Imaging of MPO. Since MPO is the most abundant protein in azurophilic granules of neutrophils, an MPO-specific luminal-bioluminescence study was carried out in support of the accumulation and activation of neutrophils in the PMA-treated ear. The mice were injected with 200 μL of luminol (5 mg/0.1 L DMF) intraperitoneally 22 h after PMA application. Immediately after luminal injection, a 40 min kinetic bioluminescence scan was performed on Xenogen

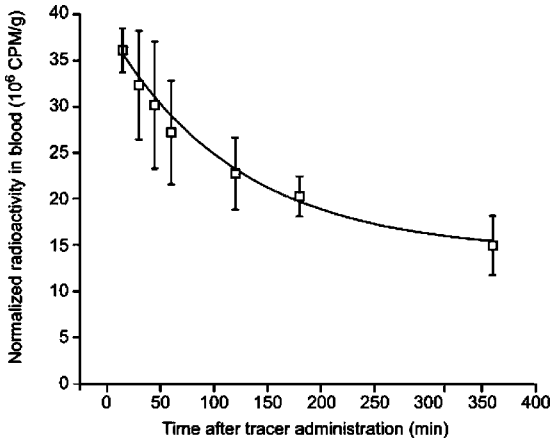


Figure 1. Monoexponential blood clearance curve of cFLFLF-PEG_{12}-TKPPR-^{99m}Tc in control mice ($n = 3$): the normalized blood radioactivity was plotted against various time points after tail vein injection of the tracer.

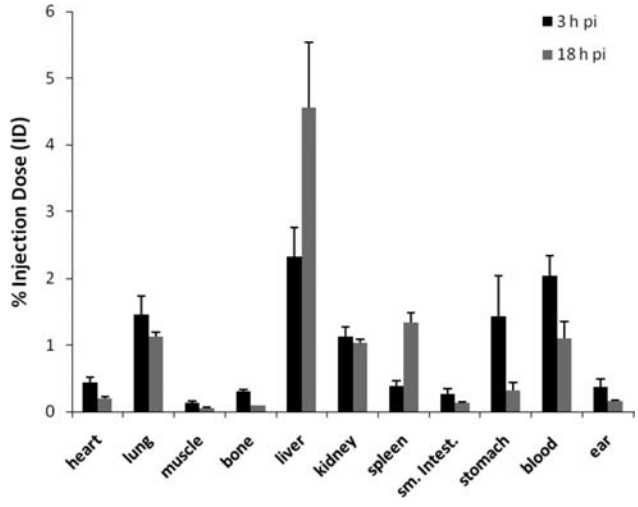


Figure 2. Tissue and organ accumulation of cFLFLF-PEG_{12}-TKPPR-^{99m}Tc at 3 and 18 h post-injection of normal mice ($n = 3$) expressed as the percent injected dose per gram of tissue (decay corrected).

IVIS Spectrum (Caliper life science, CA) and processed on *Live Image* software (Caliper life science) with open filter and exposure time of 60 s.

SPECT/CT Imaging. Twenty-four hours after PMA challenge, 3.7 MBq (1 mCi) of cFLFLF-PEG_{12}-TKPPR-^{99m}Tc in 200 μL of saline was administered via tail vein. Three hours later, CT/SPECT imaging was performed using the microSPECT/CT scanner described above. Anesthesia (1−2% isoflurane in oxygen) was delivered throughout the imaging procedure. CT projection data acquisition used the CMOS X-ray detector and obtained 200 evenly spaced projections spanning 240° over approximately 5 min. For SPECT scanning, 60 evenly spaced views were obtained over 180° using two opposing gamma cameras simultaneously, resulting in a total of 120 projections over 360° at an angular increment of 3°. The acquisition time was approximately 45 min. The two cameras were fitted with 0.5-mm-diameter tungsten pinholes. The reconstructed CT voxel size was $0.164 \times 0.164 \times 0.164$ mm^3 on a $320 \times 320 \times 384$ image matrix. The reconstructed SPECT voxel size was $0.4 \times 0.4 \times 0.4$ mm^3 on a $60 \times 60 \times 60$ image matrix. All SPECT images were corrected for radioactivity decay but not for gamma ray attenuation.

Image Analysis. Co-registration of SPECT and CT images was performed using *ASIPRO* software (Siemens Medical Solutions USA, Inc., Knoxville, TN) and a transformation matrix previously obtained with a dual modality phantom. To characterize the accumulation of the tracer in the ears, volume-of-interest (VOI) analysis was performed to identify the number of detected counts originating in the ears. CT images were used to identify voxels lying within the ear and the corresponding SPECT voxels were included in each VOI. Inflamed VOI was drawn tightly around the ear inflammation area on the SPECT transaxial image slice and copied to the control ear. Six slices were taken in both ears. The upper 60% signal (in counts/mL) was taken into calculation in each slice. The known gamma camera detection efficiency was used to compute the activity contained in the ears. This activity was expressed as a percentage of the injected dose per mouse body mass (%ID/g).

RESULTS AND DISCUSSION

The precursors, cFLFLF-PEG_n-K(HYNIC)TKPPR **6** and **7**, were synthesized using standard Fmoc peptide chemistry on resin. Briefly, starting from arginine residue loaded on resin at carboxyl group, the TK(*t*-Boc)PPR peptide was constructed first, an additional lysine residue [Lys(ivDDE)] was added to form intermediate **2** prior to addition of varied pegylated linker. Then, on the other side of the PEG the second cFLFLF peptide was built to produce the desired peptide sequence **4**. Finally, the removal of the ivDDE protecting group of the lysine linker using basic hydrazine conditions released the side chain ω-NH_2 derivative **5** for conjugation with HYNIC. The resin-bound HYNIC conjugated bivalent peptides **6** and **7** were cleaved with standard TFA chemistry. The two precursor peptides were purified by reverse-phase HPLC with total yield in the range 20−25%. The purified peptide constructs were characterized by mass spectroscopy for its composition. The calculated and observed MALDI-TOF-MS $[M+H]^+$ were 1905 and 1906 for cFLFLF-PEG_4-K(HYNIC)TKPPR **6** and 2258 and 2258 for cFLFLF-PEG_{12}-K(HYNIC)TKPPR **7**. The two radiolabeled cFLFLF-PEG_n-K(HYNIC)-TKPPR-^{99m}Tc **(8)** ($n = 4$) and (**9**) ($n = 12$) were obtained by conjugating **6** and **7** with stannous chloride reduced [^{99m}Tc]pertechnedate with nicotinic acid and

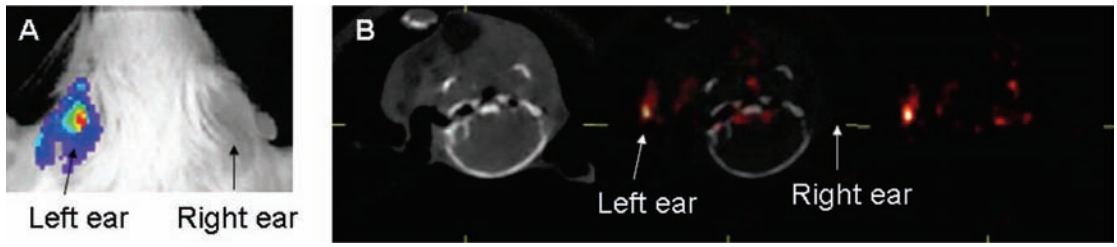


Figure 3. (A) Representative MPO-BLN image of mouse subjected to topical application of PMA on left ear for 24 h. (B) Representative transaxial images of MicroCT (left), MicroSPECT (right), and fused micro-CT and micro-SPECT (middle) of mice subjected to PMA application on left ears. Both SPECT and CT images were obtained 3 h after tail vein injection of cFLFLF-PEG_{12}-TKPPR-^{99m}Tc. SPECT scans revealed the PMA infected ear had visually more tracer uptake compared to control ear, which was quantified by ROI analysis.

tricine as coligands, respectively. The radiolabeled peptides were purified from unlabeled precursors and other reagents by reverse-phase semipreparative HPLC with radiochemical yield of >75% and radiochemical purity of 98%. The detailed synthetic method is described in Scheme 1.

The in vitro binding studies to isolated human neutrophils exhibited K_d values 47.8 and 15.1 nM for ligands **8** and **9**, respectively. The radiolabled ligand **8** was roughly 3-fold less potent than compound **9**, possibly due to the longer PEG_{12} linker allows the simultaneous binding to both the formyl peptide and the tuftsin receptors on activated neutrophils. The purified radioligands **8** and **9** were first evaluated for their Log *P* values to estimate approximate lipophilicity of the individual compounds. The observed Log *P* values for **8** and **9** are in agreement with the expected trend as PEG12 linked was found to be more hydrophilic (−0.89) compared to PEG4 derivative (−0.77). On the basis of the better solubility in water and higher binding affinity, radioligand **9** was chosen for further in vivo studies.

The cFLFLF-PEG_{12}-TKPPR-^{99m}Tc is stable for at least 6 h in serum. HPLC analysis of serum samples mixed with ligand displayed no appreciable fragments of ^{99m}Tc labeled peptide at each time point (1, 3, and 6 h).

In order to further analyze the pharmacokinetic parameters of the ligand **9**, blood clearance studies were conducted in vivo. The data revealed a monoexponential clearance of the radiotracer as shown in Figure 1. The elimination half-life for blood clearance ($T_{1/2}$) was calculated to be about 84 min.

Biodistribution of cFLFLF-PEG_{12}-TKPPR-^{99m}Tc in liver increases from 2.3 to 5.3%ID at 3 and 18 h post-injection which indicated the radiotracer is excreted mainly through the hepatobilliary pathway. The longer blood retention of cFLFLF-PEG_{12}-TKPPR-^{99m}Tc, 2.1 and 1.2%ID at 3 and 18 h post-injection vs 0.2%ID (*15*) of cFLFLFK-PEG-^{64}Cu at 18 h post-injection, correlates the longer circulation time ($T_{1/2}$) of 84 vs 55 min (Figure 2). This indicates that a longer PEG moiety might be needed for fast blood clearance of cFLFLF-PEG_n-TKPPR-^{99m}Tc and, therefore, benefit the earlier imaging quality by lowering background signals from blood.

At 22 h post PMA treatment, bioluminescence as observed by MPO assay was locally emitted from PMA-treated earlobes of FVB (female) mice after luminal administration, reaching levels 7-fold over those of vehicle-treated ears. The image (Figure 2a) 21 min after luminal injection was chosen as a representative due to the highest ratio of photons emitted from inflamed ear (left) to control ear (right). At 27 h after PMA challenge and 3 h post-injection of cFLFLF-PEG_{12}-TKPPR-^{99m}Tc, CT/SPECT imaging shows that the accumulation of the tracer measured in the inflamed ear (left) is about 3.15-fold higher than in the control ear (Figure 3b).

This preliminary data suggests that in vivo detection of inflammation through neutrophil activation and migration in live animal is feasible with gamma or SPECT modalities. In a real inflammatory situation, the intensity of radiotracer signal will be dependent on the intensity of inflammation and amount of PMN accumulation at the inflammatory site.

CONCLUSION

In conclusion, we have synthesized two neutrophil-targeting heterobivalent SPECT imaging probes: cFLFLF-PEG_4-TKPPR-^{99m}Tc and cFLFLF-PEG_{12}-TKPPR-^{99m}Tc. The peptide ligands bound to neutrophils with high affinity and demonstrated stability in serum and sufficient hydrophilicity. The cFLFLF-PEG_{12}-TKPPR-^{99m}Tc is a feasible probe for in vivo imaging of acute neutrophilic inflammation. Further biologic evaluation of this novel imaging agent is ongoing, with the goal of refining the biologic properties of the agent to facilitate studies that assess the efficacy of novel anti-inflammatory therapeutic drug candidates. On the basis of preliminary in vivo imaging results and in vitro cell function assays, this peptide appears to possess properties to be a promising new radiopharmaceutical for the in vivo imaging of neutrophils.

ACKNOWLEDGMENT

This research was supported by Nihon MediPhysics residual fund (MD-RADL Pan NMP RDC-F001917E) to D.P.. The work was also supported in part by a gift provided to S.S.B. by Philip Morris USA (The review and approval process was overseen by an External Advisory Committee without any affiliation with the University, PMUSA, or any other tobacco company. PMUSA funding for this work was based upon independent intramural and extramural reviews).

LITERATURE CITED

(1) Palestro, C. J. (2007) In vivo leukocyte labeling: the quest continues. *J. Nucl. Med. 48*, 332–334.

(2) Babich, J. W., Tompkins, R. G., Graham, W., Barrow, S. A., and Fischman, A. J. (1997) Localization of radiolabeled chemotactic peptide at focal sites of Escherichia coli infection in rabbits: evidence for a receptor-specific mechanism. *J. Nucl. Med. 38*, 1316–22.

(3) Babich, J. W., Dong, Q., Graham, W., Barzana, M., Ferril, K., Pike, M., and Fischman, A. J. (1997) A novel high affinity chemotactic peptide antagonist for infection imaging. *J. Nucl. Med. 38*, 268P.

(4) Zhang, Y., Kundu, B., Fairchild, K. D., Locke, L., Berr, S. S., Linden, J., and Pan, D. (2007) Synthesis of novel neutrophil-specific imaging agents for Positron Emission Tomography (PET) imaging. *Bioorg. Med. Chem. Lett. 17*, 6876−6878.

(5) Locke, L. W., Chordia, M. D., Zhang, Y., Kundu, B., Kennedy, D., Landseadel, J., Xiao, L., Fairchild, K. D., Berr, S. S., Linden, J., and Pan, D. (2009) A novel neutrophil-specific PET imaging agent: cFLFLFK-PEG-64Cu. *J. Nucl. Med. 50*, 790–797.

(6) Tweedle, M. F. (2006) Adventures in multivalency, the Harry S. Fischer memorial lecture CMR 2005; Evian, France. *Contr. Media Mol. Imaging 1*, 2–9.

(7) Mammen, M., Choi, S. K., and Whitesides, G. M. (1998) Polyvalent interactions in biological systems: Implications for design and use of multivalent ligands and inhibitors. *Angew. Chem., Int. Ed. 37*, 2755–2794.

(8) Ferrante, A., and Thong, Y. H. (1980) Simultaneous preparation of mononuclear and polymorphonuclear leucocytes from horse blood on ficoll-hypaque medium. *J. Immunol. Methods 34*, 279–285.

(9) Sullivan, G. W., Rieger, J. M., Scheld, W. M., Macdonald, T. L., and Linden, J. (2001) Cyclic AMP-dependent inhibition of human neutrophil oxidative activity by substituted 2-propynylcyclohexyl adenosine A(2A) receptor agonists. *Br. J. Pharmacol. 132*, 1017–26.

(10) Stolin, A., Wojcik, R., and Williams, M. (2006) in *Conference Record of the IEEE Nuclear Science Symposium and Medical Imaging Conference*, San Diego CA.

(11) Zheng, Y., Li, H., Wang, J., Stolin, A. V., Pole, D. J., and Williams, M. B. (2007) in *Proc. SPIE* 649804−1−649804−11.

(12) Gross, S., Gammon, S. T., Moss, B. L., Rauch, D., Harding, J., Heinecke, J. W., Ratner, L., Piwnica-Worms, D., Gross, S., Gammon, S. T., Moss, B. L., Rauch, D., Harding, J., Heinecke, J. W., Ratner, L., and Piwnica-Worms, D. (2009) Bioluminescence imaging of myeloperoxidase activity in vivo. *Nat. Med. 15*, 455–61.

(13) Liu, J., Wang, Z. T., Ji, L. L., Liu, J., Wang, Z. T., and Ji, L. L. (2007) In vivo and in vitro anti-inflammatory activities of neoandrographolide. *Am. J. Chin. Med. 35*, 317–28.
(14) Fretland, D., Gokhale, R., Mathur, L., Baron, D., Paulson, S., and Stolzenbach, J. (1995) Dermal inflammation in primates, mice, and guinea pigs attenuation by second-generation leukotriene B4 receptor antagonist, SC-53228. *Inflammation 19*, 333–46.
(15) Locke, L. W., Chordia, M. D., Zhang, Y., Kundu, B., Kennedy, D., Landseadel, J., Xiao, L., Fairchild, K. D., Berr, S. S., Linden, J., and Pan, D. (2009) A novel neutrophil-specific PET imaging agent: cFLFLFK-PEG-64Cu. *J. Nucl. Med. 50*, 790–7.

BC100063A

Annexin A5-Functionalized Bimodal Nanoparticles for MRI and Fluorescence Imaging of Atherosclerotic Plaques

Geralda A. F. van Tilborg,*[,†,‡] Esad Vucic,[§] Gustav J. Strijkers,[†] David P. Cormode,[§] Venkatesh Mani,[§] Torjus Skajaa,[§] Chris P. M. Reutelingsperger,[||] Zahi A. Fayad,[§] Willem J. M. Mulder,[§] and Klaas Nicolay[†]

Biomedical NMR, Department of Biomedical Engineering, Eindhoven University of Technology, Eindhoven, The Netherlands, Image Sciences Institute, University Medical Center Utrecht, Utrecht, The Netherlands, Translational and Molecular Imaging Institute, Mount Sinai School of Medicine, New York, New York, and Cardiovascular Research Institute Maastricht, Maastricht University, Maastricht, The Netherlands. Received February 16, 2010; Revised Manuscript Received July 1, 2010

Apoptosis and macrophage burden are believed to correlate with atherosclerotic plaque vulnerability and are therefore considered important diagnostic and therapeutic targets for atherosclerosis. These cell types are characterized by the exposure of phosphatidylserine (PS) at their surface. In the present study, we developed and applied a small micellar fluorescent annexin A5-functionalized nanoparticle for noninvasive magnetic resonance imaging (MRI) of PS exposing cells in atherosclerotic lesions. Annexin A5-mediated target-specificity was confirmed with ellipsometry and in vitro binding to apoptotic Jurkat cells. In vivo T_1-weighted MRI of the abdominal aorta in atherosclerotic ApoE$^{-/-}$ mice revealed enhanced uptake of the annexin A5-micelles as compared to control-micelles, which was corroborated with ex vivo near-infrared fluorescence images of excised whole aortas. Confocal laser scanning microscopy (CLSM) demonstrated that the targeted agent was associated with macrophages and apoptotic cells, whereas the nonspecific control agent showed no clear uptake by such cells. In conclusion, the annexin A5-conjugated bimodal micelles displayed potential for noninvasive assessment of cell types that are considered to significantly contribute to plaque instability and therefore may be of great value in the assessment of atherosclerotic lesion phenotype.

INTRODUCTION

Annexin A5, a 36 kDa protein belonging to the annexin family, is known to bind to the negatively charged phospholipid phosphatidylserine (PS) in the presence of Ca^{2+} (*1*, *2*). In almost all homeostatic cells, this phospholipid is restricted to the cytoplasmic leaflet of the plasma membrane and therefore inaccessible from the extracellular compartment (*3*). However, dying and activated cells, such as apoptotic cells, activated platelets (*4*, *5*), and activated macrophages (*6*), are known to expose PS also in the exoplasmic layer of the cell membrane. Furthermore, membrane integrity is lost during the process of necrosis, thereby allowing extracellular proteins to enter the cell (*7*). Therefore, annexin A5 has been proposed and exploited to function as a ligand to target apoptotic, necrotic, and other PS exposing cells for a variety of applications, including cell sorting, imaging, and drug targeting (*8*−*11*).

In atherosclerosis, a high occurrence of apoptosis and necrosis, as well as high macrophage burden, is believed to contribute significantly to plaque vulnerability and rupture (*12*−*15*). Consequently, identification of these markers using annexin A5-targeted noninvasive diagnostic imaging may contribute to discrimination between atherosclerotic lesions with a stable and unstable phenotype, which would be of great clinical value. To this aim, there have been a number of studies where technetium (^{99}Tc) or indium (^{111}In) -labeled annexin A5 has been used for imaging of vulnerable plaque or the effect of therapy with nuclear techniques in both experimental (*16*−*20*) and human atherosclerosis (*21*). Importantly, these studies demonstrated significant correlations between the extent of annexin A5 uptake, macrophage content, and the amount of apoptosis. Furthermore, all of these values were shown to increase with more advanced lesions, as classified according to the American Heart Association.

Although nuclear imaging is a very sensitive technique, it suffers from poor spatial resolution and the images lack detailed anatomical information. MRI is an imaging modality with a high spatial resolution and can discriminate among different plaque components (*22*). Nevertheless, MRI suffers from relatively low sensitivity (*23*). In targeted molecular MRI, the latter drawback is frequently compensated for by using high relaxivity (super)-paramagnetic imaging probes (*24*). These probes, usually nanoparticulate in nature, contain either (multiple) iron oxide crystals or a high payload of gadolinium. We and others previously reported on a number of such nanoparticles that have been successfully applied for MRI-based molecular imaging of atherosclerosis. These include target-specific lipid-based nanoparticles within the size range of 10−300 nm, such as micelles (*25*, *26*), high-density lipoproteins (HDL) (*27*), liposomes (*28*), and microemulsions (*29*), in which large numbers of Gd-DTPA moieties were incorporated in the lipid (bi)layer. Alternatively, iron oxide-based nanoparticles have been developed to enable molecular MRI of lipoproteins (*30*) or adhesion molecule expression in atherosclerotic plaques (*31*). For validation and co-localization purposes, the aforementioned nanoparticles can include additional fluorescent dyes, such as fluorescent lipids or quantum dots (*32*).

In the present study, we developed and characterized a small annexin A5-conjugated micellar nanoparticle, carrying multiple Gd-labeled lipids for MRI and fluorescent lipids for fluorescence microscopy or imaging. Target-specificity of this nanoparticle

* Corresponding author. Geralda A. F. van Tilborg, Image Sciences Institute, University Medical Center Utrecht, Yalelaan 2, 3584 CM Utrecht, The Netherlands. Phone: +31 30 2535515. E-mail: gtilborg@gmail.com.

[†] Eindhoven University of Technology.

[‡] University Medical Center Utrecht.

[§] Mount Sinai School of Medicine.

[||] Maastricht University.

10.1021/bc100091q © 2010 American Chemical Society
Published on Web 08/30/2010

for PS was examined with ellipsometry of PS-containing membranes, as well as CLSM of apoptotic Jurkat cells in vitro. Furthermore, in a pilot study, the nanoparticles were applied for in vivo MR imaging of phosphatidylserine exposing cells in atherosclerotic lesions of ApoE knockout ($ApoE^{-/-}$) mice. Ex vivo near-infrared fluorescence imaging of intact aortas was used to validate and quantify nanoparticle uptake in the lesions, while CLSM was employed to investigate which specific cell types bound the contrast agent.

EXPERIMENTAL PROCEDURES

Materials. 1,2-distearoyl-*sn*-glycero-3-phosphoethanolamine-*N*-[methoxy(poly(ethylene glycol))-2000] (PEG2000-DSPE), 1,2-distearoyl-*sn*-glycero-3-phosphoethanolamine-*N*-[maleimide-(poly(ethylene glycol))2000] (Mal-PEG2000-DSPE), 1,2-distearoyl-*sn*-glycero-3-phosphoethanolamine-*N*-[amino(poly(ethylene glycol))2000] (Amine-PEG2000-DSPE), and 1,2-dioleoyl-*sn*-glycero-3-phosphoethanolamine-*N*-(lissamine rhodamine B sulfonyl) (Rhodamine-PE) were obtained from Avanti Polar Lipids (Albaster, AL). Cy5.5 monoreactive NHS ester was obtained from GE Healthcare Europe GmbH (Amersham CyDye value packs, Diegem, Belgium). Gd-DTPA-di(stearylamide) (Gd-DTPA-DSA) was purchased from Gateway Chemical Technology (St. Louis, MO). HEPES was purchased from Merck (Darmstadt, Germany). All other chemicals were of analytic grade or of the best grade available. A Bradford protein assay kit was purchased from Bio-Rad laboratories (Veenendaal, The Netherlands).

Cy5.5-PEG2000-DSPE. Cy5.5-PEG2000-DSPE lipid was prepared by covalent conjugation of Cy5.5 monoreactive NHS ester to micellar Amine-PEG2000-DSPE. First, Amine-PEG2000-DSPE micelles were prepared by lipid film hydration. In short, 10 μmol Amine-PEG2000-DSPE was dissolved in 0.5 mL chloroform. Subsequently, a lipid film was obtained by rotary evaporation of the solvent, followed by additional drying under nitrogen flow. Next, the film was gently hydrated in 5 mL sodium bicarbonate solution (0.1 M $NaHCO_3$, pH 8.0) at 65 °C, until a clear solution was obtained. Once micelles were formed, 5 mg Cy5.5 monoreactive NHS ester was dissolved in 100 μL dimethyl sulfoxide (DMSO) and immediately added to the micelle-containing suspension. Coupling was performed via overnight incubation at 4 °C on a moving table. The resulting micelles were sequentially concentrated and resuspended in ultrapure water, using 20 mL vivaspin concentrators (Vivascience, Sartorius Stedim Biotech, 10 000 MWCO) at 3000 × *g* and 4 °C. At least five wash cycles were required to remove nonbound Cy5.5. Following the washing procedure, the Cy5.5-PEG2000-DSPE-micelle suspension was dried with a FreeZone 4.5 L benchtop freeze−dry system for three days (Labconco). The obtained lipid powder was dissolved in a 2:1 (v/v) mixture of chloroform and methanol, to a final Cy5.5-PEG-DSPE concentration of 1 μmol/mL.

Micellar Contrast Agent. Bimodal micelles were obtained by lipid film hydration of a lipid mixture, typically containing a total amount of 50 μmol lipids. Gd-DTPA-DSA, PEG2000-DSPE, and Mal-PEG2000-DSPE were added at a molar ratio of 0.5/0.4/0.1 and dissolved in chloroform/methanol 2:1 (v/v). Next, 1 mol % Cy5.5-PEG-DSPE or Rhodamine-PE was added to the lipid mixture for near-infrared fluorescence imaging or confocal microscopy, respectively. The solvent was removed by rotary evaporation, and additional drying of the lipid film was performed under nitrogen flow. Next, the lipid film was gently dissolved in 4 mL of warm HEPES buffered saline (20 mM HEPES and 135 mM NaCl, pH 6.7, 65 °C) during continuous heating at 65 °C until a clear solution was obtained.

Annexin A5 Coupling. The micellar contrast agent was functionalized with a variant of annexin A5 that has a single cysteine residue in the N-terminal tail (annexin A5-cys). The PS and apoptotic cell binding properties of annexin A5-cys are identical to those of recombinant human annexin A5 as previously shown by ellipsometry (*1*) and flow cytometry (*33*), respectively. Annexin A5-cys (~36 kDa) was covalently conjugated to the Mal-PEG2000-DSPE-containing micelles by sulfhydryl−maleimide coupling, as previously described for other lipid-based agents (*34*). In short, annexin A5-cys was reactivated with 10 mM DTT for 1.5 h at 37 °C. Next, 10 mM EDTA was added and DTT and EDTA were removed by extensive dialysis using a 12−14 kDa membrane (Pierce). Activated annexin A5-cys was added to the micelle suspension at a final concentration of 750 μg/μmol total lipid, and coupling was performed overnight at 4 °C. Subsequently, the annexin A5-micelles (AnxA5-micelles) were concentrated and resuspended at least 5 times in HEPES buffered saline (20 mM HEPES and 135 mM NaCl, pH 6.7) to remove nonconjugated annexin A5-cys, using 20 mL vivaspin concentrators (Vivascience, Sartorius Stedim Biotech, MWCO 100 000) at 3000 × *g* and 4 °C. Untargeted micelles were concentrated using the same protocol. A schematic of the preparation procedure of the annexin A5-micelles is shown in Figure 1.

Contrast Agent Characterization. Dynamic light scattering was performed on a Malvern instrument (Zetasizer, Nano-S) to determine the hydrodynamic diameter of control and anxA5-micelles in HEPES buffered saline (20 mM HEPES and 135 mM NaCl, pH 7.4), as deduced from the intensity-weighted particle size distribution. Final micelle concentration was determined by a phosphate analysis according to Rouser (*35*) after complete destruction with perchloric acid. Protein content of the AnxA5-micelles was measured according to a modified Bradford method (*36*), which corrects for lipid-associated background absorption at 750 nm by adding equivalent concentrations of control-micelles to calibration samples containing a known amount of annexin A5-cys. Relaxivity measurements were performed on a 60 MHz table top NMR spectrometer (Bruker, Minispec), at 25 and 37 °C. Relaxivities were obtained by measuring T_1 and T_2 values for serial dilutions of the Cy5.5-labeled micelles in the range 0.4−3.4 mM total lipid. T_1 relaxation times were obtained with an inversion recovery sequence, whereas T_2 values were measured using a CPMG sequence.

In Vitro Targeting. *Ellipsometry.* The interaction of the Cy5.5-labeled annexin A5-micelles with phosphatidylserine (PS) was monitored with ellipsometry as described in detail elsewhere (*34*). Untargeted micelles and unconjugated annexin A5-cys served as a control. In short, a silica plate was coated with a lipid bilayer of PS and phosphatidylcholine (PC) at a molar ratio of 20:80. The lipid-coated silica plate was placed in a sample container, filled with 5 mL of Ca^{2+}-containing binding buffer (10 mM HEPES, 150 mM NaCl, 5 mM KCl, 1 mM $MgCl_2$, 2.5 mM $CaCl_2$, pH 7.4). Micelles were added at a final concentration of 280 μM total lipid, while the final concentration of free annexin A5-cys protein was 56 nM. Binding of the particles was assessed by continuously measuring the polarization angle of the reflected elliptically polarized light. Once the polarization angle reached a steady-state value, 5 mM EDTA was added to investigate Ca^{2+}-dependent membrane association.

Apoptotic Cells. Target specificity for apoptotic cells was examined in the T-lymphoma cell line Jurkat (ATCC). Cells were grown in RPMI1640 medium (Gibco) at 37 °C in a humidified atmosphere and 5% CO_2. Medium was supplemented with 10% fetal calf serum and a mixture of antibiotics (100 units/mL penicillin and 0.1 mg/mL streptomycin; Biochrom AG). In order to induce a high level of apoptosis, Jurkat cells were resuspended to 1×10^6 cells/mL medium and treated with 200 ng/mL anti-Fas (CD95 human monoclonal antibody,

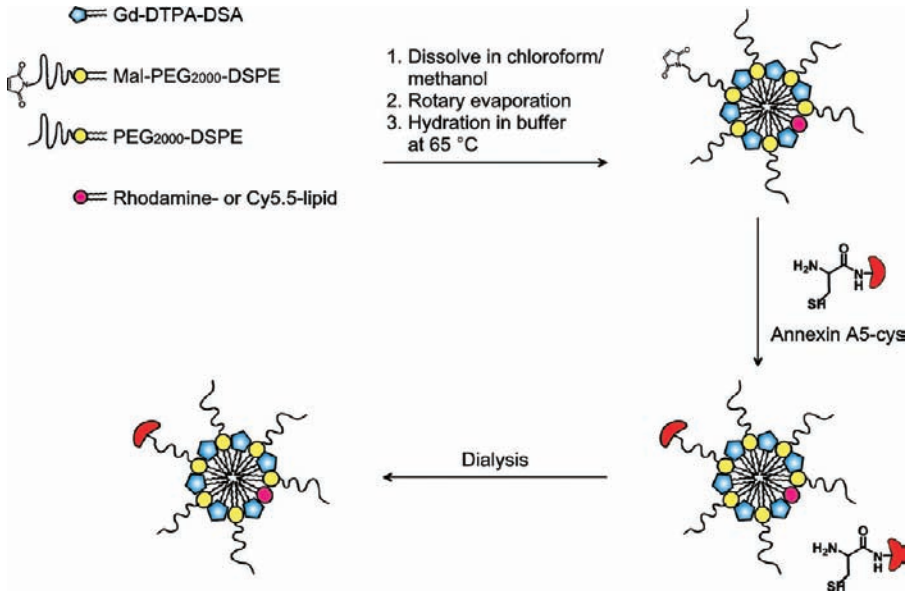


Figure 1. Schematic of nanoparticle preparation.

Beckman Coulter B.V.) for 3 h at 37 °C in a humidified atmosphere and 5% CO_2. Following this procedure, which initiated apoptosis in approximately 40−50% of the cells, cells were harvested and resuspended in Ca^{2+}-containing binding buffer to a final concentration of 2.5×10^6 cells/mL. Next, the cell suspensions were incubated with the Cy5.5-labeled annexin A5- or control-micelles for 30 min at a final concentration of 1 mM total lipid. An additional apoptotic cell sample was left untreated for comparison. Incubations were performed on a roller bench at room temperature. After the incubation procedure, cells were collected and washed at least three times in 2 mL of Ca^{2+}-containing binding buffer (300 × *g*, 5 min). Last, cells were fixed in 200 μL of 4% paraformaldehyde containing 2.5 mM $CaCl_2$.

For confocal laser scanning microscopy (CLSM), 5 μL of the resuspended fixed cell pellets were applied to poly(L-lysine) microscopy slides (Menzel-Gläser) and dried for 20 min at 55 °C. Next, the adhered cells were washed in PBS, counterstained for nuclei with DAPI (15 min; 0.1 μg/mL in PBS), washed in PBS, and mounted with Mowiol mounting medium. CLSM was performed on a Zeiss LSM 510 META NLO system (Carl Zeiss AG, Oberkochen, Germany), equipped with a multiphoton Chameleon laser and a HeNe633 laser. The Chameleon laser (780 nm) allowed excitation of DAPI, whereas the HeNe633 laser (633 nm) was used for Cy5.5 excitation. All images were obtained at 630× magnification, and imaging settings remained unchanged to allow a direct comparison of the different samples.

In Vivo Experiments. *Animals.* A total of 10 ApoE$^{-/-}$ and 2 wild-type (WT) male C57BL/6 mice were included for in vivo MRI experiments and additional ex vivo fluorescence imaging or microscopy. One additional apoE$^{-/-}$ mouse was included for ex vivo fluorescence imaging only. ApoE$^{-/-}$ mice were placed on a high-cholesterol diet (0.2% total cholesterol, Harlan Teklad, Madison, Wis) ad libitum beginning at 6 weeks until 60 to 68 weeks of age, while WT mice were maintained on a normal murine diet (Research Diets, Inc., New Brunswick, NJ). All animal experiments were approved by the ethics committee of Mount Sinai General Hospital.

MRI. In vivo MRI measurements were performed with an 89 mm vertical bore MRI system, operating at 9.4T (Bruker Instruments, Billerica, MA, USA). Mice were initially anesthetized with 4% isoflurane in oxygen (0.4 L/min) and placed head-up in a 30 mm birdcage coil for imaging (Bruker). During MRI, anesthesia was maintained using 1.5−2.0% isoflurane in oxygen (0.4 L/min) supplied through a face mask. The respiratory signal was monitored using a pressure sensor to regulate the depth of the anesthesia.

At the onset of the experiment, precontrast T_1-weighted images of the abdominal aorta in the area between the renal and aortic bifurcations were acquired using a fat-suppressed black blood spin−echo sequence with the following parameters: TR = 800 ms, TE = 8.6 ms, NEX = 16, matrix = 256 × 256, FOV = 2.6 × 2.6 cm^2, and slice thickness = 0.5 mm. For flow suppression, an inflow saturation slab of 4 mm, consisting of a 90° pulse followed by a 2 ms spoiler gradient, was positioned superior to the imaging area.

Following the precontrast scans, anesthetized mice were injected with the micellar contrast agent through the tail vein at a dose of 2.5 μmol per mouse (100 μL; 25 mM total lipid concentration). A total of 6 ApoE$^{-/-}$ mice received annexin A5-micelles fluorescently labeled with either Rhodamine-PE (n = 3) or Cy5.5-PEG2000-DSPE (n = 3). control-micelles were administrated to four ApoE$^{-/-}$ mice (Rhodamine-PE, n = 2; Cy5.5-PEG2000-DSPE, n = 2) and two WT mice received Cy5.5-labeled annexin A5-micelles.

At 24 h post-administration of the contrast agent, mice were again prepared for MR measurements. First, imaging slices were carefully matched to the precontrast images by using the unique anatomy of individual vertebrae as anatomical landmarks. Next, T_1-weighted MR images were obtained with the same parameters as used for the precontrast scans. For two ApoE$^{-/-}$ mice, the same MR protocol was additionally repeated at 48 h and 7 days after injection of the annexin A5-micelles.

Mice that underwent their last MR measurement at 24 h post-injection were immediately sacrificed by saline perfusion after the scanning procedure. Blood samples were obtained, and spleen, liver, kidney, and lung tissues were removed to investigate nanoparticle biodistribution. The abdominal aortas from mice that received Rhodamine-labeled micelles were isolated using microscopic dissection and snap-frozen in optical cutting temperature compound (Tissue Tek, Sakura Finetech) for confocal fluorescence microscopy (n = 2/group). Alternatively, whole aortas from mice that received Cy5.5-labeled micelles were excised and placed on a microscopy slide for near-infrared fluorescence imaging (NIRF, n = 2/group). For the latter procedure, the fat surrounding the abdominal aorta was carefully removed.

MR Data Analysis. Images were analyzed using *Mathematica 6* (Wolfram Research, Inc., USA). Prior to analysis, pre- and 24 h postcontrast injection measured slices were matched by the shape of the vertebrae. Slices that could not be matched were excluded from data analysis. Typically, for each ApoE$^{-/-}$ mouse 15 to 19 slices with orientations perpendicular to the abdominal aorta were analyzed. Circular regions of interest (ROIs) were drawn on the pixels in the thickened atherosclerotic vessel wall surrounding the lumen (S_w), while excluding the vessel lumen. A second ROI was drawn in a portion of the surrounding muscle (S_m). Wall signal was divided by the muscle signal to yield a normalized signal intensity $S_{norm} = S_w/S_m$ that could be compared pre- and 24 h post-contrast, as well as between mice. Signal enhancement (SE) was calculated as the average percentile difference between S_{norm} of all pre- and 24 h post-contrast slices: $[(S_{norm_post} - S_{norm_pre})/(S_{norm_pre})] \times 100\%$. WT mice were not analyzed using the above procedure, as the aortic wall in these animals could not be discriminated from surrounding tissue. Alternatively, images from WT mice were visually inspected for possible signal enhancement in the aortic wall.

Near Infrared Fluorescence Imaging. For whole-aorta near-infrared fluorescence imaging (NIRF) 1 ApoE$^{-/-}$ mouse, which received no contrast agent, was used as a control. Aortas from ApoE$^{-/-}$ mice that were injected with either control-micelles ($n = 2$) or annexin A5-micelles ($n = 2$) were collected following the in vivo MRI experiments. The dissected aortas were placed on a microscope slide and covered with gauze submerged in PBS, placed at 4 °C, and imaged within 2 h. Aortas were placed in the IVIS 200 system (Xenogen) and the Cy5.5 label was excited using a wavelength filter with a range of 615−665 nm, while the emission was recorded using a 695−770 nm filter. Fluorescent reflectance images were acquired with identical exposure times for all groups. Total photon count was determined within identical windows around the whole aorta. The mean increase in fluorescence intensity was calculated as the average percentile difference between the total photon count from the contrast-receiving group (PC_{CA}) and the total photon count from the control ApoE$^{-/-}$ mouse that received no contrast agent ($PC_{control}$): $[(PC_{CA} - PC_{control})/(PC_{control})] \times 100\%$.

Confocal Fluorescence Microscopy. 8-μm-thick frozen tissue sections were cut for confocal microscopy. Individual sections were air-dried for 10 min and blocked (PBS containing 1% BSA and 5% horse serum) for 45 min at room temperature. DNA fragmentation was detected with the TdT-mediated dUTP Nick End Labeling (TUNEL) technique, using the In Situ Cell Death Detection Kit with fluorescein isothiocyanate (FITC)-labeled dUTP (Roche, Mannheim, Germany) according to manufacturer instructions. Cells with fragmented DNA will be referred to as apoptotic. Macrophages were fluorescently stained with Alexa 647 labeled anti-CD68 antibodies (Serotec, Inc.). After washing with PBS, the sections were directly mounted with VectaShield containing 1.5 μg/mL DAPI (VectorLaboratories, Burlingame, CA) to stain cell nuclei. The sections were covered with coverslips and imaged within 12 h.

Rhodamine-labeled annexin A5-micelles and control-micelles (red) were detected and co-localized with respect to both DNA fragmentation (green) and macrophages (green) within the vessel wall 24 h after contrast agent administration using confocal laser scanning microscopy (Zeiss LSM 510 META microscope, Carl Zeiss AG, Oberkochen, Germany) in an inverted configuration. The system was equipped with four lasers and three confocal detectors, and data were captured and analyzed using Zeiss LSM 510 Meta and postprocessed with *Image Browser* software (Carl Zeiss AG, Oberkochen, Germany). All images were obtained with the same laser power and detector gain settings.

Table 1. Relaxivities of Nonspecific Control-micelles and Annexin A5-Micelles (AnxA5-micelles) in HEPES Buffered Saline at 60 MHz and Different Temperatures[a]

	25 °C		37 °C	
	r_1 (mM^{-1} s^{-1})	r_2 (mM^{-1} s^{-1})	r_1 (mM^{-1} s^{-1})	r_2 (mM^{-1} s^{-1})
Control-micelles	11.8 ± 0.1	18.5 ± 0.1	13.4 ± 0.1	20.4 ± 0.1
AnxA5-micelles	11.4 ± 0.1	19.4 ± 0.1	12.4 ± 0.1	19.9 ± 0.1

[a] Relaxivity values are based on Gadolinium concentration.

Statistics. Statistical analysis was performed for experiments with $n \geq 3$ per group. Comparisons between the two groups were performed with a Student's t test for independent samples in SPSS 16.0. $P < 0.05$ was considered significant.

RESULTS

Characterization of the Micelles. The hydrodynamic diameters of control and anxA5-micelles were 19.5 ± 0.7 nm and 22.3 ± 0.2 nm, respectively. Protein and phosphate determinations showed that on average two annexin A5-cys proteins were covalently conjugated per micelle, assuming that each micellar nanoparticle contains approximately 80 lipids (*37*). Based on the initial lipid composition, this also implies that each micelle contains approximately 1 fluorescent dye and 40 gadolinium-based lipids. The potency of a MRI contrast agent to reduce the intrinsic tissue T_1 and T_2 relaxation times, and thereby introduce tissue contrast on MR images, is described by the relaxivity values r_1 and r_2, which are expressed in mM^{-1} s^{-1}. Relaxivities r_1 and r_2 of the paramagnetic Cy5.5-labeled control-micelles and annexin A5-micelles were measured at 60 MHz and different temperatures. Importantly, similar r_1 and r_2 values were observed for the targeted versus the nontargeted micelles (Table 1). At 25 °C, the relaxivities of control-micelles were $r_1 = 11.8 \pm 0.1$ mM^{-1} s^{-1} and $r_2 = 18.5 \pm 0.1$ mM^{-1} s^{-1}, whereas for annexin A5-micelles relaxivities were $r_1 = 11.4 \pm 0.1$ mM^{-1} s^{-1} and $r_2 = 19.4 \pm 0.1$ mM^{-1} s^{-1}. These values, which are based on gadolinium concentration, are relatively high compared to clinically approved gadolinium complexes such as Gd-DTPA, for which $r_1 = 3.3$ and $r_2 = 3.9$ at 1.5 T (64 MHz) and 37 °C (*38*). An increase in temperature to 37 °C was shown to slightly elevate r_1 and r_2 for both micellar agents (Table 1).

In Vitro Targeting. Ellipsometry measurements clearly demonstrated binding of the annexin A5-micelles to a bilayer consisting of 20 mol % PS and 80 mol % phosphatidylcholine (PC), as observed by the gradually increasing polarization angle, which is known to correlate with layer thickness. The polarization angle reached a steady state at higher values compared to free annexin A5-cys (Figure 2). Binding was shown to strictly depend on annexin A5 as the polarization angle remained at baseline levels after addition of control-micelles. Furthermore, association was Ca^{2+}-dependent, as annexin A5-cys, as well as annexin A5-micelles, instantly dissociated from the bilayer upon addition of Ca^{2+}-chelating EDTA.

Micelle binding to PS-expressing cells was also examined on a Jurkat cell line using confocal laser scanning microscopy (CLSM). Apoptotic cell suspensions that were untreated (Figure 3A) or incubated with control-micelles (Figure 3B) exhibited negligible levels of Cy5.5 fluorescence, while apoptotic cells incubated with the annexin A5-micelles showed a clear cell-associated Cy5.5 signal (Figure 3C).

MRI and NIRF. In vivo precontrast T_1-weighted MR images of atherosclerotic ApoE$^{-/-}$ mice clearly revealed extensive atherosclerotic lesions in their abdominal aorta (Figure 4A,C), whereas aortas of wild-type (WT) C57BL/6 mice showed normal vessel wall morphology within the same region (Figure 4E). At 24 h post-injection of annexin A5-micelles, T_1-weighted images of the same ApoE$^{-/-}$ mice showed increased signal

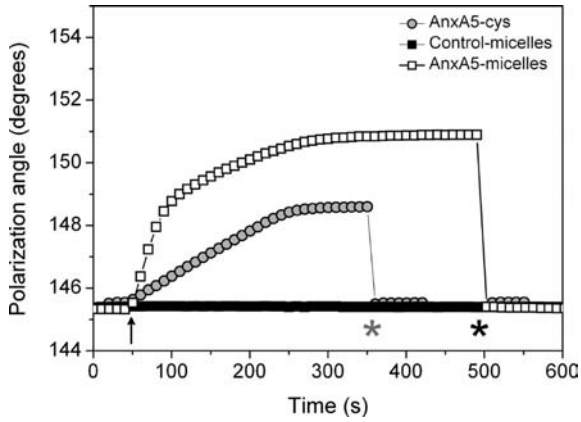


Figure 2. Ellipsometry measurements of a PS/PC (20:80) bilayer in the presence of 2.5 mM Ca^{2+} upon addition of annexin A5-cys (AnxA5-cys), annexin A5-micelles (AnxA5-micelles), and control-micelles. Micelles or protein was added at the time point indicated by the arrow. 5 mM EDTA was added at the time points indicated by the asterisks (*) to assess Ca^{2+}-dependence of binding.

intensity within the thickened aortic vessel wall (compare Figure 4C and D). Contrast enhancement within these mice persisted up to at least 7 days after injection (data not shown). Atherosclerotic lesions of $ApoE^{-/-}$ mice that were injected with control-micelles showed less signal enhancement at 24 h post-injection (compare Figure 4A and B). Moreover, no contrast changes were observed in WT mice that received annexin A5-micelles (compare Figure 4E and F).

Ex vivo near-infrared fluorescence imaging was performed on excised aortas from $ApoE^{-/-}$ mice that underwent in vivo MRI experiments and were sacrificed 24 h post-contrast agent injection. The aorta of an $ApoE^{-/-}$ mouse that received no contrast agent served as a control and showed marginal fluorescence signal due to autofluorescence (Figure 5A). In contrast, the aortas from $ApoE^{-/-}$ mice that received control-micelles (Figure 5B) or annexin A5-micelles (Figure 5C) displayed strong fluorescence signal, which was heterogeneously distributed over the entire aorta. Interestingly, aortas from mice injected with annexin A5-micelles showed multiple intense fluorescent hotspots, whereas aortas from the control micelle group revealed considerably less fluorescence in a reduced number of areas. Importantly, these hotspots were predominantly observed in areas where extensive atherosclerotic lesions were expected as described by Nakashima et al. (*39*). These areas included the aortic arch, the branching points of the renal arteries, and the aortic bifurcation (Figure 5C).

MR signal enhancement in the aortic wall also appeared highly heterogeneous throughout the examined abdominal area.

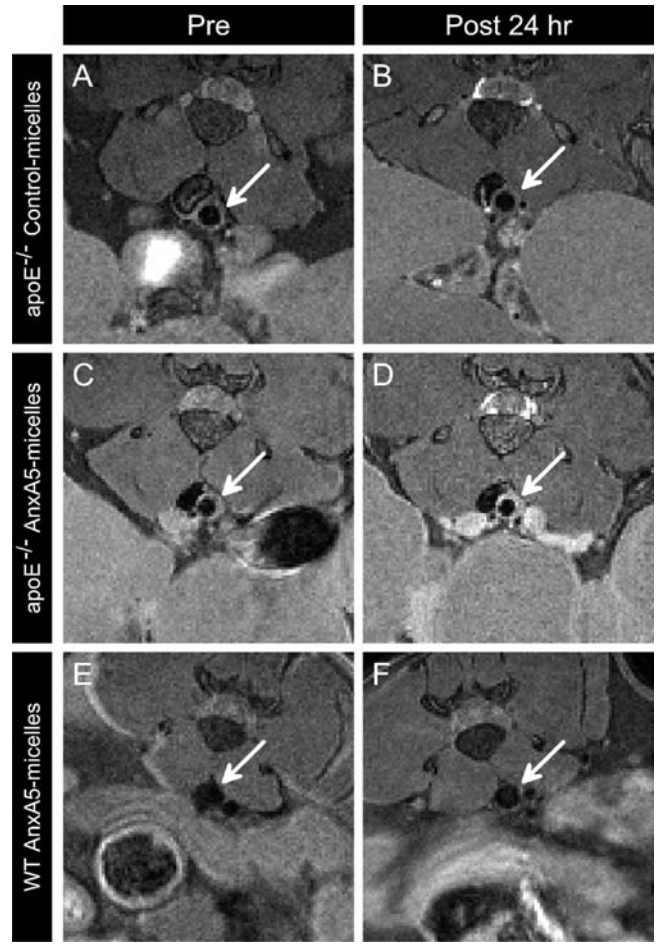


Figure 4. T_1-weighted in vivo MR images at the level of the abdominal aorta (arrow). Scans were made before (left panel) and 24 h after (right panel) contrast agent injection. $ApoE^{-/-}$ mice received either control-micelles (A,B) or annexin A5-micelles (C,D). Wild-type (WT) C57BL/6 mice only received annexin A5-micelles (E,F).

Nevertheless, all slices that were measured with in vivo MRI were used to calculate the mean signal enhancement within the vessel wall to prevent any bias by analyzing only specific slices. Mean MR signal within the examined abdominal aortic wall was calculated to be increased by $6.7 \pm 3.4\%$ and $10.7 \pm 1.7\%$ at 24 h post-administration of control or annexin A5-micelles, respectively (Figure 6A). At the same time point, the total photon count in the entire aorta was enhanced by $113.1 \pm 4.4\%$ for the control micelle group and $257.1 \pm 9.1\%$ for the annexin A5-micelle group (Figure 6B).

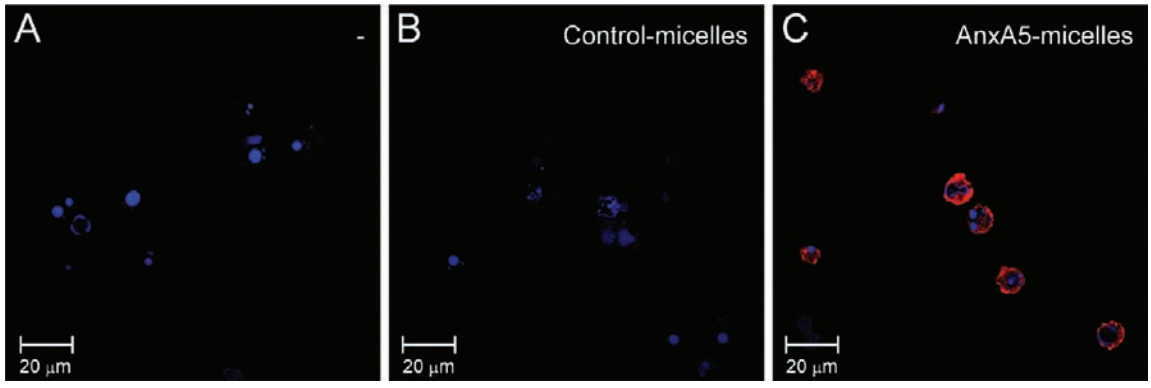


Figure 3. CLSM images of fixed apoptotic Jurkat cells after incubation with (A) no contrast agent, (B) untargeted paramagnetic control-micelles, or (C) paramagnetic annexin A5-micelles (AnxA5-micelles). Micelles contained Cy5.5-PEG2000-DSPE (red), and adhered cells were counterstained with DAPI (blue). Magnification: 630×.

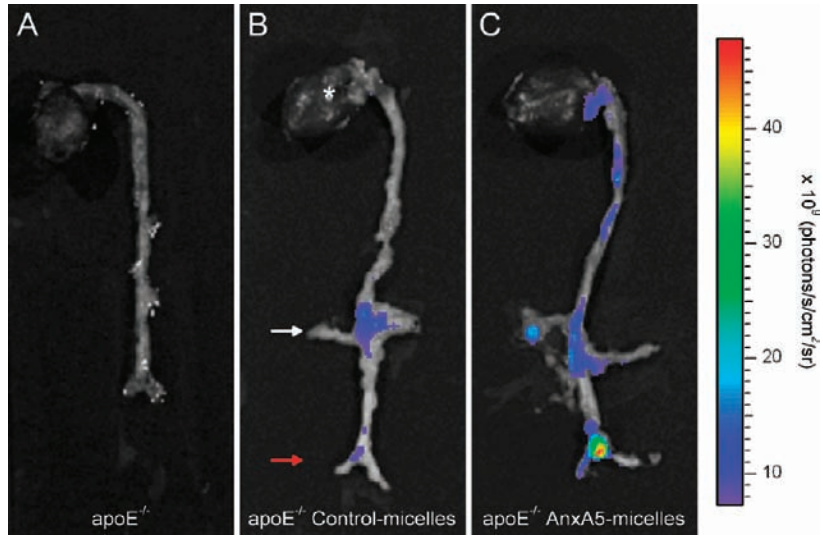


Figure 5. Ex vivo near-infrared fluorescence imaging (NIRF) of whole aortas from ApoE$^{-/-}$ mice (A) without contrast agent injection and at 24 h after injection of (B) control-micelles and (C) annexin A5-micelles. Micelles contained Cy5.5-PEG2000-DSPE. The orientation of the aorta is indicated by characteristic regions in (B), such as the heart (*), a renal branch (white arrow),and the aortic bifurcation (red arrow). In vivo MR images were acquired in the area between the white and the red arrow.

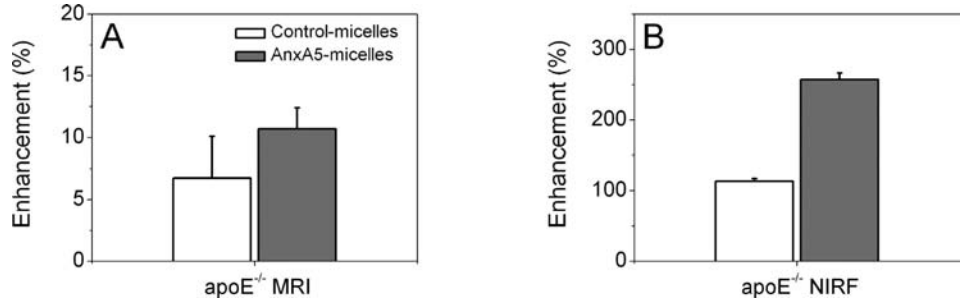


Figure 6. Quantitative analysis of MR signal enhancement in T_1-weighted images (A) and NIRF enhancement (B) at 24 h after injection of the contrast agent in ApoE$^{-/-}$ mice (B). Bars represent mean values ± SE: (A) MRI: control-micelles ($n = 4$), annexin A5-micelles ($n = 6$). NIRF: control-micelles ($n = 2$), annexin A5-micelles ($n = 2$).

Confocal Fluorescence Microscopy. Tissue sections from the abdominal aortas of the mice were examined with confocal fluorescence microscopy. Atherosclerotic lesions from ApoE$^{-/-}$ mice injected with Rhodamine-labeled control-micelles demonstrated only weak and diffuse red fluorescent signal at 24 h post-injection (Figure 7A,B), whereas bright red fluorescent hot spots were observed for ApoE$^{-/-}$ mice that received annexin A5-micelles (Figure 7C and D). In these latter mice, the annexin A5-micelles clearly colocalized with macrophages (Figure 7C) and apoptotic cells (Figure 7D) in the center of the intima. Presumably, a fraction of these macrophages are apoptotic, as previously described elsewhere (*17*). No obvious association to macrophages (Figure 7A) or apoptotic cells was observed for control-micelles (Figure 7B).

Biodistribution. At 24 h post-injection of control-micelles in ApoE$^{-/-}$ mice, the Gd content of liver and spleen was shown to be higher than that of kidneys and lungs (Figure 8A). Similar amounts of Gd were measured in the kidneys and lungs of mice that received the annexin A5-functionalized micellar contrast agent (Figure 8B). In contrast, Gd content in the liver and spleen of these mice was approximately 100% and 219% higher, respectively, compared to control-micelles. These results are in agreement with previous studies that demonstrated PS specific uptake of radiolabeled annexin A5 by the liver and spleen, while kidney accumulation appeared to be nonspecific (*40*). Importantly, preliminary studies in ApoE$^{-/-}$ mice, which were injected with the same contrast agents at equal dose, displayed similar blood clearance kinetics for control and annexin A5-micelles (data not shown). Consequently, this allows a direct comparison of the collected data from both agents.

DISCUSSION

In the current study, we developed, characterized, and evaluated the use of annexin A5-conjugated micelles for targeted MRI of atherosclerotic plaques in ApoE$^{-/-}$ mice. The micelles were composed of a paramagnetic amphiphile (Gd-DTPA-DSA) and PEGylated lipids (PEG-DSPE) in a 1:1 molar ratio. Above the so-called critical micelle concentration (CMC), PEG-DSPE forces the amphiphilic aggregation towards a micellar morphology. A near-infrared fluorophore (Cy5.5) and annexin A5 proteins were covalently conjugated to the distal ends of the PEG chains of the micelles for fluorescence imaging and target specificity, respectively. Alternatively, Rhodamine-PE, instead of Cy5.5-PEG2000-DSPE, was incorporated in the lipid monolayer for confocal fluorescence microscopy. Ellipsometry measurements on PS/PC bilayers and experiments with apoptotic Jurkat cells were performed to assess the target-specificity of the annexin A5-micelles in vitro. Furthermore, in vivo MRI of the abdominal aortas from apoA$^{-/-}$ mice and ex vivo fluorescence methods on excised aortas of the same mice were used to image the uptake of control and annexin A5-micelles in atherosclerotic lesions, as well as to validate their cellular targets following intravenous injection.

MR molecular imaging of vascular targets is usually done with nanoparticles that carry a high payload of contrast-

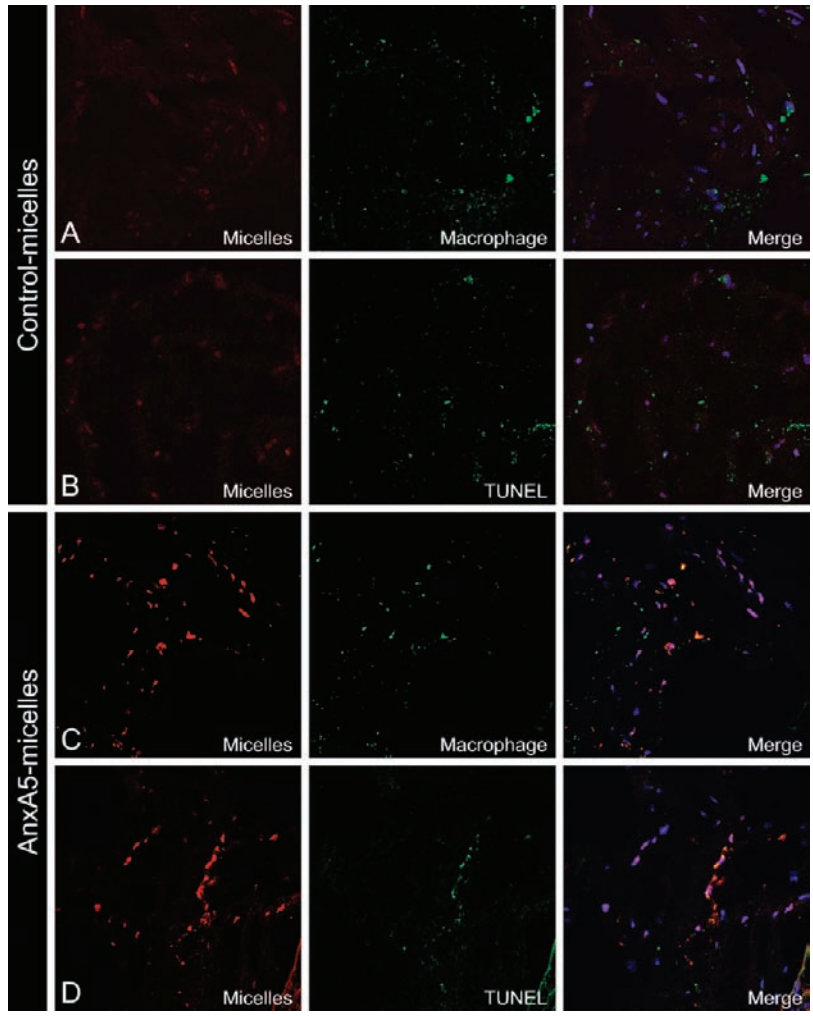


Figure 7. Confocal fluorescence microscopy of frozen sections from abdominal aortas of ApoE$^{-/-}$ mice at 24 h after administration of (A,B) control-micelles or (C,D) annexin A5-micelles (red). Sections were counterstained for (A,C) macrophages with anti-CD68 (green) or (C,D) apoptotic cells with TUNEL (green). Nuclei were stained with DAPI. Magnification: 400×.

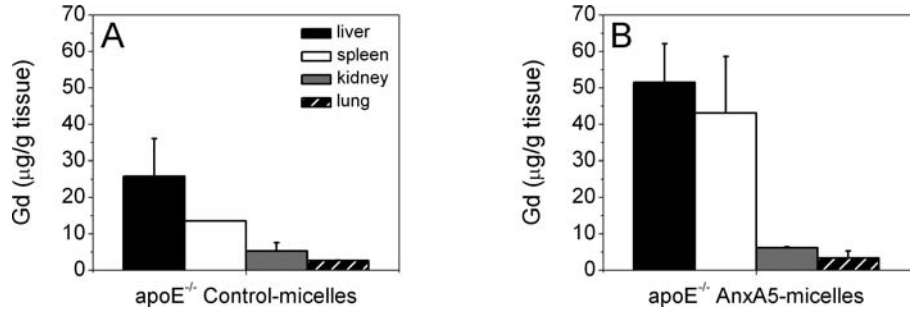


Figure 8. Biodistribution of control-micelles (A) and annexin A5-micelles (B) at 24 h post-injection in ApoE$^{-/-}$ mice, as measured by ICP-MS of Gd content indicated in micrograms per gram of tissue. Bars represent average ± SD (n = 2/group).

generating material (*41*, *42*). After intravenous administration, such nanoparticulate agents do not require extravasation from the vasculature to bind to their target, and therefore, nanoparticle size is less critical. However, when extravascular targeting is to be accomplished, e.g. in case of intraplaque targeting, a small particle size is more favorable, to allow penetration of the endothelium. Recently, Burtea et al. reported on a novel PS-specific peptide that was conjugated to a single Gd-DTPA, which successfully allowed MRI of PS exposing cells in atherosclerotic plaques (*43*). Furthermore, Schellenberger et al. reported on a PS-specific superparamagnetic iron oxide-based MRI contrast agent with a hydrodynamic diameter of approximately 15 nm, i.e. annexin A5-VSOP (*44*). However, this nanoparticle was only applied in an in vitro setting. In the current study, we developed and applied annexin A5-functionalized paramagnetic micellar nanoparticles of similar size. This relatively small size facilitates extravasation in areas with enhanced endothelial permeability, such as atherosclerotic lesions.

Ellipsometry measurements revealed a Ca^{2+}-dependent affinity of the annexin A5-conjugated micelles for a lipid bilayer that contained 20% PS, whereas nonspecific control-micelles did not bind to a similar bilayer. These results were corroborated by CLSM images of apoptotic cells, which showed abundant association of annexin A5-functionalized micelles, whereas control-micelles were barely detected.

For in vivo MRI experiments, we used a dosage that is typical for targeted MR contrast agents, i.e., 50 μmol Gd per kilogram of body weight. MRI revealed pronounced and heterogeneously distributed hyperintense areas throughout plaque-rich regions in the abdominal aorta at 24 h after administration of annexin A5-functionalized micelles. Such enhanced regions were also observed in the untargeted control micelle group, but to a lower extent. To enable comparison of both groups, the signal enhancement for each slice was calculated and averaged for all acquired imaging slices, thereby disregarding heterogeneous distribution of the contrast agent. Data analysis revealed that the mean signal enhancement throughout the abdominal aorta was nonsignificantly higher for mice that received annexin A5-micelles than for control micelle-injected mice. In both cases, the enhancement was, however, modest compared to macrophage scavenger receptor (MSR) targeted micellar contrast agents that were applied at a dose of 75 μmol Gd per kilogram of body weight (*26*).

In vivo MRI observations were compared to ex vivo fluorescence imaging of excised aortas. The mean photon count of aortas that originated from mice injected with annexin A5-micelles was at least twice that of the aortas from control micelle injected mice. In addition, near-infrared fluorescence imaging allowed us to investigate the entire aorta. The most pronounced uptake of annexin A5-micelles was observed in the aortic arch, at principal branches of the abdominal aorta, such as the renal arteries, and at the aortic bifurcation into the iliac arteries. Isobe et al. observed distinct uptake of ^{99m}Tc-labeled annexin A5 in similar regions of the aorta in ApoE$^{-/-}$ mice (*17*). Importantly, these regions are known to correspond to a high plaque burden (*39*), which was the case in this study as well. However, one should note that the in vivo MR images were acquired in the abdominal aorta in the area between the renal and aortic bifurcations. This implies that certain regions with intense uptake of the micellar contrast agent were not included in the in vivo MRI scans, which could partially explain the observed difference in signal enhancement between MRI and NIRF imaging. Future imaging studies should therefore cover a larger area of the abdominal aorta, or alternatively, another animal model could be used, with well-defined locations and phenotype of atherosclerotic plaque within the carotid artery (*45*).

Ex vivo confocal fluorescence microscopy revealed association of annexin A5-micelles to PS-expressing cells, such as apoptotic cells and macrophages, within atherosclerotic lesions in the abdominal aorta. A large fraction of these apoptotic cells are considered dying macrophages, whereas the remaining fraction most likely consists of smooth muscle cells (*46*). The annexin A5-functionalized contrast agent was most probably also associated with viable macrophages, as previously observed for biotinylated annexin A5 (*17*). Macrophages in atherosclerotic lesions are also known to nonspecifically engulf nanoparticulate agents such as USPIOs (*47*). Nevertheless, CLSM images of tissue sections from control micelle-injected mice revealed no macrophage-associated micellar fluorescence. Presumably, the cell-associated contrast agents observed in the CLSM images were internalized, which may have led to a quenched T_1 effect due to limited water exchange with the bulk (*48, 49*). Such an effect may provide a second explanation for the apparent discrepancy between the modest signal enhancement of annexin A5-micelles in the in vivo MR images and the large difference in micellar fluorescence from control and annexin A5-micelles in the ex vivo CLSM images.

At present, there is an urgent need to discriminate vulnerable atherosclerotic lesions from stable lesions. Current diagnostic methods used in the clinic are primarily focused on visualizing narrowing of the lumen but do not reveal plaque composition and thus do not predict the risk of rupture accurately (*23*). In the past decade, traditional high-resolution MRI techniques have been developed to enable plaque characterization by visualizing features such as the lipid-rich core and fibrous cap size. The biochemistry that lies at the basis of plaque formation may be investigated using MRI-based molecular imaging techniques. For example, MR imaging of the macrophage burden has been investigated with ultrasmall iron oxide nanoparticles (USPIO) (*47*), while the expression of cell adhesion molecules was visualized using VCAM-1 targeted cross-linked iron oxide nanoparticles (CLIO) (*31*). Furthermore, annexin A5-functionalized iron oxide particles were applied to image PS-expressing cells in a preliminary study on a limited number of animals (*50*). The disadvantage of such strategies is that iron oxide-based imaging relies on the use of so-called $T_2^{(*)}$-weighted MRI, in which regions of high iron oxide content appear dark. These spots are hard to localize in images that usually already have a low signal-to-noise ratio. Therefore, more recent investigations primarily focus on the application of T_1-reducing agents that appear bright in T_1-weighted MR images (*25, 29, 43*), as is the case in our study. The paramagnetic nanoparticulate agent introduced in the present study exhibited enhanced accumulation in plaque by the conjugation of annexin A5. This phenomenon may also be applied to shuttle therapeutically active compounds, such as anti-inflammatory agents or nucleotides, into plaque.

In the present study, a dose of 1.9 mg annexin A5 was administered per mouse, which was well tolerated by the animals. However, this dose is considered unfeasible in clinical studies. Ideally, small molecules such as peptides or peptidomimetics, with a high affinity for PS, need to be developed for clinical translation. Alternatively, and despite the previously mentioned disadvantages, small iron oxide nanoparticles may be employed. These nanoparticles represent a more sensitive MRI contrast agent and are typically injected at a 100-fold lower particle dose, which also decreases the Annexin A5 dose by a factor 100.

In conclusion, the present study demonstrated the potential of an annexin A5-functionalized micellar contrast agent for target-specific imaging of PS-expressing cells in atherosclerotic lesions of ApoE$^{-/-}$ mice. Such imaging strategies are of great diagnostic potential as the abundance of PS expressing cells is considered an important prognostic marker of plaque vulnerability. Interestingly, the presented nanoparticulate platform may be simultaneously exploited for therapeutic purposes, thereby facilitating a wide range of clinically relevant applications for improved diagnostics, as well as therapeutic interventions in atherosclerotic cardiovascular disease.

ACKNOWLEDGMENT

This project was funded by the BSIK program entitled Molecular Imaging of Ischemic Heart Disease (project number BSIK03033). Part of this research was funded by the ED-FP6-project DiMI, LSHB-CT-2005-512146, and carried out within the framework of the European Cooperation in the field of Scientific and Technical Research (COST) D38 Action Metal Based Systems for Molecular Imaging Applications. Furthermore, this research was supported by a travel grant awarded by The Netherlands Organization for Scientific Research (NWO). Part of this work was supported by European Union grant Euregional PACT II (IVA-VLANED-1.20).

LITERATURE CITED

(1) Andree, H. A., Reutelingsperger, C. P., Hauptmann, R., Hemker, H. C., Hermens, W. T., and Willems, G. M. (1990) Binding of vascular anticoagulant alpha (VAC alpha) to planar phospholipid bilayers. *J. Biol. Chem. 265,* 4923–8.

(2) Gerke, V., and Moss, S. E. (2002) Annexins: from structure to function. *Physiol. Rev. 82*, 331–71.
(3) Devaux, P. F., and Zachowski, A. (1994) Maintenance and consequences of membrane phospholipid asymmetry. *Chem. Phys. Lipids 73*, 107–120.
(4) Zwaal, R. F., Comfurius, P., and Bevers, E. M. (2005) Surface exposure of phosphatidylserine in pathological cells. *Cell. Mol. Life Sci. 62*, 971–88.
(5) Schroit, A. J., and Zwaal, R. F. (1991) Transbilayer movement of phospholipids in red cell and platelet membranes. *Biochim. Biophys. Acta 1071*, 313–29.
(6) Callahan, M. K., Williamson, P., and Schlegel, R. A. (2000) Surface expression of phosphatidylserine on macrophages is required for phagocytosis of apoptotic thymocytes. *Cell Death Differ. 7*, 645–53.
(7) van Engeland, M., Nieland, L. J., Ramaekers, F. C., Schutte, B., and Reutelingsperger, C. P. (1998) Annexin V-affinity assay: a review on an apoptosis detection system based on phosphatidylserine exposure. *Cytometry 31*, 1–9.
(8) Halbreich, A., Roger, J., Pons, J. N., Geldwerth, D., Da Silva, M. F., Roudier, M., and Bacri, J. C. (1998) Biomedical applications of maghemite ferrofluid. *Biochimie 80*, 379–90.
(9) Vermes, I., Haanen, C., and Reutelingsperger, C. (2000) Flow cytometry of apoptotic cell death. *J. Immunol. Methods 243*, 167–90.
(10) Boersma, H. H., Kietselaer, B. L., Stolk, L. M., Bennaghmouch, A., Hofstra, L., Narula, J., Heidendal, G. A., and Reutelingsperger, C. P. (2005) Past, present, and future of annexin A5: from protein discovery to clinical applications. *J. Nucl. Med. 46*, 2035–50.
(11) Kenis, H., Hofstra, L., and Reutelingsperger, C. P. (2007) Annexin A5: shifting from a diagnostic towards a therapeutic realm. *Cell. Mol. Life Sci. 64*, 2859–62.
(12) Davies, M. J., Richardson, P. D., Woolf, N., Katz, D. R., and Mann, J. (1993) Risk of thrombosis in human atherosclerotic plaques: role of extracellular lipid, macrophage, and smooth muscle cell content. *Br. Heart J. 69*, 377–81.
(13) Kolodgie, F. D., Narula, J., Burke, A. P., Haider, N., Farb, A., Hui-Liang, Y., Smialek, J., and Virmani, R. (2000) Localization of apoptotic macrophages at the site of plaque rupture in sudden coronary death. *Am. J. Pathol. 157*, 1259–68.
(14) Libby, P., Geng, Y. J., Aikawa, M., Schoenbeck, U., Mach, F., Clinton, S. K., Sukhova, G. K., and Lee, R. T. (1996) Macrophages and atherosclerotic plaque stability. *Curr. Opin. Lipidol. 7*, 330–5.
(15) Li, W., Hellsten, A., Jacobsson, L. S., Blomqvist, H. M., Olsson, A. G., and Yuan, X. M. (2004) Alpha-tocopherol and astaxanthin decrease macrophage infiltration, apoptosis and vulnerability in atheroma of hyperlipidaemic rabbits. *J. Mol. Cell Cardiol. 37*, 969–78.
(16) Kolodgie, F. D., Petrov, A., Virmani, R., Narula, N., Verjans, J. W., Weber, D. K., Hartung, D., Steinmetz, N., Vanderheyden, J. L., Vannan, M. A., Gold, H. K., Reutelingsperger, C. P., Hofstra, L., and Narula, J. (2003) Targeting of apoptotic macrophages and experimental atheroma with radiolabeled annexin V: a technique with potential for noninvasive imaging of vulnerable plaque. *Circulation 108*, 3134–9.
(17) Isobe, S., Tsimikas, S., Zhou, J., Fujimoto, S., Sarai, M., Branks, M. J., Fujimoto, A., Hofstra, L., Reutelingsperger, C. P., Murohara, T., Virmani, R., Kolodgie, F. D., Narula, N., Petrov, A., and Narula, J. (2006) Noninvasive imaging of atherosclerotic lesions in apolipoprotein E-deficient and low-density-lipoprotein receptor-deficient mice with annexin A5. *J. Nucl. Med. 47*, 1497–505.
(18) Haider, N., Hartung, D., Fujimoto, S., Petrov, A., Kolodgie, F. D., Virmani, R., Ohshima, S., Liu, H., Zhou, J., Fujimoto, A., Tahara, A., Hofstra, L., Narula, N., Reutelingsperger, C., and Narula, J. (2009) Dual molecular imaging for targeting metalloproteinase activity and apoptosis in atherosclerosis: molecular imaging facilitates understanding of pathogenesis. *J. Nucl. Cardiol. 16*, 753–62.
(19) Hartung, D., Sarai, M., Petrov, A., Kolodgie, F., Narula, N., Verjans, J., Virmani, R., Reutelingsperger, C., Hofstra, L., and Narula, J. (2005) Resolution of apoptosis in atherosclerotic plaque by dietary modification and statin therapy. *J. Nucl. Med. 46*, 2051–6.
(20) Sarai, M., Hartung, D., Petrov, A., Zhou, J., Narula, N., Hofstra, L., Kolodgie, F., Isobe, S., Fujimoto, S., Vanderheyden, J. L., Virmani, R., Reutelingsperger, C., Wong, N. D., Gupta, S., and Narula, J. (2007) Broad and specific caspase inhibitor-induced acute repression of apoptosis in atherosclerotic lesions evaluated by radiolabeled annexin A5 imaging. *J. Am. Coll. Cardiol. 50*, 2305–12.
(21) Kietselaer, B. L., Reutelingsperger, C. P., Heidendal, G. A., Daemen, M. J., Mess, W. H., Hofstra, L., and Narula, J. (2004) Noninvasive detection of plaque instability with use of radiolabeled annexin A5 in patients with carotid-artery atherosclerosis. *N. Engl. J. Med. 350*, 1472–3.
(22) Cappendijk, V. C., Cleutjens, K. B., Kessels, A. G., Heeneman, S., Schurink, G. W., Welten, R. J., Mess, W. H., Daemen, M. J., van Engelshoven, J. M., and Kooi, M. E. (2005) Assessment of human atherosclerotic carotid plaque components with multisequence MR imaging: initial experience. *Radiology 234*, 487–92.
(23) Sanz, J., and Fayad, Z. A. (2008) Imaging of atherosclerotic cardiovascular disease. *Nature 451*, 953–7.
(24) Mulder, W. J., Strijkers, G. J., van Tilborg, G. A., Griffioen, A. W., and Nicolay, K. (2006) Lipid-based nanoparticles for contrast-enhanced MRI and molecular imaging. *NMR Biomed. 19*, 142–64.
(25) Amirbekian, V., Lipinski, M. J., Briley-Saebo, K. C., Amirbekian, S., Aguinaldo, J. G., Weinreb, D. B., Vucic, E., Frias, J. C., Hyafil, F., Mani, V., Fisher, E. A., and Fayad, Z. A. (2007) Detecting and assessing macrophages in vivo to evaluate atherosclerosis noninvasively using molecular MRI. *Proc. Natl. Acad. Sci. U.S.A. 104*, 961–6.
(26) Mulder, W. J., Strijkers, G. J., Briley-Saboe, K. C., Frias, J. C., Aguinaldo, J. G., Vucic, E., Amirbekian, V., Tang, C., Chin, P. T., Nicolay, K., and Fayad, Z. A. (2007) Molecular imaging of macrophages in atherosclerotic plaques using bimodal PEG-micelles. *Magn. Reson. Med. 58*, 1164–70.
(27) Cormode, D. P., Chandrasekar, R., Delshad, A., Briley-Saebo, K. C., Calcagno, C., Barazza, A., Mulder, W. J., Fisher, E. A., and Fayad, Z. A. (2009) Comparison of synthetic high density lipoprotein (HDL) contrast agents for MR imaging of atherosclerosis. *Bioconjugate Chem. 20*, 937–943.
(28) Mulder, W. J., Douma, K., Koning, G. A., van Zandvoort, M. A., Lutgens, E., Daemen, M. J., Nicolay, K., and Strijkers, G. J. (2006) Liposome-enhanced MRI of neointimal lesions in the ApoE-KO mouse. *Magn. Reson. Med. 55*, 1170–4.
(29) Winter, P. M., Morawski, A. M., Caruthers, S. D., Fuhrhop, R. W., Zhang, H., Williams, T. A., Allen, J. S., Lacy, E. K., Robertson, J. D., Lanza, G. M., and Wickline, S. A. (2003) Molecular imaging of angiogenesis in early-stage atherosclerosis with alpha(v)beta3-integrin-targeted nanoparticles. *Circulation 108*, 2270–4.
(30) Cormode, D. P., Skajaa, T., van Schooneveld, M. M., Koole, R., Jarzyna, P., Lobatto, M. E., Calcagno, C., Barazza, A., Gordon, R. E., Zanzonico, P., Fisher, E. A., Fayad, Z. A., and Mulder, W. J. (2008) Nanocrystal core high-density lipoproteins: a multimodality contrast agent platform. *Nano Lett. 8*, 3715–23.
(31) Nahrendorf, M., Jaffer, F. A., Kelly, K. A., Sosnovik, D. E., Aikawa, E., Libby, P., and Weissleder, R. (2006) Noninvasive vascular cell adhesion molecule-1 imaging identifies inflammatory activation of cells in atherosclerosis. *Circulation 114*, 1504–11.
(32) Mulder, W. J., Griffioen, A. W., Strijkers, G. J., Cormode, D. P., Nicolay, K., and Fayad, Z. A. (2007) Magnetic and fluorescent nanoparticles for multimodality imaging. *Nanomedicine 2*, 307–24.

(33) Vermes, I., Haanen, C., Steffens-Nakken, H., and Reutelingsperger, C. (1995) A novel assay for apoptosis. Flow cytometric detection of phosphatidylserine expression on early apoptotic cells using fluorescein labelled Annexin V. *J. Immunol. Methods 184*, 39–51.

(34) van Tilborg, G. A., Mulder, W. J., Deckers, N., Storm, G., Reutelingsperger, C. P., Strijkers, G. J., and Nicolay, K. (2006) Annexin A5-functionalized bimodal lipid-based contrast agents for the detection of apoptosis. *Bioconjugate Chem. 17*, 741–9.

(35) Rouser, G., Fkeischer, S., and Yamamoto, A. (1970) Two dimensional thin layer chromatographic separation of polar lipids and determination of phospholipids by phosphorus analysis of spots. *Lipids 5*, 494–6.

(36) Bradford, M. M. (1976) A rapid and sensitive method for the quantitation of microgram quantities of protein utilizing the principle of protein-dye binding. *Anal. Biochem. 72*, 248–54.

(37) Ashok, B., Arleth, L., Hjelm, R. P., Rubinstein, I., and Onyuksel, H. (2004) In vitro characterization of PEGylated phospholipid micelles for improved drug solubilization: effects of PEG chain length and PC incorporation. *J. Pharm. Sci. 93*, 2476–87.

(38) Port, M., Idee, J. M., Medina, C., Robic, C., Sabatou, M., and Corot, C. (2008) Efficiency, thermodynamic and kinetic stability of marketed gadolinium chelates and their possible clinical consequences: a critical review. *Biometals 21*, 469–90.

(39) Nakashima, Y., Plump, A. S., Raines, E. W., Breslow, J. L., and Ross, R. (1994) ApoE-deficient mice develop lesions of all phases of atherosclerosis throughout the arterial tree. *Arterioscler. Thromb. 14*, 133–40.

(40) Tait, J. F., Smith, C., and Blankenberg, F. G. (2005) Structural requirements for in vivo detection of cell death with 99mTc-annexin V. *J. Nucl. Med. 46*, 807–15.

(41) Mulder, W. J., Strijkers, G. J., Habets, J. W., Bleeker, E. J., van der Schaft, D. W., Storm, G., Koning, G. A., Griffioen, A. W., and Nicolay, K. (2005 MR molecular imaging and fluorescence microscopy for identification of activated tumor endothelium using a bimodal lipidic nanoparticle. *FASEB J. 19*, 2008–10.

(42) Winter, P. M., Caruthers, S. D., Kassner, A., Harris, T. D., Chinen, L. K., Allen, J. S., Lacy, E. K., Zhang, H., Robertson, J. D., Wickline, S. A., and Lanza, G. M. (2003) Molecular imaging of angiogenesis in nascent Vx-2 rabbit tumors using a novel alpha(nu)beta3-targeted nanoparticle and 1.5 T magnetic resonance imaging. *Cancer Res. 63*, 5838–43.

(43) Burtea, C., Laurent, S., Lancelot, E., Ballet, S., Murariu, O., Rousseaux, O., Port, M., Vander Elst, L., Corot, C., and Muller, R. N. (2009) Peptidic targeting of phosphatidylserine for the MRI detection of apoptosis in atherosclerotic plaques. *Mol. Pharm. 6*, 1903–19.

(44) Schellenberger, E., Schnorr, J., Reutelingsperger, C., Ungethum, L., Meyer, W., Taupitz, M., and Hamm, B. (2008) Linking proteins with anionic nanoparticles via protamine: ultrasmall protein-coupled probes for magnetic resonance imaging of apoptosis. *Small 4*, 225–30.

(45) Cheng, C., Tempel, D., van Haperen, R., van der Baan, A., Grosveld, F., Daemen, M. J., Krams, R., and de Crom, R. (2006) Atherosclerotic lesion size and vulnerability are determined by patterns of fluid shear stress. *Circulation 113*, 2744–53.

(46) Harada, K., Chen, Z., Ishibashi, S., Osuga, J., Yagyu, H., Ohashi, K., Yahagi, N., Shionoiri, F., Sun, L., Yazaki, Y., and Yamada, N. (1997) Apoptotic cell death in atherosclerotic plaques of hyperlipidemic knockout mice. *Atherosclerosis 135*, 235–9.

(47) Ruehm, S. G., Corot, C., Vogt, P., Kolb, S., and Debatin, J. F. (2001) Magnetic resonance imaging of atherosclerotic plaque with ultrasmall superparamagnetic particles of iron oxide in hyperlipidemic rabbits. *Circulation 103*, 415–22.

(48) Strijkers, G. J., Hak, S., Kok, M. B., Springer, C. S., Jr., and Nicolay, K. (2009) Three-compartment T1 relaxation model for intracellular paramagnetic contrast agents. *Magn. Reson. Med. 61*, 1049–58.

(49) Terreno, E., Geninatti Crich, S., Belfiore, S., Biancone, L., Cabella, C., Esposito, G., Manazza, A. D., and Aime, S. (2006) Effect of the intracellular localization of a Gd-based imaging probe on the relaxation enhancement of water protons. *Magn. Reson. Med. 55*, 491–7.

(50) Smith, B. R., Heverhagen, J., Knopp, M., Schmalbrock, P., Shapiro, J., Shiomi, M., Moldovan, N. I., Ferrari, M., and Lee, S. C. (2007) Localization to atherosclerotic plaque and biodistribution of biochemically derivatized superparamagnetic iron oxide nanoparticles (SPIONs) contrast particles for magnetic resonance imaging (MRI). *Biomed. Microdevices 9*, 719–27.

BC100091Q

Carboxyl-Terminated PAMAM-SN38 Conjugates: Synthesis, Characterization, and in Vitro Evaluation

Nirmalkumar Vijayalakshmi,[†,§] Abhijit Ray,[†,§] Alexander Malugin,[†,§] and Hamidreza Ghandehari*[,†,‡,§]

Departments of Pharmaceutics and Pharmaceutical Chemistry and Bioengineering, and Utah Center for Nanomedicine, Nano Institute of Utah, University of Utah, Salt Lake City, Utah 84108. Received February 16, 2010; Revised Manuscript Received August 27, 2010

In this work, carboxyl-terminated PAMAM G-3.5 was covalently attached to SN38 via glycine and β-alanine spacers. The conjugates were stable at pH 7.4 and moderately hydrolyzed in cell culture media and rat plasma. Similarly to SN38 but to a lesser extent, both conjugates inhibited proliferation of human colorectal cancer HCT-116 cells, arrested the cell cycle in the G_2/M phase, and led to nuclear fragmentation. However, activity of the conjugate with glycine spacer (IC_{50} = 129 nM) was higher compared to that of the β-alanine linked conjugate (IC_{50} = 387 nM). These PAMAM-SN38 conjugates have the potential for targeted therapy of colorectal carcinoma.

INTRODUCTION

Polymeric drug carriers have emerged as promising alternatives to small molecule therapeutics due to their many advantages over parent drugs, which include enhanced aqueous solubility, reduced systemic toxicity, and improved efficacy (*1, 2*). In this context, dendrimers have emerged as promising candidates for targeted delivery of chemotherapeutics. They are nanometer-sized and have multiple surface groups and low polydispersity. The large number of functionalizable sites at the periphery of the dendrimers allows facile attachment of multiple drugs, targeting moieties, and imaging agents. Pharmaceutical compounds can also be physically encapsulated in the dendrimer interior to enhance water solubility and reduce toxicity (*3, 4*).

7-Ethyl-10-hydroxy camptothecin (SN38) is a chemotherapeutic agent belonging to the camptothecin family of high-potency topoisomerase I inhibitors (*5, 6*). It has extremely low water solubility and is not used directly for clinical applications. CPT-11 (Irinotecan) is the water-soluble prodrug of SN38 which is currently approved for colorectal cancer. However, it is 100−1000 times less active than SN38, causes gastrointestinal toxicity, and, similarly to SN38, has poor oral bioavailability (*7, 8*). Additionally, the pharmacologically important lactone ring in irinotecan is converted to the inactive carboxylate form in the presence of human plasma albumin (*9*). A promising approach to increase the solubility of SN38 and facilitate delivery to the site of action is attachment to water-soluble polymeric carriers (*10, 11*) or antibodies (*12*). Recently, we demonstrated that complexation of SN38 with amine-terminated generation 4 PAMAM (poly(amido amine)) dendrimers (G4-NH2) enhances water solubility of the drug and increases cellular uptake and transepithelial transport across Caco-2 cells (*13*). While such complexes show promise in oral drug delivery, covalent conjugation of SN38 to dendrimers can impart greater stability, prevent premature release, and facilitate targeted delivery (*14*). In addition, we have previously demonstrated in vitro that concentration, generation of dendrimer, and incubation time influence the toxicity observed with cationic PAMAM dendrimers, whereas under similar conditions, carboxyl-terminated anionic dendrimers have shown less toxicity yet maintained comparable transepithelial transport (*15, 16*). These observations, along with the inherent advantages of polymeric drug delivery systems, suggest that development of anionic PAMAM-SN38 conjugates can increase the bioavailability of the drug, increase its efficacy, and reduce toxicity. Here, we report the synthesis, characterization, and in vitro stability and activity of G3.5-SN38 conjugates in a colorectal cancer cell model.

EXPERIMENTAL PROCEDURES

PAMAM G3.5 dendrimer, *N*-(*tert*-butoxycarbonyl)glycine, *N*-(*tert*-butoxycarbonyl)beta alanine, *N*-ethyl-*N*′-(3-dimethylaminopropyl)carbodiimide (EDC), *N*-hydroxy succinimide (NHS), 4-(dimethylamino)pyridine (DMAP), *N*,*N*-diisopropylethylamine (DIPEA), and di-*tert*-butyl dicarbonate (Boc_2O) were obtained from Aldrich, (St. Louis, MO, USA). 7-Ethyl-10-hydroxy camptothecin (SN38) was obtained from AK Scientific Company (California, USA), and its purity was determined by ^{1}H NMR and HPLC. Anyhdrous dichloromethane (DCM) and dimethylsulfoxide (DMSO) were purchased and used without further purification.

^{1}H NMR of intermediates and conjugates was recorded on a Bruker 400 or Varian Unity 500 MHz spectrophotometer. Size exclusion chromatography (SEC) for characterization and purification of G3.5−drug conjugates were performed on an Akta fast protein liquid chromatography (FPLC) system, using Superose12 analytical and Hiload 16/60 Superdex 75 preparative-grade columns (GE, USA) respectively. The dendrimer peak was analyzed to determine the hydrodynamic radius using a Wyatt quasi-elastic light scattering detector (QELS), and the calculations were performed using the *Astra 5.3.4* software. All samples were run in triplicate. Reverse-phase high performance liquid chromatography (HPLC) was performed on a Hewlett Packard series 1100 instrument using an Agilent C18 column, 250 mm ×4.5 mm.

Synthesis of SN38-gly (3). The overall synthetic strategy is depicted in Scheme 1. SN38 derivatized at the 20-OH with a glycine spacer was synthesized according to a reported protocol

* To whom correspondence should be addressed. Hamidreza Ghandehari, Departments of Pharmaceutics and Pharmaceutical Chemistry and Bioengineering, Utah Center for Nanomedicine, Nano Institute of Utah, University of Utah. 383 Colorow Road, Salt Lake City, UT 84108. E-mail: hamid.ghandehari@pharm.utah.edu, Phone: (801) 587-1566, FAX: (801) 585-0575.

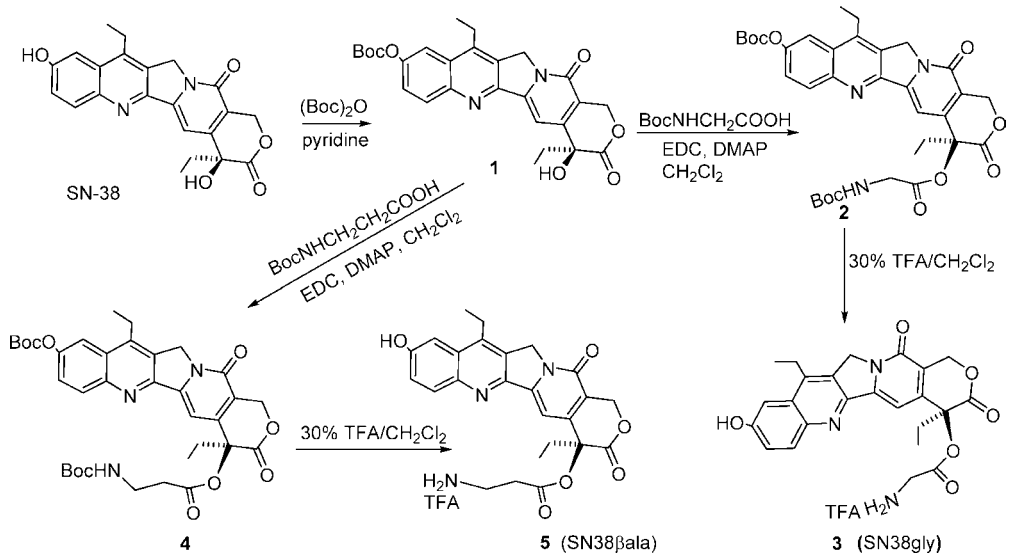
† Departments of Pharmaceutics and Pharmaceutical Chemistry.

‡ Department of and Bioengineering.

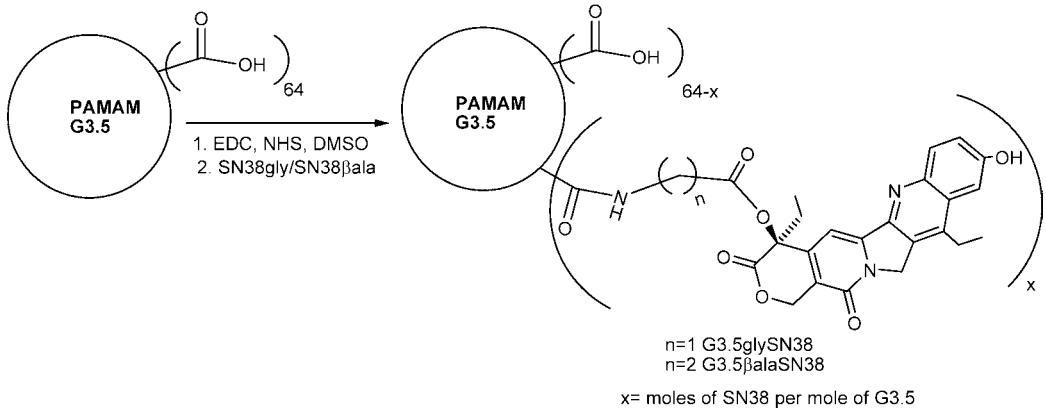
§ Utah Center for Nanomedicine.

10.1021/bc100094z © 2010 American Chemical Society
Published on Web 09/13/2010

Scheme 1. Synthesis of SN38 derivatives, SN38-gly with Glycine Spacer (3), and SN38 with *β*-Alanine Spacer (5) at the 20-OH Position



Scheme 2. Synthesis of G3.5-SN38 Conjugates



with modifications (*11*). Briefly, SN38 (0.8 g, 2.04 mmol) was stirred for 12 h with di-*tert*-butyl dicarbonate (0.579 g, 2.65 mmol) and anhydrous pyridine (4 mL, 42 mmol) in 40 mL of CH_2Cl_2 to obtain compound **1** (Scheme 1) in 90% yield. To a solution of **1** (0.5 g, 1.0 mmol) in CH_2Cl_2 (10 mL), *N*-(*tert*-butoxycarbonyl)glycine (0.5 g, 3.0 mmol), EDC (0.9 mL, 5.0 mmol), and DMAP (0.350 g, 3.0 mmol) were added and stirred for 2 h. Subsequently, the reaction mixture was washed with 0.5% $NaHCO_3$ and 0.1 N HCl. The crude product obtained was purified by column chromatography using 1−3% MeOH/$CHCl_3$ to obtain compound **2** (Scheme 1) in 63% yield. Deprotection of **2** (0.25 g, 0.3 mmol) in 30% TFA/DCM gave SN38-gly (compound **3**, 0.24 g, 95% yield). ^{1}H NMR (400 MHz, CD_3OD): δ 1.07 (t, 3H, $J = 5.8$ Hz), 1.34 (t, 3H, $J = 6.2$ Hz), 2.18−2.30 (m, 2H), 3.07−3.12 (m, 2H), 4.17 (d, 1H, $J = 14.4$ Hz), 4.27 (d, 1H, $J = 14.0$ Hz), 5.21 (s, 2H), 5.48 (d, 1H, $J = 13.2$ Hz), 5.63 (d, 1H, $J = 13.2$ Hz), 7.31 (s, 1H), 7.40−7.42 (m, 2H), 7.96 (d, 1H, $J = 7.2$ Hz). ESI-TOF MS: *m*/*z* Calc. for $C_{24}H_{23}N_3O_6 + H^+$: 450.17; Obsd. 450.12.

Synthesis of SN38-*βala* (5). In an analogous manner, compound **1** (0.4 g, 0.8 mmol) was reacted with *N*-(*tert*-butoxycarbonyl) *β*-alanine (0.28 g, 2.4 mmol) to obtain compound **4** (0.38 g, 70% yield), which upon deprotection with 30% TFA/CH_2Cl_2 gave compound **5** in 90% yield (Scheme 1). ^{1}H NMR (400 MHz, CD_3SOCD_3): δ 0.91 (t, 3H, $J = 5.6$ Hz), 1.28 (t, 3H, $J = 5.8$ Hz), 2.16−2.18 (m, 2H), 2.87−3.1 (m, 6H), 5.30 (s, 2H), 5.49 (s, 2H), 7.03 (s, 1H), 7.41 (s, 2H), 7.80 (bs, 3H), 8.0 (d, 1H, $J = 7.6$ Hz). ESI-TOF MS: *m*/*z* Calc. for $C_{24}H_{25}N_3O_6 + H^+$: 464.18; Obsd. 464.18.

Synthesis of G3.5-SN38 Conjugates. The methanolic solution of PAMAM G3.5 carboxylate equivalent to 250 mg (0.02 mmol) was evaporated under vacuum. The residue was dissolved in water, pH adjusted to 3.0, and lyophilized. To the acidified G3.5 in DMSO (15 mL) was added EDC (0.22 mL, 1.28 mmol) and NHS (0.28 g, 2.56 mmol) and the reaction mixture stirred for 10 min. To this solution, compound **3** or **5** (0.32 mmol) was added followed by DIPEA (0.07 mL, 0.32 mmol) (Scheme 2). The reaction mixture was stirred at room temperature for 8 h. DMSO was removed under high vacuum at 40 °C and residue redissolved in water, dialyzed using 3500 cutoff membrane, and sample lyophilized. The obtained product was further purified by SEC to remove low molecular weight impurities, unreacted dendrimer, and possible cross-linked impurities. The conjugates were obtained in ∼65% yield and characterized by SEC and ^{1}H NMR.

In Vitro Stability of Conjugates. Solutions of G3.5-gly-SN38 (0.75 mg/mL) and G3.5-*β*ala-SN38 (0.5 mg/mL) in PBS, pH 7.4, Mcyoy's 5A media (ATCC, Manassa, VA, USA) with 10% FBS, or 50% rat plasma (rat plasma was prepared by centrifuging rat whole blood for 10 min at 1000 rpm and the clear supernatant isolated as plasma) in PBS were incubated at 37 °C with shaking. At periodic intervals, samples (0.1 mL) were withdrawn and 0.1 mL acetonitrile added, vortexed for 30 s, and centrifuged at 1600 rpm to precipitate the proteins.

The clear supernatant was then extracted with 0.1 mL of chloroform, and the procedure was repeated in triplicate. The chloroform extracts were pooled, evaporated under nitrogen, redissolved in 80 μL of 1:1 DMSO/0.1 N HCl and analyzed by reverse-phase HPLC using a UV detector for SN38 detection. A gradient elution method of methanol/water in 0.1% TFA at a flow rate of 1 mL/min was used. The concentration of SN38 from each sample was determined from the peak areas observed, based on a calibration curve ($n = 3$) for SN38 in the concentration range 0.1−60 ug/mL. The calibration curves were plots of peak area as a function of SN38 concentration. For accurate determination of SN38 concentration in extracted samples, extraction efficiencies for SN38 using the above-described method were determined in each of the media, which were 100%, 103%, and 62% for PBS, cell culture media, and 50% rat plasma, respectively.

Evaluation of Cell Proliferation and Viability. HCT-116, human colorectal cancer cell line, was obtained from American Type Culture Collection (ATCC, Manassas, VA). The cells were cultured in Mcyoy's 5A medium (ATCC) containing 10% fetal bovine serum (FBS) at 37 °C. Cells were grown at 37 °C in a humidified atmosphere of 5% CO_2 (v/v) in air. Cell growth kinetics and viability were assessed by utilizing a highly water-soluble tetrazolium salt, WST-8 [2-(2-methoxy-4-nitrophenyl)-3-(4-nitrophenyl)-5-(2,4-disulfophenyl)-2*H*-tetrazolium, monosodium salt], as a component of Cell Counting Kit-8 from Dojindo Molecular Technologies, Inc. (Gaithersburg, MA). Cells were plated in 96 well plates (4000 cells/well) and incubated for 24 h; media was then gently aspirated, and cells were treated with different concentrations (serially diluted) of SN38, SN38-gly, SN38-βala, G3.5, G3.5-gly-SN38, or G3.5-βala-SN38 in 0.5% DMSO containing media. DMSO was used to ensure complete dissolution of SN38 in media. 0.5% DMSO did not affect cell viability. After 48 h, the cells were washed with PBS, and CCK8 reagent was added following the manufacturer's protocol. The cells were then incubated for 90 min, and absorbance at 450 nm was measured using 630 nm as reference. Cell viability was determined as percent absorbance relative to untreated control cells. Prism software (v 5.0, LaJolla, CA, USA) was used to generate the inhibition curves and IC_{50} determination.

Cell Cycle Analysis. Cell cycle progression was monitored by the flow cytometric measurement of DNA content (*17*). HCT-116 cells (0.25×10^6 cell/mL) were incubated in 6 well plates for 24 h. The cells were then exposed to free SN38 (32 nM), G3.5-gly-SN38 (240 nM), and G3.5-βala-SN38 (760 nM) for a further 24 h. Cells were then harvested, washed with 1 mL of ice-cold PBS, and fixed with 1 mL of 70% ethanol (previously frozen at −20 °C) overnight. The cells were then washed a second time with 1 mL of ice-cold PBS and treated with 0.2 mL PBS solution containing propidium iodide (Sigma-Aldrich, USA) (25 μg/mL), Triton X-100 (Sigma-Aldrich, USA) (0.05%), and RNase (Sigma-Aldrich, USA) (180 μg/mL). The solutions were incubated at room temperature in the dark for 30 min prior to analysis. Analysis of DNA content in cells stained with propidium iodide was performed using FACScan (Becton Dickinson, Mountain View, CA). The percentage of cells in each phase of the cell cycle was evaluated using the *ModFit* software (Verity Software House, Topsham, ME).

Nuclear Fragmentation Study. HCT-116 cells (0.1×10^6) were plated in 6 well plates containing coverslips and incubated for 24 h. SN38 (5 nM), G3.5-gly-SN38 (40 nM), and G3.5-βala-SN38 (120 nM) were added, and cells were incubated for 36 h. Cells were then washed with PBS three times and fixed with 4% paraformaldehyde for 10 min. Cells were again washed with PBS three times, and each coverslip was mounted on glass slide with a drop of DAPI containing mounting medium (Santacruz Biotechnology, CA, USA). Nuclear fragmentation was visualized in fixed cells stained with DAPI by a laser scanning confocal microscope Olympus FluoView FV1000 (Olympus America Corp., Center Valley, PA). The objective specifications were 60× oil immersion and numerical aperture 1.42.

Table 1. Characteristics of G3.5 PAMAM-SN38 Conjugates

compound	no. of SN38 molecules/ PAMAM[a]	wt of SN38/ wt of conjugate (%)	molecular weight[b]	elution volume (mL)	hydrodynamic radius (nm)
G3.5	-	-	12 931	13.0	1.76 ± 0.11
G3.5-gly-SN38	2.9	8.0	14 184	13.4	1.37 ± 0.06*
G3.5-βala-SN38	4.0	10.0	14 715	14.0	1.33 ± 0.05**

[a] Determined from ^{1}H NMR. [b] Determined from NMR data and reported molecular weight of PAMAM. * ($p < 0.01$) denotes significant differences of hydrodynamic radius from unconjugated G3.5. ** ($p < 0.01$) denotes significant differences of hydrodynamic radius from unconjugated G3.5.

Statistical Analysis. Statistical analysis was carried out using Student's t test with a probability value $p < 0.05$ considered statistically significant.

RESULTS AND DISCUSSION

Synthesis and Characterization. Anionic PAMAM G3.5 was covalently conjugated to SN38 via a glycine or β-alanine spacer. Amino acid linkers, particularly glycine, have been successfully used to attach SN38 and other camptothecin analogues to polymers such as poly(ethylene glycol) (PEG), poly(glutamic acid), and pegylated poly(L-lysine) dendrimer with such conjugates showing increased aqueous solubility and good in vitro and in vivo efficacy (*11*, *18*−*20*). β-Alanine differs from glycine in the presence of an additional methylene group and could thus act as a relatively extended spacer. We chose these two spacers to compare the possible effect of linker length on the extent of drug loading, rate of drug release, and activity of the conjugates. SN38 derivatives, modified at the 20-OH position via an ester linker with glycine and β-alanine, respectively, were synthesized as described in the Experimental Section (*11*). Briefly, the phenolic hydroxyl group at the 10-position of SN38 was first protected with a Boc group, and the resulting compound **1** was then reacted with N-Boc glycine to yield compound **2**. Removal of both Boc groups under acidic conditions yielded SN38-gly (compound **3**). In an analogous manner, SN38-βala (compound **5**) was also synthesized starting from SN38 (Scheme 1).

The terminal carboxyl groups of G3.5 PAMAM dendrimer were then activated using EDC/NHS and reacted with the primary amines of SN38-gly and SN38-βala, respectively, in DMSO. Thus, the dendrimer was linked via an amide bond at one end of the spacer, while the drug was attached to the same spacer via an ester bond at the other end (Scheme 2). The dendrimer was conjugated at the 20-OH end of SN38 with the aim of stabilizing the lactone form of the camptothecin derivative under physiological conditions, which is essential for antitumor activity (*9*).

The conjugates were extensively purified by dialysis followed by preparative SEC to remove low molecular weight impurities. There was an increase in the elution volume in SEC for both conjugates relative to G3.5 with the order of elution being G3.5 < G3.5-gly-SN38 < G3.5-βala-SN38. The hydrodynamic radii of both conjugates as measured by dynamic light scattering was less than that of G3.5 (Table 1). These observations suggest that, upon attachment of SN38, the dendrimer may have a more compact form to avoid unfavorable interactions between the aqueous solvent and the hydrophobic drug. It is also possible that the overall charge density on the surface of the conjugates is lowered relative to G3.5, reducing the extent of solvation in aqueous solution, which results in a lower hydrodynamic radius.

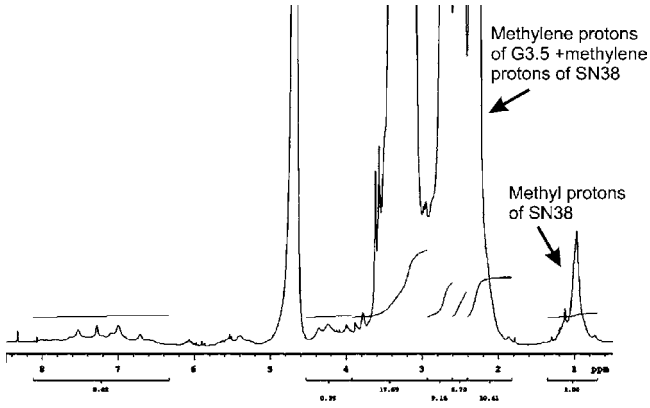


Figure 1. ^{1}H NMR spectra (500 MHz, D_2O) of G3.5-gly-SN38.

The number of drug molecules attached to the dendrimer was determined using ^{1}H NMR, by comparing the number of protons in the dendrimer to the methyl groups of SN38. The protons corresponding to PAMAM appeared between chemical shifts, 2.1−3.8 ppm, while the methyl protons appeared as a broad peak between 0.9 and 1.1 ppm (Figure 1). ^{1}H NMR was recorded at three different concentrations, 5 mg/mL, 10 mg/mL, and 25 mg/mL, and no changes in integral values corresponding to protons from the dendrimer or methyl protons of SN38 were observed. This suggested the absence of aggregation at concentrations used for NMR analysis. The drug loading per mole of dendrimer was 2.9 and 4 for G3.5-gly-SN38 and G3.5-βala-SN38, respectively (Table 1). Thus, increasing the spacer length by one methylene unit increased the drug loading slightly. For synthesis of dendrimers with the drug loadings above, 16 mol of compound gly-SN38 or βala-SN38 was used for conjugation to G3.5. Use of a further excess of drug did not improve loading, while lower stoichiometric ratios of the drug derivatives decreased loading onto PAMAM dendrimers. In order to further confirm that SN38 was covalently linked to the dendrimer, the following control experiment was performed. Acidified PAMAM G3.5 was mixed with compound gly-SN38 in DMSO and stirred under identical conditions to those of the conjugation reactions in the absence of activating reagents EDC/NHS. The resulting mixture was then purified using the same method as described for the conjugates and the isolated compound analyzed by SEC and ^{1}H NMR. The SEC profile and ^{1}H NMR were the same as for the native G3.5 PAMAM dendrimer. No peaks due to SN38 were observed in the ^{1}H NMR spectrum suggesting the absence of complexed or free drug (Supporting Information). These observations further confirm that the conjugates synthesized are not complexes and the SN38 is covalently bound to the dendrimer.

The solubility of the conjugates in water was ~140 mg/mL, which corresponds to ~10 mg/mL and ~14 mg/mL of SN38, respectively, in the cases of G3.5-gly-SN38 and G3.5-βala-SN38. SN38 has a very poor solubility of 7 μg/mL, and conjugation to the PAMAM dendrimer has considerably improved its aqueous solubility, which is higher than that of previously reported PEG-SN38 derivatives (6.7 mg/mL) (*11*).

Stability of the Conjugates. In vitro release characteristics of the conjugates was studied to assess their stability in the following physiologically relevant solutions, PBS, pH = 7.4, cell culture media: Mcyoy's 5A medium with 10% FBS and 50% rat plasma (*11*, *21*, *22*). Stability in cell culture media was studied to determine whether potential activity of the conjugates would be due to extracellular and/or intracellular release of the drug. 50% plasma was used, since in whole blood, the plasma content is about ~55%. SN38 binds strongly to plasma proteins, and the extraction efficiency in 100% rat plasma was poor (35%)

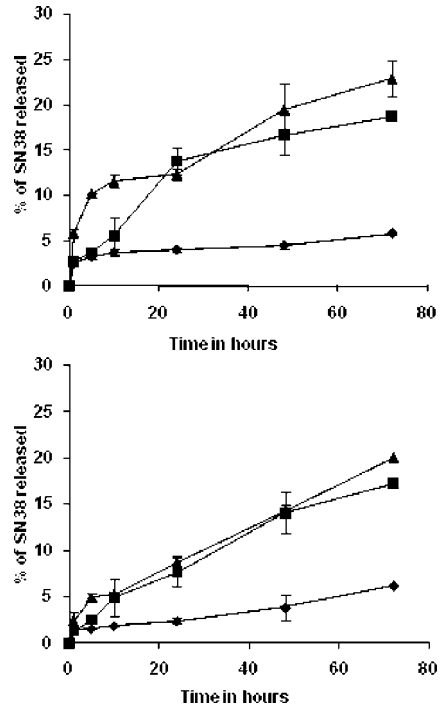


Figure 2. Stability of conjugates in different media at 37 °C. Top panel: SN38 release from G3.5-gly-SN38. Bottom panel: SN38 release from G3.5-βala-SN38. The time intervals were 0, 1, 5, 10, 24, 48, and 72 h. Each graph represents the average of two independent runs. (m ± s.d): PBS (◆), 50% rat plasma (▲), and cell culture media (■).

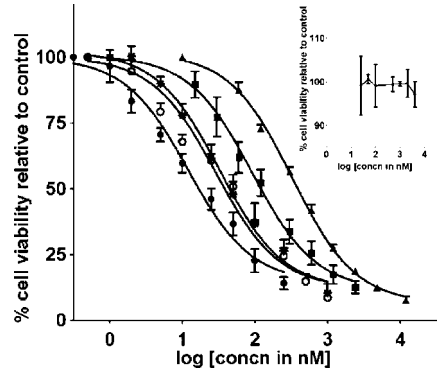


Figure 3. In vitro cytotoxicity of SN38 (•), SN38gly (○), SN38βala (*), G3.5-gly-SN38 (■), G3.5- βala-SN38 (▲) in human colorectal cancer cell line (HCT-116) after 48 h incubation. Each curve is representative of 3−5 independent experiments (m ± s.d). Inset: Inhibition curve for G3.5.

after 1 h incubation, while in 50% plasma, it was much higher (62%); and hence, the released drug could be estimated more accurately.

In PBS, both conjugates were stable with approximately 5% of the drug released in 72 h. Thus, these conjugates are more stable than the PEG-SN38 conjugates, which were reported to have a $t_{1/2}$ of only 14 h in PBS (*11*). However, in cell culture media and 50% rat plasma the extent of release was relatively higher compared to that in PBS (Figure 2). This is expected, as enzymes such as esterases are present in both plasma and 10% FBS containing media. Esterases can specifically cleave the ester bond between the spacer and the drug, whereas in PBS, the release is only due to nonspecific hydrolysis. In the case of G3.5-gly-SN38, the release in plasma was slightly higher than in cell culture medium ($p < 0.04$), but no significant difference was observed in the case of β-alanine-linked conjugate. It has been reported that increasing the length of the spacer increases the

Table 2. Cytotoxicity of Different Forms of SN38 toward Human Colorectal Carcinoma HCT-116 cells[a]

compound	IC_{50} (nM)
SN38	16 ± 3
SN38-gly	42 ± 10
SN38-βala	45 ± 6
G3.5-gly-SN38	129 ± 27*
G3.5-βala-SN38	387 ± 20**
CPT-11	$(12 \times 10^3) \pm (3.8 \times 10^3)$

[a] IC_{50} values presented as m $\pm$ s.d. of 3−5 independent experiments. * ($p < 0.001$) denotes significant difference of IC_{50} of G3.5-SN38 conjugates from SN38. ** ($p < 0.001$) denotes significant difference of IC_{50} of G3.5-SN38 conjugates from SN38.

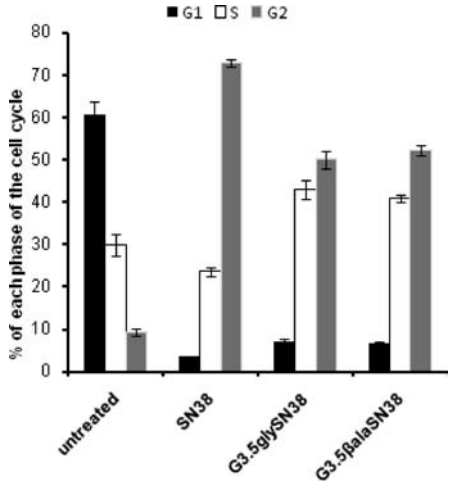


Figure 4. Effect of SN38 and G3.5-SN38 conjugates on cell cycle distribution of HCT-116 cells after 24 h incubation. Values are representative of two independent experiments, each done in duplicate (m $\pm$ s.d).

rate of hydrolysis of the ester bond due to increased accessibility to the enzyme (*22*, *23*). Upon comparing the release rates of both conjugates, we did not observe an overall, large difference in the release when increasing the linker by one methylene unit. However, it is observed that G3.5-gly-SN38 shows slightly faster release of the drug in the first 24 h than G3.5-βala-SN38 in both media and plasma ($p < 0.03$), but they return to similar rates by 48 h ($p > 0.1$). It is possible that glycine, being a natural amino acid, is a better substrate for enzymes compared to β-alanine, and hence, the glycine linked conjugate shows initially faster release rates in media containing esterases. The conjugate with glycine linker also showed a higher release of drug at pH 5 after 72 h compared to the conjugate with the β-alanine linker (see Supporting Information Figure 4). However, the dendrimer is likely to have too many different conformations in solution, such that some result in increased accessibility to the enzymes, while others lead to increased steric hindrance to ester degradation. Hence, the overall release kinetics is complex (*24*, *25*). The fact that only ~20% (Figure 2) is released even after 72 h for both conjugates in rat plasma suggests that the covalent conjugates are quite stable and hold promise as delivery systems for controlled release of the drug.

Inhibition of Cell Growth. The toxicities of the conjugates, linker modified SN38 derivatives (SN38-gly, SN38-βala), free SN38, and CPT-11 were compared upon 48 h incubation with HCT-116 cells (Figure 3). SN38 was highly toxic to the cells with IC_{50} of approximately 16 nM. It was observed that both SN38-gly and SN38-βala had similar IC_{50} values and were slightly less cytotoxic than SN38 ($p < 0.02$). This suggests that both SN38-gly and SN38-βala undergo rapid hydrolysis to release the free drug, as the IC_{50} values were only about 3 times less than that of SN38. Both conjugates were far less cytotoxic with much higher IC_{50} values compared to the free drug. However, their toxicities are still in the nanomolar range and are highly potent compared to that of CPT-11 (Table 2). PAMAM G3.5 was nontoxic in the concentration range used in the case of the conjugates (inset, Figure 3). The lower activity of the PAMAM-SN38 conjugates compared to that of SN38

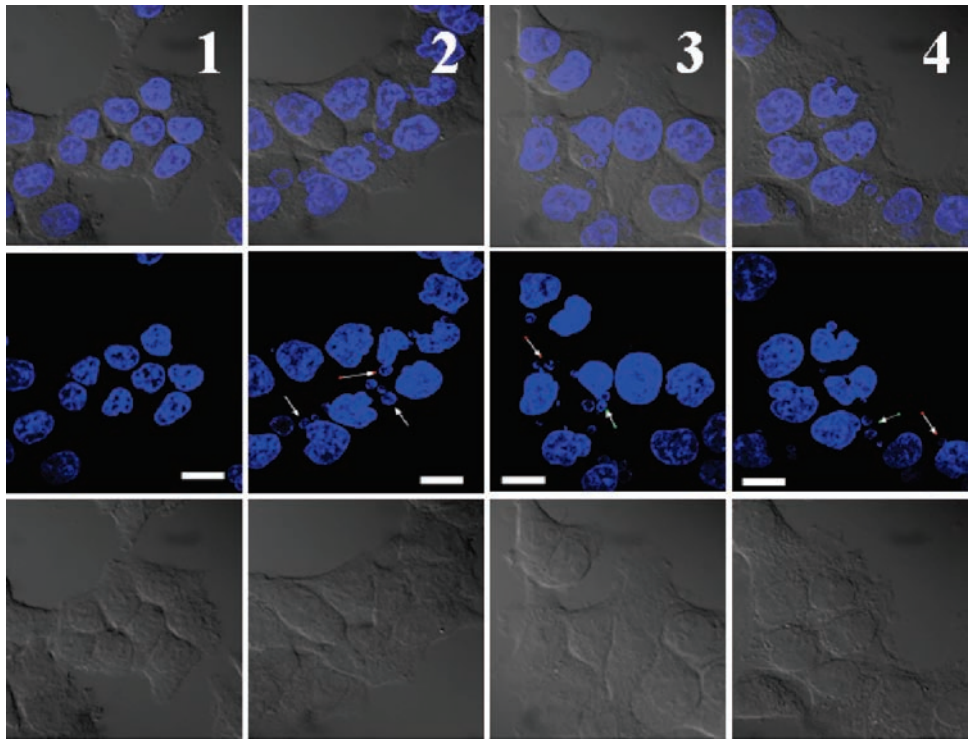


Figure 5. Nuclear fragmentation in HCT-116 cells treated with drug/conjugates. Untreated cells (column 1); 5 nM SN38 (column 2); 40 nM G3.5-gly-SN38 (column 3); 120 nM G3.5-βala-SN38 (column 4). Scale bar is 10 μm. Arrows indicate nuclear fragments. From bottom: 1st row, DIC (differential interference contrast image); 2nd row, fluorescence image; 3rd row, overlay of DIC and fluorescence images.

can be attributed to the slow release of the drug by hydrolysis of the linker from the sterically hindered dendrimer surface. G3.5-βala-SN38 exhibited lower activity as compared to G3.5-gly-SN38 ($p < 0.001$), which could perhaps be due to the observed lower initial release rate in cell culture media. There is also a possibility that the cellular uptake varies for the two different conjugates (*26*).

Induction of Cell Cycle Arrest and Nuclear Fragmentation. As both PAMAM-SN38 conjugates inhibited cell proliferation of HCT-116 cells, we further investigated the mode of action of these conjugates. SN38 is a topoisomerase I inhibitor and is known to exhibit characteristic G_2/M phase cell cycle arrest. The drug acts by covalent binding to the cleavable topoisomerase I−DNA complex, causing double-strand DNA breaks and irreversible arrest of DNA replication. These events lead to arrest in the G_2/M phase of the cell cycle (*27, 28*).

The progression of HCT-116 cells through the cell cycle after 24 h treatment with 2 × IC-50 concentration of either conjugate or free drug was evaluated using flow cytometry. As expected, SN38 caused cell cycle arrest in the G_2/M phase (73%) with considerable reduction in population of cells in the G_0/G_1 (4%) phase relative to untreated cells (61%). Upon exposure to G3.5-gly-SN38, a significant accumulation of cells in the G_2/M phase (50%) was observed with accompanying substantial decrease in G_0/G_1 (7.0%). Similarly, in the case of G3.5-βala-SN38, the accumulation of 52% cell population in the G_2 phase was observed (Figure 4). These results suggest that the dendrimer−drug conjugates have a similar mechanism of action as SN38 and the conjugates affect cells due to release of the free drug. However, compared to both conjugates, SN38 used at equitoxic 2 × IC-50 concentration induced accumulation of a larger number of cells in the G_2/M phase of the cell cycle ($p < 0.001$). This can be attributed to the slow release of drug from the conjugates.

In addition to inducing cell cycle arrest in cancer cells, anticancer drugs such as SN38 can kill cancer cells. The different modes of cell death include apoptosis, necrosis, autophagy, or mitotic catastrophe with each associated with characteristic morphological changes and biochemical markers. Few studies have shown that SN38 causes cell death mainly via an apoptotic mechanism. The morphological changes that define apoptosis include chromatin condensation, nuclear fragmentation, plasma membrane blebbing, and appearance of apoptotic bodies, while biochemical markers include formation of DNA fragment "ladders" and caspase activation (*28, 29*).

Fluorescence microscopy was used to examine and compare the effect of conjugates and free drug on cell and nuclear morphology (Figure 5). HCT-116 cells were treated for 36 h with either free SN38 or conjugates at 1/3 IC_{50}, stained with the nuclear dye, DAPI, and observed under the confocal fluorescence microscope. Untreated cells appeared mostly uniform with regularly shaped nuclei. In contrast, cells treated with either SN38 or the dendrimer−drug conjugates appeared heterogeneous. Nuclear fragments were distinctly visible, along with swollen and sparsely condensed nuclei. Mitotic cells were also occasionally seen in the treated cells. Although these observations are not conclusive evidence of apoptosis or necrosis, they do suggest that the free drug and conjugates have the same mode of action. The activity of the conjugates is due to the release of the free drug.

CONCLUSIONS

PAMAM-SN38 conjugates with ester linkers which are stable at physiological pH and in plasma with low release of drug were synthesized. Conjugation of SN38 with the dendrimer significantly increased aqueous solubility. These dendrimer−drug conjugates are potent and have IC_{50} in the nanomolar range, and show activity due to slow release of SN38. Cell cycle analysis and observed nuclear fragmentation suggest that both free drug and the drug conjugated to the dendrimer have similar mechanisms of action. These novel dendritic conjugates of SN38, coupled with our previous observations that PAMAM dendrimers are translocated across the epithelial barrier of the gut, show the potential to improve the oral bioavailability and targeted delivery of this potent drug.

ACKNOWLEDGMENT

Financial support was provided by the NIH (R01 EB007470) and Utah Science Technology and Research (USTAR). The authors appreciate the assistance of Giridhar Thiagarajan with revision of the manuscript.

Supporting Information Available: Additional ^{1}H NMR spectra, representative histograms of cell cycle analysis and drug release data for SN38 at pH 5. This material is available free of charge via the Internet at http://pubs.acs.org.

LITERATURE CITED

(1) Duncan, R. (2006) Polymer conjugates as anticancer nanomedicines. *Nat. Rev. Cancer 6*, 688–701.
(2) Li, C., and Wallace, S. (2008) Polymer-drug conjugates: recent development in clinical oncology. *Adv. Drug Delivery Rev. 60*, 886–98.
(3) Majoros, I. J., Williams, C. R., and Baker, J. R., Jr. (2008) Current dendrimer applications in cancer diagnosis and therapy. *Curr. Top. Med. Chem. 8*, 1165–79.
(4) Duncan, R., and Izzo, L. (2005) Dendrimer biocompatibility and toxicity. *Adv. Drug Delivery Rev. 57*, 2215–37.
(5) Pommier, Y. (2009) DNA topoisomerase I inhibitors: chemistry, biology, and interfacial inhibition. *Chem. Rev. 109*, 2894–902.
(6) Ulukan, H., and Swaan, P. W. (2002) Camptothecins: a review of their chemotherapeutic potential. *Drugs 62*, 2039–57.
(7) Shimada, Y., Rothenberg, M., Hilsenbeck, S. G., Burris, H. A., 3rd, Degen, D., and Von Hoff, D. D. (1994) Activity of CPT-11 (irinotecan hydrochloride), a topoisomerase I inhibitor, against human tumor colony-forming units. *Anticancer Drugs 5*, 202–6.
(8) Ulukan, H., Muller, M. T., and Swaan, P. W. (2001) Down-regulation of topoisomerase I in differentiating human intestinal epithelial cells. *Int. J. Cancer 94*, 200–7.
(9) Smith, N. F., Figg, W. D., and Sparreboom, A. (2006) Pharmacogenetics of irinotecan metabolism and transport: an update. *Toxicol. In Vitro 20*, 163–75.
(10) Caiolfa, V. R., Zamai, M., Fiorino, A., Frigerio, E., Pellizzoni, C., d'Argy, R., Ghiglieri, A., Castelli, M. G., Farao, M., Pesenti, E., Gigli, M., Angelucci, F., and Suarato, A. (2000) Polymer-bound camptothecin: initial biodistribution and antitumour activity studies. *J. Controlled Release 65*, 105–19.
(11) Zhao, H., Rubio, B., Sapra, P., Wu, D., Reddy, P., Sai, P., Martinez, A., Gao, Y., Lozanguiez, Y., Longley, C., Greenberger, L. M., and Horak, I. D. (2008) Novel prodrugs of SN38 using multiarm poly(ethylene glycol) linkers. *Bioconjugate Chem. 19*, 849–59.
(12) Moon, S. J., Govindan, S. V., Cardillo, T. M., D'Souza, C. A., Hansen, H. J., and Goldenberg, D. M. (2008) Antibody conjugates of 7-ethyl-10-hydroxycamptothecin (SN-38) for targeted cancer chemotherapy. *J. Med. Chem. 51*, 6916–26.
(13) Kolhatkar, R. B., Swaan, P., and Ghandehari, H. (2008) Potential oral delivery of 7-ethyl-10-hydroxy-camptothecin (SN-38) using poly(amidoamine) dendrimers. *Pharm. Res. 25*, 1723–9.
(14) Patri, A. K., Kukowska-Latallo, J. F., and Baker, J. R., Jr. (2005) Targeted drug delivery with dendrimers: comparison of the release kinetics of covalently conjugated drug and non-covalent drug inclusion complex. *Adv. Drug Delivery Rev. 57*, 2203–14.

(15) Kolhatkar, R. B., Kitchens, K. M., Swaan, P. W., and Ghandehari, H. (2007) Surface acetylation of polyamidoamine (PAMAM) dendrimers decreases cytotoxicity while maintaining membrane permeability. *Bioconjugate Chem. 18*, 2054–60.

(16) Kitchens, K. M., Foraker, A. B., Kolhatkar, R. B., Swaan, P. W., and Ghandehari, H. (2007) Endocytosis and interaction of poly (amidoamine) dendrimers with Caco-2 cells. *Pharm. Res. 24*, 2138–45.

(17) Shapiro, H. M. (1988) pp 353, Alan R. Liss Inc, NewYork.

(18) Singer, J. W., De Vries, P., Bhatt, R., Tulinsky, J., Klein, P., Li, C., Milas, L., Lewis, R. A., and Wallace, S. (2000) Conjugation of camptothecins to poly-(L-glutamic acid). *Ann. N. Y. Acad. Sci. 922*, 136–50.

(19) Bhatt, R., de Vries, P., Tulinsky, J., Bellamy, G., Baker, B., Singer, J. W., and Klein, P. (2003) Synthesis and in vivo antitumor activity of poly(l-glutamic acid) conjugates of 20S-camptothecin. *J. Med. Chem. 46*, 190–3.

(20) Fox, M. E., Guillaudeu, S., Frechet, J. M., Jerger, K., Macaraeg, N., and Szoka, F. C. (2009) Synthesis and in vivo antitumor efficacy of PEGylated poly(l-lysine) dendrimer-camptothecin conjugates. *Mol. Pharm. 6*, 1562–72.

(21) Chen, X., McRae, S., Parelkar, S., and Emrick, T. (2009) Polymeric phosphorylcholine-camptothecin conjugates prepared by controlled free radical polymerization and click chemistry. *Bioconjugate Chem. 20*, 2331–41.

(22) Najlah, M., Freeman, S., Attwood, D., and D'Emanuele, A. (2006) Synthesis, characterization and stability of dendrimer prodrugs. *Int. J. Pharm. 308*, 175–82.

(23) Ishikawa, T., Otsuki, M., and Iwatsuki, T. (1986) Enzymatic esterolysis of polymers containing 2-biphenylyl ester bonds in side chains. *Bull. Chem. Soc. Jpn. 59*, 3621–3624.

(24) Vicent, M. J., Greco, F., Nicholson, R. I., Paul, A., Griffiths, P. C., and Duncan, R. (2005) Polymer therapeutics designed for a combination therapy of hormone-dependent cancer. *Angew. Chem., Int. Ed. Engl. 44*, 4061–6.

(25) Khandare, J. J., Jayant, S., Singh, A., Chandna, P., Wang, Y., Vorsa, N., and Minko, T. (2006) Dendrimer versus linear conjugate: Influence of polymeric architecture on the delivery and anticancer effect of paclitaxel. *Bioconjugate Chem. 17*, 1464–72.

(26) Perumal, O., Khandare, J., Kolhe, P., Kannan, S., Lieh-Lai, M., and Kannan, R. M. (2009) Effects of branching architecture and linker on the activity of hyperbranched polymer-drug conjugates. *Bioconjugate Chem. 20*, 842–846.

(27) Tsao, Y. P., D'Arpa, P., and Liu, L. F. (1992) The involvement of active DNA synthesis in camptothecin-induced G2 arrest: altered regulation of p34cdc2/cyclin B. *Cancer Res. 52*, 1823–9.

(28) Ueno, M., Nonaka, S., Yamazaki, R., Deguchi, N., and Murai, M. (2002) SN-38 induces cell cycle arrest and apoptosis in human testicular cancer. *Eur. Urol. 42*, 390–7.

(29) Galluzzi, L., Maiuri, M. C., Vitale, I., Zischka, H., Castedo, M., Zitvogel, L., and Kroemer, G. (2007) Cell death modalities: classification and pathophysiological implications. *Cell Death Differ. 14*, 1237–43.

BC100094Z

Supporting Information

Carboxyl Terminated PAMAM-SN38 Conjugates: Synthesis, Characterization, and In vitro Evaluation.

Nirmalkumar Vijayalakshmi[1,3], Abhijit Ray[1,3], Alexander Malugin[1,3] and Hamidreza Ghandehari[*1,2,3].

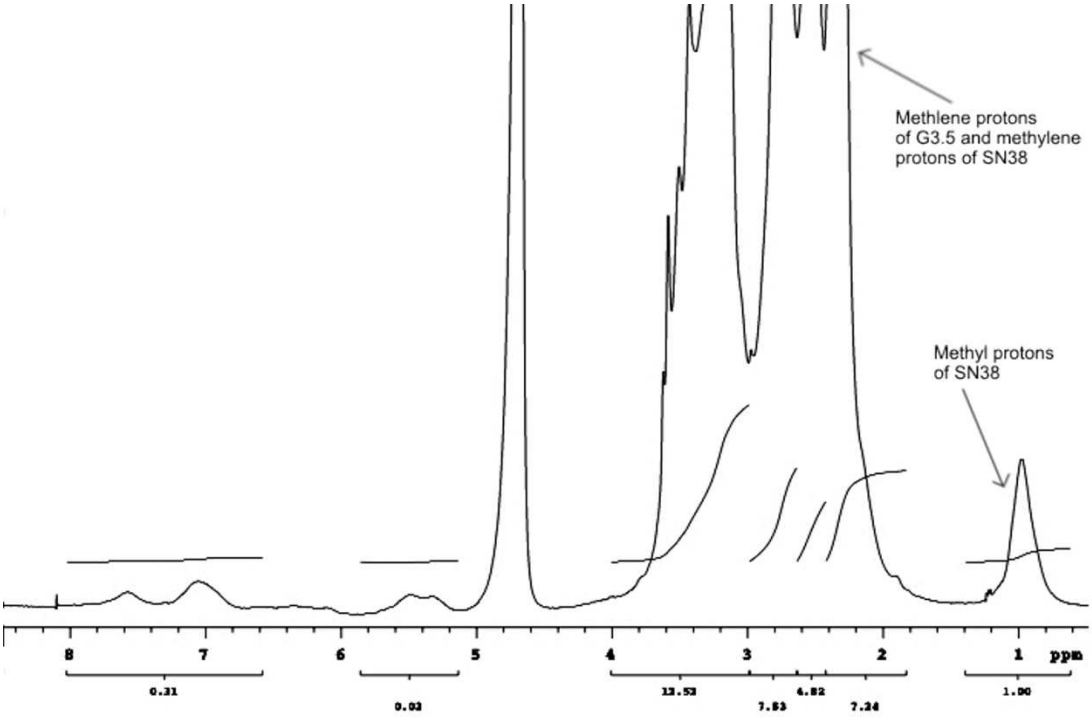
Departments of [1]Pharmaceutics and Pharmaceutical Chemistry, and [2] Bioengineering; [3]Utah Center for Nanomedicine, Nano Institute of Utah, University of Utah, Salt Lake City, UT, 84108, USA.

∗To whom correspondence should be addressed: Hamidreza Ghandehari, Departments of Pharmaceutics and Pharmaceutical Chemistry and Bioengineering, Utah Center for Nanomedicine, Nano Institute of Utah, University of Utah. 383 Colorow Road, Salt Lake City, UT 84108, USA

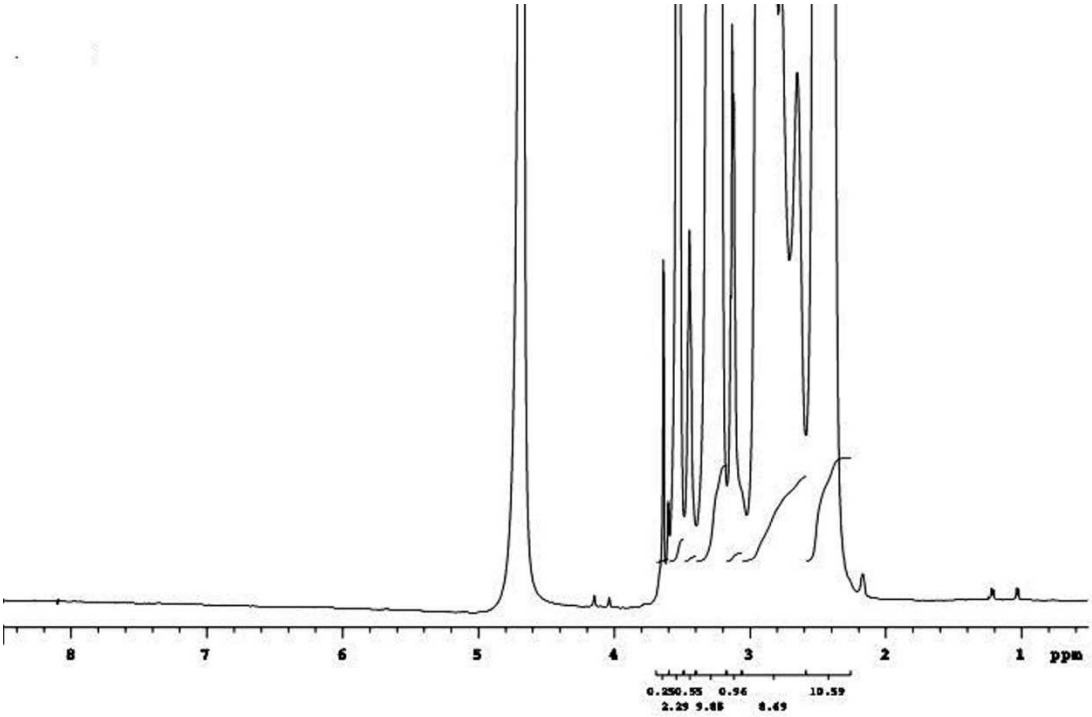
Email: hamid.ghandehari@pharm.utah.edu

Table of Contents:

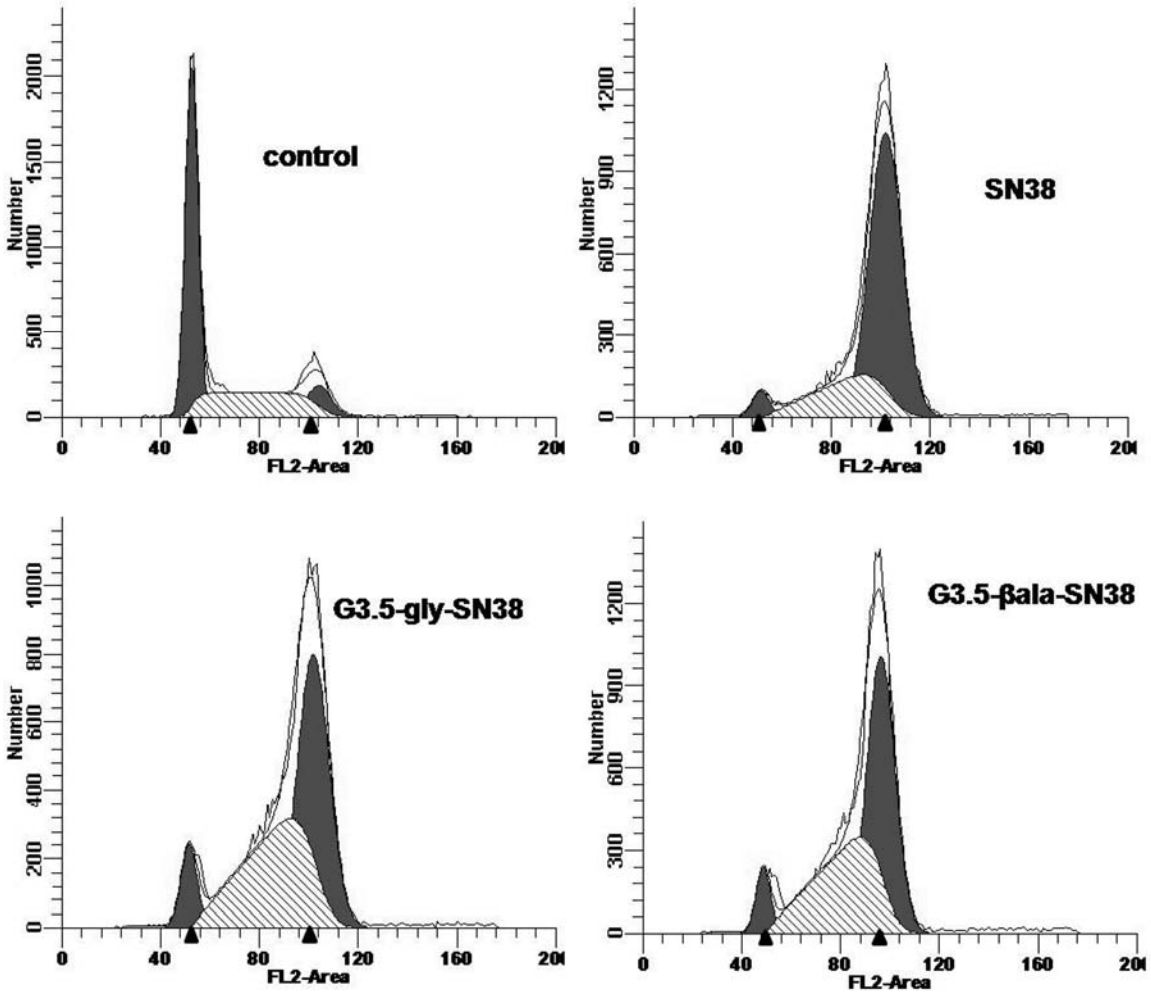
1. 1H NMR spectra of G3.5-βala-SN38 2
2. 1H NMR Spectra of G3.5 after physically mixing with SN38-gly and purification of mixture by dialysis and preparative size exclusion chromatography 2
3. Changes of DNA content in HCT-116 cells after treatment with different forms of SN38. Representative histograms from one experiment are shown. 3
4. Release of drug from conjugate at pH 5 4



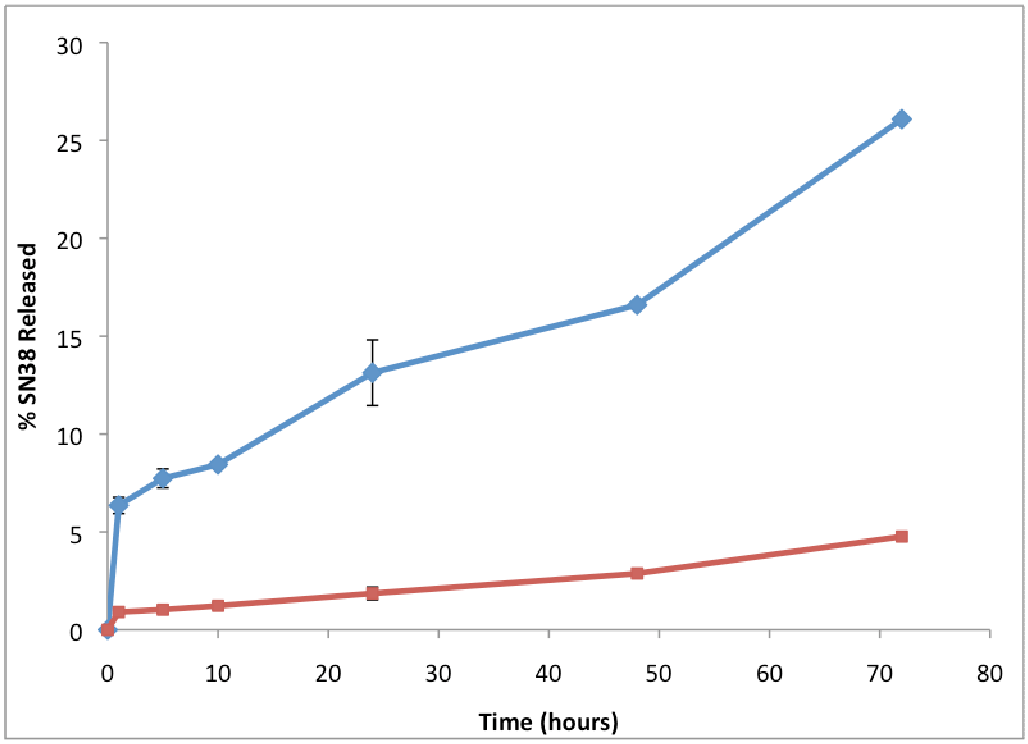
SUPPLEMENTAL FIGURE 1. 1HNMR Spectra of G3.5-βala-SN38 in D_2O



SUPPLEMENTAL FIGURE 2. 1H NMR spectra of PAMAM G3.5 after mixing with SN38-gly and purification by dialysis and preparative size exclusion chromatography. No peaks due to SN38 were observed.



SUPPLEMENTAL FIGURE 3. Changes of DNA content in HCT-116 cells after treatment with different forms of SN38. Cells were incubated with 2×IC-50 concentrations of different forms of SN38 for 24 h. Representative histograms from one experiment are shown.



SUPPLEMENTAL FIGURE 4. Release of drug from the conjugate at pH 5 over 72h. G3.5-gly-SN38 (-), G3.5-βala-SN38 (-). n = 2 at each time point.

Fast ^{18}F Labeling of a Near-Infrared Fluorophore Enables Positron Emission Tomography and Optical Imaging of Sentinel Lymph Nodes

Richard Ting,[†] Todd A. Aguilera,[†] Jessica L. Crisp,[†] David J. Hall,[‡] William C. Eckelman,[‡] David R. Vera,[‡] and Roger Y. Tsien*[,†,§]

Department of Pharmacology 0647, Department of Radiology, and Howard Hughes Medical Institute, University of California, San Diego, La Jolla, California 92093. Received March 11, 2010; Revised Manuscript Received June 24, 2010

We combine a novel boronate trap for F^- with a near-infrared fluorophore into a single molecule. Attachment to targeting ligands enables localization by positron emission tomography (PET) and near-infrared fluorescence (NIRF). Our first application of this generic tag is to label Lymphoseek (tilmanocept), an agent designed for receptor-specific sentinel lymph node (SLN) mapping. The new conjugate incorporates $^{18}F^-$ in a single, aqueous step, targets mouse SLN rapidly (1 h) with reduced distal lymph node accumulation, permits PET or scintigraphic imaging of SLN, and enables NIRF-guided excision and histological verification even after ^{18}F decay. This embodiment is superior to current SLN mapping agents such as nontargeted [^{99m}Tc]sulfur colloids and Isosulfan Blue, as well as the phase III targeted ligand [^{99m}Tc]SPECT Lymphoseek counterpart, species that are visible by SPECT or visible absorbance separately. Facile incorporation of ^{18}F into a NIRF probe should promote many synergistic PET and NIRF combinations.

INTRODUCTION

Different molecular imaging techniques have complementary advantages and disadvantages in spatial and temporal resolution, depth penetration, sensitivity, and cost (*1*). A powerful way to combine synergistic advantages is to construct synthetic probes that can be imaged by two or more modalities (*2*−*4*). Radiotracers and near-infrared fluorescence (NIRF) are particularly suitable combinations because both are sufficiently sensitive to enable direct visualization at receptor binding concentrations (nanomolar to picomolar). In contrast, magnetic resonance imaging (MRI) and X-ray contrast tomography require much higher elemental concentrations of the probe (*1*). The excellent penetration of γ-ray photons in positron emission tomography (PET) allows quantitative detection regardless of depth, making this technique ideal for whole-body scanning. NIRF offers much higher spatial and temporal resolution and cheaper instrumentation, but it is largely limited to superficial targets, making it ideal for image-guided surgery and histology.

Multimodality PET/optical probes under development currently include ^{18}F/quantum dot (QD) (*5*), ^{18}F/nanoparticle (*6*), bis(thiosemicarbazonato) ^{64}Cu chelates (*3, 7*), and ^{64}Cu/cypate (*4*) conjugates. PET bioconjugate radiochemistry is often limited to the physically more common radionuclides ^{64}Cu ($t_{1/2}$ = 762 min), ^{68}Ga ($t_{1/2}$ = 68 min), and ^{18}F ($t_{1/2}$ = 110 min), because they are easily manipulated and possess nuclear half-lives sufficiently long enough for chemical isotope manipulation and in vivo distribution. Unfortunately, each of these PET nuclides presents intrinsic complications. For example, ^{64}Cu (*3, 4, 8*) and ^{68}Ga (*9, 10*) chelates can suffer from impure isotope production as well as lowered specific activity because of impure isotope decay (*11*) and large chelation moieties that may alter ligand biodistribution and may also suffer from in vivo metal ion transchelation (*12*). Alternatively, traditional ^{18}F labeling methods (*5, 13*−*17*) relying on C−F bond formation are water-sensitive, multistep processes that often require harsh reaction conditions and long processing times that are poorly suited to the short half-life of ^{18}F.

To simplify PET chemistry, there has been recent interest in developing rapid, one-step labeling procedures from shelf-stable final target precursors with aqueous $^{18}F^-$, while reducing the side products and chromatographic purifications associated with traditional C−^{18}F labelings. Recent silica-based (*18*−*21*) and boron-based (*22*−*24*) aqueous ^{18}F capture technology allows direct preparation of isotopically pure PET compounds that are cleanly labeled, are easily purified, and have been shown to be stable in vivo (*19, 25*). We chose to generate [^{18}F]fluoroborates because they require less bulky hydrophobic substituents and potentially triple the F^- incorporation stoichiometry and attainable specific activity (*22*−*24*). A typical preparation of ^{18}F fluoride has a specific activity of ~10 Ci/μmol even if no carrier was deliberately added and therefore contains 170 atoms of ^{19}F for each atom of ^{18}F (*26*). Incorporation of three fluorine atoms triples the probability that at least one will be radioactive. We combine this boron-based ^{18}F capture technology [$t_{1/2}$ of B−F solvolysis = 5550 ± 1740 min (*23*)] with a NIR fluorophore to give a generally conjugatable PET/NIRF multimodality probe **1** (Figure 1A). Our first test of this probe is to help find and excise sentinel lymph nodes.

The current method for sentinel lymph node mapping in melanoma and breast cancer involves injection of a combination of Isosulfan Blue (*27*) and a ^{99m}Tc-labeled colloid radiopharmaceutical (*28, 29*). This pair allows for lymphoscintigraphy and absorbance-guided intraoperative lymph node excision (*30*). With little affinity for the sentinel lymph node, ^{99m}Tc-labeled colloids and Isosulfan Blue will travel past the sentinel node in a lymph chain restricting the surgeon to a small time-window within which to perform the mapping procedure. ^{99m}Tc-radiolabeled colloids are large particles that are nonspecifically trapped within lymphoid tissue. These agents are inefficient at entering lymph channels and, over time, reach distal lymph nodes. Distal colloid or dye uptake leads to the surgical removal of more lymph nodes than necessary, which increases the extent of the dissection, forces the pathologist to review a greater

* To whom correspondence should be addressed.
[†] Department of Pharmacology 0647.
[‡] Department of Radiology.
[§] Howard Hughes Medical Institute.

10.1021/bc1001328 © 2010 American Chemical Society
Published on Web 09/27/2010

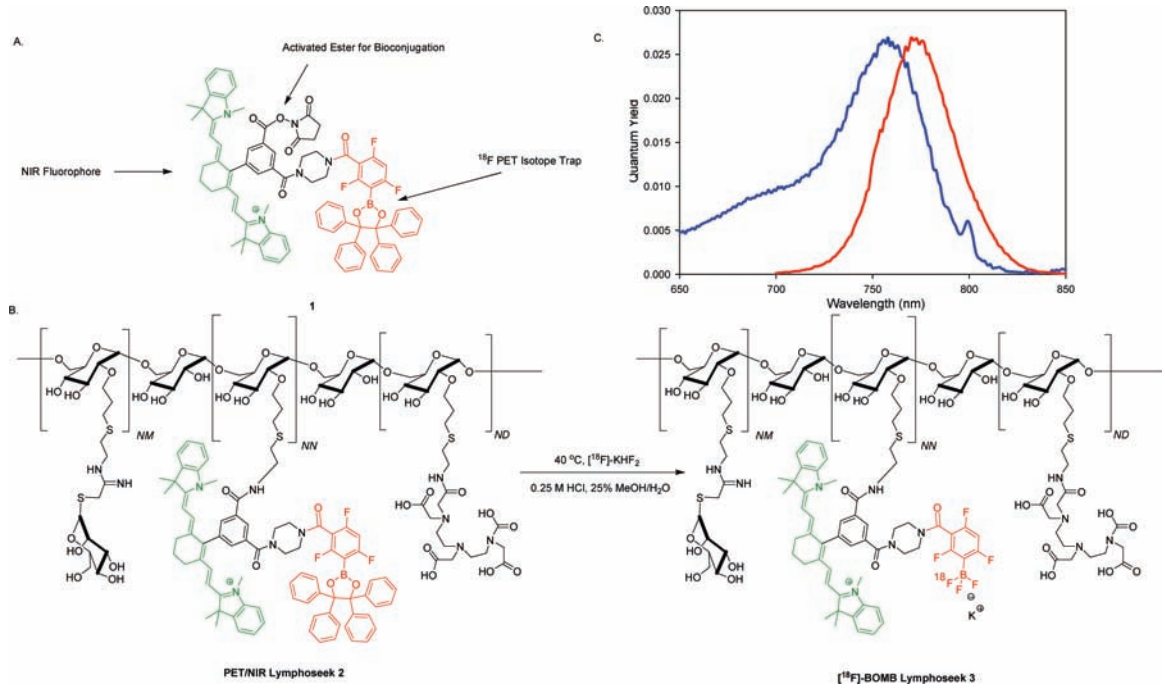


Figure 1. (A) Structure of the ^{18}F boron trap/heptamethine cyanine (C7-Cy) PET/NIR probe, [^{18}F]BOMB 1, activated as an NHS ester for general bioconjugation. The boron-based ^{18}F trap is colored red, while the NIR fluorophore is colored green. (B) Structure of PET/NIR dual probe Lymphoseek (DTPA-mannosyl-dextran) **2** and the aqueous ^{18}F labeling scheme used to generate ^{18}F-labeled [^{18}F]BOMB Lymphoseek **3**. (C) Excitation (blue) and emission (red) spectra of an aqueous solution of [^{18}F]PET/NIR-Lymphoseek **3** ($\varphi_f = 0.027$, excitation maximum = 755 nm, emission maximum = 772 nm, 1.5 μM Lymphoseek solution in water). The amine (NN), mannose (NM), and DTPA (ND) densities on Lymphoseek are 5.8, 16.5, and 4.2 mol/dextran, respectively. The average preconjugation molecular weight of Lymphoseek is 16122.

number of lymph nodes, and increases the probability of local lymphedema, a complication of lymph node resection. An alternative probe is Lymphoseek (tilmanocept), a mannosylated 16 kDa dextran conjugate, that can be labeled with ^{99m}Tc for SPECT-based imaging (*31*, *32*) and is currently in phase III clinical trials. It binds with a high affinity to cell-surface lectins [$K_D = 0.12$ nM (*33*)] and was developed specifically for sentinel lymph node mapping. ^{99m}Tc-labeled Lymphoseek has demonstrated rapid injection site clearance, a low level of distal node accumulation, a lack of local systemic toxicity, and greater specific sentinel lymph node uptake than filtered [^{99m}Tc]sulfur colloid (*32*, *34*, *35*). A version of Lymphoseek that can be viewed by both PET and NIRF would combine molecular targeting, the higher spatial resolution of PET compared to ^{99m}Tc SPECT, and the greater sensitivity and depth penetration of NIRF compared to the red absorbance of Isosulfan Blue.

Here we apply our generally conjugatable PET/NIRF probe **1** (Figure 1A) to Lymphoseek to enable multimodality-guided sentinel node visualization and excision. This [^{18}F]boron/optical multimodality beacon ([^{18}F]BOMB) is differentiated from traditional C−^{18}F PET labeling strategies (*5*, *13*−*17*) by its one-step [^{18}F]fluoride wash-in labeling. [^{18}F]BOMB Lymphoseek **3** (Figure 1B) allows rapid, receptor-specific, positive identification of the sentinel lymph node in both the NIRF and PET imaging modes while maintaining little breakthrough to distal lymph nodes. This success predicts that [^{18}F]BOMB should be generalizable to other medically relevant targets.

EXPERIMENTAL PROCEDURES

Chemical Synthesis. *PET/NIR Dual-Probe Reaction with Lymphoseek: Synthesis of PET/NIR Lymphoseek Probe **2**.* The generally conjugatable NHS ester of PET/NIR probe **1** (4 μmol) (see the Supporting Information for detailed synthesis) was added as a CH_2Cl_2 solution directly into a 1.5 mL glass vial containing 5.5 mg (0.34 μmol) of Lymphoseek bearing 5.8 amine groups per dextran (Reliable Biopharmaceuticals). This solution was concentrated to dryness and then resuspended in 100 μL of DMF. This solution was sonicated for 1 h and left to react for 18 h. The next day, 10 μL of diisopropylethylamine was added and the reaction mixture was left for an additional 2 h. The reaction mixture was then transferred to a polypropylene centrifuge tube containing 25 mL of CH_2Cl_2. A pellet of **2** was isolated following centrifugation for 20 min at 3000 rcf, washed with two more portions of CH_2Cl_2, dried under high vacuum, and resuspended in 1 mL of water. This solution was centrifuged for 2 min at 18000 rcf. Water-soluble **2** was decanted from the pellet and divided into four aliquots, which were lyophilized and stored at −78 °C. On the basis of fluorescence readings, 115.9 nmol of fluorophore-conjugated Lymphoseek **2** was isolated. On the basis of a hexose assay (*36*), 34−49 nmol of Lymphoseek was isolated as **2**. This corresponds to a 10−14% yield of **2** from unconjugated Lymphoseek. The incorporation ratio of fluorophore to Lymphoseek was 2.36 to 3.41 fluorophores per molecule of Lymphoseek. Spectrophotometric constants of a 1.5 μM solution in water were as follows: absorbance maximum = 758 nm, $\varepsilon_{758} = 110000$ cm^{-1} M^{-1} per fluorophore, excitation maximum = 757 nm, emission maximum = 777 nm, and quantum yield = 0.026.

Radiochemistry. *^{18}F-Labeled Lymphoseek **3**.* A 300−500 μL aqueous solution containing 100 mCi of $^{18}F^-$ was transferred via syringe to a 10 mL glass vial containing 0.4 μL of 0.05 M KHF_2 (40 nmol) fluoride carrier. Note that acidic solutions of H^{18}F are volatile and radioactive, and therefore, the following procedures should be performed in a vented hot cell or a fume hood with radiation shielding. This sample was heated to dryness at 140 °C under a nitrogen flow. The clear dry solid was resuspended in 5 μL of a 0.25 M HCl/25% MeOH/75% H_2O solution. This solution, containing 30 mCi, was transferred to a 600 μL microcentrifuge tube containing 10.6 nmol of lyophilized **2**. This volume was sufficient to completely solubilize **3** and was reacted at 40 °C for 1 h. Following reaction,

the reaction was quenched with 40 μL of a 1 M MOPS buffered solution (pH 7.3).

To remove unreacted [^{18}F]fluoride, 5 μL of 3.0 M KHF_2 was added, and then the entire 45 μL was transferred to a Micro Bio Spin 6 column [molecular weight cutoff of 6000 (Bio-Rad)] buffered with 10 mM Tris (pH 7.4) and centrifuged without added eluant for 4 min at 1000 rcf. To the 40 μL of eluant was added an additional 5 μL of 3.0 M KHF_2 (30 μmol) to prevent the nonspecific elution of [^{18}F]fluoride, and the solution was immediately centrifuged. This described spin column purification was repeated three more times with a fresh spin column each time. Bio-Rad P-6 columns quantitatively remove small MW organic molecule impurities (see the Supporting Information) and 93% of [^{18}F]fluoride per column (99.998% of all [^{18}F]fluoride over four columns). Chromatography took 30 min total, and the final pH of the 60 μL of Tris-buffered, eluted solution was 7−8. Fluorescence showed that 6.0 nmol of ^{18}F-labeled PET/NIRF Lymphoseek **3** was eluted from the spin columns 90 min following $^{18}F^-$ concentration. The volume was 60 μL, and the activity was 300 μCi [total preparation time (reaction and purification) of 90 min]. See the Supporting Information for final analyses.

This purified solution was divided into two 30 μL portions, each sufficient for 3 × 10 μL, 1.0 nmol injections of Lymphoseek. To one portion was added 1.0 μL of a 31 mM solution of unconjugated Lymphoseek to give enough injectate for 3 × 10 μL, 11.0 nmol injections. Injections with specific activities of 0.05 Ci/μmol for 1 nmol Lymphoseek injections and 0.005 Ci/μmol for 11 nmol Lymphoseek injections were conducted for 15−75 min following synthesis and purification (see the Supporting Information for specifics).

*^{19}F (nonradioactive) Labeling of Lymphoseek **3**.* A 10.6 nmol quantity of lyophilized **2** was dissolved in a 0.25 M HCl/25% MeOH/75% H_2O solution in a 600 μL Eppendorf tube and left to react at 40 °C for 1 h. This reaction was quenched and the solution chromatographed under conditions similar to those described above for ^{18}F labeling. Spectrophotometric constants of a 1.5 μM solution of [^{19}F]**3** in water were as follows: absorbance maximum = 756 nm, ε_{756} = 110000 cm^{-1} M^{-1} per fluorophore, excitation maximum = 755 nm, emission maximum = 772 nm, and quantum yield = 0.027 (see the Supporting Information for HPLC characterization).

In Vivo Experiments. The in vivo procedures in this study have all been approved by the University of California, San Diego, Institutional Animal Care and Use Committee. A single subcutaneous injection of **3** was made into the right rear footpad of 20−25 g, 6−8-week-old athymic nude mice (Charles River Laboratories). These mice were anesthetized 20 min prior to injection with isoflurane, taped to black cardboard, and placed in pairs on an imaging stage. Six pairs of injections were made. The injected mice received either a 1 nmol dose or a 11 nmol dose (10 μL each) of 10 mM Tris-buffered [^{18}F]Lymphoseek **3** (pH 7.3). The distribution of [^{19}F]Lymphoseek **3** proceeded for 1 h and 20 min before the mice were euthanized by isoflurane overdose followed by cervical dislocation.

Imaging. PET and CT scanning were conducted on a eXplore Vista PET scanner or eXplore Locus CT scanner from GE Healthcare. PET acquisition was conducted in a single block in static emission mode with a 100−700 keV energy window. All PET scans were 20 min unless specified otherwise. Acquisition and OSEM PET reconstruction were performed with GE Explore Vista 3.1/MMKS Image Software. This reconstructed image was fused with computed tomography (CT) images processed with GE Medical Systems eXplore Utilities. CT Image acquisition was performed at 93 μm resolution over 10 min. PET/CT image fusion was conducted with the open source program amide 0.9.1.

NIRF imaging was conducted using multiple cameras because of radioactive licensing regulations. IR image acquisition of the nonradioactive compositions in Figure 2 was performed on a Maestro small animal imaging instrument (CRI Inc.) with a 820 nm emission filter and a 710−760 nm excitation wavelength. Data were collected over a 0.5−20 s exposure. Image processing was performed with Maestro version 2.0.2 and Photoshop. The Maestro, used for Figure 2, was the best instrument for real-time, fluorescence-guided node excision, although a custom system optimized for real-time intraoperative imaging would be yet more convenient. The success of sentinel lymph node excision was 100% as determined by histology with the Maestro. Because animals containing ^{18}F could not be transported to the Maestro, NIRF in vivo image acquisition of ^{18}F-labeled compounds was performed on two systems closer to the hot cell and PET scanner. The first was an eXplore Optix (ART, Advanced Research Technologies Inc.) optical imaging system. This is a point source-detector system with a 750 nm excitation laser and a 780 nm long pass filter placed before the photomultiplier tube for single-photon fluorescence detection. The regions of interest were raster-scanned in 1.5 mm steps with laser powers ranging from 200 to 800 μW and signal integration times ranging from 200 to 1000 ms per point. Image processing was performed with Optix version 2 and Photoshop. However, the slow raster scan of the Optix made real-time, image-guided node excision difficult, so a custom full field system (*37*) was employed for faster NIRF imaging of ^{18}F-labeled compounds (Figure 3C). This system used a pulsed laser tuned to 720 nm (Mai TaiSpectraPhysics) whose output was passed through an expansion lens and diffuser for uniform area illumination. Area detection of the fluorescence intensity was acquired in reflection mode using a 780 nm fluorescence filter and standard 50 mm lens (Nikon) mounted to a microchannel plate (Picostar HRI, La Vision) for signal amplification, which was coupled to an electron-multiplying CCD camera (Andor) to capture the image. Subsequent image processing was performed with Image J and Photoshop. Both the Optix and custom systems can measure nanosecond decay kinetics to provide extra information about probe lifetime and depth, but this dimension was not exploited here.

Lymph Node Removal and Dissection. Animals were euthanized by isoflurane overdose or CO_2 inhalation followed by cervical dislocation. After the skin had been removed, fluorescent images were taken to improve the visualization of the positions of the fluorescent lymph nodes. With mice placed in prone positions, both right and left sets of lymph nodes were surgically removed in the following order: the left popliteal, the left lumbar, the right lumbar, and the right popliteal. Following excision, nodes were weighted, submersed in Optimal Cutting Temperature (OCT) Compound (Sakura Tissue-Tec # 4585) cryogenic embedding medium, and replaced next to their mouse of origin within the field of view, approximately half a centimeter below the surgical site in the corresponding mouse. In some instances where sentinel node excision was difficult, fluorescence guidance was utilized to guide surgical removal.

Following imaging, samples of blood (vena cava), liver, kidney, spleen, the hind feet (right and left), bone (contralateral femur), and muscle from the contralateral femur were collected.

Histology. Immediately following excision, lymph nodes were weighed and then coated in OCT Compound to prevent lymph nodes from becoming dehydrated during PET/CT/NIRF analysis and overnight scintillation counting. Lymph nodes were frozen at −80 °C for extended periods of time in this preservative. Frozen sections (10 μm) of the lymph nodes were imaged under NIRF conditions on a stereomicroscope (Zeiss, Lumar). Tissue was stained with hematoxylin and eosin and subsequently imaged via light microscopy (Zeiss, Axiovert). Images were

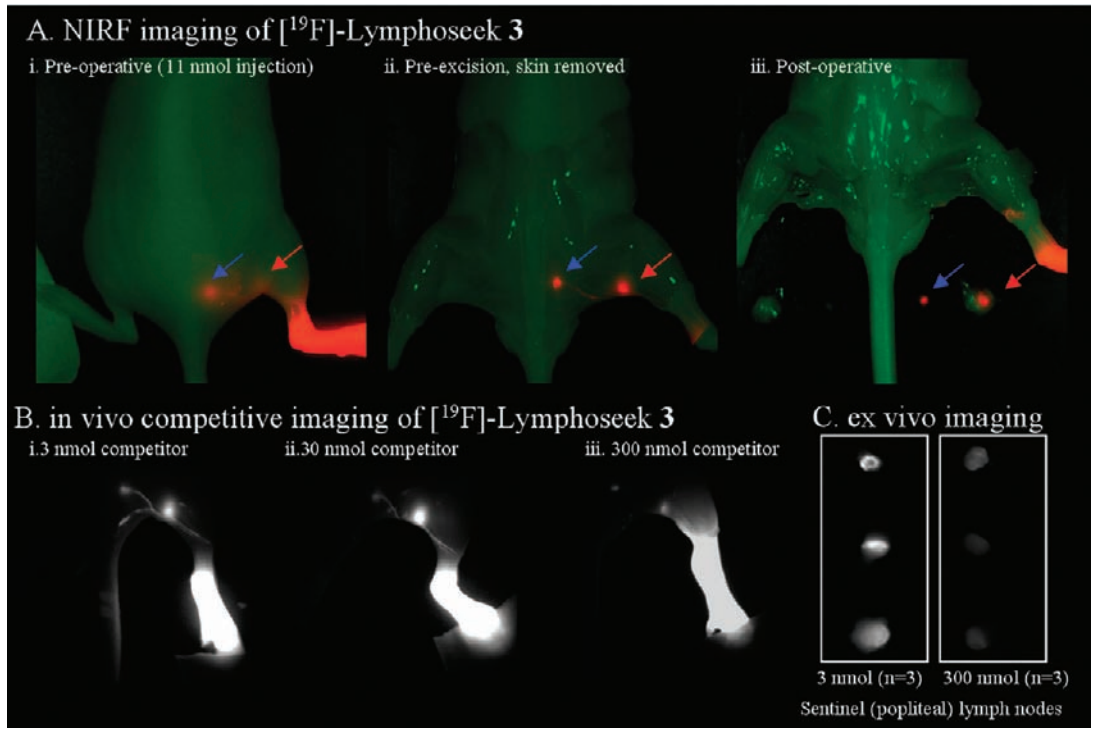


Figure 2. Nonradioactive NIRF imaging of [^{19}F]Lymphoseek **3**. (A) Typical NIRF imaging experiment of a mouse that had been injected with 1 nmol of [^{19}F]**3** diluted with 10 nmol of unconjugated Lymphoseek. The NIRF signal (colored red) is overlaid onto a bright field image (green) of a mouse. A red arrow indicates clear localization of [^{19}F]Lymphoseek **3** to the sentinel (popliteal) lymph node, while the blue arrow indicates localization to the distal (lumbar) lymph node. (i) Post-mortem skin-on image in which tissue (skin) notably interferes with the sentinel lymph node visibility. (ii) Pre-excision image (skin removed) in which the sentinel node visibility is improved and lymph drainage tracks are visible. (iii) Postoperative image in which the excised lymph nodes have been placed in the field of view. (B) In vivo imaging of [^{19}F]Lymphoseek **3**'s mannose receptor specific activity. Fluorescent [^{19}F]Lymphoseek **3** (1 nmol) was imaged in the presence of 2 (i), 29 (ii), or 300 nmol (iii) of unlabeled Lymphoseek, a competitor for lymph node mannose binding sites. Note that lymph tracks are clearly visible and that greater accumulation of fluorescent [^{19}F]Lymphoseek **3** is seen in the sentinel lymph nodes with 3 and 30 nmol injections than with 300 nmol injections because of increased competition with unlabeled Lymphoseek for sentinel lymph node mannose receptors. (C) Ex vivo imaging of [^{19}F]Lymphoseek **3**'s mannose receptor specific activity. Sentinel lymph nodes were extracted from mice and placed on a bed for analysis. Greater accumulation of fluorescent [^{19}F]Lymphoseek **3** is seen in the sentinel lymph nodes in 3 nmol injections than in 300 nmol injections (signal ratio of 3.5, $n = 3$ mice per dose, $P = 0.015$ for a two-tailed test, two-sample equal variance, quantization shown in the Supporting Information).

processed using Image J. The fluorescent histology was acquired using 710/75 nm band-pass excitation and 810/90 nm band-pass emission filters.

Biodistributions. Tissue and injectate samples of known dilutions were assayed (Gamma 9000, Beckman Instruments) for radioactivity using a 400−600 keV energy collection window.

*Nonradioactive [^{19}F]Lymphoseek **3** Dosing Experiments.* Nonradioactive [^{19}F]Lymphoseek **3** was prepared as described for its ^{18}F counterpart. This preparation was divided into 10 μL aliquots of 10 mM Tris (pH 7.3) that contained 1.0 nmol of ^{19}F-labeled Lymphoseek **3** diluted with 2, 10, 29, or 300 nmol of unlabeled Lymphoseek.

RESULTS

Synthesis and Conjugation of a General PET/NIRF NHS Probe. We appended a sufficiently electron withdrawing boronic ester (*23*) to a heptamethine cyanine, a member of a class of small-molecule dyes that possess an established safety record (*38*, *39*). Through chemistry pioneered by the Achilefu group (*40*), we modified the inexpensive synthon IR-775 (Sigma-Aldrich) into an *N*-hydroxysuccinimide (NHS)-activated pre-PET/NIRF probe **1** (Figure 1A) in three steps with a final yield of 50.7%. The resulting pre-PET/NIRF probe **1** (Figure 1A) shows long wavelength NIR fluorescence and adequate quantum yield [excitation maximum = 755 nm, emission maximum = 772 nm, and $\varphi_f = 0.027$ (Figure 1C)]. It was conjugated to Lymphoseek in a ratio of two to three molecules of fluorophore per molecule of Lymphoseek to give precursor **2** (Figure 1B). Self-quenching on **2** or **3** was not observed (see the Supporting Information).

Nonradioactive Fluorescence-Based Lymphoseek Dosing. Initial staging experiments were conducted for two purposes: (1) to determine what doses, when injected into the right rear footpad, would rapidly identify the (sentinel) popliteal lymph node and minimize flow-through to distal (lumbar) lymph nodes and (2) to determine if the conjugation of Lymphoseek to the PET/NIRF probe had altered Lymphoseek's desired pharmaceutical properties, especially mannose receptor specificity. These experiments were conducted with nonradioactive [^{19}F]Lymphoseek **3** and fluorescence equipment alone, minimizing the use of radioactivity during initial stages of this project. Lymphoseek boronate **2** (Figure 1B) was converted into fluoroborate **3**, and 1 nmol of this fluorescent material was diluted with 0, 2, 10, 29, or 300 nmol of unconjugated Lymphoseek to give 1, 3, 11, 30, or 301 nmol of total Lymphoseek but identical quantities of fluorophore. These mixtures were injected into mice (three injections per dose, 15 mice total). After 80 min, the first two lymph nodes that drain the rear-footpad injection site could be viewed by NIRF (Figure 2A,B).

In 1, 3, 11, and 30 nmol Lymphoseek injections (Figure 3 and panels Bi, A, and Bii of Figure 2, respectively), a high level of uptake in the sentinel node was observed with limited flow-through to distal lymph nodes. Injections where **3** had been diluted with 300 nmol of unlabeled Lymphoseek gave less

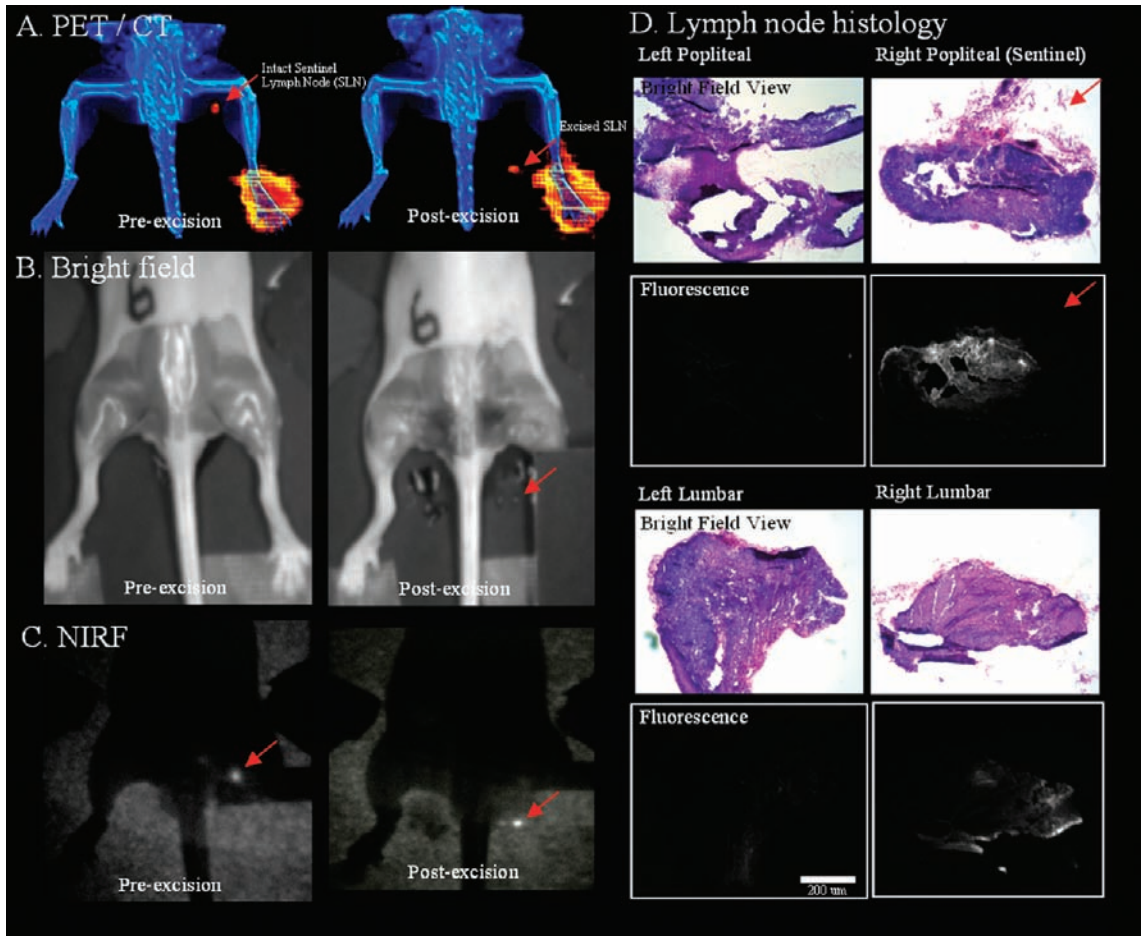


Figure 3. Multimodality imaging of a mouse injected with a 10 μL, 1 nmol, 48.1 μCi dose of ^{18}F-labeled Lymphoseek **3** (0.048 Ci/μmol). The red arrows indicates the location of the sentinel lymph node. (A) Pre-excision, live-mouse PET (red color table)/CT (blue color table) scan (left) and postoperative PET/CT scan (right) of the mouse with excised nodes (right and left lumbar and popliteal) that are placed below the excision site in the field of view. (B) Bright field images of the mouse with skin removed before (left) and after node excision (right). (C) NIRF images taken 90 min postexcision on a custom full field IR camera before (left) and after (right) lymph node excision. The injection site was covered with black cardboard to block intense signal from the foot and allow better visualization of the fluorescent lymph nodes. (D) H and E stain (top, color images) and NIRF (bottom, black and white images) histological verification of lymph node excision. A PET projection video of panel A is given as Supporting Information.

fluorescence in the sentinel lymph node of mice because of competition for SLN mannose receptors (Figure 2Biii,C). Such saturable binding of [^{19}F]Lymphoseek **3** to a limited number of SLN mannose receptors (*32, 34, 41*) suggests that conjugation to **1** does not alter Lymphoseek's mannose receptor specificity. This observation is confirmed quantitatively in separate biodistribution experiments (vide infra).

Image-guided surgical excisions of the SLN were then conducted and confirmed (Figure 2C). Real-time imaging with a NIRF camera allows for rapid and simple removal of lymph nodes, especially because the lymph tracks connecting the nodes are fully visible (Figure 2Bi,Biii). Notably, lymph tracks in mice have not been previously observed with [^{99m}Tc]Lymphoseek. The observed lymph tracks connecting injection sites and nodes should help identify the sentinel node in cases where the distinctions between distal and sentinel nodes are ambiguous.

Radiochemistry. From NIRF experiments (Figure 2), we determined that total doses of Lymphoseek of up to 30 nmol work well in imaging the SLN in mice. Using these doses, we incorporated different ^{18}F activities into **3** to determine the optimal level of radioactivity that would provide sufficient signal to image 1 nmol of Lymphoseek by PET, synthesized on a large multi-injection scale starting with only 100 mCi of $^{18}F^-$ ion. A specific activity of 1−50 Ci/mmol at the time of injection proved to be adequate for imaging ^{18}F-labeled **3** in a 20 min PET scan 1 h after injection.

Size exclusion gel chromatography in spin columns was used to remove small molecule impurities and free [^{18}F]fluoride ions from radiochemical preparations. The removal of [^{18}F]fluoride was evidenced by the absence of a bone signal in PET images (Figure 3A and Supporting Information) (*25*) and biodistribution studies (Figure 4, bone). In mouse serum, the chemical release of F^- from ^{18}F-labeled Lymphoseek **3** had a half-life of 21 h (Supporting Information), 11.6-fold slower than the radioactive decay of ^{18}F.

Multimodality PET/CT/NIRF Imaging. [^{18}F]Lymphoseek **3** was tested for in vivo multimodal imaging in 12 mice. Injections containing 1 nmol and 10−50 μCi of fluorescent **3**, with 0 or 10 nmol of added unlabeled Lymphoseek, were made into the right rear footpad of anesthetized nude mice positioned securely on trays for corroborative multimodality imaging. One hour later, a 20 min PET/CT scan was acquired (Figure 3A, left). Mice were then sacrificed by CO_2 inhalation followed by cervical dislocation; skin was removed, and NIRF images were obtained before (Figure 3C, left) and after excision of nodes, which were placed below their location of origin on the imaging tray. The bright field image of this dissection is shown in Figure 3B (before excision, left, and after excision, right). Successful node excision was confirmed by both NIRF (Figure 3C, right) and PET/CT imaging (Figure 3A, right, and Supporting Information), showing the node signal outside the body. Following image acquisition, tissues were collected for scin-

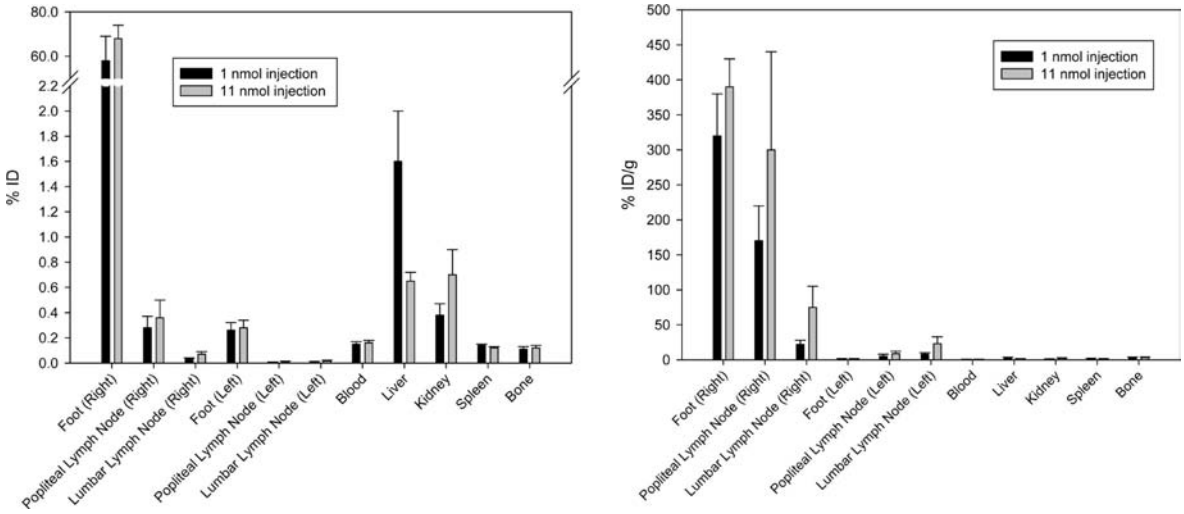


Figure 4. [^{18}F]Lymphoseek **3** tissue biodistribution in mice that were sacrificed 1 h and 20 min following injection. Units of percent injected dose (ID, left) and percent injected dose per gram (right). Biodistribution data from 12 mice were used to compile this figure.

Table 1. Distribution of Radioactive [^{18}F]Lymphoseek 3 in Mice That Were Sacrificed 80 min following Injection[a]

	percent [^{18}F]**3** activity extracted in the sentinel node	Lymphoseek in the sentinel or popliteal lymph node (pmol) (percent of detected nodal Lymphoseek)	Lymphoseek flow-through to the distal or lumbar node (pmol) (percent of detected nodal Lymphoseek)
1 nmol Lymphoseek injection	87 ± 7%	3.0 ± 0.9 (91%)	0.3 ± 0.1 (9%)
11 nmol Lymphoseek injection	74 ± 7%	40 ± 15 (83%)	8 ± 3 (17%)
t test (one-tailed two-sample unequal variance)	$P = 0.022$		$P = 0.033$

[a] Scintigraphy data from six mice were obtained per injected Lymphoseek dose (12 mice total). The percent activity extracted is defined as the difference in counts between the sentinel and distal lymph nodes minus the sum of counts in the sentinel and distal lymph nodes [(counts$_{popliteal}$ − counts$_{lumbar}$)/(counts$_{popliteal}$ + counts$_{lumbar}$)]. The percent of detected nodal Lymphoseek is defined as the amount of Lymphoseek in the lumbar lymph node divided by the sum of the Lymphoseek in both the popliteal and lumbar lymph nodes. Error = $\sigma/(n = 6)^{1/2}$.

tigraphy and histological sectioning (Figure 3D). Little or no flow-through of [^{18}F]Lymphoseek **3** to distal lymph nodes was observed in both NIRF and PET images taken under both injection conditions. PET and NIRF signals were confined to the SLN, the injection site, and, in some cases, the bladder.

Biodistribution. Scintigraphy corroborated the qualitative data observed in PET and IR images (Figure 3A,C). The [^{18}F]Lymphoseek **3** tissue distribution is shown in Figure 4 as the percent of injected dose (% ID) before (left) and after (right) normalization by tissue mass. In 1 and 11 nmol injections of Lymphoseek, the tissues of interest containing the most [^{18}F]Lymphoseek **3** are the right foot (320 ± 60 and 390 ± 40% ID/g per foot, respectively) and the right popliteal (sentinel) lymph node (170 ± 50 and 300 ± 140% ID/g per node, respectively). There is 4−7 times less [^{18}F]Lymphoseek **3** in the ipsilateral distal (lumbar) lymph nodes (22 ± 6 and 75 ± 30% ID/g, respectively) than in the sentinel lymph nodes. Much less [^{18}F]Lymphoseek accumulation is observed in contralateral nodes (5 ± 3 and 9 ± 4% ID/g for contralateral popliteal lymph nodes and 8 ± 2 and 23 ± 10% ID/g for contralateral lumbar lymph nodes, for 1 and 11 nmol injections, respectively). Nonlymphatic tissue, i.e., blood, liver, kidney, spleen, and bone, contained not more than 4% ID/g of [^{18}F]Lymphoseek **3**.

Statistical analysis verified that [^{18}F]Lymphoseek **3** retains receptor targeting properties consistent with [^{99m}Tc]Lymphoseek literature (*32*, *41*). In mice treated with 1 nmol of [^{18}F]Lymphoseek, the sentinel node extracted 87 ± 7% (Table 1) of the total lymph node accumulation, significantly greater than 74 ± 7% extracted at an 11 nmol dose. These values correspond to 3 ± 0.9 and 40 ± 15 pmol of total Lymphoseek (3 ± 0.9 and 3.6 ± 1 pmol of ^{18}F-labeled Lymphoseek **3**, respectively) in the sentinel node. These are subsaturating doses of Lymphoseek. The Lymphoseek binding capacity from a rear footpad injection in the popliteal node of mice is 49 ± 25 pmol (*41*).

Histology. NIRF histology (Figure 3D) showed that Lymphoseek **3** indeed localized to SLNs (Figure 3D), though ^{18}F activity was no longer measurable. On the basis of the specific activity of radiolabeling, the majority (>99%) of the fluorescent material was nonradioactive [^{19}F]**3** even before the ^{18}F had decayed. Hematoxylin and eosin (H and E) frozen sections of the excised lymph nodes of mice were prepared and analyzed. Specifically, lymph nodes were confirmed through the observation of an encapsulated dense mass of densely packed lymphocytes. The dense packing of these mononuclear cells includes a high nucleus:cytoplasm ratio that gives a dense basophilic/purple staining under H and E staining conditions.

DISCUSSION

We describe the novel synthesis of a small molecule NHS ester that confers both ^{18}F PET and NIRF visibility onto targeting ligands bearing free amines. Heterobifunctional adapters could easily convert the selectivity toward other reactive groups such as thiols. Because the ^{18}F is appended to the cyanine dye, only one attachment site on the targeting ligand is required. If standard NIRF and PET labels were independently affixed (*4*, *7*), at least two chemically reactive yet biologically tolerant sites on the ligand would be required. Unless regioselectivity could be tightly controlled, greater combinatorial complexity of products could result, because each site could remain unmodified or receive a NIRF or PET label. Homogeneous labeling happens not to be essential for Lymphoseek, which already contains a statistical distribution of amines, but Lymphoseek had the advantages of large-scale availability and extensive preclinical and clinical characterization. PET/NIRF-labeled Lymphoseek **3** retains the desired pharmaceutical properties of [^{99m}Tc]Lymphoseek: rapid 1 h sentinel node targeting, low level of distal lymph node accumulation, and sentinel node extraction values (1 nmol dose, 87 ± 7%; 11 nmol

dose, 74 ± 7%) that compare very well to [^{99m}Tc]Lymphoseek extraction ratios, 90 ± 10% in rabbit popliteal SLN (*31, 32*).

PET rapidly and noninvasively quantitates picomole amounts of **1** through deep tissue. An example of the superior tomographic resolution conveyed by ^{18}F PET in Figure 3A is included as an .mpg file (Supporting Information). Notably, this high-resolution projection was generated from a 20 min scan on a live mouse using only 33 μCi of activity. PET is more reliable than NIRF for imaging through deep tissue. This point is illustrated by comparing the skin-on NIRF image (Figure 2Ai) to the skin-off NIRF image (Figure 2Aii). If one were to use Figure 2Ai to evaluate Lymphoseek distribution based on relative NIRF brightness, it would incorrectly appear that the sentinel node (red arrow), buried in muscle and fat, has less Lymphoseek than the lumbar node (blue arrow), which sits next to the spine near the surface of the mouse. Following mouse sacrifice followed by skin removal (Figure 2Aii), we see that the opposite is true and that the NIRF signal is biased to tissue depth. Note that the lymph nodes seen in Figure 2 Ai would be entirely invisible by NIRF if wild-type, hair-bearing mice were used. PET is superior to NIRF in that it allows for quantitative noninvasive deep tissue three-dimensional imaging. Both the live mouse PET images shown in Figure 3 and the .mpg file included as Supporting Information illustrate this. Additional advances in PET imaging may include better CT attenuation algorithms for higher-resolution images and real-time PET reconstruction to guide surgery. If a PET scanner is not available, standard scintigraphic devices can still be used to register the positron-generated γ-rays (*42*−*44*). Consistent with previous studies of ^{18}F-labeled aryltrifluoroborates, no signal is observed in bone structure (Figures 3A and 4), demonstrating the in vivo stability of the aryl trifluoroborate to solvolysis and release of free ^{18}F (*22, 23, 45*).

The stable NIRF component on **1** also allows for NIRF-guided surgery as well as fluorescent histology long after radiotracer decay. Histological resolution (Figure 3D) and the imaging of lymph tracks (Figure 2Bi−iii) are possible only by NIRF, as these structures fall below the spatial detection limits of PET. The heterogeneous foci seen in NIRF histology (Figure 3D) identify the most probable places to find micrometastatic disease in the SLN (*46*), and their fluorescence might reduce the error in pathological evaluations. The heterogeneous distribution of **3** also suggests that only a fraction of the SLN actually filters the afferent lymph channel draining the foot. Both a 1 nmol injection of pure [^{18}F]Lymphoseek **3** and an 11 nmol injection of **3** diluted with unlabeled Lymphoseek are useful in highlighting sentinel popliteal nodes. Our use of a diluted 11 nmol injection may seem superfluous as it requires an extra step in preparation and is slightly inferior to the 1 nmol injection in terms of unwanted flow-through to distal lymph nodes (Table 1). However, the fact that the lymph node mannose receptor binding of **3** can be diluted with unlabeled Lymphoseek such that distal node flow-through is increased serves to illustrate an important trait of the dual probe, that the conjugation of targets to NHS ester **1** does not alter its target's desired diagnostic properties, in this case Lymphoseek's mannose receptor-specific targeting properties.

This PET/NIRF version of Lymphoseek **3** may improve sentinel node biopsy, because a single injection would replace the required multiple-injection combination (*47, 48*) of a radiotracer, such as [^{99m}Tc]Lymphoseek or [^{99m}Tc]sulfur colloid, with a nonspecific optical excision aid such as isosulfan blue dye. Attachment of both the positron emitter and fluorophore to a single molecularly targeted agent diminishes the risk of flow-through to distal lymph nodes and ensures perfect coregistration of the two signals, allowing PET and NIRF to complement each other. PET images would noninvasively identify sentinel nodes that drain a tumor and aid in preoperative planning. During surgery, Geiger counting of the γ-rays could help locate deeply buried nodes. Once they were exposed, higher-resolution real-time NIRF imaging would guide precision resection, including lymph tracks as well as nodes. A postoperative PET scan could confirm whether removal was complete, and NIRF would aid histological identification of metastases within the resected tissue. Successful application of PET/NIRF NHS ester **1** to a well-established, clinically interesting system suggests extension to other medically relevant targets. In previous combinations of PET and NIRF, the positron emitter and fluorophore were independently attached (*4, 7*), whereas **1** combines these capabilities in a single, versatile small molecule only slightly larger than the usual commercially available NIRF labels. It is essential that ^{18}F is incorporated into fluoroborates under mild conditions such as a weakly acidic methanol/water solution at 40 °C, because heptamethine cyanine dyes would not survive high-temperature reaction with anhydrous nucleophilic fluoride as required for traditional ^{18}F chemistries such as fluorobenzyl labeling. Despite scope for further optimization, formation of aryl fluoborate from F^- satisfies many of the criteria for "click chemistry", modularity, high yield, no offensive byproducts, mild aqueous reaction conditions, orthogonality to other functional groups, and simple product isolation (*49*). Although the B−F bond is not as chemically stable as the usual C−F bonds, appropriately substituted aryl fluoborates are stable enough that hydrolysis is negligible within the radioactive half-life of ^{18}F. Our new chemistry should facilitate the multimodality labeling of peptides, proteins, and polysaccharides, medically relevant ligands previously difficult or impossible to label by previous methods.

ACKNOWLEDGMENT

We thank Jacqueline Corbeil for excellent technical assistance with PET, CT, and NIRF imaging studies and Larry Gross for his assistance in obtaining high-resolution mass spectrometry data. This work is supported by the Howard Hughes Medical Institute (HHMI) and Grant W81XWH-05-1-0183 from the Department of Defense Breast Cancer Research Program. R.T. is supported by a Canadian Institute of Health Research (CIHR) Post-Doctoral Fellowship (MFE 83832).

Supporting Information Available: PET/CT video; PET/CT reconstructed data accessible with amide 0.9.1 (http://amide.sourceforge.net); in vivo and synthetic experimental procedures; additional multimodality PET/CT/NIRF data; fluorophore absorption, excitation, and emission spectra; Lymphoseek certificate of analysis; and Lymphoseek in vivo stability and saturation assays. This material is available free of charge via the Internet at http://pubs.acs.org.

LITERATURE CITED

(1) Tsien, R. Y. (2003) Imagining imaging's future. *Nat. Rev. Mol. Cell Biol. 9*, s16–s21.

(2) Bhushan, K. R., Mistra, P., Liu, F., Mathur, S., Lenkinski, R. E., and Frangioni, J. V. (2008) Detection of breast cancer microcalcifications using a dual-modality SPECT/NIR fluorescent probe. *J. Am. Chem. Soc. 130*, 17648–17649.

(3) Pascu, S. I., Waghorn, P. A., Conry, T. D., Betts, H. M., Dilworth, J. R., Churchill, G. C., Pokrovska, T., Christlieb, M., Aigbirhio, F. I., and Warren, J. E. (2007) Designing Zn(II) and Cu(II) derivatives as probes for in vitro fluorescence imaging. *Dalton Trans.*, 4988–4997.

(4) Edwards, W. B., Xu, B., Akers, W., Cheney, P. P., Liang, K., Rogers, B. E., Anderson, C. J., and Achilefu, S. (2008) Agonist-antagonist dilemma in molecular imaging: Evaluation of a monomolecular multimodal imaging agent for the somatostatin receptor. *Bioconjugate Chem. 19*, 192–200.

(5) Duconge, F., Pons, T., Pestourie, C., Herin, L., Theze, B., Gombert, K., Mahler, B., Hinnen, F., Kuhnast, B., Dolle, F., Dubertret, B., and Tavitian, B. (2008) Fluorine-18-labeled phospholipid quantum dot micelles for in vivo multimodal imaging from whole body to cellular scales. *Bioconjugate Chem. 19*, 1921–1926.

(6) Devaraj, N. K., Keliher, E. J., Thurber, G. M., Nahrendorf, M., and Weissleder, R. (2009) F-18 Labeled Nanoparticles for in Vivo PET-CT Imaging. *Bioconjugate Chem. 20*, 397–401.

(7) Kimura, R., Miao, Z., Cheng, Z., Gambhir, S., and Cochran, J. (2010) A Dual-Labeled Knottin Peptide for PET and Near-Infrared Fluorescence Imaging of Integrin Expression in Living Subjects. *Bioconjugate Chem. 21*, 436–444.

(8) Wu, A. M., Yazaki, P. J., Tsai, S. W., Nguyen, K., Anderson, A. L., McCarthy, D. W., Welch, M. J., Shively, J. E., Williams, L. E., Raubitschek, A. A., Wong, J. Y. C., Toyokuni, T., Phelps, M. E., and Gambhir, S. S. (2000) High-resolution microPET imaging of carcino-embryonic antigen-positive xenografts by using a copper-64-labeled engineered antibody fragment. *Proc. Natl. Acad. Sci. U.S.A. 97*, 8495–8500.

(9) Dimitrakopoulou-Strauss, A., Hohenberger, P., Haberkorn, U., Macke, H. R., Eisenhut, M., and Strauss, L. G. (2007) ^{68}Ga-labeled bombesin studies in patients with gastrointestinal stromal tumors: Comparison with ^{18}F-FDG. *J. Nucl. Med. 48*, 1245–1250.

(10) Meyer, G. J., Macke, H., Schuhmacher, J., Knapp, W. H., and Hofmann, M. (2004) ^{68}Ga-labelled DOTA-derivatised peptide ligands. *Eur. J. Nucl. Med. Mol. Imaging 31*, 1097–1104.

(11) Abbas, K., Kozempel, J., Bonardi, M., Groppi, F., Alfarano, A., Holzwarth, U., Simonelli, F., Hofman, H., Horstmann, W., Menapace, E., Leseticky, L., and Gibson, N. (2006) Cyclotron production of Cu-64 by deuteron irradiation of Zn-64. *Appl. Radiat. Isot. 64*, 1001–1005.

(12) Boswell, C. A., Sun, X. K., Niu, W. J., Weisman, G. R., Wong, E. H., Rheingold, A. L., and Anderson, C. J. (2004) Comparative in vivo stability of copper-64-labeled cross-bridged and conventional tetraazamacrocyclic complexes. *J. Med. Chem. 47*, 1465–1474.

(13) Olasz, E. B., Lang, L., Seidel, J., Green, M. V., Eckelman, W. C., and Katz, S. I. (2002) Fluorine-18 labeled mouse bone marrow-derived dendritic cells can be detected in vivo by high resolution projection imaging. *J. Immunol. Methods 260*, 137–148.

(14) Kuhnast, B., de Bruin, A., Hinnen, F., Tavitian, B., and Dolle, F. (2004) Design and synthesis of a new [F-18]fluoropyridine-based haloacetamide reagent for the labeling of oligonucleotides: 2-Bromo-N-[3-(2-[F-18]fluoropyridin-3-yloxy)propyl]acetamide. *Bioconjugate Chem. 15*, 617–627.

(15) Ross, T. L., Ermert, J., Hocke, C., and Coenen, H. H. (2007) Nucleophilic F-18-fluorination of heteroaromatic iodonium salts with no-carrier-added [F-18]fluoride. *J. Am. Chem. Soc. 129*, 8018–8025.

(16) Flavell, R. R., Kothari, P., Bar-Dagan, M., Synan, M., Vallabhajosula, S., Friedman, J. M., Muir, T. W., and Ceccarini, G. (2008) Site-specific F-18-labeling of the protein hormone leptin using a general two-step ligation procedure. *J. Am. Chem. Soc. 130*, 9106–9112.

(17) Glaser, M., and Arstad, E. (2007) "Click labeling" with 2-[F-18]fluoroethylazide for positron emission tomography. *Bioconjugate Chem. 18*, 989–993.

(18) Schirrmacher, R., Bradtmoller, G., Schirrmacher, E., Thews, O., Tillmanns, J., Siessmeier, T., Buchholz, H. G., Bartenstein, P., Wangler, B., Niemeyer, C. M., and Jurkschat, K. (2006) ^{18}F-labeling of peptides by means of an organosilicon-based fluoride acceptor. *Angew. Chem., Int. Ed. 45*, 6047–6050.

(19) Hohne, A., Mu, L., Honer, M., Schubiger, P. A., Ametamey, S. M., Graham, K., Stellfeld, T., Borkowski, S., Berndorff, D., Klar, U., Voigtmann, U., Cyr, J. E., Friebe, M., Dinkelborg, L., and Srinivasan, A. (2008) Synthesis, ^{18}F-labeling, and in vitro and in vivo studies of bombesin peptides modified with silicon-based building blocks. *Bioconjugate Chem. 19*, 1871–1879.

(20) Mu, L., Hohne, A., Schubiger, P. A., Ametamey, S. M., Graham, K., Cyr, J. E., Dinkelborg, L., Stellfeld, T., Srinivasan, A., Voigtmann, U., and Klar, U. (2008) Silicon-based building blocks for one-step ^{18}F-radiolabeling of peptides for PET imaging. *Angew. Chem., Int. Ed. 47*, 4922–4925.

(21) Schirrmacher, E., Wangler, B., Cypryk, M., Bradtmoller, G., Schafer, M., Eisenhut, M., Jurkschat, K., and Schirrmacher, R. (2007) Synthesis of p-(di-tert-butyl[^{18}F]fluorosilyl)benzaldehyde ([^{18}F]SiFA-A) with high specific activity by isotopic exchange: A convenient labeling synthon for the ^{18}F-labeling of N-aminooxy derivatized peptides. *Bioconjugate Chem. 18*, 2085–2089.

(22) Ting, R., Harwig, C. W., Lo, J., Li, Y., Adam, M. J., Ruth, T. J., and Perrin, D. M. (2008) Substituent effects on aryltrifluoroborate solvolysis in water: Implications for Suzuki-Miyaura coupling and the design of stable F-18-labeled aryltrifluoroborates for use in PET imaging. *J. Org. Chem. 73*, 4662–4670.

(23) Ting, R., Lo, J., Adam, M. J., Ruth, T. J., and Perrin, D. M. (2008) Capturing aqueous [F-18]-fluoride with an arylboronic ester for PET: Synthesis and aqueous stability of a fluorescent [F-18]-labeled aryltrifluoroborate. *J. Fluorine Chem. 129*, 349–358.

(24) Ting, R., Adam, M. J., Ruth, T. J., and Perrin, D. M. (2005) Arylfluoroborates and alkylfluorosilicates as potential PET imaging agents: High-yielding aqueous biomolecular F-18-labeling. *J. Am. Chem. Soc. 127*, 13094–13095.

(25) Ting, R., Harwig, C., auf dem Keller, U., McCormick, S., Austin, P., Overall, C. M., Adam, M. J., Ruth, T. J., and Perrin, D. M. (2008) Toward [F-18]-labeled aryltrifluoroborate radiotracers: In vivo positron emission tomography imaging of stable aryltrifluoroborate clearance in mice. *J. Am. Chem. Soc. 130*, 12045–12055.

(26) Valk, P. E., Bailey, D. L., Townsend, D. W., and Maisey, M. N. (2003) *Positron Emission Tomography: Basic Science and Clinical Practice*, Springer-Verlag, London.

(27) Hirsch, J. I., Tisnado, J., Cho, S. R., and Beachley, M. C. (1982) Use of Isosulfan Blue for Identification of Lymphatic Vessels: Experimental and Clinical Evaluation. *Am. J. Roentgenol. Radium Ther. 139*, 1061–1064.

(28) Mariani, G., Gipponi, M., Moresco, L., Villa, G., Bartolomei, M., Mazzarol, G., Bagnara, M. C., Romanini, A., Cafiero, F., Paganelli, G., and Strauss, H. W. (2002) Radioguided sentinel lymph node biopsy in malignant cutaneous melanoma. *J. Nucl. Med. 43*, 811–827.

(29) Mariani, G., Moresco, L., Viale, G., Villa, G., Bagnasco, M., Canavese, G., Buscombe, J., Strauss, H. W., and Paganelli, G. (2001) Radioguided sentinel lymph node biopsy in breast cancer surgery. *J. Nucl. Med. 42*, 1198–1215.

(30) Weaver, D. L., Krag, D. N., Ashikaga, T., Harlow, S. P., and O'Connell, M. (2000) Pathologic analysis of sentinel and nonsentinel lymph nodes in breast carcinoma: A multicenter study. *Cancer 88*, 1099–1107.

(31) Vera, D. R., Wisner, E. R., and Stadalnik, R. C. (1997) Sentinel node imaging via a nonparticulate receptor-binding radiotracer. *J. Nucl. Med. 38*, 530–535.

(32) Vera, D. R., Wallace, A. M., Hoh, C. K., and Mattrey, R. F. (2001) A synthetic macromolecule for sentinel node detection: Tc-99m-DTPA-mannosyl-dextran. *J. Nucl. Med. 42*, 951–959.

(33) Hoh, C. K., Wallace, A. M., and Vera, D. R. (2003) Preclinical studies of [Tc-99m]DTPA-mannosyl-dextran. *Nucl. Med. Biol. 30*, 457–464.

(34) Vera, D. R., Wallace, A. M., and Hoh, C. K. (2001) [Tc-99m]MAG_3-mannosyl-dextran: A receptor-binding radiopharmaceutical for sentinel node detection. *Nucl. Med. Biol. 28*, 493–498.

(35) Schoder, H., Glass, E. C., Pecking, A. P., Harness, J. K., Wallace, A. M., Hirnle, P., Alberini, J. L., Vilain, D., Larson, S. M., Hoh, C. K., and Vera, D. R. (2006) Molecular targeting of the lymphovascular system for imaging and therapy. *Cancer Metastasis Rev. 25*, 185–201.

(36) Dubois, M., Gilles, K. A., Hamilton, J. K., Rebers, P. A., and Smith, F. (1956) Colorimetric Method for Determination of Sugars and Related Substances. *Anal. Chem. 28*, 350–356.
(37) Hall, D. J., Sunar, U., Farshchi-Heydari, S., and Han, S. H. (2009) In vivo simultaneous monitoring of two fluorophores with lifetime contrast using a full-field time domain system. *Appl. Opt. 48*, D74–D78.
(38) Fox, I. J., and Wood, E. H. (1960) Indocyanine Green: Physical and Physiologic Properties. *Proc. Staff Meet. Mayo Clin. 35*, 732–744.
(39) Fox, I. J., Brooker, L. G. S., Heseltine, D. W., Essex, H. E., and Wood, E. H. (1956) New Dyes for Continuous Recording of Dilution Curves in Whole Blood Independent of Variations in Blood Oxygen Saturation. *Am. J. Physiol. 187*, 599.
(40) Lee, H., Mason, J. C., and Achilefu, S. (2006) Heptamethine cyanine dyes with a robust C-C bond at the central position of the chromophore. *J. Org. Chem. 71*, 7862–7865.
(41) Limmer, K., and Vera, D. R. Manuscript in preparation.
(42) Bax, J. J., Visser, F. C., van Lingen, A., Huitink, J. M., Kamp, O., van Leeuwen, G. R., Visser, G. W., Teule, G. J., and Visser, C. A. (1993) Feasibility of assessing regional myocardial uptake of ^{18}F-fluorodeoxyglucose using single photon emission computed tomography. *Eur. Heart J. 14*, 1675–1682.
(43) Knesaurek, K., and Machac, J. (2006) Comparison of ^{18}F SPECT with PET in myocardial imaging: A realistic thoraxcardiac phantom study. *BMC Nucl. Med. 6*, 5.
(44) Leichner, P. K., Morgan, H. T., Holdeman, K. P., Harrison, K. A., Valentino, F., Lexa, R., Kelly, R. F., Hawkins, W. G., and Dalrymple, G. V. (1995) SPECT imaging of fluorine-18. *J. Nucl. Med. 36*, 1472–1475.
(45) Bohn, P., Deyine, A., Azzouz, R., Bailly, L., Fiol-Petit, C., Bischoff, L., Fruit, C., Marsais, F., and Vera, P. (2009) Design of silicon-based misonidazole analogues and ^{18}F-radiolabelling. *Nucl. Med. Biol. 36*, 895–905.
(46) Haigh, P. I., Lucci, A., Turner, R. R., Bostick, P. J., Krasne, D. L., Stern, S. L., and Morton, D. L. (2001) Carbon dye histologically confirms the identity of sentinel lymph nodes in cutaneous melanoma. *Cancer 92*, 535–541.
(47) Chen, S. L., Iddings, D. M., Scheri, R. P., and Bilchik, A. J. (2006) Lymphatic mapping and sentinel node analysis: Current concepts and applications. *Ca—Cancer J. Clin. 56*, 292–309 (quiz 316−317).
(48) Edwards, M. J., Martin, K. D., and McMasters, K. M. (1999) Lymphatic mapping and sentinel lymph node biopsy in the staging of melanoma. *Surg. Oncol.*, 51–57.
(49) Kolb, H. C., Finn, M. G., and Sharpless, K. B. (2001) Click chemistry: Diverse chemical function from a few good reactions. *Angew. Chem., Int. Ed. 40*, 2004–2021.

BC1001328

SUPPORTING MATERIAL

IN VIVO EXPERIMENTS 2

Multi Modality Imaging: 2
PET/CT image fusion: 2
Proof of [^{19}F]-Lymphoseek-3's receptor specific binding activity 3
[^{18}F]- 3 experimental data: 5
Biodistribution: 16
Lymph node scintigraphy data: 16
Summary of Scintigraphy Data: 17

CHEMICAL SYNTHESIS: 18

General synthetic methods: 18
Dual Probe NHS ester synthesis: 18
Synthesis of dicarboxyphenyl cyanine dye (i) 19
Piperazin-1-yl(2,4,6-trifluoro-3-(4,4,5,5-tetraphenyl-1,3,2-dioxaborolan-2-yl)phenyl)methanone (ii) 20
Synthesis of carboxyphenyl piperazyl (2,4,6-trifluoro-3-(4,4,5,5-tetraphenyl-1,3,2-dioxaborolan-2-yl)phenyl)cyanine dye (iii) 23
Synthesis of N-Hydroxysuccinimide phenyl piperazyl (2,4,6-trifluoro-3-(4,4,5,5-tetraphenyl-1,3,2-dioxaborolan-2-yl)phenyl)cyanine dye 1 25
PET/NIR Dual Probe reaction with Lymphoseek: 26
Synthesis of PET/NIR- Lymphoseek probe 2 27
Characterization of Lymphoseek labeling 27
HPLC characterization of 2 and [^{19}F]-3 30

CHARACTERIZATION AND FURTHER APPLICATION 32

Final radiochemical analysis of [^{18}F]-3 32
General multimodality probe application and HPLC-MS analyses 34
Radiochemical Synthesis 36
Fluorescence and Absorption data 37

LYMPHOSEEK PLASMA STABILITY ASSAY 39

EVIDENCE OF IN VIVO ^{18}F-BORON BOND STABILITY . 40

REFERENCES: 41

IN VIVO EXPERIMENTS

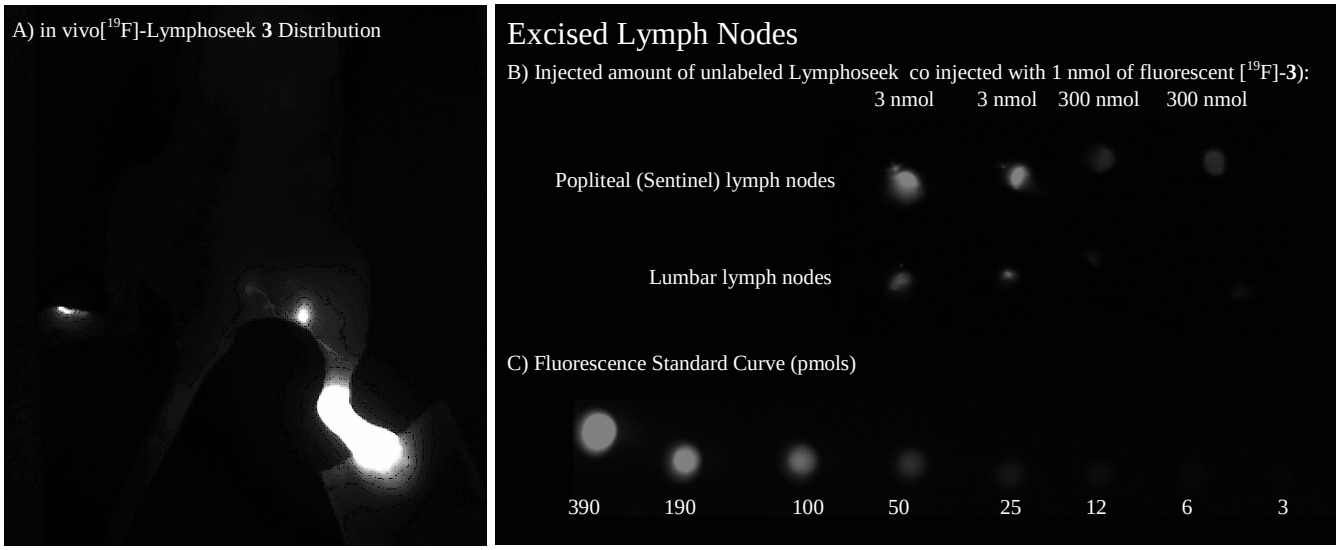
Multi Modality Imaging:

PET/CT IMAGE FUSION:

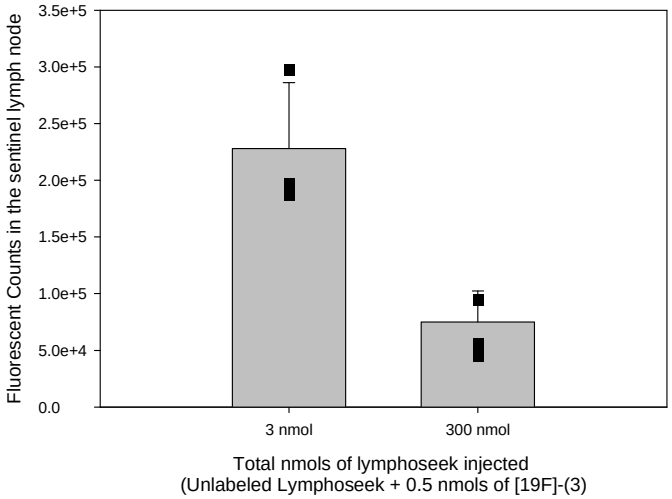
PET/CT image fusion was carried out with amide 0.9.1 open source software (http://amide.sourceforge.net). CT data in the DICOM (Digital Imaging and Communications in Medicine standard) format and PET data in .hdr (high dynamic image) format were imported into amide 0.9.1, as a new study. Inverted PET images were reflected around the x axis (right click study in study window →rotate (tab)→ change coordinate (j,y) from 1 to -1), and data was plot using a hot metal color table (right click study in study window →Colormap/Threshold (tab)→ Color Table → hot metal). Generally, PET thresholding between 1.0 and 0.0 percent was used (right click study in study window →Colormap/Threshold (tab)→ Set Max Threshold, Set Min Threshold). CT images were colormapped using a hot blue color table so that CT and PET data could be easily distinguished. Thresholding between 40 and 50 percent was sufficient to show soft tissue CT data.

To align PET and CT images, fiducidal marks were placed at appropriate locations (generally the bladder, hind right foot, right popliteal lymph node) and the alignment wizard (Tools → Alignment Wizard) was used to reconstruct an overlaid image. The overlaid image was cropped to a single mouse using Amide's cropping tool (Tools → Crop Active Data Set) and projections were generated (View → Volume Rendering). The rendered projections were exported as .jpeg files. All displayed PET images are PET/CT fused images. A sample .XIF file (PETCT.mpg) is included with this submission (Mouse 006, 1 nmol injection of **3**, note that amide 0.9.1 available at http://amide.sourceforge.net is required to open this file. This file possesses a .mpg extension and must be renamed with an .XIF extension to open.)

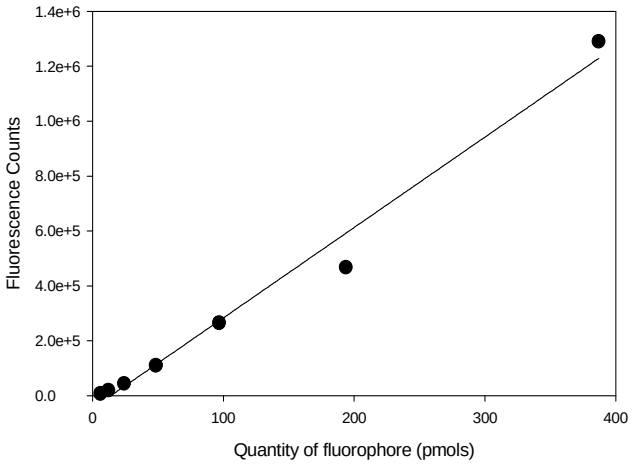
Proof of [^{19}F]-Lymphoseek-3's receptor specific binding activity



E) [^{19}F]- **3** accumulation in the **SLN** at 3 and 300 nmol



D) Standard Curve: Fluorescence Counts vs. Quantity



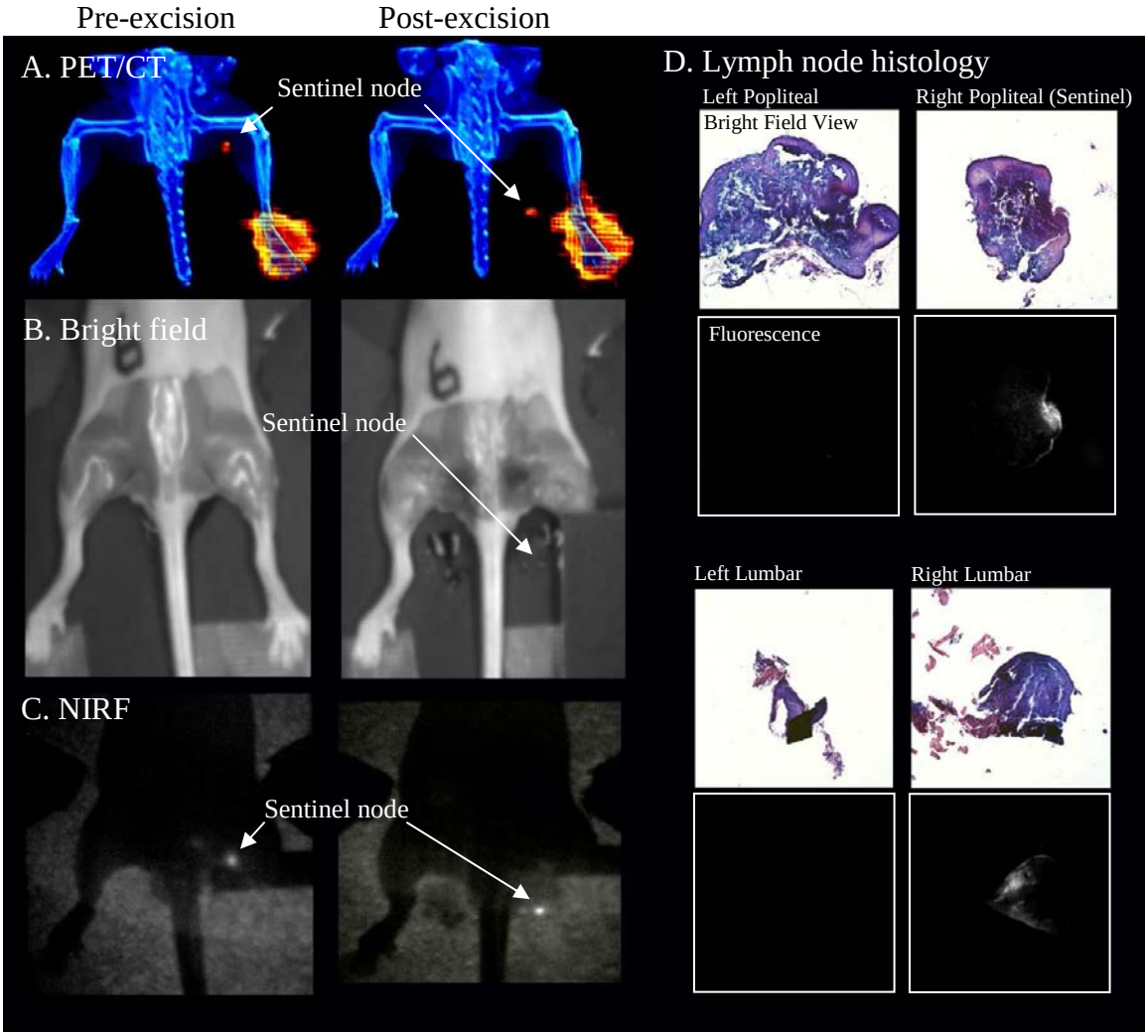
In vivo demonstration of [^{19}F]-Lymphoseek 3's receptor specific activity. Two solutions containing either 3 nmols (0.24 µL of a 12.5 nmol/µL solution) or 300 nmols (24 µL of a 12.5 nmol/µL solution) of unlabeled Lymphoseek were added to solutions containing 1 nmol (5 µL) of fluorescent [^{19}F]-Lymphoseek 3. These mixtures were diluted with water, injected into the rear footpad of mice at 30 µL volumes, and were allowed to distribute for 80 min. Three mice were injected at each dose. A) A 1 hour image skin-off in vivo image of [^{19}F]-Lymphoseek 3 prior to node extraction captured with a Maestro (CRi) 5 sec exposure. Note the clear visibility of the lymph tracks linking nodes to the foot's rear fat pad. B) Lymph nodes were extracted from mice and placed on a bed for analysis. The expected result, receptor specific accumulation, is observed. Greater accumulation of fluorescent [^{19}F]- Lymphoseek 3 is seen in the sentinel lymph nodes in 3 nmol injections than in 300 nmol injections due to increased competition with unlabeled Lymphoseek for sentinel lymph node mannose receptors. C) and D), Fluorescence [^{19}F]-3 standard curve generated with [^{19}F]-3 dissolved in 4 µL water droplets. Note that fluorescent photon quantization in tissue and standard curve conditions may differ due to the different media scattering properties, therefore fluorescence quantities in the standard curve are only relative representations of the fluorescence quantities within lymph nodes. The fluorescence response in the standard curve D) is linear therefore

fluorescence quenching at these quantities are ruled out. E) Bar graph of Lymphoseek distribution [^{19}F]-3 in the SENTINEL NODE at 3 and 300 nmol doses of Lymphoseek. A 3.5x contrast ratio is observed between the sentinel nodes in the different injection conditions (n= 3 mice per dose, P= 0.015 two tailed, two sample equal variance). Images B-C were generated with a 4 second exposure on the CRi Maestro imaging system.

[^{18}F]- 3 EXPERIMENTAL DATA:

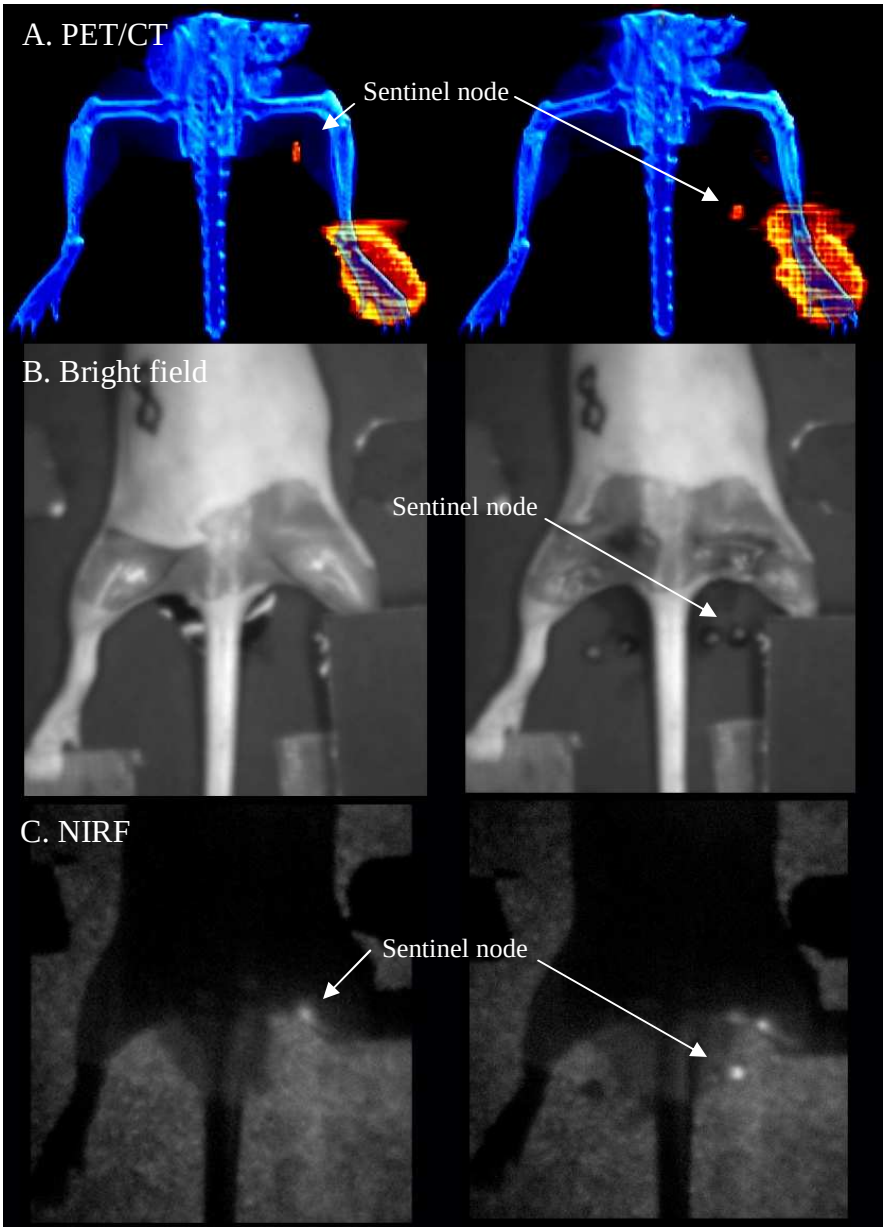
Low dose 1 nmol [^{18}F]-Lymphoseek **3** injections:

Mouse 1 of 3 low-dose 1 nmol injections of [^{18}F]-labeled Lymphoseek 3 (Mouse 006)



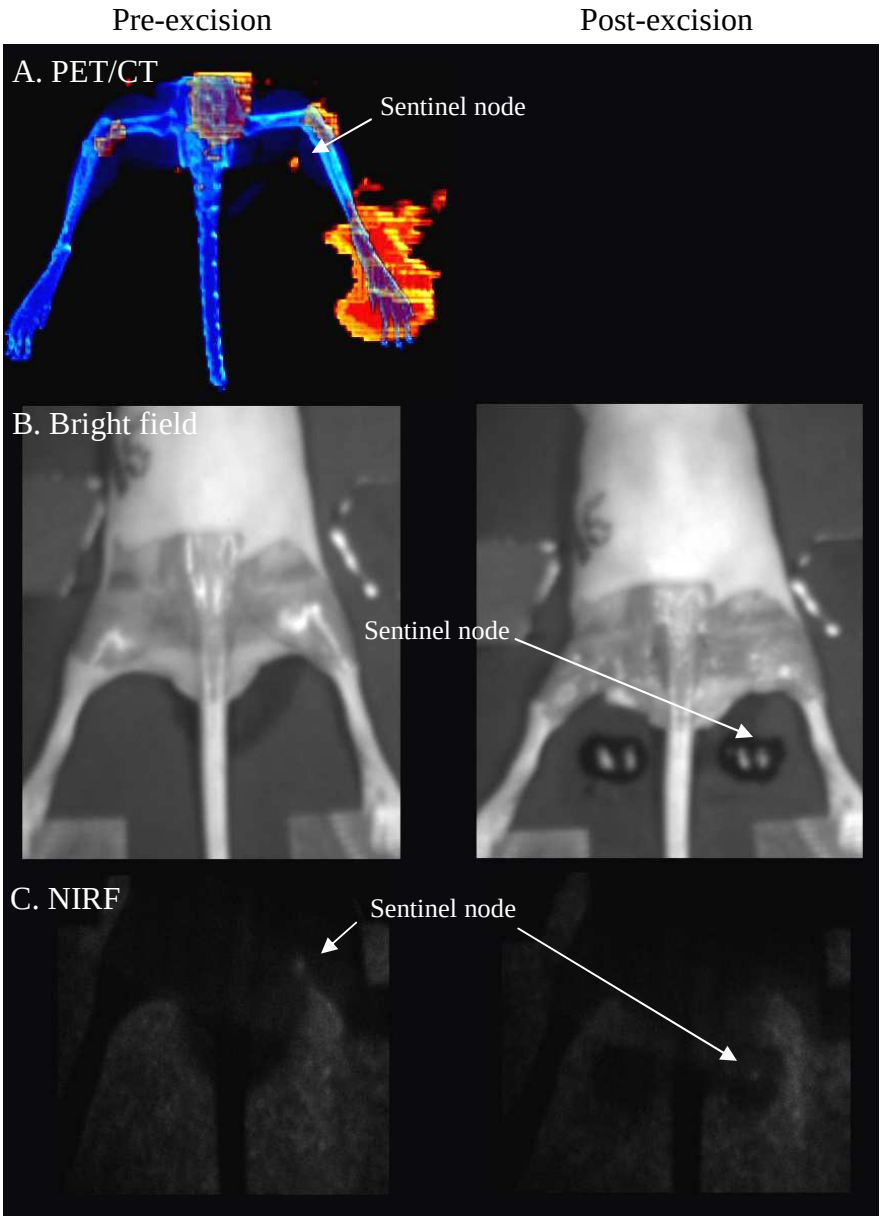
Mouse 006 was injected with a 10 µL, 1 nmol dose of [^{18}F]-labeled Lymphoseek **3** corresponding to a 48.1 µCi, 0.048 Ci/µmol ^{18}F injection at 10:19 AM, the **Time Of Injection (TOI).** The mouse was sacrificed by isofluorane overdose at 1 hour and 20 min vs. TOI. *A. top left*, 20 min pre-excision PET scan carried out 1 hour vs. TOI on 33.0 µCi of activity (decay corrected). *A. top right*, Post-excision PET scan of the mouse with resected nodes placed in the field of view. 20 min PET scan was carried out 2 hours and 57 min vs. TOI on 15.8 µCi of activity (decay corrected). *B.* Bright field image of the mouse with skin removed before *(left)* and after node resection with all resected nodes (right and left lumbar and popliteal) placed in the field of view *(right). C.* NIRF images taken at 1 hour and 33 min vs. TOI on a custom full field IR camera before *(left)* and after *(right)* lymph node resection. When identifiable, the location of the sentinel lymph node is indicated with a white arrow. *D.* Fluorescent and hematoxylin and eosin stained bright field verification of lymph node excision through histological cross sectioning of the nodes excised in B.

Mouse 2 of 3 low-dose 1 nmol injections of [^{18}F]-labeled Lymphoseek 3 (Mouse 008)



Mouse 008 was injected with a 10 µL, 1 nmol dose of [^{18}F]-labeled Lymphoseek **3** corresponding to a 42.1 µCi, 0.042 Ci/µmol ^{18}F injection at 10:50 AM, the time of injection (TOI). The mouse was sacrificed by isofluorane overdose at 1 hour and 20 min vs. TOI. *A. top left*, 20 min pre-excision PET scan carried out 1 hour vs. TOI on 28.8 µCi of activity (decay corrected). *A. top right*, Post-excision PET scan of the mouse with resected nodes placed in the field of view. 20 min PET scan was carried out 3 hours and 7 min vs. TOI on 13.0 µCi of activity (decay corrected). *B.* Bright field image of the mouse with skin removed before *(left)* and after node resection with all resected nodes (right and left lumbar and popliteal) placed in the field of view *(right). C.* NIRF images taken at 1 hour and 30 min vs. TOI on a custom full field IR camera before *(left)* and after *(right)* lymph node resection. When identifiable, the location of the sentinel lymph node is indicated with a white arrow.

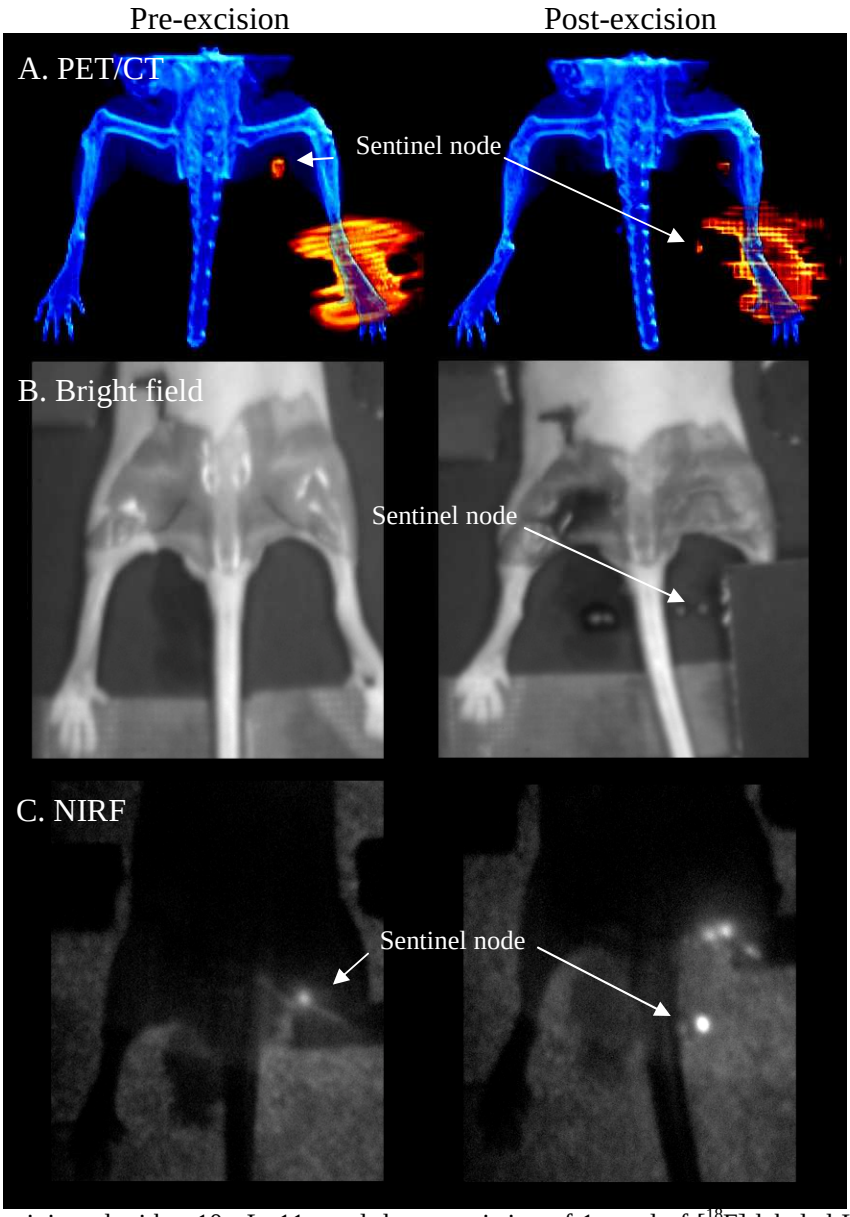
Mouse 3 of 3 low-dose 1 nmol injections of [^{18}F]-labeled Lymphoseek 3 (Mouse 016)



Mouse 010 was injected with a 10 µL, 1 nmol dose of [^{18}F]-labeled Lymphoseek **3** corresponding to a 9.7 µCi, 0.010 Ci/µmol ^{18}F injection at 3:15 PM, the time of injection (TOI). The mouse was sacrificed by isofluorane overdose at 1 hour and 20 min vs. TOI. *A. top left*, 20 min pre-excision PET scan carried out 1 hour vs. TOI on 6.6 µCi of activity (decay corrected). The mouse did not possess sufficient activity for a post-excision PET scan at 3 hours and 59 min vs. TOI (2.2 µCi of activity remained, decay corrected) but sufficient activity remained in extracted nodes for scintigraphy in biodistribution studies. *B.* Bright field image of the mouse with skin removed before *(left)* and after node resection with all resected nodes (right and left lumbar and popliteal) placed in the field of view *(right). C.* NIRF images taken at 1 hour and 24 min vs. TOI on a custom full field IR camera before *(left)* and after *(right)* lymph node resection. When identifiable, the location of the sentinel lymph node is indicated with a white arrow.

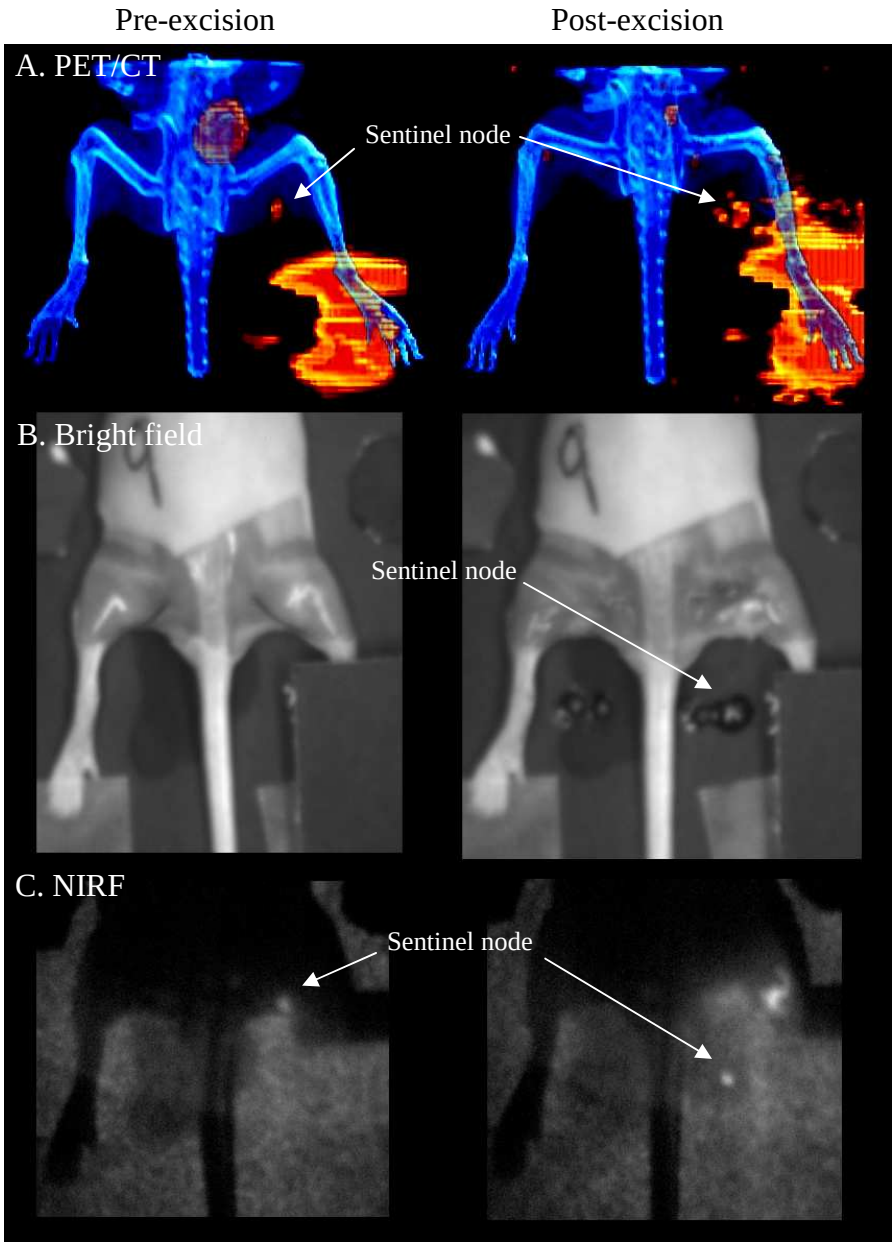
High dose 11 nmol [^{18}F]-Lymphoseek **3** injections:

Mouse 1 of 6 high-dose 11 nmol injections of [^{18}F]-labeled Lymphoseek 3 (Mouse 007)



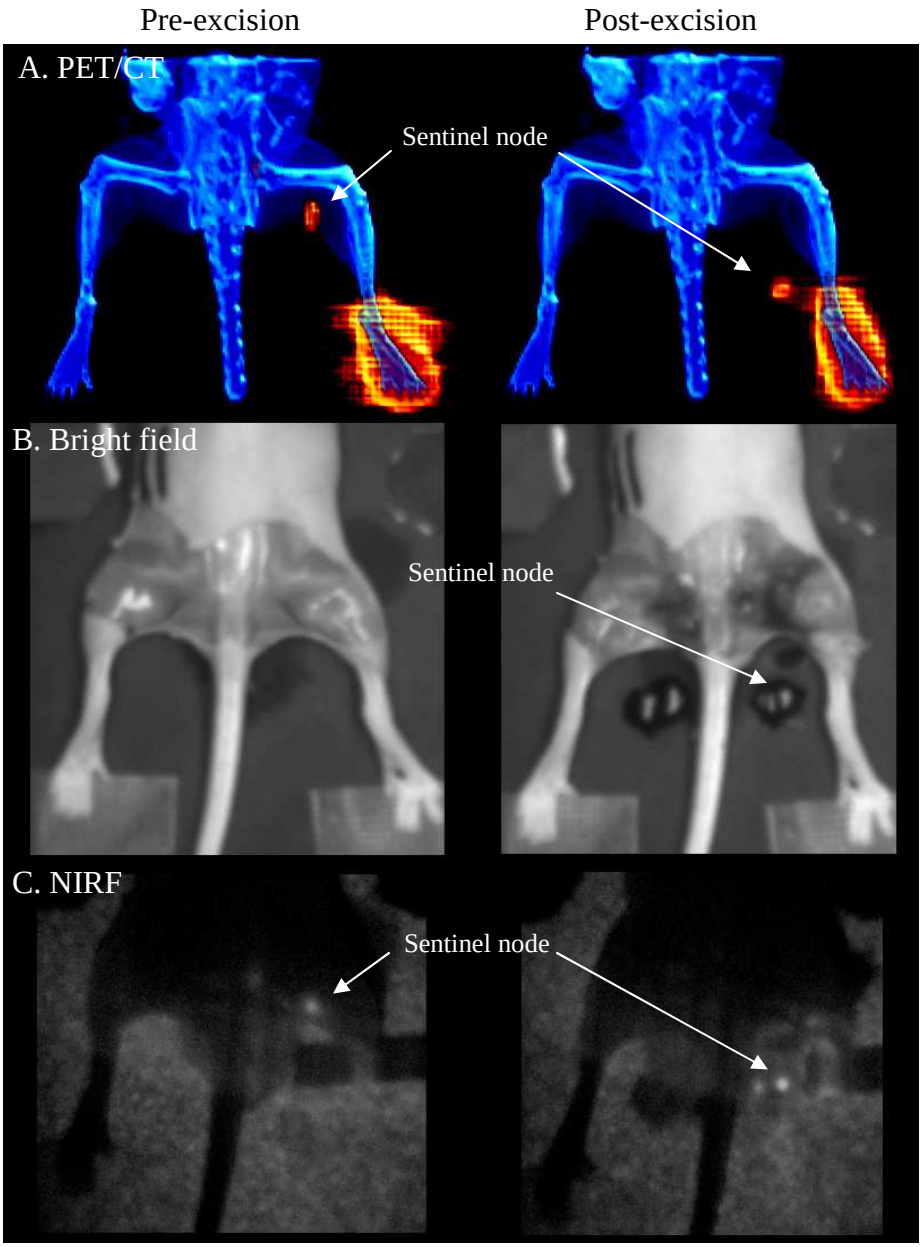
Mouse 007 was injected with a 10 µL, 11 nmol dose consisting of 1 nmol of [^{18}F]-labeled Lymphoseek **3** that had been diluted with 10 nmols of unconjugated, unlabeled Lymphoseek. This dose contained a 40.7 µCi, 0.041 Ci/µmol of ^{18}F at 10:21 AM, the time of injection (TOI). The mouse was sacrificed by isofluorane overdose at 1 hour and 20 min vs. TOI. *A. top left*, 20 min pre-excision PET scan carried out 1 hour vs. TOI on 27.9 µCi of activity (decay corrected). *A. top right*, Post-excision PET scan of the mouse with resected nodes placed in the field of view. A 20 min PET scan was carried out 2 hours and 57 min vs. TOI on 13.3 µCi of activity (decay corrected). *B.* Bright field image of the mouse with skin removed before (left) and after node resection with all resected nodes (right and left lumbar and popliteal) placed in the field of view *(right). C.* NIRF images taken at 1 hour and 33 min vs. TOI on a custom full field IR camera before *(left)* and after *(right)* lymph node resection. When identifiable, the location of the sentinel lymph node is indicated with a white arrow.

Mouse 2 of 6 high-dose 11 nmol injections of [^{18}F]-labeled Lymphoseek 3 (Mouse 009)



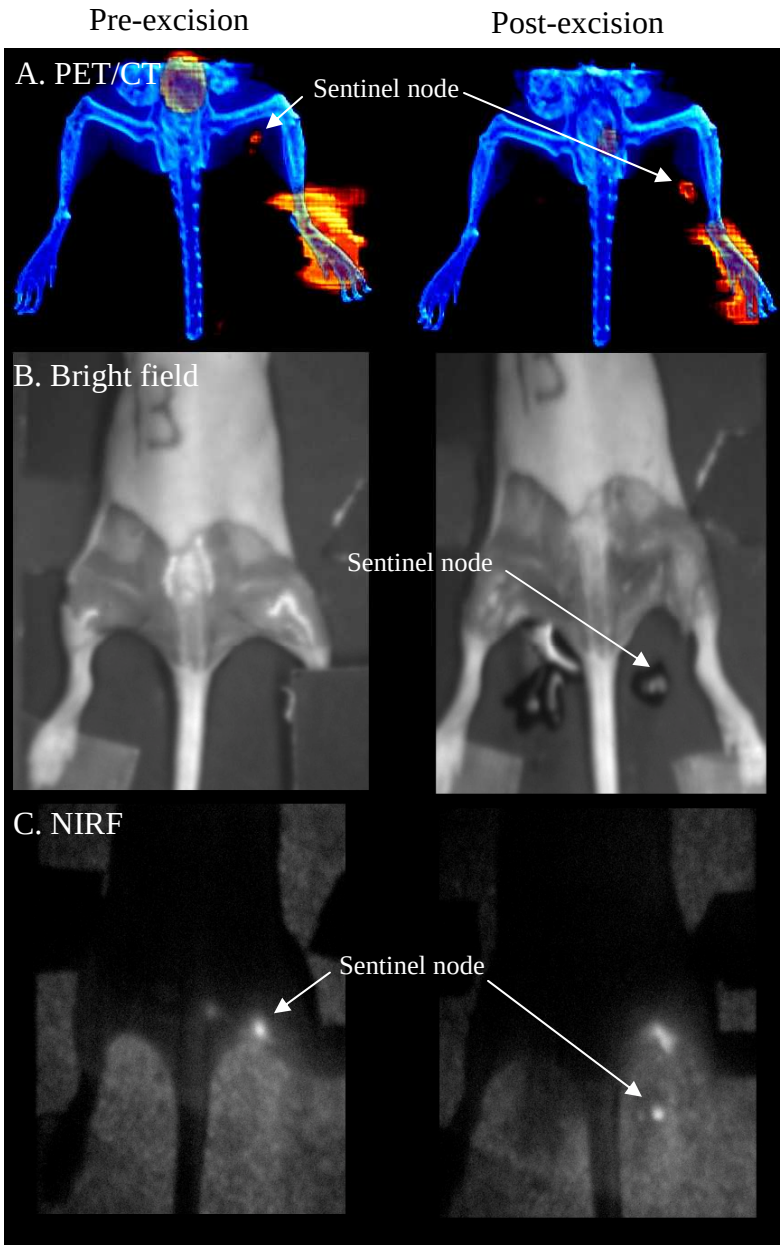
Mouse 009 was injected with a 10 µL, 11 nmol dose consisting of 1 nmol of [^{18}F]-labeled Lymphoseek **3** that had been diluted with 10 nmols of unconjugated, unlabeled Lymphoseek. This dose contained a 31.3 µCi, 0.0031 Ci/µmol of ^{18}F at 10:51 AM, the time of injection (TOI). The mouse was sacrificed by isofluorane overdose at 1 hour and 20 min vs. TOI. *A. top left*, 20 min pre-excision PET scan carried out 1 hour vs. TOI on 21.4 µCi of activity (decay corrected). *A. top right*, Post-excision PET scan of the mouse with resected nodes placed in the field of view. A 20 min PET scan was carried out 3 hours and 7 min vs. TOI on 9.6 µCi of activity (decay corrected). *B.* Bright field image of the mouse with skin removed before *(left)* and after node resection with all resected nodes (right and left lumbar and popliteal) placed in the field of view *(right). C.* NIRF images taken at 1 hour and 30 min vs. TOI on a custom full field IR camera before *(left)* and after *(right)* lymph node resection. When identifiable, the location of the sentinel lymph node is indicated with a white arrow.

Mouse 3 of 6 high-dose 11 nmol injections of [^{18}F]-labeled Lymphoseek 3 (Mouse 011)



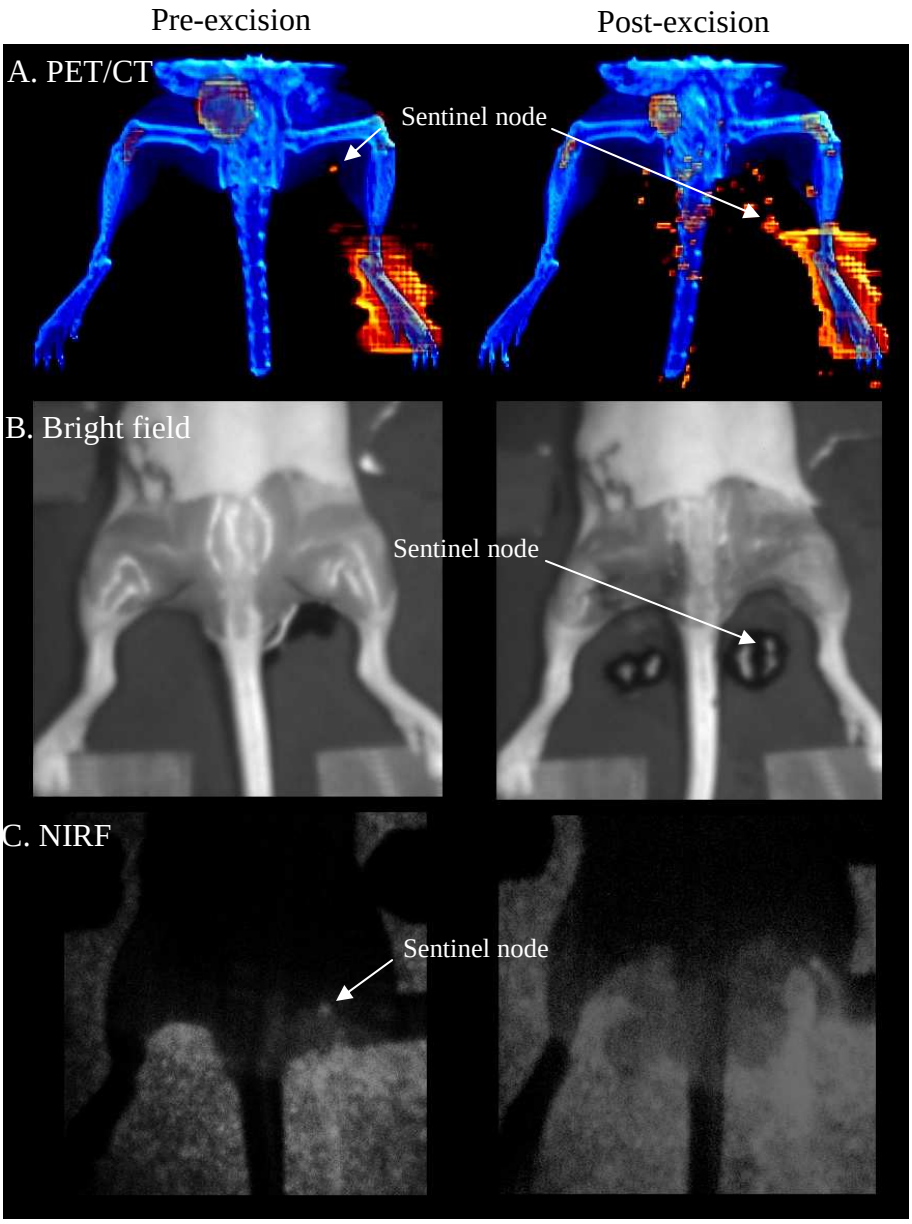
Mouse 011 was injected with a 10 µL, 11 nmol dose consisting of 1 nmol of [^{18}F]-labeled Lymphoseek **3** that had been diluted with 10 nmols of unconjugated, unlabeled Lymphoseek. This dose contained a 23.2 µCi, 0.0023 Ci/µmol of ^{18}F at 11:19 AM, the time of injection (TOI). The mouse was sacrificed by isofluorane overdose at 1 hour and 20 min vs. TOI. *A. top left*, 20 min pre-excision PET scan carried out 1 hour vs. TOI on 15.9 µCi of activity (decay corrected). *A. top right*, Post-excision PET scan of the mouse with resected nodes placed in the field of view. 20 min PET scan was carried out 3 hours and 21 min vs. TOI on 6.5 µCi of activity (decay corrected). *B.* Bright field image of the mouse with skin removed before *(left)* and after node resection with all resected nodes (right and left lumbar and popliteal) placed in the field of view *(right). C.* NIRF images taken at 1 hour and 27 min vs. TOI on a custom full field IR camera before *(left)* and after *(right)* lymph node resection. When identifiable, the location of the sentinel lymph node is indicated with a white arrow.

Mouse 4 of 6 high-dose 11 nmol injections of [^{18}F]-labeled Lymphoseek 3 (Mouse 013)



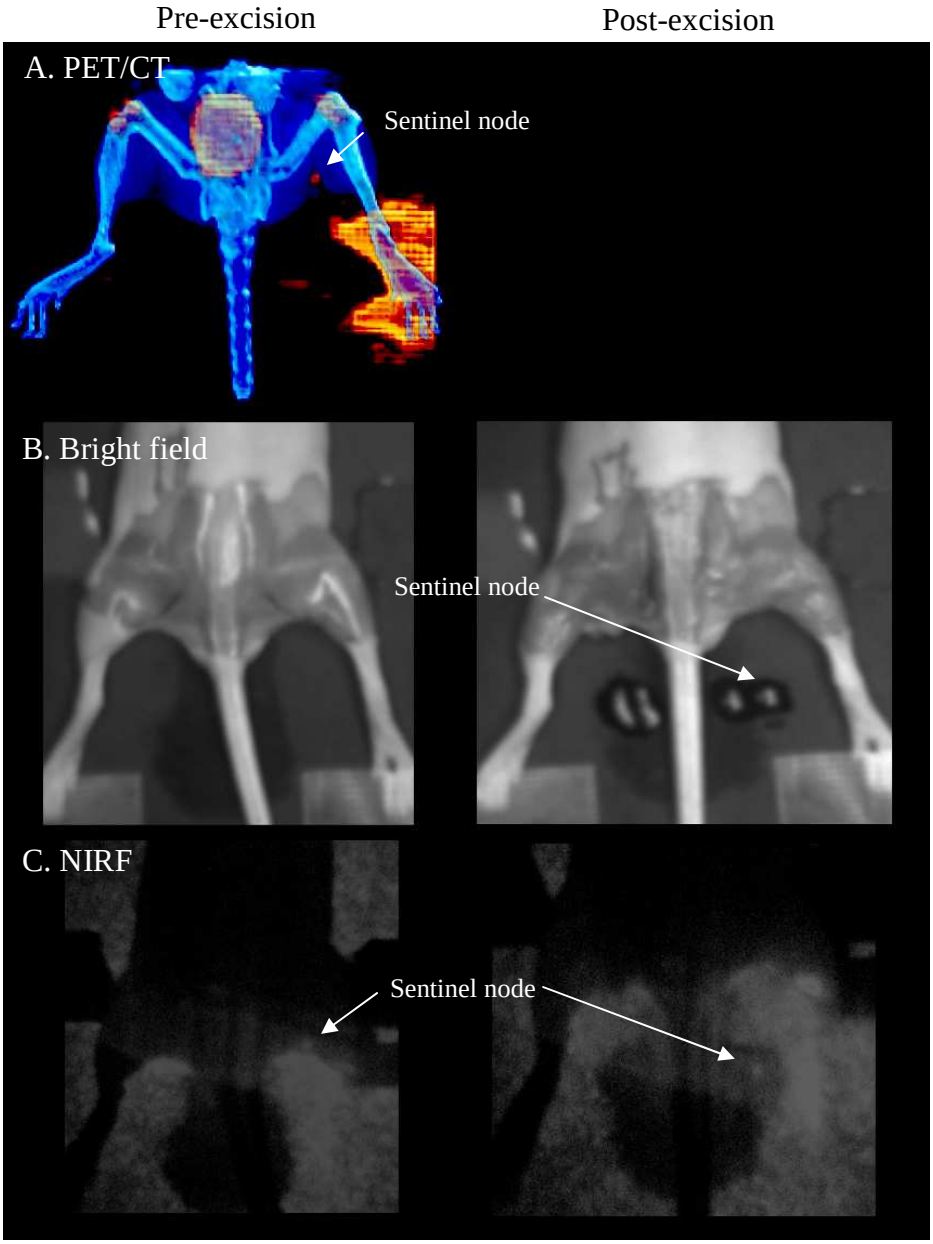
Mouse 013 was injected with a 10 µL, 11 nmol dose consisting of 1 nmol of [^{18}F]-labeled Lymphoseek **3** that had been diluted with 10 nmols of unconjugated, unlabeled Lymphoseek. This dose contained a 14.6 µCi, 0.0015 Ci/µmol of ^{18}F at 2:11 PM, the time of injection (TOI). The mouse was sacrificed by isofluorane overdose at 1 hour and 20 min vs. TOI. *A. top left*, 20 min pre-excision PET scan carried out 1 hour vs. TOI on 9.9 µCi of activity (decay corrected). *A. top right*, Post-excision PET scan of the mouse with resected nodes placed in the field of view. 30 min PET scan was carried out 3 hours and 9 min vs. TOI on 4.4 µCi of activity (decay corrected). *B.* Bright field image of the mouse with skin removed before *(left)* and after node resection with all resected nodes (right and left lumbar and popliteal) placed in the field of view *(right). C.* NIRF images taken at 1 hour and 24 min vs. TOI on a custom full field IR camera before *(left)* and after *(right)* lymph node resection. When identifiable, the location of the sentinel lymph node is indicated with a white arrow.

Mouse 5 of 6 high-dose 11 nmol injections of [^{18}F]-labeled Lymphoseek 3 (Mouse 015)



Mouse 015 was injected with a 10 µL, 11 nmol dose consisting of 1 nmol of [^{18}F]-labeled Lymphoseek **3** that had been diluted with 10 nmols of unconjugated, unlabeled Lymphoseek. This dose contained a 11.4 µCi, 0.0011 Ci/µmol of ^{18}F at 2:45 PM, the time of injection (TOI). The mouse was sacrificed by isofluorane overdose at 1 hour and 20 min vs. TOI. A. top left, A 20 min pre-excision PET scan carried out 1 hour vs. TOI on 7.8 µCi of activity (decay corrected). *A. top right*, Post-excision PET scan of the mouse with resected nodes placed in the field of view. 30 min PET scan was carried out 3 hours and 19 min vs. TOI on 3.3 µCi of activity (decay corrected). The high background in this scan is due to contamination by urine and the low amount of ^{18}F activity that was used in the scan. *B.* Bright field image of the mouse with skin removed before *(left)* and after node resection with all resected nodes (right and left lumbar and popliteal) placed in the field of view *(right). C.* NIRF images taken at 1 hour and 17 min vs. TOI on a custom full field IR camera before *(left)* and after *(right)* lymph node resection. When identifiable, the location of the sentinel lymph node is indicated with a white arrow.

Mouse 6 of 6 high-dose 11 nmol injections of [^{18}F]-labeled Lymphoseek 3 (Mouse 017)



Mouse 017 was injected with a 10 µL, 11 nmol dose consisting of 1 nmol of [^{18}F]-labeled Lymphoseek **3** that had been diluted with 10 nmols of unconjugated, unlabeled Lymphoseek. This dose contained an 11.0 µCi, 0.0011 Ci/µmol of ^{18}F at 3:16 PM, the time of injection (TOI). The mouse was sacrificed by isofluorane overdose at 1 hour and 20 min vs. TOI. *A. top left*, 20 min pre-excision PET scan carried out 1 hour vs. TOI on 7.5 µCi of activity (decay corrected). The mouse did not possess sufficient activity for a post-excision PET scan at 3 hours and 59 min vs. TOI (2.4 µCi of activity remained, decay corrected) but sufficient activity remained in extracted nodes for scintigraphy in biodistribution studies. *B.* Bright field image of the mouse with skin removed before *(left)* and after node resection with all resected nodes (right and left lumbar and popliteal) placed in the field of view *(right). C.* NIRF images taken at 1 hour and 24 min vs. TOI on a custom full field IR camera before *(left)* and after *(right)* lymph node resection. When identifiable, the location of the sentinel lymph node is indicated with a white arrow.

Biodistribution:

LYMPH NODE SCINTIGRAPHY DATA:

Processed count data for each mouse is shown in the table below:

Mouse #	Organ	%ID	Net Wt. (g)	%ID/g	Average %ID	Average Mass (mg)	Average %ID/g
Low-dose 1 nmol injections of [^{18}F]-labeled Lymphoseek (3)							
6	Foot (Right)	92.42	0.1904	485.42	58 ± 11	179 ± 5	320 ± 60
8	Foot (Right)	85.96	0.1870	459.68			
10	Foot (Right)	16.70	0.1801	92.73			
12	Foot (Right)	45.90	0.1714	267.80			
14	Foot (Right)	52.53	0.1873	280.46			
16	Foot (Right)	54.21	0.1617	335.24			
6	Popliteal Lymph Node (Right)	0.37	0.0010	370.83	0.28 ± 0.09	1.9 ± 0.4	170 ± 50
8	Popliteal Lymph Node (Right)	0.38	0.0019	197.67			
10	Popliteal Lymph Node (Right)	0.11	0.0028	39.72			
12	Popliteal Lymph Node (Right)	0.64	0.0033	194.37			
14	Popliteal Lymph Node (Right)	0.14	0.0020	72.43			
16	Popliteal Lymph Node (Right)	0.07	0.0006	124.19			
6	Lumbar Lymph Node (Right)	0.07	0.0016	46.83	0.03 ± 0.01	1.4 ± 0.2	22 ± 6
8	Lumbar Lymph Node (Right)	0.04	0.0020	22.17			
10	Lumbar Lymph Node (Right)	0.02	0.0019	10.96			
12	Lumbar Lymph Node (Right)	0.01	0.0010	9.55			
14	Lumbar Lymph Node (Right)	0.02	0.0010	16.26			
16	Lumbar Lymph Node (Right)	0.03	0.0010	29.02			
6	Ratio Popliteal/ Lumbar (Right)	4.949	0.625	7.919	16 ± 10	1.5 ± 0.4	8.3 ± 2.6
8	Ratio Popliteal/ Lumbar (Right)	8.471	0.950	8.917			
10	Ratio Popliteal/ Lumbar (Right)	5.341	1.474	3.624			
12	Ratio Popliteal/ Lumbar (Right)	67.192	3.300	20.361			
14	Ratio Popliteal/ Lumbar (Right)	8.911	2.000	4.455			
16	Ratio Popliteal/ Lumbar (Right)	2.567	0.600	4.279			
High-dose 11 nmol injections of [^{18}F]-labeled Lymphoseek (3)							
7	Foot (Right)	82.92	0.1769	468.76	68 ± 6	177 ± 5	390 ± 40
9	Foot (Right)	84.37	0.1654	510.09			
11	Foot (Right)	77.37	0.1705	453.78			
13	Foot (Right)	49.59	0.1972	251.45			
15	Foot (Right)	53.59	0.1876	285.66			
17	Foot (Right)	58.74	0.1669	351.95			
7	Popliteal Lymph Node (Right)	0.90	0.0010	897.71	0.36 ± 0.14	1.5 ± 0.3	300 ± 140
9	Popliteal Lymph Node (Right)	0.35	0.0010	348.03			
11	Popliteal Lymph Node (Right)	0.58	0.0014	412.69			
13	Popliteal Lymph Node (Right)	0.28	0.0030	92.62			
15	Popliteal Lymph Node (Right)	0.03	0.0017	17.22			
17	Popliteal Lymph Node (Right)	0.04	0.0007	59.67			
7	Lumbar Lymph Node (Right)	0.07	0.0010	70.08	0.07 ± 0.02	0.95 ± .06	75 ± 30
9	Lumbar Lymph Node (Right)	0.05	0.0007	75.24			
11	Lumbar Lymph Node (Right)	0.18	0.0009	200.53			
13	Lumbar Lymph Node (Right)	0.07	0.0011	65.22			
15	Lumbar Lymph Node (Right)	0.02	0.0011	16.92			
17	Lumbar Lymph Node (Right)	0.02	0.0009	21.77			
7	Ratio Popliteal/ Lumbar (Right)	12.809	1.000	12.809	5.0 ± 1.7	1.5 ± 0.3	4.1 ± 1.8
9	Ratio Popliteal/ Lumbar (Right)	6.608	1.429	4.625			
11	Ratio Popliteal/ Lumbar (Right)	3.201	1.556	2.058			
13	Ratio Popliteal/ Lumbar (Right)	3.873	2.727	1.420			
15	Ratio Popliteal/ Lumbar (Right)	1.573	1.545	1.018			
17	Ratio Popliteal/ Lumbar (Right)	2.132	0.778	2.741			

SUMMARY OF SCINTIGRAPHY DATA:

TISSUE	1 NMOL LYMPHOSEEK INJECTION			11 NMOL LYMPHOSEEK INJECTION		
	% ID	Mass (mg)	% ID/G	% ID	Mass (mg)	% ID/G
TISSUE BIODISTRIBUTION						
Foot (Right)	58 ± 11	179 ± 5	**320 ± 60**	68 ± 6	177 ± 5	**390 ± 40**
Popliteal Lymph Node (Right)	0.28 ± 0.09	1.9 ± 0.4	**170 ± 50**	0.36 ± 0.14	1.5 ± 0.3	**300 ± 140**
Lumbar Lymph Node (Right)	0.03 ± 0.01	1.4 ± 0.2	**22 ± 6**	0.07 ± 0.02	0.95 ± .06	**75 ± 30**
Foot (Left)	0.26 ± 0.06	168 ± 3	**1.6 ± 0.4**	0.28 ± 0.06	158 ± 4	**1.7 ± 0.3**
Popliteal Lymph Node (Left)	0.004 ± 0.004	1.3 ± 0.2	**5 ± 3**	0.010 ± 0.005	1.5 ± 0.2	**8.8 ± 3.5**
Lumbar Lymph Node (Left)	0.010 ± 0.002	1.4 ± 0.2	**8 ± 2**	0.016 ± 0.006	0.87 ± 0.09	**23 ± 10**
Blood	0.15 ± 0.02	270 ± 30	**0.61 ± 0.08**	0.16 ± 0.02	250 ± 30	**0.7 ± 0.1**
Liver	1.6 ± 0.4	520 ± 60	**3.0 ± 0.6**	0.65 ± 0.07	360 ± 30	**1.8 ± 0.2**
Kidney	0.38 ± 0.09	360 ± 20	**1.1 ± 0.3**	0.7 ± 0.2	340 ± 10	**2.2 ± 0.6**
Spleen	0.14 ± 0.01	72 ± 5	**2.0 ± 0.2**	0.12 ± 0.01	69 ± 5	**1.7 ± 0.2**
Bone	0.11 ± 0.02	39 ± 4	**3.2 ± 0.8**	0.12 ± 0.02	39 ± 3	**3.4 ± 0.7**
FOLD ACCUMULATION OF ^{18}F-3 IN THE SENTINEL NODE OVER THE DISTAL NODE	16 ± 10	1.5 ± 0.4	**8.3 ± 2.6**	5.0 ± 1.7	1.5 ± 0.3	**4.1 ± 1.8**
% ^{18}F-3 ACTIVITY EXTRACTED IN THE SENTINEL NODE VS. ALL EXTRACTED LYMPH NODES	87 ± 7 (%)			74 ± 7 (%)		

Tissue biodistribution of [^{18}F]- Lymphoseek 3 in mice that were sacrificed 1 hour and 20 min following injection. Biodistribution data from 12 mice were used to compile this table. Data from 6 mice were obtained per injected Lymphoseek dose. "Fold accumulation" is defined as the ratio of activity in the sentinel node to the distal node in individual mice. The "% activity extracted" is defined as the difference in counts between the sentinel and distal lymph nodes minus the sum of counts in the sentinel and distal lymph nodes ((Count $s_{popliteal}$ – Counts $_{lumbar}$)/ (Counts $_{popliteal}$ + Counts $_{lumbar}$). Error = $\sigma/(n=6)^{1/2}$. The probability associated with a student's t-test (one-tailed distribution, two-sample unequal variance) = 0.022.

CHEMICAL SYNTHESIS:

General synthetic methods:

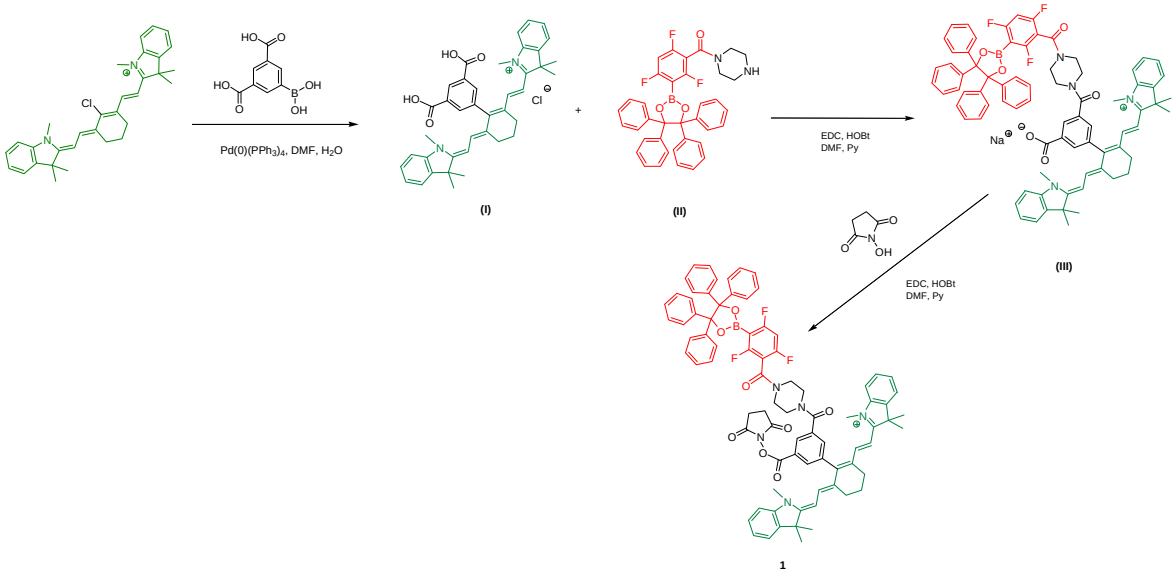
Fluoride containing compounds were purchased from Oakwood Products. Lymphoseek was received as a gift from Reliable Biopharmaceutical. Other chemicals were purchased from Aldrich, Strem, or Combi blocks. Deuterated solvents were purchased from Cambridge Isotope Laboratories.

All ^{1}H Nuclear magnetic resonance (NMR) spectra were recorded at room temperature on Varian 300 or 400 MHz Mercury or 500 MHz Joel instruments. Chemical shifts are reported using the δ scale in ppm and all coupling constants (J) are reported in hertz (Hz). ^{1}H NMR spectra are referenced to the tetramethylsilane peak (δ = 0.00) and ^{19}F NMR spectra are referenced to NEAT CF_2Cl_2 (δ = 0.00). All thin layer chromatography experiments were run on Silica Gel 60 F_{254} Glass TLC plates from EMD chemicals. Fluorescence readings were made on a Fluorolog 3 spectrophotometer with Datamax v2.2 software. High resolution mass spectrometry was performed at the University of California San Diego (UCSD) Chemistry and Biochemistry Small Molecule/Chemical Mass Spectrometry Facility.

Dual Probe NHS ester synthesis:

The synthesis of the dual probe PET/NIR NHS ester **1**, was synthesized in 3 steps. The crystallization of **(i)** is the lowest yielding step in the reaction scheme (12%). **If higher product yields are desired, direct use of (i) following acidic extraction can be carried out in lieu of crystallization. In this case the final yield of 1 is 50.7 %.**

The scheme for the synthesis of the generally conjugatable PET/NIR-probe is as shown in Scheme 1:



Scheme 1. Synthetic scheme detailing the synthesis of an activated NHS ester of the ^{18}F/ heptamethine cyanine (C7-Cy) PET/NIR probe. Boron based ^{18}F trap technology is shown in red, while the NIR fluorophore is shown in green.

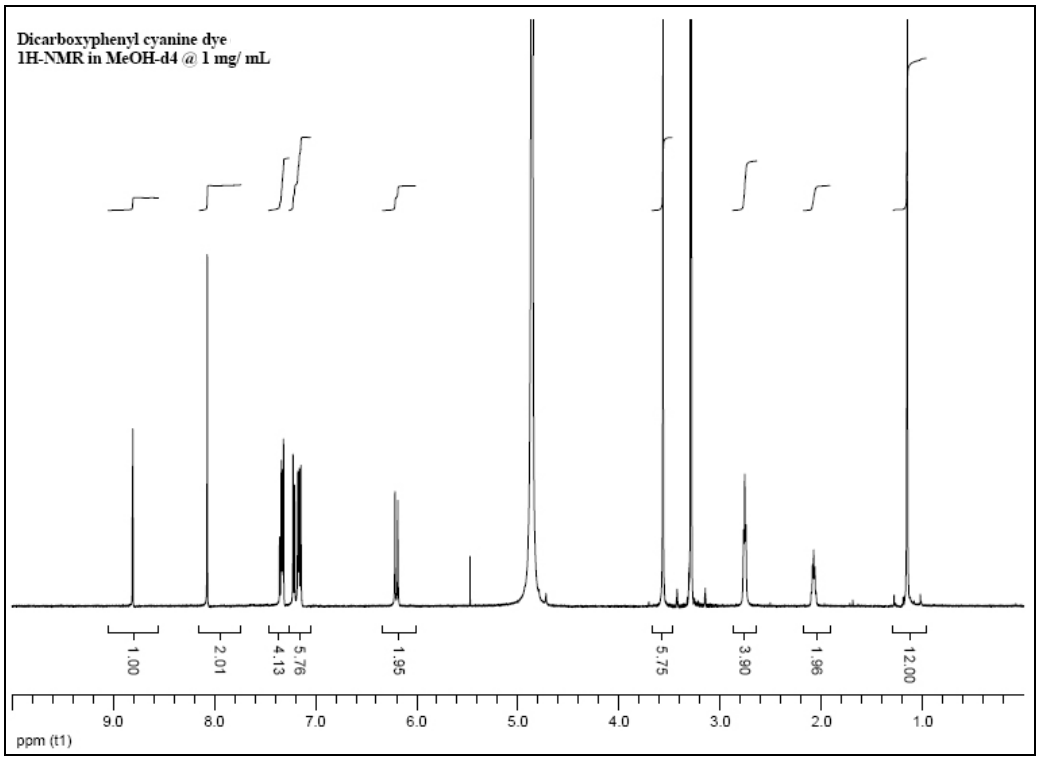
SYNTHESIS OF DICARBOXYPHENYL CYANINE DYE (I)

Reagents were added to a 25 mL round bottom flask charged with a magnetic stir bar in the following order: IR-775 (200 mg, 0.48 mmols, Sigma-Aldrich #544914), 3,5-Dicarboxyphenyl boronic Acid (200 mg, 0.97 mmols, Combi Blocks #BB-3936), Tetrakis(triphenylphosphine)palladium (0) (60 mg, 0.053 mmols, Strem #46-2150), 9 mL of MeOH, 1 mL of triethylamine, and 1 mL of H_2O. This reaction was stirred for 14 hours at room temperature and then concentrated to oil. **78% of all 775 nm absorbing material was converted to the product (i) as observed by LCMS.** The oil was resuspended in 100 mL of methylene chloride (CH_2Cl_2), and water soluble products were extracted with 50 mL of H_2O. The CH_2Cl_2 layer was washed with 100 mL of saturated ammonium chloride, 100 mL of 100 mM sodium bicarbonate, and then two washes of 100 mL of 1 M HCl. The product (i) could be converted to (ii) as is, but if pure product was desired for NMR, QY, or absorbance coefficient studies, (i) could be crystallized.

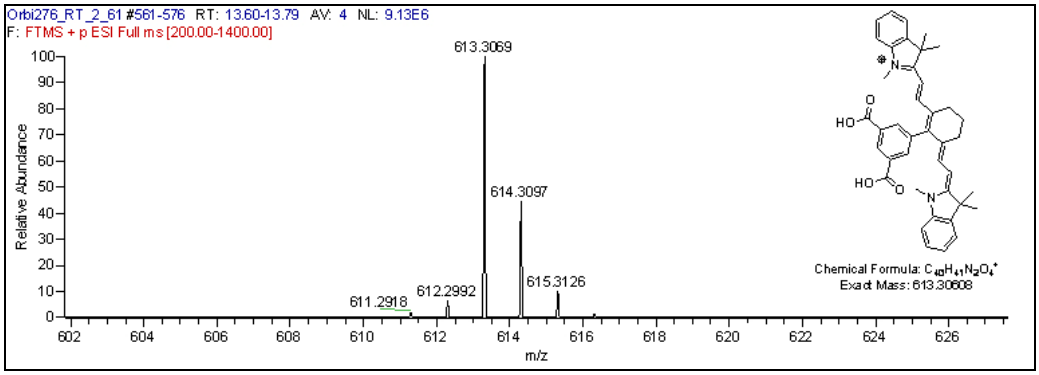
To crystallize (i), product contained in the CH_2Cl_2 layer was filtered through Whatman #5 filter paper and concentrated to ~ 5 mL at which point crystals of the **(i)** began to form. Filtration and collection of **(i)** through Whatman #5 filter paper resulted in a first crop containing 54.5 mg (0.08 mmols, 12 %) of crystalline product.

^{1}H NMR (MeOH-d4, 500 MHz, 21°C): 8.81 (*t*, J= 2 Hz, 1H), 8.07 (*d*, J= 1 Hz, 2H), 7.35-7.315 (*m*, 4H), 7.22-7.14 (*m*, 6H), 6.20 (*d*, J= 14 Hz, 2H), 3.57 (*s*, 6H), 2.76 (*t*, J= 6 Hz, 4H), 2.08 (*t*, J= 6 Hz, 2H), 1.15 (*s*, 12H). HRMS (ESI) calculated for $C_{40}H_{41}N_2O_4^+$ $(M)^+$: 613.3061, found 613.3069. Spectrophotometric constants on a 0.322 µM solution in water: λ_{max} = 749 nm, ε_{749} = 107 000 cm^{-1} M^{-1}, ex= 747 nm, em = 765 nm, and φ = 0.033.

^{1}H-NMR



HRMS-ESI^{+}



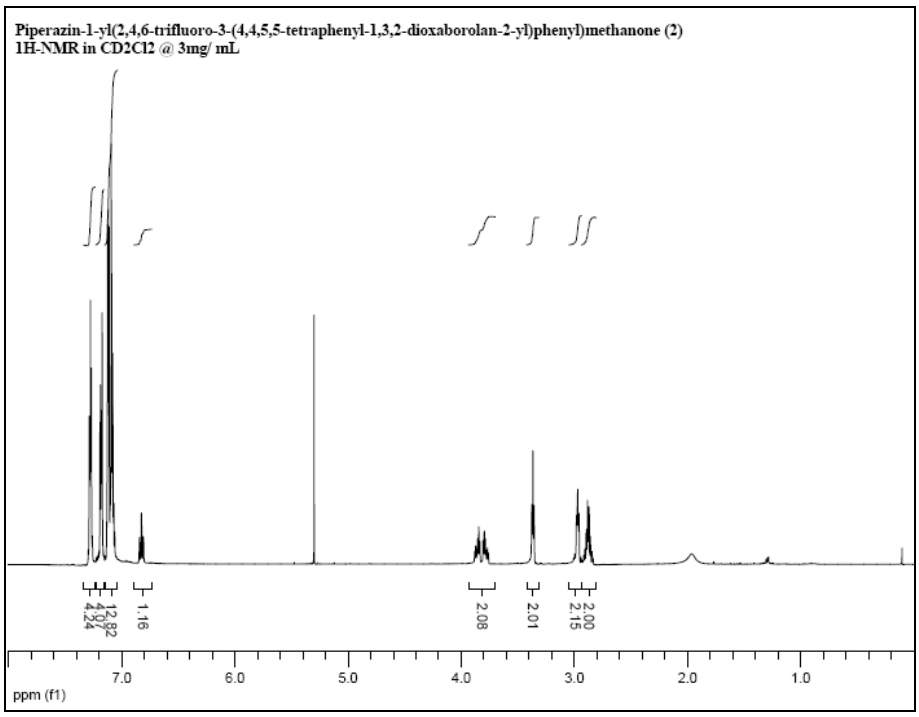
PIPERAZIN-1-YL(2,4,6-TRIFLUORO-3-(4,4,5,5-TETRAPHENYL-1,3,2-DIOXABOROLAN-2-YL)PHENYL)METHANONE (II)

Reagents were added to a 25 mL vial containing 3.55 mL of DMF in the following order: piperazine (52 mg, 0.60 mmols), pyridine (133 µL, 1.56 mmols), HOBt monohydrate (61 mg, 0.40 mmols), 2,4,6-Trifluoro-3-(4,4,5,5-tetraphenyl-1,3,2-dioxaborolan-2-yl)benzoic acid (200 mg, 0.36 mmols, synthesis (1 step from commercially available reagents, synthesis and reagent sources previously described (*1*))), and N-(3-dimethylaminopropyl)-N′-ethyl carbodiimide hydrochloride (EDC) (77 mg, 0.40 mmols). This reaction was left at room temperature for 24 hours after which it was concentrated to

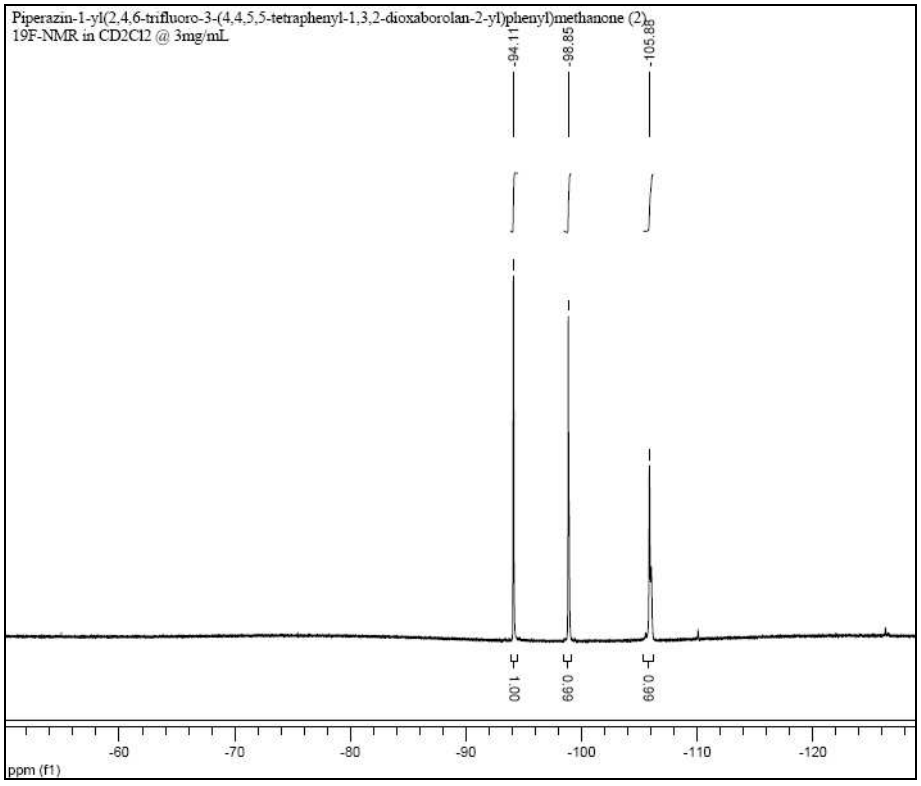
oil. A 100 mg amount of piperazine in 1 mL of CH_2Cl_2 was added to the oil to keep **(ii)** in its deprotonated state. The oil was loaded onto a 10 cm x 2.5 cm silica column where **(ii)** was eluted with 2 % MeOH/$CHCl_3$. Elution was monitored by TLC where **(ii)** displays an R_f of 0.30 in a 30 % MeOH/$CHCl_3$ v/v developing solution and gives a positive result in ninhydrin tests. The appropriate fractions were concentrated to give 136.8 mg of **(ii)** (a 61 % yield) as a white solid. The product, **(ii)**, is best stored as a 10 to 100 mM solution in CH_2Cl_2 at -78 °C.

^{1}H NMR (CD_2Cl_2, 500 MHz, 21 °C): 7.28-7.25 (*m*, 4H, CH), 7.22-7.19 (*m*, 4H, CH), 7.14-7.09 (*m*, 12H, CH), 6.87 (*t*, J= 9 Hz, 1H), 3.80-3.68 (*m*, 2H), 3.42-3.32 (*m*, 2H), 2.92-2.79 (*m*, 2H), 2.61-2.51 (*m*, 2H). ^{13}C NMR (MeOH-D4, 400 MHz): 164.9, 162.2, 145.2, 144.3, 130.2, 129.6, 129.1, 128.4, 128.1, 127.8, 125.6, 125.5, 118.8, 112.6, 96.8, 45.9, 45.3, 44.8, 40.8, 37.1, 31.8. ^{19}F NMR (CD_2Cl_2, 300 MHz): -94.11 (1F), -98.85 (1F), -105.88 (1F). HRMS (ESI) calculated for $C_{37}H_{31}BF_3N_2O_3^+$ $(M+H)^+$: 619.2374 m/z, found: 619.2394.

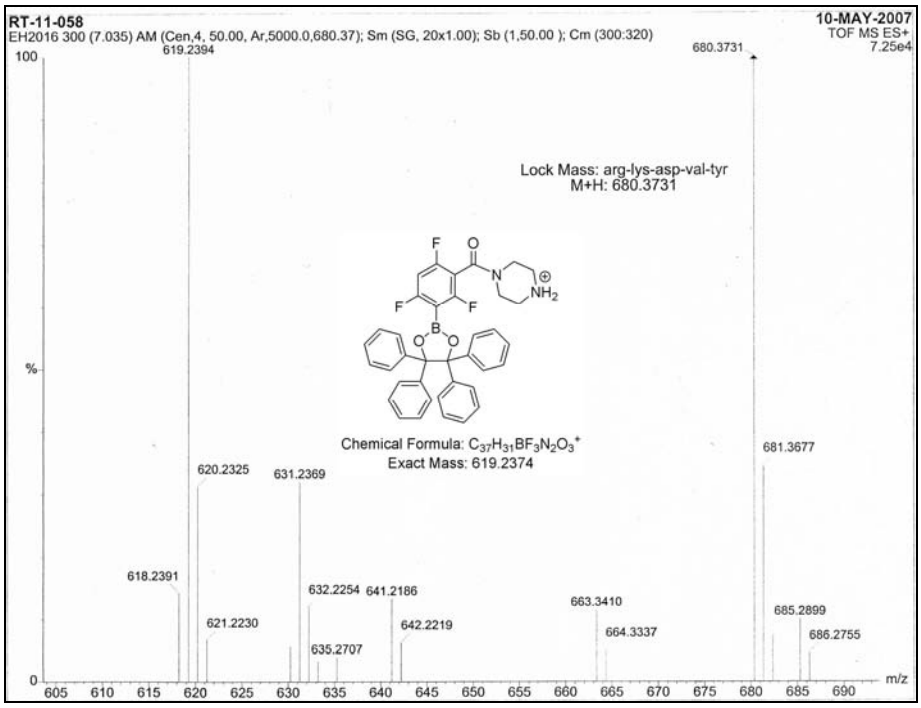
^{1}H- NMR



^{19}F- NMR



HRMS-ESI$^+$

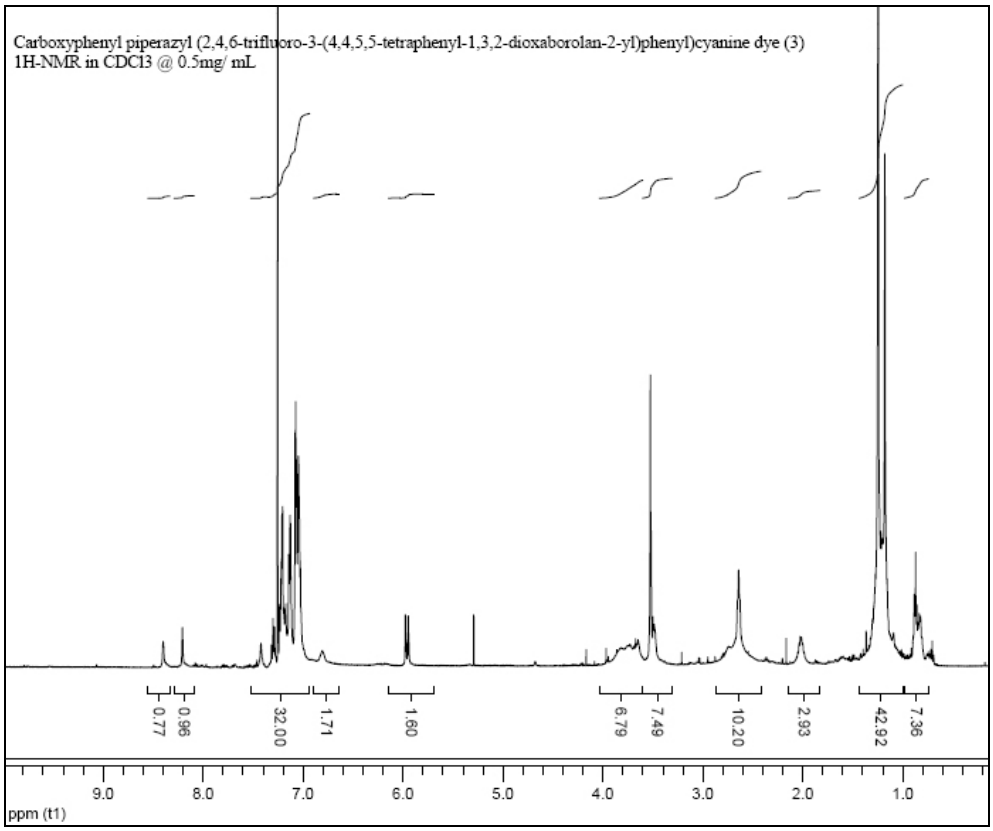


SYNTHESIS OF CARBOXYPHENYL PIPERAZYL (2,4,6-TRIFLUORO-3-(4,4,5,5-TETRAPHENYL-1,3,2-DIOXABOROLAN-2-YL)PHENYL)CYANINE DYE (III)

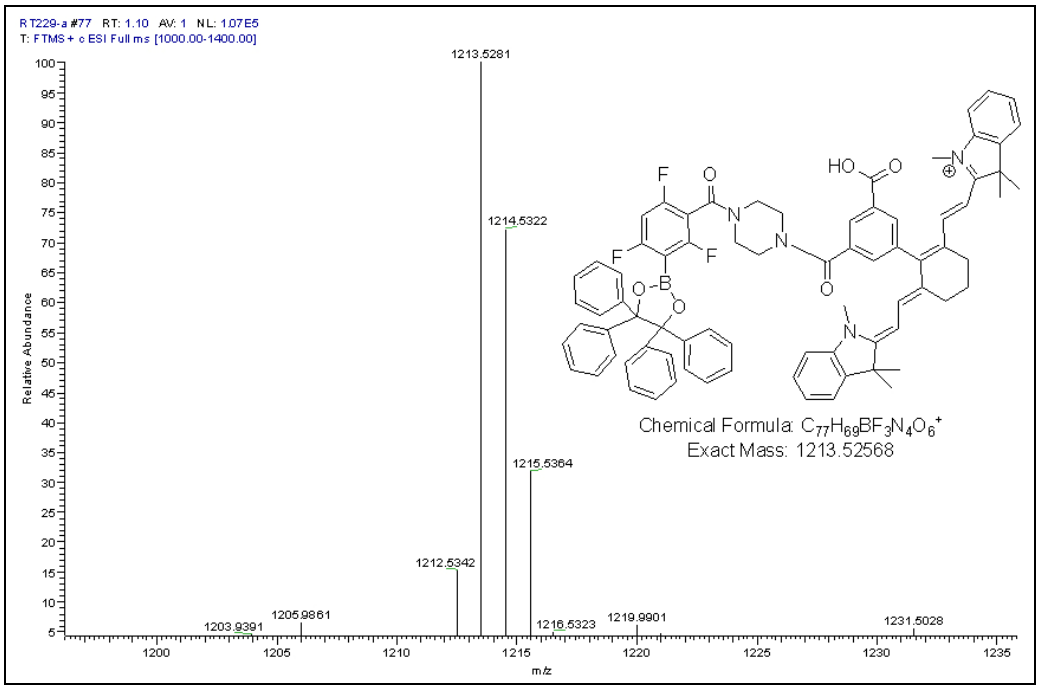
A 1.04 mL, 21.6 mM solution of **(ii)** (15 mg, 0.0225 mmols) in CH_2Cl_2 was added to **(i)** (15 mg, 0.0225 mmols). This solution was concentrated to dryness and the following reagents were added in the following order: DMF (0.9 mL), pyridine (11 µL, 0.132 mmols), HOBt monohydrate (3.45 mg, 0.0225 mmols), and N-(3-dimethylaminopropyl)-N′-ethyl carbodiimide hydrochloride (EDC) (4.5 mg, 0.0225 mmols). This reaction was sonicated for 1 hour, left at room temperature for 2 hours and then quenched with 40 mL of chloroform. This volume of chloroform was washed once with saturated aqueous ammonium chloride and twice with 40 mL of deionized water before it was concentrated. The resulting solid was loaded onto a 10 cm x 2.5 cm silica column where **(iii)** was eluted with 2 litres of 8 % MeOH/$CHCl_3$. Elution was monitored by TLC where **(iii)** displays an R_f of 0.10 with a 15 % MeOH/$CHCl_3$ v/v developing solution. The appropriate fractions were concentrated to give 17.6 mg of **(ii)** (a 65 % yield) as a stable green residue.

^{1}H NMR ($CDCl_3$, 500 MHz, 21 °C): 8.40 (*s*, 1H), 8.21 (*s*, 2H), 7.42-7.03 (*m*, 30H), 6.81 (*broad*, 1H), 5.96 (*d*, J= 7 Hz, 2H), 3.90-3.65 (*m*, 4H), 3.52 (*s*, 6H), 2.50-2.48 (*m*, 2H), 2.75-2.61 (*m*, 6H), 2.02 (*m*, 2H), 1.24-1.18 (*m*, 12H). HRMS (ESI) calculated for $C_{77}H_{69}BF_3N_4O_6^+$ $(M)^+$: 1213.5257 m/z, found: 1213.5281.

^{1}H- NMR



HRMS-ESI^{+}



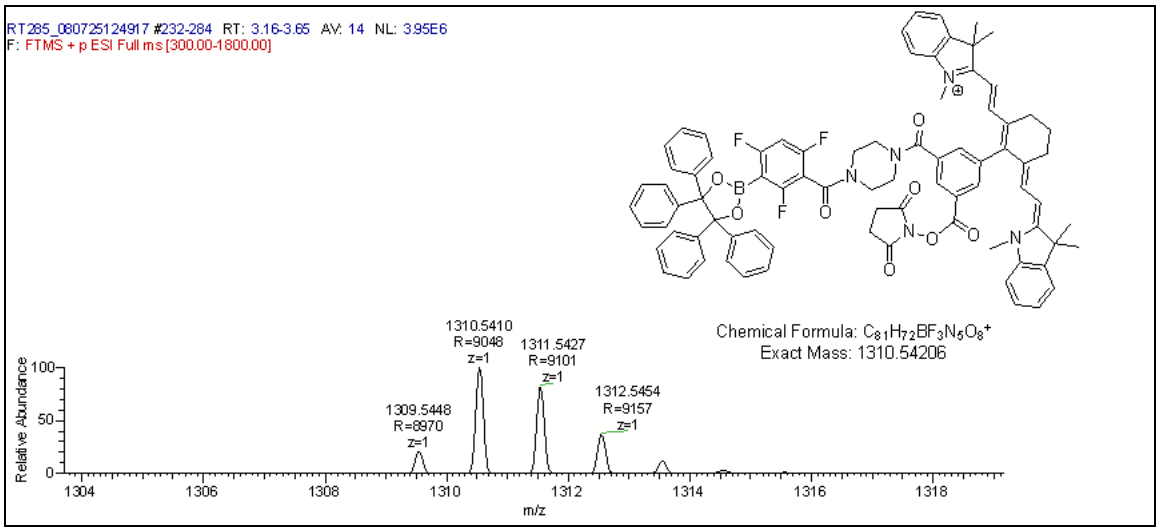
SYNTHESIS OF N-HYDROXYSUCCINIMIDE PHENYL PIPERAZYL (2,4,6-TRIFLUORO 3-(4,4,5,5-TETRAPHENYL-1,3,2-DIOXABOROLAN-2-YL)PHENYL)CYANINE DYE 1

Reagents were added to a 1.5 mL vial in the following order: **(iii)** (8.9 mg, 7.3 µmols), N-Hydroxysuccinimide (1.2 mg, 11 µmols), HOBt monohydrate (1.7 mg, 11 µmols), DMF (144 µL), pyridine (1.2 µL, 14 µmols), and N-(3-dimethylaminopropyl)-N′-ethyl carbodiimide hydrochloride (EDC) (2.2 mg, 11 µmols). This reaction was left at room temperature for 3 hours after which it was directly diluted with 2 ml of CH_2Cl_2. The CH_2Cl_2 layer was washed 3 times with 2 mL of deionized water. The CH_2Cl_2 was decanted directly into a vial and concentrated to dryness.

As a dry, crude mixture following extraction, **1** is stable and can be used as is. Unfortunately, attempts to isolate **1** as a chloride salt for ^{1}H-NMR analysis via silica chromatography gave a disproporationation product. It is speculated that the highly acidic conditions required for transforming **1** into the chloride salt induced this reactivity.

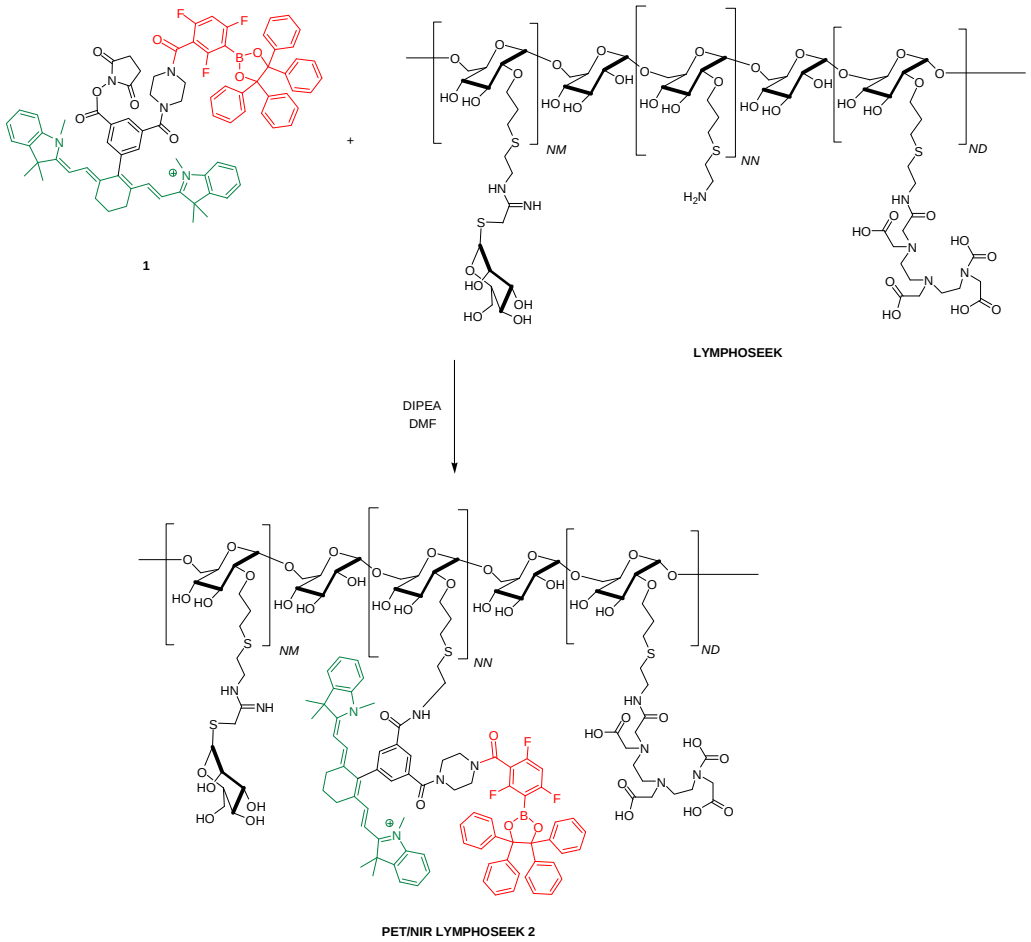
HRMS (ESI) calculated for $C_{81}H_{72}BF_3N_5O_8^+$ $(M+H)^+$: 1310.5421 m/z, found: 1310.5410.

HRMS-ESI$^+$



PET/NIR Dual Probe reaction with Lymphoseek:

The scheme for the conjugation of the PET/NIR-probe NHS ester to Lymphoseek is as shown in Scheme 2:



Scheme 2. Reaction of ^{18}F/ heptamethine cyanine (C7-Cy) PET/NIR NHS ester to DTPA-mannosyl-dextran amine (NN), mannose (NM), and DTPA (ND) (Lymphoseek). Densities were 5.8, 16.5, and 4.2 mol /dextran respectively. Exact densities were obtained from certificate of analysis (vide infra). Average molecular weight was 16122 g/mol. The boron based ^{18}F trap is shown in red, while the NIR fluorophore is shown in green.

SYNTHESIS OF PET/NIR- LYMPHOSEEK PROBE 2

A 5.5 mg quantity of unconjugated Lymphoseek ligand (0.34 µmols, Reliable Biopharmaceutical # 70-2913, vide infra for Certificate of Analysis) bearing 5.8 amine groups per mol dextran was used per synthesis of Lymphoseek **2**. The generally conjugatable NHS ester of the PET/NIR probe, **1**, was added as a 4 µmol solution in CH_2Cl_2 directly into a 1.5 mL glass vial containing 5.5 mg (0.34 µmols) of Lymphoseek. This solution was concentrated to dryness, after which the resulting solid was resuspended in 100 µL of DMF. This solution was sonicated for 1 hour and left to react for 18 hours. The next day, a 10 µL volume of diisopropyl ethyl amine (DIPEA) was added and the reaction was left for another 2 hours. The reaction was then transferred to a polypropylene centrifuge tube containing 25 mL of CH_2Cl_2. On an Allegra X-22R centrifuge, a pellet of **2** was isolated following 20 min of centrifugation at 3 000 rcf. The CH_2Cl_2 supernatant was decanted away from the pellet and fresh CH_2Cl_2 was added to the centrifuge tube. The pellet was triturated into a suspension and the centrifuge process was repeated two more times. The resulting pellet was dried under high vacuum and resuspended in a 1 mL of deionized water. This solution was transferred to a 1.5 mL eppendorf that was centrifuged for 2 min at 18 000 rcf. Water soluble **2** was decanted from the pellet and divided into 4.25 x 10.6 nmol aliquots in 600 µL microcentrifuge tubes. These aliquots were lyophilized and stored at -78 °C. Based on fluorescence readings, 115.9 nmols of fluorophore conjugated Lymphoseek **2** was isolated. Based on a glucose quantization assay (*2*), 49.16 to 33.63 nmols of Lymphoseek was isolated as **2.** This corresponds to a 10-14 % yield of **2** from unconjugated Lymphoseek.

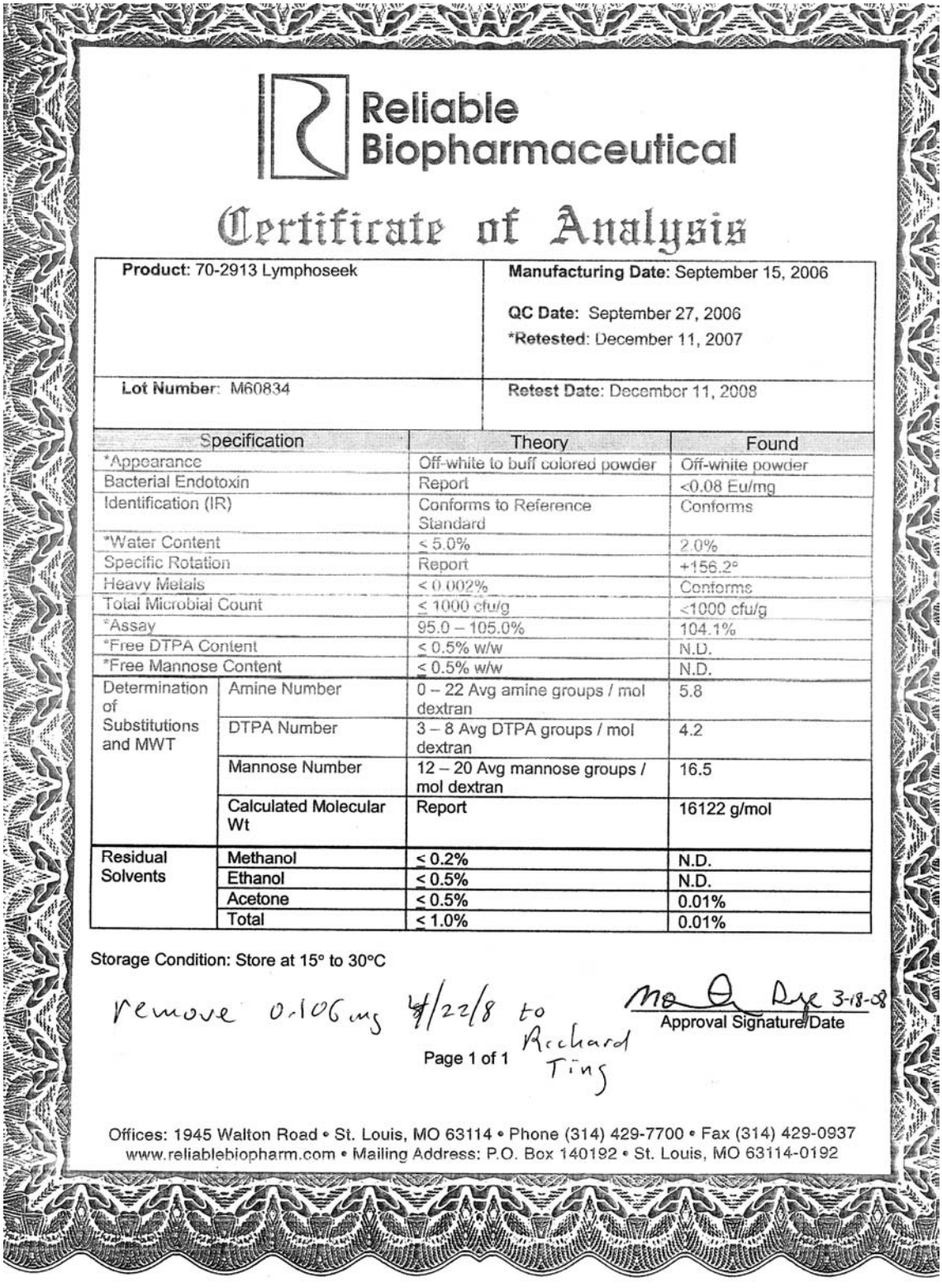
CHARACTERIZATION OF LYMPHOSEEK LABELING

In order to determine the dextran yield of **2**, a sugar assay was carried out on one aliquot of **2**. To a 10 mL test tube containing a 0.500 mL solution of **2**, 0.300 mL of a 5% phenol solution followed by 1.800 mL of 18 M H_2SO_4 were added. The exothermic reaction was vortexed for one minute and allowed to cool to room temperature after which an absorbance reading at 450 nm was taken. The amount of Lymphoseek contained in an aliquot of **2** was determined from interpolation through a standardized curve prepared from glucose assays on samples with known quantities of Lymphoseek. The reactive nature of 18 M H_2SO_4 was such that no long wavelength fluorescence was observed from **2**, therefore spectroscopic interference by the fluorophore at A_{450} was not an issue. Based on this glucose assay, 49.16 to 33.63 nmols of Lymphoseek was isolated as **2.** This corresponds to a 10-14 % yield of **2** from unconjugated, commercial Lymphoseek. The estimated molar ratio of fluorophore to Lymphoseek is 2 to 3 fluorophores per molecule of Lymphoseek. Spectrophotometric constants of a 1.5 µM solution in water: λ_{max} = 757 nm, ε_{757} = 110 000 cm^{-1} M^{-1}, ex= 757 nm, em = 777 nm, and φ = 0.026.

The estimated molar ratio of fluorophore to Lymphoseek following NHS condensation is 2 to 3 fluorophores per molecule of Lymphoseek. Although there were 5.8 amines on Lymphoseek (vide infra for certificate of analysis) and **1** was added at a ratio of 4:1 of **1** per amine, the same ratio of fluorophore: Lymphoseek labeling was always achieved.

Attempts to label a greater ratio of amines by increasing the molar ratio of **1** to facilitate greater fluorophore transfer did not change the product outcome.

Lymphoseek Certificate of Analysis:



Reliable Biopharmaceutical

Certificate of Analysis

Product: 70-2913 Lymphoseek	**Manufacturing Date**: September 15, 2006 **QC Date**: September 27, 2006 ***Retested**: December 11, 2007
Lot Number: M60834	**Retest Date**: December 11, 2008

Specification		Theory	Found
*Appearance		Off-white to buff colored powder	Off-white powder
Bacterial Endotoxin		Report	<0.08 Eu/mg
Identification (IR)		Conforms to Reference Standard	Conforms
*Water Content		≤ 5.0%	2.0%
Specific Rotation		Report	+156.2°
Heavy Metals		≤ 0.002%	Conforms
Total Microbial Count		≤ 1000 cfu/g	<1000 cfu/g
*Assay		95.0 – 105.0%	104.1%
*Free DTPA Content		≤ 0.5% w/w	N.D.
*Free Mannose Content		≤ 0.5% w/w	N.D.
Determination of Substitutions and MWT	Amine Number	0 – 22 Avg amine groups / mol dextran	5.8
	DTPA Number	3 – 8 Avg DTPA groups / mol dextran	4.2
	Mannose Number	12 – 20 Avg mannose groups / mol dextran	16.5
	Calculated Molecular Wt	Report	16122 g/mol
Residual Solvents	Methanol	≤ 0.2%	N.D.
	Ethanol	≤ 0.5%	N.D.
	Acetone	≤ 0.5%	0.01%
	Total	≤ 1.0%	0.01%

Storage Condition: Store at 15° to 30°C

remove 0.106 mg 4/22/8 to Richard Ting

Approval Signature/Date 3-18-08

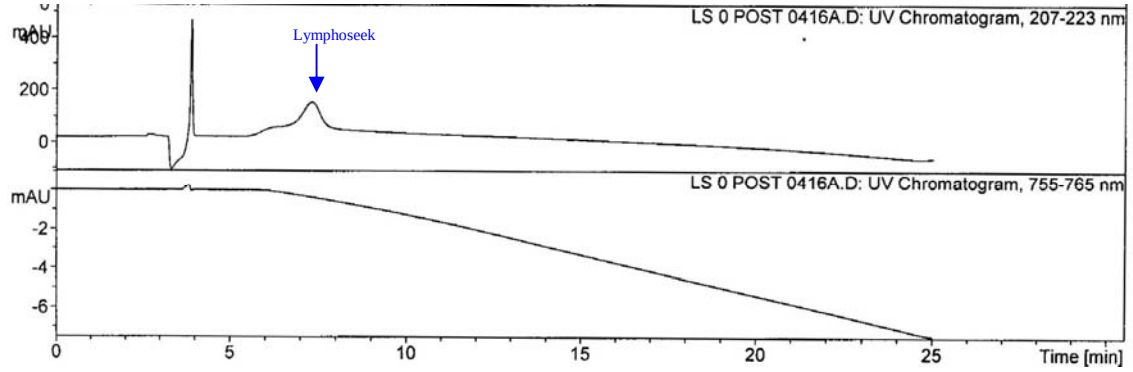
Page 1 of 1

Offices: 1945 Walton Road • St. Louis, MO 63114 • Phone (314) 429-7700 • Fax (314) 429-0937
www.reliablebiopharm.com • Mailing Address: P.O. Box 140192 • St. Louis, MO 63114-0192

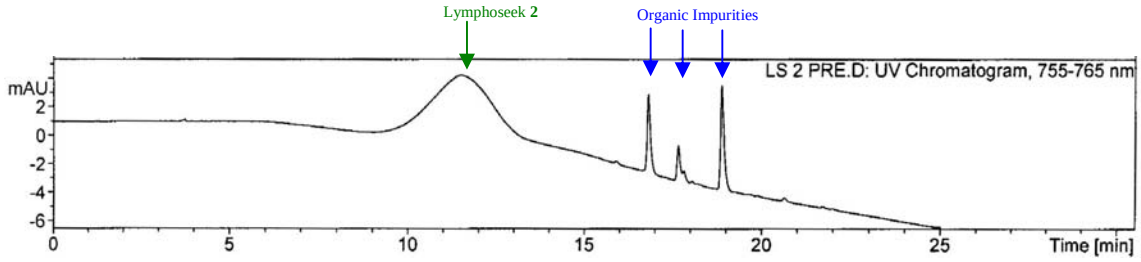
HPLC characterization of 2 and [^{19}F]-3

The HPLC characterization[†] of the reaction to give **2** and HPLC confirmation of the purity in both **2** and [^{19}F]-**3** following size exclusion chromatography are shown below.

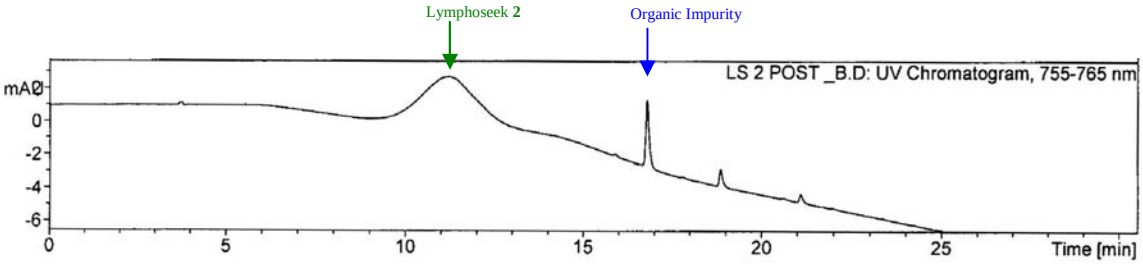
The following spectra are 215 and 780 nm absorbance HPLC elution profiles of unconjugated Lymphoseek alone. Note that Lymphoseek's elution is not sharp as it is a polymeric mixture and that Lymphoseek possesses no absorbance at 760 nm.



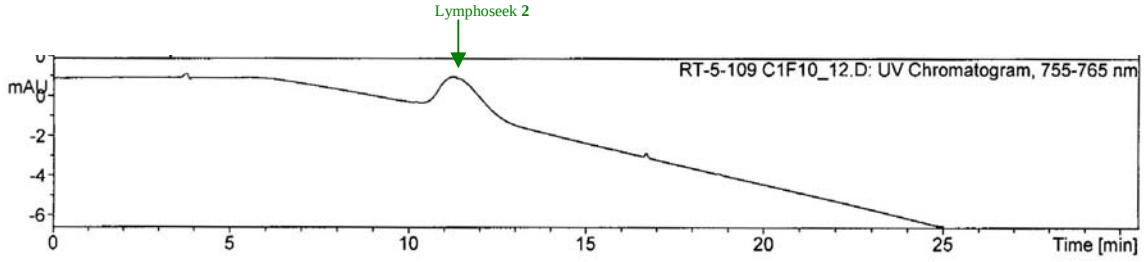
The following spectrum is the 780 nm absorbance HPLC elution profile of the crude, unpurified reaction mixture between **1** and Lymphoseek. The product, Lymphoseek **2**, absorbs at 760 nm due to labeling with **1**. Note the organic impurities at 17, 18, and 19 min from the crude, unpurified reaction mixture.



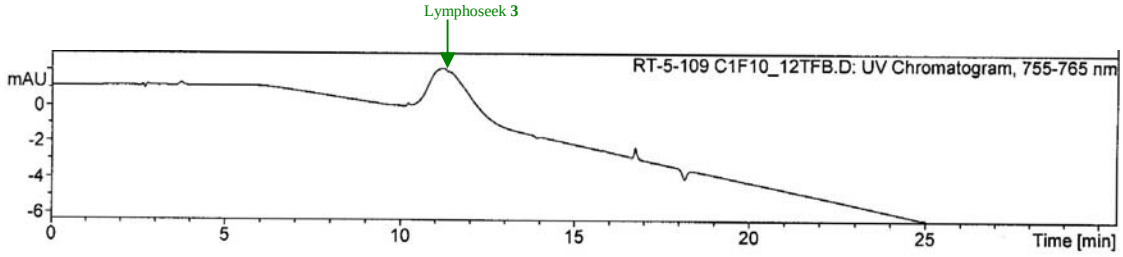
The following spectrum is the 760 nm absorbance HPLC elution profile of the crude reaction mixture containing **2** after it was extracted and passed through a single biorad-P6 size exclusion column. Note some removal of the mentioned organic impurities.



The next spectrum is the 760 nm absorbance HPLC elution profile of **2** after it was passed trough four subsequent Biorad P-6 size exclusion columns. Note the quantitative removal of organic impurities.



The final spectrum is the 760 nm absorbance HPLC elution profile of **2** after conversion to [^{19}F]-**3**, and passage trough four subsequent Biorad P-6 size exclusion columns. Again quantitative removal of organic impurities is achieved.



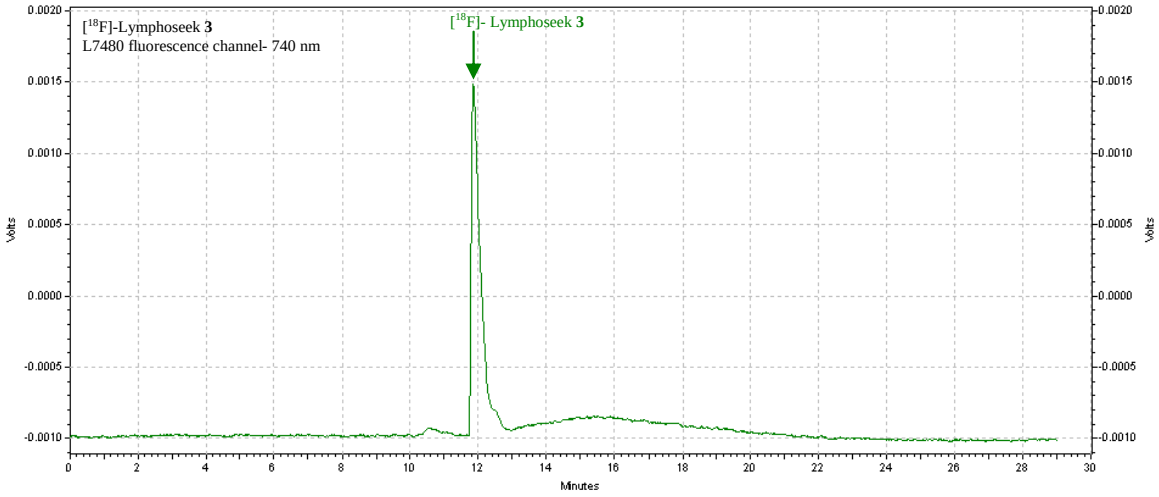
This section demonstrates by HPLC that Lymphoseek can be labeled with **1** to give **2**. It also demonstrates that **2** and **3** can be purified by size exclusion chromatography as described in the materials and methods. The transformation of **2** to **3** is difficult to characterize by MS due to the large mass of Lymphoseek and the fact that it is polymeric. Therefore, to demonstrate by MS that the trifluoroborate technology conveyed on **1** is generally applicable, a pure alterative target was labeled with **1**. MS characterization of this transformation follows the next section.

[†] HPLC Chromatography was carried out on an Agilent 1100 Series HPLC with a phenomenex Luna 5 µ C18(2) 100A 250 x 4.60 mm 5 µ column and a 1 mL/min flow rate with a 20 min, 10 to 90 % elution gradient followed by a 5 min isocratic elution with 90% acetonitrile and water where both solvents contained 0.05% trifluoroacetic acid.

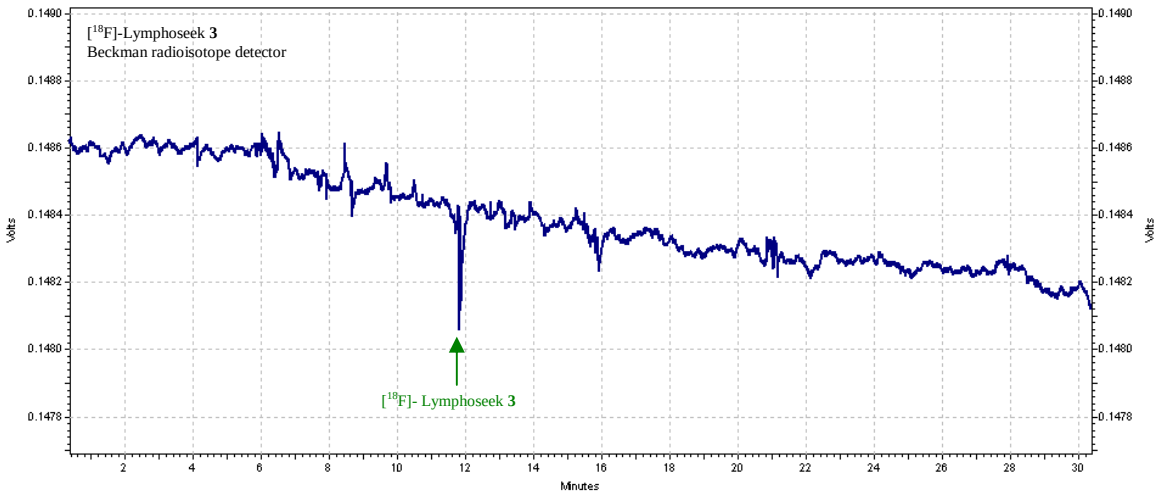
CHARACTERIZATION AND FURTHER APPLICATION

Final radiochemical analysis of [^{18}F]-3

Radiolabeled [^{18}F]-**3** was prepared as described in the materials and methods. The following HPLC analysis of [^{18}F]-**3** demonstrates its radiochemical purity. A 10 µCi amount of [^{18}F]-**3** was loaded on a Beckman Coulter System Gold HPLC equipped with a TOSOH Bioscience TSKgel G2000SW 7.8mm ID x 30 cm x 5 µ M size exclusion column, a L-7480 fluorescence detector, and a Beckman Radioisotope detector. Elution of [^{18}F]-**3** was achieved with an isocratic flow of 0.9% saline at 1 mL/min. The following figure is the elution profile of [^{18}F]-**3** as measured at 740 nm on the L7480 fluorescence detector. Note the single peak in the fluorescence channel that is indicative of a clean synthesis.

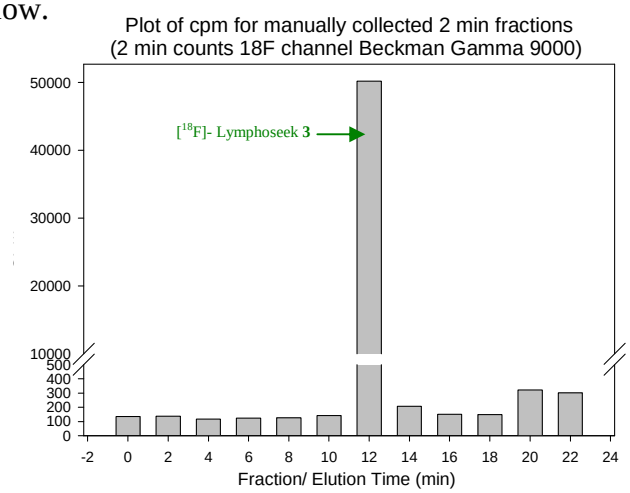


The following figure is the elution profile as observed in the Beckman radioisotope detector channel.

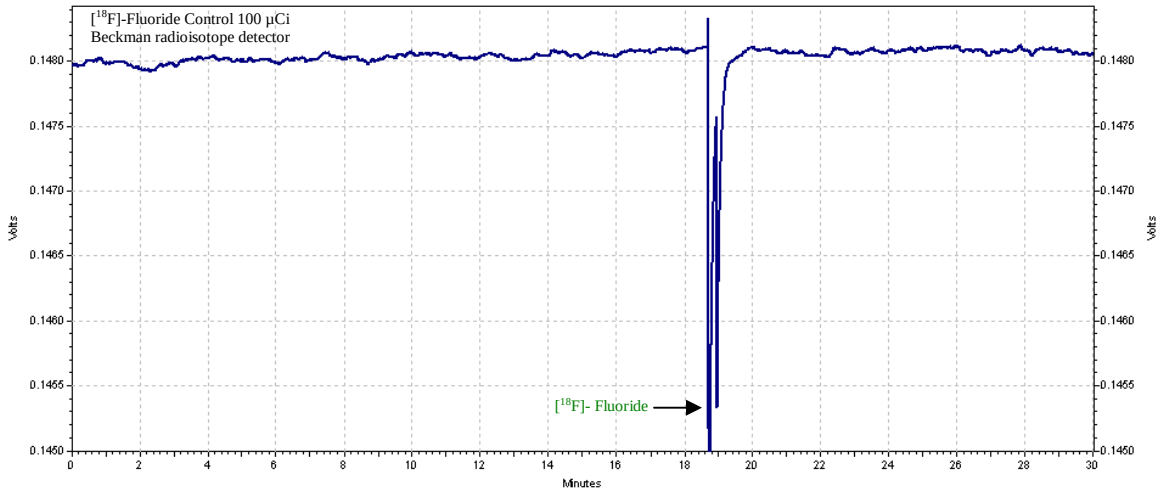


Unfortunately, the available Beckman radioisotope detector did not give a very good signal to noise ratio in the analysis of [^{18}F]-**3**. This detector is intended for use in high

activity syntheses and not for analytical preparations. To demonstrate that the fluorescent peak that is eluted at 12 min, corresponds to a pure sample of [^{18}F]-**3** with minimal radioactive contaminants**,** a 10 µCi sample of [^{18}F]-3 was injected and 2 min fractions were collected manually in eppendorf tubes. These samples were analyzed by scintillation counting on a Beckman Gamma 9000 scintillation counter. The elution profile is shown below.



Note that the majority of the radioactivity is contained within fractions 11-13. This is indicative of a radio-chemically pure species that possesses 740 nm fluorescence. As a control, a 100 µCi sample of [^{18}F]-fluoride was run and detected by the Beckman radioisotope detector. Minimal [^{18}F]-fluoride contamination is observed



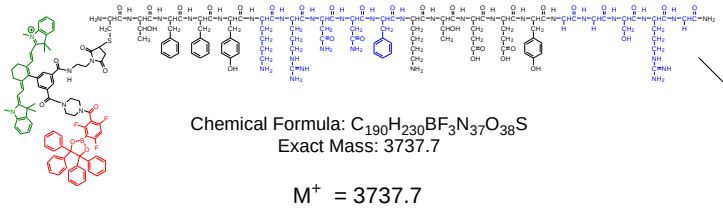
[^{18}F]-fluoride elutes at 19 min, this is consistent with the elution profile of a small molecule on a size exclusion column. The purification of [^{18}F]-**3** as described in the materials and methods gives a relatively pure compound that contains little contaminating [^{18}F]-fluoride.

General multimodality probe application and HPLC-MS analyses

The fluoridation of Lymphoseek **3**, is a perturbation that is difficult to characterize by mass spectrometry for two reasons: the large mass of the species being transformed and the polymeric nature of the species being labeled. In order to demonstrate that the trifluoroborate technology involved in transforming **2** to **3** is both clean and does not generate B-F intermediates, the following peptide was labeled with **1** and converted to a trifluoroborate under the conditions reported in this manuscript. This conversion was monitored by both MS and HPLC. The primary structure of the peptide amino acid sequence has been scrambled.

A.i

NH_2-C(FBOMB)TFFY KRNNF KTEEY GGSRG -$CONH_2$

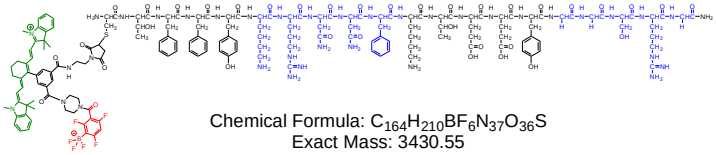


Chemical Formula: $C_{190}H_{230}BF_3N_{37}O_{38}S$
Exact Mass: 3737.7

M^+ = 3737.7
M^{2+} = 1868.8
M^{3+} = 1245.9
M^{4+} = 934.4
M^{5+} = 747.5

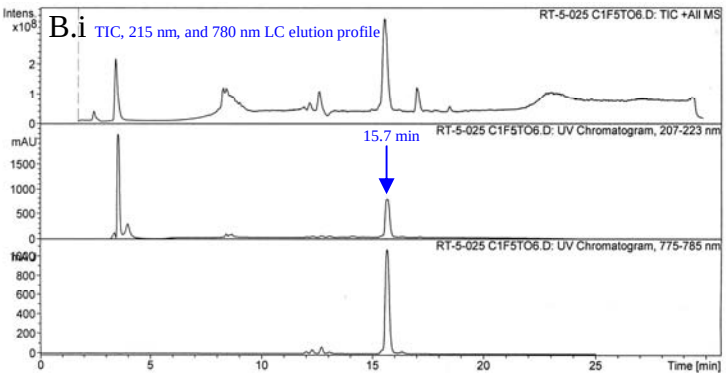
A.ii

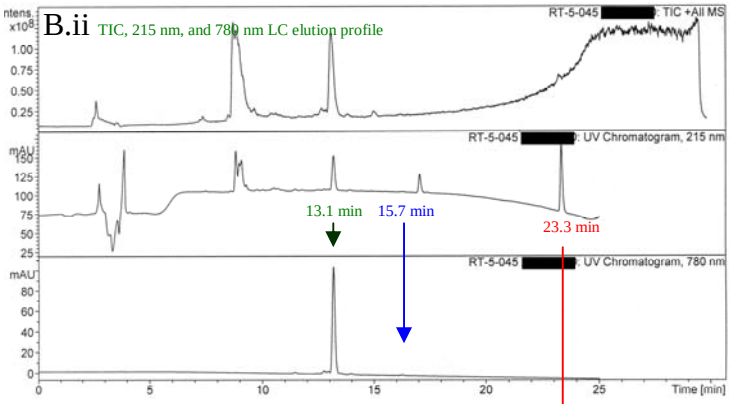
HF
HCl, H_2O
40 °C, 1h

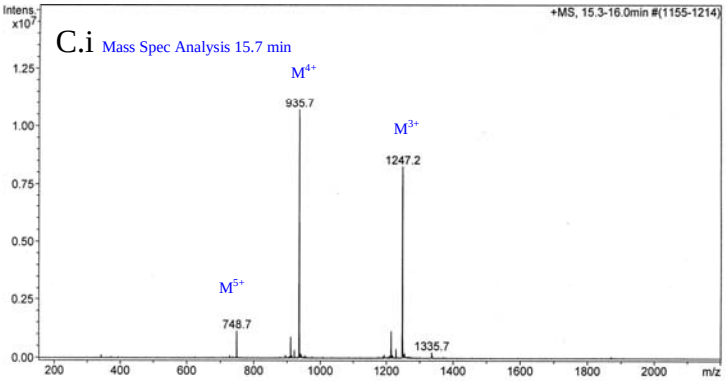


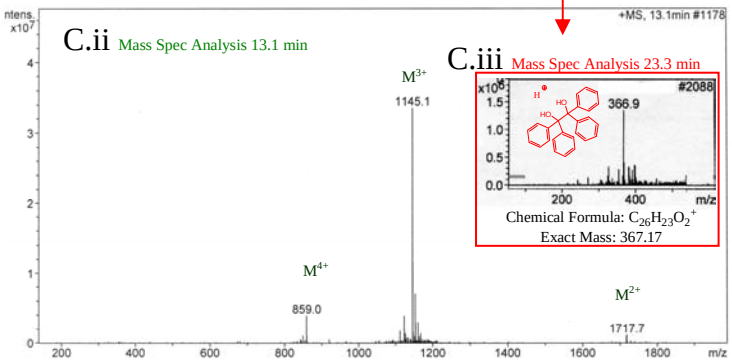
Chemical Formula: $C_{164}H_{210}BF_6N_{37}O_{36}S$
Exact Mass: 3430.55

M^+ = 3430.55
M^{2+} = 1715.3
M^{3+} = 1143.5
M^{4+} = 857.6









Chemical Formula: $C_{26}H_{23}O_2^+$
Exact Mass: 367.17

A peptide with the sequence, NH_2-(CTFFY KRNNF KTEEY GGSRG) -$CONH_2$ (Figure Ai, scrambled amino acid sequence), was labeled with **1** on its N-terminal cystine and was purified by preparative HPLC. The purified peptide-**1** is shown in figure B.i where the ionization current and the absorbance elution profiles at 780 nm and 215 nm are shown (vide infra for HPLC conditions)[†]. Note the characteristics indicative of purity including a single peak in both 780 nm (15.7 min) and 215 nm (15.7 min) absorbance spectra. The mass spectrometry profile of the peak eluted at 15.7 min is shown in figure Ci. Note a MS spectra indicative of relative purity, where M^{3+} (1247.2 M/z), M^{4+} (935.7 M/z), and M^{5+} (748.7 M/z) ions are observed, while unrelated masses are less abundant.

When the peptide is treated with aqueous fluoride, the trifluoroborate species shown in figure Aii is generated. HPLC analysis was carried out 10 min after fluoride treatment.[‡] This is clear in the HPLC absorbance elution profile at 215 nm (figure Bii), three peaks* in addition to the product (13.1 min) and the injection artifact 2-4 min are observed. Note the absence of a peak at 15.7 min indicating quantitative consumption of tetraphenyl pinacol peptide-**1** and production of [^{19}F]-trifluoroborate labeled peptide. This is observed in the absorbance elution profile at 780 nm, where the starting material at 15.7 min is completely converted to 780 nm absorbent material at 13.1 min. There is only a single peak at 13.1 min in the 780 nm spectra indicating that there are no B-^{19}F non-trifluoroborate intermediates produced (the boron on **1** is linked directly to a 780 nm fluorophore). The mass spectrometry profile of the peak eluted at 13.1 min is shown in figure Cii. Note a spectra indicative of relative purity, where M^{2+} (1717.7 M/z), M^{3+} (1145.1 M/z), and M^{5+} (859.0 M/z) ions are observed, while unrelated masses are not. The peak at 13.1 min can be purified by HPLC, stored at -20 °C, and reanalyzed by HPLC with no observed decomposition. All 215 nm absorbing peaks including peptide-**1** are removed when the reaction mixture Aii is passed through a Biorad-P6 spin column.

This HPLC-MS analysis demonstrates that the conditions for generating trifluoroborates reported in this manuscript: 1) produce trifluoroborates quantitatively, 2) do not produce B-F intermediates, and 3) are generally applicable to biomolecules other than polysaccharide polymers.

[†]Analysis was carried out on an Agilent 1100 Series HPLC equipped with a LC/MSD trap XCT. Chromatography was carried out on a phenomenex Luna 5 µ C18(2) 100A 250 x 4.60 mm 5 µ column with a 1 mL/min flow rate with a 20 min, 10 to 90 % elution gradient followed by a 5 min isocratic elution with 90% acetonitrile and water where both solvents contained 0.05% trifluoroacetic acid. Mass spectrometry was carried out through electrospray ionization in the positive mode with at trap focus at 1000 M/z. The traces shown were generated with Chemstation Rev.B.01.03[204].

[‡]The purification used for Lymphoseek **3** does not work when applied to the peptide in this analysis. This peptide has a molecular weight of 3432.51 g/mol, therefore it does not elute from the Biorad-P6 spin columns used to purify **3** in this manuscript (Biorad P6 MWCO, molecular weight cut-off,= 6000 g/mol). Preparative HPLC or the use of spin columns with a lower MWCO can be used instead in order to successfully purify low MW species.

* The new peak at 9 min in the 215 nm absorbance spectrum is not related to **1** or the fluoridation of **1** as it is not observed when other peptides of similar hydrophobicity and sequence are [^{19}F]-labeled (Data not shown). The peak at 23.3 min is attributed to tetraphenyl pinacol (figure Ciii) that is generated when the tetraphenylpinacol on peptide-**1** (15.7 min) is displaced by fluoride to form the trifluoroborate at 13.1 min.

Radiochemical Synthesis

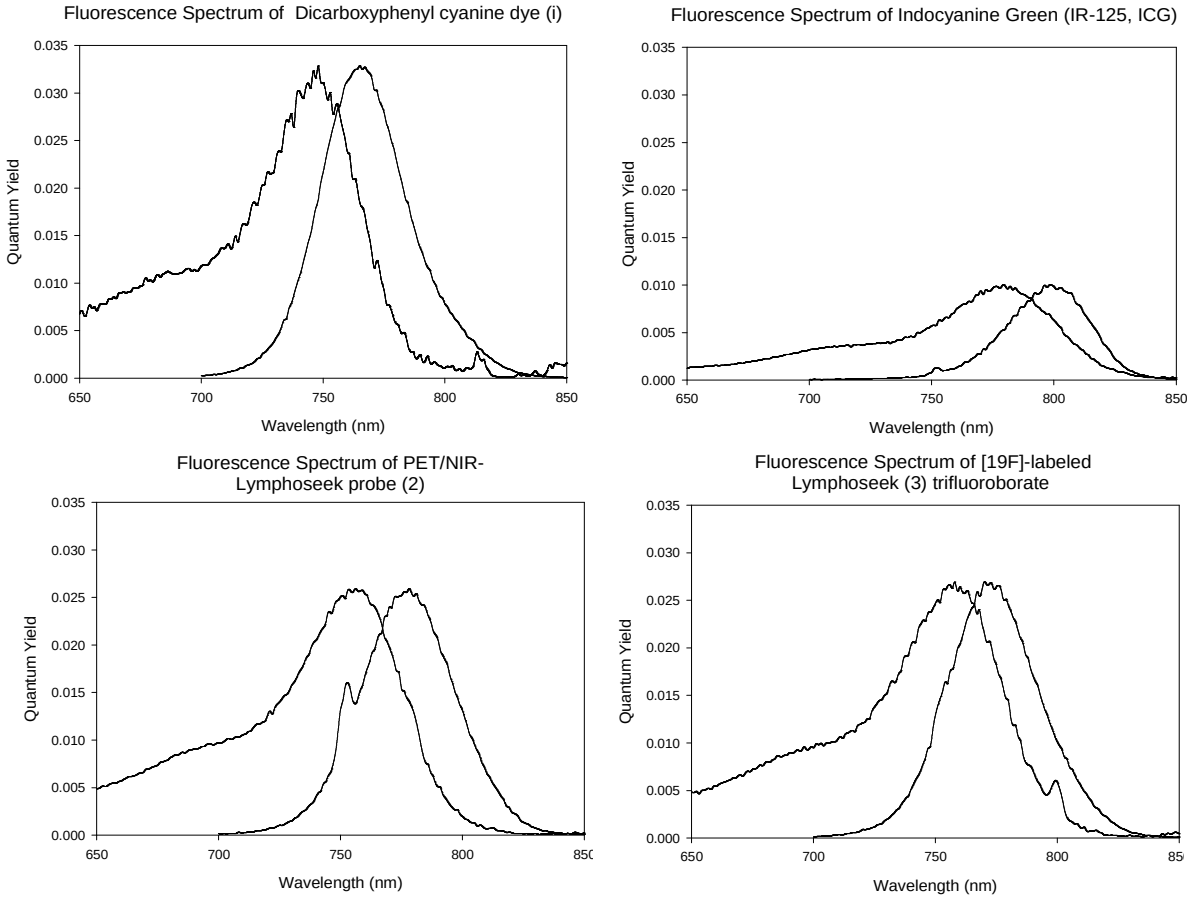
The table below summarizes the results of additional radiochemical labeling experiments that were carried out on **2** prior to the 12 mouse in vivo trial of ^{18}F labeled Lymphoseek **3** described in this manuscript. These ^{18}F labelings were carried out using protocol similar to that listed in the materials and methods unless indicated otherwise.

Experiment	Date	Reaction Volume	Activity of ^{18}F at time of addition to Lymphoseek 2	^{19}F carrier added	Moles of Lymphoseek 2	**RATIO OF FLUORIDE/ BORON**	Activity Isolated as 3	Time of synthesis (Rxn and Purification)	Specific activity (assuming 60% yield of 3 by NIRF) (Ci/µmol)	**DECAY UNCORRECTED RADIOCHEMICAL YIELD**
Section 1 : Replicate High Activity ^{18}F labeling trials @ ~4:1 Fluoride to acceptor ratio:										
RT-3-031A	Nov. 5 2008	5 µL	47.5 mCi	40 nmols	10 nmols	**4:1**	0.292 mCi	1h 10 min	0.048	**0.61 %**
RT-3-031B	Nov. 5 2008	5 µL	27.8 mCi	40 nmols	10 nmols	**4:1**	0.095 mCi	1h	0.016	**0.34 %**
RT-3-029	Sept. 3 2008	5 µL	49.6 mCi	25 nmols	5 nmols	**5:1**	0.347 mCi	1h 43 min	0.116	**0.70 %**
RT-3-027	Aug. 27 2008	5 µL	24.0 mCi	25 nmols	5 nmols	**5:1**	0.726 mCi[*]	1h 31 min	0.242	**3.02 %**[A]
Section 2: Low Activity Experimental ^{18}F labeling trials:										
RT-3-025A	Aug. 15 2008	5 µL	1.1 mCi[b]	800 nmols	0.8 nmols	**1000:1**	0.00024 mCi	1h 55 min	0.00005	**0.02%**
RT-3-025B	Aug. 15 2008	5 µL	1.1 mCi[b]	480 nmols	0.8 nmols	**600:1**	0.00028 mCi	1h 55 min	0.0006	**0.03 %**
RT-3-025C	Aug. 15 2008	5 µL	1.1 mCi[b]	160 nmols	0.8 nmols	**200:1**	0.00084 mCi	1h 55 min	0.002	**0.07 %**
RT-3-025D	Aug. 15 2008	5 µL	1.1 mCi[b]	40 nmols	0.8 nmols	**50:1**	0.00147 mCi	1h 55 min	0.003	**0.13 %**
RT-3-025E	Aug. 15 2008	5 µL	1.1 mCi[b]	10 nmols	0.8 nmols	**13:1**	0.00346 mCi	1h 55 min	0.007	**0.31 %**
Section 3: High Activity Experimental ^{18}F labeling trials:										
RT-3-021	Aug. 08 2008	5 µL	37.3 mCi	2 000 nmols	7.4 nmols	**270:1**	0.0058 mCi	3 h	0.0008	**0.02 %**
RT-3-047B	June 14 2010	8 µL	11.7 mCi	2.5 nmols	5 nmols	**0.5:1**[C]	0.169 mCi	29 min	0.056	**1.14 %**
RT-3-049	June 16 2010	5 µL	35 mCi	2.5 nmols	5 nmols	**0.5:1**[C]	0.386 mCi	34 min	0.127	**1.12 %**

[a*] [^{18}F]-Fluoride contamination verified
[b] Activity was used as is from PETNET and therefore activity was NOT dried down and resuspended at smaller volumes
[c] Stoichiometry of added fluoride to boron.

Fluorescence and Absorption data

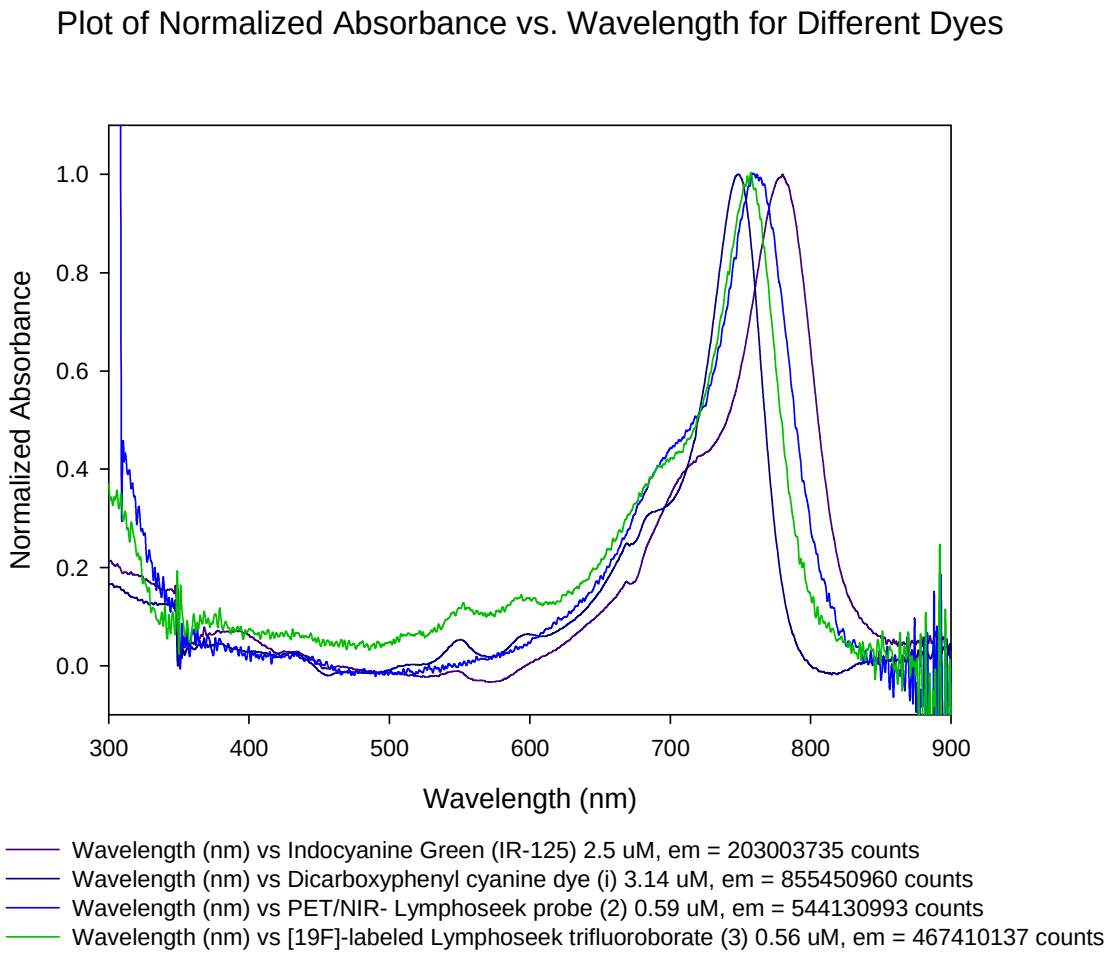
The excitation and emission spectra of (i), 2, the trifluoroborate 3, and a reference; indocyanine green (ICG, IR-125)(*3*) taken as 1-3 µM solutions in water are shown below:



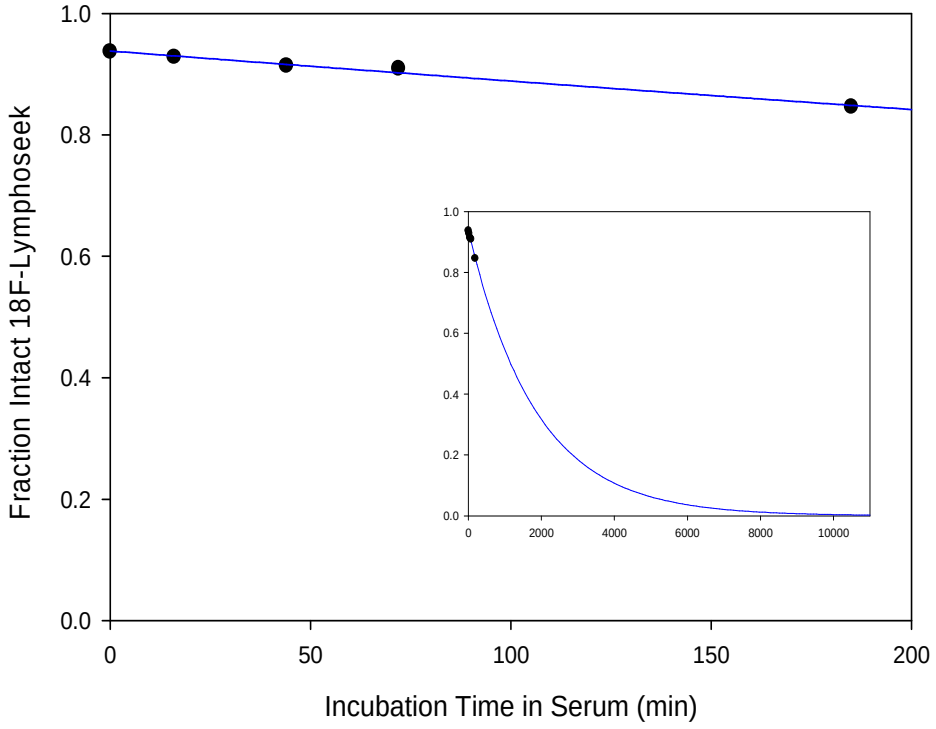
The table below details the constants associated with the described compounds (constants measured on 1-3 µM solutions in water).

Fluorophore	λ_{max} (nm) (1-3 µM solution)	**ε ($cm^{-1}M^{-1}$)** (1-3 µM solution)	Excitation (nm)	Emission (nm)	**Stokes Shift**	**Quantum Yield, φ**	**φ, relative to ICG**	**Ratio of Raw Counts em/ex**
Indocyanine Green (IR-125, ICG)	780	102 000	778	800	22	0.01(*3*)	1	702 (203003735 / 288896)
Dicarboxyphenyl cyanine dye **(i)**	749	107 000	747	765	18	0.033	3.2	490 (855450960 / 1743333)
PET/NIR- Lymphoseek probe **2**	758	110 000	757	777	20	0.026	2.6	544 (544130993 / 1000358)
[^{19}F]-labeled Lymphoseek trifluoroborate **3**	756	110 000	755	772	17	0.027	2.7	474 (467410137 / 985137)

Plot of normalized absorbance demonstrating the lack of self-quenching in Lymphoseek constructs **2** and **3**.



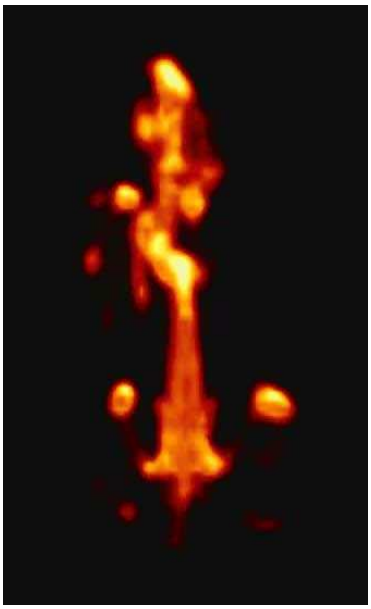
LYMPHOSEEK PLASMA STABILITY ASSAY



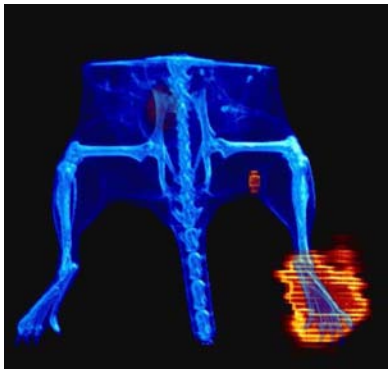
Stability plot of [^{18}F]-labeled of Lymphoseek 3. **The fraction of [^{18}F]-labeled Lymphoseek** 3 **that clears the matrix of a Bio Rad P6 size exclusion gel chromatography column (MWCO = 6000 MW) following incubation for different times in mouse serum.**

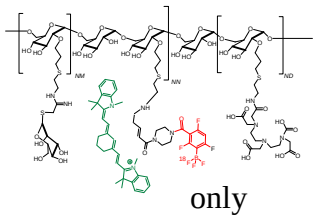
To determine the stability of [^{18}F]-labeled of Lymphoseek **3** in serum, approximately 3 nmols of labeled [^{18}F]-**3** (98 µCi @ 10:45 am) in 100 µCi of 10 mM Tris buffer pH 7.3 was added to 100 µL of mouse serum at 10:51 AM **(Start of Reaction (SOR)).** At time points corresponding to 1 min, 16 min, 44 min, 72 min, and 185 min vs. SOR, 40 µL aliquots were removed from the reaction and placed over Bio Rad Bio Gel P6 spin columns. Both the material retained in the spin column and the flow through were counted by scintillation counter. All counts were corrected for ^{18}F decay. The ratio of corrected counts obtained in the flow through divided by the sum of the counts in the flow through plus those retained in the spin column were plot against time. A non-linear regression analysis of this data was carried out using Sigma Plot 2001 v7.101. A first order decay constant of 0.00054 ± 0.00003 min^{-1} corresponding to a half-life of 1280 ± 80 min was obtained. Assuming that the material retained in the Bio Rad P6 spin column matrix represents the amount of [^{18}F]-labeled of Lymphoseek **3** that is degraded into products of molecular weight that are less than 6000 (the MWCO of the Bio Rad P6 spin columns), it can be assumed that the half-life of [^{18}F]-labeled of Lymphoseek **3** in mouse serum is 1280 ± 80 min, a value that corresponds to a very stable ^{18}F tracer considering that this value is 11.6 times that of ^{18}F nuclear decay (110 min).

EVIDENCE OF IN VIVO ^{18}F-BORON BOND STABILITY

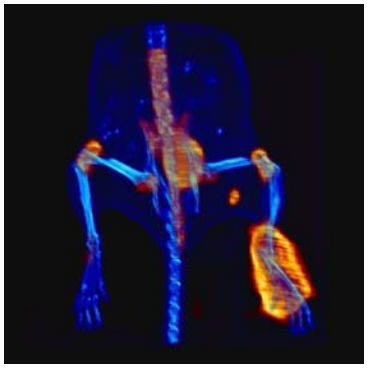


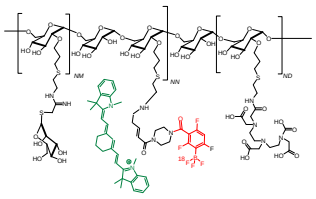
$^{18}F^-$ only





only





+

Deliberate $^{18}F^-$ contamination

The left image is of a mouse injected with ^{18}F-Fluoride after 1 hour. Note signal accumulation in bone structures and the bladder. [^{18}F]-fluoride does not accumulate in lumbar and popliteal lymph nodes. The middle image is a 1 h image of a mouse that has been injected with ^{18}F-3 in the right rear footpad. Note that this image is different from the previous image. There is specific signal accumulation in the sentinel lymph node but no signal accumulation in the knee caps or bone structures. Right image, a 1 h image of a mouse that has been injected with a sample of ^{18}F-3 that was deliberately contaminated with ^{18}F-Fluoride. Note accumulation in the sentinel lymph node as well as in the spine and kneecaps of the mouse. If ^{18}F-3 was experiencing ^{18}F-fluoride loss from F-boron bond dissociation during the in vivo PET experiment, accumulation in the spine and kneecaps of the mouse would be an expected consequence. Because the middle image, and not the right image, is typical of PET images that are acquired with ^{18}F-3, we can qualitatively conclude that the ^{18}F-boron bond is stable on ^{18}F-Lymphoseek 3 in vivo.

REFERENCES:

(1) Ting, R., Lo, J., Adam, M. J., Ruth, T. J., and Perrin, D. M. (2008) Capturing aqueous [F-18]-fluoride with an arylboronic ester for PET: Synthesis and aqueous stability of a fluorescent [F-18]-labeled aryltrifluoroborate. *Journal of Fluorine Chemistry 129*, 349-358.

(2) Dubois, M., Gilles, K. A., Hamilton, J. K., Rebers, P. A., and Smith, F. (1956) Colorimetric Method for Determination of Sugars and Related Substances. *Analytical Chemistry 28*, 350-356.

(3) Soper, S. A., and Mattingly, Q. L. (1994) Steady-State and Picosecond Laser Fluorescence Studies of Nonradiative Pathways in Tricarbocyanine Dyes - Implications to the Design of near-Ir Fluorochromes with High Fluorescence Efficiencies. *Journal of the American Chemical Society 116*, 3744-3752.

Simple Fluidic System for Purifying and Concentrating Diagnostic Biomarkers Using Stimuli-Responsive Antibody Conjugates and Membranes

Allison L. Golden,[†] Charles F. Battrell,[‡] Sean Pennell,[‡] Allan S. Hoffman,[†] James J. Lai,[†] and Patrick S. Stayton*[,†]

Department of Bioengineering, University of Washington, Seattle, Washington 98195, and Micronics, Inc., 8463 154th Avenue NE, Building G, Redmond, Washington, 98052. Received April 8, 2010; Revised Manuscript Received June 11, 2010

We report a simple fluidic system that can purify and concentrate diagnostic biomarkers through the capture and triggered release of stimuli-responsive polymer−antibody conjugates at porous membranes that are grafted with the same stimuli-responsive polymer. This technique is applied here to the capture and detection of a model streptavidin antigen and subsequently to clinical ranges of the malaria antigen *Plasmodium falciparum* histidine-rich protein 2 (PfHRP2) from spiked human plasma. The carboxyl end-groups of semi-telechelic poly(*N*-isopropylacrylamide) (pNIPAAm) synthesized by reversible addition−fragmentation chain transfer (RAFT) polymerization were modified with tetrafluorophenol to yield amine-reactive ester groups for conjugation to amine groups of anti-streptavidin and anti-PfHRP2 antibodies. Stimuli-responsive membranes were constructed from 1.2 μm pore-size, hydroxylated, nylon-6,6 filters (Loprodyne, from Pall Corporation). The surface hydroxyl groups on the filters were conjugated to a 2-ethylsulfanylthiocarbonylsulfanyl-2-methyl propionic acid (EMP) RAFT chain transfer agent, and the surface-grafted pNIPAAm was obtained by subsequent polymerization. The number average molecular weight (Mn) and polydispersity indices (PDI) of the surface grafts were characterized, and membranes with either 4100 and 8400 dalton pNIPAAm grafts showed greater than 80% anti-streptavidin capture efficiency. The 8400 dalton-graft membrane showed the highest release efficiency, and it was demonstrated that at 0.2 nM starting concentration the streptavidin could be concentrated approximately 40-fold by releasing into a small 50 μL volume. This concentrator system was applied to the capture and concentration of the PfHRP2 antigen, and results showed that the PfHRP2 antigen could be processed and detected at clinically relevant concentrations of this malaria biomarker.

INTRODUCTION

Biomarker testing can potentially help in the identification and epidemiological tracking of many diseases, as well as in their treatment monitoring. Achieving clinically relevant immunoassay limits of detection for biomarkers has typically required more time-consuming methods and specialized equipment found in centralized and higher-resource laboratory facilities. Rapid diagnostic tests (RDTs) based on lateral flow, flow-through, or dipstick approaches have greatly aided diagnosis in low-resource settings but have detection sensitivities that can limit their applications. As an example, tests for malaria are suitable for detecting higher levels of antigen released by parasitized red blood cells, but are not adequate for detection of low levels of parasitemia common with patients from non-endemic regions with clinical disease (*1*−*3*) or in cases of subpatent parasitemia levels that can serve as transmission reservoirs (*4, 5*). Additionally, they are limited in use for species discrimination, which can be necessary for correct treatment choice and monitoring (*6, 7*). By improving detection limits and incorporating multiplex assays, rapid diagnostic technologies can move to the forefront of providing accurate diagnosis across the spectrum of medical needs, rather than simply providing faster results for conventional methods.

Microfluidic assays have features desirable in a rapid diagnostic test including smaller input samples, shorter diffusion and reaction times, lower reagent consumption, and containment of biohazard waste products (*8*−*10*). However, simply reformatting current immunoassays to fit in a microfluidic device setting may prove to be insufficient for overcoming intrinsic sensitivity and assay limitations. While microfluidic volumes reduce diffusion distance, capture at the channel surface is confounded by the dominance of the advective laminar flow regime (*11*). Absolute quantities of antigen fall as the sample size is reduced and preconditioning of a sample can lead to further dilution. There is still a need for simple, integratable reagent systems that can both purify and concentrate diagnostic targets in microfluidic or flow-through diagnostic technologies.

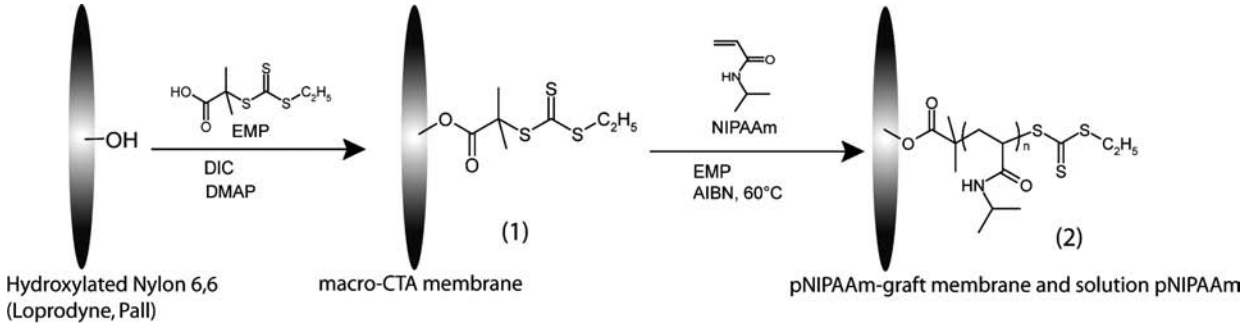
Our group has been investigating the use of "smart" polymer conjugates of biomolecules to address this need for rapid and efficient biomarker processing in microfluidic devices. In the past, there have been two primary approaches that utilized either immunoconjugates that can be phase-separated in solution and captured on surfaces or stimuli-responsive surfaces for the capture of biomolecules or cells (*12*−*20*). More recently, we have been investigating the joint application of the stimuli-responsive conjugates with stimuli-responsive microfluidic channel surfaces (*16*). Here, we have grafted polymer brushes using the reversible-addition fragmentation chain transfer (RAFT) method, which allows control of properties through control of graft molecular weight and end-groups (*21*−*23*). Grafted porous membranes incorporating stimuli-sensitive polymers have been previously used to perform separations on the basis of porosity, hydrophobicity, or surface access (*24*−*33*). These stimuli-responsive grafted membranes are particularly appealing when used jointly with stimuli-responsive antibody−polymer conjugates where the diffusion of the antigen and antibody in plasma and serum is the rate-limiting step (*34*−*36*).

Temperature-responsive micro- and nanoparticles have been previously isolated in microfluidic devices, but isolation was

* To whom correspondence should be addressed. Phone: (206) 685-8148. E-mail: stayton@u.washington.edu.
[†] University of Washington.
[‡] Micronics, Inc.

10.1021/bc100169y © 2010 American Chemical Society
Published on Web 09/16/2010

Scheme 1. Synthesis of pNIPAAm-Polymerized Membranes[a]



[a] Membranes were prepared by first coupling the EMP chain transfer agent via esterification to produce a macro-CTA membrane (1). Second, the membrane was immersed in a RAFT-mediated polymerization of NIPAAm with additional EMP and AIBN to yield solution homopolymer and covalently-linked surface polymer (2).

performed at microfluidic channel walls (*16, 37*−*39*). This requires migration of the particles away from the laminar flow stream. We present results showing that stimuli-responsive IgG and IgM antibody−pNIPAAm conjugates are efficiently captured and released at pNIPAAm-grafted nylon-6,6 membranes inserted into prefabricated microfluidic cards. The sharpness of the immunocomplex sandwich release after capture was shown to be strongly enhanced by the surface-polymerized pNIPAAm on the membrane surface during constant microfluidic flow. This system was also shown to be applicable to processing of malaria antigen from spiked human plasma samples, resulting in detection limits comparable to ELISA for the malaria *Plasmodium falciparum* histidine-rich protein 2 (PfHRP2) antigen.

EXPERIMENTAL SECTION

Materials. 2,2′-Azoisobutyronitirile (AIBN, Aldrich) was recrystallized from methanol. *N*-Isopropylacrylamide (NIPAAm, Aldrich, 97%) was recrystallized twice from hexane and dried under vacuum prior to use. Anhydrous dimethylformamide (DMF), anhydrous dimethylsulfoxide (DMSO), dichloromethane, anhydrous ethyl ether, 2,3,5,6-tetrafluorophenol (TFP), diisopropylcarbodiimide (DIC), and dimethylaminopyridine (DMAP) were purchased and used as received. Prepared 10 mM phosphate-buffered saline (PBS) and phosphate-buffered saline with 0.05% Tween-20 (PBS-T) dry reagents were purchased from Sigma and dissolved in distilled water. 3,3′,5,5′-Tetramethylbenzidine (TMB) substrate was purchased from KPL. Monoclonal mouse anti-PfHRP2 IgM antibody, monoclonal mouse anti-PfHRP2 peroxidase-conjugated detection IgG antibody, and recombinant PfHRP2 antigen were purchased from Immunology Consultants Laboratory. Polyclonal IgG antibodies against streptavidin were purchased from Abcam. Loprodyne hydroxylated nylon-6,6 membranes, 1.2 μm pore size, were from Pall. The chain transfer agent (CTA) 2-ethylsulfanylthiocarbonylsulfanyl-2-methyl propionic acid, EMP, was synthesized previously as described (*40*). Dialysis membranes were purchased from Spectrum laboratories. Prior to use, pooled human plasma (sodium EDTA, Valley Biomedical) was filtered using Whatman GD/X filters, to remove precipitate formed after thawing from the frozen aliquot, and stored at 4 °C for up to 1 week.

Preparation of pNIPAAm-Bound Membranes. Membranes with graft pNIPAAm were prepared as shown in Scheme 1. The CTA EMP (100 mM), DIC (100 mM), and DMAP (10 mM) were combined in 10 mL anhydrous DMF and added to vacuum-dried Loprodyne membrane. The reaction was stirred for 48 hours at room temperature. Membranes were washed extensively in acetone and ethanol, dried by vacuum at room temperature, and then stored under ambient conditions. Polymerization was mediated by chain transfer agent using the reversible addition−fragmentation chain transfer (RAFT) technique (*41*). Membrane with and without bound CTA were immersed in a solution polymerization vessel containing the following in DMF/EMP chain transfer agent (13.2 or 40 mmol), *N*-isopropylacrylamide monomer (0.2 g/mL), and (2.7 or 8 mmol) AIBN. Following nitrogen purging, polymerization proceeded at 60 °C for 18−24 h. Solution polymer was retained and analyzed and membranes were washed extensively with acetone and ethanol and soaked 48 h at 4 °C in several changes of distilled water to remove noncovalently adsorbed or entangled polymer.

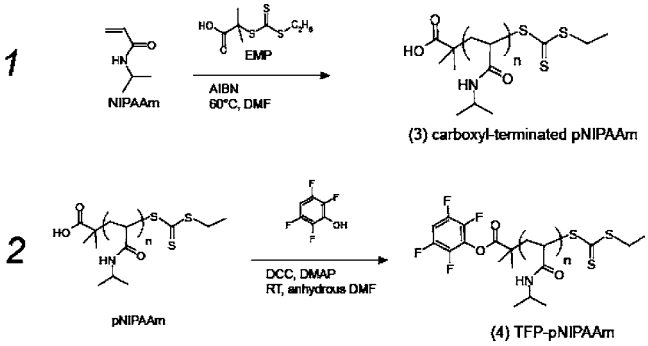
Cleavage of pNIPAAm from Surface of Membranes. 1 N sodium hydroxide solution (2 mL per cm^2 of membrane) was added to membranes and heated to 70 °C for 1 h. Solutions were neutralized with 1 N hydrochloric acid, and each membrane was washed with 2 mL of distilled water. All solutions were then combined and dialyzed against several changes of distilled water for 72 h, lyophilized, and stored dry until analysis. Polymers were dissolved in DMF and treated with immobilized TCEP for 1 h prior to characterization by gel permeation chromatography.

Synthesis of Semi-telechelic (pNIPAAm) and pNIPAAm-TFP Ester. The RAFT polymerization of *N*-isopropylacrylamide monomer included the following: 13.2 mmol EMP CTA, 0.2 g/mL NIPAAm, and 2.7 mmol AIBN. After nitrogen purging, the polymerization proceeded at 60 °C for 18 hours. The resulting polymer was precipitated from DMF twice in cold ethyl ether, filtered, dried under vacuum, and analyzed by GPC. PNIPAAm of number-average molecular weight (Mn) equal to 14 500, and polydispersity index (weight average molecular weight/number average molecular weight, or M_w/M_n) equal to 1.15 was used for preparation of TFP ester. The end carboxyl group was reacted with tetrafluorophenol (Scheme 2). The reagents pNIPAAm (1 g, 13.8 mM), DIC (42 mg, 67 mM), tetrafluorophenol (56 mg, 67 mM), and DMAP (4.1 mg, 6.7 mM) were combined in 5 mL anhydrous dichloromethane at room temperature for 24 hours. Activated polymer was then precipitated with cold anhydrous ethyl ether. Precipitates were immediately dried by vacuum and stored dry at −20 °C.

Gel Permeation Chromatography. Polymer samples from solution and surface-derived polymerizations were analyzed using gel permeation chromatography (GPC) to determine their number average molecular weight (Mn) and polydispersity index (PDI = weight average molecular weight/number average molecular weight), using Viscotek model VE2001 sampler and VE3580 refractive index (RI) detector. Samples were compared against poly(methyl methacrylate) standards to determine molecular weight.

Antibody Conjugation and Purification. One milligram of polyclonal mouse IgG antistreptavidin or monoclonal mouse

Scheme 2[a]



[a] 1. Synthesis of semi-telechelic pNIPAAm through RAFT polymerization results in carboxyl terminated pNIPAAm (**3**). 2. Tetrafluorophenol is coupled with the carboxyl end of pNIPAAm to result in TFP-pNIPAAm (**4**).

IgM anti-PfHRP2 was diluted in PBS, with 100 mM sodium bicarbonate, pH 8.5 to a final concentration of 2 mg/mL. pNIPAAm-TFP ester was dissolved in anhydrous DMSO (0.2 mg/mL). Twenty-five microliters of the pNIPAAm-TFP in DMSO was added to the antibody solution, and the reaction solution was mixed gently overnight at 4 °C. Conjugates were purified from tetrafluorophenol and excess salts with a desalting column. Conjugated antibodies were separated by heating the reaction mixture to 40 °C to induce conjugate aggregation followed by centrifugation for 2 minutes at 13,000 rpm. The supernatant was removed and the polymer pellet was resolubilized in PBS, pH 7.4. Conjugates were dialyzed against 1× PBS using 100 000 MWCO dialysis membranes over several days to reduce the content of unreacted pNIPAAm. Polymer contents of the resulting solutions were measured by UV absorbance at 307 nm against polymer concentration standards. Protein contents were determined by absorbance at 280 nm with a derived correction factor for contribution of polymer content to absorbance at 280 nm. Antibody concentrations used in immunocomplex samples were based on protein content only, since an exact molecular weight of the antibody conjugate was not established. Antibody conjugates were stored at 4 °C in PBS, pH 7.4.

Microfluidic Card Assembly. Punched pieces of membrane were positioned between two-part multilayer microchannels constructed of poly(ethylene terepthalate) (PET), and poly(methyl methacrylate) (PMMA) with an adhesive layer (excluding membrane region), shown in Figure 2. Five layers contained stacked circular cutouts to serve as a membrane well area, with inner layer diameters of 2.1 mm and outer layer diameters of 3.25 mm. Membrane pieces were positioned between two of the layers and sealed. The upper and lower membrane well layers were connected on opposing sides to rectangular channels of dimensions 9.2 mm in length, 0.36 mm in width, and 0.2 mm in height. Fluid was introduced into the lower rectangular channel to flow up and through membrane and exit through the upper rectangular channel.

Immunocomplex Samples. 100 nM of anti-streptavidin IgG polyclonal antibody conjugate (total pNIPAAm concentration of 0.58 mg/mL) was mixed with 10 nM Alexa-488 labeled streptavidin. A negative control of free pNIPAAm at 0.58 mg/mL mixed with labeled streptavidin was included as a conjugate-free control. Samples were allowed to dwell 15 min prior to running through the card. For concentration from a buffer-diluted solution, a 50 μL sample of 100 nM anti-streptavidin IgG antibody conjugate and 10nM Alexa 488-labeled streptavidin was diluted 50-fold in PBS-T to 2.5 mL.

Malaria Antigen Immunocomplex Samples. PfHRP2 antigen was spiked into >99% human plasma at concentrations of 8−200 ng/mL and mixed with anti-*Pf*HRP2 IgM pNIPAAm conjugate and anti-*Pf*HRP2 horseradish peroxidase-conjugated IgG in PBS. The final concentrations were 50% plasma, PfHRP2 antigen from 4 ng/mL (68 pM) to 100 ng/mL (1.7 nM), 14 μg/mL anti-pfHRP2-pNIPAAm conjugate (14.7 nM), and 0.4 μg/mL anti-pfHRP2 peroxidase-coupled detection antibody. Final polymer concentration was 25 μg/mL. Samples were allowed to dwell 15 minutes at room temperature prior to running.

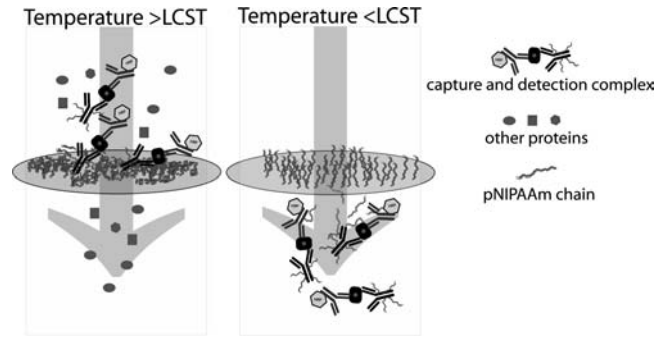


Figure 1. Schematic system design for immunocomplex capture and concentration under conditions of capture (>LCST) and release (<LCST). Covalently modified pNIPAAm-antibody, bound antigen, and detection antibody are captured at membrane during polymer aggregation above the LCST, while unconjugated plasma components flow through. When the membrane region of the device is cooled, the polymer becomes hydrophilic and molecular conjugates are released back into the flow stream, carrying their cargo of antigen and detection antibody with them.

Capture and Release in a Microfluidic Card. Capture conjugate solutions were introduced via syringe pump as a 50 μL sample plug leading wash buffer of PBS-tween (0.05%). Room-temperature samples were flowed to the membrane, wetting it, but samples did not penetrate through membrane prior to heating. For capture conditions, the entire card was heated on a solid block heater set to 40 °C. Temperature in the card was measured by a thermocouple placed through upper layer at one port. When the temperature of the thermocouple reached 35 °C (under 30 s), flow through the membrane was initiated (25 μL per minute for 2 minutes, followed by 50 μL per minute for 4 minutes), with collection of exiting 50 μL fractions. For release, the card was cooled on a 10 °C cold block until the thermocouple read 25 °C. Flow was resumed at 50 μL per minute and 15 or 50 μL fractions collected. For concentration of a diluted sample, the entire 2.5 mL sample was flowed through the membrane during heating and released upon cooling into two 50 μL fractions.

Detection of Released anti-pfHRP2 Detection Antibody. Released pfHRP2 samples were pelleted using thermal precipitation, then resuspended into 100 μL TMB substrate for color development. Reaction was stopped by 50 μL 1 N HCl. Absorbance of sample was determined using a UV−vis spectrophotometer plate reader at $A_{450\ nm} - A_{650\ nm}$. Aliquots of a dilution series of detection antibody were combined with 100 μL of TMB substrate to create a standard curve of detection antibody concentration and control for color development relative to detection antibody concentration.

RESULTS AND DISCUSSION

Construction of Stimuli-Responsive Membranes. The microfluidic system consists of two stimuli-responsive components: (1) a porous, polymer-grafted membrane and (2) antibody conjugates (Figure 1). Above the critical solution temperature (LCST), the grafted polymers on the membrane surface and the antibody conjugate polymers in the flowing solution will both phase separate, leading to capture of the antibody conjugate immunocomplex at the membrane during flow. Below the

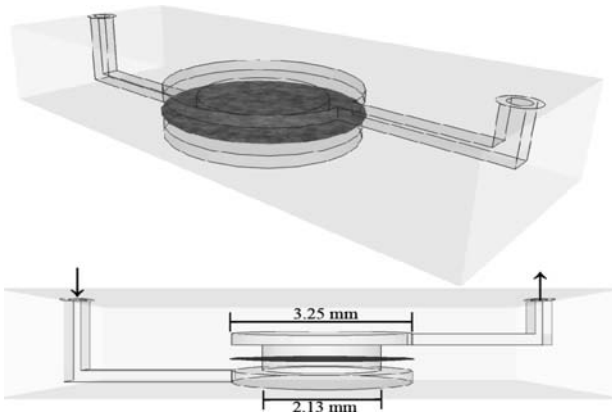


Figure 2. Schematic of microfluidic channel used in capture and release experiments, shown in isometric projection (top) and side projection (bottom) views. Stacked layers of cut poly(ethylene terepthalate) (PET) form the membrane well area, with inner layer diameters of 2.13 mm and outer layer diameters of 3.25 mm. Membrane pieces were positioned between two of the layers and sealed. The upper and lower membrane well layers are connected on opposing sides to rectangular channels of dimensions 9.2 mm in length, 0.36 mm in width, and 0.2 mm in height. Fluid is introduced into the lower rectangular channel to flow up and through membrane and exit through the upper rectangular channel.

Table 1. Chain Transfer Agent Concentration, Molecular Weight and Polydispersity Indices for Polymerization Products from Surface Grafting Reactions Used in This Study[a]

reaction	reaction EMP, mM	solution Mn (PDI)	surface Mn (PDI)
1	40 mM	3500 (1.2)	4300 (1.3)
2	13.2 mM	9500 (1.2)	8400 (1.3)
3	13.2 mM	11200 (1.2)	9000 (1.2)

[a] Solution and surface-derived polymers were analyzed by GPC. All polymerizations were performed in the presence of EMP-bound membranes, stirred at 60 °C for 18−24 h in DMF with 0.2 g/mL NIPAAm monomer and AIBN initiator equal to 0.2 times the solution EMP concentration.

LCST, the antibody conjugate immunocomplex is returned to the flow stream as the pNIPAAm chains become solvated.

As shown in Scheme 1, pNIPAAm-graft membrane material was prepared in two steps. First, the surface hydroxyl groups on 1.2 μm pore-size Loprodyne membranes were converted to RAFT CTAs using the trithiocarbonate EMP. Second, surface grafts were synthesized by immersing the macro-CTA within a polymerization solution containing additional EMP using previously identified conditions (*41*). For Mn and PDI analysis, the ester bond between the CTA and the membrane surface was hydrolyzed to cleave the grafted polymers from the membrane surface. Cleavage products derived from grafted membranes yielded milligram quantities of a soluble product per 3 cm^2 membrane material. A negative control membrane with no immobilized CTA, included in the polymerization to control for adsorbed or entangled polymer versus a covalent graft, did not yield either a measurable product or a detectable peak as analyzed by gel-permeation chromatography (GPC). By varying solution EMP concentration, molecular weights of the surface and solution polymers could be tuned. Number average molecular weight (Mn) and polydispersity indices (PDI) were analyzed for the different polymerization products (Table 1). Figure 3 shows representative GPC traces of a cleavage product with its corresponding solution polymer product. The peak shape of the surface-derived product was uniform and absent of any higher molecular weight shoulder, indicating it was not likely caused by chain−chain coupling as has been previously reported in RAFT polymerization from surfaces (*23*).

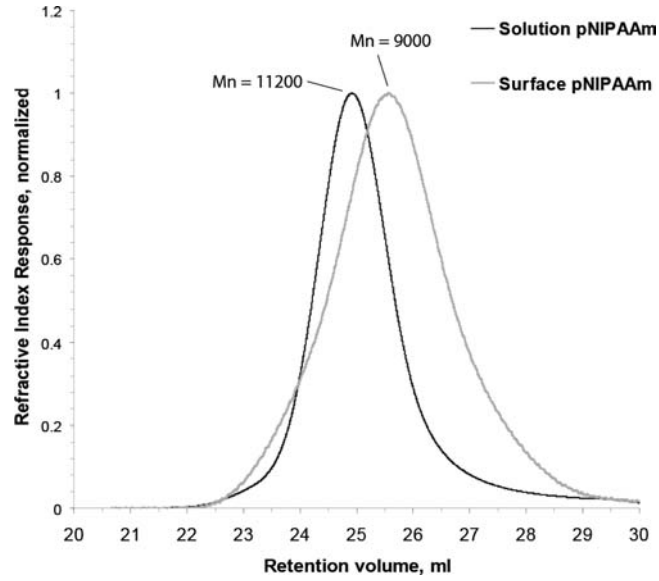


Figure 3. Analysis of grafted poly(*N*-isopropylacrylamide) and solution polymerized poly(*N*-isopropylacrylamide) by gel permeation chromatography. Normalized refractive index responses from the two syntheses are overlaid to show solution (black) and surface-cleaved (gray) polymer retention volumes, and are labeled with the calculated number-average molecular weight (Mn). Samples were derived from the same polymerization reaction containing EMP-bound 1.2 μm nylon-6,6 membranes, monomer, initiator, and solution EMP.

Covalent Antibody Conjugates. Esterification of the carboxyl end of EMP of pNIPAAm with TFP groups resulted in an amine-reactive active ester polymer (Scheme 2). Capture antibodies were reacted with the active ester polymer and the resulting product was purified from unreacted antibody through precipitation. After thermal precipitation of the reaction mixture, the pellet contained between 20% and 30% of the reacted antibody, while mock reactions with carboxyl-terminated pNIPAAm in identical quantities yielded less than 1% of the starting quantity of antibody. Reduction in polymer content after dialysis was confirmed by the decreased absorbance at 307 nm relative to the 280 nm peak, permitting quantification of both protein and polymer concentration when used in conjunction with a derived correction factor for contribution to the absorbance at 280 nm by the trithiocarbonate moiety. However, while dialysis reduced the total polymer content by over 80%, it was not complete enough based on polymer-alone dialysis (data not shown) to permit polymer-per-protein calculations.

Microfluidic Separation Efficiencies of Model Anti-Streptavidin Immunocomplex Conjugate. Fluorescently labeled streptavidin was captured with anti-streptavidin pNIPAAm antibody conjugates at membranes in microfluidic channels under flow of 50 μL per minute (Figure 4). Anti-streptavidin conjugates of pNIPAAm bound fluorescently labeled streptavidin at the membrane under heated conditions while streptavidin in a physical mixture with pNIPAAm flowed through the membrane and exited the channel as indicated by fluorescence of the flowthrough solutions. Membranes (1.2 μm pore) that were either unmodified or modified with 4100 and 8400 dalton pNIPAAm all showed greater than 80% capture efficiency. The 8400 dalton-graft membrane showed the highest release efficiency, with greater than 65% of loaded streptavidin in the first 15 μL and an overall release of approximately 80%. The immunocomplex was released from unmodified membranes much more slowly and less efficiently than from the pNIPAAm-grafted membranes, with only about 40% released in the first 15 μL. Results seen by Ebara et al. also showed slower release of pNIPAAm−streptavidin complexes from unmodified PDMS versus pNIPAAm-graft PDMS (*38*). While it was initially

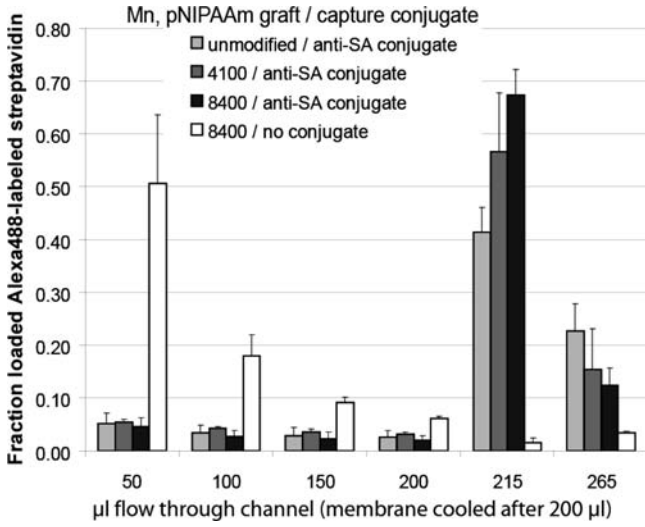


Figure 4. Anti-streptavidin antibody conjugate-bound Alexa 488-labeled streptavidin (SA) captured at membranes during heated flow (50 μL per minute) and released with cooled flow (50 μL per minute). Each 50 μL sample contained 10 nM streptavidin with either no antibody conjugate (white) or 100 nM anti-streptavidin pNIPAAm conjugate (gray to black). Membranes tested were unmodified Loprodyne (light gray), 4100 Mn-graft (medium gray), or 8400 Mn-graft (black and white) pNIPAAm-polymerized Loprodyne. Fluorescence of recovered flow fractions was measured using a plate reader fluorimeter against a standard curve.

hypothesized that the capture of conjugates with the pNIPAAm-grafted membrane would be higher than with the unmodified membrane, general hydrophobic effects and hydrogen bonding to the free amide and hydroxyl groups of the unmodified surface could explain the similar capture efficiencies. Nylon-6,6 has only a moderate affinity for dehydrated pNIPAAm, suggesting that the surface hydroxylation may play a role in the affinity (*13*, *14*). Collapse of pNIPAAm brushes on a surface is dependent on both density and molecular weight, with lower densities and smaller molecular weights exhibiting a noticeably less sharp or absent transition above the LCST (*21*, *22*). To our knowledge, no studies have been published on how such parameters affect the resolubilization of end-grafted chains. The 4100 dalton grafted membranes' release of the anti-streptavidin immunocomplex was not significantly less than that of the higher molecular weight graft membrane. However, in light of the overall trend observed, larger molecular weight graft-membranes were chosen for future work.

Capture and Enrichment of Model Antigen Using the Microfluidic Concentrator. To further test the ability of this system to concentrate antigen at the membrane surface, 100 nM anti-streptavidin conjugate and 10 nM Alexa 488-labeled streptavidin mixture were diluted 50-fold in PBS-T and flowed through heated membranes. The released antibody conjugate and antigen were concentrated approximately 40 times, from 0.2 nM to 8.5 nM in the first 50 μL released (Figure 5). The release efficiency was 84% (total released/total loaded). Evidence of concentration of the direct antibody conjugate is also seen in the reduced flowthrough concentration, indicating retention during capture conditions. The capture of the diluted solution is not expected to be mediated by particle size exclusion by the membrane pores (1.2 μm), since pNIPAAm at the concentration of the diluted solution (11.6 μg/mL) would not be expected to form particles above the nominal pore size of the membranes during the time of the capture phase, even in the absence of the antibody conjugate which would likely favor smaller particles pNIPAAm in solution (*42*). This also highlights a benefit over separation by a thermal precipitation in that much more dilute concentrations of antibody conjugate that would not be able to be separated by thermal precipitation can be efficiently separated using a membrane capture system. The mechanism of capture may be different in that the affinity between the membrane and the polymer is responsible for the capture, whereas it is a critical particle size that is responsible for precipitation in a thermal centrifugation. For the purposes of enrichment and purification of a sample, it is advantageous to reduce the need for adding additional

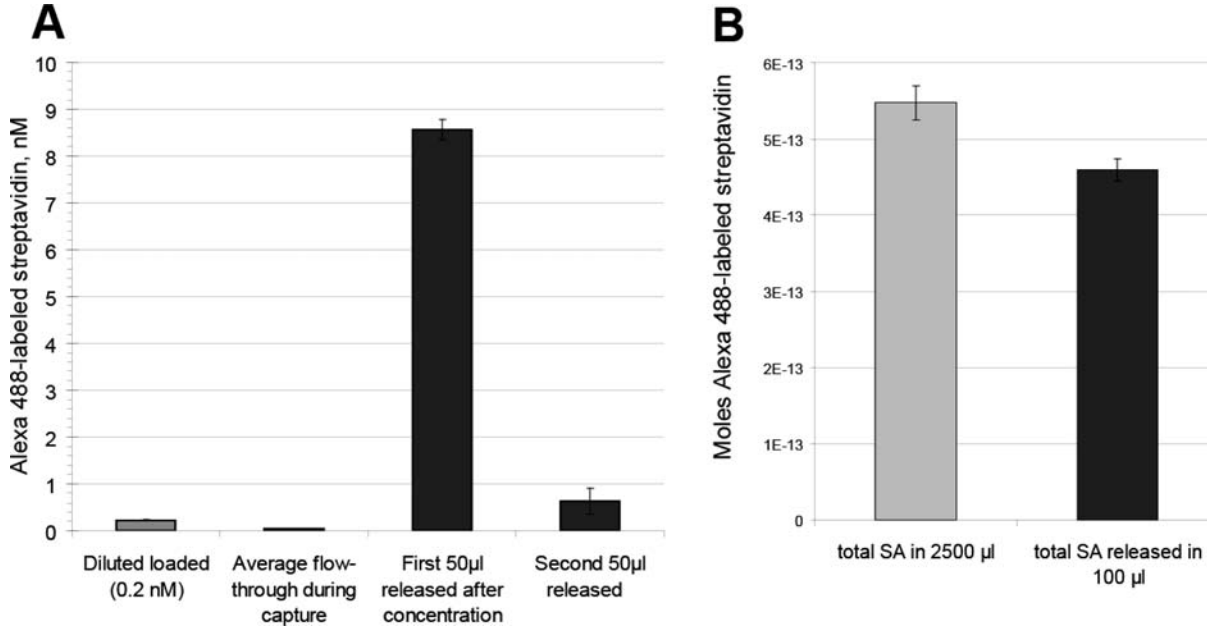


Figure 5. Concentration and enrichment of pNIPAAm-antistreptavidin immunocomplex. Samples containing 100 nM antistreptavidin antibody pNIPAAm conjugate and 10 nM Alexa 488-labeled streptavidin (SA) were diluted 50-fold into PBS-T. The entire diluted sample was flowed (100 μL per minute) through a heated membrane (pNIPAAm-modified membrane, 8400 M_n) and flow-through fractions collected (gray). After the membrane was cooled to 25 °C, 50 μL per minute flow was resumed and two 50 μL release fractions were recovered (black). (A) Concentration (nM) per 50 μL fraction was determined by measurement of fluorescence against a standard curve. (B) Right: total moles streptavidin loaded (light gray) and released (black).

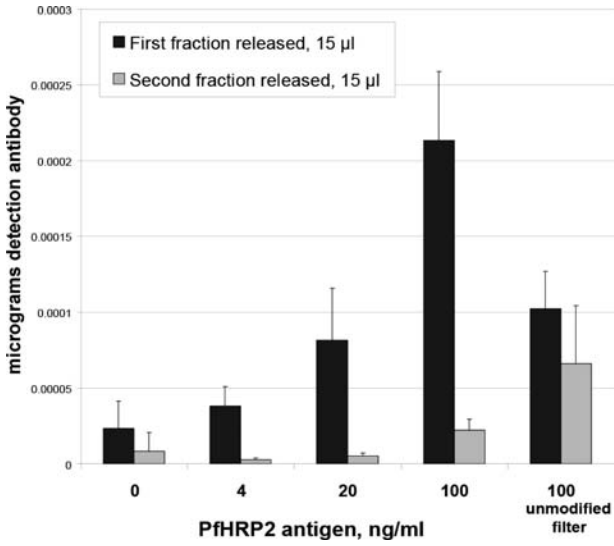


Figure 6. Released quantity of full-stack anti-PfHRP2 immunocomplex was dependent on antigen concentration and membrane modification. Samples containing anti-PfHRP2 antibody conjugate (14 μg/mL, 15 nM), PfHRP2 antigen in plasma (0−100 ng/mL range), and 0.4 μg/mL anti-PfHRP2 detection antibody were captured, washed with 400 μL PBS-T, and released into 15 μL fractions from pNIPAAm-modified membrane (M_n = 9000) or unmodified Loprodyne filter membrane. Total micrograms of peroxidase-conjugated anti-PfHRP2 detection antibody, per precipitated release fraction, was determined by measurement of TMB substrate color development against a standard curve.

polymer since it could change the solubility and viscosity of the final purified species.

Purification and Concentration of Malaria Antigen Sandwich Complex from Spiked Human Plasma. The quantity of released detection antibody was shown to be dependent on the PfHRP2 antigen concentration in the sample (Figure 6). The detection of 20 ng/mL to 100 ng/mL of PfHRP2 antigen from a 50 μL sample is within the relevant range of antigen for patient samples and comparable to the ranges detectable by standard ELISA of plasma samples (*36*). The time for the completed membrane assay was under 10 min of run time, much shorter than required for a standard ELISA, which typically consumes about 4.5 h. While the concentration of antibody−pNIPAAm conjugate used in these experiments was higher than would typically be used in a standard ELISA, this quantity could likely be reduced to a concentration similar to that used in ELISA, given the high binding affinity of the IgM antibody. The presence of pNIPAAm membrane modification resulted again in sharper release kinetics as compared to the unmodified filter membrane. Due to the concentrating capabilities of the method in this work, we expect that it may be possible to increase detection of low levels of antigen from larger plasma volumes, levels which are typically undetectable by rapid diagnostic methods and challenging as well to detect by ELISA. Data for rapid tests in terms of ng/mL concentrations of PfHRP2 antigen are not currently available. This prevents us from making any direct comparison to existing rapid assay technologies. Most literature surrounding rapid tests is expressed in parasitemia levels, which cannot be consistently correlated with PfHRP2 concentration since parasite stage and infection time would impact this number in addition to the parasite density (*43*). Future work is planned to test the performance of this system against existing malaria rapid diagnostic tests. Other candidate antigens, such as pan-*Plasmodium* lactate dehydrogenase and aldolase, may also be added for a multiplexed assay (*6*).

CONCLUSIONS

A system of stimuli-sensitive antibody conjugates and porous grafted membranes was developed for the purpose of separating and concentrating immunocomplexes within a microfluidic channel. A TFP-ester of pNIPAAm provides a facile method for conjugating pNIPAAm to amine groups on an antibody to yield phase-transition reagents suitable for capture and release of antigen. The RAFT-mediated pNIPAAm modification of a porous membrane surface results in a sharp immunocomplex release profile. We have shown this method to be capable of high-percentage capture and release of two antigens, and the ability to concentrate from dilute solutions. Full stack detection immunocomplex sandwiches identical to those used in ELISA for detection of PfHRP2 malaria antigen were separated from 50% human plasma samples. This technology has a wide range of applications for enrichment of target from samples, but can also be applied to sample preconditioning to remove specific unwanted elements from complex mixtures, such as IgG from IgM-based assays, without further diluting the sample. We have demonstrated concentration of antigen and full-stack immunocomplexes from human plasma, providing opportunities to concentrate dilute biomarkers and to expand detection ranges in microfluidic immunoassays.

ACKNOWLEDGMENT

The authors gratefully acknowledge funding from the Bill and Melinda Gates Foundation for Grand Challenges in Global Health, and the National Institutes of Health (Grant EB000252).

LITERATURE CITED

(1) Playford, E. G., and Walker, J. (2002) Evaluation of the ICT malaria P.f/P.v and the OptiMal rapid diagnostic tests for malaria in febrile returned travellers. *J. Clin. Microbiol. 40*, 4166–4171.
(2) Van Den Broek, I., Hill, O., Gordillo, F., Angarita, B., Hamade, P., Counihan, H., and Guthmann, J.-P. (2006) Evaluation of three rapid tests for diagnosis of *P. falciparum* and *P. vivax* malaria in colombia. *Am. J. Trop. Med. Hyg. 75*, 1209–1215.
(3) Ratsimbasoa, A., Fanazava, L., Radrianjafy, R., Ramilijaona, J., Rafanomezantsoa, H., and Menard, D. (2008) Short report: evaluation of two new immunochromatographic assays for diagnosis of malaria. *Am. J. Trop. Med. Hyg. 79*, 670–672.
(4) Hopkins, H., Bebell, L., Kambale, W., Dokomajilar, C., Rosenthal, P. J., and Dorsey, G. (2008) Rapid diagnostic tests for malaria at sites of varying transmission intensity in Uganda. *J. Infect. Dis. 197*, 510–518.
(5) Fogg, C., Twesigye, R., Batwala, V., Piola, P., Nabasumba, C., Kiguli, J., Mutebi, F., Hook, C., Guillerm, M., Moody, A., and Guthmann, J. P. (2008) Assessment of three new parasite lactate dehydrogenase (pan-pLDH) tests for diagnosis of uncomplicated malaria. *Trans. R. Soc. Trop. Med. Hyg. 102*, 25–31.
(6) Moody, A. (2002) Rapid diagnostic tests for malaria parasites. *Clin. Microbiol. Rev. 15*, 66-+.
(7) Murray, C. K., Gasser, R. A., Magill, A. J., and Miller, R. S. (2008) Update on rapid diagnostic testing for malaria. *Clin. Microbiol. Rev. 21*, 97-+.
(8) Weigl, B. H., and Yager, P. (1999) Microfluidics - Microfluidic diffusion-based separation and detection. *Science 283*, 346–347.
(9) Yager, P., Edwards, T., Fu, E., Helton, K., Nelson, K., Tam, M. R., and Weigl, B. H. (2006) Microfluidic diagnostic technologies for global public health. *Nature 442*, 412–418.
(10) Yager, P., Domingo, G. J., and Gerdes, J. (2008) Point-of-care diagnostics for global health. *Annu. Rev. Biomed. Eng. 10*, 107–144.

(11) Kamholz, A. E., and Yager, P. (2001) Theoretical analysis of molecular diffusion in pressure-driven laminar flow in microfluidic channels. *Biophys. J. 80*, 155–160.
(12) Auditorehargreaves, K., Houghton, R. L., Monji, N., Priest, J. H., Hoffman, A. S., and Nowinski, R. C. (1987) Phase-separation immunoassays. *Clin. Chem. 33*, 1509–1516.
(13) Monji, N., Cole, C. A., Tam, M., Goldstein, L., and Nowinski, R. C. (1990) Application of a thermally-reversible polymer-antibody conjugate in a novel membrane-based immunoassay. *Biochem. Biophys. Res. Commun. 172*, 652–660.
(14) Monji, N., Cole, C. A., and Hoffman, A. S. (1994) Activated, N-substituted acrylamide polymers for antibody coupling - application to a novel membrane-based immunoassay. *J. Biomater. Sci., Polym. Ed. 5*, 407–420.
(15) Takei, Y. G., Matsukata, M., Aoki, T., Sanui, K., Ogata, N., Kikuchi, A., Sakurai, Y., and Okano, T. (1994) Temperature-responsive bioconjugates. 3. Antibody poly(N-isopropylacrylamide) conjugates for temperature-modulated precipitations and affinity bioseparations. *Bioconjugate Chem. 5*, 577–582.
(16) Malmstadt, N., Hoffman, A. S., and Stayton, P. S. (2004) Smart" mobile affinity matrix for microfluidic immunoassays. *Lab Chip 4*, 412–415.
(17) Monji, N., and Hoffman, A. S. (1987) A novel immunoassay system and bioseparation process based on thermal phase separating polymers. *Appl. Biochem. Biotechnol. 14*, 107–120.
(18) Fong, R. B., Ding, Z. L., Hoffman, A. S., and Stayton, P. S. (2002) Affinity separation using an Fv antibody fragment-"smart" polymer conjugate. *Biotechnol. Bioeng. 79*, 271–276.
(19) Lin, P., Zheng, H., Yang, H. H., Yang, W., Zhang, C. G., and Xu, J. G. (2003) Enzyme-linked fluorescence immunoassay for human IgG by using a pH-sensitive phase separating polymer as carrier. *Chem. J. Chin. Univ.-Chin. 24*, 1198–1200.
(20) Hoffman, A. S., and Stayton, P. S. (2007) Conjugates of stimuli-responsive polymers and proteins. *Prog. Polym. Sci. 32*, 922–932.
(21) Zhu, X., Yan, C., Winnik, F. M., and Leckband, D. (2007) End-grafted low-molecular-weight PNIPAM does not collapse above the LCST. *Langmuir 23*, 162–169.
(22) Plunkett, K. N., Zhu, X., Moore, J. S., and Leckband, D. E. (2006) PNIPAM chain collapse depends on the molecular weight and grafting density. *Langmuir 22*, 4259–4266.
(23) Tsujii, Y., Ejaz, M., Sato, K., Goto, A., and Fukuda, T. (2001) Mechanism and kinetics of RAFT-mediated graft polymerization of styrene on a solid surface. 1. Experimental evidence of surface radical migration. *Macromolecules 34*, 8872–8878.
(24) Friebe, A., and Ulbricht, M. (2007) Controlled pore functionalization of poly(ethylene terephthalate) track-etched membranes via surface-initiated atom transfer radical polymerization. *Langmuir 23*, 10316–10322.
(25) Geismann, C., Yaroshchuk, A., and Ulbricht, M. (2007) Permeability and electrokinetic characterization of poly(ethylene terephthalate) capillary pore membranes with grafted temperature-responsive polymers. *Langmuir 23*, 76–83.
(26) Wu, G. G., Li, Y. P., Han, M., and Liu, X. X. (2006) Novel thermo-sensitive membranes prepared by rapid bulk photografting polymerization of N, N-diethylacrylamide onto the microfiltration membranes Nylon. *J. Membr. Sci. 283*, 13–20.
(27) Liang, L., Shi, M. K., Viswanathan, V. V., Peurrung, L. M., and Young, J. S. (2000) Temperature-sensitive polypropylene membranes prepared by plasma polymerization. *J. Membr. Sci. 177*, 97–108.
(28) Singh, N., Wang, J., Ulbricht, M., Wickramasinghe, S. R., and Husson, S. M. (2008) Surface-initiated atom transfer radical polymerization: A new method for preparation of polymeric membrane adsorbers. *J. Membr. Sci. 309*, 64–72.
(29) Ulbricht, M. (2006) Advanced functional polymer membranes. *Polymer 47*, 2217–2262.
(30) Yusof, A. H. M., and Ulbricht, M. (2008) Polypropylene-based membrane adsorbers via photo-initiated graft copolymerization: Optimizing separation performance by preparation conditions. *J. Membr. Sci. 311*, 294–305.
(31) Nagase, K., Kobayashi, J., Kikuchi, A. I., Akiyama, Y., Kanazawa, H., and Okano, T. (2008) Effects of graft densities and chain lengths on separation of bioactive compounds by nanolayered thermoresponsive polymer brush surfaces. *Langmuir 24*, 511–517.
(32) Ying, L., Yu, W. H., Kang, E. T., and Neoh, K. G. (2004) Functional and surface-active membranes from poly(vinylidene fluoride)-graft-poly(acrylic acid) prepared via RAFT-mediated graft copolymerization. *Langmuir 20*, 6032–6040.
(33) Nagase, K., Kobayashi, J., Kikuchi, A., Akiyama, Y., Annaka, M., Kanazawa, H., and Okano, T. (2008) Influence of graft interface polarity on hydration/dehydration of grafted thermoresponsive polymer brushes and steroid separation using all-aqueous chromatography. *Langmuir 24*, 10981–10987.
(34) Zorrilla, S., Hink, M. A., Visser, A., and Lillo, M. P. (2007) Translational and rotational motions of proteins in a protein crowded environment. *Biophys. Chem. 125*, 298–305.
(35) Zimmerman, S. B., and Minton, A. P. (1993) Macromolecular crowding - biochemical, biophysical, and physiological consequences. *Annu. Rev. Biophys. Biomol. Struct. 22*, 27–65.
(36) Kifude, C. M., Rajasekariah, H. G., Sullivan, D. J., Jr., Stewart, V. A., Angov, E., Martin, S. K., Diggs, C. L., and Waitumbi, J. N. (2008) Characterization of enzyme linked immunosorbent assay for plasmodium falciparum histidine-rich protein 2 in blood, plasma and serum. *Clin. Vaccine Immunol.*, CVI.00385−07.
(37) Malmstadt, N., Yager, P., Hoffman, A. S., and Stayton, P. S. (2003) A smart microfluidic affinity chromatography matrix composed of poly(N-isopropylacrylamide)-coated beads. *Anal. Chem. 75*, 2943–2949.
(38) Ebara, M., Hoffman, J. M., Hoffman, A. S., and Stayton, P. S. (2006) Switchable surface traps for injectable bead-based chromatography in PDMS microfluidic channels. *Lab Chip 6*, 843–848.
(39) Lai, J. J., Hoffman, J. M., Ebara, M., Hoffman, A. S., Estournes, C., Wattiaux, A., and Stayton, P. S. (2007) Dual magnetic-/temperature-responsive nanoparticles for microfluidic separations and assays. *Langmuir 23*, 7385–7391.
(40) Convertine, A. J., Lokitz, B. S., Vasileva, Y., Myrick, L. J., Scales, C. W., Lowe, A. B., and McCormick, C. L. (2006) Direct synthesis of thermally responsive DMA/NIPAM diblock and DMA/NIPAM/DMA triblock copolymers via aqueous, room temperature RAFT polymerization. *Macromolecules 39*, 1724–1730.
(41) Schilli, C., Lanzendorfer, M. G., and Muller, A. H. E. (2002) Benzyl and cumyl dithiocarbamates as chain transfer agent in the RAFT polymerization of N-isopropylacrylamide. In situ FT-NIR and MALDI-TOF MS investigation. *Macromolecules 35*, 6819–6827.
(42) Kulkarni, S., Schilli, C., Muller, A. H. E., Hoffman, A. S., and Stayton, P. S. (2004) Reversible meso-scale smart polymer-protein particles of controlled sizes. *Bioconjugate Chem. 15*, 747–753.
(43) Desakorn, V., Dondorp, A. M., Silamut, K., Pongtavornpinyo, W., Sahassananda, D., Chotivanich, K., Pitisuttithum, P., Smithyman, A. M., Day, N. P. J., and White, N. J. (2005) Stage-dependent production and release of histidine-rich protein 2 by Plasmodium falciparum. *Trans. R. Soc. Trop. Med. Hyg. 99*, 517–524.

BC100169Y

Novel Reduction-Responsive Cross-Linked Polyethylenimine Derivatives by Click Chemistry for Nonviral Gene Delivery

Jia Liu,[†] Xulin Jiang,*[,†] Li Xu,[†] Xianmiao Wang,[‡] Wim E. Hennink,[§] and Renxi Zhuo[†]

Key Laboratory of Biomedical Polymers of Ministry of Education and Department of Chemistry, and Modern Virology Center, College of Life Sciences, Wuhan University, Wuhan 430072, P. R. China, and Department of Pharmaceutics, Utrecht Institute for Pharmaceutical Science (UIPS), Utrecht University, P.O. Box 80082, 3508 TB, Utrecht, The Netherlands. Received April 21, 2010; Revised Manuscript Received July 5, 2010

Novel reducible disulfide-containing cross-linked polyethylenimines (PEI-SS-CLs) were synthesized via click chemistry and evaluated as nonviral gene delivery vectors. First, about four azide pendant groups were introduced into a low-molecular-weight (LMW) PEI (1.8 kDa) to get an azide-terminated PEI. Then, click reaction between a disulfide-containing dialkyne cross-linker and the azide functionalized LMW PEI resulted in a high-molecular-weight disulfide-containing cross-linked PEI composed of LMW constitute via a reducible cross-linker. The synthesized polymers were characterized by ^{1}H NMR, FTIR, and size-exclusion chromatography (SEC). It was shown that the obtained disulfide-containing cross-linked PEIs were able to condense plasmid DNA into positively charged nanoparticles. The degradation of the disulfide cross-linked polymers PEI-SS-CLs induced by DTT was confirmed by a gel retardation assay and SEC analysis. In vitro experiments revealed that the reducible PEI-SS-CLs were less cytotoxic and more effective in gene transfection (in both the presence and absence of serum) than the control nondegradable 25-kDa PEI. This study demonstrates that a reducibly degradable cationic polymer composed of LMW PEI cross-linked via a disulfide-containing linker possesses both higher gene transfection efficiency and lower cytotoxicity than PEI (25 kDa). These polymers are therefore attractive candidates for further in vivo evaluations.

INTRODUCTION

Gene therapy is a promising approach to treat human genetic and acquired diseases. The key to the success of gene therapy is the availability of safe and efficient vector systems (*1, 2*). Cationic polymers, such as poly(L-lysine) (*3*), chitosan and its derivatives (*4, 5*), poly(2-(dimethylamino)ethyl methacrylate) (pDMAEMA) (*6*−*8*), and poly(ethylene imine) (PEI) (*9*), have been widely explored as nonviral gene vectors. Among them, PEI has been regarded as the "gold" standard showing relatively high transfection efficiency, particularly in vitro, due to the proton sponge effect (*10, 11*). Although transfection efficiency of PEI-based complexes increases with PEI molecular weight (*12*), cytotoxicity of PEI also simultaneously increases. High-molecular-weight (HMW) PEIs, such as 25 kDa PEI, not only are highly effective in gene transfection, but also exhibit significant cytotoxicity. Low molecular weight (LMW) PEIs, such as 1.8 kDa PEI, are less cytotoxic but less efficient (*12, 13*).

To deal with this dilemma between transfection efficiency and cytotoxicity, biodegradable cationic polymers have been designed with either hydrolytically degradable ester groups (*8, 14*) or reducibly degradable disulfide linkages (*15*−*19*). It is expected that these polymers complexed with plasmid DNA can be degraded into less toxic low-molecular-weight structures after cellular uptake, by which the polymers lose their DNA binding capacity resulting in DNA release inside target cells. Generally, ester linkages have a pH-dependent hydrolysis with half-life time of hours to days. In contrast, disulfide linkages have been shown to be stable in blood circulation (*20*), and their degradation is rapid (minutes to hours) in the presence of reductive 1,4-dithio-DL-threitol (DTT) or glutathione (GSH) mimicking the reductive intracellular environment (*20, 21*). Therefore, the introduction of disulfide bridges in the polymer main chain (*22*−*26*) or in the cross-links of polymers (*27, 28*) has been investigated for the design of polymeric gene delivery vectors (*8*). Gopferich et al. (*29*) recently published an excellent review on the redox-sensitive, disulfide-based carriers for delivery of nucleic acids. Lee et al. (*27*) first synthesized reducible PEI derivatives using 0.8 kDa PEI reacting with homobifunctional cross-linking reagents, dithiobis(succinimidylpropionate) (DSP), or dimethyl-3,3′-dithiobis-propionimidate-2HCl (DTBP). The resulting polymers showed higher transfection efficiency compared to the parent 0.8 kDa PEI and reached transfection levels close to that of 25 kDa PEI. In a similar way, 1.8 kDa PEIs cross-linked with DTBP were able to condense DNA, and the formed polyplexes were sensitive to the GSH with significantly low cytotoxicity (*30*). Also, 5-kDa PEIs cross-linked with DSP formed stable complexes with DNA which could be destabilized by a redox trigger (*31*). Kloeckner et al. (*32*) studied a library of 37 soluble polycations synthesized by oligomerization of LMW oligoamines with different cross-linkers. They concluded that the polyplexes based on 0.8 kDa PEIs cross-linked with DSP or DTBP showed negligible toxicity and efficient reporter gene transfection at high N/P ratios. Goepferich et al. (*33*) described that linear PEIs with molecular weight of 2.6, 3.1, or 4.6 kDa cross-linked with DSP or boc-cystine resulted in branched structures. Using seven different cell lines, they showed a high transfection efficiency (about 60%) and a high

* Corresponding author. Xulin Jiang Key Laboratory of Biomedical Polymers of Ministry of Education and Department of Chemistry, Wuhan University, Wuhan 430072, P. R. China. Tel.: +86-27-68755200; fax: +86-27-68754509. E-mail address: xljiang@whu.edu.cn.

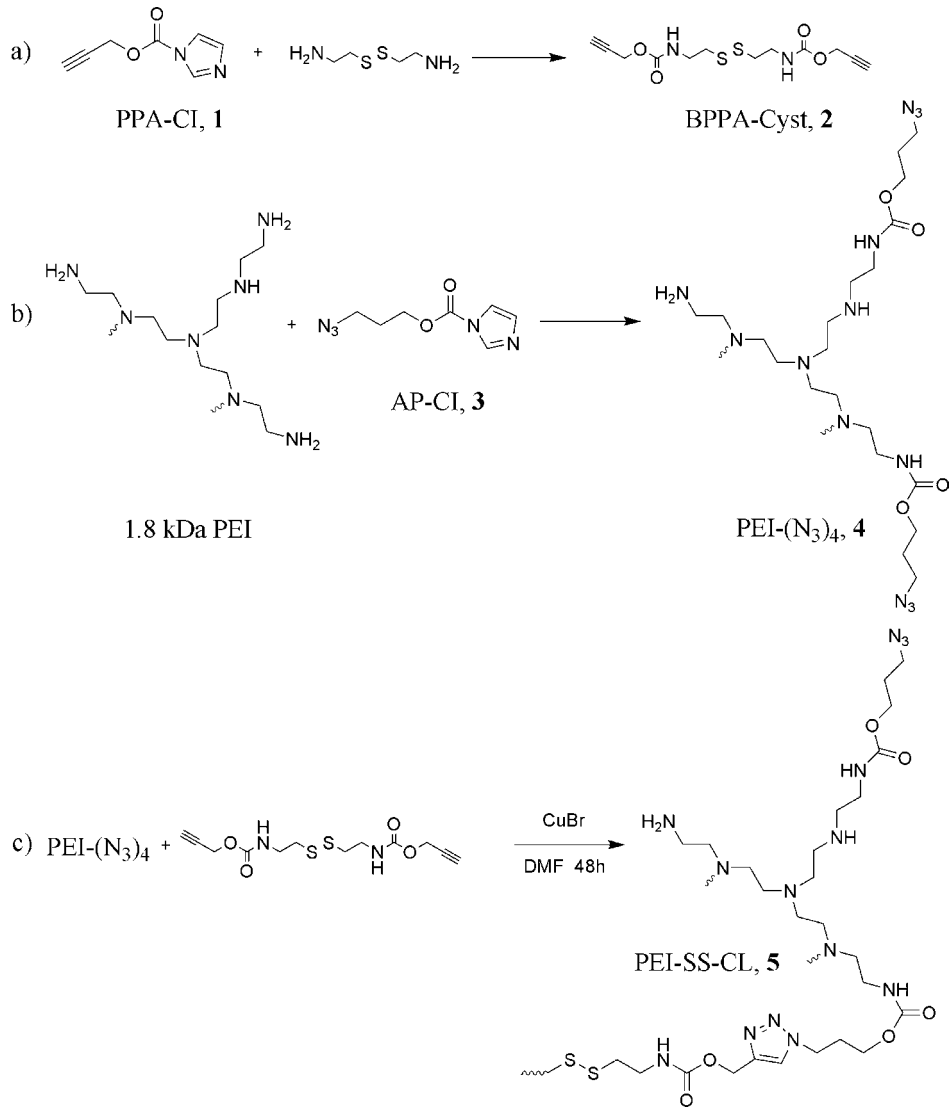
[†] Key Laboratory of Biomedical Polymers of Ministry of Education and Department of Chemistry, Wuhan University.

[‡] Modern Virology Center, College of Life Sciences, Wuhan University.

[§] Utrecht University.

10.1021/bc100191r © 2010 American Chemical Society
Published on Web 09/09/2010

Scheme 1. Synthetic Route Towards Reducible Disulfide-Contained PEI Derivatives (PEI-SS-CLs)



cell viability (>90%) of polyplexes based on the reversibly cross-linked linear PEI polymers, which was better than seven commercial transfection reagents including SuperFect, Lipofectamine, and JetPEI. It was also reported (*34*−*36*) that the disulfide cross-linked PEI derivatives using LMW PEI and DSP were highly effective as gene delivery vectors and hardly showed cytotoxicity. However, the cross-linking reaction between PEI and DSP (or DTBP) can easily lead to the formation of microgels resulting in poorly controlled molecular weight and a low yield (*35*). Peng et al. (*15*) used methylthiirane reacting with low-molecular-weight PEI to get thiolated PEIs (PEI-SHx), which were cross-linked into higher-molecular-weight PEI by oxidation of the thiol groups avoiding significantly changing the acid−base property of the PEI. However, no reducible degradation was obviously observed. They claimed that the majority of disulfide cross-links are intramolecular when the thiolation degree is high.

Recently, "click" chemistry has rapidly become a very popular method for polymer synthesis and modification due to the high selectivity and high fidelity (*8*, *37*, *38*). However, no papers using click chemistry for PEI cross-linking have been published so far. In this study, a new strategy for synthesis of disulfide cross-linked polyethylenimine (PEI-SS-CL) via click reaction is investigated, as depicted in Scheme 1. First, a LMW PEI (1.8 kDa), which has low transfection efficiency and low cytotoxicity, was modified with azide pendant groups. Then, this azide-functional PEI was reacted with disulfide-containing dialkyne cross-linker through click chemistry to obtain a reducible PEI derivative with high molecular weight. Click chemistry allows easy coupling of poly(ethylene glycol) (PEG) shielding, targeting ligands and fluorescent groups into the polyplexes for further in vivo evaluation. This paper describes the synthesis and reduction-triggered degradation of the disulfide-containing cross-linked PEI polymers and the gene transfection activities of the corresponding polyplexes.

EXPERIMENTAL PROCEDURES

Materials. Branched polyethylenimine (PEI) with molecular weight of 1.8 kDa was purchased from Alfa Aesar, and branched PEI (25 kDa) was from Sigma-Aldrich. 1,1′-Carbonyldiimidazole (CDI) (Shanghai Medpep Co., Ltd., China), propargyl alcohol (Wuhan FengFan Chemical Co., Ltd., China), cystamine dihydrochloride (Jiangsu Jintan Medicine Chemical Factory, Jiangsu, China), 1,4-dithio-DL-threitol (DTT, Shanghai Regal Biotechnology Company, China), and 3-bromopropanol (Shanghai Zhuo Rui Chemical Co., China) were used as received. *N*,*N*′-Dimethylformamide (DMF) was obtained from Shanghai Chemical Reagent Co., China, and used after distillation under reduced pressure. Plasmid pcDNA3-Luc in TE buffer with concentration of 5.0 mg/mL was from Plasmid Factory, Germany. Plasmid pEGFP encoding a red-shifted variant of wild-type green

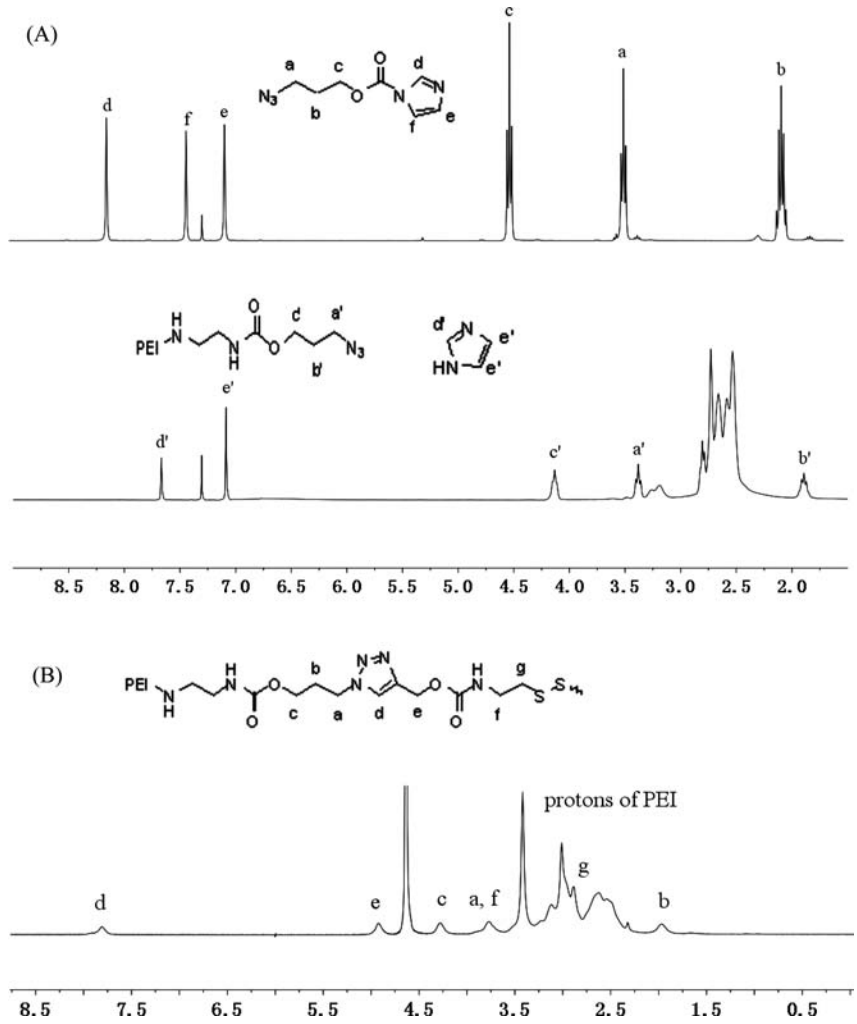


Figure 1. (A) ^{1}H NMR spectra of AP-CI and PEI-$(N_3)_4$ (with imidazole) in $CDCl_3$. (B) ^{1}H NMR spectra of PEI-SS-CL1 in D_2O.

fluorescent protein (GFP) was purchased from Clontech, Mountain View, CA, USA, and was transformed in *E. coli* DH5α and propagated in Luria−Bertani (LB) medium at 37 °C overnight. Then, the plasmids were purified by means of EndoFree plasmid purification as described previously (*39*). The purified plasmids were diluted with TE buffer solution and stored at −20 °C. The purity and concentration of plasmids were determined by ultraviolet (UV) absorbance at 260 and 280 nm. All other chemicals were analytical grade and used as received.

Synthesis of Disulfide-Containing Cross-Linked Polyethylenimine (PEI-SS-CL). *Synthesis of Bis[(Propargyl Carbamate)-Ethyl] Disulfide (BPPA-Cyst,* **2***).* Propargyl ester of carbonylimidazole (PPA-CI, **1**) was synthesized from 1,1′-carbonyldiimidazole (CDI) and propargyl alcohol (PPA) as described previously (**8**). Cystamine dihydrochloride was neutralized by 4 M NaOH and extracted with dichloromethane to yield cystamine. Then, BPPA-Cyst was synthesized from PPA-CI with the cystamine, as shown in Scheme 1. Briefly, cystamine (4.40 g, 28.52 mmol) and PPA-CI (6.93 g, 46.2 mmol) were dissolved in 50 mL dichloromethane and subsequently stirred at room temperature for 24 h. After evaporation of dichloromethane, 100 mL of 1.0 M NaH_2PO_4 (pH 4.0) was added. This aqueous solution was extracted with ethyl ether (40 mL, 3 times) to obtain, after evaporation of the solvent, BPPA-Cyst with a yield of 80.2%. ^{1}H NMR in $CDCl_3$ (Supporting Information Figure SI1): δ (ppm) 2.48 (s, 2H, ***CH***≡C), 2.82 (t, 4H, S-***CH***$_2$-C), 3.51 (app. quartet, 4H, NH-***CH***$_2$-C), 4.69(s, 4H, O-***CH***$_2$-C≡C), 5.31(s, 2H, ***NH***-C═O). IR analysis of the resulting product showed an absorption peak at 2126 cm^{-1} corresponding to the alkyne group (see Supporting Information Figure SI2, IR spectrum: 3293, 3061, 2943, 2126 ($\nu_{C\equiv C}$), and 1709 cm^{-1}).

Synthesis of 3-Azidopropyl Ester of Carbonylimidazole (AP-CI, **3***).* 3-Azidopropanol was synthesized according to the literature (*40*) with some modification. Briefly, 3-bromopropanol (3.01 g, 21.65 mmol) and sodium azide (5.62 g, 86.46 mmol) were dissolved in a mixture of 25 mL water and 10 mL acetone, stirred under reflux for 24 h in an oil bath of about 80 °C. After evaporation of acetone, the product was extracted with dichloromethane (25 mL, 3 times). The organic layer was dried over anhydrous magnesium sulfate, filtered, and evaporated to obtain colorless oil with a yield of 87.6%. ^{1}H NMR ($DCCl_3$): δ (ppm) 1.80 (app. quint, 2H, C-***CH***$_2$-C), 3.41 (t, 2H, ***CH***$_2$-N_3), 3.70 (t, 2H, **C*H*$_2$**-O).

AP-CI (**3**) was synthesized from the obtained 3-azidopropanol with carbonyldiimidazole (CDI). Briefly, a dry, round-bottomed flask was charged with CDI (4.80 g, 29.60 mmol) and 40 mL dichloromethane yielding a suspension. Next, 3-azidopropanol (1.50 g, 12.40 mmol) was added dropwise under vigorous stirring while the reaction mixture turned into a clear solution. After 4 h reaction at room temperature, the solution was washed three times with water. The organic layer was dried over anhydrous magnesium sulfate, filtered, and evaporated to obtain colorless oil with a yield of 74.3%. ^{1}H NMR in $CDCl_3$ as shown in Figure 1A: δ (ppm) 2.05 (app. quint, 2H, C-***CH***$_2$-C), 3.47 (t, 2H, N_3-***CH***$_2$), 4.50 (t, 2H, ***CH***$_2$-O), 7.06 (s, 1H, C═***CH***−N═), 7.40 (s, 1H, N−***CH***═C), 8.12 (s, 1H, N−***CH***═N).

Table 1. Characteristics of the Synthesized Disulfide Cross-Linked PEI-SS-CLs

polymers	molar feed ratios of alkyne/azide	yield(%)	M_w (kDa)	PDI
PEI-SS-CL1	1:1	59	9.4	3.12
PEI-SS-CL2	1:2	49	14.2	1.85

*Synthesis of Azide-Terminated PEI [**4**, PEI-$(N_3)_4$].* AP-CI (2.17 g, 11.13 mmol) dissolved in chloroform (20 mL) was slowly dropped (around 2 h) into a solution of 1.8 kDa PEI (5.00 g, 2.78 mmol, 29 mmol of primary amine groups, assuming that the primary amine content of the 1.8 kD PEI is 25% of the total amines (*13*) in chloroform (100 mL). Next, the reaction mixture was refluxed using an oil bath (75 °C) for 10 h. Chloroform was removed by evaporation under reduced pressure yielding a yellow liquid which was subsequently dissolved in $CDCl_3$ and characterized by ^1H NMR. No unreacted AP-CI was detected as shown in Figure 1A. The average number of azide groups per PEI molecule determined by ^1H NMR was close to 4. IR analysis of the resulting product showed an absorption peak at 2099 cm^{-1} corresponding to the asymmetric stretching vibration of the azide group (see Supporting Information Figure SI2, IR spectrum (neat): 2944, 2837, 2933, 2099 (ν_{N3}), and 1700 cm^{-1}).

Synthesis of Disulfide Cross-Linked PEI-SS-CL (5) via Click Reaction. Azide-functional PEI (PEI-$(N_3)_4$, 0.75 g, 1 equiv azide groups) and BPPA-cyst (0.16 or 0.08 g, 1 or 0.5 equiv alkyne groups) were dissolved in DMF, and CuBr (1 equiv) as catalyst was added under a nitrogen atmosphere. The reaction mixture was stirred at 50 °C for 2 days. The resulting solution was purified by dialysis against water (dialysis tube, MWCO 3.5 kDa), and the formed disulfide cross-linked PEI derivatives PEI-SS-CL1 and PEI-SS-CL2 were collected after freeze−drying. The structure of the PEI-SS-CLs was analyzed by ^1H NMR and FTIR. The molecular weights were obtained by size-exclusion chromatography−multiangle light scattering (SEC-MALLS) as described below.

Characterizations. ^1H nuclear magnetic resonance (NMR) spectra were measured with a Varian Unity 300 MHz spectrometer using $CDCl_3$ or D_2O as solvent. Fourier transformed infrared (FTIR) spectra were recorded on a Lambda Bio40 UV−vis spectrometer (Perkin-Elmer). The molecular weights and the molecular weight distributions of the polymers were evaluated by a SEC-MALLS system consisting of a Waters 2690D separations module, a Waters 2414 refractive index detector (RI), and a Wyatt DAWN EOS MALLS detector. Two chromatographic columns (Shodex OHpak SB-803 and SB-802.5, Showa Denko, Japan) with a precolumn (Shodex SB-G) were used in series. A sodium acetate (NaAc) solution was prepared by dissolving a calculated amount of sodium acetate in reverse osmosis water (0.3 M), and the pH was adjusted to 4.4 with acetic acid (*41*). A mixture of 70% 0.3 M NaAc solution, pH 4.4, and 30% acetonitrile was used as the eluent at a flow rate of 0.6 mL/min. The eluent was filtered through a 0.22 μm HPLC filter and degassed prior to use by ultrasound. The data were processed with *Astra* software (Wyatt Technology).

The reductive degradation of the disulfide cross-linked polymer PEI-SS-CL triggered by DTT was evaluated by SEC-MALLS. The polymer PEI-SS-CL (5.0 mg) was dissolved in the mobile phase (0.9 mL) followed by the addition of 0.1 mL DTT in water (1.0 mol/L). After incubation at 37 °C for 2 h, the molecular weight of the degraded polymer was determined by SEC-MALLS.

Cell Culture. Human embryonic kidney transformed (293T) cells and human cervix carcinoma (HeLa) cells were incubated in Dulbecco's Modified Eagle's Medium (DMEM) containing 10% fetal bovine serum (FBS), 100 units/mL penicillin, and 100 ug/mL streptomycin at 37 °C under a humidified atmosphere of 95% air and 5% CO_2.

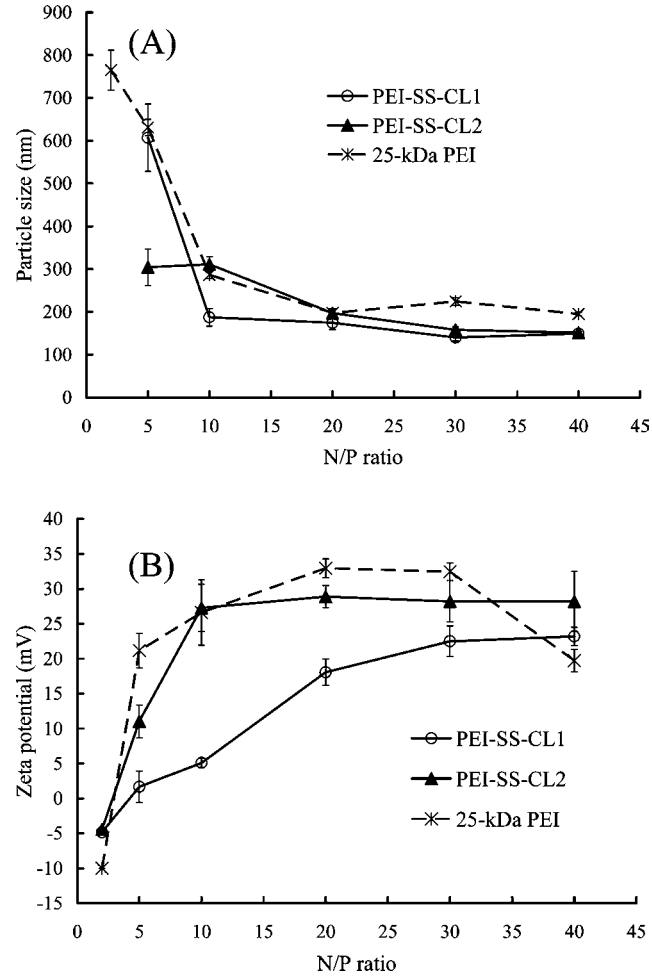


Figure 2. Size by DLS (A) and zeta potential (B) of the PEI/DNA polyplexes at various N/P ratios. Error bars are standard deviations (SD) of 3 measurements.

Cytotoxicity Assay. The cytotoxicity of the different polymers was studied using the MTT assay (*39*) on 293T cells. The cells were seeded into 96-well plates at a density of 3000 cells/well, and 100 μL DMEM containing 10% FBS was added. The cells were allowed to grow at 37 °C under a humidified atmosphere of 95% air and 5% CO_2 for 48 h. Thereafter, the medium was replaced with 100 μL of fresh medium and 100 μL solutions of PEI-SS-CLs, 25 kDa PEI and 1.8 kDa PEI, were added (final polymer concentrations ranging from 0.01 to 0.20 mg/mL). The cells were incubated for 48 h, and the medium containing polymer solution was replaced with 200 μL fresh medium. Next, the MTT reagent (20 μL in PBS, 5 mg/mL) was added to each well for further 4 h incubation at 37 °C. Then, the medium was removed and 100 μL of DMSO was added to dissolve the formed formazan crystals. The absorbance at 570 nm was recorded using a Microplate Reader (BIO-RAD 550). The relative cell viability (mean ± SD, $n = 4$) was calculated as cell viability = $(OD_{sample} - OD_{blank})/(OD_{control} - OD_{blank}) \times 100\%$, where OD_{sample} is the absorbance of solution with cells treated by polymers, $OD_{control}$ is the absorbance for untreated cells (without polymer), and OD_{blank} is the absorbance without cells.

Formation of PEI-SS-CL/DNA Polyplexes and Agarose Gel Retardation Assay. PEI-SS-CL/DNA complexes (N/P ratios ranging from 3 to 9) were prepared by addition of 5 μL polymer solution with designed concentrations in 150 mM NaCl

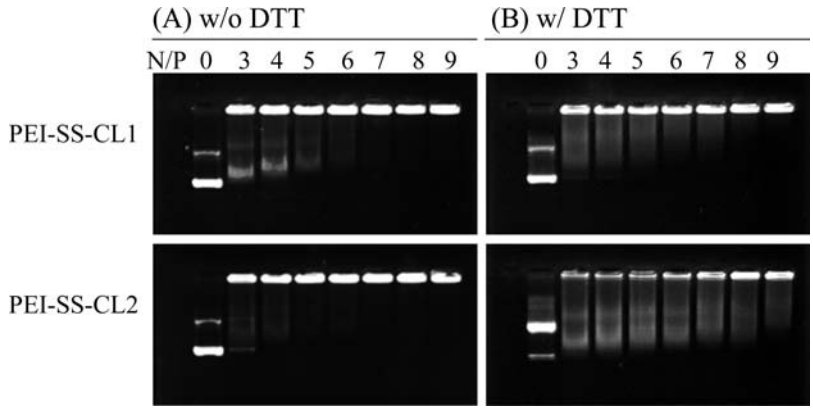


Figure 3. Agarose gel electrophoresis retardation assay of PEI-SS-CLs/DNA complexes at different N/P ratios (A) without DTT and (B) with 10 mM DTT.

(pH 7.4) to 1 μL of pcDNA3-Luc plasmid DNA (100 ng/μL in TE buffer). The resulting polyplex dispersions were incubated at 37 °C for 30 min and were then analyzed by electrophoresis in a 0.7% (w/v) agarose gel containing GelRed and in Tris-acetate (TAE) running buffer at 80 V for 60 min. DNA bands were visualized with a UV (254 nm) illuminator and photographed with a Vilber Lourmat imaging system.

The DTT triggered reductive degradation of PEI-SS-CL based polyplexes was also evaluated by agarose gel electrophoresis. To 1 mL of dispersions of PEI-SS-CL/DNA polyplexes prepared at N/P ratios ranging from 3 to 9, 100 μL of 100 mM DTT in water was added. The polyplexes were incubated at 37 °C for 30 min and were then analyzed by electrophoresis in a 0.7% (w/v) agarose gel containing GelRed and in TAE running buffer at 80 V for 60 min.

Particle Size and ζ-Potential Measurements. Polyplexes were prepared by the addition 90 μL of a PEI solution with designed concentrations (in 150 mM NaCl, pH 7.4) to 10 μL of pcDNA3-Luc plasmid DNA solution (0.1 mg/mL in 40 mM Tris-HCl buffer). The amount of polymer used was calculated on the basis of chosen N/P ratios, nitrogen atoms of the polymer over phosphates of DNA. After the complexes were incubated at 37 °C for 30 min, the polyplex dispersion was diluted with water to 1 mL prior to measurement. Particle size and ζ-potential were measured by Nano-ZS ZEN3600 (Malvern Instruments) at 25 °C.

In Vitro Transfection Activity of Polyplexes. *Luciferase Assay.* Transfection activity of polyplexes based on pcDNA3-Luc plasmid, complexed with PEI-SS-CLs, 25-kDa PEI or 1.8-kDa PEI, was evaluated in 293T and HeLa cells. The cells were seeded at a density of 70 000 cells/well in a 24-well plate. Subsequently, 1 mL of DMEM containing of 10% FBS was added, and the cells were incubated at 37 °C in a humidified atmosphere of 95% air and 5% CO_2 for 24 h. Next, the medium in each well was replaced by 0.9 mL of serum-free DMEM. The polymer/DNA polyplexes (100 μL, N/P ratios ranging from 10 to 50) prepared as described above were then added and incubated with cells for 4 h at 37 °C. The medium was replaced by fresh DMEM containing 10% FBS, and the cells were incubated for 48 h. Thereafter, the medium was removed, and the luciferase assay was performed according to manufacturer's protocols. Relative light units (RLUs) were measured with chemiluminometer (Lumat LB9507, EG&G Berthold, Germany). The total protein was measured according to a BCA protein assay kit (Pierce). Luciferase activity was expressed as RLU/mg protein.

Transfection experiments in 293T cells in the presence of serum were carried out. The protocol was the same as described above, except that the cell medium of DMEM with 10% FBS was used instead of the serum-free DMEM medium. All the transfection assays were carried out in triplicate.

Green Fluorescent Protein Assay. Transfection activity of complexes of PEI-SS-CLs with pEGFP plasmid was evaluated in 293T cells. The 293T cells were seeded at a density of 70 000 cells/well in a 24-well plate. Subsequently, 1 mL of DMEM with 10% FBS was added, and the cells were incubated at 37 °C in a humidified atmosphere of 95% air and 5% CO_2 for 24 h. Next, the cells were incubated for 4 h at 37 °C, followed by the addition of polyplexes of various N/P ratios prepared as described above. After transfection for 48 h, the cells were directly observed by an inverted microscope (Olympus IX 70). The microscopy images were obtained at the magnification of 100× and recorded using *CoolSNAP-Pro* (v 4.5.1.1) software.

RESULTS AND DISCUSSION

Synthesis and Characterization of Disulfide-Containing PEI-SS-CL. The two-step synthetic route of disulfide cross-linked polyethylenimine (PEI-SS-CL) via click reaction is illustrated in Scheme 1. First, azide pendant groups were introduced into a low-molecular-weight (LMW) PEI (1.8 kDa) to obtain PEI-(N_3)*x*, in which *x* stands for the average number of azide groups per PEI molecule. Second, the azide-functional PEI was reacted in DMF with the disulfide-containing dialkyne cross-linker BPPA-Cyst, through click chemistry with CuBr as catalyst, to obtain a reducible PEI derivative with high molecular weight.

Azide-functionalized LMW PEI was synthesized by coupling of activated azidopropanol, 3-azidopropyl ester of carbonylimidazole (AP-CI, **3**, Scheme 1), to PEI. ^{1}H NMR analysis of the obtained product (Figure 1A) shows the absence of the starting compound AP-CI (comparing the proton NMR spectra of AP-CI and PEI-(N_3)$_4$ in Figure 1A, no peaks at 8.12 (d) and 7.40 ppm (f) for PEI-(N_3)$_4$, the peaks at 4.50 (c), 3.47 (a), and 2.05 ppm (b) in AP-CI shifting to 4.09 (c′), 3.34 (a′), and 1.85 ppm (b′) for PEI-(N_3)$_4$, respectively). Also, imidazole (with one proton peak at 7.66 and two protons at 7.04 ppm) was detected in the resulting product. The IR spectrum of the resulting product shows an absorption peak at 2099 cm^{-1} corresponding to the asymmetric stretching vibration of the azide group (see Supporting Information Figure SI2). From NMR and IR analysis, it is therefore concluded that azide-functionalized PEI has been obtained. The average number of azide groups per PEI molecule (*x* in PEI-(N_3)*x*) was calculated on the basis of the ratio of the integral from 2.30 to 2.90 ppm of the PEI protons to the protons of azidopropanol at 3.34 ppm (2*H*, next to azide group), assuming that the primary amine content of the PEI (1.8 kD) is 25% of the total amines (*13, 27*). ^{1}H NMR analysis shows that *x* in PEI-(N_3)*x* is 4.1 when the AP-CI/PEI molar feed ratio was

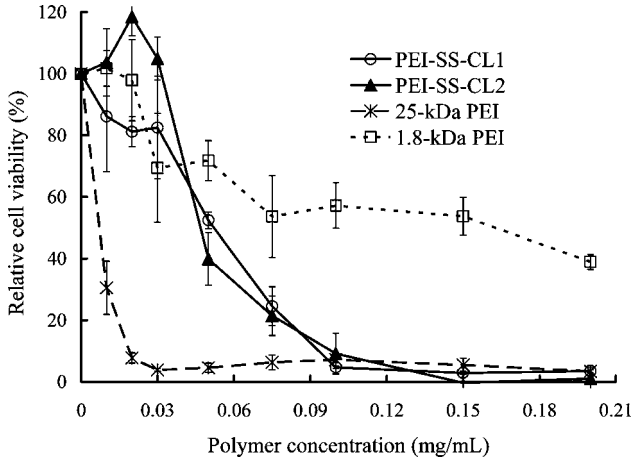


Figure 4. Cytotoxicity of cationic polymers PEI-SS-CLs and controls 1.8 kDa PEI and 25 kDa PEI to 293T cells after 48 h incubation (mean ± SD, $n = 4$).

Table 2. IC_{50} Values of PEI-SS-CLs, 1.8 kDa PEI and 25 kDa PEI

polymers	PEI-SS-CL1	PEI-SS-CL2	1.8-kDa PEI	25-kDa PEI
IC_{50} (μg/mL)	52	47	162	6

4, which indicates that AP-CI had reacted quantitatively with PEI. Because of the quantitative conversion, the reaction mixture only contains PEI-$(N_3)x$, imidazole, and solvent; no further purification was required for the next click reaction after evaporation removal of the solvent, chloroform.

The azide-functionalized LMW PEI-$(N_3)_4$ was cross-linked with disulfide-containing dialkyne BPPA-Cyst by click reaction in DMF at 50 °C for 48 h, using CuBr as catalyst, to obtain reducible HMW PEI derivative, PEI-SS-CL. Two disulfide cross-linked PEIs, named PEI-SS-CL1 and PEI-SS-CL2, were obtained with molar feed ratios of alkyne/azide of 1:1 and 1:2, respectively. Both polymers are water-soluble, which indicates that the cross-linking reactions between dialkynes and azide groups only take place within a definite number of LMW PEI molecules. However, with increasing cross-linking ratio (molar feed ratio alkyne/azide 1:0.75), microgels were formed. The soluble polymers, PEI-SS-CL1 and PEI-SS-CL2, were further investigated as gene vectors.

The structures of these soluble polymers were investigated by ^{1}H NMR and FTIR analysis. The ^{1}H NMR spectrum of PEI-SS-CL1 is shown in Figure 1B, from which it can be seen that a new peak appeared at 7.8 ppm (*H* of the triazole ring) indicating the formation of triazole groups by click reaction. The absorption peaks at 2099 cm^{-1} and 2126 cm^{-1} in the IR spectrum for polymer PEI-SS-CL1 are very weak (Supporting Information Figure SI2), which indicates that the azide groups reacted almost quantitatively with the alkyne groups.

The molecular weights and molecular weight distributions of the PEI-SS-CLs were determined by SEC-MALLS (Table 1). The weight average molecular weights of PEI-SS-CL1 and PEI-SS-CL2 were about 5 and 7 times that of the starting polymer PEI 1.8 kDa. With all ^{1}H NMR, FTIR, and SEC analysis results taken together, it can be concluded that the click reactions between BPPA-Cyst and PEI-$(N_3)_4$ were successful.

Characterization of PEI-SS-CL-Based Polyplexes. To be effective as gene delivery vectors, cationic polymers must possess the capacity to bind and condense plasmid DNA into nanoparticles which can be taken up by cells. The DNA binding and condensation properties of the starting LMW PEI (1.8 kD), the synthesized disulfide-containing PEI-SS-CLs and the branched PEI (25 kD), were investigated. It was shown by DLS measurements that 1.8 kDa PEI, even at an N/P ratio up to 50, was

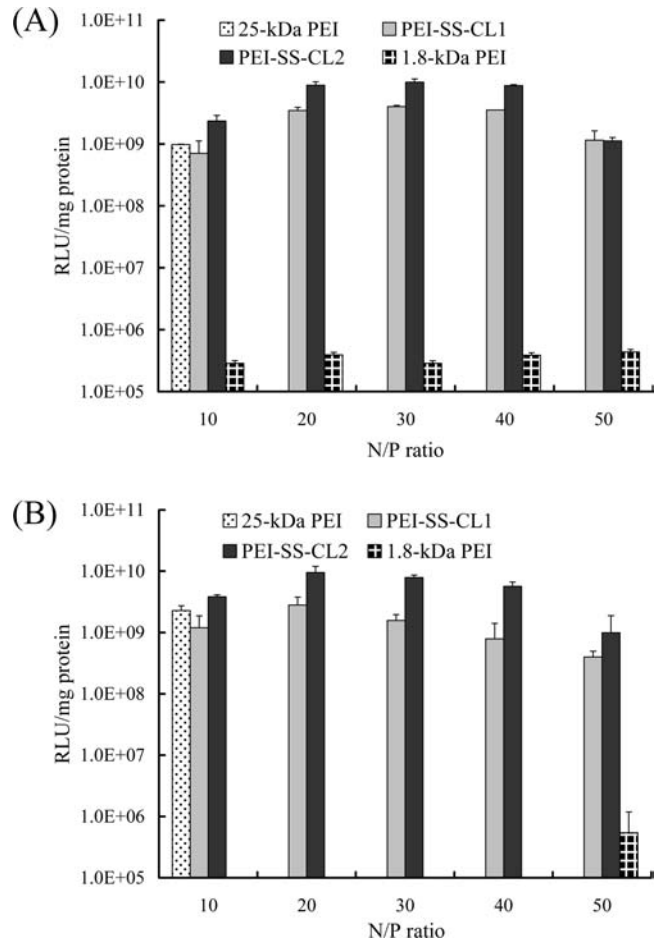


Figure 5. Luciferase expression of the PEI-SS-CL/DNA polyplexes at different N/P ratios with control 1.8 kDa PEI and 25 kDa PEI (at N/P ratio of 10) in serum-free DMEM in 293T (A) and HeLa cells (B).

unable to condense DNA. Importantly, at N/P ratios above 10, the two disulfide-containing PEI-SS-CLs prepared from the 1.8 kDa PEI were able to condense DNA into small particles with size of around 200 nm and a positive zeta potential of approximately +20 mV, similar to the 25 kDa PEI (Figure 2).

The gel retardation assay further confirmed that the two disulfide-containing PEI-SS-CLs can bind plasmid DNA efficiently and retard DNA migration at N/P ratios above 7 (Figure 3). In agreement with DLS analysis, 1.8 kDa PEI was unable to bind DNA even at an N/P ratio up to 50 (data not shown).

Reductive Degradation of the PEI-SS-CL. The DTT-induced degradation of the disulfide cross-linked PEI-SS-CLs was investigated using the agarose gel retardation assay and SEC analysis. The SEC traces of PEI-SS-CL1 and PEI-SS-CL2 in the absence and presence of DTT (Supporting Information Figure SI3) clearly show that the disulfide cross-linked polymers PEI-SS-CLs were responsive to the reductive agent DTT. After incubation with DTT for 2 h at room temperature, the weight average molecular weight of PEI-SS-CL1 decreased from 9.4 kDa (molecular weight distribution was 3.1) to 2.1 kDa (molecular weight distribution was 3.3), which is very close to M_w of PEI (1.8 kDa). Agarose gel electrophoresis (Figure 3B) shows the presence of free DNA in PEI-SS-CL/DNA polyplexes incubated with 10 mM DTT (30 min), which indicates that in a reductive environment PEI-SS-CL1 polyplexes released DNA.

In Vitro Cytotoxicity. The MTT assay for 293T cells was carried out to determine the cytotoxicity of disulfide-containing PEI-SS-CLs; 1.8 kDa PEI and 25 kDa PEI were used as controls. Figure 4 shows that the PEI-SS-CLs had a lower cytotoxicity than 25k Da PEI. The half inhibitory concentrations (IC_{50}) of

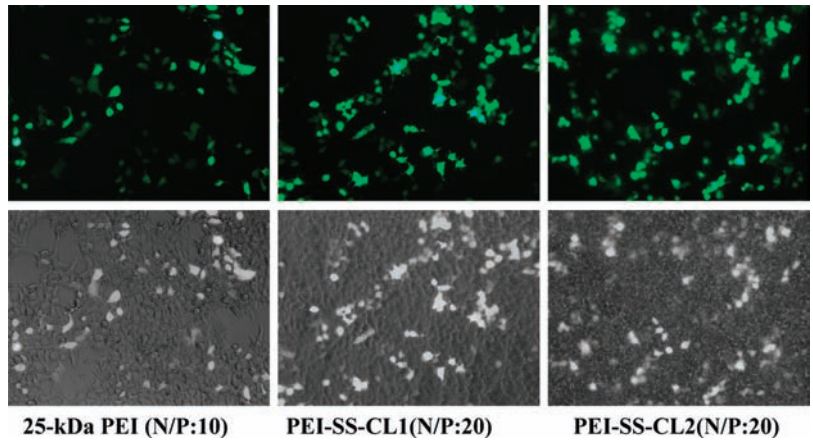


Figure 6. Fluorescent and bright-field images of enhanced green fluorescent protein expression in 293T cells for PEI-SS-CL based polyplexes (N/P ratio 20) with control 25 kDa PEI (N/P ratio 10). The images were obtained at magnification of 100×.

the polymers are summarized in Table 2 and are 52 (PEI-SS-CL1) and 47 μg/mL (PEI-SS-CL2), about 8−10× higher than that of 25 kDa PEI (6 μg/mL). The low cytocompatibility of HMW PEI is probably due to its high binding and aggregation on the cell surface and internalization, which results in significant necrosis (*13*). The low cytotoxicity of disulfide cross-linked PEI-SS-CLs indicates that, after cellular binding and internalization, they are intercellularly degraded, triggered by gluthatione, into relatively low-toxicity products.

In Vitro Transfection. The transfection activity of PEI-SS-CLs based polyplexes was evaluated in 293T and HeLa cells using the plasmid pcDNA3-Luc (expressing luciferase) and pEGFP (expressing green fluorescence) as reporter genes. Branched 25 kDa PEI and 1.8 kDa PEI, which were used for preparation of PEI-SS-CLs, were used as controls.

Figure 5 shows that PEI-SS-CL polyplexes had significantly higher transfection activity in both 293T and HeLa cells than those based on 1.8 kDa PEI. Also, incubation of cells with the PEI-SS-CL2 polyplexes resulted in about 5−10× higher luciferase expression in HeLa and in 293T cells, respectively, than polyplexes based on 25 kDa PEI, although the molecular weight of PEI-SS-CL2 is lower than that of branched PEI (25 kDa). The reason may be that PEI-SS-CLs polyplexes are degraded through cleavage of disulfide bonds inside the cells into nontoxic small PEI; DNA would be released selectively inside the cells to mediate efficient gene transfection (*15*, *25*, *27*). The transfection activity of the PEI-SS-CL2 polyplexes was higher than those of PEI-SS-CL1 at all N/P ratios studied, which can probably be ascribed to higher molecular weight of PEI-SS-CL2 .

The outstanding transfection activity of PEI-SS-CL polyplexes was visualized with a fluorescent microscope (Figure 6). The cells incubated with PEI-SS-CLs and 25-kDa PEI polyplexes showed many intracellular bright green fluorescent spots. As shown in Figure 6, substantial more fluorescent spots were observed using PEI-SS-CL1 and PEI-SS-CL2 polyplexes prepared at an N/P ratio of 20 than those based on 25-kDa PEI, which is in line with transfection data using the luciferase assay.

The transfection ability of the polyplexes of the disulfide cross-linked PEI-SS-CLs with plasmid pcDNA3-Luc in the presence of serum (10% FBS) was also investigated using 293T cells. As shown in Figure 7, the transfection efficiencies in 293T cells of the two PEI-SS-CL/DNA polyplex formulations were higher than that of the 25 kDa PEI based polyplexes in DMEM medium with 10% FBS. Especially, the PEI-SS-CL2 based polyplexes at an N/P ratio of 40 showed about an 8-fold increase in luciferase reporter gene expression compared to the control 25 kDa PEI polyplexes. This is in agreement with the reports

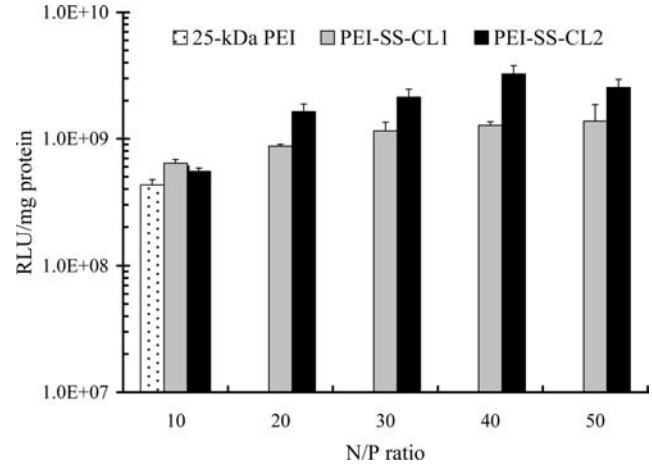


Figure 7. Luciferase expression of PEI-SS-CL/DNA polyplexes at different N/P ratios with control 25 kDa PEI (at N/P ratio of 10) in the presence of 10% FBS in 293T cells.

that the network poly(amino ester) (*42*, *43*) and disulfide cross-linked PEI (*15*) based polyplexes showed very high transfection efficiency even in the presence of serum. One possible explanation is that the cross-linked polymers have outer shells with a large proportion of the groups exposed at the surface, which may facilitate multiple simultaneous interactions with the nucleic aid phosphates and fairly maintain the stability of polymer/DNA polyplexes in the presence of serum. The other possible reason might be the introduction of reducibly cleavable disulfide bonds. Thus, importantly, the polyplexes remain active in the presence of serum proteins, which encourages further in vivo evaluation.

CONCLUSIONS

The disulfide-containing cross-linked polyethylenimine derivatives (PEI-SS-CL1 and PEI-SS-CL2) were synthesized via click reaction between disulfide-containing dialkyne cross-linker BPPA-Cyst and azide-functionalized LMW PEI. The synthesized polymers were characterized by ^{1}H NMR, FTIR, and SEC. The DNA binding and condensation properties of PEI-SS-CL were investigated for the complexes at various N/P ratios by DLS, zeta potential, and agarose gel retardation assay. We showed that the disulfide-containing PEI-SS-CLs were able to bind plasmid DNA efficiently to yield small polyplexes. The degradation of the PEI-SS-CLs in the presence of DTT was confirmed by gel retardation assay and SEC analysis. In vitro experiments demonstrated that the reducible PEI-SS-CLs not

only had much lower cytotoxicity, but also posed superior transfection activity (in both the presence and absence of serum) as compared to the control nondegradable 25 kDa PEI. Our results imply that the obtained disulfide cross-linked PEI-SS-CLs might be suitable for further in vivo gene transfection. Future work will focus on coupling of poly(ethylene glycol) (PEG) shielding, targeting ligands and fluorescent groups in the polyplexes for further in vivo evaluation.

ACKNOWLEDGMENT

This research was financially supported by the National Natural Science Foundation of China (20774068), the Ph.D. Programs Foundation of Ministry of Education of China (20070486035), and the National Key Basic Research Program of China (2005CB623903, 2009CB930300).

Supporting Information Available: Supplementary figures. This material is available free of charge via the Internet at http://pubs.acs.org.

LITERATURE CITED

(1) Mintzer, M. A., and Simanek, E. E. (2009) Nonviral vectors for gene delivery. *Chem. Rev. 109*, 259–302.

(2) Hunt, K. K., and Vorburger, S. A. (2002) Gene therapy: hurdles and hopes for cancer treatment. *Science 297*, 415–416.

(3) Trentin, D., Hubbell, J., and Hall, H. (2005) Non-viral gene delivery for local and controlled DNA release. *J. Controlled Release 102*, 263–275.

(4) Borchard, G. (2001) Chitosans for gene delivery. *Adv. Drug Delivery Rev. 52*, 145–150.

(5) Mao, S.-R., Sun, W., and Kissel, T. (2010) Chitosan-based formulations for delivery of DNA and siRNA. *Adv. Drug Delivery Rev. 62*, 12–27.

(6) Cherng, J. Y., van de Wetering, P., Talsma, H., Crommelin, D. J. A., and Hennink, W. E. (1996) Effect of size and serum proteins on transfection efficiency of poly((2-dimethylamino) ethyl methacrylate)-plasmid nanoparticles. *Pharm. Res. 13*, 1038–1042.

(7) Luten, J., Akeroyd, N., Funhoff, A., and Hennink, W. E. (2006) Methacrylamide polymers with hydrolysis-sensitive cationic side groups as degradable gene carriers. *Bioconjugate Chem. 17*, 1077–1084.

(8) Jiang, X.-L., Lok, M. C., and Hennink, W. E. (2007) Degradable-brushed pHEMA-pDMAEMA synthesized via ATRP and click chemistry for gene delivery. *Bioconjugate Chem. 18*, 2077–2084.

(9) Neu, M., Fischer, D., and Kissel, T. (2005) Recent advances in rational gene transfer vector design based on poly(ethylene imine) and its derivatives. *J. Gene Med. 7*, 992–1009.

(10) Boussif, O., Zanta, M. A., and Behr, J. P. (1996) Optimized galenics improve in vitro gene transfer with cationic molecules up to 1000-fold. *Gene Ther. 3*, 1074–1080.

(11) Akinc, A., Thomas, M., Klibanov, A. M., and Langer, R. (2005) Exploring polyethylenimine-mediated DNA transfection and the proton sponge hypothesis. *J. Gene Med. 7*, 657–663.

(12) Godbey, W. T., Wu, K. K., and Mikos, A. G. (1999) Size matters: molecular weight affects the efficiency of poly(ethylenimine) as a gene delivery vehicle. *J. Biomed. Mater. Res. 45*, 268–275.

(13) Fischer, D., Bieber, T., Li, Y., Elsasser, H. P., and Kissel, T. (1999) A novel non-viral vector for DNA delivery based on low molecular weight, branched polyethylenimine: effect of molecular weight on transfection efficiency and cytotoxicity. *Pharm. Res. 16*, 1273–1279.

(14) Luten, J., van Nostrum, C. F., De Smedt, S. C., and Hennink, W. E. (2008) Biodegradable polymers as non-viral carriers for plasmid DNA delivery. *J. Controlled Release 126*, 97–110.

(15) Peng, Q., Zhong, Z. L., and Zhuo, R. X. (2008) Disulfide cross-linked polyethylenimines prepared via thilation of low molecular weight PEI as highly efficient gene vectors. *Bioconjugate Chem. 19*, 499–506.

(16) Choi, S., and Lee, K. D. (2008) Enhanced gene delivery using disulfide-cross-linked low molecular weight polyethylenimine with listeriolysin o-polyethylenimine disulfide conjugate. *J. Controlled Release 131* (1), 70–76.

(17) Jere, D., Arote, R., Jiang, H. L., Kim, Y. K., Cho, M. H., and Cho, C. S. (2009) Bioreducible polymers for efficient gene and siRNA delivery. *Biomed. Mater. 4*, 025020.

(18) Meng, F.-H., Hennink, W. E., and Zhong, Z.-Y. (2009) Reduction-sensitive polymers and bioconjugates for biomedical applications. *Biomaterials 30*, 2180–2198.

(19) Dai, F.-Y., Sun, P., Liu, Y.-J., and Liu, W.-G. (2010) Redox-cleavable star cationic PDMAEMA by arm-first approach of ATRP as a nonviral vector for gene delivery. *Biomaterials 31*, 559–569.

(20) Saito, G., Swanson, J. A., and Lee, K.-D. (2003) Drug delivery strategy utilizing conjugation via reversible disulfide linkages: role and site of cellular reducing activities. *Adv. Drug Delivery Rev. 55*, 199–215.

(21) Schafer, F. Q., and Buettner, G. R. (2001) Redox environment of the cell as viewed through the redox state of the glutathione disulfide/glutathione couple. *Free Radic. Biol. Med. 30*, 1191–1212.

(22) Lee, Y., Koo, H., Jin, G. W., Mo, H., Cho, M. Y., Park, J.-Y., Choi, J. S., and Park, J. S. (2005) Poly(ethylene oxide sulfide): New PEG derivatives degradable in reductive conditions. *Biomacromolecules 6*, 24–26.

(23) Lin, C., Zhong, Z.-Y., Lok, M. C., Jiang, X.-L., Hennink, W. E., Feijen, J., and Engbersen, J. F. J. (2006) Linear poly(amido amine)s with secondary and tertiary amino groups and variable amounts of disulfide linkages: Synthesis and in vitro gene transfer properties. *J. Control. Release, 116*, 130–137.

(24) Lin, C., Zhong, Z.-Y., Lok, M. C., Jiang, X.-L., Hennink, W. E., Feijen, J., and Engbersen, J. F. J. (2007) Novel bioreducible poly(amido amine)s for highly efficient gene delivery. *Bioconjugate Chem. 18*, 138–145.

(25) Lee, Y., Mo, H., Koo, H., Park, J. Y., Cho, M. Y., Jin, G. W., and Park, J. S. (2007) Visualization of the degradation of a disulfide polymer, linear poly(ethylenimine sulfide), for gene delivery. *Bioconjugate Chem. 18*, 13–18.

(26) Manickam, D. S., Li, J., Putt, D. A., Zhou, Q.-H., Wu, C., Lash, L. H., and Oupický, D. (2010) Effect of innate glutathione levels on activity of redox-responsive gene delivery vectors. *J. Controlled Release 141*, 77–84.

(27) Gosselin, M. A., Guo, W.-J., and Lee, R. J. (2001) Efficient gene transfer using reversibly cross-linked low molecular weight polyethylenimine. *Bioconjugate Chem. 12*, 989–994.

(28) Miyata, K., Kakizawa, Y., Nishiyama, N., Harada, A., Yamasaki, Y., Koyama, H., and Kataoka, K. (2004) Block catiomer polyplexes with regulated densities of charge and disulfide cross-linking directed to enhance gene expression. *J. Am. Chem. Soc. 126*, 2355–2361.

(29) Bauhuber, S., Hozsa, C., Breunig, M., and Göpferich, A. (2009) Delivery of nucleic acids via disulfide-based carrier systems. *Adv. Mater. 21*, 3286–3306.

(30) Wang, Y.-X., Chen, P., and Shen, J.-C. (2006) The development and characterization of a glutathione-sensitive cross-linked polyethylenimine gene vector. *Biomaterials 27*, 5292–5298.

(31) Neu, M., Sitterberg, J., Bakowsky, U., and Kissel, T. (2006) Stabilized nanocarriers for plasmids based upon cross-linked poly(ethylene imine). *Biomacromolecules 7*, 3428–3438.

(32) Kloeckner, J., Wagner, E., and Ogris, M. (2006) Degradable gene carriers based on oligomerized polyamines. *Eur. J. Pharm. Sci. 29*, 414–425.

(33) Breunig, M., Lungwitz, U., Liebl, R., and Goepferich, A. (2007) Breaking up the correlation between efficacy and toxicity

for nonviral gene delivery. *Proc. Natl. Acad. Sci. U.S.A. 104*, 14454–14459.

(34) Breunig, M., Hozsa, C., Lungwitz, U., Watanabe, K., Umeda, I., Kato, H., and Goepferich, A. (2008) Mechanistic investigation of poly(ethylene imine)-based siRNA delivery: disulfide bonds boost intracellular release of the cargo. *J. Controlled Release 130*, 57–63.

(35) Deng, R., Yue, Y.-N., Jin, F., Chen, Y.-C., Kung, H. F., Lin, M. C. M., and Wu, C. (2009) Revisit the complexation of PEI and DNA — How to make low cytotoxic and highly efficient PEI gene transfection non-viral vectors with a controllable chain length and structure? *J. Controlled Release 140*, 40–46.

(36) Xu, P. S., Quick, G. K., and Yeo, Y. (2009) Gene delivery through the use of a hyaluronate-associated intracellularly degradable crosslinked polyethyleneimine. *Biomaterials 30*, 5834–5843.

(37) Gao, Y., Zhang, Z.-W., Chen, L.-L., Gu, W.-W., and Li, Y.-P. (2009) Synthesis of 6-N,N,N-Trimethyltriazole chitosan via "click chemistry" and evaluation for gene delivery. *Biomacromolecules 10*, 2175–2182.

(38) van Dijk, M., Rijkers, D. T. S., Liskamp, R. M. J., van Nostrum, C. F., and Hennink, W. E. (2009) Synthesis and applications of biomedical and pharmaceutical polymers via click chemistry methodologies. *Bioconjugate Chem. 20*, 2001–2016.

(39) Sun, Y.-X., Xiao, W., Cheng, S.-X., Zhang, X.-Z., and Zhuo, R.-X. (2008) Synthesis of (Dex-HMDI)-g-PEIs as effective and low cytotoxic nonviral gene vectors. *J. Controlled Release 128*, 171–178.

(40) Chung, J. E., Yokoyama, M., and Okano, T. (2000) Inner core segment design for drug delivery control of thermo-responsive polymeric micelles. *J. Controlled Release 65*, 93–103.

(41) Jiang, X.-L., van der Horst, A., van Steenbergen, M. J., van Nostrum, C. F., Schoenmakers, P. J., and Hennink, W. E. (2006) Molar-mass characterization of cationic polymers for gene delivery by aqueous SEC with online multi-angle light scattering detection. *Pharm. Res. 23*, 595–603.

(42) Lim, Y.-B., Kim, S.-M., Suh, H., and Park, J.-S. (2002) Biodegradable, endosome disruptive, and cationic network-type polymer as a highly efficient and nontoxic gene delivery carrier. *Bioconjugate Chem. 13*, 952–957.

(43) Kim, H. J., Kwon, M. S., Choi, J. S., Yang, S. M., Yoon, J. K., Kim, K., and Park, J.-S. (2006) Highly effective and slow-biodegradable network-type cationic gene delivery polymer: Small library-like approach synthesis and characterization. *Biomaterials 27*, 2292–2301.

BC100191R

Supporting Information:

Novel reduction-responsive cross-linked polyethylenimine derivatives by click chemistry for nonviral gene delivery

Jia Liu[†], *Xulin Jiang*[†,*], *Li Xu*[†], *Xianmiao Wang*[‡], *Wim E. Hennink*[§], *Renxi Zhuo*[†]

[†] Key Laboratory of Biomedical Polymers of Ministry of Education & Department of Chemistry, Wuhan University, Wuhan 430072, P. R. China

[‡] Modern Virology Center, College of Life Sciences, Wuhan University, Wuhan 430072, P. R. China

[§] Department of Pharmaceutics, Utrecht Institute for Pharmaceutical Science (UIPS), Utrecht University, P.O. Box 80082, 3508 TB, Utrecht, The Netherlands

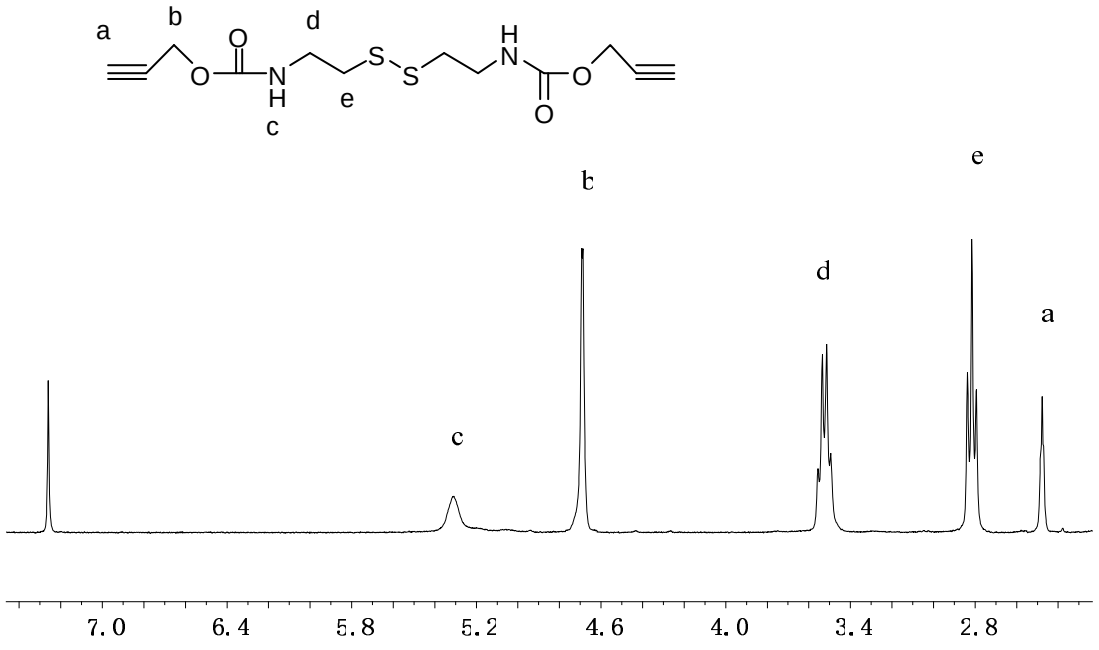


Figure SI1. H^1 NMR spectra of disulfide-containing dialkyne cross-linker BPPA-Cyst in $CDCl_3$.

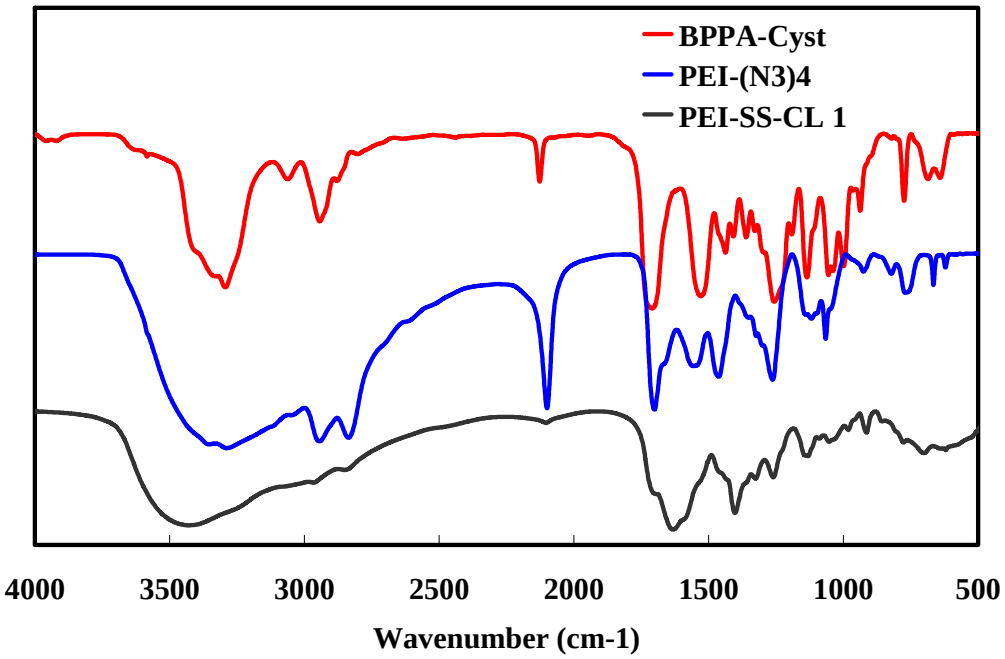


Figure SI2. FTIR spectra of BPPA-Cyst, PEI-$(N_3)_4$ and PEI-SS-CL1.

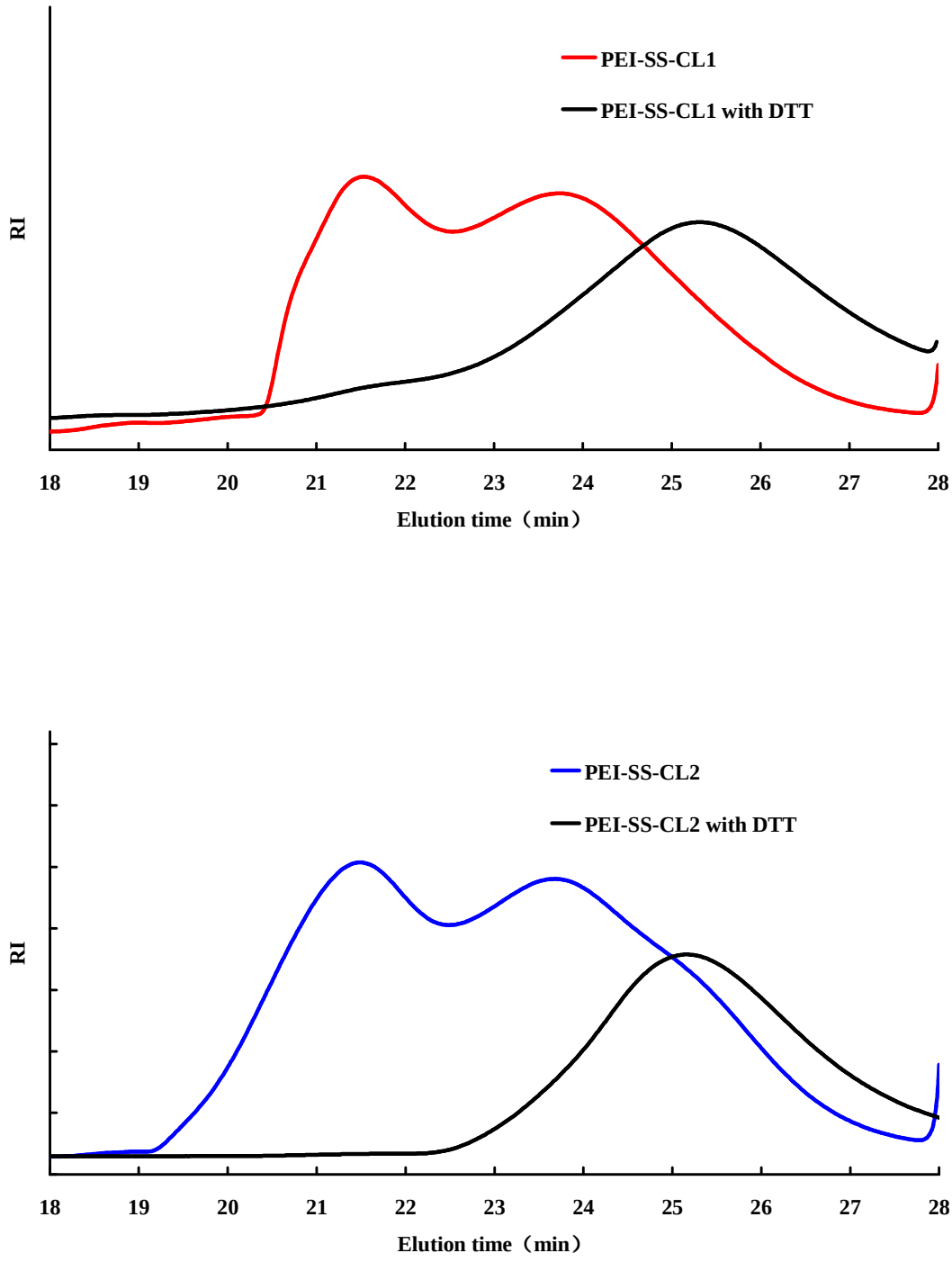


Figure SI3. The SEC traces of PEI-SS-CL1 (A) and PEI-SS-CL1 (B) in the absence and in the presence of DTT.

Isolation of Potent and Specific Trypsin Inhibitors from a DNA-Encoded Chemical Library

Luca Mannocci,*[,†,§] Samu Melkko,[†,§] Fabian Buller,[‡] Ilona Molnàr,[‡] Jean-Paul Gapian Bianké,[‡] Christoph E. Dumelin,[§] Jörg Scheuermann,[‡] and Dario Neri*[,‡]

Institute of Pharmaceutical Sciences, ETH Zürich, and Philochem AG c/o ETH Zürich, Wolfgang-Pauli-Strasse, 10, 8093 Zürich, Switzerland. Received April 23, 2010; Revised Manuscript Received July 15, 2010

Collections of chemical compounds, individually attached to unique DNA fragments serving as amplifiable identification bar codes, are generally referred to as "DNA-encoded chemical libraries". Such libraries can be used for the de novo isolation of binding molecules against target proteins of interest. Here, we describe the synthesis and use of a DNA-encoded library based on benzamidine analogues, which allowed the isolation of a trypsin inhibitor with an IC_{50} value of 3.0 nM, thus representing a >10 000-fold potency improvement compared to the parental compound. The novel trypsin inhibitor displayed an excellent selectivity toward other serine proteases. This study indicates that DNA-encoded libraries can be used for the facile "affinity maturation" of suboptimal binding compounds, thus facilitating drug development.

INTRODUCTION

The isolation of potent enzyme inhibitors is a frequent challenge in medicinal chemistry. Ligands with high binding affinity and specificity to a target enzyme typically allow the administration of low drug doses and minimize the risk of non-target-related side effects. The medicinal chemical optimization of lead compounds frequently improves drug potency by several orders of magnitude (*1*), but often requires the synthesis and screening of hundreds of synthetic derivatives. In order to facilitate the synthesis and screening of chemical libraries, the tagging of individual compounds with DNA fragments serving as amplifiable identification bar codes has been proposed (*2*−*18*). Indeed, both DNA-encoded chemical libraries displaying a single molecule on DNA ("single-pharmacophore" chemical libraries) (*13*−*18*) and libraries with a molecule at the extremity of duplex-forming complementary strands ("dual-pharmacophore" chemical libraries) (*6*−*12*) can be used. While the de novo isolation of binders from DNA-encoded chemical libraries represent a valuable tool for drug discovery, most frequently the pharmaceutical industry needs efficient methods for the improvement of lead compounds, a procedure often termed "affinity maturation". Trypsin is a good model to test chemical strategies for the development of inhibitors, since the function of the enzyme is very well understood at the molecular level (*19*, *20*) and proteases are a class of important pharmaceutical targets (*21*). Dual pharmacophore chemical libraries have previously been used for the improvement of benzamidine-based trypsin inhibitors (*11*). However, no affinity maturation procedures have so far been reported for single pharmacophore chemical libraries, which in principle should more rapidly yield molecules with the desired properties, as they do not require the optimization of linkers, joining the two individual binding fragments (*11*).

In this work, we describe the synthesis and use of a single pharmacophore DNA-encoded affinity maturation library based on benzamidine, from which we isolated a trypsin inhibitor with an IC_{50} value of 3.0 nM, thus representing a >10 000-fold potency improvement compared to benzamidine.

MATERIALS AND METHODS

Synthesis of BAM8000 compounds: The 8000 members of the BAM8000 library were synthesized in two-step "split and pool" amide-forming reactions. Initially, 40 Fmoc-protected amino acids containing a benzamidine moiety were chemically coupled to 5′-amino-modified 45-mer oligonucleotides following activation of the carboxylic acid in 70% (v/v) DMSO/water, with *N*-hydroxysulfosuccinimide, *N*-ethyl-*N*′-(3-dimethylaminopropyl)-carbodiimide and subsequent addition of aqueous triethylamine hydrochloride solution buffer, pH 10.0. The oligonucleotides had general structures: 5′-GGA GCT TGT GAA TTC TGG XXX XXX XXX GGA CGT GTG TGA ATT GTC-3′, where XXX XXX XXX unambiguously identifies the individual Fmoc-protected amino acid compound. All coupling reactions were stirred overnight at 30 °C. Subsequently, the reactions were quenched and simultaneously Fmoc deprotected by addition of piperidine in DMSO. The reactions were then purified by HPLC, and the desired fractions were dried under reduced pressure, redissolved in water and analyzed by LC-ESI-MS. Typical coupling yields were >39% overall. 4.0 nmol aliquots of each DNA−compound conjugate were pooled to generate a 40 member DNA encoded sublibrary. In the following split and pool step, the oligonucleotide sublibrary pool was aliquoted in 200 reaction vessels and an amide-forming reaction with a distinct amino reactive building block was performed following a very similar procedure as reported above (see Supporting Information). The identity of the compound used for the coupling reactions was encoded by annealing unique 44-mer oligonucleotides with general structure 5′-GTA GTC GGA TCC GAC CAC XXXX XXXX GAC AAT TCA CAC ACG TCC-3′ (where XXXX XXXX unambiguously identifies the individual carboxylic acid compound), partially complementary to the first oligonucleotide carrying the chemical

* Corresponding authors. Prof. Dr. D. Neri, Institute of Pharmaceutical Sciences, ETH Zürich, Wolfgang-Pauli-Str, 10, 8093 Zürich (Switzerland), Fax: +41-44-6331358. E-mail: dario.neri@pharma.ethz.ch. Dr. Luca Mannocci, Philochem AG c/o ETH Zürich, Wolfgang-Pauli-Str, 10, 8093 Zürich (Switzerland), E-mail: luca.mannocci@philochem.ch.

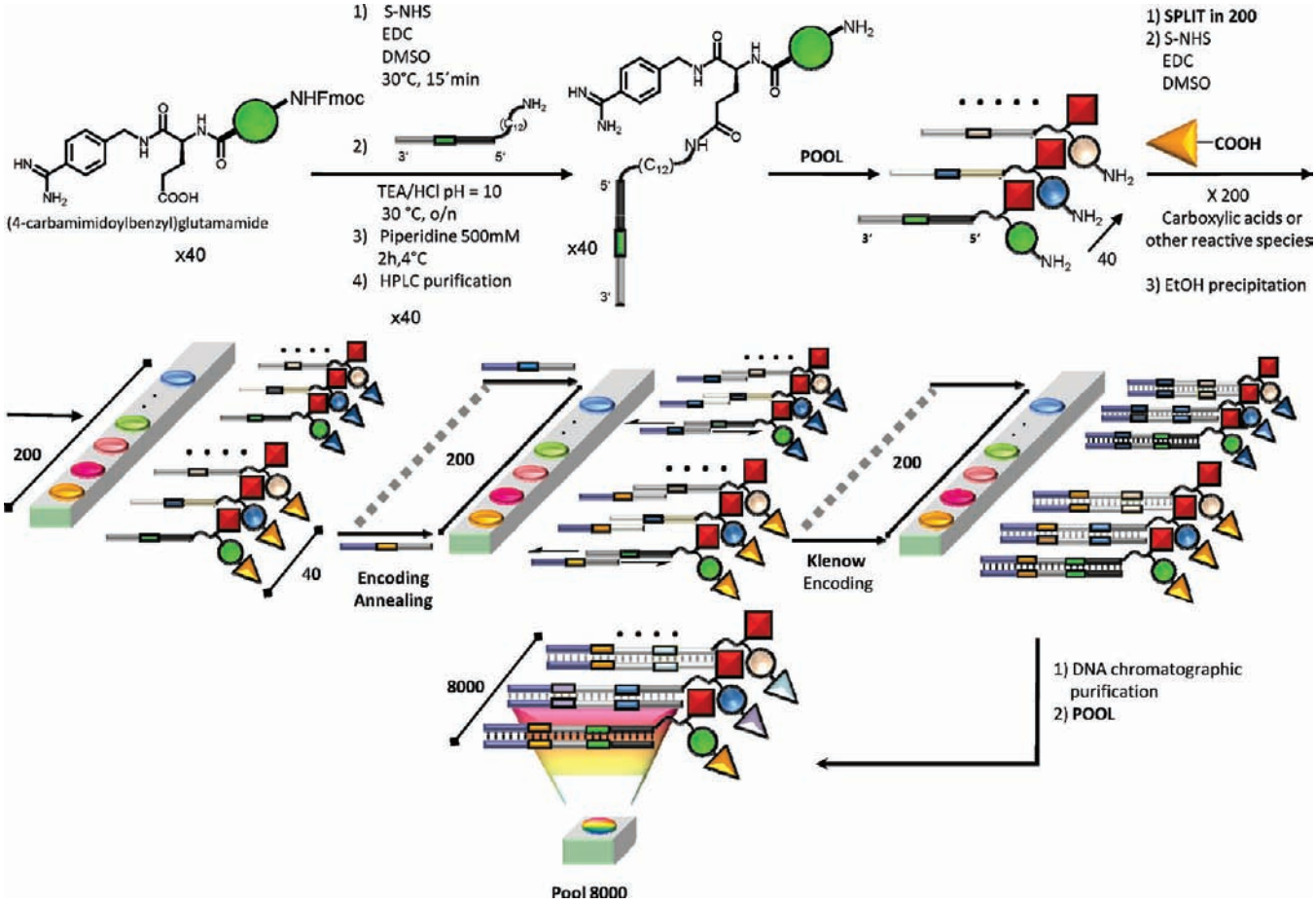
† Both authors contributed equally to the manuscript.

‡ Institute of Pharmaceutical Sciences.

§ Philochem AG.

10.1021/bc100198x © 2010 American Chemical Society
Published on Web 08/31/2010

Scheme 1. Synthesis and Encoding of the BAM8000 Library[a]



[a] Initially, 40 different Fmoc-protected amino acids, containing a benzamidine moiety, were coupled to unique oligonucleotide derivatives, carrying a primary amino group at the 5′ extremity and a 9 base pair coding region. Subsequently, the oligonucleotide conjugates were pooled and coupled to 200 amino reactive building blocks (carboxylic acid, isocyanate, sulfonyl chloride, or cyclic anhydrides) in parallel reactions. The identity of each building block was encoded by means of a Klenow polymerization step, using a set of partially complementary oligonucleotides. The procedure resulted in an 8000-member library (BAM8000), in which each chemical compound was covalently attached to a double-stranded DNA fragment, containing two coding domains which unambiguously identify the compound's structure (i.e., the two chemical moieties used for compound synthesis).

modification, and subsequently incubated with Klenow polymerase at 37 °C for 1 h. After purification on chromatographic cartridges, the 200 purified reactions were dissolved in 100 μL of water each and pooled to generate the 8000 member library (BAM8000) to a final total oligonucleotide concentration of 300 nM. Details of the synthesis, analytics, and structures of the 40 Fmoc-protected amino acids as well as the structures of the 200 amino-reactive building blocks used can be found in the Supporting Information online.

Selection and decoding experiments: 50 μL of the library BAM8000 (20 nM, total oligonucleotide concentration) was added either to 50 μL trypsin−sepharose slurry (coating density as detailed in the text) or to sepharose slurry without trypsin. Both resins were preincubated with PBS and 0.3 mg/mL herring sperm DNA. After incubation for 1 h at 25 °C, the beads were washed 4 times with 400 μL PBS (20 mM NaH_2PO_4, 30 mM Na_2HPO_4, 100 mM NaCl), and used as template for PCR amplification of the selected codes. The PCR primers had the following structure: DEL_P1_A (5′-GCC TCC CTC GCG CCA TCA GGG AGC TTG TGA ATT CTG G-3′) and DEL_P2_B (5′-GCC TTG CCA GCC CGC TCA GGT AGT CGG ATC CGA CCA C-3′). The primers additionally contain at one extremity a 19 bp domain (underlined) required for high-throughput sequencing with the 454 Genome Sequencer system. The PCR products were purified with chromatographic cartridges. Subsequent high-throughput sequencing was performed on a 454 Life Sciences-Roche FLX Sequencer platform. Analyses of the codes from high-throughput sequencing were performed by an in-house program written in C++. The frequency of each code has been assigned to each individual oligonucleotide conjugate.

Synthesis of the binding molecules: In a polypropylene syringe, either 65 mg (30 μmol) of H-Gln-2-Chlorotrityl resin (Novabiochem, cat. no 04−12−2806) or 100 mg (30 μmol) of H-Ala-2-Chlorotrityl resin (Novabiochem, cat. no 04−12−2802) was suspended in a mixture of the appropriate Fmoc-protected amino acid (60 μmol, 1 mL), HBTU (120 μmol, 1 mL), and *N*,*N*-diisopropylethylamine (240 μmol, 0.5 mL) in dry DMF. After overnight incubation at 25 °C, the resin was washed 6 times with 2 mL dry DMF, and the fmoc moiety was removed by addition of 1 mL piperidine (50% in dry DMF) for 1 h at 25 °C. After washing 6 times with 2 mL dry DMF, the corresponding compound (60 μmol, 1 mL DMF) was added, and a further amide bond formation reaction was performed either as described above (carboxylic acid compounds) or by adding DIEA (Fluka, 240 μmol, 0.5 mL) in dry DMF (sulfonyl chloride and isocyanate compounds) for 6 h at rt. The resulting product was cleaved from the resin by treating the resin 5 times with 2 mL TFA (2% in CH_2Cl_2). The methylene chloride fractions were washed 3 times with water, dried on Na_2SO_4, and concentrated in vacuo. The crude carboxylic acid product was suspended in DMF (200 μL) and a solution of *N*-hydroxysulfosuccinimide

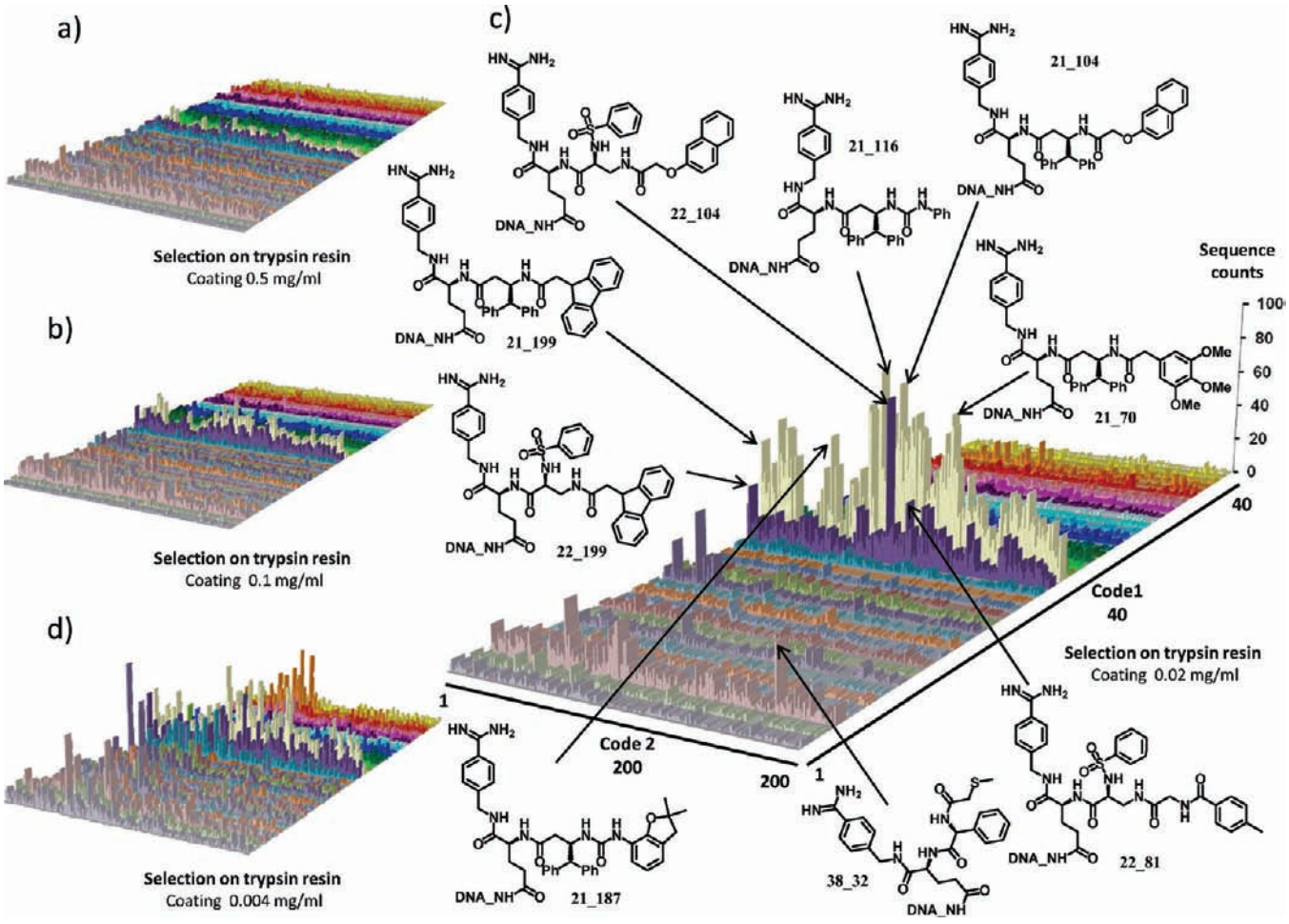


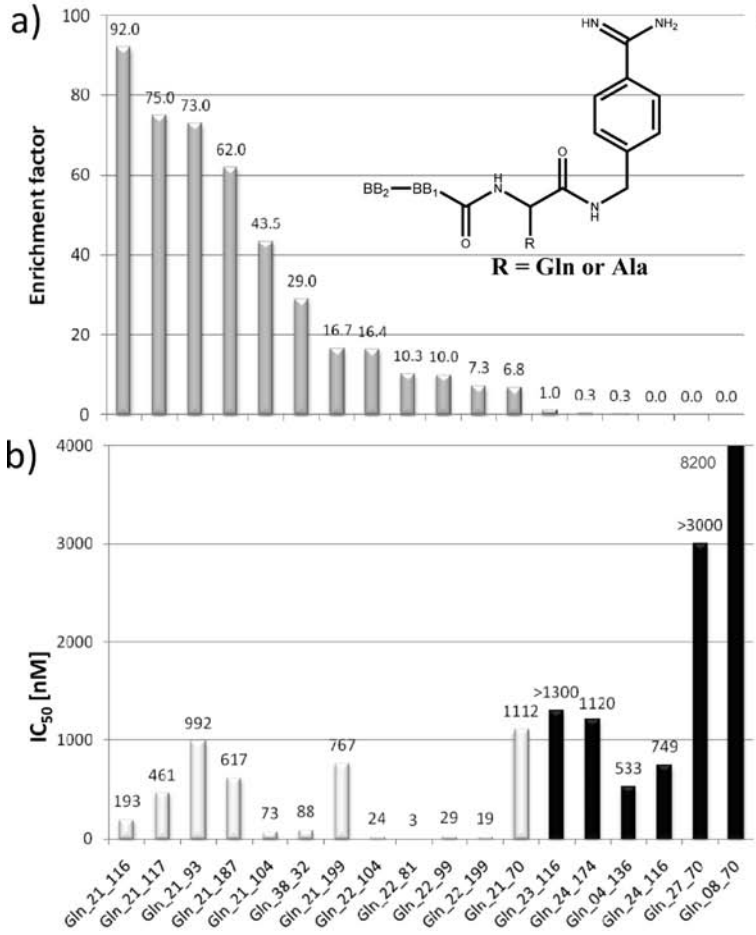
Figure 1. Plots representing the frequency (i.e., sequence counts) of the 8000 library members after selection on 4 different trypsin resins, as revealed by high-throughput 454 sequencing (*19*). The four panels are ordered from top to bottom according to decreasing protein coating density (a,b,c,d). The chemical structures of some of the most relevant trypsin binders are indicated, together with the identification number.

(36 μmol, 333 mM DMF/water, 2:1 v/v) and *N*-ethyl-*N*′-(3-dimethylaminopropyl)-carbodiimide hydrochloride (33 μmol, 100 mM DMF) was added. After 1 h at rt, 4-(aminomethyl-)benzimidamide dihydrochloride (30 μmol, ABCR, cat. no AB169853) and DIEA (180 μmol) were added. Following overnight incubation at 25 °C, HPLC purification was performed on a Synergy Prep RP18 column (5 μm, 10 × 150 mm) using a linear gradient from 20% to 100% MeCN 0.1% TFA, the desired fractions were collected and lyophilized. ESI-MS analysis confirmed the expected mass of the products. Details of the analytics can be found in the Supporting Information online.

Trypsin inhibition assay: Bovine pancreatic trypsin (1 nM) in PBS (20 mM NaH_2PO_4, 30 mM Na_2HPO_4, 100 mM NaCl [pH 7.4], containing 10% DMSO) was incubated with different concentrations of inhibitors in 384-well microtiter plates (Greiner) for 30 min at room temperature. The reaction was started by the addition of the fluorogenic substrate Z-GGR-AMC (Bachem, Bubendorf, Switzerland) dissolved in PBS and 10% DMSO to an end concentration of 0.1 mM in a total volume of 100 μL. The change of fluorescence signal (ex: 383 nm; em: 455 nm; cutoff filter: 420 nm) was recorded over 10 min using a SpectraMax microplate reader (Molecular Devices). The rate of fluorescence signal increase over time (reaction velocity v) was plotted against the corresponding inhibitor concentrations, and the IC_{50} value for the inhibitor was obtained by fitting with equation $v = a \times 0.5 \times \{-([Io] - [Eo] + IC_{50}) + [([Io] - [Eo] + IC_{50})^2 - 4 \times [Io] \times [Eo]]^{1/2}\}$; [Io] = inhibitor concentration; [Eo] = enzyme concentration = 1 nM, using the *Kaleidagraph* software package (Synergy Software, USA).

RESULTS

We have constructed a library of 8000 DNA-tagged benzamidine inhibitors based on the stepwise addition of two building blocks onto a core structure consisting of H-Glu-(4-(aminomethyl)benzamidine)-(4-(aminomethyl)benzamidine) (Scheme 1). This building block was initially coupled to 40 Fmoc-protected amino acids, and for each derivative, the side-chain carboxylic group of glutamate was deprotected and subsequently coupled to individual oligonucleotides carrying a primary amino group at the 5′ extremity. This reaction step allowed the DNA-encoding of the first building block (*13*, *15*, *16*). After Fmoc deprotection and HPLC purification (Supporting Information Table 1), the 40 oligonucleotide conjugates were pooled and split into 200 reaction vessels, where the primary amino group was covalently modified with carboxylic acids, isocyanates, sulfonyl chlorides, or cyclic anhydrides (Scheme 1). At the end of this procedure, which was already known from model reactions on oligonucleotide-tagged amines to proceed with good yields and selectivity (Supporting Information Figure 1), the second building block was encoded by hybridization of partially complementary oligonucleotides carrying an eight-base code (Scheme 1). Double-stranded DNA fragments were obtained using Klenow DNA polymerase, in full analogy to what was previously reported by our group (*13*, *15*, *16*). Fully encoded



c)

Compound (aa_BB1_BB2)	IC_{50} Trypsin (μM)	IC_{50} Thrombin (μM)	IC_{50} uPA (μM)	IC_{50} FXa (μM)
Benzamidine[12]	35	>500	35	32
Gln_22_81	0.0030	3.1	50	16
Ala_22_99	0.0052	0.052	7.9	5.9
Gln_22_199	0.019	1.9	14	11
Ala_21_116	0.023	8.2	>90	>126
Gln_22_104	0.024	0.97	7.7	6.7
Gln_22_99	0.029	0.058	42	2.1
Ala_22_104	0.034	0.094	2.8	4.1
Gln_21_104	0.073	12	6.1	11
Gln_38_32	0.088	41	>100	>173
Gln_21_116	0.193	30	8.9	21
Gln_21_117	0.461	17	58	73
Gln_04_136	0.533	7.4	50	>208
Gln_21_187	0.617	29	>250	33
Gln_24_116	0.749	185	36	>271
Gln_21_199	0.767	5.1	2.3	19
Gln_21_93	0.992	17	>33	123
Gln_24_174	1.12	56	17	>217
Gln_21_70	1.2	54	>73	>127
Gln_23_116	1.3	8.2	>74	>161
Gln_27_70	3.0	100	>85	>800
Gln_08_70	8.7	76	>145	n.d.

Figure 2. Characterization of hits from trypsin selection. (a,b) Correlation of the high-throughput sequencing enrichment factor and trypsin inhibition constant. Individual compounds identified in the trypsin selection at 0.02 mg/mL protein coating density were synthesized as glutamine derivatives and incubated at different concentrations with bovine pancreatic trypsin. The reaction was started by the addition of the fluorogenic substrate Z-GGR-AMC and the change of fluorescence signal was recorded. Inhibition constants were determined by fitting. The 18 compounds are ordered on the *x*-axis from left to right according to their enrichment factor. The enrichment factor was derived by dividing the high-throughput sequencing counts of a specific code after trypsin selection by the counts obtained after selection on empty resin (see Supporting Information Figure 2). (c) Table summarizing the inhibition constants of the 21 synthesized compounds for 4 different serine proteases (trypsin, thrombin, uPA, and FXa). Three of the best trypsin inhibitors were also synthesized as alanine derivatives in order to investigate the contribution of the glutamine linker to the inhibition. The structures of the two building blocks forming the BAM8000 library compounds can be found in Supporting Information Tables 1 and 2, respectively.

library members were purified on chromatographic cartridges, pooled, and aliquoted for library use.

The library of 8000 benzamidine derivatives was panned on sepharose resins covalently modified with a series of concentrations of trypsin (0.5, 0.1, 0.02, 0.004, and 0 mg trypsin per milliliter of CNBr-activated sepharose resin). After extensive washing, the DNA-tags of the library compounds that remained attached to the resins were used as a template for PCR amplification and the resulting amplicon mixtures were characterized by high-throughput DNA sequencing, using 454 technology (*22*) (15242, 15966, 17558, 15488, and 17145 counts, respectively, could be evaluated), in order to assess the relative abundance of individual codes for the library compounds after selection under different conditions (*13*−*16*).

Figure 1 shows that the selection performed on 0.02 mg/mL trypsin coated resin yielded the best discrimination among library compounds. Indeed, it is conceivable that at high coating density all library members may efficiently be captured with the aid of the benzamidine moiety, while at low coating density, overall capture efficiency may be insufficient even for the highest-affinity binders. Similar observations have been previously made in the field of phage display library biopanning (*23*−*28*), as well as in the screening of DNA-encoded chemical libraries (*9*).

For the first building block, moieties **21** and **22** (a diphenylmethyl and a phenylsulfonamide group, respectively) dominated the trypsin selection experiments, while various groups corresponding to the second building block were selected. Representative structures indicating some of the most frequently enriched compounds are displayed in Figure 1.

Figure 2a presents the list of the 12 most enriched compounds (sorted according to their enrichment factor, calculated as a ratio of sequence counts after selection on 0.02 mg/mL resin and after selection on empty resin; see also Supporting Information Figure 2). In addition, 6 non-enriched compounds are also considered for the comparison. The 18 compounds were resynthesized in the absence of DNA as glutamine derivatives (the most similar BAM8000 library format) and were characterized in terms of their 50% inhibitory concentration (IC_{50}) of the catalytic activity of trypsin, using a fluorogenic substrate (*11*). In general, preferentially enriched compounds exhibited better IC_{50} values compared to the nonenriched counterpart (Figure 2b). The correlation between enrichment and potency was not 1:1, as other factors (e.g., reaction yields, nonspecific interactions with the resin support) may contribute to a selection bias (*23*−*25*). However, 6 out of 12 of the preferential binders exhibited an IC_{50} value of <100 nM. Compound **22_81** exhibited the most potent trypsin inhibition, with an IC_{50} value of 3.0

nM. Importantly, the newly discovered trypsin inhibitors were highly selective, as revealed by a comparative analysis of the IC_{50} values of the 18 compounds (plus 3 analogues in which the glutamine moiety was replaced by alanine) against other serine proteases (thrombin, factor Xa, urokinase-type plasminogen activator; Figure 2c). The most potent inhibitor [((*S*)-3-(2-(4-methylbenzamido)acetamido)-2-(phenylsulfonamido)propanamido)-(*S*)-(4-carbamimidoylbenzyl)-glutamamide] displayed a selectivity of >1000-fold for trypsin, compared to the other three serine proteases.

DISCUSSION

Three main lessons could be learned from this affinity-maturation project. First, libraries containing thousands of members could be rapidly synthesized with a "split and pool" approach, which allowed the unambiguous identification and quantification of individual library members with the help of the tagging with distinctive DNA fragments serving as amplifiable identification bar codes. Second, affinity selections were best performed using a variety of experimental conditions (e.g., densities of trypsin coating on resin), in order to identify the best preferential binders and minimize resynthesis work after library selections. Third and most important, a benzamidine lead compound (which displays trypsin IC_{50} values in the 100 μM concentration range; Figure 2c) could be affinity-matured to single-digit nanomolar potency, with an excellent discrimination toward related serine proteases. We anticipate that similar affinity maturation strategies can now be routinely implemented with leads against a variety of targets of pharmaceutical interest.

ACKNOWLEDGMENT

This work was supported by Philochem AG, the Kommission für Technologie und Innovation (KTI Grant Nr. 8868.1 PFDS-LS) and the Gebert-Rüf Foundation (Grant Nr. GRS-076/06) is gratefully acknowledged. The authors declare conflict-of-interest. D.N. owns shares of Philochem AG and J.S. consults for this company.

Supporting Information Available: Detailed experimental procedure, library synthesis, high-throughput sequencing identification, enzyme inhibition assays, Supplementary Figures and Supplementary Tables. This material is available free of charge via the Internet at http://pubs.acs.org.

LITERATURE CITED

(1) Schwardt, O., Kolb, H., and Ernst, B. (2003) Drug discovery today. *Curr. Top. Med. Chem. 3*, 1–9.
(2) Brenner, S., and Lerner, R. A. (1992) Encoded combinatorial chemistry. *Proc. Natl. Acad. Sci. U.S.A. 89*, 5381–5383.
(3) Gartner, Z. J., Tse, B. N., Grubina, R., Doyon, J. B., Snyder, T. M., and Liu, D. R. (2004) DNA-templated organic synthesis and selection of a library of macrocycles. *Science 305*, 1601–1605.
(4) Halpin, D. R., and Harbury, P. B. (2004) DNA display II. Genetic manipulation of combinatorial chemistry libraries for small-molecule evolution. *PLoS Biol. 2*, E174.
(5) Melkko, S., Scheuermann, J., Dumelin, C. E., and Neri, D. (2004) Encoded self-assembling chemical libraries. *Nat. Biotechnol. 22*, 568–574.
(6) Scheuermann, J., Dumelin, C. E., Melkko, S., Zhang, Y., Mannocci, L., Jaggi, M., Sobek, J., and Neri, D. (2008) DNA-encoded chemical libraries for the discovery of MMP-3 inhibitors. *Bioconjugate Chem. 19*, 778–785.
(7) Scheuermann, J., Dumelin, C. E., Melkko, S., and Neri, D. (2006) DNA-encoded chemical libraries. *J. Biotechnol. 126*, 568–581.
(8) Melkko, S., Dumelin, C. E., Scheuermann, J., and Neri, D. (2006) On the magnitude of the chelate effect for the recognition of proteins by pharmacophores scaffolded by self-assembling oligonucleotides. *Chem. Biol. 13*, 225–231.
(9) Dumelin, C. E., Scheuermann, J., Melkko, S., and Neri, D. (2006) Selection of streptavidin binders from a DNA-encoded chemical library. *Bioconjugate Chem. 17*, 366–370.
(10) Melkko, S., Dumelin, C. E., Scheuermann, J., and Neri, D. (2007) Lead discovery by DNA-encoded chemical libraries. *Drug Discovery Today 12*, 465–471.
(11) Melkko, S., Zhang, Y., Dumelin, C. E., Scheuermann, J., and Neri, D. (2007) Isolation of high-affinity trypsin inhibitors from a DNA-encoded chemical library. *Angew. Chem., Int. Ed. Engl. 46*, 4671–4674.
(12) Dumelin, C. E., Trussel, S., Buller, F., Trachsel, E., Bootz, F., Zhang, Y., Mannocci, L., Beck, S. C., Drumea-Mirancea, M., Seeliger, M. W., et al. (2008) A portable albumin binder from a DNA-encoded chemical library. *Angew. Chem., Int. Ed. Engl. 47*, 3196–3201.
(13) Mannocci, L., Zhang, Y., Scheuermann, J., Leimbacher, M., De Bellis, G., Rizzi, E., Dumelin, C., Melkko, S., and Neri, D. (2008) High-throughput sequencing allows the identification of binding molecules isolated from DNA-encoded chemical libraries. *Proc. Natl. Acad. Sci. U.S.A. 105*, 17670–17675.
(14) Melkko, S., Mannocci, L., Dumelin, C. E., Villa, A., Sommavilla, R., Zhang, Y., Grutter, M. G., Keller, N., Jermutus, L., Jackson, R. H., et al. (2010) Isolation of a small-molecule inhibitor of the antiapoptotic protein Bcl-xL from a DNA-encoded chemical library. *ChemMedChem 5*, 584–590.
(15) Buller, F., Zhang, Y., Scheuermann, J., Schafer, J., Buhlmann, P., and Neri, D. (2009) Discovery of TNF inhibitors from a DNA-encoded chemical library based on diels-alder cycloaddition. *Chem. Biol. 16*, 1075–1086.
(16) Buller, F., Mannocci, L., Zhang, Y., Dumelin, C. E., Scheuermann, J., and Neri, D. (2008) Design and synthesis of a novel DNA-encoded chemical library using Diels-Alder cycloadditions. *Bioorg. Med. Chem. Lett. 18*, 5926–5931.
(17) Hansen, M. H., Blakskjaer, P., Petersen, L. K., Hansen, T. H., Hojfeldt, J. W., Gothelf, K. V., and Hansen, N. J. (2009) A yoctoliter-scale DNA reactor for small-molecule evolution. *J. Am. Chem. Soc. 131*, 1322–1327.
(18) Clark, M. A., Acharya, R. A., Arico-Muendel, C. C., Belyanskaya, S. L., Benjamin, D. R., Carlson, N. R., Centrella, P. A., Chiu, C. H., Creaser, S. P., Cuozzo, J. W., et al. (2009) Design, synthesis and selection of DNA-encoded small-molecule libraries. *Nat. Chem. Biol. 5*, 647–654.
(19) Craik, C. S., Largman, C., Fletcher, T., Roczniak, S., Barr, P. J., Fletterick, R., and Rutter, W. J. (1985) Redesigning trypsin: alteration of substrate specificity. *Science 228*, 291–297.
(20) Craik, C. S., Choo, Q. L., Swift, G. H., Quinto, C., MacDonald, R. J., and Rutter, W. J. (1984) Structure of two related rat pancreatic trypsin genes. *J. Biol. Chem. 259*, 14255–14264.
(21) Wood, J. M., Schnell, C. R., Cumin, F., Menard, J., and Webb, R. L. (2005) Aliskiren, a novel, orally effective renin inhibitor, lowers blood pressure in marmosets and spontaneously hypertensive rats. *J. Hypertens. 23*, 417–426.
(22) Margulies, M., Egholm, M., Altman, W. E., Attiya, S., Bader, J. S., Bemben, L. A., Berka, J., Braverman, M. S., Chen, Y. J., Chen, Z., et al. (2005) Genome sequencing in microfabricated high-density picolitre reactors. *Nature 437*, 376–380.
(23) Clackson, T., Hoogenboom, H. R., Griffiths, A. D., and Winter, G. (1991) Making antibody fragments using phage display libraries. *Nature 352*, 624–628.
(24) Marks, J. D., Ouwehand, W. H., Bye, J. M., Finnern, R., Gorick, B. D., Voak, D., Thorpe, S. J., Hughes-Jones, N. C., and Winter, G. (1993) Human antibody fragments specific for human blood group antigens from a phage display library. *Biotechnology (N Y) 11*, 1145–1149.
(25) Winter, G., Griffiths, A. D., Hawkins, R. E., and Hoogenboom, H. R. (1994) Making antibodies by phage display technology. *Annu. Rev. Immunol. 12*, 433–455.

(26) Schier, R., McCall, A., Adams, G. P., Marshall, K. W., Merritt, H., Yim, M., Crawford, R. S., Weiner, L. M., Marks, C., and Marks, J. D. (1996) Isolation of picomolar affinity anti-c-erbB-2 single-chain Fv by molecular evolution of the complementarity determining regions in the center of the antibody binding site. *J. Mol. Biol. 263*, 551–567.

(27) Schier, R., Bye, J., Apell, G., McCall, A., Adams, G. P., Malmqvist, M., Weiner, L. M., and Marks, J. D. (1996) Isolation of high-affinity monomeric human anti-c-erbB-2 single chain Fv using affinity-driven selection. *J. Mol. Biol. 255*, 28–43.

(28) Liu, B., Huang, L., Sihlbom, C., Burlingame, A., and Marks, J. D. (2002) Towards proteome-wide production of monoclonal antibody by phage display. *J. Mol. Biol. 315*, 1063–1073.

BC100198X

Supplementary Methods

General: Unless otherwise denoted, chemical compounds and proteins were purchased from Sigma-Aldrich-Fluka (Buchs, Switzerland), resin for solid phase synthesis from Novabiochem (Laufelfingen, Switzerland), enzymes from New England Biolabs (Ipswich, MA, USA) and HPLC grade lyophilized oligonucleotides were from IBA GmbH (Göttingen, Germany). SpinX columns were purchased from Corning Costar Incorporated (Acton, MA, USA) and chromatographic cartridges for DNA purification from Qiagen (Hilden, Germany), (PCR purification cat.no 28104, Nucleotides removal cat.no 28306) and used according to the protocol described by the provider. All HPLC were performed on an XTerra Prep RP_{18} column (5µm, 10x150mm) using a linear gradient from 10% to 40% MeCN in 100 mM TEAA, pH 7. LC-ESI-MS were performed on an XTerra RP_{18} column (5 µm, 4.6x20 mm) using a linear gradient from 0% to 50% MeOH in 400 mM HFIP/5 mM TEA. The mass spectra were measured from *m/z* 900 to 2000 by a Waters Quattro Micro instrument (Waters, Milford, MA, USA).

Oligonucleotide coupling reactions of 40 Fmoc-protected amino acids containing benzamidine moiety: To a reaction volume of 310 µL, containing 70% (v/v) DMSO/water, compounds were added to the respective final concentrations: Fmoc-protected amino acids DMSO solution, 30 mM; *N*-hydroxysulfosuccinimide in DMSO, 10 mM; *N*-ethyl-*N'*-(3-dimethylaminopropyl)-carbodiimide in DMSO, 4 mM; aqueous triethylamine hydrochloride solution, pH 10.0, 80 mM; oligonucleotide aqueous solution, 50 µM, (5'-GGA GCT TGT GAA TTC TGG XXX XXX XXX GGA CGT GTG TGA ATT GTC-3', XXX XXX XXX unambiguously identifies the individual Fmoc-protected amino acid compound). All coupling reactions were stirred overnight at 25 °C; residual activated species were then quenched and simultaneously Fmoc deprotected by addition of piperidine (500 mM in DMSO). Prior to HPLC purification 500 µL of 100 mM TEAA, pH 7.0, was added to the reaction mixture. The reactions were then purified by HPLC and the desired fractions were dried under reduced pressure and redissolved in 100 µL of water and analyzed by LC-ESI-MS. The samples showed the expected benzamidine Fmoc-deprotected conjugated products. Finally, 4.0 nmol of each DNA-compound conjugate were pooled to generate a 40 member DNA encoded sub-library. Typical coupling yields were between 98 % and 15% (average 56%) overall and the recoveries between 22% and 55% (average 20% overall). The structures, the matching oligonucleotide codes and the ESI-MS analysis of the 40

Fmoc-protected amino acids containing benzamidine moiety, together with the LC-MS analysis of the corresponding oligonucleotide conjugates can be found in **Supplementary Table 1**.

Coupling reactions of 200 amino reactive building blocks (carboxylic acid, isocyanate, sulfonyl chloride and cyclic anhydrides),BB2:

Carboxylic acids: To a reaction volume of 310 µL, containing 70%(v/v) DMSO/water, compounds were added to the respective final concentrations: DMSO-dissolved carboxylic acid, 30 mM; *N*-hydroxysulfosuccinimide in DMSO, 10 mM; *N*-ethyl-*N'*-(3-dimethylaminopropyl)-carbodiimide in DMSO, 4 mM; aqueous triethylamine hydrochloride, pH9.0, 80 mM; DNA-oligonucleotide sub-library pool, 1.5 µM. All coupling reactions were stirred overnight at 30 °C; residual activated species were then quenched by addition of 50 µL Tris-Cl buffer, 500 mM pH 10.0. The mixture was allowed to quantitatively precipitate by addition of 40 µL of 3 M sodium acetate buffer, pH 4.7 and 500 µL ethanol followed by 2 h incubation at -23 ºC. The DNA was centrifuged and the resulting oligonucleotide pellet was washed with ice-cold 90% (v/v) ethanol and then dissolved in 100 µL water. Test coupling reactions were also performed with the reaction conditions described above; using model 42mer 5'-Fmoc-deprotected amino acid oligonucleotide conjugates and model carboxylic acids. The reactions were analysed by HPLC and the mass of the reacted oligonucleotides detected by LC-ESI-MS. A typical reaction is reported in **Supplementary Figure 2**. The structure of the 200 compounds used as secondary building block (BB2) and the matching oligonucleotide codes are listed in **Supplementary Table 2**.

Isocyanate, sulfonyl chloride and cyclic anhydrides: To a reaction volume of 500 µL, containing 75%(v/v) DMF/water, compounds were added to the respective final concentrations: DMSO-dissolved carboxylic acid, 10 mM; $NaHCO_3$ 100 mM; DNA-oligonucleotide sub-library pool, 1.5 µM. All coupling reactions were stirred overnight at 30 °C; residual activated species were then quenched by addition of 50 µL Tris-Cl buffer, 500 mM pH 10.0. The mixture was allowed to quantitatively precipitate by addition of 40 µL of 3 M sodium acetate buffer, pH 4.7 and 500 µL ethanol followed by 2 h incubation at -23 ºC. The DNA was centrifuged and the resulting oligonucleotide pellet was washed with ice-cold 90% (v/v) ethanol and then dissolved in 100 µL water. The structure of the 200 compounds used as secondary building block (BB2) and the matching oligonucleotide codes are listed in **Supplementary Table 2**.

Synthesis of H-Glu(tBu)-(4-(aminomethyl)benzamidine)): To a solution of Fmoc-Glu(tBu)-OH (3.6 mmol, 1.53g, Bachem) in dry DMF (55 mL), *N*-hydroxysuccinimide (4.32 mmol, 500 mg) and 1-ethyl-3-(3-dimethylaminopropyl)carbodiimide hydrochloride (3.96 mmol, 760 mg) were added and the reaction stirred 1h at rt. Subsequently, the mixture was cooled on ice and 4-(aminomethyl)benzimidamide dihydrochloride (3.6 mmol, 800 mg) and *N,N*-diisopropylethylamine (14.4 mmol, 2.52 mL) were added. The reaction was stirred 3 h at 0 °C and then poured in 250 mL of water. The water phase was back extracted with ethylacetate (5 times, 60 mL). The pooled organic phases were washed 3 times with 10 mL of water, dried on Na_2SO_4 and concentrated *in vacuo*. The crude was dissolved in 40 mL dioxane and treated with piperidine (36 mmol, 3.57 mL) for 1h at rt. The mixture was then washed with ethylacetate (3 times, 10 mL) and the water phases concentrated at reduced pressure. The residue was purified by HPLC and the desired fractions were dried under reduced pressure (217 mg, C17H26N4O3 calculated: 334.2; measured: 334.8 [$M+H^+$]).

General synthesis for the 40 initial fmoc protected (4-(aminomethyl)benzamidine)-Glu acid derivatives (BB1): To the opportune fmoc-protected amino acid (36μmol) and *N*-hydroxysuccinimide (43 μmol, 5.0mg) in DMF (1mL), a solution of 1-ethyl-3-(3-dimethylaminopropyl)carbodiimide hydrochloride (40 μmol, 7.7mg) in DMF (250 μL) was added. After 1h stirring at rt, the mixture was cooled on ice. Subsequently, a solution of H-Glu(tBu)-(4-(aminomethyl)benzamidine)) (36 μmol, 12mg) in DMF (1mL) and *N,N*-diisopropylethylamine (180 μmol, 31 μL) were added. The reaction was stirred over night at 4°C and then evaporated to dryness under reduced pressure. The residue was suspended 2h at rt in TFA/water (90:10, 900 μL) prior to HPLC purification. Structures of the synthesized compounds and ESI-MS characterizations can be found in **Supplementary Table 1**.

Polymerase Klenow encoding of 200 carboxylic acids reactions: To a reaction volume of 50 μL, reagents were added to the respective final concentrations: pool 40 conjugates 320 nM, 44mer oligonucleotide (5'-GTA GTC GGA TCC GAC CAC XXXX XXXX GAC AAT TCA CAC

ACG TCC-3', XXXX XXXX unambiguously identifies the individual secondary building block, IBA) 600 nM, Klenow buffer (NEB, cat.no B7002S), dNTPs (Roche, cat.no 11969064001), 0.5 mM, Klenow Polymerase enzyme (NEB, cat.no M0210L), 5 units. The Klenow polymerization reactions were incubated at 37 ºC for 1 h and then purified on chromatographic cartridges (Qiagen, cat.no 28306). The 200 purified reactions were dissolved in 50 µL of water, each, and pooled to generate the 8000 member library (BAM8000) to a final total oligonucleotide concentration of 300 nM.

Trypsin coating of sepharose beads: 100mg CNBr-activated sepharose (GE Healthcare, Piscataway, NJ) was suspended in 1 mM HCl, washed, and mixed in separate tubes with the appropriate amount of pancreatic bovine trypsin (0.5, 0.1, 0.02, 0.004 and 0 mg/ml, Sigma, cat.no T4665) dissolved in 0.1M $NaHCO_{3aq}$ and 0.5 M NaCl. After 5 hours incubation at 4°C, the slurry was repeatedly and alternatively washed with 0.1 M Tris-Cl, 0.5 M NaCl, pH 8.3 and 0.1 M NaOAc, 0.5 M NaCl, pH 4 then stored in PBS (20mM NaH_2PO_4, 30 mM Na_2HPO_4,100 mM NaCl [pH 7.4]) at 4°C.

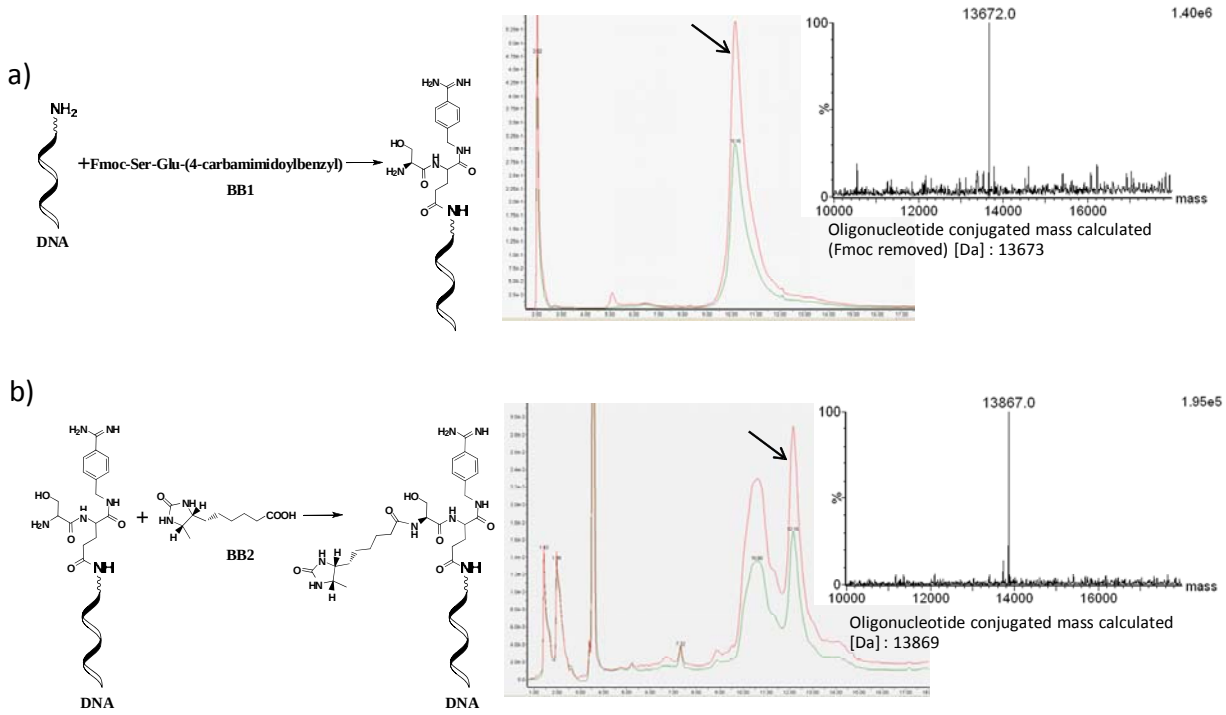
Library BAM8000 Trypsin Selections The resulting library BAM8000 (total oligonucleotide conjugate concentration 300 nM) was diluted 1:15 in PBS (20mM NaH_2PO_4, 30 mM Na_2HPO_4,100 mM NaCl [pH 7.4], 20nM final concentration). 50 µL of the library was either added to 50 µl pancreatic bovine trypsin slurry (0.5, 0.1, 0.02 and 0.004mg/ml) or to 50 µl sepharose slurry without trypsin resulting in an end concentration of 10 nM of library compounds. The resins were preincubated with PBS, 0.3 mg/mL herring sperm DNA. After incubation for 1 h at 25 ºC the mixture was transferred to a SpinX column, the supernatant was removed, and the resin washed 4 times with 400 µL PBS. After washing, the resins were resuspended in 100 µL water.

Identification of binding molecules: The codes of the oligonucleotide-compound conjugates were amplified by PCR (total volume 50 µL, 25 cycles of 1 min at 94 ºC, 1 min at 55 ºC, 40 s at 72 ºC) with either 5 µL of 100 fM BAM8000 library before selection as template, or 5 µL of each resuspended resin after selection as template. The PCR primers DEL_P1_A (5'-GCC TCC CTC GCG CCA TCA GGG AGC TTG TGA ATT CTG G-3') and DEL_P2_B (5'-GCC TTG CCA

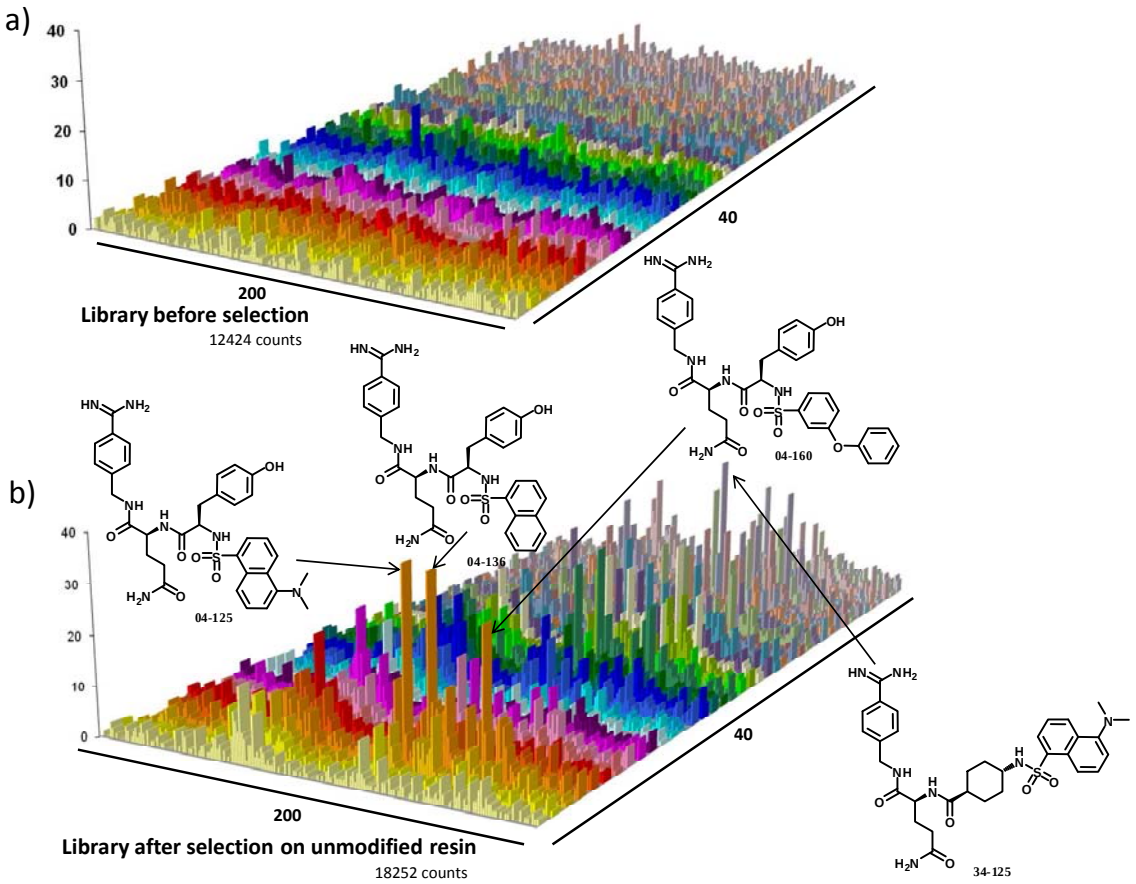
GCC CGC TCA GGT AGT CGG ATC CGA CCA C-3') additionally contain at one extremity a 19 bp domain (underlined) required for high-throughput sequencing with the 454 Genome Sequencer system. The PCR products were purified on chromatographic cartridges. Subsequent high-throughput sequencing was performed on a 454 Life Sciences-Roche FLX Sequencer platform (Sequencing by FGCZ). Analyses of the codes from high-throughput sequencing were performed by an in-house program written in C++. The frequency of each code was assigned to each individual pharmacophore.

Synthesis of the binding molecules: In a polypropylene syringe, either 50 mg (30 µmol) of H-Gln-ClTrt resin (Novabiochem, cat.no 04-12-2806) or 100 mg (30 µmol) of H-Ala-ClTrt resin (Novabiochem, cat.no 04-12-2803) were suspended in a mixture of the appropriate Fmoc-protected amino acid (60 µmol, 1 mL), HBTU (Aldrich, 120 µmol, 1 mL), and DIEA (Fluka, 240 µmol, 0.5 mL) in dry DMF. After overnight incubation at 25 °C, the resin was washed 6 times with 2 mL dry DMF and the Fmoc moiety was removed by addition of 1 mL piperidine (50% in dry DMF) for 1 h at 25 °C. After washing 6 times with 2 mL dry DMF, the opportune compound (100 µmol, 1 mL DMF) was introduced and a further amide bond formation reaction was performed either as described above (carboxylic acid compounds) or adding DIEA (Fluka, 240 µmol, 0.5 mL) in dry DMF(sulfonyl chloride and isocynate compounds) for 6 hours at rt. The resulting product was cleaved by treating the resin 5 times with 2 mL TFA (2% in CH_2Cl_2). The methylenchloride fractions were evaporated to dryness. The crude product was dissolved in DMF/water (90:10, 500 µL) and a solution of *N*-hydroxysuccinimide (72 µmol, DMF/water = 90:10, 250 µL) and of 1-ethyl-3-(3-dimethylaminopropyl)carbodiimide hydrochloride (66 µmol, 7.7 µmol) in DMF (250 µL) were subsequently added. After 2h stirring at rt, a solution of 4-(aminomethyl)benzimidamide dihydrochloride (30 µmol) and *N,N*-diisopropylethylamine (240 µmol) in DMF/water (90:10, 500 µL) were added. The pH was adjusted to pH=10 and the mixture incubated over night at rt. Prior to HPLC purification, the reaction was acidified with 250 µL of 2M HCl. The reactions were then purified by HPLC and the desired fractions were dried under reduced pressure. HPLC and ESI-MS analysis confirmed purity and the mass of the expected products (see **Supplementary Table 3**).

Enzyme inhibition assay: Either bovine pancreatic trypsin (1 nM, Sigma, cat.no T4665) or human plasma thrombin (5nM, Sigma, cat.no T6884) or factor Xa (25nM, Sigma, cat.no F9302 or human urokinase uPA (30nM, Accurate Chemical & Scientific Corporation, cat.no ACLENZ264) in PBS (20mM NaH_2PO_4, 30 mM Na_2HPO_4,100 mM NaCl [pH 7.4]), 5% DMSO) was incubated with different concentrations of inhibitors in 96-well microtiter plates (Greiner non-binding, cat.no 781900) for 30 min at room temperature (for the syntheses, see above). The reaction was started by the addition of the fluorogenic substrate Z-GGR-AMC (Bachem, Bubendorf, Switzerland) dissolved in PBS to an end concentration of 0.1 mM in a total volume of 60 ml. The change of fluorescence signal (ex: 383 nm; 455 nm; cutoff filter: 420 nm) was recorded over 25 min using a SpectraMax microplate reader (Molecular Devices). The rate of fluorescence signal increase over time (reaction velocity v) was plottedagainst the corresponding inhibitor concentrations, and the IC_{50} value for the inhibitor was obtained by fitting with equation v = a*0.5*(-([I_o]- [E_o]+ IC_{50})+sqrt(([I_o]- [E_o]+ IC_{50})^2-4*[I_o]*[E_o])) ; [I_o] = inhibitor concentration; [E_o] = enzyme concentration, using the Kaleidagraph software package (Synergy Software, USA).

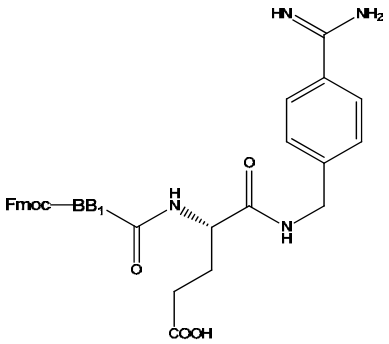


Supplementary figure 1. Typical coupling reactions using a representative 5'-amino-oligonucleotide as well as a primary and secondary building block (BB1 and BB2 respectively) to generate a model compound of the library. The HPLC chromatograms of the reactions show the traces recorded at 260nm (red) and at 280nm (green). In the side panels, the LC-ESI-MS spectrum illustrates the deconvoluted oligonucleotide conjugated masses of the products (indicated by the arrow in the chromatograms). Detailed experimental conditions are reported above in the text. a) Coupling of Fmoc-Ser-Glu-(4-carbamimidoylbenzyl) (BB1) to a representative 5'-amino-oligonucleotide. Retention time: 10.15 min, HPLC yield: 98%. b) Coupling of D-desthiobiotin (BB2) to Ser-Glu-(4-carbamimidoylbenzyl) oligonucleotide conjugated. Retention time: 12.15 min, HPLC yield 40%.

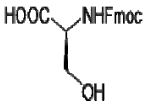
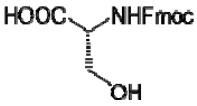
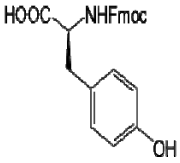
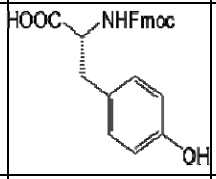
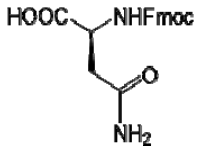
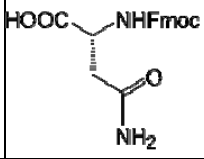
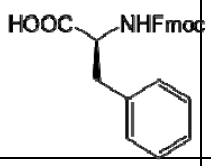
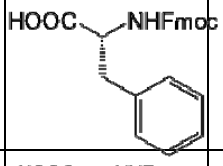
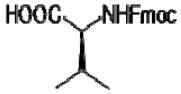


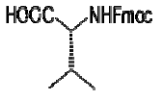
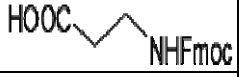
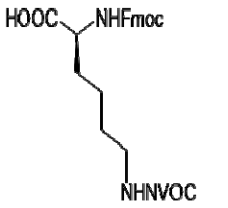
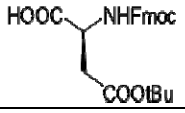
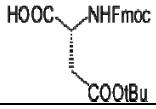
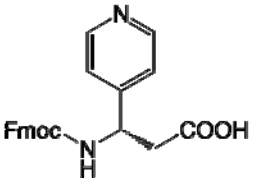
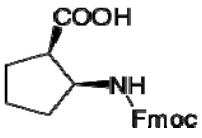
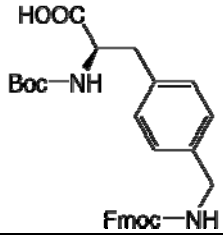
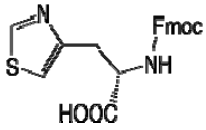
Supplementary figure 2. Plots representing the frequency (i.e., sequence counts) of the 8000 library members before selection (**a**) and after selection on unmodified resin (**b**), as revealed by high-throughput 454 sequencing.

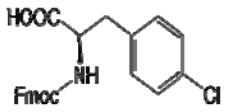
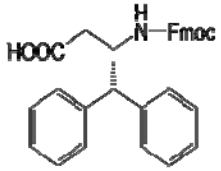
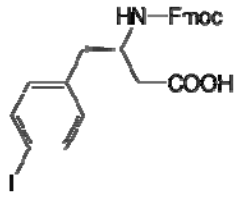
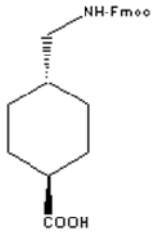
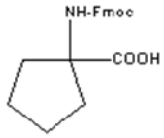
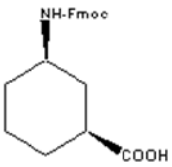
Supplemetary Table 1: The table summarizes the structures, the ESI-MS analysis and the matching oligonucleotide codes of the 40 primary building blocks (BB1) synthesized as Fmoc-protected amino acids containing benzamidine moiety. The table also contains the LC-ESI-MS analysis and the HPLC yields of the corresponding oligonucleotide conjugates used for the BAM8000 library construction.

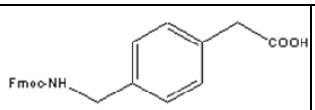
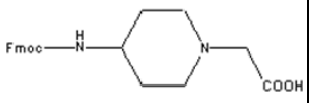
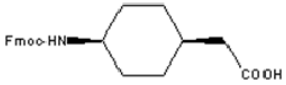
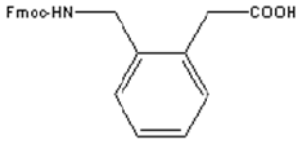
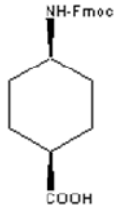
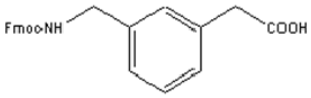
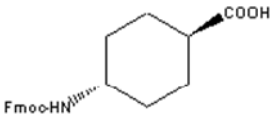
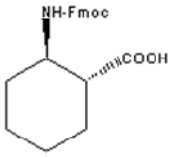
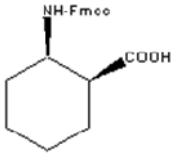


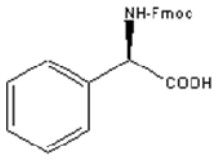
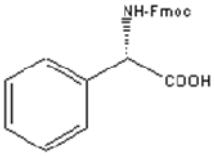
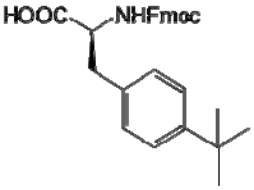
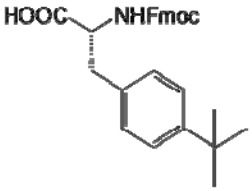
Fmoc-BB_1-Glu-(4-carbamimidoylbenzyl)

BB1	Structure (Fmoc-BB1-COOH)	Mass Calculated [Da]	Measured [M+H$^+$]	Oligonucleotide code (5'-3')	Oligonucleotide Conjugated Mass Calculated (Fmoc removed) [Da]	Oligonucleotide Conjugated Mass Deconvoluted [Da]	Yield[1] %
1		587.24	587.91	AACAAGGCA	14648	14646	98
2		587.24	588.01	AACAAGTAT	14638	14638	71
3		662.55	664.08	AACACGTGG	14730	14728	78
4		662.55	665.1	AACACTAGC	14674	14676	79
5		614.25	614.98	AACAGCGTT	14657	14656	48
6		614.25	614.98	AACATCATC	14601	14598	58
7		646.71	648.07	AACATGCCT	14649	14651	57
8		646.71	648.07	AACCAATCA	14642	14644	50
9		598.52	600.02	AACCACCGT	14586	14587	68

10		598.52	600.05	AACCCCTAA	14570	14572	76
11		557.23	557.96	AACCCTGCC	14521	14522	48
12		571.25	571.95	AACCGTCGC	14575	14576	73
13		867.73	869.28	AACCGTTCT	14861	14864	71
14		671.63	673.18	AACGATCGA	14723	14725	35
15		671.63	673.18	AACGCACAA	14692	14695	30
16		647.54	649.1	AACGGACCG	14670	14699	19
17		610.52	612.1	AACGTCTGA	14653	14653	70
18		776.71	778.26	AACTAAGCG	14828	14830	77
19		654.57	656.09	AACTACGAC	14666	14668	59

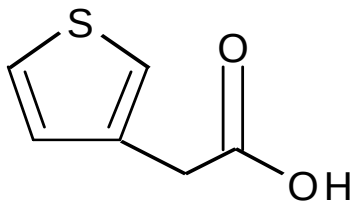
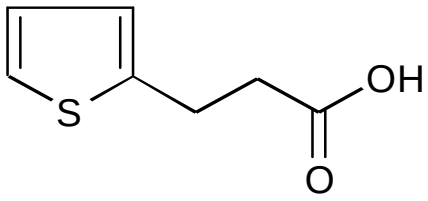
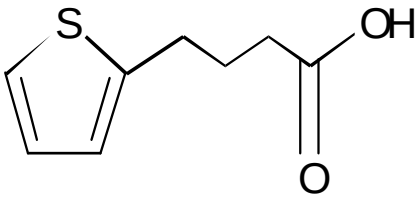
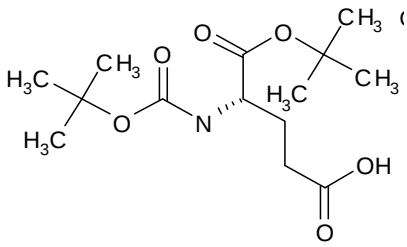
20		681	682.03	AACTCAAGG	14733	14736	67
21		736.67	738.17	AACTCGTTA	14755	14759	71
22		725.63	727.06	AACTGCCGA	14754	14758	20
23		787.48	788.04	AACTGGACG	14855	14858	68
24		638.52	640.12	AACTTGGGC	14697	14701	20
25		611.53	613.12	AAGAAGGAG	14752	14754	98
26		624.52	626.04	AAGAATTAC	14675	14678	36

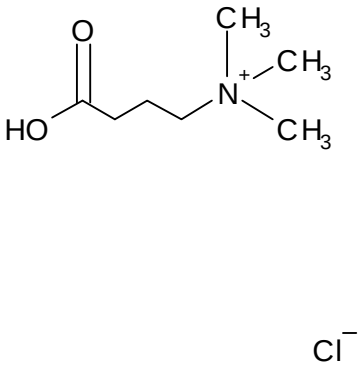
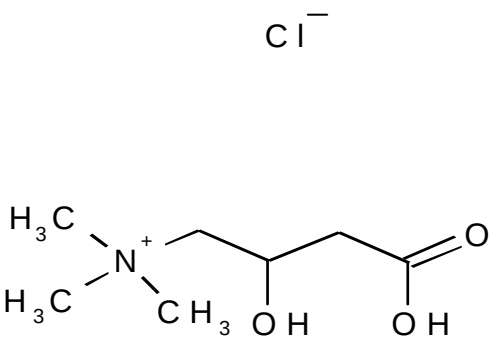
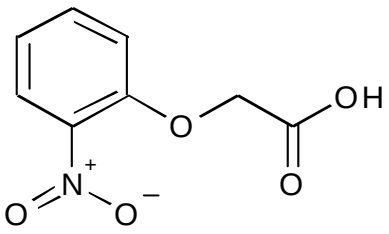
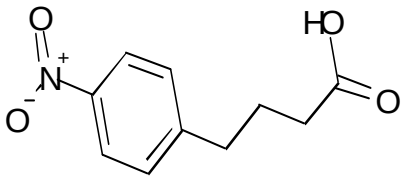
27		646.52	648.04	AAGATAAGC	14722	14722	75
28		638.62	640.12	AAGATTATT	14695	14695	73
29		639.62	641.06	AAGATTCCA	14666	14667	15
30		638.62	640.28	AAGCAACAC	14659	14661	63
31		646.52	648.26	AAGCACAAT	14682	14687	54
32		625.53	627.12	AAGCCAGAT	14677	14680	61
33		647.53	649.16	AAGCCGCAG	14700	14695	80
34		625.53	627.16	AAGCTACTT	14643	14645	56
35		625.53	627.15	AAGCTCCGC	14629	14633	63
36		625.53	627.09	AAGGAGCCG	14718	14721	57

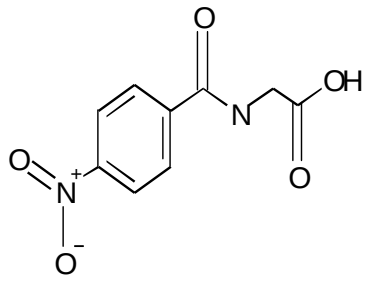
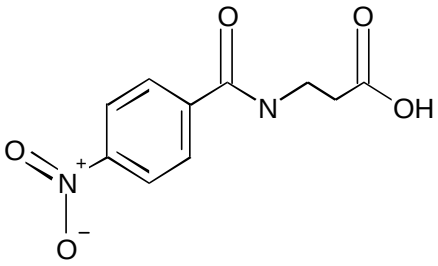
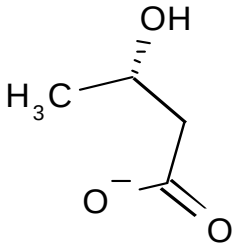
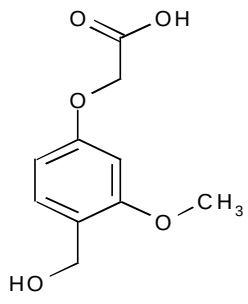
37		632.52	633.99	AAGGATGAT	14739	14739	50
38		632.52	634.05	AAGGGGATG	14780	14779	39
39		703.67	705.2	AAGGGTCTC	14762	14763	52
40		703.67	705.2	AAGGTGTGC	14802	14805	47

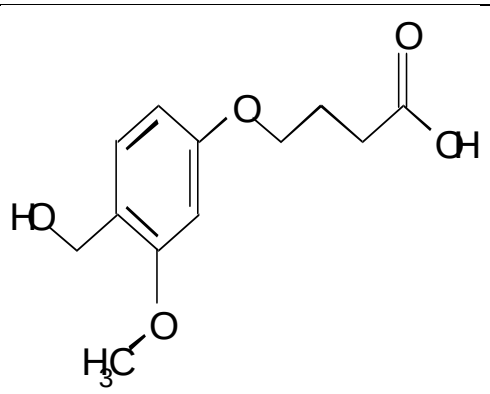
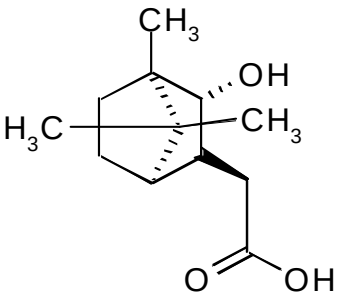
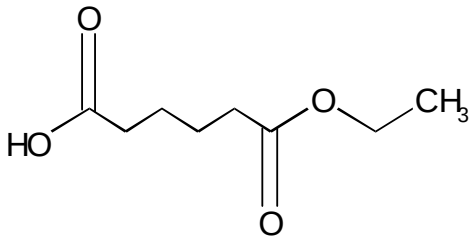
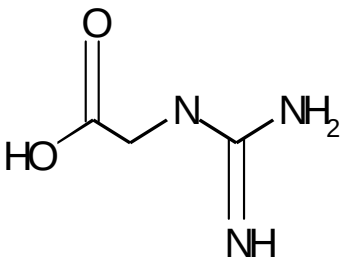
[1.] Determined by HPLC after Fmoc deprotection of the oligonucleotide conjugated compound.

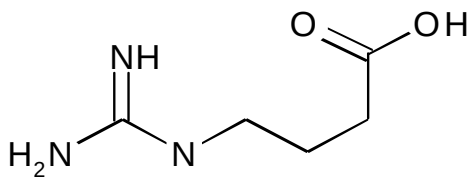
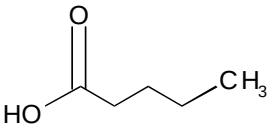
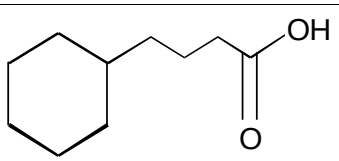
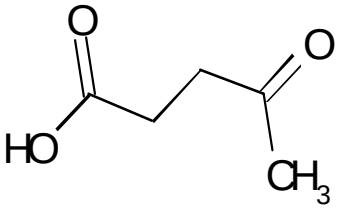
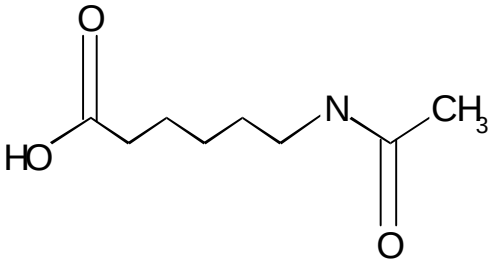
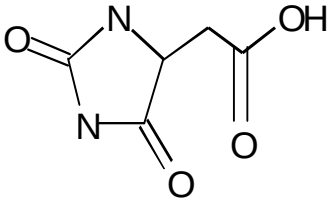
Supplemetary Table 2: The table summarizes the structures and the matching oligonucleotide codes of the 200 compounds used as secondary building block (BB2) in the BAM8000 library construction.

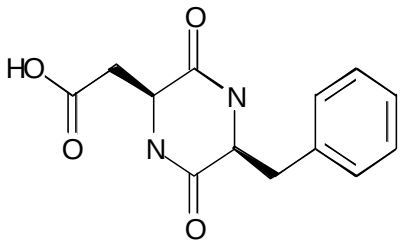
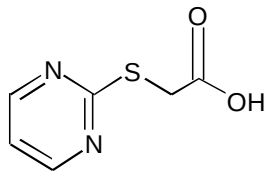
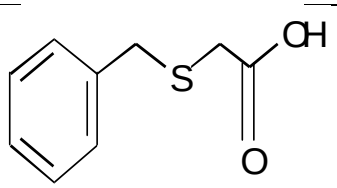
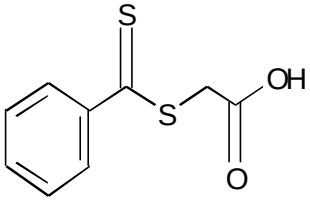
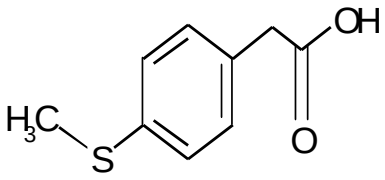
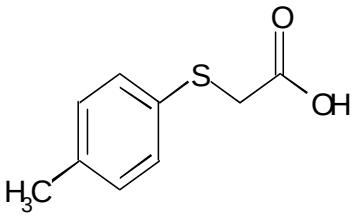
BB2	Structure	MW	Oligonucleotide code (5'-3')
1		142.2	TTCACACA
2		156.2	AAAACCCC
3		170.2	AAAAGGGG
4		303.4	AAAATTTT

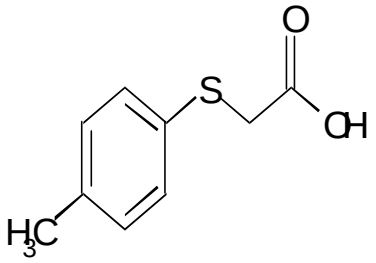
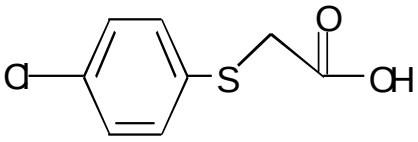
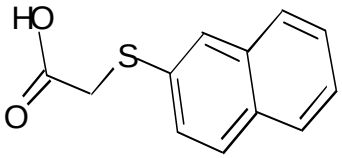
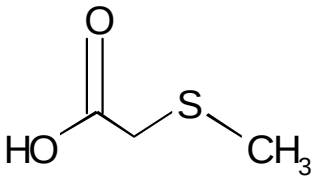
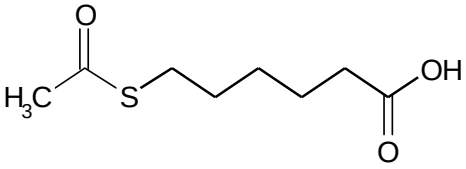
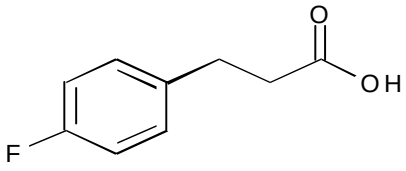
5		146.2	AAACACGT
6		162.2	AAACCATG
7		197.1	AAACGTAC
8		209.2	AAACTGCA

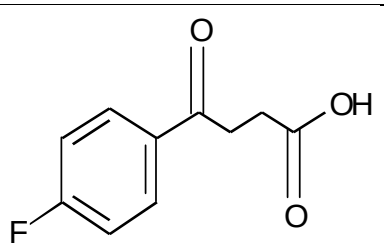
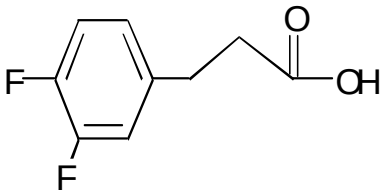
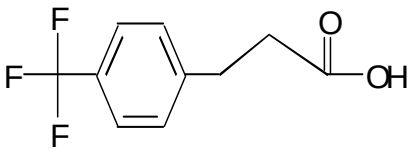
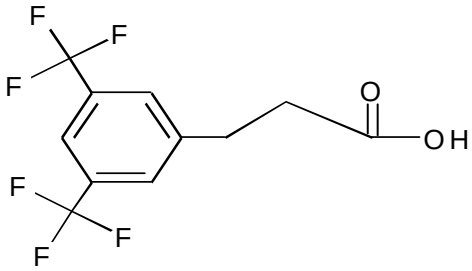
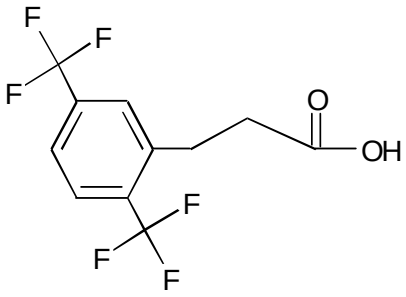
9		224.2	AAAGAGTC
10		238.2	AAAGCTGA
11		104.1	AAAGGACT
12		212.2	AAAGTCAG

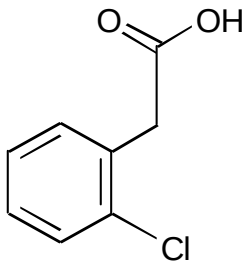
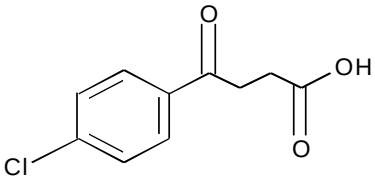
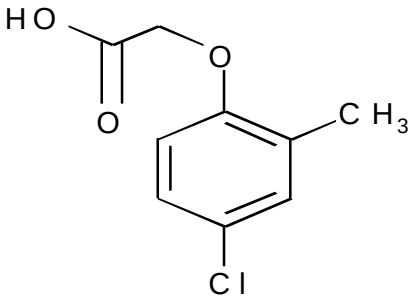
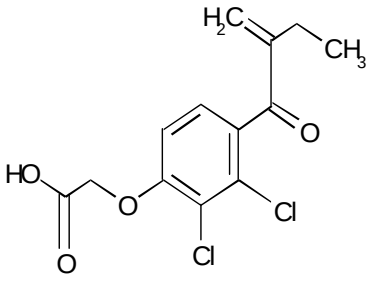
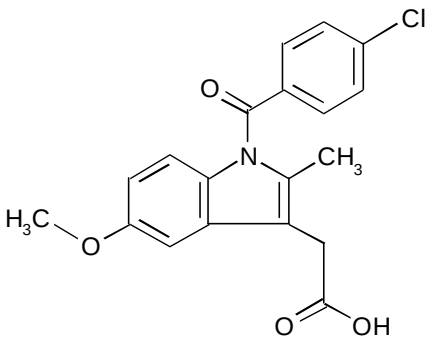
13		240.3	AAATATCG
14		212.3	AAATCGAT
15		174.2	AAATGCTA
16		117.1	AAATTAGC

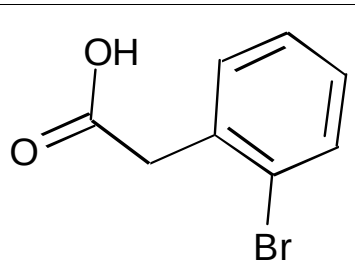
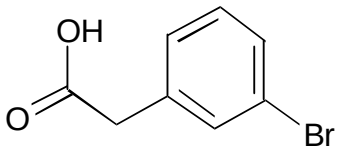
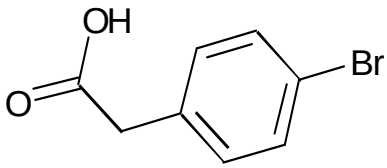
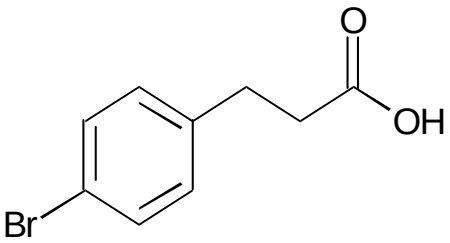
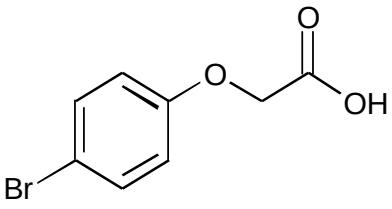
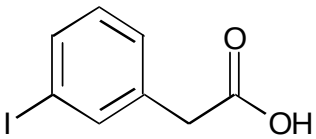
17		145.2	AACAACTG
18		102.1	AACACAGT
19		170.3	AACAGTCA
20		116.1	AACATGAC
21		173.2	AACCAACC
22		158.1	AACCCCAA

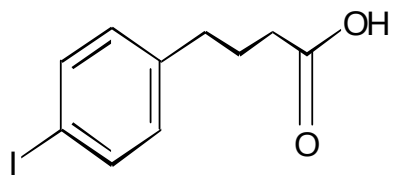
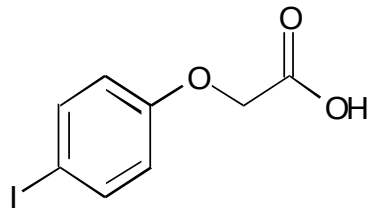
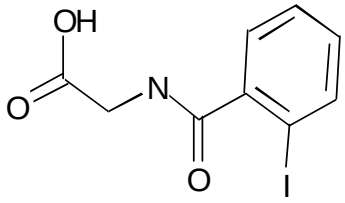
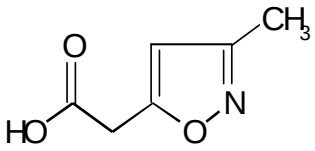
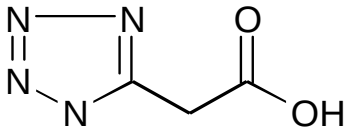
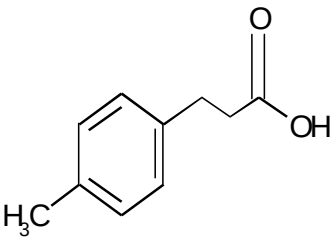
23		262.3	AACCGGTT
24		170.2	AACCTTGG
25		182.2	AACGATAT
26		212.3	AACGCGCG
27		182.2	AACGGCGC
28		182.2	AACGTATA

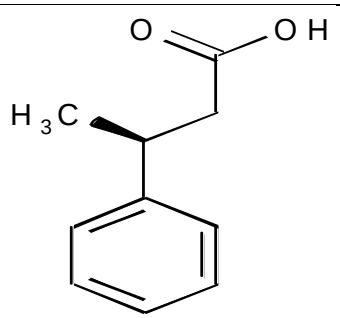
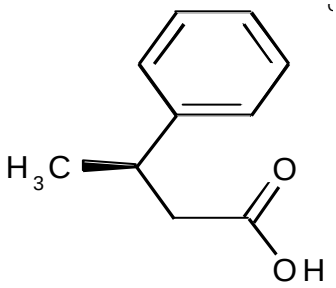
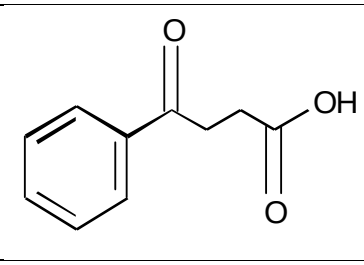
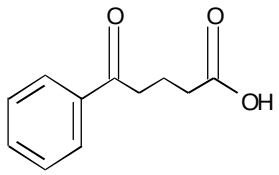
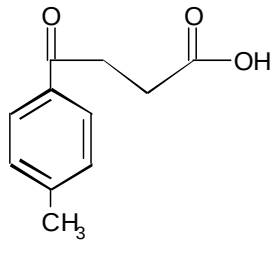
29		182.2	AACTAGGA
30		202.7	AACTCTTC
31		218.3	AACTGAAG
32		106.1	AACTTCCT
33		190.3	AAGAAGCT
34		168.2	AAGACTAG

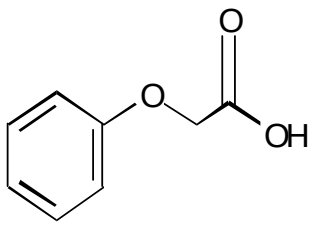
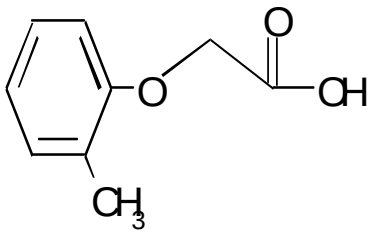
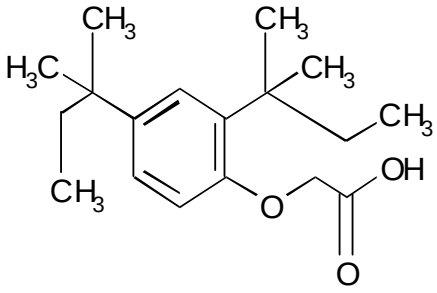
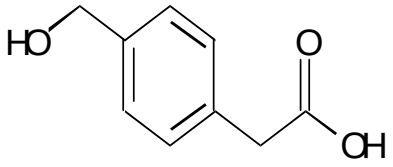
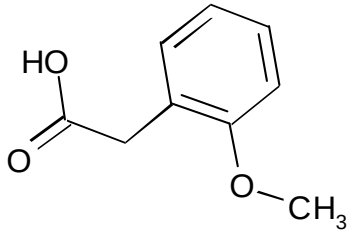
35		196.2	AAGAGATC
36		186.2	AAGATCGA
37		218.2	AAGCATTA
38		286.2	AAGCCGGC
39		286.2	AAGCGCCG

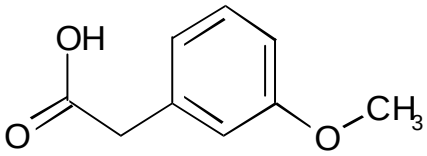
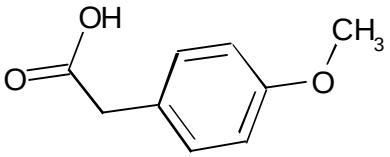
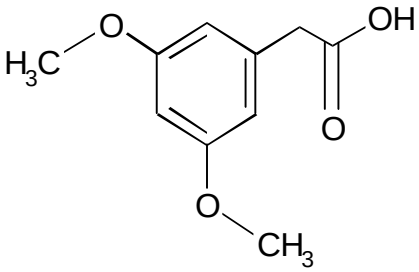
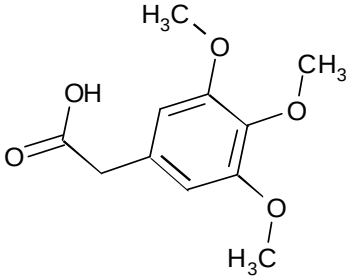
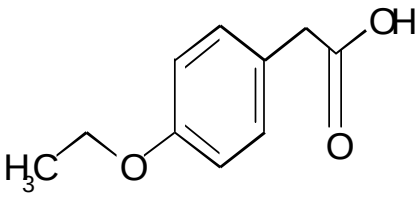
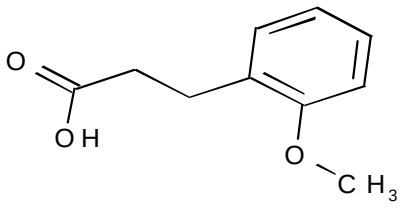
40		170.6	AAGCTAAT
41		212.6	AAGGAAGG
42		200.6	AAGGCCTT
43		303.1	AAGGGGAA
44		357.8	AAGGTTCC

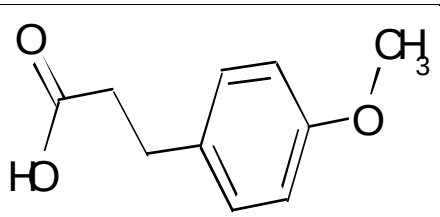
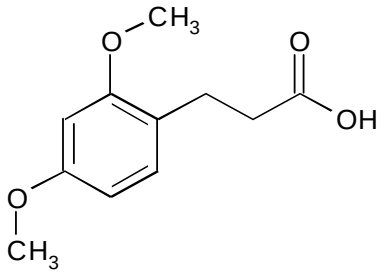
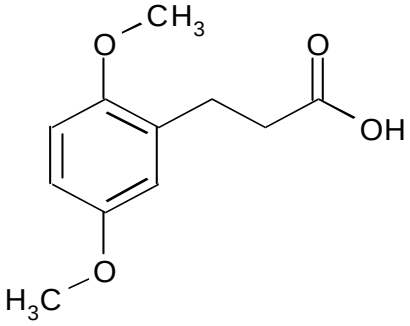
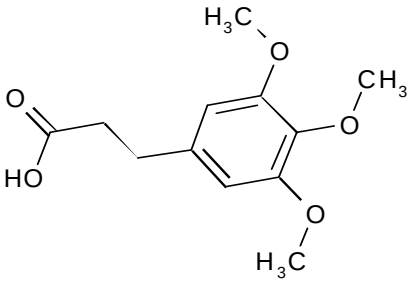
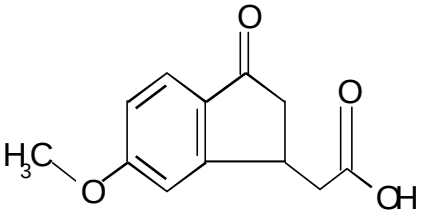
45		215.0	AAGTACAC
46		215.0	AAGTCACA
47		215.0	AAGTGTGT
48		229.1	AAGTTGTG
49		231.0	AATAATGC
50		262.0	AATACGTA

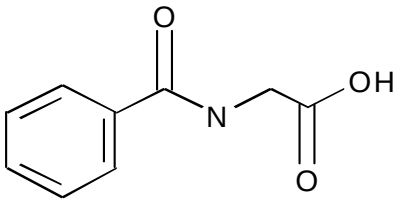
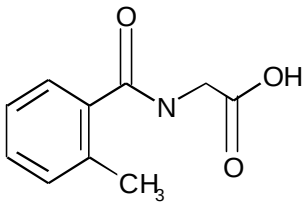
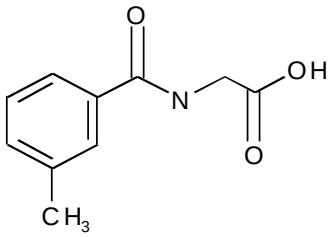
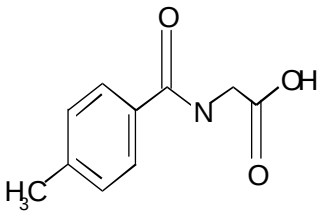
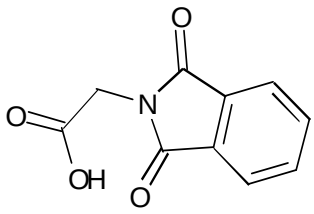
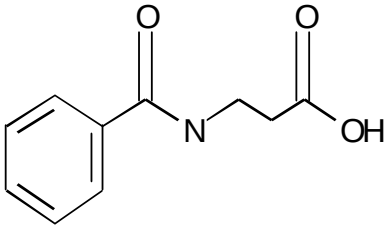
51		290.1	AATAGCAT
52		278.0	AATATACG
53		305.1	AATCAGAG
54		141.1	AATCCTCT
55		128.1	AATCGAGA
56		164.2	AATCTCTC

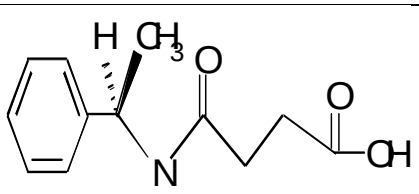
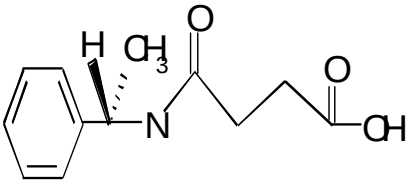
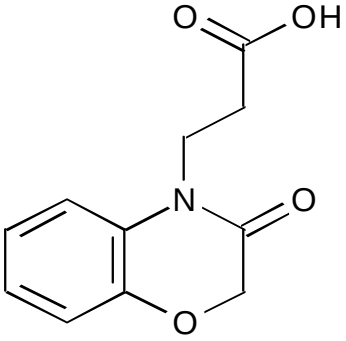
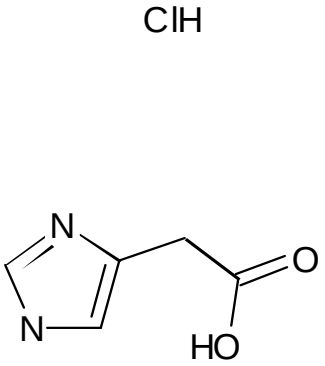
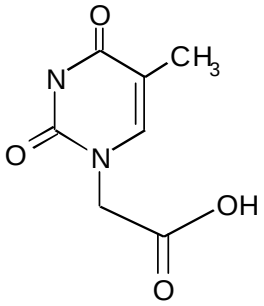
57		164.2	AATGACCA
58		164.2	AATGCAAC
59		178.2	AATGGTTG
60		192.2	AATGTGGT
61		192.2	AATTAATT

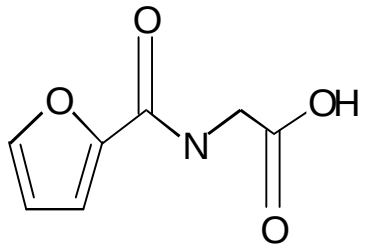
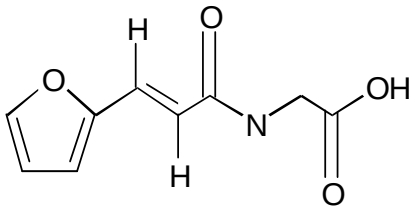
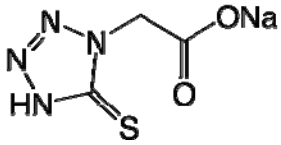
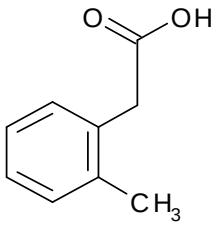
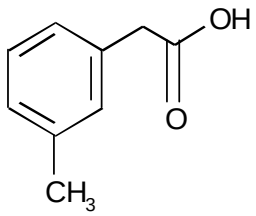
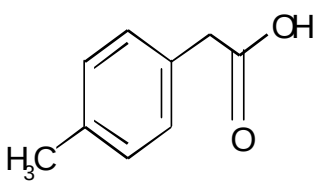
62		152.2	AATTCCGG
63		166.2	AATTGGCC
64		292.4	AATTTTAA
65		166.2	CCAAAACC
66		166.2	CCAACCAA

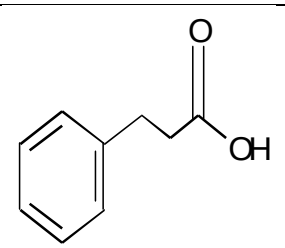
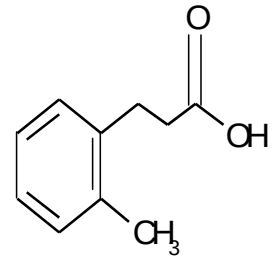
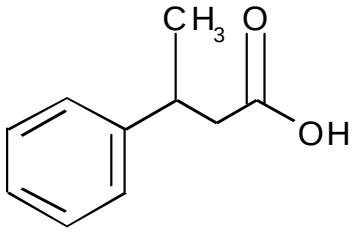
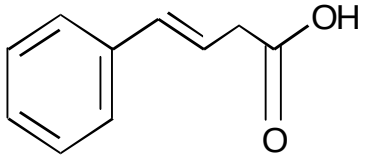
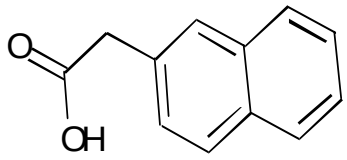
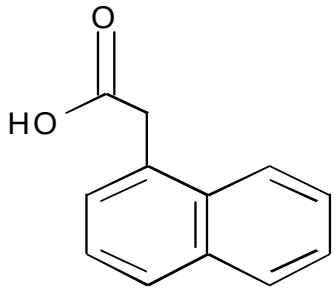
67		166.2	CCAAGGTT
68		166.2	CCAATTGG
69		196.2	CCACACTG
70		226.2	CCACCAGT
71		180.2	CCACGTCA
72		180.2	CCACTGAC

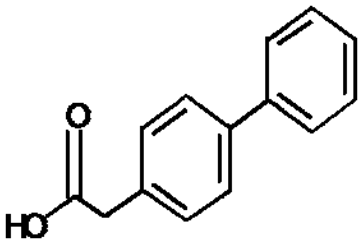
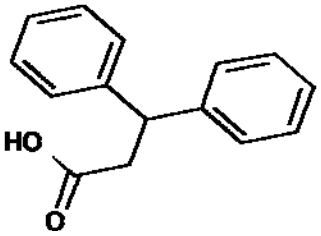
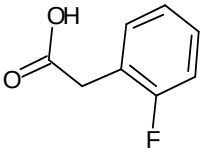
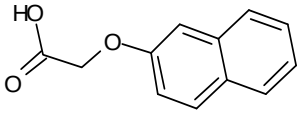
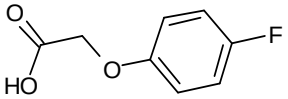
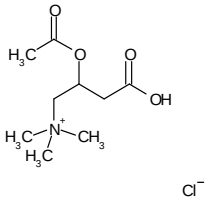
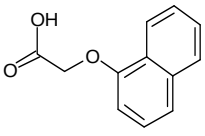
73		180.2	CCAGAGGA
74		210.2	CCAGCTTC
75		210.2	CCAGGAAG
76		240.3	CCAGTCCT
77		220.2	CCATATAT

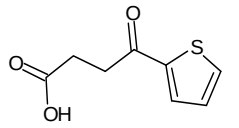
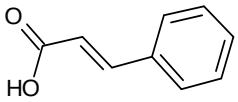
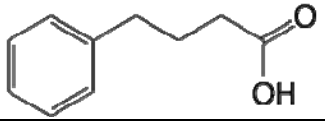
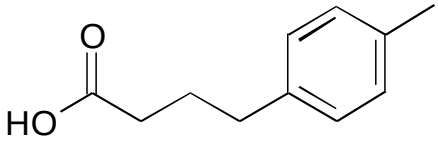
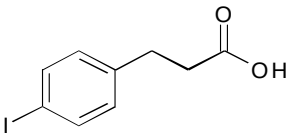
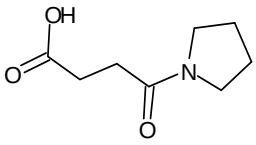
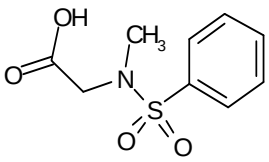
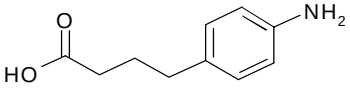
78		179.2	CCATCGCG
79		193.2	CCATGCGC
80		193.2	CCATTATA
81		193.2	CCCAACGT
82		205.2	CCCACATG
83		193.2	CCCAGTAC

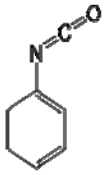
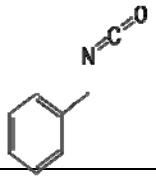
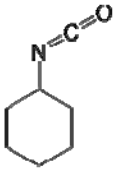
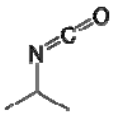
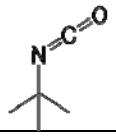
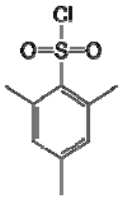
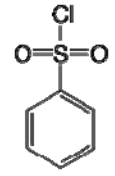
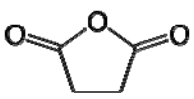
84		221.3	CCCATGCA
85		221.3	CCCCAAAA
86		221.2	TCACGAGC
87		162.6	CCCCGGGG
88		184.2	CCCCTTTT

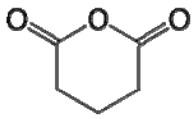
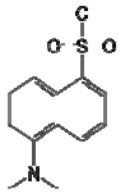
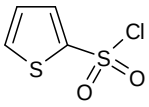
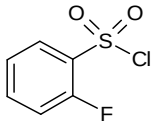
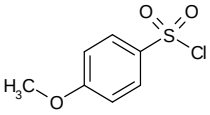
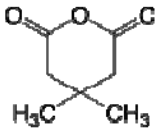
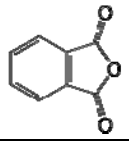
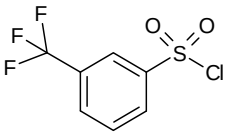
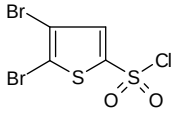
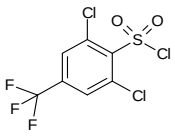
89		169.1	CCCGATCG
90		195.2	CCCGCGAT
91		184.2	CCCGGCTA
92		150.2	CCCGTAGC
93		150.2	CCCTAGTC
94		150.2	CCCTCTGA

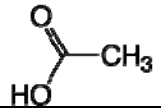
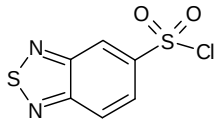
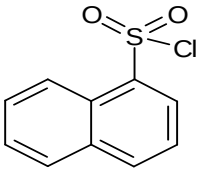
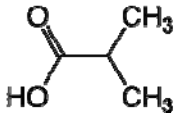
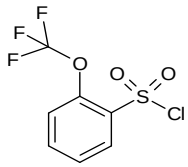
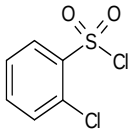
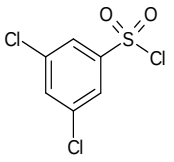
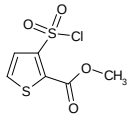
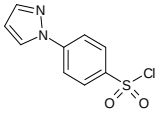
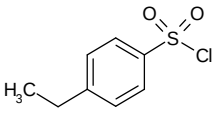
95		150.2	CCCTGACT
96		164.2	CCCTTCAG
97		164.2	CCGAAGAG
98		162.2	CCGACTCT
99		186.2	CCGAGAGA
100		186.2	CCGATCTC

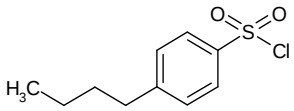
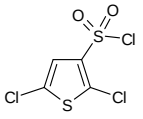
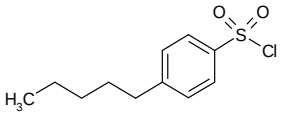
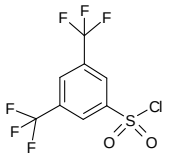
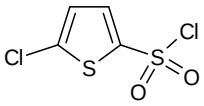
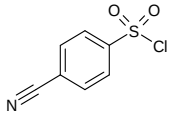
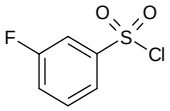
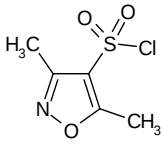
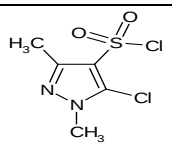
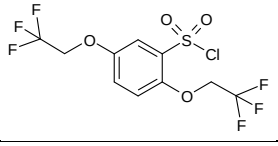
101		212.3	CCGCATGC
102		226.3	CCGCCGTA
103		154.1	CCGCGCAT
104		202.2	CCGCTACG
105		170.1	CCGGAATT
106		204.2	CCGGCCGG
107		202.2	CCGGGGCC

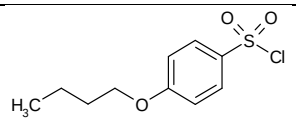
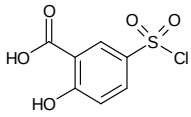
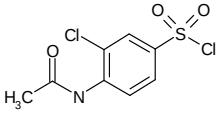
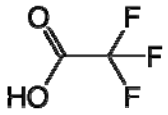
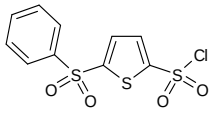
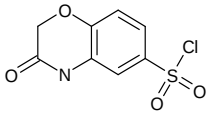
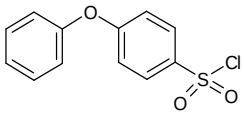
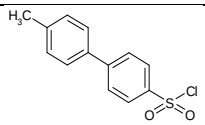
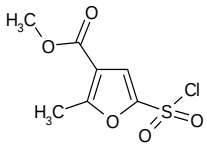
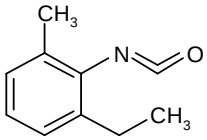
108		184.2	CCGGTTAA
109		148.2	CCGTACCA
110		164.2	CCGTCAAC
111		178.2	CCGTGTTG
112		276.1	CCGTTGGT
113		171.2	CCTAATTA
114		229.3	CCTACGGC
115		179.2	CCTAGCCG

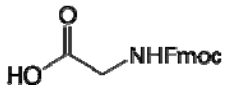
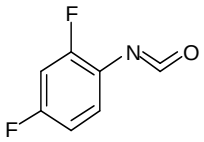
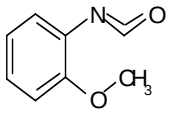
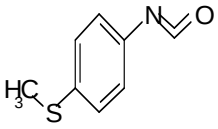
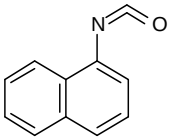
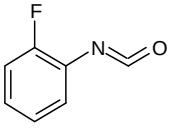
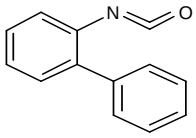
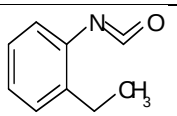
116		119.1	CCTATAAT
117		133.1	CCTCAGCT
118		125.2	CCTCGATC
119		85.1	CCTCTCGA
120		99.1	CCTGACAC
121		218.7	CCTGCACA
122		176.6	CCTGGTGT
123b		100.1	CCTGTGTG

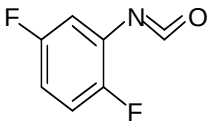
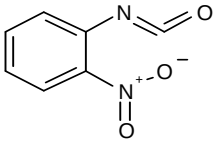
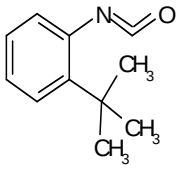
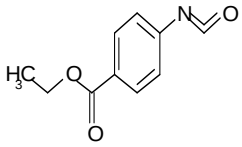
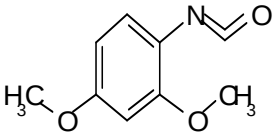
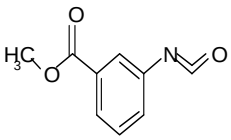
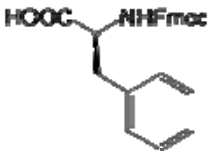
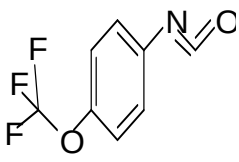
124b		114.1	CCTTCCTT
125		269.7	CCTTGGAA
126		182.7	CCTTTTCC
127		194.6	GGAAAAGG
128		206.6	GGAACCTT
129b		142.2	GGAAGGAA
130b		148,1	GGACACAC
131		244.6	GGACCACA
132		340.4	GGACGTGT
133		313.5	GGACTGTG

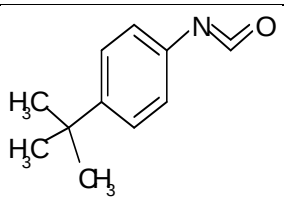
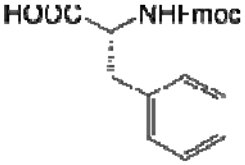
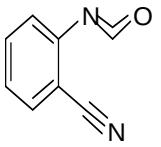
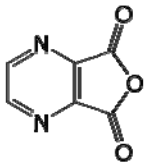
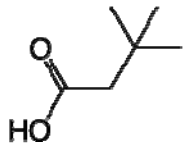
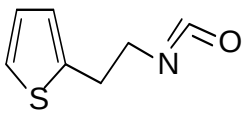
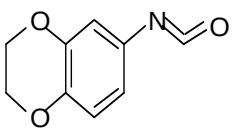
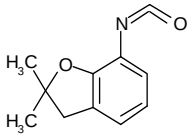
134b		60.1	GGAGAGCT
135		234.7	GGAGCTAG
136		226.7	GGAGGATC
137b		88.1	GGAGTCGA
138		260.6	GGATATTA
139		211.1	GGATCGGC
140		245.5	GGATGCCG
141		240.7	GGATTAAT
142		242.7	GGCAACCA
143		204.7	GGCACAAC

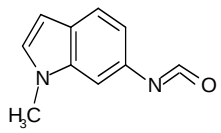
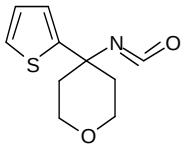
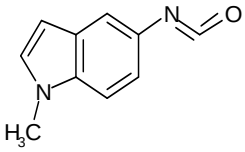
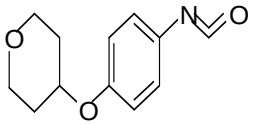
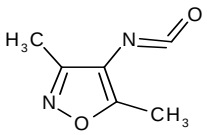
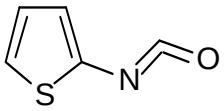
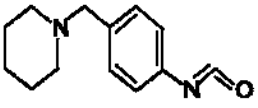
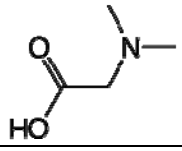
144		232.7	GGCAGTTG
145		251.5	GGCATGGT
146		246.8	GGCCAATT
147		312.6	GGCCCCGG
148		217.1	GGCCGGCC
149		201.6	GGCGATGC
150		194.6	GGCGCGTA
151		195.6	GGCGGCAT
152		229.1	GGCGTACG
153		372.7	GGCTAGAG

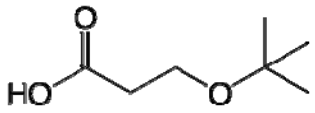
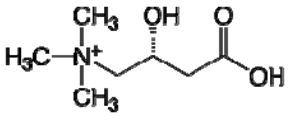
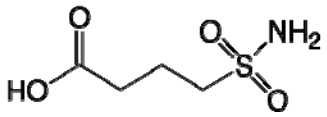
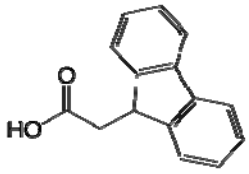
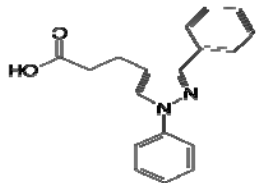
154		248.7	GGCTCTCT
155		236.6	GGCTGAGA
156		268.1	GGCTTCTC
157b		114.0	GGGAAGTC
158		322.8	GGGACTGA
159		247.7	GGGAGACT
160		268.7	GGGATCAG
161		266.7	GGGCATCG
162		238.6	GGGCCGAT
163		161.2	GGGCGCTA

164b		297.3	GGGCTAGC
165		155.1	GGGGAAAA
166		149.1	GGGGCCCC
167		165.2	GCGGCCGC
168		169.2	GGGGTTTT
169		137.1	GGGTACGT
170		195.2	GGGTCATG
171		147.2	GGGTGTAC

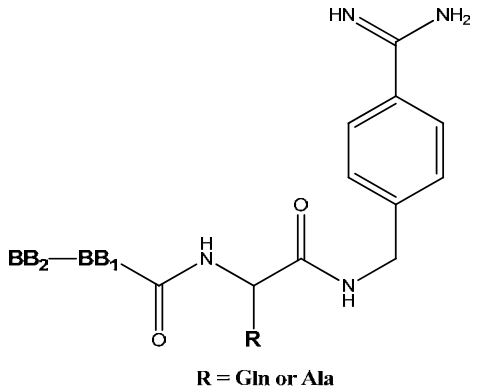
172		155.1	GGGTTGCA
173		164.1	GGTAATAT
174		175.2	GGTACGCG
175		191.2	GGTAGCGC
176		179.2	GGTATATA
177		177.2	GGTCAGGA
178b			GGTCCTTC
179		203.1	GGTCGAAG

180		175.2	GGTCTCCT
181b			GGTGACTG
182		144.1	GGTGCAGT
183b		150.1	GGTGGTCA
184b		116.2	GGTGTGAC
185		153.2	GGTTAACC
186		177.2	GGTTCCAA
187		189.2	GGTTGGTT

188		172.2	GGTTTTGG
189		209.3	TTAAAATT
190		172.2	TTAACCGG
191		219.2	TTAATTAA
192		138.1	TTACACCA
193		125.2	TTACCAAC
194		216.3	TTACGTTG
195		103.1	TTACTGGT

196		146.2	TTAGAGAG
197		161.2	TTAGCTCT
198		167.2	TTAGGAGA
199		224.3	TTAGTCTC
200		292.3	TTATATGC

Supplementary Table 3: Structures and ESI-MS analysis of the 21 synthesized trypsin inhibitors.



BB_2-BB_1-AA-(4-carbamimidoylbenzyl)

Structure ($AA_BB_1_BB_2$)	Formula	Calculated Mass	Measured $[M+H^+]$
Gln_22_81	C32H38N8O7S	678.26	679.08
Ala_22_99	C32H34N6O5S	614.23	615.3
Gln_22_199	C37H39N7O6S	709.27	710.06
Ala_21_116	C34H36N6O3	576.28	577.02
Gln_22_104	C34H37N7O7S	687.25	688.04
Gln_22_99	C34H37N7O6S	671.25	672.38
Ala_22_104	C32H34N6O6S	630.23	631.01
Gln_21_104	C41H42N6O5	698.32	699.15
Gln_38_32	C24H30N6O4S	498.2	498.88
Gln_21_116	C36H39N7O4	633.31	634.09
Gln_21_117	C37H41N7O4	647.32	648.08
Gln_04_136	C32H34N6O6S	630.23	630.98
Gln_21_187	C40H45N7O5	703.35	704.12
Gln_24_116	C28H37N7O4	535.29	536.03
Gln_21_199	C44H44N6O4	720.34	721.14
Gln_21_93	C38H42N6O4	646.33	647.22
Gln_24_174	C32H45N7O4	591.35	592.12
Gln_21_70	C40H46N6O7	722.34	723.18
Gln_23_116	C30H34IN7O4	683.17	683.91
Gln_27_70	C33H40N6O7	632.3	633.03
Gln_08_70	C33H40N6O7	632.3	633.06

Conjugation of Synthetic *N*-Acetyl-Lactosamine to Azide-Containing Proteins Using the Staudinger Ligation

Ravi S. Loka, Christopher M. Sadek, Nikolas A. Romaniuk, and Christopher W. Cairo*

Alberta Ingenuity Centre for Carbohydrate Science, Department of Chemistry, University of Alberta, Edmonton, Alberta T6G 2G2. Received April 28, 2010; Revised Manuscript Received July 1, 2010

Generation of defined glycoconjugates is necessary for the study of glycoprotein function, as well as the development of therapeutics. The biosynthesis of glycoproteins produces multiple glycoforms, proteins which differ only in the structure of the attached glycan. This inherent heterogeneity complicates the study of isolated glycans and, in particular, could obscure the role of individual glycan epitopes in biological function. We present a general strategy based on the Staudinger ligation to introduce specific glycan epitopes onto azide-containing proteins. The use of a phosphane-based Staudinger reagent allows for extremely mild reaction conditions which can be applied to aqueous proteins or cells. We demonstrate that multiple carbohydrate epitopes can be incorporated onto a protein backbone, and that the resulting glycans are competent for recognition by lectins. We propose that this general strategy will allow for testing the role of specific glycan epitopes in cellular and biochemical assays and increasing the stability of protein conjugates.

INTRODUCTION

Post-translational modification can have a dramatic influence on the function and properties of proteins (*1*). The most prevalent post-translational modification found in mammalian cells is glycosylation, whether through O- or N-linkages. Mammalian glycans are known to affect the function and recognition of proteins with roles in cellular adhesion, antigen recognition, and development (*2*). A common difficulty in the study of glycobiology is the heterogeneous nature of glycan structures. Glycoproteins isolated from natural sources are typically a mixture of glycoforms—proteins that differ only in their glycan composition. The presence of glycoforms complicates the interpretation of results from these samples. Therefore, general strategies to produce synthetic glycoconjugates with uniform glycosylation continue to be of interest.

The generation of defined glycoconjugates is critical for enabling the study of glycan function and the development of therapeutics. A variety of approaches have been employed for forming protein glycoconjugates, including amine-cross-linking, native chemical ligation, solid-phase peptide synthesis, unnatural amino acid incorporation, chemoenzymatic synthesis, and chemoselective ligation (*3*–*5*). Chemoselective ligation of glycans presents an appealing approach to the bioconjugate chemist, allowing for the combination of a biologically isolated protein with a synthetic glycan (*3*, *6*, *7*). Strategies which employ chemoselective ligation, therefore, allow the incorporation of either a known homogeneous glycan *en bloc* or the introduction of specific glycan epitopes within an existing glycan. Chemoselective modifications of glycoproteins have been demonstrated using purified glycoproteins, as well as glycoproteins in the membrane of live cells and animals (*7*–*10*).

The ability to modify glycoproteins found within the glycocalyx of living cells presents the opportunity to identify the specific roles of glycan epitopes. Chemoselective modification of cell-surface glycans, referred to as glycoform remodeling, has been used to target specific cells (*11*) and to modify the function of glycoproteins (*12*). Intriguingly, modifications of cell-surface glycans have been used to alter biological responses, inducing immune-targeting and modifying cellular adhesion (*13*, *14*). These findings suggest that chemoselective strategies can form the basis of determining the roles of specific changes in glycosylation within complex biological systems. However, the introduction of complex glycan epitopes onto a protein backbone can be challenging, and chemical methods for the synthesis of glycoproteins continue to be an active area of research (*15*–*17*).

We chose to employ a popular chemoselective strategy, the Staudinger ligation, which forms a covalent linkage between an azide and a phosphane containing an intramolecular electrophilic trap (*8*). The azide component may be introduced semisynthetically (*18*) or through the metabolic incorporation of azide-containing biosynthetic precursors (*7*, *19*). The Staudinger ligation has proven to be a robust labeling chemistry, although alternative reactions that exploit the azide functional group could also be used (*20*). Here, we describe the generation of a series of mono- and disaccharide Staudinger ligation reagents that can be used to modify azide-containing proteins. We develop an efficient route to reagents able to introduce galactose (Gal), lactose (Lac, Gal-β(1,4)-Glc), and *N*-acetyl-lactosamine (LacNAc, Gal-β(1,4)-GlcNAc) glycans. We chose to target LacNAc epitopes, as this unit is part of type 2 lactosamine repeats of N- and O-linked glycans and a component of the Lewis *x* and *y* epitopes (*21*). The resulting glycoconjugates demonstrate that the reaction is efficient and can be used to study the role of specific carbohydrate epitopes within glycoproteins.

EXPERIMENTAL PROCEDURES

General Experimental Methods. Dry solvents (CH_2Cl_2, MeOH, CH_3CN, DMF) were purchased from Sigma Aldrich in capped DriSolv bottles and used without purification and stored under argon. Toluene and pyridine were dried on molecular sieves and stored under desiccated atmosphere. Reactions were conducted under a stream of argon at ambient temperature, unless otherwise noted, and monitored by TLC on silica gel G-25 UV254 (0.25 mm). Developed TLC plates were visualized under UV lamp and charred by heating plates that were dipped in cerium molybdate stain or phosphomolybdic acid stain. NMR

* Corresponding author. Tel.: 780 492 0377; fax: 780 492 8231; e-mail: ccairo@ualberta.ca.

10.1021/bc100209r © 2010 American Chemical Society
Published on Web 09/16/2010

experiments were conducted on Varian 300, 400, or 500 MHz instruments. Chemical shifts are reported relative to the deuterated solvent peak and are in parts per million (ppm). ^{1}H NMR and ^{13}C peak assignments were made on the basis of 2D-NMR such as COSY and HSQC experiments. ESI-MS spectra were carried out on samples suspended in solvent with added NaCl. β-Lactoglobulin was obtained as a mixture of bovine A- and B-isoforms (Sigma-Aldrich) and used without further purification (*22*).

*9H-Fluoren-9-ylmethyl {2-[2-O-(2,3,4,6-Tetra-O-benzoyl-β-D-galactopyranosyl)-2-hydroxyethoxy]ethyl}carbamate (**3**).* Compound **2** (977 mg, 1.32 mmol) was dissolved in 15 mL of DCM and stirred overnight at room temperature with TMSOTf (2.34 mL, 1% in DCM, 0.13 mmol) and 9*H*-fluoren-9-yl[2-(2-hydroxy ethoxy)-ethyl]carbamate **4** (654 mg, 1.98 mmol). The solvent was removed and the product was purified by column chromatography with EtOAc/hexane (1:2) to yield 957 mg (80.1%) of **3** as a white solid. ^{1}H NMR (500 MHz, $CDCl_3$) δ 8.09 (d, J = 7.5 Hz, 2H), 8.05−8.01 (m, 2H), 7.98 (dd, J = 8.2, 1.1 Hz, 2H), 7.80 (dd, J = 8.3, 1.2 Hz, 2H), 7.77 (d, J = 7.6 Hz, 2H), 7.68−7.53 (m, 4H), 7.52−7.34 (m, 10H), 7.30 (t, J = 7.4 Hz, 2H), 7.27−7.21 (m, 2H), 6.01 (d, J = 3.4 Hz, 1H), 5.83 (dd, J = 10.4, 7.9 Hz, 1H), 5.65 (dd, J = 10.4, 3.5 Hz, 1H), 5.16 (s, 1H), 4.90 (d, J = 7.9 Hz, 1H), 4.70 (dd, J = 11.3, 6.5 Hz, 1H), 4.52−4.36 (m, 3H), 4.32 (t, J = 6.4 Hz, 1H), 4.23 (t, J = 6.9 Hz, 1H), 4.06 (dt, J = 11.1, 4.1 Hz, 1H), 3.87−3.67 (m, 1H), 3.61 (t, J = 4.1 Hz, 2H), 3.38 (t, J = 4.7 Hz, 2H), 3.29−2.96 (m, 2H); ^{13}C NMR (125 MHz, $CDCl_3$) δ 166.1, 165.6, 165.3, 156.4, 144.0, 141.3, 133.6, 133.4, 133.3, 133.29, 130.0, 129.8, 129.78, 129.7, 129.4, 129.38, 129.0, 128.8, 128.6, 128.5, 128.45, 128.3, 127.7, 127.1, 125.1, 119.9, 101.8, 71.6, 71.4, 70.2, 70.1, 69.8, 69.4, 68.1, 66.6, 62.0, 47.3, 40.8; ESIMS calculated for $C_{53}H_{47}NO_{13}Na$ $[M+Na]^+$ 928.2940, found: 928.2935.

*9H-Fluoren-9-ylmethyl {2-[2-O-(2,3,4,6-Tetra-O-benzoyl-β-D-galactopyranosyl-(1→4)-2,3,6-tri-O-benzoyl-β-D-glucopyranosyl)-2-hydroxyethoxy]ethyl}carbamate (**7**).* Compound **6** (403 mg, 0.33 mmol) was dissolved in 10 mL of DCM and stirred overnight at room temperature with TMSOTf (65 μL, 1% in DCM) and 9*H*-fluoren-9-yl[2-(2-hydroxyethoxy)ethyl]carbamate **4** (131 mg, 0.4 mmol). The solvent was removed, and the resulting solid was purified by column chromatography with EtOAc/hexane (1:1) to yield 325 mg (70.3%) of **7** as a white solid. ^{1}H NMR (500 MHz, $CDCl_3$) δ 7.99 (dt, J = 11.8, 7.0 Hz, 11H), 7.91 (d, J = 7.3 Hz, 2H), 7.83−7.72 (m, 4H), 7.72−7.53 (m, 6H), 7.48 (t, J = 7.7 Hz, 6H), 7.45−7.27 (m, 15H), 7.22 (t, J = 7.8 Hz, 2H), 7.14 (t, J = 7.7 Hz, 2H), 5.83 (t, J = 9.5 Hz, 1H), 5.74 (m, 2H), 5.50 (dd, J = 9.6, 8.1 Hz, 1H), 5.39 (dd, J = 10.3, 3.3 Hz, 1H), 5.19 (s, 1H), 4.86 (d, J = 7.8 Hz, 1H), 4.76 (d, J = 7.8 Hz, 1H), 4.62 (d, J = 11.4 Hz, 1H), 4.53 (dd, J = 12.1, 4.4 Hz, 1H), 4.47−4.31 (m, 2H), 4.31−4.13 (m, 2H), 4.01−3.78 (m, 3H), 3.78−3.58 (m, 3H), 3.51 (s, 2H), 3.34 (t, J = 4.6 Hz, 2H), 3.12 (t, J = 5.0 Hz, 2H); ^{13}C NMR (125 MHz, $CDCl_3$) δ 165.8, 165.5, 165.4, 165.38, 165.2, 164.8, 156.4, 144.0, 141.3, 133.5, 133.4, 133.3, 133.27, 133.2, 130.0, 129.8, 129.7, 129.6, 129.5, 129.4, 129.35, 128.9, 128.7, 128.6, 128.58, 128.5, 128.4, 128.3, 127.7, 127.1, 125.2, 125.1, 120.0, 101.3, 101.1, 76.1, 73.2, 72.8, 71.83, 71.8, 71.4, 70.2, 69.9, 69.88, 69.4, 67.5, 66.6, 62.4, 61.1, 47.3, 40.8; ESIMS calculated for $C_{80}H_{69}NO_{21}Na$ $[M+Na]^+$ 1402.4254, found: 1402.4256.

*9H-Fluoren-9-ylmethyl {2-[2-O-(2,3,4,6-Tetra-O-acetyl-β-D-galactopyranosyl-(1→4)-2-acetamido-3,6-di-O-acetyl-2-deoxy-β-D-glucopyranosyl)-2-hydroxyethoxy]ethyl}carbamate (**10**).* Oxazoline **9** (355 mg, 0.58 mmol) and 9*H*-fluoren-9-yl[2-(2-hydroxyethoxy)ethyl]carbamate **4** (569 mg, 1.74 mmol) were stirred with a catalytic amount of camphor sulfonic acid (CSA) (12 mg) in 12 mL of 1,2-dichloroethane under refluxing conditions (90 °C) for 2.3 h. The reaction mixture was cooled and poured over ice water and then washed successively with aqueous saturated $NaHCO_3$, then water, and then dried over anhydrous Na_2SO_4. The solvent was evaporated under vacuum, and the residue was purified by column chromatography using EtOAc to yield 427 mg (78.0%) of **10** as a yellow solid. ^{1}H NMR (500 MHz, $CDCl_3$) δ 7.77 (d, J = 7.5 Hz, 2H), 7.63 (d, J = 7.3 Hz, 2H), 7.40 (t, J = 7.5 Hz, 2H), 7.31 (tt, J = 7.5, 1.2 Hz, 2H), 5.89 (d, J = 9.0 Hz, 1H), 5.60 (s, 1H), 5.34 (d, J = 2.7 Hz, 1H), 5.11 (dd, J = 10.5, 7.9 Hz, 2H), 4.97 (dd, J = 10.5, 3.5 Hz, 1H), 4.55−4.45 (m, 3H), 4.43 (d, J = 6.9 Hz, 2H), 4.24 (t, J = 6.8 Hz, 1H), 4.13 (dd, J = 11.8, 5.4 Hz, 1H), 4.11−4.00 (m, 3H), 3.94−3.81 (m, 2H), 3.77 (t, J = 8.3 Hz, 1H), 3.69−3.56 (m, 4H), 3.53 (s, 2H), 3.44−3.23 (m, 2H), 2.14 (s, 3H), 2.10 (s, 3H), 2.05 (s, 6H), 2.03 (s, 3H), 1.97 (s, 3H), 1.94 (s, 3H); ^{13}C NMR (126 MHz, $CDCl_3$) δ 170.4, 170.3, 170.1, 170.0, 169.4, 156.8, 144.0, 141.3, 127.7, 127.1, 125.1, 120.0, 100.9, 75.6, 72.7, 72.0, 70.8, 70.7, 70.3, 70.2, 69.1, 68.5, 66.6, 66.57, 62.5, 60.8, 53.0, 50.8, 47.3, 41.1, 23.2, 20.87, 20.8, 20.7, 20.62, 20.6, 20.5; ESIMS calculated for $C_{45}H_{56}N_2O_{20}Na$ $[M+Na]^+$ 967.3319, found: 967.3307.

*Methyl 2-(Diphenylphosphino)-4-[2(2-O-β-D-galactopyranosyl-2-hydroxyethoxy)ethylcarbamoyl]benzoate (**12**).* Deprotection of compound **3** (453 mg, 0.5 mmol) was achieved under Zémplen conditions by stirring in a solution of MeOH (8 mL) with 1% NaOMe/MeOH (5.6 mL) for 4 h. The solvent was removed and a solution of DCM/H_2O (20 mL, 1:1) was added. The water layer was washed with DCM (2 × 10 mL) and lyophilized to yield 111 mg of white solid. The solid (50 mg, 0.19 mmol) was then stirred with succinimidyl-3-diphenylphosphino-4-methoxy-carbonylbenzoate **11** (*23*), (106 mg, 0.23 mmol) and two drops of triethylamine in 5 mL of DMF for 2.3 h at room temperature. The DMF was removed under vacuum, and the crude product was purified by column chromatography (Iatrobeads, Mitsubishi Kagaku Iatron, Inc.) with EtOAc/MeOH (8:2) to yield 76 mg (65%) of **12** as a yellow solid containing a small amount of the corresponding phosphine oxide. ^{1}H NMR (500 MHz, CD_3OD) δ 8.04 (dd, J = 8.0, 3.6 Hz, 1H), 7.81 (dd, J = 8.0, 1.7 Hz, 1H), 7.44 (dd, J = 3.9, 1.7 Hz, 1H), 7.39−7.31 (m, 6H), 7.26 (m, 4H), 4.24 (d, J = 7.6 Hz, 1H), 3.98 (dt, J = 10.8, 4.2 Hz, 1H), 3.81 (t, J = 3.2 Hz, 1H), 3.78−3.68 (m, 4H), 3.67 (s, 3H), 3.66−3.61 (m, 3H), 3.59 (t, J = 5.5 Hz, 2H), 3.54−3.40 (m, 7H); phosphine oxide δ 8.13 (dt, J = 8.0, 1.5 Hz, 0.2H), 7.97 (m, 0.8H), 7.70−7.59 (m, 1.3H), 7.58−7.50 (m, 0.9H); ^{13}C NMR (125 MHz, CD_3OD) δ 169.5, 168.4 (d, J_{C-P} = 2.5 Hz), 142.3 (d, J_{C-P} = 27.5 Hz), 138.9, 138.6 (d, J_{C-P} = 11.3 Hz), 138.3 (d, J_{C-P} = 20.0 Hz), 135.1 (d, J_{C-P} = 21.3 Hz), 134.5, 131.6 (d, J_{C-P} = 2.5 Hz), 130.1, 129.7 (d, J_{C-P} = 7.5 Hz), 127.9, 105.1, 76.8, 75.0, 72.6, 71.3, 70.4, 70.3, 69.8, 62.6, 52.6, 41.0; phosphine oxide δ 138.3 (d, J_{C-P} = 11.3 Hz), 133.6 (d, J_{C-P} = 3.8 Hz), 133.5 (d, J_{C-P} = 7.5 Hz), 132.9 (d, J_{C-P} = 10.0 Hz), 132.7, 132.2, 131.8 (d, J_{C-P} = 7.5 Hz), 129.9 (d, J_{C-P} = 12.5 Hz), 52.9; ^{31}P NMR (202 MHz, CD_3OD) δ 35.0 (s, 0.22P), −2.8 (s, 1.00P); ESIMS calculated for $C_{31}H_{36}PNO_{10}Na$ $[M+Na]^+$ 636.1969, found: 636.1951.

*Methyl 2-(diphenylphosphino)-4-{2[2-O-β-D-galactopyranosyl-(1→4)-β-D-glucopyranosyl-2-hydroxyethoxy]ethylcarbamoyl]}-benzoate (**13**).* Deprotection of compound **7** (325 mg, 0.24 mmol) was achieved under Zémplen conditions by stirring in a solution of MeOH (6 mL) with 1% NaOMe/MeOH (6 mL) overnight. The solvent was removed and a solution of DCM/H_2O (10 mL, 1:1) was added. The water layer was washed with DCM (2 × 5 mL) and the aqueous layer was lyophilized to yield 85 mg of a white solid. A portion of the solid (32 mg, 0.08 mmol) was stirred with succinimidyl-3-diphenylphosphino-4-methoxy-carbonylbenzoate **11** (42 mg, 0.09 mmol), and two drops of triethylamine for 3 h at room temperature in DMF (5 mL). The

solvent was removed under vacuum, and the product was purified by column chromatography (Iatrobeads) with EtOAc/MeOH (8:2) to yield 36 mg (62%) of **13** as a yellow solid containing a small amount of the corresponding phosphine oxide. ^{1}H NMR (500 MHz, CD_3OD) δ 8.04 (dd, J = 8.0, 3.6 Hz, 1H), 7.80 (dd, J = 8.0, 1.7 Hz, 1H), 7.43 (dd, J = 3.9, 1.7 Hz, 1H), 7.40−7.30 (m, 6H), 7.26 (m,4H), 4.35 (d, J = 7.6 Hz, 1H), 4.32 (d, J = 7.8 Hz, 1H), 3.96 (ddd, J = 22.3, 13.3, 8.9 Hz, 1H), 3.88 (dd, J = 12.1, 2.5 Hz, 1H), 3.84−3.75 (m, 4H), 3.74−3.68 (m, 2H), 3.68 (s, 3H), 3.67−3.62 (m, 2H), 3.61−3.57 (m, 3H), 3.56−3.41 (m, 7H), 3.38 (ddd, J = 9.2, 4.2, 2.5 Hz, 1H), 3.26−3.19 (m, 1H); phosphine oxide δ 8.13 (dt, J = 8.0, 1.6 Hz, 0.1H), 7.99 (dd, J = 8.0, 3.7 Hz, 0.1H), 7.95 (dd, J = 13.8, 1.7 Hz, 0.1H), 7.72−7.59 (m, 0.7H), 7.55 (m, 0.4H); ^{13}C NMR (125 MHz, CD_3OD) δ 169.5, 168.4 (d, J_{C-P} = 2.5 Hz), 142.3 (d, J_{C-P} = 27.5 Hz), 138.9, 138.6 (d, J_{C-P} = 10.0 Hz), 138.3 (d, J_{C-P} = 20.0 Hz), 135.1 (d, J_{C-P} = 20.0 Hz), 134.5, 131.6 (d, J_{C-P} = 2.5 Hz), 130.1, 129.7 (d, J_{C-P} = 7.5 Hz), 127.9, 105.1, 104.4, 80.7, 77.1, 76.5, 76.4, 74.9, 74.8, 72.6, 71.2, 70.4, 70.3, 69.9, 62.5, 62.0, 52.6, 41.0; ^{31}P NMR (202 MHz, CD_3OD) δ 35.0 (s, 0.10P), −2.8 (s, 1.00P); ESIMS calculated for $C_{37}H_{46}PNO_{15}Na$ $[M+Na]^+$ 798.2497, found: 798.2489.

*Methyl 2-(Diphenylphosphino)-4-{2[2-O-(β-D-galactopyranosyl-(1→4)-2-acetamido-2-deoxy-β-D-glucopyranosyl)-2-hydroxyethoxy]ethylcarbamoyl]}benzoate (***14***).* Deprotection of compound **10** (183 mg, 0.19 mmol) was achieved under Zémplen conditions by stirring in a solution of MeOH (4 mL) with 1% NaOMe/MeOH (2.3 mL) for 2.3 h. The reaction mixture was neutralized with Amberlite resin 120. The resin was washed with MeOH, stirred with 10 mL of ammonia for 30 min, and filtered. The ammonia was removed by evaporation and dried overnight under vacuum to give 52 mg of a white solid. The solid (36 mg, 0.08 mmol) was dissolved in 5 mL of DMF and stirred with succinimidyl-3-diphenylphosphino-4-methoxy-carbonylbenzoate **11** (106 mg, 0.23 mmol), and two drops of triethylamine for 4 h at room temperature. The solvent was removed under vacuum, and the material was purified by column chromatography (Iatrobeads) with DCM/MeOH (3:1) to yield 43 mg (50%) of **14** as a yellow solid containing a small amount of the corresponding phospine oxide. ^{1}H NMR (500 MHz, CD_3OD) δ 8.05 (dd, J = 8.0, 3.6 Hz, 1H), 7.82 (dd, J = 8.0, 1.7 Hz, 1H), 7.44 (dd, J = 3.9, 1.7 Hz, 1H), 7.39−7.30 (m, 6H), 7.30−7.22 (m, 4H), 4.43 (d, J = 8.4 Hz, 1H), 4.37 (d, J = 7.6 Hz, 1H), 3.96−3.89 (m, 1H), 3.88 (d, J = 2.4 Hz, 1H), 3.85−3.78 (m, 2H), 3.78−3.68 (m, 3H), 3.67 (s, 3H), 3.67−3.44 (m, 13H), 3.43−3.38 (m, 1H), 3.36 (ddd, J = 9.4, 4.4, 2.5 Hz, 1H), 1.92 (s, 3H); phosphine oxide δ 8.15 (dt, J = 8.0, 1.6 Hz, 0.2H), 8.00 (dd, J = 8.0, 3.6 Hz, 0.25H), 7.95 (dd, J = 13.8, 1.7 Hz, 0.25H), 7.68−7.58 (m, 1.4H), 7.54 (m,1H); ^{13}C NMR (125 MHz, CD_3OD) δ 173.5, 169.5, 168.5 (d, J_{C-P} = 2.5 Hz), 142.3 (d, J_{C-P} = 28.8 Hz), 138.9, 138.6 (d, J_{C-P} = 10.0 Hz), 138.26 (d, J_{C-P} = 18.7 Hz), 135.1 (d, J_{C-P} = 20.0 Hz), 134.5, 131.7 (d, J_{C-P} = 2.5 Hz), 130.1, 129.7 (d, J_{C-P} = 6.3 Hz), 127.9, 105.2, 102.8, 81.1, 77.2, 76.6, 74.9, 74.2, 72.6, 71.2, 70.4, 70.3, 70.0, 62.5, 62.0, 56.7, 52.6, 41.0, 23.1; phosphine oxide δ 139.8 (d, J_{C-P} = 7.5 Hz), 138.3 (d, J_{C-P} = 11.3 Hz), 133.6, 132.9 (d, J_{C-P} = 12.5 Hz), 129.9 (d, J_{C-P} = 12.5 Hz), 53.0; ^{31}P NMR (202 MHz, CD_3OD) δ 35.00 (s, 0.21P), −2.80 (s, 1.00P); ESIMS calculated for $C_{39}H_{49}PN_2O_{15}Na$ $[M+Na]^+$ 839.2763, found: 839.2756.

Synthesis of Azidoacetic Acid Labeled β-Lactoglobulin. Protein samples of β-lactoglobulin (5 mg, 0.3 mmol) were dissolved in borate buffer (50 mM, pH 9, 1 mL). A solution of succinimidyl 2-azidoacetate **SI1**, in dioxane, was added (27 mg mL^{-1}, 70 μL, 35 equiv) and was left at room temperature for 1 h after vortexing. The labeled protein was purified using ultracentifugation (10 kDa MW cutoff). The sample was lyophilized and stored at −20 °C.

Staudinger Ligation of Azide-Labeled Protein. Samples of azide-labeled protein (200 μg) were dissolved in 100 μL of buffer (10 mM, ammonium acetate, pH 8.9). Staudinger reagents in DMSO/H_2O (1:15, 1 mg mL^{-1}; 300 μL) were added to the protein solution and allowed to react for 12 h at room temperature. The mixture was lyophilized and dissolved in 100 μL of buffer (10 mM, ammonium acetate, pH 8.9).

LC-MS of Glycoconjugates. The LC-MS experiments were carried out on an Agilent 6220 Accurate-Mass TOF LC/MS system (Agilent Technologies, Santa Clara, California, USA). Samples were injected on a 75 × 0.5 mm Poroshell C8 column with a particle size of 5 μm (Agilent Technologies, Santa Clara, California, USA) with an Opti-pak trap cartridge kit, 5 μL bed, C8 (Optimize Technologies, Oregon City, USA). After loading of the sample, the column was flushed for 3 min at a 0.15 mL min^{-1} flow rate with 95% mobile phase A (0.1% formic acid in water) and 5% mobile phase B (0.1% FA in acetonitrile) in order to effectively remove the salts and reagents. Elution of the protein was performed by gradually increasing the concentration of phase B in the mobile phase to 95% over a period of 11 min. The column was maintained at 70 °C. Protein molecular weight information was generated using the maximum entropy deconvolution algorithm in the Agilent Mass Hunter BioConfirm software.

Lectin Blotting of Glycoconjugates. Labeled glycoprotein samples were separated by SDS-PAGE (5%/15%) and transferred to nitrocellulose. The membrane was blocked for 2 h with CarboFree Blocking Solution (Vector Laboratories) and incubated with biotinylated MAL-I lectin (Vector Laboratories) diluted in blocking solution (1 μg mL^{-1}) for 1 h. The membrane was washed with TTBS (Tris-buffered saline, 0.1% Tween 20) and incubated with streptavidin-HRP (Bio-Rad) in blocking solution for 1 h. The membrane was washed again with TTBS, and positive signals were then detected by enhanced chemiluminescence (Amersham). All incubations after protein transfer were performed at room temperature.

RESULTS AND DISCUSSION

Our conjugation strategy is summarized in Figure 1, and first required the development of suitable phosphane derivatives that could install the target carbohydrates onto a model protein. Although our primary interest is the incorporation of a LacNAc disaccharide, we also intended to make related carbohydrate structures to be used as controls in future experiments, such as a monosaccharide, galactose (Gal), and a disaccharide, lactose (Lac, Gal-β(1,4)-Glc). The target structures consist of a carbohydrate epitope, a linker, and a phosphane group. These reagents can react with any azide-containing biomolecule, such as a chemically or metabolically labeled protein, in an aqueous environment. We chose to introduce the phosphane late in the synthesis to avoid issues with oxidation commonly observed with this moiety (*24*). Therefore, we developed each of the carbohydrate epitopes as an amine that could be reacted with an activated ester of the phosphane under mild conditions. The amine was introduced as part of an ethylene glycol derived linker. This strategy is general and allows for the introduction of alternative amine-containing epitopes as desired.

Synthesis of Carbohydrate Epitopes with a Free Amine. To generate a suitable galactosyl-amine derivative, galactose was protected as the 2,3,4,6-tetrabenzoylated derivative, **1**, by perbenzoylation and selective deprotection of the anomeric position (see Supporting Information; Scheme 1) (*25*). Compound **1** was then converted to the trichloroacetimidate derivative (TCA), **2**, as a mixture of anomers using trichloroacetonitrile

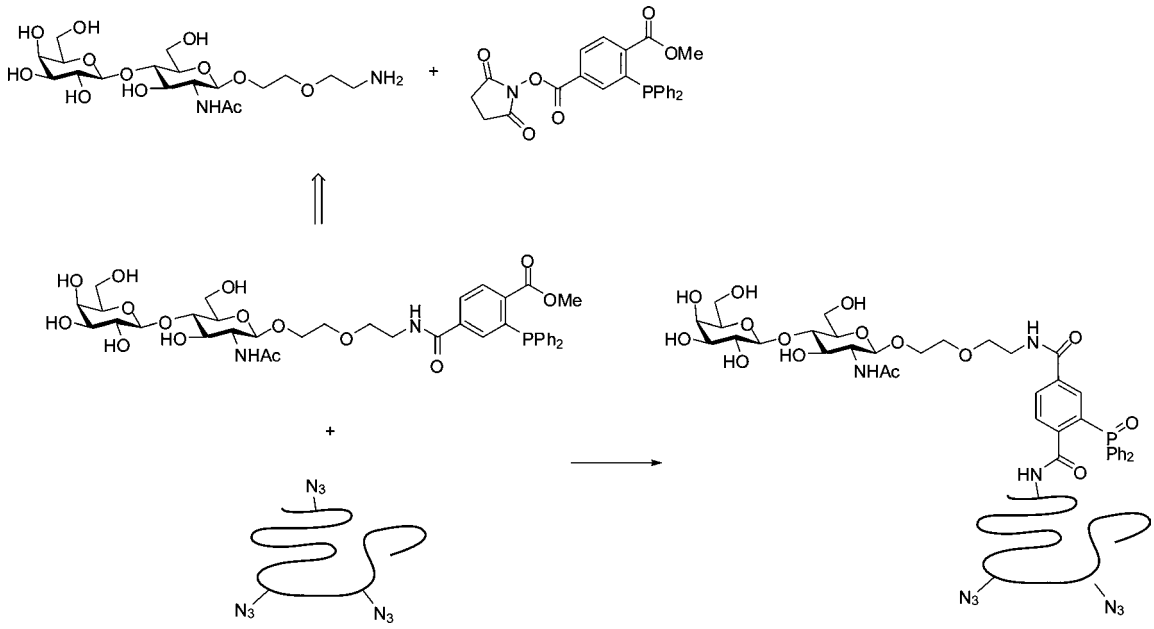
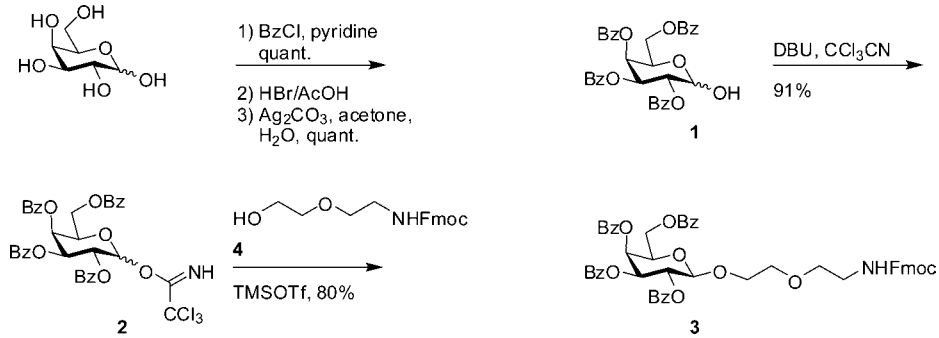
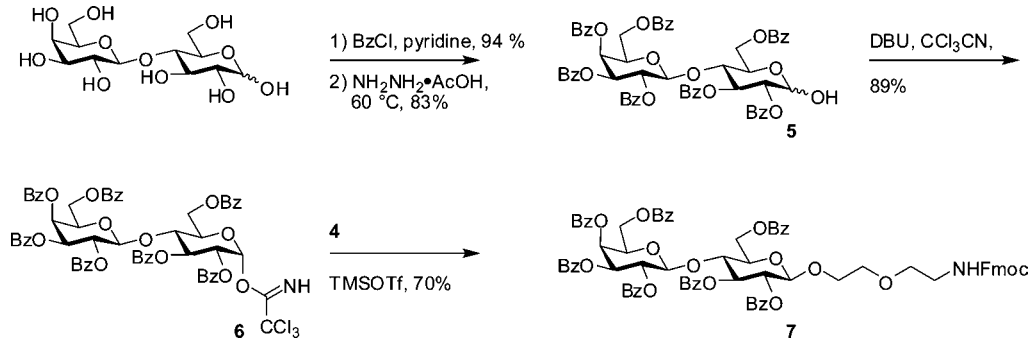


Figure 1. Glycoconjugate strategy. An azide labeled protein, generated semisynthetically or by metabolic incorporation, is reacted with a carbohydrate epitope linked to a phosphane reagent. The Staudinger ligation product is formed under mild conditions compatible with cell culture. The phosphane reagent is generated from a carbohydrate derivative containing a free amine and an NHS-ester phosphane. This strategy allows late incorporation of the phosphane, which can be sensitive to oxidation.

Scheme 1. Synthesis of Protected Galactose



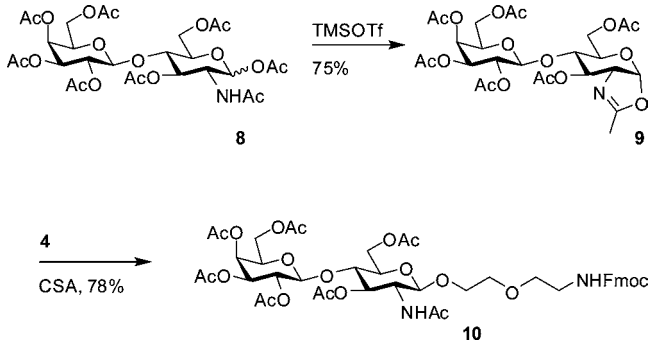
Scheme 2. Synthesis of Protected Lactose



and 1,8-diazabicycloundec-7-ene (DBU) (*25*). Glycosylation of the TCA donor, **2**, by an Fmoc-protected 2-(2-aminoethoxy)-ethanol linker, **4**, in the presence of TMSOTf proceeded in good yield, providing the fully protected compound, **3** (*26*). The lactose-containing amine was generated using a similar sequence of reactions. Perbenzoylated lactose was selectively deprotected at the anomeric position using hydrazine in acetic acid, to give compound **5** in good yield in two steps (see Supporting Information) (*27*). Treatment with DBU and trichloroacetonitrile gave the protected lactosyl-TCA derivative, **6**, as the α-anomer (*26*, *27*). Glycosylation was carried out using the protected linker (2-(2-aminoethoxy)-ethanol) **4** to provide compound **7** (Scheme 2).

The synthesis of LacNAc derivatives can be more challenging, due in part to the expense of the disaccharide as a starting material. A variety of strategies are known for generating LacNAc (*28*), either from cheaper disaccharide glycals (*29*) or from monosaccharides (*30*). We found that the method reported by Wrodnigg and Stutz (*31*, *32*) based on the Heyns rearrangement of lactulose provided excellent overall yields of lac-

Scheme 3. Synthesis of Protected LacNAc



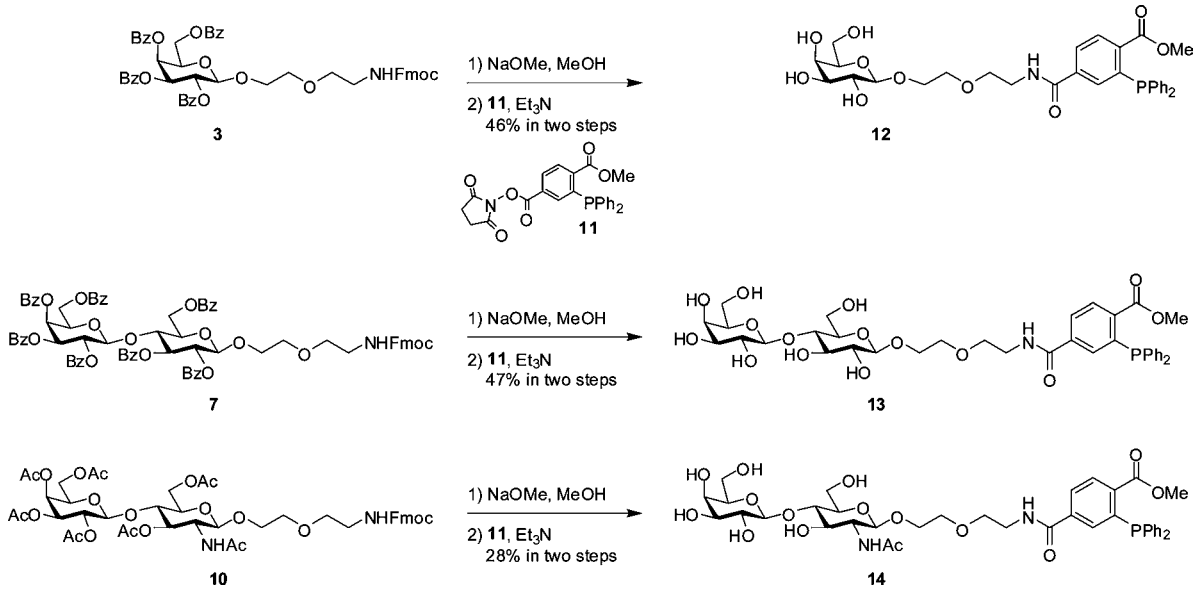
tosamine starting material. We followed the protocol of Stutz et al. for the synthesis of lactosamine as the (1,3-dimethyl-2,4,6 (1*H*,3*H*,5*H*)-trioxopyrimidine-5-ylidene)methyl (DTPM) derivative, which was easily purified by precipitation. Subsequent removal of DTPM (*33*) and acetylation provided compound **8** as a relatively economical starting material (see Supporting Information). The acetyl-protected LacNAc (**8**) was converted to oxazolidine **9** (Scheme 3) (*34*). The oxazolidine donor, **9**, was then modified to incorporate a linker, to provide the fully protected compound **10**. With three carbohydrate epitopes in their protected forms, we proceeded to convert each of **3**, **7**, and **10** to the corresponding phosphane derivatives to be used in generating protein glycoconjugates.

Synthesis of Phosphane Labeling Reagents. To convert each of the protected carbohydrate derivatives to an azide-reactive phosphane, they were first deprotected to unmask the primary amine of the linker. Alkaline deprotection conditions simultaneously removed benzoyl or acetyl and carbamate protecting groups from compounds **3**, **7**, and **10** (*35*). Each of the resulting free amines could then be acylated to generate the desired phosphane targets. Due to sensitivity of the phosphane reagent to oxidation (*24*), we chose to avoid harsh coupling conditions. Instead, the amines were acylated using an *N*-hydroxysuccinimide ester (NHS) derived phosphane **11**. This reagent was first reported by Wang et al., and we prepared the reagent from 2-(diphenylphosphanyl)-terepthalic acid 1-methyl ester reported by Kiick et al. (*10, 23*) This convergent approach provided phosphane compounds **12**, **13**, and **14** in moderate yields from their protected saccharide precursors (Scheme 4). The purity and oxidation state of the resulting phosphane compounds were confirmed using ^{31}P and ^{1}H NMR spectroscopy. Typically, we observed minor oxidation of the phosphane (ca. ~15%) based on NMR. This minor contamination of the phosphine oxide originated from the starting NHS-ester and during purification, but did not appear to be due to the coupling conditions. The phosphine oxide is expected to be unreactive for the Staudinger ligation and should not interfere with the use of these reagents for conjugation.

Conjugation of Carbohydrates to a Model Protein. With three carbohydrate-phosphane derivatives in hand, we turned our attention to the formation of glycoprotein conjugates. We sought to determine the reactivity of the reagents on a model azide-containing protein and to confirm the availability of the incorporated glycans as recognition elements within a glycoconjugate. We selected β-lactoglobulin as a model protein, due to its small size and lack of glycosylation. The protein has 178 amino acids and a molecular weight of 18 kDa (*22*). We modified lactoglobulin by acylation with an NHS-activated azido-acetic acid derivative (succinimidyl 2-azidoacetate, **SI1**) (*36*) to generate a model azide-containing protein (see Supporting Information). The sequence contains 16 lysine residues, which in addition to the *N*-terminus of the protein provide 17 possible sites for acylation.

To confirm the reactivity of phosphane reagents **12**, **13**, and **14**, each was incubated with the azide-modified lactoglobulin. The isolated protein was then analyzed by mass spectrometry (MS) to observe the formation of the desired glycoconjugates (Figure 2). For the galactose labeling reagent, **12**, we observed clear evidence of the incorporation of between 1 and 13 saccharides. The most intense peaks observed were for 8−11 sites of incorporation. Conjugation reactions performed with the LacNAc reagent, **14**, gave similar results, with incorporation of between 2 and 13 disaccharides. The most intense peaks were seen for 8−12 sites of incorporation. Similar results were found with the lactose reagent, **13** (see Supporting Information). We concluded that the Staudinger ligation reagents were efficiently incorporating the desired carbohydrate residues into the proteins. We then turned our attention to testing the availability of the glycan residues as recognition elements as part of the glycoconjugate.

Scheme 4. Synthesis of Staudinger Ligation Reagents



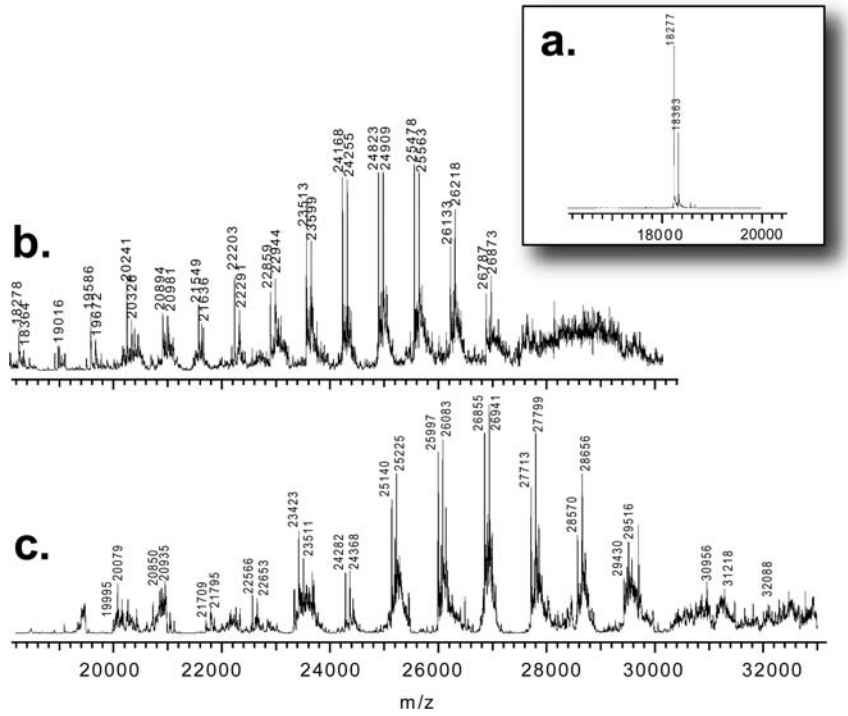


Figure 2. Mass spectral characterization of glycoconjugates. Glycoconjugates were analyzed using LC-MS to confirm the attachment of glycans. Lactoglobulin consists of A- and B-isoforms. Labeled protein samples were analyzed by LC-MS. Proteins analyzed were (a) unlabeled protein, (b) azide-labeled protein reacted with compound **12**, and (c) azide-labeled protein reacted with compound **14**. Both conjugate samples showed incorporation of as many as 13 glycans. Complete analysis of the observed peaks for all glycoconjugates are provided in Supporting Information (Tables SI1−3).

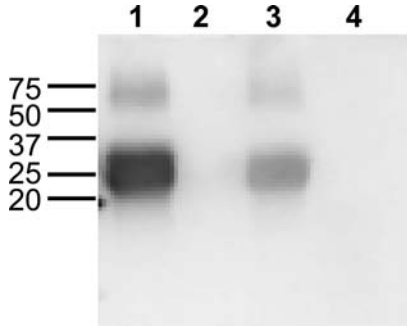


Figure 3. Lectin blotting characterization of glycoconjugates. Lactoglobulin glycoconjugates were probed with biotinylated MAL-I lectin to confirm the attachment of the desired glycans. Proteins were loaded on an SDS-PAGE gel (5−15%), transferred to nitrocellulose, and probed with MAL-I. The blot was developed with streptavidin-HRP. Lanes shown are as follows: 1, lactoglobulin-LacNAc; 2, lactoglobulin-Gal; 3, lactoglobulin-Lac; 4, azido-acetic acid labeled lactoglobulin. The expected MW for the azido-acetic acid modified lactoglobulin is 18 kDa. MW markers are 75, 50, 37, 25, and 20 kDa.

Samples of Gal-, Lac-, and LacNAc-conjugated lactoglobulin were used in a lectin-blotting experiment (*37*). The proteins were blotted onto nitrocellulose then probed with the *Maackia amurensis* lectin-I (MAL-I), which binds LacNAc and sialyl-LacNAc glycans (*38*)(Figure 3). Among the glycoconjugates studied, the lectin demonstrated a strong preference for labeling lactoglobulin which had been modified with the LacNAc reagent, **14**. Reduced staining was observed for the Lac conjugate, while neither the Gal conjugate nor the unreacted azido-lactoglobulin conjugates showed any reactivity to the lectin. These results confirm that the carbohydrate residues of the glycoconjugates are intact and capable of recognition by lectins.

Although we have only explored the use of three carbohydrate epitopes, we expect the chemistry employed here to be general and easily adapted for the incorporation of other glycan epitopes. Additionally, this modular strategy allows for only minimal development of new chemistry to generate different glycoconjugates. More complex glycans could be generated through the use of reductive amination of purified or chemoenzymatically prepared glycans (*39*). Our studies here have used purified proteins which have been acylated to incorporate azide groups. However, this approach could be adapted for the development of other protein or lipid glycoconjugates (*17, 40, 41*). An alternative strategy would be to isolate proteins or glycoproteins which have metabolically incorporated azides (*7*). This strategy could allow for selective modification of glycoproteins to test the role of specific glycan structures in biological activity. Although alternative chemistries could be employed for labeling azide-containing proteins, the Staudinger ligation strategy allows for mild conditions that are compatible with live cells.

Our group is interested in developing chemoselective strategies for increasing the proportion of specific glycan epitopes in cell-surface glycoproteins. We chose to develop chemistry for lactosamine derivatives since *N*-acetyl-lactosamine repeats are commonly found in complex N-linked glycans and O-linked glycans (*42*). Importantly, these structures can modulate the function of immunoreceptors, and the relative proportions of LacNAc incorporation can vary due to cell maturity or activation. The LacNAc epitope is essential for the recruitment of endogenous galectins to immunoreceptors, which induce cellular signals such as apoptosis and leukocyte stimulation (*42, 43*). Thus, bioconjugate methods that can modify the content of LacNAc epitopes found within glycoproteins could be used to probe the role of a single glycan epitope in biological function. Finally, the strategy described here could be used as a method

to increase the biological half-life of therapeutic proteins through attachment of defined glycans (*44–46*).

SUMMARY

We have demonstrated a general route to glycoconjugates which incorporate synthetic glycans using the Staudinger ligation. The chemistry is based on the generation of a carbohydrate epitope with a free amine, which is then acylated to incorporate a phosphane label. The resulting phosphane reagent will react with azide-containing proteins to generate a new glycoconjugate. We show that a model protein, lactoglobulin, can incorporate as many as 13 synthetic glycans, and that the resulting glycoconjugates are specifically recognized by lectins. This strategy provides a simple method of generating multisite modified glycoconjugates under extremely mild conditions which are compatible with proteins and live cells.

ACKNOWLEDGMENT

The authors would like to thank M. R. Richards, Dr. W. Peng, and Prof. T. L. Lowary (U. of Alberta) for helpful discussions and B. Reiz (U. of Alberta) for assistance with mass spectrometry. This work was funded by a grant from the Natural Sciences and Engineering Research Council of Canada (NSERC) and the Alberta Ingenuity Centre for Carbohydrate Sciences (AICCS). NAR was supported by a Queen Elizabeth II scholarship from the University of Alberta.

Supporting Information Available: Synthetic procedures, characterization, and preparation of compounds **1**, **2**, **4**, **5**, **6**, **8**, **9**, **11**, **SI1**, and synthetic intermediates. This material is available free of charge via the Internet at http://pubs.acs.org.

LITERATURE CITED

(1) Imperiali, B., and O'Connor, S. E. (1999) Effect of N-linked glycosylation on glycopeptide and glycoprotein structure. *Curr. Opin. Chem. Biol. 3*, 643–649.
(2) Dwek, R. A. (1996) Glycobiology: Toward understanding the function of sugars. *Chem. Rev. 96*, 683–720.
(3) Hang, H. C., and Bertozzi, C. R. (2001) Chemoselective approaches to glycoprotein assembly. *Acc. Chem. Res. 34*, 727–736.
(4) Peri, F., and Nicotra, F. (2004) Chemoselective ligation in glycochemistry. *Chem. Commun.* 623–627.
(5) Hecht, M. L., Stallforth, P., Silva, D. V., Adibekian, A., and Seeberger, P. H. (2009) Recent advances in carbohydrate-based vaccines. *Curr. Opin. Chem. Biol. 13*, 354–359.
(6) Carrico, I. S. (2008) Chemoselective modification of proteins: hitting the target. *Chem. Soc. Rev. 37*, 1423–1431.
(7) Luchansky, S. J., Argade, S., Hayes, B. K., and Bertozzi, C. R. (2004) Metabolic functionalization of recombinant glycoproteins. *Biochemistry 43*, 12358–12366.
(8) Saxon, E., and Bertozzi, C. R. (2000) Cell surface engineering by a modified Staudinger reaction. *Science 287*, 2007–2010.
(9) Chang, P. V., Chen, X., Smyrniotis, C., Xenakis, A., Hu, T. S., Bertozzi, C. R., and Wu, P. (2009) Metabolic labeling of sialic acids in living animals with alkynyl sugars. *Angew. Chem., Int. Ed. Engl. 48*, 4030–4033.
(10) Kiick, K. L., Saxon, E., Tirrell, D. A., and Bertozzi, C. R. (2002) Incorporation of azides into recombinant proteins for chemoselective modification by the Staudinger ligation. *Proc. Natl. Acad. Sci. U.S.A. 99*, 19–24.
(11) Mahal, L. K., Yarema, K. J., and Bertozzi, C. R. (1997) Engineering chemical reactivity on cell surfaces through oligosaccharide biosynthesis. *Science 276*, 1125–1128.
(12) Yarema, K. J., Mahal, L. K., Bruehl, R. E., Rodriguez, E. C., and Bertozzi, C. R. (1998) Metabolic delivery of ketone groups to sialic acid residues - Application to cell surface glycoform engineering. *J. Biol. Chem. 273*, 31168–31179.
(13) Lemieux, G. A., and Bertozzi, C. R. (2001) Modulating cell surface immunoreactivity by metabolic induction of unnatural carbohydrate antigens. *Chem. Biol. 8*, 265–275.
(14) Sampathkumar, S. G., Li, A. V., Jones, M. B., Sun, Z. H., and Yarema, K. J. (2006) Metabolic installation of thiols into sialic acid modulates adhesion and stem cell biology. *Nat. Chem. Biol. 2*, 149–152.
(15) Grogan, M. J., Pratt, M. R., Marcaurelle, L. A., and Bertozzi, C. R. (2002) Homogeneous glycopeptides and glycoproteins for biological investigation. *Annu. Rev. Biochem. 71*, 593–634.
(16) Bernardes, G. J. L., Castagner, B., and Seeberger, P. H. (2009) Combined approaches to the synthesis and study of glycoproteins. *ACS Chem. Biol. 4*, 703–713.
(17) Gamblin, D. P., Scanlan, E. M., and Davis, B. G. (2009) Glycoprotein synthesis: an update. *Chem. Rev. 109*, 131–163.
(18) Ochiai, H., Huang, W., and Wang, L. X. (2008) Expeditious chemoenzymatic synthesis of homogeneous N-glycoproteins carrying defined oligosaccharide ligands. *J. Am. Chem. Soc. 130*, 13790–13803.
(19) Vocadlo, D. J., Hang, H. C., Kim, E. J., Hanover, J. A., and Bertozzi, C. R. (2003) A chemical approach for identifying O-GlcNAc-modified proteins in cells. *Proc. Natl. Acad. Sci. U.S.A. 100*, 9116–9121.
(20) Sletten, E. M., and Bertozzi, C. R. (2009) Bioorthogonal chemistry: fishing for selectivity in a sea of functionality. *Angew. Chem., Int. Ed. Engl. 48*, 6974–6998.
(21) Varki, A., Cummings, R. D., Esko, J., Freeze, H. H., Hart, G., and Marth, J. (1999) *Essentials of Glycobiology*, Cold Spring Harbor Laboratory Press, Cold Spring Harbor, NY.
(22) Piez, K. A., Davie, E. W., Folk, J. E., and Gladner, J. A. (1961) β-Lactoglobulins A and B. *J. Biol. Chem. 236*, 2912–2916.
(23) Wang, C. C. Y., Seo, T. S., Li, Z., Ruparel, H., and Ju, J. (2003) Site-specific fluorescent labeling of DNA using Staudinger ligation. *Bioconjugate Chem. 14*, 697–701.
(24) Zhang, H. L., Ma, Y., and Sun, X. L. (2009) Chemically-selective surface glyco-functionalization of liposomes through Staudinger ligation. *Chem. Commun.* 3032–3034.
(25) Ivanova, I. A., Ross, A. J., Ferguson, M. A. J., and Nikolaev, A. V. (1999) Parasite glycoconjugates. Part 9. Synthesis of dec-9-enyl beta-D-galactopyranosyl-(1 -> 4)-alpha-D-mannopyranosyl phosphate and its epimers at the D-galactose moiety, substrate analogues for the elongating alpha-D-mannopyranosylphosphate transferase in the Leishmania. *J. Chem. Soc., Perkin Trans. 1* 1743–1753.
(26) Stadelmaier, A., Figueroa-Perez, I., Deininger, S., von Aulock, S., Hartung, T., and Schmidt, R. R. (2006) A Staphylococcus aureus lipoteichoic acid (LTA) derived structural variant with two diacylglycerol residues. *Bioorg. Med. Chem. 14*, 6239–6254.
(27) Biswas, G., Jeon, O. Y., Lee, W. S., Kim, D. C., Kim, K. T., Lee, S., Chang, S., and Chung, S. K. (2008) Novel guanidine-containing molecular transporters based on lactose scaffolds: lipophilicity effect on the intracellular organellar selectivity. *Chem.—Eur. J. 14*, 9161–9168.
(28) Bongat, A. F. G., and Demchenko, A. V. (2007) Recent trends in the synthesis of O-glycosides of 2-amino-2-deoxysugars. *Carbohydr. Res. 342*, 374–406.
(29) Liu, J., and Gin, D. Y. (2002) C2-amidoglycosylation. Scope and mechanism of nitrogen transfer. *J. Am. Chem. Soc. 124*, 9789–9797.
(30) Buskas, T., Konradsson, P., and Oscarson, S. (2001) Efficient synthesis of polylactosamine structures through regioselective glycosylations. *J. Carbohydr. Chem. 20*, 569–583.
(31) Wrodnigg, T. M., and Stutz, A. E. (1999) The Heyns rearrangement revisited: An exceptionally simple two-step chemical synthesis of D-lactosamine from lactulose. *Angew. Chem., Int. Ed. Engl. 38*, 827–828.
(32) Stutz, A. E., Dekany, G., Eder, B., Illaszewicz, C., and Wrodnigg, T. M. (2003) An exceptionally simple chemical synthesis of O-glycosylated D-glucosamine derivatives by Heyns rearrangement of the corresponding O-glycosyl fructoses. *J. Carbohydr. Chem. 22*, 253–265.

(33) Dekany, G., Bornaghi, L., Papageorgiou, J., and Taylor, S. (2001) A novel amino protecting group: DTPM. *Tetrahedron Lett. 42*, 3129–3132.
(34) Nishimura, S. I., Matsuoka, K., Furuike, T., Ishii, S., Kurita, K., and Nishimura, K. M. (1991) Synthetic glycoconjugates 0.2. Normal-pentenyl glycosides as convenient mediators for the syntheses of new types of glycoprotein models. *Macromolecules 24*, 4236–4241.
(35) Zemplén, G., and Pacsu, E. (1929) Über die Verseifung acetylierter Zucker und verwandter Substanzen. *Ber. Deutsch. Chem. Ges. 62*, 1613–1614.
(36) Yu, H., Yu, H., Karpel, R., and Chen, X. (2004) Chemoenzymatic synthesis of CMP-sialic acid derivatives by a one-pot two-enzyme system: comparison of substrate flexibility of three microbial CMP-sialic acid synthetases. *Bioorg. Med. Chem. 12*, 6427–6435.
(37) Freeze, H. H. (2001) Lectin Analysis of Proteins Blotted onto Filters. *Curr. Protoc. Mol. Biol.* 17.7.1−17.7.8.
(38) Yamamoto, K., Konami, Y., and Irimura, T. (1997) Sialic acid-binding motif of maackia amurensis lectins. *J. Biochem. 121*, 756–761.
(39) Chen, R., and Tolbert, T. J. Study of on-resin convergent synthesis of N-linked glycopeptides containing a large high mannose N-linked oligosaccharide. *J. Am. Chem. Soc. 132*, 3211–3216.
(40) Bennett, C. S., and Wong, C. H. (2007) Chemoenzymatic approaches to glycoprotein synthesis. *Chem. Soc. Rev. 36*, 1227–1238.
(41) Smith, M. D., Gong, D., Sudhahar, C. G., Reno, J. C., Stahelin, R. V., and Best, M. D. (2008) Synthesis and convenient functionalization of azide-labeled diacylglycerol analogues for modular access to biologically active lipid probes. *Bioconjugate Chem. 19*, 1855–1863.
(42) Earl, L. A., and Baum, L. G. (2008) CD45 Glycosylation controls T-cell life and death. *Immunol. Cell Biol. 86*, 608–615.
(43) Suzuki, O., Nozawa, Y., and Abe, M. (2006) The regulatory roles of cell surface sialylation and N-glycans in human B cell lymphoma cell adhesion to galectin-1. *Int. J. Oncol. 28*, 155–160.
(44) Jacobs, P. P., and Callewaert, N. (2009) N-glycosylation engineering of biopharmaceutical expression systems. *Curr. Mol. Med. 9*, 774–800.
(45) Sola, R. J., and Griebenow, K. (2010) Glycosylation of therapeutic proteins an effective strategy to optimize efficacy. *BioDrugs 24*, 9–21.
(46) Sinclair, A. M., and Elliott, S. (2005) Glycoengineering: The effect of glycosylation on the properties of therapeutic proteins. *J. Pharm. Sci. 94*, 1626–1635.

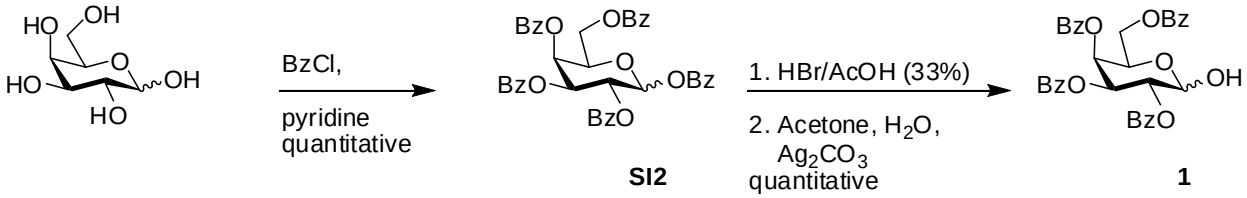
BC100209R

Supporting information for:

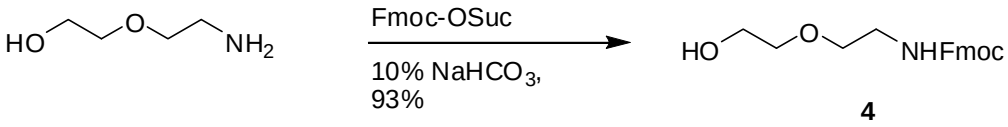
Conjugation of synthetic *N*-acetyl-lactosamine to azide-containing proteins using the Staudinger ligation

Ravi S. Loka, Christopher M. Sadek, Nikolas A. Romaniuk, and Christopher W. Cairo*

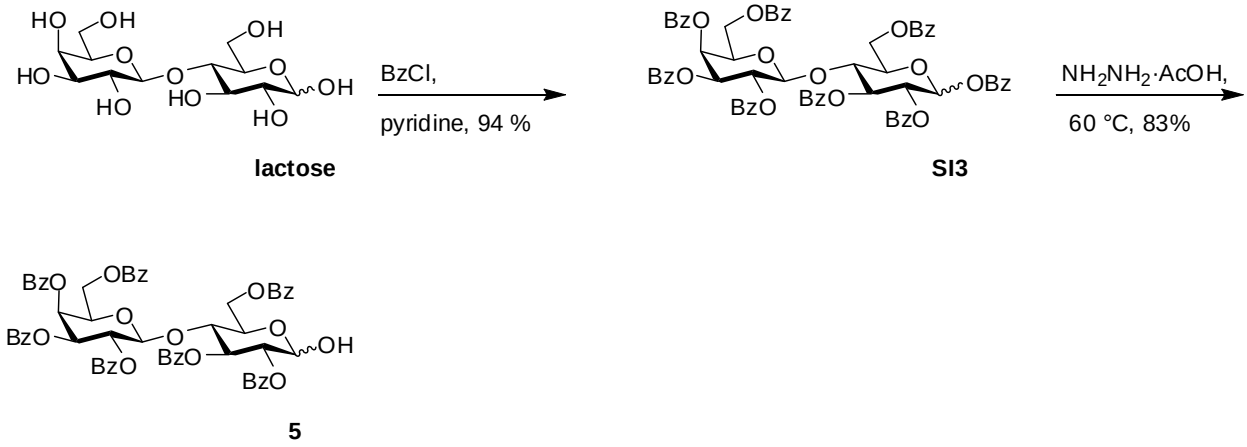
Scheme SI1: Synthesis of 2, 3, 4, 6-tetra-*O*-benzoyl-D-galactopyranoside (1)..... 2
Scheme SI2: Synthesis of protected linker (4)..... 2
Scheme SI3: Synthesis of compound 5..... 2
Scheme SI4: Synthesis of compound 8..... 2
Synthetic methods:..... 3
Table SI1: Observed mass of galactose conjugates..... 10
Table SI2: Observed mass of lactose conjugates..... 11
Table SI3: Observed mass of LacNAc conjugates..... 12
Figure SI1: Mass spectra of lactoglobulin and lactose-conjugates..... 13
^{1}H NMR of compound 3..... 14
^{13}C NMR of compound 3..... 15
^{1}H NMR of compound 4..... 16
^{13}C NMR of compound 4..... 17
^{1}H NMR of compound 7..... 18
^{13}C NMR of compound 7..... 19
^{1}H NMR of compound 10..... 20
^{13}C NMR of compound 10..... 21
^{1}H NMR of compound 11..... 22
^{31}P NMR of compound 11..... 23
^{13}C NMR of compound 11..... 24
^{1}H NMR of compound 12..... 25
^{31}P NMR of compound 12..... 26
^{13}C NMR of compound 12..... 27
^{1}H NMR of compound 13..... 28
^{31}P NMR of compound 13..... 29
^{13}C NMR of compound 13..... 30
^{1}H NMR of compound 14..... 31
^{31}P NMR of compound 14..... 32
^{13}C NMR of compound 14..... 33



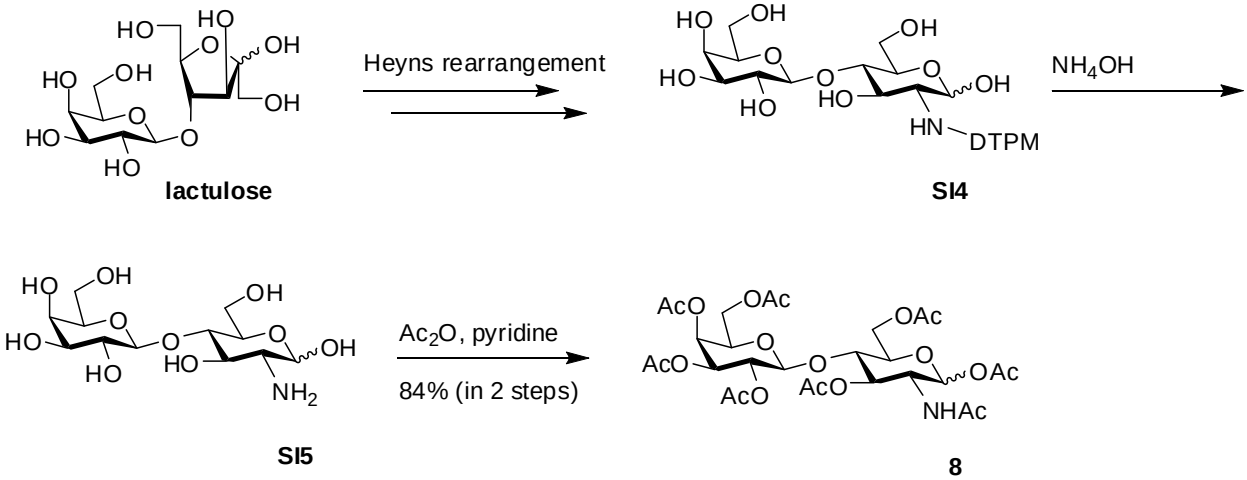
Scheme SI1: Synthesis of 2, 3, 4, 6-tetra-*O*-benzoyl-D-galactopyranoside (1)



Scheme SI2: Synthesis of protected linker (4)



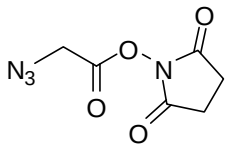
Scheme SI3: Synthesis of compound 5



Scheme SI4: Synthesis of compound 8

Synthetic methods:

Succinimidyl 2-azidoacetate (SI1):

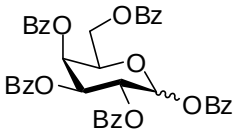


SI1

Compound **SI1** was previously reported by Yu et al. (1) Sodium azide (4.182 g, 39.3 mmol) was dissolved in 12 mL of deionized water and cooled to 0° C. Bromoacetic acid (4.456g, 32.1 mmol) was then added to the reaction, and the solution was slowly warmed to room temperature and stirred for 24 h. The mixture was acidified to pH 1 with the addition of 4 mL of HCl (1:1, HCl:H_2O). The solution was extracted with diethyl ether (3 × 30 mL). The organic layers were combined and dried over Na_2SO_4 and concentrated to give azidoacetic acid as a colorless liquid. To a solution of azidoacetic acid (1.918 g, 18.98 mmol) and NHS (2.184 g, 18.98 mmol), in anhydrous DMF (26.6 mL) under argon, was added DCC (3.916 g, 18.98 mmol) at 0 °C. The solution was stirred overnight at room temperature. The reaction was filtered to remove DCU. The filtrate was concentrated, and the product was crystallized from DCM/hexanes to give **SI1** as white solid (1) (2.230 g, 59.3% yield). ^{1}H NMR (300 MHz, $CDCl_3$) δ 4.24 (s, 2H), 2.87 (s, 4H); mp 113.9-116.1 ºC.

(1) Yu, H., Huang, S. S., Chokhawala, H., Sun, M. C., Zheng, H. J., and Chen, X. (2006) Highly efficient chemoenzymatic synthesis of naturally occurring and non-natural alpha-2,6-linked sialosides: A P. damsela alpha-2,6-sialyltransferase with extremely flexible donor-substrate specificity. *Angewandte Chemie-International Edition 45*, 3938-3944.

1, 2, 3, 4, 6-Penta-*O*-benzoyl-α/β-D-galactopyranoside (SI2):

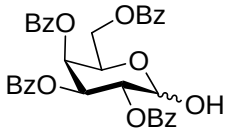


SI2

Benzoyl chloride (12.6 mL, 100 mmol) was added slowly to a suspension of galactose (3 g, 16.7 mmol) in 40 mL of pyridine and stirred at room temperature for 24 h under argon. Excess benzoyl chloride was quenched by adding 30 mL MeOH with cooling. The reaction mixture was concentrated under vacuum. The crude product was dissolved in DCM (25 mL) and washed with water (3 × 30 mL). The organic layer was dried over anhydrous Na_2SO_4. The solvent was

evaporated under vacuum and the crude residue was purified by column chromatography using EtOAc/Hexane (1:2) to yield 10.5 g (90%) of **SI2** as a white solid. ^{1}H NMR (500 MHz, $CDCl_3$) δ 8.13 (t, *J* = 6.4 Hz, 4H), 7.97 (d, *J* = 7.3 Hz, 2H), 7.88 (d, J = 7.3 Hz, 2H), 7.83 (d, *J* = 7.3 Hz, 2H), 7.65 (td, *J* = 7.4, 1.1 Hz, 2H), 7.52 (dd, *J* = 11.9, 7.6 Hz, 5H), 7.46 (t, *J* = 7.4 Hz, 2H), 7.39 (t, *J* = 7.7 Hz, 2H), 7.29 (dd, *J* = 9.7, 8.0 Hz, 4H), 6.97 (d, *J* = 3.6 Hz, 1H), 6.21 (d, *J* = 2.2 Hz, 1H), 6.14 (dd, *J* = 10.7, 3.2 Hz, 1H), 6.05 (dd, *J* = 10.7, 3.6 Hz, 1H), 4.85 (t, *J* = 6.6 Hz, 1H), 4.65 (dd, *J* = 11.3, 6.4 Hz, 1H), 4.44 (dd, *J* = 11.3, 6.9 Hz, 1H); ^{13}C NMR (125 MHz, $CDCl_3$) δ 165.9, 165.7, 165.5, 165.4, 164.5, 133.9, 133.7, 133.4, 133.3, 133.2, 130.0, 129.95, 129.8, 129.76, 129.3, 129.0, 128.98, 128.9, 128.8, 128.74, 128.7, 128.42, 128.41, 128.4, 90.7, 69.5, 68.6, 68.5, 67.7, 61.9; ESIMS calculated for $C_{41}H_{32}O_{11}Na$ $[M+Na]^+$ 723.1837, found: 723.1834.

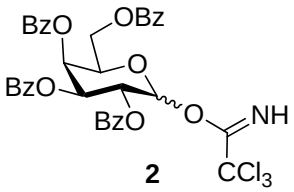
2, 3, 4, 6-Tetra-*O*-benzoyl-α/ β-D-galactopyranoside (1):



1

Penta-*O*-benzoyl galactoside, **SI2** (3 g, 4.3 mmol), was treated with 1.6 mL of HBr/AcOH (33%) in 10 mL of DCM for 1 h. The solution was washed twice with 10 mL of saturated $NaHCO_3$, NaCl, and 8 mL DI water. The DCM was evaporated and the solid was dried under vacuum. The resulting white solid was dissolved in 15 mL acetone and 0.7 mL water with Ag_2CO_3 (602 mg, 2.2 mmol). The solution was filtered through a pad of celite and dried under vacuum to yield a quantitative amount of **1** as a white solid. ^{1}H NMR (500 MHz, $CDCl_3$) δ 8.15 – 8.08 (m, 3H), 8.06 – 7.96 (m, 5H), 7.86 – 7.79 (m, 2H), 7.67 – 7.54 (m, 1H), 7.54 – 7.43 (m, 5H), 7.43 – 7.31 (m, 6H), 7.23 (t, *J* = 7.9 Hz, 3H), 6.16 - 6.11 (m,1H), 6.06 (s, 0.3H), 5.90 (s,1H), 5.77 (d, *J* = 3.5 Hz, 0.5H), 5.75 (d, *J* = 3.7 Hz, 1H),5.14 (t, *J* = 7.4 Hz, 0.3H), 4.89 (t, *J* = 6.8 Hz, 1H), 4.77 (d, *J* = 7.8 Hz, 0.3H), 4.71 (dd, *J* = 11.2, 6.3 Hz, 0.3H), 4.63 (dd, *J* = 11.3, 6.3 Hz, 1H), 4.47 (m, 0.3H), 4.40 (m, 2H); ^{13}C NMR (125 MHz, $CDCl_3$) δ 164.2, 163.8, 163.76, 163.7, 163.3, 163.2, 163.16, 131.2, 131.1, 131.05, 130.9, 130.89, 130.86, 130.8, 130.7, 127.5, 127.45, 127.4, 127.36, 127.34, 127.3, 127.26, 127.2, 126.9, 126.8, 126.75, 126.6, 126.5, 126.47, 126.2, 126.18, 126.16, 126.0, 125.95, 125.9, 125.8, 125.78, 93.7, 88.6, 69.6, 69.0, 68.8, 67.2, 66.9, 65.8, 65.7, 64.2, 59.9, 59.7; ESIMS calculated for $C_{34}H_{28}O_{10}Na$ $[M+Na]^+$ 619.1575, found: 619.1576.

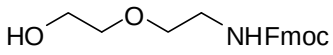
2, 3, 4, 6-Tetra-*O*-benzoyl-α/ β-D-galactopyranosyl trichloroacetamidate (2):



2

Compound **1** (1.10 g, 1.8 mmol), DBU (60 µL), and trichloroacetonitrile (2.2 mL, 4.8 mmol) were dissolved in DCM (25 mL) and stirred for 4 h at room temperature. DCM was evaporated and the residue was purified by column chromatography with EtOAc/hexane (1:2) to yield 1.214 g (91.3%) of **2** as a white solid. ^{1}H NMR (500 MHz, $CDCl_3$) δ 8.77 (s, 0.3H), 8.67 (s, 1H), 8.12 (dd, *J* = 8.2, 1.1 Hz, 3H), 8.08 (dd, *J* = 8.2, 1.2 Hz, 0.7H), 8.00 (ddd, *J* = 11.6, 8.3, 1.2 Hz, 4H), 7.94 (ddd, *J* = 20.6, 8.3, 1.2 Hz, 1.4H), 7.83 (dd, *J* = 8.3, 1.2 Hz, 2H), 7.69 – 7.63 (m, 1H), 7.63 – 7.58 (m, 1H), 7.58 – 7.49 (m, 6H), 7.48 – 7.27 (m, 11H), 6.96 (d, *J* = 3.7 Hz, 1H), 6.74 (s, 0.3H), 6.22 – 6.19 (m, 1H), 6.17 (dt, *J* = 7.0, 4.3 Hz, 0.4H), 6.12 (dd, *J* = 10.7, 3.3 Hz, 1H), 6.01 (dd, *J* = 10.7, 3.7 Hz, 1H), 5.82 (d, *J* = 4.2 Hz, 0.3H), 5.80 (s, 0.3H), 4.91 (dd, *J* = 8.8, 4.7 Hz, 1.3H), 4.85 – 4.73 (m, 1H), 4.65 (dd, *J* = 11.5, 6.9 Hz, 1H), 4.48 (dd, *J* = 11.5, 6.0 Hz, 1H); ^{13}C NMR (125 MHz, $CDCl_3$) δ 166.0, 165.9, 165.7, 165.6, 165.52, 165.51, 165.5, 165.2, 160.6, 160.3, 133.8, 133.7, 133.6, 133.4, 133.3, 133.26, 133.1, 130.05, 130.0, 129.97, 129.9, 129.86, 129.8, 129.75, 129.7, 129.5, 129.4, 129.3, 129.0, 128.9, 128.8, 128.74, 128.7, 128.5, 128.46, 128.4, 128.35, 102.9, 93.8, 91.0, 90.8, 84.6, 80.8, 77.2, 70.1, 69.8, 68.6, 68.4, 67.9, 63.4, 62.2; ESIMS calculated for $C_{36}H_{28}Cl_3NO_{10}Na$ $[M+Na]^+$ 762.0671, found: 762.0671.

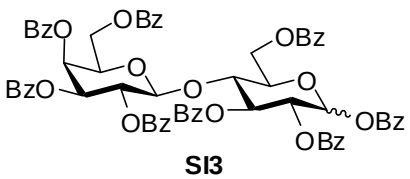
9*H*-fluoren-9-ylmethyl [2-(2-hydroxyethoxy)ethyl]carbamate (4):



4

In a round bottom flask, 23 mL of 10% $NaHCO_3$ was added to 2-(2-aminoethoxy)-ethanol (700 µL, 7 mmol) in 20 mL of dioxane. The mixture was stirred for 15 min, then 9-fluorenylmethyl-*N*-succinimidyl carbonate (2.833 g, 8.4 mmol) was added. The reaction mixture was stirred overnight then extracted with DCM (60 mL). The DCM layer was washed with water (2 x 50 mL) and dried over anhydrous Na_2SO_4. The solvent was evaporated under vacuum and the residue was purified by column chromatography using EtOAc/hexane (2:1) to yield 2.203 g (92.4%) of **4** as an off-white solid. ^{1}H NMR (400 MHz, $CDCl_3$) δ 7.76 (d, *J* = 7.5 Hz, 2H), 7.59 (d, *J* = 7.4 Hz, 2H), 7.39 (t, *J* = 7.4 Hz, 2H), 7.31 (td, *J* = 7.5, 1.2 Hz, 2H), 5.37 (s, 1H), 4.43 (d, *J* = 6.7 Hz, 2H), 4.21 (t, *J* = 6.7 Hz, 1H), 3.71 (dd, *J* = 9.3, 5.5 Hz, 2H), 3.54 (d, *J* = 4.5 Hz, 4H), 3.38 (d, *J* = 5.0 Hz, 2H), 2.44 (t, *J* = 5.8 Hz, 1H); ^{13}C NMR (100 MHz, $CDCl_3$) δ 156.6, 143.9, 141.3, 127.7, 127.0, 125.0, 120.0, 72.3, 70.1, 66.6, 61.7, 47.3, 40.9; ESIMS calculated for $C_{19}H_{21}NO_4Na$ $[M+Na]^+$ 350.1363, found: 350.1357; mp 64.3-66.9 ºC.

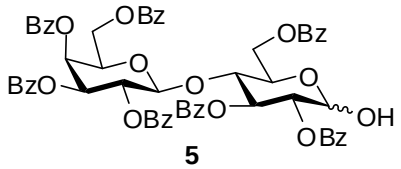
2,3,4,6-Tetra-*O*-benzoyl-β-D-galactopyranosyl-(1→4)-1,2,3,6-tetra-*O*-benzoyl-α/β-D-glucopyranose (SI3):



SI3

Benzoyl chloride was added slowly to a suspension of D-lactose (514 mg, 1.5 mmol) in 10 mL of pyridine and stirred at room temperature for 24 h under argon. Excess benzoyl chloride was quenched by adding MeOH with cooling. The reaction mixture was concentrated under high vacuum. The crude product was dissolved in DCM (25 mL) and washed with water (3 x 30 mL). The organic layer was dried over anhydrous Na_2SO_4. The solvent was evaporated under vacuum. The product was purified by column chromatography using EtOAc/hexane (1:2) to yield 1.66 g (93.9%) of **SI3** as a white solid. ^{1}H NMR (500 MHz, $CDCl_3$) δ 8.13 (dd, *J* = 8.2, 1.2 Hz, 1H), 8.08 – 7.97 (m, 13H), 7.96 – 7.85 (m, 5H), 7.77 – 7.71 (m, 3H), 7.69 – 7.25 (m, 28H), 7.20 (ddd, *J* = 11.4, 10.0, 5.6 Hz, 6H), 6.76 (d, *J* = 3.8 Hz, 0.3H), 6.21 (dd, *J* = 10.1, 9.3 Hz, 0.3H), 6.15 (d, *J* = 8.1 Hz, 1H), 5.95 (t, *J* = 9.3 Hz, 1H), 5.82 – 5.77 (m, 1.3H), 5.77 – 5.71 (m, 2.4H), 5.62 (dd, *J* = 10.3, 3.8 Hz, 0.3H), 5.39 (dd, *J* = 10.4, 3.4 Hz, 1H), 4.96 (d, *J* = 7.9 Hz, 0.3H), 4.91 (d, *J* = 7.9 Hz, 1H), 4.64 – 4.50 (m, 3H), 4.40 (td, *J* = 9.5, 3.0 Hz, 1.3H), 4.31 (dt, *J* = 10.2, 2.5 Hz, 0.3H), 4.08 (ddd, *J* = 9.9, 3.7, 1.9 Hz, 1H), 3.90 (t, *J* = 6.6 Hz, 1.4H), 3.85 – 3.76 (m, 1.5H), 3.76 – 3.68 (m, 1.3H); ^{13}C NMR (125 MHz, $CDCl_3$) δ 165.8, 165.77, 165.6, 165.5, 165.45, 165.43, 165.4, 165.3, 165.24, 165.2, 165.19, 164.9, 164.8, 164.5, 164.48, 133.9, 133.7, 133.5, 133.45, 133.4, 133.39, 133.37, 133.3, 133.26, 130.1, 130.07, 130.0, 129.8, 129.78, 129.76, 129.71, 129.7, 129.66, 129.65, 129.6, 129.57, 129.5, 129.43, 129.42, 129.4, 128.9, 128.86, 128.8, 128.7, 128.63, 128.6, 128.59, 128.56, 128.55, 128.5, 128.47, 128.4, 128.34, 128.3, 128.25, 101.3, 101.2, 92.6, 89.9, 75.7, 75.6, 73.9, 72.9, 72.0, 71.8, 71.4, 71.2, 70.7, 70.4, 70.1, 69.9, 69.8, 67.5, 62.1, 61.8, 61.0; ESIMS calculated for $C_{68}H_{54}O_{19}Na$ $[M+Na]^+$ 1197.3152, found: 1197.3142.

2,3,4,6-Tetra-*O*-benzoyl-β-D-galactopyranosyl-(1→4)-2,3,6-tri-*O*-benzoyl-α/β-D-glucopyranose (5):

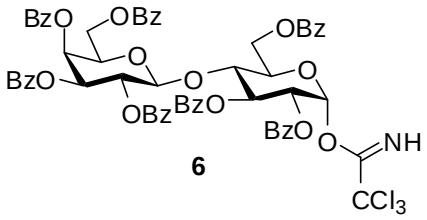


5

Hydrazine acetic acid (220 μL) was added to a solution of **SI3** (600 mg, 0.51 mmol) in DMF (10 mL) and the mixture was stirred at 60 ^{o}C for 6 h. A white solid crashed out after addition of water (20 mL) and was filtered. The solid was dissolved in DCM (10 mL) and washed with water (2 × 15 mL). The organic layer was dried over anhydrous Na_2SO_4 and evaporated under vacuum. The crude residue was purified by column chromatography using EtOAc/hexane (1:1) to yield 455 mg (83.3%) of **5** as a white solid. ^{1}H NMR (500 MHz, $CDCl_3$) δ 8.07 – 7.93 (m, 15H), 7.89 (dd, *J* = 8.3, 1.2 Hz, 3H), 7.73 (dd, *J* = 8.3, 1.2 Hz, 3H), 7.66 – 7.25 (m, 28H), 7.25 – 7.13 (m, 6H), 6.15 (dd, *J* = 9.9, 9.5 Hz, 1H), 5.87 (t, *J* = 7.47, 0.3H), 5.78 – 5.69 (m, 3H), 5.63 (d, *J* = 3.6 Hz, 1H), 5.47 – 5.36 (m, 1.5H), 5.32 – 5.28 (m, 0.3H), 5.25 (dd, *J* = 10.3, 3.7 Hz, 1H), 4.95 (d, *J* = 7.8 Hz, 1.23H), 4.93 – 4.87 (m, 0.6H), 4.58 (dd, *J* = 12.3, 1.9 Hz, 1.5H), 4.53 – 4.45 (m, *J* = 12.3, 4.1 Hz, 1.6H), 4.37 (ddd, *J* = 10.1, 3.1, 2.0 Hz, 1H), 4.31 – 4.22 (m, *J* = 9.7, 4.2 Hz, 1.5H), 3.92 (q, *J* = 6.4 Hz, 1.6H), 3.89 – 3.83 (m, 1.5H), 3.83 – 3.69 (m, *J* = 29.7, 11.3,

7.0 Hz, 2H); ^{13}C NMR (125 MHz, $CDCl_3$) δ 166.6, 166.2, 166.1, 166.0, 165.7, 165.6, 165.5, 165.47, 165.45, 165.4, 165.3, 164.9, 133.6, 133.44, 133.4, 133.37, 133.3, 133.1, 130.0, 129.95, 129.8, 129.7, 129.6, 129.5, 129.43, 129.4, 129.38, 129.1, 129.0, 128.8, 128.7, 128.6, 128.59, 128.5, 128.4, 128.3, 101.1, 95.8, 90.3, 76.1, 76.0, 74.0, 73.3, 72.6, 72.2, 72.0, 71.8, 71.4, 70.3, 70.1, 70.0, 68.4, 67.6, 67.58, 62.5, 62.45, 61.2, 61.1; ESIMS calculated for $C_{61}H_{50}O_{18}Na$ $[M+Na]^+$ 1093.2889, found: 1093.2886.

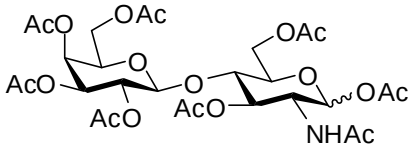
1-*O*-[2,3,4,6-Tetra-*O*-benzoyl-β-D-galactopyranosyl-(1→4)-2,3,6-tri-*O*-benzoyl-α-D-glucopyranosyl] trichloroacetimidate (6):



6

Compound **5** (430 mg, 0.4 mmol), DBU (6 µL), and trichloroacetonitrile (481 µL, 4.8 mmol) were dissolved in DCM (10 mL) and stirred for 4 h at room temperature. DCM was evaporated and the residue was purified by column chromatography with EtOAc/hexane (1:1) to yield 434 mg (89.0%) of **6** as a white solid. ^{1}H NMR (500 MHz, $CDCl_3$) δ 8.57 (s, 1H), 7.99 (dddd, *J* = 15.9, 12.8, 8.4, 1.3 Hz, 12H), 7.90 (dd, *J* = 8.3, 1.2 Hz, 2H), 7.73 (dd, *J* = 8.4, 1.3 Hz, 2H), 7.70 – 7.54 (m, 4H), 7.54 – 7.26 (m, 17H), 7.26 – 7.15 (m, 5H), 6.72 (d, *J* = 3.8 Hz, 1H), 6.20 – 6.12 (m, 1H), 5.79 – 5.71 (m, 2H), 5.55 (dd, *J* = 10.2, 3.8 Hz, 1H), 5.40 (dd, *J* = 10.3, 3.4 Hz, 1H), 4.95 (d, *J* = 7.9 Hz, 1H), 4.62 – 4.47 (m, 2H), 4.39 – 4.30 (m, 2H), 3.91 (t, *J* = 7.1 Hz, 1H), 3.83 (dd, *J* = 11.3, 6.3 Hz, 1H), 3.74 (dd, *J* = 11.3, 7.3 Hz, 1H); ^{13}C NMR (175 MHz, $CDCl_3$) δ 165.7, 165.52, 165.5, 165.4, 165.2, 165.17, 164.8, 160.7, 133.5, 133.4, 133.3, 130.0, 129.9, 129.8, 129.7, 129.65, 129.6, 129.57, 129.5, 129.4, 128.9, 128.7, 128.6, 128.57, 128.54, 128.5, 128.4, 128.3, 128.2, 101.3, 93.1, 90.7, 75.6, 71.9, 71.4, 71.35, 70.5, 70.3, 70.0, 67.5, 61.9, 61.0; ESIMS calculated for $C_{63}H_{50}Cl_3NO_{18}Na$ $[M+Na]^+$ 1236.1986, found: 1236.1997.

2-Acetamido-1,3,6-tri-*O*-acetyl-2-deoxy-4-*O*-(2,3,4,6-tetra-O-acetyl- β-D-galactopyranosyl) - α/β-D-glucopyranose (8):



8

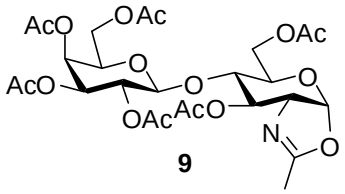
N-[1,3-Dimethyl-2,4,6 (1H, 3H, 5H)-trioxopyrimidine-5-ylidene]methyl lactosamine **SI4** (4 g, 7.9 mmol) was prepared from lactulose as described by Stutz et al. (2) The compound was suspended in 30 mL of NH_4OH and the mixture was stirred for 40 min. White precipitate was

filtered off and washed several times with distilled water. Then filtrate was (aqueous layer, 45 mL) washed with chloroform (3 x 30 mL). The aqueous layer was concentrated and dried on high vacuum for 18 h to give lactosamine **SI5** (2.4 g, 90%) as a light yellow solid. The product was confirmed by mass spectrometry (ESIMS calculated for $C_{12}H_{24}NO_{10}$ $[M+H]^+$ 342.1395, found: 342.1397.) Lactosamine (500 mg, 1.5 mmol) was then dissolved in 10 mL of pyridine and stirred with acetic anhydride (3 mL, 31.7 mmol), and a catalytic amount of DMAP for 18 h at room temperature. Excess acetic anhydride was quenched by dropwise addition of 3 mL methanol at 0 °C under constant stirring for 30 min. The solvent was removed under vacuum and the crude mixture was purified by column chromatography with EtOAc/hexane (3:1) to yield compound **8** (923 mg, 93%) as light yellow solid. Characterization of the compound was consistent with data reported by Range et al. (3). ^{1}H NMR (498 MHz, $CDCl_3$) δ 6.07 (d, *J* = 3.6 Hz, 1H), 5.86 (d, *J* = 9.7 Hz, 0.2H), 5.65 (d, *J* = 9.1 Hz, 1H), 5.61 (d, *J* = 7.7 Hz, 0.3H), 5.34 (dd, *J* = 3.3, 1.0 Hz, 1.5H), 5.21 (dd, *J* = 11.0, 8.3 Hz, 1H), 5.14 – 5.08 (m, 1.3H), 5.07 – 5.02 (m, 0.4H), 4.99 – 4.92 (m, 1.4H), 4.51 (d, *J* = 7.9 Hz, 1H), 4.47 (d, *J* = 7.9 Hz, 0.4H), 4.43 (dd, *J* = 12.0, 3.0 Hz, 0.3H), 4.41 – 4.36 (m, 1.3H), 4.35 (dd, *J* = 3.6, 1.9 Hz, 0.5H), 4.33 (d, *J* = 3.6 Hz, 0.3H), 4.26 (td, *J* = 9.4, 7.8 Hz, 0.3H), 4.17 – 4.04 (m, 4H), 3.92 – 3.80 (m, 4H), 3.76 (ddd, *J* = 8.1, 5.7, 3.1 Hz, 1H), 3.28 (d, *J* = 7.0 Hz, 0.4H), 2.16 – 1.91 (overlapped singlets, 33H); ESIMS calculated for $C_{28}H_{40}NO_{18}$ $[M+H]^+$ 678.2240, found: 678.2239.

(2) Stutz, A. E., Dekany, G., Eder, B., Illaszewicz, C., and Wrodnigg, T. M. (2003) An exceptionally simple chemical synthesis of O-glycosylated D-glucosamine derivatives by Heyns rearrangement of the corresponding O-glycosyl fructoses. *J. Carbohydr. Chem. 22*, 253-265.

(3) Range, G., Krahmer, R., Welzel, P., Muller, D., Herrmann, G. F., Kragl, U., Wandrey, C., Markus, A., vanHeijenoort, Y., and vanHeijenoort, J. (1997) A chemoenzymatic approach towards moenomycin structural analogues. *Tetrahedron 53*, 1695-1706.

2-Methyl-{3,6-di-*O*-acetyl-1,2-dideoxy-4-*O*-(2,3,4,6-tetra-*O*-acetyl-β-D-galactopyranosyl)-α-D-gluco-pyrano}-[2,1-d]-oxazoline (9):

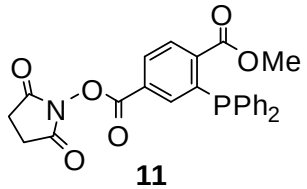


9

Peracetylated LacNAc, **8** (567 mg, 0.84 mmol), was dissolved in 10 mL of 1,2-dichloro ethane and stirred with TMSOTf (167 µL, 1.05 mmol) at 50 °C for 12 h. The reaction mixture was then warmed to room temperature. Triethylamine (0.6 mL) was added and the reaction mixture was stirred for 30 min. The solvent was removed under vacuum and the crude mixture was purified by column chromatography with toluene/EtOAc/Et_3N (100:200:1) to yield 400 mg (75%) of **9** as a yellow solid. ^{1}H NMR (498 MHz, $CDCl_3$) δ 5.90 (d, *J* = 7.3 Hz, 1H), 5.63 (s, 1H), 5.36 (d, *J* =

3.4 Hz, 1H), 5.16 (dd, *J* = 10.0, 8.3 Hz, 1H), 4.99 (dd, *J* = 10.3, 3.5 Hz, 1H), 4.64 (d, *J* = 8.0 Hz, 1H), 4.24 – 4.02 (m, 5H), 3.94 (t, *J* = 6.7 Hz, 1H), 3.64 (d, *J* = 9.5 Hz, 1H), 3.53 – 3.45 (m, 1H), 2.15 (s, 3H), 2.10 (s, 3H), 2.10 (s, 3H), 2.09 (s, 3H), 2.04 (s, 3H), 2.02 (s, 3H), 1.96 (s, 3H); ^{13}C NMR (125 MHz, $CDCl_3$) δ 170.6, 170.32, 170.3, 170.1, 169.4, 169.2, 166.8, 102.4, 99.1, 78.0, 71.0, 70.9, 70.5, 68.8, 67.5, 66.9, 65.0, 63.5, 61.1, 21.0, 20.8, 20.7, 20.66, 20.6, 20.5, 13.9; ESIMS calculated for $C_{26}H_{35}NO_{16}Na$ $[M+Na]^+$ 640.1848, found: 640.1846.

Succinimidyl 3-diphenylphosphino-4-methoxy-carbonylbenzoate (11):



11

A solution of 2-(diphenyl-phosphanyl)-terepthalic acid 1-methyl ester (1.978 g, 1 mmol), prepared according to Kiick et al. (4), was stirred with EDCI (1.244 g, 1.2 mmol) and NHS (0.684 g, 1.1 mmol) in DMF (10 mL) for one day. The reaction mixture was concentrated under reduced pressure then extracted with mixture of DCM and H_2O (50 mL). The organic layer was dried over anhydrous Na_2SO_4, and concentrated under vacuum. The residue was purified by flash column chromatography (1:1 hexane/EtOAc) to afford **11** as a yellow solid (5) (1.29 g, 52%). ^{1}H NMR (400 MHz,$CDCl_3$) δ 8.13 (s, 2H), 7.67 (d, *J* = 3.6 Hz, 1H), 7.40 – 7.26 (m, 10H), 3.76 (s, 3H), 2.84 (s, 4H);^{13}C NMR (100 MHz, $CDCl_3$) δ 168.8, 166.2 (d, J_{C-P} = 3.0 Hz), 161.0, 142.3 (d, J_{C-P} = 31.3 Hz), 139.6 (d, J_{C-P} = 19.2 Hz), 136.4 (d, J_{C-P} = 10.1 Hz), 136.0, 133.8 (d, J_{C-P} = 21.2 Hz), 130.7, 129.6, 129.1, 128.6 (d, J_{C-P} = 8.1 Hz), 127.7, 52.4, 25.5; ^{31}P NMR (162 MHz, $CDCl_3$) δ -2.9; HR-ESIMS calculated for $C_{25}H_{20}NO_6PNa(M+Na)^+$, 484.0921, found 484.0919; mp 151.2-153.6 ºC.

(4) Kiick, K. L., Saxon, E., Tirrell, D. A., and Bertozzi, C. R. (2002) Incorporation of azides into recombinant proteins for chemoselective modification by the Staudinger ligation. *Proc. Natl. Acad. Sci. U. S. A. 99*, 19-24.

(5) Wang, C. C. Y., Seo, T. S., Li, Z., Ruparel, H., and Ju, J. (2003) Site-Specific Fluorescent Labeling of DNA Using Staudinger Ligation. *Bioconjugate Chem. 14*, 697-701.

Table SI1: Observed mass of galactose conjugates

*lactoglobulin-Gal (compound **12**)*		
assignment (isoform + n)	*calculated* [a]	*observed*
B	18278	18278
A	18364	18364
A + 1	19018	19016
A + 2	19672	19672
B + 2	19586	19586
A + 3	20327	20326
B + 3	20241	20241
A + 4	20981	20981
B + 4	20895	20894
A + 5	21635	21636
B + 5	21549	21549
A + 6	22289	22291
B + 6	22203	22203
A + 7	22943	22944
B + 7	22857	22859
A + 8	23598	23599
B + 8	23512	23513
A + 9	24252	24255
B + 9	24166	24168
A + 10	24906	24909
B + 10	24820	24823
A + 11	25560	25563
B + 11	25474	25478
A + 12	26215	26218
B + 12	26129	26133
A + 13	26869	26873
B + 13	26783	26787

a. Expected masses were calculated based on the formula $M_{lac} + n*M_{linker}$, where the M_{lac} that of either β-lactoglobulin (A isoform, 18364 Da) or β-lactoglobulin (B isoform, 18278 Da), *n* is the number of sites, and M_{linker} = 654.2 Da.

Table SI2: Observed mass of lactose conjugates

*lactoglobulin-lactose (compound **13**)*		
assignment (isoform + n)	*calculated*[a]	*observed*
A + 1	19180	19181
B + 1	19094	19094
B + 2	19911	19911
A + 3	20813	20813
B + 3	20727	20727
A + 4	21629	21631
B + 4	21543	21545
B + 5	22359	22361
A + 6	23262	23264
B + 6	23176	23178
A + 7	24078	24080
B + 7	23992	23994
A + 8	24894	24898
B + 8	24808	24811
A + 9	25710	25714
B + 9	25624	25628
A + 10	26527	26530
B + 10	26441	26445
A + 11	27343	27347
B + 11	27257	27261
A + 12	28159	28165
B + 12	28073	28077
A + 14	29792	29791
A + 15	30608	30608
B + 15	30522	30528
A + 16	31424	31426

a. Expected masses were calculated based on the formula $M_{lac} + n*M_{linker}$, where the M_{lac} that of either β-lactoglobulin (A isoform, 18364 Da) or β-lactoglobulin (B isoform, 18278 Da), *n* is the number of sites, and M_{linker} = 816.3 Da.

Table SI3: Observed mass of LacNAc conjugates

*lactoglobulin-LacNAc (compound **14**)*		
assignment (isoform + n)	*calculated*[a]	*observed*
A + 2	20079	20079
B + 2	19993	19995
A + 3	20936	20935
B + 3	20850	20850
A + 4	21793	21795
B + 4	21707	21709
A + 5	22650	22653
B + 5	22564	22566
A + 6	23508	23511
B + 6	23422	23423
A + 7	24365	24368
B + 7	24279	24282
A + 8	25222	25225
B + 8	25136	25140
A + 9	26080	26083
B + 9	25994	25997
A + 10	26937	26941
B + 10	26851	26855
A + 11	27794	27799
B + 11	27708	27713
A + 12	28651	28656
B + 12	28565	28570
A + 13	29509	29516
B + 13	29423	29430

a. Expected masses were calculated based on the formula $M_{lac} + n*M_{linker}$, where the M_{lac} that of either β-lactoglobulin (A isoform, 18364 Da) or β-lactoglobulin (B isoform, 18278 Da), *n* is the number of sites, and M_{linker} = 857.3 Da.

Figure SI1: Mass spectra of lactoglobulin and lactose-conjugates

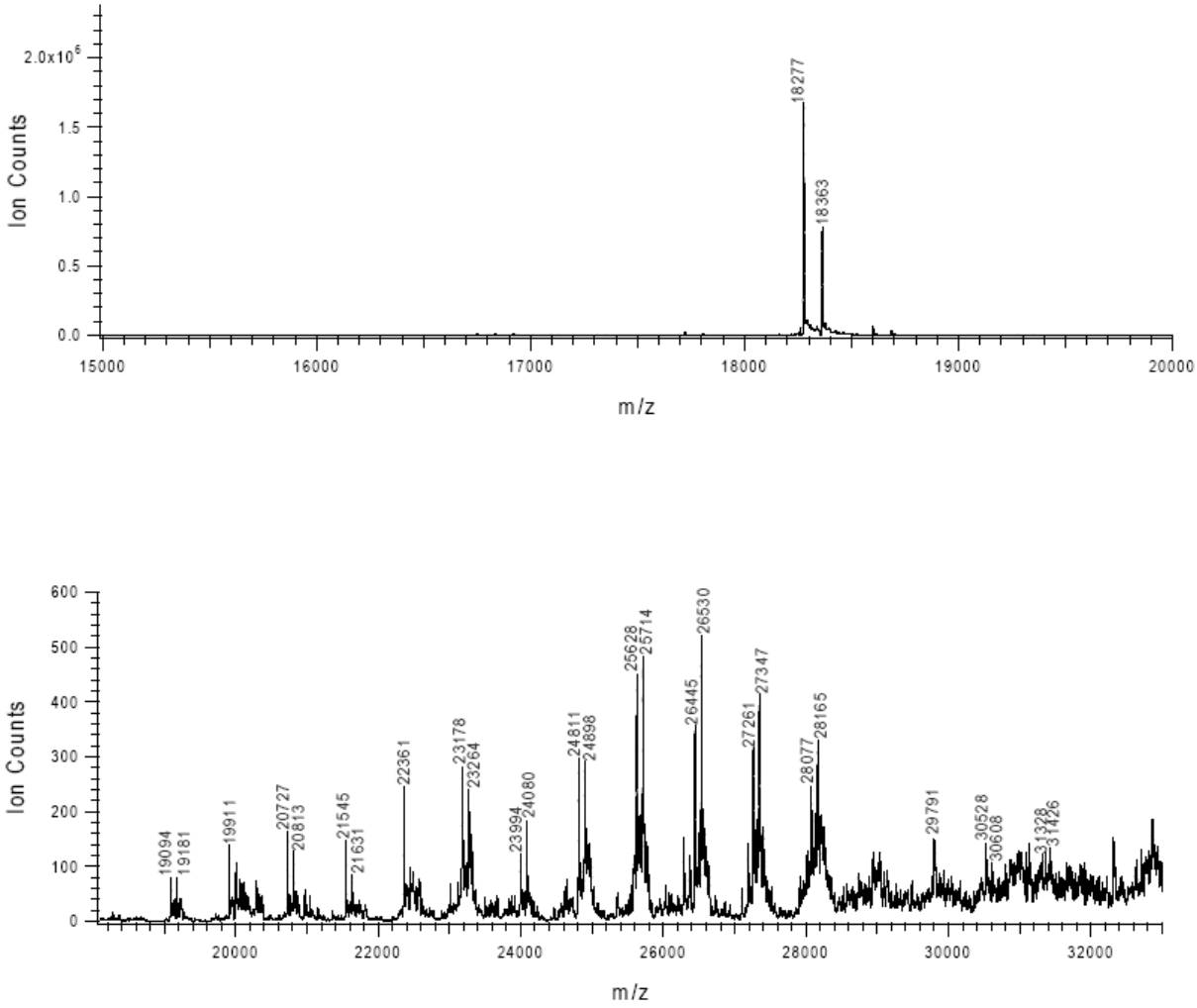
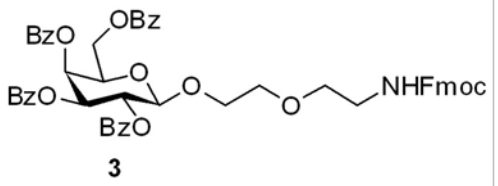
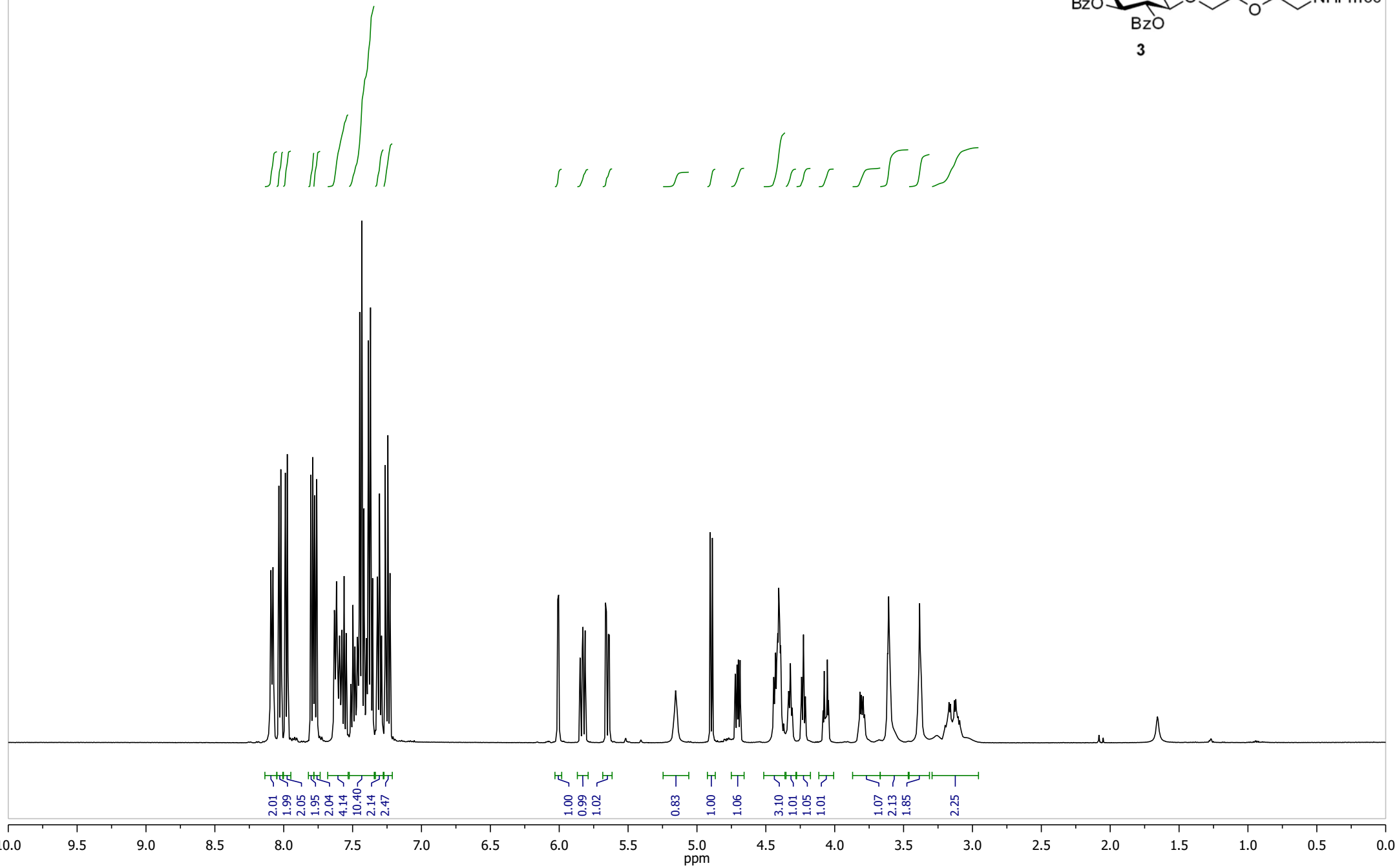


Figure SI1: Glycoconjugates were analyzed using LC-MS to confirm the attachment of glycans as described in Figure 2. Lactoglobulin consists of A- and B-isoforms. Labeled protein samples were analyzed by LC-MS. Spectra are shown for: (**a.**) unlabeled lactoglobulin, (**b.**) azide-labeled protein reacted with compound **13**. The conjugate samples observed in (**b.**) show significant incorporation of between 1-12 glycans. Also see **Table SI2** for a list of peak assignments.

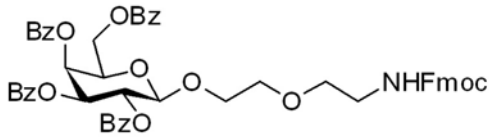
^{1}H NMR (500 MHz, $CDCl_3$)



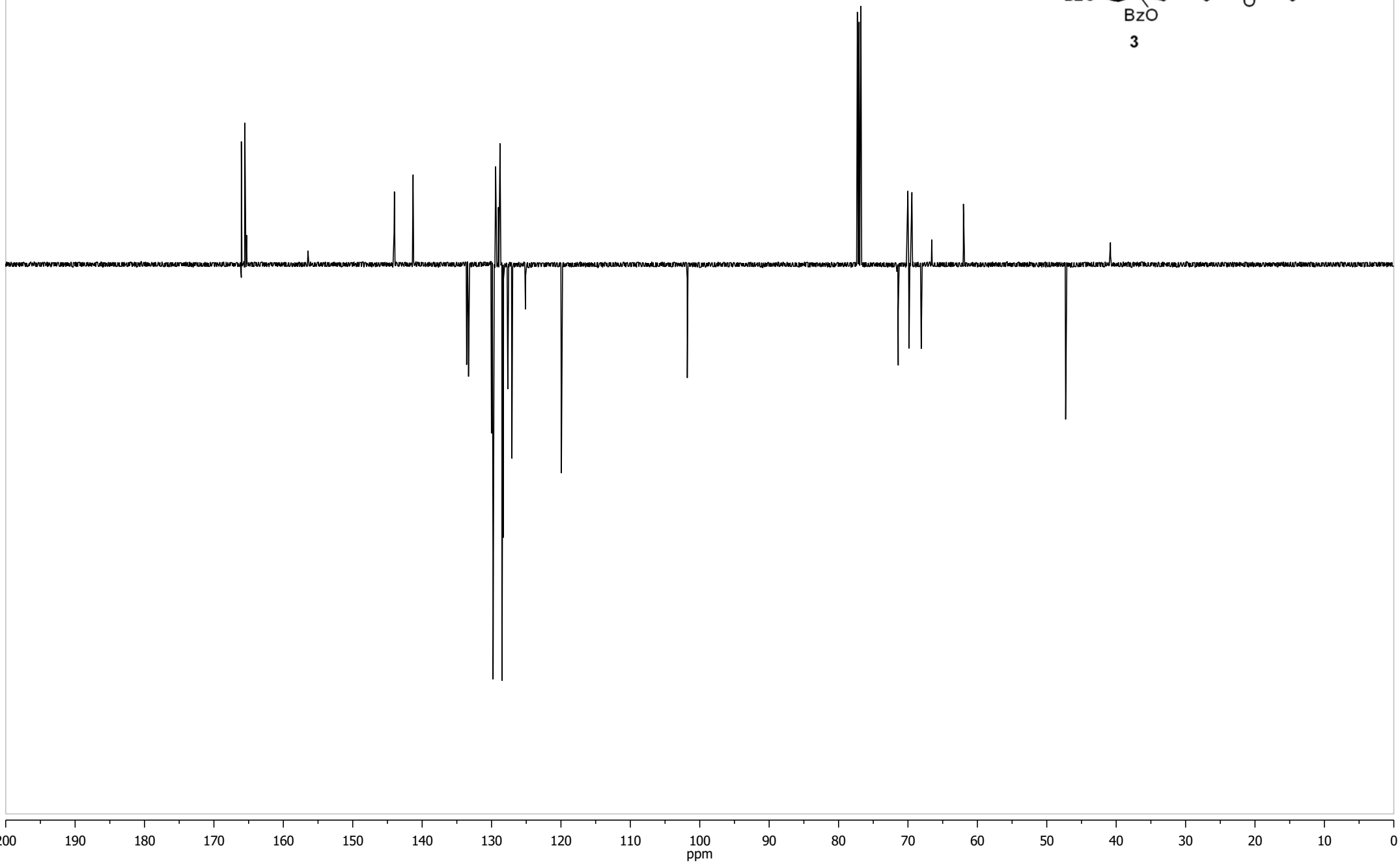
3



^{13}C NMR (125 MHz, $CDCl_3$)



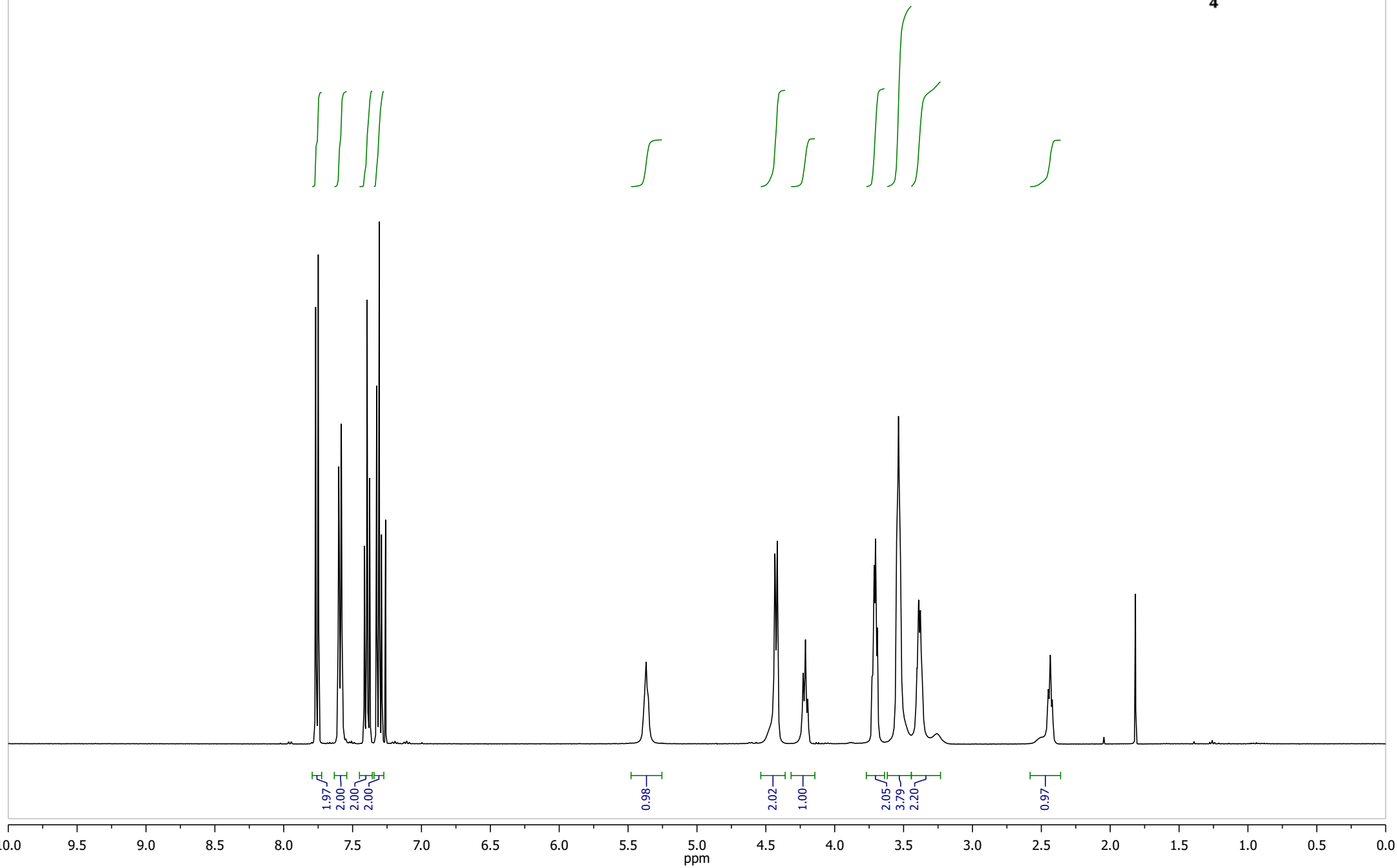
3



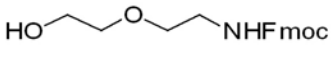
^{1}H NMR (400 MHz,$CDCl_3$)



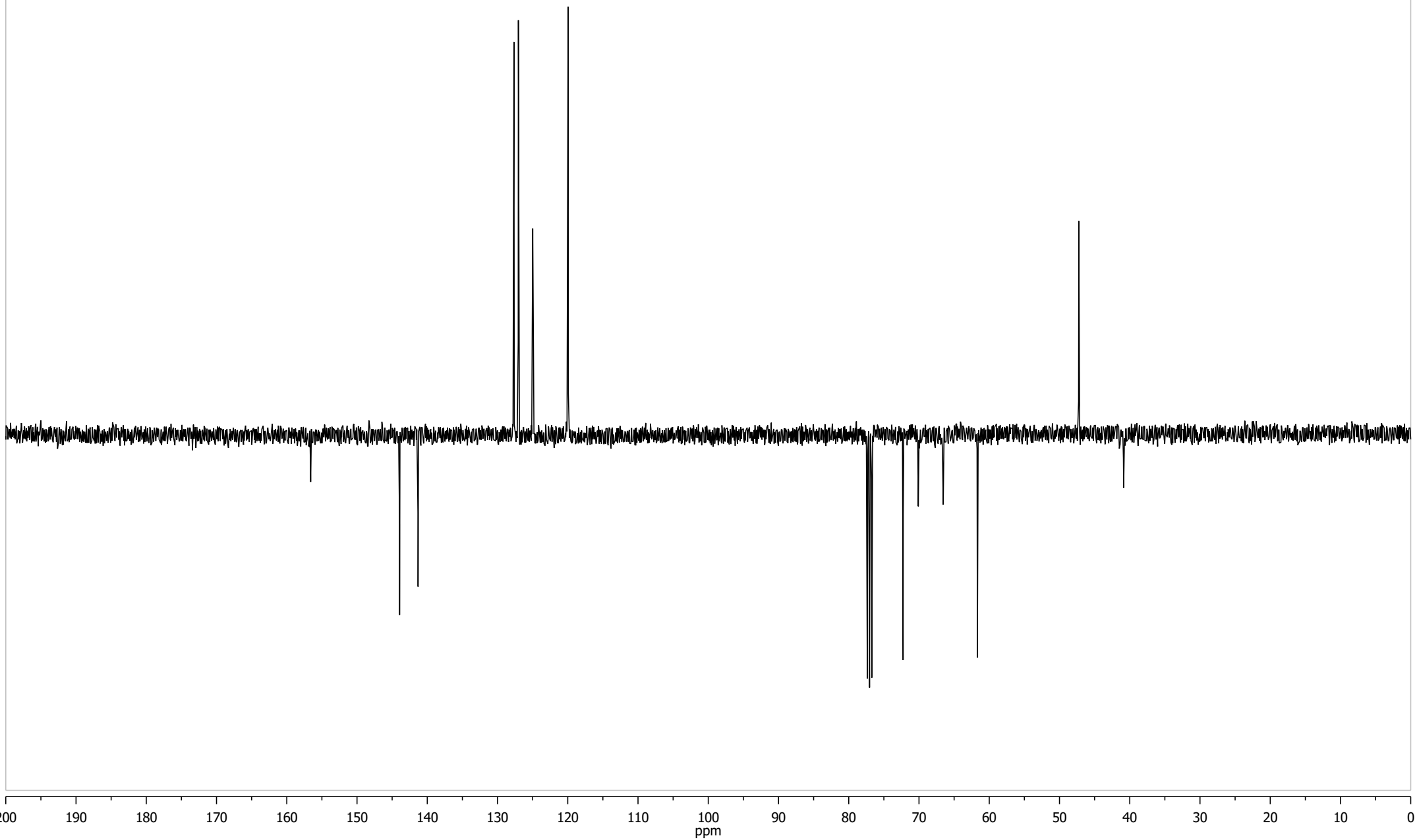
4



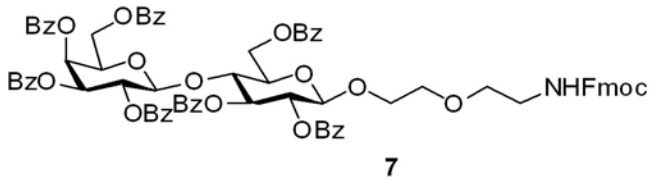
^{13}C NMR (101 MHz, $CDCl_3$)



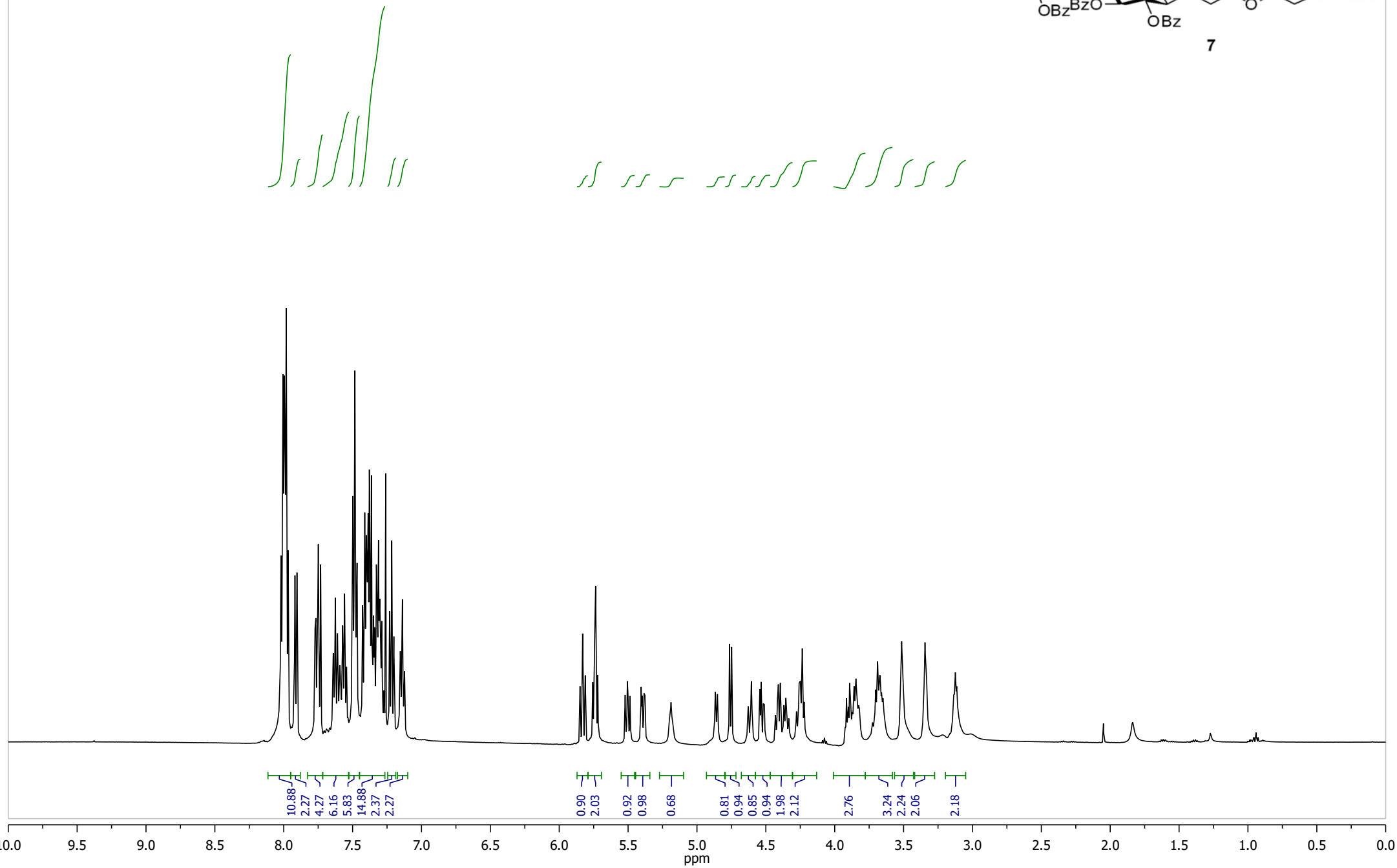
4



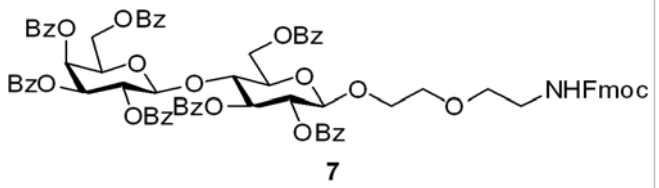
^{1}H NMR (500 MHz, $CDCl_3$)



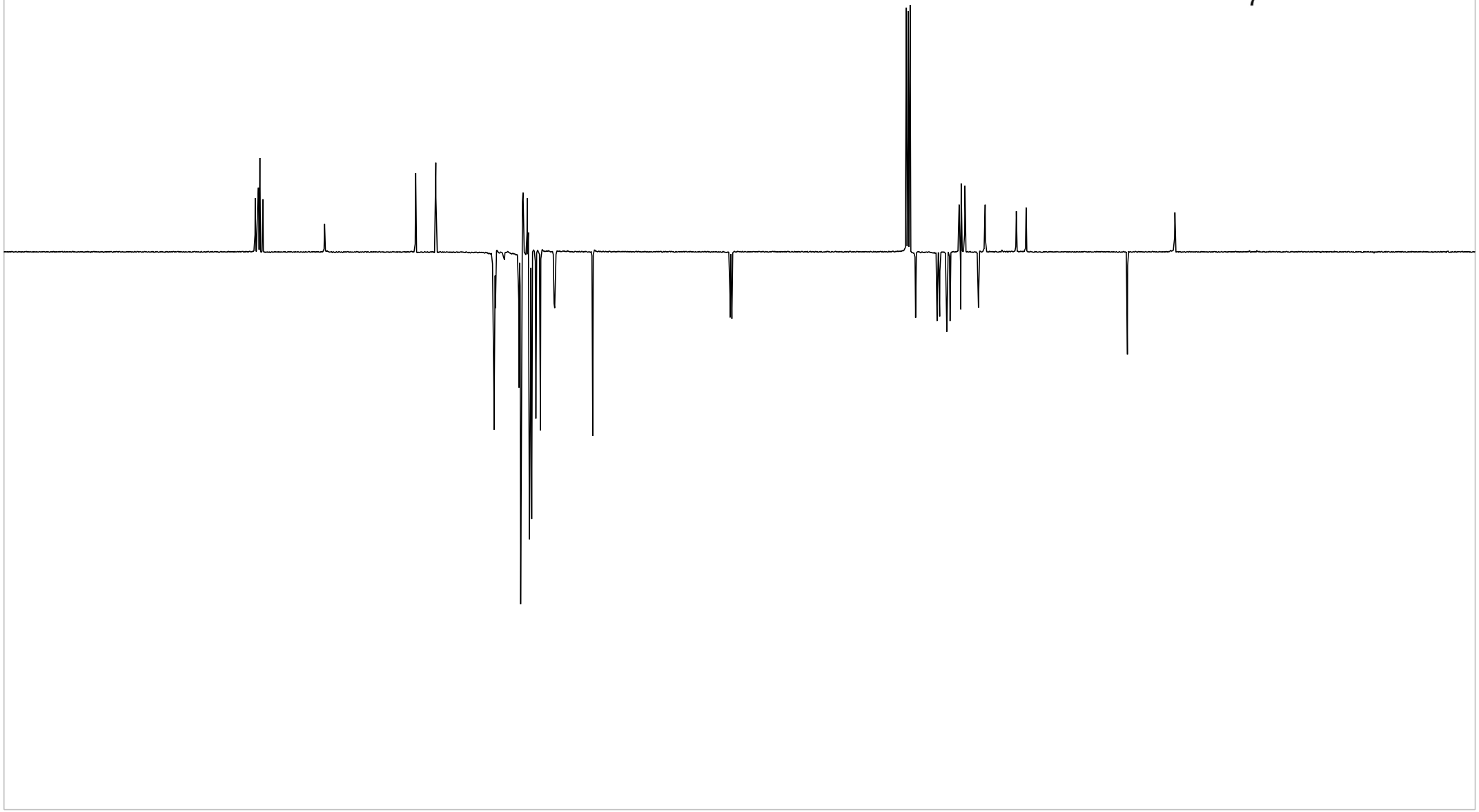
7



^{13}C NMR (125 MHz,$CDCl_3$)



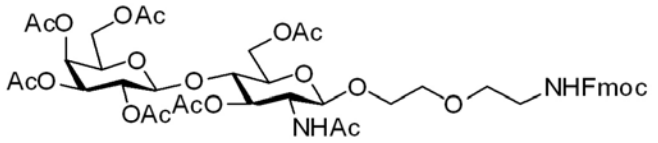
7



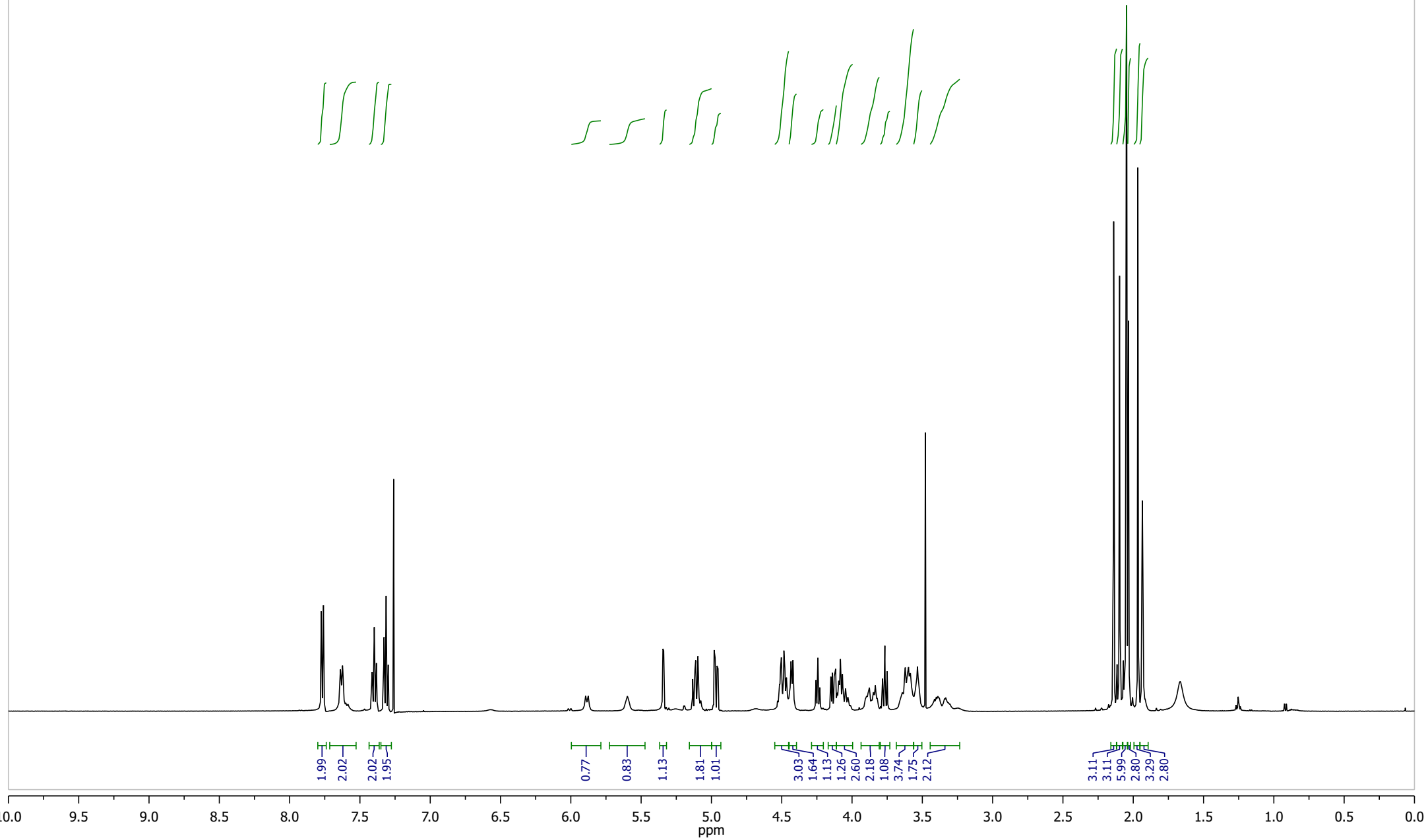
200 190 180 170 160 150 140 130 120 110 100 90 80 70 60 50 40 30 20 10 0

ppm

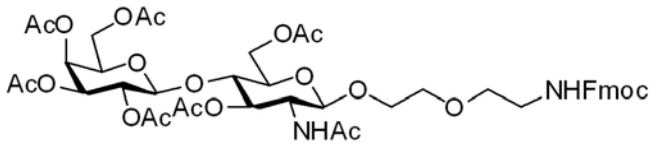
^{1}H NMR (500 MHz, $CDCl_3$)



10

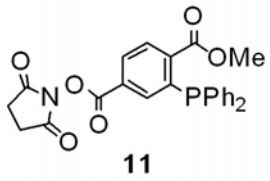


^{13}C NMR (125 MHz,$CDCl_3$)



10

^{1}H NMR (400 MHz,$CDCl_3$)



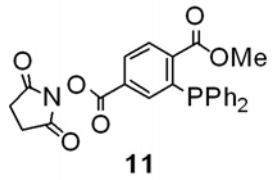
11

1.99 0.99 9.76 3.00 4.06

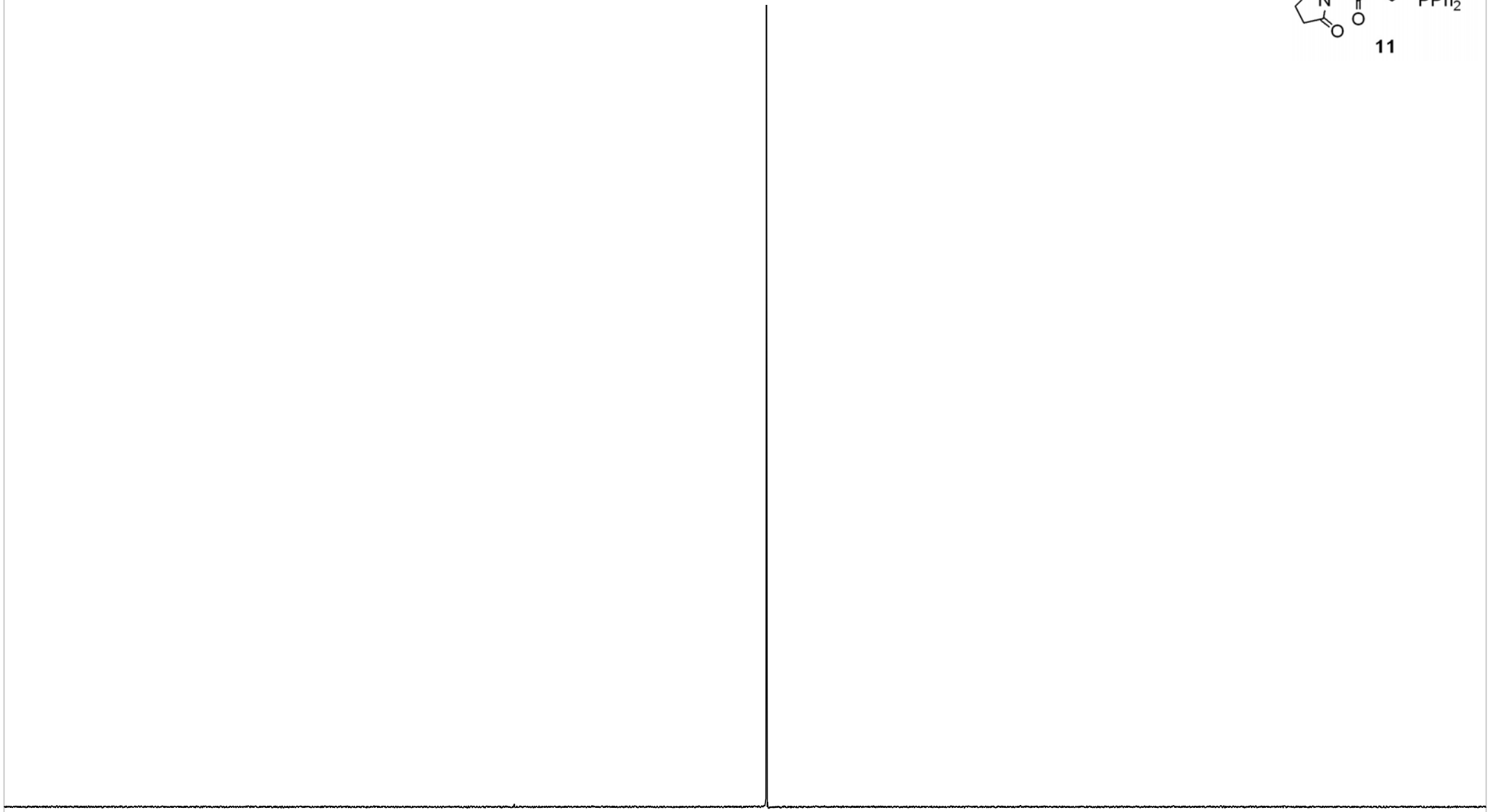
10.0 9.5 9.0 8.5 8.0 7.5 7.0 6.5 6.0 5.5 5.0 4.5 4.0 3.5 3.0 2.5 2.0 1.5 1.0 0.5 0.0

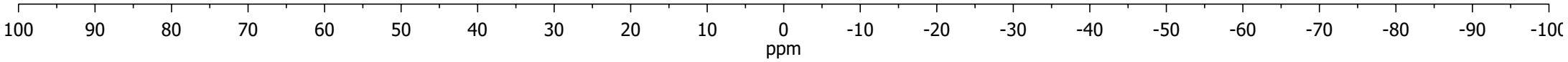
f1 (ppm)

^{31}P NMR (162 MHz, $CDCl_3$)

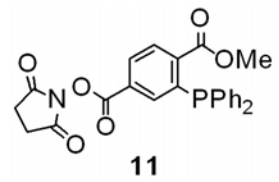


11

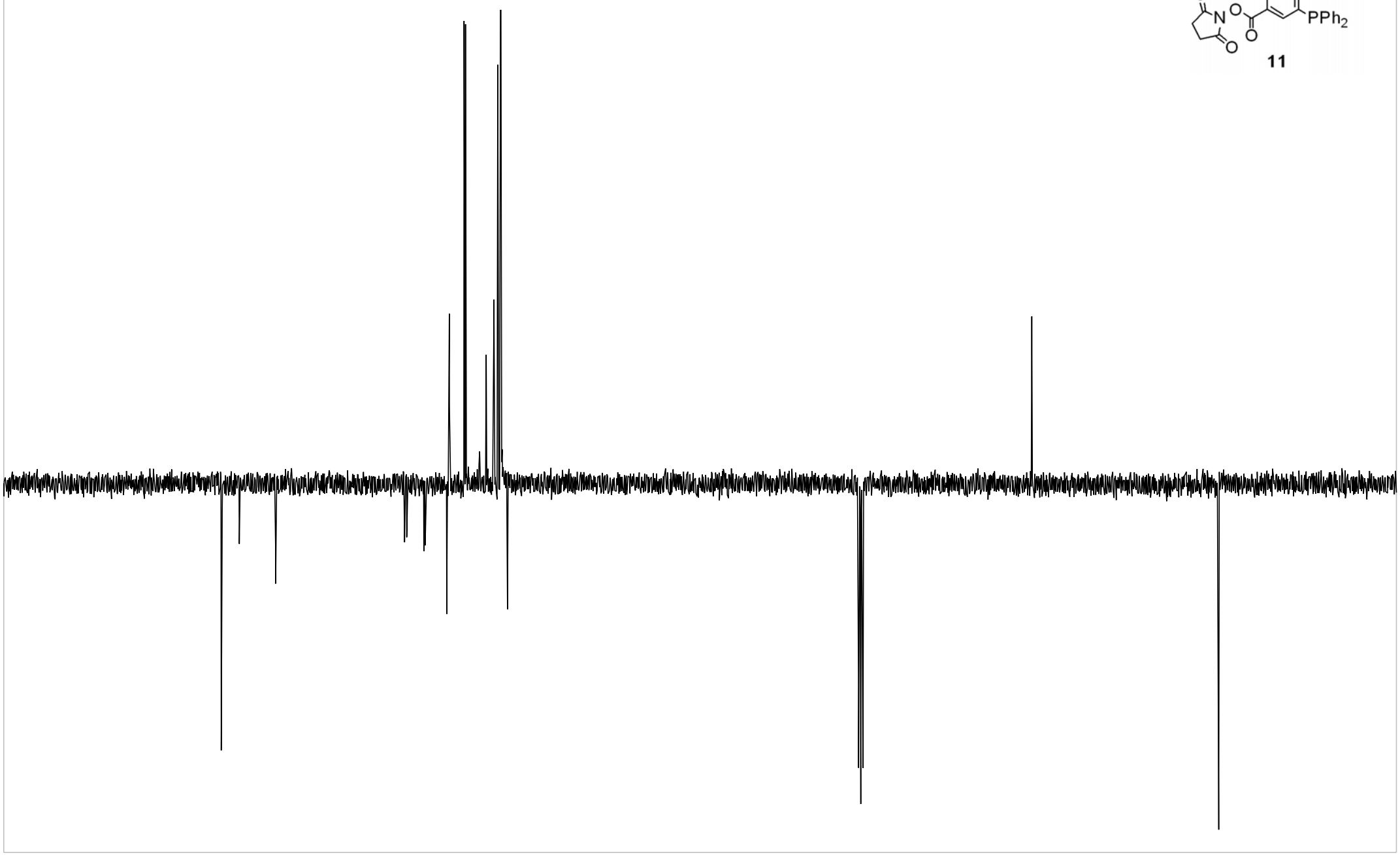




^{13}C NMR (101 MHz, $CDCl_3$)



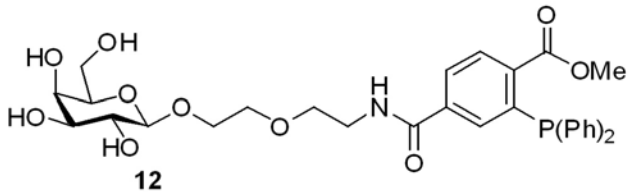
11



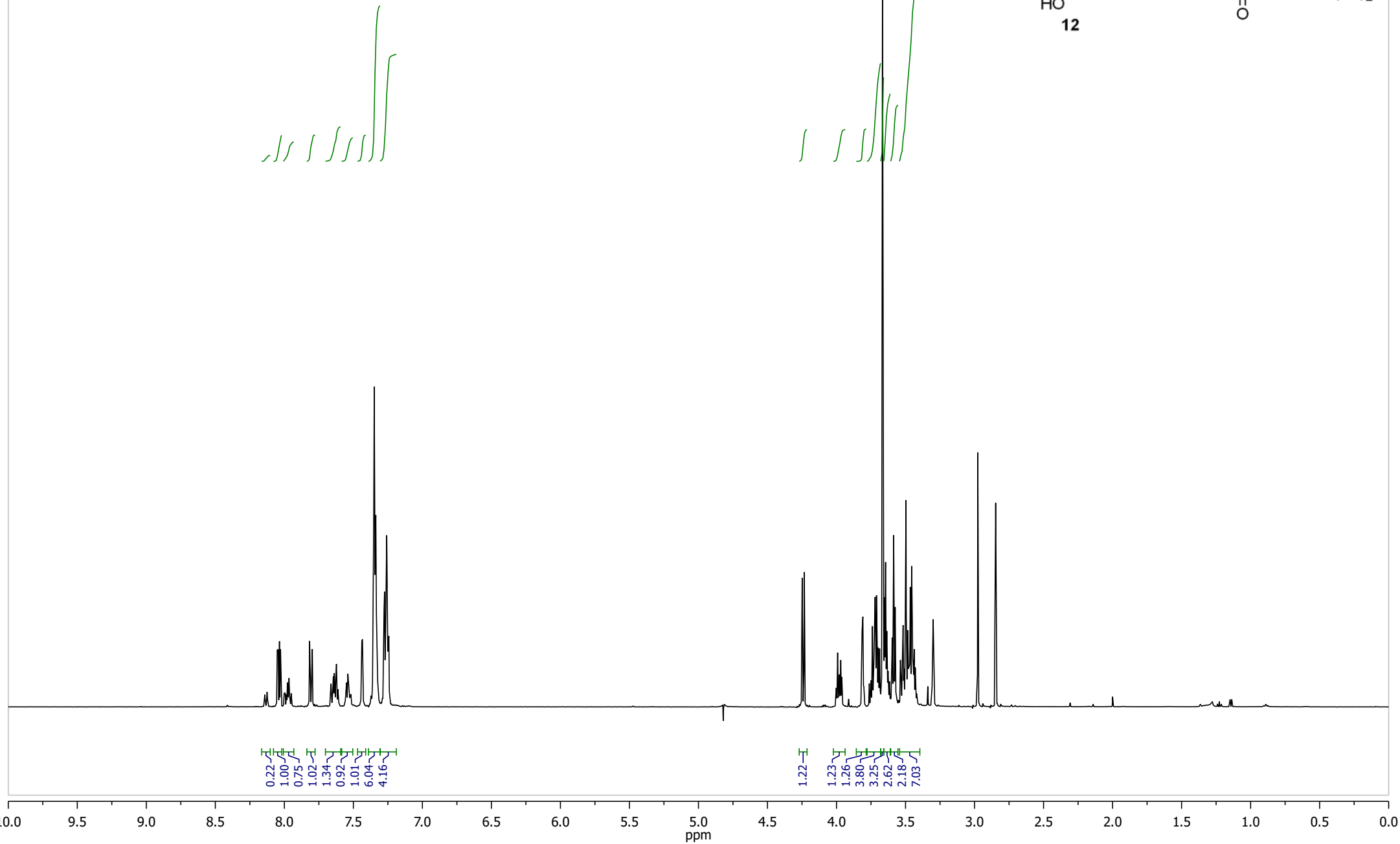
200 190 180 170 160 150 140 130 120 110 100 90 80 70 60 50 40 30 20 10 0

f1 (ppm)

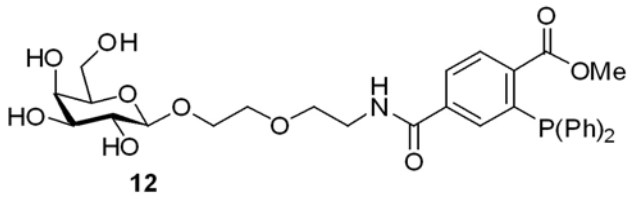
^{1}H NMR (498 MHz, CD_3OD)



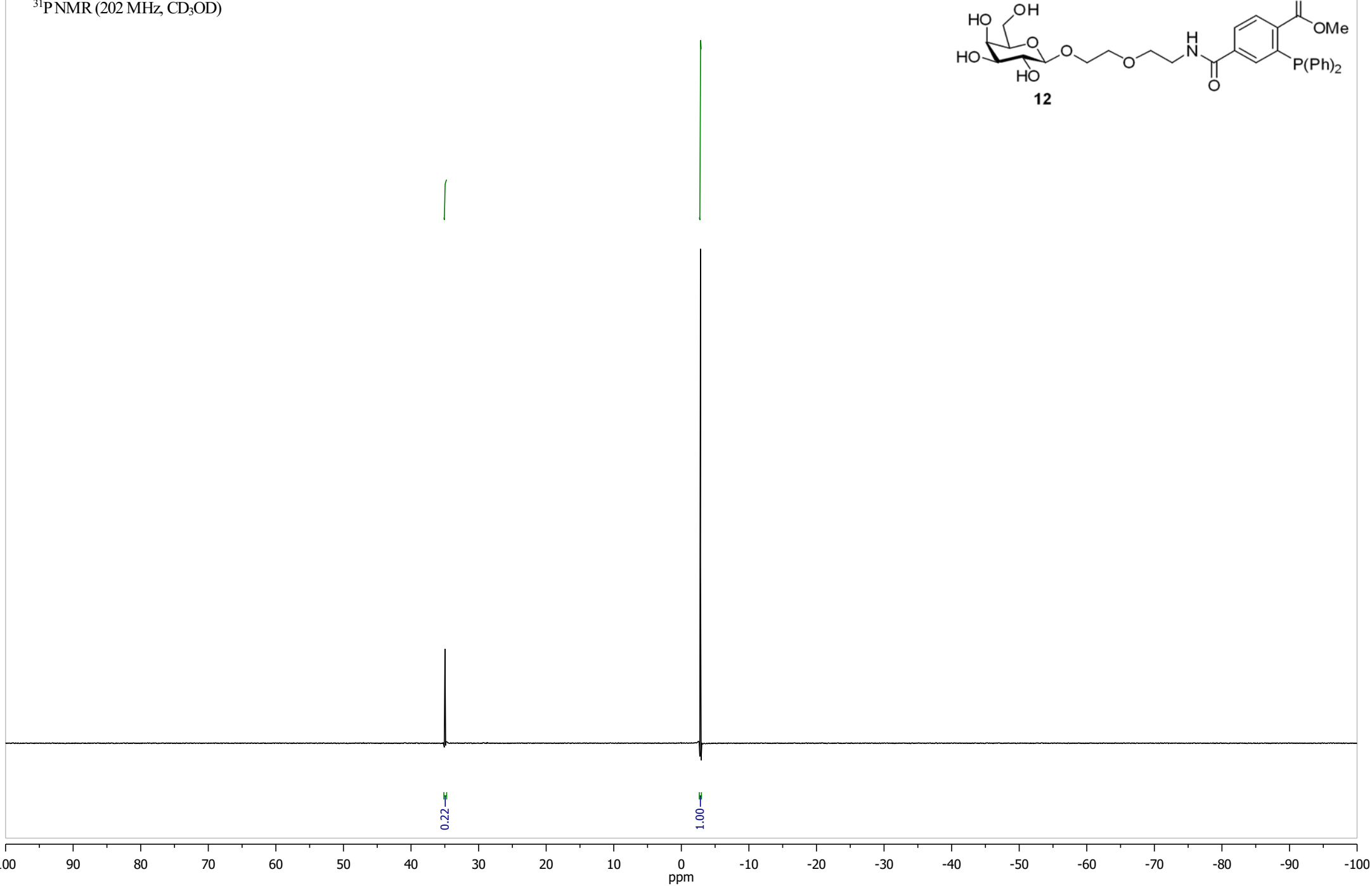
12



^{31}P NMR (202 MHz, CD_3OD)

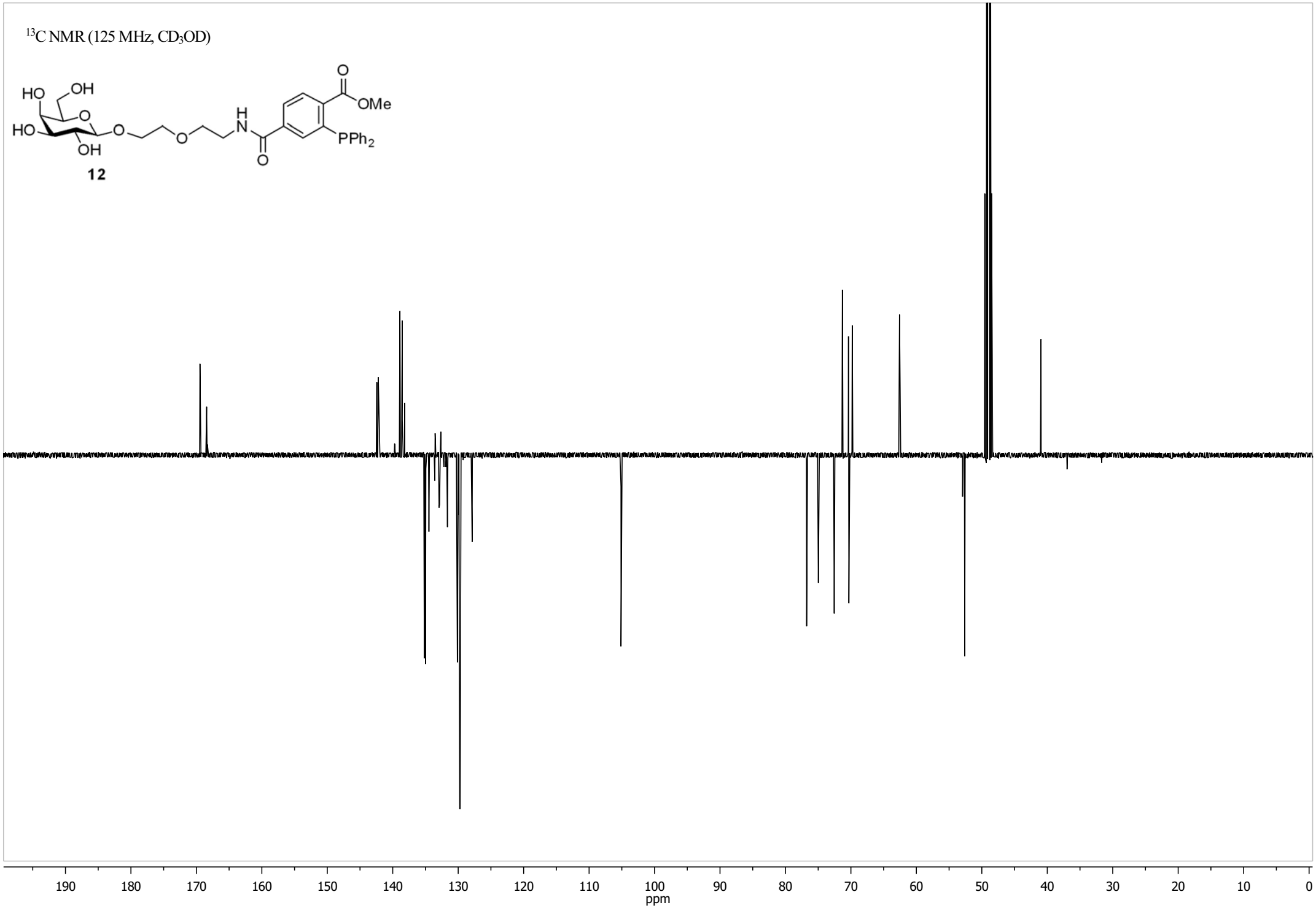


12



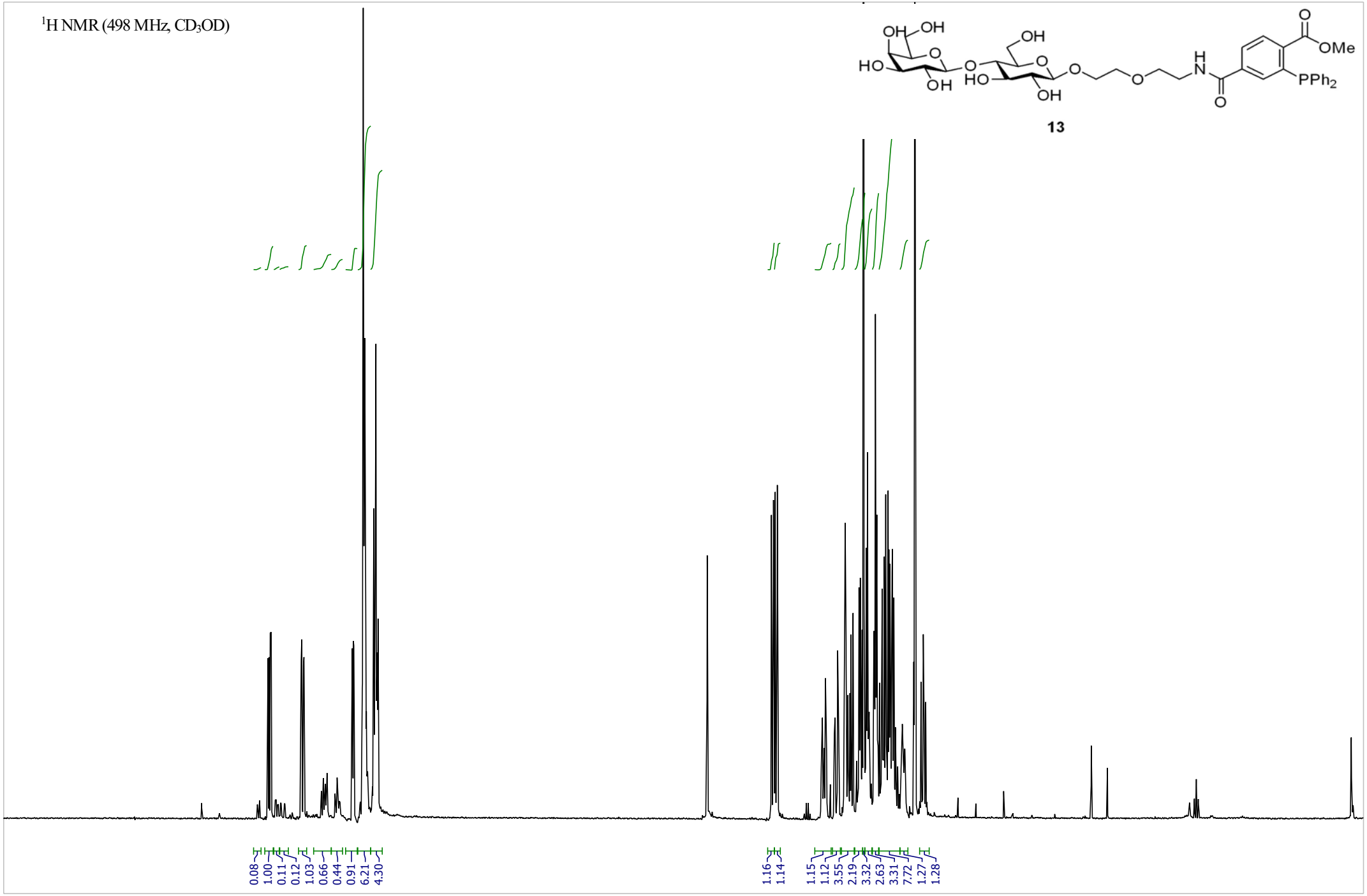
^{13}C NMR (125 MHz, CD_3OD)

12

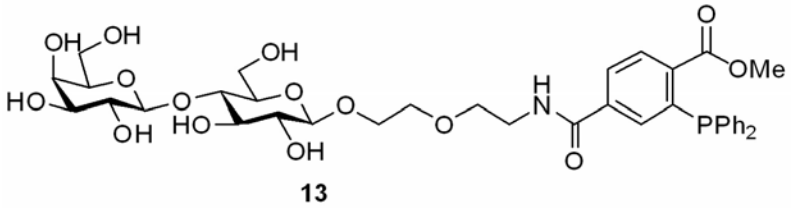


^{1}H NMR (498 MHz, CD_3OD)

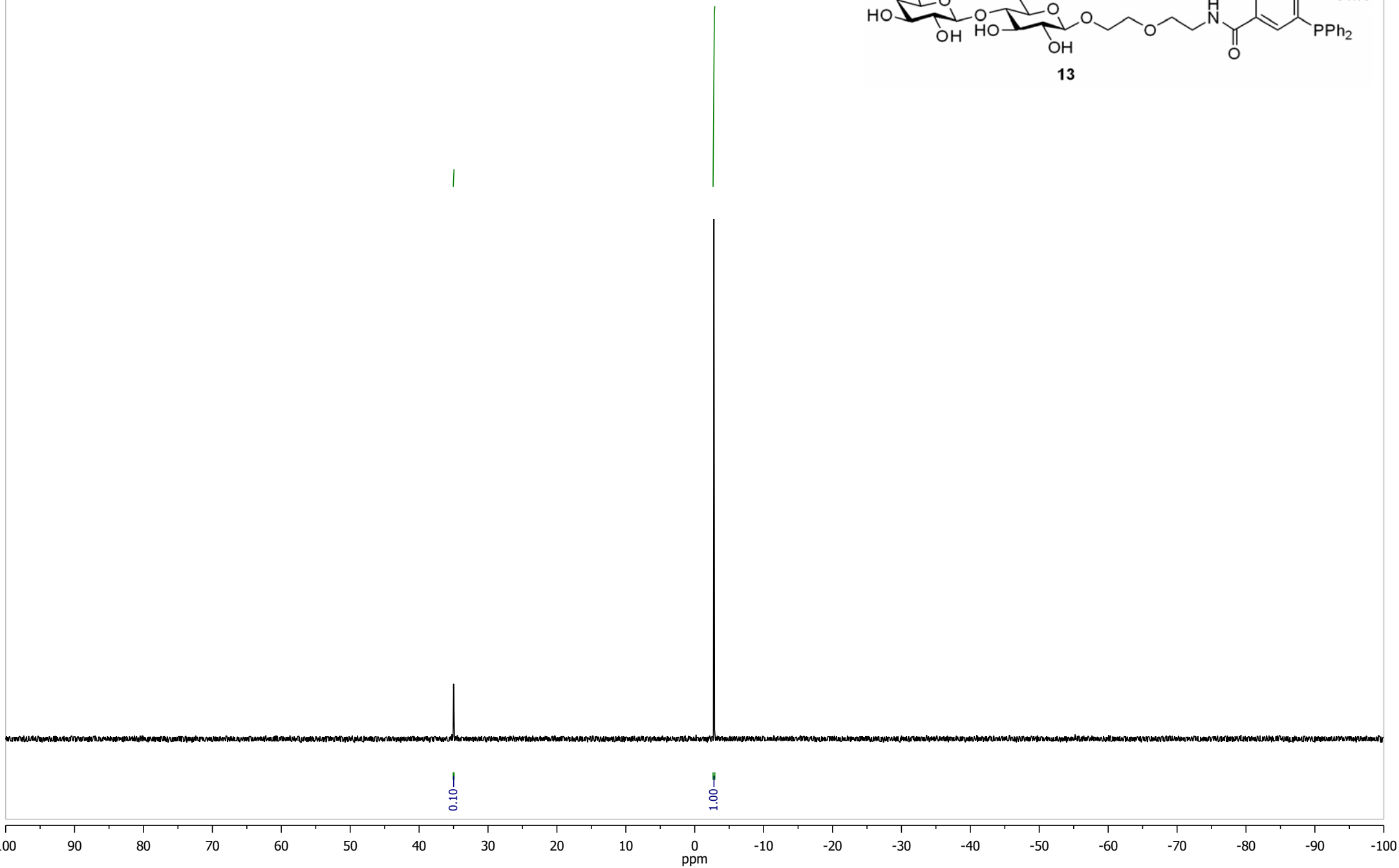
13



^{31}P NMR (202 MHz, CD_3OD)

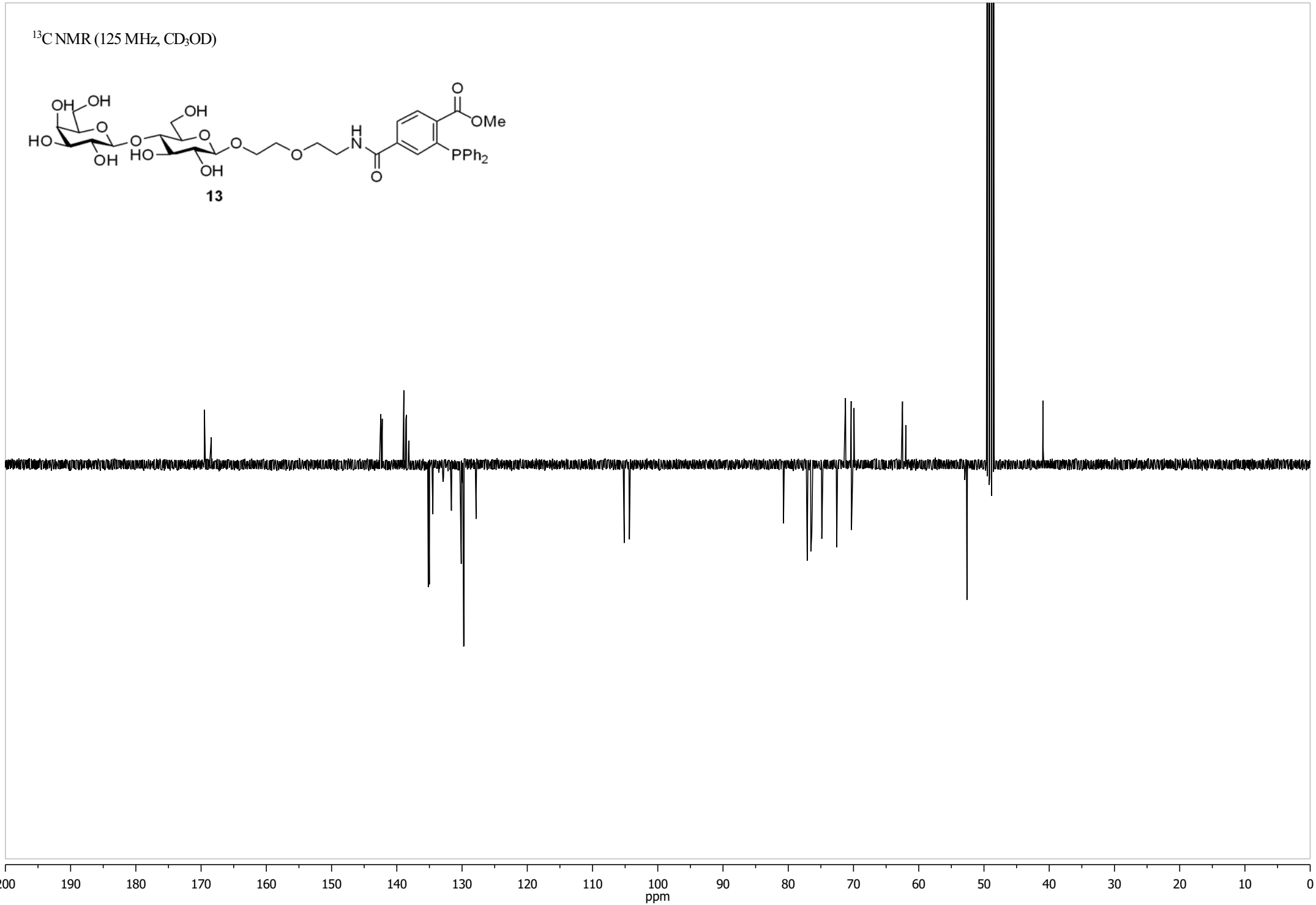


13

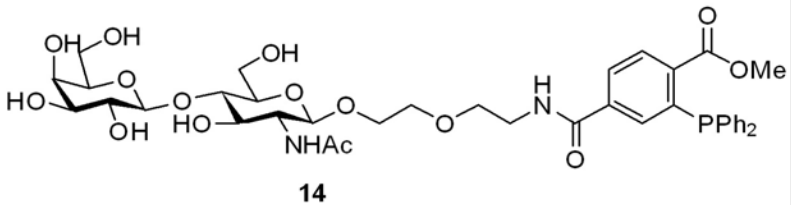


^{13}C NMR (125 MHz, CD_3OD)

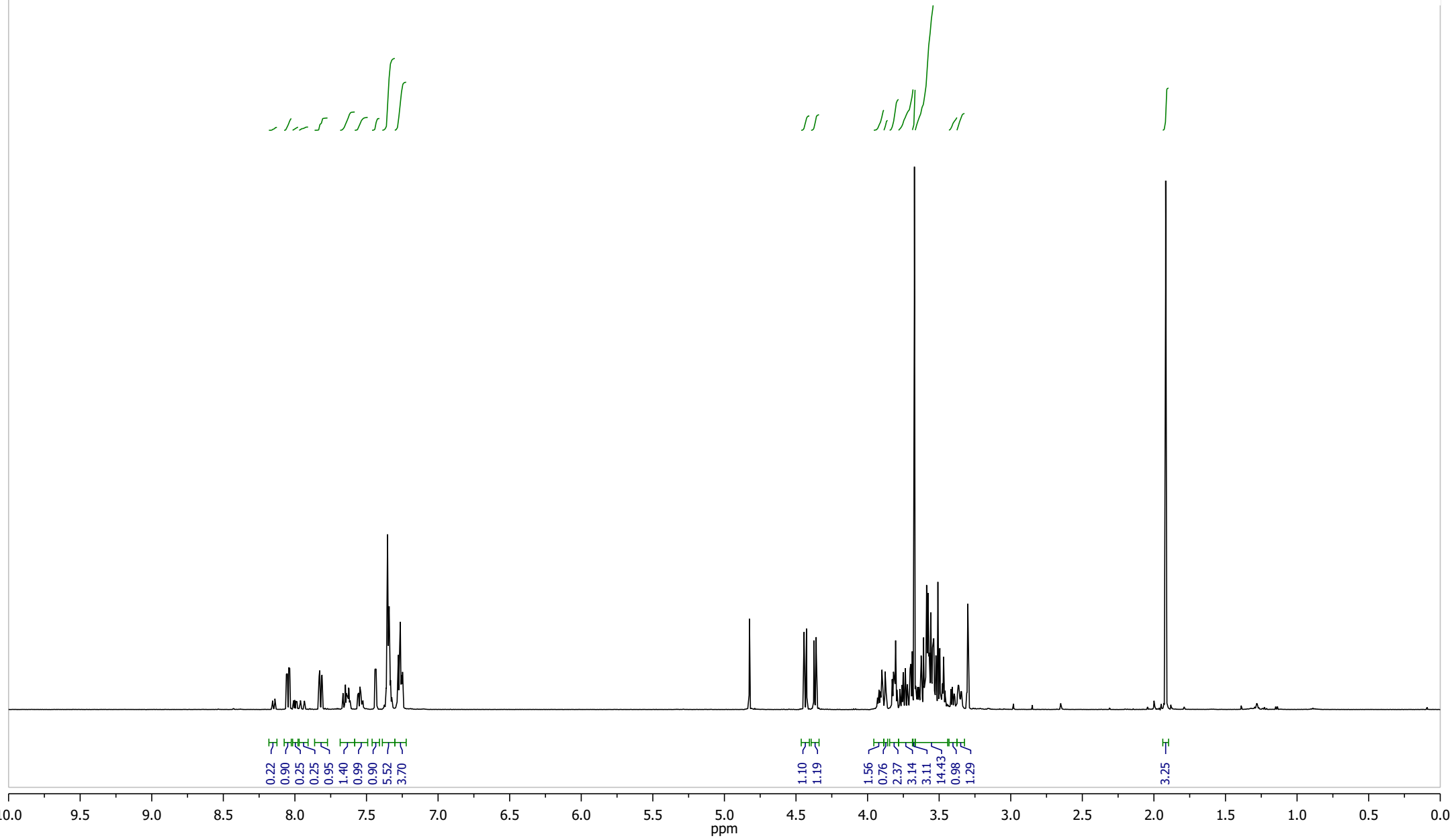
13



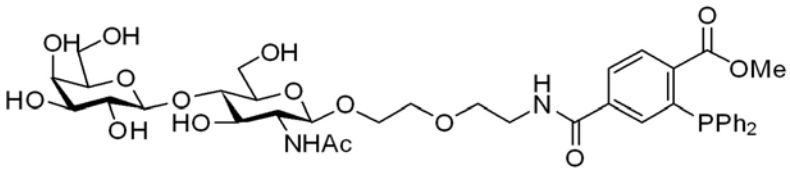
^{1}H NMR (498 MHz, CD_3OD)



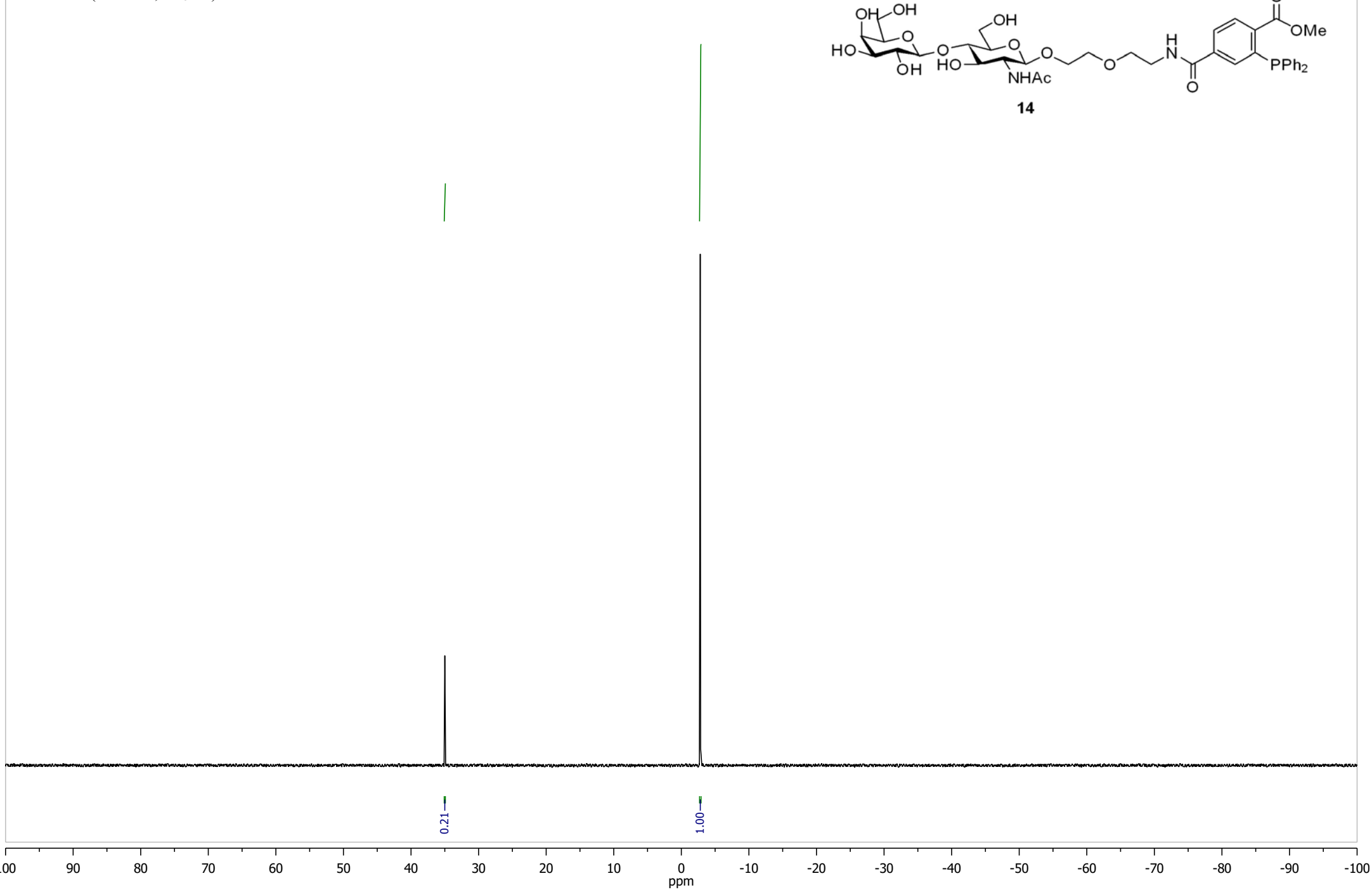
14



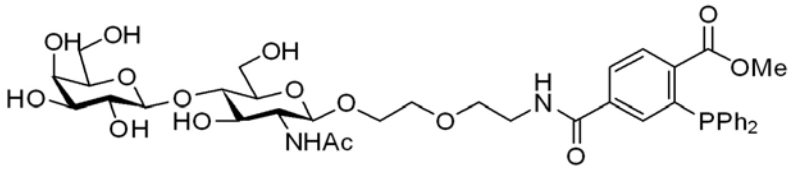
^{31}P NMR (202 MHz, CD_3OD)



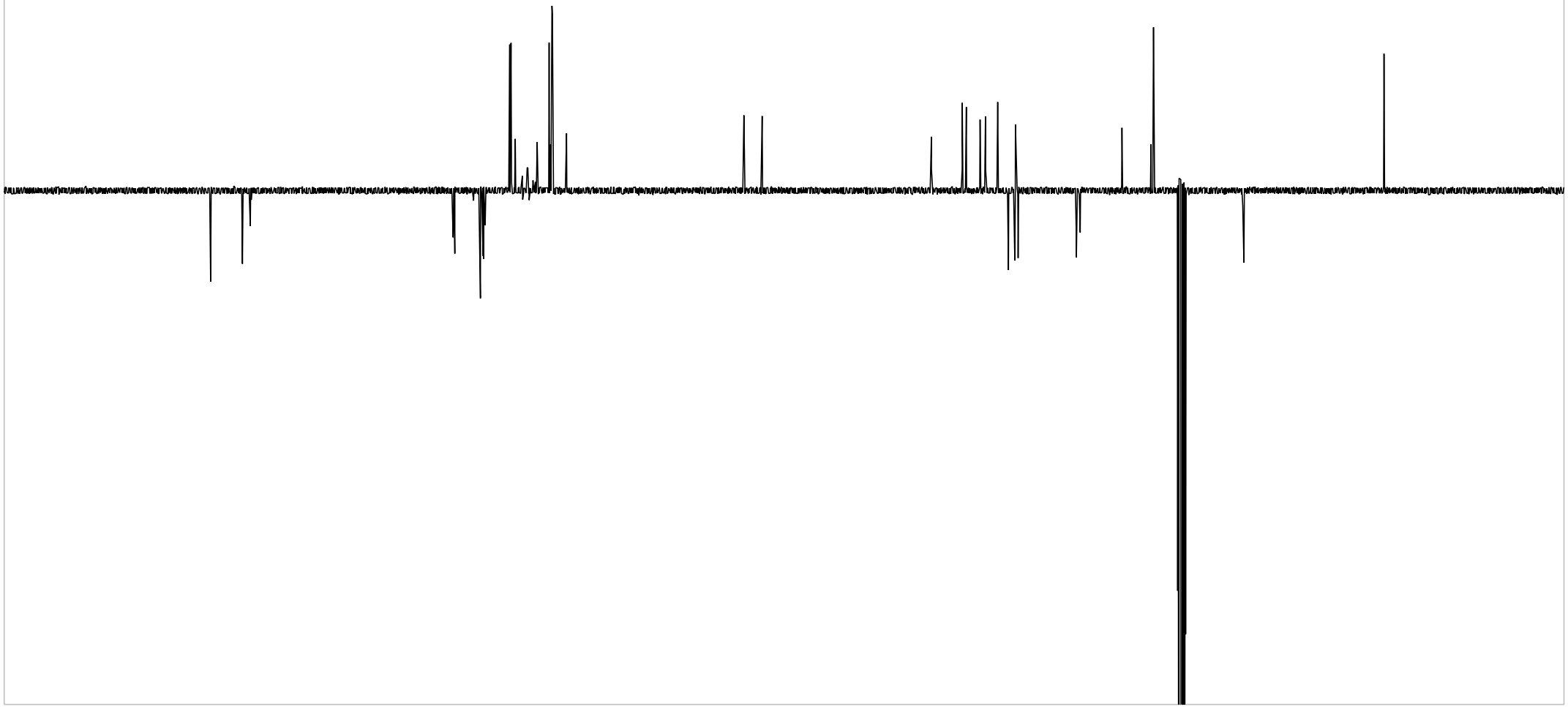
14



^{13}C NMR (125 MHz, CD_3OD)



14



200 190 180 170 160 150 140 130 120 110 100 90 80 70 60 50 40 30 20 10 0

ppm

Noncationic Dipeptide Mimic Oligomers As Cell Penetrating Nonpeptides (CPNP)

Lubomir L. Vezenkov,[†,⊥] Marie Maynadier,[‡,⊥] Jean-François Hernandez,[†] Marie-Christine Averlant-Petit,[§] Olivier Fabre,[§] Ettore Benedetti,[||] Marcel Garcia,[‡] Jean Martinez,*[,†] and Muriel Amblard*[,†]

Institut des Biomolécules Max Mousseron, UMR5247 CNRS, Universités Montpellier 1 et 2, 15 avenue Charles Flahault, 34000 Montpellier, France, IRCM, Institut de Recherche en Cancérologie de Montpellier, INSERM U896, Université Montpellier 1, CRLC Val d'Aurelle Paul Lamarque, Montpellier, F 34298, France, UMR7568 Laboratoire de Chimie-Physique Macromoléculaire (LCPM), 1 Rue Grandville, BP 20451 54001 Nancy Cedex, France, and Istituto di Biostrutture e Bioimmagini CNR and Dipartimento di Chimica Biologica, Università degli Studi di Napoli Federico II, Napoli, 80134, Italy.
Received April 28, 2010; Revised Manuscript Received July 12, 2010

Small oligomers of constrained dipeptide mimics have been synthesized as new vectors for intracellular delivery. They are highly internalized by cells and delivered to the lysosomes by an energy-dependent pathway. This new class of vectors referred to as cell penetrating nonpeptides (CPNP) possess the distinctive feature of being noncationic.

INTRODUCTION

The delivery of drugs into cells remains a major limitation in several therapies. Peptide vectors referred to as cell-penetrating peptides (CPPs) have emerged as promising tools for the intracellular delivery of bioactive cargoes (drugs, peptides, siRNA...) (*1*−*3*). Several classes of CPPs have been reported; most of them are basic or amphipathic peptides (*4*−*8*) and often display high α-helical propensity (*9*). Hydrophobic segments from protein signal sequences or membrane translocating sequences (MTS), as well as a noncharged polyproline peptide, were also described for cell membrane transport (*10, 11*). Non-natural folded oligomers termed foldamers (*12, 13*) have emerged as an important family of versatile frameworks with the first evidence of their ability to cross the cell membrane. A large number of guanidinium rich foldamers including β-peptides (*14*) and peptoids (*5*) have been reported to deliver drugs or labeled compounds into cells. Other oligomers constructed from monomers that differ significantly from α- or β-amino acids, possessing predictable helical structure and amphipathic character were also found to efficiently enter into cells (*15*−*17*). Thanks to the possibility to control their secondary structure and their resistance against protease degradation (*18*), structured oligomers constitute a privileged platform for designing cell penetrating nonpeptide compounds (CPNP). Alternatively, it has been shown that sterol derivatives could enhance molecular uptake (*19, 20*).

Taking into account these considerations, our aim was to develop a novel class of small molecules as potential vectors to mediate cell penetration. They are based on constrained dipeptide mimic oligomers. A few years ago, we showed using molecular modeling that oligomerization of constrained β-turn dipeptide mimics could induce helix-like structures (*21*). Among the different motifs selected by this program, we particularly focused on (3-*S*)[amino]-5-(carboxymethyl)-2,3-dihydro-1,5-benzothiazepin-4(5*H*)-one (DBT) described as a β-turn mimic (*22, 23*), supposedly a favorable feature to induce structured oligomers. DBT oligomers are neither polycationic nor amphipathic oligomers unlike the majority of described vectors. By virtue of their hydrophobicity, their expected ability to achieve helical type structure and resistance against protease degradation, we hypothesized that DBT oligomers should be good candidates as translocating agents. Short oligomers were synthesized and their cellular uptake and subcellular localization studied.

EXPERIMENTAL PROCEDURES

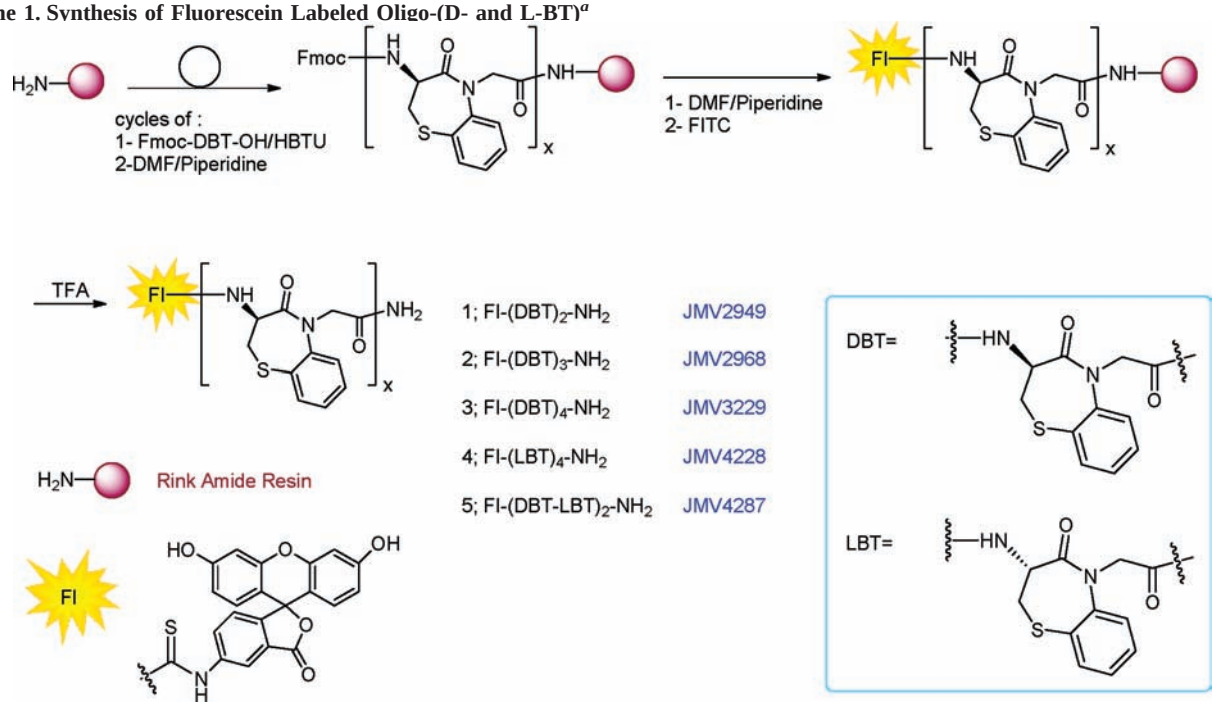
Oligomers. They were synthesized on Rink amide resin following solid phase peptide synthesis methodology and labeled at their N-terminus with fluorescein isothiocyanate (see Supporting Information). The monomeric units Fmoc-DBT-OH and Fmoc-LBT-OH were prepared as previously described (*24*).

Cell Preparation and Treatment with Oligomers. We used 1 mM stock solutions of compounds dissolved in DMSO that were further diluted with serum-free medium to obtain a final concentration of 10^{-5} M. All compounds were protected from light during the experiments, and their fluorescence values were regularly verified. Human breast cancer MDA-MB-231 cells were maintained in monolayer cultures in Dulbecco's modified Eagle's medium (DMEM) supplemented with 10% fetal bovine serum (FBS) and 50 μg/mL gentamycin at 37 °C in 5% CO_2. One day prior to the experiment, cells were harvested using trypsin in phosphate-buffered saline (PBS), centrifuged, and resuspended with culture medium. The suspension containing 10^6 cells/mL was transferred into plastic 24-well plates (Becton Dickinson, Le Pont De Claix, France) (200 μL/well) and incubated overnight until they reached >90% confluency. On the day of the experiment, the culture medium was removed, and the cells were washed once with phenol red-free DMEM. Then, 200 μL of DMEM containing 10% FBS and 10^{-5} M of compounds was dispersed on cells. Experiments were carried out in triplicate for each compound. To determine the amount of compounds assimilated by cells, including membrane-bound fractions, cells were washed twice with PBS. To determine the amount of internalized compounds, cells were washed with PBS

* To whom correspondence should be addressed. E-mail: jean.martinez@univ-montp1.fr (J.M.); muriel.amblard@univ-montp1.fr (M.A.).
† UMR5247 CNRS, Universités Montpellier.
‡ IRCM, Université Montpellier.
§ UMR7568 Laboratoire de Chimie-Physique Macromoléculaire (LCPM).
|| Università degli Studi di Napoli Federico II.
⊥ These authors contributed equally to this work.

10.1021/bc1002086 © 2010 American Chemical Society
Published on Web 09/03/2010

Scheme 1. Synthesis of Fluorescein Labeled Oligo-(D- and L-BT)[a]



[a] The scheme is given for the D series.

and then treated for 5 min with 30 μL of a solution containing 0.5 mg/mL trypsin. After trypsinization, cells were resuspended in phenol red-free DMEM and centrifuged for 5 min at 800*g*. Adherent cells or cell pellets were lysed in 200 μL of cell culture lysis reagent (Promega, Charbonnières, France). After 30 min of incubation at room temperature, 200 μL of distilled water was added before analysis on a Gemini XS spectrofluorimeter (Molecular Devices, CA, USA), with the excitation wavelength adjusted to 485 nm and emission measured at 530 nm. All fluorescence values were normalized according to the fluorescence intensity of each compound at 10^{-5} M in lysis buffer in the presence of 2×10^5 cells.

Kinetics of Internalization. One day before the experiment, 2×10^6 MDA-MB-231 cells were seeded on plastic 24-well plates. The cells were then washed with DMEM and incubated for increasing times from 1 to 24 h with 10^{-5} M oligomer at 37 °C. At the indicated time, cells were treated by trypsin and intracellular fluorescence measured as described above.

Visualization of Fluorescent Oligomers by CLSM. The day prior to the experiment, MDA-MB-231 cells were seeded onto bottom glass dishes (World Precision Instrument, Stevenage, UK) at a density of 10^6 cells per square centimeter. On the day of the experiment, cells were washed once and incubated in 1 mL phenol red-free medium containing fluorescent labeled compounds at a concentration of 10^{-5} M for 3, 16, and 24 h. Thirty minutes before the end of incubation, cells were loaded with Hoechst 33342 (Invitrogen, Cergy Pontoise, France) for nuclear staining at a final concentration of 5 μg/mL. For membrane labeling, a Vybrant lipid-raft labeling kit (Invitrogen) was used as described by the manufacturer. For endosome labeling, 20 min before the end of the experiment, 35 mg/mL of transferrin (Invitrogen) was added to the culture medium. For lysosome labeling, 3 h before the end of the experiment, 50 nM of lysotracker red DND-99 (Invitrogen) was added to phenol red-free DMEM. Before visualization, cells were washed gently with phenol red-free DMEM. Cells were then scanned with a LSM 5 LIVE confocal laser scanning microscope (Carl Zeiss, Le Pecq, France), with a slice depth (Z stack) of 0.67 μm.

RESULTS AND DISCUSSION

Design of the Target DBT Oligomers. Oligomers of different lengths were synthesized (see Supporting Information) on a solid support using Rink amide PS resin, by successive addition of N-Fmoc protected DBT (Fmoc-DBT-OH) (*24*) in the presence of HBTU as the coupling reagent (Scheme 1). In order to track their cellular internalization by fluorescence microscopy, fluorescein isothiocyanate was used to label the oligomers. The fluorescent tag was attached directly to the N-terminus of the poly(DBT) anchored to the resin (JMV2949, JMV2968 and JMV3229). The importance of the configuration and the structure of the oligomers was assessed by the preparation of the LBT derivative (JMV4228) and the D/LBT alternated oligomer (JMV4287), respectively.

Cellular Uptake of DBT Oligomers. At first, the cellular uptake in MDA-MB-231 breast cancer cells of the oligomers **1**−**5** was analyzed by fluorescence emission measurement (Figure 1) and compared to fluorescein labeled octa-arginine (*25*) (Arg_8) as a positive control and carboxyfluorescein (CF) as a negative control. In order to determine the internalized fraction of the compounds, a 5-min trypsin treatment was realized to remove membrane-bound transduction compounds (Figure 1A) (*26*). It is worth noting that the percentage of membrane-bound oligomers was not as important as in the case of the polycationic Arg_8.

The highest intracellular fluorescence intensity was found for DBT_4 (JMV3229) with a drastic decrease (>4-fold) for DBT_3 (JMV2968) and DBT_2 (JMV2949) oligomers. Thus, the cellular uptake appeared length-dependent with an increase of internalization with the oligomer size. Moreover, the amount of JMV3229 that was internalized was more significant than that of Arg_8 despite the fact that it is uncharged. Even though the increase in efficiency from DBT_2 to DBT_4 could be associated with an increase of the hydrophobicity, the high difference between DBT_3 and DBT_4 might be also attributed to a

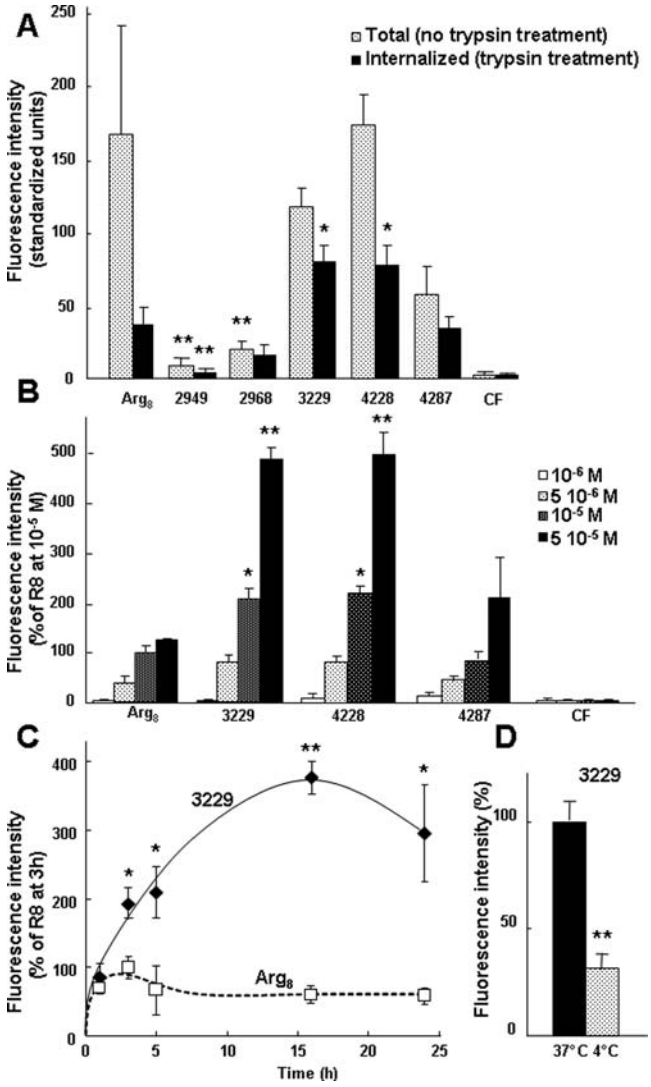


Figure 1. Uptake of Arg_8 and oligomers **1**−**5** in MDA-MB-231 cells. Data are the means ± SD from three independent experiments. In B to D, cells were treated by trypsin before fluorescence measurements. (A) Determination of total and internalized compounds after incubating cells for 3 h at 37 °C with 10^{-5} M **1**−**5**. $*p < 0.05$, $**p < 0.01$ relative to Arg_8 values with or without trypsin treatment, respectively (Student's *t* test). (B) Comparison of fluorescence emission after incubation for 3 h with several concentrations ranging from 10^{-6} to 5.10^{-5} M. $*p < 0.05$, $**p < 0.01$ relative to Arg_8 values at the same concentration (Student's *t* test). (C) Kinetics of internalization of JMV3229 and Arg_8 at 10^{-5} M. $*p < 0.05$, $**p < 0.01$ relative to Arg_8 values at the same time (Student's *t* test). (D) Effect of temperature on the cellular uptake of JMV3229 at 3 h. $**p < 0.01$ relative to Arg_8 values (Student's *t* test).

progressive organization of the oligomer structure. Compound JMV4228 constructed by oligomerization of an L-benzothiazepinone moiety was as potent as its D-counterpart suggesting that the configuration of the BT moiety was not important and that the CPNPs do not interact with a specific receptor but rather with hydrophobic plasma membrane molecules. Compound JMV4287 constructed from the alternation of D and LBT exhibited a 2-fold decreased uptake. This result could be explained by a change in the oligomer structure.

A dose−response analysis was performed to compare the uptake of the BT-oligomers with octa-arginine (Figure 1B). The penetration of all compounds appeared to be dose-dependent. However in contrast to Arg_8, uptake of JMV compounds still increased at high doses (5.10^{-5} M). The kinetics study performed with 10^{-5} M JMV3229 (Figure 1C) showed that its cellular entry was at least as efficient at 1 h as that of Arg_8. Then, JMV3229 uptake increased up to 16 h to reach a 6-fold higher concentration than Arg_8, for which maximal concentration is reached at 1 h. A temperature-dependent analysis performed at 4 and 37 °C (Figure 1D) showed that the cellular uptake exhibited a 3-fold decrease at low temperature, hence suggesting the involvement of an energy-dependent endocytotic pathway. The remaining fluorescence was most probably due to cell membrane-bound oligomers as shown in Figure 2B.

Intracellular Distribution of DBT Oligomers. Confocal laser scanning microscopy (CLSM) analyses were also performed in living cells to assess internalization and intracellular distribution. These experiments were associated with a kinetic study of DBT oligomer internalization. Figure 2A shows the internalization of JMV3229 in cellular organelles after 3 h of incubation with the highest accumulation at 16 h and an apparent decrease at 24 h in accordance with the kinetic study reported in Figure 1C. Co-staining with a membrane marker (lipid-raft labeling) indicated that this hydrophobic compound was not held in the lipid membrane. However, at 4 °C, the majority of the compound was colocalized with the membrane marker (Figure 2B) rather than internalized, confirming the temperature effect on the intracellular uptake described in Figure 1D and supporting an energy-dependent internalization mechanism.

To gain more insight into JMV3229 internalization, costainings were performed with other fluorescent markers for subcellular components such as the nucleus, endosomes, and lysosomes. The results showed that JMV3229 was mostly colocalized with an endosomal marker at 3 h (Figure 2C) and with a lysosomal marker at 16 h (Figure 2D). Similar data were obtained for the L-counterpart JMV4228 (Supporting Information). This indicated an endosomal uptake of these oligomers followed by a lysosomal accumulation.

Altogether, these data indicate the ability of these oligomers to target the endolysosomal pathway. Although most of the initial drug delivery studies aimed to avoid lysosomal addressing to prevent subsequent drug degradation, more recent studies demonstrated the relevant clinical utility to target this compartment for drug delivery in the treatment of lysosomal storage diseases, Alzheimer's disease, and cancer (*20*, *27*−*31*).

The cytotoxicity of this new class of molecules was also determined in MDA-MB-231 cells using the MTT viability assay (Supporting Information). After a 5 day-incubation, these compounds exhibited no significant effect on cell viability at the 10^{-5} M concentration used for internalization studies. These results indicated that poly-DBT could be safely used as vectors for cell drug delivery.

CONCLUSIONS

The cellular penetration efficiency of the described short DBT oligomers offers a novel class of vectors having the particularity of not being cationic. This feature should open new avenues in the field of compounds able to cross the cell membranes. The drastic increase of the cellular uptake along with the oligomer size could suggest an essential role of structuration and/or hydrophobicity for this class of compounds. Moreover, the decrease in the uptake of the D/LBT alternated oligomer should be also associated with structural features. In order to establish a relationship between their capacity to penetrate into the cell and their structural and physical features, more DBT oligomer derivatives need to be constructed. The structure of the oligomers is currently investigated using NMR spectroscopy and X-ray crystallography. The specific localization of DBT oligomers in endosomes and lysosomes has been evidenced. Studies toward the application of these CPNP as functional drug delivery vectors and the understanding of their translocation pathway are also in progress.

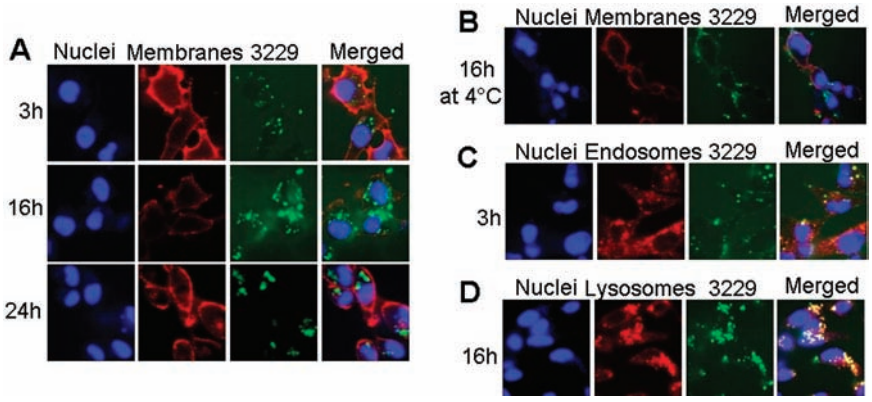


Figure 2. Confocal microscopy images of living MDA-MB-231 breast cancer cells incubated with JMV3229 compound. Images are representative of at least 3 independent experiments. (A) Distribution of JMV3229 after 3, 16, and 24 h of incubation at 37 °C. (B) Distribution of JMV3229 at 4 °C and colocalization of the oligomers with the membrane marker. (C) Co-localization of JMV3229 with the endosomal marker at 3 h at 37 °C. (D) Co-localization of JMV3229 with the lysosomal marker at 16 h at 37 °C.

ACKNOWLEDGMENT

This study was supported by the Agence Nationale de la Recherche (ANR-08-BLAN-0066-01) and ARC grant number 3953. Michel Gleizes is acknowledged for technical assistance with cell cultures.

Supporting Information Available: Solid phase supported synthesis and characterization of the different oligomers; description of the MTT assay for cellular toxicity analysis; confocal laser scanning microscopy of JMV3229 and JMV4228. This material is available free of charge via the Internet at http://pubs.acs.org.

LITERATURE CITED

(1) Joliot, A., and Prochiantz, A. (2004) Transduction peptides: from technology to physiology. *Nat. Cell Biol. 6*, 189–196.
(2) Mae, M., and Langel, U. (2006) Cell-penetrating peptides as vectors for peptide, protein and oligonucleotide delivery. *Curr. Opin. Pharmacol. 6*, 509–514.
(3) Fernandez-Carneado, J., Kogan, M. J., Pujals, S., and Giralt, E. (2004) Amphipathic peptides and drug delivery. *Biopolymers 76*, 196–203.
(4) Vives, E., Brodin, P., and Lebleu, B. (1997) A truncated HIV-1 Tat protein basic domain rapidly translocates through the plasma membrane and accumulates in the cell nucleus. *J. Biol. Chem. 272*, 16010–16017.
(5) Wender, P. A., Mitchell, D. J., Pattabiraman, K., Pelkey, E. T., Steinman, L., and Rothbard, J. B. (2000) The design, synthesis, and evaluation of molecules that enable or enhance cellular uptake: Peptoid molecular transporters. *Proc. Natl. Acad. Sci. U.S.A. 97*, 13003–13008.
(6) Derossi, D., Joliot, A. H., Chassaing, G., and Prochiantz, A. (1994) The 3rd helix of the antennapedia homeodomain translocates through biological-membranes. *J. Biol. Chem. 269*, 10444–10450.
(7) Pooga, M., Hallbrink, M., Zorko, M., and Langel, U. (1998) Cell penetration by transportan. *FASEB J. 12*, 67–77.
(8) Futaki, S. (2005) Membrane-permeable arginine-rich peptides and the translocation mechanisms. *Adv. Drug Delivery Rev. 57*, 547–558.
(9) Deshayes, S., Morris, M. C., Divita, G., and Heitz, F. (2005) Cell-penetrating peptides: tools for intracellular delivery of therapeutics. *Cell. Mol. Life Sci. 62*, 1839–1849.
(10) Hawiger, J. (1997) Cellular import of functional peptides to block intracellular signaling. *Curr. Opin. Immunol. 9*, 189–194.
(11) Crespo, L., Sanclimens, G., Montaner, B., Perez-Tomas, R., Royo, M., Pons, M., Albericio, F., and Giralt, E. (2002) Peptide dendrimers based on polyproline helices. *J. Am. Chem. Soc. 124*, 8876–8883.
(12) Gellman, S. H. (1998) Foldamers: A manifesto. *Acc. Chem. Res. 31*, 173–180.
(13) Hill, D. J., Mio, M. J., Prince, R. B., Hughes, T. S., and Moore, J. S. (2001) A field guide to foldamers. *Chem. Rev. 101*, 3893–4011.
(14) Umezawa, N., Gelman, M. A., Haigis, M. C., Raines, R. T., and Gellman, S. H. (2002) Translocation of a beta-peptide across cell membranes. *J. Am. Chem. Soc. 124*, 368–369.
(15) Gillies, E. R., Deiss, F., Staedel, C., Schmitter, J. M., and Huc, I. (2007) Development and biological assessment of fully water-soluble helical aromatic amide foldamers. *Angew. Chem., Int. Ed. 46*, 4081–4084.
(16) Okuyama, M., Laman, H., Kingsbury, S. R., Visintin, C., Leo, E., Eward, K. L., Stoeber, K., Boshoff, C., Williams, G. H., and Selwood, D. L. (2007) Small-molecule mimics of an alpha-helix for efficient transport of proteins into cells. *Nature Methods 4*, 153–159.
(17) Fernandez-Carneado, J., Van Gool, M., Martos, V., Castel, S., Prados, P., de Mendoza, J., and Giralt, E. (2005) Highly efficient, nonpeptidic oligoguanidinium vectors that selectively internalize into mitochondria. *J. Am. Chem. Soc. 127*, 869–874.
(18) Frackenpohl, J., Arvidsson, P. I., Schreiber, J. V., and Seebach, D. (2001) The outstanding biological stability of beta- and gamma-peptides toward proteolytic enzymes: An in vitro investigation with fifteen peptidases. *ChemBioChem 2*, 445–455.
(19) Hussey, S. L., and Peterson, B. R. (2002) Efficient delivery of streptavidin to mammalian cells: Clathrin-mediated endocytosis regulated by a synthetic ligand. *J. Am. Chem. Soc. 124*, 6265–6273.
(20) Rajendran, L., Schneider, A., Schlechtingen, G., Weidlich, S., Ries, J., Braxmeier, T., Schwille, P., Schulz, J. B., Schroeder, C., Simons, M., Jennings, G., Knolker, H. J., and Simons, K. (2008) Efficient inhibition of the Alzheimer's disease beta-secretase by membrane targeting. *Science 320*, 520–523.
(21) Raynal, N., Averlant-Petit, M. C., Berge, G., Didierjean, C., Marraud, M., Duru, C., Martinez, J., and Amblard, M. (2007) Molecular modeling study for a novel structured oligomer subunit selection: the example of 2-aminomethyl-phenyl-acetic acid. *Tetrahedron Lett. 48*, 1787–1790.
(22) Amblard, M., Raynal, N., Averlant-Petit, M. C., Didierjean, C., Calmes, M., Fabre, O., Aubry, A., Marraud, M., and Martinez, J. (2005) Structural elucidation of the beta-turn inducing (S)-[3-amino-4-oxo-2,3-dihydro-5H-benzo[b][1,4]thiazepin-5-yl] acetic acid (DBT) motif. *Tetrahedron Lett. 46*, 3733–3735.
(23) Amblard, M., Daffix, I., Bedos, P., Berge, G., Pruneau, D., Paquet, J. L., Luccarini, J. M., Belichard, P., Dodey, P., and Martinez, J. (1999) Design and synthesis of potent bradykinin agonists containing a benzothiazepine moiety. *J. Med. Chem. 42*, 4185–4192.

(24) Amblard, M., Calmes, M., Roques, V., Tabet, S., Loffet, A., and Martinez, J. (2002) An improved synthesis of (S)- or (R)-N-boc-protected 1,5-benzothiazepine derivatives. *Org. Prep. Proced. Int. 34*, 405–415.

(25) Wender, P. A., Galliher, W. C., Goun, E. A., Jones, L. R., and Pillow, T. H. (2008) The design of guanidinium-rich transporters and their internalization mechanisms. *Adv. Drug Delivery Rev. 60*, 452–472.

(26) Richard, J. P., Melikov, K., Vives, E., Ramos, C., Verbeure, B., Gait, M. J., Chernomordik, L. V., and Lebleu, B. (2003) Cell-penetrating peptides: A reevaluation of the mechanism of cellular uptake. *J. Biol. Chem. 278*, 585–590.

(27) Bareford, L. A., and Swaan, P. W. (2007) Endocytic mechanisms for targeted drug delivery. *Adv. Drug Delivery Rev. 59*, 748–758.

(28) Burrow, T. A., Hopkin, R. J., Leslie, N. D., Tinkle, B. T., and Grabowski, G. A. (2007) Enzyme reconstitution/replacement therapy for lysosomal storage diseases. *Curr. Opin. Pediatr. 19*, 628–635.

(29) Nixon, R. A., and Cataldo, A. M. (2006) Lysosomal system pathways: genes to neurodegeneration in Alzheimer's disease. *J. Alzheimer's Dis. 9* (3 Suppl), 277–289.

(30) Castino, R., Demoz, M., and Isidoro, C. (2003) Destination 'Lysosome': a target organelle for tumour cell killing? *J. Mol. Recognit. 16*, 337–348.

(31) Extance, A. (2009) Targeting RNA: an emerging hope for treating muscular dystrophy. *Nature Rev. Drug Discovery 8*, 917–918.

BC1002086

Non-cationic dipeptide mimic oligomers as cell penetrating non peptides (CPNP)

Lubomir Lubomirov Vezenkov, Marie Maynadier, Jean-François Hernandez, Marie-Christine Averlant-Petit, Olivier Fabre, Ettore Benedetti, Marcel Garcia, Jean Martinez, Muriel Amblard**

Table of contents

1- Synthesis of the oligomers JMV2949, JMV2968, JMV3229, JMV4228, JMV4287

2- Confocal Laser Scanning Microscopy of JMV4228

3- MTT viability assay

1- Synthesis of the oligomers JMV2949, JMV2968, JMV3229, JMV4228, JMV4287.

HBTU, DIEA, dichloromethane, methanol, acetonitrile, diethyl ether, trifluoroacetic acid, piperidine were purchased from Riedel-de Haën, Carlo Erba or Acros organics and used without purification. Fluorescein isothiocyanate (FITC) was purchased from Sigma-Aldrich, Lyon, France. Fmoc Rink amide polystyrene resin (100-200 mesh, 0.46 mmol/g) was purchased from SENN chemicals, Gentilly, France. Solvents used for HPLC and LC/MS were of HPLC grade. All final compounds were purified by reversed-phase HPLC and the purity assessed by analytical reversed-phase HPLC was found superior to 95 %

Anchoring on Rink amide-PS resin. Fmoc-Rink amide resin was conditioned for 30 minutes in DCM and submitted to the standard deprotection cycle, using DMF/ pip 80/20 solution for 30 minutes. After washing steps, the first constrained dipeptide mimetic (Fmoc-LBT-OH or Fmoc-DBT-OH) motif was loaded onto the resin through a standard coupling cycle, using HBTU (3 eq) as a coupling agent and DIEA (3 eq) as a base.

Coupling step. Coupling reaction was carried out manually in plastic syringes equipped with frits. HBTU (3 eq) as a coupling agent, DIEA (3 eq) as a base and Fmoc-DBT-OH or Fmoc-LBT-OH (3 eq) (according to resin loading) were solubilized in DMF and added to the resin. The reaction was stirred for 3 hours at room temperature. The reaction was monitored by the standard TNBS test (*1*).

Deprotection step. Fmoc deprotection was carried out using DMF/piperidine 80/20 v/v solution two times for 30 minutes.

Washing steps were performed after each coupling and deprotection steps: one time methanol, one time DCM, 3 times DMF and 3 times DCM.

FITC coupling. FITC reaction was carried out manually in plastic syringes equipped with frits. 1.5 eq of FITC and 3 eq of DIEA (according to resin loading) were solubilized in DMF and added to the resin. The reaction was stirred for 2 hours at room temperature. Due to the reddish coloration of the resin, the TNBS test was difficult to use to monitor the completion of the FITC coupling. Kaiser(*2*) test was preferred in this case.

Cleavage of Rink amide-PS resin. Oligomers were cleaved from resin for 2 hours in 99% trifluoroacetic acid. After removal of the resin by filtration, the trifluoroacetic acid was concentrated. Compounds were precipitated by addition of diethyl ether and filtrated. They were dissolved in acetonitrile/water 50/50 solution containing 0.1% TFA and freeze dried.

Purification of the compounds. All the compounds were purified by preparative HPLC (Waters 4000 apparatus) carried out on a C18 reversed-phase column (C18 Deltapak column, 100 mm x 40 mm, 15 µm, 100Å) at a flow rate of 50 mL/min of a mixture of H_2O + 0.1% TFA and CH_3CN + 0.1% TFA in gradient mode with UV detection at 214 nm.

Analysis of the compounds. HPLC: Samples were prepared in acetonitrile/water (50/50 v/v) mixture, containing 0.1% TFA. The HPLC system consisted of a Beckman 32 Karat System. All the analyses were carried out using a RP C18 VWR chromolith column, 50 mm x 3.9 mm. A flow rate of 5 mL/min and a gradient of (0–100)% B over 3 min were used. Eluent A: water/0.1% TFA; eluent B: acetonitrile/0.1% TFA. Detection was performed both at 214 nm and 254 nm.

LC/MS Analysis. Samples were prepared in acetonitrile/water (50/50 v/v) mixture, containing 0.1% TFA. The LC/MS system consisted of a Waters Alliance 2690 HPLC, coupled to a Waters-Micromass ZQ spectrometer (electrospray ionization mode, ESI+). All the analyses were carried out using a RP C18 monolithic Onyx Phenomenex 25 x 4.6 mm column. A flow rate of 3 mL/min and a gradient of (0–

100)% B over 3 min were used. Eluent A: water/0.1% formic acid; eluent B: acetonitrile/0.1% formic acid. Positive ion electrospray mass spectra were acquired at a solvent flow rate of 100–500 µL/min. Nitrogen was used for both the nebulizing and drying gas. The data were obtained in a scan mode in 0.1 s intervals; 10 scans were summed up to get the final spectrum. The yield and the purity after HPLC purification, HPLC retention time, calculated monoisotopic mass and detected mass of the compounds are reported in table 1.

Table 1.

Compound, JMV	HPLC (min)	Purity after HPLC purification	Yield	Chemical formula, MW	Ion detected (m/z)
Fl-DBT$_2$-NH$_2$ (JMV2949)	t_R =1.70	> 98%	35%	$C_{43}H_{34}N_6O_9S_3$ **874.1**	**[M+H]$^+$, 875.00**
Fl-DBT$_3$-NH$_2$ (JMV2968)	t_R =1.87	> 98%	30%	$C_{54}H_{44}N_8O_{11}S_4$ **1108.2**	**[M+H]$^+$, 1109.0**
Fl-DBT$_4$-NH2 (JMV3229)	t_R =1.80	> 98%	24%	$C_{65}H_{54}N_{10}O_{13}S_5$ **1342.2**	**[M+H]$^+$, 1343.1** **[M+2H]$^{2+}$, 672.1**
Fl-LBT$_4$-NH$_2$ (JMV4228)	t_R =1.80	> 98%	25%	$C_{65}H_{54}N_{10}O_{13}S_5$ **1342.2**	**[M+H]$^+$, 1343.2** **[M+2H]$^{2+}$, 672.3**
Fl-(DBT-LBT)$_2$-NH$_2$ (JMV4287)	t_R =1.69	> 98%	25%	$C_{65}H_{54}N_{10}O_{13}S_5$ **1342.2**	**[M+H]$^+$, 1343.2** **[M+2H]$^{2+}$, 672.2**

2- Confocal Laser Scanning Microscopy of JMV4228. Distribution of JMV4228 is reported in Figure S1.

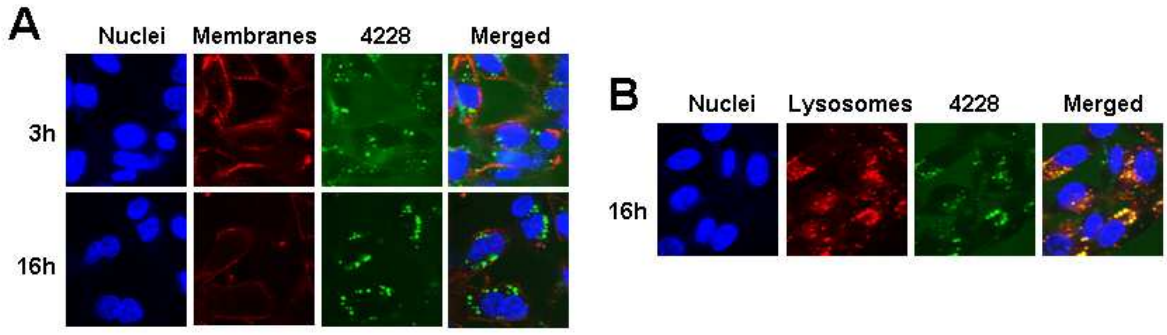


Figure S1. Confocal microscopy images of living MDA- MB-231 breast cancer cells incubated with compounds. Distribution of JMV4228 (A) at 3 h and 16 h of incubation at 37°C. To visualize

internalized compound, cells were stained with nucleus and membrane markers. Co-localization of JMV4228 (B) with the lysosome marker at 16 h at 37°C. Data are from one representative of two independent experiments.

3- MTT viability assay. Cellular toxicity of the fluorescent agents was examined using the 3-(4,5-dimethylthiazol-2-yl)-2,5-diphenyltetrazolium bromide (MTT) cell viability assay. Briefly, 5000 cells were seeded in 96-well plates. Two concentrations (10-5 and 10-6 M) of compounds were tested for 5 days. Following this incubation, the cells were incubated for 4 h with 0.5 mg/mL of MTT in media. After 4 h, the MTT/media solution was removed, and the precipitated crystals were dissolved in ethanol/DMSO (1/1). The solution absorbance was read at 540 nm. We confirmed this assay to be linear and to give comparable results as total DNA quantification by diaminobenzoic acid assay(*3*).

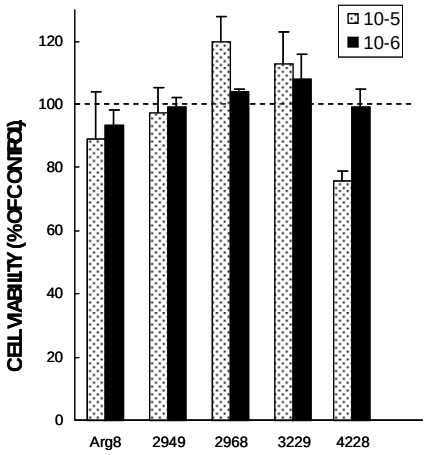


Figure S2. Cytotoxicity of compounds after a 5-day incubation at a concentration of 10^{-5} or 10^{-6} M. Values are mean ± SD of three independent experiments performed in triplicates. Values are expressed as a percentage of control cells incubated with vehicle alone (1% DMSO).

References

(1) Hancock, W. S., Battersby, J. E., and Harding, D. R. K. (1975) Use of Picric Acid as a Simple Monitoring Procedure for Automated Peptide-Synthesis. *Analytical Biochemistry 69*, 497-503.

(2) Sarin, V. K., Kent, S. B. H., Tam, J. P., and Merrifield, R. B. (1981) Quantitative Monitoring of Solid-Phase Peptide-Synthesis by the Ninhydrin Reaction. *Analytical Biochemistry 117*, 147-157.

(3) Maynadier, M., Ramirez, J. M., Cathiard, A. M., Platet, N., Gras, D., Gleizes, M., Sheikh, M. S., Nirde, P., and Garcia, M. (2008) Unliganded estrogen receptor alpha inhibits breast cancer cell growth through interaction with a cyclin-dependent kinase inhibitor (p21(WAF1)). *Faseb Journal 22*, 671-681.

In Vitro and *in Vivo* Characterization of Novel ^{18}F-Labeled Bombesin Analogues for Targeting GRPR-Positive Tumors

Linjing Mu,[†] Michael Honer,[†] Jessica Becaud,[†] Miljen Martic,[†] Pius A. Schubiger,[†] Simon M. Ametamey,*[,†] Timo Stellfeld,[‡] Keith Graham,[‡] Sandra Borkowski,[‡] Lutz Lehmann,[‡] Ludger Dinkelborg,[‡] and Ananth Srinivasan[‡]

Center for Radiopharmaceutical Sciences of ETH, PSI and USZ, CH-8093 Zurich, Switzerland, and Bayer Schering Pharma AG, Global Drug Discovery, D-13342 Berlin, Germany. Received May 6, 2010; Revised Manuscript Received July 19, 2010

The gastrin-releasing peptide receptor (GRPR) is overexpressed on a number of human tumors and has been targeted with radiolabeled bombesin analogues for the diagnosis and therapy of these cancers. Seven bombesin analogues containing various linkers and peptide sequences were designed, synthesized, radiolabeled with ^{18}F, and characterized *in vitro* and *in vivo* as potential PET imaging agents. Binding studies displayed nanomolar binding affinities toward human GRPR for all synthesized bombesin analogues. Two high-affinity peptide candidates **6b** ($K_i = 0.7$ nM) and **7b** ($K_i = 0.1$ nM) were chosen for further *in vivo* evaluation. Both tracers revealed specific uptake in GRPR-expressing PC-3 tumors and the pancreas. Compared to **[^{18}F]6b**, compound **[^{18}F]7b** was characterized by superior tumor uptake, higher specificity of tracer uptake, and more favorable tumor-to-nontarget ratios. *In vivo* PET imaging allowed for the visualization of PC-3 tumor in nude mice suggesting that **[^{18}F]7b** is a promising PET tracer candidate for the diagnosis of GRPR-positive tumors in humans.

INTRODUCTION

Bombesin (BBS) is a 14-amino acid neuropeptide that was originally isolated from the skin of the *Bombina* frog and binds with high affinity to gastrin-releasing peptide (GRP) receptors (*1*−*4*). Four subtypes of BBS/GRP receptors have been identified. The bombesin receptor subtype 2 has been shown to be overexpressed on a variety of human tumors, including small-cell lung cancer (SCLC), prostate, breast, gastric, colon, pancreatic, and gastrointestinal cancer (*5*−*9*). Thus, radiolabeled BBS analogues having high affinity for this receptor subtype can be used as radiopharmaceuticals either for the detection or treatment of these cancers (*10*−*12*).

It has been shown that the C-terminal amino acid sequences, Trp8-Ala9-Val10-Gly11-His12-Leu13-Met14-NH_2, are necessary for retaining receptor binding affinity and preserving the biological activity of BBS-like peptides; hence, the N-terminal region of the peptide can be used for radiolabeling. A number of potent BBS analogues have been labeled with various radionuclides, such as $^{99\ m}$Tc, ^{111}In, ^{90}Y, ^{64}Cu, ^{177}Lu, ^{68}Ga, or ^{18}F, for targeting GRPR-expressing cancer cells in both animal models and human subjects (*13*−*25*). Among the available PET nuclides, ^{18}F has ideal characteristics for peptide receptor imaging studies in terms of its half-life (109.7 min) and low β^+ energy (0.64 MeV) (*26*). Current known methods of radiolabeling peptides with ^{18}F rely on using prosthetic groups such as the [^{18}F]succinimidyl 4-fluorobenzoate ([^{18}F]SFB) (*27*), [^{18}F]4-fluorobenzaldehyde (*28, 29*), and thiol-selective ^{18}F-labeling reagents (*30, 31*). Although great improvements have been achieved, the established methods have disadvantages in that the synthetic methods comprise multistep radiosyntheses and time-consuming workup procedures. Therefore, several research groups focus on new synthetic strategies that avoid the use of prosthetic groups. Recent studies have demonstrated the feasibility of labeling organoboron and organosilicon bioconjugates with ^{18}F in a single step (*32*−*35*). In our laboratories, we have successfully labeled bombesin peptides with ^{18}F in one step and applying silicon−fluorine chemistry (*36*). However, the ^{18}F-labeled silicon-based peptides showed relatively low tumor accumulation and retention as well as unfavorable hepatobiliary excretion in nude mice with PC-3 xenografts. This might be due to the introduction of the highly lipophilic di-*tert*-butyl silyl labeling moiety into the peptide. In order to improve the tumor targeting and imaging potential of ^{18}F-labeled bombesin peptides, another approach via ^{18}F-for-$^{+}N(CH_3)_3$ substitution using a less lipophilic benzonitrile labeling moiety has been exploited in our laboratories (*37*). The *in vitro* binding affinity of these fluorinated bombesin peptides toward GRPR were assessed by a competitive displacement assay using [^{125}I]-Tyr^4-bombesin as the radioligand. More than 11-fold higher binding affinity with benzonitrile as the labeling moiety was obtained compared to using di-*tert*-butyl silyl as the labeling moiety with the same peptide sequence (*36*). Therefore, in this study, several new BBS peptides were synthesized and ^{18}F-labeled via the aforementioned ^{18}F-for-$^{+}N(CH_3)_3$ substitution approach. Our efforts have been focused on improving the pharmacokinetics of BBS derivatives by using different linkers, peptide sequences, and non-natural amino acids. Two bombesin analogues, one being positively and another negatively charged, were chosen for further *in vivo* evaluation in nude mice with PC-3 xenografts.

EXPERIMENTAL PROCEDURES

General. All chemicals unless otherwise stated were purchased from Sigma-Aldrich or Merck and used without further purification. Fmoc-aminoacids were purchased from IRIS Biotech except Fmoc-Statine, FA01010, and Fmoc-Ala(SO_3Na)−OH), which were purchased from NeoMPS (now Polypeptide). The solvents were of HPLC quality. Peptide syntheses were carried out using Rink-Amide resin (0.68 mmol/g) following the standard Fmoc strategy (*29*). All amino acid residues were,

* Corresponding author. Center for Radiopharmaceutical Sciences of ETH, PSI and USZ, CH-8093 Zurich, ETH Hönggerberg D-CHAB IPW HCI H427, Wolfgang-Pauli-Strasse 10, Switzerland. Tel: +41 44 633 74 63. Fax: +41 44 633 13 67. E-mail: simon.ametamey@pharma.ethz.ch.

[†] Center for Radiopharmaceutical Sciences of ETH, PSI and USZ.

[‡] Bayer Schering Pharma AG.

10.1021/bc100222u © 2010 American Chemical Society
Published on Web 09/21/2010

if not further specified, L-amino acid residues. FA01010 denotes (4*R*,5*S*)-4-amino-5-methylheptanoic acid, statine (Sta) denotes (3*S*,4*S*)-4-amino-3-hydroxy-6-methylheptanoic acid, Ala(SO_3H) denotes cysteine sulfonic acid, and Ava denotes 5-aminopentanoic acid. High-performance liquid chromatography (HPLC) analyses were performed using an ACE C18 column (50 × 4.6 mm, 3 μm) under the indicated conditions. Analytical HPLC chromatograms were obtained using an Agilent 1100 system with Gina software, equipped with UV multiwavelength and Raytest Gabi Star detectors. Semipreparative HPLC purifications were carried out using a semipreparative ACE C18 column (250 × 10 mm, 5 μm) under the indicated conditions. The semipreparative HPLC system used was a Merck-Hitachi L6200A system equipped with a Knauer variable wavelength detector and an Eberline radiation detector.

Solid-Phase Peptide Synthesis. Peptide synthesis was carried out using Fmoc-Rink Amide-linker functionalized polystyrene resin (0.68 mmol/g). The peptide chain was elongated in cycles of Fmoc deprotection, followed by coupling of the subsequent Fmoc amino acid. Acid-labile side chain protecting groups were used for the following amino acids: Fmoc-His(Trt)−OH, Fmoc-Trp(Boc)−OH, and Fmoc-Gln(Trt)−OH. Fmoc deprotection was achieved by shaking a suspension of the resin in 20% piperidine in DMF for 5 min and repeatedly doing so for another 20 min. The resin was subsequently washed with DMF (2×), CH_2Cl_2 (2×), and DMF (2×). A solution of Fmoc-Xaa−OH (Xaa = amino acid, 4 equiv), HBTU (*O*-(benzotriazol-1-yl)-*N*,*N*,*N*′,*N*′-tetramethyluronium hexafluorophosphate, 4 equiv), HOBT (1-hydroxybenzotriazole, 4 equiv), DIPEA (*N*,*N*′-di-*iso*-propylethylamine, 8 equiv) in DMF was added to the resin-bound free amine peptide and shaken for 90 min at room temperature. This step was repeated with a reaction time of 60 min, and the resin was washed with DMF (2×), CH_2Cl_2 (2×), and DMF (2×). The two steps of Fmoc-deprotection and amino-acid addition were then repeated until the final elongation of the desired peptide was achieved. The peptides were typically prepared starting with 147 mg (0.1 mmol) of the resin. The amounts of reagents and building blocks in all subsequent reactions were calculated on the basis of this amount.

Procedure for the Synthesis of (4-Trimethylammonium-3-cyano-benzoyl)-Functionalized Peptide Trifluoroacetate Salts (Precursor Compounds **1a**−**7a***).* Representative procedure: *N*-methylmorpholine (NMM, 22 μL, 0.2 mmol) was added to a solution of 2-cyano-4-carboxyl-phenyl)-trimethylammonium triflate salt (71 mg, 0.2 mmol) and 4-(4,6-dimethoxy-1,3,5-triazin-2-yl)-4-methylmorpholinium tetrafluoroborate (66 mg, 0.2 mmol) in DMF (2 mL). The mixture was added to the resin-bound, side chain protected, Fmoc-deprotected peptide (0.1 mmol, based on the initial resin loading) which was prepared by following the general procedures described above. The reaction mixture was shaken intensively for 4 h. The resin was then filtered and washed with DMF (3 × 4 mL) and CH_2Cl_2 (3 × 4 mL). The coupling step was repeated. Thereafter, the resin was treated with a mixture of trifluoroacetic acid, distilled water, phenol, and tri*iso*propylsilane (85/5/5/5, 1.5 mL) for 3 h. The mixture was added to ice cold methyl *tert*-butylether, and the precipitate was separated by centrifugation. Water was added to the pellet, and the supernatant was lyophilized. The residue was purified by preparative RP-18 HPLC-MS with a gradient of 5−30% acetonitrile in 20 min and 0.1% trifluoroacetic acid as cosolvent. The desired fraction was collected and lyophilized, and the product was analyzed by HPLC-MS.

Syntheses of Fluorinated Peptides (Reference Compounds **1b**−**7b***).* Representative procedure: A solution of 3-cyano-4-fluorobenzoic acid (66 mg, 4 equiv) (*37*), HBTU (*O*-(benzotriazol-1-yl)-*N*,*N*,*N*′,*N*′-tetramethyluronium hexafluorophosphate, 151 mg, 4 equiv), HOBT (1-hydroxybenzotriazole, 61 mg, 4 equiv), and DIPEA (*N*,*N*′-di-*iso*-propylethylamine, 70 μL, 4 equiv) in DMF (2 mL) was added to the resin-bound side chain protected peptide (0.1 mmol, based on the initial resin loading) which was prepared by following the general procedures described above. The reaction mixture was shaken intensively for 4 h. The resin was then filtered and washed with DMF (3 × 4 mL) and CH_2Cl_2 (3 × 4 mL). Thereafter, the resin was treated with a mixture of trifluoroacetic acid, distilled water, phenol, and tri*iso*propylsilane (85/5/5/5, 1.5 mL) for 3 h. The mixture was added to ice cold methyl *tert*-butylether, and the precipitate was separated by centrifugation. Water was added to the pellet, and the supernatant was lyophilized. The residue was purified by preparative RP-18 HPLC-MS with a gradient of 5−50% acetonitrile in 20 min and 0.1% trifluoroacetic acid as cosolvent. The desired fraction was collected and lyophilized, and the product was analyzed by HPLC-MS.

Radiolabeling. No-carrier added [^{18}F] fluoride was produced via the ^{18}O (p, n) ^{18}F nuclear reaction by irradiation of enriched [^{18}O] water. [^{18}F]Fluoride was immobilized on an anion-exchange cartridge (QMA light, Waters, AG) and eluted with a solution of Kryptofix $K_{2.2.2}$ (5 mg), Cs_2CO_3 (2.3 mg), or K_2CO_3 (1 mg) in acetonitrile (1.5 mL) and water (0.5 mL). The fluoride was dried by azeotropic distillation of acetonitrile at 110 °C under vacuum with a stream of nitrogen. The azeotropic drying was repeated three times with acetonitrile (3 × 1 mL). To the dried [^{18}F] fluoride complex, the TMA-based bombesin peptide precursor was added (2 mg, in 150 μL of DMSO). The reaction solution was heated at the indicated reaction temperatures. An aliquot was taken from the reaction mixture and analyzed by analytical HPLC. The identity of the tracer was confirmed by coinjection of the authentic standard on the same analytical HPLC system ACE C18 column (50 × 4.6 mm, 3 μm). Eluting conditions: 10 mM K_2HPO_4 in water (solvent A), 10 mM K_2HPO_4 in water/acetonitrile 3/7 (solvent B); 0−7.0 min, 5−95% B; 7.0−7.1 min, 95−100% B; 7.1−8.8 min, 100% B; 8.8−9.0 min, 100−5% B. The flow rate was 2 or 1.8 mL/min. Semipreparative HPLC purifications were carried out using a semipreparative ACE C18 column (250 × 10 mm, 5 μm). Elution system: 0.1% TFA in water (solvent A) and 0.1% TFA in acetonitrile/water 9/1 (solvent B).

*3-Cyano-4-[^{18}F]fluoro-benzoyl-Ava-Gln-Trp-Ala-Val-Gly-His(3Me)-Sta-Leu-NH_2 (***[^{18}F]1b***).* A solution of compound **1a** (2 mg) in anhydrous DMSO (150 μL) was added to a reaction vial containing the dry K[^{18}F]F/$K_{2.2.2}$ complex. After heating at 50 °C for 15 min, the crude reaction mixture was analyzed using an ACE C18 column. The ^{18}F-incorporation determined by HPLC was 77% (t_R = 4.92 min).

*3-Cyano-4-[^{18}F]fluoro-benzoyl-Arg-Ava-Gln-Trp-Ala-Val-Gly-His(3Me)-Sta-Leu-NH_2 (***[^{18}F]2b***).* A solution of compound **2a** (2 mg) in anhydrous DMSO (150 μL) was added to a reaction vial containing the dry Cs[^{18}F]F/$K_{2.2.2}$ complex (3.4 GBq). After heating at 70 °C for 15 min, the crude reaction mixture was analyzed using ACE C18 column. The ^{18}F-incorporation determined by HPLC was 67% (t_R = 4.87 min). The reaction mixture was diluted with water (4 mL) and injected onto an ACE semipreparative HPLC column (0.1% TFA in water (solvent A); B, 0.1% TFA in acetonitrile/water 9/1 (solvent B), 0−2.0 min, 20% B; 2.0−22.0 min, 20−60% B; 22.0−23.0 min, 60−100% B; 23.0−28.0 min, 100% B; flow rate, 3 mL/min), and the product was collected (1.1 GBq). The decay corrected radiochemical yield of the isolated product was around 47%, and radiochemical purity was greater than 99%.

*3-Cyano-4-[^{18}F]fluoro-benzoyl-Arg-βAla-Gln-Trp-Ala-Val-Gly-His(3Me)-Sta-Leu-NH_2 (***[^{18}F]3b***).* A solution of compound **3a** (2 mg) in anhydrous DMSO (150 μL) was added to a reaction vial containing dry K[^{18}F]F/$K_{2.2.2}$ complex (1.49 GBq). After heating at 50 °C for 15 min, the crude reaction mixture was

analyzed using an ACE C18 column. The ^{18}F-incorporation determined by HPLC was 56% (t_R = 4.78 min). The reaction mixture was diluted with water (4 mL) and injected onto an ACE semipreparative HPLC (0−5 min, 29% B; 5−25 min, 29−34% B; flow rate 3 mL/min). The desired ^{18}F-labeled product was collected (150 MBq, 21.1% d.c. RCY) with a specific activity of 72.5 GBq/μmol.

3-Cyano-4-[^{18}F]fluoro-benzoyl-Arg-Ser-Gln-Trp-Ala-Val-Gly-His(3Me)-Sta-Leu-NH$_2$ (**[^{18}F]4b**). A solution of compound **4a** (2 mg) in anhydrous DMSO (150 μL) was added to a reaction vial containing dry K[^{18}F]F/K$_{2.2.2}$ complex (2.9 GBq). After heating at 50 °C for 15 min, the crude reaction mixture was analyzed using ACE C18 column. The ^{18}F-incorporation determined by HPLC was 35% (t_R = 4.94 min). The reaction mixture was diluted with water (4 mL) and injected onto an ACE semipreparative HPLC (0−2 min, 35% B; 2−22 min, 35−55% B; flow rate 3 mL/min). The desired ^{18}F-labeled product was collected (28 MBq, 4% d.c. RCY).

3-Cyano-4-[^{18}F]fluoro-benzoyl-Arg-Ava-Gln-Trp-Ala-Val-Gly-His-FA01010-Leu-NH$_2$ (**[^{18}F]5b**). A solution of compound **5a** (2 mg) in anhydrous DMSO (150 μL) was added to a reaction vial containing dry K[^{18}F]F/K$_{2.2.2}$ complex (11 GBq). After heating at 70 °C for 15 min, the crude reaction mixture was analyzed using ACE C18 column. The ^{18}F-incorporation determined by HPLC was 63% (t_R = 5.51 min).

3-Cyano-4-[^{18}F]fluoro-benzoyl-Arg-Ava--Gln-Trp-Ala-Val-NMeGly-His-Sta-Leu-NH$_2$ (**[^{18}F]6b**). Radiolabeling based on the published procedure (*37*).

3-Cyano-4-[^{18}F]fluoro-benzoyl-Ala(SO$_3$H)-Ava-Gln-Trp-Ala-Val-NMeGly-His-Sta-Leu-NH$_2$ (**[^{18}F]7b**). A solution of compound **7a** (2 mg) in anhydrous DMSO (150 μL) was added to a reaction vial containing dry Cs[^{18}F]F/K$_{2.2.2}$ complex (20 GBq). After heating at 90 °C for 15 min, the crude reaction mixture was analyzed using ACE C18 column. The ^{18}F-incorporation determined by HPLC was 76% (t_R = 4.30 min). The reaction mixture was diluted with water (3 mL) and injected onto an ACE semipreparative HPLC column (0.1% TFA in water (solvent A), B, 0.1% TFA in acetonitrile/water 9/1 (solvent B), 0−2.0 min, 20% B; 2.0−22.0 min, 20−60% B; 22.0−23.0 min, 60−100% B; flow rate, 3 mL/min), and the product was collected (2.1 GBq). The decay corrected radiochemical yield of the isolated product was around 14%, and radiochemical purity was greater than 99%. Specific activity was 77 GBq/μmol at the end of the synthesis.

***In Vitro* Binding Affinity Studies.** The receptor binding affinities of bombesin (BBS) analogues **1b**−**7b** were determined in quadruplicate in a scintillation proximity assay (SPA) using cellular membranes transfected with human bombesin 2 receptors (GRPR) from PerkinElmer (RBHBS2M). The membranes and agglutinin-coupled SPA beads type A (PVT PEI Treated Wheatgerm, Amersham Bioscience) were mixed in assay buffer (50 mM Tris/HCl at pH 7.2; 5 mM $MgCl_2$; 1 mM EGTA; protease inhibitor (Roche Diagnostics GmbH; 1 tablet/50 mL); and 0.3% polyethylenemine) to give final concentrations of approximately 20 μg/mL protein and 8 mg/mL PVT-SPA beads. The ligand [^{125}I]-Tyr^4-bombesin (PerkinElmer; specific activity, 81.4 TBq/mmol) was diluted to 0.2 nM in assay buffer. The test compounds were dissolved in DMSO to give 1 mM stock solutions. They were further diluted in assay buffer to 2 pM−300 nM. Nonspecific binding was determined by an excess of 10 μM Tyr^4-bombesin (Sigma).

The assay was then performed as follows: First, 10 μL of compound solution to be tested for binding was placed in white 384 well plates (Lumitrac 200, Greiner). Next, 20 μL of the GRPR/PVT-SPA bead mixture and 20 μL of the ligand solution were added. After 120 min of incubation at room temperature, another 50 μL of assay buffer was added; the plate was sealed and centrifuged for 10 min at 520*g* at room temperature. Signals were measured in Top Count (Perkin-Elmer) for 1 min integration time per well. Nonspecific binding determined by an excess of bombesin was subtracted from total binding to yield the specific binding at each concentration. The IC_{50} and K_i values were calculated by nonlinear regression using *GraFit* 5 data analysis software (Erithacus Software Ltd.).

Lipophilicity: log $D_{7.4}$ Determination. The distribution coefficient D (log $D_{7.4}$) was determined by the "shake flask method" (*38*): the peptide was dissolved in a mixture of phosphate buffer (600 μL, pH 7.4) and *n*-octanol (600 μL) at 20 °C. The sample was equilibrated by shaking for 4 min followed by centrifugation. The concentrations of the peptide in each phase were measured by HPLC-UV absorption. The log D value was calculated as the log ratio of UV peak area at 254 nm in the organic and aqueous phases of the tested compound.

Biodistribution Studies. All animal experiments were performed in compliance with the current version of the German and Swiss law on the Protection of Animals. The biodistribution experiments were performed using nude mice bearing human prostate tumors (PC-3). For the induction of tumor xenografts, PC-3 cells (2×10^6 cells/mouse) were injected subcutaneously and allowed to grow for four to five weeks. Animals were injected intravenously with approximately 177 kBq of **[^{18}F]6b** and 230 kBq of **[^{18}F]7b** (100 μL). The animals were sacrificed at different postinjection time points (from 0.5 to 4 h, n = 3 for each time point). Organs and tissues of interest were collected and weighed. The amount of radioactivity was determined in the γ-counter to calculate the uptake (% injected dose per g tissue). In addition, three mice received 100 μg of bombesin coinjected with the radiolabeled compound and were sacrificed at 1 h postinjection to determine nonspecific uptake.

PET Study. Four nude mice were inoculated subcutaneously with PC-3 tumor cells (see above) next to the right shoulder. Animals were injected intravenously with 10−15 MBq of **[^{18}F]7b** and scanned in a whole body configuration from 60 to 105 min p.i. in the dedicated small-animal PET system quad-HIDAC. Two animals were coinjected with 50 μg of bombesin (1 mg/mL), while two animals received a corresponding volume of vehicle. PET data acquisition and monitoring of anesthesia were performed as described elsewhere (*39*). After the termination of the PET scan, animals were sacrificed at 107 min p.i. by decapitation for tissue sampling. PET data were reconstructed in a single 45 min time frame and normalized to the injected dose per body weight.

RESULTS AND DISCUSSION

Peptide Synthesis. On the basis of the amino acid sequence 7−14 of natural bombesin, we have designed and synthesized a series of new BBS analogues. To overcome the rapid degradation of natural BBS, some modifications were introduced at positions 13 and 14. Met14 was replaced by Leu for stabilization against aminopeptidase 3.4.11.1, and Leu13 was replaced by a non-natural amino acid (FA01010 or Sta) to prevent cleavage by neutral endopeptidase 3.4.24.11. Further modifications were the introduction of the methylated versions of His12 or Gly11. Additionally, a polar spacer, such as -Ava-, -Ava-Arg-, -Arg-βAla-, -Arg-Ser-, or -Ala(SO$_3$H)-Ava- was inserted between the labeling moiety and the binding sequence in order to further improve the pharmacokinetics and to avoid interference of the radiolabel with the binding region.

Nonradioactive peptides were synthesized by solid phase peptide synthesis (SPPS) following standard Fmoc strategies. Coupling of the resin-bound peptide with 3-cyano-4-fluoro-benzoic acid or 3-cyano-4-trimethylamino-benzoic acid afforded the corresponding nonradioactive (^{19}F) peptide standards and

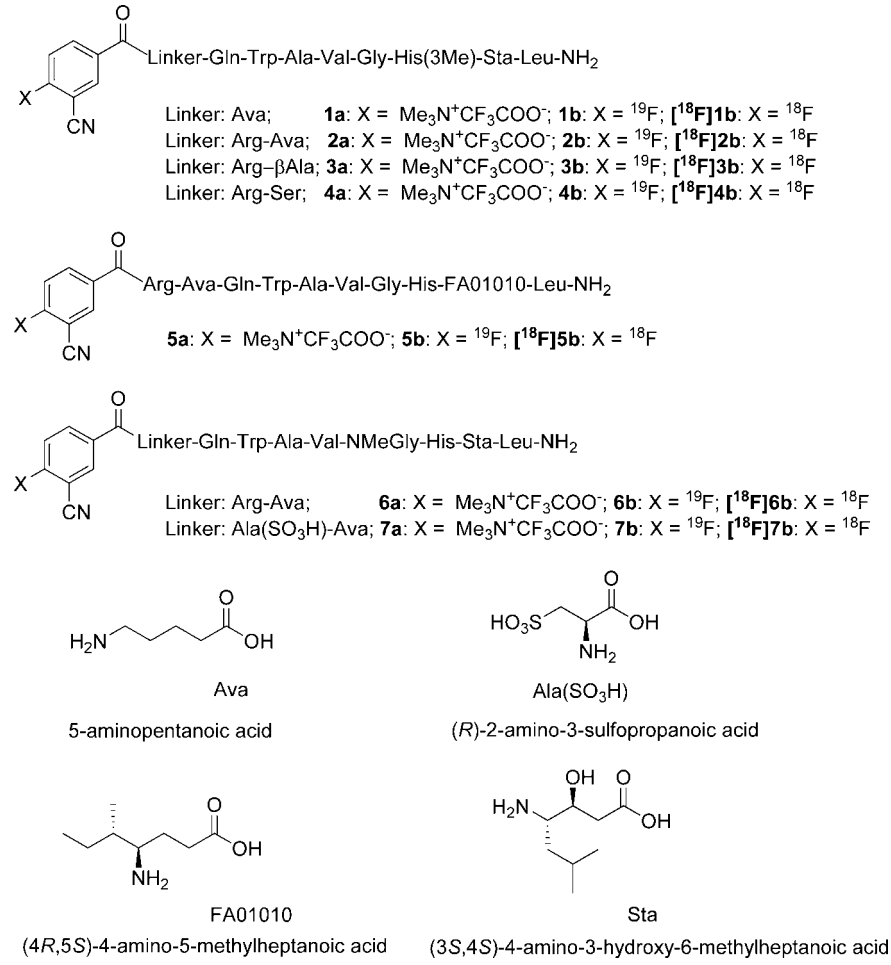


Figure 1. Synthesized bombesin analogues and structures of non-natural amino acids.

Table 1. Mass Spectrometric Analysis of Synthesized Bombesin Peptide Analogues and Their Yields[a]

peptides	molecular formula	calculated	found	yield (%)
1a	$C_{63}H_{93}N_{16}O_{12}$ (M^+)	1265.7	M^+: 1265.5	11
1b	$C_{60}H_{84}FN_{15}O_{12}$	1225.6	$[M + H]^+$: 1226.6	10
2a	$C_{69}H_{105}N_{20}O_{13}$ (M^+)	1421.8	$[(M + H)/2]^+$: 711.8	13
2b	$C_{66}H_{96}FN_{19}O_{13}$	1381.7	$[M + H]^+$: 1383.1	3
3a	$C_{67}H_{101}N_{20}O_{13}$ (M^+)	1393.8	M^+: 1393.8	22
3b	$C_{64}H_{92}FN_{19}O_{13}$	1353.7	$[M + H]^+$: 1354.8	5
4a	$C_{67}H_{101}N_{20}O_{14}$ (M^+)	1409.8	$[(M + H)/2]^+$: 705.7	20
4b	$C_{64}H_{92}FN_{19}O_{14}$	1369.7	$[(M + 2H)/2]^+$: 686.6	12
5a	$C_{68}H_{103}N_{20}O_{12}$ (M^+)	1391.8	M^+: 1391.9	8
5b	$C_{65}H_{94}FN_{19}O_{12}$	1351.7	$[M + H]^+$: 1352.9	12
6a	$C_{69}H_{105}N_{20}O_{13}$ (M^+)	1421.8	$[(M + H)/2]^+$: 711.9	11
6b	$C_{66}H_{96}FN_{19}O_{13}$	1381.7	$[(M + 2H)/2]^+$: 692.4	8
7a	$C_{66}H_{98}N_{17}O_{16}S$ (M^+)	1416.7	M^+: 1417.4	17
7b	$C_{63}H_{89}FN_{16}O_{16}S$	1376.6	$[M + H]^+$: 1378.0	34

[a] Isolated yields (not optimized; single syntheses) based on the amount and loading of commercial Fmoc-Rink-amide resin used for the synthesis.

precursors for ^{18}F-labeling, respectively. The nonradioactive BBS analogues served as a surrogate for ^{18}F-labeled compounds in the determination of binding affinity and as a standard reference for radio HPLC analysis. Figure 1 shows the sequences and the structures of the non-natural amino acid derivatives. All of the newly synthesized bombesin precursors and standard references were purified by reverse-phase HPLC and characterized by mass spectrometry (Table 1).

Radiolabeling. The direct ^{18}F-fluorination protocol developed previously in our laboratories was applied to these new bombesin peptide analogues. The synthetic scheme is depicted in Figure 2 using peptide **7a** as an example. Under the indicated radiolabeling conditions (Table 2), most peptides showed high ^{18}F-labeling efficiency. For peptide **4a**, which contains an Arg-Ser linker, a 29% ^{18}F-incorporation was obtained under mild radiolabeling conditions (50 °C, 15 min). For peptide **7a** containing the Ala(SO_3H)-Ava linker, a similar ^{18}F-labeling efficiency (26%, Table 2, entry 7) was achieved. These results successfully demonstrated that aromatic nucleophilic substitutions of ^{18}F-for-$^{+}$N(CH_3)$_3$ are feasible not only in the presence of histidine, tryptophan, and arginine amino acids but also in the presence of the unprotected acid and hydroxyl functionalities (serine amino acid). In addition, it was found that the ^{18}F-labeling efficiency could be dramatically improved from 26% to 75% by increasing the reaction temperature from 70 to 90 °C (Table 2, entries 7 and 8).

Concerning the stereochemistry of the peptides, similar peptides have been labeled under basic conditions (pH 8−10) and at elevated temperatures (75−100 °C); no racemization of the peptides was observed (*40*−*42*). Because most of our radiolabeling conditions (pH < 8, temperature 50−70 °C) are even milder than those previously reported, peptide racemization is not expected to occur under the above-mentioned radiolabeling conditions (Table 2). In addition, binding analysis of a ^{18}F-labeled peptide containing the same peptide sequence as **7b** revealed K_d and IC_{50} values of 1.43 nM and 0.94 nM, respectively, showing that the ^{18}F-labeled peptide still retains high binding affinity toward GRPR after heating at 90 °C for 10 min.

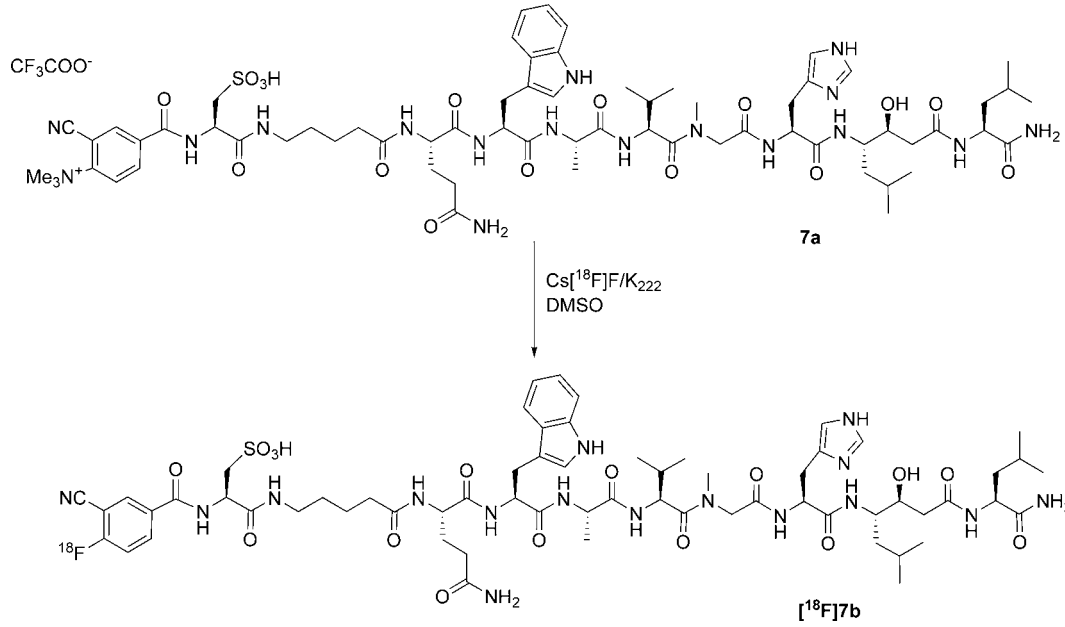


Figure 2. Synthetic scheme for the generation of **[^{18}F]7b**.

Table 2. ^{18}F-Radiolabeling of TMA-Based Bombesin Peptides[a]

entry	compd.	temp (°C)	reaction time	^{18}F-incorporation (% HPLC)	d. c. RCY (%)
1	**1a**	50	15 min	69 ± 8 (n = 2)	n.d.
2	**2a**	70	15 min	69 ± 7 (n = 3)	18%
3	**3a**	70	15 min	56 ± 1 (n = 2)	21%
4	**4a**	50	15 min	29 ± 6 (n = 2)	4%
5	**5a**	70	15 min	63 (n = 1)	n.d.
6	**6a**	70	15 min	51 ± 5 (n = 2)	20%
7	**7a**	70	15 min	26 ± 2 (n = 2)	n.d.
8	**7a**	90	15 min	74 ± 3 (n = 2)	14%

[a] ^{18}F-labeling was carried out in DMSO (150 μL) with a 2 mg amount of precursor using Cs_2CO_3 as the base. Conversion was determined from a radio-HPLC chromatogram representing the percentage of radioactivity area of the product related to the total radioactivity area. n.d.: not determined.

***In Vitro* Receptor Binding Affinity and Distribution Coefficient log $D_{7.4}$.** The binding affinities of the novel bombesin analogues toward the human GRPR were determined by a scintillation proximity assay using human GRPR-transfected cell membranes. All synthesized bombesin analogues showed nanomolar binding affinities toward human GRPR (Table 3). For peptide **1b** with Ava as a linker, a binding affinity of 28 nM was obtained. However, the attachment of one more hydrophilic amino acid Arg to the linker resulted in a more than 100 times higher binding affinity (Table 3; **2b**, K_i = 0.2 nM). Encouraged by these results, Arg-βAla and Arg-Ser were tested with the same peptide sequence. In both cases, binding affinities in the high nanomolar range were obtained (Table 3. K_i = 6.2 nM and 6.4 nM for **3b** and **4b**, respectively). With Arg-Ava as the linker, further investigations on the peptide sequence by exchanging Sta with FA01010 demonstrated that Sta was superior to FA01010 in terms of binding affinity. While the difference between the methylated His or the methylated Gly was not so obvious in this study (Table 3, K_i = 0.2 nM and 0.7 nM for **2b** and **6b**, respectively), the methylated Gly BBS analogue showed a 10-fold higher binding affinity than its corresponding methylated His analogue in our previous studies (*36*). Thus, the most promising peptide sequence toward human GRPR in this study was Gln-Trp-Ala-Val-NMeGly-His-Sta-Leu-NH_2. Further derivatization of the optimal peptide sequence by exchanging the linker Arg-Ava to Ala(SO_3H)-Ava yielded picomolar affinity (K_i = 0.1 nM) of this peptide candidate toward the GRPR.

The log $D_{7.4}$ values of the peptides are in the similar range (−0.8 to −1.4) with respect to the different polar linkers of Arg-Ava, Arg-βAla, or Ala(SO_3H)-Ava and peptide sequences. Compounds **6b** and **7b** gave the same log $D_{7.4}$ value of −1.1 (Table 3).

Biodistribution Studies. The biodistributions of **[^{18}F]6b** and **[^{18}F]7b** were carried out using nude mice bearing subcutaneous human prostate tumors (PC-3). The results are shown in Table 4. For **[^{18}F]6b**, the tumor uptake was 2.36 ± 0.47% ID/g at 30 min after injection, which slightly decreased to 1.80 ± 1.56% ID/g at 60 min postinjection and 1.61 ± 0.23% ID/g at 4 h postinjection. The binding of **[^{18}F]6b** toward GRPR could be blocked by around 40% in the tumor and 60% in the pancreas at 60 min postinjection, indicating that a large part of the tracer uptake in the tumor and pancreas can be attributed to specific GRPR binding. Besides the tumor and pancreas, the highest accumulation of the radiotracer **[^{18}F]6b** was found in excretory organs such as the gallbladder, intestine, kidneys, and liver. Activity uptake in the gall bladder and intestine was much higher than that in the kidneys, suggesting a preponderance of hepatobiliary elimination versus renal excretion. In the intestine there was, however, no differentiation between GRPR binding naturally expressed in intestinal smooth muscle cells and intestinal content. Furthermore, the increasing uptake in bone over time indicated that ^{18}F-fluoride represents a major radio metabolite. In comparison to the bombesin analogue **[^{18}F]6b**, the radiotracer **[^{18}F]7b** was characterized by clearly superior tumor targeting. The absolute tumor accumulation was more than double reaching about 5% ID/g at 30 min p.i., and this uptake was persistent over four hours. Tracer uptake in the GRPR-rich pancreas amounted to almost 50% ID/g at 1 h postinjection. Uptake of compound **[^{18}F]7b** in the tumor and pancreas was highly specific since accumulation could be effectively blocked by coadministration of unlabeled bombesin (83% and 97% specificity, respectively). The biodistribution of **[^{18}F]7b** was also characterized by a fast blood clearance leading to favorable tumor-to-blood ratios of >30 at 60 min postinjection and later. In line with compound **[^{18}F]6b**, the bombesin analogue **[^{18}F]7b** was mainly excreted via hepatobiliary pathways resulting in bile-to-tumor ratios of >20. It is clear that at physiological pH, Arg and Ala(SO_3H) become positively and negatively

Table 3. Sequence of the Tested Bombesin Analoguess and Their Binding Affinity (K_i) Towards Human GRPR and Lipophilicities (log $D_{7.4}$)

peptide	linker	peptide sequence	IC_{50} (nM)	K_i (nM)	log $D_{7.4}$
1b	Ava	Gln-Trp-Ala-Val-Gly-His(3Me)-Sta-Leu-NH_2	97	28.0	n.d.[a]
2b	Arg-Ava	Gln-Trp-Ala-Val-Gly-His(3Me)-Sta-Leu-NH_2	0.8	0.2	−1.4
3b	Arg-βAla	Gln-Trp-Ala-Val-Gly-His(3Me)-Sta-Leu-NH_2	25	6.2	−1.0
4b	Arg-Ser	Gln-Trp-Ala-Val-Gly-His(3Me)-Sta-Leu-NH_2	69	6.4	n.d.[a]
5b	Arg-Ava	Gln-Trp-Ala-Val-Gly-His-FA01010-Leu-NH_2	6.0	1.5	−0.8
6b	Arg-Ava	Gln-Trp-Ala-Val-NMeGly-His-Sta-Leu-NH_2	2.7	0.7	−1.1
7b	Ala(SO_3H)-Ava	Gln-Trp-Ala-Val-NMeGly-His-Sta-Leu-NH_2	0.4	0.1	−1.1

[a] n.d.: not determined.

Table 4. Biodistribution of [^{18}F]6b and [^{18}F]7b in Nude Mice Bearing PC-3 Xenografts at Different Times p.i.[a]

tissue	0.5 h	1.0 h	1.0 h[b]	2.0 h	4.0 h
	3-CN-4-[^{18}F]Fluoro-Bz-Arg-Ava--Gln-Trp-Ala-Val-NMeGly-His-Sta-Leu-NH_2 (**[^{18}F]6b**)				
blood	0.93 ± 0.28	0.27 ± 0.04	0.32 ± 0.02	0.15 ± 0.03	0.21 ± 0.16
kidneys	2.92 ± 0.44	1.35 ± 0.11	1.46 ± 0.13	0.87 ± 0.18	1.10 ± 0.74
liver	3.26 ± 0.60	1.23 ± 0.17	1.35 ± 0.24	0.61 ± 0.06	0.72 ± 0.39
spleen	0.56 ± 0.10	0.28 ± 0.06	0.21 ± 0.04	0.17 ± 0.03	0.19 ± 0.09
lung	1.13 ± 0.27	0.48 ± 0.16	0.69 ± 0.19	0.28 ± 0.04	0.29 ± 0.14
muscle	0.29 ± 0.03	0.15 ± 0.05	0.20 ± 0.08	0.07 ± 0.02	0.07 ± 0.02
gallbladder	82.06 ± 19.10	81.38 ± 52.78	132.49 ± 73.06	64.13 ± 34.51	58.81 ± 20.33
bone	4.36 ± 0.34	4.64 ± 0.42	4.04 ± 0.35	7.80 ± 0.89	7.98 ± 1.58
intestine	12.90 ± 1.53	6.76 ± 5.84	9.66 ± 2.06	8.92 ± 1.83	11.04 ± 0.10
pancreas	2.57 ± 0.03	1.30 ± 0.59	0.51 ± 0.10	1.26 ± 0.09	1.54 ± 0.47
adrenals	0.86 ± 0.11	0.65 ± 0.40	0.70 ± 0.39	0.26 ± 0.07	0.44 ± 0.04
tumor	2.36 ± 0.47	1.80 ± 1.56	1.11 ± 0.30	1.28 ± 0.27	1.61 ± 0.23
T/blood	2.59 ± 0.24	6.82 ± 6.19	3.46 ± 0.97	8.55 ± 2.29	11.37 ± 7.23
	3-CN-4-[^{18}F]Fluoro-Bz-Ala(SO_3H)-Ava--Gln-Trp-Ala-Val-NMeGly-His-Sta-Leu-NH_2 (**[^{18}F]7b**)				
blood	0.52 ± 0.13	0.16 ± 0.01	0.48 ± 0.21	0.10 ± 0.01	0.09 ± 0.02
kidneys	3.00 ± 2.20	0.66 ± 0.05	1.16 ± 0.48	0.42 ± 0.04	0.36 ± 0.12
liver	1.37 ± 0.18	0.50 ± 0.13	1.76 ± 0.56	0.37 ± 0.08	0.34 ± 0.12
spleen	0.63 ± 0.23	0.30 ± 0.02	1.32 ± 0.49	0.31 ± 0.12	0.28 ± 0.35
lung	0.51 ± 0.18	0.28 ± 0.03	23.04 ± 6.99	0.20 ± 0.03	0.11 ± 0.02
muscle	0.10 ± 0.01	0.05 ± 0.00	0.14 ± 0.05	0.06 ± 0.02	0.04 ± 0.02
gallbladder	230.12 ± 88.04	102.63 ± 74.25	137.40 ± 106.91	66.80 ± 54.48	137.22 ± 109.07
bone	0.84 ± 0.08	1.52 ± 0.22	1.61 ± 0.35	1.60 ± 0.12	1.75 ± 0.23
intestine	11.54 ± 2.91	11.75 ± 2.86	11.81 ± 5.52	9.88 ± 2.76	12.14 ± 2.38
pancreas	41.95 ± 5.37	49.01 ± 8.07	1.63 ± 0.65	34.49 ± 4.96	30.70 ± 5.14
adrenals	4.49 ± 1.27	3.45 ± 0.24	0.97 ± 0.10	2.31 ± 0.73	1.17 ± 0.19
tumor	4.67 ± 0.04	4.88 ± 0.36	0.84 ± 0.26	5.40 ± 0.58	5.16 ± 1.32
T/blood	9.50 ± 2.81	30.59 ± 1.05	1.80 ± 0.29	51.77 ± 2.52	55.03 ± 0.56

[a] Results are expressed as % ID/g ± SD (n = 3). [b] Blockade study: animals received 100 μg of bombesin coinjected with the radiolabeled compound.

charged, respectively. Although bearing the same binding peptide sequence and having the same lipophilicity, the charge of the linker obviously plays a major role in *in vivo* pharmacokinetics. Similar results have been reported for different bombesin analogues labeled with ^{99m}Tc, ^{64}Cu, and ^{68}Ga (*43*−*46*) suggesting that a negatively charged linker has a profound effect on the biodistribution profile of bombesin analogues. Furthermore, significant *in vivo* defluorination of compound **[^{18}F]7b** was not evident from the % ID/g values in the bone.

PET Study. The excellent tumor targeting of compound **[^{18}F]7b** encouraged us to test the capability of **[^{18}F]7b** to visualize PC3 tumors *in vivo* by PET imaging. Two nude mice bearing subcutaneous PC-3 tumor xenografts next to the right shoulder were scanned from 60 to 105 min p.i. in a dedicated small-animal PET system both under baseline and blockade conditions (Figure 3). The tumor was clearly imaged under baseline conditions, whereas no tumor visualization was possible under blocking conditions. As expected from the *ex vivo*

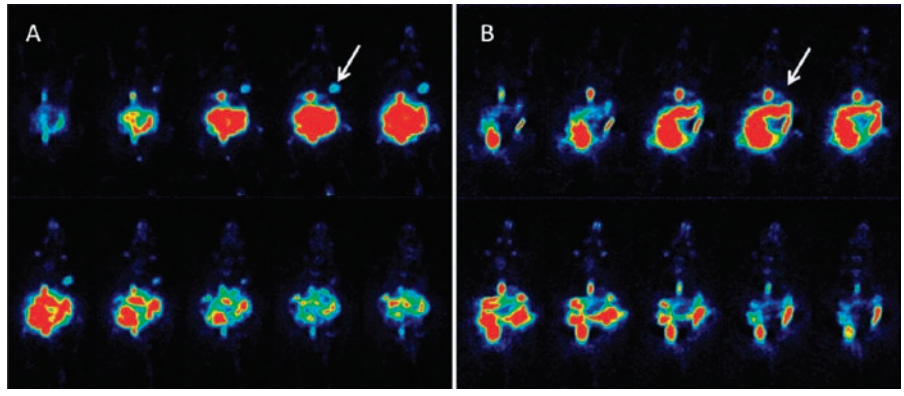


Figure 3. Series of horizontal whole body slices (ventral to dorsal) of two nude mice bearing subcutaneous PC-3 tumor xenografts next to the right shoulder (see arrows), which were injected with **[^{18}F]7b** and scanned from 60 to 105 min p.i., both under baseline (left) and blockade conditions (right). Image data were normalized to the injected dose per body weight.

biodistribution study, highest activity concentrations in the *in vivo* PET data were identified in the gall bladder and the intestine. The pancreas could not be visualized by PET due to the proximity to the bowel. Postmortem tissue sampling of these mice after PET scanning (107 min p.i.) confirmed the data which were obtained in the biodistribution study (Table 4). The absolute radioactivity uptake values in the GRPR-rich tissues were 5% ID/g for the tumor and 30% ID/g for the pancreas. The specificity of uptake amounted to 85% and 95% for the tumor and pancreas, respectively.

CONCLUSIONS

The direct ^{18}F-fluorination protocol developed previously in our lab was successfully applied to new bombesin peptide analogues. Amino acids such as histidine, tryptophan, and arginine, and non-natural amino acids such as statine and cysteine sulfonic acid in the peptide sequence did not require any protection group during radiosynthesis. *In vitro* binding studies of the synthesized bombesin analogues revealed nanomolar binding affinities toward the human GRPR. The most promising peptide sequence in this study was Gln-Trp-Ala-Val-NMeGly-His-Sta-Leu-NH_2. Two bombesin analogues containing this optimal peptide sequence, one positively (Arg-Ava) and another one negatively (Ala(SO_3H)-Ava) charged, were radiolabeled with ^{18}F and evaluated in biodistribution studies in nude mice bearing PC-3 xenografts. The comparative *in vivo* analysis of **[^{18}F]6b** and **[^{18}F]7b** showed superior characteristics for **[^{18}F]7b** with respect to (1) the total tracer accumulation in tumors and the GRPR-rich pancreas, (2) the specificity of uptake in target tissues, and (3) the target to nontarget ratios. The positive *in vivo* results of **[^{18}F]7b** suggest that this compound represents a promising PET tracer candidate for the visualization of GRPR-positive tumors in humans.

ACKNOWLEDGMENT

We thank Claudia Keller, Cindy Fischer, Selahattin, Ede, Marion Zerna, Ingo Horn, Jörg Pioch, René Zernicke, Volker Stickel, Ingolf Weber, Melanie Appel, Peter Friese, and Katrin Dinse for their excellent technical assistance.

LITERATURE CITED

(1) Anastasi, A., Erspamer, V., and Bucci, M. (1971) Isolation and structure of bombesin and alytesin, 2 analogous active peptides from skin of european amphibians *Bombina* and *Alytes*. *Experientia 27*, 166–167.

(2) Nagalla, S. R., Barry, B. J., Falick, A. M., Gibson, B. W., Taylor, J. E., Dong, J. Z., and Spindel, E. R. (1996) There are three distinct forms of bombesin: Identification of [Leu(13)]bombesin, [Phe(13)]-bombesin, and [Ser(3), Arg(10), Phe(13)]bombesin in the frog *Bombina orientalis*. *J. Biol. Chem. 271*, 7731–7737.

(3) Anastasi, A., Bucci, M., and Erspamer, V. (1972) Isolation and amino-acid sequences of alytesin and bombesin 2 analogous active tetradecapeptides from skin of european discoglossid frogs. *Arch. Biochem. Biophys. 148*, 443–446.

(4) Jensen, R. T., Battey, J. F., Spindel, E. R., and Benya, R. V. (2008) International union of pharmacology. LXVIII. Mammalian bombesin receptors: Nomenclature, distribution, pharmacology, signaling, and functions in normal and disease states. *Pharmacol. Rev. 60*, 1–42.

(5) Cornelio, D. B., Roesler, R., and Schwartsmann, G. (2007) Gastrin-releasing peptide receptor as a molecular target in experimental anticancer therapy. *Ann. Oncol. 18*, 1457–1466.

(6) Patel, O., Shulkes, A., and Baldwin, G. S. (2006) Gastrin-releasing peptide and cancer. *Biochim. Biophys. Acta 1766*, 23–41.

(7) Zhou, J. H., Chen, J., Mokotoff, M., and Ball, E. D. (2004) Targeting gastrin-releasing peptide receptors for cancer treatment. *Anti-Cancer Drugs 15*, 921–927.

(8) Markwalder, R., and Reubi, J. C. (1999) Gastrin-releasing peptide receptors in the human prostate: Relation to neoplastic transformation. *Cancer Res. 59*, 1152–1159.

(9) Reubi, J. C., Wenger, S., Schmuckli-Maurer, J., Schaer, J. C., and Gugger, M. (2002) Bombesin receptor subtypes in human cancers: Detection with the universal radioligand I-125-[D-TYR6, beta-ALA(11), PHE13, NLE14] bombesin(6−14). *Clin. Cancer Res. 8*, 1139–1146.

(10) Smith, C. J., Volkert, W. A., and Hoffman, T. J. (2003) Gastrin releasing peptide (GRP) receptor targeted radiopharmaceuticals: A concise update. *Nucl. Med. Biol. 30*, 861–868.

(11) Smith, C. J., Volkert, W. A., and Hoffman, T. J. (2005) Radiolabeled peptide conjugates for targeting of the bombesin receptor superfamily subtypes. *Nucl. Med. Biol. 32*, 733–740.

(12) Okarvi, S. M. (2004) Peptide-based radiopharmaceuticals: Future tools for diagnostic imaging of cancers and other diseases. *Med. Res. Rev. 24*, 357–397.

(13) Hoffman, T. J., Gali, H., Smith, C. J., Sieckman, G. L., Hayes, D. L., Owen, N. K., and Volkert, W. A. (2003) Novel series of In-111-labeled bombesin analogs as potential radiopharmaceuticals for specific targeting of gastrin-releasing peptide receptors expressed on human prostate cancer cells. *J. Nucl. Med. 44*, 823–831.

(14) Smith, C. J., Gali, H., Sieckman, G. L., Higginbotham, C., Volkert, W. A., and Hoffman, T. J. (2003) Radiochemical investigations of Tc-99m-N3S-X-BBN[7−14]NH2: An in vitro/in vivo structure-activity relationship study where X = 0-, 3-, 5-, 8-, and 11-carbon tethering moieties. *Bioconjugate Chem. 14*, 93–102.

(15) Smith, C. J., Gali, H., Sieckman, G. L., Hayes, D. L., Owen, N. K., Mazuru, D. G., Volkert, W. A., and Hoffman, T. J. (2003) Radiochemical investigations of Lu-177-DOTA-8-Aoc-BBN[7−14]NH2: An in vitro/in vivo assessment of the targeting ability of this new radiopharmaceutical for PC-3 human prostate cancer cells. *Nucl. Med. Biol. 30*, 101–109.

(16) Rogers, B. E., Bigott, H. M., McCarthy, D. W., Della Manna, D., Kim, J., Sharp, T. L., and Welch, M. J. (2003) MicroPET imaging of a gastrin-releasing peptide receptor-positive tumor in a mouse model of human prostate cancer using a Cu-64-labeled bombesin analogue. *Bioconjugate Chem. 14*, 756–763.

(17) Nock, B., Nikolopoulou, A., Chiotellis, E., Loudos, G., Maintas, D., Reubi, J. C., and Maina, T. (2003) [Tc-99m]Demobesin 1, a novel potent bombesin analogue for GRP receptor-targeted tumour imaging. *Eur. J. Nucl. Med. Mol. Imaging 30*, 247–258.

(18) Lin, K. S., Luu, A., Baidoo, K. E., Hashemzadeh-Gargari, H., Chen, M. K., Pili, R., Pomper, M., Carducci, M., and Wagner, H. N. (2004) A new high affinity technetium analogue of bombesin containing DTPA as a pharmacokinetic modifier. *Bioconjugate Chem. 15*, 1416–1423.

(19) Chen, X. Y., Park, R., Hou, Y. P., Tohme, M., Shahinian, A. H., Bading, J. R., and Conti, P. S. (2004) MicroPET and autoradiographic imaging of GRP receptor expression with Cu-64-DOTA-[Lys(3)]bombesin in human prostate adenocarcinoma xenografts. *J. Nucl. Med. 45*, 1390–1397.

(20) Chen, J. Q., Linder, K. E., Cagnolini, A., Metcalfe, E., Raju, N., Tweedle, M. F., and Swenson, R. E. (2008) Synthesis, stabilization and formulation of [Lu-177]Lu-AMBA, a systemic radio therapeutic agent for gastrin releasing peptide receptor positive tumors. *Appl. Radiat. Isot. 66*, 497–505.

(21) Gourni, E., Paravatou, M., Bouziotis, P., Zikos, C., Fani, M., Xanthopoulos, S., Archimandritis, S. C., Livaniou, E., and Varvarigou, A. D. (2006) Evaluation of a series of new Tc-99m-labeled bombesin-like peptides for early cancer detection. *Anticancer Res. 26*, 435–438.

(22) Zhang, H. W., Chen, J. H., Waldherr, C., Hinni, K., Waser, B., Reubi, J. C., and Maecke, H. R. (2004) Synthesis and

evaluation of bombesin derivatives on the basis of pan-bombesin peptides labeled with indium-111, lutetium-177, and yttrium-90 for targeting bombesin receptor-expressing tumors. *Cancer Res. 64*, 6707–6715.

(23) Lane, S. R., Veerendra, B., Rold, T. L., Sieckman, G. L., Hoffman, T. J., Jurisson, S. S., and Smith, C. J. (2008) (99)mTc(CO)(3)-DTMA bombesin conjugates having high affinity for the GRP receptor. *Nucl. Med. Biol. 35*, 263–272.

(24) Maecke, H. R., Hofmann, M., and Haberkorn, U. (2005) Ga-68-labeled peptides in tumor imaging. *J. Nucl. Med. 46*, 172S–178S.

(25) Nock, B. A., Nikolopoulou, A., Galanis, A., Cordopatis, P., Waser, B., Reubi, J. C., and Maina, T. (2005) Potent bombesin-like peptides for GRP-receptor targeting of tumors with Tc-99m: A preclinical study. *J. Med. Chem. 48*, 100–110.

(26) Okarvi, S. M. (2001) Recent progress in fluorine-18 labelled peptide radiopharmaceuticals. *Eur. J. Nucl. Med. 28*, 929–938.

(27) Zhang, X. Z., Cai, W. B., Cao, F., Schreibmann, E., Wu, Y., Wu, J. C., Xing, L., and Chen, X. Y. (2006) F-18-labeled bombesin analogs for targeting GRP receptor-expressing prostate cancer. *J. Nucl. Med. 47*, 492–501.

(28) Chang, Y. S., Jeong, J. M., Lee, Y. S., Kim, H. W., Rai, G. B., Lee, S. J., Lee, D. S., Chung, J. K., and Lee, M. C. (2005) Preparation of F-18-human serum albumin: A simple and efficient protein labeling method with F-18 using a hydrazone-formation method. *Bioconjugate Chem. 16*, 1329–1333.

(29) Poethko, T., Schottelius, M., Thumshim, G., Hersel, U., Herz, M., Henriksen, G., Kessler, H., Schwaiger, M., and Wester, H. J. (2004) Two-step methodology for high-yield routine radiohalogenation of peptides: F-18-labeled RGD and octreotide analogs. *J. Nucl. Med. 45*, 892–902.

(30) Toyokuni, T., Walsh, J. C., Dominguez, A., Phelps, M. E., Barrio, J. R., Gambhir, S. S., and Satyamurthy, N. (2003) Synthesis of a new heterobifunctional linker, N-[4-(aminooxy) butyl]maleimide, for facile access to a thiol-reactive F-18-Labeling agent. *Bioconjugate Chem. 14*, 1253–1259.

(31) Prante, O., Einsiedel, J., Haubner, R., Gmeiner, P., Wester, H. J., Kuwert, T., and Maschauer, S. (2007) 3,4,6-Tri-O-acetyl-2-deoxy-2-[F-18]fluoroglucopyranosyl phenylthiosulfonate: A thiol-reactive agent for the chemoselective F-18-glycosylation of peptides. *Bioconjugate Chem. 18*, 254–262.

(32) Ting, R., Adam, M. J., Ruth, T. J., and Perrin, D. M. (2005) Arylfluoroborates and alkylfluorosilicates as potential PET imaging agents: High-yielding aqueous biomolecular F-18-labeling. *J. Am. Chem. Soc. 127*, 13094–13095.

(33) Ting, R., Harwig, C., auf dem Keller, U., McCormick, S., Austin, P., Overall, C. M., Adam, M. J., Ruth, T. J., and Perrin, D. M. (2008) Toward [F-18]-labeled aryltrifluoroborate radiotracers: In vivo positron emission tomography imaging of stable aryltrifluoroborate clearance in mice. *J. Am. Chem. Soc. 130*, 12045–12055.

(34) Schirrmacher, E., Wangler, B., Cypryk, M., Bradtmoller, G., Schafer, M., Eisenhut, M., Jurkschat, K., and Schirrmacher, R. (2007) Synthesis of p-(Di-tert-butyl[(18)f]fluorosilyl)benzaldehyde ([F-18]SiFA-A) with high specific activity by isotopic exchange: A convenient Labeling synthon for the F-18-labeling of n-aminooxy derivatized peptides. *Bioconjugate Chem. 18*, 2085–2089.

(35) Mu, L. J., Hohne, A., Schubiger, R. A., Ametamey, S. M., Graham, K., Cyr, J. E., Dinkelborg, L., Stellfeld, T., Srinivasan, A., Voigtmann, U., and Klar, U. (2008) Silicon-based building blocks for one-step F-18-radiolabeling of peptides for PET imaging. *Angew. Chem., Int. Ed. 47*, 4922–4925.

(36) Hoehne, A., Mu, L., Honer, M., Schubiger, P. A., Ametamey, S. M., Graham, K., Stellfeld, T., Borkowski, S., Berndorff, D., Klar, U., Voigtmann, U., Cyr, J. E., Friebe, M., Dinkelborg, L., and Srinivasan, A. (2008) Synthesis, F-18-labeling, and in vitro and in vivo studies of bombesin peptides modified with silicon-based building blocks. *Bioconjugate Chem. 19*, 1871–1879.

(37) Becaud, J., Mu, L., Karramkam, M., Schubiger, P. A., Ametamey, S. M., Graham, K., Stellfeld, T., Lehmann, L., Borkowski, S., Berndorff, D., Dinkelborg, L., Srinivasan, A., Smits, R., and Koksch, B. (2009) Direct one-step(18)F-labeling of peptides via nucleophilic aromatic substitution. *Bioconjugate Chem. 20*, 2254–2261.

(38) Strijckmans, V. H., Dolle, F., and Coulon, C. (1996) Synthesis of a potential M(1) muscarinic agent 76Br-bromocaramiphen. *J. Labelled Compd. Radiopharm. 42*, 447–456.

(39) Honer, M., Bruhlmeier, M., Missimer, J., Schubiger, A. P., and Ametamey, S. M. (2004) Dynamic imaging of striatal D-2 receptors in mice using quad-HIDAC PET. *J. Nucl. Med. 45*, 464–470.

(40) Boswell, C. A., Regino, C. A. S., Baidoo, K. E., Wong, K. J., Bumb, A., Xu, H., Milenic, D. E., Kelley, J. A., Lai, C. C., and Brechbiel, M. W. (2008) Synthesis of a cross-bridged cyclam derivative for peptide conjugation and Cu-64 radiolabeling. *Bioconjugate Chem. 19*, 1476–1484.

(41) Van Domselaar, G. H., Okarvi, S. M., Fanta, M., Suresh, M. R., and Wishart, D. S. (2000) Synthesis and 99(m)Tc-labelling of bz-MAG3-triprolinyl-peptides, their radiochemical evaluation and in vitro receptor-binding. *J. Labelled Compd. Radiopharm. 43*, 1193–1204.

(42) Smith, C. J., Sieckman, G. L., Owen, N. K., Hayes, D. L., Mazuru, D. G., Kannan, R., Volkert, W. A., and Hoffman, T. J. (2003) Radiochemical investigations of gastrin-releasing peptide receptor-specific [Tc-99m(X)(CO)(3)-Dpr-Ser-Ser-Ser-Gln-Trp-Ala-Val-Gly-His-Leu-Met-(NH_2)] in PC-3, tumor-bearing, rodent models: Syntheses, radiolabeling, and in vitro/in vivo studies where Dpr = 2,3-diaminopropionic acid and X = H_2O or P(CH_2OH)(3). *Cancer Res. 63*, 4082–4088.

(43) Garayoa, E. G., Schweinsberg, C., Maes, V., Brans, L., Blauenstein, P., Tourwe, D. A., Schibli, R., and Schubiger, P. A. (2008) Influence of the molecular charge on the biodistribution of bombesin analogues labeled with the [Tc-99m(CO)(3)]-Core. *Bioconjugate Chem. 19*, 2409–2416.

(44) Parry, J. J., Kelly, T. S., Andrews, R., and Rogers, B. E. (2007) In vitro and in vivo evaluation of Cu-64-Labeled DOTA-linker-bombesin(7−14) analogues containing different amino acid linker moieties. *Bioconjugate Chem. 18*, 1110–1117.

(45) Schuhmacher, J., Zhang, H. W., Doll, J., Macke, H. R., Matys, R., Hauser, H., Henze, M., Haberkorn, U., and Eisenhut, M. (2005) GRP receptor-targeted PET of a rat pancreas carcinoma xenograft in nude mice with a Ga-68-labeled bombesin(6−14) analog. *J. Nucl. Med. 46*, 691–699.

(46) Fragogeorgi, E. A., Zikos, C., Gourni, E., Bouziotis, P., Paravatou-Petsotas, M., Loudos, G., Mitsokapas, N., Xanthopoulos, S., Mavri-Vavayanni, M., Livaniou, E., Varvarigou, A. D., and Archimandritis, S. C. (2009) Spacer site modifications for the improvement of the in vitro and in vivo binding properties of Tc-99m-N3S-X-bombesin[2−14] derivatives. *Bioconjugate Chem. 20*, 856–867.

BC100222U

Solid-Phase Synthesis of Azaphthalocyanine−Oligonucleotide Conjugates and Their Evaluation As New Dark Quenchers of Fluorescence

Kamil Kopecky, Veronika Novakova, Miroslav Miletin, Radim Kučera, and Petr Zimcik*

Department of Pharmaceutical Chemistry and Drug Control, Faculty of Pharmacy in Hradec Kralove, Charles University in Prague, Heyrovskeho 1203, 50005 Hradec Kralove, Czech Republic. Received May 14, 2010; Revised Manuscript Received August 30, 2010

Hydrophobic nonaggregating metal-free azaphthalocyanines (AzaPc) of the tetrapyrazinoporphyrazine type were synthesized, characterized, and used for oligonucleotide labeling. Both 3′-end and 5′-end labeling methods using solid phase synthesis suitable for automatic processes in the DNA/RNA synthesizer were developed. The hydrophobic character of AzaPc enabled the anchoring of the conjugates on reverse phase of the oligonucleotide purification cartridge, thus enabling their simple purification. AzaPc did not show any fluorescence and extremely low singlet oxygen quantum yields (Φ_Δ = 0.015−0.018 in DMF) in a monomeric state due to ultrafast intramolecular charge transfer. That is why they were investigated as a new dark quencher structural type. They profit particularly from absorption in a wide range of wavelengths (300−740 nm) that covers all fluorophores used in hybridization assays nowadays. As an example, quenching efficiency was evaluated in a simple hybridization assay using monolabeled probes. AzaPc-based probes efficiently quenched both fluorescein and Cy5 fluorescence by both resonance energy transfer and contact quenching. The results were compared with three established dark quenchers, and the AzaPc exerted better (BHQ-1 and BHQ-2) or comparable (BBQ-650) quenching efficiencies for both fluorophores.

INTRODUCTION

Modification of oligonucleotides with dyes is a commonly used procedure in genomic assays, e.g., in the monitoring of real-time polymerase chain reaction (PCR[1]). Most of the hybridization assays are based on the combination of a fluorophore with a quencher leading to the decrease of the fluorophore emission after detection of the target (*1*). The dark quenchers are a modern type of quenchers with no intrinsic fluorescence, which substantially simplifies the hybridization assays and increases their sensitivity. However, the currently used dark quenchers are based on two or three structural types, and they are often suitable only for a restricted number of fluorescent labels due to a limited spectral overlap. Therefore, the development of new highly efficient and versatile dark quenchers is desirable.

Phthalocyanines (*Pc*) and their aza-analogues azaphthalocyanines (AzaPc) are long known organic dyes with application in various areas (*2*). Despite deep investigations in *Pc* and AzaPc chemistry and applications, *Pc* conjugates with oligonucleotides were described only recently (*3*−*5*); furthermore, those using AzaPc have not been reported at all. For example, strong fluorescent properties of *Pc* were appreciated in *Pc*-oligonucleotide conjugates, and several new *Pc*-based near-infrared emitting fluorophores for DNA-hybridizations assays were developed (*6*, *7*). The use of *Pc*−oligonucleotide conjugates for a specific DNA catalytic or photosensitized modification was also described (*8*, *9*). The conjugation of *Pc* with the oligonucleotide is usually performed in a solution that requires the water solubility of the *Pc* moiety and subsequent extensive purification involving HPLC. The *Pc*−oligonucleotide labeling approaches tested until this time cover isothiocyanate (*5*) or succinimidyl methods (*6*, *10*, *11*), Huisgen cycloaddition (*12*), and reductive amination (*12*).

During our studies of AzaPc, we systematically observed that alkylamino substituted derivatives even in the strictly monomeric form are lacking any fluorescent or photosensitizing properties typical for other AzaPc derivatives (*13*). Recently, we discovered and fully explained that ultrafast intramolecular charge transfer (ICT) is responsible for the quenching of the S_1 excited state of such AzaPc (*14*). This unique mechanism of S_1 state deactivation, not yet observed at *Pc* derivatives, is responsible for the lack of fluorescence. These properties, together with strong absorption over a wide range of wavelengths, make alkylamino AzaPc ideal candidates for the modern dark quenchers. In order to confirm the hypothesis, suitable AzaPc were synthesized, simple solid-phase labeling of oligonucleotide probe was developed, and the conjugates were subjected to hybridization assays with two commonly used fluorophores.

EXPERIMENTAL PROCEDURES

All organic solvents were of analytical grade. Anhydrous butanol was stored over magnesium and distilled prior to use. Anhydrous pyridine was distilled from potassium hydroxide and stored over molecular sieves. Anhydrous tetrahydrofuran (THF) was stored over sodium and distilled prior to use. All chemicals for synthesis were obtained from established suppliers (Aldrich, Acros, Merck) and used as received. TLC was performed on Merck aluminum sheets with silica gel 60 F254. Merck

* To whom correspondence should be addressed. Tel: +420 495067257. Fax: +420 495067167. E-mail: petr.zimcik@faf.cuni.cz.

[1]Abbreviations: AzaPc, azaphthalocyanine; BBQ, BlackBerry Quencher; BHQ, Black Hole Quencher; CPG, controlled pore glass, DCC, *N*,*N*′-dicyclohexylcarbodiimide; DMF, dimethylformamide; DMSO, dimethylsulfoxide, DMTr, 4,4′-dimethoxytrityl; DMTrCl, 4,4′-dimethoxytrityl chloride; FAM, fluorescein; HBTU, *O*-(benzotriazol-1-yl)-*N*,*N*,*N*′,*N*′-tetramethyluronium hexafluorophosphate; ICT, intramolecular charge transfer; lcaa, long chain aminoalkyl; MALDI-TOF, matrix-assisted laser desorption/ionization time-of-flight; MeOH, methanol; NHS, *N*-hydroxysuccinimide; OPC, oligonucleotide purification cartridge; *Pc*, phthalocyanine; PCR, polymerase chain reaction; RET, resonance energy transfer; TFA, trifluoroacetic acid; THF, tetrahydrofuran; ZnPc, zinc phthalocyanine.

10.1021/bc100226x © 2010 American Chemical Society
Published on Web 09/20/2010

Kieselgel 60 (0.040−0.063 mm) was used for column chromatography. Long chain amino alkyl (lcaa) solid phase (500 Å controlled pore glass (CPG)) was obtained from ChemGenes Corporation (Wilmington, MA, USA). All HPLC chromatographic separations were performed on a Shimadzu chromatography system consisting of a communication bus module CBM 20A, a diode array detector SPD-M20A, two pumps LC-20AD, an autoinjector SIL-20AC, a column compartment CTO-20AC, a degasser DGU-20A_3, and a computer-based chromatographic software LC solution (Shimadzu, Tokyo, Japan). The infrared spectra were measured on IR-Spectrometer Nicolet Impact 400 in KBr pellets. The ^{1}H and ^{13}C NMR spectra were recorded on Varian Mercury-Vx BB 300 (299.95 MHz ^{1}H, and 75.43 MHz ^{13}C). The reported chemical shifts are relative to tetramethylsilane. The UV/vis spectra were recorded using a Shimadzu UV-2401PC spectrophotometer. The fluorescence spectra were obtained by an AMINCO-Bowman Series 2 luminescence spectrometer. The matrix-assisted laser desorption/ionization time-of-flight (MALDI-TOF) mass spectra of compounds **1**, **2**, and **7**−**10** were collected by a Voyager-DE STR mass spectrometer (Applied Biosystems) in α-cyano-4-hydroxycinnamic acid or *trans*-2-[3-(4-*tert*-butylphenyl)-2-methyl-2-propenylidene]-malononitrile as the matrix. Mass spectra of oligonucleotide probes were obtained using a MALDI-TOF Bruker Autoflex II mass spectrometer. Compound **3** was prepared according to Mørkved et al. (*15*), and compounds **1** (*16*) and **6** (*17*) have been published by our group earlier.

Synthesis. *Azaphthalocyanine (2).* AzaPc **1** (100 mg, 0.09 mmol) in anhydrous dichloromethane (3 mL) was added to 2-cyanoethyl-*N*,*N*-diisopropylchlorophosphoramidite (102 mg, 0.36 mmol) and diisopropylethylamine (126 μL, 0.72 mmol) in anhydrous dichloromethane (5 mL) and stirred for 2 h at rt under an argon atmosphere. Progress of the reaction was monitored on TLC (dichloromethane/acetone/methanol 50:1:1; product R_f = 0.56; compound **1** R_f = 0.12). Thereafter, the solution was washed with saturated $NaHCO_3$, dried by Na_2SO_4, and evaporated to dryness. Any possible purification on a silica column failed due to the decomposition of **2** on silica. That is why the product was used directly for oligonucleotide modification without any further purification. The similar instability of phosphoramidites on silica or alumina has been described also by other researchers (*18*). The MALDI-TOF spectra of **2** showed the mass at expected *m*/*z* = 1322.6, approximately 10% of the oxidized product at *m*/*z* = 1338.6, and a fragment at *m*/*z* = 1105.6 caused by laser ionization. Yield, 105 mg; 89% as a deep purple solid. MS (MALDI-TOF) *m*/*z* = 1105.6 (55) $[M\text{-}OPN(iPr)_2OCH_2CH_2CN]^+$, 1322.6 (100) $[M]^+$, 1338.6 (10) $[M + O]^+$.

4-[(3-Chloro-5,6-dicyanopyrazin-2-yl)methylamino]benzoic Acid (4). A mixture of compound **3** (400 mg, 2 mmol) and 4-(methylamino)benzoic acid (604 mg, 4 mmol) in THF (75 mL) was refluxed for 12 h. The reaction was cooled down and filtered, and the filtrate was purified on silica with chloroform/acetone/methanol 10:1:1 as the mobile phase. The product was recrystallized from ethanol/water. Yield, 520 mg; 83% as a yellow powder; mp 208.1−211.6 °C. ^{1}H NMR (300 MHz, [D_6] acetone): δ = 8.09 (d, ^3J(H,H) = 8.5 Hz, 2H, arom. CH); 7.48 (d, ^3J(H,H) = 8.5 Hz, 2H, arom. CH_2) and 3.66 (s, N−CH_3, 3H,) ppm. ^{13}C NMR (75 MHz, [D_6] acetone): δ = 166.7, 153.5, 149.6, 141.1, 131.9, 130.7, 130.0, 125.8, 121.9, 114.3, 114.2, and 42.6 ppm. IR (KBr): ν = 3066, 2957, 2663, 2546, 2360, 2343, 2234 (CN), 1694, 1607, 1537, 1494, 1406, and 1375 cm^{-1}.

4-[(5,6-Dicyano-3-diethylaminopyrazin-2-yl)methylamino]benzoic Acid (5). Compound **4** (312 mg, 0.89 mmol) was refluxed in THF (50 mL) with diethylamine (1.3 g 18 mmol) for 2 h. The reaction was cooled down, filtered, and the solvent evaporated. The crude product was purified on silica with a mobile phase of chloroform/methanol 10:1 and finally recrystallized from ethanol/water. Yield, 324 mg; 62% of yellow powder; mp 263.3−266.2 °C (decomp.). ^{1}H NMR (300 MHz, [D_6] DMSO−): δ = 7.79 (d, ^3J(H,H) = 8.8 Hz, 2H, arom. CH_2), 7.09 (d, ^3J(H,H) = 8.8 Hz, 2H,arom. CH), 3.48 (s, 3H, N−CH_3), 3.25 (q, ^3J(H,H) = 7 Hz, 4H, N−CH_2) and 0.78 (t, ^3J(H,H) = 7 Hz, 6H, CH_2−CH_3) ppm. ^{13}C NMR (75 MHz, [D_6] DMSO): δ = 167.0, 148.5, 147.6, 143.9, 130.9, 126.0, 124.1, 120.4, 118.3, 115.4, 115.2, 42.8, 39.2, and 12.5 ppm. IR (KBr): ν = 2976, 2936, 2876, 2360, 2229 (CN), 1686, 1607, 1533, 1501, 1404, and 1292 cm^{-1}.

2-[(4-Carboxyphenyl)methylamino]-3,9,10,16,17,23,24-heptakis(diethylamino)-1,4,8,11,15,18,22,25-(octaaza)phthalocyanine (7). Metal lithium (168 mg, 24 mmol) was added to the refluxing mixture of compounds **5** (300 mg, 0.85 mmol) and **6** (700 mg, 2.57 mmol) in anhydrous butanol (20 mL) and the reflux continued for the next 3 h. The solvent was removed under reduced pressure, dilute acetic acid (50%, 50 mL) was added, and the suspension was stirred for 30 min at rt. The crude product was filtered and washed thoroughly with water. The resulting mixture of congeners was separated on silica with dichloromethane/acetone/methanol 20:1:1 as the mobile phase. The second intense purple fraction (product) was purified again on silica with dichloromethane/acetone/methanol 30:1:1. Finally, pure compound **7** was dissolved in 5 mL of dichloromethane, dropped into 200 mL of hexane, and cooled to −30 °C overnight. The precipitated fine suspension was filtered and washed with hexane. Yield, 150 mg; 15% of deep purple solid. ^{1}H NMR (300 MHz, [D_5] pyridine): δ = 13.83 (br s, 2H; central NH), 8.48 (d, ^3J(H,H) = 9 Hz, 2H; arom. CH), 7.20 (d, overlap with solvent, 2H; arom. CH), 3.96−3.86 (m, 24H, N−CH_2), 3.85 (s, 3H; N−CH_3), 3.72 (q, ^3J(H,H) = 7 Hz, 4H; N−CH_2) and 1.27−1.06 ppm (m, 42H; CH_3). ^{13}C NMR (75 MHz, [D_5] pyridine): δ = 169.0, 153.2, 151.0, 150.9, 150.5, 146.7, 146.6, 143.0, 142.9, 141.6, 140.0, 139.9, 139.7, 139.7, 131.4, 117.3, 43.8, 43.1, 43.1, 39.1, 13.2, 13.1, and 13.1 ppm (some signals were overlapped with signals of solvent). IR (KBr): ν = 2969, 2931, 2873, 1710 (CO), 1639, 1605, and 1426 cm^{-1}. UV/vis (THF): λ_{max} (ε) = 680 (80000), 654 (66500), 622sh, 597sh, 518 (54300) and 369 nm (93200 $M^{-1}cm^{-1}$). MS (MALDI-TOF): *m*/*z* = 1168.6 $[M]^+$. Anal. ($C_{60}H_{80}N_{24}O_2$ + 2 H_2O) calcd. C 59.78, H 7.02, N 27.89; found, C 60.18, H 7.30, N 27.53.

Azaphthalocyanine (8). AzaPc **7** (290 mg, 248 μmol) was dissolved in anhydrous tetrahydrofuran (40 mL). *N*,*N*′-dicyclohexylcarbodiimide (DCC) (56.2 mg, 273 μmol) and subsequently *N*-hydroxysuccinimide (NHS) (31.4 mg, 273 μmol) were added. The reaction was stirred for 72 h at rt. The precipitated solid (*N*,*N*′-dicyclohexylurea) was filtered off and washed with THF. 3-Amino-1,2-propandiol (113 mg, 1.24 mmol) in methanol was added into the THF solution, and the reaction was stirred at rt. The reaction was protected from light by aluminum foil. After 36 h, the solvent was evaporated at reduced pressure, and the rest was suspended in water, filtered, and washed thoroughly with water. Purification was performed on silica with a dichloromethane/acetone/methanol gradient from 30:1:1 to 10:1:1. Yield, 150 mg; 49% as deep purple solid. ^{1}H NMR (300 MHz, [D_5] pyridine): δ = 13.81 (br s, 2H; central NH), 9.32 (t, ^3J(H,H) = 6 Hz, 1H; NHCO), 8.32 (d, ^3J(H,H) = 9 Hz, 2H; arom. CH), 7.17 (d, overlap with solvent, 2H; arom. CH), 4.53−4.42 (m, 1H; C*H*−OH), 4.32−4.00 (m, 4H; NH−CH_2, O−CH_2), 3.97−3.84 (m, 24H; N−CH_2), 3.83 (s, 3H, N−CH_3), 3.69 (q, ^3J(H,H) = 7 Hz; 4H, N−CH_2) 1.21 (t, ^3J(H,H) = 7 Hz, 30H; CH_3), 1.14 (t, ^3J(H,H) = 7 Hz, 6H; CH_3) and 1.06 ppm (t, ^3J(H,H) = 7 Hz, 6H; CH_3). ^{13}C NMR (75 MHz, [D_5] pyridine): δ = 168.4, 153.1, 151.0, 150.9, 150.9, 150.6, 150.5, 150.0, 147.0, 146.1, 142.8, 142.7, 141.5, 140.1, 139.9, 139.8, 139.7, 139.6, 129.4, 128.9, 128.3, 126.1, 122.9, 117.9, 116.7,

114.4, 72.2, 65.2, 43.7, 43.1, 43.0, 39.2, 30.2, 13.3, 13.1, and 13.1 ppm (some signals were overlapped with signals of solvent). IR (KBr): $\nu = 2969, 2931, 2873, 1636$ (CONH), 1607, 1506, and 1427 cm^{-1}. UV/vis (THF): λ_{max} (ε) = 681 (80000), 655 (65600), 622sh, 597sh, 518 (53500) and 370 nm (91100 $M^{-1}cm^{-1}$). MS (MALDI-TOF) m/z = 1241.3 $[M]^+$. Anal. ($C_{63}H_{87}N_{25}O_3 + 3\ H_2O$) calcd. C 58.36, H 7.23, N 27.01; found, C 58.50, H 7.33, N 26.97.

*Azaphthalocyanine (**9**).* AzaPc **8** (124 mg, 0.1 mmol), 4,4′-dimethoxytrityl chloride (DMTrCl) (44 mg, 0.13 mmol), and a catalytic amount of 4-*N*,*N*-dimethylaminopyridine were dissolved in anhydrous pyridine (20 mL) and stirred for 14 h at rt. After that time, more DMTrCl (169 mg, 0.5 mmol) was added, and the reaction was stirred further. The reaction vessel was protected from light by aluminum foil. After 24 h, TLC (dichloromethane/pyridine 40:1) indicated full conversion. The product was used directly for the subsequent reaction without any isolation. A sample was taken from the solution and analyzed using mass spectrometry. MS (MALDI-TOF) m/z 1543.7 $[M]^+$, after the addition of trifluoroacetic acid (TFA) into the matrix (deprotection of 4,4′-dimethoxytrityl (DMTr)): m/z 1241.6 $[M\text{-}DMTr]^+$.

*Azaphthalocyanine (**10**).* Succinic anhydride (100 mg, 1 mmol) was added into the previous reaction, and the mixture was heated for 12 h at 60 °C. Thereafter, the solvent was removed under reduced pressure, and the crude product was purified on silica with a step gradient: dichloromethane/pyridine 40:1, dichloromethane/pyridine 20:1, and dichloromethane/methanol/pyridine 20:1:1. Yield, 40 mg; 25% (after two steps) as a deep purple solid. ^1H NMR (300 MHz, [D_5] pyridine): δ = 13.86 (br s, 2H; central NH), 9.11 (t, ^3J(H,H) = 5 Hz, 1H; NHCO), 6.88−8.46 (m, 17H; arom. CH), 4.33−4.20 (m, 1H; C*H*-O), 3.98−3.79 (m, 26H; 1 × NH−CH_2, 12 × N−CH_2), 3.75 (s, 3H; N−CH_3), 3.73−3.56 (m, 12H; 2 × O−CH_3, 1 × O−CH_2, 2 × N−CH_2), 2.91−2.87 (m, 2H; CH_2−CO), 2.85−2.81 (m, 2H; CH_2−CO), 1.20 (t, ^3J(H,H) = 7 Hz, 30H; CH_3), 1.14 (t, ^3J(H,H) = 7 Hz, 6H; CH_3) and 1.06 ppm (t, ^3J(H,H) = 7 Hz, 6H; CH_3). ^{13}C NMR (75 MHz, [D_5] pyridine): δ = 174.4, 172.2, 167.1, 158.3, 152.4, 150.3, 150.2, 150.1, 148.5, 146.3, 145.1, 144.7, 135.7, 135.3, 134.1, 131.0, 129.9, 128.3, 127.9, 127.6, 126.4, 116.9, 113.0, 85.8, 72.4, 62.2, 54.5, 42.9, 42.4, 42.3, 38.5, 29.5, 29.3, 29.1, 12.4 ppm (some signals were overlapped with the signals of the solvent). IR (KBr): ν = 3428, 3305, 3050, 2966, 2930, 2871, 1734 (CO-O), 1640(CO-NH), 1607, 1508, 1425, and 1250 (O−CH_3) cm^{-1}. MS (MALDI-TOF): m/z = 1643.7 $[M]^+$; after the addition of TFA into the matrix, m/z = 1341.7 $[M\text{-}DMTr]^+$.

*Solid Phase Modified with Azaphthalocyanine (**11**).* AzaPc **10** (8 mg, 5 μmol), *O*-(benzotriazol-1-yl)-*N*,*N*,*N*′,*N*′-tetramethyluronium hexafluorophosphate (HBTU) (3 mg, 10 μmol), and anhydrous triethylamine (10 μL) were dissolved in anhydrous dimethylformamide (DMF) (2 mL), and 100 mg of lcaa CPG was added. The reaction vial was sealed, and the mixture was shaken for 24 h at rt on an orbital shaker protected from light. Thereafter, the solid phase was washed with DMF, acetonitrile, and diethylether and dried over the silica under reduced pressure. Unreacted amino groups were subsequently capped. A mixture of anhydrous THF, pyridine, and acetic anhydride (8:1:1 (v/v), 1 mL) was mixed with a 10% (m/m) solution of 1-methylimidazole in anhydrous THF (1 mL) and shaken with the solid phase **11** for 30 min at rt. Thereafter, the solid phase was washed with DMF, acetonitrile, and diethylether and dried over silica under reduced pressure. 4,4′-Dimethoxytrityl loading was determined as described in the following procedure. Approximately 2−3 mg of the support was accurately weighed out directly to the test tube, perchloric acid solution (10 mL, 51.4 mL of 70% $HClO_4$ + 46 mL of methanol) was added, and the test tube was sealed and shaken. The optical absorbance of the sample, diluted to fit an interval of 0.2−1.0 AU was measured at 498 nm in a 1 cm cuvette. The loading was calculated as given bellow:

$$\text{loading } (\mu\text{mol/g}) = (\text{absorbance at } 498) \times \text{dilution} \times 143/(\text{weight of support (mg)})$$

The loading of DMTr on solid phase **11** was determined to be 30.8 μmol/g.

Synthesis of Oligonucleotides. Oligonucleotides were synthesized on a Perkin-Elmer Applied Biosystems 394 DNA/RNA synthesizer. 3′-Labeling of the oligonucleotides was achieved by synthesis on modified solid phases (solid phase **11** and commercially obtained supports of Black Hole Quencher (BHQ) or BlackBerry Quencher (BBQ)). 5′-Labeling of the oligonucleotides was performed on the same synthesizer employing standard phosphoramidite chemistry and corresponding dye 2-cyanoethyl-(*N*,*N*-diisopropyl)-phosphoramidites (compound **2** and commercially obtained dyes). 3′-BHQ-1 CPG, 3′-BHQ-2 CPG, 5′-BHQ-1 phosphoramidite, 5′-BHQ-2 phosphoramidite, Cy5 phosphoramidite, and 5′-fluorescein phosphoramidite were supplied by Glen Research, Sterling, VA, USA. 3′-BBQ-650 CPG and 5′-BBQ-650 phosphoramidite were supplied by Berry & Associates, Inc., Dexter, MI, USA. The synthesis and purification of oligonucleotides labeled with commercially obtained dyes were performed according to the supplier's recommendations.

OPC Purification of Oligonucleotides S1−S6 Modified with AzaPc. Prepared oligonucleotides **S1**−**S6** with AzaPc were purified on oligonucleotide purification cartridges (OPCs), Puri-Pak cartridges, (ChemGenes Corp., Wilmington, MA, USA) directly after deprotection from the solid phase. The OPC was washed with acetonitrile (4 mL) and 2 M triethylammonium acetate (2 mL). A solution of oligonucleotide (2−3 mL) in deprotecting solution was loaded on the OPC repeatedly until all of the color was absorbed to the top of OPC. Thereafter, the OPC was washed with a diluted solution of ammonia (2.5%, 4 mL), then with 8% acetonitrile (4 mL) and 30% acetonitrile (2 mL). The desired sequence was obtained by freeze-drying the 30% acetonitrile fraction. Purified oligonucleotides were stored at −20 °C.

S1 (AzaPc): MS (MALDI-TOF), a cluster peaking at m/z 8805 $[M + H]^+$ and adducts with sodium and potassium. **S2** (AzaPc): MS (MALDI-TOF), a cluster peaking at m/z 10325 $[M + H]^+$ and adducts with sodium and potassium. **S3** (AzaPc): MS (MALDI-TOF), a cluster peaking at m/z 11846 $[M + H]^+$ and adducts with sodium and potassium. **S4** (AzaPc): MS (MALDI-TOF), a cluster peaking at m/z 8685 $[M + H]^+$ and adducts with sodium and potassium. **S5** (AzaPc): MS (MALDI-TOF), a cluster peaking at m/z 7400 $[M + H]^+$ and adducts with sodium and potassium. **S6** (AzaPc): MS (MALDI-TOF), a cluster peaking at m/z 5819 $[M + H]^+$ and adducts with sodium and potassium.

HPLC Analysis. A gradient elution was used to analyze **S1**−**S6** modified with AzaPc. The separation was performed on a Hypersil BDS C18 column (100 × 4.6 mm, 3 μm particle size) using a mobile phase consisting of acetonitrile and 50 mM triethylammonium acetate. Mobile phase A was 12% acetonitrile in 50 mM triethylammonium acetate, and mobile phase B was acetonitrile. The gradient time program was set as follows: 0−2 min 0%B; 2−18 min 0−85% B; 18−25 min 85% B; 25−25.5 min 85−0% B. The column was equilibrated for 4.5 min. The column temperature was maintained at 40 °C, and the flow rate was set at 0.7 mL/min. The compounds were analyzed by a diode array detector. The corresponding controls were analyzed separately to allow the determination of their elution patterns.

Unlabeled oligonucleotides were eluted with t_R of approximately 2 min and free dye (**1** or **8**) with t_R of approximately 23 min.

Hybridization Assays. *Absorption Spectra of Duplexes.* Spectra of duplexes were measured in hybridization buffer. Stock solutions of oligonucleotides **S1**, **S3**, and **S4** labeled with AzaPc and **SF** and **SFX** labeled with Cy5 were prepared to a concentration 100 μM. Hybridization buffer (1 mL) was transferred to a cuvette, the stock solution of oligonucleotide probe with the quencher (10 μL) was added, and the absorption spectrum was measured. Thereafter, the stock solution of the oligonucleotide labeled with fluorophore (10 μL) was added, and the solution was heated to 50 °C for 1 min. The absorption spectrum of the duplex was measured after 30 min when the sample cooled down to laboratory temperature. The final concentration of both oligonucleotides was 1 μM. Absorption spectra of **SF** and **SFX** were measured also separately after the addition of the stock solution (10 μL) to hybridization buffer (1 mL).

Determination of Quenching Efficiency. The method was adopted from Marras et al. (*1*). Oligonucleotides **S1**−**S6** modified with AzaPc, BHQ-1, BHQ-2, and BBQ-650 or without any quencher were dissolved in hybridization buffer to a stock concentration 10 μM. Oligonucleotide **SF** was dissolved in hybridization buffer to a concentration 0.05 μM and transferred to a cuvette (800 μL), and the fluorescence was measured at 663 and 517 nm for Cy5 and fluorescein (FAM), respectively (excitation wavelengths 651 and 492 nm for Cy5 and FAM, respectively). Subsequently, the oligonucleotide with the quencher (20 μL of stock solution; final concentration 0.25 μM) was added, and the solution was heated to 70 °C for 5 min and allowed to cool to laboratory temperature for 30 min (**S6** was cooled to 4 °C). Thereafter, the fluorescence of the duplex was measured. A similar procedure was used for oligonucleotide **SFX**. The quenching efficiency (*QE*) was calculated according to the following equation (*1*, *19*):

$$QE = (1 - F_X/F_0) \times 100$$

where F_0 is the fluorescence of fluorophore **SF** alone, and F_X is the fluorescence of the duplex.

Singlet Oxygen Quantum Yields and Fluorescence. Quantum yields of a singlet oxygen (Φ_Δ) of **1** and **7** were determined according to a previously published procedure (*20*) using the decomposition of 1,3-diphenylisobenzofuran in DMF. Zinc phthalocyanine (ZnPc) was used as a reference ($\Phi_\Delta = 0.56$ in DMF *21*, *22*). The absorption of the dyes in the Q-band area was set approximately to 0.1. The presented data represent the mean of three measurements.

An attempt to detect any fluorescence signals from quenchers was also made. Compounds **1** and **7** in DMF, dimethylsulfoxide (DMSO), and THF or oligonucleotides **S1**−**S6** with AzaPc in hybridization buffer were excited at the B-band (365 nm) or Q-band (650 nm). Absorption at the excitation wavelength was set to approximately 0.1. Fluorescence was monitored in a range of 550−900 nm.

RESULTS AND DISCUSSION

Synthesis. All conjugation procedures between *Pc* and oligonucleotides until now were performed in water solution with an excess of *Pc* reagent. Isolation of the desired conjugate therefore always included several steps including the final HPLC separation. Solid-phase synthesis of the conjugates allows for the reduction of the side products, and the excess of the reagent can be easily washed out. In order to further simplify the purification steps, the AzaPc labels were designed to be highly hydrophobic, and that is why the conjugates may be anchored in a short OPC allowing easy purification without the need for HPLC separation. The design of AzaPc labels was based on the following considerations: (1) the macrocycle must carry mostly hydrophobic substituents and one modifiable group; (2) the macrocycle must be substituted with alkylamino substituents in order to allow ICT to quench efficiently excited states; and (3) the hydrophobic substituents must be sufficiently bulky in order to reduce aggregation typical for planar AzaPc and *Pc* macrocycles. On the basis of these requirements, compounds **1** and **7** (Figure 1 and Schemes 1 and 2) were synthesized and further modified for both 3′- and 5′-end solid-phase labeling. Postsynthetic modification of AzaPc was easily performed because bulky *N*,*N*-diethylamino substituents reduced the aggregation to a minimum, and the typical problems with low solubility, silica binding (*22*), or tailing of AzaPc on TLC (*14*) were not observed (see Supporting Information, Figure S1).

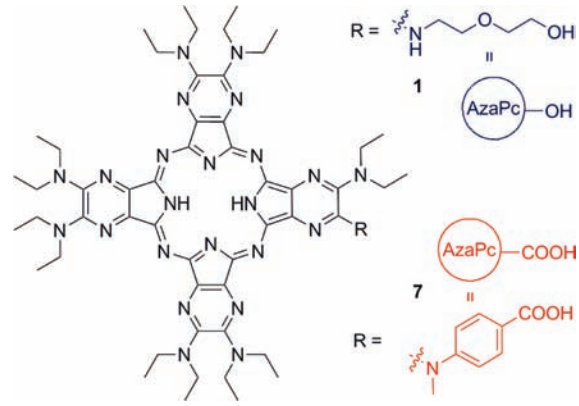
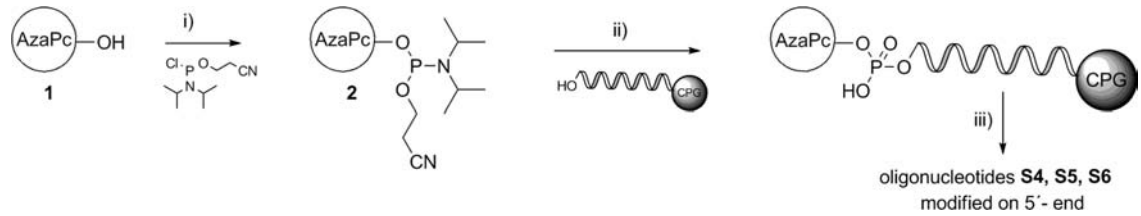


Figure 1. Structures of compounds **1** and **7**.

5′-End modified oligonucleotides **S4**−**S6** were prepared from **1** (*16*) via phosphoramidite **2** (Scheme 1). Phosphoramidites are highly reactive intermediates (*23*, *24*) finding their place in automatic DNA synthesis for both DNA elongation and labels attachment. Compound **2** was therefore introduced as the last step into the DNA/RNA synthesizer during solid-phase synthesis. Contrary to the in-solution conjugation methods, this approach simplifies the labeling and enables the general automatic processes to be used.

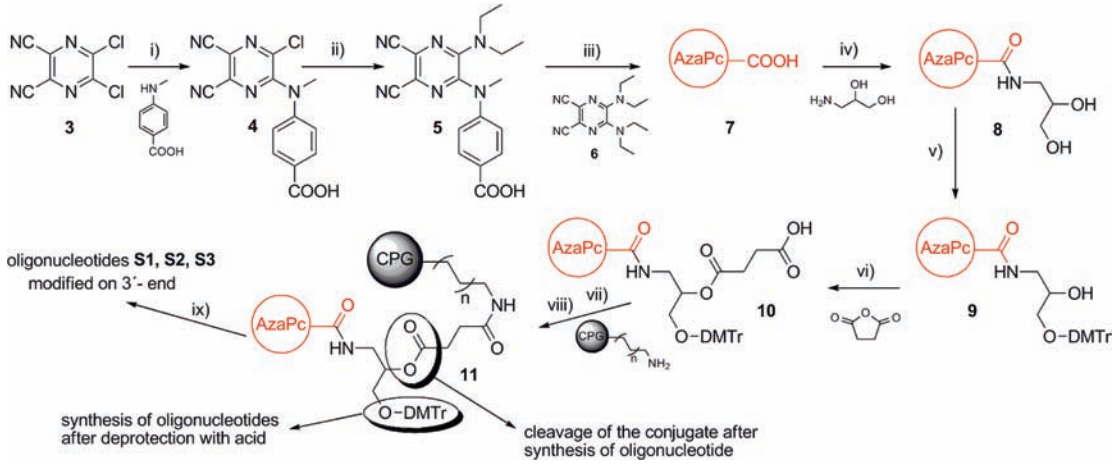
For the 3′-end labeling of oligonucleotides, the long chain aminoalkyl (lcaa) solid phase was modified by AzaPc **7** (Scheme 2) before the synthesis of the desired oligonucleotide chain (**S1**−**S3**). First, unsymmetrical AzaPc **7** was synthesized by statistical condensation of **5** and **6** and isolated from the mixture of six congeners (see Supporting Information, Figure S2) with a yield of 15%. Compound **5** was prepared by two step nucleophilic substitution of chlorine atoms in **3**. Although several selective strategies were developed for the synthesis of unsymmetrical *Pc* (*25*) including recent efforts in the improvement of solid-phase synthesis (*26*), the statistical condensation gave reasonable yields of **7** with very simple isolation of the desired congener. To verify the stability of **7** during the 3′-end labeling of oligonucleotides, the compound was subjected to the conditions occurring in the course of automated chemical oligonucleotide synthesis. It was shown to be stable in all the range of chemical conditions tested (see Supporting Information). Compound **7** was converted to dihydroxyamide **8** via an active succinimidyl ester. Protection of the primary hydroxy group with DMTrCl (**9**) allowed for selective modification of the secondary hydroxyl with succinate (**10**) and subsequent attachment of the AzaPc to lcaa solid phase (**11**). Unreacted amino groups in solid phase were capped with acetic anhydride. Solid phase **11** allows for the start of the synthesis of the DNA probe on hydroxyl after DMTr deprotection and simple cleavage of the synthesized conjugate from the solid phase by basic hydrolysis of the ester bond. Such a modified solid phase was

Scheme 1. Synthesis of 5′-End Modified Oligonucleotides Labeled with AzaPc[a]



[a] (i) anhydr. DCM, diisopropylethylamine, rt; (ii) 5-ethylthiotetrazole, anhydr. acetonitrile, DNA/RNA synthesizer; (iii) ammonia/methylamine, rt.

Scheme 2. Synthesis of 3′-End Modified Oligonucleotides Labeled with AzaPc[a]



[a] (i) THF, reflux; (ii) diethylamine, THF, reflux; (iii) anhydr. butanol, Li, reflux; (iv) DCC, NHS, anhydr. THF/methanol, rt; (v) DMTrCl, 4-(*N*,*N*-dimethylamino)pyridine, anhydr. pyridine, rt; (vi) anhydr. pyridine, 60°C; (vii) HBTU, triethylamine, anhydr. DMF, rt; (viii) acetic anhydride, 1-methylimidazole, THF/pyridine, rt; (ix) DNA synthesis in DNA/RNA synthesizer.

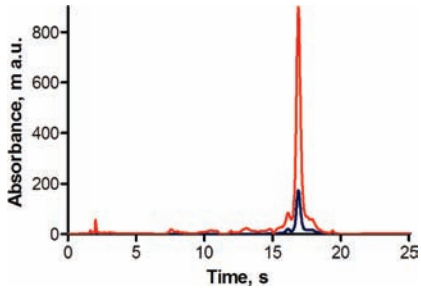


Figure 2. HPLC chromatogram of purified oligonucleotide **S3** labeled with AzaPc. Red line, 254 nm; blue line, 673 nm.

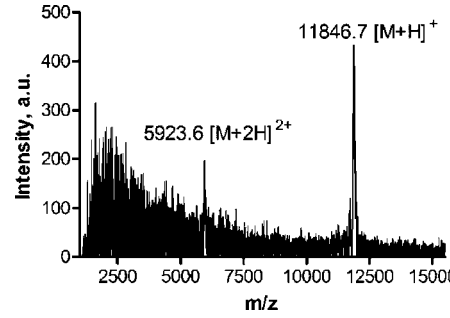


Figure 3. MALDI-TOF spectrum of oligonucleotide **S3** labeled with AzaPc.

used in a standard oligonucleotide synthesis in a DNA/RNA synthesizer. Also, this approach allows the general automatic processes in a DNA/RNA synthesizer to be used for both synthesis and cleavage of the conjugate from solid phase.

In all of the cases (**S1**−**S6**), the AzaPc conjugates cleaved from the solid phase were purified by passing through short OPC. The hydrophobic character of AzaPc labels allowed for the anchoring of the conjugates to reverse phase in OPC, and the unlabeled oligonucleotides were washed out with 8% acetonitrile. Subsequently, the increase of acetonitrile concentration to 30% released the AzaPc-oligonucleotide conjugates from OPC. The purified conjugates were analyzed by HPLC (see Figure 2), and two important peaks were detected in the chromatograms (typical retention times $t_R = 2$ min and $t_R = 17$ min). On the basis of an analysis of absorption spectra (see Supporting Information, Figure S5) and retention times of the controls, the base peak ($t_R = 17$ min) belongs to the oligonucleotide labeled with AzaPc. Unlabeled oligonucleotides were eluted in the second minute and did not exceed 4% in all cases (based on an area under the curve calculation at 254 nm). Nonconjugated AzaPc control eluted with $t_R = 23$ min and was not detected in chromatograms of AzaPc−oligonucleotide conjugates. In order to verify the composition of conjugates, MALDI-TOF spectra were recorded, and the expected mass to charge ratio was confirmed (Figure 3).

UV−Vis Spectral, Photophysical, and Photochemical Properties. Absorption spectra of AzaPc **1** and **7** were analyzed in different solvents (DMSO, THF, methanol (MeOH), DMF, and acetone). The spectra in all solvents showed the shape characteristic for monomeric species with two absorption bands typical for AzaPc or *Pc*: a high energy B-band at approximately 360 nm and a low energy Q-band at approximately 660 nm. Both compounds also showed another broad band at approximately 550 nm due to the conjugation of lone electron pairs of *N*,*N*-diethylamino substituents with a macrocyclic system (n-π^* transitions) (*14*, *27*). The Q-bands of **1** and **7** were split due to the unsymmetrical composition of the whole macrocycle because of the presence of the central hydrogens (*16*). The splitting was sharp in THF but became broad and

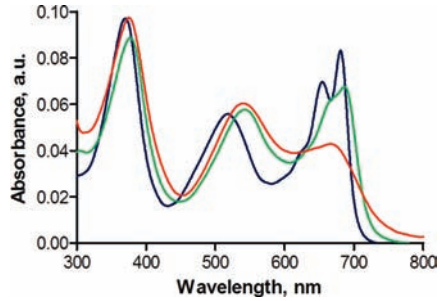


Figure 4. Absorption spectra of **7** in THF (blue), DMSO (green), and oligonucleotide **S1** with AzaPc in buffer (red) at a concentration of 1 μM.

Table 1. Spectral and Photochemical Properties of AzaPc 1 and 7

compound	λ (ε) in DMSO (nm (M^{-1} cm^{-1}))	λ (ε) in THF (nm (M^{-1} cm^{-1}))	λ (ε) in hybridization buffer (nm (M^{-1} cm^{-1}))[a]	Φ_Δ (DMF)
1	685 (57400)	677 (95300)	664 (45200)	0.015
	661 (50900)	647 (69500)	536 (66300)	
	530 (51900)	508 (58400)	373 (105900)	
	372 (84800)	365 (108000)		
7	686 (68000)	680 (86300)	668 (43000)	0.018
	542 (60000)	654 (72300)	537 (60300)	
	378 (91500)	516 (59600)	376 (97900)	
		370 (102700)		

[a] Conjugate **S1** (for **7**) or **S5** (for **1**).

featureless in solvents with increased polarity (e.g., DMSO), and completely disappeared when the conjugates where dissolved in hybridization buffer (Figure 4), indicating considerable effect of the solvent polarity on the Q-band shape. Such spectral changes in DMSO or buffer could also be attributed to aggregation, but neither the shape of the spectra nor the extinction coefficient changed in a very wide range of concentration (in DMSO 2.5×10^{-4} M-1.0×10^{-7} M). Also, no new bands at shorter or longer wavelengths corresponding to H- (*7*, *28*) or J-dimer (*29*) formation were observed. Another support for the statement that the aggregation is not responsible for the broad Q-band is that the spectra of the conjugates did not change after hybridization with complementary oligonucleotides (see, e.g., the duplex **S4**$-$**SF** in Supporting Information, Figure S6-c).

Photophysical and photochemical parameters of AzaPc **1** and **7**, which are important for their prospective use as dark quenchers, were determined. No fluorescence of either AzaPc **1** and **7** in THF, DMF, DMSO, or the AzaPc labeled probes **S1**$-$**S6** in hybridization buffer was detected. Singlet oxygen, usually strongly produced by AzaPc after illumination (*30*), is a highly reactive species that may destroy oligonucleotide probes or the target sequence (*8, 31*), and thus, its formation is undesirable in hybridization assays. Importantly, AzaPc **1** and **7** reached very low singlet oxygen quantum yields (Φ_Δ), 0.015 and 0.018, respectively. For comparison, the Φ_Δ value for FAM, a routinely used fluorophore in hybridization assays, ranges from 0.03 to 0.1 (*32*). It must be noted that no aggregates were detected during measurements, and therefore, the lack of any detectable fluorescence can be attributed solely to the deactivation of the S_1 excited state by ICT (*14*). Spectral and photochemical data of compounds **1** and **7** are summarized in Table 1.

DNA Hybridization Assays and Quenching Efficiency. The absorption spectra of AzaPc$-$oligonucleotide conjugates **S1**$-$**S6** in hybridization buffer show a wide range of absorption from 300 to 740 nm due to the AzaPc moiety (Figure 5). Thus, it efficiently overlaps the emission spectra of all fluorophores currently used in hybridization assays. Such versatility cannot be found in any other structural type of dark quenchers and makes these compounds highly promising for future development. In order to prove the quenching ability of AzaPc, oligonucleotide **SF** labeled with two commonly used fluorophores was chosen for hybridization assays. For example, FAM (λ_{em} = 517 nm) emits at short wavelengths, while Cy5 (λ_{em} = 663 nm) emits at long wavelengths. For comparative purposes, the oligonucleotides **S1**$-$**S6** were labeled with the currently used dark quenchers BHQ-1, BHQ-2, and BBQ-650, which are highly efficient at the quenching of FAM or Cy5 (*33*).

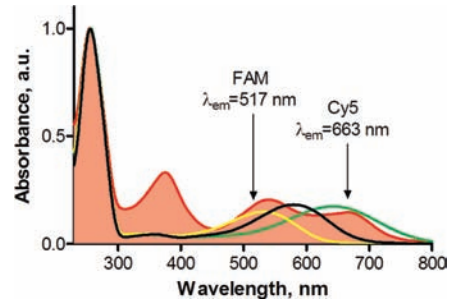


Figure 5. Absorption spectra of oligonucleotide **S1** labeled with AzaPc (red line, filled area), BHQ-1 (yellow), BHQ-2 (black), and BBQ-650 (green). The spectra were normalized to the same absorption at 254 nm (which is due to the oligonucleotides). The arrows indicate emission maxima of FAM and Cy5 fluorophores.



Figure 6. Sequences of modified oligonucleotides. F = fluorophore (FAM or Cy5), and Q = quencher (AzaPc, BHQ-1, BHQ-2, or BBQ-650).

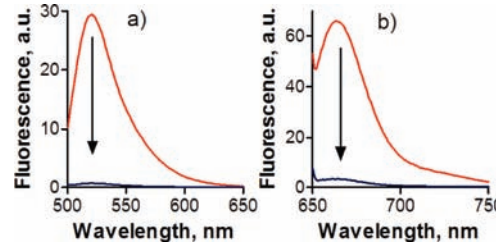


Figure 7. Fluorescence emission spectra of oligonucleotide **SF** with FAM (a) and Cy5 (b) before (red) and after (blue) the addition of the complementary oligonucleotide **S1** with AzaPc.

Oligonucleotides **S1**$-$**S6** (Figure 6) were designed to investigate both mechanisms of quenching utilized in hybridization assays. Resonance energy transfer (RET) requires the emission spectrum of a fluorophore and the absorption spectrum of a quencher to overlap with the effective distance between labeling dyes being 20$-$100 Å (*19*). During contact quenching, the fluorophore and the quencher must be very close to each other in order to form a ground-state complex that does not emit any light. Overlap of the spectra is not required in this mechanism (*19*, *34*). According to Marras et al. (*1*), the oligonucleotide **S1** can be used for the detection of the contact quenching after hybridization with **SF** because the fluorophore and the quencher may form the nonemitting heterodimer. **S3** is designed to allow purely RET quenching, and **S2** may involve both mechanisms. However, the absorption spectra of the duplex of AzaPc-labeled **S3** with Cy5-labeled **SF** revealed the presence of a certain level

Table 2. Quenching Efficiency (%)[a]

fluorophore (**SF**)	quencher	**S1**	**S2**	**S3**	**S4**	**S5**	**S6**	**S1 + SFX**
FAM	AzaPc	97.0 ± 0.12	92.3 ± 0.23	84.5 ± 0.74	35.8 ± 1.19	34.9 ± 2.11	54.9 ± 0.44	
	BHQ-1	98.5 ± 0.05	94.9 ± 0.08	88.4 ± 0.45	21.4 ± 3.73	28.0 ± 2.38	48.5 ± 0.69	
	BHQ-2	98.6 ± 0.02	95.7 ± 0.03	89.3 ± 0.10	9.9 ± 1.30	18.5 ± 1.61	48.5 ± 0.35	
	BBQ-650	97.6 ± 0.02	90.3 ± 0.11	78.9 ± 0.13	30.7 ± 0.32	36.6 ± 0.52	49.9 ± 0.03	
	no quencher	15.2 ± 0.71	5.5 ± 1.31	9.6 ± 2.15				
Cy5	AzaPc	93.8 ± 0.15	95.1 ± 0.11	96.9 ± 0.04	27.5 ± 1.55	25.1 ± 0.87	45.1 ± 0.42	−9.5 ± 10.2
	BHQ-1	96.9 ± 0.05	95.7 ± 0.08	86.9 ± 0.51	−0.5 ± 3.65	3.5 ± 5.36	4.1 ± 1.00	−4.5 ± 8.45
	BHQ-2	92.5 ± 0.28	96.3 ± 0.07	96.7 ± 0.08	5.5 ± 1.49	11.7 ± 0.95	33.1 ± 0.57	−9.1 ± 10.8
	BBQ-650	98.2 ± 0.04	96.3 ± 0.14	82.2 ± 0.06	18.6 ± 0.76	26.1 ± 0.19	46.5 ± 0.38	6.05 ± 1.01
	no quencher	3.0 ± 1.42	−35.0 ± 1.07	−38.1 ± 1.76				4.6 ± 15.5

[a] The mean of three measurements ± SD. The mathematical symbol minus means that fluorescence increased after hybridization.

of the heterodimer suggesting a looping of freely rotating 10T overhang (see Supporting Information, Figure S6). The heterodimer has a different absorption spectrum than a simple sum of the fluorophore and the quencher absorption spectra. Thus, **S3** cannot be used in this case for the detection of pure RET-based quenching.

In order to overcome this problem, oligonucleotides **S4**−**S6** were investigated in hybridization assays as well. The rigid double strand of their duplexes with **SF** prevents looping and thus permits the determination of pure RET quenching. At the same time, it enables the investigation of the quenching efficiency at a longer distance. The absorption spectra of the duplexes **S4**−**SF** corresponded well with a simple sum of spectra of **S4** and **SF** indicating the absence of the heterodimer (Supporting Information, Figure S6).

After hybridization, all of the prepared AzaPc-labeled oligonucleotides **S1**−**S6** efficiently decreased the fluorescence signal of **SF**, either Cy5 or FAM-containing (Figure 7). The quenching efficiency (*1*, *19*) is shown in Table 2. While all tested quenchers were highly efficient and comparable at a shorter distance (**S1**−**S3**), marked differences appeared at a longer distance between the fluorophore and the quencher (**S4**−**S6**). BHQ-1 quenched only FAM emission, BHQ-2 quenched both FAM and Cy5 emission, but its efficiency considerably decreased with distance. The AzaPc quencher was able to quench the fluorescence of both Cy5 and FAM with higher efficiency than the above-mentioned BHQ dyes and with efficiency comparable to that of the BBQ-650 quencher. This is most likely a consequence of better overlap of the AzaPc quencher absorption and fluorophore emission spectra (Figure 5).

In order to exclude nonselective quenching, two kinds of controls were involved. The decrease of **SF** fluorescence emission by the **S1**−**S3** sequence without any attached quencher was negligible (Table 2). Nonspecific quenching of fluorescence was excluded using Cy5-labeled oligonucleotide **SFX** that was not complementary to **S1**. No quenching occurred for any of the quenchers tested (Table 2).

CONCLUSIONS

In conclusion, novel highly efficient structural type of dark quenchers from the group of AzaPc with advantageous properties was described. A solid-phase method for labeling oligonucleotides by AzaPc quenchers and a simple and fast purification method without a need of HPLC separation were developed. Of particular notice is that the solid-phase conjugation presented here allows for the utilization of automatic processes in DNA/RNA synthesizers for both 3′- and 5′-end labeling by AzaPc.

The prepared AzaPc-based probes efficiently quench both FAM and Cy5 fluorescence in DNA hybridization probes by both RET and contact quenching. The AzaPc quencher profits from absorption in a wide range of wavelengths that covers all fluorophores used in hybridization assays nowadays. Thus, AzaPc may become the quenchers of choice for any kind of routinely used fluorophore and any hybridization assay. Finally, AzaPc represents flexible macrocycles with the possibility of shifting their absorption maximum over 750 nm (*17*). Therefore, they appear to have a great potential in genetic analysis, especially for the imaging of gene expression in living cells, where excitation and emission at long wavelengths is highly desired.

ACKNOWLEDGMENT

The work has been supported by grant KJB401100801 (The Grant Agency of the Academy of Sciences of the CR), by Research Project MSM0021620822, and by grant SVV-2010-261-001. We gratefully thank Jiří Kuneš for the measurements of NMR spectra.

Supporting Information Available: TLC of the AzaPc **7** in a mixture before isolation, structures of the AzaPc congeners from statistical condensation, stability tests of compound **7**, absorption spectra from HPLC analysis, and absorption spectra of duplexes. This material is available free of charge via the Internet at http://pubs.acs.org.

LITERATURE CITED

(1) Marras, S. A., Kramer, F. R., and Tyagi, S. (2002) Efficiencies of fluorescence resonance energy transfer and contact-mediated quenching in oligonucleotide probes. *Nucleic Acids Res. 30*, e122.

(2) Kadish, K. M., Smith, K. M., and Guilard, R., Eds. (2003) *The Porphyrin Handbook.*, Vol. 15−20, Academic Press, New York.

(3) Kuznetsova, A. A., Solov'eva, L. I., and Fedorova, O. S. (2008) Single-stranded DNA modification by an oligonucleotide-phthalocyanine Fe(II) conjugate: the kinetic features and the process mechanism. *Russ. J. Bioorg. Chem. 34*, 613–624.

(4) Kuznetsova, A. A., Chernonosov, A. A., Kuznetsov, N. A., Koval, V. V., Knorre, D. G., and Fedorova, O. S. (2006) Kinetic study of DNA modification by phthalocyanine derivative of the oligonucleotide. *Bioinorg. Chem. Appl.*, DOI: 10.1155/BCA/2006/23560.

(5) Hammer, R. P., Owens, C. V., Hwang, S. H., Sayes, C. M., and Soper, S. A. (2002) Asymmetrical, water-soluble phthalocyanine dyes for covalent labeling of oligonucleotides. *Bioconjugate Chem. 13*, 1244–1252.

(6) Nesterova, I. V., Erdem, S. S., Pakhomov, S., Hammer, R. P., and Soper, S. A. (2009) Phthalocyanine dimerization-based molecular beacons using near-IR fluorescence. *J. Am. Chem. Soc. 131*, 2432–2433.

(7) Nesterova, I. V., Verdree, V. T., Pakhomov, S., Strickler, K. L., Allen, M. W., Hammer, R. P., and Soper, S. A. (2007) Metallophthalocyanine near-IR fluorophores: Oligonucleotide conjugates and their applications in PCR assays. *Bioconjugate Chem. 18*, 2159–2168.

(8) Chernonosov, A. A., Koval, V. V., Knorre, D. G., Chernenko, A. A., Derkacheva, V. M., Lukyanets, E. A., and Fedorova, O. S. (2006) Conjugates of phthalocyanines with oligonucleotides as

reagents for sensitized or catalytic DNA modification *Bioinorg. Chem. Appl.*, DOI: 10.1155/BCA/2006/63703.

(9) Kuznetsova, A. A., Lukyanets, E. A., Solovyeva, L. I., Knorre, D. G., and Fedorova, O. S. (2008) DNA-binding and oxidative properties of cationic phthalocyanines and their dimeric complexes with anionic phthalocyanines covalently linked to oligonucleotides. *J. Biomol. Struct. Dyn. 26*, 307–319.

(10) Devlin, R., Studholme, R. M., Dandliker, W. B., Fahy, E., Blumeyer, K., and Ghosh, S. S. (1993) Homogeneous detection of nucleic-acids by transient-state polarized fluorescence. *Clin. Chem 39*, 1939–1943.

(11) Koval, V. V., Chernonosov, A. A., Abramova, T. V., Ivanova, T. W., Fedorova, O. S., Derkacheva, V. M., and Lukyanets, E. A. (2001) Photosensitized and catalytic oxidation of DNA by metallophthalocyanine-oligonucleotide conjugates. *Nucleosides, Nucleotides Nucleic Acids 20*, 1259–1262.

(12) Erdem, S. S., Nesterova, I. V., Soper, S. A., and Hammer, R. P. (2009) Mono-amine functionalized phthalocyanines: microwave-assisted solid-phase synthesis and bioconjugation strategies. *J. Org. Chem. 74*, 9280–9286.

(13) Zimcik, P., Miletin, M., Kostka, M., Schwarz, J., Musil, Z., and Kopecky, K. (2004) Synthesis and comparison of photodynamic activity of alkylheteroatom substituted azaphthalocyanines. *J. Photochem. Photobiol., A 163*, 21–28.

(14) Novakova, V., Zimcik, P., Miletin, M., Vachova, L., Kopecky, K., Lang, K., Chábera, P., and Polívka, T. (2010) Ultrafast Intramolecular charge transfer in tetrapyrazinoporphyrazines controls the quantum yields of fluorescence and singlet oxygen. *Phys. Chem. Chem. Phys. 12*, 2555–2563.

(15) Mørkved, E. H., Holmaas, L. T., Kjøsen, H., and Hvistendahl, G. (1996) Preparation of magnesium azaphthalocyanines by cyclotetramerisation of S-substituted 4,5-disulfanylpyrazine-2,3-dicarbonitriles. *Acta Chem. Scand. 50*, 1153–1156.

(16) Kopecky, K., Zimcik, P., Novakova, V., Miletin, M., Musil, Z., and Stribna, J. (2008) The synthesis and characterization of metal-free, unsymmetrical azaphthalocyanines with hydroxy groups and their complex formation with pyridine. *Dyes Pigm. 78*, 231–238.

(17) Musil, Z., Zimcik, P., Miletin, M., Kopecky, K., and Lenco, J. (2007) Synthesis, separation and UV/Vis spectroscopy of pyrazino-quinoxalino-porphyrazine macrocycles. *Eur. J. Org. Chem.* 4535–4542.

(18) Modak, A. S., Gard, J. K., Merriman, M. C., Winkeler, K. A., Bashkin, J. K., and Stern, M. K. (1991) Toward chemical ribonucleases 0.2. Synthesis and characterization of nucleoside-bipyridine conjugates: hydrolytic cleavage of RNA by their copper(II) complexes. *J. Am. Chem. Soc. 113*, 283–291.

(19) Lakowicz, J. R. (2006) *Principles of Fluorescence Spectroscopy*, 3rd ed., Springer, New York.

(20) Musil, Z., Zimcik, P., Miletin, M., Kopecky, K., Link, M., Petrik, P., and Schwarz, J. (2006) Synthesis and singlet oxygen production of azaphthalocyanines bearing functional derivatives of carboxylic acid. *J. Porphyrins Phthalocyanines 10*, 122–131.

(21) Ogunsipe, A., Maree, D., and Nyokong, T. (2003) Solvent effects on the photochemical and fluorescence properties of zinc phthalocyanine derivatives. *J. Mol. Struct. 650*, 131–140.

(22) Zimcik, P., Miletin, M., Musil, Z., Kopecky, K., Kubza, L., and Brault, D. (2006) Cationic azaphthalocyanines bearing aliphatic tertiary amino substituents-Synthesis, singlet oxygen production and spectroscopic studies. *J. Photochem. Photobiol., A 183*, 59–69.

(23) Caruthers, M. H., Barone, A. D., Beaucage, S. L., Dodds, D. R., Fisher, E. F., Mcbride, L. J., Matteucci, M., Stabinsky, Z., and Tang, J. Y. (1987) Chemical synthesis of deoxyoligonucleotides by the phosphoramidite method. *Methods Enzymol. 154*, 287–313.

(24) Theisen, P., Mccollum, C., Upadhya, K., Jacobson, K., Vu, H. N., and Andrus, A. (1992) Fluorescent dye phosphoramidite labeling of oligonucleotides. *Tetrahedron Lett. 33*, 5033–5036.

(25) De La Torre, G., Claessens, C. G., and Torres, T. (2000) Phthalocyanines: The need for selective synthetic approaches. *Eur. J. Org. Chem.* 2821–2830.

(26) Erdem, S. S., Nesterova, I. V., Soper, S. A., and Hammer, R. P. (2008) Solid-phase synthesis of asymmetrically substituted "AB(3)-type" phthalocyanines. *J. Org. Chem. 73*, 5003–5007.

(27) Musil, Z., Zimcik, P., Miletin, M., Kopecky, K., Petrik, P., and Lenco, J. (2007) Influence of electron-withdrawing and electron-donating substituents on photophysical properties of azaphthalocyanines. *J. Photochem. Photobiol., A 186*, 316–322.

(28) George, R. D., Snow, A. W., Shirk, J. S., and Barger, W. R. (1998) The alpha substitution effect on phthalocyanine aggregation. *J. Porphyrins Phthalocyanines 2*, 1–7.

(29) Novakova, V., Zimcik, P., Kopecky, K., Miletin, M., Kuneš, J., and Lang, K. (2008) Self-assembled azaphthalocyanine dimers with higher fluorescence and singlet oxygen quantum yields than the corresponding monomers. *Eur. J. Org. Chem. 2008*, 3260–3263.

(30) Zimcik, P., Miletin, M., Novakova, V., Kopecky, K., Nejedla, M., Stara, V., and Sedlackova, K. (2009) Effective monofunctional azaphthalocyanine photosensitizers for photodynamic therapy. *Aust. J. Chem. 62*, 425–433.

(31) Boutorine, A. S., Brault, D., Takasugi, M., Delgado, O., and Helene, C. (1996) Chlorin-oligonucleotide conjugates: Synthesis, properties, and red light-induced photochemical sequence-specific DNA cleavage in duplexes and triplexes. *J. Am. Chem. Soc. 118*, 9469–9476.

(32) Redmond, R. W., and Gamlin, J. N. (1999) A compilation of singlet oxygen yields from biologically relevant molecules. *Photochem. Photobiol. 70*, 391–475.

(33) Marras, S. A. E. (2008) Interactive fluorophore and quencher pairs for labeling fluorescent nucleic acid hybridization probes. *Mol. Biotechnol. 38*, 247–255.

(34) Johansson, M. K., and Cook, R. M. (2003) Intramolecular dimers: A new design strategy for fluorescence-quenched probes. *Chem.—Eur. J. 9*, 3466–3471.

BC100226X

Bioconjugate Chemistry

Supporting Information

Solid-phase synthesis of azaphthalocyanine-oligonucleotide conjugates and their evaluation as new dark quenchers of fluorescence

Kamil Kopecky, Veronika Novakova, Miroslav Miletin, Radim Kučera, Petr Zimcik*

Content

TLC of the mixture of AzaPc congeners S3

Structures of congeners appearing in the mixture after statistical condensation S4

Stability of compound **7** in reagents used during automatic DNA synthesis in DNA/RNA synthesizer..... S5

Absorption spectra from HPLC chromatogram S7

Absorption spectra of duplexes S8

References for Supporting Information S9

TLC of the mixture of AzaPc congeners

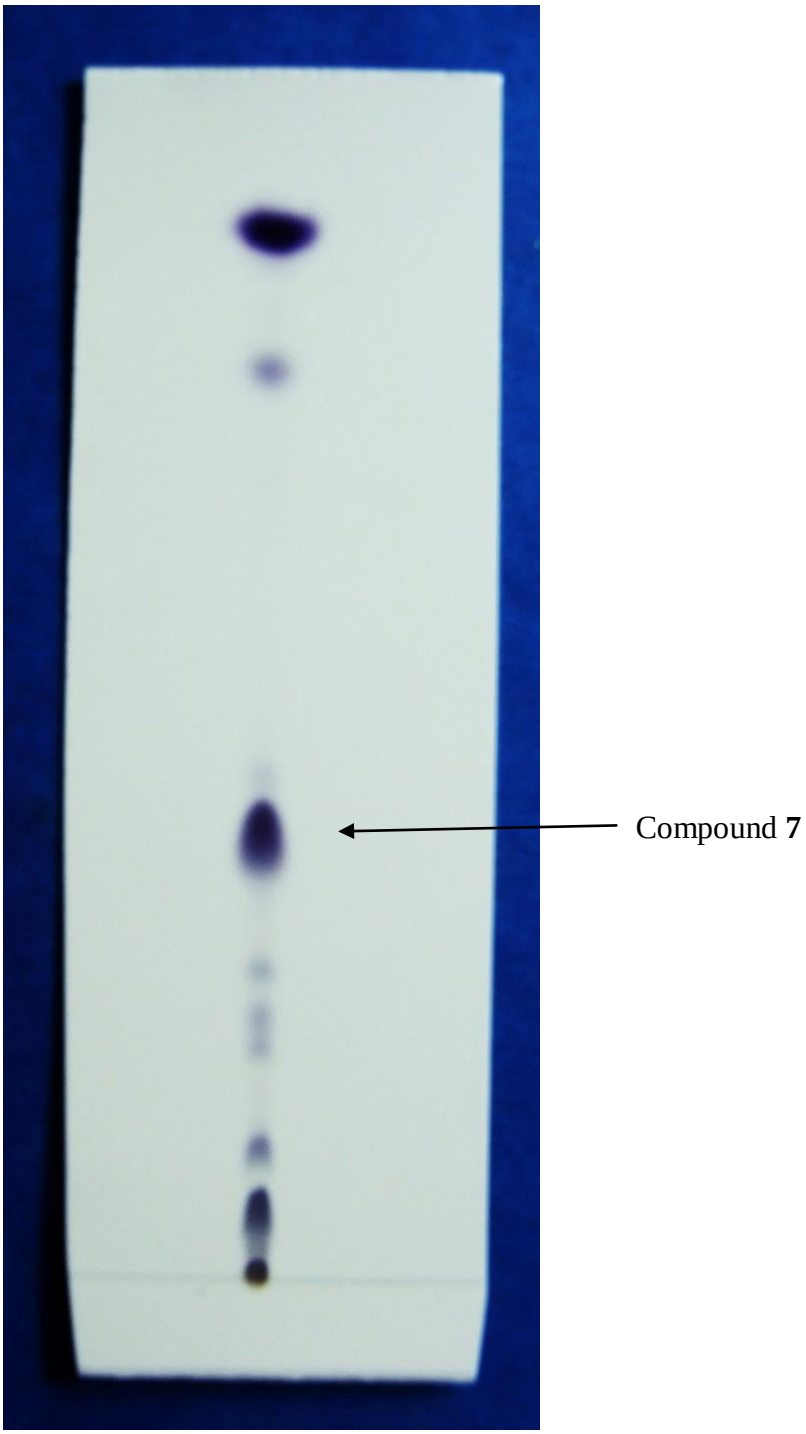


Figure S1. TLC of the mixture of AzaPc congeners after statistical condensation during synthesis of compound **7**. Note the nice round-shaped stains of AzaPc. TLC was performed on silica (Merck TLC silica gel 60 F_{254} plates) in dichloromethane/acetone/methanol 20:1:1 mobile phase.

Structures of congeners appearing in the mixture after statistical condensation

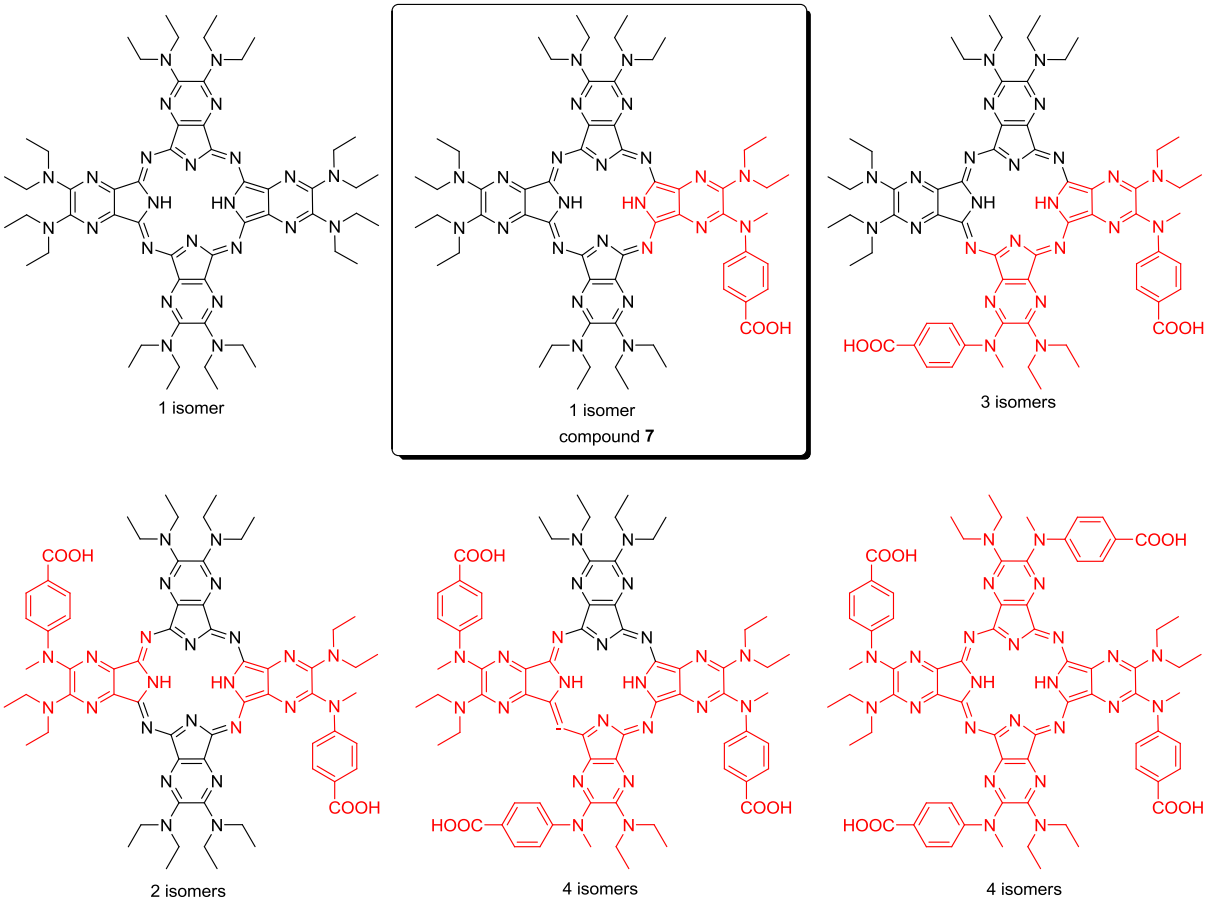


Figure S2. Possible congeners appearing in the mixture after statistical condensation during synthesis of **7**. See also Figure S1. For each congener, also number of possible structural isomers is mentioned (only one isomer is drawn).

Stability of compound 7 in reagents used during automatic DNA synthesis in DNA/RNA synthesizer.

Table S1. Reagents used in typical DNA/RNA synthesizer and typical exposure times during synthesis of standard 20-mer DNA probe.

Reagent	Composition	Times (min)[c]
A	3% (m/m) trichloroacetic acid in dichloromethane	25
B	0.25 M 5-(ethylthio)-1H-tetrazole in acetonitrile	20
C[a]	10% (m/m) 1-methylimidazole in tetrahydrofuran	15
D[a]	tetrahydrofuran / pyridine / acetic anhydride 8:1:1	15
E	0.02 M iodine in tetrahydrofuran / pyridine / water 7:2:1	15
F[b]	32% ammonia / 40% methylamine 1:1	90
G[b]	0.05 M K_2CO_3 in methanol	240-720

[a] reagents C and D are mixed before the reaction. [b] Either F or G are used for deprotection of oligonucleotide and its cleavage from solid phase. [c] typical for Perkin Elmer ABI 392/394 DNA/RNA synthesizer.

Procedure: Stock solutions of the compound **7** were prepared in concentration approx. 1×10^{-5} M in dichloromethane (for reagent A), acetonitrile (reagent B), tetrahydrofuran (reagents C+D and E) and methanol (reagent G). Reagents were prepared at double concentration than used in DNA/RNA synthesizer. Reagent F was prepared at concentration used in real conditions because preparation of higher concentrations is technically impossible. For measurements, 10 ml of dye stock solution was mixed with 10 ml of the reagent to give final concentration of the dye 5×10^{-6} M and the proper concentration of the reagent (see Table S1). The solutions were stirred at r.t. during whole experiment. 2.5 ml were taken (after 0, 2, 6, 22 and 24 h) and the UV-vis spectra were measured.

Results: No changes were observed in absorption spectra of **7** in reagents B, C+D or E within 24 hours of testing. Changes in the shape of the UV-vis spectra were observed immediately after addition of the reagent A (Figure S3). Neither the shape nor the intensity of absorption changed further even after 24 h. The change is reversible and the shape of the spectra was restored to normal after washing of the tested solution with aq. NaOH. Reagent A is a strong organic acid and lead to protonation of the *N,N*-diethylamino nitrogens in the tested dye that is accompanied by changes of the absorption spectra (*1*). Similarly, reagent G as a base caused immediate spectral changes (Figure S3) due to deprotonation of acidic central NH groups (*1, 2*). Also in this case, the spectra did not shown any further progress and the change was fully reversible after addition of few drops of acetic acid. Compound **7** could not be tested in reagent F due to insolubility in water based medium. That is why, structurally similar compound **X1** (Figure S4) synthesized in our lab earlier (*3*) was tested in this medium (dissolved directly in reagent F) . Spectral changes were similar to those observed for

compound **7** in reagent G and did not indicate any decomposition even after 24 h. Stability of compounds **7** and **X1** was tested also on TLC and its examination did not indicate any decomposition. As a conclusion, the AzaPc quencher was not decomposed in any of the reagents used during automatic DNA synthesis even when the typical exposure times were exceeded several times.

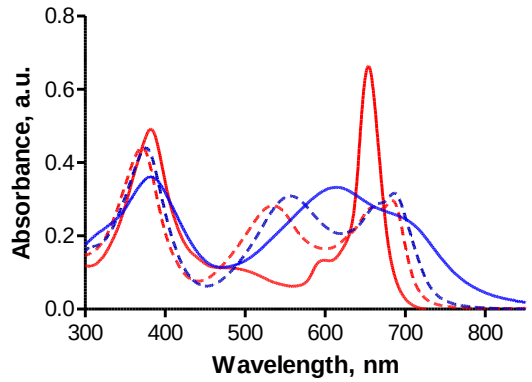
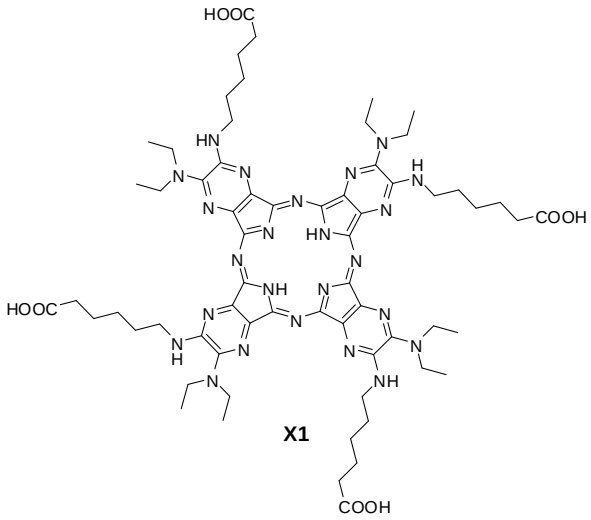


Figure S3. Absorption spectra of compound **7** in methanol (red, dotted), dichloromethane (blue, dotted), reagent A (blue, full line), reagent G (red, full line). Concentration approx. 5×10^{-6} M.



X1

Figure S4. Structure of compound **X1**.

Absorption spectra from HPLC chromatogram

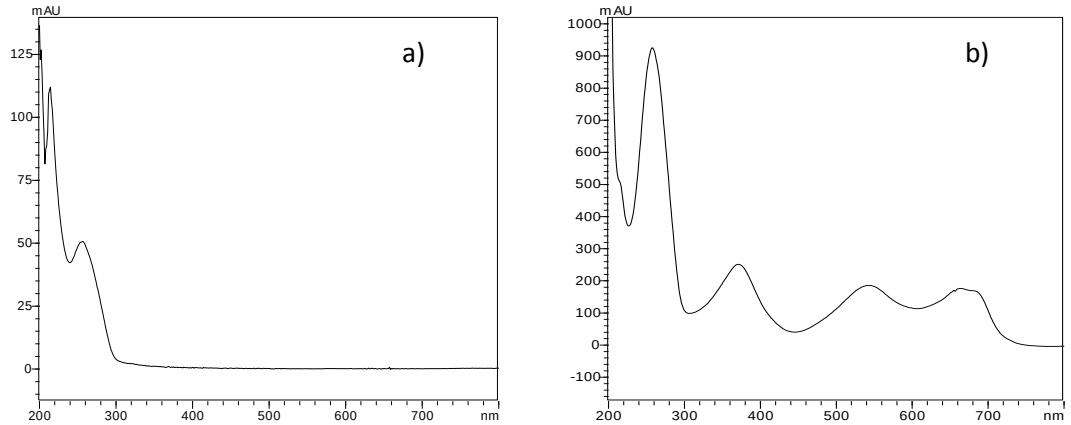


Figure S5. Absorption spectra at peaks at t_R=2.0 min (a) and t_R=16.9 min (b) of the HPLC chromatogram from Figure 2 (see article), corresponding to unlabeled oligonucleotide and AzaPc-modified oligonucleotide, respectively.

Absorption spectra of duplexes

Spectra of duplexes were measured in hybridization buffer. Stock solutions of oligonucleotides **S1**, **S3** and **S4** labeled with AzaPc and **SF** and **SFX** labeled with Cy5 were prepared to concentration 100 µM. Hybridization buffer (1 ml) was transferred to a cuvette, stock solution of oligonucleotide probe with quencher (10 µl) was added and absorption spectrum was measured. Thereafter, stock solution of oligonucleotide labeled with fluorophor (10 µl) was added and solution was heated to 50°C for 1 minute. Absorption spectrum of duplex (Figure S6) was measured after 30 minutes when the sample cooled down to laboratory temperature. Final concentration of both oligonucleotides was 1 µM. Absorption spectra of **SF** and **SFX** were measured also separately after addition of stock solution (10 µl) to hybridization buffer (1 ml).

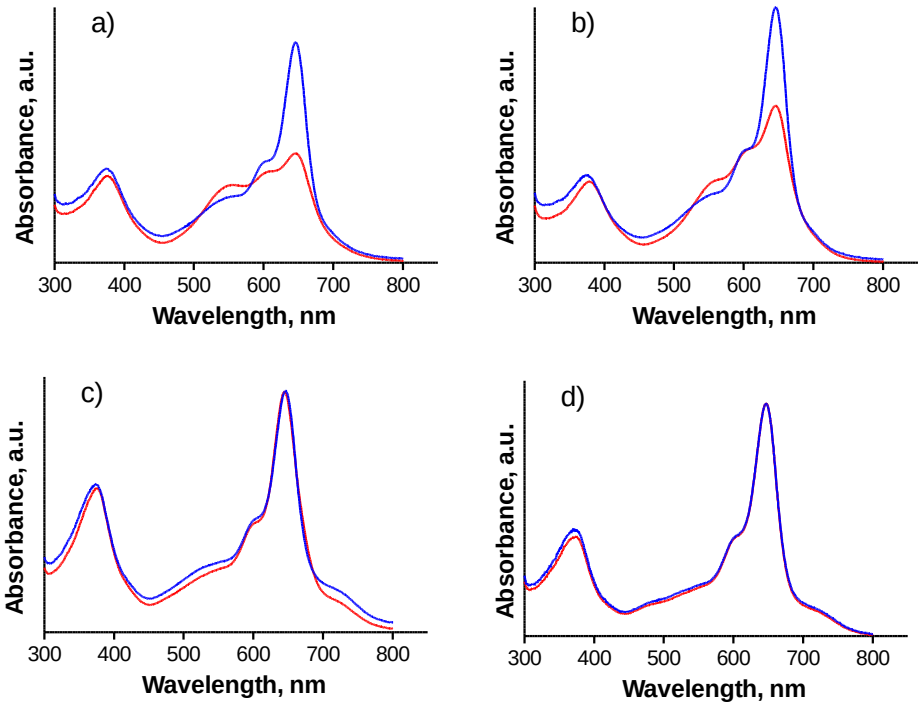


Figure S6. Red lines – measured absorption spectra of duplexes **SF** (Cy5) with **S1** (a), **S3** (b), **S4** (c) modified with AzaPc and (d) absorption spectrum of mixture of **SFX** (Cy5) with **S4** (AzaPc). Blue lines – simple sum of absorption spectra of individual oligonucleotides. In case of **S1** and **S3** the measured spectra did not correspond to calculated ones indicating presence of heterodimer Cy5-AzaPc. In case of **S4**, the heterodimers are not formed due to rigid double strand separating both dyes. Data from graph d) excludes any uncontrolled formation of the heterodimer without hybridization.

References for Supporting Information

(1) Petrik, P., Zimcik, P., Kopecky, K., Musil, Z., Miletin, M., and Loukotova, V. (2007) Protonation and deprotonation of nitrogens in tetrapyrazinoporphyrazine macrocycles. *J. Porphyrins Phthalocyanines 11*, 487-495.

(2) Kopecky, K., Zimcik, P., Novakova, V., Miletin, M., Musil, Z., and Stribna, J. (2008) The synthesis and characterization of metal-free, unsymmetrical azaphthalocyanines with hydroxy groups and their complex formation with pyridine. *Dyes Pigment. 78*, 231-238.

(3) Zimcik, P., Miletin, M., Ponec, J., Kostka, M., and Fiedler, Z. (2003) Synthesis and studies on photodynamic activity of new water-soluble azaphthalocyanines. *J. Photochem. Photobiol. A: Chem. 155*, 127-131.

Probing the Topological Tolerance of Multimeric Protein Interactions: Evaluation of an Estrogen/Synthetic Ligand for FK506 Binding Protein Conjugate

Terry W. Moore,† Jillian R. Gunther, and John A. Katzenellenbogen*

Department of Chemistry, University of Illinois at Urbana−Champaign, 600 South Mathews Avenue, Urbana, Illinois 61801, United States. Received June 10, 2010; Revised Manuscript Received September 2, 2010

Bivalent small molecules composed of a targeting element and an element that recruits endogenous proteins have been shown to block protein−protein interactions in some systems. We have attempted to apply such an approach to disrupt the interaction of the estrogen receptor α with either its associated coactivators or its dimerization partner (i.e., another estrogen receptor). We show here that a conjugate capable of simultaneously binding both the estrogen receptor and a recruited protein (FK506 Binding Protein 12 kDa) is, however, incapable of disrupting the multimeric estrogen receptor dimer/coactivator complex both in vitro and in cell-based reporter gene assays. We postulate why it may not be possible to disrupt this particular protein−protein complex—as well as other systems having high topological tolerance—with such bivalent inhibitors.

INTRODUCTION

The estrogen receptor α (ERα) is a ligand-activated transcription factor whose activity in regulating gene expression relies on two key molecular interactions: homodimerization of the ER itself and interaction of the ER dimer with its associated coactivators (e.g., the steroid receptor coactivators (SRCs)). The monomers of ERα are linked as homodimers by hydrophobic interactions among residues on two long α-helices arranged in parallel at the dimer interface, flanked across the dimer interface by both hydrophobic and polar interactions between other helical elements. The binding affinity of ERα dimerization has been estimated to be subnanomolar (*1*). In the interaction of ER with the coactivator, one molecule of an SRC binds to an ER dimer by placing two turns of an amphipathic α-helix into a hydrophobic groove on the surface of the ligand-binding domain of each monomer of the agonist-bound ER dimer. These α-helical elements contain three conserved leucine residues arranged in an LXXLL motif (L is leucine; X is typically a polar amino acid). The affinity of each LXXLL motif for ERα is characterized by a K_D of ca. 700 nM, with the bivalent interaction once estimated to have an avidity below 30 nM (*2*) but more recently found to be ca. 1 nM, with affinity being dependent to some extent on ligand structure (M. Jeyakumar and J. A. Katzenellenbogen, unpublished). ERα interaction with SRC has strict ligand dependence; it requires that the ERs be occupied by an agonist ligand, and it is disabled when the ER is either unliganded or liganded, in most circumstances, by an antagonist ligand. By contrast, ERα dimers form in vitro whether the ER is unliganded or liganded with either an agonist or antagonist ligand, although ligand binding modulates dimerization affinity to some degree (*1*).

We and others have postulated that these two protein−protein interaction "hot-spots"—the ER/ER dimer interface or the ER/SRC interface—could serve as therapeutic targets for cancers in which the estrogen receptor is upregulated, but that are nonresponsive to traditional antagonist regimens, as is the case in antiestrogen-resistant breast cancer (*3*−*6*). In fact, it is the ER/SRC interaction that is targeted in conventional ER antagonism with antiestrogens, although this inhibition proceeds through an allosteric mechanism whereby antagonist binding in the internal ligand binding pocket induces a conformational change on the receptor surface that prevents SRC binding (*7*). Thus, targeting this interaction with small molecule inhibitors is well-validated, although those that act by a direct mechanism of inhibition are much less developed (*3, 8, 9*). Oftentimes, however, protein−protein interactions of this type are viewed as intractable targets in drug discovery, because the interactions typically occur over large surface areas, as is the case with the ER dimer interface, or may be highly dynamic, as is the case with the ER/SRC interaction (*10, 11*). Because small molecules are, by definition, low-molecular-weight compounds, they may lack sufficient steric bulk to inhibit the interaction.

Gestwicki et al. (*12*) have elaborated an interesting "Trojan horse" (or heterobivalent ligand) approach to this general problem: It involves tethering a weak protein−protein interaction inhibitor to a second ligand molecule that, after gaining access to the cell, would recruit extra steric bulk in the form of a ubiquitous, endogenous protein, thereby increasing the effective size and, consequently, the potency and/or efficacy of the inhibitor (*13*). The group demonstrated this concept by disrupting the aggregation of the Aβ peptide that leads to formation of β-amyloid, a polymer implicated in the pathologic fibrillogenesis of Alzheimer's disease. They tethered Congo Red, which, in turn, binds rather poorly to β-amyloid (i.e., $IC_{50} = 2$ μM), to SLF (synthetic ligand for FK-506 binding proteins [FKBPs]). In the presence of the ubiquitous and abundant cellular protein FKBP12, some of these conjugates (e.g., **I**, Chart 1) inhibited the aggregation of β-amyloid with IC_{50} values of 50 nM, a 40-fold increase in potency compared to Congo Red. The effect was not seen in the absence of FKBP12, suggesting that the mechanism of inhibition was dependent on the steric hindrance of FKBP12 that followed from its recruitment by the SLF element in the Congo Red conjugate. This finding was a landmark because it suggested a perhaps generalizable mechanism for inhibiting protein−protein interactions.

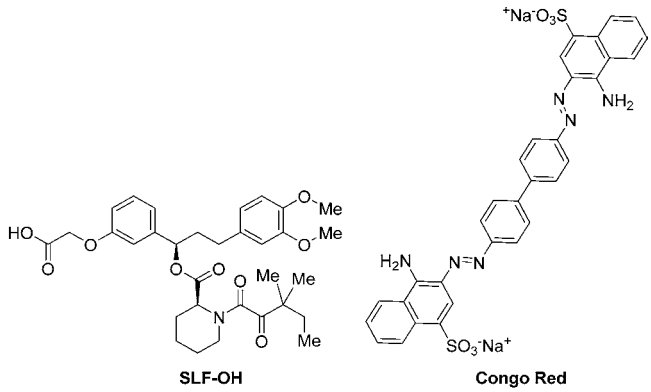
We saw an opportunity to use this technology in a conceptually similar yet mechanistically distinct manner to develop a ligand that would have context-dependent estrogenic properties—

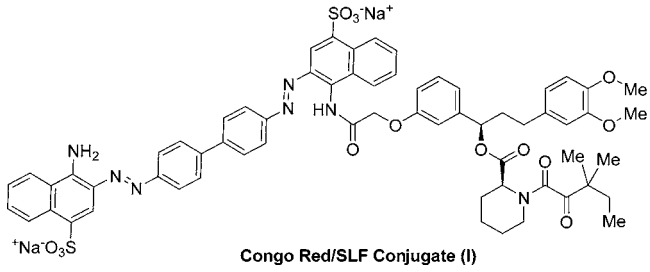
* For correspondence, contact: John A. Katzenellenbogen Department of Chemistry University of Illinois 600 South Mathews Avenue Urbana, IL 61801. phone 217 333 6310; e-mail jkatzene@uiuc.edu.

† Current address: Emory Institute for Drug Discovery, 1515 Dickey Dr., Atlanta, GA 30322.

10.1021/bc100266v © 2010 American Chemical Society
Published on Web 10/04/2010

Chart 1. Structures of SLF, Congo Red, and SLF-Congo Red Conjugate I





that is, a molecule that would allow ER to recruit its dimerization partner and coactivator, and thus function as an agonist, in the absence of FKBP, but that would function as an antagonist in the presence of FKBP. In addition, this novel approach to inhibition of estrogen signaling might prove more robust against the development of acquired resistance which typically develops following endocrine therapy of breast cancer with standard antagonists such as tamoxifen (*14*).

The native agonist for the estrogen receptor, 17β-estradiol (E2), is known to tolerate substitution at the 17α position without experiencing substantial loss in affinity, while retaining agonist activity for the ER (*15*, *16*). Thus, we examined whether an estradiol−SLF conjugate linked through the 17α position would by itself function as an ER agonist, engendering formation of the ER/SRC assembly, but, upon recruitment of FKBP, would place ER in an antagonized state resulting from FKBP disruption of the multimeric ER/SRC assembly. Curiously, what we have found is that the ER, when liganded with an estradiol−SLF conjugate, was not only capable of binding its dimerization partner and a coactivator fragment, but also was able to recruit FKBP, thus indicating that this multimeric protein complex exhibits a high topological tolerance. We describe the design, synthesis, and extensive biological evaluation of these compounds, and hypothesize why inhibition of this interaction might not be amenable to this Trojan horse-type strategy.

EXPERIMENTAL PROCEDURES

General Considerations. Reagents were obtained from Aldrich Chemical Co., TCI America, or Fisher Scientific and were used without further purification. Anhydrous solvents were purchased from Aldrich or obtained from a Solvent Dispensing System fabricated by J. C. Meyer, based on a design published by Pangborn et al. (*17*). Anhydrous DMF was vacuum-distilled over molecular sieves.

Reaction progress was monitored using thin-layer chromatography (TLC) on silica gel 60 F_{254} glass-backed plates from EM Science. Visualization was achieved by UV light (254 nm) or phosphomolybdic acid or potassium permanganate indicator. Flash column chromatography was performed with Woelm silica gel (0.040−0.063 mm) packing (*18*).

^{1}H and ^{13}C NMR spectra were recorded on either 400 or 500 MHz Varian FT-NMR spectrometers. Chemical shifts (δ) are reported in parts per million (ppm) by reference to proton resonances resulting from incomplete deuteration of the NMR solvent. High- and low-resolution electrospray ionization mass spectra were obtained on either a Micromass Quattro or Micromass Q-Tof Ultima mass spectrometer. Melting points were measured using a Thomas-Hoover capillary melting point apparatus and are uncorrected.

Chemical Synthesis. SLF-OH was synthesized according to a known procedure (*19*, *20*). The ethynylestradiol precursor was prepared (Scheme 1) by reacting 17α-ethynylestradiol with methyl 4-iodobenzoate using Sonagashira reaction conditions, to give, after saponification of the ester, an acid-functionalized estrogen. The acid was converted to the succinimid-1-yl ester **1** using dicyclohexylcarbodiimide as the dehydrating agent.

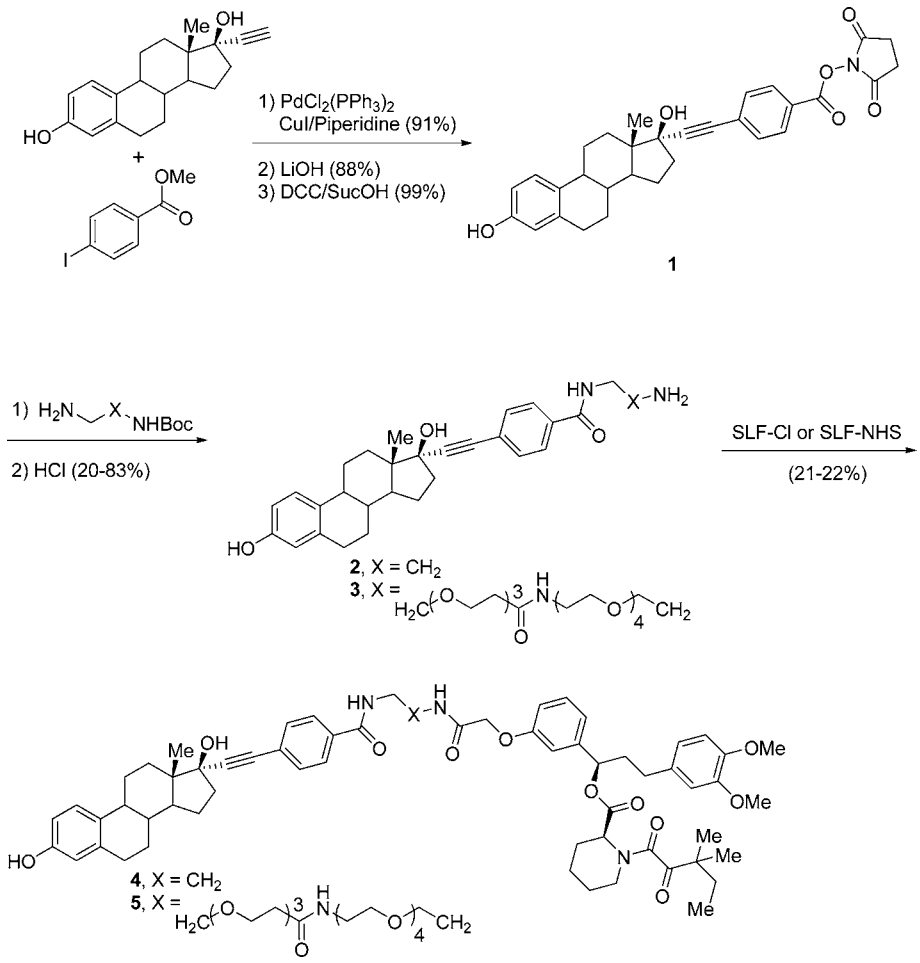
The estrogen prepared above was tethered to the SLF moiety by adding a monoprotected diamine to give, after deprotection of the remaining amine, amides **2** and **3**. The amines were coupled to the acid functionality of **SLF-OH**, to give conjugates **4** and **5**, by activating the acid as either the acyl chloride or an activated ester.

Succinimid-1-yl 3-(3,14-Dihydroxy-13-methyl-7,8,9,11,12,13,14,15,16,17-decahydro-6*H*-cyclopenta[*a*]phenanthren-17-ylethynyl)-benzoate (1). 17α-Ethynylestradiol (1.00 g, 1.0 equiv) was dissolved in anhydrous THF (10 mL). To this solution was sequentially added CuI (96 mg, 0.15 equiv), piperidine (0.842 mL, 2.0 equiv), methyl *p*-iodobenzoate (883 mg, 1.0 equiv), and $PdCl_2(PPh_3)_2$ (236 mg, 0.10 equiv). The solution was allowed to stir at RT for 12 h and was then heated to reflux for an additional 4 h. The crude reaction mixture was filtered through Celite and then purified using silica gel column chromatography (20% EtOAc/hexanes to 30% EtOAc/hexanes) to give a dark solid, which was recrystallized from boiling benzene to give 1.40 g (96% yield) of white flakes. ^{1}H NMR (400 MHz, $CDCl_3$) δ: 8.00 (d, J = 8.1 Hz, 2 H), 7.50 (d, J = 8.1 Hz, 2 H), 7.18 (d, J = 8.6 Hz, 1 H), 6.67 (d, J = 8.6 Hz, 1 H), 6.57 (s, 1 H),4.78 (s, 1H), 3.93 (s, 3H), 2.93−2.79 (m, 2 H), 2.51−2.32 (m, 2 H), 2.30−1.69 (m, 8 H), 1.63 (s, 1 H), 1.58−1.30 (m, 5 H), 0.95 (s, 3 H); HRMS calcd for $C_{28}H_{30}O_4Na$, 453.2042; found, 453.2037.

The methyl ester (1.22 g, 1.0 equiv) prepared above was dissolved in 25 mL methanol and cooled to 0 °C. LiOH (5 mL of 2.1 M; 3.6 equiv) was added, and the solution was allowed to come to RT and was stirred for 72 h. The methanol was removed under reduced pressure, and 10 mL more water was added. HCl (1 M) was added dropwise until no more solid precipitated from solution. The white solid (1.04 g, 88% yield) was filtered and dried. ^{1}H NMR (400 MHz, $CDCl_3$) δ: 8.04 (d, J = 8.1 Hz, 2 H), 7.52 (d, J = 8.1 Hz, 2 H), 7.16 (d, J = 8.6 Hz, 1 H), 6.65 (d, J = 8.6 Hz, 1 H), 6.58 (s, 1 H), 2.86−2.79 (m, 2 H), 2.49−2.30 (m, 2 H), 2.29−1.68 (m, 8 H), 1.59−1.31 (m, 5 H), 0.95 (s, 3 H); HRMS calcd for $C_{27}H_{28}O_4Na$, 439.1885; found, 439.1887.

The acid prepared above (1.00 g, 1.0 equiv), *N*-hydroxysuccinimide (1.38 g, 5.0 equiv), dicyclohexylcarbodiimide (0.90 g, 1.8 equiv) and 4-(*N*,*N*-dimethlyamino)pyridine (50 mg) were dissolved in CH_2Cl_2 and were stirred at RT. After 4 h, the solution was filtered, and the filtrate was evaporated. After dissolving the crude material in EtOAc (50 mL) and filtering again, the organic layer was washed with water (3 × 50 mL), dried ($MgSO_4$), filtered, and concentrated to give 1.23 g (99% yield) of a viscous, colorless liquid that was used without further purification. ^{1}H NMR (400 MHz, $CDCl_3$) δ: 8.05 (d, J = 8.06 Hz, 2 H), 7.54 (d, J = 8.06 Hz, 2 H), 7.13 (d, J = 8.55 Hz, 1 H), 6.62 (dd, J = 8.55, 2.69 Hz, 1 H), 6.55 (d, J = 2.69 Hz, 1 H), 6.31 (t, J = 6.23 Hz, 1 H), 5.76 (br. s., 1 H), 2.98−2.70

Scheme 1. Synthesis of Estrogen−SLF Conjugates



(m, 6 H), 2.48−2.31 (m, 3 H), 2.27−1.63 (m, 8 H), 1.54−1.31 (m, 2 H), 0.94 (s, 3 H); ^{13}C NMR (100 MHz, $CDCl_3$) δ: 169.30, 169.17, 161.33, 153.63, 138.04, 131.99, 131.85, 130.35, 129.81, 126.42, 124.15, 115.20, 112.69, 97.50, 84.88, 80.38, 49.87, 47.73, 43.55, 39.41, 38.97, 37.30, 33.79, 33.08, 29.57, 27.17, 26.38, 25.62, 25.52, 25.40, 24.82, 22.91, 12.86; HRMS calcd for $C_{31}H_{31}NO_6Na$, 536.2049; found, 536.2047.

EE2-Amine 2. The previously prepared NHS ester **1** (200 mg, 1.0 equiv) was dissolved in dry THF (0.3 mL), and diisopropylethylamine (90 μL, 1.3 equiv) was added to the solution, followed by *N*-Boc-ethylenediamine (75 mg, 1.2 equiv) in 0.5 mL dry THF. The solution was stirred at RT for 13 h, at which point another equivalent of *N*-Boc-ethylenediamine was added, because the reaction was not finished. The reaction appeared complete within 10 min after the addition of the second molar equivalent of amine. The THF was evaporated, and the gummy residue left was extracted from water (25 mL) with ethyl acetate (3 × 25 mL). The combined organic extracts were dried over $MgSO_4$, filtered, and concentrated; HRMS calcd for $C_{34}H_{43}N_2O_5$, 559.3172; found, 559.3176. The product was dissolved in ether, and then precipitated with hexanes and filtered. Then, 1 mL 4 M HCl in dioxane was added, and the product was allowed to stand at RT for 1 h. The solvents were evaporated, to give 44 mg (20% yield) of a white solid that was used without further purification. ^{1}H NMR (500 MHz, CD_3OD) δ: 7.80 (d, J = 8.3 Hz, 2 H), 7.50 (d, J = 8.3 Hz, 2 H), 7.08 (d, J = 8.5 Hz, 1 H), 6.54 (dd, J = 8.2, 2.1 Hz, 1 H), 6.47 (d, J = 1.5 Hz, 1 H), 3.44 (t, J = 6.3 Hz, 2 H), 2.83 (t, J = 6.2 Hz, 2 H), 2.80−2.72 (m, 2 H), 2.39−2.31 (m, 2 H), 2.19−1.66 (m, 8 H), 1.50−1.26 (m, 4 H), 0.91 (s, 3 H); ^{13}C NMR (125 MHz, CD_3OD) δ: 169.83, 156.13, 138.91, 135.05, 132.61, 132.50, 128.59, 128.12, 127.42, 116.21, 113.92, 97.19, 85.77, 81.00, 68.25, 51.37, 49.03, 45.31, 43.75, 42.11, 41.29, 40.06, 34.89, 34.58, 30.87, 28.78, 27.91, 26.88, 26.20, 24.01, 13.67; HRMS calcd for $C_{29}H_{35}N_2O_3$, 459.2648; found, 459.2647.

EE2-SLF Conjugate 4. SLF-OH (11.5 mg, 1.0 equiv) was converted to the acid chloride by dissolving in dry dichloromethane (0.2 mL), cooling to 0 °C, and adding thionyl chloride (3.5 mg, 1.3 equiv). After 5 min, the solvents were evaporated, and 0.2 mL more dry dichloromethane was added, the solution was cooled to 0 °C, and thionyl chloride (3.5 mg, 1.3 equiv) was again added. The reaction was allowed to come to RT and then to sit for 10 h, at which point the solvents were evaporated. Then, a solution of amine **2** (11 mg, 1.2 equiv) and diisopropylethylamine (10.7 μL, 3.0 equiv) in 0.3 mL dry DMF was added to the acid chloride, and the solution was stirred for 5.5 h at RT. The reaction mixture was then applied to a preparative thin-layer chromatography plate and eluted (CH_2Cl_2/methanol 90:10), and the topmost band was scraped from the plate. The product was extracted from the silica gel using dichloromethane/methanol (90:10) to give 4.5 mg (22% yield) of a white solid. ^{1}H NMR (500 MHz, $CDCl_3$) δ: 7.68 (d, J = 8.4 Hz, 2 H), 7.46 (d, J = 8.4 Hz, 2 H), 7.42−7.19 (m, 3 H), 7.15 (d, J = 8.6 Hz, 1 H), 6.95−6.60 (m, 4 H), 6.57 (d, J = 2.4 Hz, 1 H), 5.75 (dd, J = 8.0, 5.5 Hz, 1 H), 5.26 (d, J = 5.6 Hz, 1 H), 4.51 (d, J = 4.9 Hz, 2 H), 4.12 (d, J = 8.8 Hz, 1 H), 3.84 (s, 3 H), 3.84 (s, 3 H), 3.67−3.58 (m, 4 H), 3.35 (d, J = 12.0 Hz, 1 H), 3.18−3.12 (m, 1 H), 2.85−2.78 (m, 2 H), 2.63−2.48 (m, 2 H), 2.46−2.30 (m, 3 H), 2.14−1.23 (m, 24 H), 1.20 (s, 3 H), 1.19 (s, 3 H), 0.95 (s, 3 H), 0.87 (t, J = 7.4 Hz, 3 H); LR-ESI-MS: $[M+H]^+$ = 1024.5.

EE2 Amine 3. A prepared amine (32 mg, 1.3 equiv; see Supporting Information) was dissolved in 0.2 mL dry THF, and diisopropylethylamine (12 μL, 1.4 equiv) was added to this solution. Then, NHS ester **1** (23 mg, 1.0 equiv) was added, and the solution was stirred at RT for 6 h. The reaction mixture was then applied to a preparative thin-layer chromatography plate and eluted (90:10 acetonitrile/methanol). The topmost band was scraped from the plate, and the silica gel was extracted with acetonitrile/methanol (90:10) to give 20 mg (46% yield; HRMS calcd for $C_{51}H_{76}N_3O_{13}$, 938.5378; found, 938.5367) of product, which was then subjected to 0.4 mL 4 M HCl in dioxane (6 h), which, after evaporation of the solvents, gave 15 mg (83% yield) of amine **3**. ^{1}H NMR (500 MHz, CD_3OD) δ: 7.79 (d, J = 7.3 Hz, 2 H), 7.09 (d, J = 8.6 Hz, 1 H), 6.53 (d, J = 6.6 Hz, 1 H), 6.46 (d, J = 1.9 Hz, 1 H), 3.84−3.32 (m, 30 H), 3.12 (br. s., 2 H), 2.76 (br. s., 2 H), 2.54−2.28 (m, 4 H), 2.22−1.71 (m, 8 H), 1.53−1.18 (m, 7 H), 0.92 (s, 3 H); LR-ESI-MS: $[M+H]^+$ = 838.6.

EE2-SLF Conjugate 5. SLF-OH (17 mg, 1.0 equiv), *N*-hydroxysuccinimide (7 mg, 2.0 equiv), and dicyclohexylcarbodiimide (8 mg, 1.2 equiv) were dissolved in 0.5 mL dichloromethane and were stirred together for 6 h. The product was then passed through a short plug (ca. 1 in.) of silica gel using 100% ethyl acetate as the eluant to give, after evaporation of solvents, 16 mg (80% yield) of a solid which was used immediately in the next step. The previously formed amine **3** (15 mg, 1.0 equiv) and the previously formed NHS ester **1** were dissolved in 0.2 mL dichloromethane, and diisopropylethylamine (16 μL, 3.5 equiv) was added to the solution. The mixture was stirred for 20 h, and the reaction mixture was transferred to a preparative thin-layer chromatography plate using acetonitrile/methanol (90:10) as eluant. The topmost band was scraped off of the plate, and the compound was extracted from the silica gel with acetonitrile/methanol (90:10) to give, after evaporation of the solvents, 5 mg (21% yield) of the conjugate **5**. ^{1}H NMR (500 MHz, $CDCl_3$) δ: 7.78 (d, J = 8.5 Hz, 2 H), 7.49 (d, J = 8.5 Hz, 2 H), 7.35−7.28 (m, 2 H), 7.20−6.54 (m, 8 H), 5.83−5.73 (m, 1 H), 5.36−5.28 (m, 1 H), 4.51 (s, 2 H), 4.35−4.22 (m, 1 H), 3.93−3.83 (m, 8 H), 3.76−3.34 (m, 32 H), 3.23−3.14 (m, 1 H), 2.97−1.29 (m, 31 H), 1.23 (s, 3 H), 1.21 (s, 3 H), 1.19−1.06 (m, 2 H), 0.94 (s, 3 H), 0.89 (t, J = 7.4 Hz, 3 H); HR-ESI-MS: calcd for $C_{78}H_{107}N_4O_{19}$, 1403.7530; found, 1403.7504.

Estrogen Receptor Ligand-Binding Domain Expression and Labeling. N-Terminally His-tagged constructs in pET15b plasmids for ERα-417 and SRC3 were prepared as previously described. The ligand binding domain of ERα-417 (amino acids 304−554; C381,530S) with a single reactive cysteine at C417 or the nuclear receptor domain of SRC3 encompassing three nuclear receptor (NR) boxes (amino acids 627−829) was transformed into *E. coli* BL21(DE3)pLysS, grown at 37 °C to OD_{600} ~0.5, induced with 1 mM IPTG, and grown for 4 h at 28 °C, as previously reported (*21*).

For protein isolation, a cell pellet was suspended in 5 mL buffer (50 mM Tris buffer, pH 7.5, 10% glycerol, 0.1 mM TCEP) per gram and sonicated (Vibra cell sonicator with a micro probe; Sonic Materials, Inc., Danbury, CT) for 10 s at 60% power. After centrifugation for 30 min at 30 000 *g*, the supernatant was purified to near-homogeneity by batchwise adsorption onto a nickel-charged nitrilotriacetic acid-agarose resin (Ni-NTA-agarose; Qiagen Inc., Santa Clarita, CA), following standard protocols (*1, 21*).

Site-specific ER labeling was accomplished using 30 equiv of a thiol-reactive biotin derivative (MAL-dPEG4-biotin, Quanta BioDesign) while His_6-tagged ERα-417 LBD was immobilized on the Ni-NTA resin. The SRC3-NRD was likewise labeled using the recommended equivalents of a thiol-reactive Cy5 derivative (Cy5Maleimide Mono-Reactive Dye Pack, Amersham Biosciences). Labeling reactions were incubated overnight at 4 °C in Tris-glycerol buffer (50 mM Tris, pH 7.0, 10% glycerol, 0.1 mM tris(2-carboxyethylphosphine, TCEP). Excess fluorophore was removed by washing the protein-bound resin with wash buffer (50 mM Tris buffer, pH 7.5, 10% glycerol, and 10 mM mercaptoethanol) before eluting the labeled receptor using a solution of 100 mM EDTA, 0.5 M NaCl, and 20 mM Tris pH 8.0 (*1, 21*).

FKBP12 Expression and Labeling. A stab culture of *E. coli* that had been transformed with the pGEX-2T plasmid for GST-FKBP12 was obtained from the laboratory of Dr. Jie Chen at the University of Illinois at Urbana−Champaign. A 5 mL culture on a standard LB growth media supplemented with 100 μg/mL ampicillin was started by inoculating a single *E. coli* BL21 colony and agitated for approximately 16 h at 37 °C. The bacteria were diluted (1:100) into standard LB medium and grown at 37 °C until $OD_{600\ nm}$ of ~0.7. Protein expression was induced with 0.1 mM IPTG. After 4 h of incubation at 37 °C, all cells were harvested by centrifugation at 5000 × *g* for 15 min at 4 °C. The pellet was resuspended in 5 mL 1 × PBS buffer (pH 7.4) and 5 mM DTT. After addition of a 10 mg lysozyme (Sigma) per 1 g of bacteria, the resuspension was sonicated ten times for 2 s on ice. The fusion protein from the clear supernatant was batch purified using a 1 mL Glutathione Sepharose 4B (Amersham Biosciences), equilibrated in 5 mL ice-cold binding buffer (1 × PBS, pH 7.3) containing 5 mM DTT. The protein was allowed to bind for 4 h at 4 °C before elution with 300 μL 50 mM Tris-HCl, pH 8.0, containing 10 mM reduced glutathione and 5 mM DTT. The presence and purity of eluted GST-FKBP12 was evaluated by SDS-PAGE (*22*).

To produce fluorescein-labeled FKBP12, the protein was labeled nonspecifically with iodoacetamide−fluorescein (Invitrogen) while on the glutathione resin using the same protocol for labeling ER and SRC proteins as described above.

FRET Assay of Estradiol-SLF Binding to ER by Recruitment of Fluorescein-SRC3. Purified biotin-ERα-417 and fluorescein-SRC3-NRD were used in time-resolved FRET assays previously described (*23*) and adapted for the ER/FKBP system. A stock solution (5 μL) of ERα-417 (8 nM) and LanthaScreen Streptavidin-Terbium (Invitrogen) (2 nM) in TR-FRET buffer (20 mM Tris, pH 7.5, 0.01% NP40, 50 mM NaCl) was placed in separate wells of a black 96-well Molecular Devices HE high-efficiency microplate (Molecular Devices, Inc., Sunnyvale, CA). In a second 96-well Nunc polypropylene plate (Nalge Nunc International, Rochester, NY), a solution of each tested compound (0.001 M stock in DMF) was serially diluted in a 1:10 fashion into DMF. Each concentration of compound was then diluted 1:10 into TR-FRET buffer, and 10 μL of this solution or vehicle was added to the stock ER solution in the 96-well plate. After a 2 min incubation, 5 μL of 200 nM fluorescein-SRC3-NRD was added to each well. This mixture was allowed to incubate for 1 h at RT in the dark. TR-FRET was measured using an excitation filter at 340/10 nm and emission filters for terbium and fluorescein at 495/20 and 520/25 nm, respectively. The final concentrations of the reagents were as follows: ERα-417 (2 nM), streptavidin−terbium (0.5 nM), test compound (0−50 μM), SRC3-Fl (50 nM) (*9*).

FRET Assay of Estradiol-SLF Binding to FKBP. Purified FKBP12-GST and a fluorescein-labeled SLF compound were used for this time-resolved FRET assay. A stock solution (5 μL) of FKBP12-GST (20 nM) and LanthaScreen anti-GST-terbium antibody (Invitrogen) (20 nM) in TR-FRET buffer (20 mM Tris, pH 7.5, 0.01% NP40, 50 mM NaCl) was placed in separate wells of a black 96-well microplate. The test compounds were prepared as described above and added to the

protein solution. After a 2 min incubation, 5 μL of 400 nM fluorescein−SLF was added to each well. This mixture was allowed to incubate for 1 h at RT in the dark. TR-FRET was measured as described above. The final concentrations of the reagents were as follows: FKBP12-GST (5 nM), anti-GST-terbium (5 nM), test compound (0−50 μM), and SLF-Fl (100 nM).

FRET Assay of Agonist−SLF Binding to both ER and FKBP. This assay was conducted according to the protocol used for the above experiment "FRET Assay of Estradiol-SLF Binding to ER by Recruitment of Fluorescein-SRC" replacing the 50 nM SRC3-Fl with 50 nM FKBP12-Fl. All other concentrations and measures remained identical.

FRET Assay of ER-SRC Binding in the Presence of FKBP. This assay was performed in the same format as the experiment above "FRET Assay of Estradiol-SLF Binding to ER by Recruitment of Fluorescein-SRC" with the following changes. Unlabeled FKBP12 and SRC3 were each titrated into TR-FRET buffer and added to the well of a microplate. A stock solution of ERα-417 (8 nM), compound **4** (25 μM), and streptavidin−terbium (2 nM) was incubated for 10 min, and 5 μL of this solution was then added to each well of protein. Finally, 5 μL of 200 nM SRC3-Fl was added to each well and allowed to incubate for 20 min before the fluorescence was read.

FRET Assay of ER Dimerization in the Presence of FKBP. This assay was performed according to the protocol "FRET Assay of ER-SRC binding in the presence of FKBP" with the exchange of 50 nM SRC3-Fl for 50 nM ERα-Fl in the final assay concentrations. Also, both compound **2** and estradiol were used as test compounds in this assay to provide additional positive and negative controls.

Luciferase Reporter Gene Assay. Human endometrial cancer cells were maintained in culture as described and transfected in 24 well plates (*24*). A mixture of HBSS (50 μL/well), Holo-transferrin (Sigma T1408) (20 μL/well), and lipofectin (Invitrogen #18292−011) (5 μL/well) was incubated at RT for 5 min. The DNA mixture was made by adding 200 ng of pCMVβ-galactosidase as internal control, 500 ng of the estrogen-responsive reporter gene plasmid 2ERE Luc, and 100 ng of full-length ER alpha expression vector with 75 μL HBSS per well and, after addition to the first mixture, allowed to incubate for 20 min at RT. The cell media was changed to Opti-MEM (350 μL/well) and 150 μL of the transfection mixture was added to each well. The cells were incubated at 37 °C in a 5% CO_2 containing incubator for 6 h. The medium was then replaced with fresh medium containing 5% charcoal-dextran-treated calf serum and the desired treatments of compounds. Reporter gene activity was assayed at 24 h after ligand addition. Luciferase activity, normalized for the internal control β-galactosidase activity, was assayed as described (*24*).

RESULTS

Conjugate Design and Synthesis. The recruiting element/protein partner pair we chose, SLF/FKBP, was the same one used in the previously reported β-amyloid study (*12*), because of the advantages the pair confers: (a) FKBPs are ubiquitously expressed in various mammalian tissues, including breast cancer cells (e.g., FKBP52 makes up 1.0−1.5% of the total protein concentration in ER+ breast cancer cells (*25*)); (b) SLF, which is effectively one structural half of the natural product FK506, binds to FKBPs with high affinity ($K_d \approx 20$ nM) (*19, 26*) but is incapable of recruiting calcineurin, the interaction partner for FKBP, and, therefore, should have no confounding biological effects; (c) accessible methods have been described for the synthesis of SLF (*19, 20*); and finally, (d) because the SLF/FKBP pair proved effective in blocking protein−protein interactions in the β-amyloid case, we were hopeful that it would be a fruitful starting point for this project.

The position on the estradiol skeleton chosen for derivatization was the 17α position, an alteration typically known to give agonists (*15*). The NHS ester **1** was prepared by reacting 17α-ethynylestradiol with methyl 4-iodobenzoate using Sonogashira conditions, to give, after saponification of the methyl ester and activation, the NHS ester **1**. This activated ester **1** was reacted with monoprotected diamines, which after deprotection, gave the amine-functionalized estrogens **2** and **3**. Reaction of these amines with SLF electrophiles, prepared according to known methods (*19, 20*), gave the desired estrogen−SLF conjugates **4** and **5**.

Assay Design. In following the different protein−protein or protein−small molecule interactions in our studies described below, we have used various versions of a time-resolved fluorescence resonance energy transfer (TR-FRET) assay (*23*). In these assays, one of the protein partners, appropriately functionalized, is labeled with a FRET donor in one of two ways—by binding either a terbium strepavidin chelate (SA-Tb) or a terbium-labeled anti-GST antibody. The other partner, either a protein or small molecule, is labeled with the FRET acceptor fluorescein. In these experiments, an increase in FRET corresponds to a complex wherein both FRET donor and acceptor are in close proximity, meaning that both proteins are within the same complex. For further details, see our previous report (*23*).

EE2-SLF Conjugate 4 Binds ER and Recruits SRC3. As seen in Figure 1A, the short-tether EE2-SLF conjugate **4** was able to recruit a fluorescein-labeled SRC3 (SRC3-Fl) fragment to an ERα-LBD/SA-Tb complex, as judged by the dose-dependent increase in FRET signal seen with increasing concentrations of **4**. This result suggests that, as we had hoped, the conjugate **4** acts as an agonist, since antagonists are incapable of recruiting SRC to the ER in reconstituted in vitro systems. The potency of compound **4** is in general agreement with the results from a radiometric binding assay (*21, 27*), routinely carried out in our laboratories, which showed the relative binding affinity of **4** to be 1.5% that of estradiol, which corresponds to a K_D of 13 nM (data not shown).

Interestingly, conjugate **5**, having a longer tether joining the SLF and EE2 portions of the molecule, was much less capable of recruiting the SRC3 fragment to the ERα-LBD. We believe this may be due to the nonspecific interactions between the long tether and the proteins in the system that prevent the ligand from accessing the binding site.

EE2-SLF Conjugates Bind FKBP12. In a related TR-FRET experiment (Figure 1B), we showed that conjugate **4** is also capable of binding FKBP12, as judged by the dose-dependent competition of the ligand with a fluorescein-labeled SLF (SLF-Fl). In this experiment, FKBP12-GST was labeled with an anti-GST-Tb chelate. A decrease in FRET is expected if the molecule competes with SLF-Fl ($K_D = 30$ nM, data not shown) for binding to the FKBP12-Tb complex. The most potent FKBP12 binder was the unsubstituted **SLF-OH** ($IC_{50} = 200$ nM). Conjugates **4** and **5** bound to FKBP somewhat less well, with IC_{50} values of 1.7 and 1.8 μM, respectively.

EE2-SLF Conjugate 4 Binds ER and FKBP12 Simultaneously. Having established that each half of the conjugate **4** is able to independently bind to its respective partner, it was then important to establish that the conjugates were capable of binding both protein partners simultaneously. In a TR-FRET assay (Figure 1C), increasing concentrations of conjugate **4** were able to recruit fluorescein-labeled FKBP12 (FKBP12-Fl; labeled nonspecifically through available cysteine residues) to the Tb-ER complex. In this experiment, the negative control (the unfunctionalized **SLF-OH**) and the longer-tethered **5** were incapable of recruiting FKBP12 to the ER-Tb complex. This is in good agreement with the previous section, wherein **5** was

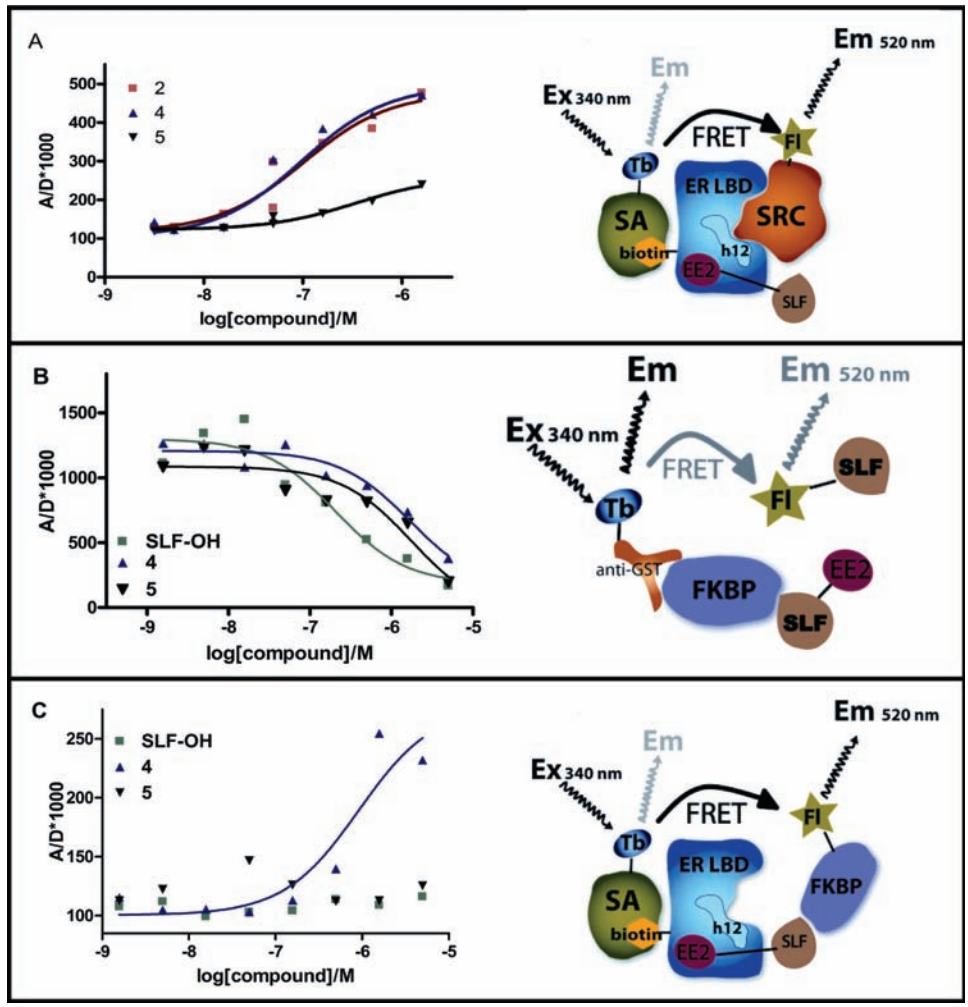


Figure 1. Time-resolved fluorescence resonance energy transfer assays. (A) Titration (ER-Tb/SRC3-Fl) of **2** (red squares), **4** (blue triangles), and **5** (black triangles) showing SRC recruitment to ER when liganded with conjugate **4**. (B) Titration (FKBP-Tb/SLF-Fl) of **SLF-OH** (green squares), **4**, and **5** showing increasing concentrations of compounds competing for SLF-Fl. (C) Titration (ER-Tb/FKBP12-Fl) of **SLF-OH**, **4**, and **5** showing recruitment of FKBP12-Fl to ER when liganded with **4**.

shown to be a poor ER binder (Figure 1A). Importantly, the results of this experiment establish that the bivalent ligand **4**, EE2-SLF, is able to bind to both of its intended protein targets, ERα and FKBP12, and bring them into one complex.

SRC3 Is Recruited to the ER/Conjugate 4/FKBP12 Complex. Conjugate **4** was capable of binding both ER and FKBP12 (Figure 1C); therefore, if it is incapable of recruiting SRC3 to ER in the presence of FKBP12, we can assume that this lack of recruitment is due to the recruited steric bulk of FKBP12. As seen in Figure 2A, ER-Tb saturated with conjugate **4** (25 μM) was capable of recruiting SRC3-Fl (high FRET), and this binding was reversible in the presence of increasing concentrations of unlabeled SRC3 (solid triangles). There was, however, no dose-dependent blockade of ER/SRC in the presence of increasing concentrations of unlabeled FKBP12 (open triangles). At the highest concentration of FKBP12 used (50 μM), no reduction is seen in the FRET signal, even though this concentration was shown to be adequate in saturating the conjugate in the previous experiment (Figure 1B). Thus, it seems that, when the ER is bound with the conjugate **4**, it can accommodate both SRC3 and FKBP12: The former is recruited due to the agonist character of the ethynylestradiol ligand (Figure 1A) and the latter can bind through the ligand component.

Conjugate 4 Is Also Incapable of Inhibiting ER Dimer Formation. In the previous experiment, ER was shown to bind a number of different proteins, but it was unclear whether a dimer or monomer of ER was responsible for this array of binding events. On the basis of structural studies of ER, dimer disruption might be more feasible than SRC inhibition, because X-ray crystallographic structures show that the 17α-phenylethynyl group of the conjugates likely exits from the binding pocket on the side of ER opposite that of the coactivator binding groove, but nearer the long helix 11, where ER dimerization takes place (*28*). If helix 11 were to be sufficiently perturbed by the recruitment of FKBP12, this could have an effect on the ability of ER to dimerize.

To probe this question, the ER-Tb complex (1 nM) was incubated with conjugate **4** (10 μM) and fluorescein-labeled ER (ER-Fl; 50 nM), such that a decrease in FRET would occur if dimer formation were to be disrupted (Figure 2B). In the positive controls, ER dimerization was disrupted (observed by a dose-dependent decrease in FRET) in the presence of increasing concentrations of unlabeled ER using either estradiol or conjugate **4**. These compounds do not, however, give this characteristic decrease in FRET in the presence of increasing concentrations of FKBP12 (open diamonds). Therefore, FKBP12 does not inhibit the formation of the ER dimer.

Conjugate 4 Is Incapable of Downregulating an ER-Regulated Reporter Gene. Regardless of its activity in in vitro assays, we thought that the conjugate might have unexpected activity in cell-based assays of ER-mediated transcription. When we treated transiently transfected HEC-1 cells with conjugate

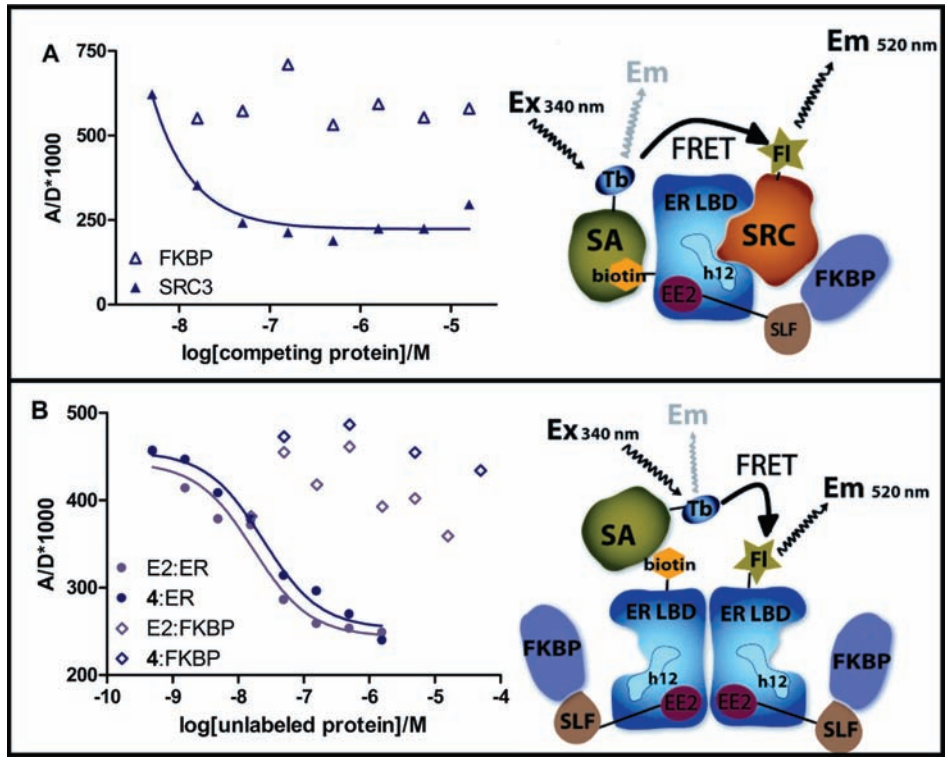


Figure 2. Time-resolved fluorescence resonance energy transfer assays. (A) Titration (conjugate **4**/ER-Tb/SRC3-Fl) of either FKBP12 (open triangles) or SRC3 (closed triangles) showing that unlabeled SRC3 displaces SRC3-Fl, but FKBP12 does not. (B) Titration (ER-Tb/ER-Fl) of conjugate **4** (blue) or estradiol (E2; purple) showing that unlabeled ER (closed circles) is able to disrupt dimer formation, but FKBP12 (open diamonds) is not.

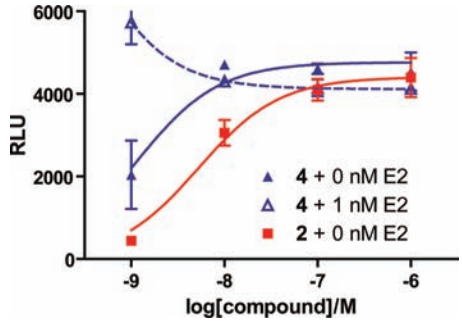


Figure 3. Luciferase reporter gene assay with **4** (closed blue triangles), **2** (closed red squares), and **4** + 1 nM E2 (open blue triangles), Increasing concentrations of **4** activate the ER-regulated luciferase gene, rather than downregulating luciferase expression.

4 (*24*), we saw, however, a dose-dependent increase in luciferase expression that was almost identical to the negative control **2**, which lacks an SLF group (Figure 3). Thus, both of these compounds behave as conventional ER agonists that are unaffected by the presence of FKBP and consistent with their ability to recruit SRC (cf. Figure 1B). When competing against 1 nM estradiol, the conjugate **4** showed no significant dose-dependent decrease in luciferase production. The small decrease in signal from −9 (1 nM) to −8 (10 nM) is most likely due to the lesser efficacy of compound **4** in comparison to estradiol as the ligands are exchanged, rather than true inhibition based on recruitment of FKBP. These data lead us to conclude that the ability of conjugate **4** to bind FKBP does not affect its efficacy, in agreement with the in vitro experiments detailed above.

DISCUSSION

The experiments detailed above yield a rather surprising finding: the ER can serve as a nexus for a remarkable number of binding events and still retain its activity, namely, binding of SA-Tb, conjugate **4**, SRC3, FKBP12, and another ER monomer occurs simultaneously and without antagonistic consequence. While this is not the finding for which we had hoped, it is an interesting one nevertheless, given that the ER-LBD is only 31 kDa, yet is able to recruit and bind approximately 145 kDa of other protein fragments simultaneously (FKBP12-GST (38 kDa), SRC3-NRD (24 kDa), streptavidin (53 kDa)). Thus, the estrogen receptor appears to be a protein with a high topological tolerance in its interactions with protein binding partners and thereby appears to be quite resistant to the disruption of its normal, functional interactions by recruitment of FKBP12 using heterobifunctional ligand−SLF conjugates.

There are a number of differences between the system we have investigated and the β-amyloid system on which this project was founded (*12*), and a comparison is instructive. Perhaps most salient is that we have not used this method to fortify the affinity of a weak, direct protein−protein interaction inhibitor, such as coactivator binding inhibitors we have studied (*8*, *9*). Rather, we have based our heterobifunctional conjugates on estradiol, a high-affinity ligand that binds to the ligand binding pocket. We were hopeful that the higher affinity of estradiol for the ligand-binding pocket of the receptor, compared to the relatively weak affinity of the known direct ER/SRC inhibitors (*8*, *9*), might serve as a better starting point for developing these types of inhibitors. Our inability to block either of these interactions with an inhibitor that binds to the ER with low nanomolar affinity, as does ours, would bode especially poorly for approaches that construct heterobifunctional conjugates from molecules that bind to the ER with only micromolar affinity, as do the currently available direct inhibitors of coactivator binding (*8*, *9*, *29*, *30*).

An additional difference between the Aβ system and ours is the size of the components involved. An oligomer of Aβ weighs only ca. 1 kDa, and its oligomerization is being inhibited by a

recruited FKBP twelve times its mass (*12*). In an in vitro sense, our system uses a 31 kDa construct of the ER-ligand binding domain and a 24 kDa SRC3 fragment. These are of comparable size to the FKBP-GST fusion protein used in our assays. Thus, it is conceivable that, although the FKBP-GST is being recruited, it is just too small to block the interaction of the larger-sized proteins. Some breast cancer cell lines, such as MCF-7, express larger FKBPs (e.g., FKBP51 or 52) that could be implemented in experiments similar to those described in this report (*25*); however, we do not believe that the steric bulk of these proteins would be significantly greater than the FKBP12-GST fusion protein (MW 38 kDa) that we have used here.

It is known that the affinities of the ER for its dimerization partner and SRC fragment are both very high ($K_d \approx$ <1 nM for both). It is not clear from the literature what the affinity of Aβ is during oligomerization, but various groups have demonstrated that appreciable oligomerization occurs at concentrations of 1−5 nM (*31, 32*), although higher concentrations (70 μM − 2 mM) are typically used when larger assemblies, such as prefibrillar and fibrillar oligomers and fibrils, are formed (*33*). The SLF-Congo Red conjugate described by Gestwicki was capable of inhibiting formation of aggregates up to ca. 28 nm^2 in size in the presence of FKBP, suggesting that the compound is not capable of disrupting the bimolecular Aβ/Aβ interaction, but rather the formation of these larger, possibly lower-affinity assemblies (*12*).

The position chosen for tethering SLF to the estradiol skeleton (17α) is an appropriate position for blocking ER dimerization, as the dimer interface occurs along the axis of helix 11 (*28*). Thus, it is surprising that the ER is able to bind its dimeric partner and FKBP simultaneously. By contrast, because SRC binds on a different face of the receptor, it might be difficult to access the ER/SRC interaction site with these types of inhibitors. It was for this reason that we created the longer-tethered conjugate **5**, in the hope that it might be able to extend further around the receptor to block the ER/SRC interaction. Unfortunately, we found that including this longer tether reduced the affinity of the molecule for the ER to levels that precluded it from being examined in our assays.

Another option in designing estrogen-SLF conjugates would be to supplement the activity of an antiestrogen by appending an SLF moiety; in fact, such a design has been reported for the androgen receptor (*34*). We have attempted to create such compounds for the estrogen receptor, but we have had difficulty in synthesizing one that has sufficient ER affinity to be examined in our assays.

More recently, heterobivalent molecules linking SLF with other ligands have been prepared (*13, 35*). These conjugates bind either to FKBP12 or to the other target protein (dihydrofolate reductase or cytochrome P450, respectively) when the two proteins are present separately, but they do not bind to both simultaneously when both are present. The steric occlusion encountered with these heterobivalent ligands is different from the behavior of the ligands, originally reported by Gestwicki et al. (*12*), that bind to FKBP and at the same time are able to interfere with the polymerization of Aβ. Our heterobivalent ligands too are able to bind to both ER and FKBP, but they do not prevent ER from interacting with other proteins (SRC or itself).

Of the heterobivalent ER ligands that have been reported in the literature, most are cytotoxic estrogens that typically contain alkylating agents tethered to estrogens (*36*−*39*); as such, they are not particularly germane to this discussion. The one exception of which we are aware is a geldanamycin-estradiol conjugate designed and synthesized by Danishefsky and coworkers (*40*). Meant to inhibit Hsp90 function and selectively degrade ER, the conjugate does seem to be selective for ER over other targets of Hsp90 inhibition (i.e., Raf-1, IGF1R) at very high concentrations (1 mM); however, no mechanistic studies were done to determine how the conjugate functions at a molecular level. It would be interesting to know whether this conjugate is also capable of simultaneously binding ER and Hsp90, whether simultaneous binding is necessary for its biological activity, and whether interruption of ER-associated protein−protein interactions contributes to its activity.

There have also been heterobivalent estrogen conjugates reported in the literature that are used in yeast-three hybrid assays, implying that the estrogen receptor is capable of binding to two different proteins simultaneously, although the interaction partner in this assay is streptavidin. This conjugate would presumably have no biological activity arising from multivalent interactions, as mammalian cells do not express avidins (*41*). We acknowledge a number of other factors (e.g., targeting element, recruiting element, tether length and composition, substitution site, enhanced affinity) one might change in creating inhibitors of the type mentioned here, but we wanted to share here our experience thus far—that a conjugate capable of binding both FKBP and ER simultaneously is incapable of inhibiting two different ER-associated protein−protein interactions.

Obviously, all of these factors merit careful consideration in the design of heterobivalent ligands, but beyond this, the overall topology of the protein−protein interaction is likely to be a critically important determinant of the feasibility and potential success of the Trojan horse approach to disruption of protein−protein interactions. The importance of the Congo Red−SLF conjugates is undeniable; however, the ER, long known as a proof-of-principle target in chemical biology experiments because of its therapeutic importance and well-studied biology, appears to have considerable topological tolerance in its interaction with its functional partner proteins (e.g., SRC). Therefore, it may not be the next logical conceptual target for this type of inhibition, and our experience suggests ways in which this Trojan horse approach may be limited.

ACKNOWLEDGMENT

The authors thank Kathryn Carlson for performing radiometric ligand-binding assays, Jie Chen for providing the FKBP12 constructs, Sung Hoon Kim for obtaining mass spectral data, and Manuel Rodriguez for assistance in synthesis. This research was supported by a grant from the National Institutes of Health (PHS 5R37 DK015556 to J.A.K.). J.R.G. received additional support from a David Robertson Fellowship, an NIH Fellowship NRSA 1 F30 ES016484-01, and Training Grant NRSA 5 T32 GM070421.

Supporting Information Available: Synthesis of the long oligoethyleneglycol tether is described. This material is available free of charge via the Internet at http://pubs.acs.org.

LITERATURE CITED

(1) Tamrazi, A., Carlson, K. E., Daniels, J. R., Hurth, K. M., and Katzenellenbogen, J. A. (2002) Estrogen receptor dimerization: ligand binding regulates dimer affinity and dimer dissociation rate. *Mol. Endocrinol. 16*, 2706–2719.

(2) Gee, A. C., Carlson, K. E., Martini, P. G., Katzenellenbogen, B. S., and Katzenellenbogen, J. A. (1999) Coactivator peptides have a differential stabilizing effect on the binding of estrogens and antiestrogens with the estrogen receptor. *Mol. Endocrinol. 13*, 1912–23.

(3) Moore, T. W., and Katzenellenbogen, J. A. (2009) Inhibitors of Nuclear Hormone Receptor/Coactivator Interactions. *Annu. Rep. Med. Chem. 44*, 443–457.

(4) Vaz, B., Mocklinghoff, S., Brunsveld, L. (2008) Targeting the nuclear receptor-cofactor interaction, in *Nuclear Receptors as*

Drug Targets (Ottow, F., and Weinmann, H., Eds.) pp 25−45, Wiley-VCH, Weinheim, Germany.
(5) Yudt, M. R., and Koide, S. (2001) Preventing estrogen receptor action with dimer-interface peptides. *Steroids 66*, 549–58.
(6) Moore, T. W., Mayne, C. G., and Katzenellenbogen, J. A. (2010) Minireview: not picking pockets: nuclear receptor alternate-site modulators (NRAMs). *Mol. Endocrinol. 24*, 683–695.
(7) Shiau, A. K., Barstad, D., Loria, P. M., Cheng, L., Kushner, P. J., Agard, D. A., and Greene, G. L. (1998) The structural basis of estrogen receptor/coactivator recognition and the antagonism of this interaction by tamoxifen. *Cell 95*, 927–37.
(8) Parent, A. A., Gunther, J. R., and Katzenellenbogen, J. A. (2008) Blocking estrogen signaling after the hormone: pyrimidine-core inhibitors of estrogen receptor-coactivator binding. *J. Med. Chem. 51*, 6512–6530.
(9) Rodriguez, A. L., Tamrazi, A., Collins, M. L., and Katzenellenbogen, J. A. (2004) Design, synthesis, and in vitro biological evaluation of small molecule inhibitors of estrogen receptor α coactivator binding. *J. Med. Chem. 47*, 600–611.
(10) Arkin, M. R., and Wells, J. A. (2004) Small-molecule inhibitors of protein-protein interactions: progressing towards the dream. *Nat. Rev. Drug Discovery 3*, 301–17.
(11) Wells, J. A., and McClendon, C. L. (2007) Reaching for high-hanging fruit in drug discovery at protein-protein interfaces. *Nature 450*, 1001–9.
(12) Gestwicki, J. E., Crabtree, G. R., and Graef, I. A. (2004) Harnessing chaperones to generate small-molecule inhibitors of amyloid beta aggregation. *Science 306*, 865–869.
(13) Gestwicki, J. E., and Marinec, P. S. (2007) Chemical control over protein-protein interactions: beyond inhibitors. *Comb. Chem. High Throughput Screen. 10*, 667–75.
(14) Arpino, G., Wiechmann, L., Osborne, C. K., and Schiff, R. (2008) Crosstalk between the estrogen receptor and the HER tyrosine kinase receptor family: molecular mechanism and clinical implications for endocrine therapy resistance. *Endocr. Rev. 29*, 217–33.
(15) Anstead, G. M., Carlson, K. E., and Katzenellenbogen, J. A. (1997) The estradiol pharmacophore: Ligand structure-estrogen receptor binding affinity relationships and a model for the receptor binding site. *Steroids 62*, 268–303.
(16) Gao, H., Katzenellenbogen, J. A., Garg, R., and Hansch, C. (1999) Comparative QSAR analysis of estrogen receptor ligands. *Chem. Rev. 99*, 723–744.
(17) Pangborn, A. B., Giardello, M. A., Grubbs, R. H., Rosen, R. K., and Timmers, F. J. (1996) Safe and convenient procedure for solvent purification. *Organometallics 15*, 1518–1520.
(18) Still, W. C., Kahn, M., and Mitra, A. (1978) Rapid chromatographic technique for preparative separations with moderate resolution. *J. Org. Chem. 43*, 2923–25.
(19) Holt, D. A., Luengo, J. I., Yamashita, D. S., Oh, H. J., Konialian, A. L., Yen, H. K., Rozamus, L. W., Brandt, M., Bossard, M. J., Levy, M. A., Eggleston, D. S., Liang, J., Schultz, L. W., Stout, T. J., and Clardy, J. (1993) Design, synthesis, and kinetic evaluation of high-affinity FKBP Ligands and the X-ray crystal-structures of their complexes with FKBP12. *J. Am. Chem. Soc. 115*, 9925–9938.
(20) Keenan, T., Yaeger, D. R., Courage, N. L., Rollins, C. T., Pavone, M. E., Rivera, V. M., Yang, W., Guo, T., Amara, J. F., Clackson, T., Gilman, M., and Holt, D. A. (1998) Synthesis and activity of bivalent FKBP12 ligands for the regulated dimerization of proteins. *Bioorg. Med. Chem. 6*, 1309–35.
(21) Carlson, K. E., Choi, I., Gee, A., Katzenellenbogen, B. S., and Katzenellenbogen, J. A. (1997) Altered ligand binding properties and enhanced stability of a constitutively active estrogen receptor: Evidence that an open pocket conformation is required for ligand interaction. *Biochemistry 36*, 14897–14905.
(22) Vilella-Bach, M., Nuzzi, P., Fang, Y. M., and Chen, J. (1999) The FKBP12-rapamycin-binding domain is required for FKBP12-rapamycin-associated protein kinase activity and G(1) progression. *J. Biol. Chem. 274*, 4266–4272.
(23) Gunther, J. R., Du, Y., Rhoden, E., Lewis, I., Revennaugh, B., Moore, T. W., Kim, S. H., Dingledine, R., Fu, H., and Katzenellenbogen, J. A. (2009) A set of time-resolved fluorescence resonance energy transfer assays for the discovery of inhibitors of estrogen receptor-coactivator binding. *J. Biomol. Screen. 14*, 181–193.
(24) Sun, J., Meyers, M. J., Fink, B. E., Rajendran, R., Katzenellenbogen, J. A., and Katzenellenbogen, B. S. (1999) Novel ligands that function as selective estrogens or antiestrogens for estrogen receptor-alpha or estrogen receptor-beta. *Endocrinology 140*, 800–804.
(25) Ward, B. K., Mark, P. J., Ingram, D. M., Minchin, R. F., and Ratajczak, T. (1999) Expression of the estrogen receptor-associated immunophilins, cyclophilin 40 and FKBP52, in breast cancer. *Breast Cancer Res. Treat. 58*, 267–80.
(26) Clackson, T., Yang, W., Rozamus, L. W., Hatada, M., Amara, J. F., Rollins, C. T., Stevenson, L. F., Magari, S. R., Wood, S. A., Courage, N. L., Lu, X., Cerasoli, F., Jr., Gilman, M., and Holt, D. A. (1998) Redesigning an FKBP-ligand interface to generate chemical dimerizers with novel specificity. *Proc. Natl. Acad. Sci. U.S.A. 95*, 10437–42.
(27) Katzenellenbogen, J. A., Johnson, H. J., and Carlson, K. E. (1973) Studies on uterine, cytoplasmic estrogen binding protein - thermal-stability and ligand dissociation rate - assay of empty and filled sites by exchange. *Biochemistry 12*, 4092–4099.
(28) Nettles, K. W., Bruning, J. B., Gil, G., O'Neill, E. E., Nowak, J., Guo, Y., Kim, Y., DeSombre, E. R., Dilis, R., Hanson, R. N., Joachimiak, A., and Greene, G. L. (2007) Structural plasticity in the oestrogen receptor ligand-binding domain. *EMBO Rep. 8*, 563–8.
(29) LaFrate, A. L., Gunther, J. R., Carlson, K. E., and Katzenellenbogen, J. A. (2008) Synthesis and biological evaluation of guanylhydrazone coactivator binding inhibitors for the estrogen receptor. *Bioorg. Med. Chem. 16*, 10075–10084.
(30) Shao, D., Berrodin, T. J., Manas, E., Hauze, D., Powers, R., Bapat, A., Gonder, D., Winneker, R. C., and Frail, D. E. (2004) Identification of novel estrogen receptor α antagonists. *J. Steroid Biochem. Mol. Biol. 88*, 351–360.
(31) Kelley, N. W., Vishal, V., Krafft, G. A., and Pande, V. S. (2008) Simulating oligomerization at experimental concentrations and long timescales: A Markov state model approach. *J. Chem. Phys. 129*, 214707.
(32) Garzon-Rodriguez, W., Sepulveda-Becerra, M., Milton, S., and Glabe, C. G. (1997) Soluble amyloid Abeta-(1−40) exists as a stable dimer at low concentrations. *J. Biol. Chem. 272*, 21037–44.
(33) Wu, J. W., Breydo, L., Isas, J. M., Lee, J., Kuznetsov, Y. G., Langen, R., and Glabe, C. Fibrillar oligomers nucleate the oligomerization of monomeric amyloid beta but do not seed fibril formation. *J. Biol. Chem. 285*, 6071–9.
(34) Singh, P., Hallur, G., Anchoori, R. K., Bakare, O., Kageyama, Y., Khan, S. R., and Isaacs, J. T. (2008) Rational design of novel antiandrogens for neutralizing androgen receptor function in hormone refractory prostate cancer. *Prostate 68*, 1570–81.
(35) Marinec, P. S., Lancia, J. K., and Gestwicki, J. E. (2008) Bifunctional molecules evade cytochrome P(450) metabolism by forming protective complexes with FK506-binding protein. *Mol. Biosyst. 4*, 571–8.
(36) Katzenellenbogen, J. A., and Zablocki, J. A. (1987) Cytotoxic Oestrogens and Antioestrogens: Concepts, Progress and Evaluation, in *Pharmacology and clinical uses of inhibitors of hormone secretion and action* (Furr, B. J. A., and Wakeling, A. E., Eds.) pp 41−59, Bailliere Tindall, London.
(37) Kim, E., Rye, P. T., Essigmann, J. M., and Croy, R. G. (2009) A bifunctional platinum(II) antitumor agent that forms DNA adducts with affinity for the estrogen receptor. *J. Inorg. Biochem. 103*, 256–261.
(38) Mitra, K., Marquis, J. C., Hillier, S. M., Rye, P. T., Zayas, B., Lee, A. S., Essigmann, J. M., and Croy, R. G. (2002) A rationally designed genotoxin that selectively destroys estrogen

receptor-positive breast cancer cells. *J. Am. Chem. Soc. 124*, 1862–1863.
(39) Rink, S. M., Yarema, K. J., Solomon, M. S., Paige, L. A., Tadayoni-Rebek, B. M., Essigmann, J. M., and Croy, R. G. (1996) Synthesis and biological activity of DNA damaging agents that form decoy binding sites for the estrogen receptor. *Proc. Natl. Acad. Sci. U.S.A. 93*, 15063–15068.
(40) Kuduk, S. D., Zheng, F. F., Sepp-Lorenzino, L., Rosen, N., and Danishefsky, S. J. (1999) Synthesis and evaluation of geldanamycin-estradiol hybrids. *Bioorg. Med. Chem. Lett. 9*, 1233–8.
(41) Hussey, S. L., Muddana, S. S., and Peterson, B. R. (2003) Synthesis of a β-estradiol-biotin chimera that potently heterodimerizes estrogen receptor and streptavidin proteins in a yeast three-hybrid system. *J. Am. Chem. Soc. 125*, 3692−3693.

BC100266V

SUPPORTING INFORMATION

for

Probing the Topological Tolerance of Multimeric Protein Interactions:

Evaluation of an Estrogen/Synthetic Ligand for FK506 Binding Protein Conjugate

by

Terry W. Moore,[a] Jillian R. Gunther and John A. Katzenellenbogen*

***tert*-Butyl 1-amino-13-oxo-3,6,9,16,19,22,25-heptaoxa-12-azaheptacosan-27-ylcarbamate:** NHS ester **26** (610 mg, 1.0 eq) was dissolved in anhydrous THF (3.0 mL) and amino alcohol **27** (500 mg, 2 eq) was added to this solution, followed by diisopropylethylamine (454 μL, 2.0 eq). This solution was stirred for 12 h, and the THF was evaporated. The compound was dissolved in ethyl acetate, and a small amount of water was added; the layers were separated, and the aqueous layer was extracted three additional times with ethyl acetate to give, after drying over $MgSO_4$ and evaporation of solvent, 550 mg (78% yield) of a viscous oil. This product was then activated as the methanesulfonate by adding in methanesulfonyl chloride (94 μL, 1.2 eq) and excess NEt_3 in dichloromethane. The solution was stirred for 4 h, and was then extracted using water and dichloromethane. The combined organic extracts were dried over $MgSO_4$ and concentrated to give 230 mg (36% yield) of the mesylate. The mesylate was then dissolved in DMF, and excess sodium azide (230 mg) was added to

the solution. The solution was stirred at RT for 4 h, and the product was extracted using ethyl acetate and brine. The organic extracts were dried over $MgSO_4$ and concentrated to give 170 mg (79% yield) of a viscous oil. Finally, the organic azide was dissolved in 20 mL methanol, and reduced for 2 h under 30 psi H_2 in a Parr shaker apparatus using 10 mol% Pd/C. The solution was filtered through celite, and the solvents were evaporated to give 150 mg (97% yield) of a viscous oil. ^{1}H NMR (500 MHz, $CDCl_3$) δ: 3.81 - 3.74 (m, 2 H), 3.73 - 3.67 (m, 2 H), 3.65 - 3.61 (m, 2 H), 3.62 - 3.50 (m, 21 H), 3.50 - 3.43 (m, 3 H), 3.41 - 3.33 (m, 3 H), 3.23 (d, *J*=4.5 Hz, 2 H), 3.17 - 3.11 (m, 2 H), 2.51 (t, *J*=6.1 Hz, 1 H), 1.35 (s, 9 H); ^{13}C NMR (125 MHz, $CDCl_3$) δ: 171.84, 156.01, 78.92, 70.30, 70.09, 70.00, 69.90, 69.79, 69.59, 67.24, 66.41, 40.00, 39.64, 38.97, 36.38, 28.22; HR-ESI MS $[M + H^+]^+$: calcd for 540.3496; found, 540.3496.

Solid-Supported Synthesis and Click Conjugation of 4′-*C*-Alkyne Functionalized Oligodeoxyribonucleotides

Anu Kiviniemi,* Pasi Virta, and Harri Lönnberg

Department of Chemistry, University of Turku, FIN-20014 Turku, Finland. Received June 11, 2010; Revised Manuscript Received August 23, 2010

4′-*C*-[*N*,*N*-Di(4-pentyn-1-yl)aminomethyl]thymidine and 4′-*C*-[*N*-methyl-*N*-(4-pentyn-1-yl)aminomethyl]thymidine 3′-(2-cyanoethyl-*N*,*N*-diisopropyl)phosphoramidites (**1**, **2**) were synthesized, and one or two such monomers were incorporated into a 15-mer oligodeoxyribonucleotide. After chain assembly, azido-functionalized ligands, including appropriate derivatives of 1,4-phenylenedimethaneamine, mannose, paromamine, and neomycin, were conjugated to the alkynyl groups by the click chemistry on a solid support. The influence of the 4′-modifications on the melting temperature with DNA and 2′-*O*-methyl RNA targets was studied. Oligonucleotides containing one to four mannose ligands in the central part of the chain (up to two 4′-*C*-[*N*,*N*-di(4-pentyn-1-yl)aminomethyl]thymidine units) form equally stable duplexes with complementary 2′-OMe RNA as the corresponding unmodified DNA sequence. At high salt content, the mannose conjugation is even stabilizing. On using a DNA target, a modest destabilization occurs. All the amino group bearing conjugates stabilized the duplexes, the DNA·DNA duplexes more than the DNA·2′-*O*-methyl RNA duplexes.

INTRODUCTION

Conjugation to peptides, carbohydrates, or small molecule compounds has been extensively studied as a possible way to improve the delivery and targeting of siRNA and antisense oligonucleotides (*1*−*15*), and the synthesis of such conjugates has been recently reviewed (*16*−*21*). Both carbohydrate−carbohydrate (*22, 23*) and carbohydrate−protein interactions (*24*−*26*) are known to play a central role in cellular recognition. These interactions are multipodal; simultaneous interaction with several monosaccharide ligands is required for high-affinity binding (*27*−*30*). Accordingly, the most attention has been paid to preparation of oligonucleotide conjugates bearing a multiarmed glycocluster at either terminus of the chain (*31*−*36*). As far as glycotargeting of siRNA is concerned, another approach appears, however, possible, viz., decoration of the sense strand with sugars. A prerequisite for this approach is that the sugar ligands do not markedly destabilize the duplex. In other words, the sense strand is aimed at serving as a scaffold to which the lectin-binding sugar ligands are tethered at appropriate distances throughout the molecule. Since the carrier is simultaneously able to hybridize with the antisense strand, the latter becomes enriched at the cell surface and, hence, internalizated by receptor-mediated endocytosis.

Several examples of oligonucleotide glycoconjugates bearing the sugars at intrachain positions have been published. These cannot, however, be exploited as sense strands in siRNA, since the sugar ligands are attached either to base moieties (*37*−*41*) or to non-nucleosidic units incorporated in the sugar−phosphate backbone (*42*−*44*). Both of these conjugations markedly destabilize the duplex. In fact, the only example of conjugation that does not markedly affect the duplex stability is offered by 4′-*C*-tethered glycoconjugates obtained by subjecting a 4′-*C*-azidomethyl incorporating oligonucleotide to Cu(I) catalyzed 1,3-dipolar cycloaddition, the so-called click reaction (*45, 46*), with an alkyne-derivatized sugar (*47*). The latter approach, however, suffers from the limitation that the 4′-*C*-azidomethyl unit has to be introduced into the chain by H-phosphonate coupling, since the intramolecular Staudinger reaction prevents preparation of the phosphoramidite building block. In the present study, the corresponding alkyne-derivatized nucleosides, viz., 4′-*C*-[*N*,*N*-di(4-pentyn-1-yl)aminomethyl]thymidine and 4′-*C*-[*N*-methyl-*N*-(4-pentyn-1-yl)aminomethyl]thymidine monomers (**1**, **2**), have been synthesized and incorporated into oligonucleotides by phosphoramidite chemistry. The 4-pentynyl group was chosen as the alkyne spacer to provide the 4′-*C*-modified nucleoside with sufficient flexibility to ensure efficient click reaction with azides (*48*) and proper alignment of the conjugate groups upon duplex formation. A related strategy has previously been applied to solid-supported derivatization of oligonucleotides containing ω-alkynylated nucleobases (*48, 49*). Monomers **1** and **2** allowed the attachment of two or one conjugative group per modified residue, respectively (Figure 1). The ligands used for the conjugation included azido derivatives of mannose (**3**), *p*-aminomethylbenzene (**4**), and aminoglycosides paromamine (**5**) and neomycin (**6**). The effects of these conjugate groups on the melting temperature of the duplexes with cDNA and 2′-*O*-methyl RNA sequences were determined to assess the contributions of electrostatic interactions and sterical factors to the efficiency of hybrization.

EXPERIMENTAL PROCEDURES

General Remarks. The NMR spectra were recorded at 500 MHz. The mass spectra were recorded using EI or ESI ionization. The RP HPLC analyses of the oligonucleotide conjugates were performed using a Thermo ODS Hypersil C18 (250 × 4.6 mm, 5 μm) analytical column, gradient elution from 0% to 50% MeCN in 0.1 mol L^{-1} triethylammonium acetate (aq) buffer over 60 min, flow rate 1 mL min^{-1}, and detection at 260 nm.

4′-*C*-Aminomethyl-3′-*O*-(4,4′-dimethoxytrityl)thymidine (8). 4′-*C*-Azidomethyl-3′-*O*-(4,4′-dimethoxytrityl)thymidine (2.14 g, 3.6 mmol) (*47*) was dissolved in THF (24 mL). Triphenylphosphine (1.50 g, 5.7 mmol), water (64 μL), and a drop of 33% aq NH_3 (∼20 μL) was added, and the reaction was stirred overnight. The reaction mixture was evaporated to dryness and purified by silica gel chromatography (10−20% MeOH in DCM containing 0.1% triethylamine). The yield was 1.54 g (75%) as a white solid foam. ^{1}H NMR (500 MHz, CD_3CN) δ_{ppm} 7.50−7.47

10.1021/bc100268w © 2010 American Chemical Society
Published on Web 09/09/2010

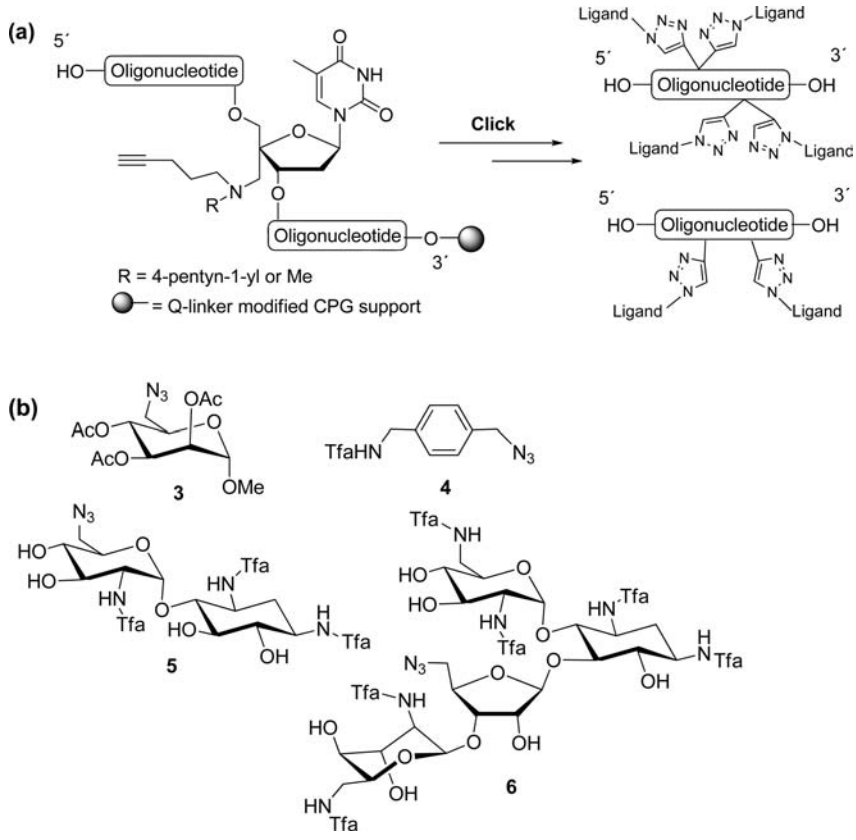


Figure 1. (a) Solid-supported conjugation of oligodeoxyribonucleotides by the click reaction. (b) Azido-functionalized ligands used in the click reaction.

(m, 2H), 7.40−7.32 (m, 6H), 7.27 (m, 1H), 7.09 (br d, 1H, J = 1.0 Hz), 6.93−6.88 (m, 4H), 6.12 (dd, 1H, J = 8.0 Hz, 4.0 Hz), 4.34 (dd, 1H, J = 7.5 Hz, 7.5 Hz), 3.79 (s, 3H), 3.78 (s, 3H), 3.60 (d, 1H, J = 12.0 Hz), 3.40 (d, 1H, J = 12.0 Hz), 3.34 (d, 1H, J = 13.5 Hz), 3.09 (d, 1H, J = 14.0 Hz), 1.98 (m, 1H), 1.78 (br d, 3H, J = 1.0 Hz), 1.32 (ddd, 1H, J = 14.5 Hz, 8.3 Hz, 4.3 Hz). ^{13}C NMR (125 MHz, CD_3CN) δ_{ppm} 163.7, 159.0, 159.0, 150.6, 145.6, 136.4, 136.1, 136.0, 130.5, 130.5, 128.2, 128.0, 127.1, 113.2, 113.2, 110.4, 87.4, 87.2, 83.6, 73.7, 64.6, 55.0, 43.5, 38.2, 11.5. ESI-MS: $[M + Na]^+$ $C_{32}H_{35}N_3NaO_7$ requires 596.2367, found 596.2376.

4′-*C*-[*N*,*N*-Di(4-pentyn-1-yl)aminomethyl]thymidine (9). Compound **8** (1.4 g, 2.4 mmol) was dissolved in MeOH (40 mL) and 4-pentynal (0.4 g, 4.9 mmol), $NaBH_3CN$ (0.46 g, 7.3 mmol), and acetic acid (140 μL) were added on an ice bath. The reaction was allowed to proceed overnight at room temperature. To remove the 4,4′-dimethoxytrityl group, 80% aqueous acetic acid was added, and after 2 h, the reaction mixture was evaporated to dryness. The residue was purified by silica gel chromatography (5−20% MeOH in DCM) yielding product **9** (0.65 g, 66%) as a powder. ^{1}H NMR (500 MHz, CD_3CN) δ_{ppm} 7.59 (d, 1H, J = 1.0 Hz), 6.28 (dd, 1H, J = 7.8 Hz, 6.3 Hz), 4.41 (dd, 1H, J = 5.0 Hz, 3.0 Hz), 3.61 (d, 1H, J = 11.5 Hz), 3.52 (d, 1H, J = 11.5 Hz), 2.92 (d, 1H, J = 14.5 Hz), 2.86 (d, 1H, J = 14.5 Hz), 2.78−2.71 (m, 2H), 2.68−2.61 (m, 2H), 2.32−2.20 (m, 6H), 2.19 (t, 2H, J = 2.8 Hz), 1.86 (br d, 3H, J = 1.0 Hz), 1.76−1.66 (m, 4H). ^{13}C NMR (125 MHz, CD_3CN) δ_{ppm} 163.9, 150.6, 136.3, 109.9, 87.3, 84.9, 84.0, 74.1, 69.0, 65.8, 56.7, 53.9, 40.2, 25.4, 15.7, 11.6. HRMS (EI): M^+ $C_{21}H_{29}N_3O_5$ requires 403.2107, found 403.2113.

4′-*C*-[*N*,*N*-Di(4-pentyn-1-yl)aminomethyl]-5′-*O*-(4,4′-dimethoxytrityl)thymidine (12). To a solution of compound **9** (0.39 g, 1.0 mmol) in 20 mL of dry pyridine, 4,4′-dimethoxytrityl chloride (0.35 g, 1.0 mmol) was added and the mixture was stirred overnight at room temperature. The volatiles were removed under reduced pressure, and the residue was purified by silica gel chromatography (50−90% ethyl acetate in petroleum ether + 0.1% triethylamine). The yield was 0.29 g (42%) as a white solid foam. ^{1}H NMR (500 MHz, $CDCl_3$) δ_{ppm} 7.40−7.37 (m, 2H), 7.33−7.23 (m, 8H), 6.87−6.82 (m, 4H), 6.46 (dd, 1H, J = 9.0 Hz, 5.5 Hz), 4.69 (dd, 1H, J = 4.0 Hz, 4.0 Hz), 3.79 (s, 6H), 3.12 (d, 1H, J = 9.5 Hz), 3.03 (d, 1H, J = 14.5 Hz), 3.01 (d, 1H, J = 9.5 Hz), 2.91−2.83 (m, 2H), 2.80 (d, 1H, J = 14.0 Hz), 2.58−2.50 (m, 2H), 2.38 (m, 1H), 2.25−2.10 (m, 5H), 1.95 (t, 2H, J = 2.8 Hz), 1.77−1.65 (m, 4H), 1.54 (d, 3H, J = 1.0 Hz). ^{13}C NMR (125 MHz, $CDCl_3$) δ_{ppm} 163.7, 158.8, 150.3, 144.1, 135.5, 135.2, 135.0, 130.1, 128.1, 128.1, 127.3, 113.3, 110.9, 87.2, 86.1, 84.9, 83.6, 76.1, 69.0, 67.2, 58.0, 55.3, 53.9, 41.4, 25.1, 16.4, 12.0. HRMS (EI): M^+ $C_{42}H_{47}N_3O_7$ requires 705.3414, found 705.3403.

3′-*O*-[(2-Cyanoethoxy)-(*N*,*N*-diisopropylamino)phosphinyl]-4′-C-[*N*,*N*-di(4-pentyn-1-yl)aminomethyl]-5′-*O*-(4,4′-dimethoxytrityl)thymidine (1). Compound **12** (0.25 g, 0.35 mmol) was dried over P_2O_5 in a vacuum desiccator and dissolved in dry DCM (5 mL). Triethylamine (248 μL, 1.8 mmol) and 2-cyanoethyl *N*,*N*-diisopropylphosphoramidochloridite (94.5 μL, 0.4 mmol) were added to the reaction solution under nitrogen. After 1 h, the reaction was completed and the mixture was eluted through a short, dried silica gel column (50% ethyl acetate in hexane, 0.1% triethylamine). The faster-eluting diastereomer I was partly obtained as a pure compound, while diastereomer II remained contaminated by diastereomer I (see Supporting Information). Yield was 0.29 g (91%) as colorless oil. Diastereomer I: ^{1}H NMR (500 MHz, CD_3CN) δ_{ppm} 9.42 (s, 1H), 7.68 (br d, 1H, J = 1.0 Hz), 7.53−7.49 (m, 2H), 7.41−7.32 (m, 6H), 7.28 (m, 1H), 6.93−6.89 (m, 4H), 6.24 (dd, 1H, J = 6.5

Hz, 5.5 Hz), 5.01 (ddd, 1H, J = 10.5 Hz, 7.0 Hz, 7.0 Hz), 3.80 (s, 6H), 3.74−3.58 (m, 5H), 3.13 (d, 1H, J = 11.0 Hz), 2.68−2.46 (m, 8H), 2.32 (m, 2H), 2.10 (t, 2H, J = 2.8 Hz), 2.07−1.94 (m, 4H), 1.52−1.40 (m, 4H), 1.39 (br d, 3H, J = 1.0 Hz), 1.21 (d, 6H, J = 6.5 Hz), 1.20 (d, 6H, J = 6.5 Hz); ^{13}C NMR (125 MHz, CD_3CN) δ_{ppm} 163.9, 158.8, 150.5, 145.1, 136.0, 135.8, 135.7, 130.3, 130.3, 128.2, 127.9, 127.0, 118.3, 113.1, 113.1, 109.9, 88.7, 88.7, 86.6, 84.5, 83.0, 72.5, 72.4, 68.7, 64.7, 58.6, 58.5, 55.8, 55.0, 54.2, 43.1, 43.0, 38.6, 38.5, 26.5, 24.0, 24.0, 24.0, 23.9, 20.1, 20.1, 15.7, 11.2; ^{31}P NMR (200 MHz, $CDCl_3$) δ_{ppm} 148.7. Diastereomer II: ^{1}H NMR (500 MHz, CD_3CN) δ_{ppm} 9.45 (s, 1H), 7.67 (s, 1H), 7.53−7.47 (m, 2H), 7.41−7.31 (m, 6H), 7.27 (m, 1H), 6.94−6.87 (m, 4H), 6.28 (dd, 1H, J = 6.0 Hz, 6.0 Hz), 4.95 (ddd, 1H, J = 9.5 Hz, 6.8 Hz, 6.8 Hz), 3.87 (m, 1H), 3.83−3.71 (m, 7H), 3.68−3.55 (m, 3H), 3.12 (d, 1H, J = 10.5 Hz), 2.72−2.42 (m, 8H), 2.30 (m, 2H), 2.09 (t, 2H, J = 2.8 Hz), 2.06−1.93 (m, 4H), 1.51−1.38 (m, 7H), 1.18 (d, 6H, J = 6.5 Hz), 1.10 (d, 6H, J = 6.5 Hz); ^{13}C NMR (125 MHz, CD_3CN) δ_{ppm} 163.9, 158.8, 150.5, 145.1, 136.1, 135.7, 135.6, 130.3, 130.3, 128.2, 127.9, 127.0, 118.6, 113.2, 113.1, 110.1, 88.4, 88.4, 86.7, 84.4, 82.9, 73.7, 73.6, 68.7, 64.9, 58.2, 58.0, 55.8, 55.0, 54.2, 43.1, 43.1, 38.8, 26.5, 24.3, 24.2, 23.8, 23.8, 20.2, 20.1, 15.7, 11.2; ^{31}P NMR (200 MHz, CD_3CN) δ_{ppm} 148.9. ESI-MS: $[M+H]^+$ $C_{51}H_{65}N_5O_8P$ requires 906.4565, found 906.4552.

4′-*C*-[*C*-(4-Pentyn-1-yl)aminomethyl]thymidine (10). Compound **8** (0.92 g, 1.6 mmol) was dissolved in MeOH (20 mL) and 4-pentynal (0.18 g, 2.2 mmol), $NaBH_3CN$ (0.30 g, 4.8 mmol) and acetic acid (92 μL) were added on an ice bath. The reaction was allowed to proceed overnight at room temperature. To remove the 4,4′-dimethoxytrityl group, 80% aqueous acetic acid was added, and after 2 h, the reaction mixture was evaporated to dryness. The residue was purified by silica gel chromatography (5−20% MeOH in DCM), giving compound **10** in 94% yield (0.51 g) as a white powder. ^{1}H NMR (500 MHz, MeOD/CD_3Cl (1:1)) δ_{ppm} 7.61 (s, 1H), 6.38 (dd, 1H, J = 8.3 Hz, 6.3 Hz), 4.53 (dd, 1H, J = 4.0 Hz, 4.0 Hz), 3.65 (s, 2H), 3.37 (m, 1H), 3.23−3.13 (m, 3H), 2.48 (m, 1H), 2.38−2.31 (m, 3H), 2.20 (br s, 1H), 1.96 (m, 2H), 1.91 (s, 3H); ^{13}C NMR (125 MHz, MeOD/CD_3Cl (1:1)) δ_{ppm} 164.7, 151.2, 136.5, 111.4, 86.1, 85.7, 81.5, 74.1, 70.7, 65.1, 49.7, 47.8, 39.4, 24.1, 15.6, 12.0. ESI-MS: $[M+H]^+$ $C_{16}H_{24}N_3O_5$ requires 338.1711, found 338.1725.

4′-*C*-[*N*-Methyl-*N*-(4-pentyn-1-yl)aminomethyl]thymidine (11). Compound **10** (0.45 g, 1.3 mmol) was dissolved in MeOH (10 mL), and paraformaldehyde (44 mg), $NaBH_3CN$ (92 mg, 1.5 mmol), and acetic acid (76 μL) were added on an ice bath. The mixture was stirred at room temperature over the weekend, and paraformaldehyde (22 mg) and $NaBH_3CN$ (50 mg, 0.8 mmol) were added to complete the reaction. The reaction was evaporated to dryness and purified by silica gel chromatography (10−20% MeOH in DCM). The yield was 0.44 g (93%). ^{1}H NMR (500 MHz, CD_3CN) δ_{ppm} 7.48 (s, 1H), 6.40 (dd, 1H, J = 8.5 Hz, 6.0 Hz), 4.45 (dd, 1H, J = 4.5 Hz, 4.5 Hz), 3.66 (d, 1H, J = 11.5 Hz), 3.61 (d, 1H, J = 12.0 Hz), 3.41 (d, 1H, J = 14.0 Hz), 3.31 (m, 1H), 3.17 (m, 2H), 2.86 (s, 3H), 2.44−2.28 (m, 5H), 1.95−1.87 (m, 5H); ^{13}C NMR (125 MHz, CD_3CN) δ_{ppm} 163.7, 150.6, 136.1, 110.5, 85.9, 85.6, 82.5, 74.3, 70.1, 65.3, 59.0, 58.1, 43.6, 38.8, 23.2, 15.2, 11.6. ESI-MS: $[M+H]^+$ $C_{17}H_{26}N_3O_5$ requires 352.1867, found 352.1849.

4′-*C*-[*N*-Methyl-*N*-(4-pentyn-1-yl)aminomethyl]-5′-*O*-(4,4′-dimethoxytrityl)thymidine (13). To a solution of compound **11** (0.36 g, 1.0 mmol) in 15 mL of dry pyridine, 4,4′-dimethoxytrityl chloride (0.42 g, 1.2 mmol) was added, and the mixture was stirred overnight at room temperature. The reaction mixture was evaporated and purified by silica gel chromatography (5% MeOH in DCM + 0.1% triethylamine). The yield was 0.27 g (40%) as a white solid foam. ^{1}H NMR (500 MHz, CD_3CN) δ_{ppm} 7.49−7.45 (m, 2H), 7.37−7.31 (m, 7H), 7.26 (m, 1H), 6.92−6.87 (m, 4H), 6.29 (dd, 1H, J = 7.5 Hz, 6.5 Hz), 4.63 (dd, 1H, J = 5.5 Hz, 3.5 Hz), 3.79 (s, 6H), 3.22 (d, 1H, J = 10.0 Hz), 3.10 (d, 1H, J = 10.0 Hz), 2.85 (d, 1H, J = 14.0 Hz), 2.69 (d, 1H, J = 14.5 Hz), 2.56 (m, 1H), 2.45 (m, 1H), 2.30−2.20 (m, 5H), 2.16−2.10 (m, 3H), 1.62 (m, 2H), 1.54 (s, 3H); ^{13}C NMR (125 MHz, CD_3CN) δ_{ppm} 163.8, 158.8, 150.6, 144.9, 135.8, 135.7, 135.5, 130.2, 130.2, 128.1, 128.0, 127.0, 113.2, 110.1, 86.8, 86.7, 84.2, 84.1, 74.4, 68.9, 66.5, 59.9, 57.8, 55.0, 42.9, 40.4, 26.0, 15.6, 11.4. ESI-MS: $[M+Na]^+$ $C_{38}H_{43}N_3NaO_7$ requires 676.2993, found 676.2997.

3′-*O*-[(2-Cyanoethoxy)-(*N*,*N*-diisopropylamino)phosphinyl)]-4′-*C*-[*N*-methyl-*N*-(4-pentyn-1-yl)aminomethyl]-5′-*O*-(4,4′-dimethoxytrityl)thymidine (2). Compound **13** (0.27 g, 0.4 mmol) was dried over P_2O_5 in a vacuum desiccator and dissolved in dry DCM (5 mL). Triethylamine (293 μL, 2.1 mmol) and 2-cyanoethyl *N*,*N*-diisopropylphosphoramidochloridite (111 μL, 0.5 mmol) were added to the reaction solution under nitrogen. After 1 h, the reaction was completed and the mixture was eluted through a short, dried silica gel column (50% ethyl acetate in hexane, 0.1% triethylamine). The faster eluting diastereomer I was partly obtained as a pure compound, while diastereomer II remained contaminated by diastereomer I (see Supporting Information). Yield was 0.31 g (87%) as a white solid foam. Diastereomer I: ^{1}H NMR (500 MHz, CD_3CN) δ_{ppm} 8.89 (s, 1H), 7.54−7.49 (m, 3H), 7.40−7.32 (m, 6H), 7.28 (m, 1H), 6.92−6.88 (m, 4H), 6.24 (dd, 1H, J = 7.0 Hz, 5.0 Hz), 4.98 (ddd, 1H, J = 10.5 Hz, 7.3 Hz, 7.3 Hz), 3.80 (s, 6H), 3.75−3.59 (m, 4H), 3.42 (d, 1H, J = 10.5 Hz), 3.22 (d, 1H, J = 10.5 Hz), 2.62−2.47 (m, 6H), 2.41−2.29 (m, 2H), 2.20 (s, 3H), 2.09−2.03 (m, 3H), 1.53 (m, 2H), 1.44 (br d, 3H, J = 1.0 Hz), 1.21 (d, 6H, J = 7.5 Hz), 1.20 (d, 6H, J = 7.0 Hz); ^{13}C NMR (125 MHz, CD_3CN) δ_{ppm} 163.6, 158.8, 150.3, 145.1, 135.8, 135.8, 135.7, 130.3, 128.2, 127.9, 127.0, 118.6, 113.1, 110.0, 88.9, 88.8, 86.5, 84.4, 83.2, 72.7, 72.5, 68.6, 64.3, 58.7, 58.5, 58.0, 55.0, 43.4, 42.9, 38.5, 26.5, 24.0, 23.9, 20.1, 20.1, 15.6, 11.3; ^{31}P NMR (200 MHz, CD_3CN) δ_{ppm} 148.6. Diastereomer II: ^{1}H NMR (500 MHz, CD_3CN) δ_{ppm} 8.94 (s, 1H), 7.52−7.48 (m, 3H), 7.38−7.31 (m, 6H), 7.27 (m, 1H), 6.91−6.87 (m, 4H), 6.27 (dd, 1H, J = 7.0 Hz, 6.0 Hz), 4.90 (ddd, 1H, J = 9.5 Hz, 7.0 Hz, 6.0 Hz), 3.87 (m, 1H), 3.79 (s, 6H), 3.77−3.56 (m, 3H), 3.43 (d, 1H, J = 10.5 Hz), 3.21 (d, 1H, J = 10.0 Hz), 2.69 (t, 2H, J = 6.0 Hz), 2.62−2.47 (m, 4H), 2.42−2.26 (m, 2H), 2.20 (s, 3H), 2.09−2.02 (m, 3H), 1.52 (m, 2H), 1.45 (br d, 3H, J = 1.0 Hz), 1.19 (d, 6H, J = 6.5 Hz), 1.12 (d, 6H, J = 6.5 Hz); ^{13}C NMR (125 MHz, CD_3CN) δ_{ppm} 163.5, 158.8, 150.3, 145.1, 135.8, 135.8, 135.7, 130.3, 128.2, 127.9, 127.0, 118.6, 113.1, 110.2, 88.5, 88.4, 86.6, 84.4, 83.1, 74.0, 73.9, 68.6, 64.5, 58.8, 58.2, 58.0, 54.9, 43.4, 43.0, 38.6, 26.5, 24.2, 24.1, 23.8, 23.8, 20.2, 20.1, 15.6, 11.2; ^{31}P NMR (200 MHz, CD_3CN) δ_{ppm} 148.9. ESI-MS: $[MH]^+$ $C_{47}H_{61}N_5O_8P$ requires 854.4252, found 854.4247.

***N*-[4-(azidomethyl)benzyl]-2,2,2-trifluoroacetamide (4).** *N*-[4-(Azidomethyl)benzyl]-(4-methoxytrityl)amine (**15**) was first synthesized from *N*-(4-methoxytrityl)-1,4-phenylenedimethanamine (**14**). Compound **14** (1.00 g, 2.4 mmol) was dissolved in DCM (4 mL), and an aqueous solution of K_2CO_3 (3.7 mmol)/$CuSO_4$ (15 μmol) (7 mL) and MeOH (30 mL) were added. Triflyl azide (4.9 mmol, theoretical amount calculated from trifluoromethanesulfonyl anhydride used in the preparation) was prepared as previously reported (*50*) and added to the reaction mixture. The reaction was stirred overnight at room temperature and evaporated to dryness. The residue was dissolved in ethyl acetate and extracted with water. The organic fraction was dried with Na_2SO_4, evaporated, and purified by silica gel chromatography (10−20% ethyl acetate in petroleum ether, 0.1%

triethylamine). Compound **15** was obtained in 96% yield (1.03 g) yield. ^{1}H NMR (500 MHz, $CDCl_3$) δ_{ppm} 7.57−7.52 (m, 4H), 7.47−7.40 (m, 4H), 7.32−7.24 (m, 6H), 7.22−7.17 (m, 2H), 6.85−6.81 (m, 2H), 4.32 (s, 2H), 3.79 (s, 3H), 3.34 (s, 2H), 1.84 (br s, 1H); ^{13}C NMR (125 MHz, $CDCl_3$) δ_{ppm} 158.0, 146.2, 141.4, 138.1, 129.8, 128.5, 128.4, 128.3, 127.9, 126.3, 113.2, 70.5, 55.2, 54.6, 47.6. To the solution of compound **15** (0.95 g, 2.2 mmol) in 10 mL of DCM, trifluoroacetic acid (0.34 mL, 4.4 mmol) and MeOH were added. After 1 h stirring at room temperature, the reaction mixture was evaporated. Without further purification, the detritylated product was subjected to trifluoroacetylation with methyl trifluoroacetate (1.60 g, 12.5 mmol) in a mixture of triethylamine (1.6 mL) and MeOH (9 mL). After 2.5 h, the mixture was evaporated and purified by silica gel chromatography (5−50% ethyl acetate in petroleum ether). The yield was 0.50 g (88%) as a yellowish solid foam. ^{1}H NMR (500 MHz, $CDCl_3$) δ_{ppm} 7.35−7.30 (m, 4H), 6.65 (br s, 1H), 4.54 (d, 2H, J = 6.0 Hz), 4.35 (s, 2H); ^{13}C NMR (125 MHz, $CDCl_3$) δ_{ppm} 157.2, 136.0, 135.7, 128.9, 128.5, 115.8, 54.3, 43.6. ESI-MS: $[M+Na]^+$ $C_{10}H_9F_3N_4NaO$ requires 281.0621, found 281.0602.

1,3,2′-Tri-*N*-trifluoroacetylparomamine (17). Paromamine trihydrochloride (**16**) was obtained by hydrolysis of paromomycin sulfate under acidic conditions (1 mol L^{-1} HCl aq in MeOH, reflux overnight), as described previously (*51*). To the suspension of compound **16** (2.96 g, 6.8 mmol) in a mixture of MeOH (60 mL) and triethylamine (14.4 mL), methyl trifluoroacetate (8.76 g, 68.4 mmol) was added. After a few minutes, the solution cleared for a while, but soon the product began to precipitate. The reaction was stirred for 1 h at room temperature, and the precipitated product was filtered and washed with MeOH. Compound **17** was received in 76% yield (3.20 g) as a white powder. ^{1}H NMR (500 MHz, D_2O/acetone-d_6) δ_{ppm} 5.38 (d, 1H, J = 3.5 Hz), 4.02 (m, 1H), 3.90 (dd, 1H, J = 10.5 Hz, 3.5 Hz), 3.84 (m, 1H), 3.73−3.65 (m, 4H), 3.58 (dd, 1H, J = 9.5 Hz, 9.0 Hz), 3.55−3.40 (m, 3H), 1.93 (m, 1H), 1.70 (ddd, 1H, J = 12.5 Hz, each); ^{13}C NMR (125 MHz, D_2O/acetone-d_6) δ_{ppm} 97.6, 79.4, 76.9, 73.6, 73.0, 70.5, 70.0, 60.6, 54.7, 50.1, 49.3, 31.9 (peaks referring to Tfa are not listed). ESI-MS: $[M+Na]^+$ $C_{18}H_{22}F_9N_3NaO_{10}$ requires 634.1054, found 634.1052.

6′-*O*-(4,4′-Dimethoxytrityl)-1,3,2′-tri-*N*-trifluoroacetylparomamine (18). Compound **17** (1.96 g, 3.2 mmol) was dried over P_2O_5 in a vacuum and dissolved in dry pyridine (70 mL). 4,4′-Dimethoxytrityl chloride (1.09 g, 3.2 mmol) was added and the mixture was stirred overnight at room temperature. After evaporation, the residue was partitioned between ethyl acetate and saturated aq $NaHCO_3$. The organic fraction was dried with Na_2SO_4, evaporated, and purified by silica gel chromatography (10% MeOH in DCM + 0.1% triethylamine) yielding product **18** (2.00 g, 68%) as a purplish foam. ^{1}H NMR (500 MHz, CD_3CN) δ_{ppm} 8.07 (br d, 1H, J = 7.0 Hz), 7.54 (br d, 2H, J = 8.5 Hz), 7.52−7.49 (m, 2H), 7.39−7.32 (m, 6H), 7.26 (m, 1H), 6.92−6.88 (m, 4H), 5.30 (d, 1H, J = 3.0 Hz), 4.05−3.92 (m, 2H), 3.89−3.75 (m, 10H), 3.70−3.61 (m, 3H), 3.53 (dd, 1H, J = 9.5 Hz, 9.0 Hz), 3.49 (m, 1H), 3.42−3.34 (m, 2H), 3.27 (dd, 1H, J = 10.0 Hz, 3.5 Hz), 3.23 (dd, 1H, J = 10.0 Hz, 2.5 Hz), 2.01 (ddd, 1H, J = 13.0 Hz, 4.5 Hz, 4.5 Hz), 1.71 (ddd, 1H, J = 13.0 Hz, each); ^{13}C NMR (125 MHz, CD_3CN) δ_{ppm} 158.6, 145.3, 136.2, 136.2, 130.2, 128.2, 127.8, 126.7, 113.0, 98.4, 85.6, 80.1, 76.5, 73.7, 72.0, 71.5, 70.3, 62.0, 54.9, 54.8, 50.1, 49.6, 31.5 (peaks referring to Tfa are not listed). ESI-MS: $[M+Na]^+$ $C_{39}H_{40}F_9N_3NaO_{12}$ requires 936.2360, found 936.2349.

6′-*O*-(4,4′-Dimethoxytrityl)-5,6,3′,4′-tetra-*O*-acetyl-1,3,2′-tri-*N*-trifluoroacetylparomamine (19). Compound **18** (1.68 g, 1.8 mmol) was dissolved in dry pyridine and acetic anhydride (1.4 mL, 14.8 mmol), and a catalytic amount of 4-dimethylaminopyridine was added. The mixture was heated at 60 °C for 3 h and evaporated to dryness. The residue was dissolved in ethyl acetate and extracted with saturated aq $NaHCO_3$. The organic fraction was dried with Na_2SO_4, evaporated, and purified by silica gel chromatography (30% ethyl acetate in DCM + 0.1% triethylamine). The product (**19**, 1.96 g) was isolated as white foam in 98% yield.^{1}H NMR (500 MHz, CD_3CN) δ_{ppm} 7.72 (d, 1H, J = 9.0 Hz), 7.56 (d, 1H, J = 9.0 Hz), 7.52−7.48 (m, 2H), 7.39−7.30 (m, 7H), 7.27 (m, 1H), 6.95−6.90 (m, 4H), 5.42 (dd, 1H, J = 10.0 Hz, 9.5 Hz), 5.36 (d, 1H, J = 3.5 Hz), 5.31 (dd, 1H, J = 10.0 Hz, 9.5 Hz), 5.08 (dd, 1H, J = 10.0 Hz, 10.0 Hz), 5.06 (dd, 1H, J = 10.5 Hz, 10.0 Hz), 4.43 (ddd, 1H, J = 10.0 Hz, 9.5 Hz, 3.8 Hz), 4.29 (m, 1H), 4.20 (m, 1H), 4.07 (dd, 1H, J = 10.0 Hz, 10.0 Hz), 3.87 (m, 1H), 3.81 (s, 3H), 3.81 (s, 3H), 3.47 (dd, 1H, J = 10.5 Hz, 1.5 Hz), 2.83 (dd, 1H, J = 10.5 Hz, 2.5 Hz), 2.10 (ddd, 1H, J = 13.0 Hz, 4.5 Hz, 4.5 Hz), 2.02−1.94 (m, 7H), 1.92 (s, 3H), 1.71 (s, 3H); ^{13}C NMR (125 MHz, CD_3CN) δ_{ppm} 170.3, 170.2, 169.4, 168.7, 158.7, 158.7, 144.9, 136.1, 135.6, 130.1, 130.0, 128.1, 127.9, 126.9, 113.1, 113.0, 96.1, 85.6, 75.1, 74.6, 72.9, 70.9, 69.4, 67.4, 60.2, 55.0, 52.0, 48.6, 48.1, 31.1, 20.0, 19.8, 19.8, 19.7 (peaks referring to Tfa are not listed). ESI-MS: $[M+Na]^+$ $C_{47}H_{48}F_9N_3NaO_{16}$ requires 1104.2783, found 1104.2695.

5,6,3′,4′-Tetra-*O*-acetyl-1,3,2′-tri-*N*-trifluoroacetylparomamine (20). A solution of 3% dichloroacetic acid in DCM (30 mL) was added to compound **19** (1.90 g, 1.8 mmol) and MeOH was added. The reaction was stirred at room temperature for 4 h and evaporated to dryness. The residue was dissolved in ethyl acetate and extracted with saturated aq $NaHCO_3$. The organic fraction was dried with Na_2SO_4, evaporated, and purified by silica gel chromatography (70% ethyl acetate in petroleum ether). The product (**20**, 1.27 g) was isolated in 92% yield. ^{1}H NMR (500 MHz, CD_3CN) δ_{ppm} 7.84 (d, 1H, J = 9.0 Hz), 7.58 (d, 1H, J = 8.5 Hz), 7.30 (d, 1H, J = 9.0 Hz), 5.31 (dd, 1H, J = 9.5 Hz, 9.5 Hz), 5.27 (d, 1H, J = 4.0 Hz), 5.14 (dd, 1H, J = 10.5 Hz, 9.5 Hz), 5.07 (dd, 1H, J = 10.0 Hz, 9.5 Hz), 5.03 (dd, 1H, J = 10.5 Hz, 10.5 Hz), 4.38−4.17 (m, 3H), 4.09 (dd, 1H, J = 10.0 Hz, 9.5 Hz), 3.81 (ddd, 1H, J = 10.0 Hz, 4.0 Hz, 2.0 Hz), 3.66 (ddd, 1H, J = 12.5 Hz, 6.5 Hz, 2.0 Hz), 3.53 (ddd, 1H, J = 12.5 Hz, 6.0 Hz, 4.0 Hz), 2.96 (t, 1H, J = 6.3 Hz), 2.13 (ddd, 1H, J = 13.5 Hz, 4.5 Hz, 4.5 Hz), 2.04−1.96 (m, 4H), 1.96 (s, 3H), 1.95 (s, 6H); ^{13}C NMR (125 MHz, CD_3CN) δ_{ppm} 170.5, 170.2, 169.8, 169.4, 96.1, 75.5, 74.5, 72.9, 70.5, 70.3, 67.6, 59.7, 52.1, 48.7, 48.0, 31.2, 19.9, 19.8, 19.8, 19.7 (peaks referring to Tfa are not listed). ESI-MS: $[M+Na]^+$ $C_{26}H_{30}F_9N_3NaO_{14}$ requires 802.1476, found 802.1474.

6′-Azido-6′-deoxy-5,6,3′,4′-tetra-*O*-acetyl-1,3,2′-tri-*N*-trifluoroacetylparomamine (21). Compound **20** (0.73 g, 0.9 mmol) was dried over P_2O_5 in a vacuum and dissolved in dry DCM (6 mL). 10% DBU (1,8-diazabicyclo[5.4.0]undec-7-ene, 1.4 mL, 0.9 mmol) solution in MeCN and trifluoromethanesulfonyl anhydride (0.19 mL, 1.1 mmol) were added on an ice bath. After 30 min, the ice bath was removed, and the reaction was stirred at room temperature for 1.5 h. The reaction mixture was partitioned between ethyl acetate and water. The organic phase was separated, dried with Na_2SO_4, and evaporated to dryness. The residue was purified by silica gel chromatography (50% ethyl acetate in hexane) yielding triflate product (0.46 g, 53%), which was directly subjected to azidation step. To a solution of triflate product (0.45 g, 0.5 mmol) in dry DMF (3 mL), sodium azide (0.16 g, 2.5 mmol) was added and the mixture was stirred overnight at room temperature. The reaction mixture was partitioned between diethyl ether and water. The organic phase was separated, dried with Na_2SO_4, and evaporated to dryness. The residue was purified by silica gel chromatography (50% ethyl acetate in petroleum ether) yielding product **21** (0.39 g, 98%). ^{1}H NMR (500 MHz, CD_3CN) δ_{ppm} 7.83 (d, 1H. J = 9.0 Hz), 7.58 (d, 1H, J = 8.0 Hz), 7.31 (d, 1H, J = 8.5

Hz), 5.32 (dd, 1H, J = 10.0 Hz, 9.5 Hz), 5.28 (d, 1H, J = 4.0 Hz), 5.15−5.07 (m, 2H), 5.04 (dd, 1H, J = 10.5 Hz, 10.5 Hz), 4.40−4.27 (m, 2H), 4.22 (m, 1H), 4.06 (dd, 1H, J = 10.0 Hz, 9.5 Hz), 3.92 (m, 1H), 3.56 (dd, 1H, J = 13.5 Hz, 2.5 Hz), 3.36 (dd, 1H, J = 13.5 Hz, 4.3 Hz), 2.13 (ddd, 1H, J = 13.0 Hz, 4.8 Hz, 4.8 Hz), 2.04 (ddd, 1H, J = 13.0 Hz each), 1.99 (s, 3H), 1.96 (s, 3H), 1.95 (s, 3H), 1.94 (s, 3H); ^{13}C NMR (125 MHz, CD_3CN) δ_{ppm} 170.4, 170.2, 169.4, 96.0, 75.8, 74.5, 72.9, 70.1, 69.3, 68.1, 52.0, 50.1, 48.7, 48.0, 31.1, 19.9, 19.8, 19.7, 19.7 (peaks referring to Tfa are not listed). ESI-MS: $[M+Na]^+$ $C_{26}H_{29}F_9N_6NaO_{13}$ requires 827.1541, found 827.1496.

6′-Azido-6′-deoxy-1,3,2′-tri-*N*-trifluoroacetylparomamine (5). To a solution of compound **21** (0.40 g, 0.5 mmol) in dry MeOH (12 mL), sodium methoxide (160 μL of 0.6 mol L^{-1} solution in MeOH) was added. After 1 h, the mixture was neutralized with a strong cation-exchange resin (Dowex 50WX8−200, H^+-form) and filtered. The solution was evaporated, yielding pure product **5** (0.28 g, 88%) as a solid powder. ^{1}H NMR (500 MHz, CD_3CN + drop of CD_3OD) δ_{ppm} 8.54 (d, 1H. J = 9.0 Hz), 8.15 (d, 1H, J = 9.0 Hz), 8.01 (d, 1H, J = 8.0 Hz), 5.21 (d, 1H, J = 3.5 Hz), 4.02 (m, 1H), 3.95 (m, 1H), 3.84 (m, 1H), 3.69 (ddd, 1H, J = 10.0 Hz, 3.0 Hz, 3.0 Hz), 3.63−3.56 (m, 2H), 3.54 (dd, 1H, J = 13.5 Hz, 2.5 Hz), 3.50 (dd, 1H, J = 9.5 Hz, 9.0 Hz), 3.47−3.41 (m, 2H), 3.34 (dd, 1H, J = 10.0 Hz, 9.5 Hz), 2.00 (ddd, 1H, J = 13.0 Hz, 4.3 Hz, 4.3 Hz), 1.68 (ddd, 1H, J = 13.0 Hz each); ^{13}C NMR (125 MHz, CD_3CN + drop of CD_3OD) δ_{ppm} 98.6, 81.2, 76.2, 73.7, 72.0, 71.0, 70.3, 54.7, 50.5, 50.1, 49.5, 31.6 (peaks referring to Tfa are not listed). ESI-MS: $[M+Na]^+$ $C_{18}H_{21}F_9N_6NaO_9$ requires 659.1119, found 659.1122.

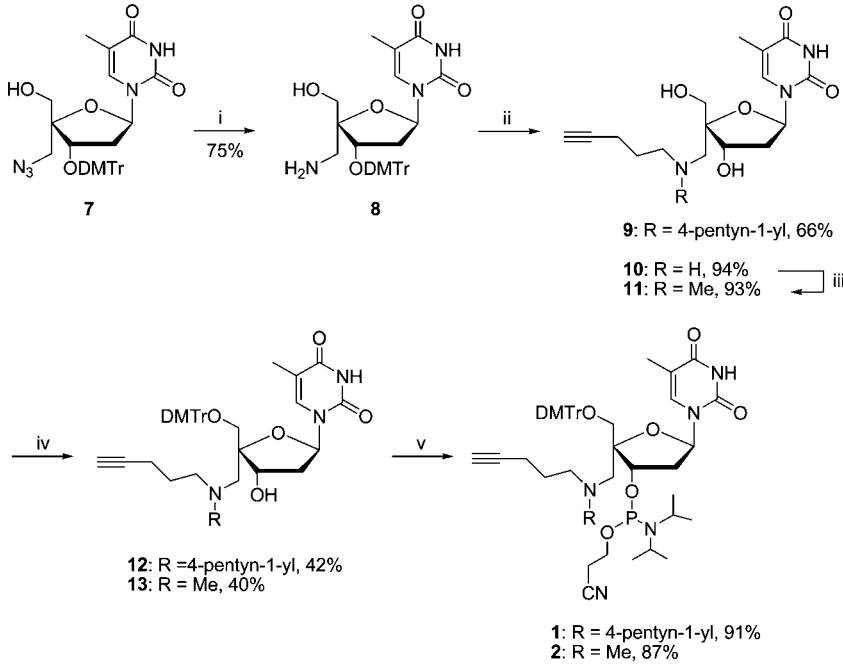
5″-*O*-(4,4′-Dimethoxytrityl)-1,3,2′,6′,2‴,6‴-hexa-*N*-trifluoroacetylneomycin (23). Triethylamine (3.6 mL, 26 mmol) and methyl trifluoroacetate (2.6 mL, 26 mmol) were added to a mixture of neomycin trisulfate (**22**, 2.0 g, 2.2 mmol) and MeOH (10 mL). The mixture was stirred overnight at room temperature and evaporated to dryness. Saturated $NaHCO_3$ was added, and the crude product was extracted with ethyl acetate. The organic layers were combined, dried over Na_2SO_4, filtered, and evaporated to dryness. The residue was further dried by coevaporation with dry pyridine and dissolved in dry pyridine, and then 4,4′-dimetoxytrityl chloride (0.80 g, 2.4 mmol) was added to the mixture. After overnight reaction, saturated $NaHCO_3$ was added to the mixture and the product was extracted with ethyl acetate. The organic layers were combined, dried over anhydrous Na_2SO_4, filtered, and evaporated to dryness. The residue was purified by silica gel chromatography (10% MeOH, 1% triethylamine in DCM) to yield 2.35 g (73%) of the product (**23**) as white foam.^{1}H NMR (500 MHz, CD_3OD) δ_{ppm} 7.46 (m, 2H), 7.36−7.30 (m, 6H), 7.21 (m, 1H), 6.90 (m, 4H), 5.78 (d, 1H, J = 3.3 Hz), 5.16 (d, 1H, J = 4.6 Hz), 5.09 (d, 1H, J = 1.5 Hz), 4.29 (dd, 1H, J = 4.8 Hz, both), 4.21−4.20 (m, 2H), 4.14 (m, 1H), 4.11 (dd, 1H, J = 6.7 Hz, both), 4.01 (m, 1H), 3.97 (m, 1H), 3.92 (m, 1H), 3.87 (dd, 1H, J = 9.9 and 8.8 Hz), 3.80 (s, 6H), 3.75−3.63 (m, 5H), 3.60 (dd, 1H, J = 13.5 and 7.4 Hz), 3.56−3.51 (m, 2H), 3.35−3.31 (m, 3H), 3.19 (dd, 1H, J = 10.5 and 3.1 Hz), 2.00 (ddd, 1H, J = 12.9 Hz, 4.2 and 4.2 Hz), 1.77 (ddd, 1H, J = 12.7 Hz, each); ^{13}C NMR (125 MHz, CD_3OD) δ_{ppm} 157.93, 157.85, 145.0, 136.0, 135.6, 130.2, 129.9, 128.0, 127.4, 126.3, 112.7, 109.0, 97.6, 96.3, 87.4, 86.3, 81.9, 76.9, 75.6, 74.8, 73.0, 72.1, 71.5, 70.3, 69.8, 69.2, 67.1, 62.5, 54.3, 53.5, 51.3, 49.6, 49.1, 40.4, 39.6, 31.5 (peaks referring to Tfa are not listed). ESI-MS: $[M+Na]^+$ $C_{56}H_{58}F_{18}N_6NaO_{21}$ requires 1515.3260, found 1515.3239.

5″-Azido-5″-deoxy-6,3′,4′,2″,3‴,4‴-hexa-*O*-acetyl-1,3,2′,6′,2‴,6‴-hexa-*N*-trifluoroacetylneomycin (25). Compound **23** (4.60 g, 3.1 mmol) was dried over P_2O_5 in vacuum and dissolved in dry pyridine (10 mL). Acetic anhydride (3.5 mL, 37.0 mmol) and a catalytic amount of 4-dimethylaminopyridine were added, and the reaction was stirred overnight at room temperature. After evaporation, the residue was partitioned between ethyl acetate and saturated aq $NaHCO_3$. The organic phase was separated, dried with Na_2SO_4, and evaporated to dryness. The residue was dissolved in 3% dichloroacetic acid in DCM (40 mL) and MeOH was added. After stirring the reaction 3 h at room temperature, the mixture was evaporated and extracted with ethyl acetate and saturated aq $NaHCO_3$. The organic phase was dried with Na_2SO_4, evaporated to dryness, and purified by silica gel chromatography (5−10% MeOH in DCM) to yield 3.90 g (87%) of the product **24** as a white foam. ^{1}H NMR (500 MHz, $CDCl_3$ + drop of CD_3OD) δ_{ppm} 5.84 (d, 1H, J = 2.0 Hz), 5.17 (d, 1H, J = 2.5 Hz), 5.14 (dd, 1H, J = 9.5 Hz, 9.5 Hz), 4.97 (dd, 1H, J = 3.0 Hz, 3.0 Hz), 4.91 (m, 1H), 4.89−4.81 (m, 2H), 4.80 (d, 1H, J = 1.5 Hz), 4.76 (dd, 1H, J = 5.8 Hz, 2.3 Hz), 4.37−4.24 (m, 2H), 4.17−4.05 (m, 4H), 3.99 (m, 1H), 3.95 (dd, 1H, J = 9.5 Hz, 8.5 Hz), 3.78 (dd, 1H, J = 13.0 Hz, 2.5 Hz), 3.74−3.64 (m, 3H), 3.63−3.53 (m, 2H), 3.32 (dd, 1H, J = 14.3 Hz, 5.8 Hz), 3.23 (dd, 1H, J = 14.0 Hz, 9.5 Hz), 2.18 (s, 3H), 2.15 (s, 3H), 2.10 (s, 3H), 2.08−2.02 (m, 7H), 1.99 (s, 3H), 1.81 (ddd, 1H, J = 13.0 Hz each); ^{13}C NMR (125 MHz, $CDCl_3$ + drop of CD_3OD) δ_{ppm} 171.0, 170.8, 170.5, 170.3, 168.7, 168.5, 107.4, 97.4, 95.0, 82.8, 80.9, 75.1, 75.0, 74.9, 73.3, 72.3, 69.9, 69.5, 68.2, 66.8, 66.2, 59.0, 51.7, 48.6, 48.1, 47.4, 40.1, 39.9, 31.3, 20.5, 20.2, 20.2, 20.2 (peaks referring to Tfa are not listed).

Compound **24** (1.07 g, 0.7 mmol) was dried over P_2O_5 in vacuum and dissolved in dry DCM (5 mL). 10% DBU (1.1 mL, 0.7 mmol) in MeCN and trifluoromethanesulfonyl anhydride (0.15 mL, 0.9 mmol) were added on an ice bath. After 30 min, the ice bath was removed and the reaction was stirred at room temperature for 2 h. The reaction mixture was partitioned between ethyl acetate and water. The organic phase was separated, dried with Na_2SO_4, and evaporated to dryness. The residue was purified by silica gel chromatography (50−80% ethyl acetate in hexane) yielding the triflate product (0.59 g, 50%) as reddish foam. The crude product was subjected as such to azidation. Accordingly, to a solution of the triflate product (0.59 g, 0.4 mmol) in dry DMF (3.5 mL), sodium azide (0.13 g, 2.0 mmol) was added, and the mixture was stirred overnight at room temperature. The reaction mixture was partitioned between diethyl ether and water. The organic phase was collected, dried with Na_2SO_4, and evaporated to dryness. The residue was purified by silica gel chromatography (50−70% ethyl acetate in hexane) yielding **25** (0.38 g, 69%). ^{1}H NMR (500 MHz, CD_3CN) δ_{ppm} 7.87 (d, 1H, J = 9.5 Hz), 7.59 (br t, 1H), 7.54 (d, 1H, J = 8.5 Hz), 7.50−7.42 (m, 2H), 7.23 (d, 1H, J = 9.5 Hz), 5.86 (d, 1H, J = 3.5 Hz), 5.24−5.17 (m, 2H), 4.99 (d, 1H, J = 3.0 Hz), 4.98−4.84 (m, 5H), 4.44−4.34 (m, 2H), 4.28 (m, 1H), 4.22 (m, 1H), 4.13−4.04 (m, 3H), 4.01 (ddd, 1H, J = 10.5 Hz, 3.5 Hz, 3.5 Hz), 3.89−3.81 (m, 2H), 3.69 (dd, 1H, J = 13.5 Hz, 3.0 Hz), 3.62 (ddd, 1H, J = 14.5 Hz, 5.0 Hz, 3.0 Hz), 3.56−3.41 (m, 4H), 2.12 (s, 3H), 2.10 (s, 3H), 2.08−2.04 (m, 4H), 2.03 (s, 3H), 2.02 (s, 3H), 2.00 (s, 3H), 1.96 (m, 1H); ^{13}C NMR (125 MHz, CD_3CN) δ_{ppm} 170.4, 170.3, 170.2, 170.0, 169.2, 168.7, 107.8, 96.9, 95.5, 82.7, 79.5, 76.5, 74.8, 74.7, 74.6, 71.3, 69.9, 68.4, 68.1, 67.6, 65.5, 51.7, 50.5, 48.8, 48.5, 47.6, 39.5, 38.9, 30.8, 20.1, 20.1, 19.9, 19.8, 19.8, 19.7 (peaks referring to Tfa are not listed). ESI-MS: $[M+Na]^+$ $C_{47}H_{51}F_{18}N_9NaO_{24}$ requires 1490.2652, found 1490.2649.

5″-Azido-5″-deoxy-1,3,2′,6′,2‴,6‴-hexa-*N*-trifluoroacetylneomycin (6). To a solution of compound **25** (0.43 g, 0.3 mmol) in dry MeOH (7 mL), sodium methoxide (200 μL of 0.6 mol L^{-1} solution in MeOH) was added. After 6 h, the mixture was neutralized with a strong cation-exchange resin (Dowex 50WX8−200, H^+-form) and filtered. The solution was evapo-

Scheme 1[a]



[a] Reagents: (i) PPh_3, H_2O, NH_3 (aq), THF; (ii) 4-pentynal (1 or 2 equiv), $NaBH_3CN$, AcOH, MeOH; (iii) paraformaldehyde, $NaBH_3CN$, AcOH, MeOH; (iv) DMTrCl, pyridine; (v) 2-cyanoethyl *N*,*N*-diisopropylphosphoramidochloridite, Et_3N, DCM.

rated yielding pure product **6** (0.34 g, 95%) as a solid powder. ^{1}H NMR (500 MHz, CD_3OD) δ_{ppm} 9.35 (d, 1H, J = 9.0 Hz), 9.27 (t, 1H, J = 5.5 Hz), 9.23 (d, 1H, J = 8.0 Hz), 8.82 (t, 1H, J = 5.5 Hz), 8.73 (d, 1H, J = 9.5 Hz), 8.33 (d, 1H, J = 9.5 Hz), 5.73 (d, 1H, J = 3.0 Hz), 5.12−5.08 (m, 2H), 4.23−4.08 (m, 5H), 4.05 (ddd, 1H, J = 10.0 Hz, 10.0 Hz, 4.0 Hz), 3.97−3.87 (m, 3H), 3.80−3.51 (m, 11H), 3.42 (dd, 1H, J = 13.3 Hz, 3.3 Hz), 3.23 (dd, 1H, J = 9.5 Hz, 9.0 Hz), 1.99 (ddd, 1H, J = 13.0 Hz, 4.3 Hz, 4.3 Hz), 1.73 (ddd, 1H, J = 12.5 Hz each); ^{13}C NMR (125 MHz, CD_3OD) δ_{ppm} 110.3, 97.6, 96.5, 87.6, 79.9, 76.2, 74.6, 73.6, 72.0, 71.7, 70.3, 70.2, 69.3, 67.7, 53.7, 51.3, 51.2, 49.8, 49.0, 40.4, 40.0, 31.5 (peaks referring to Tfa are not listed). ESI-MS: $[M+Na]^+$ $C_{35}H_{39}F_{18}N_9NaO_{18}$ requires 1238.2018, found 1238.2027.

Synthesis of Oligodeoxyribonucleotides. The modified oligodeoxyribonucleotides were synthesized on an Applied Biosystems 392 DNA synthesizer in a 1.0 μmol scale using commercial 500 Å CPG-Q-adenosine support (Q = hydroquinone-*O*,*O*′-diacetate). For phosphoramidites **1** and **2** (0.13 mol L^{-1} solution in dry MeCN), a prolonged coupling time of 10 min was used. Otherwise, standard DNA protocol was applied. The oligonucleotides were released from the support with concentrated ammonia (33% aqueous NH_3) at 55 °C overnight. For the click reactions, the support-bound material **26**−**29** were treated for 5−8 min with 10% DBU in MeCN (1 mL, dried over molecular sieves), after which the support was sequentially washed with MeCN, DMF, MeOH, water, and MeOH.

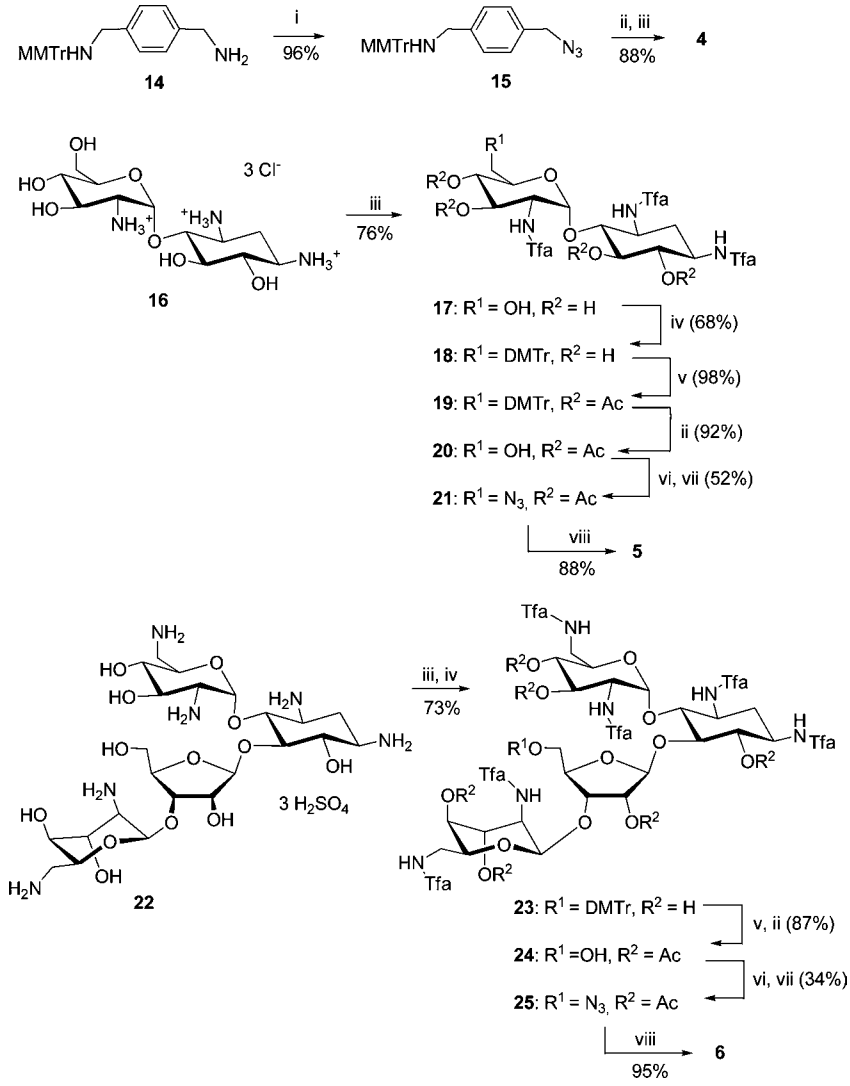
Click Conjugation. Azide-functionalized ligands, **3**−**6**, were conjugated to the alkynyl groups of oligonucleotides **26**−**29**. The solutions of ligands (50 mmol L^{-1}) in MeOH were added onto the support-bound oligonucleotides as follows: 15 equiv for **27**, 30 equiv for **26** and **29**, and 40 equiv for **28**. After that, $CuSO_4$ and tris[(1-benzyl-1,2,3-triazol-4-yl)methyl]amine (TBTA-ligand) were added as a 25 mmol L^{-1} solution in a 12:3:1 mixture of water, DMSO, and 2-butanol. The amounts added were as follows: 7.5 equiv for **27**, 15 equiv for **26** and **29**, and 20 equiv for **28**. Finally, sodium ascorbate (15, 30, and 40 equiv for **27**, **26**, **29**, and **28**, respectively) as 0.1 mol L^{-1} aqueous solution was added. The mixture was shaken at room temperature for 5 h. The support was collected by filtration and washed first with water, DMF, and MeOH. To remove the copper salt and TBTA ligand as quantitatively as possible, the support was then treated for 10 min with aq EDTA solution (0.1 mol L^{-1}), washed with water, and then for another 10 min with aqueous solution of neomycin trisulfate (0.1 mol L^{-1}). Finally, the support was washed with water, DMF, DCM, MeOH, and MeCN and subjected to standard ammonolytic release. After evaporation, the oligonucleotide conjugate was purified by RP HPLC.

Melting Temperature Studies. The melting curves (absorbance versus temperature) were measured at 260 nm on a Perkin-Elmer Lambda 35 UV−vis spectrometer equipped with a multiple cell holder and a Peltier temperature-controller. The temperature was changed at a rate of 0.5 °C/min (from 20 to 90 °C). The measurements were performed in 10 mmol L^{-1} potassium phosphate buffer (pH 7) containing 0.1 mol L^{-1} or 1.0 mol L^{-1} NaCl. The oligonucleotide conjugates and their cDNA or 2′-*O*-methyl RNA targets were used at a concentration of 2 μmol L^{-1}. T_m values were determined as the maximum of the first derivate of the melting curve.

RESULTS AND DISCUSSION

Synthesis of 4′-*C*-[*N*,*N*-di(4-pentyn-1-yl)aminomethyl]thymidine and 4′-*C*-[*N*-methyl-*N*-(4-pentyn-1-yl)aminomethyl]thymidine 3′-(2-Cyanoethyl-*N*,*N*-diisopropylphosphoramidites (1, 2). 4′-*C*-Azidomethyl-3′-*O*-(4,4′-dimethoxytrityl)-thymidine (**7**) was synthesized in good yield (75%) from 4′-*C*-hydroxymethylthymidine as described previously (*47*). Because the azido group can be easily converted to amino group by Staudinger reaction, it allows further functionalization. Accordingly, 4′-*C*-aminomethyl-3′-*O*-(4,4′-dimethoxytrityl)thymidine (**8**) was obtained by the reaction of compound **7** with triphenylphosphine and water (Scheme 1). Compound **8** was then subjected to reductive alkylation in the presence of $NaBH_3CN$ under acidic conditions. On using 2 equiv of 4-pentynal (*52*), 4′-*C*-[*N*,*N*-di(4-pentyn-1-yl)aminomethyl]thymidine (**9**) was ob-

Scheme 2[a]



[a] Reagents: (i) TfN_3, K_2CO_3, $CuSO_4$, H_2O, MeOH, DCM; (ii) DCA, DCM, MeOH; (iii) TfaOMe, Et_3N, MeOH; (iv) DMTrCl, pyridine; (v) Ac_2O, DMAP, pyridine; (vi) Tf_2O, 10% DBU in MeCN, DCM; (vii) NaN_3, DMF; (viii) NaOMe, MeOH.

tained. 4′-*C*-[*N*-Methyl-*N*-(4-pentyn-1-yl)aminomethyl]thymidine (**11**) was, in turn, prepared by two consecutive alkylation steps. Reaction with 4-pentynal gave 4′-*C*-[*N*-(4-pentyn-1-yl)aminomethyl]thymidine (**10**), which was then *N*-methylated with paraformaldehyde. After the reductive alkylations, the 3′-*O*-4,4′-dimethoxytrityl group was removed with 80% acetic acid. Compounds **9** and **11** were then converted to 5′-*O*-(4,4′-dimethoxytrityl) ethers (**12**, **13**) and phosphitylated to phosphoramidites **1** and **2**.

Synthesis of Ligands 3−6. The azido-functionalized ligands (**4**−**6**) used in the click conjugation were synthesized as outlined in Scheme 2. The azidation of previously synthesized (*47*) *N*-(4-methoxytrityl)-1,4-phenylenedimethanamine (**14**) was carried out by the Cu^{2+}-catalyzed diazo transfer described in the literature (*50*). The acid-labile trityl protection of the product (**15**) was changed to a base-labile trifluoroacetyl protection, removable by the conventional ammonolysis used for the release and deprotection of support-bound oligonucleotides.

Paromamine trihydrochloride (**16**) was obtained by acidic hydrolysis of commercially available paromomycin sulfate (*51*). After trifluoroacetylation of the amino groups, the primary 6′-hydroxyl group was protected as a 4,4′-dimethoxytrityl ether (**18**) and the remaining hydroxyl functions were acetylated. The 6′-position was then detritylated, sulfonated, and subjected to azidation. Since the azidation gave poor yields using mesyl esters as a starting material, conversion of the 6′-hydroxyl group to a triflate was attempted. The conventional treatment with triflic anhydride in the presence of pyridine, however, yielded a 6′-pyridinium salt instead of the desired product. Replacement of pyridine by less nucleophilic DBU then provided the desired triflate, which may be azidated to product **21** in 52% overall yield. This was finally deacetylated by methoxide ion-catalyzed transesterification in methanol to obtain product **5**, applicable to postsynthetic conjugation of the alkynylated oligonucleotides. 5″-Azido-1,3,2′,6′,2‴,6‴-hexa-*N*-trifluoroacetylneomycin (**6**) was synthesized starting from neomycin trisulfate (**22**) according to the same protocol as described for the paromamine derivative **5** above. The mannose-derived ligand, methyl 2,3,4-tri-*O*-acetyl-6-azido-6-deoxy-α-D-mannopyranoside (**3**), was prepared as previously reported (*53*).

Oligonucleotide Synthesis and Click Conjugation. 4′-*C*-[*N*,*N*-Di(4-pentyn-1-yl)aminomethyl]thymidine and 4′-*C*-[*N*-methyl-*N*-(4-pentyn-1-yl)aminomethyl]thymidine monomers **1** and **2** were incorporated into 15-mer oligodeoxyribonucleotides **26**−**29** using standard phosphoramidite coupling chemistry except for a prolonged 10 min coupling time. The coupling yields were 97%. Interestingly, we noticed that these modified oligonucleotides did not withstand solid-supported click con-

Scheme 3. Synthesis of the Conjugated Oligodeoxyribonucleotides Containing One 4′-*C*-Modified Monomer

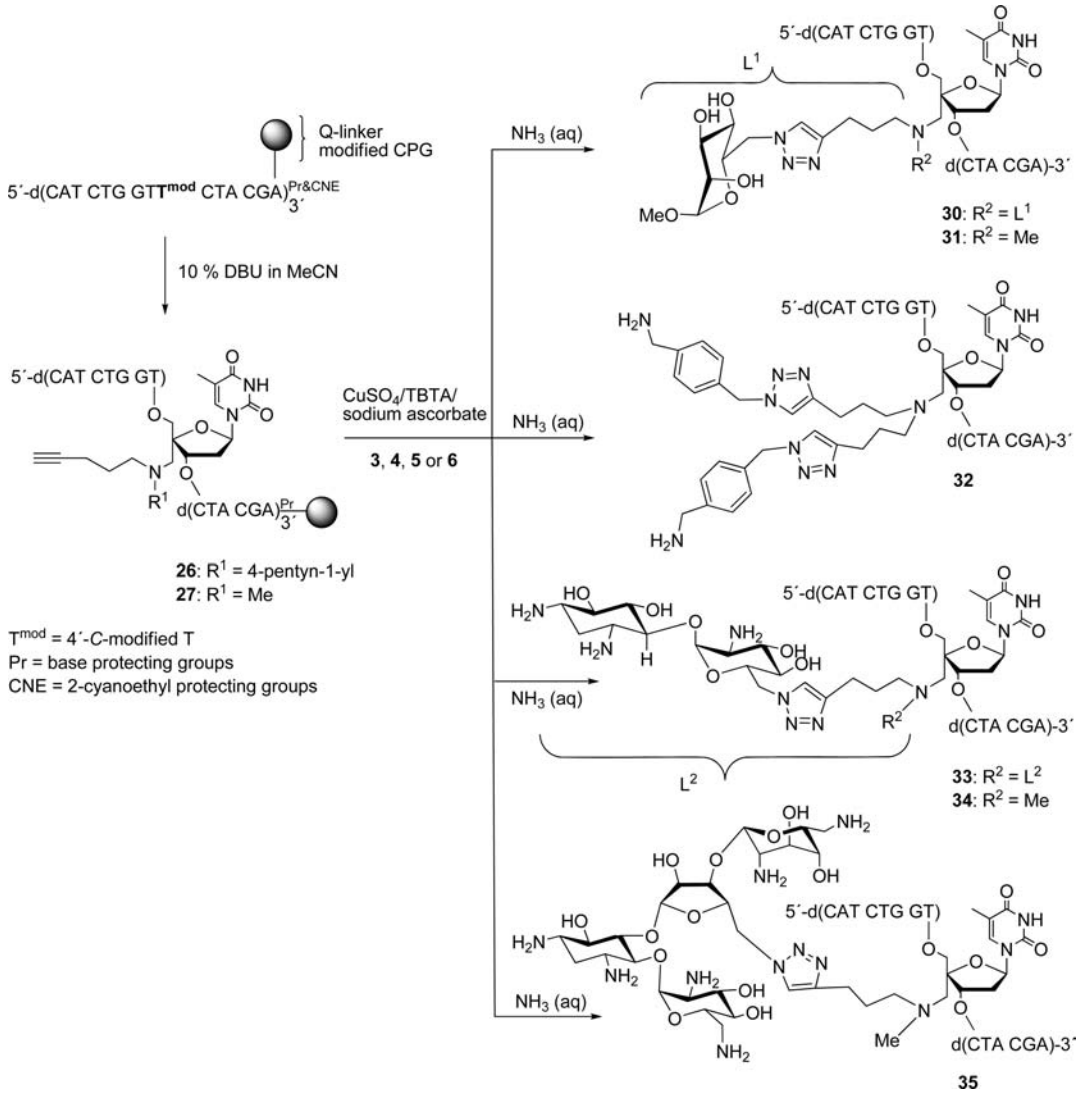


Table 1. Melting Experiments of the Oligonucleotide Conjugates and Their Complementary DNA or 2′-*O*-Methyl-RNA Sequences[a]

	compl. DNA T_m/°C and (Δ T_m/°C)		compl. 2′-*O*-methyl RNA T_m/°C and (Δ T_m/°C)	
	0.1 mol L^{-1} NaCl	1.0 mol L^{-1} NaCl	0.1 mol L^{-1} NaCl	1.0 mol L^{-1} NaCl
5′-CAT CTG GTT CTA CGA	52.8	61.9	54.1	65.0
5′-CAT CTG GT**B**CTA CGA (**26**)	54.5 (+1.7)	61.3 (−0.6)	54.7 (+0.6)	65.1 (+0.1)
5′-CAT C**B**G GTT C**B**A CGA (**28**)	52.5 (−0.3)	59.7 (−2.2)	53.0 (−1.1)	65.4 (+0.4)
5′-CAT CTG GT**D** CTA CGA (**27**)	54.6 (+1.8)	62.5 (+0.6)	55.7 (+1.6)	66.4 (+1.4)
5′-CAT C**D**G GTT C**D**A CGA (**29**)	53.5 (+0.7)	61.6 (−0.3)	52.4 (−1.7)	64.7 (−0.3)
5′-CAT CTG GT**E** CTA CGA (**30**)	53.8 (+1.0)	62.1 (+0.2)	54.3 (+0.2)	65.5 (+0.5)
5′- CAT C**E**G GTT C**E**A CGA (**36**)	51.3 (−1.5)	59.6 (−2.3)	53.8 (−0.3)	66.1 (+1.1)
5′-CAT CTG GT**F** CTA CGA (**31**)	54.6 (+1.8)	62.2 (+0.3)	54.6 (+0.5)	65.3 (+0.3)
5′-CAT CTG GT**H** CTA CGA (**32**)	57.9 (+5.1)	63.7 (+1.8)	54.2 (+0.1)	64.3 (−0.7)
5′-CAT C**H**G GTT C**H**A CGA (**37**)	62.0 (+9.2)	66.6 (+4.7)	56.7 (+2.6)	66.5 (+1.5)
5′- CAT C**I**G GTT C**I**A CGA (**38**)	61.0 (+8.2)	66.5 (+4.6)	57.3 (+3.2)	67.1 (+2.1)
5′- CAT CTG GT**J** CTA CGA (**33**)	57.9 (+5.1)	62.2 (+0.3)	53.2 (−0.9)	64.8(−0.2)
5′-CAT CTG GT**K** CTA CGA (**34**)	57.8 (+5.0)	63.5 (+1.6)	54.1 (±0.0)	65.1 (+0.1)
5′- CAT C**K**G GTT C**K**A CGA (**39**)	58.2 (+5.4)	62.8 (+0.9)	55.1 (+1.0)	65.2 (+0.2)
5′-CAT CTG GT**L** CTA CGA (**35**)	56.1 (+3.3)	62.1 (+0.2)	52.5 (−1.6)	64.2 (−0.8)

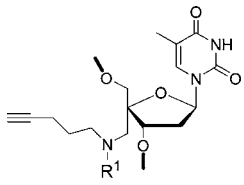
[a] In 10 mmol L^{-1} potassium phosphate buffer (pH 7) containing 0.1 mol L^{-1} or 1.0 mol L^{-1} NaCl. The oligonucleotide conjugates and their cDNA or 2′-*O*-methyl RNA targets were used a concentration of 2 μmol L^{-1}.

jugation as long as their phosphate groups were 2-cyanoethyl protected, but a chain cleavage took place leaving the modified monomer attached to the 5′-terminus of the support-bound oligonucleotide. By contrast, the 4-pentyn-1-yl functionalized oligonucleotides that had not been subjected to the conditions of click reaction could be isolated in intact form by conventional ammonolysis. To carry out the click reaction on a solid support, the 2-cyanoethyl groups had to be removed prior to the click reaction, which was achieved by treatment with 10% DBU in MeCN (5−8 min). Since the

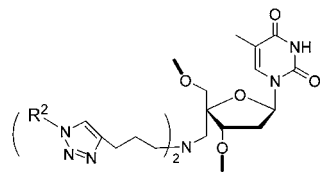
succinyl linker is not fully compatible with the DBU treatment, but undergoes a premature cleavage via succinimide formation (*54*), all the conjugate syntheses were carried out on a Q-linker loaded CPG support (*55*). After exposure of the internucleosidic linkages as phosphodiesters, the azido-functionalized ligands **3**−**6** were attached by the click reaction ($CuSO_4$/TBTA/sodium ascorbate, 5 h, r.t) and the conjugates obtained were released from the support and deprotected by ammonolysis (Scheme 3). The crude products (**30**−**39**; see Table 1) were purified by RP-HPLC, and their identity was verified by ESI-MS. Figure 2 shows representative examples of the HPLC traces of the crude oligonucleotides **35**, **36**, and **39** and the homogeneous products after purification. In each case, the desired conjugate was clearly a main product.

In our previous study on oligonucleotides containing the 4′-*C*-azidomethylthymidine monomer, we were not able to achieve homogeneous products by the solid-supported click conjugation in case the ligand contained amino groups in their structure, but capillary electrophoresis revealed the presence of two peaks with the same molecular mass. When the reactions were performed in solution, this problem was not encountered. With 4′-*C*-[*N*,*N*-di(4-pentyn-1-yl)aminomethyl]thymidine and 4′-*C*-[*N*-methyl-*N*-(4-pentyn-1-yl)aminomethyl]thymidine monomers (**1**, **2**) used in the present study, capillary electrophoretic, HPLC, and ESI-MS data all indicated the presence of only one pure conjugate for each oligonucleotide. Accordingly, all conjugations could now be conveniently made on a solid support without complications.

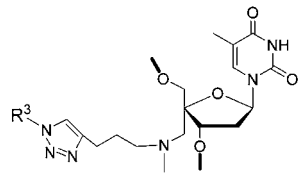
Melting Temperature Studies. Melting temperatures (T_m) for the duplexes of oligonucleotides **26**−**29** and their conjugates **30**−**39** with the cDNA and 2′-*O*-methyl RNA sequences were measured at pH 7 at the ionic strength of 0.1 and 1.0 mol L^{-1} (Table 1).



B: R^1 = 4-pentyn-1-yl
D: R^1 = Me



E: R^2 = mannose (deprotected **3**)
H: R^2 = *p*-aminomethylbenzene (deprotected **4**)
J: R^2 = paromamine (deprotected **5**)



F: R^3 = mannose (deprotected **3**)
I: R^3 = *p*-aminomethylbenzene (deprotected **4**)
K: R^3 = paromamine (deprotected **5**)
L: R^3 = neomycin (deprotected **6**)

When one 4′-*C*-modified monomer, **B** (**26**) or **D** (**27**), was incorporated into the DNA strand, the stability of the duplex increased with both DNA and 2′-*O*-Me RNA. When two such monomers were incorporated in the sequence (**28**, **29**), a slight destabilization took place.

With mannose-conjugated oligonucleotides containing a single modified monomer, either **E** (**30**) or **F** (**31**), the T_m of the DNA-hybrid was again increased, but the presence of two modified units (**36**) is destabilizing. By contrast, on using a 2′-*O*-methyl RNA target, the conjugate containing two **E** monomers and, hence, four mannose residues hybridized almost as well as the corresponding unmodified 15-mer oligodeoxyribonucleotide. At high salt concentration, the hybridization was even slightly more efficient compared to the unmodified DNA sequence.

All conjugates bearing amino groups (**32**−**35**, **37**−**39**) markedly stabilized the duplex with DNA target. With the *p*-aminomethylbenzene conjugates, the DNA-hybrids incorporating one or two **H** (**32**, **37**) or **I** (**38**) monomers were stabilized by 4−5 °C/modification. Toward 2′-*O*-methyl RNA, the stabilization was less prominent. The stabilization was more marked at low ionic strength, but it still existed at high ionic strength. Undoubtedly, the major part of the stabilization results from reduced electrostatic repulsion between negatively charged sugar−phosphate backbones and positively charged amino groups present at neutral pH. This influence plays a more important role at low ionic strength.

When one paromamine derived monomer, **J** (**33**) or **K** (**34**) was incorporated into the strand, the DNA-hybrid was stabilized by 5 °C, but the second monomer (**39**) did not result in any extra stabilization. With 2′-*O*-Me RNA target, two monomers **K** were needed to achieve even a modest increase in T_m (ΔT_m = +1.0 °C). Compared to the paromamine monomers, the neomycin group (monomer **L** in **35**) was less stabilizing than the paromamine group (monomer **K** in **34**) toward DNA, and toward 2′-*O*-Me-RNA, the effect is even destabilizing. Similarly to the *p*-aminomethylphenyl ligands, the duplex stabilizing effect of the aminoglycosides ligands is more marked at low ionic strength.

The hybridization properties of the 4′-modified oligonucleotides are encouraging. Evidently the 4′-position, facing the minor groove upon hybridization, can accommodate even rather large molecule clusters without appreciable destabilization of the duplex. The 4′-*C*-[*N*,*N*-di(4-pentyn-1-yl)aminomethyl]thymidine monomer (**1**) allows attachment of two ligands per residue, which may well be useful when applying the glycotargeting concept. A short segment of the duplex may be decorated with several sugar units. The results received with the mannose conjugated oligonucleotide, **36**, lend some support to the feasibility of sugar-coated oligonucleotides as carriers of RNA-type oligonucleotides. On the other hand, 4′-*C*-[*N*-methyl-*N*-(4-pentyn-1-yl)aminomethyl]thymidine monomer (**2**) can be preferable for attachment of bulky ligands such as neomycin derivatives to oligonucleotides. Among the amino group-bearing ligands, the most remarkable hybridization enhancement was obtained with *p*-aminomethylphenyl conjugates (**32**, **37**, **38**). Sterically more demanding aminoglycoside ligands (**33**−**35**, **39**) stabilized the DNA·DNA duplex less, but still notably. All amino group-bearing conjugates preferred DNA over 2′-OMe RNA. Compared to the results of the present paper, the previously observed duplex stabilizations achieved with some conjugates of the 4′-*C*-azidomethylthymidine incorporating oligonucleotides are modest (*47*). This implies that the alkyl chain of the 4′-*C*-(4-pentyn-1-ylaminomethyl)thymidine monomers (**1**, **2**) allows a more flexible alignment of the triazole ring and conjugate groups upon hybridization. The tertiary amino group, which probably is protonated under physiological conditions, further stabilizes the duplex formation by diminishing the electrostatic repulsion between the complementary chains, as evidenced by the fact that the melting temperatures observed for the oligonucleotides containing 4′-*C*-(alkynylaminomethyl)thymidine units (**26**−**29**) are higher than those observed for their 4′-*C*-azidomethylthymidine counterparts.

CONCLUSION

4′-*C*-[*N*,*N*-Di(4-pentyn-1-yl)aminomethyl]thymidine and 4′-*C*-[*N*-methyl-*N*-(4-pentyn-1-yl)aminomethyl]thymidine 3′-phos-

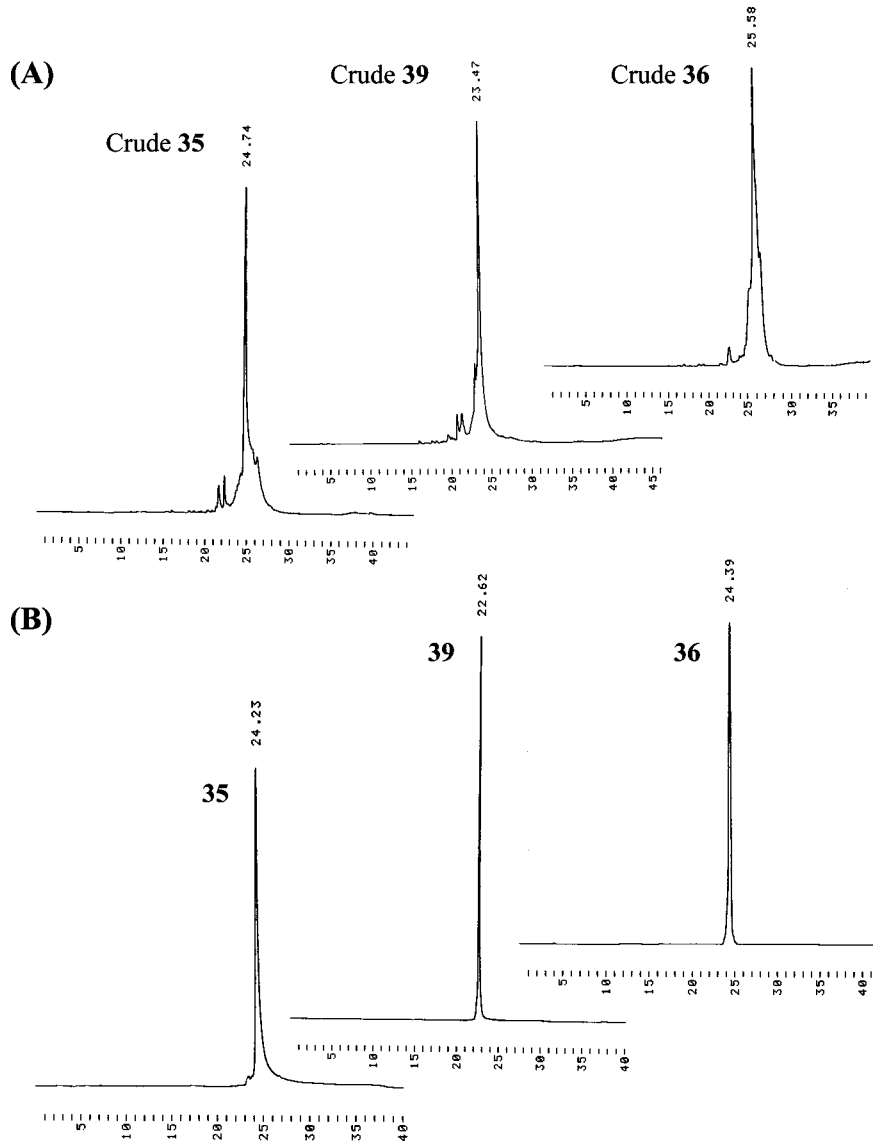


Figure 2. RP HPLC traces of the crude (A) and purified (B) oligonucleotide conjugates **35**, **36**, and **39**.

phoramidites (**1**, **2**) have been synthesized as a continuation of the previously reported preparation of 4′-*C*-azidomethylthymidine 3′-hydrogenphosphonate. Together, these building blocks enable the exploitation of the click conjugation on both ways, i.e., to have azido function present on either the oligonucleotide or ligand side. Nucleoside **1** bearing two 4-pentyn-1-yl groups is designed for high-density functionalization of modified oligonucleotides, whereas nucleoside **2** allows one-armed conjugations. Azido-derivatized ligands may be efficiently conjugated to the alkynyl groups of these monomers by the click chemistry on a solid support. However, the 2-cyanoethyl protections must be removed from the phosphates prior to the click conjugation, since the 4′-modifications used here under the click reaction conditions cause cleavage of the 5′-linked phosphate triester bond. Melting temperature studies reveal that oligonucleotides containing one to four mannose ligands in the central part of the chain (i.e., one or two modified nucleoside residue) form equally stable duplexes with complementary 2′-OMe RNA as the corresponding unmodified DNA sequence. At high salt content, the mannose conjugation is even stabilizing. The results with the space-demanding aminoglycoside ligands further demonstrate the utility of 4′-modified nucleosides **1** and **2** in glycoconjugations. All amino group-bearing conjugates stabilized the DNA·DNA duplex significantly and the DNA·2′-*O*-methyl RNA duplex notably.

ACKNOWLEDGMENT

Financial support from the Academy of Finland is gratefully acknowledged.

Supporting Information Available: NMR spectral data for **1**, **2**, **4**−**6**, **12**, and **13**. ESI-MS and RP HPLC data for oligonucleotides **26**−**39**. In addition, examples of melting temperature curves for **26**−**39** are presented. This material is available free of charge via the Internet at http://pubs.acs.org.

LITERATURE CITED

(1) Jeong, J. H., Mok, H., Oh, Y.-K., and Park, T. G. (2009) siRNA conjugate delivery systems. *Bioconjugate Chem. 20*, 5–14.
(2) Kurreck, J. (2009) RNA interference: from basic research to therapeutic applications. *Angew. Chem., Int. Ed. 48*, 1378–1398.
(3) Castanotto, D., and Rossi, J. J. (2009) The promises and pitfalls of RNA-interference-based therapeutics. *Nature 457*, 426–433.
(4) Grosshans, H., and Filipowicz, W. (2008) Molecular biology: The expanding world of small RNAs. *Nature 451*, 414–416.

(5) Corey, D. R. (2007) RNA learns from antisense. *Nat. Chem. Biol. 3*, 8–11.
(6) Kim, D. H., and Rossi, J. J. (2007) Strategies for silencing human disease using RNA interference. *Nat. Rev. Genetics 8*, 173–184.
(7) de Fougerolles, A., Vornlocher, H.-P., Maraganore, J., and Lieberman, J. (2007) Interfering with disease: a progress report on siRNA-based therapeutics. *Nat. Rev. Drug Discovery 6*, 443–453.
(8) Yan, H., and Tram, K. (2007) Glycotargeting to improve cellular delivery efficiency of nucleic acids. *Glycoconj. J. 24*, 107–123.
(9) Wilson, C., and Keefe, A. D. (2006) Building oligonucleotide therapeutics using non-natural chemistries. *Curr. Opin. Chem. Biol. 10*, 607–614.
(10) Sasaki, S., and Nagatsuki, F. (2006) Application of unnatural oligonucleotides to chemical modification of gene expression. *Curr. Opin. Chem. Biol. 10*, 615–621.
(11) Bumcrot, D., Manoharan, M., Koteliansky, V., and Sah, D. W. Y. (2006) RNAi therapeutics: a potential new class of pharmaceutical drugs. *Nat. Chem. Biol. 2*, 711–719.
(12) Dykxhoorn, D. M., Palliser, D., and Lieberman, J. (2006) The silent treatment: siRNAs as small molecule drugs. *Gene Ther. 13*, 541–552.
(13) Leung, R. K. M., and Whittaker, P. A. (2005) RNA interference: from gene silencing to gene-specific therapeutics. *Pharm. Ther. 107*, 222–239.
(14) Aboul-Fadl, T. (2005) Antisense oligonucleotides: The state of the art. *Curr. Med. Chem. 12*, 2193–2214.
(15) Manoharan, M. (2002) Oligonucleotide conjugates as potential antisense drugs with improved uptake, biodistribution, targeted delivery, and mechanism of action. *Antisense Nucleic Acids Drug Dev. 12*, 103–108.
(16) Ku, K., Duan, Q.-P., Ma, L., and Zhao, D.-X. (2010) Chemical strategies for the synthesis of peptide-oligonucleotide conjugates. *Bioconjugate Chem. 21*, 187–202.
(17) Singh, Y., Murat, P., and Defrancq, E. (2010) Recent developments in oligonucleotide conjugation. *Chem. Soc. Rev 39*, 2054–2070.
(18) Lönnberg, H. (2009) Solid-phase synthesis of oligonucleotide conjugates useful for delivery and targeting of potential nucleic acid therapeutics. *Bioconjugate Chem. 20*, 1065–1094.
(19) Eritja, R. (2007) Solid-phase synthesis of modified oligonucleotides. *Int. J. Pept. Res. Therapeut. 13*, 53–68.
(20) Venkatesan, N., and Kim, B. H. (2006) Peptide conjugates of oligonucleotides: synthesis and applications. *Chem. Rev. 106*, 3712–3761.
(21) Zatsepin, T. S., and Oretskaya, T. S. (2004) Synthesis and applications of oligonucleotide-carbohydrate conjugates. *Chem. Biodivers. 1*, 1401–1416.
(22) Bucior, I., and Burger, M. M. (2004) Carbohydrate-carbohydrate interaction as a major force initiating cell-cell recognition. *Glycoconj. J. 21*, 111–123.
(23) Hakomori, S. (2004) Carbohydrate-to-carbohydrate interaction, through glycosynapse, as a basis of cell recognition and membrane organization. *Glycoconj. J. 21*, 125–137.
(24) Ernst, B., and Magnani, J. L. (2009) From carbohydrate leads to glycomimetic drugs. *Nat. Rev. Drug Discovery 8*, 661–677.
(25) Gabius, H.-J., Siebert, H.-C., André, S., Jiménez-Barbero, J., and Rüdiger, H. (2004) Chemical biology of the sugar code. *ChemBioChem 5*, 740–764.
(26) Dwek, R. A. (1996) Glycobiology: Toward understanding the function of sugars. *Chem. Rev. 96*, 683–720.
(27) Dam, T. K., and Brewer, C. F. (2010) Multivalent lectin-carbohydrate interactions: energetics and mechanisms of binding. *Adv. Carbohydr. Chem. Biochem. 63*, 139–164.
(28) Kiessling, L. L., Gestwicki, J. E., and Strong, L. E. (2006) Synthetic multivalent ligands as probes of signal transduction. *Angew. Chem., Int. Ed. 45*, 2348–2368.
(29) Ambrosi, M., Cameron, N. R., and Davis, B. G. (2005) Lectins: tools for the molecular understanding of the glycocode. *Org. Biomol. Chem. 3*, 1593–1608.
(30) Lundquist, J. J., and Toone, E. J. (2002) The cluster glycoside effect. *Chem. Rev. 102*, 555–578.
(31) Karskela, M., Helkearo, M., Virta, P., and Lönnberg, H. (2010) Synthesis of oligonucleotide glycoconjugates using sequential click and oximation ligations. *Bioconjugate Chem. 21*, 748–755.
(32) Pourceau, G., Meyer, A., Vasseur, J.-J., and Morvan, F. (2009) Synthesis of mannose and galactose oligonucleotide conjugates by bi-click chemistry. *J. Org. Chem. 74*, 1218–1222.
(33) Moni, L., Pourceau, G., Zhang, J., Meyer, A., Vidal, S., Souteyrand, E., Dondoni, A., Morvan, F., Chevolot, Y., Vasseur, J.-J., and Marra, A. (2009) Design of triazole-tethered glycoclusters exhibiting three different spatial arrangements and comparative study of their affinities towards PA-IL and RCA 120 by using a DNA-based glycoarray. *ChemBioChem 10*, 1369–1378.
(34) Bouillon, C., Meyer, A., Vidal, S., Jochum, A., Chevolot, Y., Cloarec, J.-P., Praly, J.-P., Vasseur, J.-J., and Morvan, F. (2006) Microwave assisted "click" chemistry for the synthesis of multiple labeled-carbohydrate oligonucleotides on solid support. *J. Org. Chem. 71*, 4700–4702.
(35) Singh, Y., Renaudet, O., Defrancq, E., and Dumy, P. (2005) Preparation of a multitopic glycopeptide-oligonucleotide conjugate. *Org. Lett. 7*, 1359–1362.
(36) Dubber, M., and Frechet, J. M. J. (2003) Solid-phase synthesis of multivalent glycoconjugates on a DNA synthesizer. *Bioconjugate Chem. 14*, 239–246.
(37) Matsuura, K., Hibino, M., Ikeda, T., Yamada, Y., and Kobayashi, K. (2004) Self-organized glycoclusters along DNA: Effect of the spatial arrangement of galactoside residues on cooperative lectin recognition. *Chem.—Eur. J. 10*, 352–359.
(38) Turner, J. J., Meeuwenoord, N. J., Rood, A., Borst, P., van der Marel, G. A., and van Boom, J. H. (2003) Reinvestigation into the synthesis of oligonucleotides containing 5(β-D-glucopyranosyloxymethyl)-2′-deoxyuridine. *Eur. J. Org. Chem.* 3832–3839.
(39) Matsuura, K., Hibino, M., Yamada, Y., and Kobayashi, K. (2001) Construction of glycol-clusters by self-organization of site-specifically glycosylated oligonucleotides and their cooperative amplification of lectin recognition. *J. Am. Chem. Soc. 123*, 357–358.
(40) Tona, R., Bertolini, R., and Hunziker, J. (2000) Synthesis of aminoglycoside-modified oligonucleotides. *Org. Lett. 2*, 1693–1696.
(41) Hunzinker, J. (1999) Synthesis of 5-(2-amino-2-deoxy-β-D-glucopyranosyloxymethyl)-2′-deoxyuridine and its incorporation into oligothymidylates. *Bioorg. Med. Chem. Lett. 9*, 201–204.
(42) Karskela, M., Virta, P., Malinen, M., Urtti, A., and Lönnberg, H. (2008) Synthesis and cellular uptake of fluorescently labeled multivalent hyaluronan disaccharide conjugates of oligonucleotide phosphorothioates. *Bioconjugate Chem. 19*, 2549–2558.
(43) Katajisto, J., Heinonen, P., and Lönnberg, H. (2004) Solid-phase synthesis of oligonucleotide glycoconjugates bearing three different glycosyl groups: orthogonally protected bis(hydroxymethyl)-*N*, *N*′-bis(3-hydroxypropyl)malondiamide phosphoramidite as key building block. *J. Org. Chem. 69*, 7609–7615.
(44) Katajisto, J., Virta, P., and Lönnberg, H. (2004) Solid-phase synthesis of multiantennary oligonucleotide glycoconjugates utilizing on-support oximation. *Bioconjugate Chem. 15*, 890–896.
(45) Rostovtsev, V. V., Green, L. G., Fokin, V. V., and Sharpless, K. B. (2002) A stepwise Huisgen cycloaddition process: Copper(I)-catalyzed regioselective "ligation" of azides and terminal alkynes. *Angew. Chem., Int. Ed. 41*, 2596–2599.
(46) Tornoe, C. W., Christensen, C., and Meldal, M. (2002) Peptidotriazoles on solid phase: [1,2,3]-triazoles by regiospecific copper(I)-catalyzed 1,3-dipolar cycloadditions of terminal alkynes to azides. *J. Org. Chem. 67*, 3057–3064.

(47) Kiviniemi, A., Virta, P., and Lönnberg, H. (2008) Utilization of intrachain 4′-*C*-azidomethylthymidine for preparation of oligonucleotide conjugates by click chemistry in solution and on a solid support. *Bioconjugate Chem. 19*, 1726−1734.

(48) Gierlich, J., Burley, G. A., Gramlich, P. M. E., Hammond, D. M., and Carell, T. (2006) Click chemistry as a reliable method for the high-density postsynthetic functionalization of alkyne-modified DNA. *Org. Lett. 8*, 3639–3642.

(49) Sirivolu, V. R., Chittepu, P., and Seela, F. (2008) DNA with branched internal side chains: Synthesis of 5-tripropargylamine-dU and conjugation by an azide-alkyne double click reaction. *ChemBioChem 9*, 2305–2316.

(50) Alper, P. B., Hung, S.-C., and Wong, C.-H. (1996) Metal catalyzed diazo transfer. *Tetrahedron Lett. 37*, 6029−6032.

(51) Simonsen, K. B., Ayida, B. K., Vourloumis, D., Takahashi, M., Winters, G. C., Barluenga, S., Qamar, S., Shandrick, S., Zhao, Q., and Hermann, T. (2002) Novel paromamine derivatives exploring shallow-groove recognition of ribosomal- decoding-site RNA. *ChemBioChem 3*, 1223–1228.

(52) Subramaniam, C. S., Thomas, P. J., Mamdapur, V. R., and Chadha, M. S. (1979) Simple syntheses of dihydrojasmone and *cis*-jasmone *via* 1,4-diketones. *J. Chem. Soc., Perkin Trans. 1*, 2346–2348.

(53) Ito, Y., Okuda, T. (1967) 6-Amino-6-deoxy-D-mannose, Jpn. Tokkyo Koho/JP patent 42008003 19670331.

(54) Brown, T., Pritchard, C. E., Turner, G., and Salisbury, S. A. (1989) A new base-stable linker for solid-phase oligonucleotide synthesis. *J. Chem. Soc., Chem. Commun.* 891–893.

(55) Pon, R. T., and Yu, S. (1997) Hydroquinone-*O*,*O*′-diacetic acid ('Q-linker') as a replacement for succinyl and oxalyl linker arms in solid phase oligonucleotide synthesis. *Nucleic Acids Res. 25*, 3629–3635.

BC100268W

Solid-supported synthesis and click conjugation of 4´-*C*-alkyne functionalized oligodeoxyribonucleotides

Anu Kiviniemi, * Pasi Virta and Harri Lönnberg

Department of Chemistry, University of Turku, FIN-20014 Turku, Finland

SUPPORTING INFORMATION

Table of Contents

General procedures S2

Figure S1. ^{1}H and ^{13}C NMR ($CDCl_3$) spectrum of **12** S3

Figure S2. ^{1}H, ^{13}C and ^{31}P NMR (CD_3CN) spectrum of **1** S4-5

Figure S3. ^{1}H and ^{13}C NMR (CD_3CN) spectrum of **13** S6

Figure S4. ^{1}H, ^{13}C and ^{31}P NMR (CD_3CN) spectrum of **2** S7-8

Figure S5. ^{1}H and ^{13}C NMR ($CDCl_3$) spectrum of **4** S9

Figure S6. ^{1}H and ^{13}C NMR (CD_3CN + drop of CD_3OD) spectrum of **5** S10

Figure S7. ^{1}H and ^{13}C NMR (CD_3OD) spectrum of **6** S11

Figure S8. MS(ESI) spectrum and HPLC chromatograph of pure **26** S12

Figure S9. MS(ESI) spectrum and HPLC chromatograph of pure **27** S13

Figure S10. MS(ESI) spectrum and HPLC chromatograph of pure **28** S14

Figure S11. MS(ESI) spectrum and HPLC chromatograph of pure **29** S15

Figure S12. MS(ESI) spectrum and HPLC chromatograph of pure **30** S16

Figure S13. MS(ESI) spectrum and HPLC chromatograph of pure **31** S17

Figure S14. MS(ESI) spectrum and HPLC chromatograph of pure **32** S18

Figure S15. MS(ESI) spectrum and HPLC chromatograph of pure **33** S19

Figure S16. MS(ESI) spectrum and HPLC chromatograph of pure **34** S20

Figure S17. MS(ESI) spectrum and HPLC chromatograph of pure **35** S21

Figure S18. MS(ESI) spectrum and HPLC chromatograph of pure **36** S22

Figure S19. MS(ESI) spectrum and HPLC chromatograph of pure **37** S23

Figure S20. MS(ESI) spectrum and HPLC chromatograph of pure **38** S24

Figure S21. MS(ESI) spectrum and HPLC chromatograph of pure **39** S25

Figure S22. T_m curves of **26**-**29** with cDNA S26

Figure S23. T_m curve of **30**, **31** and **36** with 2´-*O*-methyl RNA S27
Figure S24. T_m curve of **32**, **37** and **38** with cDNA S28
Figure S25. T_m curve of **33**, **34** and **39** with cDNA S29
Figure S26. T_m curve of **35** with cDNA S29

General procedures

The NMR spectra of **1**, **2, 4-6, 12** and **13** were recorded at 500 MHz. The mass spectra of the oligonucleotides **26-39** were recorded by ESI ionization method. RP HPLC chromatographs of pure **26-39** were performed using Thermo ODS Hypersil C18 (250 × 4.6 mm, 5 μm) analytical column, a gradient elution from 0% to 50% MeCN in 0.1 mol L^{-1} TEAA (aq) buffer over 60 min, flow rate 1 mL min^{-1} and detection at 260 nm. The melting curves (absorbance versus temperature) were measured at 260 nm on a Perkin-Elmer Lambda 35 UV-vis spectrometer equipped with a multiple cell holder and a Peltier temperature-controller. The temperature was changed at a rate of 0.5 ºC / min (from 20 to 90 ºC). The measurements were performed in 10 mmol L^{-1} potassium phosphate buffer (pH 7) containing 0.1 mol L^{-1} or 1.0 mol L^{-1} NaCl. The oligonucleotide conjugates and their complementary DNA or 2´-*O*-methyl RNA targets were used at a concentration of 2 μmol L^{-1}.

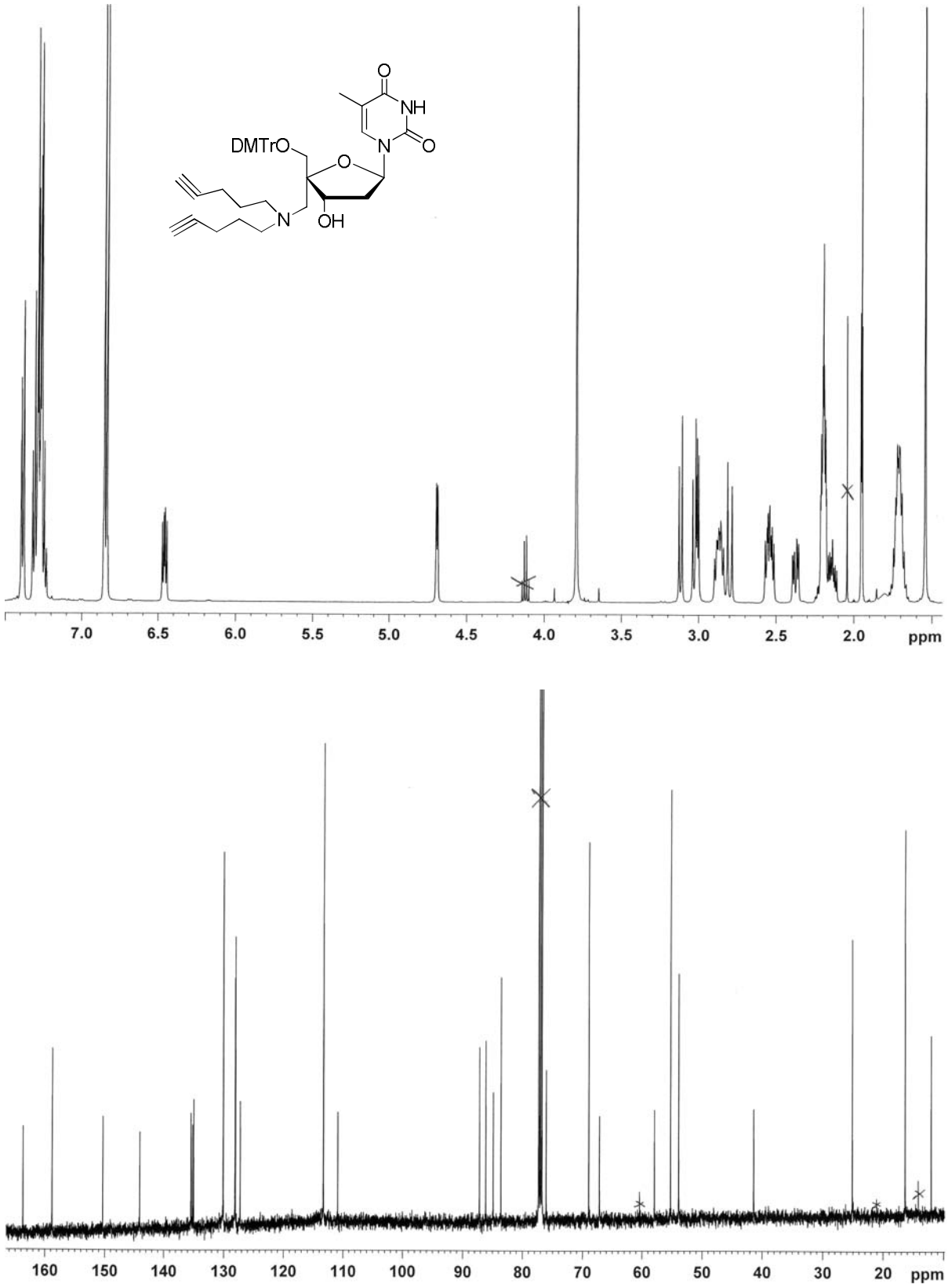
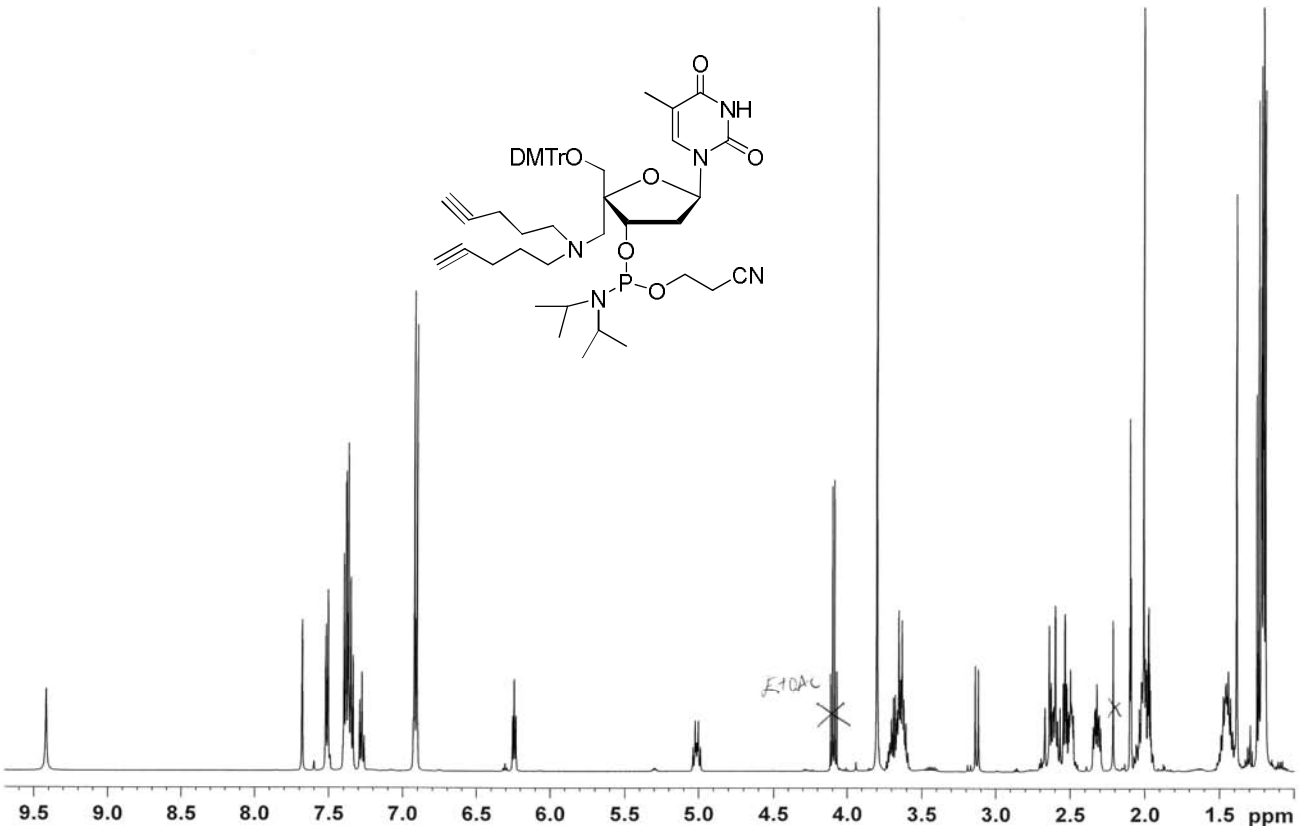
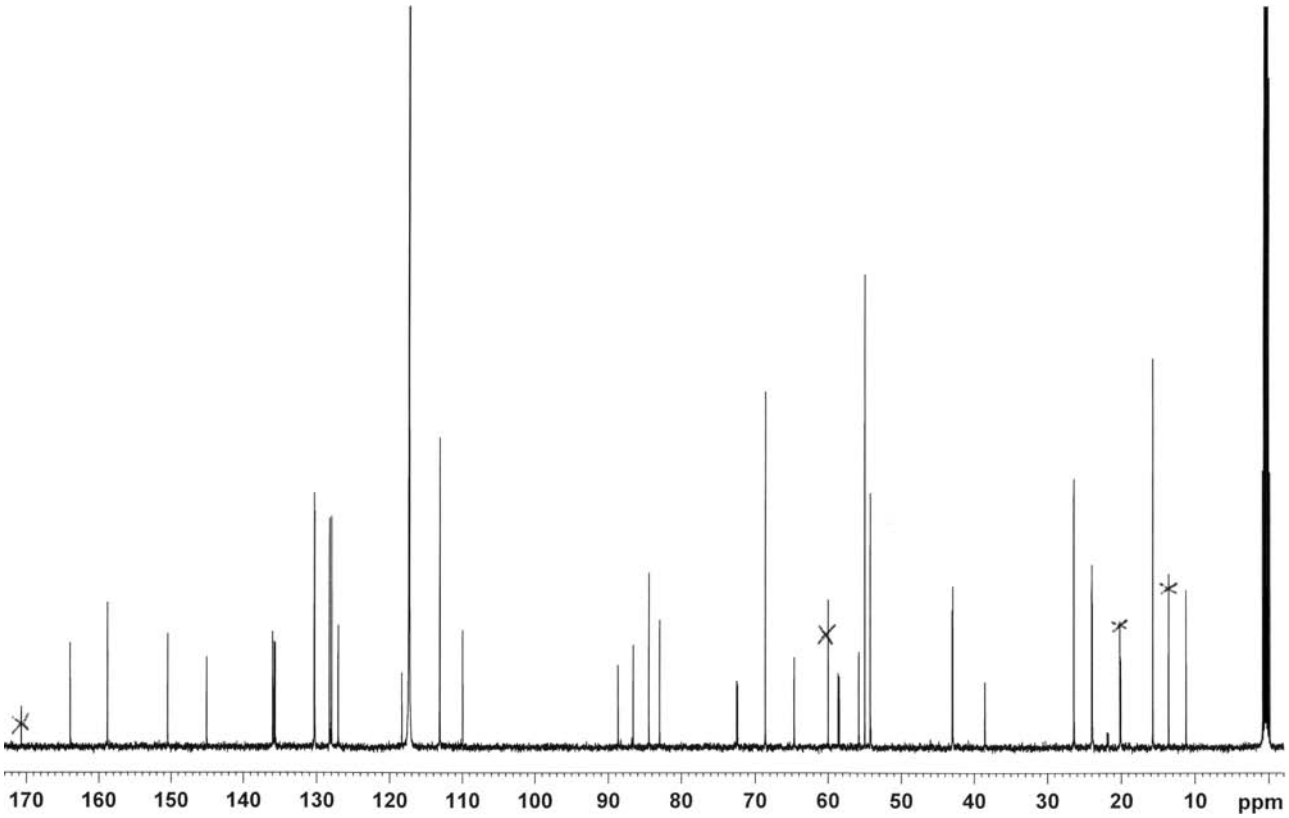


Figure S1. ^{1}H and ^{13}C NMR ($CDCl_3$) spectrum of **12**.


O
NH
DMTrO
O
N
O
N
O
P
O
CN
N
EtOAc
9.5 9.0 8.5 8.0 7.5 7.0 6.5 6.0 5.5 5.0 4.5 4.0 3.5 3.0 2.5 2.0 1.5 ppm


170 160 150 140 130 120 110 100 90 80 70 60 50 40 30 20 10 ppm

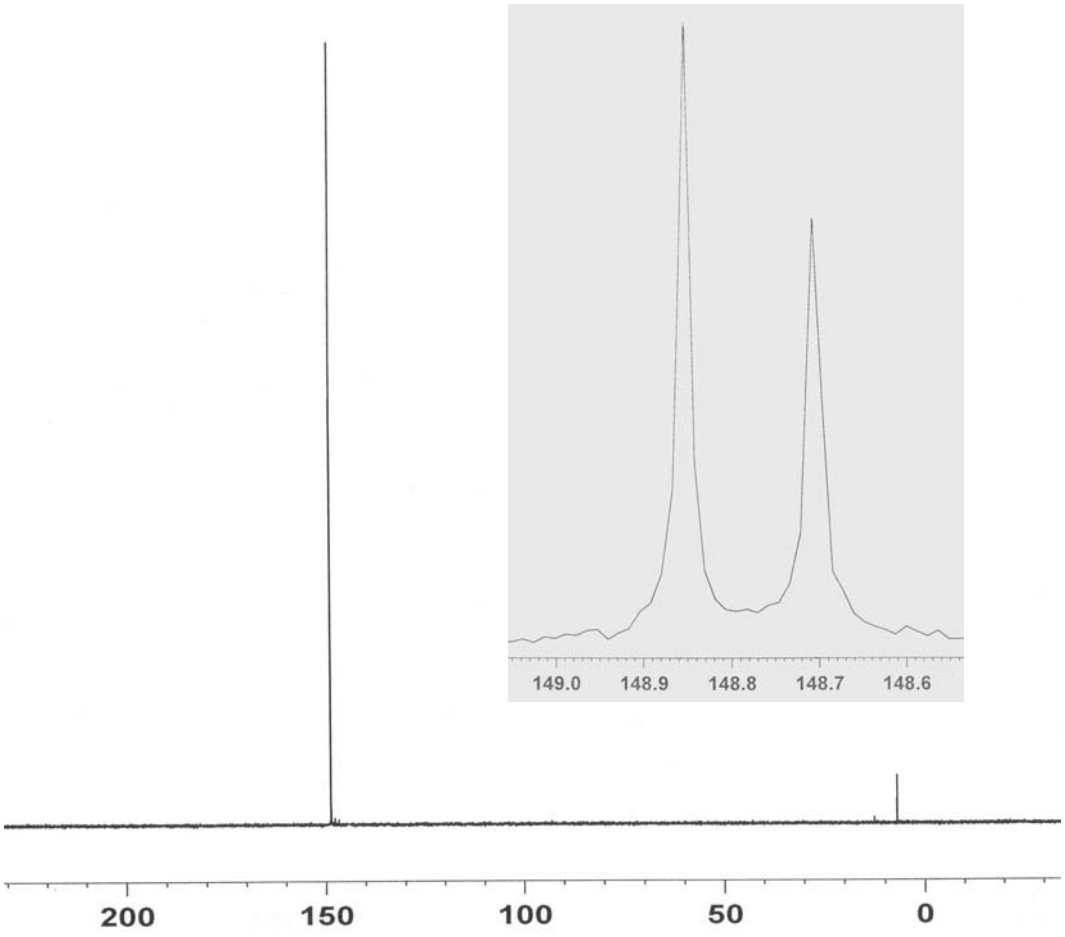


Figure S2. ^{1}H and ^{13}C NMR (CD_3CN) spectrum of compound **1** (diastereomer *I*) and ^{31}P NMR including both diastereomers.

During the purification of phosphoramidite, the diastereomer *I* was partly received as a pure compound (^{1}H and ^{13}C NMR spectrum above). Although the fraction containing the diastereomer *II*, included also some diast. *I*, the NMR data analysis was possible for both diastereomers individually.

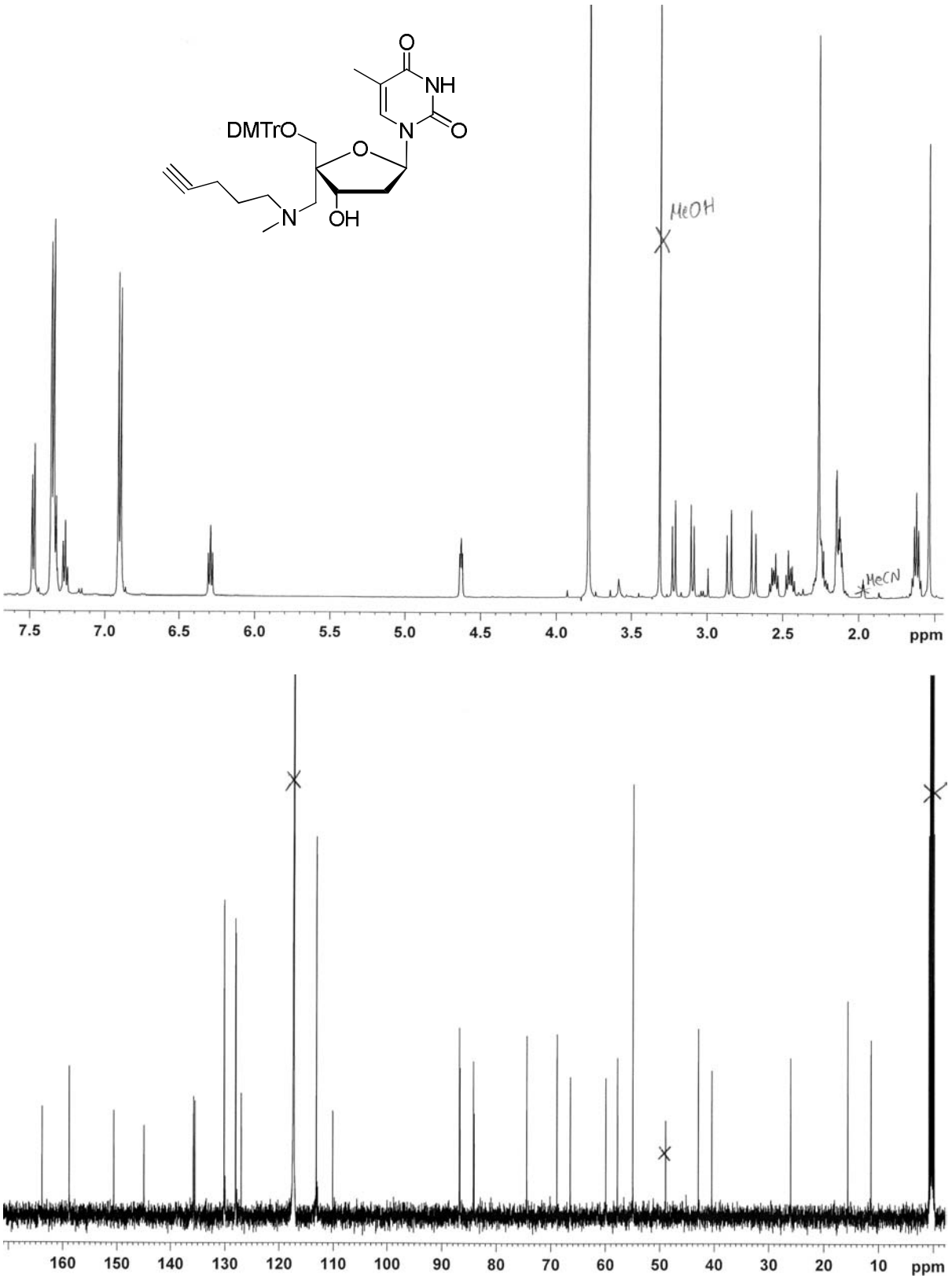
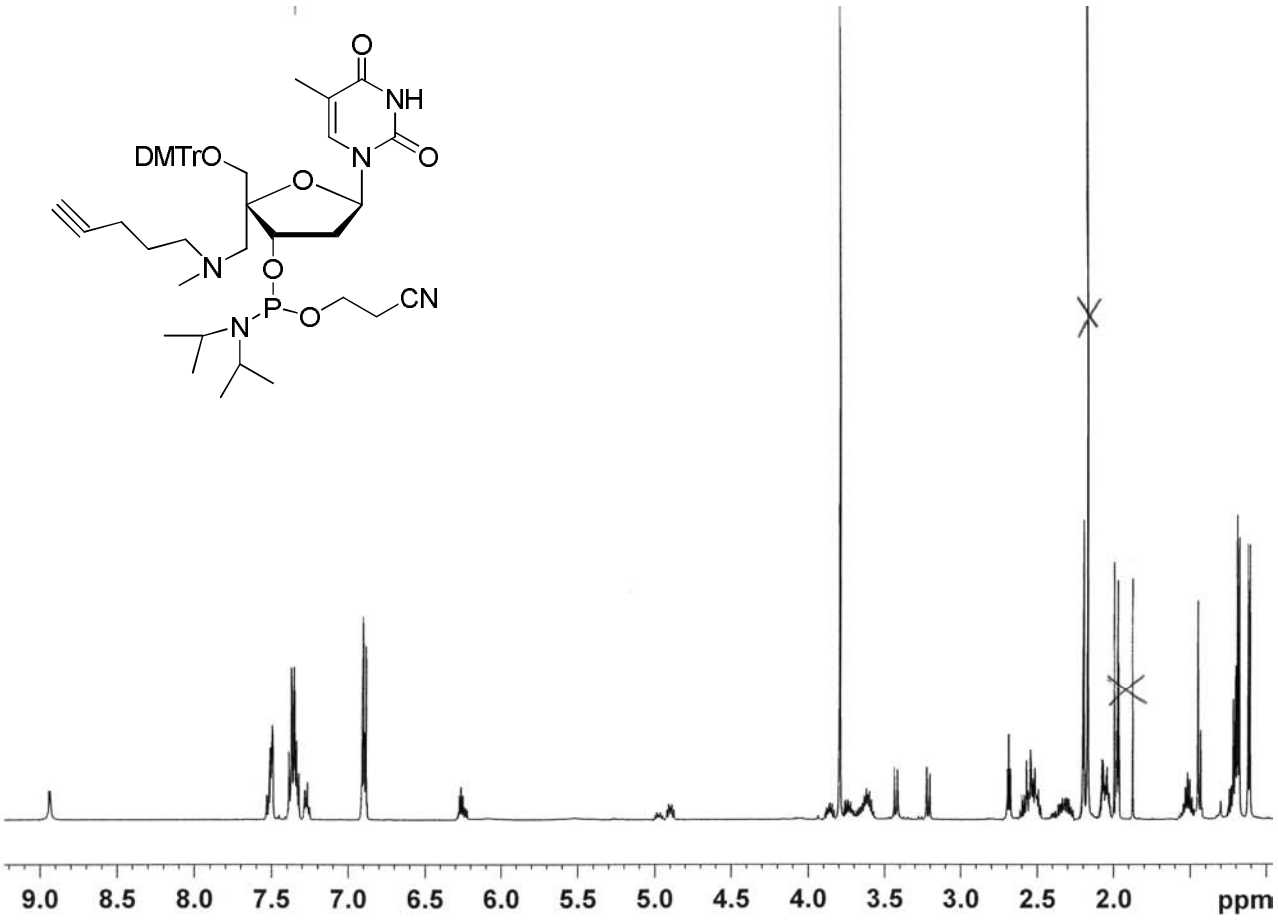
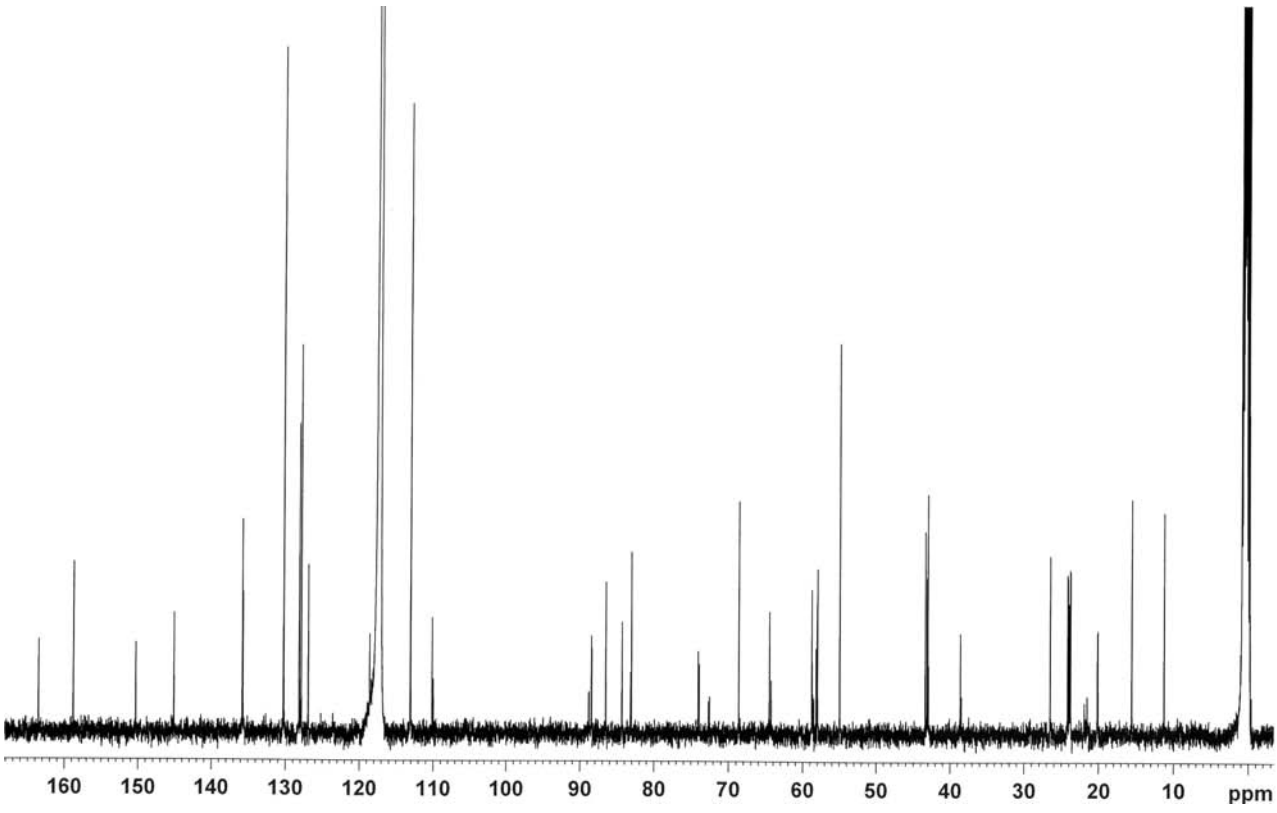


Figure S3. ^{1}H and ^{13}C NMR (CD_3CN) spectrum of **13**.


O
NH
DMTrO
N
O
O
N
O
P
O
CN
N
9.0
8.5
8.0
7.5
7.0
6.5
6.0
5.5
5.0
4.5
4.0
3.5
3.0
2.5
2.0
ppm


160
150
140
130
120
110
100
90
80
70
60
50
40
30
20
10
ppm

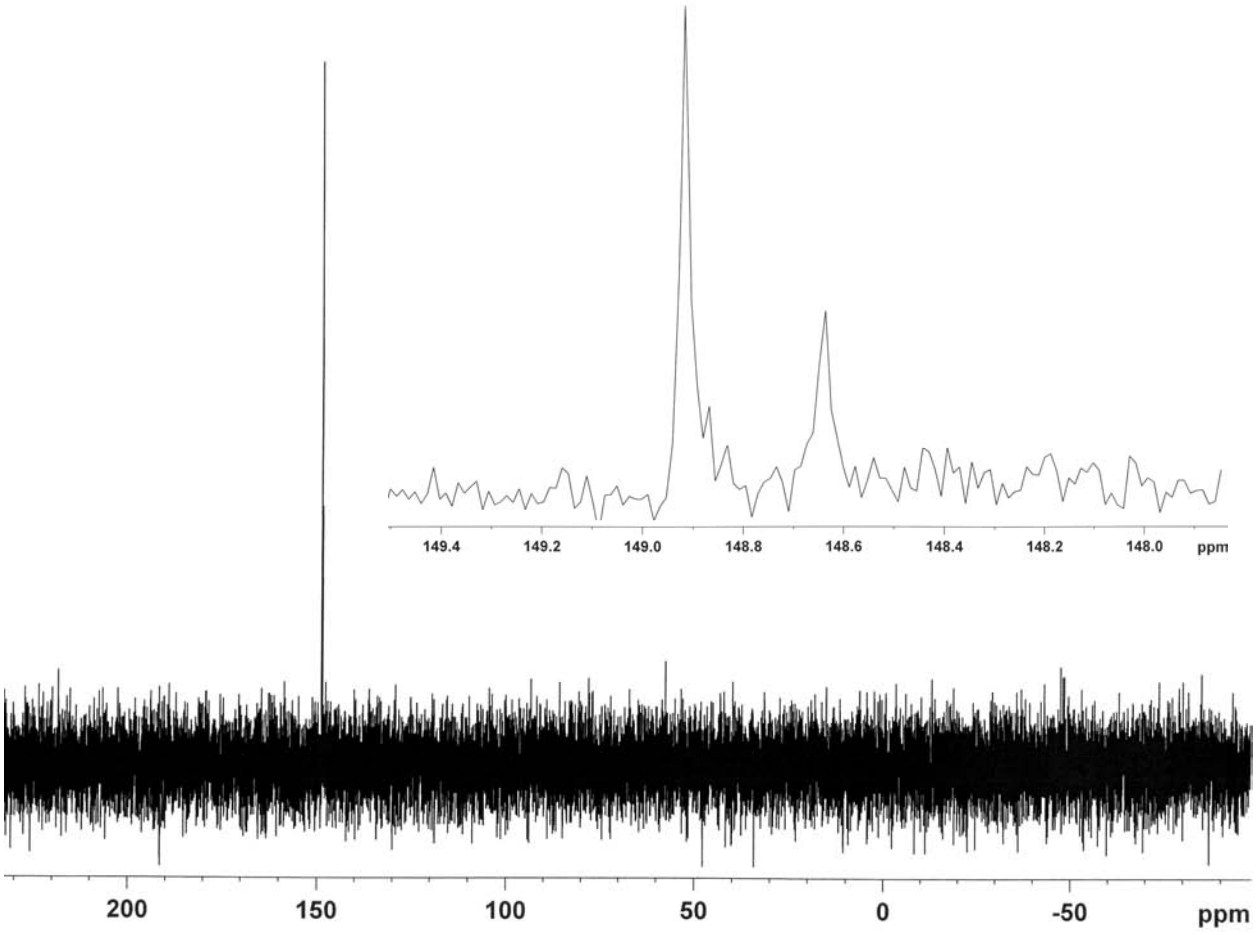


Figure S4. ^{1}H, ^{13}C and ^{31}P NMR (CD_3CN) spectrum of **2** including both diastereomers (in the NMR sample, the amount of diast. *II* is greater than diast. *I*).

During the purification of phosphoramidite, the diastereomer *I* was partly received as a pure compound. Although the fraction containing the diastereomer *II*, included also some diast. *I* (as represented in the example spectrum above), the NMR data analysis was possible for both diastereomers individually.

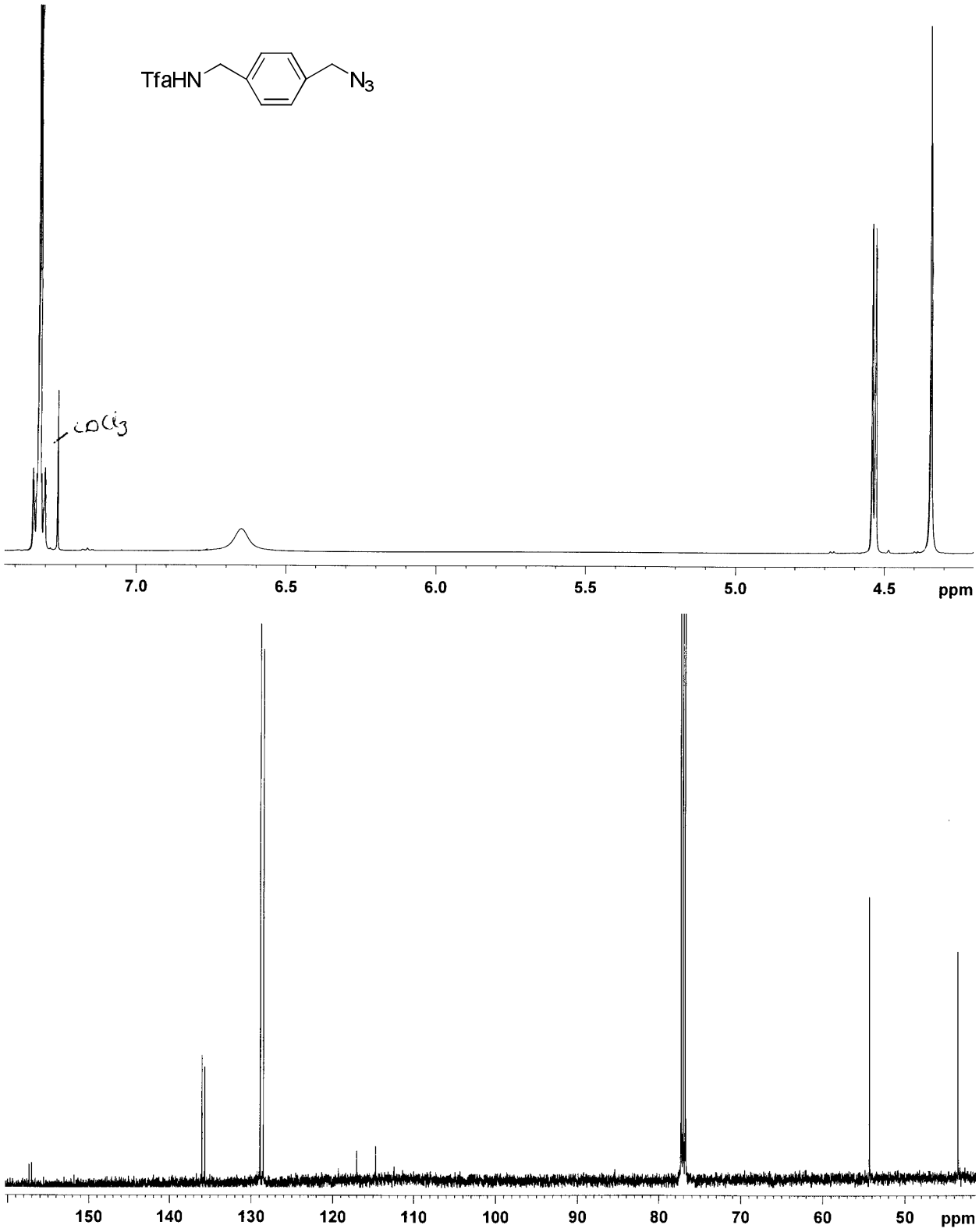


Figure S5. ^{1}H and ^{13}C NMR ($CDCl_3$) spectrum of **4**.

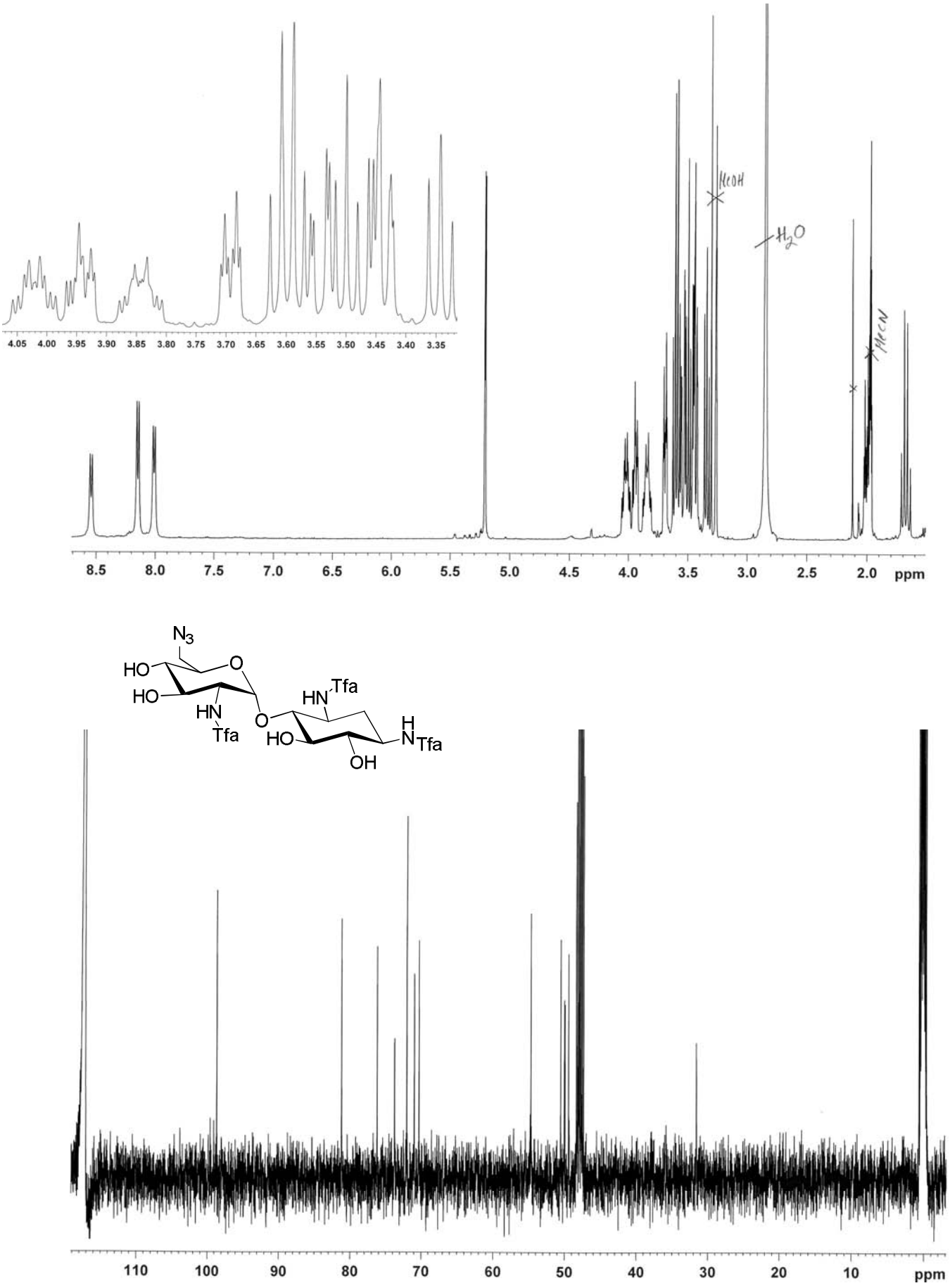


Figure S6. ^{1}H and ^{13}C NMR (CD_3CN + drop of CD_3OD) spectrum of **5**.

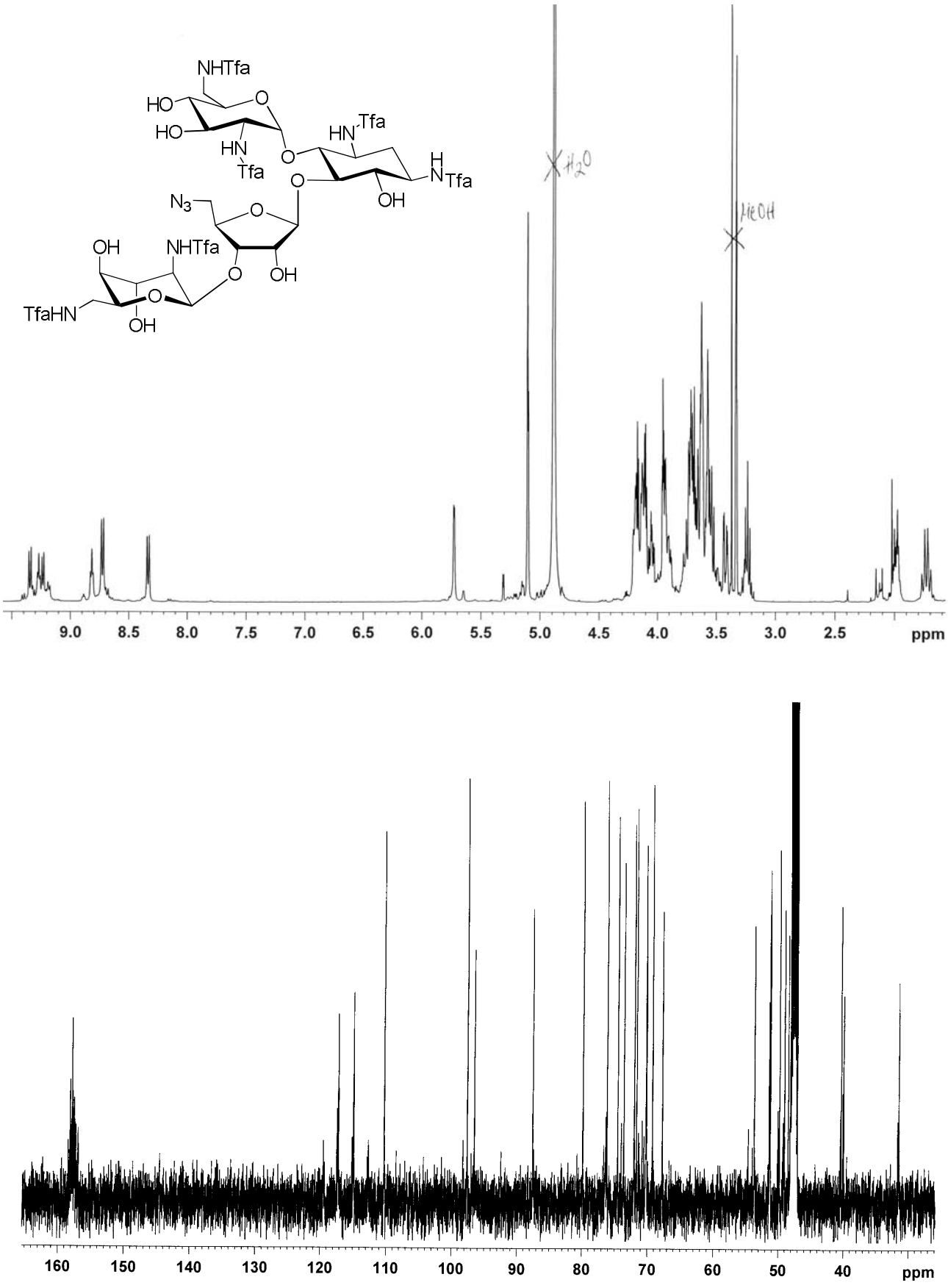


Figure S7. ^{1}H and ^{13}C NMR (CD_3OD) spectrum of **6**.

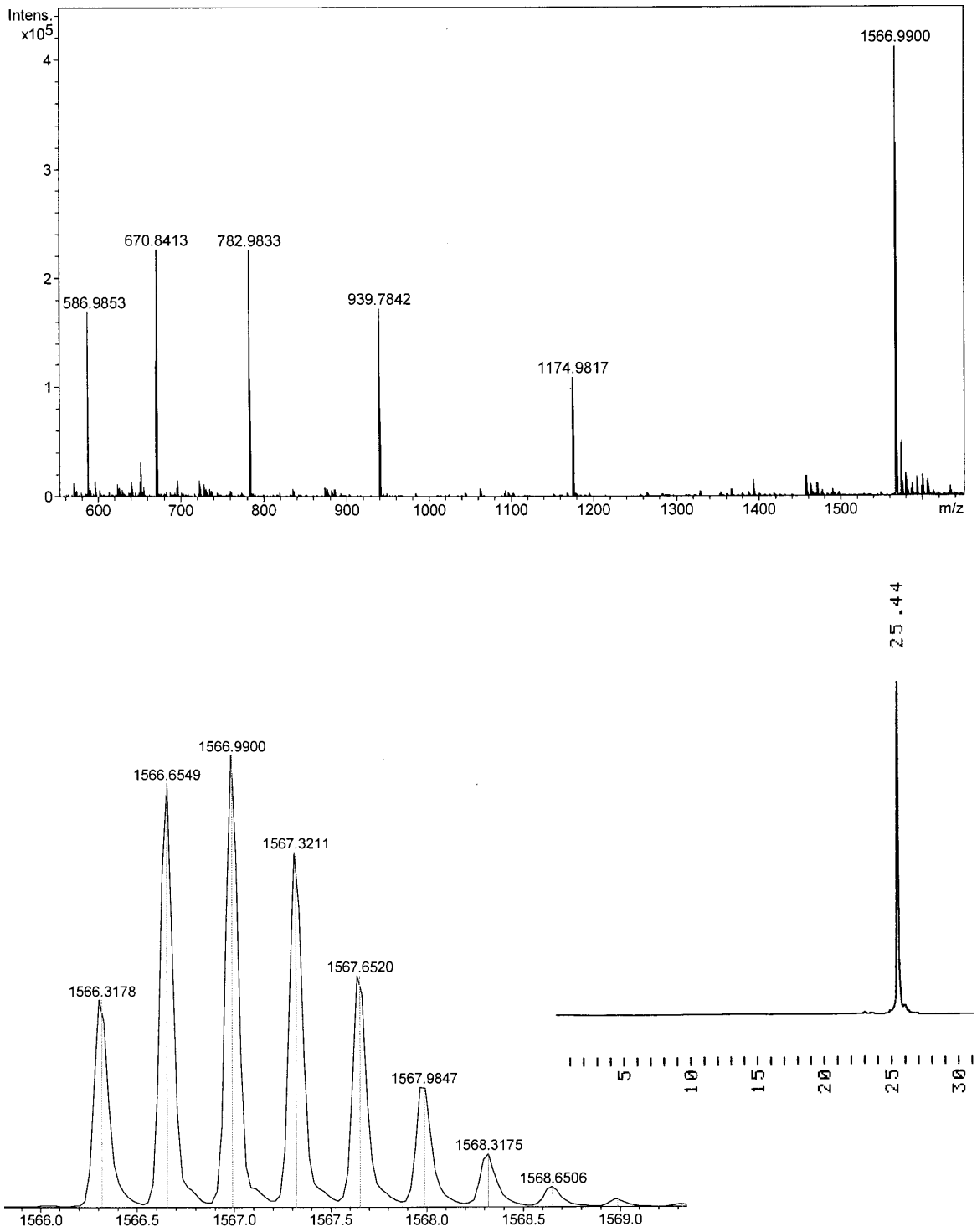


Figure S8. MS(ESI) spectrum and HPLC chromatograph of pure **26**.

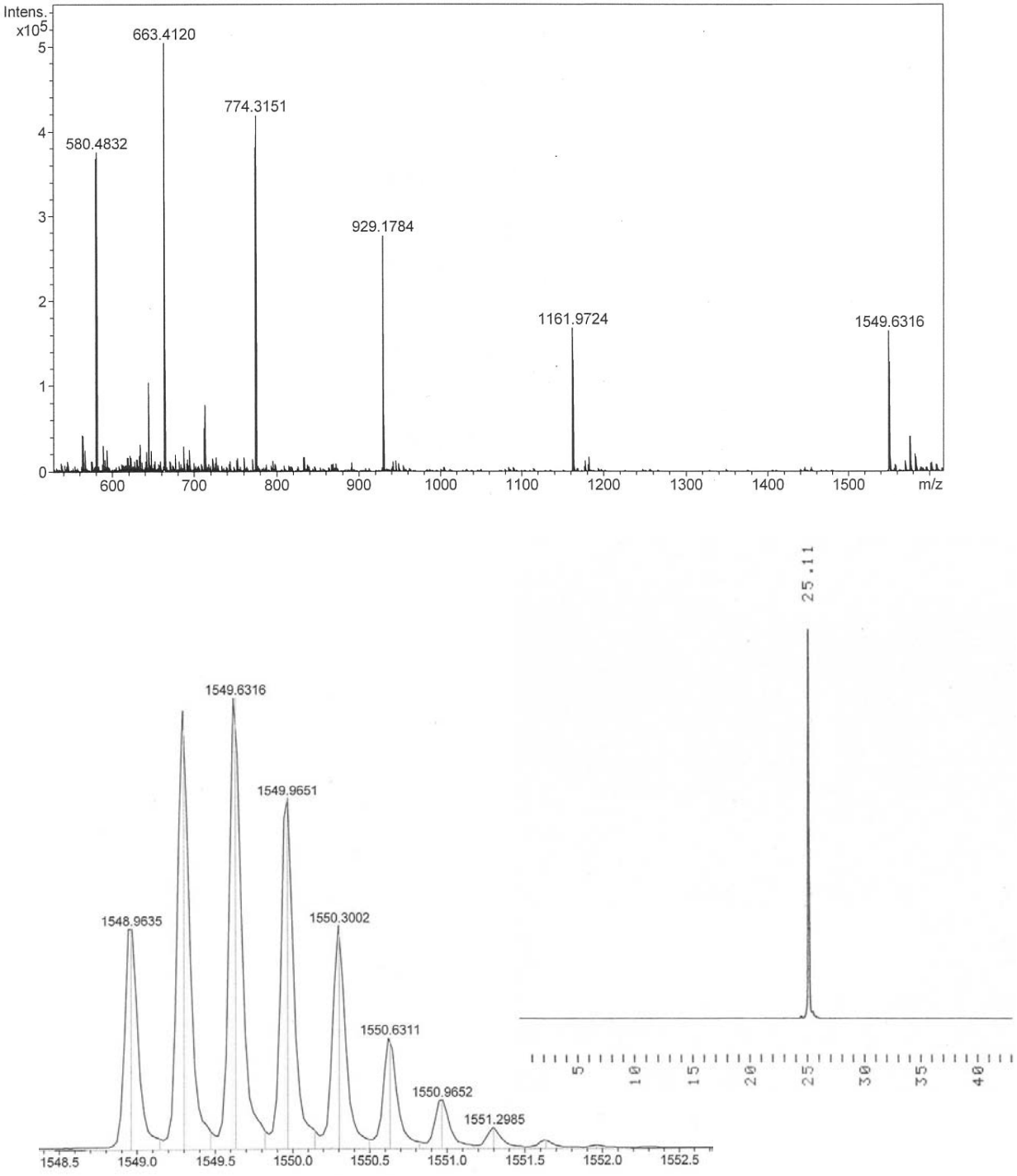


Figure S9. MS(ESI) spectrum and HPLC chromatograph of pure **27**.

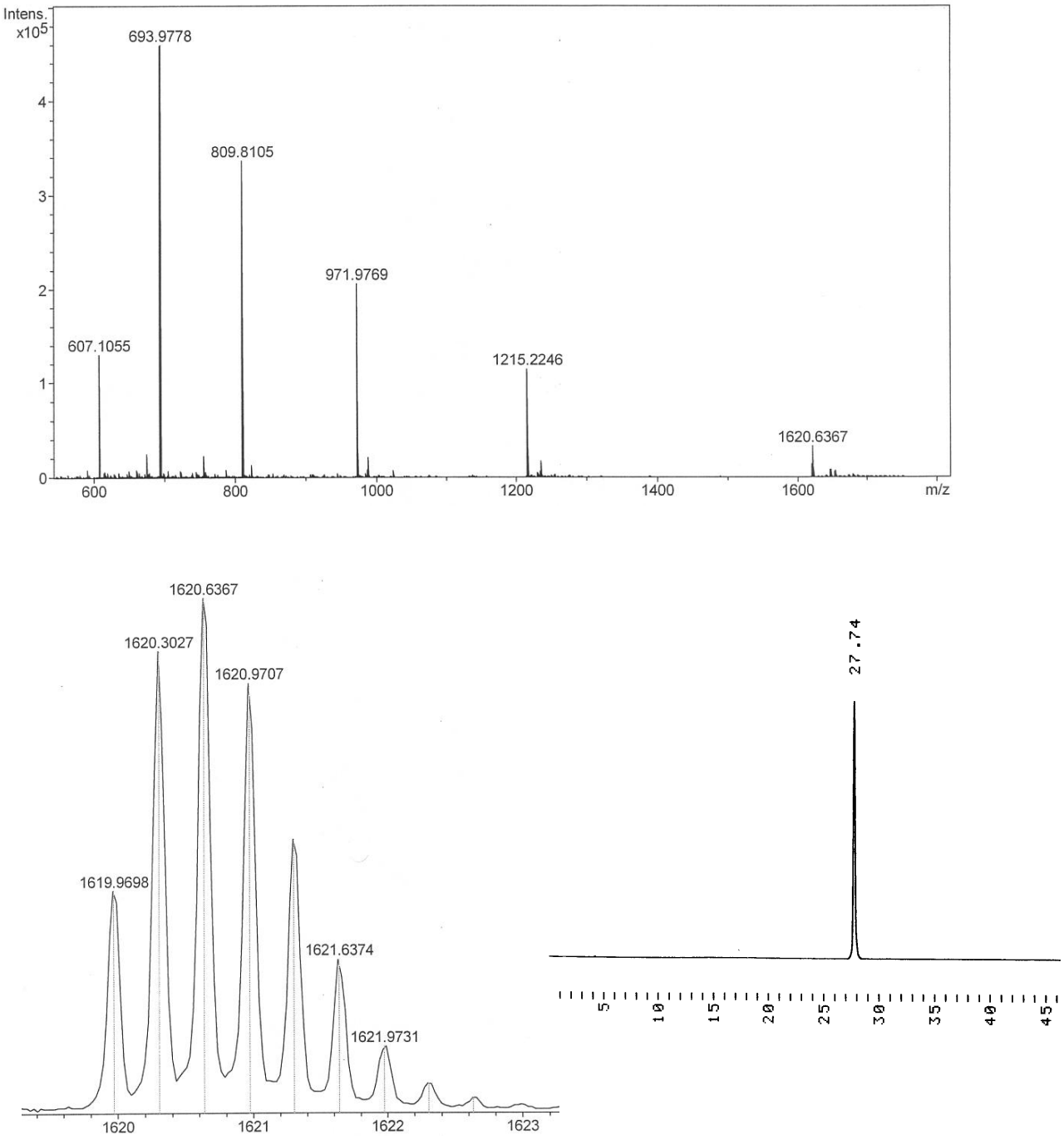


Figure S10. MS(ESI) spectrum and HPLC chromatograph of pure **28**.

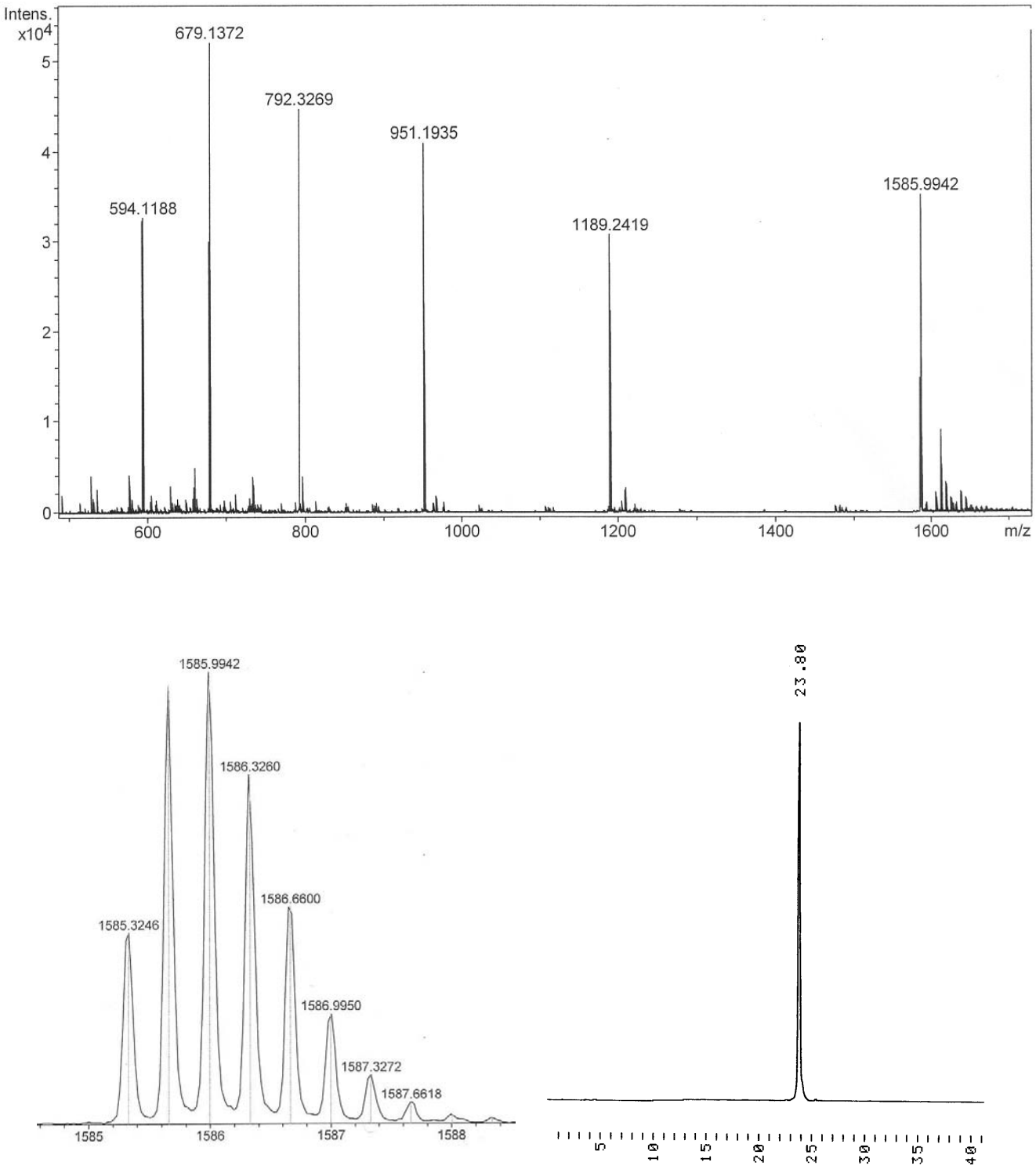


Figure S11. MS(ESI) spectrum and HPLC chromatograph of pure **29**.

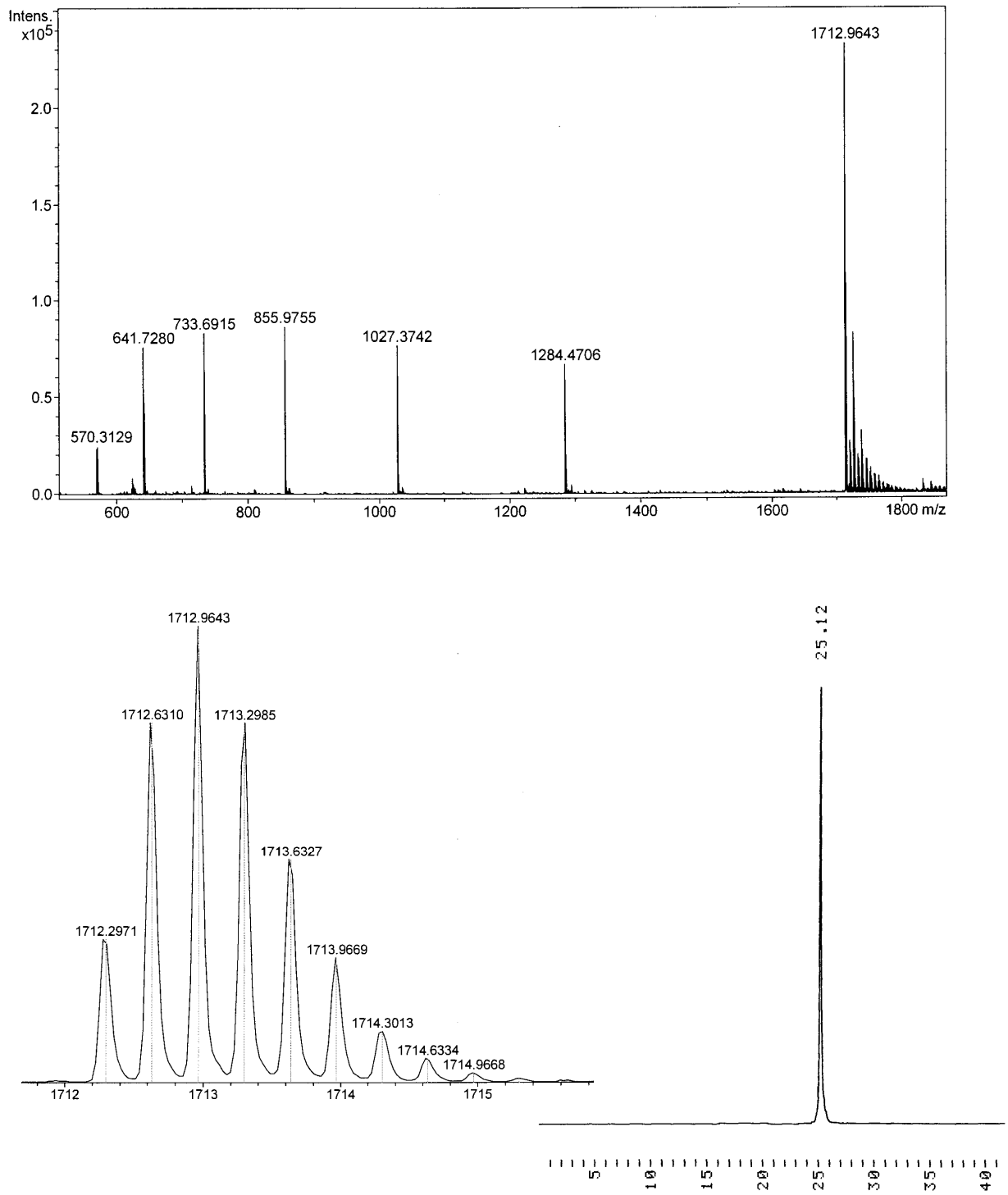


Figure S12. MS(ESI) spectrum and HPLC chromatograph of pure **30**.

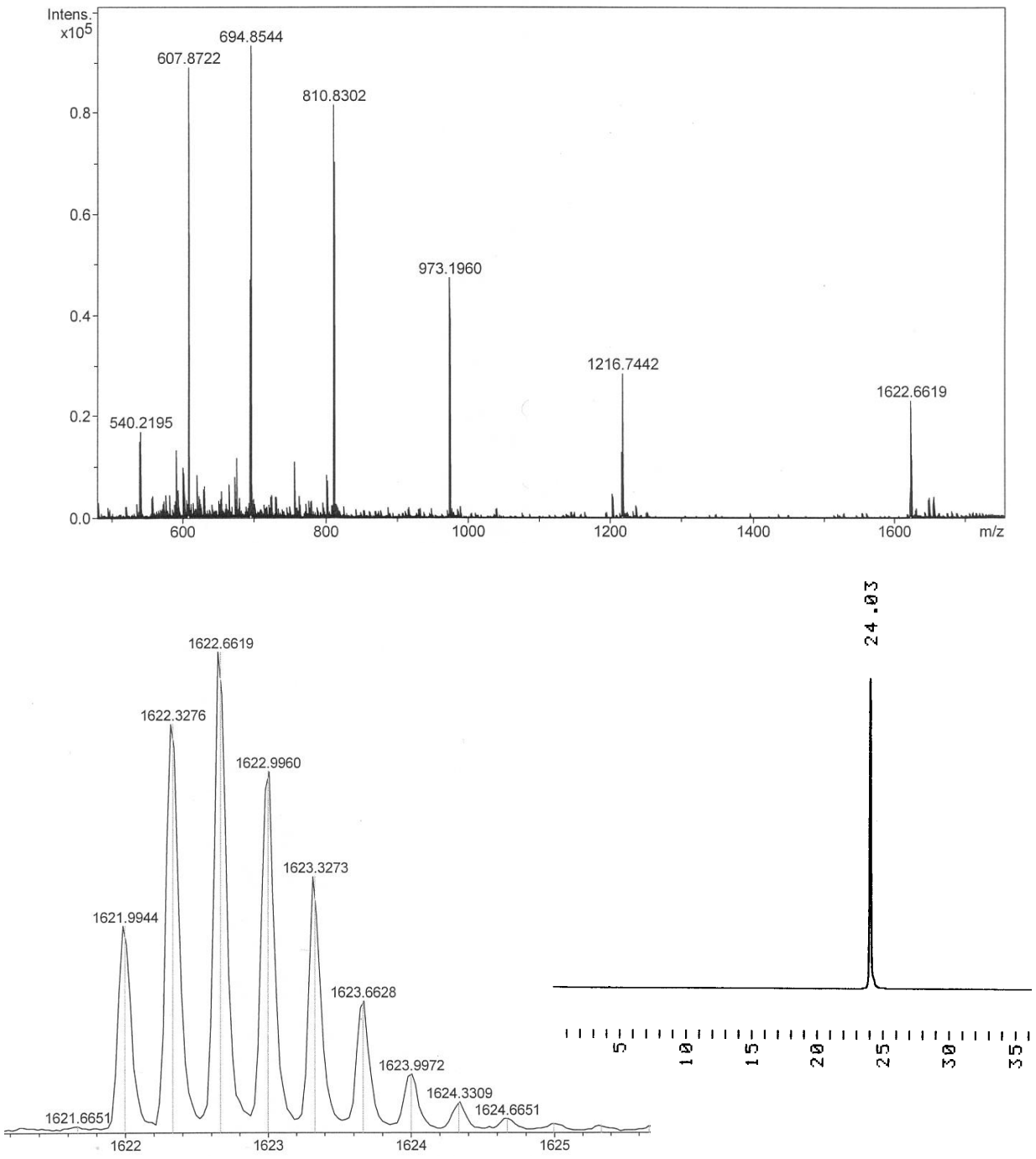


Figure S13. MS(ESI) spectrum and HPLC chromatograph of pure **31**.

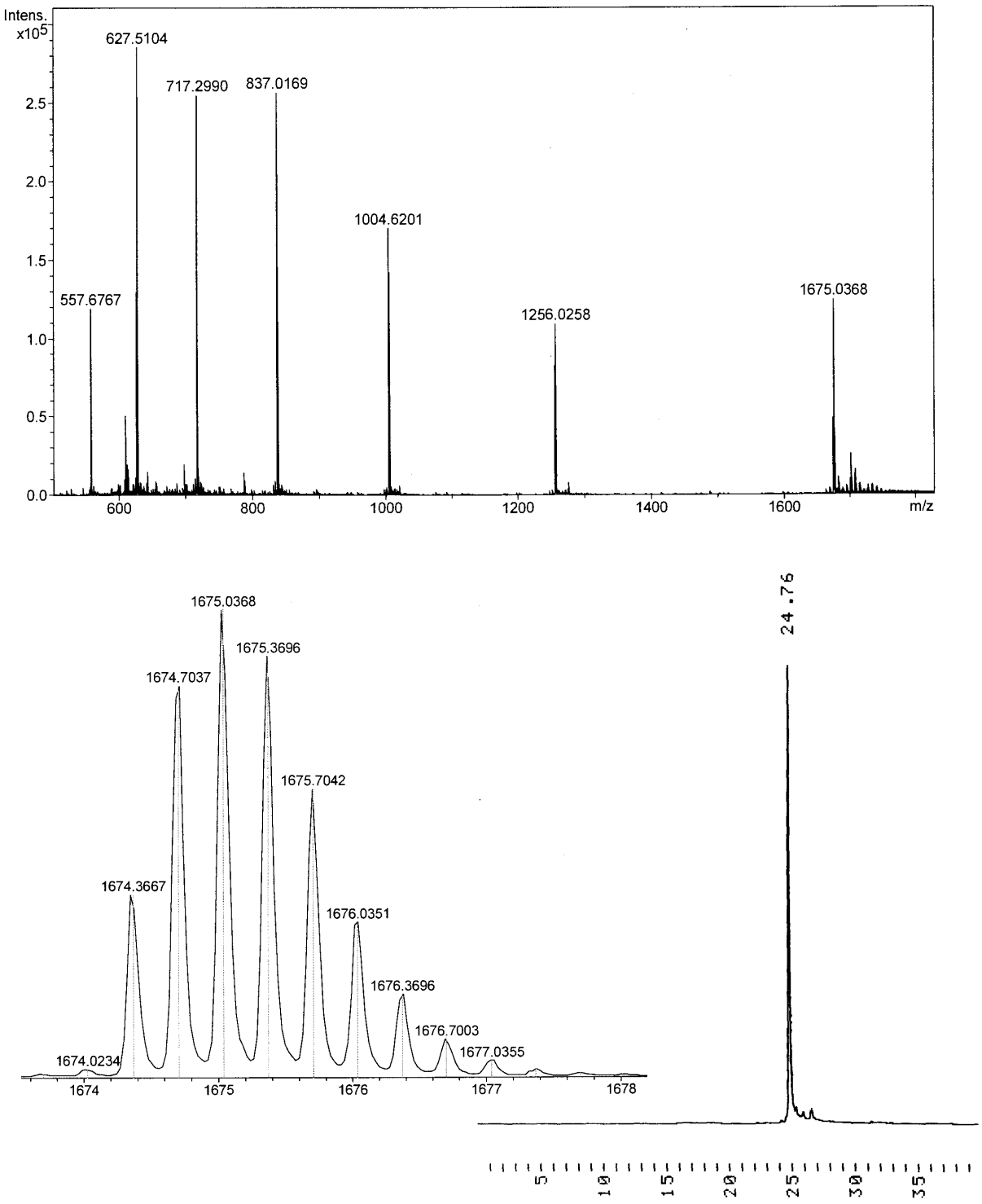


Figure S14. MS(ESI) spectrum and HPLC chromatograph of pure **32**.

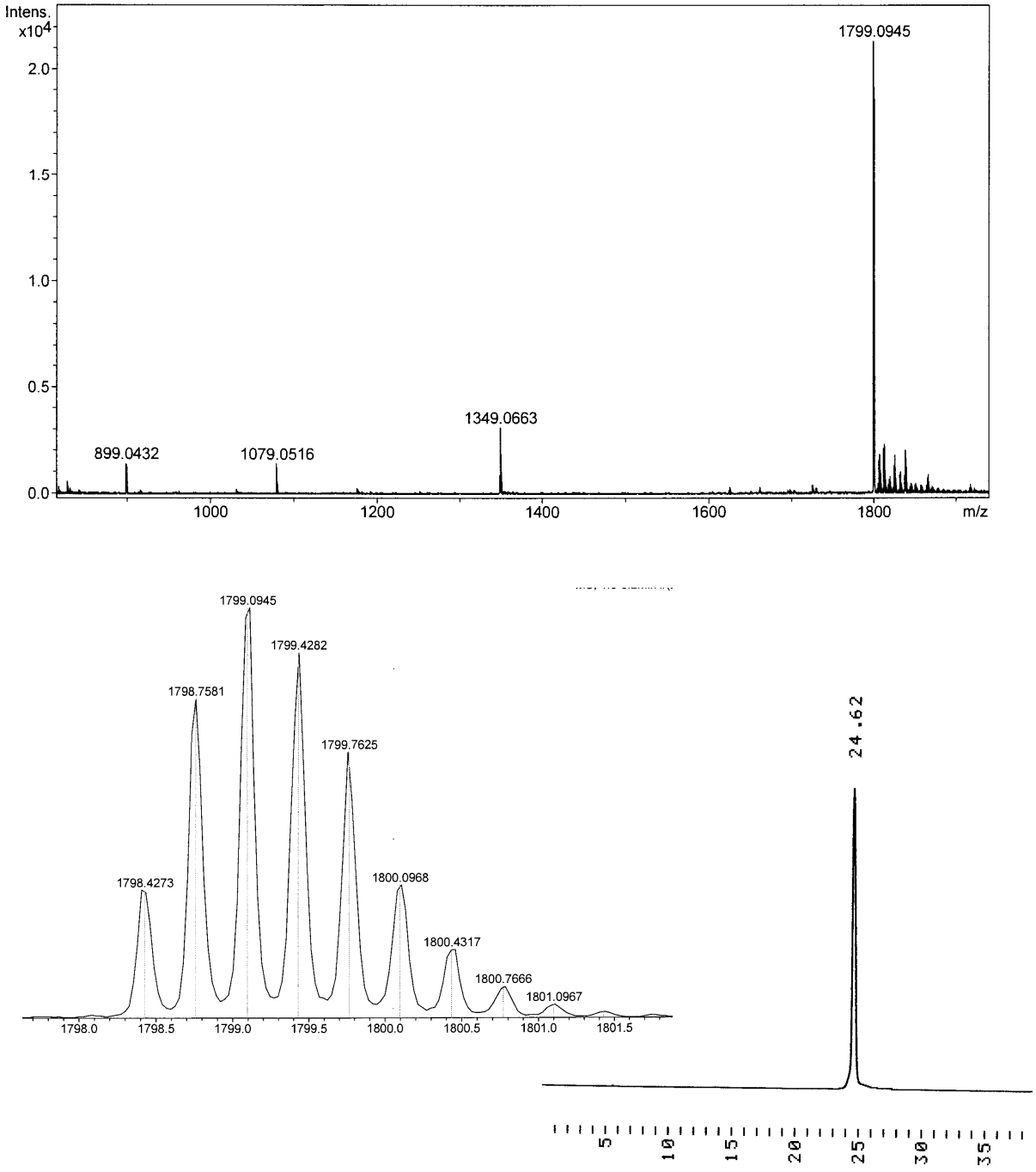


Figure S15. MS(ESI) spectrum and HPLC chromatograph of pure **33**.

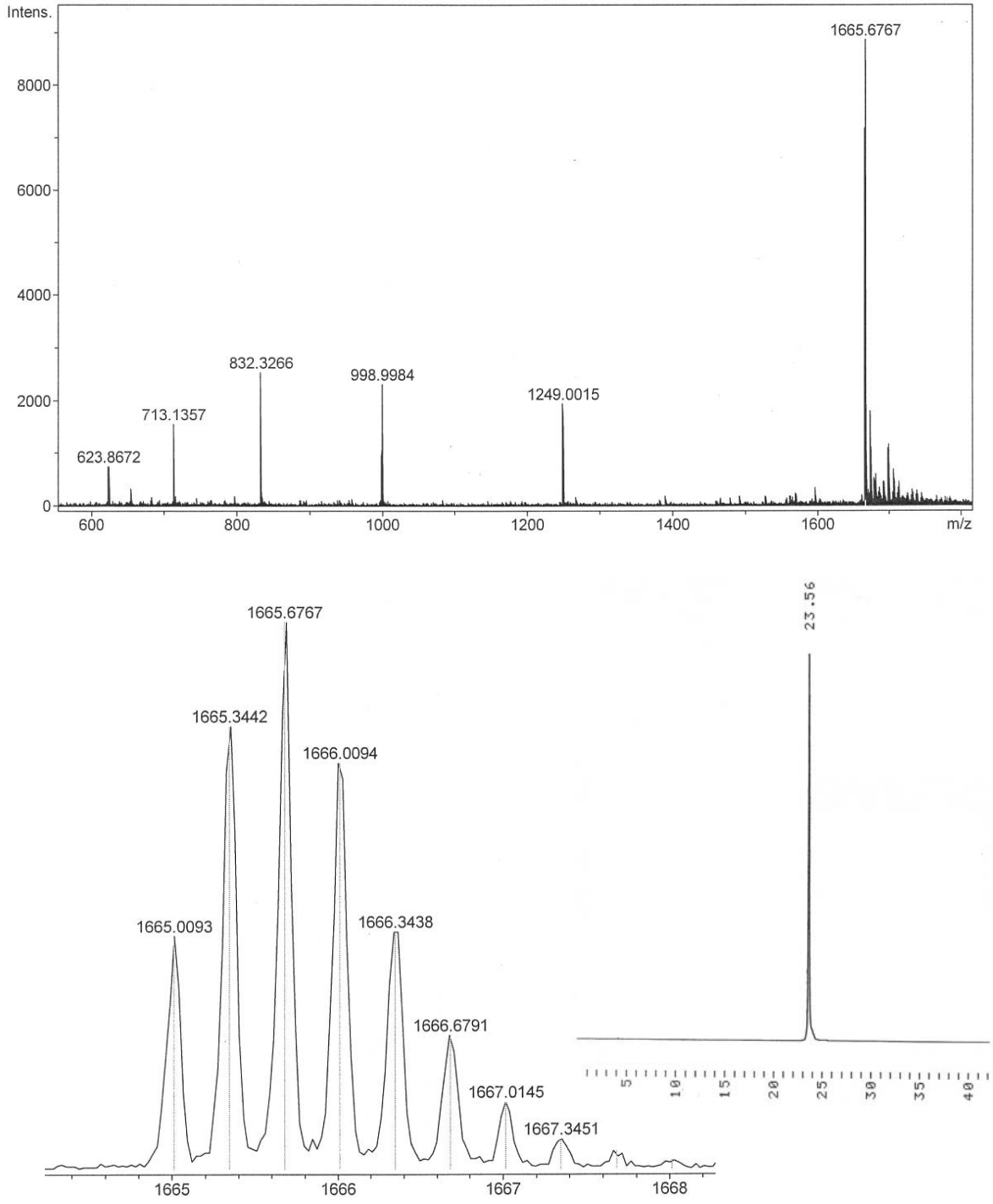


Figure S16. MS(ESI) spectrum and HPLC chromatograph of pure **34**.

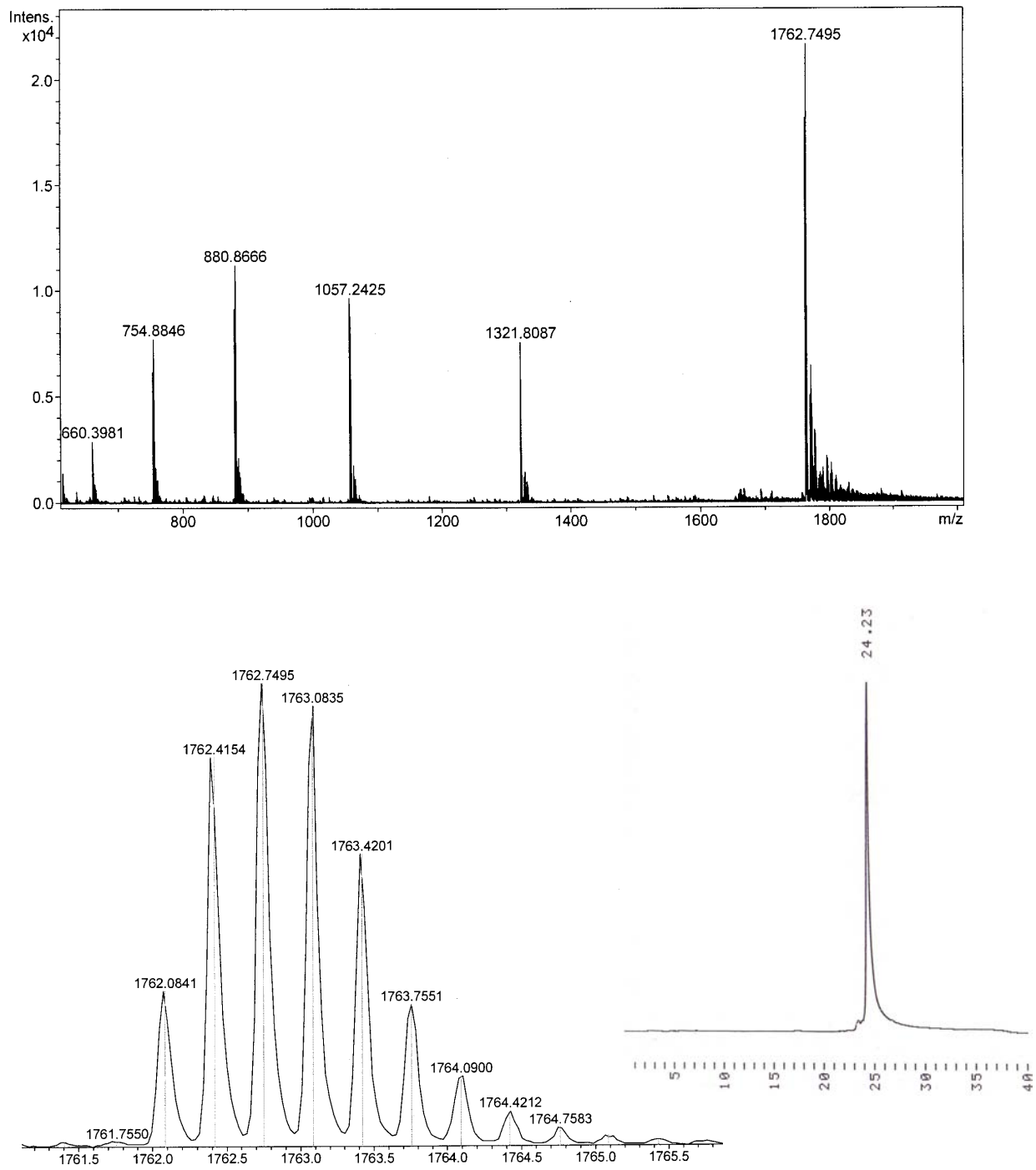


Figure S17. MS(ESI) spectrum and HPLC chromatograph of pure **35**.

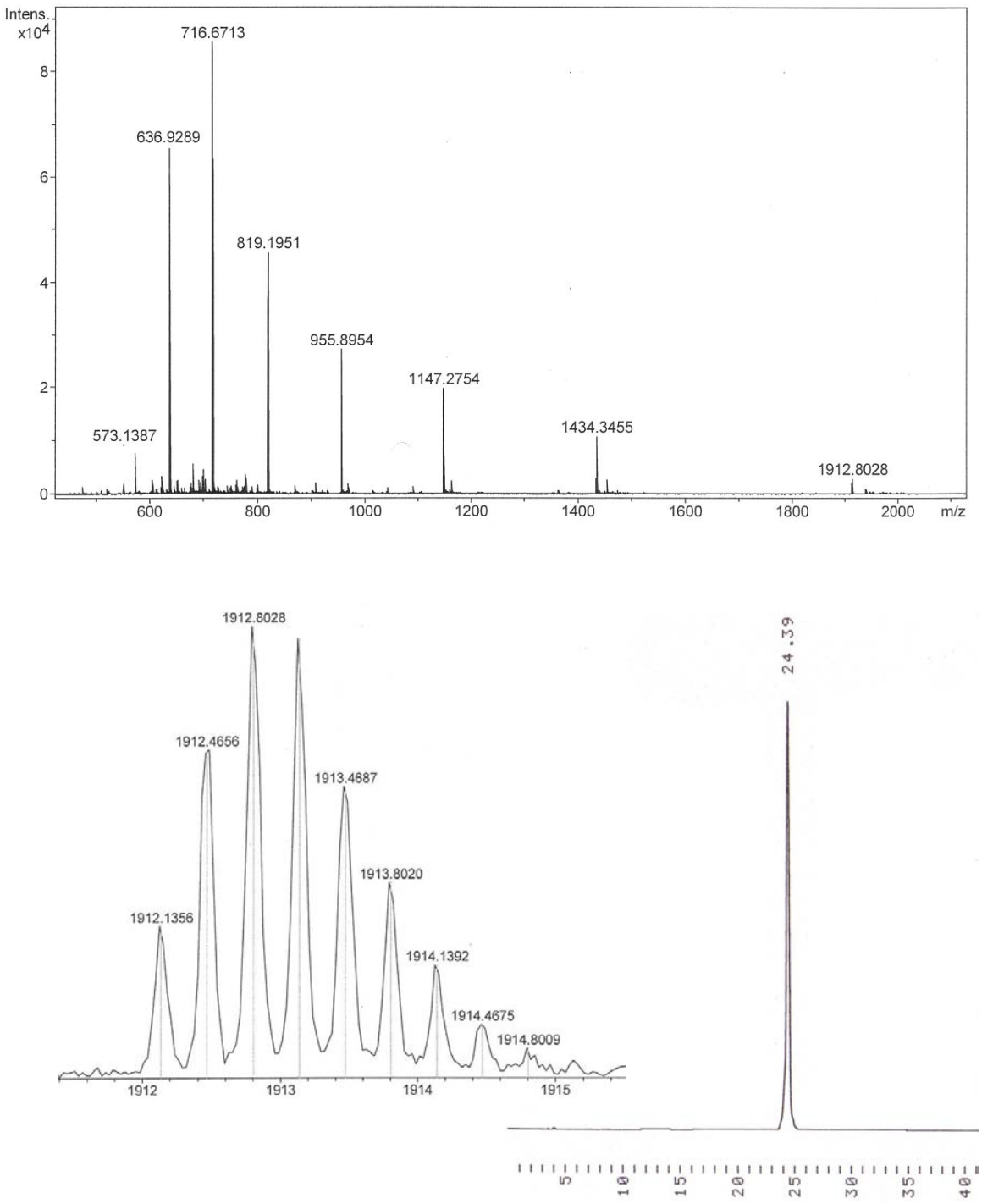


Figure S18. MS(ESI) spectrum and HPLC chromatograph of pure **36**.

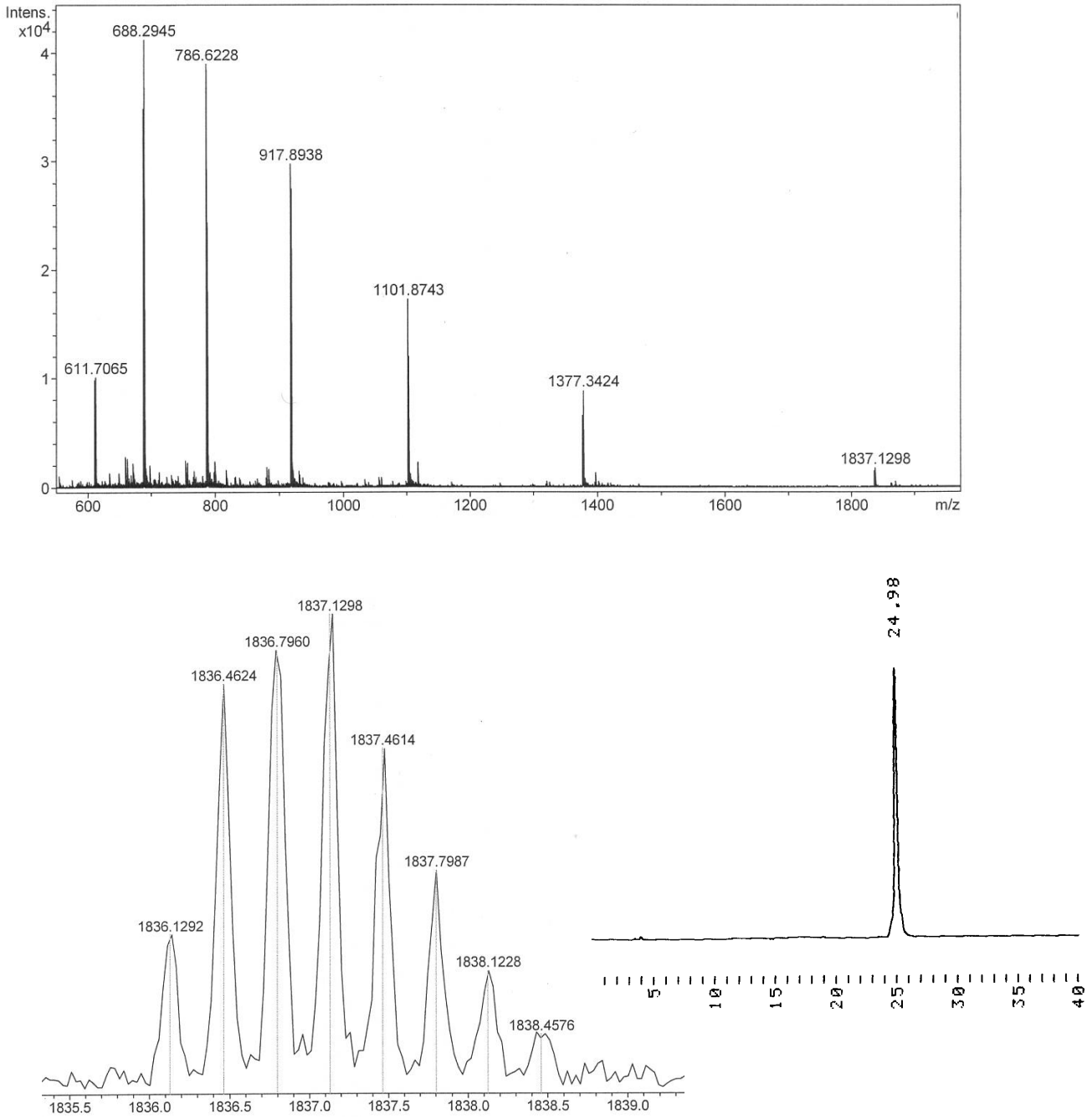


Figure S19. MS(ESI) spectrum and HPLC chromatograph of pure **37**.

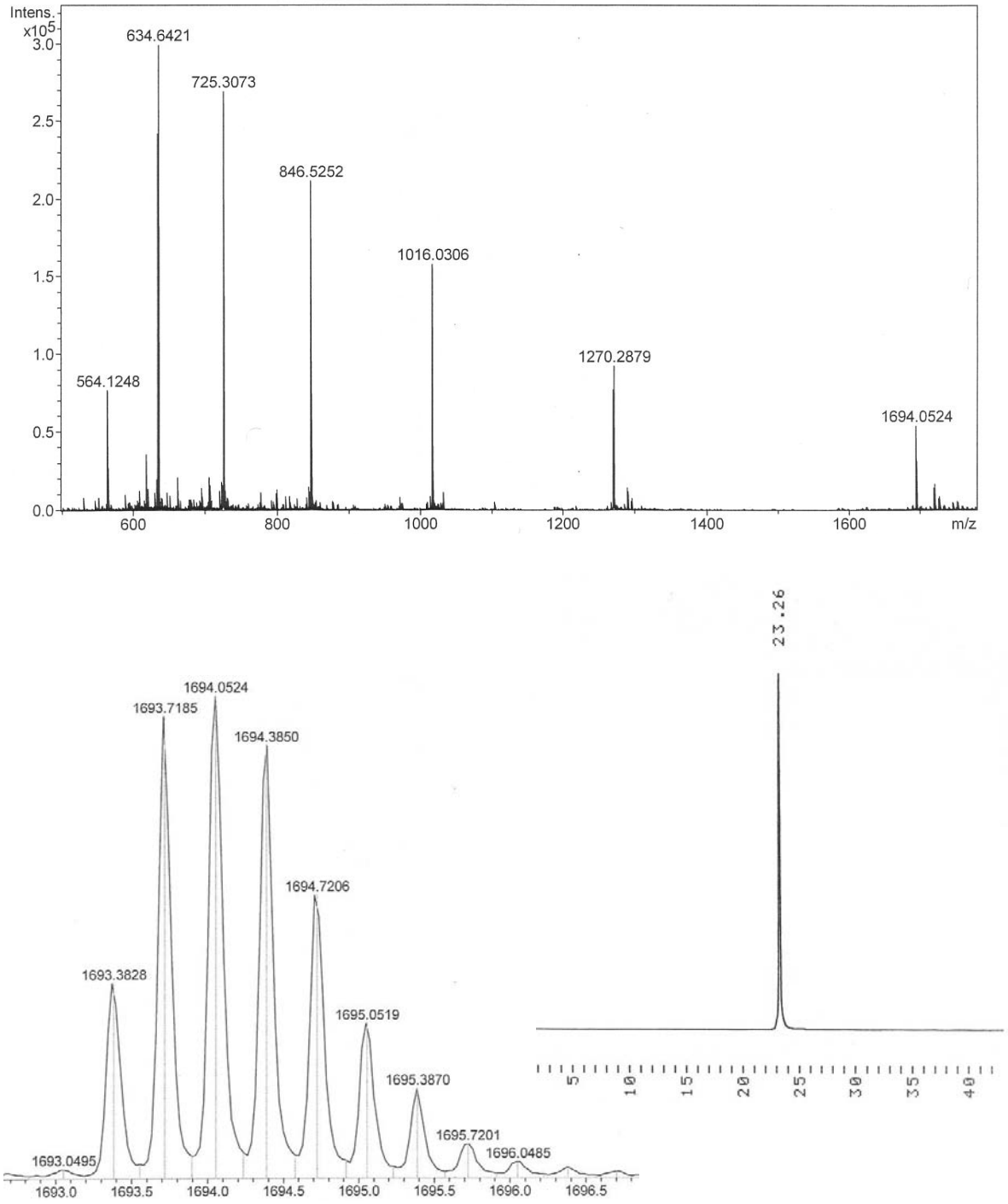


Figure S20. MS(ESI) spectrum and HPLC chromatograph of pure **38**.

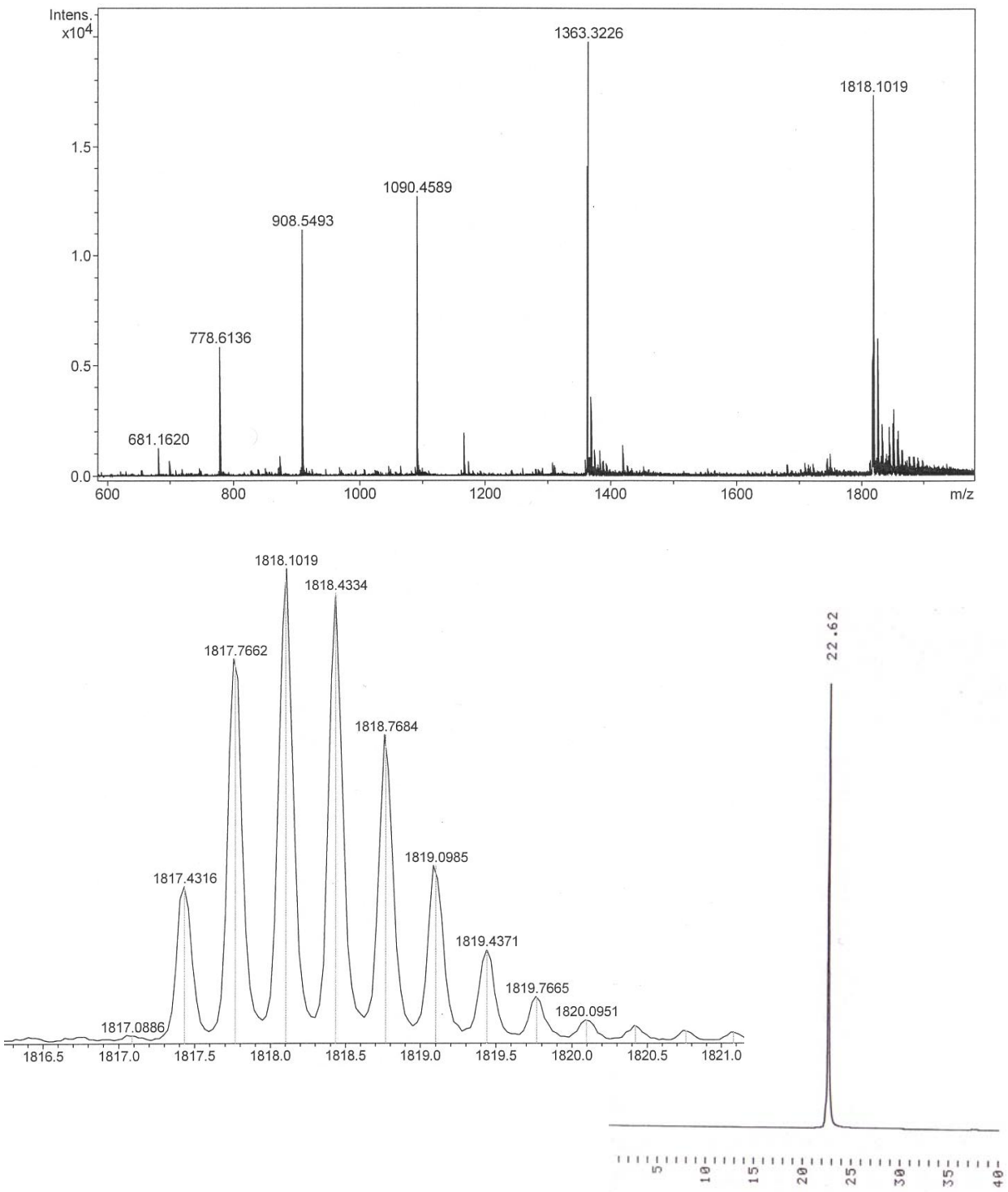


Figure S21. MS(ESI) spectrum and HPLC chromatograph of pure **39**.

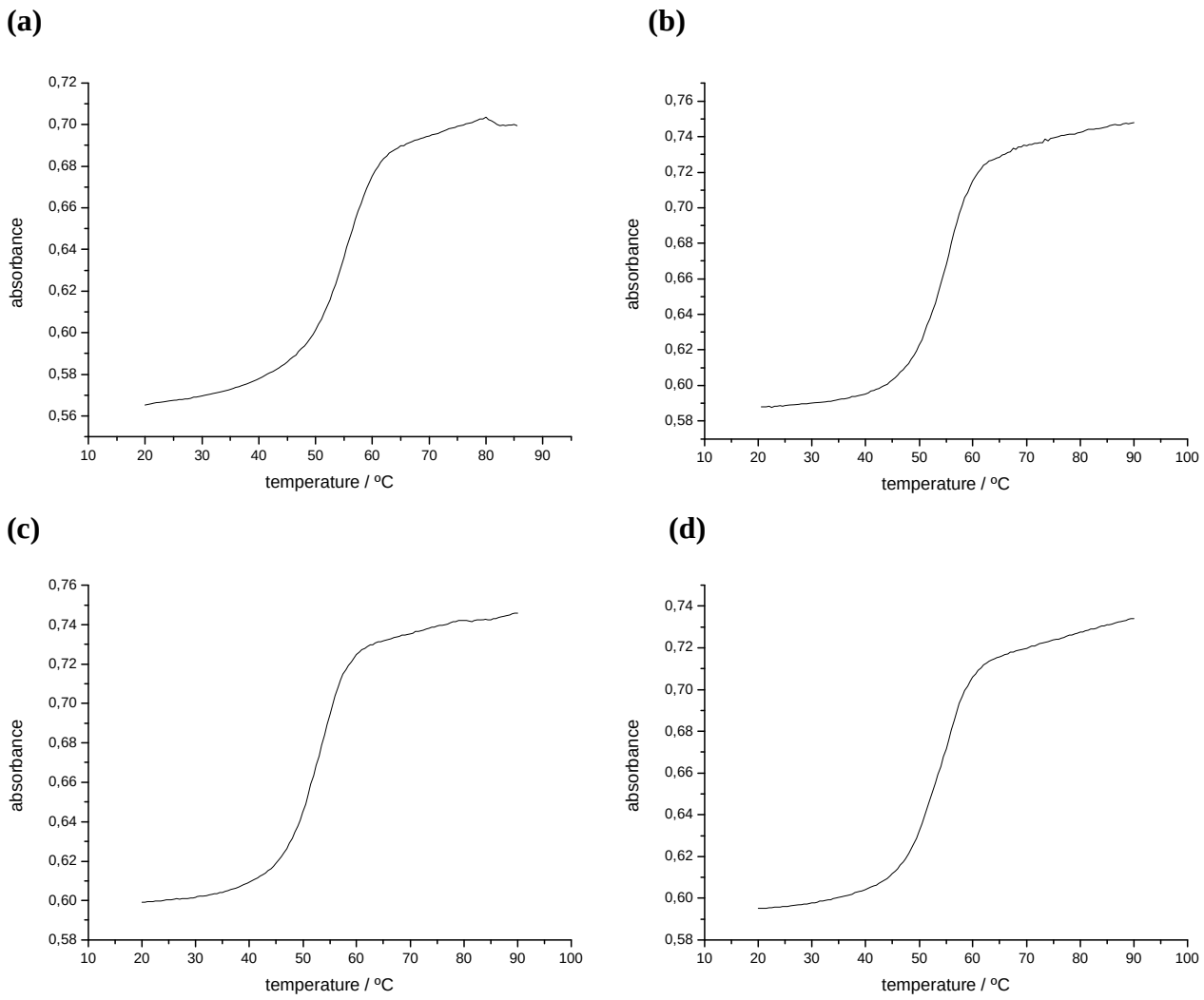


Figure S22. UV-melting profiles of the oligonucleotide conjugates **26** (a), **27** (b), **28** (c) and **29** (d) with cDNA. (Salt concentration: 0.1 mol L^{-1} NaCl)

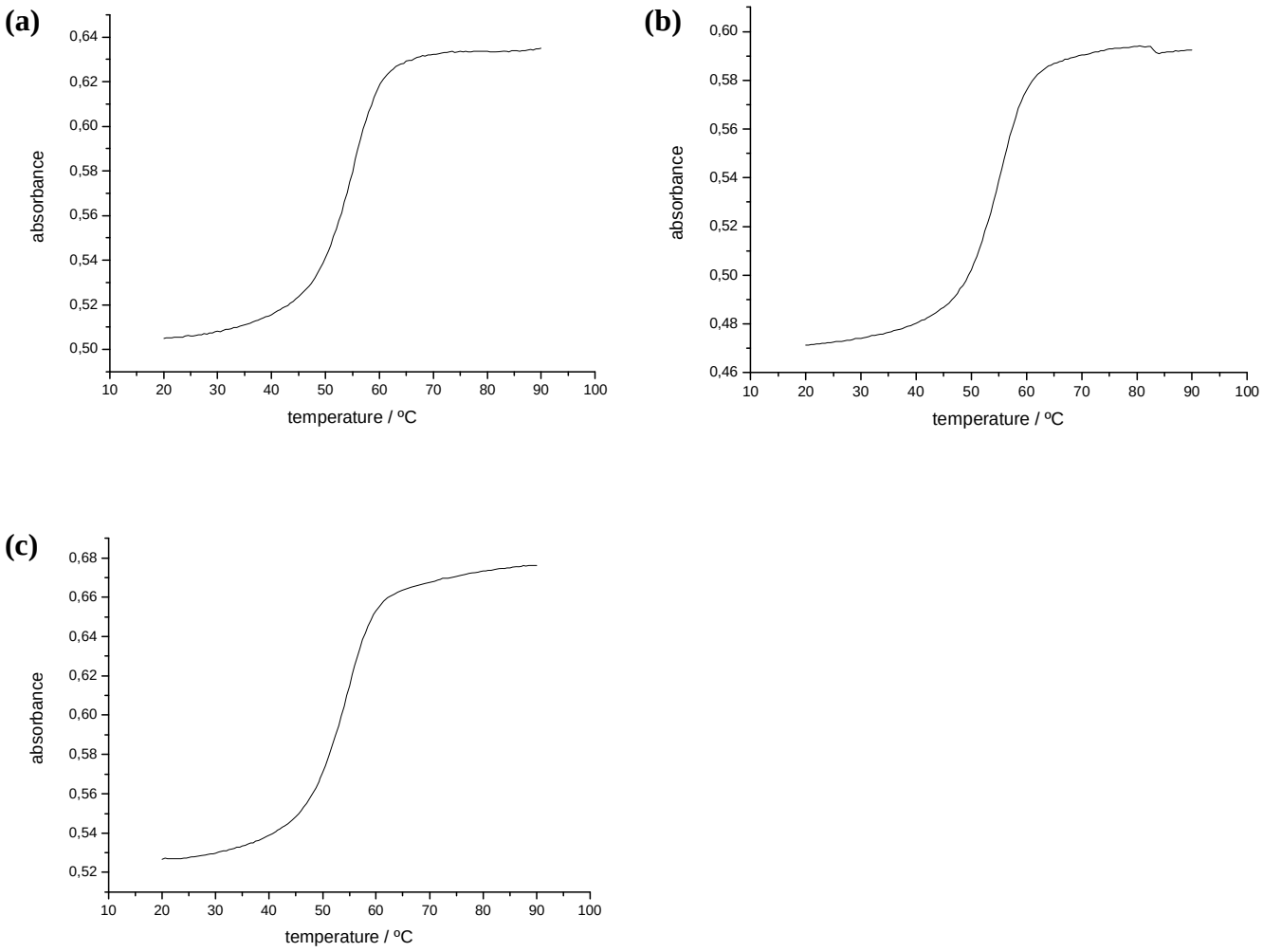


Figure S23. UV-melting profiles of the mannose conjugated oligonucleotides **30** (a), **31** (b) and **36** (c) with complementary 2´-*O*-methyl RNA. (Salt concentration: 0.1 mol L^{-1} NaCl)

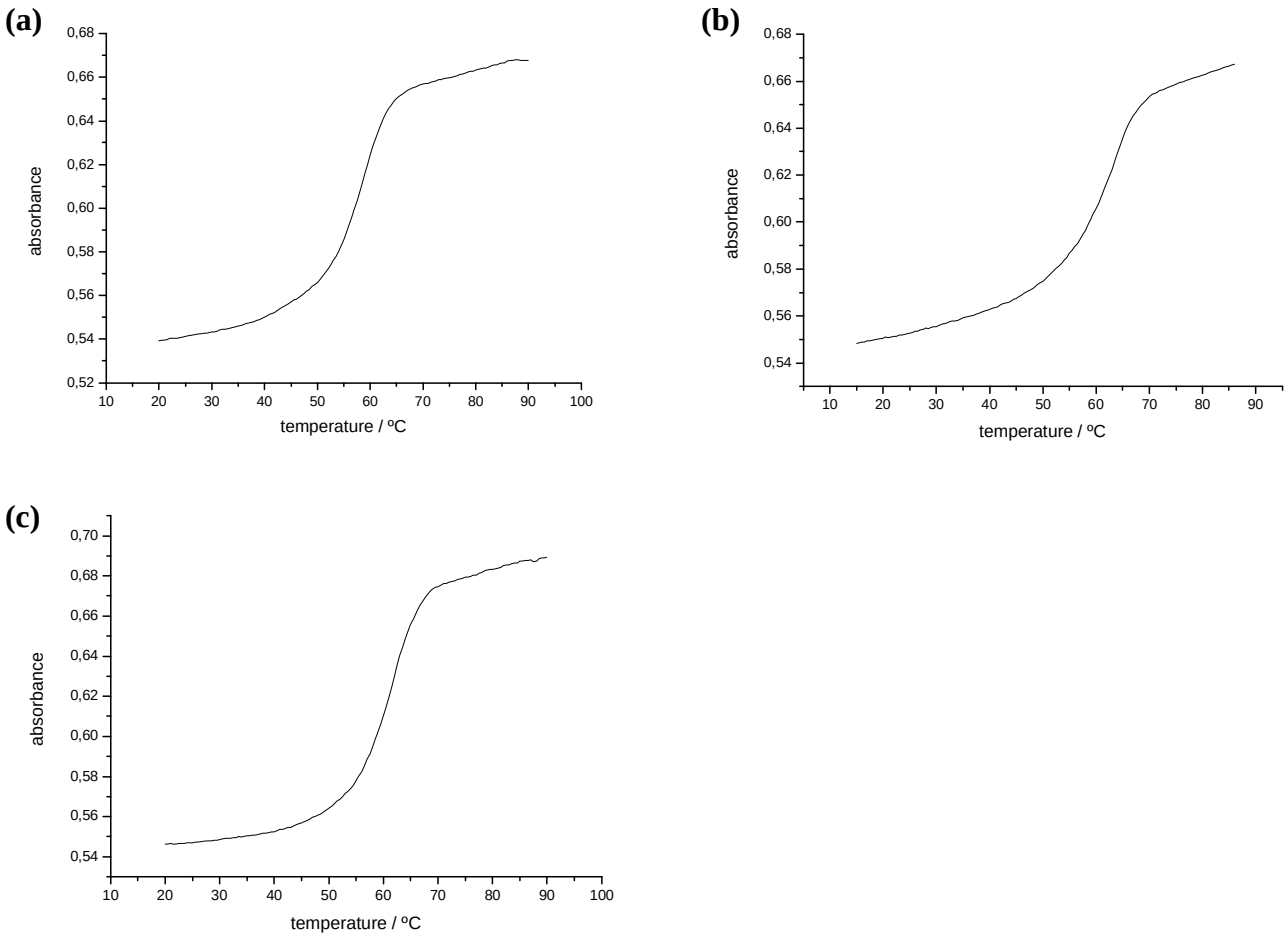


Figure S24. UV-melting profiles of the *p*-aminomethylbenzene conjugated oligonucleotides **32** (a), **37** (b) and **38** (c) with cDNA. (Salt concentration: 0.1 mol L^{-1} NaCl)

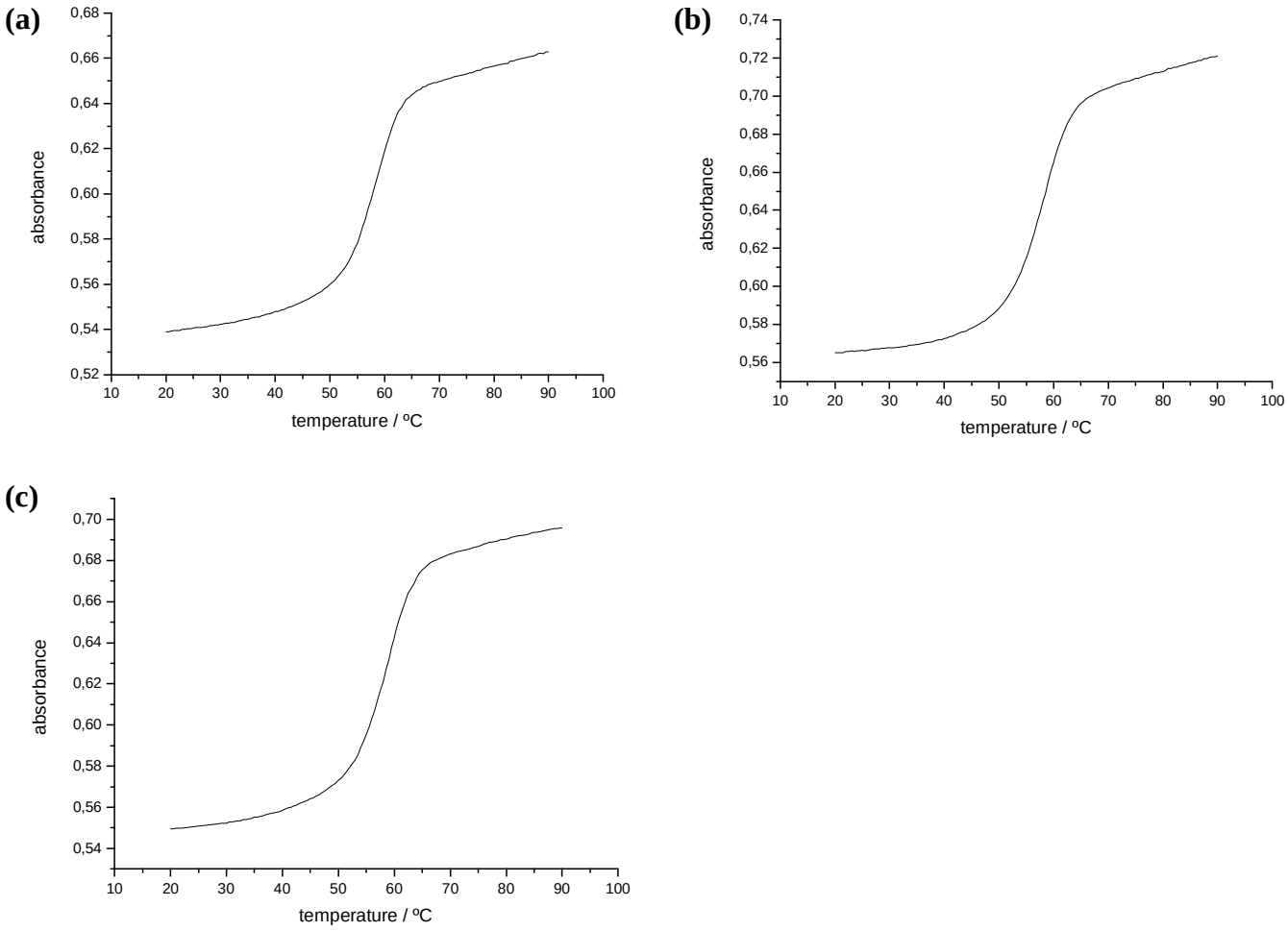


Figure S25. UV-melting profiles of the paromamine conjugated oligonucleotides **33** (a), **34** (b) and **39** (c) with cDNA. (Salt concentration: 0.1 mol L^{-1} NaCl)

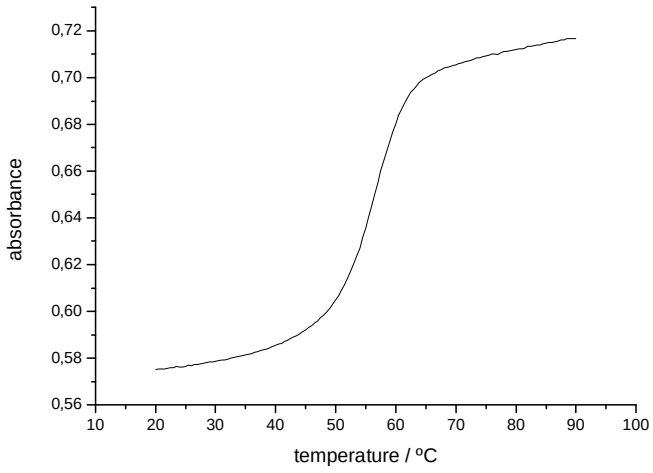


Figure S26. UV-melting profile of the neomycin conjugated oligonucleotide **35** with cDNA. (Salt concentration: 0.1 mol L^{-1} NaCl)

Synthesis and Splice-Redirecting Activity of Branched, Arginine-Rich Peptide Dendrimer Conjugates of Peptide Nucleic Acid Oligonucleotides

Amer F. Saleh,[†] Andrey Arzumanov,[†] Rachida Abes,[§] David Owen,[†] Bernard Lebleu,[§] and Michael J. Gait*[,†]

Medical Research Council, Laboratory of Molecular Biology, Hills Road, Cambridge, CB2 0QH, United Kingdom, and UMR 5235 CNRS, Université Montpellier 2, Place Eugene Bataillon, 34095 Montpellier cedex 5, France. Received June 17, 2010; Revised Manuscript Received September 7, 2010

Arginine-rich cell-penetrating peptides have found excellent utility in cell and in vivo models for enhancement of delivery of attached charge-neutral PNA or PMO oligonucleotides. We report the synthesis of dendrimeric peptides containing 2- or 4-branched arms each having one or more R-Ahx-R motifs and their disulfide conjugation to a PNA705 splice-redirecting oligonucleotide. Conjugates were assayed in a HeLa pLuc705 cell assay for luciferase up-regulation and splicing redirection. Whereas 8-Arg branched peptide−PNA conjugates showed poor activity compared to a linear $(R\text{-Ahx-R})_4$−PNA conjugate, 2-branched and some 4-branched 12 and 16 Arg peptide−PNA conjugates showed activity similar to that of the corresponding linear peptide−PNA conjugates. Many of the 12- and 16-Arg conjugates retained significant activity in the presence of serum. Evidence showed that biological activity in HeLa pLuc705 cells of the PNA conjugates of branched and linear (R-Ahx-R) peptides is associated with an energy-dependent uptake pathway, predominantly clathrin-dependent, but also with some caveolae dependence.

INTRODUCTION

Cell-penetrating peptides (CPPs) have proven extremely valuable for enhancing the cell delivery of a range of biomolecules either as covalent conjugates or as noncovalent complexing agents (*1*). Among the biocargoes that are well-suited for CPP conjugation are antisense oligonucleotide (ON) analogues that are used to target RNAs inside cells (*2, 3*). Particularly good results have been obtained in cell delivery when CPPs are conjugated to charge-neutral peptide nucleic acid (PNA) and phosphorodiamidate morpholino oligonucleotides (PMO) that are used for non-RNase-H steric block antisense applications (*4, 5*). Such ON analogues are metabolically stable inside cells and in tissues, and retain very good sequence specificity in binding to RNA targets. Peptide conjugates of PNA and PMO are now being investigated in therapeutic applications, for example, for redirecting RNA splicing in diseases such as Duchenne muscular dystrophy (DMD) (*6, 7*).

A wide range of CPPs has been proposed for PNA and PMO conjugation, some of which are derived from small transduction domains of proteins (Tat (48−60), Penetratin), and many others are composite or synthetically designed (*2, 3*). Most CPPs are cationic, and often, they also contain regions of hydrophobic amino acids. Cationic charge helps the binding of the CPP to the cell surface glycosaminoglycans. However, the mechanisms of cell uptake following cell surface binding are diverse and in some cases have proven controversial. It is commonly recognized that in most cases at modest concentrations (1 μM or less) and, especially when conjugated to an ON cargo, endocytotic uptake mechanisms of CPPs predominate, rather than direct translocation (*2, 3*). Cationic and hydrophobic elements in the CPP are also thought to help to enhance their release from endosomes into the cytosol, but the exact spatial parameters for optimal release are not well understood.

* Corresponding author. Michael J. Gait, Tel: +44 1223 402473; fax: +44 1223 420270; E-mail: mgait@mrc-lmb.cam.ac.uk.

[†] Medical Research Council, Laboratory of Molecular Biology.

[§] UMR 5235 CNRS.

It has become well accepted that when viewed by live-cell confocal microscopy fluorescently tagged cationic CPP-ON conjugates usually become sequestered within endosomal compartments (*8*). However, to interact with mRNA or pre-mRNA targets, ONs must reach the cytosol or nucleus, respectively. In order to better understand what parameters within an attached CPP are required to help endosomal release and thus allow the attached ON to reach its RNA target, it is necessary to utilize a biological assay that is characteristic of the cell compartment. Kole and colleagues developed such an assay for the nucleus, whereby HeLa cells contain an integrated pLuc705 plasmid coding for a firefly luciferase gene within which is embedded an aberrant β-globin intron. To produce firefly luciferase, it is necessary to deliver into the nucleus of the HeLa cells an 18-mer synthetic ON (which is targeted to the 705 site) to restore correct splicing of the pre-mRNA and hence a functional luciferase mRNA (*9*). This assay is straightforward and has a high dynamic range, which allows both high and low activity levels to be measured quantitatively as a positive luminescence readout. In addition, the EC_{50} of the splicing redirection can be assessed readily at the RNA level by an RT-PCR assay.

By use of the HeLa pLuc705 assay, we have reported that Arg-rich peptides are particularly valuable as delivery agents into cells when covalently conjugated to PNA or PMO ON cargoes in the absence of any transfection or other delivery agent. For example, we found that $(R\text{-Ahx-R})_4$-PNA705 and $(R\text{-Ahx-R})_4$-PMO705 conjugates (Ahx = aminohexanoic acid) were able to redirect splicing more efficiently than conjugates of Tat, Penetratin, or oligo-Arg classical CPPs (*10*−*12*). The interspersing of the non-natural Ahx amino acids is advantageous in providing an optimal spatial distribution of guanidinium side chains, in increasing metabolic stability, and in decreasing cytotoxicity (*13, 14*).

Further, the active fraction of such conjugates appears to enter HeLa pLuc705 cells predominantly by energy-dependent endocytosis (*10*), similarly to that found previously for PNA conjugates of Tat peptide (*15*). In addition, Arg-rich conjugates of

10.1021/bc100275r © 2010 American Chemical Society
Published on Web 09/29/2010

PMO ONs have been shown to be highly effective in enhancing muscle cell delivery and exon skipping in a *mdx* mouse model of Duchenne muscular dystrophy (DMD), and such conjugates are in preclinical development (*6*). Other candidate Arg-rich peptides (such as Pip peptides and B-MSP) also utilize R-Ahx-R or R-β-R (β = beta-alanyl) motifs and have been used successfully to deliver PMO with even higher activity in *mdx* mice (*16, 17*).

We described recently a synthetic, Arg-rich tetramerizing peptide R10p53^{tet} where ten Arg residues were added to the *N*-terminus of the well-defined tetramerization domain of p53 protein (*18*). The peptide was conjugated close to its C-terminus to the PNA705 18-mer used in splice-redirecting studies. The splicing redirection efficiency of the PNA705 when added to HeLa pLuc705 cells was found to be much greater for the R10p53^{tet} conjugate than for R10p53^{mono}, a point mutant in the p53 domain that had been shown previously to be unable to tetramerize. The R10p53^{tet}-PNA705 conjugate was more active than any of the conjugates to CPPs previously tested by us in this assay, such as Tat (*12, 19*), Penetratin (*19*), R_6-Penetratin (*19*), and Pip2b (*16*). However, the R10p53^{tet} peptide was long (50 amino acids) and the synthetic yields were not high, and therefore, this paradigm does not seem likely to be readily adaptable for in vivo studies. Nevertheless, the principle of multivalency seemed to be highly beneficial as originally suggested (*20*).

Several years ago, Futaki and colleagues reported branched-chain arginine peptides where 4 or 8 short oligo-Arg chains were constructed based on chain branching through both the α and ε positions of Lys residues (*21*). The best translocation into HeLa cells was observed when the Arg residues were interspersed with three Gly residues (RG_3R) and placed on a four-armed structure, resulting in a branched 8-arginine configuration. This branched peptide was conjugated either directly to fluorescein or to the protein carbonic anhydrase labeled with fluorescein, and the translocation was visualized by confocal microscopy. Unfortunately, at that time confocal microscopy was carried out in the presence of a cell fixative (acetone/methanol), conditions now known to result in artifactual cell uptake and intracellular redistribution of cationic peptides (*8*). More recently, 4-branched RG_3R peptides with an Alexa fluorescent dye attached were shown to locate in endosomal compartments using live-cell imaging (*22*). However, no activity data for any attached cargo were reported.

Another recent development has been the use of a synthetic dendrimer where eight guanidine moieties were arranged to branch from a central triazine core by means of hexyl spacers (*23*). When attached to PMO oligonucleotides, the octa-guanidino dendrimer was able to enhance cell delivery of the PMO in cultured cells in the presence of serum and also enhance delivery in vivo in a wide range of tissues (*23, 24*). These conjugates are sold commercially as "Vivo-morpholinos". Thus, the concept of spacing arginine (or guanidine) moieties in a three-dimensional dendrimer configuration seemed worth exploring further.

We now describe straightforward solid-phase techniques for the chemical synthesis of 2- and 4-branched Arg-rich peptide dendrimers where such branches contain multiple (R-Ahx-R) motifs. Such branched peptides were conjugated to a charge-neutral PNA705 cargo and evaluated for their splice-redirecting activity in a HeLa pLuc705 system in comparison to equivalent linear peptides. Whereas 8-Arg branched peptide−PNA conjugates showed poor activity compared to linear peptide−PNA conjugate, 2-branched and some 4-branched 12 and 16 Arg peptide−PNA conjugates showed activities similar to those of the corresponding linear peptide−PNA conjugates. Many of the 12- and 16-Arg conjugates retained significant activity in the presence of serum. Evidence was shown that biological activity of the peptide−PNA in HeLa cells is associated primarily with an energy-dependent uptake pathway, predominantly clathrin-dependent, but that caveolae can also play a role.

EXPERIMENTAL PROCEDURES

Synthesis of Linear and Branched (R-Ahx-R)-Containing Peptides. Peptide syntheses were carried out using a CEM Liberty microwave peptide synthesizer by Fmoc chemistry. Linear peptides were synthesized starting with 100 μmol of functionalized Fmoc-PAL-PEG-PS solid support (Applied Biosystems), 2-branched peptides were synthesized starting with 50 μmol of support, and 4-branched peptides starting with 25 μmol of support. For all branched peptide syntheses, each Fmoc amino acid derivative was made up to the same concentration as if it was a standard 100 μmol-scale linear synthesis. Thus, for a 2-branched peptide, the excess activated Fmoc amino acid over growing chains in the coupling reactions after the chain branching step was 10-fold, and for a 4-branch peptide, the excess after two branching steps was 5-fold. Coupling reactions were carried out using Fmoc-amino acids in DMF activated with 0.99 equiv of PyBop in DMF and 1.98 equiv of diisopropylethylamine (DIPEA) in *N*-methylpyrrolidone (NMP). The branch point amino acid derivative was Fmoc-Lys(Fmoc)−OH (Novabiochem). Fmoc-Arg(Pbf)−OH (Novabiochem) was used for Arg couplings with the microwave double-coupling protocol previously reported (*25*). Fmoc-deprotection at each cycle was carried out using 20% piperidine in DMF containing 0.1 M hydroxybenzotriazole (HOBT). The final peptidyl resin was washed with DMF and then dichloromethane and dried in vacuo.

Cleavage and deprotection were carried out using TFA/water/ethanedithiol/triethylsilane (94:2.5:2.5:1, 20 mL) for 2 h, the resin removed by filtration and washed with TFA (ca. 5 mL) and the filtrate sparged with nitrogen to obtain a small volume. The peptide was precipitated by addition of cold diethyl ether, collected by centrifugation, and the pellet washed a further 5 times with cold ether (25 mL).

Preparative HPLC was carried out using a Phenomenex Jupiter 10 μ C18 column (250 × 10 mm): buffer A, 0.1% TFA in water; buffer B, acetonitrile containing 10% buffer A. Elution was with a linear gradient of 15−50% buffer B over 25 min. Detection was at 215/230 nm (diode array) with a flow rate of 3.5 mL min^{-1}. Analytical HPLC used the same column type (5 μ, 250 × 4.6 mm) and similar buffer and 10−40% B over 25 min gradient conditions (1.5 mL min^{-1}). Representative HPLC traces for branched peptides are shown in Supporting Information Figure 1. MALDI-TOF mass spectral analysis used a Voyager DE Pro BioSpectrometry workstation with a matrix of α-cyano-4-hydroxycinnamic acid, 10 mg mL^{-1} in acetonitrile−0.1% aqueous TFA (1:1 v/v). The accuracy of mass measurement is regarded as ±0.05%.

PNA Synthesis. NH_2-Cys(NPys)-Lys-CCTCTTACCTCAGTTACA-Lys-amide (PNA705) was synthesized by the Fmoc/Bhoc method using PNA monomers obtained from Link Technologies Ltd. (Lanarkshire, Scotland) on a Liberty microwave peptide synthesizer, purified by HPLC, and characterized by MALDI-TOF mass spectrometry as previously described (*16, 18, 26*).

Conjugation of Peptides to PNA705. Disulfide conjugation between the single Cys residue on the peptide component and the single NPys-Cys residue on the PNA705 was carried out essentially as described previously using a 2.5-fold excess of peptide over PNA705 (*16, 19, 27*). Purification of conjugates by reversed-phase HPLC was carried out using buffers identical to those used for peptide purification and linear gradients, with diode array monitoring at 215 and 260 nm. Products were obtained by lyophilization of desired HPLC fractions. Representative examples of peptide−PNA conjugate crude and puri-

Table 1. List of Branched and Linear Peptides Synthesized and their EC_{50} Values in the RT-PCR Assay in the HeLa pLuc705 Cells

Peptide	Structure	EC50 (μM)
8 Arginines		
RXR4-4B1	R-X-R R-X-R-**K** R-X-R-**K**-**K**-X-β-C R-X-R	> 3
RXR4-4B2	R-X-R-X R-X-R-X-**K** R-X-R-X-**K**-**K**-X-β-C R-X-R-X	> 3
RXR4-4B3	R-X-R R-X-R-**K**-X R-X-R-**K**-X-**K**-X-β-C R-X-R	> 3
RXR4-2B	R-X-R-R-X-R R-X-R-R-X-R-**K**-X-β-C	> 3
RXR4	$(RXR)_4$XC	> 3
12 Arginines		
RXR6-4B	R-X-R-R-X-β R-X-R-R-X-β-**K** R-X-R-R-X-β-**K**-**K**-X-β-C R-X-R-R-X-β	> 3
RXR6-2B	R-X-R-R-X-R-R-X-R R-X-R-R-X-R-R-X-R-**K**-X-β-C	1.3 ± 0.2
RXR6	$(RXR)_6$XβC	1.0 ± 0.1
16 Arginines		
RXR8-4B1	R-X-R-R-X-R R-X-R-R-X-R-**K** R-X-R-R-X-R-**K**-**K**-X-β-C R-X-R-R-X-R	1.2 ± 0.3
RXR8-4B2	R-X-R-R-X-R-X-β R-X-R-R-X-R-X-β-**K** R-X-R-R-X-R-X-β-**K**-**K**-X-β-C R-X-R-R-X-R-X-β	1.3 ± 0.2
RXR8-2B	R-X-R-R-X-R-R-X-R-R-X-R R-X-R-R-X-R-R-X-R-R-X-R-**K**-X-β-C	0.7 ± 0.2
RXR8	$(RXR)_8$XβC	0.8 ± 0.1

fied products are shown in Supporting Information Figure 2. All conjugates were characterized by MALDI-TOF mass spectrometry as described previously (*16, 19, 27*).

Cell Culture and Splicing Redirection Assays. This was carried out similarly to that described previously (*16, 19, 27*). Peptide−PNA conjugates were incubated for 4 h in 0.35 mL OptiMEM medium with exponentially growing HeLa pLuc705 cells (1.25×10^5 cells/well seeded and cultivated overnight in 24 well plates). The medium was removed, 1 mL complete medium (DMEM plus 10% fetal bovine serum) was added, and incubation continued for 20 h. Cells were washed twice with ice-cold PBS and lysed with Reporter Lysis Buffer (Promega, Madison, WI). Luciferase activity was quantified with a Berthold Centro LB 960 luminometer (Berthold Technologies, Bad Wildbad, Germany) using the Luciferase Assay System substrate (Promega, Madison, WI). Cellular protein concentrations were measured with the BCA Protein Assay Kit (Pierce, Rockford, IL) and read using an ELISA plate reader (Dynatech MR 5000, Dynatech Laboratories, Chantilly, VA) at 550 nm. Levels of luciferase expression are shown as relative luminescence units (RLU) per microgram of protein or as fold increase in luminescence over background. All experiments were carried out in triplicate. Each data point was averaged over the three replicates.

For dose-dependence experiments, cells were treated as described above with increasing concentrations of conjugates. After carrying out the luciferase assay and BCA Protein Assay, the remaining cell lysates (about 270 μL) were transferred into 2 mL microfuge tubes, and total RNA was extracted with 1 mL TRI Reagent (Sigma). Minor changes to the manufacturer's protocol were made to accommodate the presence of Reporter Lysis Buffer. Thus, 0.3 mL of chloroform was used for extraction, and the amount of isopropanol for RNA precipitation was increased to give a 1:1 mixture with the aqueous phase. The extracted RNA was examined by RT-PCR (SuperScript III One-Step RT PCR with Platinum Taq, Invitrogen; Genius Techne Thermal cycler) with forward primer 5′-TTG ATA TGT GGA TTT CGA GTC GTC-3′ and reverse primer 5′-TGT CAA TCA GAG TGC TTT TGG CG-3′. The products were analyzed on a 2% agarose gel, which was scanned using *Gene Tools Analysis* Software (SynGene, Cambridge, UK).

Cell Culture and Splicing Redirection Assays at Low Temperature. This was carried out as described previously (*18, 19*). HeLa pLuc705 cells were preincubated for 30 min in OptiMEM at 37 or 4 °C. The conjugate was then added and incubation continued for 1 h before assay for luciferase activity was measured as above.

Cell Culture and Splicing Redirection in the Presence of Endocytosis Inhibitors. This was carried out similarly to the method described previously (*19*). HeLa pLuc705 cells were preincubated in OptiMEM at 37 °C for 20 min with one of the following inhibitors: chlorpromazine (30 μM), methyl-β-cyclodextrin (MBCD) (2.5 mM), nystatin (50 μM), or ammonium chloride (50 mM). Cells were washed twice with PBS and incubated in OptiMEM with the same concentrations of the inhibitors in the presence of 1 μM of peptide−PNA conjugate at 37 °C for 30 min. Cells were washed twice with PBS, 1 mL of DMEM complete medium was added, and incubation continued for 23 h. Each experiment was in triplicate. Luciferase expression was quantified as described above. At these concentrations of inhibitors and under the incubation conditions used, good cell viability was obtained in all cases (data not shown).

RESULTS

Synthesis of PNA705 Conjugates of Linear and Branched (R-Ahx-R)-Containing Peptides. Although the concept of chain branching through α and ε positions of Lys via use of Fmoc Lys(Fmoc)−OH was described first by Futaki (*21*), there were a number of significant differences in our methodology. First, we introduced proteolysis resistant Arg-Ahx-Arg (RXR) units as repeating units instead of oligo-Arg or Arg-$(Gly)_3$-Arg units. Second, we used the proteolysis resistant Ahx-βAla (Xβ) spacer between the branches and the C-terminal Cys residue used for conjugation to cargo, and we also varied the spacing within branches by addition of further X or β units. Third, we investigated 2-branched as well as 4-branched structures. Finally, we attached a PNA cargo via a disulfide bond and used the well-known HeLa pLuc705 cell reporter assay that is a measure of the ability of the peptide dendrimer structure to deliver the

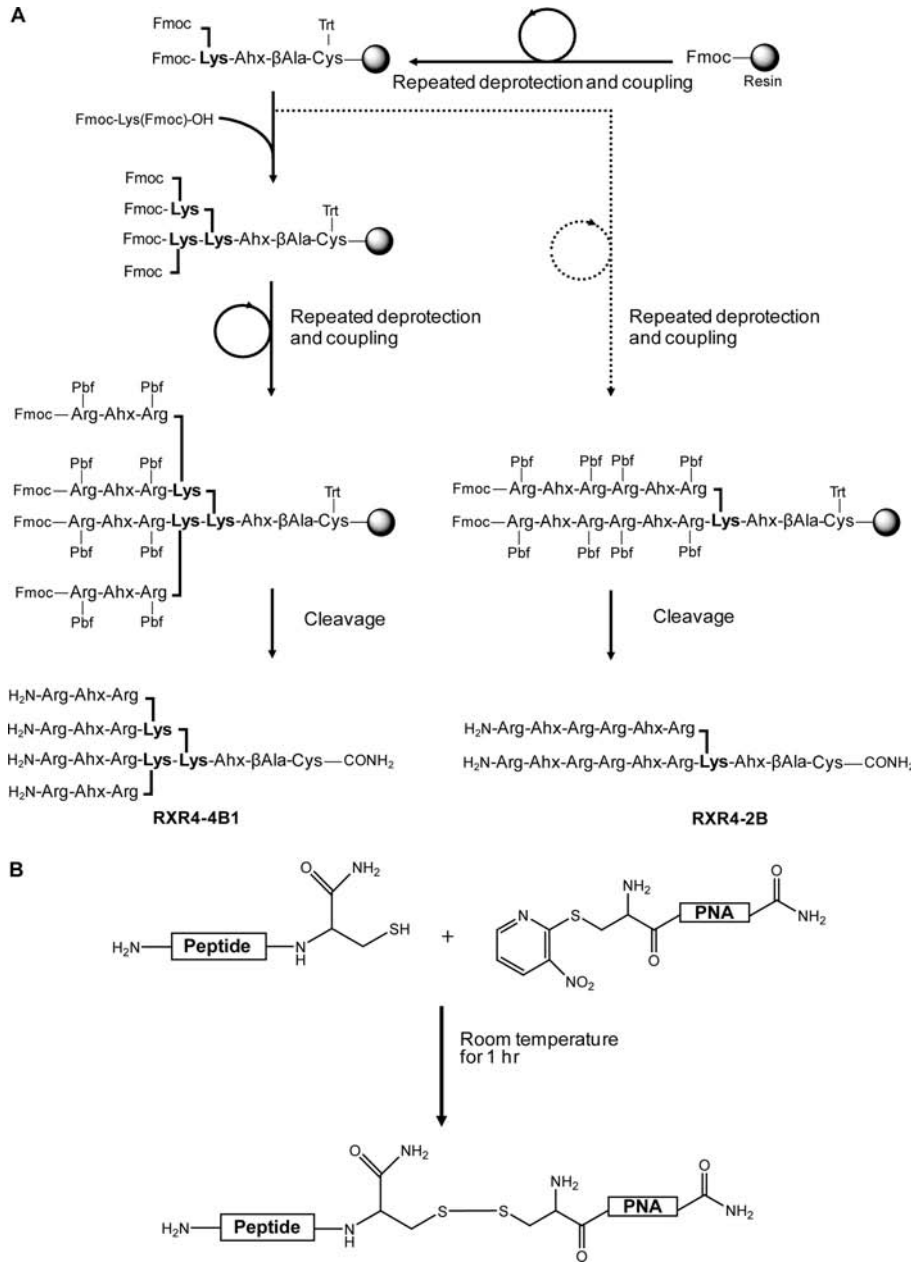


Figure 1. (A) Scheme of solid-phase peptide synthesis of branched peptides RXR4−4B1 and RXR4−2B as representative examples of the strategy of synthesis via branching with Fmoc-Lys (Fmoc)−OH and arms of R-Ahx-R units. Reagents and resin are as described in the Experimental section. (B) Scheme of the disulfide conjugation method used where the PNA contains a NPys-Cys functionality and the peptide a C-terminal free Cys functionality.

cargo to the nucleus. We compared linear (R-Ahx-R) peptides with branched analogues containing the same number of Arg residues, starting with 8-Arg residues $(R\text{-Ahx-R})_4$ and increasing the numbers of Arg residues to 12 and 16. The dendrimer structures and linear peptides RXR4, RXR6 and RXR8 are shown in Table 1.

Synthesis of branched peptide dendrimers (Figure 1A) was carried out very conveniently by microwave-aided solid-phase synthesis using the Fmoc method with a different solid support and different activation agent than reported by Futaki et al. (*21*). The coupling reactions were all very efficient, and only single couplings were needed except for Arg residues. It should be noted that we took account of the need to maintain at least a 5-fold excess of amino acids over solid-support-bound growing chains in coupling reactions at all times by reduction of the amount of solid support for 2- and 4-branched syntheses (see Experimental Procedures). The high yields and efficient syntheses are demonstrated by the HPLC traces obtained for the crude products of synthesis (Supporting Information Figure 1, showing representative 4- and 2-branched dendrimer peptide crude and purified products and MALDI-TOF analysis). Note that it was not necessary to use 5% pyridine/DMF solvent and extended (21 h) coupling times in the FmocArg(Pbf)−OH coupling reactions as previously reported (*21*). Instead, the use of microwave heating and a double coupling protocol proved highly effective (*25*).

Conjugation of purified branched and linear peptides to PNA was carried out through disulfide bond by reaction of each C-terminal Cys-containing peptide with the N-terminal Cys(N-Pys) PNA705 18-mer sequence (Figure 1B) as previously described for other linear cell-penetrating peptides (*16, 18, 19, 27*). Highly efficient conjugations were obtained with only small amounts of unconjugated peptide and PNA remaining (Supporting Information Figure 2 shows representative HPLCs for crude products and purified conjugates for RXR8−4B1-PNA705 and RXR8−2B-PNA705). Note that a disulfide linkage has the

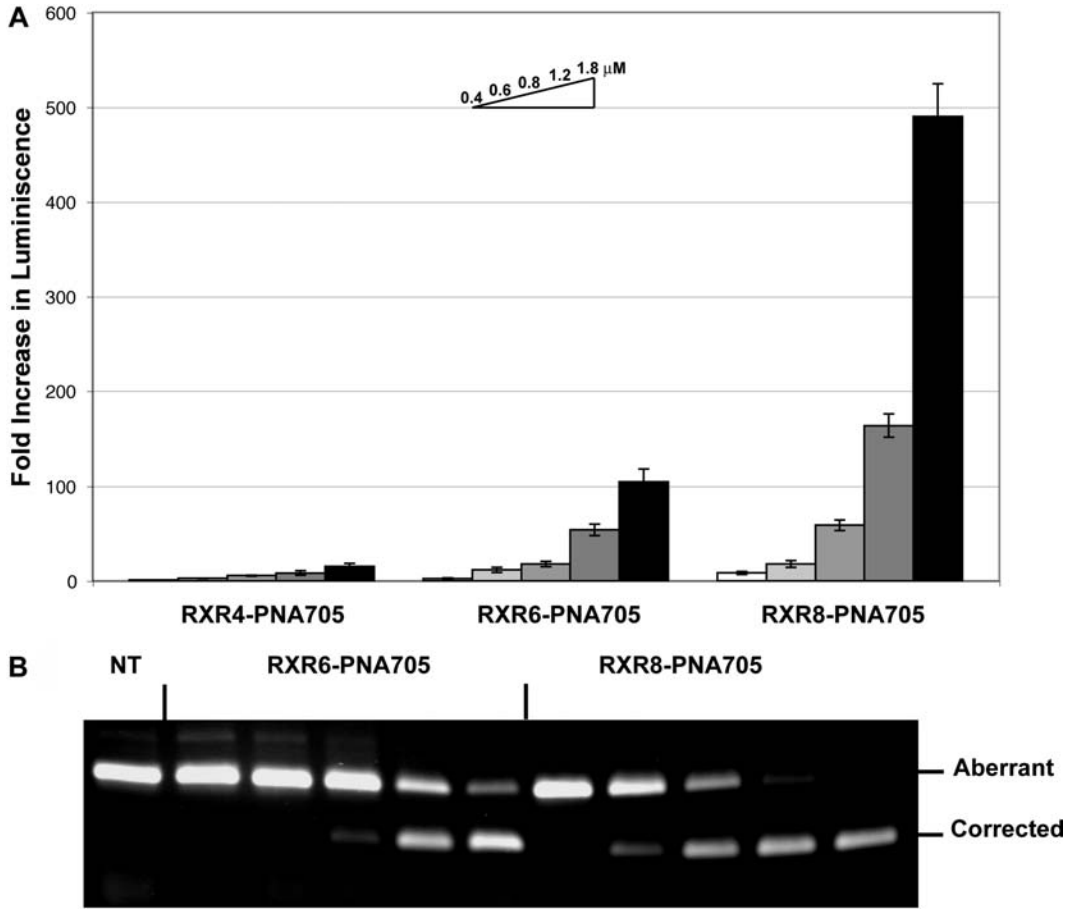


Figure 2. (A) Fold increase in luciferase expression induced by splicing redirection by incubation of RXR4-PNA705, RXR6-PNA705, and RXR8-PNA705 with HeLa pLuc705 cells. Concentrations of conjugates in each case (left to right) are 0.4, 0.6. 0.8. 1.2, and 1.8 μM. (B) RT-PCR analysis showing aberrant and redirected levels of RNA as a function of concentrations of RXR6-PNA705 or RXR8-PNA705. Concentrations of conjugates (left to right) are the same as in (A), namely, 0.4, 0.6, 0.8, 1.2, and 1.8 μM. NT = cells not treated.

advantage that, in principle, the cargo can be released from the peptide vector once inside cells because of the reducing environment, as we have used for our previous R10p53^{tet} dendrimer system (*18*).

Splice-Redirection Activity of Linear and Branched Peptide−PNA Conjugates. We reported previously the splice-redirection activity of linear $(RXR)_4$-PNA and linear $(RXR)_4$-PMO conjugates in the HeLa pLuc705 cell assay (*10, 12*). Although significantly better than $(Lys)_8$, Tat (48−60), Penetratin, and oligoArg conjugates (*12, 19, 28*), EC_{50} values using an RT-PCR assay for the amount of splice-redirected mRNA remained in the micromolar range. To our knowledge, splice-redirection of PNA conjugates to peptide containing a larger number of Arg residues has not been reported previously. We found that for the linear (R-Ahx-R) peptides an increase in the number of Arg residues to 12 (RXR6-PNA705) resulted in a significantly more active conjugate in the luciferase up-regulation assay than RXR4-PNA705, with a further increase in activity for 16 Arg residues (RXR8-PNA705) (Figure 2a). EC_{50} values (Table 1) were determined from the RT-PCR assay by scanning of the agarose gel electrophoregrams (Figure 2b). The biggest improvement in activity was between RXR4 (EC_{50} > 3 μM) and RXR6 (1.0 ± 0.1 μM), whereas a more modest improvement was seen for RXR8 (0.8 ± 0.1 μM).

PNA705 conjugates of 4-branched constructs of RXR4 where each arm contained a single RXR (RXR4−4B1), or a single RXRX (RXR4−4B2), or where additional X spacing was included between the first and second branch points (RXR4−4B3), or a 2-branch analogue with RXRRXR on each branch (RXR4−2B) all showed a dramatic loss of splice-redirecting activity, such that even at 3 μM concentration the luciferase expression activity was barely above background (Figure 3A). Likewise, a 4-branched structure containing four RXRRXβ arms (RXR6−4B) had very poor activity (Figure 3B, Table 1). By contrast, for PNA705 conjugates of RXR6 branched analogues, a 2-branched structure containing arms of RXRRXRRXR (RXR6−2B) gave rise to luciferase expression levels only a little lower than that of the linear RXR6 (Figure 3B, Table 1).

The PNA705 conjugate of RXR8 2-branched analogue (RXR8−2B) showed luciferase expression levels very similar to that for the linear RXR8 (Figure 3C), whereas the 4-branched RXR8 analogues (RXR8−4B1 and RXR8−4B2) were only slightly reduced in activity compared to the linear RXR8 (Figure 3C). The EC_{50} values (Table 1) for splice-redirected RNA measured by the RT-PCR assay in general reflected the same trends as for luciferase up-regulation results, with values for PNA705 conjugates of 2-branched peptides with 12 and 16 residues being very similar to their linear counterparts. Overall, chain branching appears to be best tolerated when the number of Arg residues is 16. For both 12 and 16 Arg residues, 2-branched structures are more active than 4-branched structures and are similar to their linear counterparts in activity. None of the 12 and 16 Arg residue conjugates showed significant toxicity, and the cell viability remained good in an MTS assay up to 3 μM with HeLa pLuc705 cells (Figure 4).

We also carried out the same luciferase and RT-PCR assays for RXR8−4B-PNA705, RXR8−2B-PNA705, and RXR8-PNA705 using a human melanoma tumor cell line containing the same integrated pLuc705 plasmid, namely, A375SM-Luc705-B cells (*29*). The results were broadly similar to the

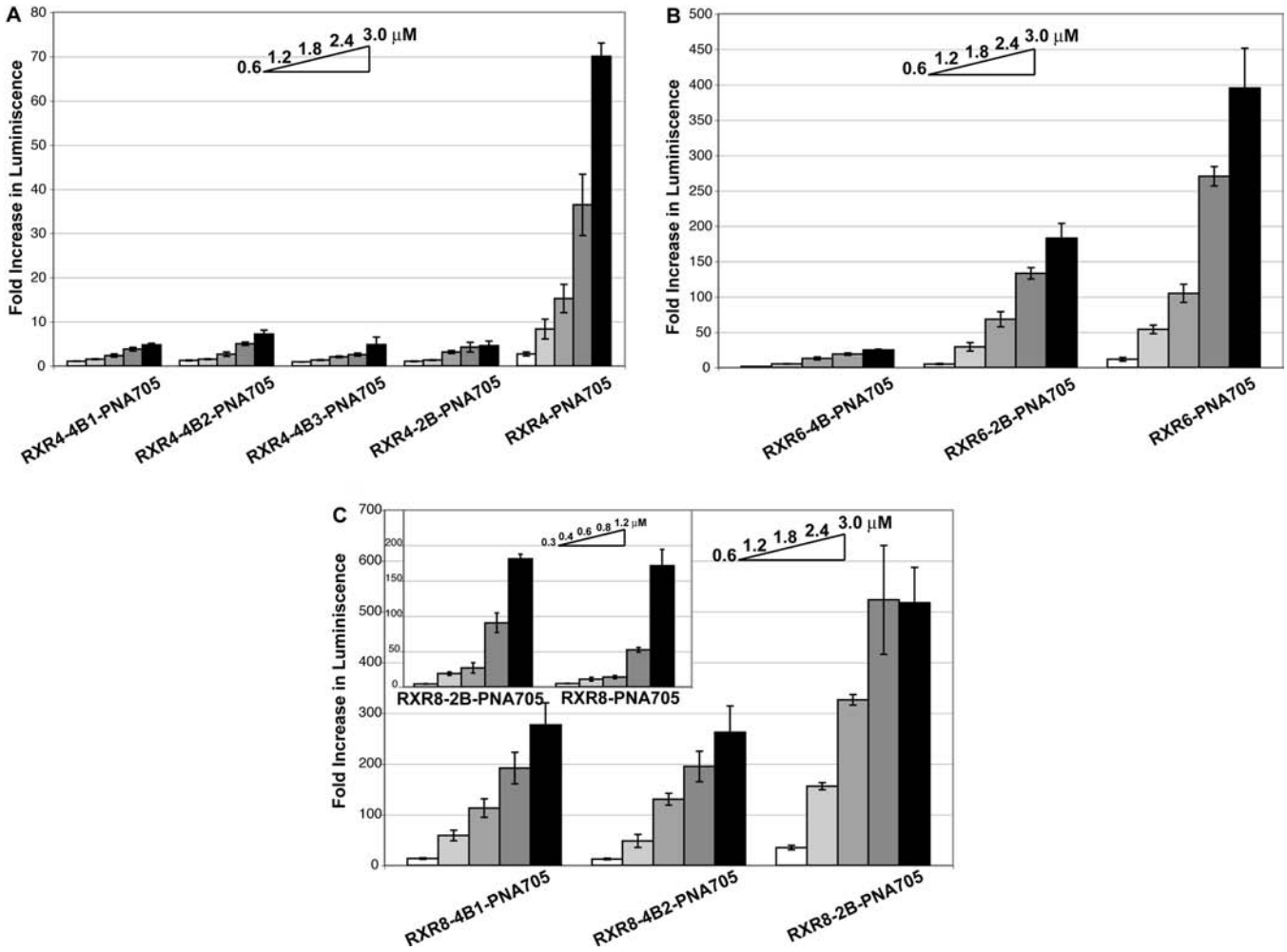


Figure 3. Fold increase in luciferase expression induced by splicing redirection in HeLa pLuc705 cells over the conjugate concentration range 0.6−3.0 μM: (A) branched and linear RXR4-PNA705 derivatives, (B) branched and linear RXR6-PNA705 derivatives, and (C) branched RXR8-PNA705 derivatives (inset shows a comparison of RXR8-2B-PNA705 and linear RXR8-PNA705 over a different concentration range 0.3−1.2 μM).

HeLa cell results in splice-redirecting activity, but in each case, the EC_{50} values in the RT-PCR assay were lower than for the HeLa cells (RXR8−4B1, 0.51 ± 0.03 μM; RXR8−2B, 0.35 ± 0.02 μM; RXR8, 0.42 ± 0.05 μM), probably reflecting a lower copy number of integrated pLuc705 plasmid in the melanoma cell line, but cell viability dropped significantly at 1 μM and higher concentrations for all these peptide−PNA conjugates (data not shown).

In addition, we carried out the HeLa pLuc705 cell luciferase assays at 1.2 μM concentration for 4 h in the presence of 10% fetal bovine serum (FBS). Interestingly, in most cases for 12 Arg and 16 Arg conjugates of PNA705 there was significant activity retained in the presence of serum, compared to serum-free media, especially for the 2-branched and the linear constructs (Supporting Information Figure 3). This is in contrast to unbranched peptide−PNA conjugates containing fewer Arg residues such as RXR4-PNA and R6Pen-PNA, where we had previously found very poor activity in the presence of serum (Arzumanov, A., Abes, R., Gait, M. J., and Lebleu, B., unpublished data).

Thus, we also synthesized a 25-mer PMO conjugate of RXR8−2B targeted to exon 23 of a mutated mouse dystrophin gene by the method previously described (*16*). At 1 μM concentration of incubation with differentiated *mdx* mouse cells in the presence of 10% FBS, but in the absence of any transfection agent, we were able to obtain >70% exon skipping in this model system, higher than for previously studied linear RXR peptide−PMO constructs (data not shown). This demonstrates that there are potential advantages of a higher number of Arg residues in the peptides in terms of activity levels in the presence of serum, which could be crucial for clinical applications.

Mechanism of Cell Uptake in HeLa pLuc705 Cells. The internalization mechanism of CPPs has been questioned ever since the first peptides were discovered. Initially, the consensus in the field was for direct translocation across the plasma membrane, but nowadays, endocytosis is considered the major pathway for many CPPs at low concentrations (*2*). We thus felt it necessary to determine whether increased biological activity of our branched peptide conjugates in comparison with the linear forms could be due to the use of a different cell uptake route. We first examined the splicing redirection activity of these peptide conjugates at low temperature of 4 °C (conditions preventing any form of endocytosis) and physiological temperature 37 °C. Cells were preincubated at 4 or 37 °C during 30 min and then incubated with the different branched peptide conjugates at 1 μM during 1 h at 4 or 37 °C. The results showed a decrease of the activity at low temperature, suggesting that the internalization of the branched peptide conjugates is predominantly energy dependent (Figure 5).

Likewise, controversies remain concerning the endocytotic pathway used for the cell internalization pathway of CPP−cargo conjugates with data advocating all three major routes (*2, 3*). We thus investigated the effects of typical inhibitors of clathrin-dependent, caveolae-dependent, and macropinocytosis pathways,

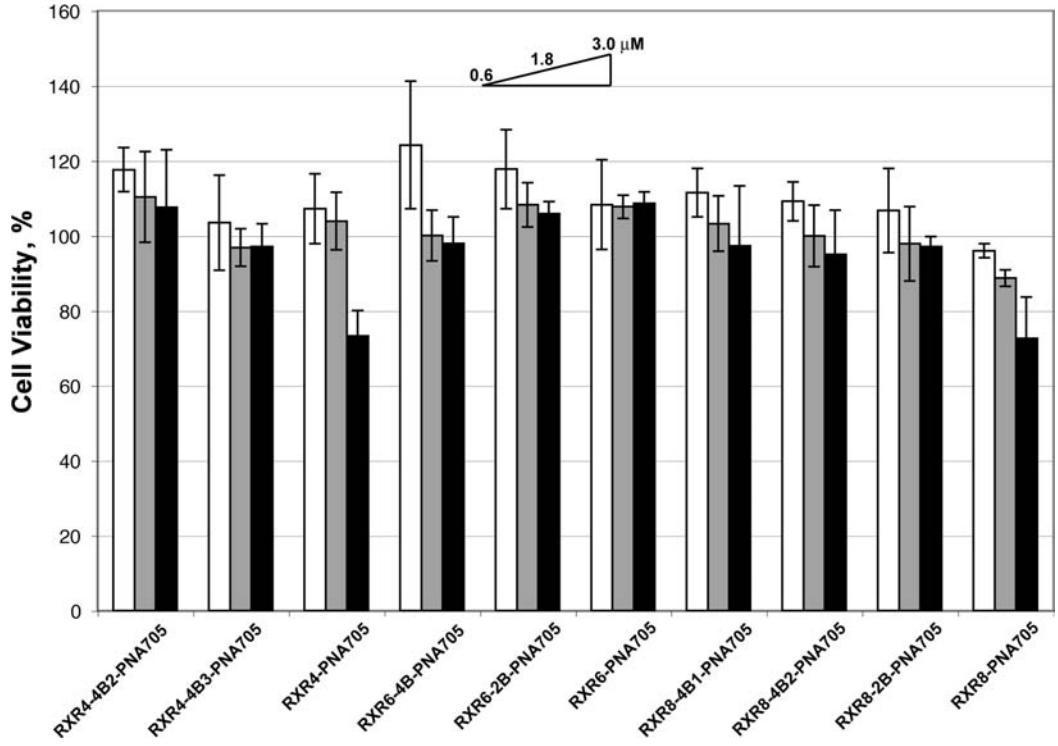


Figure 4. Percentage cell viability for branched and linear peptide-PNA705 conjugates as measured by the MTS assay. To each well of cells treated for 4 h with 0.6, 1.8, or 3.0 μM conjugate in OptiMEM (100 μL, 96 well plate) was added 20 μL of CellTiter 96 Aqueous One solution cell proliferation assay (Promega) and the color intensity measured by plate reader (Tecan, Switzerland) at 490 nm as compared to a control of cells which were not treated with conjugate. Experiments were carried out in triplicate.

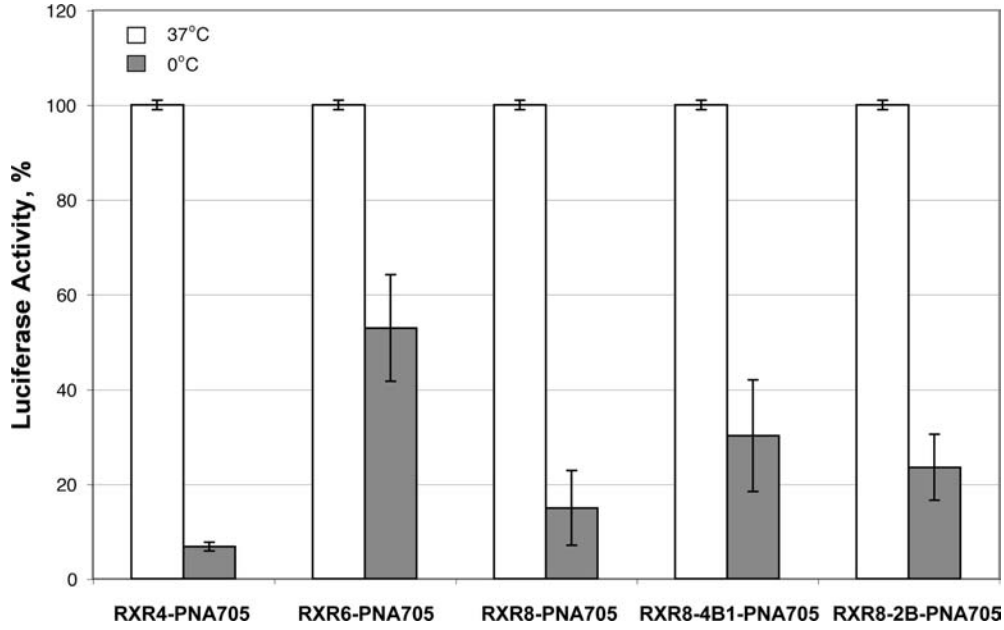


Figure 5. Low-temperature study (37 and 4 °C). Cells were preincubated at 37 °C (white bars) or 4 °C (gray bars) for 1 h and further incubated in the same conditions with PNA705 conjugates of RXR4, RXR6, RXR8, RXR8−4B1, or RXR8−2B, peptides conjugates at 1 μM. Luciferase expression assays were carried out after 24 h as indicated in the Experimental Procedures. Experiments were made in triplicate, and error bars are indicated. Data are expressed as the percentage of luciferase activity.

which are chlorpromazine, nystatin, and methyl-β-cyclodextrin (MBCD), respectively. The importance of acidification of endocytotic vesicles was evaluated with NH_4Cl. For these experiments, incubation times were reduced in order to avoid cytotoxicity of the inhibitors. Interestingly, splicing redirection efficiency by branched CPPs remained unchanged when reducing the incubation time to 30 min as compared to the 4 h incubations generally used in our studies. This is very different from the situation observed with RXR4-PMO conjugate, for example (data not shown).

Nystatin addition resulted in some reduction in the biological activity of both linear and branched peptides (Figure 6). Since nystatin complexes cholesterol and alters the structure and function of glycolipid microdomains, caveolae seem to be involved. Somewhat surprisingly, the activity increased using methyl-β-cyclodextrin, suggesting that branched peptides may

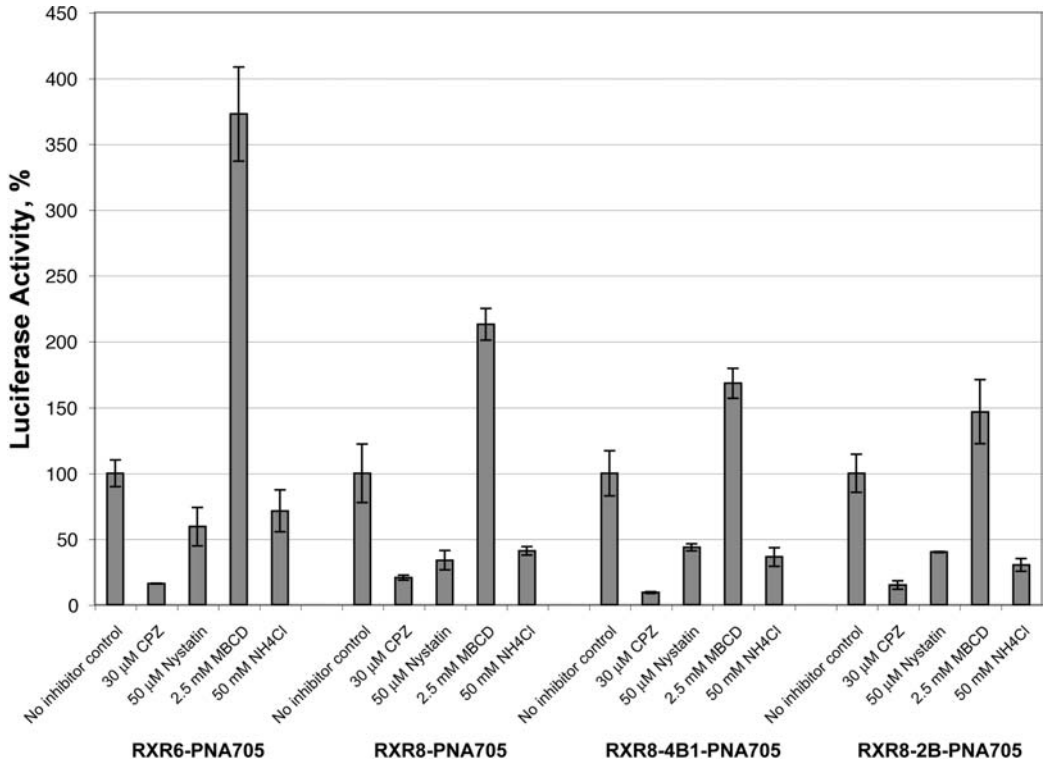


Figure 6. Luciferase activity of PNA705 conjugates of RXR6, RXR8, RXR8−4B1, or RXR8−2B using endocytosis inhibitors. Cells were preincubated at 37 °C for 20 min with chlorpromazine (30 μM), methyl-β-cyclodextrin (MBCD) (2.5 mM), nystatin (50 μM), or ammonium chloride (50 mM). Cells were further incubated in the same conditions with the peptide conjugates at 1 μM for 30 min. Luciferase expression assays were carried out after 24 h as indicated in the Experimental Procedures. Experiments were made in triplicate, and error bars are indicated. Data are expressed as the percentage of luciferase activity.

become internalized by direct membrane translocation into the cytoplasm when the membrane cholesterol is depleted, as previously reported for oligoArg (*30*). By contrast, chlorpromazine exerted a very strong effect on the biological activity with almost 90% decrease for RXR8−2B-PNA and RXR8−4B1-PNA (Figure 6). Together, these data support the notion that the clathrin-dependent uptake pathway is prominently and preferentially involved in the internalization of the branched peptides, as has already been documented for linear RXR4-PMO (*11*), Pip peptide−PNA conjugates (*16*), and Tat peptide (*15*), but with some caveolae dependence also.

Cells were also treated with NH_4Cl, which is known to neutralize the acidification of endosomal and lysosomal compartments (*31*). NH_4Cl (50 mM) caused a strong reduction in the splicing redirection activity of both linear and branched peptides with 16 Arg residues suggesting there is an accumulation in acidic compartment as shown previously for Tat−PNA conjugates (*15*) and a requirement for endosomal acidification for endosomal escape (Figure 6).

DISCUSSION

Synthesis of branched dendrimer peptides using R-Ahx-R repeating units proved very straightforward by the use of microwave-aided Fmoc solid-phase synthesis techniques. Indeed, the number of coupling steps in branched peptide syntheses is less than that for the equivalent linear peptide syntheses containing the same number of Arg residues, and the HPLC traces of the crude products all showed very high overall yields (Supporting Information Figure 1). Disulfide conjugations to PNA were just as effective as for linear peptides (Supporting Information Figure 2).

The use of a HeLa pLuc705 splice-redirecting assay for assessment of CPPs is particularly valuable to judge delivery efficacy because of its convenience, large dynamic range and its ability to measure activity in the cell nucleus for attached PNA or PMO through assays at both the RNA and protein expression levels. In our opinion, a functional assay of this type is superior to the use of fluorescent labels and observation of cell localization by confocal microscopy, because it is a true measure of the ability of a cargo to be delivered in a biologically relevant way, in this case to the cell nucleus. Thus, despite the apparently promising results of Futaki et al. for a 4-branched RG_3R peptide with 8-Arg residues in total where substantial cell uptake of the peptide was observed when a fluorescent label was attached (*21, 22*), by contrast, we found extremely poor luciferase up-regulation in the HeLa cell assay for PNA705 conjugates of both 2-branched and 4-branched peptide with only 8 Arg residues and much poorer than the linear RXR4-PNA. This suggests that branching the 8 Arg residues in this way does not trigger sufficient endosomal escape of the PNA cargo and represents a good example of how following the uptake of fluorescently labeled peptides by confocal microscopy is not predictive of subsequent biological function. We already observed a lack of correlation between cell uptake and biological activity in our SAR studies of a series of linear RXR−PMO conjugates (*13*).

As the number of Arg residues is increased to 12 and 16, however, not only does the overall level of luciferase up-regulation and splicing correction increase significantly with the number of Arg residues, but chain branching is now increasingly tolerated (Figures 2 and 3). An increase in splice-redirecting activity as the number of Arg residues is raised from 8 to 12 and 16 is not surprising, since the overall cell uptake for oligo-Arg peptides of 5 to 8 residues was shown to increase as a function of the number of Arg residues (*32*). However, the number of Arg residues and the precise three-dimensional configuration within the peptide may also affect other steps in the delivery to the nucleus. In general, we found that the longer

the run of R-Ahx-R motifs on each arm, the better the activity for the same total number of Arg residues. In the linear $(R\text{-}Ahx\text{-}R)_4$ peptide, we found previously that aminohexanoic acid spacing between guanidinium groups was optimal for splice-redirecting activity for an attached PMO oligonucleotide compared to shorter or longer spacers (*13*). Further work will be necessary to understand if this finding also holds true for the branched peptides.

However, a differential level of overall cell uptake by linear and branched peptides cannot be ruled out, especially since it has been shown for fluorescently labeled branched 8-Arg peptides that they are more dependent on interaction with membrane-associated heparan sulfate proteoglycans on the cell surface compared to linear R_8 peptides (*22*). Nevertheless, our data are consistent with the notion that the active fraction of branched Arg-rich peptide−PNAs does not use a different pathway of uptake compared to the linear R-Ahx-R peptides. This is evidenced by the very similar deleterious effects on luciferase up-regulation activity seen upon lowering the temperature of the splice correction assay to 4 °C and the similar behavior upon coincubation with endocytosis inhibitors for both branched and linear peptide−PNA constructs (Figures 5 and 6).

The very large effect of chlorpromazine on 16-Arg branched and linear peptide−PNA conjugates (Figure 6) was similar to the effects we previously observed in the same HeLa pLuc705 cells for other highly cationic peptide conjugates of PNA and PMO, such as linear RXR4-PMO (*11*), Pip peptide-PNA (*16*), and Tat peptide (*15*). We conclude as before that clathrin-dependent uptake predominates. However, the effect of nystatin on the luciferase up-regulation was much larger in the cases of both linear and branched RXR−PNA conjugates compared to the only small effects observed of nystatin on uptake and activity of the Tat peptide (*15*) and on Pip-PNA (*16*). This surprising result suggests that caveolae may play some part in uptake where there are a larger number of Arg residues, as has already been shown for Tat fusion proteins (*33*). This could account for the moderate effect of NH_4Cl in some cases, since caveolae-mediated endocytosis does not involve acidic compartments (*34*).

Our results are not entirely consistent with inhibitor experiments in the same cell assay for PNA705 conjugates of moderately cationic, Arg-containing peptides Penetratin and M918, where macropinocystosis was suggested as the major uptake pathway and clathrin-dependent endocytosis predominated only for the more hydrophobic TP10-PNA conjugate (*35*). The concentration of chlorpromazine used in our case was 30 μM, whereas in the case of Lundin et al., it was only 10 μM, and the peptide−PNA concentrations used in our case were 5-fold lower. Poon et al. reported for R_8-functionalized liposome uptake that endocytotic uptake switches from clathrin-dependent to macropinocytosis as peptide density on the liposome surface was increased (*36*), and a mechanism switch is one possible explanation for the discrepancy between our studies and those of Lundin et al. Another possibility is that the choice of uptake pathway is more subtly affected by the different relative positions of the hydrophobic and cationic elements in M918 and Penetratin as compared to the R-Ahx-R constructs. The possible sensitivity of inhibitor use to different cellular conditions, as well as possible subtle effects of amino acid composition and positioning, makes it hard to draw too definitive conclusions about the endocytosis pathways used by cationic CPPs in this class when conjugated to PNA. Further, our result that MBCD addition significantly stimulated luciferase up-regulation suggests that, when one pathway is inhibited, it is possible for cells to utilize or stimulate an alternative uptake pathway. More sophisticated cell techniques will be needed to clarify the dominant endocytotic uptake pathways for particular peptide−cargo conjugates.

A major aim of our experiments was to determine whether branched R-Ahx-R peptides could prove suitable for future development in a therapeutic context. We were particularly heartened that significant splice-redirecting activity was retained in the HeLa cell assay in the presence of 10% serum for many of the 12-Arg and 16-Arg containing conjugates (Supporting Information Figure 3), and we obtained extremely high exon skipping for RXR8−2B-PMO in a *mdx* mouse muscle cell assay that is used as a model for DMD (data not shown). However, we became concerned about the possibility of increased toxicity resulting from the use of larger numbers of Arg residues in the peptides. Although we did not observe toxicity up to 3 μM in the HeLa pLuc705 cell assay (Figure 4), we did see significant loss of cell viability at 1 μM in A375SM-Luc705-B melanoma cells for all 12 and 16 Arg conjugates (data not shown). Further, a very recent report has suggested that at high doses in both mice and monkeys some kidney toxicity is apparent when an 8-Arg peptide-PMO is injected intravenously (*6*). Thus, despite the substantial increase in cell delivery potential afforded by such dendrimeric peptide constructs, peptide conjugates with high Arg content must be used with caution in therapeutic development until the sources of these toxicities (both cellular and in vivo) can be controlled. In the case of cells, more detailed studies of membrane leakage or other specific cell toxicity assays could prove instructive.

Nevertheless, our studies have been useful in understanding some of the three-dimensional requirements for cell uptake and splice-redirecting activity of Arg-rich peptides based on an R-Ahx-R motif, and we have demonstrated that chain branching is well-tolerated when the number of Arg residues is high, especially for 2-branched peptide structures. We have shown also how such peptide chain branching is readily accessible chemically and in high yield. In principle, our methods could be used also to introduce other multiple motifs such as cell-specific uptake sequences (*17*) as conjugates of PNA or PMO cargoes. Our work expands the three-dimensional space available for CPP development.

ACKNOWLEDGMENT

We thank Rudy Juliano (University of North Carolina) for the cell line A375SM pLuc705-B. Amer Saleh was supported in part by a grant from MRC-Technology and Rachida Abes by a PhD fellowship from the Ligue Nationale contre le Cancer. We thank Donna Williams for chemical synthesis of PNA705.

Supporting Information Available: HPLC purifications of representative synthesis of branched peptides and peptide-PNA conjugates, and luciferase up-regulation results for 16-Arg constructs in HeLa pLuc705 cells in the presence of 10% FBS. This material is available free of charge via the Internet at http://pubs.acs.org.

LITERATURE CITED

(1) Langel, U. (2007) *Handbook of Cell Penetrating Peptides*, p 600, CRC Press, Boca Raton.

(2) Lebleu, B., Moulton, H. M., Abes, R., Ivanova, G. D., Abes, S., Stein, D. A., Iversen, P. L., Arzumanov, A., and Gait, M. J. (2008) Cell penetrating peptide conjugates of steric block oligonucleotides. *Adv. Drug Delivery Rev. 60*, 517–529.

(3) Said Hassane, F., Saleh, A. F., Abes, R., Gait, M. J., and Lebleu, B. (2010) Cell penetrating peptides: overview and applications to the delivery of oligonucleotides. *Cell. Mol. Life Sci. 67*, 715–726.

(4) Fabani, M. M., Ivanova, G. D., and Gait, M. J. (2008) Peptide-peptide nucleic acid conjugates for modulation of gene expres-

sion, in *Therapeutic Oligonucleotides* (Kurreck, J., Ed.) pp 80−102, Royal Society of Chemistry, Cambridge, U.K.
(5) Moulton, H. M., and Moulton, J. D. (2008) Antisense morpholino oligomers and their peptide conjugatesin, in *Therapeutic Oligonucleotides* (Kurreck, J., Ed.) pp 43−79, Royal Society of Chemistry, Cambridge, U.K.
(6) Moulton, H. M., and Moulton, J. D. (2010) Morpholinos and their peptide conjugates: therapeutic promise and challenge for Duchenne muscular dystrophy. *Biochim. Biophys. Acta*, doi: 10.1016/j.bbamem.2010.02.012.
(7) Wood, M. J. A. (2010) Towards an oligonucleotide therapy for Duchenne muscular dystrophy: a complex development challenge. *Sci. Translat. Med. 2*, 25ps15.
(8) Richard, J.-P., Melikov, K., Vivès, E., Ramos, C., Verbeure, B., Gait, M. J., Chernomordik, L. V., and Lebleu, B. (2003) Cell-penetrating peptides. A re-evaluation of the mechanism of cellular uptake. *J. Biol. Chem. 278*, 585–590.
(9) Kang, S.-H., Cho, M.-J., and Kole, R. (1998) Up-regulation of luciferase gene expression with antisense oligonucleotides: implications and applications in functional assay development. *Biochemistry 37*, 6235–6239.
(10) Abes, R., Arzumanov, A., Moulton, H. M., Abes, S., Ivanova, G. D., Iversen, P. L., Gait, M. J., and Lebleu, B. (2007) Cell-penetrating-peptide-based delivery of oligonucleotides: an overview. *Biochem. Soc. Trans. 35*, 775–779.
(11) Abes, S., Moulton, H. M., Clair, P., Prevot, P., Youngblood, D. S., Wu, R. P., Iversen, P. L., and Lebleu, B. (2006) Vectorization of morpholino oligomers by the (R-Ahx-R)$_4$ peptide allows efficient splicing correction in the absence of endosomolytic agents. *J. Controlled Release 116*, 304–313.
(12) Abes, S., Moulton, H. M., Turner, J. J., Clair, P., Richard, J.-P., Iversen, P. L., Gait, M. J., and Lebleu, B. (2007) Peptide-based delivery of nucleic acids: design, mechanism of uptake and applications to splice-correcting oligonucleotides. *Biochem. Soc. Trans. 35*, 53–55.
(13) Abes, R., Moulton, H. M., Clair, P., Yang, S. T., Abes, S., Melikov, K., Prevot, P., Youngblood, D. S., Iversen, P. L., Chernomordik, L. V., and Lebleu, B. (2008) Delivery of steric block morpholono oligomers by (R-X-R)4 peptides: structure-activity studies. *Nucleic Acids Res. 36*, 6343–6354.
(14) Wender, P. A., Mitchell, D. J., Pattabiraman, K., Pelkey, E. T., Steinman, L., and Rothbard, J. B. (2000) The design, synthesis, and evaluation of molecules that enable or enhance cellular uptake: peptoid molecular transporter. *Proc. Natl. Acad. Sci. U.S.A. 97*, 13003–13008.
(15) Richard, J. P., Melikov, K., Brooks, H., Prevot, P., Lebleu, B., and Chernomordik, L. V. (2005) Cellular uptake of unconjugated TAT peptide involves clathrin-dependent endocytosis and heparan sulfate receptors. *J. Biol. Chem. 280*, 15300–15306.
(16) Ivanova, G. D., Arzumanov, A., Abes, R., Yin, H., Wood, M. J. A., Lebleu, B., and Gait, M. J. (2008) Improved cell-penetrating peptide-PNA conjugates for splicing redirection in HeLa cells and exon skipping in *mdx* mouse muscle. *Nucleic Acids Res. 36*, 6418–6428.
(17) Yin, H., Moulton, H. M., Betts, C., Seow, Y., Boutilier, J., Iversen, P. L., and Wood, M. J. A. (2009) A fusion peptide directs enhanced systemic dystrophin exon skipping and functional restoration in dystrophin-deficient *mdx* mice. *Hum. Mol. Genet. 18*, 4405–4414.
(18) Said Hassane, F., Ivanova, G. D., Bolewska-Pedyczak, E., Abes, R., Arzumanov, A., Gait, M. J., Lebleu, B., and Gariépy, J. (2009) A peptide-based dendrimer that enhances the splice-redirecting activity of PNA conjugates in cells. *Bioconjugate Chem. 20*, 1523–1530.
(19) Abes, S., Turner, J. J., Ivanova, G. D., Owen, D., Williams, D., Arzumanov, A., Clair, P., Gait, M. J., and Lebleu, B. (2007) Efficient splicing correction by PNA conjugation to an R_6-Penetratin delivery peptide. *Nucleic Acids Res. 35*, 4495–4502.
(20) Kawamura, K. S., Sung, M., Bolewska-Pedyczak, E., and Gariépy, J. (2006) Probing the impact of valency on the routing of arginine-rich peptides into eukaryotic cells. *Biochemistry 45*, 1116–1127.
(21) Futaki, S., Nakase, I., Suzuki, T., Youjun, Z., and Sugiura, Y. (2002) Translocation of branched-chain arginine peptides through cell membranes: flexibility in the spacial disposition of positive charges in membrane-permeable peptides. *Biochemistry 41*, 7925–7930.
(22) Nakase, I., Tadokoro, A., Kawabata, N., Takeuchi, T., Katoh, H., Hiramoto, K., Negishi, M., Nomizu, M., Sugiura, Y., and Futaki, S. (2007) Interaction of arginine-rich peptides with membrane-associated proteoglycans is crucial for induction of actin organization and macropinocytosis. *Biochemistry 46*, 492–501.
(23) Li, Y.-F., and Morcos, P. A. (2008) Design and synthesis of dendritic molecular transporter that achieves efficient *in vivo* delivery of morpholino antisense oligo. *Bioconjugate Chem. 19*, 1464–1470.
(24) Wu, B., Li, Y.-F., Morcos, P. A., Doran, T. J., Lu, P., and Lu, Q. L. (2009) Octa-guanidine morpholino restores dystrophin expression in cardiac and skeletal muscles and ameliorates pathology in dystrophic mdx mice. *Mol. Ther. 17*, 864–871.
(25) Banerjee, J., Hanson, A. J., Muhonen, W. W., Shabb, J. B., and Mallik, S. (2010) Microwave-assisted synthesis of triple-helical collagen-mimetic lipopeptides. *Nat. Protoc. 5*, 39–50.
(26) Fabani, M. M., Abreu-Goodger, C., Williams, D., Lyons, P. A., Torres, A., Smith, K. G. C., Enright, A. J., Gait, M. J., and Vigorito, E. (2010) Efficient inhibition of miR-155 function in vivo by Peptide Nucleic Acids. *Nucleic Acids Res. 38*, 4466–4475.
(27) Turner, J. J., Ivanova, G. D., Verbeure, B., Williams, D., Arzumanov, A., Abes, S., Lebleu, B., and Gait, M. J. (2005) Cell-penetrating peptide conjugates of peptide nucleic acids (PNA) as inhibitors of HIV-1 Tat-dependent trans-activation in cells. *Nucleic Acids Res. 33*, 6837–6849.
(28) Abes, S., Williams, D., Prevot, P., Thierry, A. R., Gait, M. J., and Lebleu, B. (2006) Endosome trapping limits the efficiency of splicing correction by PNA-oligolysine conjugates. *J. Controlled Release 110*, 595–604.
(29) Alam, M. R., Dixit, V., Kang, H., Li, Z.-B., Chen, X., Trejo, J., Fisher, M., and Juliano, R. L. (2008) Intracellular delivery of an anionic antisense oligonucleotide via receptor mediated endocystosis. *Nucleic Acids Res. 36*, 2764–2776.
(30) Futaki, S., Nakase, I., Tadokoro, A., Takeuchi, T., and Jones, A. T. (2007) Arginine-rich peptides and their internalization mechanisms. *Biochem. Soc. Trans. 35*, 784–787.
(31) Zhang, X., Jin, Y., Plummer, M. R., Pooyan, S., Gunaseelan, S., and Sinko, P. J. (2009) Endocytosis and membrane potential are required for HeLa cell uptake of R.I.-CKTat9, a retro-inverso Tat cell penetrating peptide. *Mol. Pharmaceutics 6*, 836–848.
(32) Goun, E. A., Pillow, T. H., Jones, L. R., Rothbard, J. B., and Wender, P. A. (2006) Molecular transporters: synthesis of oligoguanidinium transporters and theor application to drug delivery and real-time imaging. *ChemBioChem 7*, 1497–1515.
(33) Ferrari, A., Pellegrini, V., Arcangeli, C., Fittipaldi, A., Giacci, M., and Beltram, F. (2003) Caveolae-mediated internalization of extracellular HIV-1 Tat fusion proteins visualized in real time. *Mol. Ther. 8*, 284–294.
(34) Pelkmans, L., Kartenbeck, J., and Helenius, A. (2001) Caveolar endocytosis of simian virus 40 reveals a new two-step vesicular transport pathway to the ER. *Nat. Cell Biol. 3*, 473–483.
(35) Lundin, P., Johansson, H., Guterstam, P., Holm, T., Hansen, M., Langel, U., and El-Andalousi, S. (2008) Distinct uptake routes of cell-penetrating peptide conjugates. *Bioconjugate Chem. 19*, 2535–2542.
(36) Poon, G. M. K., and Gariépy, J. (2007) Cell-surface proteoglycans as molecular portals for cationic peptide and polymer emtry into cells. *Biochem. Soc. Trans. 35*, 788–793.

BC100275R

SUPPPLEMENTARY INFORMATION

Synthesis and splice-redirecting activity of branched, arginine-rich peptide dendrimer conjugates of Peptide Nucleic Acid oligonucleotides

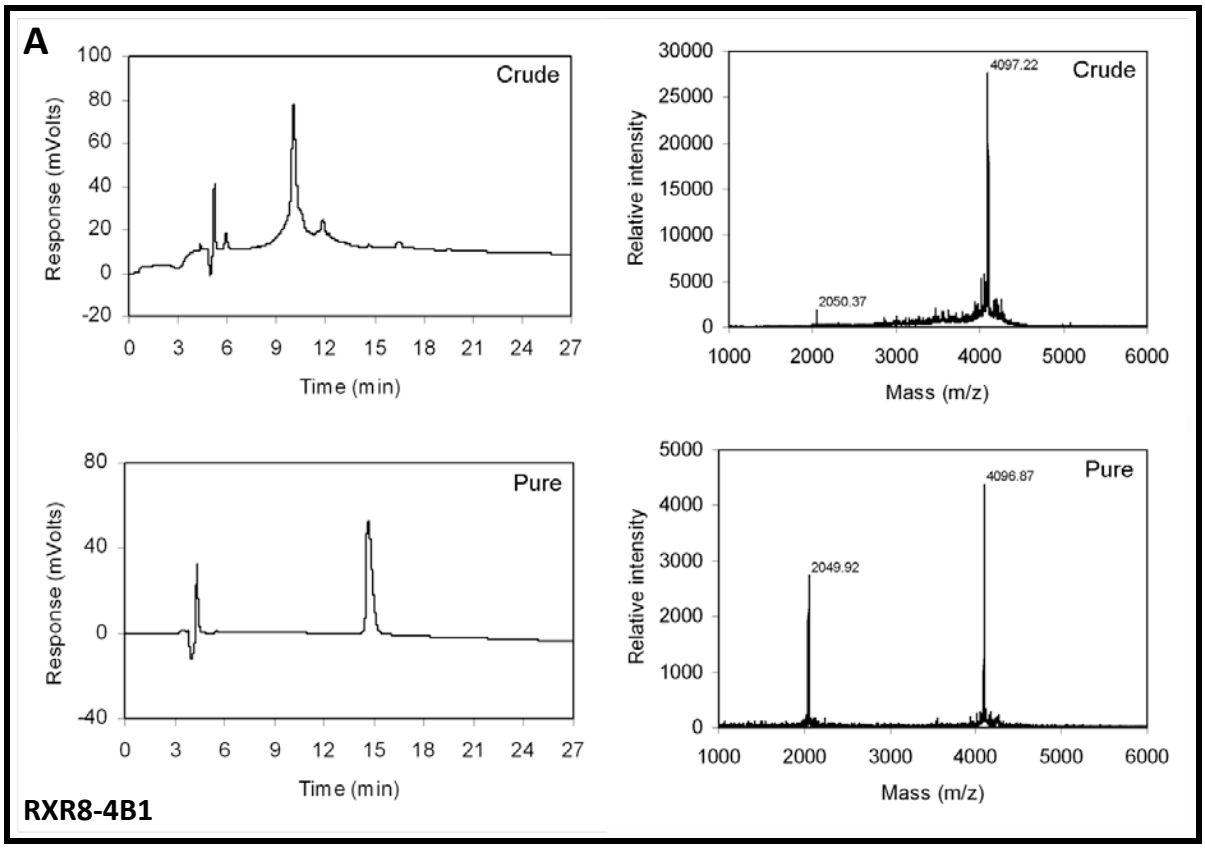
Amer Saleh[†], Andrey Arzumanov[†], Rachida Abes[§], David Owen[†], Bernard Lebleu[§] and Michael J. Gait†*

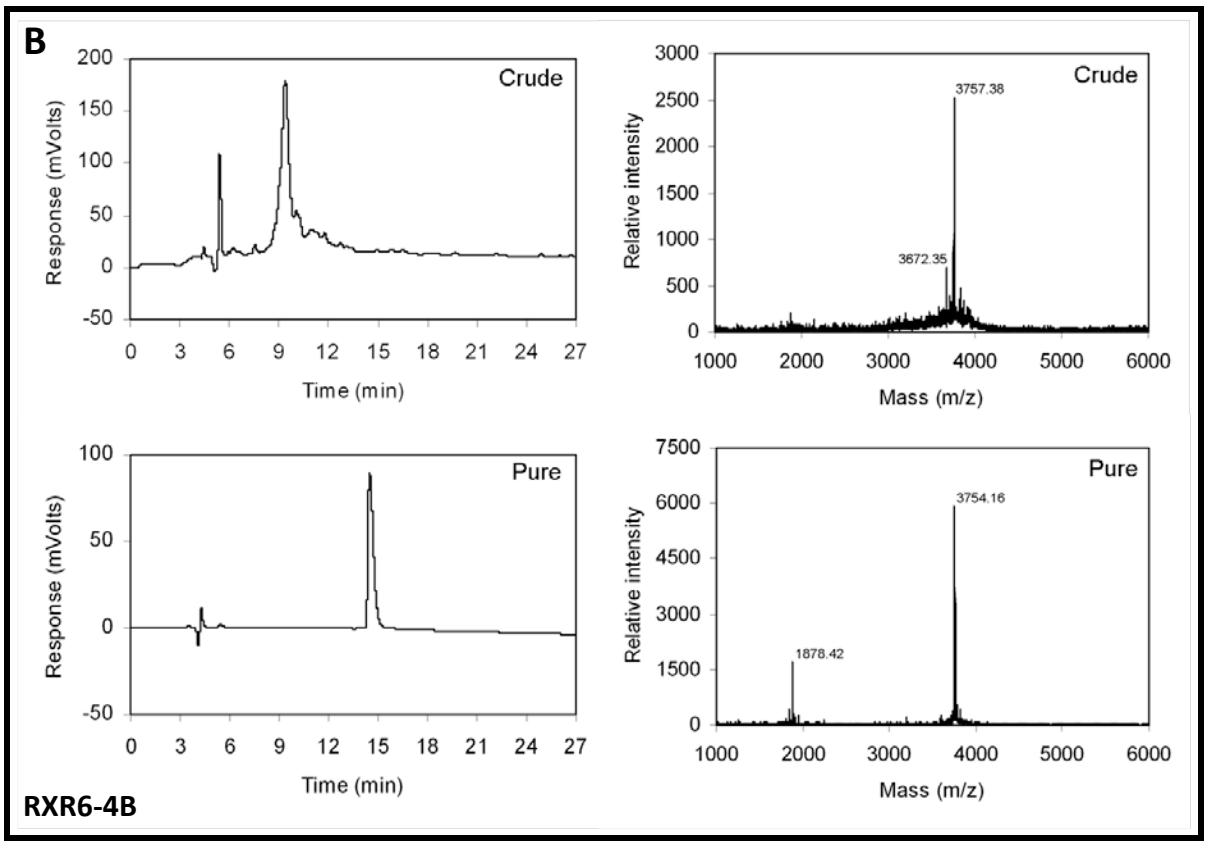
CONTENTS Page

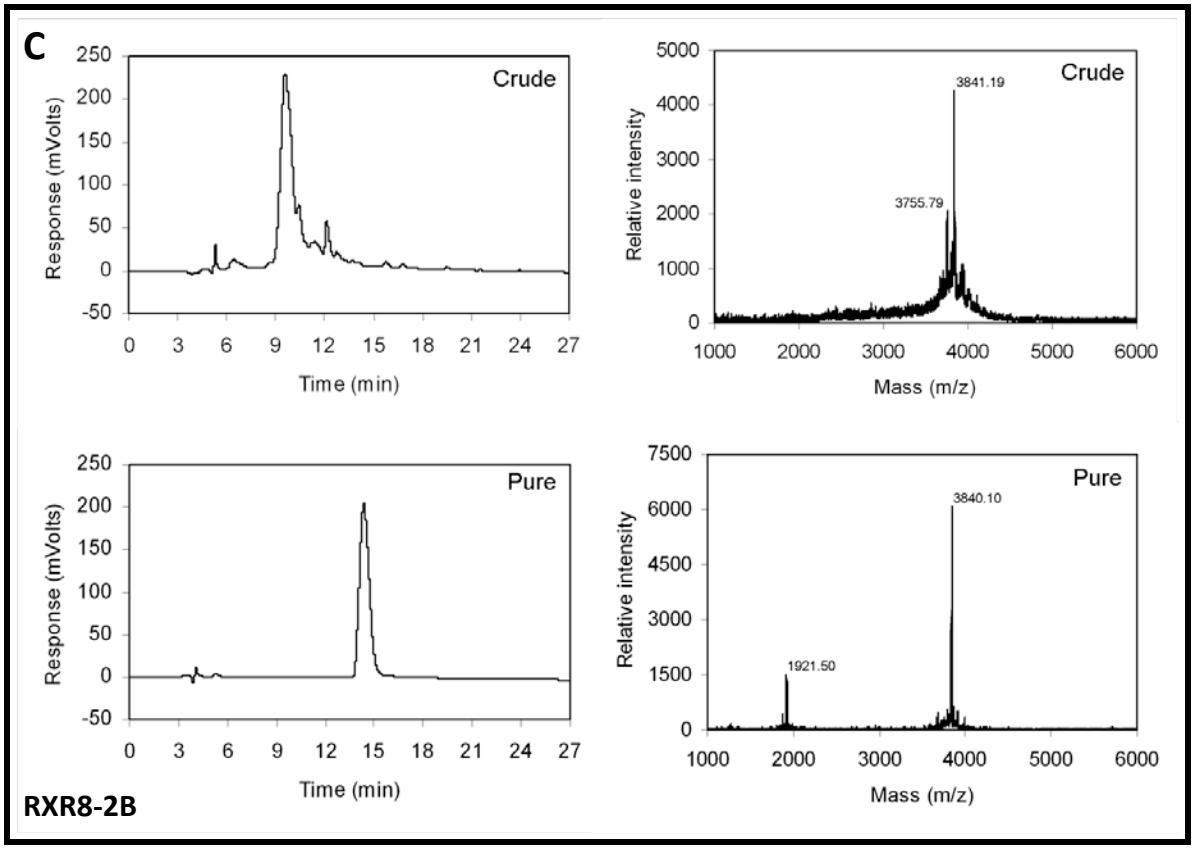
Supplementary Figure 1. Reversed-phase HPLC traces and MALDI-TOF mass spectra of 3 branched peptides. 2-3

Supplementary Figure 2. Reversed-phase HPLC traces and MALDI-TOF mass spectra of peptide-PNA705 conjugates. 4

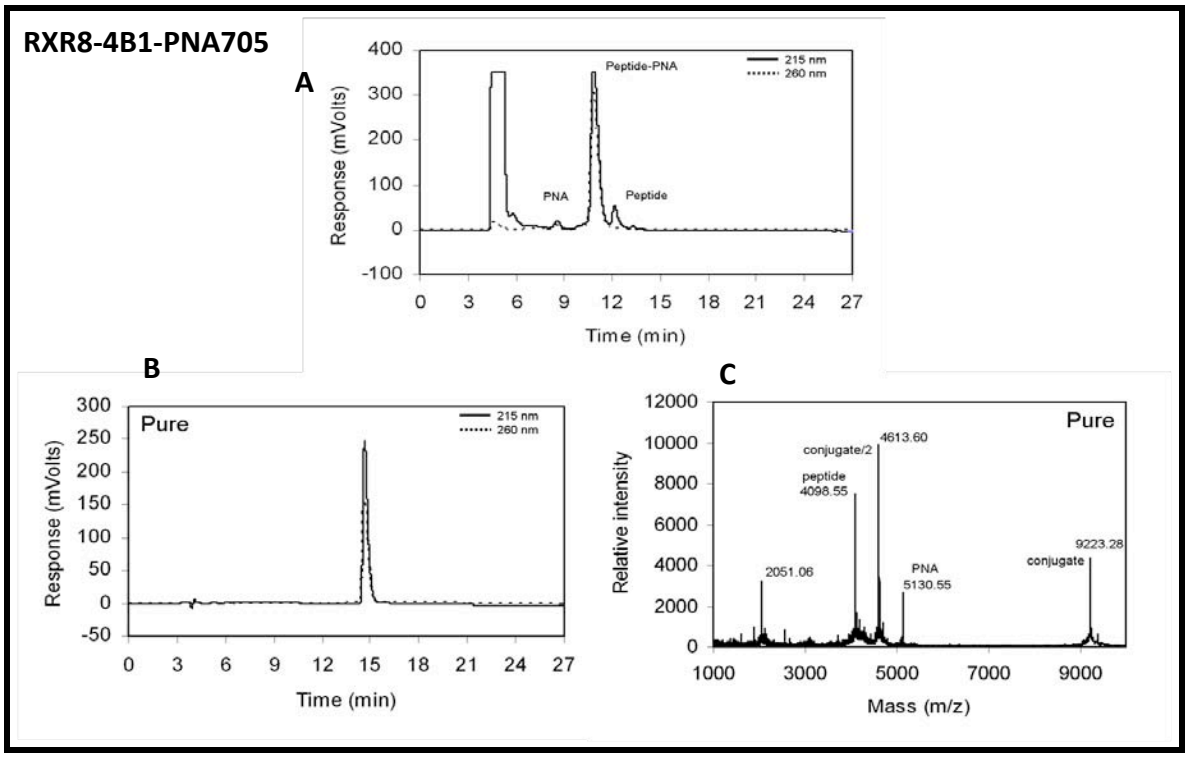
Supplementary Figure 3. Fold increase in luminescence in the luciferase assay for peptide-PNA705 conjugates in the presence or absence of 10% FBS 5

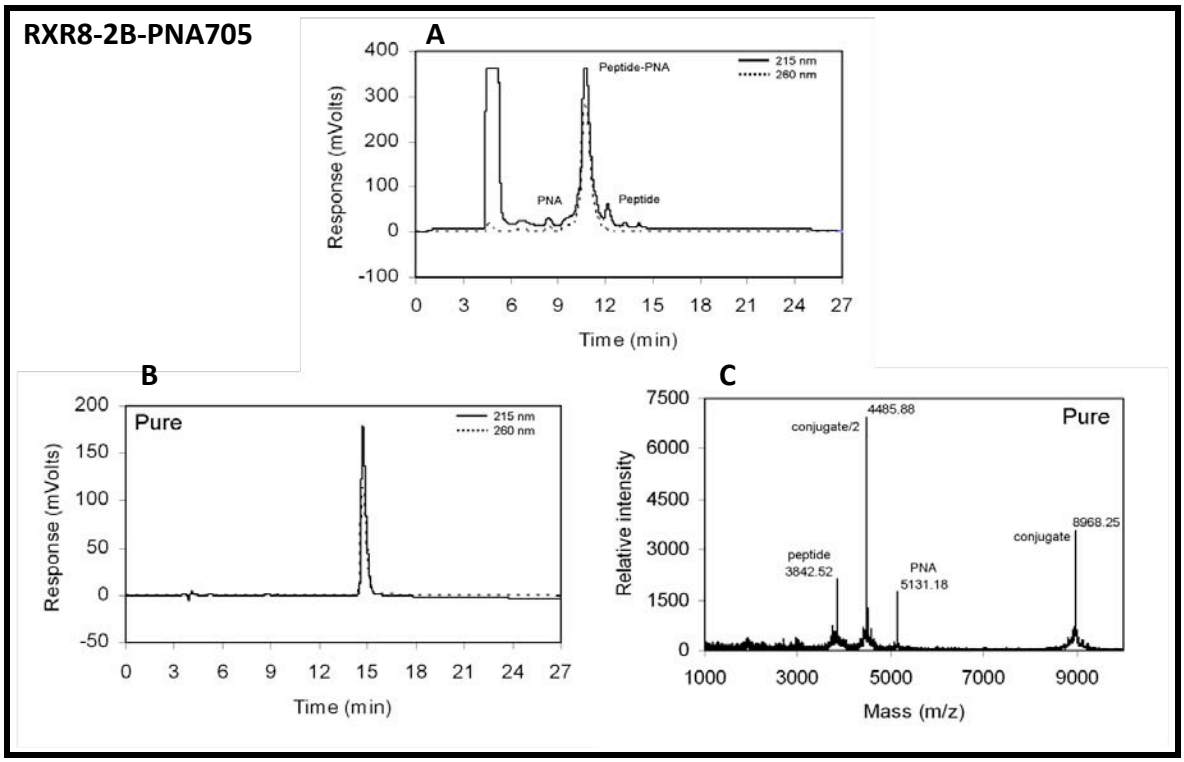

A
Crude
Response (mVolts)
Time (min)
Relative intensity
4097.22
2050.37
Mass (m/z)
Pure
4096.87
2049.92
RXR8-4B1


B
Crude
Response (mVolts)
Time (min)
Relative intensity
3757.38
3672.35
Mass (m/z)
Pure
3754.16
1878.42
RXR6-4B

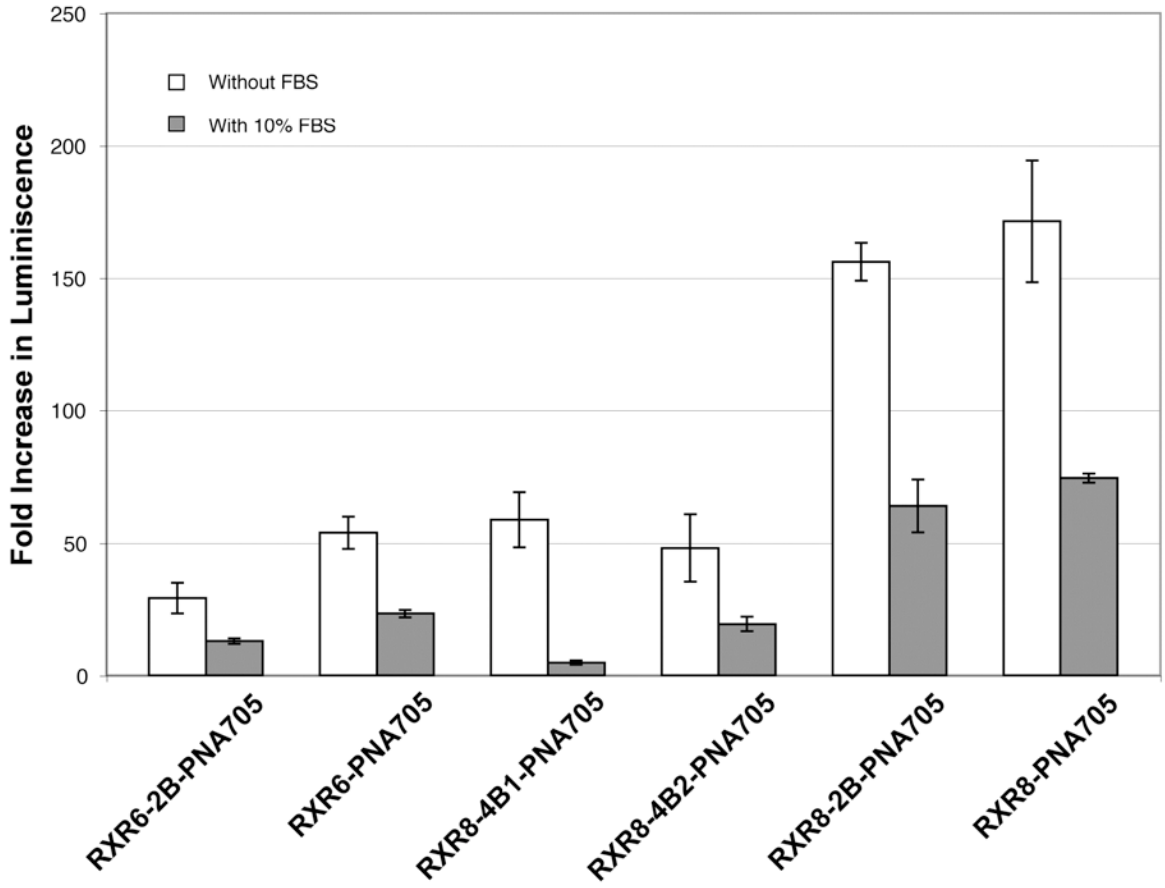


Supplementary Figure 1. HPLC traces (left) and MALDI-TOF mass spectra (right) of crude products and purified peptides (**A**) RXR8-4B1, (**B**) RXR6-4B and (**C**) RXR8-2B. Each crude peptide was purified by RP-HPLC on a 10 x 250 mm C18 column (buffer A: 0.1% TFA, buffer B: 90% acetonitrile, 10% solvent A) using 15-50% B in 25 minutes. The purified peptide was analysed by RP-HPLC on a 4.6 x 250 mm C18 column (buffer A: 0.1% TFA, buffer B: 90% acetonitrile, 10% solvent A) using 10-40% B in 25 minutes.





Supplementary Figure 2. Synthesis of conjugates RXR8-4B1-PNA705 (**Top panel**) and RXR8-2B-PNA705 (**Bottom panel**) **A**) Reversed-phase HPLC of crude products on a 10 x 250 mm C18 column (buffer A: 0.1% TFA, buffer B: 90% acetonitrile, 10% solvent A) using 15-40% B in 25 minutes. (**B**) Analysis of the purified conjugate by RP-HPLC on a 4.6 x 250 mm C18 column (buffer A: 0.1% TFA, buffer B: 90% acetonitrile, 10% solvent A) using 10-40% B in 25 minutes. (**C**) MALDI-TOF mass spectrum of the conjugate.



Supplementary Figure 3. Fold increase in luminescence obtained for selected peptide-PNA705 conjugates in the luciferase assay. Peptide-PNA conjugates (1.2 µM) were incubated for 4 h in 0.35 ml OptiMEM medium with exponentially growing HeLa pLuc705 cells (1.25 x 10^5 cells/well seeded and cultivated overnight) in 24 wells plates either with or without 10% fetal bovine serum (FBS). The medium was removed, 1 ml complete medium (DMEM plus 10% FBS) was added and incubation continued for 20 h. The luciferase assay was carried out as described in the Experimental Procedures.

Labeling Live Cells by Copper-Catalyzed Alkyne−Azide Click Chemistry

Vu Hong,[§,†] Nicole F. Steinmetz,[§,‡] Marianne Manchester,[||] and M. G. Finn*[,†]

Department of Chemistry and The Skaggs Institute for Chemical Biology, Department of Cell Biology and Center for Integrative Molecular Biosciences, The Scripps Research Institute, 10550 North Torrey Pines Road, La Jolla, California, Skaggs School of Pharmacy and Pharmaceutical Sciences, University of California San Diego, 9500 Gilman Drive, La Jolla, California.
Received June 17, 2010; Revised Manuscript Received August 24, 2010

The copper-catalyzed azide−alkyne cycloaddition (CuAAC) reaction, optimized for biological molecules in aqueous buffers, has been shown to rapidly label mammalian cells in culture with no loss in cell viability. Metabolic uptake and display of the azide derivative of *N*-acetylmannosamine developed by Bertozzi, followed by CuAAC ligation using sodium ascorbate and the ligand tris(hydroxypropyltriazolyl)methylamine (THPTA), gave rise to abundant covalent attachment of dye−alkyne reactants. THPTA serves both to accelerate the CuAAC reaction and to protect the cells from damage by oxidative agents produced by the Cu-catalyzed reduction of oxygen by ascorbate, which is required to maintain the metal in the active +1 oxidation state. This procedure extends the application of this fastest of azide-based bioorthogonal reactions to the exterior of living cells.

INTRODUCTION

To understand the roles of proteins, DNA, RNA, lipids, and glycans in a wide variety of cellular processes, imaging of biomolecules in their native environment using a spectroscopic probe has become increasingly popular (*1*−*3*). For proteins, genetically encoded tags such as GFP are routinely used. When smaller and less structurally perturbing labels are required, the target protein can be endowed with a peptide sequence that is selectively addressed with a small-molecule probe by either chemical or enzymatic reaction (*4*−*9*). These and other examples of chemoselective labeling of biomolecules in vivo are furthered by the development of bioorthogonal ligation reactions (*10*).

Cycloaddition reactions are attractive in this context, since they usually involve weakly polarized reactants, minimizing undesired side reactions with biomolecules. Recent examples include the reactions of strained olefins with nitrile oxides (*11*) or tetrazines (*12*), as well as unstrained olefins with photogenerated nitrile imines (*13*). Azide-based click reactions (*14*) are particularly applicable, since the azide group is stable and easy to introduce into biomolecules or probe molecules without dramatically changing their functional properties. The Staudinger ligation with phosphine esters and cycloaddition reactions with strained cyclic alkynes have been used to excellent effect, led by Bertozzi and co-workers (*15*−*19*), and augmented by others (*20, 21*).

While ligand-accelerated catalysis allows the copper-mediated azide−alkyne cycloaddition (CuAAC) reaction to achieve very high rates for in vitro bioconjugation reactions (*22*−*24*), the Cu(I) catalyst is regarded as toxic and therefore incompatible with living cells. Since both azide and alkyne groups (*25*−*27*) can be appended to biomolecules without altering their function or metabolic processing, it would be very useful if the CuAAC reaction could be adapted for this purpose. As a first step toward this goal, we describe here the application of optimized CuAAC reaction conditions (*24*) to the rapid and efficient labeling of cell-surface glycans on mammalian cells in culture.

EXPERIMENTAL PROCEDURES

Cell-Surface Labeling of Azido Glycans on HeLa and CHO Cells and Imaging by Confocal Microscopy. Cells were seeded at 1×10^5 cells/mL on glass-bottom Petri dishes (35 mm) and grown overnight at 37 °C and 5% CO_2 in growth medium (MEM medium containing 10% fetal calf serum, 1% glutamine, and 1% penstrep) with or without 50 μM Ac_4ManNAz for 2 days. The medium was gently aspirated, and the cells were washed two times with 1 mL of DPBS. In an eppendorf tube, $CuSO_4$ and THPTA in a 1:5 molar ratio were added to DPBS at 4 °C containing dye−alkynes **1** or **2** (final concn 25 μM) and aminoguanidine (final concn 1 mM). A freshly prepared stock solution of sodium ascorbate (100 mM) was added to establish a final ascorbate concentration of 2.5 mM. This reaction mixture was incubated on ice for 10 min at 4 °C before adding to the cells. After incubation at 4 °C for 1 or 5 min, the cells were washed and fixed with a mixture of 3% paraformaldehyde, 0.3% glutaraldehyde, and 1 mM $MgCl_2$ in DBPS for 10 min at room temperature. Cell nuclei were stained by adding 4′,6-diamidino-2-phenylindole (DAPI). Between each step, the slides were rinsed three times with DPBS. Slides were mounted using Vecta Shield mounting medium (Vector Laboratories, Burlingame, CA). Sections were imaged using a Biorad 2100 confocal microscope with a 60× oil objective. Data were analyzed and images were created using *ImageJ* (http://rsbweb.nih.gov/ij/). For dual labeling studies, the cells were washed twice with 1 mL of growth medium after the labeling reaction and returned to medium containing 50 μM Ac_4ManNAz for another 20 h. Optimized conditions for cell-surface labeling were 25 μM alkyne-488, $CuSO_4$ (50 μM), THPTA (250 μM), aminoguanidine (1 mM), and sodium ascorbate (2.5 mM) for 1 to 5 min in medium at 4 °C.

Cell-Surface Labeling of Azido Glycans on Jurkat Cells with Biotinylated Conjugates. Jurkat cells were grown in RPMI medium containing 10% fetal calf serum, 1% glutamine, and 1% penstrep with or without 10 μM Ac4ManNAz. Cells were collected using enzyme-free Hank's based cell

* mgfinn@scripps.edu.
[§] Both authors contributed equally to this work.
[†] Department of Chemistry and The Skaggs Institute for Chemical Biology, The Scripps Research Institute.
[‡] Department of Cell Biology and Center for Integrative Molecular Biosciences, The Scripps Research Institute.
[||] University of California San Diego.

10.1021/bc100272z © 2010 American Chemical Society
Published on Web 10/01/2010

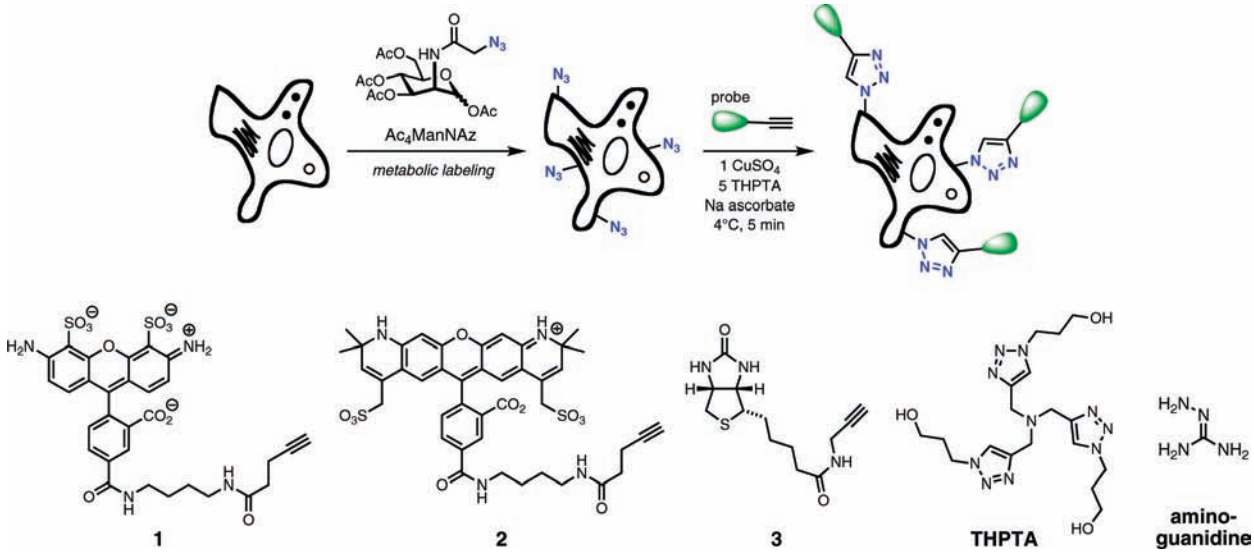


Figure 1. (Top) Cell labeling steps. (Bottom) Alkynyl probe reagents and catalyst additives.

dissociation buffer, distributed in 200 μL portions at a concentration of 5×10^6 cells/mL in the wells of a 96-well V-bottom-shaped microtiter plate, pelleted (1500 $\times$ *g*, 3 min), and washed twice with 200 μL of labeling buffer DPBS. On a separate 96-well plate, premixed $CuSO_4$ and THPTA at a 1:5 molar ratio were added to DPBS at 4 °C containing biotin−alkyne **3** (final concn 50 μM) and aminoguanidine (final concn 1 mM). A freshly prepared stock solution of sodium ascorbate (100 mM, 2.5 μL) was added to establish a final ascorbate concentration of 2.5 mM. The reaction mixture was incubated on ice for 60 min before adding to the cells. After incubation for 5 min at 4 °C, the cells were washed two times with DPBS buffer containing 1 mM EDTA pH 8.0, 25 mM HEPES pH 7.5, and 1% fetal bovine serum, fixed with 2% (v/v) formaldehyde in DPBS for 10 min at room temperature, and resuspended in the same buffer containing FITC−streptavidin (1:250 dilution) for 20 min at 4 °C. Cells were analyzed using a FACS Calibur instrument (BD Biosciences, Franklin Lakes, NJ). At least 10 000 events were collected. Experiments were repeated at least twice, and triplicates of each sample were measured and data analyzed using *FlowJo 8.7.1* software (Tree Star, Inc., Ashland, OR).

Cell Viability Assay. Cells were incubated for 2 days in untreated medium or medium containing 10 μM−50 μM Ac_4ManNAz on 96-well plates. The medium was gently aspirated, and the cells were washed twice with 200 μL of DPBS. In an eppendorf tube, premixed $CuSO_4$ and THPTA at 5:1 ratio were added to DPBS at 4 °C containing aminoguanidine (1 mM) to the desired copper concentrations. Sodium ascorbate (100 mM) was added to the final concentration of 2.5 mM. The reaction mixture was incubated on ice for 10 min at 4 °C before adding to the cells. After incubation for 5 min, the cells were washed twice with the labeling buffer and returned to growth medium for 24 h. An equal volume of premixed Cell Titer-Glo Reagent from Promega was added, plates were shaken for 10 min at room temperature, and luminescence was monitored.

Synthesis of Alexa Fluor Derivatives. To a solution of the appropriate Alexa Fluor cadaverine (1.0 equiv) in DMSO (final concentration of 0.05 M) was added a solution of *N*-(4-pentynoyloxy)succinimide (10.0 equiv) and then *N*,*N*-diisopropylethylamine (10.0 equiv). The solution was stirred at room temperature overnight in the dark, diluted in 9:1 water/acetonitrile, purified by reversed-phase HPLC using water and acetonitrile, and lyophilized to a fine powder. Electrospray−ionization mass spectrometry (negative ion detection): Alexa 488-alkyne parent ion $[\mathbf{1}\cdot H^+]^-$ $(C_{30}H_{27}N_4O_{11}S_2)^-$, calcd 683.1, found 683.1; Alexa 568-alkyne parent ion $[\mathbf{2}\cdot H^+]^-$ $(C_{42}H_{43}N_4O_{11}S_2)^-$, calcd 843.2, found 843.2.

RESULTS AND DISCUSSION

While many enzymes require copper, including cytochrome oxidase, Cu/Zn superoxide dismutase, and lysyl oxidase (*28, 29*), copper ions can be harmful to cells, mostly because they catalyze the production of reactive oxygen species (ROS) from atmospheric oxygen. Therefore, free Cu is essentially absent inside cells of aerobic organisms (*30*), but the overall intracellular copper concentration is approximately 70 μM (*31*), all bound up as Cu^I among proteins that constitute a well-developed and highly conserved system for importing and distributing this essential ion (*32*).

The Cu^I oxidation state required for the CuAAC reaction is most often achieved and/or maintained by the reduction of Cu^{II} with ascorbate. The Cu/ascorbate system is a prodigious generator of oxygen radicals and other reactive species in air (*33*−*38*). We have previously shown that a water-soluble derivative of the tris(triazolylmethyl)amine family of ligands (*39*) intercepts reactive oxygen species generated in the coordination sphere of the metal and accelerates Cu-mediated peroxide degradation (*24*). The additive aminoguanidine was also shown to capture dehydroascorbate and its decomposition products before they can react with protein side chains. The combined use of these two additives gave rise to a robust protocol to label proteins, polynucleotides, and other biomolecules in aqueous buffers with high yield and efficiency in the presence of air (*24*).

The applicability of this protocol to live cells was tested by metabolic labeling using peracetylated *N*-azidoacetylmannosamine (Ac_4ManNAz), which is taken up and incorporated into cell-surface sialylated (SiaNAz) glycans (Figure 1) (*40*−*42*). In order to gauge the effect of THPTA on eliminating the toxicity of copper and sodium ascorbate, HeLa, Chinese hamster ovary (CHO), and Jurkat cells were incubated at 4 °C with these click reaction components. Preliminary exploratory experiments showed 5 min to be an incubation period in which significant protective effects from the ligand could be observed, and we knew from previous studies that the CuAAC reaction is fast enough to provide extensive labeling in this amount of time. Longer incubations gave rise to increasing cytotoxicity under

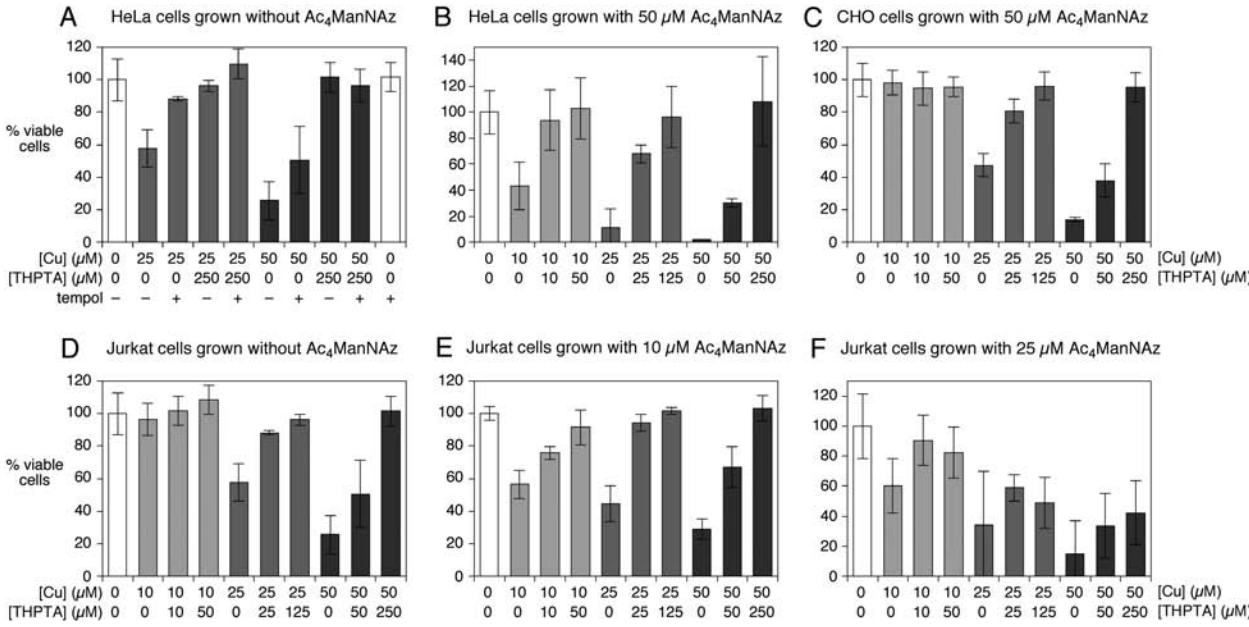


Figure 2. Viability of mammalian cells after Cu-ascorbate treatment ([$CuSO_4$] and [THPTA] as indicated, [Na ascorbate] = 2.5 mM, DPBS, 4 °C, 5 min), followed by washing in buffer and incubation in growth media for 24 h. Cell viability was determined by CellTiter-Glo Luminescent Cell Viability Assay (Promega, Madison, WI) (*43*). (B,C,E) Cells were grown for two days in the presence or absence of Ac_4ManNAz, as indicated, before Cu treatment. Error bars indicate standard deviation from the averaging of results from at least three independent experiments.

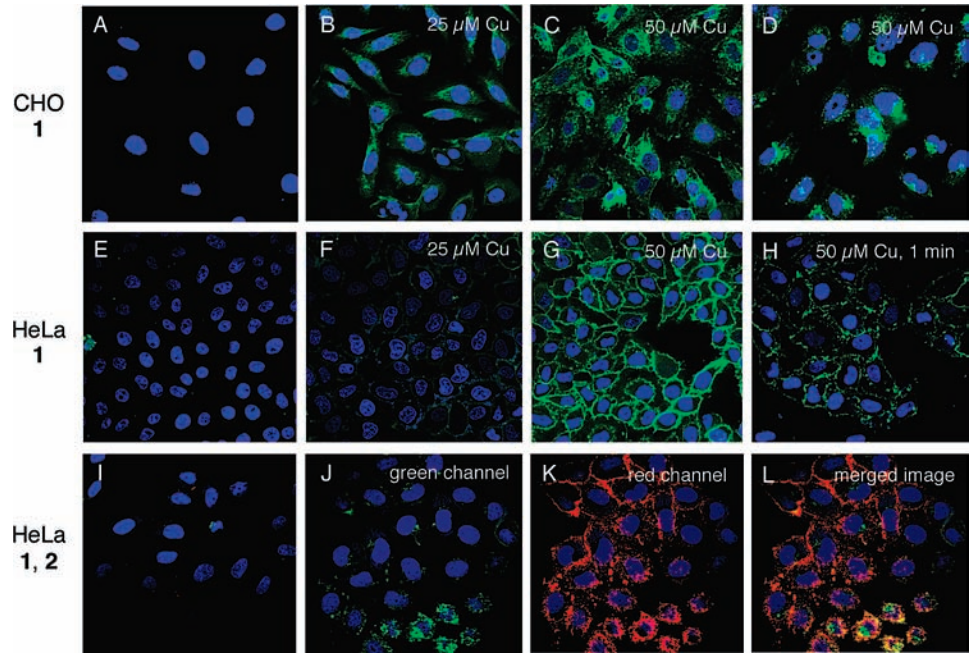


Figure 3. Representative labeling of cells (grown in the presence of 50 μM Ac_4ManNAz for 48 h) with the indicated dye−alkynes (25 μM), in the presence of Cu catalyst (5 equiv THPTA, 2.5 mM Na ascorbate, 1 mM aminoguanidine), in PBS pH 7.4 at 4 °C. The CuAAC reaction was conducted for 5 min unless otherwise noted, followed by washing in buffer and fixation for confocal microscopy imaging after incubation in fresh media for 15 min (except for panel D, for which the cells were incubated for 24 h before fixation and imaging). Nuclei were stained with DAPI (blue). Panels A, E, and I show the result of CuAAC labeling treatment with **1** on cells lacking the azido sugar, showing that nonspecific adsorption or labeling with dye does not occur. The procedure for labeling of cells shown in panels J−L is described in the text. All images are 155 × 155 μm.

most conditions. Thus, variations in Cu and ligand concentrations were explored for 5 min incubations, after which the cells were washed, placed back in media for 24 h at 37 °C and 5% CO_2, and then assessed for viability (Figure 2). In each case, the Cu/ligand/ascorbate mixture was allowed to stand for 10 min before introduction to the cells in order to allow the catalyst to quench the ROS and peroxide species generated in the reduction of dissolved oxygen (*24*).

As expected, in the absence of ligand, increasing copper concentration induced increased cell death for each cell type. Growth in the presence of the azido−sugar made the cells significantly more sensitive to Cu-ascorbate (Figure 2A vs B, D vs E,F), presumably because the health of the cells or integrity of the membrane is compromised by the incorporation of the non-natural glycan, or because the added Cu complex somehow engages the surface azide groups to the detriment of the cell.

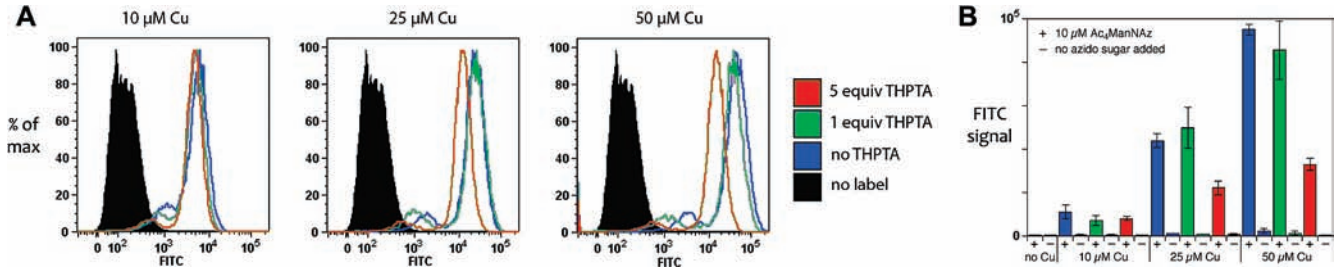


Figure 4. Flow cytometry analysis of Jurkat cells, preincubated for 48 h in growth medium containing 10 μM Ac_4ManNAz, and then labeled with **3** (50 μM) under standard conditions ($CuSO_4$ and THPTA at the indicated concentrations, 2.5 mM Na ascorbate, 1 mM aminoguanidine, in DPBS, 4 °C, 5 min). (A) All samples were analyzed in triplicate; 10 000 events were recorded in each case; and representative histograms are shown. (B) Mean fluorescence intensities with error bars representing standard deviations (statistical analysis performed using *FlowJo* software v 8.7.1).

The latter possibility is unlikely, given the fact that organic azides are not consumed by treatment with Cu^I complexes in the absence of terminal alkynes. The ligand proved to be largely protective: THPTA reversed the toxic effect of Cu-ascorbate effect in a dose-dependent manner, a 5:1 ligand:Cu ratio preserving the viability of all cell types at each Cu concentration tested (Figure 2). This is consistent with the previous observations concerning the ability of the ligand to intercept the formation of oxygen radicals with maximum efficiency (*24*).

Treatment of the Ac_4ManNAz-treated cells with dye−alkynes under the above CuAAC conditions resulted in extensive labeling, as shown in Figures 3 and 4. We chose to perform the CuAAC reactions at 4 °C to eliminate internalization of cell-surface species during this process and inhibit energy-dependent internalization of reactants. As has been previously described for in vitro bioconjugation reactions (*24*), the Cu^I•THPTA system functions best at 50 μM Cu or greater, showing much greater labeling of SiaNAz-bearing CHO and HeLa cells than 25 μM (Figure 3C vs B, G vs F). A reaction time of just 1 min gave substantial labeling, but 5 min was far better (Figure 3G vs H). In each case, evenly distributed labeling over the cell surface was observed, consistent with the expected distribution of the azido sugar throughout the exterior of the cell membrane. The viability of the cells 24 h after labeling was confirmed as above, with the same results of complete protection against ROS-induced toxicity in the presence of 5 equiv of THPTA ligand. As shown in panel D, CHO cells returned to the growth medium for 24 h after labeling showed the dye distributed in the cell interior, reflecting the expected internalization of the sialylated proteins.

The same pattern was observed in HeLa cells, which were further characterized by a two-color sequential labeling experiment. HeLa cells grown for 48 h in the presence of Ac_4ManNAz were labeled with Alexa-488 alkyne **1** at 4 °C, washed, and returned to growth media containing the azido sugar for 24 h to install additional SiaNAz residues. The cells were then labeled a second time with Alexa-568 alkyne **2** and imaged, with the results shown in Figure 3J−L. After 24 h, the initially labeled (green) sialic acid residues had trafficked largely to the inside of the cells, whereas the freshly labeled (red) sugars were distributed on the cell surface. These results suggest that the labeling protocol does not significantly perturb glycan trafficking on the time scale of the experiment.

The nonadherent Jurkat cells were analyzed by flow cytometry after the same labeling procedure described above. Ac_4ManNAz proved to be toxic to these cells at 50 μM, and cells grown in the presence of 25 μM of the sugar were more sensitive to copper than others (Figure 2F). Labeling studies were therefore performed after growth in the presence of 10 μM Ac_4ManNAz. The cells were labeled by CuAAC reaction with biotin alkyne **3**, and the label was subsequently detected with a fluorescein−streptavidin conjugate (see Experimental Section). As shown in Figure 4, labeling was most effective with 50 μM Cu, and surprisingly, the ligand could either be omitted or used in equimolar amounts with respect to Cu to achieve maximum signal. In the case of this two-step assay, however, the relationship between output signal and the degree of surface labeling may not be direct. For example, the omission of ligand could result in more cell damage and membrane permeability, and therefore in a greater signal in CuAAC labeling.

We demonstrate here a robust and general method for the surface labeling of live cells in culture using the CuAAC click reaction. The toxicity commonly attributed to copper results from the production of reactive oxygen species by Cu, ascorbate, and atmospheric oxygen. The important features of the cell labeling protocol are the use of a water-soluble accelerating ligand (THPTA) that also acts as a sacrificial reductant for oxidative species as they are produced in the coordination sphere of the metal and aminoguanidine to intercept strongly electrophilic byproducts of dehydroascorbate. The rapid nature of the reaction that allows for efficient labeling in a short time, preserving cell viability.

ACKNOWLEDGMENT

This work was supported by the NIH (R01 CA112075 to M.M. and M.G.F.; K99 EB009105 to N.F.S.), an American Heart Association Postdoctoral Fellowship (N.F.S.), the Skaggs Institute for Chemical Biology, and the W.M. Keck Foundation. We thank Prof. Peng Wu (Albert Einstein College of Medicine) for helpful discussions.

LITERATURE CITED

(1) Foley, T. L., and Burkart, M. D. (2007) Site-specific protein modification: advances and applications. *Curr. Opin. Chem. Biol. 11*, 12–19.

(2) Terpe, K. (2003) Overview of tag protein fusions: from molecular and biochemical fundamentals to commercial systems. *Appl. Microbiol. Biotechnol. 60*, 523–533.

(3) Shaner, N. C., Steinbach, P. A., and Tsien, R. Y. (2005) A guide to choosing fluorescent proteins. *Nat. Methods 2*, 905–909.

(4) Tsukiji, S., and Nagamune, T. (2009) Sortase-mediated ligation: a gift from Gram-positive bacteria to protein engineering. *ChemBioChem 10*, 787–798.

(5) Gautier, A., Juillerat, A., Heinis, C., Correa, I. R., Jr., Kindermann, M., Beaufils, F., and Johnsson, K. (2008) An engineered protein tag for multiprotein labeling in living cells. *Chem. Biol. 15*, 128–136, and references therein.

(6) Zhou, Z., Cironi, P., Lin, A. J., Xu, Y., Hrvatin, S., Golan, D. E., Silver, P. A., Walsh, C. T., and Yin, J. (2007) Genetically encoded short peptide tags for orthogonal protein labeling by Sfp and AcpS phosphopantetheinyl transferases. *ACS Chem. Biol. 2*, 337–346.

(7) Tanaka, F., Fuller, R., Asawapornmongkol, L., Warsinke, A., Gobuty, S., and Barbas, C. F., III (2007) Development of a small

peptide tag for covalent labeling of proteins. *Bioconjugate Chem. 18*, 1318–1324.
(8) Fernández-Suárez, M., Baruah, H., Martínez-Hernández, L., Xie, K. T., Baskin, J. M., Bertozzi, C. R., and Ting, A. Y. (2007) Redirecting lipoic acid ligase for cell surface protein labeling with small-molecule probes. *Nat. Biotechnol. 25*, 1483–1487.
(9) Duckworth, B. P., Zhang, Z., Hosokawa, A., and Distefano, M. D. (2007) Selective labeling of proteins by using protein farnesyltransferase. *ChemBioChem 8*, 98–105.
(10) Sletten, E. M., and Bertozzi, C. R. (2009) Bioorthogonal chemistry: fishing for selectivity in a sea of functionality. *Angew. Chem., Int. Ed. 48*, 6974–6998, and references therein.
(11) Gutsmiedl, K., Wirges, C. T., Ehmke, V., and T., C. (2009) Copper-free "click" modification of DNA via nitrile oxide-norbornene 1,3-dipolar cycloaddition. *Org. Lett. 4*, 2405–2408.
(12) Blackman, M. L., Royzen, M., and Fox, J. M. (2008) Tetrazine ligation: fast bioconjugation based on inverse-electron-demand Diels-Alder reactivity. *J. Am. Chem. Soc. 130*, 13518–13519.
(13) Song, W., Wang, Y., and Lin, Q. (2008) Selective functionalization of a genetically encoded alkene-containing protein via 'photo-click chemistry' in bacterial cells. *J. Am. Chem. Soc. 130*, 9654–9655.
(14) Kolb, H. C., Finn, M. G., and Sharpless, K. B. (2001) Click chemistry: diverse chemical function from a few good reactions. *Angew. Chem., Int. Ed. 40*, 2004–2021.
(15) Mahal, L. K., Yarema, K. J., and Bertozzi, C. R. (1997) Engineering chemical reactivity on cell surfaces through oligosaccharide biosynthesis. *Science 276*, 1125–1128.
(16) Kiick, K. L., Saxon, E., Tirrell, D. A., and Bertozzi, C. R. (2002) Incorporation of azides into recombinant proteins for chemoselective modification by the Staudinger ligation. *Proc. Natl. Acad. Sci. U.S.A. 99*, 19–24.
(17) Agard, N. J., Baskin, J. M., Prescher, J. A., Lo, A., and Bertozzi, C. R. (2006) A comparative study of bioorthogonal reactions with azides. *ACS Chem. Biol. 1*, 644–648.
(18) Laughlin, S. T., Baskin, J. M., Amacher, S. L., and Bertozzi, C. R. (2008) In vivo imaging of membrane-associated glycans in developing zebrafish. *Science 320*, 664–667.
(19) Chang, P. V., Prescher, J. A., Sletten, E. M., Baskin, J. M., Miller, I. A., Agard, N. J., Lo, A., and Bertozzi, C. R. (2010) Copper-free click chemistry in living animals. *Proc. Natl. Acad. Sci. U.S.A. 107*, 1821–1826.
(20) Ning, X., Guo, J., Wolfert, M. A., and Boons, G.-J. (2008) Visualizing metabolically labeled glycoconjugates of living cells by copper-free and fast Huisgen cycloadditions. *Angew. Chem., Int. Ed. 47*, 2253–2255.
(21) Jewett, J. C., Sletten, E. M., and Bertozzi, C. R. (2010) Rapid Cu-free click chemistry with readily synthesized biarylazacyclooctynones. *J. Am. Chem. Soc. 132*, 3688–3690.
(22) Sen Gupta, S., Kuzelka, J., Singh, P., Lewis, W. G., Manchester, M., and Finn, M. G. (2005) Accelerated bioorthogonal conjugation: a practical method for the ligation of diverse functional molecules to a polyvalent virus scaffold. *Bioconjugate Chem. 16*, 1572–1579.
(23) Rodionov, V. O., Presolski, S., Díaz, D. D., Fokin, V. V., and Finn, M. G. (2007) Ligand-accelerated Cu-catalyzed azide-alkyne cycloaddition: a mechanistic report. *J. Am. Chem. Soc. 129*, 12705–12712.
(24) Hong, V., Presolski, S. I., Ma, C., and Finn, M. G. (2009) Analysis and optimization of copper-catalyzed azide-alkyne cycloaddition for bioconjugation. *Angew. Chem., Int. Ed. 48*, 9879–9883.
(25) Chang, P., Chen, X., Smyrniotis, C., Hu, T., Bertozzi, C. R., and Wu, P. (2009) Metabolic labeling of sialic acids in living animals with alkynyl sugars. *Angew. Chem., Int. Ed. 48*, 4030–4033.
(26) Hsu, T.-L., Hanson, S. R., Kishikawa, K., Wang, S.-K., Sawa, M., and Wong, C.-H. (2007) Alkynyl sugar analogs for the labeling and visualization of glycoconjugates in cells. *Proc. Natl. Acad. Sci. U.S.A. 104*, 2614–2619.
(27) Yap, M. C., Kostiuk, M. A., Martin, D. D., Perinpanayagam, M. A., Hak, P. C., Siddam, A., Majjigapu, J. R., Rajaiah, G., Keller, B. O., J.A., P., Wu, P., Bertozzi, C. R., Falck, J. R., and Berthiaume, L. G. (2010) Rapid and selective detection of fatty acylated proteins using omega-alkynyl-fatty acids and click chemistry. *J. Lipid Res. 51*, 1566–1580.
(28) Kaim, W., and Rall, J. (1996) Copper - a "modern" bioelement. *Angew. Chem., Int. Ed. 35*, 43–60.
(29) Rosenzweig, A. C., and O'Halloran, T. V. (2000) Structure and chemistry of the copper chaperone proteins. *Curr. Opin. Chem. Biol. 4*, 140–147.
(30) Yang, L., McRae, R., Henary, M. M., Patel, R., Lai, B., Vogt, S., and Fahrni, C. J. (2005) Imaging of the intracellular topography of copper with a fluorescent sensor and by synchrotron X-ray fluorescence microscopy. *Proc. Natl. Acad. Sci. U.S.A. 102*, 11179–11184.
(31) Rae, T. D., Schmidt, P. J., Pufahl, R. A., Culotta, V. C., and O'Halloran, T. V. (1999) Undetectable intracellular free copper: the requirement of a copper chaperone for superoxide dismutase. *Science 284*, 805–808.
(32) Luk, E., Jensen, L. T., and Culotta, V. C. (2003) The many highways for intracellular trafficking of metals. *J. Biol. Inorg. Chem. 8*, 803–809.
(33) Houghton, E. A., and Nicholas, K. M. (2009) In vitro reactive oxygen species production by histatins and copper(I, II). *J. Biol. Inorg. Chem. 14*, 243–251.
(34) Barnham, K. J., Masters, C. L., and Bush, A. I. (2004) Neurodegenerative diseases and oxidative stress. *Nat. Rev. Drug Discovery 3*, 205–214.
(35) Khossravi, M., and Borchardt, R. T. (1998) Chemical pathways of peptide degradation: IX. Metal-catalyzed oxidation of histidine in model peptides. *Pharm. Res. 15*, 1096–1102.
(36) Serrano, J., Jové, M., Boada, J., Bellmunt, M. J., Pamplona, R., and Portrero-Otín, M. (2009) Dietary antioxidants interfere with Amplex Red-coupled-fluorescence assays. *Biochem. Biophys. Res. Commun. 388*, 443–449.
(37) Liu, P.-Y., Jiang, N., Zhang, J., Wei, X.-H., Lin, H.-H., and X.-Q., Y. (2006) The oxidative damage of plasmid DNA by ascorbic acid derivatives in vitro: the first research on the relationship between the structure of ascorbic acid and the oxidative damage of plasmid DNA. *Chem. Biodivers. 3*, 958–965.
(38) Khossravi, M., and Borchardt, R. T. (2000) Chemical pathways of peptide degradation. X: Effect of metal-catalyzed oxidation on the solution structure of a histidine-containing peptide fragment of human relaxin. *Pharm. Res. 17*, 851–858.
(39) Chan, T. R., Hilgraf, R., Sharpless, K. B., and Fokin, V. V. (2004) Polytriazoles as copper(I)-stabilizing ligands in catalysis. *Org. Lett. 6*, 2853–2855.
(40) Luchansky, S. J., Argade, S., Hayes, B. K., and Bertozzi, C. R. (2003) Constructing azide-labeled cell surfaces using polysaccharide biosynthetic pathways. *Methods Enzymol. 362*, 249–272.
(41) Prescher, J. A., Dube, D. H., and Bertozzi, C. R. (2004) Chemical remodelling of cell surfaces in living animals. *Nature 430*, 873–877.
(42) Dube, D. H., and Bertozzi, C. R. (2003) Metabolic oligosaccharide engineering as a tool for glycobiology. *Curr. Opin. Chem. Biol. 7*, 616–625.
(43) Niles, A. L., Moravec, R. A., and Riss, T. L. (2008) Update on *in vitro* cytotoxicity assays for drug development. *Expert Opin. Drug Discovery 3*, 655–669.

BC100272Z

Photocleavable Peptide-Conjugated Magnetic Beads for Protein Kinase Assays by MALDI-TOF MS

Guangchang Zhou,[†,‡] Xiaoliang Yan,[†] Ding Wu,[†] and Stephen J. Kron*[,†,‡]

Ludwig Center for Metastasis Research and Department of Molecular Genetics and Cell Biology, The University of Chicago, Chicago, Illinois 60637. Received July 6, 2010; Revised Manuscript Received August 30, 2010

Peptides were immobilized onto superparamagnetic beads via photocleavable linkers. This enabled simple, rapid, and label-free protein kinase assays via MALDI-TOF MS detection of substrate peptide phosphorylation. Abltide, a model substrate for the Abl protein tyrosine kinase model, was coupled onto amine-terminated beads, incubated with ATP and recombinant c-Abl kinase, and released and further detected to determine phosphorylation. Abltide phosphorylation was found to depend significantly on the length and composition of linkers to the bead surface. Inserting a diblock spacer of poly(glycine) and poly(ethylene glycol) segments markedly enhanced phosphorylation. To validate the assay, the activity of two small-molecule kinase inhibitors, imatinib and dasatinib, which target the oncogenic mutant tyrosine kinase Bcr-Abl to treat chronic myeloid leukemia (CML), was tested. Examining inhibition of the purified c-Abl or Bcr-Abl in K562 CML cell extracts, IC_{50} values were determined to be consistent with the literature. This simple, label-free, MALDI-based protein kinase assay can be readily adapted to allow multiplexed assays of multiple peptide substrates and/or analysis of alternative post-translational modifications as a tool for drug discovery and clinical testing.

INTRODUCTION

Protein kinases play critical roles in cellular signal transduction by regulating intracellular processes such as cell growth, proliferation, differentiation, and apotosis (*1*−*3*). Deregulation of protein kinase activities and resulting perturbations of downstream targets in phosphorylation cascades have been implicated as underlying causes of a number of diseases, including cancer, diabetes, and chronic inflammation (*4*−*7*). Thus, protein kinases have emerged as a major class of drug targets, leading to several small-molecule kinase inhibitors already in use, and many more in clinical trials (*8*−*12*). Multiple technologies have been developed for analyzing protein kinase activities and screening of small molecules for inhibition of protein kinases (*13*−*23*).

A key challenge in protein kinase assays lies in the detection of the formation of the phosphorylated product by transfer of the ATP γ-phosphate to the unphosphorylated substrate. A reasonable goal is to detect the activity and inhibition of a kinase in its cellular context, but this requires extraordinary sensitivity and specificity, given the ubiquitous nature of protein phosphorylation and the expression of hundreds of different kinases in many cells. Heterogeneous kinase assays, where kinase-specific protein or peptide substrates are tethered to the surface of solid supports, have unique advantages over homogeneous assays for this purpose. The added steps of substrate immobilization and separation and/or washing are offset by enhanced sensitivity and specificity offered by ready discrimination of phosphorylated products from the many phosphorylated proteins in a cell extract. Diverse strategies are described for immobilization of peptides or proteins on solid supports, including in situ peptide synthesis (*24*, *25*), noncovalent attachment via streptavidin−biotin interaction, and covalent chemistries such as NHS−amine reaction (*26*), Diel-Alder reaction (*13*), native chemical ligation (*27*), and Michael addition (*28*−*30*). However, direct attachment of peptide substrates to the support surface may limit accessibility of kinases to their substrates. Indeed, inserting a spacer between the peptide substrate and the support surface can significantly improve phosphorylation efficiency and reduce background (*31*−*34*).

Most heterogeneous kinase assays adapted to screening exploit indirect detection of phosphorylation via labels (*35*−*37*). Traditional kinase assays based on transfer of radioactive (thio)phosphate from γ-labeled ATP to peptide or protein substrates are sensitive and quantitative but not well-suited to analysis of cell extracts. Antibodies that recognize substrate phosphopeptides offer sufficient sensitivity and specificity but require additional binding and washing steps and offer limited quantitation. An attractive label-free approach is mass spectrometry (MS), which offers independent, quantitative detection of both phosphorylated and unphosphorylated substrate, and offers potential for multiplexed assays with high sensitivity, selectivity, and speed (*38*, *39*). Direct MS analysis of kinase reaction mixtures suffers from signal suppression due to salt and detergent interference and is confounded by the complexity of cell extracts. Direct matrix-assisted laser desorption ionization (MALDI) analysis of substrates immobilized via tethering to self-assembled monolayers (*40*) or onto gold nanoparticles coated onto glass slides (*32*) has demonstrated the potential of mass spectrometry for heterogeneous kinase assays.

Photocleavable linkers offer a number of advantages, because light is easy to apply, relatively harmless to living organisms, and importantly controllable both spatially and temporally (*41*). *o*-Nitrobenzyl ether derivatives are especially convenient photocleavable moieties and have been used in a variety of fields including live cell culture and imaging due to unique properties that include stability under ambient light, clean cleavage via two-photon photolysis mechanism upon exposure to UV irradiation, and fast fragmentation reactions (within nanoseconds) upon photoexcitation (*42*−*44*). Previously, we reported a chip-based kinase assay using substrate peptides copolymerized into a hydrogel via a UV-photocleavable linker (*45*). After release by 365 nm light, peptide phosphorylation can be readily detected by

* To whom correspondence should be addressed. Tel. 773-834-0250, Fax: 773-702-4394, E-mail: skron@uchicago.edu.

[†] Ludwig Center for Metastasis Research.

[‡] Department of Molecular Genetics and Cell Biology.

10.1021/bc1003058 © 2010 American Chemical Society
Published on Web 09/22/2010

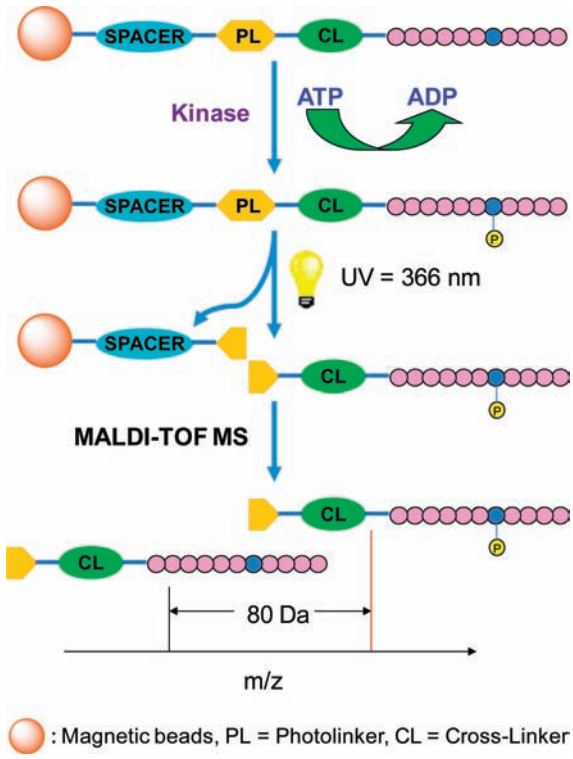


Figure 1. Schematic representation of the new label-free MALDI-based protein kinase assay technique using magnetic beads as a solid-phase analysis platform to facilitate separation and photocleavable linkers as a trigger to release peptide substrates under UV light for MALDI detection. Both phosphorylated and unphosphorylated substrate peptides can be detected by MALDI with a characteristic 80 Da difference in mass between the two peaks.

MALDI-TOF MS. Although hydrogel arrays offer a robust and inert surface that can support a high peptide density, adaptation to high-throughput screening is not straightforward. As an alternative strategy to decrease background after phosphorylation, biotin-tagged peptide substrates can be captured onto streptavidin-coated magnetic beads (*46*) prior to MALDI-TOF analysis. We recently extended this work to create a practical kinase activity screening assay and demonstrated rapid determination of IC_{50} for small-molecule kinase inhibitors (*47*). In this study, we have used Fmoc solid-phase peptide synthesis to install diblock linkers terminated by a photocleavable group onto paramagnetic particles, tethered substrate peptides, and validated these conjugates as reporters of protein kinase activity and inhibition using a MALDI-TOF readout (Figure 1). Our data suggest that this approach may be readily adapted to high-throughput, highly multiplexed analysis of kinases in whole cell lysates.

EXPERIMENTAL PROCEDURES

Materials. Fmoc-aminoethyl photolinker (4-[4-(1-(Fmoc-amino)ethyl)-2-methoxy-5-nitrophenoxy)] butanoic acid, ≥96%, Novabiochem), Fmoc-Gly-OH (N-α-Fmoc-glycine, Peptides International), HCTU coupling reagent (1-[bis(dimethylamino)methylene]-5-chlorobenzotriazolium-3-oxide hexafluorophosphate, Peptides International), 4-methylmorpholine (NMM, 99.5+%, Sigma-Aldrich), piperidine (99%, Sigma-Aldrich), *N*,*N*-dimethylformamide (DMF, anhydrous, 99.8%, Acros Organics), *N*-[*p*-maleimidophenyl]isocyanate (PMPI, Pierce), N-Fmoc-amido-dPEG$_4$-acid, N-Fmoc-amido-dPEG$_8$-acid, N-Fmoc-amido-dPEG$_{12}$-acid (Quanta Biodesign), BcMag amine-terminated magnetic beads (1 μm, Bioclone Inc.), BupH phosphate buffered saline (0.1 M sodium phosphate, 0.15 M NaCl, pH 7.2) (Pierce), and recombinant c-Abl (Upstate) were used as received. Imatinib mesylate (Novartis) was provided by Wendy Stock (The University of Chicago). Dasatinib (free base) was purchased from LC Laboratories (Woburn, MA). Cysteine-terminated G_4SG_3 Abltide substrate (CGGGGSGGGKGEAIYAAP-FAKKKG) and K562 cell lysate (human chronic myelogenous leukemia cell extract) were prepared as reported previously (*28*).

Surface Modification of Magnetic Beads. BcMag particles are uniform superparamagnetic beads consisting of silica-coated iron oxide, presenting surface primary amino groups (**MNP@NH$_2$**). The beads were washed in turn with water and DMF, and diluted to a concentration of 5 mg/mL in DMF. 500 μL of washed beads (equivalent to 0.625 μmol NH_2 groups) was added to a mixture of 100 μL of 240 mM Fmoc-Gly-OH and 900 μL of coupling reagent solution containing 0.76 M HCTU, 1.60 M NMM in DMF. The coupling reaction mixture was rotated at room temperature for 40 min; then, the beads were separated and washed with DMF three times to remove excess reactants. The Fmoc protection group was removed by treatment with 20% piperidine in DMF for 30 min. After deprotection, beads were washed with DMF three times. Four additional cycles of coupling and deprotection reactions were performed in the same manner. As a result, beads with surface poly(glycine) spacers (**MNP@Gly$_5$-NH$_2$**) were obtained and further washed with DMF.

300 μL of surface poly(glycine) spacer-modified beads (**MNP@Gly$_5$-NH$_2$**) in DMF (equivalent 0.375 μmol of free NH_2 groups) was added to a mixture of 20 μL of 400 mM N-Fmoc-amido-dPEG$_4$-acid and 780 μL of coupling reagent solution containing 0.76 M HCTU, 1.60 M NMM in DMF. The coupling reaction was again carried out at room temperature for 40 min, and deprotection for 30 min, as above. After washing with DMF, beads with surface spacers consisting of both poly(glycine) and poly(ethylene glycol) segments (**MNP@Gly$_5$-PEG$_4$-NH$_2$**) were produced.

Superparamagnetic beads with poly(ethylene glycol) spacers of different length (**MNP@PEG$_n$-NH$_2$**, n = 4, 8, 12) were prepared using three different PEG linkers (N-Fmoc-amido-dPEG$_4$-acid, N-Fmoc-amido-dPEG$_8$-acid, and N-Fmoc-amido-dPEG$_{12}$-acid) according to the above-described procedure.

Preparation of Photocleavable Abltide-Conjugated Superparamagnetic Beads. Beads with different surface spacer structures (**MNP@NH$_2$**, **MNP@Gly$_5$-NH$_2$**, **MNP@Gly$_5$-PEG$_4$-NH$_2$**, and **MNP@PEG$_n$-NH$_2$**, n = 4, 8, 12) were used for preparation of photocleavable Abltide-conjugated beads with different spacer linkers. 300 μL of each kind of bead with amino groups (equivalent to 0.375 μmol of free NH_2 groups) were added to a mixture of 60 μL of 180 mM Fmoc-aminoethyl photolinker in DMF and 540 μL of coupling reagent solution containing 0.76 M HCTU, 1.60 M NMM in DMF. The coupling reaction was carried out at room temperature for 40 min. Excess reactants were removed by washing with DMF. The removal of the Fmoc group was completed by treating the beads with 20% piperidine in DMF for 30 min. The deprotected beads were washed in turn with DMF and anhydrous DMF, and reacted with the heterobifunctional cross-linker PMPI in a 1:30 ratio of amino group to isocyanate group over 13 h. After completion of the reaction, beads were washed successively with DMF and BupH PBS buffer (pH 7.2). The maleimide-functionalized beads were reacted with the cysteine-terminated G_4SG_3 Abltide (3.33 equiv to maleimide groups) in BupH PBS buffer medium for 2.5 h. The resulting photocleavable Abltide-conjugated superparamagnetic beads were washed with water and stored in water at 4 °C.

In Vitro Kinase Assay. On-bead phosphorylation reactions by c-Abl kinase and K562 cell lysates were performed. Kinase assays using c-Abl were as reported (*47*). For kinase assays using K562 cell lyaste, a typical 50 μL kinase reaction contained 50 mM Tris-Cl (pH 7.5), 10 mM $MgCl_2$, 1 mM EGTA, 2 mM DTT, 0.01% Brij-35, 50 μM ATP, 0.50 mg/mL BSA-blocked photocleavable Abltide beads with 100 μg/mL K562 cell lysate,

and 1× complete protease inhibitor cocktail (Roche) and was incubated at 37 °C for 1 h. After the kinase reactions, beads were separated from the reaction buffer, washed twice with water, and subjected to MALDI-TOF MS analysis.

In Vitro Inhibition Assay. Dasatinib and imatinib were assayed in vitro using both recombinant c-Abl and K562 cell lysate. Assays with c-Abl or K562 cell lysate were as above with the addition of varying concentrations of inhibitors. A series of kinase reactions with 50 μM ATP and 0, 1, 10, 100, 500, 10^3, 10^4, or 10^5 nM Imatinib and 10 μM ATP and 0, 0.2, 0.5, 1, 2, 5, 10, 100, or 1000 nM Dasatinib were performed for 1 h using c-Abl at 30 °C and K562 cell lysate at 37 °C, respectively. After the kinase reactions, the beads were separated and washed with water twice, and stored in 5 μL of water at 4 °C. The degree of phosphorylation for each sample was determined by MALDI-TOF MS.

MALDI-TOF MS Analysis. Sample preparation for MALDI-TOF analysis was as described (*47*), except that the dry spotted samples were irradiated by UV light of 366 nm for 20 min prior to addition of α-cyano-4-hydroxycinnamic acid (CHCA) matrix solution onto each sample spot and analysis on a Voyager DE. The phosphorylation ratio of Abltide immobilized on magnetic beads was determined according to the previously described computational method (*47*).

RESULTS

We used solid-phase peptide synthesis to immobilize a tyrosine kinase peptide substrate with a photocleavable linker onto silica-coated superparamagnetic beads to enable simple and straightforward kinase assays (Figure 1). After the kinase reaction, both phosphorylated and unphosphorylated substrate peptide are released from the beads by UV photocleavage and then detected by MALDI-TOF MS. The phosphorylated and unphosphorylated peptide peaks are offset by 80 Da (*48*, *49*) and the degree of phosphorylation can be estimated by the relative intensities of the two peaks.

To test the new protein kinase assay technique, we chose the model system of the oncogenic protein kinase, Bcr-Abl, and a synthetic substrate peptide, Abltide. Bcr-Abl is a fusion gene product resulting from the Ph1 reciprocal 9:22 translocation (*50*, *51*), and its constitutive activity is responsible for cancer onset and progression in CML (*52*). Bcr-Abl kinase from cell extracts of the K562 cell line derived from human chronic myeloid leukemia and its counterpart recombinant c-Abl kinase were both used for this study. With this model system, Abltide was readily immobilized on magnetic beads and phosphorylated by kinases. After the reaction, MALDI-TOF MS could detect both phosphorylated and unphosphorylated peptides cleaved from the magnetic beads upon UV light exposure (λ = 366 nm).

Currently, two kinds of spacer linkers have been extensively used to distance peptides from solid supports: (i) poly(ethylene glycol) (PEG) linkers, well-known for their ability to prevent nonspecific interactions, also act as hydrophilic spacers minimizing any detrimental interaction between the attached peptide and solid surface (*53*−*55*); and (ii) glycine spacers, generally inserted into the peptide sequence, can improve the accessibility of enzymes to peptide substrates (*56*). To optimize the kinase reactions, we investigated the effect of two different linkers on

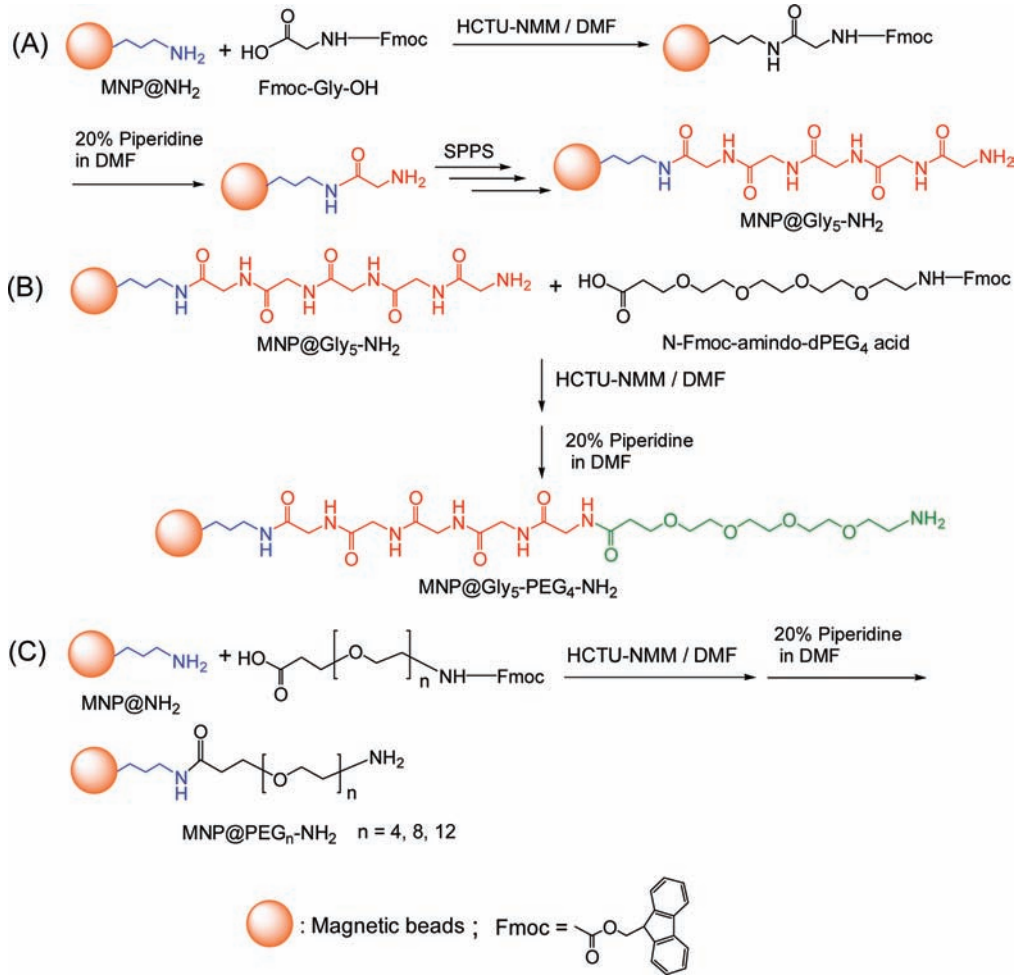


Figure 2. Structural design and synthesis of magnetic beads bearing different surface spacers via the solid-phase peptide synthesis (SPPS) technique. (A) Pentaglycine spacers. (B) Diblock spacers consisting of PEG and pentaglycine segments. (C) Single PEG spacers with different lengths.

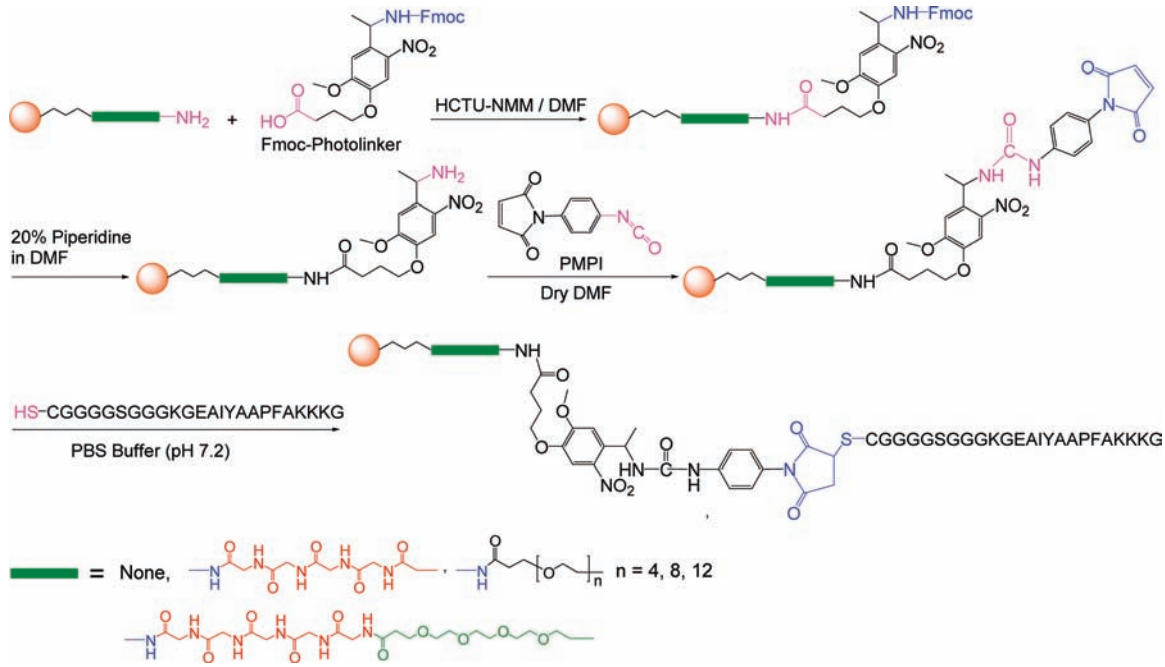


Figure 3. General synthetic route for photocleavable Abltide-conjugated magnetic beads with different surface spacer structures (pentaglycine spacer, single PEG spacers with different lengths, and diblock spacer consisting of PEG and polyglycine) through successive coupling−deprotection, amino−isocyanate, and highly selective thiol−maleimide reactions starting from magnetic beads bearing different surface spacers (denoted by the green bar).

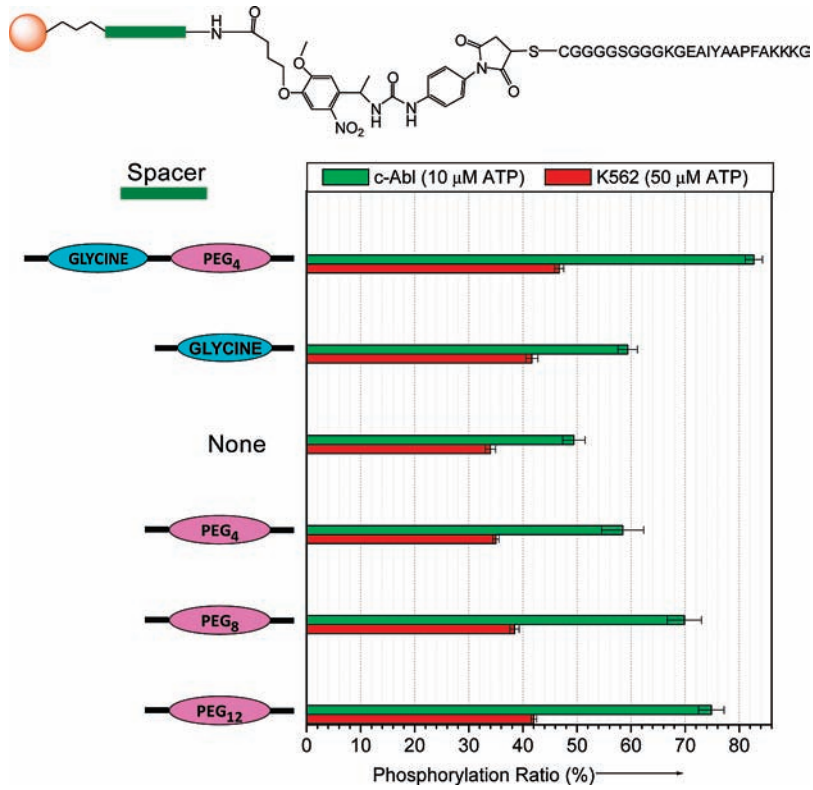


Figure 4. Effect of the surface spacer between the Abltide substrate and magnetic bead support on phosphorylation of Abltide by both c-Abl at 30 °C and K562 cell lysate at 37 °C for 1 h, respectively. The general structure of photocleavable abltide-conjugated magnetic beads was given in the upper panel, and the green bar represents different surface spacer structures shown in the lower left panel. The phosphoryaltion ratios corresponding to each surface spacer by both c-Abl and K562 cell lysate were determined by MALDI according to the intensity of phosphorylated and unphosphorylated peaks. Each experiment represented in the lower right panel was performed in triplicate.

phosphorylation of peptide substrates. First, the surface of amino-functionalized silica-coated superparamagnetic beads (**MNP@NH$_2$**) was modified by introducing a five glycine spacer (Gly_5) by a five-step standard solid-phase peptide synthesis (SPPS) procedure shown in Figure 2A. Glycine spacer-modified beads (**MNP@Gly$_5$-NH$_2$**) were further modified by insertion of a PEG linker using N-Fmoc-amino-dPEG$_4$ acid according to the standard SPPS protocol (Figure 2B). As a result, dual spacer-modified beads (**MNP@Gly$_5$-PEG$_4$-NH$_2$**) were produced. For comparison, the beads were also modified by single PEG spacers

of varying lengths (Figure 2C). The beads with different surface spacers, **MNP@NH$_2$**, **MNP@Gly$_5$-NH$_2$**, **MNP@PEG$_n$-NH$_2$**, and **MNP@Gly$_5$-PEG$_4$-NH$_2$**, were then coupled to an Fmoc-photolinker and deprotected and the amino groups reacted with *N*-[*p*-maleimidophenyl]isocyanate to form surface maleimide-functionalized beads. The maleimide-functionalized beads were then reacted with the amino-terminal cysteine on CG$_4$SG$_3$-Abltide (**C**GGGGSGGG*KEAIYAAPFAKKK*G) in PBS buffer to produce photocleavable Abltide-conjugated superparamagnetic beads with different surface spacer linkers (Figure 3). These beads were examined in kinase assays.

Abltide conjugated to superparamagnetic beads was phosphorylated in kinase buffer for 1 h with c-Abl at 30 °C or K562 cell lysate at 37 °C. The degree of phosphorylation of peptide substrates conjugated to beads via different linkers was determined by the relative intensity of phosphorylated and unphosphorylated peptide peaks in the MALDI spectrum, as summarized in Figure 4. It is clear that both single glycine and PEG spacers are able to improve the phosphorylation efficiency, most likely due to the increase in molecular mobility of the substrate peptide and kinase accessibility to peptide. The number of PEG units in the spacer had a measurable effect on phosphorylation, with longer spacers yielding a slightly higher phosphorylation ratio. We found that insertion of PEG$_{12}$ between the peptide and solid support yielded optimal phosphorylation efficiency, consistent with Katayama et al. (*33*). In particular, the diblock spacer consisting of poly(glycine) and PEG markedly increased the phosphorylation efficiency of peptide substrates, perhaps due to the complementary features of the two spacers. Therefore, the photocleavable Abltide-conjugated magnetic beads with a diblock spacer of poly(glycine) and PEG were used for the kinase inhibition assays.

A common application for assays reporting the phosphorylation of peptides is to evaluate the inhibitory ability of different drugs on protein kinases. Two clinically useful Abl kinase inhibitors, imatinib and dasatinib, have been used in the treatment of CML via targeting the oncogenic Bcr-Abl kinase. Imatinib and dasatinib were evaluated using our magnetic bead-based kinase assays. The Abltide-conjugated beads were incubated for 1 h with c-Abl kinase at 30 °C or K562 cell lysate at 37 °C with 50 μM ATP + 0−100 μM for imatinib, and with 10 μM ATP + 0−1 μM for dasatinib. The peptides were then released and analyzed by MALDI-TOF MS. Figure 5A shows a representative set of MALDI spectra of Abltide released from beads after phosphorylation by c-Abl kinase at different imatinib concentrations. The expected 80 Da increase in mass relative to the unmodified peptide was observed after peptides were phosphorylated, yielding two singly charged peaks at m/z = 2478.22 and 2398.35. With no addition of inhibitor, the Abltide substrate was 86% phosphorylated, calculated according to the relative intensity of the phosphorylated and unphosphorylated peptide ions. The c-Abl kinase activity was gradually inhibited with the increase of imatinib concentration, and fully blocked at 10 μM imatinib (Figure 5A). There is a minor peak (denoted by a star) at m/z = 2355.70 attributed to fragmentation at a site other than the site predicted for photocleavage (Figure 5B). We found that minor peak intensity depends on the completion of photocleavage prior to analysis, as well as the amount of matrix spotted and laser intensity during MALDI analysis. We found that the relative intensity ratio of the minor peaks formed from phosphorylated and unphosphorylated peptides was equal to the major ones. Therefore, the phosphorylation ratio of Abltide substrate was calculated according to the relative intensities of the major phosphorylated and unphosphorylated peaks. A dose-dependent effect on phosphorylation of Abltide by c-Abl or K562 cell lysate was observed for each inhibitor (Figure 6), and IC$_{50}$ values were calculated by fitting to sigmoidal

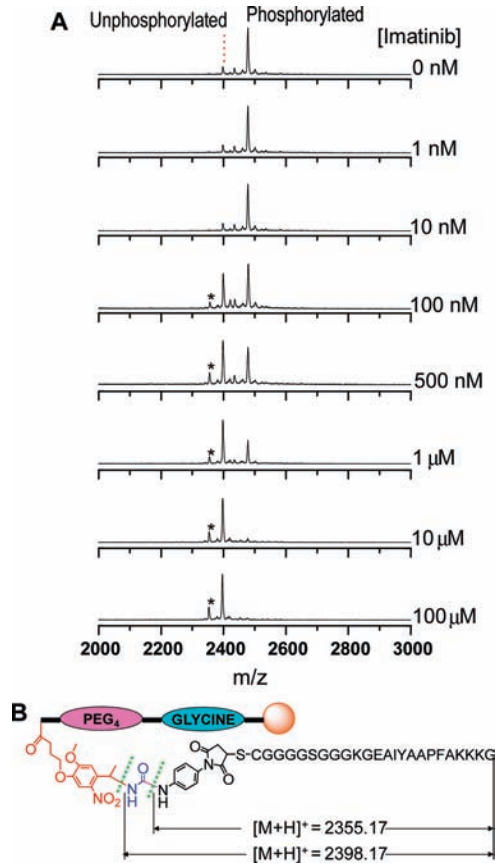


Figure 5. (A) A representative set of MALDI-TOF MS spectra of the photocleavable Abltide-conjugated magnetic beads after 1 h phosphorylation by c-Abl at different imatinib concentrations. The peaks of phosphorylated and unphorylated peptide substrates were observed at m/z = 2478.22 and 2398.35, respectively. The minor peak (denoted by a star) at m/z = 2355.70 is attributed to fragmentation at a site other than that predicted for photocleavage. (B) Predicted photocleavage and minor cleavage sites and theoretical exact mass of their corresponding generated peptide substrate fragments.

dose−response curves (Table 1). The IC$_{50}$ values of imatinib against c-Abl and K562 cell lysate were 0.53 and 1.10 μM, respectively. These values are higher than the literature IC$_{50}$ values, perhaps reflecting the use of a higher ATP concentration, 50 μM, in our experiments. However, for dasatinib, where we used 10 μM ATP, the IC$_{50}$ values against c-Abl and K562 cell lysate of 12.0 and 2.3 nM are close to reported values.

DISCUSSION

Although much progress has been made in developing protein kinase assay techniques for understanding biological regulatory pathways, many challenges still exist (*57*). Only a fraction of techniques are compatible with cell lysates or within cells (*57*). It has become clear that MALDI-based label-free heterogeneous kinase assays may have a significant application value in this field. In this study, we explored the use of magnetic beads for heterogeneous kinase assays. We chose magnetic beads as solid supports, because they can greatly facilitate on-bead preparation of peptide conjugates and rapid separation of phosphorylated products as well as being amenable to automated processing. In addition, they can promote the ionization of phosphorylated products during the process of MALDI analysis and further increase assay sensitivity (*58*). However, the immobilization of peptide substrates on the solid support plays a key role in the overall heterogeneous kinase assays. There are many strategies for immobilization of peptide substrates onto solid supports (*30*, *59*). However, our magnetic bead-based SPPS strategy has

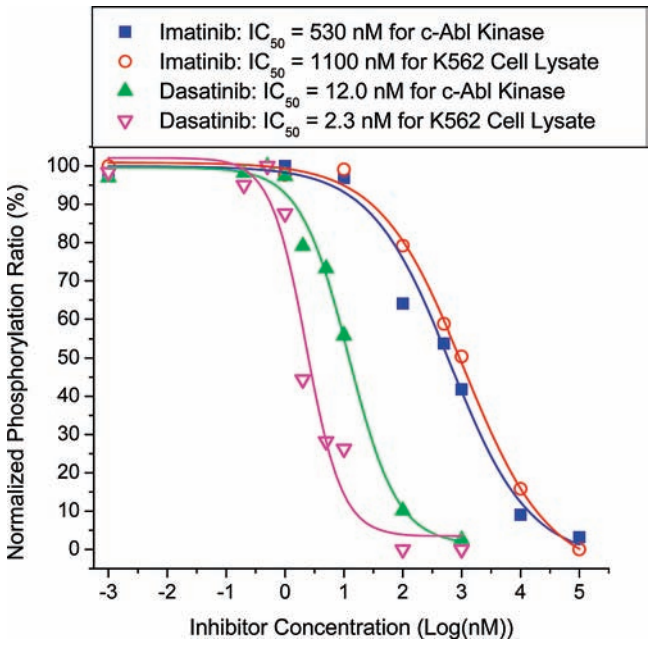


Figure 6. Inhibition assays using imatinib and dasatinib against c-Abl kinase and K562 cell lysate using the photocleavable substrate on magnetic beads, and MALDI-TOF MS analysis. The degree of phosphorylation was calculated from the ratio of phosphorylated and unphosphorylated peak intensities. Each data point is the average of three spectra. ATP concentrations for imatinib and dasatinib inhibition assays were 50 μM and 10 μM, respectively.

Table 1. IC_{50} of Inhibitors

	IC_{50} (nM), found		IC_{50} (nM), reported	
inhibitor	c-Abl	K562	c-Abl	K562
imatinib	530	1100	440 (*60*)	560 (*61*), 945 (*62*)
dasatinib	12	2.3	9 (*63*),14 (*64*)	1.0 (*65*), 16 (*62*)

shown distinct advantages over the published approaches, because it conveniently inserts different spacers between the peptide substrate and magnetic beads.

We performed a systematic study by introducing different spacers between peptide substrates and magnetic beads to understand their influence on the kinase assays. For this purpose, poly(glycine), PEG spacers, and their combinations were employed. Without spacers, the phosphorylation ratios of peptide substrates were quite low. Both the single pentaglycine spacer and PEG spacer were able to enhance the phosphorylation ratios of peptide substrates. Notably, a diblock spacer consisting of polyglycine and PEG prepared in situ by the magnetic bead-based SPPS strategy greatly improved the phosphorylation ratios as compared with the other spacers due to the synergic effects of the two types of spacers. The introduction of the diblock spacer made the MALDI-based kinase assays work well with both recombinant kinases and cell lysates. As this new kinase assay technique can rapidly quantify protein kinase activities directly from complex cellular mixtures, it provides a reasonable strategy for the development of cell-based screens for drug discovery. Unlike traditional methods, MALDI can differentiate multiple peptides and their modified forms. Thus, the use of the label-free MALDI detection tool provides this new kinase assay with the potential for quantitative evaluation of the relative potencies of a drug to different kinases.

CONCLUSIONS

We have developed a new label-free protein kinase assay technique in which magnetic beads were used as an analytical platform to immobilize peptide substrates via photocleavable linkers and released by UV light for MALDI detection. Both poly(glycine) and PEG spacers are able to improve phosphorylation efficiency and a diblock poly(glycine) and PEG spacer was found to be even more efficient than any single spacers. This simple and efficient assay technique may be adapted to high-throughput screening and generalized to a wide range of multiple post-translational modification analysis.

ACKNOWLEDGMENT

We thank Wendy Stock for kindly providing imatinib and Jonathan Goya for his helpful comments on the manuscript. This work was supported by National Institutes of Health grants HG003864, GM074691, and CA126764.

LITERATURE CITED

(1) Lu, Z. M., and Hunter, T. (2009) Degradation of activated protein kinases by ubiquitination. *Annu. Rev. Biochem. 78*, 435–475.
(2) Hunter, T. (2000) Signaling - 2000 and beyond. *Cell 100*, 113–127.
(3) Manning, G., Whyte, D. B., Martinez, R., Hunter, T., and Sudarsanam, S. (2002) The protein kinase complement of the human genome. *Science 298*, 1912–1934.
(4) Noble, M. E. M., Endicott, J. A., and Johnson, L. N. (2004) Protein kinase inhibitors: insights into drug design from structure. *Science 303*, 1800–1805.
(5) Alonso, A., Sasin, J., Bottini, N., Friedberg, I., Osterman, A., Godzik, A., Hunter, T., Dixon, J., and Mustelin, T. (2004) Protein tyrosine phosphatases in the human genome. *Cell 117*, 699–711.
(6) Cohen, P. (2002) Protein kinases - the major drug targets of the twenty-first century? *Nat. Rev. Drug Discovery 1*, 309–315.
(7) Swanson, C. D., Paniagua, R. T., Lindstrom, T. M., and Robinson, W. H. (2009) Tyrosine kinases as targets for the treatment of rheumatoid arthritis. *Nat. Rev. Rheumatol. 5*, 317–324.
(8) Zhang, J. M., Yang, P. L., and Gray, N. S. (2009) Targeting cancer with small molecule kinase inhibitors. *Nat. Rev. Cancer 9*, 28–39.
(9) Druker, B. J., Tamura, S., Buchdunger, E., Ohno, S., Segal, G. M., Fanning, S., Zimmermann, J., and Lydon, N. B. (1996) Effects of a selective inhibitor of the Abl tyrosine kinase on the growth of Bcr-Abl positive cells. *Nat. Med. 2*, 561–566.
(10) Grant, S. (2009) Therapeutic protein kinase inhibitors. *Cell. Mol. Life Sci. 66*, 1163–1177.
(11) Johnson, L. N. (2009) Protein kinase inhibitors: contributions from structure to clinical compounds. *Q. Rev. Biophys. 42*, 1–40.
(12) Sebolt-Leopold, J. S., and English, J. M. (2006) Mechanisms of drug inhibition of signalling molecules. *Nature 441*, 457–462.
(13) Houseman, B. T., Huh, J. H., Kron, S. J., and Mrksich, M. (2002) Peptide chips for the quantitative evaluation of protein kinase activity. *Nat. Biotechnol. 20*, 270–274.
(14) Rathore, R., Corr, J., Scott, G., Vollmerhaus, P., and Greis, K. D. (2008) Development of an inhibitor screening platform via mass spectrometry. *J. Biomol. Screen 13*, 1007–1013.
(15) Kondo, N., and Nishimura, S. I. (2009) MALDI-TOF mass-spectrometry-based versatile method for the characterization of protein kinases. *Chem.—Eur. J. 15*, 1413–1421.
(16) von Ahsen, O., and Bomer, U. (2005) High-throughput screening for kinase inhibitors. *ChemBioChem 6*, 481–490.
(17) Shults, M. D., Janes, K. A., Lauffenburger, D. A., and Imperiali, B. (2005) A multiplexed homogeneous fluorescence-based assay for protein kinase activity in cell lysates. *Nat. Methods 2*, 277–283.
(18) Zondlo, S. C., Gao, F., and Zondlo, N. J. (2010) Design of an encodable tyrosine kinase-inducible domain: detection of tyrosine kinase activity by terbium luminescence. *J. Am. Chem. Soc. 132*, 5619–5621.

(19) Placzek, E. A., Plebanek, M. P., Lipchik, A. M., Kidd, S. R., and Parker, L. L. (2010) A peptide biosensor for detecting intracellular Abl kinase activity using matrix-assisted laser desorption/ionization time-of-flight mass spectrometry. *Anal. Biochem. 397*, 73–78.

(20) Wu, D., Sylvester, J. E., Parker, L. L., Zhou, G., and Kron, S. J. (2010) Peptide reporters of kinase activity in whole cell lysates. *Biopolym. (Pept. Sci.) 94*, 475–486.

(21) Mand, M. R., Wu, D., Veach, D. R., and Kron, S. J. (2010) Cell treatment and lysis in 96-well filter-bottom plates for screening Bcr-Abl activity and inhibition in whole-cell extracts. *J. Biomol. Screen 15*, 434–440.

(22) Sylvester, J. E., and Kron, S. J. (2010) A bead-based activity screen for small-molecule inhibitors of signal transduction in chronic myelogenous leukemia cells. *Mol. Cancer Ther. 9*, 1469–1481.

(23) Kim, M., Shin, D.-S., Kim, J., Yoon-Sik Lee, Y.-S. (2010) Substrate screening of protein kinases: Detection methods and combinatorial peptide libraries *Pept. Sci*. DOI: 10.1002/bip.21506.

(24) Reineke, U., Volkmer-Engert, R., and Schneider-Mergener, J. (2001) Applications of peptide arrays prepared by the SPOT-technology. *Curr. Opin. Biotechnol. 12*, 59–64.

(25) Fodor, S. P. A., Read, J. L., Pirrung, M. C., Stryer, L., Lu, A. T., and Solas, D. (1991) Light-directed, spatially addressable parallel chemical synthesis. *Science 251*, 767–773.

(26) MacBeath, G., and Schreiber, S. L. (2000) Printing proteins as microarrays for high-throughput function determination. *Science 289*, 1760–1763.

(27) Lesaicherre, M. L., Uttamchandani, M., Chen, G. Y. J., and Yao, S. Q. (2002) Developing site-specific immobilization strategies of peptides in a microarray. *Bioorg. Med. Chem. Lett. 12*, 2079–2083.

(28) Wu, D., Mand, M. R., Veach, D. R., Parker, L. L., Clarkson, B., and Kron, S. J. (2008) A solid-phase Bcr-Abl kinase assay in 96-well hydrogel plates. *Anal. Biochem. 375*, 18–26.

(29) Uttamchandani, M., and Yao, S. Q. (2008) Peptide microarrays: Next generation biochips for detection, diagnostics and high-throughput screening. *Curr. Pharm. Des. 14*, 2428–2438.

(30) Kohn, M. (2009) Immobilization strategies for small molecule, peptide and protein microarrays. *J. Pept. Sci. 15*, 393–397.

(31) Ding, H., Prodinger, W. M., and Kopecek, J. (2006) Identification of CD21-binding peptides with phage display and investigation of binding properties of HPMA copolymer-peptide conjugates. *Bioconjugate Chem. 17*, 514–523.

(32) Kim, Y. P., Oh, E., Oh, Y. H., Moon, D. W., Lee, T. G., and Kim, H. S. (2007) Protein kinase assay on peptide-conjugated gold nanoparticles by using secondary-ion mass spectrometric imaging. *Angew. Chem., Int. Ed. 46*, 6816–6819.

(33) Inamori, K., Kyo, M., Matsukawa, K., Inoue, Y., Sonoda, T., Tatematsu, K., Tanizawa, K., Mori, T., and Katayama, Y. (2008) Optimal surface chemistry for peptide immobilization in on-chip phosphorylation analysis. *Anal. Chem. 80*, 643–650.

(34) Ding, H., Prodinger, W. M., and Kopecek, J. (2006) Two-step fluorescence screening of CD21-binding peptides with one-bead one-compound library and investigation of binding properties of N-(2-hydroxypropyl)methacrylamide copolymer-peptide conjugates. *Biomacromolecules 7*, 3037–3046.

(35) Li, Y. J., Xie, W. H., and Fang, G. J. (2008) Fluorescence detection techniques for protein kinase assay. *Anal. Bioanal. Chem. 90*, 2049–2057.

(36) Olive, D. M. (2004) Quantitative methods for the analysis of protein phosphorylation in drug development. *Expert Rev. Proteomics 1*, 327–341.

(37) Ma, H. C., Deacon, S., and Horiuchi, K. (2008) The challenge of selecting protein kinase assays for lead discovery optimization. *Expert Opin. Drug Discovery 3*, 607–621.

(38) McLachlin, D. T., and Chait, B. T. (2001) Analysis of phosphorylated proteins and peptides by mass spectrometry. *Curr. Opin. Chem. Biol. 5*, 591–602.

(39) Reinders, J., and Sickmann, A. (2005) State-of-the-art in phosphoproteomics. *Proteomics 5*, 4052–4061.

(40) Min, D. H., Tang, W. J., and Mrksich, M. (2004) Chemical screening by mass spectrometry to identify inhibitors of anthrax lethal factor. *Nat. Biotechnol. 22*, 717–723.

(41) Kostiainen, M. A., Smith, D. K., and Ikkala, O. (2007) Optically triggered release of DNA from multivalent dendrons by degrading and charge-switching multivalency. *Angew. Chem., Int. Ed. 46*, 7600–7604.

(42) Yan, F. N., Chen, L. H., Tang, Q. L., and Rong, W. (2004) Synthesis and characterization of a photocleavable cross-linker and its application on tunable surface modification and protein photodelivery. *Bioconjugate Chem. 15*, 1030–1036.

(43) Saran, D., and Burke, D. H. (2007) A versatile photocleavable bifunctional linker for facile synthesis of substrate-DNA conjugates for the selection of nucleic acid catalysts. *Bioconjugate Chem. 18*, 275–279.

(44) Kloxin, A. M., Kasko, A. M., Salinas, C. N., and Anseth, K. S. (2009) Photodegradable hydrogels for dynamic tuning of physical and chemical properties. *Science 324*, 59–63.

(45) Parker, L. L., Brueggemeier, S. B., Rhee, W. J., Wu, D., Kent, S. B. H., Kron, S. J., and Palecek, S. P. (2006) Photocleavable peptide hydrogel arrays for MALDI-TOF analysis of kinase activity. *Analyst 131*, 1097–1104.

(46) Kinumi, T., Niki, E., Shigeri, Y., and Matsumoto, H. (2005) Affinity-tagged phosphorylation assay by matrix-assisted laser desorption/ionization time-of-flight mass spectrometry (ATPA-MALDI): Application to calcium/calmodulin-dependent protein kinase. *J. Biochem. 138*, 791–796.

(47) Zhou, G.; Sylvester, J. E.; Wu, D.; Veach, D. R.; Kron, S. J. (2010) A magnetic bead-based protein kinase assay with dual detection techniques. *Anal. Biochem.*, doi:10.1016/j.ab.2010.08.034.

(48) Parker, L., Engel-Hall, A., Drew, K., Steinhardt, G., Helseth, D. L., Jabon, D., McMurry, T., Angulo, D. S., and Kron, S. J. (2008) Investigating quantitation of phosphorylation using MALDI-TOF mass spectrometry. *J. Mass Spectrom. 43*, 518–527.

(49) Annan, R. S., and Carr, S. A. (1996) Phosphopeptide analysis by matrix-assisted laser desorption time-of-flight mass spectrometry. *Anal. Chem. 68*, 3413–3421.

(50) Rowley, J. D. (1973) New consistent chromosomal abnormality in chronic myelogenous leukemia identified by quinacrine fluorescence and giemsa staining. *Nature 243*, 290–293.

(51) Nagar, B., Hantschel, O., Young, M. A., Scheffzek, K., Veach, D., Bornmann, V., Clarkson, B., Superti-Furga, G., and Kuriyan, J. (2003) Structural basis for the autoinhibition of c-Abl tyrosine kinase. *Cell 112*, 859–871.

(52) Warmuth, M., Danhauser-Riedl, S., and Hallek, M. (1999) Molecular pathogenesis of chronic myeloid leukemia: implications for new therapeutic strategies. *Ann. Hematol. 78*, 49–64.

(53) Cheung, C. L., Camarero, J. A., Woods, B. W., Lin, T. W., Johnson, J. E., and De Yoreo, J. J. (2003) Fabrication of assembled virus nanostructures on templates of chemoselective linkers formed by scanning probe nanolithography. *J. Am. Chem. Soc. 125*, 6848–6849.

(54) Camarero, J. A., Kwon, Y., and Coleman, M. A. (2004) Chemoselective attachment of biologically active proteins to surfaces by expressed protein ligation and its application for "protein chip" fabrication. *J. Am. Chem. Soc. 126*, 14730–14731.

(55) Niculescu-Duvaz, D., Getaz, J., and Springer, C. J. (2008) Long functionalized poly(ethylene glycol)s of defined molecular weight: Synthesis and application in solid-phase synthesis of conjugates. *Bioconjugate Chem. 19*, 973–981.

(56) Wegner, G. J., Lee, H. J., and Corn, R. M. (2002) Characterization and optimization of peptide arrays for the study of epitope-antibody interactions using surface plasmon resonance imaging. *Anal. Chem. 74*, 5161–5168.

(57) Jia, Y., Gu, X. J., Brinker, A., and Warmuth, M. (2008) Measuring the tyrosine kinase activity: a review of biochemical

and cellular assay technologies. *Expert Opin. Drug Discovery 3*, 959–978.

(58) Ficarro, S. B., Adelmant, G., Tomar, M. N., Zhang, Y., Cheng, V. J., and Marto, J. A. (2009) Magnetic bead processor for rapid evaluation and optimization of parameters for phosphopeptide enrichment. *Anal. Chem. 81*, 4566–4575.

(59) Rusmini, F., Zhong, Z. Y., and Feijen, J. (2007) Protein immobilization strategies for protein biochips. *Biomacromolecules 8*, 1775–1789.

(60) Brasher, B. B., and Van Etten, R. A. (2000) c-Ab1 has high intrinsic tyrosine kinase activity that is stimulated by mutation of the Src homology 3 domain and by autophosphorylation at two distinct regulatory tyrosines. *J. Biol. Chem. 275*, 35631–35637.

(61) Radujkovic, A., Schad, M., Topaly, J., Veldwijk, M. R., Laufs, S., Schultheis, B. S., Jauch, A., Melo, J. V., Fruehauf, S., and Zeller, W. J. (2005) Synergistic activity of imatinib and 17-AAG in imatinib-resistant CML cells overexpressing BCR-ABL - Inhibition of P-glycoprotein function by 17-AAG. *Leukemia 19*, 1198–1206.

(62) De Keersmaecker, K., Versele, M., Cools, J., Superti-Furga, G., and Hantschel, O. (2008) Intrinsic differences between the catalytic properties of the oncogenic NUP214-ABL1 and BCR-ABL1 fusion protein kinases. *Leukemia 22*, 2208–2216.

(63) Rix, U., Hantschel, O., Duernberger, G., Rix, L. L. R., Planyavsky, M., Fernbach, N. V., Kaupe, I., Bennett, K. L., Valent, P., Colinge, J., Kocher, T., and Superti-Furga, G. (2007) Chemical proteomic profiles of the BCR-ABL inhibitors imatinib, nilotinib, and dasatinib, reveal novel kinase and nonkinase targets. *Blood 110*, 4055–4063.

(64) Hantschel, O., Rix, U., Schmidt, U., Burckstummer, T., Kneidinger, M., Schutze, G., Colinge, J., Bennett, K. L., Ellmeier, W. R., Valent, P., and Superti-Furga, G. (2007) The Btk tyrosine kinase is a major target of the Bcr-Abi inhibitor dasatinib. *Proc. Natl. Acad. Sci. U.S.A. 104*, 13283–13288.

(65) Okabe, S., Tauchi, T., and Ohyashiki, K. (2008) Characteristics of dasatinib- and imatinib-resistant chronic myelogenous leukemia cells. *Clin. Cancer Res. 14*, 6181–6186.

BC1003058

Biodistribution and Excretion of Monosaccharide−Albumin Conjugates Measured with in Vivo Near-Infrared Fluorescence Imaging

Thomas E. McCann,[†] Nobuyuki Kosaka,[†] Makoto Mitsunaga,[†] Peter L. Choyke,[†] Jeffrey C. Gildersleeve,[‡] and Hisataka Kobayashi*[,†]

Molecular Imaging Program, Center for Cancer Research, National Cancer Institute, National Institutes of Health, 10 Center Drive, Bethesda, Maryland 20892-1088, and Chemical Biology Laboratory, Center for Cancer Research, National Cancer Institute-Frederick, National Institutes of Health, 376 Boyles Street, Frederick, Maryland 21702. Received July 9, 2010; Revised Manuscript Received August 22, 2010

Target specific small molecules as modulators of drug delivery may play a significant role in the future development of therapeutics. Small molecules can alter the in vivo pharmacokinetics of therapeutic macromolecules leading to more efficient drug delivery with less systemic toxicity. The potential of creating a more effective drug delivery system through glycosylation has led, for instance, to the addition of galactose to increase drug delivery to the liver. However, there are many other monosaccharides with potentially useful targeting properties that require further characterization. Here, we investigate the potential of glycosylation to guide molecular therapies using five different monosaccharides conjugated to human serum albumin (HSA). Additionally, we investigate how the amount of glycosylation may alter the pharmacokinetic profile of HSA. We introduce the use of in vivo near-infrared optical imaging to characterize the effect of differential glycosylation on the pharmacokinetics of macromolecules.

INTRODUCTION

Target-organ or cell specific drug delivery can alter the pharmacokinetics of macromolecules including proteins or nanoparticles, thus changing drug catabolism and excretion with possible improvements in the therapeutic index (i.e., improved target delivery with decreased off-target toxicity). Conjugation of drugs with small molecules such as sugars, short peptides, or folic acid can dramatically alter the pharmacokinetics (*1*). Glycosylation, in particular, has been investigated for targeting hepatocytes, macrophages, vascular endothelial cells, and various cancer cells via the so-called "lectin" family of sugar receptors, commonly overexpressed on cancer cells (*2*−*5*). For example, radiolabeled galactose conjugated to albumin has been used to assess hepatocyte function. Fluorescence-labeled galactosamine conjugated albumin has recently been found to specifically bind, internalize, and visualize the peritoneal dissemination of various ovarian cancer nodules with high specificity and sensitivity (*6*). Through these studies, it becomes clear that galactose conjugation dramatically alters the biodistribution of the molecule to which it is bound. Other monosaccharides may lead to similar alterations in catabolism and excretion.

The effect of a variety of different types and amounts of monosaccharides has not been systematically studied. Here, we conjugate low (ranging 3 to 5) and high (ranging 23 to 25) numbers of various monosaccharides (galactose-β, glucose-α, mannose-α, and fucose α and β) to human serum albumin (HSA), which is also labeled with a near-infrared (NIR) fluorescent probe. These conjugates were then used to evaluate the change in pharmacokinetic and excretion using NIR fluorescence imaging.

* Correspondence to Hisataka Kobayashi, M.D., Ph.D., Molecular Imaging Program, National Cancer Institute, NIH, Building 10, Room B3B69, MSC1088, Bethesda, MD 20892-1088. Phone: 301-451-4220; Fax: 301-402-3191; E-mail: kobayash@mail.nih.gov.

[†] Molecular Imaging Program.

[‡] Chemical Biology Laboratory.

EXPERIMENTAL PROCEDURES

Synthesis and Quality Control of Monosaccaride Conjugated Albumin. Linker-modified monosaccharides (Figure 1) were prepared as reported previously, and conjugation to HSA was carried out as reported previously for bovine serum albumin conjugates (*7*, *8*). Briefly, linker-modified monosaccharides were dissolved in a 50/50 mixture of DMF/H_2O at a final concentration of 150 mM. *N*-(3-Dimethylaminopropyl)-*N*′-ethyl-carbodiimide hydrochloride (EDC, Sigma-Aldrich, St. Louis, MO) was dissolved in a 50/50 mixture of DMF/H_2O at a final concentration of 300 mM. *N*-Hydroxysuccinimide (NHS, Sigma-Aldrich) was dissolved in DMF at a final concentration of 300 mM. The NHS ester was preformed by combining the carbohydrate, EDC, and NHS in an Eppendorf tube at a ratio of 2:1:1 and allowing the reaction to stand at room temperature with occasional gentle mixing. After 60 min, each reaction mixture was added to a solution of HSA (4 mg/mL in 10 mM sodium borate, 90 mM NaCl, pH 8.0, Sigma-Aldrich) that had been precooled to 4 °C to give a final ratio of carbohydrate to HSA of approximately 5−8:1 to produce low-density conjugates or 37−72:1 to produce high-density conjugates. After 15 min, the solution was warmed to room temperature and allowed to stand for 1 h (Figure 1). HSA conjugates were then dialyzed extensively against water containing 6 mM NaCl (SpectraPor 7, MWCO = 10 000). The extent of conjugation (Figure 2) was evaluated by measuring the average mass of each conjugate by MALDI-MS (Applied Biosystems Voyager-DE Pro time-of-flight mass spectrometer, Life Technologies Co., Carlsbad, CA) and then determining the mass shift relative to that of unmodified HSA (Table 1; also see Supporting Information Figure 1).

Synthesis of Fluorophore Conjugated Glycosylated HSA Probes. The NHS ester of IRDye 800CW (IR800) was purchased from LI-COR Co. (Lincoln, NE). Glycosylated HSA and non-glycosylated samples (6 nmol) were incubated with

10.1021/bc100313p This article not subject to U.S. Copyright. Published 2010 by the American Chemical Society
Published on Web 09/20/2010

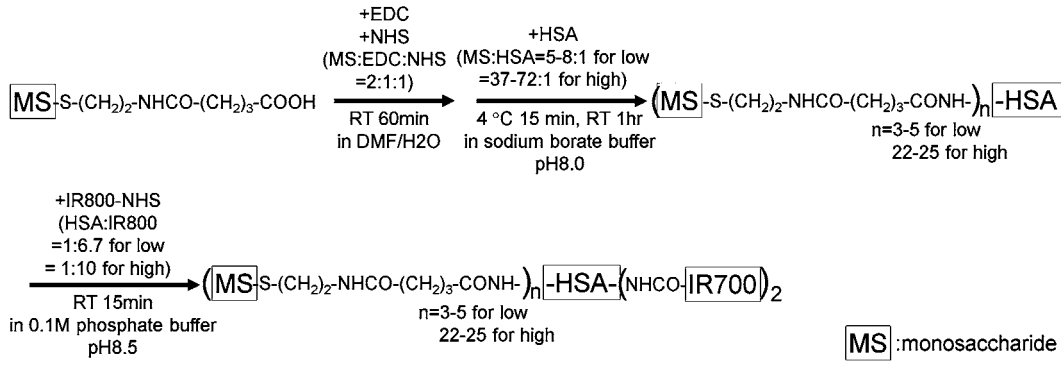


Figure 1. Synthetic scheme for conjugation and labeling.

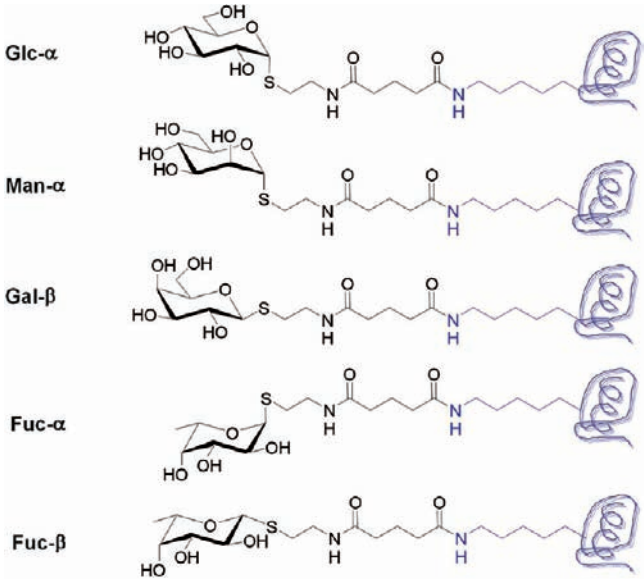


Figure 2. Chemical structure of linkage between sugar and albumin.

Table 1. Summary of the Characterization Data for the Conjugates

name	avg mass (by MALDI)	change	each saccharide adds	ratio of saccharide to HSA	density
Glc-α 23-HSA	74100	7624	335	23	high
Glc-α 05-HSA	68088	1612	335	5	low
Man-α 22-HSA	73844	7368	335	22	high
Man-α 05-HSA	67941	1465	335	5	low
Gal-β 25-HSA	74869	8393	335	25	high
Gal-β 05-HSA	68123	1647	335	5	low
Fuc-α 23-HSA	73841	7365	319	23	high
Fuc-α 03-HSA	67333	857	319	3	low
Fuc-β 24-HSA	74051	7575	319	24	high
Fuc-β 04-HSA	67767	1291	319	4	low

NHS ester of IR800 (40 nmol for low sugar and 60 nmol for high sugar) in 0.1 M Na_2HPO_4 (pH 8.5) at room temperature for 15 min. Each mixture was purified with a Sephadex G25 column (PD-10; GE Healthcare, Piscataway, NJ) (Figure 1). The protein concentration was determined by measuring the absorption at 280 nm with a UV−vis system (8453 Value UV−visible Value System; Agilent Technologies, Santa Clara, CA). The concentration of IR800 was measured by absorption with the UV−vis system to confirm the number of fluorophore molecules conjugated to each glycosylated HSA (*9*). The number of fluorophore molecules per all HSA conjugates was ∼1.7−2.3.

In Vivo Imaging. All procedures were carried out in compliance with the Guide for the Care and Use of Laboratory Animal Resources (1996), National Research Council, and approved by the local Animal Care and Use Committee.

Forty micrograms of either high or low IR800-HSA-glucose-α (Glc-α), IR800-HSA-mannose-α (Man-α), IR800-HSA-galactose-*β* (Gal-*β*), IR800-HSA-fucose-α (Fuc-α), IR800-HSA-fucose-*β* (Fuc-*β*), or IR800-HSA (control) was injected intravenously into the tail vein of female nude mice (National Cancer Institute Animal Production Facility, Frederick, MD) ($n = 3-4$ in each group). Mice were anaesthetized with isoflurane, and serial images of the dorsal and ventral surfaces were obtained using the Pearl Imager (LI-COR). The instrument has a light-tight chamber equipped with a cooled charge-coupled device camera. Illumination is with diode lasers, and the excitation and emission filters are specifically tuned for IR800. Images were acquired and processed using *Pearl Cam Software* v 1.0 (LI-COR). Longitudinal images were acquired at 10 min, 6 h, 24 h, and 48 h after injection of the imaging probe; and mice were anesthetized with vaporized isoflurane via nose cone for all imaging. To perform the quantification of signals, regions of interest (ROIs) of equal sizes were drawn and placed over areas representative of background, neck, liver, abdomen, and bladder. Total intensity for each ROI was normalized to the sum of the total intensity of all the ROIs drawn per animal, and the normalized values were used for statistical analysis.

Ex Vivo Organ Imaging. After imaging at the 48 h time point, the mice were euthanized with carbon dioxide inhalation, and liver, spleen, kidneys, blood, bone, bowel, stomach, and pancreas were removed. Organs were placed on a nonfluorescent black plate and imaged with the Pearl Imager. However, for all conditions except with the IR800-HSA probe, only the liver could be depicted. So, we then compared uptake of each glycosylated conjugate on an organ by organ basis.

For performing the quantitative analysis, identically sized ROIs were drawn on comparable parts of each corresponding organ. Total intensity for each ROI was used for statistical analysis. Sugar to sugar comparison was performed with a one-way analysis of variance (ANOVA) with Tukey's multiple comparisons post-test. High vs low sugar comparison was performed with an unpaired, two-tailed *t* test. All statistical analysis was performed using GraphPad *Prism* v 4.0c for Macintosh (GraphPad Software, San Diego, CA, www.graphpad.com).

RESULTS

In Vivo Biodistribution Study Using NIR Fluorescence Imaging. *Findings with HSA-IR800 (Control).* To assess the influence of IR800 conjugation on HSA biodistribution, we carried out serial in vivo imaging studies using an HSA-IR800 probe without glycosylation (Figure 3). At 10 min, diffuse distribution was observed throughout the body of the mouse. The primary location of the HSA at 10 min was in the vasculature, as demonstrated by clear visualization of the blood vessels (Figure 3). The liver was also identified, most likely due to the high blood volume in the liver. At 6 h, we observed

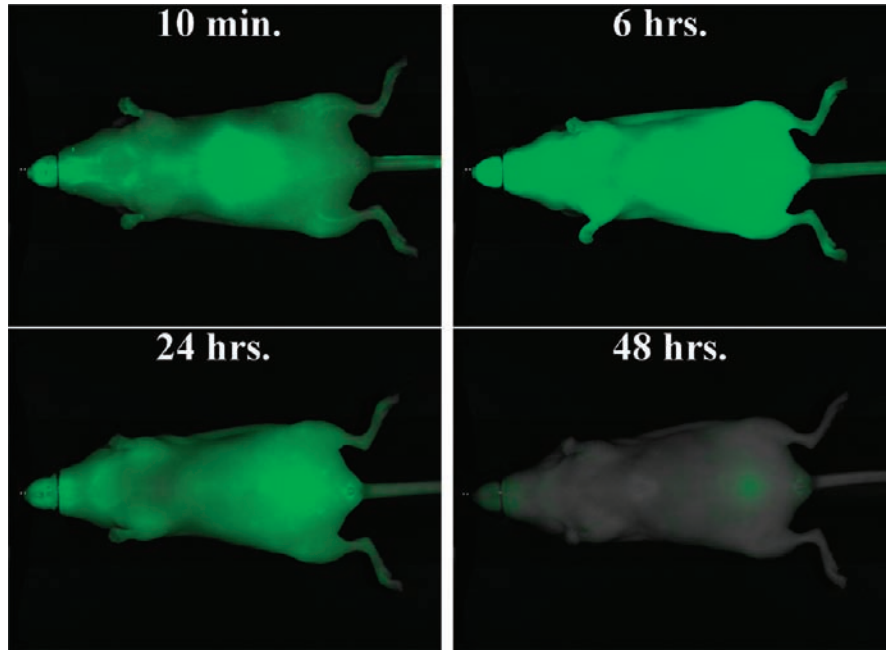


Figure 3. Time course of non-glycosylated HSA labeled with the NIR fluorophore, IR800, at 10 min, 6 h, 24 h, and 48 h after injection demonstrating a lack of targeted HSA delivery.

a diffuse signal with loss of the vessel delineation, likely representing leakage of IR800-HSA into the extracellular space and capillary beds near the skin. At 24 and 48 h, a similar diffuse pattern was observed that differed only in intensity. By 48 h, signal was barely visible.

Low Sugar-HSA-IR800 Probes. The time course of fluorescence intensity was obtained after injection of IR800-HSA labeled with low sugar numbers (3−5/HSA) of Glc-α, Man-α, Gal-β, Fuc-α, or Fuc-β (Figure 4a). Rapid accumulation of fluorescence was noted in the liver just 10 min after injection for all of the low sugar probes. Also at 10 min, the IR800-HSA low sugar probe was seen in the vessels with a minimal bladder signal. The vasculature disappeared by 6 h. At 6 h, in addition to intense liver signal, Glc-α and Gal-β labeled probes demonstrated high bowel (arrows) and some bladder signal, while Fuc-α, Fuc-β, and Man-α showed only signal in the liver and bladder (not bowel) at 6 h. Another observation is that, for all of the low sugar conjugates, the intensity of signal around the liver and abdomen was brighter at 6 h than at 10 min. At 24 h, all low sugar conjugates showed only liver signal with slight bladder signal associated with an overall decrease in fluorescence intensity. At 48 h, all sugar conjugates demonstrated minimal liver signal, although Fuc-α and Fuc-β displayed higher liver signal than Glc-α, Gal-β, and Man-α.

High Sugar-HSA-IR800 Probes. The high sugar probes (high sugar HSA-IR800) demonstrated rapid accumulation in the liver at 10 min (Figure 5a). However, unlike the low sugar probes, the blood vessels were not clearly seen 10 min after injection. Further, all high sugar probes showed some bladder signal at 10 min. At 6 h, Glc-α, Gal-β, and Fuc-β demonstrated high liver, bowel (arrow), and bladder signal. In contrast, Man-α and Fuc-α did not demonstrate bowel signal. By 24 h, the high sugar probes show only faint liver and bladder signal with Gal-β demonstrating the lowest liver signal intensity. At 48 h postinjection, the high sugar probes were no longer visible.

In the quantitative comparison of both the low (Figure 4b) and high (Figure 5b) sugar probes, the only significant difference was observed in the signal within the abdomen at 6 h. Similar results were obtained between high and low sugar probes, with Glc-α and Gal-β demonstrating the highest relative percentage of total intensity at 6 h. In both the high and low sugar groups, Gal-β abdomen intensity was statistically significantly higher compared to Man-α, Fuc-α, and Fuc-β ($p < 0.05$).

Ex Vivo Organ Analysis. Only the liver and spleen showed a difference between the probes (Figures 6 and 7). The low Gal-β probe demonstrated the lowest relative intensity of the low sugar probes at 48 h (Figure 6b). However, this difference is only statistically significant in comparison to low Glc-α ($p < 0.05$) (Figure 6d). The rest of the low sugar probes were similar in intensity. The high Gal-β probe also had the lowest relative intensity when compared to the other high sugar probes (Figure 6c). This is statistically significant in comparison to high Glc-α, Man-α, and Fuc β ($p < 0.05$) (Figure 6e). The other organ that showed a difference was the spleen. In the low sugar probes, low Man-α had the highest total intensity (Figure 7b). This increase was statistically significant relative to low Glc-α, Gal-β, and Fuc-β ($p < 0.05$) (Figure 7d). Low Fuc-α is relatively greater in intensity than low Glc-α, Gal-β, and Fuc-β, but that difference was not statistically significant. The high sugar probes have similar intensities in the spleen (Figure 7c and e).

When comparing liver signal between low and high sugar conjugates using the same sugar in ex vivo organs at 48 h, all low sugar conjugates had higher total intensity than the high sugar conjugates (Figure 6f). Low Glc-α, Man-α, Gal-β, Fuc-α, and Fuc-β all had significantly higher total intensity than the high conjugates with *P* values of 0.02, 0.03, 0.01, 0.009, and 0.01, respectively. When comparing splenic signal in ex vivo organs at 48 h, all low sugar conjugates had a relatively higher total intensity than the high sugar conjugates (Figure 7f). Low Glc-α is the only sugar conjugate that did not show statistical significance. Low Man-α, Gal-β, Fuc-α, and Fuc-β all have significantly higher total intensity than the high conjugates with *P* values of 0.0011, 0.0079, 0.014, and 0.0042, respectively.

DISCUSSION

Here, we used optical imaging to observe the biodistribution and excretion patterns associated with molecular probes composed of HSA conjugated to high and low numbers of various monosaccharides: Glc-α, Gal-β, Man-α, Fuc-α, and Fuc-β, all conjugated with identical conjugation chemistry. HSA is a

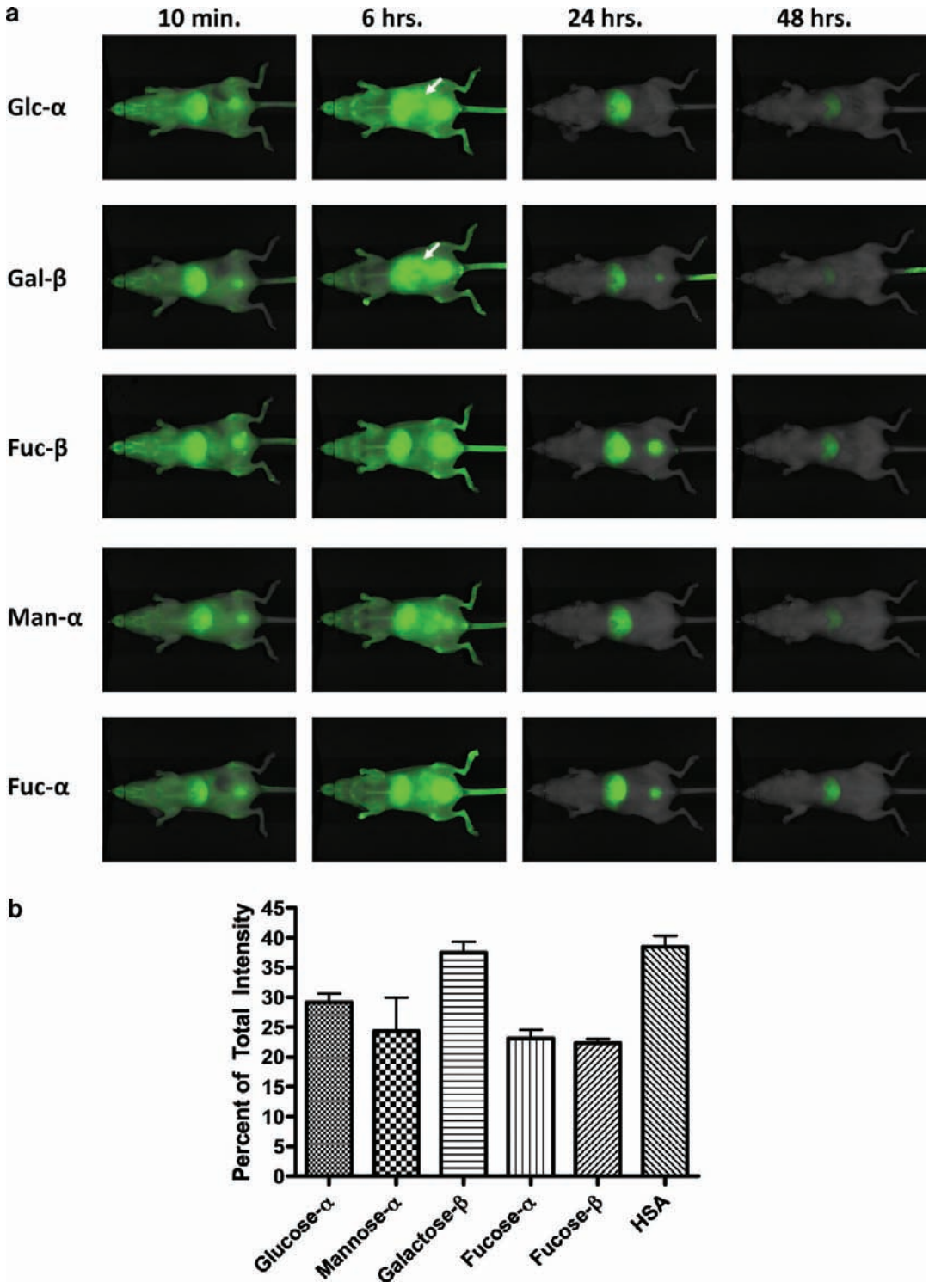


Figure 4. Time course mouse images of HSA glycosylated with a low sugar number at 10 min, 6 h, 24 h, and 48 h after injection are shown in (a). Rapid liver uptake can be appreciated as early as 10 min after injection in all sugar-conjugated albumin compared with unconjugated albumin shown in Figure 2. At 6 h, low Glc-α and Gal-β demonstrate activity present in the bowel (arrows). This is different when compared to the other sugars, and this difference is quantified and graphically represented in (b).

representative soluble protein that has high bioavailability, is nonimmunogenic, and demonstrates good in vivo stability with an average half-life of 19 days (*10*). The conjugation of IR800 to HSA demonstrated distribution throughout the body with little specificity suggesting that the addition of the NIR probe minimally changed the biodistribution of HSA. However, the conjugation of either low numbers or high numbers of sugar molecules led to rapid and specific changes in biodistribution, particularly to the liver and spleen. Similar observations have been made using radiolabeled BSA conjugated to galactose, fucose, and mannose (*11*−*13*). The effect of the amount of sugar residue conjugated to BSA on binding properties has been studied and reveals that mannosylated BSA demonstrated a higher rate of uptake as the number of mannose residues per BSA molecule increased with a plateau effect (*13*). Similarly, we found that conjugation of HSA to a low number of sugar molecules leads to slower clearance of the probe from the circulation compared to HSA conjugated to a high number of

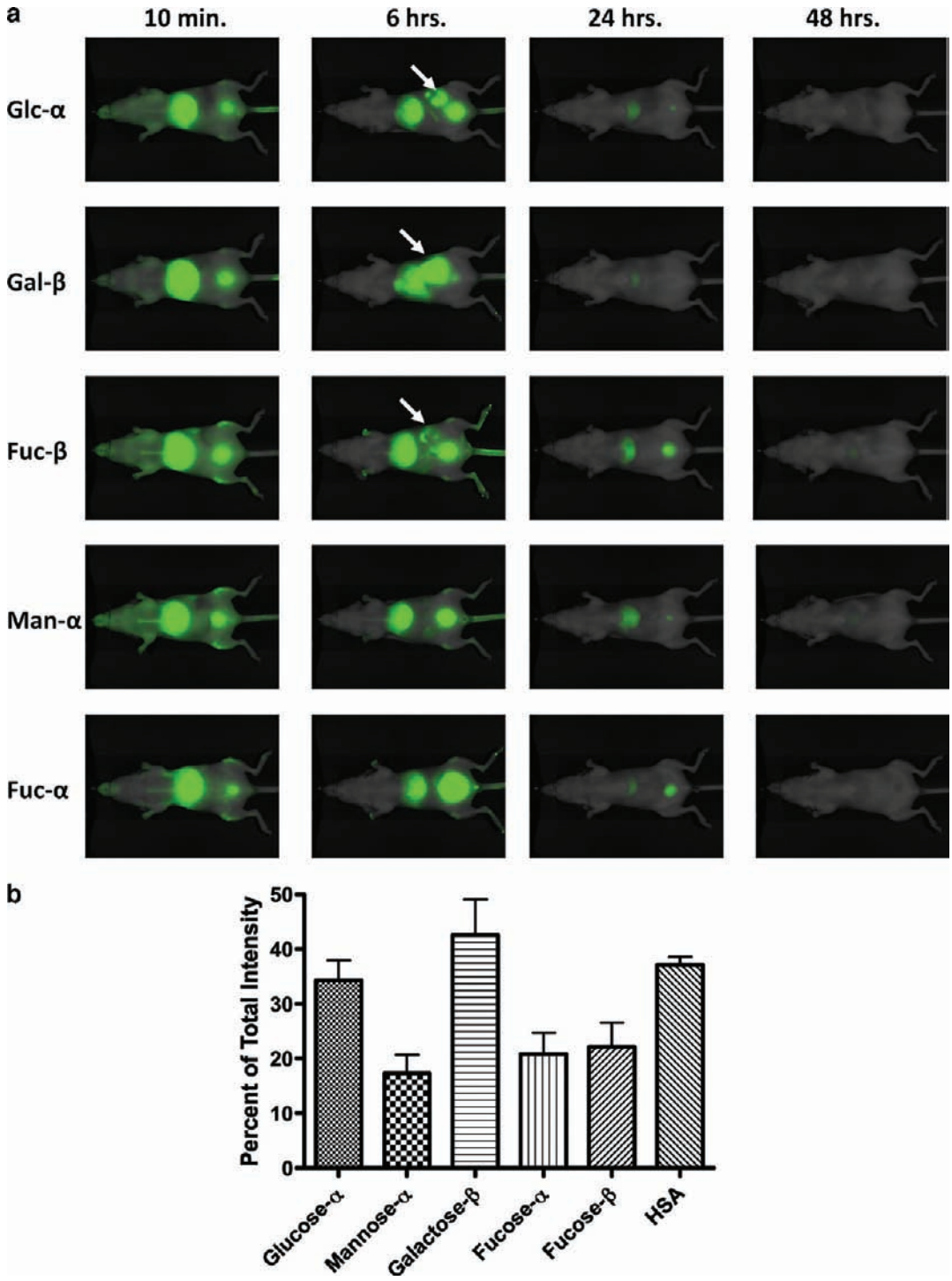


Figure 5. (a) Time course of HSA glycosylated with a high sugar number at 10 min, 6 h, 24 h, and 48 h after injection demonstrating rapid liver accumulation after just 10 min. Six hours after injection, high Glc-α, Gal-β, and Fuc-β have activity present in the bowel (arrows). (b) Graphical representation quantifying the differences in intensity of the bowel signal. Also, note that fluorescence signal is not detected at 48 h.

sugar molecules. This is demonstrated by the observation that, at 10 min, the blood vessels can still be observed in all low sugar HSA conjugates but not in high sugar HSA conjugates.

With these conjugation and labeling methods, both reactions can use amino groups at the side chain of lysine or at the N-terminal. There are 60 lysines in the HSA; therefore, theoretically 61 available conjugation sites exist in a single albumin molecule. In the previous literature, a maximum of 35 molecules of diethylenetriamine pentaacetic acid (DTPA) were conjugated with a single albumin molecule via the same amine groups for the use of macromolecular MRI contrast agents (*14*). In our experience, a maximum of 28 galactosamine and glucosamine molecules were conjugated with a single albumin molecule among 63 theoretically available carboxyl groups of glutamate using a similar direct amidation method using EDC (*15*). Therefore, although numbers of available conjugation sites are varied depending on molecules to be conjugated and conjugation chemistry, about half of the theoretically available functional groups might be practically conjugatable probably because of steric hindrance.

The current study suggests that different organs have different overall receptor specificity for different glycosylated probes. The hepatocytes, for instance, demonstrate an affinity for galactose, and this is mainly through the asialoglycoprotein receptor (*16*).

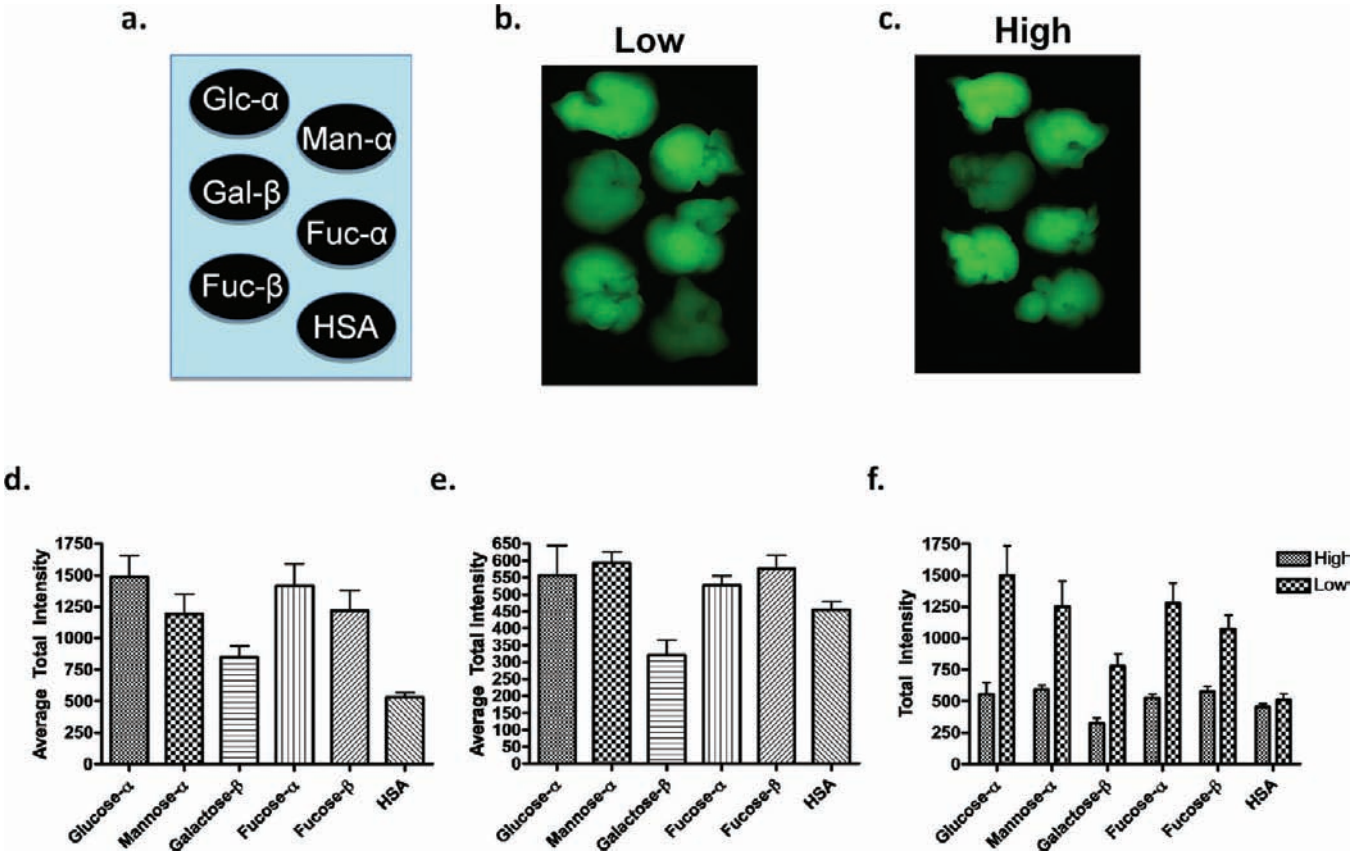


Figure 6. Ex vivo quantitation of liver intensity 48 h after injection. (a) Schematic of where (b) low or (c) high sugar conjugated HSA distributes. (d) Low and (e) high sugar quantitation is also represented graphically. (f) At 48 h, low sugar conjugates are brighter than high sugar conjugates in the liver.

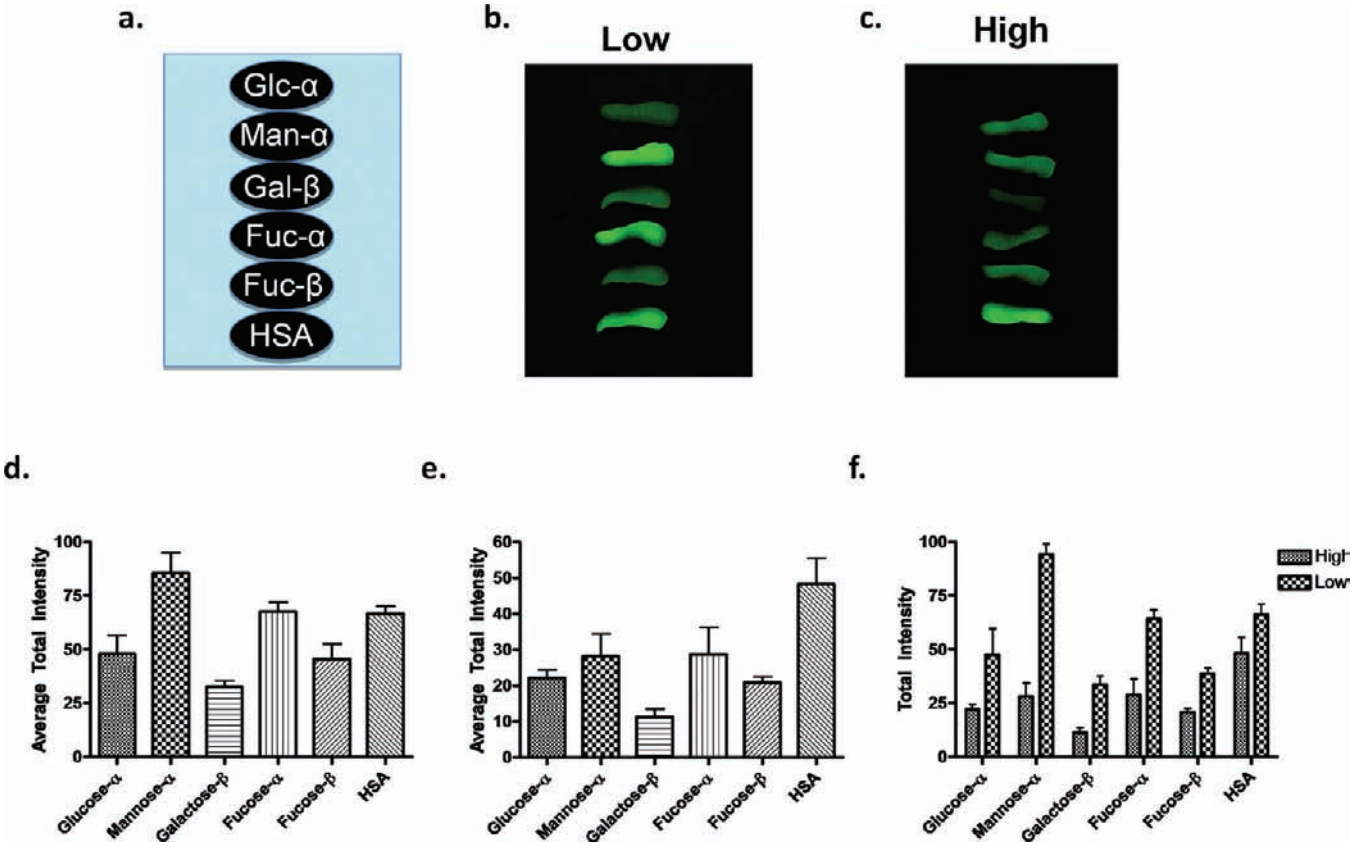


Figure 7. Ex vivo quantitation of spleen intensity 48 h after injection. (a) Schematic to illustrate where (b) low and (c) high sugar conjugated HSA is located. (d) Low and (e) high sugar quantitation is represented graphically. (f) Comparison at 48 h illustrates that low sugar conjugates are brighter than high sugar conjugates in the spleen.

Nonparenchymal cells in the liver include sinusoidal endothelial cells and Kupffer cells. Mannose receptors are expressed on both of these nonparenchymal cell types (*17*). However, there is a lectin only expressed by Kupffer cells that demonstrates high affinity for fucose and galactose but not mannose (*18*). Cultured rat sinusoidal endothelial cells and Kupffer cells were used to distinguish between the binding characteristics of BSA conjugated mannose and fucose (*17*). It was demonstrated that both mannosylated and fucosylated BSA were taken up by sinusoidal endothelial cells, and this uptake was inhibited by excess mannose or fucose but not by galactose. They further demonstrated that Kupffer cells could take up mannosylated and fucosylated BSA, but the uptake of fucosylated BSA could be inhibited by galactose (*17*).

The specific binding of glycosylated HSA molecules to cell surface receptors is supported by the excretion profiles exhibited by the different sugar conjugates. Glc-α and Gal-*β* demonstrate rapid liver uptake and excretion into the gut. This supports the concept that Glc-α and Gal-*β* may be preferentially taken up by hepatocytes, eventually culminating in hepatobiliary excretion. Man-α and Fuc-α, however, do not demonstrate gut excretion observed by Glc-α and Gal-*β*, suggesting that these sugars may lead to specific uptake into the liver via a different receptor. It would make sense that uptake of Man-α and Fuc-α by nonparenchymal cells via the mannose receptor leads to excretion by routes other than bile. Additionally, the presence of the mannose receptor on macrophages in the spleen explains the increased signal observed by low Man-α and low Fuc-α on ex vivo organ studies.

An additional challenge to using optical imaging probes is their inability to accurately quantitate signal compared with radionuclide imaging including single photon emission tomography (SPECT) and positron emission tomography (PET). This limitation is minimized with NIR probes which have much better light transmission properties in tissue than do visible range probes. Nonetheless, absolute molecule quantitation, similar to what can be done with radioisotopes, cannot be achieved using the current model. However, our semiquantitative results correlate with previous studies using radiolabeling. Quantitation with radiolabeling of albumin conjugated to sugars has some limitations, especially since catabolism in the liver or the RES may lead to separation of the radiolabel and the albumin. Moreover, this effect varies with the radioisotope employed. For instance, the difference in the biodistribution of galactosylated BSA among labeling with ^{125}I, ^{131}I, and ^{111}In (*12*) demonstrated that the choice of radioisotope alters the accuracy of quantitative pharmacokinetics. Regardless of the catabolism in hepatocytes or macrophages, radio-iodines are dehalogenated immediately after the internalization and excreted into the urine; in contrast, ^{111}In is trans-chelated and stays in the bound cells (*19*).

Unlike indocyanine green (ICG), IR800 is mostly excreted into the urine (*20*). Therefore, once macrophages catabolize the albumin conjugate, catabolized IR800 re-enters the circulation and is excreted into the urine. However, once hepatocytes catabolize the albumin conjugate, catabolized IR800 can be excreted into the bile. Therefore, we observed the intestinal activity only with Man-α and Fuc-α conjugates.

In conclusion, we demonstrate that labeling with different sugars and altering the number of sugars per molecule dramatically changes the pharmacokinetics and excretion of albumin labeled with IR800 and detected with NIR fluorescence imaging. Gal-*β* and Glc-α conjugates were excreted into the intestine suggesting uptake and catabolism by hepatocytes. In contrast, Man-α and Fuc-α conjugates were excreted into the urine suggesting that catabolism occurred mainly in macrophages. The differences of the splenic accumulation in the ex vivo organ study supported this hypothesis. The sugar conjugation might be useful for changing the catabolism and excretion route of a native compound and might lead to optimization of the dose to maximize efficacy while minimizing toxicity.

ACKNOWLEDGMENT

This research was supported by the Intramural Research Program of the NIH, National Cancer Institute, Center for Cancer Research. This research year was made possible through the Clinical Research Training Program, a public−private partnership supported jointly by the NIH and Pfizer Inc (via a grant to the Foundation for NIH from Pfizer Inc).

Supporting Information Available: Analytical mass spectroscopy conditions and data of all conjugates. This material is available free of charge via the Internet at http://pubs.acs.org.

LITERATURE CITED

(1) Wolfenden, M. L., and Cloninger, M. J. (2006) Carbohydrate-functionalized dendrimers to investigate the predictable tunability of multivalent interactions. *Bioconjugate Chem. 17*, 958–66.

(2) Kudo, M., Vera, D. R., Trudeau, W. L., and Stadalnik, R. C. (1991) Hepatic uptake of [99mTc]galactosyl-neoglycoalbumin is sensitive to receptor quantity. *Int. J. Radiat. Appl. Instrum., Part B 18*, 663–6.

(3) Sheng, K. C., Kalkanidis, M., Pouniotis, D. S., Esparon, S., Tang, C. K., Apostolopoulos, V., and Pietersz, G. A. (2008) Delivery of antigen using a novel mannosylated dendrimer potentiates immunogenicity in vitro and in vivo. *Eur. J. Immunol. 38*, 424–36.

(4) Hama, Y., Urano, Y., Koyama, Y., Choyke, P. L., and Kobayashi, H. (2006) Targeted optical imaging of cancer cells using lectin-binding BODIPY conjugated avidin. *Biochem. Biophys. Res. Commun. 348*, 807–13.

(5) Gunn, A. J., Hama, Y., Koyama, Y., Kohn, E. C., Choyke, P. L., and Kobayashi, H. (2007) Targeted optical fluorescence imaging of human ovarian adenocarcinoma using a galactosyl serum albumin-conjugated fluorophore. *Cancer Sci. 98*, 1727–33.

(6) Hama, Y., Urano, Y., Koyama, Y., Choyke, P. L., and Kobayashi, H. (2007) D-galactose receptor-targeted in vivo spectral fluorescence imaging of peritoneal metastasis using galactosamin-conjugated serum albumin-rhodamine green. *J. Biomed. Opt. 12*, 051501.

(7) Manimala, J. C., Li, Z., Jain, A., VedBrat, S., and Gildersleeve, J. C. (2005) Carbohydrate array analysis of anti-Tn antibodies and lectins reveals unexpected specificities: implications for diagnostic and vaccine development. *ChemBioChem 6*, 2229–41.

(8) Manimala, J. C., Roach, T. A., Li, Z., and Gildersleeve, J. C. (2006) High-throughput carbohydrate microarray analysis of 24 lectins. *Angew. Chem., Int. Ed. Engl. 45*, 3607–10.

(9) Ogawa, M., Kosaka, N., Choyke, P. L., and Kobayashi, H. (2009) Tumor-specific detection of an optically targeted antibody combined with a quencher-conjugated neutravidin "quencher-chaser": a dual "quench and chase" strategy to improve target to nontarget ratios for molecular imaging of cancer. *Bioconjugate Chem. 20*, 147–54.

(10) Kratz, F. (2008) Albumin as a drug carrier: design of prodrugs, drug conjugates and nanoparticles. *J. Controlled Release 132*, 171–83.

(11) Lehrman, M. A., Pizzo, S. V., Imber, M. J., and Hill, R. L. (1986) The binding of fucose-containing glycoproteins by hepatic lectins. Re-examination of the clearance from blood and the binding to membrane receptors and pure lectins. *J. Biol. Chem. 261*, 7412–8.

(12) Staud, F., Nishikawa, M., Morimoto, K., Takakura, Y., and Hashida, M. (1999) Disposition of radioactivity after injection of liver-targeted proteins labeled with 111In or 125I. Effect of labeling on distribution and excretion of radioactivity in rats. *J. Pharm. Sci. 88*, 577–85.

(13) Jansen, R. W., Molema, G., Ching, T. L., Oosting, R., Harms, G., Moolenaar, F., Hardonk, M. J., and Meijer, D. K. (1991) Hepatic endocytosis of various types of mannose-terminated albumins. What is important, sugar recognition, net charge, or the combination of these features. *J. Biol. Chem. 266*, 3343–8.

(14) Aicher, K. P., Dupon, J. W., White, D. L., Aukerman, S. L., Moseley, M. E., Juster, R., Rosenau, W., Winkelhake, J. L., and Brasch, R. C. (1990) Contrast-enhanced magnetic resonance imaging of tumor-bearing mice treated with human recombinant tumor necrosis factor alpha. *Cancer Res. 50*, 7376–81.

(15) Regino, C. A., Ogawa, M., Alford, R., Wong, K. J., Kosaka, N., Williams, M., Feild, B. J., Takahashi, M., Choyke, P. L., and Kobayashi, H. (2010) Two-step synthesis of galactosylated human serum albumin as a targeted optical imaging agent for peritoneal carcinomatosis. *J. Med. Chem. 53*, 1579–86.

(16) Ashwell, G., and Harford, J. (1982) Carbohydrate-specific receptors of the liver. *Annu. Rev. Biochem. 51*, 531–54.

(17) Higuchi, Y., Nishikawa, M., Kawakami, S., Yamashita, F., and Hashida, M. (2004) Uptake characteristics of mannosylated and fucosylated bovine serum albumin in primary cultured rat sinusoidal endothelial cells and Kupffer cells. *Int. J. Pharm. 287*, 147–54.

(18) Lehrman, M. A., Haltiwanger, R. S., and Hill, R. L. (1986) The binding of fucose-containing glycoproteins by hepatic lectins. The binding specificity of the rat liver fucose lectin. *J. Biol. Chem. 261*, 7426–32.

(19) Naruki, Y., Carrasquillo, J. A., Reynolds, J. C., Maloney, P. J., Frincke, J. M., Neumann, R. D., and Larson, S. M. (1990) Differential cellular catabolism of 111In, 90Y and 125I radiolabeled T101 anti-CD5 monoclonal antibody. *Int. J. Radiat. Appl. Instrum., Part B 17*, 201–7.

(20) Marshall, M. V., Draney, D., Sevick-Muraca, E. M., and Olive, D. M. (2010) Single-dose intravenous toxicity study of IRDye 800CW in Sprague-Dawley rats. *Mol. Imaging Biol.* .

BC100313P

Supplementary information:

Biodistribution, catabolism and excretion of monosaccharides-albumin conjugates measured with *in vivo* near infrared fluorescence imaging.

Thomas E. McCann, Nobuyuki Kosaka, Makoto Mitsunaga, Peter L. Choyke, Jeffrey C. Gildersleeve, Hisataka Kobayashi*

Molecular imaging program, Center for Cancer Research, National Cancer Institute, National Institutes of Health, 10 Center Dr., Bethesda, MD 20892-1088

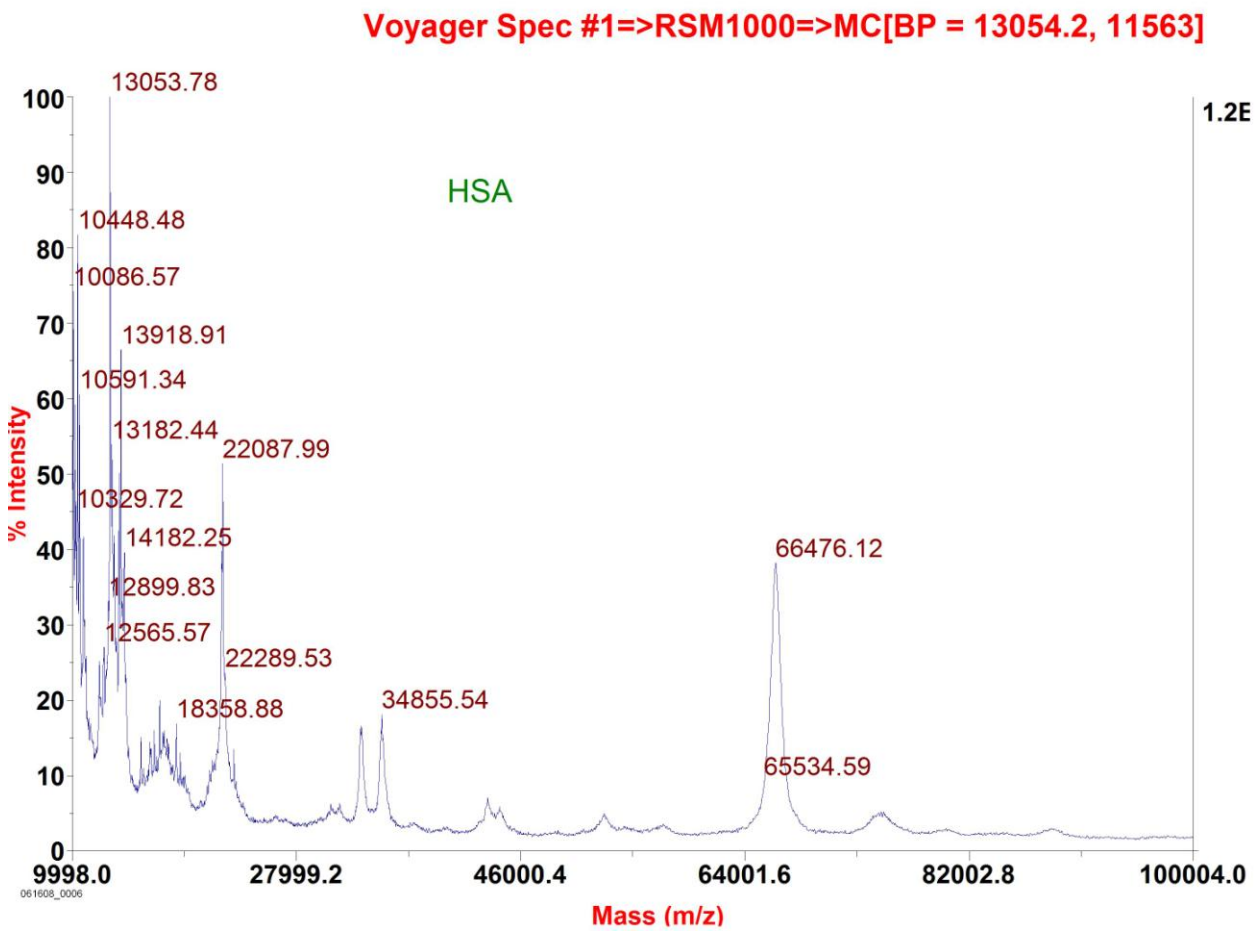
Chemical Biology Laboratory, Center for Cancer Research, National Cancer Institute-Frederick, National Institutes of Health, 376 Boyles St, Frederick, MD 21702

***Correspondence to:** Hisataka Kobayashi, M.D., Ph.D. Molecular Imaging Program, National Cancer Institute, NIH, Building 10, Room B3B69, MSC1088, Bethesda, MD 20892-1088. Phone: 301-451-4220; Fax: 301-402-3191; E-mail: kobayash@mail.nih.gov

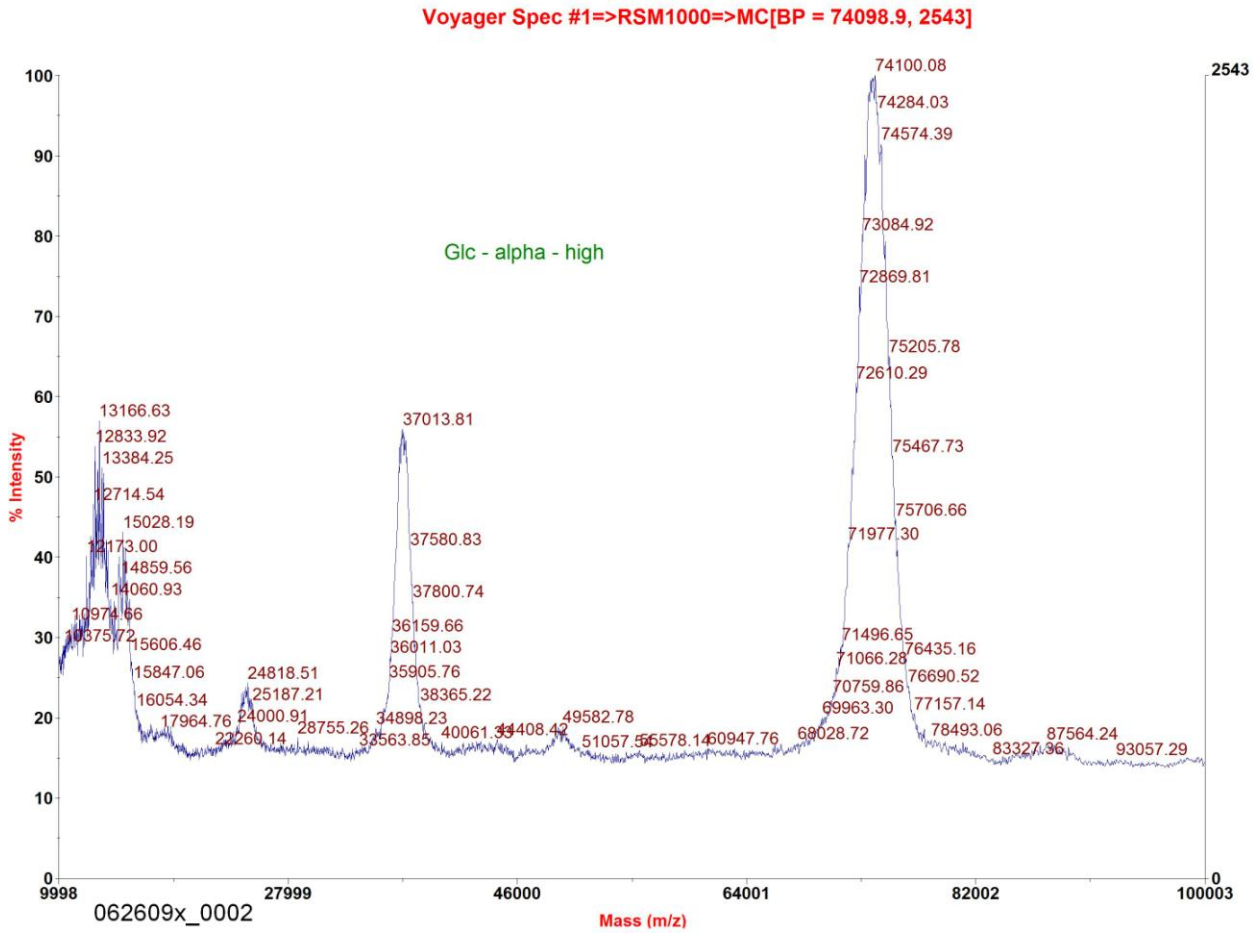
Supplementary figure 1

MALDI-MS data (Applied Biosystems Voyager-DE Pro time-of-flight mass spectrometer, Life Technologies Co., Carlsbad, CA) to evaluate the average mass of each monosaccharide-HSA conjugate (b-k) for determining the mass shift relative to unmodified HSA (a).

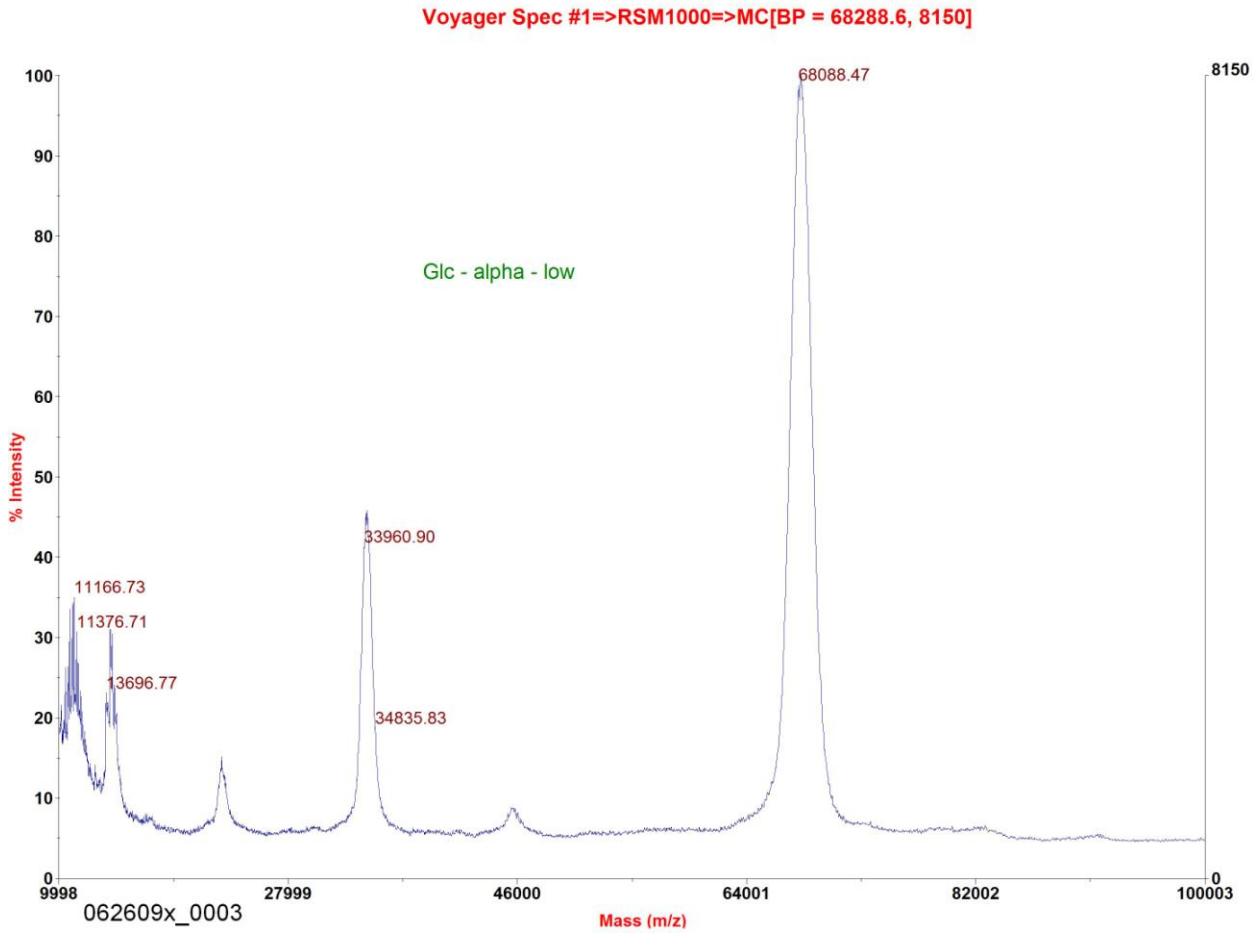
a. non-glycosylated HSA



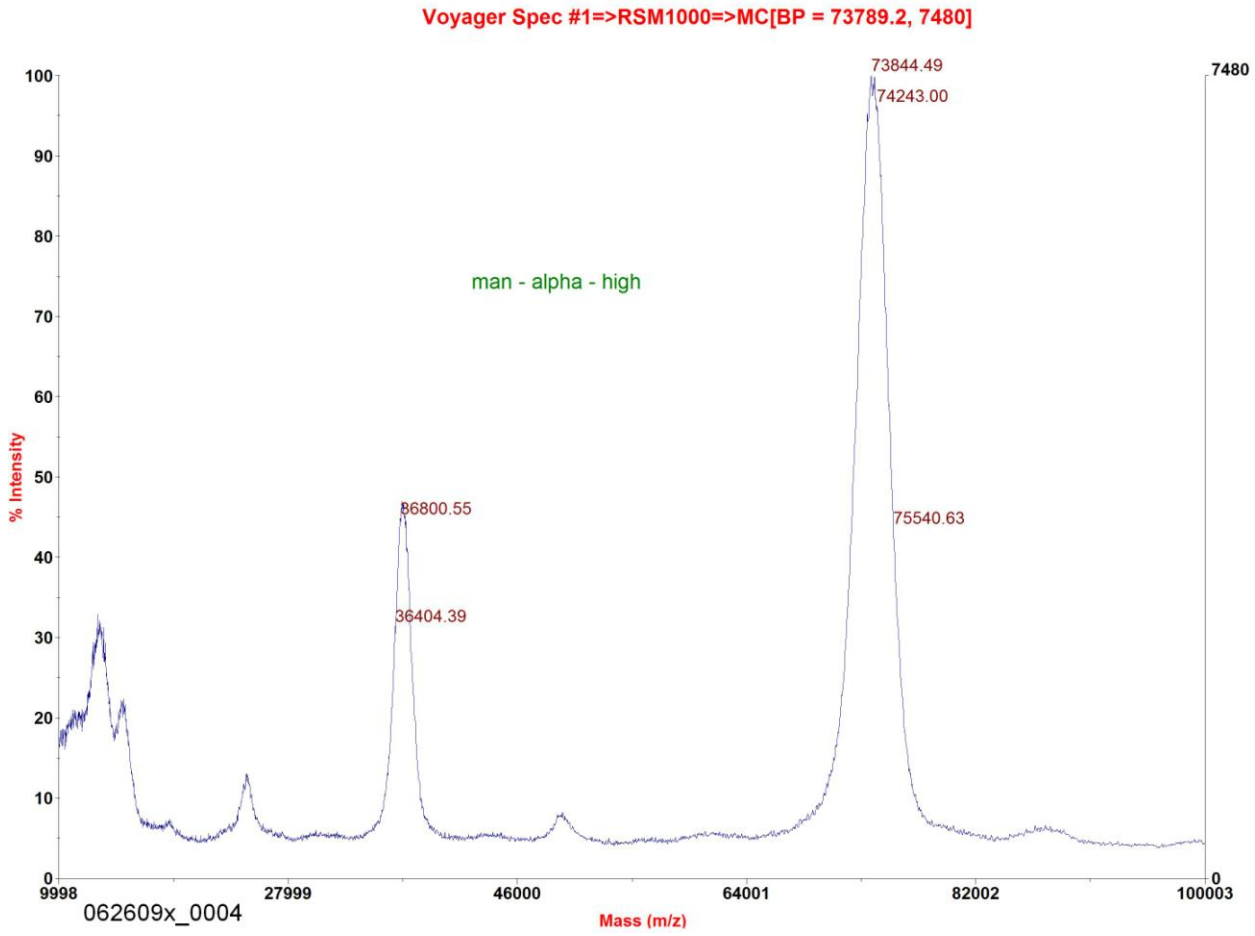
b. High Glc-α-HSA



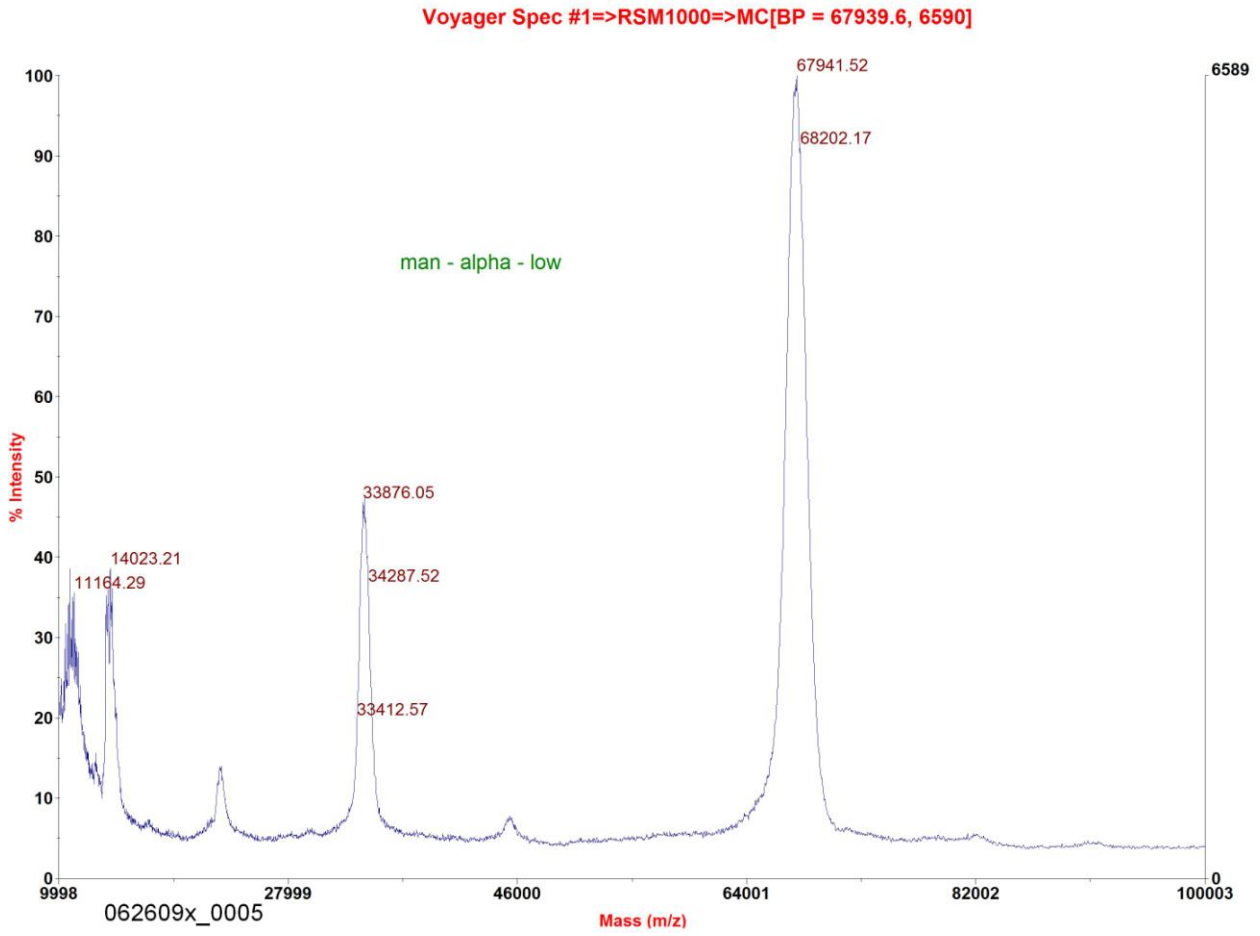
c. Low Glc-α-HSA



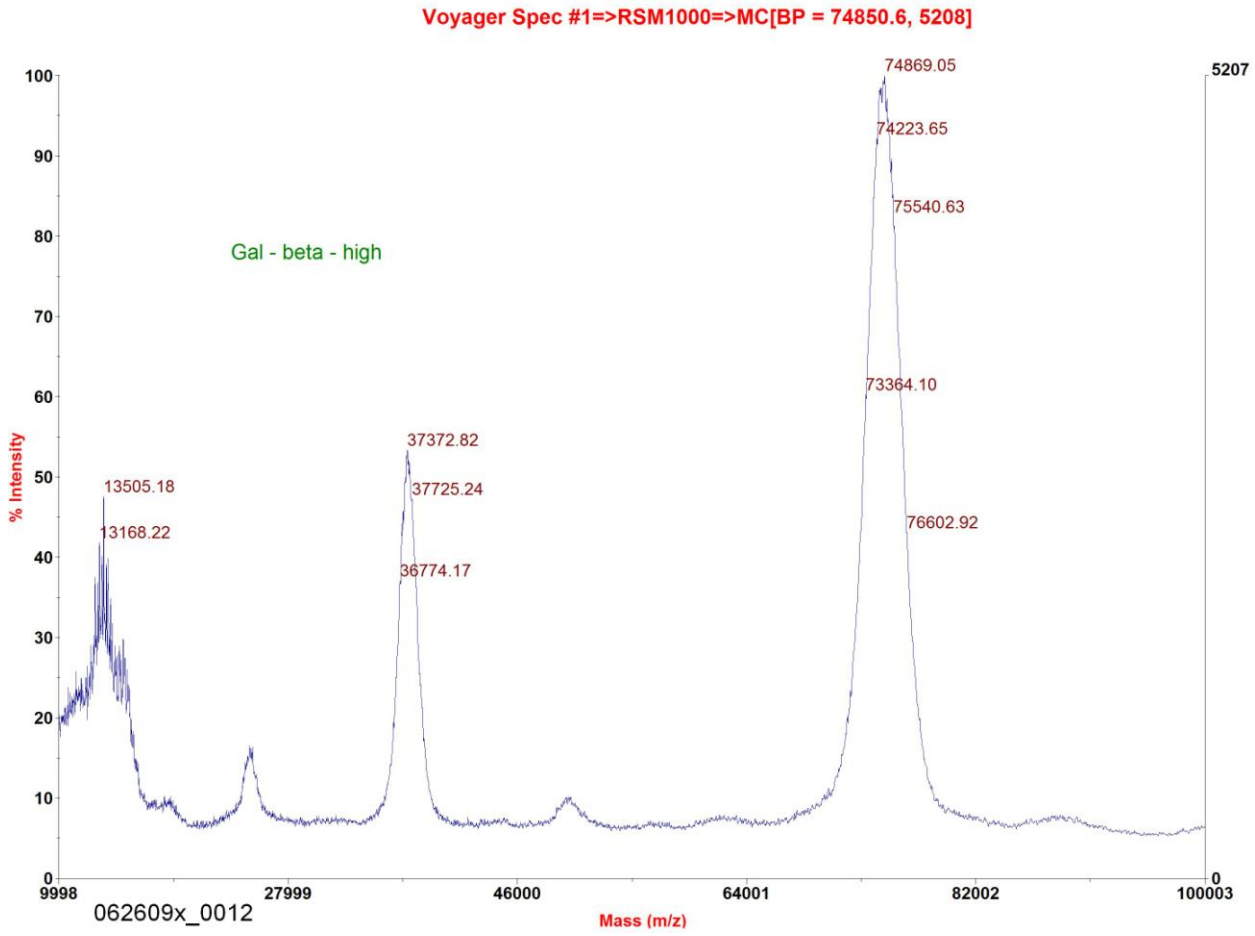
d. High Man-α-HSA



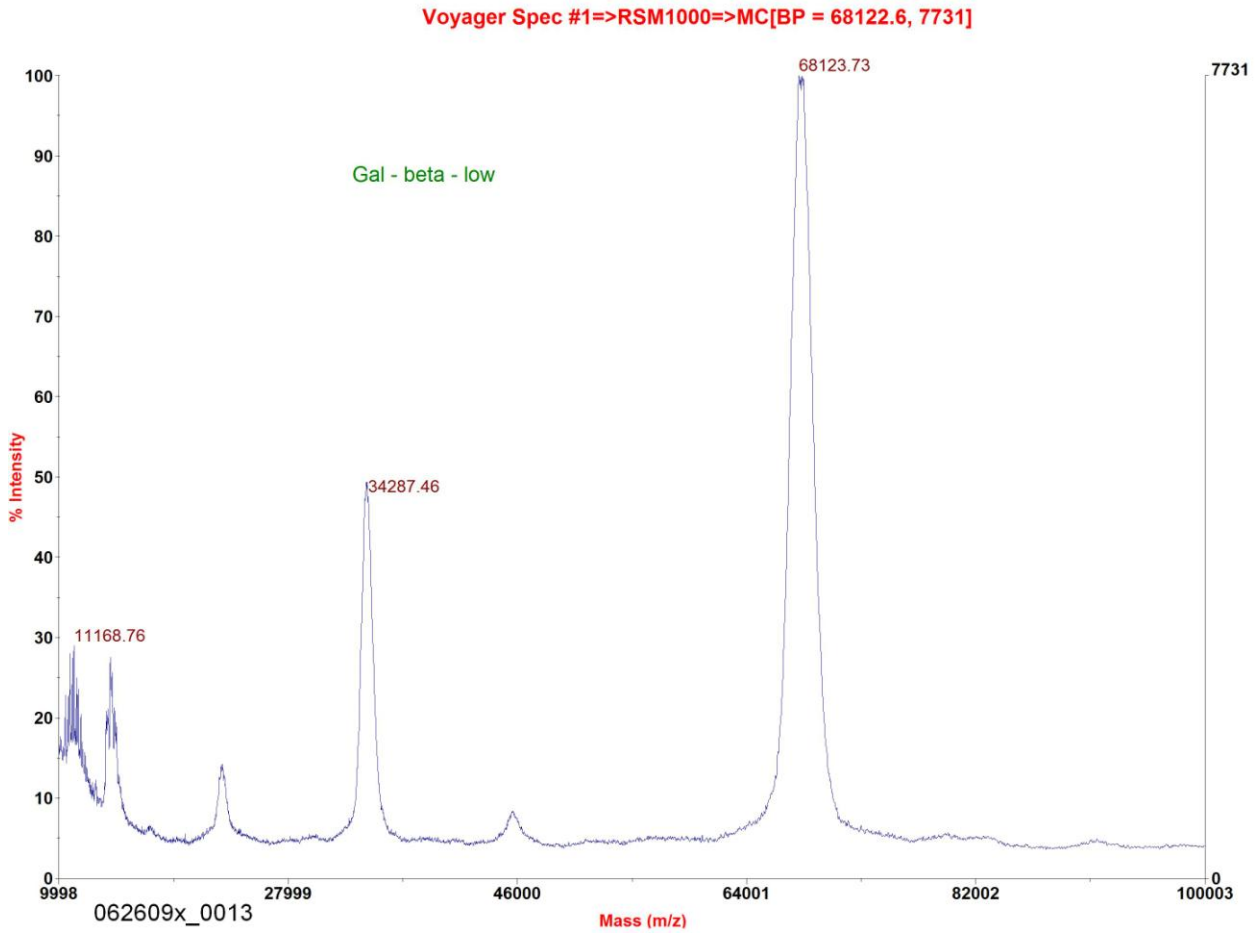
e. Low Man-α-HSA



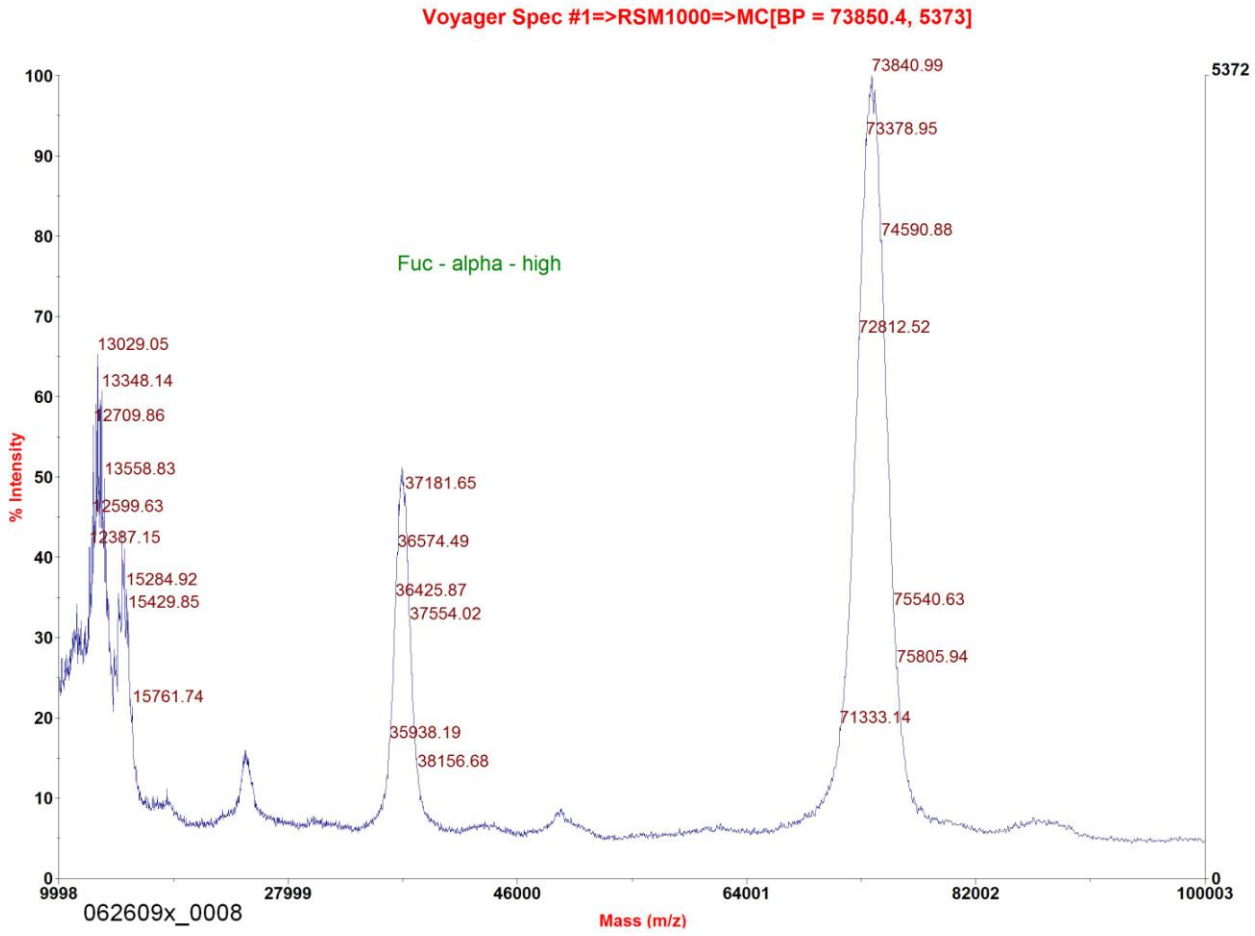
f. High Gal-β-HSA



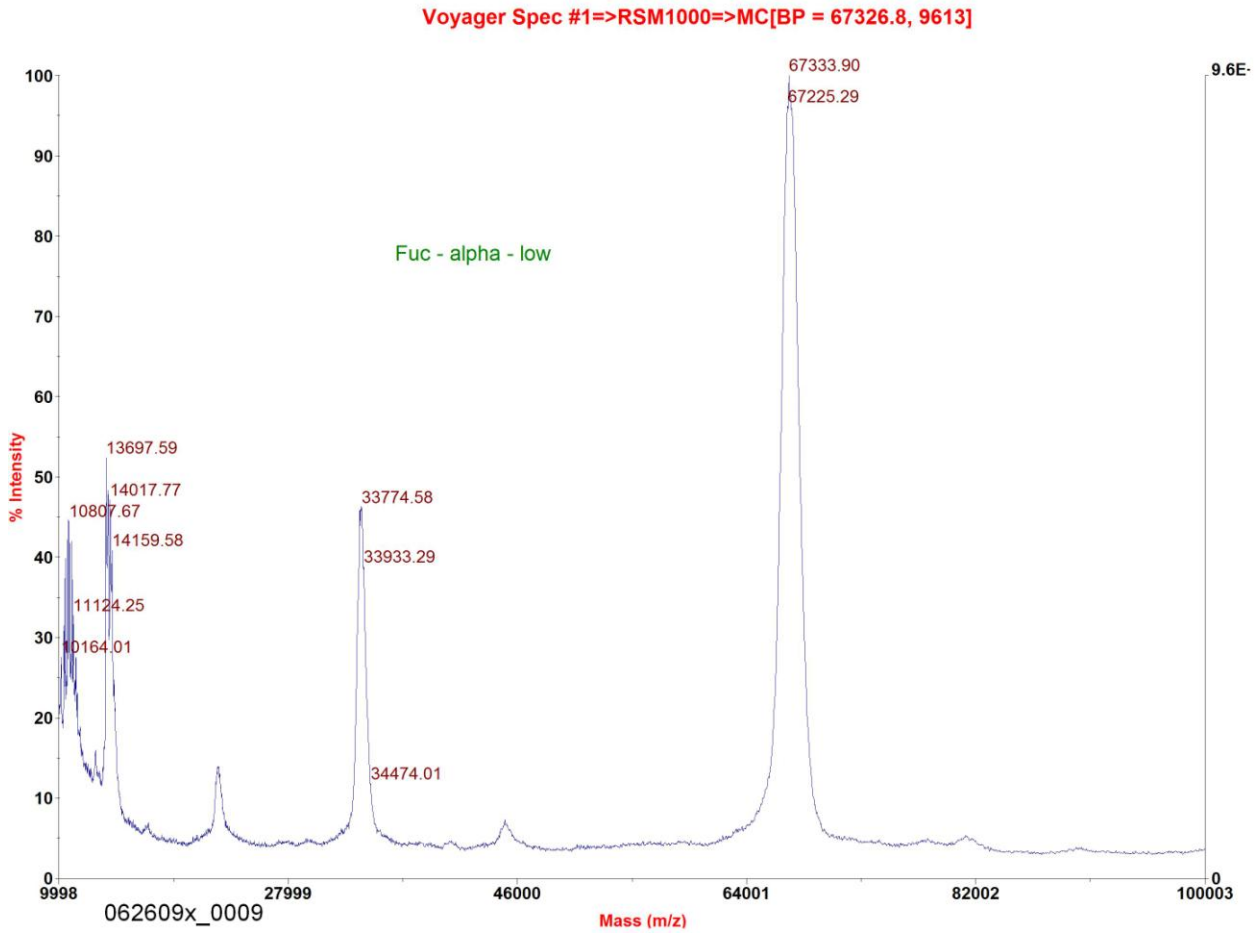
g. Low Gal-β-HSA



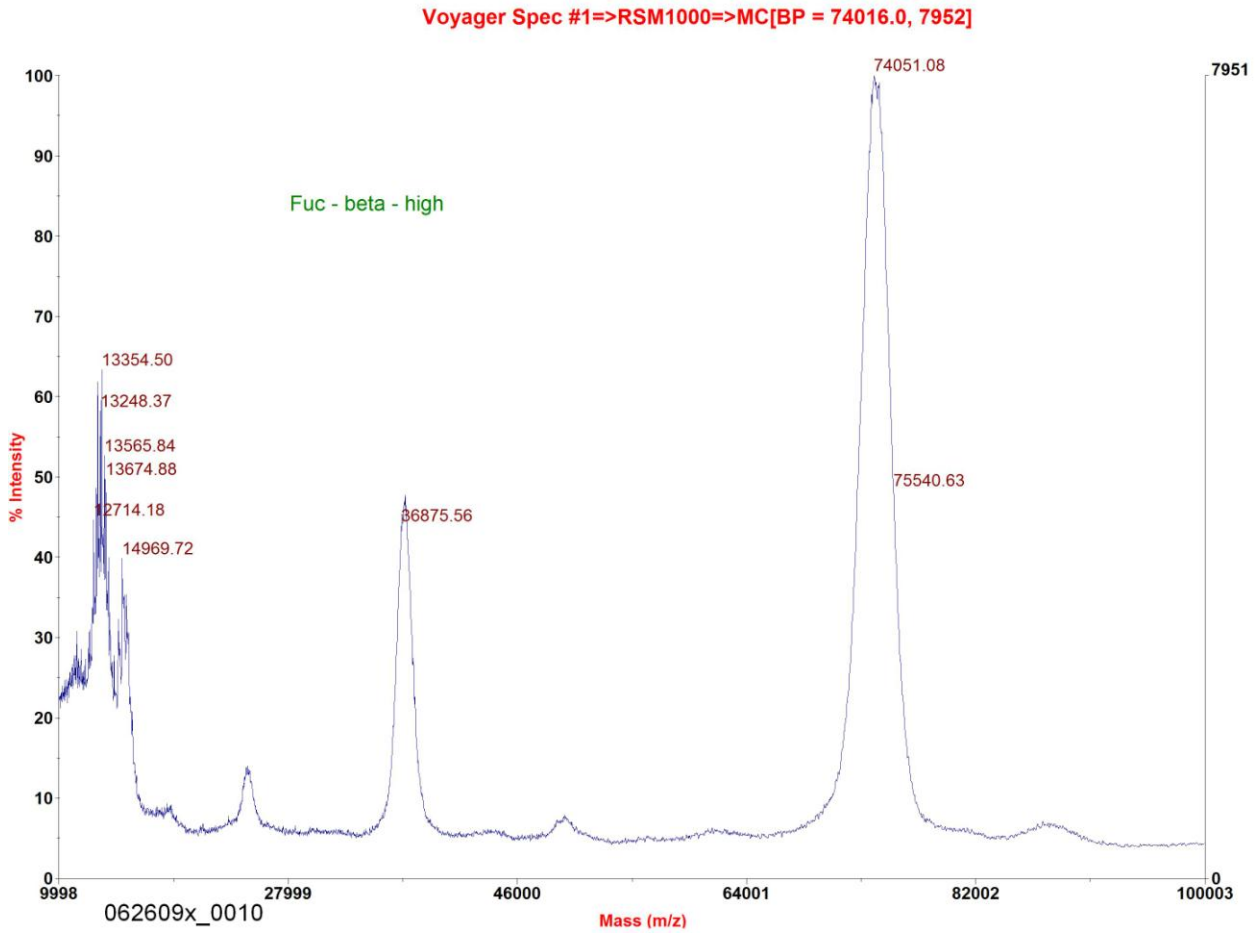
h. High Fuc-α-HSA



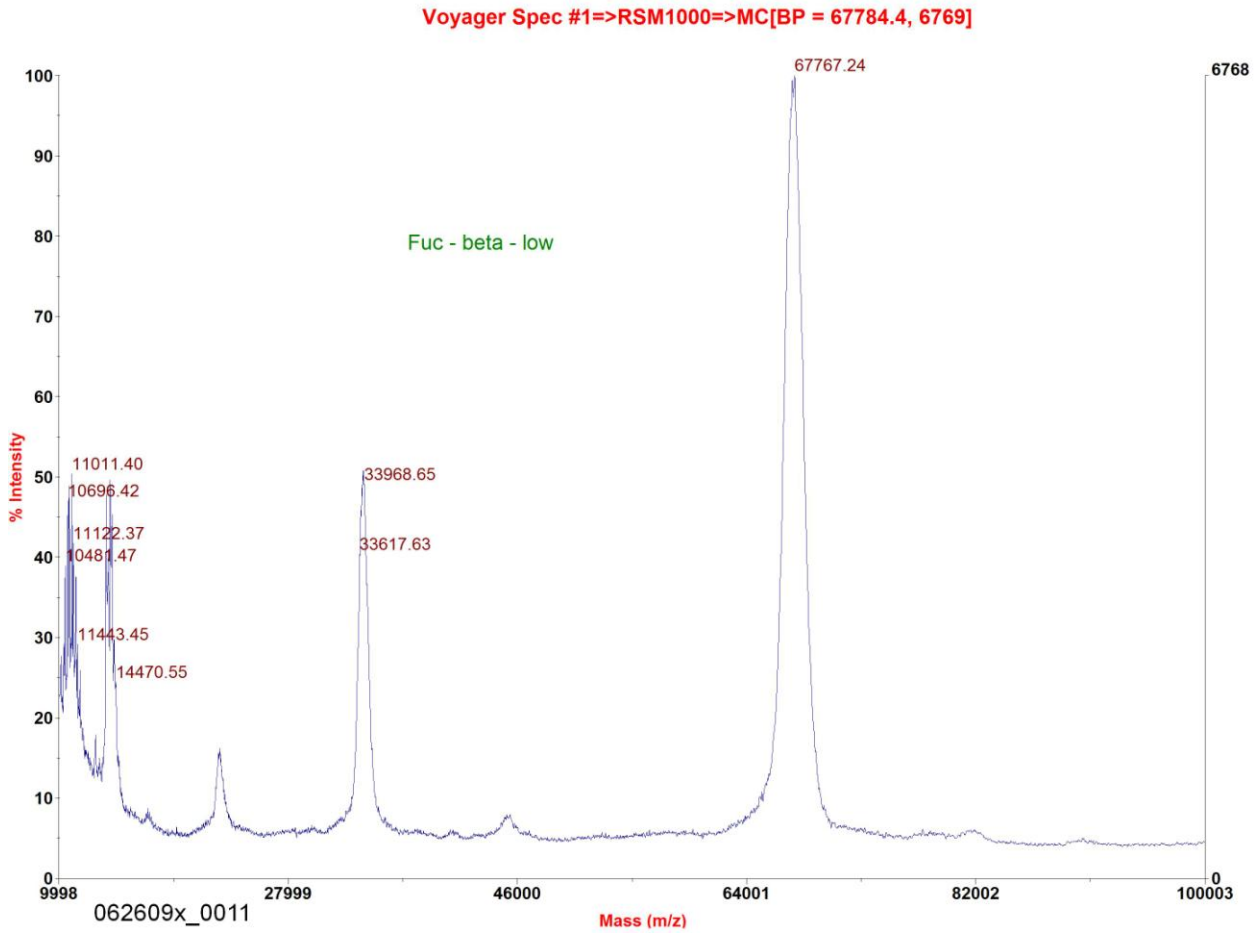
i. Low Fuc-α-HSA



j. High Fuc-β-HSA



k. High Fuc-β-HSA



Cellular Delivery and Antisense Effects of Peptide Nucleic Acid Conjugated to Polyethyleneimine via Disulfide Linkers

Peter R. Berthold,[†] Takehiko Shiraishi,[†] and Peter E. Nielsen*[,†,‡]

Department of Cellular and Molecular Medicine, Faculty of Health Sciences, The Panum Institute, University of Copenhagen, Blegdamsvej 3c, DK-2200, Copenhagen N, Denmark, and Department of Medicinal Chemistry, Faculty of Pharmaceutical Sciences, University of Copenhagen, Universitetsparken 2, DK-2100 Copenhagen, Denmark. Received August 6, 2010; Revised Manuscript Received August 24, 2010

Peptide nucleic acid (PNA) is potentially an attractive antisense and antigene agent for which more efficient cellular delivery systems are still warranted. The cationic polymer polyethylenimine (PEI) is commonly used for cellular transfection of DNA and RNA complexes, but is not readily applicable for PNA due to the (inherent) charge neutrality of PNA. However, PEI could function as an efficient scaffold for PNA via chemical conjugation. Accordingly, we modified PEI with the amine-reactive heterobifunctional linker agent *N*-succinimidyl-3-(2-pyridyldithio)propionate (SPDP) (with and without a PEG moiety) and further reacted this with a cysteine PNA. The level of modification was determined spectrophotometrically with high accuracy, and the PNA transfection efficiency of the conjugates was evaluated in an antisense luciferase splice-correction assay using HeLa pLuc705 cells. We find that PEI is an efficient vector for PNA delivery yielding significantly higher (up to 10-fold) antisense activity than an analogous PNA−octaarginine conjugate, even in the presence of chloroquine, which only slightly enhances the PEI-PNA activity. The PEI-PEG conjugates are preferred due to lower acute cellular toxicity. Finally, the method can be easily modified to allow for co-conjugation of other small molecules in a high-throughput screening assay that does not require a purification step.

INTRODUCTION

Peptide nucleic acids (PNAs[1]) have many of the properties desired of a gene targeting and antisense agent (*1*−*3*), but efficient cellular delivery and in vivo bioavailability are still a challenge despite the development of a variety of delivery techniques, including the use of cationic cell penetrating peptides (*4*−*7*) and cationic lipid transfection (*8*−*11*).

Polyethylenimine (PEI) is widely used as an efficient, nonviral complexation transfection agent for RNA and plasmid DNA (*12,13*), and it is commercially available in average polymer sizes ranging from ∼0.5 to 800 kDa (*14*). The high transfection efficiency of PEI is considered to arise from what has been coined the "proton sponge" effect (*12, 15*); the high amine content and buffering capacity of PEI results in endosomal import of protons, high osmotic pressure, and subsequent rupture of the endosomes. The endocytotic pathway is not yet clear but has been suggested to be caveolar, since modified PEI directed to clathrin and caveolar pathways is only effective in the latter (*16*). Furthermore, the endocytotic route and endosomal escape may be affected by the DNA/RNA cargo (*13, 17, 18*).

PEI could also be an attractive candidate for PNA delivery. However, because PNA is inherently charge neutral, chemical conjugation rather than simple complexation to PEI is required. The high primary amine content of PEI allows conjugation of a large number of (PNA) ligands using commercially available amine reactive linkers.

PEI transfection efficiency (and toxicity) is mutually correlated to the polymer size and structure, but branched PEI with a molecular weight of 25 kDa (PEI25) is an acceptable compromise between toxicity and transfection efficiency (*19*−*21*). Furthermore, several PEI derivatives with reduced toxicity but retained efficacy have been described, namely, cross-linked PEI (*22*−*24*) or grafted PEI onto less cytotoxic polymers like chitosan (*25*). Thus, we chose PEI25 as a suitable scaffold for PNA conjugation. Finally, modification of PEI with poly(ethylene glycol) (PEG) reduces toxicity of PEI in vitro (*26*−*28*) and in vivo (*29*−*31*), and we therefore decided to also include a PEG containing linker for PNA conjugation.

MATERIALS AND METHODS

Stock solutions of polyethylenimine, M_w 25 kDa (PEI25) and M_w 1.3 kDa (PEI1.3), both from Sigma, were prepared by neutralizing with HCl and accurately diluting to 50 mg/mL.

N-Succinimidyl-3-(2-pyridyldithio)propionate (SPDP) from CalBioChem and SPDP-dPEG$_8$-NHS ester (SPDP-PEG$_8$) from Quanta Biodesign were diluted in dry dimethyl sulfoxide (DMSO, Merck) immediately before use. Buffers used were as follows: 10× phosphate buffered saline (PBS) (100 mM Na_2HPO_4, 20 mM KH_2PO_4, 30 mM KCl, 1.4 M NaCl; all from Merck) adjusted to pH 7.4; HEPES buffer (Sigma), 200 mM, pH 7.4, and borate buffer (0.5 M boric acid (Sigma), pH 9.3). 2,4,6-Trinitrobenzenesulfonic acid (TNBS; Fluka) was used as 0.1 M aliquots, *o*-phthalaldehyde (OPA; Sigma) as 1 M aliquots, and dithiothreitol (DTT; BioUltra, Sigma) as 0.1 M aliquots at pH 9; all were stored at −20 °C.

PNAs were synthesized by standard t-Boc chemistry as previously described (*32*, *33*), purified by HPLC, and characterized by MALDI-TOF. Arg$_8$-PNA (PNA2787): H-(D-Arg)$_8$-Gly-CCT CTT ACC TCA GTT ACA-NH_2 (M_w: 6068.5 Da (calc:

* Corresponding author. Department of Cellular and Molecular Medicine, Panum Institute, University of Copenhagen, Blegdamsvej 3C, DK-2200 Copenhagen N, Denmark. Phone: +45 35 32 77 62. Fax: +45 35 32 60 42. E-mail: ptrn@sund.ku.dk.

[†] Faculty of Health Sciences, The Panum Institute.

[‡] Faculty of Pharmaceutical Sciences.

[1] Abbreviations: PNA, peptide nucleic acid; PEI, polyethylenimine; PEI25, branched PEI with M_w 25 kDa; PEG, poly(ethylene glycol); SPDP, *N*-succinimidyl-3-(2-pyridyldithio)propionate; PEI-P, PEI25 with variable ratios of amine linked PDP; PEI-PEGP, same as PEI-P with an 8mer PEG spacer.

10.1021/bc1003586 © 2010 American Chemical Society
Published on Web 09/27/2010

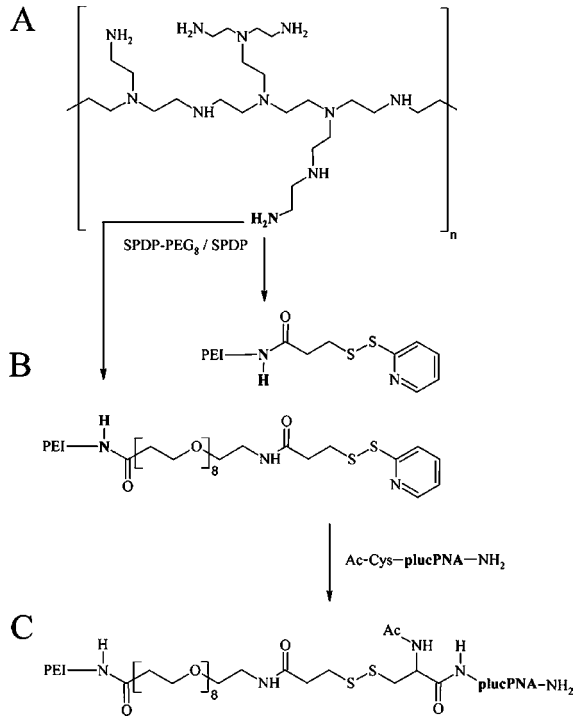


Figure 1. Synthesis and structures of PEI conjugates. Partial structure of polyethylenimine (A) and synthesis strategy. Primary amines were reacted with SPDP or SPDP-PEG_8 reagents containing an *N*-hydroxysuccinimide (NHS) ester and a sulfhydryl-reactive pyridyl disulfide group (B) which could further be reacted with a cysteine-PNA (C). PEI25 was modified to variable degrees with SPDP or SPDP-PEG_8; $n_{average}$ = ca. 15, 30, 68 (see Table 1).

6071.97). Cys-PNA (PNA3140): Ac-Cys-CCT CTT ACC TCA GTT ACA-NH_2 (M_w: 4916.15 Da (calc. 4910.59). C-teminals were amidated and N-terminal cysteine was acetylated. Cys-PNA solutions were stored at −20 °C to avoid disulfide formation.

Quantification of Polyethylenimine. PEI was quantified from primary amine content using a modified version of the TNBS assay (*34*).

PEI, diethylenetriamine (DETA), and ethylenediamine (EDA) (Sigma) were diluted to appropriate concentration in 0.1 M borate buffer, pH 9.3, containing 3% Tween 20 (Merck) and 1 mM TNBS. Following 120 min reaction, UV−vis absorbance spectra were recorded (Cary 300, Varian Inc.).

Preparation of PDP-Functionalized Polyethylenimine. Five milligrams of PEI25 (0.2 μmol) was dissolved in 1.8 mL 1× PBS, pH 7.4, and SPDP (or SPDP-PEG_8) (5 to 20 μmol in 200 μL dry DMSO) corresponding to a theoretical modification of 25−100 linkers per PEI was added. The reaction was stopped after 8 h by gel filtration using Sephadex G-25 Super Fine (G-25SF, GE Healthcare). The Sephadex was swelled according to manufacturer's protocol and preconditioned overnight with PEI1.3 and PEI25, 1 mg each/g of dry Sephadex. Seven milliliters of swelled gel was packed in handmade columns plugged with glass wool and washed thoroughly with HEPES buffer (20 mM, pH 7.4, filtered and degassed) before applying the sample. Fractions were collected in low-bind 1.5 mL polypropylene tubes using a peristaltic pump at 2.5 mL/min by elution with the HEPES buffer. Fractions containing PEI25 conjugates were pooled and dialyzed (Spectra/Por 2, MWCO 12−14 kDa, Spectrum Laboratories.) for 4 h + 12 h (250× volume, buffer change after 4 h) at 4 °C against ddH_2O. The dialysis membranes were pretreated with OPA in 50% ethanol and DETA to remove unspecified traces of sulfur, and washed thoroughly prior to dialysis.

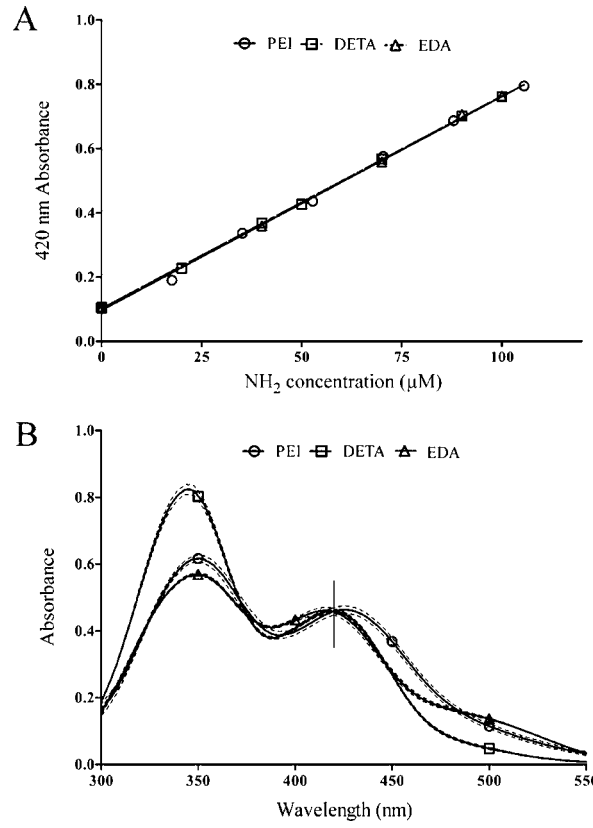


Figure 2. Standard curves (A) and absorption spectra (B) of PEI, DETA, and EDA. Absorption spectra at different concentrations of PEI, DETA, and EDA reacted with TNBS in borate buffer with 3% Tween 20 were recorded after 120 min, and absorbance at 420 nm (A) was plotted against theoretical primary amine concentration (see text for further explanation). TNBS in borate buffer with 3% Tween 20 at 120 min was used as [NH_2] = 0. (B) TNBS absorbance was subtracted from raw data and averaged spectra correspond to concentrations of 70 μM NH_2 ($n \geq 4$). Error lines (dashed) = standard deviation.

Transfection Experiments with PEI-P/PEGP. HeLa pLuc705 (Gene Tools LLC) were grown at 37 °C with 5% CO_2 in RPMI1640 medium (Sigma) supplemented with 10% fetal bovine serum (FBS) (Sigma), 1% GlutaMAX (Gibco), 100 U/mL penicillin (Gibco), and 100 μg/mL streptomycin (Gibco). The day before transfection, cells were seeded in 96-well plates (Nunc), without antibiotics, at 8×10^3 cells per well.

PEI-P/PEGP-PNA conjugates were prepared in 96-well plates; one well was prepared per triplicate transfection. Cys-PNA was left to react with PEI-P/PEGP in 20 mM HEPES in the well for 1 h. At the time of transfection, media was removed and 25 μL of the unpurified PEI-P/PEGP-PNA conjugates were diluted to 100 μL in OPTI-MEM (Gibco), and were transferred to the cells. After 6 h, cells were supplemented with 100 μL of 20% FBS and 1% GlutaMAX in RPMI-1640 and incubated for additional 18 h. For lactate dehydrogenase (LDH) leakage assays (CytoTox-ONE, Promega), 50 μL medium was recovered for analysis. After incubation, the transfection solution was removed, and then 50 μL passive lysis buffer (Promega) was added to the cells, followed by a freeze/thaw cycle, and the lysate was subjected to the further analysis. Ten microliters of lysate was diluted with 40 μL H_2O and analyzed for ATP content (CellTiter-Glo, Promega), while remaining lysate was assayed for luciferase activity (Bright-Glo, Promega). All assays were handled according to manufacturer.

RESULTS AND DISCUSSION

For conjugation to PNA, we chose to focus on PEI25, since it is a well-known standard in transfection with cationic poly-

Table 1. PEI Conjugates Used for Transfection[a]

linker	PEI25 conjugate	PDP/PEI (±SD)
SPDP	PEI-P14	14.4 ± 0.4
	PEI-P29	28.5 ± 0.9
	PEI-P68	68.4 ± 1.9
SPDP-PEG_8	PEI-PEGP15	15.5 ± 0.3
	PEI-PEGP30	29.6 ± 0.4
	PEI-PEGP66	66.1 ± 2.1

[a] Conjugates were characterized by TNBS assay and P2T release by DTT cleavage. SD = standard deviation.

mers and makes a reasonable compromise between transfection efficiency and toxicity. In order to obtain a cleavable complex, we chose to use a SPDP linker which upon reaction with cystein-containing PNA will form disulfide linkages (Figure 1B−C), and we also decided to include a PEG containing SPDP linker for possible reduction of cellular toxicity. In efforts to quantify PEI modification, we found that authentic quantification using the standard TNBS assay (*34*) was not accurate, since amine derivatives of TNBS differ significantly in reaction kinetics and extinction coefficients depend on the compounds to react with TNBS (*35*). Furthermore, trinitrophenylation of PEI caused precipitation when the majority of primary amines were reacted. However, PEI precipitation was averted by supplementing the TNBS reaction (in borate buffer at pH 9.3) with 3% Tween 20, which did not change the absorbance of the reaction products with the simple PEI model compounds EDA and DETA (*36*), as compared to borate buffer alone (not shown). Under these conditions, absorbance at 420 nm correlated linearly with primary amine content of PEI, EDA, and DETA (Figure 2A), and eq 1 was derived ($R^2 = 0.997$, valid range = [5−110 μM]) from the standard curve. The absorbance at 420 nm was used because the absorption spectra of trinitrophenylated (TNP)-PEI, -DETA, and -EDA differed significantly at 340 nm and above 430 nm with TNP-PEI being a hybrid spectrum of TNP-DETA, TNP-EDA, and TNP-$NHCH_2CH_2NR_2$ ($R \neq H$), but coalesced at 420 nm (Figure 2B).

$$[NH_2](\mu M) = \frac{(\text{Abs } 420\text{ nm}) - 85.5 \times 10^{-3}}{6.92 \times 10^{-3}} \quad (1)$$

The primary amine content of PEI25 was estimated to be ~175/polymer by comparison with TNP-DETA and TNP-EDA, which is in good agreement with the results of Harpe et al. (*14*).

Three preparations of sulfhydryl reactive 3-(2-pyridyldithio)-propionate (PDP) PEI differing in the degree of modification (14−68 per PEI) were made with both primary amine reactive SPDP and SPDP-PEG_8 linkers (Figure 1B). The conjugates were purified on Sephadex G-25SF preconditioned with PEI to block unspecific adsorption. Preconditioning the columns with PEI was critical in reducing nonspecific adsorption and significant sample loss, which was apparent when using a fluorophore-label PEI25 (not shown). We therefore assumed adsorption kinetics and capacity were analogous to those of cellulose fibers (*37*) and handled the beads accordingly, thereby reducing column loss to a minimum (as judged by control experiments using fluorescein-labeled PEI25 (results not shown).

The collected fractions were submitted to dialysis. The conjugates were characterized spectrophotometrically using the 3% Tween 20, borate buffered TNBS assay, and by measuring pyridine-2-thione (P2T) released by DTT treatment of the samples. The primary amine content ([NH_2]) was estimated from eq 1 and PEI concentration and the degree of modification

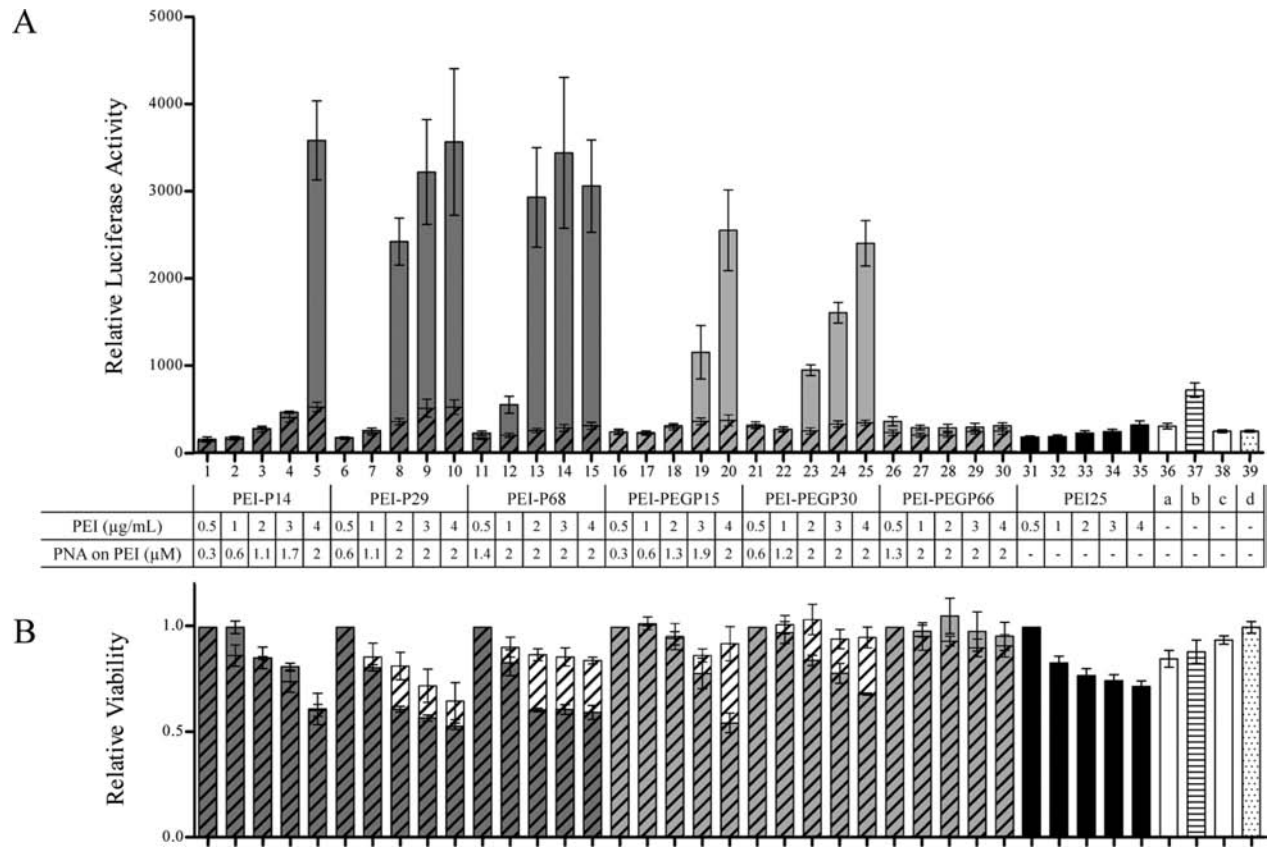


Figure 3. Effects of PEI modification. Transfections were carried out with a constant PNA concentration of 2 μM and varying concentration of functionalized PEI from 0.5 to 4 μg/mL. DTT controls were prepared for each sample (hatched overlay) in which PNA was cleaved from the PEI before transfection. Controls are 4 μM Arg_8-PNA (a), 4 μM Arg_8-PNA with chloroquine (75 μM) (b), 4 μM Cys-PNA (c), and 20 mM HEPES (1:3, v/v) in OPTI-MEM (d). Relative luciferase activity is corrected for ATP content. Error = SEM, $n = 3$.

({PDP/PEI}) from eqs 2 ([P2T] (μM) = (Δ343 nm)/(8.08×10^{-3})) and 3, respectively (Table 1).

$$[\text{PEI}] = \frac{([\text{NH}_2] + [\text{P2T}])}{175} \quad (2)$$

$$\{\text{PDP/PEI}\} = \frac{[\text{P2T}]}{[\text{PEI}]} \quad (3)$$

The modification degree and standard deviation (Table 1) were determined by unpaired comparison of triplicate TNBS and P2T release measurements, and the amine coupling efficiency (assuming 100% P2T cleavage) averaged 62%.

The PDP activated PEI was reacted with Cys-PNA (Figure 1C) in the wells in HEPES buffer and was used without further purification. Thus, samples were conveniently prepared in a 96-well format. We evaluated the transfection capacities of PEI-P/PEGP conjugates in the well-established HeLa pLuc705 splice correction assay (*38*) using a PNA targeted to the aberrant splice site (plucPNA; Ac-Cys-CCTCTTACCTCAGTTACA-NH_2), and the luciferase activity was corrected for cell viability using ATP content (rather than standard BCA assay), as this is more conveniently done in a 96-well format.

The conjugates were initially evaluated by keeping the total PNA concentration constant at 2 μM and varying the PEI concentration in the conjugation (Figure 3A). All samples were prepared with a corresponding DTT control, which was treated with 1 mM DTT prior to transfection to measure background transfection of nonconjugated PNA and PEI (Figure 3, hatched overlays). The results showed a very significant increase (up to <20-fold above background) in luciferase activity induced by the PNA upon conjugation to PEI, and this effect is virtually abolished after treatment with DTT, demonstrating the necessity of the covalent disulfide linkage for activity. The activity of the PNA-PEI conjugates is somewhat dependent on the degree of PEI modification (Figure 3A, PEI-P14, columns 1−5, vs PEI-P29 and -P68, columns 5−10 and 11−15, respectively), and the simple SPDP conjugates appear more active than the corresponding SPDP-PEG_8 conjugates (Figure 3A, PEI-P68 vs PEI-PEGP66, columns 1−15 and 16−30, respectively). In particular, the SPDP-PEG_8 conjugates are virtually inactive at the higher modification degree (Figure 3A, PEI-PEGP66, columns 26−30), although PEG-modification alleviates cellular toxicity to some extent. One possible explanation for this reduced efficiency of PEG-modified PEI is shielding of the PEI amines. Furthermore, all PEI preparations showed a dose-dependent cell toxicity (Figure 3B), and it is interesting that toxicity seems reduced upon treatment with DTT, indicating that the PNA conjugation increases the general cellular toxicity of PEI. From these results with constant PNA concentration for the conjugation (Figure 3), we found that the optimal PDP:PNA ratio was 1.2:1, which was therefore used in the dose−response experiments (Figure 4A−B).

The antisense activity of the apparently most potent and less toxic conjugates, PEI-P29, PEI-PEGP15, and PEI-PEGP30 were studied in more detail. A dose−response dependence on PNA concentration showed a close to linear relationship of all three conjugates, with the PEI-PEGP15 conjugate being twice as active as the two others most likely reflecting the reduced PEI loading and thus double PEI concentration (Figure 4A). Thus, the PEI-PEGP15 conjugate was chosen for a direct comparison with a reference CPP conjugated PNA, Arg_8-PNA (*6*−*8*) (Figure 4B). These results show that the PEI-PEGP15-PNA conjugate is about 10-fold more active than the Arg_8-PNA and up to 3−4-fold more active, even when the effect of Arg_8-PNA is enhanced with the lysosomolytic agent chloroquine (CQ) (*6*). Furthermore,

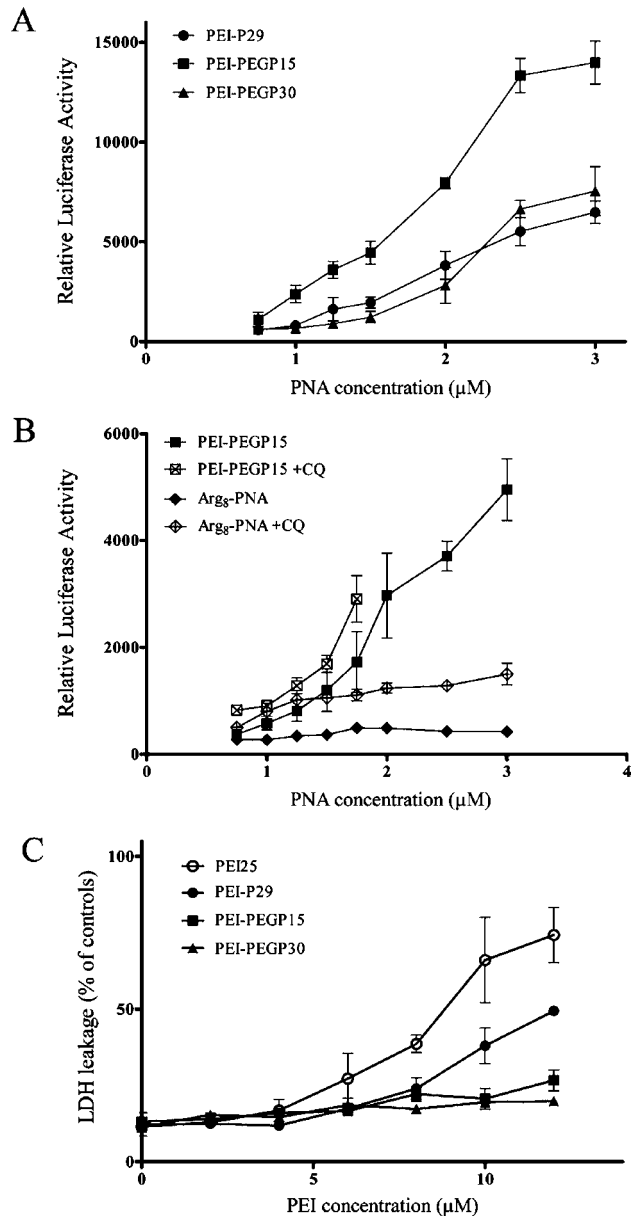


Figure 4. Dose response and acute toxicity. (A) Antisense activity of PEI-P29-, PEI-PEGP15-, and PEI-PEGP30-PNA conjugates. (B) Antisense activity of PEI-PEGP15-PNA conjugate and Arg_8-PNA in the absence or presence of chloroquine (CQ). CQ and PEI-PEGP15-PNA corresponding to PNA concentrations above 1.75 μM were highly toxic and are omitted. (C) Acute toxicity at 2 h as measured by LDH leakage. For (A) and (B), the PEI-P/PEGP concentration was determined by a PDP:PNA ratio of 1.2: 1. Relative luciferase activity is corrected for ATP content. Error = SEM, $n = 3$.

and most interestingly, the addition of chloroquine has only minimal activating effect on the PEI-PEGP15-PNA conjugate, but very significantly increases the toxicity of this (>50% for 2 μM PNA; Figure 4B).

Finally, whereas cell viability after 24 h (Figure 3B) as measured by the ATP assay did not differ much between PEI and PEI-PEG conjugates, the PEI-PEG conjugates showed significantly less acute toxicity (2 h) as measured by LDH leakage (Figure 4C). The reduced acute toxicity of SPDP-PEG_8 modified PEI25 together with the decrease in toxicity of DTT cleaved conjugates after 24 h of transfection, especially for PEI-PEGP30 and 66 (Figure 3B, columns 21−30), could indicate that the $[PEG]_8$ linker leads to reduced initial membrane damage (and possibly lower transfection efficacy when cleaved), while the delayed cytoplasmic toxicity could be caused by pertained mitochondrial damage (*19*). This is

further supported by the negligible difference between high and low modification degree with SPDP.

CONCLUSIONS

The present results clearly show that properly optimized, in terms of conjugation degree, PEI is an efficient cellular delivery agent for (antisense) PNA not requiring additional lysosomolytic activity. We also note that the experimental setup allows for high-throughput screening optimization and discovery of novel active PEI-conjugates using a variety of other bioactive ligands, such as morpholino oligomers (*39*) and minor groove binding (hairpin) polyamides (*40*). Furthermore, the system also conveniently allows for studies and optimization of heterogeneous conjugates using gene targeting agents (e.g., PNA) in combination with auxiliary agents, which have previously proven successful in improving transfection efficiency of PEI:DNA polyplexes, such as specific receptor targeting peptides (e.g., FGF) (*41, 42*), cell penetrating peptides (CPPs) (*43*−*45*), and lipids (e.g., cholesterol) (*46*), in order to optimize and tailor-make the conjugates, and exploiting the possible synergy of the agents. The ratio between the various ligands in the PEI conjugate will (to a first degree) be controlled by their ratio (as thiol derivatives) in the conjugation reaction mixture. Finally, the employment of orthogonal conjugation methods (e.g., click chemistry) would allow discrimination of ligands attached by cleavable or noncleavable linkers.

ACKNOWLEDGMENT

This work was supported by the Lundbeck Foundation.

LITERATURE CITED

(1) Nielsen, P. E. (2008) Modulating Gene Function with Peptide Nucleic Acids (PNA). *Antisense drug technology: principles, strategies, and applications* (Crooke, S. T., Ed.) pp 507−518, Chapter 18, Taylor & Francis Group, CRC Press.

(2) Nielsen, P. E. (2010) Sequence-selective targeting of duplex DNA by peptide nucleic acids. *Curr. Opin. Mol. Ther. 12*, 184–191.

(3) Lundin, K. E., Good, L., Strömberg, R., Gräslund, A., and Smith, C. I. E. (2006) Biological activity and biotechnological aspects of peptide nucleic acid. *Adv. Genet. 56*, 1–51.

(4) Lebleu, B., Moulton, H. M., Abes, R., Ivanova, G. D., Abes, S., Stein, D. A., Iversen, P. L., Arzumanov, A. A., and Gait, M. J. (2008) Cell penetrating peptide conjugates of steric block oligonucleotides. *Adv. Drug Delivery Rev. 60*, 517–529.

(5) Lundin, P., Johansson, H., Guterstam, P., Holm, T., Hansen, M., Langel, U., and EL Andaloussi, S. (2008) Distinct uptake routes of cell-penetrating peptide conjugates. *Bioconjugate Chem. 19*, 2535–2542.

(6) Shiraishi, T., Pankratova, S., and Nielsen, P. E. (2005) Calcium ions effectively enhance the effect of antisense peptide nucleic acids conjugated to cationic tat and oligoarginine peptides. *Chem. Biol. 12*, 923–929.

(7) Shiraishi, T., and Nielsen, P. E. (2006) Photochemically enhanced cellular delivery of cell penetrating peptide-PNA conjugates. *FEBS Lett. 580*, 1451–1456.

(8) Koppelhus, U., Shiraishi, T., Zachar, V., Pankratova, S., and Nielsen, P. E. (2008) Improved cellular activity of antisense peptide nucleic acids by conjugation to a cationic peptide-lipid (CatLip) domain. *Bioconjugate Chem. 19*, 1526–1534.

(9) Hamilton, S. E., Simmons, C. G., Kathiriya, I. S., and Corey, D. R. (1999) Cellular delivery of peptide nucleic acids and inhibition of human telomerase. *Chem. Biol. 6*, 343–351.

(10) Shiraishi, T., Bendifallah, N., and Nielsen, P. E. (2006) Cellular delivery of polyheteroaromate-peptide nucleic acid conjugates mediated by cationic lipids. *Bioconjugate Chem. 17*, 189–194.

(11) Shiraishi, T., Hamzavi, R., and Nielsen, P. E. (2008) Subnanomolar antisense activity of phosphonate-peptide nucleic acid (PNA) conjugates delivered by cationic lipids to HeLa cells. *Nucleic Acids Res. 36*, 4424–4432.

(12) Boussif, O., Lezoualc'h, F., Zanta, M. A., Mergny, M. D., Scherman, D., Demeneix, B., and Behr, J. P. (1995) A versatile vector for gene and oligonucleotide transfer into cells in culture and in vivo: polyethylenimine. *Proc. Natl. Acad. Sci. U.S.A. 92*, 7297–301.

(13) Malek, A., Czubayko, F., and Aigner, A. (2008) PEG grafting of polyethylenimine (PEI) exerts different effects on DNA transfection and siRNA-induced gene targeting efficacy. *J. Drug Targeting 16*, 124–139.

(14) von Harpe, A., Petersen, H., Li, Y., and Kissel, T. (2000) Characterization of commercially available and synthesized polyethylenimines for gene delivery. *J. Controlled Release 69*, 309–322.

(15) Akinc, A., Thomas, M., Klibanov, A. M., and Langer, R. (2005) Exploring polyethylenimine-mediated DNA transfection and the proton sponge hypothesis. *J. Gene Med. 7*, 657–663.

(16) Gabrielson, N. P., and Pack, D. W. (2009) Efficient polyethylenimine-mediated gene delivery proceeds via a caveolar pathway in HeLa cells. *J. Controlled Release 136*, 54–61.

(17) Bieber, T., Meissner, W., Kostin, S., Niemann, A., and Elsasser, H. (2002) Intracellular route and transcriptional competence of polyethylenimine-DNA complexes. *J. Controlled Release 82*, 441–454.

(18) Godbey, W. T., Wu, K. K., and Mikos, A. G. (1999) Tracking the intracellular path of poly(ethylenimine)/DNA complexes for gene delivery. *Proc. Natl. Acad. Sci. U.S.A. 96*, 5177–5181.

(19) Moghimi, S. M., Symonds, P., Murray, J. C., Hunter, A. C., Debska, G., and Szewczyk, A. (2005) A two-stage poly(ethylenimine)-mediated cytotoxicity: implications for gene transfer/therapy. *Mol. Ther. 11*, 990–995.

(20) Godbey, W. T., Wu, K. K., and Mikos, A. G. (1999) Size matters: Molecular weight affects the efficiency of poly(ethylenimine) as a gene delivery vehicle. *J. Biomed. Mater. Res. 45*, 268–275.

(21) Wightman, L., Kircheis, R., Rössler, V., Carotta, S., Ruzicka, R., Kursa, M., and Wagner, E. (2001) Different behavior of branched and linear polyethylenimine for gene delivery in vitro and in vivo. *J. Gene Med. 3*, 362–372.

(22) Gosselin, M. A., Guo, W., and Lee, R. J. (2001) Efficient gene transfer using reversibly cross-linked low molecular weight polyethylenimine. *Bioconjugate Chem. 12*, 989–994.

(23) Breunig, M., Lungwitz, U., Liebl, R., and Goepferich, A. (2007) Breaking up the correlation between efficacy and toxicity for nonviral gene delivery. *Proc. Natl. Acad. Sci. U.S.A. 104*, 14454–14459.

(24) Thomas, M., Ge, Q., Lu, J. J., Chen, J., and Klibanov, A. (2005) Cross-linked small polyethylenimines: while still nontoxic, deliver dna efficiently to mammalian cells in vitro and in vivo. *Pharm. Res. 22*, 373–380.

(25) Wong, K., Sun, G., Zhang, Dai, H., Liu, Y. He, and Leong, K. W. (2006) PEI-g-chitosan, a novel gene delivery system with transfection efficiency comparable to polyethylenimine in vitro and after liver administration in vivo. *Bioconjugate Chem. 17*, 152–158.

(26) Sung, S., Min, S. H., Cho, K. Y., Lee, S., Min, Y., Yeom, Y. I., and Park, J. (2003) Effect of polyethylene glycol on gene delivery of polyethylenimine. *Biol. Pharm. Bull. 26*, 492–500.

(27) Mishra, S., Webster, P., and Davis, M. E. (2004) PEGylation significantly affects cellular uptake and intracellular trafficking of non-viral gene delivery particles. *Eur. J. Cell Biol. 83*, 97–111.

(28) Zhang, X., Pan, S., Hu, H., Wu, G., Feng, M., Zhang, W., and Luo, X. (2008) Poly(ethylene glycol)-block-polyethylenimine copolymers as carriers for gene delivery: Effects of PEG molecular weight and PEGylation degree. *J. Biomed. Mater. Res., Part A 84A*, 795–804.

(29) Ogris, M., Brunner, S., Schüller, S., Kircheis, R., and Wagner, E. (1999) PEGylated DNA/transferrin-PEI complexes: reduced interaction with blood components, extended circulation in blood and potential for systemic gene delivery. *Gene Ther. 6*, 595–605.

(30) Kircheis, R., Schüller, S., Brunner, S., Ogris, M., Heider, K., Zauner, W., and Wagner, E. (1999) Polycation-based DNA complexes for tumor-targeted gene delivery in vivo. *J. Gene Med. 1*, 111–120.

(31) Ogris, M., Walker, G., Blessing, T., Kircheis, R., Wolschek, M., and Wagner, E. (2003) Tumor-targeted gene therapy: strategies for the preparation of ligand-polyethylene glycol-polyethylenimine/DNA complexes. *J. Controlled Release 91*, 173–181.

(32) Christensen, L., Fitzpatrick, R., Gildea, B., Petersen, K. H., Hansen, H. F., Koch, T., Egholm, M., Buchardt, O., Nielsen, P. E., Coull, J., and Berg, R. H. (1995) Solid-phase synthesis of peptide nucleic acids. *J. Pept. Sci. 1*, 175–183.

(33) Hyrup, B., and Nielsen, P. E. (1996) Peptide nucleic acids (PNA): Synthesis, properties and potential applications. *Bioorg. Med. Chem. 4*, 5–23.

(34) Snyder, S. L., and Sobocinski, P. Z. (1975) An improved 2,4,6-trinitrobenzenesulfonic acid method for the determination of amines. *Anal. Biochem. 64*, 284–288.

(35) Means, G. E., Congdon, W. I., and Bender, M. L. (1972) Reactions of 2,4,6-trinitrobenzenesulfonate ion with amines and hydroxide ion. *Biochemistry 11*, 3564–3571.

(36) Suh, J., Paik, H. J., and Hwang, B. K. (1994) Ionization of poly(ethylenimine) and poly(allylamine) at various pH's. *Bioorg. Chem. 22*, 318–327.

(37) Petlicki, J., and van de Ven, T. (1994) Adsorption of polyethylenimine onto cellulose fibers. *Colloids Surf., A 83*, 9–23.

(38) Kang, S. H., Cho, M. J., and Kole, R. (1998) Up-regulation of luciferase gene expression with antisense oligonucleotides: implications and applications in functional assay development. *Biochemistry 37*, 6235–9.

(39) Moulton, H. M., Fletcher, S., Neuman, B. W., McClorey, G., Stein, D. A., Abes, S., Wilton, S. D., Buchmeier, M. J., Lebleu, B., and Iversen, P. L. (2007) Cell-penetrating peptide-morpholino conjugates alter pre-mRNA splicing of DMD (Duchenne muscular dystrophy) and inhibit murine coronavirus replication in vivo. *Biochem. Soc. Trans. 35*, 826–828.

(40) Dervan, P. B., and Edelson, B. S. (2003) Recognition of the DNA minor groove by pyrrole-imidazole polyamides. *Curr. Opin. Struct. Biol 13*, 284–299.

(41) Li, D., Yu, H., Huang, H., Shen, F., Wu, X., Li, J., Wang, J., Cao, X., Wang, Q., and Tang, G. (2007) FGF receptor-mediated gene delivery using ligands coupled to polyethylenimine. *J. Biomater. Appl. 22*, 163–180.

(42) Li, D., Tang, G. P., Li, J. Z., Kong, Y., Huang, H. L., Min, L. J., Zhou, J., Shen, F. P., Wang, Q. Q., and Yu, H. (2007) Dual-targeting non-viral vector based on polyethylenimine improves gene transfer efficiency. *J. Biomater. Sci. Polym. Ed. 18*, 545–560.

(43) Kleemann, E., Neu, M., Jekel, N., Fink, L., Schmehl, T., Gessler, T., Seeger, W., and Kissel, T. (2005) Nano-carriers for DNA delivery to the lung based upon a TAT-derived peptide covalently coupled to PEG-PEI. *J. Controlled Release 109*, 299–316.

(44) Nguyen, J., Xie, X., Neu, M., Dumitrascu, R., Reul, R., Sitterberg, J., Bakowsky, U., Schermuly, R., Fink, L., Schmehl, T., Gessler, T., Seeger, W., and Kissel, T. (2008) Effects of cell-penetrating peptides and pegylation on transfection efficiency of polyethylenimine in mouse lungs. *J. Gene Med. 10*, 1236–1246.

(45) Kilk, K., EL-Andaloussi, S., Järver, P., Meikas, A., Valkna, A., Bartfai, T., Kogerman, P., Metsis, M., and Langel, Ü. (2005) Evaluation of transportan 10 in PEI mediated plasmid delivery assay. *J. Controlled Release 103*, 511–523.

(46) Wang, D., Narang, A. S., Kotb, M., Gaber, A. O., Miller, D. D., Kim, S. W., and Mahato, R. I. (2002) Novel branched poly(ethylenimine)-cholesterol water-soluble lipopolymers for gene delivery. *Biomacromolecules 3*, 1197–1207.

BC1003586

Caspase Sensitive Gold Nanoparticle for Apoptosis Imaging in Live Cells

In-Cheol Sun,[†] Seulki Lee,[‡] Heebeom Koo,[†] Ick Chan Kwon,[†] Kuiwon Choi,[†] Cheol-Hee Ahn,*[,§] and Kwangmeyung Kim*[,†]

Biomedical Research Center, Korea Institute of Science and Technology, 39-1 Hawolgok-dong, Seongbuk-gu, Seoul, 136-791, Korea, Laboratory of Molecular Imaging and Nanomedicine, National Institute of Biomedical Imaging and Bioengineering (NIBIB), National Institutes of Health (NIH), 31 Center Drive, Suite 1C14, Bethesda, Maryland 20892-2281, United States, and Research Institute of Advanced Materials (RIAM), Department of Materials Science and Engineering, Seoul National University, San 56-1, Sillim, Gwanak, Seoul, 151-744, Korea. Received July 12, 2010; Revised Manuscript Received October 1, 2010

We developed a new apoptosis imaging probe with gold nanoparticles (AuNPs). A near-infrared fluorescence dye was attached to AuNP surface through the bridge of peptide substrate (DEVD). The fluorescence was quenched in physiological conditions due to the quenching effect of AuNP, and the quenched fluorescence was recovered after the DEVD had been cleaved by caspase-3, the enzyme involved in apoptotic process. The adhesion of DEVD substrates on AuNP surface was accomplished by conjugation of the 3,4-dihydroxy phenylalanine (DOPA) groups which are adhesive to inorganic surface and rich in mussels. This surface modification with DEVD substrates by DOPA groups resulted in increased stability of AuNP in cytosol condition for hours. Moreover, the cleavage of substrate and the dequenching process are very fast, and the cells did not need to be fixed for imaging. Therefore, the real-time monitoring of caspase activity could be achieved in live cells, which enabled early detection of apoptosis compared to a conventional apoptosis kit such as Annexin V-FITC. Therefore, our apoptosis imaging has great potential as a simple, inexpensive, and efficient apoptosis imaging probe for biomedical applications.

Apoptosis is an important physiological mechanism to maintain homeostasis of multicellular organisms by elimination of infected or damaged cells and regulation of cell number (*1, 2*). Various imaging techniques were developed to image this process, because it could provide a monitoring tool for therapeutic effect of cancer treatment, efficacy of new drugs, or quality of protein therapeutics produced in mammalian cell culture. In particular, the TUNEL (TdT-mediated dUTP nick end labeling) assay is a typical method to label DNA fragmentation which occurs during apoptosis. However, many reaction steps are involved in this method and internucleosomal DNA breaks were not always associated with apoptosis (*3, 4*). Annexin V/FITC (fluorescein isothiocyanate) conjugate is another widely used method for apoptosis imaging due to its binding affinity to negatively charged phosphatidylserine (PS) exposed on the apoptotic cell membrane. However, this binding is not specific to apoptosis, because PS exposure can occur in other biological situations like myotube formation and necrosis (*5, 6*). To overcome the limitation of conventional imaging methods and to enable the early diagnosis of diseases or fast evaluation of therapeutic effect, it is necessary to develop a caspase enzyme-sensitive imaging probe, because activation of caspases is the initial stage of apoptotic process and responsible for the cell changes during apoptosis such as DNA fragment, nuclear chromatin condensation, and plasma membrane blebbing (*7*).

For this reason, we synthesized a caspase-sensitive fluorescence imaging probe using gold nanoparticles (AuNPs). Caspase-3 cleavable motifs (*8*) combined with mussel-inspired adherent peptides, 3,4-dihydroxy phenylalanines (DOPA), and lysines (Gly-Asp-Glu-Val-Asp-Ala-Pro-DOPA-Lys-DOPA-Lys-DOPA, the cleavage site is between Asp and Ala) were purchased, and a near-infrared fluorescence (NIRF) dye, Cy5.5, was conjugated to the N-terminus of peptide sequence. DOPAs and lysines (DOPAK) at the C-terminus of caspase-3 cleavable motifs played an important role in adhesion of peptides on the surface of AuNP. The Cy5.5-conjugated peptide (Cy5.5-DEVD-DOPAK) was used to modified the surface of citrated-stabilized AuNPs by a simple mixing method (Scheme 1). At the N-terminus of DEVD, three 3,4-dihydroxy phenylalanines and lysines (DOPAKs) were chemically conjugated to increase the adherence between the surface of AuNP and peptide. DOPA has been known to be rich in mussel foot protein and has excellent adhesive properties to the surface of various materials (*9*). AuNP carried out a role as a quencher of Cy5.5 for its strong surface energy transfer (*10, 11*). This nanoprobe facilitated detection and monitoring of enzymatic activity of caspase, because its NIRF emission was selectively turned on after degradation of DEVD sequence by caspase-3. Our probe has unique features such as sensitive and fast imaging, direct imaging of caspase-3 enzyme activity, and real-time imaging of apoptotic cells.

For the biological application, the stability of AuNPs in the physiological condition should be guaranteed because aggregation of them impedes their long circulation and full function in the body. The stability of Cy5.5-DEVD-DOPAK coated AuNPs (DEVD-AuNPs) was confirmed through UV−vis absorption spectroscopy in caspase buffer condition (Figure 1A; see the Supporting Information for details of caspase buffer). The spectrum showed a unique surface plasmon resonance peak of DEVD-AuNPs at 523 nm, and it was no different from that of the uncoated AuNPs even in the caspase-containing buffer. However, in the case of the uncoated AuNPs, they aggregated and the UV−vis absorbance was reduced after incubation in caspase buffer. The stability of DEVD-AuNPs was also verified by observation of the morphology in the TEM images (Figure 1B). As seen in Figure 1B, DEVD-AuNPs were uniformly dispersed and no aggregation was found. The size of DEVD-

* To whom correspondence should be addressed. Phone: (+82) 2-958-5916, (+82) 2-880-5791, Fax: (+82) 2-958-5909, (+82) 2-883-8197. E-mail: (K.K.) kim@kist.re.kr; (C.-H.A.) chahn@snu.ac.kr.

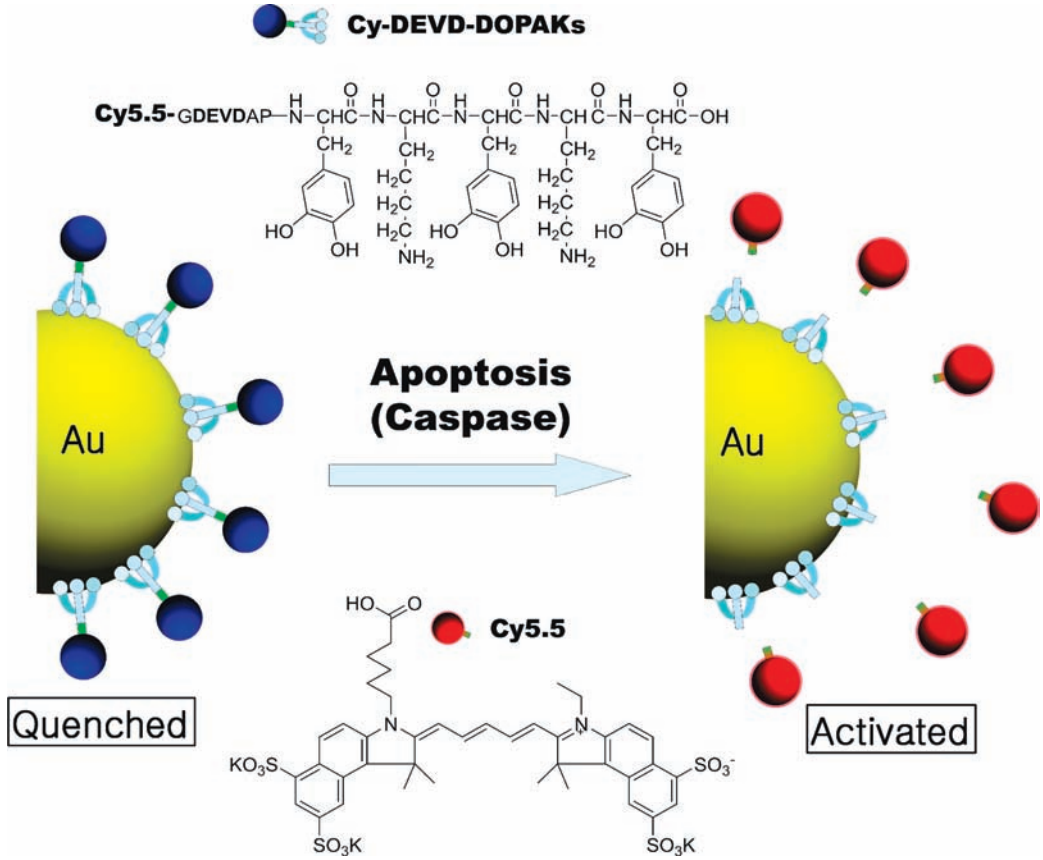
[†] Korea Institute of Science and Technology.

[‡] NIBIB, NIH.

[§] Seoul National University.

10.1021/bc1003026 © 2010 American Chemical Society
Published on Web 10/11/2010

Scheme 1. Schematic Diagram of Cy5.5 and DEVD Peptide Conjugated Gold Nanoparticles (DEVD-AuNPs)[a]



[a] Blue spheres indicated quenched state of Cy5.5 and red ones represented recovered fluorescence.

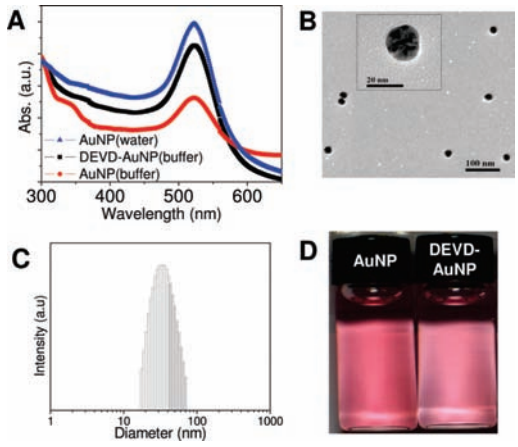


Figure 1. (A) UV−vis absorption spectrum of bare AuNP in water (blue), caspase buffer (red), and DEVD-AuNP in buffer (black). (B) TEM images of DEVD-AuNP. (C) Particle size distribution measured with DLS (D) Optical image of AuNP and DEVD-AuNP.

AuNP in the buffer was measured with dynamic light scattering, and it showed the size distribution of 37.8 ± 14.1 nm (Figure 1C). The increment of diameter was due to the hydrophilicity of peptide and not caused by aggregation of AuNPs. The enhanced stability of DEVD-AuNP was also examined by the naked eye, because it retained the unique red color during the coating process (Figure 1D). From these results of DEVD-AuNPs, it was inferred that DEVD peptide on the surface did not affect the stability of AuNPs but also stabilized AuNPs even in the caspase buffer environment. In addition, the amount of DEVD substrate bound to the AuNP surface was calculated through the measurement of UV−vis absorption of unreacted Cy5.5-DEVD during the coating process. The UV−vis absorbance at 675 nm was calibrated with a standard curve of Cy5.5, and we estimated that about 1.2×10^2 molecules of DEVD were attached to each AuNP (0.095 49 molecules/nm^2).

The feasibility of DEVD-AuNP for optical imaging probe of apoptosis was investigated. The difference of NIRF intensity of Cy5.5 was measured before and after incubation of DEVD-AuNP with caspase-3. NIRF was quenched before the addition of caspase-3 due to the nonradiative energy transfer properties of AuNP (*12*). The quenched fluorescence was recovered after the DEVD substrates on the AuNPs were degraded by caspase-3. The cleavage of DEVD increased the distance between fluorophore and AuNP, and the NIRF signal was recovered because the quenching effect of AuNP was reduced. These results were imaged with NIRF imaging system (Kodak Image Station 4000MM, New Haven, CT, USA), a function of concentration of DEVD-AuNP (Figure 2A). Due to the strong quenching effect of AuNPs, the detection of recovered fluorescence was corrupted after incubation with caspase-3 when the concentration of DEVD-AuNP had been greatly increased. For comparison, the NIRF images were obtained from the decanted solution after incubation with caspase-3 followed by centrifugation. The quantitative measurement of NIRF using a spectrofluorometer at a fixed excitation wavelength of 675 nm showed that the signal-to-background ratio could be increased by concentration of DEVD-AuNP up to 1.0 mg/mL and NIRF signal saturation appeared due to the self-quenching of Cy5.5 dyes detached from DEVD-AuNP (Figure 2B). The recovered NIRF intensity was also dependent on concentration of caspase-3 as shown in Figure 2C, and DEVD-AuNP could detect and generate fluorescence in response to only about 1 nM of caspase-3. Figure 2D shows that the fluorescence recovery of DEVD-

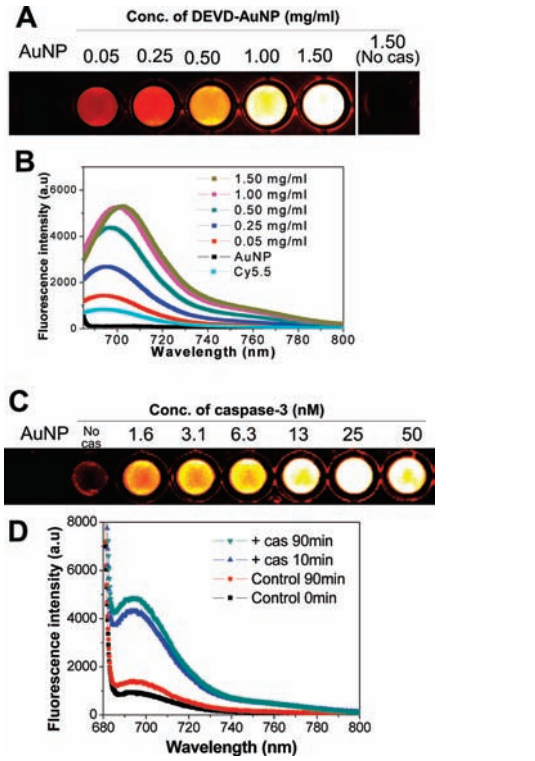


Figure 2. (A) NIRF images of DEVD-AuNP in 96-well microplate containing various concentrations of DEVD-AuNP with or without caspase-3. (B) Fluorescence spectra of DEVD-AuNP as a function of probe concentration incubated with caspase-3. (C) NIRF images of DEVD-AuNP with various concentrations of caspase-3. (D) Fluorescence spectra of DEVD-AuNP as a function of incubation time with caspase-3.

AuNP was made very quickly in response to caspase-3 and had already occurred at 10 min.

For real-time apoptosis imaging with DEVD-AuNPs in live cells, apoptosis was induced with tumor necrosis factor-related apoptosis-inducing ligand (TRAIL) in HeLa cells. TRAIL has been known to induce apoptosis effectively in various cell lines include HeLa cells (*13*). After DEVD-AuNPs were taken up by HeLa cells by coincubation for 1 h, TRAIL was treated and the cells were observed with microscopy to obtain real-time fluorescent images. Even before the formation of apoptotic body, the NIRF signal of Cy5.5 appeared after 30 min of TRAIL treatment (Figure 3A). This signal was condensed after the apoptotic body was formed in 120 min. In contrast, NIRF signal was not observed for 120 min when the cells were not treated with TRAIL. In addition, it was seen that cell death was delayed and the NIRF intensity was reduced when the cells were exposed to the inhibitor of caspase-3 (Z-DEVD-FMK, R&D Systems, Minneapolis, MN, USA) for 30 min prior to TRAIL treatment. This result was further investigated with DAPI (4′,6-diamidino-2-phenylindole) staining, which binds strongly to DNA and forms a fluorescent complex in nuclei. It is well-known that caspase cascade is activated in the cytosol area (*1, 8*), so the recovered fluorescence of Cy5.5 in the cytosol should not overlap with that of DAPI in the nuclei as shown in Figure 3B. In addition, the existence of DEVD-AuNP was monitored through a dark-field microscope. The signal of DEVD-AuNP in the dark-field image was detected only in the cytosol area of HeLa cells, which was coincident with previous results (Figure 3C). These results clearly showed that the DEVD-AuNP probe has enhanced optical functionality and specificity against caspase enzyme and it was activated only through the caspase cascade occurring in the cytoplasm.

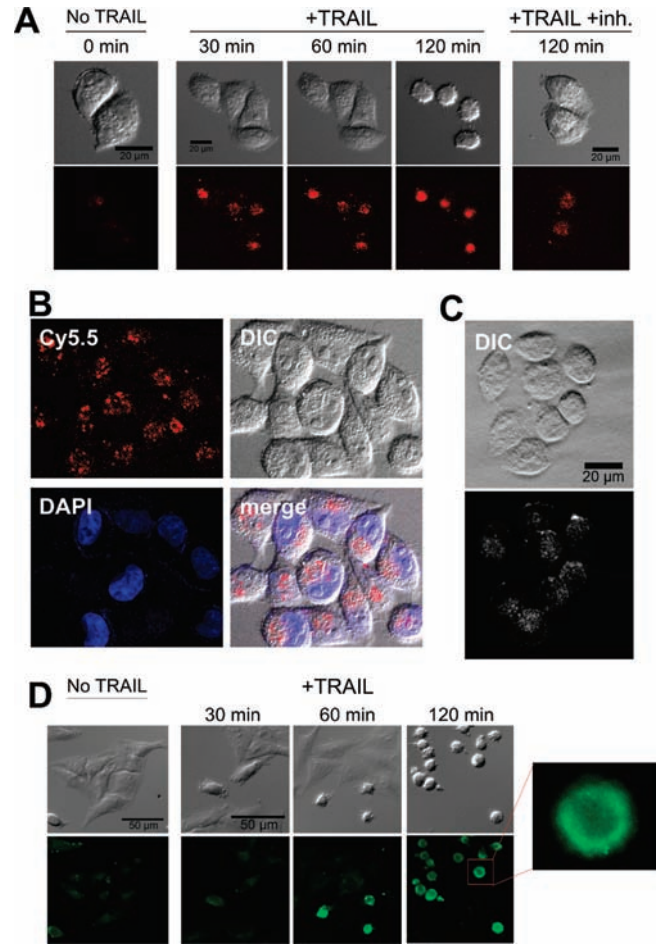


Figure 3. Microscopic images of HeLa cells after uptake of DEVD-AuNP and induction of apoptosis with TRAIL. (A) DIC and NIRF (Cy5.5) microscopic images of nonapoptotic (no TRAIL) and apoptotic (+TRAIL, +TRAIL+inh) cells treated with DEVD-AuNP. (B) DIC and fluorescence images of DEVD-AuNP treated apoptotic cells after DAPI staining (C) Dark-field images of apoptotic cell. (D) Annexin-V/FITC treated apoptotic HeLa cells before (no trail) and after (+TRAIL) treatment of TRAIL.

To show the feasibility of DEVD-AuNP for the rapid visualization and real-time detection of early apoptosis, the same experimental condition was applied to Annexin V assay (Figure 3D). The commercially available Annexin V-FITC assay was treated after induction of apoptosis in HeLa cells, but the real-time imaging was not possible because the cells should be fixed before treatment of annexin V. Even before the TRAIL was treated, a faint background fluorescenct signal of FITC was observed. After 30 min of TRAIL treatment, the morphology of the cells was slightly changed but a strong FITC signal was not detected. Strong fluorescence of FITC was seen after 60 min of TRAIL when some cells already formed apoptotic bodies. A strong FITC signal was emitted exclusively from them, which was clear 120 min after TRAIL treatment when all of the HeLa cells died from apoptotic cell death. The morphology of FITC fluorescence from the apoptotic bodies was different from that of DEVD-AuNP in Figure 3A of apoptotic HeLa cells. The NIRF of DEVD-AuNP emitted from the inside of the cell due to the uptake by HeLa cells, whereas fluorescence of annexin V was concentrated around the cell membrane because annexin V is combined with phosphatidylserine, which was exposed to the external cellular environment in apoptosis.

In conclusion, the apoptosis was successfully monitored in live cells with a molecular optical imaging technique using AuNP-based NIRF probe. It allowed rapid visualization and

detection of early apoptosis, which was not possible through the conventional apoptosis kits such as Annexin V-FITC. Moreover, the real-time monitoring of caspase activity was enabled because the fluorescence of DEVD-AuNP was activated only by caspase enzyme. In light of its simple, inexpensive, and efficient properties for an apoptosis imaging probe, DEVD-AuNP has great potential in biomedical applications.

ACKNOWLEDGMENT

This research was financially supported by the Real-Time Molecular Imaging Project, GRL Program, M.D.-Ph.D. Program (2010-0019863, 2010-0019864) of MEST, and by a grant (A062254) of the Korea Health 21 R&D Project.

Supporting Information Available: Experimental procedures. This material is available free of charge via the Internet at http://pubs.acs.org.

LITERATURE CITED

(1) Ishaque, A., and Al-Rubeai, M. (2005) Monitoring of apoptosis, In *Cell Engineering* (Al-Rubeai, M., and Fussenegger, M., Eds.) pp 281−306, Kluwer Academic Publishers, Dordrecht.

(2) Vaux, D. L., and Korsmeyer, S. J. (1999) Cell death in development. *Cell 96*, 245–254.

(3) Collins, R. J., Harmon, B. V., Gobe, G. C., and Kerr, J. F. R. (1992) Internucleosomal DNA cleavage should not be the sole criterion for identifying apoptosis. *Int. J. Radiat. Biol. 61*, 451–453.

(4) Enright, H., Hebbel, R. P., and Nath, K. A. (1994) Internucleosomal cleavage of DNA as the sole criterion for apoptosis may be artifactual. *J. Lab. Clin. Med. 124*, 63–68.

(5) van den Eijnde, S. M., van den Hoff, M. J. B., Reutelingsperger, C. P. M., van Heerde, W. L., Henfling, M. E. R., Vermeij-Keers, C., Schutte, B., Borgers, M., and Ramaekers, F. C. S. (2001) Transient expression of phosphatidylserine at cell-cell contact areas is required for myotube formation. *J. Cell Sci. 114*, 3631–3642.

(6) Krysko, O., de Ridder, L., and Cornelissen, M. (2004) Phosphatidylserine exposure during early primary necrosis (oncosis) in JB6 cells as evidenced by immunogold labeling technique. *Apoptosis 9*, 495–500.

(7) Thornberry, N. A., and Lazebnik, Y. (1998) Caspases: Enemies within. *Science 281*, 1312–1316.

(8) Sauerwald, T. M., and Betenbaugh, M. J. (2005) The role of caspases in apoptosis and their inhibition in mammalian cell culture, In *Cell Engineering* (Al-Rubeai, M., and Fussenegger, M., Eds.) pp 181−210, Kluwer Academic Publishers, Dordrecht.

(9) Lee, H., Dellatore, S. M., Miller, W. M., and Messersmith, P. B. (2007) Mussel-inspired surface chemistry for multifunctional coatings. *Science 318*, 426–430.

(10) Mayilo, S., Kloster, M. A., Wunderlich, M., Lutich, A., Klar, T. A., Nichtl, A., Kuürzinger, K., Stefani, F. D., and Feldmann, J. (2009) Long-range fluorescence quenching by gold nanoparticles in a sandwich immunoassay for cardiac troponin T. *Nano Lett. 9*, 4558–4563.

(11) Lee, S., Cha, E.-J., Park, K., Lee, S.-Y., Hong, J.-K., Sun, I.-C., Kim, Sang, Y., Choi, K., Kwon, I. C., Kim, K., and Ahn, C.-H. (2008) A near-infrared-fuorescence-quenched gold-nanoparticle imaging probe for in vivo drug screening and protease activity determination. *Angew. Chem., Int. Ed. 47*, 2804–2807.

(12) Dubertret, B., Calame, M., and Libchaber, A. J. (2001) Single-mismatch detection using gold-quenched fluorescent oligonucleotides. *Nat. Biotechnol. 19*, 365–370.

(13) Lin, J. Q., Zhang, Z. Z., Zeng, S. Q., Zhou, S. X., Liu, B. F., Liu, Q., Yang, J., and Luo, Q. M. (2006) TRAIL-induced apoptosis proceeding from caspase-3-dependent and -independent pathways in distinct HeLa cells. *Biochem. Biophys. Res. Commun. 346*, 1136–1141.

BC1003026

Gold Nanoparticle for Apoptosis Molecular Imaging

In-Cheol Sun, Seulki Lee, Ick Chan Kwon, Cheol-Hee Ahn and Kwangmeyung Kim**

Supporting informations

Experimental methods

Materials. Gold nanoparticles (AuNPs, 0.05 mg Au/ml) with diameters of 20 nm were purchased from Sigma (St. Louis, MO, USA). Protected caspase-3 substrates (DEVD-DOPAKs), Gly-Asp-Glu-Val-Asp-Ala-Pro-DOPA-Lys-DOPA-Lys-DOPA and Cy5.5 mono acid were obtained from Peptron (Daejon, Korea) and Amersham Biosciences (Buchinghamshire, UK) respectively. Tumor necrosis factor-related apoptosis-inducing ligand (TRAIL), Caspase-3 enzyme and its inhibitor, Z-DEVD-FMK, were bought from R&D Systems (Minneapolis, MN, USA). 1-Ethyl-3-(3-dimethylamino-propyl) carbodiimide hydrochloride (EDC), N-hydroxy succinimide (NHS; 98%), diisopropyl-ethylamine (DIPEA), Dimethyl sulfoxide (DMSO), Dimethyl-formamide (DMF), ethyl acetate (EA), HEPES sodium salt hydrate, ethylenediaminetetraacetic acid (EDTA), 3-[(3-cholamidopropyl)-dimethylammonio]-1-propanesulfonic acid (CHAPS) and glycerol(99+%) were acquired from Sigma. Dipyrrolidino (N-succinimidyloxy) carbenium hexafluorophosphate (HSPyU) and sodium chloride (NaCl) were products form Fluka (Milwaukee, WI) and Junsei (Japan), respectively. Water (DW) used in the

experiment was double-distilled and all other chemicals were used as received without any purification.

Preparation of Cy5.5-NHS. Cy5.5 mono acid (100 mg, 0.14 mmol) was dissolved in anhydrous DMSO and DMF (50:50, 7 ml) followed by addition of DIPEA (75 µl). HSPyU (91mg, 0.22 mmol) was added to the reaction mixture and stirred at room temperature in the dark. After 30 minutes, samples were diluted with 0.1M acetic acid for characterization with HPLC (elution: 20% to 40% acetonitrile vs. 0.1M triethyl ammonium acetate (TEAA) in water over 20 minutes at a flow rate of 1.0 ml/min.) After complete activation, the Cy5.5-NHS was precipitated by adding anhydrous EA. The precipitate was washed with EA and dried in vacuum. Purity (> 95%) was confirmed by analytical reversed-phase HPLC (Agilent 1200 series, Agilent Technologies, Palo Alto, CA, USA)

Preparation of Cy5.5-labeled caspase-3 substrate (Cy5.5-DEVD-DOPAK). Cy5.5-NHS (11 mg, 11.2 µmol) was coupled to the N-terminus of the protected DEVD-DOPAK (18 mg, 8.6 µmol) in anhydrous DMF (300 µl) containing N-methyl morpholine and 4-dimethyl amino pyridine at room temperature in the dark with shaking for 2 hours. The Cy5.5-DEVD-DOPAK (protected) product was purified by semi-preparative reversed-phase HPLC; 35% to 100% acetonitrile vs. 0.1M TEAA in water over 20 minutes at a flow rate of 5.0 ml/min. The peptide of purified product was deprotected with anisol (10 µl) and DW(10 µl) in 2 ml of trifluoroacetic acid (TFA). After 1 h of stirring, TFA was evaporated and purified with HPLC under the same condition. Purity (> 95%) was confirmed by analytical reversed-phase HPLC. Eluent was removed by freeze-drying and the mass of product was analyzed with Voyage-DE™ STR matrix-assisted laser desorption ionization with time of flight (MALDI-

TOF) mass spectrometer (Applied Biosystems, Foster City, CA, USA). Mass: calculated/found, 2504/2513.

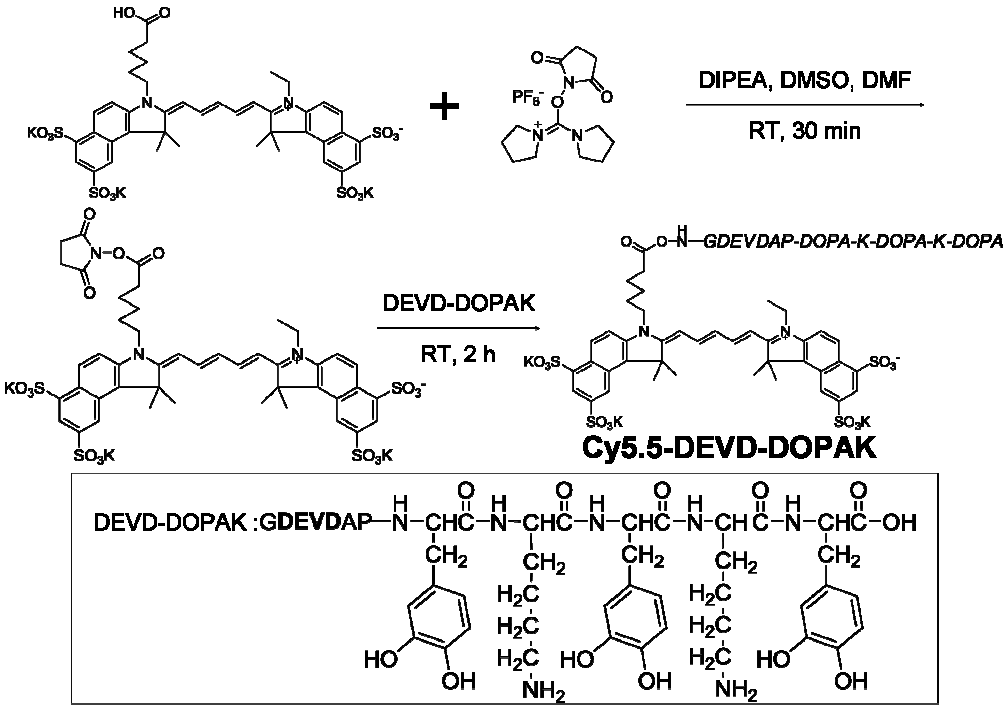


Figure S1. Schematic diagram of synthesis of Cy5.5-NHS and Cy5.5-labeled caspase-3 substrate (Cy5.5-DEVD-DOPAK)

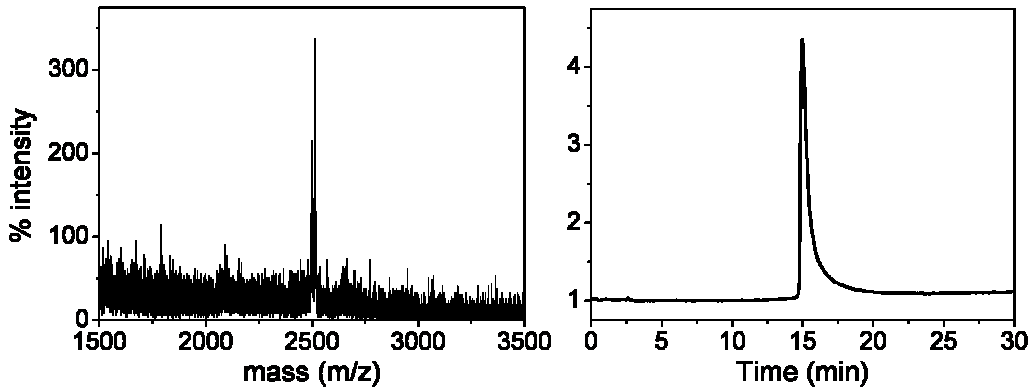


Figure S2. MALDI-TOF mass spectrum and HPLC chromatogram of Cy-DEVD-DOPAK after deprotection

Preparation of Cy5.5-DEVD-DOPAK coated AuNPs probe (DEVD-AuNPs).

Cy5.5-labeled caspase-3 substrate (Cy5.5-DEVD-DOPAK) was used to coat AuNPs by

simple mixing method. Briefly, 0.1 ml of Cy5.5-DEVD-DOPAK (100 μg/ml) solution was added dropwise to 5 ml citrated reduced gold colloid. The solution was kept in the absence of light at 25°C under stirring for 12 h. After the reaction, the solution was centrifuged (12000 rpm, 12 min) and washed with DW 3 times to remove free Cy5.5-DEVD-DOPAK. For *in vitro* enzyme test, the DEVD-AuNPs were resuspended in caspase buffer containing 50mM HEPES, 100 mM NaCl, 1 mM EDTA, 10 % glycerol and 0.1 % CHAPS and sonicated for 1 min to keep the nanoparticles uniformly dispersed. Finally the dispersed DEVD-AuNPs were stored at 4 °C before use.

Characterization of DEVD-AuNPs. The amount of Cy5.5-DEVD-DOPAK on the AuNPs surface was calculated by measuring the fluorescence signal intensity of unreacted Cy5.5-DEVD-DOPAK before and after coating process and it was compared with standard curve of Cy5.5. The fluorescence was measured with F-7000 fluorescence spectrometer (Hitachi, Tokyo, Japan). The excitation wavelength was fixed at 675 nm and emission spectra recorded from 680 to 800 nm. Under the optimal condition, 1.2×10^2 molecules of Cy5.5-DEVD-DOPAK were attached onto each AuNP particle. The spherical morphology and particle dispersion of the DEVD-AuNPs was determined by transmission electron microscopy (TEM). The TEM images were obtained from JEM-3010 (JEOL, Tokyo, Japan) operating at 300 kV. The TEM samples were prepared on the carbon-coated, 200-mesh copper grids and dried in a vacuum oven for 24 h. The size and its distributions of DEVD-AuNPs in DW were measured with dynamic light scattering (DLS) using ELS-Z2 (Otsuka, Osaka, Japan). UV-vis spectra were recorded from Optizen 2120UV (Mecasys, Daejeon, Korea) which scanned over the range of 300 ~ 700 nm.

***In vitro* enzyme test**

In vitro enzyme test was performed in caspase buffer containing HEPES (50 mM), NaCl (100 mM), EDTA (1 mM), glycerol (10% v/v) and CHAPS (0.1 % v/v) without DTT. The detection sensitivity of DEVD-AuNP probe was studied with different concentration of caspase-3 and DEVD-AuNP. DEVD-AuNP probe was examined in a 1 ml cuvette by co-incubating AuNP probe (0.5 mg Au/ml) with 1.6, 3.1, ,6.3, 13, 25 and

50 nM of caspase-3, respectively. Also 50 nM of caspase-3 enzyme was activated in 0.05, 0.25, 0.5, 1 and 1.5 mg Au/ml of DEVD-AuNP colloid. The fluorescence signal was detected with with fluorescence spectrometer. Optical NIRF imaging was performed using a Kodak Image Station 4000MM Digital Imaging System (Kodak, New Haven, CT, USA) consisting of a light-tight box equipped with a 150 W halogen lamp and an excitation filter system for Cy5.5 (Omega optical, Brattleboro, VT, USA).

Cell imaging. HeLa cells (obtained from ATCC, Rockville, MD, USA) were cultured in Dubecco's modified Eagle's medium (DMEM; Gibco, Grand Island, NY, USA) containing 10% (v/v) FBS (Gibco) and 1% (w/v) penicillin/streptomycin at 37 °C in a humidified atmosphere of 5 % CO_2. Cells were seeded at a density of 5×10^4 cells/dish in 35-mm coverglass-bottom dishes (SPL Life Sciences, Seoul, Korea) and allowed to adhere for 2 days. The cells were washed twice with phosphate-buffered saline (PBS) and 1.8 ml of DMEM (without FBS) was replenished before addition of 0.2 ml of DEVD-AuNPs (0.25 mg Au/ml). After 30 min of incubation at 37 °C, the medium was aspirated and the cells were washed twice with PBS to remove excess nanoparticles. TRAIL dissolved in DMEM (with FBS, AA) was treated to HeLa cells for induction of apoptosis. Final concentration of TRAIL and DEVD-AuNP were 300 ng/ml (13 M) and 0.025 mg Au/ml, respectively. As a control, cells were incubated with 1.34 μg (100 μM) of caspase-3 inhibitor Z-DEVD-FMK before uptake of nanoparticles. The sample was observed through IX81 fluorescence microscope (Olympus, Tokyo, Japan) equipped with a dark-field condenser.

Annexin V assay. Annexin V-FITC fluorescence microscopy kit (BD Bioscience, San Jose, CA, USA) was used according to the protocol provided by manufacturer. Briefly, apoptotic HeLa cells were washed once with Annexin V Binding Buffer after fixation. Then, the cells were stained with Annexin V-FITC solution for 10 min. The Annexin V-FITC solution was removed and washed with Binding Buffer once for the observation under the microscopy. The cells were visualized with excitation at 488 nm and emission at 530 nm.

Synthesis of N-Terminally Linked Protein and Peptide Dimers by Native Chemical Ligation

Junpeng Xiao,[†] Brian S. Hamilton,[†] and Thomas J. Tolbert*[,†,‡]

Interdisciplinary Biochemistry Graduate Program and Department of Chemistry, Indiana University, Bloomington, Indiana 47405, United States. Received August 12, 2010; Revised Manuscript Received October 6, 2010

Dimerization can be utilized to double the molecular weight of proteins and peptides and potentially increase their avidity of binding to target receptors. These dimerization effects may be utilized to increase in vivo half-lives in a manner similar to PEGylation and may also improve biological activity. In this paper, we report a new strategy for the synthesis of N-terminally linked protein and peptide homodimers utilizing native chemical ligation to conjugate a short dithioester linker to the N-terminal cysteines of protein and peptide monomers to form dimers in a single step. This strategy is general and has been applied to the production of dimers from three recombinantly expressed polypeptides, the IgG binding domain Protein G, an HIV entry inhibitor peptide C37H6, and human interleukin-1 receptor antagonist (IL-1ra). The biological activities of the C37H6 and IL-1ra dimers produced by these methods were retained or even slightly increased when compared to their corresponding monomers.

Dimeric forms of proteins and peptides play important roles in biological systems by participating in many processes including signal transduction, gene expression, enzyme regulation, and viral inhibition (*1*−*7*). One effect of dimerization of monomeric ligands is that it can increase the avidity of binding of ligands to receptors through divalent interactions, which when applied to proteins and peptides can contribute to increased biological activity (*2*). For example, anti-HIV infection activity has been enhanced by dimerization of protein ligands which bind to the HIV envelope glycoprotein gp120, such as the synthetic CD4-mimetic miniprotein CD4M9 (*8*) and the recombinant mannose binding protein cyanovirin-N (*9*). In addition to increasing avidity of binding, dimerization of proteins and peptides also doubles their molecular weight, and consequently can increase their in vivo half-lives in a manner similar to PEGylation. Although PEGylation can dramatically increase the circulation half-life of protein and peptide drugs (*10, 11*), it also has some drawbacks. PEGylation often results in a loss of binding affinity and biological activity due to steric interference of the PEG polymer (*12, 13*). Also, accumulation of large quantities of PEG in vivo can induce the formation of anti-PEG antibodies, which accelerate the clearance of PEGylated proteins (*14, 15*), and may also have long-term detrimental effects (*16*). In contrast to PEGylation, dimerization of proteins and peptides with a short synthetic linker can potentially increase in vivo half-lives by doubling molecular weight, while also maintaining or even increasing biological activity through divalent interactions. Replacement of a large PEG modification with a short linker also minimizes the potential for anti-PEG antibody formation. Because of this, there is significant interest in the development of general methods for the synthesis of dimeric proteins and peptides.

Several solid-phase peptide synthesis based approaches have been developed to form peptide dimers and even dendrimers through triazole (*17*), oxime (*18*), disulfide (*19*), thioether (*8, 20*), and thiazolidine forming reactions (*21*). However, triazole and oxime formation requires non-natural amino acids, and disulfide and thioether formation has no selectivity on proteins which contain multiple cysteine residues. Although thiazolidine formation is selective for N-terminal cysteines, the reaction is usually performed at acidic pH in an organic/water cosolvent for best efficiency, and under these reaction conditions, proteins may be denatured (*21, 22*). Consequently, the application of these approaches is limited to small synthetic peptides and single cysteine containing proteins. To expand dimer formation beyond small synthetic peptides, Kent and co-workers have utilized chemoselective thioester formation and disulfide bond formation to produce chemically synthesized tethered dimers of HIV-1 protease, where the C-terminus of one monomer is linked to the N-terminus of the second monomer through a disulfide bond (*23*). They have recently expanded this methodology by applying native chemical ligation in a convergent synthesis to link four synthetic peptides to form a "covalent dimer" of HIV-1 protease where the monomers are linked C to N with native peptide bonds (*24*). The C to N linkages of the HIV-1 protease dimers produced by the Kent lab are the same linkages that would occur in a recombinantly expressed dimer, but with the possibility of incorporating synthetic modifications selectively into the protein backbone (*25*). Dimer formation has also been applied to large recombinant proteins which contain multiple cysteine residues by utilizing expressed protein ligation (*26*) to prepare C-terminally conjugated recombinant protein dimers or dendrimers (*27, 28*). This approach produces C-terminally linked dimers, but not all proteins and peptides are suitable for conjugation at the C-terminus. For instance, conjugation at the C-terminus of HIV entry inhibitor peptide T20 significantly decreased its antiviral activity, whereas retention of antiviral activity was observed when it is conjugated at the N-terminus (*29*).

Previously, we reported a strategy to produce N-terminally linked expressed protein dimers and trimers using a combination of native chemical ligation and Cu(I)-catalyzed azide−alkyne cycloaddition click chemistry (CuAAC) (*30*). This strategy is useful for the synthesis of expressed protein heterodimers that are usually difficult to prepare using other strategies, but it also has some disadvantages. First, it requires two steps: (1) incorporation of azide and alkyne groups onto a protein's

* To whom correspondence should be addressed. Thomas J. Tolbert, Department of Chemistry, 800 E. Kirkwood Ave., Indiana University, Bloomington, IN 47405. E-mail: tolbert@indiana.edu. Tel: 812-856-1887. Fax: 812-855-8300.

[†] Interdisciplinary Biochemistry Graduate Program.

[‡] Department of Chemistry.

10.1021/bc100370j © 2010 American Chemical Society
Published on Web 10/25/2010

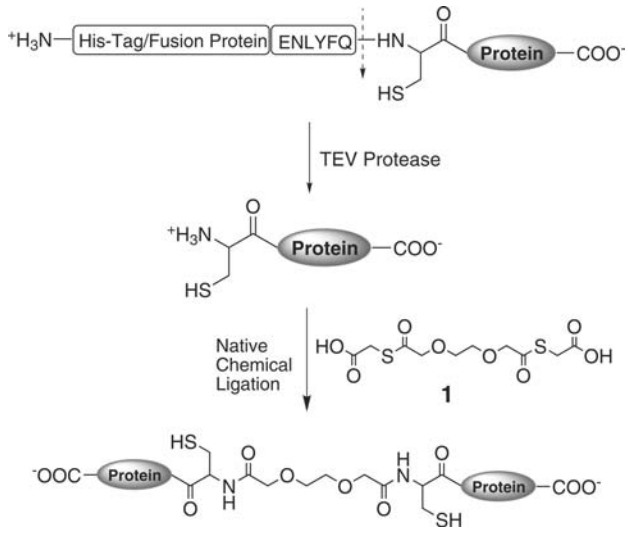


Figure 1. Strategy for the synthesis of expressed protein dimer.

N-terminus using native chemical ligation and (2) coupling of the azide and alkyne monomers together through CuAAC to form the triazole linked dimer. A second disadvantage is the use of copper in CuAAC, which may cause methionine oxidation and which we have also observed to cause difficulties when applied to triazole formation with proteins containing multiple cysteine residues (unpublished observations). Herein, we develop a more general and straightforward single-step strategy for the synthesis of N-terminally linked protein homodimers using native chemical ligation. This strategy utilizes native chemical ligation (*31*) to conjugate a monoethylene glycol dithioester linker to the N-terminal cysteines of two protein monomers forming a dimer linked together by stable peptide bonds. Native chemical ligation is a highly selective reaction between a thioester and a N-terminal cysteine, and internal cysteines do not interfere with this reaction. Thus, this strategy is general and can be applied to both small peptides and large proteins containing multiple cysteines.

In our strategy, a target protein is first recombinantly expressed as a fusion protein that contains a tobacco etch virus NIa (TEV) protease cleavage sequence between a His-tag or fusion partner and the target protein. TEV protease cleavage of the fusion protein produces the target protein with a N-terminal cysteine (*32*). The N-terminal cysteines of two protein monomers are then conjugated together with a monoethylene glycol dithioester linker via native chemical ligation to form the N-terminally linked homodimer (Figure 1). During native chemical ligation, the internal cysteines are unreactive, and therefore, our strategy can be applied to expressed peptides and proteins containing single or multiple cysteine residues.

A sequential two-step ligation strategy (ligation of one protein onto one end of the dithioester linker first, purification, and then ligation of the second protein onto the other end) is not suitable for the dithioester linker because thioester moieties are hydrolytically labile. Because of this, the second thioester would be hydrolyzed to a carboxylic acid before it could be utilized to form a dimer. Thus, a one-step synthesis strategy was investigated for dimer formation using dithioester linkers. In this strategy, excess protein rather than the dithioester linker was used to force the protein to be ligated onto the both ends of the dithioester linker simultaneously.

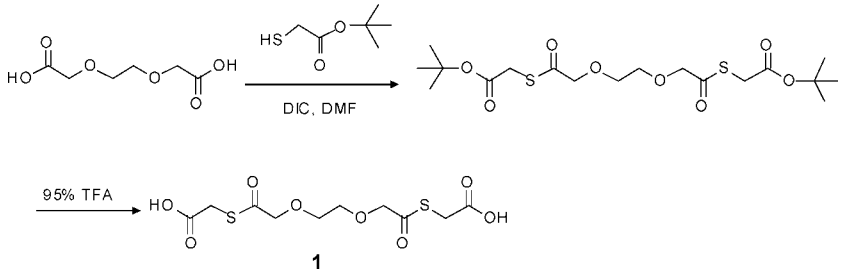
Synthesis of the monoethylene glycol dithioester linker **1** was accomplished by coupling 3,6-dioxaoctanedioic acid with 4 equiv of *t*-butyl mercaptoacetate using 4 equiv of 1,3-diisopropylcarbodiimide as the coupling reagent. This formed a *t*-butyl protected dithioester linker, which was purified by flash chromatography. The *t*-butyl protecting group was then removed by treatment with 95% trifluoroacetic acid and purified by reverse-phase HPLC to afford the dithioester linker **1** with an overall 28% yield (Scheme 1).

To work out the one-step dimer synthesis strategy, a small protein, the C2 domain of Protein G, which is an immunoglobulin-binding protein found in group G streptococci (*33*), was chosen as a model protein. Protein G was expressed as a fusion protein with a TEV protease cleavable His-tag in *E. coli* (*34*). After purification by Ni^{2+}-NTA affinity chromatography, the fusion protein was concentrated to 6 mg/mL (0.5 mM) and treated with TEV protease at room temperature for 24 h to generate the desired Protein G with a N-terminal cysteine. The cleaved Protein G was then dialyzed against ligation buffer (5 mM betaine, 20 mM sodium phosphate at pH 7.5) at 4 °C overnight and used directly in the dimer formation reaction without further purification.

The dimer formation reaction was carried out by incubation of 4 mL of 0.5 mM cleaved Protein G solution with 0.25 equiv of dithioester linker **1** (50 μL of 10 mM stock solution) and 30 mM sodium 2-mercaptoethanesulfonate at room temperature. The reaction was quenched by addition of 10 mM DTT after 24 h. The resulting Protein G dimer was separated from the excess Protein G monomer by size exclusion chromatography. After purification, 4.2 mg of Protein G dimer was obtained, giving a 62% yield based on the amount of **1** as the limiting reagent. The Protein G dimer was characterized by SDS-PAGE and ESI-MS analysis. On the SDS-PAGE gel (Figure 2, lane 2), only one band appeared after size exclusion chromatography, indicating that the protein G dimer is pure after size exclusion chromatography. The expected molecular weight of the Protein G dimer is 13 615 Da. Although the Protein G dimer migrated between the 20.0 kDa and 14.3 kDa protein markers on the SDS-PAGE gel, the ESI-MS analysis of the Protein G dimer gave a molecular weight of 13 614 Da, which is consistent with the expected molecular weight (Figure 3A and Supporting Information Figure S4). All these results indicated that the desired Protein G dimer was formed and was pure.

Since the one-step dimer synthesis strategy worked well on the small model Protein G, we went further and applied this strategy to a smaller biologically active peptide, C37H6, and a larger biologically active protein, interleukin-1 receptor antagonist (IL-1ra). C37H6 is an HIV entry inhibitor peptide derived

Scheme 1. Synthesis of the Monoethylene Glycol Dithioester Linker 1



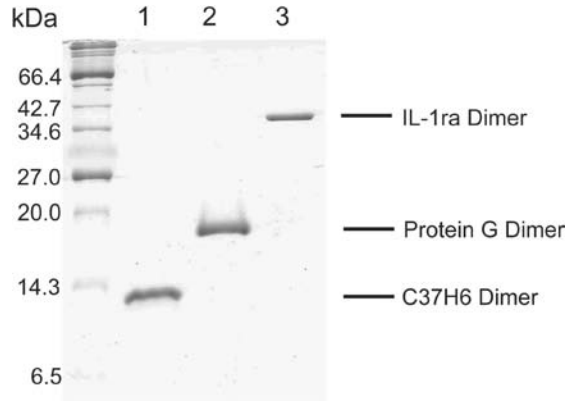


Figure 2. SDS-PAGE of purified dimers: (lane 1) C37H6 dimer, (lane 2) Protein G dimer, (lane 3) IL-1ra dimer.

from the HIV gp41 (*35*, *36*). IL-1ra is an inhibitor of the proinflammatory action of interleukin-1 and has been used as a drug for the treatment of rheumatoid arthritis (*37*, *38*). The cys-IL-1ra protein used in this paper also contains four cysteine residues and so allowed us to test this one-step dimer synthesis approach with a multicysteine containing protein.

The C37H6 peptide was expressed and purified as a fusion protein with xanthine-guanine phosphoriboysyltransferase (GPRT) as described previously (*36*). After purification, the GPRT-C37H6 fusion protein was concentrated to 12 mg/mL (0.5 mM) and treated with TEV protease to generate N-terminal cysteine containing C37H6. Next, 4 mL of the 0.5 mM cleaved C37H6 was incubated for 24 h with 0.25 equivalents of **1** (50 μL of 10 mM stock solution) in the presence of 30 mM sodium 2-mercaptoethanesulfonate. The resulting C37H6 dimer was purified by size exclusion chromatography, yielding 3.2 mg of the C37H6 dimer (56% yield). ESI-MS analysis (Figure 3B and Supporting Information Figure S5) of the C37H6 dimer gave only one molecular weight of 11 397 Da, which is consistent with the expected molecular weight of 11 398 Da. The SDS-PAGE gel also showed only one band that migrated to the approximate mass of the product. Thus, the desired, pure C37H6 dimer was also produced using this strategy.

In a manner similar to that for Protein G, the IL-1ra protein was also expressed and purified as a fusion protein with a TEV protease cleavable His-tag and concentrated to 0.5 mM (11 mg/mL). TEV protease cleavage and the dimer formation reaction to form an IL-1ra dimer were carried out as reported for Protein G. However, size exclusion chromatography purification did not separate the IL-1ra dimer from monomer well. Therefore, a SP-sepharose anion exchange column was applied twice to completely separate the IL-1ra dimer from the excess monomer and resulted in 4.9 mg of purified product (28% yield). ESI-MS analysis (Figure 3C and Supporting Information Figure S6) of IL-1ra dimer gave a molecular weight of 35 061 Da, which is consistent with the expected molecular weight of 35 057 Da. The SDS-PAGE gel also demonstrated that the IL-1ra dimer was pure. All these results demonstrated that our protein dimer synthesis strategy can be applied to both expressed small peptides and large proteins.

To determine if dimer formation altered the biological activities of C37H6 and IL-1ra, biological assays of HIV entry inhibition and IL-1ra antagonism of the IL-1 receptor were conducted. The inhibitory activities of the C37H6 monomer and dimer were examined using a luciferase based cell−cell fusion inhibition assay (*39*). In this assay, fusion between HL2/3 cells and TZM-bl cells was inhibited by C37H6 peptides which resulted in a decrease of luciferase activity (Figure 4A). On the basis of three independent assays, the C37H6 dimer showed an IC_{50} value of 2.33 ± 0.08 nM, which is 1.9-fold more potent

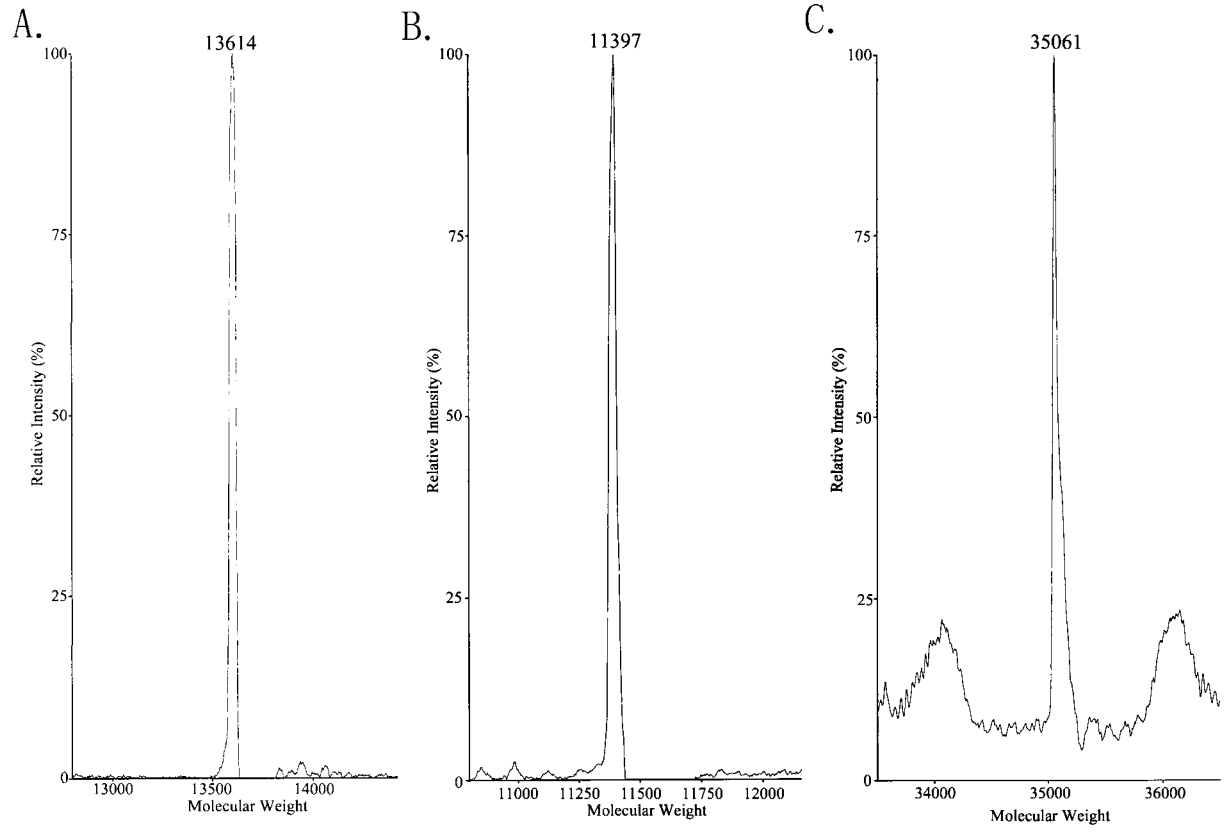


Figure 3. Reconstructed ESI mass spectra of (A) Protein G dimer, calcd 13 615 Da, found 13 614 Da; (B) C37H6 dimer, calcd 11 398 Da, found 11 397 Da; (C) IL-1ra dimer, calcd 35 057 Da, found 35 061 Da.

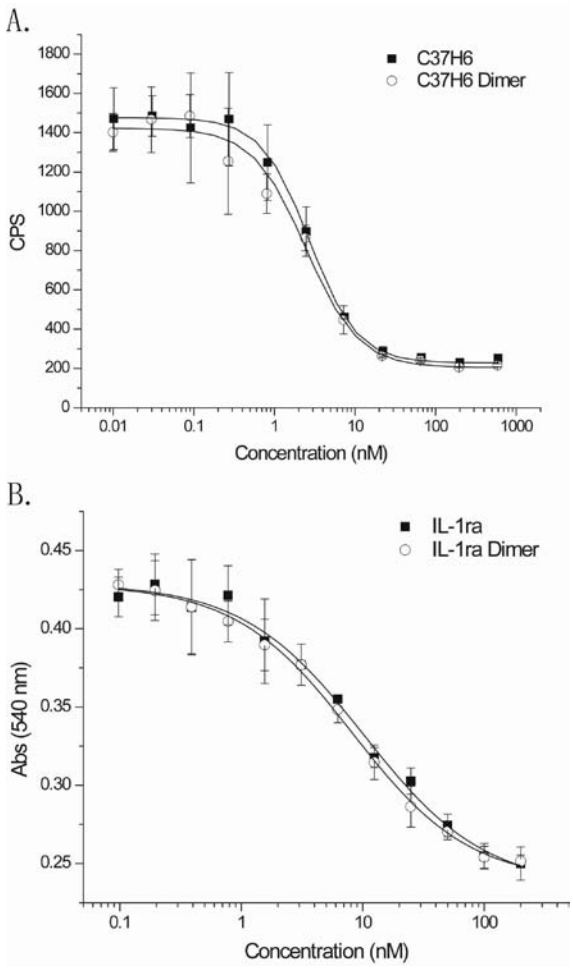


Figure 4. (A) Results from a typical cell−cell fusion inhibition assay of C37H6 monomer (solid square) and C37H6 dimer (open circle); (B) results from a typical competition assay of interleukin-1β induced proliferation with the IL-1ra monomer (solid square) and IL-1ra dimer (open circle).

than the C37H6 monomer (IC_{50}: 4.40 ± 0.10 nM). The biological activities of the IL-1ra monomer and dimer were determined using a proliferation assay, in which the interleukin-1β induced proliferation of the mouse D10.G4.1 T cell line was inhibited by IL-1ra proteins (Figure 4B) (*40*). The IL-1ra dimer resulted in an IC_{50} value of 7.63 ± 0.62 nM and the activity is similar (1.2-fold more potent than) to the monomeric IL-1ra (IC_{50}: 9.02 ± 1.11 nM). The dimer formation only slightly increased the activity of the C37H6 and IL-1ra dimers, which might due to the short linker length of **1**. Their activities might be improved more by using longer PEG linkers. Additionally, dimer formation doubled their molecular weights from 5628 Da and 17 458 Da to 11 398 Da and 35 057 Da for C37H6 and IL-1ra, respectively. In the case of IL-1ra, the increased molecular weight of the IL-1ra dimer could potentially slow down the glomerular filtration by the kidney and consequently increase its in vivo half-live.

In conclusion, a strategy for the synthesis of N-terminally linked dimeric expressed proteins and peptides was developed. This one-step strategy utilizes native chemical ligation to conjugate the N-terminal cysteine of two proteins together through a monoethylene glycol dithioester linker with a stable peptide bond linkage. The strategy is highly efficient in aqueous solution at neutral pH and can be applied to both small peptides and large proteins. It also works with proteins that contain multiple cysteine residues, as demonstrated by the synthesis of the IL-1ra dimer. Slightly increased activity of the dimeric forms of C37H6 and IL-1ra were observed in bioassays. Although the activities of the C37H6 dimer and IL-1ra dimer were not increased greatly, the linker could be easily altered by using a longer PEG linker to potentially improve their biological activities. Moreover, dimer formation doubles the molecular weight of bioactive peptides and proteins with a minimal ethylene glycol synthetic modification, which could potentially increase in vivo half-lives of proteins without forming anti-PEG antibodies.

ACKNOWLEDGMENT

We gratefully acknowledge Dr. Vasily Gelfanov and Dr. Richard DiMarchi for cell culture discussions and facilities. The following reagents were obtained through the AIDS Research and Reference Reagent Program, Division of AIDS, NIAID, NIH: HL2/3 from Dr. Barbara K. Felber and Dr. George N. Pavlakis; TZM-bl from Dr. John C. Kappes, Dr. Xiaoyun Wu, and Tranzyme Inc. This work was supported by Indiana University.

Supporting Information Available: Experimental procedures, ^{1}H and ^{13}C NMR spectra of the dithioester linker **1**, ESI-MS of Protein G dimer, C37H6 dimer and IL-1ra dimer. This material is available free of charge via the Internet at http://pubs.acs.org.

LITERATURE CITED

(1) Klemm, J. D., Schreiber, S. L., and Crabtree, G. R. (1998) Dimerization as a regulatory mechanism in signal transduction. *Annu. Rev. Immunol. 16*, 569–592.
(2) Mammen, M., Choi, S.-K., and Whitesides, G. M. (1998) Polyvalent interactions in biological systems: implications for design and use of multivalent ligands and inhibitors. *Angew. Chem., Int. Ed. 37*, 2754–2794.
(3) Marianayagam, N. J., Sunde, M., and Matthews, J. M. (2004) The power of two: protein dimerization in biology. *Trends Biochem. Sci. 29*, 618–625.
(4) Casado, V., Cortes, A., Mallol, J., Perez-Capote, K., Ferre, S., Lluis, C., Franco, R., and Canela, E. I. (2009) GPCR homomers and heteromers: a better choice as targets for drug development than GPCR monomers? *Pharmacol. Ther. 124*, 248–257.
(5) Amoutzias, G. D., Robertson, D. L., Van de Peer, Y., and Oliver, S. G. (2008) Choose your partners: dimerization in eukaryotic transcription factors. *Trends Biochem. Sci. 33*, 220–229.
(6) Wang, J., Chun, H. J., Wong, W., Spencer, D. M., and Lenardo, M. J. (2001) Caspase-10 is an initiator caspase in death receptor signaling. *Proc. Natl. Acad. Sci. U.S.A. 98*, 13884–13888.
(7) Renatus, M., Stennicke, H. R., Scott, F. L., Liddington, R. C., and Salvesen, G. S. (2001) Dimer formation drives the activation of the cell death protease caspase 9. *Proc. Natl. Acad. Sci. U.S.A. 98*, 14250–14255.
(8) Li, H., Song, H., Heredia, A., Le, N., Redfield, R., Lewis, G. K., and Wang, L. X. (2004) Synthetic bivalent CD4-mimetic miniproteins show enhanced anti-HIV activity over the monovalent miniprotein. *Bioconjugate Chem 15*, 783–789.
(9) Matei, E., Zheng, A., Furey, W., Rose, J., Aiken, C., and Gronenborn, A. M. (2010) Anti-HIV activity of defective cyanovirin-N mutants is restored by dimerization. *J. Biol. Chem. 285*, 13057–13065.
(10) Hamidi, M., Azadi, A., and Rafiei, P. (2006) Pharmacokinetic consequences of pegylation. *Drug Delivery 13*, 399–409.
(11) Veronese, F. M., and Mero, A. (2008) The impact of PEGylation on biological therapies. *BioDrugs 22*, 315–329.
(12) Fishburn, C. S. (2008) The pharmacology of PEGylation: balancing PD with PK to generate novel therapeutics. *J. Pharm. Sci. 97*, 4167–4183.
(13) Pisal, D. S., Kosloski, M. P., and Balu-Iyer, S. V. Delivery of therapeutic proteins. *J. Pharm. Sci. 99*, 2557–2575.

(14) Cheng, T. L., Wu, P. Y., Wu, M. F., Chern, J. W., and Roffler, S. R. (1999) Accelerated clearance of polyethylene glycol-modified proteins by anti-polyethylene glycol IgM. *Bioconjugate Chem. 10*, 520–528.

(15) Sroda, K., Rydlewski, J., Langner, M., Kozubek, A., Grzybek, M., and Sikorski, A. F. (2005) Repeated injections of PEG-PE liposomes generate anti-PEG antibodies. *Cell Mol. Biol. Lett. 10*, 37–47.

(16) Webster, R., Elliott, V., Park, B. K., Walker, D., Hankin, M., and Taupin, P. (2009) PEG and PEG conjugates toxicity: towards an understanding of the toxicity of PEG and its relevance to PEGylated biologicals, in *PEGylated Protein Drugs: Basic Science and Clinical Applications* (Veronese, F. M., Ed.) pp 127−146, Birkhäuser Basel, Boston, Berlin.

(17) Franke, R., Doll, C., and Eichler, J. (2005) Peptide ligation through click chemistry for the generation of assembled and scaffolded peptides. *Tetrahedron Lett. 46*, 4479–4482.

(18) Canne, L. E., Ferre- D'Amare, A. R., Burley, S. K., and Kent, S. B. H. (1995) Total chemical synthesis of a unique transcription factor-related protein: cMyc-Max. *J. Am. Chem. Soc. 117*, 2998–3007.

(19) Yang, R., Yang, J., and Weliky, D. P. (2003) Synthesis, enhanced fusogenicity, and solid state NMR measurements of cross-linked HIV-1 fusion peptides. *Biochemistry 42*, 3527–3535.

(20) Morii, T., Saimei, Y., Okagami, M., Makino, K., and Sugiura, Y. (1997) Factors governing the sequence-selective DNA binding of geometrically constrained peptide dimers. *J. Am. Chem. Soc. 119*, 3649–3655.

(21) Tam, J. P., and Yu, Q. (2002) A facile ligation approach to prepare three-helix bundles of HIV fusion-state protein mimetics. *Org. Lett. 4*, 4167–4170.

(22) Rao, C., and Tam, J. P. (1994) Synthesis of peptide dendrimer. *J. Am. Chem. Soc. 116*, 6975–6976.

(23) Baca, M., Muir, T. W., Schnoelzer, M., and Kent, S. B. H. (1995) Chemical ligation of cysteine-containing peptides: synthesis of a 22 kDa tethered dimer of HIV-1 protease. *J. Am. Chem. Soc. 117*, 1881–1887.

(24) Torbeev, V. Y., and Kent, S. B. (2007) Convergent chemical synthesis and crystal structure of a 203 amino acid "covalent dimer" HIV-1 protease enzyme molecule. *Angew. Chem., Int. Ed. 46*, 1667–1670.

(25) Baca, M., and Kent, S. B. H. (2000) Protein backbone engineering through total chemical synthesis: new insight into the mechanism of HIV-1 protease catalysis. *Tetrahedron 56*, 9503–9513.

(26) Muir, T. W., Sondhi, D., and Cole, P. A. (1998) Expressed protein ligation: a general method for protein engineering. *Proc. Natl. Acad. Sci. U.S.A. 95*, 6705–6710.

(27) van Baal, I., Malda, H., Synowsky, S. A., van Dongen, J. L., Hackeng, T. M., Merkx, M., and Meijer, E. W. (2005) Multivalent peptide and protein dendrimers using native chemical ligation. *Angew. Chem., Int. Ed. 44*, 5052–5057.

(28) Ziaco, B., Pensato, S., D'Andrea, L. D., Benedetti, E., and Romanelli, A. (2008) Semisynthesis of dimeric proteins by expressed protein ligation. *Org. Lett. 10*, 1955–1958.

(29) Stoddart, C. A., Nault, G., Galkina, S. A., Thibaudeau, K., Bakis, P., Bousquet-Gagnon, N., Robitaille, M., Bellomo, M., Paradis, V., Liscourt, P., Lobach, A., Rivard, M. E., Ptak, R. G., Mankowski, M. K., Bridon, D., and Quraishi, O. (2008) Albumin-conjugated C34 peptide HIV-1 fusion inhibitor: equipotent to C34 and T-20 in vitro with sustained activity in SCID-hu Thy/Liv mice. *J. Biol. Chem. 283*, 34045–34052.

(30) Xiao, J., and Tolbert, T. J. (2009) Synthesis of N-terminally linked protein dimers and trimers by a combined native chemical ligation-CuAAC click chemistry strategy. *Org. Lett. 11*, 4144–4147.

(31) Dawson, P. E., Muir, T. W., Clark-Lewis, I., and Kent, S. B. (1994) Synthesis of proteins by native chemical ligation. *Science 266*, 776–779.

(32) Tolbert, T. J. and Wong, C. H. (2002) New methods for proteomic research: preparation of proteins with N-terminal cysteines for labeling and conjugation. *Angew. Chem., Int. Ed. 41*, 2171−2174.

(33) Sauer-Eriksson, A. E., Kleywegt, G. J., Uhlen, M., and Jones, T. A. (1995) Crystal structure of the C2 fragment of streptococcal protein G in complex with the Fc domain of human IgG. *Structure 3*, 265–278.

(34) Xiao, J., and Tolbert, T. J. (2009) Synthesis of polymerizable protein monomers for protein-acrylamide hydrogel formation. *Biomacromolecules 10*, 1939–1946.

(35) Root, M. J., Kay, M. S., and Kim, P. S. (2001) Protein design of an HIV-1 entry inhibitor. *Science 291*, 884–888.

(36) Tolbert, T. J., Franke, D., and Wong, C. H. (2005) A new strategy for glycoprotein synthesis: ligation of synthetic glycopeptides with truncated proteins expressed in E. coli as TEV protease cleavable fusion protein. *Bioorg. Med. Chem. 13*, 909–915.

(37) Calabrese, L. H. (2002) Anakinra treatment of patients with rheumatoid arthritis. *Ann. Pharmacother. 36*, 1204–1209.

(38) Hamilton, B. S., Brede, Y., and Tolbert, T. J. (2008) Expression and characterization of human glycosylated interleukin-1 receptor antagonist in Pichia pastoris. *Protein Expr. Purif. 59*, 64–68.

(39) Wexler-Cohen, Y., and Shai, Y. (2007) Demonstrating the C-terminal boundary of the HIV 1 fusion conformation in a dynamic ongoing fusion process and implication for fusion inhibition. *FASEB J. 21*, 3677–3684.

(40) Takii, T., Honda, H., Sasayama, S., Kobayashi, T., Ikezawa, H., Udaka, S., Oomoto, Y., and Onozaki, K. (1999) Human interleukin-1 receptor antagonist: large-scale expression in Bacillus brevis 47−5Q. *J. Interferon Cytokine Res. 19*, 1325–1331.

BC100370J

SUPPORTING INFORMATION

Synthesis of N-terminally Linked Protein and Peptide Dimers by Native Chemical Ligation

Junpeng Xiao,[†] Brian S. Hamilton,[†] and Thomas J. Tolbert*[,†,‡]

Interdisciplinary Biochemistry Graduate Program[†] and Department of Chemistry[‡],

Indiana University, Bloomington, Indiana 47405

List of Contents

Experimental Procedures

Figure S1. Analytical HPLC trace of Mono-Ethylene Glycol Dithioester Linker **1**.

Figure S2. ^{1}H NMR (300 MHz, D_2O) spectra of **1**

Figure S3. ^{13}C NMR (300 MHz, D_2O) spectra of **1**

Figure S4. ESI-MS of Protein G dimer

Figure S5. ESI-MS of C37H6 dimer

Figure S6. ESI-MS of IL-1ra dimer

Materials. 3,6-Dioxaoctanedioic acid, 1,3-diisopropylcarbodiimide (DIC), betaine, and sodium 2-mercaptoethanesulfonate were purchased from Sigma-Aldrich. Anhydrous solvents were purchased and used without purification. Dulbecco's modified Eagle's medium (DMEM), RPMI 1640 medium, fetal bovine serum (FBS), penicillin, and streptomycin were obtained from Hyclone Laboratories, Inc. ^{1}H and ^{13}C NMR spectra were recorded on a 300 MHz Varian Gemini 2000 NMR spectrometer. High resolution CI mass spectrometry was performed on a Thermo Electron Corporation MAT 95XP-Trap. Low resolution ESI mass spectrometry was performed on a PE Sciex API III.

Synthesis of Mono-Ethylene Glycol Dithioester Linker 1, 4,11-Dioxo-6,9-dioxa-3,12-dithiatetradecane-1,14-dioic acid. 3,6-Dioxaoctanedioic acid (178 mg, 1.0 mmol), *t*-butyl mercaptoacetate (*1*) (593 mg, 4.0 mmol) and DIC (505 mg, 4.0 mmol) were dissolved in DMF anhydrous (10 mL). After stirring at room temperature for 24 h under N_2, the solvent was removed by rotavapor. The residue was purified by flash chromatography (ethyl acetate/hexane 20:80). After removal of solvents, the residue was dissolved in 95% TFA (10 mL) and stirred at room temperature for 30 min. The TFA and water were then azeotroped with toluene by rotavapor and the residue was purified by C18 reverse phase HPLC (Alltech Hyper Prep C18 column, 10 mm I.D., 250 mm length, gradient 5-75% acetonitrile in H_2O, 0.1% TFA over 40 min with a flow rate of 4 mL/min, detection at 220 nm), affording 90 mg of the dithioester PEG linker **1** as a colorless oil (28% yield). ^{1}H NMR (300 MHz, D_2O): δ 4.21 (s, 4H), δ 3.71 (s, 4H), δ 3.61 (s, 4H; ^{13}C NMR (300 MHz, D_2O): δ 202.53,

173.50, 75.56, 71.49, 30.91; HR-CI-MS (m/z): calcd for $C_{10}H_{15}O_8S_2$ $(M+H)^+$ 327.0203, obsd 327.0205.

Expression and Purification of GRT-C37H6 and Protein G Fusion Protein. The GPRT-C37H6 fusion protein and His-tag fused Protein G fusion protein were expressed and purified as described previously (*2, 3*). After purification, the GPRT-C37H6 and Protein G fusion proteins were concentrated to 0.5 mM (12 mg/mL and 6 mg/mL, respectively) by centrifugation at 12,390 g using a centrifugation vial containing a 10,000 Da molecular weight cutoff membrane (Amicon/Millipore).

Cloning of IL-1ra Fusion Protein. Primers were designed based on the human gene sequence (ATCC # 10658607, MGC-10430) of interleukin-1 receptor antagonist (IL-1ra). An EcoR I restriction site sequence, TEV protease site sequence, and codons for a Cys followed by four Gly residues were added to the IL-1ra DNA sequence in the 5'-primer (gaaaacctgtattttcagtgcggtggaggtggacgaccctctgggagaaaatcc). A Not I restriction site sequence was added to the 3'-primer after IL-1ra encoding DNA (gcggccgcctactcgtcctcctggaagtagaa). The IL-1ra gene was subcloned into the bacterial expression vector pET28a (Novagen) by digestion of complementary restriction sites and subsequent ligation using T4 DNA ligase (New England Biolabs). The ligation mixture was electroporated (BioRad micropulser) into Top 10 f' *E. coli* (Invitrogen) using a 0.1 cm electroporation cuvette. The resulting bacterial solution was selected on a LB (50 μg/mL kanamycin) plate. The successful insertion and absence of mutations for a selected bacterial colony was determined by DNA sequencing. The resulting

construct was named Cys-ILra-pet28a. The Cys-ILra-pet28a construct was transformed into Rosetta-gami2 (DE3) *E. coli* for protein expression.

Expression and Purification of IL-1ra Fusion Protein. An IL-1ra expressing bacterial colony was inoculated into 5 mL of Luria-Bertani (LB) media containing kanamycin (50 μg/mL), chloroamphenicol (34 μg/mL), and tetracycline (10 μg/mL). The 5 mL culture was incubated, with shaking overnight at 37º C. The dense 5 mL culture was transferred into 50 mL of LB media containing the antibiotics described above and incubated, with shaking overnight at 37º C. The dense 50 mL culture was then transferred into 1 L of LB media containing the antibiotics described above and incubated at 37º C, with shaking until the OD_{600nm} reached 0.9. IL-1ra expression was induced by the addition of 0.5 mM β-D-1-thiogalactopyranoside (IPTG) and incubated, with shaking for 12 hr at 25º C before harvesting. The bacteria culture was pelleted by centrifugation at 12,390 g for 20 min (Beckman Coulter, J2-HS). The pellet was resuspended in 30 mL of buffer A (50 mM tris, pH = 7.8) and lysed by sonication. The cell debris was then pelleted by centrifuged at 38,720 g for 20 min. The resulting solution was then loaded onto a (pre-equilibrated with buffer A, 5 mL bed volume) Ni^{2+} NTA agarose resin column and washed with buffer B (50 mM tris, 300 mM NaCl, 1 mM imidazole, pH = 7.8) to remove nonspecifically bound proteins. IL-1ra was eluted with buffer C (50 mM tris, 250 mM imidazole, pH = 7.8) and collected into 2 mL fractions. The IL-1ra containing fractions, as assessed by SDS-PAGE, were pooled and concentrated to 11 mg/mL (0.5 mM) by centrifugation at 12,390 g using a centrifugation vial containing a 10,000 Da molecular weight cutoff membrane

(Amicon/Millipore).

General Procedure for TEV Protease Cleavage. TEV protease was obtained by bacterial expression (*4*). 0.5 mM of fusion protein was placed into a 3,500 Da molecular weight cutoff dialysis bag and 200 units of TEV protease were added. The dialysis bag was placed into 1 L of buffer D (20 mM sodium phosphate buffer pH 7.5, 2 mM β-ME). The TEV protease cleavage reaction was gently stirred and incubated at room temperature for 24 h to generate the N-terminal cysteine containing protein.

General Procedure for Dimer Formation by Native Chemical Ligation. 4 mL of TEV protease cleaved protein (0.5 mM) was dialyzed into 1 L of ligation buffer (5 mM betaine, 20 mM sodium phosphate at pH 7.5) at 4 °C for 12 h using 3,500 Da molecular weight cutoff dialysis bag and then transferred into a 15 mL centrifuge tube for native chemical ligation. The ligation reaction was initiated by adding 50 μL of 10 mM dithioester linker **1** (0.25 equiv) and 450 μL of 300 mM sodium 2-mercaptoethanesulfonate (30 mM final concentration) into the protein solution, and this mixture was incubated at room temperature. After 24 h incubation, the dimerization reaction was quenched by adding 10 mM DTT.

Purification of C37H6 Dimer and Protein G Dimer. The C37H6 dimer and Protein G dimer were purified using the same procedure described below. The dimerization reaction mixture was dialyzed into 1 L of buffer D at 4 °C overnight using 6,000-8,000 Da molecular weight cutoff dialysis bag. The protein sample was then applied to a size exclusion column (100 mL bed volume of Bio-Gel P-10, Bio-Rad, pre-equilibrated with buffer D). Buffer D was used to elute the column and 2 mL

fractions were collected throughout the purification. The protein dimer containing fractions, as assessed by SDS-PAGE, were pooled together. 1 mg samples of the purified protein dimers were desalted by C18 (Alltech, 250 mm x 4.5 mm) reverse phase HPLC (10-80% acetonitrile in H_2O, 0.1% TFA) and were then analyzed by low resolution ESI mass spectrometry.

Purification of IL-1ra Dimer. The IL-1ra dimerization reaction mixture was dialyzed overnight in buffer E (10 mM potassuim phosphate, 1 mM β-mercaptoethanol, pH = 6.0) using 6,000-8,000 Da molecular weight cutoff dialysis bag. The protein sample was then loaded onto a SP-sepharose anion exchange column (40 mL bed volume, Sigma, pre-equilibrated with buffer E). Dimeric IL-1ra was then eluted using a 500 mL gradient (0-0.25 M NaCl) and collected in 15 mL fractions. The IL-1ra containing fractions, as assessed by SDS-PAGE, were then pooled and dialyzed overnight in buffer E. The protein sample was then reapplied to the SP-sepharose column to completely separate the IL-1ra dimer from the monomer. The same method described above was used for the elution of the dimer. The IL-1ra dimer was then concentrated to 0.5 mg/mL using an ultrafiltration vial containing a 30,000 Da molecular weight cutoff membrane (Amicon/Millipore). A 1 mg sample of the purified IL-1ra dimer was desalted by C18 (Alltech, 250 mm x 4.5 mm) reverse phase HPLC (10-80% acetonitrile in H_2O, 0.1% TFA) and was then analyzed by low resolution ESI mass spectrometry.

Cell-Cell Fusion Inhibition Assay of C37H6. The luciferase-based cell-cell fusion assay was performed as described previously (*5*). HL2/3 and TZM-bl cells were

obtained from the NIH AIDS Research and Reference Reagent Program. The HL2/3 cell line stably expresses HIV Gag, Env, Tat, Rev and Nef proteins. The TZM-bl indicator cell line stably expresses large amount of CD4 and CCR5, and contains integrated copies of the luciferase genes under control of the HIV-1 promoter. Both of the cells were cultured in DMEM medium containing 10% FBS, 100 U/ml penicillin, and 100 U/ml streptomycin in 37 °C, 5% CO_2 incubator. The TZM-bl cells were seeded in a 96-well plates (40 μL per well, 2.5×10^4 cells per well) and incubated in 37 °C, 5% CO_2 incubator for overnight. Then, the HL2/3 cells were added into the plate (40 μL per well, 2.5×10^4 cells per well) and co-cultured with the TZM-bl cells in 37 °C, 5% CO_2 incubator for 6 h in the absence or presence of various peptide concentrations in duplication (20 μL per well). The cell-cell fusion was measured by a luciferase enzyme assay using the Steady-Glo Luciferase Assay System and following the instruction of the manufacturer (Promega, Madision, WI, USA). Background luminescence in TZM-bl was measured without the addition of HL2/3 cells in the plate. The data were obtained by a DTX 880 multimode detector (Beckman Coulter) and the IC_{50} values were calculated by Origin using sigmoidal fit. The final presented IC_{50} values represent the average of three independent assays.

Cloning, Expression and Purification of Interleukin-1β. Primers were designed based on the human gene sequence (MGC-9216) of interleukin-1β (IL-1β). An Nco I restriction site was added to the 5'-primer (ccatggcagcacctgtacgatcactgaactgcacgc) and a EcoRI restriction site was the 3'-primer (gcggccgcttaggaagacacaaattgc). The IL-1β gene was subcloned into the bacterial expression vector pET28a by digestion with

complimentary restriction sites and subsequent ligation using T4 DNA ligase. The resulting reaction mixture was transformed into Top 10 f' *E. coli* by electroporation using a 0.1 cm electroporation cuvette. The resulting bacterial solution was selected on LB plates containing kanamycin (50 μg/mL). The successful insertion and absence of mutations of a selected bacterial colony was determined by DNA sequencing. The resulting construct was named IL1-pet28a.

IL1-pet28a was electroporated into Rosetta-gami2 (DE3) *E. coli* for protein expression. The protein expression methods described above were used for the production of IL-1β. The cells were pelleted by centrifugation at 12,390 g for 20 min and resuspended in 30 mL of buffer F (10 mM potassium phosphate, pH = 6.0) and lysed by sonication. The cell debris was pelleted by centrifugation at 38,720 g for 20 min and the supernatant was dialyzed overnight in buffer F using 3,500 Da molecular weight cutoff dialysis bag.

The protein solution was loaded onto a (30 ml bed volume, pre-equilibrated with buffer F) DEAE (Toyopearl, Tosoh) cation exchange column and washed with buffer F. IL-1β passed through the column, which allowed for separation from the proteins that bound to the DEAE column. The IL-1β containing solution was then loaded onto a (40 mL bed volume, pre-equilibrated with buffer F) SP-sepharose column and eluted using a 500 mL (0-0.5 M NaCl) gradient where 15 mL fractions were collected. The IL-1β containing fractions, as assessed by SDS-PAGE, were pooled and concentrated to 5 mL by centrifugation at 12,390 g using a centrifugation vial containing a 10,000 Da molecular weight cutoff membrane. The sample was then dialyzed overnight in buffer F

using 3,500 Da molecular weight cutoff dialysis bag. The IL-1β containing solution was then loaded onto a (150 mL bed volume, pre-equilibrated with buffer F) size exclusion column (HiPrep, S-100) and eluted using buffer F at a flow rate of 0.5 mL/min. The IL-1β containing fractions, as assessed by SDS-PAGE, were pooled and loaded onto a (pre-equilibrated with H_2O, 5 mL bed volume) endotoxin removing column (Detoxi-Gel, Thermo Scientific) and washed with H_2O. IL-1β passed through the column and so the flow through and column wash were collected and concentrated to 10 mL by centrifugation at 12,390 g using a centrifugation vial containing a 10,000 Da molecular weight cutoff membrane. The IL-1β solution was then sterilized using a 0.2 micron filter in preparation for cell culture.

Biological Assay of IL-1ra. The mouse T cell line, D10.G4.1 (ATCC # TIB-224) was used to determine the inhibitory effect of IL-1β dependent proliferation of both monomeric and dimeric IL-1ra. The cells were cultured in RPMI 1640 medium containing 10% FBS, 100 U/ml penicillin, 100 U/ml streptomycin, 500 pM IL-1β, and 10% T-STIM (BD Biosciences) in 37 °C, 5% CO_2 incubator. The methods for conducting the competition assay were followed as described previously (*6*). The final presented IC_{50} values represent the average of three independent assays.

LITERATURE CITED

(1) Woulfe, S. R., and Miller, M. J. (1986) The synthesis of substituted [[3(S)-(acylamino)-2-oxo-1-azetidinyl]thio]acetic acids. *J. Org. Chem. 51*, 3133-3139.

(2) Tolbert, T. J., Franke, D., and Wong, C. H. (2005) A new strategy for glycoprotein synthesis: ligation of synthetic glycopeptides with truncated proteins expressed in E. coli as TEV protease cleavable fusion protein. *Bioorg. Med. Chem. 13*, 909-915.

(3) Xiao, J., and Tolbert, T. J. (2009) Synthesis of Polymerizable Protein Monomers for Protein-Acrylamide Hydrogel Formation. *Biomacromolecules 10*, 1939-1946.
(4) Tolbert, T. J., and Wong, C. H. (2002) New Methods for Proteomic Research: Preparation of Proteins with N-Terminal Cysteines for Labeling and Conjugation. *Angew. Chem., Int. Ed. 41*, 2171-2174.
(5) Wexler-Cohen, Y., and Shai, Y. (2007) Demonstrating the C-terminal boundary of the HIV 1 fusion conformation in a dynamic ongoing fusion process and implication for fusion inhibition. *FASEB J. 21*, 3677-3684.
(6) Takii, T., Honda, H., Sasayama, S., Kobayashi, T., Ikezawa, H., Udaka, S., Oomoto, Y., and Onozaki, K. (1999) Human interleukin-1 receptor antagonist: large-scale expression in Bacillus brevis 47-5Q. *J. Interferon Cytokine Res. 19*, 1325-1331.

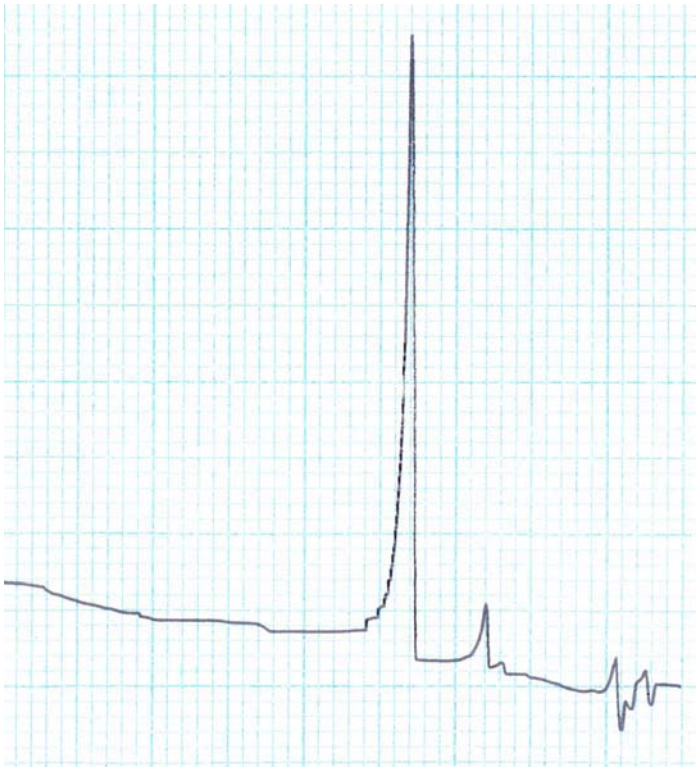


Figure S1. Analytical HPLC trace of Mono-Ethylene Glycol Dithioester Linker **1**. HPLC conditions: Alltech Hypersil ODS C18 column, 4.6 mm I.D., 250 mm length, gradient 5-75% acetonitrile in H_2O, 0.1% TFA over 40 minutes with a flow rate of 1 mL/min, detection at 220 nm. Retention time for **1** under these conditions is 18.2 min.

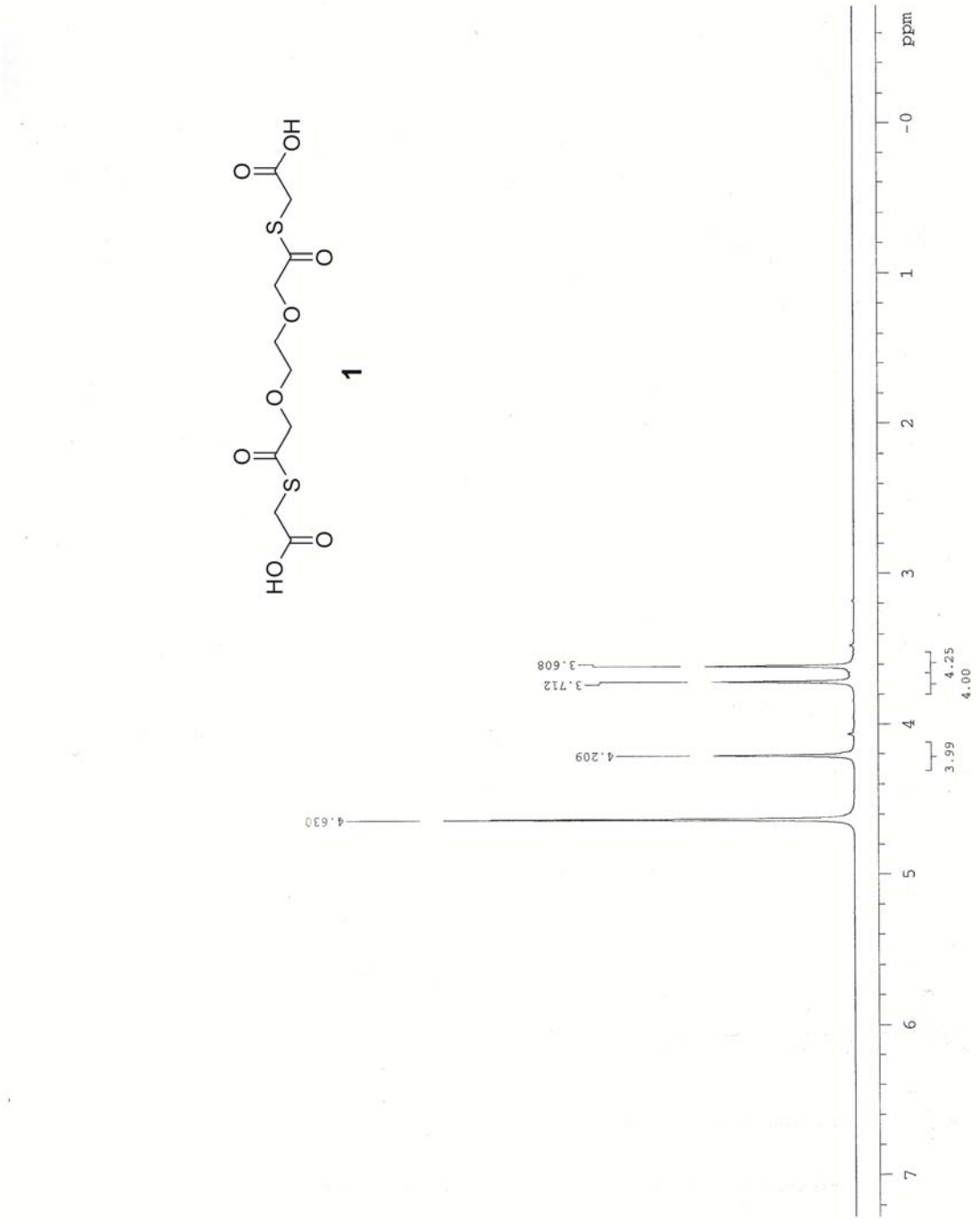


Figure S2. ^{1}H NMR (300 MHz, D_2O) spectra of **1**

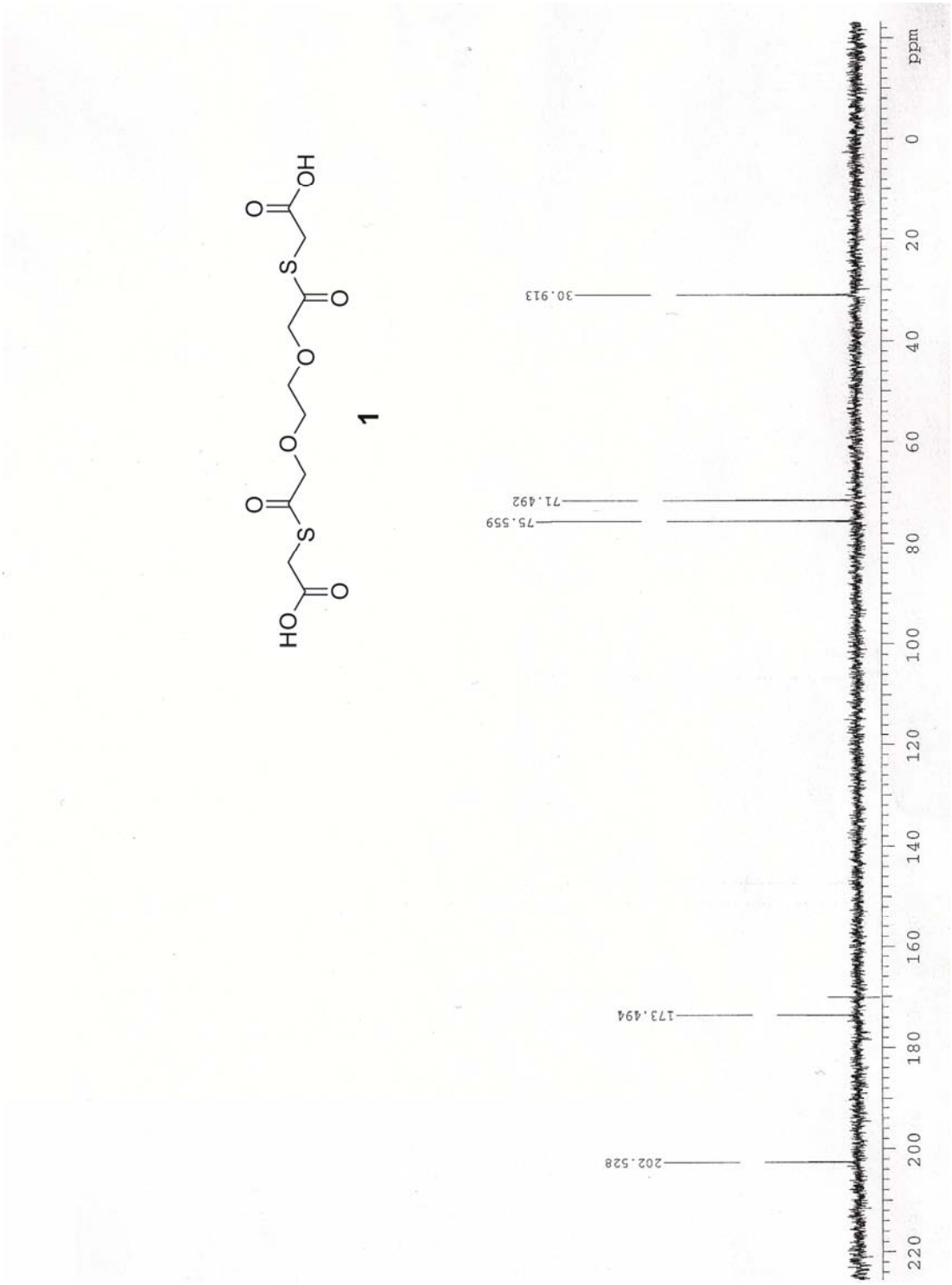


Figure S3. ^{13}C NMR (300 MHz, D_2O) spectra of **1**

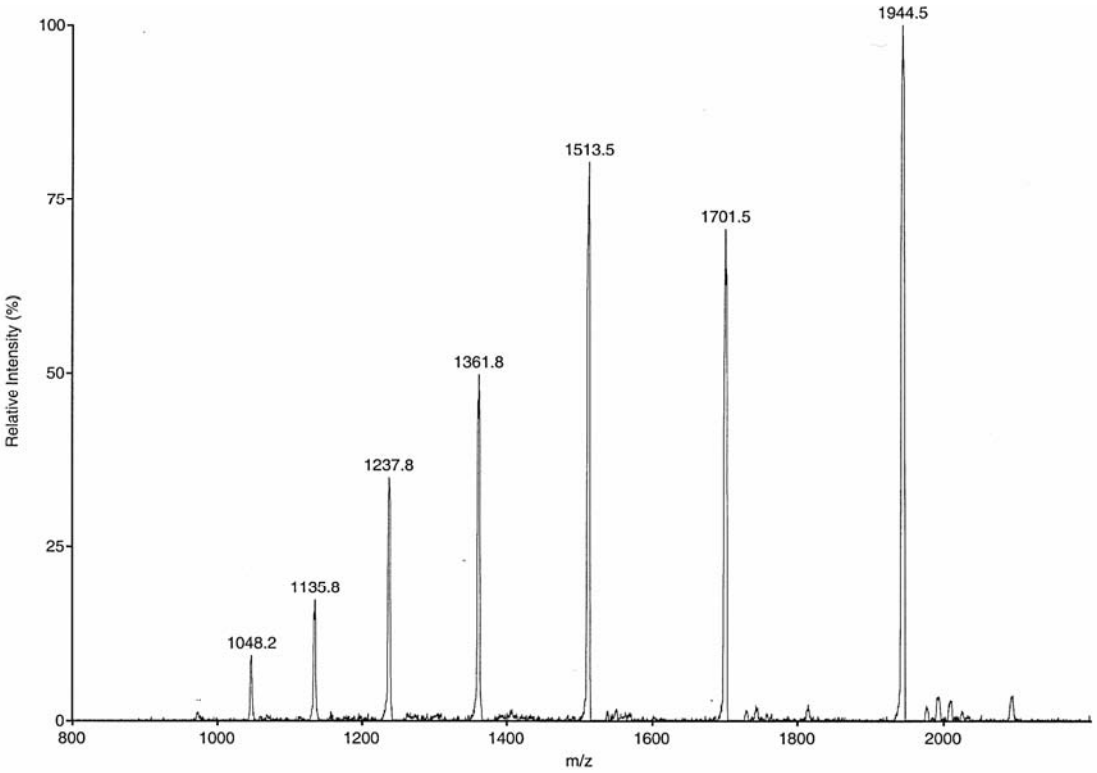


Figure S4. ESI-MS of Protein G dimer

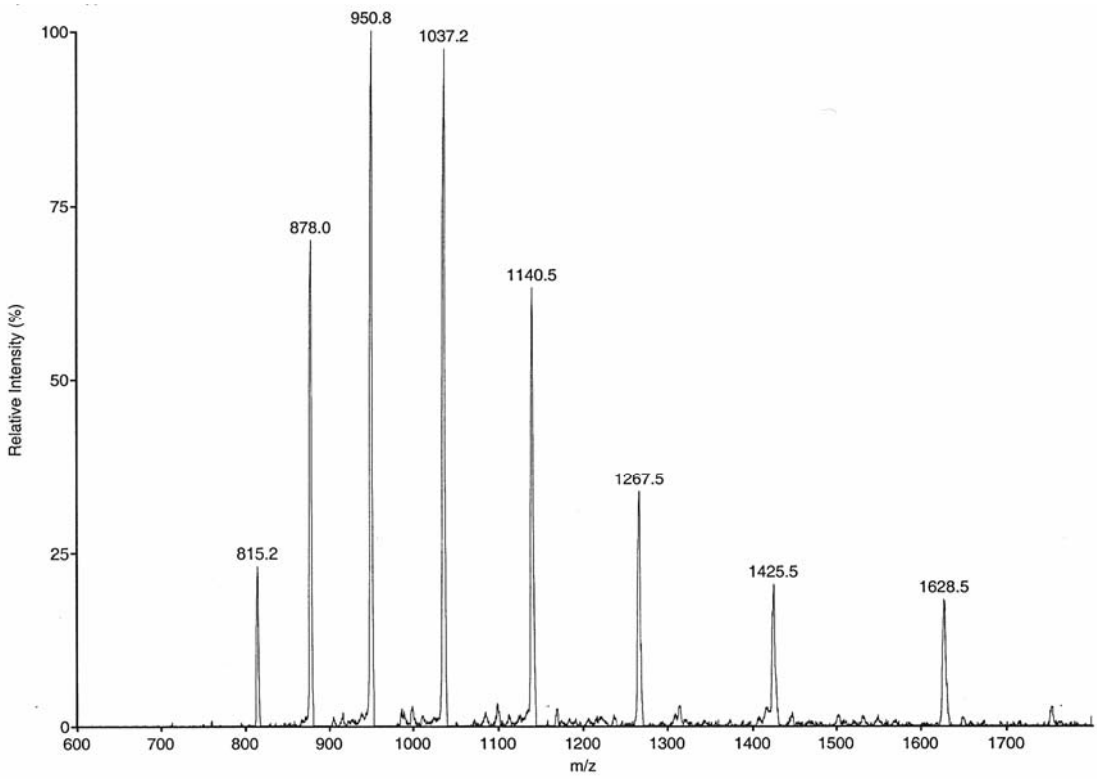


Figure S5. ESI-MS of C37H6 dimer

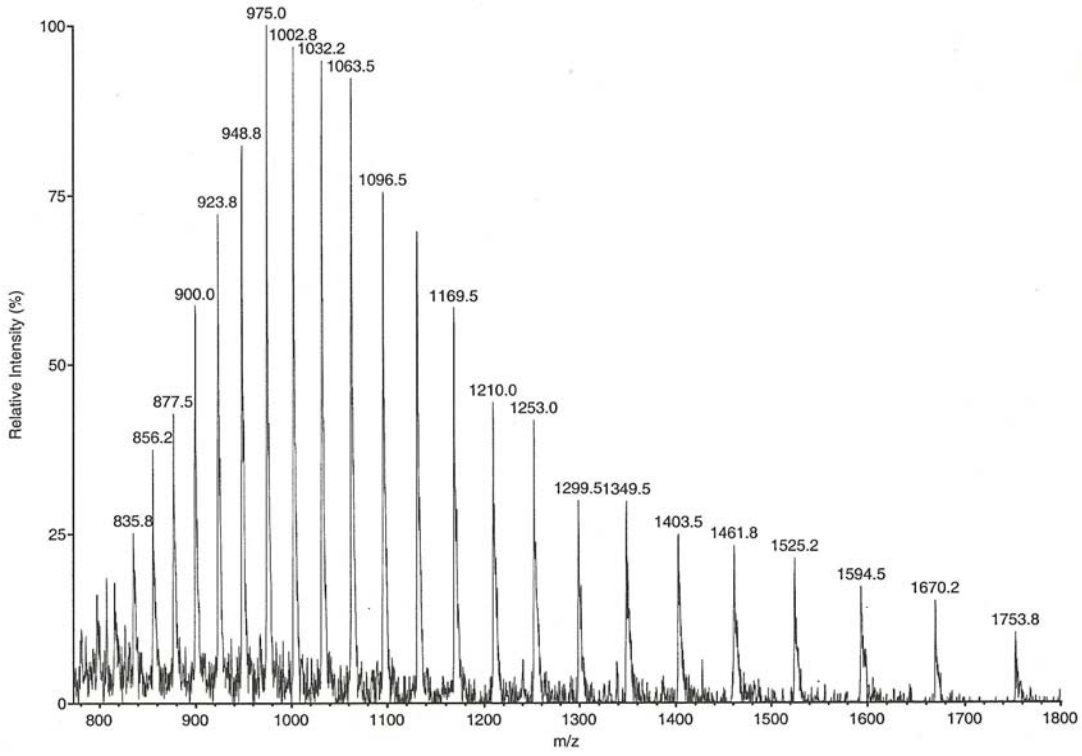


Figure S6. ESI-MS of IL-1ra dimer

Synthesis and in Vitro Antitumor Effect of Vinblastine Derivative−Oligoarginine Conjugates

Zoltán Bánóczi, Álmos Gorka-Kereskényi, Judit Reményi, Erika Orbán, László Hazai, Natália Tőkési, Judit Oláh, Judit Ovádi, Zoltán Béni, Viktor Háda, Csaba Szántay, Jr., Ferenc Hudecz,* György Kalaus, and Csaba Szántay

Research Group of Peptide Chemistry, Eötvös Loránd University (ELTE), Hungarian Academy of Sciences, Budapest 112, P.O. Box 32, H-1518, Hungary, Department of Organic Chemistry and Technology, Budapest University of Technology and Economics, Budapest, Gellért tér 4, H-1521 Hungary, Research Group for Alkaloid Chemistry, Hungarian Academy of Sciences, University of Technology and Economics, Budapest, Gellért tér 4, H-1521 Hungary, Institute of Enzymology, Biological Research Center, Hungarian Academy of Sciences, Budapest, Karolina u 29, H-1113 Hungary, Spectroscopic Research, Gedeon Richter Plc., Budapest 10, P.O. Box 27, H-1475 Hungary, and Department of Organic Chemistry, Eötvös Loránd University (ELTE), Budapest, Pázmány P. s. 1./a, H-1117 Hungary. Received January 15, 2010; Revised Manuscript Received July 12, 2010

Vinblastine is a widely used anticancer drug with undesired side effects. Its conjugation with carrier molecules could be an efficient strategy to reduce these side effects. Besides this, the conjugate could exhibit increased efficiency against resistant cells, e.g., due to the altered internalization pathway. Oligoarginines, as cell-penetrating peptides, can transport covalently attached compounds into different kinds of cells and enhance the efficiency of those compounds. We report here the coupling of vinblastine through its carboxyl group at position 16 with the *N*-terminal amino function of L-Trp methyl ester. After hydrolysis of the ester group, 17-desacetylvinblastineTrp was conjugated to the *N*-terminal amino group of oligoarginine via the *C*-terminal carboxyl group of the Trp moiety in solution. The antitumor effect of conjugates was studied on sensitive and resistant human leukemia (HL-60) cells in vitro. Our data suggest that all conjugates investigated possess an antiproliferative effect against the studied cells. However, the effect was dependent on the number of Arg residues in the conjugates: $Arg_8 > Arg_6 \gg Arg_4$. The conjugate with Arg_8 exhibited similar efficicacy as compared with free 17-desacetylvinblastineTrp. The in vitro studies also showed that the tubulin binding ability of vinblastine was essentially preserved even in the octaarginine conjugate. We also observed that two isomers were formed during conjugation. These isomers showed different levels of activity against tubulin polymerization in vitro and in vivo. The 17-desacetylvinblastineTrp-Arg_8-1 isomer conjugate possessed high selectivity against the mitotic spindles. HRMS and NMR data suggest that 17-desacetylvinblastineTrp-Arg_8-1 and 17-desacetylvinblastineTrp-Arg_8-2 are epimers at the tryptophan α carbon atom.

INTRODUCTION

Vinca-alkaloids (e.g., vincristine, vinblastine) are widely used antitumor drugs isolated first from the leaves of *Catharanthus roseus* (L.) G. Don. They cause a cytotoxic effect by disturbing the dynamics of the microtubular system (*1, 2*). In vivo, these compounds interact with tubulin at the ends of microtubules in mitotic spindles and promote microtubule instability (*3*). They are bisindole alkaloids containing a rearranged catharanthine and a vindoline moiety. Vindoline, a major alkaloid of *Catharanthus roseus*, constitutes the most complex half of vinblastine, and it is both a biosynthetic and synthetic precursor of the natural product. Upon studying the tubulin binding ability of the two parts separately, it turned out that only the catharanthine part could bind to tubulin, but this interaction is weaker than that for the bisindole alkaloids (*4*). It was concluded that the indole part of catharanthine could be responsible for the binding of vinblastine/vincristine to tubulin and the vindoline moiety could function as an anchoring residue.

The structure of vinblastine and vincristine differs only in the nature of the substituent, a methyl or a formyl group, respectively, on the vindoline *N*-atom, but this "minor" difference leads to different antitumor efficacies, potencies, and toxicities. Vinblastine is in clinical use with success in the treatment of testicular cancer, non-Hodgkin's lymphoma, and breast cancer. However, vincristine is more effective against Hodgkin's disease and pediatric solid tumors. Vinblastine treatment can result in leucopenia, while vincristine might be neurotoxic. These differences indicate that there is a marked relationship between the chemical structure and the biological effect of these alkaloids. To eliminate or reduce the side effects of these potent vinca-alkaloids, much effort has been directed toward the synthesis of new derivatives.

In the first experiments, Barnett et al. synthesized 17-desacetylvinblastine-amide (vindesine) by modifying the methyl ester group at position C-16 of the vindoline part. Vindesine and vincristine exhibited very similar biological activity spectra in animal experiments, but the neurotoxicity of the former was lower (*5*). Further compounds were prepared by modification of the amide group by incorporating different alkyl groups (*6*) or amino acids (*7*). Among the amino acid derivatives, the hydrophobic amino acid (Leu, Ile, Val, and Trp) containing derivatives showed pronounced activity. The Trp-OEt derivative had an outstanding effect on P388 and L1210 leukemias implanted intravenously in DBA_2 mice (*7*).

Various bioconjugates of vinblastine derivatives were also prepared for targeting. Conjugates with tumor-specific antibodies (*8*), for example, KS1/4 (*9*), carcinoembryonic antigen (CEA) (*10*), epidermal growth factor receptor (*11*), or PF1/D, a squamous carcinoma-reactive monoclonal antibody (*12*), were also produced and tested extensively. In other experiments, 17-desacetylvinblastine monohydrazide was coupled with folic acid

* Address correspondence to Ferenc Hudecz, Tel.: +36-1-2090-555/6428, Fax: +36-1-372-2620; E-mail: fhudecz@caesar.elte.hu.

10.1021/bc100028z © 2010 American Chemical Society
Published on Web 10/25/2010

as a targeting unit via a peptide spacer (*13, 14*). The conjugate could bind to the folate receptor positive cells and produced specific, dose-responsive activity in vitro. In vivo tests confirmed the activity of the conjugate in both syngeneic and xenograft models with minimal to moderate toxicity.

Oligoarginines are members of the cell-penetrating oligopeptide family. These synthetic or natural peptides permeate the cell membrane and transport the covalently attached cargoes into the cytosole. Among oligoarginines, hexa-, hepta-, and octaarginine showed the most effective internalization (*15, 16*). Different oligoarginines were used efficiently to transport genetically or chemically attached protein, peptide, and noncovalently bound plasmid DNA into cells (*17*). Oligoarginines can also be used to transport covalently coupled small molecules into cells, like cyclosporin A (*18*), ferrocene (*19*), and daunomycin (*20*) derivatives or bisubstrate-analogue inhibitors of basophilic protein kinases (adenosine, 5′-adenosine-carboxic acid) (*21*).

In this work, we report on the synthesis of oligoarginine (Arg_n, where $n = 4$, 6, or 8) conjugates with the Trp-derivative of vinblastine via amide bond formation in solution. We observed and isolated two isomers after conjugation. The effect of these compounds on sensitive and resistant HL-60 (human leukemia) cells was studied. Furthermore, we described our findings on the influence of conjugates on the in vitro and in vivo tubulin polymerization. Data suggest that the cytotoxicity of the conjugates was dependent on the chain length of the peptides. Moreover, only the 17-desacetylvinblastineTrp-Arg_8-1 conjugate exhibited the capability to destroy only the mitotic spindle and cause the apoptosis of the cells that are in mitosis. On the basis of HRMS and NMR data, we also report on the structure identification of the isomers proposing that 17-desacetylvinblastineTrp-Arg_8-1 and 17-desacetylvinblastineTrp-Arg_8-2 are epimers at the α-carbon atom of the Trp residue.

EXPERIMENTAL PROCEDURES

Fmoc-Arg(Pbf)-OH was purchased from Novabiochem (Läufelfingen, Switzerland), while thioanisole, 1,2-ethanedithiol (EDT), *N*-diisopropyl-ethylamine (DIEA), 1-hidroxybenztriazole (HOBt), *N,N′*-diisopropylcarbodiimide (DIC), trifluoracetic acid (TFA), phenol, ninhydrine, piperidine, 1,8-diazabicyclo[*5.4.0*]undec-7-ene (DBU) were Fluka (Buchs, Switzerland) products. The Rink-amid MBHA resin was from Novabiochem (Läufelfingen, Switzerland). Reagents and solvents used in the biological assays were purchased from Sigma-Aldrich Ltc (Budapest, Hungary). Solvents (dimethyl formaide (DMF), dichloromethane (DCM), diethyl ether, acetonitrile (AcN)) for syntheses and purification were obtained from Reanal (Budapest, Hungary).

General Procedures. Analytical RP-HPLC was performed on a Knauer (Herbert Knauer GmbH, Berlin, Germany) system using a Phenomenex SYNERGI MAX-RP column (250 × 4.6 mm I.D., 4 μm silica, 80 Å pore size) (Torrance, CA, USA) as a stationary phase. Linear gradient elution (0 min 0% B; 5 min 0% B; 50 min 90% B) was generated using 0.1% TFA in water as eluent A and 0.1% TFA in acetonitrile−water (80:20, V/V) as eluent B. Flow rate of 1 mL/min was applied at ambient temperature. The samples were dissolved in eluent B. The crude products were purified on a semipreparative Phenomenex Jupiter C18 column (250 × 10 mm I.D., 10 μm silica, 300 Å pore size) (Torrance, CA, USA). The flow rate was 4 mL/min. Peaks were detected at λ=220 nm. Positive ion electrospray ionization mass spectrometric analysis was performed on a Bruker Esquire 3000 plus (Germany). The samples were dissolved in acetonitrile−water (50:50, V/V), containing 0.1% acetic acid. High-resolution MS measurements were carried out on a Thermo LTQ FT Ultra mass spectrometer using ESI (source voltage, 4.2 kV; capillary voltage, 43 V; capillary temperature, 200 °C; sheath gas flow rate, 10 arb; aux gas flow rate, 2 arb; sweep gas flow rate, 2 arb; solvent, MeOH/H_2O 1:1 + 1 v/v % cc. AcOH) ionization technique.

All NMR measurements were performed on a Varian 800 MHz NMR spectrometer equipped with a ^{13}C enhanced HCN cold probe. $^1H-^1H$, direct $^1H-^{13}C$, long-range $^1H-^{13}C$ scalar, and dipolar spin−spin connectivities were established from ^1H, 2D-GHSQCAD, GCOSY, 2D-GHMBCAD, and 2D-ROESY NMR experiments, respectively. All pulse sequences were applied by using the standard spectrometer software package.

Synthesis of Oligoarginines. Oligoarginines (tetra-, hexa-, and octaarginine) were synthesized manually by solid-phase methodology on Rink-amide resin (0.3 g, 0.69 mmol/g) using Fmoc/^{t}Bu strategy. The side chain of Arg was protected with 2,2,4,6,7-pentamethyldihydrobenzofuran-5-sulfonyl group. N^{α}-Fmoc group was removed with 2% piperidine plus 2% DBU in DMF (2 + 2+5 + 10 min) followed by washing with DMF (8 × 0.5 min). For coupling, the Arg derivative and DIC and HOBt dissolved in DMF were used in 3-fold molar excess for the resin capacity. The reaction proceeded at RT for 60 min. Then, the resin was washed (DMF 2 × 0.5 min, DCM 3 × 0.5 min). The efficiency of coupling was checked by ninhydrin assay (*22*). The amount of resin was divided into three parts during the synthesis. After assembly, the peptide was cleaved from the resin by 10 mL of TFA using 0.75 g of phenol, 0.5 mL of distilled water, 0.5 mL of thioanisole, and 0.25 mL of 1,2-ethandithiol as scavengers. The crude product was precipitated by dry diethyl ether, dissolved in 10% acetic acid, and freeze−dried. Purification was done by RP-HPLC as described above. The following gradients were applied for purification: 0 min 0% B; 5 min 0% B; 50 min 50% B.

Synthesis of Conjugates. First, 17-desacetylvinblastineTrp was prepared by coupling the unprotected 17-desacetylvinblastine to Trp as described earlier (*7*) with some modifications. Briefly, vinblastine was refluxed in an ethanol−chloroform mixture with 98% hydrazine monohydrate instead of anhydrous hydrazine used in the published paper mentioned above. The corresponding acid azide was prepared with sodium nitrite in the presence of hydrochloric acid. The latter compound, without isolation, was allowed to react with L-Trp methyl ester in dichloromethane at 4 °C to give the Trp derivative of 17-desacetylvinblastine (*23*). After hydrolysis of the carboxylic ester, the corresponding 17-desacetylvinblastineTrp carboxylic acid (3 mg, 3.15 μmol) was coupled to oligoarginines (Arg_n, where $n = 4$, 6, or 8) (6.3 μmol) by DCC (1.3 mg, 6.3 μmol); HOBt (1 mg, 6.3 μmol) in the presence of DIEA (1.1 μL, 6.3 μmol) in 0.5 mL DMF. The reaction proceeded at RT for 4 h. The DMF was evaporated and conjugates were purified by RP-HPLC using the following gradient: 0 min 5% B; 5 min 5% B; 50 min 80% B as described above.

Cell Cultures. HeLa (ATCC, CCL-2) cells were grown in DME/F-12 medium supplemented with 10% FCS, 1 mM sodium pyruvate, 100 U/mL streptomycin, and 100 μg/mL penicillin (all from Sigma) (complete medium) in a humidified 37 °C incubator with 5% CO_2. The sensitive and resistant HL-60 human leukemia cells (ATCC: CCL-240) were cultured in RPMI-1640 medium supplemented with 10% FCS, 2 mM L-glutamine, and 160 μg/mL gentamycin. The cell culture was maintained at 37 °C in a humidified atmosphere with 5% CO_2.

MTT Assay. For cytostatic studies, sensitive and resistant HL-60 cells were placed in a 96-well plate with each well containing 5 × 10^3 cells. After incubation at 37 °C for 24 h, the cultured cells were treated with the solution of conjugates in serum-free RPMI-1640 medium for 3 h. Compounds were used at the $c = 2 \times 10^{-3}$ to 8 × 10^2 μM range. In control experiments, cells were treated with serum-free medium at 37 °C for 3 h. After incubation, cells were washed with serum-

free medium three times, and serum-containing medium was added to the cells. After 3 days at 37 °C, the 3-(4,5-dimethylthiazol-2-yl)-2,5-diphenyltetrazolium bromide (MTT) assay was carried out. The yellow solution of MTT at a concentration of 0.2 mg/mL was added to each well. The obtained purple crystal was dissolved in DMSO, and the optical density (OD) of the samples was measured at $\lambda = 540$ nm using ELISA Reader (Labsystems MS Reader, Finland). The percentage of the antitumor effect was calculated using the following equation:

$$\text{antitumor effect } \% = (1 - \text{OD}_{\text{treated}}/\text{OD}_{\text{control}}) \times 100$$

where $\text{OD}_{\text{treated}}$ and $\text{OD}_{\text{control}}$ correspond to the optical densities of the treated cells and the control cells, respectively, at $\lambda = 540$ nm. Results obtained from in vitro cytotoxicity measurements were analyzed using sigmoidal curve fitting.

Tubulin Preparation. Microtubule-associated protein (MAP)-depleted tubulin was purified from bovine brain by the method of Na and Timasheff (*24*) and stored in 10 mM phosphate buffer, pH 7.0, containing 1 M of sucrose, 0.5 mM of $MgCl_2$, and 1 mM of GTP at −80 °C. Purified tubulin showed no contamination with MAPs on overloaded SDS-PAGE. Before use, stored tubulin was dialyzed against 50 mM of 4-morpholine ethanesulfonic acid (MES) buffer, pH 6.8, at 4 °C for 3 h and then centrifuged at 100 000 *g* at 4 °C for 20 min.

Polymerization Assay. Ten micromoles of tubulin was assembled to microtubules at 37 °C in polymerization buffer (50 mM of MES buffer, pH 6.6, containing 1 mM of dithioerythritol, 1 mM of $MgCl_2$, 1 mM of EGTA (ethylene glycol tetraacetic acid), and 100 mM of KCl. The polymerization was initiated with 20 μM of paclitaxel at 37 °C. Vinblastine, 17-desacetylvinblastineTrp, and 17-desacetylvinblastineTrp−octaarginine conjugates in the 0.05−2 μM concentration range were incubated with tubulin at 37 °C for 5 min before starting the polymerization. For turbidity measurements, the absorbance was monitored at $\lambda = 350$ nm with a Cary 100 spectrophotometer (Varian, Mulgrave, Victoria, Australia). The error margin of the turbidity measurements was ±5% within a series of experiments.

Immunocytochemistry. For microscopic studies, HeLa cells were grown on 12 mm diameter coverslips. The vinblastine, 17-desacetylvinblastineTrp, and 17-desacetylvinblastineTrp−octaarginine conjugates were added to the complete medium of the cells in the 0.25−5 μM concentration range for 24 h and then were fixed with ice-cold methanol for 15 min and immunostained for α-tubulin as described by Lehotzky et al. (*25*). Nuclei were counterstained with 4′,6-diamidino-2-phenylindole (DAPI) after coverslips were mounted on an Aqua Poly/Mount medium (Sigma). Images were taken on a Leica DMLS microscope (Leica Microsystems, Wetzlar, Germany) equipped with a cooled CCD camera (Spot, Digital Instruments, Sterling Heights, MI, USA). Statistical analysis was performed manually by investigating random microscopic fields. Data were analyzed with Microsoft *Excel*. Images were processed with *ImageJ* software.

RESULTS AND DISCUSSION

To avoid the undesired effect of antitumor drugs and to increase their efficiency against resistant cells is a difficult task to achieve. The conjugation of small drug molecules to carriers could be considered as a potential strategy for utilization. In this paper, we describe the synthesis and in vitro antitumor effect of oligoarginine conjugates of the Trp derivative of 17-desacetylvinblastine. The influence of these compounds on the tubulin polymerization was also studied in vitro and in vivo.

Synthesis of Conjugates. Among the amino acid ester derivatives of viblastine, the tryptophan derivative showed the highest antitumor effect in mice (*7*). Accordingly, for the present studies 17-desacetylvinblastineTrp (*7*, *23*, *26*) was prepared with a modified procedure using 17-desacetylvinblastine (*26*), as the major metabolite of vinblastine in humans considering its pharmacological equivalency with vinblastine (*27*) (Scheme 1).

Scheme 1. Synthesis of 17-DesacetylvinblastineTrp

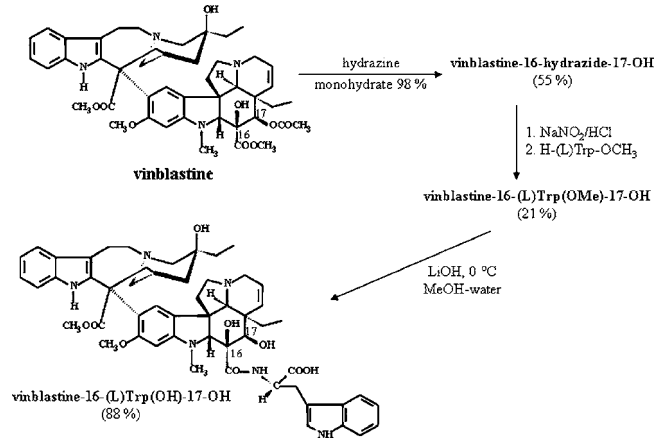


Table 1. Characteristics of 17-DesacetylvinblastineTrp−Oligoarginine Conjugates

conjugate	R_t[a] (min)	$[M+H]^+$,[b] cal. [meas.]
17-desacetylvinblastineTrp-Arg_4-1	27.9	1564.9 (1564.3)
17-desacetylvinblastineTrp-Arg_4-2	26.3	1564.9 (1564.3)
17-desacetylvinblastineTrp-Arg_6-1	26.0	1877.3 (1876.7)
17-desacetylvinblastineTrp-Arg_6-2	26.3	1877.3 (1876.7)
17-desacetylvinblastineTrp-Arg_8-1	26.3	2189.6 (2189.1)
17-dezacetylvinblasztinTrp-Arg_8-2	26.6	2189.6 (2189.1)

[a] RP-HPLC retention time, column: Phenomenex SYNERGI MAX-RP (250 × 4.6 mm I.D., 4 μm silica, 80 Å pore size). Linear gradient elution 0 min 0% B; 5 min 0% B; 50 min 90% B using 0.1% TFA in water as eluent A and 0.1% TFA in acetonitrile−water (80:20, V/V) as eluent B. [b] ESI-MS.

17-DesacetylvinblastineTrp was conjugated with tetra-, hexa-, or octaarginine in solution. First, the oligoarginines were built up on Rink-amide resin by Fmoc/^{t}Bu strategy, and after cleavage from the resin by TFA, the unprotected and purified *C*-terminal peptide amides were used for the conjugation. 17-DesacetylvinblastineTrp was coupled to the peptides by the active ester method using DCC/HOBt coupling reagents in DMF in the presence of DIEA as base. The conjugates were characterized by analytical RP-HPLC and ESI-MS (Table 1 and Figure 1 in Supporting Information).

The conjugation reaction resulted in two isomers with different retention times, but with the same molecular mass in all three cases. The isomers were separated, isolated, and characterized, and their biological effects were examined. To identify the structure of the two isomer conjugates, these compounds were studied by high-resolution MS and NMR.

Identification of the Structure of the Two Isomers of the Octaarginine Conjugates. The two compounds (17-desacetylvinblastineTrp-Arg_8-1 and 17-desacetylvinblastineTrp-Arg_8-2) obtained during the preparation of the 17-desacetylvinblastineTrp octaarginine conjugate were investigated after HPLC separation.

High-Resolution Mass Spectrometry. In the direct ESI mass spectra of the samples 17-desacetylvinblastineTrp-Arg_8-1 and 17-desacetylvinblastineTrp-Arg_8-2 multiply charged ions of $[M+4H]^{4+}$, $[M+5H]^{5+}$ and $[M+6H]^{6+}$ can be detected. The monoisotopic mass values were obtained by the deconvolution of the mass spectra (using Xtract in *Xcalibur 2.0.7*): 17-DesacetylvinblastineTrp-Arg_8-1: *m*/*z* 2188.29693, calculated value for $C_{102}H_{161}O_{16}N_{39}$: 2188.29780 ($\delta$ −0.4 ppm). 17-

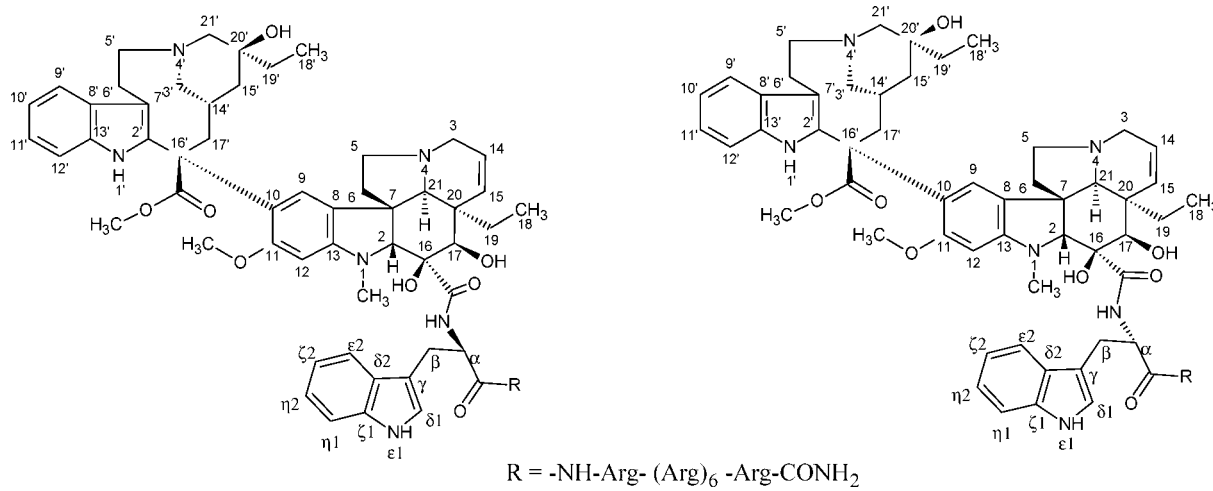


Figure 1. Structures proposed for the two isomeric Arg8 conjugates of 17-desacetylvinblastineTrp: 17-desacetylvinblastineTrp-Arg$_8$-1 (left) and 17-desacetylvinblastineTrp-Arg$_8$-2 (right).

DesacetylvinblastineTrp-Arg$_8$-2: *m/z* 2188.29728, calculated value for $C_{102}H_{161}O_{16}N_{39}$: 2188.29780 ($\delta$ −0.2 ppm).

The most intense $[M+5H]^{5+}$ ion peaks were fragmented by CID (collision induced dissociation) at a normalized collision energy of 25%. The monoisotopic mass values of the main fragment ions in the deconvoluted MS-MS spectra are the following: 17-DesacetylvinblastineTrp-Arg$_8$-1: *m/z* 2129.25013, 2015.17064, 1876.09619, 1702.96880, 1660.94691, 1537.91516, 1501.89406, 1348.74426, 1234.66543, 1192.64356, 1174.63301, 1078.56404, 648.36752, 523.28346. 17-DesacetylvinblastineTrp-Arg$_8$-2: *m/z* 2129.25155, 2015.17057, 1876.09677, 1234.66544, 1192.64463, 1174.63280, 953.63348, 894.46857, 708.38901, 648.36785.

On the basis of the accurate mass values of the fragment ions in the MS−MS spectra, elemental compositions were calculated using the *Xcalibur 2.0.7* software. In the range of 0.2−1.5 ppm mass accuracy, plausible elemental compositions could be obtained for all of the fragment ions. All of these elemental compositions are in agreement with the expected 17-desacetylvinblastineTrpArg$_8$ chemical structure. However, when comparing the MS-MS spectra of the two samples some differences can be noticed regarding the obtained fragment ions and their relative abundance values. Most of the fragment ions were obtained by the cleavage of the Arg$_8$ part of the molecule for both samples. In the case of 17-desacetylvinblastineTrp-Arg$_8$-1, more fragment ions were produced by the cleavage of the vindoline C ring (cleavage of the C_2-C_{16} and $C_{17}-C_{20}$ bonds), while exclusively for 17-desacetylvinblastineTrp-Arg$_8$-2, a single minor fragment ion was observed in the deconvoluted mass spectrum, which can originate from a C−C cleavage beside the carbonyl group of the Tryptophan. According to these MS data, compounds 17-desacetylvinblastineTrp-Arg$_8$-1 and 17-desacetylvinblastineTrp-Arg$_8$-2 are two stereoisomers of 17-desacetyvinblastineTrpArg$_8$.

NMR. Since both compounds 17-desacetylvinblastineTrp-Arg$_8$-1 and 17-desacetylvinblastineTrp-Arg$_8$-2 were available only in a limited amount for NMR measurements, only limited spectroscopic information could be obtained on an affordable time scale even on our ultrasensitive 800 MHz NMR spectrometer. Furthermore, due to their conformational dynamics both compounds gave broad ^{1}H NMR resonances in all common NMR solvents (such as DMSO-d_6, $CDCl_3$, ACN-d_3, MeOD-d_4, or D_2O), which prohibited easy access to the desired spectroscopic information (see Supporting Information Figure 2 as an example) in this concentration. Finally, a solvent mixture containing ACN-d_3 and D_2O in a one-to-one ratio was chosen as the most suitable medium. Although most of the resonances (mainly those belonging to the vindoline half of the two molecules) were still significantly broadened in this solvent mixture, structurally informative spectral information could nevertheless be obtained. In accordance with the HRMS results, these data suggest that 17-desacetylvinblastineTrp-Arg$_8$-1 and 17-desacetylvinblastineTrp-Arg$_8$-2 are epimers at the tryptophan α-carbon atom (Figure 1).

Partial ^{1}H and ^{13}C NMR assignments (determined from ^{1}H, 2D-GHSQCAD, GCOSY, 2D-GHMBCAD, and 2D-ROESY NMR spectra) that are indicative of the proposed epimeric structures are listed in Table 1 in Supporting Information. These structures are supported via the following argument. The chemical shifts of the catharantine parts of 17-desacetylvinblastineTrp-Arg$_8$-1 and 17-desacetylvinblastineTrp-Arg$_8$-2 (note that an almost complete assignment could be achieved for the catharantine moieties) are practically the same, telling us that the structural difference is located elsewhere in the two molecules.

Due to the low sample concentrations and to the significant broadening of some of the resonances belonging to the vindoline half of the molecules, assignments for this part of the compounds could not be given completely. Nevertheless, the similarity of the signals due to the detectable and assignable functional groups [the C(14)═C(15) double bond, the C(20)-Et, C(11)-OMe, and N(1)-Me functions], as well as those belonging to the aromatic resonances (*8, 9*) of the indole part, indicate that the vindoline parts also remained intact during the formation of the conjugates.

The most significant differences were detected in signals belonging to the tryptophan moieties, especially those belonging to the Trp α and β protons of these residues. Not only do the chemical shifts of the Trp α (5.09 and 4.84 ppm in 17-desacetylvinblastineTrp-Arg$_8$-2 and 17-desacetylvinblastineTrp-Arg$_8$-1, respectively) and β protons (3.73 ppm in 17-desacetylvinblastineTrp-Arg$_8$-2 and 3.58 and 3.72 ppm in 17-desacetylvinblastineTrp-Arg$_8$-1) differ significantly, but the coupling patterns differ as well (Figure 3 in Supporting Information). In 17-desacetylvinblastineTrp-Arg$_8$-2, the Trp α proton resonance appears as a triplet with a coupling constant of 5.9 Hz, while that in 17-desacetylvinblastineTrp-Arg$_8$-1 is a doublet of doublet with coupling constants of 10.4 and 5.6 Hz. These findings indicate that during the formation of the Arg conjugates inversion of the Trp α carbon occurred. The Trp moieties are expected to be in different conformational states in the two epimers, which accounts for the observed difference in the coupling patterns of the Trp α proton resonances.

In order to identify the two epimers, we recorded the ^{1}H NMR spectra of two smaller model systems containing only the

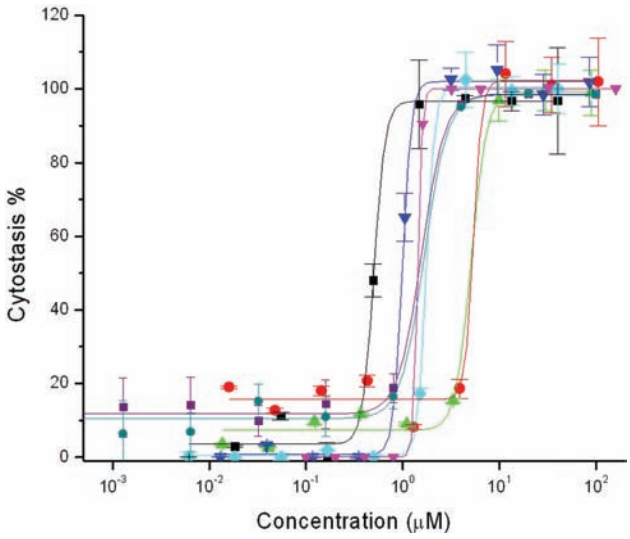


Figure 2. Cytostatic activity of vinblastine sulfate, 17-desacetylvinblastine, and its conjugates on sensitive HL-60 cells. The cells were incubated with the compound for 3 h, after growth in serum-containing medium for 3 days. The IC_{50} values were determined by MTT assay as described in the text: black -■-, 17-desacetylvinblastineTrp, $IC_{50} = 0.49$ μM; magenta -▼-, vinblastine sulfate, $IC_{50} = 1.26$ μM; red -●-, 17-desacetylvinblastineTrp-Arg_4-1, $IC_{50} = 5.25$ μM; green -▲-, 17-desacetylvinblastineTrp-Arg_4-2, $IC_{50} = 4.97$ μM; cyan -◆-, 17-desacetylvinblastineTrp-Arg_6-1, $IC_{50} = 0.97$ μM; blue -▼-, 17-desacetylvinblastineTrp-Arg_6-2, $IC_{50} = 1.75$ μM; purple -■-, 17-desacetylvinblastineTrp-Arg_8-1, $IC_{50} = 1.61$ μM; teal -●-, 17-desacetylvinblastineTrp-Arg_8-2, $IC_{50} = 1.59$ μM.

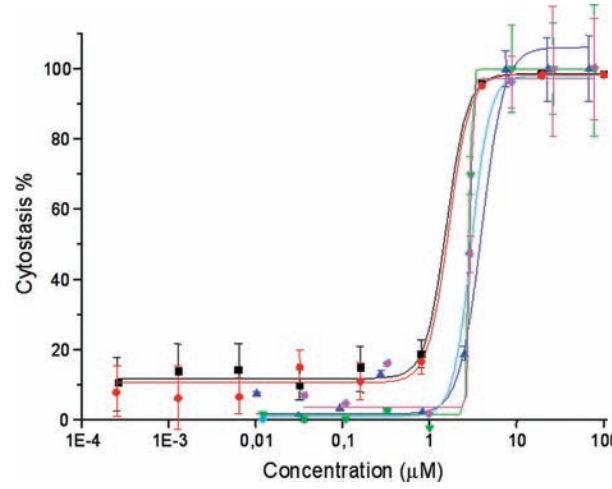


Figure 3. Cytostatic activity of 17-desacetylvinblastineTrp-Arg_8 conjugates on sensitive and resistant HL-60 cells. The cells were incubated with the compound for 3 h, after grown in serum-containing medium for 3 days. The IC_{50} values were determined by MTT assay as described in the text: black -■-, 17-desacetylvinblastineTrp-Arg_8-1/HL-60, $IC_{50} = 1.61$ μM; red -●-, 17-desacetylvinblastineTrp-Arg_8-2/HL-60, $IC_{50} = 1.59$ μM; blue -▲-, 17-desacetylvinblastineTrp-Arg_8-1/HL-60-MDR1, $IC_{50} = 2.62$ μM; green -▼-, 17-desacetylvinblastineTrp-Arg_8-2/HL-60-MDR1, $IC_{50} = 2.94$ μM; cyan -◆-, 17-desacetylvinblastineTrp-Arg_8-1/HL-60-MRP1, $IC_{50} = 2.94$ μM; magenta -▼-, 17-desacetylvinblastineTrp-Arg_8-2/HL-60-MRP1, $IC_{50} = 3.78$ μM.

"vindoline" half bound to D- and L-tryptophan (unpublished synthetic results), having the structures shown in Figure 4 in Supporting Information. In the vindoline−L-tryptophan model, the α proton appears as a triplet (5.8 Hz) similarly to epimer 17-desacetylvinblastineTrp-Arg_8-2, while in the vindoline−D-tryptophan model, it appears as a doublet of doublets (8.9 and 4.8 Hz) similarly to epimer 17-desacetylvinblastineTrp-Arg_8-1 (Figure 5 in the Supporting Information). These similarities indicate that 17-desacetylvinblastineTrp-Arg_8-2 and 17-desacetylvinblastineTrp-Arg_8-1 contain the L- and D-tryptophan moieties, respectively.

Additional synthetic and spectroscopic investigations are in progress to further verify the proposed structures as well as to explore the nature of and reasons behind the observed epimerization of Trp octaarginine during its coupling to 17-desacetylvinblastine.

Cytostatic Effect of Conjugates on HL-60 Human Leukemia Cells. The cytostatic effect of conjugates as well as of the control compounds was studied on sensitive and resistant HL-60 cells using MTT assay. The cells were treated with vinblastine sulfate, 17-desacetylvinblastineTrp, and its conjugates at different concentrations for 3 h, and then, the number of living cells was determined after 72 h. Data are summarized in Figure 2. In contrast to vinblastine sulfate ($IC_{50} = 1.26$ μM), the 17-desacetylvinblastine has more marked activity on sensitive HL-60 cells ($IC_{50} = 0.0043$ μM). The presence of Trp residue in the amino acid conjugate decreased the activity by 2 orders of magnitude ($IC_{50} = 0.49$ μM), but it is still more effective than vinblastine sulfate. On sensitive HL-60 cells, the increasing number of Arg residues enhanced the cytostatic effect of the conjugate. The octa- and hexaargininеTrp conjugate isomers have slightly higher activity ($IC_{50} = 1.61$ μM and 1.59 μM, for octaargininеTrp conjugate and $IC_{50} = 0.97$ μM and 1.75 μM for hexaargininеTrp conjugates) as compared to the tetraargininеTrp conjugates ($IC_{50} = 5.25$ μM and 4.97 μM). It is interesting to note that the octa- and hexaargininеTrp conjugate isomers almost preserve the activity of 17-desacetylvinblastineTrp, and these values are comparable with those of vinblastine sulfate ($IC_{50} = 0.97-1.75$ μM for octa- and hexaargininеTrp conjugates and $IC_{50} = 1.26$ μM for vinblastine sulfate).

The activity of compounds was studied on HL-60/MDR1 and HL-60/MRP1 resistant cells, too. The effect of vinblastine sulfate on resistant HL-60/MRP1 cells ($IC_{50} = 1.31$ μM) is similar to that of sensitive HL-60 cells ($IC_{50} = 1.26$ μM), but its efficacy was somewhat lower in the case of resistant HL-60/MDR1 cells ($IC_{50} = 2.96$ μM).

The effect of 17-desacetylvinblastine decreased markedly ($IC_{50} = 1.78$ for MDR1 and 0.24 μM for MRP1), showing that it is a good substrate of the MDR1 and MRP1 transporter proteins, somewhat better than vinblastine sulfate. The efficiency of the Trp derivative diminished dramatically in the presence of the MDR1 protein ($IC_{50} = 59.6$ μM), but the effect of the MRP1 protein was less marked ($IC_{50} = 3.98$ μM).

The antitumor effect of the conjugates increased with the number of Arg residues present in the conjugates on both resistant cell lines, but the IC_{50} values are somewhat higher than in the case of the sensitive cells. The two isomer conjugates (except the compounds with four Arg residues) show similar effects on the resistant cells. The IC_{50} values of octaarginine conjugates are shown in Figure 3.

Our results show that 17-desacetylvinblastine significantly inhibits the division of sensitive human leukemia cells. This effect, which is higher than that of vinblastine sulfate, decreases if the molecule is modified by a Trp. The conjugation of 17-desacetylvinblastineTrp to oligoarginine resulted in an antitumor effect which is dependent on the number of Arg residues. The presence of hexa- and octaarginine in the conjugates has almost no effect—these compounds exhibit essentially the same level of antitumor activity. However, tetraarginine reduces the activity significantly.

17-Desacetylvinblastine has significant cytotoxicity, higher than that of vinblastine. While the attachment of Trp dramatically decreases the effect of 17-desacetylvinblastine, this derivative still has a similar activity to vinblastine. The IC_{50} values of octa- and hexaargininеTrp conjugates suggest that these

compounds exhibit in vitro an antitumor effect similar to that of vinblastine.

In the case of resistant cells, the effect of 17-desacetylvinblastine is dramatically decreased, and the activity of both the Trp derivative and its octaarginine conjugate is similar in the case of HL-60/MRP1. The HL-60/MDR1 cells pump out the Trp derivative so effectively that its activity decreases to one tenth, while the octaarginineTrp conjugates show comparable effect with 17-desacetylvinblastine. Interestingly, the effect of vinblastine sulfate is reduced only by MDR1 proteins and only to a little extent. The biggest effect is measured in the presence of the MDR1 protein when the cells are treated by vinblastine derivatives. In the case of conjugates, the MRP1 proteins result in a bigger reduction in the activity. These results show that 17-desacetylvinblastine is a very good substrate of the transporter proteins. Considering the decreased effect of the conjugates, it is attractive to speculate that the transport proteins can also pump out the conjugated 17-desacetylvinblastine from the cells. The extent of efflux increased in the case of conjugates with a shorter oligoarginine, which could suggest that the character of conjugates became similar to that of the drug. On the other hand, the efficacy of the MRP1 protein to 17-desacetylvinblastineTrp is increased by the conjugation. In the resistant cells, the proteins pump out the compounds and the resulting concentration reduction inhibits the effect of the drugs. Because the cytotoxicity of 17-desacetylvinblastine and the octaarginineTrp conjugate are almost similar on resistant cells, it can be supposed that the reason for the significant difference in the case of the sensitive cells is the difference between the concentrations of active 17-desacetylvinblastine in the cells. In the case of 17-desacetylvinblastine, the achieved effective intracellular concentration is determined only by the diffusion rate. However, with the conjugates at least two different processes are involved, namely, the internalization of the conjugates and the interaction of the released (free) or conjugated drug with the microtubular system at the site of action. In order to analyze the influence of the presence of oligoarginine, the effect of the conjugates was studied on tubulin polymerization in vitro and in vivo.

In Vitro and in Vivo Effect of Vinblastine Derivatives on Tubulin Polymerization. In order to characterize the effect of vinblastine and its conjugate derivatives on a microtubule assembly, the polymerization of tubulin heterodimers was investigated in vitro at different drug concentrations.

Figure 4 shows that vinblastine and its derivatives inhibit paclitaxel-induced tubulin polymerization; however, this effect was dependent upon the nature of the derivatives. The dose−response curves obtained by plotting the polymerization rate as a function of drug concentrations reveal that the inhibitory effects of 17-desacetylvinblastineTrp and the 17-desacetylvinblastineTrp-Arg_8-2 conjugates are comparable to those of vinblastine in the polymerization assay. However, the inhibitory potency of the 17-desacetylvinblastineTrp-Arg_8-1 conjugate on the microtubule assembly was less pronounced. It should be noted that with the mixture of the two Trp-Arg_8-containing isomers (before their HPLC separation) we obtained a lower inhibitory effect than with 17-desacetylvinblastineTrp-Arg_8-2, but a higher effect than with 17-desacetylvinblastineTrp-Arg_8-1. This result suggests that the 17-desacetylvinblastineTrp-Arg_8-1 conjugate is not a potential antimitotic agent. However, the effect observed in an in vitro system with purified tubulin cannot provide information on the specificity of the drugs. Specificity, i.e., the antimicrotubular activity of the drug, was studied at a cellular level using HeLa cells by investigating both the interphase and spindle microtubules in parallel.

The majority of the eukaryote cells are at interphase, and only the minority are in mitosis—at a certain point in time—even

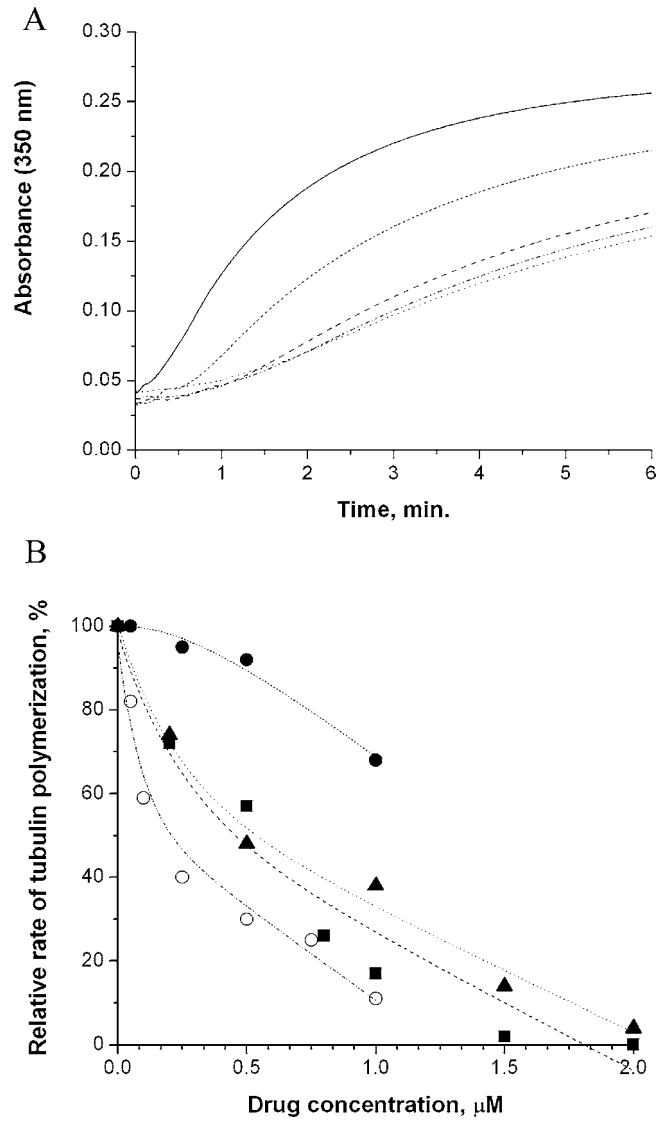


Figure 4. Effect of vinblastine and its conjugate derivatives on tubulin polymerization. (A) Turbidimetric assay. The paclitaxel-induced tubulin polymerization was followed at $\lambda = 350$ nm. The concentration of vinblastine and its derivatives was 1 μM. Tubulin control (solid line), vinblastine (dashed line), 17-desacetylvinblastineTrp (dotted line), 17-desacetylvinblastineTrp-Arg_8-1 (short dashed line), 17-desacetylvinblastineTrp-Arg_8-2 (dash-dot-dotted line). (B) The relative effect of vinblastine and its derivatives on tubulin polymerization as a function of drug concentration. (■, dashed line) vinblastine, (▲, dotted line) 17-desacetylvinblastineTrp, (●, short dashed line) 17-desacetylvinblastineTrp-Arg_8-1, (○, dash-dot-dotted line) 17-desacetylvinblastineTrp-Arg_8-2.

in cancer cells, which are characterized by rapid proliferation. Therefore, if a drug specifically targets the mitotic microtubule spindle, this effect is not necessarily reflected at a cellular level by the cytotoxicity index.

In order to characterize the antimicrotubule activities of vinblastine and its conjugate derivatives at a cellular level, we performed comparative studies in human cervical carcinoma (HeLa) cells. The drugs were added to the medium of the growing cells at different concentrations. After 24 h, the microtubular network of the cells was immunostained with antitubulin antibody and visualized by immunofluorescence microscopy.

Figure 5 shows that the interphase microtubular network can be characterized by three well-defined stages: (i) Normal stage (Figure 5a): the microtubular network is assembled into bundled fibers of highly ordered fashion. The fibers originate from the

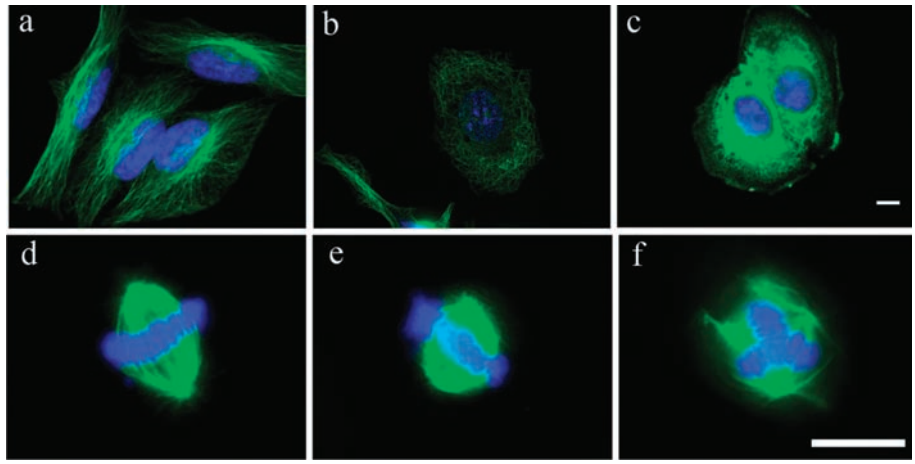


Figure 5. Characteristic pictures for interphase (a−c) and mitotic (d−f) microtubule network formations in HeLa cells immunostained for α-tubulin (green); normal, control (a and d), fragmentated (b) induced by 2.5 μM 17-desacetylvinblastineTrp, depolymerized (c) induced by 2.5 μM vinblastine, asymmetric (e) induced by 0.25 μM, and multipolar (f) induced by 2.5 μM 17-desacetylvinblastineTrp treatment. Blue: DAPI. Bar: 5 μm.

Table 2. Effect of Vinblastine and 17-Desacetylvinblastine Derivatives on the Spindle and Interphase Microtubule Ultrastructures[a]

	vinblastine		17-desacetylvinblTrp		17-desacetylvinblTrpArg$_8$-**2**		17-desacetylvinblTrpArg$_8$-**1**	
	aberrant mitosis (%)	interphase microtubules	aberrant mitosis (%)	interphase microtubules	aberrant mitosis (%)	interphase microtubules	aberrant mitosis (%)	interphase microtubules
control	2	normal	2	normal	2	normal	2	normal
0.25 μM	100	depolymerized	47	normal	22	normal	n. d.[b]	n. d.
1 μM	100	depolymerized	100	fragmented	75	normal	45	normal
2.5 μM	100	depolymerized	100	fragmented	98	fragmented	75	normal
5 μM	100	depolymerized	100	depolymerized	100	fragmented	100	normal

[a] HeLa cells were treated with the drugs at different concentrations for 24 h. The percentage distribution of the aberrant mitotic spindle among all cells in the phase of mitosis was quantified by investigating random microscopic fields. The structure of the interphase and mitotic microtubules was visualized by immunofluorescence microscopy using monoclonal antitubulin antibody. [b] n.d: not defined.

microtubule organizing center and are concentrated around the nucleus. Their free ends radiate outward toward the cell membrane, forming a network. In drug-treated cells, microtubules undergo significant reorganizations. (ii) Fragmented stage (Figure 5b): long bundles of microtubules are fragmented into short, disorganized fibers which radiate to the cell periphery in a criss−cross fashion. In the vicinity of nuclei, the microtubules acquire an amorphous appearance. The microtubule organizing centers are no longer apparent. (iii) Depolymerized stage (Figure 5c): all microtubules are disassembled; the depolymerized microtubules show homogeneous cytosolic distribution.

We also studied the changes of the spindle structures in parallel with those of the interphase at various drug concentrations. Treatment of the cells with vinblastine or its derivatives caused significant alterations in the spindle structures. Typical structures visualized in the drug-treated samples are shown in Figure 5: normal, symmetric (Figure 5d), asymmetric (Figure 5e), and multipolar (Figure 5f).

For evaluation of the specificity of the vinblastine derivatives, we quantified the relative amount (%) of the aberrant mitotic spindles as compared to all mitotic cells. In addition, the ultrastructures of the interphase microtubules were visualized and ranked according to the categories presented in Figure 5.

According to the data summarized in Table 2, vinblastine, even at the lowest concentration used in this study, depolymerized the microtubular network completely; the tubulin homogeneously distributed within the cytosol corresponding to Figure 5c. 17-DesacetylvinblastineTrp causes much less damage to the microtubular network than vinblastine, and 47% of the mitotic cells are aberrant at 0.25 μM. The two Trp-Arg$_8$ conjugates displayed distinct effects, while the 17-desacetylvinblastineTrp-Arg$_8$-2 isomer conjugate caused significant fragmentation of the interphase microtubule at 2.5 μM, the 17-desacetylvinblastineTrp-Arg$_8$-1 isomer conjugate did not affect them at all even at a 5 μM concentration. These results clearly show that the 17-desacetylvinblastineTrp-Arg$_8$-1 isomer conjugate is highly selective against the mitotic spindles and destroys only these structures in the mitotic cells. As among tumor cells there are more cells in mitosis at a certain time point than among normal cells, these data suggest that the 17-desacetylvinblastineTrp-Arg$_8$-1 isomer conjugate may have a selective cytotoxic effect against tumor cells and may thus have lower side effects. As the isomers are different in the configuration of Trp, further studies are needed to rationalize this selectivity.

CONCLUSIONS

Vinblastine is an efficient antitumor agent, but its side effects and resistance can restrict its use. A promising approach to avoid the harmful effects is its conjugation with an appropriate partner compound. The coupling of 17-desacetylvinblastineTrp with cell-penetrating oligoarginines results in conjugates whose biological effectiveness correlates with the chain length of peptides. The octa- and hexaarginine conjugates preserve the cytotoxicity of the original drug on both sensitive and resistant HL-60 cells. Moreover, the 17-desacetylvinblastineTrp-Arg$_8$-1 isomer conjugate preferentially destroys the mitotic spindle, at least in the case of cancerous HeLa cells, resulting in cell cycle inhibition. Further studies should be performed to demonstrate that this conjugate can exclusively target the tumor cells and is less toxic to normal cells in many other cases.

ACKNOWLEDGMENT

These studies were supported by grants from the Hungarian Research Fund (OTKA, no. K68285 and K68734), Hungarian Ministry of Education (NKFP Medichem 2), and from the Hungarian Ministry of Health (ETT 209/2009). The authors are grateful to Dr. Szilvia Bősze for the helpful discussion and to

Gedeon Richter Plc. (Budapest, Hungary) for sponsorship. Moreover, one of the authors (Á. G.-K.) is indebted to the József Varga Foundation for financial support.

Supporting Information Available: NMR data and spectra, analytical HPLC chromatograms. This material is available free of charge via the Internet at http://pubs.acs.org.

LITERATURE CITED

(1) Owellen, R. J., Jr., Owens, A. H., and Donigian, D. W. (1972) The binding of vincristine, vinblastine and colchicine to tubulin. *Biochem. Biophys. Res. Commun. 47*, 685–691.

(2) Owellen, R. J., Hartke, C. A., Dickerson, R. M., and Hains, F. O. (1976) Inhibition of tubulin-microtubule polymerization by drugs of the vinca alkaloid class. *Cancer Res. 36*, 1499–1502.

(3) Toso, R. J., Jordan, M. A., Farrell, K. W., Matsumoto, B., and Wilson, L. (1993) Kinetic stabilization of microtubule dynamic instability in vitro by vinblastine. *Biochemistry 32*, 1285–1293.

(4) Prakash, V., and Timasheff, N. S. (1991) Mechanism of interaction of vinca alkaloids with tubulin: catharanthine and vindoline. *Biochemistry 30*, 873–880.

(5) Barnett, J. C., Cullinan, J. G., Gerzon, K., Hoying, R. C., Jones, W. E., Newlon, W. M., Poore, G. A., Robison, R. L., Sweeney, M. J., Todd, G. C., Dyke, R. W., and Nelson, R. L. (1978) Structure-activity relationships of dimeric Catharanthus alkaloids. 1. Deacetylvinblastine amide (vindesine) sulfate. *J. Med. Chem. 21*, 88–96.

(6) Conrad, A. R., Cullinan, J. G., Gerzon, K., and Poore, A. G. (1979) Structure-activity relationships of dimeric catharanthus alkaloids. 2. Experimental antitumor activities of N-substituted deacetylvinblastine amide (Vindesine) su1fates. *J. Med. Chem. 22*, 391–400.

(7) Bhushana Rao, K. S. P., Collard, M-P. M., Dejonghe, J. P. C., Atassi, G., Hannart, J. A., and Trouet, A. (1985) Vinblastin-23-oyl amino acid derivatives: chemistry, physicochemical data, toxicity, and antitumor activities against P388 and L1210 leukemias. *J. Med. Chem. 28*, 1079–1088.

(8) Laguzza, C. B., Nichols, L. C., Briggs, L. S., Cullinan, J. G., Johnson, A. D., Starling, J. J., Baker, L. A., Bumol, F. T., and Corvalant, F. R. J. (1989) New antitumor monoclonal antibody-vinca conjugates LY203725 and related compounds: design, preparation, and representative in vivo activity. *J. Med. Chem. 32*, 548–555.

(9) Apelgren, D. L., Zimmerman, L. D., Briggs, L. S., and Bumol, F. T. (1990) Antitumor activity of the monoclonal antibody-vinca alkaloid immunoconjugate LY203725 (KSl/4−4-Desacetylvinblastine-3-carboxhydrazide) in a Nude Mouse Model of human ovarian cancer. *Canser Res. 50*, 3540–3544.

(10) Starling, J. J., Maciak, S. M., Hinson, A. N., Nichols, L. C., Briggs, L. S., Laguzza, C. B., Smith, W., and Corvalan, F. R. J. (1992) In vivo antitumor activity of a panel of four monoclonal antibody-vinca alkaloid immunoconjugates which bind to three distinct epitopes of carcinoembryonic antigen. *Bioconjugate Chem. 3*, 315–322.

(11) Gutowski, C. M., Briggs, L. S., and Johnson, A. D. (1991) Epidermal growth factor receptor-reactive monoclonal antibodies: xenograft antitumor activity alone and as drug immunoconjugates. *Cancer Res. 51*, 5471–5475.

(12) Johnson, A. D., and Laguzza, C. B. (1987) Antitumor xenograft activity with a conjugate of a vinca derivative and the squamous carcinoma-reactive monoclonal antibody PF1/D. *Cancer Res. 47*, 3118–3122.

(13) Vlahov, R. I., Santhapuram, R. K. H., Kleindl, J. P., Howard, J. S., Stanford, M. K., and Leamon, P. C. (2006) Design and regioselective synthesis of a new generation of targeted chemotherapeutics. Part 1: EC145, a folic acid conjugate of desacetylvinblastine monohydrazide. *Bioorg. Med. Chem. Lett. 16*, 5093–5096.

(14) Leamon, P. C., Reddy, A. J., Vlahov, R. I., Kleindl, J. P., Vetzel, M., and Westrick, E. (2006) Synthesis and biological evaluation of EC140: a novel folate-targeted vinca alkaloid conjugate. *Bioconjugate Chem. 17*, 1226–1232.

(15) Mitchell, D. J., Kim, D. T., Steinman, L., Fathman, C. G., and Rothbard, J. B. (2000) Polyarginine enters cells more efficiently than other polycationic homopolymers. *J. Pept. Res. 56*, 318–325.

(16) Futaki, S., Suzuki, T., Ohashi, W., Yagami, T., Tanaka, S., Ueda, K., and Sugiura, Y. (2001) Arginine-rich peptides. An abundant source of membrane-permeable peptides having potential as carriers for intracellular protein delivery. *J. Biol. Chem. 276*, 5836–5840.

(17) Hudecz, F., Bánóczi, Z., and Csík, G. (2005) Medium-sized peptides as built in carriers for biologically active compounds. *Med. Res. Rev. 25*, 679–736.

(18) Rothbard, J. B., Garlington, S., Lin, Q., Kirschberg, T., Kreider, E., McGrane, P. L., Wender, P. A., and Khavari, P. A. (2000) Conjugation of arginine oligomers to cyclosporin A facilitates topical delivery and inhibition of inflammation. *Nat. Med. 6*, 1253–1257.

(19) Miklán, Zs., Szabó, R., Zsoldos-Mády, V., Reményi, J., Bánóczi, Z., and Hudecz, F. (2007) New ferrocene containing peptide conjugates: Synthesis and effect on human leukemia (HL-60) cells. *Biopolymers. 88*, 108–114.

(20) Bánóczi, Z., Peregi, B., Orbán, E., Szabó, R., and Hudecz, F. (2008) Synthesis of Daunomycin containing oligoarginine conjugates and their effect on Human leukemia cells (HL-60). *Arkivoc iii*, 140–153.

(21) Enkvist, E., Lavogina, D., Raidaru, G., Vaasa, A., Viil, I., Lust, M., Viht, K., and Uri, A. (2006) Conjugation of adenosine and hexa-(D-arginine) leads to a nanomolar bisubstrate-analog inhibitor of basophilic protein kinases. *J. Med. Chem. 49*, 7150–7159.

(22) Kaiser, E., Colescott, R. L., Bossinger, C. D., and Cook, P. I. (1970) Color test of detection of free amino groups in the solid phase synthesis of peptides. *Anal. Biochem. 34*, 595–598.

(23) The ethyl ester derivative of 3 is known as an antitumor agent vintriptol investigated in phase I and II clinical studies, see also Oosterkamp, H. M., Vlasveld, L. Th., Wanders, J., Beijnen, J. H., Van Tellingen, Dubbelman, O., A. C., Simonetti, G. P. C., Franklin, H. R., Vermorken, J. B., and Ten, W. W. (1991) Phase I study of vintriptol, a tryptophan ester of vinblastin. *Eur. J. Cancer Clin. Oncol. 27*, 1222–1226.

(24) Na, C. N., and Timasheff, S. N. (1986) Interaction of vinblastine with calf brain tubulin: multiple equilibria. *Biochemistry 25*, 6214–6222.

(25) Lehotzky, A., Tirián, L., Tökési, N., Lénárt, P., Szabó, B., Kovács, J., and Ovádi, J. (2004) Dynamic targeting of microtubules by TPPP/p25 affects cell survival. *J. Cell Sci. 117(Pt 25)*, 6249–6259.

(26) Hannart, J. A., Bhushana Rao, K. S. P., and Trouet, A. (1981) *N*-(Vinblastinoyl-23) derivatives of amino acids and peptides and their preparation, EP0041935.

(27) Brady, S. F., Pawluczyk, J. M., Lumma, P. K., Feng, D.-M., Wai, J. M., Jones, R., DeFeo-Jones, D., Wong, B. K., Miller-Stein, C., Lin, J. H., Oliff, A., Freidinger, R. M., and Garsky, V. M. (2002) Design and synthesis of a pro-drug of vinblastine targeted at treatment of prostate cancer with enhanced efficacy and reduced systemic toxicity. *J. Med. Chem. 45*, 4706–4715.

BC100028Z

Synthesis and *in vitro* antitumor effect of vinblastine derivative-oligoarginine conjugates

Zoltán Bánóczi[†], Álmos Gorka-Kereskényi[‡], Judit Reményi[†], Erika Orbán[†], László Hazai[‡, $], Natália Tőkési[§], Judit Oláh[§], Judit Ovádi[§], Zoltán Béni[&], Viktor Háda[&], Csaba Szántay[&] Jr., Ferenc Hudecz*[†,#], György Kalaus[$] and Csaba Szántay[‡,$]

[†] *Research Group of Peptide Chemistry, Eötvös Loránd University (ELTE), Hungarian Academy of Sciences, Budapest 112, P.O. Box 32, H-1518, Hungary,*

[‡] *Department of Organic Chemistry and Technology, Budapest University of Technology and Economics, Budapest, Hungary,*

[$] *Research Group for Alkaloid Chemistry, Hungarian Academy of Sciences, University of Technology and Economics, Budapest, Hungary*

[§] *Institute of Enzymology, Biological Research Center, Hungarian Academy of Sciences, Budapest, Hungary,*

[&] *Spectroscopic Research, Gedeon Richter Plc., H-1475 Budapest 10, P.O.Box 27 , Hungary,*

[#] *Department of Organic Chemistry, Eötvös Loránd University (ELTE), Budapest Hungary,*

Content

Table 1. 3

Figure 1 4

Figure 2 5

Figure 3 6

Figure 4 7

Figure 5 8

Table 1. Partial ^{1}H and ^{13}C NMR assignments of the two Arg8 conjugates

	17-desacetylvinblastineTrp-Arg_8-2		17-desacetylvinblastineTrp-Arg_8-1	
Position	^{1}H (ppm)	^{13}C (ppm)	^{1}H	^{13}C (ppm)
2	3.77 s	82.9	Nd	nd
3'	3.14 m & 4.21 m	48.0	3.08 m & 4.21 m	48.1
5'	3.92 m & 4.00	59.6	3.94 m	59.5
6'	3.73 & 4.84 m	23.3	3.70 m & 4.77 m	23.2
14	6.23 dd	nd	6.21 dd	nd
15	6.06 br d	133.2	5.98 br	nd
14'	1.71	29.2	1.63 m	29.4
15'	1.96 m & 2.06 m	39.4	1.97 m & 2.02 m	39.2
17	3.92 s	75.6	4.08 s	76.5
17'	2.79 & 4.16 m	38.0	2.70 & 4.13 m	38.1
18	1.11 t	10.6	1.14 t	10.6
19	1.52 m & 1.86 m	35.7	1.52 m & 1.92m	35.2
18'	1.28 t	9.1	1.29 t	8.9
19'	1.86 m	37.3	1.87 m	37.1
20		45.7		45.4
20'		70.5		70.3
21'	3.55 m	63.7	3.49 m & 3.56 m	63.6
9	7.12	126.9	6.89 br	nd
12	6.69	98.4	6.44 s	94.6
9'	7.96 d	120.9	7.93 d	120.4
10'	7.51 t	122.7	7.58 t	122.0
11'	7.58 t	126.1	7.54 t	125.3
12'	7.72 d	114.5	7.65 d	113.8
α	5.09 t	58.9	4.85 dd	58.9
β	3.73 m	29.8	3.58 dd & 3.72 dd	30.2
δ1	7.57 s	127.3	7.65 s	126.7
ε2	7.96 d	120.9	8.09 d	121.0
ζ2	7.19 t	122.5	7.49 t	121.7
η1	7.84 d	114.9	7.77 d	114.2
η2	7.57 t	127.3	7.49 t	124.2
N-Me	2.84 s	42.2	2.13 br s	40.0
16-COOMe	4.05 s	59.0	3.97 s	58.8
11-OMe	4.19 s	55.6	4.10 s	55.6
Arg α*	4.64 m (4.50 dd)	56.0 (56.5)	4.64 m (4.59)	56.0
Arg β*	2.04 m & 2.14 m	31.4	2.05 m & 2.15 m	31.5
Arg γ*	1.93 m & 1.96 m	27.5	1.96 & 1.93	27.4
Arg δ*	3.50 m (3.40 t)	43.6	3.50 (3.44)	43.5

nd: not determined;

* Approximate chemical shifts of the Arg residues (congested signals); some of the signals belonging to the *N*-terminal Arg are separately detectable, these are given in parentheses.

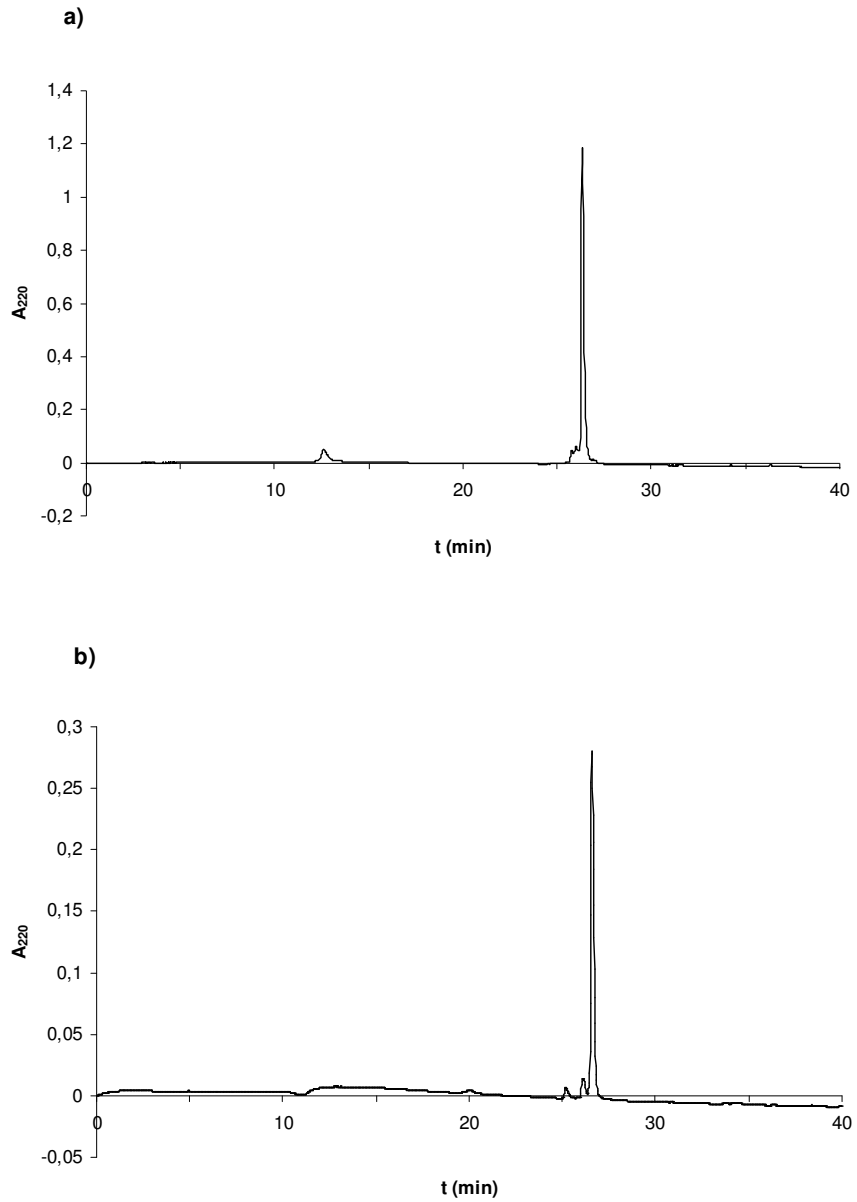


Figure 1. Analytical chromatogram of a) 17-desacetylvinblastineTrp-Arg_8-1 and b) 17-desacetylvinblastineTrp-Arg_8-2. Column: Phenomenex SYNERGI MAX-RP (250 x 4.6 mm I.D., 4 µm silica, 80 Å pore size). Linear gradient elution 0 min 0% B; 5 min 0% B; 50 min 90% B using 0.1% TFA in water as eluent A and 0.1% TFA in acetonitrile-water (80:20, V/V) as eluent B

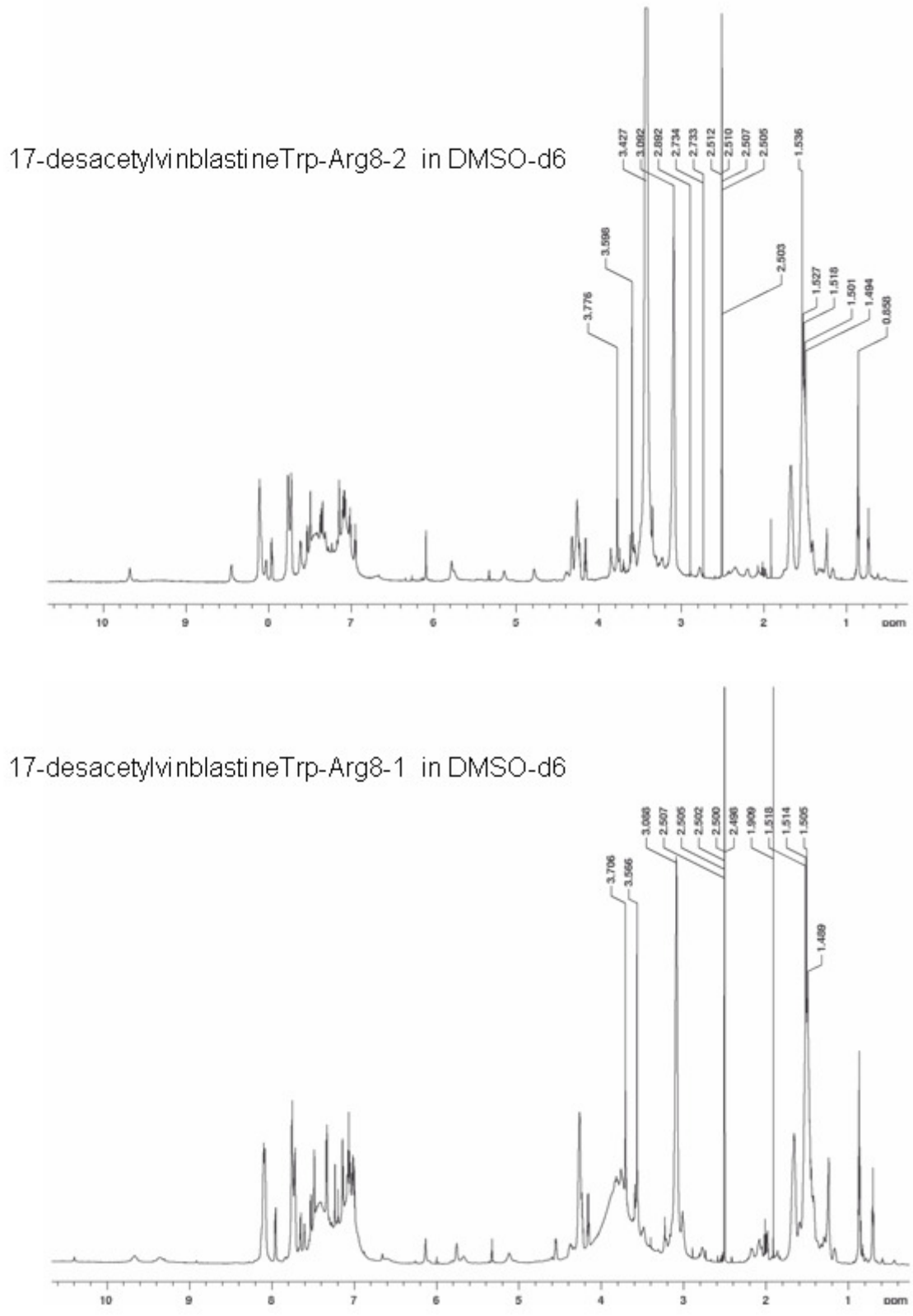


Figure 2. ^{1}H NMR spectra of the octaarginie epimers **17-desacetylvinblastineTrp-Arg$_8$-2** (above) and **17-desacetylvinblastineTrp-Arg$_8$-1** (below) in DMSO-*d6*

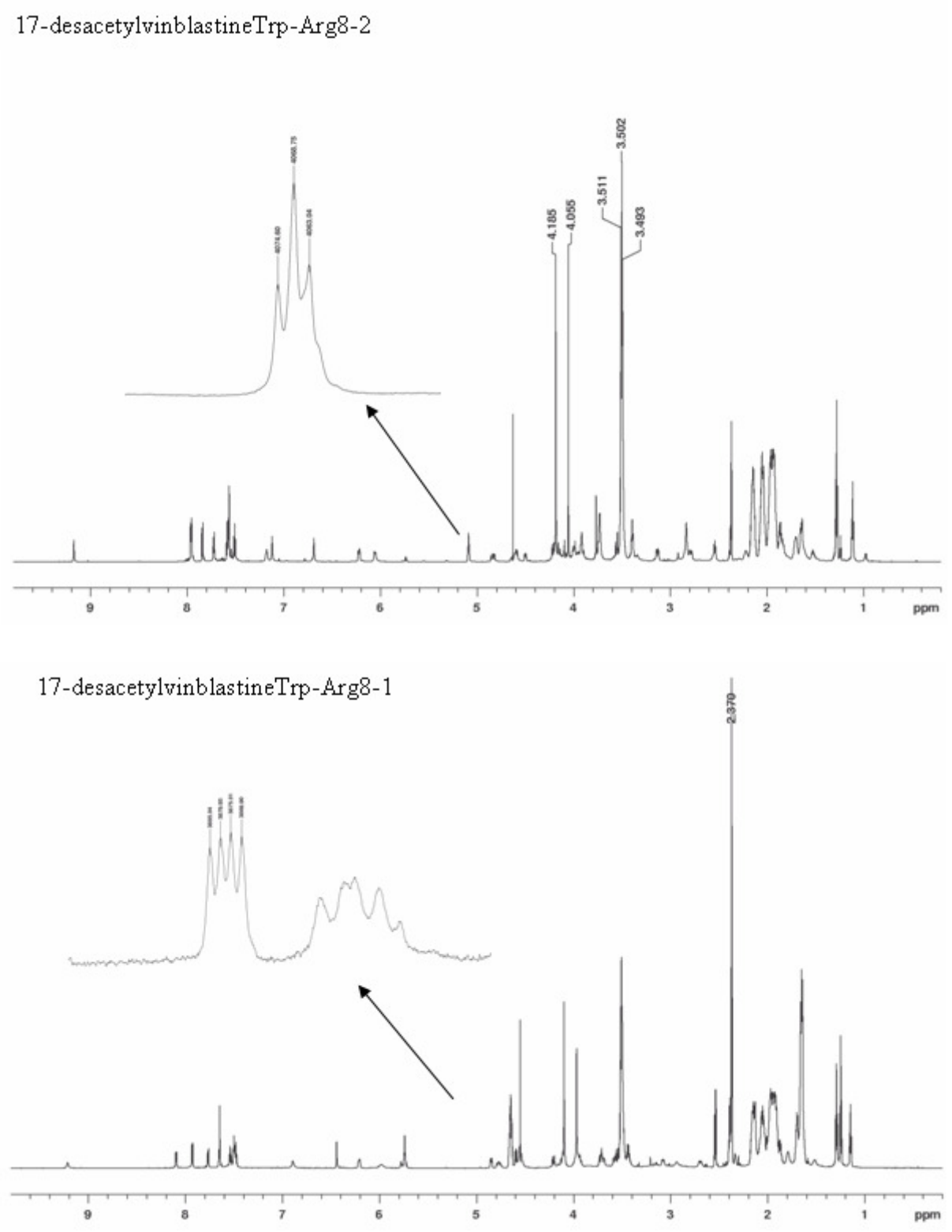


Figure 3. ^{1}H NMR spectra of the octaarginine epimers **17-desacetylvinblastineTrp-Arg$_8$-2** (upper trace) and **17-desacetylvinblastineTrp-Arg$_8$-1** (lower trace).

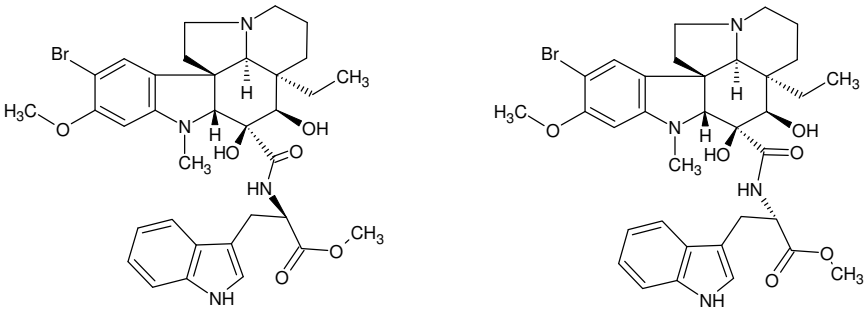


Figure 4. Structure of the “vindoline”-L-Trp (right) and of “vindoline”-D-Trp (left) conjugate used as model compounds.

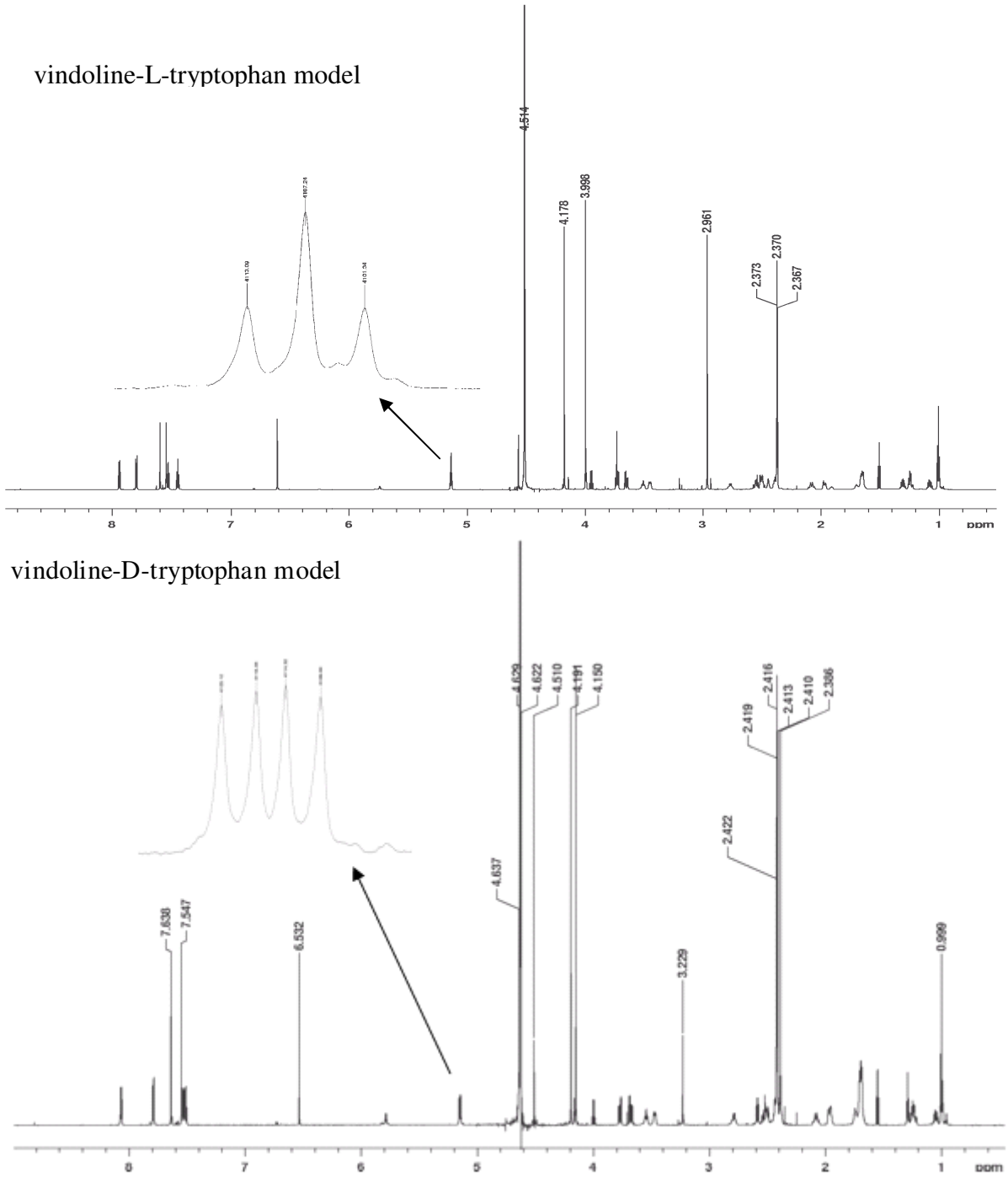


Figure 5. ^{1}H NMR spectra of the vindoline–L-Trp (upper trace) and of vindoline–D-Trp (lower trace) conjugate used as model compounds.

Conjugates of a Novel 7-Substituted Camptothecin with RGD-Peptides as $\alpha_v\beta_3$ Integrin Ligands: An Approach to Tumor-Targeted Therapy

Alma Dal Pozzo,*,† Emiliano Esposito,† Minghong Ni,† Laura Muzi,† Claudio Pisano,‡ Federica Bucci,‡ Loredana Vesci,‡ Massimo Castorina,‡ and Sergio Penco‡

Istituto di Ricerche Chimiche e Biochimiche G. Ronzoni, via G. Colombo, 81, 20133, Milano, Italy, and Area of Oncology Research and Development, Sigma-Tau, Pomezia, Roma, Italy. Received February 24, 2010; Revised Manuscript Received September 30, 2010

Eight conjugates of a novel camptothecin derivative (Namitecan, NMT) with RGD peptides have been synthesized and biologically evaluated. This study focused on factors that optimize the drug linkage to the transport vector. The different linkages investigated consist of heterofunctional glycol fragments and a lysosomally cleavable peptide. The linkage length and conformation were systematically modified with the purpose to understand their effect on receptor affinity, systemic stability, cytotoxicity, and solubility of the corresponding conjugates. Among the new conjugates prepared, **C6** and **C7** showed high receptor affinity and tumor cell adhesion, acceptable stability in murine blood, and high cytotoxic activity ($IC_{50} = 8$ nM). The rationale, synthetic strategy, and preliminary biological results will be presented.

INTRODUCTION

The antitumor efficacy of clinically used anticancer drugs is limited by their nonspecific toxicity to normal cells, resulting in a low therapeutic index. Therefore, great efforts are being devoted to the aim of targeting therapeutics preferentially to tumors, sparing physiological tissues and decreasing side effects. In late years, several different approaches to this problem have been studied, which mainly focused on conjugating cytotoxic agents with macromolecules such as monoclonal antibodies (mAbs) or polymeric materials (*1*−*5*). First successes have been achieved with mAbs immunoconjugates, and some of them are currently in clinical trials. However, there are factors restricting the scope of this approach: the antigen-dependent drug delivery to target tumor cell population can be limited by the cell surface density of expressed antigens and by saturation of the receptors with immunoconjugates that are endocytosed at a given rate. The new generation immunoconjugates have incorporated drugs that are considerably more potent than the standard anticancer agents. Among them, the anti-CD33-calicheamicin (Mylotarg) has been approved by FDA for treatment of acute myeloid leukemia (*6*).

During the past two decades, the understanding of many receptors overexpressed by tumor cells during proliferation has given impetus to the development of low-molecular-weight selective ligands. Therefore, following a trend toward replacing the antibody scaffolds with small molecules, several peptides have been proposed as tumor-targeting tools, to be used as receptor imaging or as therapeutics when conjugated with antitumor agents; for recent reviews on this topic, see ref 7, 8. Small receptor-binding peptides offer the advantage of being easily synthesized, modified, and characterized in order to optimize their affinity to specific receptors.

Cyclic peptides containing the RGD (Arg-Gly-Asp) sequence are well-known as specific ligands of the $\alpha_v\beta_3$ integrin cell surface receptor. This integrin has a predominant role in tumor-induced angiogenesis and is overexpressed on the activated endothelial cells in several tumor forms, but expressed at a low level on normal and mature endothelial cells. Inhibition of angiogenesis has been shown to prevent tumor growth and even cause tumor regression in various experimental models (*9*). However, antiangiogenic therapy usually is not sufficient to eradicate tumors in the late stage. Thus, combination of antiangiogenic agents with either chemo or radiation therapy has demonstrated enhanced activity in multiple tumor systems (*10*). Ruoslathi et al. first raised the idea of conjugating a cytotoxic agent with RGD-containing peptides (*11*−*13*). Later on, many RGD peptides have been evaluated for their potential as antiangiogenic agents or integrin-targeted radiotracers and/or therapeutics (*14*−*19*).

We were interested in studying the effect of RGD cyclopeptides in conjugation with a new potent antitumoral drug belonging to the camptothecin family, Namitecan, NMT (*20*). A number of camptothecin prodrugs and delivery systems have been developed to improve the pharmacokinetic profile of this anticancer drug (*21*−*23*). We have previously reported on the synthesis and biological evaluation of a number of RGD−NMT conjugates (*24*), where the targeting RGD peptide was attached to the drug by either amide or hydrazone bond; in theory, both linkages should be potentially stable at physiological pH, whereas the main difference between them lies in the acid stability. During that study, we demonstrated that the amide bond-containing conjugates maintained good affinity to integrin receptors and accumulated in tumor cells after internalization, but showed no appreciable activity both in vitro and in vivo, indicating that the amide bond is too stable to promptly release the drug into the tumor cells. On the contrary, the hydrazone bond-containing conjugates exhibited high in vitro cytotoxicity, but their stability at pH 7.4 was much lower than expected; as a consequence, their activity has been mostly attributed to the NMT prematurely liberated within the cell culture medium. Thus, it was concluded that both types of linkage are not suitable for these low-molecular-weight conjugates. Moreover, all conjugates prepared were not soluble enough for a complete in vivo study, likely because the proximity of ligand and drug

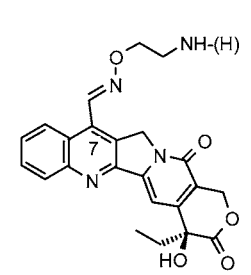
* To whom correspondence should be addressed. Dr. Alma Dal Pozzo, Ist. Di Ricerche Chimiche e Biochimiche G. Ronzoni, via Colombo 81, 20133 Milano, Italy. Tel.: +39-02-70600223; Fax: +39-02-70641634, e-mail: dalpozzo@ronzoni.it.

† Istituto di Ricerche Chimiche e Biochimiche G. Ronzoni.

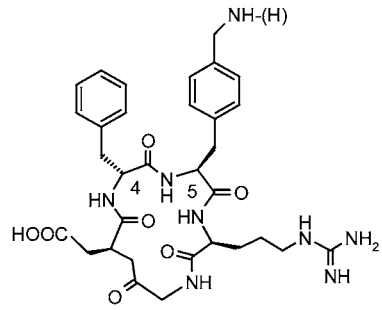
‡ Area of Oncology Research and Development.

10.1021/bc100097r © 2010 American Chemical Society
Published on Web 10/15/2010

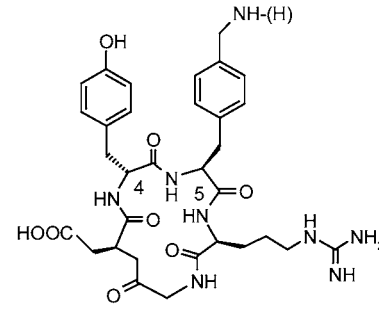
Chart 1. Structure of NMT, Cyclopeptides P1 and P2, and Conjugates C1−C7



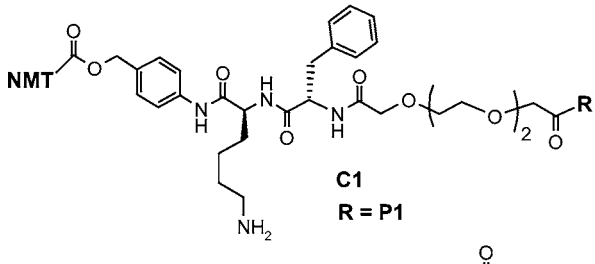
NMT (ST1968, Namitecan)



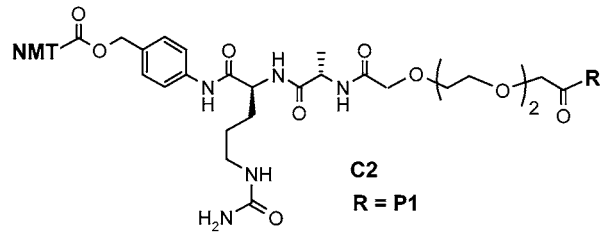
P1



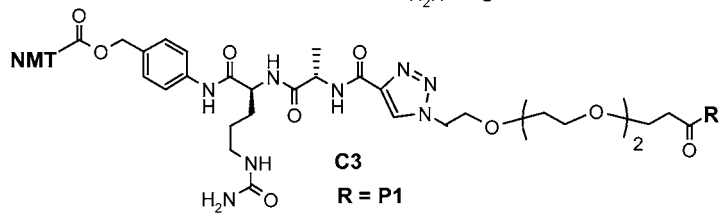
P2



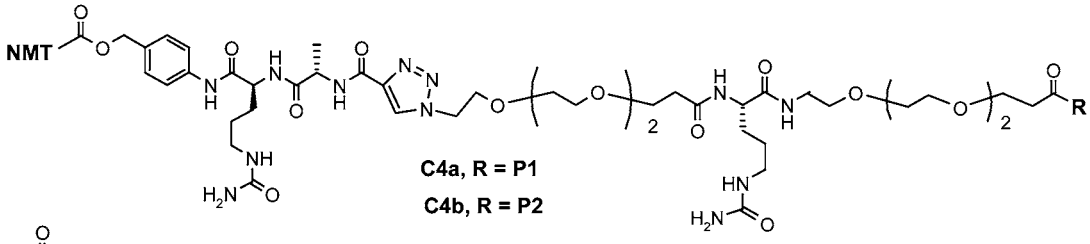
C1
R = P1



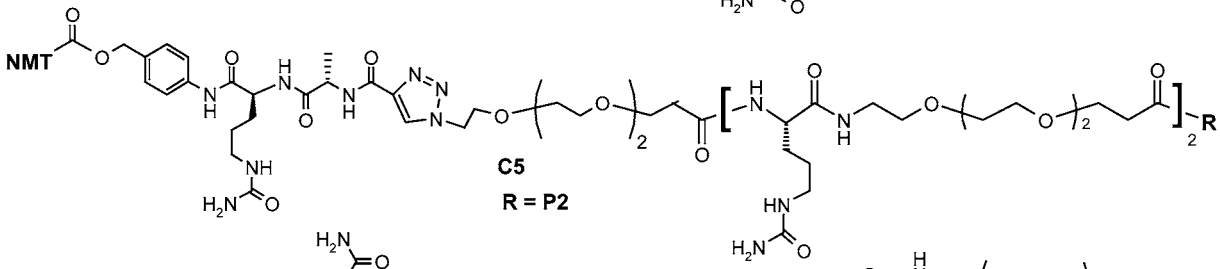
C2
R = P1



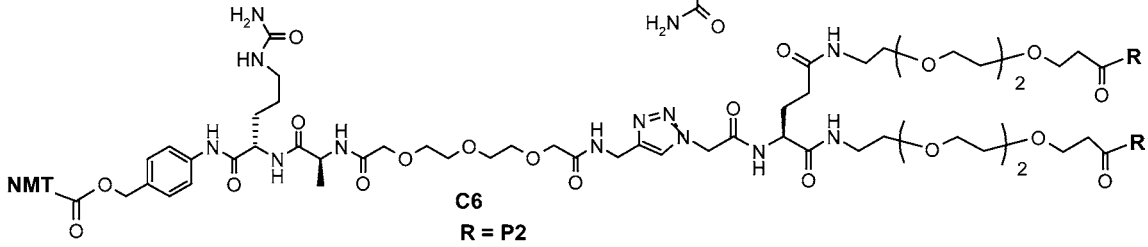
C3
R = P1



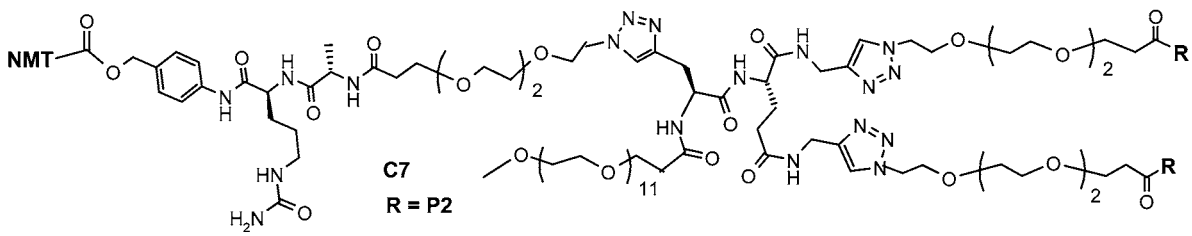
C4a, R = P1
C4b, R = P2



C5
R = P2

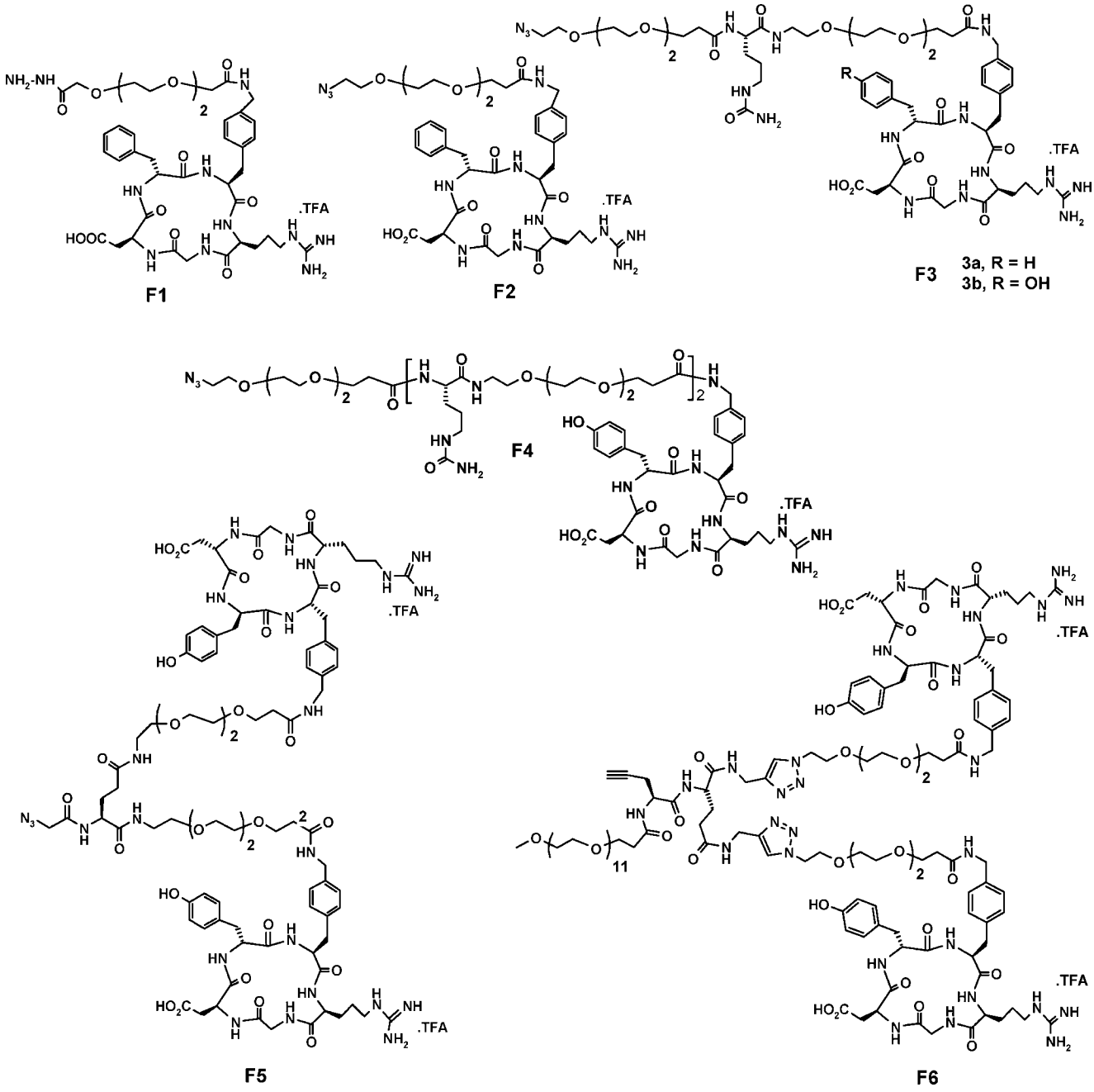


C6
R = P2



C7
R = P2

Chart 2. Structure of Fragments F1−F6, Containing Cyclopeptides



forms efficient intramolecular stacking interactions. Inspired by these results, we sought to verify another interesting approach, proposed in the literature and based on the introduction of selective protease-sensitive peptides into tumor-targeted conjugate spacers. These peptides have been claimed to be specific substrates of enzymes overexpressed within the lysosomal compartment of tumor cells, but rather stable to proteases in the systemic circulation (*25*−*28*).

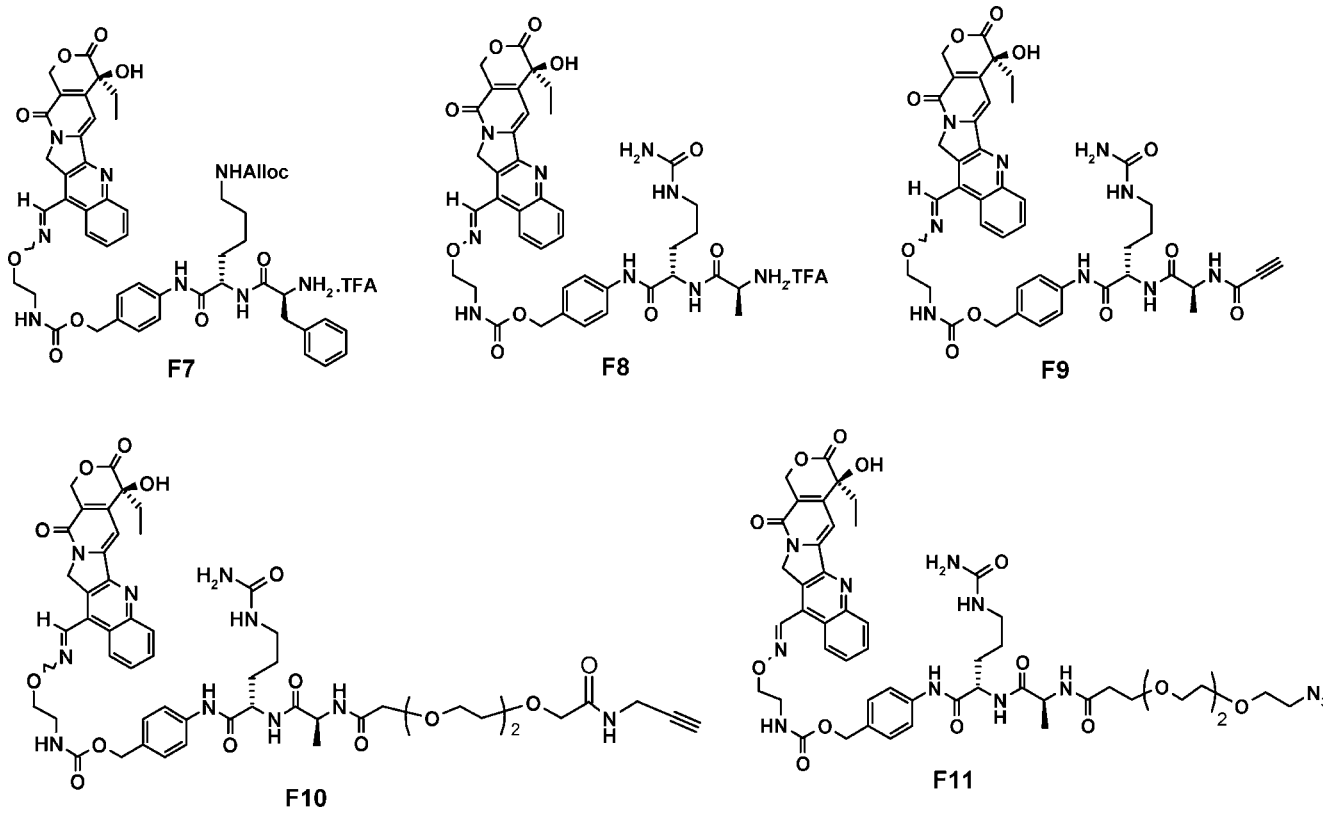
Because of our interest in the potential of this approach, we have undertaken the development of a series of tumor-targeted conjugates containing an $\alpha_v\beta_3$ integrin recognition moiety connected to NMT by different molecular bridges as spacers. The structure of these spacers include a peptide, that is enzymatically cleavable, but stable enough in the systemic circulation, and a number of glycol residues, whose length and conformation were systematically modified, in order to enhance solubility, without disturbing the binding of the RGD ligand to the receptor.The objective of the work described in this article was to study the effect of the spacer modifications on receptor affinity, stability in murine blood, cytotoxicity, and solubility of the new conjugates.

Among a series of RGD cyclopeptide analogues of Cilengitide (*29*), designed and synthesized in our laboratories for the purpose of this study, we identified **P1** and **P2** to be used as targeting ligands, owing to their optimal stability and affinity to α_v integrins (*30*). Peptide ligands, camptothecin derivative NMT, and conjugate structures are illustrated in Chart 1. The structure of the fragments used for assembling the conjugates is illustrated in Charts 2 and 3. Each pair of fragments, which were coupled together to obtain the desired conjugate, is described in Table 1.

EXPERIMENTAL PROCEDURES

Materials and Instruments. All reagents and solvents were reagent grade and were distilled prior to use. All natural amino

Chart 3. Structure of Fragments F7−F11, Containing the Cytotoxic Drug NMT



acids and resin were purchased from Bachem (Switzerland). Fmoc-4-aminomethyl-phenylalanine (Amp) was purchased from PepTech Corporation, Burlington, MA, USA; the corresponding building blocks, Fmoc-Amp-glycol-R (where R can be amino, hydrazido, or azido group), were easily synthesized by standard methods. PEG derivatives were purchased from Iris Biotech GMBH (Germany). Namitecan (ST1968) was synthesized in Sigma-Tau laboratories (*20*). Microwave-assisted reactions were performed on a CEM MW instrument. Compounds were purified and characterized by a RP-HPLC 600 Waters instrument, equipped with a semipreparative column Alltima, Alltech, RP18, 10 μ, 22 × 250 mm, or an analytical column Gemini, Phenomenex, C18, 5 μ, 4.6 × 250 mm, at $\lambda = 220$ nm, using acetonitrile/water with 0.1% trifluoroacetic acid as mobile phase. ^{1}H NMR spectra were recorded on an AC300 Bruker instrument. Mass spectra were recorded on Bruker Autoflex Maldi-Tof or Micro-Tof Q instruments. Flash chromatography was carried out on silica gel Merck 230−400 mesh.

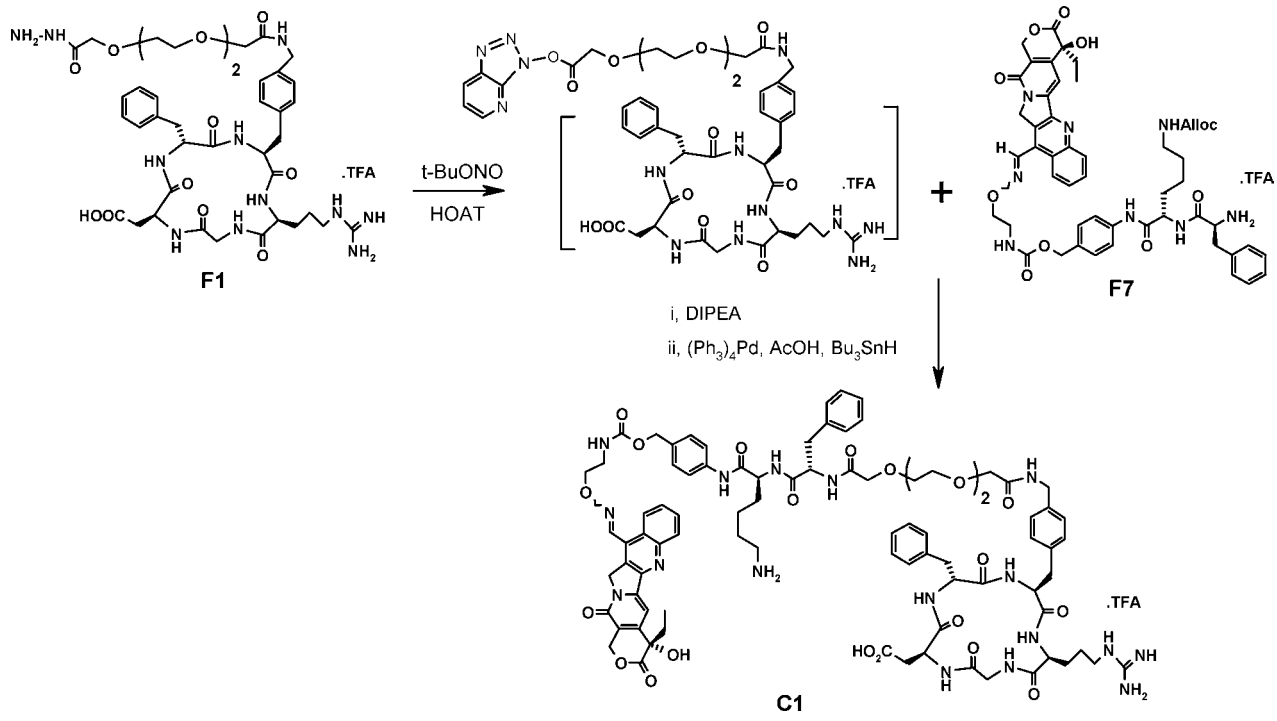
Synthesis of Conjugate C1. (Method A) As described in Scheme 1, fragment **F1** (350 mg, 0.319 mmol) and HOAT (259 mg, 1.91 mmol) were dissolved with 7 mL DMF; then, *t*-butyl nitrite (45 μL, 0.383 mmol) was added and the mixture left under stirring at room temperature. After 30 min, 1 equiv of DIPEA was added, and the reaction mixture was poured into a solution containing fragment **F7** (337 mg, 0.319 mmol) in 2 mL DMF; pH was adjusted to 7.5 with DIPEA and the mixture left under stirring at room temperature, protected from light. After 2 h, an additional equivalent of the activated ester, prepared in situ as described above, was added, pH adjusted at 7.5, and left overnight. The solvent was removed at reduced pressure, and the residue was purified by preparative HPLC (40% CH_3CN in H_2O + 0.1% TFA). To remove the *N*-Alloc group, the compound was dissolved in 1 mL DMF, under argon, together with 2.5 mg of $(Ph_3P)_4Pd$, AcOH (12 μL), and Bu_3SnH (25 μL), and stirred for 1 h. The final conjugate **C1** was obtained after repeated precipitations with cool diethyl ether followed by lyophilization, with 97% purity.

Synthesis of Conjugate C2. Coupling between fragments **F1** and **F8** was performed following the procedure described for conjugate **C1**. After purification by preparative HPLC and lyophilization, the compound was obtained with 97.6% purity.

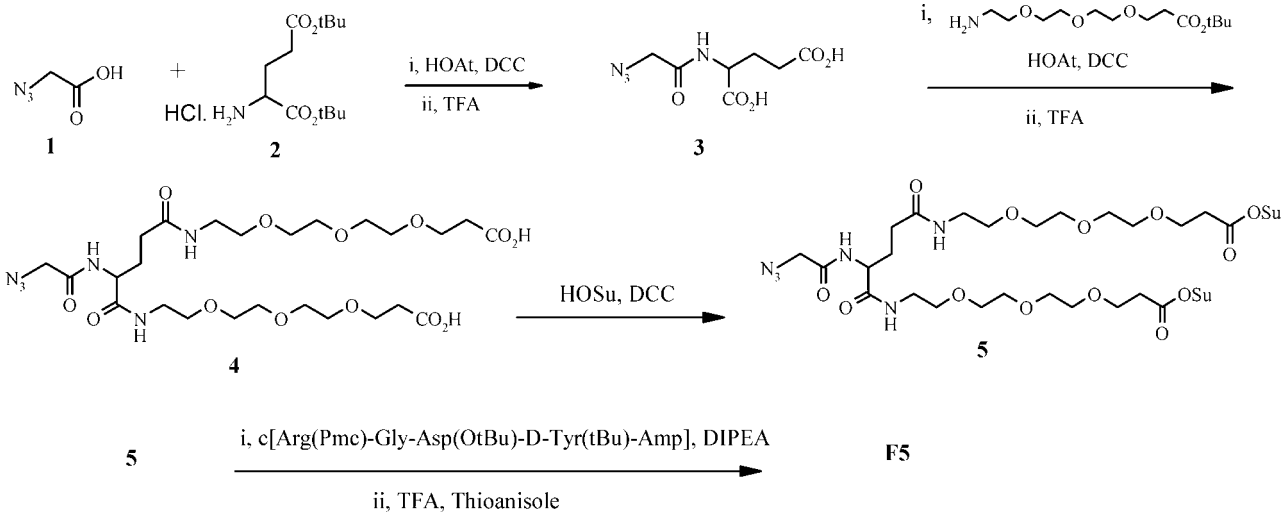
Synthesis of Conjugates C3−C7. (Method B) General procedure. Two fragments, containing an alkyne and an alkylazido group, respectively, were assembled by Huisgen 1,3-dipolar cycloaddition. Equimolar amounts of the two desired fragments were dissolved in DMF. Aqueous solutions of sodium ascorbate (1 equiv) and $CuSO_4 \cdot 5H_2O$ (0.1 equiv) were added, pH was adjusted to 6 by addition of NaOH, and the suspension was stirred at room temperature overnight. When necessary to speed up the reaction, the mixture was submitted to microwave irradiation, 90 W for 2 min (T_{max} obs 120 °C) once or twice until completion of the reaction, as monitored by HPLC. Final conjugates were obtained with >98% purity, after preparative HPLC and lyophilization.

MW-Assisted Solid-Phase Synthesis of Cyclopeptides. *General Procedure.* Solid-phase synthesis followed the standard Fmoc-protocol, starting from Fmoc-Gly-SASRIN. The amino acids (2 equiv) were added in the following order: Fmoc-Arg(Pmc)-OH, Fmoc-Amp(building block)-OH, Fmoc-D-Phe-OH (or Fmoc-D-Tyr(tBu)-OH), and Fmoc-Asp(OtBu)-OH. At each step, Fmoc deprotection was carried out with 20% piperidine. Energy applied: 30 W for 5 min (t_{max} obs. 70 °C) for couplings and 25 W for 3 min (t_{max} obs. 40 °C) for deprotections. For cleavage of the peptides, the resin was treated with 1% TFA in DCM during 15 min for 5 times and the filtrates immediately neutralized with pyridine. The collected filtrates were taken to dryness under vacuum, and the linear peptides were dissolved with acetonitrile containing 1% DIPEA to obtain a 1.5×10^{-3} M solution, then added with 3 equiv TBTU/HOBT and stirred for 1 h, until complete cyclization, as monitored by HPLC. After evaporation of the solvent, the cyclopeptides were

Scheme 1. Synthesis of the Conjugate C1



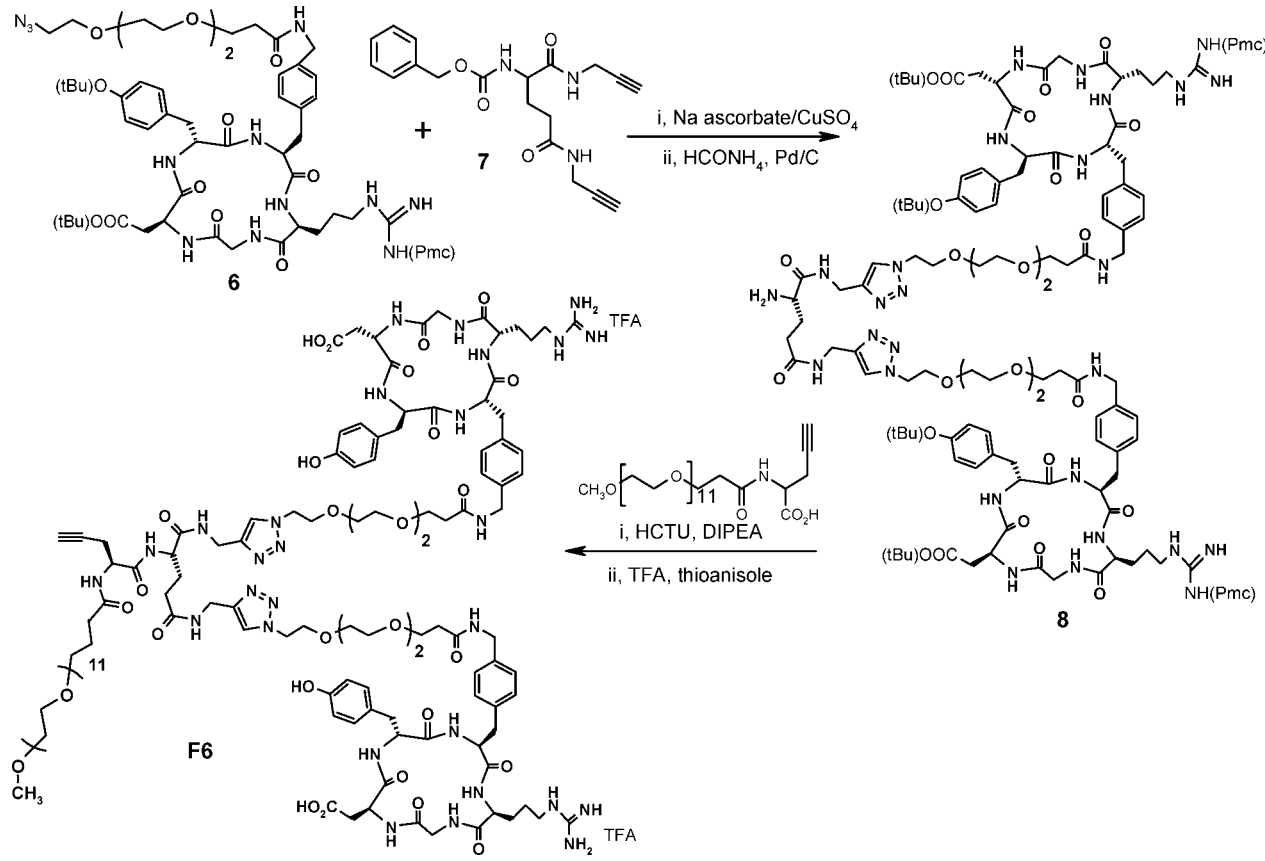
Scheme 2. Synthesis of Fragment F5



dissolved with DCM and washed (water, 0.1 N HCl, water). The organic phase, after drying with Na_2SO_4, was concentrated and the residue purified by flash chromatography (mobile phase, 95:5 → 85:15 DCM/MeOH). Removal of the protecting groups was performed with 95:5 TFA/H_2O within 1 h. After concentration to small volume, the products were further purified by repeated precipitations with dry and cold diethyl ether. Total yields were around 50%, calculated on the amount of starting resin.The cyclopeptides prepared with this method differ from each other for the presence of D-Phe **(P1)** or D-Tyr (**P2**) at position 4 and for the Amp-building blocks at position 5.

Synthesis of Fragment F5. As described in the Scheme 2, DCC (84 mg, 0.405 mmol) was added to a cold solution of azidoacetic acid **1** (41 mg, 0.405 mmol), glutamic acid di-*tert*-butyl ester. HCl **2** (100 mg, 0.338 mmol), HOAT (0.405 mmol), and DIPEA (127 mL, 0.744 mmol) in 5 mL DCM. The reaction was stirred at room temperature for 2.5 h and after filtration was diluted up to 30 mL and washed with water, 0.1 N HCl, 5% $NaHCO_3$, and water. After removing the solvent, the residue was treated with 3 mL of TFA for 1 h to afford 2-(2-azidoacetylamino)-pentanedioic acid **3**, which was dissolved with 45 mL of 8:1 DCM/DMF and coupled with *tert*-butyl 12-amino-4,7,10-trioxadodecanoate (281 mg, 1.01 mmol), HOAT (137 mg, 1.014 mmol), DIPEA (174 mL), and DCC (209 mg, 1.014 mmol) by the standard method to give a crude product that was purified by flash chromatography (95:5 DCM/MeOH) to obtain 175 mg of a solid white powder. Yield 68% (calc. for 3 steps). After deprotection with TFA, the bis-carboxylic intermediate **4** (0.234 mmol**)** was dissolved with 5 mL of DMF and treated with *N*-hydroxysuccinimide (108 mg, 0.936 mmol) and DCC (145 mg, 0.700 mmol) by stirring overnight. Solvent was removed and the succinimide **5**, dissolved with 8 mL DCM, was added to a solution of the partially protected cyclopeptide c[Arg(Pmc)-Gly-Asp(OtBu)-D-Tyr(tBu)-Amp], 728 mg, 0.66 mmol and DIPEA (113 μL, 0.66 mmol) in 14 mL of DMF. After 1.5 h, solvent was removed and the residue purified by preparative HPLC (69% CH_3CN). Yield 48%. Total deprotection was performed with 1:1 TFA/DCM containing 220 equiv of

Scheme 3. Synthesis of Fragment F6



thioanisole. The pure fragment **F5** was obtained as a white solid after evaporation of the solvents and subsequent precipitations from cold diethyl ether. Yield 79%.

Synthesis of Fragment F6. As reported in Scheme 3, the totally protected cyclopeptide c{Arg(Pmc)-Gly-Asp(OtBu)-D-Tyr(OtBu)-Amp[CO-$(CH_2)_2$-(O-CH_2-CH_2)-O-$(CH_2)_2$-N_3]} **6** (572 mg, 0.448 mmol) and 1,3-bis-(prop-2-ynylcarbamoyl-propyl)-carbamic acid benzyl ester **7** (72.5 mg, 0.206 mmol) were dissolved with 12 mL of 7:5 DMF/H_2O. Then, 2.5 M sodium ascorbate (90 μL) and 0.5 M $CuSO_4 \cdot 5H_2O$ (45 μL) were added, and the mixture submitted to microwave irradiation (90 W, T_{max} obs. 121 °C). The same operation was repeated three times until complete disappearance of the starting material, which was monitored by HPLC (35% CH_3CN). After removing the solvent under reduced pressure, the crude residue was purified by flash chromatography (93:7 → 90:10 → 80:20 DCM/MeOH). Yield 71%. ESI mass: 1453.6 (*m*/*z* 2+), 969.4 (*m*/*z* 3+). 406 mg of this product was dissolved with 3:5 DMF/MeOH and orthogonally deprotected by means of ammonium formate (44 mg, 0.7 mmol) and Pd/C (200 mg). After 3 h stirring, the reaction was filtered, and the filtrate concentrated to give the intermediate **8**, which was dissolved with 3 mL DMF and used for the next step. *N*-(Methyl-PEG_{11}-carboxy)-propargylglycine (102 mg, 0.149 mmol in 4.5 mL DCM) followed by HCTU (62 mg, 0.149 mmol) and DIPEA (51 μL, 0.298 mmol) were added, and the resulting solution stirred for 2 h. After evaporation, the residue was redissolved with 300 mL of DCM and washed with water (2 × 50 mL).The organic phase was evaporated, and the fragment fully deprotected by means of a mixture of TFA/DCM/thioanisole (1:1:0.3). After taking to dryness, the residue was purified by repeated precipitations from TFA with cold diethyl ether, to afford 245 mg of fragment **F6**, with 41% yield (calculated from 3 steps).

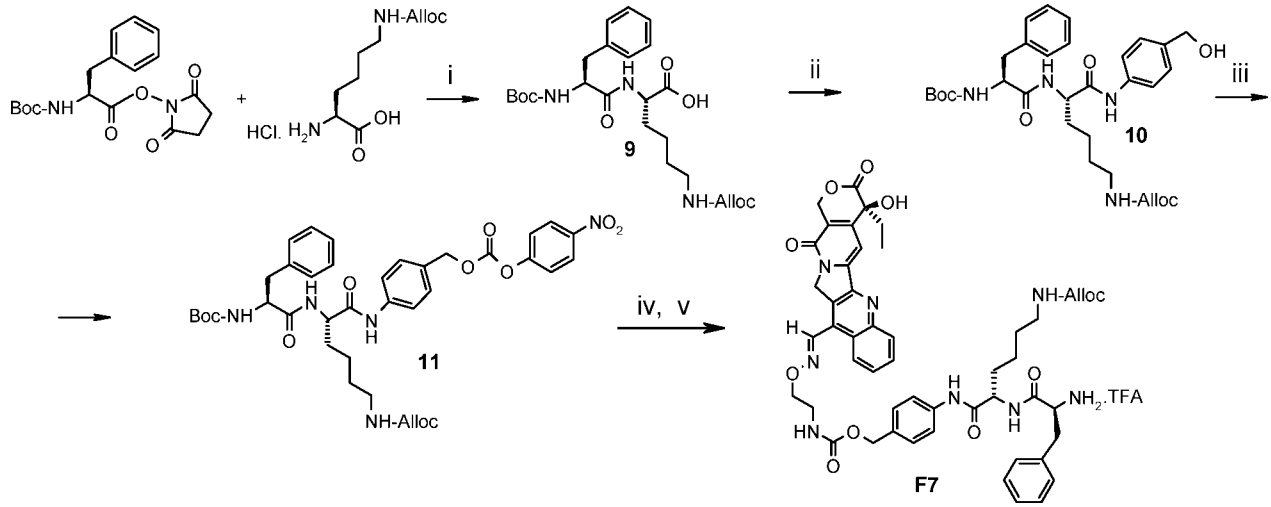
Conjugates Binding to $\alpha_v\beta_3$ Integrin, Tumor Cell Adhesion, and in Vitro Cytotoxicity. These assays were performed following the experimental procedures already published (*24*), and the results are reported in the Tables 5 and 7.

Conjugate Stability in Murine Blood. The blood of untreated healthy mice was collected in tubes containing 2% EDTA.The sample molecules were added to obtain a concentration of 5 μM.The tubes were incubated at 37 °C under rotation for different sampling times during an interval of 3 h. At each time point, the samples were centrifuged at 1000*g* for 10 min, and the supernatants transferred in new tubes and stored at −20 °C. Plasma (100 μL) was processed by adding 700 μL of a cold mixture of 0.1% acetic acid and methanol (1:5 v/v). After vortexing, samples were kept at 20 °C for 10 min and then centrifuged at 14 000*g* for 10 min at 4 °C. The supernatants were analyzed by RP-HPLC-FL Beckman; column, Discovery HS-F5, 100 × 4.6 mm, 5 μ, Supelco; mobile phase, A = 0.1 M AcOH + 0.1% TEA, B = CH_3CN; flow rate, 1 mL/min; spectrofluorometric detector, RF-10AXL Shimadzu; wavelengths, λ_{ex} 370 nm and λ_{em} 510 nm. A gradient elution was employed ranging from 25% to 33% B within 30 min. Data were acquired by computer system and processed by 32Karat Software, Beckman. Calibration curves were performed in plasma, and peak areas were used to calculate each calibration curve intercept and the slope of each calibration curve equation by weighted least-squares method, using l/*y* as weighting factor. All peaks were well-resolved from impurities of plasma and methods were linear in the tested range ($r^2 > 0.985$), with results suitable for quantification. Results are reported in Table 6 as a percentage of residual amounts found at each sampling time versus time zero (calculated using mean values of triplicate samples).

RESULTS

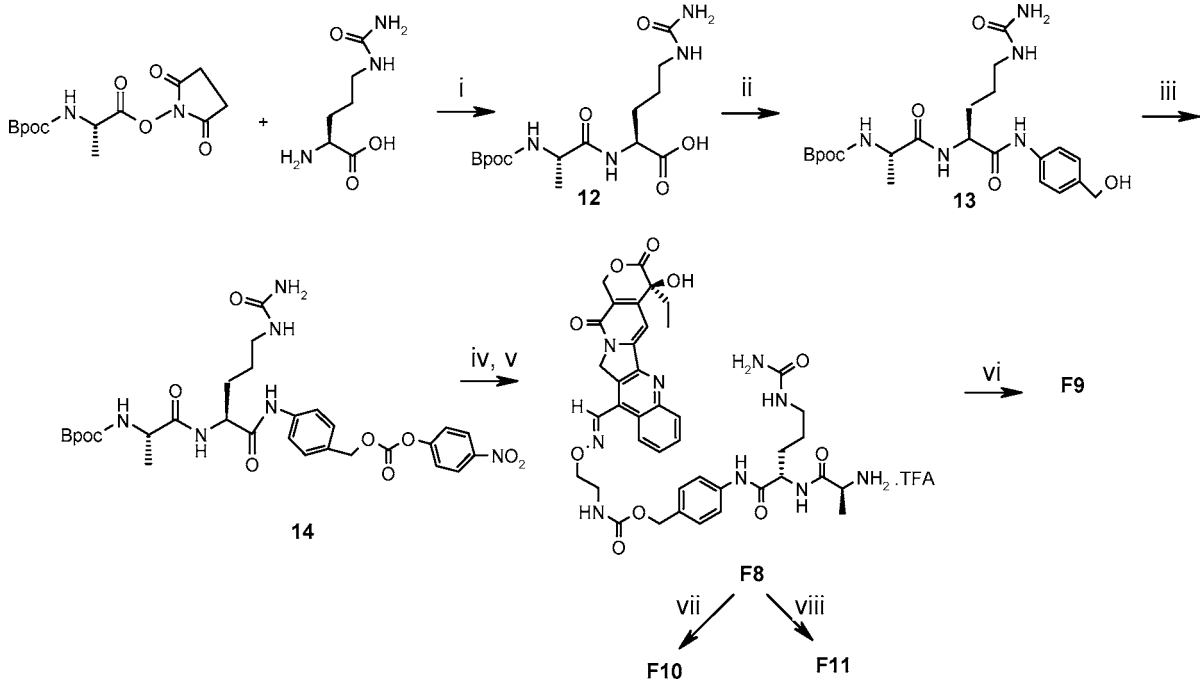
Synthesis. Two groups of fragments have been prepared: the fragments **F1**−**F6** of the first group (Chart 2) contain one or

Scheme 4. Synthesis of Fragment F7[a]



[a] Reagents and conditions: (i) LiOH·H_2O; (ii) 4-aminobenzylalcohol, HOAT, DCC; (iii) 4-nitrophenylchloroformate, py; (iv) 7-(2-aminoethoxyimine)-methyl-camptothecin.HCl, TEA, DMF; (v) TFA/DCM 1:1. Total yield 46.8%.

Scheme 5. Synthesis of Fragments F8−F11[a]



[a] Reagents and conditions: (i) LiOH·H_2O; (ii) 4-aminobenzylalcohol, HOAT, DCC; (iii) 4-nitrophenylchloroformate, py; (iv) NMT, TEA; (v) 0.5% TFA in trifluoroethanol, 30 min, total yield 56.2%; (vi) propiolic acid, HOAT, DCC; yield 72.6%; (vii) HCC-CH_2-NH-CO-CH_2-O-(CH_2-CH_2O)$_2$-CH_2-COOH, DCC, yield 63.5%; (viii) N_3-$(CH_2)_2$-O-(CH_2-CH_2-O)$_2$-$(CH_2)_2$-COOH, DCC, yield 62.8%.

two RGD cyclopeptides, which differ from each other for the amino acid in position 5 bearing glycol chains of different length and conformation. These fragments were built with good yields by MW-assisted SPPS, following cyclization in solution. In the case of the dimeric fragments **F5** and **F6**, two cyclopeptides were connected in solution through a dendron based on glutamic acid. The experimental procedures are given in detail and illustrated in Schemes 2 and 3. Fragments **F7**−**F11** of the second group (Chart 3) contain the camptothecin derivative and the lysosomally cleavable dipeptide sequence.The dipeptide is connected to the *N*-terminal of the drug through 4-aminobenzylalcohol (PABA). PABA is a known self-immolative entity (*31*) that accomplishes a double function, to increase the distance between peptide and cytotoxic drug, allowing a better recognition by the endopeptidases, and to guarantee prompt release of the parent drug through a 1,6-elimination mechanism, only after the enzymatic hydrolysis. The fragments belonging to the latter group were all prepared with similar synthetic procedures, except for minor modifications. In fact, during the synthesis of the first fragment **F7** (Scheme 4), deprotection of the terminal *N*-Boc caused a loss of about 10% of NMT, even reducing the TFA treatment to a few minutes. Therefore, *N*-Bpoc protection was used for fragments **F8**−**F11** (Scheme 5), because it can be removed with 0.5% TFA in trifluoroethanol without any cleavage of the carbamate bond.

In each fragment of both groups, a unique amino, hydrazido, azido, or alkyne function was introduced for further reaction with the corresponding counterpart to give the desired conjugates **C1**−**C7** (Chart 1). Each pair of fragments used for the synthesis of each conjugate is indicated in Table 1. The formation of

Table 1. Reacting Fragments, Coupling Methods Used in the Synthesis of Conjugates C1−C7 and Yields

fragments	conjugates	yields %
F1 + F7	**C1**[a]	46.6
F1 + F8	**C2**[a]	55.0
F2 + F9	**C3**[b]	44.0
F3a + F9	**C4a**[b]	42.5
F3b + F9	**C4b**[b]	45.0
F4 + F9	**C5**[b]	39.0
F5 + F10	**C6**[b]	41.0
F6 + F11	**C7**[b]	42.0

[a] Method A. [b] Method B.

conjugates needs a chemoselective synthesis. In fact, the reacting fragments must be used in a totally deprotected form, because the carbamate bond between NMT and the rest of the molecule is very sensitive to all late deprotection conditions. Two different methods were used: the conjugates **C1** and **C2** were synthesized via the acylazide method from the initial hydrazide, using the transfer active ester condensation procedure (TAEC) introduced by Ramage et al. (*32*), as described in Scheme 1 (Method 1). Later on, for conjugates **C3−C7**, we found more convenient the use of Huisgen 1,3-dipolar reaction (*33*), (Method B). In fact, this cycloaddition affords cleaner products, because of its mild nature; moreover, grafting of the residual alkyne with the azide-terminated molecule enables the use of equivalent amounts of the two fragments, whereas the acylazide reaction requires two equivalents of the RGD counterpart. In the case of the bulkier conjugates, MW irradiation was applied to accelerate the reaction. Physico-chemical characterization of all fragments and conjugates is reported in the Tables 2, 3, and 4.

Effect of Spacer on the Conjugate Receptor Affinity, Tumor Cell Adhesion, and Stability in Murine Blood. The effects of spacer modifications on the behavior of the conjugates RGD−NMT are illustrated in Tables 5, 6, and 7. All spacers contain the dipeptide alanine-citrulline as a lysosomally cleavable sequence, except for **C1**, which contains phenylalanine-lysine. Within the series **C2−C5**, the spacers differ from each

Table 2. Physico-Chemical Characterization of Conjugates C1−C7

entry	HPLC[a], rt, min[b]	Maldi mass $[M+H]^+$	^{1}H NMR
C1	9.0, 12.0 (35%)	1696.6	(DMSO-d_6 + D_2O) δ 9.29 (s, 1H), 8.60 (d, 1H; J = 9.4), 8.22 (d, 1H, J = 9.4), 7.87 (t, 1H, J = 8.2), 7.73 (t, 1H, J = 8.2), 7.40 (s, 1H), 7.25 (d, 2H, J = 8.2), 7.20−7.10 (m, 14H), 7.03 (d, 2H; J = 8.2), 5.42−5.30 (m, 4H), 5.02 (s, 2H), 4.71−4.58 (m, 2H), 4.48−4.32 (m, 4H), 4.30−4.23 (m, 2H), 4.20−4.00 (m, 4H), 3.93 (s, 2H), 3.89−3.72 (m, 4H), 3.63−3.11 (m, 10H), 2.92−2.63 (m, 9H), 2.40−2.21 (m, 1H), 1.95−1.80 (m, 2H), 1.65−1.30 (m, 10H), 0.88 (t, 3H, J = 7.4).
C2	7.96, 10.4 (34%)	1650.71	(DMSO-d_6 + D_2O): δ 9.29 (s, 1H), 8.60 (d, 1H, J = 9.4), 8.22 (d, 1H, J = 9.4), 7.87 (t, 1H, J = 8.2), 7.73 (t, 1H, J = 8.2), 7.36 (s, 1H), 7.24 (d, 2H, J = 8.5), 7.15−7.11 (m, 9H), 7.03 (d, 2H, J = 8.5), 5.42 (s, 2H), 5.36 (s, 2H), 4.95 (s, 2H), 4.64−4.60 (m, 1H), 4.45−4.27 (m, 8H), 4.07−4.00 (m, 3H), 3.94 (s, 2H), 3.90 (s, 2H), 3.59−3.46 (m, 10H), 3.09−2.66 (m, 9H), 2.40−2.33 (m, 1H), 1.90−1.86 (m, 2H), 1.75−1.38 (m, 8H), 1.24 (d, 3H, J = 6.9), 0.89 (t, 3H, J = 7.3).
C3	7.7, 9.9 (34%)	1745.7	(DMSO-d_6 + D_2O) δ 9.19 (s, 1H), 8.50−8.40 (m, 2H), 8.19 (d, 1H, J = 8.4), 7.80 (t, 1H, J = 8.2), 7.74 (t, 1H, J = 8.2), 7.45 (d, 2H, J = 8.5), 7.39 (s, 1H), 7.19−6.95 (m, 11H), 5.48−5.30 (m, 3H), 5.19 (s, 1H), 4.89 (s, 2H), 4.69 (s, 1H), 4.60−4.24 (m, 8H), 4.20 (s, 2H), 4.13 (m, 1H), 4.02−3.98 (m, 2H), 3.89−3.75 (m, 2H), 3.52−3.37 (m, 10 H), 3.30−3.22 (m, 2H), 3.10−2.62 (m, 9H), 2.40−2.30 (m, 3H), 1.91−1.81 (m, 2H), 1.76−1.38 (m, 8H), 1.34 (d, 3H, J = 6.9), 0.86 (t, 3H, J = 7.3).
C4a	11.2, 15.4 (30%)	2106.0	(DMSO-d_6 + D_2O) δ 9.13 (s, 1H), 8.47−8.35 (m, 2H), 8.20−8.09 (m, 1H), 7.90−7.81 (m, 1H), 7.79−7.69 (m, 1H), 7.45−7.30 (m, 3H), 7.19−6.90 (m, 11H), 5.49−5.20 (m, 4H), 4.86 (s, 2H), 4.60−3.90 (m, 15H), 3.65−3.50 (m, 4H), 3.49−3.33 (m, 20H), 3.32−3.10 (m, 4H), 3.08−2.60 (m, 10H), 2.45−2.20 (m, 6H), 1.92−1.37 (m, 14H), 1.33 (d, 3H, J = 5.1), 0.85 (t, 3H, J = 5.7).
C4b	10.8, 15.2 (29%)	2120.89	(DMSO-d_6) δ 9.94 (s, 1H), 9.28 (s, 1H), 9.04 (s, 1H), 8.58 (d, 1H, J = 9.1), 8.52 (s, 1H), 8.30−8.16 (m, 3H), 8.15−7.98 (m, 2H), 7.97−7.72 (m, 5H), 7.62−7.48 (m, 3H), 7.37 (s, 1H), 7.25 (d, 2H, J = 8.5), 7.20−6.90 (m, 7H), 6.82 (d, 2H, J = 7.8), 6.56 (d, 2H, J = 7.6), 6.41 (s, 1H), 5.98−5.83 (m, 2H), 5.48−5.20 (m, 8H), 4.95 (s, 2H), 4.65−4.53 (m, 3H), 4.52−4.32 (m, 4H), 4.31−4.12 (m, 4H), 4.11−3.96 (m, 4H), 3.84 (t, 2H, J = 5.1), 3.65−3.35 (m, 24H), 3.20−2.80 (m, 16H), 2.45−2.33 (m, 4H), 1.98−1.83 (m, 2H), 1.82−1.40 (m, 12H), 1.35 (d, 3H, J = 7), 0.89 (t, 3H, J = 7.2).
C5	11.4, 16.2 (28%)	2480.0	(D_2O) δ 8.73 (s, 1H), 8.52 (s, 1H), 7.83 (s, 1H), 7.75 (s, 1H), 7.62 (s, 1H), 7.39 (s, 1H), 7.19 (d, 2H, J = 7.9), 7.05 (d, 2H, J = 7.9), 7.00−6.80 6H), 6.63 (d, 2H, J = 8.3), 5.65−5.40 (m, 4H), 5.05−4.85 (m, 2H), 4.70−4.62 (m, 2H), 4.60−4.25 (m, 14H), 4.10−4.00 (m, 2H), 3.95−3.35 (m, 34H), 3.30−3.10 (m, 10H), 3.00−2.50 (m, 16H), 2.15−2.05 (m, 2H), 2.00−1.45 (m, 17H), 1.15−1.05 (m, 3H).
C6	9.2, 12.6 (29%)	2988.78	(DMSO-d_6 + D_2O) δ 9.30 (s, 1H), 8.57 (d, 1H, J = 8.2), 8.40 (s, 1H), 8.22 (d, 1H, J = 8.2), 7.91 (t, 1H, J = 7.1), 7.71 (t, 1H, J = 7.3), 7.52 (d, 2H, J = 8.5), 7.38 (s, 1H), 7.23 (d, 2H, J = 8.5), 7.18−7.04 (m, 8H), 6.81 (d, 4H, J = 8), 6.56 (d, 4H, J = 8.2), 5.42 (s, 2H), 5.38 (s, 2H), 5.22 (s, 1H), 5.10 (s, 2H), 4.93 (s, 1H), 4.74 (s, 1H), 4.38−4.34 (m, 9H), 4.26−4.14 (m, 7H), 4.06−4.03 (m, 2H), 3.90 (s, 4H), 3.91−3.83 (m, 2H), 3.62 (t, 4H, J = 6.1), 3.55−3.36 (m, 10H), 3.29−2.79 (m, 20H), 2.39 (t, 4H, J = 6.1), 2.20−2.08 (m, 2H), 1.89−1.82 (m, 3H), 1.75−1.33 (m, 13H), 1.23 (d, 3H, J = 6.9), 0.90−0.84 (m, 3H).
C7	10.0, 12.5 (29%)	3721.0	(DMSO-d_6 + D_2O) δ 9.05 (s, 1H), 8.31 (d, 1H, J = 8.2), 8.10 (d, 1H, J = 8.2), 7.80 (t, 1H, J = 7.2), 7.77 (s, 1H), 7.73−7.61 (m, 3H), 7.40 (s, 1H), 7.43−7.29 (m, 2H), 7.06−6.99 (m, 10H), 6.80 (d, 4H, J = 8.2), 6.53 (d, 4H, J = 8.2), 5.49 (s, 2H), 5.43−5.11 (m, 4H), 4.79 (s, 1H), 4.57 (s, 1H), 4.43−4.11 (m, 24H), 3.70 (s, 6H), 3.60−3.30 (m, 78H), 3.17 (s, 3H), 3.05−2.70 (m, 20H), 2.40−2.22 (m, 10H), 2.20−1.23 (m, 16H), 1.19 (d, 3H, J = 7), 0.82 (t, 3H, J = 7).

[a] The conjugates show two peaks corresponding to *E*/*Z* isomers of the original cytotoxic molecule. [b] Acetonitrile % in the mobile phase is indicated in brackets.

Table 3. Physico-Chemical Characterizations of Fragments F1−F6, Containing Cyclopeptide Residues

entry	HPLC[a], rt, min	Maldi mass $[M + H]^+$	^{1}H NMR
F1	9.14 (20%)	870.13	(DMSO-d_6 + D_2O) δ 7.14−7.09 (m, 5H), 7.02−6.97 (m, 4H), 4.57−4.52 (m, 2H), 4.46−4.44 (m, 2H, 4.26 (s, 2H), 4.00 (d, 1H, J = 15), 3.95−3.90 (m, 2H), 3.57−3.51 (m, 8H), 3.26 (d, 1H, J = 15), 3.04 (t, 2H, J = 6.7), 2.87−2.64 (m, 5H), 2.38−2.33 (m, 1H), 1.75−1.72 (m, 1H), 1.51−1.47 (m, 1H), 1.34−1.32 (m, 2H).
F2	8.3 (30%)	881.0	(DMSO-d_6 + D_2O) δ 7.13−6.98 (m, 9H), 4.57−4.52 (m, 1H), 4.47−4.40 (m, 1H), 4.31−4.28 (m, 1H), 4.27 (s, 2H), 4.03−3.98 (m, 2H), 3.62−3.48 (m, 12H), 3.32 (t, 2H, J = 5), 3.30 (d,1H, J = 9), 3.04 (t, 2H, J = 6), 2.93−2.60 (m, 5H), 2.54−2.35 (m, 3H), 1.85−1.67 (m, 1H), 1.65−1.45 (m, 1H), 1.43−1.35 (m, 2H).
F3a	10.8 (25%)	1241.0	(D_2O) δ 7.29−7.11 (m, 9H), 4.65 (t, 1H, J = 8.2), 4.40 (s, 2H), 4.35−4.17 (m, 4H), 3.76−3.56 (m, 24H), 3.49 (t, 2H, J = 4.7), 3.39−3.36 (m, 2H), 3.18−3.06 (m, 4H), 2.97−2.83 (m, 4H), 2.75−2.65 (m, 1H), 2.58 (t, 3H, J = 7.6), 1.85−1.34 (m, 8H).
F3b	8.9 (22%)	1256.96	(D_2O) δ 7.43 (d, 2H, J = 8.2), 7.30 (d, 2H, J = 8.2), 7.18 (d, 2H, J = 8.8), 6.94 (d, 2H, J = 8.8), 4.93 (t, 1H, J = 6.5), 4.59 (s, 2H), 4.53−4.36 (m, 4H), 4.01−3.74 (m, 26H), 3.67 (t, 2H, J = 4.7), 3.59−3.52 (m, 2H), 3.35 (t, 2H, J = 7.0), 3.27 (t, 2H, J = 7.0), 3.14−3.04 (m, 5H), 2.95−2.87 (m, 1H), 2.79−2.72 (m, 4H), 2.03−1.58 (m, 8H).
F4	11.6 (21%)	1617.31	(D_2O), δ 7.25 (d, 2H, J = 8.2), 7.12 (d, 2H, J = 8.2), 7.00 (d, 2H, J = 8.8), 6.76 (d, 2H, J = 8.8), 4.60 (t, 1H, J = 6.5), 4.42 (s, 2H), 4.31−4.19 (m, 6H), 3.83−3.57 (m, 40H), 3.52−3.40 (m, 5H), 3.36 (s, 4H), 3.21−3.07 (m, 6H), 2.96- 2.67 (m, 2H), 2.62−2.51 (m, 6H), 1.92−1.30 (m, 12H).
F5	10.9 (22%)	1935.22	
F6	8.7 (26%)	2679.79	(DMSO-d_6 + D_2O) δ 7.78 (s, 1H), 7.76 (s, 1H), 7.08 (d, 4H, J = 7.7), 7.01 (d, 4H, J = 8.2), 6.78 (d, 4H, J = 8.3), 6.54 (d, 4H, J = 8.2), 4.52−4.44 (m, 2H), 4.42−4.00 (m, 16H), 3.73 (t, 4H, J = 5.3), 3.60−3.54 (m, 7H), 3.50−3.37 (m, 67H), 3.31 (s, 1H), 3.26 (s, 1H), 3.20 (s, 3H), 3.02 (t, 5H, J = 6.5), 2.90−2.52 (m, 11H), 2.36 (t, 8H, J = 6.5), 2.19−2.10 (m, 2H), 2.0−1.90 (m, 1H), 1.80−1.68 (m, 4H), 1.55−1.42 (m, 2H), 1.35−1.28 (m, 4H)

[a] Acetonitrile % in the mobile phase is indicated in brackets.

Table 4. Physico-Chemical Characterization of Fragments F7−F11, Containing the Cytotoxic Drug NMT

entry	HPLC[a], rt, min[b]	mass	^{1}H NMR
F7	18.0, 25.0 (35%)	965.0[c]	(DMSO-d_6) δ 9.96 (s, 1H), 9.28 (s, 1H), 8.56 (d, 1H, J = 8.5), 8.28 (s, 1H), 8.21 (d, 1H, J = 8.5), 8.05−8.00 (m, 1H), 7.90 (t, 1H, J = 7.4 Hz), 7.75 (t, 1H, J = 7.4), 7.52 (d, 1H, J = 8.4), 7.36 (s, 2H), 7.30−7.19 (m, 9H), 6.41 (s, 1H), 5.86−5.80 (m, 1H), 5.42−5.36 (m, 2H), 5.26−5.11 (m, 2H), 4.95 (s, 2H), 4.43−4.37 (m, 6H), 3.48 (t, 2H, J = 5.7), 3.00−2.61 (m, 4H), 1.90−1.82 (m, 2H), 1.74−1.50 (m, 2H), 1.49−1.35 (m, 2H), 1.30−1.18 (m, 2H), 0.82 (t, 3H, J = 7.2).
F8	12.0, 16.9 (26%)	812.32[d]	(DMSO-d_6) δ 10.10 (s, 1H), 9.31 (s, 1H), 8.59 (d, 1H, J = 8.6), 8.22 (d, 1H, J = 8.5), 8.04 (s, 3H), 7.91 (t, 1H, J = 7.9), 7.76 (t, 1H, J = 8.1), 7.54 (d, 2H, J = 8.2), 7.36 (s, 1H), 7.25 (d, 2H, J = 8.6), 6.51 (s, 1H), 6.02 (t, 1H, J = 6.3), 5.45 (s, 2H), 5.42 (s, 2H), 5.36 (s, 2H), 4.95 (s, 2H), 4.50−4.47 (m, 1H), 4.37 (t, 2H, J = 5.6), 3.95−3.85 (m, 1H), 3.49−3.42 (m, 2H), 3.10−2.92 (m, 2H), 1.91−1.82 (m, 2H), 1.75−1.38 (m, 4H), 1.34 (d, 3H, J = 6.9), 0.88 (t, 3H, J = 7.2).
F9	11.4, 16.2 (31%)	885.8[c]	
F10	11.6, 16.3 (32%)	1053.4[d]	(DMSO-d_6) δ 9.89 (s, 1H), 9.28 (s, 1H), 8.58 (d, 1H, J = 8.2), 8.22 (d, 1H, J = 8.2), 8.11 (d, 1H, J = 7.8), 8.03−7.99 (m, 1H), 7.90 (t, 1H, J = 7.9), 7.76 (t, 1H, J = 7.9), 7.64 (d, 1H, J = 7.2), 7.55 (d, 2H, J = 8.4), 7.37 (s, 1H), 7.24 (d, 2H, J = 8.4), 6.41 (s, 1H), 5.91 (t, 1H, J = 5.7), 5.42 (s, 2H), 5.37 (s, 2H), 5.32 (s, 2H), 4.95 (s, 2H), 4.43−4.36 (m, 3H), 3.92 (s, 2H), 3.89 (s, 4H), 3.88−3.86 (m, 1H), 3.60−3.58 (m, 8H), 3.48−3.44 (m, 2H), 3.01−2.95 (m, 3H), 1.92−1.86 (m, 2H), 1.70−1.38 (m, 4H), 1.25 (d, 3H, J = 6.9), 0.89 (t, 3H, J = 7.3).
F11	9.0, 12.0 (36%)	1041.4[d]	(DMSO-d_6) δ 9.81 (s, 1H), 9.28 (s, 1H), 8.51 (d, 1H, J = 9.0), 8.20 (d, 1H, J = 8.1), 7.89 (t, 1H, J = 7.1), 7.86−7.75 (m, 2H), 7.49 (d, 2H, J = 8.1), 7.39 (s, 1H), 7.21 (d, 2H, J = 8.4), 6.40 (s, 1H), 5.90−5.88 (m, 1H), 5.42 (s, 2H), 5.37 (s, 2H), 5.31 (s, 2H), 4.95 (s, 2H), 4.39−4.27 (m, 4H), 3.60−3.49 (m, 14H), 3.37 (t, 2H, J = 4.8), 3.01−2.95 (m, 2H), 2.40−2.38 (m, 2H), 1.90−1.86 (m, 2H), 1.71−1.38 (m, 4H), 1.20 (d, 3H, J = 7.0), 0.89 (t, 3H, J = 7.2).

[a] Acetonitrile % in the mobile phase is indicated in brackets. [b] These fragments show two peaks corresponding to *E*/*Z* isomers of the original cytotoxic molecule. [c] Maldi $[M + Na]^+$. [d] Esi $[M + H]^+$.

other for the length and disposition of the hydrophilic glycol chains, whereas the spacers of conjugates **C6** and **C7** contain two RGD ligands connected to the drug through multiple glycol chains in a branched conformation. In Table 5, the conjugate affinity to $\alpha_v\beta_3$ integrin and their tumor cell adhesion is reported in parallel with the ligand cyclopeptides and the drug alone. **C1**−**C3**, bearing a short glycol between ligand and drug, showed very poor solubility and lost affinity to the receptor if compared with the ligand alone, most probably due to steric hindrance induced by the drug. However, when the glycol spacers were elongated in **C4**−**C5**, affinity and solubility improved, but the stability decreased, as it is possible to observe in Table 6. This is consistent with the results reported in Table 7: as stability decreased, cytotoxicity increased, obviously due to some amounts of the free drug in the culture media. Only the dimeric conjugates **C6** and **C7** exhibited good receptor affinity and cytotoxicity, together with sufficient stability and optimal solubility.

Cell adhesion of the conjugates resulted generally increased with respect to RGD peptides alone, and this may be attributed to cooperative adhesion of the whole molecule.

DISCUSSION

In the present work, RGD peptides as targeting moieties were conjugated to the cytotoxic agent Namitecan through

Table 5. Binding to Isolated $\alpha_v\beta_3$ Integrin[a] of Conjugates C1−C7 and Their Effect on Adhesion to PC3 (Prostatic Carcinoma) and A2780 (Ovarian Carcinoma) Cell Lines, in the Presence of Vitronectin, after 3 h Treatment

	binding, IC_{50} nM	cell adhesion, IC_{50} μM	
entry	$\alpha_v\beta_3$	PC3	A2780
P1	1.70 ± 0.10	23.20 ± 5.02	3.80 ± 0.30
P2	1.08 ± 0.12	25.20 ± 4.50	4.50 ± 0.20
C1	9.71 ± 0.06	1.80 ± 0.40	2.70 ± 0.30
C2	30.40 ± 2.25	2.10 ± 0.20	0.90 ± 0.05
C3	11.00 ± 0.81	0.56 ± 0.07	0.67 ± 0.02
C4a	2.99 ± 0.26	1.60 ± 0.80	1.70 ± 0.20
C4b	4.36 ± 0.22	0.50 ± 0.09	1.70 ± 0.10
C5	9.38 ± 0.17	1.40 ± 0.20	5.40 ± 0.30
C6	3.00 ± 0.10	0.39 ± 0.09	0.45 ± 0.02
C7	6.20 ± 0.08	1.00 ± 0.05	1.00 ± 0.00
NMT	no binding	no adhesion	

[a] Nonspecific binding was determined in the presence of 1 μM Echistatin.

Table 6. Stability of Conjugates C1−C7 in the Whole Blood of CD1 Mice, Expressed as Percentage of Residual Amounts Found at Different Hours vs Time Zero

entry	1 h	2 h	3 h
C1	1.8	n.d.	n.d.
C2	100	100	100
C3	56	34	20
C4a	34	8	0.9
C4b	35	9	1.5
C5	38	11	2.5
C6	76	73	67
C7	67	61	51

Table 7. Cytotoxicity of Conjugates C1−C7, after 3 h Treatment, IC_{50} μM

entry	PC3	A2780
C1	0.22 ± 0.003	0.0084 ± 0.0006
C2	4.60 ± 0.80	0.095 ± 0.02
C3	1.00 ± 0.10	0.03 ± 0.003
C4a	2.50 ± 0.70	0.009 ± 0.0007
C4b	0.84 ± 0.20	0.013 ± 0.0006
C5	0.42 ± 0,05	0.02 ± 0.003
C6	1.00 ± 0.02	0.008 ± 0.0005
C7	1.00 ± 0.01	0.008 ± 0.0001
NMT	0.36 ± 0.05	0.0049 ± 0.0003
P1	>3000	>3000
P2	>3000	>3000

different spacers, consisting of linear or branched glycol residues and a peptide suitable for releasing the drug by enzymatic hydrolysis inside the tumor cell. The products were evaluated for their in vitro tumor cell-targeting efficacy, stability in murine blood, solubility, and cytotoxicity, with the purpose of studying their structure−activity relationship. Since the spacers between carrier and drug play the main role in the fate of small targeted drug conjugates, we systematically modified these molecular bridges in a continuing effort to reach a fine balance between sufficient systemic stability and cleavability inside the tumor cells, while preserving high receptor affinity and solubility of the whole conjugate. In the first conjugate **C1**, a spacer containing the Phe-Lys dipeptide was introduced, because this sequence had been proposed by Dubowchick et al. (*26, 27*) for rapid lysosomal hydrolysis and high human plasma stability. However, we assisted at the total cleavage of **C1** within one hour in the murine blood. In a search for more stable peptides, we evaluated other peptide sequences (such as D-Ala-Phe-Lys, Val-Cit, Aib-Cit, Tic-Cit), but with negative results (Dal Pozzo, A., Ni, M., and Bucci, F. Data not published. We also confirmed with our representative examples that compounds lacking the PABC self-immolative group do not release CPT, probably because of the steric crowding of the bulky drug), even though some of them have been used with success in the literature, mainly for immunoconjugates. Finally, the Ala-Cit dipeptide was found to have a significantly longer life in murine blood, together with sufficient cleavability by tumor cell associated proteases, as demonstrated by the cytotoxic activity of the corresponding conjugates; thus, Ala-Cit was adopted in all subsequent conjugate spacers. However, the stability was greatly influenced by the rest of the molecule, and this is observable with conjugates **C3**−**C5**, where elongation of the hydrophilic glycol chains led to a decrease of the half-life in the murine blood (see Table 6). To improve the solubility, we chose to substitute the commonly used large poly(ethylene glycol)s (PEGs) with a number of small glycol chains. In fact, PEGs, which are unique water-solubilizing agents currently employed for bioactive systems, are commercially available as polydisperse oligomers, and would yield undesirable heterogeneous products; moreover, because of their conformational flexibility, they tend to create bulky loops that can interfere with the ligand binding to the receptor. On the contrary, short glycols can be distributed on strategical positions of the molecular construct with respect to both the targeting and cleavable peptides. At first, we introduced in the spacers short glycol fragments connected in series through citrulline residues, which, beyond increasing hydrophilicity, should impart rigidity to the chain by their amide bonds, without shielding the ligand from recognition. Nevertheless, this strategy proved unsuccessful: in fact, as solubility improved, stability decreased, and cytotoxicity increased, due to the presence of significant amounts of the parent drug. This behavior indicates that the cleavable peptide is more exposed to the blood proteases. A deshielding effect is also observable in the conjugate **C3**, where the rigid triazole linkage orients the spacer chain away from the cleavable dipeptide moiety, where it is more accessible. On the other hand, solubility issues are a potentially negative aspect that could be a serious obstacle for preclinical development, and introduction of hydrophilic moieties is unavoidable. In an attempt to increase pegylation, while maintaining plasma stability and affinity to the receptor, we designed dimeric conjugates containing two RGD linked to a dendron unit bearing different glycol chains, to obtain a multifunctional platform where different pendant domains can be strategically allocated, without disturbing each other. Moreover, this approach exploits the multivalency effect on the ligand affinity (*16, 18, 34*). In this way, we could find conjugates **C6** and **C7**, endowed with the desired characteristics (increased avidity for the receptor together with appreciable stability and solubility), which demonstrated superior in vitro efficacy.

CONCLUSION

Our study highlights the crucial role of the spacer between targeting device and drug in tumor-targeted conjugates. Unlike immunoconjugates (where the bulky nature of the targeting molecule is less sensitive to the influence of the drug and spacer counterparts, and can shield and stabilize the connecting bond from premature hydrolysis), engineering conjugates with low-molecular-weight ligands is a most challenging problem, its success depending on a plateau of different factors. In fact, the small targeting molecule must retain tumor binding after substitution with molecules, that may be of similar or larger size, and the addition of new domains results in the modification of existing domains affecting their properties. Accordingly, careful selection of the enzymatically cleavable peptide and the length and disposition of the hydrophilic chains shoud be necessary for

the development of each single small targeting molecule for therapeutic application, since the strategy is not generalizable. We tried to help bring order to this sometimes unruly subject, and optimized the properties of our conjugates after a systematic in vitro study. Our results demonstrate the potential of tumor-targeted delivery of conjugates based on the specific recognition of the integrin RGD ligands and selective release of the drug by tumor-associated enzymes. However, we are aware of possible in vivo problems, such as the following: (1) Partial distribution of free drug generated through extracellular proteases cannot be ruled out. (2) The hydrophilic compounds synthesized may undergo rapid renal clearance, and larger PEGs would be needed to enhance the retention time in the circulation and allow proper tumor accumulation. Nevertheless, an improved therapeutic index could be expected by tumor specific delivery of at least a part of the targeted drug, resulting in lower and therefore less toxic systemic doses necessary to obtain the antitumor effect. Further evaluation of conjugates **C6** and **C7** in preclinical animal models for tumor growth inhibition and acute toxicity studies are currently in progress.

ACKNOWLEDGMENT

We are grateful to Sigma-Tau, Roma, Italy, for financial assistance. We thank Gianni Dottori for technical assistance.

LITERATURE CITED

(1) Doronina, S. O., Toki, B. E., Torgov, M. Y., Mendelsohn, B. A., Cerveny, C. G., Chace, D. F., DeBlank, R. I., Gearing, R. P., Bovee, T. D., Siegall, C. B., Francisco, J. A., Wahl, A. F., Meyer, D. I., and Senter, P. D. (2003) Development of potent monoclonal antibody auristatin conjugates for cancer therapy. *Nat. Biotechnol. 21*, 778–784.

(2) Jaracz, S., Chen, J., Kuznetsova, L. V., and Ojima, I. (2005) Recent advances in tumor- targeting drug conjugates. *Biorg. Med. Chem. 13*, 5043–5054.

(3) Temming, K., Meyer, D. L., Zabinski, R., Dijkers, E. C. F., Poelstra, K., Molema, G., and Kok, R. J. (2006) Evaluation of RGD-targeted albumin carriers for specific delivery of auristatin E to tumor blood vessels. *Bioconjugate Chem 17*, 1385–1394.

(4) Chari, R. V. J. (2008) Targeted cancer therapy: conferring specificity to cytotoxic drugs. *Acc. Chem. Res. 41*, 98–107.

(5) Ducry, L., and Stump, B. (2010) Antibody-drug conjugates: linking cytotoxic payloads to monoclonal antibodies. *Bioconjugate Chem. 21*, 5–13.

(6) Hamman, P. R., Hinman, L. M., Hollander, I., Beyer, C. F., Lindh, D., Holcomb, R., Hallett, W., Tsou, H. R., Upeslacis, J., Shochat, D., Mountain, A., Flowers, D. A., and Bernstein, I. (2002) Gentuzumab ozogamicin: a potent and selective anti-CD33 antibody-calicheamicin conjugate for treatment of acute myeloid leukemia. *Bioconjugate Chem 13*, 47–58.

(7) Okarvi, S. M. (2004) Peptide-based radiopharmaceutical; future tools for diagnostic imaging of cancer and other diseases. *Med. Res. Rev. 24*, 357–397.

(8) Zaccaro, L., del Gatto, A., Pedone, C., and Saviano, M. (2009) Peptides for tumor therapy and diagnosis: current status and future directions. *Curr. Med. Chem. 16*, 780–795.

(9) Cristofanilli, M., Charnsangavej, C., and Hortobagyi, G. N. (2002) Angiogenesis modulation in cancer research: novel clinical approaches. *Nat. Rev. Drug Discovery 1*, 415–426.

(10) Jain, R. K. (2003) Molecular regulation of vessel maturation. *Nat. Med. 9*, 685–693.

(11) Ruoslathi, E., and Pierschbacher, M. D. (1987) New perspective in cell adhesion RGD and integrins. *Science 238*, 491–497.

(12) Pasqualini, R., Koivunen, E., and Ruoslathi, E. (1997) α_v integrins as receptors for tumor targeting by circulating ligands. *Nat. Biotechnol. 15*, 542–546.

(13) Arap, W., Pasqualini, R., and Ruoslathi, E. (1998) Cancer treatment by targeted drug delivery to tumor vasculature in a mouse model. *Science 279*, 377–380.

(14) Haubner, R., and Wester, H. J. (2004) Radiolabelled traces for imaging of tumor angiogenesis and evaluation of antiangiogenic therapies. *Curr. Pharm. Des. 10*, 1439–455.

(15) Temming, K., Schiffelers, R. M., Molema, G., and Kok, R. J. (2005) RGD-based strategies for selective delivery of therapeutics and imaging agents to the tumor vasculature. *Drug Resistance Updates 8*, 381–402.

(16) Chen, X., Plasencia, C., Hou, Y., and Neamati, N. (2005) Synthesis and biological evaluation of dimeric RGD peptide-paclitaxel conjugate as a model for integrin-targeted drug delivery. *J. Med. Chem. 48*, 1098–1106.

(17) Meyer, A., Auernheimer, J., Modlinger, A., and Kessler, H. (2006) Targeting RGD recognizing integrins: drug development, biomaterial research, tumor imaging and targeting. *Curr. Pharm. Des 12*, 2723–2747.

(18) Ryppa, C., Mann-Steinberg, H., Fichtner, I., Weber, H., Satchi-Fainaro, R., Biniossek, M. L., and Kratz, F. (2008) In vitro and in vivo evaluation of doxorubicin conjugates with the divalent peptide E-[c(RGDfK)$_2$)] that targets integrin $\alpha_v\beta_3$. *Bioconjugate Chem. 19*, 1414–422.

(19) McNerny, A. M., Kukowska-Latallo, J. F., Mullen, D. G., Wallace, J. M., Desai, A. M., Shukla, R., Huang, B., Holl, M. M. B., and Baker, J. R. (2009) RGD dendron bodies: synthetic avidity agents with defined and potentially interchangeable effector sites that can substitute for antibodies. *Bioconjugate Chem. 20*, 1853–1859.

(20) Pisano, C., De Cesare, M., Beretta, G. L., Zuco, V., Pratesi, G., Penco, S., Vesci, L., Foderà, R., Ferrara, F. F., Guglielmi, M. B., Carminati, P., Dalla valle, S., Morini, G., Merlini, L., Orlandi, A., and Zumino, F. (2008) Preclinical profile of antitumor activity of a novel Hydrophilic camptothecin, ST1968. *Mol. Cancer Ther. 7*, 2051–2059.

(21) Conover, C. D., Greenwald, R. B., Pendri, A., Gilbert, K. W., and Shum, K. L. (1998) Camptothecin delivery systems. Enhanced efficacy and tumor accumulation of camptothecin following its conjugation to poly(ethylene glycol) via a glycine linker. *Cancer Chemother. Pharmacol 42*, 407–414.

(22) Caiolfa, V. R., Zamai, M., Fiorino, A., Frigerio, E., Pellizzoni, C., d'Argi, R., Ghigleri, A., Castelli, M. G., Farao, M., Pesenti, E., Gigli, M., Angelucci, F., and Suarato, A. (2000) Polymer-bound camptothecin: initial biodistribution and antitumor activity studies. *J. Controlled Release 65*, 105–119.

(23) Lerchen, H. G., Baumgarten, J., von dem Bruch, K., Lehmann, T. E., Sperzel, M., Kempka, G., and Fiebig, H. H. (2001) Design and optimization of 20-O-linked camptothecin glycoconjugates as anticancer agents. *J. Med. Chem. 44*, 4186–4195.

(24) Dal Pozzo, A., Ni, M. H., Esposito, E., Dallavalle, S., Musso, L., Bargiotti, A., Pisano, C., Vesci, L., Bucci, F., Castorina, M., Foderà, R., Giannini, G., and Penco, S. (2010) Novel tumor-targeted RGD peptide-camptothecin conjugates: synthesis and biological evaluation. *Biorg. Med. Chem. 18*, 64–72.

(25) Duncan, R., Cable, H. C., Lloyd, J. B., Rejmanova, P., and Kopecek, J. (1983) Polymers containing enzymatically degradable bond, 7. Design of oligopeptides side chains in poly N-2-hydroxypropyl)methacrylamide copolymers to promote degradation by lysosomal enzymes. *Macromol. Chem. 184*, 1997–2008.

(26) Dubowchik, G. M., and Firestone, R. A. (1998) Cathepsin B-sensitive dipeptide prodrugs. 1. A model study of structural requirements for efficient release of Doxorubicin. *Biorg. Med-.Chem. Lett. 8*, 3341–3346.

(27) Dubowchik, G. M., Firestone, R. A., Padilla, L., Willner, D., Hofstead, S. J., Mosure, K., Knipe, J. O., Lash, S. J., and Trail, P. A. (2002) Cathepsin B-labile dipeptide linkers for lysosomal release of doxorubicin from internalizing immunoconjugates: model studies of enzymatic drug release and antigen-specific in vitro antitumor activity. *Bioconjugate Chem. 13*, 858–869.

(28) Shiose, Y., Kuga, H., Ohki, H., Ikeda, M., Yamashita, F., and Hashida, M. (2009) Systematic research of peptide spacers controlling drug release from macromolecular prodrugs system, carboxymethyldextran-polyalcohol-peptide drug conjugates. *Bioconjugate Chem. 20*, 60–70.

(29) Haubner, R., Finsinger, D., and Kessler, H. (1997) Stereoisomeric peptide libraries and peptidomimetics for designing selective inhibitors of the $\alpha_v\beta_3$ integrin for a new cancer therapy. *Angew. Chem. 36*, 1374–1389.

(30) Dal Pozzo, A., Penco, S., Giannini, G., Tinti, O., Pisano, C., Vesci and L., Ni, M. H. Cyclopeptide derivatives with anti-integrin activity, EP 1 751 176 B1, October 3, 2010.

(31) Carl, P. L., Chakravarty, P. K., and Katzenellenbogen, J. A. (1980) A novel connector linkage applicable in prodrug design. *J. Med. Chem. 24*, 479–480.

(32) Wang, P., Layfield, R., Landon, M., Mayer, R. J., and Ramage, R. (1998) Transfer active ester condensation: A novel technique for peptide segment coupling. *Tetrahedron Lett. 85*, 8711–8714.

(33) Kolb, H. C., and Sharpless, K. B. (2003) The growing impact of click chemistry on drug discovery. *Drug Discovery Today. 8*, 1128–1137.

(34) Kitov, P. I., and Bundle, D. R. (2003) On the nature of multivalency effect: a thermodynamic model. *J. Am. Chem. Soc. 125*, 16271–16284.

BC100097R

Multiphoton-Absorption-Induced-Luminescence (MAIL) Imaging of Tumor-Targeted Gold Nanoparticles

Matthew B. Dowling,[†] Linjie Li,[‡] Juhee Park,[‡] George Kumi,[‡] Anjan Nan,[§] Hamid Ghandehari,[||] John T. Fourkas,[‡,⊥] and Philip DeShong*[,†,‡]

Department of Bioengineering, Department of Chemistry and Biochemistry, University of Maryland, College Park, Maryland 20742-2111, United States, School of Pharmacy, University of Maryland, Baltimore, Maryland 21201, United States, and Department of Bioengineering, University of Utah, Salt Lake City, Utah 84101, United States. Received March 3, 2010; Revised Manuscript Received September 16, 2010

We demonstrate that multiphoton-absorption-induced luminescence (MAIL) is an effective means of monitoring the uptake of targeted nanoparticles into cells. Gold nanoparticles (AuNPs) with diameters of 4.5 and 16 nm were surface-functionalized with monocyclic RGDfK, an RGD peptide analogue that specifically targets the $\alpha_v\beta_3$ integrin, a membrane protein that is highly overexpressed in activated endothelial cells during tumor angiogenesis. To determine whether cyclic RGD can enhance the uptake of the functionalized AuNPs into activated endothelium, human umbilical vein endothelial cells (HUVECs) were used as a model system. MAIL imaging of HUVECs incubated with AuNPs demonstrates differential uptake of AuNPs functionalized with RGD analogues: RGDfK-modified nanoparticles are taken up by the HUVECs preferentially compared to AuNPs modified with linear RGD (GRGDSP) conjugates or with no surface conjugates. The luminescence counts observed for the AuNP-RGDfK conjugates are an order of magnitude greater than for AuNP-GRGDSP conjugates. Transmission electron microscopy shows that, once internalized, the AuNP-RGDfK conjugates remain primarily within endosomal and lysosomal vesicles in the cytoplasm of the cells. Significant aggregation of these particles was observed within the cells. MAIL imaging studies in the presence of specific uptake inhibitors indicate that AuNP-RGDfK conjugate uptake involves a specific binding event, with $\alpha_v\beta_3$ integrin-mediated endocytosis being an important uptake mechanism.

INTRODUCTION

The development of techniques for targeting of multifunctional nanostructures to specific locations in vivo is a major goal in nanomedicine (*1*−*4*). Once these nanostructures reach their destination, they should be able to perform additional tasks, such as releasing a payload or being taken up into specific cells via endocytosis. The design of effective nanovectors for targeting applications (diagnostics, imaging, or drug delivery) would benefit greatly from methods that allow the direct probing of these processes. Within the field of single molecule/particle tracking, there are two classes of probes, (1) organic fluorophores and (2) quantum dots, which have generated the majority of the interest. However, despite the clear advances in their associated imaging techniques, both classes present major disadvantages that limit their practical applications as trackable probes within biological systems. Organic fluorophores are subject to photobleaching within time scales that are much shorter than many important biological processes (*5, 6*). Quantum dots experience blinking upon sustained excitation, and they are synthesized from cytotoxic materials (*7, 8*). Additionally, the chemistries involved in attaching targeting agents and/or therapeutic molecules to quantum dots are generally complex and not well-understood (*9, 10*).

Noble metal nanostructures such as gold and silver represent a third major class of nanovectors for direct probing. Unlike organic fluorophores or quantum dots, these structures do not experience photobleaching or blinking upon sustained excitation (*5*). Furthermore, the chemistries of noble metals are well-understood, and they present minimal toxicity and/or inflammatory concerns. Hence, photoinduced luminescence from noble metals has attracted attention for use in biomedical imaging, particularly as this method has become increasingly efficient over the past few decades. In 1986, Boyd et al. discovered that gold surfaces exhibit a 10^6-fold enhancement in luminescence intensity when subjected to two-photon excitation as opposed to single-photon excitation (*11*). More recently, it has been demonstrated that noble metal nanoparticles also exhibit efficient luminescence upon multiphoton excitation. Farrer et al. demonstrated that multiphoton-absorption-induced luminescence (MAIL[1]) from AuNPs is generated efficiently with 800 nm laser intensities that are lower than those typically used for two-photon imaging of living cells (*5*). For AuNPs, this luminescence spans the visible spectrum and was shown to arise from three-photon absorption when excited with 800 nm light (*5*). Similar results have been found for silver nanoparticles (*12*). We have recently shown, by correlating MAIL intensity with SEM

* Corresponding author. Philip DeShong, 2101 Building 091, College of Chemical and Life Sciences, Department of Chemistry and Biochemistry, University of Maryland, College Park, MD 20742. Phone: (301) 405-1892, Fax: (301) 314-9121. E-mail: deshong@umd.edu.

[†] Department of Bioengineering, University of Maryland.

[‡] Department of Chemistry and Biochemistry, University of Maryland.

[§] School of Pharmacy, University of Maryland.

[||] University of Utah.

[⊥] Prof. John T. Fourkas is also affiliated with (1) Institute of Physical Science and Technology, (2) Center for Nanophysics and Advanced Materials, (3) Maryland NanoCenter, University of Maryland, College Park, MD 20742.

[1] Abbreviations: MAIL (multiphoton-absorption-induced-luminescence), HUVECs (human umbilical vein endothelial cells), RGD (arginine-glycine-aspartic acid peptide), RGDfk (arginine-glycine-aspartic acid-phenylalanine-lysine monocylic peptide), AuNPs (gold nanoparticles).

10.1021/bc100115m © 2010 American Chemical Society
Published on Web 10/21/2010

images, that aggregates of AuNPs show even stronger MAIL signals than individual particles (*13*).

MAIL from gold nanostructures shows considerable promise for biomedical applications. Durr et al. have shown that luminescence from gold nanorods can be orders of magnitude brighter than autofluorescence from cancer cells (*14*). Wang et al. were able to image gold nanorods within cancer cells in vitro and flowing in a mouse ear blood vessel in vivo using MAIL (*15*). Park et al. used MAIL to perform three-dimensional imaging of gold nanoshells within mouse tumor tissue (*16*). Qu et al. have used MAIL to image AuNPs targeted to lymphoma cells (*17*). In addition, Nagesha et al. have used MAIL to visualize AuNPs in *Dictyostelium discoideum* cells and murine embryonic stem cells (*6*).

Here, we also use MAIL, but instead to monitor the targeting and endocytosis of AuNPs of different sizes to human umbilical vein endothelial cells (HUVECs), which serve as an in vitro model for the activated endothelium of tumor angiogenesis. The targeting moiety of interest in this study is RGDfK, a cyclic RGD analogue. This peptide has a large binding affinity for the $\alpha_v\beta_3$ integrin, a membrane protein that is overexpressed in the activated endothelium and thus represents a potential target for chemotherapy (*18*−*23*). Fani et al. showed that free RGDfK peptide displays approximately 4-fold preferential uptake into tumor tissue as compared to a linear RGD control peptide (*24*). Additionally, we have previously shown that water-soluble polymers with side chains terminated in RGDfK localize efficiently within solid tumors in vivo (*19*−*23*). A number of other groups have demonstrated that the RGD peptide is generally an effective targeting moiety for therapeutic molecules and nanoparticles to the activated endothelium (*25*−*28*).

AuNPs provide a platform for targeted drug delivery and tumor ablation. However, the fate of AuNP-RGDfK systems in endothelial cells is unknown (*18, 23*). In this study, we conjugate AuNPs with the targeting peptide RGDfK or, as a control, with a linear RGD peptide. AuNPs are attractive for targeting applications because they are highly stable and biocompatible, have well-established surface chemistry, and can exhibit strong MAIL signals. We demonstrate that MAIL imaging methodology can monitor the uptake of AuNPs functionalized with RGD peptide analogues. The collected images indicate that the AuNPs undergo differential uptake into HUVECs based upon both particle size and surface conjugate, and that the uptake is largely a receptor-mediated process. In addition, we benchmark the MAIL imaging with transmission electron microscopy, and demonstrate that the two techniques give complementary results. This suggests that MAIL may be used for rapid, routine screening of the efficacy of a given targeting moiety attached to AuNPs. It is also worth noting that the MAIL imaging reported in this manuscript uses low power and thus is capable of real-time, 3D imaging of living cells.

EXPERIMENTAL PROCEDURES

Chemicals. Linear GRGDSP was obtained from Calbiochem, Inc. (La Jolla, CA). RGDfK (M_w 604.5) was obtained from Anaspec, Inc. (San Jose, CA). Fibrinogen, sodium azide, bovine serum albumin, paraformaldehyde, MTT, and doxorubicin were each purchased from Sigma. Hydrogen tetrachloroaurate (III) was obtained from Alfa Aesar. All chemicals for the preparation of AuNPs and surface functionalization with peptide conjugates were purchased from commercial suppliers and used without further purification unless noted otherwise. Milli-Q water (Millipore, 18 MΩ) was used throughout.

Preparation of Citrate-Stabilized AuNPs. Water-soluble AuNPs were prepared according to the method reported by Natan (*29*) for 4.5 nm size and a modification of the method reported by Frens (*30*) for 16 nm size.

4.5-nm-Diameter Gold Nanoparticles. A solution of $HAuCl_4$ (1.00 mL, 29.4 mM in H_2O, Alfa Aesar) was added into 90 mL of H_2O at room temperature. After the solution had been stirred for 1 min, a solution of sodium citrate (2.00 mL, 38.8 mM in H_2O) was added, followed by a fresh solution of $NaBH_4$ (1.00 mL, 0.075% in 38.8 mM of sodium citrate). The red colloidal suspension was stirred for 10 min and stored at 4 °C.

16-nm-Diameter Gold Nanoparticles. To a refluxing solution of $HAuCl_4$ (100 mL, 1.47 mM in H_2O) was added a solution of sodium citrate (2.00 mL, 0.340 M in H_2O). The resulting red colloidal suspension was stirred at reflux for 20 min, cooled to room temperature, and stored at 4 °C.

General Procedure for the Synthesis of RGD Peptide Conjugates. Peptide conjugates were prepared using a modification of the reported conjugation procedure developed in the DeShong lab (*31*). A solution of RGD peptide (1.0 equiv) in HEPES buffer (0.1 M, pH 7.4) was mixed with a solution of the *N*-hydroxy succinimidyl thioctic ester (1.3 equiv) in acetone. The resulting mixture was stirred at room temperature for 24 h, and the acetone was removed in vacuo. The aqueous layer was acidified with aq HCl (0.2 M) to pH 3, washed with organic solvent (EtOAc or ether), and neutralized with aq NaOH (0.2 M). The remaining organic solvent was removed in vacuo, and the final solution was filtered through a 200 nm membrane filter. This RGD peptide conjugate solution in HEPES buffer was used for the surface functionalization of AuNPs without further purification.

Linear RGD Peptide Conjugate. Linear RGD peptide (5.0 mg, GRGDSP, Calbiochem) in 4.0 mL of buffer was treated with *N*-hydroxy succinimidyl thioctic ester (3.4 mg) in 2.0 mL of acetone. After purification as described above in the General Procedure, the final solution was filtered with a total volume of 5.0 mL.

Cyclic RGD Peptide Conjugate. Cyclic RGD peptide (2.4 mg, RGDfK, Anaspec) in 2.0 mL of buffer was treated with *N*-hydroxy succinimidyl thioctic ester (1.6 mg) in 2.0 mL of acetone. After purification as described above in the General Procedure, the final solution was filtered as described above with a total volume of 7.0 mL.

General Procedure for the Surface Functionalization of AuNPs with RGD Peptide Conjugates. A solution of citrate-stabilized AuNPs was mixed with a solution of RGD peptide conjugate. Self-assembly of peptide conjugate onto the surface of AuNPs was accomplished by leaving the solution at room temperature for 24 h. The functionalized particles were then purified by centrifugal filtering (Centriplus YM-30, Amicon). The process was repeated two times with H_2O. The residue in the centriplus filter was additionally purified by gel filtration (prepacked column, PD-10, GE Healthcare). The final volume of particle solution was adjusted with H_2O and stored at 4 °C.

4.5-nm-Diameter AuNPs Functionalized with Linear RGD Peptide. To a solution of citrate-stabilized AuNPs (5.0 mL) was added a solution of linear RGD peptide conjugate in HEPES buffer (0.25 mL). After purification as described above in the General Procedure, the final volume of purified functionalized nanoparticle solution is 5.0 mL in H_2O.

4.5-nm-Diameter AuNPs Functionalized with Cyclic RGD Peptide. To a solution of citrate-stabilized AuNPs (5.0 mL) was added a solution of cyclic RGD peptide conjugate in HEPES buffer (0.50 mL). After purification as described above in the General Procedure, the final volume of purified functionalized nanoparticle solution is 5.0 mL in H_2O.

16-nm-Diameter AuNPs Functionalized with Linear RGD Peptide. A solution of linear RGD peptide conjugate in HEPES buffer (0.5 mL) was diluted with HEPES buffer (7.5 mL, 20 mM, pH 7.4), and the resulting solution was then mixed with a solution of citrate-stabilized AuNPs (4.0 mL). After purification

as described above in the General Procedure, the final volume of purified functionalized nanoparticle solution is 16 mL in H_2O.

16-nm-Diameter AuNPs Functionalized with Cyclic RGD Peptide. A solution of cyclic RGD peptide conjugate in HEPES buffer (0.5 mL) was diluted with HEPES buffer (3.5 mL, 20 mM, pH 7.4), and the resulting solution was then mixed with a solution of citrate-stabilized AuNPs (2.0 mL). After purification as described above in the General Procedure, the final volume of purified functionalized nanoparticle solution is 8.0 mL in H_2O.

Characterization of AuNPs. UV−visible absorption spectra were recorded using an Ocean Optics USB 2000 spectrometer. Transmission electron microscopy (TEM) measurements were performed using a ZEISS EM10 CA. Samples were prepared by drop casting 5 μL of the sample onto a Formvar coated copper grid. The distribution of particle sizes was determined using *ImageJ*.

Cell Lines. HUVECs (human umbilical vein endothelial cells, [Lonza] Cambrex Biosciences, Walkersville, MD) were cultured in endothelial growth media at 37 °C in a humidified atmosphere of 5% CO_2 (v/v). The growth media consisted of 500 mL of endothelial cell basal media (EBM) supplemented with 10 ng/mL recombinant epidermal growth factor (hEGF), 1 μg/mL hydrocortisone, 12 μg/mL bovine brain extract, 25 U/mL heparin, 50 μg/mL amphotericin B, and 2% fetal bovine serum. The cells were detached and harvested using 0.05% trypsin/0.02% EDTA in PBS.

Cell Viability. To determine cell cytotoxicitiy/viability, the cells were plated at a density of 1×10^4 cells/well in a 96-well plate at 37 °C in 5% CO_2 atmosphere. After 24 h of culture, the medium in the wells was replaced with fresh medium containing nanoparticles in varying concentrations. After 24 h, 100 μL of MTT solution (5 mg/mL in phosphate buffer pH 7.4, MTT Sigma-Aldrich) was added to each well. After 3 h incubation at 37 °C and 5% CO_2 for exponentially growing cells and 15 min for steady-state confluent cells, the medium was removed and formazan crystals were solubilized with 100 μL of DMSO, and the solution was vigorously mixed to dissolve the reacted dye. The absorbance of each well was read on a microplate reader at 560 nm. The spectrophotometer was calibrated to zero absorbance, using culture medium without cells. The relative cell viability (%) related to control wells containing cell culture medium without nanoparticles was calculated by $[A]_{test}/[A]_{control} \times 100$. As a positive control, 100 μM doxorubicin (DOX) was added to an extra set of plated culture wells in conjunction with each test sample.

Transmission Electron Microscopy (TEM) of Cells. The medium containing the gold nanoparticles not taken up by the cells was discarded, and the cells were thoroughly washed with PBS buffer. Cells were scraped from the culture dish and centrifuged at 5000 *g* for 5 min, and the supernatant was removed. The cell pellets were fixed in a 0.1 M PBS solution containing 2.5% glutaraldehyde and 4% paraformaldehyde for 1 h. The pellets were then rinsed with 0.1 M PBS, embedded in 2% agarose gel, postfixed in 4% osmium tetroxide solution for 1 h, rinsed with distilled water, stained with 0.5% uranyl acetate for 1 h, dehydrated in a graded series of ethanol (30%, 60%, 70%, 90%, and 100%), and embedded in epoxy resin. The resin was polymerized at 60 °C for 48 h. Ultrathin sections (50−70 nm) obtained with a LKB ultramictrotome were stained with 5% uranyl acetate and 2% aqueous lead citrate and imaged via transmission electron microscopy. One representative image out of 30 captured images at the same magnification (61600×) is shown in the results and discussion sections for each experimental condition studied.

Amino Acid Analysis. Amino acid content analysis of the AuNP−peptide conjugates was performed by Commonwealth Biotechnologies, Inc. (Richmond, VA), by chromatographic measurement of derivatized peaks after hydrolysis of the sample in 6 N HCl at 110 °C for 20 h.

MAIL Imaging of Cells. Cells were plated at a density of 5×10^4 cells/mL in four-chamber tissue culture slides (BD Falcon); each chamber had been treated with 1 mL of fibrinogen (200 μg/mL) for 24 h at 4 °C prior to seeding the cells. After 24 h of culture, the medium in the chambers was replaced with fresh medium containing nanoparticles of three varieties, separately: (1) bare Au citrate NPs, (2) linear RGD conjugated AuNPs, and (3) monocyclic RGD conjugated AuNPs. One chamber per slide was refilled with fresh media containing no nanoparticles to serve as a control. After incubation for a particular time interval (e.g., 2 h, 6 h, 24 h), the media were removed from the chambers and cells were fixed by treatment with paraformaldehyde (4% v/v in PBS) for 10 min. The cells were then washed twice with 25 mM glycine in PBS to remove unreacted paraformaldehyde. Again, one representative image out of a set of 30 captured images at the same magnification (40×) is displayed in the results and discussion section for each experimental condition studied.

Apparatus. The multiphoton microscope has been described in detail previously (*32*), and so we present only brief details here. The excitation source was a Coherent Mira 900-F Ti:sapphire laser that produced pulses with a duration of approximately 150 fs at a center wavelength of 800 nm. The laser was focused into the sample through a 40× microscope objective with a numerical aperture of 0.75 (Zeiss Plan Neofluar). An excitation power of 1.5 mW was used. MAIL emission was collected by the same objective and was detected by single-photon-counting avalanche photodiodes. Light with wavelengths of 750 nm and longer was filtered out before detection. Images were collected by scanning the laser beam across the sample using a pair of galvanometric mirrors. A program written in LabView was used to control the scanning and to monitor the luminescence counts as a function of position on the sample. In the resulting MAIL images, a color is assigned to each pixel based upon the luminescence counts collected at that pixel position. Hence, the images give an immediate indication of the location and intensity of AuNP structures present within the captured frame.

Integration of MAIL Image Intensities. In order to generate semiquantitative data from each MAIL image, pixel values were integrated in a program written in LabView. The program discarded values lower than 15, which were considered to be random noise present even on sample chamber slides to which no gold had been added. All remaining pixel values were summed and assigned to the corresponding image.

Blocking of AuNP Uptake into HUVECs. Cells were cultured in fibrinogen-treated four-chamber slides for 24 h. After that period, three wells were treated with different blocking agents and one was left as an untreated control. The blocking agents used were sodium azide (0.1%), bovine serum albumin (3%), and free cyclic RGDfK (1 μM). Cells were treated with blocking agent for 10 min and then washed twice with PBS. AuNPs with surface-conjugated RGDfK were added to all wells in 1 mL of growth media. After an additional 24 h, cells were fixed with paraformaldehyde and subsequently imaged by MAIL.

RESULTS AND DISCUSSION

We studied AuNPs of two different diameters, 4.5 and 16 nm, to determine whether the size of the particle, and correspondingly the number of peptide conjugates attached, would have an effect on the uptake results. Figure 1 shows TEM images of these particles ex vivo and corresponding UV absorption spectra. Figures 1b and 1e show the cyclic RGD conjugates for 4.5 and 16 nm particles, respectively, demonstrat-

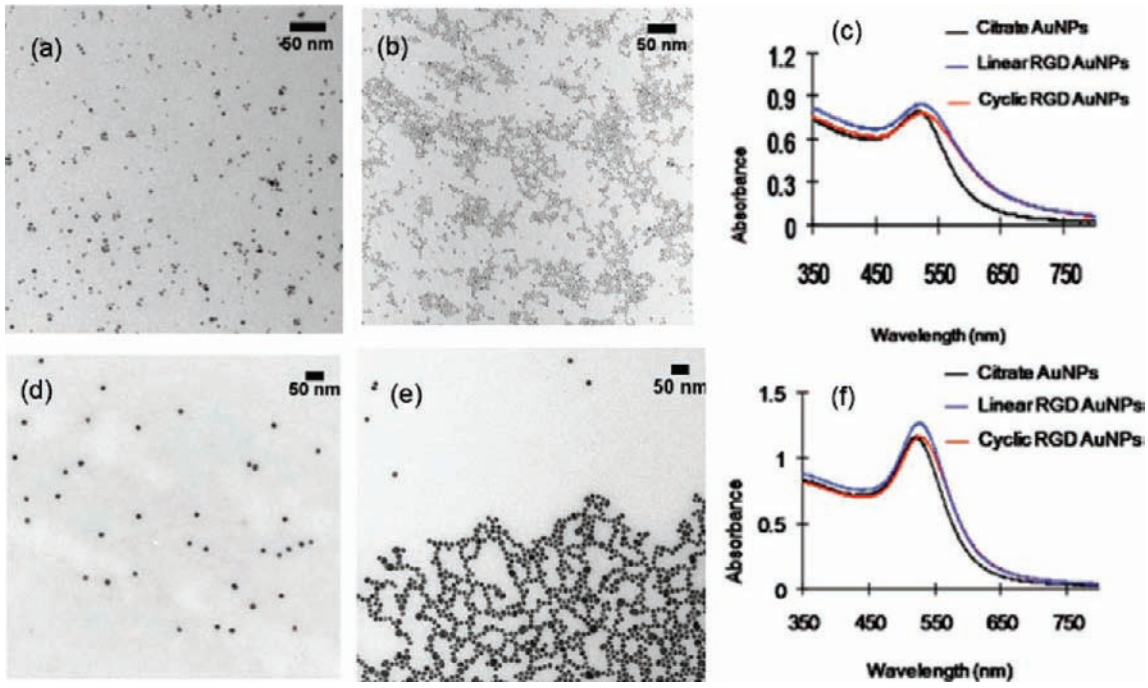


Figure 1. TEM images and UV−vis absorption spectra of AuNPs: (a) citrate-stabilized AuNPs (average diameter, 4.5 ± 1.4 nm); (b) cyclic RGD peptide-functionalized AuNPs; (c) 4.5 nm citrate-stabilized AuNPs (in black, λ_{max} = 520 nm), linear RGD peptide-functionalized AuNPs (in blue, λ_{max} = 523 nm), and cyclic RGD peptide-functionalized AuNPs (in red, λ_{max} = 523 nm); (d) citrate-stabilized AuNPs (average diameter, 15.8 ± 1.6 nm); (e) cyclic RGD peptide-functionalized AuNPs; (f) 15.8 nm citrate-stabilized AuNPs (in black, λ_{max} = 520 nm), linear RGD peptide-functionalized AuNPs (in blue, λ_{max} = 526 nm), and cyclic RGD peptide-functionalized AuNPs (in red, λ_{max} = 526 nm).

ing a significant amount of aggregation relative to their bare citrate counterparts in Figures 1a and 1d. The increased aggregation of the peptide-functionalized AuNPs can be attributed to hydrogen bonding occurring between surface conjugates on adjacent particles, as water was removed from the system by vacuum prior to TEM analysis. Aggregation of functionalized AuNPs on TEM grids has been observed for many derivatives. Analysis of the solutions prior to deposition by dynamic light scattering indicated that aggregation in solution is minimal.

The wavelength of maximum absorption for both particle sizes remains constant at 525 nm for bare citrate AuNPs, linear RGD conjugated AuNPs, and cyclic RGD conjugated AuNPs, although the absorbance values increase slightly over the measured wavelength range for both the linear and cyclic RGD-conjugated AuNPs. Absorption peaks for aggregated samples are broadened and shifted significantly to longer wavelengths. As our observed UV absorbance peaks are sharp and are consistent with values reported previously for stable AuNP suspensions, aggregation in solution is likely to be insignificant. Furthermore, it has been previously demonstrated that AuNPs do not aggregrate in serum-completed cell growth media (*33*).

Figure 2 summarizes the results of the MTT cytotoxicity assay for 4.5 nm AuNPs incubated with HUVECs. Even at a concentration of 39 μg/mL of AuNPs, which is significantly higher than what would be possible in a biologically relevant setting, the AuNPs were nontoxic to the HUVECs. However, DOX mixed with any AuNP sample diminishes cell survival to below 2%. There are two key points to take from the results of this experiment. First, 4.5 nm AuNPs, which are comparable in size to many cellular proteins, do not harm the target cells. Second, the addition of targeting peptides to the surfaces of the AuNPs does not lead to measurable toxicity of the nanovector under the conditions used in this study. This preliminary toxicological screening result is promising for the potential use of surface-functionalized particles as in vivo targeting agents. We also note that similar results were found for the 16 nm

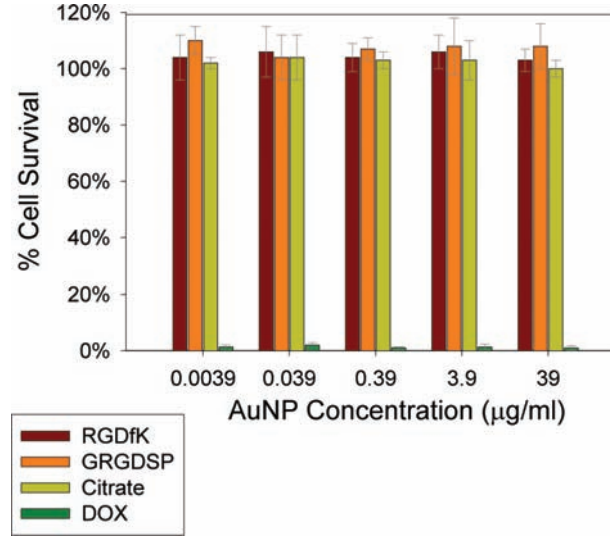


Figure 2. MTT assay of peptide-targeted AuNPs incubated with HUVECs.4.5 nm particles of three different types, (1) AuNP-RGDfK conjugates (maroon bars), (2) AuNP-GRGDSP conjugates (orange bars), and (3) bare citrate-stabilized AuNPs (gold bars), were each incubated with HUVECs for a 72 h MTT assay. Doxorubicin (DOX; 100 μM) was incubated with the HUVECs as a positive control (green bars).

AuNPs, both bare and with the targeting peptides conjugated to the particle surfaces (data not shown for brevity).

Table 1 summarizes the results of amino acid analysis on the AuNP−peptide conjugates for the 4.5 nm AuNPs. The grafting density of linear RGD peptides on the AuNPs was approximately 5 times as large as that of cyclic RGD peptides. This finding is reasonable, since the cyclic peptide conjugate takes up a significantly larger effective area than the linear peptide counterparts. Since the peptide conjugates were reacted with the AuNPs in large excess, it is assumed that saturation of the particle surfaces was achieved, and so the greater surface

Table 1. Amino Acid Analysis of Peptide-Conjugated AuNPs (4.5 nm)[a]

conjugate type	(avg no. of conjugated peptides)/particle	(avg no. of conjugated peptides)/nm^2
cyclic RGD peptide	124.6 ± 29.3	2.0 ± 0.5
linear RGD peptide	610.7 ± 92.9	9.6 ± 1.5

[a] Particle/peptide conjugates were treated in highly acidic conditions to hydrolyze the bound amino acids, whose mass was subsequently measured. It is shown that the average number of peptide conjugates per particle is nearly five times as high for the linear RGDs as compared to the cyclic RGDfKs (indicated error is s.d.).

density of linear peptides resulted. The average number of conjugated peptides per unit area for 4.5 nm AuNPs is shown in Table 1, and the surface densities for 16 nm AuNPs are expected to be similar, but were not determined in this study.

MAIL Detection of Particle Uptake into Cells. MAIL imaging was performed on HUVECs incubated for 6 and 24 h with 4.5 nm AuNPs and with 16 nm AuNPs. Note that all MAIL images in this study show one representative cell from a single image out of the correspondingly treated cell population, although many images were collected. Shown in Figure 3 are MAIL images and corresponding transmission optical images at 6 h incubation with 4.5 nm AuNPs. Figure 4 shows HUVECs incubated with the same AuNPs for 24 h. The cells incubated with the AuNPs with cyclic RGD conjugates (Figures 3a and 4a) exhibit a greater luminescence signal than those cells

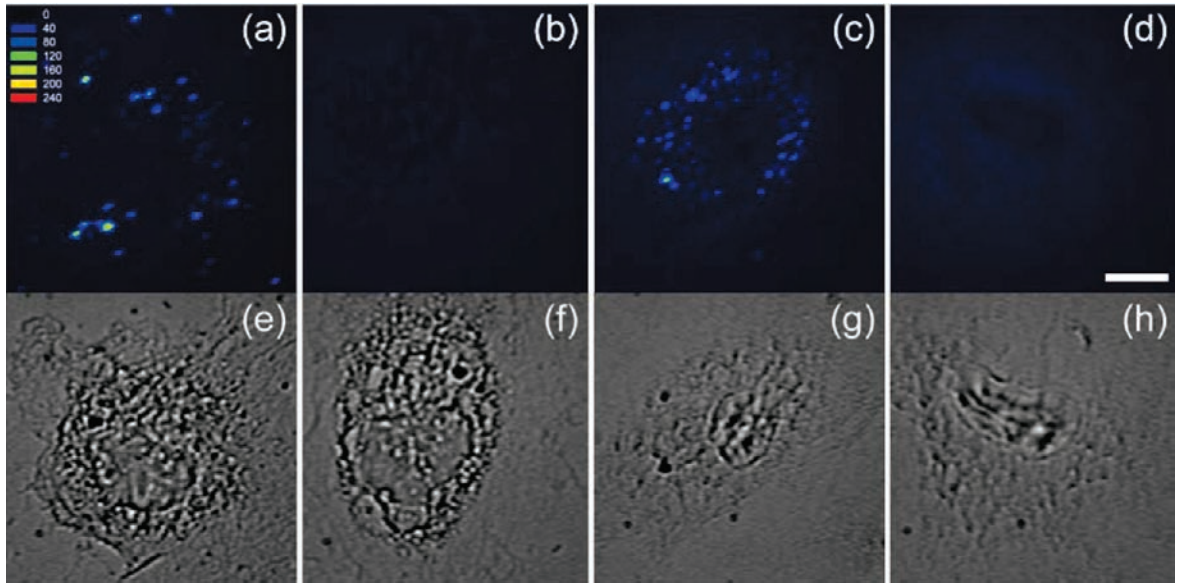


Figure 3. MAIL/transmission optical (40×) images for 6 h uptake of targeted 4.5 nm AuNPs into HUVECs. (a) MAIL image of 4.5 nm AuNPs with cyclic RGD conjugates; (b) MAIL image of 4.5 nm AuNPs with linear RGD conjugates; (c) MAIL image of bare citrate 4.5 nm AuNPs; (b) MAIL image of controls, i.e., no AuNPs incubated with HUVECs; (e) transmission image of 4.5 nm AuNPs with cyclic RGD conjugates; (f) transmission image of 4.5 nm AuNPs with linear RGD conjugates; (g) transmission image of bare citrate 4.5 nm AuNPs; (h) transmission image of control sample. The scale bar is 10 μm.

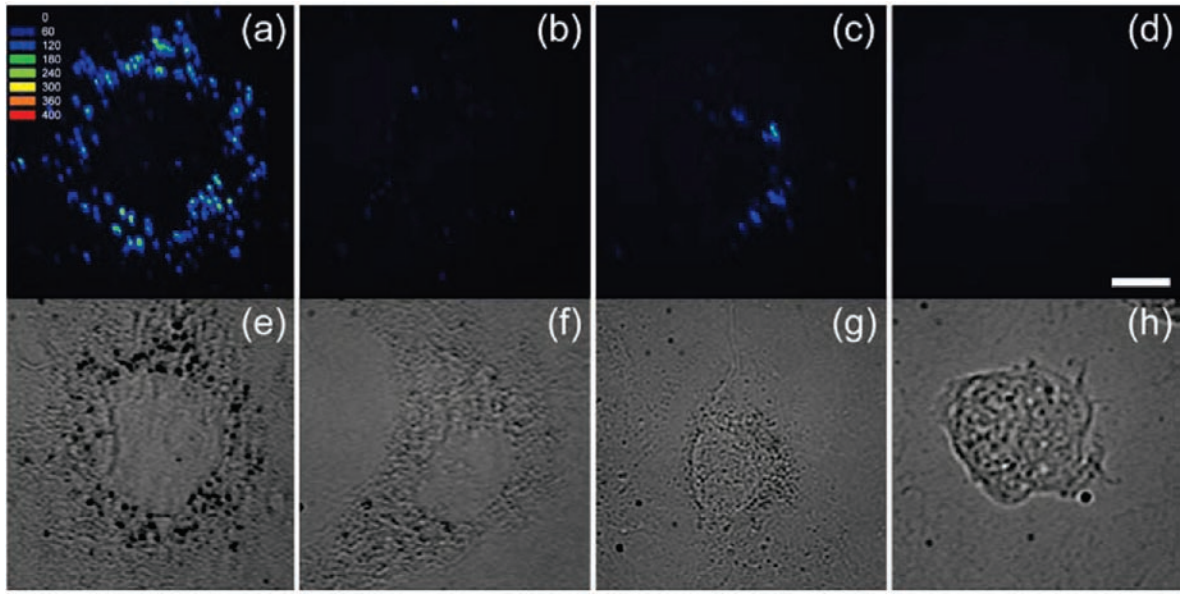


Figure 4. MAIL/transmission optical (40×) images for 24 h uptake of targeted 4.5 nm AuNPs into HUVECs. (a) MAIL image of 4.5 nm AuNPs with cyclic RGD conjugates; (b) MAIL image of 4.5 nm AuNPs with linear RGD conjugates; (c) MAIL image of bare citrate 4.5 nm AuNPs; (b) MAIL image of controls, i.e. no AuNPs incubated with HUVECs; (e) transmission image of 4.5 nm AuNPs with cyclic RGD conjugates; (f) transmission image of 4.5 nm AuNPs with linear RGD conjugates; (g) transmission image of bare citrate 4.5 nm AuNPs; (h) transmission image of control sample. The scale bar is 10 μm.

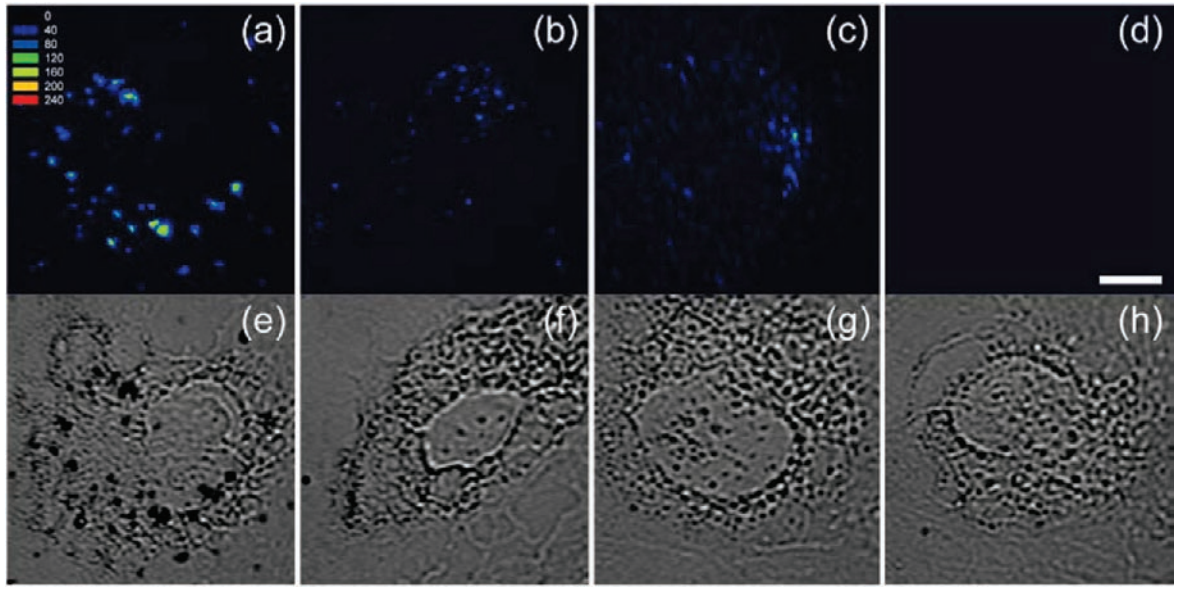


Figure 5. MAIL/transmission optical (40×) images for 6 h uptake of targeted 16 nm AuNPs into HUVECs. (a) MAIL image of 16 nm AuNPs with cyclic RGD conjugates; (b) MAIL image of 16 nm AuNPs with linear RGD conjugates; (c) MAIL image of bare citrate 16 nm AuNPs; (b) MAIL image of controls, i.e., no AuNPs incubated with HUVECs; (e) transmission image of 16 nm AuNPs with cyclic RGD conjugates; (f) transmission image of 16 nm AuNPs with linear RGD conjugates; (g) transmission image of bare citrate 16 nm AuNPs; (h) transmission image of control sample. The scale bar is 10 μm.

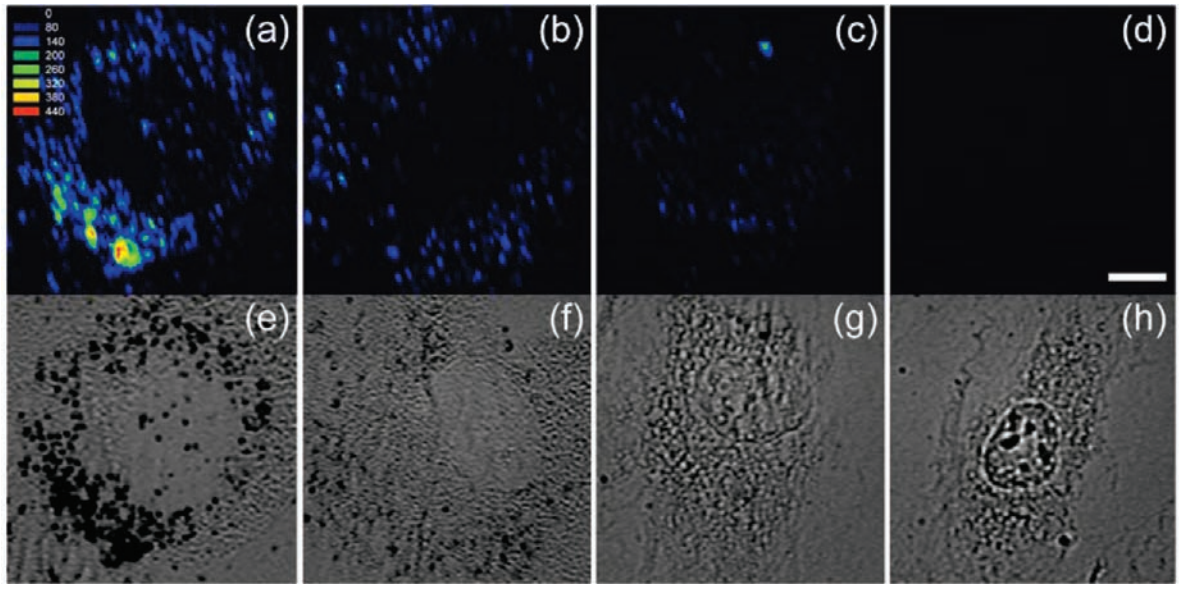


Figure 6. MAIL/transmission optical (40×) images for 24 h uptake of targeted 16 nm AuNPs into HUVECs. (a) MAIL image of 16 nm AuNPs with cyclic RGD conjugates; (b) MAIL image of 16 nm AuNPs with linear RGD conjugates; (c) MAIL image of bare citrate 16 nm AuNPs; (b) MAIL image of controls, i.e., no AuNPs incubated with HUVECs; (e) transmission image of 16 nm AuNPs with cyclic RGD conjugates; (f) transmission image of 16 nm AuNPs with linear RGD conjugates; (g) transmission image of bare citrate 16 nm AuNPs; (h) transmission image of control sample. The scale bar is 10 μm.

incubated with either AuNPs functionalized with linear RGD conjugates (Figures 3b and 4b) or bare citrate AuNPs (Figures 3c and 4c).

Figures 5 and 6 show images of HUVECs incubated with 16 nm AuNPs after 6 h and 24 h of incubation, respectively. Again, a greater luminescence signal is observed in the samples containing the AuNPs with cyclic RGD conjugates (Figures 5a and 6a), and uptake increases significantly over the 24 h period. The MAIL signals for 16 nm AuNPs are stronger than those for 4.5 nm AuNPs. This effect could be intrinsic to the AuNPs or could be due to a more effective exocytotic mechanism for smaller particles by the HUVECs. Note that the concentration of particles incubated with the HUVECs was 39 μg/mL, which was the upper limit value for the 72 h MTT assay. Thus, a large number of the targeted AuNPs are getting into the cells, but they do not appear to harm the cells in any significant way.

Figure 7 displays a histogram of the integrated MAIL counts from treated cell populations corresponding to representative images displayed in Figures 3−6. While the intensity values in this figure do not give an absolute quantitative measure of the number AuNPs within the cell, the data clearly indicate that differential uptake is observed among the experimental conditions. The 16 nm AuNP−RGDfK conjugates at 24 h displayed the highest intensity value (1.31×10^6) among the tested samples. The data also indicate that large increase in intensity was observed over an 18 h period (between the 6 and 24 h test points) for the 4.5 nm AuNP−RGDfK conjugates and the 16 nm AuNP−RGDfK conjugates at 12.36-fold and 13.17-fold,

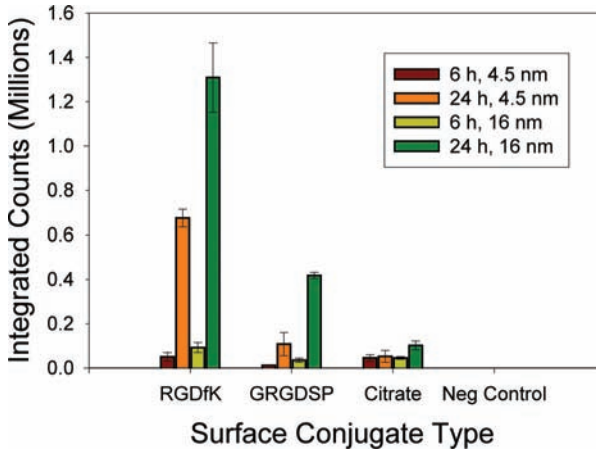


Figure 7. Integrated counts from MAIL images of targeted AuNPs (Corresponding representative images shown in Figures 3−6).

respectively. Again, as anticipated from the images at 24 h, the AuNP−RGDfK conjugate samples had significantly higher average luminescence counts (1.31×10^6 [16 nm] and 6.75×10^5 [4.5 nm]) than the AuNP−GRGDSP (4.18×10^5 [16 nm] and 1.08×10^5 [4.5 nm]) or citrate-stabilized AuNP (1.01×10^5 [16 nm] and 5.23×10^4 [4.5 nm]) controls of the same particle size. For the 6 h time interval, preferential uptake of the 4.5 nm citrate-stabilized AuNPs compared to the 4.5-nm AuNP−GRGDSP conjugate was unexpected. There are three possible explanations for this observation. First there should be a large difference in zeta potential (surface charge) between the functionalized and unfunctionalized gold nanoparticles that may influence uptake. Alternatively, preferential uptake of the citrate nanoparticles may arise from the saturation of the linear RGD peptide on surface of the gold nanoparticles, which would interfere with single peptide−receptor binding events via steric hindrance. Finally, the 4.5 nm particles may be more susceptible to exocytosis mechanisms during the initial uptake period (*33*). At this point, it is not possible to differentiate among these three explanations without significant experimentation. These additional studies are underway and will be reported in due course.

Determination of the Cellular Uptake Mechanism. Figures 8 and 9 show HUVEC cells incubated with AuNP−RGDfK conjugates for 24 h in the presence of different uptake-blocking agents for 4.5 and 16 nm AuNPs, respectively. The leftmost images are controls in which the HUVECs have not been treated with a blocking agent. We observe significantly greater luminescence in these images (Figures 8a and 9a), indicating that the blocking agents alter the uptake of the AuNP−RGDfK conjugates. In Figures 8b and 9b, the cells have been treated with 0.1 wt % sodium azide, an endocytosis inhibitor, for 10 min prior to addition of AuNP−RGDfKs. The luminescence signal is diminished significantly for both 4.5 and 16 nm AuNPs, although some small patches of signal are still observed for these samples.

The cells in Figures 8c and 9c have been treated for 10 min with 3% BSA, which blocks nonspecific binding to the cells. For both samples, a smaller luminescence signal was observed, although this signal was more comparable to that of the untreated controls. This inhibition study indicates that a large fraction of the functionalized AuNPs is taken up into the cells via specific binding to a cell-surface receptor followed by receptor-mediated endocytosis. Figures 8d and 9d demonstrate that treatment of the cells with 1 μM RGDfK to block $\alpha_v\beta_3$ integrins significantly decreases the intensity of the luminescent signals relative to the untreated controls. This result implies that the majority of uptake must involve endocytosis via the $\alpha_v\beta_3$ integrin.

Figure 10 displays a histogram of the integrated MAIL counts from the treated cell populations corresponding to the representative images shown in Figures 8 and 9. As expected, the untreated HUVEC samples had the highest integrated counts at 5.28×10^5 and 1.09×10^6 for 4.5 and 16 nm AuNPs, respectively. AuNP−RGDfK conjugates taken up into HUVECs pretreated with 3% BSA displayed the next highest intensity values, with a 64% drop-off in intensity for 4.5 nm AuNP−RGDfKs (1.91×10^5 counts) and a 68% drop-off in intensity for 16 nm AuNP−RGDfKs (3.54×10^5 counts) relative to the untreated HUVEC controls. For both 4.5 nm and 16 nm

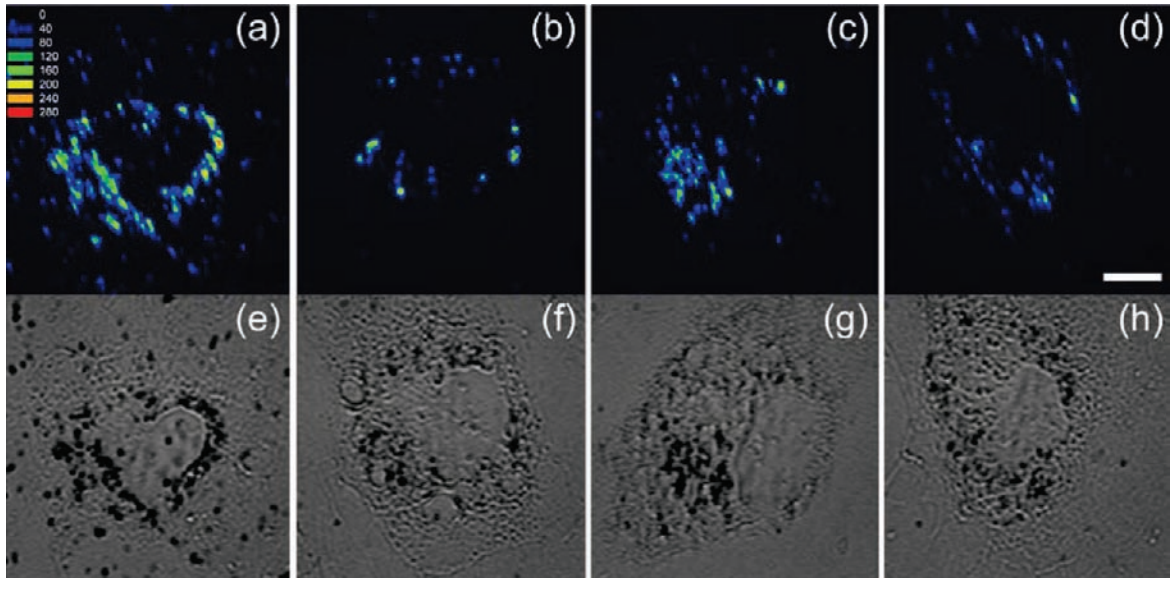


Figure 8. MAIL/transmission optical (40×) images for 24 h uptake of targeted 4.5 nm AuNPs into HUVECs. (a) MAIL image 4.5 nm AuNPs with cyclic RGD conjugates (no treatment); (b) MAIL image of 4.5 nm AuNPs with cyclic RGD conjugates, HUVECs treated with sodium azide; (c) MAIL image of 4.5 nm AuNPs with cyclic RGD conjugates, HUVECs blocked with BSA; (d) MAIL image of 4.5 nm AuNPs with cyclic RGD conjugates, HUVECs treated with free RGDfK; (e) transmission image of 4.5 nm AuNPs with cyclic RGD conjugates (no treatment); (f) transmission image of 4.5 nm AuNPs with cyclic RGD conjugates, HUVECs treated with sodium azide; (g) transmission image of 4.5 nm AuNPs with cyclic RGD conjugates, HUVECs blocked with BSA; (h) transmission image of 4.5 nm AuNPs with cyclic RGD conjugates, HUVECs treated with free RGDfK. The scale bar is 10 μm.

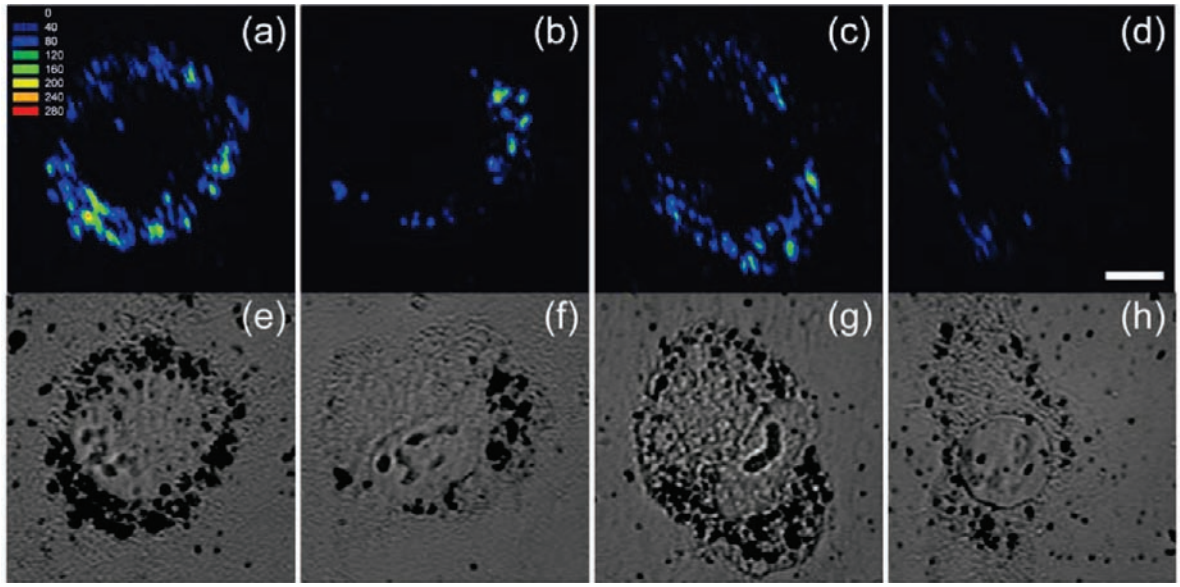


Figure 9. MAIL/transmission optical (40×) images for 24 h uptake of targeted 16 nm AuNPs into HUVECs. (a) MAIL image 16 nm AuNPs with cyclic RGD conjugates (no treatment); (b) MAIL image of 16 nm AuNPs with cyclic RGD conjugates, HUVECs treated with sodium azide; (c) MAIL image of 16 nm AuNPs with cyclic RGD conjugates, HUVECs blocked with BSA; (d) MAIL image of 16 nm AuNPs with cyclic RGD conjugates, HUVECs treated with free RGDfK; (e) transmission image of 16 nm AuNPs with cyclic RGD conjugates (no treatment); (f) transmission image of 16 nm AuNPs with cyclic RGD conjugates, HUVECs treated with sodium azide; (g) transmission image of 16 nm AuNPs with cyclic RGD conjugates, HUVECs blocked with BSA; (h) transmission image of 16 nm AuNPs with cyclic RGD conjugates, HUVECs treated with free RGDfK. The scale bar is 10 μm.

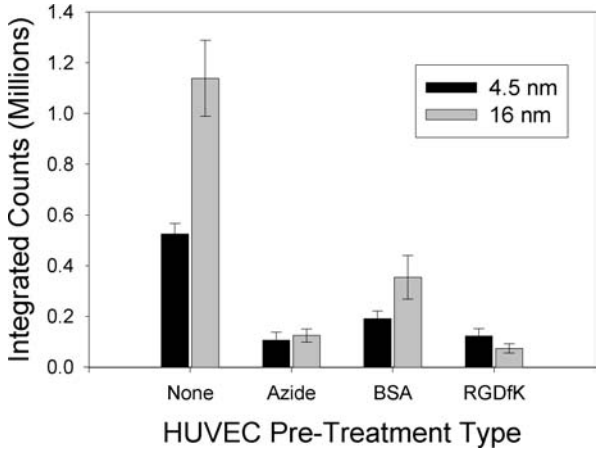


Figure 10. Integrated counts from MAIL images of AuNP−RGDfK conjugates pretreated with blocking agents (corresponding representative images in Figures 8−9, a−d).

AuNP−RGDfKs taken up in HUVECs pretreated with BSA, intensity values 2.5 to 4 times higher were measured relative to the sodium azide and free RGDfK pretreated HUVECs incubated with the same AuNPs. The individual values suggest that this preferential uptake is due to a specific binding event between the AuNP−RGDfKs and cell surface receptors, while smaller amounts of signal may be attributed to nonspecific uptake (free RGDfK blocking) and nonspecific binding to the cell surface (free RGDfK blocking and sodium azide treatment).

Detection of Particle Uptake into Cells via TEM imaging. Figure 11 shows TEM images of HUVECs incubated with 4.5 and 16 nm AuNPs with surface conjugated RGDfK for a period of 72 h. These images demonstrate that the nanoparticles are taken primarily into endosomal and lysosomal vesicles. Aggregation of the AuNPs is observed within the vesicle. This intracellular destabilization may arise from ligand exchange reactions within the cell, as suggested by Rotello et al., (*35*) or may be the result of digestion of the ligand shell by proteases within the endosomes and lysosomes, a mechanism proposed by Nativo et al. in an AuNP uptake study on human fibroblasts

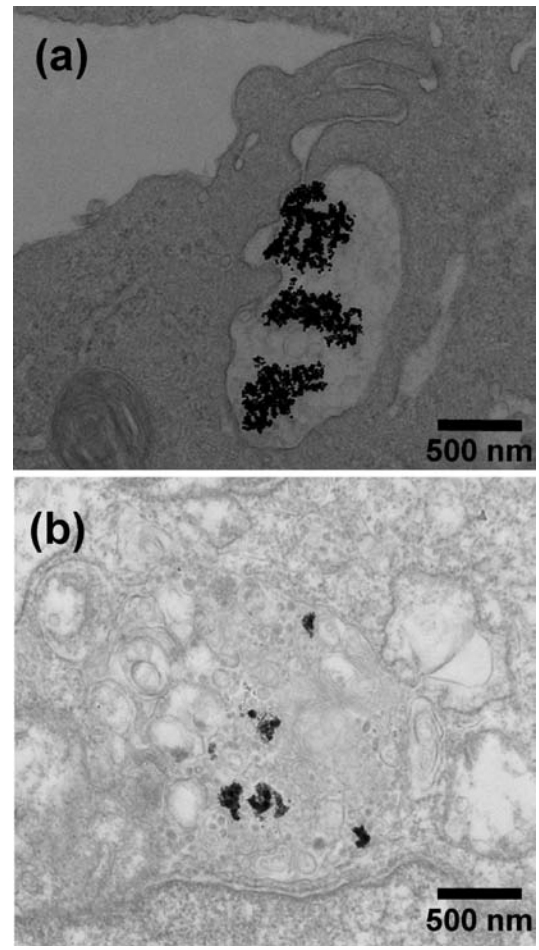


Figure 11. TEM images of AuNPs taken up by HUVECs. (a) 16 nm AuNPs with surface conjugated cyclic RGD peptide incubated with HUVECs for 72 h; AuNPs are seen to be uptaken into an endosomal compartments. (b) 4.5 nm AuNPs with surface conjugated cyclic RGD peptide incubated with HUVECs for 72 h; AuNPs are also observed clustered within endosomal compartments.

(*36*). These TEM studies serve as a benchmark to demonstrate that MAIL imaging can provide similar information to electron microscopy, but with the potential of performing imaging in real time and on live cells.

CONCLUSIONS

We have shown via MAIL imaging that AuNPs of two different diameters, 4.5 and 16 nm, can be targeted specifically to activated endothelial cells by covalent conjugation of RGD peptides to the surface of the nanoparticle. Detected signal from these particles within the cells depended on two factors: (1) the size of the particle, 4.5 nm vs 16 nm, and (2) the structure of the RGD analog. AuNP−RGDfK conjugates exhibit highly differential nanoparticle uptake when compared to AuNPs conjugated with linear RGD or bare AuNPs. The integrated counts for MAIL images of the targeted HUVECs were an order of magnitude higher for the AuNP−RGDfK conjugates than for the AuNP−GRGDSP controls. Also, cells incubated with 16 nm AuNPs exhibit significantly higher MAIL signals than those incubated with the smaller 4.5 nm AuNPs. Additional experiments in which uptake into HUVECs was blocked with BSA, sodium azide, or free RGDfK, indicated that AuNP−RGDfK conjugates are internalized following a specific binding event and that $\alpha_v\beta_3$ integrin-mediated endocytosis is an important uptake mechanism. Results from MAIL studies were verified by comparison to TEM images, which revealed that the endocytosed AuNPs remain primarily within endosomal and lysosomal vesicles.

The studies reported here demonstrate that MAIL is a powerful tool for monitoring targeting and determining uptake mechanisms of surface-functionalized nanostructures. Given the capability of MAIL for rapid, three-dimensional imaging with high resolution, this technique shows great promise for applications in nanomedicine.

ACKNOWLEDGMENT

P.D. and H.G. thank the NSF-NIRT (CHE 0511219478) for generous financial support. In addition, M.B.D. would like to thank the Fischell Fellowship in Biomedical Engineering for graduate support. The authors would also like to acknowledge Dr. Ru-Ching Hsia at the University of Maryland Baltimore School of Dentistry EM facility for assistance in TEM sample preparation and imaging.

LITERATURE CITED

(1) Cun, D., Jensen, L. B., Nielsen, H. M., Moghimi, M., and Foged, C. (2008) Polymeric nanocarriers for siRNA delivery: challenges and future prospects. *J. Biomed. Nanotechnol. 4*, 258–275.

(2) Hervella, P., Lozano, V., and Garcia-Fuentes, M. (2008) Nanomedicine: new challenges and opportunities in cancer therapy. *J. Biomed. Nanotechnol. 4*, 276–292.

(3) Bianco, A., Kostarelos, K., and Prato, M. (2008) Opportunities and challenges of carbon-based nanomaterials for cancer therapy. *Expert Opin. Drug Delivery 5*, 331–342.

(4) Venugopal, J., Prabhakaran, M. P., Low, S., Choon, A. T., Zhang, Y. Z., Deepika, G., and Ramakrishna, S. (2008) Nanotechnology for nanomedicine and delivery of drugs. *Curr. Pharm. Des. 14*, 2184–2200.

(5) Farrer, R. A., Butterfield, F. L., Chen, V. W., and Fourkas, J. T. (2005) Highly efficient multiphoton-absorption-induced luminescence from gold nanoparticles. *Nano Lett. 5*, 1139–1142.

(6) Nagesha, D., Laevsky, G. S., Lampton, P., Banyal, R., Warner, C., DiMarzio, C., and Sridhar, S. (2007) In vitro imaging of embryonic stem cells using multiphoton luminescence of gold nanoparticles. *Int. J. Nanomed. 2*, 813–819.

(7) Bruchez, M., Moronne, M., Gin, P., Weiss, S., and Alivisatos, A. P. (1998) Semiconductor nanocrystals as fluorescent biological labels. *Science 281*, 2013–2016.

(8) Chan, W. C. W., Maxwell, D. J., Gao, X. H., Bailey, R. E., Han, M. Y., and Nie, S. M. (2002) Luminescent quantum dots for multiplexed biological detection and imaging. *Curr. Opin. Biotechnol. 13*, 40–46.

(9) Gao, X. H., Chan, W. C. W., and Nie, S. M. (2002) Quantum-dot nanocrystals for ultrasensitive biological labeling and multicolor optical encoding. *J. Biomed. Opt. 7*, 532–537.

(10) Seydel, C. (2003) Quantum dots get wet. *Science 300*, 80–81.

(11) Boyd, G. T., Yu, Z. H., and Shen, Y. R. (1986) Photoinduced luminescence from the noble-metals and its enhancement on roughened surfaces. *Phys. Rev. B 33*, 7923–7936.

(12) Kempa, T., Farrer, R. A., Giersig, M., and Fourkas, J. T. (2006) Photochemical synthesis and multiphoton luminescence of monodisperse silver nanocrystals. *Plasmonics 1*, 45–51.

(13) Nah, S., Li, L. J., and Fourkas, J. T. (2009) Field-enhanced phenomena of gold nanoparticles. *J. Phys. Chem. A 113*, 4416–4422.

(14) Durr, N. J., Larson, T., Smith, D. K., Korgel, B. A., Sokolov, K., and Ben-Yakar, A. (2007) Two-photon luminescence imaging of cancer cells using molecularly targeted gold nanorods. *Nano Lett. 7*, 941–945.

(15) Wang, H. F., Huff, T. B., Zweifel, D. A., He, W., Low, P. S., Wei, A., and Cheng, J. X. (2005) In vitro and in vivo two-photon luminescence imaging of single gold nanorods. *Proc. Natl. Acad. Sci. U.S.A. 102*, 15752–15756.

(16) Park, J., Estrada, A., Sharp, K., Sang, K., Schwartz, J. A., Smith, D. K., Coleman, C., Payne, J. D., Korgel, B. A., Dunn, A. K., and Tunnell, J. W. (2008) Two-photon-induced photoluminescence imaging of tumors using near-infrared excited gold nanoshells. *Opt. Express 16*, 1590–1599.

(17) Qu, X. C., Wang, J., Yao, C. P., and Zhang, Z. X. (2008) Two-photon imaging of lymphoma cells targeted by gold nanoparticles. *Chin. Opt. Lett. 6*, 879–881.

(18) Assa-Munt, N., Jia, X., Laakkonen, P., and Ruoslahti, E. (2001) Solution structures and integrin binding activities of an RGD peptide with two isomers. *Biochemistry 40*, 2373–2378.

(19) Borgman, M. P., Coleman, T., Kolhatkar, R. B., Geyser-Stoops, S., Line, B. R., and Ghandehari, H. (2008) Tumor-targeted HPMA copolymer-(RGDfK)-(CHX-A'-DTPA) conjugates show increased kidney accumulation. *J. Controlled Release 132*, 193–199.

(20) Line, B. R., Mitra, A., Nan, A., and Ghandehari, H. (2005) Targeting tumor angiogenesis: Ccomparison of peptide and polymer-peptide conjugates. *J. Nucl. Med. 46*, 1552–1560.

(21) Mitra, A., Coleman, T., Borgman, M., Nan, A., Ghandehari, H., and Line, B. R. (2006) Polymeric conjugates of mono- and bi-cyclic alpha(V)beta(3) binding peptides for tumor targeting. *J. Controlled Release 114*, 175–183.

(22) Mitra, A., Mulholland, J., Nan, A., McNeill, E., Ghandehari, H., and Line, B. R. (2005) Targeting tumor angiogenic vasculature using polymer-RGD conjugates. *J. Controlled Release 102*, 191–201.

(23) Mitra, A., Nan, A., Papadimitriou, J. C., Ghandehari, H., and Line, B. R. (2006) Polymer-peptide conjugates for angiogenesis targeted tumor radiotherapy. *Nucl. Med. Biol. 33*, 43–52.

(24) Fani, M., Psimadas, D., Zikos, C., Xanthopoulos, S., Loudos, G. K., Bouziotis, P., and Varvarigou, A. D. (2006) Comparative evaluation of linear and cyclic Tc-99m-RGD peptides for targeting of integrins in tumor angiogenesis. *Anticancer Res. 26*, 431–434.

(25) Frochot, C., Di Stasio, B., Vanderesse, R., Belgy, M. J., Dodeller, M., Guillemin, F., Viriot, M. L., and Barberi-Heyob, M. (2007) Interest of RGD-containing linear or cyclic peptide targeted tetraphenylchlorin as novel photosensitizers for selective photodynamic activity. *Bioorg. Chem. 35*, 205–220.

(26) Rehor, A., Schmoekel, H., Tirelli, N., and Hubbell, J. A. (2008) Functionalization of polysulfide nanoparticles and their

performance as circulating carriers. *Biomaterials 29*, 1958–1966.

(27) Singh, S. R., Grossniklaus, H. E., Kang, S. J., Edelhauser, H. F., Ambati, B. K., and Kompella, U. B. (2009) Intravenous transferrin, RGD peptide and dual-targeted nanoparticles enhance anti-VEGF intraceptor gene delivery to laser-induced CNV. *Gene Ther. 16*, 645–659.

(28) Suk, J. S., Suh, J., Choy, K., Lai, S. K., Fu, J., and Hanes, J. (2006) Gene delivery to differentiated neurotypic cells with RGD and HIV Tat peptide functionalized polymeric nanoparticles. *Biomaterials 27*, 5143–5150.

(29) Brown, K. R., Walter, D. G., and Natan, M. J. (2000) Seeding of colloidal Au nanoparticle solutions. 2. Improved control of particle size and shape. *Chem. Mater. 12*, 306–313.

(30) Frens, G. (1973) Controlled nucleation for regulation of particle-size in monodisperse gold suspensions. *Nat. Phys. Sci. 241*, 20–22.

(31) Cuatreca, P., and Parikh, I. (1972) Adsorbents for affinity chromatography - use of N-hydroxysuccinimide esters of agarose. *Biochemistry 11*, 2291.

(32) Farrer, R. A., Previte, M. J. R., Olson, C. E., Peyser, L. A., Fourkas, J. T., and So, P. T. C. (1999) Single-molecule detection with a two-photon fluorescence microscope with fast-scanning capabilities and polarization sensitivity. *Opt. Lett. 24*, 1832–1834.

(33) Chithrani, B. D., Ghazani, A. A., and Chan, W. C. W. (2006) Determining the size and shape dependence of gold nanoparticle uptake into mammalian cells. *Nano Lett. 6*, 662–668.

(34) Chithrani, B. D., and Chan, W. C. W. (2007) Elucidating the mechanism of cellular uptake and removal of protein-coated gold nanoparticles of different sizes and shapes. *Nano Lett. 7*, 1542–1550.

(35) Hong, R., Han, G., Fernandez, J. M., Kim, B. J., Forbes, N. S., and Rotello, V. M. (2006) Glutathione-mediated delivery and release using monolayer protected nanoparticle carriers. *J. Am. Chem. Soc. 128*, 1078–1079.

(36) Nativo, P., Prior, I. A., and Brust, M. (2008) Uptake and intracellular fate of surface-modified gold nanoparticles. *Acs Nano 2*, 1639–1644.

BC100115M

Self-Protecting Bactericidal Titanium Alloy Surface Formed by Covalent Bonding of Daptomycin Bisphosphonates

Chang-Po Chen and Eric Wickstrom*

Department of Biochemistry and Molecular Biology, Thomas Jefferson University, Philadelphia, Pennsylvania 19107, United States.
Received March 12, 2010; Revised Manuscript Received September 24, 2010

Infections are a devastating complication of titanium alloy orthopedic implants. Current therapy includes antibiotic-impregnated bone cement and antibiotic-containing coatings. We hypothesized that daptomycin, a Gram-positive peptide antibiotic, could prevent bacterial colonization on titanium alloy surfaces if covalently bonded via a flexible, hydrophilic spacer. We designed and synthesized a series of daptomycin conjugates for bonding to the surface of 1.0 cm^2 Ti6Al4V foils through bisphosphonate groups, reaching a maximum yield of 180 pmol/cm^2. Daptomycin-bonded foils killed 53 ± 5% of a high challenge dose of 3×10^5 cfu *Staphylococcus aureus* ATCC 29213.

INTRODUCTION

The introduction of medical implants has revolutionized the field of medicine. Orthopedic implants, dental implants, vascular grafts, heart valves, and stents have extended life spans and the quality of life (*1*). However, implant-associated infections are serious complications of all those medical devices (*2*). The current arthroplasty infection rate ranges 1−5%, but the infection rate is much higher in trauma patients and in populations at risk for infection (*3*). Implant removal is usually the only clinical option because bacterial biofilm formation on the surface of the implant protects the microorganisms from the immune system and antibiotic therapy (*4, 5*). A number of local antibiotic delivery systems, such as antibiotic-containing poly(methyl methacrylate) cement (*6*) or biopolymers (*7*), have been developed to prevent orthopedic implant-associated infections. These approaches suffer from the limitation that the antibiotics can only be released to the surroundings over a short time. In some cases, the porous material holding the antibiotics has to be removed by a second surgery (*2*).

In order to address the problems faced by local delivery systems, covalent modification of orthopedic implants has been investigated with a variety of antibacterial materials. Quaternary ammonium salts, such as poly(4-vinyl-*N*-alkylpyridinium bromide) and 3-(trimethoxysilyl)propyldimethyloctadecyl ammonium chloride, were covalently bonded to glass, metal, and polymer surfaces to provide bactericidal activity (*8, 9*). An antimicrobial peptide LL-37 has also been attached to the surface of titanium alloy implants to prevent infections (*10, 11*). The peptide has a broad-spectrum activity against bacteria and fungi through peptide−membrane interactions leading to membrane permeation. Ampicillin has been used to modify the surface of polytetrafluoroethylene to effect surface antibiotic activity (*12, 13*).

Recently, we reported the covalent modification of titanium powder and titanium alloy pins by vancomycin, a Gram-positive peptide antibiotic that blocks peptidoglycan cross-linking (*14*), via a flexible, hydrophilic spacer (*15, 16*). The surfaces of the titanium alloy pins were uniformly oxidized with a hydrogen peroxide/sulfuric acid mixture, then functionalized with aminopropyltriethyoxysilane. After amide bonding of two aminoethoxyethoxyacetates to the surface aminopropyl groups, vancomycin was coupled to the titanium alloy surface via a third amide bond. The covalently attached vancomycin prevented *Staphylococcus aureus* (*17*) and *S. epidermidis* (*18*) colonization and biofilm formation on the titanium alloy surfaces.

This approach should be effective against most Gram-positive infections today, since resistance to vancomycin is relatively rare. Nevertheless, resistance to vancomycin is becoming more prevalent (*19, 20*), and we must prepare for the time when vancomycin will be much less effective. Treatment with daptomycin, a recently discovered antibacterial cyclic lipopeptide (*21*), might be a candidate for a second-generation antibiotic, as there have been no reports yet of resistance. Daptomycin appears to function by penetrating the bacterial cell membrane and causing rapid depolarization, resulting in a loss of membrane potential, leading to inhibition of protein, DNA, and RNA synthesis, thereby killing the bacteria (*22*).

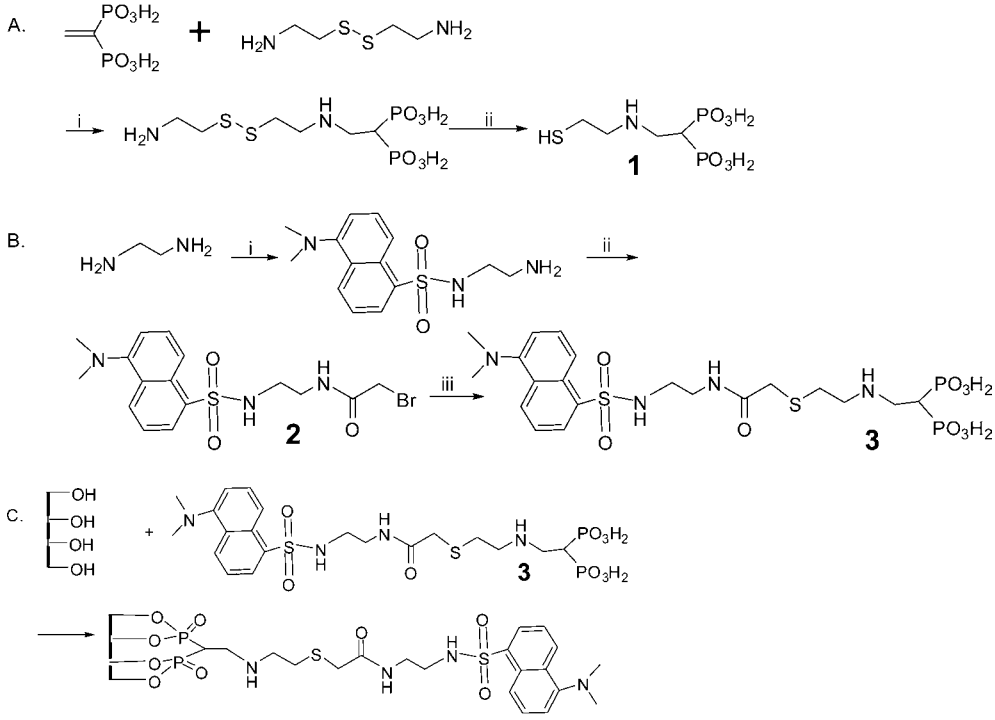
Bisphosphonates bind strongly to metal surfaces and bone tissue (*23, 24*), and have been successfully integrated into bone-specific drug delivery systems to target protein, peptide, estrogen, antibiotics, antitumor and radioactive pharmaceutics to bone tissue (*25*). Recently, bisphosphonate has been conjugated with poly(ethylene glycol) or alkanes to directly modify titanium surfaces (*26*), and an RGD[1]peptide was bound to the titanium implants by conjugating with four phosphonic acid groups (*27*). Because of the strong and selective affinity of phosphonates to the oxidized surface of titanium (*25*), we hypothesized that a phosphonate derivative of daptomycin could bond readily to the surface of Ti6Al4V titanium alloy to form an antibiotic monolayer. This approach could reduce the number

* To whom correspondence should be addressed, at Department of Biochemistry and Molecular Biology, Thomas Jefferson University, Bluemle 219, 233 South 10th Street, Philadelphia, PA 19107. Tel: 1.215.955.4578. Fax: 1.215.955.4580. E-mail: eric@tesla.jci.tju.edu.

[1]Abbreviations: Boc, *t*-butyloxycarbonyl; CF_3CO_2H, trifluoroacetic acid; CH_2Cl_2, dichloromethane; CH_3CN, acetonitrile; DCC, *N*,*N*′-dicyclohexylcarbodiimide; EtOAc, ethyl acetate; Et_2O, diethyl ether; Fmoc, fluorenylmethoxycarbonyl; HATU, 2-(7-aza-1*H*-benzotriazole-1-yl)-1,1,3,3-tetramethyl-uronium hexa-fluorophosphate; H_2NEtNH_2, ethylenediamine, H_2O_2, hydrogen peroxide; H_2SO_4, sulfuric acid; HPLC, high performance liquid chromatography; iPrOH, isopropanol; iPr_2NEt, diisopropylethylamine; iPr_3SiH, triisopropylsilane; MALDI-TOF, matrix-assisted laser desorption-ionization time-of-flight; MeOH, methanol; Me_2NCHO, *N*,*N*-dimethylformamide; Me_2SO, dimethylsulfoxide; MIC, minimum inhibitory concentration; mp, melting point; Na_2CO_3, sodium carbonate, Na_2SO_4, sodium sulfate, NHS, *N*-hydroxysuccinimide; RGD, arginine-glycine-aspartate; rt, room temperature; TEG, tetra(ethylene glycol).

10.1021/bc100136e © 2010 American Chemical Society
Published on Web 10/15/2010

Scheme 1. Synthesis of Dansyl Bisphosphonic Acid (3) and Attachment to the Oxidized Surface of Ti6Al4V Foil[a]



[a] A. 2-(2-Mercaptoethylamino)ethylidene-1,1-bisphosphonic acid (**1**): (i) water, 110 °C, 6 h. (ii) Me_3P. B. Dansyl bisphosphonic acid (**3**): (i) dansyl chloride, rt 2 h. (ii) bromoacetic acid, DCC, EtOAc. (iii) 2-(2-Mercaptoethylamino)ethylidene-1,1-bisphosphonic acid (**1**), 50% Me_2NCHO/50% water. C. Attachment to Ti6Al4V foil.

of chemical synthetic steps required, relative to our vancomycin construct (*16*), and make sterilization feasible during production.

MATERIALS AND METHODS

Materials. Daptomycin was purchased from Cubist Pharmaceuticals. Fmoc-Lys(εBoc)-OH and HATU were purchased from Novobiochem. Bromoacetic acid, CF_3CO_2H, CH_2Cl_2, CH_3CN, DCC, Et_2O, EtOAc, hexane, H_2NEtNH_2, iPr_2NEt, iPrOH, iPr_3SiH, Me_2NCHO, and MeOH were purchased from Sigma-Aldrich. Müller-Hinton broth was purchased from Becton-Dickinson. Mal-dPEG4 NHS ester (#10214) (succinimidyl-TEG-maleimide) was purchased from Quantum Biodesign Ltd. 2-(2-Mercaptoethylamino) ethylidene-1,1-bisphosphonic acid (**1**), prepared as described (*28*) (Scheme 1), was the generous gift of Dr. Ivan S. Alferiev of the Children's Hospital of Philadelphia.

Chromatography. Normal-phase flash chromatography of crude products was carried out on a 2.5 × 60 cm silica gel column eluted with 75% hexane/25% EtOAc or 95% CH_2Cl_2/5% MeOH.

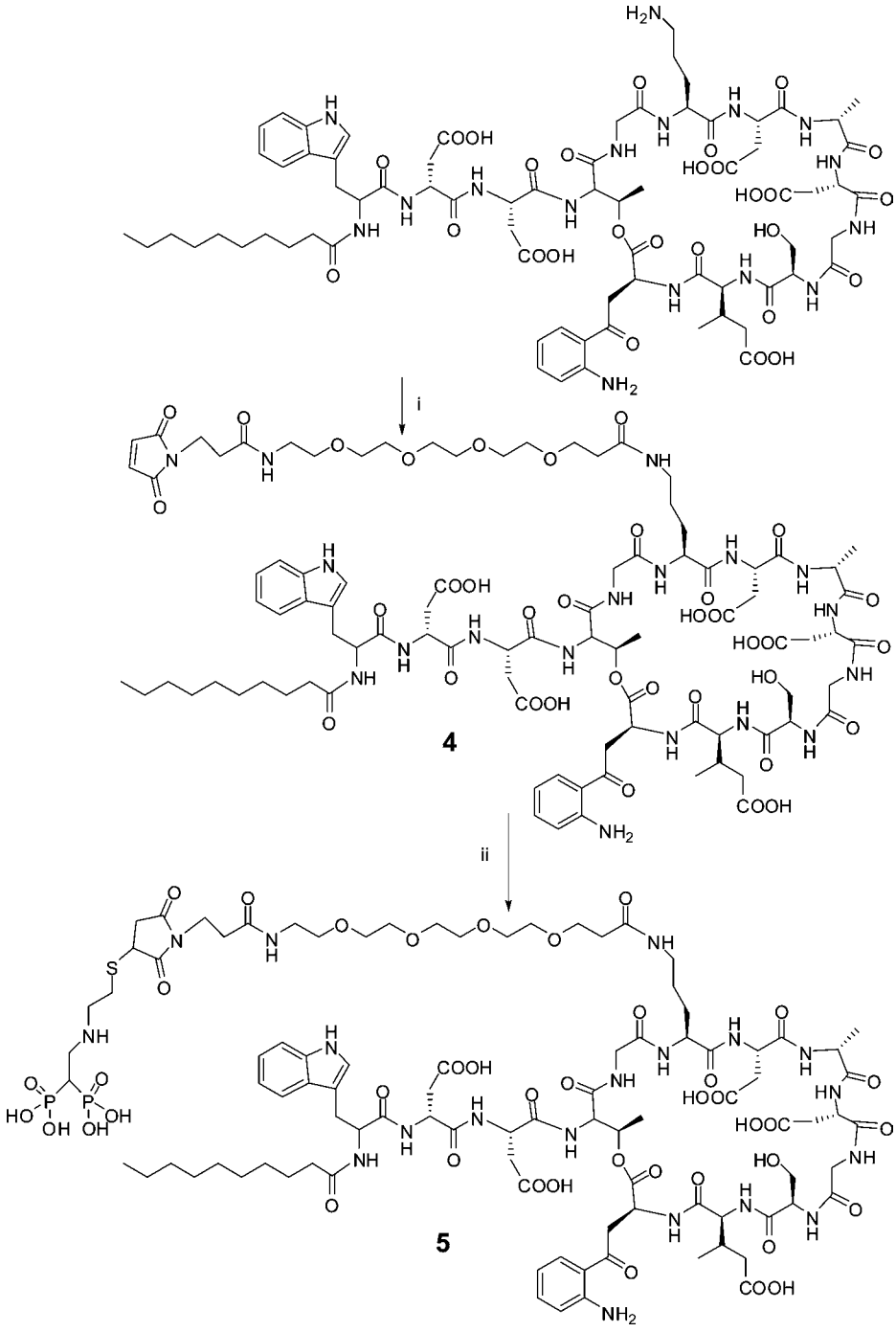
Preparative reversed-phase high-performance liquid chromatography (HPLC) of intermediates was performed on an Alltech Alltima C_{18} 5 μ column, 250 × 22 mm, coupled to a UV detector at 254 nm, eluted with a linear gradient of 10−50% CH_3CN in water containing 0.1% CF_3CO_2H in 30 min at a flow rate 6 mL/min. The analysis was performed with a Waters 600E system, using Alltech C18 5 μ, 250 × 4.6 mm column coupled to a Waters 486 detector at 254 nm. Sample was eluted with a linear gradient of 20−70% CH_3CN in water containing 0.1% CF_3CO_2H in 30 min with a flow rate of 1 mL/min. Thin layer chromatography of intermediates was done on Baker Si250F silica gel TLC plates developed with MeOH/CH_2Cl_2 solvent system, then visualized with a Mineralight 254 nm lamp.

Apparatus. ^{1}H NMR spectra were recorded with a Varian INOVA 400 MHz spectrometer (Palo Alto, CA). Molecular weight analysis was performed on an Ettan MALDI-TOF mass spectrometer (GE Healthcare, Piscataway, NJ). Lyophilization was performed using a Christ Alpha 2−4 freeze-dryer (Martin Christ, Osterode am Harz, Germany) equipped with a Pfeiffer Vacuum Pump (Asslar, Germany). Fluorescence readings were performed on a QuantaMaster double monochromator fluorimeter (Photon Technologies, Birmingham, NJ). Deionized water was produced using a Milli-Q water purification system (Millipore, Bedford, MA).

Synthesis. *1-Bromoacetyl-2-dansyl-ethylenediamine (**2**).* To 20 mL of H_2NEtNH_2 was added dansyl chloride (1.079 g, 4 mmol) in 30 min under stirring (Scheme 1). The reaction was stirred for 2 h at room temperature, followed by removal of unreacted H_2NEtNH_2 under reduced pressure. The residual syrup was dissolved in 20 mL EtOAc, washed with saturated aqueous Na_2CO_3 solution (3 × 5 mL), and water (3 × 5 mL). The organic phase was dried with Na_2SO_4, filtered, and the solvent removed by rotary evaporation. The residual product was redissolved in dry EtOAc, followed by addition of bromoacetic acid (555.6 mg, 4 mmol) and DCC (824 mg, 4 mmol). The mixture was stirred at room temperature for 3 h, after which the precipitate was removed by filtration. The filtrate was then washed with saturated aqueous Na_2CO_3 solution (3 × 5 mL), and water (3 × 5 mL). The organic phase was dried with Na_2SO_4. The desired product (*2*) was purified by flash chromatography on a silica gel column eluted with 75% hexane/25% EtOAc. Yield: 1.57 g (94.7%). ^{1}H NMR (400 MHz, $CDCl_3$), δ = 8.62 (d, 1H), 8.25−8.30 (m, 2H), 7.55−7.62 (m, 2H), 7.25 (br, 1H), 6.71 (br, 1H), 5.33 (br, 1H), 3.69 (s, 1H), 3.33−3.37 (m, 2H), 3.07−3.11 (m, 2H), 2.94 (s, 6H). ^{13}C NMR (100 MHz, $CDCl_3$), δ = 166.8, 155.0, 153.6, 134.5, 130.8, 130.0, 129.6, 128.8, 123.7, 118.6, 115.7, 45.8, 43.2, 40.1, 28.8. MALDI-TOF MS, calc. 414.32 Da, found 414.52 Da.

*Dansyl-bisphosphonic Acid (**3**).* 2-(2-Mercaptoethylamino)-ethylidene-1,1-bisphosphonic acid (**1**) (265 mg, 1 mmol) was dissolved in 5 mL of 67% Me_2NCHO/33% water and adjusted to pH 7.0 with NaOH under the protection of argon. Then, 1-bromoacetyl-2-dansyl-ethylenediamine (**2**) (414 mg, 1 mmol)

Scheme 2. Synthesis of Daptomycin-TEG-bisphosphonic Acid (5)[a]



[a] (i) 1.1 equiv of succinimidyl TEG maleimide, Me_2NCHO, r.t. (ii) 2-(2-Mercaptoethylamino) ethylidene-1,1-bisphosphonic acid (**1**), 50% Me_2NCHO/50% water.

was dissolved in 2 mL Me_2NCHO and added dropwise to (**1**) under the protection of argon (Scheme 1). The mixture was stirred at room temperature for 2 h. The solvent was then removed by rotary evaporation under vacuum. Finally, the residue was dissolved in 10% aqueous CH_3CN and purified by preparative reversed-phase HPLC. The eluent peak corresponding to the product 2-(9-dansyl-6,9-diaza-5-oxo-3-thia-nonanyl)-ethylidene-1,1-bisphosphonic acid (**3**) was pooled, concentrated, and lyophilized. ^{1}H NMR (400 MHz, Me_2SO), δ = 8.48 (d, 1H), 8.29 (d, 1H), 8.13−8.11 (m, 2H), 8.05 (t, 1H), 7.67−7.60 (m, 2H), 7.29 (d, 1H), 3.34−3.27 (m, 2H), 3.22 (t, 2H), 3.12−3.09 (m, 4H), 2.85 (s, 6H), 2.85−2.83 (m, 4H), 2.52−2.51 (m, 1H), 2.44−2.36 (m, 1H). ^{13}C NMR (100 MHz, $CDCl_3$), δ = 169.0, 157.9, 151.3, 135.7, 129.5, 129, 128.3, 127.9, 123.7, 119.1, 115,2, 45.6, 45.1, 44.3, 41.7, 40.3, 35.5, 33.5, 27.7. ^{31}P NMR (Me_2SO): δ = 17.15 (^{1}H decoupled: s). MALDI-TOF MS, calc. 598.57 Da, found 598.86 Da. Yield: 546 mg (91%).

*Daptomycin-TEG-maleimide (**4**).* Daptomycin (100 mg, 0.062 mmol) was dissolved in 1 mL Me_2NCHO and added to 1.1 equiv of succinimidyl-TEG-maleimide (Scheme 2). The mixture was stirred at room temperature overnight. The product was precipitated by Et_2O and purified by analytical reversed-phase HPLC. The eluent peak corresponding to the product daptomycin-TEG-maleimide (**4**) was pooled, concentrated, and lyophilized. The purified sample was characterized by analytical HPLC (Figure 4B). MALDI-TOF MS, calc. for $C_{90}H_{126}N_{18}O_{35}$ 2020.01 Da, found $[M+H]^+$ 2021.53 Da. Yield: 112 mg (89%).

*Bisphosphonic Acid Derivative of Daptomycin (**5**).* To a solution of daptomycin-TEG-maleimide (**4**) (100 mg, 49.5 μmol) in 1 mL water was added 14.4 mg of 2-(2-mercaptoethylamino)ethylidene-1,1-bisphosphonic acid (**1**) in 1 mL water (pH 7.0, adjusted by sodium hydroxide) under the protection of argon (Scheme 2). The mixture was stirred at room temperature for 1 h. The sample was purified by analytical reversed-phase HPLC. The eluent peak corresponding to the product daptomycin-TEG-bisphosphonic acid (**5**) was pooled, concentrated, and lyophilized. The purified sample was characterized by analytical HPLC (Figure 4C). MALDI-TOF MS calc. for $C_{94}H_{139}N_{19}O_{41}P_2S$ 2285.24 Da, found $[M+H]^+$ 2286.13 Da. Yield: 105 mg (93%).

*Dansyl-Lys(εBoc)-OH (**6**).* To a solution of α-H_2N-Lys(εBoc)-OH (492.6 mg, 2 mmol) in CH_2Cl_2 (5 mL) was added 10 mmol of iPr_2NEt, followed by addition of 2.1 mmol of dansyl chloride (dissolved in 2 mL CH_2Cl_2) dropwise over 10 min (Scheme 3). The mixture was stirred at room temperature for 2 h. The solvent was removed by rotary evaporation, and the residue was dissolved in 10 mL EtOAc, washed with water, and then dried with Na_2SO_4. The solvent was evaporated, and the resulting product dansyl-Lys(εBoc)-OH (**6**) was purified with flash chromatography with 95% CH_2Cl_2/5% MeOH ($R_f = 0.12$). ^{1}H NMR (400 MHz, Me_2SO), δ = 8.53 (d, 1H), 8.32−8.38 (m, 1H), 8.27 (d, 1H), 7.59−7.49 (m, 2H), 7.20 (d, 1H), 5.93 (s, 1H), 4.43 (s, 1H), 3.97−3.89 (m, 2H) 2.89 (s, 6H), 2.8−2.7 (m, 2H), 1.68−1.6 (m, 2H), 1.38 (s, 9H), 1.22−1.1 (m, 4H). ^{13}C NMR (100 MHz, $CDCl_3$), δ = 174.2, 158.1, 156.2, 151.6, 134.1, 130.7, 129.8, 129.7, 128.4, 123.2, 119.3, 115.3, 81.1, 55.5, 45.8, 39.9, 32, 28.4, 21.7. MALDI-TOF MS calc. for $C_{23}H_{33}N_3O_6S$ 479.59 Da, found $[M+H]^+$ 480.62 Da. Yield: 765 mg (87%).

*Dansyl-Lys-daptomycin (**7**).* Dansyl-Lys(εBoc)-OH (**6**) (23.6 mg, 49 μmol), NHS (7.4 mg, 55 μmol), and DCC (11.2 mg 54 μmol) were dissolved in 5 mL anhydrous EtOAc in darkness. After stirring for 2 h at room temperature, the precipitate was removed by filtration, and the solvent was evaporated. The resultant NHS active ester was dissolved in 1 mL anhydrous Me_2NCHO and added to a solution of 100 mg daptomycin in 1 mL Me_2NCHO (Scheme 3). The mixture was stirred at room temperature overnight. The product was precipitated by Et_2O, sedimented, and dried under vacuum. The residue was incubated with 2 mL 95% CF_3CO_2H/2.5% water/2.5% iPr_3SiH at room temperature for 1 h to deprotect the Boc group. The deprotected derivative was precipitated by Et_2O and purified by analytical reversed-phase HPLC. The eluent peak corresponding to the product dansyl-Lys-daptomycin (**7**) was pooled, concentrated, and lyophilized. The purified sample was characterized by analytical HPLC and MALDI-TOF MS. Calc. for $C_{90}H_{125}N_{19}O_{27}S$, 1937.13 Da, found $[M+H]^+$ 1938.09 Da. Yield: 105 mg (88%).

*Dansyl-Lys-daptomycin-TEG-maleimide (**8**).* Dansyl-Lys-daptomycin (**7**) (120 mg, 0.062 mmol) was dissolved in 1 mL Me_2NCHO and added to 1.1 equiv of succinimidyl-TEG-maleimide in 1 mL Me_2NCHO (Scheme 3). The mixture was stirred at room temperature overnight. The product was precipitated by Et_2O and purified by analytical reversed-phase HPLC. The eluent peak corresponding to the product dansyl-Lys-daptomycin-TEG-maleimide (**8**) was pooled, concentrated, and lyophilized. The purified sample was characterized by analytical HPLC and MALDI-TOF MS. Calc for $C_{108}H_{149}N_{21}O_{38}S$, 2381.52 Da, found $[M+H]^+$ 2383.10 Da. Yield: 128 mg (87%).

*Dansyl-Lys-daptomycin-TEG-bisphosphonic Acid (**9**).* The conjugation of 2-(2-mercaptoethylamino)-ethylidene-1,1-bisphosphonic acid (**1**) with **8** to give the dansyl-Lys-daptomycin-TEG-bisphosphonic acid derivative (**9**) (Scheme 3) was carried out according to the procedure described above for preparing **5**. The purified dansyl-Lys-daptomycin-TEG-bisphosphonic acid (**9**) was characterized by analytical HPLC (Figure 4D). MALDI-TOF MS: calc. for $C_{112}H_{162}N_{22}O_{44}P_2S_2$ 2646.68 Da, found $[M+H]^+$ 2648.02 Da.

Methods. *Oxidation of Ti6Al4V Foil Surface.* Ti6Al4V foil (0.6 mm thickness) was cut into 1 × 1 cm squares and washed twice with acetone, then once each with double-deionized water, saturated aqueous Alconox, and 0.1 M NaOH. Finally, the foils were washed with 50% concentrated HCl/50% MeOH at room temperature for 30 min with sonication every 5 min, followed by three washes with double-deionized water. The cleaned foil surfaces were then oxidized in 50% H_2O_2/50% concentrated H_2SO_4 at 4 °C for 4 h. The oxidized foils were washed four times with water, Me_2NCHO, and water, dried overnight under vacuum, and placed in the argon atmosphere chamber of an MO-20M glovebox (*29*).

*Attachment of Dansyl-bisphosphonic Acid (**3**) to Ti6Al4V Foils.* 2-(9-Dansyl-6,9-diaza-5-oxo-3-thia-nonanyl)-ethylidene-1,1-bisphosphonic acid (**3**) (5 mg/mL) was incubated with oxidized Ti6Al4V foils in water (pH was adjusted to 7.0 using 1 M NaOH) at room temperature for 16 h (Scheme 1) with intermittent shaking.

Stability of Dansyl-bisphosphonic Acid (3) on the Surface of Titanium Foil. After washing with water and PBS, the dansyl-bisphosphonate foils were immersed in PBS, pH 7.4, and kept at 37 °C to investigate the stability of the linkage between titanium and dansyl. The dansyl-bisphosphonate residues released into the solution were measured by total fluorescence (λ_{ex} 337 nm and λ_{em} 520 nm) (*30*) at several time points over one month.

After one month of incubation at pH 7.4, 1 M NaOH was added to the PBS buffer to adjust the pH to 12, and the foils were incubated with the basic solution for 4 h at room temperature, with intermittent sonication, to release all the remaining dansyl moieties from the surface of the foils, as described (*30*). Dansyl moieties in solution were measured by fluorescence as before. In each batch of foils, the total fluorescence stripped from the foil was treated as 100%.

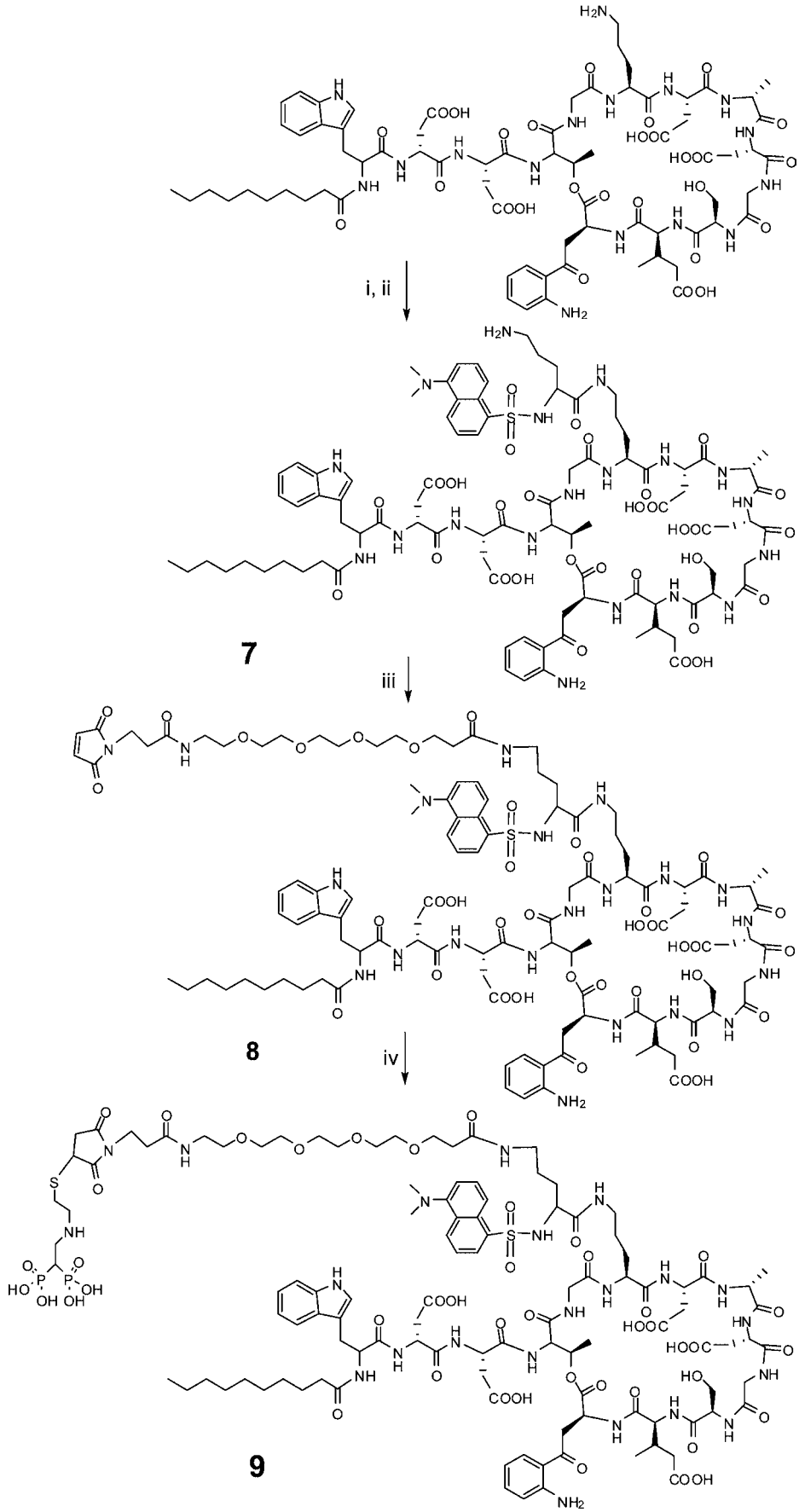
*Attachment of Daptomycin-TEG-bisphosphonic Acid (**5**) to Ti6Al4V Foils.* Daptomycin-TEG-bisphosphonic acid (**5**) (2 mg, 0.88 μmol) was dissolved in 1 mL water, and the pH was adjusted to 7.0 with 1 M NaOH. Six foils (1 × 1 × 0.06 cm^3) were immersed in the solution and kept at room temperature for 16 h with intermittent gentle shaking, avoiding foil-to-foil contact. The solution was removed, and the foils were washed with water (3 × 1.5 mL), Me_2NCHO (3 × 1.5 mL), and water (3 × 2 mL). The foils were dried under vacuum at room temperature.

Fluorescent Quantitation of Daptomycin Derivatives on the Titanium Foil Surface. Dansyl-Lys-daptomycin-TEG-bisphosphonic acid (**9**) (5 mg/mL) was incubated with 20 Ti6Al4V foils at pH 7 at room temperature for 16 h, followed by washing with water, Me_2NCHO, and water. The modified foils were then incubated with 0.01 M NaOH at room temperature for 4 h. The fluorescence was recorded with λ_{ex} 337 nm and λ_{em} 520 nm (*30*), quantitated against a standard curve of known dansyl concentrations, as before (*16*).

Minimum Inhibitory Concentrations. Minimum inhibitory concentrations (MIC) were determined by broth microdilution according to NCCLS guidelines (*31*) except that the Müller-Hinton Broth was supplemented to 50 mg/L Ca^{2+} and all assays were performed at 37 °C with *S. aureus* ATCC 29213.

Antibacterial Activity Assay on Daptomycin-TEG-bisphosphonate-Ti6Al4V Foils. Each dried foil was adhered in place in an individual well of a 24-well plate by low-melting-point wax with the upper surface uncovered (Figure 1). The upper

Scheme 3. Synthesis of *N*-Dansyl Daptomycin Bisphosphonic Acid (9)[a]



[a] (i) Dansyl-Lys (Boc)-NHS ester, Me_2NCHO, r.t, overnight. (ii) CF_3CO_2H/water/iPr_3SiH (95:2.5:2.5), rt, 1 h. (iii) succinimidyl-TEG-maleimide, Me_2NCHO, rt, overnight. (iv) 2-(2-Mercaptoethylamino)ethylidene-1,1-bisphosphonic acid, 50% Me_2NCHO/50% water.

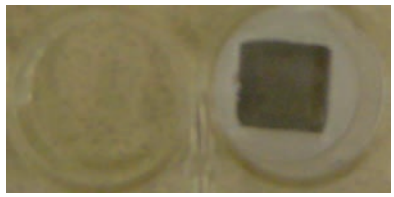


Figure 1. Each dried Ti6Al4V foil was adhered in place in an individual well of a 24-well plate by low-melting-point wax for antibiotic activity evaluation with the upper surface uncovered. Left, empty well; right, one piece of Ti6Al4V foil adhered in the well using low-melting-point wax.

surfaces of the foils were sterilized with 70% iPrOH for 30 min at room temperature, followed by rinsing with sterile broth three times. Then, 200 μL aliquots of Müller-Hinton broth (complemented with Ca^{2+}) containing 3×10^5 cfu were transferred into each well containing a foil and incubated at 37 °C for 16 h (same time point with that used in MIC test). The broth in the wells was diluted with 800 μL of fresh Müller-Hinton broth, and the optical density at 600 nm was recorded. The experiment was carried out with nonimmobilized daptomycin-modified foils and immobilized blank foils as controls.

Statistical Analysis. Data were expressed as mean ± SE. The significance of differences between means of experimental groups was determined by using Student's *t* test.

RESULTS

Design and Synthesis of Dansyl-bisphosphonic Acid (3) as a Fluorescent Model for Ti6Al4V Bonding. The reaction of dansyl chloride with a large excess of H_2NEtNH_2 provided dansylamidoethylamine as the main product, and the residual H_2NEtNH_2 could be collected for further use (Scheme 1). The reaction of dansylamidoethylamine and bromoacetic acid gave 1-bromoacetyl-2-dansyl-ethylenediamine (**2**). The dansyl-bisphosphonic acid derivative (**3**) was prepared by selective reaction of 1-bromoacetyl-2-dansyl-ethylenediamine (**2**) with 2-(2-mercaptoethylamino)ethylidene-1,1-bisphosphonic acid (**1**) under basic conditions (Scheme 1).

Attachment of Dansyl-bisphosphonic Acid (3) to Ti6Al4V Foils. 2-(9-Dansyl-6,9-diaza-5-oxo-3-thianonanyl)-ethylidene-1,1-bisphosphonic acid (**3**) (5 mg/mL) was incubated with oxidized Ti6Al4V foils in water (pH was adjusted to 7.0 using 1 M NaOH) at room temperature for 16 h (Scheme 1) with intermittent shaking. The time course of attachment is shown in Figure 2. Coupling was largely complete by 1 h, and leveled off by 10 h.

Stability of Dansyl-bisphosphonic Acid (3) on the Surface of Titanium Foil. The dansyl-bisphosphonate residues released into the pH 7.4 PBS solution at 37 °C were measured by total fluorescence (λ_{ex} 337 nm and λ_{em} 520 nm) (*30*) at several time points over one month (Figure 3). In each batch of foils, the total fluorescence stripped from the foil was treated as 100%. The data showed that about 25% percent of the dye was released in the first 10 h of incubation in pH 7.4 phosphate saline buffer. No more dansyl was released to the buffer in one month. It seems likely that the rapidly eluted dansyl moieties were only adsorbed, not covalently bonded. The results imply that the covalently attached dansyl-bisphosphonic acid was stable on the surface of titanium foils in PBS at 37 °C.

Design and Synthesis of of Bisphosphonic Acid Derivative of Daptomycin (5) for Bonding to Ti6Al4V Foils. Daptomycin is a cyclic lipopeptide antibiotic with one primary amino group, four carboxylic acid groups, and one sensitive indole ring (*21*). A study of N-acylated ornithine analogues of daptomycin indicated that acylation of the ε-amino group on ornithine did not significantly influence the antibacterial activity (*32, 33*). Only the ε-amino group on ornithine reacted with NHS active esters. Electron density on the aromatic amine of the daptomycin anthraniloyl residue is more delocalized than usual by the neighboring carbonyl function. The resulting low nucleophilicity greatly disfavors reaction with NHS esters.

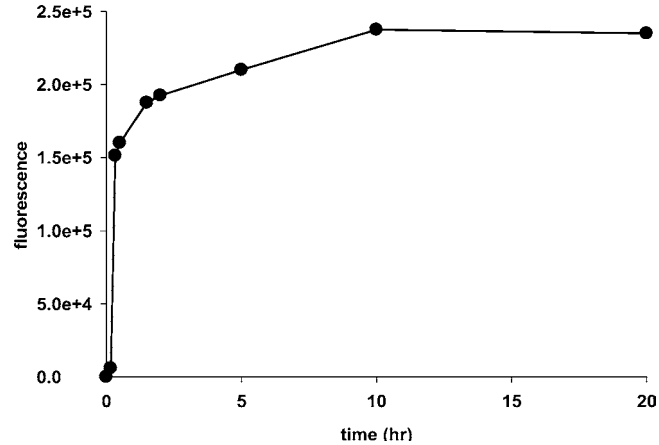


Figure 2. Time course of attachment of dansyl bisphosphonic acid bound to the surface of Ti6Al4V foils at different time points. The passivated foils were incubated with dansyl bisphosphonic acid (pH 7.4, 2.5 mg/mL) at room temperature. The foils were removed from the solution at a series of time points and then washed with Me_2NCHO and water, followed by incubation with 1 mL 0.01 M NaOH at room temperature for 3 h. The fluorescence in the NaOH solution was recorded with λ_{ex} 337 nm and λ_{em} 520 nm (*30*).

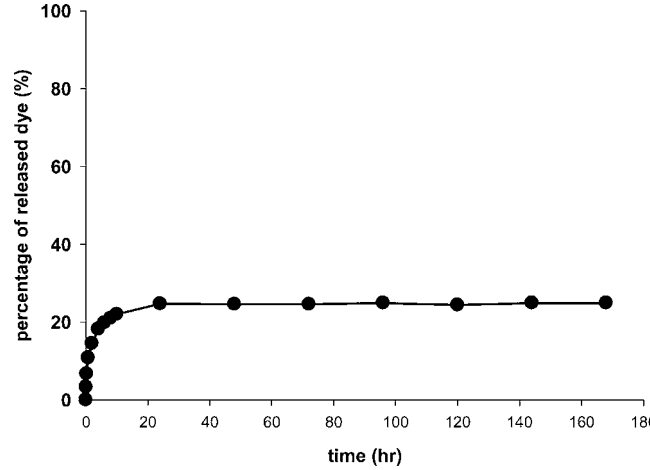


Figure 3. Release kinetics of dansyl bisphosphonic acid on the surface of Ti6Al4V foil. The foil was incubated in 1 mL phosphate buffer (pH 7.4) at 37 °C. Dansyl fluorescence was recorded with λ_{ex} 337 nm and λ_{em} 520 nm. The data were expressed as release % = $(F_{sample} - F_0)/(F_{final} - F_0)$. F_{sample}, the fluorescence at a certain time point; F_0, background of phosphate buffer; F_{final}, fluorescence of the loading dansyl bisphosphonic acid.

In order to increase the flexibility of attached daptomycin on the surface of titanium foil, bifunctional TEG with maleimide and NHS groups was selected to conjugate with daptomycin to form daptomycin-TEG-maleimide (**4**) overnight in Me_2NCHO, after which the maleimide specifically reacted with sulfhydryl group of 2-(2-mercaptoethylamino)ethylidene-1,1-bisphosphonic acid daptomycin-TEG-maleimide (**1**) at pH 7.0 with a yield of 93% (Scheme 2).

Dansyl-Lys-daptomycin-TEG-bisphosphonic Acid (9). The antimicrobial activity of daptomycin prompted us to prepare dansyl-daptomycin bisphosphonates to enable fluorescent monitoring of foil bonding. In order to introduce the dansyl group, the ε-amine of lysine was coupled with dansyl, while the

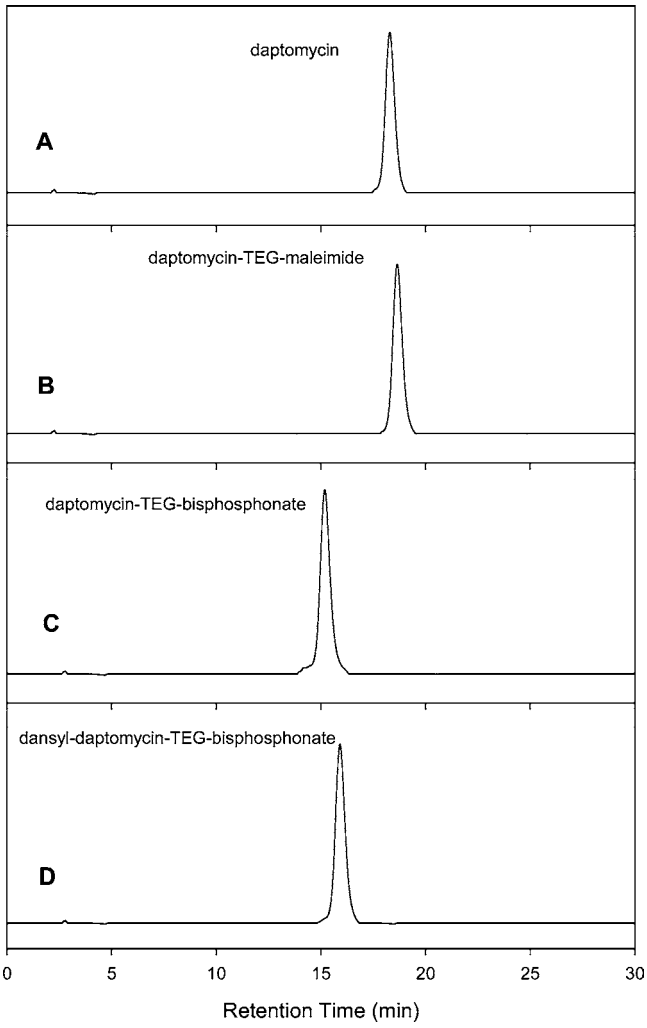


Figure 4. Analytical HPLC of daptomycin (A), daptomycin-TEG-maleimide (B), daptomycin-TEG-bisphosphonate (C), and dansyl-daptomycin-TEG-bisphosphonate (D). The analysis was performed with a Waters 600E system, using Alltech C18 5 μ, 250 $\times$ 4.6 mm column coupled to a Waters 486 detector at 254 nm. Sample was eluted with a linear gradient of 20−70% CH_3CN in water containing 0.1% CF_3CO_2H in 30 min with a flow rate of 1 mL/min. The retention times for the peaks in A, B, C, and D were 18.3, 18.4, 15.5, and 15.9 min, respectively.

ε-amine side chain of lysine was protected with Boc (Scheme 3). To prepare dansyl-Lys-daptomycin (**7**), the α-dansyl-Lys-εBoc (**6**) was converted to a succinimidyl active ester and used to acylate the ornithine residue of daptomycin (Scheme 3). The deprotected lysine ε-amino side chain in **7** was reacted with succinimidyl-TEG-maleimide to give dansyl-Lys-daptomycin-TEG-maleimide (**8**). The conjugation of 2-(2-mercaptoethylamino)ethylidene-1,1-bisphosphonic acid (**1**) with **8** to give the dansyl-Lys-daptomycin-TEG-bisphosphonic acid derivative (**9**) (Scheme 3) was carried out according to the procedure described above for preparing **5**. The purified dansyl-Lys-daptomycin-TEG-bisphosphonic acid (**9**) was characterized by analytical HPLC (Figure 4D).

Fluorescent Quantitation of Daptomycin Derivatives on the Titanium Foil Surface. After confirming the antibacterial activity of attached daptomycin on the surface of titanium foils, dansyl-Lys-daptomycin-TEG-bisphosphonic acid (**9**) was synthesized and was used as a model to investigate how much daptomycin was coupled to the solid surface. The daptomycin loading fell in the range 0.06−0.18 nmol/cm^2, below the theoretical maximum of adducts that could be coupled to the surface of titanium foil, 0.22 nmol/cm^2 (*34*).

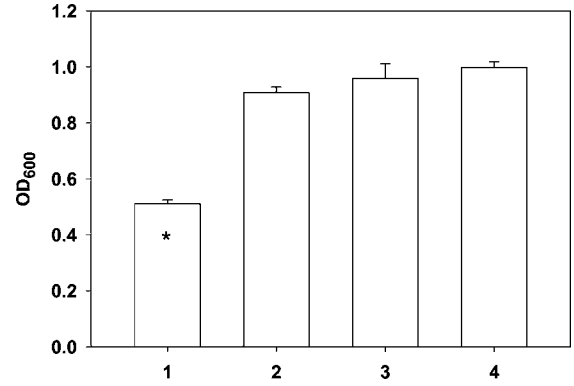


Figure 5. Histogram of antibacterial activity of daptomycin bisphosphonic acid covalently bound to the surface of Ti6Al4V foils. 1, daptomycin modified foils adhered by wax, covered by 200 μL of broth containing 3 $\times$ 10^5 cfu *S. aureus*; 2, nonadhered daptomycin modified foils floating in 200 μL of broth containing 3 $\times$ 10^5 cfu *S. aureus*; 3, adhered blank foils incubated with 200 μL of broth containing 3 $\times$ 10^5 cfu *S. aureus*; 4, 200 μL of broth containing 3 $\times$ 10^5 cfu *S. aureus.* Symbol * indicates statistically significant differences ($p < 0.05$) from the other groups. The *y*-axis is the optical density of the bacteria-containing broth at 600 nm.

Antibacterial Activity of Surface-Tethered Daptomycin. The MIC of DAP-TEG-bisphosphonic acid (**5**) was 8.0 μg/mL with *S. aureus* ATCC 29213 as the model bacterium in calcium-complemented Müller-Hinton broth, compared with an MIC of 0.8 μg/mL for daptomycin (Supporting Information). The mass of daptomycin attached to a single 1.0 cm^2 Ti6Al4V foil at the maximum observed yield of 0.18 nmol/cm^2 is 0.83 μg. If that amount of **5** was released into the 200 μL of broth applied to each foil, the concentration of **5** in solution would only be 4.2 μg/mL, lower than 8.0 μg/mL (MIC of daptomycin-TEG-bisphosphonic acid).

However, the covalently bound daptomycin on the solid-phase foil surfaces killed 53 $\pm$ 5% of the high challenge dose of 3 $\times$ 10^5 cfu in the 200 μL of broth applied to each foil (Figure 5). The data showed that there was a significant difference (p = 0.000 01) between the bacterial growth inhibition activities of the DAP-TEG-bisphosphonate surface and the nonmodified control surfaces. No significant antibacterial activity difference (p = 0.20, 0.49, 0.20) was observed among the nonmodified or nonadhered control surfaces.

DISCUSSION

The gold standard for implants is titanium because of its biocompatibility and osseointegrating ability (*35*). Much effort has been paid to the surface modification of titanium implants to enhance osseointegration, and biofuctionalization of the titanium implant surface by attaching therapeutic proteins, peptides, or antibiotics has attracted the attention of scientists from metallurgy and medicinal chemistry (*36*). We have linked vancomycin to titanium powder and pins by aminopropylation of the surface with aminopropyltriethoxysilane and attaching the antibiotics to the functionalized surface via a pair of di(ethylene glycol) spacers to extend the drug away from the metal surface. The attached antibiotics significantly inhibited the growth of bacteria on the metal surface (*15, 16*). The extensive chemical manipulations and the incompatibility of metallurgy and organic chemistry prompted us to investigate a more convenient and compatible method. In fact, functionalization of titanium alloy surfaces using a "dip and rinse" protocol that combines the goals of efficacy and convenience is being sought by those working in this area (*27*).

Bisphosphonate binds strongly to metal surfaces and bone tissue (*23, 24*), so it became our first choice in the design and

preparation of a daptomycin conjugate to be attached to Ti6Al4V alloy through the "dip and rinse" process. The preparation reported here of dansyl-TEG-bisphosphonic acid and its stable attachment to the surface of oxidized Ti6Al4V demonstrates the practicality of "dip and rinse" modification by daptomycin−bisphosphonate conjugates. The bioactivity and stability results indicated that bisphosphonate derivatives of daptomycin could effectively attach to Ti6Al4V foils and provide significant antibacterial activity. It is inevitable that some daptomycin bisphosphonates will dissociate from the metal surfaces over time. However, the dissociated daptomycin bisphosphonates are likely to be trapped by the surrounding bone tissue, thereby reducing systemic distribution, because of the bone-targeting activity of bisphosphonates after systemic administration of drug−bisphosphonate conjugates (*25*). By changing the number of phosphonates linked with the drugs, the stability might be adjustable in order to meet different requirements.

The selection of antibiotics to be covalently attached to the surface of implants is key to surface antibacterial activity. Current strategies to prevent implant-related infections include antibiotic-eluting bioceramics, drug-impregnated bone cements, and natural and synthetic polymers loaded with antimicrobials (*37*). Erythromycin, tobramycin, gentamicin, cephalexin, norfloxacin, sulbactam-cefoperazone, sulbactam-ampicillin, and antimicrobial peptides have been used in the delivery system. These materials deliver active drugs only from the time of implantation, lasting at most only through the immediate postoperative period, and deliver a relatively low solution concentration.

Covalent attachment of antibiotics to the surface of implants is the new direction in the development of self-protecting bactericidal implants. Amipicillin (*38*), vancomycin (*15*), and antimicrobial peptides (*11*) have been reported to be attached to the surface of implant materials such as polytetrafluoroethylene and titanium alloys. There are several factors that should be taken into consideration to select the antibiotics to be attached to the surface of an implant. The antimicrobial should ideally act at the bacterial cell surface, such as β-lactams, vancomycin, quaternary ammonium, or antimicrobial peptides. If the site of action is inside the bacterium, permanent bonding would significantly reduce bioactivity. We observed that phenomenon previously when we explored the attachment of minocycline to the surface of Ti6Al4V foils through an acid-labile linkage that could be broken in response to the lower pH caused by a local bacterial infection (*39*). It will also be valuable to investigate the effect of longer or shorter spacers.

The second important characteristic is that the interaction of the antimicrobial with the bacteria should be noncovalent, so that the antibiotic remains unchanged and active after each bacterial challenge. Even though ampicillin and other β-lactam antibiotics were effective against Gram-positive and some Gram-negative bacteria, the β-lactam interaction with bacterial transpeptidases opens the lactam ring to covalently modify the enzyme, so that the antibiotics can only be used once. Daptomycin, however, acts in the bacterial membrane, leading to a change in cell polarity and permeability that kills the bacteria (*22*). The interaction of daptomycin with bacteria depends only on physical binding. As a result, daptomycin could retain its structural integrity and bactericidal activity against successive bacterial challenges, as we observed with vancomycin bound to titanium alloy surfaces (*15, 17, 18*).

The daptomycin bonded to the Ti6Al4V surfaces killed 53 $\pm$ 5% of the high challenge dose of bacteria suspended in a drop of broth applied to each foil. Under the conditions of our experiments, the surface was exposed to 1.5×10^6 cfu/mL, many more than in clinical practice, where most circulating bacteria will be suppressed by systemic antibiotics, and only a limited number of opportunistic bacteria first attack an implant.

In conclusion, bisphosphonic acid derivatives of daptomycin were synthesized. The conjugates were stably attached to Ti6Al4V surfaces and provided antibacterial activity against high doses of *S. aureus*. The antibiotics can stay bonded to the alloy for an extended period to prevent infections on the surfaces of implants. The integration of bisphosphonates with antibiotics opens a new way for covalent protection of implants.

ACKNOWLEDGMENT

We thank Dr. Richard Wassell and Mr. Zhixian Lu of the Thomas Jefferson University Proteomics Center for assistance in mass spectrometry, and Dr. Ivan S. Alferiev of Division of Cardiology, the Children's Hospital of Philadelphia, for his generous gift of 2-(2-mercaptoethylamino) ethylidene-1,1-bisphosphonic acid. This work was supported by a grant from Cubist Pharmaceuticals to E.W. and a grant from the National Institutes of Health (AR051303) to Dr. Irving Shapiro. Conflicts of interest: E.W. is a cofounder of SecureImplant LLC, which might ultimately benefit from the results of this investigation, but did not support the work.

Supporting Information Available: Determination of minimum inhibitory concentrations. This material is available free of charge via the Internet at http://pubs.acs.org.

LITERATURE CITED

(1) Moss, A. J., Hamburger, S., Moore, R. M., Jr., Jeng, L. L., and Howie, L. J. (1991) Use of selected medical device implants in the United States, 1988. *Adv. Data* 1–24.

(2) Garvin, K. L., and Hanssen, A. D. (1995) Infection after total hip arthroplasty: Past, present, and future. *J. Bone Joint Surg. 77A*, 1576–1588.

(3) Mahan, J., Seligson, D., Henry, S. L., Hynes, P., and Dobbins, J. (1991) Factors in pin tract infections. *Orthopedics 14*, 305–308.

(4) Duggan, J. M., Georgiadis, G. M., and Kleshinski, J. F. (2001) Management of prosthetic joint infections. *Infect. Med. 18*, 534–541.

(5) Zimmerli, W., Trampuz, A., and Ochsner, P. E. (2004) Prosthetic-joint infections. *N. Engl. J. Med. 351*, 1645–54.

(6) Huang, Y. Y., and Chung, T. W. (2001) Microencapsulation of gentamicin in biodegradable PLA and/or PLA/PEG copolymer. *J. Microencapsulation 18*, 457–465.

(7) Mi, F. L., Shyu, S. S., Lin, Y. M., Wu, Y. B., Peng, C. K., and Tsai, Y. H. (2003) Chitin/PLGA blend microspheres as a biodegradable drug delivery system: a new delivery system for protein. *Biomaterials 24*, 5023–5036.

(8) Isquith, A. J., Abbott, E. A., and Walters, P. A. (1972) Surface-bonded antimicrobial activity of an organosilicon quaternary ammonium chloride. *Appl. Environ. Microbiol. 24*, 859–863.

(9) Tiller, J. C., Liao, C. J., Lewis, K., and Klibanov, A. M. (2001) Designing surfaces that kill bacteria on contact. *Proc. Natl. Acad. Sci. U.S.A. 98*, 5981.

(10) Boman, H. G. (2003) Antibacterial peptides: basic facts and emerging concepts. *J. Internal Med. 254*, 197–215.

(11) Gabriel, M., Nazmi, K., Veerman, E. C., NieuwAmerongen, A. V., and Zentner, A. (2006) Preparation of LL-37-grafted titanium surfaces with bactericidal activity. *Bioconjugate Chem. 17*, 548–550.

(12) Aumsuwan, N., Heinhorst, S., and Urban, M. W. (2007) The effectiveness of antibiotic activity of penicillin attached to expanded poly(tetrafluoroethylene) (ePTFE) surfaces: A quantitative assessment. *Biomacromolecules 8*, 3525–3530.

(13) Aumsuwan, N., Danyus, R. C., Heinhorst, S., and Urban, M. W. (2008) Attachment of ampicillin to expanded poly(tetrafluoroethylene): surface reactions leading to inhibition of microbial growth. *Biomacromolecules 9*, 1712–1718.

(14) Kahne, D., Leimkuhler, C., Lu, W., and Walsh, C. (2005) Glycopeptide and lipoglycopeptide antibiotics. *Chem. Rev. 105*, 425–48.

(15) Jose, B., Antoci, J. V., Zeiger, A. R., Wickstrom, E., and Hickok, N. J. (2005) Vancomycin covalently bonded to titanium beads kills *Staphylococcus aureus*. *Chem. Biol. 12*, 1041–1048.

(16) Edupuganti, O. P., Antoci, V., Jr., King, S. B., Jose, B., Adams, C. S., Parvizi, J., Shapiro, I. M., Zeiger, A. R., Hickok, N. J., and Wickstrom, E. (2007) Vancomycin covalently bound to Ti6Al4V pins provides longterm inhibition of *Staphylococcus aureus* colonization. *Bioorg. Med. Chem. Lett. 17*, 2692–2696.

(17) Antoci, V., Jr., King, S. B., Jose, B., Parvizi, J., Zeiger, A. R., Wickstrom, E., Freeman, T. A., Composto, R. J., Ducheyne, P., Shapiro, I. M., Hickok, N. J., and Adams, C. S. (2007) Vancomycin covalently bonded to titanium alloy prevents bacterial colonization. *J. Orthop. Res. 25*, 858–866.

(18) Antoci, V., Jr., Adams, C. S., Parvizi, J., Davidson, H. M., Composto, R. J., Freeman, T. A., Wickstrom, E., Ducheyne, P., Jungkind, D., Shapiro, I. M., and Hickok, N. J. (2008) The inhibition of *Staphylococcus epidermidis* biofilm formation by vancomycin-modified titanium alloy and implications for the treatment of periprosthetic infection. *Biomaterials 29*, 4684–4690.

(19) Weigel, L. M., Clewell, D. B., Gill, S. R., Clark, N. C., McDougal, L. K., Flannagan, S. E., Kolonay, J. F., Shetty, J., Killgore, G. E., and Tenover, F. C. (2003) Genetic analysis of a high-level vancomycin-resistant isolate of Staphylococcus aureus. *Science 302*, 1569–71.

(20) Brandl, K., Plitas, G., Mihu, C. N., Ubeda, C., Jia, T., Fleisher, M., Schnabl, B., DeMatteo, R. P., and Pamer, E. G. (2008) Vancomycin-resistant enterococci exploit antibiotic-induced innate immune deficits. *Nature 455*, 804–7.

(21) Hancock, R. E. W. (2005) Mechanisms of action of newer antibiotics for Gram-positive pathogens. *Lancet Infect. Dis. 5*, 209–218.

(22) Steenbergen, J. N., Alder, J., Thorne, G. M., and Tally, F. P. (2005) Daptomycin: a lipopeptide antibiotic for the treatment of serious Gram-positive infections. *J. Antimicrob. Chemother. 55*, 283–8.

(23) Ehrick, R. S., Capaccio, M., Puleo, D. A., and Bachas, L. G. (2008) Ligand-modified aminobisphosphonate for linking proteins to hydroxyapatite and bone surfaces. *Bioconjugate Chem 19*, 315–321.

(24) Auernheimer, J., and Kessler, H. (2006) Benzylprotected aromatic phosphonic acids for anchoring peptides on titanium. *Bioorg. Med. Chem. Lett. 16*, 271–273.

(25) Zhang, S., Gangal, G., and Uludag, H. (2007) 'Magic bullets' for bone diseases: progress in rational design of bone-seeking medicinal agents. *Chem. Soc. Rev. 36*, 507–531.

(26) Gawalt, E. S., Avaltroni, M. J., Koch, N., and Schwartz, J. (2001) Self-assembly and bonding of alkanephosphonic acids on the native oxide surface of titanium. *Langmuir 17*, 5736–5738.

(27) Auernheimer, J., Zukowski, D., Dahmen, C., Kantlehner, M., Enderle, A., Goodman, S. L., and Kessler, H. (2005) Titanium implant materials with improved biocompatibility through coating with phosphonate-anchored cyclic RGD peptides. *ChemBioChem 6*, 2034–2040.

(28) Alferiev, I. S., Connolly, J. M., and Levy, R. J. (2005) A novel mercapto-bisphosphonate as an efficient anticalcification agent for bioprosthetic tissues. *J. Organomet. Chem. 690*, 2543–2547.

(29) Antoci, V., Jr., Adams, C. S., Hickok, N. J., Shapiro, I. M., and Parvizi, J. (2007) Vancomycin bound to Ti rods reduces periprosthetic infection: preliminary study. *Clin. Orthop. Relat. Res. 461*, 88–95.

(30) Silverman, B. M., Wieghaus, K. A., and Schwartz, J. (2005) Comparative properties of siloxane vs phosphonate monolayers on a key titanium alloy. *Langmuir 21*, 225–228.

(31) Jorgensen, J. H., Cleeland, W. A., Craig, G., Doern, M., Ferraro, J., Finegold, C. M., Hansen, S. L., Jenkins, S. G., Novick, W. J., and Pfaller, M. A. (1993) Methods for dilution antimicrobial susceptibility tests for bacteria that grow aerobically, 3rd approved standard. *National Committee for Clinical Laboratory Standards 13*, 1–12.

(32) Hill, J., Siedlecki, J., Parr, I., Morytko, M., Yu, X., Zhang, Y., Silverman, J., Controneo, N., Laganas, V., and Li, T. (2003) Synthesis and biological activity of N-acylated ornithine analogues of daptomycin. *Bioorg. Med. Chem. Lett. 13*, 4187–4191.

(33) Siedlecki, J., Hill, J., Parr, I., Yu, X., Morytko, M., Zhang, Y., Silverman, J., Controneo, N., Laganas, V., and Li, T. (2003) Array synthesis of novel lipodepsipeptide. *Bioorg. Med. Chem. Lett. 13*, 4245–4249.

(34) Xiao, S. J., Textor, M., Spencer, N. D., Wieland, M., Keller, B., and Sigrist, H. (1997) Immobilization of the cell-adhesive peptide Arg-Gly-Asp-Cys (RGDC) on titanium surfaces by covalent chemical attachment. *J. Mater. Sci. Mater. Med. 8*, 867–72.

(35) Liu, X., Chu, P. K., and Ding, C. (2004) Surface modification of titanium, titanium alloys, and related materials for biomedical applications. *Mater. Sci. Eng., R 47*, 49–121.

(36) Schliephake, H., and Scharnweber, D. (2008) Chemical and biological functionalization of titanium for dental implants. *J. Mater. Chem. 18*, 2404–2414.

(37) Wu, P., and Grainger, D. W. (2006) Drug/device combinations for local drug therapies and infection prophylaxis. *Biomaterials 27*, 2450–2467.

(38) Aumsuwan, N., Heinhorst, S., and Urban, M. W. (2007) Antibacterial surfaces on expanded polytetrafluoroethylene; penicillin attachment. *Biomacromolecules 8*, 713–718.

(39) Chen, C.-P., Zeiger, A. R., and Wickstrom, E. (2007) Bactericidal activity of extended 9-glycyl-minocycline derivatives. *Bioorg. Med. Chem. Lett. 17*, 6558–6562.

BC100136E

Supplemental Information for

Self-Protecting Bactericidal Titanium Alloy Surface Formed by Covalent Bonding of Daptomycin Bisphosphonates

Chang-Po Chen, Eric Wickstrom*

Department of Biochemistry and Molecular Biology, Thomas Jefferson University, Philadelphia, PA 19107

* To whom correspondence should be addressed, at Department of Biochemistry and Molecular Biology, Thomas Jefferson University, Bluemle 219, 233 South 10th Street, Philadelphia, PA 19107. Tel: 1.215.955.4578. Fax: 1.215.955.4579. E-mail: eric@tesla.jci.tju.edu

Minimum inhibitory concentrations. Minimum inhibitory concentrations (MIC) were determined with *Staphylococcus aureus* strain 25923 (ATCC, Germantown, MD), by broth microdilution according to NCCLS guidelines (*1*) for aerobic Gram-positive organisms. *S. aureus* were maintained in Müller-Hinton broth supplemented with 50 mg/L calcium chloride, according to the Cubist Pharmaceuticals protocol, at a final *S. aureus* titer of 5×10^5 cfu/ml, using daptomycin (**1**) as the positive control. All assays were performed in triplicate at 37˚C.

Table 1. MIC of daptomycin and its derivatives

Compound Name	MIC, μg/ml
Daptomycin **1**	0.8
DAP-TEG-bisphosphonic acid, **5**	8.0

(1) Jorgensen, J. H., Cleeland, W. A., Craig, G., Doern, M., Ferraro, J., Finegold, C. M., Hansen, S. L., Jenkins, S. G., Novick, W. J., and Pfaller, M. A. (1993) Methods for dilution antimicrobial susceptibility tests for bacteria that grow aerobically, 3rd approved standard. *National Committee for Clinical Laboratory Standards 13*, 1-12.

Quantitative Detection of Single Molecules Using Enhancement of Dye/DNA Conjugate-Labeled Nanoparticles

Qingwang Xue,[†] Dafeng Jiang,[†] Lei Wang,*[,‡] and Wei Jiang*[,†]

School of Chemistry and Chemical Engineering, Shandong University, 250100 Jinan, P.R. China, and School of Pharmacy, Shandong University, 250012 Jinan, P.R. China. Received April 29, 2010; Revised Manuscript Received September 27, 2010

An ultrasensitive fluorescence immunoassay method for quantitative detection of single molecules is developed on the basis of counting single magnetic nanobeads (MNBs) with combined amplification of DNA and dye/DNA conjugate. Highly amplified fluorescence signal and low background signal are achieved by using mutilabel bioconjugates made by linking multiple dye/DNA conjugates to streptavidin-coated magnetic nanobeads (SA-MNBs) and magnetic separation. In this method, human IgG (Ag) is captured on the silanized glass substrate surface, followed by immunoreaction with biotinylated mouse antihuman antibody (BT-Ab). Then, SA-MNBs are attached to the BT-Ab through the biotin/streptavidin interaction at a ratio of 1:1. Subsequently, a 30 base pair double-stranded oligonucleotide terminated with biotin (BT-dsDNA) is conjugated to the SA-MNBs. The resultant Ag-BT-Ab-SA-MNBs/BT-dsDNA/SYBR Green I is achieved after a fluorescent DNA probe, SYBR Green I, is added to the substrate and bound to the oligonucleotide at high ratios. Finally, epifluorescence microscopy coupled with a high-sensitivity electron multiplying charge-coupled device is employed for human IgG fluorescence imaging and detection. The number of fluorescent spots corresponding to single protein molecules on the images is counted. It is found that the number of fluorescent spots resulting from the SA-MNBs/BT-dsDNA/SYBR Green I immuotargeted on the glass slides is correlated with the concentration of human IgG target antigen in the range 3.0−50 fM.

INTRODUCTION

Recently, single-molecule detection (SMD), based on the analysis of individual molecules, has attracted a great deal of attention in the area of analytical chemistry and life science (*1, 2*). In analytical chemistry, single-molecule detection (SMD) is the ultimate limit of detection (*3*). Fluorescence detection techniques combined with capillary or microchannels (*4*−*8*), confocal fluorescence microscopy (*9*−*16*), total internal reflection fluorescence microscopy (TIRFM) (*17*−*23*), and epifluorescence microscopy (EFM) (*24, 25*) are the most popular techniques in SMD. Of these SMD studies with fluorescence quantitative detection, all research performed the counting of single fluorescence molecules for quantitative analysis at the single-molecule level. The SMD quantitative research technique relies on directly counting one by one the number of target molecules rather than measuring signal intensity to quantitative analysis of the concentration, which is suitable for ultralow concentrations of target biological macromolecule identification and detection. As for SMD-based quantitative research, on the assumption of target biological macromolecules being identified, the most important advantage of the quantitative technique that relies on counting single molecules is that the detected signal intensity is not important, which guarantees the reliability of the quantitative determination (*3*). To ensure that the target biological macromolecule can be identified, a better signal-to-noise (*S*/*N*) ratio is needed, which can improve the sensitivity.

Fluorescent antibodies have been widely used in single-molecule fluorescence immunodetection. The fluorescent labels for the labeling of antibodies, which provide exquisite sensitivity (*26*) and guarantee the reliability of quantitative determination, should be bright and stable enough in single-molecule fluorescence detection. Usually, a fluorescent dye molecule is coupled to the target molecules to generate a detectable signal. However, two major difficulties limit the sensitivity when these fluorophores are used. The first difficulty is the relatively low fluorescence signal intensity. Because one antibody can only be labeled with one or a few fluorophores, the fluorescence signal is too weak to be detected when the target concentration is low. The second difficulty is the poor photostability of many fluorophores. Most organic dyes suffer serious photobleaching. To improve the sensitivity of single-molecule fluorescence immunodetection by using highly fluorescent and photostable fluorescence labels, quantum dots (QDs) have been developed and explored as novel signal labels for single-molecule fluorescence immunodetection (*23, 26*−*29*). Although QDs have many unique prominent properties, there are many problems involved in using QDs as fluorescence labels, such as the stability of multifunctionalized QDs in different reaction systems, the toxity of heavy metal ions, and the blinking and physical adsorption (*27, 30*). Thus, efforts to develop novel fluorescence labels to reduce the background signal from nonspecific adsorption of labels and increase fluorescence signal intensity have gained considerable momentum in single-molecule fluorescence detection.

Along with the efficient magnetic particle amplification strategy for sensitive detection of biomolecules (*31, 32*), a magnetic particle amplification strategy could be also applied to single-molecule immunodetection. The magnetic particle acts as a carrier and a bridge when functionalized magnetic particles are used as signal labels. On one hand, the significant signal intensity could be gained from the application of amplification strategy. On the other hand, the background signals from nonspecific adsorption of labels could be reduced because of the application of magnetic particles. Recently, Jin's group (*3*)

* Corresponding author. W.J.: Tel +86 531 88363888; fax +86 531 88564464; e-mail wjiang@sdu.edu.cn. L.W.: Tel +86 531 88382330; e-mail wangl-sdu@sdu.edu.cn.

[†] School of Chemistry and Chemical Engineering.

[‡] School of Pharmacy.

10.1021/bc100212w © 2010 American Chemical Society
Published on Web 10/27/2010

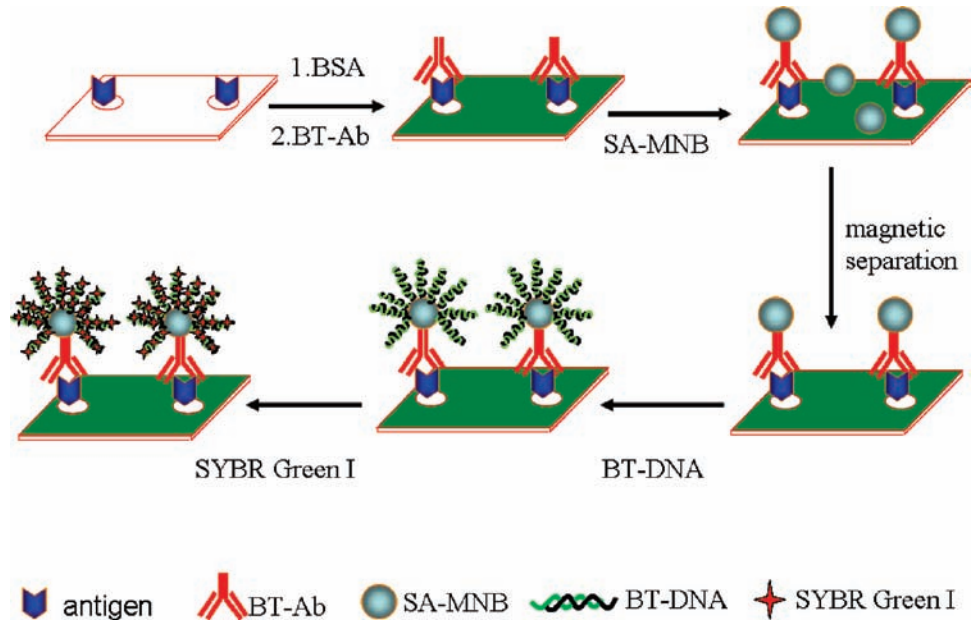


Figure 1. Schematic representation of the process of immunoassay labeling format by using the conjugate SA-MNBs/BT-dsDNA/SYBR Green I label.

developed an electrochemical immunoassay strategy for quantitative detection of single molecules based on counting the magnetic nanobeads released from a substrate with the combination of DNA amplification and enzyme amplification. If SA-MNB does not need to be dissociated, further sensitivity improvement may be obtained by directly counting the number of functionalized magnetic nanobeads attached to single antibodies for quantitative detection of single molecules in a fluorescence image.

In this work, we present an ultrasensitive fluorescence immunoassay method for quantitative detection of single molecules based on counting of single magnetic nanobeads with combined amplification of DNA and DNA/SYBR Green I conjugate. The principle of this method is shown in Figure 1. In this method, we employed a streptavidin-coated magnetic nanobead as a carrier for the conjugation of multiple fluorescent BT-dsDNA/SYBR Green I conjugates. It was attached to a biotin-modified mouse antihuman antibody through the high-specificity, high-affinity biotin−streptavidin interaction at a ratio of 1:1. Human IgG captured on the silanized glass substrate surface was detected by its immunoreaction with biotinylated mouse antihuman antibody. EFM with EMCCD was employed for human IgG fluorescence imaging and detection. In this case, only one MNB is bound to one single protein. Each fluorescent spot corresponds to one SA-MNB/BT-dsDNA/SYBR Green I immuotargeted on the glass slides. Finally, the number of fluorescent spots corresponding to single protein molecules on the images was counted. It is found that the number of fluorescent spots resulting from the SA-MNBs/BT-dsDNA/SYBR Green I immuotargeted on the glass slides could be applied to the quantitative detection of human IgG target antigen.

EXPERIMENTAL SECTION

Materials and Instrumentation. Human immunoglobulin G (IgG), monoclonal antihuman IgG-Biotin conjugate (Clone HP-6017), 3-glycidyloxypropyltrimethoxysilane, and bovine serum albumin were purchased from Sigma-Aldrich Co. (St. Louis, MO, USA). Strand A, biotin-5′-TTT TTT TTT GCG GGT AAC GTC AAT ATT AAC TTT ACT CCC-3′, and strand B, 5′-GGG AGT AAA GTT AAT ATT GAC GTT ACC CGC-3′, were obtained from the Genscript Corporation (Nanjing, China). Streptavidin−MNBs (350 nm diameter, 1.343 g mL^{-1}, aqueous suspension containing 0.1% bovine serum albumin (BSA), 0.05% Tween-20, and 10 μM EDTA at a concentration of 3.324×10^{11} beads mL^{-1}) from Bangs Laboratories Inc. (Fishers, IN), Tris (>99.8%) from Amresco Inc. (Solon, OH), and Tween-20 from Sigma (St. Louis, MO) were used in the work. Other chemicals (analytical grade) were obtained from standard reagent suppliers. Microscope cover glasses (22×22 mm^2) were purchased from Cole-Parmer (Illinois, USA).

The physiological buffer saline (PBS) consisted of 0.15 M NaCl, 7.6 mM NaH_2PO_4, and 2.4 mM Na_2HPO_4 (pH 7.4). PBS−T buffer consisted of 0.15 M NaCl, 7.6 mM Na_2HPO_4, 2.4 mM NaH_2PO_4, and 0.05% Tween-20 (pH 7.4). TE buffer consisted of 10 mM Tris−HCl and 1.0 mM Na_2EDTA (pH 8.0). TTL buffer consisted of 0.10 M Tris−HCl (pH 8.0), 0.1% Tween-20, and 1.0 M LiCl. TT buffer consisted of 0.25 M Tris−HCl (pH 8.0) and 0.1% Tween-20. TTE buffer consisted of 0.25 M Tris−HCl (pH 8.0), 0.1% Tween-20, and 20 mM Na_2EDTA (pH 8.0). A phosphate buffer (pH 7.0) containing 1% BSA was used as a buffer for blocking.

We used an inverted microscope (model IX81, Olympus, Tokyo, Japan) equipped with a high-numerical-aperture 40× objective lens (PlanApo, Olympus, Tokyo, Japan), a mercury lamp (OSRAM, HBO, 103w/2, Germany), a mirror unit consisting of a 470−490 nm excitation filter (BP470−490), a 505 nm dichromatic mirror (DM 505), a 510−550 nm emission filter (IF510−550), and a 16 bit thermoelectrically cooled EMCCD (Cascade 512B, Tucson, AZ, USA). The EMCCD was used for collecting the fluorescent images. Imaging acquisition and data analysis were performed using the *MetaMorph* software (Universal Imaging, Downingtown, PA, USA).

DNA Hybridization. A 30 base pair biotinylated double-stranded oligonucleotide (BT-dsDNA) was obtained by hybridizing two complementary single-stranded oligonucleotides. The two oligonucleotides were mixed in 2 × SSC buffer, denatured at 95 °C for 5 min (*33*), annealed at 72 °C for 10 min, and naturally cooled down to 48 °C for 6 h.

Substrate Preparation and Antigen Coating. The epoxy-functionalized glass surfaces were prepared according to the modification described in the literature (*27*). The freshly prepared substrate surface was coated with 100 μL human IgG

solutions of various concentrations (50, 30, 10, 8.0, 5.0, 3.0 fM). The substrate was immediately placed in a sealed Petri dish at 37 °C for 5 h. After that, the substrate was washed three times with PBS-T washing buffer to remove unbound human IgG and impurities.

Blocking. We used a phosphate buffer containing 1% BSA as a blocking buffer. To the substrate of antigen coating was added 100 μL of blocking, and then, the substrate was incubated for 3 h. After that, the substrate was washed three times with PBS-T washing buffer.

Immunoreaction. Antihuman IgG-Biotin solution was 40-fold diluted with a phosphate buffer (pH 7.4) before being used, and 100 μL of the diluted solution of various concentrations (2, 1.2, 0.4, 0.32, 0.2, 0.12 pM) was then added to the substrate. The biotinylated monoclonal antihuman IgG (BT-Ab) molecule was bound to the human IgG through the immunoreaction. After that, the substrate was deposited hermetically for 2 h at 37 °C. Finally, nonspecifically absorbed antibodies were washed by PBS-T washing buffer.

Binding of SA-MNBs to BT-Ab. Five microliters of streptavidin-MNB suspension (3.324×10^{11} beads/mL) was washed five times with 400 μL of TTL buffer to remove surfactants. Then, 50 μL of TTL buffer was added. Subsequently, streptavidin−MNB was conjugated to the biotinylated monoclonal antihuman IgG molecules by adding 16 μL of streptavidin−MNB suspension (0.52×10^9 beads) and incubating for 2 h at 37 °C. After the incubation, the redundant MNB were separated magnetically from the substrate using a neodymium−boron (Nd−B) magnet that produced an inhomogeneous magnetic field on the top of the sample cell for 5 min. Then, the substrate of the cell was gently rinsed eight times with 200 μL of PBS-T by drawing these solutions out along the wall of the cell. Finally, nonspecifically absorbed SA-MNBs were removed with magnetic separation.

Modification of SA-MNBs with BT-DNA. 100 μL of 0.14 μM BT-DNA solution was added to the substrate, and then the substrate was incubated hermetically for 2 h at 37 °C. Double-stranded oligonucleotides terminated with biotin (BT-dsDNA) were conjugated to the streptavidin−MNBs. Finally, the unreacted biotin−dsDNA was washed away with 400 μL PBS-T washing buffer. Then, the substrate was washed twice with 400 μL of TT buffer and twice with 400 μL of TTE buffer.

SYBR Green I Adding and Fluorescence Image Detection. 100 μL 2.0 μM of SYBR Green I was added to the substrate and incubated for 10 min. SYBR Green I was bound to the oligonucleotide at high ratios by the specific binding interaction with the oligonucleotide. The resultant Ag-BT-Ab-SA-MNBs/BT-dsDNA/SYBR Green I was formed. All images were taken using an Olympus IX81 microscope (40× objective) equipped with a 16 bit thermoelectrically cooled EMCCD. The fluorescence images were obtained by the excitation light within the wavelength 470−490 nm of the mercury lamp and exposure time of 100 ms. Thirty images on the coverslip substrate were acquired one by one by moving the coverslip. Finally, the bright spots corresponding to single protein molecules on all the images were counted.

RESULTS AND DISCUSSION

Binding one MNB to One IgG onto the Substrate. Human IgG was captured on the epoxy-functionalized glass surfaces as the substrate by the covalent cross-linking reaction. The basic assumption in this method is that one protein brings one MNB onto the substrate. This assumption can be satisfied when the distance between two adjacent proteins captured on the substrate is larger than that between two adjacent MNBs. Thus, the concentration of protein should be low enough. It can be roughly calculated that 0.52×10^9 MNBs with a diameter of 350 nm can completely occupy the substrate within an area of 50 mm^2. This means that the amount of protein should be lower than 86 fM. In our experiments, 100 μL of human IgG solutions with concentrations lower than 50 fM was used. Thus, if all proteins are captured on the substrate, the average distance between two proteins is longer than the diameter of the MNB. Although there are many streptavidin binding sites on each MNB, it is not possible that one MNB is bound to more than two human IgG molecules because the space between two adjacent human IgG molecules is big enough. In order to prove this assumption, we measured the average distance between two adjacent proteins using EFM that can take a single-molecule image. To do so, the antigen captured on the substrate was labeled with QDs using biotin−antibody and SA-QDs. The fluorescence image for 50 fM target protein is shown in Figure 2. In the image, each bright spot corresponds to a target protein. It is obvious that the interspot distance is greater than 4 μm, which is much bigger than the diameter between two adjacent MNBs. Thus, we can conclude that one target protein should bring one MNB onto the substrate when the concentration of target protein is lower than 50 fM. This conclusion was demonstrated by a control experiment, in which the target protein solution was replaced by a buffer. In this case, only 10−11 bright spots were observed in 25 images, i.e., < 0.5 spot appeared in an image on average, which was in accordance with the result mentioned in Jin's literature (*3*).

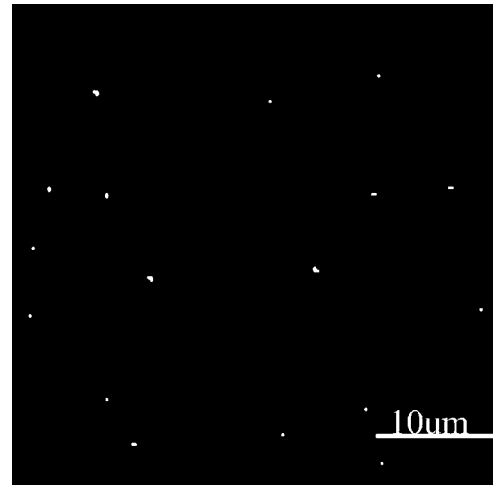


Figure 2. EFM fluorescence image of single QD-labeled human IgG on the substrate using 50 fM human IgG.

Reducing the Background Signal with Magnetic Separation. In this experiment, it has been roughly calculated that 0.52×10^9 MNBs with a diameter of 350 nm could completely occupy the substrate within an area of 50 mm^2. 100 μL of human IgG solutions with concentrations lower than 50 fM was used. This means that the amount of protein is lower than the number of MNB. Through the irreversible interaction between streptavidin and biotin, the 350-nm-diameter SA-MNB was conjugated to BT-Ab. Along with reducing the amount of protein, the MNB was far more than the antigen. The BT-dsDNA/SYBR Green I conjugate that was subsequently added to the substrate was easily bound to the redundant MNB on the substrate, leading to the background effect. To address this problem, we employed magnetic separation to remove the unbound MNB on the substrate. With the same experimental conditions, the fluorescence intensity images of the substrate of negative experiments for 50 fM target proteins without and with magnetic separation are shown in Figure 3, which indicated that the redundant MNB could be removed from the substrate with magnetic separation.

Multilabel Amplification. The high available surface-to-volume ratio of the streptavidin magnetic bead provides more

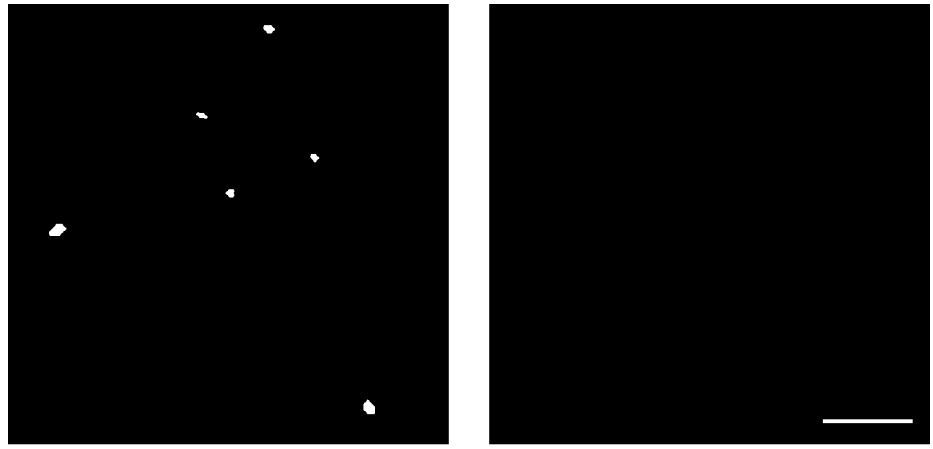


Figure 3. Fluorescent intensity subframe image of negative experiment for 50 fM target proteins in solution. Conditions: (A) without magnetic separation, (B) with magnetic separation. Scale bar, 30 pixel.

binding sites for analysis. We attached multiple BT-DNA/SYBR Green I conjugates to the streptavidin magnetic bead surfaces to increase fluorescence intensity and to improve the sensitivity. The biotinylated double-stranded oligonucleotide (BT-dsDNA) was obtained by hybridizing two complementary single-stranded oligonucleotides. The BT-dsDNA has a sequence with 9 thymine nucleotides at the biotin end acting as a spacer to reduce the steric hindrance between BT-dsDNA and the surface-confined streptavidin of MNB interaction. Through the irreversible interaction between streptavidin and biotin ($K_a = 10^{15}/M^{-1}$) with rapid binding kinetics and strong affinity, biotin−dsDNA combines with the 350 nm diameter streptavidin−MNB and produces the resultant Ag-BT-Ab-SA-MNB/BT-dsDNA. In this method, the primary amplification factor of the final detection fluorescence intensity is correlated with the number of BT-dsDNA on one MNB. The average number biotin binding sites on the surface (*m*) of one streptavidin−MNB was calculated using the equation reported in the manufacture's instructions of MagPrep streptavidin beads (Bangs Laboratories Inc., Fishers, IN). With the binding capacity (*g*) of the streptavidin-coated magnetic bead, the molecular weight (*M*) of biotin−FITC and the number (*C*) of magnetic beads per milligram, *m* could be estimated to be 2.25×10^4. The average biotin binding sites on the surface of one streptavidin−MNB is ∼30 000 based on the data provided in the manufacturer's instructions. In order to ensure all binding sites on the surface of one streptavidin−MNB conjugated with biotin-dsDNA, the amount of biotin-dsDNA used for reaction here is 10 times over the biotin binding sites.

The amount of BT-dsDNA per unit weight of magnetic beads was determined by measuring the concentration of DNA solution added and washed down after magnetic separation, which was determined by the absorbance at 260 nm using ultraviolet spectrophotometry. According to the difference at the two concentrations, we worked out the number of BT-dsDNA per magnetic bead to be ∼3000, which was in accordance with the data mentioned in Jin's report (*3*), implying an amplification factor of ∼3000 for DNA amplification. Although the measured value was different from that offered by the manufacturer's instructions, the large amplification factor was achieved. Magnetic beads of diameter 350 nm provided a very high number of labels on the surface and gave better sensitivities and detection limits.

Assembly of Fluorescent DNA Nanotags. In the systems reported here, DNA nanostructures serve as a template for assembling the intercalating dyes into fluorescent arrays. High densities of fluorophores are assembled in a very small region

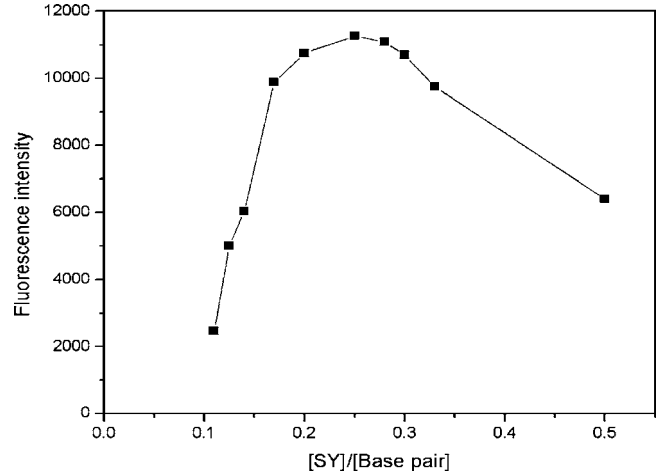


Figure 4. Dependence of maximum fluorescence intensity on ratio of intercalating SY groups per DNA base pair. Conditions: 13.9 nM dsDNA.

of base pairs in the DNA helix, yet the DNA template keeps them far enough away from each other to prevent self-quenching. A common feature of organic dyes is that they tend to aggregate in aqueous solution, which usually leads to self-quenching of fluorescence. Steric constraints impede multiple dyes from binding at the same intercalation site. As illustrated in Figure 4, the fluorescence increased monotonically when the fluorescence probe was titrated into the BT-DNA solution at increasing dye-to-base pair ratios (dbpr), the fluorescence saturated at approximately 0.25 dye/base pair. The quenching observed for SYBR Green I at ratios in excess of 0.25 is likely the result of alternative, nonintercalative binding that can occur at relatively high loading. Nevertheless, working at a ratio of 0.25 or lower yields highly fluorescent DNA-templated dye arrays.

Fluorescence Imaging Analysis. For the optimal fluorescence image, the study was optimized at a variety of imaging conditions. First, the effects of exposure time and intensifier gain were investigated, and the optimized setting values were 100 ms and 2000, respectively. In this case, the optimal fluorescence image was obtained. Second, in the experiment, the fluorescence intensity must be uniform. The intensity of the excitation light on the area illuminated by the mercury lamp through the objective was not uniform inside an area of $201 \times 201\ \mu m^2$ (512×512 pixels), as shown in Figure 5A. The light

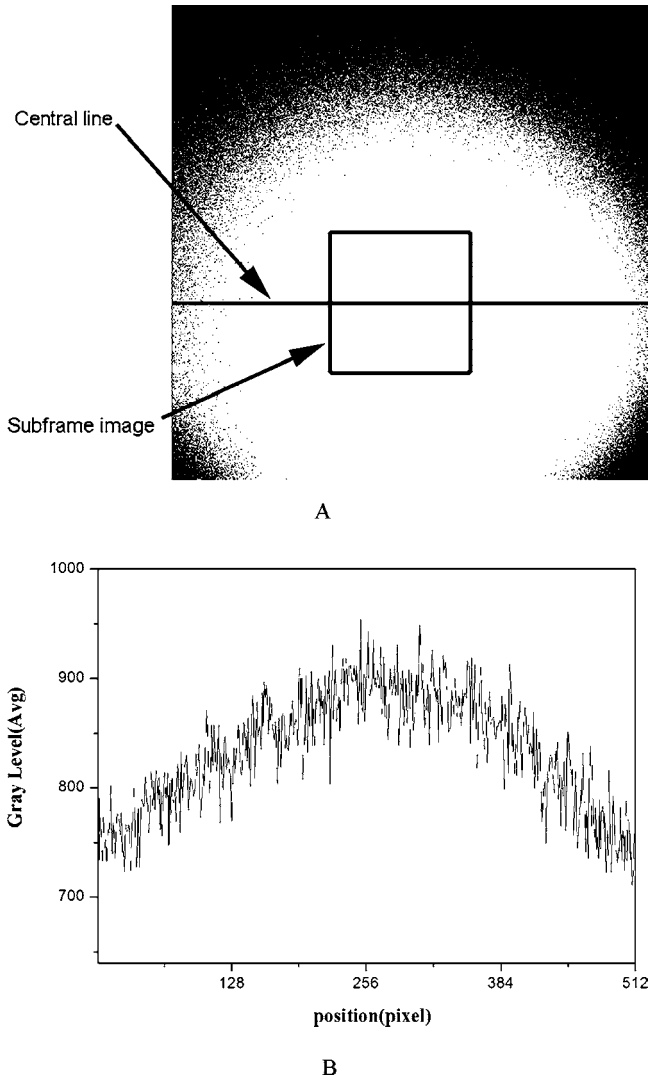


Figure 5. (A) Blank image and (B) distribution of light intensity along the central line of the bright region indicated in A in the *x* direction. Conditions: laser power of 103 W/2 mW; excitation wavelength 470−490 nm; emission wavelength of 510 nm; exposure time of 100 ms.

intensity dispersed from the center. The distribution of the fluorescence intensity corresponding to the central line in the χ direction of the light spot was given in Figure 5B. It was obvious that the light intensity dispersed from the center. In order to solve this problem, we chose a 150 × 150 pixel subregion at the center of the light spot for measuring the fluorescence intensity image. The intensity deviation inside an area of 59 × 59 μm^2 (150 × 150 pixels) at the center of the light spot was less than 5%. The threshold for image acquirement was chosen at a value of 3 times the standard deviation of the background noise for 10 blank images. For each concentration, 30 (three images of each location) images were obtained from location to location on the substrate surface, which was performed by moving the *XY* sample stage, as shown in Figure 6.

The typical fluorescence subframe images of SA-MNB/BT-dsDNA/SYBR Green I conjugate at different concentrations of human IgG in the range from 3.0 to 50 fM were shown in Figure 6. At the higher concentration, it was noted that the fluorescence intensities of some bright spots were 2−3 times higher than the mean intensity of a bright spot corresponding to a single MNB, which was obtained in lower concentrations (<10 fM) for IgG. A possible reason was that the steric hindrance among SA-MNBs made the number of BT-dsDNA per magnetic bead

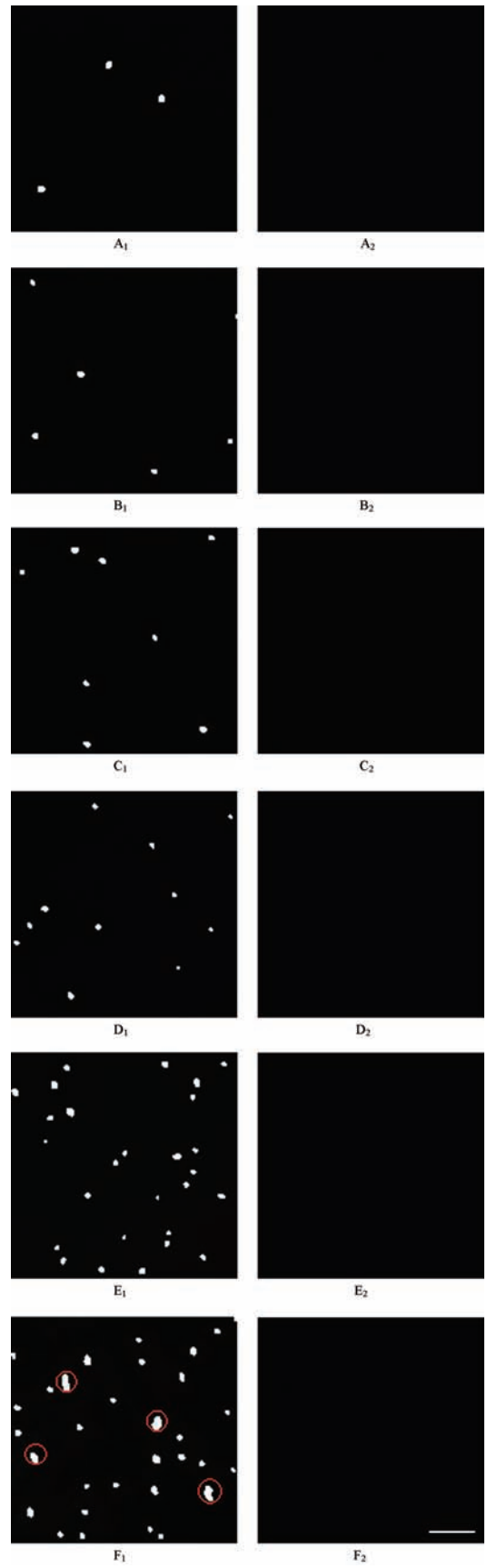


Figure 6. Fluorescent subframe image of human IgG molecules in solution at different concentrations. Conditions: human IgG concentration (fM): (A_1) 3.0, (B_1) 5.0, (C_1) 8.0, (D_1) 10, (E_1) 30, (F_1) 50, (A_2, B_2, C_2, D_2, E_2, F_2,) the corresponding negative control experiment. The bright spots of two nearest-neighbor MNBs aggregated one brighter spot (marked with red circle) in (F_1). Scale bar, 30 pixels.

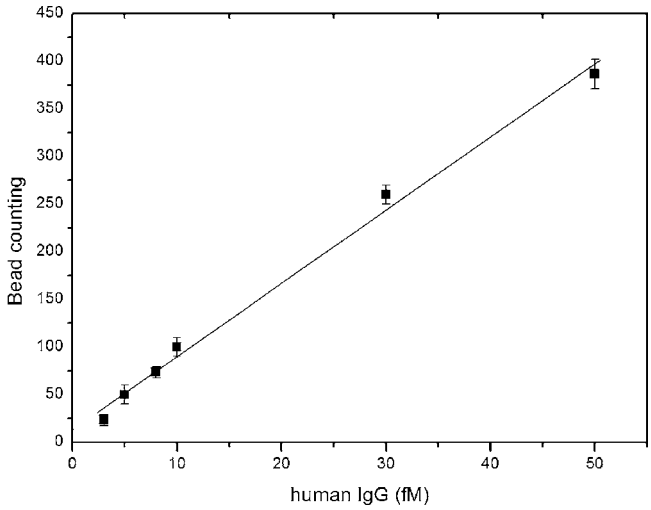


Figure 7. Linear relationship between the number of beads and the concentration of human IgG ($n = 3$). Conditions: Each data point represents an average of 3 measurements (each error bar indicates the standard deviation).

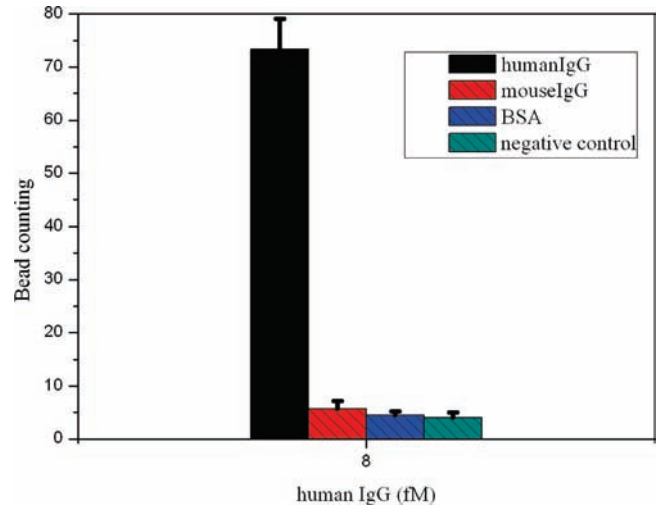


Figure 8. Comparison of fluorescence immunoassay for human-IgG (black column), mouse IgG (red column), BSA (blue column), and negative control (green column) on a silanized glass subframe using the SA-MNBs/BT-dsDNA/SYBR Green I conjugate label. Conditions: Each data point represents an average of 3 measurements (each error bar indicates the standard deviation); 10 images each measurement.

slightly different. Another possible reason was that, when the distance of two neighbor MNBs was small, the bright spots of two nearest-neighbor MNBs aggregated at one brighter spot due to diffraction of the fluorescence image. In the lower concentration, the fluorescence intensity of bright spots was rather uniform. However, as to the SMD-based quantitative methods, when the condition that one MNB was bound to one human IgG molecule onto the substrate was satisfied, the detected signal intensity was rather unimportant.

Quantification of Human IgG by SA-MNB/BT-dsDNA/SYBR Green I Conjugate. Human IgG concentration was quantified by counting the number of bright spots corresponding to single molecules on the fluorescence subframe images. Under the optimal conditions, the number of bright spots was proportional to the human IgG concentration. The typical fluorescence subframe images of Ag-BT-Ab-SA-MNB/BT-dsDNA/SYBR Green I at different concentrations in the range from 3.0 to 50 fM are shown in Figure 6. At the higher concentrations, it was noted that the fluorescence intensities of some bright spots were 2−3 times higher than the mean intensity of a bright spot corresponding to a single MNB. To solve this problem, the 30 positive images taken by the EMCCD were investigated in lower concentrations (<10 fM) for IgG. It was found that the bright spots on the subframe images were dispersive and each bright spot corresponding to a single MNB took up roughly a 6×6 pixel area, meaning that a fluorescence spot from a single functionalized MNB corresponding to a single human IgG molecule occupied roughly a 6×6 pixel area. While some bright spots in higher concentrations (>30 fM) exceed the 6×6 pixel grid of the image, taking the number of pixels occupied by the bright spots as the number of single IgG molecules was more accurate than taking the number of bright spots, even if the calibration was somewhat rough. The fluorescence intensity of bright spots (marked with red circle) in higher concentrations (>30 fM) that exceeded a 6×6 pixel area was assumed to come from two nearest-neighbor MNBs. When the concentrations exceeded 30 fM, the distance of two neighbor MNBs was small. The bright spots of two nearest-neighbor MNBs aggregated to one brighter spot due to diffraction of the fluorescence image. Figure 7 showed the linear relationship between the number of beads and human IgG concentration in the range 3.0−50 fM. The linear regression equation for human IgG in the range 3.0−50 fM was determined to be $y = 13.135 + 7.684 \times 10^{15}x$ ($R = 0.996$). The present approach improved the sensitivity by 4 orders of magnitude compared to the IgG(H+L)-Alexa Fluor 488 labeling for adsorption equilibrium strategy (*23*) and by 1.5 orders of magnitude approximately compared to the biotinylated monoclonal antihuman IgG molecules immobilized on the glass substrate surface by the streptavidin-coated quantum dot labeling strategy (*27*, *30*). A major factor in increased sensitivity is likely to be that highly amplified fluorescence signal and low background signal are achieved by using mutilabel bioconjugates made by linking multiple dye/DNA conjugates to streptavidin-coated magnetic nanobeads (SA-MNBs) and magnetic separation. The improved photostability is likely to be the number of dsDNA/SYBR Green I bound per bead in the labeling development step. By comparison, the SA-MNB/dsDNA/SYBR Green I conjugate approach reported in this paper uses all the common reagents such as biotin, oligonucleotides, streptavidin-coated magnetic nanobead, and fluorescent DNA probes.

To evaluate the specificity of the assay for human IgG, an experiment was carried out in which the surface-immobilized protein was replaced with either mouse IgG or BSA, while keeping the protein concentration the same as that for human IgG. The subsequent assay procedure was also the same as for human IgG. As illustrated in Figure 8, at a protein concentration of 8.0 fM, 30 images were obtained from location to location on the substrate surface. The fluorescence spots of either mouse IgG or BSA sample are very low by comparison with that of human IgG. The result indicates that the immunoassay is highly specific for human IgG.

CONCLUSION

In this paper, we reported an ultrasensitive fluorescence immunoassay for quantitative detection of single protein molecules based on counting of single magnetic nanobeads corresponding to single proteins with combined amplification of DNA and BT-DNA/SYBR Green I conjugate. As described above, the method offers several significant advantages. First, our strategy is to use a magnetic nanobead as a bridge carrier to attach multiple BT-DNA/SYBR Green I conjugates to an antibody at a single site, that is to say, many multiple BT-DNA/SYBR Green I conjugates are attached to an antigen to generate a strong detectable signal. Second, such a low background is attributed to a blocking step and extensive washing steps with

magnetic separation. Third, the BT-DNA/SYBR Green I conjugate is not pre-synthesized, but rather formed in situ as part of the immunoassay. A fluorescent DNA probe was bound to the oligonucleotide at high ratio. The binding stoichiometry is preferably high to ensure the high ratio, and the quantum yield of SYBR Green I is also high. The unbound probe does not emit fluorescence, and measurements can be performed without a wash step. Fourth, the multiple labeling approach uses readily available reagents and MNBs that are commercially available.

ACKNOWLEDGMENT

This project was supported by the National Natural Science Foundation of China (Grant Nos. 20775043, 20875056) and the Natural Science Foundation of Shandong Province in China (Grant No. Z2008B05). The authors would also like to acknowledge funding from the Graduate Independent Innovation Foundation of Shandong University.

LITERATURE CITED

(1) Weiss, S. (1999) Fluorescence spectroscopy of single biomolecules. *Science 283*, 1676–1683.
(2) Liu, S. P., Yang, Z., Liu, Z. F., Liu, J. T., and Shi, Y. (2006) Resonance Rayleigh scattering study on the interaction of gold nanoparticles with berberine hydrochloride and its analytical application. *Anal. Chim. Acta 572*, 283–289.
(3) Zhang, X., Li, L., Li, L., Chen, J., Zou, G., Si, Z., and Jin, W. (2009) Ultrasensitive electrochemical DNA assay based on counting of single magnetic nanobeads by a combination of DNA amplification and enzyme amplification. *Anal. Chem. 81*, 1826–1832.
(4) Anazawa, T., Matsunaga, H., and Yeung, E. S. (2002) Electrophoretic quantitation of nucleic acids without amplification by single-molecule imaging. *Anal. Chem. 74*, 5033–5038.
(5) Zheng, J., and Yeung, E. S. (2002) Anomalous radial migration of single DNA molecules in capillary electrophoresis. *Anal. Chem. 74*, 4536–4547.
(6) Li, H., Xue, G., and Yeung, E. S. (2001) Selective detection of individual DNA molecules by capillary polymerase chain reaction. *Anal. Chem. 73*, 1537–1543.
(7) Lagally, E. T., Medintz, I., and Mathies, R. A. (2001) Single-molecule DNA amplification and analysis in an integrated microfluidic device. *Anal. Chem. 73*, 565–570.
(8) Shortreed, M. R., Li, H., Huang, W. H., and Yeung, E. S. (2000) High-throughput single-molecule DNA screening based on electrophoresis. *Anal. Chem. 72*, 2879–2885.
(9) Sun, B., and Chiu, D. T. (2005) Determination of the encapsulation efficiency of individual vesicles using single-vesicle photolysis and confocal single-molecule detection. *Anal. Chem. 77*, 2770–2776.
(10) Prummer, M., Sick, B., Renn, A., and Wild, U. P. (2004) Multiparameter microscopy and spectroscopy for single-molecule analytics. *Anal. Chem. 76*, 1633–1640.
(11) Byassee, T. A., Chan, W. C., and Nie, S. (2000) Probing single molecules in single living cells. *Anal. Chem. 72*, 5606–5611.
(12) Haab, B. B., and Mathies, R. A. (1999) Single-molecule detection of DNA separations in microfabricated capillary electrophoresis chips employing focused molecular streams. *Anal. Chem. 71*, 5137–5145.
(13) Shelby, J. P., and Chiu, D. T. (2003) Mapping fast flows over micrometer-length scales using flow-tagging velocimetry and single-molecule detection. *Anal. Chem. 75*, 1387–1392.
(14) Tadakuma, H., Yamaguchi, J., Ishihama, Y., and Funatsu, T. (2001) Imaging of single fluorescent molecules using video-rate confocal microscopy. *Biochem. Biophys. Res. Commun. 287*, 323–327.
(15) Dorre, K., Stephan, J., Lapczyna, M., Stuke, M., Dunkel, H., and Eigen, M. (2001) Highly efficient single molecule detection in microstructures. *J. Biotechnol. 86*, 225–236.
(16) Li, H., Zhou, D., Browne, H., Balasubramanian, S., and Klenerman, D. (2004) Molecule by molecule direct and quantitative counting of antibody-protein complexes in solution. *Anal. Chem. 76*, 4446–4451.
(17) Li, H. W., and Yeung, E. S. (2005) Direct observation of anomalous single-molecule enzyme kinetics. *Anal. Chem. 77*, 4374–4377.
(18) Singh-Zocchi, M., Dixit, S., Ivanov, V., and Zocchi, G. (2003) Single-molecule detection of DNA hybridization. *Proc. Natl. Acad. Sci. U.S.A. 100*, 7605–7610.
(19) Kang, S. H., and Yeung, E. S. (2002) Dynamics of single-protein molecules at a liquid/solid interface: implications in capillary electrophoresis and chromatography. *Anal. Chem. 74*, 6334–6339.
(20) Ma, Y., Shortreed, M. R., and Yeung, E. S. (2000) High-throughput single-molecule spectroscopy in free solution. *Anal. Chem. 72*, 4640–4645.
(21) Xu, X. H., and Yeung, E. S. (1998) Long-range electrostatic trapping of single-protein molecules at a liquid-solid interface. *Science 281*, 1650–1653.
(22) Xu, X. H., and Yeung, E. S. (1997) Direct measurement of single-molecule diffusion and photodecomposition in free solution. *Science 275*, 1106–1109.
(23) Wang, L., Xu, G., Shi, Z., Jiang, W., and Jin, W. (2007) Quantification of protein based on single-molecule counting by total internal reflection fluorescence microscopy with adsorption equilibrium. *Anal. Chim. Acta 590*, 104–109.
(24) Hanley, D. C., and Harris, J. M. (2001) Quantitative dosing of surfaces with fluorescent molecules: characterization of fractional monolayer coverages by counting single molecules. *Anal. Chem. 73*, 5030–5037.
(25) Agrawal, A., Zhang, C., Byassee, T., Tripp, R. A., and Nie, S. (2006) Counting single native biomolecules and intact viruses with color-coded nanoparticles. *Anal. Chem. 78*, 1061–1070.
(26) Hahn, M. A., Tabb, J. S., and Krauss, T. D. (2005) Detection of single bacterial pathogens with semiconductor quantum dots. *Anal. Chem. 77*, 4861–9.
(27) Jiang, D., Wang, L., and Jiang, W. (2009) Quantitative detection of antibody based on single-molecule counting by total internal reflection fluorescence microscopy with quantum dot labeling. *Anal. Chim. Acta 634*, 83–88.
(28) Stavis, S. M., Edel, J. B., Samiee, K. T., and Craighead, H. G. (2005) Single molecule studies of quantum dot conjugates in a submicrometer fluidic channel. *Lab Chip 5*, 337–343.
(29) Zhang, C. Y., and Johnson, L. W. (2008) Simple and accurate quantification of quantum dots via single-particle counting. *J. Am. Chem. Soc. 130*, 3750–3751.
(30) Jiang, D., Liu, C., Wang, L., and Jiang, W. Fluorescence single-molecule counting assays for protein quantification using epi-fluorescence microscopy with quantum dots labeling. *Anal. Chim. Acta 662*, 170–176.
(31) Willner, I., and Katz, E. (2003) Magnetic control of electrocatalytic and bioelectrocatalytic processes. *Angew. Chem., Int. Ed. Engl. 42*, 4576–4588.
(32) Weizmann, Y., Patolsky, F., Katz, E., and Willner, I. (2003) Amplified DNA sensing and immunosensing by the rotation of functional magnetic particles. *J. Am. Chem. Soc. 125*, 3452–3454.
(33) Zhang, Q., and Guo, L. H. (2007) Multiple labeling of antibodies with dye/DNA conjugate for sensitivity improvement in fluorescence immunoassay. *Bioconjugate Chem 18*, 1668–1672.

BC100212W

Surface-Bound Cytomimetic Assembly Based on Chemoselective and Biocompatible Immobilization and Further Modification of Intact Liposome

Yong Ma, Hailong Zhang, and Xue-Long Sun*

Department of Chemistry, Cleveland State University 2121 Euclid Avenue, Cleveland Ohio 44115, United States. Received May 5, 2010; Revised Manuscript Received September 20, 2010

A surface-bound cytomimetic assembly based on chemically selective and biocompatible immobilization and further modification of intact liposome is described. Liposomes carrying PEG-triphenylphosphine were chemoselectively immobilized onto azide-modified glass slides through Staudinger ligation, followed by modification with azide-modified lactose as a model biomolecule through Staudinger ligation to afford the surface-bound cytomimetic assembly. The intact liposome immobilized and modified and its protein binding activity were confirmed by fluorescence imaging, fluorescent dye releasing kinetics, and AFM techniques. The resultant surface-bound cytomimetic assembly showed sustained stability and fluorescent dye releasing kinetics and specific protein binding activity. The reported method provides a robust platform for preparation of a complex immobilized liposome system with multifunctional components, which mimics the cell surface in both geographical and content features and thus will find important biomedical applications.

INTRODUCTION

Cell surface biomolecules, especially glycans, have become attractive biomimetic targets for potential biomedical applications, since they act as receptors for a variety of protein ligands and are involved in a wide range of biological processes, including immune recognition events (*1*) and virus and bacterial invasion (*2*), as well as tissue growth and repair (*3*). On the other hand, cell surface glycosylated molecules play a significant role in maintaining the nonadhesive/nonthrombogenic property of the native intravascular luminal wall (*4*). Therefore, mimicking cell surface glycan structure by immobilizing glycan onto solid surface, namely, glycosurface has been explored extensively for biosensors and functional and biocompatible biomaterial surface engineering applications (*5, 6*). However, in most cases, glycans are directly conjugated onto the solid surfaces, which lack cell surface glycoconjugates' three-dimensional (3D) structure properties and cell lipid membrane's supplement effect and thus showed lower activity in both affinity and selectivity points and had limited success.

For cell surface mimetic engineering, surface chemistry characterized by the type of cell-binding ligand (carbohydrates, proteins, etc.) and their surface density (*7*), spatial distribution (*8*), and conformation (*9*) have been demonstrated to be important surface cues. Immobilization of liposome onto solid surface has shown great potential in biological and biomedical research and applications (*10*). This discipline has been inspired by the fact that liposome structurally retains the properties inherent in natural lipid membranes and functionally can serve as a biomembrane model and can encapsulate both hydrophobic and hydrophilic compounds such as drug and gene for delivery applications (*11*). For example, immobilized liposomes have been investigated as model systems presenting lipid membranes for bioseparation (*12*), biosensor (*13*), and nanobioreactor (*14*) applications. Recently, immobilized liposomes have been explored for medical device surface functionalization for sustained drug elution at the site of interest (*15*). Crucial to the further development of immobilized liposomes for practical application is their stability and the immobilization methods that allow chemoselective and biocompatible attachment of the intact liposomes with multifunctional components. Early studies using physisorptive entrapment (*12, 15*) for liposome immobilization suffered from their low reproducibility and stability due to their nonspecific interaction features. In response to these problems, biotin−streptavidin/avidin (*13, 14*) and oligonucleotide-based specific binding (*16*), histidine-nickel (*17*), and covalent immobilization strategies such as using glutaraldehyde (*18*), disulfide linkage (*19*), carbamate (*20*), and carbodiimide (*21*) chemistry have been explored. The major limitations to all these approaches lie in the fact that the immobilized liposomes tend to unravel, rupture, and fuse with other surrounding liposomes during and after the immobilization process, as well as nonselective and harsh reaction conditions. In addition, to the best of our knowledge, there has been no report on further covalent modification of the immobilized liposome. Herein, a chemically selective and biocompatible immobilization and further modification of intact liposome was investigated for preparation of a surface-bound cytomimetic assembly. The immobilized and functionalized liposome-based system mimics the cell surface in both geographical and content features and thus is expected to have high biological activity. Specifically, liposomes carrying PEG-triphenylphosphine were chemoselectively immobilized onto azide-PEG-modified glass slides through Staudinger ligation and were further modified with azide-modified glycans through Staudinger ligation with triphenyphosphine localized on the immobilized liposome exterior surface (Figure 1). This strategy fulfills the following important design criteria: (1) PEG spacers on both glass side and liposome surface will stabilize the immobilized liposome (*22*); (2) the azide group tolerates a diverse array of other functionalities in the complex and undergoes chemoselective Staudinger ligation with triphenylphosphine under mild conditions. Several research groups have demonstrated the superior chemoselectivity and biocompatibility of Staudinger ligation, for example, in the recently highlighted metabolic engineering of cell surface (*23*), microarray (*24*), and liposome surface functionalization (*25*) applications. In addition, Staudinger ligation is a catalyst-free

* Address correspondence to Xue-Long Sun, Ph.D., 2121 Euclid Avenue SI 313, Cleveland, OH 44115. Phone: (216) 687-3919. Fax: (216) 687-9298. E-mail: x.sun55@csuohio.edu.

10.1021/bc100220j © 2010 American Chemical Society
Published on Web 10/12/2010

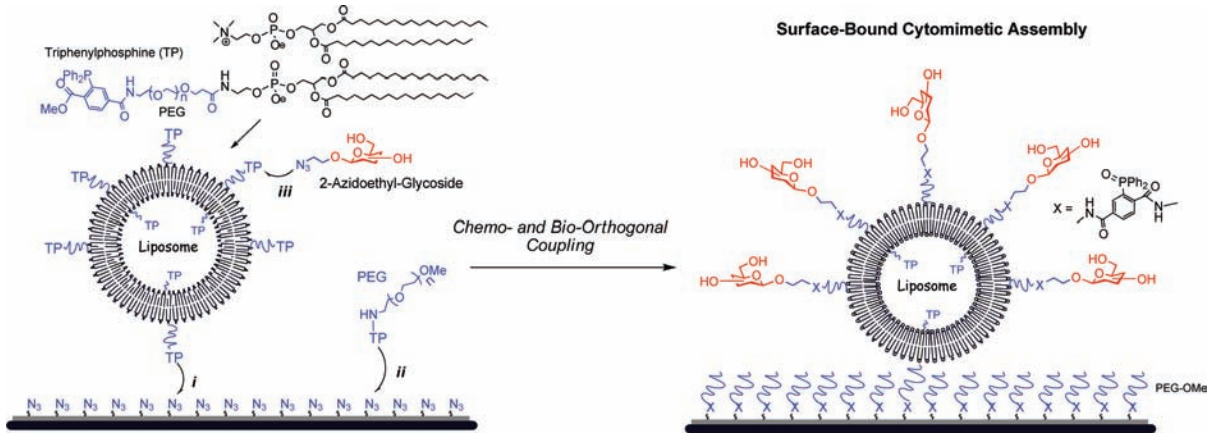


Figure 1. Illustration of chemoselective and biocompatible immobilization and further glyco-modification of intact liposome based on Staudinger ligation and PEG chemistry.

coupling reaction and thus does not bring in any residue to the immobilized liposome during the reaction. Therefore, the reported method will provide a robust platform for preparation of a complex immobilized liposome system with multifunctional components for a variety of biological and biomedical research and practices.

MATERIALS AND METHODS

Materials. 1,2-Distearoyl-*sn*-glycero-3-phosphocholine (DSPC) and 1,2-distearoyl-*sn*-glycero-3-phosphoethanolamine-*N*-(lissamine rhodamine B sulfonyl) (ammonium salt) (DSPE-Rodamine) were purchased from Avanti Polar Lipids (Alabaster, AL, USA). Cholesterol, 5,6-carboxyfluorescein, and lectin (Arachis hypogae, FITC-labeled) were purchased from Sigma (USA). All other solvents and reagents were purchased from commercial sources and were used as received, unless otherwise noted. Deionized water was used as a solvent in all experiments. DSPE-PEG_{2000}-triphenylphosphine, MeO-PEG_{2000}-triphenylphosphine, azide-PEG_6-Glass slide, and 2-azideethyle-lactoside were synthesized as described in the Supporting Information.

General Measurement. The fluorescence imaging experiments of the immobilized liposomes on a glass slide were performed by using Typhoon 9410 variable mode imager (Amersham Biosciences, USA). A two-channel stage-scanning fluorescent image was used. Channel 1 used 521 nm output (526 nm) from laser blue 2 to selectively excite 5,6-CF encapsulated inside the liposome, and Channel 2 used 571 nm output (580 nm) from laser green to selectively excite Liss Rhod-DSPE embedded in the lipid membrane. AFM imaging experiments of the immobilized liposomes on a glass slide were performed by using PicoPlus 3000 (Molecular Imaging, USA).

Liposome Preparation. DSPC (15 mg, 20.4 μmol), cholesterol (4 mg, 10.2 μmol), and DSPE-PEG_{2000}-Triphenylphosphine (0.9 mg, 0.3 μmol) (2:1:1% molar ratio) were dissolved in 3.0 mL of chloroform. The solvent was gently removed on an evaporator under reduced pressure to form a thin lipid film on the flask wall, which was kept in a vacuum chamber overnight. The lipid film was swelled with 2.5 mL of PBS (pH 7.4) buffer containing 5,6-carboxyfluorescein (50 mM for fluorescence imaging or 85 mM for releasing study) to form the multilamellar vesicle suspension, followed by 10 freeze−thaw cycles involving quenching in liquid N_2 and then immersion in a 65 °C water bath. The lipid suspension thus formed was extruded through polycarbonate membranes (pore size 600, 200, and 100 nm, gradually) to afford small unilamellar vesicles (SUVs). Non-entrapped CF was separated from the 5,6-CF-encapsulated vesicles with Sephadex G-50 gel chromatography (1.5 × 20 cm column) using PBS (pH 7.4) buffer as eluent. For fluorescence imaging study, 1 mol % of DSPE-Rodamine was embedded in the lipid membrane as the same liposome preparation above. For liposome size determination, 20 μL of extruded liposome sample was diluted to 2 mL with PBS (pH 7.4) buffer and then measured with a 90plus particle size analyzer (Brookhaven Co., USA).

Staudinger Immobilization of Liposome. The liposome prepared above was diluted to desired lipid concentration (2.0 mg/mL, total lipid concentration) by PBS (pH 7.4) buffer and then was incubated on an azide-PEG6-functionalized glass slide for 2.0 h at room temperature. Next, MeO-PEG_{2000}-triphenylphosphine was added (20 μg/mL) to quench the azide group left on the glass slide for 2 h at room temperature, followed by removing the glass slide from the reaction solution. Finally, the liposome-immobilized glass slide was washed by rinsing with PBS (pH 7.4) buffer for 2.0 h, repeated three times.

Staudinger Glyco-Functionalization of Immobilized Liposome. The immobilized liposome carrying triphenylphosphine was incubated with 2-azidoethyllactoside in PBS buffer (pH 7.4, 40 mg/mL) at room temperature for 2.0 h, followed by removing the glass slide from the reaction solution. The glass slide was washed by rinsing with PBS (pH 7.4) buffer for 2.0 h, repeated three times.

Specific Lectin Binding onto Lactosylated Immobilized Liposome. The lactosylated liposomes immobilized onto a glass slide were incubated with lectin (Arachis hypogae, FITC-labeled, Sigma) in PBS (pH 7.4) buffer solution (50 μg/mL) at room temperature for 2.0 h, followed by removing the glass slide from the reaction solution. The glass slide was washed by rinsing with PBS (pH 7.4) buffer for 2.0 h, repeated three times. The control experiment was performed with lectin-FITC presaturated with free lactose (0.1 mM in PBS (pH 7.4) buffer).

Measurement of Release of 5,6-CF from Liposome. 5,6-CF released from free liposomes, immobilized liposomes, and glycosylated immobilized liposomes in PBS (pH 7.4) buffer at room temperature was measured over time. The excitation and emission wavelengths of 5,6-CF were 497 and 520 nm, respectively. The variation of the fluorescent intensity with release time was calculated according to the equation below

$$\text{fraction of CF remaining in liposomes} = 1 - F/F_0$$

where F is the fluorescent intensity measured at any time during the experiment and F_0 is the total fluorescent intensity measured

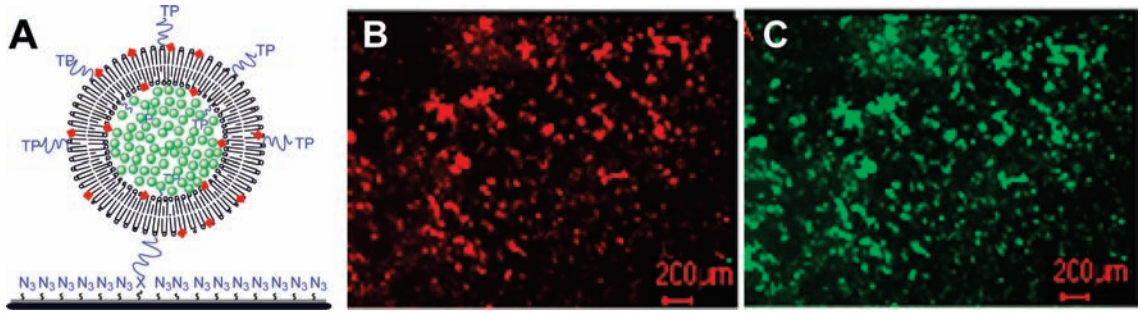


Figure 2. Fluorescent-labeled immobilized liposome (A); fluorescence images of immobilized liposomes obtained for selectively exciting PE-Rhodamine embedded in the liposome membrane (B) and for selectively exciting 5,6-CF encapsulated in the liposome (C). Bar size: 200 μm.

after disrupting liposomes completely with 0.5% Triton X-100 in PBS (pH 7.4) buffer.

RESULTS AND DISCUSSION

The synthesis of surface-immobilized liposomes starts with the synthesis of anchor group modified liposomes followed by attachment onto a solid surface carrying a counterpart group of the anchor group on the liposome surface. The anchor lipid DSPE-PEG_{2000}-Triphenylphosphine was synthesized by amidation of commercially available DSPE-PEG_{2000}-NH_2 (Avanti Polar Lipid, Inc.) with 3-diphenylphosphino-4-methoxycarbonylbenzoic acid NHS active ester (see the Supporting Information). Small unilamellar vesicles composed of DSPC and cholesterol (2:1 mol ratio) and 1.0 mol % of the anchor lipid in PBS (pH 7.4) buffer were prepared by rapid extrusion through polycarbonate membrane with pore size of 600, 200, and 100 nm diameter, sequentially at 65 °C. In the present study, DSPC was used as a model lipid; different lipids such as unsaturated lipids will be used to mimic the real cellular surface in continued study. This produced small unilamellar vesicles show an average mean diameter of 120 $\pm$ 5 nm as determined by dynamic light scattering (see Supporting Information). On the other hand, the azid-PEG_6-glass slide was used as model surface and was prepared by amidation of commercially available amine glass slide (Xenopore, Co) with azido-PEG_6-COO-NHS (see the Supporting Information). Next, immobilization of the preformed liposomes was performed by incubating azide-PEG-glass slides with preformed liposomes in PBS (pH 7.4) buffer (2 mg/mL of total lipid concentration) for 2.0 h at room temperature, followed by addition of MeO-PEG_{2000}-triphenylphosphine (20 μg/mL) to quench the azide group left on the glass slide for 2 h at room temperature. Finally, removing the glass slide from the reaction solution followed by washing with PBS (pH 7.4) buffer three times to remove the unreacted liposomes afforded immobilized liposomes.

To confirm the intact liposome immobilized on the glass slide surface, a fluorescence imaging study was conducted first. DSPE-Rodamine (1 mol %, Avanti Polar Lipid, Inc.) was doped in the liposomes so as to label the lipid membrane, and 5,6-carboxyfluorescein (5,6-CF, Sigma) (50 mM) was encapsulated into the liposome so as to image the inner compartment of the liposome (Figure 2A). As a result, detecting either Rhodamine (Figure 2B) or 5,6-CF (Figure 2C) yielded a fluorescence image of the immobilized liposome for an azide-PEG glass slide treated with liposomes carrying anchor group triphenylphosphine, while there was no apparent fluorescence image observed for an azide-PEG glass slide treated with liposomes without anchor group triphenylphosphine (data not shown). These results indicated that the immobilization of intact liposomes was achieved through Staudinger ligation. Both fluorescence images were not so uniform. This might be due to non-uniform functionalization of the glass slide surface or the original glass slide surface being bumpy.

To examine whether the immobilization reaction condition could provoke liposome disruption, fluorescent dye releasing kinetics from the liposome during immobilization reaction was investigated. Briefly, we have exposed our standard conditions to the same type of liposomes but with encapsulated self-quenching concentration (85 mM) of 5,6-CF. On the basis of the fluorescence quenching determinations (Figure 3A), we could demonstrate that less than 7.2% leakage of the total loading was triggered during the immobilization reaction (2.0 h) compared with 5.2% leakage for the same liposome during storage without reaction (2.0 h). The leakage percentiles were calculated by destroying liposomes with surfactant 0.5% Triton X-100 in PBS (pH 7.4) buffer to release all 5,6-CF encapsulated after 2.0 h reaction. These results indicated that the immobilization reaction condition is harmless for liposome integrity. Continually, the subsequent fluorescent dye releasing kinetics over time for the non-destroyed immobilized liposomes was examined to verify the stability of the intact immobilized liposome in PBS (pH 7.4) buffer at room temperature. It was found that immobilized liposome showed a constant leakage of approximately 25%/day for three days (Figure 3B), whereas free liposome in PBS (pH 7.4) solution showed a leakage rate of approximately 20%/day (Figure 3C), which is slightly less than that of immobilized liposome. The extended fluorescent dye releasing results further demonstrated that intact liposomes had been successfully immobilized onto the glass slide and showed sustained stability as well.

Furthermore, atomic force microscopy (AFM) was used to confirm the intact liposomes immobilized on the glass slide surface, since it is a powerful tool for investigating surface-related physical and chemical properties in the nanoscale. Typical AFM images of immobilized liposomes were observed on the azide-PEG glass slide treated with liposomes carrying anchor group triphenylphosphine (Figure 4B), while there were no immobilized liposomes observed for the azide-PEG glass slide treated with liposomes without anchor group triphenylphosphine (Figure 4A). These results further indicated the successful immobilization of intact liposomes via Staudinger ligation.

Lactose was chosen as a model glycan for chemoselective modification of the immobilized liposome since it serves as ligand for lectin (*26*) and cells such as hepatocytes that express galactose-specific binding receptor asialoglycoproteins on the surface (*27*). Briefly, glyco-modification was performed by incubation of the immobilized liposomes carrying triphenylphosphine on the exterior surface with 2-azidoethyllactoside (*28*) in PBS buffer (pH 7.4) at room temperature under an argon atmosphere for 2 h. Similarly, fluorescent dye releasing kinetics from the glycosylated immobilized liposome was examined by using liposome encapsulating self-quenching concentrations (85 mM) of 5,6-CF (Figure 3D). It was found that the 5,6-CF releasing kinetics from the glycosylated immobilized liposome is slower than that of its precursor, but slightly faster than that

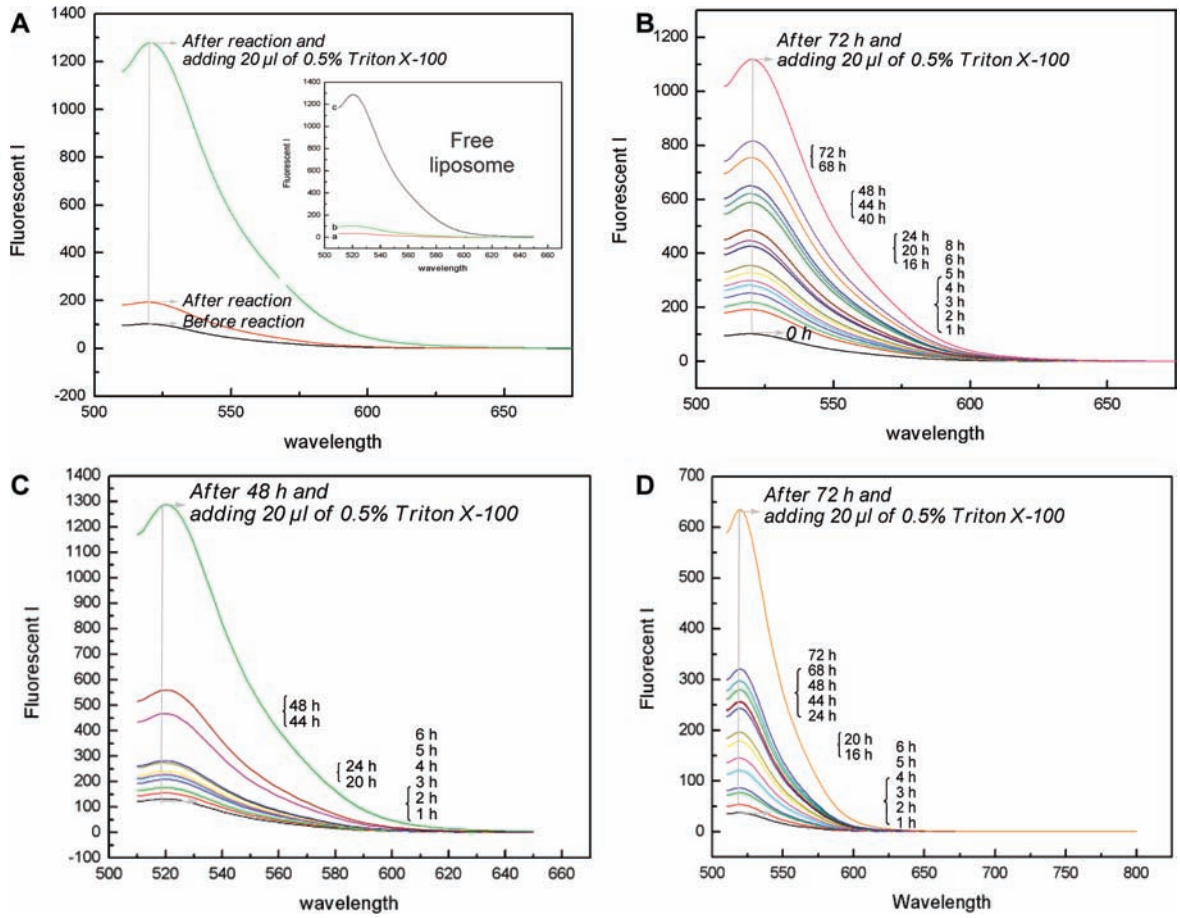


Figure 3. 5,6-CF releasing from liposome during the immobilization reaction: before reaction, after reaction, and after adding 20 μL of 0.5% Triton X-100 (A); the 5,6-CF releasing kinetics from immobilized liposome (B); the 5,6-CF releasing kinetics from free liposome (C); and the 5,6-CF releasing kinetics from glycosylated immobilized liposome (D) during storage in PBS (pH 7.4) buffer at rt during 0−72 h, and after adding 20 μL of 0.5% Triton X-100 at the final point.

of free liposome (Figure 5A), which indicated that glycosylated immobilized liposome showed sustained stability. It can be explained by the fact that liposome surface glycans prevent 5,6-CF release and stabilize the immobilized liposome. Furthermore, the glyco-stabilizing function was defined by a detergent rupturing experiment (*29*), in which the immobilized liposomes were ruptured by adding surfactant 0.5% Triton X-100 immediately after immobilization and glycosylation reaction, respectively. As shown in Figure 5B, 90% of encapsulated 5,6-CF was released from the non-glycosylated immobilized liposomes in 30 min, while it took 120 min for the glycosylated immobilized liposomes. In other words, the glycosylated immobilized liposomes released encapsulated 5,6-CF much more slowly than its precursor did. This result demonstrated the capacity of the surface glycans to protect liposomes against the action of surfactant, which is consistent with the literature report (*29*).

Next, to determine whether the grafted lactose residues are easily accessible at the surface of the immobilized liposomes, specific lectin binding assay was conducted by incubating lactosylated immobilized liposomes in the presence of β-galactose binding lectin (*Arachis hypogae,* 120 kDa, FITC-Labeled, Sigma) in PBS (pH 7.4) buffer at room temperature for 2.0 h. As shown in Figure 6, the specific binding of fluorescent-labeled lectin was observed on the lactosylated immobilized liposome (Figure 6A), while no fluorescent image was observed on non-glycosylated immobilized liposomes treated with the same lectin (Figure 6B). Furthermore, lectin binding was not observed when lactose-saturated lectin was used (Figure 6C). These results indicated specific binding of lectin onto the lactosylated immobilized liposomes. Finally, AFM images were investigated to confirm lactosylated immobilized liposomes as well as its lectin binding. As result, there is no apparent size change after lactosylation of the immobilized liposomes (Figure 4C); however, morphological change was observed after lectin binding to the lactosylated immobilized liposomes (Figure 4D). This phenomenon can be explained as the glycosylated immobilized liposome might be ruptured due to specific multivalent binding interaction between grafted lactoses on the immobilized liposome surface and lectin. These results further demonstrated the successful glyco-functionalization of the immobilized liposome and its lectin binding capacity.

CONCLUSION

A surface-bound cytomimetic assembly was demonstrated by chemically selective and biocompatible immobilization and further glyco-modification of intact liposome through Staudinger ligation and PEG chemistry. The integrity and stability of the intact glycosylated immobilized liposomes and its specific lectin binding were confirmed by fluorescence imaging, fluorescent dye releasing kinetics, and AFM techniques. The high specificity and efficiency and biocompatible reaction conditions make the present approach an attractive alternative to all currently used protocols for liposome immobilization and modification. Continued study on maximum and optimized density of immobilized liposomes and the glycans on the surface of the immobilized liposomes correlating to its stability and biological activity are under investigation and will be reported accordingly. The reported method will provide a robust platform for preparation of immobilized liposome systems with multifunctional compo-

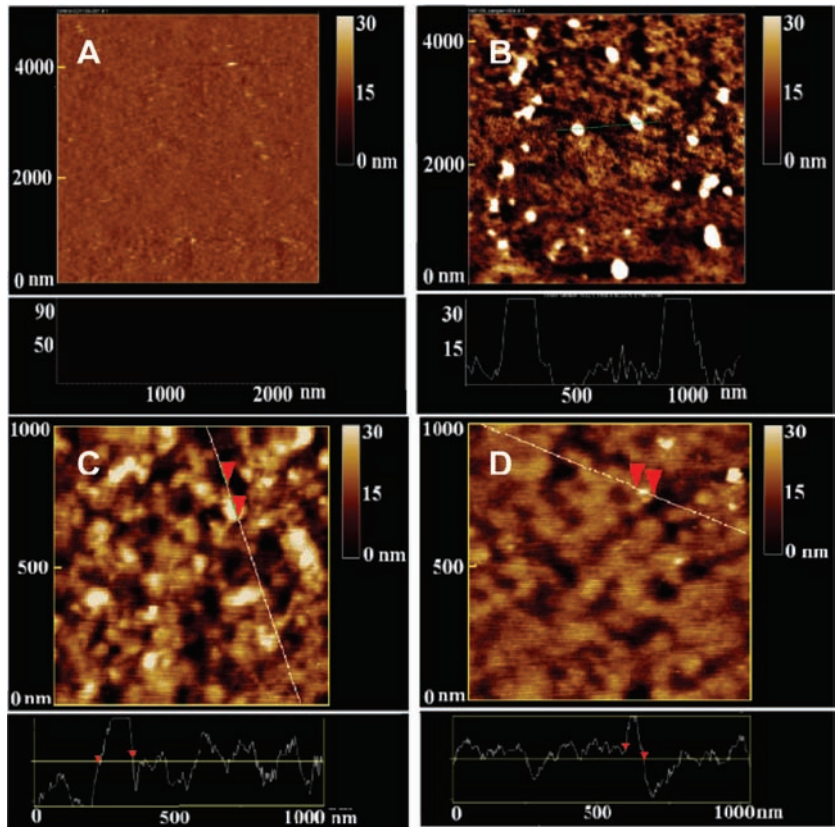


Figure 4. AFM image of immobilized intact liposomes onto glass slide: azide-PEG-glass slide incubated with liposomes without DSPE-PEG2000-TP (A), azide-PEG-glass slide incubated with liposomes carring PEG2000-TP (B), glycosylated immobilized liposome (C), glycosylated immobilized liposome after lectin binding (D).

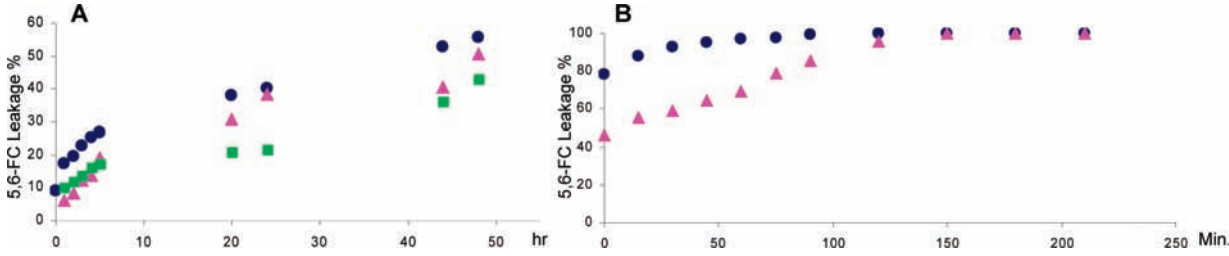


Figure 5. 5,6-CF releasing kinetics from liposomes during storage (A): free liposome (green square), immobilized lipsomes (blue dot), glycosylated immobilized liposomes (pink triangle). 5,6-CF releasing kinetics from liposome after adding 20 μL of 0.5% Triton X-100 in PBS (pH 7) buffer (B): immobilized liposomes (blue dot), glycosylated immobilized liposomes (pink triangle).

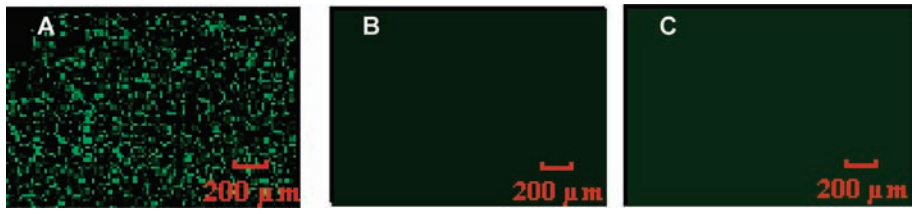


Figure 6. Fluorescent image of lectin (FITC-labeled *Arachis hypogaea*) binding onto the immobilized liposome surface: lactosylated immobilized liposomes (A); bare glass slide (B), lactosylated immobilized liposomes incubated with free lactose presaturated lectin (C). Bar size: 200 μm.

nents that can be used in cell surface models and biosensors and biomedical device surface functionalization and will find important use in biological and biomedical research and applications.

ACKNOWLEDGMENT

This work was financially supported by the grant from NIH (1R01HL102604-01), American Health Assistance Foundation (AHAF-H2007027), and the Startup Fund from Cleveland State University. Thanks to Dr.s Su-Tung Yau and Mekki Bayachou at CSU for AFM study.

Supporting Information Available: Syntheses of DSPE-PEG_{2000}-triphenylphosphine, azide-PEG_6-Glass slide, and 2-azidoethyllactoside. This material is available free of charge via the Internet at http://pubs.acs.org.

LITERATURE CITED

(1) Sodetz, J. M., Paulson, J. C., and McKee, P. A. (1979) Carbohydrate composition and identification of blood group A, B, and H oligosaccharide structures on human Factor V_{III}/von Willebrand factor. *J. Biol. Chem. 254*, 10754–10760.

(2) Karlsson, K. A. (1995) Microbial recognition of target-cell glycoconjugates. *Curr. Opin. Struct. Biol. 5*, 622–635.

(3) Varki, A. (1993) Biological roles of oligosaccharides: all of the theories are correct. *Glycobiology 3*, 97–130.

(4) Evans, W. H., and Graham, J. M. (1991) *Membrane structure and function*, pp 1−86, Oxford University Press, New York.

(5) Zhang, Y., Luo, S., Tang, Y., Yu, L., Hou, K., Cheng, J., Zhang, Y., Telyatnikov, V., Sathe, M., Zeng, X. Q., and Wang, P. G. (2003) Studying the interaction of α-gal carbohydrate antigen and proteins by quartz-crystal microbalance. *J. Am. Chem. Soc. 125*, 9292–92933.

(6) Gupta, A. S., Wang, S., Link, E., Anderson, E. H., Hofmann, C., Lewandowski, J., Kottke-Marchant, K., and Marchant, R. E. (2006) Glycocalyx-mimetic dextran-modified poly(vinyl amine) surfactant coating reduces platelet adhesion on medical-grade polycarbonate surface. *Biomaterials 27*, 3084–3095.

(7) Michael, K. E., Vernekar, V. N., Keselowsky, B. G., Meredith, J. C., Latour, R. A., and Garcia, A. J. (2003) Adsorption-induced conformational changes in fibronectin due to interactions with well-defined surface chemistries. *Langmuir 19*, 8033–8040.

(8) Rajagopalan, P., Marganski, W. A., Brown, X. Q., and Wong, J. Y. (2004) Direct comparison of the spread area, contractility, and migration of balb/c 3T3 fibroblasts adhered to fibronectin- and RGD-modified substrata. *Biophys. J. 87*, 2818–2827.

(9) Luk, Y. Y., Kato, M., and Mrksich, M. (2000) Self-assembled monolayers of alkanethiolates presenting mannitol groups are inert to protein adsorption and cell attachment. *Langmuir 16*, 9604–9608.

(10) Christensen, S. M., and Stamou, D. (2007) Surface-based lipid vesicle reactor systems: fabrication and applications. *Soft Matter 3*, 828–836.

(11) Torchilin, P. V. (2005) Recent advances with liposomes as pharmaceutical carriers. *Nat. Rev. Drug Discovery 4*, 145–160.

(12) Zhang, Y. X., Aimoto, S., Lu, L., Yang, Q., and Lundahl, P. (1995) Immobilized liposome chromatography for analysis of interactions between lipid bilayers and peptides. *Anal. Biochem. 229*, 291–298.

(13) Ngo, A. T., Karam, P., Fuller, E., Burger, M., and Cosa, G. (2008) Liposome encapsulation of conjugated polyelectrolytes: Toward a liposome beacon. *J. Am. Chem. Soc. 130*, 457–459.

(14) Jung, S. L., Shumaker-Parry, S. J., Campbell, T. C., Yee, S. S., and Gelb, H. M. (2000) Quantification of tight binding to surface-immobilized phospholipid vesicles using surface plasmon resonance: Binding constant of phospholipase A2. *J. Am. Chem. Soc. 122*, 4177–4184.

(15) Kallinteri, P., Antimisiaris, S. G., Tsota, I., Kalogeropoulou, C., Karnabatidis, D., and Siablis, D. (2002) Dexamethasone incorporating liposomes: An in vitro study of their applicability as a slow release delivery system of dexamethasone from covered metallic stents. *Biomaterials 23*, 4819–4826.

(16) Yoshina-Ishii, C., and Boxer, S. G. (2003) Arrays of mobile tethered vesicles on supported lipid bilayers. *J. Am. Chem. Soc. 125*, 3696–3697.

(17) Stora, T., Dienes, Z., Vogel, H., and Duschl, C. (2000) Histidine-tagged amphiphiles for the reversible formation of lipid bilayer aggregates on chelator-functionalized gold surfaces. *Langmuir 16*, 5471–5478.

(18) Yoshimoto, M., Wang, S., Fukunaga, K., Fournier, D., Walde, P., Kuboi, R., and Nakao, K. (2005) Novel immobilized liposomal glucose oxidase system using the channel protein OmpF and catalase. *Biotechnol. Bioeng. 90*, 231–238.

(19) Khaleque, M. A., Okamura, Y., Yabushita, S., and Mitani, M. (2003) Liposome immobilization on polymer gel particles by in situ formation of covalent linkages. *Chem. Lett. 32*, 416–417.

(20) Lunelli, L., Pasquardini, L., Pederzolli, C., Vanzetti, L., and Anderle, M. (2005) Covalently anchored lipid structures on amine-enriched polystyrene. *Langmuir 21*, 8338–8343.

(21) Morita, S., Nukui, M., and Kuboi, R. (2006) Immobilization of liposomes onto quartz crystal microbalance to detect interaction between liposomes and proteins. *J. Colloid Interface Sci. 298*, 672–678.

(22) Allen, T. (1996) Nanocompartments enclosing vesicles, colloids, and macromolecules via interdigitated lipid bilayers. *Curr. Opin. Colloid Interface Sci. 1*, 645–651.

(23) Prescher, A. J., Dube, H. D., and Bertozzi, R. C. (2004) Chemical remodelling of cell surfaces in living animals. *Nature 430*, 873–877.

(24) Stamou, D., Duschl, C., Delamarche, E., and Vogel, H. (2003) Staudinger ligation: a new immobilization strategy for the preparation of small-molecule arrays. *Angew. Chem., Int. Ed. 42*, 5830–5834.

(25) Zhang, H., Ma, Y., and Sun, X.-L. (2009) Chemically-selective surface glyco-functionalization of liposomes through staudinger ligation. *Chem. Commun.* 3032–3034.

(26) Sun, X.-L., Cui, W., Haller, C., and Chaikof, E. L. (2004) Site-specific multivalent carbohydrate labeling of quantum dots and magnetic beads. *ChemBioChem 5*, 1593–1596.

(27) Wu, J., Nantz, M. H., and Zern, M. A. (2002) Targeting hepatocytes for drug and gene delivery: emerging novel approaches and applications. *Front. Biosci. 7*, d717−d725.

(28) Sun, X.-L., Grande, D., Baskaran, S., and Chaikof, E. L. (2002) Glycosaminoglycan mimetic biomaterials. 4. Synthesis of sulfated lactose-based glycopolymers that exhibit anticoagulant activity. *Biomacromolecules 3*, 1065–1070.

(29) Maza, A., López, O., Cócera, M., and Parra, J. L. (2000) Protection of liposomes against triton X-100 by means of the new exopolymer excreted by Pseudoalteromonas antarctica NF3. *J. Colloid Surf. A 166*, 91–99.

BC100220J

Surface-Bound Cytomimetic Assembly Based on Chemoselcetive and Biocompatible Immobilization and Further Modification of Intact Liposome

Yong Ma, Hailong Zhang and Xue-Long Sun*

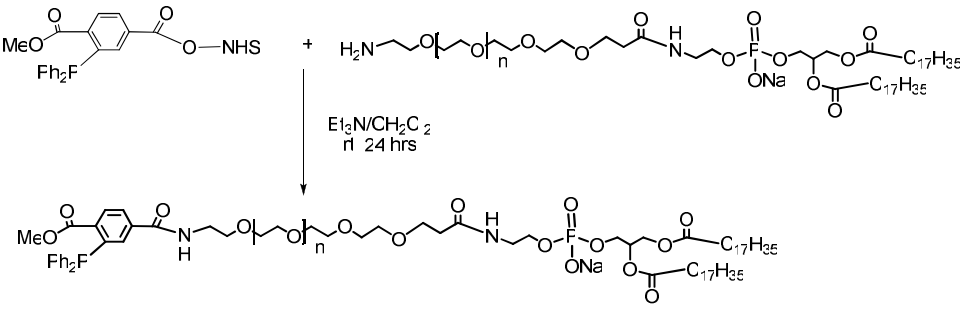
Supporting Information

Materials. All solvents and reagents were purchased from commercial sources and were used as received, unless otherwise noted. Deionized water with a resistivity of 18Ω was used as a solvent in all polymerization reactions.

Method. Thin-layer chromatography (TLC) was performed on Whatman silica gel aluminum backed plates of 250 μm thickness on which spots were visualized with UV light or by charring the plate after dipping in 10% H_2SO_4 in methanol. ^{1}H NMR spectra were recorded with a Varian INOVA 300 MHz spectrometer. In all cases, the sample concentration was 10 mg/mL, and the appropriate deuterated solvent was used as an internal standard.

1. 1-Succinimidyl 3-diphenylphosphino-4-methoxycarbonylbenzoate was synthesized as literature method.[1]

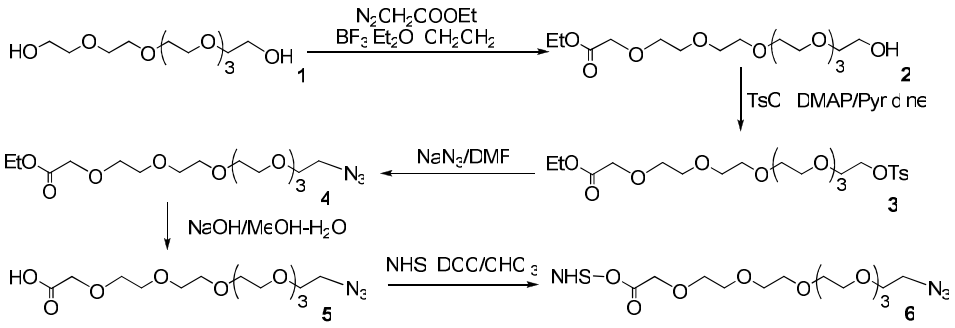
2. Synthesis of DSPE-PEG$_{2000}$-Triphenylphosphine



Scheme 1. Synthesis of DSPE-PEG$_{2000}$-Triphenylphosphine

DSPE-PEG2000-NH_2 (100 mg, 35.8 μmol) was dissolved in 20 mL of CH_2Cl_2, and 0.2 mL of Et_3N was added. After stirring for 30 min at room temperature, a solution of succinimidyl 3-diphenylphosphino-4-methoxycarbonylbenzoate (33 mg, 71.6 μmol) in 5 mL of CH_2Cl_2 was added. The reaction mixture was stirred at room temperature for 24 h and then concentrated under vacuum to give a residue, which was purified by silica gel chromatography using chloroform/methanol (4:1, v/v) as elute to afford DSPE-PEG$_{2000}$-Triphenyphosphine (45 mg, 42%), ^{1}H NMR ($CDCl_3$, 300 MHz) δ: 8.06 (m, 1H), 7.79 (m, 1H), 7.66 (m, 2H), 7.52-7.42 (m, 2H), 7.28-7.34 (m, 8H), 6.64 (m, 1H), 5.19 (s, 1H), 4.34-4.20 (m, 3H), 3.95-3.80 (m, 3H), 3.80-3.50 (br. S, 100H, O-CH_2-CH_2-O), 3.40-3.20 (m, 3H), 2.28 (br.s, 4H), 1.58 (br.s, 4H), 1.36-1.20 (s, 32H), 0.89 (t, *J*, 6.9 , 6H) ppm, ^{31}P NMR ($CDCl_3$, 121 MHz) δ: -2.70 ppm.

3. Synthesis of Azido-PEG$_6$-COO-NHS ester



Scheme 2. Synthesis of Azido-PEG6-COO-NHS ester

Synthesis of Hexa (ethylene glycol) monoester (2): Ethyl diazoacetate (0.47 mL, 4.42 mmol) was added dropwise to a solution of hexa(ethylene glycol) (10 g, 35.3 mmol) and BF_3•Et_2O (0.056 mL, 0.442 mmol) in dichloromethane (12 mL) at 0 ^oC. The reaction mixture was allowed to proceed for 15 min at room temperature and then saturated NH_4Cl (6 mL) was added. The reaction solution was placed in a separatory funnel and was extracted with dichloromethane (3 × 20 mL). The combined organic phase was concentrated in vacuum to afford yellow oil, which was purified with silica gel chromatography (3:1 (v/v) EtOAc:hexanes → EtOAc) to afford **2** as a clear oil (2.90 g, 23%). ^{1}H-NMR ($CDCl_3$, 300 MHz) δ: 4.16 (q, *J* = 7.14 Hz, 2H), 4.10 (s, 2H), 3.62-3.70 (m, 22H), 3.56 (t, *J* = 4.24 Hz, 2H), 2.78 (br, s, 1H), 1.23 (t, *J* = 7.14 Hz, 3H) ppm.

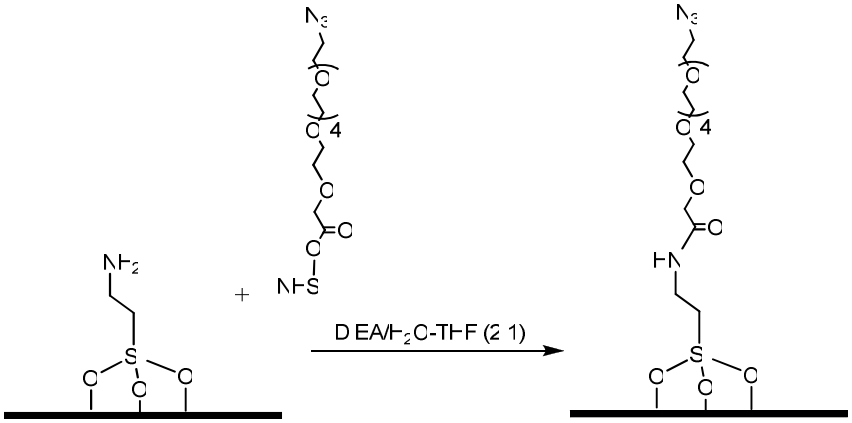
Synthesis of O-Toluenesulfonyl-hexa(ethylene glycol) ethyl ester (3): *P*-toluenesulfonyl chloride (2.25 g, 11.80 mmol) and DMAP (65 mg, 0.54 mmol) were added to a solution of **2** (2.90 g, 7.84 mmol) in 1:1 (v/v) of pyridine/dichloromethane (25 mL). After 5 hr, the reaction solution was poured into ice-cold water (50 mL), and the aqueous phase was extracted with dichloromethane (3 × 40 mL). The combined organic phases were washed with NH_4Cl (20 mL) and brine (20 mL), dried over Na_2SO_4, and concentrated. The resultant yellow oil was chromatographed on silica gel (EtOAc: *n*-Hexanes, 3:1, v/v) to afford **3** as a clear oil (1.56 g, 40%). ^{1}H-NMR ($CDCl_3$, 300 MHz) δ: 7.73 (d, *J* = 8.30 Hz, 2H), 7.28 (d, *J* = 8.30 Hz, 2H), 4.14 (q, *J* = 7.14 Hz, 2H), 4.08 (s, 2H), 3.52-3.68 (m, 22H), 2.39 (s, 3H), 1.22 (t, *J* = 7.14 Hz, 3H) ppm.

Synthesis of Ethyl 14-azido-3, 6, 9-hexaaoxatetradecan-1-oate (4): Sodium azide (0.400 g, 6.16 mmol) was added to a solution of **3** (0.78 g, 1.53 mmol) in DMF (20 mL). The reaction mixture was stirred at 70 ^oC overnight then cooled to room temperature, water (10 mL) was added and extracted with Et_2O (3 × 20 mL). The combined Et_2O layer was backwashed by saturated NaCl (2 × 10 mL). The diethyl ether extraction was dried by anhydrous Na_2SO_4 and concentrated to afford crude yellow oil, which was purified with silica gel chromatography with Hexane/Ethyl aceate (1:4, v/v) as elute to afford **4** (0.48 g, 80%) as near colorless oil. ^{1}H-NMR ($CDCl_3$, 300 MHz) δ: 4.14 (q, *J* = 7.2 Hz, 2H), 4.07 (s, 2H), 3.70-3.55 (m, 22H), 3.31 (t, *J* = 5.0 Hz, 2H), 1.20 (t, *J* = 7.1 Hz, 3H), 1.20 (t, *J* = 7.1 Hz, 3 H) ppm.

Synthesis of 14-azido-3, 6, 9-hexaaoxatetradecan-1-oic acid (5): The azide compound **4** (0.48 g, 1.22 mmol) was dissolved in 5 mL of methanol. 4.5 mL of 1N NaOH was added to the solution at 0 °C and the mixture was stirred for 21 h at room temperature. Then reaction solution was concentrated under reduced pressure to obtain a residue. 1N HCl was added to the residue until pH 2, and then was extracted with chloroform (3 x 20 mL). The organic phase was washed once by a saturated saline solution, and dried with an anhydrous Na_2SO_4. The organic phase was concentrated under reduced pressure to obtain a colorless liquid serving as compound **5** (0.40 g, 90%). ^{1}H-NMR ($CDCl_3$, 300 MHz) δ: 4.16 (s, 2H), 3.68 (m, 22H), 3.41 (t, *J* = 6.1 Hz, 2H) ppm.

Synthesis of Azido-PEG$_6$-COO-NHS ester (6): 400 mg (1.0 mmol) of azide-PEG6-COOH (5) and 271 mg (1.30 mmol) of DCC were dissolved in 10 mL $CHCl_3$ and then stir at 0 °C for 30 min. After adding 152 mg (1.30 mmol) of *N*-hydroxysuccinimide, the mixture was stirred at room temperature over night. The chloroform was evaporated to provide the yellow crystalline product, which was purified by a silica gel column ($CHCl_3$ → EtOAc) to afford pure product **6** (620 mg, 89%). ^{1}H-NMR ($CDCl_3$, 300 MHz) δ 3.71-3.52 (m, 22H), 3.37 (m, 4H), 3.28 (m, 2H), 2.81 (s, 2H) ppm.

4. Preparation of Azide-PEG$_6$-Glass slide



Scheme 3. Preparation of Azide-PEG$_6$-Glass slide

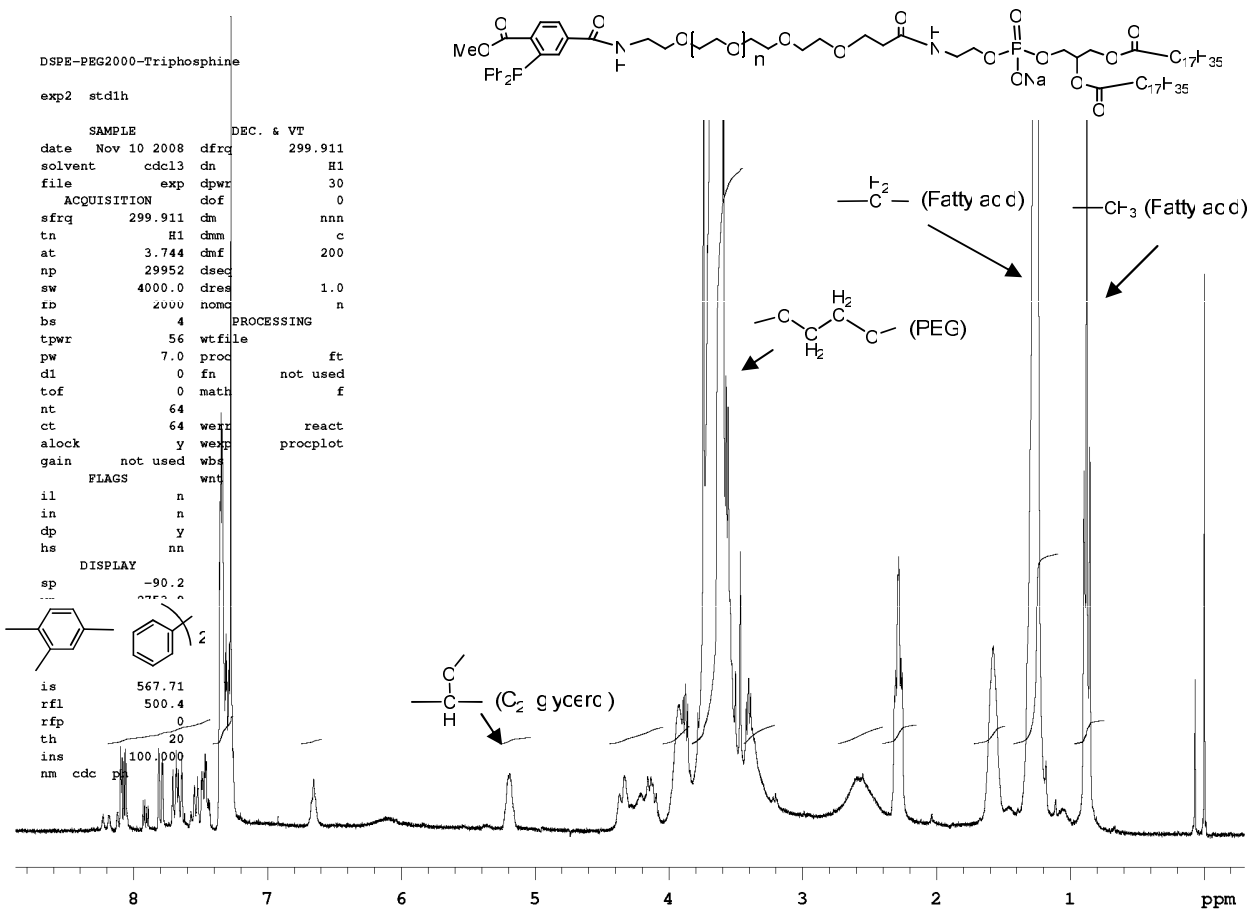
N_3-PEG$_6$-NHS (10 mg) was dissolved in 4.0 mL of THF, 0.5 mL of *N*,*N*-disopropylethyl-amine (DIEA) was added and then diluted to 8.0 mL by H_2O, followed by incubation of amine functionalized glass slide for 8 h at room temperature. The glass slide was rinsed with THF (3 times, 5 min each), water (3 times, 5 min each), then dried under N_2 atmosphere.

5. 2-azidoethyl-lactoside was synthesized as literature method.[2]

Reference:

1. C. C.-Y. Wang, T. S. Seo, Z. Li, H. Ruparel, J. Ju, *Bioconjugate Chem*. **2003**, *14*, 697.
2. X.-L. Sun, D. Grande, S. Baskaran, and E. L. Chaikof, *Biomacromolecules*, **2002**, *3*, 1065.

^{1}H NMR spectrum of DSPE-PEG$_{2000}$-triphenylphosphine in CDCl$_3$

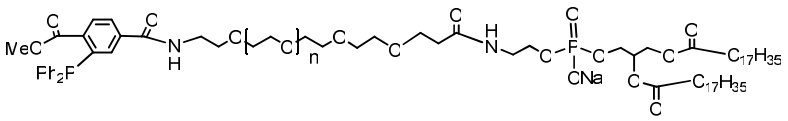


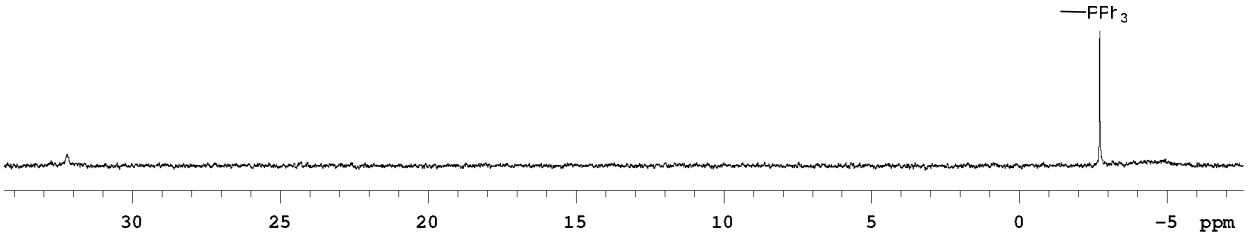
^{31}P NMR spectrum of DSPE-PEG$_{2000}$-triphenyl phosphine in $CDCl_3$

DSPE-PEG2000-Triphosphine

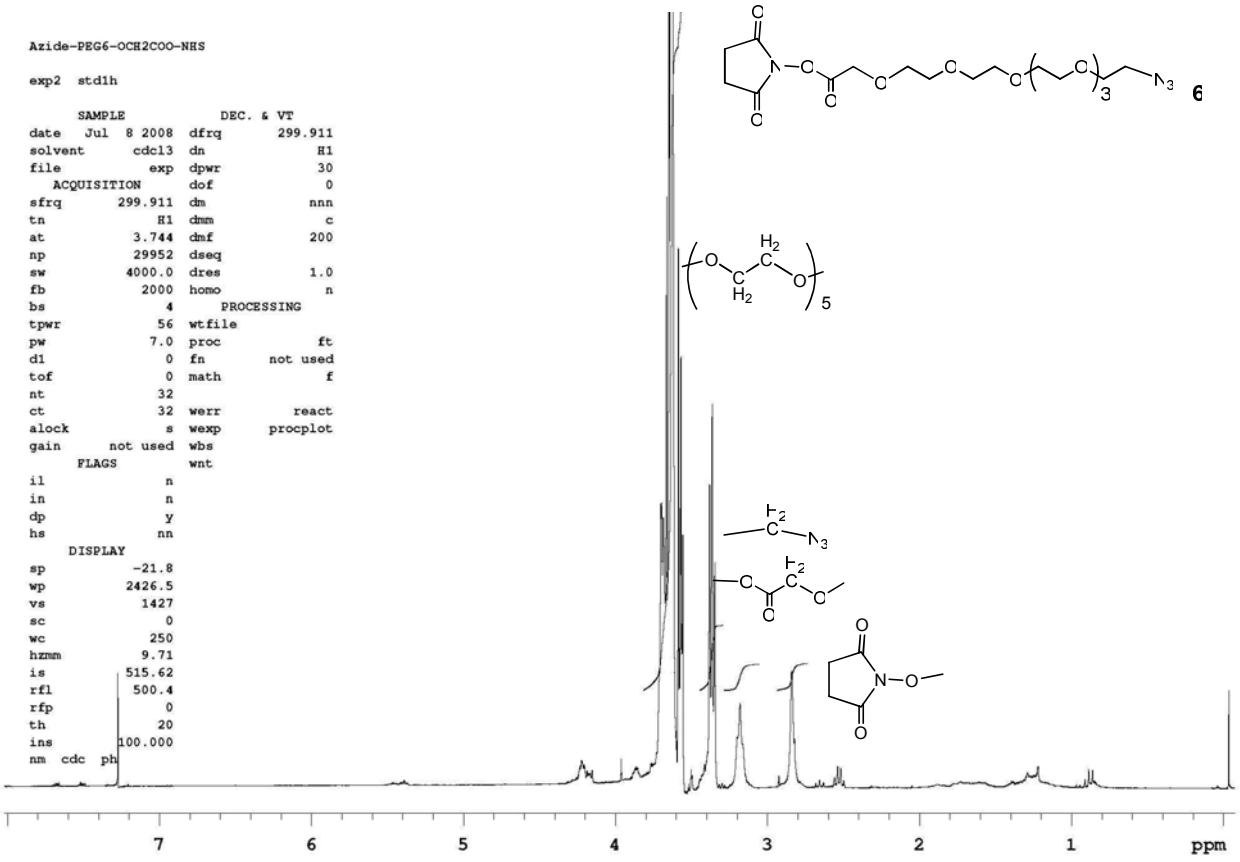
exp2 s2pul

SAMPLE		SPECIAL	
date	Nov 10 2008	temp	not used
solvent	CDCl3	gain	not used
file	exp	spin	not used
ACQUISITION		hst	0.008
sw	26711.2	pw90	10.500
at	1.600	alfa	20.000
np	85476	FLAGS	
fb	15000	il	n
bs	64	in	n
d1	1.000	dp	y
nt	128	hs	nn
ct	128	PROCESSING	
TRANSMITTER		lb	2.00
tn	P31	fn	not used
sfrq	121.416	DISPLAY	
tof	10602.7	sp	-919.4
tpwr	52	wp	5089.0
pw	4.083	rfl	2429.1
DECOUPLER		rfp	0
dn	H1	rp	77.5
dof	0	lp	-205.4
dm	yyy	PLOT	
dmm	w	wc	250
dpwr	40	sc	0
dmf	10000	vs	382
		th	12
		ai no ph	



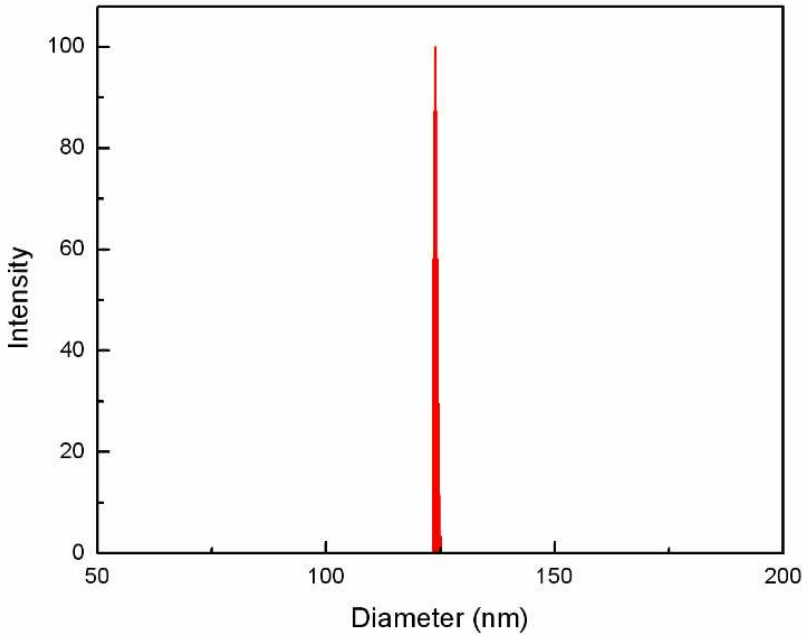


^{1}H NMR spectrum of Azido-PEG$_6$-COO-NHS:



4. Dynamic Light Scattering (DLS) experiment to determine liposome size

20 μL of extruded liposome sample was diluted to 2 mL with PBS (pH 7.4) buffer and then measured with 90plus particle size analyzer (Brookhaven Co., USA).



Influence of the Backbone Structure on the Release of Bioactive Volatiles from Maleic Acid-Based Polymer Conjugates

Damien L. Berthier,* Nicolas Paret, Alain Trachsel, and Andreas Herrmann*

Firmenich SA, Division Recherche et Développement, B.P. 239, CH-1211 Genève 8, Switzerland. Received May 7, 2010; Revised Manuscript Received September 22, 2010

Poly(maleic acid monoester)-based β-mercapto ketones were synthesized and investigated as potential delivery systems for the controlled release of bioactive, volatile, α,β-unsaturated enones (such as damascones and damascenones) by retro 1,4-addition. The bioconjugates were prepared in a one-pot synthesis using 2-mercaptoethanol as a linker. The thiol group of 2-mercaptoethanol adds to the double bond of the enone to form a β-mercapto ketone, which was then grafted via nucleophilic ring-opening of the remaining alcohol function onto a series of alternating copolymers of maleic anhydride and 1-octadecene, ethylene, isobutylene, and methyl vinyl ether. The influence of copolymer backbones on the release of δ-damascone was investigated in buffered aqueous solution as a function of pH and time. In the presence of a cationic surfactant, the polymer conjugates were transferred from an aqueous medium to a cotton surface. The deposition and the release of δ-damascone from the cotton surface as a function of the polymer backbone structure were measured by fluorescence spectroscopy and dynamic headspace analysis, respectively. All polymer conjugates were found to deliver higher amounts of the volatile into the headspace than the reference consisting of unmodified δ-damascone. Polymers with a hydrophobic backbone were generally efficiently deposited on the cotton surface, but released δ-damascone only moderately in solution. Conjugates with a more hydrophilic backbone release the active compound more efficiently in water, but are deposited to a lower extent onto the target surface. A good balance of the hydrophobicity and hydrophilicity of the polymer backbone is the key factor to maximize the deposition of the conjugates on the target surface and to optimize the release of the bioactive volatiles.

INTRODUCTION

Semiochemicals are highly volatile, biologically active organic compounds that serve for interspecies communication via evaporation and transportation through the air by diffusion (*1–3*). Many of these compounds have been used as fragrances since antiquity (*4, 5*), and advances in organic synthesis have resulted in the introduction of new volatile compounds to the palette of the modern perfumer (*6–9*). As a consequence of their high volatilities (vapor pressures) (*10, 11*), the perception of these compounds is usually transient. Bearing in mind that the longevity of fragrance perception is an important factor in the appreciation of perfumed consumer articles (*12*), and that perfumes are generally complex mixtures of fragrance ingredients having different volatilities, water solubilities, and chemical functions (*4, 6–9*), the stability of these ingredients during storage, their efficient delivery, and their resilience in application are very important.

Physical (encapsulation-based) (*13, 14*) or chemical (precursors) (*15*) delivery systems have been developed to improve substantivity, which is defined as the ability to be deposited on different substrates and the retention of volatile perfumery ingredients. Because of their particular physicochemical properties, a broad variety of polymers (*12, 16–20*) and polymer conjugates (*15, 21–30*) have been described as suitable carrier materials to control the release of fragrances. These materials can disperse hydrophobic volatile molecules in aqueous media and enhance their deposition on various substrates.

Physical delivery systems are based on the preparation of polymer matrices (*12, 16–19*) or core−shell structures (*20*), which stabilize sensitive compounds whose slow diffusion out of the encapsulating matrix or capsule improves the duration of fragrance perception.

In contrast, chemical delivery systems, so-called profragrances, use mild ambient conditions to cleave the covalent bond of the volatile conjugated to a precursor substrate (*15*). Reaction conditions allowing the cleavage of a chemical bond between a substrate and a targeted molecule comprise changes in temperature, hydrolysis or change of pH, oxidation, and exposure to daylight or enzymes. Because of their macromolecular structure, polymer conjugates were generally found to slow down the release of volatiles compared with the corresponding monomeric, low-molecular-weight analogues (*22–29*). Changes in the polymer structure with respect to the hydrophilicity or hydrophobicity of the polymer backbone (*28–30*), as well as the presence of specific chemical functionalities in close proximity to the release unit (*29*), were found to strongly influence the release rates of the volatiles from their precursors.

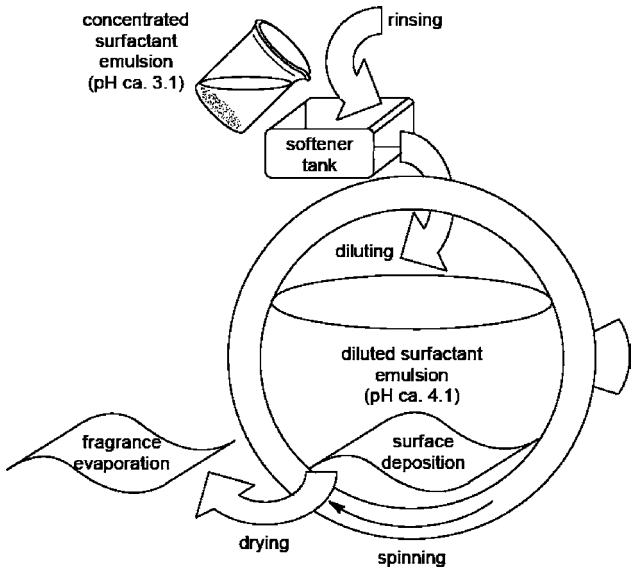
Endo and co-workers prepared a series of amphiphilic poly(methacrylate) copolymers with different ratios of hydrophobic fragrance-releasing acetal side chains and hydrophilic poly(ethylene glycol) (PEG) side chains (*30*). They found that the polymers aggregate to micelles, which strongly influenced the cleavage of the acid-labile acetal side chain and thus the release of the fragrance. With the polymer aggregation being temperature dependent, application of heating and cooling cycles allowed control of the rate of fragrance release from the polymeric profragrances.

Recently, Fehr and Galindo (*31*) reported the Michael-type 1,4-addition of carboxylic acids or thiols to enones, such as damascones or damascenones, the so-called rose ketones (*32, 33*). The β-mercapto ketone obtained by condensation of 1-dodecanethiol and δ-damascone was especially found to be very

* To whom correspondence should be addressed. E-mail: damien.berthier@firmenich.com, andreas.herrmann@firmenich.com. Fax: +41 22 780 33 34.

10.1021/bc100223s © 2010 American Chemical Society
Published on Web 10/11/2010

Scheme 1. Fabric Softening Process in a Washing Machine



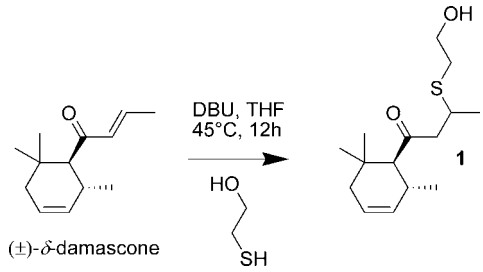
efficient as a fragrance precursor and has now been commercialized (*31*). From these results, we became interested in preparing polymeric fragrance delivery systems that released rose ketones by retro 1,4-addition and in investigating the influence of structural modifications on the surface deposition of the polymers from an aqueous environment and the release efficiency of the bioactive volatile.

A recent study reported the pH-dependent release of δ-damascone from amphiphilic random copolymers of a β-acyloxy ketone derivative of δ-damascone and methacrylic acid (*28*). Poly(methacrylate)-based profragrances were synthesized via an aldol condensation of the corresponding methyl ketone with acetaldehyde, followed by esterification of the resultant β-hydroxy ketones with methacrylic acid (*28, 31*). Subsequent copolymerization with methacrylic acid, at different molar ratios to adjust the polarity of the polymer backbone, controlled the surface adsorption/deposition of the polymer on various substrates and its dispersion in aqueous media. Although this procedure provided access to a very efficient pH-dependent delivery system for δ-damascone by retro 1,4-addition, the preparation of the intermediate 3-hydroxy ketone of δ-damascone is costly and difficult to scale up.

Because alternating copolymers of maleic anhydride can be easily modified by ring-opening of the reactive anhydride unit with alcohols or amines (*34, 35*), these are suitable substrates for the grafting of bioactive compounds and, at the same time, for fine-tuning the physicochemical properties of the resulting conjugate. Accordingly, various maleic acid monoesters were prepared by reaction with monomeric or polymeric alcohols (*36–41*) to afford a series of versatile, biocompatible delivery systems (*42, 43*).

To be perceived, fragrance molecules have to be evaporated from a surface. In fine perfumery, surface deposition is easily achieved by spraying the volatiles together with a solvent onto the target surface (e.g., skin, fabric). However, in other types of application, surface deposition is less evident and becomes an important issue to control the release of volatiles. Scheme 1 shows a typical fabric softening process in a washing machine. A concentrated surfactant emulsion, serving as the softening agent, is rinsed into a larger volume of water corresponding to a dilution by a factor of ca. 300. The active agent is then deposited from this diluted surfactant emulsion onto the fabric (cotton) surface. After stirring for a short time, the emulsion is withdrawn and the fabric dried. To achieve a controlled release effect, it is important to understand and control the release

Scheme 2. Preparation of β-Mercapto Ketone 1 by 1,4-Addition of 2-Mercaptoethanol to δ-Damascone



properties of the delivery system in aqueous solution (during the washing cycle), the amount of its deposition onto the fabric, as well as the evaporation kinetics on dry fabric (after the washing cycle).

In this study, we thus prepared a series of maleic anhydride-based δ-damascone conjugates in an easy one-pot, two-step process using 2-mercaptoethanol as a linker. 1,4-Addition of the thiol group to the enone double bond of δ-damascone gave β-mercapto ketone **1** (Scheme 2), which then reacted by nucleophilic ring-opening with poly(maleic anhydride) copolymers.

The release of the fragrances by retro 1,4-addition was investigated in solution as a function of pH by solvent extraction. The copolymer conjugates were labeled with pyren-1-ylmethanol (*44*) to quantify their deposition from an aqueous dispersion onto a cotton surface in the presence of a cationic surfactant. Finally, the influence of the polymer backbone structure on the amount of polymer deposition and release of δ-damascone was investigated by dynamic headspace analysis (*45–47*) on dry cotton.

EXPERIMENTAL PROCEDURES

General. Commercially available reagents and solvents were used without further purification if not stated otherwise. Reactions were carried out in standard glassware under N_2 or Ar, and yields were not optimized. Demineralized H_2O: Millipore-Synergy-185 water purifier. IR Spectra: Perkin-Elmer-1600-FTIR spectrometer; $\tilde{\nu}$ of weak (w), medium (m), or strong (s) bands in cm^{-1}. ^1H and ^{13}C NMR spectra: Bruker-DPX-400 spectrometer; δ in ppm downfield from Me_4Si as internal standard, J in Hz. High-resolution mass spectra (HRMS) were recorded in the multimode (MM) on an Agilent 1200 RR high-performance liquid chromatograph, equipped with an Agilent Eclipse Plus C18 column (2.1 × 100 mm inner diameter (i.d.)), eluted at 0.5 mL min^{-1} with a gradient of water (containing 0.1% of formic acid)/acetonitrile at 50 °C and coupled to a MSD TOF HR G3250A mass spectrometer (MM source, dual mode positive) at 250 °C, with the N_2 flow at 5 mL min^{-1}, the nebulizer pressure at 40 psi, the capillary voltage at 3000 V, and the fragmentor voltage at 140 V.

Analytical Size-Exclusion Chromatography (SEC). SEC analyses were carried out at room temperature (ca. 22 °C) with a system composed of a Thermo Finnigan Surveyor vacuum online degasser, quaternary LC pump, autosampler, and UV/vis detector, combined with a Thermo Separation Products (tsp) Spectra System IR 150 refractometer and a Viscotek 270 Dual Detector viscometer. Samples were eluted from a Macherey Nagel Nucleogel GPC 104-5 column (300 × 7.7 mm i.d., particle size 5 μm) at a flow rate of 1.0 mL min^{-1} by using HPLC-grade tetrahydrofuran (THF) from SDS. Universal calibrations were performed with the viscometer and the RI detector using commercial poly(styrene) standards from Fluka. Ca. 40 mg of the polymer standard was accurately weighed and dissolved in 10 mL of THF; then 50 μL aliquots of those solutions were injected for the calibration. Molecular weights of poly(maleic anhydrides) were given by the manufacturer to

be M_n = 30 000−50 000 g mol^{-1} (**2**), M_w = 60 000 g mol^{-1} (**3**), M_w = 100 000−500 000 g mol^{-1} (**4**), and M_w = 200 000 g mol^{-1} (**5**).

3-(2-Hydroxy-ethylsulfanyl)-1-(2,6,6-trimethyl-cyclohex-3-enyl)-butan-1-one (1). (*E*)-1-(2,6,6-Trimethylcyclohex-3-enyl)-but-2-en-1-one (δ-damascone, 10.0 g, 52.1 mmol) and 1,8-diazabicyclo[5.4.0]undec-7-ene (DBU, 0.78 mL, 5.21 mmol) were dissolved in THF (50 mL) prior to the dropwise addition of a solution of 2-mercaptoethanol (3.5 mL, 50 mmol) in THF (20 mL) at 45 °C; the mixture was then stirred for 12 h. Treatment with 5% aqueous HCl, extraction with Et_2O, and consecutive washing of the organic phase with a saturated aqueous solution of $NaHCO_3$ and a saturated solution of NaCl afforded an organic phase which was dried (Na_2SO_4), filtered, and concentrated to give a colorless oil (13.8 g, 99%). ^{1}H NMR (400 MHz, $CDCl_3$): δ 5.53 (m, 1H), 5.45 (m, 1H), 3.77 (m, 2H), 3.35 (sext., 6.9 Hz, 1H), 2.96 (m, 1H), 2.88 (m, 1H), 2.86−2.63 (m, 3H), 2.60−2.45 (m, 2H), 2.23 (m, 1H), 1.97 (m, 1H), 1.70 (m, 1H), 1.31 (m, 3H), 1.02 (m, 1H), 0.96 (m, 5H), 0.92 (d, 6.9 Hz, 2H), 0.88 (d, 6.9 Hz, 1H) ppm. ^{13}C NMR (100.6 MHz, $CDCl_3$): δ 212.76 (s), 212.61 (s), 131.81 (d), 131.68 (d), 124.23 (d), 124.13 (d), 67.96 (t), 62.89 (d), 61.15 (t), 61.13 (t), 55.13 (t), 41.75 (t), 41.70 (t), 36.48 (q), 34.38 (t), 34.27 (t), 34.05 (d), 33.98 (d), 33.20 (q), 33.13 (q), 31.75 (d), 31.69 (d), 31.44 (d), 31.38 (d), 29.85 (q), 29.75 (q), 25.60 (t), 22.32 (q), 22.14 (q), 20.75 (q), 20.73 (q), 19.92 (q), 19.88 (q) ppm. IR (neat): 3415w, 3018w, 2956m, 2928m, 2871m, 2830w, 1703s, 1667m, 1625w, 1457m, 1430w, 1386m, 1366s, 1286w, 1250w, 1212w, 1153m, 1115m, 1044s, 999s, 953w, 932w, 895w, 843w, 690s cm^{-1}. HRMS: *m*/*z* calcd. for $C_{15}H_{27}O_2S$, $[M + H]^+$ 271.17263, found 271.17080.

General Procedure to Prepare Alternating Copolymers of Maleic Acid-Based Profragrances. δ-Damascone (2.68 g, 13.94 mmol), 2-mercaptoethanol (1.08 g, 13.80 mmol), and 2,3,4,6,7,8,9,10-octahydropyrimido[1,2-*a*]azepine (0.21 mL, 1.39 mmol) were dissolved in acetone (50 mL) to give a colorless solution. The solution was stirred at 45 °C for 2 h. Thin layer chromatography (TLC) in ethyl acetate showed a complete conversion; no more 2-mercaptoethanol was detected (rf = 0.15). Pyren-1-ylmethanol (31.70 mg, 0.14 mmol) was added to the solution before one of the copolymers **2**−**5** (13.94 mmol of maleic anhydride unit) in acetone (30 mL) was added dropwise. The reaction mixture was stirred at 45 °C for 48 h. Copolymers **6**−**9** were obtained by precipitation from pentane or diethyl ether, filtered, and dried under vacuum at 50 °C for 24 h.

Alternating Copolymer of 1-Octadecene and Maleic Acid Mono-{2-[1-methyl-3-oxo-3-(2,6,6-trimethyl-cyclohex-3-enyl)-propylsulfanyl]ethyl} Ester Labeled with Pyren-1-ylmethanol (6). Precipitation afforded a white solid (4.82 g, 70%, conversion (of **1**) 51%). ^{1}H NMR (DMSO-d_6, 400 MHz): δ 8.46−8.22 (br. m, 0.08H), 7.02 (br. m, 0.01H), 5.52 (m, 1H), 5.46 (m, 1H), 4.09 (m, 1.5H), 3.51 (m, 1H), 3.28 (m, 6H), 2.96 (s, 6H), 2.74 (m, 4H), 2.59 (m, 1.5H), 2.43−2.15 (br. m, 4H), 1.93 (m, 3H), 1.63 (m, 5H), 1.18 (m, 60H), 0.96 (m, 4H), 0.82 (m, 13H) ppm. ^{13}C NMR (DMSO-d_6, 100.6 MHz): δ 162.64 (s), 131.54 (d), 124.13 (d), 62.97 (d), 61.37 (t), 54.45 (t), 45.33 (t), 40.97 (t), 36.42 (q), 33.88 (t), 32.52 (t), 31.41 (t), 31.34 (d), 31.02 (q), 29.24 (t), 22.09 (t), 21.40 (q), 20.52 (q), 20.36 (q), 19.34 (q) ppm. IR (neat): 3634 to 2324m, 3018w, 2922s, 2852s, 2605w, 2498w, 1778w, 1726m, 1710m, 1649m, 1625w, 1567m, 1464m, 1397w, 1386m, 1366m, 1323w, 1167s cm^{-1}. M_w = 68 600 g mol^{-1}. M_n = 28 000 g mol^{-1}.

Alternating Copolymer of Isobutylene and Maleic Acid Mono-{2-[1-methyl-3-oxo-3-(2,6,6-trimethyl-cyclohex-3-enyl)-propylsulfanyl]ethyl} Ester Labeled with Pyren-1-ylmethanol (7). Precipitation afforded a white solid (1.91 g, 65%, conversion (of **1**) 20%). ^{1}H NMR (DMSO-d_6, 400 MHz): δ 8.63−8.19 (br. m, 0.05H), 7.71 (m, 0.01H), 7.04 (m, 0.03H), 5.54 (m, 1H), 5.46 (m, 1H), 4.95 (m, 3H), 4.08 (m, 2H), 3.61 (m, 2H), 3.54 (m, 6H), 3.48 (m, 6H), 3.30 (m, 3H), 2.68 (m, 9H), 2.31 (m, 9H), 1.97 (m, 18H), 1.06 (br. m, 24H) ppm. ^{13}C NMR (DMSO-d_6, 100.6 MHz): δ 165.31 (s), 162.25 (s), 131.56 (d), 124.13 (d), 61.45 (d), 41.77 (d), 23.40 (br. d) ppm. IR (neat): 3768 to 2495w, 2959m, 2937w, 2879m, 1786s, 1731s, 1646s, 1585w, 1469m, 1394m, 1371m, 1321m, 1175s cm^{-1}.

Alternating Copolymer of Ethylene and Maleic Acid Mono-{2-[1-methyl-3-oxo-3-(2,6,6-trimethyl-cyclohex-3-enyl)propylsulfanyl]ethyl} Ester Labeled with Pyren-1-ylmethanol (8). Precipitation afforded a white solid (3.27 g, 89%, conversion (of **1**) 50%). ^{1}H NMR (DMSO-d_6, 400 MHz): δ 8.52−8.16 (br. m, 0.17H), 5.54 (m, 1H), 5.47 (m, 1H), 4.09 (m, 2H), 3.52 (m, 4H), 3.25 (m, 3H), 3.01 (m, 2H), 2.87 (m, 10H), 2.71 (m, 4H), 2.32 (m, 3H), 2.12 (m, 3H), 1.93 (m, 3H), 1.63 (m, 5H), 1.43 (m, 5H), 1.24 (m, 4H), 0.95 (m, 3H), 0.84 (m, 6H) ppm. ^{13}C NMR (DMSO-d_6, 100.6 MHz): δ 211.93 (s), 176.46 (s), 131.53 (d), 124.15 (d), 63.02 (t), 61.31 (t), 60.96 (d), 54.36 (t), 54.19 (t), 53.25 (d), 49.64 (t), 42.72 (d), 37.53 (d), 34.00 (s), 32.52 (d), 31.57 (d), 31.13 (d), 31.03 (t), 28.16 (t), 25.82 (t), 23.27 (q), 21.49 (q), 21.30 (q), 20.31 (q), 19.38 (q), 18.82 (q), 9.36 (q) ppm. IR (neat): 3750 to 2162m, 2952m, 2933m, 2871m, 1786w, 1722s, 1705s, 1649m, 1562w, 1455m, 1387m, 1361m, 1156s cm^{-1}.

Alternating Copolymer of Methoxyethylene and Maleic Acid Mono-{2-[1-methyl-3-oxo-3-(2,6,6-trimethyl-cyclohex-3-enyl)propylsulfanyl]ethyl} Ester Labeled with Pyren-1-ylmethanol (9). Precipitation afforded a white solid (4.89 g, 95%, conversion (of **1**) 30%). ^{1}H NMR (DMSO-d_6, 400 MHz): δ 8.46−8.02 (br. m, 0.11H), 7.22 (m, 0.01H), 5.54 (m, 1H), 5.47 (m, 1H), 4.11 (m, 2H), 3.52 (m, 4H), 3.26 (m, 12H), 2.88 (m, 2H), 2.74 (m, 4H), 2.63 (m, 2H), 2.31 (m, 2H), 1.95 (m, 2H), 1.64 (m, 3H), 1.23 (m, 3H), 0.95 (m, 3H), 0.84 (m, 6H) ppm. ^{13}C NMR (DMSO-d_6, 100.6 MHz): δ 211.70 (s), 172.67 (s), 165.30 (s), 131.46 (d), 124.67 (d), 64.80 (d), 63.23 (d), 61.30 (s), 54.16 (t), 53.32 (t), 47.78 (t), 40.91 (t), 37.49 (d), 33.99 (d), 32.54 (d), 31.65 (q), 23.20 (t), 21.47 (q), 20.47 (q), 19.36 (q) ppm. IR (neat): 3750 to 2323m, 3016w, 2956m, 2932m, 2884w, 2831w, 1855w, 1778m, 1728s, 1704s, 1648m, 1587w 1454m, 1441m, 1386m, 1366m, 1165s cm^{-1}. M_w = 315 000 g mol^{-1}. M_n = 53 000 g mol^{-1}.

Alternating Copolymer of Methoxyethylene and Maleic Acid Mono-(α-methoxy-poly(ethylene oxide)) And Mono-{2-[1-methyl-3-oxo-3-(2,6,6-trimethyl-cyclohex-3-enyl)propylsulfanyl]ethyl} Esters Labeled with Pyren-1-ylmethanol (10). Copolymer **5** (10 mmol) was dissolved in acetone (40 mL) prior to the dropwise addition of a solution of **1** (8 mmol), pyren-1-ylmethanol (0.01 mmol), and α-methoxy-poly(ethylene glycol) (2 mmol, M_n = 550 g mol^{-1}) in acetone (30 mL) and a solution of triethylamine (10 mmol) and 4-dimethylaminopyridine (DMAP, 61 mg, 0.5 mmol) in acetone (30 mL) at 0 °C. The mixture was heated at 40 °C for 24 h. The cooled mixture was then diluted with dichloromethane and extracted with aqueous HCl (5%), dried (Na_2SO_4), filtered, concentrated, and precipitated from pentane to afford a red solid (4.69 g, 88%, conversion (of **1**) 75%). ^{1}H NMR (DMSO-d_6, 400 MHz): δ 8.46−8.02 (br. m, 0.09H), 7.22 (m, 0.02H), 5.54 (m, 1H), 5.45 (m, 1H), 4.78 (m, 0.3H), 4.57 (m, 0.3H), 4.09 (m, 1.8H), 3.51 (m, 15H), 3.33 (m, 28H), 2.88 (m, 1.3H), 2.74 (m, 3H), 2.61 (m, 2H), 2.32 (m, 2H), 1.94 (m, 2H), 1.65 (m, 3H), 1.24 (m, 3H), 0.94 (m, 3H), 0.83 (m, 6H) ppm. ^{13}C NMR (DMSO-d_6, 100.6 MHz): δ 211.71 (s), 165.31 (s), 131.51 (d), 124.10 (d), 71.16 (t), 69.66 (t), 63.18 (d), 61.30 (s), 60.99 (t), 40.99 (q), 37.54 (d), 34.02 (d), 33.85 (s), 32.57 (t), 32.51 (t), 31.64 (t), 31.14 (t), 31.02 (t), 29.04 (s), 27.81 (t), 21.45 (br. q), 20.45 (q), 19.33 (q) ppm. IR

(neat): 3675 to 2323m, 2953m, 2930m, 2884m, 2831w, 1727s, 1705s, 1648m, 1587w, 1453m, 1386w, 1365m, 1323w, 1172s cm^{-1}.

Controlled Release of δ-Damascone From Copolymers 6−10 in Buffered Solutions. According to the molecular mass of their repeat unit, copolymers **6**−**10** were dispersed in a buffered aqueous solution (CertiPUR from Merck, 5 mL) at pHs 4, 7, and 10, respectively. The solutions thus contained equimolar concentrations of δ-damascone (0.045 mmol mL^{-1} or 8.7 mg mL^{-1}). Samples were stirred for 1 h to obtain a solution or a homogeneous dispersion. Each solution or dispersion was divided into four samples of 1 mL and mixed with 1 mL of a solution of 1,4-dibromobenzene at 150 mg L^{-1} (internal standard) in a mixture of isooctane/diethyl ether (9:1). The samples were stirred at 25 °C in a water bath for 1, 3, and 6 days. The δ-damascone content in the organic phase was analyzed by gas chromatography (GC) using a GC 7890A system equipped with an auto sampler 7683 series from Agilent Technologies (1 μL injected) and a HP-5 column (30 m, i.d. 0.32 mm, film thickness 0.25 μm). The volatiles were analyzed by GC at 100 °C for 1 min and then heated to 170 at 10 °C min^{-1}, for a total run time of 8 min. Helium was the mobile gas phase; the split ratio was 50:1. A calibration curve was measured and used to quantify δ-damascone. All samples were analyzed in triplicate.

Thermogravimetric Analysis (TGA). Solid contents were measured by thermogravimetry using an organic phase solution (20 μL) and placed with a precision syringe (Hamilton - Bonaduz, Switzerland, 25 μL) inside an aluminum pan (Mettler-Toledo ME-26763 40 μL) that had been previously weighed on a precision balance (Mettler-Toledo XP204S). Measurements were carried out under a constant nitrogen flow (20 mL min^{-1}) with a thermogravimetric analyzer (Mettler-Toledo TGA/SDTA851ᵉ) equipped with a microbalance (accuracy: 1 μg) and an accurate oven having an internal volume of 35 mL. Temperatures were increased from 25 to 80 °C at 10 °C min^{-1} and kept at 80 °C for 25 min and 30 s. All measurements were performed in triplicate.

The stability of copolymers **6** and **9** (data not shown) was measured by thermogravimetry. Solids were placed inside an aluminum pan that had been previously weighed on a precision balance. Temperatures were increased from 20 to 270 at 10 °C min^{-1} under a constant nitrogen flow (20 mL min^{-1}).

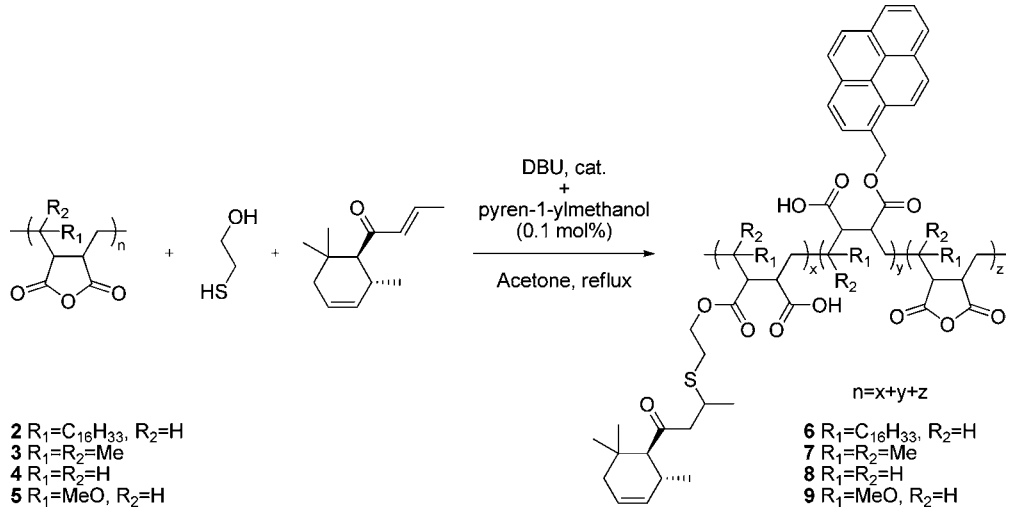
Preparation of Aqueous Surfactant Emulsions. A cationic surfactant containing emulsion with the following composition was prepared: Stepantex VK90 (Stepan) 16.5%, calcium chloride 0.2%, water 83.3%. A total of 1.0% to 5.5%, depending on the δ-damascone content of the polymers, of poly(maleic acid)-based copolymers was added to the softener formulation. All values are given in % by weight.

Procedure for Polymer Deposition on Cotton. The fabric softening process in a washing machine as illustrated in Scheme 1 was transferred to a laboratory scale. In a beaker (1 L), poly(maleic acid)-based copolymers **6**−**10** (**6**, 43.6 mg (2.4%) in THF (3 mL); **7**, 48.3 mg (2.7%) in methanol (5 mL); **8**, 23.5 mg (1.3%) in methanol (5 mL); **9**, 348.7 mg (10% in dipropylene glycol (DIPG), 1.9%); **10**, 312.5 mg (10% in DIPG, 1.7%), all of which can release a total amount of 8.7 mg of δ-damascone) were added to the aqueous concentrated surfactant emulsion (1.80 g, pH ca. 3.1), respectively, and the resulting mixtures stirred for 18 h. The emulsions were then placed in a beaker (1 L) and diluted with demineralized cold tap water (600 g). One cotton sheet (Eidgenössische Materialprüfanstalt (EMPA, Switzerland), cotton test cloth Nr. 221, cut to ca. 12 × 12 cm^2 sheets (average mass ca. 3.5 g) and prewashed with an unperfumed detergent powder (perfumery application laboratories)) was added in a beaker to the diluted surfactant emulsion (pH ca. 4.1) and manually stirred for 3 min, left standing for 2 min, and then wrung out by hand and weighed (average mass ca. 7 g) to estimate the quantity of residual water and to ensure that each cotton sheet was loaded with the same amount of diluted surfactant emulsion. As a reference sample, a solution (1 mL) containing an equimolar amount of unmodified δ-damascone (87.2 mg in 10 mL of acetone) was added to another 1.80 g of the original fabric softener formulation, which was treated as described above. All cotton sheets were line dried for 3 days.

Procedure for Fluorescence Measurements. Poly(maleic acid)-based copolymers **6**−**10** were added to the aqueous surfactant emulsion and diluted with demineralized cold tap water as described above. Several aliquots of the emulsions were pipetted off (1.0, 0.5, and 0.1 mL) and adjusted to 1.0 mL with the diluted aqueous surfactant emulsion. For the verification of the linearity of the fluorescence intensity with respect to the copolymer concentration, additional points using 0.75 and 0.25 mL of the emulsion were recorded. All samples were then further diluted with demineralized water by a factor of 100 and analyzed by fluorescence spectroscopy. Measurements were carried out on a Jobin Yvon Fluorolog-3 spectrometer equipped with DataMax software. The average spectra of three scans were recorded between 370 and 400 nm, with an excitation wavelength of 334 nm, increment 0.5 nm, integration time 0.5 s, slit excitation 1.5 nm, and slit emission 1.5 nm. Data were analyzed at 378, 384, 389, and 398 nm. The fluorescence intensity measured for the 1.00 mL aliquot served as the reference corresponding to 0% of deposition and the other aliquots as external standard calibration of the corresponding polymer. Then, one cotton sheet (see above) was added to each beaker containing the diluted emulsions with the copolymer, and manually stirred for 3 min, left standing for 2 min, and then wrung out by hand, and line-dried for 3 days (see above). The remaining emulsion (1.00 mL) was diluted by a factor of 100 and analyzed by fluorescence spectroscopy as described above to determine the amount of remaining nondeposited copolymer. The missing amount with respect to the first fluorescence measurement was assumed as being deposited on the fabric surface. All measurements were carried out in duplicate.

Procedure for Dynamic Headspace Sampling. One of the dry cotton sheets was put into a headspace sampling cell (internal volume ca. 160 mL), thermostatted at 25 °C, and exposed to a constant airflow (200 mL min^{-1}), respectively (*48*). The air was filtered through active charcoal and aspirated through a saturated solution of NaCl, corresponding to a constant humidity of ca. 75% (*49*). For 15 min, the volatiles were adsorbed onto a waste Tenax cartridge and then for 15 min onto a clean Tenax cartridge. The sampling was repeated seven times every 60 min (45 min trapping on the waste cartridge and 15 min on a clean cartridge) (*48*); the waste cartridges were discarded. The cartridges with the volatiles were desorbed on a Perkin-Elmer TurboMatrix ATD 350 desorber coupled to a Perkin-Elmer Autosystem XL gas chromatograph equipped with a J&W Scientific DB1 capillary column (30 m, i.d. 0.25 mm, film thickness 0.25 μm) and a Perkin-Elmer Turbomass Upgrade mass spectrometer. The volatiles were analyzed by GC using a two-step temperature gradient starting from 70 to 130 °C at 3 °C min^{-1} and then heating to 260 at 25 °C min^{-1}. The injection temperature was at 240 °C and the detector temperature at 260 °C. External standard calibrations were carried out using six different concentrations of δ-damascone in acetone (varying between 1.96×10^{-6} and 9.26×10^{-4} mol L^{-1}). Each calibration solution (2 μL) was injected with a microliter syringe onto three clean Tenax cartridges, respectively. All the cartridges were desorbed immediately under the same conditions as those resulting from the headspace sampling (see above). Because

Scheme 3. Preparation of Poly(maleic acid monoester)-Based δ-Damascone Conjugates 6 ($x = 55$, $y = 0.1$, $z = 50$), 7 ($x = 65$, $y = 0.3$, $z = 260$), 8 ($x = 640$, $y = 1$, $z = 640$), and 9 ($x = 320$, $y = 1$, $z = 750$)



the quantities of released compounds were monitored at very low concentrations, the calibration curve was forced through the origin of the coordinate system. Plotting the concentrations (in ng L^{-1}) against the peak areas gave a straight line with a correlation coefficient of $r^2 > 0.9990$. All experiments were carried out in duplicate.

RESULTS AND DISCUSSION

Preparation of Poly(maleic acid)-Based Profragrances. Poly(maleic acid)-based conjugates of δ-damascone were prepared in a one-pot procedure consisting of two reaction steps. In the first step, 2-mercaptoethanol, serving as a linker (*50*), was reacted with a slight excess of δ-damascone to give 1,4-addition product **1** in very good yields (Scheme 2). This reaction step was carried out in the presence of catalytic amounts of DBU as a base (*31*). β-Mercapto ketone **1** was isolated for full characterization. ^{1}H NMR analysis showed the disappearance of the enone double bond and the appearance of two signals corresponding to the formation of the thioether (a sextuplet at 3.3−3.4 ppm for the CH group of the rose ketone moiety and a multiplet at 2.5−2.8 for the CH_2 group of the ethylene linker), whereas the signals of the other double bonds remained unchanged.

After complete reaction of the mercaptoethanol, as shown by TLC in ethyl acetate, one of the commercially available poly(maleic anhydride) copolymers **2**−**5**, respectively, was added as the second reaction step to react with the primary alcohol function of **1** upon ring-opening of the maleic anhydride function (Scheme 3).

Copolymers **2**−**5**, obtained by copolymerization of maleic anhydride with 1-octadecene, isobutylene, ethylene, or methyl vinylether, respectively, are commercially available. Alternating copolymer **5**, for example, is supplied by ISP Technologies under the trade name Gantrez and used as an ingredient in toothpaste and various pharmaceutical products (*43*).

Depending on the solubility of the copolymers, different solvents (DMF, THF, or acetone) were used for the reaction with β-mercapto ketone **1**. Four different bases, namely, pyridine, tributylamine, triisobutylamine, and triethylamine (Et_3N), with a catalytic amount of DMAP, were tested to open the maleic anhydride moiety of **2**−**5** with **1** to give polymer conjugates **6**−**10** (Scheme 3); triethylamine led to the best conversions (*36*–*41*).

In this work, the one-pot two-step preparation of copolymers **6**−**10** was carried out in acetone, which is a convenient solvent for an industrial scaleup. Intermediate **1** was synthesized in situ by adding 2-mercaptoethanol to δ-damascone in the presence of DBU as catalyst. When the conversion was completed, the acetone solutions of copolymers **2**−**5** were added to **1**. We observed that the presence of DBU as a base was sufficient to reach acceptable conversion (see Experimental Procedures).

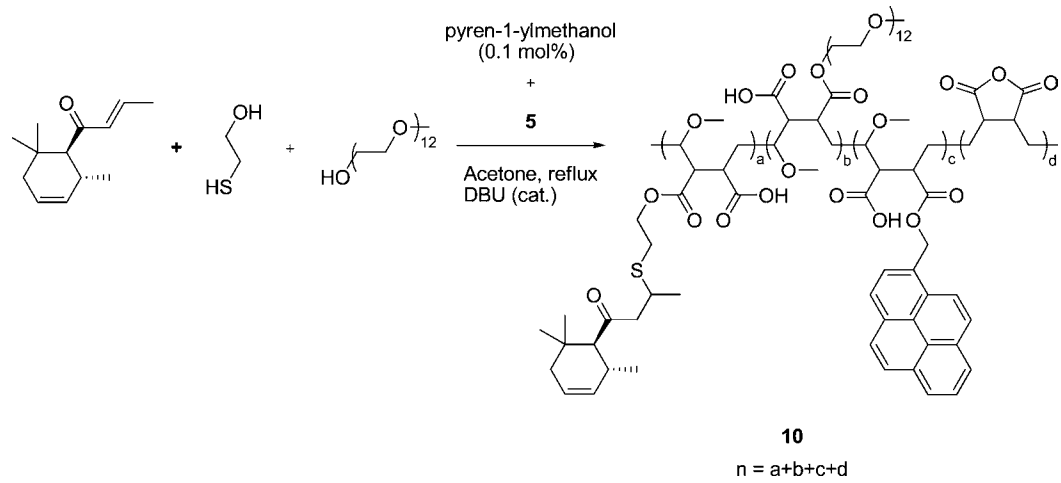
Grafting a fluorescent marker onto the polymer backbone (*44*) is convenient to measure the deposition on various surfaces. We labeled our polymer conjugates by adding pyren-1-ylmethanol to the reaction mixture (*51*). Its concentration was limited to 0.1 mol % to avoid saturation of the fluorescent signal and to keep the physical properties of copolymers **6**−**10**. Amphiphilic polymer conjugates are known to aggregate in surfactant emulsions (*52*). However, this aspect was not studied in the context of this work because it requires higher grafting of the fluorescence moiety.

The conversion of the grafting reaction was analyzed by ^{1}H NMR spectroscopy by integrating the signals of the cyclohexene double bonds (between 5.45 and 5.85 ppm) of alcohol **1** and comparing them with characteristic resonances from the different copolymers **2**−**5**, such as the signal of the methyl group of the alkyl chain of 1-octadecene in **2** (at 0.87 ppm), the signal of the dimethyl group of the isobutylene unit in **3** (at 1.07 ppm), the broad signal of the poly(ethylene) backbone in **4** (1.40 to 2.15 ppm), and the signal of the methyl ether (at 3.36 ppm) of copolymer **5**.

Despite the fact that ring-opening of maleic anhydride creates carboxylic acid functions that increase the polarity of the polymer backbone, this effect was counterbalanced by the introduction of the rather hydrophobic rose ketone release unit. In contrast to copolymer **9**, conjugates **6**−**8** were found to be almost insoluble in aqueous media and gave only dispersions. This solubility profile indicates that minor structural modifications of the copolymer structure have an important influence on the physicochemical properties of the resulting conjugate (*28*, *29*). The release of δ-damascone from the thioether conjugate is pH dependent. Although relatively stable under acidic conditions, the precursors slowly release the bioactive compound at pH values above 6 (*31*). Furthermore, for an efficient release, the polymer must be soluble, or at least well-dispersed, in water (*28*).

To fine-tune the water solubility, we grafted poly(ethylene glycol) side chains onto the polymer backbone by using the same one-pot synthesis described above. PEG is a water-soluble and biocompatible polymer that has already been used to modify

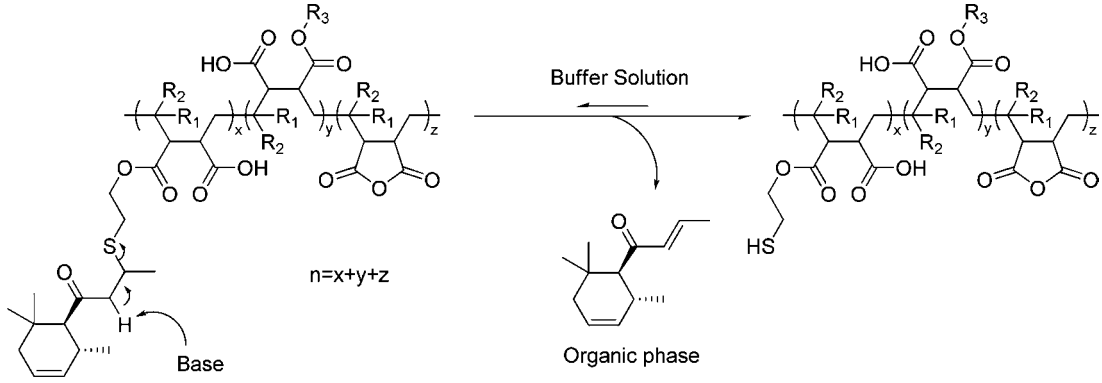
Scheme 4. Preparation of Poly(maleic acid monoester)-Based δ-Damascone Conjugate 10 ($a = 800$, $b = 215$, $c = 1$, $d = 59$)



10

n = a+b+c+d

Scheme 5. Mechanism of Release of δ-Damascone from Copolymers 6 ($x = 55$, $y = 0.1$, $z = 50$), 7 ($x = 65$, $y = 0.3$, $z = 260$), 8 ($x = 640$, $y = 1$, $z = 640$), 9 ($x = 320$, $y = 1$, $z = 750$), and 10 ($x = 1015$ ($x = a + b$, see Scheme 4), $y = 1$ ($= c$), $z = 59$ ($= d$))



6 R_1=$C_{16}H_{33}$, R_2=H, R_3=pyren-1-ylmethanol
7 R_1=R_2=Me, R_3=pyren-1-ylmethanol
8 R_1=R_2=H, R_3=pyren-1-ylmethanol
9 R_1=MeO, R_2=H, R_3=pyren-1-ylmethanol
10 R_1=MeO, R_2=H, R_3=PEG or pyren-1-ylmethanol

different poly(maleic anhydride) copolymers of styrene (*53*), 1-hexene (*54*), and methyl vinyl ether (*55*). We thus prepared a PEG-modified analogue of copolymer **9** by adding a mixture of a poly(ethylene glycol) monomethyl ether (20 mol % with respect to the maleic anhydride unit) and **1** (80 mol %) to polymer **5** to afford conjugate **10** (Scheme 4). The grafting of the PEG chains on **5** was complete, and conversion of **1** was estimated at 75 mol %.

Measurement of the Controlled Release of δ-Damascone from Poly(Maleic Acid)-Based Conjugates in Buffered Solutions at pH 4, 7, and 10 as a Function of Time. In technical applications or under physiological conditions, Michael-type 1,4-addition of thiols to α,β-unsaturated ketones can be reversible, as described for the reaction of prostaglandins with various thiols (*56*). In the present study, the release of δ-damascone from copolymers **6**−**10** is presumably also controlled by this mechanism (Scheme 5).

The influence of the copolymer structure on the release of δ-damascone from conjugates **6**−**10** was first studied in buffered aqueous solution at different pH values. The pH influences the kinetics of the retro 1,4-addition. Furthermore, the solubility of the different delivery systems in aqueous media is impacted by the pH because the carboxylic acid functions can be deprotonated under neutral or alkaline conditions (*28*). The amount of each polymer was chosen to release the same concentration of δ-damascone in all samples, that is to say, 8.7 mg mL^{-1} or 8700 ng μL^{-1}. In order to prevent equilibration, a nonmiscible organic solvent, a mixture of isooctane/diethyl ether (9:1), was added to the system to continuously extract the released δ-damascone (*30*). Organic and water phases were gently stirred so as not to mix with each other at pH 4 (the pH of fabric softener applications), 7, and 10 (the pH of liquid detergent applications) for different times. The quantity of δ-damascone released into the organic phase was analyzed by GC. Results were plotted as a function of pH for copolymers **6**−**10** after 1, 3, and 6 days (Figures 1a−d).

In solution, the release of δ-damascone is strongly influenced by the polymer backbone. When the polymer contained methyl groups or hydrogen atoms, as in copolymers **7** and **8**, respectively, the solubility in the buffered solutions was very limited, especially at low pH. Both copolymers **7** and **8** gave stable dispersions at pH 4 and 7, and were soluble only at pH 10. They released only 253.9 and 325.2 ng μL^{-1} of δ-damascone at pH 10 after 6 days, which corresponded to 2.9% and 3.7% of δ-damascone grafted on the copolymers, respectively.

When the comonomer of the backbone contained a methoxy group, the resulting copolymer **9** was soluble at all pH values. A faster release was observed with a δ-damascone concentration of 999.5 ng μL^{-1} measured at pH 10 after 6 days. This trend suggests that the higher solubility of a copolymer facilitates the release by retro 1,4-addition. This result was confirmed at the example of copolymer **10**, which was modified with PEG side

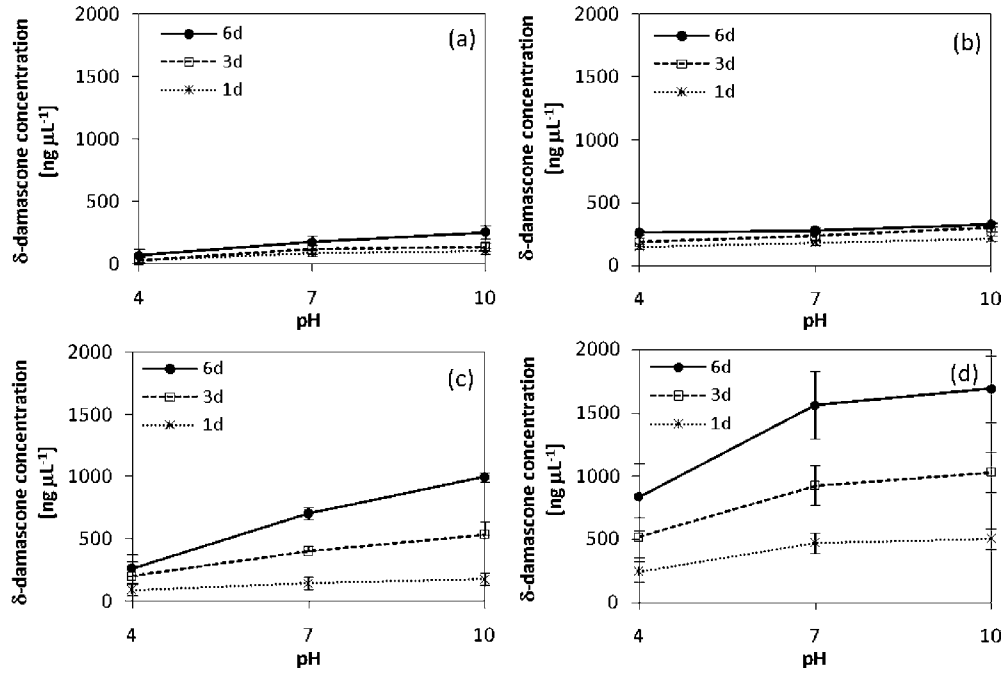


Figure 1. a−d. Concentrations of δ-damascone released from copolymers **7** (a, $R_1 = R_2 =$ Me), **8** (b, $R_1 = R_2 =$ H), **9** (c, $R_1 =$ MeO), and **10** (d, $R_1 =$ MeO + PEG chain ester) as a function of pH after 1, 3, and 6 days as determined by GC analysis.

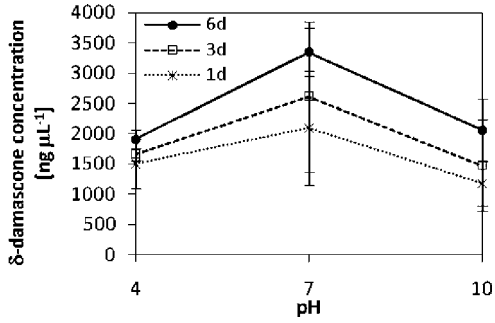


Figure 2. Concentrations of δ-damascone released from copolymer **6** as a function of pH after 1, 3, and 6 days as determined by GC analysis.

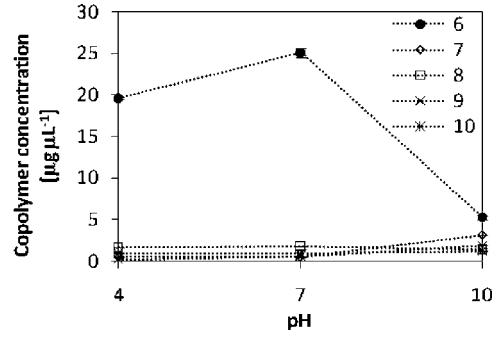


Figure 3. Concentrations (in mg mL^{-1}) of copolymers **6−10** extracted from buffered aqueous solutions into the organic phase as a function of pH after 1 day as determined by thermogravimetric analysis.

chains. Its solubility was significantly improved, and the amount of δ-damascone released from copolymer **10** increased faster than in the case of the unmodified copolymer **9**, even at pH 4 (Figure 1d). The measured δ-damascone concentrations varied between 836.2 ng μL^{-1} at pH 4 and 1689.9 ng μL^{-1} at pH 10, corresponding to a release of 19.4%.

Nonetheless, high water solubility might prevent an efficient deposition of the copolymers on a fabric surface. Therefore, we were also interested in understanding the release from more hydrophobic structures, such as copolymer **6** with a hexadecyl side chain. As observed with copolymers **7−10**, the release of δ-damascone from **6** increased with time at different pH values (Figure 2). However, after 1 and 3 days, we observed a more important δ-damascone release at pH 4 than at pH 10. These results are different from those obtained with copolymers **7−10** and in contradiction with the mechanism of release (Scheme 5). In addition, high variability of the data was observed, indicating an uncontrolled process.

In comparison with copolymers **7−10**, the presence of the hexadecyl side chain should change the solubility profile of copolymer **6**, and we expected that a large part of the copolymer was dissolved in the organic phase. The solubility of all copolymers was thus estimated by thermogravimetry. We placed 20 μL of the organic phase (isooctane/diethylether 9:1) inside an aluminum pan, which was dried in a thermogravimeter at 80 °C for 30 min. A plateau was reached, indicating that the samples were dried. The experiment was repeated with the pure extraction solvent, which served as the reference. The difference between both plateaus corresponds to the concentration of polymer in the organic phase. Data obtained from measurements performed after one day are reported in Figure 3.

Concentrations of copolymers were measured at different pH values as a function of time (Table 1). As expected, the concentrations of copolymers **7−10** in the organic phase are relatively low. The concentration of copolymer **7** in the organic phase was at maximum 1−2%. The concentration of copolymer **8** leveled off at around 6−7%, indicating a saturation of the organic phase, even after 1 day. Solubilization of copolymers **9** and **10** in the organic phase increased slowly with time but did not exceed 8% and 7%, respectively.

In contrast, 45% and 58% of copolymer **6** were detected in the organic phase at pH 4 and 7, respectively (Table 1). These concentrations increased with time to reach a maximum at about 78% at pH 7 after 6 days and decreased to 12% at pH 10. At this pH, the carboxylic acid functions of the copolymer are mostly deprotonated, which makes the polymer less soluble in the organic phase. Furthermore, the release of δ-damascone increases the polarity of the polymer and thus decreases its solubility in the organic phase.

Table 1. Concentrations (in μg μL^{-1} and %) of Copolymers 6−10 in the Organic Phase as a Function of pH and Time

		copolymers dissolved in organic phase [μg μL^{-1}] ([%])				
pH	day #	**6**	**7**	**8**	**9**	**10**
	1	19.63 (45.2)	0.50 (1.0)	1.62 (6.9)	0.22 (0.6)	0.97 (2.2)
4	3	22.08 (50.9)	0.14 (0.3)	1.51 (6.4)	0.44 (1.3)	2.67 (6.1)
	6	24.00 (55.3)	0.29 (0.6)	1.35 (5.7)	2.71 (7.8)	1.78 (6.7)
	1	25.13 (57.6)	0.52 (1.1)	1.79 (7.5)	0.55 (1.6)	0.90 (2.1)
7	3	31.75 (73.2)	0.48 (1.0)	1.69 (7.2)	0.73 (2.1)	1.35 (3.1)
	6	33.70 (77.7)	0.67 (1.4)	1.35 (5.7)	1.43 (4.1)	1.27 (4.0)
	1	5.25 (12.1)	0.35 (0.7)	1.41 (6.0)	1.87 (5.4)	1.20 (2.8)
10	3	1.00 (2.3)	0.19 (0.4)	1.44 (6.1)	0.68 (2.0)	1.42 (3.3)
	6	0.91 (2.1)	0.31 (0.7)	1.48 (6.3)	1.84 (5.3)	2.22 (7.0)

These results suggest that a large part of copolymer **6** was dissolved in the organic phase at pH 4 and 7. Its concentration in buffered aqueous solution must thus have decreased, which then slowed down the release of δ-damascone (Figure 2). The concentration of δ-damascone extracted from the aqueous phase was determined by GC analysis using a calibrated flame ionization detector (FID). The presence of copolymer **6** in the organic phase suggests that, at an injection temperature of 250 °C, additional amounts of δ-damascone and other volatiles might be generated by thermal degradation of the polymer conjugate. Therefore, we measured the stability of the copolymer at this temperature by using TGA. Pure copolymer **6** was placed inside an aluminum pan, which was transferred into the TGA. The temperature was increased from 25 to 270 at 10 °C min^{-1} and the mass loss measured as a function of time (Figure 4). A significant mass loss was detected in the range from 150 to 270 °C, corresponding to 38% of the total polymer mass. The same experiment was carried out with the starting copolymer **2**, and a mass loss of only 8% was measured in this case. This result demonstrated that copolymers of maleic acid were not stable at 250 °C (injector temperature represented by a dotted line in Figure 4) and that they degraded (*57*). We assume that this degradation first releases precursor **1**, which then further degrades (Scheme 6). This was confirmed by TGA analysis of **1** for which a complete mass loss was measured at 270 °C, suggesting either evaporation or degradation of **1**. With the boiling point of δ-damascone being 253 °C, we thus assume that copolymer **6** degrades, in fact, in two steps, as illustrated in Scheme 6. The thermal degradation of copolymer **6** extracted into the organic phase thus explains the large amount of δ-damascone detected in our GC measurements.

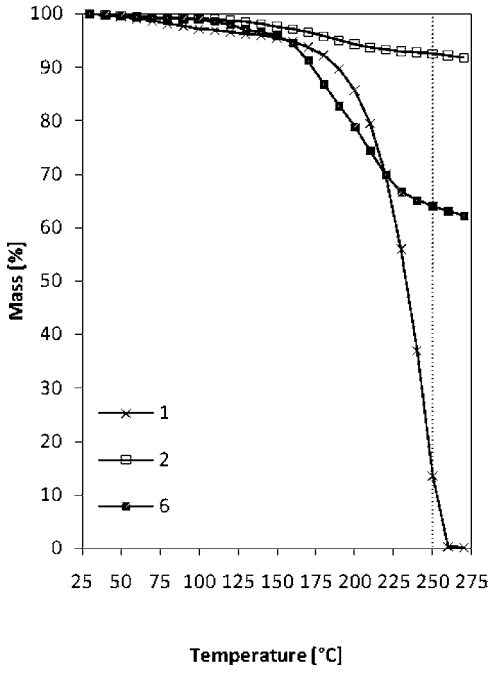


Figure 4. Thermogravimetric analysis of β-mercapto ketone **1** and copolymers **2** and **6** from 25 to 270 °C at 10 °C min^{-1}.

With the ester bond being much more stable than the β-mercapto ketone moiety (*15*), we did not expect the release of 2-mercaptoethanol under the mild reaction conditions found in the targeted application. This was confirmed by the fact that no smell arising from sulfur compounds was detected in the applications.

However, even if we were not able to accurately measure the release of δ-damascone from **6** at pH 4 and 7, the low concentration of this copolymer in the organic phase at pH 10 (Table 1), combined with the high concentration of released δ-damascone, suggested that copolymer **6** might nevertheless be a suitable δ-damascone delivery system in practical applications. The efficient release of δ-damascone at pH 10 emphasizes the importance of the polarity of the backbone on the release rate. The tendency observed at pH 10 was confirmed (at lower extent) at pH 4, which is the pH of our model application.

Deposition of the Copolymers from an Aqueous Environment onto Cotton. To test the potential of the different δ-damascone conjugates for practical applications in functional perfumery, we investigated the release of the active volatile in a fabric softening composition. Fabric softeners are particularly interesting in the context of this project, as they are usually acidic (pH ca. 3.1), which means that the polymer conjugates are expected to be stable during storage. In use (e.g., during a normal washing cycle), the fabric softener is diluted with water, resulting in an increase of pH to ca. 4.1, which should trigger the release of the damascone. Fabric softener formulations typically consist of about 16% by weight of a cationic surfactant in water, such as a quaternized triethanolamine ester of a fatty acid (TEA-esterquat) (*58*, *59*). Cationic surfactants are efficiently deposited onto cotton surfaces (*58*–*61*) and therefore facilitate the transport of apolar organic molecules such as fragrances from an aqueous environment onto textiles (*62*–*65*). It can be expected that the polymer conjugates are also deposited with the surfactant onto cotton surfaces. To ensure that the quantity of polymer deposited onto the cotton depends on the polymer structure and not on the deposition process, the amount of the diluted surfactant emulsion deposited on the cotton sheet was controlled (by weighing a constant amount of remaining water). As outlined above, the polymer deposition should depend on the copolymer structure and should thus be influenced by the nature of the comonomer (*28*). The polarity of the copolymer is expected to be further influenced by the pH of the system.

Besides the choice of the linker (*66*) and efficient deposition on the target surface, the amount of δ-damascone released into the headspace also depends on the release kinetics of the active compound from the corresponding polymer conjugate; these are dependent on the water solubility of the polymer, as previously shown for a series of poly(methacrylate) derivatives (*28*). At acidic pH, as in the softener formulation, the carboxylic acid functions of polymers **6**−**10** are protonated. The pK_a of the maleic acid units is a function of the degree of dissociation and

Scheme 6. Proposed Mechanism of Degradation of Copolymer 6 ($x = 55$, $y = 0.1$, $z = 50$) at 250°C in the GC Injector

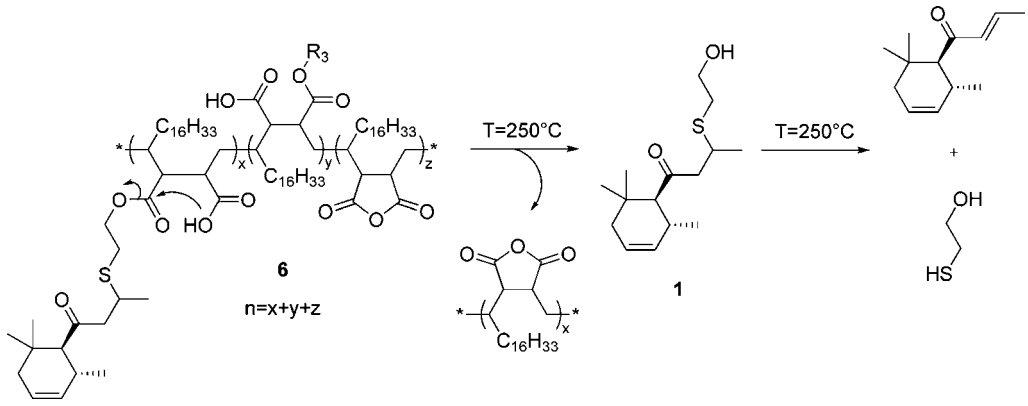


Table 2. Amount of Deposition of Pyrene-Labeled Poly(maleic acid)-Based δ-Damascone Conjugates 6−10 on Cotton as Determined by Fluorescence Spectroscopy (data recorded at 389 nm, excitation at 334 nm)

copolymer	deposition determined with respect to reference [%]	deposition determined by external standard calibration [%]	average deposition [%]	amount of conjugated δ-damascone deposited onto the cotton surface [%]
6	44	43	44	3.83
7	28	41	35	3.05
8	40	50	45	3.92
9	29	32	31	2.70
10	23	25	24	2.09

has been reported to be between 4 and 8 (*67*). Therefore, upon dilution during the application, the pH increases and the polymers become partially deprotonated, which results in an increased solubility of the conjugates in the aqueous medium. With the release being pH dependent (Figure 1) and triggered at a pH of ca. 6.5 and above (*31*), additional carboxylic acid functions are generated on the polymer backbone (Scheme 5). The water solubility of the polymer still increases, which should then accelerate the release of the active volatile.

The amount of polymer deposition on the cotton surface was determined with the help of the fluorescence label of copolymers **6**−**10**. In a typical experiment, equimolar amounts of copolymers with respect to the total amount of active compound to be released were solubilized in an appropriate solvent and pipetted into an aqueous emulsion of a TEA-esterquat, corresponding to a total of ca. 1.0−5.5% by weight of polymer in the surfactant emulsion. After the emulsion was stirred for several hours, it was diluted with tap water and a small aliquot pipetted off. The measured fluorescence intensity served as the reference, corresponding to 0% of deposition. Then, one cotton sheet was added and stirred manually for 5 min (to allow for the deposition of the surfactant and the polymer conjugate onto the cotton surface). The cotton sheet was removed before another aliquot of the surfactant emulsion was pipetted off, and then the cotton sheet was wrung out by hand and line-dried for 3 days. The measured fluorescence intensity reflected the quantity of the remaining nondeposited copolymer in the surfactant emulsion. The missing amount with respect to the reference measurement was assumed as being deposited on the fabric surface. The release of δ-damascone from the dry cotton surface was then analyzed by dynamic headspace analysis as described below.

Despite the fact that the fluorescence label corresponded to only about 0.1 mol % by weight of the total mass of the copolymer, its concentration in the surfactant emulsion was by far too high for accurate fluorescence measurements. A nonlinear fluorescence response was obtained by diluting the sample by a factor varying between 2 and 10. The surfactant emulsions were thus diluted by a factor of 100 and the fluorescence spectra recorded between 370 and 400 nm with an excitation at 334 nm. Additionally, the difference in fluorescence intensity measured at different wavelengths before and after addition of the cotton sheet was compared with data obtained by external standard calibration. Data were analyzed at 378, 384, 389, and 398 nm. The dependence of the fluorescence intensity at the different wavelengths with respect to the amount of polymer in the emulsion, after dilution by a factor 100, was verified with the example of δ-damascone conjugate **9**.

At all wavelengths, a linear relationship was observed when varying the polymer concentration over 1 order of magnitude, thus covering a range corresponding to 0−90% of deposition. Extrapolation of the fluorescence intensities to zero polymer concentration revealed some remaining fluorescence at 378 nm, whereas at the other wavelengths, the fluorescence decreased to a fluorescence intensity value close to zero. With the curve recorded at 389 nm having the steepest slope, we selected this wavelength for further analysis.

Table 2 lists the data obtained for the deposition of poly(maleic acid)-based δ-damascone conjugates **6**−**10** on cotton and indicates the total amount of conjugated δ-damascone transferred to the cotton surface. Our measurements confirmed the expected dependence of the polymer structure on the amount of surface deposition.

According to the copolymer structures, different amounts of the conjugates were deposited on the cotton surface, varying between 24% for the more hydrophilic polymer **10** and 45% for the more apolar structures **6** and **8**, thus confirming an inverse correlation of the deposition with the ease of dispersion of the materials in an aqueous environment, which was also reported previously for a series of poly(methacrylate) derivatives (*28, 30*).

Nevertheless, for practical application, the amount of δ-damascone to be delivered from the target surface is the most important factor to be considered for the efficiency of a delivery system. Increasing the deposition on the target substrate is the first step of optimization; controlling the rate of the covalent bond cleavage reaction is another parameter to be considered. The latter strongly depends on the local environment of the release site (*28–30*). As the next step, we thus determined the release of δ-damascone from the different poly(maleic acid) conjugates by dynamic headspace analysis after deposition of the polymers from an aqueous environment onto a cotton

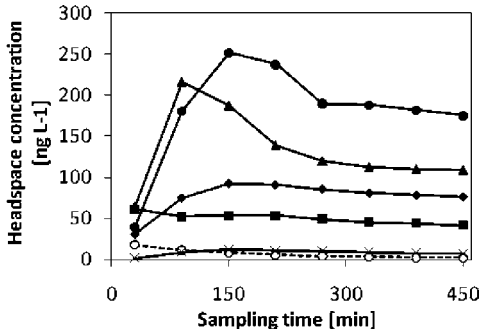


Figure 5. Headspace concentrations (in ng L^{-1} of air) measured for the evaporation of δ-damascone from poly(maleic acid)-based conjugates **6** (-◆-), **7** (-×-), **8** (-■-), **9** (-•-), and **10** (-▲-) on dry cotton after 3 days with respect to unmodified δ-damascone as the reference (---○---).

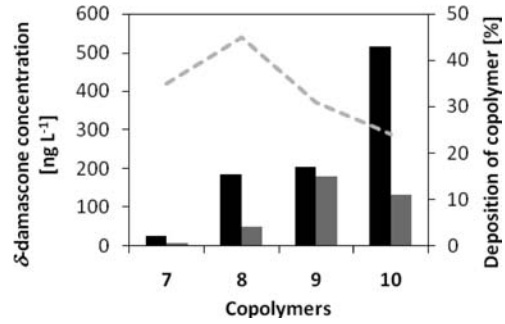


Figure 6. Correlation of δ-damascone concentrations measured in buffered aqueous solution (pH 4, after 3 days, black bars), in the headspace above the cotton surface (after 3 days of line-drying, gray bars) with the amount of polymer deposited onto the surface (dotted line) for copolymers **7**−**10**.

surface, and we tried to correlate the amount of deposition with the release efficiency.

Dynamic Headspace Analysis of the Controlled Release of δ-Damascone from Poly(maleic acid)-Based Conjugates on Dry Cotton. δ-Damascone conjugates **6**−**10** were deposited from a TEA-esterquat emulsion onto the cotton surface as described above. After line-drying for 3 days, one of the dry towels was put into a headspace sampling cell that was controlled for temperature and relative humidity of the air (*48*). A constant flow of air of ca. 200 mL min^{-1} was continuously pumped across the cell. After equilibrating the system, the volatiles were adsorbed onto a clean Tenax cartridge for 15 min and then onto a waste cartridge for 45 min. The sampling was repeated seven times at constant time intervals every 60 min. At the end of the experiment, the sample cartridges were thermally desorbed and the volatiles quantified by GC analysis (*48*). The absolute headspace concentrations of δ-damascone were determined by external standard calibration. All experiments were carried out in duplicate and compared with a reference sample composed of unmodified δ-damascone, which was prepared and analyzed under the same conditions as the polymer conjugates. The measured headspace concentrations of δ-damascone released from polymers **6**−**10** or from the reference sample on dry cotton after 3 days are illustrated in Figure 5.

The data show that the headspace concentrations were higher when δ-damascone was released from either one of the polymeric precursors **6**−**10** as compared with the unmodified δ-damascone used as the reference, thus confirming the expected resiliency of fragrance release. The release of δ-damascone was found to be particularly efficient from polymer conjugates **6**, **9**, and **10**, with increased headspace concentrations (measured at the end of the experiment after 450 min, Figure 5) by a factor of 30, 75, or 50, respectively, with respect to the δ-damascone reference. With a human group olfactory threshold for δ-damascone of 0.021 ng L^{-1} air (*32, 33*), all detected concentrations lie above the human detection limit and are therefore easily perceived by humans (Figure 5).

The observed constant increase of some of the concentration curves of δ-damascone released from the precursors at the beginning of the experiment may result from the changing conditions at the cotton surface from the line-drying to the headspace sampling cell (*48*). A constant airflow at ca. 75% of humidity was aspirated through the headspace sampling cell. Although the ambient humidity during the line-drying of the fabric was estimated as being quite high, the cotton sheets may still take up some humidity during the experiment, which in return may trigger some fragrance release. After ca. 200 min, a constant or slightly decreasing amount of δ-damascone was released from the samples. Due to the fact that the headspace above the cotton surface, and thus the δ-damascone evaporated from the surface, was constantly removed, the system is not at equilibrium. The observed constant release at the end of the measurements thus corresponds to a constant release rate over time.

Comparison of the release rates observed by dynamic headspace analysis (Figure 5) with those from solution measurements (Figure 1) generally showed a good correlation. With the exception of copolymer **6** (which was extracted into the organic phase and thermally degraded in the GC injector), the relative amount of δ-damascone released was found to low for copolymer **7** as compared to copolymers **8**−**10**. This was the case for both headspace analysis and solution experiments. Despite its better deposition, copolymer **8** released less δ-damascone than copolymers **9** and **10**, which correlates to a less efficient release in solution. In contrast, copolymer **10** with a faster release in solution released less δ-damascone into the headspace than copolymer **9** due to its lower deposition on the cotton surface.

Considering the amount of deposition of the different polymers (Table 2) and the efficiency of release observed in solution (Figure 1), one can see that these two parameters have an opposite influence on the amount of δ-damascone released into the headspace. In solution, polymer conjugate **10** with hydrophilic PEG chains near the releasing unit was found to release the highest amount of δ-damascone of the series of compounds tested in this work. However, as a result of a limited deposition on the cotton surface, its final performance was found to be comparable to copolymer **6** with hydrophobic alkyl side chains. The latter is suspected to release the volatile less efficiently in solution, at pH between 4 and 7, but was better deposited onto cotton.

Our measurements carried out in aqueous-buffered solution have shown that the structure of the polymer influences the rates of release, independently of other parameters such as the surface deposition. We therefore expected that copolymer **10** should give rise to a higher release of δ-damascone than copolymers **7**−**9**. The headspace concentrations of δ-damascone released from the polymers on the cotton surface were then measured after line-drying for 3 days. These concentrations correspond to the momentaneous release at the given time. The total amount released over time was influenced by the polymer structures (release efficiency) and depended on the amount of polymer deposited onto the surface (maximum amount to be released). The maximum amount of δ-damascone that can be released into the air (as required for the practical application) was estimated from measurement of the deposition of the polymers on the target surface (Table 2). Figure 6 correlates the concentrations of δ-damascone released in solution (at pH 4 after 3 days, Figure 1) and the momentaneous headspace concentration measured

above the cotton surface (constant value measured after 3 days of line-drying and 450 min of sampling, Figure 5) together with the deposition (data determined by fluorescence measurements, Table 2) for polymers **7**−**10** (horizontal axis).

Accordingly, a well-adjusted balance between hydrophobicity (deposition) and hydrophilicity (solubility, release kinetics) is presumably the most important criterion for the choice of the appropriate delivery system with respect to the targeted application. The presence of PEG side chains favors the release but not the deposition. Therefore, polymer conjugate **9** seems to represent the best structural compromise of the delivery systems investigated in this work by giving rise to the highest headspace concentrations of δ-damascone after 3 days. The ease of structural modifications, allowing fine-tuning of the physicochemical properties of bioconjugates, makes polymeric delivery systems particularly interesting for the controlled release of bioactive compounds in various applications.

CONCLUSION

Besides prolonging the duration of evaporation, polymeric bioconjugates have additional advantages as delivery systems for bioactive volatiles such as fragrances. Labile covalent bonds to be cleaved in the conjugate to release bioactive compounds can be stabilized by the encapsulating polymer matrix, and thus, degradation can be (partially) prevented during storage in harsh media. Furthermore, the ease of structural modification by choosing suitable co-monomers allows preparation of copolymers with enhanced surface deposition and/or better dispersion in aqueous media.

Damascones or damascenones, the so-called rose ketones, are important fragrance raw materials frequently used in perfumery. With 2-mercaptoethanol as a linker, α,β-unsaturated enones such as δ-damascone form the corresponding β-mercapto ketone, which then reacts under mild conditions with poly(maleic anhydride) copolymers to afford the corresponding conjugates in a two-step, one-pot procedure with very good yields and high conversions.

The release of δ-damascone from the polymer conjugates by retro 1,4-Michael-type addition was investigated in buffered aqueous solution as a function of pH and time, as well as after deposition onto a cotton surface in the presence of a cationic surfactant. Grafting a fluorescence label to the polymer backbone allowed quantification of polymer deposition from an aqueous environment on a cotton surface.

The most efficient release of δ-damascone was achieved for a polymer conjugate representing a well-balanced compromise of hydrophilicity (giving rise to high release rates) and hydrophobicity (increased surface deposition) of the polymer backbone. Our data thus show that the detailed understanding of the influence of the polymer structure on the deposition and the reactivity of the conjugates is the most important prerequisite toward the design of new polymer-based bioconjugates.

Poly(maleic acid)-based copolymers were found to be particularly suitable as profragrances because they can be easily modified to cover a broad range of polarity and structural functionality within the polymer backbone. A series of these compounds with different backbone functionalities are widely available and thus allow easy access to a broad variety of structures. Therefore, the polymer conjugates described in this work (*68*) might be easily adapted for the release of bioactive compounds in various biomedical applications.

ACKNOWLEDGMENT

The authors thank Philippe Chevalier for his assistance with the polymer synthesis, Daniel Grenno for recording the high-resolution mass spectra, and Dr. Roger Snowden for constructive comments on the manuscript.

Supporting Information Available: Numerical data for Figures 1 and 5, and fluorescence spectra of the deposition measurements listed in Table 2. This material is available free of charge via the Internet at http://pubs.acs.org.

LITERATURE CITED

(1) Pichersky, E., Noel, J. P., and Dudareva, N. (2006) Biosynthesis of plant volatiles: nature's diversity and ingenuity. *Science 311*, 808–811.

(2) Baldwin, I. T., Halitschke, R., Paschold, A., von Dahl, C. C., and Preston, C. A. (2006) Volatile signaling in plant-plant interactions: "talking trees" in the genomics era. *Science 311*, 812–815.

(3) Bergström, L. G. W. (2008) Chemical communication by behaviour-guiding olfactory signals. *Chem. Commun.* 3959–3979.

(4) Arctander, S. (1969) *Perfume and Flavor Chemicals*, Vol. 1 (A-J) and 2 (K-Z), published by the author, Montclair, NJ.

(5) Surburg, H., and Panten, J. (2006) *Common Fragrance and Flavor Materials*, 5th ed. (Surburg, H., and Panten, J., Eds.) pp 1−318, Wiley-VCH, Weinheim.

(6) Kraft, P., Bajgrowicz, J. A., Denis, C., and Fráter, G. (2000) Odds and trends: recent developments in the chemistry of odorants. *Angew. Chem., Int. Ed. 39*, 2980–3010.

(7) Brenna, E. (2003) Enzyme-mediated syntheses of chiral communication substances: fragrances for perfumery applications. *Curr. Org. Chem. 7*, 1347–1367.

(8) Chapuis, C., and Jacoby, D. (2001) Catalysis in the preparation of fragrances and flavours. *Appl. Catal., A 221*, 93–117.

(9) Saudan, L. (2007) Hydrogenation processes in the synthesis of perfumery ingredients. *Acc. Chem. Res. 40*, 1309–1319.

(10) Friberg, S. E. (1998) Fragrance compounds and amphiphilic association structures. *Adv. Colloid Interface Sci. 75*, 181–214.

(11) Zhang, Z., Friberg, S. E., and Aikens, P. A. (2000) Change of amphiphilic association structures during evaporation from emulsions in surfactant-fragrance-water systems. *Int. J. Cosmet. Sci. 22*, 181–199.

(12) Milotic, D. (2003) The impact of fragrance on consumer choice. *J. Consum. Behav. 3*, 179–191.

(13) Ness, J., Simonsen, O., and Symes, K. (2003) Microcapsules for household products. *Microspheres, Microcapsules Liposomes 6*, 199–234.

(14) Park, S.-J., and Arshady, R. (2003) Microcapsules for fragrances and cosmetics. *Microspheres, Microcapsules Liposomes 6*, 157–198.

(15) Herrmann, A. (2007) Controlled release of volatiles under mild reaction conditions: from nature to everyday products. *Angew. Chem., Int. Ed. 46*, 5836–5863.

(16) Saito, Y., Miura, K., Tokuoka, Y., Kondo, Y., Abe, M., and Sato, T. (1996) Volatility and solubilization of synthetic fragrances by Pluronic® P-85. *J. Dispersion Sci. Technol. 17*, 567–576.

(17) Suzuki, K., Saito, Y., Tokuoka, Y., Abe, M., and Sato, T. (1997) Poly(ethylene oxide)/poly(propylene oxide)/poly(ethylene oxide) triblock copolymer as a sustained-release carrier for perfume compounds. *J. Am. Oil Chem. Soc. 74*, 55–59.

(18) Kayali, I. (2003) Solubilization of fragrance compounds in block copolymer/water system. *Jordan. J. Appl. Sci. 5*, 42–49.

(19) Berthier, D. L., Schmidt, I., Fieber, W., Schatz, C., Furrer, A., Wong, K., and Lecommandoux, S. (2010) Controlled release of volatile fragrance molecules from PEO-*b*-PPO-*b*-PEO block copolymer micelles in ethanol-water mixtures. *Langmuir 26*, 7953–7961.

(20) Ternat, C., Ouali, L., Sommer, H., Fieber, W., Velazco, M. I., Plummer, C. J. G., Kreutzer, G., Klok, H.-A., Månson, J.-A. E., and Herrmann, A. (2008) Investigation of the release of bioactive volatiles from amphiphilic multiarm star-block copolymers by thermogravimetry and dynamic headspace analysis. *Macromolecules 41*, 7079–7089.

(21) Perry, R. J. (2005) "Pro-fragrant" silicone delivery polymers. *Delivery System Handbook for Personal Care and Cosmetic*

Products: Technology, Applications, and Formulations (Rosen, M. R., Ed.) pp 667−682, William Andrew Publishing, Norwich.

(22) Kamogawa, H., Okabe, S., and Nanasawa, M. (1976) Synthesis of polymerizable acetals. I. Vinylbenzaldehyde acetals with perfume alcohols. *Bull. Chem. Soc. Jpn. 49*, 1917–1919.

(23) Kamogawa, H., Haramoto, Y., and Nanasawa, M. (1979) Synthesis of polymerizable acetals. II. Readily hydrolyzable acetals from citronellol and vitamins. *Bull. Chem. Soc. Jpn. 52*, 846–848.

(24) Kamogawa, H., Mukai, H., Nakajima, Y., and Nanasawa, M. (1982) Chemical release control - Schiff bases of perfume aldehydes and aminostyrenes. *J. Polym. Sci., Polym. Chem. Ed. 20*, 3121–3129.

(25) Kamogawa, H., Haramoto, Y., Misaka, Y., Asada, Y., Ohno, Y., and Nanasawa, M. (1985) Chemical release control: sulfonate esters from perfume and herbicide alcohols and p-styrenesulfonyl chloride. *J. Polym. Sci., Polym. Chem. Ed. 23*, 1517–1526.

(26) Galioğlu, O., and Akar, A. (1988) Perfume alcohols supported to sulfochlorinated poly(styrene-co-divinyl benzene) beads. *J. Polym. Sci., Part A: Polym. Chem. 26*, 2355–2357.

(27) Kamogawa, H., Kohno, H., and Kitagawa, R. (1989) Chemical release control: carbamates of 3-vinylphenyl and 2-methacryloyloxyethyl isocyanates and perfume and herbicide alcohols. *J. Polym. Sci., Part A: Polym. Chem. 27*, 487–495.

(28) Berthier, D., Trachsel, A., Fehr, C., Ouali, L., and Herrmann, A. (2005) Amphiphilic polymethacrylate- and polystyrene-based chemical delivery systems for damascones. *Helv. Chim. Acta 88*, 3089–3108.

(29) Trachsel, A., de Saint Laumer, J.-Y., Haefliger, O. P., and Herrmann, A. (2009) Parameters influencing the release of tertiary alcohols from the surface of "spherical" dendrimers and "linear" stylomers by neighbouring-group-assisted hydrolysis of 2-carbamoylbenzoates. *Chem.—Eur. J. 15*, 2846–2860.

(30) Morinaga, H., Morikawa, H., Wang, Y., Sudo, A., and Endo, T. (2009) Amphiphilic copolymer having acid-labeile acetal in the side chain as a hydrotrope: controlled release of aldehyde by thermoresponsive aggregation-dissociation of polymer micelles. *Macromolecules 42*, 2229–2235.

(31) Fehr, C., and Galindo, J. (2005) Aldols by Michael addition: application of the retro-Michael addition to the slow release of enones. *Helv. Chim. Acta 88*, 3128–3136.

(32) Kastner, D. (1994) 25 Jahre Rosenketone - Thema mit Variationen. *Parfuem. Kosmet. 75* (3), 170–81.

(33) Williams, A. (2002) Rose ketones: celebrating 30 years of success. *Perfum. Flavor. 27* (2), 18–32.

(34) Shulkin, A., and Stöver, H. D. H. (2002) Polymer microcapsules by interfacial polyaddition between styrene-maleic anhydride copolymers and amines. *J. Membr. Sci. 209*, 421–432.

(35) Donati, I., Gamini, A., Vetere, A., Campa, C., and Paoletti, S. (2002) Synthesis, characterization, and preliminary biological study of glyconjugates of poly(styrene-co-maleic acid). *Biomacromolecules 3*, 805–812.

(36) Boztuğ, A., and Basan, S. (2003) Synthesis and characterization of maleic anhydride-styrene-allyl propionate terpolymer ester derivatives. *J. Appl. Polym. Sci. 89*, 296–299.

(37) Xi, F., Basset, Jr, W., and Vogl, O. (1983) Esters of alternating copolymers of maleic or 2,3-dimethylmaleic anhydride with alkyl vinyl ethers. *J. Polym. Sci., Part A: Polym. Chem. 21*, 891–911.

(38) Chiellini, E. M., Leonardi, G., Giannasi, D., and Solaro, R. (1992) Partial esters of alternating copolymers of maleic anhydride and alkyl vinyl ethers for pharmaceutical applications. *J. Bioact. Compat. Polym. 7*, 161–174.

(39) Zatz, J. L., Weiner, N. D., and Gibaldi, M. (1968) Monomolecular film properties of protective and enteric film formers I. Effect of polymer side chain on surface pressure-area isotherms. *J. Pharm. Sci. 57*, 1440–1442.

(40) Zatz, J. L., Weiner, N. D., and Gibaldi, M. (1970) Orientation of monolayers of half-esters of poly(methyl vinyl ether maleic anhydride). *J. Colloid Interface Sci. 33*, 1–7.

(41) Finne, U., Kyyrönen, K., and Urtti, A. (1989) Drug release from monoisopropyl ester of poly(vinyl methyl ether-maleic anhydride) can be modified by basic salts in the polymer matrix. *J. Controlled Release 10*, 189–194.

(42) Uglea, C. V., Panaitescu, L., Spridon, D., Ursu, D., Popa, I., and Ottenbrite, M. (1996) Biological activity of maleic anhydride copolymers. I. Biocompatibility and antitumoural effects of maleic anhydride-vinyl acetate, maleic anhydride-methyl methacrylate and maleic anhydride-styrene copolymers. *J. Biomater. Sci., Polym. Ed. 8*, 269–280.

(43) Plochocka, K. (2001) Polymeric delivery and release systems for oral care actives (to ISP Investments Inc.), US Patent 6,315,987, *Chem. Abstract 135*, 362395.

(44) Winnik, F. M., and Regismond, S. T. A. (1996) Fluorescence methods in the study of the interactions of surfactants with polymers. *Colloids Surf., A 118*, 1–39.

(45) Vitenberg, A. G. (2003) Equilibrium model in the description of gas extraction and headspace analysis. *J. Anal. Chem. 58*, 2–15.

(46) Snow, N. H., and Slack, G. C. (2002) Head-space analysis in modern gas chromatography. *Trends Anal. Chem. 21*, 608–617.

(47) Penton, Z. E. (2002) Headspace gas chromatography. *Compr. Anal. Chem. 37*, 279–296.

(48) Levrand, B., Fieber, W., Lehn, J.-M., and Herrmann, A. (2007) Controlled release of volatile aldehydes and ketones from dynamic mixtures generated by reversible hydrazone formation. *Helv. Chim. Acta 90*, 2281–2314.

(49) Nyqvist, H. (1983) Saturated salt solutions for maintaining specified relative humidities. *Int. J. Pharm. Technol. Prod. Manuf. 4*, 47–48.

(50) Davaran, S., Rashidi, M. R., and Hashemi, M. (2003) Synthesis and hydrolytic behaviour of 2-mercaptoethyl ibuprofenate-polyethylene glycol conjugate as a novel transdermal prodrug. *J. Pharm. Pharmacol. 55*, 513–517.

(51) Burattini, S., Colquhoun, H. M., Greenland, B. W., Hayes, W., and Wade, M. (2009) Pyrene-functionalised, alternating copolymimide for sensing nitroaromatic compounds. *Macromol. Rapid Commun. 30*, 459–463.

(52) Yamamoto, H., Mizusaki, M., Yoda, K., and Morishima, Y. (1998) Fluorescence studies of hydrophobic association of random copolymers of sodium 2-(acrylamido)-2-methylpropanesulfonate and *N*-dodecylmethacrylamide in water. *Macromolecules 31*, 3588–3594.

(53) Zhu, L.-P., Yi, Z., Liu, F., Wei, X.-Z., Zhu, B.-K., and Xu, Y.-Y. (2008) Amphiphilic graft copolymers based on ultrahigh molecular weight poly(styrene-alt-maleic anhydride) with poly(ethylene glycol) side chains for surface modification of polyethersulfone membranes. *Eur. Polym. J. 44*, 1907–1914.

(54) Mazi, H., Kibarer, G., Emregül, E., and Rzaev, Z. M. O. (2006) Bioengineering functional copolymers. IX. Poly[(maleic anhydride-co-hexene-1)-*g*-poly(ethylene glycol)]. *Macromol. Biosci. 6*, 311–321.

(55) Ding, L. M., Shi, J., and Yang, C. Z. (1997) Ion-conducting polymers based on modified alternating maleic anhydride copolymer with oligo(oxyethylene) side chains. *Synth. Met. 87*, 157–163.

(56) Suzuki, M., Mori, M., Niwa, T., Hirata, R., Furuta, K., Ishikawa, T., and Noyori, R. (1997) Chemical implications for antitumor and antiviral prostaglandins: reaction of Δ^7-prostaglandin A_1 and prostaglandin A_1 methyl esters with thiols. *J. Am. Chem. Soc. 119*, 2376–2385.

(57) Ladavière, C., Delair, T., Domard, A., Pichot, C., and Mandrand, B. (1999) Studies of the thermal stability of maleic anhydride co-polymers in aqueous solution. *Polym. Degrad. Stab. 65*, 231–241.

(58) Levinson, M. I. (1999) Rinse-added fabric softener technology at the close of the twentieth century. *J. Surfactants Deterg. 2*, 223–235.

(59) Mishra, S., and Tyagi, V. K. (2007) Esterquats: the novel class of cationic fabric softeners. *J. Oleo Sci. 56*, 269–276.

(60) Berg, J. C. (1985) The role of surfactants. *Absorbency* (Chatterjee, P. K., Ed.) pp 149−195, Elsevier, New York.
(61) Laughlin, R. G. (1991) Fabric softening. *Cationic Surfactants - Physical Chemistry, Surfactant Sci. Ser.*, Vol. 37 (Rubingh, D. N., Holland, P. M., Eds.), pp 449−467, Dekker, New York.
(62) Escher, S., and Oliveros, E. (1994) A quantitative study of factors that influence the substantivity of fragrance chemicals on laundered and dried fabrics. *J. Am. Oil Chem. Soc. 71*, 31–40.
(63) Stora, T., Escher, S., and Morris, A. (2001) The physico-chemical basis of perfume performance in consumer products. *Chimia 55*, 406–412.
(64) Liu, H., Obendorf, S. K., Leonard, M. J., Young, T. J., and Incorvia, M. J. (2005) Adsorption of aroma chemicals on cotton fabric from aqueous systems. *J. Surfactants Deterg. 8*, 311–317.
(65) Obendorf, S. K., Liu, H., Tan, K., Leonard, M. J., Young, T. J., and Incorvia, M. J. (2009) Adsorption of aroma chemicals on cotton fabric in different aqueous environments. *J. Surfactants Deterg. 12*, 43–58.
(66) Schoenmakers, R. G., van de Wetering, P., Elbert, D. L., and Hubbell, J. A. (2004) The effect of the linker on the hydrolysis rate of drug-linked ester bonds. *J. Controlled Release 95*, 291–300.
(67) Delben, F., Paoletti, S., Porasso, R. D., and Benegas, J. C. (2006) Potentiometric titrations of maleic acid copolymers in dilute aqueous solution: experimental results and theoretical interpretation. *Macromol. Chem. Phys. 207*, 2299–2310.
(68) Berthier, D., and Herrmann, A. (2008) Polymer conjugates for a controlled release of active molecules (to Firmenich SA), WO 2008/044178, *Chem. Abstract 148*, 472574.

BC100223S

Influence of the Backbone Structure on the Release of Bioactive Volatiles from Maleic Acid-Based Polymer Conjugates

Damien L. Berthier, Nicolas Paret, Alain Trachsel, and Andreas Herrmann**

Firmenich SA, Division Recherche et Développement, B.P. 239, CH-1211 Genève 8, Switzerland

SUPPORTING INFORMATION

Table S1. Conversions of the grafting reaction of β-mercapto ketone **1** onto alternating poly(maleic acid)-based copolymers **2**-**5**, determined by ^{1}H-NMR spectroscopy.

Formation of	**6**	**7**	**8**	**9**	**10**
Conversion [mol%]	51	20	50	30	75

Table S2. Concentrations of δ-damascone released from copolymers **6**-**10**, measured by GC after 1, 3, and 6 days at pH 4, 7, and 10 in ng μL^{-1} and % (in brackets) of grafted δ-damascone (see Figure 1).

	Concentration of released δ-damascone after 1, 3, and 6 days [ng μL^{-1}] ([%])					
pH	day #	**6**	**7**	**8**	**9**	**10**
4	1	1509.2 (17.3)	28.0 (0.3)	148.7 (1.7)	59.5 (0.7)	244.7 (2.8)
	3	1663.1 (19.0)	27.9 (0.3)	185.7 (2.1)	204.3 (2.3)	515.8 (5.9)
	6	1915.8 (22.0)	70.6 (0.8)	260.9 (3.0)	260.9 (3.0)	836.2 (9.6)
7	1	2092.3 (24.0)	91.9 (1.1)	180.5 (2.1)	148.5 (1.7)	472.9 (5.4)
	3	2611.8 (30.0)	118.1 (1.4)	236.8 (2.7)	403.7 (4.6)	928.6 (10.7)
	6	3342.2 (38.4)	176.2 (2.0)	279.2 (3.2)	706.4 (8.1)	1562.2 (18.0)
10	1	1183.9 (13.6)	108.3 (1.2)	214.2 (2.5)	143.0 (1.6)	502.5 (5.8)
	3	1477.3 (16.9)	136.9 (1.6)	299.8 (3.4)	536.4 (6.2)	1030.8 (11.8)
	6	2060.7 (23.7)	253.9 (2.9)	325.2 (3.7)	999.5 (11.5)	1689.9 (19.4)

Table S3. Headspace concentrations of δ-damascone released from poly(maleic acid)-based precursors **6**–**10** with respect to unmodified δ-damascone as the reference on dry cotton after 3 days. All data are average values of several measurements (see Figure 5).

Sampling time [min]	Amount of δ-damascone released [ng L^{-1}] of air from					
	reference	**6**	**7**	**8**	**9**	**10**
30	18.2	31.2	2.2	60.9	39.8	64.7
90	11.4	74.8	9.3	52.2	181.1	216.4
150	8.4	93.0	12.5	53.5	251.7	187.7
210	5.9	91.1	11.3	53.4	237.7	138.9
270	4.2	85.6	10.7	49.0	189.9	120.1
330	3.3	81.1	9.5	45.8	188.0	112.7
390	2.7	78.5	8.2	44.4	182.4	110.2
450	2.3	76.2	7.4	41.7	175.2	109.1

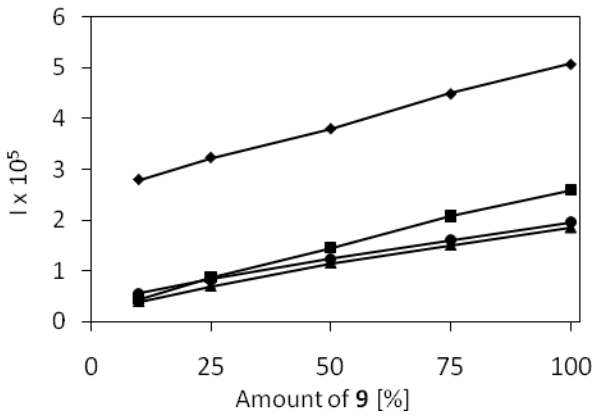


Figure S1. Fluorescence intensities (arbitrary units) measured for different amounts of poly(maleic acid)-based conjugate **9** at 378 (—♦—), 384 (—●—), 389 (—▲—), and 398 nm(—■—) in a water-based cationic surfactant emulsion (excitation at 334 nm).

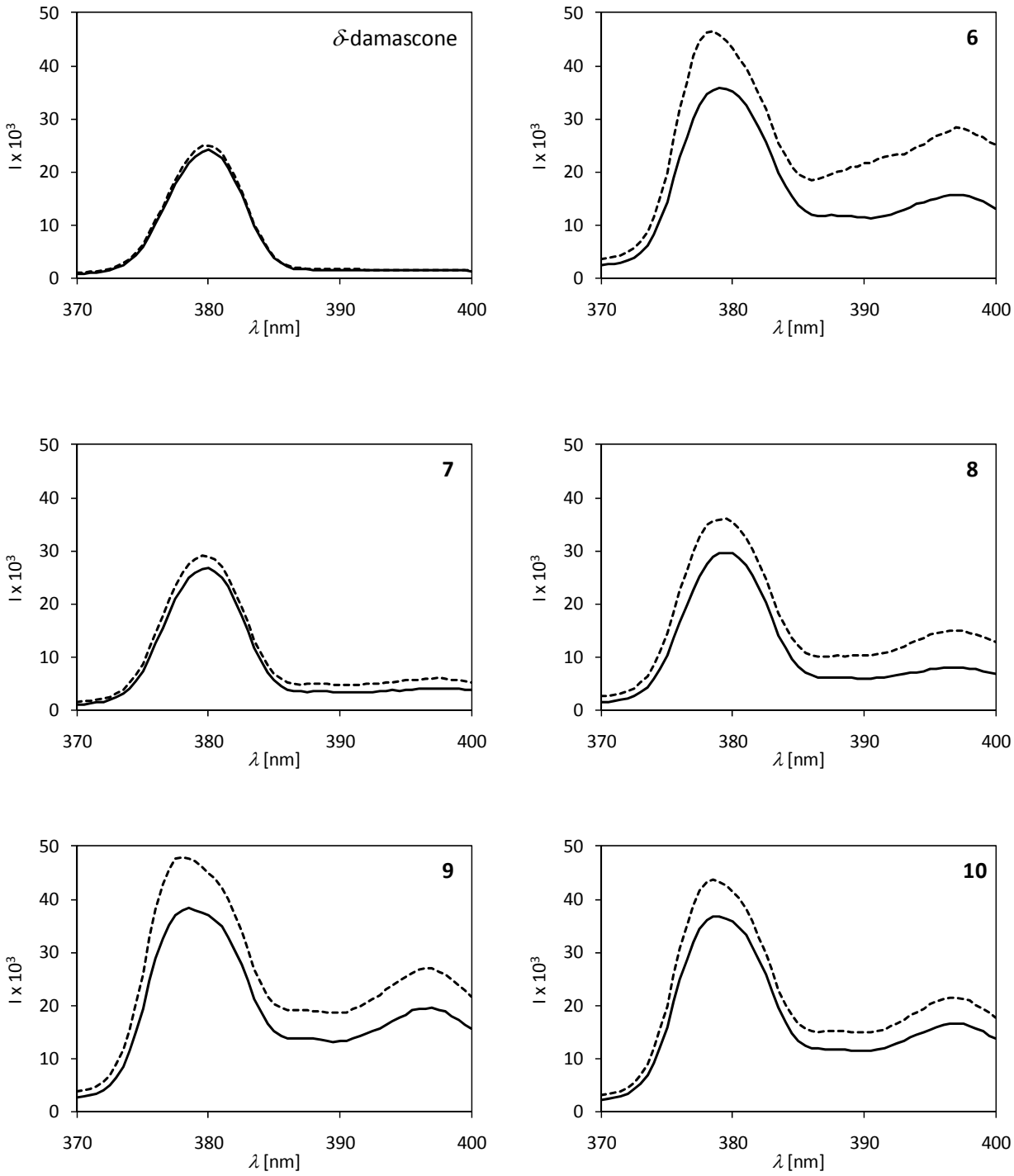


Figure S2. Fluorescence spectra (arbitrary units for I) recorded for diluted surfactant solutions in the presence of copolymers **6**-**10**, or δ-damascone as the reference, before (-----) and after (——) addition of a cotton sheet (average values of two measurements, see Table 2).

HEHEHE-Tagged Affibody Molecule May Be Purified by IMAC, Is Conveniently Labeled with $[^{99m}Tc(CO)_3]^+$, and Shows Improved Biodistribution with Reduced Hepatic Radioactivity Accumulation

Vladimir Tolmachev,*[,†,‡] Camilla Hofström,[§] Jennie Malmberg,[†] Sara Ahlgren,[‡] Seyed Jalal Hosseinimehr,[†,||] Mattias Sandström,[⊥] Lars Abrahmsén,[#] Anna Orlova,[†] and Torbjörn Gräslund[§]

Division of Biomedical Radiation Sciences, Rudbeck Laboratory, and Division of Nuclear Medicine, Department of Medical Sciences, Uppsala University, Uppsala, Sweden, Department of Molecular Biotechnology, Royal Institute of Technology, Stockholm, Sweden, Department of Radiopharmacy, Faculty of Pharmacy, Mazandaran University of Medical Sciences, Sari, Iran, Hospital Physics, Department of Oncology, Uppsala University Hospital, Uppsala, Sweden, and Affibody AB, Stockholm, Sweden. Received May 20, 2010; Revised Manuscript Received September 23, 2010

Affibody molecules are a class of small (ca. 7 kDa) robust scaffold proteins suitable for radionuclide molecular imaging of therapeutic targets in vivo. A hexahistidine tag at the N-terminus streamlines development of new imaging probes by enabling facile purification using immobilized metal ion affinity chromatography (IMAC), as well as convenient $[^{99m}Tc(CO)_3]^+$-labeling. However, previous studies in mice have demonstrated that Affibody molecules labeled by this method yield higher liver accumulation of radioactivity, compared to the same tracer lacking the hexahistidine tag and labeled by an alternative method. Two variants of the HER2-binding Affibody molecule $Z_{HER2:342}$ were made in an attempt to create a tagged tracer that could be purified by immobilized metal affinity chromatography, yet would not result in anomalous hepatic radioactivity accumulation following labeling with $[^{99m}Tc(CO)_3]^+$. In one construct, the hexahistidine tag was moved to the C-terminus. In the other construct, every second histidine residue in the hexahistidine tag was replaced by the more hydrophilic glutamate, resulting in a HEHEHE-tag. Both variants, denoted $Z_{HER2:342}$-H_6 and $(HE)_3$-$Z_{HER2:342}$, respectively, could be efficiently purified using IMAC and stably labeled with $[^{99m}Tc(CO)_3]^+$ and were subsequently compared with the parental H_6-$Z_{HER2:342}$ having an N-terminal hexahistidine tag. All three variants were demonstrated to specifically bind to HER2-expressing cells in vitro. The hepatic accumulation of radioactivity in a murine model was 2-fold lower with $[^{99m}Tc(CO)_3]^+$-$Z_{HER2:342}$-H_6 compared to $[^{99m}Tc(CO)_3]^+$-H_6-$Z_{HER2:342}$, and more than 10-fold lower with $[^{99m}Tc(CO)_3]^+$-$(HE)_3$-$Z_{HER2:342}$. These differences translated into appreciably superior tumor-to-liver ratio for $[^{99m}Tc(CO)_3]^+$-$(HE)_3$-$Z_{HER2:342}$ compared to the alternative conjugates. This information might be useful for development of other scaffold-based molecular imaging probes.

INTRODUCTION

Malignant transformation of cells is often associated with overexpression of cell surface proteins, such as different growth factor receptors. The use of antitumor agents with the ability to selectively target such overexpressed proteins increases the specificity of cancer treatment, resulting in improved therapy (*1*−*3*). Obviously, only tumors with the relevant alteration on the cell surface respond to the targeted therapy. For this reason, molecular profiling of tumors is necessary to select suitable patients. The commonly used biopsy-based methods are associated with false-negative findings due to inter- and intratumoral heterogeneity of cell surface protein exposure (*4*, *5*). An attractive alternative is in vivo radionuclide molecular imaging (RMI), which is global, minimally invasive, and less sensitive to target expression heterogeneity, and may be used repeatedly to follow the course of the disease (*6*−*8*). The precondition of successful application of RMI is high sensitivity and specificity of the imaging agent, which is provided by high accumulation in tumors and low uptake in healthy organs and tissues. High tumor uptake and rapid clearance of nonbound radiolabeled scaffold proteins provide high imaging contrast, increasing the sensitivity of imaging.

Previous studies with antibody-based imaging agents have demonstrated that imaging contrast is favored by a small size of the targeting probe (*9*). This prompted the development of protein-based imaging agents smaller than the smallest binding antibody fragment (*10*). One example is the Affibody molecules, containing only 58 amino acids (approximately 7 kDa), based on a single polypeptide, three-helix bundle domain derived from staphylococcal protein A. They lack backbone cysteines and are capable of rapid folding. Affibody molecules with high affinity and selectivity for different targets have previously been selected by phage display from libraries made by randomizing 13 surface-exposed residues on helices 1 and 2, i.e., the 2 N-terminal helices (*11*). The successful development of Affibody-based imaging agents is exemplified by $Z_{HER2:342}$, which binds to human epidermal receptor type 2 (HER2) with high affinity (K_D 22 pM) (*12*). HER2 is a relevant target for RMI since it is overexpressed in a significant fraction of many carcinomas, and since different HER2-targeted therapeutics are available (*13*).

Technetium-99m ($T_{1/2}$ = 6.0 h) is widely used in radionuclide diagnostics because of favorable energy of emitted γ-quanta

* Corresponding author. Vladimir Tolmachev, Biomedical Radiation Sciences, Rudbeck Laboratory, Uppsala University, S-751 81 Uppsala, Sweden. Phone: +46 18 471 3414, Fax: + 46 18 471 3432, E-mail: vladimir.tolmachev@bms.uu.se.

† Rudbeck Laboratory, Uppsala University.

‡ Department of Medical Sciences, Uppsala University.

§ Royal Institute of Technology.

|| Mazandaran University of Medical Sciences.

⊥ Uppsala University Hospital.

Affibody AB.

10.1021/bc1002357 © 2010 American Chemical Society
Published on Web 10/22/2010

GSSHHHHHHLQVDNKFNKEMRNAYWEIALLPNLNNQQKRAFIRSLYDDPS
QSANLLAEAKKLNDAQAPKVD

AENKFNKEMRNAYWEIALLPNLNNQQKRAFIRSLYDDPSQSANLLAEAKK
LNDAQAPKVDGSHHHHHH

MHEHEHEAENKFNKEMRNAYWEIALLPNLNNQQKRAFIRSLYDDPSQSAN
LLAEAKKLNDAQAPKVD

Figure 1. Sequences of studied proteins.

and low radiation absorbed dose burden to patients, combined with low price and a wide availability of $^{99}Mo/^{99m}Tc$ generators. An attractive approach for obtaining a protein-based imaging agent suitable for labeling with technetium-99m is to produce the tracer protein recombinantly with a hexahistidine-tag. This tag can be used both for efficient purification by immobilized metal ion affinity chromatography (IMAC) and for chelation of ^{99m}Tc-tricarbonyl ($[^{99m}Tc(CO)_3]^+$) (*14*). This very elegant labeling technique has been applied on a number of targeting proteins (*15*−*18*) to provide stable and site-specific labeling, giving uniform conjugates with reproducible chemical and pharmacological proprieties. Importantly, no additional coupling of chelators is required, and the proteins can be labeled directly after purification. This simple procedure is suitable for development of protein-based imaging agents binding new molecular targets, facilitating comparison of alternative variants of the tracer protein. However, evaluation of the dimeric His_6-$(Z_{HER2:4})_2$ anti-HER2 Affibody molecule demonstrated that $[^{99m}Tc(CO)_3]^+$-His_6-$(Z_{HER2:4})_2$ yielded high accumulation of radioactivity in the liver (*19*). Since the liver is a major metastatic site for many carcinomas, a high liver uptake is an undesirable property of any imaging agent, and hence, correct assessment of this property is very important when comparing alternative variants of a labeled tracer.

Previous studies have shown that different chelators and labeling chemistry may influence the excretion pathway and hepatic uptake of Affibody molecules. For example, increasing the hydrophilicity of the chelator reduced the hepatobiliary excretion of ^{99m}Tc-radioactivity, when the peptide-based N_3S chelators mercaptoacetyl-X-X-X (maXXX, where X is Gly, Ser, Glu, or Lys) were located at the N-terminus (*20*−*23*). In contrast, alternative amino acids in the C-terminal chelating sequence X-X-Cys (where X is Val, Asp, Ser, or Glu) yielded a similar level of hepatobiliary excretion of the radioactivity from ^{99m}Tc (*24*, *25*). Taken together, these data suggested that the properties of the N-terminal portion of the molecule are more crucial for hepatic uptake and hepatobiliary excretion than the properties of the C-terminus when chelating ^{99m}Tc by an N_3S chelator. Furthermore, comparison of the same Affibody molecule with or without an N-terminal hexahistidine tag and site-specifically labeled at the C-terminus with ^{111}In (by maleimido-DOTA) or ^{99m}Tc (by cysteine-containing peptide-based N_3S chelator) clearly showed that the presence of the hexahistidine tag led to much higher accumulation of radioactivity in the liver (*24*, *26*). Thus, the presence of an N-terminal hexahistidine tag leads to a higher uptake in the liver.

The present study was performed to test the hypothesis that the problem with high accumulation of radioactivity in the liver might be solved by either relocating the hexahistidine tag or making it more hydrophilic. The hypothesis was tested by constructing two novel affibody tracers. In the first construct, the tag was moved from the N-terminus to the C-terminus. In the second construct, the hydrophilicity of the N-terminal tag was increased by replacing three of the six histidine residues by glutamic acid residues, resulting in a HEHEHE-tag (Figure 1). Both molecules denoted $Z_{HER2:342}$-H_6 and $(HE)_3$-$Z_{HER2:342}$, respectively, could be purified by IMAC and labeled with $[^{99m}Tc(CO)_3]^+$, and both constructs yielded less radioactivity in the liver in a murine model: 2-fold and more than 10-fold less than the parent tracer, respectively. This was reflected in a significant improvement of tumor-to-liver ratio in tumor xenograft-bearing mice.

MATERIALS AND METHODS

General. Buffers were prepared using common methods from chemicals supplied by Merck (Darmstadt, Germany). High-quality Milli-Q water (resistance higher than 18 MΩ/cm) was used for preparing solutions. The IsoLink labeling kit was purchased from Covidien. NAP-5 size exclusion columns were from GE Healthcare, Uppsala, Sweden. ^{99m}Tc was obtained as pertechnetate from an Ultra-TechneKow generator (Covidien) by elution with sterile 0.9% NaCl. The yield, radiocolloid content, and radiochemical purity of the labeled Affibody constructs were analyzed using 150−771 DARK GREEN, Tec-Control Chromatography strips from Biodex Medical Systems (New York, USA) as described (*20*). Cells used during in vitro experiments were detached using trypsin−EDTA solution (0.25% trypsin, 0.02% EDTA in buffer, Biochrom AG, Berlin, Germany). For in vivo experiments, Ketalar (50 mg/mL, Pfizer, NY, USA), Rompun (20 mg/mL, Bayer, Leverkusen, Germany), and Heparin (5000 IE/mL, Leo Pharma, Copenhagen, Danmark) were used. Data on cellular uptake and biodistribution were assessed by an unpaired, two-tailed Student's *t*-test using GraphPad *Prism* (v 4.00 for Windows GraphPad Software, San Diego, California, USA) in order to determine any significant differences ($p < 0.05$).

Instrumentation. The radioactivity was measured using an automated gamma-counter with a 3 in. NaI(Tl) detector (1480 WIZARD, Wallac Oy, Turku, Finland). The distribution of radioactivity along the thin layer chromatography strips and SDS-PAGE gels was measured on a Cyclone Storage Phosphor System and analyzed using the *OptiQuant* image analysis software. Cells were counted using an electronic cell counter (Beckman Coulter).

Production and Purification of Affibody Molecules, $Z_{HER2:342}$-H_6 and $(HE)_3$-$Z_{HER2:342}$. The gene encoding $Z_{HER2:342}$ was PCR amplified from vector pAY1069-$(Z_{HER2:342})_2$ (*12*) to introduce the amino acid sequence GSHHHHHH at the C-terminus (denoted $Z_{HER2:342}$-H_6) or the amino acid sequence MHEHEHE at the N-terminus (denoted $(HE)_3$-$Z_{HER2:342}$). PCR fragments were fitted with the restriction sites for *Hin*dIII and NdeI, which were subsequently used to subclone the fragments into the expression vector pET21a(+), containing a T7 promoter (Novagen, Darmstadt, Germany). Correct DNA sequences were verified by cycle sequencing using an ABI Prism 3700 Analyzer (Applied Biosystems, CA).

The H_6-$Z_{HER2:342}$ Affibody molecule having a His_6-tag at N-terminus was produced as described by Orlova and co-workers (*12*). The molecules $Z_{HER2:342}$-H_6 and $(HE)_3$-$Z_{HER2:342}$ were produced in *Escherichia coli* strain BL21(DE3) essentially as previously described for other Affibody molecules (*27*). After fermentation, cells were harvested by centrifugation, and cell pellets were resuspended in washing buffer (50 mM Na_2HPO_4, 300 mM NaCl, pH 7). Cells were disrupted by sonication, and cell debris was removed by centrifugation.

The $Z_{HER2:342}$-H_6 Affibody molecule was recovered by IMAC purification on a Talon Metal Affinity Resin (BD Bioscience, San Jose, CA) column under native conditions essentially as recommended by the manufacturer, using acid elution (50 mM sodium acetate, 300 mM NaCl, pH 4.8).

The cleared cell lysate containing $(HE)_3$-$Z_{HER2:342}$ was heat-treated (60 °C for 10 min) followed by centrifugation (35 000 *g*, 20 min, 4 °C). The supernatant was subsequently filtered through a 0.45 μm filter (Sartorius Stedim Biotech, Aubagne

Cedex, France) before loading onto a column containing Chelating Sepharose Fast Flow (GE Healthcare, Uppsala, Sweden) with immobilized Ni^{2+}-ions. The protein was recovered by IMAC purification under native conditions using an imidazole gradient (0−500 mM) for elution, according to the manufacturer's instructions. The process was monitored using an ÄKTA explorer 100 system (GE Healthcare).

Eluted fractions containing Affibody molecules were pooled and concentrated using Vivaspin2 centrifugal concentrators (Vivascience, Hannover, Germany). The buffer was changed to PBS (137 mM NaCl, 8 mM Na_2HPO_4, 1.5 mM KH_2PO_4, 2.7 mM KCl, pH 7.4) by dialysis overnight at 4 °C using SnakeSkin Pleated Dialysis Tubing (Pierce, Rockford, IL). Protein concentrations were determined from the absorbance at 280 nm and by amino acid analysis (Amino Acid Analysis Center, Uppsala University).

Sample Purity Analysis. Analytic reverse-phase high-performance liquid chromatography (RP-HPLC) was used to investigate sample purity and the retention times of $Z_{HER2:342}$-H_6, $(HE)_3$-$Z_{HER2:342}$, and H_6-$Z_{HER2:342}$ using a C18 column on an Agilent 1200 HPLC system (Agilent Technologies, Santa Clara, CA). Samples containing 0.2 mg Affibody molecule were injected sequentially onto the column and eluted using a 20 min gradient of 20−65% B (A, 0.1% trifluoroacetic acid (TFA) in H_2O; B, 0.1% TFA in CH_3CN), with a flow rate of 0.8 mL/min. Each integrated peak area corresponding to the Affibody molecule was compared to the area of all peaks to calculate the purity.

Mass Spectrometry Analysis. The molecular mass of $Z_{HER2:342}$-H_6 and $(HE)_3$-$Z_{HER2:342}$ was determined by mass spectrometry analysis using a 6520 Accurate-Mass Q-TOF LC/MS instrument (Agilent Technologies, Santa Clara, CA). The molecular masses were retrieved using Agilent *MassHunter B.02.00* software (Agilent Technologies) yielding the isotopic and charge state information.

Biosensor Analysis. Affinity constants were measured by real-time biospecific interaction analyses using a Biacore 2000 instrument (Biacore AB, Uppsala, Sweden). The extracellular portion of human HER2 fused to the Fc region of human IgG (R&D Systems, Minneapolis, MN) was immobilized (∼1000 RU) on a flow-cell surface of a CM5 sensor chip (Biacore Life Science, GE Healthcare, Uppsala, Sweden) by amine coupling, according to the manufacture's instructions. Another sensor chip was activated and deactivated for use in the reference flow-cell. Dilution series consisting of five different concentrations were prepared for each Affibody construct and injected in duplicates over the flow-cells with a flow rate of 50 μL/min. The concentration ranges used were 90 pM to 1.5 nM for $Z_{HER2:342}$-H_6, 65 pM to 1 nM for $(HE)_3$-$Z_{HER2:342}$, and 200 pM to 2.9 nM for H_6-$Z_{HER2:342}$. After each sample injection, the flow-cell surface was regenerated by 20 μL of 15 mM HCl. The dissociation equilibrium constant (K_D), the association rate constant (k_a), and the dissociation rate constant (k_d) were calculated using *BIAevaluation 3.2* software (Biacore Life Science, GE Healthcare, Uppsala, Sweden), assuming a one-to-one interaction model.

Melting Point Analysis. Variable temperature measurements of $Z_{HER2:342}$-H_6 and $(HE)_3$-$Z_{HER2:342}$ were performed using a JASCO J-810 spectropolarimeter instrument (JASCO, Tokyo, Japan). Samples were diluted to a concentration of 60 μM in PBS, and the absorbance was measured at 221 nm during a temperature gradient increasing 5 °C/min ranging from 20 to 90 °C. Circular dichroism spectra were also recorded from 250 to 195 nm at 20 °C, before and after each variable temperature measurement.

Labeling of H_6-$Z_{HER2:342}$, $Z_{HER2:342}$-H_6, $(HE)_3$-$Z_{HER2:342}$. Labeling of H_6-$Z_{HER2:342}$, $Z_{HER2:342}$-H_6, and $(HE)_3$-$Z_{HER2:342}$ with $[^{99m}Tc(CO)_3]^+$ was performed as described by Orlova and co-workers (*19*). Briefly, 500 μL (350 MBq-2 GBq) of $^{99m}TcO_4^-$-containing generator eluate was added to a vial with the IsoLink kit. The mixture was incubated at 100 °C during 20 min. Thereafter, 40 μL of mixture were transferred to a tube containing 50 μg (∼6.8 nmol) Affibody molecule in 40 μL PBS and incubated at 50 °C. The labeling yield after incubation for 10, 20, 40, and 60 min was monitored by ITLC to assess labeling kinetics. When the ITLC strips were eluted with PBS pertechnetate, as well as carbonyl and histidine complexes of ^{99m}Tc migrated with the eluent front (R_f = 1.0), while Affibody molecules do not migrate under these conditions (R_f = 0.0). To determine the presence of reduced hydrolyzed technetium, ITLC was eluted with pyridine/acetic acid:water (5:3:1.5). When this eluent was used, the technetium colloids stayed at the application point (R_f = 0.0), while radiolabeled Affibody molecules, as well as pertechnetate and carbonyl complexes of ^{99m}Tc, migrated with the solvent front (R_f = 1.0). The experiments were performed in quadruplicate. In addition, blank experiments were performed, where the Affibody molecules were omitted.

For in vitro and in vivo studies, labeling during 60 min was selected. The labeled Affibody molecules were purified using NAP-5 desalting columns (GE Healthcare), pre-equilibrated and eluted with PBS. The purity of each preparation was evaluated using thin layer chromatography.

To evaluate storage stability (shelf life), the purified radiolabeled conjugates were kept at ambient temperature (23 °C) and analyzed after 1, 2, 6, and 24 h. To predict in vivo stability of the ^{99m}Tc-label, a histidine challenge (*14*) of conjugates was performed. Briefly, a 500- and 5000-fold excess of histidine was added to the conjugate. After incubation at 37 °C during 1 h, the mixture was analyzed using radio-ITLC. The incubation time was selected on the basis of previous data on the biodistribution of Affibody molecules, showing that more than 95% of Affibody-related radioactivity was cleared from the blood 1 h after injection, irrespectively of label (*21*, *26*, *28*). SDS-PAGE analysis was performed to confirm the stability test data. Two samples of each labeled conjugate were incubated at 37 °C with 5000-fold excess of histidine during 1 h. After incubation, samples were analyzed by SDS-PAGE on NuPAGE 4−12% Bis-Tris Gel (Invitogen) in MES buffer (200 V constant). To facilitate interpretation of the result, a sample of ^{99m}Tc-pertechnetate and a sample of the same conjugate not treated with histidine were analyzed in parallel with the test samples on the same gel. Distribution of radioactivity along the SDS-PAGE gels was measured using a Cyclone Storage Phosphor System.

In Vitro Studies. The in vitro HER2 specificity of the ^{99m}Tc-labeled Affibody molecules was evaluated using SKOV-3 ovarian carcinoma cell line and two prostate cancer cell lines, DU-145 and PC-3. All cell lines were purchased from American Type Tissue Culture Collection (ATCC) via LGC Promochem, Borås, Sweden. SKOV-3 was selected because it has a high level of HER2 expression (1.2×10^6 receptors per cell) (*29*) and was used in our earlier studies on radiolabeled Affibody molecules. Prostate cancer cell lines (both expressing $\sim 5 \times 10^4$ receptors per cell, A. Orlova and J. Malmberg, unpublished results) were selected because of our intention to visualize HER2-expression in prostate cancer in future studies. In vitro specificity testing was performed according to the methods described earlier (*24*). Briefly, a solution of each conjugate (concentration 0.2 nM) was added to six Petri dishes (ca. 10^6 cells in each). A 1000-fold excess of nonlabeled recombinant $Z_{HER2:342}$ was added 5 min before the radiolabeled conjugates to saturate the receptors in blocking experiments. The cells were

incubated during 1 h in a humidified incubator at 37 °C. Thereafter, the media were collected, the cells were detached by trypsin−EDTA solution, and the radioactivity in cells and media was measured to calculate the fraction of cell-bound radioactivity.

The cellular retention and internalization of radioactivity were evaluated as described by Wållberg and Orlova (*22*) using the SKOV-3 cell line. Tumor cells were incubated with radiolabeled conjugate (1 nM) for 1 h at 4 °C. Thereafter, the incubation media was discarded and the cells were washed three times using ice-cold serum-free medium. After addition of 1 mL complete medium, the cells were further incubated at 37 °C. Three dishes were analyzed for cell-associated radioactivity at predetermined time points, up to 24 h. Medium was collected, and the cells were washed three times with ice-cold serum-free medium—these two steps were omitted for the zero time point—and treated with 0.5 mL of 4 M urea solution in 0.2 M glycine buffer, pH 2.5, for 5 min on ice. The acid fraction was collected, and cells were washed with another 0.5 mL acid solution. The radioactivity in the acid wash fraction was considered to be membrane-bound radioactivity. After addition of 0.5 mL of 1 M NaOH, the cells were incubated at 37 °C for at least 0.5 h and the basic wash solution collected. Dishes were washed with an additional 0.5 mL of basic solution. The radioactivity in the alkaline fractions was considered to be internalized radioactivity.

The antigen-binding capacity (ABC) was analyzed according to the method described and validated by Wållberg and co-workers (*30*). The SKOV-3 cells were scraped from culture flasks, and three cell pellets containing 10^7 cells were formed by gentle centrifugation. A solution of radiolabeled Affibody molecules in cell culture medium (1 mL, 0.26 pmol) was added to each pellet to provide approximately a 100-fold molar access of receptor over conjugate. The cells were gently resuspended and incubated for 1 h at 4 °C under gentle shaking. After incubation, cells were pelleted and 0.5 mL of the supernatant was transferred to new tubes. The radioactivity of the samples was measured, and the ABC was calculated as

$$\mathrm{ABC} = (A_{\mathrm{pellet+media}} - A_{\mathrm{media}})/(A_{\mathrm{pellet+media}} + A_{\mathrm{media}}) \times 100\%$$

In Vivo Studies. All animal experiments were planned and performed in accordance with national legislation on laboratory animals' protection and were approved by the Local Ethics Committee for Animal Research.

Male NMRI mice (18 weeks old, weight 32.4 ± 1.7 g) were used in the biodistribution studies. The animals were intravenously injected with 520 kBq (1 μg, 0.125 nmol) of $[^{99m}Tc(CO)_3]^+$-H_6-$Z_{HER2:342}$, $[^{99m}Tc(CO)_3]^+$-$Z_{HER2:342}$-H_6, or $[^{99m}Tc(CO)_3]^+$-$(HE)_3$-$Z_{HER2:342}$ diluted in 100 μL PBS. Mice were sacrificed and dissected at 4 or 24 h after injection.

The mice were euthanized at predetermined time points by an intraperitoneal injection of Ketalar-Rompun solution (20 μL of solution per gram body weight: Ketalar, 10 mg/mL; Rompun, 1 mg/mL) followed by heart puncture with a 1 mL syringe rinsed with Heparine (5000 IE/mL). Blood and organ samples—lung, liver, spleen, stomach, kidneys, salivary gland, thyroid, muscle, bone, intestines (with content)—and the remaining carcass were collected, weighed, and the radioactivity measured as described above. The organ uptake values are expressed as percent of injected dose per gram of tissue (% ID/g), except for the intestines and the remaining carcass where values are expressed as % ID per whole sample.

Male outbreed NMRI *nu*/*nu* mice were used in tumor targeting experiments. Approximately 10^6 LS174T colon adenocarcinoma cells (ATCC) (expressing ~6×10^4 receptors per cell; A. Orlova, unpublished results) were subcutaneously implanted in the right hind leg. At the time of the biodistribution experiment, the average tumor size was 0.74 ± 0.39 g.

Animals were randomized into groups of four and injected intravenously with 1 μg $[^{99m}Tc(CO)_3]^+$-H_6-$Z_{HER2:342}$, $[^{99m}Tc(CO)_3]^+$-$Z_{HER2:342}$-H_6, or $[^{99m}Tc(CO)_3]^+$-$(HE)_3$-$Z_{HER2:342}$ conjugate (40 kBq) in 100 μL PBS. To verify the specificity of targeting by $[^{99m}Tc(CO)_3]^+$-$(HE)_3$-$Z_{HER2:342}$, HER2 receptors were presaturated in one additional group of mice by a subcutaneous injection with 500 μg of unlabeled H_6-$Z_{HER2:342}$ 45 min before injection of the labeled conjugate. The animals were euthanized at 4 h p.i., and the biodistribution was studied as described above.

For gamma camera imaging, two mice bearing LS174T xenografts were injected with 1.5 MBq (1 μg) $[^{99m}Tc(CO)_3]^+$-H_6-$Z_{HER2:342}$ or an equal amount of $[^{99m}Tc(CO)_3]^+$-$(HE)_3$-$Z_{HER2:342}$, respectively. The animals were euthanized at 4 h p.i. by overdosing Ketalar/Rompun. After euthanasia, the urinary bladders were dissected. Imaging of both mice was performed simultaneously at the department of Nuclear Medicine at Uppsala University Hospital using a Millenium VG gamma camera (General Electric) equipped with a low-energy, high-resolution (LEHR) collimator. Acquisition of static images was performed with a 256 × 256 matrix and a zoom factor of 3. The energy window settings were 140 keV, 15%.

RESULTS

Production and Purification of Affibody Molecules with Different Histidine Tags. The affibody tracers were produced recombinantly in *Escherichia coli* followed by cell disruption by sonication. $Z_{HER2:342}$-H_6 was directly purified from the lysate by IMAC using a column with immobilized Co^{2+}. Purification of $(HE)_3$-$Z_{HER2:342}$ was performed by heat-treating the lysate at 60 °C for 10 min to precipitate endogenous *E. coli* proteins followed by centrifugation and purification by IMAC using a column with immobilized Ni^{2+}. Purification of $Z_{HER2:342}$-H_6 resulted in an essentially pure protein of the expected molecular mass (Figure 2). Samples taken after the different steps in the purification of $(HE)_3$-$Z_{HER2:342}$ were analyzed by SDS-PAGE and showed that the heat-treatment resulted in reduction of endogenous *E. coli* proteins and that the pooled and concentrated material after IMAC was essentially pure with only one band having the expected molecular mass (Figure 2).

Analysis of Physical Properties of Purified Affibody Constructs. Analytic RP-HPLC analysis showed a purity for both $Z_{HER2:342}$-H_6 and $(HE)_3$-$Z_{HER2:342}$ of over 90% (Table 1). The molecular masses of $Z_{HER2:342}$-H_6 and $(HE)_3$-$Z_{HER2:342}$ were determined by mass spectrometry analysis and showed a good correlation with the theoretical values (Table 1). The K_D value for H_6-$Z_{HER2:342}$ interacting with HER2 was determined to be 23 pM, essentially identical to the previously determined 22 pM (*12*). The K_D values obtained for $Z_{HER2:342}$-H_6 and $(HE)_3$-$Z_{HER2:342}$ were similar, 20 and 18 pM, respectively (Table 1), indicating that neither the location nor the composition of the histidine tag influenced the HER2 binding.

$Z_{HER2:342}$-H_6 and $(HE)_3$-$Z_{HER2:342}$ were also analyzed by circular dichroism, showing that both molecules had a melting temperature of 65 °C (Table 2), correlating well with the previously reported value for H_6-$Z_{HER2:342}$ (63 °C) (*12*). Also, both Affibody molecules gave CD spectra showing high α-helical content, similar to those previously determined for H_6-$Z_{HER2:342}$. The spectra recorded for both constructs before and after heating to 90 °C were highly similar, indicating that both molecules refolded efficiently (Figure 2).

Labeling of H_6-$Z_{HER2:342}$, $Z_{HER2:342}$-H_6, $(HE)_3$-$Z_{HER2:342}$. The use of labeling conditions optimized by Orlova and co-workers (*19*) enabled efficient labeling, resulting in a radiochemical yield of more than 80% after 60 min of incubation with $[^{99m}Tc(CO)_3(H_2O)_3]^+$ for all conjugates (Figure 3). Labeling of H_6-$Z_{HER2:342}$ was somewhat more efficient than labeling of

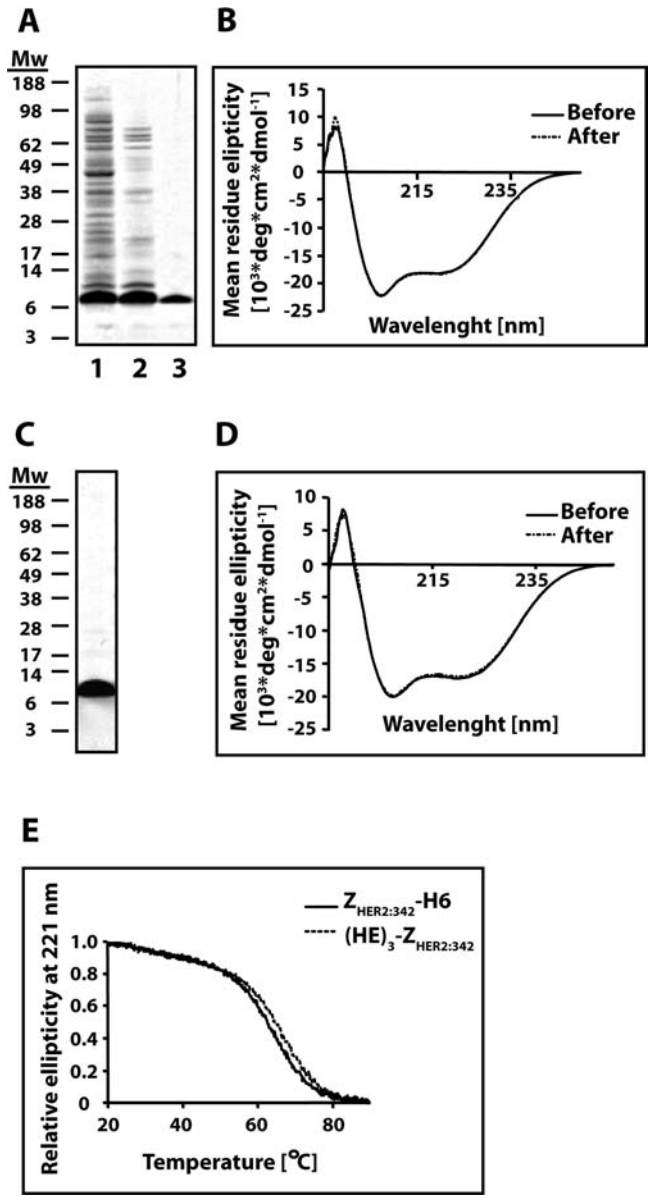


Figure 2. Analysis of $Z_{HER2:342}$-H6 and HEHEHE-$Z_{HER2:342}$ Affibody molecules. SDS-PAGE analysis of samples taken during the purification of HEHEHE-$Z_{HER2:342}$ is shown in panel A. Lane 1, sample after cell lysis and initial clarification; lane 2, sample after heat-treatment; lane 3, sample after IMAC purification. Panel B: an overlay of CD-spectrum recorded before and after thermal unfolding (as in panel E) of HEHEHE-$Z_{HER2:342}$. Panel C: SDS-PAGE analysis of a sample of the eluted material after IMAC purification of $Z_{HER2:342}$-H6. Panel D: an overlay of CD-spectrum recorded before and after thermal unfolding (as in panel E) of $Z_{HER2:342}$-H6. Panel E: overlay of the relative ellipticity measured by CD-spectrometry at 221 nm as a function of temperature for HEHEHE-$Z_{HER2:342}$ and $Z_{HER2:342\text{-}H6}$.

Table 1. Characteristics of Affibody Molecules

	Affibody molecule		
	$(HE)_3$-$Z_{HER2:342}$	$Z_{HER2:342}$-H_6	H_6-$Z_{HER2:342}$
calculated M_w (Da)	7835	7872	8215
found M_w (Da)	7836	7873	8215
sample purity (%)	92.6	95.6	98.0
RP-HPLC retention time (min)	15.6	15.3	15.6
T_m (°C)	65	65	63
K_D (pM)	18	20	23
K_a (M^{-1} s^{-1})	7.0×10^6	2.2×10^7	4.0×10^6
K_s (s^{-1})	1.2×10^{-4}	4.5×10^{-4}	8.79×10^{-5}

$Z_{HER2:342}$-H_6 and $(HE)_3$-$Z_{HER2:342}$. A simple purification using a disposable desalting column provided isolated yield of 75 ± 7%, 71 ± 12%, and 77 ± 4% for $[^{99m}Tc(CO)_3]^+$-H_6-$Z_{HER2:342}$, $[^{99m}Tc(CO)_3]^+$-$Z_{HER2:342}$-H_6, and $[^{99m}Tc(CO)_3]^+$-$(HE)_3$-$Z_{HER2:342}$, respectively (mean ± standard deviation, $n = 3$). The radiochemical purity was over 95%, and the specific radioactivity was in the range 1.7−2 MBq/μg (14−15.8 GBq/μmol). Radiocolloid formation was very low, less than 1.5% with all three constructs.

Table 2. In Vitro Stability of $[^{99m}Tc(CO)_3]^+$-H_6-$Z_{HER2:342}$, $[^{99m}Tc(CO)_3]^+$-$Z_{HER2:342}$-H_6, and $[^{99m}Tc(CO)_3]^+$-$(HE)_3$-$Z_{HER2:342}$[a]

	stability in PBS at ambient temperature		
	$[^{99m}Tc(CO)_3]^+$-H_6-$Z_{HER2:342}$	$[^{99m}Tc(CO)_3]^+$-$Z_{HER2:342}$-H_6	$[^{99m}Tc(CO)_3]^+$-$(HE)_3$-$Z_{HER2:342}$
0	99.9 ± 0.9	98.2 ± 0.2	99.3 ± 0.1
1 h	99.8 ± 0.2	97.8 ± 0.2	98.6 ± 0.1
2 h	99.0 ± 0.2	98.1 ± 0.2	99.7 ± 0.2
6 h	99.6 ± 0	97.7 ± 0.6	99.5 ± 0.3
24 h	97.2 ± 0.2	96.7 ± 0	98.5 ± 0.8
	Histidine Challenge (1 h at 37 °C)		
control	99.1	96.5	99.0
500-fold excess histidine	98.5 ± 0.2	95.2 ± 0.7	98.4 ± 0.5
5000-fold excess histidine	98.2 ± 0.2	95.1 ± 0.9	98.4 ± 0.2

[a] Each data point represents an average from three samples ± standard deviation.

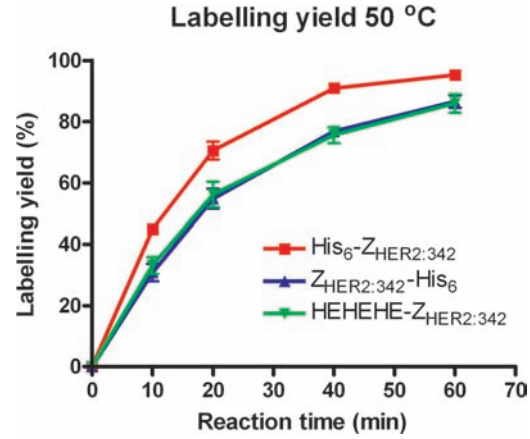


Figure 3. Labeling kinetics of Affibody molecules using IsoLink at 50 °C. $[^{99m}Tc(CO)_3(H_2O)_3]^+$ was added to 50 μg of Affibody molecules in 40 + l PBS. After 10, 20, 40, and 60 min of incubation, samples of the reaction mixture were analyzed using thin-layer chromatography. Labeling yields are presented as an average from four independent experiments with the error bars corresponding to ±1 standard deviation.

The results from the stability tests are presented in Table 2 and Figure 4, showing that all conjugates demonstrated a remarkably high stability. The loss of radioactivity was about 1% after 24 h incubation in PBS at room temperature. All constructs showed a high stability of label attachment in the histidine challenge; the release of technetium-99m was only minor and independent of the excess of free histidine. The results were comparable with previously published data for ^{99m}Tc His-tag-labeled compounds (*14, 19*). Figure 4 shows a representative radioactivity pattern after SDS-PAGE analysis of a sample from 60 min incubation of ($[^{99m}Tc(CO)_3]^+$-$(HE)_3$-$Z_{HER2:342}$) with 5000-fold excess of histidine at 37 °C. ^{99m}Tc-pertechnetate and a control sample incubated in PBS at room temperature were included for comparison. The main peak corresponds to migration of a monomeric Affibody molecule. The only other radioactivity peak corresponds to low-molecular-weight compounds, such as ^{99m}Tc-pertechnetate. This peak did not contain more than 1.1% of the total activity after the challenge, showing high stability of the complex.

In Vitro Studies. Binding specificity tests (Table 3) indicated that the binding of all ^{99m}Tc-labeled Affibody constructs to living HER2-expressing cells was receptor mediated; saturation of the

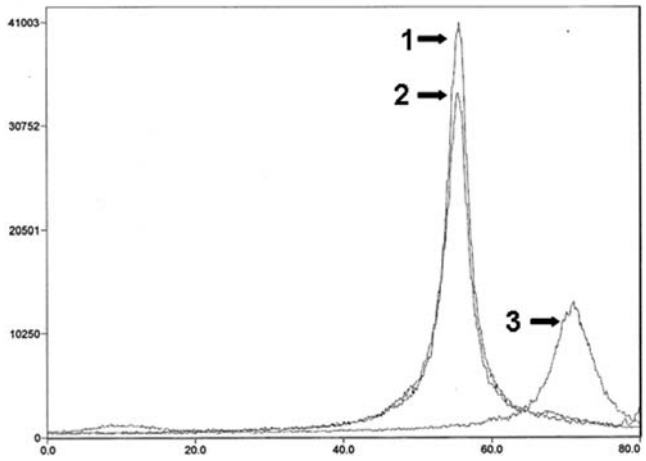


Figure 4. SDS-PAGE analysis of $[^{99m}Tc(CO)_3]^+$-$(HE)_3$-$Z_{HER2:342}$ stability under histidine challenge. Distribution of radioactivity along lanes was visualized and quantified using Cyclone Storage Phosphor System. 1, $[^{99m}Tc(CO)_3]^+$-$(HE)_3$-$Z_{HER2:342}$ control sample, which was incubated in PBS at room temperature for 1 h; 2, $[^{99m}Tc(CO)_3]^+$-$(HE)_3$-$Z_{HER2:342}$ sample, which was incubated in 5000-fold excess of histidine at 37 °C for 1 h; 3, ^{99m}Tc-pertechnetate was used as a marker for low-molecular-weight compounds.

Table 3. Specificity of Binding of Technetium-99m-Labeled Affibody Molecules to HER2-Expressing Cells in Vitro[a]

	nonblocked	blocked	*p*-value
SKOV-3			
$[^{99m}Tc(CO)_3]^+$-H_6-$Z_{HER2:342}$	48.9 ± 0.8	2.3 ± 0.5	<0.0005
$[^{99m}Tc(CO)_3]^+$-$Z_{HER2:342}$-H_6	46 ± 2	3.0 ± 0.1	<0.0005
$[^{99m}Tc(CO)_3]^+$-$(HE)_3$-$Z_{HER2:342}$	48 ± 2	0.9 ± 0.1	<0.0005
DU-145			
$[^{99m}Tc(CO)_3]^+$-H_6-$Z_{HER2:342}$	6.1 ± 0.2	3.0 ± 0.3	<0.0005
$[^{99m}Tc(CO)_3]^+$-$Z_{HER2:342}$-H_6	9.0 ± 0.4	3.1 ± 0.2	<0.0005
$[^{99m}Tc(CO)_3]^+$-$(HE)_3$-$Z_{HER2:342}$	3.19 ± 0.04	1.4 ± 0.3	<0.0005
PC-3			
$[^{99m}Tc(CO)_3]^+$-H_6-$Z_{HER2:342}$	6.7 ± 0.1	3.6 ± 0.1	<0.0005
$[^{99m}Tc(CO)_3]^+$-$Z_{HER2:342}$-H_6	6.8 ± 1.0	3.4 ± 0.2	<0.005
$[^{99m}Tc(CO)_3]^+$-$(HE)_3$-$Z_{HER2:342}$	3.0 ± 0.2	0.8 ± 0.1	<0.0005

[a] The test was performed on the ovarian cancer cell line, SKOV-3 (high expression level) and prostate cancer cell lines, DU-145 and PC-3 (both with low expression level). For pre-saturation of antigens, a 1000-fold molar excess of nonradioactive Affibody molecules was added. Data are presented as mean values of percent added radioactivity that is cell-bound from three cell dishes and standard deviations.

receptors by preincubation with nonlabeled $Z_{HER2:342}$ significantly decreased the binding of the radiolabeled Affibody molecules. The level of cell-associated radioactivity was appreciably lower for both prostate cancer cell lines PC-3 and DU-145 compared to the ovarian carcinoma cell line SKOV-3, reflecting the lower expression level of HER2.

The cellular retention and internalization test showed that all conjugates were efficiently retained by HER2-expressing cells (Figure 5). The cellular retention of total radioactivity was generally high, with 80.1 ± 0.5%, 47.7 ± 0.1%, and 65.3 ± 1.1% cell-associated after 24 h of incubation at 37 °C, for $[^{99m}Tc(CO)_3]^+$-H_6-$Z_{HER2:342}$, $[^{99m}Tc(CO)_3]^+$-$Z_{HER2:342}$-H_6, and $[^{99m}Tc(CO)_3]^+$-$(HE)_3$-$Z_{HER2:342}$, respectively. In contrast, the internalization rate differed, being highest for $[^{99m}Tc(CO)_3]^+$-H_6-$Z_{HER2:342}$ and lowest for $[^{99m}Tc(CO)_3]^+$-$Z_{HER2:342}$-H_6. The overall cellular retention correlated directly with the internalization rate of the conjugates.

The antigen binding capacity after labeling was retained to a very high extent. The fraction of conjugate bound to approximately 100-fold receptor excess was 79.6 ± 0.6%, 80.5 ± 0.4%, and 70.3 ± 7.3% for $[^{99m}Tc(CO)_3]^+$-H_6-$Z_{HER2:342}$, $[^{99m}Tc(CO)_3]^+$-$Z_{HER2:342}$-H_6, and $[^{99m}Tc(CO)_3]^+$-$(HE)_3$-$Z_{HER2:342}$, respectively. These values are similar to those previously observed for ^{99m}Tc-labeled Affibody molecules (*21*, *22*).

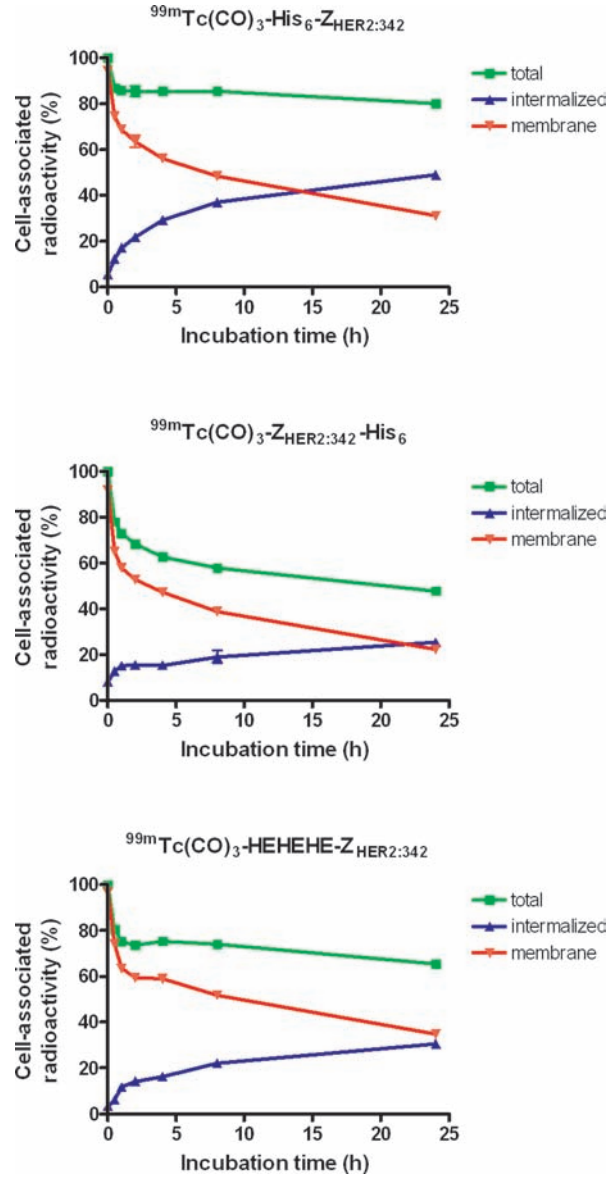


Figure 5. Cell-associated radioactivity as a function of time after interrupted incubation of SKOV-3 cells with $[^{99m}Tc(CO)_3]^+$-H6-$Z_{HER2:342}$, $[^{99m}Tc(CO)_3]^+$-$Z_{HER2:342}$-H6, or $[^{99m}Tc(CO)_3]^+$-$(HE)_3$-$Z_{HER2:342}$. The cell-associated radioactivity at time zero after the interrupted incubation was defined as 100%. The radioactivity that was removed from cells by treatment with 4 M urea solution in 0.2 M glycine buffer, pH 2.0, was considered membrane-bound and the rest internalized. Data are presented as an average value from 3 dishes ± standard deviation. Due to the small standard deviation, not all error bars are visible behind the symbols.

In Vivo Studies. Data on the comparative biodistribution of $[^{99m}Tc(CO)_3]^+$-H_6-$Z_{HER2:342}$, $[^{99m}Tc(CO)_3]^+$-$Z_{HER2:342}$-H_6, and $[^{99m}Tc(CO)_3]^+$-$(HE)_3$-$Z_{HER2:342}$ in male NMRI mice at 4 and 24 h after intravenous injection are presented in Table 4 and Table 5, respectively. The general pattern of all three conjugates was typical for Affibody molecules, with rapid clearance from blood, nonspecific compartments, and the carcass. The renal clearance was accompanied by reabsorption, which resulted in an appreciable accumulation of radioactivity in the kidneys (80−100% ID/g at 4 h after injection). The average radioactivity in the gastrointestinal tract, including content, was below 5% for all

Table 4. Biodistribution of ^{99m}Tc-Labeled Affibody Molecules in Male NMRI Mice, 4 h after Intravenous Injection[a]

	$[^{99m}Tc(CO)_3]^+$-H_6-$Z_{HER2:342}$	$[^{99m}Tc(CO)_3]^+$-$Z_{HER2:342}$-H_6	$[^{99m}Tc(CO)_3]^+$-$(HE)_3$-$Z_{HER2:342}$
blood	0.19 ± 0.06^b	0.9 ± 0.4^d	0.28 ± 0.04^c
lung	0.6 ± 0.1^b	0.9 ± 0.1^d	0.24 ± 0.02^c
liver	10 ± 3^b	5 ± 1^d	0.9 ± 0.2^c
spleen	1.3 ± 0.3^b	0.8 ± 0.1^d	0.17 ± 0.03^c
stomach	0.6 ± 0.3	0.7 ± 0.2^d	0.20 ± 0.08
kidney	92 ± 23	100 ± 16	80 ± 4
salivary gland	0.51 ± 0.10	0.6 ± 0.1^d	0.19 ± 0.01^c
thyroid*	0.01 ± 0.01	0.01 ± 0.01^d	0.004 ± 0.001
muscle	0.13 ± 0.03^b	0.20 ± 0.02^d	0.052 ± 0.005^c
intestines (with content)*	1.9 ± 0.2	2.5 ± 0.6	3 ± 2
carcass*	4.9 ± 1.0^b	7.2 ± 1.0^d	2.2 ± 0.4^c

[a] The concentration of radioactivity in different organs is expressed as % ID/g, and presented as an average value from 4 animals ± standard deviation. * data for thyroid, intestines with content and carcass are presented as % of injected radioactivity per whole sample;. [b] Significant difference between $[^{99m}Tc(CO)_3]^+$-H_6-$Z_{HER2:342}$ and $[^{99m}Tc(CO)_3]^+$−$Z_{HER2:342}$-H_6. [c] Significant difference between $[^{99m}Tc(CO)_3]^+$-H_6-$Z_{HER2:342}$ and $[^{99m}Tc(CO)_3]^+$-$(HE)_3$-$Z_{HER2:342}$. [d] Significant difference between $[^{99m}Tc(CO)_3]^+$-$Z_{HER2:342}$-H_6 and $[^{99m}Tc(CO)_3]^+$-$(HE)_3$-$Z_{HER2:342}$.

Table 5. Biodistribution of ^{99m}Tc-Labeled Affibody Molecules in Male NMRI Mice, 24 h after Intravenous Injection[a]

	$[^{99m}Tc(CO)_3]^+$-H_6-$Z_{HER2:342}$	$[^{99m}Tc(CO)_3]^+$-$Z_{HER2:342}$-H_6	$[^{99m}Tc(CO)_3]^+$-$(HE)_3$-$Z_{HER2:342}$
blood	0.07 ± 0.02^b	0.19 ± 0.04^d	0.10 ± 0.02^c
lung	0.34 ± 0.03^b	0.46 ± 0.06^d	0.12 ± 0.02^c
liver	7 ± 1^b	2.9 ± 0.5^d	0.61 ± 0.08^c
spleen	0.8 ± 0.1^b	0.47 ± 0.07^d	0.10 ± 0.02^c
stomach	0.21 ± 0.06	0.28 ± 0.03^d	0.07 ± 0.02^c
kidney	45 ± 6	56 ± 10	43 ± 6
salivary gland	0.24 ± 0.04	0.25 ± 0.03^d	0.06 ± 0.01^c
thyroid*	0.0041 ± 0.0009	0.006 ± 0.003	NM
muscle	0.07 ± 0.01	0.09 ± 0.02^d	0.024 ± 0.003^c
intestines (with content)*	1.10 ± 0.09	1.0 ± 0.2^d	0.39 ± 0.05^c
carcass*	2.7 ± 0.3	3.3 ± 0.4^d	0.92 ± 0.08^c

[a] The concentration of radioactivity is expressed as % ID/g, and presented as an average value from 4 animals ± standard deviation. * data for thyroid, intestines with content, and carcass are presented as % of injected radioactivity per whole sample. NM = not measurable. [b] Significant difference between $[^{99m}Tc(CO)_3]^+$-H_6-$Z_{HER2:342}$ and $[^{99m}Tc(CO)_3]^+$−$Z_{HER2:342}$-H_6. [c] Significant difference between $[^{99m}Tc(CO)_3]^+$-H_6-$Z_{HER2:342}$ and $[^{99m}Tc(CO)_3]^+$-$(HE)_3$-$Z_{HER2:342}$. [d] Significant difference between $[^{99m}Tc(CO)_3]^+$-$Z_{HER2:342}$-H_6 and $[^{99m}Tc(CO)_3]^+$-$(HE)_3$-$Z_{HER2:342}$.

conjugates, showing minimal excretion of conjugates or their radiocatabolites via the bile. The radioactivity uptake in stomach, salivary gland, and thyroid was low for all three conjugates, indicating that no pertechnetate was released in vivo. However, some differences in biodistribution were seen between conjugates (see Table 4 and Table 5). For example, the blood clearance of $[^{99m}Tc(CO)_3]^+$-H_6-$Z_{HER2:342}$ was the most rapid. However, the most remarkable difference in biodistribution was the large difference in hepatic accumulation of radioactivity. Four hours after injection, the concentration of radioactivity in the liver was 2-fold lower with $[^{99m}Tc(CO)_3]^+$-$Z_{HER2:342}$-H_6 than with $[^{99m}Tc(CO)_3]^+$-H_6-$Z_{HER2:342}$ (5.3 ± 1.1% ID/g compared to 10.3 ± 2.8% ID/g; $p < 0.05$). At the same time point, the concentration of radioactivity in the liver with $[^{99m}Tc(CO)_3]^+$-$(HE)_3$-$Z_{HER2:342}$ was more than 10-fold lower than with $[^{99m}Tc(CO)_3]^+$-H_6-$Z_{HER2:342}$ (0.93 ± 0.15% ID/g; $p < 0.0005$), and nearly 6-fold lower than with $[^{99m}Tc(CO)_3]^+$-H_6-$Z_{HER2:342}$ ($p < 0.0005$).

Comparison of biodistribution data for 4 and 24 h pi shows 1.5−1.8-fold decrease of hepatic radioactivity and 1.8−2-fold decrease of renal radioactivity, suggesting a moderately residualizing character of all labels.

The biodistribution data from nude NMRI mice bearing tumor xenografts (4 h pi) and the results of their statistical treatment are presented in Tables 6 and 7. The data are in very good agreement with the data from immunocompetent mice at the same time point (taking into account strain-to-strain variability and difference in animal size). The uptake of radioactivity in normal organs and tissues followed the pattern found in normal NMRI mice. The accumulation of radioactivity in the liver was again the lowest with $[^{99m}Tc(CO)_3]^+$-$(HE)_3$-$Z_{HER2:342}$, 9.2-fold lower than with $[^{99m}Tc(CO)_3]^+$-H_6-$Z_{HER2:342}$ and 4.9-fold lower than with $[^{99m}Tc(CO)_3]^+$-$Z_{HER2:342}$-H_6. Accordingly, the hepatic uptake in the case of $[^{99m}Tc(CO)_3]^+$-$Z_{HER2:342}$-H_6 was nearly 2-fold lower than the uptake seen with the counterpart having an N-terminally located hexahistidine tag. At the same time, the clearance of radioactivity from blood was the slowest for $[^{99m}Tc(CO)_3]^+$-$Z_{HER2:342}$-H_6. Overall, $[^{99m}Tc(CO)_3]^+$-$(HE)_3$-$Z_{HER2:342}$ provided the most rapid clearance from normal organs and tissues. Preinjection of a large amount of H_6-$Z_{HER2:342}$ significantly reduced tumor uptake of $[^{99m}Tc(CO)_3]^+$-$(HE)_3$-$Z_{HER2:342}$, demonstrating targeting specificity. There was no significant difference in the tumor uptake between the conjugates. However, the lower accumulation in normal tissue provided appreciable better tumor-to-organ ratio with $[^{99m}Tc(CO)_3]^+$-$(HE)_3$-$Z_{HER2:342}$ compared to the two other conjugates (except from the kidneys) (Table 7). The most spectacular difference seen between the conjugates was the tumor-to-liver ratio: the value was 0.29 ± 0.04 with $[^{99m}Tc(CO)_3]^+$-H_6-$Z_{HER2:342}$ (i.e., negative contrast) and 3.0 ± 0.5 with $[^{99m}Tc(CO)_3]^+$-$(HE)_3$-$Z_{HER2:342}$.

Gamma-camera imaging, performed at 4 h pi (Figure 6), confirmed the results of the biodistribution experiments. The most prominent sites of radioactivity accumulation with both $[^{99m}Tc(CO)_3]^+$-H_6-$Z_{HER2:342}$ and $[^{99m}Tc(CO)_3]^+$-$(HE)_3$-$Z_{HER2:342}$ were in the kidneys. The HER2-expressing tumor xenografts were visualized using both conjugates. However, a high liver accumulation exceeding the accumulation in tumor was observed for $[^{99m}Tc(CO)_3]^+$-H_6-$Z_{HER2:342}$, but not with $[^{99m}Tc(CO)_3]^+$-$(HE)_3$-$Z_{HER2:342}$.

DISCUSSION

Development of imaging agents often requires in vivo comparison of several variants with similar properties (*12, 16*). The evaluation procedure is appreciably facilitated by the use of a technique that enables labeling of the different variants without additional modification, i.e., coupling of a chelator or prosthetic group. A hexahistidine tag allows for facile labeling with $^{99m}Tc(CO)_3^+$ and may also be used for easy and highly efficient purification. The drawback with an N-terminal hexahistidine tag on an Affibody molecule is high hepatic accumulation of radioactivity. Our hypothesis was that hepatic accumulation of the radioactivity is caused by high uptake of the tracer in the liver, which in turn is caused by the relatively hydrophobic nature of the tag labeled with $^{99m}Tc(CO)_3^+$ (*31*). Indeed, there are several observations of higher hepatic uptake of $[^{99m}Tc(CO)_3]^+$-labeled hexahistidine-labeled imaging agents compared to what was expected with the corresponding protein (*32, 33*) or compared to what had been seen with an alternative labeling method (*15, 19*). Interestingly, Ruscowski and coauthors (*34*) have previously suggested that the handling of proteins in the liver is more influenced by the presence of "hydrophobic patches", i.e., areas with high density of hydrophobic side chains, than the overall lipophilicity of the protein. Although histidine is not generally considered hydrophobic, it can most likely not balance the hydrophobic nature of technetium tricarbonyl.

Thus, the $^{99m}Tc(CO)_3^+$ labeled hexahistidine tag may create a "hydrophobic" patch at the N-terminal end of the Affibody molecule which promotes uptake of the tracer in the liver. This is further supported by previous observations of large effect of single amino acid substitutions in the N-terminus of the affibody molecule on biodistribution properties (*20*−*23*). However,

Table 6. Biodistribution of ^{99m}Tc-Labeled Affibody Molecules in Male NMRI *nu*/*nu* Mice Bearing LS174T Xenografts, 4 h after Intravenous Injection[a]

	$[^{99m}Tc(CO)_3]^+$-H_6-$Z_{HER2:342}$	$[^{99m}Tc(CO)_3]^+$-$Z_{HER2:342}$-H_6	$[^{99m}Tc(CO)_3]^+$-$(HE)_3$-$Z_{HER2:342}$	$[^{99m}Tc(CO)_3]^+$-$(HE)_3$-$Z_{HER2:342}$ blocking**
blood	0.54 ± 0.10^b	1.1 ± 0.2^d	0.33 ± 0.02^c	0.37 ± 0.03
lung	0.7 ± 0.1	1.2 ± 0.4^d	0.28 ± 0.05^c	0.34 ± 0.04
liver	8.1 ± 0.8^b	4.3 ± 0.8^d	0.88 ± 0.05^c	1.05 ± 0.09
spleen	1.3 ± 0.5	0.8 ± 0.3^d	0.20 ± 0.05^c	0.3 ± 0.1
kidney	82 ± 9	67 ± 13	70 ± 10	72 ± 6
tumor	2.2 ± 0.3	3.2 ± 0.9	2.6 ± 0.4	0.33 ± 0.04^e
muscle	0.11 ± 0.02	0.19 ± 0.06^d	0.07 ± 0.01^c	0.10 ± 0.09
bone	0.4 ± 0.1	0.34 ± 0.08^d	0.15 ± 0.04^c	0.16 ± 0.04
intestines*	4.1 ± 0.7	5.1 ± 0.6	6 ± 1	5.2 ± 0.9
carcass*	5.6 ± 0.2^b	9 ± 2^d	2.8 ± 0.2^c	3.1 ± 0.2

[a] The concentration of radioactivity is expressed as % ID/g, and presented as an average value from 4 animals ± standard deviation. * data for intestines with content and carcass are presented as % of injected radioactivity per whole sample. ** blocking of HER2 in tumors was obtained by pre-injection of 1 mg of nonlabeled H_6-$Z_{HER2:342}$. [b] Significant difference between $[^{99m}Tc(CO)_3]^+$-H_6-$Z_{HER2:342}$ and $[^{99m}Tc(CO)_3]^+$-$Z_{HER2:342}$-H_6. [c] Significant difference between $[^{99m}Tc(CO)_3]^+$-H_6-$Z_{HER2:342}$ and $[^{99m}Tc(CO)_3]^+$-$(HE)_3$-$Z_{HER2:342}$. [d] Significant difference between $[^{99m}Tc(CO)_3]^+$-$Z_{HER2:342}$-H_6 and $[^{99m}Tc(CO)_3]^+$-$(HE)_3$-$Z_{HER2:342}$. [e] Significant difference between $[^{99m}Tc(CO)_3]^+$-$(HE)_3$-$Z_{HER2:342}$ with and without blocking.

Table 7. Tumor-to-Organ Ratios for ^{99m}Tc-Labeled Affibody Molecules in Male NMRI *nu*/*nu* Mice Bearing LS174T Xenografts, 4 h after Intravenous Injection[a]

	$[^{99m}Tc(CO)_3]^+$-H_6-$Z_{HER2:342}$	$[^{99m}Tc(CO)_3]^+$-$Z_{HER2:342}$-H_6	$[^{99m}Tc(CO)_3]^+$-$(HE)_3$-$Z_{HER2:342}$
blood	4.5 ± 0.1^b	3.0 ± 0.4^c	81 ± 2^d
lung	3.4 ± 0.1	2.9 ± 1.0^c	9.6 ± 0.7^d
liver	0.29 ± 0.04^b	0.7 ± 0.1^c	3.0 ± 0.5^d
spleen	2.3 ± 0.4^b	3.8 ± 0.5^c	14 ± 3^d
kidney	0.028 ± 0.002^b	0.047 ± 0.006	0.038 ± 0.009
muscle	21.0 ± 0.2	17 ± 3^c	40 ± 3^d
bone	7 ± 2	9 ± 2^c	18 ± 5^d

[a] Data presented as an average value from 4 animals ± standard deviation. [b] Significant difference between $[^{99m}Tc(CO)_3]^+$-H_6-$Z_{HER2:342}$ and $[^{99m}Tc(CO)_3]^+$-$Z_{HER2:342}$-H_6. [c] Significant difference between $[^{99m}Tc(CO)_3]^+$-H_6-$Z_{HER2:342}$ and $[^{99m}Tc(CO)_3]^+$-$(HE)_3$-$Z_{HER2:342}$. [d] Significant difference between $[^{99m}Tc(CO)_3]^+$-$Z_{HER2:342}$-H_6 and $[^{99m}Tc(CO)_3]^+$-$(HE)_3$-$Z_{HER2:342}$.

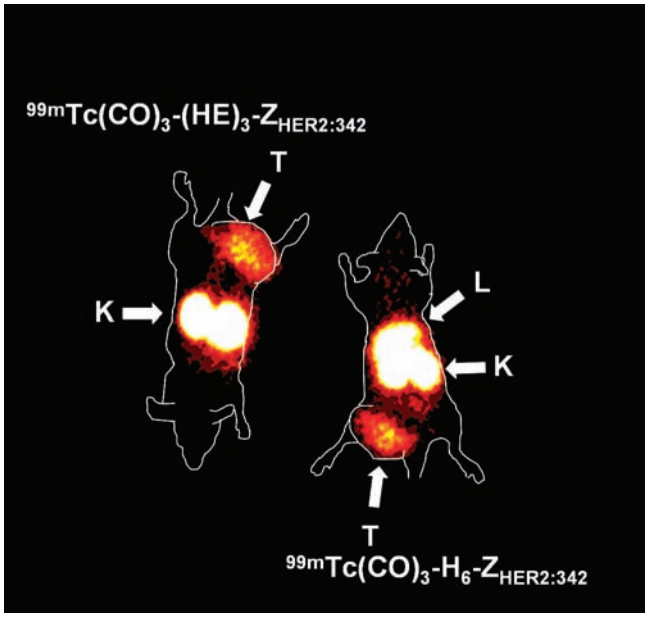


Figure 6. Imaging of HER2 expression in LS174T xenografts in NMRI nude mice using $[^{99m}Tc(CO)_3]^+$-H_6-$Z_{HER2:342}$ and $[^{99m}Tc(CO)_3]^+$-$(HE)_3$-$Z_{HER2:342}$. Planar gamma-camera images were acquired 4 h after administration of the tracers. Arrows point to tumors (T), liver (L), and kidneys (K).

similar amino acid replacements in the C-terminus gave only small effects (*24*−*26*). Since the C-terminus is spatially distant from the N-terminus in this antiparallel triple helical protein, we therefore hypothesized that placing hexahistidine tag at the C-terminus instead of at the N-terminus might make a difference in the biodistribution properties, without changing the overall hydrophobicity of the protein. The results from the present study confirmed this hypothesis, showing that the $[^{99m}Tc(CO)_3]^+$-labeled $Z_{HER2:342}$-H_6 yielded a 2-fold lower hepatic radioactivity concentration compared to the parent $[^{99m}Tc(CO)_3]^+$-labeled H_6-$Z_{HER2:342}$, in both normal and tumor-bearing mice. However, the positive effect of the C-terminal location of hexahistidine tag on overall biodistribution was modest and associated with some negative effects, such as appreciably elevated blood radioactivity concentration. The latter is not due to lower stability, as shown by histidine challenge. The concentration of radioactivity in the intestine and carcass is also slightly higher, which may indicate not only that the favorable lowering of the hepatic radioactivity concentration is due to reduced uptake of $[^{99m}Tc(CO)_3]^+$-labeled $Z_{HER2:342}$-H_6, but also that lower hepatic retention of radioactivity might be involved. More detailed studies are needed to fully elucidate this issue.

The other approach investigated to reduce liver uptake was to increase the hydrophilicity in the N-terminal portion of the tracer, by introducing charged residues in the hexahistidine tag, while retaining the possibility for IMAC purification and labeling with $[^{99m}Tc(CO)_3]^+$. Previous studies of N-terminally located N_3S chelators consisting of the sequence mercaptoacetyl-X-X-X (where X is Glu, Ser, or Lys) have shown that the overall biodistribution is more favorable if glutamate is included compared to lysine (*35*). Therefore, the negatively charged amino acid glutamate was chosen to increase the hydrophilicity. Furthermore, labeling with $[^{99m}Tc(CO)_3]^+$ seems only to require an H-X-H-motif (*36*) indicating that every second histidine in the hexahistidine tag could be substituted for glutamate without affecting its chelating properties. We therefore chose to add the motif H-E-H-E-H-E to the Affibody tracer. Like the His_6-tag, this motif will probably also be surface exposed allowing purification by IMAC, for example, by a resin containing immobilized iminodiacetic acid (IDA)/Ni^{2+}-ions. The results exceeded expectations, and this tracer could be efficiently purified by IMAC and labeled by $[^{99m}Tc(CO)_3]^+$, and when used in vivo, the hepatic concentration of radioactivity was more than 10-fold lower with $[^{99m}Tc(CO)_3]^+$-$(HE)_3$-$Z_{HER2:342}$ compared to that with $[^{99m}Tc(CO)_3]^+$-H_6-$Z_{HER2:342}$, both at 4 and 24 h. A slightly slower blood clearance could be seen with $[^{99m}Tc(CO)_3]^+$-$(HE)_3$-$Z_{HER2:342}$, but the concentration of radioactivity was lower in all tissues already at 4 hour after injection, and much lower at 24 hours after injection. Besides a low uptake value for the liver, rapid clearance was also reflected in lower values in the carcass and intestine, disregarding the intestine at 4 h after injection of $[^{99m}Tc(CO)_3]^+$-$(HE)_3$-$Z_{HER2:342}$ where no reliable value was obtained. Importantly, the HEHEHE tag is not less stable toward histidine challenge than the hexahistidine tag, supporting the conclusion that the effects seen are directly related to much lower hepatic uptake of $[^{99m}Tc(CO)_3]^+$-$(HE)_3$-

$Z_{HER2:342}$. Furthermore, no correlation could be seen between the retention time of Affibody molecules on reversed-phase HPLC (Table 1) and liver uptake. This suggests that the observed differences in hepatic uptake are due to differences in local rather than overall hydrophobicity. This observation is in agreement with the hypothesis of Ruscowski and coauthors (*34*) concerning the importance of "hydrophobic patches" for hepatic uptake of radiolabeled peptides.

Taken together, purification on IMAC worked equally well for all three constructs. Labeling using $[^{99m}Tc(CO)_3]^+$ was nearly as efficient with Z_{HER2}-H_6 and $(HE)_3$-Z_{HER2} as labeling of H_6-$Z_{HER2:342}$, and all three labeled constructs were equally stable in PBS and toward a histidine challenge. Furthermore, specific binding to HER2-expressing cells was seen with all three labeled tracer, at levels in agreement with the receptor density of the selected cell-lines (Table 3.). Significant differences were only seen in the biodistribution of radioactivity, believed to be primarily due to differences in the uptake of the labeled tracers by the liver, as outlined above. The renal excretion and retention seem to be virtually identical; for example, a 2-fold decrease of kidney values between 4 and 24 h were seen with all three variants of $Z_{HER2:342}$. This suggests that all three labels possess similar, moderately residualizing properties. This provides further support for the assumption that hepatic uptake, not hepatic retention, differs among the labeled tracers. Radioactivity uptake with $[^{99m}Tc(CO)_3]^+$-$(HE)_3$-$Z_{HER2:342}$ at 4 h pi (a time point relevant for imaging using ^{99m}Tc) was significantly lower in lungs, spleen, stomach, salivary gland, and muscles in comparison with $[^{99m}Tc(CO)_3]^+$-H_6-$Z_{HER2:342}$ and $[^{99m}Tc(CO)_3]^+$-$Z_{HER2:342}$-H_6.

The findings from biodistribution experiments in normal mice were confirmed in an experiment on tumor-bearing mice. The data for normal organs and tissues were in very good agreement. All conjugates were capable of targeting LS174T xenografts with moderate expression of HER2 in these cells. One might expect somewhat higher uptake of $[^{99m}Tc(CO)_3]^+$-$(HE)_3$-$Z_{HER2:342}$ in the tumor because of increased bioavailability. However, this did not happen, possibly because of better retention of $[^{99m}Tc(CO)_3]^+$-H_6-$Z_{HER2:342}$ by cancer cells (Figure 5). Nevertheless, the favorable biodistribution properties of $[^{99m}Tc(CO)_3]^+$-$(HE)_3$-$Z_{HER2:342}$ provided the best tumor-to-organ ratios in comparison with the other conjugates. The most important difference was in the tumor-to-liver ratio, determining the sensitivity of liver metastasis detection. In the case of $[^{99m}Tc(CO)_3]^+$-H_6-$Z_{HER2:342}$, the concentration of radioactivity in the tumor was only one-third of the concentration in the liver. Relocation of the hexahistidine tag to the C-terminus improved the tumor-to-liver ratio, and $[^{99m}Tc(CO)_3]^+$-$Z_{HER2:342}$-H_6 might provide a positive contrast over the liver for tumors with a higher level of HER2 expression. $[^{99m}Tc(CO)_3]^+$-$(HE)_3$-$Z_{HER2:342}$ gave a positive contrast (tumor-to-liver ratio of 3.0 ± 0.5) in the present experiment using low HER2 expressing LS174T xenografts.

In conclusion, this study demonstrated that both the position and composition of a histidine tag may influence the hepatic uptake of $[^{99m}Tc(CO)_3]^+$-labeled Affibody molecules in vivo. The use of the hydrophilic and negatively charged HEHEHE-tag provided by far the lowest level of hepatic uptake, as well as the lowest accumulation of radioactivity in other organs and tissues. In fact, the biodistribution data obtained with this ^{99m}Tc-labeled variant of $Z_{HER2:342}$ are in line with the data obtained with the best nonhistidine tag containing constructs labeled with ^{99m}Tc (*22*, *24*, *25*). Thus, this molecule might be a good clinical imaging agent, not just an example of a favorable procedure for evaluating alternative variants of a novel tracer. We hope that these observations can also be helpful for development of other targeting scaffold proteins for in vivo radionuclide imaging.

ACKNOWLEDGMENT

This work was supported by grants from Swedish Research Council (Vetenskapsrådet) and Swedish Cancer Society (Cancerfonden).

LITERATURE CITED

(1) Zafir-Lavie, I., Michaeli, Y., and Reiter, Y. (2007) Novel antibodies as anticancer agents. *Oncogene 26*, 3714–3733.
(2) Collins, I., and Workman, P. (2006) New approaches to molecular cancer therapeutics. *Nat. Chem. Biol. 2*, 689–700.
(3) Hartmann, J. T., Haap, M., Kopp, H. G., and Lipp, H. P. (2009) Tyrosine kinase inhibitors - a review on pharmacology, metabolism and side effects. *Curr. Drug. Metab. 10*, 470–481.
(4) Dei Tos, A. P., and Ellis, I. (2005) Assessing epidermal growth factor receptor expression in tumours: what is the value of current test methods? *Eur. J. Cancer 41*, 1383–92.
(5) Apple, S. K., Lowe, A. C., Rao, P. N., Shintaku, I. P., and Moatamed, N. A. (2009) Comparison of fluorescent in situ hybridization HER-2/neu results on core needle biopsy and excisional biopsy in primary breast cancer. *Mod. Pathol. 22*, 1151–9.
(6) Kelloff, G. J., Krohn, K. A., Larson, S. M., Weissleder, R., Mankoff, D. A., Hoffman, J. M., Link, J. M., Guyton, K. Z., Eckelman, W. C., Scher, H. I., O'Shaughnessy, J., Cheson, B. D., Sigman, C. C., Tatum, J. L., Mills, G. Q., Sullivan, D. C., and Woodcock, J. (2005) The progress and promise of molecular imaging probes in oncologic drug development. *Clin. Cancer Res. 11*, 7967–7985.
(7) McLarty, K., and Reilly, R. M. (2007) Molecular imaging as a tool for personalized and targeted anticancer therapy. *Clin. Pharmacol. Ther. 81*, 420–424.
(8) Tolmachev, V., Stone-Elander, S., and Orlova, A. (2010). Radiolabelled receptor-tyrosine-kinase targeting drugs for patient stratification and monitoring of therapy response: prospects and pitfalls. *Lancet. Oncol. 11*, 992−1000.
(9) Kenanova, V., and Wu, A. M. (2006) Tailoring antibodies for radionuclide delivery. *Expert Opin. Drug Delivery 3*, 53–70.
(10) Van de Wiele, C., Revets, H., and Mertens, N. (2004) Radioimmunoimaging. Advances and prospects. *Q. J. Nucl. Med. Mol. Imaging 48*, 317–325.
(11) Nygren, P. A. (2008) Alternative binding proteins: Affibody binding proteins developed from a small three-helix bundle scaffold. *FEBS J. 275*, 2668–2676.
(12) Orlova, A., Magnusson, M., Eriksson, T. L., Nilsson, M., Larsson, B., Hoiden-Guthenberg, I., Widström, C., Carlsson, J., Tolmachev, V., Ståhl, S., and Nilsson, F. Y. (2006) Tumor imaging using a picomolar affinity HER2 binding affibody molecule. *Cancer Res. 66*, 4339–4348.
(13) Tolmachev, V. (2008) Imaging of HER-2 overexpression in tumors for guiding therapy. *Curr. Pharm. Des. 14*, 2999–3011.
(14) Waibel, R., Alberto, R., Willuda, J., Finnern, R., Schibli, R., Stichelberger, A., Egli, A., Abram, U., Mach, J. P., Plücthun, A., and Schubiger, P. A. (1999) Stable one-step technetium-99m labe ling of His-tagged recombinant proteins with a novel Tc(I)-carbonyl complex. *Nat. Biotechnol. 17*, 897–901.
(15) Berndorff, D., Borkowski, S., Moosmayer, D., Viti, F., Müller-Tiemann, B., Sieger, S., Friebe, M., Hilger, C. S., Zardi, L., Neri, D., and Dinkelborg, L. M. (2006) Imaging of tumor angiogenesis using 99mTc-labeled human recombinant anti-ED-B fibronectin antibody fragments. *J. Nucl. Med. 47*, 1707–1716.
(16) Gainkam, L. O., Huang, L., Caveliers, V., Keyaerts, M., Hernot, S., Vaneycken, I., Vanhove, C., Revets, H., De Baetselier, P., and Lahoutte, T. (2008) Comparison of the biodistribution and tumor targeting of two 99mTc-labeled anti-EGFR nanobodies in mice, using pinhole SPECT/micro-CT. *J. Nucl. Med. 49*, 788–795.
(17) Tavaré, R., Torres Martin De Rosales, R., Blower, P. J., and Mullen, G. E. (2009) Efficient site-specific radiolabeling of a modified C2A domain of synaptotagmin I with [99mTc(CO)3]+:

a new radiopharmaceutical for imaging cell death. *Bioconjugate Chem. 20*, 2071–2081.
(18) Zahnd, C., Kawe, M., Stumpp, M. T., de Pasquale, C., Tamaskovic, R., Nagy-Davidescu, G., Dreier, B., Schibli, R., Binz, H. K., Waibel, R., and Plückthun, A. (2010) Efficient tumor targeting with high-affinity designed ankyrin repeat proteins: effects of affinity and molecular size. *Cancer Res. 70*, 1595–1605.
(19) Orlova, A., Nilsson, F. Y., Wikman, M., Widström, C., Ståhl, S., Carlsson, J., and Tolmachev, V. (2006) Comparative *in vivo* evaluation of technetium and iodine labels on an anti-HER2 affibody for single-photon imaging of HER2 expression in tumors. *J. Nucl. Med. 47*, 512–519.
(20) Engfeldt, T., Tran, T., Orlova, A., Widstrom, C., Feldwisch, J., Abrahmsen, L., Wennborg, A., Karlstrom, A. E., and Tolmachev, V. (2007) ^{99m}Tc-chelator engineering to improve tumour targeting properties of a HER2-specific Affibody molecule. *Eur. J. Nucl. Med. Mol. Imaging 34*, 1843–1853.
(21) Ekblad, T., Tran, T., Orlova, A., Widström, C., Feldwisch, J., Abrahmsen, L., Wennborg, A., Karlström, A. E., and Tolmachev, V. (2008) Development and preclinical characterisation of ^{99m}Tc-labelled Affibody molecules with reduced renal uptake. *Eur. J. Nucl. Med. Mol. Imaging 35*, 2245–2255.
(22) Tran, T., Engfeldt, T., Orlova, A., Sandström, M., Feldwisch, J., Abrahmsén, L., Wennborg, A., Tolmachev, V., and Karlström, A. E. (2007) ^{99m}Tc-maEEE-$Z_{HER2:342}$, an Affibody molecule-based tracer for the detection of HER2 expression in malignant tumors. *Bioconjugate Chem. 18*, 1956–1964.
(23) Tran, T., Ekblad, T., Orlova, A., Widström, C., Feldwisch, J., Wennborg, A., Abrahmsén, L., Tolmachev, V., and Eriksson Karlström, A. (2008) Effects of Lysine-containing mercaptoacetyl-based Chelators on the Biodistribution of ^{99m}Tc-labeled anti-HER2. *Bioconjugate Chem. 19*, 2568–2576.
(24) Ahlgren, S., Wållberg, H., Tran, T. A., Widström, C., Hjertman, M., Abrahmsén, L., Berndorff, D., Dinkelborg, L. M., Cyr, J. E., Feldwisch, J., Orlova, A., and Tolmachev, V. (2009) Targeting of HER2-expressing tumors using a site-specifically ^{99m}Tc-labeled recombinant Affibody molecule $Z_{HER2:2395}$ with C-terminal engineered cysteine. *J. Nucl. Med. 50*, 781–789.
(25) Tran, T. A., Rosik, D., Abrahmsén, L., Sandström, M., Sjöberg, A., Wållberg, H., Ahlgren, S., Orlova, A., and Tolmachev, V. (2009) Design, synthesis and biological evaluation of a HER2-specific affibody molecule for molecular imaging. *Eur. J. Nucl. Med. Mol. Imaging 36*, 1864–1873.
(26) Ahlgren, S., Orlova, A., Rosik, D., Sandström, M., Sjöberg, A., Baastrup, B., Widmark, O., Fant, G., Feldwisch, J., and Tolmachev, V. (2008) Evaluation of maleimide derivative of DOTA for site-specific labeling of recombinant affibody molecules. *Bioconjugate Chem. 19*, 235–243.
(27) Lundberg, E., Brismar, H., and Gräslund, T. (2009) Selection and characterization of Affibody ligands to the transcription factor c-Jun. *Biotechnol. Appl. Biochem. 52*, 17–27.
(28) Tolmachev, V., Mume, E., Sjöberg, S., Frejd, F. Y., and Orlova, A. (2009) Influence of valency and labelling chemistry on in vivo targeting using radioiodinated HER2-binding. *Eur. J. Nucl. Med. Mol. Imaging 36*, 692–701.
(29) Persson, M., Tolmachev, V., Andersson, K., Gedda, L., Sandström, M., and Carlsson, J. (2005) [(177)Lu]pertuzumab: experimental studies on targeting of HER-2 positive tumour cells. *Eur. J. Nucl. Med. Mol. Imaging 32*, 1457–1462.
(30) Wållberg, H., and Orlova, A. (2008) Slow internalization of anti-HER2 synthetic affibody monomer ^{111}In-DOTA-$Z_{HER2:342-pep2}$: implications for development of labeled tracers. *Cancer Biother. Radiopharm. 23*, 435–42.
(31) Ballinger, J. R., Cooper, M. S., and Mather, S. J. (2004) Re: controversies - $[Tc(CO)_3]^+$ chemistry: a promising new concept for SPET? *Eur. J. Nucl. Med. Mol. Imaging 31*, 304–305.
(32) Francis, R. J., Mather, S. J., Chester, K., Sharma, S. K., Bhatia, J., Pedley, R. B., Waibel, R., Green, A. J., and Begent, R. H. (2004) Radiolabelling of glycosylated MFE-23::CPG2 fusion protein (MFECP1) with 99mTc for quantitation of tumour antibody-enzyme localisation in antibody-directed enzyme prodrug therapy (ADEPT). *Eur. J. Nucl. Med. Mol. Imaging 31*, 1090–1096.
(33) Pimentel, G. J., Vazquez, J. E., Quesada, W., Felipe, Y., Carderón, C., Freyre, F. M., Oliva, J. P., and Gavilondo, J. V. (2001) Hexa-histidine tag as a novel alternative for one-step direct labelling of a single-chain Fv antibody fragment with 99m Tc. *Nucl. Med. Commun. 22*, 1089–1094.
(34) Rusckowski, M., Qu, T., Gupta, S., Ley, A., and Hnatowich, D. J.(. (2001) A comparison in monkeys of (99m)Tc labeled to a peptide by 4 methods. *J. Nucl. Med. 42*, 1870–1877.
(35) Tolmachev, V., and Orlova, A. (2009) Update on Affibody molecules for in vivo imaging of targets for cancer therapy. *Minerva Biotecnol. 21*, 21–30.
(36) Novak-Hofer, I., Waibel, R., Zimmermann, K., Schibli, R., Grünberg, J., Chester, K. A., Murray, A., Lo, B. K., Perkins, A. C., and Schubiger, P. A. (2004) Radiometal labeling of antibodies and antibody fragments for imaging and therapy. *Methods Mol. Biol. 248*, 481–494.

BC1002357

Chemically Modified Firefly Luciferase Is an Efficient Source of Near-Infrared Light

Bruce R. Branchini,* Danielle M. Ablamsky, and Justin C. Rosenberg

Department of Chemistry, Connecticut College, New London, Connecticut 06320, United States. Received June 5, 2010; Revised Manuscript Received September 14, 2010

Bioluminescence and bioluminescence resonance energy transfer (BRET) are two naturally occurring light emission phenomena that have been adapted to a wide variety of important research applications including in vivo imaging and enzyme assays. The luciferase enzyme from the North American firefly, which produces yellow−green light, is a key component of many of these applications. Recognizing the heightened interest in the potential of near-infrared (nIR) light to improve these technologies, we have demonstrated that spectral emissions with maxima of 705 and 783 nm can be efficiently produced by a firefly luciferase variant covalently labeled with nIR fluorescent dyes. In one case, an outstanding BRET ratio of 34.0 was achieved emphasizing the importance of selective labeling with fluorescent dyes and the efficiency provided by the intramolecular BRET process. Additionally, we constructed a biotinylated fusion protein that similarly produced nIR light. This novel material was immobilized on solid supports containing streptavidin, demonstrating, in principle, that it may be used for receptor-based imaging. Also, the matrix-bound labeled fusion protein was used to measure factor Xa activity at physiological concentrations in blood. We believe this to be the first report of bright nIR light sources produced by chemical modification of a beetle luciferase.

INTRODUCTION

A wide variety of biological organisms emit light spanning the visible spectrum. Bioluminescence emission maxima ranging from 450 to 625 nm have been recorded (*1*) for species of crustaceans and beetles. Moreover, the 705 nm peak luminescence emanating from the light organs of several dragonfish (*2*) extends bioluminescence beyond human vision into the near-infrared (nIR) 700−1000 nm. In the dragonfish, the emitter is likely a secondary pigment (*2*) excited via bioluminescence resonance energy transfer (BRET), the natural process responsible for the green glow of the aequorin−GFP complex (*3, 4*). BRET-based assays, in which a bioluminescence donor excites a fluorescent acceptor, have been developed for a variety of applications (*5*) including measuring protease activity (*6*) and detecting protein−protein interactions (*7*−*9*). In the field of in vivo imaging, there is heightened interest in the nIR region because it can enable deeper imaging owing to lower background and minimized signal loss from light absorption and scattering (*10*). Promising BRET-based imaging results have been reported with quantum dot (QD)-*Renilla* luciferase (rLuc) conjugates (*11, 12*), including a recently described bioinorganic hybrid structure that emits at ∼800−1050 nm (*13*), and with a *Cypridina* luciferase (cLuc) containing fusion proteins modified with an indocyanine dye emitting at 675 nm (*14*).

Our interest is in developing new biomaterials with photonic properties that may be suitable for improved biomarker and biosensor applications focusing on the firefly luciferase system from *Photinus pyralis* (Luc). The firefly enzyme produces yellow−green light (Figure 1a) through a series of reactions that require substrates firefly (beetle) luciferin (LH_2), Mg-ATP, and oxygen. This process is generally considered to have the highest known quantum yield (41 ± 7.4%) (*15*) of any bioluminescence system based on the conversion of substrate (luciferin) into photons. Additional advantages of working with Luc are the superior stability and relatively low cost of LH_2. While notable applications of BRET-based red sources have been reported (*11, 12, 14*), we have developed Luc-based BRET systems with greater BRET efficiencies that provide improved signal-to background ratios. The efficiency of BRET is dependent on the spectral overlap, relative orientation, and the distance between the bioluminescence donor and the fluorescence acceptor. We set out to determine whether the Luc system could be used to produce efficient BRET-based sources of nIR light. Our strategy was to optimize spectral overlap with the long-wavelength acceptor absorption spectra typical of nIR fluorescent dyes by starting with a recombinant *P. pyralis* luciferase containing the mutations Thr214Ala, Ala215Leu, Ile232Ala, Ser284Thr, Phe295Leu, Arg330Gly, Ile351Val, and Phe465Arg (Ppy RE8), our recently developed (*16*) thermostable Luc variant, which emits red light (617 nm) (Figure 1b). We investigated two acceptors, the Alexa Fluor nIR dyes AF680 and AF750 with excitation maxima of 680 and 750 nm and emission maxima of 705 and 780 nm, respectively. Using versions of these dyes containing maleimide groups, we covalently attached the nIR dyes to Ppy RE10, a variant of Ppy RE8 containing two surface Cys residues at positions 169 and 399, and achieved highly efficient nIR emission by an intramolecular BRET process that minimized donor−acceptor distance. We report here the design, construction, and characterization of soluble and immobilized Luc-based sources of nIR light. Additionally, we demonstrate that the novel materials can be applied to the assay of factor Xa activity and we provide information from model studies with blood designed to assess the potential advantage of nIR transmittance. The measurement of factor Xa activity has become increasingly common in clinical laboratories, because it is an effective means to monitor heparin

* Corresponding author. Bruce Branchini, Department of Chemistry, Connecticut College, 270 Mohegan Avenue, New London, CT 06320. Ph: +1 860 439 2479, Fax: +1 860 439 2477, E-mail: brbra@conncoll.edu.

10.1021/bc100256d © 2010 American Chemical Society
Published on Web 10/11/2010

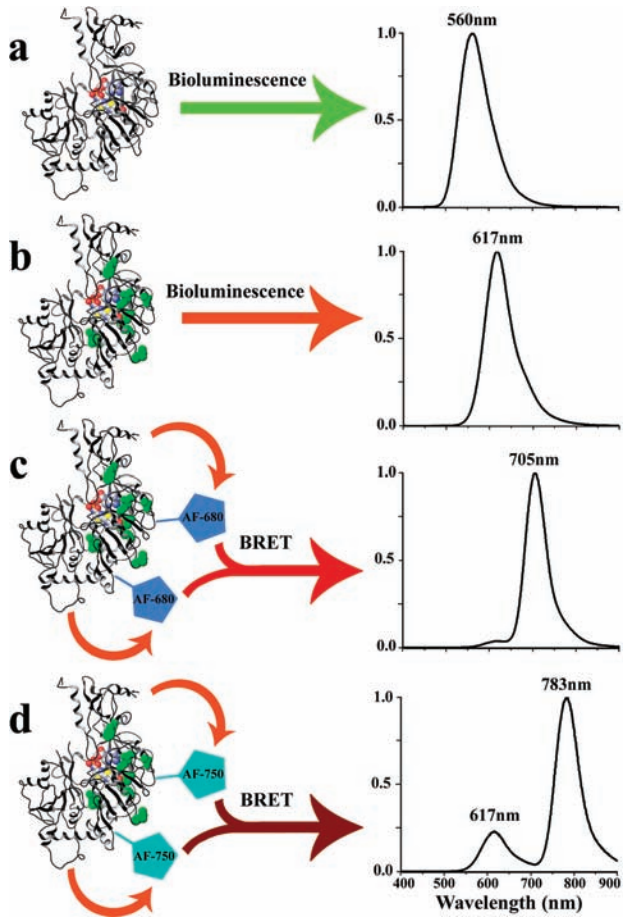


Figure 1. Normalized bioluminescence and BRET emission spectra of (a) Luc, (b) Ppy RE8, and Ppy RE10 labeled with (c) AF680 or (d) AF750. Reactions were initiated by the addition of LH_2 and Mg-ATP at pH 7.8. Ribbon diagrams are based on a Luc-DLSA crystal structure (Branchini, B. R., Southworth, T. L., and Gulick, A. M. Unpublished results) (*25*) showing mutated residues (green) and DLSA as CPK models.

anticoagulant therapy used for treatment and prevention of thromboembolic disease (*17*).

EXPERIMENTAL PROCEDURES

Materials. The following materials were obtained from the sources indicated: Mg-ATP (bacterial source) from Sigma-Aldrich (St. Louis, MO); Alexa Fluor 680 C2-maleimide (AF680) and Alexa Fluor 750 C5-maleimide (AF750) dyes from Invitrogen (Carlsbad, CA); NanoLinK streptavidin magnetic microspheres from SoluLinK Biosciences (San Diego, CA); and Streptavidin agarose resin from Thermo Scientific (Rockford, IL). The recombinant GST-fusion proteins Ppy RE8 (*16*) and Ppy RE10 were expressed and purified as previously reported (*16, 18*−*21*). LH_2 was a generous gift from Promega (Madison, WI), and the pET-KBPT-Luc plasmid (*22*) was a generous gift from E. S. Yeung, Iowa State University.

General Methods. Concentrations of unlabeled proteins were determined using the Bio-Rad Protein Assay system using BSA as the standard. Unless otherwise specified, specific activity measurements, heat inactivation studies, and steady-state kinetics constants were determined as previously reported (*18, 19, 21, 23*). Mass spectral analyses were performed by tandem HPLC−electrospray ionization mass spectrometry (LC/ESMS) using a ThermoFinnigan Surveyor HPLC system and a ThermoFinnigan LCQ Advantage mass spectrometer. The found molecular masses (Da) of the newly reported luciferase variants were within the allowable experimental error (0.01%) of the calculated values (in parentheses): Ppy RE8-Thr169Cys, 61000 ± 6 (60998); Ppy RE8-Phe368Cys, 60961 ± 6 (60956); Ppy RE8-Ser399Cys, 61021 ± 6 (61016); and Ppy RE10, 61020 ± 6 (61014).

Covalent Labeling of Luciferase Enzymes with Alexa Fluor Maleimide Dyes. Stock solutions (10 mM, determined by UV−vis spectroscopy) of the AF680 ($\varepsilon_{684\ nm} = 175\ 000\ M^{-1}\ cm^{-1}$) and AF750 ($\varepsilon_{753\ nm} = 290\ 000\ M^{-1}\ cm^{-1}$) dyes (*24*) were prepared in sterile deionized water, divided into 30 μL aliquots, lyophilized, and stored at −20 °C. All labeling reactions were performed at 10 °C in 20 mM sodium phosphate buffer, pH 7.2 containing 150 mM NaCl, 5 mM EDTA and 0.8 M ammonium sulfate (PBSA buffer). Using Slide-A-Lyzer 10K MWCO dialysis cassettes (Thermo Scientific, Rockford IL), stock luciferase solutions (~2 mg/mL) in 20 mM Tris-HCl (pH 7.0) containing 150 mM NaCl, 1 mM EDTA, and 1 mM DTT were dialyzed against PBSA buffer (5 changes, 1 L each) to remove DTT and introduce 0.8 M ammonium sulfate. The inclusion of ammonium sulfate in PBSA effectively reduced noncovalent dye incorporation that can result from hydrophobic interactions between the dyes and the proteins. Labeling reactions were initiated by the addition of 1 mL of 30 μM enzyme in PBSA buffer to a lyophilized aliquot of AF680 or AF750 (final concentration 300 μM) and gently mixed for 15 min. Reactions were quenched by addition of 20 μL of 100 mM glutathione in PBSA buffer, incubated for 15 min, and dialyzed against PBSA buffer (8 changes, 1 L each). The nIR dye-labeled proteins could be stored in PBSA buffer at 5 °C for at least 6 weeks without the loss of more than 10% activity. For long-term storage, labeled and unlabeled proteins were dialyzed into 20 mM sodium phosphate buffer, pH 7.2, containing 150 mM NaCl and 5 mM EDTA, flash-frozen in liquid N_2, and stored at −80 °C with complete retention of activity.

Determination of Fluorescent Dye Labeling Stoichiometry. The degree of nIR dye labeling was estimated by UV−vis spectroscopy by measuring the micromoles of dye (using the molar absorptivity coefficients above) bound to micromole samples of labeled luciferases. A Micro BCA Protein Assay Kit (Thermo Scientific, Rockford IL) was used to determine the quantity of enzyme with readings taken at 540 nm to avoid interference with dye absorption bands. Additionally, LC/ESMS analysis of the labeled luciferases was performed using a BioBasic-C4 (100 × 1 mm) column eluted at a flow rate of 50 μL/min using an acetonitrile gradient of 10%/min. Elution was monitored by absorbance at 260 and 680 nm or 750 nm. With all labeled enzymes, long-wavelength absorption associated with the Alexa Fluor dyes was only observed coeluting with protein indicating the absence of any noncovalently attached label. If present, fluorescent dyes not covalently attached to protein would be observed eluting prior to the covalently labeled enzymes (Supporting Information Figure S1). Dye/protein incorporation ratios were determined from the observed masses of each covalently labeled protein. Protein mass increases of 979 Da (AF680) and 1048 Da (AF750) were taken as 1:1 dye/protein incorporation ratios, while mass increases of 1958 Da (AF680) and 2096 Da (AF750) corresponded to 2:1 dye/protein incorporation ratios. Postrun data analysis was performed using ThermoFinnigan *BioWorks Browser 3.0* deconvolution software.

Identification of Ppy RE10 Residues Labeled with Fluorescent Dyes. Samples (200 μg) of Ppy RE10 labeled as described above with AF680 or AF750 were digested with thermolysin (protease/protein, 1:10, w/w) in 50 mM ammonium bicarbonate, pH 8.0, for 6 h at 37 °C. Peptides were separated on a Gemini-NX 5 μ C18 110 Å column (50 × 2.00 mm) at a flow rate of 50 μL/min using 0.1% aqueous TFA containing linear gradients of acetonitrile: 5% (v/v) initially for 5 min, 50%

after 90 min, and 95% after 110 min. Elution was monitored by absorbance at 214 nm, 260 nm, and either 680 or 750 nm for AF680 or AF750 labeled peptides, respectively. Each digest of nIR dye-labeled enzyme produced two major peaks with long-wavelength absorbance attributable to the dyes. For the AF680-labeled luciferase, masses of 1199 ± 0.1 and 1344 ± 0.1 Da were found corresponding to the mass of the dye plus Val168Cys169 and Ile397Met398Cys399, respectively. For the AF750-labeled enzyme, masses of 1268 ± 0.1 and 1413 ± 0.1 Da were observed that were consistent with the mass of the dye plus Val168Cys169 and Ile397Met398Cys399, respectively. While the presence of Val80Cys81 is a potential source of ambiguity, Ppy RE8, which lacks Cys at position 169, did not incorporate the Alexa Fluor dyes. Additionally, the labeled peptide sequences were confirmed by MS/MS analysis in which masses of 1100 ± 0.1 and 1169 ± 0.1 Da, corresponding to Cys covalently bound to AF680 and AF750, respectively, were observed. Upon prolonged standing at room temperature, proteolysis mixtures produced additional peaks corresponding to mass additions of 18, suggesting hydrolytic ring-opening of the maleimide group. Since the dyes are presumably attached through thioether linkages, maleimide ring-opening would not release the dyes.

Bioluminescence and BRET Emission Spectra. Bioluminescence emission spectra were obtained using a Horiba Jobin-Yvon iHR imaging spectrometer equipped with a liquid N_2 cooled CCD detector and the excitation source turned off. Data were collected at 25 °C (in a 0.8 mL quartz cuvette) over the wavelength range 400−935 nm with the emission slit width set to 25 nm and were corrected for the spectral response of the CCD using a correction curve provided by the manufacturer. Reactions (0.525 mL final volume) were initiated by addition of 5 μL aliquots of luciferase in PBSA buffer (0.2−0.3 μM final concentration) to solutions containing LH_2 (150 μM) and Mg-ATP (2 mM) in 25 mM glycylglycine buffer, pH 7.8. The pH values of the reaction mixtures were confirmed before and after spectra were obtained. BRET ratios were calculated from emission spectra by dividing the area under the BRET emission peak by the area under the residual bioluminescence peak.

Immobilization of BXRE-680 onto Streptavidin Supports. Biotinylated BXRE10, the fusion protein consisting of an N-terminus hexa-His tagged biotin binding domain (BBD) joined to Ppy RE10 through the peptide linker GSGSIEGRGSGS, was chemically modified with AF680 as described above yielding BXRE-680, the corresponding biotinylated fusion protein with AF680 covalently bound in a 2:1 dye/protein ratio. Streptavidin-coated magnetic microspheres and agarose resin were each prepared by aliquoting 0.1 mL portions of bead slurry, separating and removing the supernatant (via magnet for magnetic beads, quick desktop centrifugation for agarose resin), and washing three times with 0.1 mL portions of PBSA buffer. The supernatant was removed, and the beads were stored on ice. BXRE-680 was bound to the supports by adding 0.1 mL of an ∼1.5 mg/mL protein solution in PBSA to the prewashed beads, which were then incubated with gentle mixing for 10 min on ice. The supernatant was removed, and the immobilized BXRE-680 beads were washed five times with 0.1 mL portions of PBSA buffer. The materials were resuspended in PBSA buffer to a total volume of 0.1 mL and stored in PBSA buffer at 5 °C. An equally effective procedure to prepare immobilized BXRE-680 was to add the streptavidin-coated supports to labeling mixtures of nIR dye and BXRE10 (see above), followed by washing with ten 0.1 mL aliquots of PBSA. Excess label and unreacted glutathione were effectively removed while avoiding the exhaustive dialysis step. Alternatively, biotinylated BXRE10 can be bound to the insoluble supports and then labeled with AF680 followed by repeated washing with PBSA buffer.

Estimation of Specific Activities of Immobilized Fusion Proteins. Integrated specific activities of bead-bound fusion protein samples were estimated using a Horiba Jobin-Yvon Fluorolog-3 with the excitation source shunted. A "flea"-sized magnetic stir bar was used to suspend the immobilized material throughout the 15 min measurement. A volume of bead solution equivalent to ∼2 μg of protein was mixed with 0.4 mL of 0.6 mM LH_2 in a 0.8 mL quartz cuvette. The reactions were initiated at 25 °C by injection of 120 μL of 18 mM Mg-ATP solution through a modified lid. Signal intensity was measured over 15 min by centering the emission monochromator to the appropriate peak wavelength (617 nm for BXRE10, 706 nm for BXRE-680). The emission slit width was set to the maximum of 29.4 nm, and emission intensities were corrected for the spectral response of the R928 photomultiplier tube, and for the relative percentage of the overall emission profile observable through the 29.4 nm window.

Transmittance of Bioluminescence through Blood. Solutions (5 mL) of 2 mM Mg-ATP and 0.60 mM LH_2 in PBS, pH 7.3, were diluted with equal volumes of PBS or citrated human blood, and the pH of each was adjusted to 7.3. Aliquots (520 μL) of PBS- or blood-containing solutions were added to cuvettes, and bioluminescence was initiated by addition of 3 μg of luciferase at 25 °C. After 10 s, bioluminescence emission was recorded with a CCD detector as described above. Percent light transmittance through 50% blood solution was calculated from the ratio of the integrated intensities of the signals transmitted through blood and PBS.

Factor Xa Assay. Assays of factor Xa activity from a commercial sample of authentic material were performed in either PBSA buffer or citrated human blood. The specific activity of the sample was confirmed by assay with the chromogenic substrate Bz-Ile-Glu(γ-OR)-Gly-Arg-pNA·HCl (Kabi Diagnostica, Stockholm, Sweden). A sample of BXRE-680 immobilized onto agarose beads (Agarose-SA:BXRE-680), prepared as described above, was divided into 0.1 mL aliquots that were briefly centrifuged. The supernatants were removed and replaced with 0 to 20 μg/mL of factor Xa in 0.1 mL of either PBSA or blood. The solutions were resuspended and gently mixed while incubating at 25 °C. At various time intervals, the suspensions were briefly centrifuged, 5 μL aliquots were withdrawn, and incubation was continued after the mixtures were resuspended. To simulate performing the bioluminescence measurements in blood, assay solutions containing 0.25 mL of blood and 0.25 mL of 1.0 mM Mg-ATP and 0.3 mM LH_2 in PBS were used. Light reactions were initiated by the addition the 5 μL aliquots of supernatant and were monitored with a liquid N_2 cooled CCD as described above. Emission intensity was determined by integrating the resulting bioluminescence emission spectra. Light reactions performed in PBSA (no added blood) were monitored using a photomultiplier tube as described above.

RESULTS AND DISCUSSION

Ppy RE8 Cysteine Variants. With the goal of developing efficient intramolecular BRET-based sources of nIR light using the firefly luciferase system, we initiated our studies with the recently developed thermostable Luc variant Ppy RE8 (*16*), which emits red light (617 nm) (Figure 1b) with 63% bioluminescence specific activity compared to wild-type Luc (Ppy WT) (Table 1). The red-shifted emission of Ppy RE8 provided better donor−acceptor overlap with the nIR fluorescent dyes AF680 and AF750 than was possible with Luc, 59% with AF680 and 29% with AF750 compared to 40% and 15%, respectively (Figure 2). The commercially available AlexaFluor dyes afford nIR fluorescence with good quantum yields of 0.36 (AF680) and 0.12 (AF750) (*24*), and excellent labeling specificity for Cys residues provided by the appended maleimide groups.

Table 1. Properties of Firefly Luciferase Variants

enzyme	relative specific activity[a]	decay time[b] (min)	K_m (μM)		bioluminescence λ_{max} (nm, fwhm[c])	thermal inactivation[d] (h)
			LH_2	Mg-ATP		
Ppy WT	100	0.10	15 ± 2	160 ± 20	560 (73)	0.26
Ppy RE8	63	0.26	77 ± 8	391 ± 39	617 (73)	3.50
Ppy RE8/C169	78	3.10	138 ± 9.6	450 ± 45	617 (72)	4.00
Ppy RE8/C368	84	3.90	105 ± 13	523 ± 50	617 (72)	1.10
Ppy RE8/C399	94	2.30	113 ± 13	517 ± 48	617 (71)	3.50
Ppy RE10	97	1.70	175 ± 16	422 ± 41	617 (71)	3.60

[a] Specific activity based on 15 min integration assays performed as previously described (*23*). The error of the triplicate measurements was less than 10% of the measured value. [b] Time for maximum signal intensity to decay to 15% of the initial value. [c] Full width at half-maximum intensity. [d] Time for the maximum initial activity to decay to 50% at 37 °C.

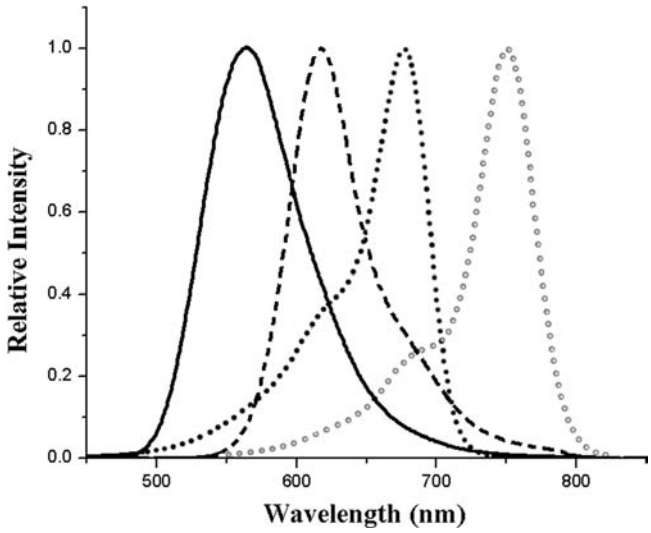


Figure 2. Overlap of normalized bioluminescence emission spectra of Luc (solid line), Ppy RE8 (dashed line), and Ppy RE10 (dashed line) with the normalized excitation (absorption) spectra of AF680 (closed circles) and AF750 (open circles).

Although Ppy RE8 contains four native Cys residues, molecular modeling based on a crystal structure (*1*) of Luc in complex with the inhibitor DLSA (*25*), an N-acylsulfamate analogue of LH_2-AMP, indicated that the thiols were not in solvent-exposed surface positions. As anticipated, control experiments with Ppy RE8 and the AlexaFluor nIR dyes produced neither measurable BRET signals nor any covalent incorporation of dye as determined by LC/ESMS (data not shown). Next, molecular modeling was used to select residues Thr169, Ser185, Ser307, Phe368, and Ser399 for mutation to Cys based on their surface locations, proximity to (but not part of) the active site, and, with the exception of Phe368, structural similarity to Cys. The single Cys Ppy RE8 variants were obtained as pure proteins in yields of 5−10 mg/0.25 L culture, and the characterization of the bioluminescence properties of the three most promising ones is presented in Table 1. Significantly, the introduction of a single Cys residue at positions 169, 368, or 399 produced luciferases with bioluminescence emission maxima of 617 nm, a value identical to that of the template enzyme Ppy RE8. The K_m values of the single Cys mutants were slightly elevated up to 2.3-fold for LH_2 and 1.3-fold for Mg-ATP, while the specific activities determined from 15 min integrated light emission were somewhat enhanced. Since the overall stability of the Cys368 enzyme, estimated from 37 °C thermal inactivation data (Table 1), was significantly lower than that of Ppy RE8 and the other Cys variants, we did not study it further. Instead, we added both the T169C and S399C mutations to Ppy RE8 and expressed and purified the resulting Ppy RE10 protein obtaining 7 mg from 0.25 L culture. The protein has 1.4-fold enhanced specific activity and is otherwise quite similar to Ppy RE8.

Covalent Labeling of Luciferases with Alexa Fluor Maleimide Dyes Produces nIR BRET Emission. The Ppy RE8 Cys169 and Cys399 enzymes along with Ppy RE10 were covalently labeled with AF680 and AF750 by incubating 30 μM protein solutions in PBSA buffer with a 10-fold molar excess of dye for 15 min at 10 °C. Ppy RE8/C169 and Ppy RE8/C399 have similar activity and thermostability properties (Table 1) and nIR dye labeling produced BRET emission at ~705 nm (with AF680) and ~780 nm (with AF750). However, the BRET efficiencies obtained with these proteins were quite different (Table 2). The BRET ratios of the position 399 labeled enzymes were ~5- to 9-fold greater than those of the corresponding position

Table 2. Properties of Luciferase Variants and Fusion Proteins Labeled with Alexa Fluor nIR Dyes

enzyme[a]	relative specific activity[b]	decay time[c] (min)	thermal inactivation[d] (h)	BRET λ_{max} (nm, fwhm[e])	BRET ratio[f]	labeling stoichiometry[g]
Ppy WT	100	0.10	0.26		-	-
Ppy RE8	63	0.26	3.50	-	-	-
Ppy RE10	97	1.7	3.60	-	-	-
BXRE10[h]	60	2.0	3.5	-	-	-
Ppy RE8/C169-AF750	19	5.3	2.3	778 (71)	0.5	1.0 (1:1)
Ppy RE8/C399-AF750	86	2.4	2.8	780 (70)	2.1	1.3 (1:1)
Ppy RE10-AF750	41	4.4	3.0	783 (60)	4.0	1.8 (2:1)
Ppy RE8/C169-AF680	132	2.4	3.3	704 (59)	4.5	1.1 (1:1)
Ppy RE8/C399-AF680	180	1.5	1.3	705 (60)	10.0	1.4 (1:1)
Ppy RE10-AF680	164	7.4	3.5	705 (57)	34.0	2.1 (2:1)
BXRE-680	115	5.7	1.5	706 (49)	14.0	2.0 (2:1)[i]
MagSphere-SA:BXRE-680	34	13.6	-	706 (49)	11.0	-
Agarose-SA:BXRE-680	76	13.0	-	708 (48)	13.7	-

[a] AF750 and AF680 refer to the fluorescent dyes covalently attached to the respective enzymes. [b] Specific activity based on 15 min integration assays performed as previously described (*23*). The error of the triplicate measurements was less than 10% of the measured value. [c] Time for maximum signal intensity to decay to 15% of the initial value. [d] Time for the maximum initial activity to decay to 50% at 37 °C. [e] Full width at half-maximum intensity. [f] BRET ratios were calculated from emission spectra by dividing the area under the BRET emission peak by the area under the residual bioluminescence peak. [g] The number of dye molecules incorporated per molecule of enzyme was calculated by UV−vis absorption as described in the Experimental Procedures. The error in the UV−vis based determination is ~20%. The ratios in parentheses are based on the masses associated with the only peaks detected using LC/ESMS. [h] Contains bound biotin. [i] The BXRE-680 LC peak contained a second minor mass indicative of 1:1 dye/protein labeling.

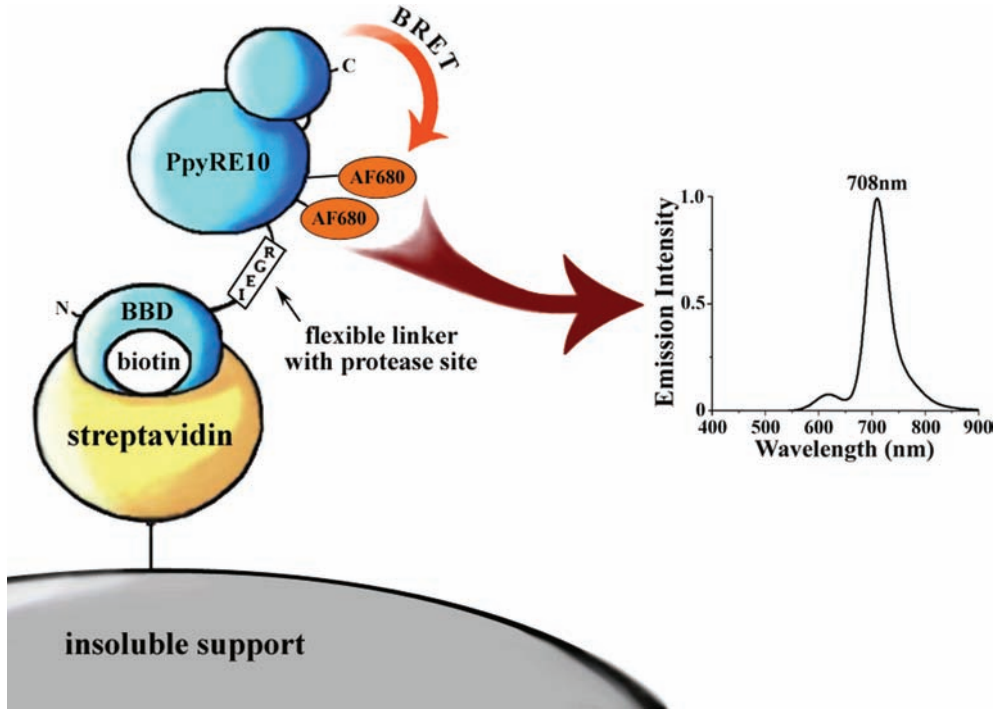


Figure 3. BRET emission spectrum of BXRE-680 immobilized on Agarose-SA. The fusion protein contains biotin bound to a biotin binding domain that is connected through a 12 amino acid linker (containing a factor Xa protease site) to Ppy RE10 labeled with AF680. The emission spectrum was recorded by suspending an aliquot of the immobilized material in a pH 7.8 buffer containing LH_2 and Mg-ATP.

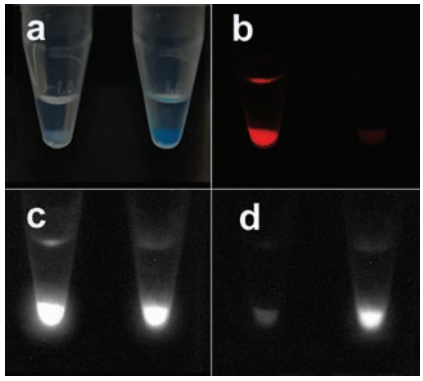


Figure 4. Visible and nIR light emission produced by unlabeled and labeled immobilized fusion proteins. In each panel, the tubes contain ~20 μL of Agarose-SA bound substrate (right tubes, BXRE-680; and left tubes, the immobilized fusion protein with no AF680 attached) that settled from 70 μL pH 7.8 buffered suspensions after brief centrifugation. The protein concentrations in the 20 μL of settled resin are ~40 μM. In panels (a) and (b), photographs were taken with a Nikon D80 equipped with a stock IR filter (a) in ambient light prior to addition of LH_2 and Mg-ATP and (b) in the dark at 15 s exposure following addition of the substrates and showing only visible light emission. In panels (c) and (d) photographs were taken with an iGen NV 20/20 camera with night vision (infrared) capability (c) capturing total light emission; and in (d) using a Schott 695 nm long-pass filter showing only nIR emission.

169 enzymes (Table 2). Since the dyes attached to Cys399 are estimated to be 15 Å closer (20 Å versus 35 Å) to the emitter oxyluciferin, the higher BRET ratios associated with the labeling of Cys399 are expected, because resonance energy transfer efficiency is inversely proportional to and heavily weighted by the distance between the donor and the acceptor.

We reproducibly and quantitatively labeled milligram quantities of Ppy RE10 by attaching AF680 or AF750 to both the Cys169 and Cys399 residues (Table 2). Thermolysin proteolysis and LC/ESMS analyses verified the covalent attachment of the nIR dyes to the expected Cys169 and Cys399 residues (Experimental Procedures), presumably through thioether linkages. The dye-modified luciferases displayed emission maxima shifted to 705 and 783 nm with BRET ratios of 35.0 and 4.1, respectively (Figure 1c and d). Integrated light emission was 4.0-fold greater for Ppy RE10 labeled with AF680 compared to the AF750 labeled enzyme, representing a 1.7-fold increase and 2.4-fold decrease with respect to the Ppy RE10 template. The nIR dye-labeled Ppy RE10 enzymes provided an excellent combination of high BRET ratios, retention of enzyme activity, minimal nonspecific dye incorporation, long-wavelength emission maxima, and extended glow kinetics. Importantly, the two additional engineered Cys residues did not alter the 617 nm bioluminescence maximum of precursor Ppy RE8, nor did they adversely affect specific activity.

While the BRET ratio of 4.0 with the attached AF750 label is very good and is similar to results obtained with quantum dot (QD)−rLuc mutant conjugates (*12*), the 34.0 value obtained with AF680 is extraordinary. Moreover, the bioluminescence maximum of Luc has been red-shifted 223 nm by the combined effects of mutagenesis (57 nm) and BRET (166 nm) in the AF750 labeled enzyme. The nIR dye-labeled Ppy RE10 enzymes were stable for at least 6 weeks when stored in solution at 5 °C, and they could be flash frozen, stored at −80 °C, and thawed without loss of activity. Additionally, the BRET activity was retained at levels greater than 50% for ~3 h at 37 °C. To the best of our knowledge, this is the first report of bright nIR light sources produced by chemical modification of a beetle luciferase. The outstanding BRET ratio (34.0) achieved with AF680 labeling of Ppy RE10 emphasizes the importance of selective labeling with fluorescent dyes.

We considered the basis of the appreciably different labeling results, particularly the 4.0-fold higher specific activity and 8.5-fold greater BRET ratio obtained with Ppy RE10 labeled with AF680 and AF750, respectively (Table 2). Since the dyes are approximately the same size, have similar chemical structures (preliminary structure assignments based on HRMS and NMR) and are attached to the same Ppy RE10 thiols, distances from the emitter can be ruled out, although differences in spatial

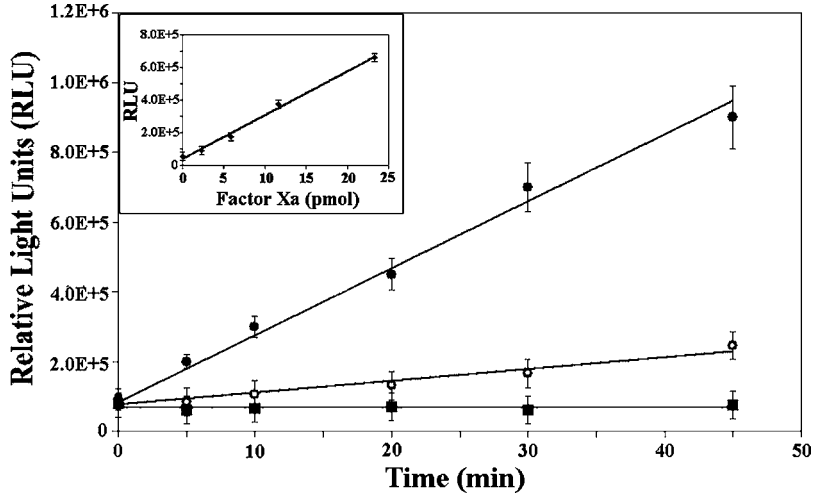


Figure 5. Bioluminescence assays of factor Xa activity in whole blood. Stirred suspensions of aliquots of Agarose-SA:BXRE-680 in whole blood (0.1 mL) were incubated at 20 °C with factor Xa: (filled squares) 0 μg/mL; (open circles) 2.5 μg/mL; and (filled circles) 10 μg/mL. Aliquots (5 μL) were withdrawn and assayed at the times shown as described in detail in the Experimental Procedures. The inset shows bioluminescence end point assay data collected 30 min after incubation of factor Xa in stirred substrate suspensions of Agarose-SA:BXRE-680.

orientation of the dyes may be a contributing factor. Instead, it is likely that the variation in the specific activities can largely be accounted for by the 3-fold higher fluorescence quantum yield of AF680 (0.36) compared to AF750 (0.12) (*24*). That is, even if the energy transfer efficiencies were identical, the AF680 labeled enzyme would be expected to produce ~3-fold more BRET emission than the AF750 labeled protein. While the difference in the quantum yields of the nIR dyes also contributes to the superior BRET ratio of the AF680 labeled Ppy RE10, the 2-fold greater spectral overlap of Ppy RE10 bioluminescence with the AF680 excitation spectrum is also an important contributing factor. Additionally, the AF680 labeled enzymes produced integrated specific activities (based on total photons emitted) that were greater than that of Ppy WT (Table 2). This is most likely due to improved turnover. Under the assay conditions employed in the measurement of the integration-based activities, Luc is inhibited by the formation of dehydroluciferyl-AMP, a side product naturally formed during the oxidation of LH_2 (*26*−*28*), that binds tightly and dissociates very slowly (K_D = 0.5 nM) from the active site. Possibly, the binding of AF680 on the surface of the Luc variants results in conformational changes that caused an increase in the K_D of the inhibitor.

Immobilized AF680-Labeled Ppy RE10 Fusion Proteins. To demonstrate that a Luc-based BRET source could be applied where nIR emission would be advantageous, e.g., in receptor-based imaging and for enzyme assays in whole blood, we constructed the fusion protein BXRE-680 and immobilized it to streptavidin (SA) bound to agarose or magnetic microspheres (Figure 3). Modeled after a similar fusion protein containing Luc immobilized on magnetic beads (*22*), BXRE-680 contains biotin bound to a biotin binding domain connected to AF680-labeled Ppy RE10 through a12 amino acid residue linker sequence that includes the IleGluGlyArg factor Xa protease site. Reaction of AF680 with the biotinylated fusion protein BXRE10 produced BXRE-680 with an ~2-fold greater specific activity, likely resulting from the slower decay of luminescence (Table 2). The linker peptide and BBD do not contain Cys residues and LC/ESMS analysis of BXRE-680 confirmed the incorporation of 2 nIR dyes/fusion protein. After attachment to both agarose and magnetic microspheres through the strong streptavidin (SA)−biotin interaction (*29*), matrix-bound BXRE-680 produced BRET ratios of 13.7 (708 nm maximum) and 11.0 (706 nm maximum), respectively (Table 2). While immobilization reduced specific activity 1.5- and 3.4-fold for the agarose and magnetic bead bound materials, respectively, the materials are bright sources of red and nIR light as illustrated with Agarose-SA:BXRE-680 (Figure 4). Yeung and co-workers reported (*22*) making a biotinylated fusion protein of Luc with an attached BBD that was then immobilized on SA-containing beads. The modified beads were attached to cell surfaces and employed to image ATP release from live astrocyte cells upon addition of LH_2 using a CCD camera (*22*). The construction of the biotinylated BXRE-680 fusion protein and demonstration that it efficiently emits nIR light while immobilized through the streptavidin−biotin interaction (Figures 3 and 4) established, in principle, that our material can be applied similarly for receptor imaging of genetically encoded streptavidin sites. However, one drawback of the chemical labeling approach used to produce our materials is that they cannot be genetically encoded, thereby limiting their usefulness for in vivo applications. Nevertheless, Ohmiya and co-workers recently demonstrated (*14*) the targeting and tumor imaging capabilities of a biotinylated nIR dye labeled-cLuc conjugate in live mice. This was accomplished by first linking the labeled cLuc conjugate to an avidin-monoclonal antibody against a cell surface tumor marker. Injection of this biotin−avidin complex, followed by injection of the cLuc substrate coelenterazine produced BRET signals (λ_{max} = 675 nm) that enabled tumor detection and imaging (*14*). These interesting results strongly support the feasibility of applying BXRE-680 fusion proteins for similar purposes. Moreover, since the cited applications (*14, 22*) employ CCD cameras, the longer wavelength emission and superior BRET ratio of BXRE-680 (e.g., 40- to 50-fold greater than the cLuc-containing material) may provide enhanced sensitivity in environments containing interfering visible light absorbing substances. However, additional experiments must be undertaken to determine whether the potential advantages of BXRE-680 can be realized.

Factor Xa Assays with Agarose-SA:BXRE-680. We also explored the use of the agarose bound BXRE-680 material (Figure 3) as a substrate for assaying factor Xa activity. Briefly, various concentrations (1−20 μg/mL) of commercial factor Xa were incubated at 25 °C in citrated human blood containing the resin-bound substrate. The assay principle is that factor Xa cleavage of BXRE-680 releases AF680-labeled Ppy RE10 from the matrix into the blood medium. Physiologically significant levels of factor Xa activity were proportional to the light intensity produced by the solubilized BRET source (after brief centrifugation to separate unreacted matrix-bound substrate) upon addition of substrates LH_2 and Mg-ATP (Figure 5). The advantage provided by the nIR source was that there was

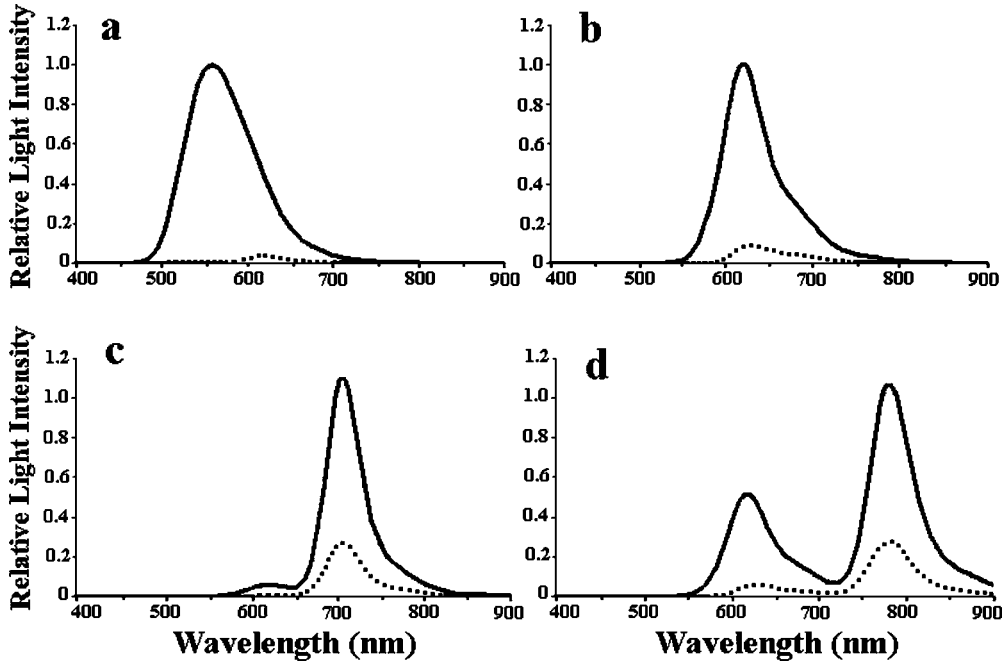


Figure 6. Relative transmittance of bioluminescence through citrated human blood. The emission spectra shown in all panels were initiated by addition of solutions of Mg-ATP (2 mM) and LH_2 (0.60 mM) in PBS to citrated human blood (dashed lines) or PBS (solid lines) containing (a) Ppy GR-TS (*18*); (b) Ppy RE10; (c) Ppy RE10-AF680; and (d) PpyRE10-AF750 as described in detail in the Experimental Procedures.

sufficient sensitivity to detect 1 μg/mL of factor Xa from aliquots of blood diluted only 1:1 with substrate solution. Emission spectra showing the attenuation of green (Ppy GR-TS), red (Ppy RE10), and nIR (Ppy RE10-AF680 and Ppy RE10-AF750) signals by whole human blood diluted 1:1 with an isotonic buffer are presented in Figure 6. Since the bioluminescence measurements were made with the proteins in direct contact with the blood components, attenuation may result not only from the absorption of light emission, but also from nonspecific effects, e.g., adsorption of the enzymes, and from quenching of bioluminescence and/or fluorescence of the nIR dyes. Strong hemoglobin absorption (*30*) is likely an important factor in the nearly complete loss (~97%) of the green signal (Figure 6a) and the 550−600 nm component of the Ppy RE10 emission (Figure 6b). However, interference of Ppy RE10 bioluminescence also occurs as the total bioluminescence signal has been attenuated ~90%. The loss of Ppy RE10 bioluminescence intensity no doubt contributes to the reduced intensity of the nIR signals produced by BRET (Figure 6c,d); however, the relative intensities produced by the AF-680 and AF-750 labeled enzymes in blood were ~23% and ~25%. This result very likely reflects the greater transmission of nIR light in a medium containing hemoglobin. Immobilized versions of the fusion protein with linkers containing other specific cleavage sites should provide new substrates for protease assays as demonstrated with factor Xa, possibly in media like blood where interference with visible light is a serious problem. Additional potential applications (*31*) include immunoassays and biosensors.

ACKNOWLEDGMENT

The authors gratefully acknowledge the financial support provided by the Air Force Office of Scientific Research (FA9550-07-1-0043 and FA9550-10-1-0174), the National Science Foundation (MCB0842831), and the Hans & Ella McCollum ′21 Vahlteich Endowment.

Supporting Information Available: Experimental Procedures including materials and general methods for cloning of Ppy RE8 variants, cloning of fusion protein BXRE10, expression and purification of biotinylated fusion protein BXRE10 and relative quantum yield measurements; HPLC chromatograms of Ppy RE10-AF750. This material is available free of charge via the Internet at http://pubs.acs.org.

LITERATURE CITED

(1) Hastings, J. W. (1996) Chemistries and colors of bioluminescent reactions- a review. *Gene 173*, 5–11.
(2) Widder, E. A., Latz, M. I., Herring, P. J., and Case, J. F. (1984) Far red bioluminescence from 2 deep-sea fishes. *Science 225*, 512–514.
(3) Morin, J. G., and Hastings, J. W. (1971) Energy transfer in a bioluminescent system. *J. Cell Physiol. 77*, 313–8.
(4) Shimomura, O., Johnson, F. H., and Saiga, Y. (1962) Extraction, purification and properties of aequorin, a bioluminescent protein from the luminous hydromedusan, Aequorea. *J. Cell. Comp. Physiol. 59*, 223–39.
(5) Roda, A., Michelini, E., Magliulo, M., and Guardigli, M. (2006) Novel BRET-based biosensors with a new bioluminescent donor, Gaussia luciferase, for oestrogen and androgen receptor ligands. *Luminescence 21*, 289–290.
(6) Dacres, H., Dumancic, M. M., Horne, I., and Trowell, S. C. (2009) Direct comparison of fluorescence- and bioluminescence-based resonance energy transfer methods for real-time monitoring of thrombin-catalysed proteolytic cleavage. *Biosens. Bioelectron. 24*, 1164–1170.
(7) De, A., Ray, P., Loening, A. M., and Gambhir, S. S. (2009) BRET3: a red-shifted bioluminescence resonance energy transfer (BRET)-based integrated platform for imaging protein-protein interactions from single live cells and living animals. *Faseb J. 23*, 2702–2709.
(8) Pfleger, K. D., and Eidne, K. A. (2006) Illuminating insights into protein-protein interactions using bioluminescence resonance energy transfer (BRET). *Nat. Methods 3*, 165–174.
(9) Prinz, A., Diskar, M., and Herberg, F. W. (2006) Application of bioluminescence resonance energy transfer (BRET) for biomolecular interaction studies. *ChemBioChem 7*, 1007–1012.
(10) Rao, J. H., Dragulescu-Andrasi, A., Yao, H. Q., and Yao, H. Q. (2007) Fluorescence imaging in vivo: recent advances. *Curr. Opin. Biotechnol. 18*, 17–25.

(11) So, M. K., Xu, C. J., Loening, A. M., Gambhir, S. S., and Rao, J. H. (2006) Self-illuminating quantum dot conjugates for in vivo imaging. *Nat. Biotechnol. 24*, 339–343.
(12) Xing, Y., So, M. K., Koh, A. L., Sinclair, R., and Rao, J. H. (2008) Improved QD-BRET conjugates for detection and imaging. *Biochem. Biophys. Res. Commun. 372*, 388–394.
(13) Ma, N., Marshall, A. F., and Rao, J. H. (2010) Near-infrared light emitting luciferase via biomineralization. *J. Am. Chem. Soc. 132*, 6884–6885.
(14) Wu, C., Mino, K., Akimoto, H., Kawabata, M., Nakamura, K., Ozaki, M., and Ohmiya, Y. (2009) In vivo far-red luminescence imaging of a biomarker based on BRET from Cypridina bioluminescence to an organic dye. *Proc. Natl. Acad. Sci. U.S.A. 106*, 15599–15603.
(15) Ando, Y., Niwa, K., Yamada, N., Enomot, T., Irie, T., Kubota, H., Ohmiya, Y., and Akiyama, H. (2008) Firefly bioluminescence quantum yield and colour change by pH-sensitive green emission. *Nat. Photonics 2*, 44–47.
(16) Branchini, B. R., Ablamsky, D. M., Davis, A. L., Southworth, T. L., Butler, B., Fan, F., Jathoul, A. P., and Pule, M. A. (2010) Red-emitting luciferases for bioluminescence reporter and imaging applications. *Anal. Biochem. 396*, 290–297.
(17) Ignjatovic, V., Summerhayes, R., Gan, A., Than, J., Chan, A., Cochrane, A., Bennett, M., Horton, S., Shann, F., Lane, G., Ross-Smith, M., and Monagle, P. (2007) Monitoring unfractionated heparin (UFH) therapy: which anti-factor Xa assay is appropriate? *Thromb. Res. 120*, 347–351.
(18) Branchini, B. R., Ablamsky, D. M., Murtiashaw, M. H., Uzasci, L., Fraga, H., and Southworth, T. L. (2007) Thermostable red and green light-producing firefly luciferase mutants for bioluminescent reporter applications. *Anal. Biochem. 361*, 253–262.
(19) Branchini, B. R., Ablamsky, D. M., Rosenman, J. M., Uzasci, L., Southworth, T. L., and Zimmer, M. (2007) Synergistic mutations produce blue-shifted bioluminescence in firefly luciferase. *Biochemistry 46*, 13847–13855.
(20) Branchini, B. R., Magyar, R. A., Murtiashaw, M. H., Anderson, S. M., and Zimmer, M. (1998) Site-directed mutagenesis of histidine 245 in firefly luciferase: A proposed model of the active site. *Biochemistry 37*, 15311–15319.
(21) Branchini, B. R., Southworth, T. L., Murtiashaw, M. H., Wilkinson, S. R., Khattak, N. F., Rosenberg, J. C., and Zimmer, M. (2005) Mutagenesis evidence that the partial reactions of firefly bioluminescence are catalyzed by different conformations of the luciferase C-terminal domain. *Biochemistry 44*, 1385–1393.
(22) Zhang, Y., Phillips, G. J., Li, Q. X., and Yeung, E. S. (2008) Imaging localized astrocyte ATP release with firefly luciferase beads attached to the cell surface. *Anal. Chem. 80*, 9316–9325.
(23) Branchini, B. R., Southworth, T. L., Khattak, N. F., Michelini, E., and Roda, A. (2005) Red- and green-emitting firefly luciferase mutants for bioluminescent reporter applications. *Anal. Biochem. 345*, 140–148.
(24) Haugland, R. P., Spence, M. T. Z., Johnson, I. D., and Basey, A. (2005) *The handbook: a guide to fluorescent probes and labeling technologies*, 10th ed., Molecular Probes, Eugene, OR.
(25) Branchini, B. R., Murtiashaw, M. H., Carmody, J. N., Mygatt, E. E., and Southworth, T. L. (2005) Synthesis of an N-acyl sulfamate analog of luciferyl-AMP: A stable and potent inhibitor of firefly luciferase. *Bioorg. Med. Chem. Lett. 15*, 3860–3864.
(26) Rhodes, W. C., and McElroy, W. D. (1958) The synthesis and function of luciferyl-adenylate and oxyluciferyl-adenylate. *J. Biol. Chem. 233*, 1528–1537.
(27) Fraga, H., Esteves Da Silva, J. C. G., and Fontes, R. (2004) Identification of luciferyl adenylate and luciferyl coenzyme A synthesized by firefly luciferase. *ChemBioChem 5*, 110–115.
(28) Fraga, H., Fernandes, D., Fontes, R., and Esteves da Silva, J. C. G. (2005) Coenzyme A affects firefly luciferase luminescence because it acts as a substrate and not as an allosteric effector. *FEBS J. 272*, 5206–5216.
(29) Green, N. M. (1990) Avidin and streptavidin. *Methods Enzymol. 184*, 51–67.
(30) Shah, K., and Weissleder, R. (2005) Molecular optical imaging: applications leading to the development of present day therapeutics. *NeuroRx 2*, 215–25.
(31) Roda, A., Guardigli, M., Michelini, E., and Mirasoli, M. (2009) Bioluminescence in analytical chemistry and in vivo imaging. *Trends Anal. Chem. 28*, 307–322.

BC100256D

SUPPORTING INFORMATION

Chemically Modified Firefly Luciferase Is an Efficient Source of Near-Infrared Light

Bruce R. Branchini, Danielle M. Ablamsky and Justin C. Rosenberg*

Department of Chemistry, Connecticut College, New London, Connecticut 06320

* To whom correspondence should be addressed: brbra@conncoll.edu

CONTENTS:

1. Materials and General Methods
2. Cloning of Ppy RE8 Variants
3. Cloning of Fusion Protein BXRE10
4. Expression and Purification of Biotinylated Fusion Protein BXRE10
5. Table S1:
6. Figure S1:
7. Figure S2:
8. Figure S3:
9. Figure S4:
10. SI References

1. Materials and General Methods

Materials. The following materials were obtained from the sources indicated: Mg-ATP (bacterial source) from Sigma-Aldrich (St. Louis, MO); Glutathione Sepharose 4B media and pGEX-6P-2 expression vector from GE Healthcare (Piscataway, NJ); pQE30 expression vector from Qiagen (Valencia, CA); QuikChange® Lightning Site-Directed Mutagenesis kit from Stratagene (La Jolla, CA); Alexa Fluor® 680 C2-maleimide (AF680) and Alexa Fluor® 750 C5-maleimide (AF750) dyes from Invitrogen (Carlsbad, CA); NanoLinK™ streptavidin magnetic microspheres from SoluLinK Biosciences (San Diego, CA); and Streptavidin agarose resin from Thermo Scientific (Rockford, IL). The recombinant GST-fusion proteins Ppy RE8 (S1) (*15*) and Ppy RE10 were expressed and purified as previously reported (S1-S5) (*15-19*). LH_2 was a generous gift from Promega (Madison, WI) and the pET-KBPT-Luc plasmid (S7) (*20*) was a generous gift from E. S. Yeung, Iowa State University.

General Methods. Concentrations of unlabeled proteins were determined using the Bio-Rad Protein Assay system using BSA as the standard. DNA sequencing to verify all mutations, insertions and ligation sites was performed at the W. M. Keck Biotechnology Laboratory at Yale University. Unless otherwise specified, specific activity measurements, heat inactivation studies and steady-state kinetics constants were determined as previously reported (S2, S3, S5, S6) (*16, 17, 19, 21*).

2. Cloning of Ppy RE8 Variants.

Starting with the DNA encoding Ppy RE8 in the pGEX-6P-2 vector (S2), the QuikChange Lightning Site-Directed Mutagenesis kit was used to introduce the following single mutations using the indicated primers and their respective reverse complements: Thr169Cys 5´- CAG TCG ATG TAC ACG TTC GTC TGC TCT CAT CTA CCT CCC GGT TTT AAT G - 3´ [AleI]; Phe368Cys, 5´ - GGT AAA GTT GTT CCA TGT TTT GAA GCC AAG GTT GTG GAT CTG - 3´ [BstXI]; and Ser399Cys 5´-T GTC AGA GGG CCC ATG ATT ATG TGC GGT TAT GTA AAC AAT CCG - 3´ [ApaI] (bold represents the mutated codons, underline represents silent changes to create a unique screening

endonuclease site and brackets indicate the screening endonuclease). The gene encoding Ppy RE10 was made by sequential introduction of the Thr169Cys and Ser399Cys changes into the Ppy RE8 DNA.

3. Cloning of Fusion Protein BXRE10.

The vector containing the gene encoding a fusion protein (BXRE10), consisting of an N-terminus hexa-His tagged biotin binding domain joined to Ppy RE10 through the peptide linker –GSGSIEGRGSGS-, was constructed as follows. First the Qiagen pQE30 plasmid was modified to enable the insertion of the gene for Ppy RE10 flanked by BamHI and XhoI sites in the pGEX-6P-2 vector (see above). The existing XhoI site in the pQE30 plasmid was removed and a new one was created in the multiple cloning site downstream of the already present BamHI site using the following primers and their respective reverse complements: 5´- ACG AGG CCC TTT CGT CTT CAC CTG GAG AAA TCA TAA AAA - 3´and 5´- CAC GGA TCC GCA TGC GAG CTC GAG ACC CCG GGT CGA CCT - 3´, respectively. The gene encoding Ppy RE10 was isolated from the pGEX-6p-2 plasmid by digestion with BamHI and XhoI and was then ligated into the modified pQE30 vector, which had been digested with the same restriction enzymes. The modified pQE30 plasmid containing the Ppy RE10 gene was further altered by introducing the PmlI and SpeI restriction sites upstream of the luciferase gene to enable insertion of the DNA encoding the biotin binding domain (BBD, residues Met12-Val76 in the pET-KPBT-Luc plasmid) using the following primer and its respective reverse complement: 5´ - CAC CAT CAC CAT CAC GTG AGC ACT AGT GGA TCC ATG GAA GAC - 3´ (bold represents the inserted codons and the PmlI and SpeI endonuclease sites are underlined). The BBD was amplified from the pET-KPBT-Luc plasmid by PCR (initial denaturation at 95 °C for 2 min; a 60-cycle amplification of 95 °C for 30 s, 55 °C for 30 s and 68 °C for 1.75 min; and a final extension at 68 °C for 5 min) with the primers 5´- CAT CAT CAC GTG ATG GCT AGA GTC GAC GTC AGC - 3´ and 5´- CCA CCA GTA CTA GTA GTA ACG GCC GCC AGT GTG C - 3´ (bold represents the introduced endonuclease sites for insertion of the BBD). The PCR product was cleaned with the Qiagen QIAquick PCR purification kit, digested with PmlI and SpeI and ligated into the modified pQE30 vector

containing the Ppy RE10 DNA, which had been treated with the same restriction endonucleases, yielding pQE30-BBD-RE10. Using the primer 5´ - A CTG GCG GCC GTT ACT ACT GGA TCC GGA TCC ATC GAA GGT CGT GGA AGT GGA TCC AT - 3´ (bold represents the inserted codons) and its reverse complement, a 12 amino acid linker containing the factor Xa protease site IleGluGlyArg was inserted between the BBD and Ppy RE10 genes yielding pQE30-BXRE10. This plasmid encodes the fusion protein BBD-GSGSIEGRGSGS-Ppy RE10 containing a hexa-His-tag at the N-terminus (BXRE10).

3. Expression and Purification of Biotinylated Fusion Protein BXRE10.

Cultures (250 mL of Luria-Bertani media supplemented with 100 mg/mL ampicillin, 25 mg/mL kanamycin and 50 mM biotin) of transformed E. coli BL21 (pREP4) cells containing the pQE30-BXRE10 plasmid were grown in 1 L flasks at 37 °C to mid log phase ($A_{600\ nm}$ ~ 0.6), moved to a 22 °C incubator, allowed to equilibrate for 10 min, induced with 0.1 mM IPTG and incubated at 22 °C for 16-18 h. Cells were harvested by centrifugation at 4 °C and then frozen at -80 °C for 15 min. The cell pellet was resuspended in 25 mL of 150 mM sodium chloride, 100 mM sodium phosphate buffer, pH 7.3 (PBS) containing 0.1 mM phenylmethylsulfonyl fluoride and 5 mM imidazole. After the addition of 2.5 mL lysozyme (10 mg/mL in PBS), the cells were lysed by sonication and treated with DNase (5 mg/mL) and RNase (10 mg/mL) for 5 min on ice. Triton X-100 was added (1% final volume) and the whole-cell extracts were isolated by centrifugation at 20000 x g for 45 min. The biotinylated His-tagged fusion protein was purified using Ni-NTA agarose (Qiagen) affinity chromatography according to the manufacturer's instructions. Fractions eluted with 250-500 mM imidazole were pooled (2 mL) and dialyzed (2 changes, 1 L each) against 20 mM sodium phosphate buffer, pH 7.2 containing 150 mM NaCl, 5 mM EDTA and 0.8 M ammonium sulfate (PBSA buffer). Biotinylation was confirmed by LC/ESMS analysis showing a single eluting peak of 74592 ± 7 Da corresponding to the predicted mass of BXRE10 plus biotin (74348 + 244 = 74592 Da). The protein was stored at 5 °C in PBSA buffer (~2mg/mL) and retained 90% activity for at least 6 weeks.

SI References.

S1) Branchini, B. R., Ablamsky, D. M., Davis, A. L., Southworth, T. L., Butler, B., Fan, F., Jathoul, A. P., and Pule, M. A. (2010) Red-emitting luciferases for bioluminescence reporter and imaging applications. *Analytical Biochemistry 396*, 290-297.

S2) Branchini, B. R., Ablamsky, D. M., Murtiashaw, M. H., Uzasci, L., Fraga, H., and Southworth, T. L. (2007) Thermostable red and green light-producing firefly luciferase mutants for bioluminescent reporter applications. *Analytical Biochemistry 361*, 253-262.

S3) Branchini, B. R., Ablamsky, D. M., Rosenman, J. M., Uzasci, L., Southworth, T. L., and Zimmer, M. (2007) Synergistic mutations produce blue-shifted bioluminescence in firefly luciferase. *Biochemistry 46*, 13847-13855.

S4) Branchini, B. R., Magyar, R. A., Murtiashaw, M. H., Anderson, S. M., and Zimmer, M. (1998) Site-directed mutagenesis of histidine 245 in firefly luciferase: A proposed model of the active site. *Biochemistry 37*, 15311-15319.

S5) Branchini, B. R., Southworth, T. L., Murtiashaw, M. H., Wilkinson, S. R., Khattak, N. F., Rosenberg, J. C., and Zimmer, M. (2005) Mutagenesis evidence that the partial reactions of firefly bioluminescence are catalyzed by different conformations of the luciferase C-terminal domain. *Biochemistry 44*, 1385-1393.

S6) Branchini, B. R., Southworth, T. L., Khattak, N. F., Michelini, E., and Roda, A. (2005) Red- and green-emitting firefly luciferase mutants for bioluminescent reporter applications. *Analytical Biochemistry 345*, 140-148.

S7) Zhang, Y., Phillips, G. J., Li, Q. X., and Yeung, E. S. (2008) Imaging Localized Astrocyte ATP Release with Firefly Luciferase Beads Attached to the Cell Surface. *Analytical Chemistry 80*, 9316-9325.

Enhanced Target-Specific Accumulation of Radiolabeled Antibodies by Conjugating Arginine-Rich Peptides as Anchoring Molecules

Rei Miyamoto,[†] Hiromichi Akizawa,[‡] Takeshi Nishikawa,[†] Tomoya Uehara,[†] Yusuke Azuma,[§] Ikuhiko Nakase,[§] Shiroh Futaki,[§] Hirofumi Hanaoka,[||] Yasuhiko Iida,[⊥] Keigo Endo,[||] and Yasushi Arano*[,†]

Graduate School of Pharmaceutical Sciences, Chiba University, 1-8-1 Inohana, Chuo-ku, Chiba 260-8675, Japan, Graduate School of Pharmaceutical Sciences, Health Sciences University of Hokkaido, 1757 Kanazawa, Tobetsu-cho, Ishikari-gun, Hokkaido 061-0293, Japan, Institute for Chemical Research, Kyoto University, Gokasho, Uji, Kyoto 611-0011, Japan, Graduate School of Medicine, Gunma University, 39-22, Showa-machi 3-chome, Maebashi, Gunma 371-8511, Japan, and Suzuka University of Medical Science, 1001-1 Kishioka-cho, Suzuka, Mie 510-0293, Japan. Received June 8, 2010; Revised Manuscript Received August 23, 2010

We have devised and estimated a new strategy to prolong the residence time of radiolabeled antibodies in tumor in which an octaarginine peptide (R_8) was used as an anchoring molecule to fix antibodies against CD20 (NuB2; IgG2a) on tumor cells. Conjugation of R_8 with antibodies was performed by maleimide−thiol chemistry using thiol groups generated by reducing the disulfide bonds of the antibody. The R_8-conjugated NuB2 was then reacted with succinimidyl *meta*-[^{125}I]iodobenzoate to prepare [^{125}I]SIB-NuB2$_I$ (0.92 R_8/NuB2) and [^{125}I]SIB-NuB2$_{III}$ (3.38 R_8/NuB2). Both SIB-NuB2$_I$ and SIB-NuB2$_{III}$ exhibited size-exclusion HPLC elution profiles and immunoreactivity to CD20-positive cells similar to those of NuB2. NuB2$_I$ also possessed isoelectric focusing (IEF) profile similar to NuB2. However, NuB2$_{III}$ registered a broad IEF band toward higher pI. When incubated with CD20-positive cells, [^{125}I]SIB-NuB2$_I$ and [^{125}I]SIB-NuB2$_{III}$ exhibited 1.4 and 4.0 times higher cell-associated radioactivity than [^{125}I]SIB-NuB2. After the cells were washed and reincubated in a fresh medium for 3 h, [^{125}I]SIB-NuB2$_I$ and [^{125}I]SIB-NuB2$_{III}$ exhibited significantly higher cell-associated radioactivity than [^{125}I]SIB-NuB2. In biodistribution studies in normal mice, while both [^{125}I]SIB-NuB2$_I$ and [^{125}I]SIB-NuB2 exhibited similar biodistribution profiles, [^{125}I]SIB-NuB2$_{III}$ showed faster clearance from the blood and higher hepatic radioactivity levels than [^{125}I]SIB-NuB2. In SCID mice bearing CD20-positive xenografts, [^{131}I]SIB-NuB2$_I$ exhibited significantly higher radioactivity in xenografts than those of [^{125}I]SIB-NuB2 with no significant increase being observed in other tissues. The findings indicate that appropriate R_8 modification of antibodies satisfies both specific targeting ability of antibody and strong cell-association property of R_8, which was reflected in the increased radioactivity levels in tumor. These findings supported the applicability of this approach to enhance target-specific accumulation of radiolabeled antibodies.

INTRODUCTION

Radioimmunotherapy (RIT) is a cancer therapeutic modality that combines the specific tumor targeting of immunotherapeutics and cytotoxic radiation mechanisms. Encouraging results have been reported in patients with hematologic malignancies treated with ^{90}Y- and ^{131}I-labeled antibodies against CD20 (*1*−*4*), due to their intrinsic high radiosensitivity and relatively good access of the radiolabeled antibodies to the cancer cells (*5*, *6*). Despite numerous efforts, the treatment of solid tumors with radiolabeled antibodies resulted in limited success, due to poor localization of radiolabeled antibodies in the tumors (*7*−*9*). Thus, the enhancement of tumor accumulation and retention of radiolabeled antibodies constitutes a prime requisite for successful RIT.

Numerous factors have been presented as being responsible for tumor accumulation and retention of radiolabeled antibodies (*8*). Since the mechanism of accumulation of radiolabeled antibodies is based on their specific but reversible binding to antigens in tumor tissues, a strategy that shifts the equilibrium to antigen association was considered of prime importance to enhancing tumor accumulation. The use of antibodies internalized to target cells would prolong residence time in the tumor, since these molecules will be resistant to being cleared by washout. The conjugation of arginine-rich cell-penetrating peptides (AR-CPPs) to antibodies has been conducted as a means to facilitate internalization of antibodies and to increase tumor accumulation. Indeed, a prior study reported an increase in tumor accumulation of AR-CPP-conjugated antibodies in vitro (*10*). However, in vivo studies showed increased accumulation in nontarget tissues such as the liver with decreased accumulation in tumors. A prior study also described that the tumor targeting ability of an antibody construct (scFv) was completely abolished following conjugation with AR-CPP (*11*).

Meanwhile, an increase in avidity of antibodies constitutes another strategy to enhance tumor accumulation, as observed in antibody constructs with multivalent binding domains (*8*, *12*, *13*). An increase in tumor uptake was also observed with divalent radiolabeled haptens in pretargeting strategy (*14*). These studies suggested that chemical modification of antibodies with anchoring molecules that possess strong interaction with cell surface molecules or cell membrane may also be useful to shift the equilibrium to antigen association in tumor tissues.

* Corresponding author. Yasushi Arano, Ph.D. Graduate School of Pharmaceutical Sciences, Chiba University, 1-8-1 Inohana, Chuo-ku, Chiba 260-8675, Japan. Phone: +81-43-226-2896; Fax: +81-43-226-2897; E-mail: arano@p.chiba-u.ac.jp.

[†] Chiba University.

[‡] Health Sciences University of Hokkaido.

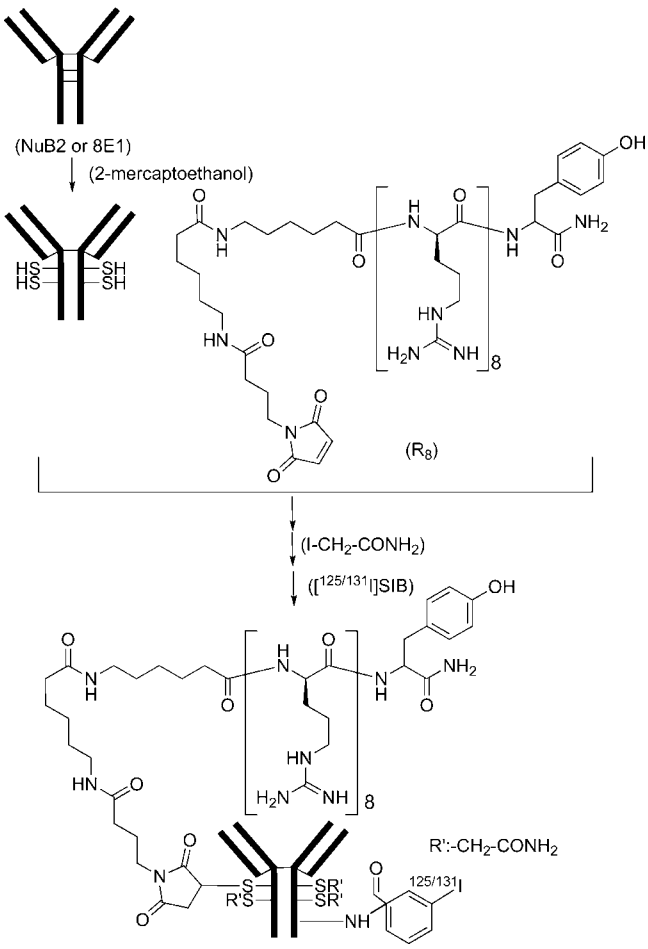
[§] Kyoto University.

[||] Gunma University.

[⊥] Suzuka University of Medical Science.

10.1021/bc100259q © 2010 American Chemical Society
Published on Web 10/25/2010

Scheme 1



The AR-CPPs possess strong interaction with phosphate groups, sulfates, and carboxylates on cellular components (*15*−*18*). The electrostatic interaction between AR-CPPs and cell membrane is so strong that complete removal of AR-CPPs from the cell surface is difficult to perform (*19*−*21*). Such characteristics render AR-CPPs applicable as an anchoring molecule to shift the equilibrium to antigen association for prolonged retention of radiolabeled antibodies in tumors. In addition, the strong electrostatic interaction between AR-CPPs and cellular components suggested that AR-CPPs would exert their anchoring ability at conjugation levels much lower than those used for facilitating internalization.

In this study, an octaarginine peptide was selected as an anchoring molecule, and the peptide was derivatized with a maleimide group to conjugate with a relevant or irrelevant antibody against CD20 (Scheme 1). After radiolabeling of the modified antibodies with succinimidyl *meta*-[$^{125/131}$I]iodobenzoate ([$^{125/131}$I]SIB), the effect of the octaarginine conjugation on specific binding to target cells, dissociation rates from the cells, and biodistribution was determined with special emphasis being laid on the relationship between the anchoring ability of R_8 and the number of R_8 molecules attached per molecule of the antibody. The applicability of the new approach using an AR-CPP as an anchoring molecule to prolong residence time of radiolabeled antibodies in tumor will be discussed.

EXPERIMENTAL PROCEDURES

Reagents and Chemicals. Na[^{125}I]I and Na[^{131}I]I were obtained from MP Biomedicals (Irvine) and Perkin-Elmer (Yokohama, Japan), respectively. The stannyl precursor of the radioiodination reagents, *N*-succinimidyl-3-(tri-*n*-butylstannyl)-benzoate (ATE) was synthesized as reported previously (*22*). Size-exclusion high-performance liquid chromatography (SE-HPLC) was performed using a Cosmosil Diol-300 (7.5 × 600 mm, Nacalai Tesque, Kyoto, Japan) column at a flow rate of 1 mL/min with 0.1 M phosphate buffer (PB, pH 6.8) as an eluent. Each eluent was collected with a fraction collector (RediFlac, GE Healthcare Bioscience, Tokyo, Japan) at 1 min intervals. The radioactivity counts in each fraction (1 mL) were determined with an autowell γ counter (ARC-380M, Aloka, Tokyo). TLC analyses were performed with silica plates (Silica Gel 60 F_{254}, Merck, Tokyo). Isoelectric focusing (IEF) was conducted using a Tefco STC808 mini electrophoresis cell (Tefco, Tokyo) with a precast polyacrylamide gel isoelectric focusing (IEF-PAGE) mini isocratic gel (pH 3−10) (Tefco, Tokyo). Other reagents were of reagent grade and were used as received.

Cells and Antibodies. The CD20 positive human peripheral lymphocyte line RPMI 1788 cells were incubated with RPMI-1640 medium (Sigma-Aldrich Co, St. Louis, MO, USA) supplemented with 10% fetal calf serum and were used for the studies.

The monoclonal antibodies used in this study were a murine monoclonal antibody (NuB2; IgG2b) that reacts specifically with CD20 as a relevant antibody and a murine monoclonal antibody (8E1; IgG2a) specific to a neural protein as an irrelevant one, respectively, since both subclasses possess similar quaternary structures and the interchain disulfide bonds are the primary sites of chemical reduction for both antibodies (*23*). Both antibodies were kindly supplied from Immuno-Biological Laboratories Co, Ltd., (Takasaki, Japan).

Synthesis of Mal-(Acp)$_2$-(D-Arg)$_8$-(D-Tyr) (R_8). We employed D-octaarginine peptide as an AR-CPP, and the peptide with N-terminal bis-aminocaproate linker was coupled with *N*-(4-maleimidebutyryloxy)succinimide for antibody conjugation (Scheme 1).

The peptide chain of R_8 was constructed by Fmoc (9-fluorenylmethyloxycarbonyl) solid-phase peptide synthesis on a TGS-RAM resin (Shimadzu, Kyoto) using Shimadzu PSSM8 peptide synthesizer (Shimadzu, Kyoto) with its standard protocol. A 1-[bis(dimethylamino)methylene]-1*H*-benzotriazolium 3-oxide hexafluorophosphate/1-hydroxybenzotriazole/*N*,*N*-diisopropylethylamine coupling system was employed as the coupling system. As amino acid derivatives, Fmoc-Acp, Fmoc-D-Arg(Pdf), and Fmoc-D-Tyr(^{t}Bu) were used (Acp = 6-aminocaproic acid). The peptide resin was then treated with *N*-(4-maleimidobutyryloxy)succinimide (3 equiv) and *N*-methylmorpholine (3 equiv) in DMF at 37 °C for 20 min to yield a peptide resin bearing a maleimide moiety on its N-terminus. The final deprotection of the peptide resin using trifluoroacetic acid (TFA)−H_2O (95:5) at room temperature for 3 h followed by reverse-phase HPLC purification with a Cosmosil Protein-R (10 × 250 mm, Nacalai Tesque, Kyoto) at a flow rate of 1 mL/min with a gradient mobile phase starting from 14% A (H_2O containing 0.1% TFA) and 86% B (CH_3CN containing 0.1% TFA) to 44% A and 56% B in 15 min. The product was ascertained by matrix-assisted laser desorption ionization time-of-flight mass spectrometry (MALDI-TOFMS, Voyager-DE STR, Applied Biosystems, Tokyo). MALDI-TOFMS: 1822.14 [Calcd for $(M + H)^+$: 1822.16].

Preparation of R_8-Modified Antibodies. Two R_8-modified NuB2s with different R_8-conjugation levels ($NuB2_I$ and $NuB2_{III}$) were prepared by reducing the disulfide bonds of NuB2 as reported previously with some modifications (Scheme 1) (*22*). Briefly, NuB2 was concentrated in a nitrogen atmosphere to 6.0 mg/mL in well-degassed 0.1 M PB (pH 7.0) containing 2 mM EDTA. The antibody (1.0 mL) was allowed to react with 2-mercaptoethanol (2-ME, 1000 molar excess) by gently stirring at room temperature for 30 min. Excess 2-ME was then removed

by a centrifuged column procedure using Sephadex G-50 Fine (GE Healthcare, Tokyo) equilibrated and eluted with 0.1 M PB (pH 6.0) containing 2 mM EDTA. A small aliquot of the filtrate was sampled, and the number of exposed thiol groups was determined with 2,2-dipyridyl disulfide (*24*). The filtrate was then added to a reaction vial containing 1.5-fold R_8 (42.8 μL, 85.7 μg) for $NuB2_I$ or 5-fold R_8 for $NuB2_{III}$ in 0.1 M PB (pH 6.0). After the reaction mixture was agitated gently for 1.5 h at 25 °C, 500-fold molar excess of iodoacetamide (269 μL, 2.68 mg) in 0.1 M PB (pH 6.0) was added. The reaction mixture was further incubated for 30 min to alkylate the unreacted thiol groups. $NuB2_I$ and $NuB2_{III}$ were finally purified by the centrifuged column procedure, equilibrated, and eluted with PBS (0.01 M, pH 7.4; Wako, Tokyo). Both $8E1_I$ and $8E1_{III}$ were prepared according to the procedure described above except for using 8E1 in place of NuB2.

Preparation of [$^{125/131}$I] *N*-Succinimidyl 3-Iodobenzoate (SIB)-Labeled Antibodies. *N*-Succinimidyl 3-(tri-*n*-butylstannyl)benzoate (ATE) was synthesized and radio-iodinated in the presence of *N*-chlorosuccinimide (NCS) as described previously (*25*). Briefly, ATE was dissolved in methanol containing 1% acetic acid (0.45 mg/mL), and 16.2 μL of this solution was mixed with 4.4 μL of NCS in methanol (0.5 mg/mL) in a sealed vial, followed by addition of Na[^{125}I]I (2 μL). After incubation at room temperature for 45 min, the reaction was quenched with aqueous sodium bisulfite (2.2 μL, 0.72 mg/mL). The radiochemical yield of [^{125}I]SIB was determined by TLC developed with ethyl acetate. The solvent was removed under a stream of N_2 prior to subsequent conjugation reaction with the antibodies. Conjugation of [^{125}I]SIB with antibodies was performed according to our previous procedure (*22*), with slight modifications as follows: A solution of $NuB2_I$, $NuB2_{III}$, $8E1_I$, or $8E1_{III}$ (120 μL, 2.5 mg/mL) in 0.2 M borate buffer (pH 8.5) was added to the dried residue of crude [^{125}I]SIB. After gentle incubation for 1 h at room temperature, [^{125}I]SIB-labeled antibodies were purified by the centrifuged column procedure, equilibrated, and eluted with PBS. Radioiodination of ATE with Na[^{131}I]I was performed as described above except for using Na[^{125}I]I in place of Na[^{131}I]I. Radiochemical purities of radiolabeled antibodies were also determined by SE-HPLC and TLC developed with 80% methanol/H_2O.

Preparation of ^{125}I-NuB2. Direct radioiodination of NuB2 was performed by the chloramine T method (*22*). To a solution of NuB2 (0.25 mg/mL; 200 μL) in 0.3 M PB (pH 7.5) was added 5 μL of Na[^{125}I]I. Chloramine T (0.1 mg/mL, 25 μL), freshly prepared in the same buffer, was then added. After incubation of the mixture for 10 min at room temperature, the reaction was terminated by an addition of 6 μL of aqueous sodium bisulfite (0.7 mg/mL). ^{125}I-NuB2 was purified by the centrifuged column procedure. The radiochemical purity was determined by SE-HPLC and TLC developed with 80% methanol/H_2O.

Preparation of Fluoresced Antibodies. NuB2, $NuB2_I$, and $NuB2_{III}$ were also labeled with Alexa Fluor 488 (AF, Molecular Probes, Tokyo). The fluorophore was dissolved in dimethylformamide at a concentration of 10 mg/mL, and the conjugation reaction was performed with a 5-fold molar excess of the fluorophore in 0.1 M sodium carbonate−sodium bicarbonate buffer (pH 9.0). After 1 h at room temperature, the reaction was terminated by an addition of freshly prepared 1.5 M hydroxylamine, and the fluorescent antibodies were purified by the centrifuged column procedure. The protein concentration in the purified conjugates was determined spectrophotometrically by subtracting 0.11 $A_{495\ nm}$ of the fluorophore from the $A_{280\ nm}$ of the antibody. The degree of labeling was calculated by dividing the $A_{495\ nm}$ of the fluorophore by the molar concentration of the antibodies and the dye extinction coefficient of 71 000 M^{-1} cm^{-1}.

Immunoreactivity. The immunoreactivity of radiolabeled NuB2s was assessed by the competitive immunoassay (*26*). To minimize nonspecific binding of radioiodinated antibodies to plastic tubes, the tubes were presaturated with a freshly prepared solution of 1% bovine serum albumin in PBS for 30 min, followed by three washes with PBS (*27*). Nonradioactive SIB-NuB2, SIB-$NuB2_I$, and SIB-$NuB2_{III}$ were prepared by experimental procedures similar to those used for [^{125}I]SIB-labeled antibodies, except that nonradioactive NaI was used in place of Na[^{125}I]I. A mixed solution of 50 μL ^{125}I-NuB2 and 50 μL nonradioactive SIB-NuB2, SIB-$NuB2_I$ or SIB-$NuB2_{III}$ (0.05−10 μg) was incubated in the presence of 1×10^6 RPMI 1788 cells suspended in 100 μL of PBS at 37 °C for 1 h. After centrifugation at 10 000 × *g* for 5 min, supernatant was discarded and the cell-associated radioactivity was determined using an auto γ counter.

RPMI 1788 Cell Binding and Retention. The cell binding of [^{125}I]SIB-labeled antibodies was also evaluated according to the procedure of Foulon et al. with slight modification (*28*). Approximately 1 μg each of [^{125}I]SIB-labeled antibodies was incubated with 1×10^6 RPMI 1788 cells for 1 h at 37 °C. Aliquots of cells in triplicate were removed, centrifuged, and washed with cold media. Then, the cell-associated radioactivity was determined as described above. Similar studies were conducted in the presence of 1000-fold excess of unlabeled NuB2.

The rest of the cells were resuspended in RPMI 1640 media containing 10% fetal bovine serum and 20 mM HEPES to a density of 3×10^6 cells/mL. After incubation for 1 and 3 h, aliquots of cells in triplicate were removed, centrifuged, and washed twice with cold media, and the cell-associated radioactivity was determined.

Confocal Microscopy. For each assay, 6×10^6 cells were plated into 35 mm glass-bottomed dishes. The cells were then incubated at 37 °C for 1 h with a fresh solution of NuB2, $NuB2_I$, or $NuB2_{III}$ (60 μL, 0.1 mg/mL) in cold RPMI 1640 media containing 10% FCS and 20 mM HEPES. The cells were washed twice with the same medium at 4 °C. The acidotropic dye LysoTracker Red DND-99 (Molecular Probes, Eugene, OR) was diluted in DMSO. The cells were resuspended in prewarmed (37 °C) medium containing 50 nM LysoTracker Red for 30 min. For live-cell imaging, aliquots of cells in 35 mm glass-based dishes were analyzed by confocal microscopy using a Fluoview FV500 (Olympus, Tokyo). Images were obtained at low-power laser (0.3−3.0% laser) using the 488 nm line of an argon laser. All images were obtained as 10 μm thicknesses of one planar (*xy*) section. The cells were maintained at 37 °C in a temperature-controlled box.

In Vivo Studies. Animal studies were conducted in accordance with our institutional guidelines and were approved by Chiba University Animal Care Committee. Biodistribution studies were performed by intravenous administration of a PBS solution of [^{125}I]SIB-NuB2, [^{125}I]SIB-$NuB2_I$, or [^{125}I]SIB-$NuB2_{III}$ to 6-week-old male ddY mice (Japan SLC Inc., Shizuoka, Japan). Groups of five mice, each receiving 0.3 μCi (20 μg/100 μL) of the antibodies, were used for the experiments. Organs of interest were removed and weighed, and the radioactivity counts were determined with an autowell γ counter at 1, 3, and 24 h postinjection.

Severe combined immunodeficiency (SCID) mice (C.B-17/IcrCrj-scid, Charles River Japan, Kanagawa, Japan) bearing xenograft of RPMI 1788 cells were also treated with a mixed solution of [^{131}I]SIB-$NuB2_I$ and [^{125}I]SIB-NuB2. The biodistribution of radioactivity after i.v. administration of the mixture

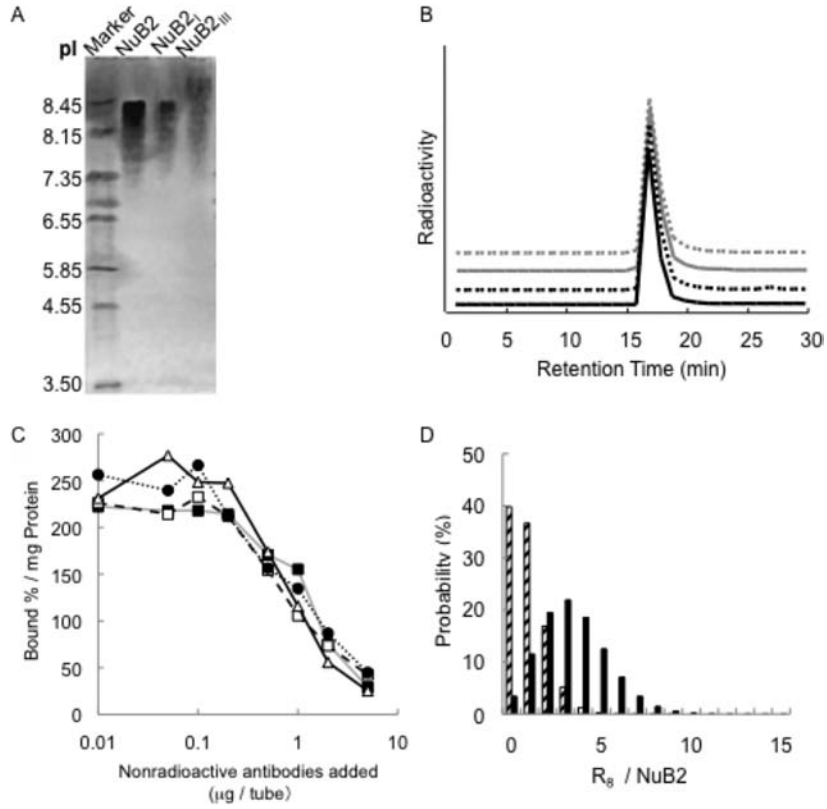


Figure 1. Characterization of R_8-conjugated antibodies ($NuB2_I$ and $NuB2_{III}$). (A) Isoelectric focusing. While both NuB2 and $NuB2_I$ showed similar profiles, a wider band toward higher pI was observed with $NuB2_{III}$. (B) Size-exclusion HPLC profiles. ^{125}I-NuB2: black solid line. [^{125}I]SIB-NuB2: black broken line. [^{125}I]SIB-$NuB2_I$: gray solid line. [^{125}I]SIB-$NuB2_{III}$: gray broken line. All the radioiodinated NuB2s exhibited similar elution profiles. (C) Competitive immunoassay to RPMI 1788 cells. Increasing concentrations of nonradioactive iodine-labeled NuB2s (NuB2 (solid square), SIB-NuB2 (square), SIB-$NuB2_I$ (circle), SIB-$NuB2_{III}$ (triangle)) and 1×10^6 RPMI 1788 cells were incubated in the presence of [^{125}I]-labeled NuB2. No significant differences were observed among the four NuB2s. (D) Poisson distribution profiles of $NuB2_I$ (hatched column) and $NuB2_{III}$ (solid column).

to 8-week-old SCID mice was monitored at 24, 48, 72, and 96 h postinjection. Groups of 5−7 mice, each receiving 0.3 μCi (10 μg each) of antibodies, were used for the experiments. Organs of interest were removed and weighed, and the radioactivity counts were determined with an autowell γ counter. A window from 29 to 97 keV was used for counting ^{125}I, whereas one from 280 to 440 keV was used for ^{131}I. Correlation factors to eliminate crossover of ^{131}I activity into ^{125}I were determined by counting ^{131}I standard in each window. The crossover of ^{125}I into the ^{131}I channel was negligible.

Statistical Analysis. Data are expressed as means ± standard deviation where appropriate. Results were statistically analyzed with an unpaired Student's *t*-test using the Microsoft *Excel* program. Differences were considered statistically significant when the *p* value was less than 0.05.

RESULTS

Preparation of Conjugates. Conjugation of NuB2 or 8E1 with R_8 was performed by maleimide−thiol chemistry using thiol groups generated by reducing the disulfide bonds of the antibody molecule. The numbers of R_8 molecule attached per molecule of NuB2 were determined to be 0.92 for $NuB2_I$ and 3.38 for $NuB2_{III}$. Similar procedures were employed for the preparation of $8E1_I$ and $8E1_{III}$ where the number of R_8 per molecule of 8E1 was estimated to be 0.98 and 3.85, respectively. The pI values of NuB2, $NuB2_I$, and $NuB2_{III}$ were determined by the isoelectric focusing and found to be 7.5−8.6, 7.5−8.6, and 7.5−9.0, respectively (Figure 1A). All [$^{125/131}$I]SIB-labeled antibodies had radiochemical purities over 95% when determined by the SE-HPLC (Figure 1B) and TLC. ^{125}I-NuB2 was prepared by the chloramine T method with radiochemical purity of 99%. AF-NuB2, AF-$NuB2_I$, and AF-$NuB2_{III}$ were labeled with Alexa Fluor 488 with a conjugation level of 3.67, 3.89, and 3.57 molecules of the fluorophore per molecule of each antibody.

Immunoreactivity Measurement. Figure 1C shows the RPMI 1788 cell binding of ^{125}I-NuB2 in the presence of unlabeled NuB2, nonradioactive SIB-conjugated NuB2, SIB-$NuB2_I$, and SIB-$NuB2_{III}$. Unlabeled NuB2 almost completely inhibited the binding of ^{125}I-NuB2 to RPMI 1788 cells, and no significant differences were observed in the inhibitory curves among the nonradioactive SIB-NuB2, SIB-$NuB2_I$, and SIB-$NuB2_{III}$. Similar results were observed with AF-labeled antibodies (data not shown).

Localization of the Antibodies in RPMI 1788 Cells. Figure 2A shows the localization of NuB2, $NuB2_I$, and $NuB2_{III}$ in living cells when determined by confocal microscopy. All AF-labeled antibodies (green) were present on the cell membrane. Under the conditions, LysoTracker (red) was observed in acidic compartment of the cells such as endosome and lysosome.

In Vitro Cell Binding and Retention. When the radiolabeled antibodies were incubated with the RPMI 1788 cell at 1 h at 37 °C, [^{125}I]SIB-$NuB2_I$ and [^{125}I]SIB-$NuB2_{III}$ showed 1.4 and 4.3 times higher cell-associated radioactivity than [^{125}I]SIB-NuB2 (Figure 2B). When the radiolabeled antibodies were incubated in the presence of 1000-fold excess of NuB2, significant reduction in the cell-associated radioactivity was observed with [^{125}I]SIB-NuB2 and [^{125}I]SIB-$NuB2_I$. However, [^{125}I]SIB-$NuB2_{III}$ still registered high cell-associated radioactivity. Similarly, higher cell-associated radioactivity was observed

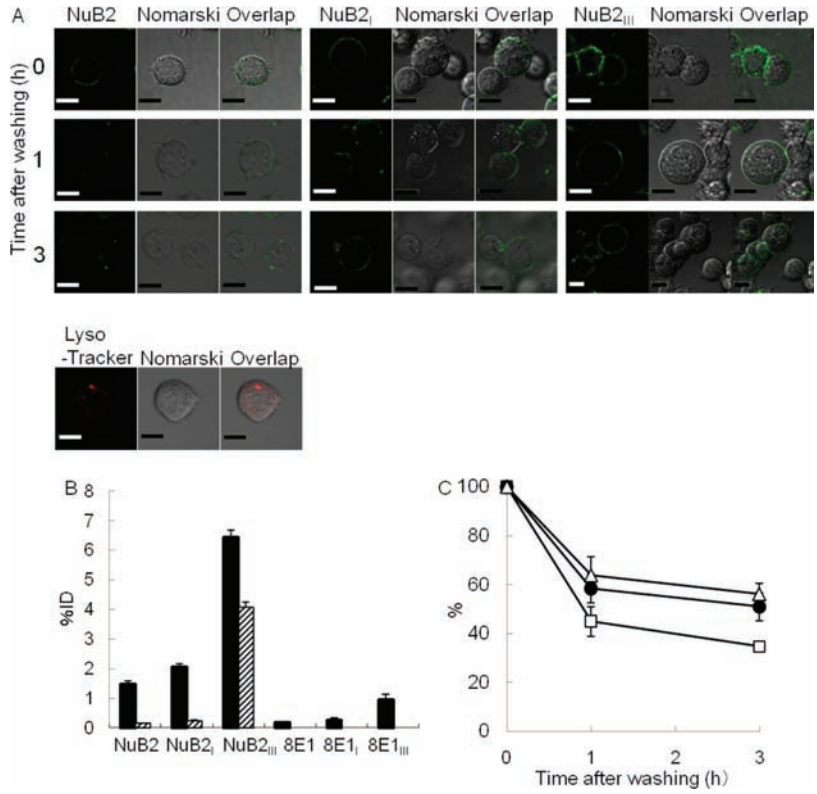


Figure 2. Cellular processing of [^{125}I]SIB-NuB2s. (A) Confocal microscopy to detect NuB2s localization (green) in RPMI 1788 cells as a function of incubation intervals at 37 °C; bars, 10 μm. (B) RPMI 1788 cell-associated radioactivity after 1 h incubation of [^{125}I]SIB-NuB2s at 37 °C (solid column). Similar experiments were performed in the presence of 1000-fold excess of NuB2 (hatched column). (C) Retention of [^{125}I]SIB-labeled NuB2s ([^{125}I]SIB-NuB2 (square), [^{125}I]SIB-NuB2$_I$ (solid circle), [^{125}I]SIB-NuB2$_{III}$ (triangle)) on RPMI 1788 cells after washing and reincubation in a fresh medium for 1 and 3 h (average of triplicates and SD).

in [^{125}I]SIB-8E1$_{III}$ when compared with [^{125}I]SIB-8E1 and [^{125}I]SIB-8E1$_I$.

Figure 2C shows the retention of [^{125}I]SIB-NuB2, [^{125}I]SIB-Nub2$_I$, and [^{125}I]SIB-NuB2$_{III}$ from RPMI 1788 cells as a function of reincubation times. While [^{125}I]SIB-NuB2 showed 44.3% and 34.2% of the initial radioactivity levels at 1 and 3 h postincubation, [^{125}I]SIB-NuB2$_I$ exhibited the cell-bound radioactivity of 59.1% and 51.2% at the same postincubation times. [^{125}I]SIB-NuB2$_{III}$ showed radioactivity levels of 67.8% and 61.3% at 1 and 3 h postincubation, respectively.

In Vivo Studies. The biodistribution of radioactivity after intravenous injection of [^{125}I]SIB-NuB2, [^{125}I]SIB-NuB2$_I$, and [^{125}I]SIB-NuB2$_{III}$ to normal mice is summarized in Table 1. Both [^{125}I]SIB-NuB2 and [^{125}I]SIB-NuB2$_I$ showed similar radioactivity levels in the blood, liver, kidney, and intestine. However, [^{125}I]SIB-NuB2$_{III}$ exhibited faster clearance of the radioactivity from the blood with higher radioactivity levels in the liver throughout the postinjection time examined. As a result, [^{125}I]SIB-NuB2$_{III}$ exhibited higher liver-to-blood ratios of the radioactivity.

Table 2 shows the biodistribution of the radioactivity after simultaneous injection of [^{125}I]SIB-NuB2 and [^{131}I]SIB-NuB2$_I$ in SCID mice bearing RPMI 1788 cells. [^{131}I]SIB-NuB2$_I$ exhibited significantly higher radioactivity levels in the tumor than those observed with [^{125}I]SIB-NuB2 from 48 to 96 h postinjection. [^{131}I]SIB-NuB2$_I$ exhibited similar radioactivity levels in other tissues such as the blood, liver, kidney, and intestine when compared with [^{125}I]SIB-NuB2.

Table 1. Biodistribution of Radioactivity after Intravenous Injection of [^{125}I]SIB-NuB2, [^{125}I]SIB-NuB2$_I$, and [^{125}I]SIB-NuB2$_{III}$ in Normal Mice[a]

	time after injection		
	1 h	3 h	24 h
	[^{125}I]SIB-NuB2		
blood	26.51 (0.99)	22.37 (1.33)	12.63 (0.48)
liver	7.65 (0.49)	5.99 (0.34)	3.34 (0.29)
kidney	5.92 (0.43)	5.46 (1.68)	3.31 (0.15)
stomach[b]	0.56 (0.55)	0.84 (0.08)	1.27 (0.44)
intestine	1.30 (0.07)	1.69 (0.15)	1.36 (0.33)
liver/blood	0.29 (0.03)	0.27 (0.00)	0.26 (0.01)
	[^{125}I]SIB-NuB2$_I$		
blood	26.26 (0.83)	20.70 (0.14)	10.54** (0.61)
liver	7.03 (0.3)	5.72 (0.33)	2.81 (0.40)
kidney	6.85* (0.31)	5.38 (0.50)	3.37 (0.35)
stomach[b]	0.58 (0.06)	1.01* (0.07)	1.89 (0.95)
intestine	1.15 (0.17)	1.68 (0.04)	0.95 (0.16)
liver/blood	0.27 (0.01)	0.28 (0.02)	0.27 (0.03)
	[^{125}I]SIB-NuB2$_{III}$		
blood	20.32 (3.79)	15.45** (1.36)	8.08** (0.49)
liver	17.91** (0.42)	14.71** (0.46)	5.85** (0.69)
kidney	6.50 (0.73)	5.80 (0.57)	3.42 (0.17)
stomach[b]	0.86** (0.05)	1.30* (0.25)	1.66 (0.67)
intestine	1.01 (0.08)	1.42 (0.30)	0.82 (0.17)
liver/blood	0.90** (0.14)	0.96** (0.12)	0.72** (0.05)

[a] Tissue radioactivity is expressed as percent of injected dose per gram of wet tissue. Results are expressed as means (SD) of three animals each point. [b] Expressed as percent of injected dose per tissue. Significances determined by unpaired Student's *t*-test. * $p < 0.05$ compared to [^{125}I]SIB-NuB2. ** $p < 0.01$ compared to [^{125}I]SIB-NuB2.

DISCUSSION

In this study, we estimate the ability of an octaarginine peptide, R_8, as an anchoring molecule to enhance target accumulation of radiolabeled antibodies. The spatial location of the anchoring molecules attached to an antibody was considered of importance to maintain antigen binding properties, specific binding, and biodistribution profiles of the parental

Table 2. Biodistribution of Radioactivity after Intravenous Injection of [^{125}I]SIB-NuB2 and [^{131}I]SIB-NuB2$_I$ in RPMI1788 Cell-Bearing SCID Mice[a]

	time after injection			
	24 h	48 h	72 h	96 h
	[^{125}I]SIB-NuB2			
blood	14.05 (1.02)	8.64 (1.18)	4.79 (1.22)	3.02 (0.39)
xenograft	4.54 (0.68)	5.36 (1.03)	3.95 (1.08)	4.81 (0.78)
liver	5.01 (0.82)	3.04 (0.39)	1.68 (0.27)	1.01 (0.10)
kidney	4.56 (0.67)	3.09 (0.50)	1.70 (0.35)	1.08 (0.22)
stomach[b]	0.33 (0.05)	0.20 (0.04)	0.38 (0.06)	0.09 (0.01)
intestine	1.15 (0.13)	1.05 (0.18)	0.58 (0.11)	0.36 (0.08)
xenograft/blood	0.32 (0.06)	0.62 (0.09)	0.83 (0.03)	1.59 (0.35)
liver/blood	0.36 (0.07)	0.35 (0.01)	0.35 (0.04)	0.33 (0.04)
	[^{131}I]SIB-NuB2$_I$			
blood	14.60 (0.57)	8.17 (1.14)	4.58 (0.72)	2.78 (0.33)
xenograft	6.20* (0.92)	7.52* (1.19)	6.04* (1.21)	7.20** (1.32)
liver	4.33 (0.49)	2.42* (0.29)	1.39 (0.10)	0.80** (0.08)
kidney	4.78 (0.71)	2.95 (0.47)	1.57 (0.18)	1.03 (0.22)
stomach[b]	0.36 (0.06)	0.20 (0.04)	0.37 (0.07)	0.08 (0.01)
intestine	1.34 (0.19)	1.03 (0.18)	0.59 (0.08)	0.35 (0.09)
xenograft/blood	0.42 (0.07)	0.92** (0.11)	1.31** (0.11)	2.59* (0.64)
liver/blood	0.30 (0.03)	0.30** (0.01)	0.30 (0.03)	0.29 (0.03)

[a] Tissue radioactivity is expressed as percent of injected dose per gram of wet tissue. Results are expressed as means (SD) of five to six animals for each point. [b] Expressed as percent injected dose. Significances determined by unpaired Student's *t*-test. * $p < 0.05$ compared to [^{125}I]SIB-NuB2. ** $p < 0.01$ compared to [^{125}I]SIB-NuB2.

antibodies. It was speculated that the attachment of anchoring molecules close to an antibody molecule may cause less interaction with cell surface molecules or cell membrane of target cells, whereas attachment of linkers that place the anchoring molecules at a distance from the antibody molecule may increase nonspecific binding. We selected a butyryl-bis(aminocaproate) linkage between a maleimide moiety and an octaarginine peptide with an expectation that the octaarginine moiety would not interact directly with a cell but interact strongly after the specific binding of antibody takes place. Since the importance of the density of AR-CPP molecules in an antibody was well-documented (*10, 11*), two R_8-conjugated antibodies holding different numbers of R_8 per molecule of the antibody were prepared (Scheme 1).

The R_8 conjugation and subsequent iodination reactions did not affect the SE-HPLC profiles of NuB2 (Figure 1B). The three SIB-labeled NuB2s possessed similar immunoreactivity to the antigen-positive tumor cells (Figure 1C). However, the heavy conjugation of R_8 to NuB2 increased the bandwidth of isoelectric focusing and raised pI of the resulting NuB2$_{III}$ (Figure 1A). The reaction of R_8 derivatives and an antibody can be better understood by considering the example of a perfectly random reaction (*29*). Poisson distribution can be used to predict how the R_8 molecules will be distributed among the individual antibody molecules. According to the calculation (Figure 1D), the majority of NuB2$_I$ contained up to 2 molecules of R_8 per molecule of NuB2. On the other hand, NuB2$_{III}$ consisted of a variety of conjugates ranging from 1 to 7 R_8 molecules per molecule of NuB2 with over 65% of NuB2$_{III}$ containing more than 3 R_8 molecules per molecule of NuB2, which accounts for the wide bandwidth of the isoelectric focusing.

The effect of R_8 conjugation levels on the target cell binding was assessed using CD20 positive cells. [^{125}I]NuB2$_{III}$ exhibited high cell-bound radioactivity levels even in the presence of a 1000-fold excess of cold NuB2. Since the cell-bound radioactivity levels of [^{125}I]SIB-8E1$_{III}$ were much lower than those of [^{125}I]SIB-NuB2$_{III}$, the majority of the cell-associated radioactivity of [^{125}I]NuB2$_{III}$ would be attributable to the specific antigen binding, followed by the strong interaction of the R_8 moieties with the cell. The low cell-bound radioactivity of [^{125}I]SIB-NuB2$_I$ in the presence of excess NuB2 suggested slower interaction kinetics of R_8 moieties with the cell, following the specific binding. However, when the dissociation rates from the cells were compared, not only [^{125}I]SIB-NuB2$_{III}$ but also [^{125}I]SIB-NuB2$_I$ exhibited much longer residence times in the CD20 positive tumor cells than [^{125}I]SIB-NuB2 (Figure 2C). The confocal microscopy confirmed that both NuB2$_I$ and NuB2$_{III}$ were present on the cell membrane (Figure 2A). These studies supported the hypothesis that the conjugation of anchoring molecules that possess strong interaction with cell surface molecules or cell membrane prolonged the retention of radiolabeled antibodies on tumor cells by fixing the antigen-bound antibodies on target cells, although the binding kinetics of anchoring molecules with the cell was affected by their density. This also suggested that further improvement of spatial location of the R_8 molecule may increase the binding kinetics.

Despite favorable anchoring ability, the heavy conjugation of R_8 affected biodistribution profiles of the parental antibody. As shown in Table 1, [^{125}I]SIB-NuB2$_{III}$ displayed faster clearance from the blood and higher accumulation in the liver in normal mice, as also observed in prior studies (*30*). On the other hand, both [^{125}I]SIB-NuB2 and [^{125}I]SIB-NuB2$_I$ displayed similar biodistribution (Table 1). These results reinforced the importance of the number of R_8 molecules attached per molecule of an antibody to retain its in vivo behavior (*10, 11*) and showed that the present conjugation of up to 2 R_8 molecules per molecule of NuB2 did not induce any significant changes in biodistribution. Recently, we have observed that the biodistribution of PAMAM dendrimers is predominantly determined by their net molecular charge as measured by both zeta potential and pI values (*31*). The present study also suggests that the determination of net molecular charge of AR-CPP-modified antibodies may be useful to predict their pharmacokinetics.

The biodistribution studies in tumor-bearing SCID mice were investigated with [^{125}I]SIB-NuB2 and [^{131}I]SIB-NuB2$_I$ since they exhibited similar pharmacokinetics in normal mice. To minimize individual differences, the biodistribution studies were conducted after injection of a mixed solution of [^{131}I]SIB-NuB2$_I$ and [^{125}I]SIB-NuB2. As shown in Table 2, the role played by R_8 conjugation on tumor accumulation was clearly demonstrated in the biodistribution studies, where [^{131}I]SIB-NuB2$_I$ exhibited significantly higher radioactivity levels in the xenograft than those of simultaneously administrated [^{125}I]SIB-NuB2 with no significant increase being observed in the radioactivity levels of blood, liver, and other tissues between the two. When considering the in vitro studies, these results would be attributable to the delayed dissociation rates of [^{131}I]SIB-NuB2$_I$ from the target cells in vivo.

In conclusion, the findings in this study indicated that the conjugation of anchoring molecules to an antibody that possesses a strong interaction with cell surface molecules or cell membrane enhanced accumulation in target tissues by fixing antigen-bound antibodies on target cells. This study also showed that conjugation of up to 2 molecules of R_8 per molecule of NuB2 satisfied both target-specific binding of antibodies and strong cell binding property of R_8. Further optimization of the conjugation chemistry would be required to provide uniform conjugates with appropriate linkage structure between R_8 and an antibody. These findings strongly suggested the application of AR-CPP to enhance specific accumulation of antibodies in target for more effective RIT.

ACKNOWLEDGMENT

The authors appreciated to Immuno-Biological Laboratories Co, Ltd., for supplying the relevant and irrelevant antibodies. Y. Azuma is grateful for the JSPS Research Fellowship for Young Scientists. This work was supported in part by a Grant-in-Aid for Scientific Research (B), for Exploratory Research,

for Development of Systems and Technology for Advanced Measurement and Analysis, and by Special Funds for Education and Research (Development of SPECT Probes for Pharmaceutical Innovation) from the Ministry of Education, Culture, Sports, Science, and Technology, Japan. This work was dedicated to our distinguished colleague, the late Mr. Yuichiro Taira.

LITERATURE CITED

(1) Fisher, R. I., Kaminski, M. S., Wahl, R. L., Knox, S. J., Zelenetz, A. D., Vose, J. M., Leonard, J. P., Kroll, S., Goldsmith, S. J., and Coleman, M. (2005) Tositumomab and iodine-131 tositumomab produces durable complete remissions in a subset of heavily pretreated patients with low-grade and transformed non-Hodgkin's lymphomas. *J. Clin. Oncol. 23*, 7565–7573.

(2) Vose, J. M. (2004) Bexxar: novel radioimmunotherapy for the treatment of low-grade and transformed low-grade non-Hodgkin's lymphoma. *Oncologist 9*, 160–172.

(3) Gordon, L. I., Molina, A., Witzig, T., Emmanouilides, C., Raubtischek, A., Darif, M., Schilder, R. J., Wiseman, G., and White, C. A. (2004) Durable responses after ibritumomab tiuxetan radioimmunotherapy for $CD20^+$ B-cell lymphoma: long-term follow-up of a phase 1/2 study. *Blood 103*, 4429–4431.

(4) Witzig, T. E., White, C. A., Wiseman, G. A., Gordon, L. I., Emmanouilides, C., Raubitschek, A., Janakiraman, N., Gutheil, J., Schilder, R. J., Spies, S., Silverman, D. H., Parker, E., and Grillo-Lopez, A. J. (1999) Phase I/II trial of IDEC-Y2B8 radioimmunotherapy for treatment of relapsed or refractory CD20(+) B-cell non-Hodgkin's lymphoma. *J. Clin. Oncol. 17*, 3793–803.

(5) von Mehren, M., Adams, G. P., and Weiner, L. M. (2003) Monoclonal antibody therapy for cancer. *Annu. Rev. Med. 54*, 343–369.

(6) Goldenberg, D. M. (2001) The role of radiolabeled antibodies in the treatment of non-Hodgkin's lymphoma: the coming of age of radioimmunotherapy. *Crit. Rev. Oncol. Hematol. 39*, 195–201.

(7) Boswell, C. A., and Brechbiel, M. W. (2007) Development of radioimmunotherapeutic and diagnostic antibodies: an inside-out view. *Nucl. Med. Biol. 34*, 757–778.

(8) Jain, M., Venkatraman, G., and Batra, S. K. (2007) Optimization of radioimmunotherapy of solid tumors: biological impediments and their modulation. *Clin. Cancer Res. 13*, 1374–1382.

(9) Tempero, M., Leichner, P., Baranowska-Kortylewicz, J., Harrison, K., Augustine, S., Schlom, J., Anderson, J., Wisecarver, J., and Colcher, D. (2000) High-dose therapy with ^{90}Yttrium-labeled monoclonal antibody CC49: a phase I trial. *Clin. Cancer Res. 6*, 3095–3102.

(10) Anderson, D. C., Nichols, E., Manger, R., Woodle, D., Barry, M., and Fritzberg, A. R. (1993) Tumor cell retention of antibody Fab fragments is enhanced by an attached HIV TAT protein-derived peptide. *Biochem. Biophys. Res. Commun. 194*, 876–884.

(11) Niesner, U., Halin, C., Lozzi, L., Günthert, M., Neri, P., Wunderli-Allenspach, H., Zardi, L., and Neri, D. (2002) Quantitation of the tumor-targeting properties of antibody fragments conjugated to cell-permeating HIV-1 TAT peptides. *Bioconjugate Chem 13*, 729–736.

(12) Batra, S. K., Jain, M., Wittel, U. A., Chauhan, S. C., and Colcher, D. (2002) Pharmacokinetics and biodistribution of genetically engineered antibodies. *Curr. Opin. Biotechnol. 13*, 603–608.

(13) Goel, A., Colcher, D., Baranowska-Kortylewicz, J., Augustine, S., Booth, B. J., Pavlinkova, G., and Batra, S. K. (2000) Genetically engineered tetravalent single-chain Fv of the pancarcinoma monoclonal antibody CC49: improved biodistribution and potential for therapeutic application. *Cancer Res. 60*, 6964–6971.

(14) Boerman, O. C., van Schaijk, F. G., Oyen, W. J., and Corstens, F. H. (2003) Pretargeted radioimmunotherapy of cancer: progress step by step. *J. Nucl. Med. 44*, 400–411.

(15) Rothbard, J. B., Jessop, T. C., Lewis, R. S., Murray, B. A., and Wender, P. A. (2004) Role of membrane potential and hydrogen bonding in the mechanism of translocation of guanidinium-rich peptides into cells. *J. Am. Chem. Soc. 126*, 9506–9507.

(16) Sakai, N., Takeuchi, T., Futaki, S., and Matile, S. (2005) Direct observation of anion-mediated translocation of fluorescent oligoarginine carriers into and across bulk liquid and anionic bilayer membranes. *ChemBioChem 6*, 114–122.

(17) Nakase, I., Takeuchi, T., Tanaka, G., and Futaki, S. (2008) Methodological and cellular aspects that govern the internalization mechanisms of arginine-rich cell-penetrating peptides. *Adv. Drug Delivery Rev. 60*, 598–607.

(18) Goncalves, E., Kitas, E., and Seelig, J. (2005) Binding of oligoarginine to membrane lipids and heparan sulfate: structural and thermodynamic characterization of a cell-penetrating peptide. *Biochemistry 44*, 2692–2702.

(19) Kaplan, I. M., Wadia, J. S., and Dowdy, S. F. (2005) Cationic TAT peptide transduction domain enters cells by macropinocytosis. *J. Controlled Release 102*, 247–253.

(20) Nakase, I., Niwa, M., Takeuchi, T., Sonomura, K., Kawabata, N., Koike, Y., Takehashi, M., Tanaka, S., Ueda, K., Simpson, J. C., Jones, A. T., Sugiura, Y., and Futaki, S. (2004) Cellular uptake of arginine-rich peptides: roles for macropinocytosis and actin rearrangement. *Mol. Ther. 10*, 1011–1022.

(21) Richard, J. P., Melikov, K., Vives, E., Ramos, C., Verbeure, B., Gait, M. J., Chernomordik, L. V., and Lebleu, B. (2003) Cell-penetrating peptides. A reevaluation of the mechanism of cellular uptake. *J. Biol. Chem. 278*, 585–590.

(22) Arano, Y., Wakisaka, K., Ohmono, Y., Uezono, T., Akizawa, H., Nakayama, M., Sakahara, H., Tanaka, C., Konishi, J., and Yokoyama, A. (1996) Assessment of radiochemical design of antibodies using an ester bond as the metabolizable linkage: evaluation of maleimidoethyl 3-(tri-n-butylstannyl)hippurate as a radioiodination reagent of antibodies for diagnostic and therapeutic applications. *Bioconjugate Chem. 7*, 628–637.

(23) Percy, M. E., Baumal, R., Dorrington, K. J., and Percy, J. R. (1976) Covalent assembly of mouse immunoglobulin G subclasses in vitro: application of a theoretical model for interchain disulfide bond formation. *Can. J. Biochem. 54*, 675–87.

(24) Grassetti, D. R., and Murray, J. F., Jr. (1967) Determination of sulfhydryl groups with 2,2′- or 4,4′-dithiodipyridine. *Arch. Biochem. Biophys. 119*, 41–49.

(25) Zalutsky, M. R., and Narula, A. S. (1987) A method for the radiohalogenation of proteins resulting in decreased thyroid uptake of radioiodine. *Int. J. Rad. Appl. Instrum. A 38*, 1051–1055.

(26) Koizumi, M., Endo, K., Kunimatsu, M., Sakahara, H., Nakashima, T., Kawamura, Y., Watanabe, Y., Saga, T., Konishi, J., and Yamamuro, T. (1988) ^{67}Ga-labeled antibodies for immunoscintigraphy and evaluation of tumor targeting of drug-antibody conjugates in mice. *Cancer Res. 48*, 1189–1194.

(27) Samnick, S., Schaefer, A., Siebert, S., Richter, S., Vollmar, B., and Kirsch, C. M. (2001) Preparation and investigation of tumor affinity, uptake kinetic and transport mechanism of iodine-123-labelled amino acid derivatives in human pancreatic carcinoma and glioblastoma cells. *Nucl. Med. Biol. 28*, 13–23.

(28) Foulon, C. F., Reist, C. J., Bigner, D. D., and Zalutsky, M. R. (2000) Radioiodination via D-amino acid peptide enhances cellular retention and tumor xenograft targeting of an internalizing anti-epidermal growth factor receptor variant III monoclonal antibody. *Cancer Res. 60*, 4453–4460.

(29) Meares, C. F., and Goodwin, D. A. (1984) Linking radiometals to proteins with bifunctional chelating agents. *J. Protein Chem. 3*, 215–228.

(30) Kameyama, S., Horie, M., Kikuchi, T., Omura, T., Takeuchi, T., Nakase, I., Sugiura, Y., and Futaki, S. (2006) Effects of cell-permeating peptide binding on the distribution of ^{125}I-labeled Fab fragment in rats. *Bioconjugate Chem. 17*, 597–602.

(31) Uehara, T., Ishii, D., Uemura, T., Suzuki, H., Kanei, T., Takagi, K., Takama, M., Murakami, M., Akizawa, H., and Arano, Y. (2010) gamma-Glutamyl PAMAM dendrimer as versatile precursor for dendrimer-based targeting devices. *Bioconjugate Chem. 21*, 175–181.

BC100259Q

Structural Requirements of the ASBT by 3D-QSAR Analysis Using Aminopyridine Conjugates of Chenodeoxycholic Acid

Xiaowan Zheng,[‡] Yongmei Pan,[‡] Chayan Acharya,[†] Peter W. Swaan, and James E. Polli*

Department of Pharmaceutical Sciences, School of Pharmacy, University of Maryland, 20 Penn Street, Baltimore, Maryland 21201, United States. Received June 17, 2010; Revised Manuscript Received August 26, 2010

The human apical sodium-dependent bile acid transporter (ASBT) is a validated drug target and can be employed to increase oral bioavailability of various drug conjugates. The aim of the present study was to investigate the chemical space around the 24-position of bile acids that influences both inhibition and uptake by the transporter. A series of 27 aminopyridine and aminophenol conjugates of glutamyl-chenodeoxycholate were synthesized and their ASBT inhibition and transport kinetics (parametrized as K_i, K_t, and J_{max}) measured using stably transfected ASBT-MDCK cells. All conjugates were potent ASBT inhibitors. Monoanionic conjugates exhibited higher inhibition potency than neutral conjugates. However, neutral conjugates and chloro-substituted monoanionic conjugates were not substrates, or at least not apparent substrates. Kinetic analysis of substrates indicated that similar values for K_i and K_t implicate substrate binding to ASBT as the rate-limiting step. Using 3D-QSAR, four inhibition models and one transport efficiency model were developed. Steric fields dominated in CoMFA models, whereas hydrophobic fields dominated CoMSIA models. The inhibition models showed that a hydrophobic or bulky substitute on the 2 or 6 position of a 3-aminopyridine ring enhanced activity, while a hydrophobic group on the 5 position was detrimental. Overall, steric and hydrophobic features around the 24 position of the sterol nucleus strongly influenced bile acid conjugate interaction with ASBT. The relative location of the pyridine nitrogen and substituent groups also modulated binding.

INTRODUCTION

Bile acids are primarily absorbed in the terminal ileum via the apical sodium-dependent bile acid transporter (ASBT; SLC10A2) (*1*, *2*), which displays high transport capacity and efficiency (*3*). This transporter may also be employed as a prodrug target for enhancing oral drug bioavailability of poorly permeating compounds, where drug is conjugated to bile acid and bile acid allows for the conjugate to be taken up by ASBT (*3*). However, the lack of knowledge of ASBT substrate requirements has impeded progress in rational prodrug design to target ASBT. Structure−activity studies have largely employed ASBT inhibition rather than substrate uptake, perhaps due to inhibition studies being more facile. Various transport studies have been performed over 30 years using animal tissues and organs, but the interpretability of the bile acid transport by ASBT has been confounded by other intestinal and hepatic transporters (*4*).

Our laboratory previously developed a stably transfected ASBT-MDCK monolayer to evaluate ASBT-mediated transport of solutes (*5*). Using a series of native bile acids to evaluate ASBT binding properties, we found that chenodeoxycholate (CDCA) was the most potent inhibitor among native bile acids and conjugation through C-24 of CDCA with taurine or glycine enhanced binding affinity (*6*). A series of C-24 CDCA conjugates were then synthesized using glutamic acid or lysine as a linker, and the results showed that only conjugates with one negative charge and a single bulky ester substituent proximal or distal to the C-24 region were ASBT substrates (*7*). Furthermore, a C-24 bile acid prodrug of valacyclovir enhanced oral bioavailability by 2-fold, compared to acyclovir in rats (*8*). Overall, ASBT permits bile acid conjugates with substitutions at the C-24 side chain region, but the chemistry space extending beyond the C-24 region needs to be further explored, especially for ASBT substrates. In fact, several quantitative structure−activity relationships studies have been reported for general ASBT inhibition. Thus, we sought to apply 3D-QSAR approaches to elucidate the substrate requirements in the space extending beyond the C-24 region using comparative molecular field analysis (CoMFA) (*9*) and comparative molecular similarity indices analysis (CoMSIA) (*10*). These algorithms are particularly useful when the structure of a target protein is unknown and may be applied for lead compound optimization (*11*).

The objective of this study was to synthesize and characterize substrate uptake and inhibition properties of C-24 bile acid probe moiety conjugates, and subsequently develop comprehensive 3D-QSAR models to elucidate the substrate requirements on positions beyond C-24 region. Pyridine and phenol are common chemical scaffolds in drug structures (*12*). Therefore, C-24 aminopyridine and aminophenol conjugates of glutamyl-CDCA were synthesized and their inhibition and uptake kinetics were evaluated. Pyridine and phenol probes were functionalized using different ring substitutions in order to study chemical substituent effect on ASBT inhibition and uptake. Using a combination of inhibition and uptake studies, we differentiate ASBT inhibitors from substrates and developed 3D-QSAR models for both classes of bile analogues. These studies provide new insight into the substrate requirements for ASBT uptake and shed light on the design of bile acid conjugates that can increase intestinal drug permeability and bioavailability.

EXPERIMENTAL PROCEDURES

Materials. [^{3}H]-Taurocholic acid was purchased from Perkin-Elmer (Waltham, MA). Taurocholic acid was purchased from Sigma (St. Louis, MO). CDCA was obtained from TCI America

* To whom correspondence should be addressed. E-mail: jpolli@rx.umaryland.edu. Tel. +1410-706-8292; Fax: +1 410-706-5017.

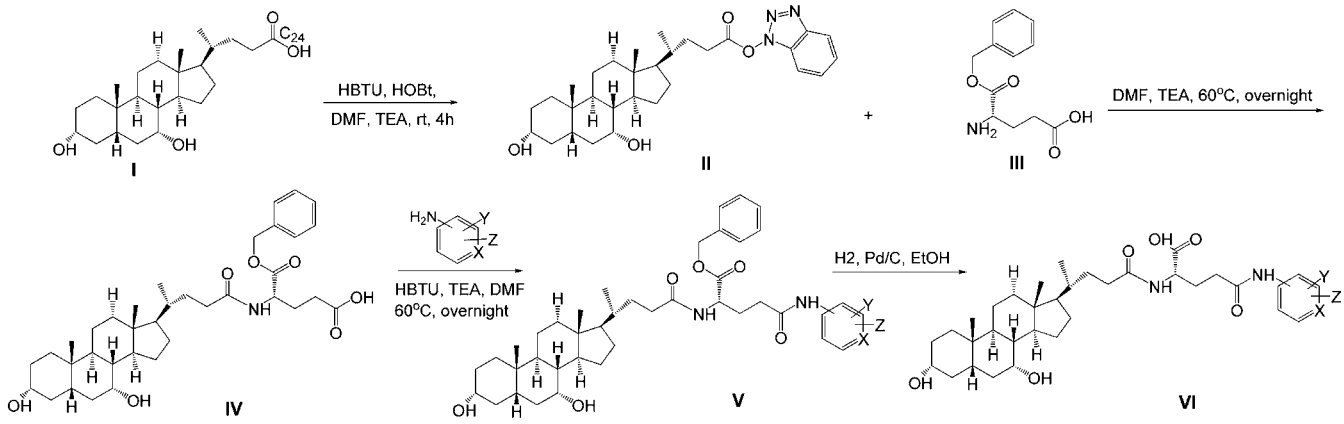
[‡] Xiaowan Zheng and Yongmei Pan contributed equally to this work.

[†] Present Address: Institut Européen de Chimie et Biologie, Université Bordeaux 1, 2 rue Robert Escarpit, 33607 Pessac Cedex, France.

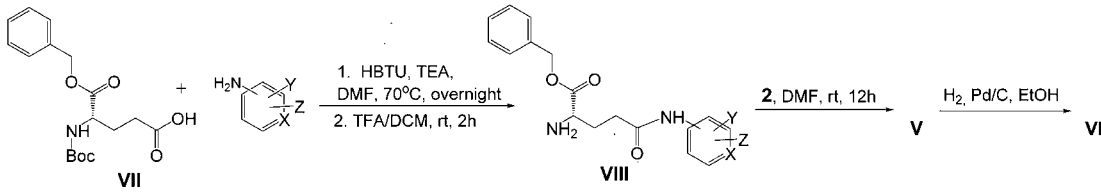
10.1021/bc100273w © 2010 American Chemical Society
Published on Web 10/22/2010

Scheme 1. General Synthetic Approaches to Obtain CDCA-Glutamyl-Pyridine or CDCA-Glytamyl-Phenol Conjugates[a]

Approach 1.



Approach 2.



[a] X = N, H; Y = H, CH_3, OCH_3, NH_2, OH, Cl, F, Br; Z = H, CH_3.

(Portland, OR). Protected glutamic acid analogues were from Novabiochem (Gibbstown, NJ). Aminopyridine analogues were purchased from Sigma Aldrich (St. Louis, MO) and Matrix Scientific (Columbia, SC). Fetal bovine serum (FBS), trypsin, and Dulbecco's modified Eagle's medium (DMEM) were purchased from Invitrogen Corporation (Carlsbad, CA). All other reagents and chemicals were of the highest purity commercially available.

Synthetic Procedures. A series of aminopyridines were conjugated to CDCA using glutamic acid as a linker. Two synthetic approaches were employed (Scheme 1). Among the native bile acids, CDCA was selected on the basis of its favorable transport across ASBT-MDCK monolayers (*6*).

*N-Hydroxybenzotriazole (HOBT) Esters of CDCA (**II**).* CDCA **I** (5 g) was activated with HOBT (0.5 equiv) and HBTU (1.2 mmol) in 20 mL of anhydrous dimethylformamide (DMF) along with 1.2 equiv of triethylamine (TEA) at RT for 4 h to form CDCA-OBt ester **II**. The reaction was terminated by adding 50 mL of water. Subsequently, the reaction mixture was extracted with ethyl acetate (EtOAc) (3×). The combined organic layer was washed with brine (1×), dried with anhydrous sodium sulfate, filtered, and evaporated under vacuum to yield a white fluffy solid CDCA-OBt ester **II** (90% yield). Mass spectrometry (MS) showed appropriate peaks: $[M+H]^+$ 510.81, $[M+Na]^+$ 532.81. **II** was used in approaches A and B.

*Synthesis of CDCA-α-Benzyl-Glutamyl Probe (**V**).* Approach 1 was applied as shown in Scheme 1. **II** (5.0 g) was reacted with to 0.8 equiv of L-α-benzyl glutamic acid **III** in 30 mL of anhydrous DMF along with 1 equiv of TEA at 60 °C overnight. Reaction was terminated by adding 50 mL of water. The reaction mixture was extracted with EtOAc (3×). The combined organic layer was washed with 1 N HCl (3×) and brine (1×). Then, the organic extract was dried with anhydrous sodium sulfate, filtered, and evaporated under vacuum to yield off-white solid glutamyl-CDCA conjugates **IV** (75% yield). MS showed appropriate peaks: $[M+H]^+$ 612.81, $[M+Na]^+$ 634.81.

IV (1.0 g) was activated with 1.2 equiv of HBTU in 15 mL of anhydrous DMF along with 1.2 equiv of TEA for 10 min followed by addition of appropriate aminopyridine or aminophenol probes at 60 °C overnight. Reaction was terminated by adding 30 mL of water. The reaction mixture was extracted with EtOAc (3×). The combined organic layer was washed with 1 N HCl (3×), 1 N NaOH (3×), and brine (1×). Then, the organic extract was dried with anhydrous sodium sulfate and filtered. The EtOAc extract was evaporated under vacuum to yield thick, yellow oil. The crude product was further purified by silica gel column chromatography using a mobile phase of EtOAc and hexane (95:5). Fractions were collected and solvent evaporated to yield the neutral conjugate **V**. Purity of the conjugate was characterized by TLC and MS techniques.

Approach 2 was applied as shown in Scheme 1. First, 2.0 g of N-boc-α-benzyl-glutamic acid **VII** was coupled to aminopyridine or aminophenol probes (1.1 equiv) using HBTU (1.2 equiv) as coupling reagents in 10 mL of anhydrous DMF along with of 2.2 equiv of TEA at 70 °C overnight. Reaction was terminated by adding 30 mL of water. The reaction mixture was extracted with EtOAc (3×). The combined organic layer was washed with 1 N HCl (3×), 1 N NaOH (3×), and brine (1×). Then, the organic extract was dried with anhydrous sodium sulfate, filtered, and evaporated under vacuum to yield orange oil. The crude product was further purified by silica gel column chromatography using a mobile phase of EtOAc and hexane (90:10). Fractions were collected and solvent evaporated to give a solid, white intermediate. Purity of the intermediate conjugates was characterized by TLC and MS techniques. The intermediate was then selectively N-deprotected using 25% trifluoroacetic acid (TFA) in anhydrous dichloromethane (DCM) at RT for 1−2 h. Solvent was evaporated under vacuum to yield off-white solid **VIII**.

VIII (1.0 g) was reacted with 1.2 equiv of CDCA-OBt ester **II**, along with 1 equiv of TEA in 15 mL of anhydrous DMF at RT overnight. Reaction was terminated by adding 50 mL of water. The reaction mixture was purified as described above (see synthetic approach **I**) to yield the neutral conjugate **V**.

Synthesis of CDCD-Glutamyl Probe (VI). The neutral conjugates **V** were subjected to catalytic hydrogenation for the removal of the benzyl ester using 10% Pd/charcoal in ethanol at 50 psi overnight. Suspension was filtered through Celite and solvent evaporated under vacuum to yield the final conjugates **VI**. For chloro- and bromo-substituted neutral conjugates **V**, the benzyl ester was removed in 10 mL 33% hydrobromic acid in acetic acid at RT for 2 h. Reaction was terminated by adding 30 mL of EtOAc. The reaction mixture was extracted with water (3×). The organic layer was washed with brine (1×), dried with anhydrous sodium sulfate, filtered, and evaporated under vacuum to yield the final conjugates **VI**.

Characterization of Conjugates. Identity and purity of bile acid conjugates was characterized by TLC, MS, and ^{1}H NMR (proton, COSY). MS was performed on a LCQ ESI-MS (Thermo Fisher Scientific Inc., Waltham, MA). ^{1}H NMR spectra were recorded on a Varian Inova 500 MHz (Varian Inc., Palo Alto, CA). The mass spectra in all cases gave a molecular ion in agreement with the calculated mass of the conjugates. No CDCA impurity was detected in any final conjugate (*13*). LC-MS/MS and ^{1}H NMR results are compiled in Supporting Information Table S1. The chemical shifts are reported in parts per million (ppm) relative to tetramethylsilane (TMS) ($\delta = 0.0$ ppm).

Cell Culture. Stably transfected ASBT-MDCK cells were grown as previously described (*14*). Briefly, cells were grown at 37 °C, 90% relative humidity, 5% CO_2 atmosphere and fed every two days. Media comprised DMEM supplemented with 10% FBS, 50 units/mL penicillin, and 50 μg/mL streptomycin. Cells were passaged after reaching 90% confluency.

Inhibition Study. To characterize compound binding affinities to ASBT, cis-inhibition studies of taurocholate uptake were conducted as previously described (*15*). Briefly, cells were seeded in 12 well cluster plates (Corning; NY) at a density of 1.5 million cells/well. Inhibition studies were performed on the fifth day in Hank's Balance Salts Solution (HBSS). Cells were exposed to donor solution containing 2.5 μM taurocholate (spiked with 0.5 μCi/mL [^{3}H]-taurocholate) in the presence of a conjugate at eight concentrations (0−100 μM) for 10 min. Cells were lysed using NaOH. Cell lysate was counted for taurocholate radioactivity using a liquid scintillation counter (Beckmann Instruments, Inc., Fullerton, CA). For neutral conjugates, 2.5% DMSO was included in transport buffer, which has been shown to not affect ASBT kinetics (*16*).

Uptake Study. The uptake of conjugates by ASBT, representing cellular absorption mediated by the transporter, was evaluated. Cells were seeded as above for inhibition studies. Uptake studies employed HBSS buffer or modified HBSS buffer (i.e., sodium-free). Since ASBT is a sodium-dependent transporter, studies using sodium-free buffer enabled passive permeability measurement of conjugate. Cells were exposed to donor solution contain eight different conjugate concentrations (1−500 μM). Subsequently, cells were lysed as previous described (*16*) by adding 0.25 mL acetonitrile to each well, following evaporation at RT. A solution (1 mL) containing 50% water and 50% acetonitrile was added to each well for 10 min. Sample was stored in −80 °C until analysis by LC-MS/MS. Taurocholate uptake was measured on each study occasion as a control.

Analytical Methods. The conjugate was quantified by LC-MS on a Thermo Finnigan Surveyor HPLC system, equipped with a Thermo Finnigan Surveyor autosampler and a Thermo TSQ quantum mass spectrometer (Thermo Fisher Scientific Inc., Waltham, MA). The column used was a Phenomenex Luna C8 (50 × 2.0 mm, 3 μm; Phenomenex; Torrance, CA, USA) heated to 45 °C. The mobile phase was A, 0.1% formic acid in water; and B, 0.1% formic acid in acetonitrile, with a flow rate of 0.4 mL/min. The injection volume was 10 μL. Detection was achieved under positive ion electrospray tandem mass spectrometry using $[M+H]^+$ peak for all conjugates. The mobile phase and retention time for each conjugate are detailed in Supporting Information Table S1. The limit of quantification for all conjugates was between 1 and 2.5 nM.

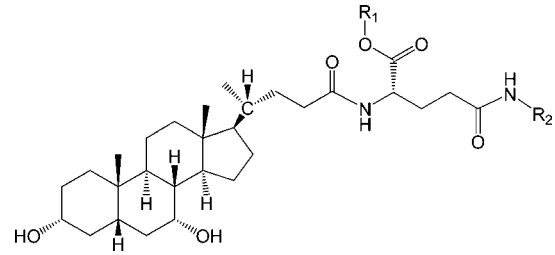


Figure 1. General structure of CDCA-glutamyl-probe (pyridines, phenol) conjugates. Database alignment employed the sub-structure CDCA-glutamate.

Kinetic Analysis. Inhibition data were analyzed in terms of inhibition constant K_i and used a modified Michaelis−Menten competitive inhibition model, as previously described, taking into account aqueous boundary layer (ABL) resistance (*17*).

Uptake data were analyzed in terms of K_t, J_{max}, $normJ_{max}$, and P_p, where J_{max} is the transport capacity; $normJ_{max}$ is normalized conjugate J_{max} against taurocholate J_{max} from the same occasion; K_t is the Michaelis−Menten coefficient for ASBT-mediated transport; and P_p is the conjugate passive permeability coefficient. For **18**, estimated K_t was less than 0.1 μM, such that K_t was assigned a value of 0.1 μM, due to the limited ability to accurately estimate potent K_t values (*17*). Data were analyzed using WinNonlin Professional (Pharsight Corporation; Mountain View, CA).

3D-QSAR Analysis. 3D-QSAR models were developed for K_i and $normJ_{max}/K_t$. The inhibition constant K_i reflects compound binding affinity to ASBT, with smaller values denoting greater binding. $normJ_{max}/K_t$ reflects the efficiency of conjugate translocation by ASBT.

The implementation of the CoMFA and CoMSIA techniques was performed as described previously (*18, 19*). Briefly, conjugates were sketched with *Sybyl 7.2* (Tripos Inc., St. Louis, MO). Each structure was minimized using the Powell method and Tripos force field (*20*) with maximum iterations of 2000 steps and termination gradient of 0.001 kcal/mol. Partial atomic charges were computed by the Gasteiger-Hückel method (*21*). Conjugates were aligned via "database alignment" based on a template structure in Figure 1. The reference compound during alignment was **12** for K_i models and **15** for the $normJ_{max}/K_t$ model. A regularly placed grid of 2.0 Å was created around aligned molecules. An sp^3 carbon atom with charge +1.00 was used as a probe atom. The steric and electrostatic fields were truncated at +30.00 kcal/mol. In contour maps of models, areas with above 80% favorability among the fields being viewed were regarded as beneficial for the biological activity, while those with field values below 20% were regarded as detrimental. The attenuation factor was 0.3. Models were obtained using the partial-least-squares (PLS) analysis (*22*). Leave-one-out cross validation (LOO) was performed to determine the optimum number of components, and nonvalidation PLS was applied to obtain the final model. Models were evaluated by the cross-validated standard coefficient q^2 and correlation coefficient r^2. A model with high q^2 (above 0.5), high r^2, low standard error of prediction (SEP), and low standard error of estimate (SEE) was considered to possess good predictability. Models were also evaluated using a test set of four randomly selected conjugates.

RESULTS AND DISCUSSION

Synthesis. A series of aminopyridine and aminophenol conjugates of glutamyl-CDCA were synthesized. The general

Table 1. Structures and the Biological Activities of the Bile Acid Conjugates[a]

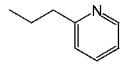
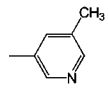
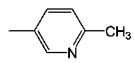
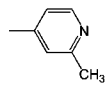
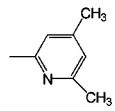
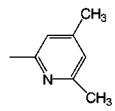
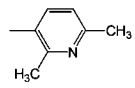
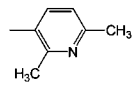
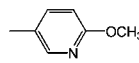
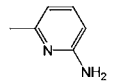
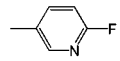
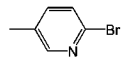
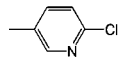
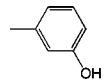
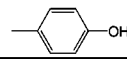
Comp.	R_1	R_2	K_i (μM)	K_t (μM)	normJ_{max}[b]	normJ_{max}/K_t (μM^{-1})	$P_p \times 10^7$ (cm/s)	ClogP
1	−H		5.28 (±0.84)	9.88 (±2.33)	0.616 (±0.033)	0.0620 (±0.0151)	5.36 (±0.26)	2.87
2[c]	−H		1.51 (±0.24)	1.06 (±0.71)	0.298 (±0.010)	0.281 (±0.189)	2.01 (±0.21)	2.87
3	−H		8.73 (±1.49)	21.6 (±4.8)	0.435 (±0.029)	0.0201 (±0.0047)	2.28 (±0.22)	2.87
4	−H		7.13 (±1.18)	17.4 (±3.0)	0.330 (±0.074)	0.0190 (±0.0054)	1.70 (±0.15)	1.90
5	−H		4.66 (±0.53)	11.2 (±3.6)	0.0791 (±0.0097)	0.00705 (±0.00243)	1.19 (±0.09)	2.72
6	−H		11.1 (±1.1)	77.3 (±26.7)	0.300 (±0.043)	0.00388 (±0.00146)	2.57 (±0.28)	2.72
7	−H		23.6 (±1.4)	21.2 (±4.4)	0.413 (±0.036)	0.0195 (±0.0044)	2.16 (±0.21)	3.37
8	−H		7.87 (±1.00)	24.6 (±4.4)	0.293 (±0.013)	0.0119 (±0.0022)	2.01 (±0.13)	3.37
9	−H		2.81 (±0.21)	9.80 (±3.83)	0.196 (±0.012)	0.0200 (±0.0079)	4.65 (±0.29)	3.37
10	−H		6.61 (±0.98)	7.44 (±2.20)	0.716 (±0.042)	0.0962 (±0.0290)	4.45 (±0.54)	3.87
11	$-CH_2C_6H_5$		122 (±19)	ND[d]	ND	ND	ND	5.21
12	−H		1.91 (±0.41)	92.2 (±14.7)	0.511 (±0.034)	0.00554 (±0.00096)	1.55 (±0.21)	3.22
13	$-CH_2C_6H_5$		28.1 (±4.43)	ND	ND	ND	ND	4.56
14	−H		8.94 (±1.11)	1.20 (±0.38)	0.242 (0.013)	0.202 (±0.065)	3.53 (±0.16)	3.71
15	−H		13.2 (±2.2)	4.44 (±0.42)	1.44 (±0.017)	0.324 (±0.031)	3.78 (±0.19)	2.54
16	−H		3.07 (±0.36)	2.80 (±1.19)	0.404 (0.025)	0.144 (±0.062)	2.57 (±0.33)	3.39
17	$-CH_2C_6H_5$		17.8 (±2.0)	NM[e]	NM	NM	62.3 (±4.1)	4.73
18[c]	−H		5.80 (±0.68)	0.1	2.67 (±0.24)	26.7	8.77 (±4.83)	2.53

Table 1. Continued

Comp.	R_1	R_2	K_i (μM)	K_t (μM)	normJ_{max} [b]	normJ_{max}/K_t (μM^{-1})	$P_p \times 10^7$ (cm/s)	ClogP
19	−H		6.84 (±0.76)	4.30 (±1.21)	0.361 (±0.052)	0.0840 (±0.0265)	11.6 (±0.5)	3.13
20	−H		5.74 (±1.02)	11.7 (± 2.4)	0.307 (±0.023)	0.0262 (±0.0057)	4.40 (±0.18)	3.13
21	−H		21.1 (±3.13)	33.0 (±28.1)	0.670 (±0.050)	0.0203 (±0.017)	48.9 (±2.5)	3.85
22[c]	−H		4.96 (±0.77)	83.6 (±43.2)	3.47 (±0.63)	0.0415 (±0.0227)	100 (±4)	3.85
23	−H		7.92 (±1.4)	NM	NM	NM	33.8 (±0.9)	3.7
24	−H		7.87 (±1.72)	NM	NM	NM	39.7 (±0.7)	2.85
25[c]	−H		3.54 (±0.50)	5.57 (±1.09)	1.46 (±0.06)	0.262 (±0.052)	6.01 (±0.34)	3.1
26	−H		2.43 (±0.39)	3.29 (±1.15)	0.464 (0.151)	0.141 (±0.067)	7.95 (±0.80)	2.87
27	−H		7.18 (±0.98)	15.3 (±2.4)	0.437 (0.027)	0.0286 (±0.0036)	7.65 (±0.73)	2.87

[a] Data were summarized as mean (±SEM) of three measurements. [b] To correct for variation in ASBT expression levels across studies, J_{max} of each bile acid was normalized against taurocholate J_{max} from the same occasion. [c] **2**, **18**, **22**, and **25** were used as the test set. The other 23 compounds were used as the training set. [d] Not determinable owing to high passive permeability. [e] Not measurable due to lack of transportation by ASBT.

structure is depicted in Figure 1, and all conjugate structures are drawn in Table 1. The synthetic strategy was based on coupling the carboxyl group at the C-24 position of CDCA to the amino group of the common drug scaffolds pyridine or phenol, using glutamic acid as a linker (Scheme 1). A negative charge around the C-24 region was designed to promote ASBT translocation (*7, 23*). The corresponding neutral analogues with α-benzyl protection on the glutamic acid linker were also synthesized. Unsubstituted, monosubstituted, and disubstituted pyridine and phenol were employed as functioned probe moieties that yielded conjugates with varying chemistry in the region beyond C-24.

ASBT Inhibition. Table 1 lists K_i values of the 27 conjugates, which included 24 pyridine-based conjugates and 3 phenol-based conjugates. Neutral conjugates with α-benzyl protection on C-24 were poorly water-soluble. Therefore, among the 24 neutral conjugates that were synthesized, only **11**, **13**, and **17** allowed K_i to be measured.

All 24 monoanionic conjugates were potent inhibitors with K_i ranging from 1.51 to 23.6 μM with CDCA-glutamyl-3-aminopyridine **2** being the most potent inhibitor. They are in the range of native bile acids. The three neutral conjugates were less potent than their corresponding monoanionic conjugates by approximately 10−20-fold.

ASBT Uptake. While all 27 conjugates exhibited high inhibition potency, only 22 showed to be substrates. Table 1 lists kinetic parameters K_t, *norm*J_{max}, *norm*J_{max}/K_t, and P_p. K_t represents transporter affinity. To accommodate variation in ASBT expression levels across studies, J_{max} of each bile acid was normalized against taurocholate J_{max} from the same occasion yielding *norm*J_{max}. The *norm*J_{max}/K_t value represents the ASBT mediated transport efficiency. Neutral compound **17** exhibited a high passive permeability, such that it was not able to be assessed as a substrate or not. The other two neutral compounds, **11** and **13**, were not further evaluated. Results from **17** were consistent with previous findings that a negative charge around the C-24 region is required for translocation (*7*).

K_t values ranged from 0.1 μM for **18** to 92.2 μM for **12**. *norm*J_{max} ranged from 0.0791 for **5** to 2.67 for **18**. *norm*J_{max}/K_t ranged from 0.00388 μM^{-1} for **6** to 26.7 μM^{-1} for **18**. P_p ranged from 1.19×10^{-7} cm/s for **5** to 100×10^{-7} cm/s for **22**. Figure 2A shows the uptake profile of **18**, which was the most potent substrate in terms of both K_t and *norm*J_{max}; Figure 2B shows the nonsubstrate **23**.

Ring substituent position had an important effect on transport efficiency. For example, for 3-aminopyridine conjugates, substitution at position 2 led to more potent substrate compared to other positions, e.g., **5** (11.2 μM) vs **7** (21.2 μM), and **18** (0.1 μM) vs **19** (4.30 μM) when substitution is moved from 2 to 5 position. Substitution at position 6 significantly decreased activity, when **8** (24.6 μM) is compared with **5** and **7**; **20** (11.7 μM) is compared with **18** and **19**; **12** (92.2 μM) is compared with **5**; **22** (83.6 μM) is compared with **21** (33.0 μM). The type of substituent group also influenced K_t. For example, all fluoro-substituted conjugates were potent substrates, bromo-substituted conjugates were weak substrates, while chloro-substitution abolished uptake.

Comparison of Inhibition Kinetics vs Transporter Kinetics. Transporter-mediated translocation minimally involves substrate binding to the transporter, transporter conformation changes involving substrate translocation, dissociation of substrate from transporter, and transporter conformation restoration.

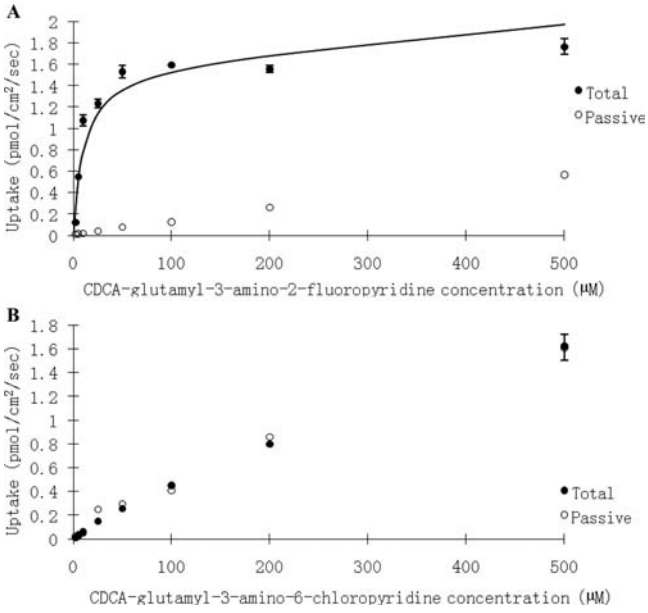


Figure 2. Concentration-dependent uptake of (A) CDCA-glutamyl-3-amino-2-fluoropyridine **18** and (B) CDCA-glutamy-3-amino-6-chloropyridine **23** into ASBT-MDCK monolayers. The conjugate was measured at varying concentrations (2.5−500 μM) in the presence and absence of sodium to delineate ASBT-mediated and passive uptake components. Data indicate total uptake in the presence of sodium (•) and passive uptake in the absence of sodium (○). Uptake of **18** was several-fold higher in the presence of sodium than in the absence of sodium, reflecting ASBT-mediated uptake. Uptake of **23** was the same in the presence and absence of sodium; passive uptake was high, such that the compound was either not a substrate or not measurable as a substrate due to high passive permeability.

The initial binding step is assessed by K_i. Results show that ASBT inhibition requirements were different from the ASBT-mediated transport requirements. A potent inhibitor may be a weak substrate, such as **6**, **12**, and **22**. Figure 3A illustrates the relationship of transporter affinity K_t and inhibition potency K_i for all 22 substrates. Figure 3B excludes **6**, **12**, and **22**, where K_t was notably weaker than K_i. For these 19 conjugates in Figure 3B, there was a modest association between K_t and K_i with linear slope = 0.995, $r^2 = 0.403$, and $p = 0.003$. Qualitatively, most conjugates yielded similar potency of K_t and K_i, suggesting that conjugate binding was broadly the slow kinetic step for conjugate translocation. These results agree with previous native bile acid findings (*6*). It should be noted that **14** and **18** yielded K_t values that were over 7-fold more potent than K_i although they both were potent inhibitors and substrates (e.g., K_i and K_t < 10 μM). For **6**, **12**, and **22**, where K_t was far less potent than K_i, postbinding events were rate-limiting.

Figure 4 shows that transport capacity was not associated with inhibitory potency. Capacities of most conjugates spanned a narrow range and were less than taurocholate. However, $normJ_{max}$ of **15**, **18**, **22**, and **25** were higher than that of taurocholate. Supporting Information Figures S1 and S2 show that transport capacity and transport efficiency were not related to K_t or K_i, respectively.

ASBT Inhibition 3D-QSAR Models. Figure 5 shows the superimposition of all 27 compounds for inhibition model development. Twenty-three compounds were included in the training set. The remaining, randomly selected four compounds (i.e., **2**, **18**, **22**, and **25**) were used as the test set. Four 3D-QSAR models, including one CoMFA and three CoMSIA models, were developed using pK_i data (Table 2). CoMSIA-1 included electrostatic and steric fields, whereas CoMSIA-2 included an additional hydrophobic field. CoMSIA-3 included the three molecular descriptors from models 1 and 2, as well as hydrogen bond donor and acceptor fields.

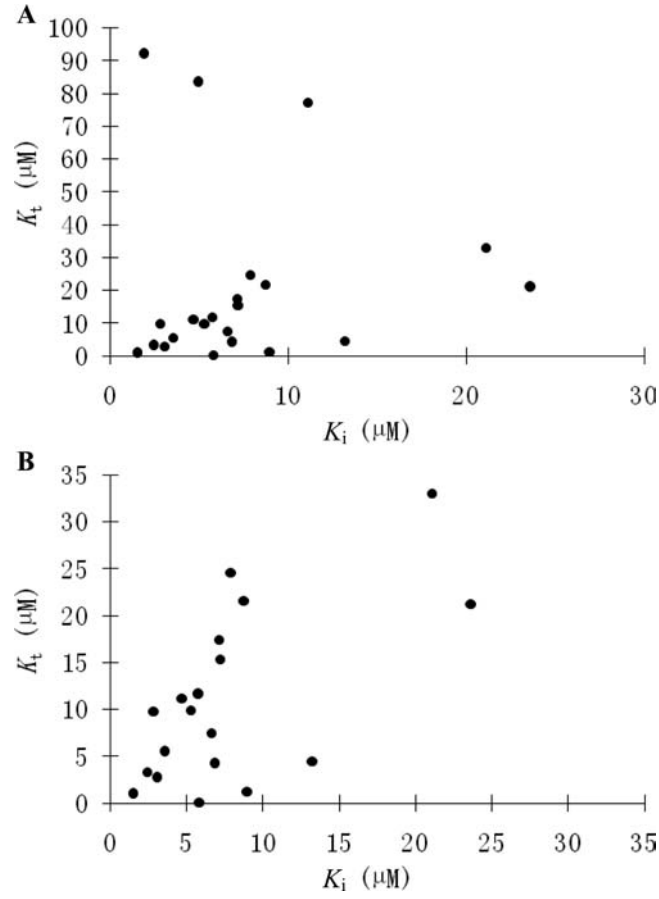


Figure 3. Relationship of K_t and K_i. (A) For all 22 bile acid conjugates that were substrates, K_t vs K_i are plotted. **6**, **12**, and **22** exhibited several-fold higher K_t values than K_i values. (B) With **6**, **12**, and **22** removed, most conjugates yielded similar K_t and K_i. Linear regression showed slope = 0.995, $r^2 = 0.403$, and $p = 0.003$. **14** and **18** yielded $K_t \ll K_i$, although all were <10 μM.

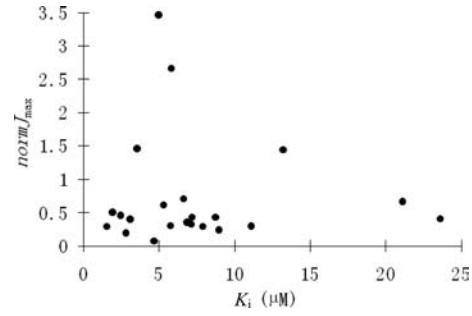


Figure 4. Relationship between $normJ_{max}$ and K_i. Transporting capacity was not associated with inhibition potency. Linear regression showed a slope of -0.008 μM^{-1} and $r^2 = 0.003$. **15**, **18**, **22**, and **25** yielded J_{max} higher than taurocholate. All other conjugates exhibited J_{max} less than taurocholate J_{max}, and ranged from 0.0791 to 0.716.

CoMFA and CoMSIA models were comparable in terms of their predictability of pK_i, with CoMFA-1 ($q^2 = 0.675$, $r^2 = 0.965$) and CoMSIA-3 ($q^2 = 0.612$, $r^2 = 0.958$) being the best inhibition models (Table 2). Figure 6 shows the relationship of observed versus predicted pK_i for training set and test set of CoMFA-1 and CoMSIA-3. The corresponding data are listed in Supporting Information Table S2. Both models accurately predicted activities of three out of the four test compounds. **2** was underpredicted by both models, where the observed K_i was 1.51 μM and predicted K_i were 8.13 μM and 11.7 μM by CoMFA-1 and CoMSIA-3, respectively.

Table 2 also shows the relative contributions of specific fields to the inhibition activities. For CoMFA-1, the steric feature

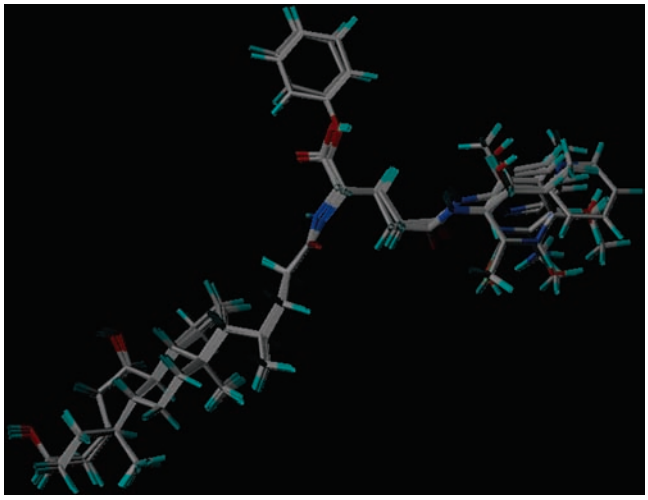


Figure 5. Superimposition of training set and test set compounds for inhibition model development.

Table 2. Result from CoMFA and CoMSIA Analysis

	CoMFA-1[a]	CoMSIA-1[a]	CoMSIA-2[a]	CoMSIA-3[a]	CoMFA-2[b]
q^2	0.675	0.388	0.572	0.612	0.538
SEP[c]	0.255	0.349	0.292	0.278	0.550
r^2	0.965	0.879	0.959	0.958	0.999
SEE[c]	0.004	0.155	0.091	0.091	0.025
NOC[c]	5	5	5	5	9
			Fraction		
steric	0.731	0.377	0.120	0.084	0.612
electronic	0.269	0.623	0.378	0.202	0.388
hydrophobic			0.502	0.408	
donor				0.131	
acceptor				0.173	

[a] Models for pK_i. [b] Model for log($normJ_{max}/K_i$). [c] SEP: standard error of prediction; SEE: standard error of estimate; NOC: number of components.

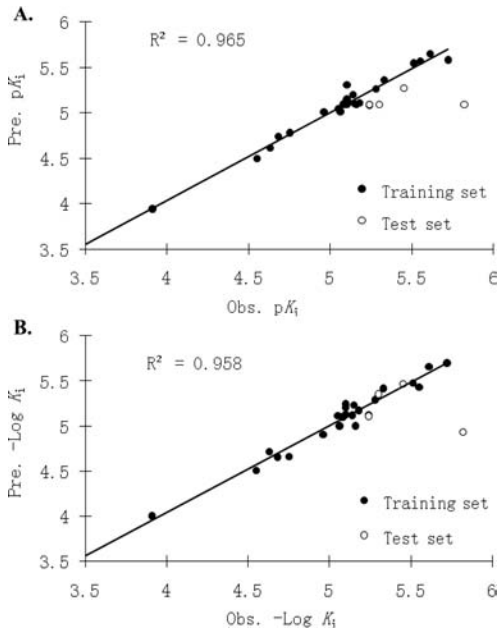


Figure 6. Observed versus predicted pK_i plot of the CoMFA-1 (A) and CoMSIA-3 (B) using 23 training set conjugates (•) and 4 test set conjugates (○). The solid line is the regression for the training set. The regression line has a slope = 0.965 and r^2 = 0.965 for CoMFA-1, and 0.959 and 0.958 for CoMSIA-3, respectively.

dominated (73.1% contribution) the electrostatic feature. For all CoMSIA models, the steric feature was less important than the electrostatic feature. For example, the contributions of steric and electrostatic features in CoMSIA-1 were 37.7% and 62.3%, respectively. The different effects of steric and electrostatic fields between CoMFA and CoMSIA are attributed to their energy function forms. The contribution of the steric feature in CoMSIA is further reduced when the hydrophobic field was added, with 12.0% and 8.4% for CoMSIA-2 and CoMSIA-3, respectively. For these two models, the hydrophobic was the most determining feature that contributed 50.2% and 40.8%, respectively. Considering the improved q^2 in CoMSIA-2 and CoMSIA-3 vs CoMSIA-1, the hydrophobic feature was the major contributor to improve pK_i predictability. Hydrogen bond donor and acceptor in CoMSIA-3 contributed 13.1% and 17.3%, respectively, and account for the slight q^2 increase from 0.572 in CoMSIA-2 to 0.612 in CoMSIA-3.

3D-QSAR Contour Maps for Inhibition. Figures 7 and 8 illustrate features of the CoMFA-1 and CoMSIA-3 models, respectively. Contour maps were drawn relative to CDCA-glutamyl-3-amino-2,6-dimethylpyridine **12**.

CoMFA Contour Maps. The steric contours from CoMFA-1 (Figure 7A) reveal that bulky groups at the 2 or 6 position (green region) of 3 aminopyridine afford beneficial steric interactions for inhibition, whereas bulky substitutes on position 5 (yellow region) are detrimental. The contours explain the higher activity of 2,6-dimethyl-substituted **12** (K_i = 1.94 μM) over 2-methyl substituted **8** (7.87 μM) and 6-methyl substituted **5** (4.66 μM). The two green regions also accounted for the higher activity of **5** and **8** than **6** (11.1 μM) and **7** (23.64 μM), where the methyl group is moved from 2 or 6 to 4 or 5. The same pattern is evident for bromo substitution. When bromine is moved from position 6 in **22** to 5 in **21**, the activity decreased from 4.96 to 21.1 μM. The electrostatic contour from CoMFA-1 (Figure 7B) indicates that an electropositive group near the −COO (blue region) will be favorable. Considering that a hydroxyl hydrogen on a carboxylic group bears a positive charge, this blue area reflects that a carboxylic acid near C-24 improved inhibition more than the corresponding conjugates with α-benzyl protection. Inhibition potency decreased from 6.61 to 122 μM comparing **10** to **11**, from 1.94 to 28.1 μM comparing **12** to **13**, and from 3.07 to 17.78 μM comparing **16** to **17**. These findings agree with previous observations that a negative charge near C24 region is preferred (*7*). In Figure 7B, the red contour region behind the 2 position and a blue contour region near the 6 position of the 3-aminopyridine ring indicate that an electronegative or electropositive group enhanced inhibition.

CoMSIA Contour Maps. Steric contour maps from CoMSIA-3 (Figure 8A) reveal that the green regions are patterned similarly to those from CoMFA-1 (Figure 7A). However, CoMSIA-3 provides two additional yellow contours above the carboxylate group indicating that a steric interaction near −COO is unfavorable. The yellow areas are consistent with the blue electrostatic contour of CoMFA-1 (Figure 7B), where α-benzyl protection of the carboxylate decreased the inhibition potency (i.e., **10** vs **11**, **12** vs **13**, and **16** vs **17**). Electrostatic contours (Figure 8B) are consistent with the patterns observed in CoMFA-1 (Figure 7B), e.g., red and blue regions around 2 and 6 position of the 3-aminipyridine ring. Hydrophobic contour plots (Figure 8C) indicate that hydrophobic substitution on the 2 or 6 position enhances inhibition (orange regions), whereas such substitution on the 5 position reduces potency (white contour). This result is consistent with steric contours of CoMFA-1 (Figure 7A). Hydrogen bond donor contours (Figure 8D) suggest that a −OH in the carboxyl group can be regarded as a hydrogen bond donor. The cyan area near the −COO group agrees with the steric (Figure 8A) and hydrophobic contours (Figure 8C), indicating that the α-benzyl group on −COO remarkably reduced the inhibition activities. The purple area near the pyridine ring indicates that a hydrogen-bond donor

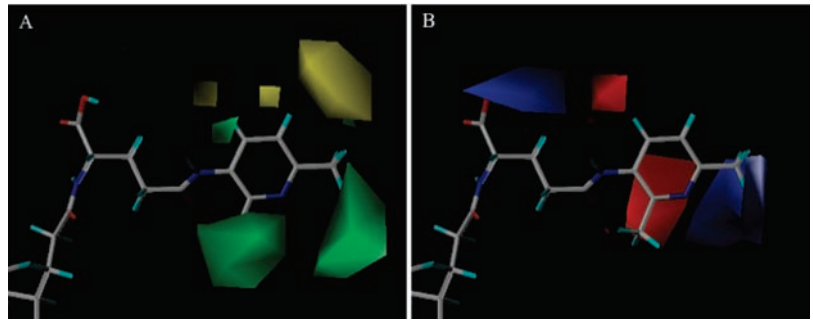


Figure 7. Steric (A) and eletrostatic (B) contour maps around compound CDCA-glutamyl-3-amino-2,6-dimethylpyridine **12** for CoMFA-1 inhibition model. In panel A, green contours show where bulky substitute favored inhibition, while yellow contours were disfavored. In panel B, blue region represents favorable electropositive interaction for inhibition, while red shows disfavored electropositive character.

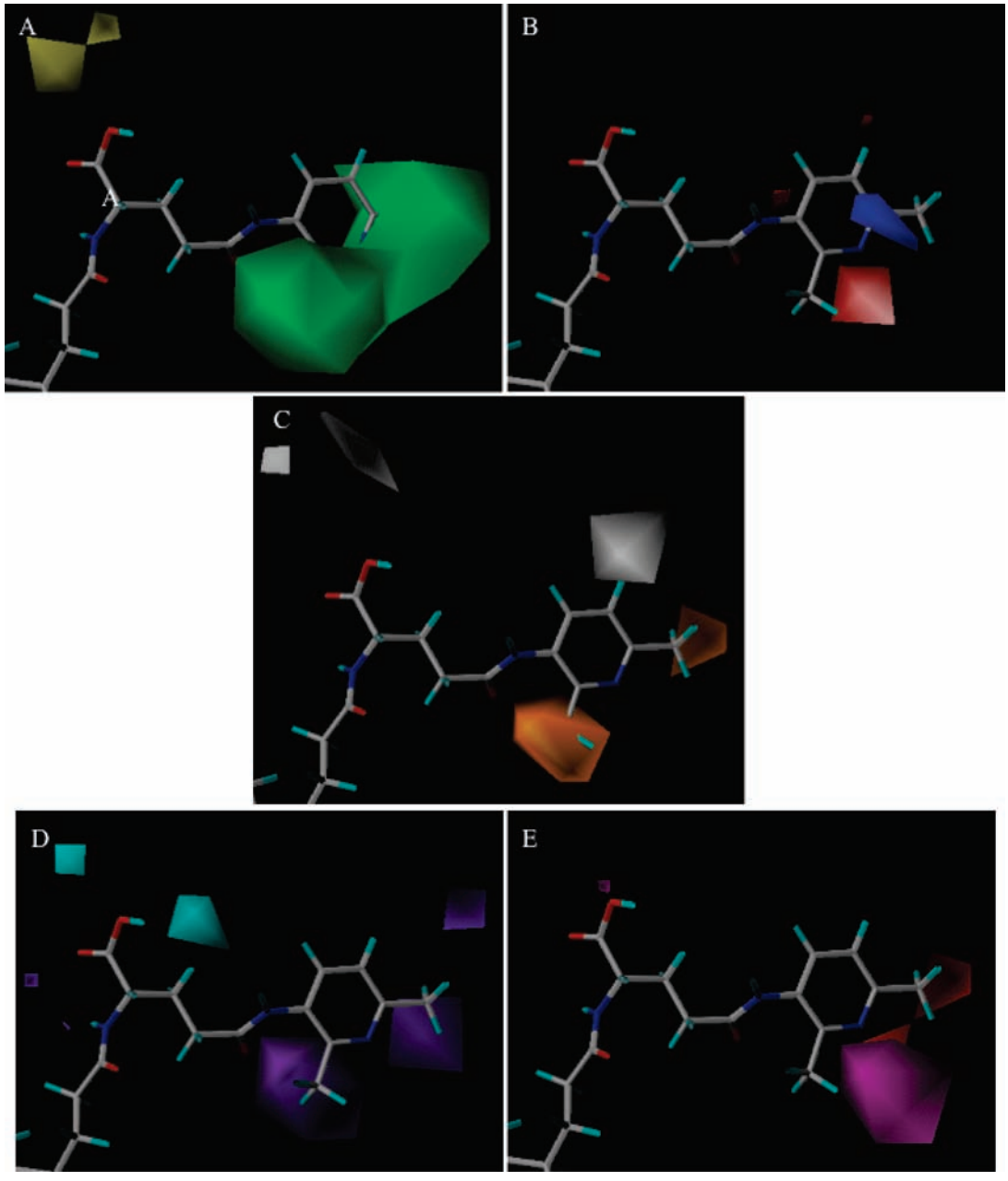


Figure 8. Steric (A), electrostatic (B), hydrophobic (C), hydrogen bond donor (D), and hydrogen bond acceptor (E) contour maps around CDCA-glutamyl-3-amino-2,6-dimethylpyridine **12** for CoMSIA-3 inhibition model. In panel A, green and yellow contours represent favorable and unfavorable bulky substituent interaction regions for inhibition. In panel B, blue and red contours represent regions that favor electropositive and electronegative groups, respectively. In panel C, orange and white contours are areas where hydrophobic groups enhance and diminish activity. In panel D, cyan and purple contours indicate regions where an inhibitor's hydrogen bond donor is favored and disfavored, respectively. In panel E, magenta and red contours represent favorable and unfavorable hydrogen-bond acceptor regions, respectively.

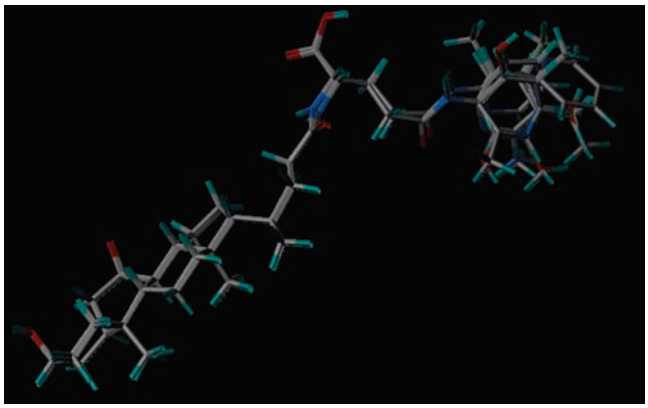


Figure 9. Superimposition of training set and test compounds for transport efficiency model development.

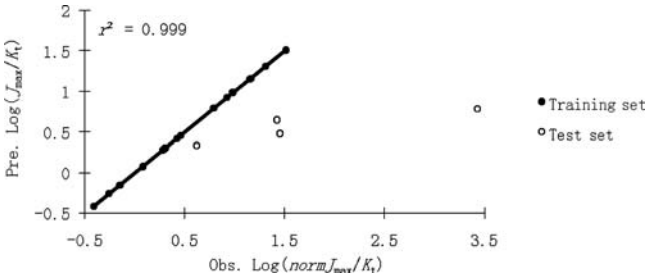


Figure 10. Observed vs predicted log($normJ_{max}/K_t$) plot of the CoMFA-2 using 18 training set conjugates (•) and 4 test set conjugates (○). The solid line is the regression for the training set. The regression line has slope = 1.00 and r^2 = 0.999.

behind the 2 and 6 positions of the 3-aminopyridine ring is detrimental. Hydrogen bond acceptor contours (Figure 8E) determine favorable (magenta) areas near the pyridine nitrogen and a red (disfavored) area around the 6 position on 3-aminopyridine ring, reflecting the decreased activity from 2.43 to 7.18 μM when a hydroxyl group is moved from the meta position in **26** to the para in **27** on the phenol ring.

Comparison of CoMFA and CoMSIA Models for Inhibition. CoMFA-1 possessed slightly greater predictability than CoMSIA-3 in terms of q^2 (0.675 and 0.612, respectively). However, the advantage of CoMSIA is the employment of a Gaussian-type energy calculation and additional molecular descriptors, including hydrophobic fields, hydrogen bond acceptor, and hydrogen bond donor. For example, the influence of the α-benzyl group is not accommodated by the steric contour of CoMFA-1 (Figure 7A), but is accommodated by the steric and hydrophobic contours of CoMSIA-3 (Figure 8A,B). The hydrophobic contour of CoMSIA-3 had a similar pattern to the steric contour of CoMFA-1, indicating that the hydrophobic field of CoMSIA-3 may share common features with the steric field of CoMFA-1. The similarity is not surprising, because a large hydrophobic substitution may have significant steric effects.

ASBT Transport Efficiency Model. As with the inhibition models, **2**, **18**, **22**, and **25** were reserved as test compounds for transport efficiency modeling. Figure 9 shows the superimposition of all 22 compounds for transport efficiency model development. No QSAR model was derived from K_t data with significant q^2.

A comprehensive CoMFA model (CoMFA-2) was derived from log($normJ_{max}/K_t$) (Table 2). The q^2 and r^2 values were 0.538 and 0.999, respectively. Similar to CoMFA-1, steric fields dominated the electrostatic fields for transport efficiency with contributions of 61.2% and 38.8%, respectively. Figure 10 shows the relationship between observed and predicted uptake efficiencies of the training and test set (corresponding data in Supporting Information Table S2). The uptake efficiencies of test sets **22** and **25** were underestimated by 2- and 6-fold, respectively. **2** and **18** were significantly underestimated by approximately 9- and 400-fold, respectively. A potential contributing factor to the prediction error of **18** is that its uptake efficiency was over 100-fold greater than that of all other conjugates. The underestimated activity of compound **2** might be due to chemical or physical features beyond the predictive capacity of CoMFA and CoMSIA models.

CoMFA Model Contours for Transport Efficiency. Figure 11 shows steric and electrostatic contours of CoMFA-2 relative to CDCA-glutamyl-2,6-diaminopyridine **15**, the most efficient ASBT substrate within the training set ($normJ_{max}/K_t$ = 0.324 μM^{-1}). As above, a large green contour near positions 5 and 6 on the pyridine ring in Figure 11A indicates that a bulky group is beneficial. Compared to other position 6 substituents, transport efficiency of **14** with a methoxy group at position 6 on the 3-aminopyridine ring ($normJ_{max}/K_t$ = 0.202 μM^{-1}) was high compared to **8** (methyl substituted, 0.0119 μM^{-1}), **20** (fluoro, 0.0262 μM^{-1}), and **22** (bromo, 0.0415 μM^{-1}). The other green region near 1 and 6 positions on the pyridine ring of **15** indicates that steric interaction is favorable. A yellow contour between 4 and 5 positions indicates that a steric substituent will decrease efficiency. For example, fluoro substitution exhibited higher efficiencies than corresponding bromo substitution (**19** vs **21**). Figure 11B shows the electrostatic contour. The large blue region near the 4 and 5 positions on the 2,6-aminopyridine ring reflects the lower efficiency of the para hydroxyl in **27** compared to the ortho hydroxyl in **25** or the meta hydroxyl in **26**. The small blue region under the 6 position of **15** agrees with its high efficiency, compared to compounds lacking a 6-amino substitute such as **1**. The red region near the 4 position of **15** indicates that an electronegative substitute at the 4 position on 2-aminopyridine could enhance the transport efficiency.

LogP Effects on ASBT Inhibition and Transport. Partition coefficient (LogP) is a measurement of compound solubility and lipophilicity (*24*). Since CoMFA and CoMSIA models indicated that steric and hydrophobic features strongly influenced conjugate interaction with ASBT, LogP may explain inhibition or transport efficiency. Calculated LogP (CLogP) was computed

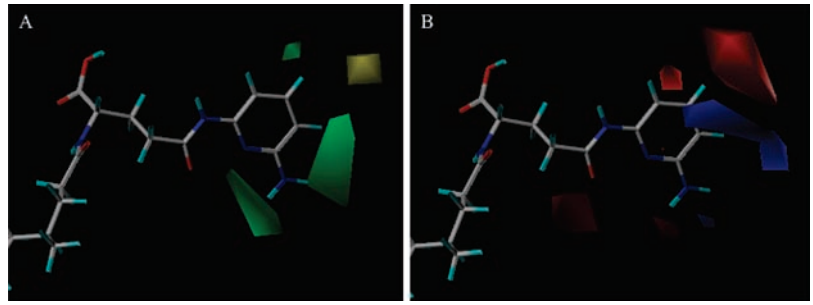


Figure 11. Steric (A) and eletrostatic (B) contour maps around CDCA-glutamyl-2,6-diaminopyridine **15** for CoMFA-2 transport efficiency model. In panel A, green contours show where bulky substitute favored inhibition, while yellow contours were disfavored. In panel B, the blue region represents favorable electropositive interaction for inhibition, while red shows disfavored electropositive character.

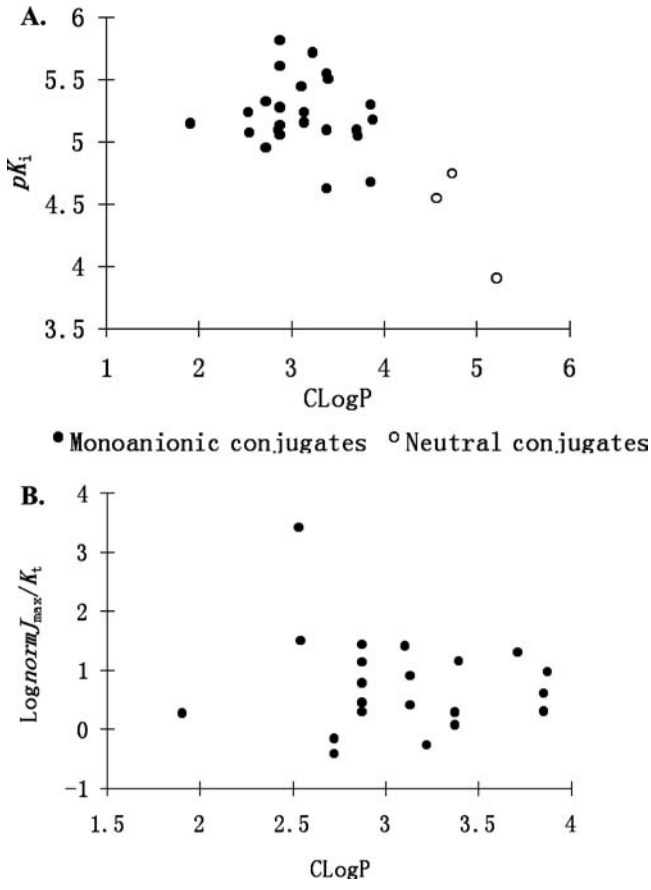


Figure 12. Influence of LogP on ASBT inhibition (A) and transport efficiency (B). (A) Observed pK_i vs ClogP shows a fairly negative correlation between pK_i and CLogP (slope = −0.331, $r^2 = 0.367$, and $p = 0.0008$). However, there was no simple correlation ($r^2 = 0.021$) among the 24 monoanionic conjugates when the three neutral conjugates (i.e., the α-benzyl substituted conjugates **11**, **13**, and **17**) were eliminated. (B) Observed log($normJ_{max}/K_t$) vs ClogP shows no relationship between log($normJ_{max}/K_t$) and CLogP with $r^2 = 0.015$ and $p = 0.586$.

using SYBYL according to Hansch and colleagues (*24, 25*) (Table 1). Plots of observed pK_i vs CLogP (Figure 12A) shows a fairly negative correlation between pK_i and CLogP with $r^2 = 0.367$ and $p = 0.0008$ (i.e., lipophilicity reduced binding potency). Comparison of α-benzyl-substituted conjugates to their nonsubstituted counterparts (**11** vs **10**, **13** vs **12**, and **17** vs **16**) essentially accounted for this trend. However, elimination of these three neutral conjugates (open circles in Figure 12A) leads to no relationship between pK_i and CLogP ($r^2 = 0.021$) among the 24 monoanionic conjugates (filled circles in Figure 12A). This lack of simple correlation between inhibition and CLogP is supportive of COMFA and COMSIA findings that hydrophobicity played differing roles in conjugate binding (i.e., hydrophobic or bulky substitute on the 2 or 6 position of a 3-aminopyridine ring enhanced activity, while a hydrophobic group on the 5 position was detrimental).

There was no correlation between Log($normJ_{max}/K_t$) and CLogP, with $r^2 = 0.015$ (Figure 12B). Additionally, no correlation was observed between K_t vs CLogP and $normJ_{max}$ vs CLogP as well with $r^2 = 0.037$ and 0.005, respectively. The lack of correlation between transport parameters and CLogP indicates that other physicochemical and structural variables impact transport beyond hydrophobicity, and further suggests a greater complexity in conjugate translocation compared to conjugate binding.

Comparison to Previous ASBT Models. Several computational models have been developed to study structural requirements of ASBT inhibition. Baringhaus and co-workers (*26*) explored the chemical features of ASBT inhibitors with 3D pharmacophore using structurally diverse molecules. 3D pharmacophore and Bayesian models were derived and applied by our lab to identify novel ASBT inhibitors among commercial drugs (*15*). However, the above studies do not systemically involve C-24 conjugated bile acid analogues, nor do they address the more complex process of ASBT-mediated uptake. Swaan and colleagues (*27*) applied CoMFA analysis on a series of bile acid−peptide analogues and found that inhibition was favored by an electron donor group between C-24 and C-27 and steric bulk at the end of the side chain. These results corroborate our present findings.

3D-QSAR models using a conformationally sampled pharmacophore (CSP) approach were developed for inhibition requirements using C-24 bile acid conjugates that employed piperidines as probe moieties (*28*). Results here using pyridines and phenols as probe moieties in part agree with these piperidine findings, where hydrophobicity favored inhibition activity. In contrast to piperidine findings, the results showed a position effect, where the relative location of the pyridine nitrogen and substituent groups modulated the conjugate ASBT inhibition and translocation.

C-24 bile acid conjugates have previously been shown to be ASBT substrates (*7, 29−31*). One of these studies was a SAR study involving a series of C-24 cholic acid conjugates and found that the C-24 side chain can be 14 Å in length or longer for translocation and that large hydrophobic moieties increase binding to ASBT (*29*). In another study, C-24 conjugation with glutamic acid and lysine also found that charge and hydrophobicity around the 24 position influenced translocation (*7*). Results of this study are in agreement with these prior findings that a negative change near C-24 promotes substrate translocation and that steric bulk at certain positions of the aminopyridine ring beyond C-24 also favors translocation.

CONCLUSION

With the view that bile acid conjugates can serve as prodrugs that target ASBT to increase oral drug permeability and bioavailability, a series of aminopyridine or aminophenol conjugates of glutamyl-bile acids were synthesized. Their ASBT inhibition and transport efficiency were evaluated to investigate their interaction beyond the C-24 region of CDCA with ASBT. Similar values for K_i and K_t indicate that substrate binding to ASBT was generally the rate-limiting step in overall substrate transport. 3D-QSAR models were developed for ASBT inhibition. The steric field dominated in the CoMFA model, whereas the hydrophobic field dominated other features in the CoMSIA models. Monoanionic conjugate exhibited higher inhibition potency than neutral conjugate. A hydrophobic or bulky substituent on the 2 or 6 position of a 3-aminopyridine ring enhanced inhibition, while a hydrophobic group on the 5 position was detrimental. Both inhibition models predicted test set inhibition. Recently, the value of inhibition-only QSAR models for drug transporters has been questioned (*32*), which prompted us to also develop ASBT models for transport efficiency. 3D-QSAR has not previously been applied to ASBT substrate studies. Similar to the inhibition models, the steric field was the predominant contributor; however, we demonstrate that steric contributions to ASBT transport cannot be explained simply by lipophilicity. Overall, these 3D-QSAR models provide new insight into the substrate requirements for ASBT uptake and shed light on the design of bile acid conjugates that can increase intestinal drug permeability and bioavailability.

ACKNOWLEDGMENT

This work was support in part by National Institutes of Health grants DK67530 (to J.E.P.) and DK61425 (to P.W.S.). The

author gratefully acknowledges Dr. Gasirat Tririya and Rana Rais for their assistance in chemical synthesis and Dr. Guoyun Bai for NMR assignment assistance.

Supporting Information Available: Additional related tables and figures. This material is available free of charge via the Internet at http://pubs.acs.org.

LITERATURE CITED

(1) Dawson, P. A., and Oelkers, P. (1995) Bile acid transporters. *Curr. Opin. Lipidol. 6*, 109–114.

(2) Dawson, P. A., Lan, T., and Rao, A. (2009) Bile acid transporters. *J. Lipid Res.*

(3) Balakrishnan, A., and Polli, J. E. (2006) Apical sodium dependent bile acid transporter (ASBT, SLC10A2): a potential prodrug target. *Mol. Pharmaceutics 3*, 223–230.

(4) Lack, L. (1979) Properties and biological significance of the ileal bile salt transport system. *Environ. Health Perspect. 33*, 79–89.

(5) Balakrishnan, A., Sussman, D. J., and Polli, J. E. (2005) Development of stably transfected monolayer overexpressing the human apical sodium-dependent bile acid transporter (hASBT). *Pharm. Res. 22*, 1269–1280.

(6) Balakrishnan, A., Wring, S. A., and Polli, J. E. (2006) Interaction of native bile acids with human apical sodium-dependent bile acid transporter (hASBT): influence of steroidal hydroxylation pattern and C-24 conjugation. *Pharm. Res. 23*, 1451–1459.

(7) Balakrishnan, A., Wring, S. A., Coop, A., and Polli, J. E. (2006) Influence of charge and steric bulk in the C-24 region on the interaction of bile acids with human apical sodium-dependent bile acid transporter. *Mol. Pharmaceutics 3*, 282–292.

(8) Tolle-Sander, S., Lentz, K. A., Maeda, D. Y., Coop, A., and Polli, J. E. (2004) Increased acyclovir oral bioavailability via a bile acid conjugate. *Mol. Pharmaceutics 1*, 40–48.

(9) Cramer, R. D., Patterson, D. E., and Bunce, J. D. (1988) Comparative molecular-field analysis (Comfa) 0.1. Effect of shape on binding of steroids to carrier proteins. *J. Am. Chem. Soc. 110*, 5959–5967.

(10) Klebe, G., Abraham, U., and Mietzner, T. (1994) Molecular similarity indexes in a comparative-analysis (Comsia) of drug molecules to correlate and predict their biological-activity. *J. Med. Chem. 37*, 4130–4146.

(11) Martin, Y. C. (1998) 3D QSAR: current state, scope, and limitations. *Drug Discovery Des. 12*, 3–23.

(12) Bemis, G. W., and Murcko, M. A. (1996) The properties of known drugs. 1. Molecular frameworks. *J. Med. Chem. 39*, 2887–2893.

(13) Gonzalez, P., and Polli, J. E. (2008) Impact of impurity on kinetic estimates from transport and inhibition studies. *J. Pharmacol. Exp. Ther. 326*, 296–305.

(14) Balakrishnan, A., Sussman, D. J., and Polli, J. E. (2005) Development of stably transfected monolayer overexpressing the human apical sodium-dependent bile acid transporter (hASBT). *Pharm. Res. 22*, 1269–1280.

(15) Zheng, X., Ekins, S., Raufman, J. P., and Polli, J. E. (2009) Computational models for drug inhibition of the human apical sodium-dependent bile acid transporter. *Mol. Pharmaceutics 6*, 1591–1603.

(16) Rais, R., Gonzalez, P. M., Zheng, X., Wring, S. A., and Polli, J. E. (2008) Method to screen substrates of apical sodium-dependent bile acid transporter. *AAPS J. 10*, 596–605.

(17) Balakrishnan, A., Hussainzada, N., Gonzalez, P., Bermejo, M., Swaan, P. W., and Polli, J. E. (2007) Bias in estimation of transporter kinetic parameters from overexpression systems: Interplay of transporter expression level and substrate affinity. *J. Pharmacol. Exp. Ther. 320*, 133–144.

(18) McKay, D. B., Chang, C., Gonzalez-Cestari, T. F., McKay, S. B., El-Hajj, R. A., Bryant, D. L., Zhu, M. X., Swaan, P. W., Arason, K. M., Pulipaka, A. B., Orac, C. M., and Bergmeier, S. C. (2007) Analogs of methyllycaconitine as novel noncompetitive inhibitors of nicotinic receptors: pharmacological characterization, computational modeling, and pharmacophore development. *Mol. Pharmacol. 71*, 1288–1297.

(19) Kaler, G., Truong, D. M., Khandelwal, A., Nagle, M., Eraly, S. A., Swaan, P. W., and Nigam, S. K. (2007) Structural variation governs substrate specificity for organic anion transporter (OAT) homologs. Potential remote sensing by OAT family members. *J. Biol. Chem. 282*, 23841–23853.

(20) Clark, M., Cramer, R. D., and Vanopdenbosch, N. (1989) Validation of the general-purpose Tripos 5.2 force-field. *J. Comput. Chem. 10*, 982–1012.

(21) Gasteiger, J., and Marsili, M. (1980) Iterative partial equalization of orbital electronegativity: A rapid access to atomic charges. *Tetrahedron 36*, 3219–3228.

(22) Wold, S., Ruhe, A., Wold, H., and Dunn, W. (1984) Collinearity problem in linear regression. The partial least squares (pls)> approach to generalized inverses. *SIAM J. Sci. Stat. Comput. 5*, 735–743.

(23) Lack, L., and Weiner, I. M. (1966) Intestinal bile salt transport: structure-activity relationships and other properties. *Am. J. Physiol. 210*, 1142–1152.

(24) Leo, A., Hoekman, D. H., and Hansch, C. (1995) Exploring QSAR, hydrophobic, electronic, and steric constants, American Chemical Society, Washington, DC.

(25) Leo, A., Hansch, C., and Ekins, D. (1971) Partition coefficients and their uses. *Chem. Rev. 71*, 525–616.

(26) Baringhaus, K. H., Matter, H., Stengelin, S., and Kramer, W. (1999) Substrate specificity of the ileal and the hepatic Na(+)/bile acid cotransporters of the rabbit. II. A reliable 3D QSAR pharmacophore model for the ileal Na(+)/bile acid cotransporter. *J. Lipid Res. 40*, 2158–2168.

(27) Swaan, P. W., Szoka, F. C., Jr., and Oie, S. (1997) Molecular modeling of the intestinal bile acid carrier: a comparative molecular field analysis study. *J. Comput.-Aided Mol. Des. 11*, 581–588.

(28) Gonzalez, P. M., Acharya, C., Mackerell, A. D., Jr., and Polli, J. E. (2009) Inhibition requirements of the human apical sodium-dependent bile acid transporter (hASBT) using aminopiperidine conjugates of glutamyl-bile acids. *Pharm. Res. 26*, 1665–1678.

(29) Kagedahl, M., Swaan, P. W., Redemann, C. T., Tang, M., Craik, C. S., Szoka, F. C., Jr., and Oie, S. (1997) Use of the intestinal bile acid transporter for the uptake of cholic acid conjugates with HIV-1 protease inhibitory activity. *Pharm. Res. 14*, 176–180.

(30) Mills, C. O., Milkiewicz, P., Saraswat, V., and Elias, E. (1997) Cholyllysyl fluroscein and related lysyl fluorescein conjugated bile acid analogues. *Yale J. Biol. Med. 70*, 447–457.

(31) Swaan, P. W., Hillgren, K. M., Szoka, F. C., Jr., and Oie, S. (1997) Enhanced transepithelial transport of peptides by conjugation to cholic acid. *Bioconjugate Chem. 8*, 520–525.

(32) Giacomini, K. M., Huang, S. M., Tweedie, D. J., Benet, L. Z., Brouwer, K. L., Chu, X., Dahlin, A., Evers, R., Fischer, V., Hillgren, K. M., Hoffmaster, K. A., Ishikawa, T., Keppler, D., Kim, R. B., Lee, C. A., Niemi, M., Polli, J. W., Sugiyama, Y., Swaan, P. W., Ware, J. A., Wright, S. H., Yee, S. W., Zamek-Gliszczynski, M. J., and Zhang, L. (2010) Membrane transporters in drug development. *Nat. Rev. Drug Discovery 9*, 215–236.

BC100273W

Supporting Information

Structural Requirements of the ASBT by 3D-QSAR Analysis Using Aminopyridine Conjugates of Chenodeoxycholic Acid

Xiaowan Zheng, Yongmei Pan, Chayan Acharya[†], Peter W. Swaan, James E. Polli*

Department of Pharmaceutical Sciences, School of Pharmacy, University of Maryland, 20 Penn Street, Baltimore, MD 21201, USA.

[†]Present Address: Institut Européen de Chimie et Biologie, Université Bordeaux 1, 2 rue Robert Escarpit, 33607 Pessac Cedex, France

*To whom correspondence should be addressed. (e-mail: jpolli@rx.umaryland.edu); Tel. +1410-706-8292; Fax: +1 410-706-5017

Xiaowan Zheng and Yongmei Pan contributed equally to this work.

Running Title: conjugate QSAR for ASBT transporter

Table S1. Physicochemical characteristics of conjugates.

Comp.	LC-MS/MS					^{1}H-NMR (DMSO-*d*6)[d]
	Exact Mass [a]	Q1 Mass (m/z) [b]	Q3 Mass (m/z) [b]	Retention Time (min)	X-Initial B% in gradient[c]	
1	597.38	598.30	94.90	1.04	35%	12.52 (1H, s, β), 10.44 (1H, s, γ), 8.29 (1H, d, α), 8.06 (1H, d, α), 8.00 (1H, d, γ), 7.75 (1H, t, α), 7.07 (1H, t, α), 4.17 (1H, m, θ)
2	597.38	598.41	221.00	1.24	40%	12.34 (1H, s, β), 10.21 (1H, s, γ) 8.74 (1H, s, α) 8.26 (1H, d, α), 8.05 (1H, d, α), 8.00 (1H, d, γ) 7.35 (1H, t, α), 4.20 (1H, m, θ)
3	597.38	598.41	221.00	2.24	30%	12.63 (1H, s, β), 10.55 (1H, s, γ), 8.45 (2H, d, α), 8.09 (1H, d, γ), 7.66 (2H, d, α), 4.23 (1H, m, θ)
4	625.41	626.31	189.01	1.23	33%	12.50 (1H, s, β), 8.74 (1H, d, 7), 8.22 (1H, t, α), 8.09 (1H, d, γ), 8.05 (1H, t, γ), 7.72 (1H, t, α) 7.25 (1H, d, α), 4.12 (1H, m, θ) 3.52 (1H, m, α) 3.09 (1H, t, α)
5	611.39	612.30	238.03	1.55	35%	12.41 (1H, s, β), 9.45 (1H, s, γ), 8.23 (1H, d, α), 8.08 (1H, d, γ), 7.78 (1H, d, α), 7.20 (1H, t, α), 4.22 (1H, m, θ), 2.39 (3H, s, α)
6	611.39	612.25	238.03	1.00	40%	12.43 (1H, s, β), 9.51 (1H, s, γ), 8.49 (1H, s, α), 8.23 (1H, d, α) 8.09 (1H, d, γ) 7.24 (1H, d, α), 4.25 (1H, m, θ), 2.19 (3H, s, α)
7	611.39	612.45	108.91	1.43	40%	12.21 (1H, s, β), 10.08(1H, s, γ), 8.50 (1H, s, α), 8.03 (1H, d, γ), 8.07 (1H, s, α), 7.87 (1H, s, α), 4.31 (1H, m, θ), 2.40 (3H, s, α)
8	611.39	612.25	237.99	1.38	35%	12.01 (1H, s, β), 10.03 (1H, s, γ), 8.57 (1H, s, α), 8.02 (1H, d, γ), 7.88 (1H, d, α), 7.16 (1H, d, α) 4.21 (1H, m, θ), 2.38 (3H, s, α)
9	611.39	612.30	108.97	1.98	32%	12.03 (1H, s, β), 10.24 (1H, s, γ), 8.26 (1H, d, α), 8.03 (1H, d, γ), 7.43 (1H, s, α), 7.34 (1H, d, α) 4.31

						(1H, m, θ) 2.39(3H, s, α)
10	625.41	626.81	234.04	1.46	35%	11.57 (1H, s, β) 10.31 (1H, s, γ), 7.89 (1H, d, γ), 7.75 (1H, s, α), 6.78 (1H, s, α), 4.27 (1H, m, θ) 2.32 (3H, s, α), 2.24 (3H, s, α)
11	715.46	716.54	NA	NA	NA	10.30 (1H, s, γ), 8.20 (1H, d, γ), 7.74 (1H, s, α), 7.35 (5H, s, β), 6.78 (1H, s, α), 5.09 (2H, s, β), 4.29 (1H, m, θ), 2.33 (3H, s, α), 2.24 (3H, s, α)
12	625.41	626.41	123.00	1.10	32%	11.48 (1H, s, β), 10.01 (1H, s, γ), 7.71 (1H, d, α), 7.43 (1H, d, γ), 7.01 (1H, d, α), 4.11 (H, m, θ), 2.35 (3H, s, α), 2.37 (3H, s, α)
13	715.46	716.57	NA	NA	NA	9.38 (1H, s, γ), 8.25 (1H, d, γ), 4.31 (1H, m, θ), 7.60 (1H, d, α), 7.35 (5H, s, β), 7.03 (1H, d, α), 5.12 (2H, s, β), 2.38 (3H, s, α), 2.31 (3H, s, α)
14	627.39	628.40	124.92	1.39	45%	12.40 (1H, s, β), 9.92 (1H, s, γ), 8.33 (1H, s, **7**), 8.04 (1H, d, γ), 7.87 (1H, d, α), 6.77 (1H, d, α), 4.19 (1H, m, θ), 3.80 (3H, s, α)
15	612.39	613.40	220.50	1.76	35%	12.56 (1H, s, β), 10.29 (1H, s, γ), 8.12 (1H, d, γ), 7.52 (1H, t, α), 7.31 (2H, s, α) 6.34 (1H, d, α), 5.93 (1H, d, α), 4.24 (1H, m, θ)
16	613.37	614.40	221.97	1.18	40%	12.59 (1H, s, β), 10.25 (1H, s, γ), 8.09 (1H, d, γ), 7.90 (1H, d, α), 7.30 (1H, d, α), 7.18 (1H, t, α) 5.47 (1H, s, α), 4.18 (1H, m, θ)
17	703.42	704.41	312.07	2.55	48%	10.20 (1H, s, γ), 8.25 (1H, d, γ), 7.88 (1H, d, α), 7.35 (5H, s, β), 7.27 (1H, d, α), 7.14 (1H, t, α), 5.11 (2H, s, β), 4.30 (1H, m, θ)
18	615.37	616.40	112.91	1.36	45%	12.50 (1H, s, β), 9.93 (1H, s, γ), 8.41 (1H, d, α), 8.06 (1H, d, γ), 7.92 (1H, d, α), 7.33 (1H, t, α), 4.19 (1H, m, θ)
19	615.37	616.41	112.98	1.52	40%	12.48 (1H, s, β), 10.70 (1H, s, γ), 8.58 (1H, s, α), 8.26 (1H, s, α), 8.13 (1H, d, γ), 8.08 (1H, s, α), 4.21 (1H, m, θ)

20	615.37	616.40	224.80	1.59	40%	12.57 (1H, s, β), 10.25 (1H, s, γ), 8.42 (1H, s, α), 8.17 (1H, d, α), 8.11 (1H, d, γ), 7.17 (1H, d, α), 4.34 (1H, m, θ)
21	675.29	676.3/678.30	599.40	4.73	45%	12.56 (1H, s, β), 10.35 (1H, s, γ), 9.35 (1H, s, α), 8.09 (1H, d, γ), 8.63 (1H, s, α), 8.36 (1H, s, α), 4.24 (1H, m, θ)
22	675.29	676.3/678.26	172.81	5.69	45%	12.54 (1H, s, β), 10.27 (1H, s, γ), 8.57 (1H, s, α), 8.09 (1H, d, γ), 7.96 (1H, d, α), 7.56 (1H, d, α), 4.23 (1H, m, θ)
23	631.34	632.30/634.30	540.16	4.87	40%	12.56 (1H, s, β), 10.29 (1H, s, γ), 8.58 (1H, s, α), 8.10 (1H, d, γ), 8.06 (1H, d, α), 7.45 (1H, d, α) 4.24 (1H, m, θ)
24	631.34	632.30/634.40	128.92	4.45	43%	12.51 (1H, s, β), 11.45 (1H, s, γ), 8.84 (1H, s, α), 8.68 (1H, d, α), 8.18 (1H, d, γ), 8.04 (1H, d, α), 4.22 (1H, m, θ)
25	612.38	613.40	221.12	2.72	35%	12.49 (1H, s, β), 9.76 (1H, s, γ), 8.06 (1H, s, γ), 7.66 (1H, d, α), 6.93 (1, t, α), 6.84 (1H, d, α), 6.75 (1H, t, α), 4.30 (1H, m, θ)
26	612.38	613.30	220.94	1.83	40%	12.58 (1H, s, β), 9.82 (1H, s, γ), 8.07 (1H, d, γ), 7.21 (1H, s, α), 7.08 (1H, t, α), 6.97 (1H, d, α), 6.46 (1H, d, α), 4.15 (1H, m, θ)
27	612.38	613.31	220.81	1.44	45%	12.53 (1H, s, β), 9.63 (1H, s, γ) 8.06 (1H, d, γ), 7.34 (2H, d, α), 6.68 (2H, d, α), 4.20 (1H, m, θ)

[a] Calculated monoisotopic mass.

[b] Q1 and Q3 mass are experimental mass $[M+H]^+$.

[c] The mobile phase was A, 0.1% formic acid in water; and B, 0.1% formic acid in acetonitrile. The gradient times were listed as percent organic phase, B%. 0–0.2 (X%), 0.2–3.0 (X–95%), 3.0–4.0 (95%), 4.0–4.2 (95-X%), and 4.2–7.0 min (X%)

[d] Only characteristic peaks are shown, CDCA region and methylene peaks are not shown; values are in ppm relative to TMS; β indicates assignment to proton peaks in R_1; α indicates assignment to protons in R_2; γ indicates assignment to protons in amide, θ indicates the proton in α carbon.

Table S2. 3D-QSAR models for inhibition and transport efficiency.

Comp.	Obs. pK_i[a]	Pre. pK_i		Obs. Log(J_{max}/K_t)[b]	Pre. Log(J_{max}/K_t)
		CoMFA-1	CoMSIA-3		CoMFA-2
1	5.28	5.26	5.29	0.790	0.794
2[c]	5.82	5.09	4.93	1.45	0.479
3	5.06	5.02	5.00	0.300	0.307
4	5.15	5.10	5.23	0.280	0.279
5	5.33	5.36	5.42	-0.150	-0.151
6	4.96	5.01	4.91	-0.410	-0.412
7	4.63	4.62	4.71	0.290	0.289
8	5.1	5.31	5.20	0.0800	0.0770
9	5.55	5.57	5.43	0.300	0.298
10	5.18	5.11	5.17	0.980	0.984
11	3.91	3.94	4.00	ND	ND
12	5.72	5.58	5.70	-0.260	-0.257
13	4.55	4.50	4.51	ND	ND
14	5.05	5.05	5.11	1.31	1.31
15	5.08	5.10	5.10	1.51	1.51
16	5.51	5.55	5.48	1.16	1.16
17	4.75	4.78	4.66	NM	NM
18[c]	5.24	5.09	5.11	3.43	0.783
19	5.16	5.09	5.00	0.920	0.925
20	5.24	5.09	5.12	0.420	0.418
21	5.3	5.09	5.36	0.310	0.308
22[c]	4.68	4.74	4.67	0.620	0.331
23	5.1	5.10	5.25	NM	NM
24	5.1	5.15	5.13	NM	NM
25[c]	5.45	5.27	5.47	1.42	0.649
26	5.61	5.65	5.66	1.15	1.15
27	5.14	5.20	5.12	0.460	0.457

[a] –log(K_i) calculated from observed K_i.

[b] Calculated from log($normJ_{max}/K_t \times 100$)

[c] **2**, **18**, **22**, and **25** were used as test set.

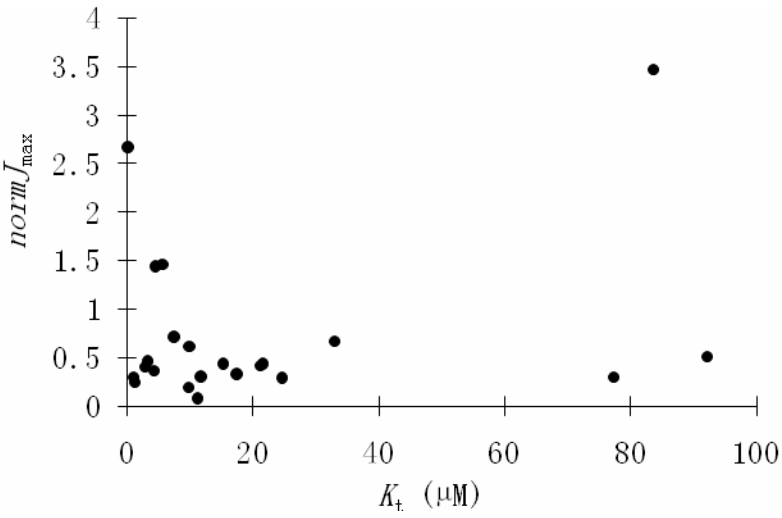


Figure S1. Relationship between $normJ_{max}$ and K_t. Transporting capacity was not associated with transporter affinity. Linear regression showed a slope of 0.008 μM^{-1} and r^2 of 0.064. **15**, **18**, **22**, and **25** yielded J_{max} higher than taurocholate. All other conjugates exhibited J_{max} less than taurocholate J_{max}, and ranged from 0.0791 to 0.716.

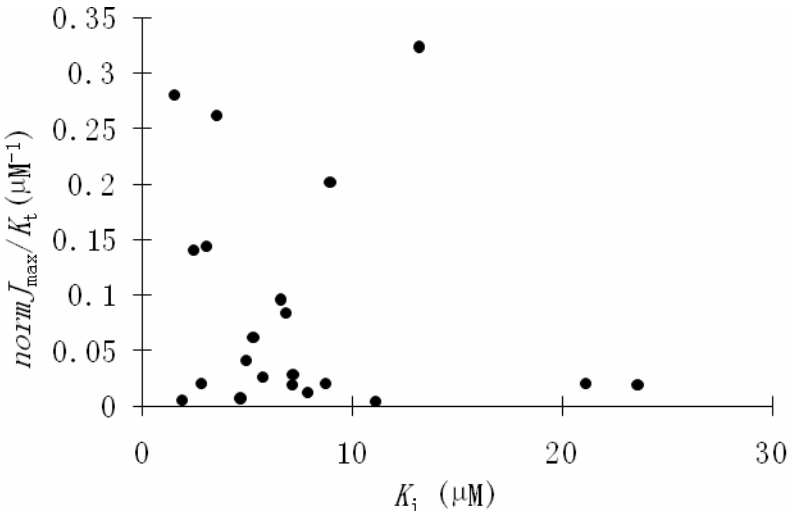


Figure S2. Relationship between $normJ_{max}/K_t$ and K_t. Linear regression showed a slope of -0.003 μM^{-2} and r^2 of 0.028. Transporting efficiency was not associated with inhibition potency. **18** was removed from the plot due to its high $normJ_{max}/K_t$ value of 26.7.

Active Accumulation of Gold Nanorods in Tumor in Response to Near-Infrared Laser Irradiation

Atsushi Shiotani,[†] Yasuyuki Akiyama,[†] Takahito Kawano,[†] Yasuro Niidome,[†] Takeshi Mori,[†,‡] Yoshiki Katayama,[†,‡] and Takuro Niidome*[,†,‡,§]

Department of Applied Chemistry, Faculty of Engineering, and Center for Future Chemistry, Kyushu University, 744 Motooka, Nishi-ku, Fukuoka 819-0395, Japan, and PRESTO, Japan Science and Technology Corporation, Kawaguchi 332-0012, Japan.
Received June 25, 2010; Revised Manuscript Received September 21, 2010

Gold nanorods, rod-shaped gold nanoparticles, have strong absorbance in the near-infrared region, and the absorbed light energy can be converted to heat, the so-called photothermal effect. The gold nanorods were coated with thermoresponsive polymers, which have different phase transition temperatures that were controlled by adding comonomers, *N*,*N*-dimethylacrylamide (DMAA) or acrylamide (AAm) to *N*-isopropylacrylamide (NIPAM). The phase transition temperatures of poly(NIPAM-DMAA) and poly(NIPAM-AAm)-coated gold nanorods were 38 and 41 °C, respectively, while polyNIPAM-coated gold nanorods showed phase transition at 34 °C. Irradiation of the coated gold nanorods using the near-infrared laser induced a decrease in their sizes due to a phase transition of the polymer layers. Poly(NIPAM-AAm)-coated gold nanorods stably circulated in the blood flow without a phase transition after intravenous injection. Irradiation of near-infrared light at a tumor after the injection resulted in the gold specifically accumulating in the tumor. This novel accumulation technique which combines a thermoresponsive polymer and the photothermal effect of the gold nanorods should be a powerful tool for targeted delivery in response to light irradiation.

INTRODUCTION

Gold nanorods, rod-like shaped gold nanoparticles, have attracted increasing attention in recent years. Gold nanorods show unique optical properties, including two absorption bands corresponding to the transverse and longitudinal surface plasmon oscillations of free electrons in the visible (∼520 nm) and near-infrared (∼900 nm) regions, respectively (*1, 2*). Furthermore, absorbed light energy is converted efficiently into heat via the so-called photothermal effect (*3*). Since near-infrared light is ideally suited for in vivo imaging and laser therapy due to its high tissue penetration (*4*), gold nanorods are expected to act both as contrast agents for bioimaging and as thermal converters for photothermal therapy (*5, 6*).

Thermoresponsive polymers such as *N*-isopropylacrylamide (NIPAM) show a discontinuous volume phase transition, and their hydrophobicity changes in response to temperature increases (*7, 8*). These properties have been applied in the design of controlled drug release systems (*9*−*11*). Raucher et al. reported that the resulting hydrophobicity induced the uptake of the polymers to tumor cells in vitro (*12*). After intravenous injection of the polymers into tumor-bearing mice, they were accumulated in the tumor where it was locally heated (*13*). If thermoresponsive polymers can be conjugated to gold nanorods, the photothermal effect of gold nanorods actuated by irradiating the near-infrared light can induce the phase transition of the polymers. Gorelikov et al. prepared submicrometer-sized spheres of poly(NIPAM-*co*-acrylic acid) gels containing gold nanorods stabilized by cationic surfactant (*14*). Volume phase transition in response to near-infrared laser light was observed. Wei et al. prepared poly(NIPAM) (PNIPAM)-modified gold nanorods by surface-initiated atom transfer radical polymerization (*15*). They loaded norvancomycin, a widely used glycopeptide antibiotic against methicillin-resistant *Staphylococcus aureus*, into the PNIPAM layer on the gold nanorod. The PNIPAM layer retained the norvancomycin, and near-infrared laser irradiation enhanced its release, which was monitored by absorption at 260 nm.

Recently, our group succeeded in coating a PNIPAM gel on the surface of the gold nanorods, named PNIPAM-coated gold nanorods (*16*). They showed reversible shrinking of the gel layer triggered by near-infrared laser irradiation. The core−shell structure of PNIPAM-coated gold nanorods was prepared by colloid-template polymerization. After intravenous injection of PNIPAM-coated gold nanorods into mice, near-infrared laser light was irradiated to the right kidney for 10 min. At 30 min after the injection, significant accumulation of the gold nanorods was observed in the irradiated kidney. Thus, active accumulation mediated by the photothermal effect of the gold nanorods was confirmed. However, larger amounts of the injected gold nanorods were detected in the lungs in addition to the irradiated kidney (*16*). This is likely due to the phase transition of the PNIPAM layer which typically occurs at about 34 °C, which is lower than the body temperature of mice (37 °C). Therefore, after the injection, the hydrophobicity of the PNIPAM layer increased, and then, the gold nanorods were trapped in the capillary vessels in the lungs.

To maintain the stability of the gold nanorods in the circulating blood and demonstrate phase transition above the body temperature of the mice, the phase transition temperature should be adjusted to include a relevant range between 37 °C to represent a typical body temperature and 43 °C to account for a situation where the tissue is thermally damaged. Some research groups have succeeded in controlling the phase transition temperature of PNIPAM by adding a hydrophilic monomer such as *N*,*N*-dimethylacrylamide (DMAA) (*17*) or acrylamide (AAm) (*18*). Resultant copolymers, P(NIPAM-DMAA) and P(NIPAM-AAm), showed higher phase transition temperatures than the PNIPAM, because the hydrophilic units impede aggregation of NIPAM units in the polymer. In this

* To whom correspondence should be addressed. Phone and Fax: +81-92-802-2851. E-mail: niidome.takuro.655@m.kyushu-u.ac.jp.
[†] Faculty of Engineering, Kyushu University.
[‡] Center for Future Chemistry, Kyushu University.
[§] Japan Science and Technology Corporation.

10.1021/bc100284s © 2010 American Chemical Society
Published on Web 10/06/2010

study, we prepared thermoresponsive polymer-coated gold nanorods that show phase transition at temperatures above the normal body temperature of mice. Active accumulation of the gold nanorods to the tumor site triggered by the near-infrared laser irradiation was observed.

EXPERIMENTAL PROCEDURES

Materials. Gold nanorods were supplied by Mitsubishi Materials Corp. (Tokyo, Japan) and Dai Nippon Toryo Co. Ltd. (Osaka, Japan). The gold nanorods dispersed by cetyltrimethylammonium bromide (CTAB) were prepared by our previous methods (*19*). The average length and width of the as-supplied gold nanorods were 48.8 ± 7.9 nm and 9.0 ± 1.2 nm, respectively (aspect ratio: 5.4). Thiol-terminated poly(ethylene glycol) (PEG) (MW ca. 20 000 Da) was purchased from NOF Co., Ltd. (Tokyo, Japan). Tetraethyl orthosilicate (TEOS) was purchased from Tokyo Chemical Industry Co., Ltd. (Tokyo, Japan). 3-(Methacryloxy) propyl triethoxysilane (MPS) was purchased from Gelest, Inc. (Morisville, PA, USA). *N*-Isopropylacrylamide (NIPAM), *N*,*N*-dimethylacrylamide (DMAA), sodium dodecyl sulfate (SDS), 25% ammonia solution, and ethanol (99.5%) were purchased from Wako Pure Chemical Industries, Ltd. (Osaka, Japan). Acrylamide (AAm) and *N*,*N*′-methylenebisacrylamide (MBA) were purchased from Nacalai Tesque, Inc. (Kyoto, Japan). Potassium persulfate (KPS) was purchased from Sigma-Aldrich, Inc. (Missouri, USA). Phosphotungstic acid was purchased from TAAB Laboratories Equipment Ltd. (Berkshire, UK).

Preparation of Silica-Coated Gold Nanorods. PEG-modified gold nanorods were prepared by a method previously reported (*20*). A solution of gold nanorods containing CTAB was centrifuged at 14 000 × *g* for 10 min, decanted, and resuspended in distilled water to remove excess CTAB. A total of 10 mL of a solution of 1 mM gold nanorods (concentration of gold atom) was added to 2 mL of 1 mM thiol-terminated PEG (MW ca. 20 000 Da). The mixture was stirred overnight at room temperature and was dialyzed. PEG-modified gold nanorods were coated with a silica layer using the modified Stöber method, which is based on the hydrolysis of TEOS in ethanol/water mixture in the presence of gold nanorods, which act as seeds (*21, 22*). A solution of the prepared PEG-modified gold nanorods was concentrated by centrifugation. A total of 1 mL of a solution of 10 mM PEG-modified gold nanorods (as gold atoms) was diluted with 7.8 mL of ethanol. The mixture was added to 200 μL of 5% ammonia solution, and 1 mL of 50 mM TEOS was added. The reaction was allowed to proceed for 24 h at room temperature. The reaction mixture was added to 1 mL of 100 mM MPS to graft methacryl groups on the surface. The mixture was stirred for 24 h and dialyzed against ethanol/water solution (9/1) to remove excess MPS.

Preparation of Thermoresponsive Polymer-Coated Gold Nanorods. Thermoresponsive polymer-coated gold nanorods were prepared by following our previous report (*16*). All thermoresponsive polymer-coated gold nanorods were prepared by free radical precipitation polymerization. The resulting solution of the silica-coated gold nanorods grafted with MPS was centrifuged and resuspended in water. In the polymerization procedure, silica-coated gold nanorods grafted with MPS were used as seeds for the precipitation polymerization of NIPAM, 16 mol % of either comonomer (DMAA and AAm), and MBA using SDS as a stabilizer and KPS as an initiator. The mixture was bubbled through nitrogen for 10 min to remove residual oxygen. The reaction was allowed to proceed for 4 h at 70 °C. Then, the reaction mixture was dialyzed to remove the remaining monomers and initiator.

Characterization and Measurements. Absorption spectra of gold nanorods from the visible to near-infrared light region were measured with a spectrophotometer, Jasco V-670 (Tokyo, Japan). Morphologies of gold nanorods were observed with a transmission electron microscope (TEM) JEOL JEM-2010 (Tokyo, Japan) after staining with 1% phosphotungstic acid. Sizes of thermoresponsive polymer-coated gold nanorods in water were evaluated by the dynamic light scattering analysis with the Malvern Zetasizer Nano ZS (Worcestershire, UK). *Z*-average was used as an average diameter. Thermoresponsive polymer-coated gold nanorod solutions were diluted to 0.6 μg/mL (as gold weight) to avoid aggregate formation of the particles, and temperature of the sample was increased in a stepwise manner by 2 °C from 20 to 60 °C. After increasing the temperature by 2 °C, the sample was allowed to equilibrate at temperature for 5 min before data collection of scattered light from a He−Ne laser (633 nm). Photothermally driven size change of thermoresponsive polymer-coated gold nanorods was also measured with the Zetasizer Nano ZS. The thermoresponsive polymer-coated gold nanorod solutions (6 μg/mL (as gold weight; it is still enough to avoid aggregate formation), 700 μL) were irradiated using a near-infrared continuous-wave diode laser of wavelength at 807 nm (2.5 W/cm^2) (Alfalight Corporation, Madison, WI, USA). The laser was irradiated from the top of the solution in a cuvette for the dynamic light scattering analysis. The laser was turned off during the measurements because the effects of scattered light produced by the laser disturbed the measurements.

Animals. Male ddY mice (Kyudo Co., Ltd., Saga, Japan) were used in all experiments. Five-week old mice were maintained in a temperature controlled environment at 24 °C with a 12 h light/dark cycle and were provided with drinking water and food ad libitum. Animal experiments were performed according to the Guidelines for Animal Care and Use Committee, Kyushu University.

Implantation of Tumor Cells into Mice. Mouse rectum carcinoma colon-26 cells were cultured in RPMI-1640 containing 10% fetal bovine serum and 60 μg/mL kanamycin sulfate. The dishes containing cells were maintained at 37 °C in an incubator under a 5% CO_2 atmosphere. Tumor-bearing mice were prepared as follows. Colon-26 cells were injected subcutaneously into the right and left sides of the abdomen of a mouse (ddY, male, 5 weeks, 23−26 g) at a dose of 1 × 10^6 cells in 100 μL Hank's balanced salt solution per injection, then allowed to grow for 5 days, after which time the tumors had reached a size of 5−10 mm in diameter.

Biodistribution of P(NIPAM-AAm)-Coated Gold Nanorods in Mice. Normal mice and mice having two tumors at the right and left sides of the abdomen were anesthetized, then P(NIPAM-AAm)-coated gold nanorods (120 μg/mL (as gold weight), 10 μL/g of mice weight) were injected intravenously into the mice. In the case of the tumor-bearing mice, at 1 min after the injection, a near-infrared laser light (wavelength, 807 nm; power, 3.8 W/cm^2) irradiated the right tumor for 10 min. Mice were sacrificed at 30 min and 72 h after injection. Blood and major organs (liver, lung, spleen, kidney, and tumor) were collected. The samples were added to approximately 4 mL aqua regia and then heated overnight at 95 °C. The organic compounds were completely oxidized, and the gold was ionized. Finally, the samples were condensed to less than 0.5 mL by further heating at 120 °C for 2 h. The residues were diluted to 10 mL of 0.5 M HCl and sonicated for 10 min. Quantitative analysis of gold was performed by inductively coupled plasma mass spectrometry (ICP-MS) using the Agilent 7500c model ICP-MS (Agilent, CA, USA).

RESULTS AND DISCUSSION

Preparation of Thermosensitive Polymer-Coated Gold Nanorods. First, the gold nanorods stabilized by CTAB as shown in Figure 1A were modified with PEG, and then, the

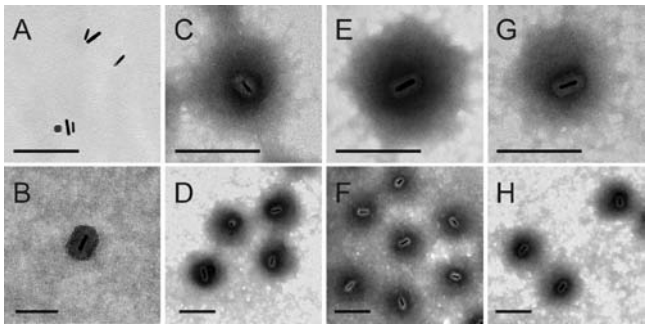


Figure 1. TEM images of gold nanorods. (A) Gold nanorods dispersed by CTAB. (B) Silica-coated gold nanorods grafted with MPS. (C,D) PNIPAM-coated gold nanorods. (E,F) P(NIPAM-DMAA)-coated gold nanorods. (G,H) P(NIPAM-AAm)-coated gold nanorods. Scale bars indicate 200 nm.

Table 1. Composition of Reaction Mixtures to Prepare Thermoresponsive Polymer-Coated Gold Nanorods, Which Have Different Phase Transition Temperatures

coated polymer	NIPAM (mM)	DMAA (mM)	AAm (mM)	MBA (mM)	SDS (mM)	KPS (mM)
PNIPAM	50			5	1	1
P(NIPAM-DMAA)	41	9		5	1	1
P(NIPAM-AAm)	41		9	5	1	1

PEG-modified gold nanorods were coated with a silica layer using a modified Stöber method. Thickness of the resultant silica layer on the gold nanorods was 50−60 nm. This corresponded to that of the PEG layer of the original PEG-modified gold nanorods (Figure 1B). After coating with silica shells, the gold nanorods were dispersed without forming aggregates in a solution of 90% ethanol in water and were used in the following step. The silane-coupling agent MPS was used to modify the surface of the silica-coated gold nanorods with methacryl groups. Silica-coated gold nanorods grafted with MPS were modified with thermoresponsive polymers which have different phase transition temperatures. To alter the phase transition temperature of the PNIPAM, a hydrophilic monomer, 16 mol % of DMAA or AAm, was added to reaction mixtures of NIPAM polymerization as shown in Table 1. Figure 1C−H shows TEM images of the polymer-coated gold nanorods. The single core of a silica-coated gold nanorod modified with a single shell of the thermoresponsive polymer was observed in each case. There was no difference in the morphology among these variations, PNIPAM-coated gold nanorods (Figure 1C,D), P(NIPAM-DMAA)-coated gold nanorods (Figure 1E,F), and P(NIPAM-AAm)-coated gold nanorods (Figure 1G,H). After modifying the gold surface with the silica layer, a slight red shift of the absorption in the near-infrared light region (∼900 nm) was observed (Figure 2). Modifications with the thermoresponsive polymers caused a blue shift of the absorption. This is likely due to changes in the local refractive index around the gold nanorods produced by the silica shells and the thermoresponsive polymer layers (*23*). The increase of absorption in the visible region (∼500 nm) would be due to light scattering of the polymer layers.

Temperature-Induced Size Change of the Thermoresponsive Polymer-Coated Gold Nanorods. Size changes in the thermoresponsive polymer-coated gold nanorods induced by increasing their temperatures were measured by dynamic light scattering (DLS) (Figure 3). To avoid aggregation, experiments were performed at a low concentration (0.6 μg/mL of gold weight) of the gold nanorods. All thermoresponsive polymers showed discontinuous phase transition behavior. The volume phase transition of PNIPAM-coated gold nanorods occurred at about 34 °C, in agreement with a previous study (*16*). The phase transition temperatures of copolymerized thermoresponsive

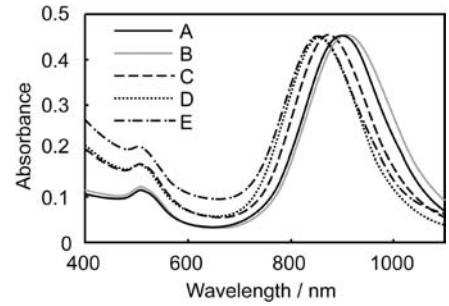


Figure 2. Absorption spectra of gold nanorods. (A) Gold nanorods dispersed by CTAB. (B) Silica-coated gold nanorods grafted with MPS. (C) P(NIPAM-AAm)-coated gold nanorods. (D) P(NIPAM-DMAA)-coated gold nanorods. (E) PNIPAM-coated gold nanorods.

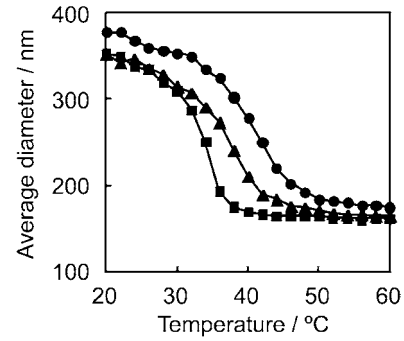


Figure 3. Temperature dependence of hydrodynamic diameters of thermoresponsive polymer-coated gold nanorods. Squares: PNIPAM-coated gold nanorods. Triangles: P(NIPAM-DMAA)-coated gold nanorods. Circles: P(NIPAM-AAm)-coated gold nanorods.

polymers, P(NIPAM-DMAA) and P(NIPAM-AAm)-coated gold nanorods, were about 38 and 41 °C, respectively. P(NIPAM-DMAA) and P(NIPAM-AAm)-coated gold nanorods showed slightly broader phase transition curves than PNIPAM-coated gold nanorods. Interruption of PNIPAM chain segments by other monomers would cause broadening of the phase transition of the polymers (*24*). Considering that the phase transition temperature is lowered by about 2.5 °C in the blood, i.e., physiological conditions (osmotic pressure maintained by ionic concentration equivalent to 150 mM NaCl) (*25*), P(NIPAM-AAm)-coated gold nanorods are expected to show phase transition at the desired range 38−42 °C in blood after intravenous injection.

Laser Irradiation-Induced Change in Size of the Thermoresponsive Polymer-Coated Gold Nanorods. We examined the phase transition behavior of the thermoresponsive polymer-coated gold nanorods by irradiation using a focused near-infrared laser at a wavelength of 807 nm (Figure 4). The PNIPAM-coated gold nanorods shrank from ∼330 to ∼130 nm after laser irradiation (2.5 W/cm^2) for 10 min, corresponding to a ∼95% decrease in the total volume of the coated gold nanorods. P(NIPAM-DMAA)-coated gold nanorods shrank from ∼330 to ∼170 nm, corresponding to a ∼86% decrease in the volume. P(NIPAM-AAm)-coated gold nanorods shrank from ∼350 to ∼230 nm, corresponding to a ∼70% decrease in the volume, which was lower than P(NIPAM-DMAA)- and PNIPAM-coated gold nanorods. The sizes of the polymer-coated gold nanorods after the light irradiation corresponded to those at about 44 °C as shown in Figure 3 indicating that temperatures of the samples were increased to about 44 °C after the laser irradiation for 10 min. Actually, the temperature of the samples after light irradiation for 10 min was between 45 and 47 °C (data not shown). If thermal damage of tissue is desired, as in the case of hyperthermia, the temperature increase is sufficient. A cycle of shrinkage and swelling

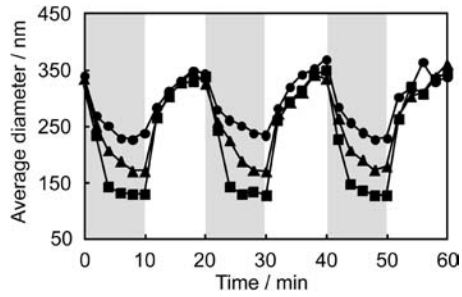


Figure 4. Changes in hydrodynamic diameters of thermoresponsive polymer-coated gold nanorods upon irradiation using a near-infrared laser. Squares: PNIPAM-coated gold nanorods. Triangles: P(NIPAM-DMAA)-coated gold nanorods. Circles: P(NIPAM-AAm)-coated gold nanorods. Periods of laser irradiation are indicated by the gray area.

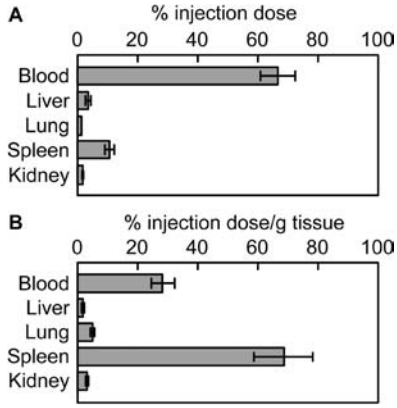


Figure 5. Biodistribution of P(NIPAM-AAm)-coated gold nanorods at 30 min after intravenous injection to mice. Amounts of gold in blood and tissues were evaluated by ICP-MS. Panels A and B indicate % injected dose and % injected dose per gram of tissue, respectively. Data represent mean values for $n = 3$ and bars are standard errors of the mean.

induced by switching the laser on and off could be repeated. This result indicated that the optical property of the gold nanorods and characters of the thermoresponsive polymer layers were not affected by the laser irradiation.

Biodistribution of P(NIPAM-AAm)-Coated Gold Nanorods. Since P(NIPAM-AAm)-coated gold nanorods are expected to maintain the hydrophilic surface at the body temperature of a mouse (37 °C) and undergo phase transition after laser irradiation in the temperature range 38−42 °C, P(NIPAM-AAm)-coated gold nanorods were employed for examination of biodistribution after intravenous injection. P(NIPAM-AAm)-coated gold nanorods were systemically injected into normal mice, and then blood and major organs were collected at 30 min after the injection. The amount of the gold (% injected dose) in the organs was evaluated by inductively coupled plasma mass spectrometry (ICP-MS) (Figure 5A). A total of 66% of the injected dose of gold was found in the blood. As we already reported in the previous paper (*16*), in the case of PNIPAM-coated gold nanorods, about 1% of the injected dose of gold was detected in the blood at 30 min, and about 45% of the injected dose of gold was found in the lung. It was believed that phase transition of the PNIPAM layer on the gold nanorods was induced by the body temperature after the injection and then the surface hydrophobicity caused aggregation of the gold nanorods. Finally, the gold nanorods became trapped in the capillary vessels in the lungs and/or interacted with the cellular surface through hydrophobic interactions. In contrast, P(NIPAM-AAm)-coated gold nanorods that have a higher phase transition temperature than the body temperature showed stable circulation in the blood flow at least 30 min after the intravenous injection. The amount of the gold per gram of tissue was calculated from

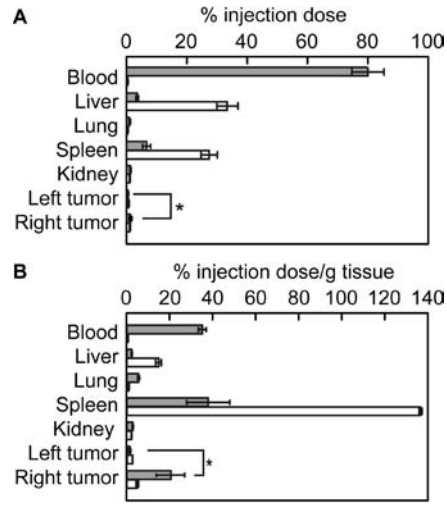


Figure 6. Biodistribution of P(NIPAM-AAm)-coated gold nanorods at 30 min (gray bars) and 72 h (open bars) after intravenous injection to mice that have two tumors at their abdomen. A near-infrared laser light at a power density of 3.8 W/cm^2 was applied to tumor for 10 min after the injection. Amounts of gold in blood and tissues were evaluated by ICP-MS. Panels A and B indicate % injected dose and % injected dose per gram of tissue, respectively. Data represent mean values for $n = 3$ and bars are standard errors of the mean. $^*P < 0.05$.

the data shown in Figure 5A (Figure 5B). The highest accumulation of the gold nanorods was found in the spleen, likely because nanoparticles larger than 200 nm like the P(NIPAM-AAm)-coated gold nanorods are known to be trapped by splenic physical filtration (*26*−*28*). Very small amounts of gold were observed in other organs.

Next, we examined the active accumulation of P(NIPAM-AAm)-coated gold nanorods in a tumor irradiated by the near-infrared laser light in vivo. P(NIPAM-AAm)-coated gold nanorods were intravenously injected into mice that have two tumors at the abdomen. The right tumor was irradiated using the near-infrared laser (807 nm, 3.8 W/cm^2) for 10 at 1 min after the injection. Organs were collected at 30 min and 72 h after the injection, and the amounts of the gold nanorods (% injected dose) in the organs were evaluated by ICP-MS (Figure 6A). A total of 80% of the injected dose of gold was found in the blood at 30 min. In the case of the normal mice without laser irradiation, 66% of the gold was observed (Figure 5A). Although existence of the tumor may affect the biodistribution of the gold nanorods in mice, the volumes of the tumors used in this study would be too small (less than 1% of body weight) to affect it. Furthermore, it is also supposed that the laser power used (807 nm, 3.8 W/cm^2, 10 min) would not affect the blood circulation of the mice. Therefore, this inconsistency would be due to experimental error. In the irradiated right tumor, a significantly larger amount of the gold (1.1 ± 0.4%) was detected compared with the left tumor (0.06 ± 0.03%), although the absolute amount of gold was lower than that of the spleen (6.5 ± 1.3%). At 72 h, a small amount of gold was observed in the blood, while most of the gold accumulated in the liver and the spleen. In the left tumor, the amount of gold was increased to 0.42 ± 0.05%. This may be due to the EPR effect; however, the absolute amount of the gold was extremely low. In the irradiated right tumor, 0.88 ± 0.09% of gold was detected. This was not significantly different from the accumulation at 30 min (1.1 ± 0.4%), indicating that most of the gold was retained in the right tumor for 72 h.

The calculation of the amount of gold per gram of tissue (Figure 6B) indicates a clear difference in the accumulations between the right and left tumors at 30 min, and the accumulation in the right tumor (20%/g tissue) was higher than the case

of the PEG-modified gold nanorods accumulating in the tumor by EPR effect (15%/g tissue), which was enough to show photothermal tumor damage (*29*). On the other hand, the accumulation in the right tumor was comparable to that in the blood and the spleen. As described previously, the mechanism of the accumulation is believed to involve the hydrophobic surface of the P(NIPAM-AAm)-coated gold nanorods after the phase transition induced by the photothermal effect of the gold nanorods triggered aggregate formation at the light irradiated site. For example, in the case of the right tumor, the gold nanorods became trapped in the capillary vessels in the tumor and/or interacted with the cellular surface and the extracellular matrix through the hydrophobic interactions. At 72 h, the amount of the gold per gram of tissue in the right tumor was lower than that at 30 min. The reason the value was decreased is that the tumor had grown for 72 h without a decrease in the absolute amount of gold in the tumor.

Although further optimization of several factor, e.g., inject does of the polymer-coated gold nanorods, condition of the laser irradiation, and further surface modification to improve the accumulation in the tumor, are required, this novel accumulation technique which combines a thermoresponsive polymer and the photothermal effect of the gold nanorods will be a powerful tool for targeting the gold nanorods for purposes of photothermal therapy. As well, this technique may be useful for targeted delivery and controlled release of drugs at the site of light irradiation if drugs can be successfully encapsulated in the polymer layer as previously reported by Wei et al. (*15*).

CONCLUSION

Thermoresponsive polymer-coated gold nanorods with different phase transition temperatures were prepared by adding comonomers, DMAA and AAm, to the polymerization of NIPAM. P(NIPAM-AAm)-coated gold nanorods underwent phase transition at temperatures above the normal body temperature of mice. Active accumulation of the gold nanorods in the tumor in response to the near-infrared light irradiation was demonstrated in tumor-bearing mice after intravenous injection. This combination of a thermoresponsive polymer and the photothermal effect of the gold nanorods should provide clues for the development of novel therapeutic techniques controlled by light.

ACKNOWLEDGMENT

This research was supported by the Precursory Research for Embryonic Science and Technology (PRESTO) from the Japan Science and Technology Agency, a Grant-in-aid for Scientific Research (B) (No. 19300172) from the Japan Society for the Promotion of Science (JSPS), and JSPS Research Fellowships for Young Scientists.

LITERATURE CITED

(1) Yu, Y. Y., Chang, S. S., Lee, C. L., and Wang, C. R. C. (1997) Gold nanorods: electrochemical synthesis and optical properties. *J. Phys. Chem. B 101*, 6661–6664.

(2) Link, S., Mohamed, M. B., and El-Sayed, M. A. (1999) Simulation of the optical absorption spectra of gold nanorods as a function of their aspect ratio and the effect of the medium dielectric constant. *J. Phys. Chem. B 103*, 3073–3077.

(3) Chou, C. H., Chen, C. D., and Wang, C. R. C. (2005) Highly efficient, wavelength-tunable, gold nanoparticle based optothermal nanoconvertors. *J. Phys. Chem. B 109*, 11135–11138.

(4) Weissleder, R. (2001) A clearer vision for *in vivo* imaging. *Nat. Biotechnol. 19*, 316–317.

(5) Niidome, T., Akiyama, Y., Shimoda, K., Kawano, T., Mori, T., Katayama, Y., and Niidome, Y. (2008) In vivo monitoring of intravenous injected gold nanorods using near-infrared light. *Small 4*, 1001–1007.

(6) Dickerson, E. B., Dreaden, E. C., Huang, X., El-Sayed, I. H., Chu, H., Pushpanketh, S., McDonald, J. F., and El-Sayed, M. A. (2008) Gold nanorod assisted near-infrared plasmonic photothermal therapy (PPTT) of squamous cell carcinoma in mice. *Cancer Lett. 269*, 57–66.

(7) Hirotsu, S., Hirokawa, Y., and Tanaka, T. (1987) Volume-phase transitions of ionized *N*-isopropylacrylamide gels. *J. Chem. Phys. 87*, 1392–1395.

(8) Schild, H. G. (1992) Poly(*N*-isopropylacrylamide): experiment, theory and application. *Prog. Polym. Sci. 17*, 163–249.

(9) Wei, H., Zhang, X. Z., Zhou, Y., Cheng, S. X., and Zhuo, R. X. (2006) Self-assembled thermoresponsive micelles of poly(*N*-isopropylacrylamide-*b*-methyl methacrylate). *Biomaterials 27*, 2028–2034.

(10) Huang, X., and Lowe, T. L. (2005) Biodegradable thermoresponsive hydrogels for aqueous encapsulation and controlled release of hydrophilic model drugs. *Biomacromolecules 6*, 2131–2139.

(11) Huang, G., Gao, J., Hu, Z., John, J. V., St onder, B. C., and Moro, D. (2004) Controlled drug release from hydrogel nanoparticle networks. *J. Controlled Release 94*, 303–311.

(12) Raucher, D., and Chilkoti, A. (2001) Enhanced uptake of a thermally responsive polypeptide by tumor cells in response to its hyperthermia-mediated phase transition. *Cancer Res. 61*, 7163–7170.

(13) Dreher, M. R., Liu, W., Michelich, C. R., Dewhirst, M. W., and Chilkoti, A. (2007) Thermal cycling enhances the accumulation of a temperature-sensitive biopolymer in solid tumors. *Cancer Res. 67*, 4418–4424.

(14) Gorelikov, I., Field, L. M., and Kumacheva, E. (2004) Hybrid microgels photoresponsive in the near-infrared spectral range. *J. Am. Chem. Soc. 126*, 15938–15939.

(15) Wei, Q., Ji, J., and Shen, J. (2008) Synthesis of near-infrared responsive gold nanorod/PNIPAAm core/shell nanohybrids via surface initiated ATRP for smart drug delivery. *Macromol. Rapid Commun. 29*, 645–650.

(16) Kawano, T., Niidome, Y., Mori, T., Katayama, Y., and Niidome, T. (2009) PNIPAM gel-coated gold nanorods for targeted delivery responding to a near-infrared laser. *Bioconjugate Chem. 20*, 209–212.

(17) Kohori, F., Sakai, K., Aoyagi, T., Yokoyama, M., Yamato, M., Sakurai, Y., and Okano, T. (1999) Control of adriamycin cytotoxic activity using thermally responsive polymeric micelles composed of poly(*N*-isopropylacrylamide-*co*-*N*, *N*-dimethylacrylamide)- b-poly(D, L-lactide). *Colloids Surf., B 16*, 195–205.

(18) Mayer, D. E., Shin, B. C., Kong, G. A., Dewhirst, M. W., and Chilkoti, A. (2001) Drug targeting using thermally responsive polymers and local hyperthermia. *J. Controlled Release 74*, 213–224.

(19) Niidome, Y., Nishioka, K., Kawasaki, H., and Yamada, S. (2003) Rapid synthesis of gold nanorods by combination of chemical reduction and photoirradiation processes; morphological changes depending on the growing processed. *Chem. Commun. 18*, 2376–2377.

(20) Niidome, T., Yamagata, M., Okamoto, Y., Akiyama, Y., Takahashi, H., Kawano, T., Katayama, Y., and Niidome, Y. (2006) PEG-modified gold nanorods with a stealth character for in vivo applications. *J. Controlled Release 114*, 343–347.

(21) Pastoriza-Santos, I., Pérez-Juste, J., and Liz-Marzán, L. M. (2006) Silica-coating and hydrophobation of CTAB-stabilized gold nanorods. *Chem. Mater. 18*, 2465–2467.

(22) Stöber, W., Fink, A., and Bohn, E. J. (1968) Controlled growth of monodisperse silica spheres in the micron size range. *Colloid Interface Sci. 26*, 62–69.

(23) Liz-Marzán, L. M., Giersig, M., and Mulvaney, P. (1996) Synthesis of nanosized gold-silica core-shell particles. *Langmuir 12*, 4329–4335.

(24) Das, M., Sanson, N., Fava, D., and Kumacheva, E. (2007) Microgels loaded with gold nanorods: photothermally triggered volume transitions under physiological conditions. *Langmuir 23*, 196–201.

(25) Freitag, R., and Garret-Flaudy, F. (2002) Salt effects on the thermoprecipitation of poly-(*N*-isopropylacrylamide) oligomers from aqueous solution. *Langmuir 18*, 3434–3440.

(26) Moghimi, S. M., Hunter, A. C., and Murray, J. C. (2001) Long-circulation and target-specific nanoparticles: theory to practice. *Pharmacol. Rev. 53*, 283–318.

(27) Moghimi, S. M., Porter, C. J. H., Muir, I. S., Illum, L., and Davis, S. S. (1991) Non-phagocytic uptake of intravenously injected microspheres in rat spleen: influence of particle size and hydrophilic coating. *Biochem. Biophys. Res. Commun. 177*, 861–866.

(28) Chen, L. T., and Weiss, L. (1973) The role of the sinus wall in the passage of erythrocytes through the spleen. *Blood 41*, 529–537.

(29) Niidome, T., Akiyama, Y., Yamagata, M., Kawano, T., Mori, T., Niidome, Y., and Katayama, Y. (2009) Poly(ethylene glycol)-modified gold nanorods as a photothermal nano-device for hyperthermia. *J. Mater. Sci. Polym. Ed. 20*, 1203–1215.

BC100284S

Synthesis, Characterization, and Thermodynamic Study of a Polyvalent Lytic Peptide−Polymer Conjugate As Novel Anticancer Agent

Jieying Zhong[†] and Ying Chau*[,‡]

Bioengineering Graduate Program and Department of Chemical and Biomolecular Engineering, The Hong Kong University of Science and Technology. Received June 25, 2010; Revised Manuscript Received September 27, 2010

We designed and synthesized a new polyvalent lytic peptide−polymer conjugate as a novel chemotherapeutic agent capable of overcoming multidrug resistance. A hexapeptide (KWKWKW or $(KW)_3$) was designed and conjugated to dextran in multiple copies to afford a polyvalent conjugate. A robust synthesis procedure involving click chemistry and the detailed characterization of the conjugate were reported here. The conjugate Dex-$(KW)_3$ exhibited significantly enhanced anticancer potency in vitro by up to 500-fold compared to monomeric $(KW)_3$. The LC_{50} value was comparable to that of conventional lytic peptides which have more than 20 residues. No hemolytic activity was shown by the conjugates up to 300 μM. Thermodynamic study indicated that the binding of conjugates was predominantly entropy-driven while the binding of free peptides was mainly enthalpy-driven, implying a deeper penetration of conjugate into the core of lipid bilayer. The binding affinity of conjugate to neutral membrane is much higher than that to free peptide ($K_{conj} \approx 8822.9\ M^{-1}$, $K_{pep} \approx 1884.7\ M^{-1}$). In binding to negatively charged membrane, the conjugate surpassed free peptides at high concentrations when the binding of free peptides became saturated. The higher binding capability, attributed to the high local concentration of peptides mounted on a polymer backbone, explains the superior anticancer activity of polyvalent Dex-$(KW)_3$.

INTRODUCTION

For cancers that are homological or metastatic, chemotherapy is almost the only choice of treatment. However, multidrug resistance remains an impediment to successful chemotherapy (*1*). Resistant cancer cells can diminish or even neutralize the therapeutic effect by increasing the efflux and/or reducing the uptake of drug, thus greatly impair the effectiveness of conventional chemotherapeutics. This problem brings a strong demand for novel chemotherapeutics. In antibiotic research, another field also facing the problem of drug resistance, a group of antimicrobial peptides are considered promising (*2*). More recently, their potential as anticancer agents is being recognized (*3, 4*).

These peptides widely exist in nature as an important component of innate immune system against infection (*5*). Their action is fast, direct, and broad-spectrum, complementary to the adaptive immune system, which is specific but requires more time to mobilize. The cytotoxicity of peptides is mediated by the disruption of cytoplasmic membrane. Models on the mechanism have been proposed (*6, 7*). Most of these peptides are amphipathic and cationic. The cationic charge allows peptides to accumulate on the membrane surface, and the side chains of hydrophobic residues subsequently insert into the outer layer of the membrane. The expansion of the outer layer places lateral pressure on the lipid bilayer to bend inward. It is important to have sufficient peptides in close proximity to create enough strain on the curvature of the lipid layer to break down the membrane. When the number of inserted peptides is above a certain limit, the formation of pores or the global decomposition of membrane leads to cell death. The activity of lytic peptides is independent of the extracellular recognition or intracellular uptake. Its target is not any specific molecule or pathway but the cell membrane, which is a relatively conservative structure so that resistance cannot be easily acquired. This unique feature renders this family of molecules an advantage in overcoming multidrug resistance.

However, lytic peptides require a minimal length and local concentration to be effective. Though the effective length varies from sequence to sequence, these peptides usually have more than 10 residues. For peptides without modification, the critical concentration at the target site can only be driven by high bulk concentration at which peptides may cause unwanted toxicity such as hemolysis. Besides, peptides may suffer from degradation by proteases, inactivation by serum proteins, and fast elimination in the blood circulation. These create additional hurdles to achieving effective concentration at the target sites. Therefore, antibiotic peptides succeeded in clinical trials only as topical agents. Another issue accompanying long sequences and low efficiency is high cost. The strategy of polyvalency was employed by several studies for it is known to be able to increase the avidity of weak monomeric ligands dramatically (*8*). Antimicrobial potency was significantly enhanced by mounting multiple copies of lytic peptides to a core or a scaffold (*9*−*11*). These reports support the hypothesis that clustering and sufficient local concentration are essential to the activity of lytic peptides, suggesting polyvalent design as a solution to fulfill the therapeutic promise of membrane lytic peptides.

In this study, we aim to demonstrate that polyvalency increases the anticancer potency of membrane lytic peptides. We will address the underlying mechanism via the thermodynamics measurement of the interaction between cell membranes and peptides. To these ends, a peptide−polymer conjugate was synthesized by coupling multiple copies of short lytic sequences to a dextran backbone. With this design, we expect not only an enhanced effectiveness due to polyvalency, but also an improve-

* Correspondence address: Department of Chemical and Biomolecular Engineering, Hong Kong University of Science and Technology, Clear Water Bay, Hong Kong SAR, China, E-mail: ying.chau@ust.hk, Tel: (852) 2358 8935, Fax: (852) 2358 0054.

[†] Bioengineering Graduate Program.

[‡] Department of Chemical and Biomolecular Engineering.

10.1021/bc1002899 © 2010 American Chemical Society
Published on Web 10/21/2010

ment in stability, tumor targeting, and pharmacokinetic properties due to polymeric conjugation (*12*).

MATERIALS AND METHODS

Reagents. Dextran T-70, *N*-(3-dimethylaminopropyl)-*N*′-ethylcarbodiimide (EDC), 2,4,6-trinitrobenzene sulfonic acid (TNBSA), 1,2-dioleoyl-*sn*-glycero-3-phosphocholine (DOPC), 1,2-dioleoyl-*sn*-glycero-3-phospho-*rac*-(1-glycerol) sodium salt (DOPG), trifluoroacetic acid (TFA), sodium azide, copper sulfate, and deuterium oxide were purchased from Sigma (St. Louis, USA). Propargylamine, 3-bromopropionic acid, and Gly-Gly were from Fluka (St. Louis, USA). DMSO, chloroacetic acid, and ascorbic acid sodium were obtained from Acros (Geel, Belgium). Acetonitrile was from Duksan (Gyeonggi-do, Korea). 3-(4,5-Dimethyl-2-thiazolyl)-2,5-diphenyl-2*H*-tetrazolium bromide (MTT) and all the cell culture reagents were bought from Invitrogen (Carlsbad, USA). Human breast cancer cell line MCF-7 and prostate cancer cell line PC-3 were kindly provided by Prof. Kathy Luo (Nanyang Technological University, Singapore) and Prof. Patrick Ling (The University of Hong Kong, Hong Kong), respectively.

Synthesis. *Preparation of Azido Peptide.* The peptides were synthesized based on the solid-phase peptide synthesis procedure. Briefly, Fmoc- Amide AM resin was mixed in DMF in a plastic peptide vessel (1 h), then subjected to Fmoc-deprotection and coupling. The Fmoc-protection group was removed by incubating resin in a piperidine/DMF mixture (25:75, v/v, 10 mL/g of resin) under agitation for 15 min. The vessel was drained via vacuum and washed with DMF (6×). The Fmc-protected amino acid (5 equiv), HBTU (4.5 equiv), and HOBT (4.5 equiv) were dissolved in DMF (5 mL/g of resin) followed by the addition of DIPEA (10 equiv). This mixture was quickly added to the resin and agitated for 3 h. After coupling, the resin was washed with DMF (3×). The Fmoc-deprotection and coupling were repeated for each amino acid until the desired sequence was assembled. At the end of peptide prolongation, the N-terminal was capped with 3-bromopropionic acid with the same coupling method as amino acid. The resin was then thoroughly washed with DMF, DCM, and methanol (3× each) and dried in high vacuum overnight. The resulting sequence was then deprotected and cleaved from resin by adding a cleavage cocktail (TFA/TIPS/water, 95:2.5:2.5, v/v) to the vessel. After 3 h incubation with agitation, the mixture was filtered. The filtrate was concentrated under a nitrogen stream. Cold diethyl ether was added to the filtrate to precipitate raw peptide $Br(CH_2)_2CONH\text{-}KWKWKW\text{-}NH_2$. The terminal bromine was converted to azide after overnight incubation in DMSO containing sodium azide (25 mg/mL) at room temperature in the dark. Purification was performed on a silica C18 column (1 × 25 cm, Grace Vydac 218TP) connected to an HPLC delivery system equipped with a UV detector (Waters, Milford, USA). The chromatographic separation was run at 5 mL/min using water and acetonitrile, both supplemented with 0.1% TFA, as mobile phases A and B, respectively. After sample injection, the column was rinsed with 5% mobile phase B for 10 min, followed by a gradient from 5% B to 30% B in 10 min and then to 80% B in 60 min. Absorbance at 220 and 280 nm was monitored. Eluted fractions were collected. Peptide identity was confirmed by MALDI mass spectroscopy analysis (Calc.: 1056.6, found: 1056.7). Analytical HPLC indicated that the purity was higher than 95%.

Preparation of Carboxymethyl Dextran (CM-Dextran). Dextran T-70 (2 g) was dissolved in 6 M sodium hydroxide solution (10 mL) to yield a clear solution. Chloroacetic acid (116.5 mg) was then added. The resulting mixture was held at 90 °C with vigorous stirring for 3 h. HCl (5 M) was added to neutralize and terminate the reaction. The product was purified by ultrafiltration against DI water. Briefly, the reaction mixture as aqueous solution was put in a cup-like ultrafilter equipped with a semipermeable membrane (cutoff: 10 000 Da) (SINAP Membrane Science & Technology Co., Ltd., Shanghai, China). Hydrostatic pressure was applied by connecting the interior of ultrafilter to compressed nitrogen. Salt, catalyst, and unreacted reagents passed through the membrane with water while polymers were retained. DI water was refilled before the solution was too concentrated. The ultrafiltration was stopped when the volume of filtrate was six times the volume of the original mixture. The lyophilized polymer appeared as a fluffy white powder.

Preparation of Alkynyl Dextran. Carboxylmethyl groups were further modified with alkynyl groups according to the procedure below. CM-dextran (2 g, 0.244 mmol carboxylmethyl) and propargyl amine (0.63 mL, 9.8 mmol) were dissolved in water (20 mL). The pH of the mixture was tuned to 5 with HCl. EDC (2.35 g, 12.25 mmol in total) was added to the mixture in 5 aliquots in 48 h. Excessive amounts of propargyl amine and EDC were used to drive the completeness of conversion. The reaction was held at room temperature. The polymer was purified by ultrafiltration as previously described and lyophilized for storage.

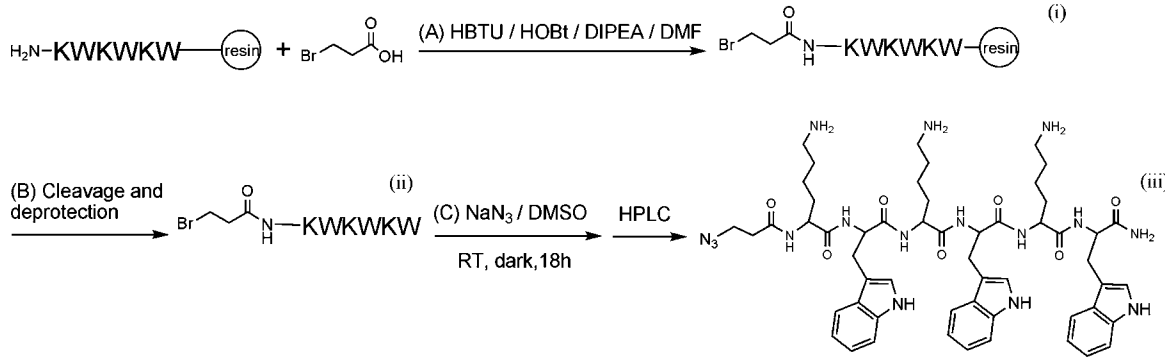
Preparation of Conjugate Dex-$(KW)_3$. Propargyl dextran (91.2 mg, 0.011 mmol alkyne) and azido $(KW)_3$ (17.7 mg, 0.017 mmol) were dissolved in DI water and mixed thoroughly. Copper sulfate pentahydrate (2.77 mg, 0.011 mmol) and sodium ascorbate (4.4 mg, 0.022 mmol) were subsequently added to the mixture. The reaction was carried out in a nitrogen atmosphere at 40 °C for 48 h. The product was then dialyzed against DI water using cellulose dialysis membrane tubing (Spectrum Laboratories, Rancho Dominguez, CA, USA) with a molecular weight cutoff at 3000−8000 Da for 3 days. On the second day of dialysis, the solution was taken out and centrifuged at 4500 rpm for 10 min to remove the insoluble copper ions. The supernatant was then dialyzed again. A white fluffy powder was obtained after lyophilization.

NMR Spectroscopy. ^1H NMR spectra were recorded on 400 MHz spectrometer (JNM EX-400, JEOL Ltd., Tokyo, Japan). All samples were dissolved in D_2O for spectral acquisition.

Determination of Peptide Loading (TNBSA assay). TNBSA reacts readily and exclusively with primary amine at pH 8 to form yellow adducts which can be monitored at 335−345 nm (*13*). Since there are plenty of primary amines at the side chain of lysine in the sequence, we used this method to quantify the loading of $(KW)_3$ on conjugate. Dipeptide Gly-Gly was used as a standard. A concentration series of Gly-Gly and conjugates were prepared in 0.1 M sodium bicarbonate. The volume of each standard and sample was 0.5 mL. To each standard and sample was added 0.25 mL of TNBSA (0.01% w/v, in 0.1 M sodium bicarbonate). After incubation in a 37 °C water bath for two hours, 0.25 mL of SDS (10% w/v, in water) and 0.125 mL of HCl (1 M) were added and mixed thoroughly. Absorbance was measured at 335 nm with a microplate reader (Varian Cary 50, Palo Alto, USA). A standard curve was constructed by plotting the amine concentration of Gly-Gly standards against the absorbance reading.

Cell Culture. Human breast cancer cell line MCF-7 was maintained in MEM. Prostate cancer cell line PC-3 was maintained in RPMI 1640 medium. Mouse embryo fibroblast NIH/3T3 was maintained in DMEM. The drug-resistant cell line MES-SA/Dx5 and its parental cell line MES-SA were cultured in McCoy's 5A medium. All media were supplemented with 10% fetal bovine serum, except the medium for NIH/3T3 was supplemented with 10% bovine calf serum. Cells were cultured at 37 °C in 5% CO_2 atmosphere.

Scheme 1. Synthesis Procedure of Azide-Terminated Lytic Peptide[a]



[a] Reactants and products: (i) bromine-terminated $(KW)_3$ on resin; (ii) bromine-terminated $(KW)_3$; (iii) azide-terminated $(KW)_3$. Reaction conditions: (A) HBTU/HOBT/DIPEA coupling in DMF; (B) dilute trifluoroacetic acid cleavage from resin and deprotection of peptide side chains; (C) substitution of bromine by azide in DMSO and purification by reversed-phase HPLC. Typical yield of step C is ∼70%.

In Vitro Cytotoxicity Test (MTT assay). Cells were seeded on a 96-well plate at a density of 15 000 (PC-3, MCF-7, and NIH/3T3) or 20 000 (MES-SA and MES-SA/Dx5) cells per well. After overnight incubation, the growth medium was replaced with 100 μL of serum-free medium containing peptides or conjugates at the indicated concentrations. After 3 h of incubation, 10 μL of MTT was added to each well to achieve a final concentration of 0.5 mg/mL. The plate was then incubated at 37 °C for 4 h. 100 μL of SDS solution (10% w/v in 0.01 M HCl) was added to each well to dissolve the purple crystals of formazan. After overnight incubation, the absorbance at 595 nm was measured with a plate reader (Wallac Victor^3 1420, PerkinElmer, MA, USA). The percentage viability was calculated as follows:

$$\text{viability}(\%) = (A_s - A_0)/(A_c - A_0) \times 100\%$$

where A_s is the absorbance value of sample, A_c is the absorbance of control where cells were untreated, and A_0 is the absorbance of cell-free background. Each experiment was repeated three times independently.

Hemolysis Assay. Heparinized fresh rabbit blood was centrifuged at 2000 rpm for 10 min. The supernatant was removed. The red blood cells were then resuspended in warm PBS. The procedure was repeated three times to rinse the red blood cells prior to use. Peptides were added to erythrocyte suspension to obtain the designated peptide concentrations and a final erythrocyte concentration of 4% (v/v). The resulting suspensions were incubated at 37 °C for 1 h at 300 rpm agitation. Samples were then centrifuged at 2000 rpm for 10 min. The absorbance of supernatant at 540 nm was measured to examine the release of hemoglobin and the damage of erythrocyte membrane. Zero hemolysis and 100% hemolysis consisted of erythrocyte suspended in PBS and 1% Triton X-100, respectively. The percentage of hemolysis was determined as follows:

$$\text{hemolysis}(\%) = (A_s - A_0)/(A_{100} - A_0) \times 100\%$$

where A_s is the absorbance value of the sample, A_{100} is the absorbance of completely lysed RBC in 1% Triton X-100, and A_0 is the absorbance of zero hemolysis. Each experiment was repeated at least three times independently.

Small Unilamellar Vesicles (SUVs) Preparation. The phospholipid DOPC and DOPG were dissolved in dichloromethane and mixed in a 75/25 molar ratio. The mixture was dried under a nitrogen stream and subsequently under a high vacuum overnight. The weight of the mixed lipid was measured. For DOPC SUV, lipid was directly weighed and used. The dry film was dissolved in phosphate buffer (20 mM, 100 mM NaCl, pH 7.4) to obtain a final lipid concentration of 10 mM. The suspension was then vortexed rigorously for 2 h for hydration. Sonication was applied with a probe tip-type sonicator (Sonifier 450, Branson, Danbury, CT, USA). The lipid suspension was sonicated in an ice bath (output = 5, duty cycle = 35) until a clear solution was obtained. Debris was removed by centrifugation at 14 000 rpm for 10 min. The concentration of SUV suspension was calculated according to the weight of lipid measured prior to preparation.

Particle Size and Potential Measurement by Dynamic Light Scattering (DLS). The particle size and surface potential of lipid vesicles, polymers, and conjugates were measured by laser-light scattering with a zeta potential analyzer (ZetaPlus, Brookhaven Instruments Corporation, NY, USA). All the samples were prepared in PBS (20 mM, 100 mM NaCl, pH7.4). Polymers and conjugates were measured at 10 mg/mL. SUV samples were measured at a lipid concentration of 5 mM.

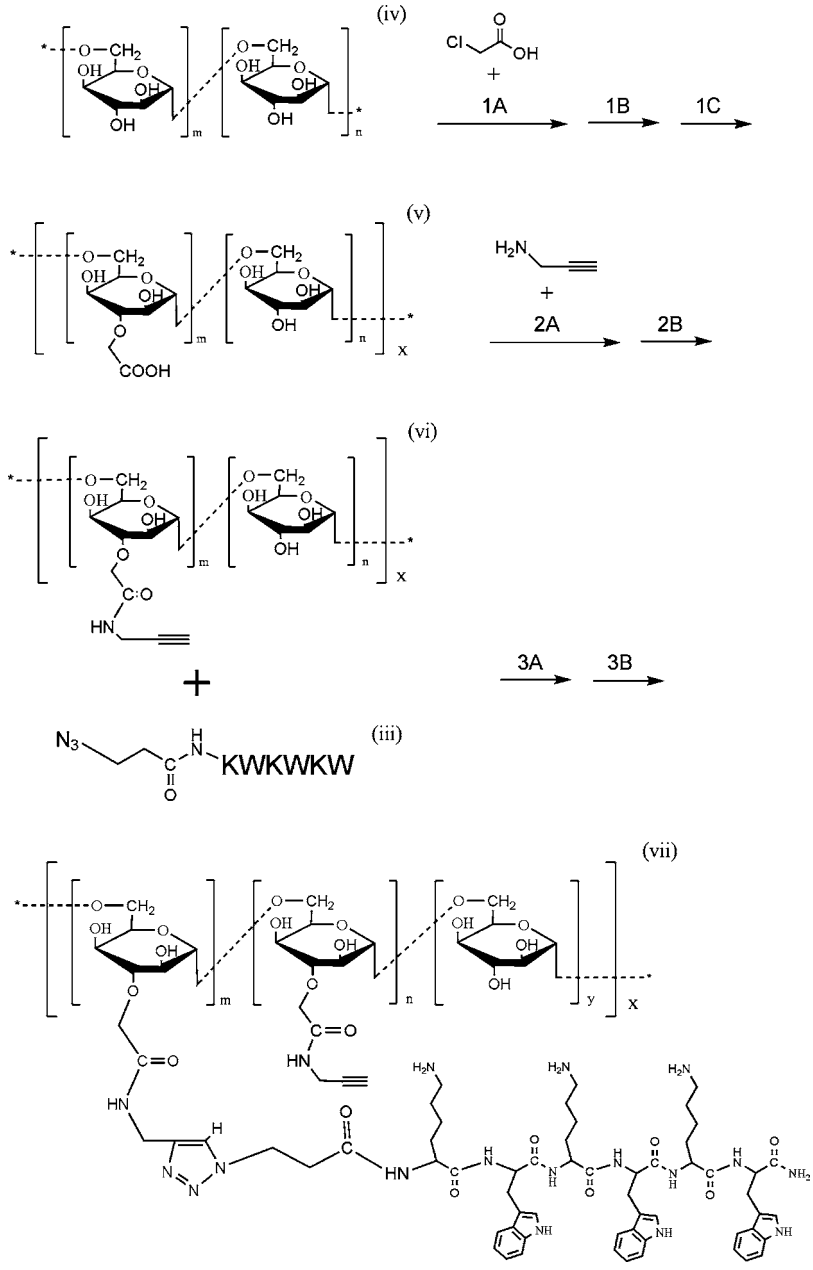
Isothermal Titration Calorimetry. Experiments were performed using an isothermal titration calorimeter (VP-ITC, MicroCal, NJ, USA) at 25 °C. PBS (20 mM, pH 7.4, 100 mM NaCl) was used as the working buffer. All the samples were degassed prior to use. SUV suspension (10 mM lipid concentration) was injected in 6 μL increments into a solution of peptides or conjugates (2 or 10 μM equivalent peptide concentration according to the respective affinity) in the calorimeter cell (cell volume = 1.4561 mL). The heat liberated from the binding of peptides to lipids in each injection was recorded. The titration continued until the released heat approached zero. The heat of dilution was determined by the titration of SUV suspension into buffer. Heats of dilution were relatively small but nevertheless subtracted. Binding isotherms were constructed as described (*14*). The procedure was summarized in the Supporting Information.

RESULTS

Design and Synthesis of Lytic Peptide−Polymer Conjugate Dex-$(KW)_3$. A hexapeptide, Lys-Trp-Lys-Trp-Lys-Trp ($(KW)_3$), was designed as the lytic sequence based on the principle of amphipathicity. Tryptophan is a hydrophobic amino acid with a bulky ring at the side chain. The importance of tryptophan to lysing activity has been reported by previous studies (*15, 16*). Lysine and arginine were widely used as the source of positive charge in synthetic antimicrobial peptides. The lysine-containing sequence is less cationic but prone to inducing membrane disruption instead of penetration compared to an arginine-containing analogue (*17*). With consideration of the aim of this work, lysine was selected.

Since there are multiple active amine groups at both the N-terminal and side chains, a conjugation method that can be restricted at the terminal is required. Moreover, because the

Scheme 2. Synthesis Procedure of Dextran-$(KW)_3$ Conjugate[a]



[a] Reactants and products: (iv) Dextran of MW 70 000 Da; (v) carboxylmethyl dextran; (vi) alkynyl dextran; (vii) conjugate Dex-$(KW)_3$. Reaction conditions and step yields: 1A, carboxylmethyl modification in 6 M NaOH solution at 90 °C; 1B, termination and neutralization with 5 M HCl; 1C, ultrafiltration against water, yield of step 1 = ~80%; 2A, coupling with propargyl amine under catalysis of EDC in water; 2B, ultrafiltration against water, yield of step 2 = ~90%; 3A, conjugation by Cu(I)-catalyzed cycloaddition; 3B, dialysis against DI water, yield of step 3 = ~70%.

resulting conjugates are going to be tested in vitro, the minimized use of organic solvent and harsh conditions will be preferred. Cu(I)-catalyzed Huisgen 1,3-dipolar cycloaddition between azide and alkyne was adopted for conjugation. As one of the click chemistry reactions, it provides the advantages of high specificity and mild conditions.

Azide-terminated peptide was prepared according to Scheme 1. The sequence $(KW)_3$ was synthesized on resins, and the N-terminal was capped with 3-bromopropionic acid at the end of peptide prolongation. Since positive charge is essential to peptide activity, the C-terminal was amidated to mask the negatively charged carboxyl group. After cleavage from resins, the terminal bromine was substituted with azide for subsequent conjugation. The reaction yield was ~70%.

Dextran T-70 was modified with pendant carboxymethyl (Scheme 2 reaction 1). The reaction was examined by ^{1}H NMR. In the spectrum, the peak of the C1 proton of glucose structural units (-O−C*H*−O-, δ = 5.0 ppm) shifts upon carboxylmethyl modification (-O−C*H*−O-, δ = 5.2 ppm) (Supporting Information Figure S1(A)). The substitution degree of carboxylmethyl groups could be tuned by adjusting the feed ratio of chloroacetic acid.

CM-dextran was further converted to alkynyl dextran (Scheme 2 reaction 2). Because unmasked carboxyl groups may impair the activity of lytic sequence, to which positive charge is important, an excessive amount of propargyl amine was added to drive the completeness of reaction. The success of the reaction was confirmed by the signal of alkyne proton (C*H*≡C-, δ = 2.65 ppm) in the ^{1}H NMR spectrum (Supporting Information Figure S1(B)). The alkyne proton was estimated and compared with the C1 proton of carboxylmethyl glucose structural units

Table 1. Summary of the Characterization Results of Polymers and Conjugate

	loading of functional group or peptide (mmol/gram)	zeta potential (mV)	diameter (nm)
dextran T-70	−	1.29 ± 2.51	9.48 ± 0.25
carboxylmethyl−dextran	∼0.122	-7.02 ± 2.11	14.59 ± 0.35
alkynyl−dextran	∼0.122	0.35 ± 2.03	11.57 ± 0.24
Dex-$(KW)_3$	∼0.05	8.13 ± 2.63	8.19 ± 0.42

The loading of carboxylmethyl and alkynyl groups on dextran was estimated by comparing the signals of the functional groups to the signal of glucose units in the ^{1}HNMR spectrum. The loading of peptides on dextran was calculated by measuring the primary amine groups on peptide side chains with a colorimetric assay. All the samples for DLS were prepared in PBS buffer (20 mM, 100 mM NaCl, pH 7.4). Polymers and conjugates were measured at 10 mg/mL. SUV samples were prepared at a lipid concentration of 5 mM.

(-O−C*H*−O-, $\delta = 5.2$ ppm). The result suggested that the conversion was close to 100%.

Cu(I)-catalyzed Huisgen 1,3-dipolar cycloaddition was applied to graft $(KW)_3$ to dextran (Scheme 2 reaction 3). The occurrence of conjugation was indicated by the decrease of alkyne proton signal at δ 2.65 ppm and the appearance of peptide amine protons and triazole proton signal in the range δ 7−8 ppm in the ^{1}H NMR spectrum of the conjugate (Supporting Information Figure S1(C)). Not all the triple bonds were reacted since the alkyne proton signal, though decreased, could still be detected. The conversion from alkyne to triazole linkage was ∼50%.

Conjugate Characterization: Peptide Loading, Particle Size, and Charge. According to ^{1}H NMR, the amount of pendant carboxylmethyl in structure v (Scheme 2) and alkynyl groups in structure vi (Scheme 2) was around 0.122 mmol per gram of polymer. The precise peptide loading was measured by TNBSA assay. The loading was around 0.05 mmol peptide per gram of conjugate (Scheme 2 structure vii). The variation of loading was within 10% from batch to batch. The degree of modification, size, and charge of polymers and conjugate were summarized in Table 1.

Cytotoxicity against Cancer Cells. Dex-$(KW)_3$ was tested for its anticancer activity in vitro and compared with free peptide Ac-$(KW)_3$-$CONH_2$. The conjugate and free $(KW)_3$ were tested at equivalent peptide concentrations in human prostate cancer cells PC-3 and breast cancer cells MCF-7 (Figure 1A,B). Free $(KW)_3$ exhibited toxicity only at extremely high concentrations with LC_{50} higher than 500 μM. However, Dex-$(KW)_3$ was much more active toward both cell lines with LC_{50} less than 10 μM. This value is comparable to most conventional lytic peptides of more than 20 residues (*18*). The result showed that a polyvalent presentation significantly enhanced the potency of a short lytic peptide by 50- and 500-fold, respectively, in PC-3 and MCF-7. We also constructed a conjugate analogue Dex-$(KW)_4$ to study the effect of increasing the length of peptide on cytotoxicity (Figure 1B). Dex-$(KW)_4$ and free $(KW)_4$ were subjected to the same test. Dex-$(KW)_4$ was slightly more active at low concentrations than Dex-$(KW)_3$, but free $(KW)_4$ acquired moderate activity with an extra (KW) unit with LC_{50} between 30 and 100 μM. In systemic administration, peptides prematurely detached from the conjugate can interact with nontargeted cells before they are directed to tumor tissues. To avoid undesirable side effects, an ideal lytic sequence should be inactive in free form and exhibit high potency when conjugated. $(KW)_3$ was preferred, because it showed a larger contrast in activity between its free form and conjugated form.

Ability to Overcome Multidrug Resistance. After confirming the anticancer activity, we further investigated the potential of Dex-$(KW)_3$ in killing cancer cells that have acquired drug resistance. MES-SA is a human uterine sarcoma cell line that is sensitive to chemotherapeutic agents. MES-SA/Dx5 is a subline of MES-SA with multidrug resistance, established by growing parental MES-SA cells in the presence of doxorubicin of gradually increased concentration over a prolonged period. MES-SA/Dx5 exhibits a marked cross-resistance to a number of chemotherapeutics. We confirmed the drug resistance of MES-SA/Dx 5 in our lab and found that the IC_{50} of doxorubicin was 10-fold higher in MES-SA/Dx5 than in MES-SA (data not shown). Dex-$(KW)_3$ and free peptide were applied to both cell lines, and their activities were measured by MTT assay (Figure 2). The result indicated that the cytotoxicity profiles were very similar in the cells with and without resistance. It suggested that the anticancer activity of the new conjugate was not affected by multidrug resistance, consistent with previous reports about lytic peptides. Again, the potency of conjugates was significantly increased compared with free peptides.

To exclude the possibility that the toxicity resulted from the polymer backbone or the unmasked alkynyl groups, cell lines were exposed to alkynyl dextran at equivalent polymer concentration to that of the conjugate. The result confirmed that the polymer was nontoxic to all the cancer cells used in this study at tested concentrations and therefore not the reason for the observed cytotoxicity (Supporting Information Figure S2).

Effect of Dex-$(KW)_3$ on Noncancer Cells. Hemolysis is one of the potential risks when lytic peptide-based therapeutics are administrated systemically. To investigate the effect of the new conjugate on red blood cells, Dex-$(KW)_3$ was incubated with a red blood cell suspension under agitation to mimic the situation in the circulation system. Free $(KW)_3$ and alkynyl dextran were subjected to the same test. Over the concentration range tested (5−300 μM), the percentages of hemolysis in all the samples were less than 3% (Table 2). The cytotoxicity test was also conducted on a fibroblast cell line NIH/3T3 to examine the effect of conjugate on normal cells. The activity profile was similar to the one against cancer cells, though the potency was slightly lower (Supporting Information Figure S3).

Isothermal Titration Calorimetry. Small unilamellar vesicle (SUV) was used as a model of the cell membrane to investigate the interaction between conjugates and cell membranes. Neutral DOPC vesicles and negatively charged DOPC/DOPG (75:25) vesicles were prepared. Their size and zeta potential were measured prior to titration. The measurement showed that vesicles were approximately 30 nm in diameter. The zeta potentials of DOPC and DOPC/DOPG vesicles were 3.28 ± 1.23 mV and -19.48 ± 1.61 mV, respectively.

Because the disruption of lipid vesicles will generate extra heat flow, which is difficult to dissect from the heat of binding, the concentrations of lipids, conjugates, and peptides were carefully chosen prior to the titration experiments to ensure that the vesicles would remain intact even at the highest peptide/lipid molar ratio during the first injection (Supporting Informations Table S1). In this way, the measurement reflected only the binding interaction of the conjugates or free peptides with the membrane.

Lipid vesicle suspensions were titrated into the conjugate or free peptide solution. The heat flow in each injection was recorded. As the titration proceeded, the amount of peptide available for binding decreased. Therefore, the measured heat of binding decreased with consecutive lipid injections (Supporting Information Figure S4). The titration continued until the enthalpy change approached zero.

Binding isotherms was constructed by plotting the binding degree (X_b: molar ratio of bound peptide to lipid) as a function of the equilibrium concentration of unbound peptide in the solution (C_f) (Figure 3A). In the titration of negatively charged DOPC/DOPG (75:25) SUVs, the isotherm of free $(KW)_3$ is a smooth curve with decreasing slope. Consistent with previous

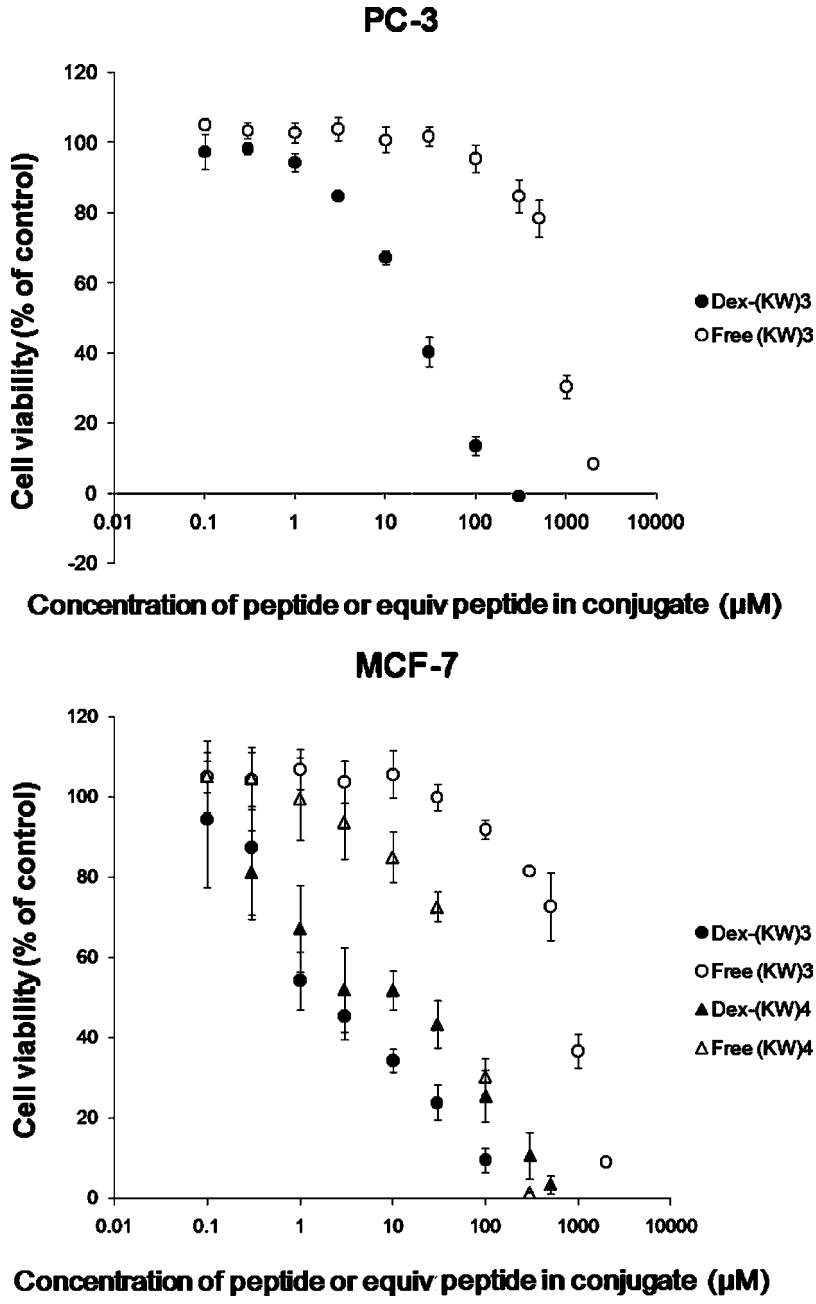


Figure 1. In vitro cytotoxicity against cancer cells. Dex-$(KW)_3$ was applied to (A) human prostate cancer cells PC-3 and (B) breast cancer cells MCF-7 at indicated equivalent peptide concentrations and incubated for 3 h. The cytotoxicity was determined by MTT assay. Free $(KW)_3$ was subjected to the same procedure for comparison. Dex-$(KW)_4$ and free $(KW)_4$ were tested on MCF-7 to investigate the effect of peptide length on anticancer activity. Cell viability was normalized by control and shown as the percentage of viability. The result is an average of at least three independent tests.

reports (*19*), the apparent binding constant (K_{app}) of free $(KW)_3$ decreased with increasing peptide concentration. This is because binding was predominantly driven by the electrostatic interaction between cationic peptides and the negative membrane surface. As the peptide concentration increased and the binding proceeded, the negatively charged surface of lipid vesicle was gradually screened by bound peptides. The weakened attraction is translated into a lowered binding constant. In contrast to free $(KW)_3$, the conjugate gave a relatively steady binding constant over the course of titration. Therefore, the conjugate eventually surpassed the free peptide in binding affinity at high concentrations. The isotherm of the conjugate was roughly treated as a straight line, and an apparent binding constant of 9728 M^{-1} was obtained from linear regression. This approach for estimating binding constant is not applicable to the whole isotherm of free peptides, but apparent binding constants in the ranges of initial binding (20 574 M^{-1}) and saturated binding (2254 M^{-1}) were calculated. It was found that the apparent binding constant of free $(KW)_3$ decreased by almost 1 order of magnitude from the beginning to the end of titration.

To further investigate the binding thermodynamics in the absence of electrostatic attraction, neutral DOPC SUVs were employed. Dex-$(KW)_3$ yielded an isotherm similar to the one with DOPC/DOPG SUVs and gave a binding constant of 8822.8 M^{-1} (Figure 3B). However, for the free $(KW)_3$, the isotherm was remarkably different upon removal of electrostatic interaction. The isotherm is almost linear, and the binding constant was estimated to be 1884.7 M^{-1}, significantly lower than the conjugate. It should be noted that the end of titration was defined as the point where all the peptides or conjugates were consumed for binding and the release of heat approached zero. In the previous three titration experiments, 10 μM was used as the

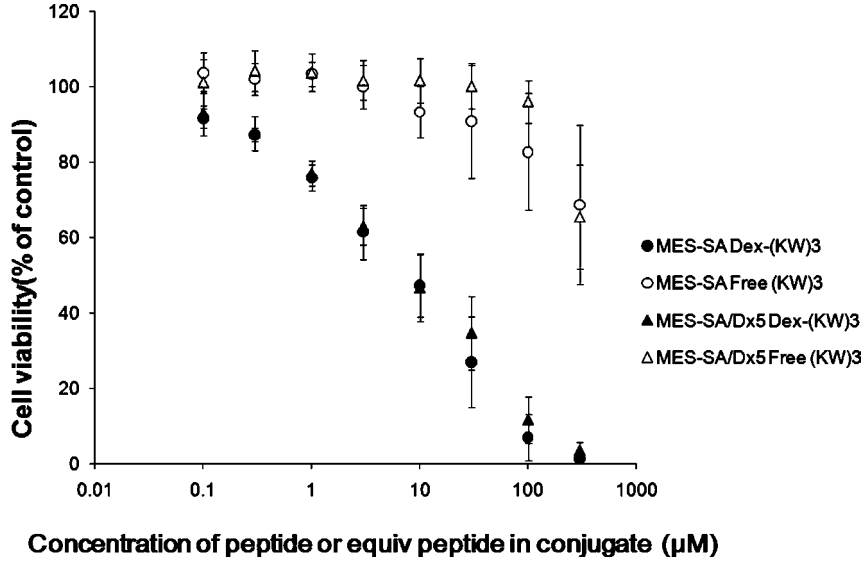


Figure 2. Ability to overcome multidrug resistance. Dex-$(KW)_3$ was applied to human uterine sarcoma cell line MES-SA and its resistant subline MES-SA/Dx5 at indicated equivalent peptide concentrations and allowed for 3 h incubation. Cytotoxicity was measured by MTT assay. Free $(KW)_3$ was subjected to the same procedure for comparison. Cell viability was normalized by control and shown as the percentage of viability. The result is an average of at least three independent tests.

Table 2. Values of % Hemolysis at the Highest Tested Concentration of Conjugate, Free Peptide, and Corresponding Precursor Polymer

	Dex-$(KW)_3$	free $(KW)_3$	alkynyl dextran
% hemolysis	1.9 ± 0.2%	1.2 ± 0.9%	2.0 ± 0.9%

Fresh rabbit red blood cell suspension (4% v/v in PBS) was incubated with Dex-$(KW)_3$, free $(KW)_3$, and alkynyl dextran for 2 h in agitation prior to the measurement of released hemoglobin. Data in Table 2 show the percent hemolysis at 300 μM peptide concentration (equiv peptide concentration for Dex-$(KW)_3$ and equiv polymer concentration for alkynyl dextran). Results are the average of three independent assays.

initial peptide concentration in the reaction cell. Because free $(KW)_3$ showed low affinity and slow binding rate with neutral membranes, we used 2 μM as the initial concentration of free $(KW)_3$ in DOPC SUVs titration to ensure that the titration can be completed in a reasonable number of injections. This is the reason the isotherm of free $(KW)_3$-DOPC binding covers a smaller concentration range in Figure 3B.

From the ITC experiments, thermodynamic parameters related to the membrane binding can be calculated (Table 3). By comparison of the change of free energy (ΔG), there is a trend among different combinations of titrant and titrand: peptide (low conc.)/DOPC/G < conjugate/DOPC/G ≈ conjugate/DOPC < peptide (high conc.)/DOPC/G ≈ peptide/DOPC. Though in all the titrations the binding is favored by both enthalpy and entropy, there is a substantial difference in the relative contributions of these two components to ΔG. Generally speaking, the conjugate has a more negative entropy component ($-T\Delta S$) and free peptide has a more negative enthalpy term (ΔH) regardless of the type of SUVs (Figure 4).

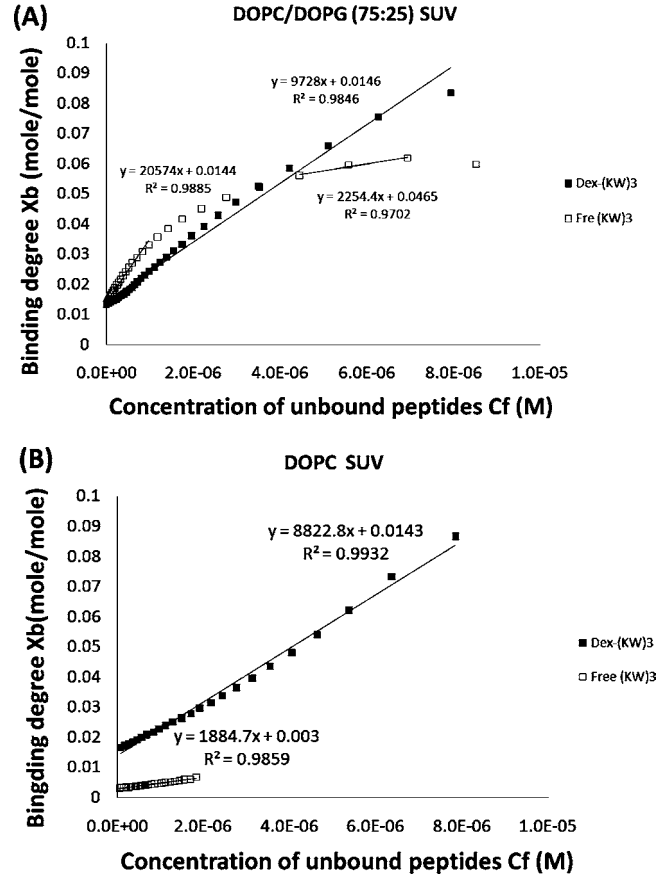


Figure 3. Binding isotherms of lipid−conjugate interaction and lipid−peptide interaction Conjugate Dex-$(KW)_3$ and free peptide $(KW)_3$ were titrated into the suspension of negatively charged lipid vesicles (A) and neutral lipid vesicles (B). The binding isotherm was obtained by plotting the degree of binding X_b against the concentration of unbound peptide C_f as described in Supporting Information. The straight lines are linear regression of the binding isotherms. The slope gave an estimation of the apparent binding constants (K_{app}).

DISCUSSION

A procedure was developed to synthesize a new lytic peptide−polymer conjugate. The lytic sequence $(KW)_3$ was chosen based on previous structure−activity relationship studies about the critical structural requisite of an active lytic peptide (*20*−*22*). Despite the high variability in the peptide sequence, there are two determinants of membrane activity: (1) the presence of cationic charge and hydrophobic residues in a balanced ratio and (2) the capability to rearrange the residues in an amphipathic way by segregating basic and hydrophobic residues on the opposite sides of peptide surface. Lysine was used to provide the positive charge necessary for membrane absorption, and tryptophan with a bulky, lipophilic indole ring

Table 3. Thermodynamic Parameters for Conjugate−SUV and Peptide−SUV Binding

condition	sample	SUV	ΔH (kcal/mol)	ΔG (kcal/mol)	ΔS (cal/(mol*K))	$-T\Delta S$ (kcal/mol)	K(1/M)
1	Dex-$(KW)_3$	DOPC	−1.33	−7.76	21.57	−6.43	8822.8
2	Dex-$(KW)_3$	DOPC/DOPG (75:25)	−3.57	−7.81	14.23	−4.24	9728.0
3	free $(KW)_3$	DOPC	−4.20	−6.84	8.86	−2.64	1884.7
4	free $(KW)_3$ (high conc.)	DOPC/DOPG (75:25)	−6.00	−6.95	3.19	−0.95	2254.4
5	free $(KW)_3$ (low conc.)	DOPC/DOPG (75:25)	−6.00	−8.26	7.58	−2.26	20574.0

ΔH values were calculated from the sum of corrected heats of reaction. Typically, 6 μL of SUV suspension (c_l = 10 mM) was injected into a peptide or conjugate solution (c_p or equiv c_p = 10 μM, except in condition 3, c_p = 2 μM) at 25 °C. Apparent binding constants (K_{app}) were estimated from the corresponding binding isotherm. The changes of free energies (ΔG) and entropies (ΔS) were calculated using the equations $\Delta G = -RT \ln 55.5K$ and $\Delta G = \Delta H - T\Delta S$. The factor 55.5 is the molar concentration of water. $K^* = 55.5K_{app}$ is the binding constant if the concentration of peptide is referenced to 1 mol H_2O (*19*).

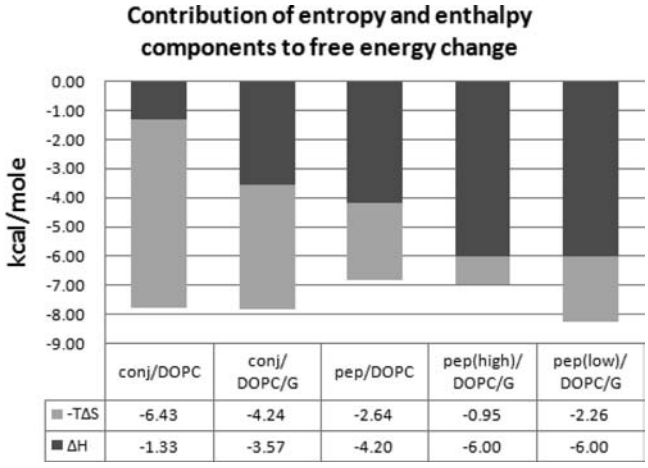


Figure 4. Relative contribution of entropy ($-T\Delta S$, dark column) and enthalpy (ΔH, light column) components to free energy change ($\Delta G = \Delta H - T\Delta S$, stacked column) is shown in a stacked column chart and the values are summarized in the table below. Abbreviations: conj, Dex-$(KW)_3$; pep, free $(KW)_3$; DOPC, small unilamellar vesicles composed of DOPC; DOPC/G, small unilamellar vesicles composed of DOPC and DOPG (75:25).

was employed for the insertion and perturbation to membrane lipid matrix. Since the amino acid residues can rotate along peptide backbone, we expected $(KW)_3$ to be capable of rearranging the side chains in a way to exhibit amphipathicity (Scheme 1). 1,3-Dipolar cycloaddition between alkyne and azide, known as one of the "click" reactions, was applied for conjugation (Scheme 2), though the reaction efficiency (~50%) was not as high as expected. The conjugate is about 8 nm in diameter, within the size range suitable for passive tumor targeting according to the effect of enhanced permeation and retention (EPR) (*12*).

The effect of polyvalency on anticancer activity of conjugates was investigated in different cancer cell lines. $(KW)_3$ is designed to be a potential membrane-lytic sequence. The in vitro test indicated that the hexapeptide was mild unless at extremely high concentrations (LC_{50} > 500 μM), which may be due to the short length. However, the potency of the conjugate was greatly enhanced by around 50-fold in PC-3 and even higher in MCF-7 with an increase up to 500-fold (Figure 1A,B). According to the compatibility test of the precursor polymer, the cytotoxicity was not caused by the polymer backbone. The enhancement of activity should be mainly attributed to the polyvalency of peptides on conjugation. The activity of free peptide was length-dependent. An analogue sequence $(KW)_4$ showed moderate activity with an extra (KW) unit. The potency of Dex-$(KW)_4$ was only slightly increased compared with that Dex-$(KW)_3$ (Figure 1B). $(KW)_3$ is a better choice because shorter length means a reduced risk of immunogenicity. Most importantly, $(KW)_3$ gave a better contrast between conjugate and free peptide, which helps to lower the risk of nonspecific toxicity caused by prematurely detached peptides in the systemic administration without compromising the conjugate activity.

One of the motivations for developing membrane-active anticancer peptides is to overcome the problem of multidrug resistance in chemotherapy. We examined the activity of Dex$(KW)_3$ in drug-resistant cancer cells MES/SA-Dx5 and the drug-sensitive counterpart MES/SA, then compare the results (Figure 2). The anticancer activity of the conjugate was not impaired by the drug resistance phenotype. This result is consistent with previous reports on antimicrobial peptides and anticancer peptides. The target of most lytic peptides is cytoplasmic membrane, the outermost structure of a cell, and the lytic activity does not rely on any specific signal pathway. As a result, the efflux pump of resistant cells cannot diminish the peptide activity. Besides, membrane is a conservative cellular structure so that acquiring resistance by genetic mutation is much more difficult.

The enhancement in membrane activity of polyvalent antimicrobial peptides has been reported by several groups (*9*−*11*). In the current study, we also observed similar trends in anticancer effects. Hints all point to an idea that the polyvalent presentation of peptides should surmount the hurdle of assembly by prenucleating on a scaffold (polymer). However, this hypothesis has not been experimentally verified and this motivates us to perform a thermodynamic analysis to compare monomeric peptide and polyvalent conjugate in the capability of binding with lipid membranes. To focus on the binding step, the lipid vesicles were kept intact by keeping the peptide concentration below the threshold for lysis.

According to the Shai-Matsuzaki-Huang (SMH) model, the interaction of peptides and the membrane goes through two sequential stages before lysis actually happens (*5*). The initial association is mediated by the electrostatic interaction. At this "absorption" stage, peptides associate with the membrane either superficially or embedded just below the aqueous interface (*23*). The basic residues form a hydrogen bond and/or a salt bridge with the lipid head groups, which contribute to the negative ΔH. This is supported by the result of our thermodynamic study. When the vesicles are negatively charged, the increase of electrostatic interaction is always accompanied with a more negative ΔH for both conjugates and free peptides (Figure 4). A lack of hydrophobic interaction is involved at this stage, and the lipids remain well-packed. As the peptide concentration continues to increase, the binding enters the "integration" stage where the nonpolar side chains insert into the hydrophobic core of the membrane and perturb the lipid matrix. In this stage, the entropy takes the lead in driving the binding. There are two reasons for entropy contribution to dominate in this stage. First, the packing of the lipid layer is greatly impaired; and second, large amounts of water originally organized around the hydrophobic side chains are released upon the burial of side chains in the core of the membrane ("solvation" effect (*8*)). The "absorption" and "integration" represent different depth in binding.

In our system, the binding of peptide and conjugate with the membrane also went through these two stages. The contribution of entropy and enthalpy to free energy was summarized in Figure 4. Regardless of the type of vesicle, it was found that the binding of conjugates is mainly entropy-driven, while the binding of free peptides is mainly enthalpy-driven. We hypothesize that conjugates were primarily in the "integration" stage with deeper penetration into the phospholipid bilayer. Under the same conditions, most free peptides tended to be in the "absorption" stage where peptides were in a shallow location and less disturbance to the membrane was caused. Since peptide concentration is the force that drives binding and lysing to proceed, the high local concentration of peptide mounted on a polymer scaffold leads to a deeper penetration of conjugate and enhances the lysing activity. The prenucleation or preassembly of the conjugated peptides is another reason for the more positive ΔS of Dex-$(KW)_3$. Upon binding to the membrane, peptides become more restricted, and this loss of freedom contributes to a decrease of entropy, a situation that applies to both conjugated and free peptides. Because the peptides in the conjugate were in an initial status of higher order, the entropy penalty is accordingly smaller compared to that of free peptides.

From the isotherm of free peptide−DOPC/DOPG SUV binding (Figure 3A), the binding capability of free $(KW)_3$ was significantly weakened at high concentrations due to electrostatic repulsion, and binding became almost saturated even though the vesicles were still intact. In contrast, the binding behavior of the conjugate was barely affected by the electrostatic effect. It is probably because the initially bound peptides can bring the rest of the peptides on the same polymer backbone into the vicinity of cell membrane. The polyvalent design thus facilitates the subsequent binding and counteracts the effect of repulsion.

Interestingly, though the enhanced activity of Dex-$(KW)_3$ was shown in both cytotoxicity and thermodynamic studies, the hemolysis activity of the conjugate was almost negligible at the concentrations tested (5−300 μM) (Table 2). In other multivalent lytic peptides as antibiotics, the relatively low hemolytic activity compared to antibacterial activity was also observed (*10*, *11*). The erythrocyte membrane is known for a high content of cholesterol compared to other cell types (*24*). It has been reported that there is an inverse relationship between the rate of hemolysis and the cholesterol content in the membrane (*25*). The stability of the erythrocyte membrane is mainly responsible for the selectivity. Considering that the conjugate binding is entropy driven, we reason that it may suffer from a greater loss of activity when exposed to a less fluid membrane due to increased resistance against deep peptide penetration. This property of the conjugate is advantageous to systemic administration as the risk of hemolysis is minimized. In a fibroblast cell line NIH/3T3, which is a normal cell but shares more similarity with cancer cells in structure than erythrocyte, the activity of Dex-$(KW)_3$ is comparable to those observed in cancer cells (Supporting Information Figure S3). The lack of selectivity resulted from the subtle differences between transformed and nontransformed cells in the plasma membrane. Though it has been reported that acidic components such as phosphatidylserine and O-glycosulated mucin increased in and around the cancer cell membrane (*26*), which leads to increased membrane potential and thus preferential interaction of cancer cells with cationic lytic peptides, these differences were not significant enough to provide robust specificity. A tumor-targeting conjugate is currently being constructed in our lab to address the selectivity issue.

To conclude, a polyvalent lytic peptide−polymer conjugate Dex-$(KW)_3$ was designed, synthesized, and characterized. The new conjugate showed significantly enhanced activity against cancer cells compared to monomeric peptides, and the anticancer activity was not affected by the acquisition of multidrug resistance in cancer cells. The detrimental effect on erythrocytes was negligible. The encouraging in vitro data showed the potential of this new conjugate for systemic treatment against drug-resistant cancer. For the first time, the mechanism of polyvalency-mediated activity enhancement of lytic peptides was investigated by quantitative thermodynamic study. At the same bulk concentration, the polyvalent conjugate caused a stronger perturbation of membrane structure, which should be attributed to the increased local concentration of peptides in a polyvalent conjugate.

ACKNOWLEDGMENT

Peptides were synthesized using solid-phase synthesis by Dr. Sunny Cheung, the University of Hong Kong. Dr. Zhongyu Li in our group provided advice on the conjugation chemistry. Clara Eng, California Institute of Technology, contributed to the ITC investigation as part of her undergraduate summer research project. Hong Kong Research Grant Council (Earmarked Research Grant HKUST 6407/06M) provided financial support to this project.

Supporting Information Available: Binding isotherm construction procedure, NMR spectra of modified polymers and conjugate (Figure S1), effect of precursor polymer on cell viability (Figure S2), cytotoxicity test on noncancer fibroblast cell line NIH/3T3 (Figure S3), isothermal titration calorimetry of Dex-(KW)3 and free (KW)3 with lipid vesicles (Figure S4), integrity test of lipid vesicles at the highest peptide/lipid ratio in isothermal titration (Table S1). These materials are available free of charge via the Internet at http://pubs.acs.org.

LITERATURE CITED

(1) Gottesman, M. M., Fojo, T., and Bates, S. E. (2002) Multidrug resistance in cancer: Role of ATP-dependent transporters. *Nat. Rev. Cancer 2*, 48–58.
(2) Hancock, R. E. W., and Sahl, H. G. (2006) Antimicrobial and host-defense peptides as new anti-infective therapeutic strategies. *Nat. Biotechnol. 24*, 1551–1557.
(3) Leuschner, C., and Hansel, W. (2004) Membrane disrupting lytic peptides for cancer treatments. *Curr. Pharm. Des. 10*, 2299–2310.
(4) Papo, N., and Shai, Y. (2005) Host defense peptides as new weapons in cancer treatment. *Cell. Mol. Life Sci. 62*, 784–790.
(5) Zasloff, M. (2002) Antimicrobial peptides of multicellular organisms. *Nature 415*, 389–395.
(6) Shai, Y. (2002) Mode of action of membrane active antimicrobial peptides. *Biopolymers 66*, 236–248.
(7) Matsuzaki, K. (1999) Why and how are peptide-lipid interactions utilized for self-defense? Magainins and tachyplesins as archetypes. *Biochim. Biophys. Acta 1462*, 1–10.
(8) Mammen, M., Choi, S. K., and Whitesides, G. M. (1998) Polyvalent interactions in biological systems: Implications for design and use of multivalent ligands and inhibitors. *Angew. Chem., Int. Ed. 37*, 2755–2794.
(9) Arnusch, C. J., Branderhorst, H., De Kruijff, B., Liskamp, R. M. J., Breukink, E., and Pieters, R. J. (2007) Enhanced membrane pore formation by multimeric/oligomeric antimicrobial peptides. *Biochemistry 46*, 13437–13442.
(10) Liu, Z. G., Deshazer, H., Rice, A. J., Chen, K., Zhou, C. H., and Kallenbach, N. R. (2006) Multivalent antimicrobial peptides from a reactive polymer scaffold. *J. Med. Chem. 49*, 3436–3439.
(11) Tam, J. P., Lu, Y. A., and Yang, J. L. (2002) Antimicrobial dendrimeric peptides. *Eur. J. Biochem. 269*, 923–932.
(12) Maeda, H. Tumor-selective delivery of macromolecular drugs via the EPR effect: background and future prospects, *Bioconjugate Chem. 21*, 797−802.

(13) Snyder, S. L., and Sobocinski, P. Z. (1975) An improved 2,4,6 trinitrobenzenesulfonic acid method for the determination of amines. *Anal. Biochem. 64*, 284–288.
(14) Seelig, J. (1997) Titration calorimetry of lipid-peptide interactions. *Biochim. Biophys. Acta 1331*, 103–116.
(15) Chen, P. W., Shyu, C. L., and Mao, F. C. (2003) Antibacterial activity of short hydrophobic and basic-rich peptides. *Am. J. Vet. Res. 64*, 1088–1092.
(16) Schibli, D. J., Epand, R. F., Vogel, H. J., and Epand, R. M. (2002) Tryptophan-rich antimicrobial peptides: comparative properties and membrane interactions. *Biochem. Cell Biol. 80*, 667–677.
(17) Almeida, P. F., and Pokorny, A. (2009) Mechanisms of antimicrobial, cytolytic, and cell-penetrating peptides: from kinetics to thermodynamics. *Biochemistry 48*, 8083–8093.
(18) Ohsaki, Y., Gazdar, A. F., Chen, H. C., and Johnson, B. E. (1992) Antitumor-activity of magainin analogs against human lung-cancer cell-lines. *Cancer Res. 52*, 3534–3538.
(19) Seelig, J. (2004) Thermodynamics of lipid-peptide interactions. *Biochim. Biophys. Acta 1666*, 40–50.
(20) Dathe, M., Nikolenko, H., Klose, J., and Bienert, M. (2004) Cyclization increases the antimicrobial activity and selectivity of arginine- and tryptophan-containing hexapeptides. *Biochemistry 43*, 9140–9150.
(21) Haug, B. E., Stensen, W., Stiberg, T., and Svendsen, J. S. (2004) Bulky nonproteinogenic amino acids permit the design of very small and effective cationic antibacterial peptides. *J. Med. Chem. 47*, 4159–4162.
(22) Sundriyal, S., Sharma, R. K., Jain, R., and Bharatam, P. V. (2008) Minimum requirements of hydrophobic and hydrophilic features in cationic peptide antibiotics (CPAs): pharmacophore generation and validation with cationic steroid antibiotics (CSAs). *J. Mol. Model. 14*, 265–278.
(23) Sato, H., and Felix, J. B. (2006) Peptide-membrane interactions and mechanisms of membrane destruction by amphipathic alpha-helical antimicrobial peptides. *Biochim. Biophys. Acta 1758*, 1245–1256.
(24) Yeagle, P. L. (1985) Cholesterol and the cell membrane, *Biochim. Biophys. Acta 822*.
(25) Araki, K., and Rifkind, J. M. (1980) Erythrocyte membrane cholesterol: An explanation of the aging effect on the rate of hemolysis. *Life Sci.* 26.
(26) Sarah, R., Dennison, M. W., Harris, F., and Phoenix, D. A. (2006) Anticancer α-helical peptides and structure/function relationships underpinning their interactions with tumor cell membranes, *Curr. Protein Pept. Sci. 7*.

BC1002899

Synthesis, characterization and thermodynamic study of a polyvalent lytic peptide-polymer conjugate as novel anticancer therapeutics

Jieying ZHONG, Ying CHAU*

Figure S1(A). ^{1}HNMR spectrum of carboxylmethyl dextran……...2

Figure S1(B). ^{1}HNMR spectrum of alkynyl dextran…….2

Figure S1(C). ^{1}HNMR spectrum of conjugate Dex-$(KW)_3$……...……3

Figure S2. Effect of precursor polymer on cell viability……...3

Figure S3. Effect of Dex-$(KW)_3$ on non-cancer fibroblast cell line NIH/3T3…...…4

Figure S4. Isothermal titration calorimetry of Dex-$(KW)_3$ and free $(KW)_3$ with lipid vesicles …….5

Table S1. Diameter of lipid vesicles at the highest peptide/lipid ratio in isothermal titration……...6

Isotherm construction……..6

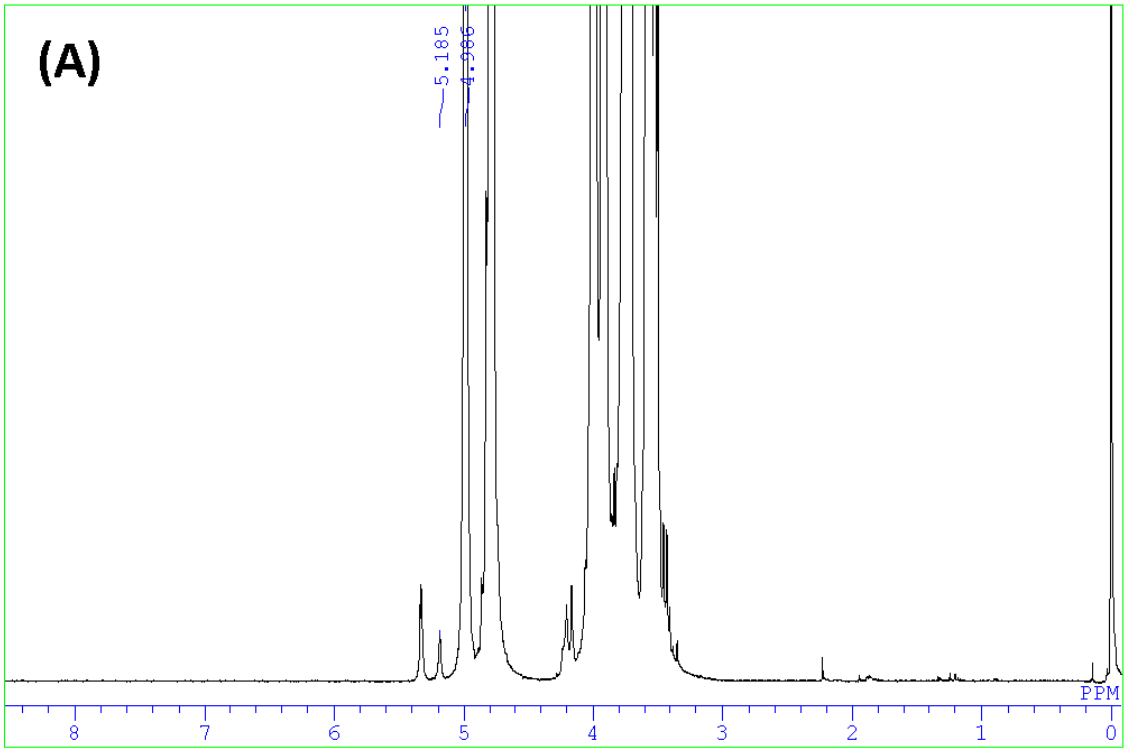


Figure S1(A). ^{1}HNMR spectrum of carboxylmethyl dextran

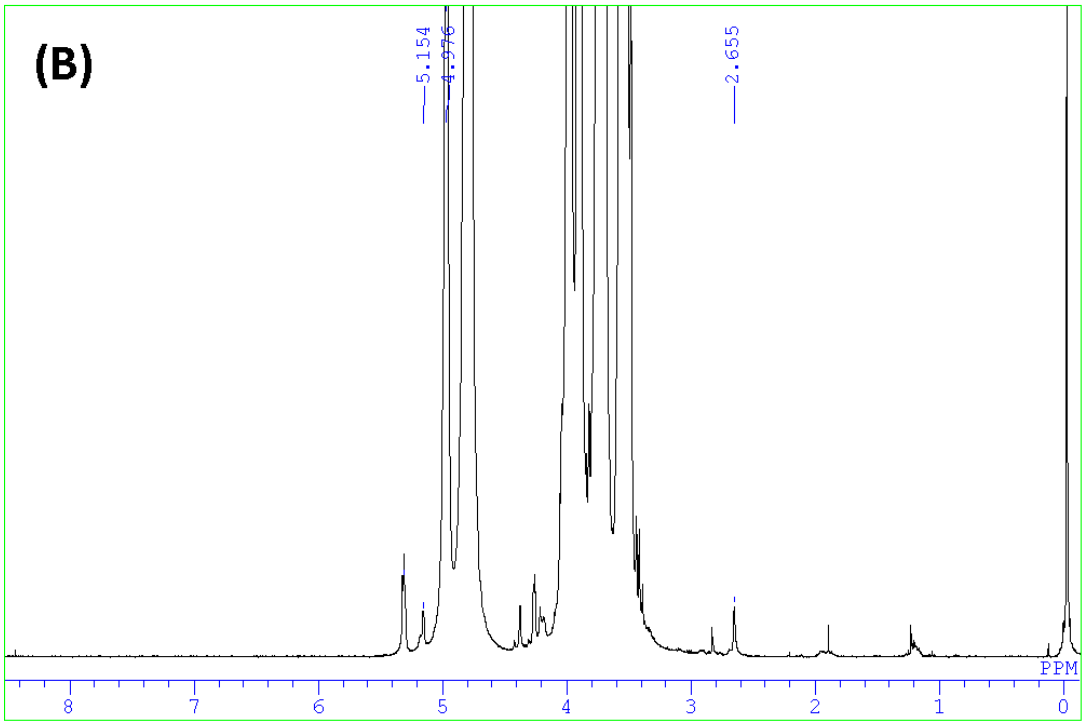


Figure S1(B). ^{1}HNMR spectrum of alkynyl dextran

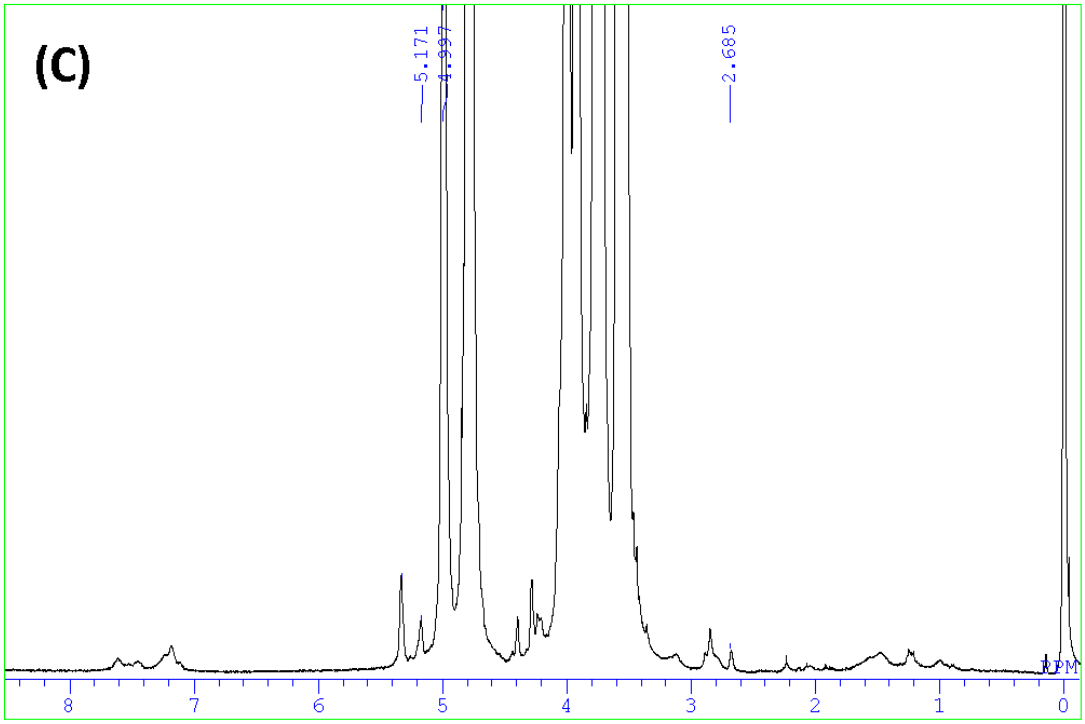


Figure S1(C). ^{1}HNMR spectrum of conjugate Dex-$(KW)_3$

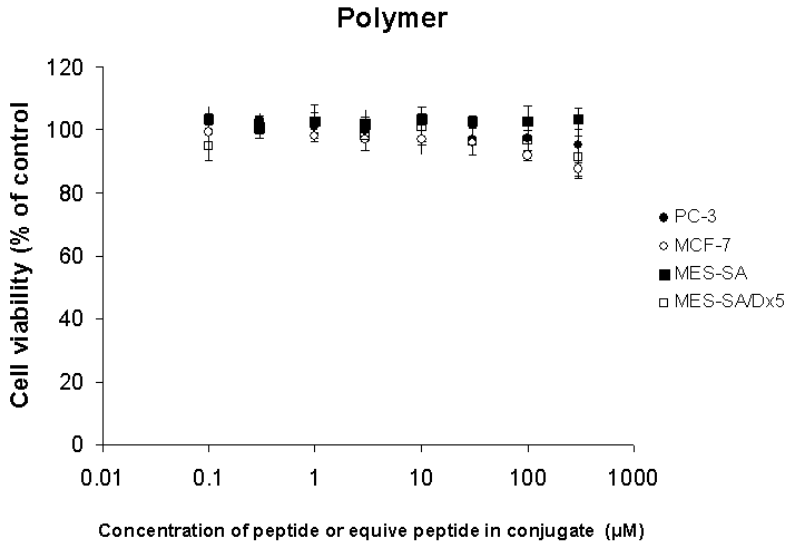


Figure S2. Effect of precursor polymer on cell viability

Alkynyldextran of equivalent polymer concentration to conjugate was applied to all the cancer cell lines that have been used in this study. The effect of precursor polymers on cell viability was measured by MTT assay after 3-hour incubation. Cell viability was normalized by control and shown as the percentage of viability. The result is the average of three independent tests.

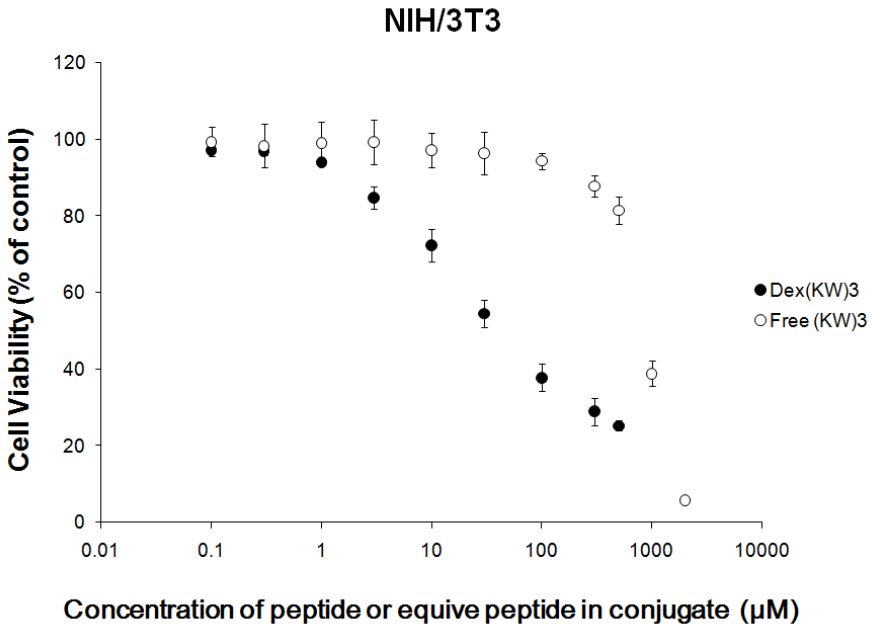


Figure S3. Effect of Dex-$(KW)_3$ on non-cancer fibroblast cell line NIH/3T3

Dex-$(KW)_3$ was applied to non-transformed fibroblast cell line NIH/3T3 at indicated equivalent peptide concentrations and allowed for 3-hour incubation. Cytotoxicity was measured by MTT assay. Free $(KW)_3$ was subjected to the same procedure for comparison. Cell viability was normalized by control and shown as the percentage of viability. The result is an average of at least three independent tests.

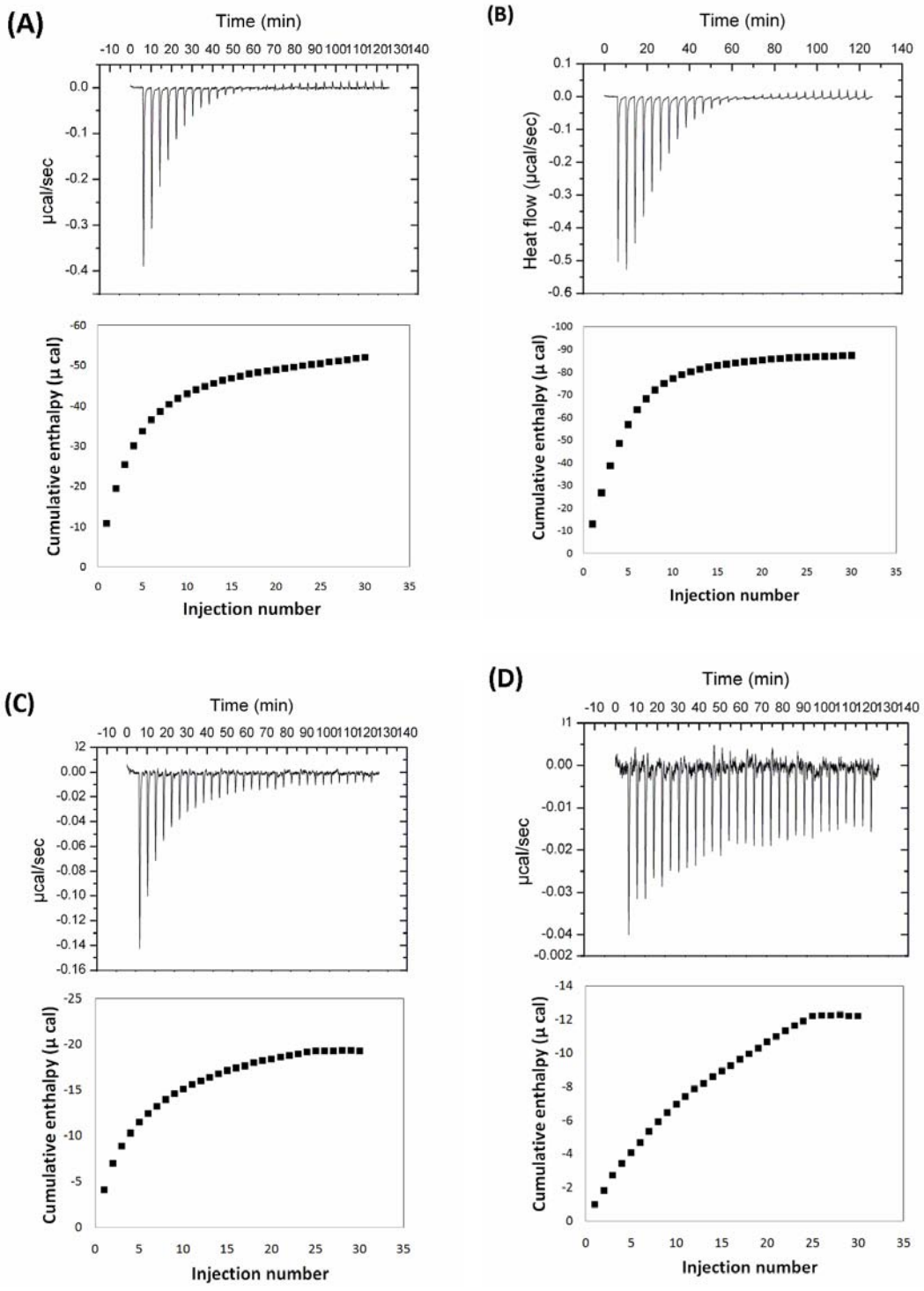


Figure S3. Isothermal titration calorimetry of Dex-$(KW)_3$ and free $(KW)_3$ with lipid vesicles.

The upper panel of each figure shows the calorimeter traces. Each peak represents an injection of 6 µL of small unilamellar vesicles suspension (lipid concentration = 10

mM) into the calorimeter cell containing conjugate or free peptide solution (equivalent peptide concentration = 10 μM, except (D) where peptide concentration = 2 μM). The lower panel shows the cumulative reaction enthalpy（$\sum_1^k \Delta h_k$）after each injection. (A) DOPC/DOPG(75:25) SUV/Dex-$(KW)_3$; (B) DOPC/DOPG(75:25) SUV/free $(KW)_3$; (C) DOPC SUV/ Dex-$(KW)_3$; (D) DOPC SUV/ free $(KW)_3$.

Table S1. Diameter of lipid vesicles at the highest peptide/lipid ratio in isothermal titration

	DOPC SUV	**DOPC/DOPG SUV (75:25)**
Buffer	32.2 ± 2.7 nm	26.2 ± 3.3 nm
Dex-$(KW)_3$	31.5 ± 0.4 nm	31.0 ± 1.2 nm
	31.2 ± 0.8 nm	31.0 ± 4.4 nm
	31.3 ± 0.6 nm	33.1 ± 2.3 nm
Free $(KW)_3$	33.0 ± 4.1 nm	31.0 ±11.9 nm
	30.1 ± 1.1 nm	28.7 ± 9.6 nm
	30.0 ± 1.4 nm	29.6 ± 7.3 nm

SUVs (41.2 μM lipid concentration) were mixed with conjugate and free peptide (10 μM equiv peptide concentration) respectively. The mixture resembles the condition in the reaction cell of isothermal titration calorimeter after the first injection of SUVs, when the ratio of lipid/peptide has the highest value. The diameter of SUVs in buffer indicates the original size of vesicles. Vesicles were subjected to particle sizing by dynamic light scattering (DLS). The effect of conjugate and peptide on vesicle integrity at the particular titration conditions were evaluated by comparing the size of lipid vesicles in the presence and absence of peptide or conjugate. MeasurementS were repeated three times for conjugate or peptide treated vesicles.

Isotherm construction

The experimentally measured heat of reaction at the kth injection is denoted as Δh_{k}, while $\sum_1^{\mathrm{k}} \Delta h_k$ is the cumulative heat of the first k injections and $\sum_1^{\mathrm{n}} \Delta h_{\mathrm{n}}$ is the total heat of all injections (provided $\Delta h_{\mathrm{n}} = 0$). After k injections, the fraction of peptide bound to the lipid membrane is given by

$$X_{\mathrm{p}}^{(k)} = n_{\mathrm{p}}^{(k)}/n_{\mathrm{p}} = \sum_1^k \Delta h_k \;/\; \sum_1^n \Delta h_k$$

Here $n_{\mathrm{p}}^{(k)}$ is the molar amount of bound peptide after k injections and $\mathrm{n_p}$ is the total amount of peptide in the calorimeter cell. $X_{\mathrm{p}}^{(k)}$ approaches its maximal value 1 at the end of titration since all the peptides have bound to the membrane. The

concentration of peptide free for binding $c_f^{(k)}$ after each injection can be calculated according to

$$c_f^{(k)} = c_p^o \left(1 - X_p^{(k)}\right)$$

where c_p^o is the initial peptide concentration in calorimeter cell. The lipid concentration after kth injection $n_L^{(k)}$ can be calculated by

$$n_L^{(k)} = k \cdot V_{inj} \cdot c_L^o$$

where V_{inj} is the injection volume per titration step and c_L^o is the concentration of stock lipid solution in the needle. Usually peptides cannot interact with the lipids inside, only the lipid molecules in the outer leaflet are available for peptide binding. It was reported that for the SUVs produced by sonication with the diameter about 30 nm, the molar fraction of lipid molecules in the outer leaflet is about 60% (*1*). The degree of binding after *k*th injection $X_b^{(k)}$ is defined as the molar ratio of bound peptide and total available lipid as below

$$X_b^{(k)} = n_p^{(k)} / \left(n_L^{(k)} \cdot 0.6\right)$$

where 0.6 is the correction factor that takes into account the accessible lipid on the outside layer. The isotherm is obtained by plotting the degree of binding $X_b^{(k)}$ as a function of the concentration of peptide free for binding $c_f^{(k)}$. The apparent binding constant, K_{app}, is given by the slope of the curve.

$$K_{app} = X_b / C_f$$

The change of free energy and entropy were calculated by

$$\Delta G = -RT(\ln 55.5K)$$

$$\Delta G = \Delta H - T\Delta S$$

where R is the gas constant, factor 55.5 is the molar concentration of water, $K^* = 55.5K_{app}$ is the binding constant if the concentration of peptide is referred to 1 mol H_2O.

(1) Beschiaschvili, G., and Seelig, J. (1992) PEPTIDE BINDING TO LIPID BILAYERS - NONCLASSICAL HYDROPHOBIC EFFECT AND

MEMBRANE-INDUCED PK SHIFTS. *Biochemistry 31*, 10044-10053.

Bishydrazide Glycoconjugates for Lectin Recognition and Capture of Bacterial Pathogens

Avijit Kumar Adak,[†] Alexei P. Leonov,[†] Ning Ding,[‡] Jyothi Thundimadathil,[§] Sumith Kularatne,[†] Philip S. Low,[†] and Alexander Wei*[,†]

Department of Chemistry, 560 Oval Drive, Purdue University, West Lafayette, Indiana 47907-2084, United States. Received June 30, 2010; Revised Manuscript Received September 11, 2010

Bishydrazides are versatile linkers for attaching glycans to substrates for lectin binding and pathogen detection schemes. The α,ω-bishydrazides of carboxymethylated hexa(ethylene glycol) (**4**) can be conjugated at one end to unprotected oligosaccharides, then attached onto carrier proteins, tethered onto activated carboxyl-terminated surfaces, or functionalized with a photoactive cross-linking agent for lithographic patterning. Glycoconjugates of bishydrazide **4** can also be converted into dithiocarbamates (DTCs) by treatment with CS_2 under mild conditions, for attachment onto gold substrates. The immobilized glycans serve as recognition elements for cell-surface lectins and enable the detection and capture of bacterial pathogens such as *Pseudomonas aeruginosa* by their adsorption onto micropatterned substrates. A detection limit of 10^3 cfu/mL is demonstrated, using a recently introduced method based on optical pattern recognition.

INTRODUCTION

Pathogenic microorganisms are an omnipresent threat to global biosecurity, and effective biodetection strategies are necessary to control the spread of infectious diseases. One viable approach to pathogen detection is to develop diagnostic technologies based on "immutable" recognition of ligands presented on cell surfaces, a vital first step in the cycle of infection. These recognition elements are often low molecular weight molecules such as glycans, which are exploited by pathogens for gaining entry into their host cells. Pathogens must maintain this ligand affinity in order to remain virulent, as those which undergo mutations that disable recognition can no longer infect their target cells. Glycan-based strategies have proven to be particularly successful in detecting bacteria that use lectins for adhesion to host cell membranes (*1*−*8*). Furthermore, the immutability of this functional recognition provides an important advantage over antibody-based detection schemes, which are susceptible to nonfunctional mutations that are often irrelevant to pathogen virulence.

Glycoconjugates are also of considerable importance for high-throughput diagnostics or screening of carbohydrate-binding proteins associated with various biological functions or disease states (*9*−*12*). Several different covalent chemistries have been successfully implemented for surface functionalization, such as thiol−ene and thiol−maleimide additions (*13*−*16*), Diels−Alder or Cu-catalyzed Huisgen cycloadditions (*17*−*19*), nucleophilic addition to epoxides and isothiocyanates (*20, 21*), amide bond ligation (*22, 23*), and Staudinger ligation (*24*). However, many of these methods require that glycans be in a protected form prior to linker installation and may involve multiple synthetic or purification steps.

Chemoselective coupling of bifunctional linkers to underivatized glycans is an attractive option, particularly if the reducing-end sugar can be retained in its native cyclized form. Traditional methods involve covalent attachment to the free hemiacetal via reductive amination or glycation, but while the conditions are mild, they sacrifice the reducing-end sugar by generating an open-chain structure (*25, 26*). However, weakly basic nucleophiles like aminooxy ethers (H_2NO-R, MeHNO-R) and hydrazides (H_2NNHCO-R) have been shown to condense with hemiacetals in aqueous solutions for efficient glycoconjugation (*27*−*39*). Hydrazides have been widely used for bioconjugation onto aldehyde- or carboxyl-presenting surfaces (*25*); conversely, hydrazides can also be presented on substrates for the specific generation of carbohydrate microarrays.

Here, we investigate α,ω-bishydrazides as bifunctional linkers for conjugating underivatized glycans onto various substrates and present several surface functionalization methods with application toward the binding of lectins and pathogenic bacteria. Bishydrazides can be useful as chelating agents or as supramolecular recognition motifs (*40, 41*), but are most often applied as polymer or biopolymer cross-linking agents (*42*−*44*). At first glance, bishydrazides appear to be an unlikely choice for heterofunctionalization; however, we find that they can be selectively monofunctionalized and are versatile linkers for glycoconjugate chemistry.

In this work, we use glycan-bishydrazide conjugates to target specific lectins and adhesins found in *Pseudomonas aeruginosa*, an opportunistic, Gram-negative bacteria often found in hospital settings. Nosocomial *Pseudomonas* infections have become increasingly drug-resistant and can be especially pernicious in immunocompromised patients or those suffering from cystic fibrosis, so there is a strong need to develop detection platforms against this pathogen. Epidemiological studies suggest that the risk of *Pseudomonas* infections in healthy individuals increases with environmental pathogen counts above 10^3 cfu/mL (*45, 46*).We aim to address this important public health concern by focusing on glycan recognition as a mechanism for detecting virulent pathogens such as *Pseudomonas* at densities as low as 10^3 cfu/mL, the estimated threshold for nosocomial infection.

EXPERIMENTAL PROCEDURES

General Procedures. All starting materials and reagents were obtained from commercial sources and used as received unless otherwise noted. Fuc(α1→2)Gal(β1→4)Glc (2′-fucosyllactose

* To whom correspondence should be addressed. E-mail: alexwei@purdue.edu; Tel: (765) 494-5257; Fax: (765) 494-0239.

[†] Purdue University.

[‡] Present address: Department of Medicinal Chemistry, School of Pharmacy, Fudan University, Shanghai 201203, P.R. China.

[§] Present address: Peptisyntha, Inc., Torrance, CA 90501.

10.1021/bc100288c © 2010 American Chemical Society
Published on Web 10/06/2010

3) was purchased from V-laboratories, Inc., and GalNAc(β1→4)-Gal(β1→4)Glc (pulmonary trisaccharide **2**) was prepared by multistep synthesis (see below). Bovine serum albumin (BSA), galactose-binding lectin from *Arachis hypogaea* (peanut lectin), antilectin rabbit IgG, and FITC-labeled antirabbit goat IgG were purchased from Sigma and used as received. *Pseudomonas aeruginosa* (PA01 strain) was obtained from ATCC and grown overnight on agar plates (15 g/L of Bacto Agar, 8 g/mL of Difco Nutrient Broth) at 37 °C. CS_2, CH_2Cl_2, and CH_3CN were freshly distilled from CaH_2 before use; anhydrous and anaerobic MeOH and THF were passed through activated alumina and dipensed from a solvent purification system (MBraun). Reactions were carried out in oven-dried glassware under an inert atmosphere, and solvents were freshly distilled from CaH_2 prior to use. ^1H and ^{13}C NMR spectra were recorded on a Bruker DRX 400 spectrometer operating at 400 and 100 MHz respectively. Chemical shifts (δ) are reported in ppm and referenced to the solvent used ($CDCl_3$, δ 7.24 and 77.23; CD_3OD, δ 3.31 and 49.15; D_2O, δ 4.80), with coupling constants (*J*) reported in Hz. Deionized water with a resistivity of >18 MΩ·cm was obtained from an ultrafiltration system (Milli-Q, Millipore) and passed through a 0.22 μm filter to remove particulate matter. Silica gel chromatography was performed using ICN SiliTech 32−63 D; reverse-phase HPLC was performed using a Phenomenex Synergi C-18 column (250 × 21.2 mm, 4 μM, 80 Å) with UV detection at 214 nm, using an aqueous CH_3CN solvent gradient with a linear flow rate of 10 mL/min.

Neoglycoprotein Formation. In a typical experiment, a freshly prepared solution of BSA (10 mg) in phosphate buffered solution (PBS, pH 7.4, 200 μL) was treated with 1-ethyl-3-(3-dimethylaminopropyl)carbodiimide hydrochloride (EDC·HCl, 3 mg in 50 μL PBS) and gently stirred at rt for 1 h. The activated protein solution was then treated with pulmonary trisaccharide−hydrazide conjugate **7** (5.1 mg) in 200 μL PBS, then stirred for another 2 h, followed by membrane dialysis and passage through a 0.45 μm filter to remove aggregates and particulate matter. These BSA glycoconjugates could be stored safely at 4 °C for several months.

In Situ Dithiocarbamate (DTC) and Monolayer Formation (*47, 48*). In a typical experiment, a 10 mM solution of lactose−bishydrazide conjugate **6** in deaerated methanol (1.5 mg in 200 μL) was treated with 10 mM solutions of CS_2 (200 μL) and Et_3N (200 μL), then stirred at rt for 1 h in a capped vial prior to use (see below). In situ DTC formation was monitored by diluting aliquots of the reaction mixture in deionized water, then measuring increases in characteristic absorption peak intensities at 250 and 292 nm using a Cary-50 spectrophotometer (cell path length = 1 cm).

DTC-anchored monolayers (DAMs) were produced from a freshly prepared solution of **6**-DTC, diluted 10-fold with deionized water to a final concentration of 1 mM. A 30 μL aliquot of this stock solution was spread across a lightly oxidized PDMS stamp, then patterned onto Au substrates by microcontact printing (see below). Lactose-terminated DAMs were treated with a solution of peanut lectin (50 μg/mL) and visualized by fluorescence immunostaining. The robustness of the patterned DAMs was evaluated by measuring changes in relative emission intensities over time, with exposure to 2-mercaptoethanol (10 or 100 μM) in PBS. Mean luminosity values and standard deviations were taken from selected regions on the printed substrate using Photoshop v.7.0.1 (Adobe Systems).

UV Photolithography. Glass substrates coated with a 50 nm Au layer (1.2 × 1.2 cm^2, Reichert) were cleaned with a piranha solution (2 parts 18 M H_2SO_4, 1 part 30% H_2O_2) for 3 min, then thoroughly rinsed with deionized water and dried under a stream of argon. (Caution: Piranha solution is a strong oxidizing agent, and should be handled with extreme care.) Freshly cleaned substrates were coated with BSA by soaking in a 1 wt % solution in PBS for several hours at rt, followed by immersion in a solution of photoactive glycoconjugate (20 mM in 2:1 MeOH/CH_2Cl_2) for 5 min. The dried films were covered by a quartz photomask having linewidths of 10 or 15 μm and grating periods of 20 μm (Advanced Reproductions Corp.), then exposed to a short-wave ultraviolet lamp (Spectroline, ENF-240C) operating at 254 nm for 25 min, followed by a rinse with MeOH. Microcontact printing (see below) could also be used for patterning photoactive glycoconjugates onto BSA-coated glass slides.

Microcontact Printing (μCP). A freshly prepared poly(dimethylsiloxane) (PDMS) stamp (grating period a = 20 μm; line width = 15 μm) was lightly oxidized by a 15 s exposure in a plasma cleaner, then coated with 30 μL of an aqueous solution of **6**-DTC for 2 min (see above for preparation of stock solution). The PDMS stamp was dried in air after blotting excess solution, then pressed lightly onto a roughened Au substrate (see below) at an applied pressure of 6 kPa for 3 s, as measured by a mechanical stamper developed in our laboratories. A brass plate was placed at the top of the stamp for even distribution of pressure, and the stamp remained in conformal contact with the substrate for an additional 5 min.

Similar μCP conditions were used to pattern BSA glycoconjugates onto smooth Au substrates. A 30 μL aliquot of a 1 wt % BSA−lactose hydrazide conjugate (**6**-BSA) in PBS was cast onto a lightly oxidized PDMS stamp as described above and allowed to sit for 2 min prior to blotting. The PDMS stamp was dried in air, pressed lightly onto the substrate at an applied pressure of 6−12 kPa for 3 s, and then allowed to remain in conformal contact without added pressure for another 5 min. The micropatterned substrate was washed sequentially with PBS, PBS containing 0.05% Tween-20, and then deionized water. The patterned substrate was further incubated with a 5% BSA solution in PBS for 2 h, then washed as above prior to use.

Glycan-Directed Affinity Binding and Imaging. Micropatterned glycoconjugates were exposed to either soluble lectins or to live bacterial cultures and visualized by immunofluorescent staining (bound lectin) or darkfield microscopy (bound bacteria) using an upright microscope (Olympus BH2-RFL-T3) equipped with a darkfield condensor, a high-pressure Hg lamp and filter set for FITC emission, and a DP70 camera for image acquisition. Fluorescence imaging was performed either on glass or on roughened Au substrates; the latter were prepared by immersing clean Au substrates into a solution of $AgNO_3$ (3.7 mM) and hydroquinone (120 mM) in 1.3 M citric acid buffer (pH 3.5) for 1.5 min, followed by a quick rinse with deionized water and immersion in an aqueous $HAuCl_4$ solution (0.5 mM) for 30 min. Roughened Au substrates were dried in air, prior to use.

For affinity patterning with proteins, micropatterned substrates were incubated with a dilute solution of lectin from *Arachis hypogaea* (peanut lectin, 50 μg/mL in PBS) for 2 h at 4 °C. The chip was washed with PBS, then treated with a solution of antipeanut lectin rabbit IgG (1 μg/mL in PBS) for 2 h at 4 °C, then washed again and treated with a solution of FITC-labeled antirabbit goat IgG (1 μg/mL in PBS) for another 2 h at 4 °C. The chip was washed with PBS, deionized water, and then dried under a stream of air prior to fluorescence imaging.

For affinity patterning with bacteria, *Pseudomonas aeruginosa* (PA01 strain, ATCC) was cultured in NB broth containing choline (0.2% w/v), the latter being necessary for the ectopic expression of fucose-binding lectin PA-IIL (*49*). Micropatterned substrates were incubated with suspensions of live *Pseudomonas* for 1 h at room temperature, at concentrations ranging from 10^8 to 10^2 cfu/mL. After incubation, the chip was washed with PBS and deionized water prior to darkfield imaging. The density

of live *Pseudomonas* was estimated by correlating turbidity measurements (ca. 10^9 cfu/mL at O.D. 1) with colony counts obtained by plating serial dilutions. Fluorescent staining of active cultures (SYTO 9/propidium iodide (PI) stains, Invitrogen) confirmed that >90% of the bacteria were alive prior to their exposure to glycan-patterned substrates.

Darkfield images were subjected to fast Fourier transform (FFT) for pattern demodulation to reveal characteristic peaks in reciprocal lattice space ($k = 1/a$) indicating pathogen capture, according to a recently established protocol (*50*). Standard sizes and magnification were established for each micropatterned image, so that the units defining periodicity (in μm) were correctly translated into reciprocal lattice units (in μm^{-1}) in the spectra derived from the FFT images. Signal-to-noise (*S*/*N*) levels were determined as the ratio of the peak value at 0.05 μm^{-1} (after background subtraction) to the standard deviation of background intensity; signal qualities were considered acceptable above $S/N = 3$.

Glycoconjugate-Lectin Binding Immunoassays. Each incubation was performed for 2 h at rt, followed by rinsing three times with PBS to remove excess proteins prior to the next step. 96-well microtiter plates were coated with **6**-BSA conjugate (10 mg/mL), blocked with a 1% BSA solution to minimize nonspecific protein adsorption, and then incubated with increasing concentrations of peanut lectin in the presence or absence of 100-fold excess lactose. Wells were then treated with antilectin rabbit IgG (1 μg/mL), followed by antirabbit horseradish peroxidase (HRP) IgG (1 μg/mL). The optical absorbances of the wells were analyzed using a microplate reader (VERSA$_{max}$, Molecular Devices) following addition of the HRP substrate (100 μL). Untreated and antilectin rabbit IgG treated wells (without primary antibody) in PBS served as negative controls.

For flow cytometry, carboxylic acid functionalized microspheres were conjugated to lactose−bishydrazide **6** via standard EDC coupling for 16 h at rt, followed by multiple washes with PBS. The lactose-conjugated microspheres were dispersed in PBS (1.2 mL) and split into several Eppendorf tubes, which were incubated with increasing concentrations of peanut lectin in the presence or absence of 100-fold excess lactose. After incubating for 2 h at rt, tubes were rinsed and subjected to sequential incubation with antilectin rabbit IgG and antirabbit FITC IgG as described above. The microspheres were then analyzed for fluorescent immunolabeling using a flow cytometer (Cytomics F500, Beckman Coulter, 10^4 microspheres/sample). Untreated and antilectin rabbit IgG (without primary antibody) treated microspheres in PBS served as negative controls.

*Hexa(ethylene glycol)-Linked Bishydrazide (**4**).* A solution of hexa(ethylene glycol) (5.0 g, 17.70 mmol) in dry THF (50 mL) at room temperature was treated portionwise with potassium *tert*-butoxide (9.92 g, 88.54 mmol) at rt, then stirred for 30 min. The reaction mixture was treated dropwise with ethyl bromoacetate (20 mL, 170 mmol), then stirred at reflux for 20 h. The reaction mixture was cooled to rt, filtered and concentrated, and then purified by silica gel chromatography (EtOAc/hexanes 1:1) to yield pure diethyl ester as a colorless oil (5.5 g, 68%). ^{1}H NMR (400 MHz, $CDCl_3$) δ 4.62 (s, 4H), 4.17 (q, 4H, J = 7.2 Hz), 3.71−3.69 (m, 4H), 3.66−3.63 (m, 8H), 3.61−3.59 (m, 12H), 1.23 (t, 6H, J = 7.2 Hz). ^{13}C NMR (100 MHz, $CDCl_3$) δ 170.01, 167.44, 71.01, 70.85, 70.63, 68.88, 68.36, 61.60, 60.79, 14.16. MS (ESI) calcd for $C_{20}H_{38}O_{11}[M]^+$ *m*/*z* 454.24; found: *m*/*z* 454.98.

The hexa(ethylene glycol)-linked diester (1.0 g, 2.2 mmol) was dissolved in MeOH (20 mL) passed through an activated alumina column (MBraun) and treated with anhydrous hydrazine (0.34 mL, 11.0 mmol). The reaction mixture was stirred at rt for 24 h, then concentrated followed by the azeotropic removal of hydrazine using toluene (3 × 10 mL), and finally dried in vacuo to afford a light yellow oil (0.92 g, 98%). The resulting bishydrazide could be used to prepare glycoconjugates without further purification. ^{1}H NMR (400 MHz, $CDCl_3$) δ 8.61 (br s, 2H), 4.06 (s, 4H), 3.74−3.58 (m, 28H). ^{13}C NMR (100 MHz, CD_3OD) δ 173.72, 171.15, 73.66, 72.10, 71.51, 71.44, 71.75, 62.12. MS (ESI) calcd for $C_{16}H_{34}N_4O_9Na$ $[M+Na]^+$ *m*/*z* 449.44; found: *m*/*z* 449.02.

*Heptanediol-Linked Bishydrazide (**5**).* Heptane-1,7-diol (1.1 g, 7.56 mmol) was treated with ethyl bromoacetate (4.35 mL, 37.82 mmol) as described above, followed by workup and silica gel purification (EtOAc/hexanes 1:2) to yield the pure diester as a colorless oil (0.92 g, 36%). ^{1}H NMR (400 MHz, $CDCl_3$) δ 4.15 (t, 4H, J = 6.7 Hz), 3.81 (s, 4H), 3.61 (t, 4H, J = 6.1 Hz), 1.63 (quint, 4H, J = 6.4 Hz), 1.53 (quint, 4H, J = 6.7 Hz), 1.34 (3, 6H), 1.26 (m, 2H). ^{13}C NMR (100 MHz, $CDCl_3$) δ 167.52, 66.54, 63.04, 32.77, 29.10, 28.48, 26.13, 25.87, 25.76.

Anhydrous hydrazine (0.185 mL, 5.91 mmol) was treated with heptanediol-linked diester (0.36 g, 1.18 mmol) in methanol (10 mL), according to the reaction conditions described above. After azeotropic removal of the volatiles using toluene, bishydrazide **5** was obtained as an oil (0.32 g, 92%) and could be used to prepare glycoconjugates without further purification. ^{1}H NMR (400 MHz, CD_3OD) δ 3.40 (t, 4H, J = 6.4 Hz), 1.40 (quint, 4H, J = 6.6 Hz), 1.25−1.21 (m, 10H). ^{13}C NMR (100 MHz, CD_3OD) δ 173.73, 172.39, 62.94, 33.57, 30.38, 26.90. MS (ESI) calcd for $C_{11}H_{24}N_4O_4$ $[M]^+$ *m*/*z* 276.17; found 276.76.

*Hexa(ethylene glycol)-Linked Lactose-Bishydrazide Conjugate (**6**).* A mixture of lactose (10 mg, 0.029 mmol) and bishydrazide linker **4** (124.6 mg, 0.29 mmol) in NaOAc buffer (1 mL, pH 4.2) was stirred at 70 °C for 2 days. The reaction mixture was evaporated under reduced pressure, then purified by reverse-phase HPLC (1−30% aq CH_3CN gradient over 60 min) to afford **6** as colorless oil (18.9 mg, 86%). ^{1}H NMR (400 MHz, CD_3OD) δ 4.62 (s, 1H), 4.34 (d, 1H, J = 7.5 Hz), 4.14 (d, 1H, J = 8.6 Hz), 4.09−4.03 (m, 3H), 3.98 (dd, 1H, J = 4.0, 12.0 Hz), 3.92 (dd, 1H, J = 4.0, 8.0 Hz), 3.84−3.79 (m, 2H), 3.78−3.74 (m, 2H), 3.70−3.65 (m, 22H), 3.59−3.52 (m, 6H), 3.49−3.46 (m, 2H). ^{13}C NMR (100 MHz, CD_3OD) δ 172.32, 171.81, 105.10, 91.89, 80.45, 77.76, 77.11, 76.63, 74.81, 73.66, 73.53, 72.51, 72.14, 72.07, 71.54, 71.31, 70.75, 70.29, 62.48, 62.21, 62.12. MS (ESI) calcd for $C_{28}H_{54}N_4O_{19}Na$ $[M+Na]^+$ *m*/*z* 773.32; found: *m*/*z* 773.37.

*Hexa(ethylene glycol)-Linked Pulmonary Trisaccharide-Bishydrazide Conjugate (**7**).* This compound was prepared according to the procedure above, starting from pulmonary trisaccharide **2** (32 mg, 0.058 mmol) and bishydrazide linker **4** (60.0 mg, 0.14 mmol). Purification by RP-HPLC (1−30% aq CH_3CN gradient over 60 min) yielded glycoconjugate **7** as a light-yellow oil (32 mg, 58%). ^{1}H NMR (400 MHz, CD_3OD) δ 4.61 (d, 1H, J = 8.3 Hz), 4.32 (d, 1H, J = 7.6 Hz), 4.14 (d, 1H, J = 5.5 Hz), 4.08−3.97 (m, 10H), 3.89−3.47 (m, 36H), 2.05 (s, 3H). ^{13}C NMR (100 MHz, CD_3OD) δ 180.31, 175.05, 105.05, 104.44, 93.98, 78.18, 76.80, 76.23, 75.98, 74.69, 74.14, 73.57, 73.07, 72.60, 71.44, 69.53, 62.61, 61.72, 55.05, 24.15, 23.18. MS (ESI) calcd for $C_{36}H_{67}N_5O_{24}Na$ $[M+Na]^+$ *m*/*z* 976.40; found: *m*/*z* 976.18.

*Hexa(ethylene glycol)-Linked 2′-Fucosyllactose-Bishydrazide Conjugate (**8**).* This compound was prepared according to the procedure above, starting from commercially available 2′-fucosyllactose (2.5 mg, 5.1 μmol) and bishydrazide linker **4** (21.8 mg, 51 μmol). Purification by RP-HPLC (1−40% aq CH_3CN gradient over 60 min) yielded glycoconjugate **8** as a colorless oil (2.9 mg, 51%). ^{1}H NMR (300 MHz, D_2O) δ 5.17 (d, 1H, J = 3.1 Hz), 4.38 (d, 1H, J = 7.7 Hz), 4.10 (m, 1H), 4.02−3.98 (m, 4H), 3.82 (m, 1H), 3.75−3.71 (m, 2H), 3.67−3.43 (m, 41H), 3.29 (m, 1H), 3.23 (m, 1H), 1.09 (d, 1.7H,

J = 6.6 Hz), 1.03 (d, 1.3H, J = 6.6 Hz). MS (ESI) calcd for $C_{34}H_{64}N_4O_{23}Na$ $[M+Na]^+$ *m/z* 919.38; found: *m/z* 919.70.

*Heptanediol-Linked Lactose-Bishydrazide Conjugate (**9**).* This compound was similarly prepared as that described above, starting from lactose (50 mg, 0.146 mmol) and 1,7-heptanediol bishydrazide **5** (201 mg, 0.736 mmol). Purification by RP-HPLC (1−50% aq CH_3CN gradient over 45 min) yielded glycoconjugate **9** as a light-yellow oil (54 mg, 62%). ^1H NMR (400 MHz, CD_3OD) δ 4.30 (d, 1H, J = 7.6 Hz), (d, 1H, J = 8.2 Hz), (d, 1H, J = 4.4 Hz), 3.97 (s, 2H), 3.83−3.77 (m, 2H), 3.67−3.59 (m, 4H), 3.54−3.45 (m, 4H), 3.41−3.35 (m, 2H), 3.22−3.19 (m, 1H), 1.92−1.69 (m, 14H). ^{13}C NMR (100 MHz, CD_3OD) δ 181.97, 173.86, 103.51, 89.97, 78.93, 76.39, 75.95, 75.52, 73.09, 71.55, 70.84, 69.18, 61.66, 61.01, 60.84, 23.98, 20.65, 20.44, 20.37. MS (ESI) calcd for $C_{23}H_{45}N_4O_{14}$ $[M+H]^+$ *m/z* 601.28; found: *m/z* 601.09.

*2-Deoxy-3,4,6-tri-O-acetyl-2-trichloroacetamido-β-D-galactopyranosyl-(1→4)-2,4,6-tri-O-benzyl-β-D-galactopyranosyl-(1→4)-1,2,3,6-tetra-O-benzyl-D-glucopyranose (**12**).* D-Galactosamine thiophenyl glycoside **10** (*51*) (36.8 mg, 0.066 mmol) and lactose derivative **11** (*52*) (43.0 mg, 0.044 mmol) were stirred under argon in dry CH_2Cl_2 (2 mL) for 30 min at rt in the presence of freshly activated, powdered 4 Å molecular sieves. The reaction mixture was cooled to −70 °C, then treated with *N*-iodosuccinimide (NIS, 17.8 mg, 0.079 mmol) and a catalytic amount of triflic acid (TfOH, 2.0 mg, 0.0132 mmol). The reaction mixture was slowly warmed to 0 °C, then stirred for an additional 4 h at rt. The reaction mixture was then neutralized with a few drops of triethylamine and filtered over a pad of Celite with rinsing by CH_2Cl_2. The mixture was washed with a 10% Na_2SO_3 solution followed by water, and the aqueous layer was extracted twice with CH_2Cl_2. The organic phases were collected and dried over anhydrous Na_2SO_4 and concentrated then purified by silica gel chromatography (EtOAc/hexanes 2:3) to afford trisaccharide **12** as a yellow oil (52.2 mg, 84%). ^1H NMR (400 MHz, $CDCl_3$) δ 7.44−7.25 (m, 35H, ArH), 6.23 (d, 1H, J = 10 Hz, NH), 5.26 (d, 1H, J = 2.8 Hz), 4.97 (d, 2H, J = 12.0 Hz), 4.94 (d, 2H, J = 12.0 Hz), 4.88 (d, 2H, J = 8.0 Hz), 4.85 (d, 2H, J = 8.0 Hz), 4.81 (d, 2H, J = 9.6 Hz), 4.78 (d, 2H, J = 8.0 Hz), 4.71 (d, 2H, J = 8.0 Hz), 4.66 (d, 2H, J = 12.0 Hz), 4.51 (d, 1H, J = 8.0 Hz), 4.49 (d, 1H, J = 8.0 Hz), 4.44 (d, 2H, J = 12.0 Hz), 4.13−3.98 (m, 5H), 3.90 (dd, 2H, J = 6.0, 11.2 Hz), 3.74−3.67 (m, 2H), 3.62−3.59 (m, 1H), 3.56 (d, 2H, J = 9.2 Hz), 3.49 (t, 1H, J = 7.6 Hz), 3.36 (d, 1H, J = 9.6 Hz), 2.09 (s, 3H), 2.03 (s, 3H), 1.99 (s, 3H). ^{13}C NMR (100 MHz, $CDCl_3$) δ 170.49, 170.44, 170.30, 162.00, 139.15, 138.66, 137.84, 137.56, 129.00, 128.88, 128.57, 128.42, 128.30, 128.16, 128.00, 127.94, 127.83, 127.70, 127.59, 102.77, 99.51, 92.53, 82.53, 81.76, 82.53, 81.76, 76.11, 75.43, 75.06, 74.32, 73.88, 71.29, 70.64, 69.95, 68.20, 66.31, 60.87, 53.43, 20.87, 20.78, 20.68. MS (MALDI-TOF) calcd for $C_{75}H_{80}Cl_3NO_{19}Na$ $[M+Na]^+$ *m/z* 1426.4287; found: *m/z* 1426.4573.

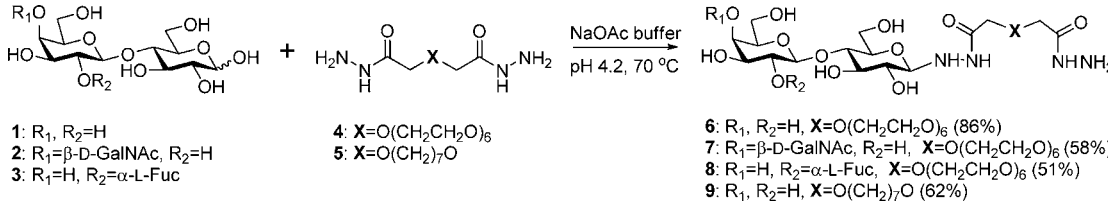
*2-Acetamido-2-deoxy-3,4,6-tri-O-acetyl-β-D-galactopyranosyl-(1→4)-2,4,6-tri-O-benzyl-β-D-galactopyranosyl-(1→4)-1,2,3,6-tetra-O-benzyl-D-glucopyranose (**13**).* A solution of trichloroacetamide **12** (50 mg, 0.036 mmol) in dry benzene (1 mL) was treated with tributyltin hydride (52.4 mg, 0.18 mmol) and 2,2′-azobis(isobutyronitrile) (AIBN, 5.86 mg, 0.036 mmol). The mixture was degassed for 15 min with argon, then heated to reflux for 1 h, cooled to rt, and poured into an aq solution of $NaHCO_3$, and extracted with CH_2Cl_2. The combined extracts were washed with brine, dried over anhydrous Na_2SO_4, and concentrated under reduced pressure. Purification of the residue by silica gel chromatography (EtOAc/hexanes 1:1) afforded acetamide **13** as a yellow oil (32.5 mg, 70%). ^1H NMR (400 MHz, $CDCl_3$) δ 7.53−7.23 (35H, ArH), 5.47 (d, 1H, J = 8.9 Hz, N*H*), 5.32 (d, 1H, J = 2.7 Hz), 4.97 (d, 1H, J = 8.0 Hz), 4.91 (d, 2H, J = 11.2 Hz), 4.87 (d, 1H, J = 8.6 Hz), 4.82 (d, 2H, J = 9.3 Hz), 4.78 (d, 2H, J = 10.6 Hz), 4.75 (d, 1H, J = 11.2 Hz), 4.65 (d, 2H, J = 11.2 Hz), 4.61 (d, 2H, J = 8.6 Hz), 4.57 (d, 1H, J = 4.0 Hz), 4.49 (d, 1H, J = 7.8 Hz), 4.42 (d, 1H, J = 10.2 Hz), 4.39 (d, 1H, J = 6.4 Hz), 4.34 (d, 1H, J = 12.0 Hz), 4.24 (d, 2H, J = 12.0 Hz), 4.20 (d, 1H, J = 10.6 Hz), 4.07 (dd, 1H, J = 5.8, 11.2 Hz), 4.00 (d, 1H, J = 4.0 Hz), 3.95 (t, 1H, J = 12.0 Hz), 3.84 (t, 1H, J = 7.4 Hz), 3.77 (dd, 1H, J = 4.0, 10.0 Hz), 3.70 (d, 1H, J = 9.8 Hz), 3.65−3.62 (m, 1H), 3.55 (t, 1H, J = 8.9 Hz), 3.50 (d, 1H, J = 7.5 Hz), 3.46 (d, 1H, J = 8.0 Hz), 3.42 (dd, 1H, J = 2.6, 8.0 Hz), 3.37−3.32 (m, 2H), 2.19 (s, 3H), 2.01 (s, 3H), 1.95 (s, 3H), 1.60 (s, 3H). ^{13}C NMR (100 MHz, $CDCl_3$) δ 170.72, 170.31, 170.22, 169.91, 138.79, 138.53, 138.40, 138.34, 138.22, 137.44, 137.25, 129.04, 128.94, 128.71, 128.32, 128.19, 127.93, 127.87, 127.73, 127.53, 127.34, 127.07, 103.32, 102.76 (2C), 82.79, 81.95, 80.78, 76.10, 75.58, 75.33, 74.45, 73.51, 73.38, 72.07, 71.19, 70.96, 68.75, 68.31, 66.71, 61.35, 51.01, 23.41, 21.08, 20.87. MS (ESI) 1324.25 $[M+Na]^+$. MS (MALDI-TOF) calcd for $C_{75}H_{83}NO_{19}Na$ $[M+Na]^+$ *m/z* 1324.5456; found: *m/z* 1324.5573.

*2-Acetamido-2-deoxy-β-D-galactopyranosyl-(1→4)-β-D-galactopyranosyl-(1→4)-D-glucopyranose (**2**).* A solution of triacetate **13** (100 mg, 0.076 mmol) in dry methanol (5.0 mL) was treated at rt with a catalytic amount of NaOMe in methanol (1 M, 32 μL). The reaction mixture was stirred for 1 h at rt and then treated with Dowex 50WX8 (H^+) resin (500 mg), filtered, and concentrated to dryness. The partially deprotected trisaccharide was dissolved in MeOH (5 mL) and treated with a catalytic amount of $Pd(OH)_2$ on charcoal (80 mg, 20% on active carbon), purged with H_2, and stirred under an H_2 atmosphere for 12 h. The catalyst was filtered through a pad of Celite, and the filtrate was concentrated to yield pulmonary trisaccharide **2**, as an off-white solid (38 mg, 90% over two steps). ^1H NMR (400 MHz, CD_3OD) δ 4.61 (dd, 1H, J = 2.9, 8.4 Hz), 4.48 (d, 1H, J = 7.2 Hz), 4.33 (d, 1H, J = 7.7 Hz), 4.00 (d, 1H, J = 1.7 Hz), 3.90−3.82 (m, 4H), 3.79−3.75 (m, 2H), 3.71−3.64 (m, 2H), 3.62−3.58 (m, 4H), 3.51−3.46 (m, 4H), 3.42−3.39 (m, 1H), 2.02 (s, 3H). ^{13}C NMR (100 MHz, CD_3OD) δ 175.12, 105.12, 104.43, 99.25, 93.69, 80.93, 78.29, 76.82, 76.49, 76.27, 76.00, 74.68, 74.38, 72.59, 69.91, 62.63, 61.95, 61.62, 55.27, 23.15. MS (ESI) calcd for $C_{20}H_{35}NO_{16}Na$ $[M+Na]^+$ *m/z* 568.47; found: *m/z* 568.11.

*Fluorescein-Labeled 2′-Fucosyllactose Bishydrazide Conjugate (**14**).* A solution of glycoconjugate **8** (2.2 mg, 2.4 μmol) and fluorescein isothiocyanate (FITC, 1.14 mg, 2.9 μmol) in anhydrous methanol was treated with *N,N*-diisopropylethylamine (1.2 μL, 9.8 μmol) and stirred for 10 h at rt. The reaction mixture was concentrated and the residue was purified by RP-HPLC (1−30% aq CH_3CN gradient over 45 min) to yield FITC conjugate **14** as a greenish-yellow solid (2.1 mg, 67%). ^1H NMR (400 MHz, CD_3OD) δ 8.18 (d, 1H, J = 8.9 Hz), 7.50 (d, 1H, J = 2.0 Hz), 7.36 (d, 1H, J = 8.8), 4.21 (br s, 2H), 4.14 (d, 1H, J = 9.4 Hz), 4.05 (d, 1H, J = 9.3 Hz), 3.79−3.78 (m, 4H), 3.74−3.62 (m, 37H), 3.52−3.50 (m, 2H), 3.45−3.42 (m, 1H), 3.24−3.23 (m, 2H), 3.21−3.17 (m, 2H), 3.12−3.09 (m, 1H), 2.00 (3, 3H). MS (MALDI) calcd for $C_{55}H_{76}N_5O_{28}S$ $[M+H]^+$ *m/z* 1290.43; found: *m/z* 1290.27.

*Photoactive Glycan-Bishydrazide Conjugates (**15**−**17**).* In a typical reaction, a solution of pulmonary trisaccharide−bishydrazide conjugate **7** (11 mg, 11.5 μmol) and *N*-5-azido-2-nitrobenzoyloxy-succinimide (ANB-NOS, 5.3 mg, 17.3 μmol) in anhydrous DMF (1 mL) was treated with *N,N*-diisopropylethylamine (2.0 μL, 12.7 μmol) and stirred for 12 h at rt, protected from light. The reaction mixture was concentrated, and the residue was purified by RP-HPLC (1−30% aq CH_3CN gradient over 45 min) to afford ANS conjugate **16** as a brown

Scheme 1. Synthesis of Glycan−Bishydrazide Conjugates

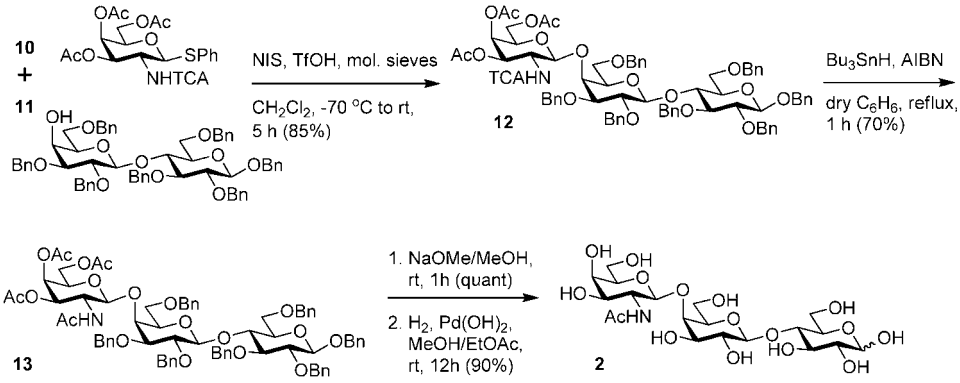


1: R_1, R_2=H
2: R_1=β-D-GalNAc, R_2=H
3: R_1=H, R_2=α-L-Fuc

4: **X**=O(CH$_2$CH$_2$O)$_6$
5: **X**=O(CH$_2$)$_7$O

6: R_1, R_2=H, **X**=O(CH$_2$CH$_2$O)$_6$ (86%)
7: R_1=β-D-GalNAc, R_2=H, **X**=O(CH$_2$CH$_2$O)$_6$ (58%)
8: R_1=H, R_2=α-L-Fuc, **X**=O(CH$_2$CH$_2$O)$_6$ (51%)
9: R_1, R_2=H, **X**=O(CH$_2$)$_7$O (62%)

Scheme 2. Synthesis of Pulmonary Trisaccharide[a]



[a] TCA = trichloroacetyl.

solid (8.4 mg, 63%). ^{1}H NMR (400 MHz, CD_3OD) δ 8.08 (s, 1H), 7.89 (br s, 1H), 7.69 (d, 1H, J = 8.0 Hz), 7.41 (d, 1H, J = 7.9 Hz), 7.14 (t, 1H, J = 7.9 Hz), 6.53−6.51 (m, 3H), 5.20 (s, 1H), 4.53 (s, 1H), 4.43 (d, 1H, J = 8.0 Hz), 4.17−4.13 (m, 2H), 4.06−4.05 (m, 2H), 4.03−4.01 (m, 2H), 3.77−3.57 (m, 35H), 3.53−3.48 (m, 4H), 1.16 (d, 1H, J = 6.4 Hz), 1.10 (d, 1H, J = 7.4 Hz). MS (ESI) calcd for $C_{43}H_{70}N_9O_{27}Na$ $[M+H]^+$ m/z 1144.43; found: m/z 1144.87.

RESULTS AND DISCUSSION

Synthesis and Reactivity of Bishydrazide Glycoconjugates. The preparation of bishydrazide cross-linkers have been previously reported in the literature, but with little detail regarding their purification (*53*). We found bis(carboxymethyl) esters to be practical intermediates for bishydrazide formation, but hydrazinolysis should be performed under strictly anhydrous conditions to avoid the generation of byproducts during glycoconjugate formation. Bishydrazide linkers **4** and **5** were synthesized from their corresponding α,ω-diols by base-promoted carboxymethylation with ethyl bromoacetate in THF, followed by treatment with excess hydrazine in anhydrous methanol under an inert atmosphere. The bishydrazides prepared in this manner could be collected in nearly quantitative yields simply by removing all volatiles by azeotropic drying with toluene, then used to generate glycoconjugates without further purification.

Glycan−bishydrazide conjugates were prepared by adapting the conditions reported by Shin and co-workers (Scheme 1) (*20, 21*). After an extensive evaluation of reaction conditions using hexa(ethylene glycol)-linked bishydrazide **4** and commercial-grade lactose, we determined that the highest yields were obtained by treating 1 equiv of glycan in AcOH/NaOAc buffer (pH 4.2) with 10 equiv of bishydrazide linker at 70 °C for 48 h. The glycoconjugates were readily separated from the excess linker by preparative reverse-phase HPLC using an aqueous CH_3CN gradient. ^{13}C NMR analysis of lactose−bishydrazide conjugate **6** indicated the anomeric carbons to have the expected chemical shifts for *O,O*- and *N,O*-acetals (δ_c 105.10 and 91.89 ppm, respectively), confirming the pyranosidic nature of the reducing-end sugar. ^{1}H NMR coupling constant analysis indicated that the bishydrazides form β-glycoside linkages, in accord with earlier reports (*54*−*57*). It should be noted that the formation of bishydrazide glycoconjugates **7** and **8** is not always complete after 48 h under these conditions; on the other hand, the formation of glycan dimers is negligible, circumventing the need for heterobifunctional linkers.

Glycan−bishydrazide conjugates **7** and **8** were prepared using GalNAc(β1→4)-Gal(β1→4)Glc (**2**) and 2′-fucosyllactose (Fuc-(α1→2)Gal(β1→4)Glc, **3**), with the former obtained through multistep organic synthesis (see below). Trisaccharide **2** is a common substructure in the glycans presented on the epithelial lining of the pulmonary tract and is a high-affinity ligand for adhesins presented on the pili of virulent *Pseudomonas* (*58, 59*). Fucose-presenting glycans such as **3** have been shown to be potent ligands for the lectin PA-IIL, also expressed by *Pseudomonas* (*60, 61*). These glycans presented us an opportunity to evaluate the bishydrazide glycoconjugate chemistry in the context of bacterial pathogen detection.

Briefly, pulmonary trisaccharide **2** was synthesized by the coupling of *N*-trichloroacetyl-protected GalNAc donor **10** (*51*) with lactose-derived acceptor **11** (*52*) and *N*-iodosuccinimide-triflic acid activation conditions, yielding the desired β-glycoside **12** in 86% yield (Scheme 2, see Experimental Procedures section for details). Reductive dechlorination with tributyltin hydride, followed by methanolic deacetylation and global debenzylation, yielded trisaccharide **2** in excellent overall yields.

The glycan−bishydrazide conjugates react readily with standard labeling and bioconjugation reagents. Fluorescent glycoconjugate **14** was generated by treatment of 2′-fucosyllactose-bishydrazide **8** with fluorescein isothiocyanate (FITC), whereas photoreactive glycoconjugates **15**−**17** were produced by coupling bishydrazide-linked glycans **6**−**8** with *N*-(5 azido-2-nitrobenzoyloxy)succinimide (ANB-NOS) (Figure 1). In both of these cases, hydrazide coupling was most efficient in anhydrous polar solvents such as DMF and MeOH, using *N,N*-diisopropylethylamine as the base (see Experimental Procedures section for details). Neoglycoproteins could also be formed in phosphate-buffered saline (PBS) solutions at physiological pH using typical EDC coupling conditions (*39*), and stored at 4 °C for several months.

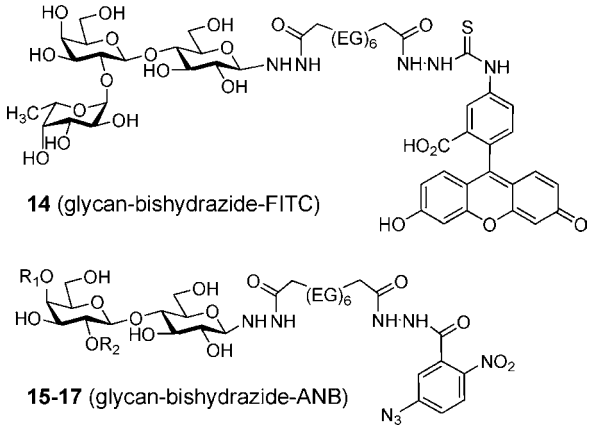


Figure 1. Glycan−bishydrazide conjugates labeled with fluorescent or photoreactive chromophores. $(EG)_6 = -O(CH_2CH_2O)_6-$. **15**: R_1, R_2 = H. **16**: R_1 = β-D-GalNAc, R_2 = H. **17**: R_1 = H, R_2 = α-L-Fuc.

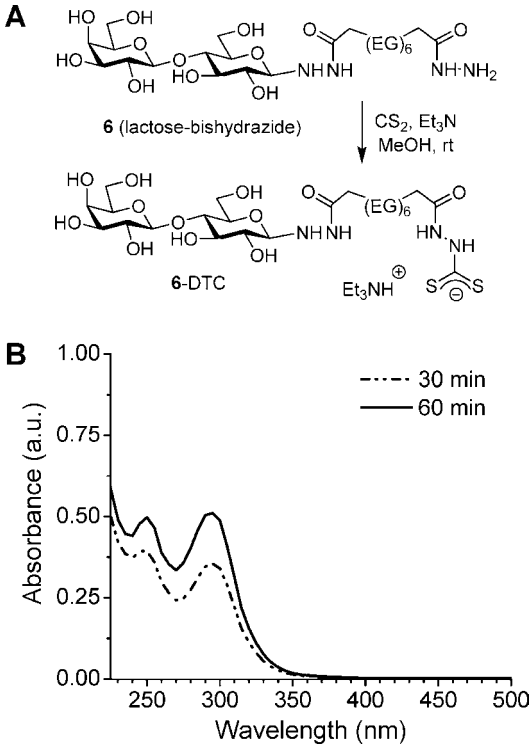


Figure 2. (A) In situ DTC formation starting from lactose−bishydrazide conjugate **6**; $(EG)_6 = O(CH_2CH_2O)_6$. (B) UV absorption spectra of **6**-DTC in dilute aqueous solution, taken during in situ DTC formation. No further increases in peak intensities were observed after 60 min.

The hydrazide-terminated glycoconjugates are also amenable to in situ dithiocarbamate (DTC) formation, a recently established method for anchoring amine-terminated ligands onto metal surfaces (*47*, *48*, *62*−*69*). DTCs are conveniently prepared by the addition of nucleophilic amines to CS_2 in polar organic or aqueous media and exhibit a strong binding affinity for gold and several types of inorganic oxides. Bishydrazide−DTCs can be prepared in a similar fashion: in this work; an equimolar mixture of lactose−bishydrazide conjugate **6**, CS_2, and Et_3N in methanol resulted in essentially quantitative formation of DTC triethylammonium salt within 1 h under ambient conditions (**6**-DTC, Figure 2). The reaction time was determined by using UV absorption spectroscopy to monitor hydrazide−DTC formation based on increases in characteristic peak intensities at 250 and 292 nm (*70*).

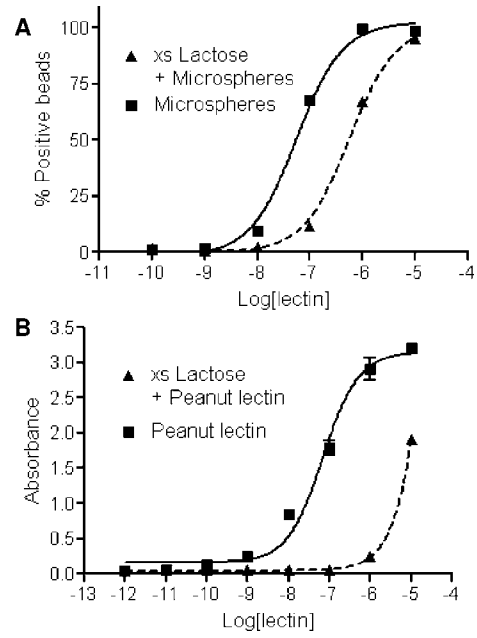


Figure 3. (A) Affinity and lactose competition assay of peanut lectin binding to microspheres conjugated with lactose−bishydrazide **6** using flow immunocytometry. (B) ELISA and competition assay of peanut lectin binding to immobilized **6**-BSA.

Lectin and Bacterial Binding by Bishydrazide Glycoconjugates. Bishydrazide glycoconjugates can be directly attached onto surface-active substrates for the selective capture of lectins and subsequent binding immunoassays. For example, lactose−bishydrazide **6** was attached onto NHS-activated latex microspheres in order to measure the binding affinity of peanut lectin by flow immunocytometry (K_d = 50 nM), using a FITC-labeled secondary antibody for fluorescence detection (Figure 3A and Supporting Information Figure S1). Selective binding was established by a competition assay against 1 mM lactose, which increased K_d by 10-fold. However, in some cases the use of carrier proteins such as BSA is more convenient for surface functionalization by simple physisorption. An ELISA of **6**-BSA conjugate indicates its affinity for peanut lectin to be the same as that measured for lactose-conjugated microspheres.

Glycoconjugates can also be covalently tethered onto protein layers and other organic substrates by photo-cross-linking, which provides opportunities to create glycan microarrays and micropatterns by photolithography (*71*−*75*). Au substrates coated with a monolayer of BSA were immersed in a solution of lactose-bishydrazide-ANB conjugate **15**, then dried in air and exposed to UV irradiation through a photomask. The intermediate nitrenes that are generated upon UV irradiation (*76*) presumably insert into the amino acid side chains of the immobilized BSA, resulting in a patterned array of glycans after washing away the unexposed ligands. Incubation with peanut lectin followed by fluorescence immunostaining revealed well-defined line patterns, defined by the photomask features (Figure 4).

A similar approach was used to generate photopatterned arrays of the pulmonary trisaccharide and 2′-fucosyllactose on BSA-coated substrates, using glycan-bishydrazide-ANB conjugates **16** and **17**, respectively. These micropatterned substrates were exposed to the opportunistic pathogen *Pseudomonas aeruginosa* at 10^6−10^8 cfu/mL, then washed and imaged by optical darkfield microscopy to visualize patterns of glycan-immobilized bacteria in a label-free manner (Figure 5 and Supporting Information Figures S2 and S3). Specificity for **16** and **17** was confirmed by introducing *Pseudomonas* to control substrates patterned with lactose−bishydrazide conjugate, which resulted in no apparent binding. Furthermore, only live *Pseudomo-*

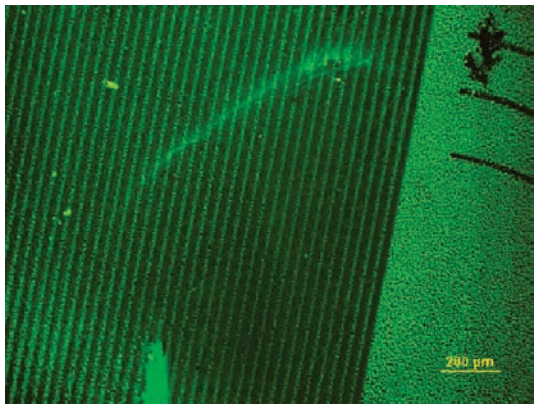


Figure 4. Fluorescence immunostaining of peanut lectin bound to lactose-bishydrazide-ANB conjugate **15**, photopatterned onto a BSA-coated substrate by UV irradiation ($\lambda = 254$ nm) through a quartz mask.

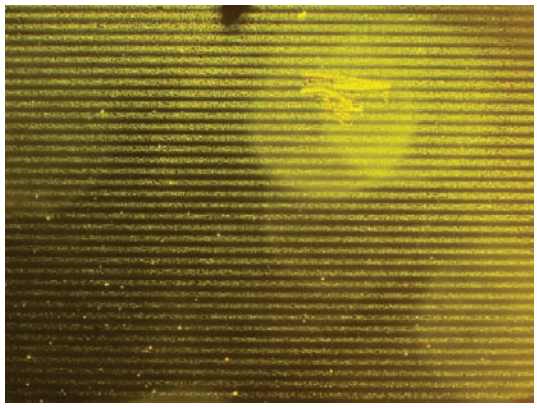


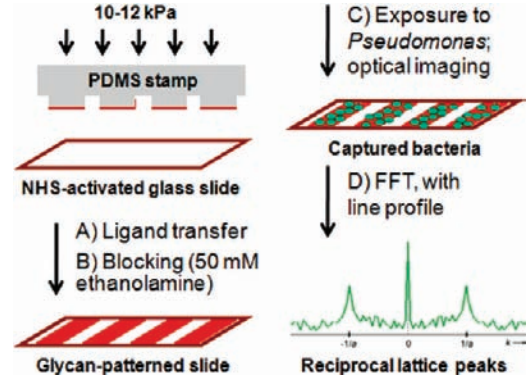
Figure 5. Capture of *Pseudomonas* on BSA-coated substrates with photopatterned glycan-bishydrazide-ANB conjugate, imaged by darkfield microscopy. Bacterial capture mediated by 2′-fucosyllactose conjugate **17** at 10^8 cfu/mL; grating period $a = 20$ μm. Additional images in Supporting Information (Figures S2−S4).

nas were captured by the trisaccharide ligands; exposing the bacteria to UV irradiation for 2 h prior to their introduction resulted again in no observable pattern (Supporting Information Figure S4). We note that the patterns formed by bacterial adhesion at lower pathogen densities can be well below saturation levels; however, our pathogen detection method only requires a fill factor of a few percent for pattern recognition, as will be demonstrated shortly.

Glycan−bishydrazide conjugates could also be patterned onto substrates by microcontact printing (μCP), a well-established "soft lithography" technique based on microfabricated polydimethylsiloxane (PDMS) stamps for the physical transfer of organic or biomolecular ligands, including glycans (*77*−*81*). Stamps imprinted with 20 μm gratings were coated with solutions of **7**-BSA or **8**-BSA in phosphate buffer, then dried in air and placed in conformal contact with activated glass slides under lightly applied pressure (see Scheme 3 and Experimental Procedures section). The substrates were blocked then exposed for 1 h to *Pseudomonas* at 10^2−10^8 cfu/mL, then evaluated for evidence of patterned pathogen capture (Figure 6). On average, we find the pattern transfer of **7**-BSA by μCP to be more consistent than that produced by photolithography, and remarkably reliable for mediating bacterial adhesion at low pathogen densities.

Visual inspection of the patterned glycan slides can indicate *Pseudomonas* capture at a concentration of 10^5 cfu/mL (Figure 6D). However, image processing by fast Fourier transform

Scheme 3[a]



[a] (A,B) Glycan-patterned slides by microcontact printing of BSA glycoconjugates onto NHS-activated glass substrates, followed by a blocking step. (C) Patterned capture slides were exposed to *Pseudomonas* at variable concentrations, then imaged under darkfield condtions. (D) Image processing by FFT analysis produced reciprocal lattice peaks at $k = \pm 1/a$ in spectral format; central peak ($k = 0$) scales with spatially averaged intensity of original image; noise from nonspecific binding is dispersed throughout *k*-space.

allows the linear array of scattering signals to be analyzed as reciprocal lattice peaks, enabling much lower limits of detection (*50*). These demodulated signals are largely separated from background noise and can be presented with much greater contrast than the original darkfield images (Figure 6A−H, insets). As a result, we find that slides patterned with **7**-BSA can detect *Pseudomonas* capture in a label-free manner, with acceptable signal-to-noise (*S*/*N*) ratios down to 10^3 cfu/mL (Figure 6F).

Interestingly, we observe that our *Pseudomonas* cultures have a much lower avidity for 2′-fucosyllactose **8** than for pulmonary trisaccharide **7**, which are recognized by adhesins that are constitutively presented at the tips of bacterial pili (*82*). Whereas affinity for **7**-BSA is robust and minimally affected by the presence of competing GalNAc or lactose up to 100 mM (Supporting Information, Figure S5), affinity for **8**-BSA is observed only when the bacteria has been cultured in the presence of choline (*49*). It has been shown that the expression of the fucose-binding lectin PA-IIL is regulated by quorum sensing circuitry (*las* and *rhl*), which are activated in an environmentally dependent (paracrinal) fashion (*83, 84*).

Presentation of Glycan-Bishydrazides on Metal Surfaces by in Situ Dithiocarbamate Formation. Biosensor applications are often performed with gold substrates, like those based on surface plasmon resonance (SPR) and quartz crystal microbalance (QCM) (*85*, *86*). For short-term biosensing studies, it is often appropriate to employ chemisorptive ligands such as ω-functionalized alkanethiols, which are well-known to form self-assembled monolayers (SAMs) on gold surfaces (*87*). However, alkanethiol-based SAMs can have limited stability when exposed to even mildly oxidizing conditions (*88*), so it is worth considering other types of chemisorptive ligands that can support robust surface functionalization under variable environments or in physiological settings.

DTC-anchored monolayers (DAMs) are useful alternatives to thiol-based SAMs, as they have been shown to have greater resistance to surface desorption or oxidative degradation (*47*). Although earlier studies involving in situ DTC and DAM formation have been conducted with alkyl- and dialkylamines (*47*, *48*, *62*−*69*), hydrazide−DTCs can be formed just as easily and may also serve as chemisorptive ligands. Lactose−bishydrazide **6** was thus converted into the corresponding DTC (Figure 2), then diluted in water and deposited onto a PDMS stamp for pattern transfer onto a chemically roughened Au surface by μCP. The

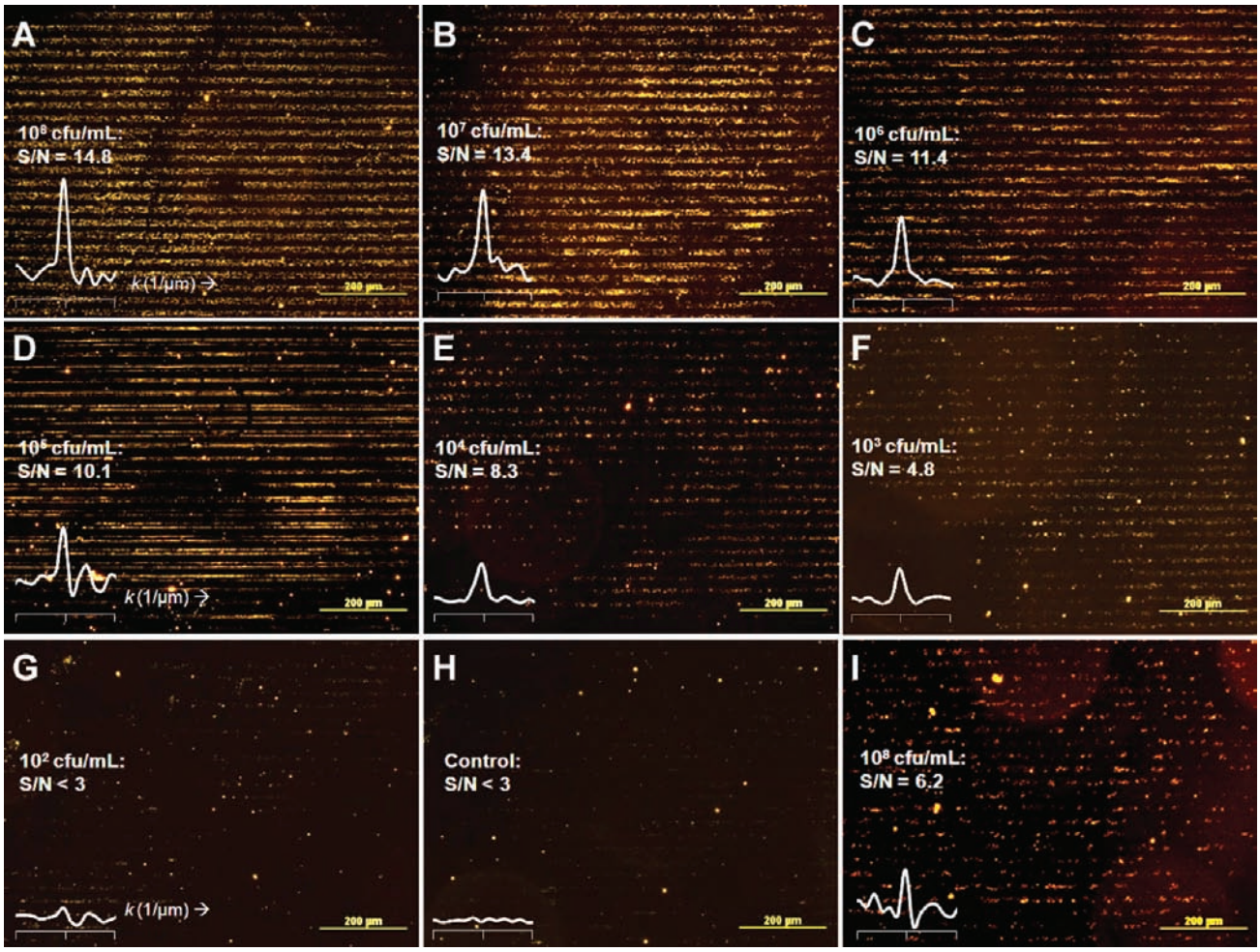


Figure 6. Capture of live *Pseudomonas* on glass substrates patterned with BSA−glycan bishydrazide conjugates using μCP, as imaged by darkfield microscopy. (A−G) Substrates patterned with pulmonary trisaccharide conjugate **7**-BSA after a 1-h exposure to *Pseudomonas*, at concentrations ranging from 10^8 to 10^2 cfu/mL. Pattern contrast correlates with signal-to-noise (*S*/*N*) ratio defined by reciprocal lattice peak produced by FFT ($k = 0.05\ \mu m^{-1}$). (H) Substrate patterned with **7**-BSA without exposure to bacteria (control). (I) *Pseudomonas* capture mediated by 2′-fucosyllactose conjugate **8**-BSA, in the presence of choline (10^8 cfu/mL).

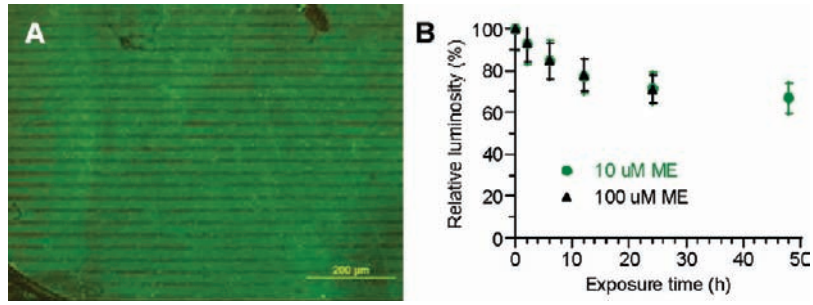


Figure 7. (A) Fluorescence immunostaining of peanut lectin bound to lactose conjugate **6**-DTC, presented as DAMs on Au substrates by μCP. (B) Stability profile of hydrazide−DTC patterns on roughened Au in PBS containing ME (10 or 100 μM), based on changes in relative luminosity.

patterned substrates were blocked by BSA and incubated with peanut lectin, whose binding to lactose-terminated DAMs was visualized by immunofluorescent staining (Figure 7). It is important to note that Au substrates are often incompatible with fluorescence imaging due to their propensity to quench emission; however, radiative decay rates can be accelerated on roughened Au substrates by coupling with local plasmon modes and may even produce a net gain in emission (*89*).

As expected, the oriented presentation of **6**-DTC on Au surfaces is well-suited for the immobilization of multivalent lectins, and patterned substrates can be soaked in PBS for extended periods without concern for degradation. To further establish whether glycan−bishydrazide DAMs are capable of providing robust support as carbohydrate microarrays for protein screening or pathogen binding, we investigated their stability in the presence of 2-mercaptoethanol (ME), a polar thiol that is frequently used to displace alkanethiol-based SAMs from Au surfaces (*90*). This displacement assay is important in the context of physiological sensing, as biogenic thiols such as cysteine and glutathione can also be considered as competing adsorbates. The immunofluorescent patterns on roughened Au substrates were thus exposed to 10 μM or 100 μM ME in PBS at room temperature for 2 days, with monitoring of selected regions at different exposure times by fluorescence microscopy (Supporting

Information, Figure S6). Both conditions produced very gradual decay profiles, with an estimated halflife of over 80 h (Figure 7B). It should be mentioned that displacement assays with millimolar levels of ME could not be performed in this case, as this was sufficient to cause degradation of the roughened Au substrates themselves. Nevertheless, exposure of **6**-DTC ligands to ME at these levels has minimal detrimental effect on DAM stability and merits further investigation. A direct comparison between SAMs and DAMs is in progress and will be reported in due course.

CONCLUSIONS

α,ω-Bishydrazides are useful and versatile linkers for attaching glycans onto substrates for bacterial pathogen detection and lectin profiling. Unprotected glycans are conjugated straightforwardly to bishydrazides with retention of the native pyranose conformation at the reducing end, and can be further conjugated to amine-reactive substrates, carrier proteins, and to metal surfaces by in situ DTC formation. With respect to the latter, glycan-bishydrazide-DTCs form robust attachments to roughened gold substrates and are able to withstand displacement by competing thiols under physiologically relevant conditions. Glycan−bishydrazide conjugates can be subsequently employed in microfabrication schemes involving photolithography or PDMS-based microcontact printing for the facile detection of glycan-binding proteins and pathogens, as demonstrated by the patterned adsorption of peanut lectin and *Pseudomonas*. We anticipate using this methodology to support real-time biosensing applications involving protein biomarker or pathogen detection.

ACKNOWLEDGMENT

The authors gratefully acknowledge financial support from the National Institutes of Health (GM-069862), the National Science Foundation (CHE-0243496), the Department of Defense (W911SR-08-C-0001) administered through the U.S. Army RDECOM (Edgewood Contracting Division), and the Center for Sensing Science and Technology at Purdue University. We thank David Lyvers and Ron Reifenberger for their contributions toward FFT analysis, and Youngsoon Kim and James Newton for helpful discussions and assistance with microcontact printing, bacteria culture, and quantitative bacterial cell culture analysis.

Supporting Information Available: Representative data from flow immunocytometry (Figure S1); control experiments for specificity of pathogen capture (Figures S2−S5); additional immunofluorescence images of lectins bound to DTC-anchored glycan bishydrazides on Au substrate (Figure S6); ^{1}H and ^{13}C NMR spectra of all new compounds. This material is available free of charge via the Internet at http://pubs.acs.org.

LITERATURE CITED

(1) Stevens, J., Blixt, O., Paulson, J. C., and Wilson, I. A. (2006) Glycan microarray technologies: tools to survey host specificity of influenza viruses. *Nat. Rev. Microbiol. 4*, 857–864.

(2) Wang, H. F., Gu, L. R., Lin, Y., Lu, F. S., Meziani, M. J., Luo, P. G. J., Wang, W., Cao, L., and Sun, Y. P. (2006) Unique aggregation of anthrax (*Bacillus anthracis*) spores by sugarcoated single-walled carbon nanotubes. *J. Am. Chem. Soc. 128*, 13364–13365.

(3) El-Boubbou, K., Gruden, C., and Huang, X. (2007) Magnetic glyco-nanoparticles: A unique tool for rapid pathogen detection, decontamination, and strain differentiation. *J. Am. Chem. Soc. 129*, 13392–13393.

(4) Kale, R. R., Mukundan, H, Price, D. N., Harris, J. F., Lewallen, D. M., Swanson, B. I., Schmidt, G. J., and Iyer, S. S. (2008) Detection of intact influenza viruses using biotinylated biantennary *S*-sialosides. *J. Am. Chem. Soc. 130*, 8169–8171.

(5) Liu, L.-H., Dietsch, H., Schurtenberger, P., and Yan, M. (2009) Photoinitiated coupling of unmodified monosaccharides to iron oxide nanoparticles for sensing proteins and bacteria. *Bioconjugate Chem. 20*, 1349–1355.

(6) Disney, M. D., and Seeberger, P. H. (2004) The use of carbohydrate microarrays to study carbohydrate-cell interactions and to detect pathogens. *Chem. Biol. 11*, 1701–1707.

(7) Ngundi, M. M., Kulagina, N. V., Anderson, G. P., and Taitt, C. R. (2006) Nonantibody-based recognition: alternative molecules for detection of pathogens. *Exp. Rev. Proteom. 3*, 511–524.

(8) Kulkarni, A. A., Weiss, A. A., and Iyer, S. S. (2010) Glycan-based high-affinity ligands for toxins and pathogen receptors. *Med. Res. Rev. 30*, 327–393.

(9) Wu, C.-Y., Liang, P.-H., and Wong, C.-H. (2009) New development of glycan arrays. *Org. Biomol. Chem. 7*, 2247–2254.

(10) Laurent, N., Voglmeir, J., and Flitsch, S. L. (2008) Glycoarrays - tools for determining protein-carbohydrate interactions and glycoenzyme specificity. *Chem. Commun.* 4400–4412.

(11) Park, S., Lee, M.-R., and Shin, I. (2008) Carbohydrate microarrays as powerful tools in studies of carbohydrate-mediated biological processes. *Chem. Commun. 37*, 4389–4399.

(12) Horlacher, T., and Seeberger, P. H. (2008) Carbohydrate arrays as tools for research and diagnostics. *Chem. Soc. Rev. 37*, 1414–1422.

(13) Park, S., Lee, M.-R., Pyo, S. J., and Shin, I. (2004) Carbohydrate chips for studying high-throughput carbohydrate-protein interactions. *J. Am. Chem. Soc. 126*, 4812–4819.

(14) Park, S., and Shin, I. (2002) Fabrication of carbohydrate chips for studying protein-carbohydrate interactions. *Angew. Chem., Int. Ed. 41*, 3180–3182.

(15) Ratner, D. M., Adams, E. W., Disney, M. D., and Seeberger, P. H. (2004) Tools for glycomics: mapping interactions of carbohydrates in biological systems. *ChemBioChem 5*, 1375–1383.

(16) Houseman, B. T., Gawalt, E. S., and Mrksich, M. (2003) Maleimide-functionalized self-assembled monolayers for the preparation of peptide and carbohydrate biochips. *Langmuir 19*, 1522–1531.

(17) Houseman, B. T., and Mrksich, M. (2002) Carbohydrate arrays for the evaluation of protein binding and enzymatic modification. *Chem. Biol. 9*, 443–454.

(18) Bryan, M. C., Fazio, F., Lee, H. K., Huang, C. Y., Chang, A., Best, M. D., Calarese, D. A., Blixt, C., Paulson, J. C., Burton, D., Wilson, I. A., and Wong, C. H. (2004) Covalent display of oligosaccharide arrays in microtiter plates. *J. Am. Chem. Soc. 126*, 8640–8641.

(19) Michel, O., and Ravoo, B. J. (2008) Carbohydrate microarrays by microcontact "click" chemistry. *Langmuir 24*, 12116–12118.

(20) Lee, M.-R., and Shin, I. (2005) Fabrication of chemical microarrays by efficient immobilization of hydrazide-linked substances on epoxide-coated glass surfaces. *Angew. Chem., Int. Ed. 44*, 2881–2884.

(21) Park, S., and Shin, I. (2007) Carbohydrate microarrays for assaying galactosyltransferase activity. *Org. Lett. 9*, 1675–1678.

(22) Blixt, O., Head, S., Mondala, T., Scanlan, C., Huflejt, M. E., Alvarez, R., Bryan, M. C., Fazio, F., Calarese, D., Stevens, J., Razi, N., Stevens, D. J., Skehel, J. J., van Die, I., Burton, D. R., Wilson, I. A., Cummings, R., Bovin, N., Wong, C. H., and Paulson, J. C. (2004) Printed covalent glycan array for ligand profiling of diverse glycan binding proteins. *Proc. Natl. Acad. Sci. U.S.A. 101*, 17033–17038.

(23) De Paz, J. L., Noti, C., and Seeberger, P. H. (2006) Microarrays of synthetic heparin oligosaccharides. *J. Am. Chem. Soc. 128*, 2766–2767.

(24) Köhn, M., Wacker, R., Peters, C., Schröder, H., Soulère, L., Breinbauer, R., Niemeyer, C. M., and Waldmann, H. (2003) Staudinger ligation: a new immobilization strategy for the preparation of small-molecule arrays. *Angew. Chem., Int. Ed. 42*, 5830–5834.

(25) Hermanson, G. T. (2008) *Bioconjugate Techniques*, 2nd ed., Academic Press, San Diego.
(26) Xia, B. Y., Kawar, Z. S., Ju, T. Z., Alvarez, R. A., Sachdev, G. P., and Cummings, R. D. (2005) Versatile fluorescent derivatization of glycans for glycomic analysis. *Nat. Methods 2*, 845–850.
(27) Lee, M.-R., and Shin, I. (2005) Facile preparation of carbohydrate microarrays by site-specific, covalent immobilization of unmodified carbohydrates on hydrazide-coated glass slides. *Org. Lett. 7*, 4269–4272.
(28) Park, S., Lee, M.-R., and Shin, I. (2009) Construction of carbohydrate microarrays by using one-step direct immobilizations of diverse unmodified glycans on solid surfaces. *Bioconjugate Chem. 20*, 155–162.
(29) Zhi, Z. L., Powell, A. K., and Turnbull, J. E. (2006) Fabrication of carbohydrate microarrays on gold surfaces: Direct attachment of nonderivatized oligosaccharides to hydrazide modified self-assembled monolayers. *Anal. Chem. 78*, 4786–4793.
(30) Bohorov, O., Andersson-Sand, H., Hoffmann, J., and Blixt, O. (2006) Arraying glycomics: a novel bi-functional spacer for one-step microscale derivatization of free reducing glycans. *Glycobiology 16*, 21C–27C.
(31) Liu, Y., Feizi, T., Campanerorhodes, M., Childs, R., Zhang, Y., Mulloy, B., Evans, P., Osborn, H., Otto, D., and Crocker, P. (2007) Neoglycolipid probes prepared via oxime ligation for microarray analysis of oligosaccharide-protein interactions. *Chem. Biol. 14*, 847–859.
(32) Chen, G., and Pohl, N. (2008) Synthesis of fluorous tags for incorporation of reducing sugars into a quantitative microarray platform. *Org. Lett. 10*, 785–788.
(33) Cló, E., Blixt, O., and Jensen, K. J. (2010) Chemoselective reagents for covalent capture and display of glycans in microarrays. *Eur. J. Org. Chem.* 540–554.
(34) Thygesen, M. B., Sauer, J., and Jensen, K. J. (2009) Chemoselective capture of glycans for analysis on gold nanoparticles: carbohydrate oxime tautomers provide functional recognition by proteins. *Chem.—Eur. J. 15*, 1649–1660.
(35) Cervigni, S. E., Dumy, P., and Mutter, M. (1996) Synthesis of glycopeptides and lipopeptides by chemoselective ligation. *Angew. Chem., Int. Ed. 35*, 1230–1232.
(36) Zhao, Y. M., Kent, S. B. H., and Chait, B. T. (1997) Rapid, sensitive structure analysis of oligosaccharides. *Proc. Natl. Acad. Sci. U.S.A. 94*, 1629–1633.
(37) Zhi, Z. L., Laurent, N., Powell, A. K., Karamanska, R., Fais, M., Voglmeir, J., Wright, A., Blackburn, J. M., Crocker, P. R., Russell, D. A., Flitsch, S., Field, R. A., and Turnbull, J. E. (2008) A versatile gold surface approach for fabrication and interrogation of glycoarrays. *ChemBioChem 9*, 1568–1575.
(38) Guillaumie, F., Thomas, O. R. T., and Jensen, K. J. (2002) Immobilization of pectin fragments on solid supports: novel coupling by thiazolidine formation. *Bioconjugate Chem. 13*, 285–294.
(39) Lohse, A., Martins, R., Jørgensen, M. R., and Hindsgaul, O. (2006) Solid-Phase oligosaccharide tagging (SPOT): validation on glycolipid-derived structures. *Angew. Chem., Int. Ed. 45*, 4167–4172.
(40) Bacchi, A., Carcelli, M., Pelizzi, G., Solinas, C., and Sorace, L. (2006) Trinuclear copper(II) complexes of bis(acylhydrazone) ligands. Structural analysis and magnetic properties of a sulfato-bridged hexanuclear dimer. *Inorg. Chim. Acta 359*, 2275–2280.
(41) Dydio, P., Zieliński, T., and Jurczak, J. (2009) Bishydrazide derivatives of isoindoline as simple anion receptors. *J. Org. Chem. 74*, 1525–1530.
(42) Bystrický, S., Machová, E., Malovíková, A., and Kogan, G. (1999) Determination of the cross-linking effect of adipic acid dihydrazide on glycoconjugate preparation. *Glycoconjugate J. 16*, 691–695.
(43) Urmenyi, A. M., Poot, A. A., Wessling, M., and Mulder, M. H. V. (2005) Affinity membranes for hormone removal from aqueous solutions. *J. Membr. Sci. 259*, 91–102.
(44) Ono, T., Fujii, S., Nobori, T., and Lehn, J.-M. (2007) Soft-to-hard transformation of the mechanical properties of dynamic covalent polymers through component incorporation. *Chem. Commun.* 46–48.
(45) Price, D., and Ahearn, D. G. (1988) Incidence and persistence of *Pseudomonas aeruginosa* in whirlpools. *J. Clin. Microbiol. 26*, 1650–1654.
(46) *Guidelines for safe recreational water environments. Vol 2: Swimming pools and similar environments* (2006) pp 43−45, World Health Organization, Geneva.
(47) Zhao, Y., Pérez-Segarra, W., Shi, Q., and Wei, A. (2005) Dithiocarbamate assembly on gold. *J. Am. Chem. Soc. 127*, 7328–7329.
(48) Zhu, H., Coleman, D. M., Dehen, C. J., Geisler, I. M., Zemlyanov, D., Chmielewski, J., Simpson, G. J., and Wei, A. (2008) Assembly of dithiocarbamate-anchored monolayers on gold surfaces in aqueous solutions. *Langmuir 24*, 8660–8666.
(49) Gilboa-Garber, N. (1982). Pseudomonas aeruginosa lectins. *Methods in Enzymology. Vol. 83: Complex Carbohydrates, Part D* (Kaplan, N. P., Colowick, N. P., and Ginsburg, V., Eds.) pp 378−385, Chapter 32, Academic Press, San Diego.
(50) Doorneweerd, D. D., Henne, W. A., Reifenberger, R. G., and Low, P. S. (2010) Selective capture and identification of pathogenic bacteria using an immobilized siderophore. *Langmuir 26*, 15424−15429.
(51) Bélot, F., and Jacquinet, J.-C. (2000) Unexpected stereochemical outcome of activated 4,6-O-benzylidene derivatives of the 2-deoxy-2-trichloroacetamido-D-*galacto* series in glycosylation reactions during the synthesis of a chondroitin 6-sulfate trisaccharide methyl glycoside. *Carbohydr. Res. 325*, 95–106.
(52) Matsuoka, K., Goshu, Y., Takezawa, Y., Mori, T., Sakamoto, J.-I., Yamada, A., Onaga, T., Koyama, T., Hatano, K., Snyder, P. W., Toone, E. J., and Daiyo Terunuma, D. (2007) Practical synthesis of fully protected globotriaose and its glycopolymers. *Carbohydr. Polym. 69*, 326–335.
(53) Vercruysse, K. P., Marecak, D. M., Marecek, J. F., and Prestwich, G. D. (1997) Synthesis and *in vitro* degradation of new polyvalent hydrazide cross-linked hydrogels of hyaluronic acid. *Bioconjugate Chem. 8*, 686–694.
(54) Leteux, C., Childs, R. A., Chai, W., Stoll, M. S., Kogelberg, H., and Feizi, T. (1998) Biotinyl-l-3-(2-naphthyl)alanine hydrazide derivatives of *N*-glycans: versatile solid-phase probes for carbohydrate-recognition studies. *Glycobiology 8*, 227–236.
(55) Shinohara, Y., Sota, H., Gotoh, M., Hasebe, M., Tosu, M., Nakao, J., and Hasegawa, Y. (1996) Bifunctional labeling reagent for oligosaccharides to incorporate both chromophore and biotin groups. *Anal. Chem. 68*, 2573–2579.
(56) Ojala, C. R., Ostman, J. M., and Ojala, W. H. (2002) The saccharide-hydrazide linkage: molecular and crystal structures of the semicarbazide derivatives of D-glucose, D-galactose, and D-xylose, including a 'forbidden' conformation of the galactose derivative. *Carbohydr. Res. 337*, 21–29.
(57) Flinn, N. S., Quibell, M., Monk, T. P., Ramjee, M. K., and Urch, C. J. (2005) A single-step method for the production of sugar hydrazides: intermediates for the chemoselective preparation of glycoconjugates. *Bioconjugate Chem. 16*, 722–728.
(58) Krivan, H. C., Roberts, D. D., and Ginsburg, V. (1988) Many pulmonary pathogenic bacteria bind specifically to the carbohydrate sequence GalNAcβ1−4Gal found in some glycolipids. *Proc. Natl. Acad. Sci. U.S.A. 85*, 6157–6161.
(59) Yu, L., Lee, K. K., Hodges, R. S., Paranchych, W., and Irvin, R. T. (1994) Adherence of *Pseudomonas aeruginosa* and *Candida albicans* to glycosphingolipid (Asialo-GM1) receptors is achieved by a conserved receptor-binding domain present on their adhesions. *Infect. Immunol. 62*, 5213–5219.
(60) Mitchell, E., Houles, C., Sudakevitz, D., Wimmerova, M., Gautier, C., Perez, S., Wu, A. M., Gilboa-Garber, M., and Imberty, A. (2002) Structural basis for oligosaccharide-mediated adhesion of *Pseudomonas aeruginosa* in the lungs of cystic fibrosis patients. *Nat. Struct. Biol. 9*, 918–921.

(61) Imberty, A., Wimmerova, M., Mitchell, E. P., and Gilboa-Garber, N. (2004) Structures of the lectins from *Pseudomonas aeruginosa*: Insights into the molecular basis for host glycan recognition. *Microb. Infect. 6*, 221–228.

(62) Huff, T. B., Hansen, M. H., Zhao, Y., Cheng, J.-X., and Wei, A. (2007) Controlling the cellular uptake of gold nanorods. *Langmuir 23*, 1596–99.

(63) Huff, T. B., Tong, L., Zhao, Y., Hansen, M. N., Cheng, J.-X., and Wei, A. (2007) Hyperthermic effects of gold nanorods on tumor cells. *Nanomedicine 2*, 125–132.

(64) Zhao, Y., Newton, J. N., Liu, J., and Wei, A. (2009) Dithiocarbamate-coated SERS substrates: sensitivity gain by partial surface passivation. *Langmuir 25*, 13833–13839.

(65) Guerrini, L., Garcia-Ramos, J. V., Domingo, C., and Sanchez-Cortes, S. (2009) Sensing polycyclic aromatic hydrocarbons with dithiocarbamate-functionalized Ag nanoparticles by surface-enhanced Raman scattering. *Anal. Chem. 81*, 953–960.

(66) Cao, R., Jr., Diaz, A., Cao, R., Otero, A., Cea, R., C. R.-A., Maria, and Serra, C. (2007) Building layer-by-layer a bis(dithiocarbamato)copper(II) complex on Au{111} surfaces. *J. Am. Chem. Soc. 129*, 6927–6930.

(67) Park, M. H., Ofir, Y., Samanta, B., and Rotello, V. M. (2009) Robust and responsive dendrimer-gold nanoparticle nanocomposites via dithiocarbamate crosslinking. *Adv. Mater. 21*, 2323–2325.

(68) Patel, G., Kumar, A., Pal, U., and Menon, S. (2009) Potassium ion recognition by facile dithiocarbamate assembly of benzo-15-crown-5-gold nanoparticles. *Chem. Commun.* 1849–1851.

(69) Morf, P., Raimondi, F., Nothofer, H.-G., Schnyder, B., Yasuda, A., Wessels, J. M., and Jung, T. A. (2006) Dithiocarbamates: functional and versatile linkers for the formation of self-assembled monolayers. *Langmuir 22*, 658–663.

(70) Lee, A. W. M., Chan, W. H., Chiu, C. M. L., and Tang, K. T. (1989) Ultraviolet spectrophotometric determination of primary and secondary aliphatic amines by formation of dithiocarbamates. *Anal. Chim. Acta 218*, 157–160.

(71) Ito, Y. (2006) Photoimmobilization for microarrays. *Biotechnol. Prog.* 924–932.

(72) Carroll, G. T., Wang, D. N., Turro, N. J., and Koberstein, J. T. (2008) Photons to illuminate the universe of sugar diversity through bioarrays. *Glycoconjugate J. 25*, 5–10.

(73) Carroll, G. T., Wang, D. N., Turro, N. J., and Koberstein, J. T. (2006) Photochemical micropatterning of carbohydrates on a surface. *Langmuir 22*, 2899–2905.

(74) Liu, L.-H., Dietsch, H., Schurtenberger, P., and Yan, M. (2009) Photoinitiated coupling of unmodified monosaccharides to iron oxide nanoparticles for sensing proteins and bacteria. *Bioconjugate Chem. 20*, 1349–1355.

(75) Norberg, O., Deng, L., Yan, M., and Ramström., O. (2009) Photo-Click immobilization of carbohydrates on polymeric surfacess: a quick method to functionalize surfaces for biomolecular recognition studies. *Bioconjugate Chem. 20*, 2364–2370.

(76) Lewis, R. V., Roberts, M. F., Dennis, E. A., and Allison, W. S. (1977) Photoactivated heterobifunctional cross-linking reagents which demonstrate the aggregation state of phospholipase A_2. *Biochemistry 16*, 5650–5654.

(77) Kumar, A., and Whitesides, G. M. (1993) Features of gold having micrometer to centimeter dimensions can be formed through a combination of stamping with an elastomeric stamp and an alkanethiol "ink" followed by chemical etching. *Appl. Phys. Lett. 63*, 2002–2004.

(78) Bernard, A., Renault, J. P., Michel, B., Bosshard, H. R., and Delamarche, E. (2000) Microcontact printing of proteins. *Adv. Mater. 12*, 1067–1070.

(79) Inerowicz, H. D., Howell, S., Regnier, F. E., and Reifenberger, R. (2002) Multiprotein immunoassay arrays fabricated by microcontact printing. *Langmuir 18*, 5263–5268.

(80) Godula, K., Rabuka, D., Nam, K. T., and Bertozzi, C. R. (2009) Synthesis and microcontact printing of dual end-functionalized mucin-like glycopolymers for microarray applications. *Angew. Chem., Int. Ed. 48*, 4973–4976.

(81) Wendeln, C., Heile, A., Arlinghaus, H. F., and Ravoo, B. J. (2010) Carbohydrate microarrays by microcontact printing. *Langmuir 26*, 4933–4940.

(82) Keizer, D. W., Slupsky, C. M., Kalisiak, M., Campbell, A. P., Crumpi, M. P., Sastry, P. A., Hazes, B., Irvin, R. T., and Sykes, B. D. (2001) Structure of a pilin monomer from *pseudomonas aeruginosa*. *J. Biol. Chem. 276*, 24186–24193.

(83) Winzer, K., Falconer, C., Garber, N.-C., Diggle, S. P., Camara, M., and Williams, P. (2000) The *Pseudomonas aeruginosa* lectins PA-IL and PA-IIL are controlled by quorum sensing and by RpoS. *J. Bacteriol. 182*, 6401–6411.

(84) Duan, K., and Surette, M. G. (2007) Environmental regulation of *Pseudomonas aeruginosa* PAO1 Las and Rhl quorum-sensing systems. *J. Bacteriol. 189*, 4827–4836.

(85) Homola, J. (2008) Surface plasmon resonance sensors for detection of chemical and biological species. *Chem. Rev. 108*, 462–493.

(86) Marx, K. A. (2003) Quartz crystal microbalance: a useful tool for studying thin polymer films and complex biomecolecular systems at the solution-surface interface. *Biomacromolecules 4*, 1099–1120.

(87) Love, C. J., Estroff, L. A., Kriebel, J. K., Nuzzo, R. G., and Whitesides, G. M. (2005) Self-assembled monolayers of thiolates on metals as a form of nanotechnology. *Chem. Rev. 105*, 1103–1170.

(88) Flynn, N. T., Tran, T. N., Cima, M. J., and Langer, R. (2003) Long-term stability of self-assembled monolayers in biological media. *Langmuir 19*, 10909–10915.

(89) Lakowicz, J. R. (2001) Radiative decay engineering: biophysical and biomedical applications. *Anal. Biochem. 298*, 1–24.

(90) Castelino, K., Kannan, B., and Majumdar, A. (2005) Characterization of grafting density and binding efficiency of DNA and proteins on gold surfaces. *Langmuir 21*, 1956–1961.

BC100288C

Bishydrazide Glycoconjugates for Lectin Recognition and Capture of Bacterial Pathogens

Avijit Kumar Adak, Alexei P. Leonov, Ning Ding, Jyothi Thundimadathil, Sumith Kularatne, Philip S. Low, and Alexander Wei

Supporting Information

1. Figure S1 ---------- S1
2. Figure S2---------- S2
3. Figure S3 ---------- S2
4. Figure S4 ---------- S2
5. Figure S5 ---------- S3
6. Figure S6 ---------- S3
7. NMR spectra of hexa(ethylene glycol)-linked diester ---------- S4
8. NMR spectra of hexa(ethylene glycol)-linked bishydrazide (**4**) ---------- S5
9. NMR spectra of heptanediol-linked diester ---------- S6
10. NMR spectra of heptanediol-linked bishydrazide (**5**) ---------- S7
11. NMR spectra of lactose–bishydrazide conjugate (**6**) ---------- S8
12. NMR spectra of pulmonary trisaccharide–bishydrazide conjugate (**7**) -- S9
13. NMR spectra of heptanediol-linked lactose–bishydrazide conjugate (**9**) S10
14. NMR spectra of pulmonary trisaccharide intermediate (**12**) ---------- S11
15. NMR spectra of pulmonary trisaccharide intermediate (**13**) ---------- S12
16. NMR spectra of (β-GalNAc(1→4)β-Gal(1→4)β-Glc) (**2**) ---------- S13

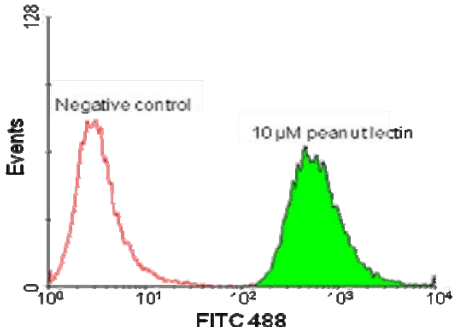


Figure S1: Representative data from flow immunocytometry demonstrating peanut lectin binding to microspheres conjugated with lactose–bishydrazide **6** (cf. Figure 3). Positive binding determined by degree of peak overlap between immunolabeled beads and negative control.

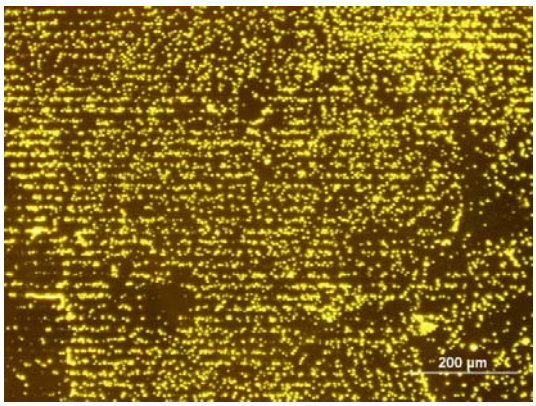


Figure S2: Capture of *Pseudomonas* on BSA-coated substrates with photopatterned glycan–bishydrazide–ANB conjugate, imaged by darkfield microscopy. Bacterial capture at 10^6 cfu/mL, using pulmonary trisaccharide conjugate **16.**

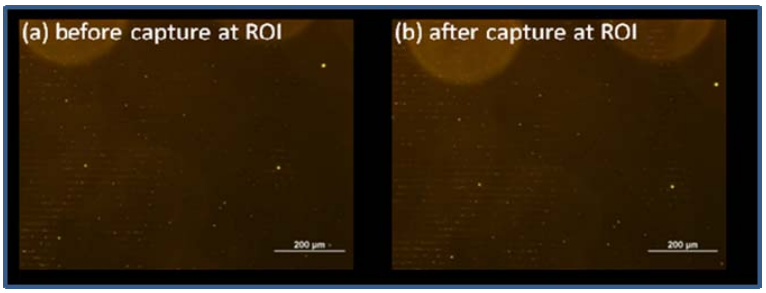


Figure S3: Control study showing no *Pseudomonas* capture by substrates patterned with lactose–bishydrazide conjugate. Darkfield images of patterned region of interest (ROI), (a) before and (b) after exposure to *Pseudomonas* for 1 hour at 10^6 cfu/mL.

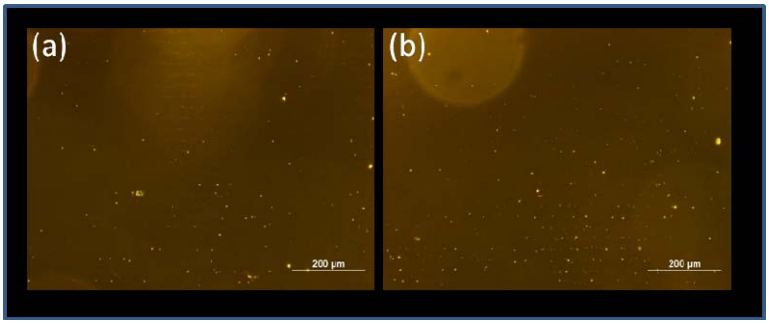


Figure S4: Control study showing no capture of UV-irradiated *Pseudomonas* (2 hours, λ_{max} = 254 nm) by substrate patterned with pulmonary trisaccharide–BSA conjugate (**7**–BSA). Darkfield images of patterned ROI, (a) before and (b) after exposure to UV-irradiated *Pseudomonas* (10^6 cfu/mL).

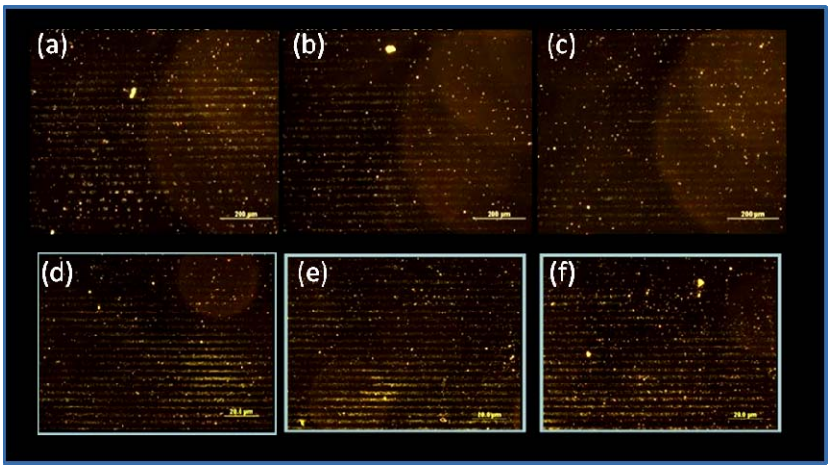


Figure S5: Control study showing capture of *Pseudomonas* by substrate patterned with **7**–BSA, in the presence of excess lactose (a–c) or GalNAc (d–f). (a) 100 mM lactose; (b) 50 mM lactose; (c) 1 mM lactose; (d) 100 mM GalNAc; (e) 50 mM GalNAc; (f) 1 mM GalNAc.

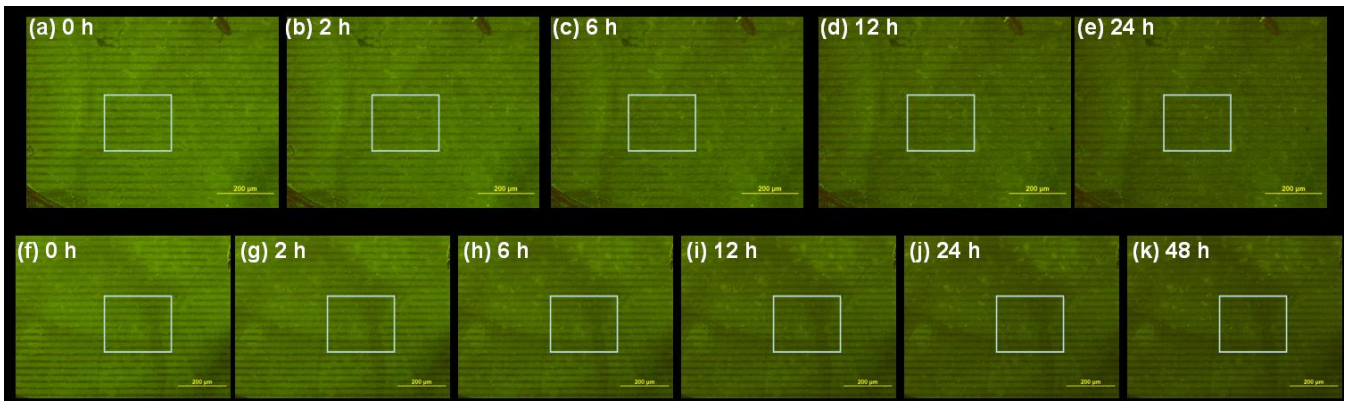
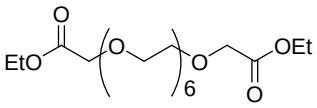
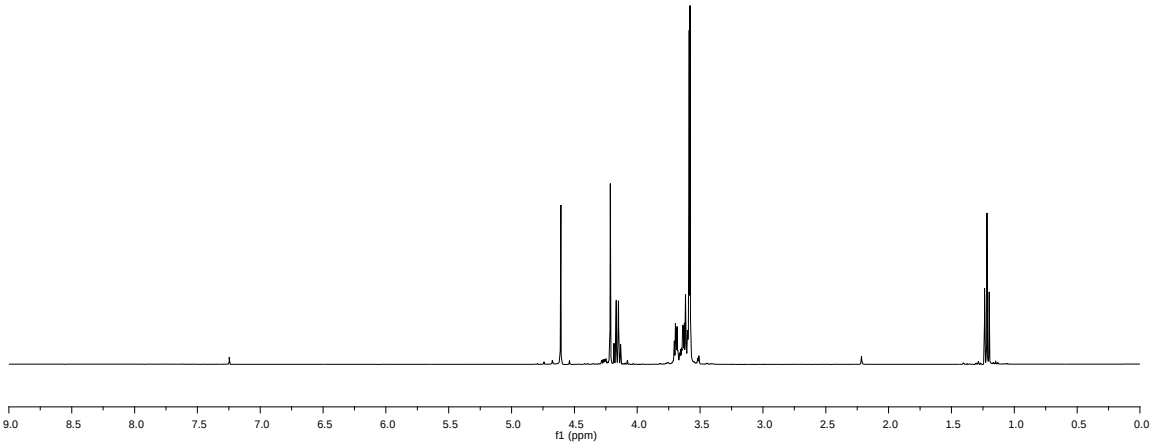


Figure S6: Fluorescence microscopy images of the immunocomplexes exposed to different concentration of ME. Top: (a-e) images exposed to 100 μM ME for 2-24 h. Bottom: (f-k) images exposed to 10 μM ME for 2-48h. Square regions (256x256 pixels) in each image were analyzed (by Adobe Photoshop) for changes in luminosities.

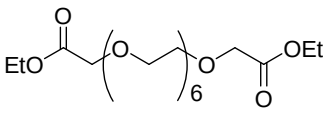
Hexa(ethylene glycol)-linked bis-ethyl(carboxymethyl)ester

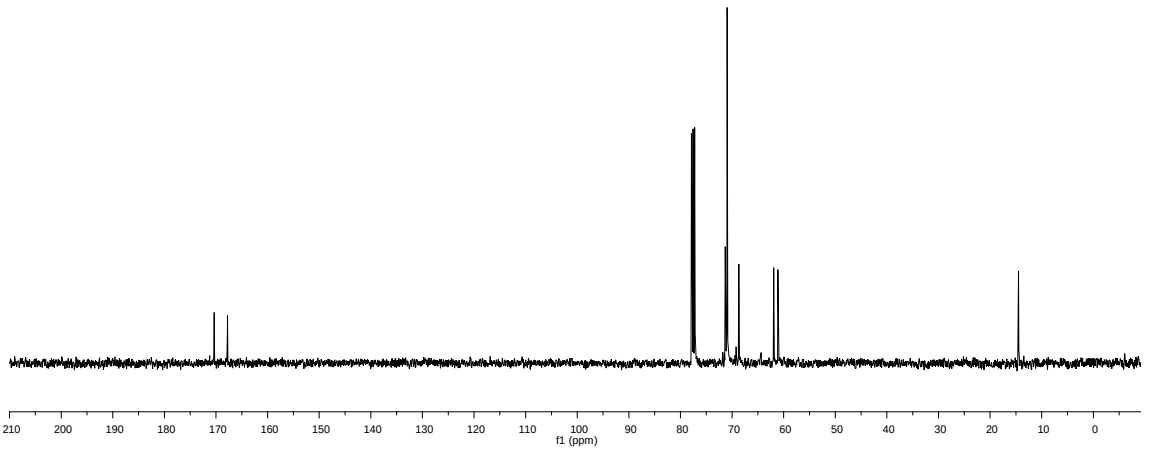
^{1}H NMR (400 MHz, $CDCl_3$)





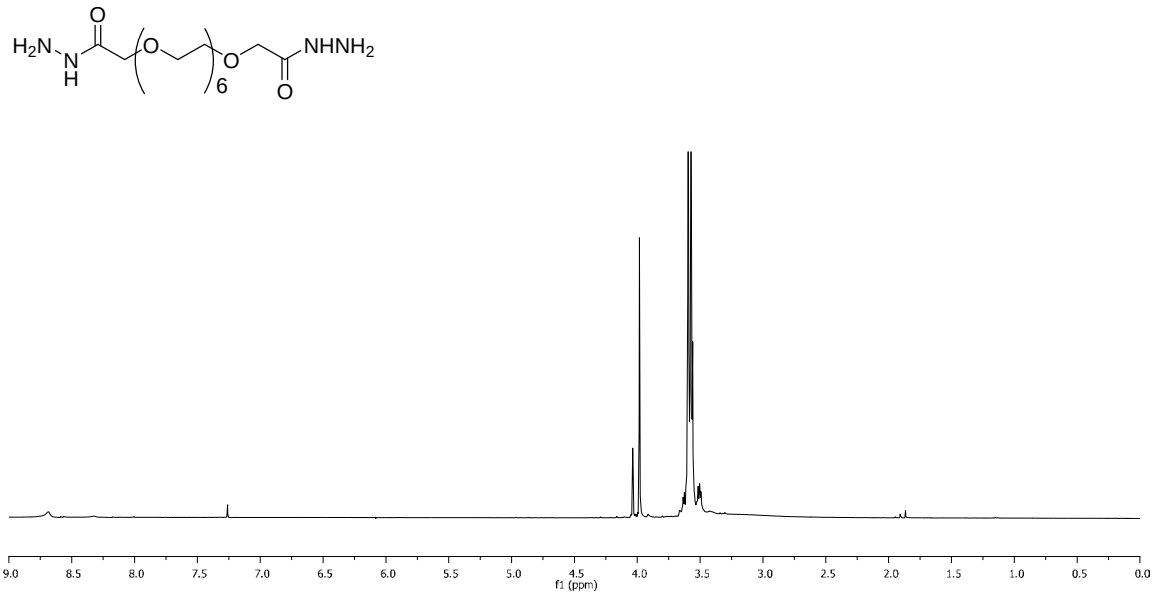
^{13}C NMR (100 MHz, CD_3OD)



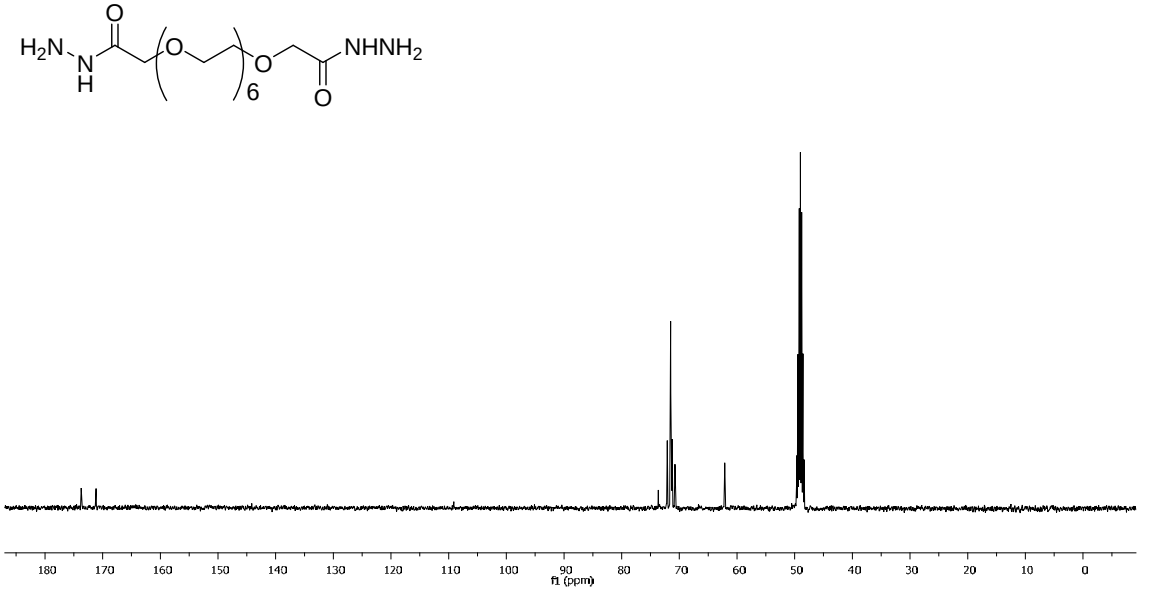


Hexa(ethylene glycol)-linked bishydrazide (**4**)

^{1}H NMR (400 MHz, $CDCl_3$)

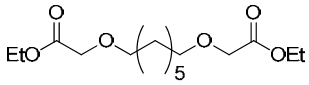


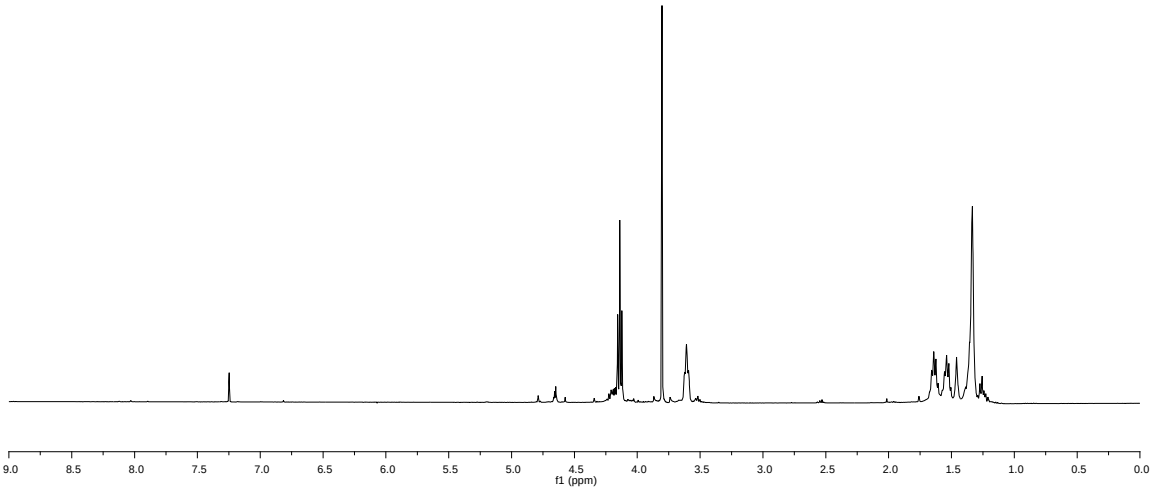
^{13}C NMR (100 MHz, CD_3OD)



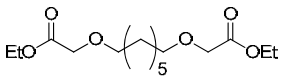
Heptanediol-linked bis-ethyl(carboxymethyl)ester

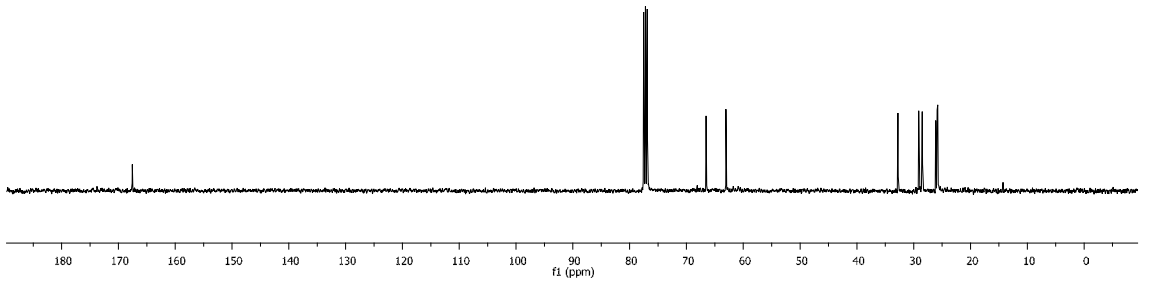
^{1}H NMR (400 MHz, $CDCl_3$)





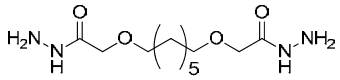
^{13}C NMR (100 MHz, $CDCl_3$)

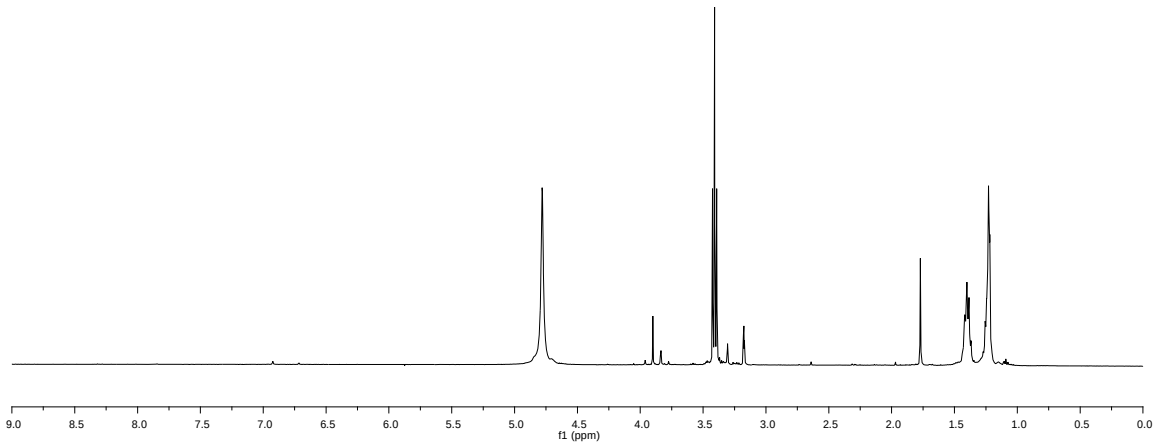




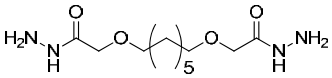
Heptanediol-linked bishydrazide (**7**)

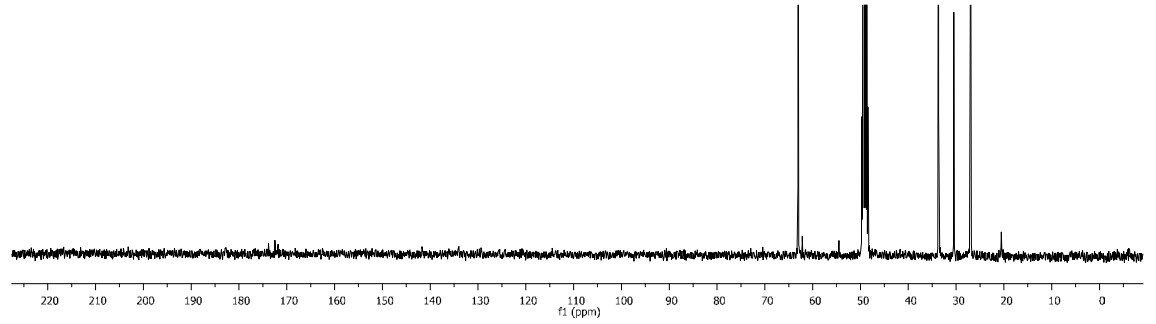
^{1}H NMR (400 MHz, $CDCl_3$)





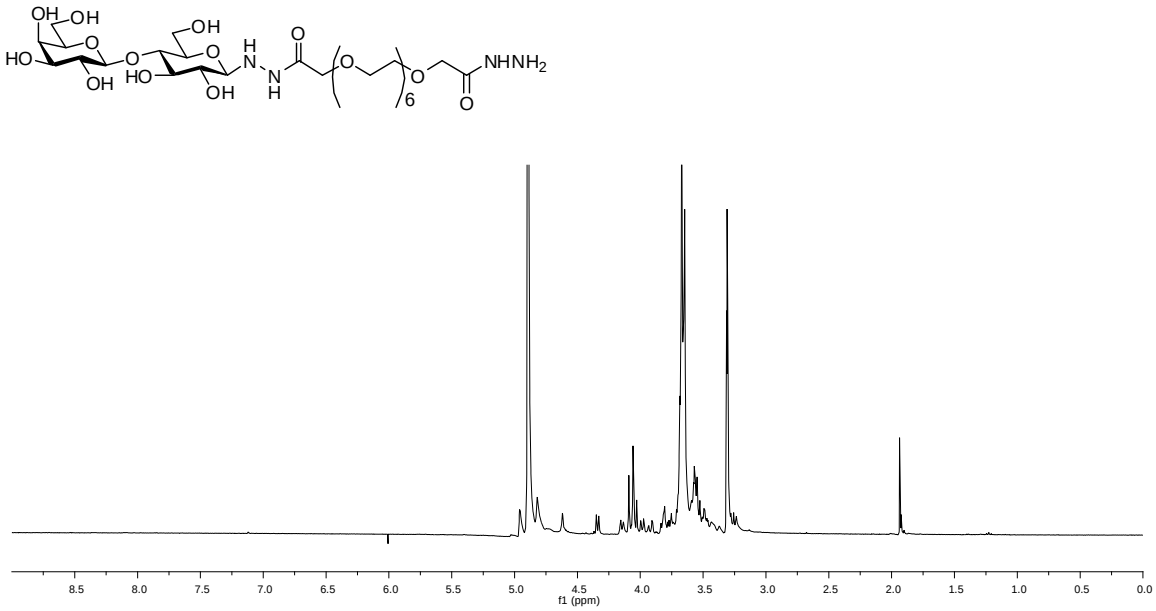
^{13}C NMR (100 MHz, $CDCl_3$)



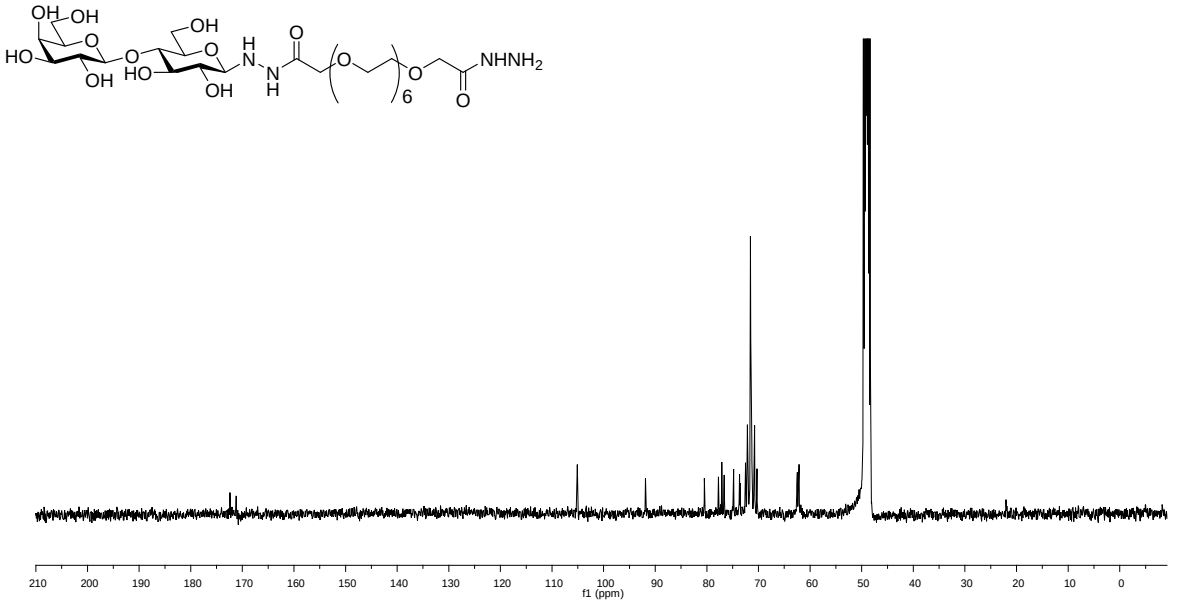


Lactose–bishydrazide conjugate (**6**)

^{1}H NMR (400 MHz, CD_3OD)

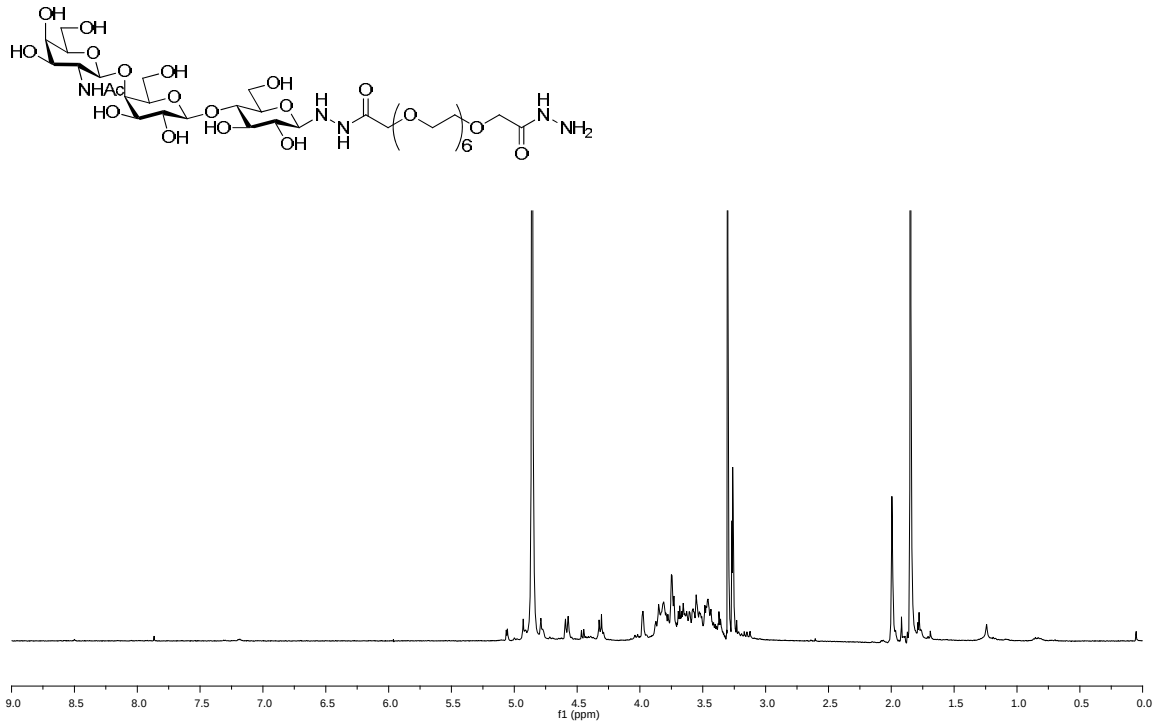


^{13}C NMR (100 MHz, CD_3OD)

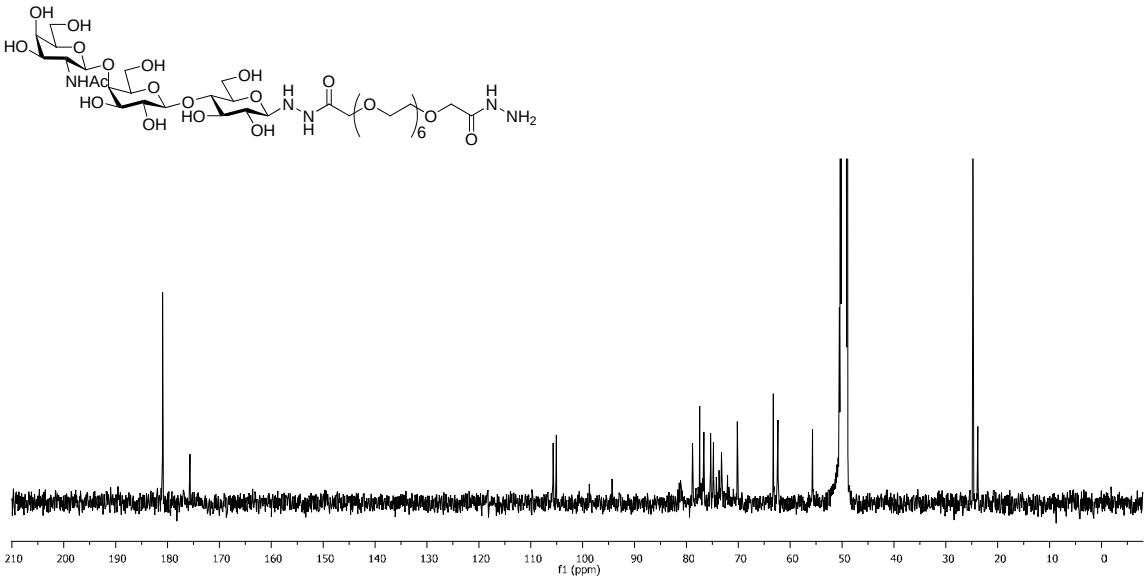


Pulmonary trisaccharide–bishydrazide conjugate (**7**)

^{1}H NMR (400 MHz, CD_3OD)

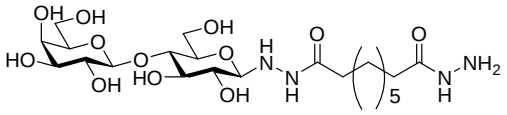


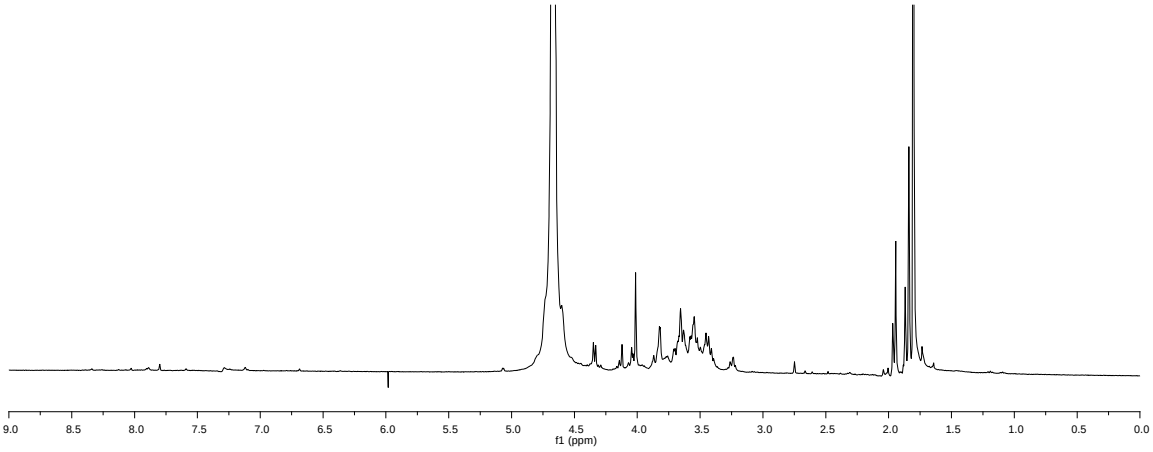
^{13}C NMR (100 MHz, CD_3OD)



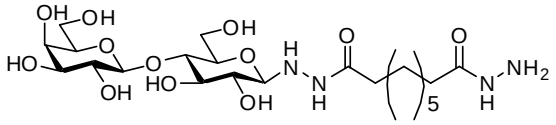
Heptanediol-linked lactose–bishydrazide conjugate (**9**)

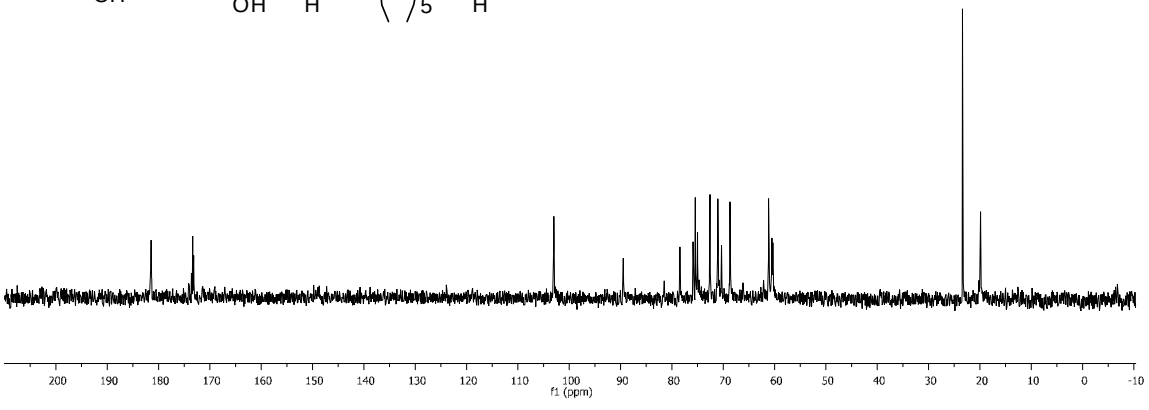
^{1}H NMR (400 MHz, D_2O)





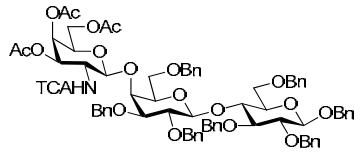
^{13}C NMR (100 MHz, D_2O)

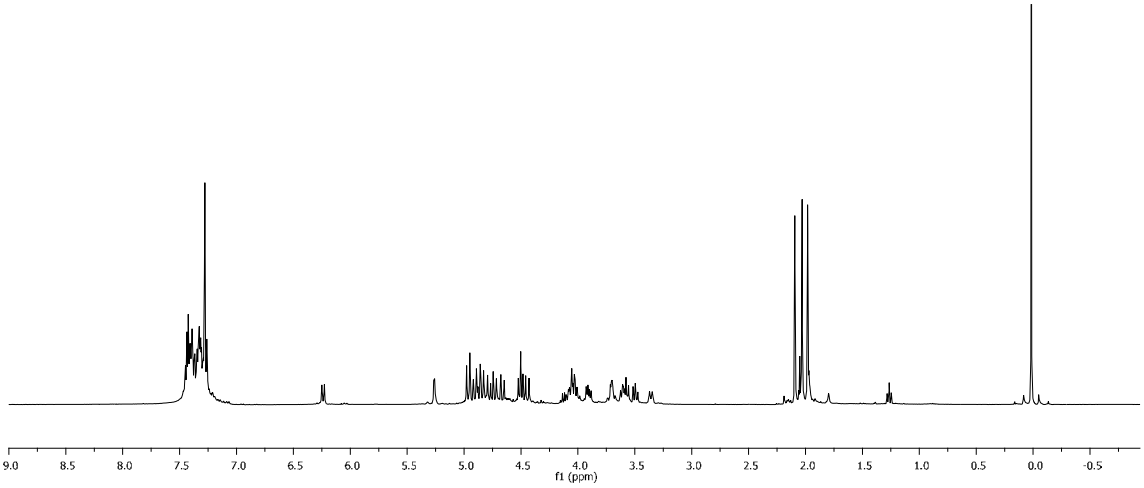




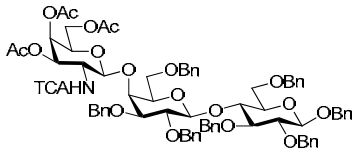
Pulmonary trisaccharide (β-GalNAc(1→4) β-Gal(1→4)β-Glc), trichloroacetamide (**12**)

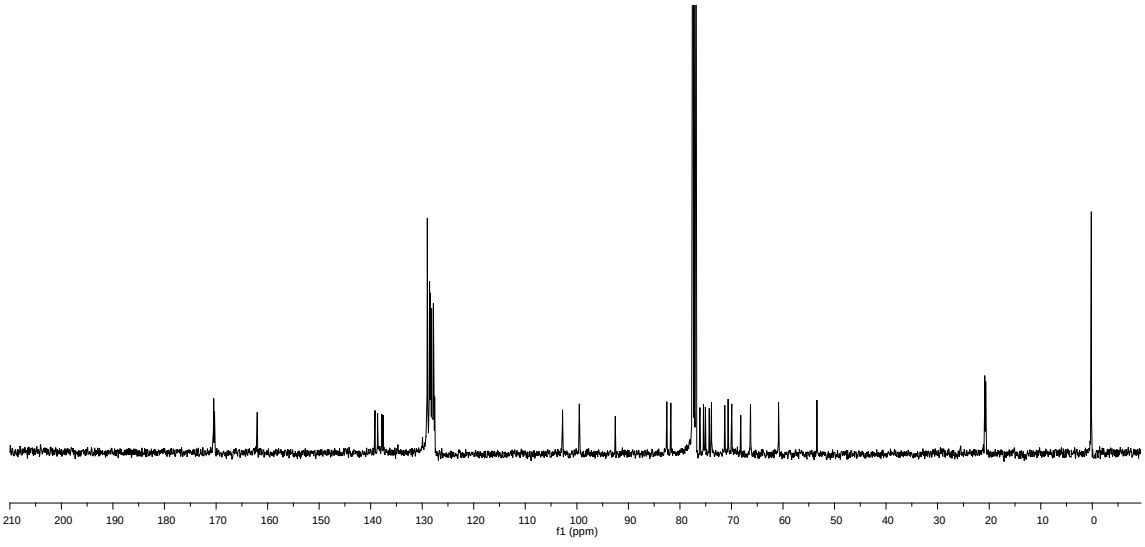
^{1}H NMR (400 MHz, $CDCl_3$)





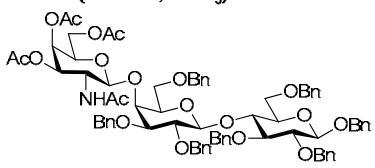
^{13}C NMR (100 MHz, $CDCl_3$)

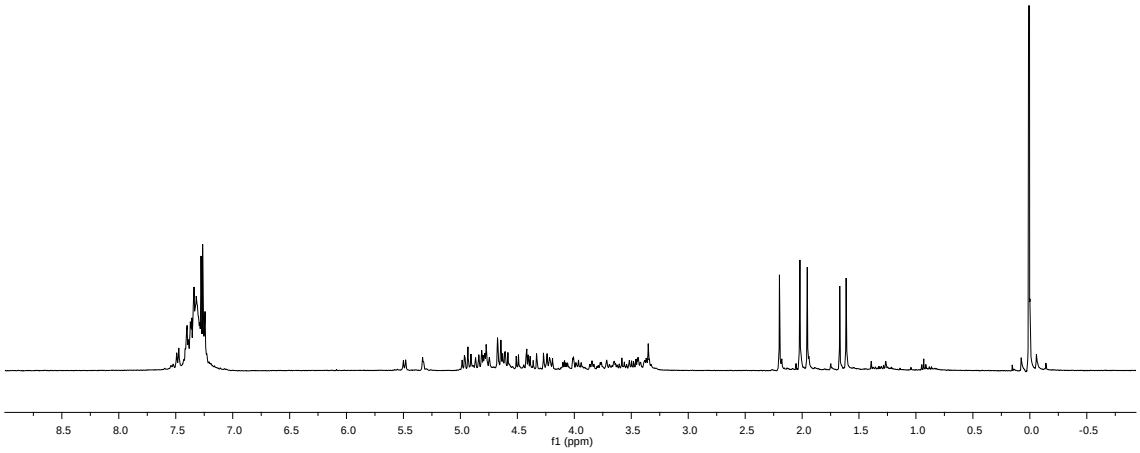




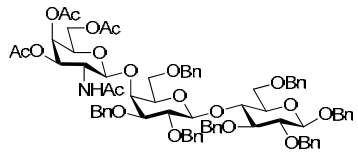
Pulmonary trisaccharide (β-GalNAc(1→4) β-Gal(1→4)β-Glc), protected derivative (**13**)

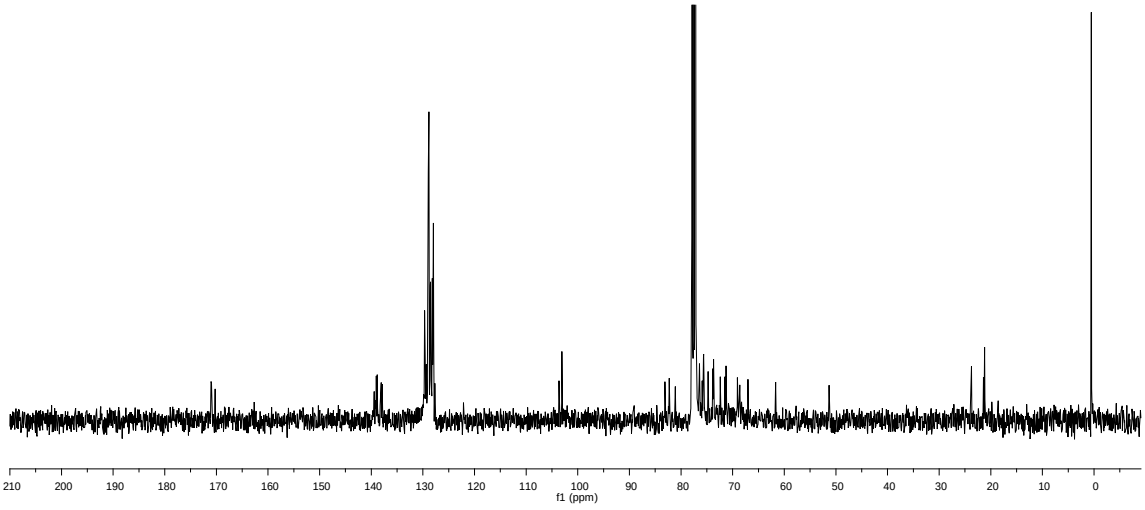
^{1}H NMR (400 MHz, $CDCl_3$)





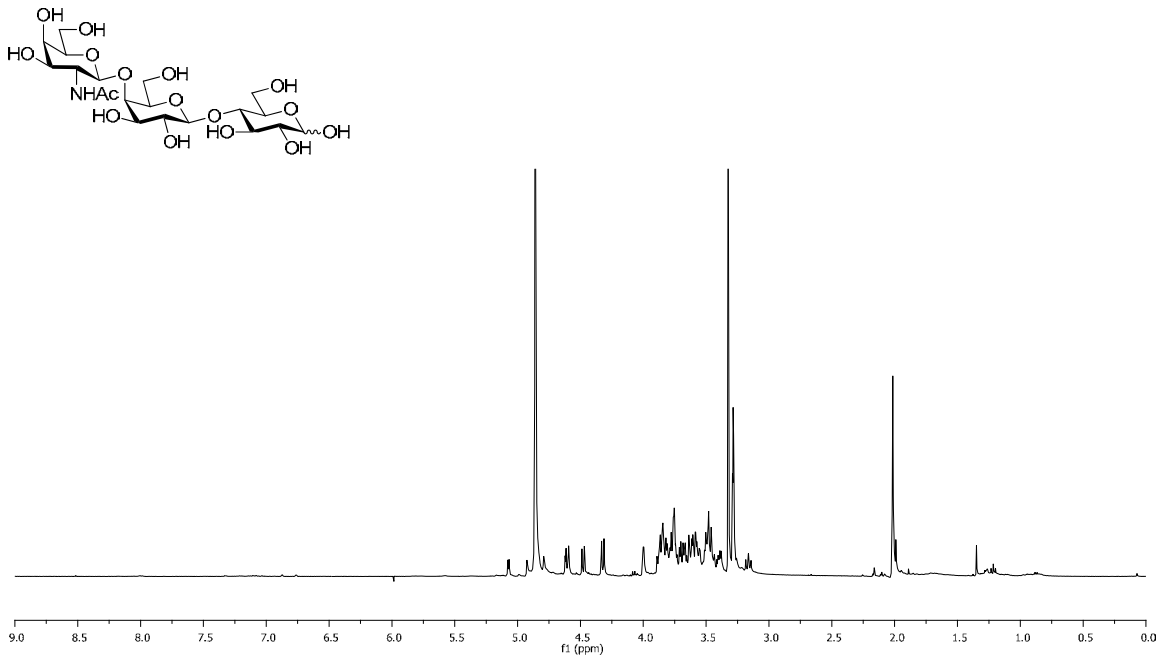
^{13}C NMR (100 MHz, $CDCl_3$)



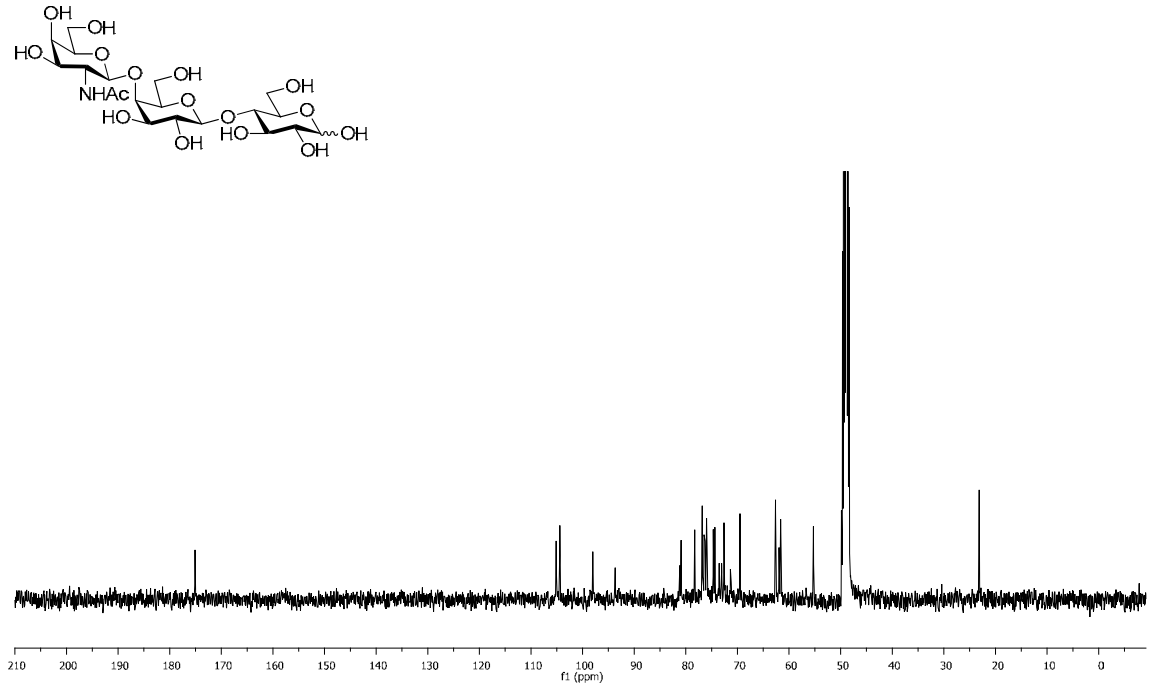


Pulmonary trisaccharide (β-GalNAc(1→4) β-Gal(1→4)β-Glc) (**2**)

^{1}H NMR (400 MHz, CD_3OD)



^{13}C NMR (100 MHz, CD_3OD)



Surface Functionalization Using Catalyst-Free Azide−Alkyne Cycloaddition

Alexander Kuzmin,[†] Andrei Poloukhtine,[†] Margreet A. Wolfert,[‡] and Vladimir V. Popik*,[†]

Department of Chemistry and Complex Carbohydrate Research Center, University of Georgia, 315 Riverbend Road, Athens, Georgia 30602, United States. Received July 6, 2010; Revised Manuscript Received September 29, 2010

The utility of catalyst-free azide−alkyne [3 + 2] cycloaddition for the immobilization of a variety of molecules onto a solid surface and microbeads was demonstrated. In this process, the surfaces are derivatized with aza-dibenzocyclooctyne (ADIBO) for the immobilization of azide-tagged substrates via a copper-free click reaction. Alternatively, ADIBO-conjugated molecules are anchored to the azide-derivatized surface. Both immobilization techniques work well in aqueous solutions and show excellent kinetics under ambient conditions. We report an efficient synthesis of aza-dibenzocyclooctyne (ADIBO), thus far the most reactive cyclooctyne in cycloaddition to azides. We also describe convenient methods for the conjugation of ADIBO with a variety of molecules directly or via a PEG linker.

INTRODUCTION

Surface immobilization of biomolecules is a very important step in the manufacturing of biosensors, microbeads, biochips, probe arrays, medical implants, and other devices (*1*−*5*). The key requirements for this process are the preservation of biochemical properties of immobilized substrates and robustness of the linkage. Copper(I)-catalyzed Huisgen 1,3-dipolar cycloaddition of azides to terminal acetylenes has emerged as one of the most convenient methods for the functionalization of various surfaces (*3, 5*−*10*). The triazol linker formed in the azide "click" reaction has excellent chemical stability due to the aromatic character of the heterocycle. Azide tags can be incorporated into biomolecules using a variety of different strategies, such as postsynthetic modification (*11*−*13*), in vitro enzymatic transfer (*14, 15*), the use of covalent inhibitors (*16*), and metabolic labeling by feeding cells a biosynthetic precursor modified with azido functionality (*17*). While conventional copper(I)-catalyzed click chemistry has become commonplace in surface derivatization, as well as in polymer and materials synthesis (*6*−*10, 18*−*20*), the use of metal catalyst often limits the utility of the method. Copper ions are cytotoxic (*21*), can cause degradation of DNA molecules (*22, 23*), and induce protein denaturation (*24*). In addition, the use of catalysts complicates kinetics of the immobilization process, requires polar solvents, and can alter surface properties (*25*).

Conventional copper-catalyzed azide click coupling methods employ terminal acetylenes, since internal alkynes react with azides only at elevated temperatures. Cyclooctynes, on the other hand, are known to form triazoles without a catalyst under ambient conditions, albeit at a rather slow rate (*26*). The triple bond incorporated into an eight-membered ring is apparently already bent into a geometry resembling the transition state of the cycloaddition reaction, thus reducing its activation barrier (*27*). Recently developed cyclooctyne derivatives are substantially more reactive toward azides and offer a convenient metal-free alternative to the copper-catalyzed click reaction (*28*−*33*). Metal-free click chemistry has been successfully employed for the modification of luminescent quantum dots (*25*) and protein labeling and purification (*34*−*37*), as well as for the introduction of fluorescent tags into live cells (*25, 38, 39*) and organisms (*40, 41*).

* E-mail: vpopik@chem.uga.edu.
[†] Department of Chemistry.
[‡] Complex Carbohydrate Research Center.

Among reactive cyclooctyne derivatives, dibenzocyclooctynes are synthetically more accessible (*42*). The major limitation of these click reactants is the relatively low rate of azide cycloaddition (ca. 0.05 M^{-1} s^{-1}) (*34*−*37*). Substitution of one of the saturated carbons in the cyclooctyne ring for a nitrogen atom not only improves its reactivity, but also simplifies the synthesis (*28*−*33*). To extend the arsenal of bioorthogonal copper-free click reagents, we have developed an efficient synthesis of aza-dibenzocyclooctyne-containing compounds for azide-coupling reactions. In the present report, we describe a novel approach to efficient surface-functionalization using a catalyst-free azide click reaction. This method allows for the site-specific covalent anchoring of proteins and other substrates to various surfaces. The same metal-free click reaction is employed for the PEGylation of nonfunctionalized areas of the surface. Such treatment allows for a dramatic reduction or complete elimination of nonspecific binding. The copper-free click immobilization strategy discussed in the present report can be applied to the preparation of various types of arrays, as well as to the derivatization of microbeads and nanoparticles.

EXPERIMENTAL PROCEDURES

Materials and Methods. Purification of products by column chromatography was performed using 40−63 μm silica gel. All NMR spectra were recorded on a 400 MHz instrument in $CDCl_3$ and referenced to TMS unless otherwise noted. Images of fluorophore-patterned slides were recorded, and fluorescence intensity was quantified using a Typhoon 9400 variable mode imager (GE Healthcare) at an excitation/emission setting appropriate for fluorescein (488/520 nm) or Lissamine rhodamine B (532/580 nm) fluorophores in PBS solution; images of fluorescent microbeads were obtained using Zeiss Observer AX10 inverted microscope with an X-cite series 120 fluorescent light source and Chroma Technology filters. The relative fluorescent intensity (spot/background) was quantified using *ImageJ* program (NIH).

Tetrahydrofuran was distilled from a sodium/benzophenone ketyl; ether and hexanes were distilled from sodium; *N*,*N*-dimethylformamide (DMF) was dried by passing through an alumina column. Biotin-dPEG3+4-azide and Biotin-PEG4-acid were purchased from Quanta BioDesign; fluorescein SE, Oregon Green SE, Lissamine rhodamine B sulfonyl chloride, and FITC-Avidin were obtained from Invitrogen; (3-glycidyloxypropyl)-

10.1021/bc100306u © 2010 American Chemical Society
Published on Web 10/21/2010

dimethoxymethylsilane was purchased from TCI America; 0.0067 M phosphate buffered saline (PBS) with pH 7.4 was obtained from Thermo Scientific. Bovine serum albumin (BSA) was obtained from Fisher BioReagents. Other reagents were purchased from Aldrich or VWR and used as received unless otherwise noted. Polished glass slides were obtained from VWR; NanoLink streptavidin magnetic microspheres (1% aqueous suspension) were purchased from SoluLink Biosciences. Aza-dibenzocycloctyne **6** conjugates with fluorescein (ADIBO-fluor, **10**), Oregon green (ADIBO-OG, **11**), and Lissamine rhodamine B (ADIBO-Rhodamine, **12**) were prepared by treating **6** with equimolar amounts of fluorescein SE, Oregon Green SE, Lissamine rhodamine B sulfonyl chloride, respectively, in DMF in the presence of DIEA (ethyldiisopropylamine). Oregon green azide (**13**) and Lissamine rhodamine B azide (**14**) were prepared by reacting equimolar amounts of Oregon green SE or Lissamine rhodamine B sulfonyl chloride with 3-azidopropyl amine in DMF in the presence of DIEA. Conjugates **10**−**14** were purified by chromatography ($CHCl_3$/MeOH/AcOH 100:5:0.5) and their purity was confirmed by HPLC analysis. 1-Amino-11-azido-3,6,9-trioxaundecane (AminoPEG_4azide) (*43*) and 6-azidohexylamine (*44*) were prepared according to literature procedures.

*5,6-Dihydrodibenzo[b,f]azocine (**2**).* A solution of dibenzosuberenone (25 g, 121 mmol) and hydroxylamine hydrochloride (6.81 mL, 164 mmol) in pyridine (70 mL) was refluxed for 20 h. The reaction mixture was concentrated and poured into 5% aqueous hydrochloric acid (with crushed ice), stirred for 20 min, filtered, and dried in the air to provide 28.1 g of crude dibenzosuberenone oxime, as a white precipitate. Dibenzosuberenone oxime (16 g, 72.3 mmol) was added to 250 mL polyphosphoric acid at 125 °C; the reaction mixture was stirred for 60 min at this temperature, poured onto crushed ice (∼700 mL), stirred for another 30 min, and filtered. The filter cake was washed with water and dried under vacuum to provide crude dibenzo[*b*,*f*]azocin-6(5H)-one **1** (11.6 g, 52.4 mmol, 73%) as a gray powder.

A suspension of **1** (7.4 g, 33.4 mmol) and lithium aluminum hydride (2.494 mL, 66.9 mmol) in anhydrous ether (200 mL) was refluxed for 15 h. The reaction mixture was quenched by water and filtered, and the filter cake was washed with ether. The filter cake was dispersed in ether (100 mL), stirred for 10 min, and filtered. The combined organic layers were dried over $MgSO_4$, solvent was removed under vacuum, and the product was purified by chromatography (hexanes/ethyl acetate 2:1) to provide 4.04 g (19.49 mmol, 58%) of 5,6-dihydrodibenzo[*b*,*f*]-azocine (*2*). ^{1}H NMR: δ 7.27−7.23 (m, 1 H), 7.2−7.1 (m, 3 H), 6.96−6.9 (m, 1 H), 6.9−6.8 (m, 1 H), 6.65−6.55 (m, 1 H), 6.54−6.48 (m, 1 H), 6.40 (d, J = 8 Hz, 1 H), 6.38−6.29 (m, 1 H), 4.51 (d, J = 6.8 Hz, 2 H), 4.2 (br s, 1 H). ^{13}C NMR: δ 147.3, 139.3, 138.3, 134.9, 132.7, 130.3, 129.0, 128.1, 127.8, 127.6, 127.5, 121.8, 118.1, 117.9, 49.6. HRMS (ESI+) calcd for $C_{15}H_{14}N$ $[M+H]^+$ 208.1126, found 208.1120.

*N-(6-(Dibenzo[b,f]azocin-5(6H)-yl)-6-oxohexyl)trifluoroacetamide (**3**).* 6-(Trifluoroacetamido)hexanoyl chloride (*45*) (0.984 g, 4.52 mmol) was added to a solution of **2** (0.75 g, 3.62 mmol) and pyridine (0.859 g, 10.86 mmol) in CH_2Cl_2 (ca. 10 mL) at rt and stirred for 30 min. The reaction mixture was diluted with CH_2Cl_2 (ca. 20 mL), washed with water (2 × 30 mL), and dried over anhydrous $MgSO_4$, and the solvent was removed under reduced pressure. The residue was purified by chromatography (hexanes/ethyl acetate 2:3) to provide 1.064 g (2.56 mmol, 71%) of **3** as yellowish oil. ^{1}H NMR: δ 7.32−7.22 (m, 4 H), 7.19−7.11 (m, 4 H), 6.77 (d, J = 13.2 Hz, 1 H), 6.58 (d, J = 13.2 Hz, 1 H), 5.46 (d, J = 14.8 Hz, 1 H), 4.20 (d, J = 14.8 Hz, 1 H), 3.29−3.15 (m, 2 H), 2.09−2.02 (m, 1 H), 1.93−1.85 (m, 1 H), 1.51−1.32 (m, 4 H), 1.25−1.04 (m, 2 H). ^{13}C NMR: δ 172.7, 157.5, 141.1, 136.1, 135.8, 134.8, 132.4, 131.8, 130.5, 128.5, 128.2, 128.1, 128.0, 127.3, 127.2, 117.5, 114.6, 54.8, 39.6, 34.3, 28.2, 25.9, 24.3. HRMS (ESI+) *m*/*z* calcd for $C_{23}H_{24}F_3N_2O_2$ $[M+H]^+$ 417.1790, found 417.1783.

*N-(6-Trifluoroacetamidohexanoyl)-5,6-dihydro-11,12-didehydrodibenzo[b,f]azocine (**5**).* Pyridine hydrobromide perbromide (0.948 g, 2.97 mmol) was added to a solution of **3** (1.05 g, 2.70 mmol) in CH_2Cl_2 (4 mL) at rt, and the reaction mixture was stirred overnight. The reaction mixture was diluted with CH_2Cl_2 (20 mL), washed with 5% aqueous hydrochloric acid (20 mL), dried over $MgSO_4$, and solvent removed under vacuum. The residue was passed through a short pad of silica gel (CH_2Cl_2) to give 1.2 g of crude *N*-(trifluoroacetamidohexanoyl)-5,6,11,12-tetrahydro-11,12-dibromodibenzo[*b*,*f*]azocine (*4*) as an oil. A solution of crude **4** (1.2 g, 2.08 mmol) in THF (5 mL) was added to a solution of potassium *t*-butoxide (0.584 g, 5.21 mmol) in THF (10 mL) at rt; the reaction mixture was stirred for 1 h, diluted with ethyl acetate (20 mL), washed with 5% aqueous hydrochloric acid and brine, then dried over $MgSO_4$, and the solvent was removed under reduced pressure. The crude product was purified by chromatography (hexanes/ethyl acetate, 2:1 to 1:1) to afford 0.76 g (1.83 mmol, 88%) of **5** as brown oil. ^{1}H NMR: δ 7.68 (d, J = 7.6 Hz, 1 H), 7.45−7.21 (m, 7 H), 6.79 (br s, 1 H), 5.16 (d, J = 14.4 Hz, 1 H), 3.67 (d, J = 13.6 Hz, 1 H), 3.22−3.14 (m, 1 H), 3.11−3.02 (m, 1 H), 2.24−2.16 (m, 1 H), 1.41−1.22 (m, 4 H), 1.11−0.9 (m, 2 H). MS: *m*/*z* 414 $[M^+]$. Calcd for $C_{23}H_{21}F_3N_2O_2$ 414.

*N-(6-Aminohexanoyl)-5,6-dihydro-11,12-didehydrodibenzo-[b,f]azocine (ADIBO-C6-amine, **6**).* A solution of K_2CO_3 (2 g, 14.47 mmol) in 15 mL of water was added to a solution of *N*-(6-trifluoroacetamido hexanoyl)-5,6-dihydro-11,12-didehydrodibenzo[*b*,*f*]azocine (**5**, 2.95 g, 7.12 mmol) in MeOH (30 mL) at rt and stirred overnight. Solvents were removed under reduced pressure, the residue was redissolved in CH_2Cl_2/ethyl acetate (1:4), then washed with brine and water. The organic layer was dried over anhydrous Na_2SO_4 and concentrated in vacuum. The crude product was purified by chromatography (CH_2Cl_2/MeOH 10:1 to 10:4) to provide 1.31 g (4.11 mmol, 58%) of **6** as slightly yellow oil. ^{1}H NMR: δ 7.71 (d, J = 7.6 Hz, 1 H), 7.45−7.21 (m, 7 H), 5.18 (d, J = 14.4 Hz, 1 H), 3.63 (d, J = 13.6 Hz, 1 H), 3.32 (br, 2 H), 2.67 (t, J = 5.6 Hz, 1 H), 2.52 (t, J = 5.6 Hz, 1 H), 2.21−2.19 (m, 1 H), 1.95−1.90 (m, 1 H), 1.45−1.35 (m, 2 H) 1.28−1.20 (m, 2 H), 1.11−0.9 (m, 2 H). ^{13}C NMR: δ 173.3, 151.8, 147.8, 132.3, 132.1, 128.9, 128.2, 128.0, 127.8, 127.5, 126.5, 122.1, 123.0, 114.8, 107.9, 55.8, 41.4, 34.7, 31.9, 26.0, 24.8. HRMS (ESI+) *m*/*z* calcd for $C_{21}H_{23}N_2O$ $[M+H]^+$ 319.1810, found 319.1799.

*N-(3-Aminopropionyl)-5,6-dihydro-11,12-didehydrodibenzo[b,f]azocine (ADIBO-C3-amine, **7**).* **7** was prepared following the same protocol as the preparation of **6**. ^{1}H NMR (500 MHz): δ 7.68 (d, J = 7.5 Hz, 1 H), 7.45−7.33 (m, 5 H), 7.29 (t, J = 7.5 Hz, 1 H), 7.25 (t, J = 7 Hz, 1 H), 5.15 (d, J = 14 Hz, 1 H), 3.16 (d, J = 14 Hz, 1 H), 2.82−2.67 (m, 2H), 2.45−2.35 (m, 1 H), 2.01−1.92 (m, 1 H), 1.6−1.4 (br s, 2 H). ^{13}C NMR: δ 172.14, 151.48, 148.01, 132.12, 129.08, 128.29, 128.21, 127.99, 127.63, 127.01, 125.43, 122.85, 122.57, 114.97, 107.66, 55.25, 38.25, 38.15. HRMS (ESI+) calcd for $C_{18}H_{17}N_2O$ $[M+H]^+$ 277.1341, found 277.1339.

*Aza-dibenzocyclooctyne−Biotin Conjugate (ADIBO-biotin, **8**).* HBTU (1.916 g, 5.05 mmol) was added to a solution of biotin-PEG4-acid (1.9 g, 3.87 mmol) and DIEA (0.647 g, 5.61 mmol) in CH_2Cl_2 (15 mL) at rt and stirred for 15 min. A solution of **7** (1.238 g, 4.48 mmol) in CH_2Cl_2 (2 mL) was added dropwise, the reaction mixture was stirred for 3 h and concentrated under reduced pressure. The product was purified by chromatography (CH_2Cl_2 to CH_2Cl_2/MeOH 20:1 to 100:15) to provide 2.44 g (3.26 mmol, 87%) of **8** as colorless semisolid. ^{1}H NMR (500 MHz, $CDCl_3$): δ 7.66 (d, J = 7 Hz, 1 H),

7.42−7.3 (m, 7 H), 7.28−7.25 (m, 1 H), 7.05−6.99 (m, 1 H), 6.79−6.75 (m, 1 H), 6.61 (br s, 1 H), 5.13 (d, J = 14 Hz, 1 H), 4.5−4.45 (m, 1 H), 4.32−4.25 (m, 1 H), 3.68 (d, J = 14 Hz, 1 H), 3.65−3.45 (m, 17 H), 3.44−3.36 (m, 2 H), 3.32−3.22 (m, 2 H), 3.15−3.07 (m, 2 H), 2.9−2.82 (m, 1 H), 2.75−2.65 (m, 1 H), 2.55−2.46 (m, 1 H), 2.33 (q, J = 6 Hz, 2 H), 2.2 (t, J = 7.5 Hz, 2 H), 2.0−1.92 (m, 1 H), 1.75−1.6 (m, 4 H), 1.45−1.35 (m, 5 H). ^{13}C NMR: δ 173.51, 171.99, 171.13, 164.01, 151.1, 148.09, 132.13, 129.14, 128.68, 128.21, 127.83, 127.19, 125.58, 123.07, 122.45, 114.72, 107.86, 70.45, 70.43, 70.39, 70.3, 70.17, 70.03, 69.98, 97.17, 61.83, 60.26, 55.69, 55.52, 53.67, 42.0, 40.52, 39.14, 36.79, 35.89, 35.26, 34.71, 28.29, 28.11, 25.63, 18.59, 17.44, 11.88. HRMS (ESI+) m/z calcd for $C_{39}H_{53}N_5O_8S$ $[M+H]^+$ 750.3537, found 750.3542.

*Aza-dibenzocyclooctyne-PEG$_4$-Amine (ADIBO-PEG$_4$-amine, **9**).* EDC (0.75 g, 4.68 mmol) was added to a solution of Boc-NH-$(CH_2CH_2O)_4$-$CH_2CH_2CO_2H$ (*46*) (1.57 g, 4.32 mmol) in CH_2Cl_2 (15 mL) and DIEA (0.7 g, 5.4 mmol) at rt and stirred for 15 min. A solution of ADIBO-amine **7** (1 g, 3.6 mmol) in CH_2Cl_2 (1 mL) was added to the reaction mixture and stirred for 4 h, at which time the solvent was removed under reduced pressure and the crude product purified by chromatography (ethyl acetate/hexanes 1:1 to 9:1) to provide 1.8 g (2.8 mmol, 80%) of crude *N*-Boc-protected ADIBO-PEG$_4$-amine (9-Boc) as yellow oil.

A solution of TFA (0.48 g, 4.2 mmol) in THF (15 mL) was added to a solution of **9-Boc** (1.8 g, 2.8 mmol) in THF (30 mL) at rt. The reaction mixture was stirred overnight, and the solvent was removed under reduced pressure. The residue was purified by chromatography (CH_2Cl_2/MeOH 10:1 to 10:4) to provide 1.15 g (2.2 mmol, 79%) of ADIBO-PEG$_4$-amine (**9**) as slightly yellow oil. ^{1}H NMR (500 MHz): δ 7.67 (d, J = 7.5 Hz, 1 H), 7.43−7.34 (m, 5 H), 7.31 (t, J = 7.5 Hz, 1 H), 7.29−7.24 (m, 1 H), 6.95−6.88 (m, 1 H), 5.13 (d, J = 14 Hz, 1 H), 4.45−4.2 (br s, 2 H), 3.7−3.5 (m, 22 H), 3.37−3.2 (m, 3 H), 2.68 (t, J = 5 Hz, 2 H), 2.57−2.42 (m, 1 H), 2.4−2.32 (m, 2 H), 2.02−1.92 (1 H). ^{13}C NMR (100 MHz, $CDCl_3$): 172.13, 171.21, 151.20, 148.16, 129.3, 129.2, 128.78, 128.44, 128.31, 127.9, 127.29, 127.25, 125.68, 123.16, 122.55, 114.81, 107.92, 70.46, 70.39, 70.35, 70.32, 70.30, 70.26, 70.1, 55.62. 48.86, 36.69, 35.41, 34.67. HRMS (ESI+) m/z calcd for $C_{29}H_{38}N_3O_6$ [M+H] 524.2761, found 524.2756. (Note: Integration of ^{1}H spectra of compounds containing PEG commonly overestimates the number of protons due to the presence of tightly bound water and/or hydroxylic solvents.)

Cleaning and Activation of Glass Slide Surfaces. All glass slides were sonicated for 30 min in methanol, rinsed with acetone, and dried in an oven at 145 °C for 1 h. Piranha solution (90 mL) was prepared by the addition of H_2O_2 (25 mL of 35% v/v) in one portion to 65 mL of conc H_2SO_4 in a 100 mL Pyrex beaker, which was kept in a water bath (**Caution:** Piranha solution reacts violently with organic compounds and should be handled with extreme care. Wear thick plastic gloves, lab coat, and safety glasses. Any piranha solutions should be handled in a fume hood at all times). The solution was carefully stirred with a glass rod, followed by inserting glass slides into the solution. After 1 h, slides were removed from the solution and rinsed with copious amounts of distilled water, then acetone, and dried in an oven for 20 min at 145 °C. Glass slides prepared in this fashion were submitted to derivatization procedures immediately.

Preparation of Epoxy-Derivatized Glass Slides. Freshly activated glass slides were immersed in a solution of freshly distilled (3-glycidyloxypropyl)dimethoxy-methylsilane (1% v/v) and DIEA (1% v/v) in dry toluene (100 mL) at 25 °C for 16 h. Slides were sonicated two times in methanol for 15 min, thoroughly rinsed with acetone, and dried under a stream of nitrogen.

Preparation of Aza-dibenzocyclooctyne (ADIBO, 6)-Coated Glass Slides. Freshly prepared epoxy-coated glass slides were placed in a solution of aza-dibenzocyclooctyne amine **6** (75 mg) and DIEA (1 mL) in DMF (100 mL) and incubated overnight at rt. Slides were then rinsed with acetone, sonicated for 15 min in methanol, rinsed with acetone, and dried under a stream of nitrogen.

Preparation of Azide-Coated Glass Slides. Freshly prepared epoxy-coated glass slides were immersed in a solution of 6-azidohexylamine (1 mL) and DIEA (1 mL) in DMF (100 mL) overnight at rt. The slides were then sonicated for 15 min in methanol, rinsed with acetone, and dried under a stream of nitrogen.

Patterned Derivatization of Glass Slides with Aza-dibenzocyclooctyne 6. One microliter drops of a 10 mM PBS solution of dibenzocyclooctyne **6** were spotted using a micropipet on a freshly prepared epoxy-coated slide, followed by incubation in a humidity chamber containing PBS buffer for 12 h at rt. The slide was washed with copious amounts of acetone, then water, and sonicated in DMF for 30 min.

Patterned Immobilization of Fluorescent Dyes on ADIBO-Coated Slides. Solutions of Oregon green azide (**13**, 0.1 mM and 1 mM in PBS) or Lissamine rhodamine B azide (**14**, 0.1 mM) were spotted using a pipet (2 μL) on a freshly prepared dibenzocyclooctyne plate and incubated in a humidity chamber for various periods of time (vide infra). Slides were rinsed with acetone, then sonicated for 15 min in methanol, rinsed with acetone, and dried under a stream of nitrogen.

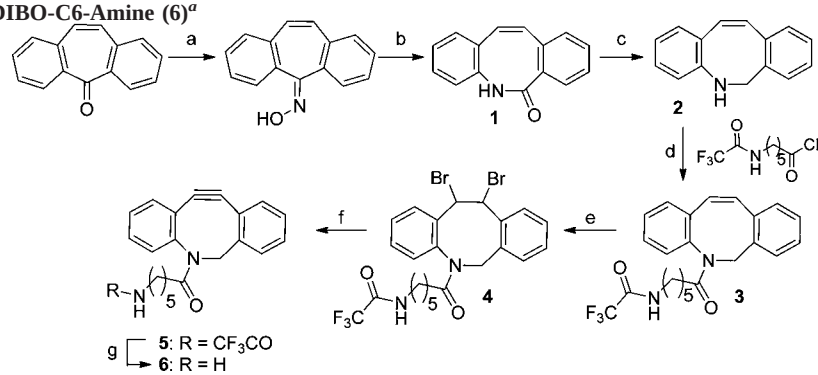
Patterned Immobilization of Avidin on ADIBO-Coated Slides. One microliter drops of biotin-dPEG3+4-azide PBS solutions of different concentrations (10 mM, 1 mM, and 0.1 mM) were spotted on a ADIBO-coated glass slide. Slides were incubated in a humidity chamber for 1 h at rt, rinsed with copious amounts of acetone, then water, and sonicated in DMF for 30 min. Slides were then immersed in a blocking solution containing 1% aminoPEG$_4$azide in DMF and incubated overnight at rt. The slides were then rinsed with acetone, sonicated in DMF for 30 min, and rinsed with distilled water, followed by immersion into a solution of avidin-FITC (50 μL of 2 mg/mL in 10 mL of PBS) at 2 °C for 15 min. The slides were sonicated in PBS containing 0.1% Tween 20 for 30 min, washed with distilled water, incubated in PBS containing 0.1% of BSA for 12 h at 2 °C, sonicated again in PBS (1% of Tween 20) for 30 min, and rinsed with distilled water.

Patterned Immobilization of Fluorescent Probes on Azide-Coated Slides. One microliter drops of 1 mM of ADIBO-fluor (**10**) solution in PBS were spotted on an azide plate, followed by incubation in a humidity chamber for 12 h at rt. Slides were rinsed with acetone, then sonicated for 15 min in methanol, rinsed with acetone, and dried under a stream of nitrogen.

For two-color derivatization, azide-coated slides patterned with ADIBO-fluor (**10**) spots as described above were immersed in a solution of ADIBO-Rhodamine (**12**, 1 mM in PBS) and incubated for 3 h at rt. Slides were rinsed with acetone, then sonicated for 15 min in methanol, rinsed with acetone, and dried under a stream of nitrogen.

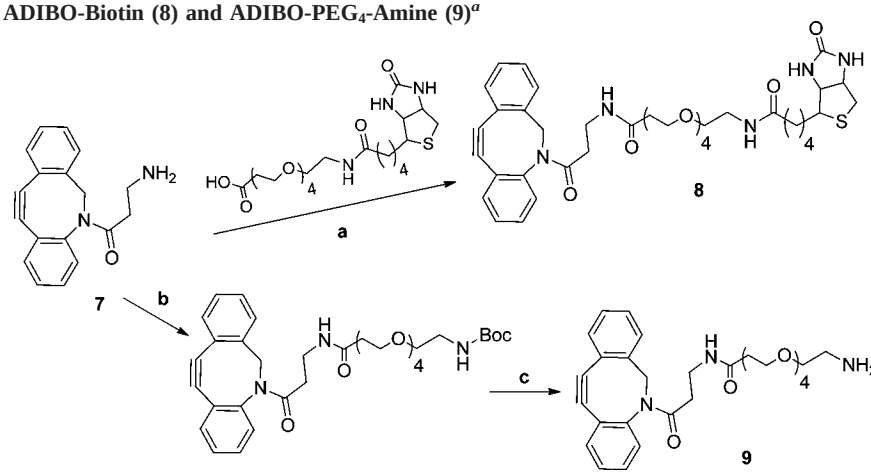
Patterned Immobilization of Avidin on Azide-Coated Slides. One microliter drops of ADIBO-biotin (**8**) solutions of different concentrations (10 mM, 1 mM, 0.1 mM, and 0.01 mM in PBS) were spotted on an azide-coated glass slide. Slides were incubated in a humidity chamber for 1 h at rt, rinsed with copious amounts of acetone, then water, and sonicated in DMF for 30 min. Slides were then immersed in a blocking solution containing 0.1% ADIBO-PEG4-amine (**9**) in DMF and incu-

Scheme 1. Synthesis of ADIBO-C6-Amine (6)[a]



[a] Reagents and conditions: (a) $NH_2OH.HCl$, pyridine, 60%; (b) PPA, 125 °C, 73%; (c) $LiAlH_4$, ether, 58%; (d) pyridine, CH_2Cl_2, 71%; (e) pyridinium tribromide, 78%; (f) *t*-BuOK, THF, 88%; (g) K_2CO_3, aq MeOH, 58%.

Scheme 2. Synthesis of ADIBO-Biotin (8) and ADIBO-PEG_4-Amine (9)[a]



[a] Reagents and conditions: (a) HBTU, DIEA, CH_2Cl_2, 89%; (b) Boc-NH-$(CH_2CH_2O)_4$-$CH_2CH_2CO_2H$, EDC, DIEA, CH_2Cl_2, 80%; (c) TFA, THF, 79%.

bated overnight at rt. The slides were rinsed with acetone, sonicated in DMF for 30 min, and rinsed with distilled water, followed by immersion into a solution of avidin-FITC (50 μL of 2 mg/mL in 10 mL PBS) at 2 °C for 15 min. The slides were sonicated in a PBS solution containing 0.1% Tween 20 for 30 min, washed with distilled water, incubated in PBS containing 0.1% BSA for 12 h at 2 °C, sonicated again in PBS (1% Tween 20) for 30 min, and rinsed with distilled water.

Preparation of ADIBO-Coated Magnetic Beads. A solution of ADIBO−biotin conjugate (**8**) (25 μL, 10 mM in PBS) was added to a suspension of streptavidin-coated magnetic beads (25 μL of 10 mg/mL) in 450 μL PBS. The resulting mixture was stirred by shaking for 2 h at rt. The reaction mixture was centrifuged at 11 000 rpm for 2 min, the supernatant liquid was decanted, and the pellet resuspended in PBS (450 μL). The washing step was repeated two times.

Preparation of Azide-Coated Magnetic Beads. A solution of Biotin-dPEG3+4-azide (25 μL, 10 mM in PBS) was added to a suspension of streptavidin-coated magnetic beads (25 μL of 10 mg/mL) in 450 μL PBS. The resulting mixture was stirred by shaking for 2 h at rt. The reaction mixture was centrifuged at 11 000 rpm for 2 min, the supernatant liquid was decanted, and the pellet resuspended in PBS (450 μL, pH 7.4). The washing step was repeated twice.

Fluorescent Labeling of ADIBO-Coated Magnetic Beads. A solution of Oregon Green-azide (**13**) (10 mM in PBS) was added to a suspension of ADIBO-coated magnetic beads (25 μL of 10 mg/mL) and incubated for 3 h at rt. Beads were centrifuged at 11 000 rpm for 1 min, the supernatant liquid was decanted, and the pellet was resuspended in 450 μL PBS containing 0.1% Tween 20, centrifuged, washed with PBS, centrifuged, and resuspended in 450 μL PBS for fluorescent microscopy imaging.

Fluorescent Labeling of Azide-Coated Magnetic Beads. A solution of ADIBO-fluor (**10**, 25 μL of 10 mM in PBS) was added to a suspension of azide-coated magnetic beads (25 μL of 10 mg/mL) in 450 μL PBS and incubated for 3 h at rt. Beads were centrifuged at 11 000 rpm for 1 min, the supernatant liquid was decanted, and the pellet was resuspended in 450 μL PBS containing 0.1% of Tween 20, centrifuged, washed with PBS, centrifuged, and resuspended in 450 μL PBS for fluorescent microscopy imaging.

RESULTS AND DISCUSSION

Synthesis of Aza-dibenzocyclooctyne−Amine Conjugate (ADIBO-amine, 6). The efficient preparation of ADIBO-amine developed in our lab is outlined in Scheme 1. It starts with the polyphosphoric acid-catalyzed Beckman rearrangement of dibenzosuberenone oxime, which is readily prepared by treating commercially available dibenzosuberenone with hydroxylamine. The lactam **1** produced in this reaction is then reduced with lithium aluminum hydride to give dihydrodibenzo[*b*,*f*]azocine (**2**). The secondary amino group in **2** is converted to amide **3** by reacting with 1.25 equiv of 6-(trifluoroacetamido)hexanoyl chloride in the presence of pyridine. The olefin in **3** is smoothly converted into an acetylene moiety via a bromination−dehydrobromination procedure to give aza-dibenzocyclooctyne **5** in excellent yield (88%). Saponification of the trifluoroacetamide moiety with potassium carbonate in aqueous methanol gives

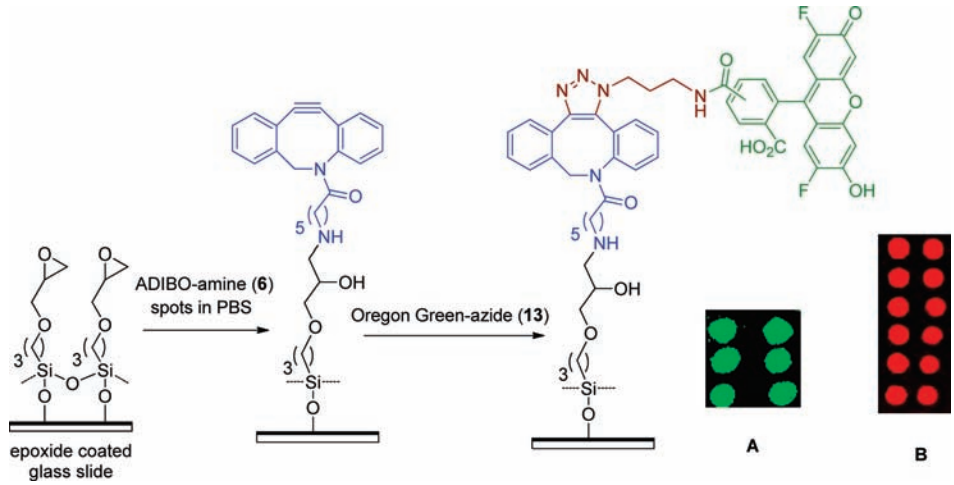


Figure 1. Schematic representation of ADIBO derivatization of an epoxy-coated slide followed by copper-free click immobilization of Oregon green dye. Inserts show fluorescent images ADIBO slides patterned with (A) Oregon green azide (**13**) and (B) Lissamine rhodamine B azide (*14*).

target ADIBO-C6-amine (**6**). ADIBO-amine with a shorter aminoakyl side chain, ADIBO-C3-amine (**7**), was prepared following the same synthetic sequence by replacing 6-(trifluoroacetamido)hexanoyl chloride in step "d" with 3-(trifluoroacetamido)propionyl chloride.

Aza-dibenzocyclooctyne−Biotin Conjugate (ADIBO-biotin, 8). 8 was prepared by HBTU (1-[bis(dimethylamino)methylene]-1*H*-benzotriazolium-3-oxide hexafluorophosphate)-promoted coupling of ADIBO-C3-amine (*7*) with biotin-PEG4-acid (Scheme 2). EDC-induced coupling of compound **7** with *N*-Boc-15-amino-4,7,10,13-tetraoxapentadecanoic acid, followed by trifluoroacetic acid-catalyzed removal of *N*-Boc protection gave Aza-dibenzocyclooctyne-PEG_4-amine (ADIBO-PEG_4-amine, **9**, Scheme 2).

ADIBO and Azide Functionalization of Glass Slides. Derivatization experiments were performed on glass surfaces due to the ready availability, low cost, high mechanical stability, low intrinsic fluorescence, and easy surface modification techniques of the glass substrate. Freshly prepared epoxide-coated slides were incubated in a DMF solution of ADIBO-amine **6** or 6-azidohexylamine in the presence of Hünig's base (*N*-ethyl-*N*,*N*-diisopropylamine) overnight and washed with acetone, then methanol (Figures 1 and 5).

Oregon Green azide (**13**) was used as a model compound to assess the efficiency and kinetics of the metal-free azide click immobilization on ADIBO-coated slides. To ensure that a fluorescent dye is immobilized on the slides only by the click reaction and not due to physical absorption or other chemical reactions, we spotted the epoxy-coated plate with ADIBO-amine (**6**). After overnight incubation and washing, these plates were immersed in a PBS solution of Oregon green azide (**13**, 0.01 mM) for 100 min and washed with acetone, then sonicated for 15 min in methanol, rinsed with acetone, and dried under a stream of nitrogen. The fluorescence image of the resulting slide demonstrates that dye **13** specifically binds to the ADIBO-derivatized surface and not to the rest of the slide (Figure 1, insert A). While the value of relative fluorescence intensity (spot versus background) depends on the starting epoxy plate (we have also tested VWR Microarray Epoxy 2 Slides and Corning Epoxide Slides), Oregon green spots always showed bright fluorescence with 2000−6000 contrast ratio. In the following fluorescent dye patterning experiments, 2 μL drops of 0.1 mM or 0.01 mM PBS solutions of azide−dye conjugate were applied onto ADIBO-derivatized slides. Thus, 0.1 mM solution of Lissamine rhodamine B azide (**14**) was spotted on the ADIBO-

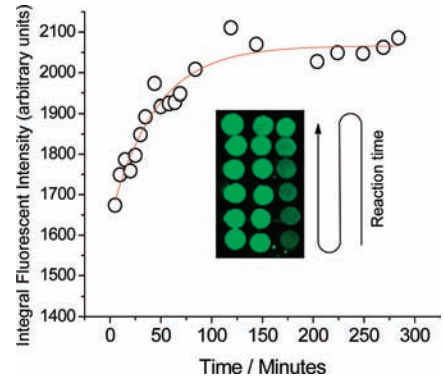


Figure 2. Integral fluorescent intensity of Oregon green azide (**13**) spots on ADIBO-derivatized slide versus reaction time.

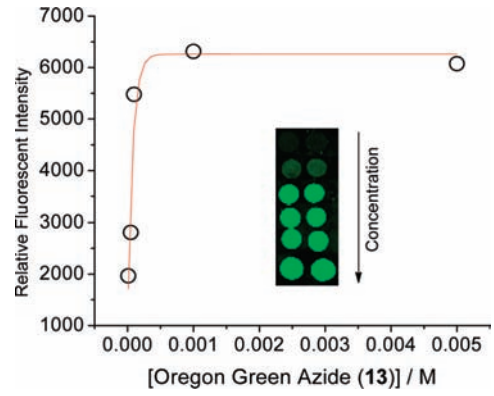


Figure 3. Integral fluorescent intensity of Oregon green azide (**13**) spots on ADIBO-derivatized slide versus concentration (10 μM, 50 μM, 0.1 mM, 1 mM, and 5 mM).

slide, incubated for 1 h, and thoroughly washed. The fluorescence image also has a good contrast ratio (Figure 1, insert B).

Kinetics of Metal-Free Click Immobilization. To evaluate the kinetics of the ADIBO−azide reaction on the surface, we spotted 2 μL drops of a 0.1 mM Oregon green azide (**13**) PBS solution onto ADIBO-derivatized slides. The first spot was allowed to react for 284 min; subsequent drops were applied at different times, with the last drop applied just 5 min before washing. The slides were stored in a humidity chamber during this procedure. The immobilization reaction shows excellent kinetics. Within 5 min, the relative fluorescent intensity reaches

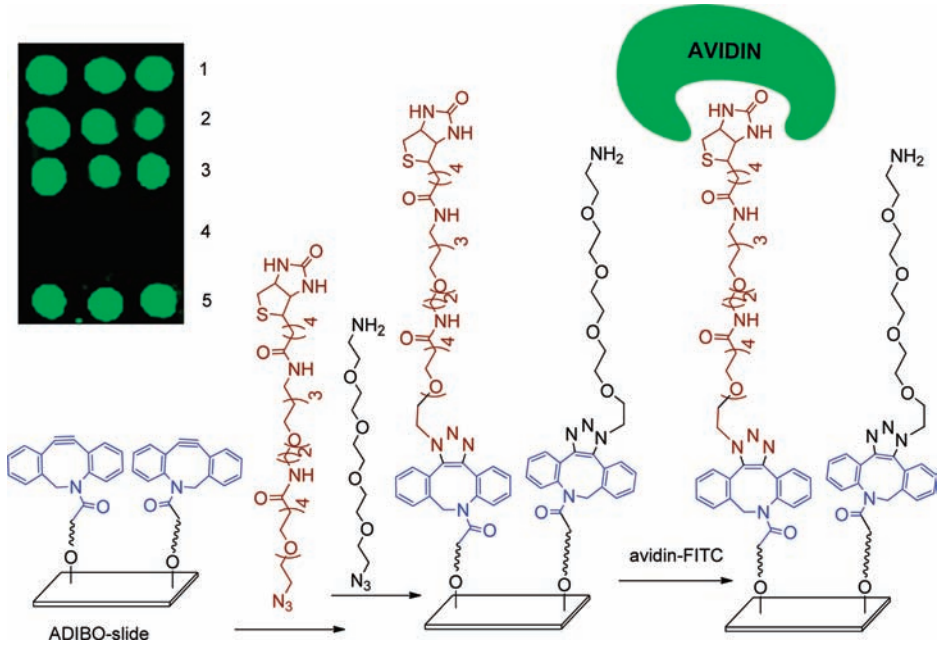


Figure 4. Schematic representation of patterned biotinylation of ADIBO-coated slide followed by selective immobilization of avidin-FITC. The insert shows the fluorescent image of ADIBO-slide spotted with 1 μL of the following solutions: lanes 1−3, 10 mM, 1 mM, and 0.1 mM PBS solutions of Biotin-dPEG3 + 4-azide; lane 4, 1 mM biotin-PEG$_4$-C≡CH; lane 5, 0.1 mM of Oregon green azide (**13**). The slide was then treated with aminoPEG$_4$azide and developed with avidin−FITC solution.

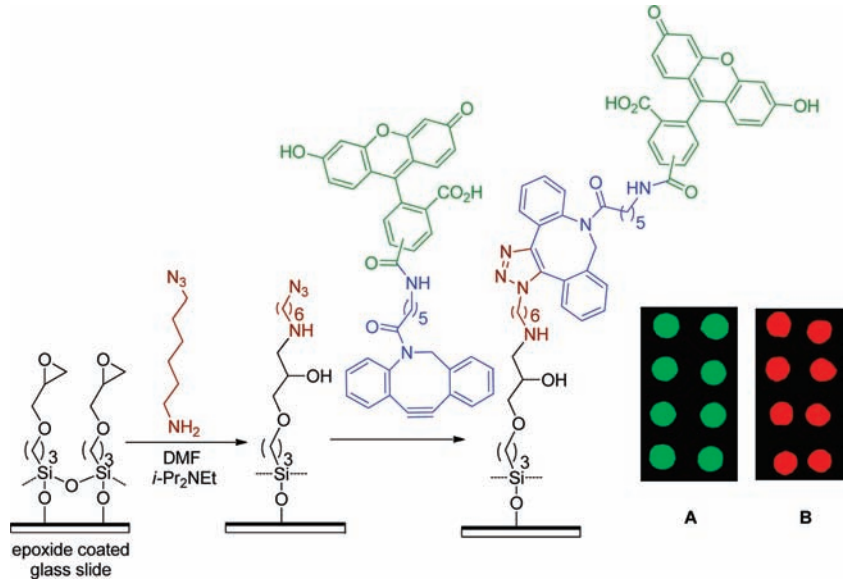


Figure 5. Schematic representation of azide derivatization of an epoxy-coated slide followed by copper-free click immobilization of ADIBO-fluor (*10*). Inserts show fluorescent images of azide slides patterned with (A) ADIBO-fluor (*10*) and (B) ADIBO-Rhodamine (*12*).

44−80% of the maximum value, and saturation of fluorescence is achieved at ca. 100 min at 0.1 mM of azide (Figure 2). As a result, incubation with the coupling reagent for 100 min was selected as a standard procedure for subsequent experiments.

To optimize the concentration of the substrate for the metal-free click immobilization, we spotted an ADIBO slide with PBS solutions of various concentration of Oregon green azide (**13**): 10 μM, 50 μM, 0.1 mM, 1 mM, and 5 mM. After incubation for 100 min and washing, the image of the slide was recorded and the integral fluorescent intensity analyzed (Figure 3). The saturation of Oregon green fluorescence is achieved at approximately 0.1 mM concentration of the azide **13**.

Biotinylation of ADIBO-Slides and Immobilization of Avidin. The exceptional selectivity and high binding constant between avidin and biotin (dissociation constant = 10^{-15} M) (*47*) is widely used in bioconjugation and surface immobilization applications (*1*−*5*, *10*, *48*−*53*). Therefore, we decided to test the efficiency of surface biotinylation using a copper-free azide click reaction. As shown in Figure 4, 1 μL drops of three different concentrations (10 mM, 1 mM, and 0.1 mM) of biotin-dPEG3+4-azide solutions in PBS were applied onto an ADIBO-functionalized glass slide. For a comparison, 1 μL drops of a 0.1 mM PBS solution of Oregon green azide (**13**) were also spotted on the slide. To test for the possibility of nonspecific absorption of biotin conjugates on the ADIBO slides, a 1 mM PBS solution of biotin-PEG$_4$-C≡CH was also spotted on the slide. After an hour-long incubation and washing, slides were immersed in a 1% DMF solution of aminoPEG$_4$azide and incubated overnight. Our initial experiment showed that dibenzocyclooctynes have significant affinity toward proteins. Ex-

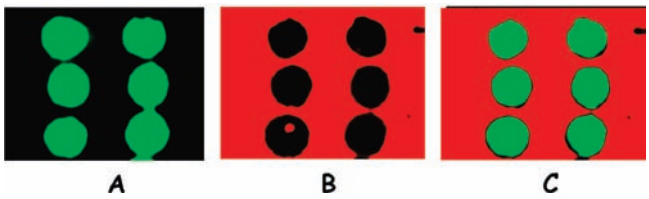


Figure 6. Two-color derivatization of azide slides. The slide was spotted with ADIBO-fluor (**10**), washed, and immersed in a solution of ADIBO-Rhodamine (*12*). (A) Fluorescent image recorded using 495/520 nm filter; (B) image recorded using 532/580 nm filter; (C) images A and B merged.

posure to the aminoPEG$_4$azide solution converts unreacted aza-dibenzocyclooctyne fragments into triazole−PEG conjugates. Patterned biotinylated slides were developed with an avidin-FITC PBS solution for 15 min at 2 °C and washed thoroughly. The fluorescent image of this slide shows selective immobilization of the protein in the biotinylated areas, while nonspecific binding of avidin was not observed (Figure 4). Incubation of the avidin-FITC-patterned slides in a PBS solution containing BSA does not reduce the fluorescence, confirming the immobilization of avidin via specific biotin−avidin interactions.

Patterning of Fluorescent Dyes on Azide-Coated Slides. To assess the efficiency of a reverse copper-free click surface derivatization, we prepared azide-coated glass slides (vide supra). Such a surface provides a convenient platform for immobilization using both conventional (i.e., copper-catalyzed) and catalyst-free azide click reactions. One microliter drops of a 1 mM PBS solutions of aza-dibenzocyclooctyne **6** conjugates with fluorescein (ADIBO-fluor, **10**) or with Lissamine rhodamine B (ADIBO-Rhodamine, **12**) were allowed to react for 12 h, then washed thoroughly. Fluorescent images of the resulting slides with fluorescein (Figure 5, insert A) and Lissamine rhodamine B (Figure 5, insert B) illustrate the efficiency of substrate immobilization on the azide-derivatized surface using metal-free click chemistry.

After immobilization, slides are often subjected to vigorous washing procedures, including the use of detergents and sonication in aqueous solutions and organic solvents. To test the stability of the azide surface to the washing procedures and to explore the feasibility of multisubstrate surface derivatization using copper-free click chemistry, we studied the sequential immobilization of two fluorescent dyes. The azide-coated glass slide was initially spotted with 1 μL drops of a 1 mM PBS solution of ADIBO-fluor (**10**) and incubated in a humidity chamber for 12 h at rt. The slide was rinsed with acetone, sonicated in DMF for 30 min, and rinsed with distilled water, then immersed in a 0.1 mM solution of ADIBO-Rhodamine (**12**) for another 12 h, then thoroughly washed. The fluorescent image recorded with a green (495−520 nm) filter clearly shows a pattern of fluorescein-immobilized spots (Figure 6A). The bright background of Lissamine rhodamine B fluorescence and dark spots, where azide groups were consumed in the first step, are visible on the image recorded with a red (532−580 nm) filter (Figure 6B). Figure 6C shows merged images A and B, which demonstrates that reactivity of an azide-derivatized surface is not significantly affected by washing procedures.

Patterned Biotinylation of Azide-Slides and Selective Immobilization of Avidin. To further demonstrate the versatility of the copper-free click reaction for protein immobilization, we have conducted patterned biotinylation of azide-derivatized slides, followed by the immobilization of avidin. Azide-functionalized glass slides were spotted with 1 μL drops of four different concentrations (10 mM, 1 mM, 0.1 mM, and 0.01 mM) of a PBS solution of ADIBO−biotin (*8*). Slides were incubated in a humidity chamber for 30 min, 2.5 h, and 3.5 h and washed with copious amounts of acetone, then water, and sonicated in DMF. To reduce nonspecific binding of the protein, slides were immersed in a blocking solution containing 0.1% ADIBO-PEG$_4$-amine (**9**) in DMF and kept overnight. The slides were then washed, incubated

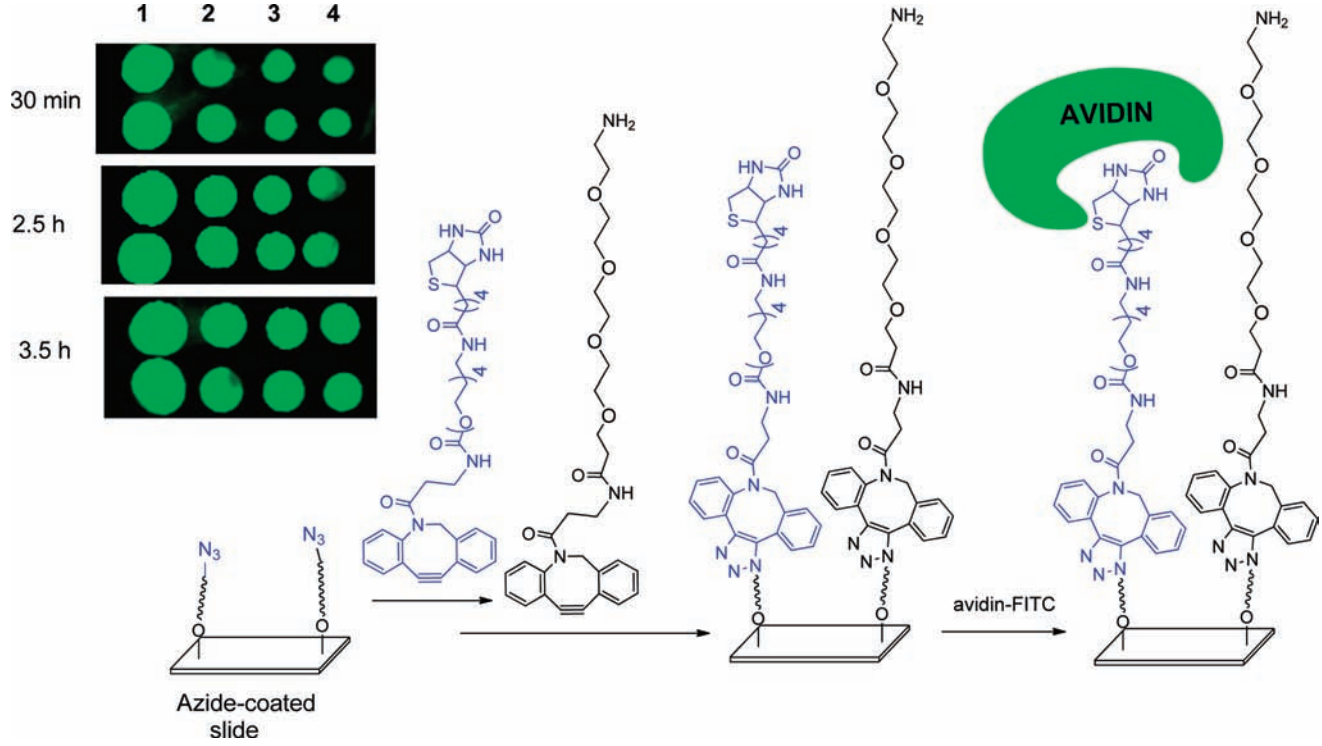


Figure 7. Schematic representation of patterned biotinylation of azide-coated slides followed by selective immobilization of avidin-FITC. The insert shows the fluorescent image of azide-derivatized slide spotted with 1 μL of ADIBO-biotin (**8**) solutions of the following concentrations: (1) 10 mM; (2) 1 mM; (3) 0.1 mM; (4) 0.01 mM. The first slide was incubated for 30 min, the second for 2.5 h, and the third for 3.5 h. Slides were then immersed in a solution of ADIBO-PEG$_4$-amine and developed with a solution of avidin-FITC.

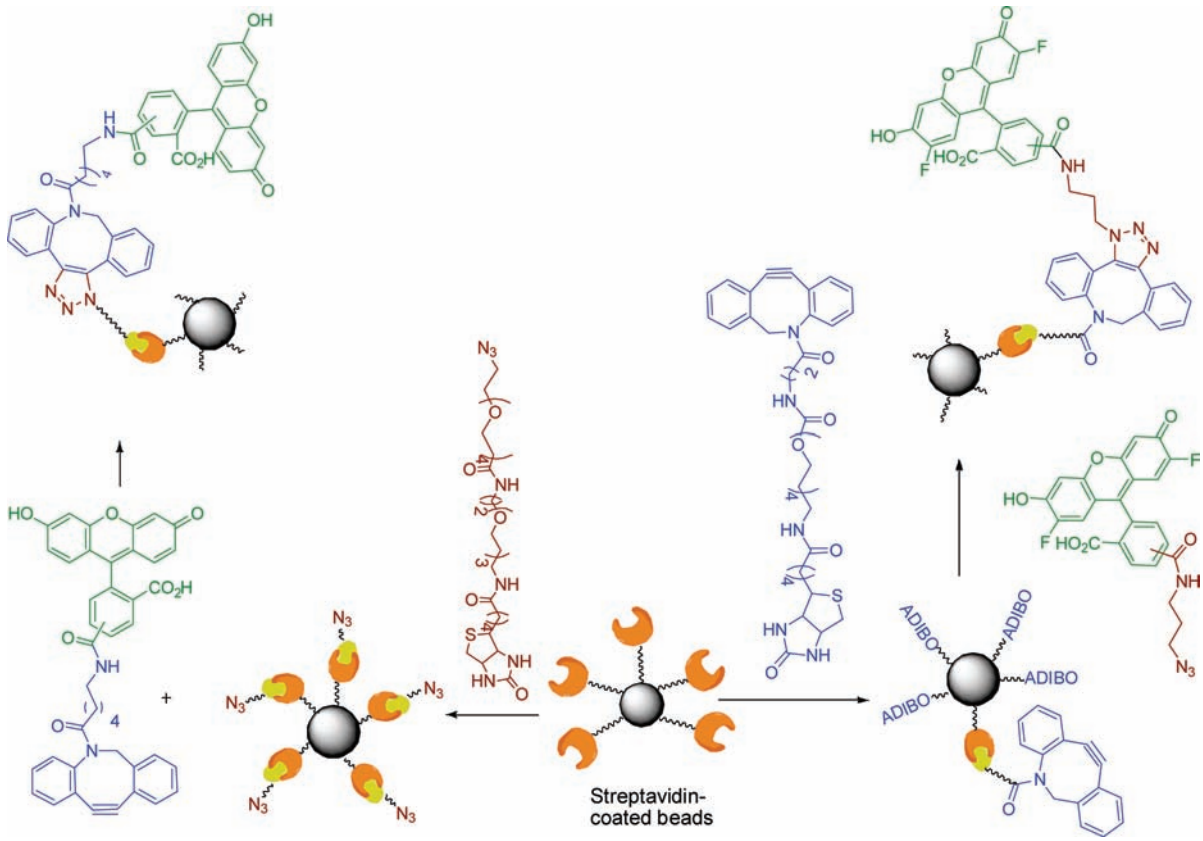


Figure 8. Schematic representation of derivatization of streptavidin-coated magnetic beads with azide and aza-dibenzocyclooctyne moieties, followed by the metal-free azide click coupling to fluorescent dyes.

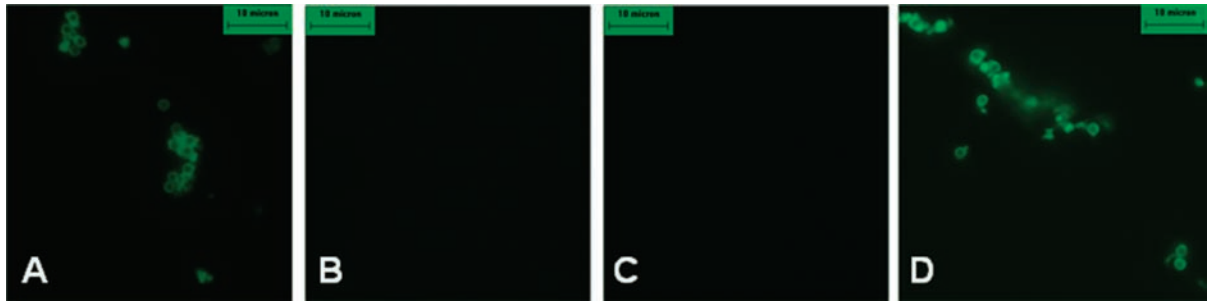


Figure 9. Fluorescent confocal microscope images of PBS suspensions of streptavidin-coated magnetic beads: (A) treated with ADIBO−biotin (**8**) followed by reaction with Oregon green azide (**13**); (B) treated with biotin-PEG_4-C≡CH and then with Oregon green azide (*13*); (C) incubated with ADIBO-fluor only (**10**); (D) treated with biotin-dPEG3 + 4-azide and then with incubated ADIBO-fluor (*10*).

in a solution of avidin-FITC at 2 °C for 15 min, and washed again. As in the case of patterned biotinylation of ADIBO slides, fluorescent images show selective immobilization of the fluorescently labeled protein in biotinylated areas. No significant nonspecific binding of avidin to the slides was observed (Figure 7). Fluorescent intensity of the spots produced at various concentrations of ADIBO-biotin and incubation time illustrate the efficiency of the reaction. Even at 10 μM concentration of ADIBO-biotin (**8**), a 30 min incubation produces a brightly fluorescent spot after avidin-FTIC development.

Catalyst-Free Derivatization of Microbeads. To demonstrate the utility of the copper-free azide click reaction for the modification of microparticle surfaces, we have explored the application of this reaction to the fluorescent labeling of streptavidin-coated magnetic beads. The surface of the beads was derivatized with azide groups by treating a suspension of the beads with biotin-dPEG3+4-azide (Figure 8). The aza-dibenzocyclooctyne functionalization of streptavidin beads was achieved by reacting the former with ADIBO-biotin (**8**, Figure 8).

The ADIBO-functionalized streptavidin beads were suspended in a PBS solution of Oregon green azide (**13**) and incubated for 3 h at rt. Beads were washed and resuspended in PBS for imaging via fluorescent confocal microscopy. Figure 9A shows the bright fluorescence of these Oregon green-labeled beads. The starting (unmodified) streptavidin magnetic beads treated with **13** under the same conditions show no detectable emission. As an additional control experiment, we have derivatized the beads with terminal acetylene groups by treating streptavidin beads with biotin-PEG_4-C≡CH. Incubation of the resulting particles in an Oregon green azide (**13**) solution, followed by thorough washing, did not induce detectable fluorescence in the beads (Figure 9B). Azide-derivatized microbeads were labeled with fluorescein by reacting them with an ADIBO−fluorescein

conjugate (**10**, Figure 9C). Magnetic streptavidin beads directly treated with ADIBO-fluor (**10**) showed no fluorescence (Figure 9D).

CONCLUSIONS

We have described an efficient synthesis of aza-dibenzocyclooctynes (ADIBO) starting from inexpensive precursors. This method allows for preparation of ADIBO derivatives on a large scale. The utility and excellent kinetics of catalyst-free ADIBO-azide cycloaddition for the patterned derivatization of glass slides and streptavidin beads has been demonstrated. The same metal-free click reaction was employed for the PEGylation of unfunctionalized areas of the surface. Such treatment allowed for dramatic reduction or complete elimination of nonspecific binding of proteins to the surface. The strategy described in this report provides a convenient tool for the site-specific covalent immobilization of various biomolecules. These procedures can be especially useful in cases where the presence of copper ions has to be avoided.

ACKNOWLEDGMENT

Authors thank Ms. Sara Orski and Dr. Jason Locklin for the useful discsussions and assistance in surface characterization; Georgia Cancer Coalition for the support of this project.

Supporting Information Available: NMR spectra of newly synthesized compounds. This material is available free of charge via the Internet at http://pubs.acs.org.

LITERATURE CITED

(1) Nebhani, L., and Barner-Kowollik, C. (2009) Orthogonal transformations on solid substrates: efficient avenues to surface modification. *Adv. Mater. 21*, 3442–3468.

(2) Wong, L. S., Khan, F., and Micklefield, J. (2009) Selective covalent protein immobilization: strategies and applications. *Chem. Rev. 109*, 4025–4053.

(3) Iha, R. K., Wooley, K. L., Nyström, A. M., Burke, D. J., Kade, M. J., and Hawker, C. J. (2009) Applications of orthogonal "click" chemistries in the synthesis of functional soft materials. *Chem. Rev. 109*, 5620–5686.

(4) Ratner, B. D., Hoffman, A. S., Schoen, F. J., and Lemons, J. E. (2004) *Biomaterials science: an introduction to materials in medicine*, Academic Press, San Diego, CA.

(5) Im, S. G., Bong, K. W., Kim, B.-S., Baxamusa, S. H., Hammond, P. T., Doyle, P. S., and Gleason, K. K. (2008) Patterning nanodomains with orthogonal functionalities: solventless synthesis of self-sorting surfaces. *J. Am. Chem. Soc. 130*, 14424–14425.

(6) Fleischmann, S., Hinrichs, K., Oertel, U., Reichelt, S., Eichhorn, K.-J., and Voit, B. (2008) Modification of polymer surfaces by click chemistry. *Macromol. Rapid Commun. 29*, 1177–1185.

(7) Fournier, D., Hoogenboom, R., and Schubert, U. S. (2007) Clicking polymers: a straightforward approach to novel macromolecular architectures. *Chem. Rev. Soc. 36*, 1369–1380.

(8) Michel, O., and Ravoo, B. J. (2008) Carbohydrate microarrays by microcontact "click" chemistry. *Langmuir 24*, 12116–12118.

(9) Ku, S.-Y., Wong, K.-T., and Bard, A. J. (2008) Surface patterning with fluorescent molecules using click chemistry directed by scanning electrochemical microscopy. *J. Am. Chem. Soc. 130*, 2392–2393.

(10) Sun, X.-L., Stabler, C. L., Cazalis, C. S., and Chaikof, E. L. (2006) Carbohydrate and protein immobilization onto solid surfaces by sequential diels-alder and azide-alkyne cycloadditions. *Bioconjugate Chem. 17*, 52–57.

(11) Gramlich, P. M. E., Wirges, C. T., Manetto, A., and Carell, T. (2008) Postsynthetic DNA modification through the copper-catalyzed azide-alkyne cycloaddition reaction. *Angew. Chem., Int. Ed. 47*, 8350–8358.

(12) Weisbrod, S. H., and Marx, A. (2008) Novel strategies for the site-specific covalent labelling of nucleic acids. *Chem. Commun.* 5675–5685.

(13) Sletten, E., and Bertozzi, C. (2009) Bioorthogonal chemistry: fishing for selectivity in a sea of functionality. *Angew. Chem., Int. Ed. 48*, 6974–6998.

(14) Fernandez-Suarez, M., Baruah, H., Martinez-Hernandez, L., Xie, K. T., Baskin, J. M., Bertozzi, C. R., and Ting, A. Y. (2007) Redirecting lipoic acid ligase for cell surface protein labeling with small-molecule probes. *Nat. Biotechnol. 25*, 1483–1487.

(15) Ochiai, H., Huang, W., and Wang, L.-X. (2008) Expeditious chemoenzymatic synthesis of homogeneous N-glycoproteins carrying defined oligosaccharide ligands. *J. Am. Chem. Soc. 130*, 13790–13803.

(16) Speers, A. E., Adam, G. C., and Cravatt, B. F. (2003) Activity-based protein profiling in vivo using a copper(I)-catalyzed azide-alkyne [3 + 2] cycloaddition. *J. Am. Chem. Soc. 125*, 4686–4687.

(17) Baskin, J. M., and Bertozzi, C. R. (2007) Bioorthogonal click chemistry: covalent labeling in living systems. *QSAR Comb. Sci. 26*, 1211–1219.

(18) Rostovtsev, V. V., Green, L. G., Fokin, V. V., and Sharpless, K. B. (2002) A stepwise Huisgen cycloaddition process: copper(I)-catalyzed regioselective "ligation" of azides and terminal alkynes. *Angew. Chem., Int. Ed. 41*, 2596–2599.

(19) Hein, J. E., and Fokin, V. V. (2010) Copper-catalyzed azide-alkyne cycloaddition (CuAAC) and beyond: new reactivity of copper(I) acetylides. *Chem. Soc. Rev. 39*, 1302–1315.

(20) Mamidyala, S. K., and Finn, M. G. (2010) In situ click chemistry: probing the binding landscapes of biological molecules. *Chem. Soc. Rev. 39*, 1252–1261.

(21) Gaetke, L. M., and Chow, C. K. (2003) Copper toxicity, oxidative stress, and antioxidant nutrients. *Toxicology 189*, 147–163.

(22) Gierlich, J., Burley, G. A., Gramlich, P. M. E., Hammond, D. M., and Carell, T. (2006) Click chemistry as a reliable method for the high-density postsynthetic functionalization of alkyne-modified DNA. *Org. Lett. 8*, 3639–3642.

(23) Burrows, C. J., and Muller, J. G. (1998) Oxidative nucleobase modifications leading to strand scission. *Chem. Rev. 98*, 1109–1152.

(24) Wang, Q., Chan, T. R., Hilgraf, R., Fokin, V. V., Sharpless, K. B., and Finn, M. G. (2003) Bioconjugation by copper(I)-catalyzed azide-alkyne [3 + 2] cycloaddition. *J. Am. Chem. Soc. 125*, 3192–3193.

(25) Bernardin, A., Cazet, A. l., Guyon, L., Delannoy, P., Vinet, F., Bonnaff, D., and Texier, I. (2010) Copper-free click chemistry for highly luminescent quantum dot conjugates: application to in vivo metabolic imaging. *Bioconjugate Chem 21*, 583–588.

(26) Wittig, G., and Krebs, A. (1961) On the existence of low-membered cycloalkynes. *Chem. Ber. 94*, 3260–3275.

(27) Ess, D. H., Jones, G. O., and Houk, K. N. (2008) Transition states of strain-promoted metal-free click chemistry: 1,3-dipolar cycloadditions of phenyl azide and cyclooctynes. *Org. Lett. 10*, 1633–1636.

(28) Baskin, J. M., Prescher, J. A., Laughlin, S. T., Agard, N. J., Chang, P. V., Miller, I. A., Lo, A., Codelli, J. A., and Bertozzi, C. R. (2007) Copper-free click chemistry for dynamic in vivo imaging. *Proc. Natl. Acad. Sci. U.S.A. 104*, 16793–16797.

(29) Sletten, E. M., and Bertozzi, C. R. (2008) A hydrophilic azacyclooctyne for Cu-free click chemistry. *Org. Lett. 10*, 3097–3099.

(30) Codelli, J. A., Baskin, J. M., Agard, N. J., and Bertozzi, C. R. (2008) Second-generation difluorinated cyclooctynes for copper-free click chemistry. *J. Am. Chem. Soc. 130*, 11486–11493.

(31) Jewett, J. C., Sletten, E. M., and Bertozzi, C. R. (2010) Rapid Cu-free click chemistry with readily synthesized biarylazacyclooctynones. *J. Am. Chem. Soc. 132*, 3688–3690.

(32) Ning, X., Guo, J., Wolfert, M. A., and Boons, G.-J. (2008) Visualizing metabolically labeled glycoconjugates of living cells

by copper-free and fast huisgen cycloadditions. *Angew. Chem., Int. Ed. 47,* 2253–2255.

(33) Debets, M. F., van Berkel, S. S., Schoffelen, S., Rutjes, F. P. J. T., van Hest, J. C. M., and van Delft, F. L. (2010) Aza-dibenzocyclooctynes for fast and efficient enzyme PEGylation via copper-free (3 + 2) cycloaddition. *Chem. Commun 46*, 97–99.

(34) Link, A. J., Vink, M. K. S., Agard, N. J., Prescher, J. A., Bertozzi, C. R., and Tirrell, D. A. (2006) Discovery of aminoacyl-tRNA synthetase activity through cell-surface display of non-canonical amino acids. *Proc. Natl. Acad. Sci. U.S.A. 103*, 10180–10185.

(35) Fernandez-Suarez, M., Baruah, H., Martinez-Hernandez, L., Xie, K. T., Baskin, J. M., Bertozzi, C. R., and Ting, A. Y. (2007) Redirecting lipoic acid ligase for cell surface protein labeling with small-molecule probes. *Nat. Biotechnol. 25*, 1483–1487.

(36) Zou, Y., and Yin, J. (2008) Cu-free cycloaddition for identifying catalytic active adenylation domains of nonribosomal peptide synthetases by phage display. *Bioorg. Med. Chem. Lett. 18*, 5664–5667.

(37) Nessen, M. A., Kramer, G., Back, J., Baskin, J. M., Smeenk, L. E. J., de Koning, L. J., van Maarseveen, J. H., de Jong, L., Bertozzi, C. R., Hiemstra, H., and de Koster, C. G. (2009) Selective enrichment of azide-containing peptides from complex mixtures. *J. Proteome Res. 8*, 3702–3711.

(38) Wilson, J. T., Krishnamurthy, V. R., Cui, W., Qu, Z., and Chaikof, E. L. (2010) Noncovalent cell surface engineering with cationic graft copolymers. *J. Am. Chem. Soc. 132*, 2845–2845.

(39) Poloukhtine, A. A., Mbua, N. E., Wolfert, M. A., Boons, G.-J., and Popik, V. V. (2009) Selective labeling of living cells by a photo-triggered click reaction. *J. Am. Chem. Soc. 131*, 15769–15776.

(40) Laughlin, S. T., Baskin, J. M., Amacher, S. L., and Bertozzi, C. R. (2008) In vivo imaging of membrane-associated glycans in developing zebrafish. *Science 320*, 664–667.

(41) Chang, P. V., Prescher, J. A., Sletten, E. M., Baskin, J. M., Miller, I. A., Agard, N. J., Lo, A., and Bertozzi, C. R. (2010 Copper-free click chemistry in living animals. *Proc. Nat. Acad. Sci. U.S.A. 107*, 1821–1826.

(42) Seitz, G., Pohl, L., and Pohlke, R. (1969) 5,6-Didehydro-11,12-dihydrodibenzo[a,e]-cyclooctene. *Angew. Chem., Int. Ed. 8*, 447–448.

(43) Schwabacher, A. W., Lane, J. W., Schiesher, M. W., Leigh, K. M., and Johnson, C. W. (1998) Desymmetrization reactions: efficient preparation of unsymmetrically substituted linker molecules. *J. Org. Chem. 63*, 1727–1729.

(44) Lee, J. W., Jun, S. I., and Kim, K. (2001) An efficient and practical method for the synthesis of mono-N-protected a,w-diaminoalkanes. *Tetrahedron Lett. 42*, 2709–2711.

(45) Clark, J. S., Hodgson, P. B., Goldsmith, M. D., and Street, L. J. (2001) Rearrangement of ammonium ylides produced by intramolecular reaction of catalytically generated metal carbenoids. Part 1. Synthesis of cyclic amines. *J. Chem. Soc. Perkin Trans. 1*, 3312–3324.

(46) Pessi, A., Bianchi, E., and Ingallinella, P. (2009) Preparation of cholesterol derivatives of peptidyl inhibitors of viral fusion. *PCT Int. Appl.* 39.

(47) Green, N. M. (1990) Avidin and streptavidin. *Methods Enzymol. 184*, 51–67.

(48) Jacobs, A. T., and Marnett, L. J. (2010) Systems analysis of protein modification and cellular responses induced by electrophile stress. *Acc. Chem. Res. 43*, 673–683.

(49) Wilchek, M., and Bayer, E. A. (1990) Introduction to avidin-biotin technology. *Methods Enzymol. 184*, 5–13.

(50) Mader, H. S., Link, M., Achatz, D. E., Uhlmann, K., Li, X., and Wolfbeis, O. S. (2010) Surface-modified upconverting microparticles and nanoparticles for use in click chemistries. *Chem.—Eur. J. 16*, 5416–5424.

(51) Böttcher, T., and Sieber, S. A. (2010) Showdomycin as a versatile chemical tool for the detection of pathogenesis-associated enzymes in bacteria. *J. Am. Chem. Soc. 132*, 6964–6972.

(52) Landi, F., Johansson, C. M., Campopiano, D. J., and Hulme, A. N. (2010) Synthesis and application of a new cleavable linker for "click"-based affinity chromatography. *Org. Biomol. Chem. 8*, 56–59.

(53) Zhang, J., Wang, X., Wu, D., Liu, L., and Zhao, H. (2009) Bioconjugated Janus particles prepared by in situ click chemistry. *Chem. Mater. 21*, 4012–4018.

BC100306U

Supporting Information

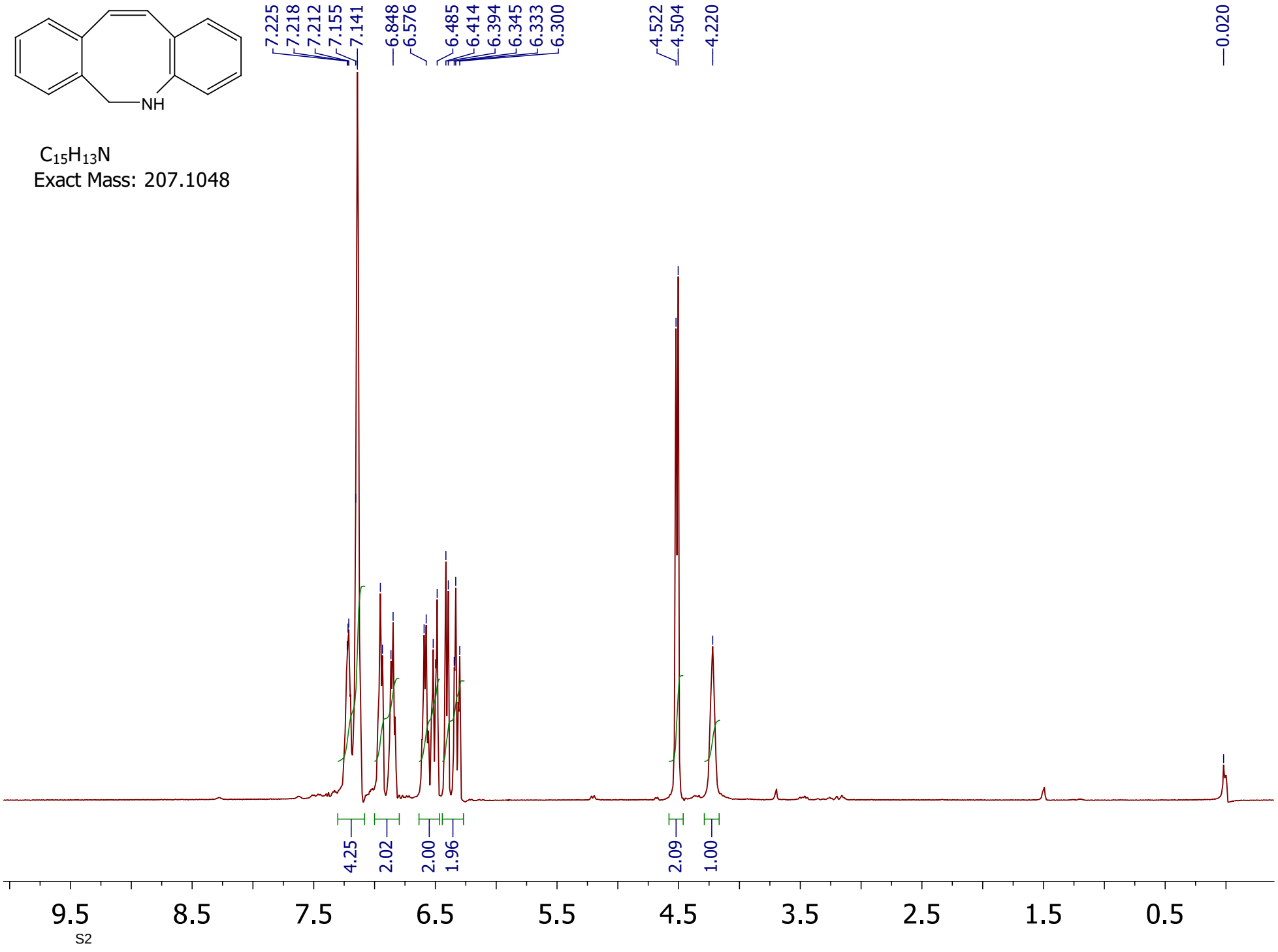
for

Surface Functionalization Using Catalyst-Free Azide – Alkyne Cycloaddition

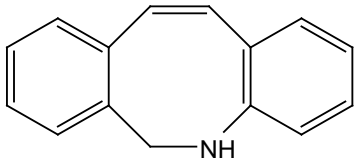
by Alexander Kuzmin, Andrei Poloukhtine, Margreet A. Wolfert, Vladimir V.Popik

vpopik@chem.uga.edu

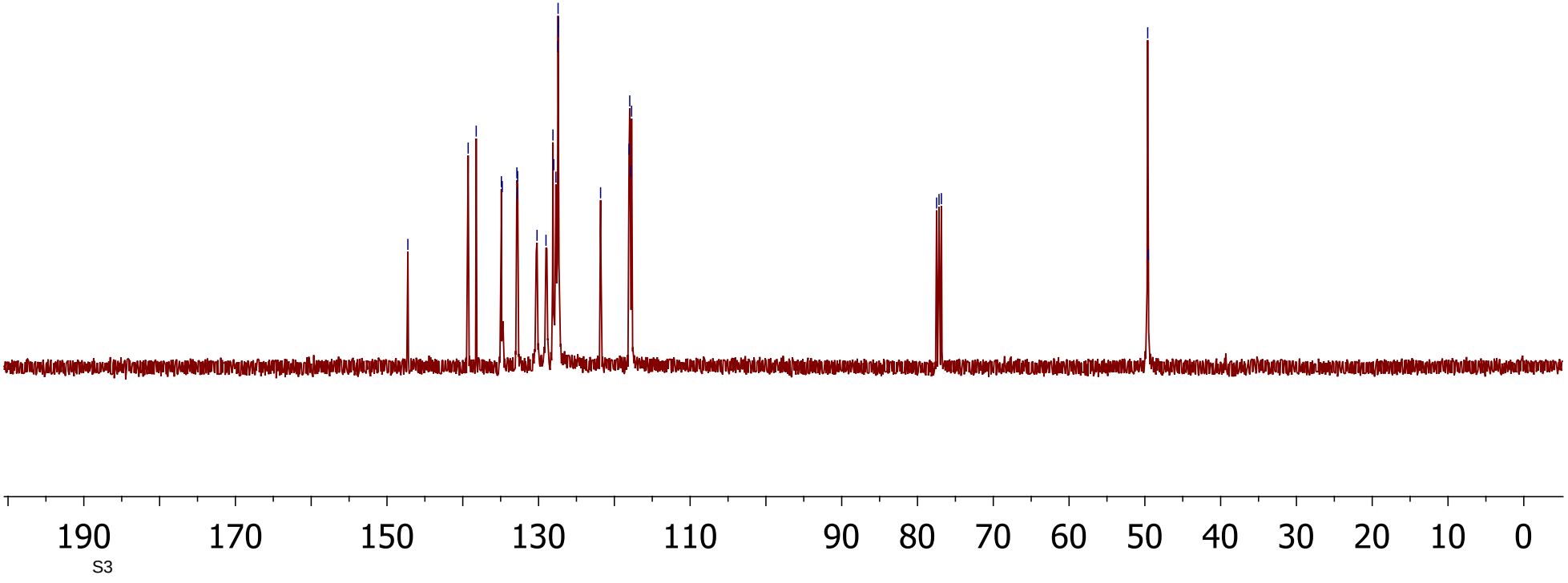
$C_{15}H_{13}N$
Exact Mass: 207.1048

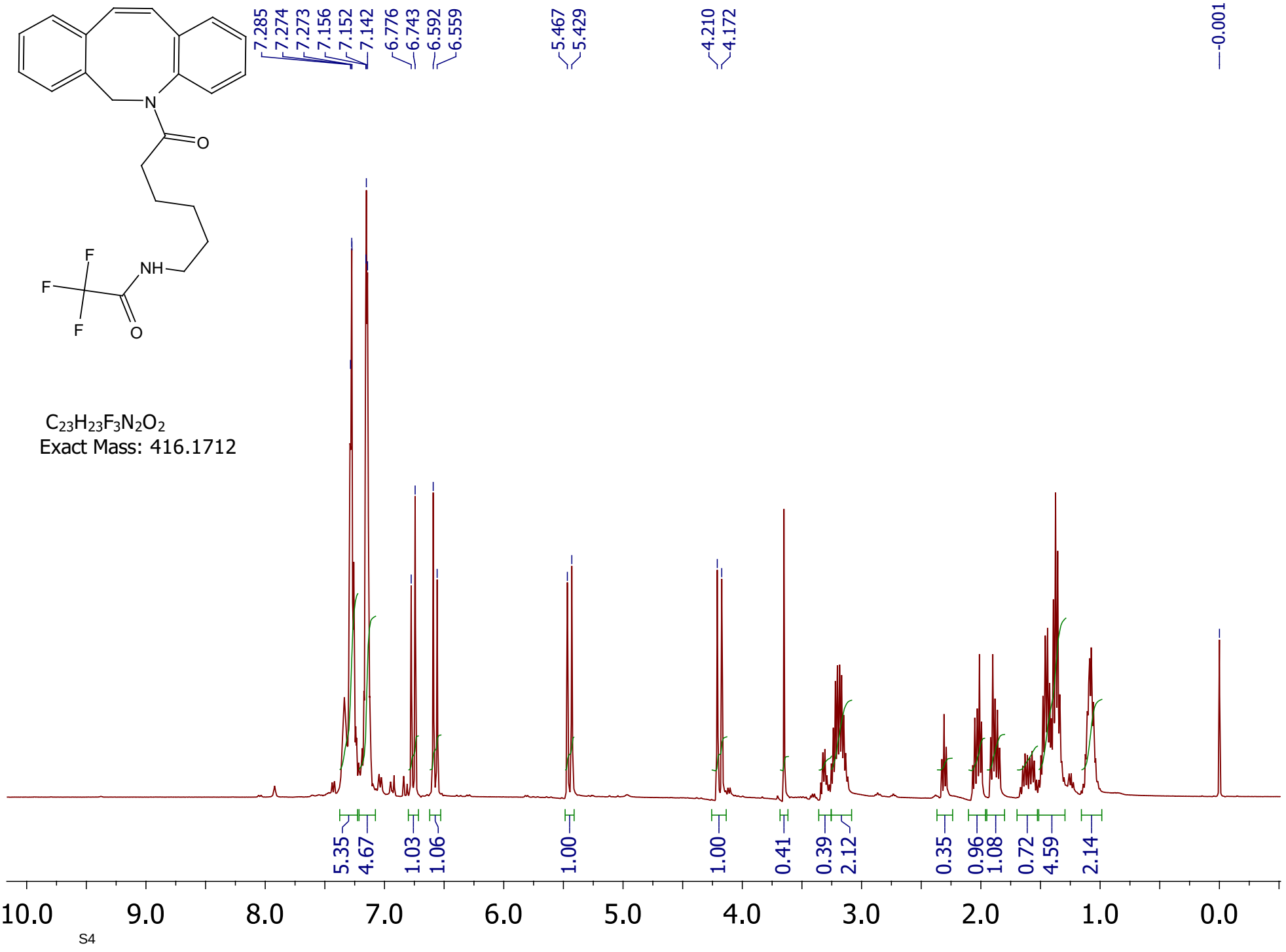


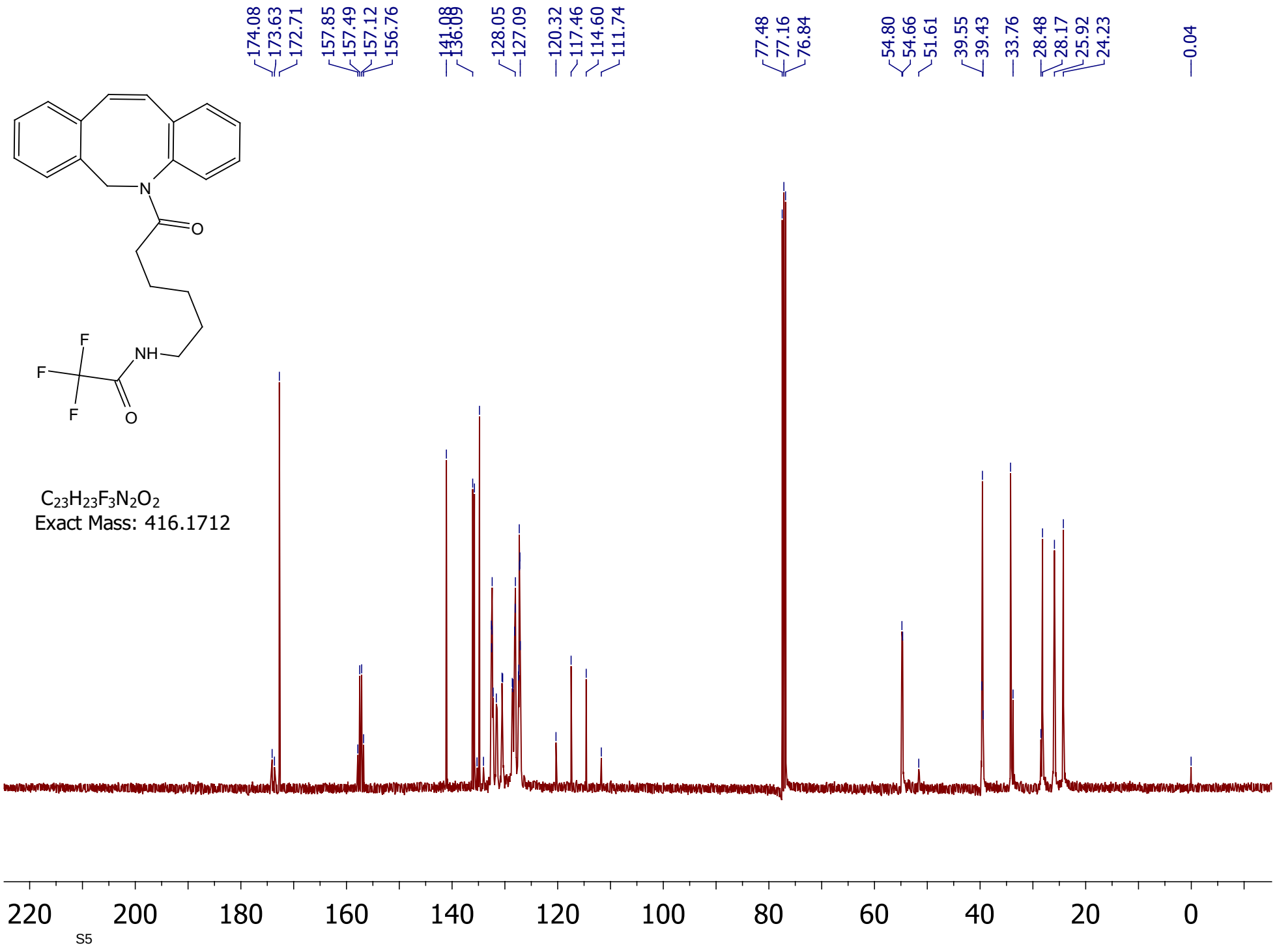
147.25
139.29
132.76
128.10
127.46
127.38
121.82
118.06
117.97
117.82
117.72
77.48
77.16
76.85
49.62
49.53



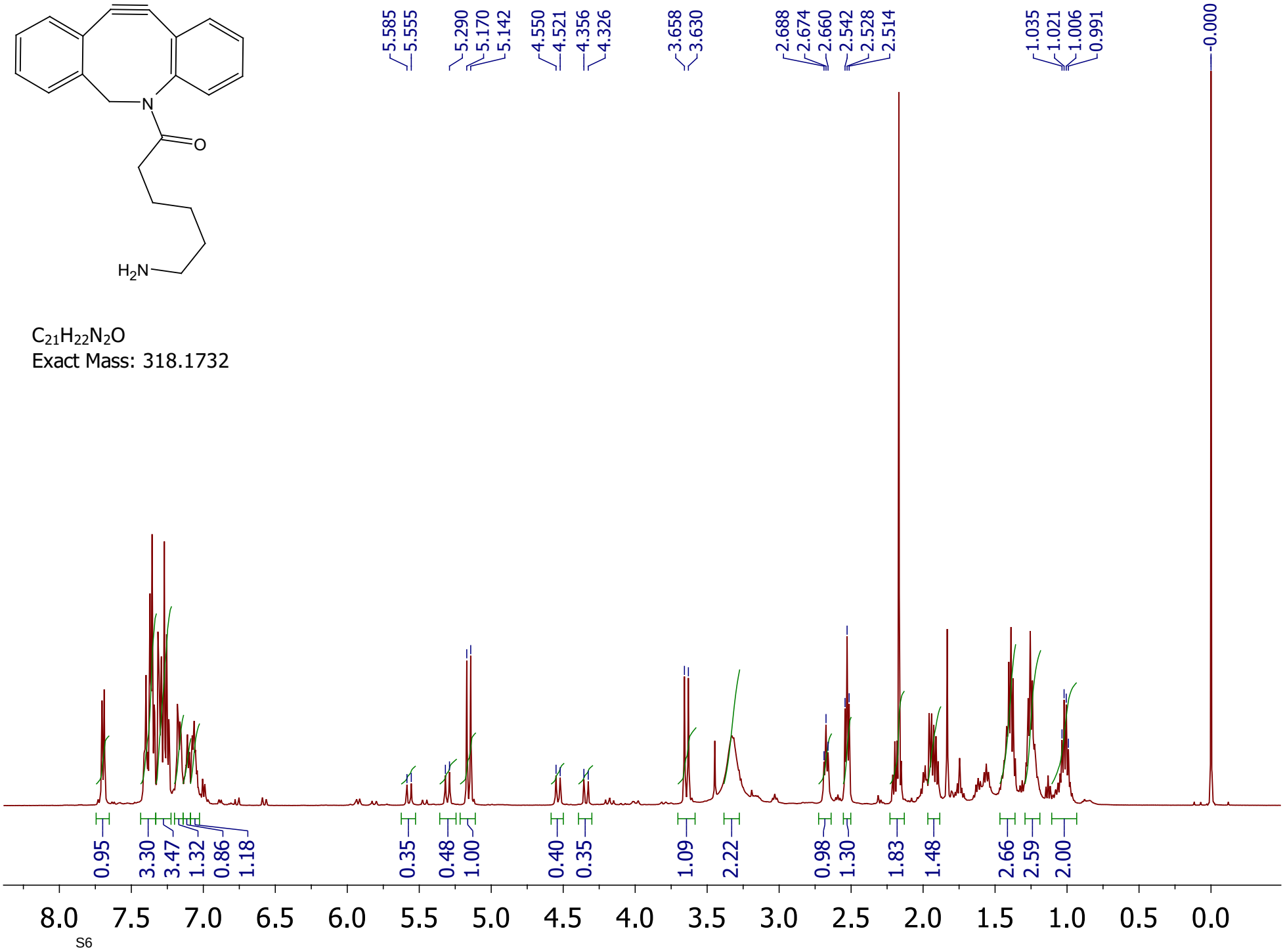
$C_{15}H_{13}N$
Exact Mass: 207.1048



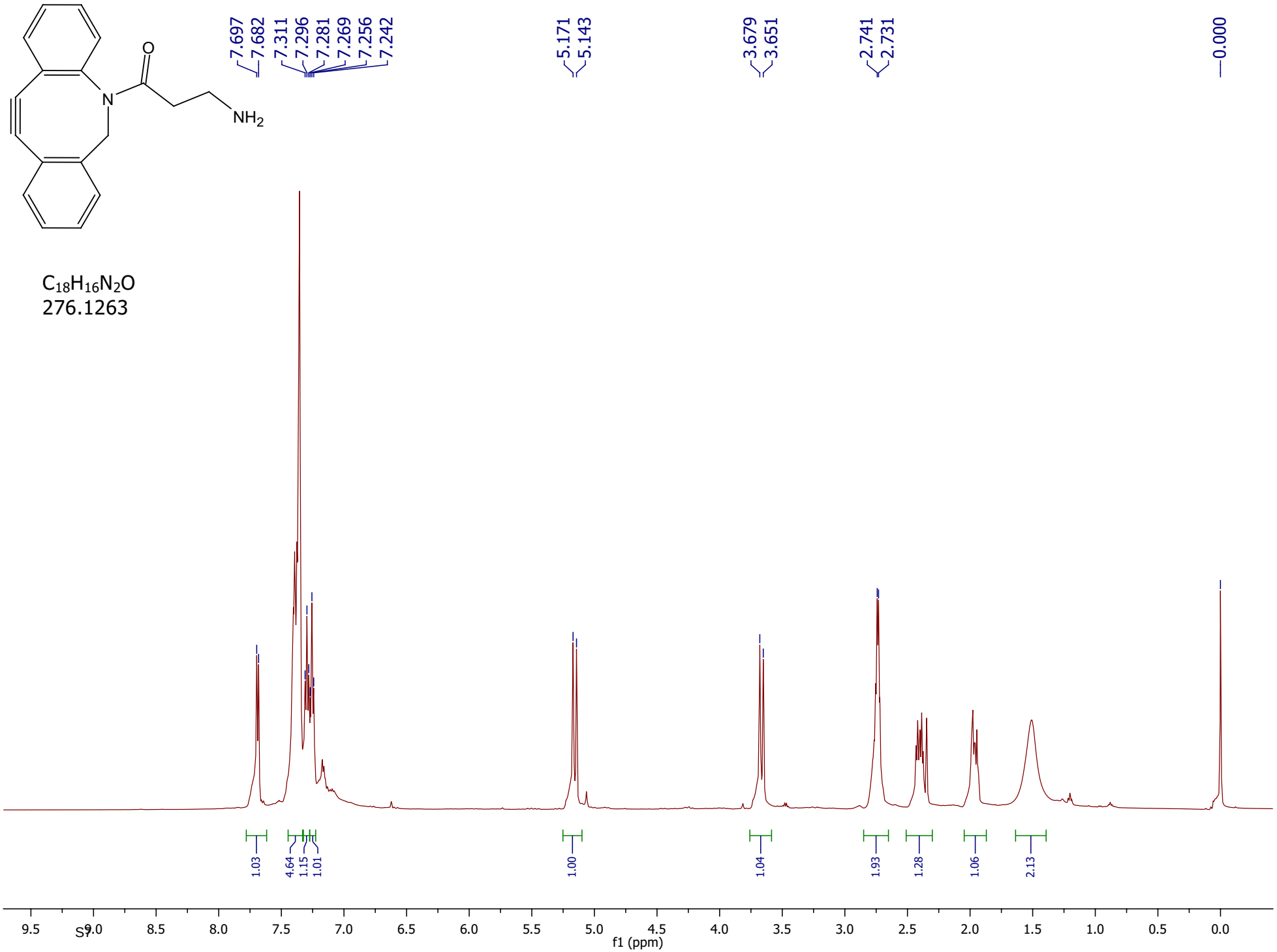

7.285
7.274
7.273
7.156
7.152
7.142
6.776
6.743
6.592
6.559
5.467
5.429
4.210
4.172
-0.001
N
O
NH
F
F
F
O
C23H23F3N2O2
Exact Mass: 416.1712
5.35
4.67
1.03
1.06
1.00
1.00
0.41
0.39
2.12
0.35
0.96
1.08
0.72
4.59
2.14
10.0
9.0
8.0
7.0
6.0
5.0
4.0
3.0
2.0
1.0
0.0

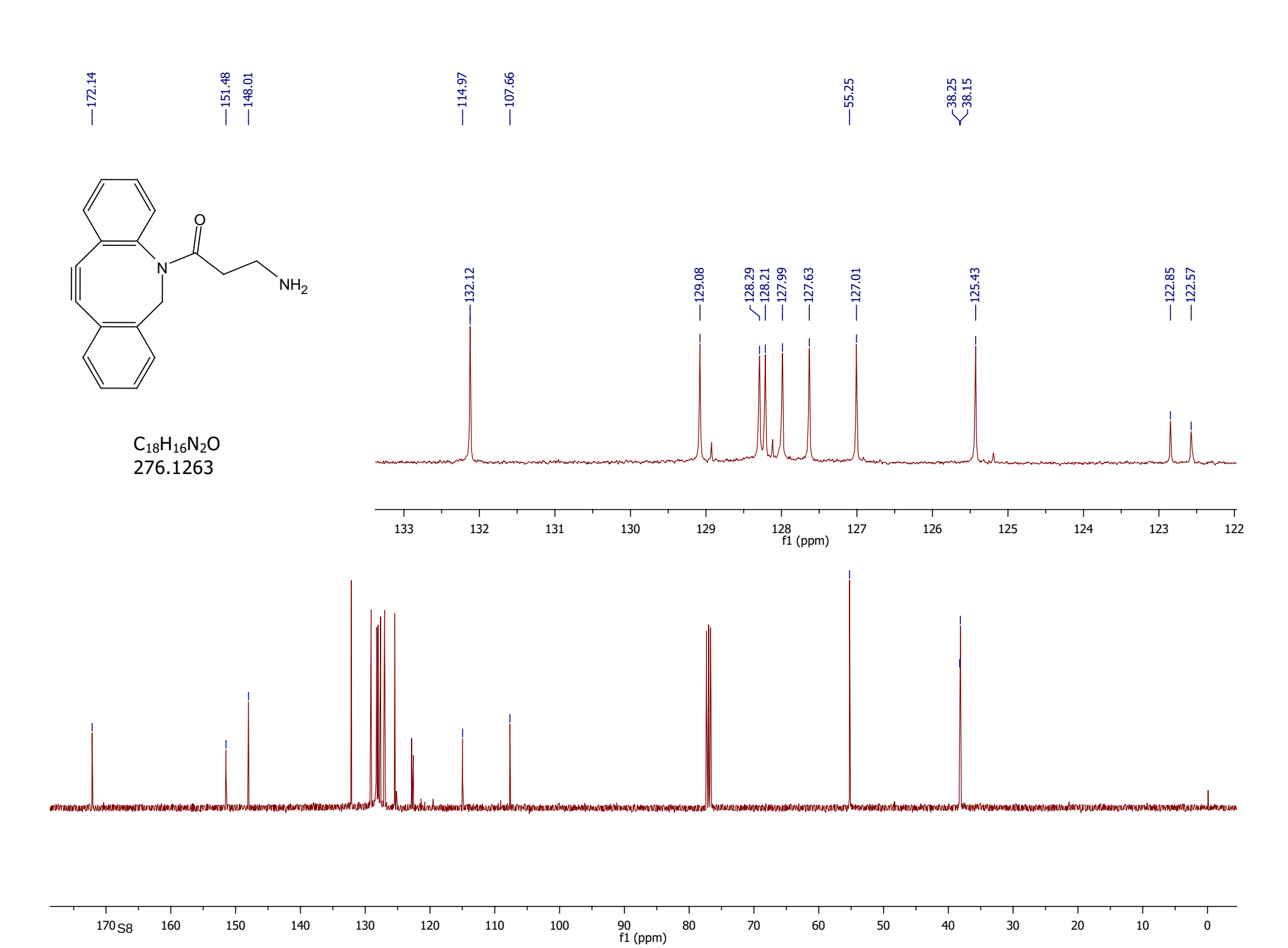

174.08
173.63
172.71
157.85
157.49
157.12
156.76
141.08
136.09
128.05
127.09
120.32
117.46
114.60
111.74
77.48
77.16
76.84
54.80
54.66
51.61
39.55
39.43
33.76
28.48
28.17
25.92
24.23
0.04
N
O
NH
F
F
F
O
C23H23F3N2O2
Exact Mass: 416.1712
220
200
180
160
140
120
100
80
60
40
20
0

$C_{21}H_{22}N_2O$
Exact Mass: 318.1732

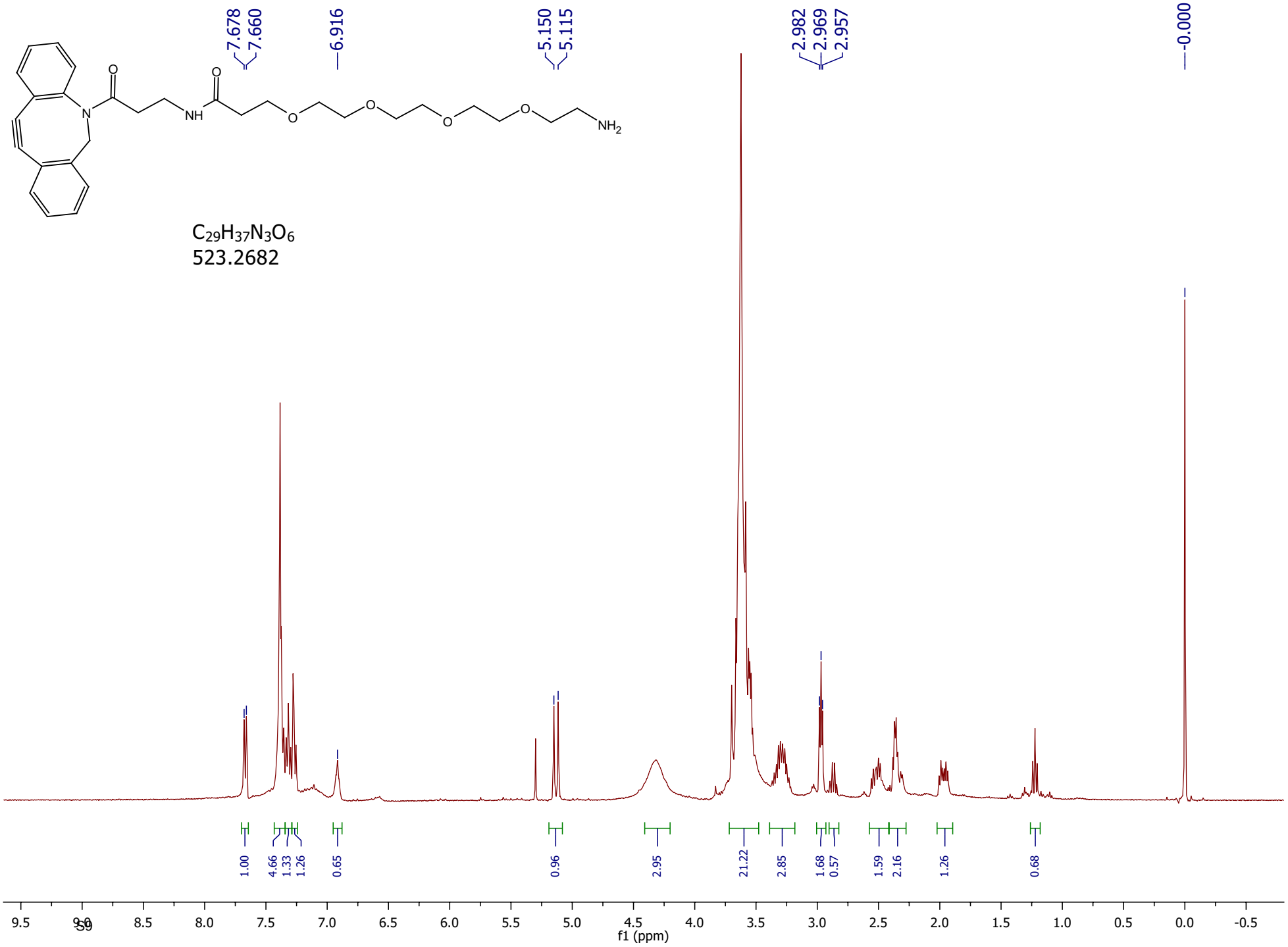


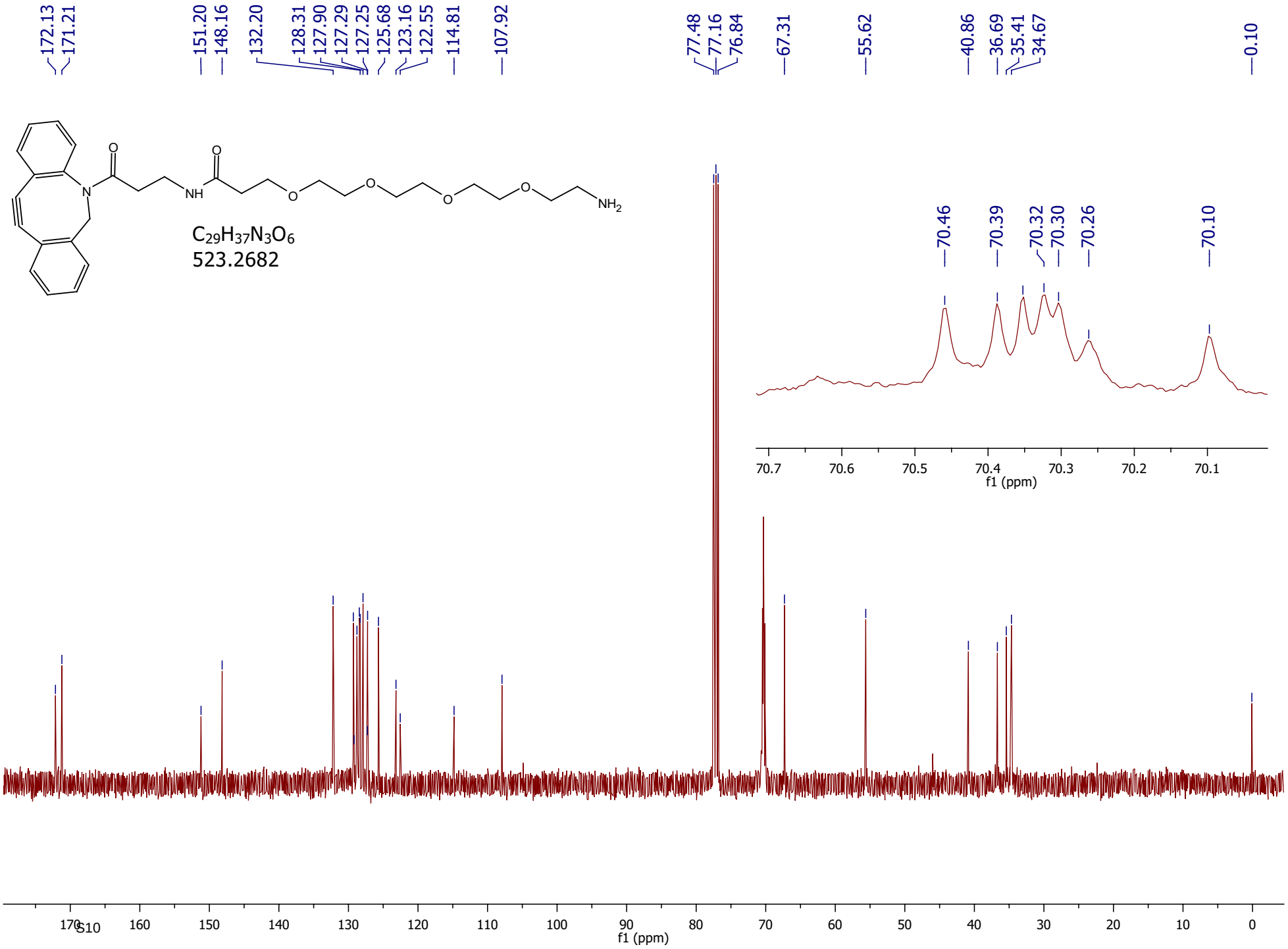
$C_{18}H_{16}N_2O$
276.1263

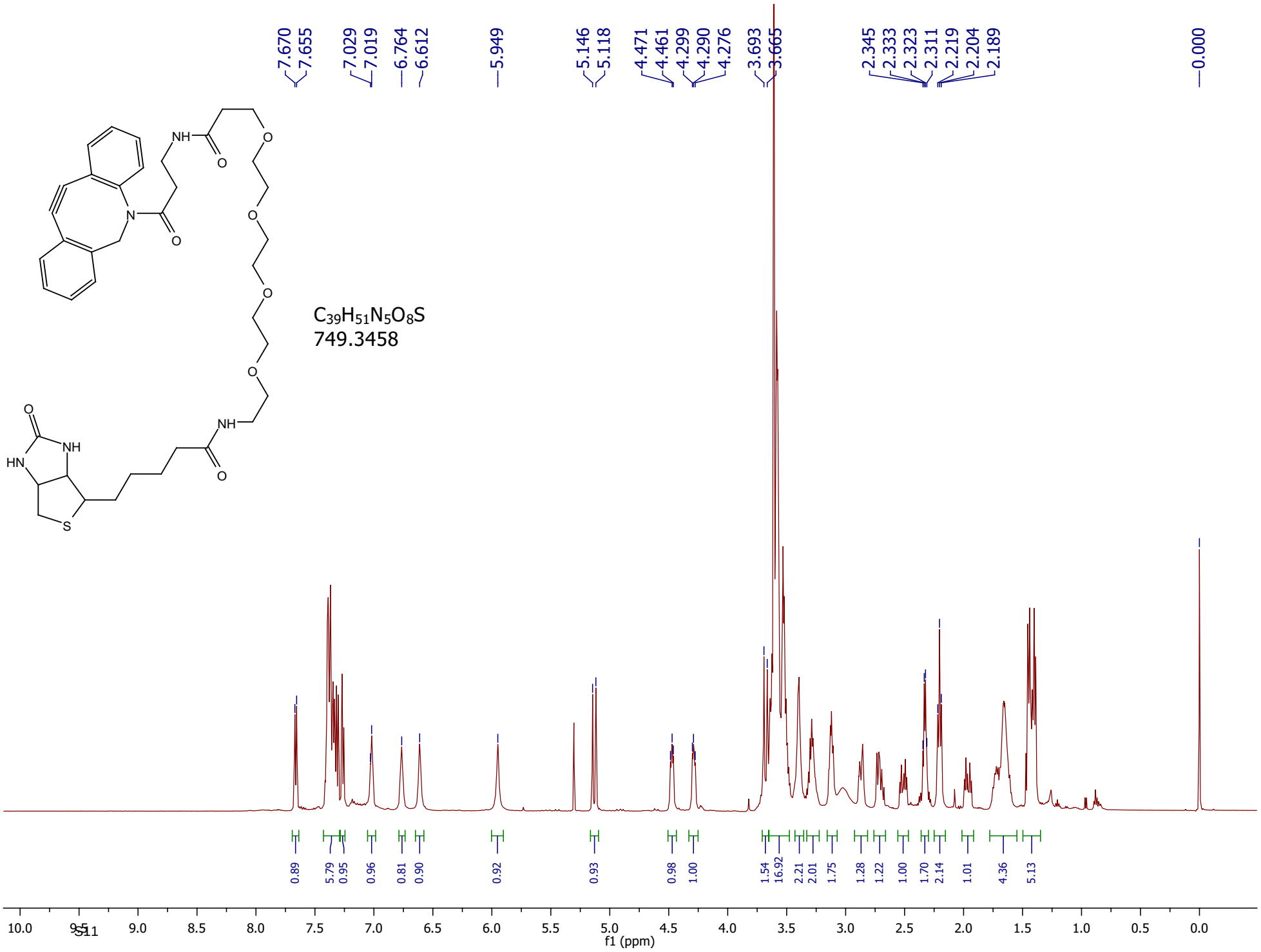


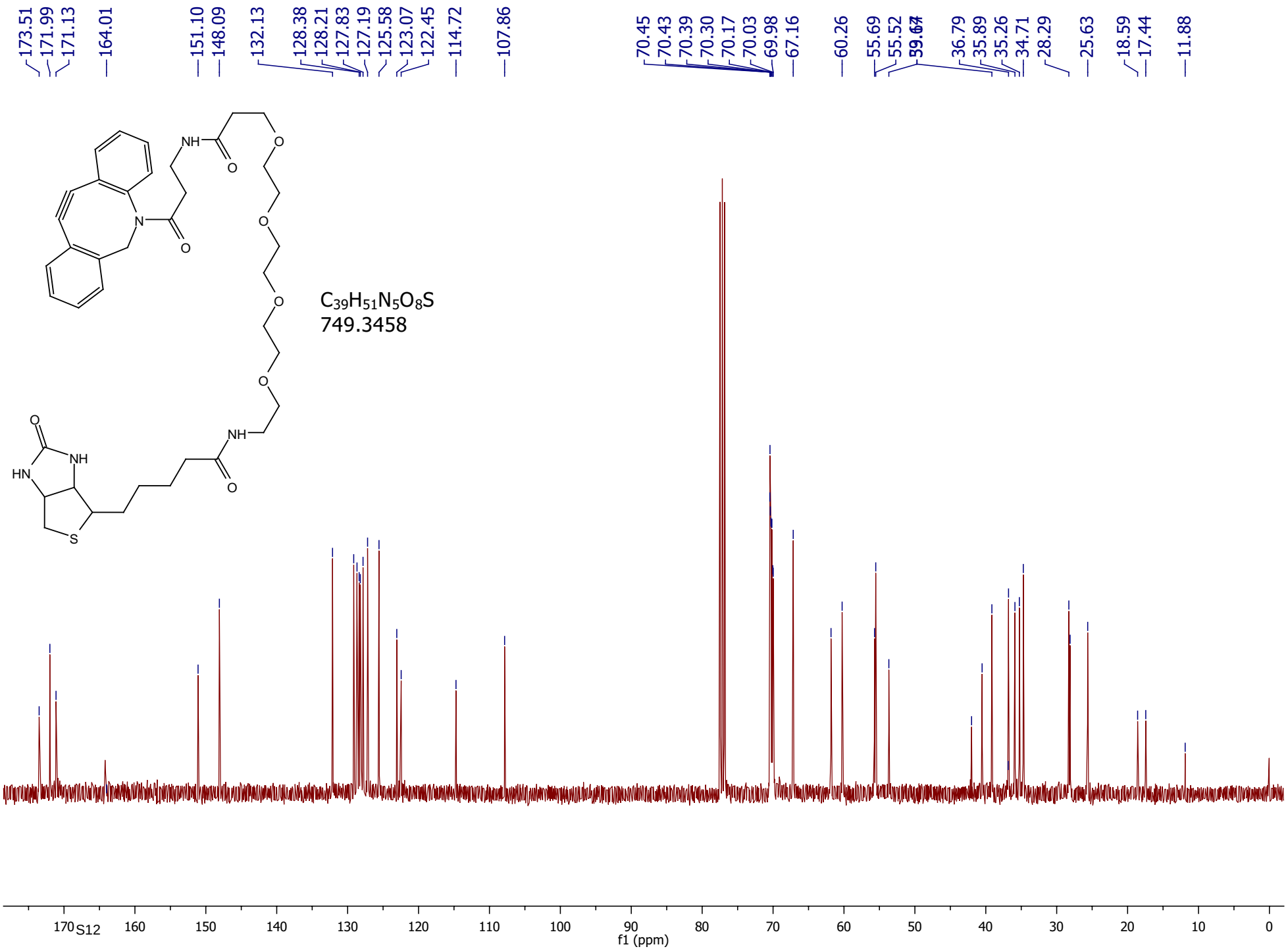

172.14
151.48
148.01
114.97
107.66
55.25
38.25
38.15
O
N
NH2
C18H16N2O
276.1263
132.12
129.08
128.29
128.21
127.99
127.63
127.01
125.43
122.85
122.57
133
132
131
130
129
128
127
126
125
124
123
122
f1 (ppm)
170
160
150
140
130
120
110
100
90
80
70
60
50
40
30
20
10
0
f1 (ppm)

$C_{29}H_{37}N_3O_6$
523.2682




172.13
171.21
151.20
148.16
132.20
128.31
127.90
127.29
127.25
125.68
123.16
122.55
114.81
107.92
77.48
77.16
76.84
67.31
55.62
40.86
36.69
35.41
34.67
0.10
O
O
N
NH
O
O
O
O
O
NH2
C29H37N3O6
523.2682
70.46
70.39
70.32
70.30
70.26
70.10
70.7
70.6
70.5
70.4
70.3
70.2
70.1
f1 (ppm)
170
160
150
140
130
120
110
100
90
80
70
60
50
40
30
20
10
0
f1 (ppm)


7.670
7.655
7.029
7.019
6.764
6.612
5.949
5.146
5.118
4.471
4.461
4.299
4.290
4.276
3.693
3.665
2.345
2.333
2.323
2.311
2.219
2.204
2.189
0.000
C39H51N5O8S
749.3458
0.89
5.79
0.95
0.96
0.81
0.90
0.92
0.93
0.98
1.00
1.54
16.92
2.21
2.01
1.75
1.28
1.22
1.00
1.70
2.14
1.01
4.36
5.13
f1 (ppm)


173.51
171.99
171.13
164.01
151.10
148.09
132.13
128.38
128.21
127.83
127.19
125.58
123.07
122.45
114.72
107.86
70.45
70.43
70.39
70.30
70.17
70.03
69.98
67.16
60.26
55.69
55.52
36.79
35.89
35.26
34.71
28.29
25.63
18.59
17.44
11.88
NH
O
O
O
O
O
O
O
NH
O
NH
HN
O
S
N
O
C39H51N5O8S
749.3458
170
160
150
140
130
120
110
100
90
80
70
60
50
40
30
20
10
0
f1 (ppm)

Self-Assembled Terplexes for Targeted Gene Delivery with Improved Transfection

Qiao Zhang, Si Chen, Ren-Xi Zhuo, Xian-Zheng Zhang, and Si-Xue Cheng*

Key Laboratory of Biomedical Polymers of Ministry of Education, Department of Chemistry, Wuhan University, Wuhan 430072, People's Republic of China. Received July 7, 2010; Revised Manuscript Received September 20, 2010

To improve transfection efficiency and to incorporate target ligands to the gene delivery systems, heparin and heparin−biotin were introduced to complexes of polyamidoamine dendrimer and DNA (PAMAM/DNA) via electrostatic interactions to form self-assembled PAMAM/DNA/heparin and PAMAM/DNA/heparin−biotin terplexes, respectively. The self-assembled terplexes were characterized by agarose gel electrophoresis and particle size analysis. The MTT assay indicated that, after incorporation of heparin and heparin−biotin, the terplexes exhibited decreased cytotoxicity. In addition, as compared with PAMAM/DNA and PAMAM/DNA/heparin complexes, the PAMAM/DNA/heparin−biotin complexes exhibited much higher cellular uptake into HeLa cells due to the specific interactions between biotin and biotin receptors on HeLa cells, which led to the enhanced transfection activity. The PAMAM/DNA/heparin−biotin complexes would be a promising targeting gene delivery system.

INTRODUCTION

Gene therapy is a promising approach for the treatment of incurable diseases and genetic disorders such as cancers (*1, 2*). The efficient and safe gene transfer vectors are of critical importance for the applications of gene therapy. Nonviral vectors such as cationic liposomes and polycations have attracted much attention because of their low immune response and safety. However, the low transfection efficiency greatly limits their clinical applications (*3*).

To improve the performance of nonviral vectors and to overcome the barriers in gene delivery, many modification strategies have been developed. Among them, incorporation of various ligands to the polycation vectors could effectively enhance the cellular uptake and achieve improved transfection efficiency for the targeted cells (*4*). The frequently reported targeting ligands include monoclonal antibodies, peptides (*5*), carbohydrates such as galactose for hepatocyte targeting (*6*), and vitamins such as folate (*7*). Most commonly, the targeting ligands are incorporated to the polymer vectors through covalent bonds.

Molecular self-assembly is a rapid and powerful method for fabricating nanosized materials with various supramolecular architectures. In comparison with the chemical reactions, the self-assembly is more convenient, flexible, and favorable for keeping the bioactivity of the ligands. As far as we know, the studies on incorporation of target ligands to gene delivery systems through self-assembly are very limited. In this study, we developed a new strategy to introduce ligands to gene delivery systems through electrostatic interactions; i.e., heparin−biotin was introduced to the complexes of PAMAM/DNA via electrostatic interactions to from PAMAM/DNA/heparin−biotin terplexes. For comparison, PAMAM/DNA/heparin terplexes without the targeting ligand were also prepared through self-assembly. Biotin (vitamin H) is an essential vitamin for the division of all cells, especially for the rapid proliferations of tumor cells. The cancer cells often overexpress biotin receptors on the cell surface. There are many reports on the incorporation of biotin as cell targeting ligands for targeted drug delivery (*8–11*). The reported biotin targeted tumor cell lines include L1210FR, Ov2008, M109, 4T1 (*8*), HeLa (*9*), JC, MCF-7 (*10*), and HepG2 (*11*). Heparin as one of the most potent anticoagulants has been widely used to enhance the blood compatibility of biomaterials (*12*). The conjugation of heparin to polyethylenimine (PEI) can inhibit the adsorption of serum proteins to the PEI surface and improve the in vivo gene transfection efficiency (*13*). In addition, the negatively charged heparin can form complexes with polycations such as PEI and PAMAM (*14–16*). In the current study, heparin was used to improve the biocompatibility and partially shield the positive charge of PMAMA/DNA complexes to reduce the cytotoxicity. Biotin was used as a cell targeting ligand to enhance the cellular uptake for particular cancer cells. The existence of heparin or heparin−biotin lowered the cytotoxicity and enhanced the transfection efficiencies of the terplexes. In addition, the transfection activity of PAMAM/DNA/heparin−biotin terplexes in particular tumor cells could be further improved due to the increased biotin receptor mediated cell uptake. The terplexes have promising applications in targeting gene delivery to cancer cells.

EXPERIMENTAL PROCEDURES

Materials. Poly(amidoamine) (PAMAM) dendrimer (generation 5 with 128 surface amino groups) was purchased from Aldrich. Heparin sodium and heparin−biotin sodium (molecular weight 15 000 Da) were obtained from Sigma. 3-(4,5-Dimethylthiazol-2-yl)-2,5-diphenyltetrazolium bromide (MTT) was from Amresco. Dimethylsulfoxide (DMSO) was from Sigma.

The reporter plasmids, pGL3-Luc and pEGFP-C1, were purchased from Promega and Invitrogen, respectively. Plasmids were amplified in *Escherichia coli* and extracted and purified by E.Z.N.A. Fastfilter Endo-free Plasmid Maxi Kit (Omega). Plasmids were suspended in deionized water and stored at −20 °C.

HeLa, HEK293T, and COS-7 cells were obtained from China Center for Typical Culture Collection (Wuhan, China) and cultured in Dulbecco's Modified Eagle's Medium (DMEM) (Gibco), supplemented with 10% fetal bovine serum (FBS), 2

* Corresponding author. Tel./fax: +8627 6875 4509. E-mail address: chengsixue@hotmail.com, chengsixue@whu.edu.cn (S.X. Cheng).

10.1021/bc100309e © 2010 American Chemical Society
Published on Web 10/08/2010

mg/mL $NaHCO_3$, and 100 unit/mL penicillin/streptomycin. Cells were incubated at 37 °C in humidified air/5% CO_2.

Formation of PAMAM/DNA/Heparin and PAMAM/DNA/Heparin−Biotin Terplexes. PAMAM was diluted to an appropriate concentration in deionized water and stored at 4 °C until use. PAMAM/DNA complexes were made up by adding the aqueous solution of PAMAM to an equal volume of plasmid DNA in deionized water at a particular N/P ratio, followed by incubation at 37 °C for 30 min. The N/P ratio was based on the calculation of the number of terminal -NH_2 groups on the dendrimer versus the number of phosphate groups of the DNA.

PAMAM/DNA/heparin and PAMAM/DNA/heparin−biotin terplexes were prepared by mixing the PAMAM/DNA complexes containing aqueous solution with an aqueous solution of heparin or heparin−biotin of equal volume and then incubating at 37 °C for 30 min.

Agarose Gel Electrophoresis. Terplexes with different compositions were evaluated by agarose gel retardation assay. Five microliters of complexes containing solution with 0.1 μg DNA was electrophoresed on the 0.7% (w/v) agarose gel containing GelRed with Tris-acetate-EDTA (TAE) running buffer at 80 V for 80 min. DNA was visualized on a Vilber Lourmat UV-transilluminator.

Size and Zeta Potential Measurements. The size and zeta potential of complexes were measured using a Nano-ZS ZEN3600 (Malvern Instruments). The complexes contained solution containing 4 μg pGL3-Luc were diluted by deionized water to 0.8 mL for the size and zeta potential measurements. The data are given as mean ± standard deviation (SD) based on three independent measurements.

Cytotoxicity. The cytotoxicities of PAMAM/DNA complexes, PAMAM/DNA/heparin, and PAMAM/DNA/heparin−biotin complexes with the heparin/DNA or heparin−biotin/DNA weight ratio of 2 at various N/P ratios were examined by MTT assay. The HeLa cells were seeded in the 96-well plates at a density of 6×10^3 cells/well in 200 μL of DMEM containing 10% FBS. After incubation for 24 h, the medium was replaced by 200 μL of serum-free DMEM. Then, the complexes containing solution (20 μL containing 0.2 μg DNA) was added into the well. After coincubation at 37 °C for 48 h, the medium was removed and 20 μL of MTT (5 mg/mL) solution was added to each well and further incubated for 4 h. Thereafter, the medium was removed carefully, and 150 μL DMSO was added to each well to dissolve the formazan crystals. The absorbance was measured at 570 nm by a microplate reader (Biorad 550). The cells without coincubation with the complexes were used as the control. The data are given as mean ± standard deviation (SD) based on five measurements.

In Vitro Transfections. The transfection activities of various complexes in HeLa, COS-7, and 293T cells were examined. Unless otherwise mentioned, the transfections were carried out in serum-free media. The detailed transfection procedure is as follows. The cells were seeded at a density 5×10^4 cells per well in a 24-well plate with 1 mL of DMEM containing 10% FBS and incubated at 37 °C. After incubation for 24 h, the medium was replaced by 1 mL of serum-free DMEM. Then, the complexes containing solution (100 μL containing 1 μg DNA) was added into the well and incubated at 37 °C for 4 h. After that, the serum-free DMEM was replaced with fresh DMEM containing 10% FBS, and the cells were further incubated for 44 h. (For the transfections carried out in serum containing media, the cells and the complexes were coincubated in DMEM containing 10% FBS for 4 h. Other conditions were the same as that for the transfections carried out in serum-free media.)

To assay the expression of pGL3-Luc, the medium was removed and the cells were rinsed gently by phosphate buffered saline (PBS, 0.1 M, pH 7.4). After thorough lysis of the cells with reporter lysis buffer (Promega) (200 μL/well), the luciferase activity was determined by detecting the light emission from an aliquot of cell lysate incubated with 100 μL of luciferin substrate (Promega) in a luminometer (Lumat LB9507, Berthold). The protein content of the cell lysate was determined by BCA protein assay kit (Pierce). The optical density (OD) value was determined at 570 nm using a microplate reader (Biorad 550). The data are given as mean ± standard deviation (SD) based on three independent measurements.

To assay the expression of pEGFP-C1, the cells expressing green fluorescent proteins were directly observed by an inverted microscope (IX 70, Olympus) with a digital color camera (Roper CoolSnap Color). The micrographs were obtained at the magnification of 100× and recorded using *Image-Pro Plus* software.

Cellular Uptake Study. The uptake of complexes into HeLa cells was studied by confocal microscopy. YOYO-1 was used as molecular probe to label pGL3-Luc. One microgram of pGL3-Luc plasmid was mixed with 2.5 μL YOYO-1 solution (10 μM) and incubated for 15 min at 37 °C. The cells were seeded at a density of 5×10^4 cells per well in a 24-well plate with 1 mL of complete growth medium containing 10% FBS and incubated at 37 °C. After incubation for 24 h, the medium was replaced by 1 mL serum-free DMEM. Then, the complexes (100 μL containing 1 μg DNA) were added into the well and incubated at 37 °C for 4 h. After that, the medium was removed, the cells were washed twice with PBS, and then 200 μL DMEM containing 10% FBS and 20 μL Hoechst 33258 solution (10 mg/mL) were added and incubated at 37 °C for 20 min to stain nuclei of the cells. Finally, the solution was removed, cells were washed with PBS twice, and 1 mL of fresh DMEM containing 10% FBS was added. The cells were observed under excitation at 488 nm using a confocal laser scanning microscope (Nikon C1-si TE2000). The micrographs were obtained at the magnification of 800× and recorded using Nikon EZ-C1 *FreeViewer* software.

RESULTS AND DISCUSSION

Formation and Characterization of PAMAM/DNA/Heparin and PAMAM/DNA/Heparin−Biotin Terplexes. PAMAM dendrimers are a class of spherical, nanoscopic, highly ordered polymers with primary amino groups on the surface, which have lower cytotoxicity compared with PEI and have been extensively investigated as gene vectors (*17*). Heparin is a highly sulfated anionic polysaccharide. It was reported that PAMAM and heparin can form complexes through electrostatic interactions (*15, 16*). As we know, in order to condense DNA effectively, the complexes of polycation/DNA for gene delivery usually have a positive charge on the surface. In the current study, after mixing the positively charged PAMAM/DNA complexes with the negatively charged heparin and heparin−biotin, PAMAM/DNA/heparin and PAMAM/DNA/heparin−biotin terplexes were formed, respectively.

It was reported that heparin could replace DNA in the polycation/DNA complexes by vigorously mixing. In this study, the stability of different complexes was assessed by the agarose gel retardation assay and the results are shown in Figure 1. For PAMAM/DNA/heparin terplexes with a heparin/DNA weight ratio of 2 (Figure 1a), when the PAMAM/DNA N/P ratios were in the range 5−60, the complexes were able to completely bind DNA. Similarly, for PAMAM/DNA/heparin−biotin terplexes with a heparin−biotin/DNA weight ratio of 2 (Figure 1b), they could efficiently bind DNA at the PAMAM/DNA N/P ratio from 5 to 60. However, for PAMAM/DNA/heparin−biotin terplexes with a PAMAM/DNA N/P ratio of 20 (Figure 1c), PAMAM/DNA/heparin−biotin could not completely prevent DNA from

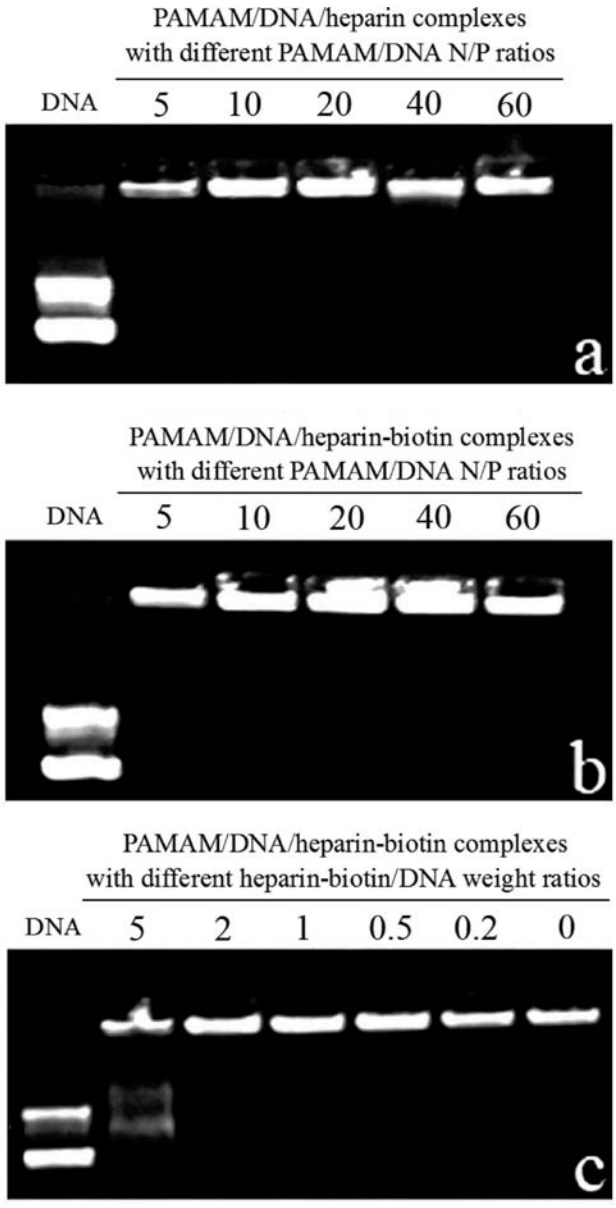


Figure 1. Agarose gel retardation assay of different complexes: (a) PAMAM/DNA/heparin complexes with a heparin/DNA weight ratio of 2 and different PAMAM/DNA N/P ratios, (b) PAMAM/DNA/heparin−biotin complexes with a heparin−biotin/DNA weight ratio of 2 and different PAMAM/DNA N/P ratios, and (c) PAMAM/DNA/heparin−biotin complexes with a PAMAM/DNA N/P ratio of 20 and different heparin−biotin/DNA weight ratios.

migrating into the gel when the weight ratio of heparin−biotin/DNA was 5, indicating that, in order to bind DNA completely, the weight ratio of heparin−biotin/DNA should be less than 5.

The particle sizes of different complexes were measured as shown in Figure 2. All sizes of PAMAM/DNA complexes at different N/P ratios were less than 200 nm, which indicated DNA could be effectively condensed by PAMAM at the N/P ratio higher than 5. As compared with the sizes of PAMAM/DNA complexes, the sizes of PAMAM/DNA/heparin slightly increased. This is due to the fact that the negatively charged heparin was attached to the surface of PAMAM/DNA complexes, leading to the increased sizes. Compared with PAMAM/DNA complexes, the size of PAMAM/DNA/heparin−biotin also increased. Compared with PAMAM/DNA/heparin terplexes, most commonly the sizes of PAMAM/DNA/heparin−biotin terplexes were smaller. The possible reason for this phenomenon is the hydrophobic nature of biotin moiety, which resulted in a

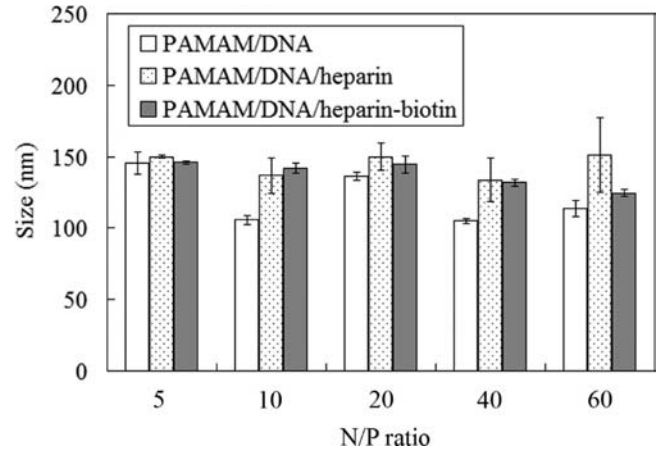


Figure 2. Particle sizes of different complexes with different PAMAM/DNA N/P ratios. The weight ratio of heparin/DNA and heparin−biotin/DNA is 2.

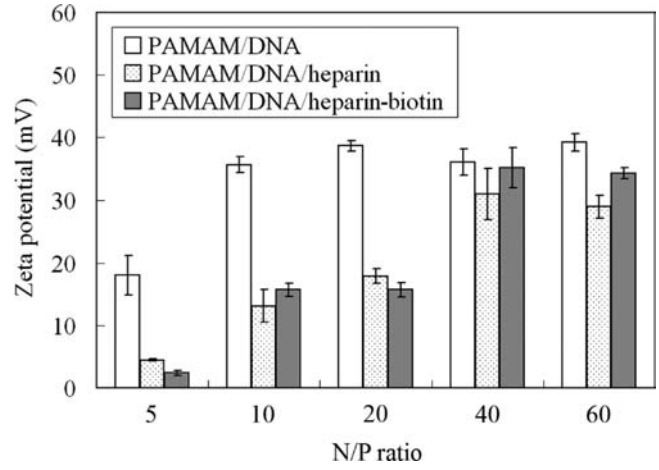


Figure 3. Zeta potentials of different complexes with different PAMAM/DNA N/P ratios. The weight ratio of heparin/DNA and heparin−biotin/DNA is 2.

less extended configuration of heparin−biotin chains on the surface of the terplexes. Nevertheless, the size differences between different complexes were not large, and all complexes had the mean sizes less than 200 nm.

The zeta potentials of different complexes are shown in Figure 3. The zeta potentials of all complexes were positive. Because of the positive surface charge caused by the excess PAMAM and the strong electrostatic interactions between PAMAM/DNA complexes and heparin or heparin−biotin, the heparin and heparin−biotin in the systems could form terplexes and the free heparin and heparin−biotin could be ignored. The zeta potentials of the complexes increased with increasing PAMAM/DNA N/P ratio when the N/P ratio was less than 20. Compared with PAMAM/DNA, the zeta potential of PAMAM/DNA/heparin and PAMAM/DNA/heparin−biotin decreased significantly, especially at the relatively low N/P ratios, because the negatively charged heparin or heparin−biotin was attached to the surface of PAMAM/DNA complexes. As a result, the positive surface charges of the PAMAM/DNA complexes were partially neutralized. The positive zeta potential values of all complexes were in good agreement with the result of agarose gel retardation assay, which also indicated that PAMAM/DNA/heparin and PAMAM/DNA/heparin−biotin terplexes with different N/P ratios were stable when the weight ratio of heparin/DNA and heparin−biotin/DNA was 2.

In Vitro Cytotoxicity. The cytotoxicity of different complexes in HeLa cells was evaluated by MTT assay. As presented

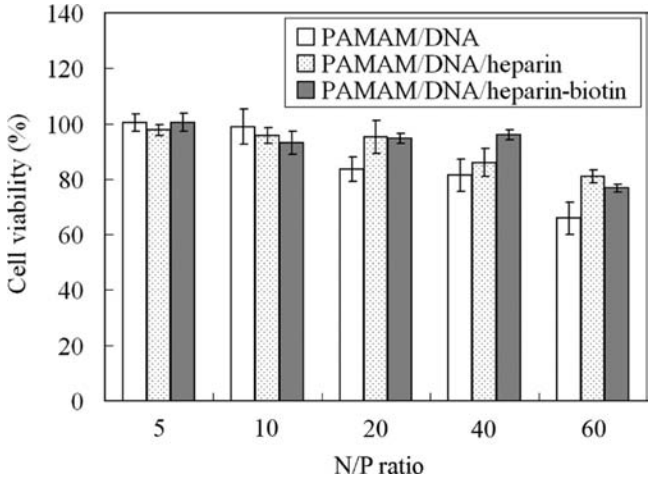


Figure 4. Cell viability of HeLa cells after coincubation with different complexes with different PAMAM/DNA N/P ratios. The weight ratio of heparin/DNA and heparin−biotin/DNA is 2.

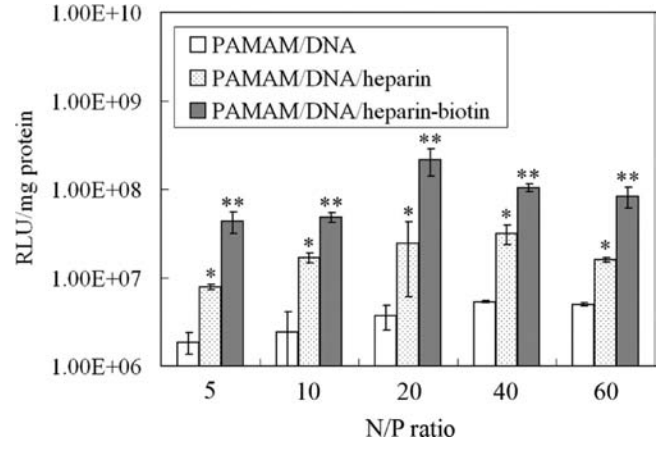


Figure 5. Luciferase expression in HeLa cells transfected with different complexes with different PAMAM/DNA N/P ratios. The weight ratio of heparin/DNA and heparin−biotin/DNA is 2. (* $p < 0.05$ as compared with the data of PAMAM/DNA complexes at the same N/P ratio, and ** $p < 0.05$ as compared with the data of PAMAM/DNA/heparin complexes at the same N/P ratio.)

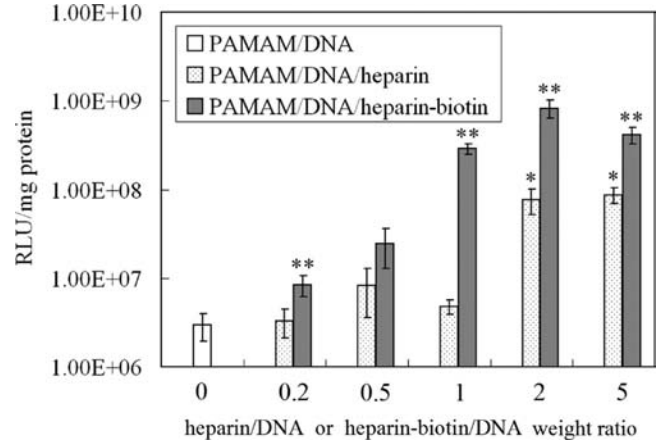


Figure 6. Luciferase expression in HeLa cells transfected with different complexes with different heparin/DNA or heparin−biotin/DNA weight ratios. The PAMAM/DNA N/P ratio is 20. (* $p < 0.05$ as compared with the data of PAMAM/DNA complexes, ** $p < 0.05$ as compared with the data of PAMAM/DNA/heparin complexes at the same heparin/DNA or heparin−biotin/DNA weight ratio.)

in Figure 4, for PAMAM/DNA complexes, with an increase in N/P ratio, the cell viability decreased. As expected, generally the cytotoxicities of PAMAM/DNA/heparin and PAMAM/DNA/heparin−biotin terplexes were lower than that of the PAMAM/DNA complexes, especially at the high N/P ratios. As we know, during the gene transfection, the positive charge on the surface of complexes is essential for binding the negatively charged cell membranes and thus being taken up via an endocytic mechanism. However, the higher positive surface charge means higher cytotoxicity of the complexes, and the high cytotoxicity of the polycations limits their clinical applications as gene vectors. One of the strategies to reduce the cytotoxicity is to neutralize or partially shield the positive charge on the polycation/DNA complexes. For example, the PEG chains grafted to polycations could shield the positive surface charge and thus reduce the cytotoxicity while maintaining the efficient transfection ability of the polycations (*18–20*). In this study, heparin and heparin−biotin were used to partially neutralize the positive charge of PAMAM/DNA complexes. The resultant terplexes showed relatively lower zeta potential as compared with PAMAM/DNA, which resulted in their lowered cytotoxicity.

In Vitro Transfection. The luciferase expressions in HeLa cells transfected with different complexes with the heparin/DNA or heparin−biotin/DNA weight ratio of 2 and different PAMAM/DNA N/P ratios are shown in Figure 5. For all N/P ratios, as compared with PAMAM/DNA complexes, PAMAM/DNA/heparin terplexes exhibited a much higher gene transfection activity. In addition, the gene expression levels mediated by PAMAM/DNA/heparin−biotin terplexes could obviously be further improved. Both comparisons between the data of PAMAM/DNA and PAMAM/DNA/heparin and the data of PAMAM/DNA/heparin and PAMAM/DNA/heparin−biotin showed $p < 0.05$, indicating that the differences were statistically significant. As we know, heparin is one of the most potent anticoagulants and has been widely used to enhance the blood compatibility of biomaterials. According to previous studies of other researchers, the conjugation of heparin to PEI or physical modification of PEI with heparin via electrostatic interactions can improve the cytocompatibility and transfection efficiency (*13, 14*). Our results are in accordance with the previous studies.

Biotin is an essential vitamin for the division of all cells, especially for the rapid proliferations of tumor cells. The cancer cells often overexpress biotin receptors on the cell surface. The improvement of gene expression mediated by PAMAM/DNA/heparin−biotin suggested that the presence of biotin moiety facilitated the uptake of terplexes in tumor cells due to the specific interactions between biotin and its receptors on HeLa cells (*9*) and led to the improved transfection efficiency. Our results are in agreement with the previous literature. As reported, the biotin conjugated PAMAM (G5) exhibited enhanced cellular uptake of HeLa cells, i.e., about 2 times higher than that without incorporation of biotin as determined by the mean fluorescence (*9*). In our study, the luciferase expressions in HeLa cells transfected with PAMAM/DNA/heparin−biotin were about 2 to 6 times higher than that transfected with PAMAM/DNA/heparin when the N/P ratios were in the range 5−60 (Figure 5).

From Figure 5, the gene expressions increased with increasing N/P ratio at the N/P ratio ranging from 5 to 20. A further increase in N/P ratio did not result in an obvious improvement in the transfection. This is because the complexes with a low N/P ratio could not efficiently mediated gene expressions, while the N/P ratio of more than 20 was too high, which caused the low cell viability after transfection. Thus, we fixed the N/P ratio at 20 for further study.

As shown in Figure 6, when fixing the PAMAM/DNA N/P ratio at 20, the gene expressions mediated by PAMAM/DNA/

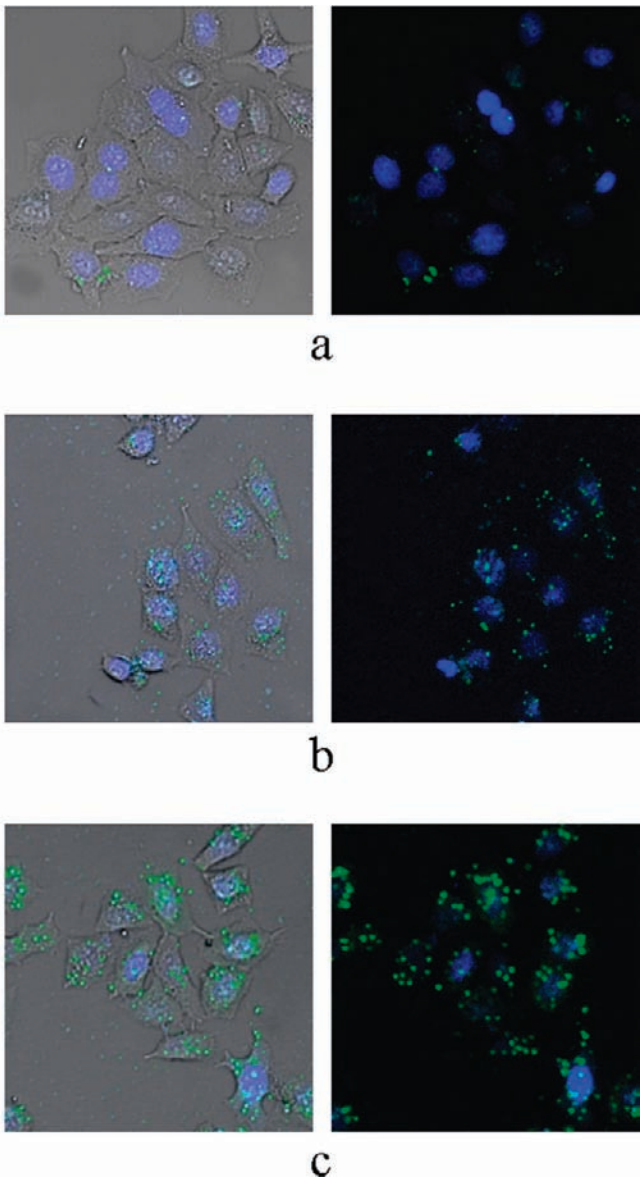


Figure 7. Confocal images of HeLa cells after incubation with (a) PAMAM/DNA, (b) PAMAM/DNA/heparin, and (c) PAMAM/DNA/heparin−biotin complexes. The PAMAM/DNA N/P ratio is 20, and the weight ratio of heparin/DNA and heparin−biotin/DNA is 2.

heparin and PAMAM/DNA/heparin−biotin terplexes increased with increasing weight ratio of heparin/DNA or heparin−biotin/DNA, reached maximum values at the heparin/DNA or heparin−biotin/DNA weight ratio of 2, implying that the heparin/DNA or heparin−biotin/DNA weight ratio at 2 was high enough to improve the transfection activity of the terplexes. For the different complexes at each particular heparin/DNA or heparin−biotin/DNA weight ratio, the same trend could be found, i.e., the transfection level increased significantly by binding heparin or heparin−biotin on the surface of PAMAM/DNA complexes, and the PAMAM/DAN/heparin−biotin complexes exhibited the highest transfection efficiency.

To further confirm the mechanism of the improvement of transfection in the presence of biotin moiety, we used confocal microscopy to visualize the cell uptake of different complexes. As shown in Figure 7, after coincubation with PAMAM/DNA complexes for 4 h, only a few green fluorescence dots could be observed in HeLa cells (Figure 7a), while more green fluorescence dots could be observed for the cells treated with PAMAM/DNA/heparin terplexes (Figure 7b), suggesting that adding

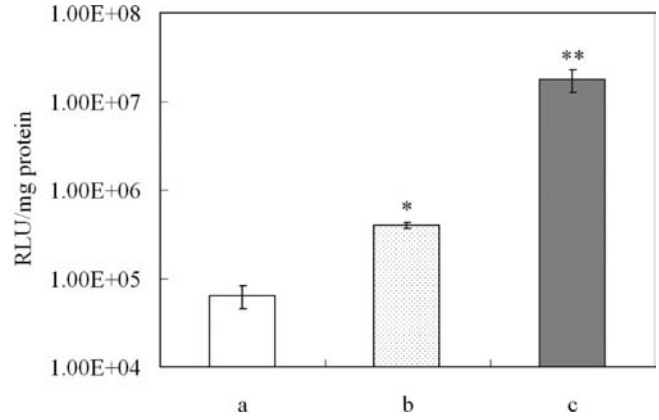


Figure 8. Luciferase expression in HeLa cells transfected with (a) PAMAM/DNA, (b) PAMAM/DNA/heparin, and (c) PAMAM/DNA/heparin−biotin complexes in DMEM containing 10% FBS. The PAMAM/DNA N/P ratio is 20, and the weight ratio of heparin/DNA and heparin−biotin/DNA is 2. (* $p < 0.05$ as compared with the data of PAMAM/DNA complexes, ** $p < 0.05$ as compared with the data of PAMAM/DNA/heparin complexes.)

appropriate heparin increased the cellular uptake. According to the earlier reports, anionic dendrimer could result in a markedly improved cellular uptake of oligonucleotide, and the positive surface charge is not the sole factor determining the cell uptake (*21*). Our result was consistent with the literature. The intensity of fluorescence was highest for the cells treated with PAMAM/DNA/heparin−biotin terplexes (Figure 7c), indicating that the existence of the biotin moiety played an important role in the cell uptake and the PAMAM/DNA/heparin−biotin terplexes could enter the cells through specific interactions between biotin and its receptors. The confocal microscopic observation clearly indicated that the level of cellular uptake in HeLa cells markedly increased by the presence of heparin and especially heparin−biotin. These results were in good agreement with the results of the in vitro transfection.

As it is well know that the presence of serum could reduce the transfection efficiency of polycations, the excess positive charge on the surface of the polycation/DNA complexes results in nonspecific adsorption of plasma proteins in serum. Heparin could inhibit the adsorption of serum proteins to the surfaces of liposomes and PEI (*13*, *22*). In this study, the transfection mediated by different complexes in the serum-contained media was investigated. As shown in Figure 8, the gene expression level increased significantly with the presence of heparin or heparin−biotin in the complexes. However, the expression levels decreased greatly in the serum-containing media (Figure 8) as compared with that in the serum-free media (Figure 5c). This is probably because all the terplexes were still positively charged, and their transfection efficacy was also affected by the presence of serum.

To further assess the transfection activities of terplexes in HeLa cells, another plasmid pEGFP-C1 was used to form PAMAM/DNA/heparin and PAMAM/DNA/heparin−biotin terplexes. Being consistent with gene transfection results using plasmid pGL3-Luc, the images in Figure 9 also showed that the PAMAM/DNA/heparin terplexes exhibited enhanced transfection activity and the PAMAM/DNA/heparin−biotin terplexes had the highest transfection activity, because the weakest fluorescence emission was observed for the HeLa cells transfected by PAMAM/DNA, whereas the highest fluorescent density was observed for the cells transfected with PAMAM/DNA/heparin−biotin.

In order to evaluate the transfection activity of the terplexes, the in vitro transfections were carried out in both 293T cells

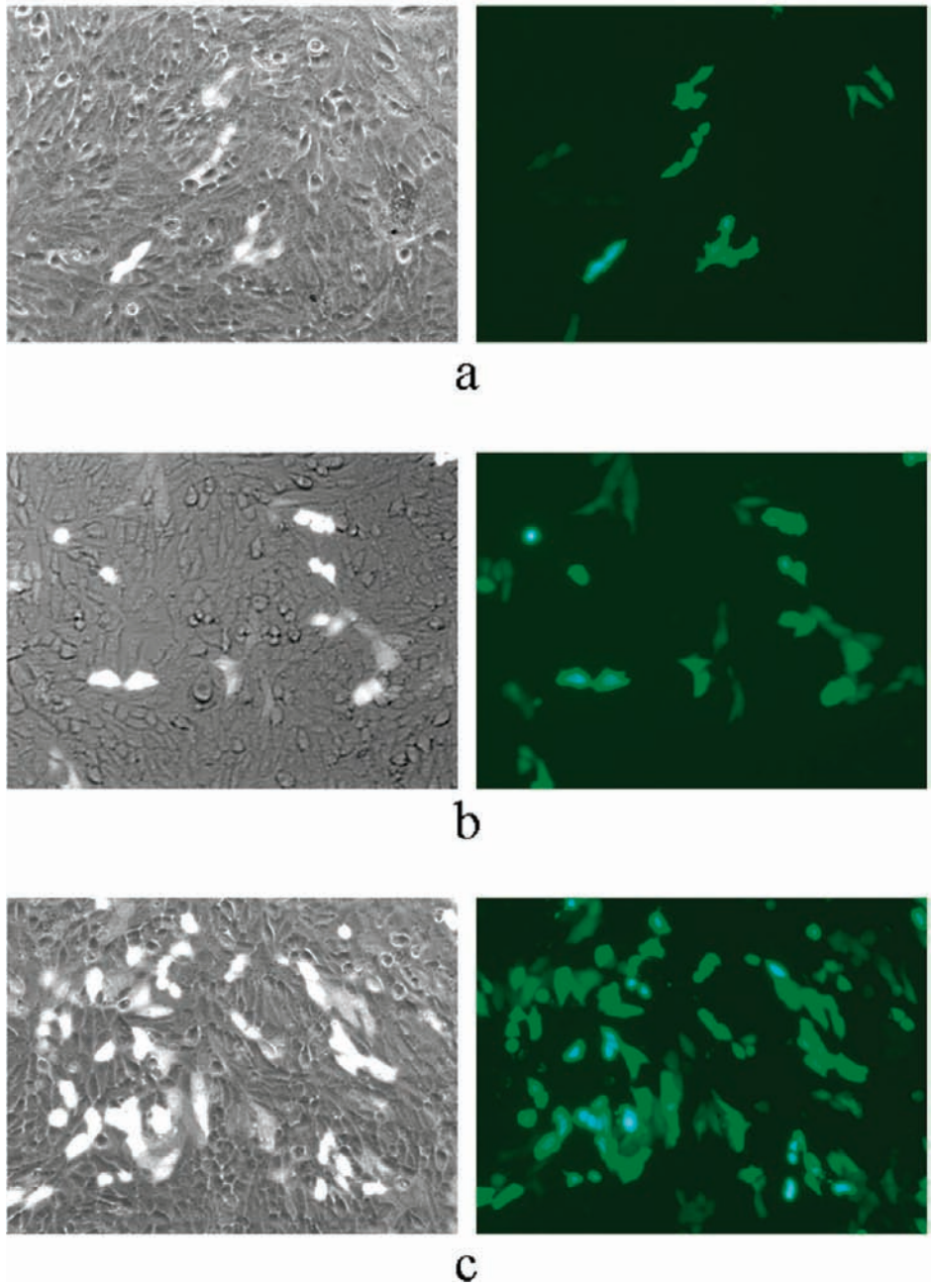


Figure 9. Enhanced green fluorescent protein expression in HeLa cells transfected with (a) PAMAM/DNA, (b) PAMAM/DNA/heparin, and (c) PAMAM/DNA/heparin−biotin complexes. The PAMAM/DNA N/P ratio is 20, and the weight ratio of heparin/DNA and heparin−biotin/DNA is 2.

(Figure 10) and COS-7 cells (Figure 11). The transfection activities of PAMAM/DNA/heparin terplexes and PAMAM/DNA/heparin−biotin terplexes were also statistically significantly higher than that of PAMAM/DNA complexes ($P < 0.05$). These results suggested that the presence of heparin or heparin−biotin was favorable for the transfection in these cells. According to the literature (*8–11*), most tumor cell types overexpress receptors involved in vitamin uptake such as biotin, although some tumor cell types do not overexpress biotin receptors, and normal cells do not overexpress biotin receptors. In our study, the transfection activity of PAMAM/DNA/heparin−biotin terplexes was almost the same as that of PAMAM/DNA/heparin terplexes in 293T and COS-7 cells. The presence of biotin on the surface of the complexes could not further enhance the transfection, implying that biotin receptors were not overexpressed in 293T and COS-7 cells, which were nontumor cells.

CONCLUSIONS

In this study, heparin and heparin−biotin were introduced to the complexes of PAMAM/DNA via electrostatic interactions. The presence of appropriate amounts of heparin and heparin−biotin did not affect the DNA condense ability of PAMAM and could lead to lowered cytotoxicities and improved gene transfection activities for the self-assembled PAMAM/DNA/heparin and PAMAM/DNA/heparin−biotin terplexes. The PAMAM/DNA/heparin−biotin terplexes exhibited an enhanced cellular uptake into HeLa cells due to the specific interactions between biotin and biotin receptors on HeLa cells, and thus led to further improvement in the gene transfection in HeLa cells as compared with PAMAM/DNA/heparin. These results indicated that PAM-

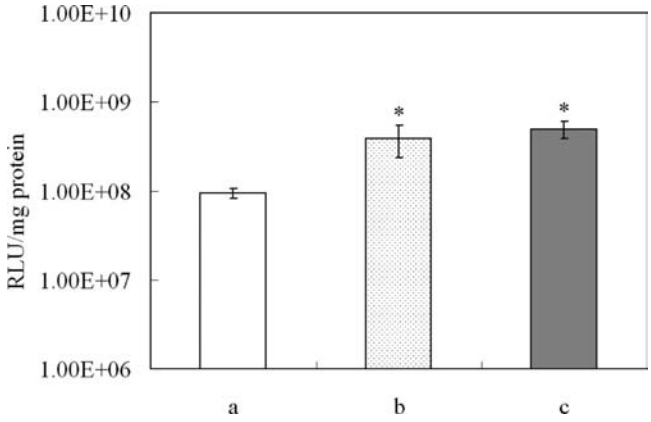


Figure 10. Luciferase expression in 293T cells transfected with (a) PAMAM/DNA, (b) PAMAM/DNA/heparin, and (c) PAMAM/DNA/heparin−biotin complexes. The PAMAM/DNA N/P ratio is 20, and the weight ratio of heparin/DNA and heparin−biotin/DNA is 2. (* $p < 0.05$ as compared with the data of PAMAM/DNA complexes.)

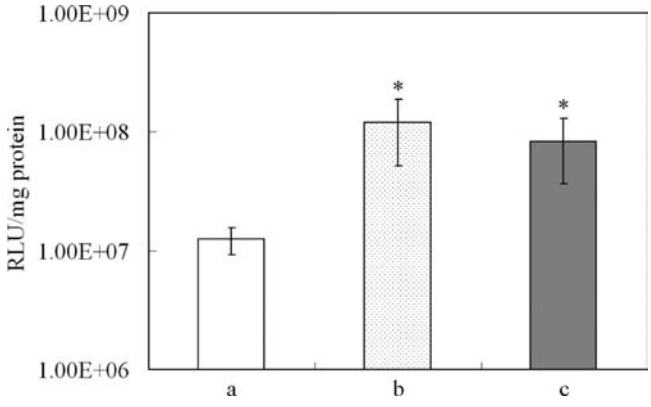


Figure 11. Luciferase expression in COS-7 cells transfected with (a) PAMAM/DNA, (b) PAMAM/DNA/heparin, and (c) PAMAM/DNA/heparin−biotin complexes. The PAMAM/DNA N/P ratio is 20, and the weight ratio of heparin/DNA and heparin−biotin/DNA is 2. (* $p < 0.05$ as compared with the data of PAMAM/DNA complexes.)

AM/DNA/heparin−biotin terplexes would have promising potential applications in targeting gene delivery to cancer cells.

ACKNOWLEDGMENT

Financial supports from National Natural Science Foundation of China (20774070 and 21074099) and Ministry of Science and Technology of China (National Basic Research Program of China 2009CB930300) are gratefully acknowledged.

LITERATURE CITED

(1) Dominik, E. D., and Nettelbeck, D. M. (2009) Targeting cancer by transcriptional control in cancer gene therapy and viral oncolysis. *Adv. Drug Delivery Rev. 61*, 554–571.

(2) Waehler, R., Russell, S. J., and Curiel, D. T. (2007) Engineering targeted viral vectors for gene therapy. *Nat. Rev. Gene 8*, 573–587.

(3) Mintzer, M. A., and Simanek, E. E. (2009) Nonviral vectors for gene delivery. *Chem. Rev. 109*, 259–302.

(4) Zhang, S., Zhao, Y., Zhao, B., and Wang, B. (2010) Hybrids of nonviral vectors for gene delivery. *Bioconjugate Chem. 21*, 1003–1009.

(5) Mendonca, L. S., Firmino, F., Moreira, J. N., Pedroso de Lima, M. C., and Simoes, S. (2010) Transferrin receptor-targeted liposome encapsulating anti-BCR-ABL siRNA or asODN for chronic myeloid leukemia treatment. *Bioconjugate Chem. 21*, 157–168.

(6) Zhang, X. Q., Wang, X. L., Zhang, P. C., Liu, Z. L., Zhuo, R. X., Mao, H. Q., and Leong, K. W. (2005) Galactosylated ternary DNA/polyphosphoramidate nanoparticles mediate high gene transfection efficiency in hepatocytes. *J. Controlled Release 102*, 749–763.

(7) Cheng, H., Zhu, J. L., Zeng, X., Jing, Y., Zhang, X. Z., and Zhuo, R. X. (2009) Targeted gene delivery mediated by folate-polyethylenimine-block-poly(ethylene glycol) with receptor selectivity. *Bioconjugate Chem. 20*, 481–487.

(8) Gregory, R. J., McTavish, K., McEwan, J., Rice, J., and Nowotnik, D. (2004) Vitamin-mediated targeting as a potential mechanism to increase drug uptake by tumours. *J. Inorg. Biochem. 98*, 1625–1633.

(9) Yang, W. J., Cheng, Y. Y., Xu, T. W., Wang, X. Y., and Wen, L. P. (2009) Targeting cancer cells with biotin-dendrimer conjugates. *Eur. J. Med. Chem. 44*, 862–868.

(10) Patil, Y., Sadhukha, T., Ma, L., and Panyam, J. (2009) Nanoparticle-mediated simultaneous and targeted delivery of paclitaxel and tariquidar overcomes tumor drug resistance. *J. Controlled Release 136*, 21–29.

(11) Na, K., Lee, T. B., Park, K. H., Shin, E. K., Lee, Y. B., and Choi, H. K. (2003) Self-assembled nanoparticles of hydrophobically-modified polysaccharide bearing vitamin H as a targeted anti-cancer drug delivery system. *Eur. J. Pharm. Sci. 18*, 165–173.

(12) Andersson, J., Sanchez, J., Ekdahl, K. N., Elgue, G., Nilsson, B., and Larsson, R. (2003) Optimal heparin surface concentration and antithrombin binding capacity as evaluated with human non-anticoagulated blood in vitro. *J. Biomed. Mater. Res. A 67*, 458–466.

(13) Jeon, O., Yang, H. S., Lee, T. J., and Kim, B. S. (2008) Heparin-conjugated polyethylenimine for gene delivery. *J. Controlled Release 132*, 236–242.

(14) Hu, C. H., Zhang, L., Wu, D. Q., Cheng, S. X., Zhang, X. Z., and Zhuo, R. X. (2009) Heparin-modified PEI encapsulated in thermosensitive hydrogels for efficient gene delivery and expression. *J. Mater. Chem. 19*, 3189–3197.

(15) Bai, S. H., Thomas, C. D., and Ahsan, F. (2007) Dendrimers as a carrier for pulmonary delivery of enoxaparin a low-molecular weight heparin. *J. Pharm. Sci. 96*, 2090–2106.

(16) Bai, S. H., and Ahsan, F. (2009) Synthesis and evaluation of pegylated dendrimeric nanocarrier for pulmonary delivery of low molecular weight heparin. *Pharm. Res. 26*, 539–548.

(17) Dufes, C., Uchegbu, I. F., and Schatzlein, A. G. (2005) Dendrimers in gene delivery. *Adv. Drug Delivery Rev. 57*, 2177–2202.

(18) Luo, D., Haverstick, K., Belcheva, N., Han, E., and Saltzman, W. M. (2002) Poly(ethylene glycol)-conjugated PAMAM dendrimer for biocompatible, high-efficiency DNA delivery. *Macromolecules 35*, 3456–3462.

(19) Kojima, C., Kono, K., Maruyama, K., and Takagishi, T. (2000) Synthesis of polyamidoamine dendrimers having poly(ethylene glycol) grafts and their ability to encapsulate anticancer drugs. *Bioconjugate Chem. 11*, 910–917.

(20) Lee, Y., Miyata, K., Oba, M., Ishii, T., Fukushima, S., Han, M., Koyama, H., Nishiyama, N., and Kataoka, K. (2008) Charge-conversion ternary polyplex with endosome disruption moiety: a technique for efficient and safe gene delivery. *Angew. Chem., Int. Ed. 47*, 5163–5166.

(21) Hussain, M., Shchepinov, M. S., Sohail, M., Benter, I. F., Hollins, A. J., Southern, E. M., and Akhtar, S. (2004) A novel anionic dendrimer for improved cellular delivery of antisense oligonucleotides. *J. Controlled Release 99*, 139–155.

(22) Han, H. D., Lee, A., Song, C. K., Hwang, T., Seong, H., Lee, C. O., and Shin, B. C. (2006) In vivo distribution and antitumor activity of heparin-stabilized doxorubicin-loaded liposomes. *Int. J. Pharm. 313*, 181–188.

BC100309E

Synthesis, Characterization, and in Vitro Evaluation of Long-Chain Hyperbranched Poly(ethylene glycol) as Drug Carrier

Yan Pang,[§,†] Jinyao Liu,[§,†] Jieli Wu,[‡] Guolin Li,[†] Ruibin Wang,[†,‡] Yue Su,[‡] Peng He,[||] Xinyuan Zhu,*[,†,‡] Deyue Yan, and Bangshang Zhu*[,‡]

School of Chemistry and Chemical Engineering and Instrumental Analysis Center, Shanghai Jiao Tong University, 800 Dongchuan Road, Shanghai 200240, People's Republic of China, and Department of Biological and Environmental Engineering, Cornell University, Ithaca, New York 14853, United States. Received July 18, 2010; Revised Manuscript Received September 11, 2010

A series of novel long-chain hyperbranched poly(ethylene glycol)s (LHPEGs) with biodegradable connections were designed and synthesized in one pot through proton-transfer polymerization using PEG and commercial glycidyl methacrylate as monomers and potassium hydride as catalyst. The LHPEGs were hydrolyzed at neutral pH resulting in the decrease of molecular weights. In vitro evaluation demonstrated that LHPEGs were biocompatible and displayed negligible hemolytic activity. The efficient cellular uptake of LHPEGs was confirmed by flow cytometry and confocal laser scanning microscopy. Moreover, conjugation of a model hydrophobic anticancer drug methotrexate to LHPEGs inhibited the proliferation of a human cervical carcinoma Hela cell line. MTT assay indicated that the conjugated methotrexate dose required for 50% cellular growth inhibition against Hela cells was 20 μg/mL. By combining the advantages of long-chain hyperbranched structure and PEG, LHPEG provides a promising drug carrier for therapeutic fields.

INTRODUCTION

Poly(ethylene glycol) (PEG) has attracted great attention in biomedical fields due to its good hydrophilicity, biocompatibility, nonimmunogenicity, ion-transporting ability, and chemical stability under basic or neutral conditions (*1*−*13*). The conjugation of PEG has been used to various investigational and clinical compounds, such as peptides, proteins, oligodeoxynucleotides, antibodies, polymers, liposomes, and inorganic/organic nanoparticles (*14*−*22*). It is worth noting that PEG is often the first choice in the biopharmaceutical industry for the improvement of pharmacological properties (*23, 24*). PEG−drug conjugates can change the physical and chemical properties of the linked drugs, including the conformation, electrostatic binding, and hydrophilic−hydrophobic balance. More significantly, PEG can increase the stability and retention time in the blood of the conjugated drug, as well as reduce the proteolysis, renal excretion, and immunogenicity (*25*). However, a major problem for PEG as a drug carrier lies in the fact that linear PEG possesses a limited attachment capacity, with only one or two end groups depending on the inherent structure of polymer chain (*25, 26*). Therefore, PEG with many functional groups is highly attractive for drug delivery applications.

In contrast to linear polymers, dendritic polymers including dendrimers and hyperbranched polymers are highly branched macromolecules with low viscosity, good solubility, and plenty of terminal functional groups (*27*−*33*). Recently, dendritic polymers have been widely used for drug conjugates, because they can carry multiple copies of drug and/or targeting/imaging ligands (*34*). In the past few years, hyperbranched polyglycerols and PEG-methacrylate polymers with cross-linkers have been produced as PEG-mimic hyperbranched polymers (*26, 35*−*39*). Due to their structural similarity to PEG and highly branched nature, these mimics exhibit a broad range of potential applications in medicine and pharmacology. On the other hand, long-chain hyperbranched polymers are particularly interesting and have received growing attention because of their unique long-chain and hyperbranched structures (*40*−*49*). For example, Hutchings and co-workers developed the "macromonomer" approach to prepare long-chain hyperbranched polymers (*49*). By employing a Williamson coupling reaction of α,ω,ω'-trifunctional AB_2 macromonomers, a series of long-chain hyperbranched polymers have been obtained. However, to the best of our knowledge, a drug carrier based on PEG with a long-chain hyperbranched structure has not yet been reported. Herein, through the molecular design, a novel long-chain hyperbranched PEG which integrates the advantages of long-chain hyperbranched structure and PEG has been prepared in one pot via proton-transfer polymerization of PEG and commercial glycidyl methacrylate with the help of potassium hydride. The transformation of PEG from the conventional linear structure to the unique long-chain hyperbranched architecture with biodegradable connection provides a promising material for drug carriers.

MATERIALS AND METHODS

Materials. Potassium hydride (KH, 30 wt % dispersion in mineral oil, Acros), acridine orange (AO, Aldrich), ethidium bromide (EB, Aldrich), polyethylenimine (PEI, M_w = 25 kDa, Aldrich), *N*-hydroxysuccinamide (NHS, Acros), *N*,*N*-dicyclohexylcarbodiimide (DCC, Aldrich), 4-dimethylamino-pyridine (DMAP, Aldrich), and 3-(4,5-dimethyl-thiazol-2-yl)-2,5-diphenyl tetrazolium bromide (MTT, Aldrich) were used as received. PEG (M_n = 600, Acros) was dried by azeotropical distillation from anhydrous toluene. Glycidyl methacrylate (GMA, Acros) and dimethyl sulfoxide (DMSO) were dried over calcium hydride (CaH_2) and distilled under reduced pressure. Tetrahydrofuran (THF) was dried by refluxing over fresh sodium benzophenone complex (a deep purple color indicating an oxygen- and moisture-free solvent) and distilled just before polymerization. Methotrexate (MTX) was purchased from

* E-mail: xyzhu@sjtu.edu.cn.
§ These authors are joint first authors.
† School of Chemistry and Chemical Engineering, Shanghai Jiao Tong University.
‡ Instrumental Analysis Center, Shanghai Jiao Tong University.
|| Cornell University.

10.1021/bc100325a © 2010 American Chemical Society
Published on Web 10/05/2010

Sangon Biotech (Shanghai) Co., Ltd. Clear polystyrene tissue culture treated 12-well and 96-well plates were obtained from Corning Costar. All other reagents and solvents were purchased from the domestic suppliers and used as received.

Synthesis of Long-Chain Hyperbranched PEG (LHPEG). A suspension of KH in mineral oil (30% in weight) was introduced in a dry, preweighed 100 mL Schlenk flask under argon (Ar). The mineral oil was removed by three extractions with THF, and the remaining THF was removed by vacuum. When KH was completely dried, the flask was weighted again to determine the amount of KH (0.542 g, 13.5 mmol). Then, 30 mL DMSO and PEG600 (16.2 g, 27.0 mmol) were introduced into the flask (Caution: hydrogen gas was generated). The solution was stirred for 2 h to form the potassium alcoholate. Subsequently, GMA (3.84 g, 27.0 mmol) was added by syringe and the polymerization was conducted at 80 °C for 48 h. Upon completion of the polymerization, the mixture was precipitated into 1000 mL acetone/diethyl ether (v/v = 1/4). The product was redissolved in methanol and neutralized by filtration over cation-exchange resin. The obtained polymer was precipitated twice from methanol solution into cold diethyl ether. The residues were dissolved in distilled water. Exhaustive dialysis against exchanged distilled water was carried out for 7 days, followed by lyophilization to give the LHPEG (yield: 12.9 g, 64.5%).

Rhodamine B Labeled LHPEG (LHPEG-RB). A typical rhodamine B (RB) conjugation reaction is described as follows: NHS (130.0 mg, 1.132 mmol) and RB (542 mg, 1.132 mmol) were dissolved in 20 mL of DMF, and then DCC (256.6 mg, 1.246 mmol) and DMAP (276.3 mg, 2.265 mmol) were added to the solution. The mixture was stirred at 50 °C overnight. LHPEG (830 mg, 0.126 mmol) in 10 mL DMF was added to the reaction solution. The reaction was conducted at room temperature for another 48 h. Then, the insoluble substance was filtered and DMF was removed by rotary evaporation. The residues were dissolved in distilled water. Exhaustive dialysis against exchanged distilled water was carried out for 7 days, followed by lyophilization to give the LHPEG-RB.

MTX Conjugated LHPEG (LHPEG-MTX). In a typical experiment, MTX (665.2 mg, 1.46 mmol), LHPEG (878.2 mg, 0.133 mmol), DCC (316.6 mg, 1.54 mmol), and DMAP (178.6 mg, 1.46 mmol) were mixed in a 100 mL flask with 20 mL DMF. The solution was stirred for 48 h at room temperature under a nitrogen atmosphere. Then, the insoluble dicyclohexylurea was filtered and DMF was removed by rotary evaporation. The crude product was purified by repeatedly dissolved in methanol and then precipitated in diethyl ether. The residues were dissolved in distilled water. Exhaustive dialysis against exchanged distilled water was carried out for 7 days, followed by lyophilization to give LHPEG-MTX.

Characterization of Polymers. ^{1}H and ^{13}C NMR spectra of the polymers were recorded using Bruker Avance III 400 spectrometer with dimethyl sulfoxide-d_6 (DMSO-d_6) as a solvent. Quantitative ^{13}C NMR spectra were measured by the method of inverse gated ^{1}H decoupling. In DEPT experiments, the ^{1}H tip angle θ was set to 135° to determine carbon multiplicities with CH, CH_3 up, and CH_2 down. ^{1}H, ^{1}H-COSY and ^{13}C, ^{1}H-HSQC spectra were recorded using the standard pulse sequence provided by Bruker. Fourier transformed infrared (FTIR) spectrum measurements were performed on a Bruker Equinox-55 FTIR spectrometer with a disk of KBr. The molecular weights and polydispersity indexes (PDIs) were determined by gel permeation chromatography (GPC). GPC was performed on a Perkin-Elmer series 200 system (10 μm PL gel 300 × 7.5 mm mixed-B and mixed-C column, PEG calibration) equipped with a refractive index (RI) detector. DMF contained 0.01 mol/L lithium bromide was used as the mobile phase at a flow rate of 1 mL/min at 70 °C. The glass transition temperature (T_g) and melting behavior of polymers were measured with a TA Instruments Q2000 differential scanning calorimeter (DSC) under nitrogen (N_2) atmosphere. All samples were heated from −80 to 100 °C at a heating rate of 20 °C/min. The midpoint of the slope change of the heat capacity plot of the second heating scan was taken as T_g. UV−vis measurements were performed on a Perkin-Elmer Lambda 20 UV−vis spectrometer in the range 300−500 nm.

Degradation of LHPEG. Degradation behavior of LHPEG was estimated by the measurement of molecular weights. In brief, 0.2 g LHPEG was dissolved in 10 mL PBS and incubated at 37 °C with shaking. A series of 1 mL solutions were extracted and lyophilized after appropriate time intervals. The molecular weights of the lyophilized samples were measured by GPC analysis.

Cell Cultures. NIH 3T3 cells (a mouse embryonic fibroblast cell line) and Hela cells (a human cervical carcinoma cell line) were cultured in DMEM (Dulbecco's modified Eagle's medium) supplied with 10% FBS (fetal bovine serum) and antibiotics (50 units/mL penicillin and 50 units/mL streptomycin) at 37 °C in a humidified atmosphere containing 5% CO_2.

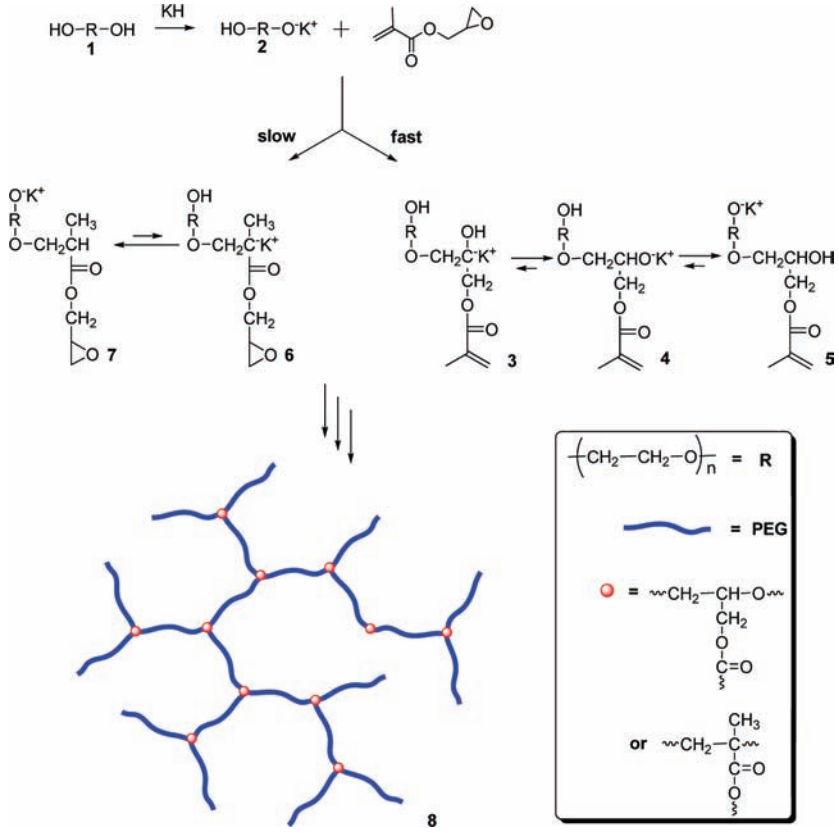
Cytotoxicity of LHPEG. NIH 3T3 cells were seeded into 96-well plates at an initial seeding density of 8.0×10^3 cells/well in 200 μL medium. After 24 h incubation, the culture medium was removed and replaced with 200 μL medium containing serial dilutions of LHPEG. The cells were grown for another 24 h. Then, 20 μL of 5 mg/mL MTT assays stock solution in phosphate buffered saline (PBS) was added to each well. After incubating the cells for 4 h, the medium containing unreacted dye was removed carefully. The obtained blue formazan crystals were dissolved in 200 μL per well DMSO, and the absorbance was measured in a BioTek Elx800 at a wavelength of 490 nm.

AO/EB Double Staining. NIH 3T3 cells were seeded in 6-well plates at 5×10^5 cells per well in 1 mL complete DMEM and cultured for 24 h, followed by removing culture medium and adding 1 mL LHPEG solutions (in DMEM medium) with the concentration of 1 mg/mL. After 24 h incubation, cells were rinsed by PBS twice and incubated in PBS containing AO (5 μg/mL) and EB (5 μg/mL) at 37 °C in 5% CO_2 for 10 min. Then, the cells were rinsed by PBS twice and directly imaged by an Olympus BX61 fluorescence microscope.

Hemolysis Assay. The blood was drawn from the ear vein of a male New Zealand white rabbit (2.5 kg body weight). A 2% (w/v) suspension of red blood cells (RBCs) was isolated through the following procedure. First, the blood was centrifuged at 2000 rpm for 5 min at 4 °C, and the plasma and top of the pellet were discarded. The pellet was resuspended in PBS (pH = 7.4) that had been prechilled to 4 °C. The suspension was subjected to another repeating centrifugation step as described. Finally, the pellet was resuspended in a volume appropriate to 2% (w/v) suspension using PBS (pH = 7.4). Samples were dissolved at concentrations of 2 mg/mL in PBS and added to an equal volume of 2% (w/v) RBC suspension in PBS. Dextran and PEI were used as reference controls, and Triton X-100 (1% v/v) was used to give a 100% hemolysis value. Hemoglobin release was determined by a Perkin-Elmer Lambda 20 UV−vis spectrometer at 545 nm and expressed as a percentage of hemoglobin release relative to the Triton X-100 control.

Cell Internalization. Cell internalization was characterized by flow cytometry and confocal laser scanning microscopy (CLSM). Flow cytometry was used to provide statistics on the uptake of LHPEG into Hela cells. Hela cells (5.0×10^5 cells per well) were seeded in a 6-well tissue culture plate. After 24 h culture, the RB labeled P1 dissolved in DMEM culture

Scheme 1. Detailed Proton-Transfer Polymerization Mechanism of LHPEG



medium with a concentration of 1 mg/mL was added to different wells and the cells were incubated at 37 °C for predetermined time intervals. After the incubation, samples were prepared for flow cytometry analysis by removing the cell growth media, rinsing with PBS buffer, and treating with trypsin. Data for 1.0 $\times$ 10^4 gated events were collected, and analysis was performed by means of a BD FACSCalibur flow cytometer and *CELLQuest* software.

For CLSM, Hela cells (2.0 $\times$ 10^5 cells per well) were seeded on coverslips in a 6-well tissue culture plate. After 24 h culture, the LHPEG-RB dissolved in DMEM culture medium with a concentration of 1 mg/mL was added to different wells and the cells were incubated at 37 °C for predetermined time intervals. After being washed with PBS, the cells were fixed with 4% formaldehyde for 30 min at room temperature, and the slides were rinsed with PBS three times. Finally, the cells were stained with 2-(4-amidinophenyl)-6-indolecarbamidine dihydrochloride (DAPI) for 10 min, and the slides were rinsed with PBS three times. The slides were mounted and observed by a LSM 510META.

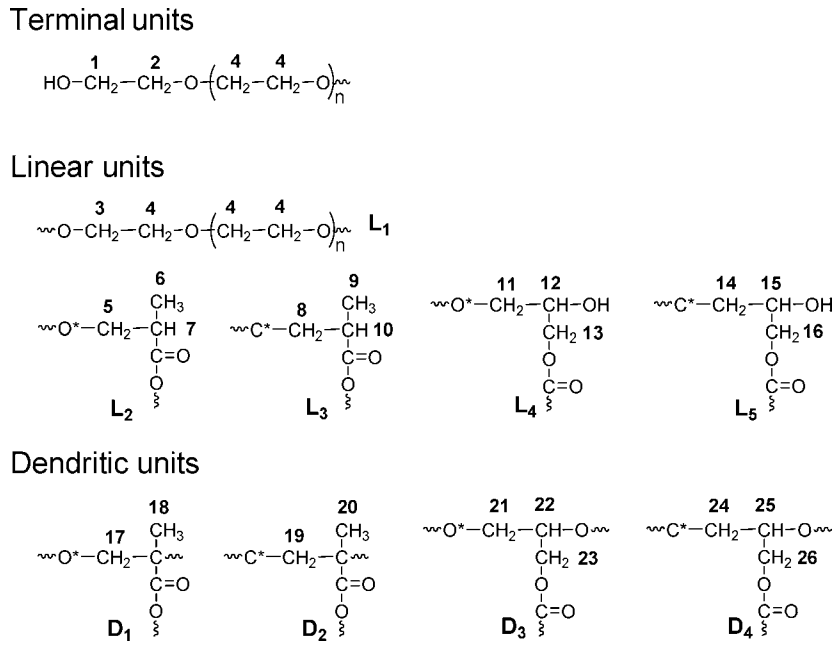


Figure 1. Various structural units of LHPEG.

Table 1. Reaction Conditions and Results of Proton-Transfer Polymerization of PEG and GMA

entry[a]	P/G[b]	M_w[c] ($\times 10^3$)	M_n[c] ($\times 10^3$)	M_w/M_n[c]	DB[d]	T_g[e] (°C)	T_m[e] (°C)
P1	1:1	19.9	6.6	3.02	0.57	−48.7	13.3
P2	1.1:1	18.4	6.2	2.96	0.61	−49.1	15.0
P3	1.2:1	15.7	5.6	2.81	0.65	−49.3	17.0

[a] The polymer obtained from the corresponding condition listed. [b] The molar ratio of PEG to GMA. [c] Molecular weights and polydispersities were determined by GPC. [d] The degree of branching (DB) was calculated from quantitative ^{13}C NMR analysis. [e] T_g and T_m were measured by DSC.

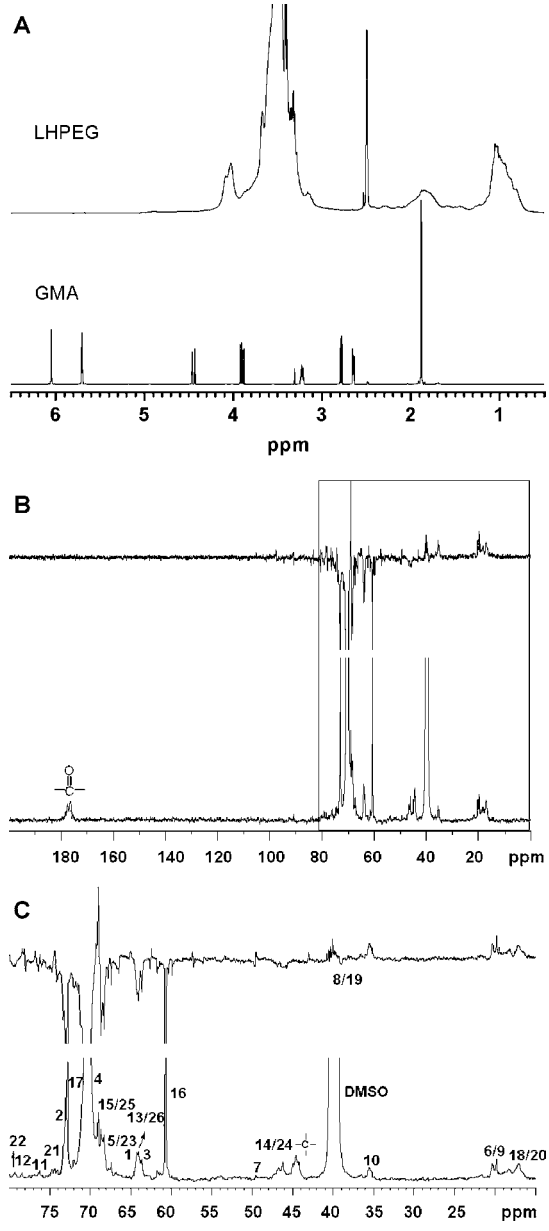


Figure 2. ^1H NMR spectra of P1 and GMA (A), ^{13}C DEPT-135 NMR spectrum of P1 (B), and the enlargement of spectrum B from 15 to 80 ppm (C).

Activity Analyses. The inhibition of LHPEG-MTX against Hela cells was evaluated in vitro by MTT assay, using free MTX with the same concentrations as the control. Hela cells were seeded into 96-well plates at an initial seeding density of 5.0×10^3 cells/well in 200 μL medium. After 24 h incubation, the culture medium was removed and replaced with 200 μL medium containing serial concentrations of free MTX or conjugated MTX. The cells were grown for another 72 h. The culture

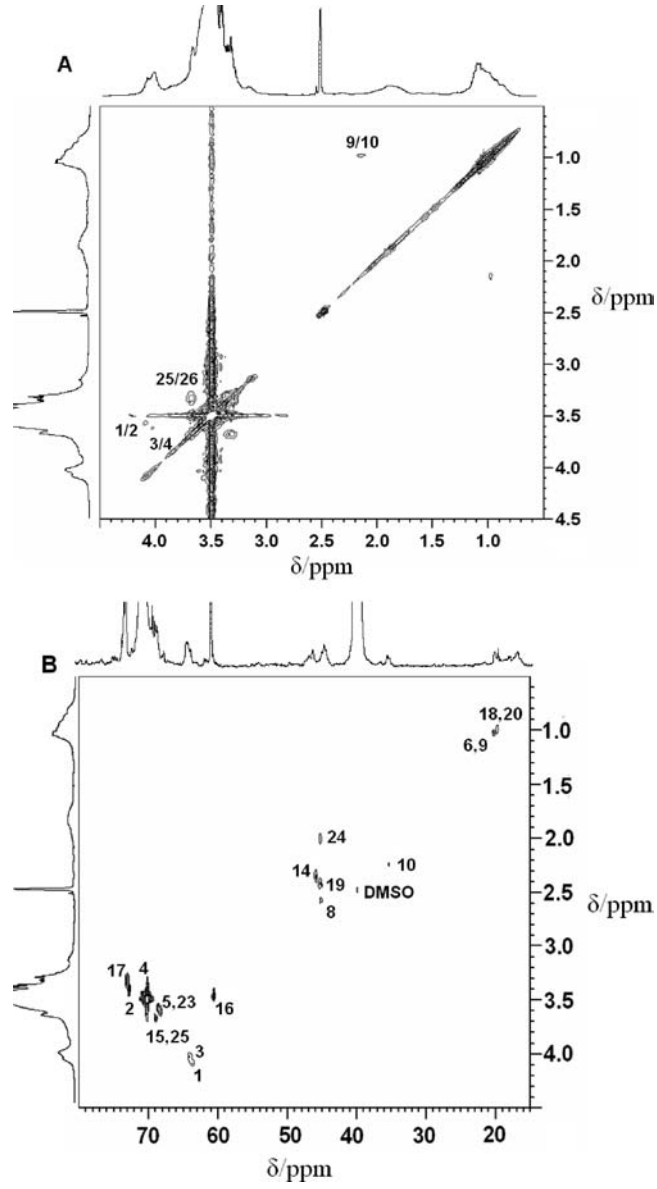


Figure 3. 2D NMR spectra of P1: (A) ^1H, ^1H-COSY spectrum, (B) ^{13}C, ^1H-HSQC spectrum.

medium was replenished with fresh DMEM after 48 h incubation. Then, 20 μL of 5 mg/mL MTT assay stock solution in PBS was added to each well. After incubating the cells for 4 h, the medium containing unreacted MTT was removed carefully. The obtained blue formazan crystals were dissolved in 200 μL per well DMSO, and the absorbance was measured in a VarioskanFlash at a wavelength of 570 nm.

RESULTS AND DISCUSSION

Synthesis and Characterization of LHPEG. On the basis of the molecular design, LHPEGs were synthesized through proton-transfer polymerization by oxyanionic initiation. GMA is a typical monomer for proton-transfer polymerization, because of the existence of two different reactive groups, namely, a vinyl group and an epoxy group. Both the epoxy group and the double bond of GMA could be polymerized through oxyanionic initiation (*50*). Correspondingly, the ester bond introduced in the backbone can make the polymer degradable in biological milieu. PEG was used as an oxyanionic active center to initiate the proton-transfer polymerization of GMA with the help of KH catalyst.

The detailed proton-transfer polymerization mechanism of LHPEG from PEG and GMA through oxyanionic initiation is shown in Scheme 1. The hydroxyl groups of PEG **1** are easily initiated by KH, producing the initiator **2** with the release of hydrogen gas (H_2). Because GMA has a vinyl group and an epoxy group, there are two possibilities for the reaction of **2** with GMA. **2** initiates the epoxy group of GMA leading to **3**, while **2** reacts with the vinyl group of GMA producing **6**. It has been extensively reported that the active anion center of the secondary alkoxide or carbonanion can transfter immediately to the more stable primary alkoxide through proton transfer (*51*−*53*). Thus, the intermidiate compounds **4**, **5**, and **7** are expected. Further polymerization of **3**, **4**, **5**, **6**, and **7** gives the LHPEG **8**. Highly viscous product was obtained after the polymerization was carried out in DMSO at 80 °C for 48 h. The reaction proceeded homogeneously, and no gelation took place throughout the polymerization. Table 1 summarizes the experimental conditions and corresponding characterization data.

Figure 1 displays the structural units of LHPEG synthesized from PEG and GMA. To confirm the existence of these structures, both ^{1}H and ^{13}C NMR experiments were performed. ^{1}H NMR spectra were used to investigate the conversion of GMA into the polymer (Figure 2A). The peaks at 6.05 and 5.70 ppm corresponding to the vinyl group of GMA and peaks at 3.23, 2.78, and 2.65 ppm corresponding to the epoxide group of GMA disappear completely in the ^{1}H NMR spectrum of LHPEG. As expected, a new signal around 1.04 ppm assigning to the methyl group of GMA units appears and the resonances around 2.50 and 1.84 ppm assigned to the methylene of GMA units are strengthened in the spectrum of LHPEG. These data indicate that the GMA monomer has been successfully converted to LHPEG polymer. Figure 2B,C gives a DEPT-135 spectrum to distinguish methylene and methane or methine carbons. The peaks 6, 9, 18, and 20 are assigned to the methyl groups from GMA units. To further verify the branched topology of the polymerized product, the two-dimensional NMR (2D-NMR) technique was used (*54*). Figure 3A,B gives the ^{1}H, ^{1}H-COSY and ^{13}C, ^{1}H-HSQC spectra, respectively. It can be found that 1-H/2-H, 3-H/4-H, 9-H/10-H, and 25-H/26-H are in different spin systems. On the basis of the information from the ^{1}H, ^{1}H-COSY and ^{13}C, ^{1}H-HSQC spectra, the detailed assignment is shown in Figure 3. According to the following equation proposed by Fréchet (*55*), the degree of branching (DB) for LHPEG can be determined

$$\mathrm{DB} = (D + T)/(D + T + L)$$

where D, T, and L represent the fractions of the dendritic, terminal, and linear units, respectively. Table 1 shows the DBs of the polymerized samples. The DBs of these polymers are at 0.57−0.65, suggesting the formation of long-chain hyperbranched products.

FTIR results provide the additional chemical structure information of LHPEG (Figure 4A). The strong absorption peak at 1092 cm^{-1} is attributed to the C−O−C stretching vibrations. The band at 1466 cm^{-1} results from the asymmetric deformation vibration of the $-CH_2-$ groups. The band around 2868 cm^{-1} corresponds to the $-CH_2-$ vibrations of PEG, while the broad O−H stretching vibration around 3494 cm^{-1} indicates the appearance of many hydroxyl groups. In contrast to PEG, an apparent strong ester carbonyl band at 1727 cm^{-1} emerges, confirming the presence of ester bonds in LHPEG. Furthermore, DSC analyses verify the hyperbranched structures of LHPEGs. As shown in Figure 4B, the DSC curve of PEG600 shows one melting endotherm at 20.9 °C. For LHPEGs, the introduction of branched GMA units weakens the regular stacking ability of PEG chains. Therefore, the melting endotherm decreases to 17.0, 15.0, and 13.3 °C for P3, P2, and P1, respectively. In the meantime, both the glass transition temperatures (T_g) at about −49 °C and the cold crystallization peak around −10 °C can be observed for all LHPEG samples. In addition, the molecular weights and PDI values of these polymers were measured by GPC, and the data are summarized in Table 1. In detail, the molecular weights of P1, P2, and P3 are 6600, 6200, and 5600 g/mol, with the PDI values of 3.02, 2.96, and 2.81, respectively. The real molecular weights of LHPEGs may be even larger than the values estimated by GPC analysis using linear PEG as the calibration, because dendritic polymers generally have smaller sizes than linear polymers with the same molecular weight and can hardly be expanded in solution (*56*). These results further testify to the successful preparation of LHPEGs.

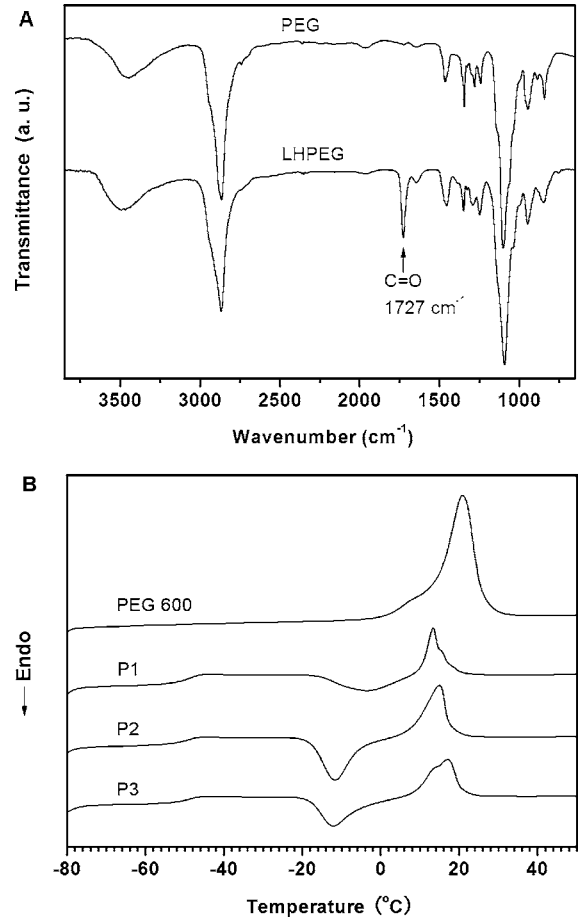


Figure 4. FTIR spectra of PEG and P1 (A); DSC curves of LHPEGs and PEG600 (B).

Degradation and Cytotoxicity. The biodegradability of polymeric materials is of great importance for biomedical applications. As is well-known, the degradation of polymers decreases the cytotoxicity and makes them easy to eliminate through the excretion pathway in vivo (*57*, *58*). Here, the degradation abilities of LHPEGs were determined by incubation at 37 °C in PBS to simulate the in vivo environment. Samples of the degradation products were extracted at appropriate time intervals and analyzed by the GPC technique. The GPC results of degraded polymers at different time points suggest that the ester bonds in the backbone of LHPEG are susceptible to hydrolysis at physiological conditions to form low molecular weight products (Figure S1 in Supporting Information).

The relative cytotoxicity of LHPEG was estimated by MTT assay and AO/EB double staining methods. NIH 3T3 cells were cultured for 24 h to permit cell attachment. After this time, the culture medium was removed and replaced with culture medium containing serial dilutions of LHPEG. The cells were grown

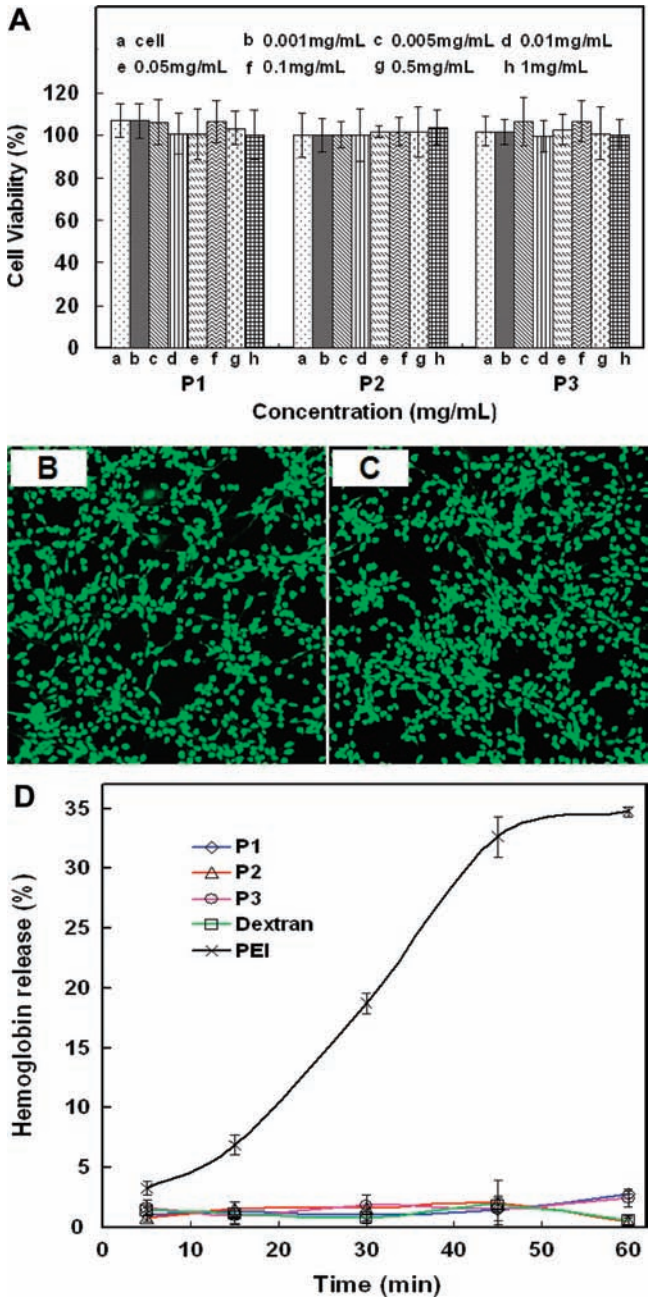


Figure 5. Cytotoxicity of LHPEGs determined by MTT assay against NIH 3T3 cells (A), fluorescence images of NIH 3T3 cells after incubation without (B) or with (C) 1 mg/mL LHPEG for 24 h (cells were stained by AO and EB), (D) hemolysis assay of 1 mg/mL LHPEG at different time intervals compared to PEI and dextran (Triton X-100 was used as a 100% hemolysis value).

for another 24 h. Figure 5A shows the cell viability after 24 h incubation with LHPEG at different concentrations from 0.001 to 1 mg/mL. The results demonstrate that NIH 3T3 cells cultured with LHPEG remain near 100% viability when the polymer concentration is up to 1 mg/mL. That is to say, the obtained LHPEG exhibits nontoxicity to NIH 3T3 cells. Furthermore, AO/EB double-staining results demonstrate the cell compatibility of LHPEG directly. Healthy cells have green nuclei and uniform chromatin with intact cell membrane. On the contrary, the cells undergoing apoptosis have orange nuclei and condensed chromatin with nuclear shrinkage. Moreover, the cells in necrosis or in the late stage of apoptosis have red nuclei with damaged cell membranes (*59*). As an example, the NIH 3T3 cells after incubation with the LHPEG of 1 mg/mL for 24 h are all healthy

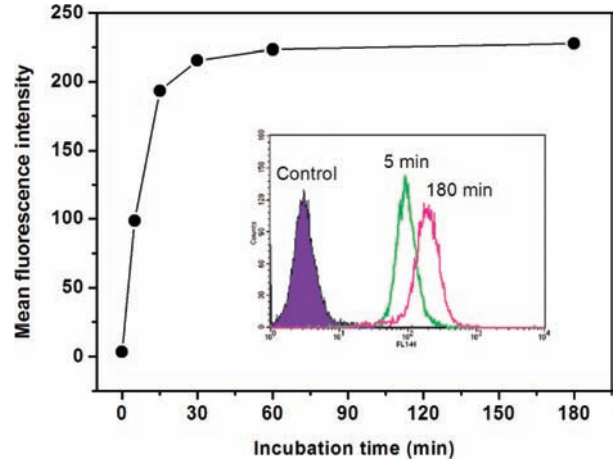


Figure 6. Cellular uptake of LHPEG-RB by Hela cells versus the incubation time by flow cytometry analysis. Insert is the representative flow cytometry histogram profiles of Hela cells cultured with LHPEG-RB for 5 and 180 min, respectively.

with green nuclei in comparison to the untreated cells, which indicates the good viability of cells (Figure 5B,C).

It is well-known that PEG can provide a long circulation time in blood, which makes it a good candidate for drug conjugates. The stability of LHPEG in physiological conditions was evaluated through red blood hemolysis assay, which also served as a model to assess cell membrane toxicity of LHPEG (*60, 61*). The P1, P2, and P3 were dissolved at a concentration of 2 mg/mL in PBS and added to an equal volume of 2% (w/v) red blood cell (RBCs) suspension in PBS. Dextran and PEI were used as reference controls, and Triton X-100 (1% v/v) was used as a 100% hemolysis value. All samples were stored at 37 °C for predetermined time intervals. Hemolysis was evaluated by measuring the amount of hemoglobin released in the supernatant at 545 nm. Under these conditions, LHPEGs show comparable hemoglobin release to dextran, which is significantly lower than the corresponding incubation time of PEI (Figure 5D). PEI causes a serious hemoglobin release, indicating that it damages the erythrocytes (*60*). When incubated for 1 h, PEI causes 80 times higher hemoglobin release than that of LHPEGs. The hemolysis assays demonstrate negligible hemolytic activity of LHPEG compared to those of blank values.

Cell Internalization Studies. To study the cellular transport of LHPEG, RB was used as a fluorescence probe and conjugated to the polymers. The cellular uptake of LHPEG was determined by measuring the intracellular fluorescence intensity using flow cytometry. Cells without any treatment were used as a blank control. It is obvious that the fluorescence is found within 5 min and the fluorescence intensity increases rapidly over a period of 15 min (Figure 6). After incubation for 15 min, the relative geometrical mean fluorescence intensity (GMFI) of polymer pretreated cells is about 55-fold that of nonpretreated cells. The fast enhancement of fluorescence signals indicates high cellular uptake of LHPEGs by Hela cells. With the incubation time increasing to 180 min, the GMFI of Hela cells increases from 3 to 228. Rejman examined the internalization rate of the fluorescent latex beads by murine melanoma cells, and found that smaller objects were taken up more rapidly (*62*). Thus, we speculate that the efficient intracellular uptake of LHPEGs can be attributed to the global molecular structure as well as the small hydrodynamic volume (*63*).

Moreover, the cellular uptake of LHPEGs by Hela cells was also evaluated by CLSM. Both the red fluorescence from RB and the blue fluorescence from DAPI were used to study the localization of LHPEG within the cells. First, Hela cells were incubated with RB-labeled LHPEGs for different time intervals.

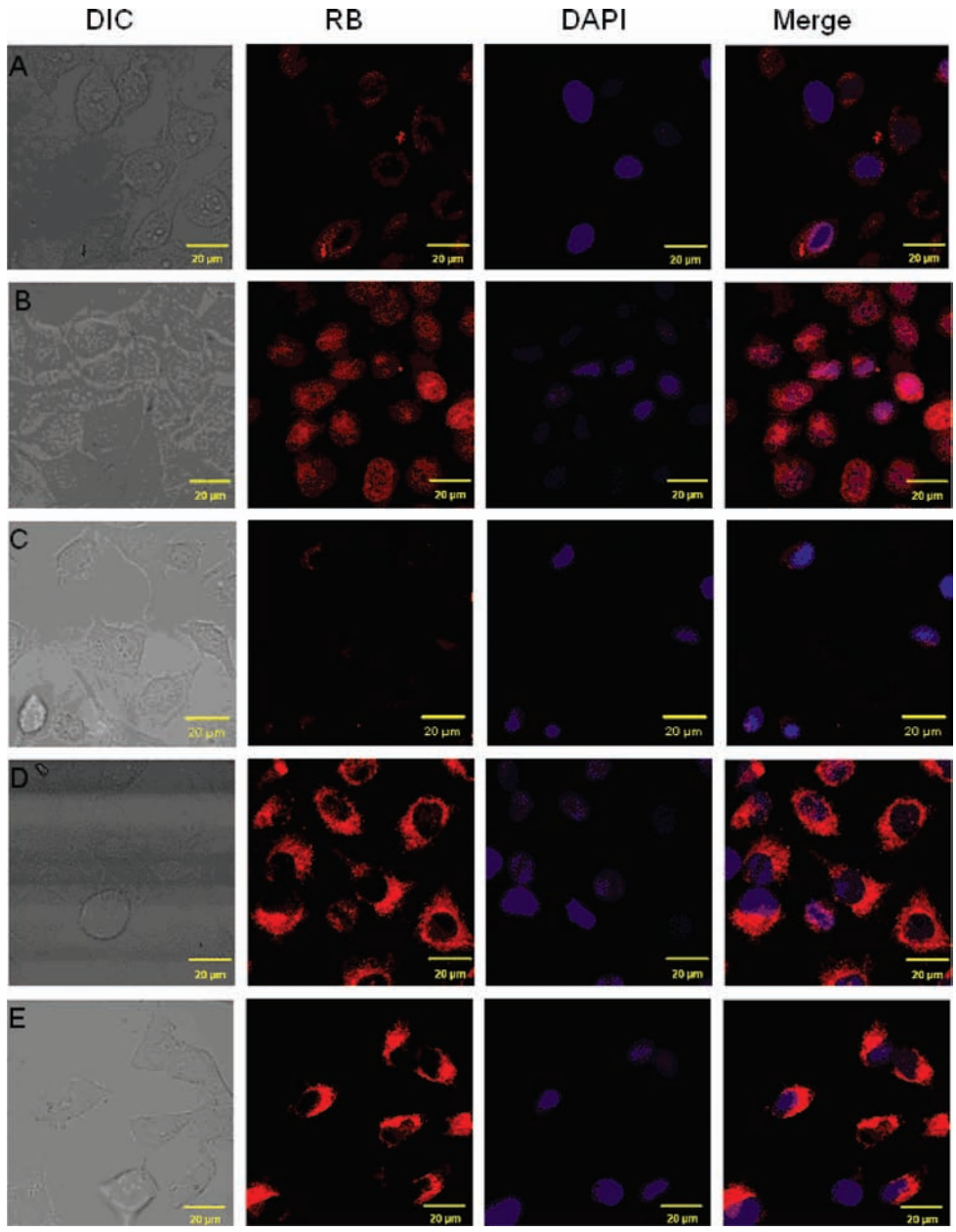
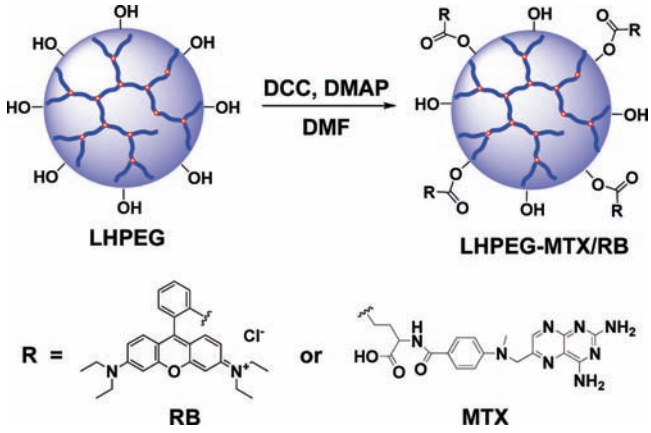


Figure 7. CLSM photos of Hela cells incubated with free RB or LHPEG-RB for different intervals. The pictures from left to right are differential interference contrast (DIC), RB fluorescence, DAPI fluorescence, and the merged image, respectively. (Cell nucleuses were stained with DAPI). (A) RB treated cells for 5 min, (B) RB treated cells for 60 min, (C) LHPEG-RB treated cells for 5 min, (D) LHPEG-RB treated cells for 60 min, (E) LHPEG-RB treated cells for 180 min.

Meanwhile, free RB was used as a control. Subsequently, the cell nucleus was stained by DAPI, and then the treated cells were fixed with formaldehyde. As shown in Figure 7A, red fluorescence was predominantly localized in the cytosol compared with blue nucleus after the cells incubated with free RB for 5 min. When prolonging the incubation time to 1 h, the localization of RB fluorescence in cells was changed and accumulated mainly in the nucleus (Figure 7B). On the other hand, the detectable red RB fluorescence of the cells incubated with LHPEG-RB for 5 min were similarly located in the perinuclear region instead of the nucleus (Figure 7C). However, with the incubation time increasing to 180 min, the red fluorescence of LHPEG-RB in cells still emerged at the cytosol rather than the nucleus. This result may be attributed to the endocytosis mechanism of the cellular internalization of LHPEG (*64*, *65*). Hence, the LHPEG can be efficiently transported by living cells.

Drug Conjugate and Tumor Cell Proliferation Inhibition. The good biocompatibility and efficient living cell transportation of LHPEGs encouraged us to further evaluate their potential as a polymeric drug carrier. Methotrexate (MTX), a folic acid antagonist, is a widely used agent for the treatment of certain human cancers (*66*). As displayed in Scheme 2, the LHPEG-MTX was prepared by coupling the end hydroxyl groups of LHPEG with the γ-carboxyl groups of MTX in the present of DCC and DMAP in dry DMF. The resulting conjugate was purified by repeatedly dissolving in methanol and precipitating in diethyl ether, and then exhaustive dialysis against water. NMR analysis was performed to evaluate the drug content of the final obtained conjugate (Figure 8). Calculating from the ^{1}H NMR spectrum of LHPEG-MTX, the MTX content was determined to be 20.5 wt % by calculating the relative intensity of the peak at 7.71 or 6.81 ppm (protons from the phenyl group in MTX) and the peak around 4.03 ppm (methylene groups in

Scheme 2. Synthetic Route of LHPEG-MTX/RB Conjugates



the end of the PEG chain). That is to say, one LHPEG carrier conjugates three MTX molecules. The drug content was also confirmed by GPC chromatography. As shown in Figure S2 in the Supporting Information, the molecular weight is increased by 1500 after the conjugation of MTX with LHPEG. The GPC analysis indicates that one LHPEG-MTX possesses about three MTX molecules. In addition, the drug content of the LHPEG-MTX was further measured by UV−vis spectra at 400 nm (Figure S3 in Supporting Information). According to the calibration curve of MTX in DMF, the drug content is determined to be about 20 wt % in LHPEG-MTX, which is consistent with the results of NMR and GPC techniques.

To demonstrate the therapeutic potential of LHPEG-MTX, in vitro evaluation was performed by MTT assay against Hela cells. It is worth pointing out that LHPEG shows nontoxicity against Hela cells with the concentration up to 1 mg/mL (Figure S4 in Supporting Information). To compare the cytotoxic activity of LHPEG-MTX with that of the free drug, MTX in the free form was used as a control. The Hela cell proliferation results are shown in Figure 9. It is found that the conjugated MTX dose required for 50% cellular growth inhibition (IC_{50}) is 20 μg/mL. This result indicates that LHPEG-MTX is able to enter the cell and produce the desired pharmacological action. On the other hand, the IC_{50} of free MTX is 5 μg/mL, which exhibits higher inhibition compared with conjugated MTX. It has been well-documented that the free drug is more potent than the conjugated drug (*67*). The antiproliferation effect of LHPEG-MTX might be attributed to the drug release from the conjugate in the course of incubation. Once the conjugate enters the cell, it

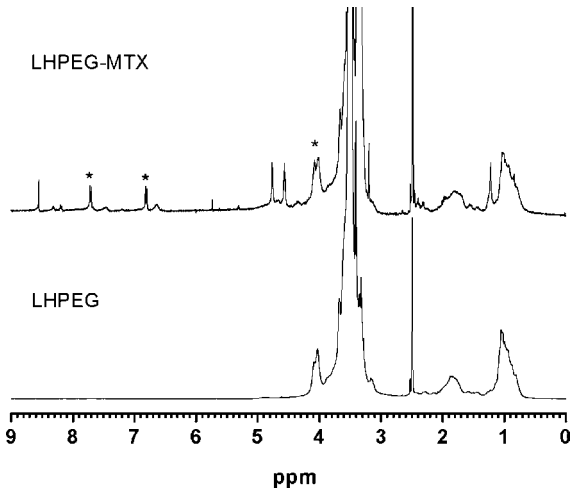


Figure 8. ^{1}H NMR spectra of LHPEG and LHPEG-MTX in DMSO-d_6.

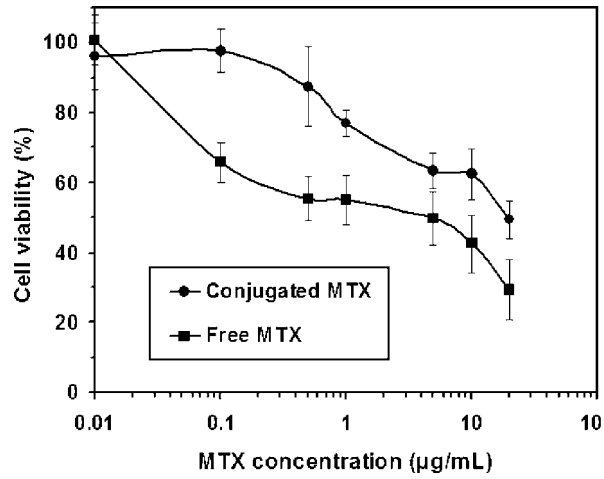


Figure 9. Inhibition proliferation of free MTX and conjugated MTX against Hela cells measured by MTT assay. Each data point represents an average of three measurements with standard error bars.

is conceivable that the acidic pH and the enzymes in the endosomes would eventually hydrolyze the ester bond and slowly release MTX, which provides the therapeutic effect (*68, 69*).

CONCLUSIONS

A series of novel long-chain hyperbranched poly(ethylene glycol)s were prepared in one pot through proton-transfer polymerization by oxyanionic initiation using PEG and GMA as monomer with the help of KH catalyst. The polymer structure and properties were analyzed by NMR, FTIR, GPC, and DSC techniques. The DBs of these polymers were at 0.57−0.65, and their molecular weights were around 6000 g/mol with PDI about 3.0. GPC measurements revealed that these polymers were hydrolyzed. DSC curves showed that LHPEGs had a T_g of about −49 °C and a T_m of ∼15 °C. Moreover, in vitro MTT and AO/EB double-staining assays demonstrated that HPEGs were nontoxic against NIH 3T3 cells even at a high dose of 1 mg/mL. Hemolysis assay confirmed that these polymers possessed negligible hemolytic activity comparable to those of blank values. That is to say, these HPEGs had no cell membrane toxicity. Furthermore, flow cytometry and CLSM analysis suggested that LHPEGs could be easily internalized by Hela cells and preferentially accumulated in the cytoplasm instead of the nucleus. In addition, conjugation of MTX to LHPEGs inhibited the proliferation of Hela cells. MTT assay indicated that the conjugated MTX dose required for 50% cellular growth inhibition against Hela cells was 20 μg/mL. As it combines the advantages of long-chain hyperbranched structure and PEG together, LHPEG provides a promising material for a drug carrier.

ACKNOWLEDGMENT

This work is sponsored by the National Natural Science Foundation of China (20974062, 50773037, 50633010) and National Basic Research Program 2009CB930400, the Fok Ying Tung Education Foundation (111048), Shuguang Program (08SG14), and Shanghai Leading Academic Discipline Project (Project Number: B202).

Supporting Information Available: Calculation of degree of branching, degradation rate of LHPEG, GPC curves, and UV−vis spectra of LHPEG and LHPEG-MTX, and in vitro cytotoxicity of LHPEG against Hela cells. This material is available free of charge via the Internet at http://pubs.acs.org.

LITERATURE CITED

(1) Ambade, A. V., Savariar, E. N., and Thayumanavan, S. (2005) Dendrimeric micelles for controlled drug release and targeted delivery. *Mol. Pharm. 2*, 264–272.

(2) Ke, W., Shao, K., Huang, R., Han, L., Liu, Y., Li, J., Kuang, Y., Ye, L., Lou, J., and Jiang, C. (2009) Gene delivery targeted to the brain using an angiopep-conjugated polyethyleneglycol-modified polyamidoamine dendrimer. *Biomaterials 30*, 6976–6985.

(3) Kojima, C., Kono, K., Maruyama, K., and Takagishi, T. (2000) Synthesis of polyamidoamine dendrimers having poly(ethylene glycol) grafts and their ability to encapsulate anticancer drugs. *Bioconjugate Chem. 11*, 910–917.

(4) Liu, M., Kono, K., and Fréchet, J. M. J. (2000) Water-soluble dendritic unimolecular micelles: their potential as drug delivery agents. *J. Controlled Release 65*, 121–131.

(5) Paleos, C. M., Tsiourvas, D., and Sideratou, Z. (2007) Molecular engineering of dendritic polymers and their application as drug and gene delivery systems. *Mol. Pharm. 4*, 169–188.

(6) Coombes, A. G., Tasker, S., Lindblad, M., Holmgren, J., Hoste, K., Toncheva, V., Schacht, E., Davies, M. C., Illum, L., and Davis, S. S. (1997) Biodegradable polymeric microparticles for drug delivery and vaccine formulation: the surface attachment of hydrophilic species using the concept of poly(ethylene glycol) anchoring segments. *Biomaterials 18*, 1153–1161.

(7) Vandermeulen, G. W. M., and Klok, H.-A. (2004) Peptide/Protein hybrid materials: enhanced control of structure and improved performance through conjugation of biological and synthetic polymers. *Macromol. Biosci. 4*, 383–398.

(8) Fleming, A. B., Haverstick, K., and Saltzman, W. M. (2004) *In vitro* cytotoxicity and in vivo distribution after direct delivery of PEG-camptothecin conjugates to the rat brain. *Bioconjugate Chem. 15*, 1364–1375.

(9) Kallinteri, P., Higgins, S., Hutcheon, G. A., St. Pourcain, C. B., and Garnett, M. C. (2005) Novel functionalized biodegradable polymers for nanoparticle drug delivery systems. *Biomacromolecules 6*, 1885–1894.

(10) Han, H. D., Shin, B. C., and Choi, H. S. (2006) Doxorubicin-encapsulated thermosensitive liposomes modified with poly(N-isopropylacrylamide-co-acrylamide): drug release behavior and stability in the presence of serum. *Eur. J. Pharm. Biopharm. 62*, 110–116.

(11) Al-Jamal, W. T., Al-Jamal, K. T., Cakebread, A., Halket, J. M., and Kostarelos, K. (2009) Blood circulation and tissue biodistribution of lipid-quantum dot (L-QD) hybrid vesicles intravenously administered in mice. *Bioconjugate Chem. 20*, 1696–1702.

(12) Pantos, A., Tsiourvas, D., Sideratou, Z., Paleos, C. M., Giatrellis, S., and Nounesis, G. (2004) Interactions of complementary PEGylated liposomes and characterization of the resulting aggregates. *Langmuir 20*, 6165–6172.

(13) Davis, F. F., Abuchowski, A., van Es, T., Palczuk, N. C., Chen, R., Sarcova, K., and Wieder, K. (1978) Enzyme-polyethylene glycol adducts: modified enzymes with unique properties. *Enzyme Eng. 4*, 169–173.

(14) Filpula, D., and Zhao, H. (2008) Releasable PEGylation of proteins with customized linkers. *Adv. Drug Delivery Rev. 60*, 29–49.

(15) Duncan, R. (2003) The dawning era of polymer therapeutics. *Nat. Rev. Drug Discovery 2*, 347–360.

(16) Harris, J. M., and Chess, R. B. (2003) Effect of PEGylation on pharmaceuticals. *Nat. Rev. Drug Discovery 2*, 214–221.

(17) Veronese, F. M., and Harris, J. M. (2008) Peptide and protein PEGylation III: advances in chemistry and clinical applications. *Adv. Drug Delivery Rev. 60*, 1–2.

(18) Tseng, Y. L., Liu, J. J., and Hong, R. L. (2002) Translocation of liposomes into cancer cells by cell-penetrating peptides penetratin and tat: a kinetic and efficacy study. *Mol. Pharmacol. 62*, 864–872.

(19) Maeda, T., and Fujimoto, K. (2006) A reduction-triggered delivery by a liposomal carrier possessing membrane-permeable ligands and a detachable coating. *Colloid Surf., B 49*, 15–21.

(20) Lee, L. S., Conover, C., Shi, C., Whitlow, M., and Filpula, D. (1999) Prolonged circulating lives of single-chain fv proteins conjugated with polyethylene glycol: a comparison of conjugation chemistries and compounds. *Bioconjugate Chem. 10*, 973–981.

(21) Chirila, T. V., Rakoczy, P. E., Garrett, K. L., Lou, X., and Constable, I. J. (2002) The use of synthetic polymers for delivery of therapeutic antisense oligodeoxynucleotides. *Biomaterials 23*, 321–342.

(22) Banerjee, P., Weissleder, R., Jr., and Bagdanov, A. (2006) Linear polyethyleneimine grafted to a hyperbranched poly(ethylene glycol)-like core: a copolymer for gene delivery. *Bioconjugate Chem. 17*, 125–131.

(23) Greenwald, R. B. (2001) PEG drugs: an overview. *J. Controlled Release 74*, 159–171.

(24) Duncan, R. (2006) Polymer conjugates as anticancer nanomedicines. *Nat. Rev. Cancer 6*, 688–701.

(25) Veronese, F. M., and Mero, A. (2008) The impact of PEGylation on biological therapies. *Biodrugs 22*, 315–329.

(26) Calderón, M., Quadir, M. A., Sharma, S. K., and Haag, R. (2010) Dendritic polyglycerols for biomedical applications. *Adv. Mater. 22*, 190–218.

(27) Tomalia, D. A., and Fréchet, J. M. J. (2002) Discovery of dendrimers and dendritic polymers: a brief historical perspective. *J. Polym. Sci., Part A: Polym. Chem. 40*, 2719–2728.

(28) Bosman, A. W., Janssen, H. M., and Meijer, E. W. (1999) About dendrimers: structure, physical properties, and applications. *Chem. Rev. 99*, 1665–1688.

(29) Gao, C., and Yan, D. Y. (2004) Hyperbranched polymers: from synthesis to applications. *Prog. Polym. Sci. 29*, 183–275.

(30) Voit, B. I., and Lederer, A. (2009) Hyperbranched and highly branched polymer architectures-synthetic strategies and major characterization aspects. *Chem. Rev. 109*, 5924–5973.

(31) Carlmark, A., Hawker, C., Hult, A., and Malkoch, M. (2009) New methodologies in the construction of dendritic materials. *Chem. Soc. Rev. 38*, 352–362.

(32) Saha, A., and Ramakrishnan, S. (2008) AB_2 + A type copolymerization approach for the preparation of thermosensitive PEGylated hyperbranched polymers. *Macromolecules 41*, 5658–5664.

(33) Hawker, C. J., Chu, F., Pomery, P. J., and Hill, D. J. T. (1996) Hyperbranched poly(ethylene glycol)s: a new class of ion-conducting materials. *Macromolecules 29*, 3831–3838.

(34) Esfand, R., and Tomalia, D. A. (2001) Poly(amidoamine) (PAMAM) dendrimers: from biomimicry to drug delivery and biomedical applications. *Drug Discovery Today 6*, 427–436.

(35) Wilms, D., Stiriba, S. E., and Frey, H. (2010) Hyperbranched polyglycerols: from the controlled synthesis of biocompatible polyether polyols to multipurpose applications. *Acc. Chem. Res. 43*, 129–141.

(36) Klier, J., Scranton, A. B., and Peppas, N. A. (1990) Self-associating networks of poly(methacry1ic acid-g-ethylene glycol). *Macromolecules 23*, 4944–4949.

(37) Mathura, A. M., Hammondsa, K. F., Klier, J., and Scrantona, A. B. (1998) Equilibrium swelling of poly(methacrylic acid-g-ethylene glycol) hydrogels effect of swelling medium and synthesis conditions. *J. Controlled Release 54*, 177–184.

(38) Hassan, C. M., Doyle, F. J., III, and Peppas, N. A. (1997) Dynamic behavior of glucose-responsive poly(methacrylic acid-g-ethylene glycol) hydrogels. *Macromolecules 30*, 6166–6173.

(39) Torres-Lugo, M., and Peppas, N. A. (1999) Molecular design and in vitro studies of novel pH-sensitive hydrogels for the oral delivery of calcitonin. *Macromolecules 32*, 6646–6651.

(40) Teertstra, S. J., and Gauthier, M. (2004) Dendrigraft polymers: macromolecular engineering on a mesoscopic scale. *Prog. Polym. Sci. 29*, 277–327.

(41) Muchtar, Z., Schappacher, M., and Deffieux, A. (2001) Hyperbranched nanomolecules: regular polystyrene dendrigrafts. *Macromolecules 34*, 7595–7600.

(42) Schappacher, M., Deffieux, A., Putaux, J. L., Viville, P., and Lazzaroni, R. (2003) Synthesis and characterization of water-soluble amphipatic polystyrene-based dendrigrafts. *Macromolecules 36*, 5776–5783.

(43) Bernard, J., Schappacher, M., Viville, P., Lazzaroni, R., and Deffieux, A. (2005) Synthesis and properties of PS-PEO core-shell amphiphilic dendrigrafts. *Polymer 46*, 6767–6776.

(44) Tomalia, D. A., Hedstrand, D. M., and Ferritto, M. S. (1991) Comb-burst dendrimer topology: new macromolecular architecture derived from dendritic grafting. *Macromolecules 24*, 1435–1438.

(45) Gauthier, M., and Moller, M. (1991) Uniform highly branched polymers by anionic grafting: arborescent graft polymers. *Macromolecules 24*, 4548–4553.

(46) Puskas, J. E., and Grasmuller, M. (1998) Star-branched and hyperbranched polyisobutylenes. *Macromol. Symp. 132*, 117–126.

(47) Hutchings, L. R., Dodds, J. M., and Roberts-Bleming, S. J. (2005) HyperMacs: highly branched polymers prepared by the polycondensation of AB_2 macromonomers, synthesis and characterization. *Macromolecules 38*, 5970–5980.

(48) Hutchings, L. R., Dodds, J. M., Rees, D., Kimani, S. M., Wu, J. J., and Smith, E. (2009) HyperMacs to hyperblocks: a novel class of branched thermoplastic elastomer. *Macromolecules 42*, 8675–8687.

(49) Hutchings, L. R., and Roberts-Bleming, S. J. (2006) DendriMacs. Well-defined dendritically branched polymers synthesized by an iterative convergent strategy involving the coupling reaction of AB_2 macromonomers. *Macromolecules 39*, 2144–2152.

(50) Jia, Z. F., Li, G. L., Zhu, Q., Yan, D. Y., Zhu, X. Y., Chen, H., Wu, J. L., Tu, C. L., and Sun, J. (2009) Hybrid polymerization of vinyl and hetero-ring groups of glycidyl methacrylate resulting in thermoresponsive hyperbranched polymers displaying a wide range of lower critical solution temperatures. *Chem.—Eur. J. 15*, 7593–7600.

(51) Chang, H. T., and Fréchet, J. M. J. (1999) Proton-transfer polymerization: a new approach to hyperbranched polymers. *J. Am. Chem. Soc. 121*, 2313–2314.

(52) Sunder, A., Quincy, M. F., Mülhaupt, R., and Frey, H. (1999) Hyperbranched polyether polyols with liquid crystalline properties. *Angew. Chem., Int. Ed. 38*, 2928–2930.

(53) Imai, T., Nawa, Y., Kitajyo, Y., Satoh, T., Kaga, H., Kaneko, N., and Kakuchi, T. (2005) Synthesis of hyperbranched polytetritol by ring-opening multibranching polymerizations of 2,3-anhydroerythritol and 2,3-anhydro-dl-threitol. *Macromolecules 38*, 1648–1654.

(54) Chen, L., Zhu, X. Y., Yan, D. Y., Chen, Y., Chen, Q., and Yao, Y. F. (2006) Controlling polymer architecture through host-guest interactions. *Angew. Chem., Int. Ed. 45*, 87–90.

(55) Hawker, C. J., Lee, R., and Fréchet, J. M. J. (1991) One-step synthesis of hyperbranched dendritic polyesters. *J. Am. Chem. Soc. 113*, 4583–4588.

(56) Fang, J. H., Kita, H., and Okamoto, K. I. (2000) Hyperbranched polyimides for gas separation applications. 1. Synthesis and characterization. *Macromolecules 33*, 4639–4646.

(57) Kima, T. H., Cook, S. E., Arote, R. B., Cho, M.-H., Nah, J. W., Choi, Y. J., and Cho, C. S. (2007) A degradable hyperbranched poly(ester amine) based on poloxamer diacrylate and polyethylenimine as a gene carrier. *Macromol. Biosci. 7*, 611–619.

(58) Arote, R. B., Lee, E. S., Jiang, H. L., Kim, Y. K., Choi, Y. J., Cho, M. H., and Cho, C. S. (2009) Efficient gene delivery with osmotically active and hyperbranched poly(ester amine)s. *Bioconjugate Chem. 20*, 2231–2241.

(59) Cohen, J. J. (1993) Apoptosis. *Immunol. Today 14*, 126–130.

(60) Reul, R., Nguyen, J., and Kissel, T. (2009) Amine-modified hyperbranched polyesters as non-toxic, biodegradable gene delivery systems. *Biomaterials 30*, 5815–5824.

(61) Nguyen, J., Steele, T. W. J., Merkel, O., Reul, R., and Kissel, T. (2008) Fast degrading polyesters as siRNA nano-carriers for pulmonary gene therapy. *J. Controlled Release 132*, 243–251.

(62) Rejman, J., Oberle, V., Zuhorn, I. S., and Hoekstra, D. (2004) Size-dependent internalization of particles via the pathways of clathrin- and caveolae-mediated endocytosis. *Biochem. J. 377*, 159–169.

(63) Liu, J. Y., Huang, W., Pang, Y., Zhu, X. Y., Zhou, Y. F., and Yan, D. Y. (2010) Hyperbranched polyphosphates for drug delivery application: design, synthesis, and in vitro evaluation. *Biomacromolecules 11*, 1564–1570.

(64) Kannan, S., Kolhe, P., Raykova, V., Glibatec, M., Kannan, R. M., Lieh-Lai, M., and Bassett, D. (2004) Dynamics of cellular entry and drug delivery by dendritic polymers into human lung epithelial carcinoma cells. *J. Biomater. Sci. Polym. Ed. 15*, 311–330.

(65) Perumal, O., Khandare, J., Kolhe, P., Kannan, S., Lieh-Lai, M., and Kannan, R. M. (2009) Effects of branching architecture and linker on the activity of hyperbranched polymer-drug conjugates. *Bioconjugate Chem. 20*, 842–846.

(66) Bertino, J. R. (1993) Ode to methotrexate. *J. Clin. Oncol. 11*, 5–14.

(67) Jesús, O. L. P. D., Ihre, H. R., Gagne, L., Fréchet, J. M. J., and Szoka, F. C., Jr. (2002) Polyester dendritic systems for drug delivery applications: *in vitro* and *in vivo* evaluation. *Bioconjugate Chem. 13*, 453–461.

(68) Khandare, J., Kolhe, P., Pillai, O., Kannan, S., Lieh-Lai, M., and Kannan, R. M. (2005) Synthesis, cellular transport, and activity of polyamidoamine dendrimer-methylprednisolone conjugates. *Bioconjugate Chem. 16*, 330–337.

(69) Pang, Y., Zhu, Q., Liu, J. Y., Wu, J. L., Wang, R. B., Chen, S. Y., Zhu, X. Y., Yan, D. Y., Huang, W., and Zhu, B. S. (2010) Design and synthesis of cationic drug carriers based on hyperbranched poly(amine-ester)s. *Biomacromolecules 11*, 575–582.

BC100325A

Supporting Information

Synthesis, Characterization, and *In Vitro* Evaluation of Long-Chain Hyperbranched Poly(ethylene glycol) as Drug Carrier

Yan Pang,[†§] Jinyao Liu,[†§] Jieli Wu,[‡] Guolin Li,[†] Ruibin Wang,[†,‡] Yue Su,[†] Peng He,[II] Xinyuan Zhu,[†,‡,*] Deyue Yan,[†] Bangshang Zhu[‡,*]

[§] These authors are joint first authors.

[†] *School of Chemistry and Chemical Engineering, Shanghai Jiao Tong University, 800 Dongchuan Road, Shanghai 200240, People's Republic of China*

[‡] *Instrumental Analysis Center, Shanghai Jiao Tong University, 800 Dongchuan Road, Shanghai 200240, People's Republic of China*

[II] *Department of Biological and Environmental Engineering, Cornell University, Ithaca, NY 14853*

Calculation of the degree of branching (DB) of LHPEG

It can be seen from Figure 1 that there exist ten structural units in LHPEG: four dendritic unit (D_1, D_2, D_3, and D_4), five linear units (L_1, L_2, L_3, L_4, and L_5) and one terminal unit. The DB can be determined by the following equation:

$$DB = (D + T) / (D + T + L)$$

where,

$$D = D_1 + D_2 + D_3 + D_4 = S_{C18} + S_{C20} + S_{C21} + S_{C24}$$

$$L = L_1 + L_2 + L_3 + L_4 + L_5 = S_{C3} + S_{C6} + S_{C9} + S_{C11} + S_{C16}$$

$$T = S_{C1}$$

therefore, the DBs of LHPEGs can be calculated in details by the following equation:

$$DB = (S_{C18} + S_{C20} + S_{C21} + S_{C24} + S_{C1}) / (S_{C18} + S_{C20} + S_{C21} + S_{C24} + S_{C1} + S_{C3} + S_{C6} + S_{C9} + S_{C11} + S_{C16})$$

where,

S_{CX} are the integrated areas of the carbon peaks (x = 1, 2…) as labeled in the Figure 1.

The calculated DB values of LHPEGs can be found in Table 1.

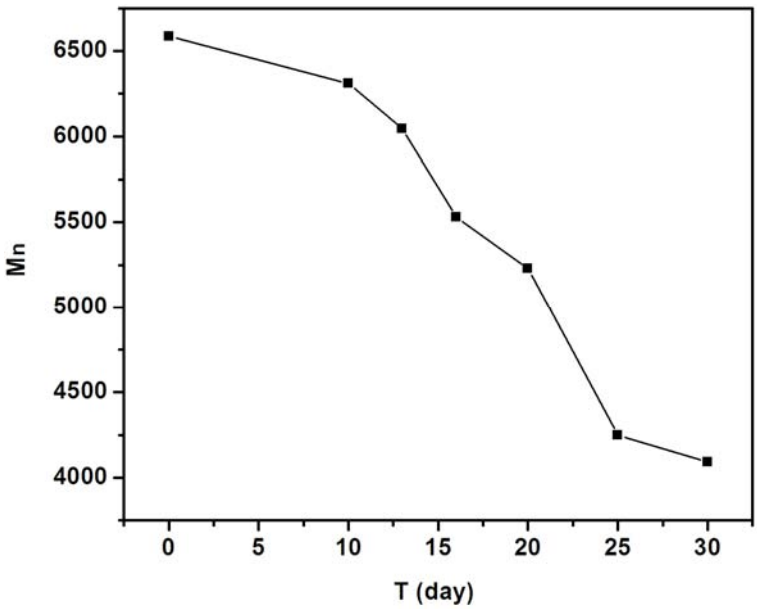


Figure S1. Molecular weight reduction of LHPEG as a function of degradation time.

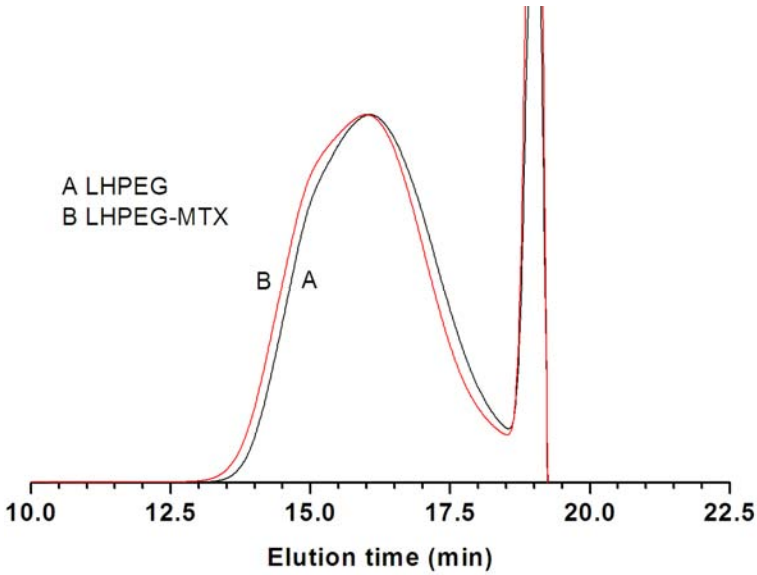


Figure S2. GPC curves of LHPEG (A) and LHPEG–MTX (B).

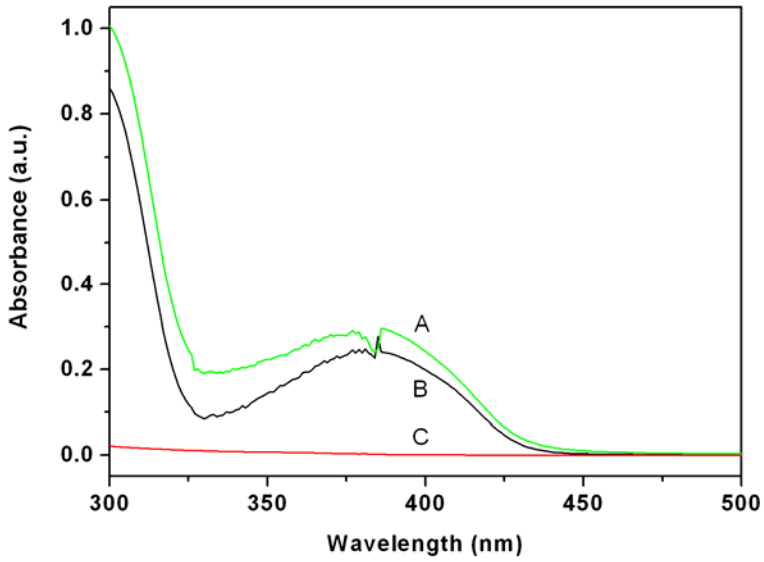


Figure S3. UV-vis spectra of LHPEG-MTX (A), MTX (B), and the mixture of LHPEG and MTX after dialysis (C).

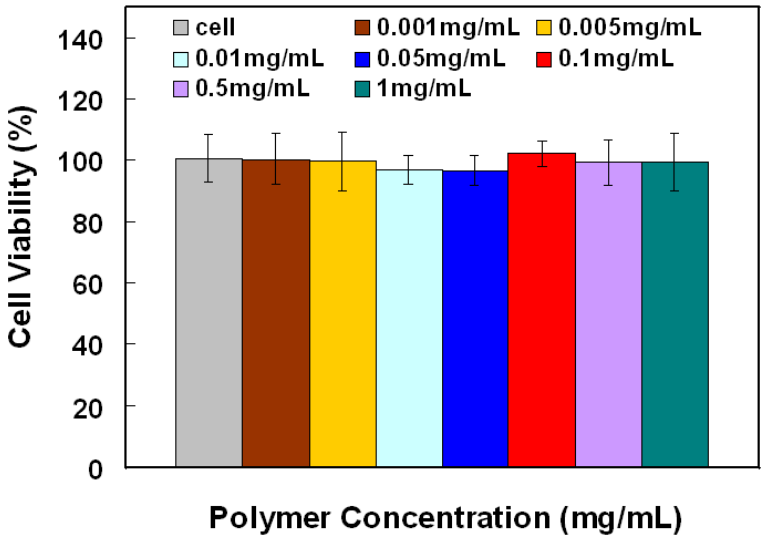


Figure S4. *In vitro* cytotoxicity of LHPEG determined by MTT assay against Hela cells.

Dual Sensing of Hairpin and Quadruplex DNA Structures Using Multicolored Peptide Nucleic Acid Fluorescent Probes

Girish Koripelly,[†] Kamel Meguellati,[†] and Sylvain Ladame*[,‡]

Institut de Science et d'Ingénierie Supramoléculaires (ISIS), CNRS UMR 7006, Université de Strasbourg, Strasbourg, France.
Received July 23, 2010; Revised Manuscript Received September 6, 2010

Synthesis of water-soluble 5-mer peptide nucleic acids (PNAs) functionalized at their 5′- and 3′-ends with two original precursors of pentamethine cyanine dye synthesis is reported. The successful use of these PNA probes for sensing DNA hairpin structures in vitro was also demonstrated where specific hairpin formation was associated with the appearance of a characteristic fluorescence signal at 660 nm. A comparative study between three different strategies where PNAs were targeting either the stem or the loop of the hairpin was carried out. Best sensitivity was obtained using PNA sequences complementary to the loop sequence and directing both functional moieties toward the base of loop. Unprecedented proof-of-concept for the simultaneous sensing of hairpin and quadruplex DNAs with a nonoverlapping two-color system (C3 and C5) is also demonstrated.

INTRODUCTION

Although the most abundant form of DNA in vivo is the double-stranded helical conformation reported for the first time in 1953 by Watson and Crick (*1*), it has been known for more than 50 years that nucleic acids can also adopt alternative (i.e., non B-DNA) secondary structures under physiological conditions. Such structures can be either single-stranded (e.g., hairpins, intramolecular G-quadruplexes, pseudoknots) or double-stranded (e.g., cruciforms, bimolecular G-quadruplexes) and have received increasing attention because of the role they were proposed to play in transcription regulatory mechanisms (*2*). For instance, it has been known for several decades that DNA sequences containing a high density of clustered guanines were able to adopt four-stranded secondary structures named guanine (G)-quadruplexes or tetraplexes in the presence of physiological cations, notably K^+ and Na^+ (Figure 1) (*3*−*7*). More recently, in silico studies have revealed the high prevalence of such G-rich DNA sequences throughout the human genome, particularly in gene promoter regions (*8*−*10*). Hairpin formation has also been demonstrated both in vitro and in vivo (*11*). Stem-loop hairpin structures are obtained by folding of a partially self-complementary or palindromic DNA sequence (Figure 1). Their presence in gene promoters (*12*) or near gene replication origins (*13*), for instance, strongly suggests that DNA hairpins could play a functional role in naturally occurring regulatory mechanisms of gene expression. For this reason, non-Watson−Crick DNA secondary structures represent attractive therapeutic targets to regulate the expression of specific genes via chemical or biochemical intervention. Successful examples of gene regulation with small molecules that bind to and stabilize hairpin or quadruplex DNA (or RNA) have been recently reported in the literature (*14*−*18*). Although these studies represent converging evidence that such structures do form in the context of the cell, there is still an urgent need for chemical probes capable of sensing the formation of nucleic acid structures both in vitro and in vivo.

There is currently a growing interest in the development of new fluorescent chemosensors based on supramolecular systems which have the ability to recognize and bind to a specific metabolite with high affinity. As a result of this interaction, the system re-equilibrates, thus leading to a change of the physical properties (i.e., changes in fluorescence intensity and/or fluorescence emission wavelength) of the medium. Since the 1960s, engineered DNA molecules have been used extensively as highly specific fluorescent probes in order to explore various biological processes (e.g., DNA transcription, DNA recombination) and more recently for genotyping applications. Among them, molecular beacons (MBs) have received particular attention because of their broad applications in modern bioresearch (*19*). Typically, MBs are DNA hairpin structures functionalized at their 5′- and 3′-ends with a fluorescence donor and a fluorescence acceptor. Binding of the MB to a DNA or RNA target, through sequence-specific hybridization, results in the opening of the MB, thus separating the fluorescence donor from its neighboring fluorescence acceptor. Other examples include the use of modified (e.g., fluorescently labeled) oligonucleotides or oligonucleotide mimics in oligonucleotide-templated reactions. In such systems, a specific reaction of dye formation occurs only upon hybridization of the probes to a complementary nucleic acid target. A characteristic fluorescent signal will then be emitted which can be directly linked to the detection of the

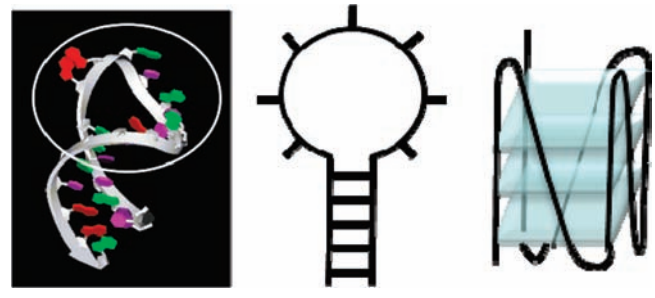


Figure 1. X-ray crystal structure and schematic representation of a DNA hairpin loop and schematic representation of a parallel-stranded intramolecular G-quadruplex (from left to right).

* To whom correspondence should be addressed. Institut de Science et d'Ingénierie Supramoléculaires (ISIS), Université de Strasbourg, CNRS UMR 7006, 8, allée Gaspard Monge, 67083 Strasbourg Cédex, France. Fax: (+33) 368855115, E-mail: s.ladame@isis.u-strasbg.fr.

[†] Both authors contributed equally to this work.

[‡] Current address: Imperial College London, Department of Bioengineering, Royal School of Mines Building, South Kensington Campus, London SW7 2AZ, U.K. E-mail: sladame@imperial.ac.uk, Phone: (+44) 2075945308.

10.1021/bc100335f © 2010 American Chemical Society
Published on Web 10/05/2010

targeted sequence and/or structure (*20*). Most recent reports of DNA-templated reactions applied to oligonucleotide sensing are based on the Staudinger reaction (*21*−*25*), aldol-type (*26*, *27*), organomercury-activated (*28*), or S_NAr (*29*) reactions.

Because peptide nucleic acids (*30*, *31*) offer the advantage of a higher stability, they have been recently used as an alternative to DNA for the design of highly specific nucleic acid probes (*32*−*36*). We recently reported the use of fluorogenic PNA probes for sensing G-quadruplex formation. Upon binding of both probes to the single-stranded flanking arms of a quadruplex, formation of a trimethine cyanine dye from two nonfluorescent precursors was templated (*27*). Herein, we describe the synthesis of a novel fluorescent Fisher's base aldehyde probe-head, its incorporation in a PNA strand, and the applications of the resulting fluorescently labeled probe for sensing hairpin DNA secondary structures. Reaction between this fluorescent Fisher's base aldehyde and a nonfluorescent indolenine molecule leads to the formation of a pentamethine cyanine dye (Cy5) absorbing and emitting at a significantly longer wavelength than its precursor. The system has been designed such that the Cy5 product forms solely upon simultaneous hybridization of both probes to either the loop or the stem of a unique hairpin DNA target. Therefore, hairpin formation will be directly linked to the appearance of a fluorescent signal at long wavelength ($\lambda_{em} > 650$ nm), well above the residual fluorescence of biological media, and above the fluorescence emission wavelength of most fluorescent products formed in oligonucleotide-templated reactions (*21*−*29*), including that previously reported by us (*27*). Simultaneous sensing of various DNA structures via a two-color (Cy3-Cy5) system will also be presented.

EXPERIMENTAL PROCEDURES

Ethyl 2-(3,3-Dimethyl-2-methyleneindolin-1-yl)-acetate (1). A mixture of 2,3,3-trimethyl-3*H*-indole (1.00 g, 6.28 mmol) and ethyl iodoacetate (1.61 g, 7.53 mmol) was heated at 80 °C for 5 h. After cooling the reaction mixture to room temperature, the red solid obtained was triturated with ether, filtered, and dried under vacuum. To the solid, 1 N NaOH (25 mL) was added and stirred for 1 h at RT. The reaction mixture was then extracted with CH_2Cl_2 (3 × 30 mL), and the combined organic layers were dried over Na_2SO_4, filtered, and concentrated in vacuo. The residue was purified by column chromatography on SiO_2 (PE/ether, 3:1; Rf = 0.48) to give the title compound (1.28 g, 83%) as a yellow oil. ^{1}H NMR (400 MHz, DMSO): δ = 7.16 (dd, J = 7.3, 0.9 Hz, 1H), 7.06 (td, J = 7.7, 1.2 Hz, 1H), 6.74 (td, J = 7.5, 0.6 Hz, 1H), 6.67 (d, J = 7.9 Hz, 1H), 4.39 (s, 2H), 4.10 (q, J = 7.2 Hz, 2H), 3.87 (d, J = 2.2 Hz, 1H), 3.81 (d, J = 2.0 Hz, 1H), 1.29 (s, 6H), 1.17 (t, J = 7.2 Hz, 3H) ppm. ^{13}C NMR (100 MHz, DMSO): δ = 168.6, 161.0, 145.4, 136.7, 127.3, 121.8, 118.8, 105.7, 74.8, 60.4, 43.6, 43.5, 29.6 (× 2) 14.1 ppm. HRMS (ESI) *m*/*z*: calcd for $C_{15}H_{19}NO_2$ $[M+H]^+$ 246.149; found 246.150.

2-(3,3-Dimethyl-2-methyleneindolin-1-yl)acetic Acid (2). To a solution of ethyl 2-(3,3-dimethyl-2-methyleneindolin-1-yl)acetate (1.30 g, 5.30 mmol) in ethanol (40 mL) was added 1 N NaOH solution (30 mL) at RT, and the mixture was stirred at the same temperature overnight. Later, the solvent was removed in vacuo, and the residue was dissolved in a minimum amount of water (15 mL) and then acidified to pH = 3 with 1 N HCl solution. The solution was concentrated, and the residue was dissolved in ethanol. The suspension was filtered, and this process was repeated at least two times. Finally, the filtrate was concentrated, and the residue was purified by column chromatography on SiO_2 (CH_2Cl_2/MeOH 8:2; Rf = 0.20) to give the title compound (860 mg, 75%) as a thick brown oil. ^{1}H NMR (400 MHz, DMSO): δ = 7.15 (dd, J = 7.3, 0.7 Hz, 1H), 7.06 (td, J = 7.7, 1.2 Hz, 1H), 6.73 (t, J = 7.2 Hz, 1H), 6.65 (d, J = 7.9 Hz, 1H), 4.26 (s, 2H), 3.85 (d, J = 2.0 Hz, 1H), 3.81 (d, J = 2.0 Hz, 1H), 1.28 (s, 6H) ppm, CO_2H signal not visible. ^{13}C NMR (100 MHz, DMSO): δ = 170.1, 160.8, 145.5, 136.7, 127.3, 121.7, 118.6, 105.6, 74.4, 43.6, 43.5, 29.7 (× 2) ppm. HRMS (ESI) *m*/*z*: calcd for $C_{13}H_{15}NO_2$ $[M+H]^+$ 218.116; found 218.119.

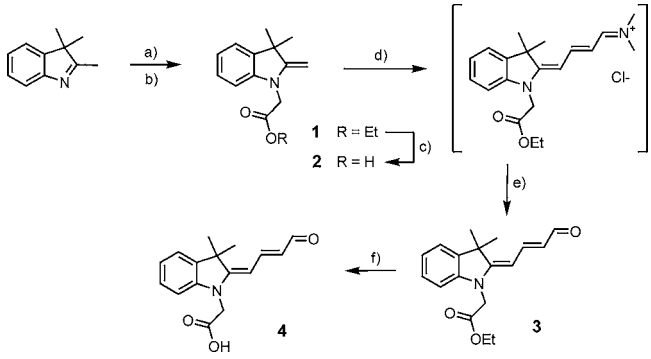
Ethyl 2-((2*E*)-2-((*E*)-3-Formylallylidene)-3,3-dimethylindolin-1-yl)acetate (3). Acetic anhydride (12.5 mL) was added dropwise to dimethylaminoacrolein (1.76 g, 1.78 mL, 17.8 mmol) and the mixture was stirred at RT for 15 min. Then, a solution of ethyl 2-(3,3-dimethyl-2-methyleneindolin-1-yl)acetate (1.25 g, 5.09 mmol) in CH_2Cl_2 (5 mL) was added dropwise. After stirring the reaction mixture for 2 d at RT, the solvent was removed in vacuo. The residue was dissolved in THF (30 mL), and a saturated solution of K_2CO_3 (60 mL) was added carefully. After stirring the mixture for 30 min at RT, the layers were separated and the aqueous layer was extracted with EtOAc (3 × 20 mL). The combined organic layers were dried over Na_2SO_4, filtered, and concentrated in vacuo. The residue was purified by column chromatography on SiO_2 (CH_2Cl_2/EtOAc 9.5:0.5; Rf = 0.20) to give the title compound (1.32 g, 86%) as a yellow oil. ^{1}H NMR (400 MHz, DMSO): δ = 9.46 (d, J = 8.3 Hz, 1H), 7.88−7.82 (m, 1H), 7.37 (d, J = 7.3 Hz, 1H), 7.19 (td, J = 7.8, 1.1 Hz, 1H), 6.98−6.93 (m, 2H), 5.81 (dd, J = 14.2, 8.3 Hz, 1H), 5.62 (d, J = 12.6 Hz, 1H), 4.70 (s, 2H), 4.14 (q, J = 7.3 Hz, 2H), 1.59 (s, 6H), 1.19 (t, J = 7.3 Hz, 3H) ppm. ^{13}C NMR (100 MHz, DMSO): δ = 192.4, 167.8, 164.6, 150.2, 143.4, 138.5, 127.8, 123.6, 121.9, 121.4, 107.8, 95.3, 61.0, 46.3, 43.7, 27.9 (× 2), 14.0 ppm. HRMS (ESI, positive mode) *m*/*z*: calcd for $C_{18}H_{21}NO_3$ $[M+H]^+$ 300.159; found 300.160.

2-((2*E*)-2-((*E*)-3-Formylallylidene)-3,3-dimethylindolin-1-yl)acetic Acid (4). To a solution of ethyl 2-((2*E*)-2-((*E*)-3-formylallylidene)-3,3-dimethylindolin-1-yl)acetate (300 mg, 1.00 mmol) in EtOH (2 mL) was added 1 N NaOH (1.5 mL) at RT and the mixture was stirred at the same temperature for 1.5 h. Later, the solvent was removed in vacuo, and the residue was dissolved in a minimum amount of water (3 mL) and then acidified to pH = 3 with 1 N HCl solution. The aqueous layer was extracted with EtOAc (4 × 10 mL). The combined organic layers were dried over Na_2SO_4, filtered, and concentrated in vacuo to give the title compound (260 mg, 96%) as a blue−green solid. The crude product was directly used for PNA coupling without further purification. ^{1}H NMR (400 MHz, DMSO): δ = 13.1 (br. s, 1H), 9.45 (d, J = 8.3 Hz, 1H), 7.88−7.81 (m, 1H), 7.36 (d, J = 7.0 Hz, 1H), 7.19 (td, J = 7.8, 1.1 Hz, 1H), 6.98−6.93 (m, 2H), 5.81 (dd, J = 14.2, 8.3 Hz, 1H), 5.62 (d, J = 12.6 Hz, 1H), 4.58 (s, 2H), 1.59 (s, 6H) ppm. ^{13}C NMR (100 MHz, DMSO): δ = 192.3, 169.1, 164.8, 150.4, 143.6, 138.6, 127.8, 123.3, 121.8, 121.3, 107.9, 95.1, 46.4, 43.7, 27.9 (× 2) ppm. HRMS (ESI, negative mode) *m*/*z*: calcd for $C_{16}H_{17}NO_3$ $[M-H]^-$ 270.112; found 270.110.

PNA Synthesis. PNAs were synthesized on a solid support using Fmoc chemistry. The PNA strand was cleaved from the resin with trifluoroacetic acid/triisopropylsilane/H_2O (95:2.5:2.5) solution and purified by HPLC. The final compounds were characterized by MALDI-TOF. **Pna1** *m*/*z*: $[M+H]^+$ calcd for $C_{87}H_{116}N_{38}O_{19}^+$ 1997.928, found 1997.718. **Pna2** *m*/*z*: $[M+H]^+$ calcd for $C_{88}H_{124}N_{39}O_{19}^+$ 2030.993, found 2030.923. **Pna3** *m*/*z*: $[M+H]^+$ calcd for $C_{84}H_{115}N_{36}O_{19}^+$ 1931.913, found 1932.082.

DNA Folding. Hairpin and quadruplex DNA folding was carried out by heating a DNA solution (5 μM) in potassium phosphate buffer (10 mM, pH 7.4 also containing 100 mM KCl) at 95 °C for 10 min and then letting it slowly cool down to room temperature over 6 h.

Scheme 1. Synthesis of 2-Methylene-Indolenin Derivative and Fischer's Base Aldehyde[a]



[a] Reagents and conditions: (a) ethyl iodoacetate, 80 °C, 5 h; (b) 1 N NaOH, EtOH, 25 °C, 1 h (83% over two steps); (c) 1 N NaOH, EtOH, 25 °C, 16 h (75%); (d) dimethylaminoacrolein, AcOH, CH_2Cl_2, 48 h; (e) sat. aq. K_2CO_3, THF, 25 °C, 1 h, (86% over two steps); (f) 1 N NaOH, EtOH, 25 °C, 1.5 h (96%).

Fluorescence Studies. Fluorescence emission spectra were recorded in quartz cells (500 μL with a 5 mm path length) at 20 °C on a Jobin Yvon Fluorolog 3.22 instrument. The excitation and emission bandwidths were fixed to 5 and 5 nm, respectively.

Ligation/Sensing Experiments. In a typical experiment, 500 μL of a mixture of **Pna1** (500 nM), **Pna2** (500 nM), and prefolded hairpin DNA (500 nM) in a potassium phosphate buffer (10 mM, pH 7.4 also containing 100 mM KCl) was prepared freshly in a fluorescence Quartz cuvette (5 mm path length) and kept sealed at 20 °C for the duration of experiment. Formation of the pentamethine cyanine dye product was then monitored by fluorescence spectroscopy (at t_0 and then every hour over 10 h).

Dual Sensing Experiments. After a screening of various concentrations of both DNA and PNA sequences, the following ratio 1:4:4:2:4 **Pna1**/**Pna2**/**Pna3**/**Hairp1a**/**Quad1** was found to give the optimal sensitivity and selectivity. Working with stoichiometric amounts of all PNA and DNA strands resulted in good sensitivity but lower selectivity (data not shown). Ligation experiments in the presence of both quadruplex and hairpin DNA were carried out in 500 μL quartz cuvettes by incubating a freshly prepared mixture of three PNA probes (**Pna1**−**3**) and two DNA targets (**Hairp1a** and **Quad1**) in potassium phosphate buffer.

RESULTS AND DISCUSSION

Design and Synthesis of the PNA Probes. Two 5-mer PNAs (**Pna1** and **Pna2**) were synthesized on solid support, which also contained two *ε*-*N*,*N*-dimethyl lysine residues to ensure solubility of both PNAs in water at near-physiological pH. These PNA probes were functionalized at their C- or N-terminus with two precursors for the synthesis of pentamethine cyanine dyes: *N*-alkyl-2,3,3-trimethylindolenine **2** and aldehyde **4**, respectively. Both precursors were synthesized from commercially available 2,3,3-trimethylindoline (Scheme 1).

Reaction of 2,3,3-trimethyl-3*H*-indole with ethyl iodoacetate gave the corresponding quarternized salt which was subsequently isomerized to 2-methylene-indolenin **1** via treatment with 1 N NaOH solution. Condensation of **1** with dimethylaminoacrolein in the presence of acetic anhydride provided the activated hemicyanine intermediate, which was then hydrolyzed into aldehyde **3** with a saturated K_2CO_3 solution. Final hydrolysis of the ethyl ester of compounds **1** and **3** using 1 N NaOH afforded both C5 precursors **2** and **4**, respectively. While indolenine **2** is nonfluorescent, aldehyde **4** emits maximally at 476 nm when excited at 410 nm. Reaction between compounds **2** and **4** leads to the formation of a symmetrical pentamethine cyanine dye (C5) characterized by its unique fluorescent properties (λ_{exc} = 625 nm, λ_{em} = 660 nm), very different from those of its two precursors.

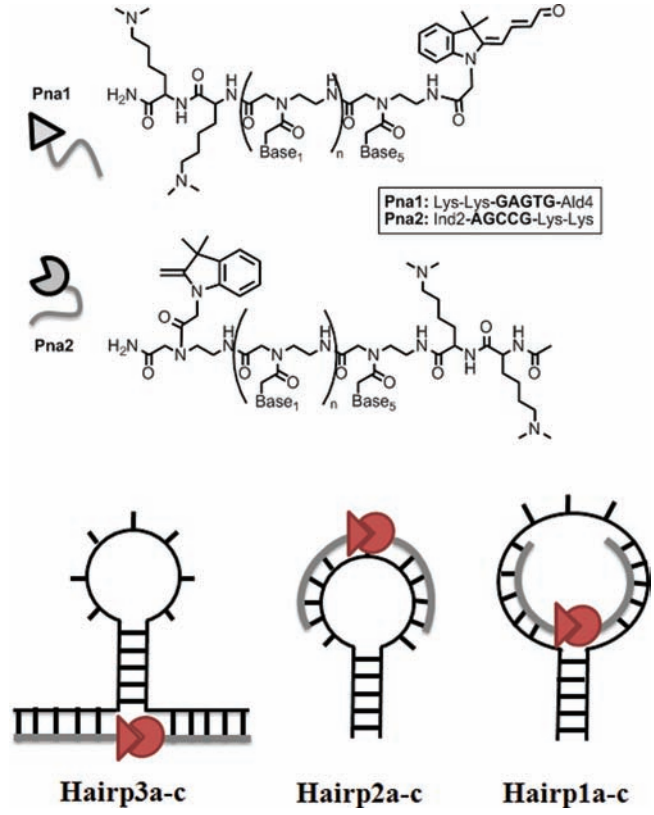


Figure 2. Structures of PNA probes **Pna1** and **Pna2** (top). Schematic representation of the hairpin DNA-templated synthesis of the pentamethine cyanine dye upon simultaneous hybridization of both PNA probes to either the hairpin flanking regions (**Hairp3a-c**) or the hairpin loop (**Hairp2a-c** and **Hairp1a-c**) (bottom).

Table 1. Oligonucleotide and PNA Sequences

	DNA[a] and PNA[b] sequences
Pna1	Lys(NMe_2)-Lys(NMe_2)-GAGTG-**Ald4**
Pna2	**Ind2**-AGCCG-Lys(NMe_2)-Lys(NMe_2)
Hairp1a	*CCTAGC*TCGGCTTTTTCTCACGCTAGG
Hairp1b	***CCTAG***CTTCGGTTTCTCACT*GCTAGG*
Hairp1c	***CCTAG***CTTTCGGCTCTCACTT*GCTAGG*
Hairp1d	***CCTAGC***TCGGCTTTTTCTCAC
Hairp2a	***CCTAGC***TTTCTCACTTTTCGGCTTT*GCTAGG*
Hairp2b	***CCTAGC***TTCTCACTTTTTCGGCTTT*GCTAGG*
Hairp2c	CCTAGCTTTTCTCACTTTCGGCTTT*GCTAGG*
Hairp3a	CTCACT*TGCGAT*ACTC*ATCGCA*TTCGGC
Hairp3b	CTCACTT*TGCGAT*ACTC*ATCGCA*TTTCGGC
Quad1	GCATCC**GGGC**GGGCGCGA**GGGAGGG**TTCGGC

[a] DNA sequences are given from the 5′- to 3′-end. [b] PNA sequences are given from the C-terminal to N-terminal end.

Although highly unfavorable in water, this aldolization−elimination reaction can be templated when carried out in a favorable chemical environment. **Pna1** and **Pna2** (see Figure 2 and Table 1 for structures and sequences) were synthesized on rink amide MBHA resin (Merck Biosciences, loading 0.56 mmol/g) using standard solid-phase Fmoc chemistry. They were subsequently purified by reversed-phase HPLC and characterized by MALDI.

5-mers PNA was chosen as the minimal length necessary for a full and sequence-specific PNA−DNA hybridization under near-physiological conditions. On the basis of the abundant literature on PNAs (*37*), it is anticipated that our short PNA/

DNA duplexes will have melting temperatures above 40 °C, indicating that almost all the PNA probes will be hybridized to the DNA target in the conditions of our experiments. It is also noteworthy that the presence of two Lysine residues is likely to increase even further the stability of the heteroduplex formed. In the case of unusually unstable (AT-rich) sequences, however, stability of the PNA−DNA heteroduplex would need to be increased. For instance, this could be achieved by increasing the length of the PNA strands, without interfering with the reaction of cyanine dye formation which occurs at the other end of the PNA.

Hairpin DNA Sensing. Reaction between stoichiometric amounts of **Pna1** and **Pna2** (500 nM each) was investigated in a 10 mM potassium phosphate solution (pH = 7.4) also containing 100 mM potassium chloride, in the presence and in the absence of various nucleic acid templates. In each case, reaction efficiency was determined by monitoring the formation of the pentamethine cyanine (product of the reaction between indolenine **2** and aldehyde **4**) by fluorescence spectroscopy over a ten hour period. In the absence of any template, and at a 500 nM concentration of both PNAs, only traces of the fluorescent cyanine dye product were ever detectable. We then investigated the possibility to use our PNA probes for sensing hairpin DNA structures. Three different strategies were developed that consisted of targeting either the hairpin single-stranded flanking arms or the hairpin loop (Figure 2). In the former approach, a hairpin structure was designed which contained two single-stranded flanking arms at its 3′- and 5′-ends, the sequences of which were complementary to those of **Pna1** and **Pna2**. This system (sequences **Hairp3a-c**, table1) was designed so that (i) **Pna1** and **Pna2** could hybridize in a sequence-specific manner to these two single-stranded arms and (ii) the reactive functionalities of both PNAs would be brought in close enough proximity to react with each other only when the hairpin was formed, while remaining separated in the absence of any DNA folding.

In the latter approach, a hairpin DNA structure was chosen that also contained a large central loop, the sequence of which included both **Pna1** and **Pna2** complementary sequences (Figure 2). Once again, only upon simultaneous hybridization of both PNA probes to their cDNA sequences located in the loop region, will the aldehyde be able to react with the 2-methylene-indolenine. Two systems were designed in which the cyanine dye was expected to form either at the center of the loop (sequences **Hairp2a-c**, Table 1) or at the intercept between the loop and the stem (sequences **Hairp1a-d**, Table 1). It is noteworthy that (i) all DNA sequences **Hairp1**−**3** were shown to form stable hairpin structures under the conditions of our experiment and in the absence of PNA probes, and (ii) DNA hairpins **Hairp1** and **Hairp2** were designed which contained larger loops than **Hairp3** in order to allow complete hybridization of both 5-mer PNAs to the hairpin loop.

The potential of **Hairp3a-c**, **Hairp2a-c**, and **Hairp1a-c** to serve as a DNA template for the reaction of cyanine dye formation was determined. Briefly, a stoichiometric mixture of **Pna1**, **Pna2**, and one hairpin DNA was reacted in potassium phosphate buffer at physiological pH, and the appearance of the cyanine dye product was monitored by fluorescence spectroscopy (λ_{exc} = 625 nm). As a control experiment, a reaction was carried out under the same conditions but lacking the DNA template. Interestingly, every hairpin DNA tested proved capable of significantly increasing the reaction efficiency, although at different levels depending on whether the PNA probes were targeting the loop or the stem of the hairpin (Figure 3). Moreover, as previously observed by us with other fluorogenic systems ((*27*) and unpublished data) and although no detectable fluorescence is observed in the absence of template (F_0 < 350),

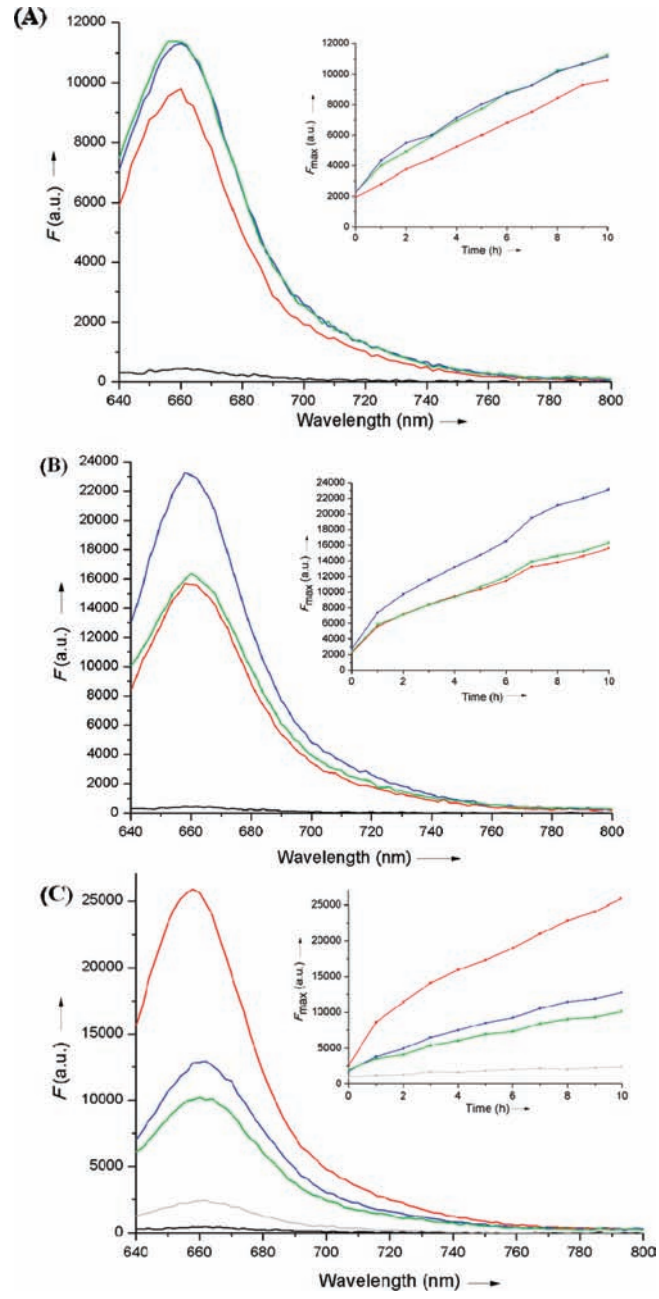


Figure 3. Fluorescence emission spectra of a stoichiometric mixture of **Pna1** and **Pna2** (500 nM each) measured after 10 h (λ_{exc} = 625 nm) in the absence (black) or in the presence of various DNA templates: (A) **Hairp3a** (red), **Hairp3b** (blue), and **Hairp3c** (green); (B) **Hairp2a** (red), **Hairp2b** (blue), **Hairp2c** (green); (C) **Hairp1a** (red), **Hairp1b** (blue), **Hairp1c** (green), **Hairp1d** (gray). Reaction time courses (maximum fluorescence intensity vs time) are also given as insets for each DNA templated reaction.

DNA-catalyzed reactions are all characterized by a fast and almost instantaneous appearance of fluorescence (F_0 > 6000) followed by a slower increase over 10−12 h. The kinetics of cyanine dye formation proved generally slow, the fluorescence intensity still rising even after 10 h, even in the presence of a template (Figure 3). However, the facts that (i) only residual amounts of fluorescent product form in the absence of DNA template (i.e., very low background signal) and (ii) a very fast initial phase of cyanine dye formation is observed in the presence of template make this chemistry suitable for the detection of DNA secondary structures. Indeed, a signal-to-noise ratio of ≥17 was obtained for all hairpin DNA-templated reactions after less than 10 min reaction.

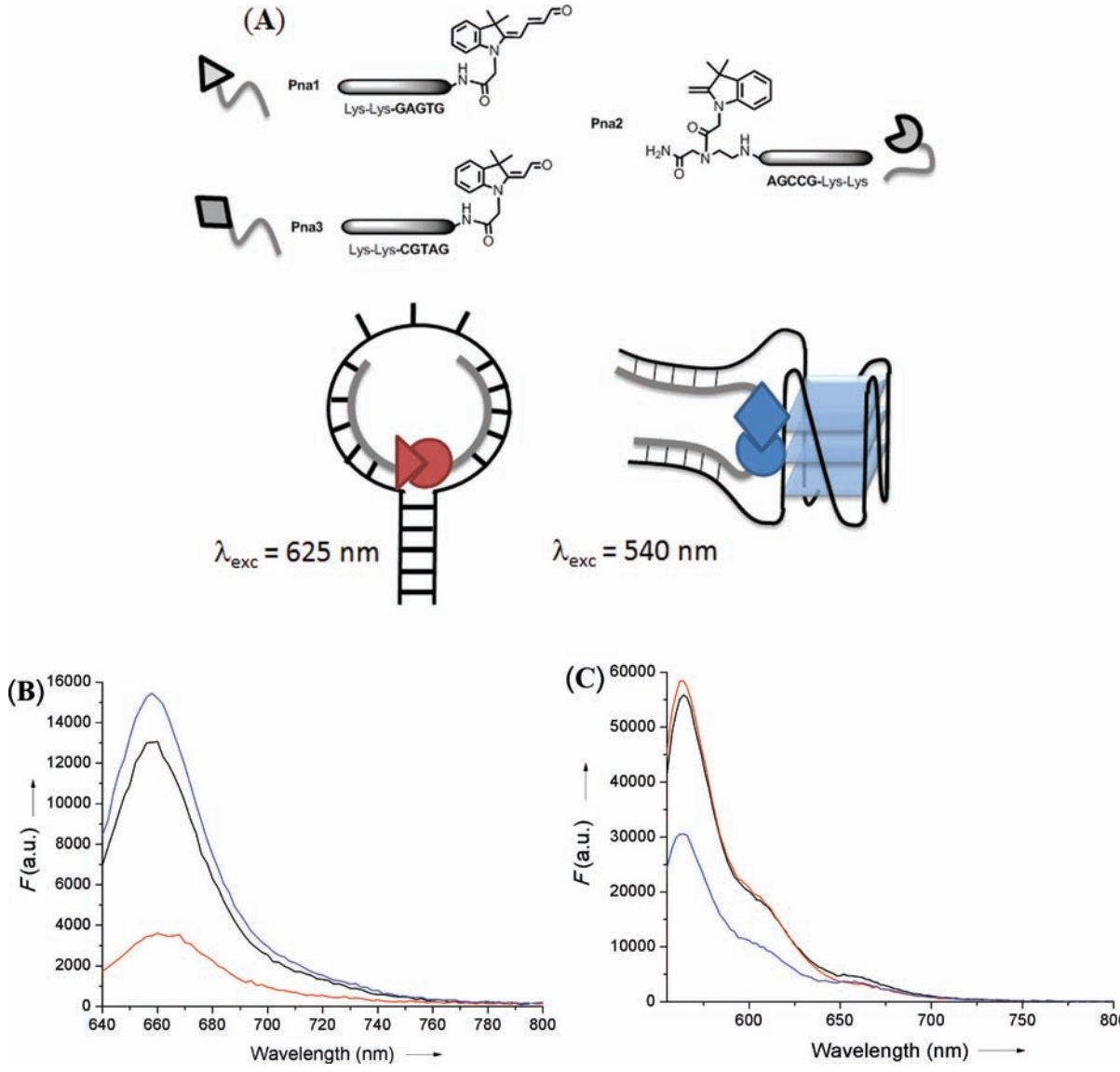


Figure 4. Schematic representation of the general system for sensing simultaneously hairpin and quadruplex DNA, based on a dual-color detection system (A). Fluorescence emission spectra (λ_{exc} = 540 nm) of a mixture of **Pna1** (250 nM), **Pna2** (1 μM), and **Pna3** (1 μM) in potassium phosphate buffer (10 mM, pH = 7.4 also containing 100 mM KCl) in the presence of 500 nM **Hairp1a** (blue), 1 μM **Quad1** (red), or a mixture of 500 nM **Hairp1a** and 1 μM **Quad1** (black). Excitation wavelengths were either λ_{exc} = 625 nm (B) or λ_{exc} = 540 nm (C). Emission spectra were recorded after 12 h incubation at room temperature.

The least effective templating effect was obtained when targeting the 3′ and 5′ single-stranded flanking ends of the hairpin (**Hairp3a**−**c**). This effect also proved almost independent of the number of nucleotides located between the PNA complementary sequences and the first nucleotide involved in the stem formation. Indeed, comparable fluorescence intensities were obtained from **Hairp3a**, **Hairp3b**, and **Hairp3c**, which contain a one-, two-, and three-nucleotide gap between the PNA/DNA duplex regions and the hairpin stem, respectively (Figure 3a).

Sensing hairpin formation proved, however, more efficient when both PNAs were directed against the hairpin loop, the amount of cyanine dye formed after 10 h of reaction being, for instance, twice as high with **Hairp1a** as with **Hairp3a**. Two slightly different approaches were considered for targeting hairpin loops, the reaction of cyanine dye formation taking place either at the center of the loop or at its base, in the vicinity of the stem. Both approaches proved equally effective (same fluorescence intensity at the maximum emission wavelength obtained after 10 h with **Hairp1a** and **Hairp2b**) although being highly dependent on the overall design. While a four-nucleotide gap between the functional ends of **Pna1** and **Pna2** led to the optimal reaction efficiency within the **Hairp2** series (**Hairp2b**, Figure 3b), hybridization of both PNAs starting from the first nucleotides constituting of the loop was found twice as effective as systems where **Pna1** and **Pna2** were separated further (**Hairp1a** versus **Hairp1b**,**c**, Figure 3c).

While **Hairp1a** and **Hairp2b** proved to be equally good templates for the aldolization−elimination reaction, they are based on two different strategies that can find distinct applications in modern bioresearch, in particular, for sensing hairpin DNA formation in vitro and maybe also in vivo. In order to demonstrate the strong link between hairpin formation and pentamethine cyanine dye formation, an analogue of **Hairp1a** was designed which was missing six nucleotides at its 3′-end in order to prevent hairpin formation. The ability of this new single-stranded DNA (so-called **Hairp1d**) to act as a template was investigated by fluorescence spectroscopy (gray curve, Figure 3c). Not surprisingly, the fluorescence intensity obtained with **Hairp1d** was ca. 10 times lower than that obtained with **Hairp1a**, thus demonstrating that the templating effect observed with the latter was indeed structure-specific.

Whether the hairpin remains "hairpin-like" or opens up upon hybridization of both PNAs to the DNA template remains to be demonstrated. **Hairp2** is likely to open after PNA ligation, as is commonly observed with MBs (thus forming a highly stable 10-mer PNA/DNA heteroduplex with single-stranded DNA flanking arms). In the case of **Hairp1** and **Hairp3**, however, the complex formed between the ligation product and the DNA template can be defined as a PNA/DNA hybrid three-way junction and could therefore be significantly more stable than the "open" structure. Additional structural studies will be required to further address this question.

Dual Hairpin + Quadruplex DNA Sensing Using a Dual-Color System. We recently demonstrated that two fluorogenic PNA probes (**Pna2** and **Pna3**, Figure 4a) could be used for sensing the formation of G-quadruplex DNA in vitro. The system was designed so that simultaneous and sequence-specific hybridization of both PNAs to a unique G-quadruplex-containing oligonucleotide were the only conditions inducing the formation of a fluorescent trimethine cyanine dye (λ_{em} = 563 nm) (*27*). Since the fluorescent properties of this trimethine cyanine dye were significantly different compared to those of **Pna1** aldehyde (λ_{em} = 476 nm) and to those of the pentamethine analogue formed when reacting **Pna1** with **Pna2** (λ_{em} = 660 nm), we reasoned that it should be possible to simultaneously detect the formation of both hairpin and quadruplex DNAs using a non-overlapping, two-color "Cy3-Cy5" system. The system was designed so that a unique nucleophilic PNA, **Pna2**, could potentially react with two electrophilic PNA aldehydes, **Pna1** and **Pna3**, to form a pentamethine (λ_{em} = 660 nm) and a trimethine (λ_{em} = 563 nm) cyanine dye, respectively. While **Pna1** and **Pna2** are directed against hairpin DNA **Hairp1a**, **Pna2** and **Pna3** are directed against quadruplex DNA **Quad1**. Hence, it was our expectation to be able to specifically correlate quadruplex and hairpin DNA formation with the appearance of characteristic fluorescence signals at λ_{em} = 563 nm and λ_{em} = 660 nm, respectively. In order to demonstrate the concept, a mixture of **Pna1** (250 nM), **Pna2** (1 μM), and **Pna3** (1 μM) was incubated under near-physiological conditions and in the presence of various DNA templates: (i) **Hairp1a** (500 nM), (ii) **Quad1** (1 μM), and (iii) a mixture of **Hairp1a** and **Quad1** (500 nM and 1 μM, respectively). In each case, the formation of the trimethine and pentamethine cyanine dyes were monitored by fluorescence spectroscopy (λ_{exc} = 540 and 625 nm, respectively) (Figure 4a). Under our experimental conditions, detection of hairpin DNA proved highly specific, even in the presence of an alternative DNA secondary structure. Indeed, comparable fluorescence intensities were obtained when using as a template either **Hairp1a** alone or a mixture of **Hair1a** and **Quad1**, while only residual fluorescence was detectable when using the quadruplex **Quad1** alone (Figure 4b).

Detection of quadruplex DNA in the presence of hairpin DNA also proved possible, the amount of trimethine cyanine dye formed decreasing by only <5% upon addition of competitor hairpin DNA (Figure 4c). However, significant background fluorescence (ca. 50%) was also obtained under our conditions, which could be interpreted as the result of a nonspecific formation of trimethine cyanine dye templated by hairpin DNA. So far, attempts to combine on a single oligonucleotide the quadruplex and hairpin forming sequences (both structures being separated by a polyT linker) in order to simultaneously detect both structures were unsuccessful due to high background signal, which is likely due to the formation of complex tertiary structures resulting in nonspecific reaction of dye (C3 and C5) formation.

CONCLUSION

Detection of nucleic acid secondary structures remains a key challenge for chemists due to their large abundance and structural diversity within the genome. Of particular interest are structures located in regions essential for DNA replication or transcription (e.g., in gene promoters) which could serve as therapeutic targets for regulating gene expression. Whether a DNA strand can potentially form into a hairpin or a quadruplex conformation based on the DNA primary sequence can now be easily predicted, and with reasonably good accuracy. However, whether these structures actually form (or not) depending on the context (in vitro or in vivo) or the experimental conditions remains much more challenging. Therefore, fluorescent probes capable of detecting the folding of specific nucleic acid sequences would represent an important way to validate the existence of such structures in vivo and also maybe to identify new targets. Herein, we reported three different strategies for sensing hairpin DNA formation by targeting either the loop or the stem with short PNAs functionalized at their 3′- or 5′-end with two precursors of a pentamethine cyanine dye. When working at low PNA concentrations (500 nM each), the aldolization−elimination reaction is highly unfavorable, thus resulting in no significant appearance of fluorescence. However, a significant increase (>50-fold) in fluorescence intensity can be obtained upon sequence-specific hybridization of both PNAs to either the loop or the stem of the hairpin target. Therefore, this PNA-based approach represents an original strategy for sensing hairpin DNA formation in vitro, the best sensitivity being obtained when targeting the hairpin loop with the cyanine dye forming in the vicinity of the hairpin stem (**Hairp1a**). Compared to other DNA-templated reactions described in the literature that also involve the formation of a fluorescent product, our system offers the significant advantages of (i) absorbing and emitting in the far-red part of the spectrum (λ_{em} = 660 nm), thus making it suitable for in vivo applications, and (ii) requiring no catalysis, thus making it biocompatible. It is also noteworthy that this unprecedented DNA-templated C5 synthesis can be orthogonal to the DNA-templated C3 synthesis recently reported by us (*27*), thus allowing simultaneous detection of at least two different structures within a two-color (C3−C5) system. Although such approach still requires optimization, we demonstrated that it was possible to use a combination of three PNA probes for sensing, within a mixture of hairpin and quadruplex DNA, either or both secondary structures. The development of PNA probes of increased specificity (e.g., longer PNAs) and higher sensitivity for in vivo applications is currently underway in our group.

ACKNOWLEDGMENT

The authors are very thankful to the Centre National de la Recherche Scientifique (CNRS) and the International Centre for Frontier Research in Chemistry (icFRC) for financial support.

LITERATURE CITED

(1) Watson, J. D., and Crick, F. H. C. (1953) Molecular structure of nucleic acids; a structure for deoxyribose nucleic acid. *Nature 171*, 737–738.
(2) Wadkins, R. M. (2000) Targeting DNA secondary structures. *Curr. Med. Chem. 7*, 1–15.
(3) *G.N. Parkinson Quadruplex Nucleic Acids* (2006) Neidle, S., and Balasubramanian, S., Eds; pp 1−30, RSC Biomolecular Sciences Publishing, Cambridge, UK.
(4) Huppert, J. L., and Balasubramanian, S. (2007) G-quadruplexes in promoters throughout the human genome. *Nucleic Acids Res. 35*, 406–413.
(5) Qin, Y., and Hurley, L. H. (2008) Structures, folding patterns, and functions of intramolecular DNA G-quadruplexes found in eukaryotic promoter regions. *Biochimie 90*, 1149–1171.

(6) Eddy, J., and Maizels, N. (2008) Conserved elements with potential to form polymorphic G-quadruplex structures in the first intron of human genes. *Nucleic Acids Res. 36*, 1321–1333.
(7) Verma, A., Yadav, V. K., Basundra, R., Kumar, A., and Chowdhury, S. (2009) Evidence of genome-wide G4 DNA-mediated gene expression in human cancer cells. *Nucleic Acids Res. 37*, 4194–4204.
(8) Wong, H. M., and Huppert, J. L. (2009) Stable G-quadruplexes are found outside nucleosome-bound regions. *Mol. BioSyst. 5*, 1713–1719.
(9) Panayotatos, N., and Fontaine, A. (1987) A native cruciform DNA structure probed in bacteria by recombinant T7 endonuclease. *J. Biol. Chem. 262*, 11364–11368.
(10) Varani, G. (1995) Exceptionally stable nucleic acid hairpins. *Annu. Rev. Biophys. Biomol. Struct. 24*, 379–404.
(11) Baker, E. S., Dupuis, N. F., and Bowers, M. T. (2009) DNA hairpin, pseudoknot, and cruciform stability in a solvent-free environment. *J. Phys. Chem. B 113*, 1722–1727.
(12) Dai, X., Greizerstein, M. B., Nadas-Chinni, K., and Rothman-Denes, L. B. (1997) Supercoil-induced extrusion of a regulatory DNA hairpin. *Proc. Natl. Acad. Sci. U.S.A. 94*, 2174–2179.
(13) Willwand, K., Mumtsidu, E., Kuntz-Simon, G., and Rommelaere, J. (1998) Initiation of DNA replication at palindromic telomeres is mediated by a duplex-to-hairpin transition induced by the minute virus of mice nonstructural protein NS1. *J. Biol. Chem. 273*, 1165–1174.
(14) Dervan, P. B., Poulin-Kerstien, A. T., Fechter, E. J., and Edelson, B. S. (2005) Regulation of gene expression by synthetic DNA-binding ligands. DNA binders and related subjects. *Top. Curr. Chem. 253*, 1–31.
(15) Caldarelli, S. A., Mehiri, M., Di Giorgio, A., Martin, A., Hantz, O., Zoulim, F., Terreux, R., Condom, R., and Patino, N. (2005) A cyclic PNA-based compound targeting domain IV of HCV IRES RNA inhibits in vitro IRES-dependent translation. *Bioorg. Med. Chem. 13*, 5700–5709.
(16) Bejugam, M., Sewitz, S., Shirude, P. S., Rodriguez, R., Shahid, R., and Balasubramanian, S. (2007) Trisubstituted isoalloxazines as a new class of G-quadruplex binding ligands: small molecule regulation of c-kit oncogene expression. *J. Am. Chem. Soc. 129*, 12926–12927.
(17) Waller, Z. A., Sewitz, S. A., Hsu, S. T., and Balasubramanian, S. (2009) A small molecule that disrupts G-quadruplex DNA structure and enhances gene expression. *J. Am. Chem. Soc. 131*, 12628–12633.
(18) Wu, P., Ma, D. L., Leung, C. H., Yan, S. C., Zhu, N., Abagyan, R., and Che, C. M. (2009) Stabilization of G-quadruplex DNA with platinum(II) Schiff base complexes: luminescent probe and down-regulation of c-myc oncogene expression. *Chem.—Eur. J. 15*, 13008–13021.
(19) Wang, K., Tang, Z., Yang, C. J., Kim, Y., Fang, X., Li, W., Wu, Y., Medley, C. D., Cao, Z., Li, J., Colon, P., Lin, H., and Tan, W. (2009) Molecular engineering of DNA: molecular beacons. *Angew. Chem., Int. Ed. 48*, 856–870.
(20) Ranasinghe, R. T., and Brown, T. (2005) Fluorescence based strategies for genetic analysis. *Chem. Commun.* 5487–5502.
(21) Cai, J., Li, X., Yue, X., and Taylor, J. S. (2004) Nucleic acid-triggered fluorescent probe activation by the Staudinger reaction. *J. Am. Chem. Soc. 126*, 16324–16325.
(22) Pianowski, Z. L., and Winssinger, N. (2007) Fluorescence-based detection of single nucleotide permutation in DNA via catalytically templated reaction. *Chem. Commun.* 3820–3822.
(23) Franzini, R. M., and Kool, E. T. (2008) 7-Azidomethoxycoumarins as profluorophores for templated nucleic acid detection. *ChemBioChem 9*, 2981–2988.
(24) Z.Pianowski, Z., Gorska, K., Oswald, L., Merten, C. A., and Winssinger, N. (2009) Imaging of mRNA in live cells using nucleic acid-templated reduction of azidorhodamine probes. *J. Am. Chem. Soc. 131*, 6492–6497.
(25) Furukawa, K., Abe, H., Hibino, K., Sako, Y., Tsuneda, S., and Ito, Y. (2009) Reduction-triggered fluorescent amplification probe for the detection of endogenous RNAs in living human cells. *Bioconjugate Chem. 20*, 1026–1036.
(26) Huang, Y., and Coull, J. M. (2008) Diamine catalyzed hemicyanine dye formation from nonfluorescent precursors through DNA programmed chemistry. *J. Am. Chem. Soc. 130*, 3238–3239.
(27) Meguellati, K., Koripelly, G., and Ladame, S. (2010) DNA-templated synthesis of trimethine cyanine dyes: a versatile fluorogenic reaction for sensing G-quadruplex formation. *Angew. Chem., Int. Ed. 49*, 2738–2742.
(28) Franzini, R. M., and Kool, E. T. (2008) Organometallic activation of a fluorogen for templated nucleic acid detection. *Org. Lett. 10*, 2935–2938.
(29) Shibata, A., Abe, H., Ito, M., Kondo, Y., Shimizu, S., Aikawa, K., and Ito, Y. (2009) DNA templated nucleophilic aromatic substitution reactions for fluorogenic sensing of oligonucleotides. *Chem. Commun.* 6586–6588.
(30) Nielsen, P. E., Egholm, M., Berg, R. H., and Buchardt, O. (1991) Sequence-selective recognition of DNA by strand displacement with a thymine-substituted polyamide. *Science 254*, 1497–1500.
(31) Egholm, M., Buchardt, O., Christensen, L., Behrens, C., Freier, S. M., Driver, D. A., Berg, R. H., Kim, S. K., Norden, B., and Nielsen, P. E. (1993) PNA hybridizes to complementary oligonucleotides obeying the Watson-Crick hydrogen-bonding rules. *Nature 365*, 566–568.
(32) Grossmann, T. N., and Seitz, O. (2009) Nucleic acid templated reactions: consequences of probe reactivity and readout strategy for amplified signaling and sequence selectivity. *Chem.—Eur. J. 15*, 6723–6730.
(33) Hansen, M. E., Bentin, T., and Nielsen, P. E. (2009) High-affinity triplex targeting of double stranded DNA using chemically modified peptide nucleic acid oligomers. *Nucleic Acids Res. 37*, 4498–4507.
(34) Wojciechowski, F., and Hudson, R. H. (2009) Peptide nucleic acid containing a meta-substituted phenylpyrrolocytosine exhibits a fluorescence response and increased binding affinity toward RNA. *Org. Lett. 11*, 4878–4881.
(35) Socher, E., Jarikote, D. V., Knoll, A., Röglin, L., Burmeister, J., and Seitz, O. (2008) FIT probes: peptide nucleic acid probes with a fluorescent base surrogate enable real-time DNA quantification and single nucleotide polymorphism discovery. *Anal. Biochem. 375*, 318–330.
(36) Oquare, B. Y., and Taylor, J. S. (2008) Synthesis of peptide nucleic acid FRET probes via an orthogonally protected building block for post-synthetic labeling of peptide nucleic acids at the 5-position of uracil. *Bioconjugate Chem. 19*, 2196–2204.
(37) Sugimoto, N., Satoh, N., Yasuda, K., and Nakano, S. (2001) Stabilization factors affecting duplex formation of peptide nucleic acid with DNA. *Biochemistry 40*, 8444–8451.

BC100335F

New Unsymmetrical Bolaamphiphiles: Synthesis, Assembly with DNA, and Application for Gene Delivery

Namrata Jain, Youri Arntz, Valérie Goldschmidt, Guy Duportail, Yves Mély, and Andrey S. Klymchenko*

Laboratoire de Biophotonique et Pharmacologie, UMR 7213 CNRS, Université de Strasbourg, Faculté de Pharmacie, 74, Route du Rhin, 67401 ILLKIRCH Cedex, France. Received July 23, 2010; Revised Manuscript Received September 20, 2010

The success in gene therapy relies strongly on new efficient gene delivery vectors. Nonviral vectors based on lipids and polymers constitute an important alternative to the viral vectors. However, the key problem with these vectors is the poor structural control of their DNA complexes. In the present work, following new design we synthesized unsymmetrical bolaamphiphiles, molecules bearing neutral sugar (gluconic acid) and dicationic ornithine head groups connected by different long hydrophobic spacers. Within this design, a positively charged headgroup is expected to bind DNA, the hydrophobic spacer is to drive the formation of a monolayer membrane shell around DNA, while the neutral group is to be exposed outside of the complex. Our fluorescence and gel electrophoresis data showed that self-assembly of bolas and their interaction with DNA depend strongly on the bola structure. The size of bola/DNA complexes (bolaplexes) estimated from dynamic light scattering data was ~100 nm at low N/P (cationic nitrogen/DNA phosphate molar ratio), while at higher N/Ps it was significantly larger due to neutralization of their surface charge. Atomic force microscopy studies revealed nanostructural rod-shaped or spherical morphology of the bolaplexes. Transfection efficiency of the bolaplexes in vitro was significant when either DOPE or chloroquine were used as helping agents, suggesting that the key barrier for their internalization is the endosomal escape. Finally, all bolas showed low cytotoxicity (cell viability >80%). The present results show that bolas are prospective candidates for construction of nonviral gene delivery vectors. We believe that further optimization of polar head groups and a hydrophobic spacer in the bolas will lead to vectors with controlled small size and high transfection efficiency.

INTRODUCTION

The vast majority of natural and synthetic lipids studied so far are "monopolar" amphiphiles, that is, molecules presenting one polar headgroup and generally two hydrophobic chains. However, bipolar amphiphiles, which are analogues of lipids presenting polar groups at the two opposite sides of the hydrophobic chain(s), so-called bolaamphiphiles (bolas), became the matter of intensive research only in the recent years (*1*). A remarkable feature of bolas is that in contrast to bilayer membranes formed by lipids they can form monolayer membranes (Figure 1), having bolas with membrane-spanning hydrophobic chains, which are believed to be responsible for enhanced physical stability of bola membranes (*1, 2*). In nature, they are mainly present in archaebacteria and ensure the integrity of the bacterial membrane at high temperature (90 °C) and low pH (1−1.5) (*3, 4*). Membranes made from synthetic bolas, forming either nanotubes or vesicles, can also show an exceptional stability, some of them being stable even in the dry phase (*5, 6*) or in some organic solvents (*7*). Unsymmetrical bolas, bearing two different polar head groups, assembled in a parallel fashion can form asymmetric membranes, so that the two opposite sides of the monolayer membrane present different functional groups (Figure 1) (*5, 6*). One of the attractive applications of bolas, which is still in its infancy stage, is gene delivery, a domain for which "monopolar" cationic lipids and other cationic agents are currently maintaining a dominant position.

Gene delivery, which is a main concern in gene therapy, relies heavily on development of new delivery vectors. Nonviral vectors based on lipids are highly attractive, since they can deliver large quantities of genetic information and are weakly immunogenic (*8*). A variety of cationic lipids for gene delivery has been developed in recent decades (*8*−*19*). Their complexes with DNA (lipoplexes) show high transfection efficiency in vitro, though their application for gene therapy in vivo remains a challenge. One of the key problems of cationic lipids is the poor structural control of their lipoplexes (*10, 20*). Indeed, symmetric lipid bilayers made of cationic lipids interact with DNA by forming infinite sandwich-like structures of high polydispersity (Figure 1) (*10*).

In this respect, unsymmetrical bolas bearing positively charged and neutral head groups could be an attractive alternative to the cationic lipids. These molecules could generate asymmetric membranes (in form of vesicles or nanotubes) having positively charged inner and neutral outer surfaces. In such a case, the inner membrane surface can be used to wrap the DNA molecule (Figure 1), while the outer neutral membrane surface, being inert to DNA, would prevent further oligomerization of the complex and could be utilized for efficient exposure of the biological signal for specific targeting. The examples of successful application of bolas for gene delivery, which has been shown only in the recent years, include synthetic unsymmetrical bolas (*21*−*25*) and archaebacteria-derived lipids (*26, 27*). Among unsymmetrical bolas, the most promising were those bearing a sugar (gluconic or lactonic acid) residue on one side and mono- or oligo-cationic ammonium-based group on the other (*21, 23*). Moreover, the galactose-bearing bolas showed some specificity to HepG2 cell line, expressing a galactose receptor of endocytosis (*21, 22*).

In the present work, three new bolaamphiphiles were synthesized, bearing neutral sugar and dicationic ornithine head groups, connected by different hydrophobic spacers. We showed

* To whom correspondence should be addressed. E-mail: andrey.klymchenko@unistra.fr. Fax: +33 368 854313. Tel: +33 368 854255.

10.1021/bc100334t © 2010 American Chemical Society
Published on Web 10/14/2010

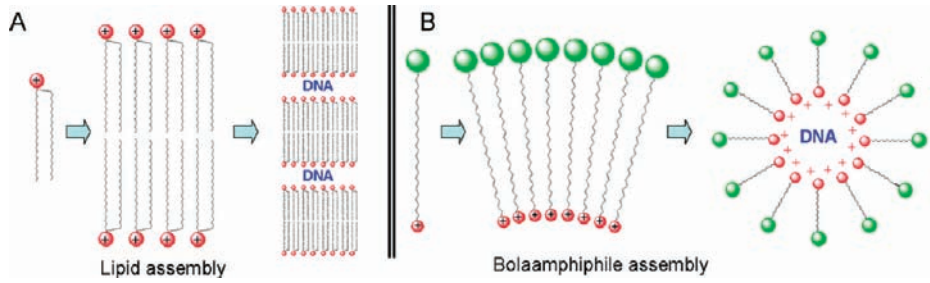


Figure 1. Lipids and bolaamphiphiles assembly with DNA. (A) Schematic presentation of bilayers formed from cationic lipids and further formation of DNA complexes, so-called lipoplexes. (B) Assembly of bolaamphiphiles into asymmetric membranes and formation of DNA complexes, so-called bolaplexes.

that the nature of spacer defines the bola self-assembly, the interaction with DNA and the morphology of the obtained complexes. Moreover, some bolas can transfect efficiently COS-7 cells in the presence of either a helper lipid (DOPE) or an endosomolytic reagent (chloroquine) (*28*). The latter indicates that the key barrier for gene delivery with the present bolas resides in the endosomal escape. This work presents new bolaamphiphile-based nonviral vectors and provides insights for further improvements of their efficiency.

MATERIALS AND METHODS

All chemicals and solvents for synthesis were purchased from Sigma-Aldrich. Mass spectra were measured using Mass Spectrometer Mariner System 5155. LC-MASS was performed on Agilent, 1956 B/MSD. ^{1}H NMR spectra were recorded on Bruker 300 MHz spectrometer.

***N*-Boc-4-aminophenol (1).** 4-Aminophenol (4 g, 36.7 mmol) and Boc_2O (8 g, 36.7 mmol) were dissolved in 30 mL of THF and left stirring overnight. Then 100 mL of water was added and the product was extracted with ethyl acetate (3 × 50 mL) and further dried with sodium sulfate. After solvent evaporation in vacuo, the crude product **1** was used without further purification.

16-(4-tert-Butoxycarbonylaminophenoxy)-hexadecanoic Acid Methyl Ester (2). Boc-protected 4-aminophenol (**1**) (1.8 g, 8.6 mmol) and 16-bromohexadecanoic acid methyl ester (3 g, 8.6 mmol, prepared by methylation of the acid in methanol and thionyl chloride) were dissolved in 10 mL of DMF and supplemented with 1.8 g (13 mmol) of potassium carbonate. After 12 h of stirring at room temperature (RT), the solution was poured in water (50 mL) and the product was extracted with dichloromethane (3 × 30 mL) and dried with sodium sulfate. Then the solvent was removed and the product **2** (1.6 g, 40%) was crystallized from ethanol. ^{1}H NMR ($CDCl_3$, 300 MHz): δ 7.24 (d, 2H), 6.82 (d, 2H), 6.4 (s, 1H), 3.91 (t, 2H), 3.67 (s, 3H), 2.31 (t, 2H), 1.82−1.58 (m, 4H), 1.55−1.48 (m, 9H), 1.46−1.2 (m, 24H). LC-MS (*m*/*z*): found $[M + 1]^+$ = 378.2; calcd for $C_{28}H_{47}NO_5^+$-$C_5H_9O_2$ (Boc) = 378.3.

16-[4-(2,5-Bis-tert-butoxycaronylamino-pentanoylamino)-phenoxy]-hexadecanoic Acid Methyl Ester (3). Boc was removed from **2** (3.14 mmol, 1.5 g) by treating with 5 mL TFA and 3% H_2O for 1 h at RT. The solvent was evaporated and 1.54 g (3.1 mmol) of the obtained deprotected amine was coupled with 2,5-bis-tert-butoxycarbonyl amino-pentanoic acid (3.57 mmol, 1.15 g) using BOP (3.44 mmol, 1.52 g), HOBt (4.3 mmol, 0.58 g), and DIEA (12.6 mmol, 2.2 mL) in DMF (15 mL) and dichloromethane (30 mL). The mixture was stirred overnight at RT. Then, solvent was evaporated and product was crystallized from acetonitrile. The precipitate was filtered off and dried to give compound **3** (1.6 g, 76%). ^{1}H NMR ($CDCl_3$, 300 MHz): δ 8.41 (s, 1H), 7.41 (d, 2H), 6.81 (d, 2H), 5.25 (s, 1H), 4.73 (s, 1H), 4.39 (s, 1H), 3.9 (t, 2H), 3.65 (s, 3H), 3.4 (s, 1H), 3.09 (s, 1H), 2.28 (t, 2H), 1.83−1.69 (m, 4H), 1.67−1.53 (m, 4H), 1.47−1.38 (m, 18H), 1.37−1.16 (m, 22H). LC-MS (*m*/*z*): found $[M + 1]^+$ = 491.2; calcd for $C_{38}H_{65}N_3O_8^+$-$C_{10}H_{18}O_4$ (2Boc) = 491.2.

(1-{4-[15-(2-Amino-ethylcarbamoyl)-pentadecyloxy]-phenylcarbamoyl}-4-tert-butoxycabonylamino-butyl)-carbamic Acid tert-Butyl Ester (4). Methyl ester of **3** (0.7 mmol, 0.5 g) was substituted with ethylenediamine (150 mmol, 10 mL) for 72 h at 70 °C. Then the excess of ethylenediamine was evaporated, 50 mL of water was added and the product **4** was filtered (0.45 g, 87%). ^{1}H NMR ($CDCl_3$, 300 MHz): δ 8.45 (s, 1H), 7.42 (d, 2H), 6.82 (d, 2H), 6.05 (s, 1H), 5.30 (s, 1H), 4.75 (s, 1H), 4.37 (s, 1H), 3.91 (t, 2H), 3.42−3.25 (m, 3H), 3.16−3.02 (m, 1H), 2.84 (t, 2H), 2.17 (t, 2H), 2.06−1.92 (m, 4H), 1.79−1.7 (m, 2H), 1.67−1.54 (m, 4H), 1.48−1.37 (m, 18H), 1.37−1.20 (m, 20H). LC-MS (*m*/*z*): found $[M + 1]^+$ = 720.4; calcd for $C_{39}H_{69}N_5O_7^+$ = 720.4.

[4-tert-Butoxylamino-4-(4-{15-[2-(2,3,4,5,6-pentahydroxy-hexanoylamino)-ethylcabamoyl]-pentadecyloxy}-phenylcarbamoyl)-butyl]-carbamic Acid tert-Butyl Ester (5). D-gluconic acid δ-lactone (0.23 mmol, 0.04 g) was added to solution of **4** (0.11 mmol, 0.1 g) in 15 mL of methanol. Then, DIEA (1.4 mmol, 0.24 mL) was added and the reaction mixture was stirred at 70 °C for about 24 h. Solvents were evaporated in vacuo. Compound **5** (0.09 g, 90%) was crystallized from methanol. ^{1}H NMR (CD_3OD, 300 MHz): δ 7.42 (d, 2H), 6.87 (d, 2H), 4.21 (s, 1H), 4.18−4.06 (m, 2H), 3.96 (t, 2H), 3.83−3.6 (m, 5H), 3.09 (t, 2H), 2.19 (t, 2H), 1.86−1.54 (m, 10H), 1.48−1.41 (m, 18H), 1.39−1.26 (m, 22H). LC-MS (*m*/*z*): found $[M + 1]^+$ = 898.57; calcd for $C_{45}H_{79}N_5O_{13}^+$ = 898.57.

16-[4-(2,5-Diamino-pentanoylamino)-phenoxy]-hexadecanoica-cid[2-(2,3,4,5,6-pentahydroxy-hexanoylamino)-ethyl]-amide (Orn-C16-G). Boc was removed from 50 mg of **5** using 0.5 mL TFA and 3% H_2O (1 h) to get the final product Orn-C16-G (27 mg, 90%). LC-MS (Bruker, HTCultra) (*m*/*z*): found $[M + 1]^+$ = 698.4; calcd for $C_{35}H_{64}N_5O_9^+$ = 698.4.

Fluorescence Measurements. Absorption spectra were recorded on a Cary 400 spectrophotometer (Varian) and fluorescence spectra either on FluoroMax 3.0 or Fluorolog (Jobin Yvon, Horiba) spectrofluorimeters. All the emission spectra were corrected from the background signal of the corresponding blank (corresponding solution without the fluorescent dye). For measurements with 1,8-ANS, 50 nM of the dye dissolved in 20 mM MES buffer (pH 7.4 or 6.0) solution was titrated with increasing quantities of the corresponding bola, added from stock solutions. All spectra were recorded 2 min after each addition. In the ethidium bromide (EtBr) exclusion assay, an aliquot of CT-DNA (final concentration 20 μM) was added to the solution of EtBr (0.4 μM). After 2 min, increasing quantities of the corresponding bola were added from stock solutions (in DMF with 10% of water). Fluorescence intensity recorded at 600 nm (excitation at 550 nm) was recorded 2 min after each addition of bola aliquot.

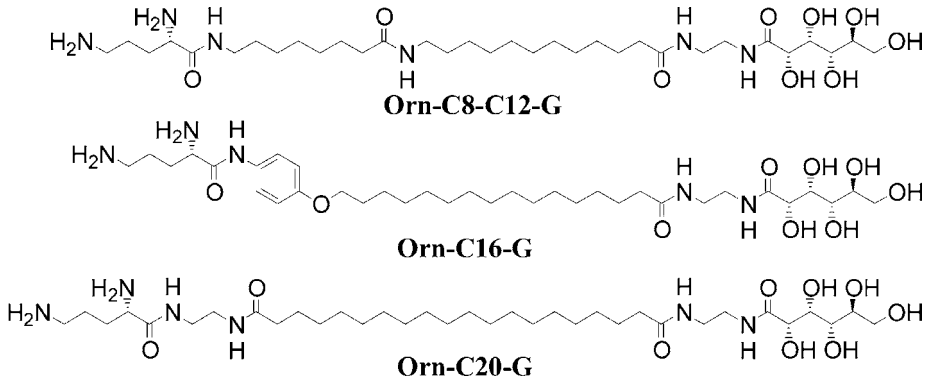


Figure 2. Chemical structures of bolaamphiphiles.

Dynamic Light Scattering (DLS) and ζ-Potential Measurements. The bolaplexes were prepared in 20 mM MES at pH 7.4 by mixing equal volumes of the solutions of calf thymus DNA (CT-DNA) or pCMV-Luc plasmid (pDNA) and the corresponding bolas. The bola solutions were prepared by adding aliquots of their stock solutions (in DMF with 10% of water) to the buffer. The final DNA concentration (expressed in phosphate) was 20 μM, while the bolas concentration was adjusted according to a desired N/P ratio. The N/P ratio between bolas and pDNA was expressed as the molar ratio between all the protonable amino groups of the bolas and the phosphate groups of the DNA. The DLS measurements were performed after 30 min of incubation at room temperature. The average size of the complexes was determined with a Zetasizer Nano ZS (Malvern Instruments) with the following specifications: sampling time, 30 s; medium viscosity, 0.8872 cP; refractive index (RI) medium, 1.33; RI particle, 1.590; scattering angle, 90°; temperature, 25 °C. For particle analysis, the statistics based on particle volume and particle number were presented. For ζ-potential measurements, the same sample preparation was done using CT-DNA at 30 μM concentration. The instrumental specifications were the same, accounting for a solvent dielectric constant of 78.5.

Gel Electrophoresis. The bolaplexes were prepared at different N/P ratios using 60 μM pCMV-Luc plasmid (final phosphate concentration), followed by 30 min incubation at room temperature. Four microliters of loading dye (Lonza, 6×) was added to 20 μL of the prepared complexes and then 12 μL of this mixture was loaded on 0.9% agarose gel prepared with 0.5X TAE (tris-acetate-ethylenediaminetetraacetic acid) buffer. In parallel, a 10 kbp DNA ladder (Lonza) was loaded on the gel. Electrophoresis was carried out with 0.5X TAE buffer at a constant voltage of 100 mV. DNA bands were visualized by UV trans-illuminator (GeneGenius, Syngene) after coloration with EtBr (0.5 μg/mL) for 15 min.

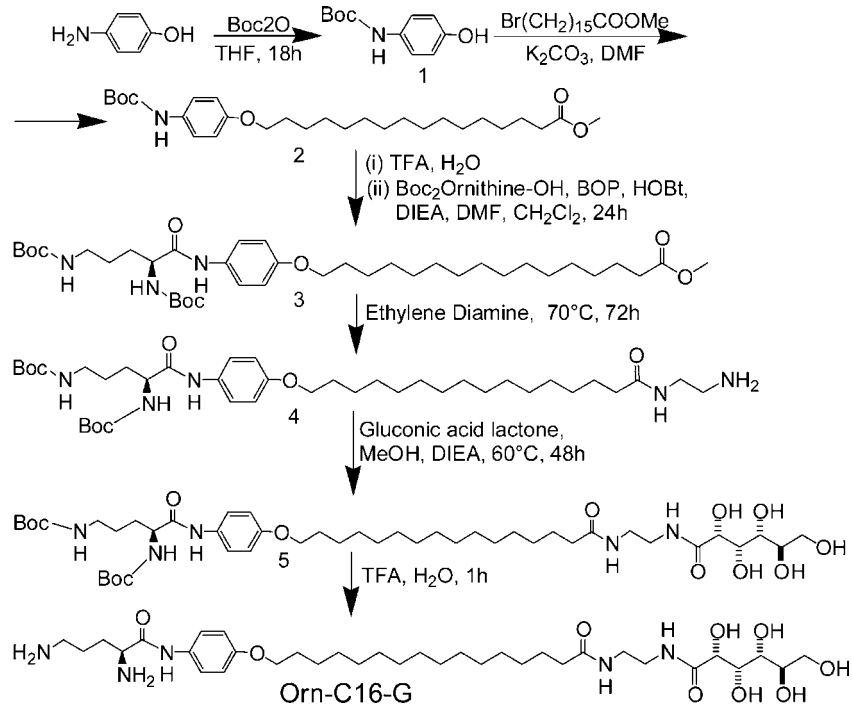
AFM Measurements. AFM measurements were performed using the Solver Pro-M (NT-MDT) instrument. The measurements were performed in liquid phase (MES buffer pH 7.4) by using the tapping mode. The cantilevers used were NSG03 type (NT-MDT) with a typical spring constant of 1.7 N/m, a resonance frequency of 32 kHz in liquid, and a tip curvature radius of 10 nm. Images were acquired with a resolution of 512 × 512 and a scan rate of 2 Hz. The samples were prepared as for DLS measurements, then 100 μL of the solution was deposited on the freshly cleaved mica followed by the addition of 10 μL of a $MgCl_2$ stock solution to obtain a final concentration of 10 mM. The measurements were performed 10 min after sample preparation.

Transfection and Cytotoxicity. COS-7 cells (African Green Monkey kidney fibroblast cell line) were grown in Dulbecco's modified Eagle's medium (Gibco-Intvitogen), supplemented with 10% fetal bovine serum (FBS, Lonza) and 100 U/ml of penicillin and streptomycin (Gibco-Intvitogen) at 37 °C in a humidified atmosphere containing 5% CO_2. Cells were seeded at a density of 1×10^5 cells in a 24-well plate, 24 h before transfection.

Transfection was done by using bola/pDNA (pCMV-Luc plasmid, 1 μg/well) complexes at different N/P ratios in serum-free Opti-MEM (Gibco-Invitrogen) or complete culture medium (DMEM containing 10% of FBS). For this purpose, bolaplexes were prepared in MES buffer (pH 7.4) as for DLS measurements and then added to the cells in Opti-MEM. Chloroquine (100 μM) or DOPE (1:1 molar ratio with respect to bola) was used to enhance transfection efficiency in some formulations. In formulations with DOPE, a mixture of DOPE and a corresponding bola in ethanol was evaporated in a round-bottom flask to obtain a film. Then, MES buffer (pH 7.4) was added and the samples were hydrated overnight at RT. Then, the samples were vortexed vigorously for 1 min and further sonicated in an ultrasonic bath for 15 min. The obtained suspensions were mixed with an equal volume of pDNA in the buffer to obtain a desired N/P ratio. All formulations were incubated at RT for 30 min before addition to the cells. After 3 h of incubation of cells with bolaplexes at 37 °C, 10% of FBS was added to serum-free samples, while for all the samples with chloroquine the transfection medium was replaced with fresh complete culture medium and then cells were cultured for another 45 h. Total incubation time for all samples was 48 h. Luciferase gene expression of lysed cells was quantified using a commercial kit (Invitrogen) and a luminometer (CentroXS^3 LB 960, BERTHOLD Technologies). Results were expressed as relative light units integrated over 10 s per mg of total cell protein lysate (RLU/mg of total protein). The experiments were repeated six times for serum-free samples and three times for samples with serum. The total protein was determined by BC assay (Protein Quantitation Kit, Interchim) using Cary 4000 spectrophotometer. As a positive control in the transfection measurements, commercially available agent jetPEI (Polyplus) was used following protocols provided in the kit.

Cytotoxicity of bolas was evaluated using 3-(4,5-dimethyl-2-thiazolyl)-2,5-diphenyltetrazolium bromide (MTT, Sigma-Aldrich) assay (*29*). COS-7 cells were seeded in a 24-well plate at 1×10^5 cells per well and after 24 h of incubation at 37 °C supplemented with bolas at different concentrations or jetPEI (150 μM, expressed as concentration of nitrogen residues) in serum-free Opti-MEM. After incubation for 3 h at 37 °C, 10% of FBS was added and cells were cultured for another 45 h. Cells were washed with phosphate buffer saline (PBS) and incubated with serum free medium containing 0.5 mg/mL MTT for 3 h at 37 °C. Media was discarded and formazan crystals were resuspended in 0.5 mL MTT solvent (Sigma-Aldrich). Absorbance of formazan solution was measured at 570 nm with

Scheme 1. Synthesis of Bola Orn-C16-G



respect to the background at 690 nm using Cary 4000 spectrophotometer. Cell viability was expressed as relative absorbance (%) of the sample versus control cells.

RESULTS AND DISCUSSION

Design and Synthesis. The basic design of bolas relies on one neutral group and one dicationic group connected by a hydrophobic spacer. As neutral group we selected a sugar residue, which is biocompatible and relatively inert. The dicationic headgroup responsible for DNA binding was the ornithine residue (Orn), featuring two amino groups separated by a 4-carbon atom distance. This distance ensures protonation of both amino groups at neutral pH and thereby efficient interaction with negatively charged DNA. On the basis of this design, three new bolaamphiphiles were synthesized, presenting different hydrophobic spacers: (a) a dipeptide composed of end-substituted amino acids of 8- and 12-carbon atoms, Orn-C8-C12-G; (b) a hydrophobic linker composed of an alkyl chain of C16-carbon atoms and an aromatic unit, Orn-C16-G; and (c) a long (20-carbon atoms) alkyl chain, Orn-C20-G (Figure 2). This variation of the hydrophobic spacer could tune the hydrophobic, H-bonding and π-stacking interactions between bolas. An example of synthesis of Orn-C16-G is presented in Scheme 1. Initially, the amino group of 4-aminophenol was protected with Boc-group (**1**) and its hydroxyl was further reacted with methyl 16-bromohexadecanoate. Then, the amino group in the obtained conjugate **2** was further deprotected and substituted with Boc-protected ornithine. The obtained conjugate **3** was further reacted with ethylene diamine giving **4**. The latter was then substituted with D-gluconic acid δ-lactone followed by Boc-removal, affording final bola Orn-C16-G. The yields of the individual steps were systematically >50% and the obtained final bolas in 100−200 mg quantities were sufficiently pure according to NMR, LC-MS and HPLC techniques (see also Supporting Information).

Self-Assembly. 1,8-ANS dye is poorly fluorescent in water, while on binding to lipid membranes it becomes strongly fluorescent (*30*). In the present work, we used this probe to study the concentration-dependent bolas assembly. Solutions at pH 7.4 and 6.0 were tested, which could alter the protonation of the amino groups of bolas in the self-assembled state. It can be seen from Figure 3 that for Orn-C16-G at pH 7.4, fluorescence intensity grows rapidly with bola concentration showing beginning of saturation at higher concentrations. In contrast, at pH 6.0, a moderate increase in fluorescence intensity is followed by rapid increase at concentrations >20 μM. These data suggest that the critical aggregation concentration (CAC) at pH 7.4 is too low to be detected with this method, while at pH 6.0 it is clearly much larger being close to 20 μM. We could speculate that the self-assembly could be accompanied by a partial deprotonation of bola amino groups, so that lower pH may favor disassembly (i.e., higher CAC). In contrast, for bola Orn-C20-G rapid increase of 1,8-ANS fluorescence intensity was observed both at pH 7.4 (see Figure S1 in Supporting Information) and 6.0 (Figure 3). This indicates that CAC of Orn-C20-G is much

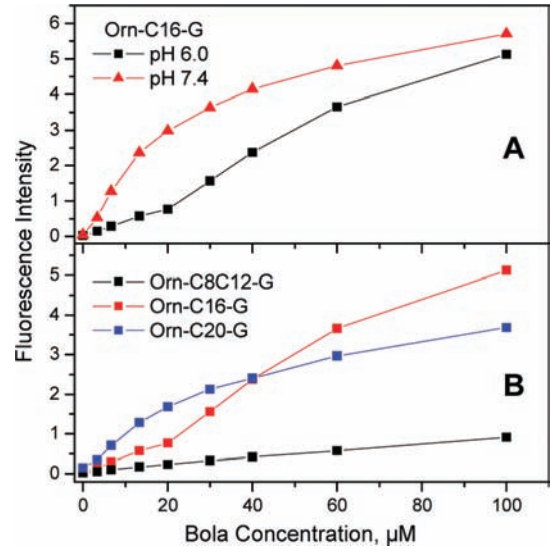


Figure 3. Fluorescence intensity of 1,8-ANS (50 nM) as a function of bolas concentration. (A) Orn-C16-G in MES buffer at pH 7.4 and 6. (B) Three different bolas at pH 6.

Table 1. Dynamic Light Scattering Data of Bolas and Bolaplexes in Aqueous Buffer (pH 7.4)

		volume analysis		
	sample	diameter, nm	amount, %	number analysis mean diameter, nm
Orn-C16-G	bola (100 μM)	110	88	73
		1450	12	
	bola/pDNA N/P 1.2 (12 μM bola)	109	95	90
	bola/pDNA	92	45	152
	N/P 2 (12 μM bola)	510	55	
	bola/pDNA N/P 2 (20 μM bola)	1550	95	1400
	bola/pDNA N/P 5 (50 μM bola)	870	100	925
	bola (100 μM)	140	15	110
		1050	85	
	bola/pDNA	97	20	90
	N/P 1.2 (12 μM bola)	930	80	
Orn-C20-G	bola/pDNA N/P 2 (12 μM bola)	970	100	900
	bola/pDNA N/P 2 (20 μM bola)	1370	100	1200
	bola/pDNA N/P 5 (50 μM bola)	1090	100	1069
	bola/DOPE (100 μM bola)	220	30	140
		1120	70	
Orn-C16-G/DOPE (1:1)	bola/DOPE/pDNA N/P 2 (20 μM bola)	220	100	218
	bola/DOPE/pDNA N/P 3 (30 μM bola)	200	20	190
		800	80	
	bola/DOPE/pDNA N/P 5 (50 μM bola)	1440	100	1350

lower than that of Orn-C16-G, probably because of its hydrophobic spacer, which is longer and does not contain bulky aromatic group, thus ensuring tight bola packing. Finally, Orn-C8-C12-G showed relatively weak increase in the fluorescence of 1,8-ANS with increasing concentration suggesting that it does not assemble at the studied concentration range. The latter result is probably connected to the presence of an amide group within the bola hydrophobic spacer, which may strongly diminish its hydrophobic interactions and thus increase its CAC.

The information about molecular order of bolas assemblies can be provided from fluorescence anisotropy of a rod-shaped molecule TMA-DPH (*31*). The observed values of fluorescence anisotropy for Orn-C16-G and Orn-C20-G assemblies at 100 μM are relatively high (0.30−0.32) at 20 °C and correspond to a rigid and highly ordered environment similar to lipid membranes in solid gel phase (0.32) for DPPC at 20 °C (data not shown) (*32*). These high values of fluorescence anisotropy suggest that bolas are probably organized in monolayers with a transmembrane spanning orientation, thus excluding possible bolas bilayer structure presenting a U-shaped conformation, as reported for some other bolas (*33*).

According to DLS data, Orn-C16-G and Orn-C20-G at 100 μM concentration form a significant fraction of small structures (around 100 nm, Table 1) in line with fluorescence data suggesting self-assembly of bolas at these conditions. These structures were stable for 1−2 h, while after longer incubation some precipitation of the bolas was observed.

Interactions with DNA. To study interactions of bolas with DNA, gel electrophoresis was first used. It can be seen from Figure 4A that Orn-C8-C12-G forms complexes with firefly luciferase plasmid DNA (pDNA) only at high N/P ratios (ratio between cationic groups of bola and phosphate groups of DNA). Indeed, only at N/P > 10 the pDNA band disappears. This indicates a relatively weak affinity of this bola to DNA. In contrast, Orn-C16-G (Figure 4B) and Orn-C20-G (Figure 4C) form complexes with pDNA at N/P values close to 1.0−1.2. It can be noted that Orn-C20-G shows a slightly stronger interaction since the DNA band disappears at lower N/P ratio (1.2) as compared to Orn-C16-G (1.6). By taking into account that all bola molecules are bearing the same dicationic ornithine residue, the stronger interaction of Orn-C16-G and Orn-C20-G with DNA is probably connected with a higher hydrophobicity of their spacers, which in turn favors their self-assembly and their cooperative interaction with DNA. Thus, we can assert that the interaction of the present bolas with DNA is controlled in part by their ability to self-assemble. Finally, a mixture of Orn-C16-G with a helper lipid DOPE (1:1 molar ratio with respect to bola), which was important in our transfection experiments (see below), showed complex formation at slightly higher N/P ratio, being completed at N/P 3 (see Figure S2 in Supporting Information).

The DNA condensation within the bolaplexes can be followed by the ethidium bromide (EtBr) exclusion assay (*34*). This dye when intercalated into DNA is highly fluorescent, while after DNA condensation it is expelled from its intercalation site, thus resulting in a strong decrease of its fluorescence intensity (up to 90%). For these studies, a linear DNA from calf thymus was used as the model. According to our data, Orn-C8-C12-G showed a relatively weak and rather linear decrease of EtBr fluorescence intensity as a function of N/P ratio (Figure 5), which is in line with the gel electrophoresis data showing its

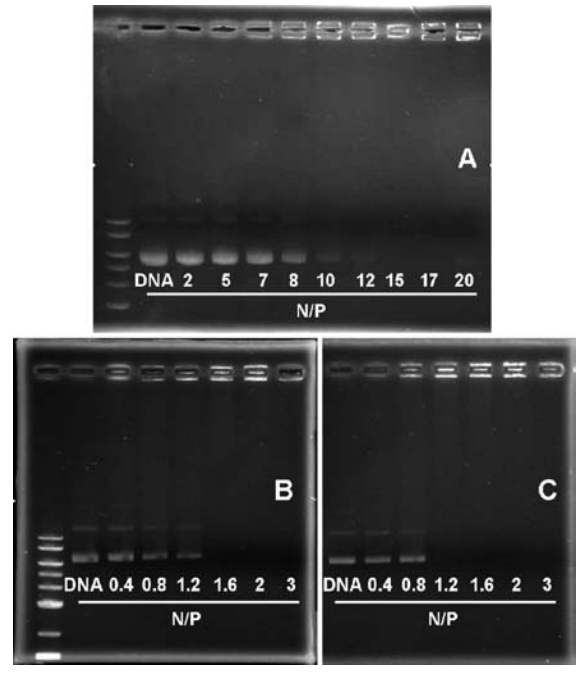


Figure 4. Agarose gel electrophoresis (0.9%) of Orn-C8-C12-G (A), Orn-C16-G (B), and Orn-C20-G (C) complexed with pDNA at different N/P ratios. Bands at the left of gels (A) and (B) correspond to 10 kbp DNA ladder.

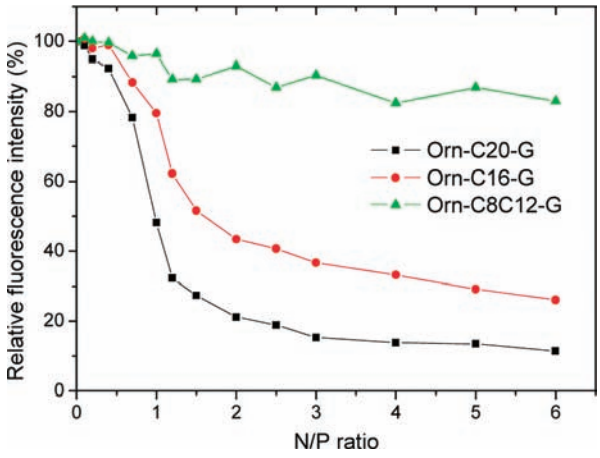


Figure 5. Exclusion of EtBr from CT-DNA complexes with bolas at different N/P ratios. The fluorescence intensity was normalized to 100% of the initial intensity.

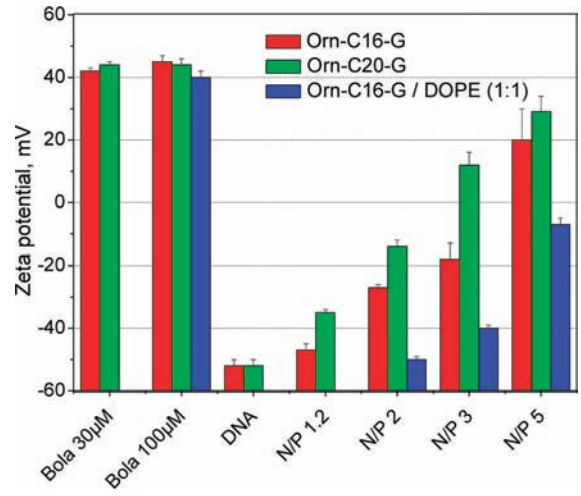


Figure 6. ζ-potential of nanostructures formed by bolas alone and by their formulations with DOPE and CT-DNA in MES buffer (pH 7.4) at different N/P ratios.

weak interaction with DNA. In contrast, both Orn-C16-G and Orn-C20-G showed a sharp decrease of EtBr fluorescence at N/P around 1. Thus, in accordance with the gel electrophoresis data it is confirmed that these bolas bind strongly to DNA by showing a significant level of DNA condensation. It can be also noticed that, similarly to the gel electrophoresis data, Orn-C20-G shows an EtBr fluorescence decrease at lower N/P ratio as compared to Orn-C16-G. Moreover, the fluorescence decrease is stronger for the former bola (ca. 85% for Orn-C20-G as compared to ca. 70% for Orn-C16-G). Thus, we can conclude that Orn-C20-G presents a stronger affinity to DNA and condense it more significantly as compared to Orn-C16-G. This conclusion corroborates with the observed stronger ability of Orn-C20-G to self-assemble without DNA evidenced by 1,8-ANS data. Since Orn-C8-C12-G shows a poor affinity to DNA and almost a negligible DNA condensation ability, we excluded this compound from further characterization, focusing only on Orn-C16-G and Orn-C20-G bolas.

Structural Characterization of Bolaplexes. To estimate the size of the obtained bolaplexes, DLS technique was used. Initially, the bolaplexes at different N/P ratios were prepared by direct addition of increasing quantities of Orn-C16-G from stock to pDNA solution. It was observed that at low N/P ratios, the particle size was relatively small (around 100 nm), while above N/P 1.2, their size increased rapidly reaching a maximum at N/P 2 (700 nm) and then further decreases until N/P 5 (see Supporting Information). In a second approach, the bolaplexes were prepared by mixing equal volumes of bolas and DNA aqueous solutions, followed by 30 min incubation at RT. This method gave similar DLS results for low N/P ratios (1.2 and 2): relatively small particles at N/P = 1.2 and much larger at N/P = 2 (Table 1). It is important to note that for Orn-C16-G at lower concentration the bolaplexes at N/P 2 (30 min incubation) showed much smaller sizes (150 nm). In contrast, after 5 min of incubation, Orn-C16-G/pDNA complexes presented similar small sizes (ca. 150 nm) for both low and high bola concentrations. Thus, the higher bola concentration probably favors aggregation of bolaplexes into larger particles. At N/P 5, this preparation method (with 30 min incubation) also gave relatively large particles as for N/P 2. The observed discrepancy between the two methods of preparation for N/P 5 is probably related to the incubation time, since in the first approach the measurements were done 5 min after each addition. The DLS data obtained with Orn-C20-G were similar to those with Orn-C16-G (Table 1), so that bolaplexes were small at N/P ratio 1.2, while their size increased significantly at higher N/P ratios. Moreover, for Orn-C16-G/DOPE mixture (1:1), a similar increase in the size of the bolaplexes was observed at higher N/P ratios (Table 1). The observation of larger complexes at higher N/Ps differs clearly from behavior of polyplexes and lipoplexes. Indeed, the latter at N/Ps close to 1 show relatively large complexes because of neutral charge of the complex, while at higher N/Ps they are much smaller because of their strong positive charge (*35*−*37*). Interestingly, our observations are in line with recent reports on other bolas featuring cationic group on one end and a neutral sugar residue on the other (*23*, *24*). Therefore, we can suggest that the increase in size of bolaplexes at higher N/Ps could be a special feature of this type of bolas, which is probably because their bolaplexes do not become positively charged at higher N/Ps. This hypothesis was verified by measuring the zeta potential of bolaplexes (Figure 6). The bolas alone showed strongly positive ζ-potentials, while the bolaplexes at low N/P ratios were negatively charged and reached neutrality at N/P ratios around 3. At N/P 5, the observed ζ-potential was positive, however, we suspect that it could be due to excess of bola molecules that do not complex with DNA, thus contributing to apparent positive potential values. For Orn-C16-G/DOPE mixture (1:1), the ζ-potentials were systematically more negative, though a clear neutralization of the complexes was observed at N/P 5 (Figure 6). We expect that, as shown in Figure 1B, the positively charged part of bola interacts with DNA, while the neutral sugar residue is exposed at the bolaplex surface. This structure may favor neutrality of the bolaplex at higher N/Ps. Presence of DOPE does not change this tendency, but only shifts the complex neutralization to higher N/P ratios.

To access the nanoscopic architecture of bolaplexes, we performed atomic force microscopy (AFM) measurements in liquid (buffer) phase on a mica surface. An efficient absorption of the bolaplexes (N/P 2 or 1.2) at the mica surface was achieved only in the presence of magnesium cations. This indicates that the bolaplexes at the studied N/P ratios are negatively charged, so that Mg^{2+} ions act as a link between bolaplexes and the negatively charged mica surface. Orn-C16-G bolaplexes with pDNA formed relatively small and spherical structures (Figure 7A). The average height and width of the particles were 12 and 120 nm, respectively, which correspond to an average particle volume of about 1.7×10^5 nm^3 and an equivalent spherical particle diameter of 70 nm. This size is smaller than the one observed by DLS for N/P 2 (12 μM bola). Several reasons may explain this discrepancy. At first, the smaller size particles observed by AFM is based on a particle by particle data analysis, while DLS measures an average size with higher sensitivity to larger particles. Indeed, the DLS data based on particle number

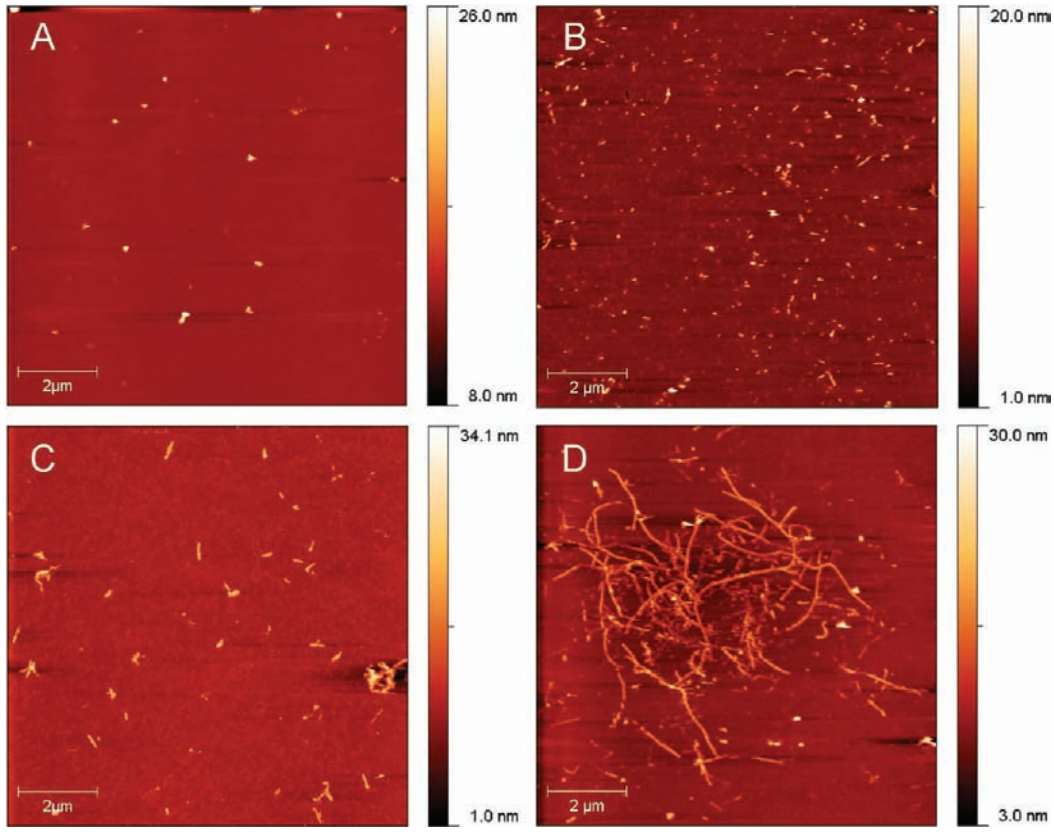


Figure 7. AFM images of Orn-C16-G (A and B, N/P 2) and Orn-C20-G (C and D, N/P 1.2) bolaplexes with pDNA (A and C) and CT-DNA (B and D). Images were obtained by tapping mode.

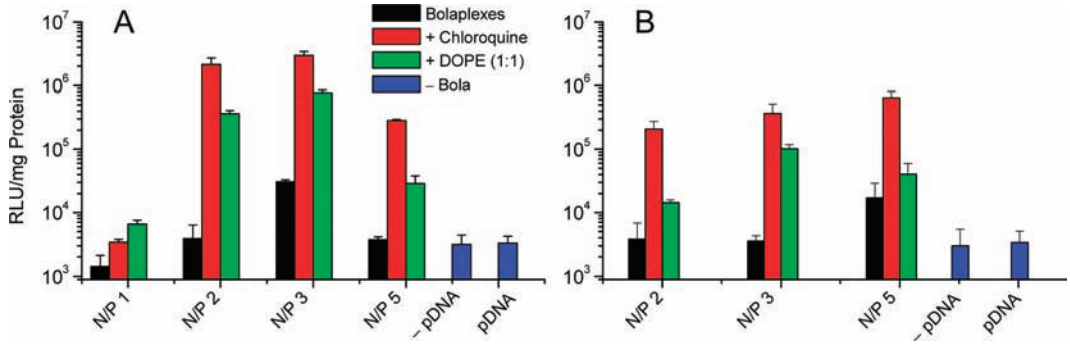


Figure 8. Transfection efficiency of the Orn-C16-G bolaplexes at different N/P ratios in COS-7 cells without (A) and with serum (B). Cells were incubated in serum-free Opti-MEM (A) or complete culture medium, DMEM containing 10% of FBS (B) with a bolaplex composed of plasmid DNA (1 μg per well), Orn-C16-G, and DOPE (when indicated). For some samples, the medium contained 100 μM chloroquine. After 3 h, 10% of FBS was added to the serum-free samples, while for all the samples with chloroquine the transfection medium was replaced with fresh complete culture medium. The luciferase activity quantification was performed after 48 h of incubation. Transfection efficiency determined from the luciferase assay was expressed as RLU/mg of protein. The negative controls were nontreated cells (-pDNA) and those transfected with naked pDNA (pDNA). The experiments were repeated six times for serum-free samples (A) and three times for samples with serum (B).

statistics is much closer to AFM data than those based on volume analysis (Table 1). Moreover, DLS data provides a hydrodynamic size of the particles, which is larger than the real size. Finally, in AFM measurements, the particles are stabilized by adsorption at the surface, while in DLS they are free in solution and can further aggregate to form larger particles. Bolaplexes of Orn-C16-G with CT-DNA showed high polydispersity and formed both spherical and short rodlike structures (Figure 7B). The presence of short rods of 8−10 nm height, 40−60 nm width, and 300−600 nm length could be explained by the linear structure of CT-DNA that favored the formation of elongated structures. In contrast, Orn-C20-G/DNA bolaplexes at N/P 2 were very large and polydisperse, in line with DLS data, which prompted us to study the bolaplexes at N/P 1.2. Remarkably, the complexes at N/P 1.2 showed predominantly rodlike structures for both pDNA and CT-DNA (Figure 7C and D). However, in the case of pDNA, the observed rods were relatively short, having height and width around 10 and 120 nm, respectively, while in the case of CT-DNA, they correspond to very long fibers of 16 nm height and 80 nm width. The formation of these "spaghetti-like" structures was previously reported for cationic lipids (*38*). It was proposed that in this kind of structure, the DNA molecule is located in the core, being surrounded by the lipid membrane. Probably, Orn-C20-G/CT-DNA bolaplexes present a similar structure, where single or multiple DNA strands are surrounded by a monolayer of bola molecules, similarly to the idealistic model in Figure 1B.

Transfection Efficiency and Cytotoxicity. The transfection efficiency of bolaplexes was in serum-free and serum-containing media for the different formulations by using the luciferase expression assay (Figure 8). For serum-free samples (Figure 8A), considerable transfection efficiency was observed for Orn-C16-G bolaplexes at N/P 2, 3, and 5 only in the presence of helper lipid DOPE or the endosomolytic reagent chloroquine (*28*). The better efficiency observed in the presence of DOPE is in line with previously reported data concerning other bolaamphiphiles (*21, 23*). DOPE probably improves the fusion of bolaplexes with cellular and endosomal membranes (*39, 40*). However, the strong effect of chloroquine on bolaplexes delivery is reported for the first time. This result clearly shows that the key barrier for internalization of bolaplexes is related to the endosomal escape. In the presence of serum, the transfection efficiency decreased significantly for all samples with DOPE (Figure 8B), which is in line with previous reports showing that DOPE-containing lipoplexes are highly sensitive to serum (*41*). In the presence of chloroquine, the effect of serum was less important, and the transfection efficiency increased systematically at higher N/P ratio. At N/P = 5, the sample with serum showed even slightly higher transfection efficiency than that without serum (Figure 8). Similar results were reported for lipoplexes, where higher N/Ps increased their resistance to serum (*42*).

On the other hand, bolaplexes of Orn-C20-G displayed relatively poor transfection efficiency for most of the formulations, which can be related to their larger size and spaghetti-like architecture (Figure 7). It should be noted that the observed values of transfection efficiency for Orn-C16-G were significantly lower than that for highly efficient commercial agent jetPEI (3×10^8 RLU/mg protein in the present study), while they were comparable with those recently reported for some other bolaamphiphiles (*21, 22*). Taking into account that the area of bolaamphiphiles as nonviral vectors is still poorly explored, we believe that there is a lot of room for improvement of their transfection efficiency. It will require optimization of bola chemical structure to achieve better control on the size and stability of the bolaplexes as well as on their ability to escape from endosomes. This work is currently in progress and will be reported in due course.

MTT-based assay suggested that new bolas do not show any considerable cytotoxicity. In the concentration range 30−200 μM of bolas with 48 h incubation, the observed cell viability was >80%, while for jetPEI (150 μM, expressed for nitrogen residues) it was only about 60% (see Supporting Information). The MTT results correlated well with the observed relatively high total protein (>80% vs. control) after 48 h of transfection with bolaplexes. This low cytotoxicity of the new bolas is an important advantage compared to polyplexes and lipoplexes. Thus, the obtained results showed the potentials of the new bolas molecules, especially Orn-C16-G, for the elaboration of highly efficient nonviral vectors.

CONCLUSIONS

We have synthesized three new bolaamphiphiles, bearing cationic and neutral groups at opposite sides of a hydrophobic spacer. The two bolaamphiphiles with more hydrophobic spacers exhibit low critical aggregation concentration and stronger affinities to DNA. At low N/P ratio (1.2), these bolas form bolaplexes of relatively small size, showing spherical and rodlike structures, while at higher N/P ratio their size increases due to neutralization of the complexes. Bolaplexes showed considerable transfection efficiency only in presence of the helper lipid DOPE or the endosomolytic agent chloroquine, indicating that the endosomal escape constitutes the main barrier to the internalization of these complexes. The present work provides strong basis for a further development of new efficient gene delivery vectors based on this original class of compounds.

ACKNOWLEDGMENT

This work was supported by Fondation pour la Recherche Médicale (FRM). We thank the groups of J.-S. Remy and B. Frisch for help with luminometry and DLS measurements. We also thank G. Zuber for fruitful discussions.

Supporting Information Available: Procedures for synthesis of Orn-C20-G and Orn-C8-C12-G. Some DLS data. Total protein and MTT-based cytotoxicity assays. This material is available free of charge via the Internet at http://pubs.acs.org.

LITERATURE CITED

(1) Fuhrhop, J. H., and Wang, T. (2004) Bolaamphiphiles. *Chem. Rev. 104*, 2901–2938.
(2) Damste, J. S. S., Schouten, S., Hopmans, E. C., Van Duin, A. C. T., and Geenevasen, J. A. J. (2002) Crenarchaeol: The characteristic core glycerol dibiphytanyl glycerol tetraether membrane lipid of cosmopolitan pelagic crenarchaeota. *J. Lipid Res. 43*, 1641–1651.
(3) Derosa, M., Gambacorta, A., and Gliozzi, A. (1986) Structure, Biosynthesis, And Physicochemical Properties Of Archaebacterial Lipids. *Microbiol. Rev. 50*, 70–80.
(4) Stetter, K. O. (1996) Hyperthermophilic procaryotes. *FEMS Microbiol. Rev. 18*, 149–158.
(5) Shimizu, T., Masuda, M., and Minamikawa, H. (2005) Supramolecular nanotube architectures based on amphiphilic molecules. *Chem. Rev. 105*, 1401–1443.
(6) Kameta, N., Masuda, M., Minamikawa, H., Mishima, Y., Yamashita, I., and Shimizu, T. (2007) Functionalizable organic nanochannels based on lipid nanotubes: Encapsulation and nanofluidic behavior of biomacromolecules. *Chem. Mater. 19*, 3553–3560.
(7) Wang, X., and Liang, Y. (2001) Formation of monolayer lipid membranes in water and ethanol from bolaamphiphiles. *J. Colloid Interface Sci. 233*, 364–366.
(8) Mintzer, M. A., and Simanek, E. E. (2009) Nonviral vectors for gene delivery. *Chem. Rev. 109*, 259–302.
(9) Martin, B., Sainlos, M., Aissaoui, A., Oudrhiri, N., Hauchecorne, M., Vigneron, J. P., Lehn, J. M., and Lehn, P. (2005) The design of cationic lipids for gene delivery. *Curr. Pharm. Des. 11*, 375–394.
(10) Safinya, C. R. (2001) Structures of lipid-DNA complexes: Supramolecular assembly and gene delivery. *Curr. Opin. Struct. Biol. 11*, 440–448.
(11) Chesnoy, S., and Huang, L. (2000) Structure and function of lipid-DNA complexes for gene delivery. *Annu. Rev. Biophys. Biomol. Struct. 29*, 27–47.
(12) Hirko, A., Tang, F., and Hughes, J. A. (2003) Cationic lipid vectors for plasmid DNA delivery. *Curr. Med. Chem. 10*, 1185–1193.
(13) Huang, L., Hung, M.-C., and Wagner, E., Eds. (1999) *Nonviral Vectors for Gene Therapy*, Academic Press, London.
(14) Demeneix, B., Hassani, Z., and Behr, J. P. (2004) Towards multifunctional synthetic vectors. *Curr. Gene. Ther. 4*, 445–455.
(15) Mastrobattista, E., van der Aa, M. A. E. M., Hennink, W. E., and Crommelin, D. J. A. (2006) Artificial viruses: a nanotechnological approach to gene delivery. *Nat. Rev. Drug Discovery 5*, 115–121.
(16) Nishikawa, M., and Huang, L. (2001) Nonviral vectors in the new millennium: Delivery barriers in gene transfer. *Hum. Gene Ther. 12*, 861–870.
(17) Zuber, G., Dauty, E., Nothisen, M., Belguise, P., and Behr, J. P. (2001) Towards synthetic viruses. *Adv. Drug Delivery Rev. 52*, 245–253.
(18) Zuber, G., Zammut-Italiano, L., Dauty, E., and Behr, J. P. (2003) Targeted gene delivery to cancer cells: Directed assembly

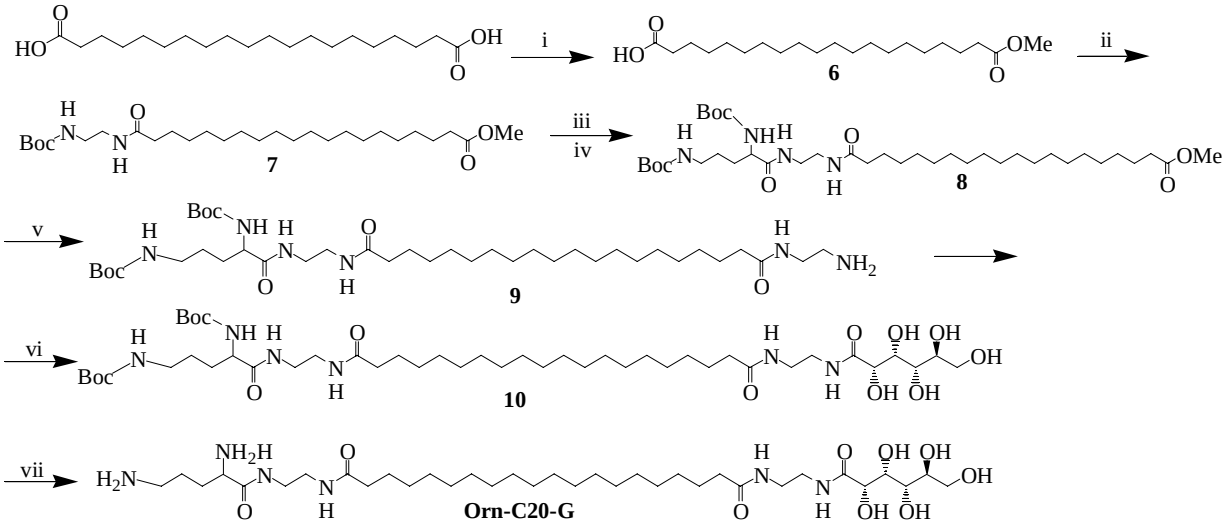
of nanometric DNA particles coated with folic acid. *Angew. Chem., Int. Ed. 42*, 2666–2669.
(19) Zhang, S., Zhao, Y., Zhao, B., and Wang, B. (2010) Hybrids of Nonviral Vectors for Gene Delivery. *Bioconjugate Chem. 21*, 1003–1009.
(20) Koltover, I., Salditt, T., Radler, J. O., and Safinya, C. R. (1998) An inverted hexagonal phase of cationic liposome-DNA complexes related to DNA release and delivery. *Science 281*, 78–81.
(21) Gaucheron, J., Santaella, C., and Vierling, P. (2001) In vitro gene transfer with a novel galactosylated spermine bolaamphiphile. *Bioconjugate Chem. 12*, 569–575.
(22) Fabio, K., Gaucheron, J., Di Giorgio, C., and Vierling, P. (2003) Novel galactosylated polyamine bolaamphiphiles for gene delivery. *Bioconjugate Chem. 14*, 358–367.
(23) Brunelle, M., Polidori, A., Denoyelle, S., Fabiano, A. S., Vuillaume, P. Y., Laurent-Lewandowski, S., and Pucci, B. (2009) A structure-activity investigation of hemifluorinated bifunctional bolaamphiphiles designed for gene delivery. *C. R. Chim. 12*, 188–208.
(24) Denoyelle, S., Polidori, A., Brunelle, M., Vuillaume, P. Y., Laurent, S., ElAzhary, Y., and Pucci, B. (2006) Synthesis and preliminary biological studies of hemifluorinated bifunctional bolaamphiphiles designed for gene delivery. *New J. Chem. 30*, 629–646.
(25) Eaton, M. A. W., Baker, T. S., Catterall, C. F., Crook, K., Macaulay, G. S., Mason, B., Norman, T. J., Parker, D., Perry, J. J. B., Taylor, R. J., Turner, A., and Weir, A. N. (2000) A new self-assembling system for targeted gene delivery. *Angew. Chem., Int. Ed. 39*, 4063–4067.
(26) Réthoré, G., Montier, T., Le Gall, T., Delépine, P., Cammas-Marion, S., Lemiègre, L., Lehn, P., and Benvegnu, T. (2007) Archaeosomes based on synthetic tetraether-like lipids as novel versatile gene delivery systems. *Chem. Commun. 20*, 2054–2056.
(27) Lainé, C., Mornet, E., Lemiègre, L., Montier, T., Cammas-Marion, S., Neveu, C., Carmoy, N., Lehn, P., and Benvegnu, T. (2008) Folate-equipped pegylated archaeal lipid derivatives: Synthesis and transfection properties. *Chem.—Eur. J. 14*, 8330–8340.
(28) Cotten, M., Langle-Rouault, F., Kirlappos, H., Wagner, E., Mechtler, K., Zenke, M., Beug, H., and Birnstiel, M. L. (1990) Transferrin-polycation-mediated introduction of DNA into human leukemic cells: Stimulation by agents that affect the survival of transfected DNA or modulate transferrin receptor levels. *Proc. Natl. Acad. Sci. U.S.A. 87*, 4033–4037.
(29) Mosmann, T. (1983) Rapid colorimetric assay for cellular growth and survival: Application to proliferation and cytotoxicity assays. *J. Immunol. Meth. 65*, 55–63.
(30) Slavik, J. (1982) Anilinonaphthalene Sulfonate as a Probe of Membrane-Composition and Function. *Biochim. Biophys. Acta 694*, 1–25.
(31) Lentz, B. R. (1993) Use of fluorescent probes to monitor molecular order and motions within liposome bilayers. *Chem. Phys. Lipids 64*, 99.
(32) M'Baye, G., Mely, Y., Duportail, G., and Klymchenko, A. S. (2008) Liquid ordered and gel phases of lipid bilayers: fluorescent probes reveal close fluidity but different hydration. *Biophys. J. 95*, 1217–1225.
(33) Meister, A., and Blume, A. (2007) Self-assembly of bipolar amphiphiles. *Curr. Opin. Colloid Interface Sci. 12*, 138–147.
(34) Lleres, D., Dauty, E., Behr, J. P., Mely, Y., and Duportail, G. (2001) DNA condensation by an oxidizable cationic detergent. Interactions with lipid vesicles. *Chem. Phys. Lipids 111*, 59–71.
(35) Pitard, B., Oudrhiri, N., Vigneron, J. P., Hauchecorne, M., Aguerre, O., Toury, R., Airiau, M., Ramasawmy, R., Scherman, D., Crouzet, J., Lehn, J. M., and Lehn, P. (1999) Structural characteristics of supramolecular assemblies formed by guanidinium-cholesterol reagents for gene transfection. *Proc. Natl. Acad. Sci. U.S.A. 96*, 2621–2626.
(36) Xu, Y., Hui, S. W., Frederik, P., and Szoka, F. C., Jr. (1999) Physicochemical characterization and purification of cationic lipoplexes. *Biophys. J. 77*, 341–353.
(37) Findeis, M. A., Ed. (2001) *Nonviral Vectors for Gene Therapy: Methods and Protocols*, Humana Press, Clifton, NJ.
(38) Sternberg, B., Sorgi, F. L., and Huang, L. (1994) New structures in complex formation between DNA and cationic liposomes visualized by freeze-fracture electron microscopy. *FEBS Lett. 356*, 361–366.
(39) Felgner, J. H., Kumar, R., Sridhar, C. N., Wheeler, C. J., Tsai, Y. J., Border, R., Ramsey, P., Martin, M., and Felgner, P. L. (1994) Enhanced gene delivery and mechanism studies with a novel series of cationic lipid formulations. *J. Biol. Chem. 269*, 2550–2561.
(40) Farhood, H., Serbina, N., and Huang, L. (1995) The role of dioleoyl phosphatidylethanolamine in cationic liposome mediated gene transfer. *Biochim. Biophys. Acta 1235*, 289–295.
(41) Li, S., Tseng, W. C., Beer Stolz, D., Wu, S. P., Watkins, S. C., and Huang, L. (1999) Dynamic changes in the characteristics of cationic lipidic vectors after exposure to mouse serum: Implications for intravenous lipofection. *Gene Ther. 6*, 585–594.
(42) Yang, J. P., and Huang, L. (1997) Overcoming the inhibitory effect of serum on lipofection by increasing the charge ratio of cationic liposome to DNA. *Gene Ther. 4*, 950–960.

BC100334T

New unsymmetrical bolaamphiphiles: synthesis, assembly with DNA and application for gene delivery

Namrata Jain, Youri Arntz, Valerie Goldschmidt, Guy Duportail, Yves Mely, Andrey S. Klymchenko

1. Synthesis of Orn-C12-G and Orn-C8-C12-G bolas.



Reagents: (i) MeOH, H_2SO_4, $C_2H_4Cl_2$, 85°C, 24h (25%) ; (ii) BOP, HOBt, DIEA, DMF, CH_2Cl_2, 24h (72%) ; (iii) TFA, H_2O, 1h; (iv) BOP, HOBt, DIEA, DMF, CH_2Cl_2, 40°C, 24h (70%) ; (v) Ethylene Diamine, 70°C, 72h (93%) ; (vi) Gluconic acid lactone, MeOH, DIEA ; (vii) TFA, H_2O, 1h (90%).

Scheme S1. Synthesis of **Orn-C20-G.**

Eicosanedioic acid monomethyl ester (6). The procedure was adapted from Ref. (1). Eicosanedioic acid (14.6 mmol, 5 g) was dissolved in 300 ml of ethylene chloride at 85°C. Methanol (7.4 mmol, 0.59 ml) was added to the clear solution, then H_2SO_4 (1.4 ml) was cautiously added, and the reaction was left for reflux overnight at 85°C. The solvent was concentrated and water was added. Three phases were obtained: aqueous, organic and slurry. To the organic phase, which contained mainly di- and mono-esters, carbon tetrachloride was added and placed in a separate funnel. The organic layer was washed with water, then dried over $MgSO_4$ and evaporated. Product was subjected to column chromatography, where di-ester was eluded with dichloromethane and the monoester **6** with ethyl acetate (25 % yield). ^{1}H NMR ($CDCl_3$, 300 MHz): 3.65 (s, 3H), 2.36-2.26 (m, 4H), 1.65-1.56 (m, 4H), 1.39-1.19 (m, 28H).

19-(2-tert-Butoxycarbonylamino-ethylcarbamoyl)-nonadecanoic acid methyl ester (7). *N*-Boc-ethylenediamine (1 mmol, 0.162 g) was coupled with mono-methyl ester **6** (0.84 mmol, 0.3 g) using BOP (0.93 mmol, 0.41 g), HOBt (1.2 mmol, 0.16 g) and DIEA (3.4 mmol, 0.6 ml) in DMF (5 ml) and dichloromethane (20 ml). The mixture was stirred overnight at room temperature. Then the solvent was evaporated and the product was crystallized from acetonitrile to give product **7** (0.3 g,

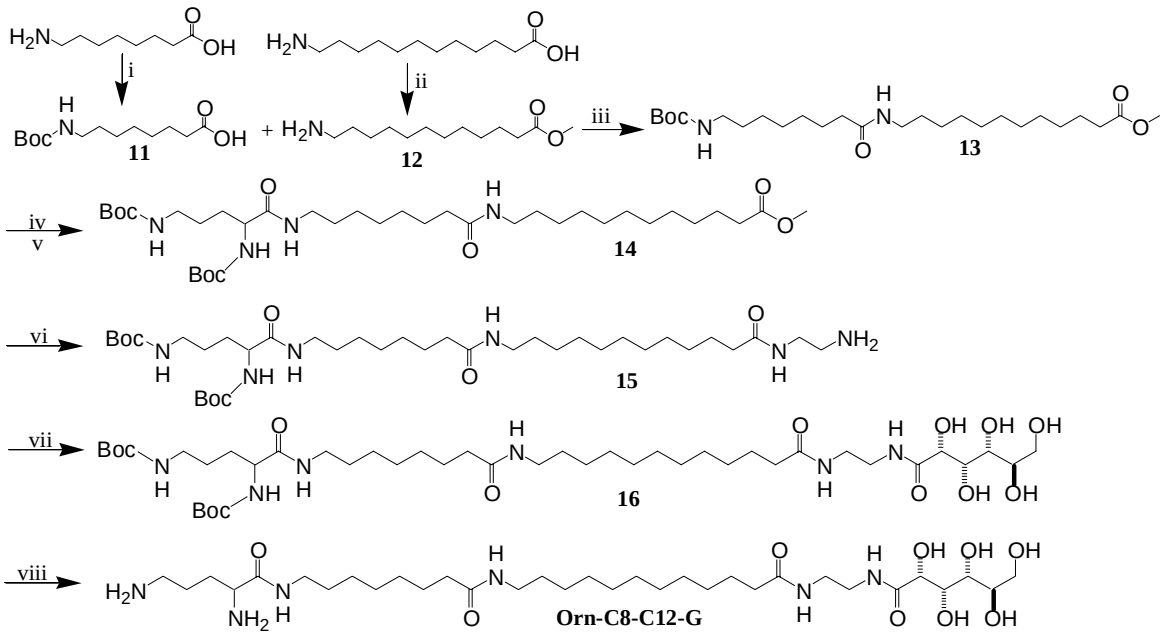
72 %). ^{1}H NMR (DMSO, 300 MHz): 7.62 (s, 1H), 6.61 (s, 1H), 3.58 (s, 3H), 3.05 (t, 2H), 2.97 (t, 2H), 2.27 (t, 2H), 2.03 (t, 2H), 1.57-1.42 (m, 4H), 1.4-1.33 (m, 9H), 1.32-1.17 (m, 28H). LC-MS: (m/z) Found $[M+1]^+$ = 399.2 (calcd for $C_{28}H_{54}N_2O_5^+$ - $C_5H_9O_2$ (Boc) = 399.3).

19-[2-(2,5-Bis-tert-butoxycarbonylamino-pentanoylamino)-ethylcarbamoyl]-nonadecanoic acid methyl ester (8). Boc-group was removed from **7** (0.54 mmol, 0.27 g) by treating with 1 ml TFA and 3% H_2O, for 1 h at RT. The solvent was evaporated and obtained de-protected amine was coupled with 2,5-Bis-tert-butoxycarbonyl-aminopentanoic acid (0.62 mmol, 0.207 g) using BOP (0.93 mmol), HOBt (1.2 mmol) and DIEA (3.4 mmol, 0.6 ml) in DMF (10 ml) and dichloromethane (10 ml). The mixture was stirred overnight at 40 °C. Then the solvent was evaporated and the product was crystallized from ethyl acetate. The precipitate was filtered off and dried to give solid crystals of compound **8** (0.34 g, 70 %). ^{1}H NMR ($CDCl_3$, 300 MHz): 6.95 (s, 1H), 6.39 (s, 1H), 5.18 (s, 1H), 4.76 (s, 1H), 4.17 (s, 1H), 3.65 (t, 3H), 3.4-3.2 (m, 5H), 3.11-2.99 (m, 1H), 2.28 (t, 2H), 2.15 (t, 2H), 1.87-1.7 (m, 2H), 1.67-1.5 (m, 8H), 1.46-1.38 (m, 18H), 1.34-1.17 (m, 30H). LC-MS: (m/z) Found $[M+1]^+$ = 613.4 (calcd for $C_{38}H_{72}N_4O_5^+$ - $C_5H_9O_2$ (Boc) = 613.4).

(1-{2-[19-[2-(2-Amino-ethylcarbamoyl)-nonadecanoylamino]-ethylcarbamoyl}-4-tert-butoxycarbonylamino-butyl)-carbamic acid tert-butyl ester (9). Methyl ester **8** (0.4 mmol, 0.3 g) was reacted with ethylenediamine (150 mmol 10 ml) for 72 h at 70°C. Then the excess of ethylenediamine was evaporated and water was poured into the reaction flask. Formed precipitate was filtered off to give compound **9** (0.29 g, 93 %). ^{1}H NMR (CD_3OD, 300 MHz): 3.96 (s, 1H), 3.05 (t, 2H), 2.73 (t, 2H), 2.23-2.16 (m, 4H), 1.67-1.5 (m, 8H), 1.46-1.44 (m, 18H), 1.39-1.23 (m, 30H). LC-MS: (m/z) Found $[M+1]^+$ = 741.4 (calcd for $C_{39}H_{76}N_6O_7^+$ = 741.5).

[4-tert-Butoxycabonylamino-4-(2-{19-[2-(2,3,4,5,6-pentahydroxy-hexanoylamino)-ethylcarbamoyl]-nonadecanoylamino}-ethylcabamoyl)-butyl]-carbamic acid tert-butyl ester (10). δ-Gulonic-γ-Lactone (0.23 mmol, 0.04 g) was added to solution of **9** (0.13 mmol, 0.1 g) in 10 ml of methanol. Then, DIEA (1.4 mmol, 0.24 ml) was added and reaction mixture was stirred at 70°C for about 24 h. Solvents were evaporated in vacuo. The obtained compound was crystallized from methanol to give product **10** (0.095 g, 95 %). ^{1}H NMR (CD_3OD, 300 MHz): 4.21 (s,1H), 4.1 (s, 1H), 3.98 (s, 1H), 3.84-3.59 (m, 5H), 3.07 (t, 2H), 2.25-2.12 (m, 4H), 1.68-1.49 (m, 8H), 1.49-1.4 (m, 18H), 1.4-1.21 (m, 30H). LC-MS: (m/z) Found $[M+1]^+$ = 919.6 (calcd for $C_{45}H_{86}N_6O_{13}^+$ = 919.6).

Eicosanedioic acid [2-(2,5-diamino-pentnoylamino)-ethyl]-amide[2-(2,3,4,5,6-pentahydroxy-hexanoylamino)-ethyl]-amide (Orn-C20-G). 40 mg of the Boc-protected product **10** was treated with 0.4 ml TFA and 3 % H2O for clean removal of Boc group to get final compound **Orn-C20-G** (27 mg, 90 %). LC-MS: (m/z) Found $[M+1]^+$ = 719.5 (calcd for $C_{35}H_{71}N_6O_9^+$ = 719.5).



Reagents: (i) Boc_2O, DMF, CH_2Cl_2, 20h (92%); (ii) $SOCl_2$, MeOH, 20h (94%); (iii) BOP, HOBt, DIEA, DMF, CH_2Cl_2, 24h (81%); (iv) TFA, CH_2Cl_2, 1h; (v) BOP, HOBt, DIEA, DMF, CH_2Cl_2, 24h (92%); (vi) $C_2H_8N_2$, 70°C, 72h (96%); (vii) MeOH, DIEA, 70°C, 24h; (viii) TFA, H_2O, 1h (92%).

Scheme S2. Synthesis of **Orn-C8-C12-G.**

8-tert-Butoxycabonylamino-octanoic acid (11). Amino group of 8-Aminooctanoic acid (31.4 mmol, 5 g) was protected by Boc using Di-tert-butyl dicarbonate (34.6 mmol, 7.54 g) in solution of DMF (30 ml) and dichloromethane (40 ml).Then, DIEA (94.2 mmol, 16.38 ml) was added and the reaction mixture was stirred for 20 h at RT. The solvent was evaporated and product was crystallized from dichloromethane. The precipitate was filtered off and dried to give compound **11** (7.5 g, 92 %). ^{1}H NMR ($CDCl_3$, 300 MHz): δ 4.55 (s, 1H), 3.07 (t, 2H), 2.3 (t, 2H), 1.67-1.5 (t, 4H), 1.56-1.37 (t, 9H), 1.37-1.21 (m, 6H).

12-Amino-dodecanoic acid methyl ester (12). Thionyl chloride (103.4 mmol, 7.5 ml) was added drop-wise to 100 ml of methanol at 0 °C and the mixture was stirred for another 20 min. Then, 10 g of 12-aminododecanoic acid (46.5 mmol) was added and reaction mixture was stirred for 20 h at RT. The solvent was evaporated and product was crystallized from heptane to give compound **12** (10 g, 94 %). ^{1}H NMR (DMSO, 300 MHz): δ 7.89 (s, 2H), 3.68 (s, 3H), 2.75 (t, 2H), 2.28 (t, 2H), 1.58-1.15 (m, 18H).

12-(8-tert-Butoxycarbonylamino-octanoylamino)-dodecanoic acid methyl ester (13). Compound **12** (6.5 mmol, 1.5 g) was coupled with **11** (7.2 mmol, 1.87 g) using BOP (7.2 mmol, 3.18 g), HOBt (8.9 mmol, 1.2 g) and DIEA (25.9 mmol, 4.5 ml) in DMF (15 ml) and dichloromethane (30 ml). The reaction mixture was stirred 24 h at RT. Then the solvents were evaporated and product was crystallized from ethyl acetate : heptane (8:2). The precipitate was filtered off and dried to give compound **13** (2.5 g, 81 %). ^{1}H NMR ($CDCl_3$, 300 MHz): δ 5.41 (s, 1H), 4.48 (s, 1H), 3.65 (s, 3H), 3.21 (t, 2H), 3.08 (t, 2H), 2.29 (t, 2H), 2.13 (t, 2H), 1.69-1.15 (m, 39H). LC-MS: (m/z) Found $[M+1]^+$ = 371.2 (calcd for $C_{26}H_{50}N_2O_5^+$ - $C_{10}H_{18}O_4$ (2Boc) = 371.2).

12-[8-(2,5-Bis-tert-butoxycarbonylamino-pentanoylamino)-octanoylamino]-dodecanoic acid methyl ester (14). Boc group of **13** (2.13 mmol, 1 g) was removed in dichloromethane (3 ml) in the presence of 2 ml of TFA for 1 h at RT. The solvent was evaporated and 1 g (2.1 mmol) of the obtained deprotected amine was coupled with 2,5-Bis-tert-butoxycarbonyl amino-pentanoic acid (2.2 mmol, 0.72 g) using BOP (2.4 mmol, 1.04 g), HOBt (2.96 mmol, 0.4 g) and DIEA (8.63 mmol, 1.5 ml) in DMF (5 ml) and dichloromethane (15 ml). The mixture was stirred overnight at RT. Then solvent was evaporated and product **14** (1.3 g, 92 %) was crystallized from acetonitrile. ^{1}H NMR ($CDCl_3$, 300 MHz): δ 6.46 (s, 1H), 5.56 (s, 1H), 5.2 (s, 1H), 4.73 (s, 1H), 4.17 (s, 1H), 3.65 (s, 3H), 3.28-3.04 (m, 6H), 2.28 (t, 2H), 2.13 (t, 2H), 1.66-1.19 (m, 50H). LC-MS: (m/z) Found $[M+1]^+$ = 585.4 (calcd for $C_{36}H_{68}N_4O_8^+$ - $C_{10}H_{18}O_4$ (2Boc) = 585.4).

(1-{7-[11-(2-Amino-ethylcarbamoyl)-undecylcarbamoyl]-heptylcarbamoyl}-4-tert-butoxycarbonylamino-butyl)-carbamic acid tert-butyl ester (15). The methyl ester of **14** (1.75 mmol, 1.2 g) was reacted with ethylenediamine (150 mmol, 10 ml) for 72 h at 70°C. Then the excess of ethylenediamine was evaporated, the water was added and the product **15** was filtered (1.2 g, 96 %). ^{1}H NMR (CD_3OD, 300 MHz): δ 3.99 (s, 1H), 3.28-3.13 (m, 6H), 3.06 (t, 2H), 2.73 (t, 2H), 2.24-2.15 (m, 4H), 1.67-1.28 (m, 50H). LC-MS: (m/z) Found $[M+1]^+$ = 713.4 (calcd for $C_{37}H_{72}N_6O_7^+$ = 713.4).

[4-tert-Butoxycabonylamino-4-(7-{11-[2-(2,3,4,5,6-pentahydroxy-hexanoylamino)-ethylcarbamoyl]-undecylcarbamoyl}-heptylcabamoyl)-butyl]-carbamic acid tert-butyl ester (16). δ-Gulonic-γ-Lactone (0.95 mmol, 0.17 g) was added to solution of **15** (0.56 mmol, 0.4 g) in 30 ml of methanol. Then, DIEA (5.64 mmol, 0.98 ml) was added and the reaction mixture was stirred at 70°C for about 24 h. Solvents were evaporated in vacuo. The obtained compound was crystallized from methanol to get product **16** (0.15 g, 88 %). ^{1}H NMR (DMSO, 300 MHz): δ 7.83-7.61 (m, 4H), 6.8-6.64 (m, 2H), 5.35 (d, 1H), 4.57-4.26 (m, 5H), 4.0-3.75 (m, 3H), 3.61-3.38 (m, 6H), 3.22-2.81 (m, 11H), 2.06-1.95 (m, 4H), 1.54-1.37 (m, 10H), 1.36-1.32 (m, 18H), 1.31-1.11 (m, 24H). LC-MS: (m/z) Found $[M+1]^+$ = 891.6 (calcd for $C_{43}H_{82}N_6O_{13}^+$ = 891.6).

12-[8-(2,5-Diamino-pentanoylamino)-octanoylamino]-dodecanoic acid[2-(2,3,4,5,6-pentahydroxy-hexanoylamino)-ethyl]-amide (Orn-C8-C12-G). Boc group of **16** was removed from 0.1 g (0.11 mmol) of the compound using 1 ml TFA and 3% of H2O to afford the final product **Orn-C8-C12-G** (0.095 g, 92 %). MS: (m/z) Found $[M+1]^+$ = 691.5 (calcd for $C_{33}H_{67}N_6O_9^+$ = 691.5). MS: (m/z) Found $[M+1]^+$ = 691.5 (calcd for $C_{33}H_{67}N_6O_9^+$ = 691.5).

2. 1,8-ANS fluorescence data.

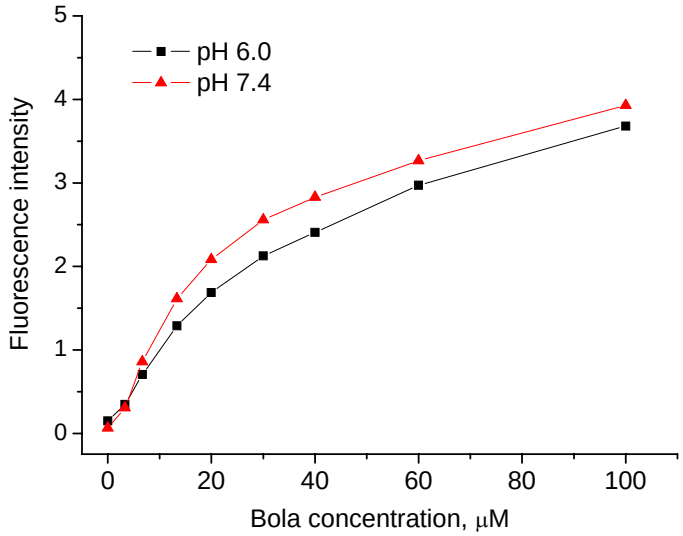


Fig. S1. Fluorescence intensity of 1,8-ANS (50 nM) as a function of Orn-C20-G bola concentration at two different pH.

3. Gel electrophoresis data.

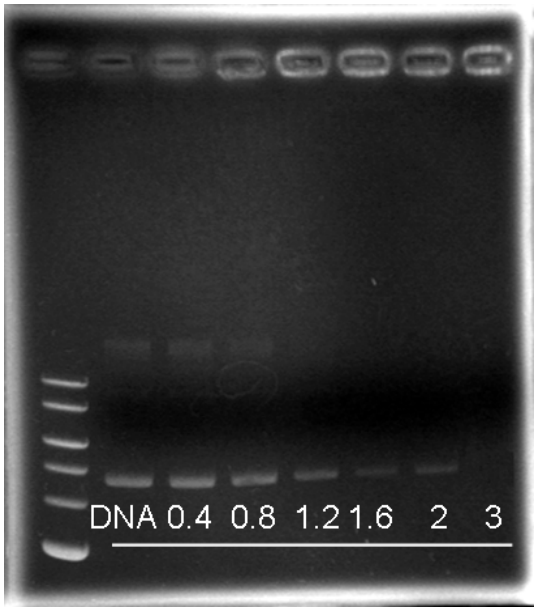


Fig. S2. Agarose gel electrophoresis (0.9%) of Orn-C16-G/DOPE (1:1) mixture complexed with pDNA at different N/P ratios. Bands at the left of the gel correspond to 10 kbp DNA ladder.

4. DLS data

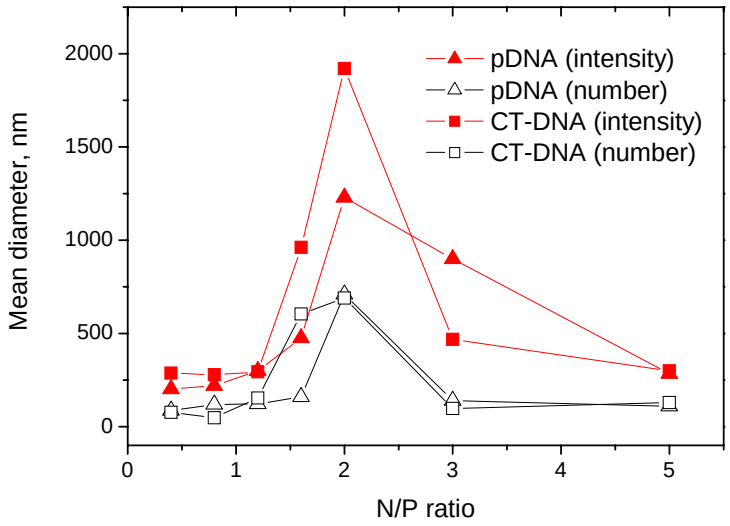
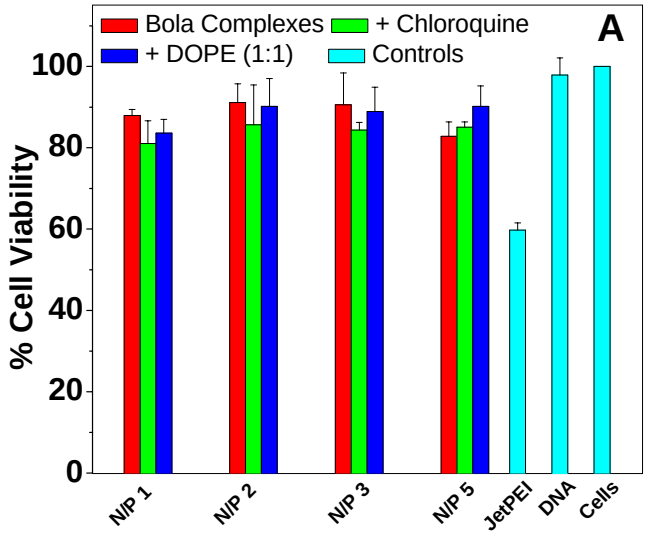


Fig. S3. Mean diameters as measured by DLS of Orn-C16-G complexes with pDNA (triangle) and CT-DNA (square) at different N/P ratios. The experiments were performed in MES buffer (pH 7.4) by addition of increasing quantities of bola stock solution (in DMF/water) to pDNA solution. Each measurement was proceeded 5 min after each addition of bola aliquot. Mean diameters are presented based on statistics of scattered intensity (filled symbols) and particle number (open symbols).

5. Cytotoxicity and total protein assays.



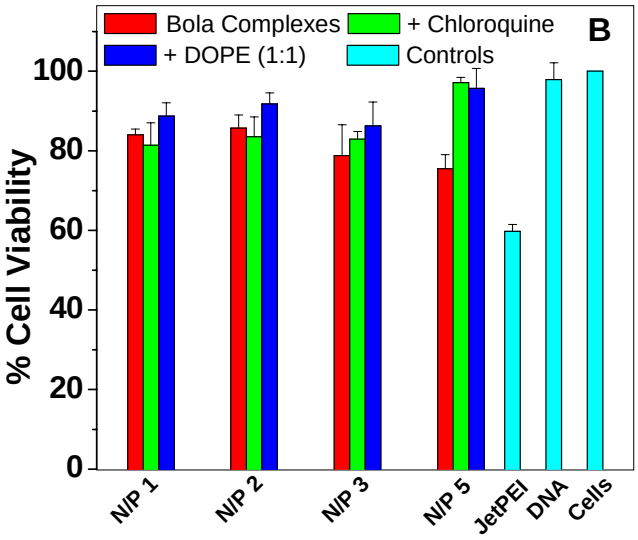


Fig. S4. Total protein concentration from the transfection experiments in COS-7 cells for **Orn-C16-G** (A) and **Orn-C20-G** (B) bolas. The data are normalized to 100% for the control non-treated cells. Cells were incubated in serum-free Opti-MEM with a bolaplex composed of plasmid DNA (1 μg per well), bola and DOPE (when indicated) at pH 7.4. Different N/P ratios were tested. After 3 h, the transfection medium was replaced with fresh complete culture medium, and cells were cultured for an additional 45 h. When indicated the medium contained 100 μM chloroquine. Then cells were lysed and the total protein was estimated using BC assay.

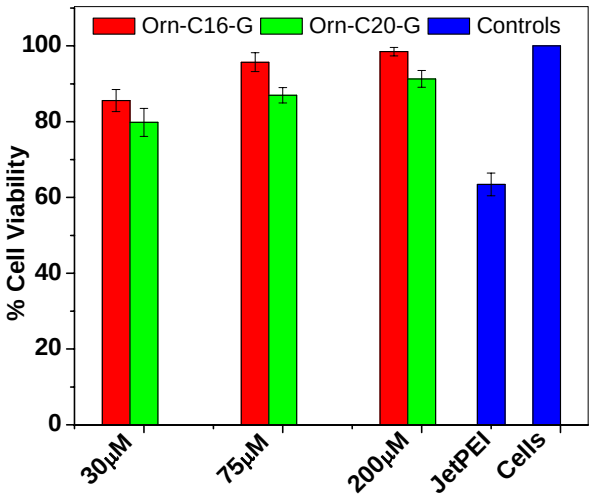


Fig. S5. Cytotoxicity of bolas based on MTT assay. COS-7 cells were incubated for 48 h with the bolas (as described in Fig. S1) at the mentioned concentrations or with JetPEI (150 μM, expressed as concentration of nitrogen residues).

References

(1) Buller, R., Cohen, H., Jensen, T. R., Kjaer, K., Lahav, M.; Leiserowitz, L. (2001) Self-Assembly of Bolaamphiphiles Forming Alternating Layer Arrangements with Lead and Copper Divalent Ions. *J. Phys. Chem. B 105*, 11447–11455.

Targeted Delivery of siRNA to Hepatocytes and Hepatic Stellate Cells by Bioconjugation

Lin Zhu and Ram I. Mahato*

Department of Pharmaceutical Sciences, University of Tennessee Health Science Center, Memphis, Tennessee 38103, United States.
Received July 28, 2010; Revised Manuscript Received September 20, 2010

Previously, we successfully conjugated galactosylated poly(ethylene glycol) (Gal-PEG) to oligonucleotides (ODNs) via an acid labile ester linker (Zhu et al., *Bioconjugate Chem.* **2008**, *19*, 290−8). In this study, sense strands of siRNA were conjugated to Gal-PEG and mannose 6-phosphate poly(ethylene glycol) (M6P-PEG) for targeted delivery of siRNAs to hepatocytes and hepatic stellate cells (HSCs), respectively. These siRNA conjugates were purified by ion exchange chromatography and verified by gel retardation assay. To evaluate their RNAi functions, the validated siRNA duplexes targeting firefly luciferase and transforming growth factor beta 1 (TGF-β1) mRNA were conjugated to Gal-PEG and M6P-PEG, and their gene silencing efficiencies were determined after transfection into HepG2 and HSC-T6 cells. The disulfide bond between PEG and siRNA was cleaved by dithiothreitol, leading to the release of intact siRNA. Both Gal-PEG-siRNA and M6P-PEG-siRNA conjugates could silence luciferase gene expression by about 40% without any transfection reagents, while the gene silencing effects reached more than 98% with the help of cationic liposomes at the same dose. Conjugation of TGF-β1 siRNA with Gal-PEG and M6P-PEG could silence endogenous TGF-β1 gene expression as well. In conclusion, these siRNA conjugates have the potential for targeted delivery of siRNAs to hepatocytes and hepatic stellate cells for efficient gene silencing in vivo.

INTRODUCTION

Significant progress has been made in enhancing the potency and specificity of RNA interference (RNAi) molecules, which include double-stranded RNA (dsRNA), small interfering RNA (siRNA) (19−23 base pairs), short hairpin RNA (shRNA), and micro RNA (miRNA). Although they are structurally different, all of these molecules induce sequence-specific gene silencing by either degrading or inhibiting the target mRNA via perfect or mismatched binding in the presence of RNA-induced silencing complex (RISC) (*1, 2*). The simplest and most effective strategy of gene silencing is to synthesize siRNAs based on the target mRNA sequence. siRNA has been shown to have the potential to treat numerous diseases, including cancer, fibrosis, genetic disorders, and viral infection (*3*−*5*). However, siRNAs have not been successfully used as clinical therapeutics due to several obstacles, including the poor enzymatic stability, short circulation time in the bloodstream, nonspecific tissue or cell targeting, and insufficient intracellular transport (*6*).

Various cationic lipids and polymers are being used as transfection reagents for siRNA delivery. siRNAs could be condensed by these carriers via electrostatic interaction into nanosized particles which are easy for cells to take up via endocytosis, membrane fusion, or both. After complex formation, siRNAs are protected from enzymatic digestion (*7*). However, cationic carriers are not suitable for in vivo delivery of siRNAs since they may bind to negatively charged serum proteins and undergo aggregation resulting in undesired distribution, and induction of inflammatory cytokines release and activation of the complement system (*8, 9*).

PEGylation is known to increase the in vitro and in vivo stability of drug molecules, as well as improve their pharmacokinetic profiles. We previously reported that the conjugation of galactose (*10*)−poly(ethylene glycol) (PEG) to oligonucleotide (ODN) using an acid-labile ester linker successfully stabilized ODN, prolonged its circulation time, and specifically delivered ODN to hepatocytes after systemic administration (*11*). The linkage between ODN and PEG could be cleaved at pH 5.5 (endosomal pH), and free ODN could be released. In a separate study, we have also demonstrated that mannose-6-phosphate (M6P) as a ligand could significantly increase the accumulation of ODN in hepatic stellate cells (HSCs) in rats.

Here, we used a similar strategy to Gal-PEG-ODN conjugate to design two siRNA conjugates, Gal-PEG-siRNA and M6P-PEG-siRNA, for targeted delivery of siRNAs to hepatocytes via asialoglycoprotein receptor-mediated endocytosis and HSCs via M6P/insulin-like growth factor-II receptor (M6P/IGF2R) mediated endocytosis, respectively. In this study, the heterobifunctional PEG, (*ortho*-pyridyl) disulfide−poly(ethylene glycol)−*N*-hydroxysuccinimidyl ester (OPSS-PEG-NHS), was used as a backbone followed by modification with either Gal or M6P at its NHS end and with the 3′-sense strand of siRNA at its OPSS end via disulfide bond. To make sure there is no loss in gene silencing due to bioconjugation, Luciferase siRNA and TGF-β1 siRNA were used as model siRNA sequences.

MATERIALS AND METHODS

Materials. OPSS-PEG-NHS (MW: 3400 Da) was purchased from Creative PEGWorks (Winston Salem, NC). Palladium (10 wt % on activated carbon), thiophosgene, dithiothreitol (DTT), L-glutathione (GSH) reduced, *p*-aminophenyl β-D-galactopyranoside, ethidium bromide (EtBr), *p*-nitrophenyl-α-D-mannopyranoside, dimethylformamide (DMF), and deuterium oxide (D_2O) were purchased from Sigma-Aldrich Chemicals (St. Louis, MO). Sodium chloride, acetic acid, and HPLC-grade water were purchased from Fisher Scientific (Fair Lawn, NJ). Luciferase assay kit, TE buffer, 6× gel loading buffer, and Tris-hydrochloride were purchased from Promega (Madison, WI).

* Corresponding author. Ram I. Mahato, Ph.D. Professor, Department of Pharmaceutical Sciences, University of Tennessee Health Science Center, 19 South Manassas St., Cancer Research Building RM 226, Memphis, TN 38103. Tel: (901) 448-6929. Fax: (901) 448-2099. E-mail: rmahato@uthsc.edu.

10.1021/bc100346n © 2010 American Chemical Society
Published on Web 10/21/2010

Human/mouse TGF-β1 ELISA kit was purchased from eBioscience (San Diego, CA). Dialysis tubing (MWCO 1000 Da) was purchased from Spectrum Laboratories, Inc. (Houston, TX). Zeba Spin Desalting Columns (MWCO: 7000 Da) was purchased from Thermo Scientific (Rockford, IL). Dulbecco's modified Eagle's medium (DMEM), penicillin streptomycin solution (100×), phosphate buffered saline (PBS), trypsin-EDTA, agarose, and Lipofectamine 2000 were purchased from Invitrogen Corporation (Carlsbad, CA). Bovine serum albumin (BSA) (fraction V, purity >98%) was purchased from Atlanta Biologicals (Lawrenceville, GA). Pyridinium cationic liposomes containing pyridinium lipid (C16:1, amide linker, trans)/DOPE (1:1 mol/mol) cationic liposomes were prepared by Zhu et al. (*12*).

Small Interfering RNAs (siRNAs). Luciferase siRNA (sense strand: CUUACGCUGAGUACUUCGA[dT][dT], antisense strand: UCGAAGUACUCAGCGUAAG[dT][dT]) was purchased from Invitrogen Corporation. TGF-β1 siRNA (*13*) (sense strand: GCUGUACAUUGACUUUAGG[dT][dT], antisense strand: CCUAAAGUCAAUGUACAGC[dT][dT]) (Accession no.: NM_021578) and the scramble siRNA were purchased from Invitrogen Corporation (Carlsbad, CA). For conjugation purposes, the sense strand of the siRNA was modified with a thiol group (-$(CH_2)_3$-S-S-$(CH_2)_3$-OH-3′) at its 3′ end by Invitrogen Corporation.

Methods. *Synthesis of p-Aminophenyl β-D-Galactopyranoside and p-Aminophenyl-6-phospho-α-D-mannopyranoside. p*-Aminophenyl β-D-galactopyranoside was synthesized according to our previous study (*11*). Briefly, p-nitrophenyl β-D-galactopyranoside was reduced with 10% palladium on activated carbon under hydrogen (1 atm) in a 1:1 (v/v) ethanol−water mixture for 2 h. The product, *p*-aminophenyl β-D-galactopyranoside, was concentrated by solvent evaporation and characterized by ^{1}H NMR and mass spectrometry after dissolving in D_2O.

p-Aminophenyl-6-phospho-α-D-mannopyranoside was synthesized according to our previous study (*14*) by dissolving *p*-nitrophenyl-α-D-mannopyranoside (pnpM) (0.3 g, 1 mmol) in the mixture of acetonitrile, pyridine, and water (1/0.4/0.04, v/v/v). Phosphorus oxide chloride (0.4 mL, 4.4 mmol) was added and stirred for 1 h on an ice−water bath. The reaction mixture was poured onto 20 g of ice. After the ice melted, pH was adjusted to 7.0 by slowly adding 2.5 M NaOH, and the solution was evaporated to dryness. The solid material was dissolved in water and crystallized at 4 °C overnight. The crystals were filtered and washed with 5 mL of absolute ethanol. The compound was recrystallized in a mixture of 1 mL of water and 10 mL of ethanol, redissolved in water, and lyophilized to give *p*-nitrophenyl-6-phospho-α-D-mannopyranoside (pnpM6P). PnpM6P was reduced with 100 mg of 10% palladium on activated carbon under H_2 (1 atm) in a 4:1 (v/v) methanol−water mixture for 2 h. After filtration, the residue was redissolved in water and lyophilized to give *p*-aminophenyl-6-phospho-α-D-mannopyranoside (papM6P). The product was characterized using ^{1}H NMR and mass spectrometry.

Synthesis of Gal-PEG-OPSS and M6P-PEG-OPSS. OPSS-PEG-NHS (50 mg) and *p*-aminophenyl β-D-galactopyranoside (50 mg) were dissolved separately in 0.4 mL of dimethylformamide (DMF), mixed together, and stirred for 6 h at room temperature under N_2 protection in the dark. The reaction mixture was dialyzed against distilled water for 48 h with MWCO 1000 to remove the unreacted *p*-aminophenyl β-D-galactopyranoside. The product Gal-PEG-OPSS was freeze−dried and characterized by ^{1}H NMR after dissolving it in D_2O.

OPSS-PEG-NHS (50 mg) were dissolved in 0.4 mL of DMF, and papM6P (50 mg) was dissolved in 0.4 mL of distilled water. Then, they were mixed and stirred for 6 h at room temperature under N_2 protection in the dark. The reaction mixture was dialyzed against distilled water for 48 h with MWCO 1000 to remove the unreacted papM6P. The product M6P-PEG-OPSS was freeze−dried and characterized by ^{1}H NMR after dissolving it in D_2O.

Synthesis of Gal-PEG-siRNA and M6P-PEG-siRNA. The lyophilized 3′ thiol-siRNA was reconstituted in TE buffer of pH 8.3−8.5 at a concentration of approximately 100 A260 units/mL. siRNA solution was then treated with 0.1 M dithiothreitol (DTT) aqueous solution at room temperature for 30 min. The excess DTT was removed by gel filtration and 3′-sulfhydryl siRNA was stored under N_2 to avoid oxidative dimerization to the disulfide before conjugation. 3′-Sulfhydryl siRNA and Gal-PEG-OPSS (or M6P-PEG-OPSS) were dissolved in 0.5 mL PBS (pH7.5) at a molar ratio of 1:100, and stirred under nitrogen at room temperature for 6 h. The reaction mixture was analyzed and purified by ion exchange high-performance liquid chromatography, which was carried on a Resource Q ion exchange column (GE Healthcare Life Sciences, Piscataway, NJ) by an HPLC system (Waters, Milford, MA) with detection at 260 nm using a gradient starting from 0% B to 80% B (A, 20 mM Tris-HCl buffer; B, 20 mM Tris-HCl buffer containing 0.1 M sodium chloride) at a flow rate of 1 mL/min at 25 °C. The purified Gal-PEG-siRNA and M6P-PEG-siRNA were desalted using Zeba Spin Desalting Column by centrifugation at the speed of 2000 *g* and freeze−dried.

Characterization of Gal-PEG-siRNA and M6P-PEG-siRNA. The concentrations of siRNA and siRNA conjugate solutions were quantitated by a UV spectrophotometer. To determine the cleavage of the disulfide bond and siRNA dissociation from Gal-PEG-siRNA and M6P-PEG-siRNA, 2 μg siRNA and the conjugates containing 2 μg siRNA were incubated in 50 mM DTT aqueous buffer for 40 min at room temperature. The DTT-treated samples and controls (nontreated siRNA and siRNA conjugate) were mixed with 6× gel loading buffer and applied on the 1% agarose gel and run at 10 V/cm for 60 min at room temperature followed by ethidium bromide (EtBr) staining and visualization under UV light.

Cell Cultures and Transfections. HepG2 cells were maintained in a complete growth medium containing DMEM medium supplemented with 10% FBS, 100 IU/mL penicillin, and 100 μg/mL streptomycin at 37 °C in a 5% CO_2 humidified atmosphere. HSC-T6 cells, kindly provided by Dr. Scott Friedman (Mount Sinai School of Medicine, New York), were maintained in the same condition as HepG2 cells. Before transfection, the cells were seeded in 24-well plates and maintained in 0.5 mL of complete growth medium at 37 °C for 24 h. The cell number was about 4×10^4 cells per well.

Luciferase expression plasmid (pDNA3-Luc) was first transfected with cells by pyridinium cationic liposomes (*12*). Briefly, 0.2 μg/well luciferase plasmid and pyridinium cationic liposomes were diluted to 25 μL by Opti-MEM I medium, respectively, and incubated for 5 min at room temperature. Lipoplexes were prepared by mixing plasmid and liposomes in equal volume and incubated for 20 min at room temperature to allow complex formation. Immediately before transfection, the medium was removed, and cells were washed gently with sterile phosphate buffered saline. Lipoplexes were added to each well and diluted to 0.5 mL by Opti-MEM I medium, and the plate was incubated under 5% CO_2 at 37 °C for 6 h. Following transfection, the culture medium was replaced with complete growth medium and maintained overnight before further treatment.

To transfect luciferase siRNA and its conjugate, two methods were used. In the first method, siRNA and its conjugates were added directly into cell cultures without the assistance of cationic liposomes. In the second method, siRNA and its conjugates were mixed with cationic liposomes to form the lipoplexes before

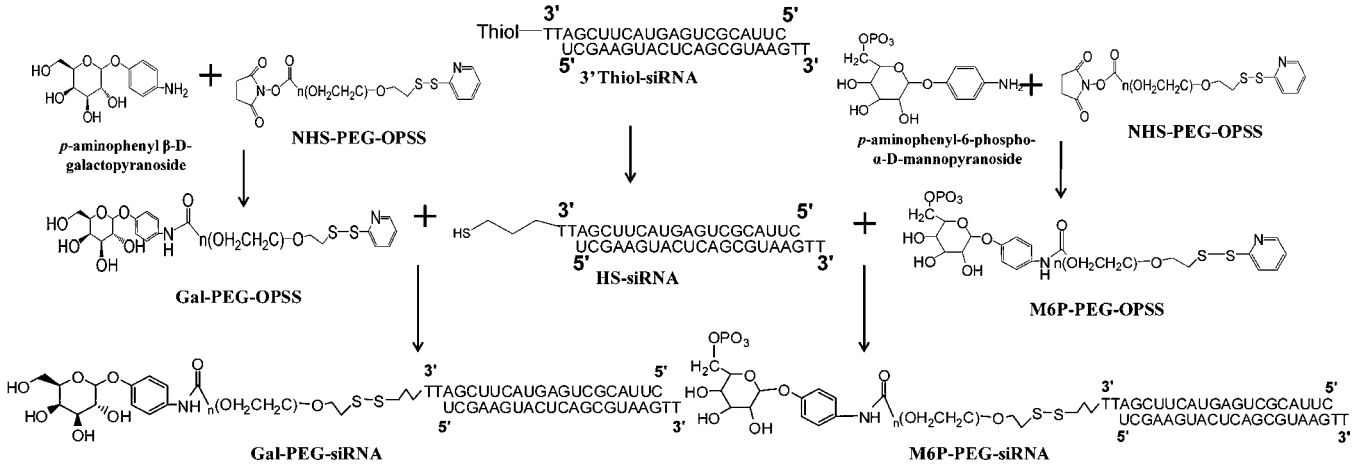


Figure 1. Synthesis scheme of Gal-PEG-siRNA and M6P-PEG-siRNA.

adding into cell cultures. After 6 h of transfection, the medium was replaced with the complete growth medium and incubated for an additional 42 h.

To determine luciferase gene expression, the cells were collected and lysed. The cell lysate was measured for luciferase gene expression by Luciferase Assay Kit (Promega, Madison, WI). The total protein concentration was measured by bicinchoninic acid (BCA) protein assay reagent (Pierce, Rockford, IL). Luciferase activity was normalized by the total protein content and expressed as relative light unit (RLU) per microgram of protein (RLU/μg protein).

To determine their gene silencing effects, TGF-β1 siRNA and its conjugates were mixed with the media and added into HepG2 cells and HSC cells. After 6 h of transfection, the medium was replaced with the complete growth medium and incubated for additional 42 h. To determine TGF-β1 gene expresstion, the supernatant was collected and measured by Human/Mouse TGF-β1 ELISA kit.

RESULTS

Synthesis of Gal-PEG-siRNA and M6P-PEG-siRNA. The synthesis scheme of Gal-PEG-siRNA and M6P-PEG-siRNA was shown in Figure 1. Before conjugation, *p*-nitrophenyl β-D-galactopyranoside was reduced to *p*-aminophenyl β-D-galactopyranoside. ESI-MS and ^{1}H NMR spectra of this intermediate product were not shown but could be found in our previous paper (*11*). *p*-Nitrophenyl-α-D-mannopyranoside (pnpM) was phosphorylated to *p*-nitrophenyl-6-phospho-α-D-mannopyranoside (pnpM6P) and pnpM6P was reduced to *p*-aminophenyl-6-phospho-α-D-mannopyranoside (papM6P). ESI-MS and ^{1}H NMR results of this intermediate product are shown in Figure 2.

Gal-PEG-OPSS and M6P-PEG-OPSS were synthesized from heterofunctional PEG derivative, NHS-PEG-OPSS and identified by ^{1}H NMR. After reaction with Gal or M6P, the two peaks (a and b positions) of the benzene ring were found in the NMR spectra. The data indicated that Gal and M6P reacted with NHS group and linked with PEG (Figure 3). Gal-PEG-OPSS and M6P-PEG-OPSS were then conjugated to 3′-sulfhydryl siRNA by disulfide exchange reaction between sulfhydryl and OPSS groups. Ion exchange HPLC was used to monitor the conjugation reaction and purify the final products. The ion exchange HPLC chromatograms of siRNA, M6P-PEG-OPSS, and M6P-PEG-siRNA were shown in Figure 4. M6P-PEG-OPSS eluted first, since they have no charge and cannot bind to anion exchange resin; free siRNA is a negatively charged molecule and bound to anion exchange resin and eluted last. After conjugation, the charge of siRNA was partially blocked by the flexible long chain of PEG and eluted between PEG and siRNA. The chromatograms of Gal-PEG-OPSS and Gal-PEG-siRNA were not shown, since they are similar to those of M6P-PEG-OPSS and M6P-PEG-siRNA. Gal-PEG-siRNA and M6P-PEG-siRNA conjugates were also identified by 1% agarose gel electrophoresis and visualized under UV light (Figure 5).

Dissociation of siRNAs from Gal-PEG-siRNA and M6P-PEG-siRNA Conjugates. To determine whether the disulfide bond between Gal-PEG or M6P-PEG and siRNA is cleavable and free siRNA can be released, siRNA and its conjugates were treated with DTT aqueous buffer for 40 min and analyzed by gel retardation assay. Gal-PEG-siRNA and M6P-PEG-siRNA conjugates migrated more slowly than free siRNA. However, after treatment with DTT for 40 min, the disulfide bond was completely cleaved and free siRNA was released and migrated at the same speed as the siRNA control (Figure 5).

Gene Silencing Study. Firefly luciferase expression plasmid was transfected into both HepG2 and HSC-T6 cells using previously optimized pyridinium cationic liposomes at the charge ratio of 3:1 (N/P) (*12*). Gene silencing efficiencies of siRNA conjugates were determined after transfection of luciferase expression plasmid. In the absence of cationic liposomes, Gal-PEG-siRNA conjugate showed luciferase gene silencing up to about 45% at the dose of 400 nM compared to the naked siRNA group and the control group (plasmid group) without siRNA treatment (Figure 6A). Addition of an excessive amount of Gal-PEG-OPSS into HepG2 cells before transfection of siRNA conjugate abolished the gene silencing ability of Gal-PEG-siRNA conjugate. Similarly, pretreatment of HSC-T6 cells with an excess amount of M6P-PEG-OPSS before the transfection of M6P-PEG-siRNA conjugate abolished the gene silencing ability of this conjugate. Target cells were pretreated with an excess amount of Gal-PEG-OPSS or M6P-PEG-OPSS to saturate the surface receptors and inhibit the receptor-mediated cellular uptake of siRNA conjugates. Since the molecular weights of galactose or mannose 6-phosphate are too small and may not be effective in saturating the target receptors, the conjugates containing the ligands are commonly used (*11*). To keep data comparable, we used 400 nM siRNA conjugates in Gal-PEG+ conjugate and M6P-PEG+conjugate groups.

Figure 6B showed the luciferase gene silencing efficiency of siRNA and Gal-PEG-siRNA. After complex formation with pyridinium cationic liposomes, the gene silencing of Gal-PEG-siRNA significantly increased and reached up to 90% even at the dose of 100 nM, while the gene silencing effect of luciferase siRNA was just about 60% at the same dose. Figure 6C showed the gene silencing ability of M6P-PEG-siRNA in HSC-T6 cells without pyridinium cationic liposomes. M6P-PEG-siRNA could

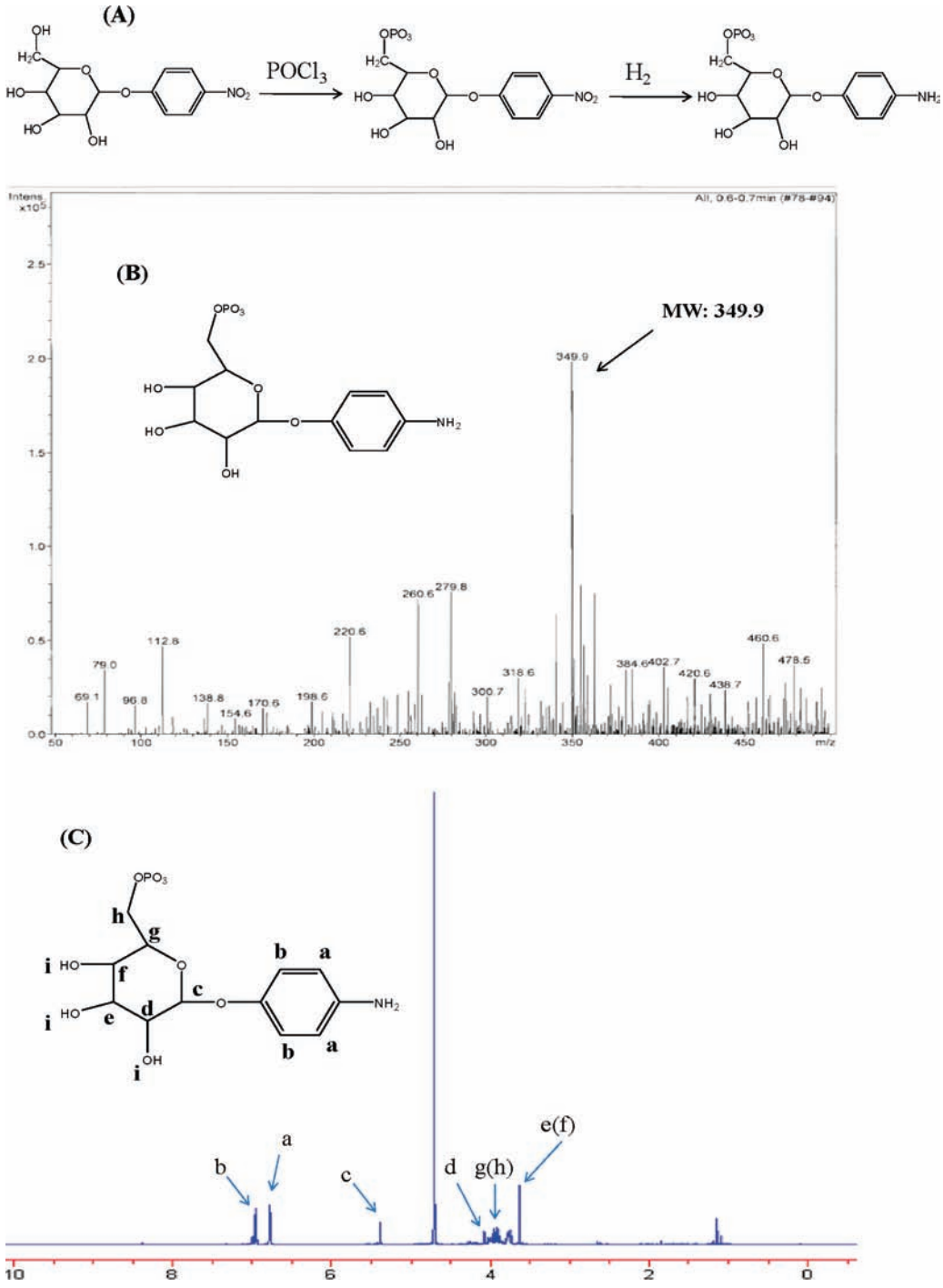


Figure 2. Synthesis and characterization of *p*-aminophenyl-6-phospho-α-D-mannopyranoside with ESI-MS and ^{1}H NMR. (A) Synthesis scheme of *p*-aminophenyl-6-phospho-α-D-mannopyranoside. (B) Electron spray ionization mass spectra were obtained after dissolving the product in a 4:1 (v/v) methanol−water mixture on an ESQUIRE-LC ion trap LC/MS sy stem in negative mode. (C) For ^{1}H NMR, samples were dissolved in D_2O, and the spectra were recorded on a Bruker ARX-500 MHz NMR spectrometer at 25 °C.

silence luciferase gene expression at a similar level to Gal-PEG-siRNA. Luciferase gene silencing was dependent on Gal-PEG-siRNA and M6P-PEG-siRNA dose in both the absence and presence of pyridinium cationic liposomes.

To determine the effect of bioconjugation on TGF-β1 gene silencing in HepG2 and HSC-T6 cells, the sense strand of a potent TGF-β1 siRNA duplex was conjugated with either Gal-PEG-OPSS or M6P-PEG-OPSS to form TGF-β1 siRNA conjugates. After transfection, the level of TGF-β1 protein in the cell medium was measured by ELISA kit. The gene silencing effects of siRNA conjugates were shown in Figure 7. Without transfection reagents, conjugation of TGF-β1 siRNA with Gal-PEG-OPSS or M6P-PEG-OPSS significantly enhanced TGF-β1 gene silencing effects up to 40% of the nontreatment group compared to TGF-β1 siRNA.

DISCUSSION

Effective delivery of siRNA to specific cell types in vivo is critical for the successful therapeutic use of siRNA. The current studies of siRNA delivery systems are focused on the electrostatic interaction with cationic liposomes and polymers, since negatively charged siRNAs are poorly taken up by the cells. Although the use of these cationic carriers is effective in vitro, an ideal siRNA carrier should not bear any positive charge, since

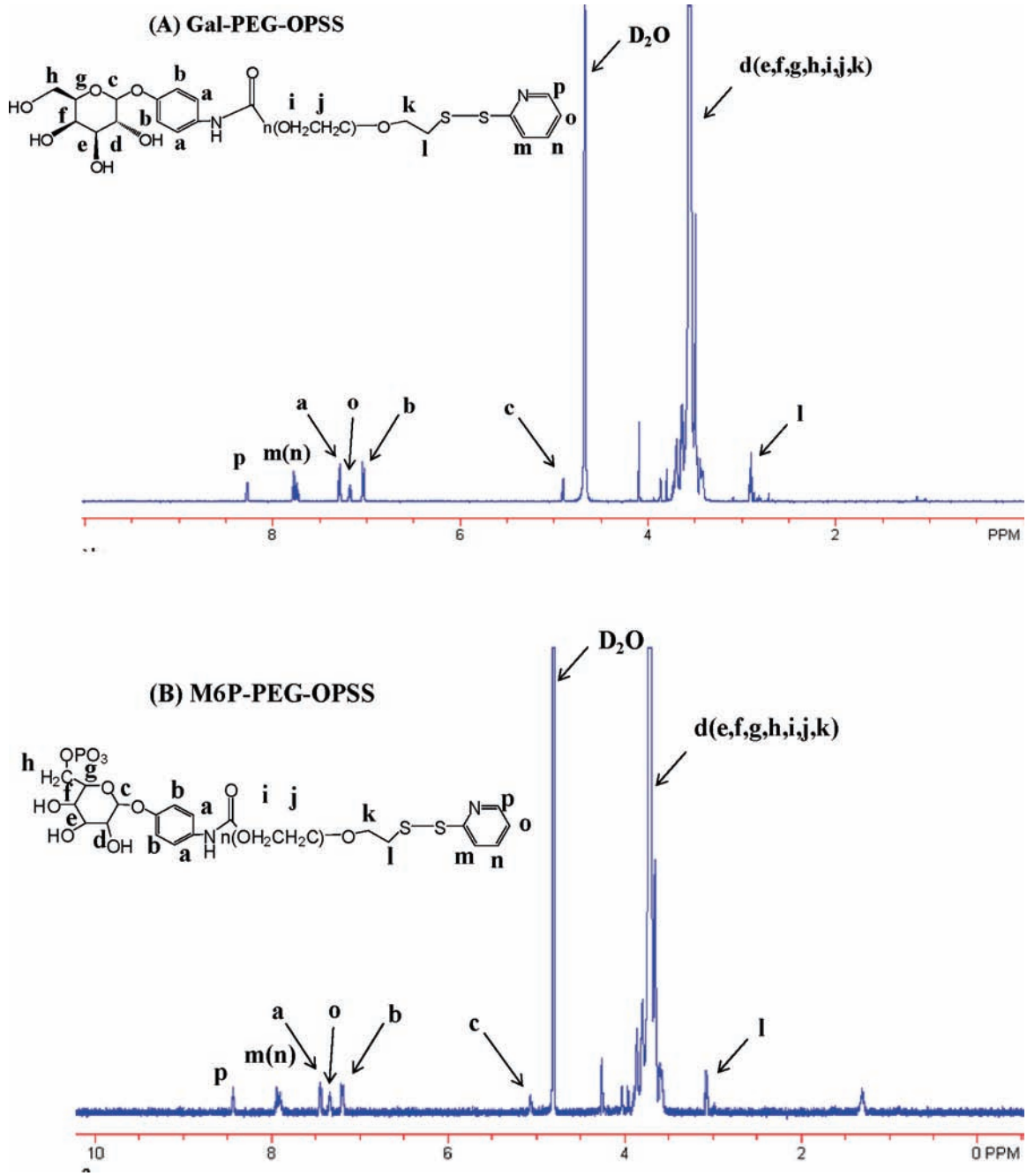


Figure 3. Characterization of Gal-PEG-OPSS (A) and M6P-PEG-OPSS (B) with ^{1}H NMR. The samples were dissolved in D_2O, and the spectra were recorded on a Bruker ARX-500 MHz NMR spectrometer at 25 °C.

it may cause an immune response and unexpected distribution due to nonspecific ionic interaction with plasma proteins. To avoid the use of polycations, Rajue et al. directly conjugated asialoglycoprotein to ODNs via disulfide bonds to target hepatocytes (*15*). Nakagawa et al. directly conjugated the small-molecule ligand, anisamide, to ODNs, to target the σ receptor on the surface of human lung cancer cells (*16*). The lipophilic molecule, α-tocopherol, was also covalently conjugated to the antisense strand of siRNA to target the liver (*17*). Although direct conjugation of ligands to ODN or siRNA increased their targeting efficiencies, it might not significantly improve the stability or dissociation of loaded ODN and siRNA. PEGylation is known to significantly enhance the stability of ODNs and siRNAagainst exonucleases and reduce renal clearance compared to unmodified ones (*18*−*20*), which improves their bioactivity by increasing plasma residence time and decreasing nuclease degradation. The flexible PEG chains also shield the inherent negative charge of these ODNs and siRNA, thereby possibly facilitating cellular uptake of the conjugated ODNs and siRNA (*21*).

Oligonucleotides and siRNA are cleared rapidly from the blood circulation and accumulated in the peripheral tissues, especially in the liver and kidney (*22*−*24*). Their in vivo activity depends on their pharmacokinetic profiles, especially the rate of excretion and degradation. In a previous study, we successfully conjugated ODN to Gal-PEG via an acid-labile linkage and demonstrated that systemic administration of Gal-PEG-ODN significantly increased accumulation in hepatocytes via galactose/asialoglycoprotein receptor-mediated endocytosis (*11*). In a separate study, we synthesized M6P-BSA and conjugated this to ODN. Systemic administration of M6P-BSA-ODN conjugate increased the accumulation of ODNs in HSCs via M6P/IGF2R mediated endocytosis compared to other types of liver cells in rats (*14*).

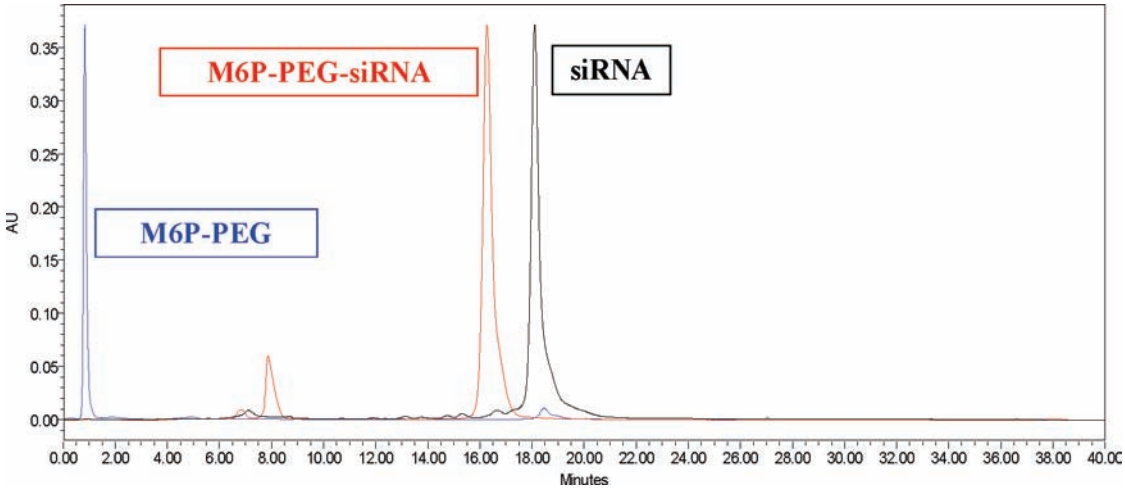


Figure 4. Purification of M6P-PEG-siRNA conjugate by ion-exchange chromatography. The reaction mixture was carried on a Resource Q ion exchange column (GE Healthcare Life Sciences, Piscataway, NJ) by an HPLC system (Waters, Milford, MA) with detection at 260 nm using a gradient starting from 0% B to 80% B (A, 20 mM Tris-HCl buffer; B, 20 mM Tris-HCl buffer containing 0.1 M sodium chloride) at a flow rate of 1 mL/min at 25 °C.

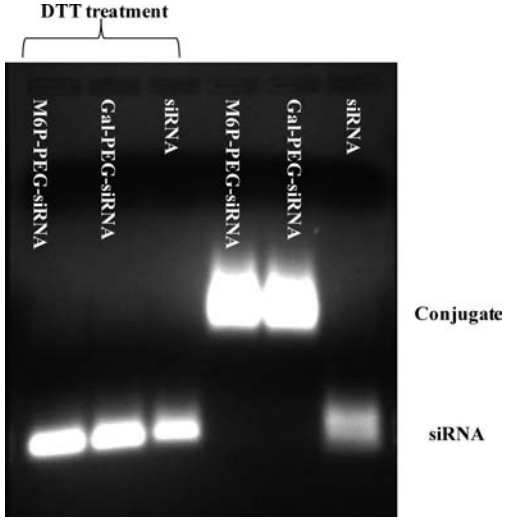


Figure 5. Identification of siRNA conjugates by gel retardation assay. Two microgram aliquots of siRNAs, Gal-PEG-siRNA, and M6P-PEG-siRNA were incubated with 50 mM DTT at room temperature for 40 min. The treated samples and nontreated controls were applied on 1% agarose gel and run at 10 V/cm for 60 min followed by EtBr staining, then visualized under UV light.

siRNAs can be covalently linked with functional molecules via either noncleavable or cleavable linkages, such as acid-labile ester (*11, 25*) and reducible disulfide bond (*19, 26*). For single-stranded ODNs, both 3′- and 5′-termini of these molecules are reported to be used as functional sites for the conjugation reaction (*11, 27*). For the siRNA duplex, however, the antisense strand of siRNA plays a key role and works as the template in RISC to perform RNAi. Improper modification of antisense strands may cause the loss of RNAi function (*28*). It was further shown that the 5′-terminus of the antisense strand was more important than the 3′-terminus and determined RNAi activity (*29*−*31*). In comparison to the antisense strand, manipulation of the sense strand of siRNA is relatively safe and effective. Both 3′- and 5′-ends of the sense strand can be used for conjugation (*32*).

In the present study, we investigated the application of a PEG-based macromolecular delivery system using two different ligands for siRNA delivery. Since the disulfide bond has been proven to be cleaved by reducing agents in the cytoplasm and was extensively used in drug delivery systems (*19, 33*−*35*), we used cleavable disulfide bonds as the linkage between siRNA and PEG to ensure the release of intact siRNA molecules from the conjugates in the reducing environment in the cytoplasm where RNAi takes action after endocytosis. This is expected to be better than the use of PEGylated cationic liposomes and PEI, where the PEG chain may influence the endosomal escape, as the PEG chain often cannot be released from the carriers.

Chronic liver injury and inflammation of hepatocytes or other hepatic cells cause liver fibrosis, resulting in excessive accumulation of extracellular matrix (ECM) proteins and activation and transformation of HSCs to proliferative myofibroblast-like cells. Many inflammatory cytokines were up-regulated during liver fibrosis. Among them, TGF-β1, which is mainly expressed by HSCs, plays a key role in initiation and maintenance of liver fibrosis (*36*). TGF-β1 gene silencing has been shown to inhibit the ECM production as well as accelerate its degradation resulting in resolution of fibrogenesis (*37*). In our previous study, we demonstrated siRNA sequence and dose-dependent TGF-β1 gene silencing and consequent inhibition of collagen synthesis (*13*). Therefore, hepatocytes and HSCs are often chosen as targets to deliver the therapeutics to treat liver fibrosis. Excessive ECM causes the loss of sinusoidal fenestrae (*38*), suggesting that liposomal and other particulate delivery systems may not be suitable for siRNA delivery to hepatic cells. In comparison to particulate delivery systems, the water-soluble delivery systems, Gal-PEG-siRNA and M6P-PEG-siRNA, are much more attractive for siRNA delivery to hepatocytes and HSCs in fibrotic liver. In this study, the 3′-thiol modifier was first reduced to a 3′-sulfhydryl group, which was active and could form a disulfide bond with an (*ortho*-pyridyl)-disulfide (OPSS) group by disulfide exchange reaction in PBS. The disulfide bond was cleaved, and free siRNAs were released after treatment with a reducing agent DTT. The gel retardation assay confirmed that, after conjugation with PEG, the migration rate of siRNA conjugates was significantly slower than that of free siRNA, but after DTT treatment, the linker between siRNA and PEG was cleaved, and the released siRNA showed a similar migration rate to unconjugated siRNA (Figure 5). We did not use mass spectrophotometry to identify the siRNA conjugates, because siRNA may get degraded during the MALDI-TOF MS test, and it requires a large amount of siRNA to get the signal (*39, 40*).

Luciferase gene silencing of siRNA conjugates indicated that siRNAs did not lose their RNAi function during conjugation and after dissociation from siRNA conjugates (Figure 6). siRNA

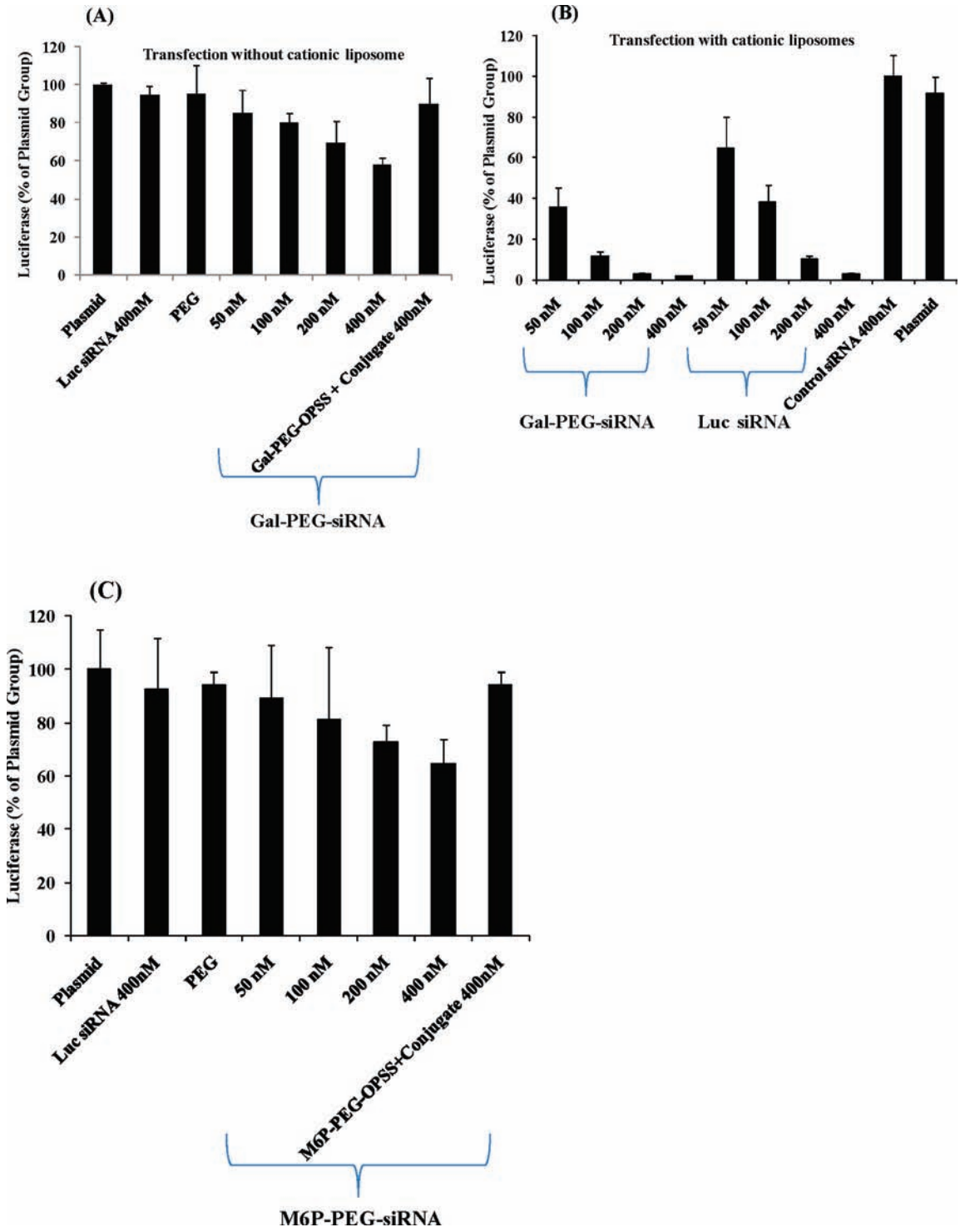


Figure 6. Luciferase gene silencing effects of Gal-PEG-siRNA and M6P-PEG-siRNA. Before the gene silencing study, luciferase plasmid was transfected into both HepG2 and HSC-T6 cells using lipoplexes formed between luciferase plasmid and pyridinium cationic liposomes at the charge ratio of 3/1 (±). The dose of plasmid was 0.2 μg per well in a 24-well plate. To study the gene silencing ability of Gal-PEG-siRNA, luciferase siRNA and its Gal-PEG-siRNA conjugate were added into HepG2 cells without (A) and with (B) the formation of siRNA/liposome complexes using pyridinium cationic liposomes. For M6P-PEG-siRNA, luciferas siRNA and its M6P-PEG-siRNA conjugate were added directly into HSC-T6 cells without cationic liposomes (C). After 6 h of transfection, the medium was replaced with the complete growth medium and incubated for additional 42 h. The cell number was about 4×10^4 cells per well in a 24-well plate.

conjugates had about 40% down-regulation of luciferase gene at the dose of 400 nM in both HepG2 and HSC-T6 cells in the absence of cationic liposomes (Figure 6A,C), while the luciferase gene was almost completely silenced in the presence of cationic liposomes at the same condition (Figure 6B). Without condensation with cationic liposomes, the flexible hydrophilic PEG chain surrounds and shields siRNA or the ligand on it from accessing the cell membrane, thereby decreasing both specific and nonspecific endocytosis. After complex formation with cationic liposomes, the lipoplexes were slightly positively charged and easy for cells to take up (nonspecific) and had high gene silencing effects. Furthermore, the combination of ligand−receptor-mediated specific endocytosis, siRNA conjugates showed higher gene silencing effect compared to naked

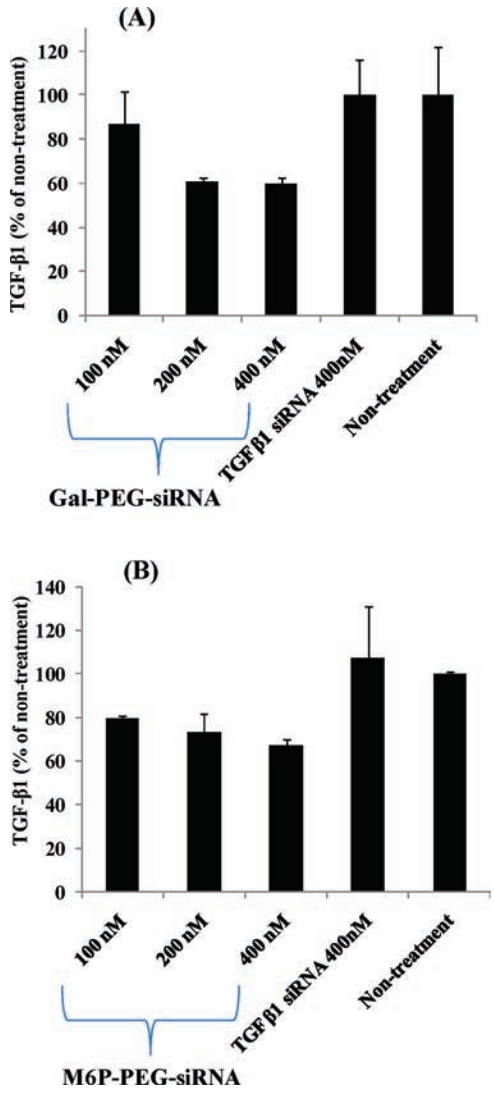


Figure 7. TGF-β1 gene silencing effects of Gal-PEG-siRNA and M6P-PEG-siRNA. (A) TGF-β1 siRNA and Gal-PEG-siRNA were added directly into HepG2 cells without cationic liposomes. (B) TGF-β1 siRNA and M6P-PEG-siRNA were added directly into HSC-T6 cells without cationic liposomes. After 6 h of transfection, the medium was replaced with the complete growth medium and incubated for an additional 42 h. There were about 4×10^4 cells per well in a 24-well plate.

siRNAs (Figure 6B). However, in the in vivo situation, PEGylated siRNAs will be retained in blood circulation and cleared very slowly compared to naked siRNAs. Our previous studies showed that pegylated ODN could significantly prolong the elimination half-life ($t_{1/2\beta}$) of ODN up to 118.61 $\pm$ 22.06 min (*11*) compared to only 34.60 $\pm$ 4.32 min of naked ODN after i.v. injection in rats (*14*). The longer residence will provide sufficient time for siRNA conjugates to access their target cells and initiate ligand−receptor-mediated endocytosis. In Figure 6A,C, preaddition of an excessive amount of Gal-PEG or M6P-PEG significantly inhibited the gene silencing effects of corresponding siRNA conjugates, which indicated that the cellular uptake of siRNA conjugates was ligand−receptor-mediated endocytosis, not nonspecific endocytosis.

To verify the function of PEG-based siRNA conjugate, we used TGF-β1 siRNA as the model sequence. The similar gene silencing effects were observed when TGF-β1 siRNA was conjugated to Gal-PEG-OPSS and M6P-PEG-OPSS (Figure 7A,B). On the basis of these results, we can predict that cation-free Gal-PEG-siRNA and M6P-PEG-siRNA conjugates will be specifically accumulated in hepatocytes or HSCs and minimize the nonspecific distribution and immunostimulatory effect in vivo.

In conclusion, we successfully conjugated siRNA to Gal-PEG-OPSS and M6P-PEG-OPSS via a disulfide bond. The gene silencing effects of these siRNA conjugates were observed in HepG2 and HSC-T6 cells. These siRNA conjugates have the potential to be used for targeted delivery of siRNAs to hepatocytes and hepatic stellate cells in vivo.

ACKNOWLEDGMENT

This study was supported by a grant EB003922 from the National Institute of Health.

LITERATURE CITED

(1) Montgomery, M. K., Xu, S., and Fire, A. (1998) RNA as a target of double-stranded RNA-mediated genetic interference in Caenorhabditis elegans. *Proc. Natl. Acad. Sci. U.S.A. 95*, 15502–7.

(2) Fire, A., Xu, S., Montgomery, M. K., Kostas, S. A., Driver, S. E., and Mello, C. C. (1998) Potent and specific genetic interference by double-stranded RNA in Caenorhabditis elegans. *Nature 391*, 806–11.

(3) Song, E., Lee, S. K., Wang, J., Ince, N., Ouyang, N., Min, J., Chen, J., Shankar, P., and Lieberman, J. (2003) RNA interference targeting Fas protects mice from fulminant hepatitis. *Nat. Med. 9*, 347–51.

(4) de Fougerolles, A., Vornlocher, H. P., Maraganore, J., and Lieberman, J. (2007) Interfering with disease: a progress report on siRNA-based therapeutics. *Nat. Rev. Drug Discovery 6*, 443–53.

(5) Oh, Y. K., and Park, T. G. (2009) siRNA delivery systems for cancer treatment. *Adv. Drug Delivery Rev. 61*, 850–62.

(6) De Paula, D., Bentley, M. V., and Mahato, R. I. (2007) Hydrophobization and bioconjugation for enhanced siRNA delivery and targeting. *RNA 13*, 431–56.

(7) Herringson, T. P., and Altin, J. G. (2009) Convenient targeting of stealth siRNA-lipoplexes to cells with chelator lipid-anchored molecules. *J. Controlled Release 139*, 229–38.

(8) Hartikka, J., Bozoukova, V., Ferrari, M., Sukhu, L., Enas, J., Sawdey, M., Wloch, M. K., Tonsky, K., Norman, J., Manthorpe, M., and Wheeler, C. J. (2001) Vaxfectin enhances the humoral immune response to plasmid DNA-encoded antigens. *Vaccine 19*, 1911–23.

(9) Moghimi, S. M., and Patel, H. M. (2002) Modulation of murine liver macrophage clearance of liposomes by diethylstilbestrol. The effect of vesicle surface charge and a role for the complement receptor Mac-1 (CD11b/CD18) of newly recruited macrophages in liposome recognition. *J. Controlled Release 78*, 55–65.

(10) Hermanson, G., Whitlow, V., Parker, S., Tonsky, K., Rusalov, D., Ferrari, M., Lalor, P., Komai, M., Mere, R., Bell, M., Brenneman, K., Mateczun, A., Evans, T., Kaslow, D., Galloway, D., and Hobart, P. (2004) A cationic lipid-formulated plasmid DNA vaccine confers sustained antibody-mediated protection against aerosolized anthrax spores. *Proc. Natl. Acad. Sci. U.S.A. 101*, 13601–6.

(11) Zhu, L., Ye, Z., Cheng, K., Miller, D. D., and Mahato, R. I. (2008) Site-specific delivery of oligonucleotides to hepatocytes after systemic administration. *Bioconjugate Chem. 19*, 290–8.

(12) Zhu, L., Lu, Y., Miller, D. D., and Mahato, R. I. (2008) Structural and formulation factors influencing pyridinium lipid-based gene transfer. *Bioconjugate Chem. 19*, 2499–512.

(13) Cheng, K., Yang, N., and Mahato, R. I. (2009) TGF-beta1 gene silencing for treating liver fibrosis. *Mol. Pharm. 6*, 772–9.

(14) Ye, Z., Cheng, K., Guntaka, R. V., and Mahato, R. I. (2005) Targeted delivery of a triplex-forming oligonucleotide to hepatic stellate cells. *Biochemistry 44*, 4466–76.

(15) Rajur, S. B., Roth, C. M., Morgan, J. R., and Yarmush, M. L. (1997) Covalent protein-oligonucleotide conjugates for efficient

delivery of antisense molecules. *Bioconjugate Chem. 8*, 935–40.

(16) Nakagawa, O., Ming, X., Huang, L., and Juliano, R. L. Targeted intracellular delivery of antisense oligonucleotides via conjugation with small-molecule ligands. *J. Am. Chem. Soc. 132*, 8848–9.

(17) Nishina, K., Unno, T., Uno, Y., Kubodera, T., Kanouchi, T., Mizusawa, H., and Yokota, T. (2008) Efficient in vivo delivery of siRNA to the liver by conjugation of alpha-tocopherol. *Mol. Ther. 16*, 734–40.

(18) Healy, J. M., Lewis, S. D., Kurz, M., Boomer, R. M., Thompson, K. M., Wilson, C., and McCauley, T. G. (2004) Pharmacokinetics and biodistribution of novel aptamer compositions. *Pharm. Res. 21*, 2234–46.

(19) Kim, S. H., Jeong, J. H., Lee, S. H., Kim, S. W., and Park, T. G. (2006) PEG conjugated VEGF siRNA for anti-angiogenic gene therapy. *J. Controlled Release 116*, 123–9.

(20) Lee, S. H., Kim, S. H., and Park, T. G. (2007) Intracellular siRNA delivery system using polyelectrolyte complex micelles prepared from VEGF siRNA-PEG conjugate and cationic fusogenic peptide. *Biochem. Biophys. Res. Commun. 357*, 511–6.

(21) Kim, S. H., Jeong, J. H., Lee, S. H., Kim, S. W., and Park, T. G. (2008) Local and systemic delivery of VEGF siRNA using polyelectrolyte complex micelles for effective treatment of cancer. *J. Controlled Release 129*, 107–16.

(22) Mahato, R. I., Rolland, A., and Tomlinson, E. (1997) Cationic lipid-based gene delivery systems: pharmaceutical perspectives. *Pharm. Res. 14*, 853–9.

(23) Graham, M. J., Crooke, S. T., Monteith, D. K., Cooper, S. R., Lemonidis, K. M., Stecker, K. K., Martin, M. J., and Crooke, R. M. (1998) In vivo distribution and metabolism of a phosphorothioate oligonucleotide within rat liver after intravenous administration. *J. Pharmacol. Exp. Ther. 286*, 447–58.

(24) Santel, A., Aleku, M., Keil, O., Endruschat, J., Esche, V., Fisch, G., Dames, S., Loffler, K., Fechtner, M., Arnold, W., Giese, K., Klippel, A., and Kaufmann, J. (2006) A novel siRNA-lipoplex technology for RNA interference in the mouse vascular endothelium. *Gene Ther. 13*, 1222–34.

(25) Oishi, M., Nagasaki, Y., Itaka, K., Nishiyama, N., and Kataoka, K. (2005) Lactosylated poly(ethylene glycol)-siRNA conjugate through acid-labile beta-thiopropionate linkage to construct pH-sensitive polyion complex micelles achieving enhanced gene silencing in hepatoma cells. *J. Am. Chem. Soc. 127*, 1624–5.

(26) Muratovska, A., and Eccles, M. R. (2004) Conjugate for efficient delivery of short interfering RNA (siRNA) into mammalian cells. *FEBS Lett. 558*, 63–8.

(27) Harrison, J. G., and Balasubramanian, S. (1998) Synthesis and hybridization analysis of a small library of peptide-oligonucleotide conjugates. *Nucleic Acids Res. 26*, 3136–45.

(28) Chiu, Y. L., and Rana, T. M. (2003) siRNA function in RNAi: a chemical modification analysis. *RNA 9*, 1034–48.

(29) Schwarz, D. S., Hutvagner, G., Du, T., Xu, Z., Aronin, N., and Zamore, P. D. (2003) Asymmetry in the assembly of the RNAi enzyme complex. *Cell 115*, 199–208.

(30) Khvorova, A., Reynolds, A., and Jayasena, S. D. (2003) Functional siRNAs and miRNAs exhibit strand bias. *Cell 115*, 209–16.

(31) Schwarz, D. S., Hutvagner, G., Haley, B., and Zamore, P. D. (2002) Evidence that siRNAs function as guides, not primers, in the Drosophila and human RNAi pathways. *Mol. Cell 10*, 537–48.

(32) Jeong, J. H., Mok, H., Oh, Y. K., and Park, T. G. (2009) siRNA conjugate delivery systems. *Bioconjugate Chem. 20*, 5–14.

(33) Rozema, D. B., Lewis, D. L., Wakefield, D. H., Wong, S. C., Klein, J. J., Roesch, P. L., Bertin, S. L., Reppen, T. W., Chu, Q., Blokhin, A. V., Hagstrom, J. E., and Wolff, J. A. (2007) Dynamic PolyConjugates for targeted in vivo delivery of siRNA to hepatocytes. *Proc. Natl. Acad. Sci. U.S.A. 104*, 12982–7.

(34) Al-Abd, A. M., Lee, S. H., Kim, S. H., Cha, J. H., Park, T. G., Lee, S. J., and Kuh, H. J. (2009) Penetration and efficacy of VEGF siRNA using polyelectrolyte complex micelles in a human solid tumor model in-vitro. *J. Controlled Release 137*, 130–5.

(35) Derfus, A. M., Chen, A. A., Min, D. H., Ruoslahti, E., and Bhatia, S. N. (2007) Targeted quantum dot conjugates for siRNA delivery. *Bioconjugate Chem. 18*, 1391–6.

(36) Bauer, M., and Schuppan, D. (2001) TGFbeta1 in liver fibrosis: time to change paradigms. *FEBS Lett. 502*, 1–3.

(37) Friedman, S. L. (2003) Liver fibrosis -- from bench to bedside. *J. Hepatol. 38* (Suppl 1), S38–53.

(38) Bataller, R., and Brenner, D. A. (2005) Liver fibrosis. *J. Clin. Invest. 115*, 209–18.

(39) Turner, J. J., Jones, S. W., Moschos, S. A., Lindsay, M. A., and Gait, M. J. (2007) MALDI-TOF mass spectral analysis of siRNA degradation in serum confirms an RNAse A-like activity. *Mol. Biosyst. 3*, 43–50.

(40) Bahr, U., Aygun, H., and Karas, M. (2008) Detection and relative quantification of siRNA double strands by MALDI mass spectrometry. *Anal. Chem. 80*, 6280–5.

BC100346N

Hyaluronic Acid Immobilized Magnetic Nanoparticles for Active Targeting and Imaging of Macrophages

Medha Kamat,[†] Kheireddine El-Boubbou,[†] David C. Zhu,[‡] Teri Lansdell,[†] Xiaowei Lu,[†] Wei Li,[§] and Xuefei Huang*,[†]

Department of Chemistry and Departments of Radiology and Psychology, Michigan State University, East Lansing, Michigan 48824, United States, and Department of Pharmaceutical Sciences, University of Tennessee Health Science Center, 847 Monroe Avenue, Memphis, Tennessee 38163, United States. Received August 2, 2010; Revised Manuscript Received September 29, 2010

Imaging and targeted delivery to macrophages are promising new approaches to study and treat a variety of inflammatory diseases such as atherosclerosis. In this manuscript, we have designed and synthesized iron oxide based magnetic nanoparticles bearing hyaluronic acid (HA) on the surface to target activated macrophages. The HA-coated nanoparticles were prepared through a co-precipitation procedure followed by postsynthetic functionalization with HA and fluorescein. The nanoparticles were characterized by transmission electron microscopy, thermogravimetric analysis, elemental analysis, dynamic light scattering, and high-resolution magic angle spinning NMR and were biocompatible with cells and colloidally stable in the presence of serum. The HA immobilized on the nanoparticles retained their specific biological recognition with the HA receptor CD44, which is present on activated macrophages in high-affinity forms. Cell uptake studies demonstrated significant uptake of HA nanoparticles by activated macrophage cell line THP-1, which enabled magnetic resonance imaging of THP-1 cells. The uptake of nanoparticles was found to be both HA and CD44 dependent. Interestingly, Prussian blue staining showed that the magnetite cores of the HA-coated nanoparticles were only transiently present inside the cells, thus reducing the potential concerns of nanotoxicity. Furthermore, fluorescein on the nanoparticle was found to be delivered to the cell nucleus. Therefore, with further development, these HA functionalized magnetic nanoparticles can potentially become a useful carrier system for molecular imaging and targeted drug delivery to activated macrophages.

INTRODUCTION

Macrophages play central roles in mediating a wide range of infectious and inflammatory diseases, such as tuberculosis, atherosclerosis, rheumatoid arthritis, multiple sclerosis, and graft rejection (*1, 2*). They are critical in the initiation and maintenance of inflammation, which can lead to tissue destruction. For example, in atherosclerotic plaque development, a large number of macrophages are recruited to the cholesterol-rich site of injured aorta, which damages the fibrous tissue capping the plaques (*3, 4*). The weakened plaques can rupture, resulting in heart attack and stroke. The presence of a large number of active macrophages in plaques can be viewed as a biomarker for plaque instability (*5*). Therefore, effective technologies for monitoring macrophages as well as delivery of drugs to modulate macrophage activities can have great diagnostic and therapeutic potentials (*1, 6*).

Recently, the use of nanoparticle systems for biological imaging and drug delivery has attracted increasing attention (*1*). With their nanometer dimensions and large surface area, nanoparticles present a powerful platform for the attachment of multiple copies of diverse ligands. Furthermore, nanoparticles can have unique magnetic, optic, or fluorescent properties, rendering them suitable for biological imaging (*7*−*9*). Although nanoparticles can be nonspecifically taken up by macrophages, the development of nanoparticles bearing specific ligands that are capable of actively targeting macrophages can potentially enhance the efficiency and selectivity of delivery.

An attractive targeting ligand is hyaluronic acid (HA[1]), a member of the glycosaminoglycan family (*10*). HA is composed of tandem disaccharide repeats of β-1,4-D-glucuronic acid-β-1,3-D-N-acetylglucosamine. As an important component of the extracellular matrix, HA has been shown to be involved in multiple cellular processes, including cell adhesion, cell migration, innate immunity, and wound healing (*10, 11*). In addition, HA is highly biocompatible and readily available. These attributes render it uniquely suited for imaging and drug delivery applications (*12*) which has been studied in cancer (*13*), cartilage (*14*), liver cirrhosis (*15*), and arthritis (*16*). However, HA has not been utilized for macrophage targeting.

Macrophages are known to express HA receptors such as CD44, the major HA receptor in human bodies (*17, 18*). The interactions between HA and CD44 are crucial for the recruitment of leukocytes and macrophages in atherosclerotic plaque development (*19*−*21*). As part of our ongoing program to study atherosclerosis, we have begun to investigate whether the HA immobilized nanoparticles can be used to actively target and

* Corresponding author. Xuefei Huang, Department of Chemistry, Michigan State University, East Lansing, MI 48824, USA, Tel: (517) 355-9715, ext 329; Fax: (517) 353-1793; E-mail: xuefei@chemistry.msu.edu.

[†] Department of Chemistry, Michigan State University.

[‡] Departments of Radiology and Psychology, Michigan State University.

[§] University of Tennessee Health Science Center.

[1] Abbreviations: CDMT, 2-chloro-4,6-dimethoxy-1,3,5-triazine; DE-SPION, dextran coated superparamagnetic iron oxide nanoparticles; FBS, fetal bovine serum; FITC, fluorescein isothiocyanate; HA, hyaluronic acid; HRMAS-NMR, high resolution magic angle spinning NMR; LPS, lipopolysaccharide; MTS, 3-(4,5-dimethylthiazol-2-yl)-5-(3-carboxymethoxyphenyl)-2-(4- sulfophenyl)-2*H*-tetrazolium; PMA, phorbol 12-myristate 13-acetate; TNF-α, tumor necrosis factor α.

10.1021/bc100354m © 2010 American Chemical Society
Published on Web 10/26/2010

image macrophages. Herein, we report our results on the uptake and intracellular distribution of HA-coated magnetic nanoparticles in macrophages.

EXPERIMENTAL PROCEDURES

Material. All chemicals were reagent grade and were used as received from the manufacturer. Dextran (MW 9−11 kDa), iron(II) chloride, ammonium hydroxide, sodium hydroxide, epichlorohydrin, bovine serum albumin, goat serum, and LPS from *E. coli* strain 0111:B4 were purchased from Sigma-Aldrich (St. Louis, MO) and used as is. Iron(III) chloride was purchased from Honeywell Riedel de Haen. Hyaluronic acid (MW 30 kDa) was purchased from Lifecore Biomedical. Fluorescein isothiocyanate (FITC), mouse antihuman CD44 monoclonal antibody (clone MEM85), and Alexa Fluor 594 goat antimouse IgG_{2b} secondary antibody were purchased from Invitrogen (Carlsbad, CA). Water used during synthesis was cell culture grade Millipore filtered water.

Cell Culture. THP-1 (human monocytic cell line), EA.hy926 (human vascular endothelial cell line), and LNCaP (human prostate cancer cell line) were purchased from American Type Culture Collection (Manassas, VA). THP-1 and LNCaP were maintained in RPMI 1640 supplemented with fetal bovine serum (10%, Sigma-Aldrich, endotoxin free), Penicillin−streptomycin−glutamine (1%), HEPES buffer (1%), and sodium pyruvate (1%). EA.hy926 cells were kept in M199 supplemented with fetal bovine serum (10%), penicillin−streptomycin−glutamine (1%), HEPES buffer (1%), and sodium pyruvate (1%). The cells were kept in an 37 °C incubator equipped with 5% CO_2. All cell culture related supplies were purchased from GIBCO (Invitrogen, Carlsbad, CA). MTS was purchased from Promega (Madison, WI) and TNF-α ELISA kit was purchased from R&D systems (Minneapolis, MN).

Synthesis of HA-DESPIONs and FITC-HA-DESPIONs. Dextran (4.5 g, MW 9−11 kDa) and iron(III) chloride (0.32 g, 1.2 mmol) were dissolved in water (10 mL), and filtered through a 0.22 μm membrane (Millipore). The mixture was cooled to 0 °C and 0.22 μm membrane filtered solution of iron(II) chloride (0.13 g, 0.63 mmol) in water (0.45 mL) was added dropwise. The reaction mixture was then neutralized by addition of ice-cold ammonium hydroxide solution (0.45 mL). This greenish suspension was heated between 75 and 85 °C for 1.5 h with continuous stirring under a nitrogen atmosphere. Upon completion, reaction was cooled to room temperature, and the excess dextran and ammonium hydroxide were removed using ultrafiltration (Millipore). The reaction mixture was further concentrated to 20 mL total volume using ultrafiltration and filtered through 0.22 μm membrane, followed by washing with water (4 mL) leading to dextran-coated superparamagnetic iron oxide nanoparticles (DESPIONs). To this nanoparticle suspension, an aqueous solution of 5 M NaOH (10 mL) was added followed by dropwise addition of epichlorohydrin (4 mL). The reaction mixture was stirred vigorously for 24 h, after which it was purified using dialysis against DI water with 5 exchanges over 24 h. The reaction was then concentrated to final volume of 30 mL using ultrafiltration. Ammonium hydroxide (8 mL) solution was then added and the reaction was heated at 37 °C for 36 h. The reaction mixture was then purified using dialysis against DI water with 10 water exchanges over 2 days producing NH_2-DESPIONs. HA was then conjugated to NH_2-DESPIONs. HA (100 mg, MW 30 kDa) was dissolved in water and mixed with Amberlite H^+ resin until pH ∼3 and stirred for 4 h to convert HA into its carboxylic acid form. Upon completion, the resin was filtered off and water was evaporated to dryness. The protonated HA was then dissolved in a mixture of 4 mL water and 2.5 mL acetonitrile, under nitrogen. To this mixture, *N*-methyl morpholine (50 μL) was added, followed by addition of 2-chloro-4,6-dimethoxy-1,3,5-triazine (CDMT, 30 mg). The reaction was stirred at RT for 1 h, after which NH_2-DESPIONs (26 mg in 10 mL water) was added. The reaction was stirred at RT for 20 h, followed by neutralization with Dowex H^+ resin. The resin was filtered off and the product was dialyzed using a 14 kDa cutoff membrane for 2 days with 10 water changes.

FITC labeling of HA-nanoparticles (HA-DESPION) was carried out by adding a solution of FITC (5 mg) in DMSO (1 mL) to an aqueous solution of HA-DESPION (30 mg, 6 mL water). As FITC has low aqueous solubility, DMSO (5 mL) was added to the reaction until a homogeneous solution was achieved. The reaction was stirred in the dark for 3 days and purified using ultrafiltration with 100 kDa cutoff membrane.

High-Resolution Magic Angle Spinning (HRMAS) NMR. HRMAS NMR experiments were carried out on a Varian Inova-500 NMR spectrometer equipped with a 4 mm gHX Nanoprobe (Variannmr Inc., Palo Alto, CA) available at the University of Tennessee Health Science Center (Memphis, TN). The HR-MAS probe with internal lock is capable of performing either direct or indirect (inverse) detection experiments. MAS experiments were performed at spinning rates of up to 2.5 kHz using a 40 μL glass rotor. The HA-DESPIONs were dissolved in D_2O solvent and were further diluted at different concentrations with D_2O to find out the concentration limit to the NMR signal broadening. HRMAS ^1H NMR spectra were obtained using 100−600 scans for each experiment. The sample temperature was regulated with an accuracy of ±0.1 °C.

Competitive Enzyme Linked Immunosorbent Assay (ELISA). In a 96 well-plate, 100 μL of goat antihuman IgG F_C γ (3 μg/well, Millipore, cat no. AP113) in PBS buffer was added to each well. The plate was covered with aluminum foil and incubated at 4 °C overnight. The wells were then washed 3 times with 200 μL PBST buffer (0.5% Tween 20) as follows: the plate was emptied by inversion over a sink, tapped against some layers of soft paper tissue to remove residual liquid, and then washed with buffer repeatedly (insufficient washings may lead to undesired high background). Blocking was completed by adding 5% BSA in PBS (200 μL) to each well followed by incubation at 37 °C for 2 h. The plate was then washed as described above. 100 μL of CD44-F_C γ chimera (0.2 μg/well, R&D systems, cat no. 3660-CD) in PBS buffer was then added to each well and incubated at 37 °C for 45 min. The plate was washed 3 times with 200 μL PBST buffer (0.05% Tween 20) as before. 100 μL of b-HA (0.5 μg/well), b-HA + HA 16 KDa (2.5 μg/well), or b-HA + HA-NPs (7.32, 3.66, 2.75, 1.5, 0.88, 0.55, 0.15, 0.088, 0.055 μg HA/well) solutions were then added to each well and incubated at room temperature for 2 h. The plate was then washed 3 times with 200 μL PBST buffer (0.05% Tween 20) and twice with PBS buffer. 100 μL Avidin-HRP in 0.2% BSA−PBS solution was then added to each well and incubated at room temperature for 1 h. The plate was then washed 3 times with 200 μL PBST buffer (0.05% Tween 20) and twice with PBS buffer. 100 μL of chromogenic TMB solution was added to each well, homogenized, and incubated for 15 min, or until a blue color appeared. The plate should be protected against light during this incubation. The reaction was then quenched by adding 0.5 M H_2SO_4 (50 μL) to each well with positive wells becoming yellow. For quantitative measurements, it was important that each well was incubated for exactly the same length of time. Optical absorbance was directly assessed through the bottom of the microwell plate using an automated ELISA plate reader (Biorad) at 450 nm.

Colloidal Stability Studies. The nanoparticles (HA-DESPIONs or FITC-HA-DESPION) were suspended in PBS or RPMI 1640 containing 10% FBS at a concentration of 1 mg/mL. The change in size was monitored by over a period of six

days using a Zetasizer Nano zs instrument. The samples were stored at RT and the FITC-HA-DESPIONs were stored in the dark at RT.

MTS Cell Viability Assay. THP-1 cells were inoculated in a 96 well plate at cell density of 4×10^5 cells/mL, 200 μL/well. They were differentiated using phorbol 12-myristate 13-acetate (PMA, 10 ng/mL) to induce adhesion. After 16 h, the supernatant was replaced by the desired incubation media (either media alone or serum free media containing 50 μg/mL HA-DESPION). The incubation was carried out for varying periods of times (see data). The supernatant was removed, cells were washed using serum containing RPMI 1640 twice, and then incubated with serum containing media for 48 h. After 48 h, 3-(4,5-dimethylthiazol-2-yl)-5-(3-carboxymethoxyphenyl)-2-(4-sulfophenyl)-2*H*-tetrazolium (MTS, 20 μL) reagent was added to each well and the plate was further incubated for 3 h. The intensity of brown color was measured using absorbance plate reader at 490 nm (Molecular Devices SpectraMax M5[e]). All the experiments were performed in triplicates.

HA-DESPION Adherence Assay with THP-1 Cells. THP-1 cells were serially diluted from a concentration of 2 million to 8600 cells/mL and plated in a 96 well plate at 200 μL/well, followed by the addition of 20 μL of MTS reagent. The cells were incubated at 37 °C for 3 h and the resulting brown color was read at 490 nm using a plate reader (Molecular Devices SpectraMax M5[e]). The readings were used to generate a standard curve of absorbance vs number of viable cells. To perform the adherence assay, a 96 well nunc plate was coated with human umbilical cord HA (5 mg/mL) overnight at 4 °C. The plate was washed 3 times with PBS to remove unattached coating. The THP-1 cells were treated with LPS (1 μg/mL) for 2 h, washed with media, counted using Trypan blue. The activated THP-1 cells were added to half the plate with unactivated THP-1 cells on the other half as a control. The plate was then incubated for1.5 h at 37 °C. Upon completion, the plate was washed with cell culture media 6 times to remove unbound cells, followed by resuspension in 200 μL of media in each well. At this time, the MTS reagent (20 μL) was added to each well and the plate was incubated for 3 h and read using a plate reader at 490 nm. The absorbance was correlated to the cell density using the previously generated standard curve. Each set was done in triplicate.

Determination of Cellular Uptake by Flow Cytometry. The cells were inoculated in a 6 well plate at a density of 5×10^5 cell/mL, treated with LPS (1 μg/mL) for 2 h at 37 °C, centrifuged to remove the supernatant media, and resuspended in serum free media containing FITC-HA-DESPION or FITC-DESPION (2.5 μg of FITC/mL of media) for 2 h at either 37 or 4 °C. Upon completion, the cells were centrifuged, washed with serum containing media twice, resuspended in 300 μL of the media, and analyzed using BD Vantage SE flow cytometer. Viability was assessed using propidium iodide. For the EA.hy926, the same procedure was used except the LPS treatment. After incubation with nanoparticles, the cells were detached using trypsin−EDTA (0.5%) and processed using the above procedure.

Cellular Uptake Monitoring by Confocal Microscopy. The cells were suspended in chambered cover glass (Nunc, FisherSci) at a density of 5×10^5 cells/mL. The THP-1 cells were treated with PMA (10 ng/mL) overnight to induce adhesion followed by LPS (1 μg/mL) treatment for 2 h at 37 °C. After one hour, the cells were treated with LysoTracker-594 DND (Invitrogen) at the final concentration of 1 μM, and the samples were incubated at 37 °C for another hour. Upon completion, the supernatants were removed and the cells were washed using PBS, fixed with 10% neutral buffered formalin for 20 min, and treated with 4′,6-diamidino-2-phenylindole (DAPI) at 300 nM concentration to stain the nuclei fluorescent blue. The samples were washed with PBS and water. Images were gathered using the Olympus FluoView 1000 LSM confocal microscope.

Prussian Blue Staining. The cells were suspended in chambered cover glass (Nunc, FisherSci) at a density of 5×10^5 cells/mL. The THP-1 cells were treated with PMA (10 ng/mL) overnight to induce adhesion followed by LPS (1 μg/mL) treatment for 2 h at 37 °C. The cells were washed to remove LPS and serum free media containing HA-DESPION or DESPION was added. The cells were incubated with the nanoparticles for half an hour, 1 h, 4 h, and 24 h, respectively, and were then washed repeatedly to remove the unbound particles. The cells were then fixed using 10% neutral buffered formalin for 20 min, washed with PBS buffer, and treated with 1:1 mixture of 4% potassium ferrocyanide and 4% HCl for 25 min at RT. Upon completion, the slides were rinsed with PBS and treated with 0.1 mL of nuclear fast red solution (Sigma) as a counterstain for 5 min, followed by rinsing with PBS. The resulting slides were observed under 40× magnification of an optical microscope.

MRI of Cells. THP-1 cells were plated at a density of 5×10^5 cells/mL in a 6 well plate, differentiated using PMA (10 ng/mL) for 16 h followed by treatment with LPS at 1 μg/mL for 2 h at 37 °C. After 2 h, the supernatant was removed and HA-DESPION (100 μg/mL, 10 μg/mL Fe) was added in serum free media to separate wells, and incubated for 2, 4, and 24 h, respectively, at 37 °C. After completion, the supernatant was removed; cells were washed with PBS to remove unbound particles, resuspended in 0.5 mL PBS, and assessed using MRI. MRI measurements were carried out on a GE 3T Signa HDx MR scanner (GE Healthcare, Waukesha, WI) with a wrist coil. Fast, spoiled gradient recalled echo 3D T_2*-weighted images were acquired with the following parameters: flip angle = 15°; echo times (TEs) = 5.9 ms, 14.5 ms, 23.0 ms, 31.6 ms, 40.2 ms, 48.7 ms, 57.3 ms, and 65.9 ms; time of repetition (TR) = 72.5 ms; receiver bandwidth (rBW) = ±15.6 kHz; field of view (FOV) = 6 cm; slice thickness = 1.5 mm; number of slices = 16; acquisition matrix = 256 × 256; number of excitation (NEX) = 1; and scan time = 1 min 39 s.

Antibody Blocking of THP-1 Cell Uptake of HA-DESPIONs. The THP-1 cells were differentiated using PMA (10 ng/mL) for 16 h at 37 °C, followed by treatment with LPS 1 μg/mL for 2 h at 37 °C. Various concentrations of mouse antihuman CD44 antibody (MEM-85 clone) were added to cells, and the cells continued to be incubated at 37 °C for 1 h. The supernatant was removed and FITC-HA-DESPION (100 μg/mL) was added in serum free media. The cells were incubated at 37 °C for one hour and then washed multiple times to remove unbound particles. Upon completion, the cells were lysed using 1% SDS and the fluorescence of the supernatant was measured using a plate reader. The experiment was performed in 5 sets for each time point.

RESULTS AND DISCUSSION

Synthesis and Characterization of HA-DESPIONs. The preparation of HA coated nanoparticles started from formation of the water-soluble nanoparticles by co-precipitating Fe^{3+} and Fe^{2+} salts in the presence of dextran (9−11 kDa) (*22*). The resulting nanoparticles (DESPIONs) were cross-linked by epichlorohydrin to improve the stability of the coating, which was followed by ammonium hydroxide treatment leading to NH_2-DESPIONs (*22*). HA (30 kDa) was then immobilized onto the nanoparticles through amide linkages promoted by CDMT (*23*) leading to magnetic nanoparticle HA-DESPIONs (Figure 1a). Dynamic light scattering data showed that the DESPION prepared has a hydrodynamic radius of 155 nm with a zeta potential of +43.4 mV. In comparison, HA-DESPION has a hydrodynamic radius of 205 nm with a zeta potential of −33.7

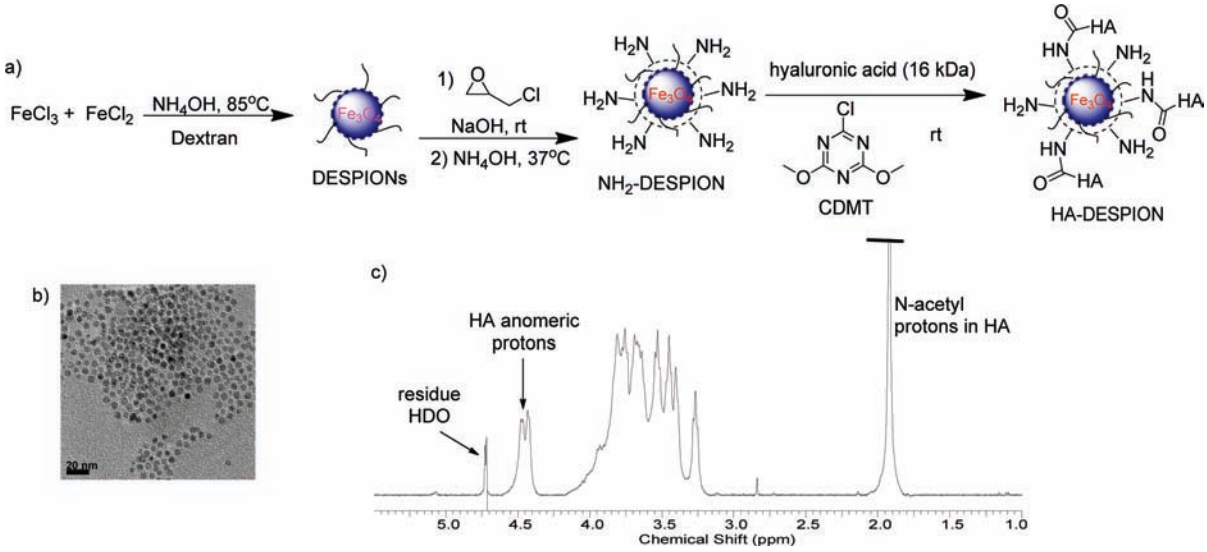


Figure 1. (a) Synthesis, (b) TEM image, and (c) ^{1}H-HRMAS NMR spectrum of HA-DESPION.

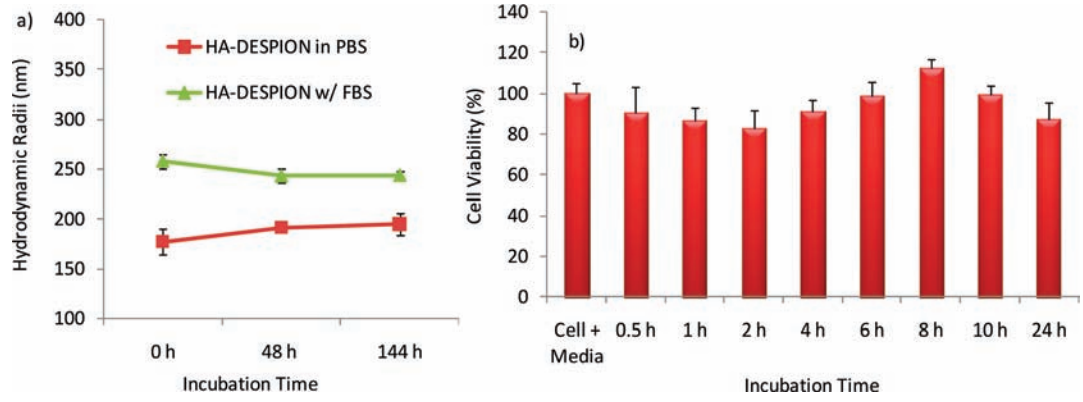


Figure 2. (a) Hydrodynamic radii (nm) of HA-DESPIONs in PBS or in 10% FBS containing media. (b) Percent of viable THP-1 cells upon incubation with HA-DESPIONs (100 μg/mL) as determined by MTS cell viability assays.

mV. The large change of zeta potential is attributed to the negatively charged nature of HA on the external surface of HA-DESPIONs. TEM revealed that the nanoparticle cores of HA-DESPIONs are quite homogeneous with an average diameter of 6 nm (Figure 1b). Under dry vacuum conditions encountered in TEM studies, the surface polysaccharides could collapse to form a tight coating, thus explaining the short interparticle distances observed in TEM images. TGA analysis showed that, upon HA incorporation, the percentage of the weight loss due to thermolysis of organics on HA-DESPIONs increased from 78% to 90% (Supporting Information Figure S1) and elemental analysis confirmed the increase of nitrogen upon HA functionalization (Supporting Information Table S1). The presence of HA on HA-DESPIONs was further ascertained by the HRMAS-NMR technique, which is a powerful method to overcome the field inhomogeneity caused by the superparamagnetic nature of the nanoparticles (*24*, *25*). ^{1}H-HRMAS NMR spectrum of the HA-DESPIONs showed resonances characteristic of HA with the anomeric protons appearing at 4.48 ppm and 4.43 ppm together with a singlet at 1.92 ppm due to the N-acetyl group (Figure 1c). On the basis of ^{1}H NMR integration as well as TGA data, the molar ratio of HA to dextran is determined to be 3:1.

In order to test whether HA immobilized on the nanoparticles can be recognized by receptors, we established a competitive ELISA procedure. CD44 was anchored onto microtiter plates in an IgG chimera form. The binding between a biotinylated HA polymer (0.5 μg/mL) and immobilized CD44 was then tested in the presence of various concentrations of HA-DESPIONs. HA-DESPIONs effectively inhibited the binding between the HA polymer and CD44 with an IC_{50} value of 0.5 μg/mL, while the DESPION without HA did not have any effect on HA-CD44 interaction even at a concentration of 50 μg/mL. This proves that HA immobilized on HA-DESPION retains its biological recognition.

Colloidal stability of nanoparticles under physiological conditions is an important factor for biological applications. The particle stability in biological media was evaluated by monitoring their hydrodynamic radii by DLS. The HA-DESPIONs maintained their sizes in both PBS buffer and culture media containing 10% fetal bovine serum (FBS) over one week, thus demonstrating that serum proteins do not induce nanoparticle aggregations (Figure 2a). HA-DESPIONs are also biocompatible, which had no effects on cell viabilities as determined through MTS cell viability assays (Figure 2b).

In order to facilitate fluorescence monitoring of cellular interactions, fluorescein was attached onto HA-DESPIONs through the reaction with FITC. The resulting FITC-HA-DESPIONs were characterized in a same manner as HA-DESPIONs and were found to have similar properties. Fluorescein can also serve as a model drug to evaluate drug delivery. Control reaction of FITC and HA alone under identical conditions gave FITC-HA conjugate with 10% of fluorescence intensity compared with that from FITC-HA-DESPION. This suggests FITC is attached to both HA and the aminated dextran on the nanoparticle surface.

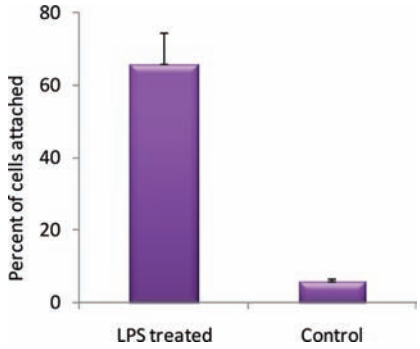


Figure 3. Percentage of differentiated THP-1 cells adhered on HA coated plates with and without LPS treatment. LPS treatment significantly enhanced THP-1 affinity with HA.

THP-1 Nanoparticle Uptake Kinetics. With the HA coated nanoparticles in hand, we examined their interactions with a human monocytic cell line THP-1. THP-1 cells can be differentiated into adherent and macrophage-like cells by exposure to PMA, which has been used quite extensively as a model for human macrophages (*26, 27*). The presence of CD44 on THP-1 cells was established by immunohistostaining. Incubation of THP-1 cells with antihuman CD44 IgG mAb followed by Alexafluor 594 labeled anti-IgG secondary antibody gave intense cell surface staining (Supporting Information Figure S2a). Western blot analysis further confirmed the presence of CD44 in THP-1 cells (Supporting Information Figure S2d).

It is known that the interactions between HA and CD44 are subject to tight regulations such that the receptor is normally maintained in a quiescent state showing little appreciable HA binding (*28*). For example, although freshly isolated peripheral blood monocytes and lymphocytes express CD44, they do not bind HA (*29*). During inflammation, however, the pro-inflammatory cytokine tumor necrosis factor α (TNF-α) induces sulfation and subsequent conformational changes of CD44, which transforms it into a form with much greater HA affinity (*21, 28, 30, 31*). To establish the THP-1 activation condition, we treated the PMA differentiated THP-1 cells with *E. coli* LPS, which led to the excretion of a large amount of TNF- α (2500 pg/mL) to the media (Supporting Information Table S2). In comparison, a very low TNF-α level (37.5 pg/mL) was detected from THP-1 culture without the addition of LPS. The high TNF- α level following LPS should turn CD44 into its high-affinity HA binding form, which was tested in a plate adhesion assay (Figure 3). Upon incubation of cells on HA coated cell culture plates, 66% of the LPS activated THP-1 cells adhered to these plates as compared to 6% of cells not treated with LPS, thus confirming the enhanced affinity of activated THP-1 cells with HA (*32*).

Next, we examined the interactions of HA-DESPIONs with THP-1 cells. LPS activated THP-1 cells were incubated with FITC-HA-DESPIONs for varying periods of time (0.5 h, 1 h, 2 h, 4 h, and 24 h), which was followed by extensive washing to remove unbound particles. The amount of fluorescence retained by the cells was then quantified. Significant amounts of the nanoparticles were rapidly uptaken by THP-1 cells, which did not change much after two hours (Figure 4a). The presence of HA on the nanoparticles was crucial for uptake, as the mean fluorescence intensity of cells incubated with FITC-DESPION without HA coating was only 20% of that with HA coated nanoparticles (Figure 4b). In addition, although other cells such as endothelial cell EA.hy926 also express CD44 (Supporting Information Figure S3), the THP-1 cells have 6-fold higher uptake capacities than EA.hy926 (Figure 4c). This suggests that the HA-DESPIONs can be used as a carrier to enhance delivery selectively to activated macrophages.

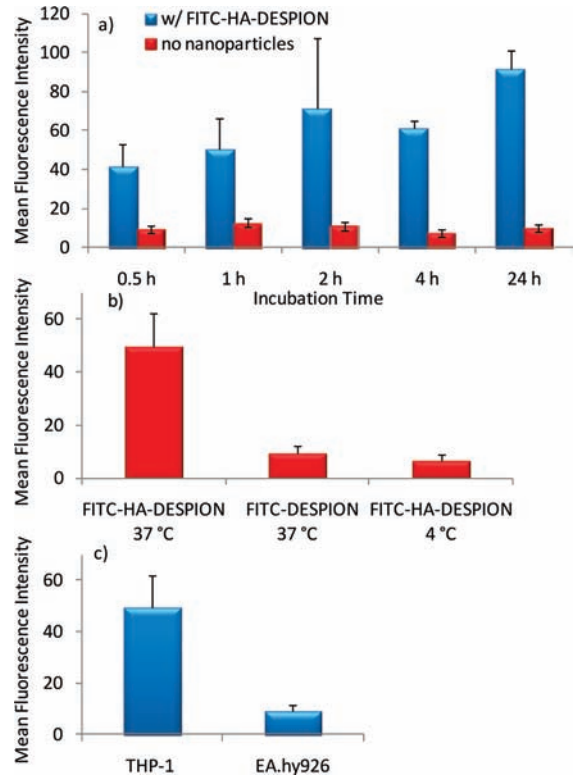


Figure 4. (a) Time-dependent uptake of FITC-HA-DESPION (100 μg/mL) by LPS activated THP-1 cell as measured by the mean fluorescence intensity of the cells. (b) Uptake comparison between FITC-HA-DESPION and FITC-DESPION as well as FITC-HA-DESPION at 37 °C vs 4 °C by activated THP-1 cells. (c) FITC-HA-DESPION uptake by THP-1 cells compared with that by CD44 expressing endothelial cell EA.hy926.

It is known that extracellular HA is typically endocytosed into lysosomes (*33*). For effective drug delivery using the HA-DESPION platform, it is important that the cargo can escape the lysosomes after internalization inside the cells. To monitor the intracellular distribution, we analyzed THP-1 cells by confocal microscopy following incubation with FITC-HA-DESPION (Figure 5). Interestingly, the green fluorescence was found concentrated in the nuclei (cyan color in Figure 5d) with some in the lysosomes. This points to the potential of using HA-DESPIONs for nuclear drug delivery such as gene therapy (*34*).

To further analyze nanoparticle uptake, we stained the THP-1 cells with Prussian blue stain, which reacts with iron ions present in the magnetite core yielding a characteristic blue color. The cells were incubated with nanoparticles for specific periods of time (0.5 h, 1 h, 4 h, and 24 h) and the unbound particles were washed off. With half-hour HA-DESPION incubation, most Prussian blue stains were found on THP-1 cell exterior surface as evident from the diffuse appearance of the blue color at cell surface (Figure 6a). With one hour incubation, the blue color appeared inside the cells indicating intracellular nanoparticle uptake (Figure 6b). Interestingly, as time went by, the blue color disappeared from inside the cells, suggesting efflux of the core of the nanoparticles from the cellular interior (Figure 6c,d). At 24 h, most of the staining was observed on the exterior cell surface. In contrast, with DESPIONs devoid of HA, the nanoparticles were retained inside the cells even after 24 h (Figure 6e), which was consistent with literature reports (*35, 36*).

An important application of magnetic nanoparticles is in MR imaging, as the magnetite nanoparticles are effective MRI contrast agents (*8, 37*). The uptake of the HA-DESPIONs by activated THP-1 cells was monitored by MRI upon incubation

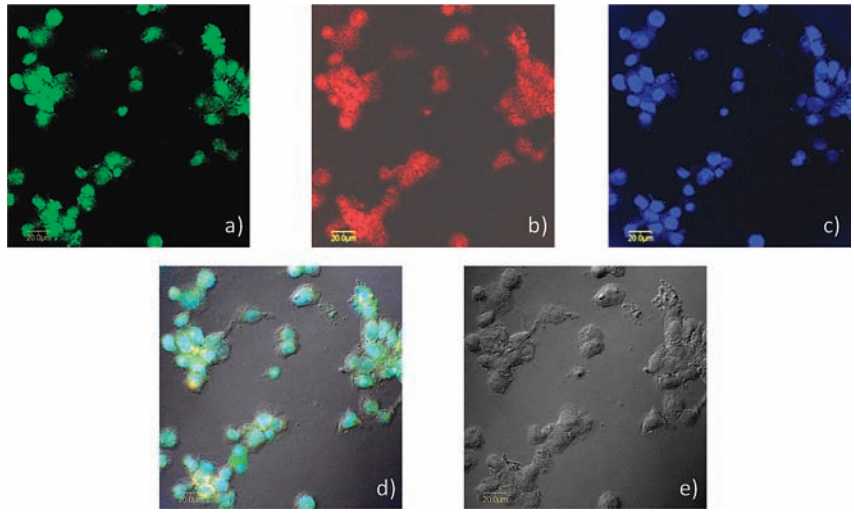


Figure 5. Confocal microscopy images of LPS activated THP-1 cells 1 h after incubation with FITC-HA-DESPION. (a) Fluorescein channel; (b) Lysotracker channel showing location of lysosomes; (c) DAPI channel showing location of nucleus; (d) overlay of a−c; (e) laser image of the cells. The image overlay indicated that the fluorescein was concentrated in the cell nuclei.

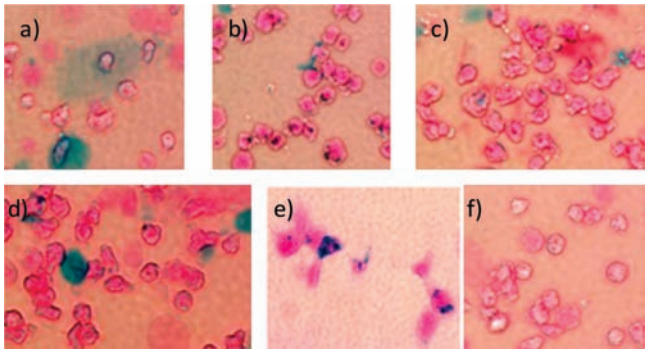


Figure 6. Prussian blue staining images of activated THP-1 cells incubated with HA-DESPIONs after (a) 0.5 h (the dispersed blue staining patterns suggested that nanoparticles were bound to the outer cell membrane); (b) 1 h; (c) 4 h; (d) 24 h followed by washing off unbound particles. The magnetite cores were found to be exocytosed out of the cells. (e) Activated THP-1 cells after 24 h incubation with DESPIONS. The intracellular staining suggested the retention of the magnetite core inside the cells. (f) Activated THP-1 cells without nanoparticle incubations.

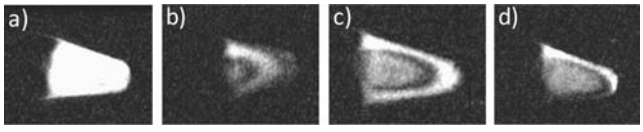


Figure 7. T2* weighted MR images of activated THP-1 cells (TE = 40.2 ms). (a) Before incubation with HA-DESPIONs, (b) 2 h, (c) 4 h, and (d) 24 h after incubation with HA-DESPIONs (100 μg/mL) followed by washing off unbound particles. The significant T2* contrast changes upon nanoparticle incubation suggested HA-DESPIONs can be used to monitor macrophages by MRI.

of HA-DESPIONs with cells for set time periods and washing off unbound particles. Significant changes in T2 weighted MR images of THP-1 cells were observed (Figure 7). Despite the fact that most HA-DESPIONs were exocytosed out of the interior of the cells with 24 h incubation (Figure 6d), sufficient amounts of HA-DESPIONs remained bound on the cell surface leading to large contrast change in MRI (Figure 7d). This suggested the potential applicability of these nanoparticles for noninvasive in vivo monitoring of macrophages. Various iron oxide nanoparticles including DESPIONs have been used previously for MR imaging (*8*, *37*). Although, in general, these nanoparticles are found to be biocompatible (*38*, *39*), side effects

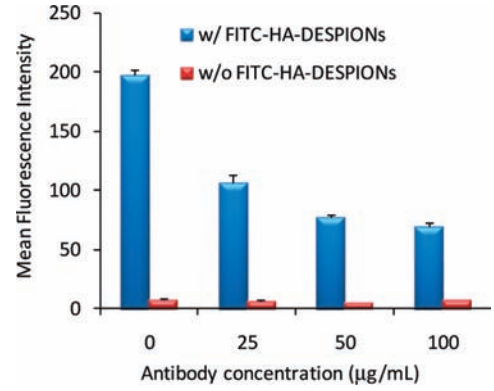


Figure 8. Mean fluorescence intensities of activated THP-1 cells incubated with various concentrations of blocking antibody MEM-85, followed by 1 h incubation with FITC-HA- DESPION (100 μg/mL) and washing off unbound particles. MEM-85 significantly reduced cell fluorescence intensities suggesting CD44 was involved in HA-DESPION uptake.

due to iron toxicities and nanotoxicities have been observed both in vitro and in vivo (*40*−*42*). For example, internalization of iron oxide nanoparticles resulted in a dose dependent reduction of the viability of growing neuron cells (*41*). Our observations that the magnetic cores of HA-DESPIONs are only transiently present inside the cells suggest the side effects from administrations of these particles will likely be small.

Mechanistic Studies of Nanoparticle Uptake. To better understand HA-DESPION uptake, we examined its temperature dependence. While significant uptake was observed at 37 °C, incubation of HA-DESPION at 4 °C reduced the uptake to the background level (Figure 4b). In addition, the phagocytosis inhibitor cytochalasin D (*43*) did not significantly affect the uptake (data not shown), which suggested that the uptake was most likely due to an energy-dependent receptor-mediated endocytosis process. In order to test the role of CD44, LPS activated THP-1 cells were incubated with anti-CD44 mAb MEM-85, which has been shown to block the binding of HA by CD44 (*44*), prior to the introduction with HA-DESPIONs. In the presence of MEM-85, the uptake was significantly decreased highlighting the important role CD44 played (Figure 8). However, other mechanisms should be operating, as there was still 30% residual uptake following MEM-85 blocking.

Fluorescein nuclear localization and exocytosis of the magnetite core can be explained by the involvement of CD44. HA-

DESPIONs bound with cell surface CD44 and were endocytosed into endosomes and lysosomes. It is known that HA can be digested inside the cells, presumably by acid-active lysosomal hyaluronidases (*45*). Thus, the HA on HA-DESPIONs can be partially cleaved, which would release HA fragments labeled with fluorescein and allow their trafficking to the nucleus. This is supported by the observation from Wight and co-workers that exogenous HA added to permeabilized fibroblast cells could be found in cell nucleus (*46*). With the large amount of HA on the exterior surface, HA-DESPIONs could remain bound to CD44 in the endosomes, recycle to the cell surface, and be released from the cells accounting for the disappearance of magnetite cores from the intracellular space.

CONCLUSIONS

We have synthesized iron oxide magnetic nanoparticles coated with HA, which have excellent colloidal stability and biocompatibility. The HA-DESPIONs retained the native biological recognition of HA by HA receptor CD44. HA-DESPIONs could be efficiently uptaken by activated macrophages, which enabled their imaging by MRI and paved the way for future in vivo studies. Furthermore, the dual labels (fluorescein and magnetite core) on the NPs enabled us to track the magnetite core and the cargo individually. This led to the unique observation that the magnetite core was only present transiently inside the cells. The cargo fluorescein was found to be delivered to the cell nucleus, unveiling the potential of using the HA-DESPION platform for nuclear drug delivery.

ACKNOWLEDGMENT

This work was supported by an NSF CAREER award (X.H.), and an American Heart Association Postdoctoral Fellowship (M.N.K.) and Predoctoral Fellowship (K.E.). We would like to thank Prof. Jetze Tepe, Michigan State University, for access to the cell culture facility and the Department of Radiology, Michigan State University, for the usage of the MRI scanner. We would like to thank Melinda Frame for her help with confocal microscopy and Dr. Louis King for FACS studies.

Supporting Information Available: TGA and elemental analysis of HA-DESPIONs; anti-TNF-α ELISA procedure and results; CD44 immunohisto-staining and Western blots of THP-1 and EA.hy926 cells. This material is available free of charge via the Internet at http://pubs.acs.org.

LITERATURE CITED

(1) Chellat, F., Merhi, Y., Moreau, A., and Yahia, L. (2005) Therapeutic potential of nanoparticulate systems for macrophage targeting. *Biomaterials 26*, 7260–7275.

(2) Lewis, C. E., and McGee, J. O. (1992) in *The Macrophage: The Natural Immune System*, Oxford University Press, New York.

(3) Lucas, A. D., and Greaves, D. R. (2001) Atherosclerosis: role of chemokines and macrophages. *Exp. Rev. Mol. Med. 3*, 1–18.

(4) Ross, R. (1999) Atherosclerosis - an inflammatory disease. *New Eng. J. Med. 340*, 115–126.

(5) Amirbekian, V., Lipinski, M. J., Briley-Saebo, K. C., Amirbekian, S., Aguinaldo, J. G. S., Weinreb, D. B., Vucic, E., Frias, J. C., Hyafil, F., Mani, V., Fisher, E. A., and Fayad, Z. A. (2007) Detecting and assessing macrophages in vivo to evaluate atherosclerosis noninvasively using molecular MRI. *Proc. Nat. Acad. Sci., U.S.A. 104*, 961–966.

(6) Ahsan, F., Rivas, I. P., Khan, M. A., and Suárez, A. I. T. (2002) Targeting to macrophages: role of physicochemical properties of particulate carriers-liposomes and microspheres-on the phagocytosis by macrophages. *J. Controlled Release 79*, 29–40.

(7) Giljohann, D. A., Seferos, D. S., Daniel, W. L., Massich, M. D., Patel, P. C., and Mirkin, C. A. (2010) Gold nanoparticles for biology and medicine. *Angew. Chem., Int. Ed. 49*, 3280–3294.

(8) Thorek, D. L. J., Chen, A. K., Czupryna, J., and Tsourkas, A. (2006) Superparamagnetic iron oxide nanoparticle probes for molecular imaging. *Ann. Biomed. Eng. 34*, 23–38.

(9) Michalet, X., Pinaud, F. F., Bentolila, L. A., Tsay, J. M., Doose, S., Li, J. J., Sundaresan, G., Wu, A. M., Gambhir, S. S., and Weiss, S. (2005) Quantum dots for live cells, in vivo imaging, and diagnostics. *Science 307*, 538–544.

(10) Lapcik, L., Jr., Lapcik, L., De Smedt, S., Demeester, J., and Chabrecek, P. (1998) Hyaluronan: preparation, structure, properties, and applications. *Chem. Rev. 98*, 2663–2684.

(11) Raman, R., Sasisekharan, V., and Sasisekharan, R. (2005) Structural insights into biological roles of protein-glycosaminoglycan interactions. *Chem. Biol. 12*, 267–277.

(12) Oh, E. J., Park, K. T., Kim, K. S., Kim, J. S., Yang, J. A., Kong, J. H., Lee, M. Y., Hoffman, A. S., and Hahn, S. K. (2010) Target specific and long-acting delivery of protein, peptide, and nucleotide therapeutics using hyaluronic acid derivatives. *J. Controlled Release 141*, 2–12, and references cited therein.

(13) Platt, V. M., Jr. (2008) Anticancer therapeutics: targeting macromolecules and nanocarriers to hyaluronan or CD44, a hyaluronan receptor. *Mol. Pharmaecutics 5*, 474–486, and references cited therein.

(14) Laroui, H., Grossin, L., Léonard, M., Stoltz, J.-F., Gillet, P., Netter, P., and Dellacherie, E. (2007) Hyaluronate-covered nanoparticles for the therapeutic targeting of cartilage. *Biomacromolecules 8*, 3879–3885.

(15) Kim, K. S., Hur, W., Park, S.-J., Hong, S. W., Choi, J. E., Goh, E. J., Yoon, S. K., and Hahn, S. K. (2010) Bioimaging for targeted delivery of hyaluronic acid derivatives to the livers in cirrhotic mice using quantum dots. *ACS Nano 6*, 3005–3014.

(16) Lee, H., Lee, K., Kim, I. K., and Park, T. G. (2008) Synthesis, characterization, and in vivo diagnostic applications of hyaluronic acid immobilized gold nanoprobes. *Biomaterials 29*, 4709–4718.

(17) Naor, D., Sionov, R. V., and Ish-Shalom, D. (1997) CD44: structure, function, and association with the malignant process. *Adv. Cancer Res. 71*, 241–319.

(18) Aruffo, A., Stamenkovic, I., Melnick, M., Underhill, C. B., and Seed, B. (1990) CD44 is the principal cell surface receptor for hyaluronate. *Cell 61*, 1303–1313.

(19) Cuff, C. A., Kothapalli, D., Azonobi, I., Chun, S., Zhang, Y., Belkin, R., Yeh, C., Secreto, A., Assoian, R. K., Rader, D. J., and Pure, E. (2001) The adhesion receptor CD44 promotes atherosclerosis by mediating inflammatory cell recruitment and vascular cell activation. *J. Clin. Invest. 108*, 1031–1040.

(20) DeGrendele, H. C., Estess, P., Picker, L. J., and Siegelman, M. H. (1996) CD44 and its ligand hyaluronate mediate rolling under physiologic flow: a novel lymphocyte-endothelial cell primary adhesion pathway. *J. Exp. Med. 183*, 1119–1130.

(21) DeGrendele, H. C., Estess, P., and Siegelman, M. H. (1997) Requirement for CD44 in activated T cell extravasation into an inflammatory site. *Science 278*, 672–675.

(22) Palmacci, S., Josephson, L., and Groman, E. V. (1995) Synthesis of polymer-covered superparamagnetic oxide colloids for magnetic resonance contrast agents or other applications; (Advanced Magnetics, Inc., USA). Patent WO/1995/005669.

(23) Bergman, K., Elvingson, C., Hilborn, J., Svensk, G., and Bowden, T. (2007) Hyaluronic acid derivatives prepared in aqueous media by triazine-activated amidation. *Biomacromolecules 8*, 2190–2195.

(24) El-Boubbou, K., Zhu, D. C., Vasileiou, C., Borhan, B., Prosperi, D., Li, W., and Huang, X. (2010) Magnetic glyconanoparticles: a tool to detect, differentiate, and unlock the glycocodes of cancer via magnetic resonance imaging. *J. Am. Chem. Soc. 132*, 4490–4499.

(25) Polito, L., Colombo, M., Monti, D., Melato, S., Caneva, E., and Prosperi, D. (2008) Resolving the structure of ligands bound to the surface of superparamagnetic iron oxide nanoparticles by

high-resolution magic-angle spinning NMR spectroscopy. *J. Am. Chem. Soc. 130*, 12712–24.
(26) Takashiba, S., Van Dyke, T. E., Amar, S., Murayama, Y., Soskolne, A. W., and Shapira, L. (1999) Differentiation of monocytes to macrophages primes cells for lipopolysaccharide stimulation via accumulation of cytoplasmic nuclear factor kB. *Infect. Immunol. 67*, 5573–5578.
(27) Park, E. K., Jung, H. S., Yang, H. I., Yoo, M. C., Kim, C., and Kim, K. S. (2007) Optimized THP-1 differentiation is required for the detection of responses to weak stimuli. *Inflamm. Res. 56*, 45–50.
(28) Nandi, A., Estess, P., and Siegelman, M. H. (2000) Hyaluronan anchoring and regulation on the surface of vascular endothelial cells is mediated through the functionally active form of CD44. *J. Biol. Chem. 275*, 14939–14948.
(29) Levesque, M. C., and Haynes, B. F. (1996) In vitro culture of human peripheral blood monocytes induces hyaluronan binding and up-regulates monocyte variant CD44 lsoform expression. *J. Immunol. 156*, 1557–1565.
(30) Brown, K. L., Maiti, A., and Johnson, P. (2001) Role of Sulfation in CD44-Mediated Hyaluronan Binding Induced by Inflammatory Mediators in Human CD14 Peripheral Blood Monocytes. *J. Immunol. 167*, 5367–5374.
(31) Maiti, A., Maki, G., and Johnson, P. (1998) TNF-alpha induction of CD44-mediated leukocyte adhesion by sulfation. *Science 282*, 941–943.
(32) Gee, K., Kozlowski, M., and Kumar, A. (2003) Tumor necrosis factor-alpha induces functionally active hyaluronan-adhesive CD44 by activating sialidase through p38 mitogen-activated protein kinase in lipopolysaccharide-stimulated human monocytic cells. *J. Biol. Chem. 278*, 37275–37287.
(33) Knudson, W., Chow, G., and Knudson, C. B. (2002) CD44-mediated uptake and degradation of hyaluronan. *Matrix Biol. 21*, 15–23.
(34) Pouton, C. W., Wagstaff, K. M., Roth, D. M., Moseley, G. W., and Jans, D. A. (2008) Targeted delivery to the nucleus. *Adv. Drug Delivery Rev. 59*, 698–717.
(35) Lee, H., Lee, E., Kim, D. K., Jang, N. K., Jeong, Y. Y., and Jon, S. (2006) Antibiofouling polymer-coated superparamagnetic iron oxide nanoparticles as potential magnetic resonance contrast agents for in vivo cancer imaging. *J. Am. Chem. Soc. 128*, 7383–7389.
(36) Raynal, I., Prigent, P., Peyramaure, S., Najid, A., Rebuzzi, C., and Corot, C. (2004) Macrophage endocytosis of superparamagnetic iron oxide nanoparticles: mechanisms and comparison of ferumoxides and ferumoxtran-10. *Invest. Radiol. 39*, 56–63.
(37) Wang, Y.-X. J., Hussain, S. M., and Krestin, G. P. (2001) Superparamagnetic iron oxide contrast agents: physicochemical characteristics and applications in MR imaging. *Eur. Radiol. 11*, 2319–2331.
(38) Kim, J. S., Yoon, T. J., Yu, K. N., Kim, B. G., Park, S. J., Kim, H. W., Lee, K. H., Park, S. B., Lee, J. K., and Cho, M. H. (2006) Toxicity and tissue distribution of magnetic nanoparticles in mice. *Toxicol. Sci. 89*, 338–347.
(39) Weissleder, R., Stark, D. D., Engelstad, B. L., Bacon, B. R., Compton, C. C., White, D. L., Jacobs, P., and Lewis, J. (1989) Superparamagnetic iron oxide: pharmacokinetics and toxicity. *Am. J. Roentgenol. 152*, 167–173.
(40) Shubayev, V. I., Pisanic II, T. R., and Jin, S. (2009) Magnetic nanoparticles for theragnostics. *Adv. Drug Delivery Rev. 61*, 467–477, and references cited therein.
(41) Pisanic II, T. R., Blackwell, J. D., Shubayev, V. I., Finõnes, R. R., and Jin, S. (2007) Nanotoxicity of iron oxide nanoparticle internalization in growing neurons. *Biomaterials 28*, 2572–2581.
(42) Fletes, R., Lazarus, J. M., Gage, J., and Chertow, G. M. (2001) Suspected iron dextran-related adverse drug events in hemodialysis patients. *Am. J. Kidney Dis. 37*, 743–749.
(43) Schrijvers, D. M., Martinet, W., De Meyer, G. R. Y., Andries, L., Herman, A. G., and Kockx, M. M. (2004) Flow cytometric evaluation of a model for phagocytosis of cells undergoing apoptosis. *J. Immunol. Methods 287*, 101–108.
(44) Bajorath, J., Greenfield, B., Munro, S. B., Day, A. J., and Aruffo, A. (1998) Identification of CD44 residues important for hyaluronan binding and delineation of the binding site. *J. Biol. Chem. 273*, 338–343.
(45) Lepperdinger, G., Strobl, B., and Kreil, G. (1998) HYAL2, a human gene expressed in many cells, encodes a lysosomal hyaluronidase with a novel type of specificity. *J. Biol. Chem. 273*, 22466–22470.
(46) Evanko, S. P., and Wight, T. N. (1999) Intracellular localization of hyaluronan in proliferating cells. *J. Histochem. Cytochem. 47*, 1331–1341.

BC100354M

Supporting information

Hyaluronic Acid Immobilized Magnetic Nanoparticles for Active Targeting and Imaging of Macrophages

Medha Kamat;[a] *Kheireddine El-Boubbou;*[a] *David C. Zhu;*[b] *Teri Lansdell;*[a] *Xiaowei Lu;*[a] *Wei Li;*[c] *Xuefei Huang*[a]*

[a]Department of Chemistry, Michigan State University, East Lansing, MI 48824, USA

[b]Departments of Radiology and Psychology, Michigan State University, East Lansing, MI 48824, USA

[c]Department of Pharmaceutical Sciences, University of Tennessee Health Science Center, 847 Monroe Avenue, Memphis, TN 38163, USA

Corresponding author:

Xuefei Huang

Department of Chemistry, Michigan State University, East Lansing, MI 48824, USA

Tel: (517) 355-9715, ext 329

Fax: (517) 353-1793

Email: xuefei@chemistry.msu.edu

Table of contents

Figure S1	S3
Figure S2	S4
Figure S3	S6
Table S1	S7
Table S2	S7

Figure S1. Thermogravimetric analysis of NH_2-DESPION and HA-DESPION. The additional weight loss upon heating of HA-DESPION compared to NH_2-DESPION was attributed to HA immobilized on the NPs.

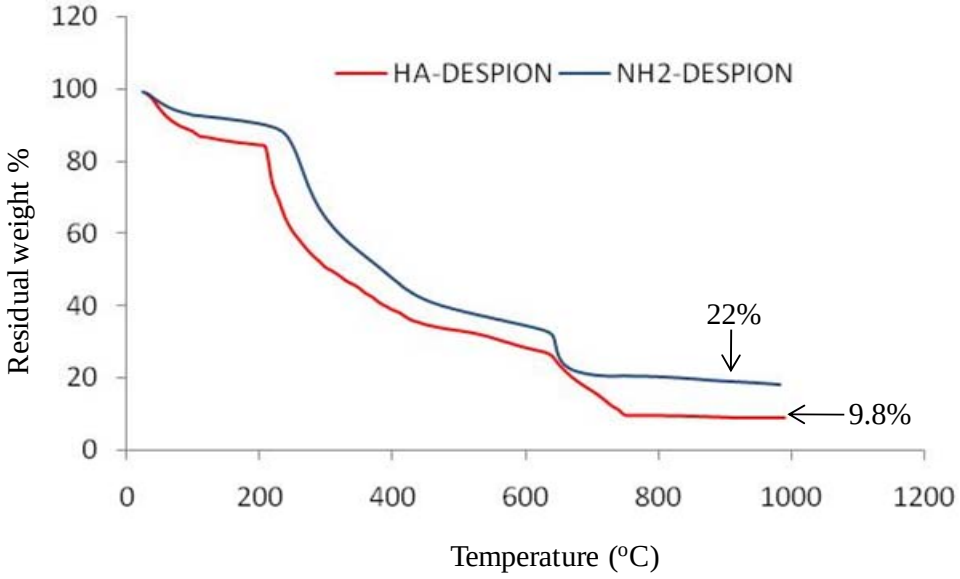
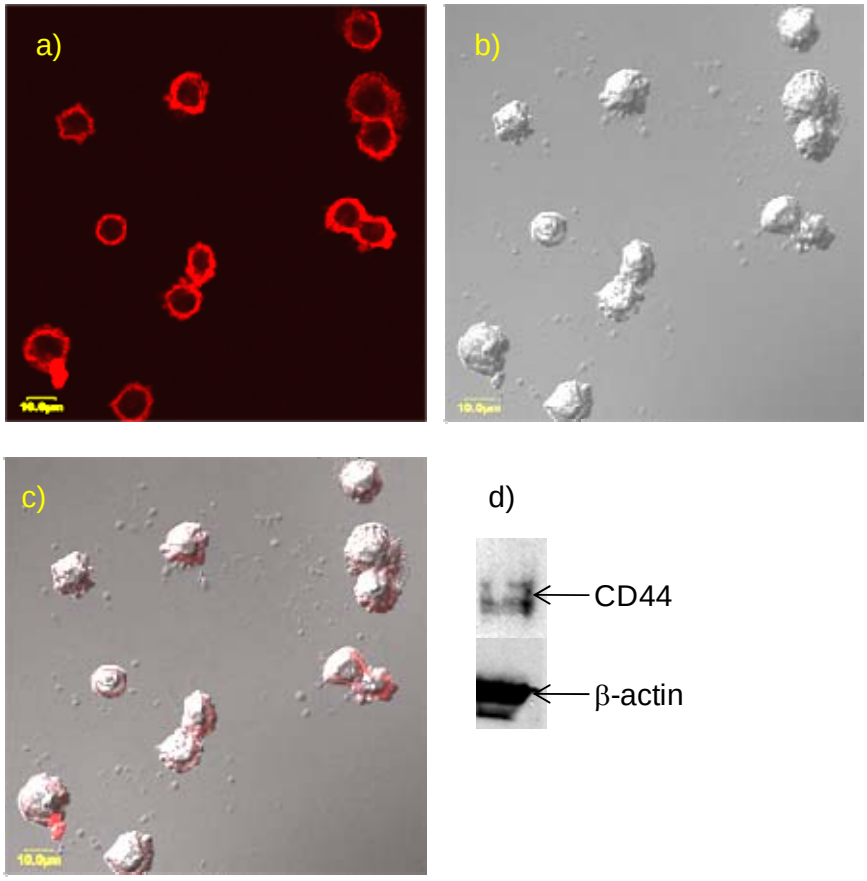


Figure S2. a) Confocal fluorescent microscopy image of THP-1 cells upon incubation with anti-human CD44 mAb followed by Alexafluor 594 labeled anti-IgG secondary antibody; b) Laser image of the cells; and c) Overlay of the fluorescent and laser images. The intense red color in a) suggested the presence of CD44 in THP-1 cells. This was confirmed by d) Western blot of THP-1 cells.



Immunohistostaining for CD44: The cells were inoculated in 4 chambered cover glass (LabTek, Fisher Science) at a cell density of $4x10^5$cells/mL. THP-1 cells were differentiated with PMA(10 μg/mL) to allow adhesion overnight. Next morning the cells were fixed using 10% neutral buffered formalin for 15min, washed with PBS containing 0.05% tween20 (Sigma) (wash buffer) twice for 10 min each. The cells were blocked using PBS containing 10% goat serum and 1% BSA for 2 h at RT. After 2 h, the blocking solution was drained and 300μL of 50μg/mL mouse anti human CD44 mAb (MEM 85, Invitrogen) diluted in PBS containing 1% BSA was added. The samples were then incubated in a moisture chamber at 4^oC for 48 h. For control, the blocking solution was used. Upon completion of incubation period, the supernatants were drained and washed with wash buffer twice for 10 min each. Chambers were dried by decanting and then were treated with 300 μL of 10 μg/mL goat antimouse IgG_{2b} secondary antibody labeled with Alexa Fluor 594 for 1 h, in dark. After an hour, the chambers were

washed buffer twice with 10 min each followed by water, in dark. Samples were imaged using confocal microscopy on Olympus Fluoview 1000 LSM.

Western Blot analysis to determine CD44 expression: The medium was removed from cell culture either by centrifugation or aspiration. The cells were washed with cold PBS twice and then lysed using a mixture of RIPA buffer, protease inhibitor phenyl methyl sulphonyl fluoride (PMSF), and phosphatase inhibitor cocktail. The lysate was centrifuged to remove cell debris. The total protein concentration was determined using Bradford assay (Bio-Rad). The samples together with high-molecular weight prestained standards were electrophoresed on non reducing 10% SDS gel, and then transferred to a PVDF membrane. The membrane was blocked using 4% non-fat milk in TBS-tween (TBST) buffer for 1 h and then treated with mouse anti-human CD44 antibody (156-3C11, Cell signaling) diluted to 1:1000 in 4% non-fat milk in TBST at 4°C overnight followed by goat anti-mouse HRP antibody (Bio-Rad) for 1 h. The blot was sprayed with chemiluminescent HRP detection reagent (Denville Scientific) and developed using autoradiography. β-actin was used as a positive control and was detected using mouse anti-human β-actin peroxidase antibody AC-15 (Sigma-Aldrich,) diluted at 1:40,000 in 4%Milk-TBSTfor 1 h at RT. The blot was developed using aforementioned protocol.

Figure S3. a) Confocal fluorescent microscopy image of EA.hy926 cells upon incubation with anti-human CD44 mAb followed by Alexafluor 594 labeled anti-IgG secondary antibody; b) Laser image of the cells; and c) Overlay of the fluorescent and laser images. The intense red color in a) suggested the presence of CD44 in EA.hy926 cells. This was confirmed by d) Western blot of EA.hy926 cells.

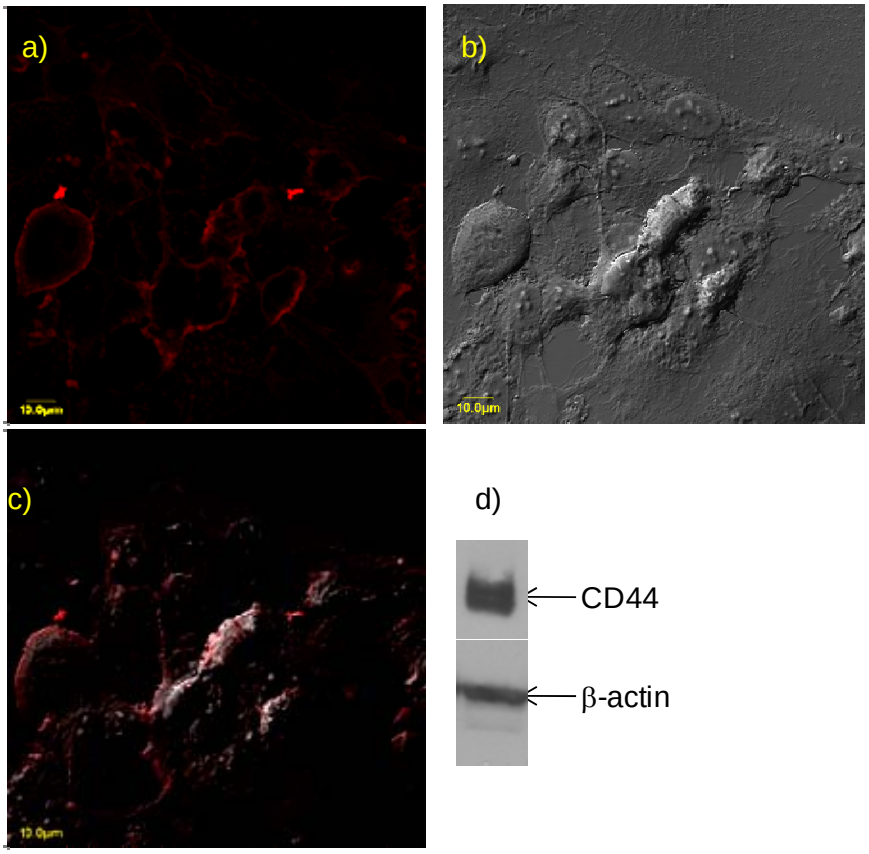


Table S1. Elemental analysis of nanoparticles. The significant increase of % of nitrogen in HA-DESPION confirmed the immobilization of HA on NPs.

Nanoparticles	C (%)	H (%)	N (%)
DESPION	45.09	6.28	0.09
NH_2-DESPION	42.42	6.09	1.02
HA-DESPION	40.09	5.81	3.03

Table S2. Concentration of TNF-α released from THP-1 cells under various conditions as determined from an anti-TNF-α ELISA.

	Treatment method	Amount of TNF-α (pg/mL)
1	Control	0
2	Media only	0
3	PMA (10 ng/mL)	37.5
4	Cholesterol (10 ng/mL)	40.5
5	PMA + LPS (10 ng/mL)	2500

Anti-TNF-α ELISA: The THP-1 cells were treated with endotoxin free media, PMA containing media (10 ng/mL, 16 h), and LPS containing media (10 ng/mL, 2 h), at a density of $5x10^5$ cells/mL. After completion of the treatment, the supernatant was collected, centrifuged to remove cellular debris, and subjected to ELISA. The ELISA was performed according to the manufacturer's instructions (R&D systems) to determine the cytokine concentration.

Synthesis and Photophysical Properties of Thioglycosylated Chlorins, Isobacteriochlorins, and Bacteriochlorins for Bioimaging and Diagnostics

Sunaina Singh,[†] Amit Aggarwal,[†] Sebastian Thompson,[†] João P. C. Tomé,[†] Xianchun Zhu,[‡] Diana Samaroo,[#] Mikki Vinodu,[†] Ruomei Gao,[‡] and Charles Michael Drain[†,§,*]

Department of Chemistry & Biochemistry, Hunter College of the City University of New York, 695 Park Avenue, New York, New York 10065, United States, Department of Chemistry and Biochemistry, Jackson State University, 1400 J. R. Lynch Street, Jackson, Mississippi 39217, United States, NYC College of Technology, 300 Jay Street, Brooklyn, New York 11201, United States, and The Rockefeller University, 1230 York Avenue, New York, New York 10065, United States. Received August 4, 2010; Revised Manuscript Received September 23, 2010

The facile synthesis and photophysical properties of three nonhydrolyzable thioglycosylated porphyrinoids are reported. Starting from *meso*-perfluorophenylporphyrin, the nonhydrolyzable thioglycosylated porphyrin ($PGlc_4$), chlorin ($CGlc_4$), isobacteriochlorin ($IGlc_4$), and bacteriochlorin ($BGlc_4$) can be made in 2−3 steps. The ability to append a wide range of targeting agents onto the perfluorophenyl moieties, the chemical stability, and the ability to fine-tune the photophysical properties of the chromophores make this a suitable platform for development of biochemical tags, diagnostics, or as photodynamic therapeutic agents. Compared to the porphyrin in phosphate buffered saline, $CGlc_4$ has a markedly greater absorbance of red light near 650 nm and a 6-fold increase in fluorescence quantum yield, whereas $IGlc_4$ has broad Q-bands and a 12-fold increase in fluorescence quantum yield. $BGlc_4$ has a similar fluorescence quantum yield to $PGlc_4$ (<10%), but the lowest-energy absorption/emission peaks of $BGlc_4$ are considerably red-shifted to near 730 nm with a nearly 50-fold greater absorbance, which may allow this conjugate to be an effective PDT agent. The uptake of $CGlc_4$, $IGlc_4$, and $BGlc_4$ derivatives into cells such as human breast cancer cells MDA-MB-231 and K:Molv NIH 3T3 mouse fibroblast cells can be observed at nanomolar concentrations. Photobleaching under these conditions is minimal.

INTRODUCTION

Chlorins are porphyrinoids with one pyrrole double bond missing. Isobacteriochlorins and bacteriochlorins are porphyrinoids with two pyrrole double bonds missing on adjacent or opposite pyrroles, respectively. Oxidative or reductive transformations of porphyrins can yield these chromophores. Porphyrins, chlorins, bacteriochlorins, and isobacteriochlorins each have unique photophysical properties that are exploited by nature and can be used for diverse applications (*1, 2*). Compared to the parent tetraarylporphyrin, the intensity of the lowest-energy UV−visible absorption band near 650 nm can increase by ∼20-fold for chlorins and by ∼5-fold for the isobacteriochlorins. For bacteriochlorins, the absorption band near 650 nm is similar to porphyrins, but an additional high-intensity absorption band appears near 730 nm. The excited-state lifetimes, singlet and triplet quantum yields, and distortion upon metal ion binding are significantly different for these three types of macrocycles (*3, 4*).

For diagnostic and photodynamic therapeutic (PDT) applications, the enhanced intensity of the low-energy absorption bands allows more efficient use of wavelengths of light that penetrate further into tissues (*5*−*8*). An example of a chlorin PDT photosensitizer is *meso*-tetrakis(3′-hydroxyphenyl)chlorin (m-THPC) and its derivatives (*9*). Other water-soluble chlorins are reported (*10*−*12*). For therapeutic uses of PDT agents, high triplet quantum yields are desirable to photosensitize the formation of singlet oxygen and other reactive oxygen species, which then cause damage to diverse cellular components. For diagnostics, the dyes appended with appropriate targeting motifs need to have greater fluorescence quantum yields for use as fluorescent tags or trackers (*13*). Fluorescent dyes with targeting motifs can be used in fluorescence guided surgery (*14*).

Porphyrins, chlorins, isobacteriochlorins, bacteriochlorins, and phthalocyanines with 1−8 appended sugar moieties can have cytotoxic activity, because the sugars can direct the chromophore to some cancer cells (*15*−*27*). However, most reported compounds have O-glyco linkages where hydrolysis may diminish in vivo effectiveness compared to corresponding nonhydrolyzable derivatives. The number, type, and position of the sugar moieties have long been known to effect cell uptake and photochemical properties (*16, 21, 28*). The synthesis of a polyglycerol dendrimer with a porphyrin core is reported (*29*), click reactions have been used to glycosylate chlorin e_6 (*30*), and polysaccharides have been appended to porphyrins (*31*).

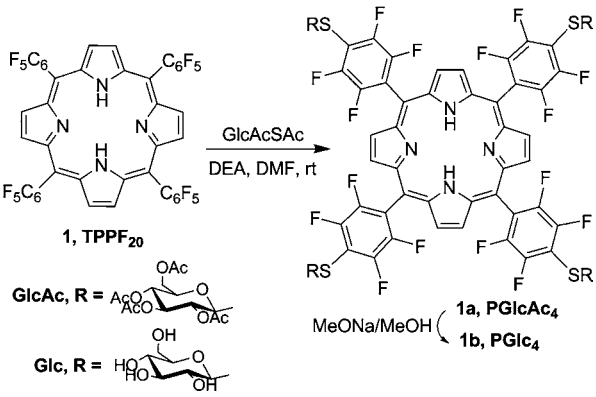
Previously, we reported the synthesis of nonhydrolyzable thioglycosylated tetraarylporphyrins and showed that the tetraglucose derivative ($PGlc_4$, Scheme 1, **1b**) is a selective and effective PDT agent in vitro using several cell lines, such as MDA-MB-231 human breast cancer cells, whereas the galactose derivative is much less effective (*32*). Also, the glycosylated compounds were taken up by transformed mouse $3Y1^{vSrc}$ cells but not taken up by normal mouse fibroblast cells (*32, 33*). We first reported the synthesis and ground-state electronic properties of a glycosylated chlorin formed using a dipolar addition to $TPPF_{20}$ to append a fused *N*-methyl-pyrrolidine moiety and the same chemistry to append the sugars (Scheme 2) (*34*).

One advantage of using the tetraperfluorophenylporphyrin ($TPPF_{20}$) is that it can serve as a core platform for a host of materials (*35, 36*) and biochemical applications because the para fluoro group can be routinely substituted with a variety of

* To whom correspondence should be addressed. (C.M.D.) Phone: 212-650-3791. Fax: 212-772-5332. E-mail: cdrain@hunter.cuny.edu.
[†] Hunter College.
[‡] Jackson State University.
[#] New York City College of Technology.
[§] Rockefeller University.

10.1021/bc100356z © 2010 American Chemical Society
Published on Web 10/21/2010

Scheme 1. Synthesis of $PGlc_4$ from Tetrakis(pentafluorophenyl)porphyrin ($TPPF_{20}$)



nucleophiles to form bioconjugates, biocompatible compounds, and combinatorial libraries (*33, 37*−*41*). For example, we have appended ethylene glycols, polyamines, lysines, alkanes, fluorous alkanes, sugars, and nucleotides using both primary amines and thiols. Subsequently, glycols with an oxygen linkage were also reported (*42*). The PDT activity of many of these derivatives has been studied with a variety of cell lines, and the glycosylated compounds affect apoptosis in several cases (*22, 42*−*44*). Also, the 16 fluoro groups make this compound amenable for in vivo ^{19}F NMR studies of localization (*45*).

Given the diversity of the targeting moieties on the core platform, it is desirable to be able to tune the photophysical properties of the chromophore for these assorted applications, and an obvious means to accomplish this is to adjust the number of double bonds in the macrocycle as is done in nature (*46*). There are many strategies to make porphyrins lacking one or two double bonds using oxidative and reductive strategies (*5, 47*). The formation of the perfluorophenylchlorin (CF_{20}), perfluorophenylisobacteriochlorin (IF_{20}), and perfluorophenylbacteriochlorin (BF_{20}) by 1,3-dipolar additions was reported by the Cavaleiro group (*48*−*52*). The advantage of this route is that it does not use toxic reagents and the products are reasonably stable chemically and to photobleaching. Vicente and co-workers exploited the thio coupling chemistry on CF_{20} to append carboranyl groups (*53*), and Hirohara has appended sugars to free base and Pt derivatives (*54, 55*) for potential therapeutic applications. We now report the synthesis, photophysical properties, and relative cell uptake of the glycosylated chlorin **2b** ($CGlc_4$), isobacteriochlorin **3b** ($IGlc_4$), and bacteriochlorin **4b** ($BGlc_4$) analogues (Scheme 2).

EXPERIMENTAL PROCEDURE

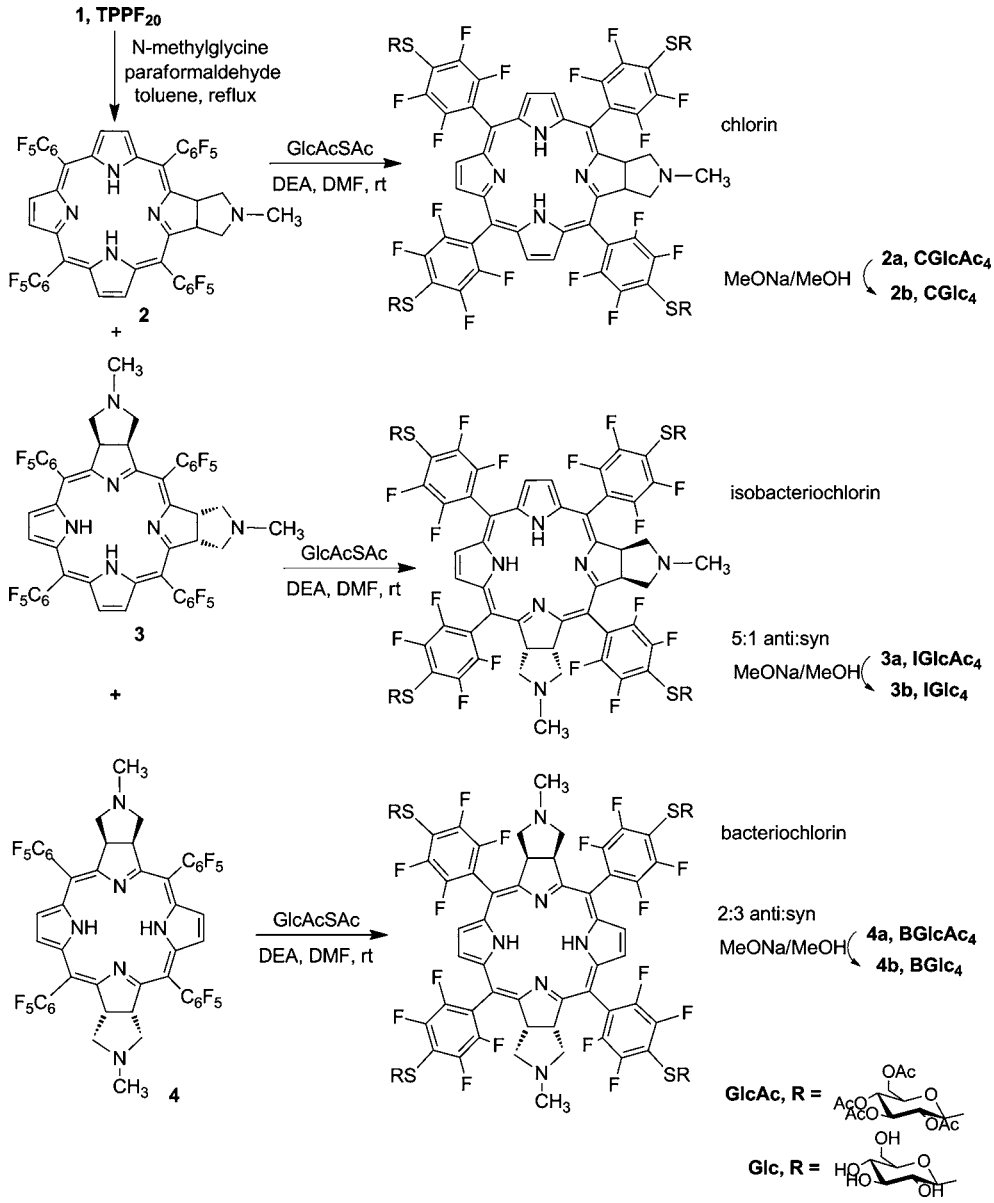
Materials and Methods. *General.* ^1H and ^{13}C NMR spectra were recorded in a Brüker Avance 500 MHz spectrometer and the ^{19}F spectra in a JEOL 400 MHz spectrometer. Electrospray ionization mass spectrometric analyses were performed at the CUNY Mass Spectrometry Facility at Hunter College using an Agilent Technologies HP-1100 LC/MSD instrument. The electrospray ionization was run in methanol, with 0.1% formic acid. UV-visible spectra were recorded on a Varian Bio3 spectrophotometer. Steady-state fluorescence (emission) spectra were measured with a Fluorolog τ3, Jobin-SPEX Instruments S.A., Inc. All reagents were obtained from commercial sources and used without further purification. $TPPF_{20}$ porphyrin was obtained from Frontier Scientific. Dulbecco's Modified Eagle Medium (DMEM), trypsin-EDTA, and antimycotic for cell culture were obtained from GibcoBRL. Hanks' balanced salt solution was obtained from Cellgro (Mediatech). Bovine calf serum was obtained from HyClone. Phosphate buffered saline (PBS) was purchased from Invitrogen. Flash column chromatography was performed using silica gel-60, and the analytical TLC was carried out on precoated sheets with silica gel (0.2 mm thick), both from Sorbent Technologies. The octanol/water partition coefficients were determined by saturating 1:1 (v/v) mixtures of the solvents with the porphyrinoid, waiting 8−10 h, and measuring the Soret and first Q-band intensities. This data were confirmed by saturating each solvent separately before mixing equal volumes.

Synthesis. *Improved Synthesis $PGlcAc_4$ (**1a**).* To a solution of $TPPF_{20}$, **1** (50 mg, 51 μmol), and 2,3,4,6-tetra-*O*-acetyl-glucosylthioacetate (90 mg, 233 μmol, 4.6 equiv) in DMF (5 mL), diethyl amine (1 mL) was added. The reaction mixture was stirred at room temperature for 1.5 h. Then, the product was precipitated with methanol/water and the solid filtered through a short column of Celite and washed with water. The crude mixture was recovered in dichloromethane and purified by flash chromatography (silica gel) using a mixture of ethyl acetate/hexanes (3:1) as eluent. The glycoporphyrin **1a** (110 mg, 92%) was obtained after crystallization in dichloromethane/hexane, as a red powder.

*Synthesis of Porphyrin $PGlc_4$ (**1b**).* Porphyrin **1a** (50 mg, 21 μmol) was dissolved in methanol/dichloromethane (3:1, 8 mL) and treated with sodium methoxide (0.5 M solution in methanol, 1 mL). The reaction mixture was stirred at room temperature for 1.5 h and then neutralized by an aqueous citric acid solution. The mixture was filtered through a Waters Sep-Pak C_{18} 35 cm^3 reverse-phase prep column and washed with water. The deprotected glycoporphyrin **1b** was then purified on flash chromatography (silica gel) eluted using a mixture of ethyl acetate/methanol (3:1) and crystallized in methanol/CH_2Cl_2 (33.5 mg, 96%). mp > 250 °C. ^{19}F NMR (DMSO-d_6): δ −133.82 to −132.57 (m, 8F, Ar-*m*-F), −139.75 to −139.50 (m, 8F, Ar-*o*-F). ^1H NMR (DMSO-d_6): δ 9.33 (bs, 8H, pyrrolic β-H), 5.78 (bs, 4H, Glc-H), 5.10−5.29 (m, 13H, Glc-H), 4.72 (bs, 4H, Glc-H), 3.82−3.84 (m, 5H, Glc-H), 3.52−3.55 (m, 6H, Glc-H), 3.18−3.23(m, 12H, Glc-H), −3.17 (s, 2H, NH).

*Synthesis of Protected Thioglycosylated Chlorin, $CGlcAc_4$ (**2a**).* Chlorin **2** was prepared as previously reported method (*48, 49*). To a solution of chlorin **2** (25 mg, 24 μmol) and 2,3,4,6-tetra-*O*-acetyl-glucosylthioacetate (42 mg, 109 μmol, 4.5 equiv) in DMF (2.5 mL) diethyl amine (0.5 mL) was added. The reaction mixture was stirred at room temperature for 1 h. Then, the reaction mixture was precipitated with methanol/water, and the solid was filtered through a short column of Celite and washed with water. The crude mixture was recovered in CH_2Cl_2 and purified by flash chromatography (silica gel) using a mixture of ethyl acetate/hexanes (3:2) as eluent. Chlorin **2a** (48 mg, 82%) was obtained after crystallization in CH_2Cl_2 /hexanes, as a green powder. Because the *N*-methyl-pyrrolidine points to one face of the chlorin and the stereo centers on the sugars, **2a** is made as a mixture of diastereomers at the β-pyrrole positions bearing the *N*-methyl-pyrrolidine moieties. These are seen in some of the resonances in the ^1H NMR and especially the complexity of the phenyl region of the ^{13}C NMR, which show the coupling to ^{19}F and the diastereomers. The peaks in the ^{19}F NMR spectrum are somewhat broader than the achiral starting material. mp > 250 °C. ^{19}F NMR (DMSO-d_6): δ −130.09 to −129.81, −130.56 to −130.25 (2m, 4F, Ar-*m*-F), −131.69 to −131.54 (m, 4F, Ar-*m*-F), −137.10 to −136.78 (m, 2F, Ar-*o*-F), −138.98 to −138.82 (m, 6F, Ar-*o*-F). ^1H NMR ($CDCl_3$): δ 8.82−8.84, 8.55−8.57, 8.48−8.50 (3m, 6H, pyrrolic β-H), 5.11−5.40 (3m, 18H, 2H β-H [C (sp^3)] and 16H, Glc-H), 4.26−4.35 (m, 8H, Glc-H), 3.88−3.91 (m, 4H, Glc-H), 2.58 and 3.16 (2t, 4H, pyrrolidine-H), 2.22 (s, 3H, NCH_3), 2.07−2.10 (m, 48H, acetyl-H), −1.74 (s, 2H, NH). ^{13}C NMR ($CDCl_3$): δ 20.6 and 20.7 (CH_3CO_2), 41.2 (NCH_3), 53.1 and 53.2 (C2 and C3), 61.7 and 61.9 (Glc), 63.0 (CH_2), 68.0, 68.1, 70.7, 73.9, 84.5 and 84.6

Scheme 2. Synthesis of $CGlc_4$, $IGlc_4$, and $BGlc_4$



(Glc), 97.5, 106.7, 106.8, 111.6, 111.8, 122.1, 122.4, 124.0, 124.3, 128.2, 128.3, 132.5, 134.9, 135.0, 140.0, 141.1, 144−149 (C_6F_4), 152.3, 168.6, 168.8, 169.4 (CH_3CO_2), 170.2 and 170.7 (CH_3CO_2). HRMS calcd for $C_{103}H_{95}F_{16}N_5O_{36}S_4$ $(M+2H)^+$ 2409.4384, found 2409.4318.

*Synthesis of Thioglycosylated Chlorin, $CGlc_4$ (**2b**).* This details what we previously reported (*34*) and was later modified by Hirohara et al (*54*). Glycochlorin **2a** (30 mg, 12.4 μmol) was dissolved in methanol/CH_2Cl_2 (3:1, 4 mL) and treated with sodium methoxide (0.5 M solution in methanol, 1 mL). The reaction mixture was stirred at room temperature for 1 h and then neutralized by an aqueous citric acid solution. The mixture is filtered through Waters Sep-Pak C_{18} 35 cm^3 reverse-phase prep column and washed with water. The deprotected glycochlorin **2b** was then eluted with methanol and purified by flash chromatography (silica gel) using a mixture of ethyl acetate/methanol (3:2) as eluent. Chlorin **2b** (20 mg, 93%) was obtained after crystallization in methanol/CH_2Cl_2, as a green powder. **2b** is also a mixture of diastereomers. These are not well-resolved in the ^{1}H NMR but are observed, especially the complexity of the phenyl region of the ^{13}C NMR, which shows the coupling to ^{19}F and the diastereomers. mp > 250 °C. ^{19}F NMR (DMSO-d_6): δ −132.67 to −132.28 (m, 4F, Ar-*m*-F), −133.79 to −133.64 (m, 4F, Ar-*m*-F), −137.90 to −137.53 (m, 2F, Ar-*o*-F), −139.93 to −139.82 (m, 6F, Ar-*o*-F). ^{1}H NMR (DMSO-d_6): δ 9.14, 8.81 and 8.74 (3bs, 6H, pyrrolic β-H), 5.02−5.10, 5.28 and 5.75 (1m and 2bs, 18H, 2H β-H [C (sp^3)] and 16H, Glc-H), 4.55−4.68 (m, 4H, Glc-H), 4.10 (m, 2H, Glc-H), 3.73−3.78, 3.51, 3.18 and 3.04 (1m and 3bs, 26H, 4H pyrrolidine-H and 22H Glc-H), 2.05 (s, 3H, NCH_3), −1.97 (s, 2H, NH). ^{13}C NMR (DMSO-d_6): δ 41.0 (NCH_3), 49.1 and 53.1 (C2 and C3), 61.7, 61.71, and 61.9 (Glc), 62.9 (CH_2), 70.57, 70.60, 70.68, 70.78, 70.8, 75.1, 75.2, 78.51, 78.54, 78.6, 79.6, 82.2, 82.3, 84.9, 85.0 and 85.2 (Glc), 97.8, 106.8, 113.8, 113.9, 114.1, 114.2, 119.5, 119.6, 119.8, 120.0, 120.2, 126.6, 129.8, 133.5, 135.1, 140.3, 143−149 (C_6F_4), 152.4, 170.2. HRMS calcd. for $C_{71}H_{62}F_{16}N_5O_{20}S_4$ $(M+H)^+$ 1736.2615, found 1736.2603.

*Synthesis of Isobacteriochlorin (**3**) and Bacteriochlorin (**4**).* These compounds are made using modifications of the previously reported procedure (*49*) and scaled up. A toluene (20 mL) solution of $TPPF_{20}$ (100 mg, 0.1 mmol), *N*-methylglycine (30 mg, 1 mmol), and paraformaldehyde (20 mg, 0.22 mmol) was heated at reflux for ca. 12 h under a nitrogen atmosphere. Further portions of *N*-methylglycine (30 mg) and

paraformaldehyde (20 mg) were again added, and the resulting mixture was refluxed for a total of 24 h (2 × 12 h). The compounds were separated by flash chromatography (silica gel) using hexane/CH_2Cl_2 (50:50 v/v) to elute the negligible amount of unreacted porphyrin **1**, followed by CH_2Cl_2 to get the chlorin **2** (45 mg, 42%) and then CH_2Cl_2/acetone (95:5) to get the isobacteriochlorin **3** (40 mg, 34%). However, we found that a small amount (ca. 10−15%) of the bacteriochlorin consistently elutes with the isobacteriochlorin under these conditions. Thus, compounds **2**, **3**, and **4** were separated using a petroleum ether/ethyl acetate gradient on a flash silica gel column. From 100 mg $TPPF_{20}$ (102.6 μmol) is obtained 70 mg of the chlorin compound **2** (67.89 μmol, 66% yield), 15 mg of the anti isobacteriochlorin compound **3** (13.77 μmol, 13% yield), and 5 mg of both the syn and anti bacteriochlorin compound **4** (4.6 μmol, 5% yield). The diastereomeric anti form of compound **3** is preferentially formed; conversely, the syn form of compound **4** is the major product (3:2 syn/anti), and the NMR, HRMS, and UV−visible spectra for **3** and **4** were consistent with the previous report (*49*).

*Synthesis of Protected Thioglycosylated Isobacteriochlorin, IGlcAc$_4$ (**3a**).* To a solution of isobacteriochlorin **3** (25 mg, 23 μmol) and 2,3,4,6-tetra-*O*-acetyl-glucosylthioacetate (40 mg, 103 μmol, 4.5 equiv) in DMF (2.5 mL), diethyl amine (0.5 mL) was added. The reaction mixture was stirred at room temperature for 4 h. The reaction mixture was precipitated with methanol/H_2O and the solid filtered through a short column of Celite and washed with water. The crude mixture was recovered in CH_2Cl_2 and purified by flash chromatography (silica gel) using a mixture of ethyl acetate/hexanes (3:1) as eluent. Isobacteriochlorin **3a** (49 mg, 86%) was obtained after crystallization in CH_2Cl_2/hexanes, as a pink powder. Because the *N*-methyl-pyrrolidine points to opposite faces of the isobacteriochlorin and of the stereo centers on the sugars, **3a** is made as a mixture of two sets of diastereomers on the four β-pyrrole positions bearing the *N*-methyl-pyrrolidine moieties. These are seen in some of the resonances in the ^{1}H NMR and especially the complexity of the phenyl region of the ^{13}C NMR, which shows the coupling to ^{19}F and the multiplicity due to the adjacent pair of diastereomers. mp > 250 °C. ^{19}F NMR (DMSO-d_6): δ −128.46 to −128.35, −128.81 to −128.70 (2m, 2F, Ar-*m*-F), −130.11 to −129.88, −130.45 to −130.35, −130.91 to −130.81 and −131.62 to −131.41 (4m, 6F, Ar-*m*-F), −136.79 to −136.64, −137.35 to −137.17, −139.42 to −139.23 and −140.04 to −139.94 (4m, 8F, Ar-*o*-F). ^{1}H NMR ($CDCl_3$): δ 7.64, 7.63, 7.22, 7.17 (4d, j = 5 Hz, 4H, pyrrolic β-H), 5.03−5.32 (m, 16H, Glc-H), 4.45−4.50 and 4.16−4.25 (2m, 14H, 4H β-H [C (sp^3)], 2H NH and 8H Glc-H), 3.83(d, j = 5 Hz, 4H, Glc-H), 2.70 and 2.88 (2t, j = 8.2 Hz, 4H, pyrrolidine-H), 2.06−2.31 (m, 58H, 4H pyrrolidine-H, 6H NCH_3, 48H, acetyl-H). ^{13}C NMR ($CDCl_3$): δ 20.6 ($\underline{C}H_3CO_2$), 41.0 (NCH_3), 47.8 and 51.7 (C2, C3, C7, and C8), 61.4, 61.8, 62.5 (CH_2 and Glc), 68.0, 70.2, 70.5, 73.81, 73.83, 76.3, 84.5 and 84.6 (Glc), 92.2, 98.2, 111.0, 111.1, 111.3, 113.6, 121.4, 121.5, 121.6, 128.5, 128.6, 144.4−148.7 (C_6F_4), 169.37, 169.38, 169.41, 170.16 and 170.62 ($CH_3\underline{C}O_2$). HRMS calcd. for $C_{106}H_{100}F_{16}N_6O_{36}S_4$ $(M)^{+\bullet}$ 2464.4806, found 2464.4700.

*Synthesis of Thioglycosylated Isobacteriochlorin, IGlc$_4$ (**3b**).* Isobacteriochlorin **3a** (30 mg, 12.1 μmol) was dissolved in methanol/CH_2Cl_2 (3:1, 4 mL) and treated with sodium methoxide (0.5 M solution in methanol, 1 mL). The reaction mixture was stirred at room temperature for 1 h and then neutralized by an aqueous citric acid solution. The mixture was filtered through Waters Sep-Pak C_{18} 35 cm^3 reverse-phase prep column and washed with water. The deprotected isobacteriochlorin **3b** was eluted with methanol and purified by flash chromatography (silica gel) using a mixture of ethyl acetate/methanol (3:2) as eluent. Isobacteriochlorin **3b** (19 mg, 88%) was obtained after crystallization in methanol/CH_2Cl_2 as a pink powder. **3b** is likewise a mixture of two sets of diastereomers. These are not resolved in the ^{1}H NMR, but are observed especially in the complexity of the phenyl region of the ^{13}C NMR, which shows the coupling to ^{19}F and the multiplicity due to the adjacent pair of diastereomers. mp > 250 °C. ^{19}F NMR (DMSO-d_6): δ −131.31 to −131.01, −132.98 to −132.25 and −133.68 to −133.43 (3m, 8F, Ar-*m*-F), −138.2 to −137.59, −140.13 to −140.04, −140.37 to −140.31 and −140.89 to −140.79 (4m, 8F, Ar-*o*-F). ^{1}H NMR (DMSO-d_6): δ 7.78 and 7.30 (2s, 4H, pyrrolic β-H), 5.67 (m, 4H, Glc-H), 5.21−5.24, 5.02−5.06 and 4.91−4.95 (3m, 12H, Glc-H), 4.40−4.44 and 4.05−4.13 (2m, 12H, 4H β-H [C (sp^3)], 2H NH, 8H Glc-H), 3.16−3.26 (m, 20H), Glc-H), 2.70, 2.57, 2.19 and 2.18 (4bs, 8H, pyrrolidine-H), 2.01 (s, 6H, NCH_3). ^{13}C NMR (DMSO-d_6/methanol-d_4): δ 40.6 (NCH_3), 47.7, 49.06 (C2, C3, C7, and C8), 61.5, 61.6, 61.7, 62.5, 70.48, 70.52, 75.0, 75.1, 78.44, 78.46, 78.48, 84.8, 85.0 (CH_2 and Glc), 92.2, 97.8 113.2, 113.3, 113.36, 113.38, 113.61, 119.0, 119.2, 146.0−148.6 (C_6F_4). HRMS calcd. for $C_{74}H_{69}F_{16}N_6O_{20}S_4$ $(M+H)^+$ 1793.3194, found 1793.3197.

*Synthesis of Protected Thioglycosylated Bacteriochlorin, BGlcAc$_4$ (**4a**).* To a solution of bacteriochlorin **4** (7 mg, 6.4 μmol) and 2,3,4,6-tetra-*O*-acetyl-glucosylthioacetate (12 mg, 29 μmol, 4.5 equiv) in DMF (0.5 mL), diethyl amine (0.1 mL) was added. The reaction mixture was stirred at room temperature for 4 h. Then, the reaction mixture was precipitated with methanol/H_2O, and the solid was filtered through a short column of Celite and washed with water. The crude mixture was recovered in CH_2Cl_2 and purified by flash chromatography (silica gel) using a mixture of ethyl acetate/hexanes (3:1) as eluent. Bacteriochlorin **4a** (13 mg, 86%) was obtained after crystallization in CH_2Cl_2/hexanes, as a green powder. Because of the stereo centers on the sugars, **4a** is made as a mixture of two sets of diastereomers. mp > 250 °C. ^{19}F NMR ($CDCl_3$): δ −129.05 to −128.15 (4m, 8F, Ar-*m*-F), −132.80 to −132.40 (m, 4F, Ar-*o*-F), −134.95 to −134.45 (m, 4F, Ar-*o*-F). ^{1}H NMR ($CDCl_3$): δ 8.30 (m, 4H, pyrrolic β-H), 5.12−5.23 (m, 20H, 16H Glc-H, 4H, β-H [C (sp^3)]), 4.15−4.30 (m, 8H Glc-H), 3.88 (m, 4H, Glc-H), 3.05−3.10 (m, 4H, pyrrolidine-H), 2.45−2.46 (m, 4H pyrrolidine-H), 2.06−2.31 (m, 54H, 6H NCH_3, 48H, 48H, acetyl-H), −1.75 (s, 2H, NH). ^{13}C NMR ($CDCl_3$): δ 20.6 (CH_3CO_2), 41.2 (NCH_3), 52.4 and 52.5 (C2, C3, C7, and C8), 61.7, 61.8 (CH_2 and Glc), 68.0, 70.6, 73.88, 76.70, 77.0, 77.3, 84.6 and 84.7 (Glc), 92.2, 99.7, 107.7, 111.4, 111.5, 115.5, 115.6, 122.6, 122.7, 136.0, 136.1, 144.4−148.7 (C_6F_4), 164.0, 169.38, 169.40, 170.19, and 170.64 (CH_3CO_2). HRMS calcd. for $C_{106}H_{100}F_{16}N_6O_{36}S_4$ $(M)^{+\bullet}$ 2464.4806, found 2464.4813.

*Synthesis of Thioglycosylated Bacteriochlorin, BGlc$_4$ (**4b**).* Bacteriochlorin **4a** (10 mg, 4.0 μmol) was dissolved in methanol/CH_2Cl_2 (3:1, 1.5 mL) and treated with sodium methoxide (0.5 M solution in methanol, 0.2 mL). The reaction mixture was stirred at room temperature for 1 h and then neutralized by an aqueous citric acid solution. The mixture is filtered through Waters Sep-Pak C_{18} 35 cm^3 reverse-phase prep column and washed with water. Though **4** has a plane of symmetry, because of the chiral centers on the sugars on **4a** and **4b**, these are prepared as a set of two diastereomers. The deprotected bacteriochlorin **4b** was eluted with methanol and purified by flash chromatography (silica gel) using a mixture of ethyl acetate/methanol (3:2) as eluent. Bacteriochlorin **4b** (6.5 mg, 88%) was obtained after crystallization in methanol/CH_2Cl_2, as a green powder. mp > 250 °C. ^{19}F NMR (MeOD): δ −134.0 to −132.5 (4m, 8F, Ar-*m*-F), −137.2 to −136.0 (m, 4F, Ar-*o*-F), −140.0 to −139.0 (m, 4F, Ar-*o*-F). ^{1}H NMR (MeOD): δ 8.42 (bs, 4H, pyrrolic β-H), 5.30−5.45 (m, 4H, Glc-H), 5.05−5.14 (m, 4H, β-H [C (sp^3)]), 3.73−3.74 and 3.63−3.65 (2m, 8H,

Glc-H), 3.49−3.54 and 3.41−3.43 (2m, 16H, 8H, and 8H Glc-H), 3.15−3.18 (m, 4H, pyrrolidine-H), 2.79−2.82 (m, 4H, pyrrolidine-H), 2.28 (s, 6H, NCH_3). ^{13}C NMR (MeOD): δ 39.8 (NCH_3), 51.8, 51.9 (C2, C3, C7, and C8), 61.6, 70.5, 74.57, 74.59, 78.3, 81.36, 81.37, 84.9, 85.12 (CH_2 and Glc), 99.91, 99.94, 100.0, 103.9, 113.32, 113.34, 113.45, 113.50, 120.86, 121.0, 136.2, 136.3, 136.4, 146.0−148.6 (C_6F_4). HRMS calcd. for $C_{74}H_{69}F_{16}N_6O_{20}S_4$ $(M+H)^+$ 1793.3194, found 1793.3179.

UV−visible, Fluorescence Spectroscopy, and Quantum Yield Calculations. UV−visible and fluorescence measurements were performed on dilute solutions, typically ~2 μM, of compounds in ethanol, phosphate buffered saline (PBS), and ethyl acetate. The UV−visible spectra were obtained from 330 to 800 nm using 1 cm quartz cuvettes. For steady-state fluorescence spectroscopy, samples were excited at 509 nm for ethyl acetate and 512 nm for PBS and ethanol where absorbencies are ≤0.1. For emission spectra, both the excitation and detection monochromators had a band-pass of 1 nm. The corrected emission (for instrument response) and absorption spectra were used to calculate the quantum yield. Fluorescence quantum yields were determined for chlorin, isobacteriochlorin, and bacteriochlorin solutions relative to TPP in toluene, which has a fluorescence quantum yield of 0.11 (*57, 58*). The quantum yields were measured indirectly using TPP; thus, these values may have some systematic error. All experiments were carried out on the same day, using identical concentrations to minimize any experimental errors. These three glycosylated conjugates are quite stable toward photobleaching. When ethanolic solution of $IGlc_4$ is exposed to sunlight with a power of ca. 40−80 W/m^2 for ca 2 h, we found only 10.5% of the compound decomposed (Supporting Information).

Quantum Yield of Singlet Oxygen Production (Φ_Δ). Φ_Δ values were determined on a relative basis by using *meso*-tetrakis(4-sulfonatophenyl)porphine dihydrochloride (TSPP) as a reference sensitizer ($\Phi_{\Delta,TSPP} = 0.7$ in methanol) (*56*). A time-resolved Nd:YAG laser (Polaris II, Electro Scientific Industries, Inc.) equipped with low-temperature cooled Ge detector (Applied Detector Corporation) was employed as an excitation source at 532 nm. All of the experiments were carried out in deuterium methanol-d_1. The absorbances from samples and TSPP at 532 nm were controlled between 0.1 and 0.5. $^1O_2$ luminescence was monitored as a function of sensitizer absorbance. Slopes were analyzed from a plot of $^1O_2$ intensity via absorbance. Φ_Δ can be calculated according to following equation:

$$\Phi_{\Delta,\text{sample}}/\Phi_{\Delta,\text{reference}} = \text{slope}_{\text{sample}}/\text{slope}_{\text{reference}}$$

Cell Culture. 3T3 K:MOLV NIH cells maintained in DMEM, 10% BCS, 1% antimycotic at 37 °C and in 5% CO_2 atmosphere were plated onto coverslips in cell culture dishes. $PGlc_4$, $CGlc_4$, and $IGlc_4$ dissolved in methanol were added to the cell cultures to a final concentration of 1 or 2.5 μM such that there was never more than 0.5% methanol in the solution. After 20 h incubation, cells were washed with PBS 3−5 times and fixed in 4% paraformaldehyde solution for 10 min at room temperature. The cells were then washed with PBS 3 times. The cells were visualized using a Nikon Optiphot 2 fluorescence microscope. Images were captured as JPEG files at 10× magnification, with a 505−565 nm excitation band-pass filter and a 565−685 nm emission band-pass filter. For each set of experiments, cells were cultured and the fluorescence images were taken under identical culture and microscopic conditions. For quantitative studies, the image intensities of the cells in the fluorescence micrographs were calculated by FLim program available at http://nathan.instras.com/projects/FLim/index.html.

Confocal Microscopy. Cells were plated onto coverslips in cell culture dishes. $BGlc_4$ dissolved in DMSO was added to the cultures to a final concentration of 10 μM (DMSO concentrations were <0.2%). After incubation for 24 h, the cells were rinsed three times with PBS and incubated with a 4% paraformaldehyde solution for 15 min at 37 °C under cell growth conditions. Cells were then washed three times with PBS, mounted in Dako fluorescence mounting medium, and visualized using a Zeiss LSM510 laser scanning confocal microscope where images were captured with excitation at 514 nm, emission used a 710−750 nm band-pass filter.

RESULTS AND DISCUSSION

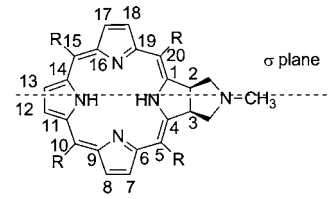
The reduction of $TPPF_{20}$ is carried out by modifications of a reported 1,3-dipolar cycloaddition reaction of an azomethine ylide with $TPPF_{20}$, **1**, to produce chlorin **2**, isobacteriochlorin **3**, and bacteriochlorin **4** (Scheme 2) (*48, 49, 51*). The reaction is scaled up by 5-fold, and the chlorin, bacteriochlorin, and isobacteriochlorin products were separated by column chromatography using a petroleum ether/ethyl acetate gradient as eluent. When compound **3** is the target, the products are formed in yields of ca. 66% for **2**, 13% yield of the anti isomer of **3**, and 5% yields for the syn and anti isomers of the bacteriochlorin **4**. These yields are somewhat different from those reported, and reflect the yield of the isobacteriochlorin to the bacteriochlorin as ca. 5:1 rather than a few percent of the latter.

The mechanism of these dipolar additions has been discussed (*51*). Interestingly, chiral HPLC assays and CD spectra indicate a trace quantity of what is likely the product of a nonconcerted addition reaction in the crude reaction mixture in the synthesis of the chlorin. This may arise because of the stability of an intermediate conferred by the macrocycle (*59, 60*), but we did not pursue this. Statistically, the second dipolar addition reaction should prefer the adjacent pyrrole 2:1 over the opposite pyrrole, but IF_{20} is formed at 3:1. As with previous reports, for IF_{20} the anti structure (Scheme 2) forms predominantly by ca. 7-fold (*48, 49*), and our preliminary dynamics calculations indicate steric crowding between the *N*-methyl-pyrrolidine methylenes, and adjacent fluorophenyls result in distortion of the macrocycle and partial blocking of the syn face. In the case of the BF_{20}, the syn isomer is the major product. The dipolar addition mechanism in terms of MO calculations was discussed (*51*).

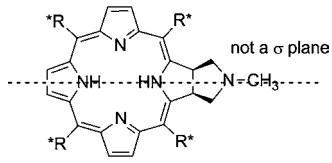
The principal goal was to obtain the four compounds in one step and in sufficient quantity for the next reactions. NMR and mass spectrometry are consistent with the previous report and attest to the purity of these porphyrinoid-F_{20} intermediates. The nucleophilic substitution of the thioglucose at the para position of the perfluorophenyl substituents of these porphyrinoids is a modification of that previously reported (*33*). Specifically, 4.5 equiv of 1-thioacetate-2,3,4,6-tetra-*O*-acetyl-β-D-glucopyranose, a greater quantity of diethylamine (DEA), in 1 h reactions yields $PGlcAc_4$ **1a**. Thus, **2a** ($CGlcAc_4$), **3a** ($IGlcAc_4$), and **4a** ($BGlcAc_4$) are obtained from **2**, **3**, and **4**, respectively (Scheme 2). More than four thiosugars can be added with greater equivalents and longer reaction times. Flash chromatography yields the protected glycosylated derivatives as the mixture of diastereomers in ca. 85% yields. The carbohydrate protection groups were removed by treating **1a**, **2a**, **3a**, and **4a** with sodium methoxide in dry methanol to obtain the glycoporphyrinoids **1b**, **2b**, **3b**, and **4b** in ca. 95−98% yield (Scheme 2) (Supporting Information).

Since the *N*-methyl-pyrrolidine points toward one face of the macrocycle, addition of moieties with chiral centers such as the sugars to chlorin **2** results in diastereomers at the *N*-methylpyrrolidine β-carbons for **2a** and **2b**, even though **2** has a plane of symmetry. Thus, **2a** and **2b** are 2R,3S diastereomers, which was not previously recognized. As pointed out in the synthesis (*51*), there is a set of enantiomers at the β-carbons for the anti conformer of **3**; thus, the addition of the sugars further

Scheme 3. $CGlc_4$ Diastereomers (see Supporting Information)



(2*R*,3*S*) - meso when R is achiral



(2*R*,3*S*) - optically active diastereomer when R* is chiral

differentiates these in **3a** and **3b** into diastereomers 2R,3S,7S,8R and 2S,3R,7R,8S. Both the syn and anti forms of bacteriochlorin **4** have a plane of symmetry, but addition of the sugars results in a set of diastereomers, 2R,3S,12S,13R and 2S,3R,12R,13S (Scheme 3).

The structures of all porphyrinoids were confirmed by NMR, UV−visible, and mass spectrometry and HRMS analysis. The ^{1}H NMR spectra of **2a**, **3a**, and **4a** show the porphyrinoid core pyrrole β protons near 8.9 ppm and the pyrrole NH protons near −2 ppm. The ^{1}H NMR spectra of all three compounds show resonance at 2.1 and 2.3 ppm, due to the acetyl protons, and the resonances of the other protons of the carbohydrate unit appear between 4 and 6 ppm. The resonances of the anomeric protons appear as doublets at 5.03 ppm to 5.40 ppm. The N-methyl groups are observed in the 2.22 ppm for **2a** and are obscured by the acetyl groups in **3a** and **4a**. While the diastereomers are observed for some resonances for the protected derivatives, they are not well-resolved for **2b**, **3b,** and **4b**.

The ^{19}F NMR spectra confirm the substitution of the para-fluorine atom by the sugar unit, showing the disappearance of the resonances due to the para-fluorine atoms in **2**, **3**, and **4** at −150 ppm. An important diagnostic is the signal due to the meta-fluorine atom shift from −160 ppm in **2**, **3**, and **4** to −130 ppm for **2a**, **3a**, and **4a**. The ortho-fluorine atom resonances remain near −140 ppm. The ^{19}F NMR spectra do not exhibit marked differences between **2a** and **2b**, **3a** and **3b**, or **4a** and **4b**, though these peaks are broadened due to the diastereomeric centers. The ^{13}C NMR clearly indicates the multiple resonances arising from the diastereomers, especially for the phenyl carbons, which remain coupled to the F-atoms, and are closest to the chiral centers of **2a**, **2b**, **3a**, **3b**, **4a**, and **4b**.

Considering the large dependence of the photophysical properties of polar chromophores on the solvent matrix and on other experimental parameters, it is important to develop a self-consistent set of data for accurate comparison of these properties and assessment of potential applications. Since the dye can partition into lipophilic, hydrophilic, or amphipathic cellular structures, we have assayed the photophysical properties in three different solvents. Thus, PBS at pH = 7.4, ethanol, and ethyl acetate solvents were used to probe the photophysical properties (the partition coefficients and photophysical properties are summarized in Tables 1 and 2). While the initial association with the cell is mediated by glucose receptors and the four glycosyl groups on the chromophore, some nonspecific partition into the membrane is also indicated. Because of the size of the molecules, uptake is unlikely to proceed by active or passive transport, but the high local concentration around the cell increases diffusion. Thus, uptake is also dependent on the relative hydrophobicity of the compounds (*61*). The octanol/water partition coefficient and R_f for the glycosylated compounds are listed in Table 1.

Table 1. Partition Coefficients

compound	octanol/water	R_f[a]
$PGlc_4$	43.9 (4.8)	0.6 (5.5)
$CGlc_4$	28.5 (3.13)	0.37 (3.4)
$IGlc_4$	9.1 (1)	0.11 (1)
$BGlc_4$	12.7 (1.4)	0.13 (1.2)

[a] Normalized values in parentheses; see Experimental Section.

The electronic spectra of **2**, **3**, and **4** and the glycosylated derivatives are significantly different from the $TPPF_{20}$. The lowest-energy Q-band of chlorin, $CGlc_4$, in PBS buffer at 649 nm has about 25-fold greater intensity than corresponding Q-band of porphyrin $PGlc_4$ at 646 nm. For isobacteriochlorin, $IGlc_4$ in the same buffer, the lowest-energy Q-band at 645 nm is 5-fold more intense than the porphyrin at the same wavelength. For $BGlc_4$, the strong lowest-energy peak is located at 730 nm improving the absorption in the red region of the spectrum. The fluorescence emission spectra for the four glycosylated porphyrinoids are correspondingly different and have a strong solvent dependence (Table 2).

There are negligible Stokes shifts for $PGlc_4$, $CGlc_4$, and $BGlc_4$ in the three solvents, indicating minimal specific solvent−solute interactions with the macrocycle effecting vibrational processes (*62*). Notably, for the $IGlc_4$ in PBS, the strongest fluorescence band λ_{max} is at 606 nm with a weaker emission centered at 650 nm, while for $BGlc_4$, the peak is presented at 725 nm. Excitation spectra all indicate the presence of only the given compounds. The 0.17 and 0.36 fluorescence quantum yields for $CGlc_4$ and for $IGlc_4$ in PBS are 6 times and 12 times, respectively, that of the porphyrin analogue $PGlc_4$, while for $BGlc_4$ it is 0.03, similar to the $PGlc_4$. There is a small decrease in fluorescence quantum yield upon replacement of the para F atom by the thiocarbohydrate group due to both electronic and heavy atom effects. The greater fluorescence quantum yield of **2b** than m-THPC (*13*) or a water-soluble dimeso substituted chlorin (*10*) likely arises from the presence of the 16 F groups and relative energies of the molecular orbitals, and is consistent with the quantum yield of singlet oxygen generation by **2** (*63*). However, tetraarylporphyrins with a tripeptide (*64*) and other meso aryl chlorins (*65*) have similar photophysical properties to what we find. The sugars have little direct effect on the photophysics but modulate the amphipathicity and enable the observed solvent dependence.

The quantum yields of singlet oxygen formation for three of the compounds in methanol-d_1 are listed in Table 2. Since the porphyrin ring is the reactive site for $^1O_2$ production, the frequency of collisions that result in the formation of $^1O_2$ is related to the probability that an $^3O_2$ molecule makes physical contact with the chromophore in the excited, triplet state. The additional steric effect of the pyrrolidine-fused rings on $CGlc_4$ and $IGlc_4$ could result in reduced collision frequencies and a lower Φ_Δ compared to $PGlc_4$. It is reasonable to expect that internal conversion is somewhat consistent between the compounds, so the increased fluorescence quantum yield means a decrease in the amount of triplet formed. The Φ_Δ data dovetail with the observe fluorescence yields, but the Φ_Δ for $IGlc_4$ in methanol is more consistent with the PBS buffer data.

Because our previous studies with thioglycosylated porphyrin $PGlc_4$ indicated good uptake and photodynamic effects on several cancer cell lines, K:Molv NIH 3T3 mouse fibroblasts (Figure 2) and the MDA-MB-231 breast cancer cell line were used to evaluate the cellular uptake of the glycosylated

Table 2. Photophysical Properties of Glycosylated Porphyrinoid Derivatives

compound	solvent	UV−visible[a]	emission λ_{max}	Φ_F[b]	$^1O_2$ Φ_Δ
$TPPF_{20}$	DMSO	412, 504, 538, 580, 632	637, 702	--	
CF_{20}	DMSO[c]	408, 504, 536, 598, 652	656	--	
m-THPC	methanol[d]		653, 720	0.09	0.43
m-THPBC	methanol[d]		612, 653, 746	0.11	0.43
$PGlc_4$	ethanol	412, 505, 535, 586, 653	653, 702	0.05	0.85[f]
	PBS buffer	410, 510, --- 576, 646(1)[a]	646, 692	0.03	
	ethyl acetate	412, 507, 450, 583, 655	649, 701	0.05	
	DMSO[c]	415, 507, 539, 581, 636	640, 705	0.06	
$CGlc_4$	ethanol	408, 507, 534, 599, 653	653, 715	0.43	0.32[f]
	PBS buffer	409, 506, 533, 597, 649(25)[a]	649, 707	0.17	
	ethyl acetate	406, 504, 531, 597, 651	653, 712	0.39	
	DMSO[e]	412, 506, 537, 598, 652	652	--	0.28
$BGlc_4$	ethanol	353, 374, 505, 732	729	0.047	--
	PBS buffer	357, 508, 730	725	0.03	
	ethyl acetate	352, 379, 508, 730	730	0.055	
$IGlc_4$	ethanol	385, 513, 548, 588, 643	596, 646, 705	0.70	0.59[f]
	PBS buffer	385, 513, 548, 593, 645(5)[a]	606, 650, 711	0.36	
	ethyl acetate	384, 510, 548, 589, 653	596, 646, 700	0.60	

[a] Relative intensity of lowest-energy Q bands. [b] Fluorescence experiments done in air. [c] Taken from ref *55*. [d] m-THPC and the bacteriochlorin m-THPBC taken from ref *13*. [e] Taken from ref *54*. [f] Excited at 532 nm in methanol-d_1.

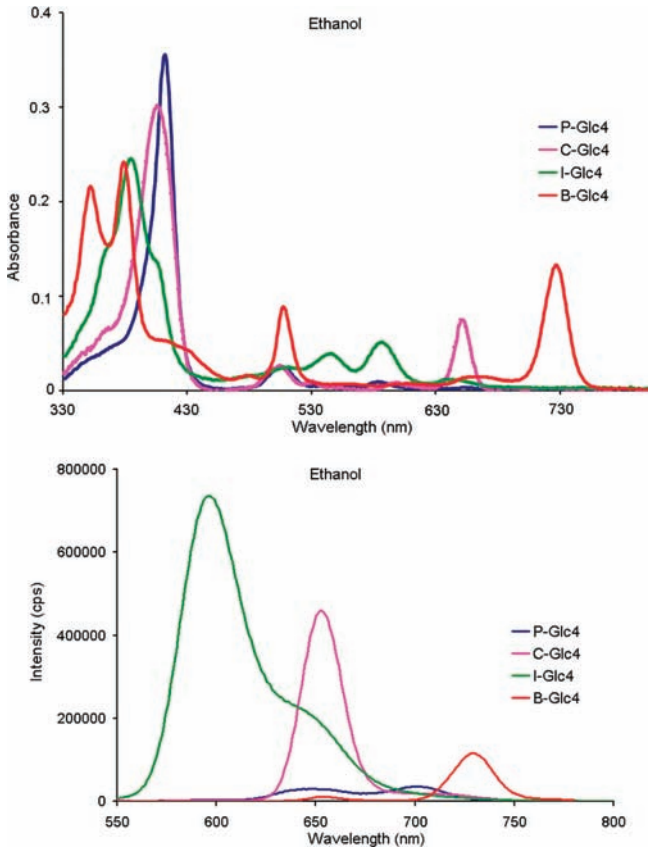


Figure 1. Top: UV−visible spectra of the compounds, 2 μM in ethanol. Bottom: emission spectra of the compounds in ethanol; excitation at 512 nm where the absorbance is ca. 0.05 for each compound.

derivatives. Our initial hypothesis was that the *N*-methylpyrrolidine moieties used to make and stabilize the chlorin, bacteriochlorin, and isobacteriochlorin (as well as the stereo centers at the β positions) would have minimal effect on cell uptake, because these are sandwiched between the glycosylated tetrafluorophenyl groups. K:Molv NIH 3T3 cells were incubated identically with 2.5 μM concentrations of $PGlc_4$, $CGlc_4$, and $IGlc_4$, rinsed with buffer, and the relative uptake was quantified by comparison of images taken by fluorescence microscopy under identical settings (*38*). Confocal microscopy using 10 μM $BGlc_4$ was used because the red absorption and emission are outside the range of our fluorescence microscope (Figure 3). The electronic spectra, fluorescence, and fluorescence microscopy studies all show that these compounds are robust to photobleaching. The remaining 16 F groups impart oxidative stability and further enhance the photonic properties.

At 2.5 μM, the relative integrated intensities for $PGlc_4$, $CGlc_4$, and $IGlc_4$ in the fluorescence micrographs of the K:Molv NIH 3T3 are 1:2:7, respectively (Figure 2). Taking into consideration both the partition coefficients and the fluorescence quantum yields, one would expect that the relative uptake of these compounds into the cells measured by fluorescence to be ca. 1:4:2 for the $PGlc_4$/$CGlc_4$/$IGlc_4$, respectively. The disparity may arise from differences in cell specificity or the degree of aggregation of the compounds in the PBS buffer and/or aggregation as the local concentration of the dyes around the cell increases (*17*). The propensity of aggregation inside the cell may also vary. Also, some diastereomers may be taken up preferentially over others. The mechanism of uptake and photodynamic effects in this and other cell lines will be reported elsewhere.

Though there may be differences in uptake among these compounds, we have shown that the $PGlc_4$ compound localizes in the endoplasmic reticulum because of the metabolic needs of this organelle (*43*). The significantly greater fluorescence quantum yield of the $IGlc_4$ system means that ca. 25 nM concentrations can be used to follow receptors and/or glycolysis processes in the cell (Figure 4). Thus, $IGlc_4$ is better suited for tagging and sensor applications. For PDT applications, sensitizers with strong red absorptions are generally considered better because these wavelengths penetrate deeper into tissue (*6, 7*). The optical cross section of $CGlc_4$ in the red region is significantly larger than the porphyrin or isobacteriochlorin analogues. Thus, if red light is used to activate the second-generation dye $CGlc_4$, the increased light absorptivity more than compensates the reduced triplet quantum yield. Given the very strong 730 nm absorption, the low fluorescence quantum yield, and the greater triplet quantum yield of $BGlc_4$, this may be the best photosensitizer for PDT of the compounds described herein. However, a more efficient synthesis and purification of the isomers and diastereomers needs to be developed for the bacteriochlorin compounds to be used. The detailed photophysics of these compounds, including in biological systems, will be the subject of future studies.

Though the fluorescence of $CGlc_4$ and $IGlc_4$ is greater than that of the parent porphyrin, there is still sufficient triplet formation to effect cell death via necrosis and/or apoptosis. This indicates that these compounds can be used as dual function

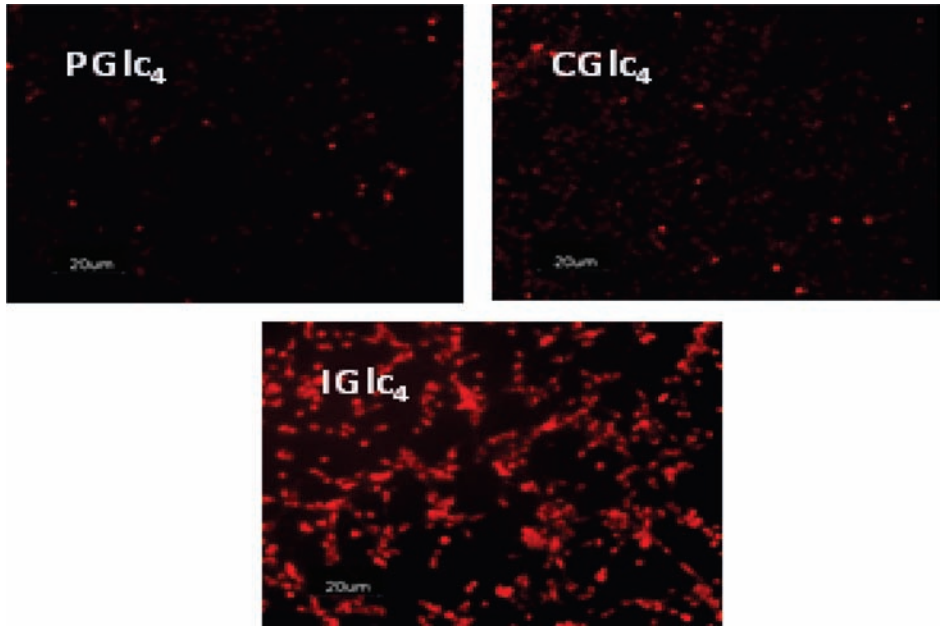


Figure 2. Fluorescence microscopy of K:Molv NIH 3T3 cells treated with 2.5 μM $PGlc_4$ (**1b**), $CGlc_4$ (**2b**), and $IGlc_4$ (**3b**). K:Molv NIH 3T3 cells were incubated for 20 h with porphyrinoids, followed by removal of unbound dye from the cell culture by repeated rinsing with PBS, and the cells were imaged under identical microscope settings and not enhanced; magnification 10×.

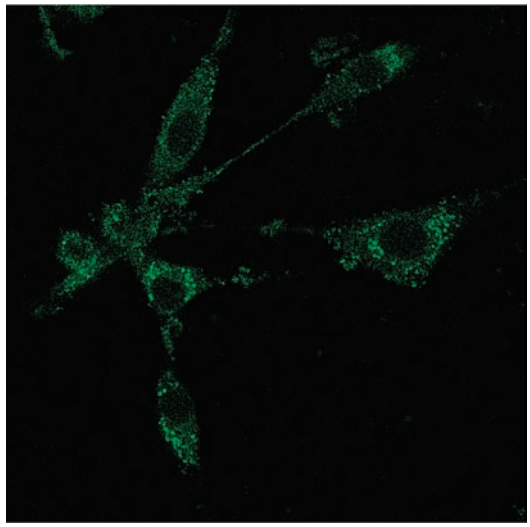


Figure 3. K:Molv NIH 3T3 cells were incubated with 10 μM $BGlc_4$ for 24 h, rinsed three times with PBS buffer, and fixed with 4% paraformaldehyde solution. Confocal microscope excitation at 514 nm, emission monitored with a 710−750 band-pass filter. No images are observed using a 610−650 nm emission band-pass filter, so fluorescence does not arise from the one of the other dye systems. The image is not enhanced; magnification is 60×.

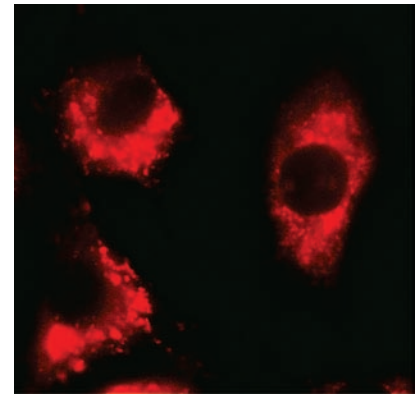


Figure 4. Fluorescence image of a MDA-MB-231 breast cancer cell treated with 25 nM $IGlc_4$ and rinsed three times with PBS buffer to remove unbound dye (see Supporting Information for comparisons to the other porphyrinoids).

agents that both locate and treat cancerous cells. To demonstrate PDT activity, $CGlc_4$ and $IGlc_4$ were tested under the same conditions as $PGlc_4$ (10 μM concentration and 10 min irradiation with white light from a 13 W fluorescent bulb). $CGlc_4$ and $IGlc_4$ induce cell death only after twice the light power is used (data not shown).

We have also made the chlorin via a gemdiol on one pyrrole unit of $TPPF_{20}$ and the corresponding tetraglycosylated derivative (*47, 66*), but the yield and stability are not as good as the those of the compounds described herein (Supporting Information). Similar to the parent $TPPF_{20}$, preliminary studies indicate the same high-yield substitution chemistry can yield an array of conjugates on these core platforms to target various tissues (*2, 34, 38*), cell types, and cellular structures (*67*).

In conclusion, these core platforms will enable rapid development of new multifunctional imaging, sensing, and therapeutic agents (*68*) for specific targets, and the ability to assess the effectiveness appended motifs in targeting. These platforms will also facilitate the development of effective probes for fundamental biochemical/biophysical studies (*44, 69*). Both $CGlc_4$ and $IGlc_4$ have significantly enhanced fluorescence quantum yields compared to $PGlc_4$, while the $BGlc_4$ derivative has a fluorescence quantum yield that is similar to the parent porphyrin. Thus, $IGlc_4$ has greatest potential use as fluorescent tags, diagnostics, or imaging agents. The intermediate fluorescence of the $CGlc_4$ system may well serve as a dual purpose agent for targeting, detecting, and treating diseased tissues. The $BGlc_4$ system has near-optimal properties as the PDT agent, but new synthetic strategies are needed to make these compounds.

ACKNOWLEDGMENT

Supported by National Institutes of Health (NIH) GM60654 to C.M.D.; KL2RR024997 for J.P.C.T. and UL1RR024996 for S.T. of the Clinical and Translational Science Center at Weill Cornell Medical College UL1-RR024996; and National Science

Foundation (NSF) CHE-0847997 to C.M.D. R.G. acknowledges support from NSF-PREM (DMR-0611539) and NIH-RCMI (2G12-RR-013459). Hunter College Chemistry infrastructure is supported by the NSF, NIH, including the RCMI program (G12-RR-03037), and the City University of New York.

Supporting Information Available: Additional spectroscopic data including ^{1}H NMR, ^{13}C NMR, ^{19}F NMR, and HRMS of all the protected and deprotected glycosylated porphyrinoids, UV−visible and fluorescence spectra in three different solvents: PBS, ethanol, and ethyl acetate, diastereomeric structures of CF_{20} and IF_{20}, CD spectra of CF_{20}, IF_{20}, and BF_{20} in chloroform, CD spectra of $CGlc_4$, $IGlc_4$, and $BGlc_4$ in methanol, cell uptake fluorescence images using MDA-MB-231 breast cancer cell line, singlet oxygen quantum yield data, and photobleaching experiment of $IGlc_4$ in sunlight. Spectroscopic characterization of the compounds and the substitution of a diol chlorin outlined. This material is available free of charge via the Internet at http://pubs.acs.org.

LITERATURE CITED

(1) Kadish, K., Smith, K. M., and Guilard, R. (2000, 2003) *The Porphyrin Handbook*, Vol. 1−20, Academic Press, New York.

(2) Drain, C. M., and Singh, S. (2010) Combinatorial libraries of porphyrins: Chemistry and applications, In *The Handbook of Porphyrin Science with Applications to Chemistry, Physics, Materials Science, Engineering, Biology and Medicine* (Kadish, K., Smith, K. M., and Guilard, R., Eds.) pp 485−537, World Scientific Publisher, Singapore.

(3) Smith, K. M. (1972) *Porphyrins and Metalloporphyrins*, Elsevier, Amsterdam.

(4) Dolphin, D. (1978) *The Porphyrins*, Academic Press, London.

(5) Sternberg, E. D., Dolphin, D., and Brückner, C. (1998) Porphyrin-based photosensitizers for use in photodynamic therapy. *Tetrahedron 54*, 4151–4202.

(6) Bonnett, R. (1995) Photosensitizers of the porphyrin the phthalocyanine series for phtodynamic therapy. *Chem. Soc. Rev. 24*, 19–33.

(7) Pandey, R. K. (2000) Recent advances in photodynamic therapy. *J. Porphyrins Phthalocyanines 4*, 368–373.

(8) Pandey, R. K., and Zheng, G. (2000) Porphyrins as photosensitizers in photodynamic therapy, In *The Porphyrin Handbook* (Kadish, K. M., Smith, K. M., and Guilard, R., Eds.) pp 157−230, Academic Press, London.

(9) Laville, I., Figueiredo, T., Loock, B., Pigaglio, S., Maillard, P., Grierson, D. S., Carrez, D., Croisy, A., and Blais, J. (2003) Synthesis, cellular internalization and photodynamic activity of glucoconjugated derivatives of tri and tetra(meta-hydroxyphenyl)chlorins. *Bioorg. Med. Chem. 11*, 1643–1652.

(10) Borbas, K. E., Chandrashaker, V., Muthiah, C., Kee, H. L., Holten, D., and Lindsey, J. S. (2008) Design, synthesis, and photophysical characterization of water-soluble chlorins. *J. Org. Chem. 73*, 3145–3158.

(11) Yihui, C., Guolin, L., and Ravindra, K. P. (2004) Synthesis of bacteriochlorins and their potential utility in photodynamic therapy (PDT). *Curr. Org. Chem. 8*, 1105–1134.

(12) Huang, Y.-Y., Mroz, P., Zhiyentayev, T., Sharma, S. K., Balasubramanian, T., Ruzi, C., Krayer, M., Fan, D., Borbas, K. E., Yang, E., Kee, H. L., Kirmaier, C., Diers, J. R., Bocian, D. F., Holten, D., Lindsey, J. S., and Hamblin, M. R. (2010) In vitro photodynamic therapy and quantitative structure-activity relationship studies with stable synthetic near-infrared-absorbing bacteriochlorin photosensitizers. *J. Med. Chem. 53*, 4018–4027.

(13) Bonnett, R., Charlesworth, P., Djelal, B. D., Foley, S., McGarvey, D. J., and Truscott, T. G. (1999) Photophysical properties of 5,10,15,20-tetrakis(*m*-hydroxyphenyl)-porphyrin (*m*-THPP), 5,10,15,20-tetrakis(*m*-hydroxyphenyl)chlorin (m-THPC) and 5,10,15,20-tetrakis(*m*-hydroxyphenyl)bacteriochlorin (m-THPBC): a comparative study. *J. Chem. Soc., Perkin Trans. 2*, 325–328.

(14) Nguyen, Q. T., Olson, E. S., Aguilera, T. A., Jiang, T., Scadeng, M., Ellies, L. G., and Tsien, R. Y. (2010) Surgery with molecular fluorescence imaging using activatable cell-penetrating peptides decreases residual cancer and improves survival. *Proc. Natl. Acad. Sci., U.S.A. 107*, 4317–4322.

(15) Mikata, Y., Onchi, Y., Tabata, K., Ogura, S.-i., Okura, I., Ono, H., and Yano, S. (1998) Sugar-dependent photocytotoxic property of tetra- and octa-glycoconjugated tetraphenylporphyrins. *Tetrahedron Lett. 39*, 4505–4508.

(16) Chen, X., and Drain, C. M. (2004) Photodynamic therapy using carbohydrate conjugated porphyrins. *Drug Des. Rev. 1*, 215–234.

(17) Csik, G., Balog, E., Voszka, I., Tölgyesi, F., Oulmi, D., Maillard, P., and Momenteau, M. (1998) Glycosylated derivatives of tetraphenyl porphyrin: photophysical characterization, self-aggregation and membrane binding. *J. Photochem. Photobiol., B 44*, 216–224.

(18) Obata, M., Hirohara, S., Sharyo, K., Alitomo, H., Kajiwara, K., Ogata, S.-i., Tanihara, M., Ohtsuki, C., and Yano, S. (2007) Sugar-dependent photodynamic effect of glycoconjugated porphyrins: A study on photocytotoxicity, photophysical properties and binding behavior to bovine serum albumin (BSA). *Biochim. Biophys. Acta 1770*, 1204–1211.

(19) Gomes, A. T. P. C., Leão, R. A. C., Silva, F. C. d., Neves, M. G. P. M. S., Faustino, M. A. F., Tomé, A. C., Silva, A. M. S., Pinheiro, S., Souza, M. C. B. V. d., Ferreira, V. F., and Cavaleiro, J. A. S. (2009) Synthesis of new glycoporphyrin derivatives through carbohydrate-substituted α-diazoacetates. *J. Porphyrins Phthalocyanines 13*, 247–255.

(20) Hirohara, S., Obata, M., Ogata, S.-i., Ohtsuki, C., Higashida, S., Ogura, S.-i., Okura, I., Takenaka, M., Ono, H., Sugai, Y., Mikata, Y., Tanihara, M., and Yano, S. (2005) Cellular uptake and photocytotoxicity of glycoconjugated chlorins in HeLa cells. *J. Photochem. Photobiol., B 78*, 7–15.

(21) Hirohara, S., Obata, M., Alitomo, H., Sharyo, K., Ogata, S.-i., Ohtsuki, C., Yano, S., Ando, T., and Tanihara, M. (2008) Structure-photodynamic effect relationships of 24 glycoconjugated photosensitizers in HeLa cells. *Biol. Pharm. Bull. 31*, 2265–2272.

(22) Maillard, P., Loock, B., Grierson, D. S., Laville, I., Blais, J., Doz, F., Desjardins, L., Carrez, D., Guerquin-Kern, J. L., and Croisy, A. (2007) In vitro phototoxicity of glycoconjugated porphyrins and chlorins in colorectal adenocarcinoma (HT29) and retinoblastoma (Y79) cell lines. *Photodiag. Photodyn. Ther. 4*, 261–268.

(23) Zorlu, Y., Ermeydan, M. A., Dumoulin, F., Ahsen, V., Savoie, H., and Boyle, R. W. (2009) Glycerol and galactose substituted zinc phthalocyanines. Synthesis and photodynamic activity. *Photochem. Photobiol. Sci. 8*, 312–318.

(24) Okada, M., Kishibe, Y., Ide, K., Takahashi, T., and Hasegawa, T. (2009) Convenient approach to access octa-glycosylated porphyrins via "click chemistry". *Int. J. Carbohydr. Chem.* 305276.

(25) Amessou, M., Carrez, D., Patin, D., Sarr, M., Grierson, D. S., Croisy, A., Tedesco, A. C., Maillard, P., and Johannes, L. (2008) Retrograde delivery of photosensitizer $(TPPp\text{-}O\text{-}beta\text{-}GluOH)_3$ selectively potentiates its photodynamic activity. *Bioconjugate Chem. 19*, 532–538.

(26) Iqbal, Z., Hanack, M., and Ziegler, T. (2009) Synthesis of an octasubstituted galactose zinc(II) phthalocyanine. *Tetrahedron Lett. 50*, 873–875.

(27) Soares, A. R. M., Tomé, J. P. C., Neves, M. G. P. M. S., Tomé, A. C., Cavaleiro, J. A. S., and Torres, T. (2009) Synthesis of water-soluble phthalocyanines bearing four or eight D-galactose units. *Carbohydr. Res. 344*, 507–510.

(28) Hirohara, S., Nishida, M., Sharyo, K., Obata, M., Ando, T., and Tanihara, M. (2010) Synthesis, photophysical properties and photocytotoxicity of mono-, di-, tri- and tetra-glucosylated fluorophenylporphyrins. *Biorg. Med. Chem. 18*, 1526–1535.

(29) Elmer, S. L., Man, S., and Zimmerman, S. C. (2008) (2008) Synthesis of polyglycerol, porphyrin-cored dendrimers using click chemistry. *Eur. J. Org. Chem.* 3845–3851.

(30) Grin, M. A., Lonin, I. S., Makarov, A. I., Lakhina, A. A., Toukach, F. V., Kachala, V. V., Orlova, A. V., and Mironov, A. F. (2008) Synthesis of chlorin-carbohydrate conjugates by 'click chemistry'. *Mendeleev Commun. 18*, 135–137.

(31) Mikata, Y., Sawaguchi, T., Kakuchi, T., Gottschaldt, M., Schubert, U. S., Ohi, H., and Yano, S. (2010) (2010) Control of the Aggregation properties of tris(maltohexaose)-linked porphyrins with an alkyl chain. *Eur. J. Org. Chem.* 663–671.

(32) Chen, X., Hui, L., Foster, D. A., and Drain, C. M. (2004) Efficient synthesis and photodynamic activity of porphyrin-saccharide conjugates: targeting and incapacitating cancer cells. *Biochemistry 43*, 10918–10929.

(33) Pasetto, P., Chen, X., Drain, C. M., and Franck, R. W. (2001) Synthesis of hydrolytically stable porphyrin C- and S-glycoconjugates in high yields. *Chem. Commun.* 81–82.

(34) Drain, C. M., Singh, S., Samaroo, D., Thompson, S., Vinodu, M., and Tomé, J. P. C. (2009) New porphyrin glyco-conjugates. *Proc. Soc. Photo Opt. Instrum. Eng.* 7380.

(35) Drain, C. M., Varotto, A., and Radivojevic, I. (2009) Self-organized porphyrinic materials. *Chem. Rev. 109*, 1630–1658.

(36) Varotto, A., Todaro, L., Vinodu, M., Koehne, J., Liu, G.-y., and Drain, C. M. (2008) Self-organization of a new fluorous porphyrin and C_{60} films on indium-tin-oxide electrode. *Chem. Commun.* 4921–4923.

(37) Samaroo, D., Soll, C. E., Todaro, L. J., and Drain, C. M. (2006) Efficient microwave-assisted synthesis of amine substituted pentafluorophenylporphyrin. *Org. Lett. 8*, 4985–4988.

(38) Samaroo, D., Vinodu, M., Chen, X., and Drain, C. M. (2007) meso-tetra(pentafluorophenyl)porphyrin as an efficient platform for combinatorial synthesis and the selection of new photodynamic therapeutics using a cancer cell line. *J. Comb. Chem. 9*, 998–1011.

(39) Shaw, S. J., Edwards, C., and Boyle, R. W. (1999) Regioselective synthesis of multifunctionalizd porphyrins - coupling of mono-(pentafluorophenyl)porphyrins to electrophiles. *Tetrahedron Lett. 40*, 7585–7586.

(40) Shaw, S. J., Elgie, K. J., Edwards, C., and Boyle, R. W. (1999) Mono-(pentafluorophenyl)porphyrins - Useful intermediates in the regioselective synthesis of multifunctionalised porphyrins. *Tetrahedron Lett. 40*, 1595–1596.

(41) Traylor, T. G., Byun, Y. S., Traylor, P. S., Battioni, P., and Mansuy, D. (1991) Polymeric polyhalogenated metalloporphyrin catalysts for hydroxylation of alkanes and epoxidation of alkenes. *J. Am. Chem. Soc. 113*, 7821–7823.

(42) Králová, J., Bříza, T., Moserová, I., Dolenský, B., Vašek, P., Poučková, P., Kejík, Z., Kaplánek, R., Martásek, P., Dvořák, M., and Král, V. (2008) Glycol porphyrin derivatives as potent photodynamic inducers of apoptosis in tumor cells. *J. Med. Chem. 51*, 5964–5973.

(43) Thompson, S., Chen, X., Hui, L., Toschi, A., Foster, D. A., and Drain, C. M. (2008) Low concentrations of a non-hydrolysable tetra-S-glycosylated porphyrin and low light induces apoptosis in human breast cancer cells via stress of the endoplasmic reticulum. *Photochem. Photobiol. Sci. 7*, 1415–1421.

(44) Plaetzer, K., Kiesslich, T., Oberdanner, C. B., and Krammer, B. (2005) Apoptosis following photodynamic tumor therapy: Induction, mechanisms and detection. *Curr. Pharm. Des. 11*, 1151–1165.

(45) Pandey, S. K., Gryshuk, A. L., Graham, A., Ohkubo, K., Fukuzumi, S., Dobhal, M. P., Zheng, G., Ou, Z., Zhan, R., Kadish, K. M., Oseroff, A., Ramaprasad, S., and Pandey, R. K. (2003) Fluorinated photosensitizers: synthesis, photophysical, electrochemical, intracellular localization, in vitro photosensitizing efficacy and determination of tumor-uptake by 19F in vivo NMR spectroscopy. *Tetrahedron 59*, 10059–10073.

(46) Mauzerall, D. C. (1998) Evolution of porphyrins. *Clin. Dermatol. 6*, 195–201.

(47) Brückner, C., McCarthy, J. R., Daniell, H. W., Pendon, Z. D., Ilagan, R. P., Francis, T. M., Ren, L., Birge, R. R., and Frank, H. A. (2003) A spectroscopic and computational study of the singlet and triplet excited states of synthetic [beta]-functionalized chlorins. *Chem. Phys. 294*, 285–303.

(48) Silva, A. M. G., Tomé, A. C., Neves, M. G. P. M. S., Silva, A. M. S., and Cavaleiro, J. A. S. (1999) meso-Tetraarylporphyrins as dipolarophiles in 1,3-dipolar cycloaddition reactions. *Chem. Commun.* 1767–1768.

(49) Silva, A. M. G., Tome', A. C., Neves, M. G. P. M. S., Silva, A. M. S., and Cavaleiro, J. A. S. (2005) 1,3-Dipolar cycloaddition reactions of porphyrins with azomethine ylides. *J. Org. Chem. 70*, 2306–2314.

(50) Cavaleiro, J. A. S., Tomé, A. C., and Neves, M. G. P. M. S. (2010) meso-Tetraarylporphyrin derivatives: New synthetic methodologies, In *The Handbook of Porphyrin Science with Applications to Chemistry, Physics, Materials Science, Engineering, Biology and Medicine* (Kadish, K., Smith, K. M., and Guilard, R., Eds.) pp 193−294, World Scientific Publisher, Singapore.

(51) Jiménez-Osés, G., García, J. I., Silva, A. M. G., Santos, A. R. N., Tomé, A. C., Neves, M. G. P. M. S., and Cavaleiro, J. A. S. (2008) Mechanistic insights on the site selectivity in successive 1,3-dipolar cycloadditions to meso-tetraarylporphyrins. *Tetrahedron 64*, 7937–7943.

(52) Maestrin, A. P. J., Ribeiro, A. O., Tedesco, A. C., Neri, C. R., Vinhado, F. S., Serra, O. A., Martins, P. R., Iamamoto, Y., Silva, A. M. G., Tomé, A. C., Neves, M. G. P. M. S., and Cavaleiro, J. A. S. (2004) A novel chlorin derivative of Meso-tris(pentafluorophenyl)-4-pyridylporphyrin: synthesis, photophysics and photochemical properties. *J. Braz. Chem. Soc. 15*, 923–930.

(53) Hao, E., Friso, E., Miotto, G., Jori, G., Soncin, M., Fabris, C., Sibrian-Vazquez, M., and Vicente, M. G. H. (2008) Synthesis and biological investigations of tetrakis(p-carboranylthio-tetrafluorophenyl)chlorin (TPFC). *Org. Biomol. Chem. 6*, 3732–3740.

(54) Hirohara, S., Obata, M., Alitomo, H., Sharyo, K., Ando, T., Tanihara, M., and Yano, S. (2009) Synthesis, photophysical properties and sugar-dependent in vitro photocytotoxicity of pyrrolidine-fused chlorins bearing S-glycosides. *J. Photochem. Photobiol., B 97*, 22–33.

(55) Hirohara, S., Obata, M., Alitomo, H., Sharyo, K., Ando, T., Yano, S., and Tanihara, M. (2009) Synthesis and photocytotoxicity of S-glucosylated 5,10,15,20-Tetrakis(tetrafluorophenyl)porphyrin metal complexes as efficient $^1O_2$-generating glycoconjugates. *Bioconjugate Chem. 20*, 944–952.

(56) Tanielian, C., Wolff, C., and Esch, M. (1996) Singlet oxygen production in water: aggregation and charge-transfer effects. *J. Phys. Chem. 100*, 6555–6560.

(57) Bonnett, R., and Martínez, G. (2001) Photobleaching of sensitizers used in photodynamic therapy. *Tetrahedron 57*, 9513–9547.

(58) Seybold, P. G., and Gouterman, M. (1969) Porphyrins XIII: Fluorescence spectra and quantum yields. *J. Mol. Spectrosc. 31*, 1–13.

(59) Vivanco, S., Lecea, B., Arrieta, A., Prieto, P., Morao, I., Linden, A., and Cossío, F. P. (2000) Origins of the loss of concertedness in pericyclic reactions: Theoretical prediction and direct observation of stepwise mechanisms in [3 + 2] thermal cycloadditions. *J. Am. Chem. Soc. 122*, 6078–6092.

(60) Tufariello, J. J., Mullen, G. B., Tegeler, J. J., Trybulski, E. J., Wong, S. C., and Ali, S. A. (1979) Synthesis in the tropane class of alkaloids. Pseudotropine and dl-cocaine. *J. Am. Chem. Soc. 101*, 2435–2442.

(61) Mishra, P. P., Patel, S., and Datta, A. (2006) Effect of increased hydrophobicity on the binding of two model amphiphilic chlorin drugs for photodynamic therapy with blood plasma and its components. *J. Phys. Chem. B 110*, 21238–21244.

(62) Drain, C. M., Gentemann, S., Roberts, J. A., Nelson, N. Y., Medforth, C. J., Jia, S., Simpson, M. C., Smith, K. M., Fajer, J.,

Shelnutt, J. A., and Holten, D. (1998) Picosecond to microsecond photodynamics of a nonplanar nickel porphyrin: solvent dielectric and temperature effects. *J. Am. Chem. Soc. 120*, 3781–3791.

(63) Obata, M., Hirohara, S., Tanaka, R., Kinoshita, I., Ohkubo, K., Fukuzumi, S., Tanihara, M., and Yano, S. (2009) In vitro heavy-atom effect of palladium(II) and platinum(II) complexes of pyrrolidine-fused chlorin in photodynamic therapy. *J. Med. Chem. 52*, 2747–2753.

(64) Boisbrun, M., Vanderesse, R., Engrand, P., Olié, A., Hupont, S., Regnouf-de-Vains, J.-B., and Frochot, C. (2008) Design and photophysical properties of new RGD targeted tetraphenylchlorins and porphyrins. *Tetrahedron 64*, 3494–3504.

(65) Gonsalves, A. M. d. A. R., Serra, A. C., and Pineiro, M. (2009) The small stones of Coimbra in the huge tetrapyrrolic chemistry building. *J. Porphyrins Phthalocyanines 13*, 429–445.

(66) Fox, S., and Boyle, R. W. (2006) Synthetic routes to porphyrins bearing fused rings. *Tetrahedron 62*, 10039–10054.

(67) Vicente, M. G. H., Nurco, D. J., Shetty, S. J., Osterloh, J., Ventre, E., Hegde, V., and Deutsch, W. A. (2002) Synthesis, dark toxicity and induction of in vitro DNA photodamage by a tetra(4-nido-carboranylphenyl)porphyrin. *J. Photochem. Photobiol., B 68*, 123–132.

(68) Zhang, X.-a., Lovejoy, K. S., Jasanoff, A., and Lippard, S. J. (2007) Water-soluble porphyrins as a dual-function molecular imaging platform for MRI and fluorescence zinc sensing. *Proc. Natl. Acad. Sci. U.S.A. 104*, 10780–10785.

(69) Morris, R. L., Azizuddin, K., Lam, M., Berlin, J., Nieminen, A.-L., Kenney, M. E., Samia, A. C. S., Burda, C., and Oleinick, N. L. (2003) Fluorescence resonance energy transfer reveals a binding site of a photosensitizer for photodynamic therapy. *Cancer Res. 63*, 5194–5197.

BC100356Z

Synthesis and Photophysical Properties of Thioglycosylated- Chlorins, Isobacteriochlorins and Bacteriochlorins for Bioimaging and Diagnostics

Sunaina Singh,[†] Amit Aggarwal,[†] Sebastian Thompson,[†] João P. C. Tomé,[†] Xianchun Zhu,[‡] Diana Samaroo,[#] Mikki Vinodu,[†] Ruomei Gao,[‡] and Charles Michael Drain[†§]*

Department of Chemistry & Biochemistry, Hunter College of the City University of New York, 695 Park Avenue, New York, New York 10065, United States, Department of Chemistry and Biochemistry, Jackson State University, 1400 J. R. Lynch Street, Jackson, Mississippi 39217, United States, NYC College of Technology, 300 Jay Street, Brooklyn, New York 11201, United States, and The Rockefeller University, 1230 York Avenue, New York, New York 10065, United States. Received August 4, 2010; Revised Manuscript Received September 23, 2010

*To whom correspondence should be addressed. (C.M.D.) Phone: 212-650-3791. Fax: 212-772-5332. Email: cdrain@hunter.cuny.edu

[†]Hunter College
[‡]Jackson State University
[#]NYC College of Technology
[§]Rockefeller University

		Figure
$PGlc_4$	^{19}F NMR, ^{1}H NMR	S1-2
$CGlcAc_4$	^{19}F NMR, ^{1}H NMR, ^{13}C NMR, HRMS	S3-6
$CGlc_4$	^{19}F NMR, ^{1}H NMR, ^{13}C NMR, HRMS	S7-10
$IGlcAc_4$	^{19}F NMR, ^{1}H NMR, ^{13}C NMR, HRMS	S11-14
$IGlc_4$	^{19}F NMR, ^{1}H NMR, ^{13}C NMR, HRMS	S15-18
$BGlcAc_4$	^{19}F NMR, ^{1}H NMR, ^{13}C NMR, HRMS	S19-22
$BGlc_4$	^{19}F NMR, ^{1}H NMR, ^{13}C NMR, HRMS	S23-26
Emission spectra in ethanol, PBS buffer, ethylacetate		S27-29
UV-visible spectra in ethanol, PBS buffer, ethylacetate		S30-32
Diastereomers		S33
CD spectra		S34
Fluorescence imaging		S35
$^{1}O_2$ quantum yield data		S36
Photobleaching of $IGlc_4$		S37
Gemdiol synthesis		S38

Spectral Data for all Compounds:

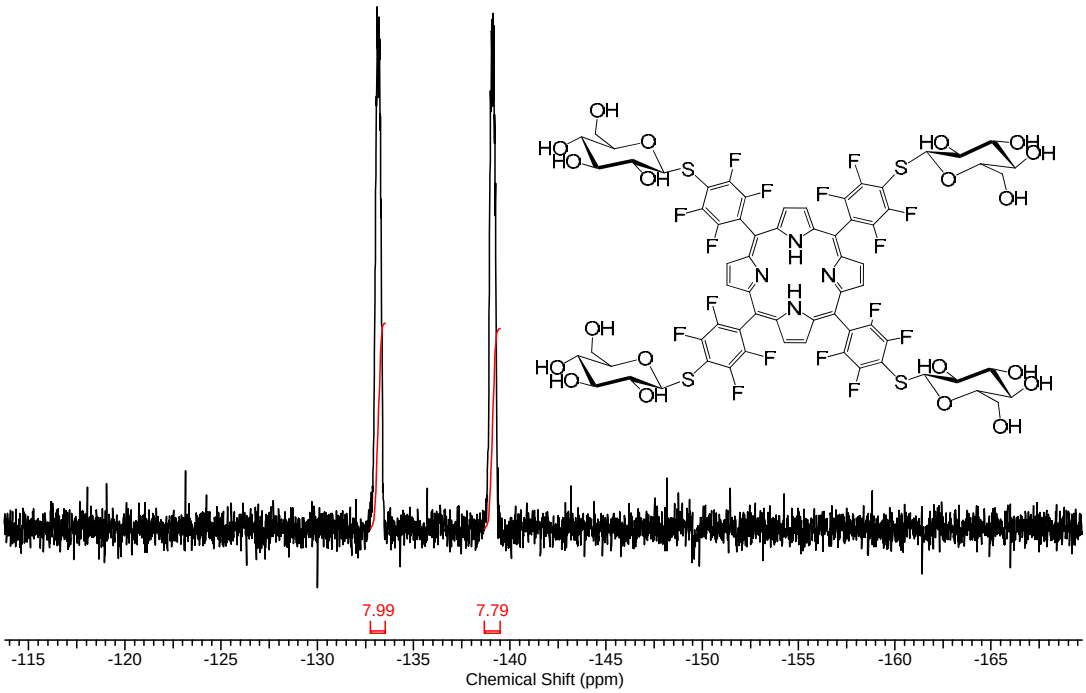


Figure S1. Porphyrin 1b ($PGlc_4$) ^{19}F NMR (DMSO-d_6).

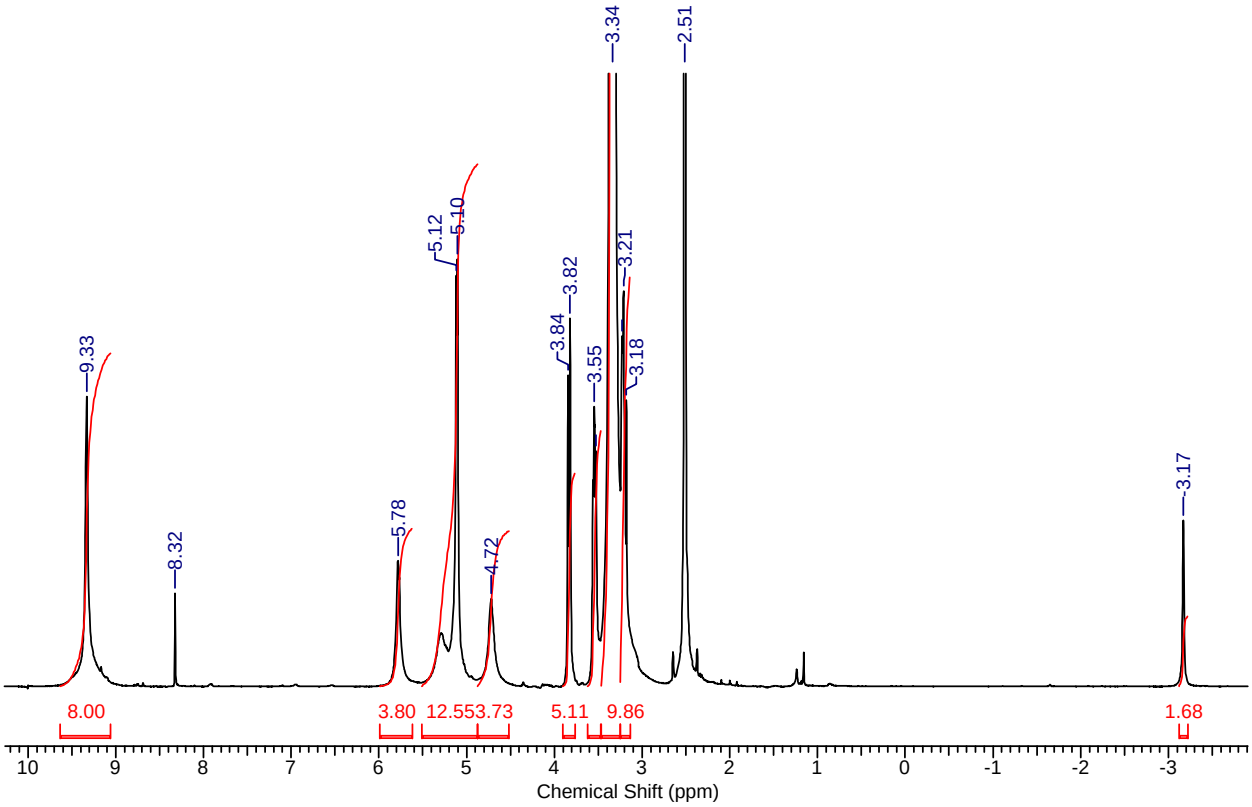


Figure S2. Porphyrin 1b ($PGlc_4$) ^1H NMR (DMSO-d_6 3.34 ppm, 2.51 water ppm).

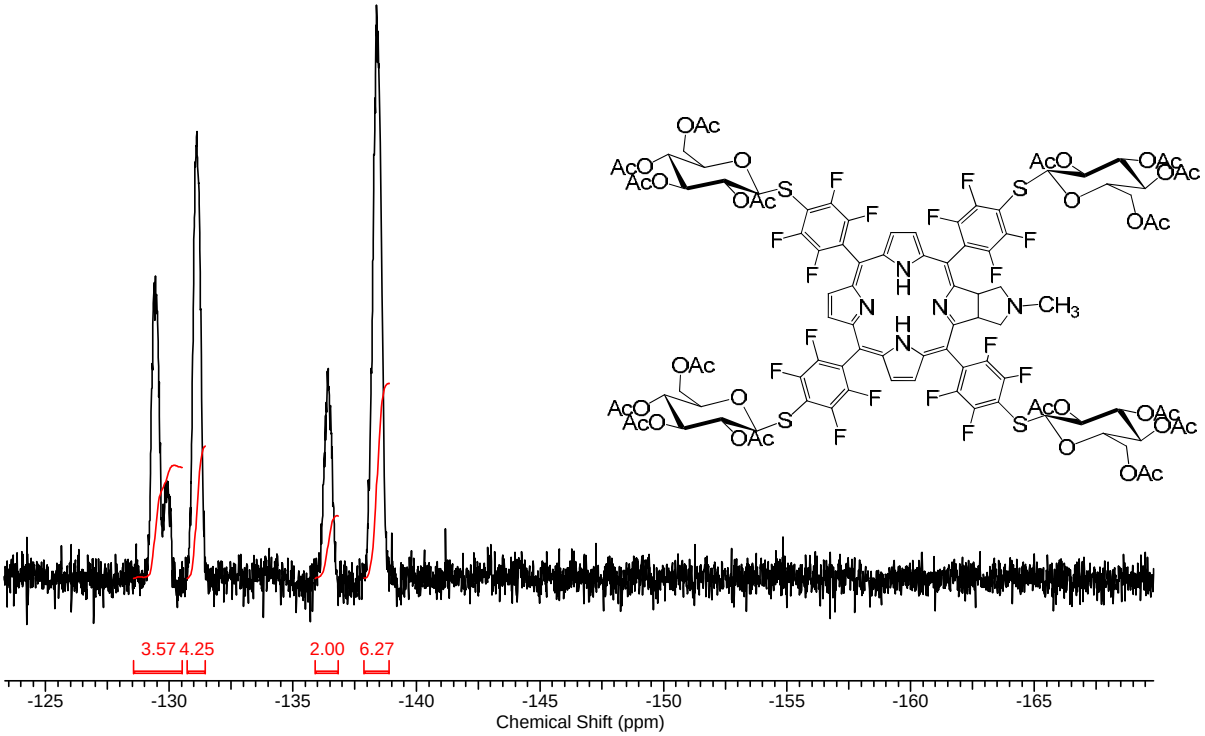


Figure S3. Chlorin 2a ($CGlcAc_4$) ^{19}F NMR ($DMSO\text{-}d_6$).

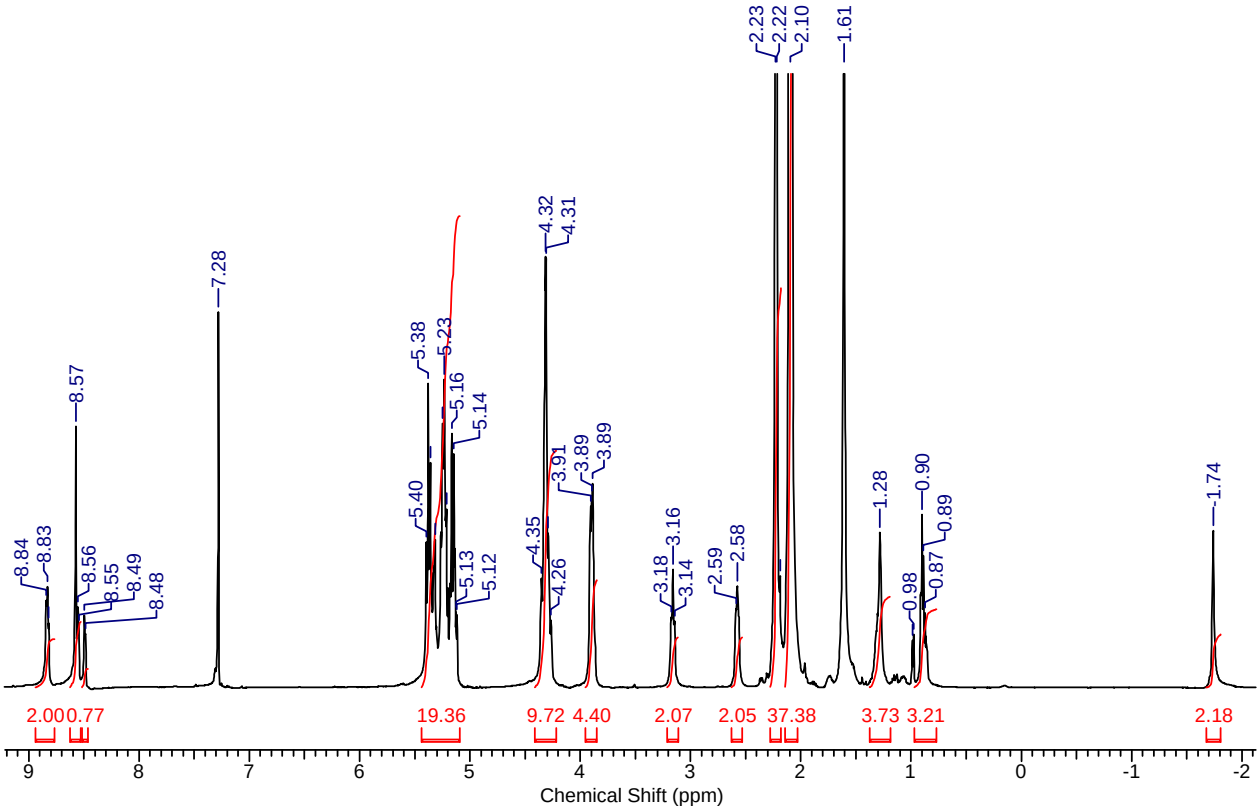


Figure S4. Chlorin 2a ($CGlcAc_4$) ^1H NMR ($CDCl_3$ 7.28 ppm, water 1.61 ppm).

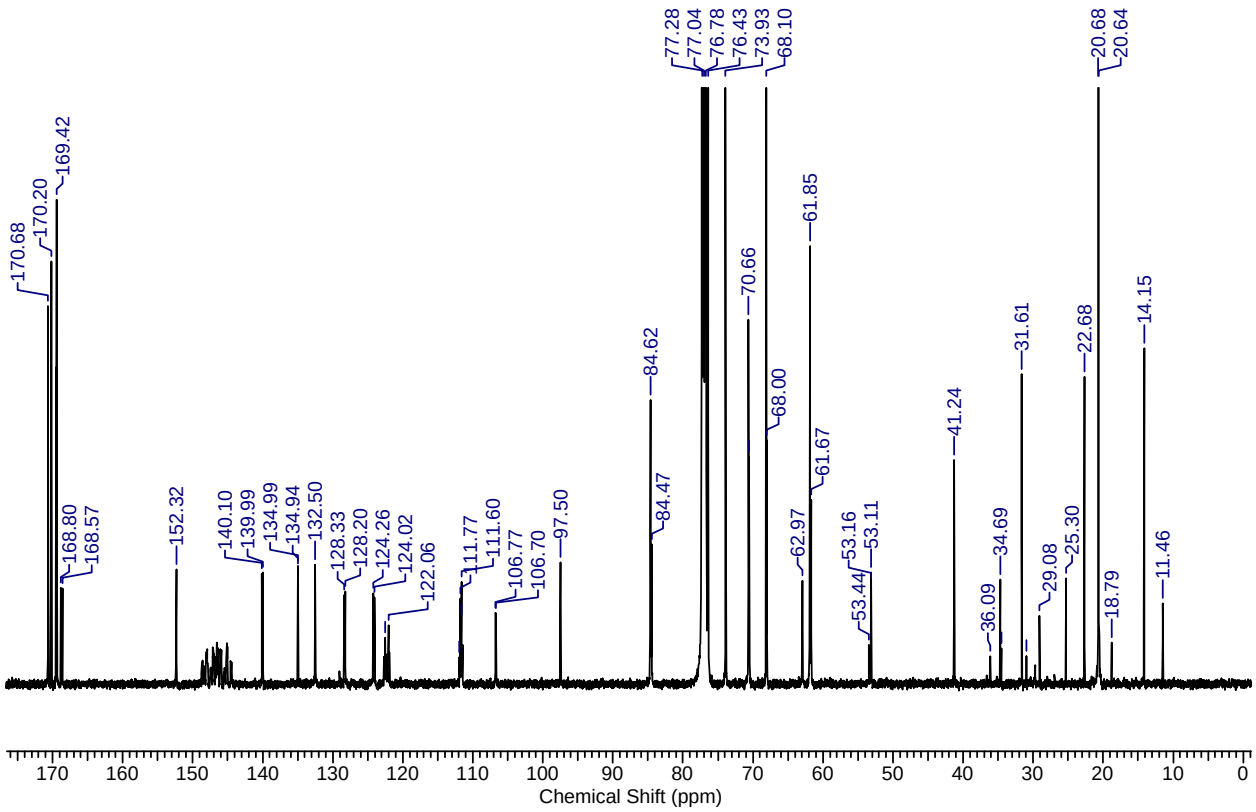
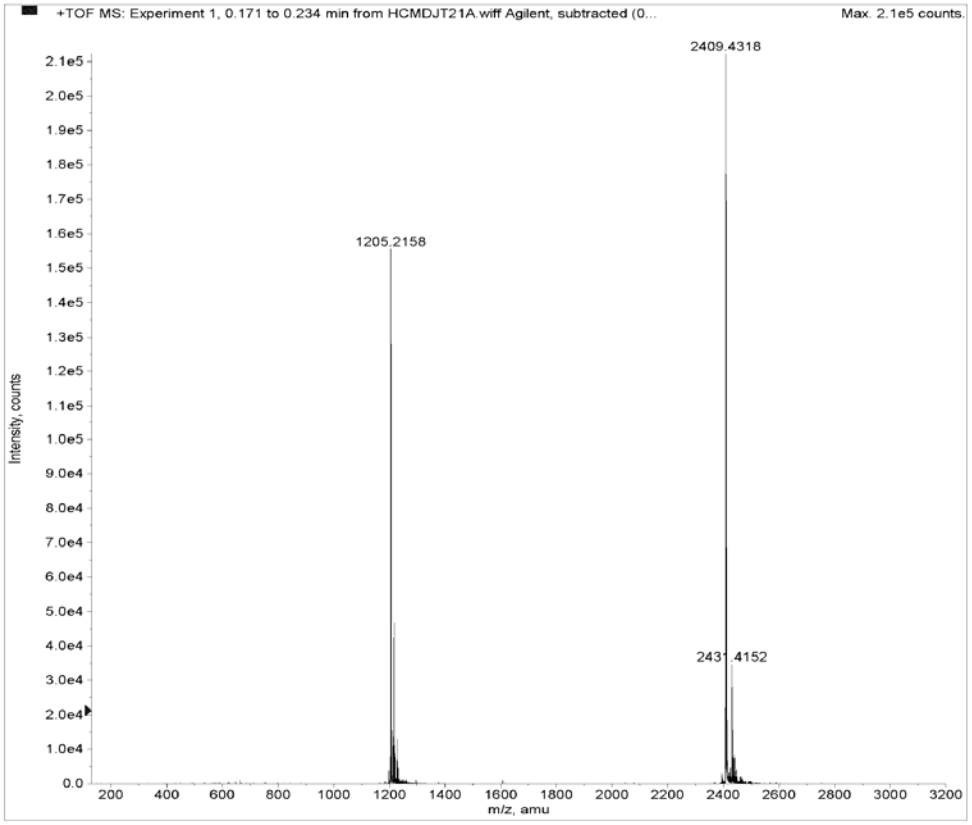


Figure S5. Chlorin 2a ($CGlcAc_4$) ^{13}C NMR ($CDCl_3$ 77 ppm).



The peak at 2431 is the sodium ion adduct, and the peak at 1205 is the doubly charged M/2 ion.

	Formula	Calculated m/z (amu)	mDa Error	PPM Error	DBE
1	C101 H95 N5 O36 F16 Na S4	2408.4276	0.0638	0.0264	48.5
2	C103 H94 N5 O36 F16 S4	2408.4300	-2.3414	-0.9721	51.5
3	C104 H82 N5 O36 F16 S4	2408.3361	91.5590	38.0160	58.5
4	C100 H107 N5 O36 F16 Na S4	2408.5215	-93.8366	-38.9617	41.5
5	C102 H83 N5 O36 F16 Na S4	2408.3337	93.9642	39.0147	55.5
6	C102 H106 N5 O36 F16 S4	2408.5239	-96.2419	-39.9604	44.5

Figure S6. Chlorin 2a ($CGlcAc_4$) HRMS.

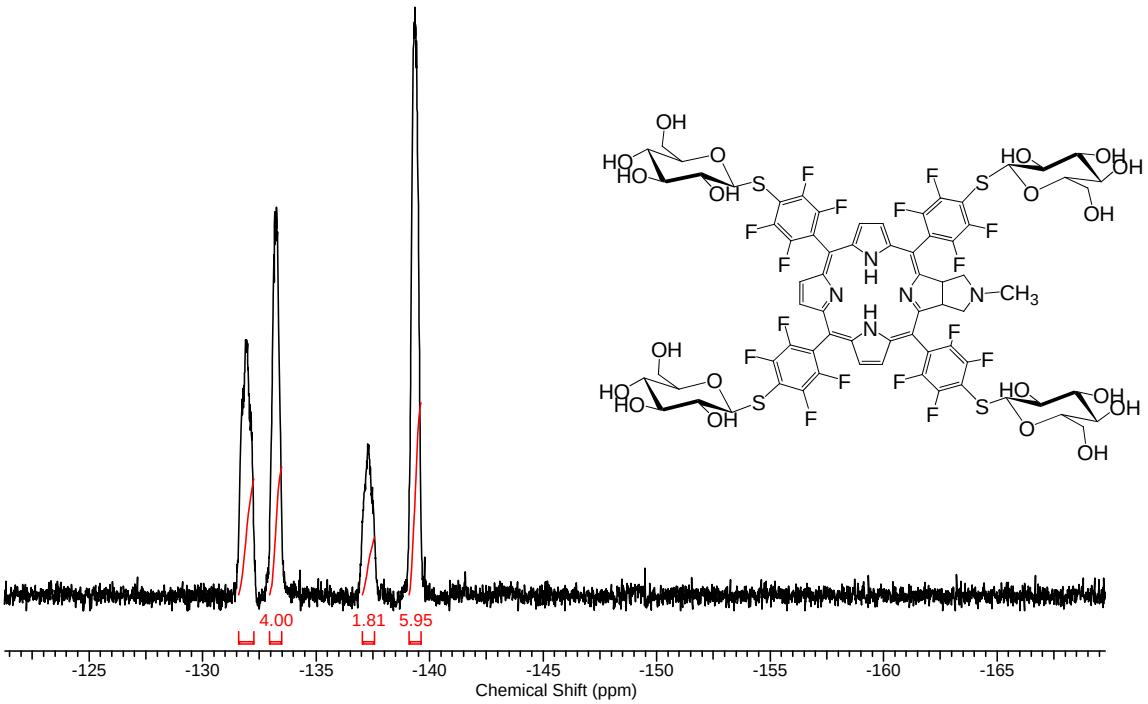


Figure S7. Chlorin 2b ($CGlc_4$) ^{19}F NMR (DMSO-d_6).

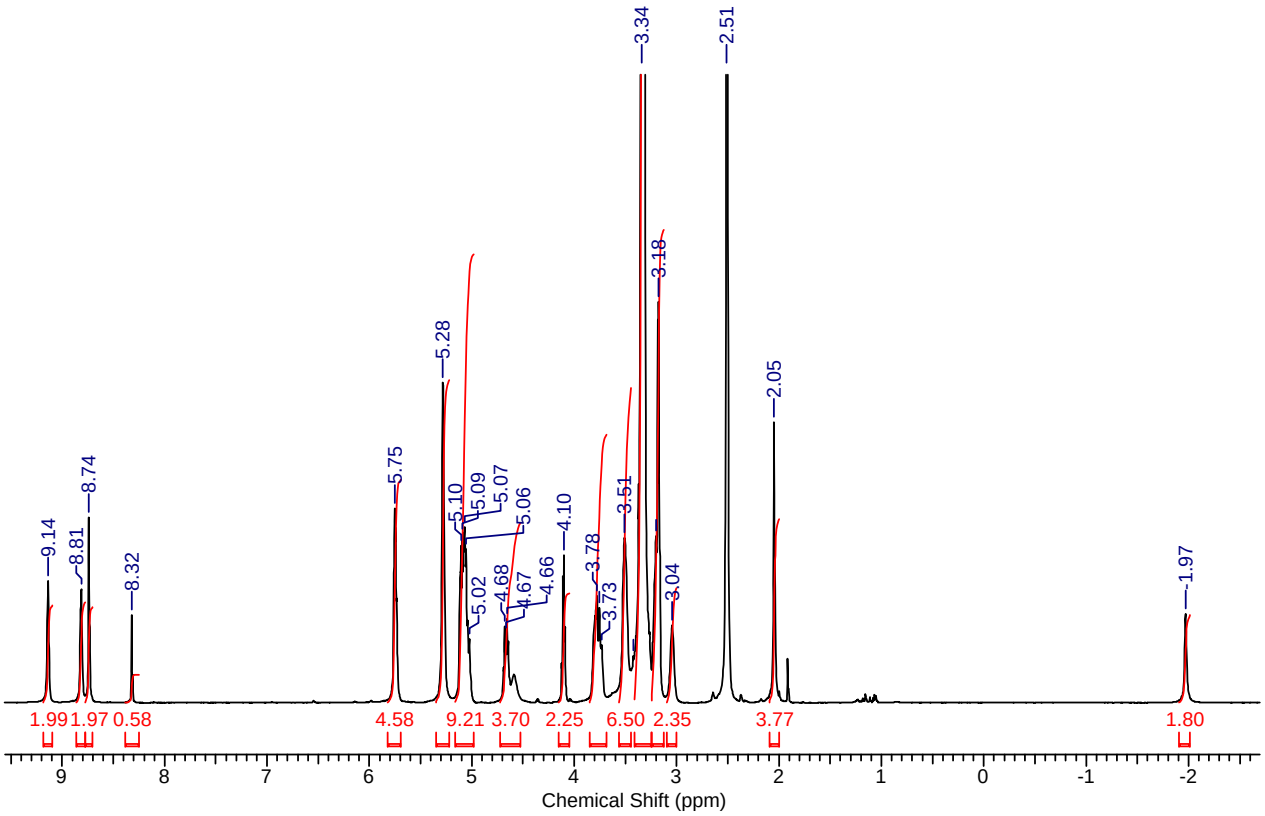


Figure S8. Chlorin 2b ($CGlc_4$) ^{1}H NMR (DMSO-d_6 3.34 ppm, 2.51 water ppm).

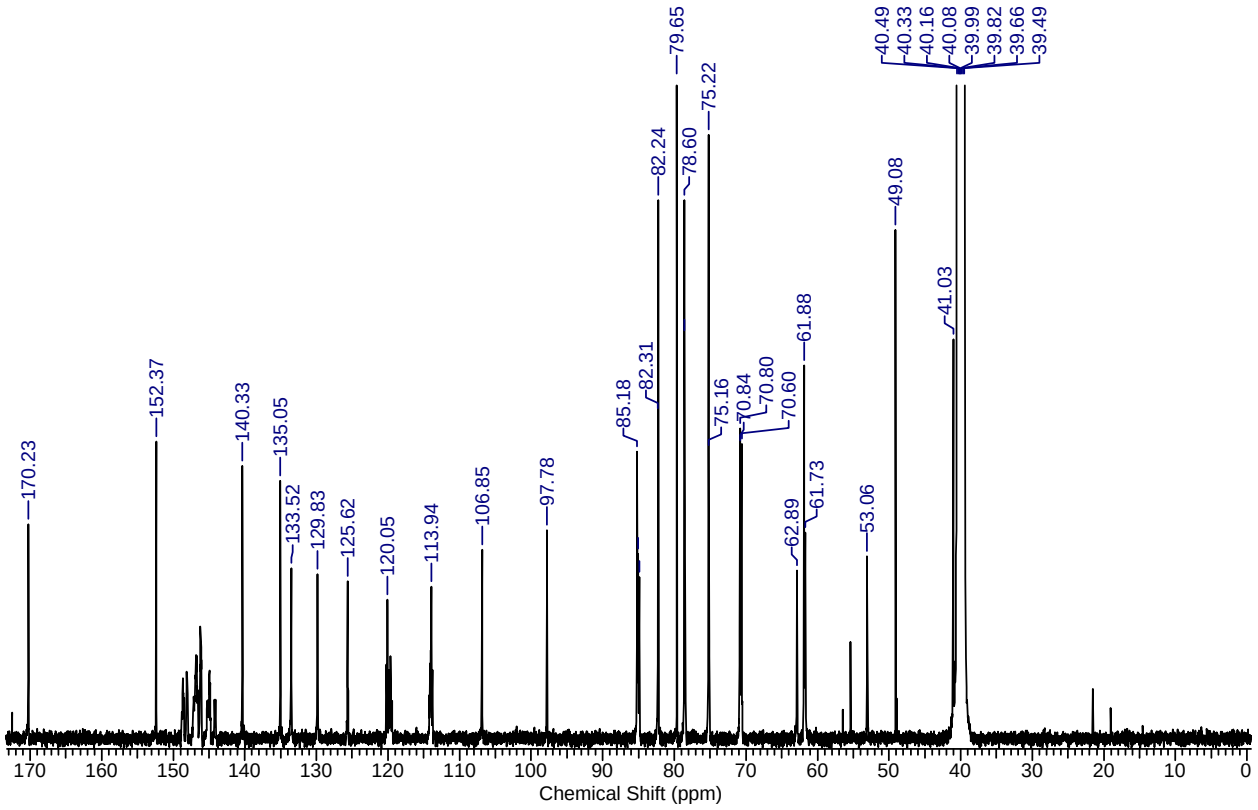
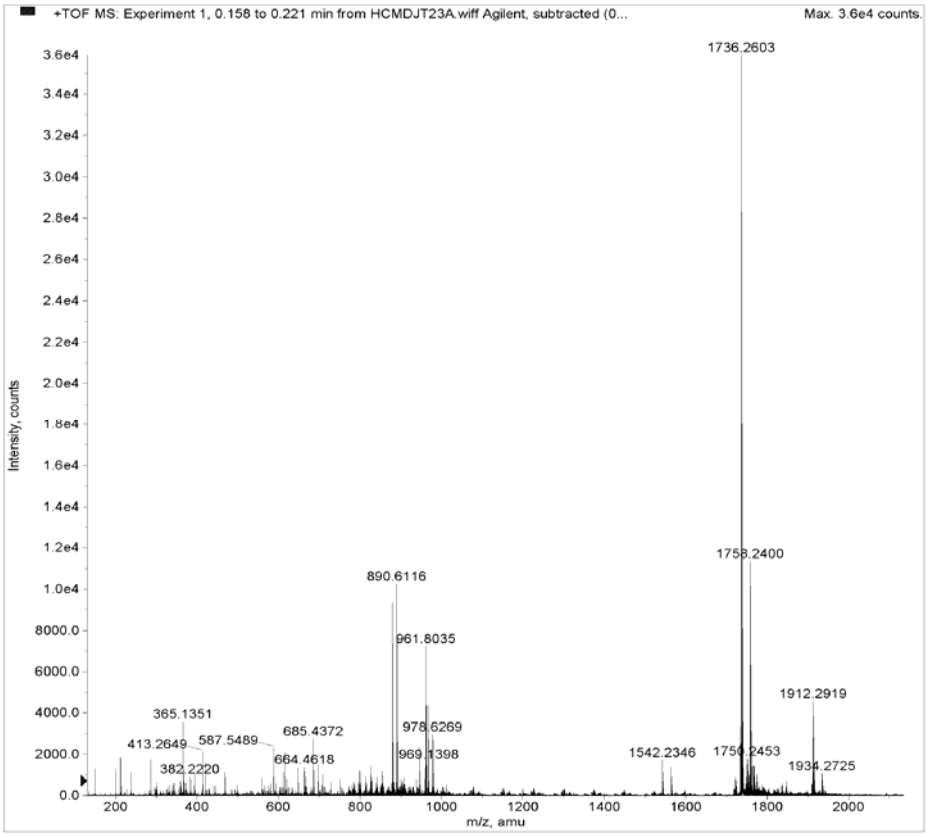


Figure S9. Chlorin 2b ($CGlc_4$) ^{13}C NMR (DMSO-d_6 40 ppm), some acetic acid is present in this sample.



	Formula	Calculated m/z (amu)	mDa Error	PPM Error	DBE
1	C71 H62 N5 O20 F16 S4	1736.2610	-1.1059	-0.6369	35.5

Figure S10. Chlorin 2b ($CGlc_4$) HRMS.

The ESI of chlorin **2b** ($CGlc_4$) was run in methanol, with 0.1% formic acid. M/z peak at 1736 is for (M+H), 1758 is for (M + Na), 1542 is for M -SGlc, 1575 for M -Glc, and 1912 is M + Na + 2,5-dihydroxybenzoic acid (calibration matrix)

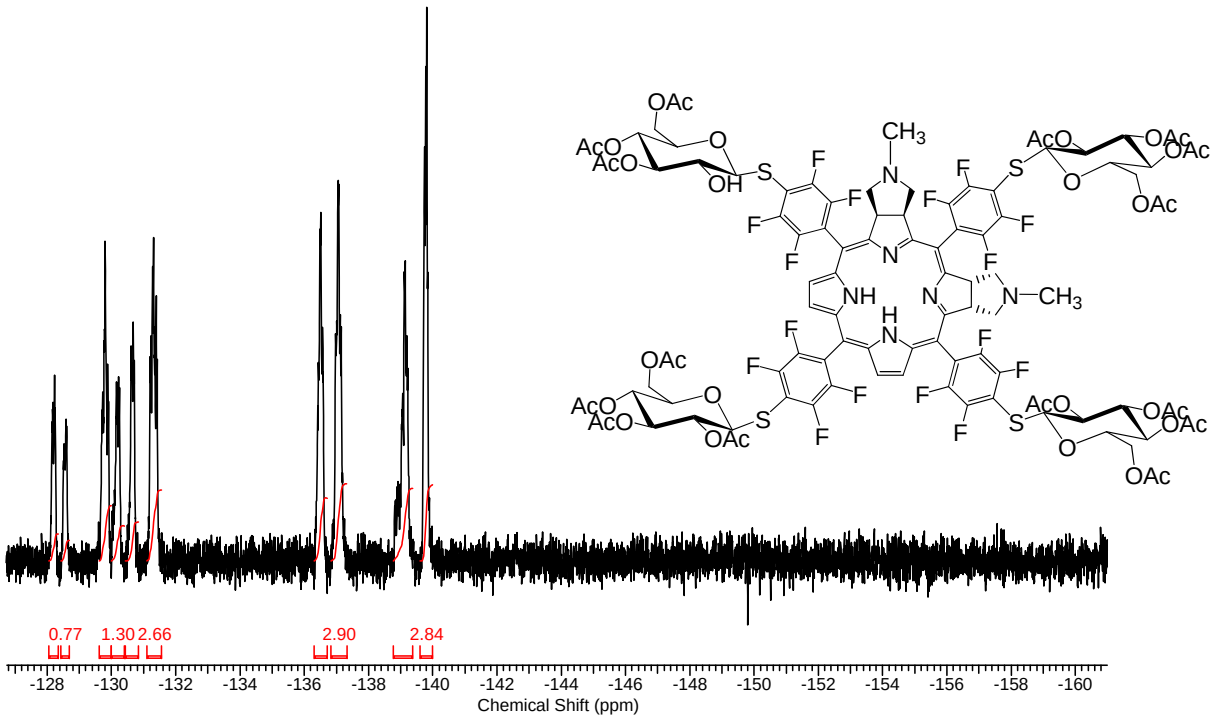


Figure S11. Isobacteriochlorin 3a ($IGlcAc_4$) ^{19}F NMR (DMSO-d_6).

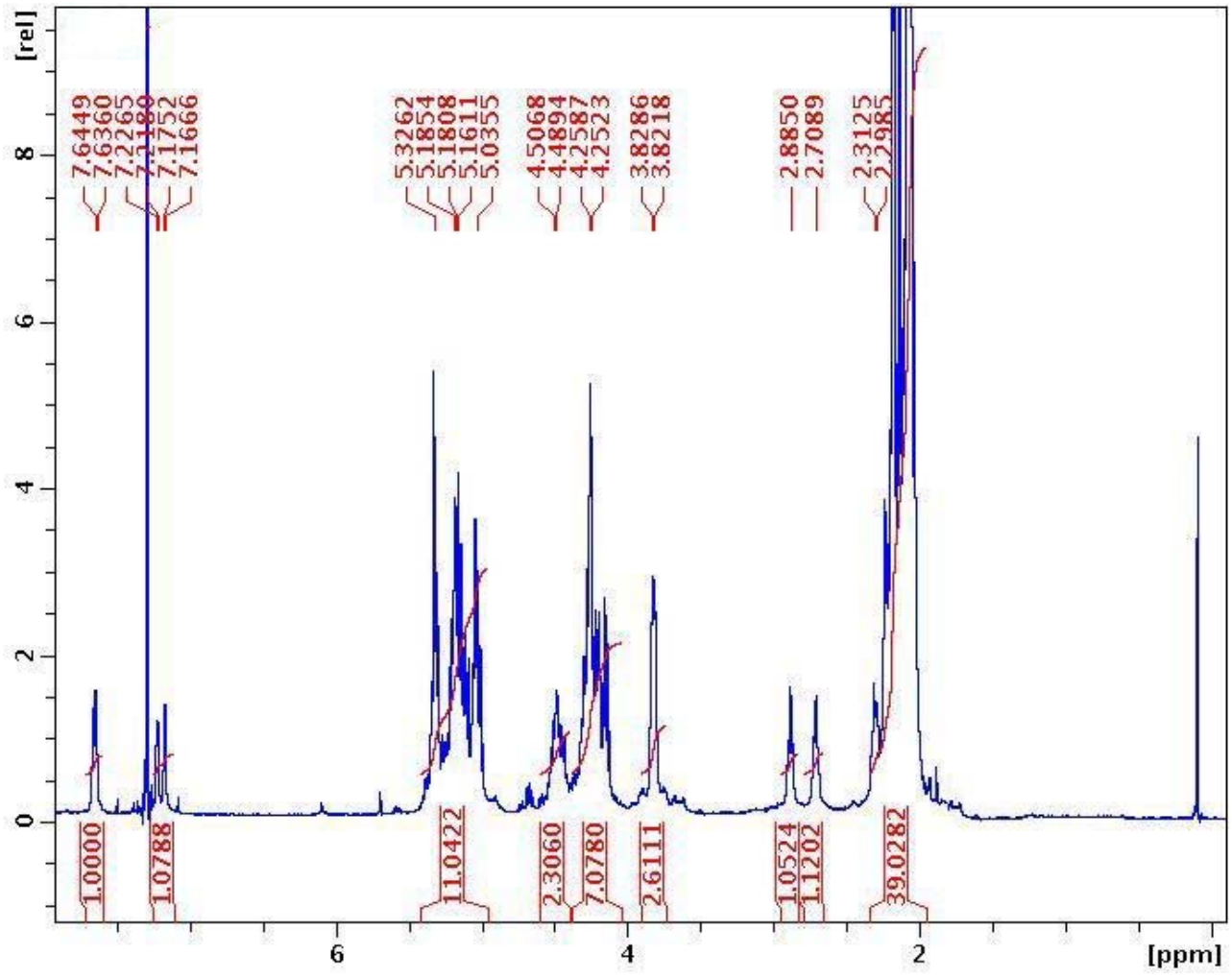


Figure S12. Isobacteriochlorin 3a ($IGlcAc_4$) ^1H NMR ($CDCl_3$ 7.29 ppm).

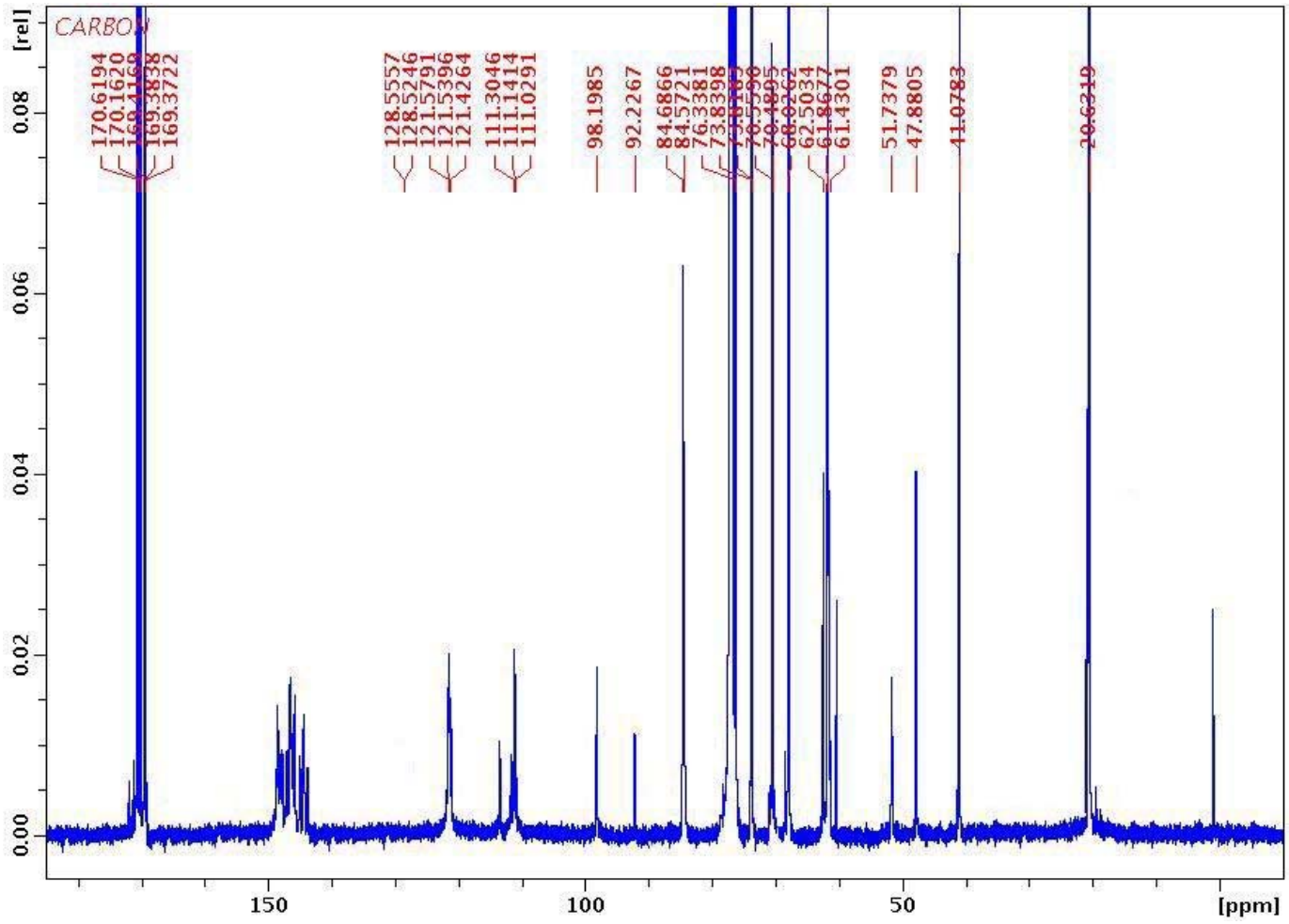
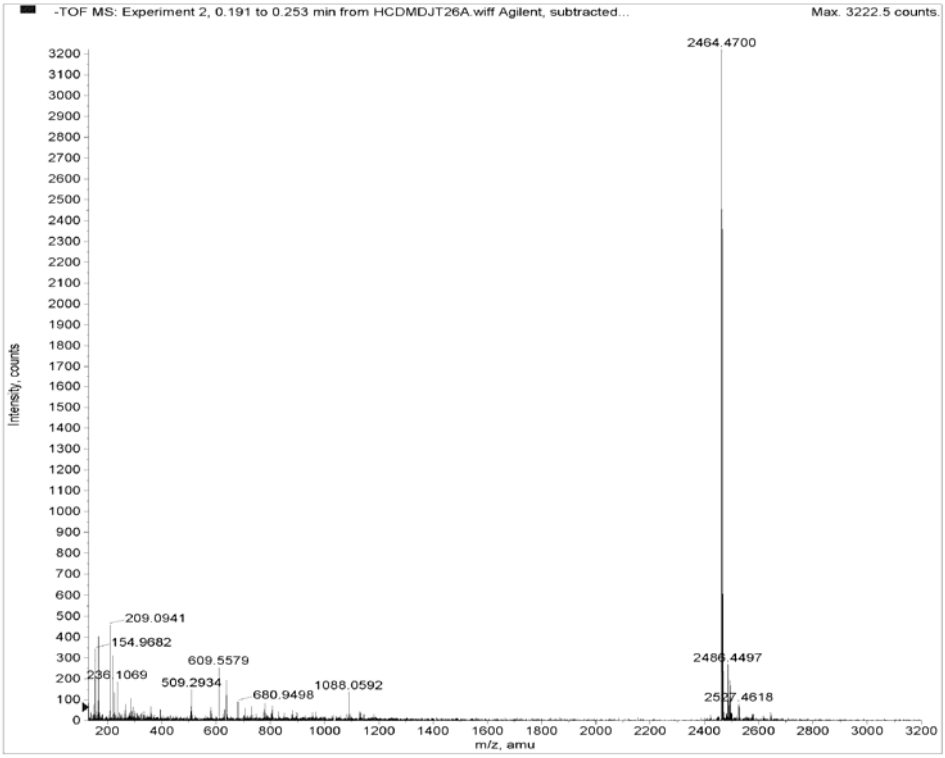


Figure S13. Isobacteriochlorin 3a ($IGlcAc_4$) ^{13}C NMR ($CDCl_3$ 76 ppm).



The peak at 2486 is the sodium ion adduct.

Elemental composition calculator

Target m/z: +2463.4666 amu
Tolerance: +3.0000 ppm
Result type: Elemental
Max num of results: 100
Min DBE: -0.5000 Max DBE: +100.0000
Electron state: Even
Num of charges: -1
Add water: N/A
Add proton: N/A
File Name: HCDMDJT26A.wiff

	Elements	Min Number	Max Number
1	C	106	106
2	Cl	0	0
3	F	16	16
4	H	98	105
5	K	0	0
6	N	6	6
7	Na	0	0
8	O	36	36
9	P	0	0
10	S	4	4

	Formula	Calculated m/z (amu)	mDa Error	PPM Error	DBE
1	C106 H99 N6 O36 F16 S4	2463.4733	-6.7378	-2.7351	52.5

Figure S14. Isobacteriochlorin 3a ($IGlcAc_4$) HRMS.

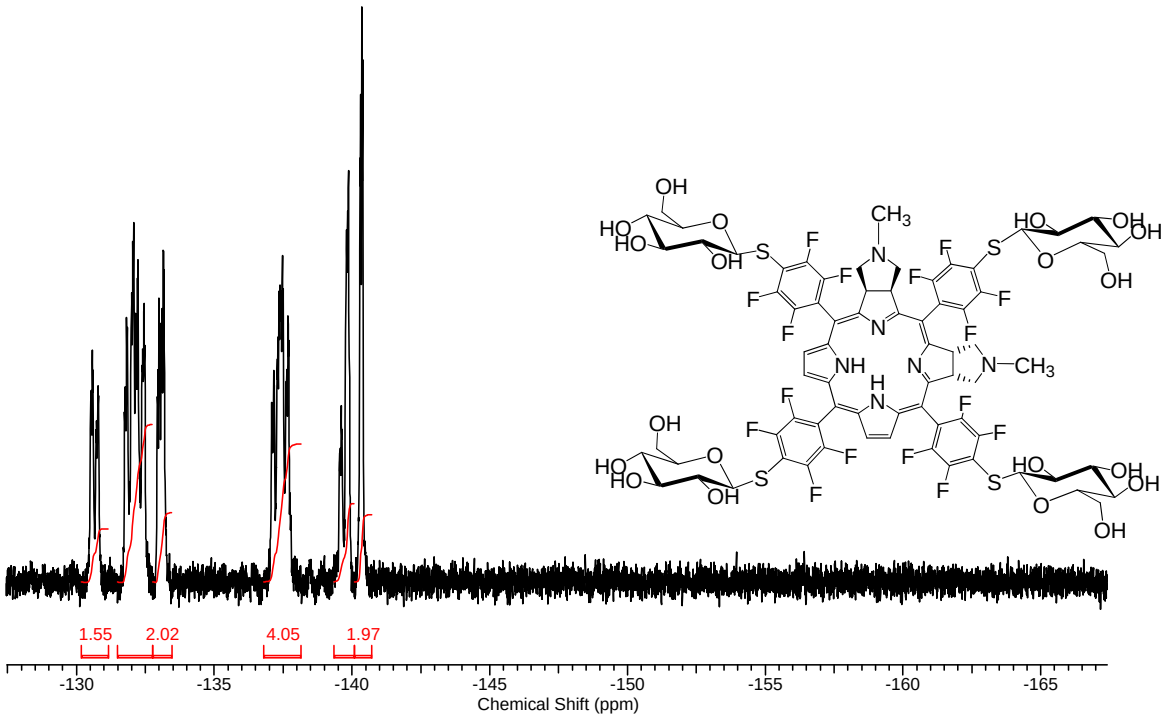


Figure S15. Isobacteriochlorin 3b ($IGlc_4$) ^{19}F NMR (DMSO-d_6).

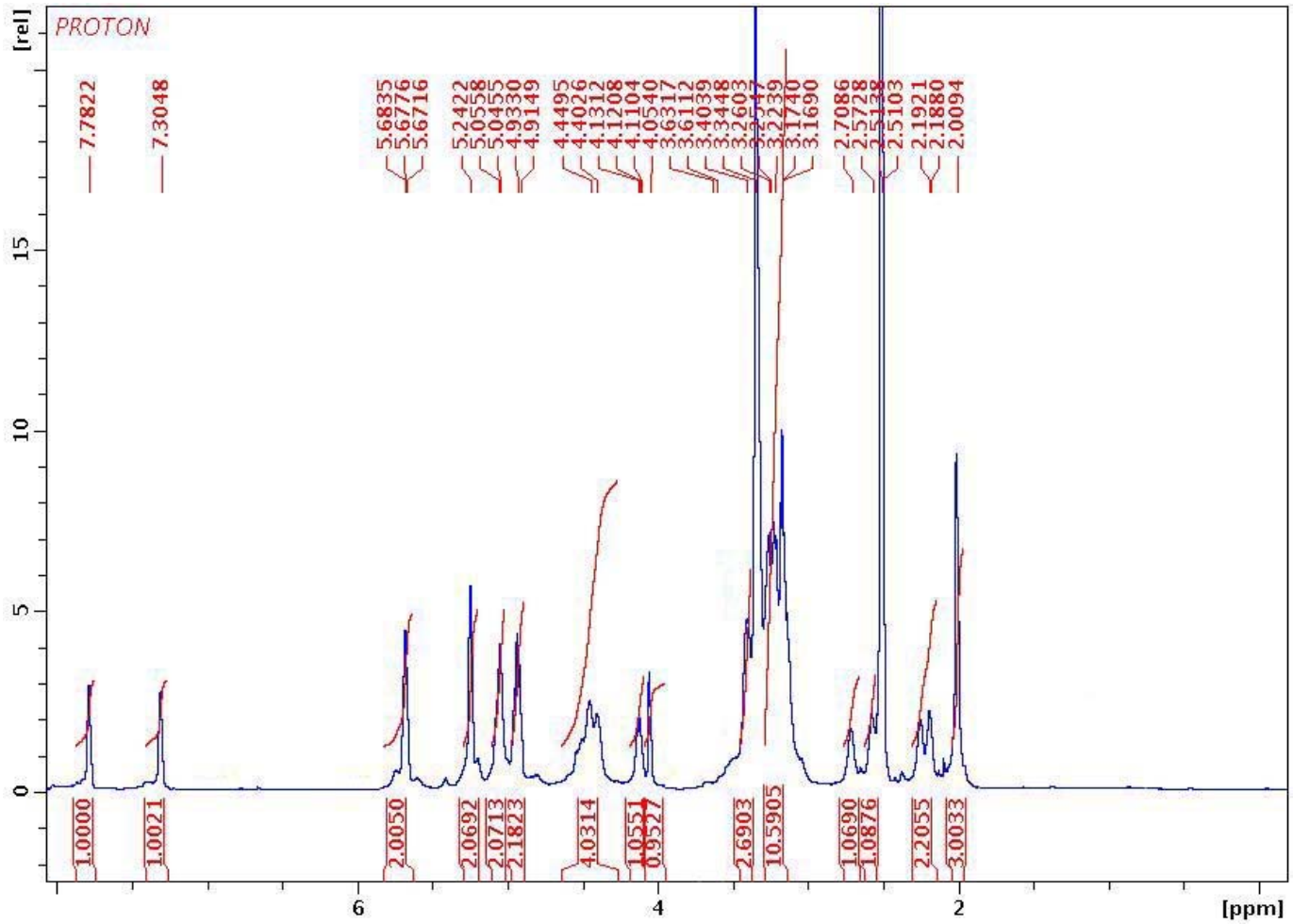


Figure S16. Isobacteriochlorin 3b ($IGlc_4$) ^{1}H NMR (DMSO-d_6 2.51 ppm, water 3.3 ppm).

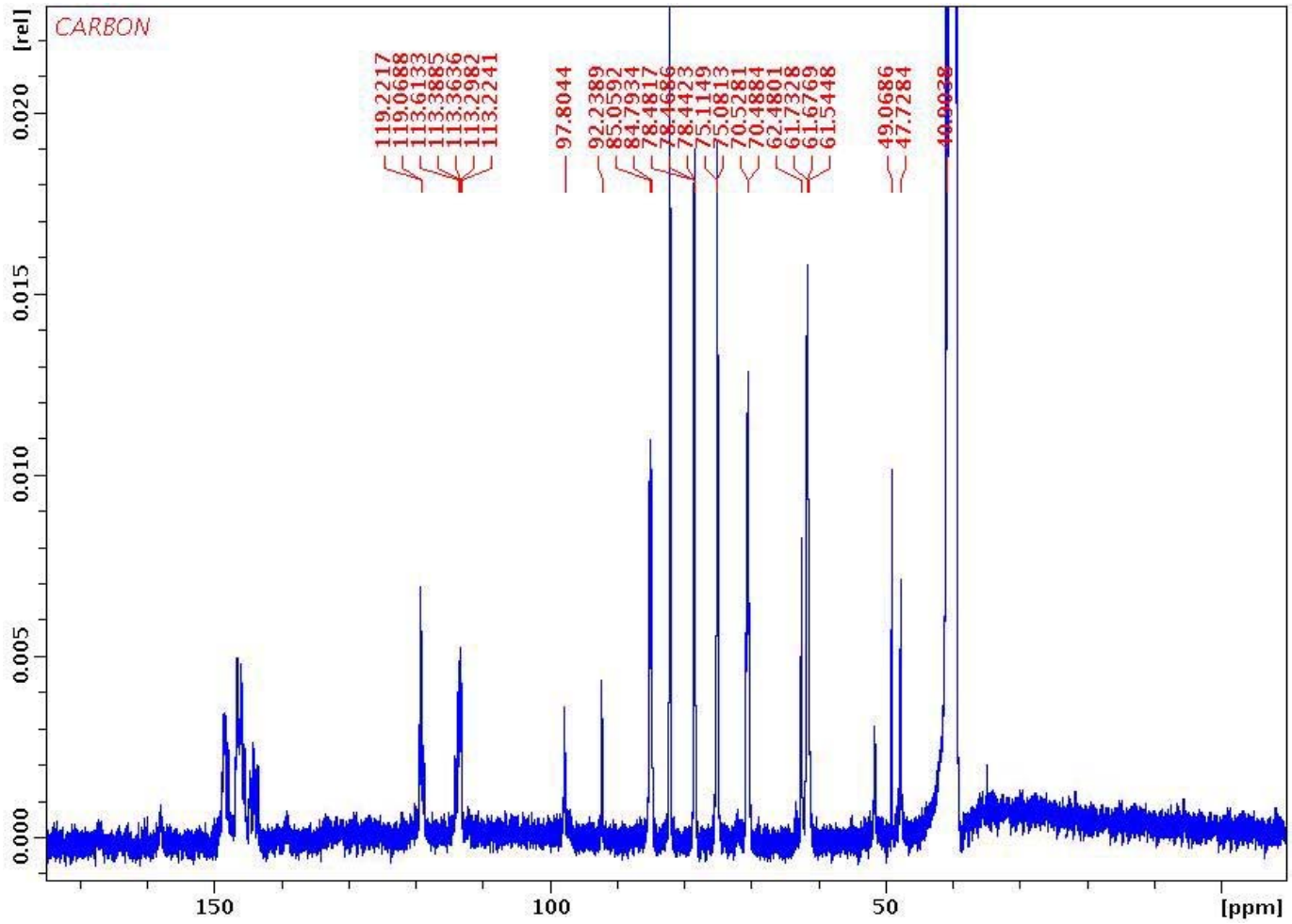
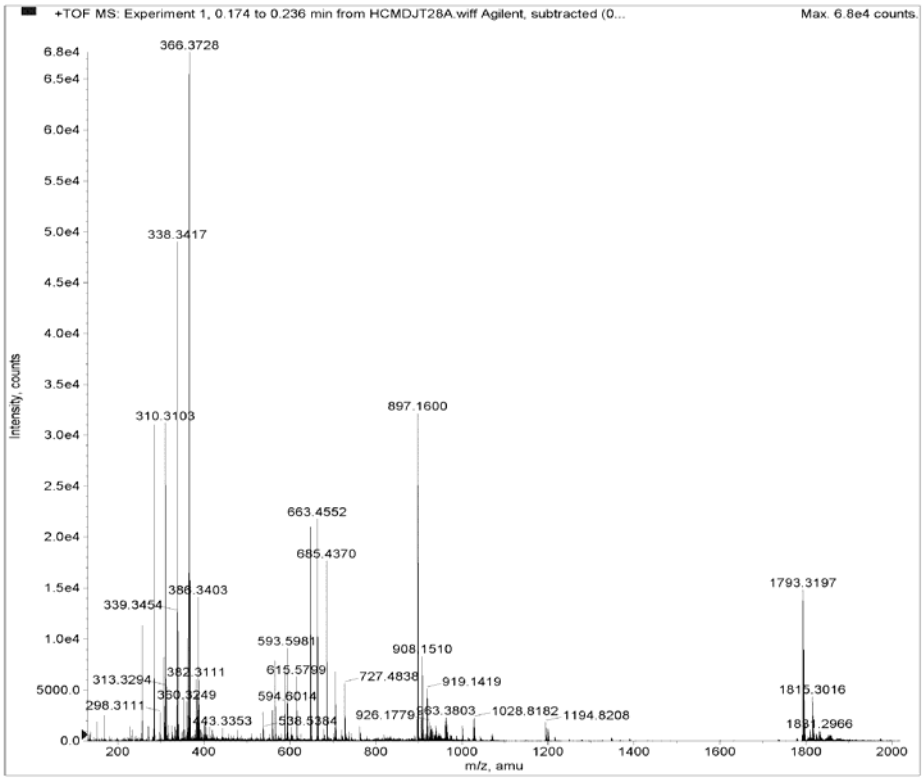


Figure S17. Isobacteriochlorin 3b ($IGlc_4$) ^{13}C NMR (DMSO-d_6 40 ppm).



	Formula	Calculated m/z (amu)	mDa Error	PPM Error	DBE
1	C74 H69 N6 O20 F16 S4	1793.3188	0.8447	0.4710	35.5

Figure S18a. Isobacteriochlorin 3b ($IGlc_4$) HRMS.

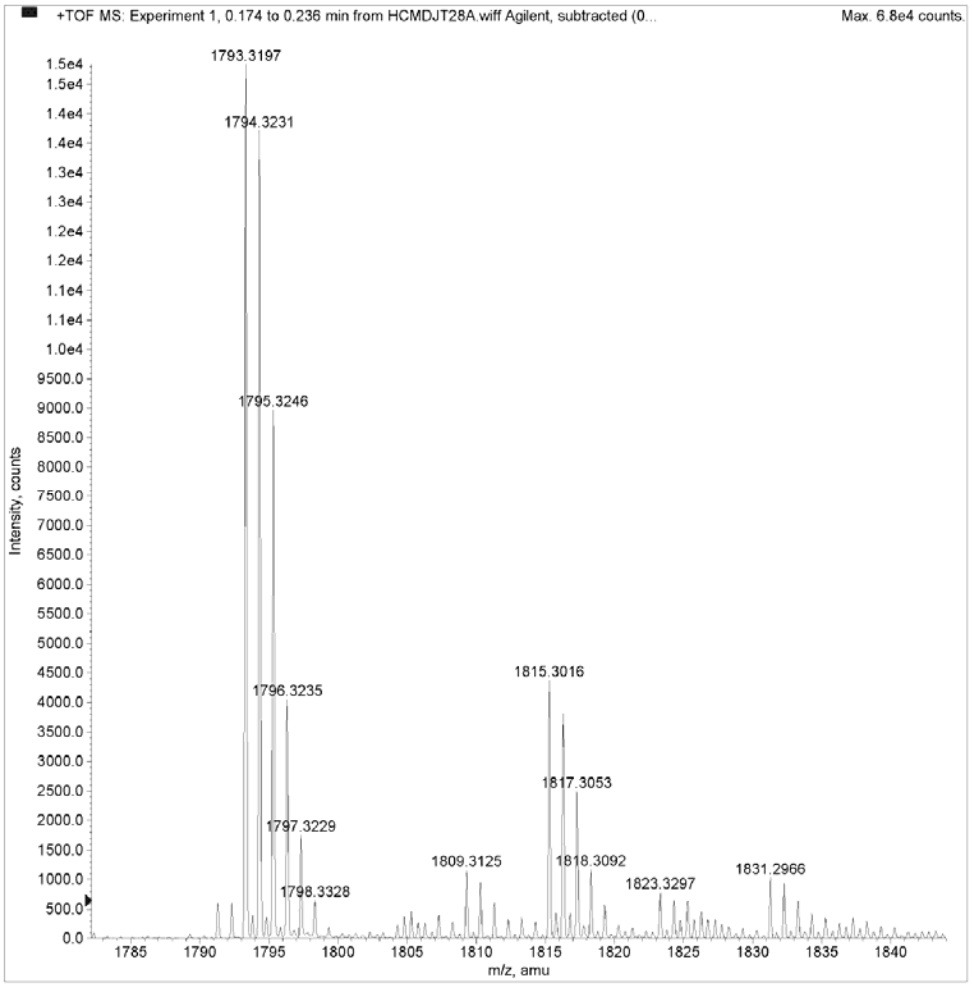
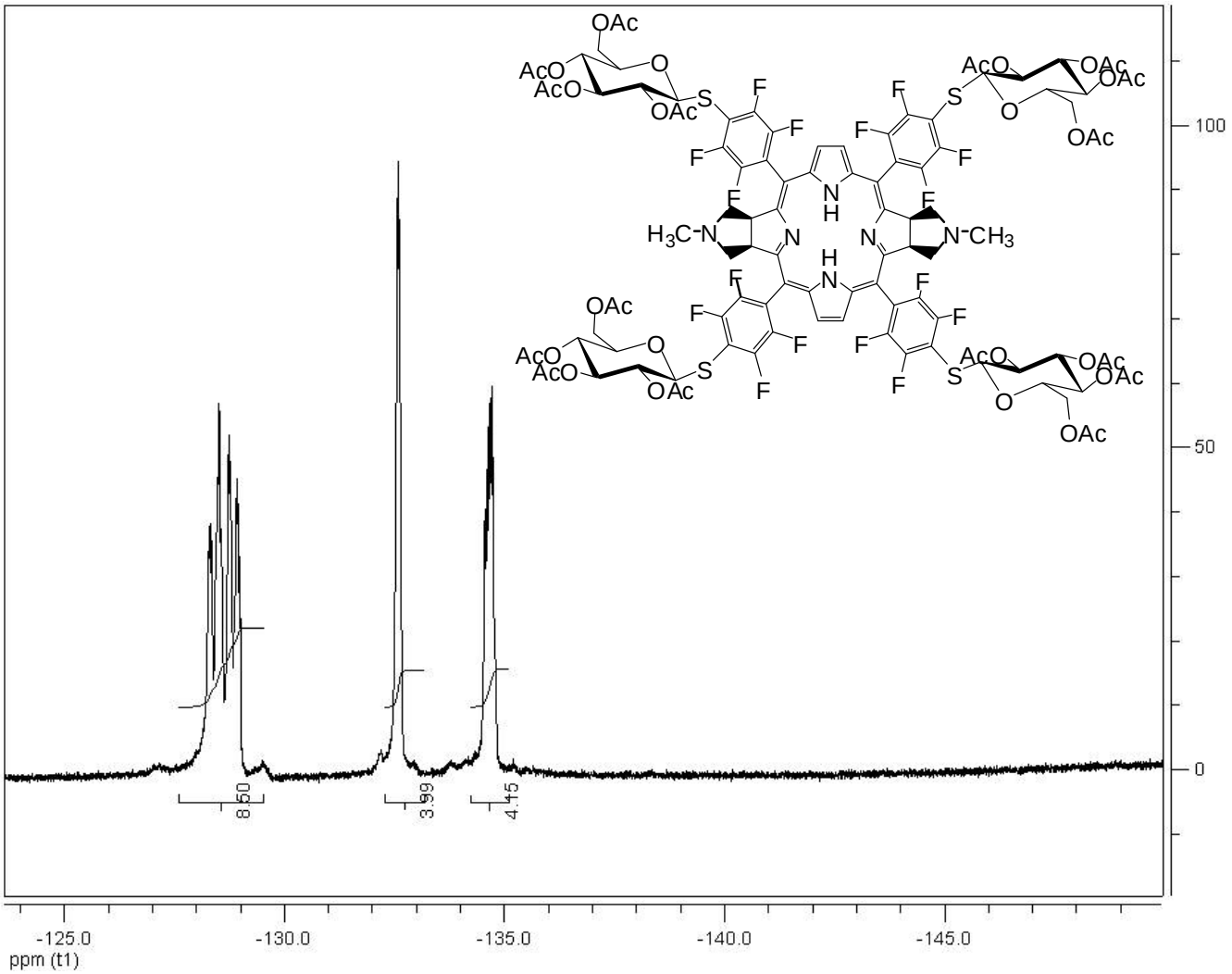


Figure S18b. Isobacteriochlorin 3b ($IGlc_4$) HRMS. The peak at 1815 is the sodium ion adduct, and the peak at 797 is the doubly charged M/2 ion.


OAc
AcO
AcO
O
OAc
S
F
F
F

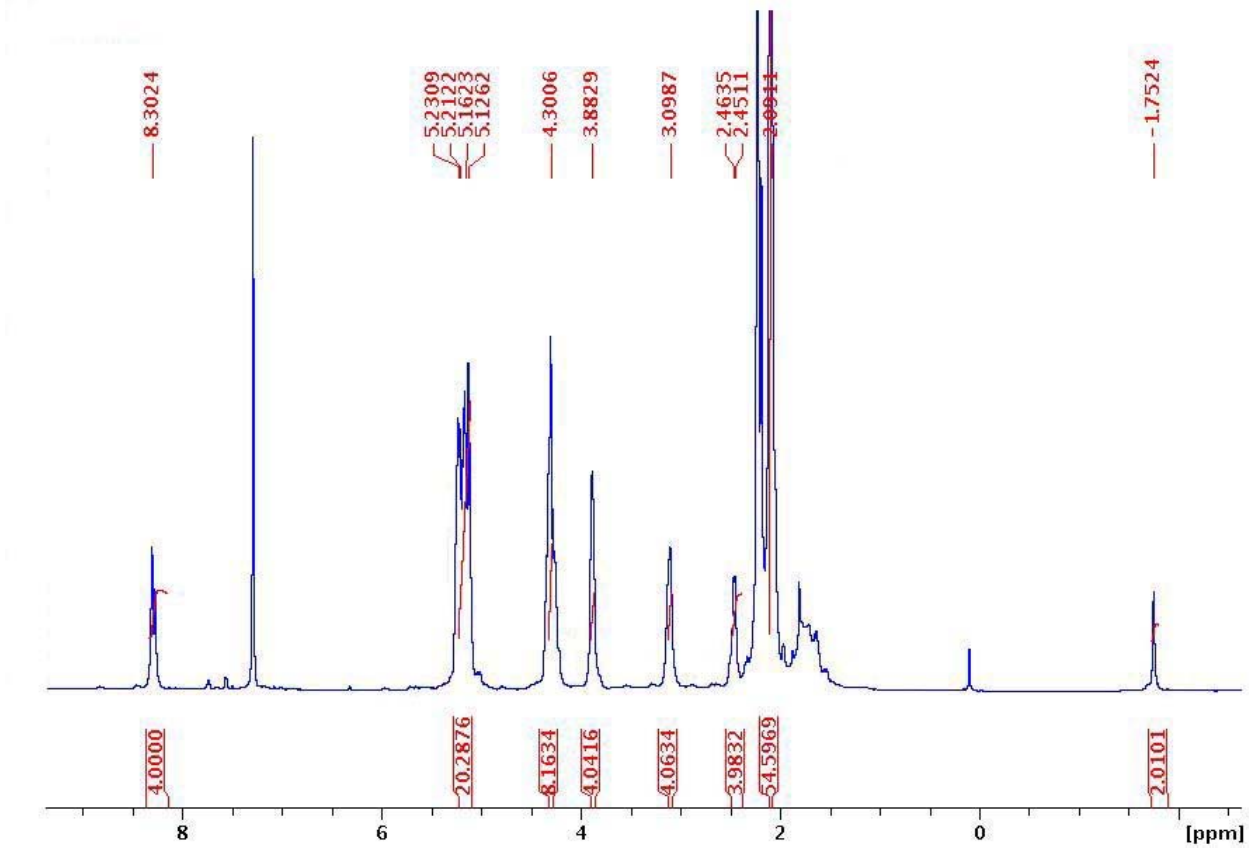


Figure S20. Bacteriochlorin 4a ($BGlcAc_4$) ^1H NMR ($CDCl_3$ 7.29 ppm)**.**

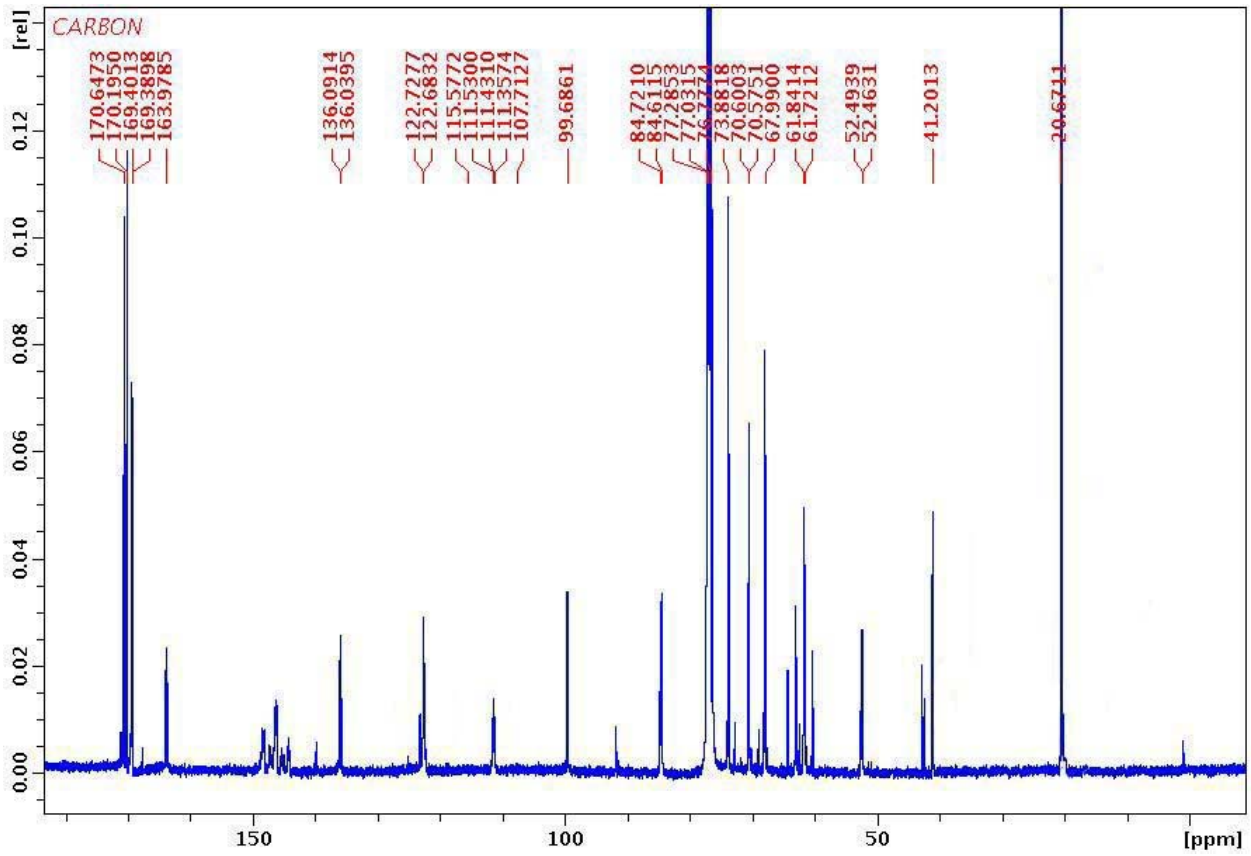


Figure S21. Bacteriochlorin 4a ($BGlcAc_4$) ^{13}C NMR ($CDCl_3$ 76 ppm).

Qualitative Compound Report

Data File	HCSS200900629_002.d	**Sample Name**	BGlac4
Sample Type	Sample	**Position**	P1-C1
Instrument Name	Instrument 1	**User Name**	Mahen
Acq Method		**IRM Calibration Status**	Success
DA Method	MahenFI.m	**Comment**	Sample M - Flow injection, ACN% MeOH

Compound Table

Compound Label	RT	Mass	Abund	Formula	Tgt Mass	Diff (ppm)
Cpd 1: C106 H100 F16 N6 O36 S4	0.2	2464.4813	11551	C106 H100 F16 N6 O36 S4	2464.4806	0.3

Compound Label	RT	Algorithm	Mass
Cpd 1: C106 H100 F16 N6 O36 S4	0.2	Find By Formula	2464.4813

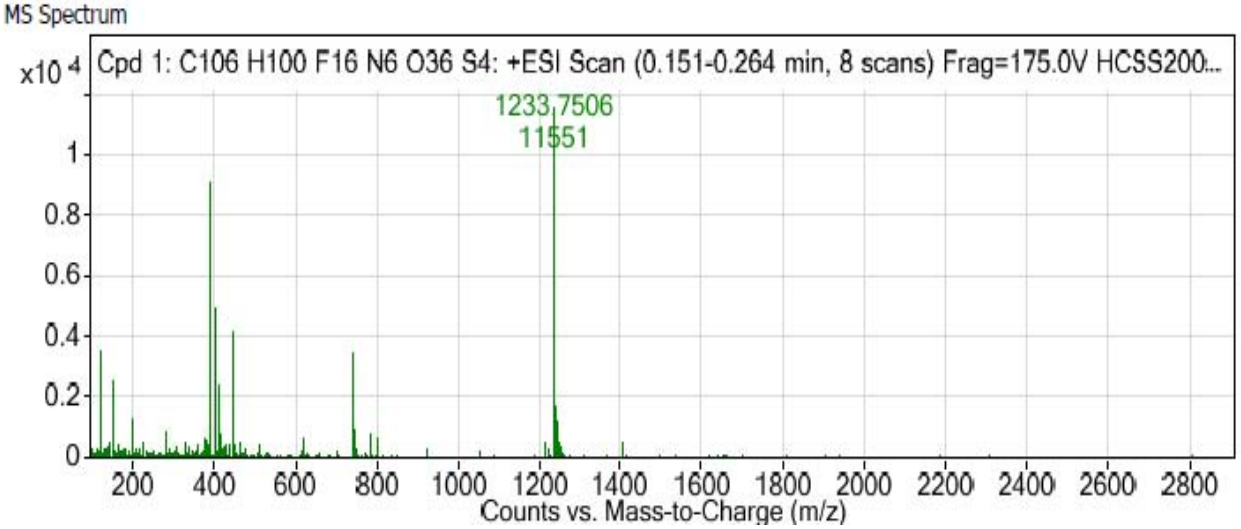


Figure S22. Bacteriochlorin 4a ($BGlcAc_4$) HRMS, the peaks at 1233 are the doubly charged species.

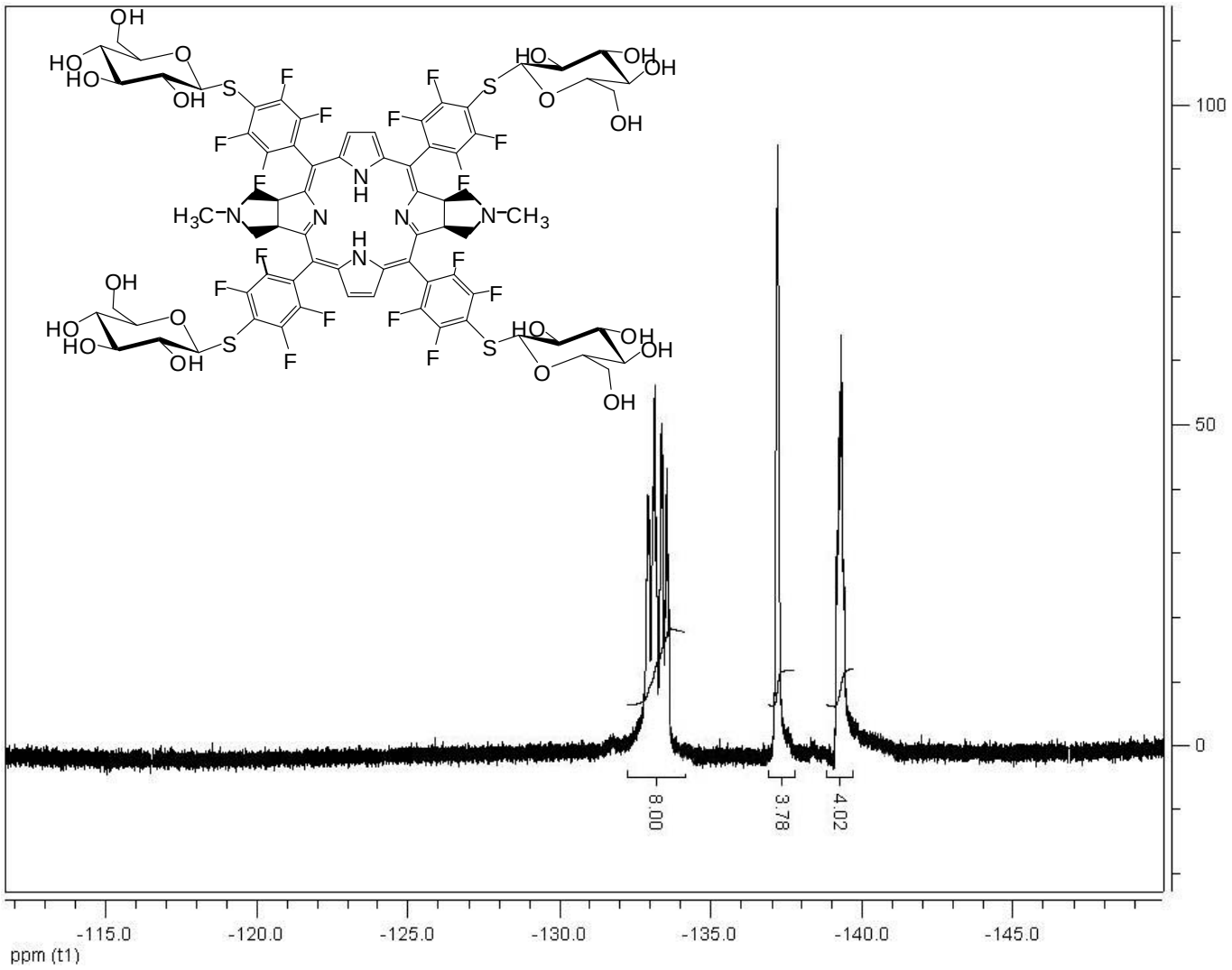


Figure S23. Bacteriochlorin 4b ($BGlc_4$) ^{19}F NMR (MeOD).

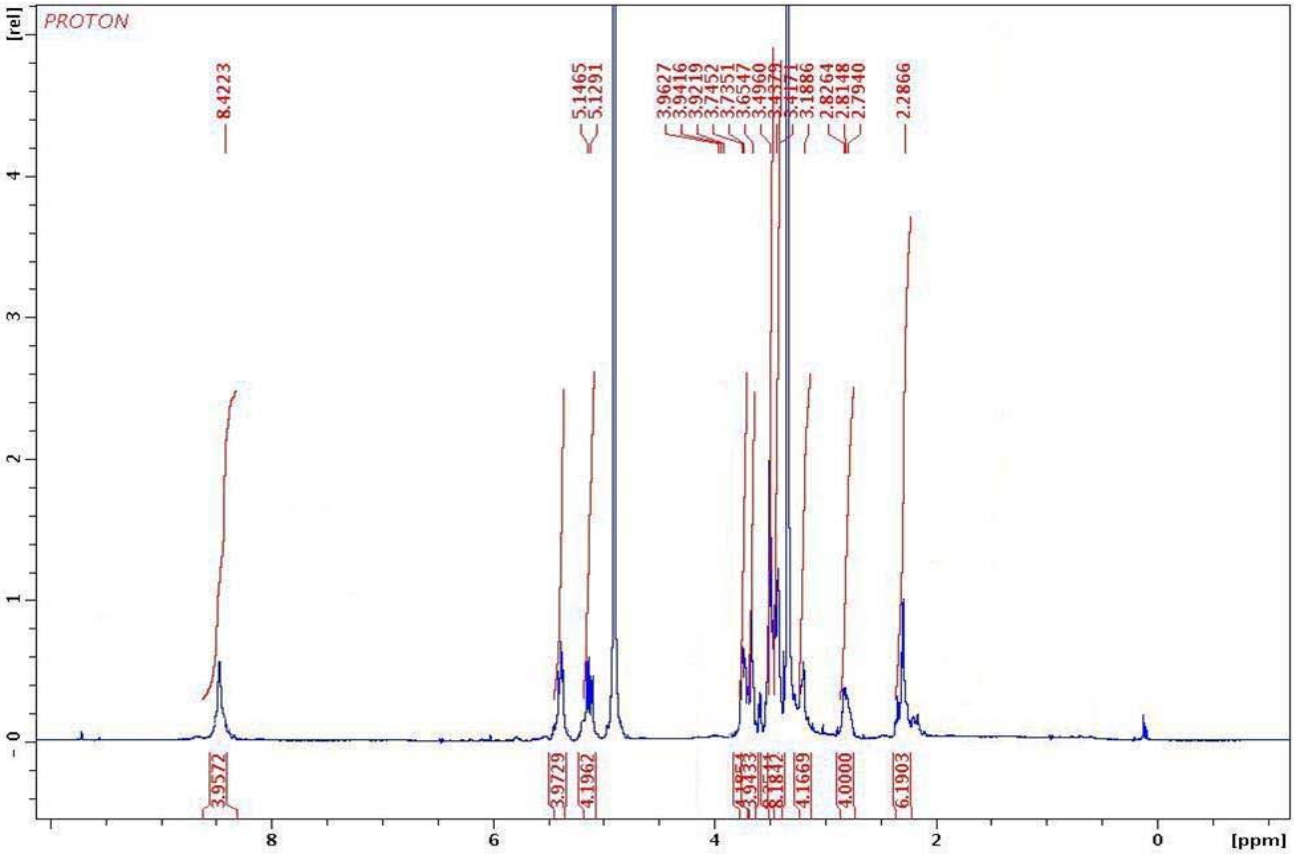


Figure S24. Bacteriochlorin 4b ($BGlc_4$) ^1H NMR (MeOD 4.87 and 3.31 ppm, water 4.9 ppm).

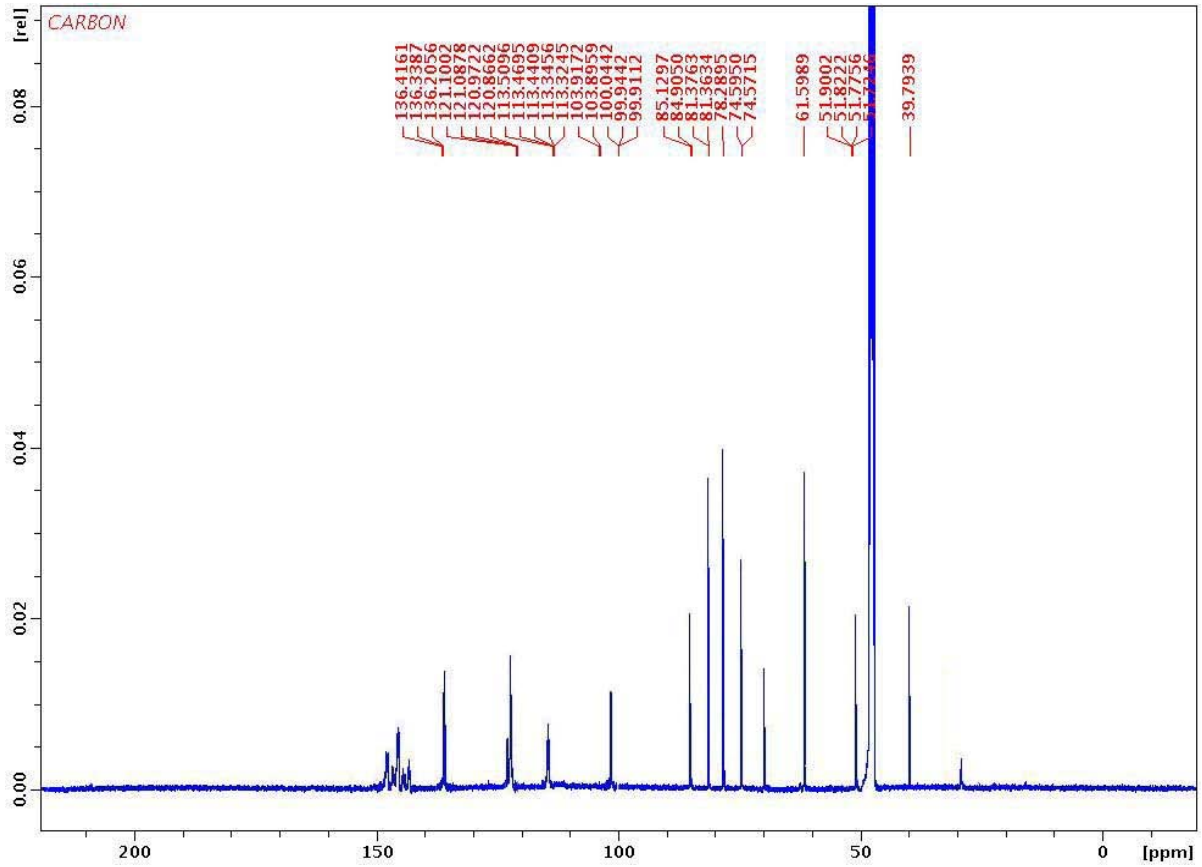


Figure S25. Bacteriochlorin 4b ($BGlc_4$) ^{13}C NMR (MeOD 49.15 ppm).

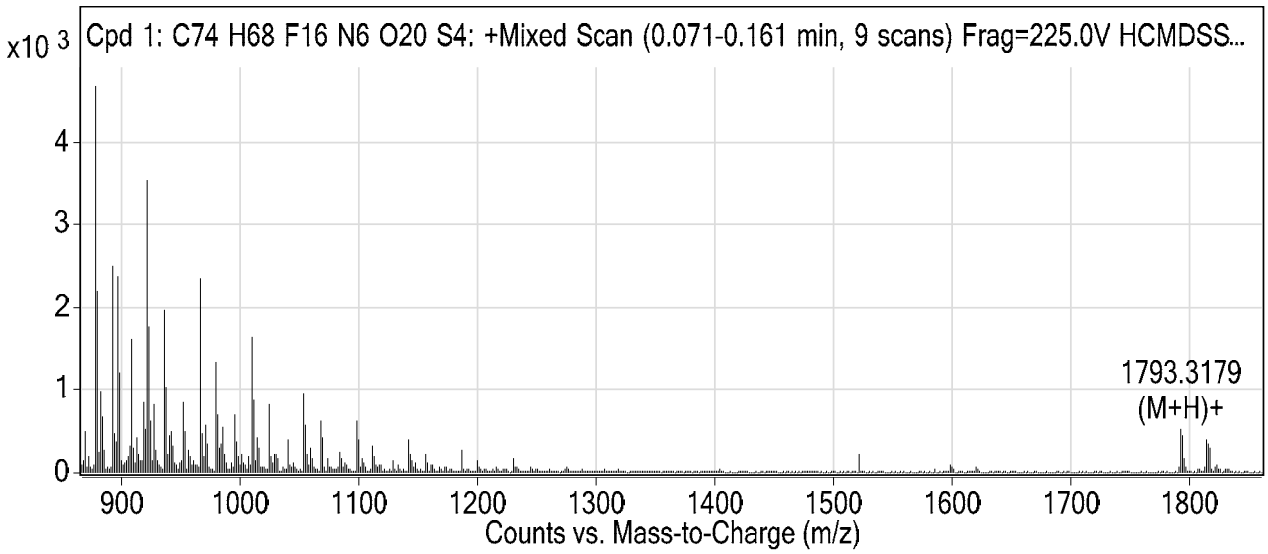


Figure S26. Bacteriochlorin 4b ($BGlc_4$) HRMS.

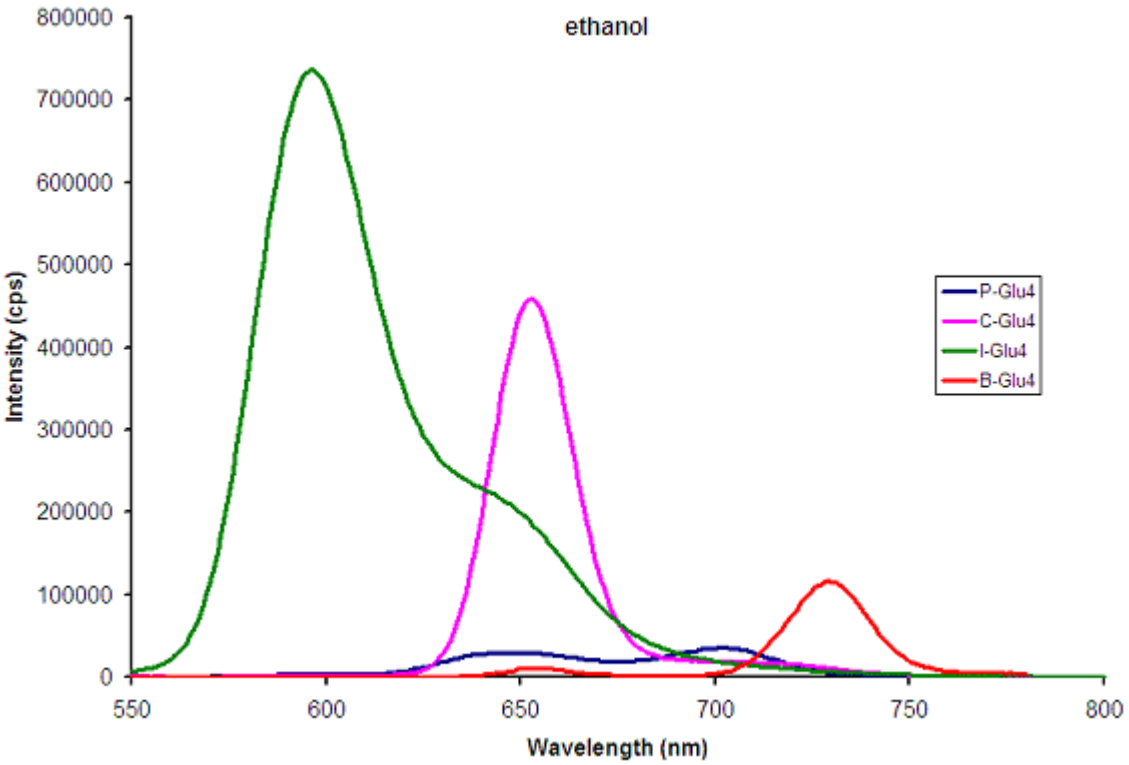


Figure S27. Emission spectra of the compounds in ethanol; excitation at 512 nm where the O.D. is ca. 0.05 for each compound.

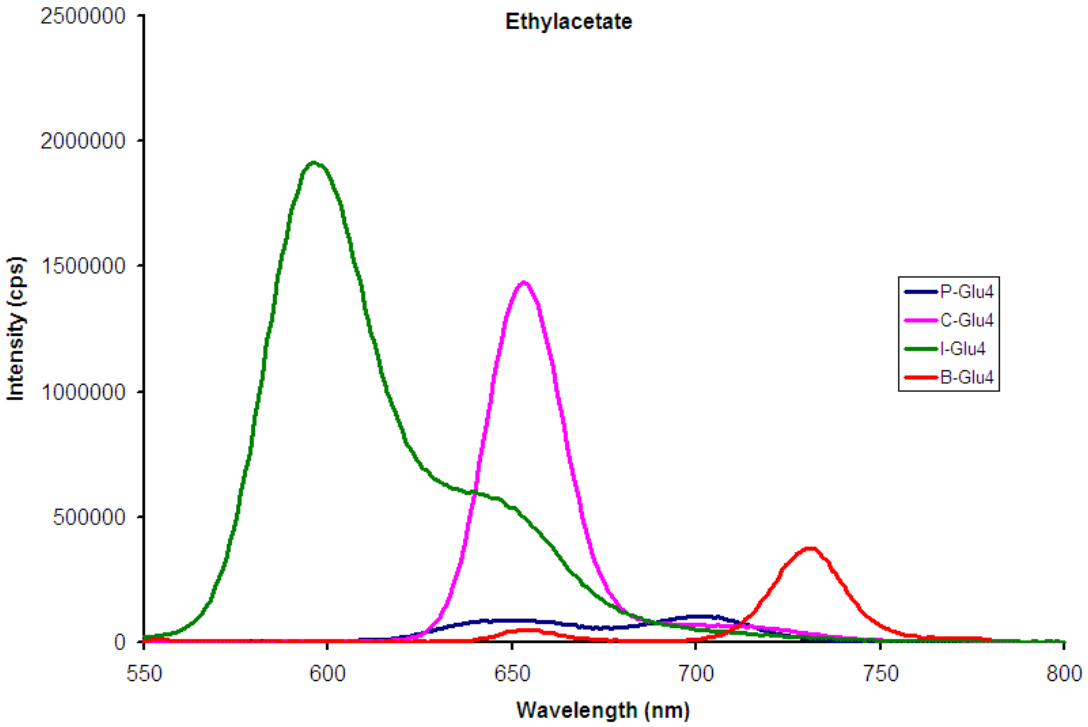


Figure S28. Emission spectra of the compounds in ethyl acetate; excitation at 509 nm where the O.D. was 0.098 for all three compounds.

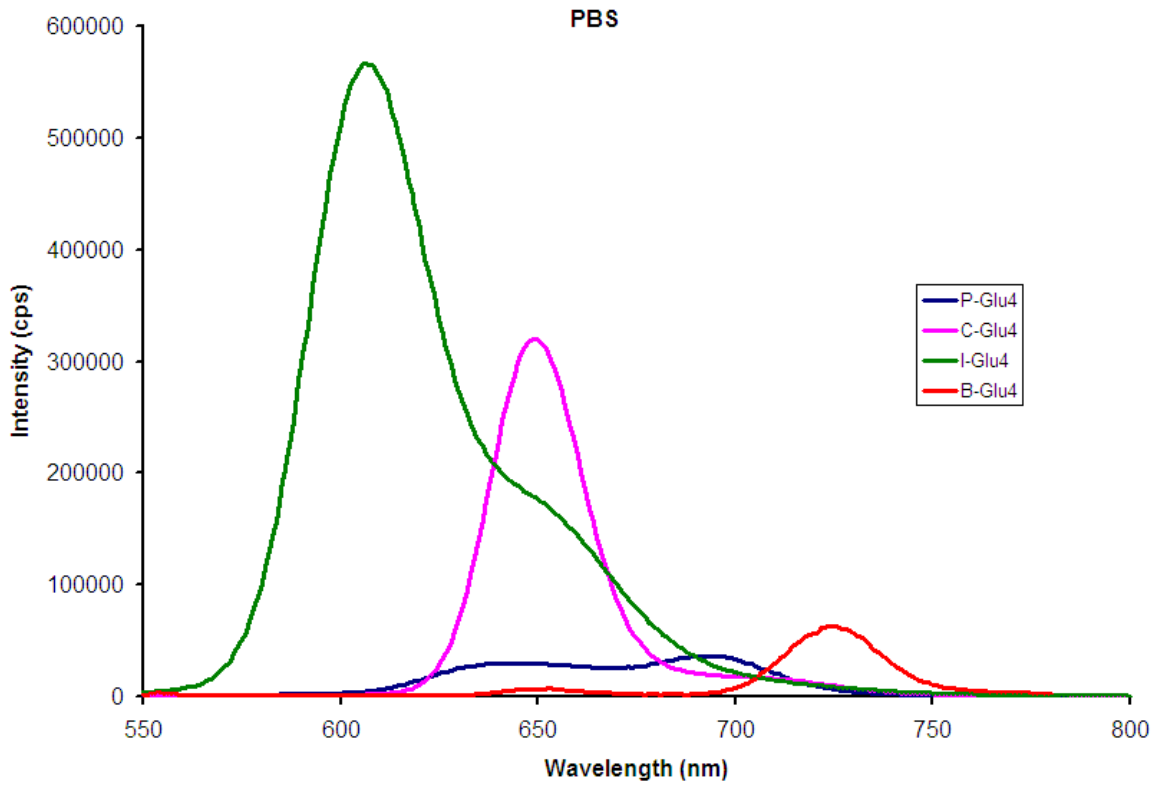


Figure S29. Emission spectra of the compounds in PBS; excitation at 512 nm, where the O.D. was 0.018 for all three compounds.

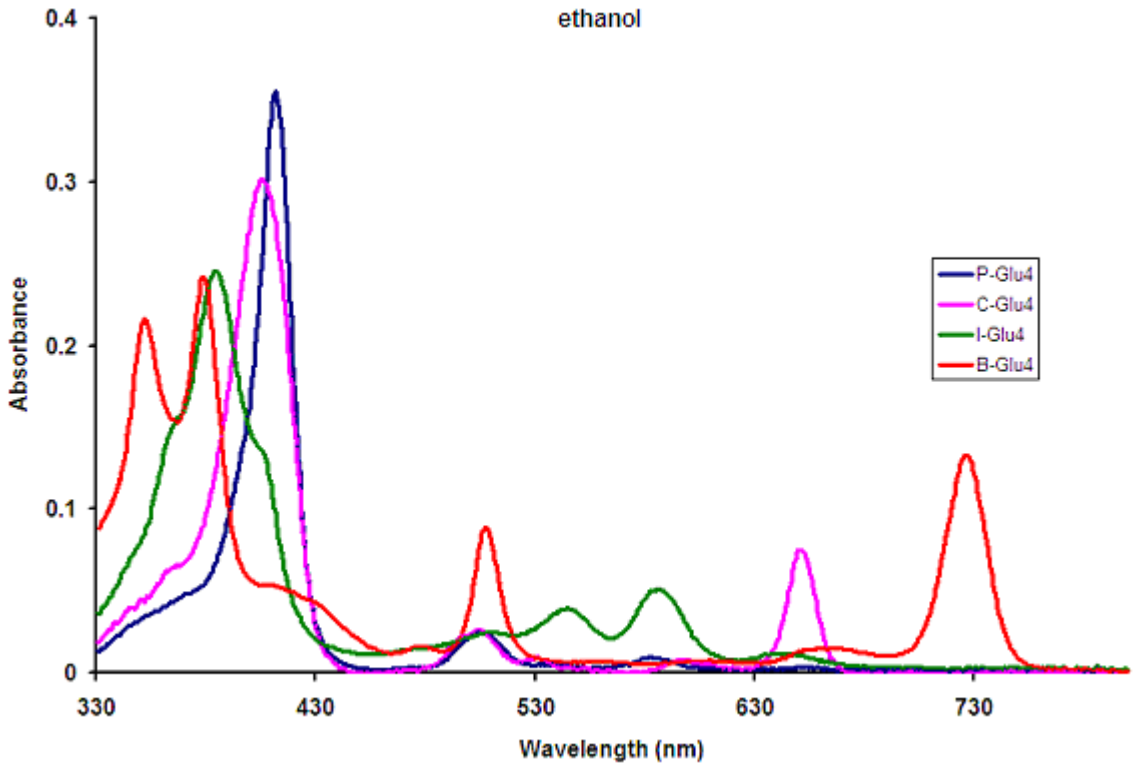


Figure S30. UV-visible spectra of the compounds, 2 µM in ethanol.

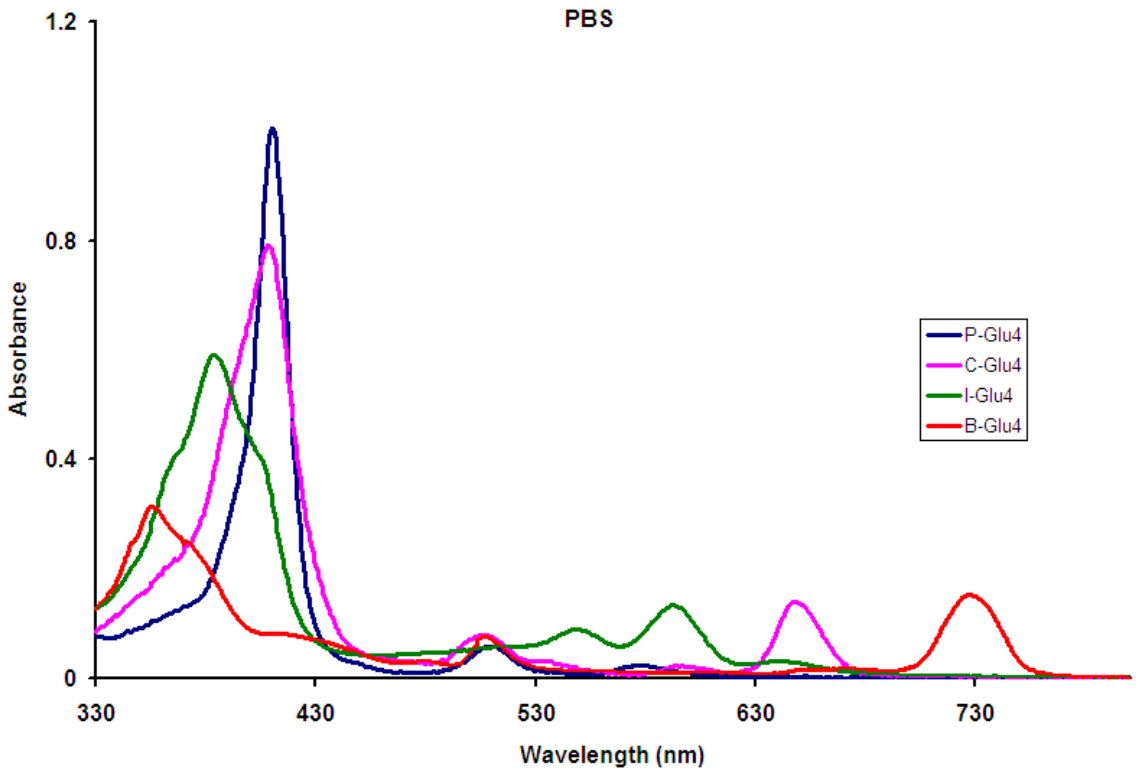


Figure S31. UV-visible spectra of the compounds, 2 µM in PBS.

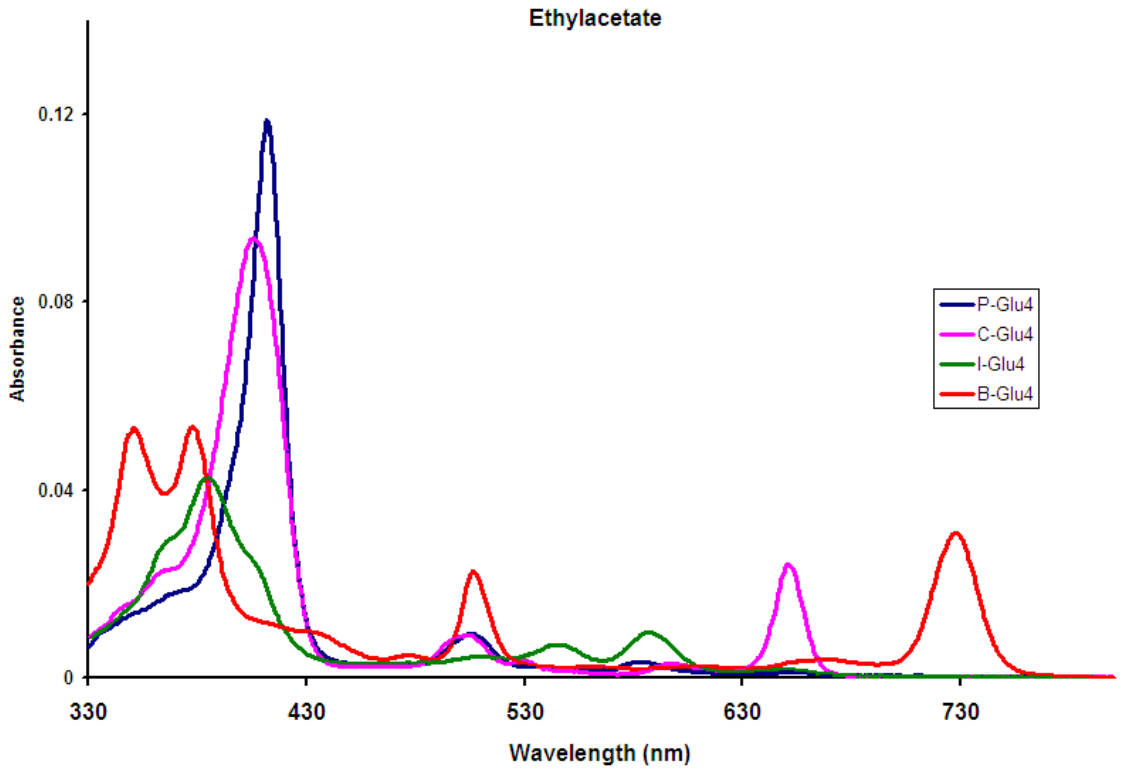


Figure S32. UV-visible spectra of the compounds, 2 µM in ethyl acetate**.**

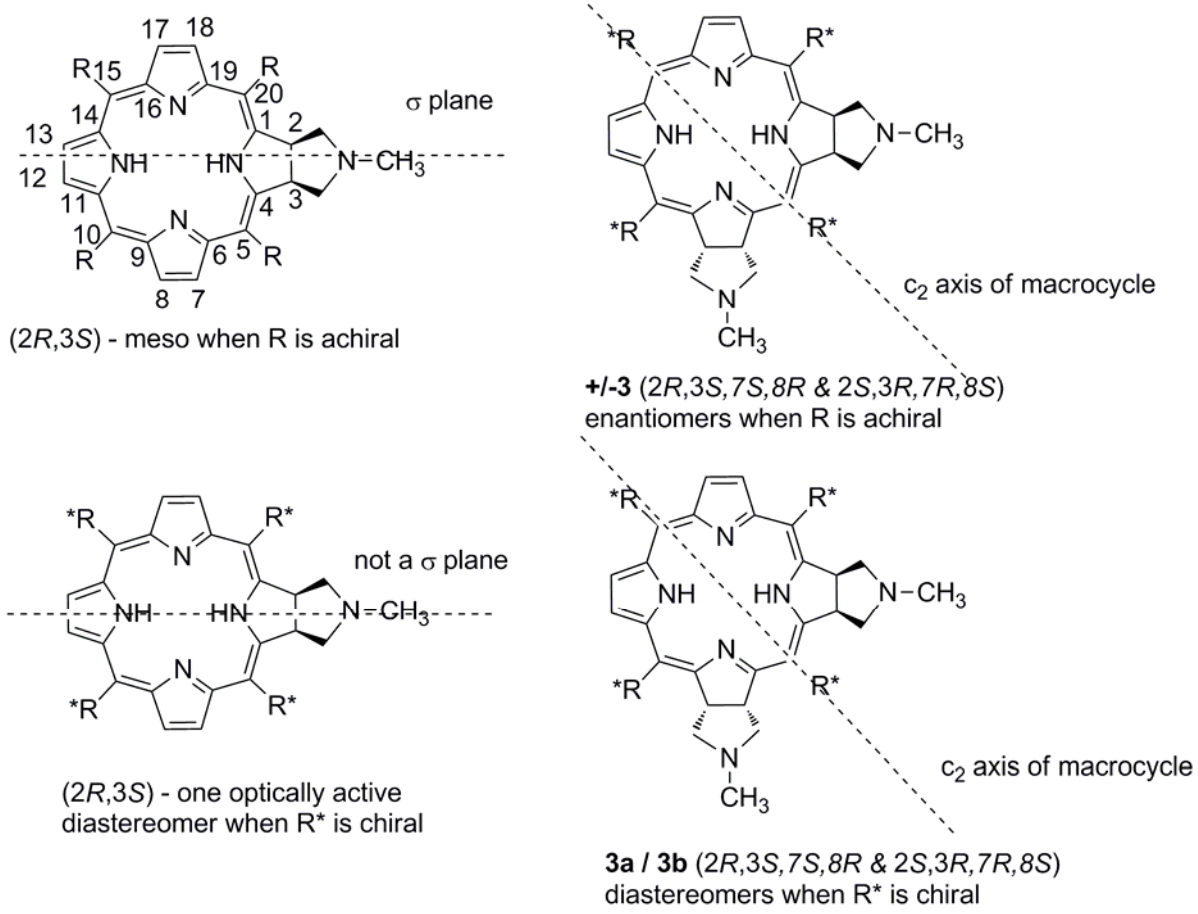


Figure S33. Formation of diastereomers. The diastereomers of IF_{20} can be separated on a chiral HPLC column.

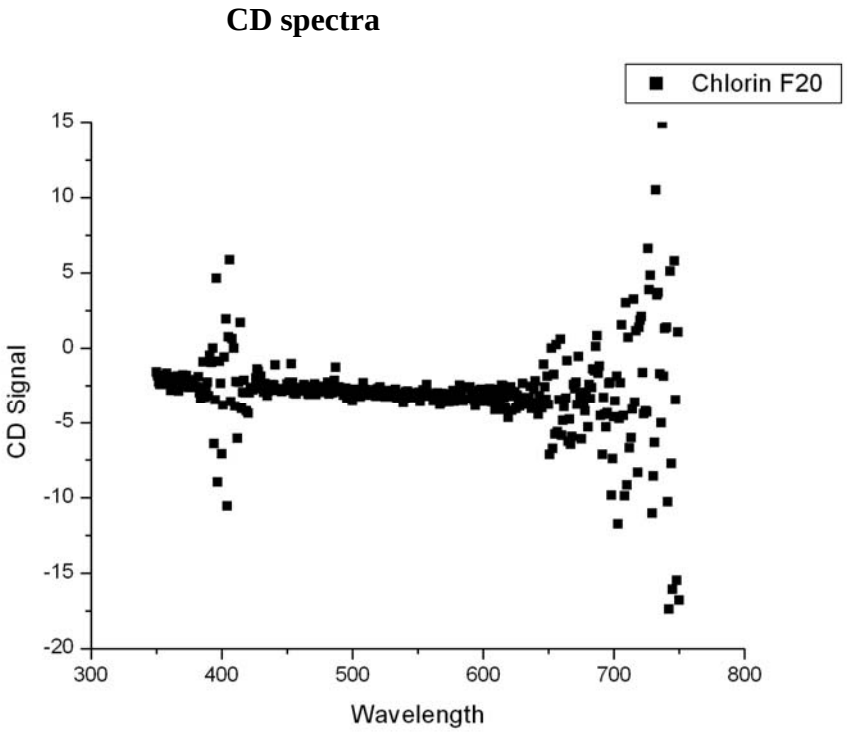


Figure S34-A. CD spectra of CF_{20} in chloroform.

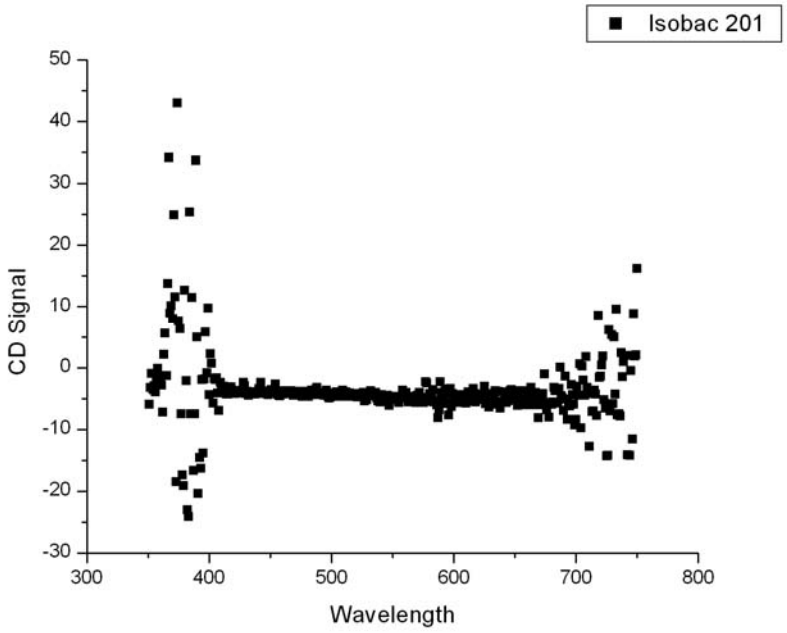


Figure S34-B: CD spectra of *anti* IF_{20} in chloroform.

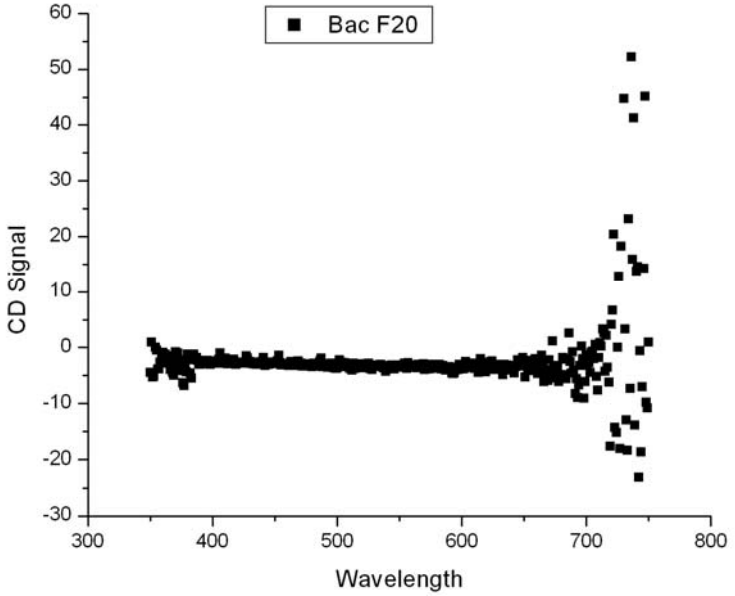


Figure S34-C. CD spectra of *syn* BF_{20} in chloroform**.**

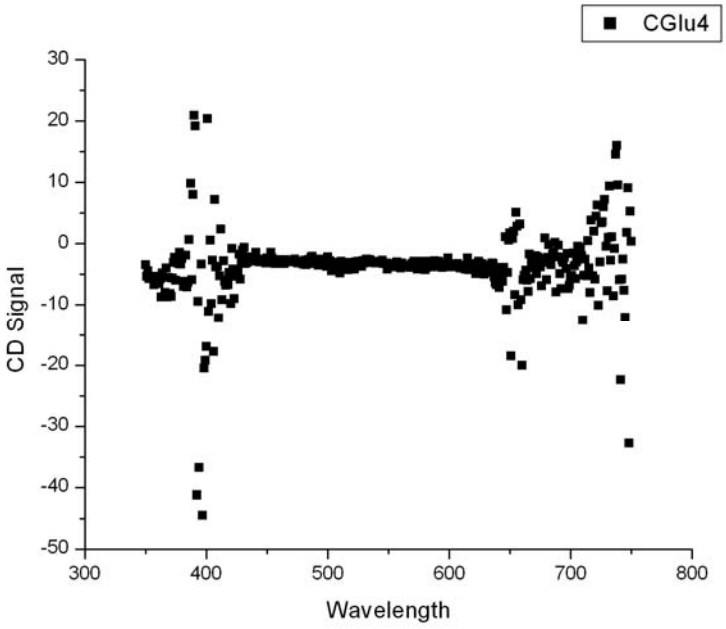


Figure S34-D: CD spectra of $CGlc_4$ in methanol.

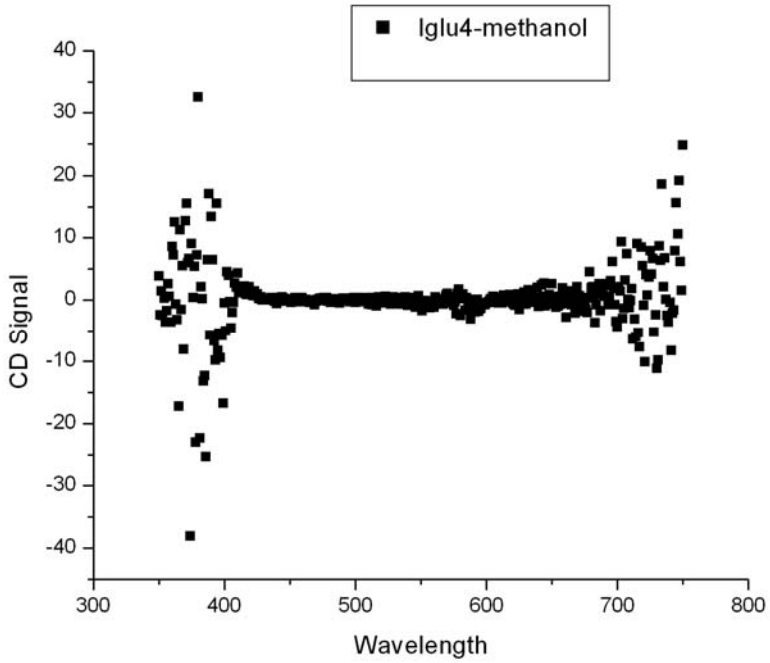


Figure S34-E: CD spectra of $IGlc_4$ in methanol.

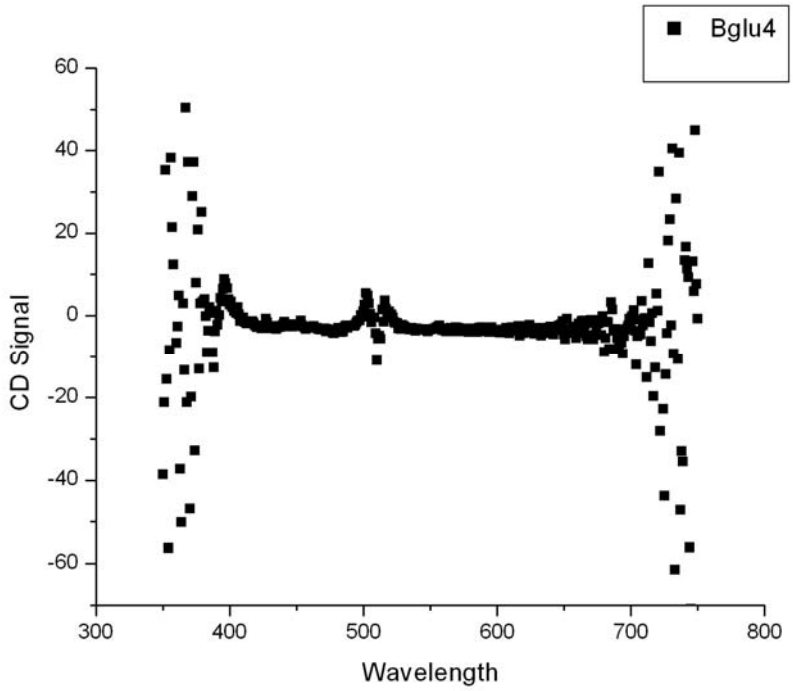
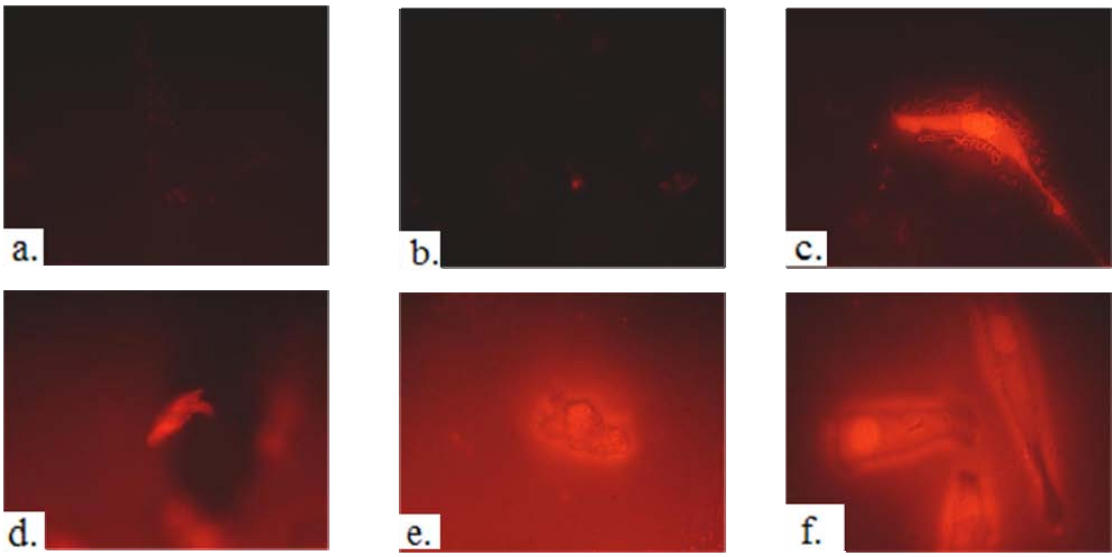


Figure S34-F: CD spectra of $BGlc_4$ in methanol.



$PGlc_4$ $CGlc_4$ $IGlc_4$

Figure S35. Cell uptake of the three $PGlc_4$, $CGlc_4$, and $IGlc_4$ by MDA-MB-231 breast cancer cells. a-c: fluorescence images after uptake from 0.05 μM solutions; d-f: cellular fluorescence after uptake from 0.5 μM solutions. 60x magnification.

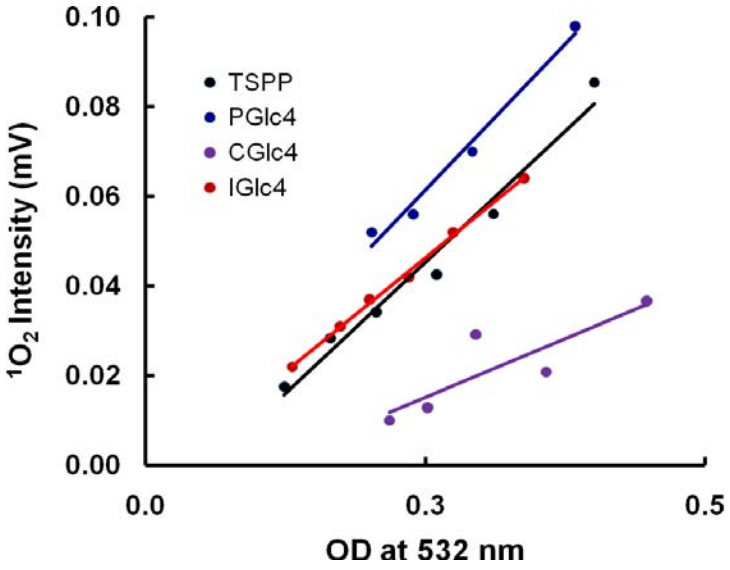


Figure S36. Changes in $^1O_2$ intensity as a function of OD at 532 nm. The lower Φ_Δ from $CGlc_4$ may partially due to the inefficient light absorption at 532 nm compared to $IGlc_4$.

Ideally, all of the lines in Figure S36 should go through zero. However, in many cases the background signals from laser pulse and detector can result in a positive intercept. This is largely accounted for since the Φ_Δ were calculated by comparing the slopes to a standard (TSPP).

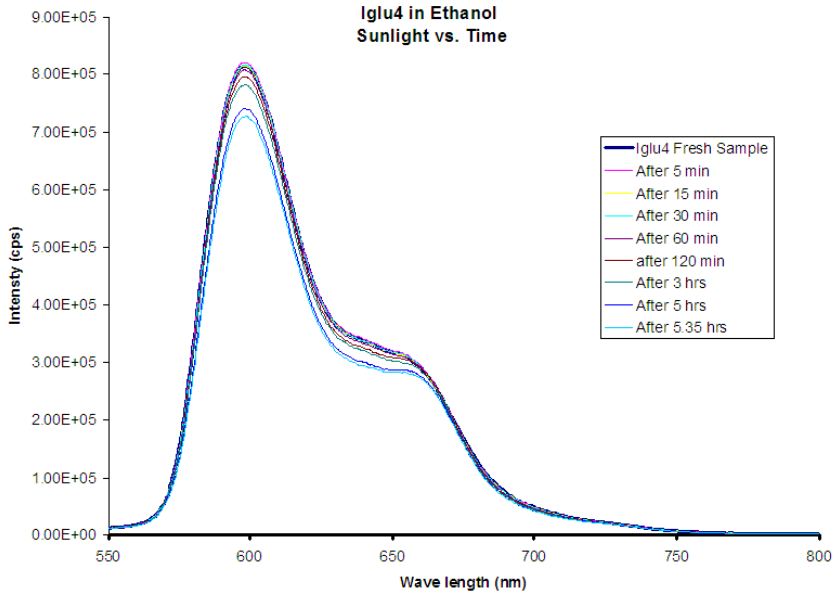


Figure S37. Emission spectra of $IGlc_4$ in ethanol in air in a closed vial shows only a small degree of photobleaching of $IGlc_4$ in sun light with time.

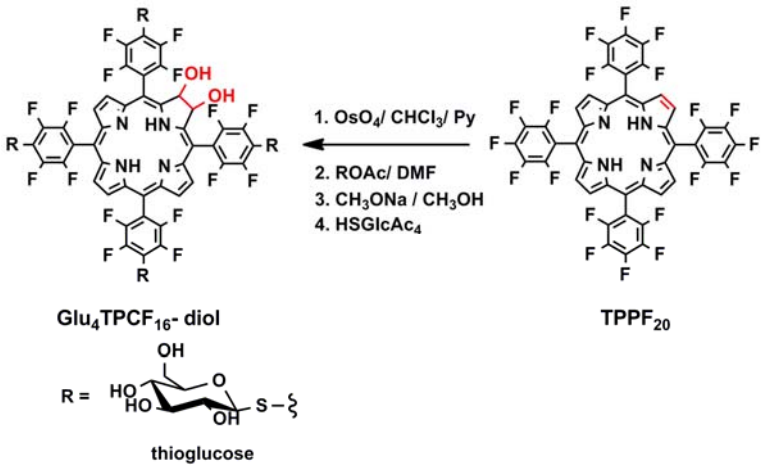


Figure S38. The para F substitution chemistry works on the diols formed using the procedures outlined in: Lara, K. K., Rinaldo, C. R., and Brückner, C. (2005) meso-Tetraaryl-7,8-diol-21,23-dithiachlorins and their pyrrole-modified derivatives: a spectroscopic comparison to their aza-analogues. *Tetrahedron 61*, 2529-2539.

Synthesis: S. Singh, J.P.C. Tome. Diol synthesis: M. Vinodu. Fluorescence microscopy images: D. Samaro, S. Thompson. Singlet oxygen studies: X. Zhu, R. Gao

Convenient Synthesis of a Propargylated Cyclic (3′-5′) Diguanylic Acid and Its "Click" Conjugation to a Biotinylated Azide

Andrzej Grajkowski,*[,‡] Jacek Cieślak,[‡] Alexei Gapeev,[§] Christian Schindler,[†] and Serge L. Beaucage[‡]

Division of Therapeutic Proteins, Center for Drug Evaluation and Research, Food and Drug Administration, 8800 Rockville Pike, Bethesda, Maryland 20892, United States, Department of Microbiology & Immunology, Columbia University, 701 West 168th Street, New York, New York 10032, United States, and Department of Chemistry and Biochemistry, University of Maryland, Baltimore County, 1000 Hilltop Circle, Baltimore, Maryland 21250, United States.
Received August 26, 2010; Revised Manuscript Received September 16, 2010

The ribonucleoside building block, N^2-isobutyryl-2′-*O*-propargyl-3′-*O*-levulinyl guanosine, was prepared from commercial N^2-isobutyryl-5′-*O*-(4,4′-dimethoxytrityl)-2′-*O*-propargyl guanosine in a yield of 91%. The propargylated guanylyl(3′-5′)guanosine phosphotriester was synthesized from the reaction of N^2-isobutyryl-2′-*O*-propargyl-3′-*O*-levulinyl guanosine with N^2-isobutyryl-5′-*O*-(4,4′-dimethoxytrityl)-2′-*O*-*tert*-butyldimethylsilyl-3′-*O*-[(2-cyanoethyl)-*N*,*N*-diisopropylaminophosphinyl] guanosine and isolated in a yield of 88% after *P*(III) oxidation, 3′-/5′-deprotection, and purification. The propargylated guanylyl(3′-5′)guanosine phosphotriester was phosphitylated using 2-cyanoethyl tetraisopropylphosphordiamidite and 1*H*-tetrazole and was followed by an in situ intramolecular cyclization to give a propargylated c-di-GMP triester, which was isolated in a yield of 40% after *P*(III) oxidation and purification. Complete *N*-deacylation of the guanine bases and removal of the 2-cyanoethyl phosphate protecting groups from the propargylated c-di-GMP triester were performed by treatment with aqueous ammonia at ambient temperature. The final 2′-desilylation reaction was effected by exposure to triethylammonium trihydrofluoride affording the desired propargylated c-di-GMP diester, the purity of which exceeded 95%. Biotinylation of the propargylated c-di-GMP diester was easily accomplished through its cycloaddition reaction with a biotinylated azide derivative under click conditions to produce the biotinylated c-di-GMP conjugate of interest in an isolated yield of 62%.

INTRODUCTION

Cyclic (3′-5′)diguanylate (c-di-GMP) was first identified in *Acetobacter xylinum* as a factor that allosterically regulates membrane cellulose synthesis (*1*−*3*). More recently, enzymes controlling the intracellular levels of c-di-GMP, particularly those including the GGDEF (Gly-Gly-Asp-Glu-Phe) and EAL (Glu-Ala-Leu) domains, which possess diguanylate cyclase and phosphodiesterase activities, respectively, have been identified in the majority of bacterial genomes (*2*). Consistent with these findings, functional studies have determined that c-di-GMP levels regulate important bacterial programs, such as those associated with a switch from planktonic to biofilm growth and those associated with virulence (*2*). Moreover, c-di-GMP has been identified as a potent adjuvant, owing to its ability to induce the expression of a number of inflammatory cytokines and chemokines (e.g., TNF-α, IL-1, IFN-*β*, IP-10, and Rantes) (*4*, *5*). More recent studies have provided evidence for a cytosolic sensor that detects c-di-GMP and initiates this inflammatory response (*5*). However, the sensor responsible for eliciting this inflammatory response, as well as many components in bacterial c-di-GMP signaling cascades, remains unidentified. The development of a biotinylated c-di-GMP conjugate provides an important tool for the identification and characterization of the proteins binding this ligand and their respective signaling pathways, both in prokaryotes and in eukaryotes. Moreover, these tools may also prove valuable in characterizing the responses associated with c-di-AMP (*6*).

Various synthetic strategies have been implemented for the synthesis of c-di-GMP and its analogues. Indeed, in addition to the hydroxybenzotriazole phosphotriester method (*7*,*8*), combinations of phosphoramidite and phosphotriester (*9*−*12*), phosphoramidite and *H*-phosphonate (*13*), or phosphotriester and *H*-phosphonate (*14*, *15*) methods have also been reported for this purpose. Interestingly, an enzymatic approach and a solid-phase approach to the synthesis of c-di-GMP have recently been described in the literature (*16*, *17*). We now report a straightforward solution-phase synthesis of the propargylated c-di-GMP **10** using exclusively, for the first time, phosphoramidite chemistry. The synthetic strategy consists of exploiting commercially available starting materials (**1** and **4**) and clustering synthetic operations in order to minimize the number of purification steps (Schemes 1−3). As outlined in Scheme 4, synthesis of the biotinylated azide **13** from commercial aminoalkylated biotin amide **12** and conversion of **13** to the biotinylated c-di-GMP **14** via a copper(I)-catalyzed [3 + 2] azide−alkyne cycloaddition reaction (CuAAC or click chemistry) (*18*, *19*) are described in detail in this report.

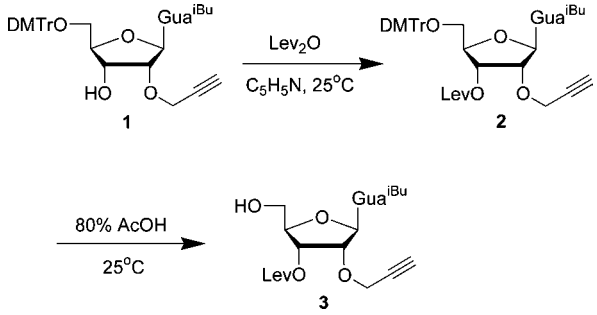
EXPERIMENTAL PROCEDURES

***N*^{2}-Isobutyryl-3′-*O*-levulinyl-2′-*O*-propargyl Guanosine (3).** To a solution of N^2-isobutyryl-5′-*O*-(4,4′-dimethoxytrityl)-2′-*O*-propargyl guanosine (**1**, 1.73 g, 2.50 mmol) in dry pyridine (10 mL) was added levulinic anhydride (*20*, *21*) (2.50 g, 10.0 mmol); the solution was stirred at ∼25 °C for 16 h and was then evaporated to a gummy material under reduced pressure. The residue was dissolved in $CHCl_3$ (30 mL) and was vigorously

* To whom correspondence should be addressed. Tel: (301)-827-1860. Fax: (301)-480-3256. E-mail: Andrzej.Grajkowski@fda.hhs.gov.
‡ Center for Drug Evaluation and Research.
§ University of Maryland.
† Columbia University.

10.1021/bc1003857 © 2010 American Chemical Society
Published on Web 10/13/2010

Scheme 1. 3′-*O*-Acylation of the Ribonucleoside 1 and 5′-*O*-Deprotection of 2[a]

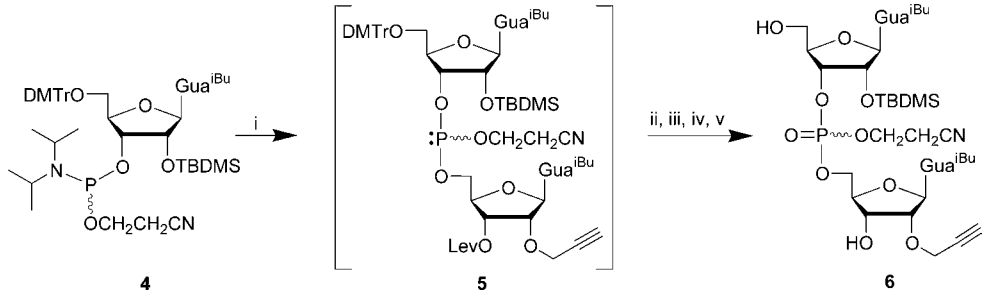


[a] Keys: DMTr, 4,4′-dimethoxytrityl; Gua, guanin-9-yl; iBu, isobutyryl; Lev_2O, levulinic anhydride; Lev, levulinyl.

mixed with water (15 mL). The organic layer was collected and evaporated under low pressure. The crude ribonucleoside **2** was dissolved in 80% AcOH (10 mL) in order to remove the 5′-protecting group; progress of the reaction was monitored by TLC, which revealed complete cleavage of the 4,4′-dimethoxytrityl (DMTr) ether after a reaction time of 3 h. The reaction mixture was concentrated under vacuum to an oil, which was dissolved in $CHCl_3$ (3 mL) and purified by chromatography on silica gel (∼40 g) using a gradient of MeOH (0 → 3%) in $CHCl_3$. Fractions containing the ribonucleoside **3** were collected and evaporated under reduced pressure to give a white solid (1.12 mg, 2.28 mmol) in a yield of 91% based on the molar amount of ribonucleoside **1** that was used as the starting material. ^{1}H NMR (300 MHz, DMSO-d_6): δ 12.1 (bs, 1H), 11.7 (bs, 1H), 8.29 (s, 1H), 5.90 (d, 1H, J = 7.7 Hz), 5.38 (m, 2H), 4.83 (dd, 1H, J = 7.7, 7.7 Hz), 4.14 (m, 3H), 3.63 (m, 2H), 3.41 (t, 1H, J = 2.4 Hz), 2.77 (m, 2H), 2.76 (sept, 1H, J = 6.7 Hz), 2.56 (m, 2H), 2.13 (s, 3H), 1.12 (d, 6H, J = 6.7 Hz). ^{13}C NMR (75 MHz, DMSO-d_6): δ 206.7, 180.1, 171.7, 154.6, 148.9, 148.4, 137.1, 119.8, 84.1, 83.9, 79.1, 78.7, 77.9, 71.4, 61.0, 57.6, 37.3, 34.7, 29.5, 27.5, 18.7. +ESI-HRMS: Calcd for $C_{22}H_{27}N_5O_8$ $[M + H]^+$, 490.1932, found 490.1935.

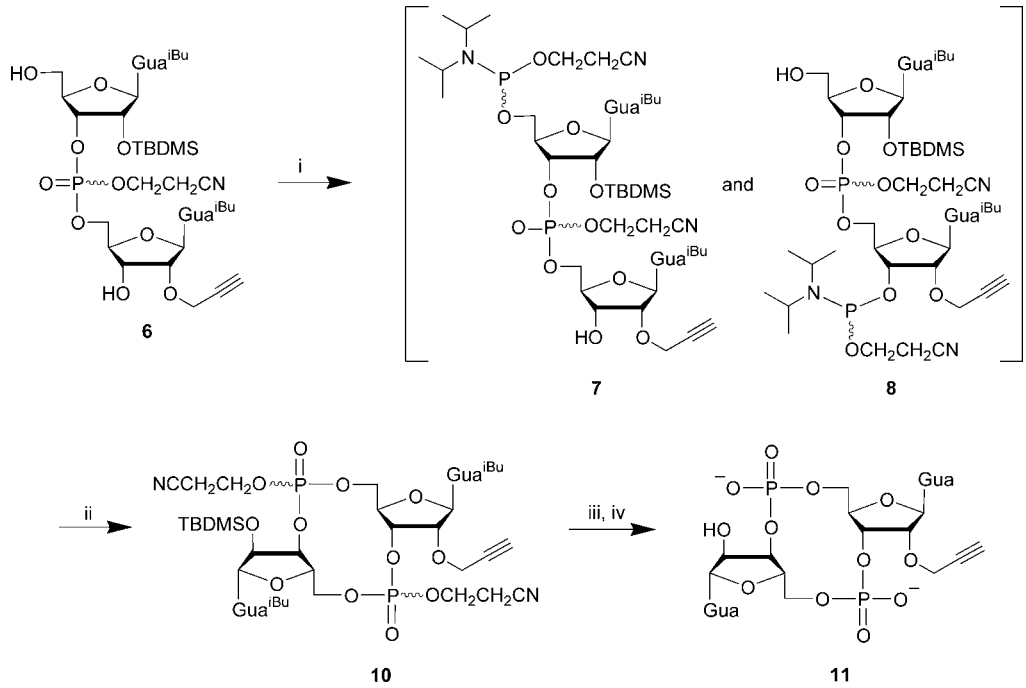
Propargylated Guanylyl(3′-5′)guanosine Phosphotriester 6. To a stirred solution of pre-dried ribonucleoside **3** (970 mg, 2.00 mmol) and phosphoramidite **4** (1.94 g, 2.00 mmol) in anhydrous MeCN (20 mL) was added solid 1*H*-tetrazole (210 mg, 3.00 mmol). ^{31}P NMR analysis of the reaction mixture showed, within 4 h at ∼25 °C, the appearance of two singlets

Scheme 2. Preparation of the Diribonucleoside Phosphotriester 6[a]



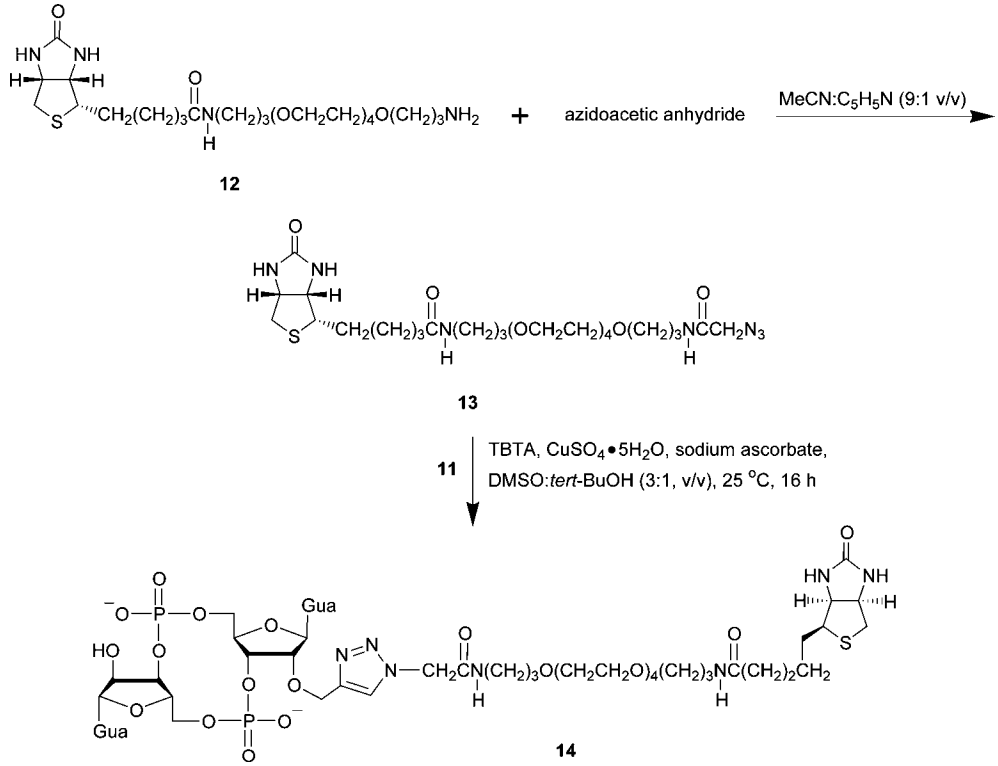
[a] Conditions: (i) **3**, 1*H*-tetrazole, MeCN, 2 h, 25 °C; (ii) *tert*-BuOOH/decane, 30 min; (iii) hydrazine hydrate/AcOH/C_5H_5N, 15 min, then 2,4-pentanedione, 5 min; (iv) chromatography on silica gel; (v) 80% AcOH, 3 h, 25 °C. Keys: DMTr, 4,4′-dimethoxytrityl; Gua, guanin-9-yl; iBu, isobutyryl; TBDMS, *tert*-butyldimethylsilyl; Lev, levulinyl.

Scheme 3. Conversion of the Diribonucleoside Phosphotriester 6 to the Propargylated c-di-GMP 11[a]



[a] Conditions: (i) $(i\text{-}Pr_2N)_2POCH_2CH_2CN$, 1*H*-tetrazole (1.0 equiv at the rate of 0.25 equiv/15 min), MeCN, 3 h; (ii) 1*H*-tetrazole (2 equiv), MeCN, 16 h; (iii) conc aq NH_3, 30 h, 25 °C; (iv) $Et_3N \cdot 3HF$, 20 h, 25 °C. Keys: Gua, guanin-9-yl; iBu, isobutyryl; TBDMS, *tert*-butyldimethylsilyl.

Scheme 4. Biotinylation of the Propargylated c-di-GMP 10[a]



[a] Keys: Gua, guanine-9-yl; TBTA, tris-(benzyltriazolylmethyl)amine.

(δ_P = 140.7 and 139.5 ppm) corresponding to the expected diastereomeric diribonucleoside phosphite triesters **5**. Addition of 5.5 M *tert*-butyl hydroperoxide in decane (730 μL) to the reaction mixture resulted in the conversion of the phosphite triesters to their diastereomeric phosphate triester derivatives within 30 min. The solution was evaporated under vacuum to an oily residue, which was treated with a solution (40 mL) of 0.5 M hydrazine hydrate in pyridine/AcOH (3:2 v/v) for 15 min; 2,4-pentanedione (2 mL) was then added to the solution in order to quench unreacted hydrazine hydrate. The volatiles were removed under reduced pressure, and the reaction product was partitioned between $CHCl_3$ (40 mL) and H_2O (20 mL). The organic phase was collected and evaporated to dryness under vacuum; the remaining material was dissolved in $CHCl_3$ (5 mL) and purified by chromatography on silica gel (~40 g) using a gradient of MeOH (0 → 5%) in $CHCl_3$. Fractions containing the 3′-deprotected dinucleoside phosphate triester were collected and evaporated under low pressure to give a yellowish powder, which was dissolved in of 80% AcOH (15 mL) and left stirring for 3 h at ~25 °C. Hexanes (25 mL) was added to the vigorously stirred reaction mixture in order to extract the 4,4′-dimethoxytrityl alcohol side product. After phase separation, the lower layer was collected and evaporated to dryness under vacuum. The thoroughly dried material was dissolved in CH_2Cl_2 (5 mL), and the solution was added dropwise to stirred hexanes (100 mL). The precipitate was filtered to give the diribonucleoside phosphate triester **6** (2.25 g, 1.76 mmol) as a white solid in a yield of 88% relative to the molar amount of ribonucleoside **3** that was used as starting material. ^{31}P NMR (121 MHz, DMSO-d_6): δ −1.96, −2.38. +ESI-HRMS: Calcd for $C_{40}H_{56}N_{11}O_{14}PSi$ $[M + H]^+$ 974.3588, found 974.3594.

Propargylated c-di-GMP 11. Vacuum-dried propargylated diribonucleoside phosphotriester **6** (973 mg, 1.00 mmol) and 2-cyanoethyl tetraisopropylphosphordiamidite (301 mg, 1.00 mmol) were dissolved in dry MeCN (20 mL) to which was added solid 1*H*-tetrazole (70 mg, 1.0 mmol) in four portions over a period of 1 h under an inert gas atmosphere. The solution was stirred for an additional 2 h at ~25 °C, and 1*H*-tetrazole (140 mg, 2.00 mmol) was then added to the reaction mixture, which was left stirring for 16 h. Without any workup, *tert*-butyl hydroperoxide (5.5 M in decane, 550 μL) was added to the stirred solution. After 30 min, the reaction mixture was concentrated under vacuum to an oil, which was dissolved in $CHCl_3$ (5 mL) and purified by chromatography on silica gel (~30 g). The product eluted from the silica gel column when employing a gradient of MeOH (0 → 8%) in $CHCl_3$. Fractions containing the propargylated c-di-GMP triester **10** were checked by TLC [R_f ($CHCl_3$/MeOH 9:1 v/v) = 0.33], collected, and evaporated under reduced pressure to give a white solid (435 mg, 400 μmol) in a yield of 40%. The purified c-di-GMP triester **10** (109 mg, 100 μmol) was treated with concentrated aqueous ammonia (3 mL) in a sealed glass vial for 30 h at ~25 °C; excess aqueous ammonia was then evaporated to dryness under reduced pressure. The material left was dissolved in neat triethylamine trihydrofluoride (4.00 mL, 24.5 mmol), and the solution was allowed to stir for 20 h at ~25 °C. The fully deprotected product was purified by RP-HPLC using a 5 μm Supelcosil LC-18S column (25 cm × 10 mm) according to the following conditions: starting from 0.1 M triethylammonium acetate pH 7.0, a linear gradient of 2.5% MeCN/min is pumped at a flow rate of 3 mL/min for 40 min. Fractions containing the product were collected and evaporated using a stream of air to give the propargylated c-di-GMP **11** in a near-quantitative yield. ^{1}H NMR (300 MHz, DMSO-d_6): δ 10.78 (bs, 1H), 9.76 (bs, 1H), 8.00 (s, 1H), 7.95 (s, 1H), 6.59 (bs, 4H), 5.85 (d, 1H, J = 4.3 Hz), 5.73 (d, 1H, J = 5.3 Hz), 4.88 (m, 1H), 4.73 (m 1H), 4.58 (t, 1H, J = 4.0 Hz), 4.53 (t, 1H, J = 5.2 Hz), 4.46 (dd, 1H, ^2J = 15.2 Hz, ^4J = 2.3 Hz), 4.38 (dd, 1H, ^2J = 15.2 Hz, ^4J = 2.3 Hz), 4.23−4.06 (m, 4H), 3.91 (m, 2H), 3.43 (t, 1H, ^4J = 2.3 Hz). ^{13}C NMR (75 MHz, DMSO-d_6): δ 156.5, 153.9, 151.1, 150.7, 135.0, 134.7, 116.24, 116.16, 86.5, 85.1, 80.4 (d, J_{C-P} = 9.2 Hz), 80.2 (d, J_{C-P} = 5.7 Hz), 79.7, 78.4, 77.6, 72.6 (d, J_{C-P} = 5.7 Hz), 72.0, 71.0, 62.8 (d, J_{C-P} = 5.7 Hz), 62.5 (d, J_{C-P} = 5.7 Hz), 57.7, 45.4, 8.44. ^{31}P NMR (121 MHz, DMSO-

d_6): δ −0.29, −1.25. +ESI-HRMS: Calcd for $C_{23}H_{26}N_{10}O_{14}P_2$ $[M + H]^+$ 729.1178 found 729.1184.

Biotinylated Azide 13. To a solution of commercial *N*-D-(+)-biotinyl-4,7,10,13,16-pentaoxa-1,19-diaminononadecane (**12**, 50 mg, 94 μmol) in 1 mL of MeCN/C_5H_5N (9:1 v/v) was added azidoacetic anhydride (35 mg, 0.19 mmol). The solution was stirred at ~25 °C for 1 h and was then concentrated to an oil using a stream of argon. The crude product was purified by chromatography on silica gel (2 g) using a gradient of MeOH (0−10%) in $CHCl_3$. Fractions containing the product were collected and evaporated under vacuum to give **13** as a solid (35 mg, 57 μmol, 61%). +ESI-HRMS: Calcd for $C_{26}H_{47}N_7O_8S$ $[M + H]^+$ 618.3280, found 618.3283.

Biotinylated c-di-GMP 14. To the propargylated c-di-GMP **11** (150 OD_{260}) was added a solution of 10 mM biotinylated azide **13** (800 μL), 100 mM $CuSO_4$ (120 μL), and 100 mM *tris*-(benzyltriazolylmethyl)amine (TBTA, 240 μL), each in DMSO/*tert*-BuOH (3:1 v/v). A solution of 400 mM sodium ascorbate in H_2O (175 μL) was then added to the reaction mixture, which was left stirring at ~25 °C for 16 h. The crude reaction product was purified by RP-HPLC under conditions identical to those described for the purification of the propargylated c-di-GMP **11**. Fractions containing the product were collected and evaporated under a stream of air to give the biotinylated c-di-GMP **14** (93 OD_{260}) in an isolated yield of 62%. ^{31}P NMR (121 MHz, D_2O): δ −1.73, −2.06. +ESI-HRMS: Calcd for $C_{49}H_{73}N_{17}O_{22}P_2S$ $[M + H]^+$ 1346.4385, found 1346.4429; $[M + 2H]^{2+}$ 673.7229, found 673.7229.

RESULTS AND DISCUSSION

Our solution-phase approach to the synthesis of the biotinylated c-di-GMP conjugate **14** began with the preparation of the ribonucleoside building block **3** (Scheme 1) from the commercially available propargylated ribonucleoside **1**, which was 3′-*O*-acylated by treatment with levulinic anhydride (*20*, *21*) in dry pyridine. After extractive workup, the fully protected ribonucleoside **2** was treated with 80% AcOH in order to remove the 5′-DMTr group. The 5′-deprotected ribonucleoside was purified by chromatography on silica gel to give pure **3** in a yield of 91%. The ribonucleoside was characterized by ^{1}H and ^{13}C NMR spectroscopies and by high-resolution mass spectrometry (HRMS).

The commercial availability of the 2′-*O*-*tert*-butyldimethylsilyl (TBDMS) ribonucleoside phosphoramidite **4** (Scheme 2) and the pervasive use of the click chemistry for labeling nucleosides and oligonucleotides with fluorophores, carbohydrates, and other functional groups (*22*, *23*) have been motivational in the development of our synthetic approach to the synthesis of **14**. Indeed, the reaction of **4** with the 5′-hydroxyl function of ribonucleoside **3** in the presence of 1.5 molar equiv of 1*H*-tetrazole in anhydrous MeCN produced the dinucleoside phosphate triester **5** (Scheme 2). After *P*(III) oxidation by *tert*-butyl hydroperoxide and upon concentration of the reaction mixture to an oil, a solution of hydrazine hydrate in pyridine and acetic acid was added in order to remove the levulinyl group from the terminal 3′-hydroxyl of the diribonucleoside phosphate triester. The hydrazinolysis reaction was stopped by the addition of 2,4-pentanedione, and following an extractive workup, the reaction product was purified by silica gel chromatography. The 5′-DMTr group of the purified material was then cleaved under acidic conditions (80% AcOH) to give, after workup and precipitation from hexanes, the propargylated diribonucleoside phosphate triester **6** in a yield of 88% relative to the molar amount of ribonucleoside building block **3** that was used as the starting material. This yield is excellent given that out of four synthetic operations only one purification step was performed. The dinucleoside phosphotriester **6** was characterized, as a mixture of two

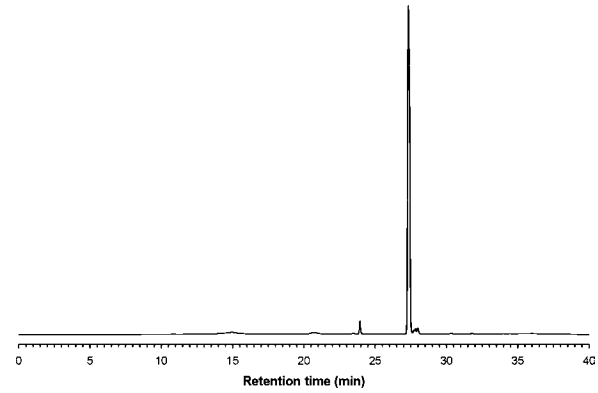


Figure 1. RP-HPLC analysis of the guanylyl(3′-5′)guanosine phosphotriester **6**. Analytical chromatographic conditions are described in the Supporting Information under Materials and Methods. Peak heights were normalized to the highest peak, which was set to 1 arbitrary unit.

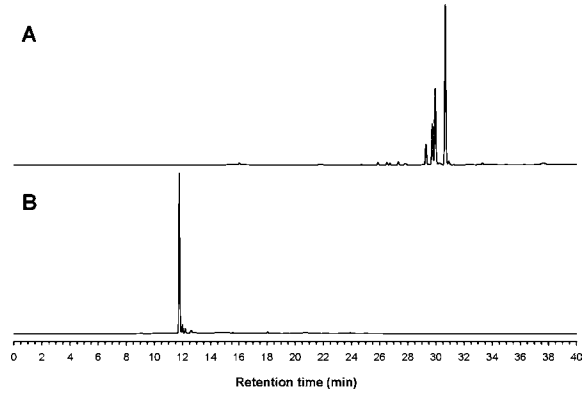


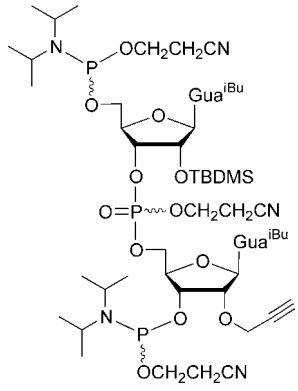
Figure 2. RP-HPLC analysis of the conversion of the propargylated c-di-GMP triester **10** to the propargylated c-di-GMP **11**. (A) Chromatogram of the silica gel-purified propargylated c-di-GMP triester **10**. (B) Chromatogram of the propargylated c-di-GMP **11** that was obtained from silica gel-purified **10** after complete deprotection, which was effected by treatment with (i) concentrated aqueous ammonia for 30 h at 25 °C and (ii) triethylamine trihydrofluoride for 20 h at 25 °C. Analytical chromatographic conditions are described in the Supporting Information under Materials and Methods. Peak heights were normalized to the highest peak, which was set to 1 arbitrary unit.

P-diastereomers, by ^{31}P NMR spectroscopy and HRMS (see Experimental Procedures section). The purity of **6** was assessed by RP-HPLC (Figure 1) and was determined to be 95%.

The preparation of the propargylated and fully protected c-di-GMP derivative **10** (Scheme 3) was carried out in MeCN by the phosphitylation of **6** with strictly 1 mol equiv of 2-cyanoethyl tetraisopropylphosphordiamidite and solid 1*H*-tetrazole, which was added at the rate of 0.25 mol equiv per 15 min under rigorously anhydrous conditions. Such a stoichiometry presumably favored the formation of the 5′-phosphoramidite **7** relative to that of the 3′-phosphoramidite **8** and 3′,5′-bis-phosphoramidite **9**, the formation of which cannot conclusively be ruled out. The intramolecular cyclization of **7** and **8** was then performed by adding two molar equivalents of solid 1*H*-tetrazole to the initial phosphitylation reaction mixture. The concentration of the reagents, with the exception of 1*H*-tetrazole, was sufficiently low (~50 mM) to favor intramolecular cyclization rather than intermolecular polymerization. The intramolecular cyclization reaction was allowed to proceed overnight (16 h) and was followed by the addition of a solution of *tert*-butyl hydroperoxide in decane in order to convert the newly formed phosphite triester function to its tetracoordinated phosphate triester state and complete the synthesis of **10**. The crude product was purified by chromatography on silica gel to give an amorphous white

solid in a yield of 40% based on the starting propargylated dinucleoside phosphate triester **6**.

The modest yield of intramolecular cyclization may be attributed to a number of factors. The use of only 1 mol equiv of 2-cyanoethyl tetraisopropylphosphordiamidite is necessary to minimize if not prevent the formation of **9**, which otherwise would result in a commensurate loss of cyclic product in addition to residual unphosphitylated **6**. Perhaps the most important factor contributing to a lower yield of **10** may be related to the presence of adventitious water in a relatively large volume of MeCN, which would lead to hydrolysis of the 1*H*-tetrazole-activated phosphoramidite functions of **7** and **8** and prevent intramolecular cyclization. However, these limitations, which are inherent to our approach to the synthesis of **10**, are clearly outweighed by the simplicity and convenience of the method.



9

RP-HPLC analysis of **10** revealed the expected presence of four diastereomers, two for each chiral phosphate function (Figure 2A). The asymmetry of **10** in addition to the chirality of its two tetracoordinated phosphate esters contributed to the complexity of its ^{1}H, ^{13}C, and ^{31}P NMR spectra. Indeed, the proton-decoupled ^{31}P NMR analysis of **10**, which revealed six out of theoretically eight signals, underscores the challenging characterization of **10** by spectroscopic techniques. In order to mitigate this difficulty, the strategy of converting **10** to the c-di-GMP **11** was adopted. Complete deprotection of **10** consisted of removing the N^2-isobutyryl and 2-cyanoethyl phosphate protecting groups first by treatment with concentrated aqueous ammonia in a sealed glass vial over a period of 30 h at ambient temperature. Lastly, the cleavage of the 2′-*O*-TBDMS group was effected by reaction with triethylamine trihydrofluoride to give, nearly quantitatively, the propargylated c-di-GMP **11**, as judged by RP-HPLC analysis of the deprotection reaction (Figure 2B). This analysis also revealed the purity of **11**, which was determined to be 95%. The propargylated c-di-GMP **11** was adequately characterized by ^{1}H, ^{13}C, and ^{31}P NMR spectroscopies and HRMS (see Experimental Procedures section).

The preparation of the biotinylated azide **13** was required for the biotinylation of **11** (Scheme 4). Acylation of the commercial aminoalkylated biotin derivative **12** with azidoacetic anhydride in a solution of 10% pyridine in MeCN over a period of 1 h at ambient temperature afforded **13** in moderate yield after purification. Azidoacetic anhydride was generated in situ from azidoacetic acid and *N*,*N*′-dicyclohexylcarbodiimide in THF under conditions similar to those employed for the preparation of levulinic anhydride (*20*, *21*). Azidoacetic acid was prepared from the reaction of bromoacetic acid and sodium azide, as described in the literature (*24*). Given the inherent complexity of the ^{1}H and ^{13}C NMR spectra of biotinylated azide **13**, its characterization by HRMS was found to be the most informative.

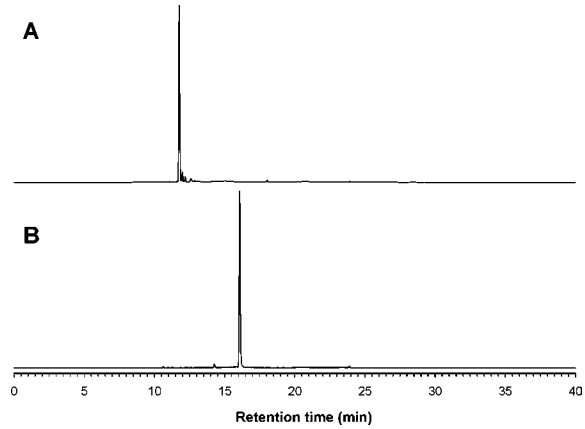


Figure 3. RP-HPLC analysis of the "click" conjugation of the propargylated c-di-GMP **11** with the biotinylated azide **13**. (A) Chromatogram of the propargylated c-di-GMP **11**. (B) Chromatogram of the purified biotinylated c-di-GMP **14** obtained from "click" conjugation of **11** with **13** under the conditions described in the Experimental Procedures section. Analytical chromatographic conditions are described in the Supporting Information under Materials and Methods. Peak heights were normalized to the highest peak, which was set to 1 arbitrary unit.

The copper(I)-catalyzed [3 + 2] cycloaddition of **13** with the propargylated c-di-GMP **11** was performed essentially as reported by Berndl et al. (*25*). The biotinylated c-di-GMP **14** was purified by RP-HPLC and was isolated in a yield of 62%, which is based on the molar amount of **11** used as the starting material. Figure 3 illustrates the "click" conjugation of the biotinylated azide **13** with the propargylated c-di-GMP **11.**

CONCLUSION

The synthetic strategy for the synthesis of the propargylated c-di-GMP **10** reported herein is based on the use of commercial starting materials including the propargylated ribonucleoside **1** and the 2′-*O*-TBDMS ribonucleoside phosphoramidite **4**. The absence of a vicinal hydroxyl function in **4** precluded the notorious migration of the TBDMS group (*26*) and formation of any isomeric side product when using this reagent. Phosphitylation of the propargylated diribonucleoside phosphate triester **6** when employing only 1 mol equiv of commercial 2-cyanoethyl tetraisopropylphosphordiamidite led to the formation of **10**, for the first time through exclusively phosphoramidite chemistry. The yield of **10** is perhaps lower than those reported using other cyclization procedures, but the convenience and simplicity of our synthetic strategy prevail over other preparative synthetic approaches in terms of the availability of starting materials, minimization of potential side reactions, and number of necessary purification steps. As mentioned above, the biological implications of the biotinylated c-di-GMP **14**, in regard to identification and characterization of the proteins recognizing and binding to c-di-GMP, are currently being investigated and may provide valuable insight into their signaling pathways and bioactivity in prokaryotes and eukaryotes. The results of these studies are beyond the scope of this report and will be communicated elsewhere. In this context, our straightforward approach to the synthesis of the propargylated c-di-GMP **11** is being exploited in the preparation of structural analogues of **11** having either one or two (2′-5′)phosphodiester linkages instead of the native (3′-5′)phosphodiester functions in order to assess whether their biotinylated conjugates may permit the identification of proteins that may or may not be similar to those associated with the recognition and binding of **11**. This work is again based on the commercial availability of both the 3′-*O*-propargylated and 3′-*O*-TBDMS isomers of ribonucleoside **1**

and ribonucleoside phosphoramidite **4**, respectively. The results of these studies will be reported in due course.

ACKNOWLEDGMENT

This work was supported in part by NIH grants R21 ES016835 and RO1 AI058211 (C.S.).

Supporting Information Available: Materials and methods; ^{1}H and ^{13}C NMR spectra of the propargylated ribonucleoside **3** and c-di-GMP **11**; ^{31}P NMR spectra of the propargylated guanylyl(3′-5′)guanosine phosphotriester **6**, fully protected c-di-GMP **10**, c-di-GMP **11** and biotinylated c-di-GMP **14**; mass spectra of **3**, **6**, **11**, **13**, and **14**; TLC analysis of **10** and detailed preparations of levulinic anhydride and azidoacetic anhydride. This material is available free of charge via the Internet at http://pubs.acs.org.

LITERATURE CITED

(1) Ross, P., Weinhouse, H., Aloni, Y., Michaeli, D., Weinberger-Ohana, P., Mayer, R., Braun, S., de Vroom, E., van der Marel, G. A., van Boom, J. H., and Benziman, M. (1987) Regulation of cellulose synthesis in *Acetobacter xylinum* by cyclic diguanylic acid. *Nature 325*, 279–281.

(2) Hengge, R. (2009) Principles of c-di-GMP signalling in bacteria. *Nat. Rev. Microbiol. 7*, 263–273.

(3) Yan, H., and Chen, W. (2010) 3′,5′-Cyclic diguanylic acid: a small nucleotide that makes big impacts. *Chem. Soc. Rev. 39*, 2914–2924.

(4) Karaolis, D. K. R., Means, T. K., Yang, D., Takahashi, M., Yoshimura, T., Muraille, E., Philpott, D., Schroeder, J. T., Hyodo, M., Hayakawa, Y., Talbot, B. G., Brouillette, E., and Malouin, F. (2007) Bacterial c-di-GMP is an immunostimulatory molecule. *J. Immunol. 178*, 2171–2181.

(5) McWhirter, S. M., Barbalat, R., Monroe, K. M., Fontana, M. F., Hyodo, M., Joncker, N. T., Ishii, K. J., Akira, S., Colonna, M., Chen, Z. J., Fitzgerald, K. A., Hayakawa, Y., and Vance, R. E. (2009) A host type I interferon response is induced by cytosolic sensing of the bacterial second messenger cyclic-di-GMP. *J. Exp. Med. 206*, 1899–1911.

(6) Woodward, J. J., Iavarone, A. T., and Portnoy, D. A. (2010) c-di-AMP secreted by intracellular *Listeria monocytogenes* activates a host type I interferon response. *Science 328*, 1703–1705.

(7) Ross, P., Mayer, R., Weinhouse, H., Amikam, D., Huggirat, Y., Benziman, M., de Vroom, E., Fidder, A., de Paus, P., Sliedregt, L. A. J. M., van der Marel, G. A., and van Boom, J. H. (1990) The cyclic diguanylic acid regulatory system of cellulose synthesis in *Acetobacter xylinum*. *J. Biol. Chem. 265*, 18933–18943.

(8) Amiot, N., Heintz, K., and Giese, B. (2006) New approach for the synthesis of c-di-GMP and its analogues. *Synthesis* 4230–4236.

(9) Hayakawa, Y., Nagata, R., Hirata, A., Hyodo, M., and Kawai, R. (2003) A facile synthesis of cyclic bis(3′→5′)diguanylic acid. *Tetrahedron 59*, 6465–6471.

(10) Kawai, R., Nagata, R., Hirata, A., and Hayakawa, Y. (2003) A new synthetic approach to cyclic bis(3′→5′)diguanilic acid. *Nucleic Acids Res. Suppl. 3*, 103–104.

(11) Hyodo, M., and Hayakawa, Y. (2004) An improved method for synthesizing cyclic bis(3′-5′)diguanylic acid (c-di-GMP). *Bull. Chem. Soc. Jpn. 77*, 2089–2093.

(12) Hyodo, M., Sato, Y., and Hayakawa, Y. (2006) Synthesis of cyclic bis(3′-5′)diguanylic acid (*c*-di-GMP) analogs. *Tetrahedron 62*, 3089–3094.

(13) Zhang, Z., Gaffney, B. L., and Jones, R. A. (2004) c-di-GMP displays a monovalent metal ion-dependent polymorphism. *J. Am. Chem. Soc. 126*, 16700–16701.

(14) Humes, E., and Yan, H. (2006) Convenient synthesis of 3′,5′-cyclic diguanylic acid (cdiGMP). *Nucleic Acids Symp. Ser. 50*, 5–6.

(15) Yan, H., and López Aguilar, A. (2007) Synthesis of 3′,5′-cyclic diguanylic acid (cdiGMP) using 1-(4-chlorophenyl)-4-ethoxypiperidin-4-yl as a protecting group for 2′-hydroxy functions of ribonucleosides. *Nucleosides, Nucleotides Nucleic Acids 26*, 189–204.

(16) Rao, F., Pasunooti, S., Ng, Y., Zhuo, W., Lim, L., Liu, A. W., and Liang, Z.-X. (2009) Enzymatic synthesis of c-di-GMP using a thermophilic diguanylate cyclase. *Anal. Biochem. 389*, 138–142.

(17) Kiburu, I., Shurer, A., Yan, L., and Sintim, H. O. (2008) A simple solid-phase synthesis of the ubiquitous bacterial signaling molecule, c-di-GMP and analogues. *Mol. BioSyst. 4*, 518–520.

(18) Rostovtsev, V. V., Green, L. G., Fokin, V. V., and Sharpless, K. B. (2002) A stepwise Huisgen cycloaddition process: Copper(I)-catalyzed regioselective "ligation" of azides and terminal alkynes. *Angew. Chem., Int. Ed. 41*, 2596–2599.

(19) Tornøe, C. W., Christensen, C., and Meldal, M. (2002) Peptidotriazoles on solid phase: [1,2,3]-triazoles by regiospecific copper(I)-catalyzed 1,3-dipolar cycloadditions of terminal alkynes to azides. *J. Org. Chem. 67*, 3057–3064.

(20) Hassner, A., Strand, G., Rubinstein, M., and Patchornik, A. (1975) Levulinic esters. Alcohol protecting group applicable to some nucleosides. *J. Am. Chem. Soc. 97*, 1614–1615.

(21) Guo, Z., and Xue, J. (2009) *Levulinic anhydride. Encyclopedia of Reagents for Organic Synthesis*, 2nd ed. (Paquette, L. A., Crich, D., Fuchs, P. L., and Molander, G., Eds.) pp 5961−5963, John Wiley & Sons, Hoboken, NJ.

(22) El-Sagheer, A. H., and Brown, T. (2010) Click chemistry with DNA. *Chem. Soc. Rev. 39*, 1388–1405, and references therein.

(23) Gramlich, P. M. E., Wirges, C. T., Manetto, A., and Carell, T. (2008) Postsynthetic DNA modification through the copper-catalyzed azide-alkyne cycloaddition reaction. *Angew. Chem., Int. Ed. 47*, 8350–8358, and references therein.

(24) Dyke, J. M., Groves, A. P., Morris, A., Ogden, J. S., Dias, A. A., Oliveira, A. M. S., Costa, M. L., Barros, M. T., Cabral, M. H., and Moutinho, A. M. C. (1997) Study of the thermal decomposition of 2-azidoacetic acid by photoelectron and matrix isolation infrared spectroscopy. *J. Am. Chem. Soc. 119*, 6883–6887.

(25) Berndl, S., Herzig, N., Kele, P., Lachmann, D., Li, X., Wolfbeis, O. S., and Wagenknecht, H.-A. (2009) Comparison of a nucleosidic vs non-nucleosidic postsynthetic "Click"modification of DNA with base-labile fluorescent probes. *Bioconjugate Chem. 20*, 558–564.

(26) Beaucage, S. L., and Reese, C. B. (2009) *Recent Advances in the Chemical Synthesis of RNA. Current Protocols in Nucleic Acid Chemistry*. (Beaucage, S. L., Bergstrom, D. E., Herdewijn, P., Matsuda, A., Eds.) pp 2.16.1−2.16.31, Chapter 2, Vol. 1,John Wiley & Sons, Hoboken, NJ.

BC1003857

Supporting Information Available

Convenient Synthesis of a Propargylated Cyclic (3'-5') Diguanylic Acid and its "Click" Conjugation to a Biotinylated Azide

Andrzej Grajkowski,[*,‡] *Jacek Cieślak,*[‡] *Alexei Gapeev,*[§] *Christian Schindler*[†] *and Serge L. Beaucage*[‡]

[‡]Division of Therapeutic Proteins, Center for Drug Evaluation and Research, Food and Drug Administration, 8800 Rockville Pike, Bethesda, Maryland 20892, and [†]Department of Microbiology & Immunology, Columbia University, 701 W. 168th St., New York, New York 10032, and [§]Department of Chemistry and Biochemistry, University of Maryland, Baltimore County, 1000 Hilltop Circle, Baltimore, Maryland 21250

Table of Contents

Materials and Methods……..S02
Preparation of levulinic anhydride……S02
Preparation of azidoacetic anhydride……S02
Figure S1. 300 MHz ^{1}H NMR spectrum of N^2-Isobutyryl-3'-*O*-levulinyl-2'-*O*-propargylguanosine (**3**) in DMSO-d_6…….....S03
Figure S2. 75 MHz ^{13}C NMR spectrum of N^2-Isobutyryl-3'-*O*-levulinyl-2'-*O*-propargylguanosine (**3**) in DMSO-d_6…….....S03
Figure S3. 121 MHz ^{31}P NMR spectrum of the propargylated guanylyl (3'-5')guanosine phosphotriester **6** in DMSO-d_6……..S04
Figure S4. 121 MHz ^{31}P NMR spectrum of the propargylated c-di-GMP **10** in MeCN……. S04
Figure S5. TLC analysis of the propargylated c-di-GMP **10** on silica gel…….. S05
Figure S6. 121 MHz ^{31}P NMR spectrum of the propargylated c-di-GMP **11** in DMSO-d_6…… S05
Figure S7. 300 MHz ^{1}H NMR spectrum of the propargylated c-di-GMP **11** in DMSO-d_6…….S06
Figure S8. 75 MHz ^{13}C NMR spectrum of the propargylated c-di-GMP **11** in DMSO-d_6……..S06
Figure S9. 121 MHz ^{31}P NMR spectrum of the biotinylated c-di-GMP **14** in D_2O…… S07
Figure S10. Low resolution mass spectrum of N^2-isobutyryl-3'-*O*-levulinyl-2'-*O*-propargylguanosine (**3**)…… S08
Figure S11. High resolution mass spectrum of the propargylated guanylyl (3'-5')guanosine phosphotriester **6**…….....S09
Figure S12. High resolution mass spectrum of the propargylated c-di-GMP **11**…….S10
Figure S13. Low resolution mass spectrum of the biotinylated azide **13**…… S11
Figure S14. High resolution mass spectrum of the biotinylated c-di-GMP **14**…….S12

Materials and Methods. Common chemicals and solvents in addition to bromoacetic acid, DMSO, *tert*-butanol, tripropargyl amine, benzyl azide, sodium azide, levulinic acid, hydrazine hydrate, 2,4-pentanedione, 1,3-dicyclohexycarbodiimide, pyridine, triethylamine trihydrofluoride, 2-cyanoethyl tetraisopropylphosphordiamidite, 1*H*-tetrazole, 5.5 M *tert*-butyl hydroperoxide in decane, tetrakis(acetonitrile)copper(I) hexafluorophosphate, copper(II) sulfate pentahydrate, sodium ascorbate, and concentrated aqueous ammonia were all purchased from commercial sources and used without further purification. Azidoacetic acid was prepared from the reaction of bromoacetic acid and sodium azide as described by Dyke, J. M. et al. (*J. Am. Chem. Soc.* **1997**, *119*, 6883-6887). *Tris*(benzyltriazolylmethyl)amine was prepared as reported by Chan, T. R. et al. (*Org. Lett*. **2004**, *6*, 2853-2855). N^2-isobutyryl-5'-*O*-(4,4'-dimethoxytrityl)-2'-*O*-propargyl guanosine, N^2-isobutyryl-5'-*O*-(4,4'-dimethoxytrityl)-2'-*O*-*tert*-butyldimethylsilyl-3'-*O*-[(2-cyanoethoxy)-*N*,*N*-diisopropylamino]phosphinyl guanosine, *N*-D(+)-biotinyl-4,7,10,13,16-pentaoxa-1,19-diaminononadecane, anhydrous solvents (MeCN, CH_2Cl_2, C_6H_6, pyridine, THF) and deuterated solvents (C_6D_6, D_2O, DMSO-d_6) were obtained from reputable sources and used as received.

Flash chromatography purifications were performed on glass columns (0.6 and 2.5 cm I.D.) packed with silica gel 60 (230-400 mesh), whereas analytical thin-layer chromatography (TLC) analyses were conducted on 2.5 cm × 7.5 cm glass plates coated with a 0.25 mm thick layer of silica gel 60 F_{254}.

Analytical RP-HPLC analyses were performed using a 5 μm Supelcosil LC-18S column (25 cm × 4.6 mm) according to the following conditions: starting from 0.1 M triethylammonium acetate pH 7.0, a linear gradient of 2.5% MeCN/min is pumped at a flow rate of 1 mL/min for 40 min. Preparative RP-HPLC purifications were performed using a 5 μm Supelcosil LC-18S column (25 cm × 10 mm) according to the following conditions: starting from 0.1 M triethylammonium acetate pH 7.0, a linear gradient of 2.5% MeCN/min is pumped at a flow rate of 3 mL/min for 40 min. 2 M Triethylammonium acetate buffer was purchased from Applied Biosystem and diluted to 0.1 M with HPLC grade water prior to use.

All NMR experiments were performed using a spectrometer at the field of 300.13, 75.47 and 121.5 MHz for one-dimensional ^{1}H, ^{1}H-decoupled ^{13}C and ^{1}H-decoupled ^{31}P, respectively. Samples were maintained at a temperature of 298 ºK. All spectra were recorded in deuterated solvents or as indicated and chemical shifts δ were reported in parts per million (ppm) relative to appropriate internal references.

High resolution mass spectra used to confirm the elemental composition of compounds **3**, **6**, **11**, **13** and **14** were obtained on a Bruker Daltonics ApexQ FT-ICR mass spectrometer equipped with a 12 T magnet. Electrospray ionization in positive ion mode was used to generate $[M+H]^+$ and $[M+Na]^+$ ions out of test samples (0.01 mg dissolved in 1 mL of 10 mM ammonium acetate in MeCN:H_2O (1:1 v/v)). Spectra were externally calibrated using 0.5 mg/mL solution of CsI in water, which yielded a series of peaks in the mass range used for analysis (200-2000 m/z).

Preparation of levulinic anhydride. To a solution of levulinic acid (3.5 g, 30 mmol) in anhydrous THF (100 mL) was added 1,3-dicyclohexylcarbodiimide (32 g, 15 mmol). The reaction mixture was stirred for 5 h at ~25 ºC and was then filtered in order to remove the solid 1,3-dicyclohexylurea side product. The filtrate was evaporated under reduced pressure. The material left was isolated in near quantitative yield and was used without further purification in the acylation of **1**.

Preparation of azidoacetic anhydride. To a solution of azidoacetic acid acid (202 mg, 2.00 mmol) in anhydrous THF (3 mL) was added 1,3-dicyclohexylcarbodiimide (206 mg, 1.00 mmol). The reaction mixture was stirred for 5 h at ~25 ºC and was then processed as described above for the preparation of levulinic anhydride. Azidoacetic anhydride was isolated in near quantitative yield and was used without further purification in the acylation of **12**.

Figure S1. 300 MHz ^{1}H NMR spectrum of N^2-isobutyryl-3'-*O*-levulinyl-2'-*O*-propargyl guanosine (3) in DMSO-d_6

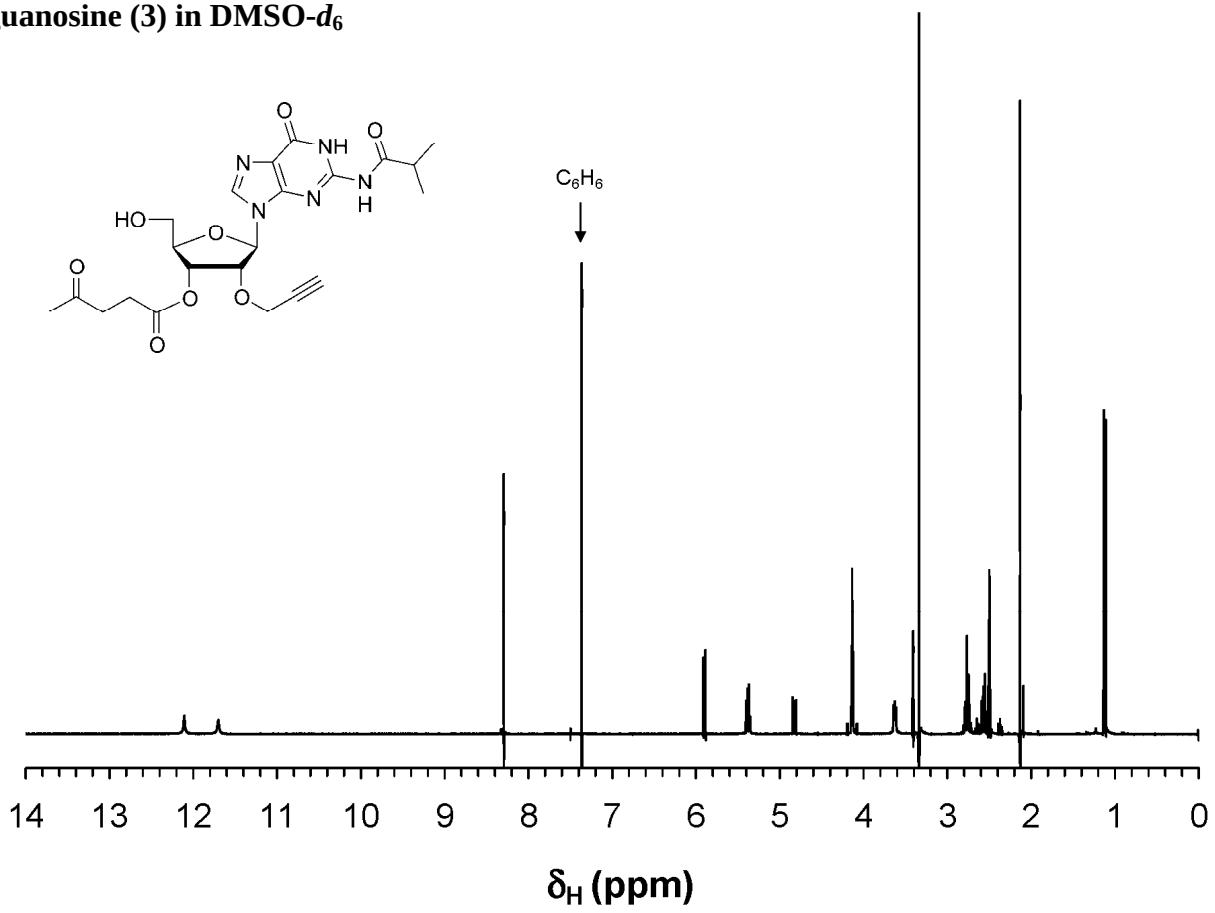


Figure S2. 75 MHz ^{13}C NMR spectrum of N^2-Isobutyryl-3'-*O*-levulinyl-2'-*O*-propargyl guanosine (3) in DMSO-d_6

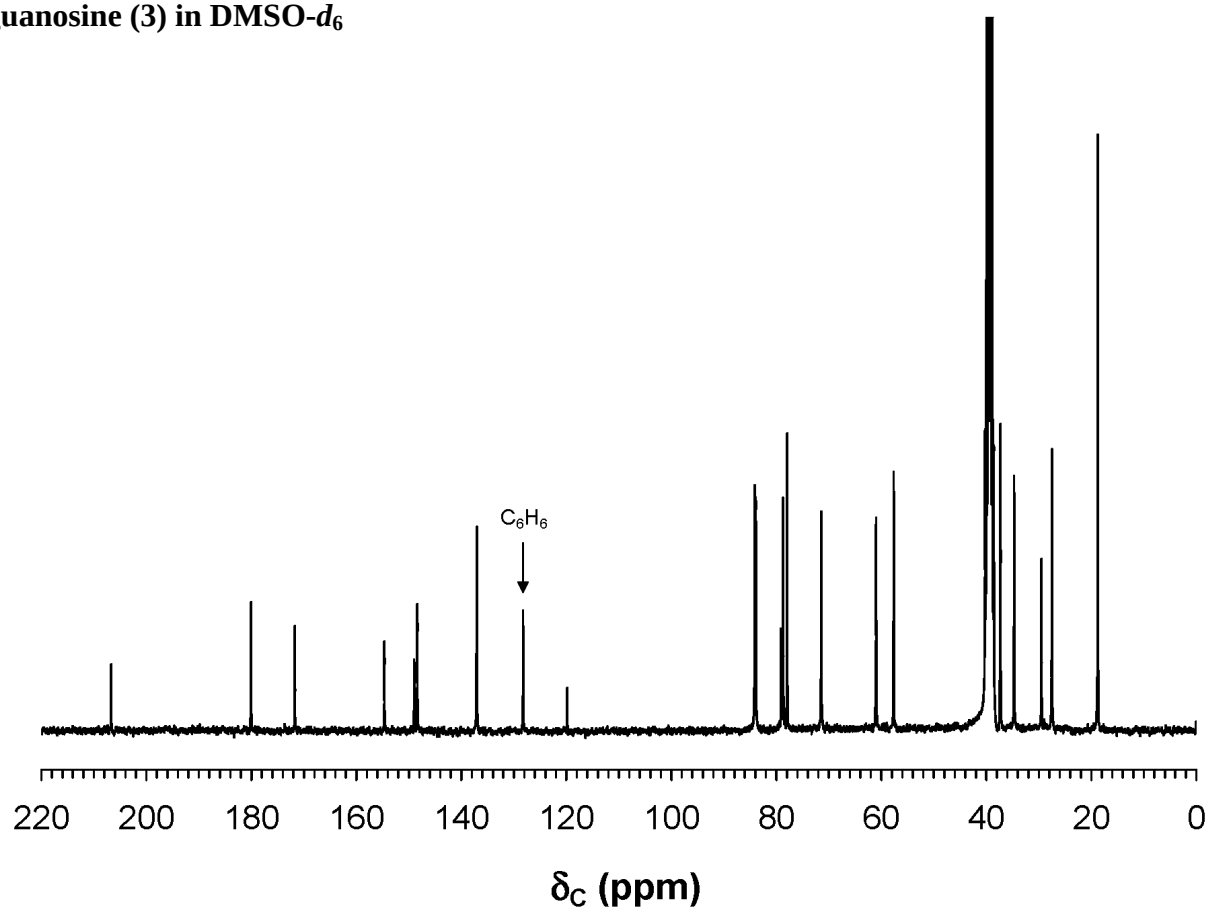


Figure S3. 121 MHz ^{31}P NMR spectrum of the propargylated guanylyl(3'-5')guanosine phosphotriester 6 in DMSO-d_6

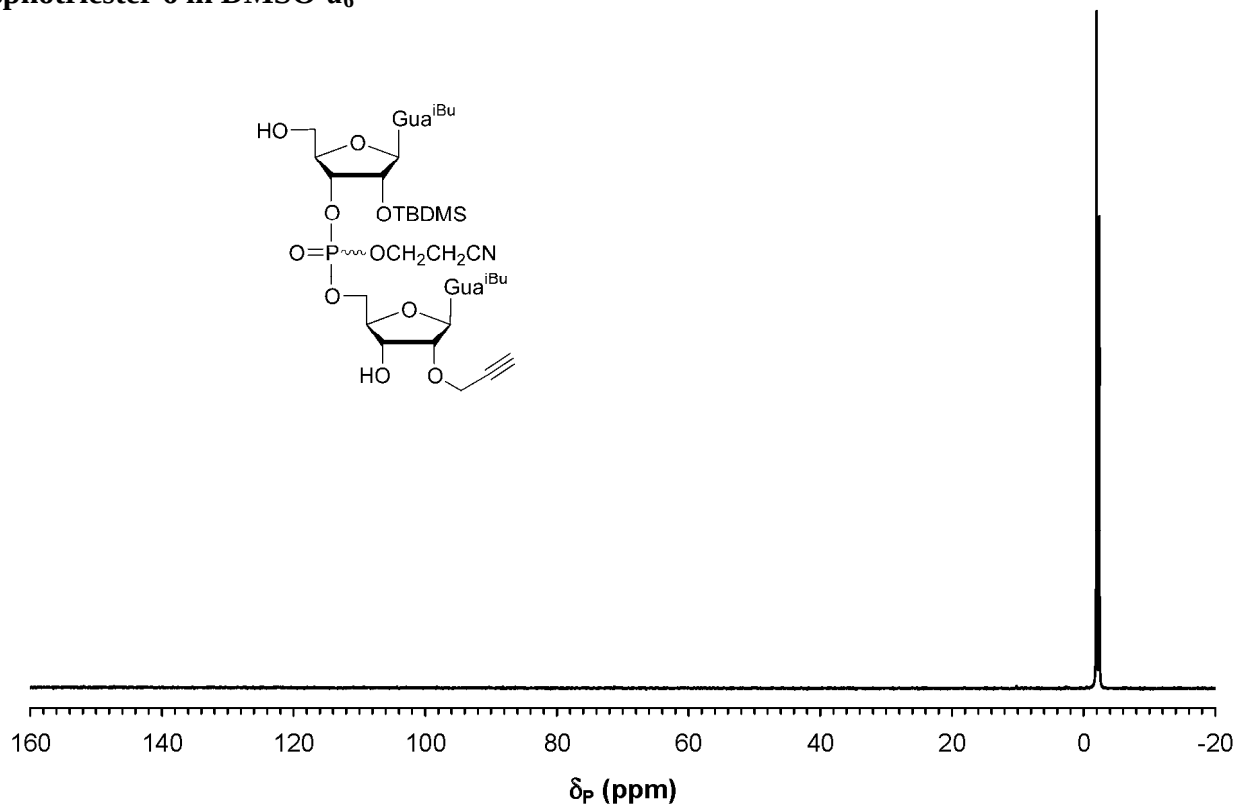


Figure S4. 121 MHz ^{31}P NMR spectrum of the silica gel-purified propargylated c-di-GMP 10 in MeCN

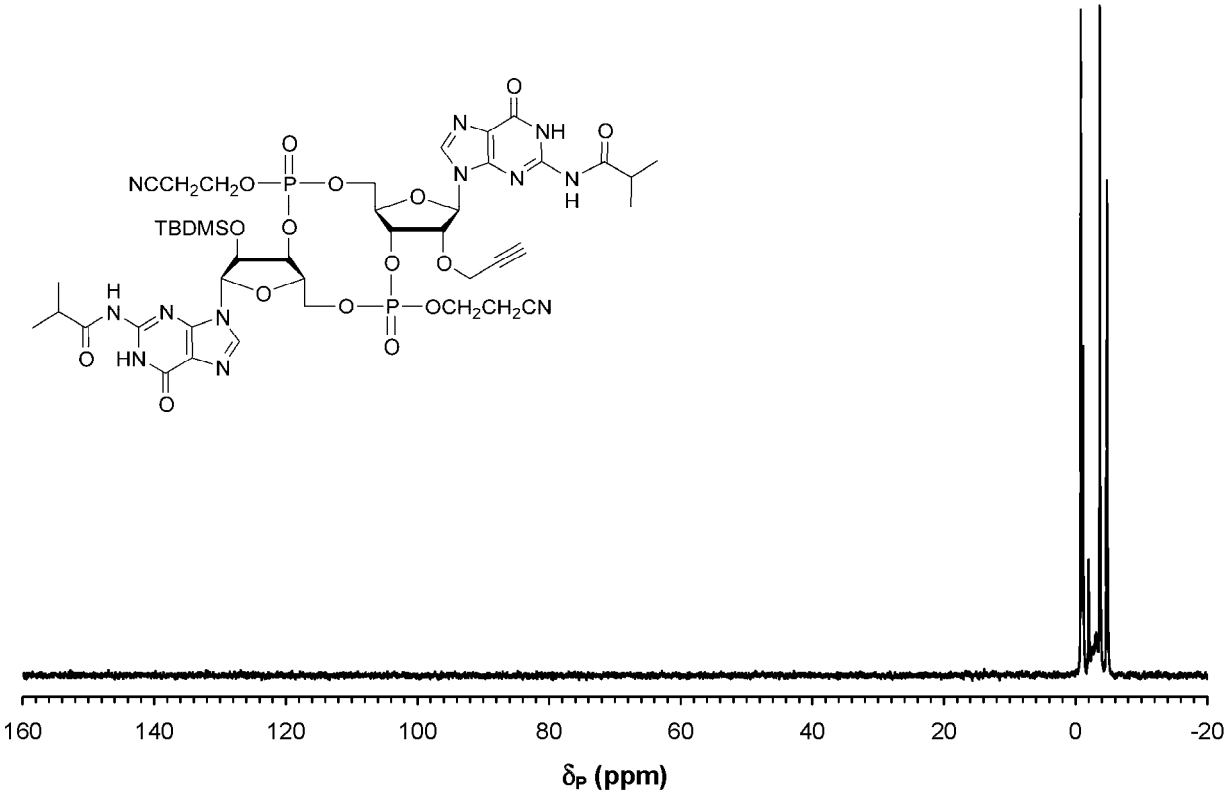
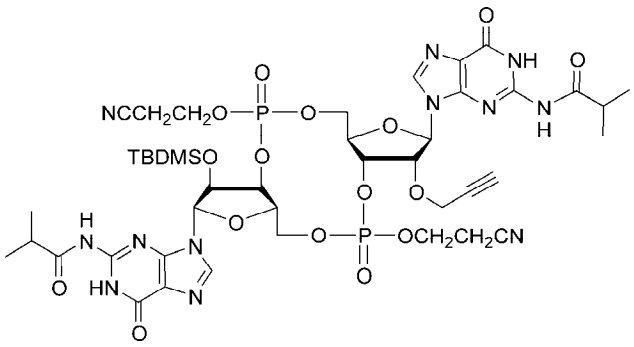


Figure S5. TLC analysis of the propargylated c-di-GMP 10 on silica gel.



R_f [$CHCl_3$:MeOH (9:1 v/v)] = 0.33

UV detection (~254 nm)

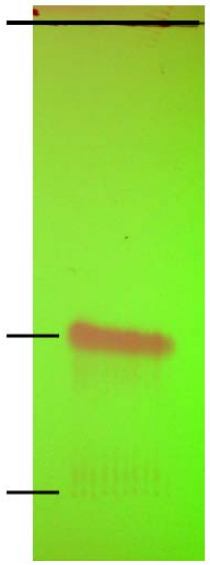


Figure S6. 121 MHz ^{31}P NMR spectrum of the propargylated c-di-GMP 11 in DMSO-d_6

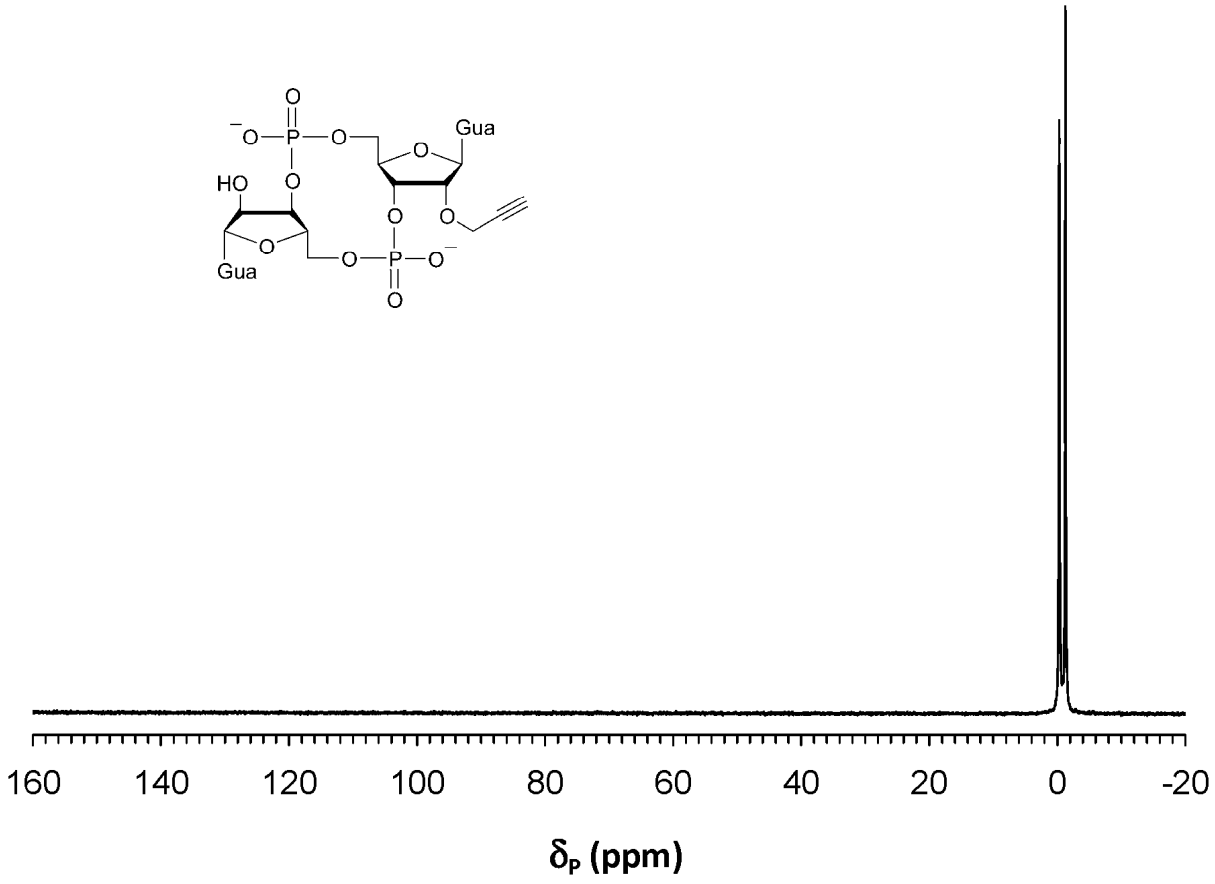


Figure S7. 300 MHz ^{1}H NMR spectrum of the propargylated c-di-GMP 11 in DMSO-d_6

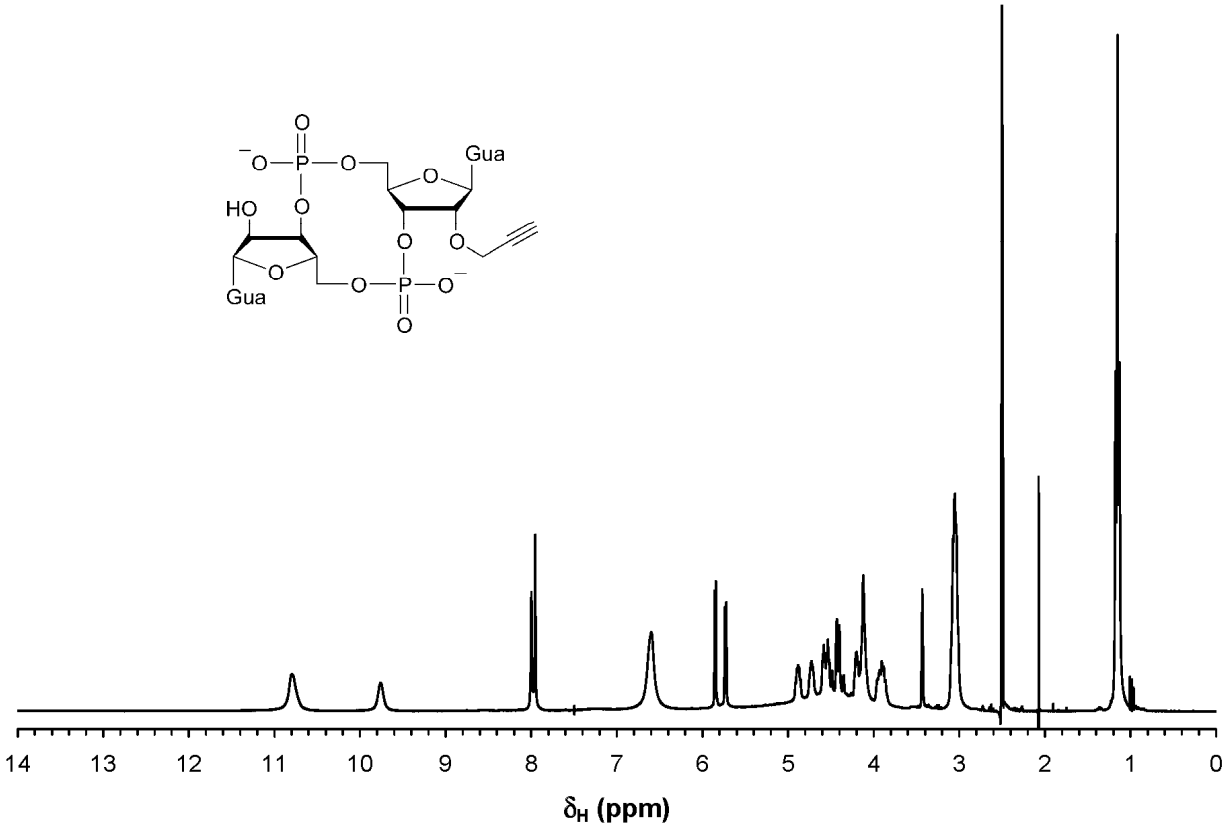


Figure S8. 75 MHz ^{13}C NMR spectrum of the propargylated c-di-GMP 11 in DMSO-d_6

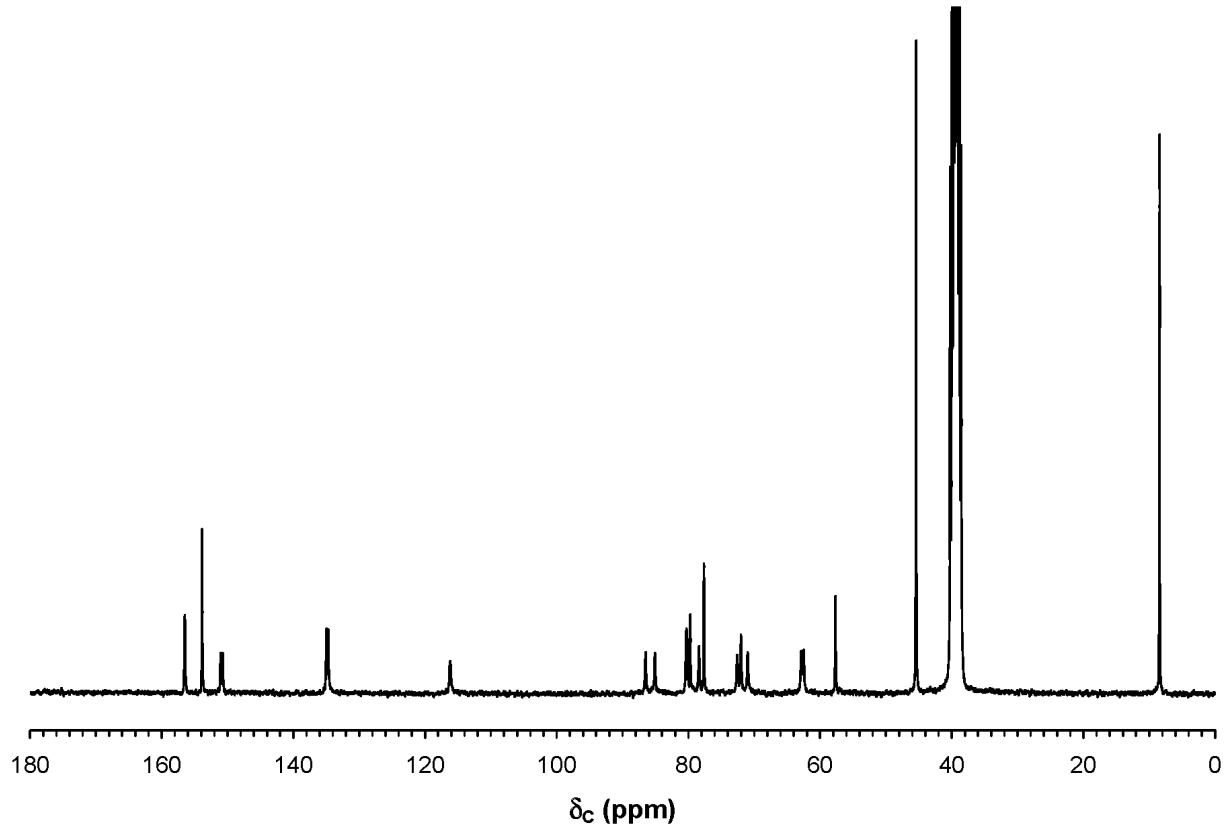


Figure S9. 121 MHz ^{31}P NMR spectrum of the biotinylated c-di-GMP 14 in D_2O

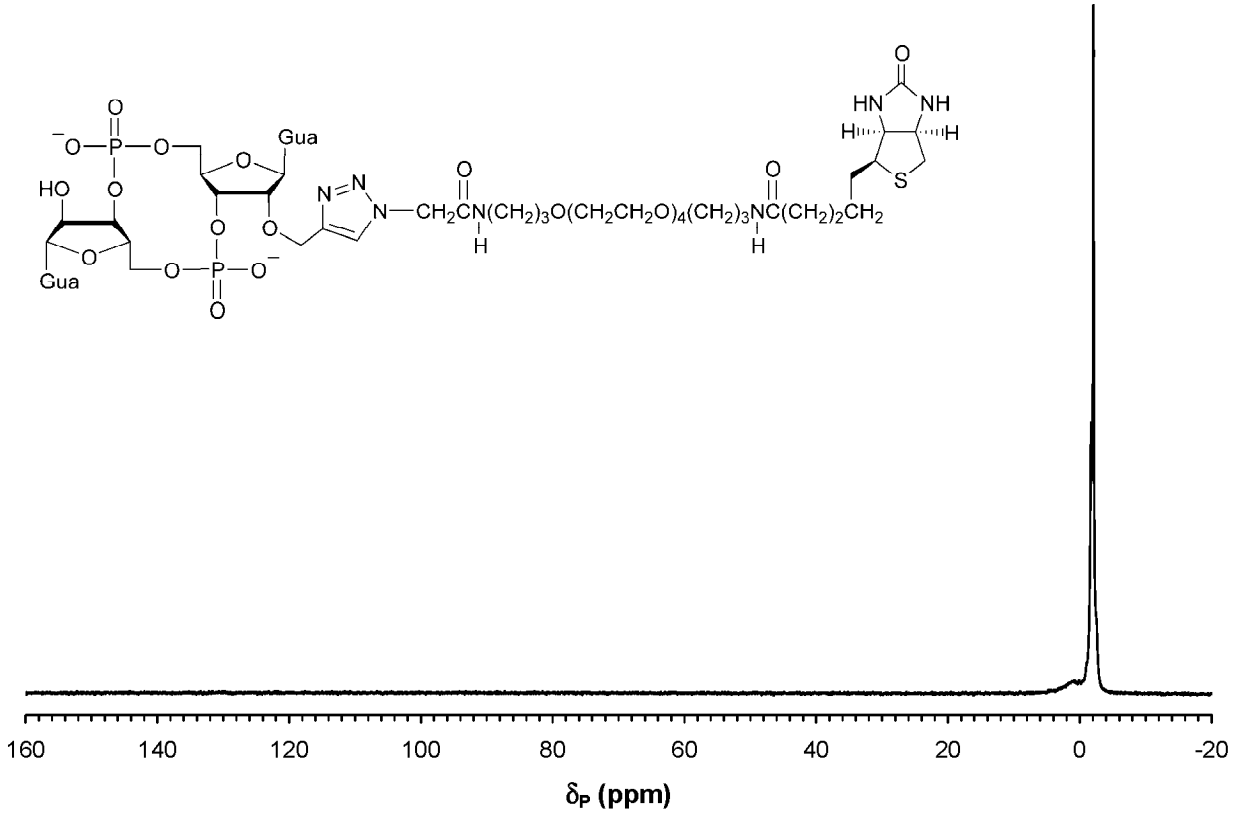


Figure S10. Low resolution mass spectrum of N^2-isobutyryl-3'-*O*-levulinyl-2'-*O*-propargyl guanosine (3)

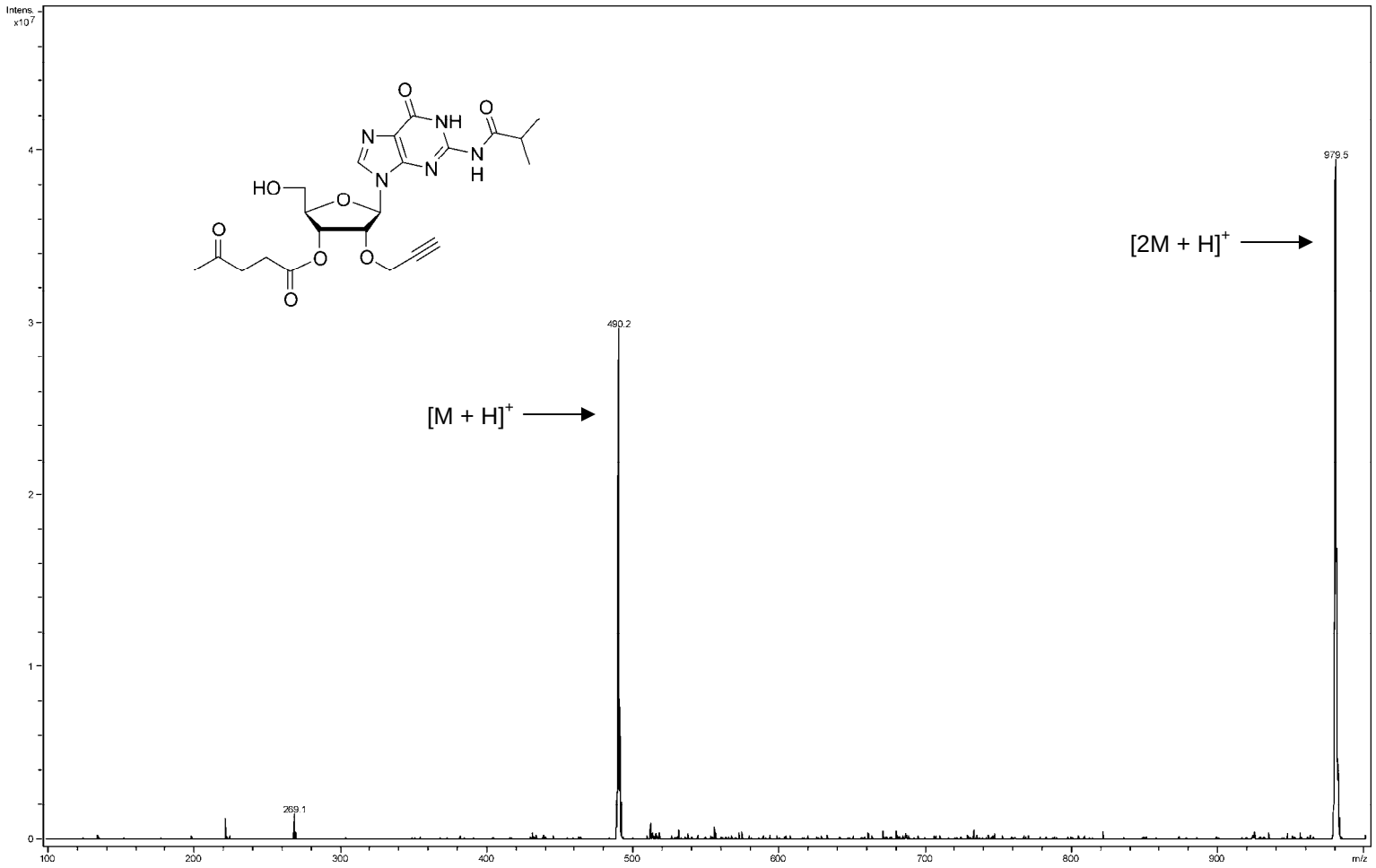


Figure S11. High resolution mass spectrum of the propargylated guanylyl(3'-5')guanosine phosphotriester 6

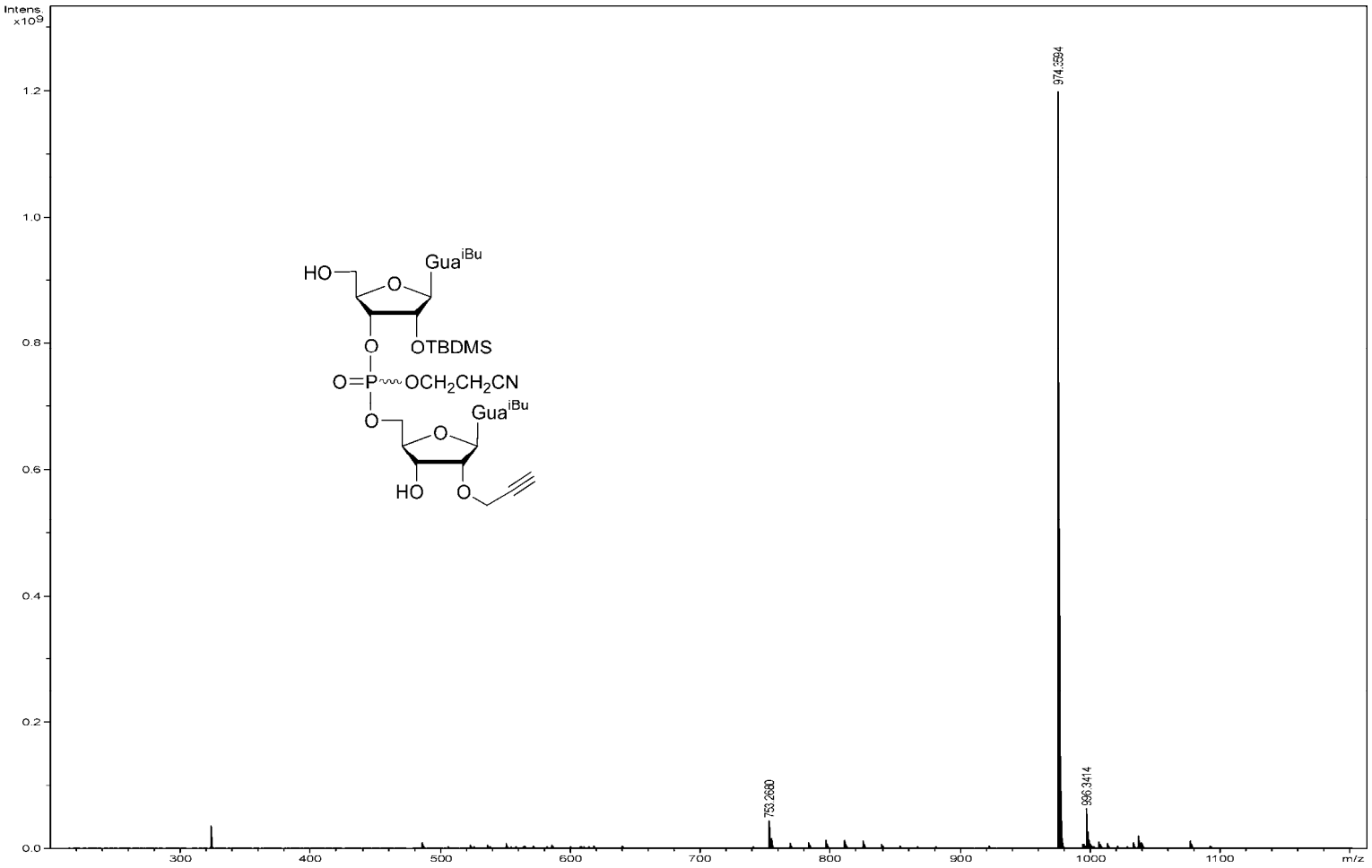


Figure S12. High resolution mass spectrum of the propargylated c-di-GMP 11

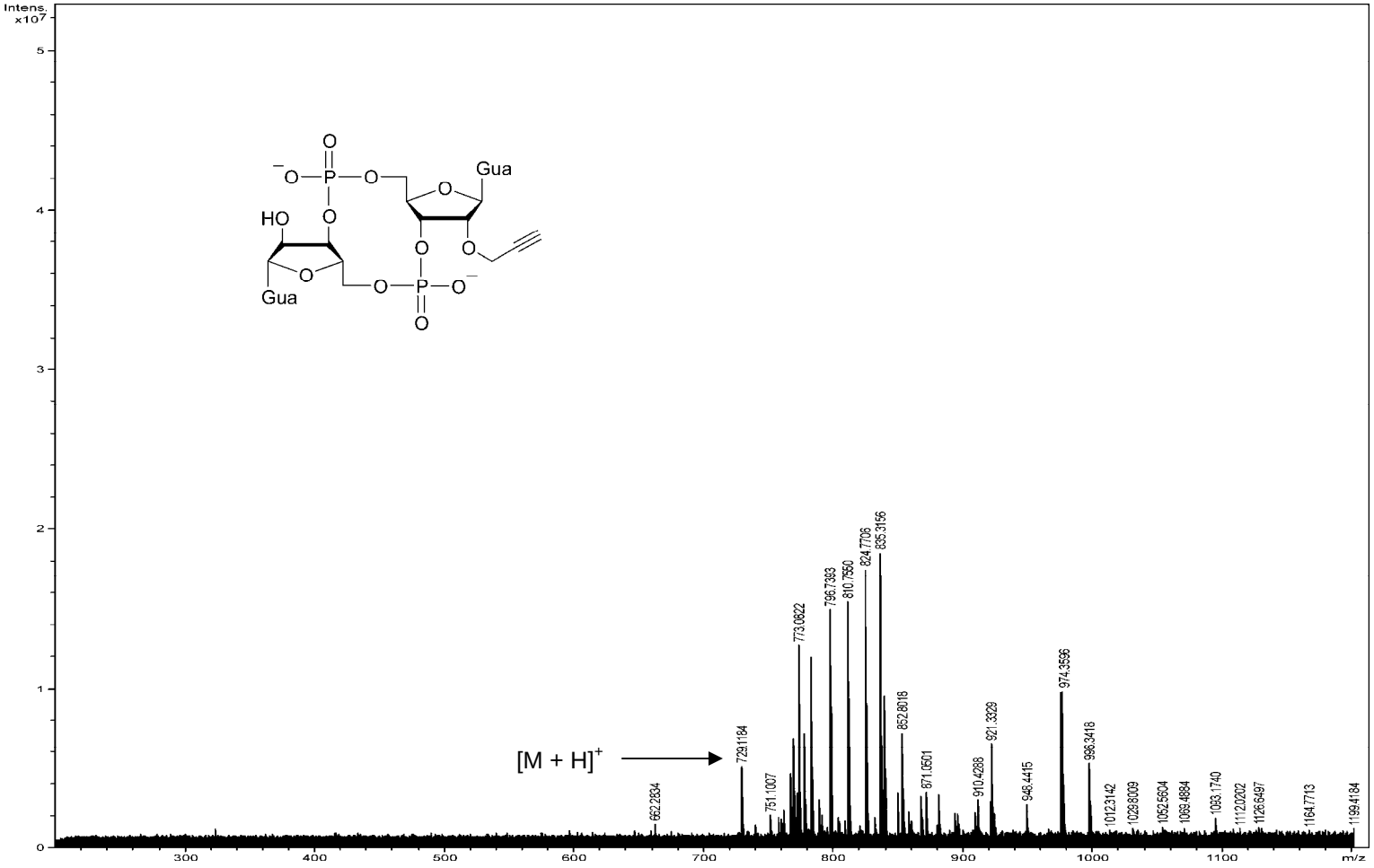


Figure S13. Low resolution mass spectrum of the biotinylated azide 13

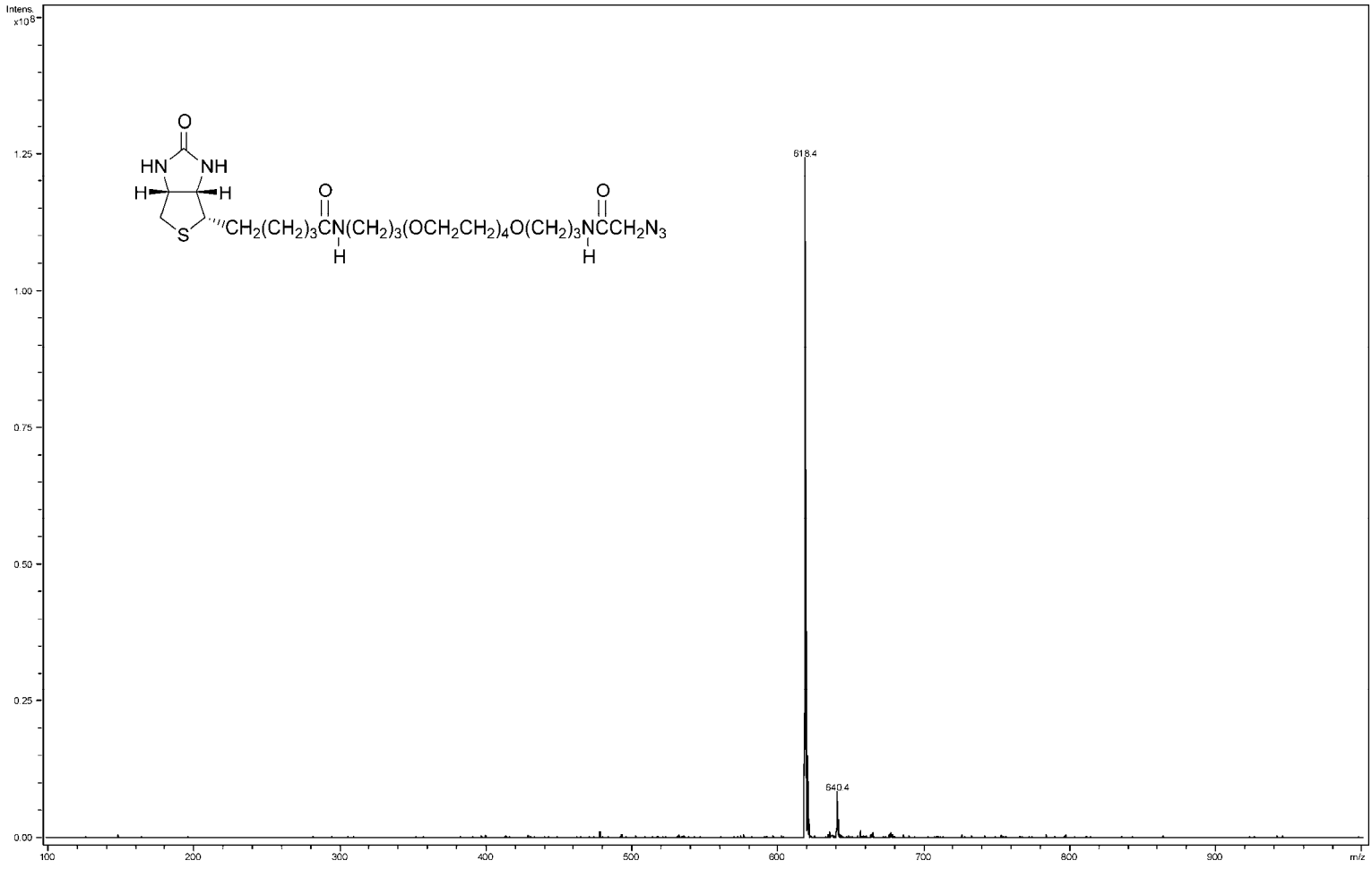
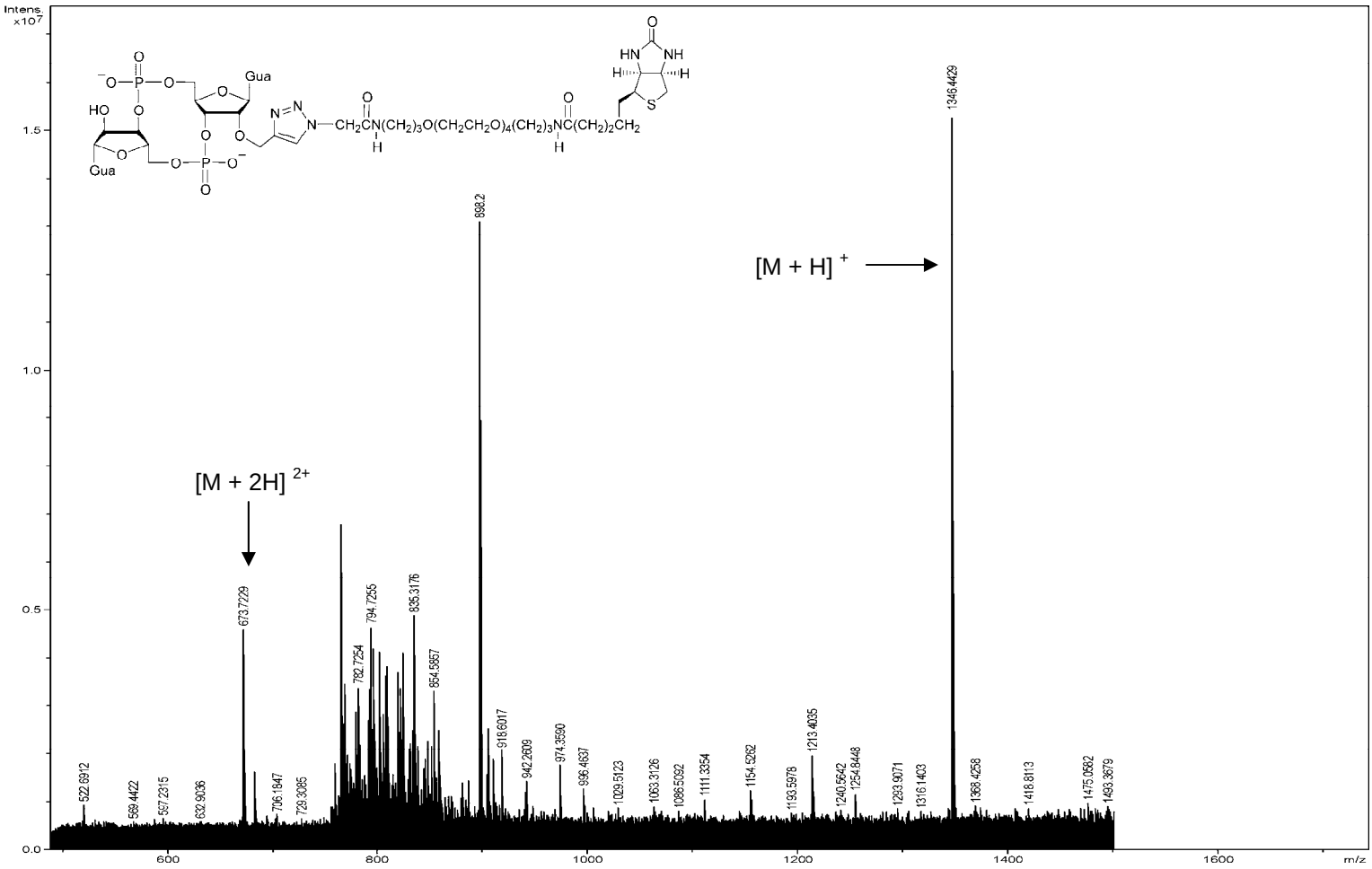


Figure S14. High resolution mass spectrum of the biotinylated c-di-GMP 14



Effects of Charge on Antibody Tissue Distribution and Pharmacokinetics

C. Andrew Boswell,[†] Devin B. Tesar,[‡] Kiran Mukhyala,[§] Frank-Peter Theil,[†] Paul J. Fielder,[†] and Leslie A. Khawli*[,†]

Department of Pharmacokinetic and Pharmacodynamic Sciences, Department of Antibody Engineering, and Department of Bioinformatics, Genentech Research and Early Development, South San Francisco, California 94080, United States. Received June 8, 2010; Revised Manuscript Received October 3, 2010

Antibody pharmacokinetics and pharmacodynamics are often governed by biological processes such as binding to antigens and other cognate receptors. Emphasis must also be placed, however, on fundamental physicochemical properties that define antibodies as complex macromolecules, including shape, size, hydrophobicity, and charge. Electrostatic interactions between anionic cell membranes and the predominantly positive surface charge of most antibodies can influence blood concentration and tissue disposition kinetics in a manner that is independent of antigen recognition. In this context, the deliberate modification of antibodies by chemical means has been exploited as a valuable preclinical research tool to investigate the relationship between net molecular charge and biological disposition. Findings from these exploratory investigations may be summarized as follows: (I) shifts in isoelectric point of approximately one pI unit or more can produce measurable changes in tissue distribution and kinetics, (II) increases in net positive charge generally result in increased tissue retention and increased blood clearance, and (III) decreases in net positive charge generally result in decreased tissue retention and increased whole body clearance. Understanding electrostatic interactions between antibodies and biological matrices holds relevance in biotechnology, especially with regard to the development of immunoconjugates. The guiding principles and knowledge gained from preclinical evaluation of chemically modified antibodies will be discussed and placed in the context of therapeutic antibodies that are currently marketed or under development, with a particular emphasis on pharmacokinetic and disposition properties.

INTRODUCTION

Antibody therapy is an increasingly important therapeutic modality based on identification and pharmacological exploitation of molecular targets associated with inflammatory, oncologic, and autoimmune diseases. Advances in hybridoma technology and molecular biology have enabled the development of murine, chimeric, humanized, and fully human monoclonal antibodies (mAb). As a result, in recent decades several novel therapeutic antibodies have been approved for the treatment of a variety of diseases and have been mass-produced as highly specific and relatively homogeneous reagents (*1, 2*). One major goal in biotechnology is to improve the clinical utility of these reagents with respect to antigen targeting and potency to encourage effective disease therapy. Achieving this goal depends not only upon a thorough understanding of molecular properties underlying antibody behavior and function, but also upon the development of techniques to manipulate these properties in such a way that specifically enhances properties desired for a particular application without exacerbating undesirable ones. For instance, pharmacodynamic (PD) response is often directly proportional to tissue exposure and, thus, plasma half-life (*3*). As such, a typical goal in biotherapeutic development is to identify a candidate molecule having desirable pharmacokinetic (PK) properties or, alternatively, to manipulate a molecule's properties to improve PK properties while preserving antigen recognition.

* Address correspondence to Leslie A. Khawli, Early Development Pharmacokinetics and Pharmacodynamics, Genentech, Inc., South San Francisco, CA 94080. Tel. 650-225-6509; Fax 650-742-5234; E-mail: khawli.leslie@gene.com.

[†] Department of Pharmacokinetic and Pharmacodynamic Sciences.

[‡] Department of Antibody Engineering.

[§] Department of Bioinformatics.

Pharmacokinetic and pharmacodynamic (PKPD) properties of antibodies are governed by both molecule-dependent and species-dependent parameters (*4*). Biological processes are important determinants in antibody PK; examples include binding to antigens (*5*) and other cognate receptors (*6*). Furthermore, an antibody's valency, shape, size, isoelectric point (pI), dosage, and injection method may also influence its disposition kinetics and clearance (*3, 7*). Molecular charge is only one of the many parameters that collectively influence antibody PK (*4, 8*), and its long-established importance (*9*) will be emphasized in this review. Following a brief overview of antibody structure and function, the results of preclinical studies involving charge-modified antibodies will be summarized. Finally, the physiological implications of electrostatic properties of antibodies will be considered at cellular and tissue levels.

ANTIBODY STRUCTURE AND FUNCTION

Immunoglobulins (Igs or antibodies) are the fundamental protein players of both innate and acquired immunity. Immunoglobulins are tetramers consisting of two light chains (LCs, ~25 kDa each) and two heavy chains (HCs, ~55 kDa each) arranged in a shape that resembles the letter "Y" (Figure 1a,b). The LCs contain an N-terminal variable domain and a C-terminal constant domain, while the HCs consist of a variable N-terminal domain and three to four C-terminal constant domains. The Fab domain (antigen binding fragment) is composed of the LC and the first two N-terminal domains of the HC. The association of the LC and HC variable domains creates an N-terminal "hypervariable region" which confers the specificity of the antibody by virtue of the interaction of amino acids within the hypervariable region with molecular components (often amino acids) of an antigen. The Fc region (crystallizing fragment) is a dimer of the two or more C-terminal domains of the HC that are not part of the Fab. Whereas the

10.1021/bc100261d © 2010 American Chemical Society
Published on Web 11/05/2010

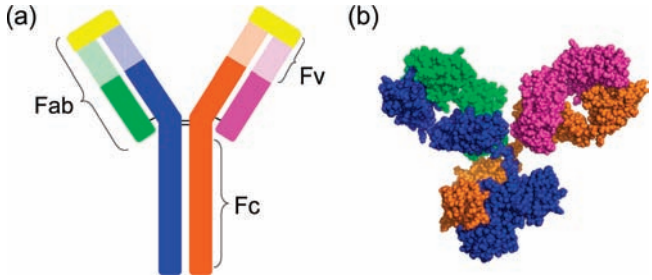


Figure 1. The four-chain structure of an immunoglobulin. The cartoon representation in (a) highlights the overall structural features of a human IgG, with CDRs depicted in yellow, and the Fab, Fv, and Fc regions indicated using brackets. The image of IgG1 (PDB code 1igy) in (b) was generated using the PyMOL molecular visualization system (*106*). In both (a) and (b), the two heavy chains are depicted in blue and orange and the two light chains in green and magenta.

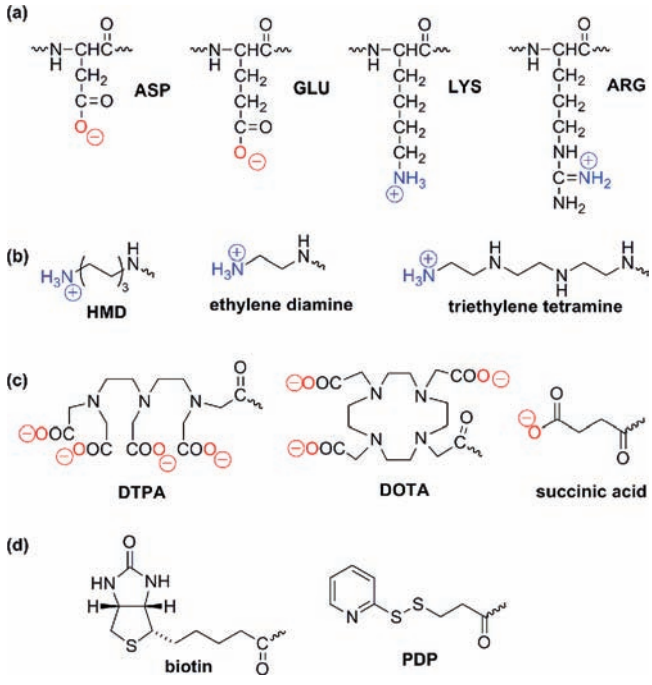


Figure 2. Natural/artificial groups contributing to antibody charge. Chemical structures of naturally occurring amino acids that are usually charged at physiological pH values (a) are shown. Also presented are structures of (b) cationic groups, (c) anionic groups, and (d) neutral groups for charge modification with wavy bonds indicating the potential site of protein conjugation. Abbreviations: HMD, hexamethylenediamine; DTPA, diethylene triamine pentaacetic acid; DOTA, 1,4,7,10-tetraazacyclododecane-1,4,7,10-tetraacetic acid; PDP, pyridyl disulfide propionate.

Fab is responsible for antigen recognition and binding, the Fc regulates the biological functions of the antibody by binding to Fc receptors and eliciting immune effector functions. Binding to Fc receptors can also mediate transport of antibodies within cells or protect them from proteolytic degradation. Of particular importance for therapeutic Abs, the Fc portion of IgG binds pH-dependently to the neonatal Fc receptor (FcRn) (*10*) which protects antibodies from degradation and partially accounts for their long serum half-lives (*6, 11*).

In mammals, IgG is the most abundant Ig in serum (~80% of total serum Ig) and is the principle Ig that participates in the adaptive immune response. There are four human IgG subclasses (IgG_1, IgG_2, IgG_3, and IgG_4), which are distinguished from one another by differences in the constant region of the HC sequence. These sequence differences affect the length of the hinge region as well as the position and number of disulfide bonds between the two HCs of the IgG molecule. Additionally,

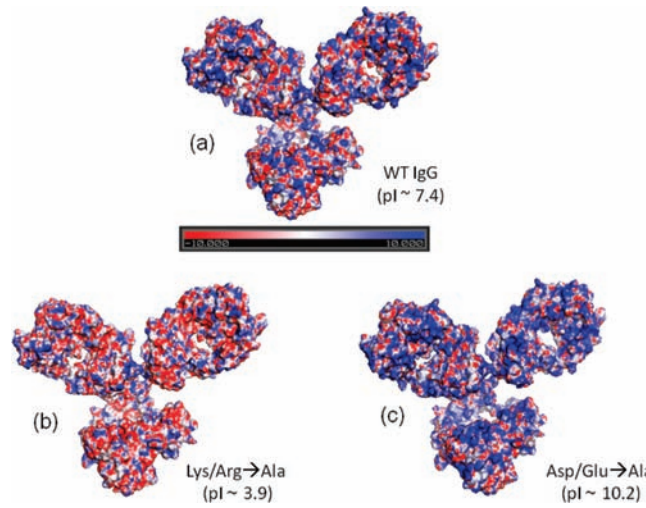


Figure 3. Graphical illustration of antibody charge modification. Electrostatic surface images of native IgG1 (PDB code 1igy) (a) and two simulated charge-modified variants (b,c) are displayed using the PyMOL molecular visualization system (*106*) to illustrate regions of neutral (white), positive (blue), and negative (red) charge. Note that, despite the extreme degree of protein modification in these simulated charge variants, the estimated pI values are roughly within the range of values shown for experimental test molecules listed in Table 2. The variant structures were created from the native protein by manual point mutation, using *DeepView* v 4.0.1 Swiss PdbViewer (http://www.expasy.org/spdbv/) (*107*), of all 86 Lys and 38 Arg residues (b) or all 60 Asp and 64 Glu residues (c) to Ala. Electrostatic potential maps were computed with default settings using the PBEQ Solver within CHARMM-GUI running from The University of Kansas Department of Molecular Biosciences Center for Bioinformatics Lab (http://www.charmm-gui.org/) (*108*). Estimated pI values were calculated from the corresponding sequences using *Scripps Protein Calculator* v 3.3 (http://www.scripps.edu/~cdputnam/protcalc.html).

different IgG subclasses bind to different Fc receptors with varying affinities. Thus, IgGs of one subclass may be more or less efficient at eliciting certain effector functions than IgGs of another subclass. For example, IgG_3 is the most effective subclass at activating the complement, followed by IgG_1 and IgG_2, whereas IgG_4 cannot activate the complement. Circulating IgG participates in adaptive immunity by binding to antigens in the circulation. Antigens are cleared through subsequent activation of complement and/or other effector functions such as opsonization (phagocytosis of antigen/pathogen by macrophages and neutrophils) and antibody-dependent cell-mediated cytotoxicity (ADCC).

ANTIBODY CHARGE: NATURAL HETEROGENEITY AND METHODS FOR MODIFICATION

Heterogeneity in the physicochemical properties of antibodies is a ubiquitous phenomenon resulting from the very complex, macromolecular nature of immunoglobulins. For instance, the influence of charged amino acids (Figure 2a) within a complex three-dimensional structure explains the presence of charged surfaces that often encourage protein−protein interactions under physiological conditions (*12*). Illustrated in Figure 3a is a typical variable charge distribution pattern that exists intramolecularly, across different surface regions of a single antibody. Note that, in some antibodies, a sizable degree of polarity may result from the presence of oppositely charged regions within different areas of the macromolecule. Furthermore, significant intermolecular heterogeneity (i.e., polydispersity) exists among different antibody molecules comprising any given preparation. A fundamental property of antibodies and other proteins is the isoelectric point (pI), which is defined as the pH at which the macromolecule carries no net electrical charge. While the approximate

Table 1. List of Available Experimental (EXP) and Theoretical (CALC) Isoelectric Point (pI) Values for Selected FDA-Approved Therapeutic Antibodies[a]

antibody	trade name	type/source	$pI_{(EXP)}$	ref.	$pI_{(CALC)}$ HC	$pI_{(CALC)}$ LC	$pI_{(CALC)}$ full
muromonab	Orthoclone	rodent	na		8.53	6.34	8.26
abciximab	ReoPro	chimeric Fab	~8.3	*99*	7.25	4.99	6.16
rituximab	Rituxan	chimeric	na		8.58	8.61	8.65
basiliximab	Simulect	chimeric	na		8.59	8.6	8.65
daclizumab	Zenapax	humanized	8.2−9.0	*100*	8.34	8.32	8.42
trastuzumab	Herceptin	humanized	8.6−9.1	*101*	8.49	7.76	8.41
			~8.6	*28*			
			9.2	*95*			
alemtuzumab	Campath	humanized	8.5−9.0	*102*	8.6	8.81	8.73
ibritumomab	Zevalin	murine	na		7.61[b]	7.8[b]	7.83[b]
adalimumab	Humira	human	8.6−9.1	*103*	na	na	na
tositumomab	Bexxar	murine	na		8.58	8.61	8.65
omalizumab	Xolair	humanized	na		8.21	5.39	7.01
bevacizumab	Avastin	humanized	8.3−8.6	*104*	na	na	na
			8.2−8.3	*105*			
cetuximab	Erbitux	chimeric	na		8.69	6.35	8.44

[a] Theoretical pI values were computed by inputting the heavy chain (HC), light chain (LC), or full protein sequence of each antibody (http://www.drugbank.ca) (*97*) into the ProtParam tool within the ExPASy Proteomics Server of the Swiss Institute of Bioinformatics (http://www.expasy.ch/tools/protparam.html) (*98*). [b] Charges imparted by the conjugated chelator, tiuxetan, were not factored into the theoretical pI calculations.

surface charge distribution (Figure 3a) and overall pI (Table 1) of an antibody can be predicted from its sequence and structure, charge variation (often in the form of covalent modification of amino acid residues or glycan moieties) is known to spontaneously arise during production and manufacturing. Such alterations vary between different production methods and is of particular relevance in the biotechnology industry (reviewed in *refs* 13−15).

Despite an inherent charge polydispersity that arises spontaneously in production, efforts to isolate charge variants and evaluate them on an individual basis suggest that differences of less than approximately one pI unit are inconsequential for PK (*16*). As such, methods have been developed for deliberately modifying the net charge of antibodies, often yielding more drastic changes in pI values (Figure 3b,c). The rationale for these efforts is twofold: (I) to permit exploratory preclinical study of the relationships between the net molecular charge and in vivo disposition kinetics and (II) to potentially improve the PK properties of antibodies for the diagnosis or treatment of disease. One promising approach to this endeavor is antibody engineering technology, which can produce changes in pI and biological clearance through substitutions involving charged amino acids (Figure 2a) (*17*). An alternative approach is the deliberate modification of antibody charge through direct chemical modification of amino acid side chains with positive (Figure 2b), negative (Figure 2c), or neutral (Figure 2d) chemical groups. Chemical modification of antibodies is commonly used to deliver payloads such as radionuclides (*18*) or toxins (*19*), but can also allow alteration of net molecular charge. As a point of reference, the amino acid modifications in Figure 3b,c would be equivalent to conjugation of 25 diethylene triamine pentaacetic acid (DTPA) molecules (Figure 2c) through Lys residues (assuming a maximum net −5 charge reduction (*20*)) or 62 hexamethylenediamine (HMD) molecules (Figure 2b) through Asp/Glu residues (assuming a maximum net +2 charge increase (*21*)), respectively. Such modifications can also produce significant changes in pI and, in turn, noticeable changes in plasma and tissue PK as demonstrated by numerous examples in the proceeding section.

PK AND TISSUE DISPOSITION OF CHARGE-MODIFIED ANTIBODIES

Deliberate chemical modifications of antibodies with a variety of acidic, basic, or neutral chemical entities have been exploited to change the net molecular charge of antibodies (Figure 2b−d) (*22*). Apart from the chemical nature of the appended functional group, the site of modification (e.g., tyrosines, lysines, cysteines, oligosaccharides) has also been shown to affect tissue distribution and elimination of modified antibodies (*23*).

Cationization. Progress in molecular biology has yielded novel therapeutic strategies including gene therapy and cellular protein delivery, which rely on the entry of charged macromolecules into intracellular compartments. Cationization of antibodies is a drug delivery strategy wherein the pI is raised, often by conversion of surface carboxyl groups to primary amines or other positively charged groups. A number of cationic groups can be utilized, including HMD, ethylene diamine, and triethylene tetramine (Figure 2b). The resulting modified proteins have demonstrated altered biological properties, with a general trend toward increased plasma clearance and volume of distribution and increased disposition in both target (e.g., tumor) and normal tissues (Table 2) (*24*−*29*). Increased volume of distribution due to cationization can be demonstrated visually by whole body radiographic imaging, such as for an indium-111 (^{111}In)-labeled murine antibody against the human epidermal growth factor receptor (EGFR) (Figure 4) (*30*).

A common goal for therapeutic antibodies is to extend plasma half-life as a means to increase exposure, often expressed in terms of the area under the plasma concentration−time curve (*6*). In contrast, cationization tends to shorten plasma half-life due to an enhancement in both the rate and the magnitude of tissue distribution. However, cationization might prove to be a useful strategy in specific applications in which prolonged antibody exposure may be sacrificed for the sake of rapid, enhanced tissue uptake (e.g., targeting antibodies to efficiently cross the blood-brain barrier (*25*)). Cationization of antibodies has also been explored as a means to encourage extravasation, antigen binding, and receptor-mediated endocytosis (*31*) of antibodies into target cells. In contrast to native Abs, which are generally excluded from cell membranes in the absence of receptor-mediated endocytosis, cationized Abs are better able to reach the intracellular space via absorptive-mediated endocytosis (*32*, *33*). Electrostatic interactions between positively charged proteins and negatively charged cell membranes (*34*) could permit cell entry via nonspecific membrane flow and have been implicated in the mechanism by which cationized antibodies are rapidly endocytosed by cells in vitro (*35*). A similar phenomenon is suggested to induce absorptive-mediated transcytosis across microvascular endothelial barriers in vivo (*36*).

Although cationization has been shown to improve endocytosis and target tissue retention, several undesirable effects have also been reported. In general, retention in nontarget tissues is also significantly increased for cationized antibodies relative to

Table 2. Summary of Reported Preclinical Studies Involving Charge-Modified Antibodies

test molecules/target (species)	modifying group/Δ pI	effect on tissue disposition	effect on blood, plasma, or whole body clearance (CL)†	ref
		Cationized Antibodies		
^{125}I-goat colchicine-specific polyclonal IgG (rat)	HMD 5.85−9.0 to 8.65−10.3	↑ (74-fold) in V_D	↑ (114-fold) in systemic CL	*24*
^{125}I-AMY33/anti-β-amyloid (BALB/c mice)	HMD 7 to 9	↑ in %ID/g (2 h) for liver, kidney, lung, heart, brain	↑ (28-fold) in plasma CL	*25*
^{111}In-AMY33/anti-β-amyloid (BALB/c mice)	HMD (but also DTPA) 7 to (n/a)	↑ in %ID/g (2 h) for liver, kidney; not in lung, heart, brain	↑ (3.2-fold) in plasma CL	*25*
^{111}In-murine anti-EGFR (SCID mice)	HMD (but also DTPA) 8.1−8.3 to 8.7	↑ in %ID/g (1 h) for liver, lung	↑ in blood CL (i.e., decrease in AUC^{SS})	*30*
^{125}I-anti-HIV immune globulin (SCID mice)	HMD 6.3−7.3 to 8.1− >9.5	↑ in V_D (2 h) for liver, kidney, lung, brain	↑ (1600-fold) in blood CL	*26*
^{125}I-murine mAb D146/ anti-*Ras* peptide (BALB/c mice)	HMD 8.5 to >9.5	↑ in V_D (2 h) for liver, kidney, lung, heart, brain	↑ (58-fold) in plasma CL	*27*
^{125}I-humanized 4D5/anti-HER2 (rat)	HMD 8.6 to >9.3	↑ in V_D (2 h) for brain, heart, lung, liver, kidney	↑ (23-fold) in plasma CL_{SS}	*28*
mouse monoclonal IgG, MOPC21 (SCID mice)	HMD 6.0 to 8.6 − 9.3	↑ in tumor microvascular permeability; P_v (10^{-7} cm s^{-1}): 4.25−5.27 vs 1.47−4.07	↑ in plasma CL (i.e., decrease in k, time constant of concentration decay in the plasma: 500−1500 vs 3400−8200 s)	*29*
		Anionized Antibodies		
mouse monoclonal IgG, MOPC21 (SCID mice)	succinate 6.0 to 3.0−3.9	↓ in tumor microvascular permeability; P_v (10^{-7} cm s^{-1}): 1.11−2.53 vs 1.47−4.07	↑ in plasma CL based on decrease in k, time constant of concentration decay in the plasma	*29*
^{111}In-rabbit IgG/antihuman serum albumin (BALB/c mice)	DTPA 9.43−4.65 to 7.9−4.27	↓ in %ID/g (4 h) for intestine, colon ↑ in %ID/g (4, 24 h) for liver	n/a	*51*
human, nonspecific, polyclonal IgG (rat)	DTPA 6.6−9.3 to 6.0−8.3	↓ in %ID/g (up to 24 h) for most tissues	No Δ in plasma CL based on terminal half-life ($t^2_{1/2}$ (h) = 20.5 ± 1.9 vs 20.7 ± 1.6)	*52*
^{111}In-bovine IgG (ddY mice)	succinate (as well as DTPA) pI values n/a	↑ in %ID (1 h) for liver Suc_{50}-IgG > Suc_{22}-IgG > IgG	↑ in total CL: CL_{total} (mL/h) at 20 mg/kg dose: 0.46 (Suc_{22}-IgG) vs 2.86 (Suc_{50}-IgG) vs 0.4 (IgG)	*53*
		Neutralized Antibodies		
^{125}I-chTNT-3/B/antihistone HI and DNA [BALB/c mice (PK); athymic nude mice (distribution)]	biotin >9.6 to 8.0−9.6	↓ in %ID/g (72 h) for most tissues	↑ in whole body CL based on whole body $t_{1/2}$: 90.0 ± 8.1 vs 134.2 ± 4.0 h	*59*
$^{125/131}$I-B72.3/murine anti-TAG72 IgG1 (BALB/c mice (PK); athymic nude mice (distribution))	SPDP 4.8−5.0 to 4.5−4.7	↓ in %ID/g (72 h) for most tissues (except tumor)	↑ in whole body CL based on whole body $t_{1/2}$: 20 vs 120 h	*60*
$^{125/131}$I-Lym-1/murine IgG2a anti-HLA-Dr (BALB/c mice (PK); athymic nude mice (distribution))	SPDP 7.2−7.8 to 5.1−6.0	↓ in %ID/g (7 d) for most tissues (except tumor)	↑ in whole body CL based on whole body $t_{1/2}$: 60 vs 144 h	*60*
$^{125/131}$I-TNT-1/antihistone HI and DNA (BALB/c mice (PK); athymic nude mice (distribution))	SPDP 5.8−6.0 to 4.8−5.1	↓ in %ID/g (72 h) for most tissues	↑ in whole body CL based on whole body $t_{1/2}$	*60*
^{125}I-TNT-1/antihistone HI and DNA (BALB/c mice (PK); athymic nude mice (distribution))	biotin >9.6 to 7.2	↓ in %ID/g (72 h) for most tissues	↓ in whole body CL based on whole body $t_{1/2}$: 17.4 ± 2.4 vs 30.4 ± 1.8 h	*58*
^{125}I-TNT-2/antihistone HI and DNA (BALB/c mice (PK); athymic nude mice (distribution))	biotin >9.6 to 8.2	↓ in %ID/g (5 d) for most tissues	No Δ in whole body CL based on whole body $t_{1/2}$ 175.1 ± 3.0 vs 178.7 ± 7.2 h	*58*
^{125}I-TNT-3/antihistone HI and DNA (BALB/c mice (PK); athymic nude mice (distribution))	biotin >9.6 to 7.2	↓ in %ID/g (72 h) for most tissues	↑ in whole body CL based on whole body $t_{1/2}$: 90.1 ± 3.8 vs 134.2 ± 4.0 h	*58*

control antibodies (Figure 4). In addition, cationized human IgGs have been shown to form soluble immune complexes that induce activation of human platelets at much lower concentrations than native, noncationized human IgGs (*37*).

Anionization. Attempts have also been made to produce anionized Abs by chemically converting neutral or positively charged groups into negatively charged groups; this modification typically increases plasma clearance while decreasing tissue uptake and retention. While it may seem counterintuitive that both cationization and anionization increase plasma clearance, different underlying mechanisms are involved: tissue sequestration in the former case, and more rapid whole body clearance in the latter. Various anionic groups may be exploited for this type of modification, including DTPA (*38*), 1,4,8,11-tetraazacyclododecane-*N*,*N*′,*N*″,*N*‴-tetraacetic acid (DOTA) (*39*, *40*), and succinic acid (*41*) (Figure 2c). Similar induction of negative charge is imparted by protein conjugation to 1,4,8,11-tetraazacyclotetradecane-*N*,*N*′,*N*″,*N*‴-tetraacetic acid (TETA) (*39*, *42*) and other polyaminopolycarboxylate chelates that are routinely used in radiopharmaceutical applications (*18*, *43*). Considering that so few macrocyclic chelates are occupied by metal cations in high-specific-activity radiotracer preparations, alteration of antibody pI occurs irrespective of the presence or absence of cationic metal radionuclides.

The majority of antibodies possess a more basic isoelectric point (pI > 6) than most serum proteins (pI < 5.5) (*44*); this is

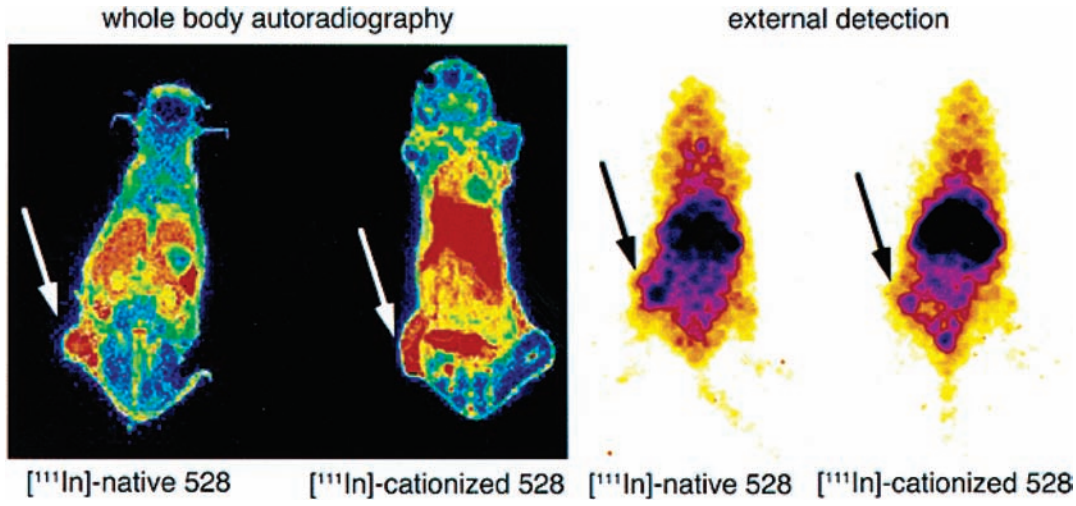


Figure 4. Effects of antibody cationization on tissue distribution. Figure reproduced with permission from Lee and Pardridge, 2003 (*30*). Whole body autoradiography (left) or gamma counter external detection (right) of female SCID mice implanted with U87 subcutaneous tumors in the right flank (arrows). Mice were injected with 50 μCi of either [^{111}In]-native 528 mAb or [^{111}In]-cationized 528 mAb. At 24 h after injection, the animals were anesthetized for external detection and then sacrificed for whole body autoradiography. The tumors were imaged 15 days after implantation.

particularly true for human IgGs (Table 1) and is a property that is in fact commonly exploited in their purification (*45*). This also makes them susceptible to ionic interactions with negatively charged glycan chains on cell surfaces (*46*) and heparin sulfate proteoglycans within the extracellular matrix (ECM) (*47*−*50*), collectively promoting higher tissue disposition and retention. Anionization partially abrogates these attractive forces, thereby reducing such non-antigen-dependent tissue uptake.

Anodal shifts in antibody pI generally induce faster blood clearance and lower tissue accumulation, with the exception of liver (Table 2) (*29, 51*−*53*). It is important to note that the increased hepatic retention of radioactivity may be due in part to transchelation of ^{111}In from the DTPA chelate to transferrin, with subsequent localization in the liver and other organs of the reticuloendothelial system (*23*). This behavior might be avoided by choosing a different radiometal/chelate pair such as ^{111}In/DOTA, taking advantage of the higher kinetic stability of the metal complex formed by this macrocyclic chelate.

It is evident that cautious interpretation is necessary when comparing uptake data obtained using both residualizing (e.g., radiometal chelate-based) and nonresidualizing (radiohalogenated tyrosine-based) probes. Specifically, it is advisible to only compare data obtained using a single labeling method when studying charge-dependent trends in tissue uptake. For instance, when antibodies conjugated to radiometal-chelate probes undergo endocytosis upon binding in antigen-expressing tissues, a greater cumulative tissue uptake of radioactivity is observed due to probe residualization following lysosomal catabolism (*54*). This effect is not related to molecular charge of the intact antibody; rather, it is driven by the inability of the resulting highly polar, charged radiometal-chelate-amino acid metabolites to cross the cell membrane, in contrast to the diffusible degradation products of antibodies that are directly radioiodinated through tyrosine residues. Radiometal-chelate probes are often preferred for tumor-targeting diagnostic and therapeutic applications for this reason. For instance, an ^{111}In-DTPA-labeled IgG against the carcinoembryonic antigen (CEA) resulted in 41% of the injected dose per gram being localized within human colorectal xenografts at 24 h compared to 9% for a nonbinding ^{111}In-DTPA-labeled control IgG and 19% for the analogous radioiodinated anti-CEA antibody (*55*). Such trends induced by probe residualization are most profound in antigen-expressing tumors or in antigen-expressing normal tissues. In contrast, non-antigen-expressing tissues have demonstrated little or no differences in levels of radioactivity between residualizing (^{111}In) and nonresidualizing (^{125}I) labeling methods (*54*).

Neutralization. Improvements in the biodistribution of antibodies have been sought using another approach in which an uncharged group is appended to a charged amino acid residue (e.g., lysine). A variety of neutral, uncharged groups may be utilized, including biotin and the heterobifunctional linker, pyridyl disulfide propionate (PDP) (Figure 2d). Additionally, PEGylation (PEG = poly(ethylene glycol)) is a broad modification strategy for therapeutics (reviewed in *refs* 56, 57). Such modifications will not be further considered here, however, as the large size (1−25 kDa) of PEG groups routinely used in antibody PEGylation often induces simultaneous changes in multiple molecular properties, including conformation, electrostatic binding, and hydrophobicity. Neutralization of positive charge (i.e., net reduction of charge) is much more common than neutralization of negative charge due to facile chemical methodologies which can be used to cap the nucleophilic amino groups of lysines.

In some cases, antigen binding may be preserved in charge-modified antibodies while still reducing nonspecific organ uptake. For instance, favorable results were obtained for a series of biotin-modified TNT mAbs, which yielded preparations having 65−69% immunoreactivity in a cell binding assay, more rapid whole body clearance, and higher tumor-to-background ratios due to lower uptake in normal tissues (Figure 5) (*58*). The masking of positive charges in proteins often produces changes in biological behavior similar to those induced by anionization (Figure 5) (Table 2) (*58*−*60*). Once again, such generalizations must be approached with caution, as the nature of the capping group can heavily influence the impact of the modification on antibody disposition.

pI/PK Relationships. By analyzing the directional changes indicated by arrows in Table 2, certain overall trends from preclinical evaluation of charge-modified antibodies should become apparent to the reader. In general, antibodies that were chemically modified to achieve higher, more basic pI values (Table 2, Cationized Antibodies) are associated with increased tissue uptake and increased blood clearance. In contrast, modified antibodies having more acidic pI values (Table 2, Anionized/Neutralized Antibodies) displayed decreased tissue uptake and increased whole-body (including blood) clearance. Nevertheless, cautious interpretation of data must be exercised

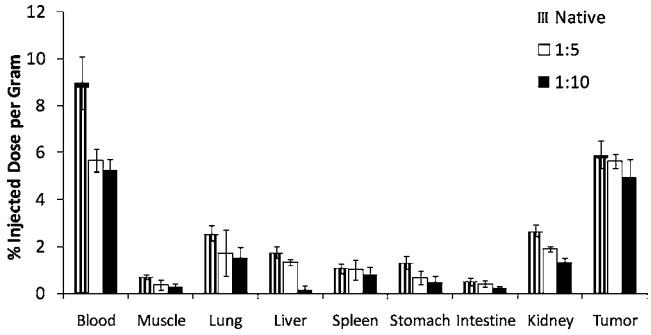


Figure 5. Effects of neutralization of positive charge in antibodies on tissue distribution. Data adapted with permission from Khawli et al. 2002 (*58*). Five-day tissue biodistribution and tumor uptake of ^{125}I-labeled parental (striped) and biotinylated (mAb/biotin ratio = 1:5, white; 1:10, black) chTNT-2 mAbs in Madison 109 murine lung adenocarcinoma-bearing BALB/c mice.

due to additional consequences of charge modification beyond electrostatic interactions, such as conformational changes in overall antibody structure and steric effects (*41*). It is also plausible that chemical modification of antibodies may, in some cases, deleteriously impact an antibody's binding affinity to FcRn (*10*) which, in turn, could trigger a reduction in serum half-life (*61*−*64*). Furthermore, the degree to which these putative changes would arise is highly dependent on the number, bulkiness, and physicochemical properties of small molecule charge modifiers attached to the protein. Another potential unwanted effect associated with antibody modification is increased immunogenicity due to creation of new antigenic determinants (*65*, *66*). Such responses might compromise antibody efficacy by direct neutralization, acceleration of clearance, prevention of further dosing, and induction of serum sickness (*67*). However, accumulating experimental data shows that incidence rates of clinical immunogenicity for some chemically modified antibodies are quite acceptable. For instance, 4% for a yttrium-90-labeled anionic chelate-modified murine anti-CD20 IgG (ibritumomab tiuxetan, i.e., Zevalin) (*68*), <2% for a somewhat hydrophobic calicheamicin-modified humanized IgG_4 (gemtuzumab ozogamicin, i.e., Mylotarg) (*68*), and 9% for a biotin-modified iodine-131-labeled chimeric tumor necrosis therapy antibody (^{131}I-TNT) (*69*).

Antibody Engineering Approches. As depicted in Figure 3, charged groups tend to be distributed randomly across the entire surface on a chemically modified antibody variant; this is governed by location of available amino acids that can undergo chemical reaction with modifying groups. In contrast, the use of modern protein engineering technologies can allow charge modification via site-directed mutagenesis. For instance, charge-modified antibodies were produced through selective point mutations of amino acids located exclusively in the variable (Fv) region (see Figure 1) and evaluated in normal and in β2-microglobulin knockout mice (*17*); these studies demonstrated a relationship between the plasma PK and pI values of antibodies that was independent of the FcRn salvage pathway (*17*). Consistent with the data in Table 2, increasing the pI value produced increases in plasma clearance; however, antibody variants with decreased pI values conversely showed enhanced plasma half-lives. The discrepancy between these observations and the data presented in Table 2 could result from charge localization within the variable region, which would affect the dipole moments (*70*) of engineered antibodies more drastically than for chemically modified variants. Alternatively, as suggested by Igawa et al., chemical modification may deleteriously affect FcRn binding and, hence, antibody PK (*17*). However, nearly a 4-fold reduction in β-phase half-life of an IgG was achieved by a single amino acid substitution in the Fc region, demonstrating that dramatic changes in PK, possibly modulated by FcRn affinity, can occur even in the absence of chemical modification (*71*). These and other plausible arguments warrant further plasma and tissue PK studies of antibody charge variants produced by both chemical and genetic means, but with full characterization of FcRn binding affinity.

pI/PK Relationships beyond IgG. Although this review is primarily focused on full-length IgG, similar charge modification strategies have been applied to a variety of antibody fragments and other macromolecules. In most cases, similar trends in blood PK and/or tissue distribution are observed. In fact, the same pI/p*K* trend observed for cationized IgG (Table 2) has also been reported for other classes of macromolecules including dextrose derivatives, for which cationization shortened the half-life in mice while anionization prolonged it (*72*). However, comparisons should be made only within a given class of molecules due to the additional influence of molecular size (*53*, *73*).

The same trend of increased plasma clearance for cationized proteins relative to native proteins has been observed for both an IgG and its corresponding Fab (*24*). It should be noted, however, that an antibody fragment is much more susceptible to electrostatic interactions within the kidneys than a full-length IgG because the fragment's size is below the glomerular filtration threshold (*18*, *74*). For instance, one study involving a series of anionized (glycolated) Fabs demonstrated that renal accumulation via reabsorption into renal proximal tubules decreased as the pI decreased (*75*); similar trends were observed for a series of glycolated disulfide-bonded variable region fragments (dsFv) (*76*). Co-administration of lysine was shown to block the renal uptake of radiolabeled dsFv, offering a strategy in lessening nephrotoxicity during radioimmunotherapy (*77*). In a somewhat related strategy, co-administration of a $sc(Fv)_2$ with a highly cationic peptide, penetratin (pI = 12.3), was able to increase tumor uptake of the protein despite the lack of a covalent bond between the two molecules, implicating electrostatic $sc(Fv)_2$−penetratin interaction as a plausible mechanism (*78*). Studies involving scFv−calmodulin fusion proteins demonstrated that derivatives having pI values between 5.0 and 9.0 had better tumor targeting ability than those with extreme pI values (*79*).

CHARGE-DEPENDENT PHYSIOLOGICAL INTERACTIONS

Positive charge on the surface of an antibody may lead to aberrant interactions with the cell membrane due to the presence of negatively charged groups that decorate the lipid bilayer surface of most mammalian cells (*22*). As such, the complex nature of biological matrices must be appreciated in order to provide a framework for interpreting charge effects in antibody PK, PD, and metabolic outcome. For instance, video microscopy has demonstrated that masking of the negative charge on the surface of red blood cells (RBCs) with a cationic polymer significantly increased RBC flow velocity through capillaries, presumably due to reduced electrostatic repulsive forces between the RBCs and negatively charged macromolecules on the surface of capillary endothelial cells (*80*). Circulating antibodies are susceptible to similar repulsive electrostatic forces but, due to their ability to permeate through openings in capillary walls, experience such forces at both the luminal and serosal surfaces of the vascular endothelial wall. In this section, the physicochemical attributes of selected physiological compartments, including the extracellular matrix, healthy tissues, and solid tumors, will be further considered.

Overview of Interstitial Space/Extracellular Matrix. Both body fluid balance and maintenance of interstitial hydration are regulated by the distribution volume of macromolecules (e.g., albumin, IgG) (*81*). In turn, the distribution volumes of

macromolecules are influenced by anionic glycosaminoglycans in the ECM (*81*). Following extravasation, antibodies experience various electrostatic forces within the interstitial fluid space due to the presence of negatively charged heparin sulfate and other anionic proteoglycans on the surface of cells within the interstitium (*47, 48, 82*). Proteoglycans are produced by most mammalian cells as components of the ECM. Diversity in the number of chains, chain lengths, and sulfation patterns allow these macromolecules to make significant contributions to ECM structure and function (*48, 82*). Electrostatic attraction between cationized molecules and anionic heparan sulfate (*82*) proteoglycans have been implicated in cellular internalization of viruses, basic peptides, and polycation-nucleic-acid complexes for gene transfer and protein delivery to mammalian cells (*47*).

Interstitial fluid volumes (V_i) measured using the extracellular space marker chromium-51-ethylenediaminetetraacetic acid (^{51}Cr-EDTA) can be combined with radiolabeled macromolecule data to derive the relative available (V_a/V_i) and excluded (V_e/V_i) interstitial volume fractions. Values of V_e/V_i for positively (pI = 8.7) and negatively (pI = 6.6) charged radioiodinated IgG were measured in rat skin (0.37 and 0.65, respectively) and in muscle (0.24 and 0.51, respectively) (*83*). Higher V_e/V_i values for anionic IgG in both tissues suggested that fixed negative charges, most likely glycosaminoglycans, discouraged interstitial antibody localization via charge repulsion, thereby regulating interstitial fluid balance (*83*).

Further insight into electrostatic interactions between antibodies and the negatively charged mammalian interstitium may be gained by considering analogous data for albumin. A higher V_e/V_i value was obtained for native (pI = 4.9) HSA than for cationized (pI = 7.6) HSA in rat skeletal muscle (0.26 and 0.16, respectively) and in rat skin (0.40 and 0.30, respectively) (*84, 85*). The magnitude of difference in V_e/V_i between the same two charged macromolecules decreased in rat dermis with increasing dehydration, likely due to a reduced hydration domain surrounding tissue and probe macromolecules in conditions of increased electrostatic interactions (*81*). Negatively charged hyaluronic acid associated with collagen was implicated as a contributing factor in the intrafibrillar volume of collagen, possibly influencing V_e/V_i (*81*).

Organ-Specific Interactions. Charge-selective renal filtration is considered to be largely facilitated by heparan sulfate in the glomerular basement membrane (GBM) (*49, 86*). Minimization of albumin loss from plasma is regulated by several mechanisms, including renal handling, charge repulsion with the capillary wall, and the FcRn-mediated salvage pathway (*87*). In addition to maintaining normal physiology, charge of antibodies can also play an important role in several disease states. For instance, the high positive charge of sugar chains on anti-DNA antibodies are involved in the pathology of renal disorders in lupus patients (*88*). Furthermore, in preclinical studies addressing the etiology of anti-GBM nephritis, glomerular deposition of cationic anti-GBM antibodies was 4-fold higher than that of anionic antibodies (*89*). Likewise, analysis of urine from patients with proximal renal tubular disease revealed that urinary IgG was reabsorbed in a cationic-preferential manner (*90*). Moreover, in an effort to avoid nephrotoxicity due to high renal accumulation of radiolabeled or toxin-conjugated small immunoproteins used for cancer therapy, positive charge can be decreased to discourage electrostatic attraction to the polyanionic brush border of the renal proximal tubules (*75, 76*).

The localization and clearance of antibodies in the liver may be affected by both hydrophobic and electrostatic interactions. The increased tendency for hydrophobic antibodies to undergo hepatobiliary excretion is widely accepted (*91, 92*); however, molecular charge may also influence the degree of hepatic uptake (*53, 93*). In lungs, the presence of negative charges on pulmonary endothelial cells, basement membranes, and interstitial matrices may attract positively charged (i.e., basic) proteins, effectively retarding their plasma-lymph transport while enhancing their extravascular distribution volume and initial clearance (*94*). Cationization of antibodies has been explored as a means to enhance transport of antibodies across the blood-brain barrier (BBB) (*25*).

Solid Tumor Interactions. To improve exposure of biologics in solid tumors, both chemical and protein engineering (*7*) strategies have been employed to manipulate the molecular size, charge, valency, and binding affinity of antibodies and other biotherapeutics. Similarly to the situation in normal tissues, electrostatic repulsion between anionic macromolecules and the negatively charged tumor ECM can limit their extravasation and/or extravascular dispersion, effectively causing them to be partially excluded from the interstitial compartment. For example, a lower V_e/V_i was observed for trastuzumab (pI = 9.2) relative to control IgG (pI = 7.6) in tumors established in rats (0.29 and 0.36, respectively) (*95*). Similarly, cationized albumin (pI = 7.6) possessed a lower V_e/V_i relative to native albumin (pI = 5.0) (0.21 and 0.38, respectively) (*95*).

An alternative interpretation of these data could be that cationized macromolecules having lower V_e/V_i values display higher vascular permeabilities. Similar conclusions were reached in a separate study, where the vascular permeabilities of HMD-cationized bovine serum albumin (BSA, pI 8.6−9.1) and IgG (pI 8.6−9.3) in human colon adenocarcinoma (LS174T) tumors were more than 2-fold higher than that of the succinylate-anionized BSA (pI ≈ 2.0) and IgG (pI 3.0−3.9) (Table 2) (*29*). Although cationized molecules extravasated more rapidly in solid tumors than similarly sized neutral or anionic derivatives, they also displayed a nearly 2-fold faster plasma clearance than succinylated molecules, as well as enhanced drug delivery to normal organs (*29*).

CONCLUDING REMARKS

The technologies driving advances in the production of therapeutic antibodies have markedly influenced the evolution of the biotechnology industry. Extensive examinations of the molecular biology, toxicology, metabolism, PK, and PD of antibodies have been conducted, yet these biological parameters are seldom related to the physicochemical properties of the macromolecules themselves. Charge-dependent interactions between antibodies and biological matrices hold relevance in biotechnology, especially with regard to the development of immunoconjugates. While antigen binding specificity and kinetics are important considerations in antibody therapy, the charge (pI) of antibodies also bears an important influence on their PK and tissue distribution.

Heterogeneity in molecular charge distribution occurs spontaneously in the routine production of antibodies, can be deliberately induced through chemical or genetic means, and can be characterized using a combination of analytical and chromatographic techniques. In particular, the deliberate modification of antibodies by chemical means has been exploited as a valuable preclinical research tool to investigate the relationship between net molecular charge and biological disposition. Findings from these exploratory investigations may be summarized as follows: (I) shifts in isoelectric point of approximately one pI unit or more can produce measurable changes in tissue distribution and kinetics, (II) increases in net positive charge generally result in increased tissue retention and increased blood clearance, and (III) decreases in net positive charge generally result in decreased tissue retention and increased whole body clearance.

The last fifteen years has produced a variety of strategies to optimize the use of antibodies in humans. The generation of

engineered forms (chimeric, humanized, human) of antibodies and the exploration of novel modifications to improve PK represent exciting areas of biotechnological research. As biotherapeutics become increasingly important in disease treatment, a more extensive investigation of the biological consequences of variations in charge and other physicochemical properties will likely be required. Insight into the underlying mechanisms behind unexpected or undesirable PK properties of antibody therapeutics may be gained by including electrostatic parameters in clinically predictive physiologically based models of disposition kinetics (*96*). Finally, charge modification of antibodies as a means of "fine tuning" plasma PK parameters and target accumulation is an exciting and potentially useful approach to the development of new biotherapeutics.

ACKNOWLEDGMENT

The authors would like to thank Allison Bruce for assistance with graphics and Wendy Putnam, Daniela Bumbaca, and Scott Northrup for helpful discussions. The authors express appreciation to their many colleagues and peers who have contributed over the years to the development of antibodies and immunoconjugates. Apologies are extended to those whose important and relevant work was omitted due to lack of space. Disclosure Statement: All authors are employees of Genentech, a member of the Roche Group, and hold financial interest in Roche.

LITERATURE CITED

(1) Christiansen, J., and Rajasekaran, A. K. (2004) Biological impediments to monoclonal antibody-based cancer immunotherapy. *Mol. Cancer Ther. 3*, 1493–501.

(2) Kohler, G., and Milstein, C. (1975) Continuous cultures of fused cells secreting antibody of predefined specificity. *Nature 256*, 495–7.

(3) Boswell, C. A., Deng, R., Lin, K., Putnam, W. S., Lei, C., Theil, F. P., Joshi, A., Fielder, P. J., and Khawli, L. A. (2009) In vitro-in vivo correlations of pharmacokinetics, pharmacodynamics and metabolism for antibody therapeutics, In *Proteins and Peptides: Pharmacokinetic, Pharmacodynamic, and Metabolic Outcomes* (Mrsny, R. J., and Daugherty, A., Eds.) Informa HealthCare, New York.

(4) Wang, W., Wang, E. Q., and Balthasar, J. P. (2008) Monoclonal antibody pharmacokinetics and pharmacodynamics. *Clin. Pharmacol. Ther. 84*, 548–58.

(5) Mager, D. E. (2006) Target-mediated drug disposition and dynamics. *Biochem. Pharmacol. 72*, 1–10.

(6) Yeung, Y. A., Leabman, M. K., Marvin, J. S., Qiu, J., Adams, C. W., Lien, S., Starovasnik, M. A., and Lowman, H. B. (2009) Engineering human IgG1 affinity to human neonatal Fc receptor: impact of affinity improvement on pharmacokinetics in primates. *J. Immunol. 182*, 7663–71.

(7) Beckman, R. A., Weiner, L. M., and Davis, H. M. (2007) Antibody constructs in cancer therapy: protein engineering strategies to improve exposure in solid tumors. *Cancer 109*, 170–9.

(8) Iznaga-Escobar, N., Mishra, A. K., and Perez-Rodriguez, R. (2004) Factors affecting pharmacokinetics of monoclonal antibodies: A review article. *Methods Find. Exp. Clin. Pharmacol. 26*, 123–7.

(9) Olitzki, L. (1933) Electric charge of antibodies. *J. Immunol. 24*, 505–512.

(10) Roopenian, D. C., and Akilesh, S. (2007) FcRn: the neonatal Fc receptor comes of age. *Nat. Rev. Immunol. 7*, 715–25.

(11) Yeung, Y. A., Wu, X., Reyes, A. E., 2nd, Vernes, J. M., Lien, S., Lowe, J., Maia, M., Forrest, W. F., Meng, Y. G., Damico, L. A., Ferrara, N., and Lowman, H. B. (2010) A therapeutic anti-VEGF antibody with increased potency independent of pharmacokinetic half-life. *Cancer Res. 70*, 3269–77.

(12) Castro, G., Boswell, C. A., and Northrup, S. H. (1998) Dynamics of protein-protein docking: cytochrome c and cytochrome c peroxidase revisited. *J. Biomol. Struct. Dyn. 16*, 413–24.

(13) Harris, R. J. (2005) Heterogeneity of recombinant antibodies: linking structure to function. *Dev. Biol. (Basel) 122*, 117–27.

(14) Putnam, W. S., Prabhu, S., Zheng, Y., Subramanyam, M., and Wang, Y. M. C. (2010) Pharmacokinetic, pharmacodynamic and immunogenicity comparability assessment strategies for monoclonal antibodies. *Trends Biotechnol. 28*, 509–516.

(15) Vlasak, J., and Ionescu, R. (2008) Heterogeneity of monoclonal antibodies revealed by charge-sensitive methods. *Curr. Pharm. Biotechnol. 9*, 468–81.

(16) Khawli, L. A., Goswami, S., Hutchinson, R., Kwong, Z. W., Yang, J., Wang, X., Yao, Z., Sreedhara, A., Cano, T., Tesar, D., Nijem, I., Allison, D. E., Wong, P. Y., Kao, Y. H., Quan, C., Joshi, A., Harris, R. J., and P., M. (2010) Charge variants in IgG1: isolation, characterization, in vitro binding properties and pharmacokinetics in rats. *mAbs 2*, 613–24.

(17) Igawa, T., Tsunoda, H., Tachibana, T., Maeda, A., Mimoto, F., Moriyama, C., Nanami, M., Sekimori, Y., Nabuchi, Y., Aso, Y., and Hattori, K. Reduced elimination of IgG antibodies by engineering the variable region. *Protein Eng. Des. Sel. 23*, 385–92.

(18) Boswell, C. A., and Brechbiel, M. W. (2007) Development of radioimmunotherapeutic and diagnostic antibodies: an inside-out view. *Nucl. Med. Biol. 34*, 757–78.

(19) Damle, N. K. (2008) Antibody-drug conjugates ace the tolerability test. *Nat. Biotechnol. 26*, 884–5.

(20) De Stefano, C., Gianguzza, A., Piazzese, D., and Sammartano, S. (2003) Interactions of diethylenetriaminepentaacetic acid (dtpa) and triethylenetetraaminehexaacetic acid (ttha) with major components of natural waters. *Anal. Bioanal. Chem. 375*, 956–67.

(21) Cascio, S., De Robertis, A., and Foti, C. (1999) Protonation of diamines H_2N-$(CH_2)_n$-NH_2 ($n = 2-10$) in NaCl aqueous solution at different ionic strengths. *J. Chem. Eng. Data 44*, 735–738.

(22) Sharifi, J., Khawli, L. A., Hornick, J. L., and Epstein, A. L. (1998) Improving monoclonal antibody pharmacokinetics via chemical modification. *Q. J. Nucl. Med. 42*, 242–9.

(23) Rodwell, J. D., Alvarez, V. L., Lee, C., Lopes, A. D., Goers, J. W., King, H. D., Powsner, H. J., and McKearn, T. J. (1986) Site-specific covalent modification of monoclonal antibodies: in vitro and in vivo evaluations. *Proc. Natl. Acad. Sci. U.S.A. 83*, 2632–6.

(24) Hong, G., Bazin-Redureau, M. I., and Scherrmann, J. M. (1999) Pharmacokinetics and organ distribution of cationized colchicine-specific IgG and Fab fragments in rat. *J. Pharm. Sci. 88*, 147–53.

(25) Bickel, U., Lee, V. M. Y., and Pardridge, W. M. (1995) Pharmacokinetic differences between ^{111}In- and ^{125}I-labeled cationized monoclonal antibody against β-amyloid in mouse and dog. *Drug Delivery 2*, 128–135.

(26) Pardridge, W. M., Kang, Y. S., Diagne, A., and Zack, J. A. (1996) Cationized hyperimmune immunoglobulins: pharmacokinetics, toxicity evaluation and treatment of human immunodeficiency virus-infected human-peripheral blood lymphocytes-severe combined immune deficiency mice. *J. Pharmacol. Exp. Ther. 276*, 246–52.

(27) Pardridge, W. M., Kang, Y. S., Yang, J., and Buciak, J. L. (1995) Enhanced cellular uptake and in vivo biodistribution of a monoclonal antibody following cationization. *J. Pharm. Sci. 84*, 943–8.

(28) Pardridge, W. M., Buciak, J., Yang, J., and Wu, D. (1998) Enhanced endocytosis in cultured human breast carcinoma cells and in vivo biodistribution in rats of a humanized monoclonal antibody after cationization of the protein. *J. Pharmacol. Exp. Ther. 286*, 548–54.

(29) Dellian, M., Yuan, F., Trubetskoy, V. S., Torchilin, V. P., and Jain, R. K. (2000) Vascular permeability in a human

tumour xenograft: molecular charge dependence. *Br. J. Cancer 82*, 1513–8.
(30) Lee, H. J., and Pardridge, W. M. (2003) Monoclonal antibody radiopharmaceuticals: cationization, pegylation, radiometal chelation, pharmacokinetics, and tumor imaging. *Bioconjugate Chem. 14*, 546–53.
(31) Wall, D. A., and Maack, T. (1985) Endocytic uptake, transport, and catabolism of proteins by epithelial cells. *Am. J. Physiol. 248*, C12–20.
(32) Basu, S. K., Goldstein, J. L., Anderson, G. W., and Brown, M. S. (1976) Degradation of cationized low density lipoprotein and regulation of cholesterol metabolism in homozygous familial hypercholesterolemia fibroblasts. *Proc. Natl. Acad. Sci. U.S.A. 73*, 3178–82.
(33) Shen, W. C., and Ryser, H. J. (1978) Conjugation of poly-L-lysine to albumin and horseradish peroxidase: a novel method of enhancing the cellular uptake of proteins. *Proc. Natl. Acad. Sci. U.S.A. 75*, 1872–6.
(34) Vorbrodt, A. W. (1989) Ultracytochemical characterization of anionic sites in the wall of brain capillaries. *J. Neurocytol. 18*, 359–68.
(35) Pardridge, W. M., Bickel, U., Buciak, J., Yang, J., Diagne, A., and Aepinus, C. (1994) Cationization of a monoclonal antibody to the human immunodeficiency virus REV protein enhances cellular uptake but does not impair antigen binding of the antibody. *Immunol. Lett. 42*, 191–5.
(36) Triguero, D., Buciak, J. B., Yang, J., and Pardridge, W. M. (1989) Blood-brain barrier transport of cationized immunoglobulin G: enhanced delivery compared to native protein. *Proc. Natl. Acad. Sci. U.S.A. 86*, 4761–5.
(37) Schattner, M., Lazzari, M., Trevani, A. S., Malchiodi, E., Kempfer, A. C., Isturiz, M. A., and Geffner, J. R. (1993) Activation of human platelets by immune complexes prepared with cationized human IgG. *Blood 82*, 3045–51.
(38) Russell, C. D., Crittenden, R. C., and Cash, A. G. (1980) Determination of net ionic charge on Tc-99m DTPA and Tc-99m EDTA by a column ion-exchange method. *J. Nucl. Med. 21*, 354–60.
(39) Boswell, C. A., Sun, X., Niu, W., Weisman, G. R., Wong, E. H., Rheingold, A. L., and Anderson, C. J. (2004) Comparative in vivo stability of copper-64-labeled cross-bridged and conventional tetraazamacrocyclic complexes. *J. Med. Chem. 47*, 1465–74.
(40) Scappaticci, F. A., Contreras, A., Boswell, C. A., Lewis, J. S., and Nolan, G. (2003) Polyclonal antibodies to xenogeneic endothelial cells induce apoptosis and block support of tumor growth in mice. *Vaccine 21*, 2667–77.
(41) Ali, J., and Younus, H. (2006) Effect of succinylation of antibodies on their conformation and interaction with the antigen. *Biochemistry (Mosc.) 71*, 1336–40.
(42) Lewis, M. R., Boswell, C. A., Laforest, R., Buettner, T. L., Ye, D., Connett, J. M., and Anderson, C. J. (2001) Conjugation of monoclonal antibodies with TETA using activated esters: biological comparison of ^{64}Cu-TETA-1A3 with ^{64}Cu-BAT-2IT-1A3. *Cancer Biother. Radiopharm. 16*, 483–94.
(43) Clifford, T., Boswell, C. A., Biddlecombe, G. B., Lewis, J. S., and Brechbiel, M. W. (2006) Validation of a novel CHX-A" derivative suitable for peptide conjugation: small animal PET/CT imaging using yttrium-86-CHX-A"-octreotide. *J. Med. Chem. 49*, 4297–304.
(44) Geerligs, I. E. J., Beijnen, J. H., Bekers, O., and Underberg, W. J. M. (1993) Quality control of protein and peptide drugs: Monoclonal antibodies and some biological response modifiers derived by recombinant DNA technology. *Drug Dev. Ind. Pharm. 19*, 33–84.
(45) Page, M., and Thorpe, R. (1998) IgG purification. *Methods Mol. Biol. 80*, 95–111.
(46) Varki, A. (2008) Sialic acids in human health and disease. *Trends Mol. Med. 14*, 351–60.
(47) Belting, M. (2003) Heparan sulfate proteoglycan as a plasma membrane carrier. *Trends Biochem. Sci. 28*, 145–51.
(48) Hardingham, T. E., and Fosang, A. J. (1992) Proteoglycans: many forms and many functions. *Faseb J. 6*, 861–70.
(49) van den Hoven, M. J., Wijnhoven, T. J., Li, J. P., Zcharia, E., Dijkman, H. B., Wismans, R. G., Rops, A. L., Lensen, J. F., van den Heuvel, L. P., van Kuppevelt, T. H., Vlodavsky, I., Berden, J. H., and van der Vlag, J. (2008) Reduction of anionic sites in the glomerular basement membrane by heparanase does not lead to proteinuria. *Kidney Int. 73*, 278–87.
(50) Wiig, H., Gyenge, C., Iversen, P. O., Gullberg, D., and Tenstad, O. (2008) The role of the extracellular matrix in tissue distribution of macromolecules in normal and pathological tissues: potential therapeutic consequences. *Microcirculation 15*, 283–96.
(51) Gangopadhyay, A., Petrick, A. T., and Thomas, P. (1996) Modification of antibody isoelectric point affects biodistribution of 111-indium-labeled antibody. *Nucl. Med. Biol. 23*, 257–61.
(52) ten Kate, C. I., Fischman, A. J., Rubin, R. H., Fucello, A. J., Riexinger, D., Wilkinson, R. A., Du, L., Khaw, B. A., and Strauss, H. W. (1990) Effect of isoelectric point on biodistribution and inflammation: imaging with indium-111-labelled IgG. *Eur. J. Nucl. Med. 17*, 305–9.
(53) Yamasaki, Y., Sumimoto, K., Nishikawa, M., Yamashita, F., Yamaoka, K., Hashida, M., and Takakura, Y. (2002) Pharmacokinetic analysis of in vivo disposition of succinylated proteins targeted to liver nonparenchymal cells via scavenger receptors: importance of molecular size and negative charge density for in vivo recognition by receptors. *J. Pharmacol. Exp. Ther. 301*, 467–77.
(54) Perera, R. M., Zoncu, R., Johns, T. G., Pypaert, M., Lee, F. T., Mellman, I., Old, L. J., Toomre, D. K., and Scott, A. M. (2007) Internalization, intracellular trafficking, and biodistribution of monoclonal antibody 806: a novel anti-epidermal growth factor receptor antibody. *Neoplasia 9*, 1099–110.
(55) Hnatowich, D. J., Layne, W. W., Childs, R. L., Lanteigne, D., Davis, M. A., Griffin, T. W., and Doherty, P. W. (1983) Radioactive labeling of antibody: a simple and efficient method. *Science 220*, 613–5.
(56) Caliceti, P., and Veronese, F. M. (2003) Pharmacokinetic and biodistribution properties of poly(ethylene glycol)-protein conjugates. *Adv. Drug Delivery Rev. 55*, 1261–77.
(57) Chapman, A. P. (2002) PEGylated antibodies and antibody fragments for improved therapy: a review. *Adv. Drug Delivery Rev. 54*, 531–45.
(58) Khawli, L. A., Mizokami, M. M., Sharifi, J., Hu, P., and Epstein, A. L. (2002) Pharmacokinetic characteristics and biodistribution of radioiodinated chimeric TNT-1, -2, and -3 monoclonal antibodies after chemical modification with biotin. *Cancer Biother. Radiopharm. 17*, 359–70.
(59) Hornick, J. L., Sharifi, J., Khawli, L. A., Hu, P., Biela, B. H., Mizokami, M. M., Yun, A., Taylor, C. R., and Epstein, A. L. (1998) A new chemically modified chimeric TNT-3 monoclonal antibody directed against DNA for the radioimmunotherapy of solid tumors. *Cancer Biother. Radiopharm. 13*, 255–68.
(60) Khawli, L. A., Glasky, M. S., Alauddin, M. M., and Epstein, A. L. (1996) Improved tumor localization and radioimaging with chemically modified monoclonal antibodies. *Cancer Biother. Radiopharm. 11*, 203–15.
(61) Ghetie, V., Hubbard, J. G., Kim, J. K., Tsen, M. F., Lee, Y., and Ward, E. S. (1996) Abnormally short serum half-lives of IgG in beta 2-microglobulin-deficient mice. *Eur. J. Immunol. 26*, 690–6.
(62) Israel, E. J., Wilsker, D. F., Hayes, K. C., Schoenfeld, D., and Simister, N. E. (1996) Increased clearance of IgG in mice that lack beta 2-microglobulin: possible protective role of FcRn. *Immunology 89*, 573–8.
(63) Junghans, R. P., and Anderson, C. L. (1996) The protection receptor for IgG catabolism is the beta2-microglobulin-containing neonatal intestinal transport receptor. *Proc. Natl. Acad. Sci. U.S.A. 93*, 5512–6.
(64) Petkova, S. B., Akilesh, S., Sproule, T. J., Christianson, G. J., Al Khabbaz, H., Brown, A. C., Presta, L. G., Meng, Y. G., and

Roopenian, D. C. (2006) Enhanced half-life of genetically engineered human IgG1 antibodies in a humanized FcRn mouse model: potential application in humorally mediated autoimmune disease. *Int. Immunol. 18*, 1759–69.

(65) Chirino, A. J., Ary, M. L., and Marshall, S. A. (2004) Minimizing the immunogenicity of protein therapeutics. *Drug Discovery Today 9*, 82–90.

(66) Hwang, W. Y., and Foote, J. (2005) Immunogenicity of engineered antibodies. *Methods 36*, 3–10.

(67) Carter, P. J. (2006) Potent antibody therapeutics by design. *Nat. Rev. Immunol. 6*, 343–57.

(68) Pendley, C., Schantz, A., and Wagner, C. (2003) Immunogenicity of therapeutic monoclonal antibodies. *Curr. Opin. Mol. Ther. 5*, 172–9.

(69) Wang, H., Cao, C., Li, B., Chen, S., Yin, J., Shi, J., Ye, D., Tao, Q., Hu, P., Epstein, A., and Ju, D. (2008) Immunogenicity of iodine 131 chimeric tumor necrosis therapy monoclonal antibody in advanced lung cancer patients. *Cancer Immunol. Immunother. 57*, 677–84.

(70) Zhou, J., Tsao, H. K., Sheng, Y. J., and Jiang, S. (2004) Monte Carlo simulations of antibody adsorption and orientation on charged surfaces. *J. Chem. Phys. 121*, 1050–7.

(71) Hornick, J. L., Sharifi, J., Khawli, L. A., Hu, P., Bai, W. G., Alauddin, M. M., Mizokami, M. M., and Epstein, A. L. (2000) Single amino acid substitution in the Fc region of chimeric TNT-3 antibody accelerates clearance and improves immunoscintigraphy of solid tumors. *J. Nucl. Med. 41*, 355–62.

(72) Tabata, Y., Kawai, T., Murakami, Y., and Ikada, Y. (1997) Electric charge influence of dextran derivatives on their tumor accumulation after intravenous injection. *Drug Delivery 4*, 213–221.

(73) Yuan, F., Dellian, M., Fukumura, D., Leunig, M., Berk, D. A., Torchilin, V. P., and Jain, R. K. (1995) Vascular permeability in a human tumor xenograft: molecular size dependence and cutoff size. *Cancer Res. 55*, 3752–6.

(74) Haraldsson, B., Nystrom, J., and Deen, W. M. (2008) Properties of the glomerular barrier and mechanisms of proteinuria. *Physiol. Rev. 88*, 451–87.

(75) Kobayashi, H., Le, N., Kim, I. S., Kim, M. K., Pie, J. E., Drumm, D., Paik, D. S., Waldmann, T. A., Paik, C. H., and Carrasquillo, J. A. (1999) The pharmacokinetic characteristics of glycolated humanized anti-Tac Fabs are determined by their isoelectric points. *Cancer Res. 59*, 422–30.

(76) Kim, I. S., Yoo, T. M., Kobayashi, H., Kim, M. K., Le, N., Wang, Q. C., Pastan, I., Carrasquillo, J. A., and Paik, C. H. (1999) Chemical modification to reduce renal uptake of disulfide-bonded variable region fragment of anti-Tac monoclonal antibody labeled with ^{99m}Tc. *Bioconjugate Chem. 10*, 447–53.

(77) Kobayashi, H., Yoo, T. M., Kim, I. S., Kim, M. K., Le, N., Webber, K. O., Pastan, I., Paik, C. H., Eckelman, W. C., and Carrasquillo, J. A. (1996) L-lysine effectively blocks renal uptake of ^{125}I- or ^{99m}Tc-labeled anti-Tac disulfide-stabilized Fv fragment. *Cancer Res. 56*, 3788–95.

(78) Jain, M., Chauhan, S. C., Singh, A. P., Venkatraman, G., Colcher, D., and Batra, S. K. (2005) Penetratin improves tumor retention of single-chain antibodies: a novel step toward optimization of radioimmunotherapy of solid tumors. *Cancer Res. 65*, 7840–6.

(79) Melkko, S., Halin, C., Borsi, L., Zardi, L., and Neri, D. (2002) An antibody-calmodulin fusion protein reveals a functional dependence between macromolecular isoelectric point and tumor targeting performance. *Int. J. Radiat. Oncol. Biol. Phys. 54*, 1485–90.

(80) Vink, H., Wieringa, P. A., and Spaan, J. A. (1995) Evidence that cell surface charge reduction modifes capillary red cell velocity-flux relationships in hamster cremaster muscle. *J. Physiol. 489* (Pt 1), 193–201.

(81) Wiig, H., Tenstad, O., and Bert, J. L. (2005) Effect of hydration on interstitial distribution of charged albumin in rat dermis in vitro. *J. Physiol. 569*, 631–41.

(82) Kreuger, J., Spillmann, D., Li, J. P., and Lindahl, U. (2006) Interactions between heparan sulfate and proteins: the concept of specificity. *J. Cell Biol. 174*, 323–7.

(83) Wiig, H., and Tenstad, O. (2001) Interstitial exclusion of positively and negatively charged IgG in rat skin and muscle. *Am. J. Physiol. Heart Circ. Physiol. 280*, H1505–12.

(84) Gyenge, C. C., Tenstad, O., and Wiig, H. (2003) In vivo determination of steric and electrostatic exclusion of albumin in rat skin and skeletal muscle. *J. Physiol. 552*, 907–16.

(85) Taylor, A. E., and Parker, J. C. (2003) Intersitial exluded volumes: the effect of charge. *J. Physiol. 553*, 333.

(86) Morita, H., Yoshimura, A., and Kimata, K. (2008) The role of heparan sulfate in the glomerular basement membrane. *Kidney Int. 73*, 247–8.

(87) Koltun, M., Nikolovski, J., Strong, K., Nikolic-Paterson, D., and Comper, W. D. (2005) Mechanism of hypoalbuminemia in rodents. *Am. J. Physiol. Heart Circ. Physiol. 288*, H1604–10.

(88) Kinoshita, K., Ikoma, S., Yamagata, T., Nozaki, Y., Sugiyama, M., and Funauchi, M. (2006) Electric charge and sugar chains of immunoglobulin G in systemic lupus erythematosus. *Clin. Exp. Nephrol. 10*, 25–32.

(89) Madaio, M. P., Salant, D. J., Adler, S., Darby, C., and Couser, W. G. (1984) Effect of antibody charge and concentration on deposition of antibody to glomerular basement membrane. *Kidney Int. 26*, 397–403.

(90) Takahashi, S., Wada, N., Harada, K., and Nagata, M. (2004) Cationic charge-preferential IgG reabsorption in the renal proximal tubules. *Kidney Int. 66*, 1556–60.

(91) Skogh, T. (1982) Tissue distribution of intravenously injected dinitrophenylated human serum albumin. Effects of specific IgG and IgA antibodies. *Scand. J. Immunol. 16*, 465–75.

(92) Skogh, T., Stendahl, O., Sundqvist, T., and Edebo, L. (1983) Physicochemical properties and blood clearance of human serum albumin conjugated to different extents with dinitrophenyl groups. *Int. Arch. Allergy Appl. Immunol. 70*, 238–44.

(93) Ghitescu, L., and Fixman, A. (1984) Surface charge distribution on the endothelial cell of liver sinusoids. *J. Cell Biol. 99*, 639–47.

(94) Parker, J. C., Gilchrist, S., and Cartledge, J. T. (1985) Plasma-lymph exchange and interstitial distribution volumes of charged macromolecules in the lung. *J. Appl. Physiol. 59*, 1128–36.

(95) Wiig, H., Gyenge, C. C., and Tenstad, O. (2005) The interstitial distribution of macromolecules in rat tumours is influenced by the negatively charged matrix components. *J. Physiol. 567*, 557–67.

(96) Boswell, C. A., Ferl, G. Z., Mundo, E. E., Schweiger, M. G., Marik, J., Reich, M. P., Theil, F. P., Fielder, P. J., and Khawli, L. A. (2010) Development and evaluation of a novel method for preclinical measurement of tissue vascular volume. *Mol. Pharm. 7*, 1848–57.

(97) Wishart, D. S., Knox, C., Guo, A. C., Cheng, D., Shrivastava, S., Tzur, D., Gautam, B., and Hassanali, M. (2008) DrugBank: a knowledgebase for drugs, drug actions and drug targets. *Nucleic Acids Res. 36*, D901–6.

(98) Wilkins, M. R., Gasteiger, E., Bairoch, A., Sanchez, J. C., Williams, K. L., Appel, R. D., and Hochstrasser, D. F. (1999) Protein identification and analysis tools in the ExPASy server. *Methods Mol. Biol. 112*, 531–52.

(99) Jordan, R., Deckelbaum, L., and Nakada, M. (2002) Appendix B to monoclonal antibody-based pharmaceuticals, Abciximab/ReoPro, In *Pharmaceutical biotechnology: an introduction for pharmacists and pharmaceutical scientists* (Crommelin, D. J. A., and Sindelar, R. D., Eds.) p *313*, Taylor & Francis, New York.

(100) Costello, M. A., Woititz, C., De Feo, J., Stremlo, D., Wen, L.-F. L., Palling, D. J., Iqbal, K., and Guzman, N. A. (1992) Characterization of humanized anti-tac monoclonal antibody by traditional separation techniques and capillary electrophoresis. *J. Liquid Chromatogr. 15*, 1081–1097.

(101) Hunt, G., Moorhouse, K. G., and Chen, A. B. (1996) Capillary isoelectric focusing and sodium dodecyl sulfate-

capillary gel electrophoresis of recombinant humanized monoclonal antibody HER2. *J. Chromatogr., A 744*, 295–301.
(102) Wan, Y., Vasan, S., Ghosh, R., Hale, G., and Cui, Z. (2005) Separation of monoclonal antibody alemtuzumab monomer and dimers using ultrafiltration. *Biotechnol. Bioeng. 90*, 422–32.
(103) Santora, L. C., Krull, I. S., and Grant, K. (1999) Characterization of recombinant human monoclonal tissue necrosis factor-alpha antibody using cation-exchange HPLC and capillary isoelectric focusing. *Anal. Biochem. 275*, 98–108.
(104) Vlckova, M., Kalman, F., and Schwarz, M. A. (2008) Pharmaceutical applications of isoelectric focusing on microchip with imaged UV detection. *J. Chromatogr., A 1181*, 145–52.
(105) Moore, J. M., Patapoff, T. W., and Cromwell, M. E. (1999) Kinetics and thermodynamics of dimer formation and dissociation for a recombinant humanized monoclonal antibody to vascular endothelial growth factor. *Biochemistry 38*, 13960–7.
(106) DeLano, W. L. (2008) The PyMOL Molecular Graphics System. DeLano Scientific LLC: Palo Alto, CA, USA. http://www.pymol.org.
(107) Guex, N., and Peitsch, M. C. (1997) SWISS-MODEL and the Swiss-PdbViewer: an environment for comparative protein modeling. *Electrophoresis 18*, 2714–23.
(108) Jo, S., Kim, T., Iyer, V. G., and Im, W. (2008) CHARMM-GUI: a web-based graphical user interface for CHARMM. *J. Comput. Chem. 29*, 1859–65.

BC100261D

Generation of Endosomolytic Reagents by Branching of Cell-Penetrating Peptides: Tools for the Delivery of Bioactive Compounds to Live Cells in Cis or Trans

Alfredo M. Angeles-Boza,[†] Alfredo Erazo-Oliveras,[†] Ya-Jung Lee, and Jean-Philippe Pellois*

Department of Biochemistry and Biophysics, 300 Olsen Boulevard, Texas A&M University, College Station, Texas 77843-2128, United States. Received March 9, 2010; Revised Manuscript Received October 19, 2010

We describe the synthesis and cellular delivery properties of multivalent and branched delivery systems consisting of cell-penetrating peptides assembled onto a peptide scaffold using native chemical ligation. A trimeric delivery system presenting three copies of the prototypical cell-penetrating peptide TAT shows an endosomolytic activity much higher than its monomeric and dimeric counterparts. This novel reagent promotes the endosomal release of macromolecules internalized into cells by endocytosis, and as a result, it can be used to achieve cytosolic delivery of bioactive but cell-impermeable macromolecules in either cis (covalent conjugation) or trans (simple coincubation).

Cell-penetrating peptides (CPPs) can be conjugated to cell-impermeable macromolecules and carry their cargo into mammalian cells (*1*−*3*). A prototypical CPP is the cationic TAT peptide (GRKKRRQRRR). TAT−macromolecule conjugates interact with cell-surface proteoglycans and are internalized into cells by TAT-induced macropinocytosis and other endocytosis mechanisms. TAT and its cargo then enter the cytosolic space of the cell by escaping from endosomes (*4*). This endosomolytic activity is however only modest, and a large fraction of macromolecules remain trapped inside endocytic organelles and unable to reach their intracellular targets (*4*, *5*). In order to increase delivery of cargo to the cytoplasm, the challenge is to enhance the endosomolytic activity of TAT. This is particularly difficult given that the exact mechanisms involved in this critical step of the delivery process are unclear. A potential solution to this problem, however, is to create multivalent delivery agents displaying multiples copies of the peptide (*6*). This is based on the principle that multivalency results in an increase of the local concentration of the CPP at the sites where the peptide interacts with cellular components. It has been clearly established that such an approach can increase the endocytic uptake of cationic peptides and that branched molecules can function and multitask in ways their linear homologues cannot (*7*−*9*). Whether multivalency enhances the endosomolytic activity of CPPs remains, however, uncertain. In this report, we hypothesize that branched TAT derivatives would also have an increased endosomolytic activity as compared to TAT and that these reagents could induce the release of macromolecules trapped inside endocytic organelles into the cytosolic space of cells. To test this hypothesis, we report a simple and modular synthetic route to generate branched multivalent CPPs carrier agents. We show that dimerization of TAT does not improved its delivery properties, while species with more than 3 branches lead to unproductive membrane binding. In contrast, a trimeric TAT translocates into live cells with much higher efficiency than its monomeric counterpart. Importantly, the endosomolytic activity of the trimeric peptide is sufficiently increased so that it is able to deliver a bioactive peptide in trans. Together, these results should be important for the future design of multivalent delivery agents and establish branched CPP species as noncytotoxic endosomolytic agents that could complement numerous delivery methodologies.

Our synthetic approach consists of assembling multiple CPPs onto scaffold peptides using native chemical ligation (NCL) (*10*). The scaffold peptides contain several lysines that have been modified at the ε NH_2 with a cysteine residue (Figure 1) (*11*). Each cysteine is available to react with TAT containing a C-terminal thioester to generate branched species. The scaffold peptides were synthesized by SPPS using standard Fmoc protocols. Two to six lysine residues bearing Mtt protecting groups at the ε NH_2 were incorporated on Rink amide resin and separated by glycine residues to reduce steric hindrance during synthesis and NCL. The lysine side chains were deprotected orthogonally with 2% TFA, and Boc-Cys(S^tBu)-OH was coupled onto the exposed ε NH_2. This was followed by N-terminal Fmoc deprotection and subsequent coupling of 5(6)-carboxyfluorescein (Fl). TFA cleavage and HPLC purification afforded the scaffold peptides containing 2 to 6 sites for NCL. TAT thioester was obtained by SPPS on a sulfamylbutyryl resin using reported protocols (*12*). The multivalent TAT compounds were obtained by reacting the scaffold peptides containing *n* cysteines with 3*n* equiv of TAT-thioester at room temperature in aqueous buffer at pH 7.5. Formation of the products, Fl-TAT*n*, was detected by HPLC as early as 1 h, and the reactions were complete in less than 12 h.

The cellular import of the multivalent compounds was first investigated by live-cell fluorescence microscopy. The fluorescein molecule installed at the N-terminus of the peptides was used as both a fluorescent label and a model of a small molecule cargo. A fluorescein labeled TAT (Fl-TAT) was evaluated as a "nonbranched" control. Fl-TAT, Fl-TAT2, and Fl-TAT3 were incubated with HeLa cells for 30 min at 1 or 5 μM. These concentrations were chosen because Fl-TAT is known to penetrate cells poorly under a concentration threshold of 5−10 μM (*13*). We therefore considered that it would be possible to observe any enhancement of activity by Fl-TAT2 and Fl-TAT3 as compared to Fl-TAT under conditions where the monomeric peptide shows low activity. After washing the cells with fresh media, cells were imaged by fluorescence confocal microscopy (Figure 1b). In the case of Fl-TAT and Fl-TAT2, a punctate distribution consistent with accumulation of the compounds inside endocytic organelles was observed at both concentrations. No accumulation of the peptides in the cytosol was detected.

* E-mail: pellois@tamu.edu, Tel: 979-845-0101, Fax: 979-862-4718.
[†] These two authors have contributed equally to this work.

10.1021/bc100130r © 2010 American Chemical Society
Published on Web 11/02/2010

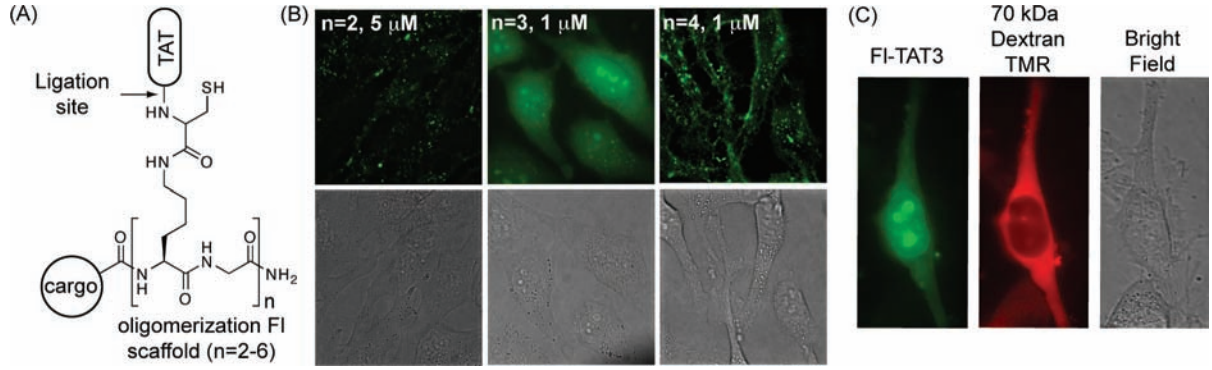


Figure 1. (A) Structure of the multivalent delivery agents Fl-TAT*n*. Multiple copies of the TAT peptide are ligated to a cysteine-containing oligomerization scaffold by NCL while a cell-impermeable cargo, fluorescein (Fl), is incorporated during SPPS. (B) Fluorescence and bright field images of live HeLa cells treated with Fl-TAT2 ($n = 2$), Fl-TAT3 ($n = 3$), and Fl-TAT4 ($n = 4$). The fluorescent cargo is trapped inside endocytic organelles with Fl-TAT2 (punctate distribution, 5 μM; same results were obtained for Fl-TAT at 5 μM) but released into the cytosol with Fl-TAT3 (diffuse distribution in cytosol and nucleus) at only 1 μM. Fl-TAT4 is bound to the plasma membrane. (C) Fluorescence images of live HeLa cells treated with Fl-TAT3 (1 μM) and 70 kDa Dextran-TMR (10 μM), a marker of pinocytosis. The cells represented in B or C were not stained by SYTOX Blue. This indicates that the membrane of these cells was not compromised.

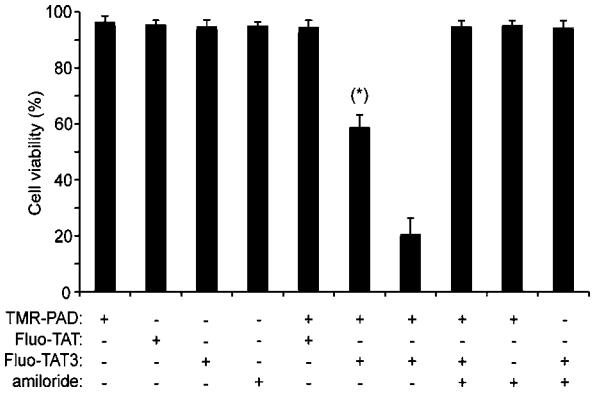


Figure 2. Delivery of TMR-PAD into HeLa cells mediated by Fl-TAT (10 μM) and Fl-TAT3 (1 μM where highlighted with * or 3 μM otherwise) as measured by a reduction in cell viability. SYTOX Blue staining was used to detect dead or dying cells 240 min after incubation with the peptides. Amiloride was used to inhibit macropinocytosis. Cell viability is expressed in % in comparison to an untreated sample. These results represent the average cell viability and corresponding standard deviation from three experiments.

In contrast, Fl-TAT3 exhibited a clear, diffuse, and cytosolic distribution at 1 or 5 μM indicative of an increase in the translocation efficiency as compared to the monomeric and dimeric compounds. Importantly, this was not accompanied by an increase in cytotoxicity of Fl-TAT3 (see next paragraph and Figure 2). The transport of Fl-TAT3 into the cytosol was inhibited by amiloride, an inhibitor of macropinocytosis. These results indicate that Fl-TAT3 is predominantly internalized by macropinocytosis and that it reaches the cytosol of cells by escaping from the endocytic pathway. Fl-TAT*n* with $n = 4$, 5, and 6 were also tested but could not be washed from the cell surface to a satisfactory level after incubation, and analysis of their transport properties was therefore difficult. These results are consistent with the work of Futaki and co-workers who have reported the synthesis of peptides with four branched chains of the type $(R_n)_4$ ($n = 1-6$) (*14*). $(R_2)_4$ was shown to internalized into cells with an efficiency similar to that of its linear homologue R_8, while $(R_6)_4$ was found to only accumulate at the plasma membrane without being able to enter cells (*15*). Likewise, Fl-TAT*n* with $n = 4$, 5, and 6 might bind to cell-surface components to such an extent that, in this case, it leads to a membrane-bound state that is not productive. Accordingly, these reagents were not considered further in our experiments.

To characterize the delivery activity of Fl-TAT3, we tested whether Fl-TAT3 might be capable of inducing the release of macromolecules from endosomes. This idea is based on the principle that, if Fl-TAT3 and a macromolecule are coincubated and accumulate together within endocytic vesicles, Fl-TAT3 might cause leakage of the endosomal membrane and release of the macromolecule into the cell (*16*). This was first suggested by the observation that 70 kDa Dextran-TMR, a marker of pinocytosis that typically accumulates inside endocytic vesicles when coincubated with cells, was present in the cytosol of cells when coincubated with Fl-TAT3 (Figure 1C). To test this hypothesis further and evaluate the delivery of a bioactive macromolecule, the pro-apoptotic peptide KLAKLAKKLAK-LAK-NH_2 (PAD) was used. PAD is cell-impermeable and has a negligible cytotoxicity toward mammalian cells (*17*). However, if delivered into the cytosol of cells, PAD permeabilizes the mitochondrial membrane and induces apoptosis (*18*, *19*). Cell death was therefore used as an indicator of the efficiency with which Fl-TAT3 might deliver PAD into cells. PAD labeled with carboxytetramethylrhodamine (TMR-PAD, 10 μM) was coincubated with Fl-TAT (1 to 10 μM) or Fl-TAT3 (1 to 3 μM) for 30 min. The import of TMR-PAD, Fl-TAT, and Fl-TAT3 into cells was monitored by confocal microscopy, and cell viability was assessed by SYTOX Blue staining. SYTOX Blue stains the nucleus of apoptotic or necrotic cells with a compromised plasma membrane without staining live cells. When TMR-PAD was coincubated with Fl-TAT, TMR-PAD was present inside endocytic organelles but did not appear to enter the cytosol of cells (as monitored by TMR fluorescence; not shown) regardless of the concentration of Fl-TAT used. In addition, the cell viability was not affected by treatment with these peptides (Figure 2). These results are consistent with a model where Fl-TAT cannot promote endosomal release of TMR-PAD, and as a result, TMR-PAD is unable to induce cell death. In contrast, cells incubated with Fl-TAT3 and TMR-PAD showed a diffuse and cytosolic distribution for both TMR-PAD and Fl-TAT3 (Figure 3). These cells were not stained by SYTOX Blue 60 min post-incubation. However, 40% and 80% of the cells became SYTOX Blue positive 240 min post-incubation when 1 or 3 μM Fl-TAT3 were used, respectively. Progression to classic morphological changes such as membrane blebbing and nuclear fragmentation further confirmed that cells were undergoing apoptosis. Treatment with amiloride inhibited delivery of Fl-TAT3 and TMR-PAD into cells as well as cell death (Figures 2 and 3). These results therefore indicate that the cytotoxicity observed when Fluo-TAT3 and TMR-PAD are coincubated arises from the delivery of TMR-PAD by Fl-TAT3

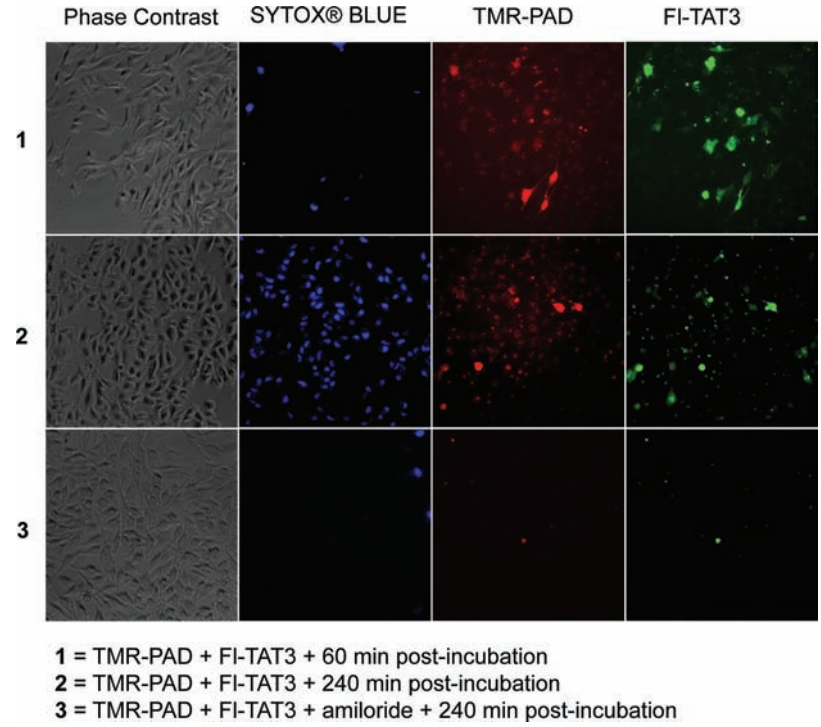


Figure 3. Images of cells incubated with TMR-PAD (10 μM), Fl-TAT3 (3 μM), and with or without the macropinocytosis inhibitor amiloride. Cells were incubated with the peptides for 30 min and washed with fresh media, and SYTOX Blue was added to detect dead cells. Images were acquired 60 or 240 min after addition of SYTOX Blue. Blue nuclei in the SYTOX Blue images represent dead or dying cells. Cells containing a cytosolic distribution of both TMR-PAD and Fl-TAT3 can be observed at 60 min.

as opposed to cytotoxic effects that might arise when the peptides are combined and not related to the transport of TMR-PAD. Together, these results support a model where Fl-TAT3 and TMR-PAD are first internalized into cells by endocytic mechanisms and where Fl-TAT3 then releases TMR-PAD into the cytosol of cells.

The NCL synthesis scheme used in this report generates Fl-TAT*n* compounds that contain *n* free thiols. On one hand, these thiols could be used to attach molecular cargos to the multivalent delivery reagents. On the other hand, the thiols, when left unmodified, could promote the aggregation of Fl-TAT*n* through the formation of intermolecular disulfide bridges. Such aggregates could participate in the cellular activities observed. The presence of aggregates could not be detected when the Fl-TAT*n* compounds dissolved in PBS were oxidized by bubbling oxygen in the media (HPLC and mass spectrometry analysis), suggesting that intramolecular disulfide bonds might form preferentially over intermolecular bonds (Supporting Information). Nonetheless, in vitro assays might not reproduce what happens inside cells, and it is possible that aggregates form in the lumen of endosomes. To address this issue, the thiols of Fl-TAT3 were blocked with iodoacetamide to form an acetamidated analogue of Fl-TAT3 (synthesis and characterization in Supporting Information). This product, Fl-TAT3-(S-CH_2-CO-NH_2)$_3$, cannot form disulfide bonds because the thiols are replaced by thioethers. To compare the delivery activity of Fl-TAT3-(S-CH_2-CO-NH_2)$_3$ with that of Fl-TAT3, Fl-TAT3-(S-CH_2-CO-NH_2)$_3$ (3 μM) and TMR-PAD (10 μM) were coincubated for 30 min with HeLa cells, and cell viability was assessed by microscopy. While incubation with Fl-TAT3-(S-CH_2-CO-NH_2)$_3$ alone resulted in a cell viability of 90%, coincubation with TMR-PAD resulted in a cell-viability of 25% 240 min post-incubation (Supporting Information). These results are similar to those obtained with Fl-TAT3. This suggests that the delivery activity of Fl-TAT3 is not a result of aggregation of the compound and that the presence of the thiols is not necessary to achieve delivery.

Overall, the trimeric TAT reported appears to have an endosomolytic activity much greater than its monomeric and dimeric counterparts without displaying the unproductive membrane binding observed for constructs containing more branches. As a result, it can deliver the small molecule cargo fluorescein in cis at concentrations much lower than that required for Fl-TAT. In addition, it can also be used to achieve delivery of a bioactive but cell-impermeable peptide in trans. This is important because this demonstrates that a macromolecule does not need to be labeled with an extraneous delivery peptide to be delivered, thereby greatly simplifying delivery protocols for in vitro applications. We are now testing the applicability of this delivery method to other macromolecules and exploring the effect of the structure and spatial orientation of the scaffold peptide on the delivery activity of the TAT trimer.

ACKNOWLEDGMENT

This work was supported by Award Number R01GM087227 from the National Institute of General Medical Sciences. A. E.-O. was supported by the Chemistry-Biology Interface training grant NIH 3 T32 GM008523.

Supporting Information Available: Full experimental procedures and compound characterization. This material is available free of charge via the Internet at http://pubs.acs.org.

LITERATURE CITED

(1) Brooks, H., Lebleu, B., and Vives, E. (2005) Tat peptide-mediated cellular delivery: back to basics. *Adv. Drug Delivery Rev. 57*, 559–77.

(2) Heitz, F., Morris, M. C., and Divita, G. (2009) Twenty years of cell-penetrating peptides: from molecular mechanisms to therapeutics. *Br. J. Pharmacol. 157*, 195–206.

(3) Nakase, I., Takeuchi, T., Tanaka, G., and Futaki, S. (2008) Methodological and cellular aspects that govern the internalization mechanisms of arginine-rich cell-penetrating peptides. *Adv. Drug Delivery Rev. 60*, 598–607.

(4) Wadia, J. S., Stan, R. V., and Dowdy, S. F. (2004) Transducible TAT-HA fusogenic peptide enhances escape of TAT-fusion proteins after lipid raft macropinocytosis. *Nat. Med. 10*, 310–5.
(5) Lee, Y. J., Datta, S., and Pellois, J. P. (2008) Real-time fluorescence detection of protein transduction into live cells. *J. Am. Chem. Soc. 130*, 2398–9.
(6) Sung, M., Poon, G. M., and Gariepy, J. (2006) The importance of valency in enhancing the import and cell routing potential of protein transduction domain-containing molecules. *Biochim. Biophys. Acta 1758*, 355–63.
(7) Kawamura, K. S., Sung, M., Bolewska-Pedyczak, E., and Gariepy, J. (2006) Probing the impact of valency on the routing of arginine-rich peptides into eukaryotic cells. *Biochemistry 45*, 1116–27.
(8) Tung, C. H., Mueller, S., and Weissleder, R. (2002) Novel branching membrane translocational peptide as gene delivery vector. *Bioorg. Med. Chem. 10*, 3609–14.
(9) Hassane, F. S., Ivanova, G. D., Bolewska-Pedyczak, E., Abes, R., Arzumanov, A. A., Gait, M. J., Lebleu, B., and Gariepy, J. (2009) A peptide-based dendrimer that enhances the splice-redirecting activity of PNA conjugates in cells. *Bioconjugate Chem. 20*, 1523–1530.
(10) Dawson, P. E., Muir, T. W., Clark-Lewis, I., and Kent, S. B. (1994) Synthesis of proteins by native chemical ligation. *Science 266*, 776–9.
(11) Alves, D. A., Esser, D., Broadbridge, R. J., Beevers, A. P., Chapman, C. P., Winsor, C. E., and Betley, J. R. (2003) Synthesis and use of a pseudo-cysteine for native chemical ligation. *J. Pept. Sci. 9*, 221–8.
(12) Szewczuk, L. M., Tarrant, M. K., Sample, V., Drury, W. J., Zhang, J., and Cole, P. A. (2008) Analysis of serotonin N-acetyltransferase regulation in vitro and in live cells using protein semisynthesis. *Biochemistry 47*, 10407–10419.
(13) Duchardt, F., Fotin-Mleczek, M., Schwarz, H., Fischer, R., and Brock, R. (2007) A comprehensive model for the cellular uptake of cationic cell-penetrating peptides. *Traffic 8*, 848–66.
(14) Futaki, S., Nakase, I., Suzuki, T., Youjun, Z., and Sugiura, Y. (2002) Translocation of branched-chain arginine peptides through cell membranes: flexibility in the spatial disposition of positive charges in membrane-permeable peptides. *Biochemistry 41*, 7925–30.
(15) Nakase, I., Tadokoro, A., Kawabata, N., Takeuchi, T., Katoh, H., Hiramoto, K., Negishi, M., Nomizu, M., Sugiura, Y., and Futaki, S. (2007) Interaction of arginine-rich peptides with membrane-associated proteoglycans is crucial for induction of actin organization and macropinocytosis. *Biochemistry 46*, 492–501.
(16) Lee, Y. J., Erazo-Oliveras, A., and Pellois, J. P. (2009) Delivery of macromolecules into live cells by simple co-incubation with a peptide. *ChemBioChem 11*, 325–330.
(17) Javadpour, M. M., Juban, M. M., Lo, W. C., Bishop, S. M., Alberty, J. B., Cowell, S. M., Becker, C. L., and McLaughlin, M. L. (1996) De novo antimicrobial peptides with low mammalian cell toxicity. *J. Med. Chem. 39*, 3107–13.
(18) Kwon, M. K., Nam, J. O., Park, R. W., Lee, B. H., Park, J. Y., Byun, Y. R., Kim, S. Y., Kwon, I. C., and Kim, I. S. (2008) Antitumor effect of a transducible fusogenic peptide releasing multiple proapoptotic peptides by caspase-3. *Mol. Cancer Therapeut. 7*, 1514–1522.
(19) Takeuchi, T., Kosuge, M., Tadokoro, A., Sugiura, Y., Nishi, M., Kawata, M., Sakai, N., Matile, S., and Futaki, S. (2006) Direct and rapid cytosolic delivery using cell-penetrating peptides mediated by pyrenebutyrate. *ACS Chem. Biol. 1*, 299–303.

BC100130R

Generation of Endosomolytic Reagents by Branching of Cell-Penetrating Peptides: Tools for the Delivery of Bioactive Compounds to Live Cells in Cis or Trans

Alfredo M. Angeles-Boza, Alfredo Erazo-Oliveras, Ya-Jung Lee and Jean-Philippe Pellois*

Department of Biochemistry and Biophysics, 300 Olsen Boulevard, Texas A&M University, College Station, TX 77843 – 2128.
E-mail: pellois@tamu.edu, Tel: 979-845-0101, Fax: 979-862-4718

SUPPORTING INFORMATION

Live-cell Imaging Experiments:

HeLa cells were seeded on 8-well chamber glass slide (Lab-Tek^{TM} Cat. No. 177402, 0.8 cm^2/well, Nunc International, Naperville, IL) at 3.0 x 10^4 cells/well in Dulbecco's modified Eagle's medium supplemented with 10% FBS and incubated for 24 h at 37°C in a humidified atmosphere containing 5% CO_2. For live-cell imaging, cells were washed and incubated with Leibovitz's L-15 Medium and placed under an inverted epifluorescence microscope (Model IX81, Olympus, Center Valley, PA) equipped with a heating stage maintained at 37°C. The microscope is configured with a spinning disk unit (DSU, Olympus) to perform both confocal and wide-field fluorescence microscopy. Images were collected using a Rolera-MGI Plus back-illuminated EMCCD camera (Qimaging, Surrey, BC, Canada) mounted on the microscope with UPlanFl 100× / 1.3 NA oil, or LCPlan 20× / 0.4 NA objectives. Images were acquired using phase contrast and three standard fluorescence filter sets: CFP (Ex = 436±20 nm / Em= 480±40 nm), Texas Red (Ex = 560±40 nm / Em= 630±75 nm), and FITC (Ex = 482±35 nm / Em= 536±40 nm). (Semrock, Rochester, NY). Cells were treated with the different peptides in L-15 medium. The concentrations of the peptides were determined by measuring the absorbance of the

fluorescein moiety at 492 nm (ε = 56000 M^{-1} cm^{-1} at pH 7.4). For macropinocytosis inhibition, cells were first pretreated with 50 μM of amiloride (Sigma, MO*)* for 30 minutes, and then with the peptides while keeping amiloride present. After incubation at 37°C for 30 minutes, the cells were washed with PBS 5 times and the medium was replaced with fresh L-15. The integrity of the plasma membrane of the cells was determined by addition of the cell-impermeable DNA stain SYTOX® Blue (5 μM, dead cells are stained in less than 5 min at this concentration). Cells were then placed on the microscope and images were acquired in the CFP fluorescence channel for detection of SYTOX® Blue. TMR was detected with the Texas Red filter set and Fl with the FITC filter set. Images were processed using the SlideBook 4.2 software (Olympus, Center Valley, PA).

For the delivery of TMR-PAD to live cells reported in Figure 2 and 3, cells were imaged with a 20 X objective by phase contrast and fluorescence imaging for up to 4 hours. Ten to twenty images were acquired for each experiment. The total number of cells in a given image was determined from the phase contrast image while the number of dead cells was determined by identifying cells containing a blue fluorescent nucleus stained by SYTOX® Blue. Cell viability was determined by first establishing a ratio of dead cells/total number of cells for each sample (1000 cells were counted in each experiments and each experiments were repeated 3 times).

Peptide Synthesis and Purification

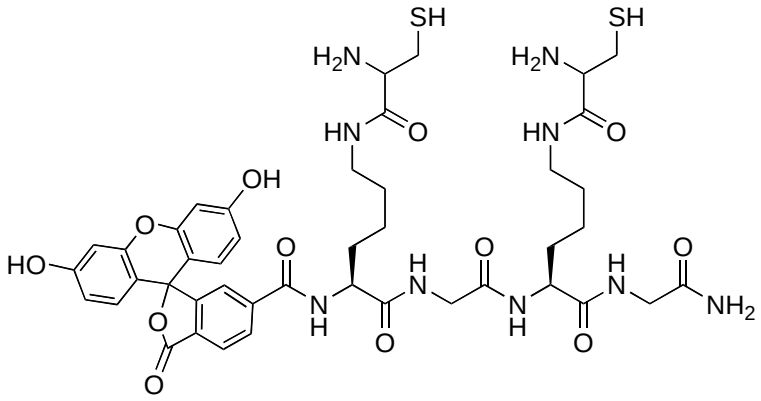
All amino acids were obtained from Novabiochem (San Diego, CA and used as received. Peptides were synthesized in-house by SPPS using standard Fmoc protocols. Fmoc-Lys(Boc)-OH, Fmoc-Lys(Mtt)-OH, Fmoc-Gly-OH, Fmoc-Arg(Pbf)-OH, Fmoc-Gln(Trt)-OH, Fmoc-Leu-OH, Fmoc-Ala-OH, and Boc-Cys(StBu) were used to assemble the peptides. Reactions were carried out in SPPS vessels at room temperature using a stream of dry N_2 to provide agitation. Fmoc deprotection was performed by addition of piperidine in DMF (20%, 5 mL) to the Fmoc-peptide resin (0.72 mmol). Deprotection was carried out for 1×3 min and 1×10 min. Coupling reactions were carried out for 2 h with a mixture of Fmoc-amino acid (2.88 mmol), HBTU (1.06 g, 2.80 mmol), and DIEA (1.25 mL, 7.2 mmol) in DMF. Upon completion of the reaction, the resin was washed with DMF. The peptides were analyzed and purified by reverse phase HPLC. HPLC analysis was performed on a Hewlett-Packard 1200 series instrument and a Vydac C18 column (5 micron, 4 x 150 mm). Flow rate was 1 mL/min and detection was at 214 nm and 450 nm. Semi-preparative HPLC was performed on a Vydac C18 10 × 250 mm column. Flow rate was 4 mL/min and detection was at 214 nm and 450 nm. All runs used linear gradients of 0.1% aqueous TFA (solvent A) and 90% acetonitrile, 9.9% water and 0.1% TFA (solvent B). The correct identity of the peptides was confirmed by time-of-flight mass spectrometry performed with a Shimadzu/Kratos instrument (AXIMA-CFR, Shimadzu, Kyoto).

Synthesis of Fl-(Kε(C)-G)$_n$-NH$_2$

The Fl-(Kε(C)-G)$_n$-NH$_2$, n=2-6, peptides were assembled using a standard Fmoc solid phase peptide synthesis strategy. Fmoc-Gly-OH was first coupled to the Rink amide resin (0.72 mmol scale). Fmoc-Lys(Mtt)-OH and Fmoc-Gly-OH were the alternatively coupled to generate the peptides Fmoc-(Kε(Mtt)-G)$_n$-Rink amide. The Mtt protecting groups were cleaved by treating the resin with 2% TFA in DCM for 30 min and Boc-Cys(S^{t}Bu)-OH (3 x n equivalents) was coupled onto the exposed ε amino groups in DMF containing DIEA and HBTU (3 x n eq.). This was followed by *N*-terminal Fmoc deprotection and subsequent overnight coupling of 5(6)-carboxyfluorescein (Fl, 1.1 eq) in DMF containing HBTU (1.1 eq.). The S-StBu

groups on the Cys side chains were cleaved on the solid phase using 100 eq of PBu_3 and 400 eq of H_2O in DMF:DCM for 4h. The peptides were cleaved from the resin with 92.5% TFA, 2.5% TIS, 2.5% EDT, and 2.5% H_2O. The crude products were precipitated and washed with cold diethyl ether and then lyophilized to yield crude peptide solids that were purified by preparative scale reverse phase HPLC using a water/acetonitrile gradient in the presence of 0.1% TFA.

Characterization of Fl-(Kε(C)-G)$_2$-NH$_2$



Chemical Formula: $C_{43}H_{53}N_9O_{12}S_2$
Molecular Weight: 952.06

Figure S1. Structure and expected molecular weight of Fl-(Kε(C)-G)$_2$-NH$_2$

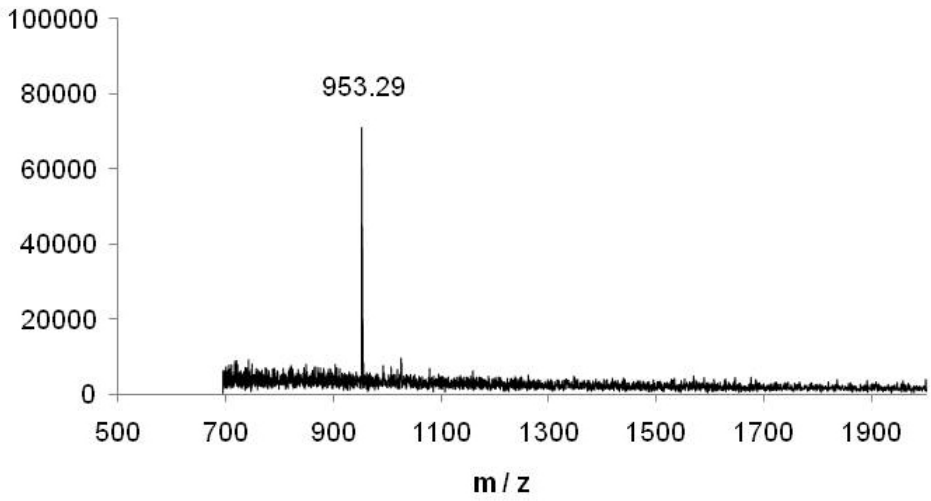
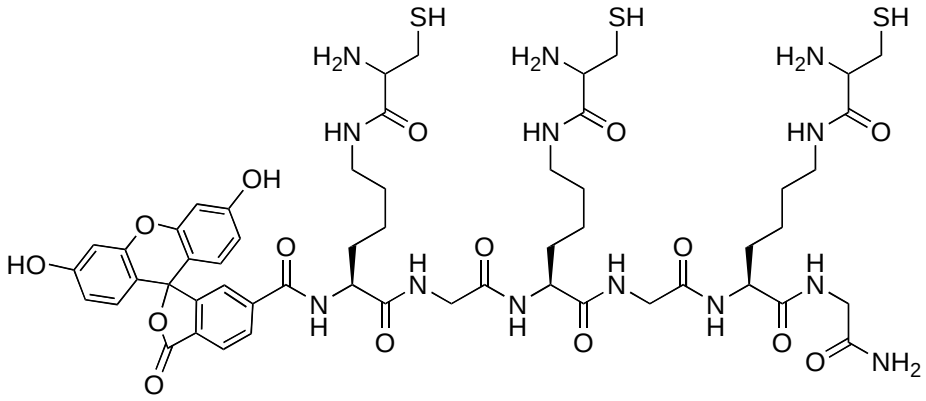


Figure S2. MALDI-TOF MS spectrum of Fl-(Kε(C)-G)$_2$-NH$_2$.

Characterization of Fl-(Kε(C)-G)$_3$-NH$_2$



Chemical Formula: $C_{54}H_{73}N_{13}O_{15}S_3$
Molecular Weight: 1240.43

Figure S3. Structure and expected molecular weight of Fl-(Kε(C)-G)$_3$-NH$_2$.

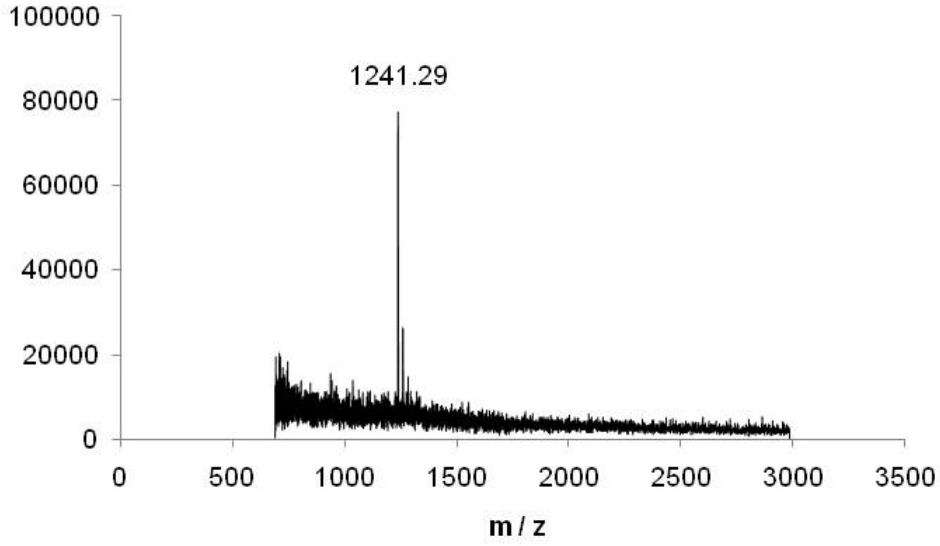
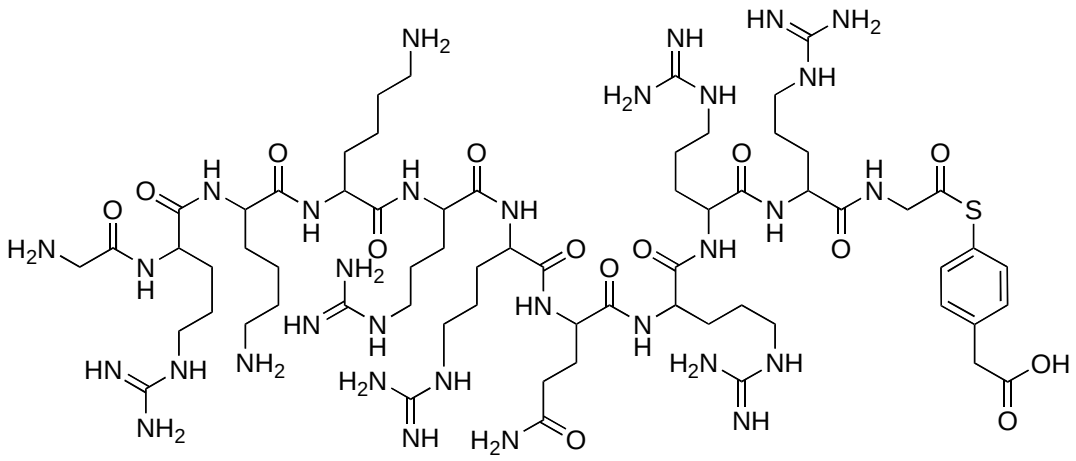


Figure S4. MALDI-MS spectrum of Fl-(Kε(C)-G)$_3$-NH$_2$.

Synthesis of TAT-thioester

The TAT peptide thioester (GRKKRRQRRRG-thioester) was readily prepared by SPPS on the 4-sulfamylbutyryl-AM resin using reported protocols.[1] The resin was pre-swollen in 10 volumes of dry methylene chloride for 1 h. During this period, Fmoc-Gly-OH (4 equiv) along with 1-methylimidazole (4 equiv) was dissolved in a 4:1 mixture of dry methylene chloride (DCM) and dimethylformamide (DMF) under a blanket of inert gas. *N*,*N*′-diisopropylcarbodiimide (DIC) was added and the solution was mixed for 5 min at room temperature. This acylation mixture was added to the drained resin. The resin was agitated with a stream of N2 for 18 h at room temperature and then drained. The resin was washed with DCM and DMF. The desired peptide is then formed via standard manual peptide synthesis. Boc-Gly-OH was used in the last coupling. The resin was washed with DMF and DCM. For activation of the resin prior to cleavage, a solution of iodoacetonitrile (25 equiv) and diisopropylethyl amine (10 equiv) in 3 mL of DMF and 1 mL of hexamethylphosphoric triamide was added to the drained resin. The resin was agitated with a stream of N2 for 18 h at room temperature. The solution was drained, and the resin was washed with DMF and DCM prior to immediate cleavage. The peptide was then cleaved from the activated resin with mercaptophenylacetic acid. First, mercaptophenylacetic acid (2.0 mmol for 0.1 mmol resin) was suspended in DCM (10 mL) in a round-bottom flask flushed with argon. The mixture was cooled to 0 °C and DIEA (1.0 mmol) was added dropwise over 5 min. The resin pre-swollen in DCM was drained and treated with the thiol solution. The resin bed was stirred for 18 h at room temperature. The resin was drained and the filtrate collected. The resin was washed with three additional portions of DCM, these being pooled with the original filtrate. The filtrate was concentrated in vacuo to provide a crude product. The residue was treated with 10 mL of a 95:2.5:2.5 TFA/water/triisopropylsilane (TIS) mixture to remove the side-chain protecting groups. The product was filtered to remove excess insoluble thiol, concentrated in vacuo, and precipitated and washed with cold diethyl ether. The peptide was purified by reversed-phase HPLC and analyzed by mass spectrometry. Expected mass: 1603.9 Da, observed mass: 1603.2 Da.

Characterization of TAT-thioester



Chemical Formula: C65H118N32O14S
Molecular Weight: 1603.90

Figure S5. Structure and expected molecular weight of TAT-MPAA thioester (GRKKRRQRRRK-MPAA).

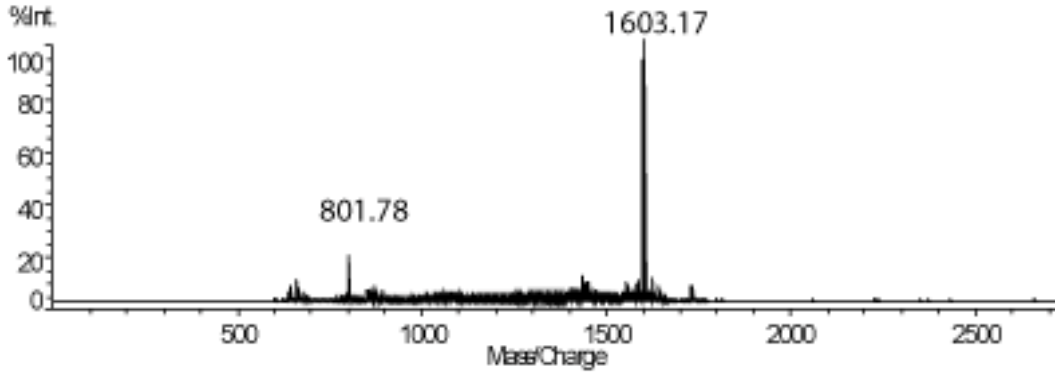
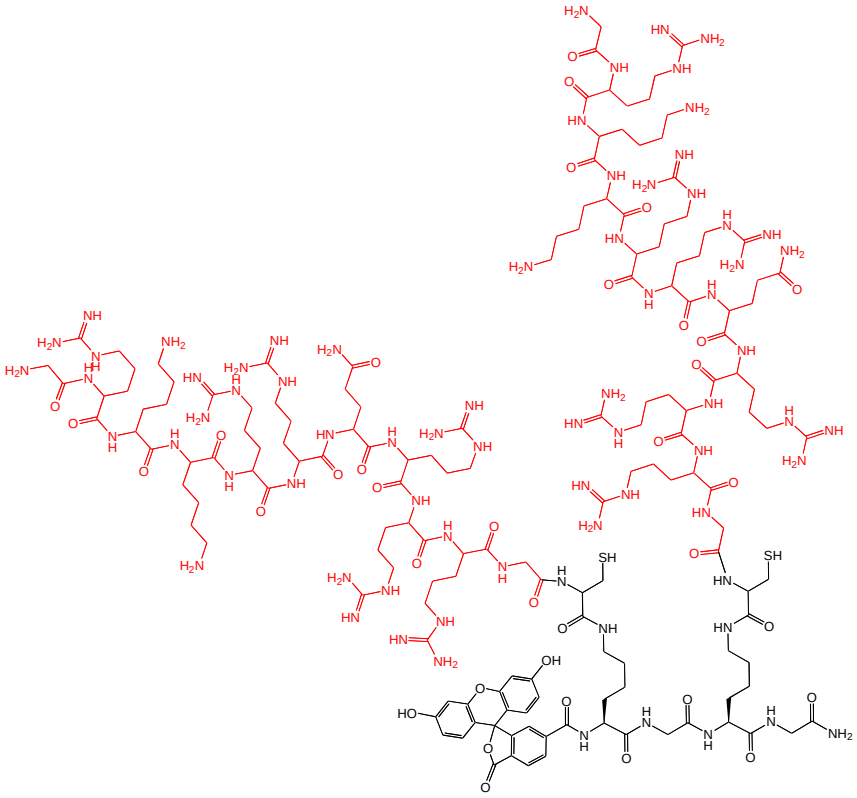


Figure S6. MALDI-MS spectrum of TAT-MPAA thioester. The peak at 801.78 corresponds to the doubly-charged product.

Synthesis of Fl-TATn

Fl-TATn was formed by addition of TAT-MPAA thioester (3 x n equivalents) to Fl-(Kε(C)-G)$_n$-NH_2 (1 mM) in 25 mM HEPES, 100 mM MESNa, and 10 mM TCEP at pH 7.5 (TAT-MPAA thioester exchanges to TAT-mercaptoethanesulfonate thioester under these conditions). After 16 hours of reaction at room temperature, the crude product was purified by preparative scale reverse phase HPLC using a water/acetonitrile gradient in the presence of 0.1% TFA.

Characterization of Fl-TAT2



Chemical Formula: $C_{157}H_{273}N_{73}O_{36}S_2$
Molecular Weight: 3823.45

Figure S7. Structure and expected molecular weight of Fl-TAT2.

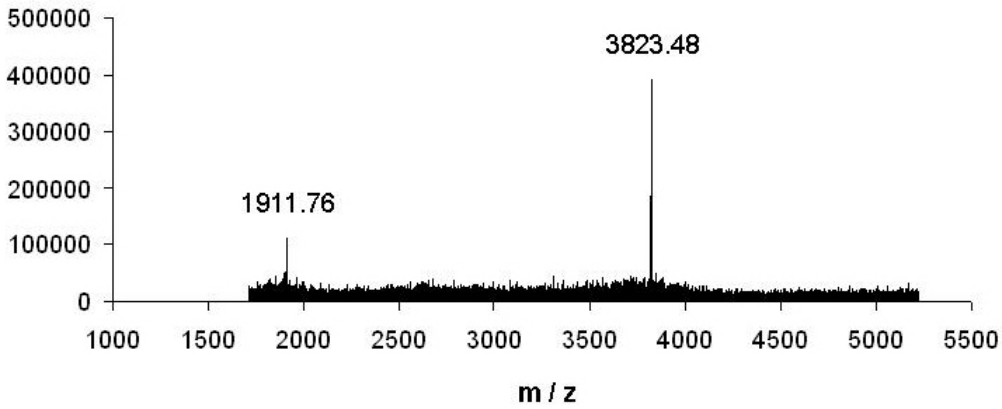
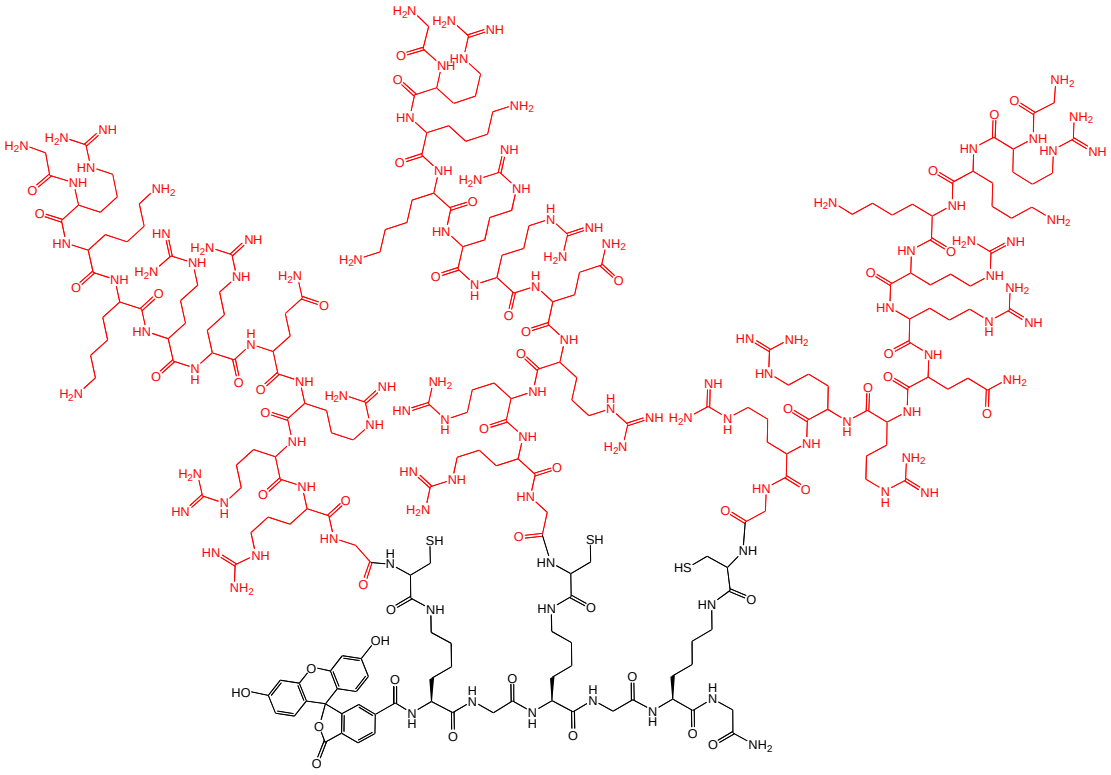


Figure S8. MALDI-TOF MS spectrum of Fl-TAT2. The peak at 1911.76 corresponds to the doubly charged product.

Characterization of Fl-TAT3



Chemical Formula: $C_{225}H_{403}N_{109}O_{51}S_3$
Molecular Weight: 5547.50

Figure S9. Structure and expected molecular weight of Fl-TAT3**.**

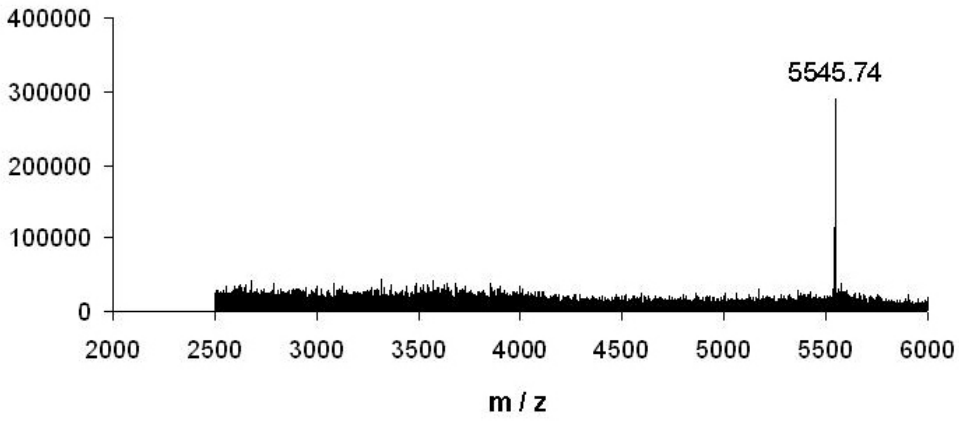


Figure S10. MALDI-TOF MS spectrum of Fl-TAT3.

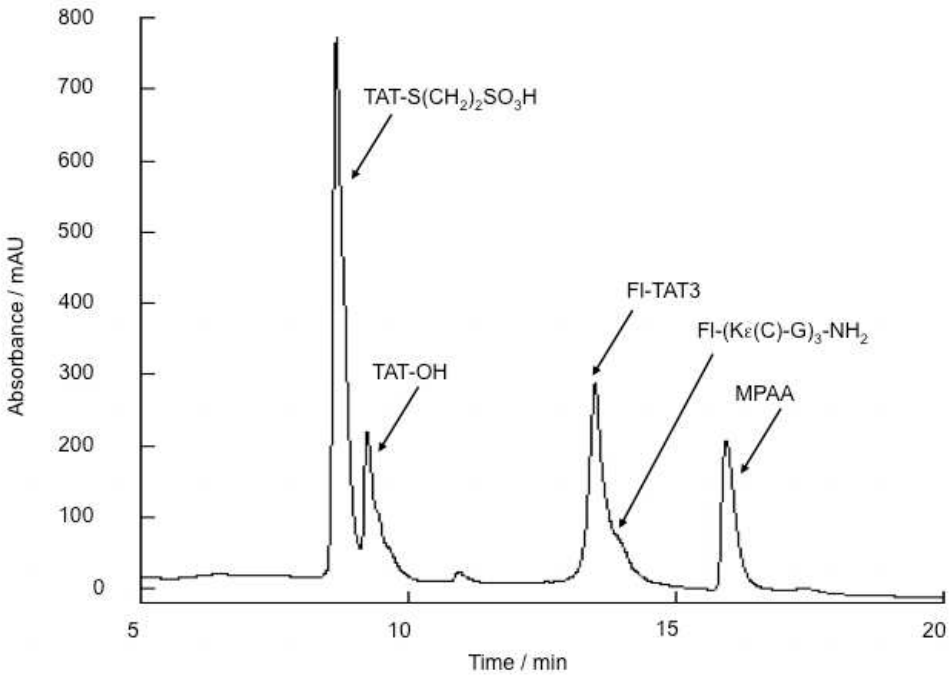
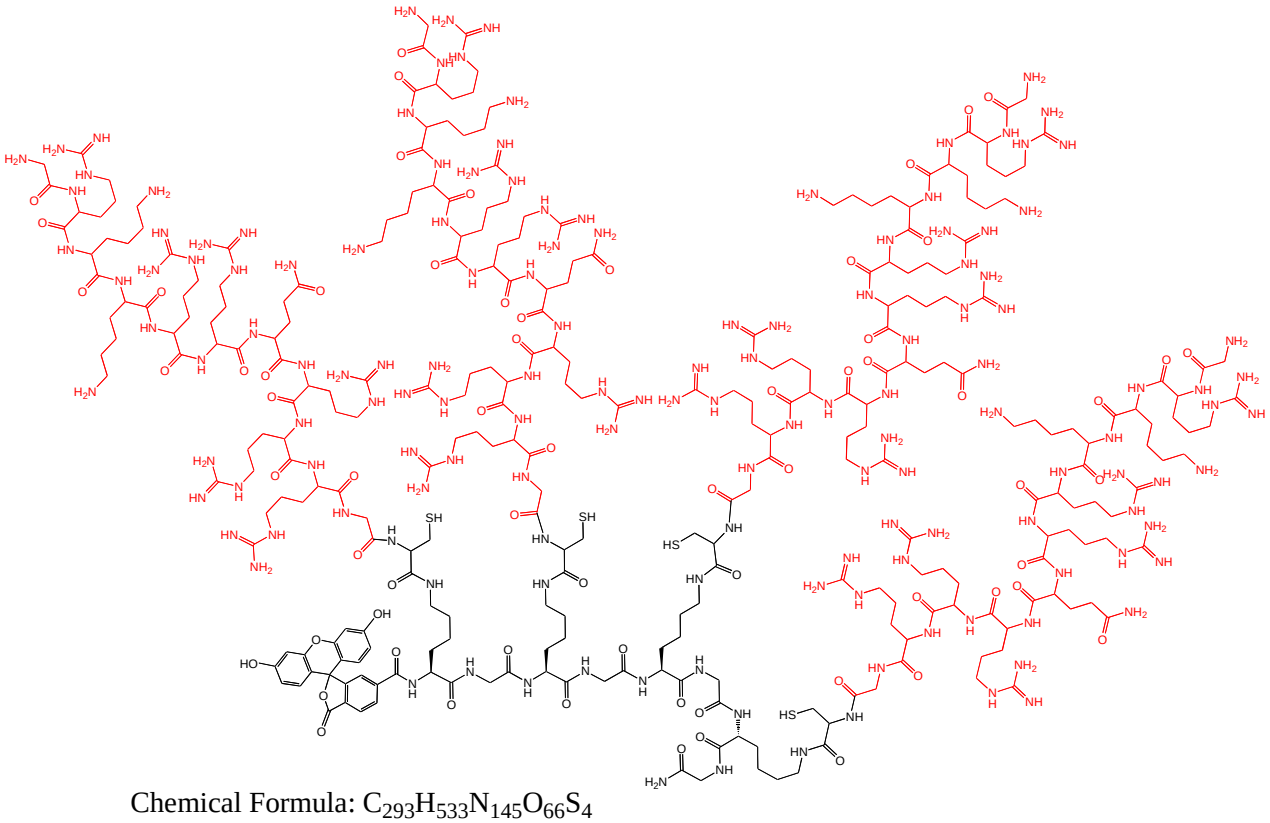


Figure S11. HPLC analysis of the reaction between Fl-(Kε(C)-G)$_n$-NH$_2$ and TAT-thioester after 2 hours of reaction. Reagents and products were identified by mass spectrometry.

Characterization of Fl-TAT4



Chemical Formula: $C_{293}H_{533}N_{145}O_{66}S_4$
Molecular Weight: 7271.56

Figure S12. Structure and expected molecular weight of Fl-TAT4**.**

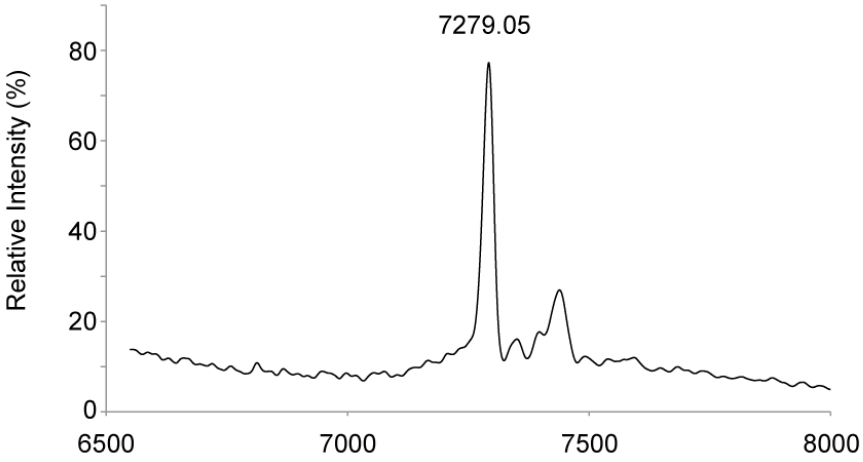
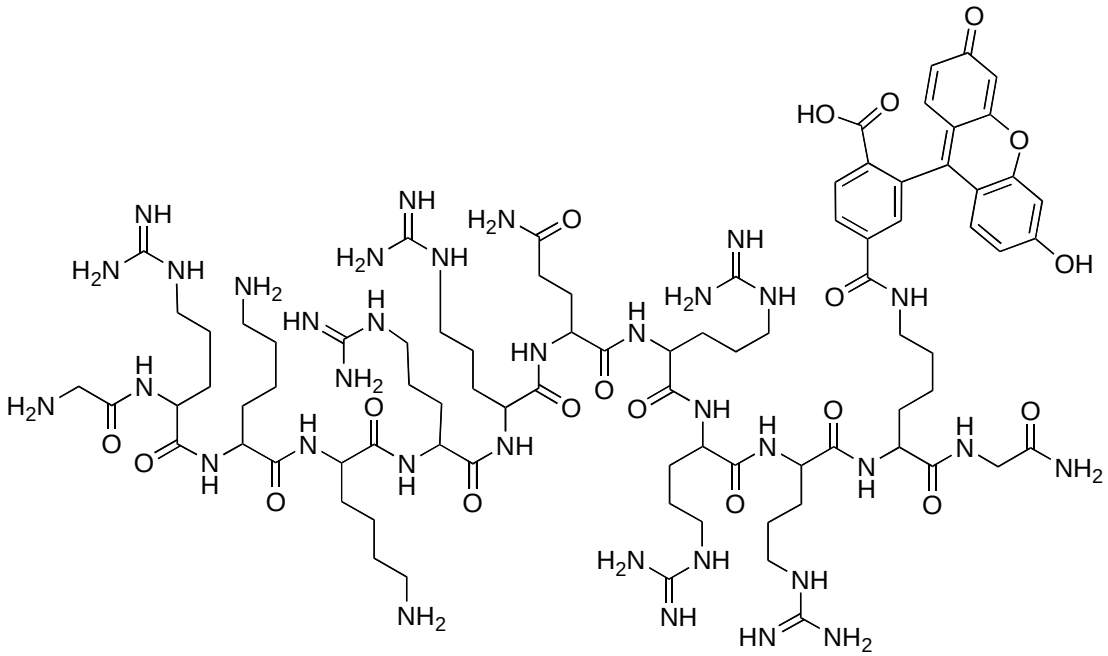


Figure S13. MALDI-TOF MS spectrum of Fl-TAT4.

Synthesis of Fl-TAT

Fl-TAT (GRKKRRQRRRK(Fl)G-NH_2) was prepared by SPPS on the Rink amide resin. Fmoc-G-R(Pbf)-K(Boc)-K(Boc)-R(Pbf)-R(Pbf)-Q(Trt)-R(Pbf)-R(Pbf)-R(Pbf)-K(Mtt)-G was first assembled on the resin. The Mtt protecting group was cleaved by treating the resin with 2% TFA in DCM for 30 min and 5(6)-carboxyfluorescein (Fl, 1.1 eq.) was coupled onto the exposed ε amino groups in DMF containing DIEA and HBTU (1.1 eq.). This was followed by *N*-terminal Fmoc deprotection with 20% piperidine in DMF. The peptide was cleaved from the resin with 92.5% TFA, 2.5% TIS, 2.5% EDT, and 2.5% H_2O. The crude product was precipitated and washed with cold diethyl ether and then lyophilized to yield crude solid that was purified by preparative scale reverse phase HPLC using a water/acetonitrile gradient in the presence of 0.1% TFA. . Expected mass: 1939.2 Da, observed mass: 1937.2 Da.

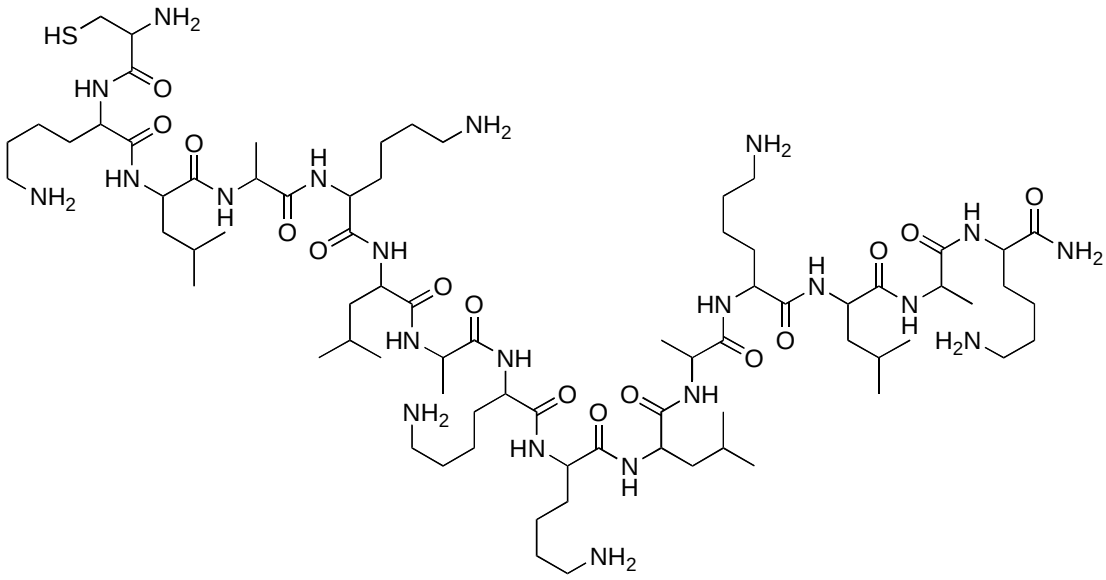


Chemical Formula: $C_{84}H_{135}N_{35}O_{19}$
Molecular Weight: 1939.19

Figure S14. Structure and expected molecular weight of Fl-TAT (GRKKRRQRRRK(Fl)G-NH_2)

Synthesis of Cys-PAD (CKLAKLAKKLAKLAK-NH_2)

The Cys-PAD (CKLAKLAKKLAKLAK) peptide was assembled using a standard Fmoc solid phase peptide synthesis strategy on a rink amide resin. The protected peptide was cleaved from the resin with 92.5% TFA, 2.5% TIS, 2.5% EDT, and 2.5% H_2O. The crude product was precipitated and washed with cold diethyl ether. The precipitated peptide was then lyophilized, dissolved in HPLC buffer and purified by preparative scale reverse phase HPLC using a water/acetonitrile gradient in the presence of 0.1% TFA. Expected mass: 1626.1 Da, observed mass: 1626.6 Da.

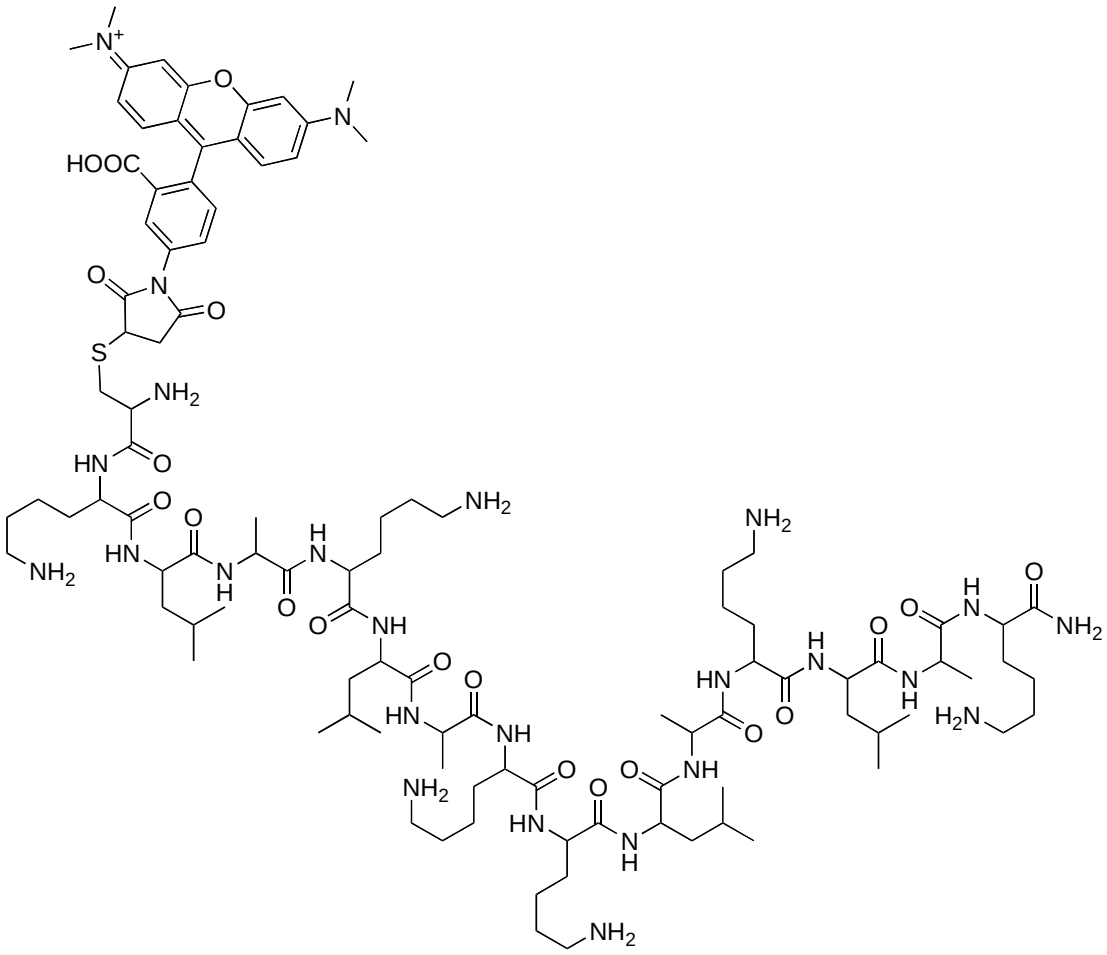


Chemical Formula: $C_{75}H_{144}N_{22}O_{15}S$
Molecular Weight: 1626.15

Figure S15. Structure and expected molecular weight of C-PAD (CKLAKLAKKLAKLAK-NH_2)

Synthesis of TMR-PAD (TMR-CKLAKLAKKLAKLAK-NH_2)

TMR-PAD (TMR-CKLAKLAKKLAKLAK-NH2) was obtained by reaction between the Cys-PAD peptide and the fluorophore tetramethylrhodamine-5(6)-maleimide. Cys-PAD (0.38 μmol) was dissolved in 25 mM Hepes at pH 7.5, 100 mM MESNa, and 20 mM TCEP (0.38 mM mM final concentration). To this was added the fluorophore tetramethylrhodamine-5(6)-maleimide (0.38 μmol). After 36 hours at 4 °C, the reaction was complete and the crude product was purified by preparative scale reverse phase HPLC using a water/acetonitrile gradient in the presence of 0.1% TFA. Expected mass, 2108.66, observed mass: 2109.40 Da.



Chemical Formula: $C_{103}H_{168}N_{25}O_{20}S^+$
Molecular Weight: 2108.66

Figure S16. Structure and expected molecular weight of TMR-PAD (TMR-CKLAKLAKKLAKLAK-NH_2)

Oxidation of Fl-TATn

To test whether the thiols present in the Fl-TATn compounds could lead to aggregate formation through the formation of intermolecular disulfide bridges, the compounds (10 μM in PBS, this concentration reflects the highest concentration used in the cell-based assays) were oxidized by bubbling O2 in the media for 1 hour. Formation of aggregates of higher molecular weights was monitored by HPLC analysis and mass spectrometry. The HPLC profiles and MS spectra of the oxidized Fl-TATn compounds were similar to those presented above and to the samples treated with the reducing agent TCEP (10 mM), indicating that no intermolecular disulfide bridges formed between the Fl-TATn molecules. Instead, intramolecular disulfide bridges might have formed. Given the close proximity of the cysteine residues in the Fl-TATn compounds, these intramolecular disulfide bonds would have a greater probability of formation than intermolecular disulfide bridges. These intramolecular disulfide bridges might however not lead to a shift in HPLC retention time. The mass spectrometry analysis was also not accurate enough to unequivocally confirm the loss of 2 H that would accompany the formation of each disulfide bridge.

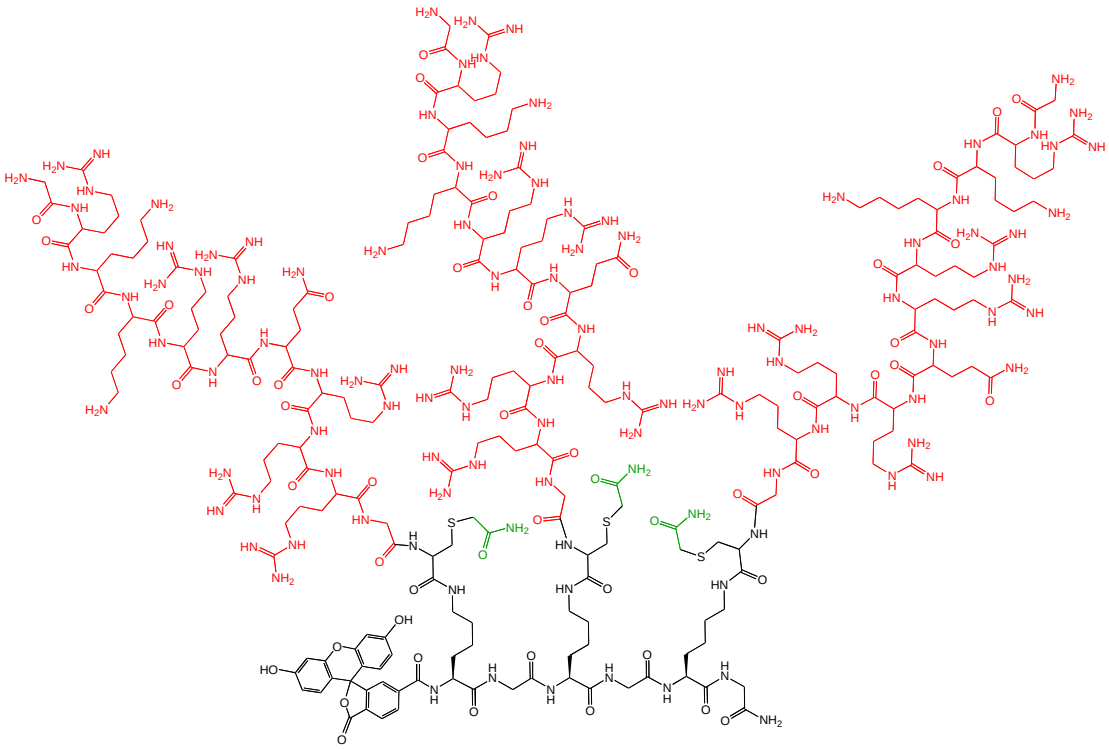
In the case of Fl-TAT2 and Fl-TAT4, oxidation of the cysteines was confirmed by monitoring the reducing activity of the compounds. Fl-TAT2 and Fl-TAT4 were first reduced with immobilized TCEP in PBS. The TCEP beads were filtered and the solution was immediately added to a solution of Aldrithiol-2 (2,2'-dithiopyridine, 100 μM). Aldrithiol forms a thiopyridone salt upon reduction and this is accompanied by an increase in absorbance at 350 nm. As expected, the reduced Fl-TAT2 and Fl-TAT4 caused an increase in the absorbance of the solution at 350 nm. In a parallel assay, the freshly reduced Fl-TAT2 and Fl-TAT4 were bubbled with O2 as described in the previous paragraph. In this case, addition of Aldrithiol did not cause an increase in the absorbance 350 nm (the absorbance of fluorescein at 490 nm was measured to confirm that the reduced and oxidized Fl-TATn compounds were used at the same concentration). These results therefore confirm that the reducing activity of Fl-TAT2 and Fl-TAT4 was abolished after the oxidation step, further confirming that intracellular disulfide bonds are formed.

In the case of Fl-TAT3, one can presume that one intramolecular disulfide bridge might form, leaving one cysteine that could potentially form an intermolecular

disulfide bond. The fact that we did not detect aggregates of high molecular weight might reflect that fact that intermolecular disulfide bond formation is sterically unfavorable. Indeed, Fl-TAT3 had the ability to reduce Aldrithiol-2 even after the oxidation step, confirming that a free thiol might remain even after bubbling oxygen (aldrithiol is a small molecule that presumably might have access to this free thiol). However, to unequivocally confirm that aggregates of the Fl-TAT3 compound were not involved in the unique delivery properties of this compound, the free thiol groups present in the molecule were capped with iodoacetamide. These results are described in the next section.

Synthesis and Characterization of Fl-TAT3-(S-CH2-CO-NH2)3 (Fl-TAT3 acetamidated with iodoacetamide to block the thiols and prevent disulfide bond formation)

Fl-TAT3-(S-CH2-CO-NH2)3 was formed after addition of iodoacetamide (50 mM) to Fl-TAT3 (1.4 mM) in 6 M GnHCl, 25 mM HEPES, and 50 mM TCEP at pH 8.5. The solution was placed on a shaker at room temperature. The reaction was monitored by analytical reversed-phase HPLC and MALDI-TOF. After 24 h, the elution peak corresponding to Fl-TAT3 had completely disappeared to lead to the formation of a single peak corresponding to the product. The product was purified by reverse-phase HPLC. The Aldrithiol test described in the previous section was used to confirm that the compound formed had no reducing activity and therefore no free thiol (Fl-TAT3 was used as a positive control). Yield: 69.3 %. Expected mass: 5718.66 Da, Observed mass: 5722.25 Da.



Chemical Formula: $C_{231}H_{412}N_{112}O_{54}S_3$
Molecular Weight: 5718.66

Figure S17. Structure and expected molecular weight of Fl-TAT3-(S-CH2-CO-NH2)3**.**

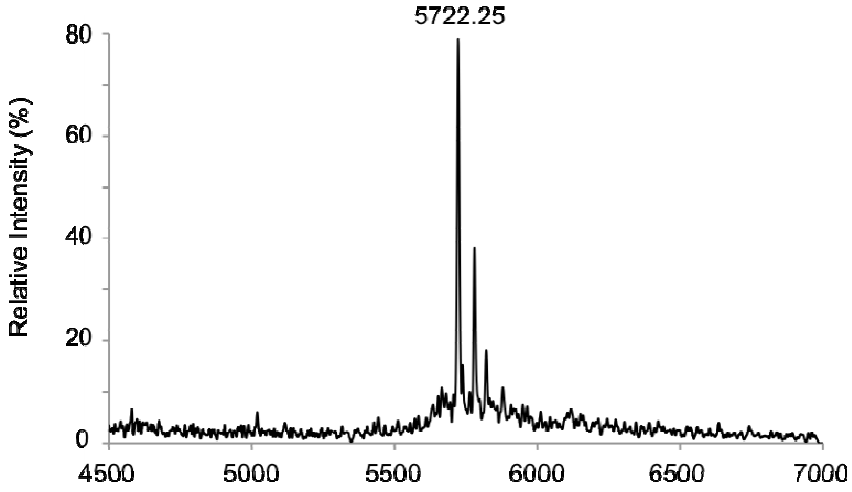


Figure S18. MALDI-TOF MS spectrum of Fl-TAT3-(S-CH2-CO-NH2)3.

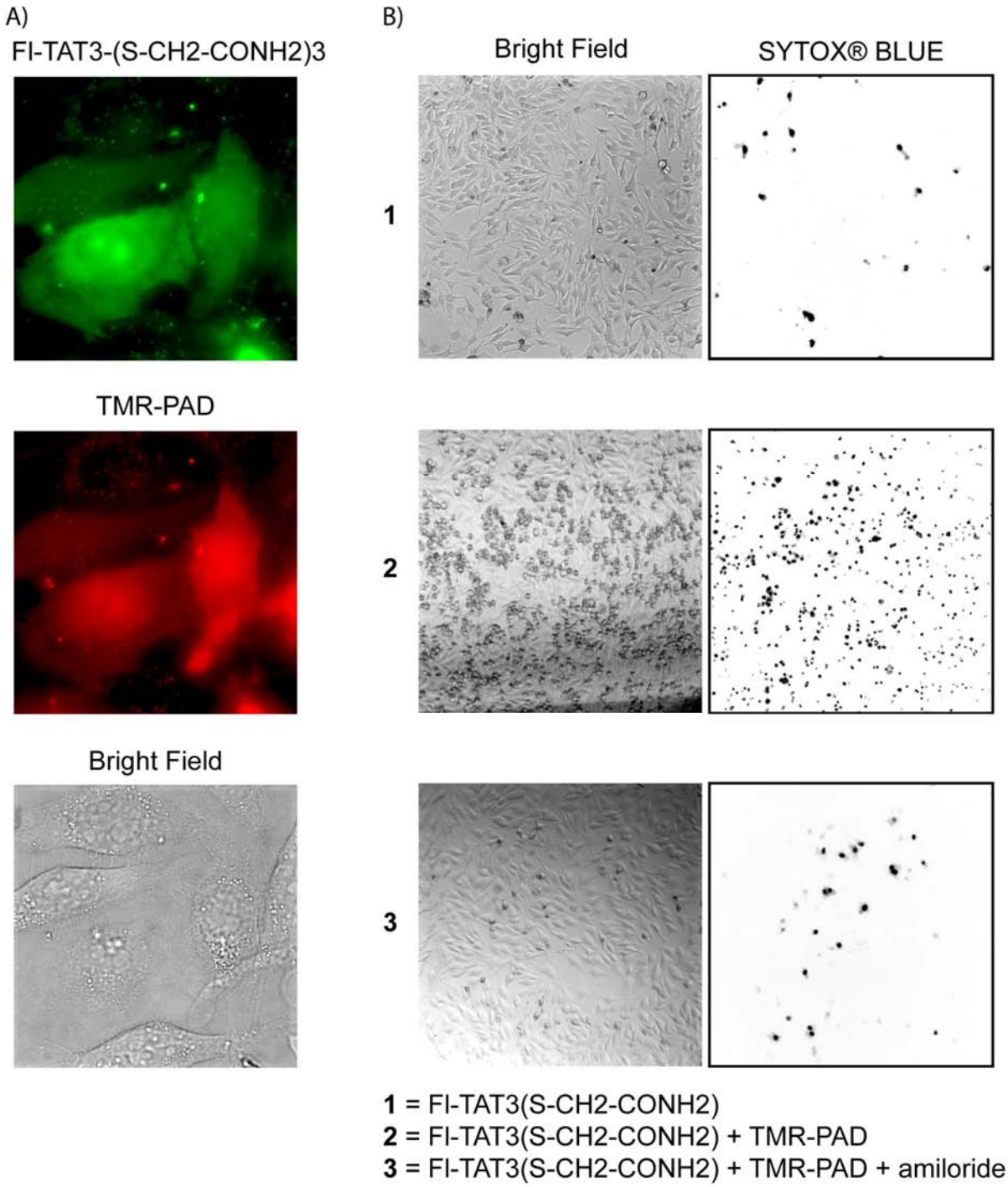


Figure S19. A) C) Fluorescence images of live HeLa cells treated with Fl-TAT3-(S-CH2-CO-NH2)3 (3 μM) and TMR-PAD (10 μM) after a 30 min co-incubation at 37°C (the objective used was 100X). The cells represented were not stained by SYTOX® Blue at this early time point. This indicates that the membrane of these cells was not compromised. B) Images of cells incubated with TMR-PAD (10 μM), Fl-TAT3-(S-CH2-CO-NH2)3 (3 μM), and with or without the macropinocytosis inhibitor amiloride. Cells were incubated with the peptides for 30 min, washed with fresh media, and SYTOX Blue was added to detect dead cells. Images were acquired 240 min after addition of SYTOX® Blue. Black nuclei in the SYTOX® Blue images represent dead or dying cells (images are represented as inverted monochrome).

As shown in Figure S19, Fl-TAT3-(S-CH2-CO-NH2)3 alone does not cause extensive cell-death (>90% viability). In contrast, co-incubation of TMR-PAD and Fl-TAT3-(S-CH2-CO-NH2)3 causes cell-death in a time-dependent manner. Figure S19 A illustrates that cells are viable immediately after incubation while Figure S19 B shows that cell viability was reduced to less than 25% after 240 min (cell viability was determined as describe in page 2 of this document). The control showing that TMR-PAD alone is not toxic to cells is shown in Figure 2. Finally, addition of amiloride to the incubation media blocks macropinocytosis and the delivery of TMR-PAD into live cells by Fl-TAT3-(S-CH2-CO-NH2)3.

(1) Szewczuk, L. M.; Tarrant, M. K.; Sample, V.; Drury, W. J., 3rd; Zhang, J.; Cole, P. A. *Biochemistry* **2008**, *47*, 10407.

Re and Tc Tricarbonyl Complexes: From the Suppression of NO Biosynthesis in Macrophages to in Vivo Targeting of Inducible Nitric Oxide Synthase

Bruno L. Oliveira,[†] Paula D. Raposinho,[†] Filipa Mendes,[†] Flávio Figueira,[†] Isabel Santos,[†] António Ferreira,[‡] Carlos Cordeiro,[‡] Ana P. Freire,[‡] and João D. G. Correia*,[†]

Unidade de Ciências Químicas e Radiofarmacêuticas, ITN, Estrada Nacional 10, 2686-953 Sacavém, Portugal, and Centro de Química e Bioquímica, Departamento de Química e Bioquímica, Faculdade de Ciências da Universidade de Lisboa, Portugal.
Received June 28, 2010; Revised Manuscript Received October 12, 2010

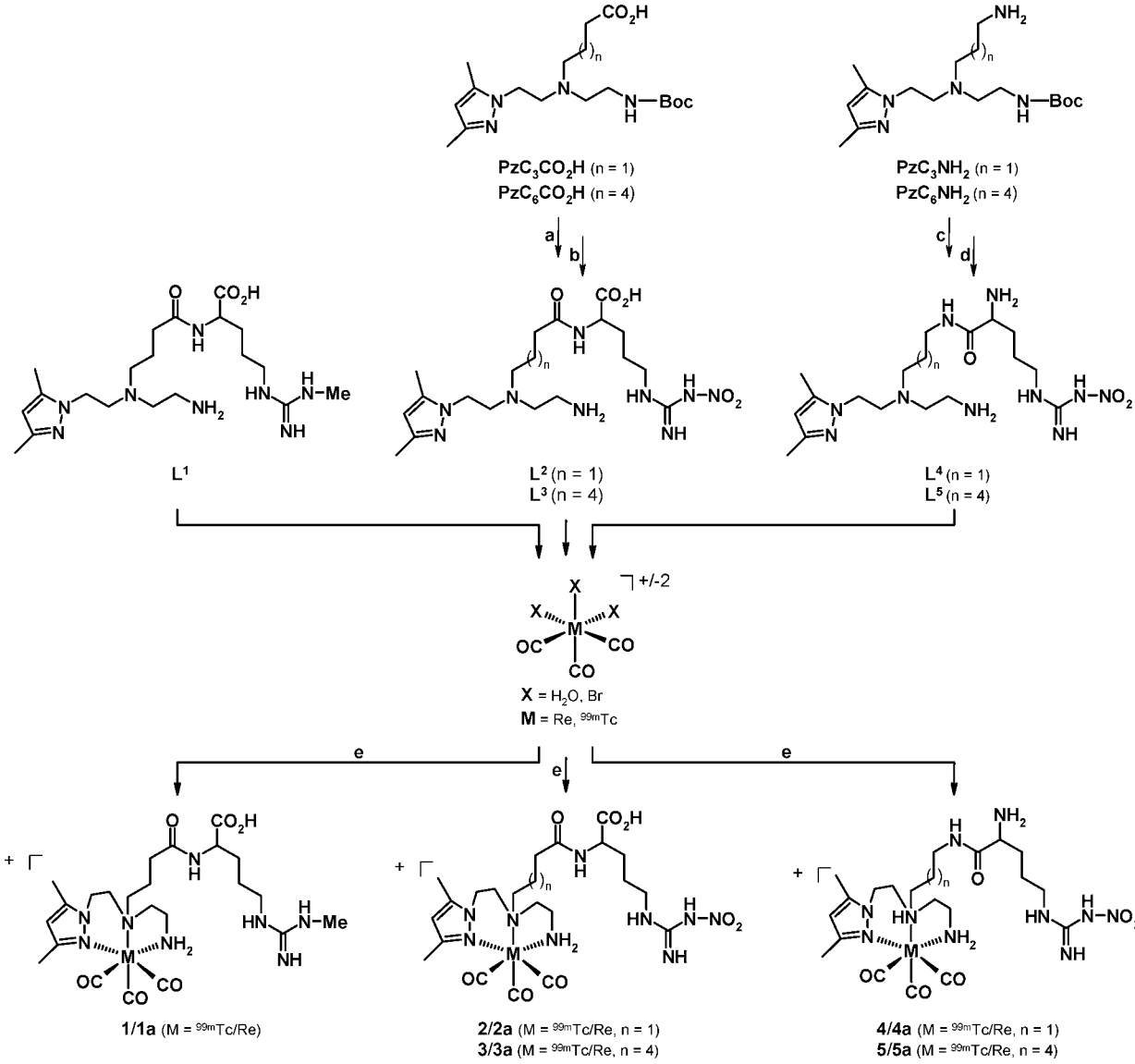
The in vivo molecular imaging of nitric oxide synthase (NOS), the enzyme responsible for the catalytic oxidation of L-arginine to citrulline and nitric oxide (NO), by noninvasive modalities could provide valuable insights into NO/NOS-related diseases. Aiming at the design of innovative ^{99m}Tc(I) complexes for targeting inducible NOS (iNOS) in vivo by SPECT imaging, herein we describe a set of novel ^{99m}Tc(CO)$_3$ complexes (**2**−**5**) and the corresponding rhenium surrogates (**2a**−**5a**) containing the NOS inhibitor N^{ω}-nitro-L-arginine. The latter is linked through its α-NH_2 or α-COOH group and an alkyl spacer of variable length to the metal center. The complexes **2a** (propyl spacer) and **3a** (hexyl spacer), in which the α-NH_2 group of the inhibitor is involved in the conjugation to the metal center, presented remarkable affinity for purified iNOS, being similar to that of the free nonconjugated inhibitor (K_i = 3−8 μM) in the case of **3a** (K_i = 6 μM). **2a** and **3a** are the first examples of organometallic complexes that permeate through RAW 264.7 macrophage cell membranes, interacting specifically with the target enzyme, as confirmed by the suppression of NO biosynthesis in LPS-treated macrophages (**2a**, ca. 30% inhibition; **3a**, ca. 50% inhibition). The ^{99m}Tc(I)-complexes **2** and **3**, stable both in vitro and in vivo, also presented the ability to cross cell membranes, as demonstrated by internalization studies in the same cell model. The biodistribution studies in LPS-pretreated mature female C57BL6 mice have shown that **2** presented an overall higher uptake in most tissues of the LPS-treated mice compared to the control group (30 min postinjection). This increase is significant in lung (3.98 ± 0.63 vs to 0.99 ± 0.13%ID/g), which is known to be the organ with the highest iNOS expression after LPS treatment. These results suggest that the higher uptake in that organ may be related to iNOS upregulation.

The in vivo molecular imaging of nitric oxide synthase (NOS), the enzyme responsible for the catalytic oxidation of L-arginine to citrulline and nitric oxide (NO), by noninvasive modalities could provide valuable insights into NO/NOS-related diseases such as cancer, neurological disorders, or vascular malfunctions, among others (*1*−*10*). So far, the main modalities explored for NOS imaging include positron emission tomography (PET) and optical imaging (OI) (*9*−*15*). The nuclear imaging modalities PET or single photon emission computed tomography (SPECT), due to their favorable features, and broad range of available probes offer high clinical potential (*16*−*18*). Technetium-99m (^{99m}Tc) is the radionuclide of choice for SPECT imaging due to its almost ideal nuclear properties ($t_{1/2}$ = 6.02 h, $E_{\gamma_{max}}$ = 140 keV) and rich chemistry, which allows modulation of the biological properties of the radioactive complexes. Taking into consideration our interest in the design of innovative ^{99m}Tc(I)-complexes for targeting molecular processes in vivo (*19*−*21*), we have recently proposed a set of novel ^{99m}Tc(CO)$_3$ complexes containing pendant L-arginine or NOS inhibitors for targeting NOS expression by SPECT imaging (*22*, *23*). Enzymatic assays of purified inducible NOS (iNOS) activity in the presence of the analogue Re(CO)$_3$-complexes, prepared as "nonradioactive" surrogates, have shown that the Re complexes **1a** (K_i = 36 μM) and **2a** (K_i = 84 μM) stabilized by bioconjugates bearing N^{ω}-monomethyl- (**L**^{1}) or N^{ω}-nitro-L-arginine pendant moieties (**L**^{2}), respectively, still presented inhibitory action (Scheme 1). Indeed, **1a** and **2a** are the first examples of organometallic complexes able to inhibit the iNOS (*22*). Interestingly, **2a** presented higher inhibitory potency than the corresponding metal-free bioconjugate **L**^{2} (K_i = 178 μM). These encouraging results prompted us to introduce structural changes in **2a** aimed at increasing the affinity of the metal complex for the enzyme. Such modifications involved, on one hand, introduction of a longer alkyl chain between the N^{ω}-nitro-L-arginine pendant arm and the chelating unit and, on the other hand, conjugation of the amino acid derivative to the metal complex trough its α-COOH group. Toward this goal, we synthesized the new bioconjugates **L**^{3}−**L**^{5} in a two-step procedure by direct conjugation of the Boc-protected precursors **PzC$_6$CO$_2$H**, **PzC$_3$NH$_2$**, and **PzC$_6$NH$_2$** to the corresponding N^{ω}-nitro-L-arginine derivative using standard coupling reagents, followed by hydrolysis of the protecting groups under acidic conditions (Scheme 1). All amino acid-containing bioconjugates were obtained as air-stable colorless oils after purification by semipreparative reversed-phase high-performance liquid chromatography (RP-HPLC) with ≥98% purity (see Supporting Information). All bioconjugates were characterized by elemental analysis, ^{1}H/^{13}C NMR (including 2D-NMR experiments such as ^{1}H-^{1}H-^{1}H COSY and ^{1}H-^{13}C HSQC) and IR spectroscopy, and electrospray ionization mass spectrometry (see Supporting Information). Reaction of **L**^{1}−**L**^{5} with the organometallic

* To whom correspondence should be addressed. Dr. João D. G. Correia, Unidade de Ciências Químicas e Radiofarmacêuticas, ITN, Estrada Nacional 10, 2686-953 Sacavém (Portugal). Phone: (+351)219946233, Fax: (+351)219946185, e-mail: jgalamba@itn.pt.
[†] Unidade de Ciências Químicas e Radiofarmacêuticas.
[‡] Faculdade de Ciências da Universidade de Lisboa.

10.1021/bc100291e © 2010 American Chemical Society
Published on Web 11/02/2010

Scheme 1. Synthesis of Bioconjugates L^2−L^5 and Organometallic Complexes 1/1a−5/5a[a]



[a] Reagents and conditions: (a) N^{ω}-nitro-L-arginine methyl ester, HBTU, Et_3N, DMF/ACN, r.t.; (b) HCl 3 N, r.t.; (c) N^{α}-Boc-N^{ω}-nitro-L-arginine, DCC, HOBt, DMF/DCM, r.t.; (d) TFA/DCM, r.t..; (e) H_2O, 100 °C. ACN = acetonitrile; Boc = *t*-butoxycarbonyl; DCC = *N*,*N*′-Dicyclohexylcarbodiimide; DCM = dichloromethane; DMF = dimethylformamide; HBTU = *O*-Benzotriazole-*N*,*N*,*N*′,*N*′-tetramethyl-uronium-hexafluoro-phosphate; HOBt = *N*-Hydroxybenzo-triazole; r.t. = room temperature; TFA = trifluoroacetic acid.

precursor *fac*-$[^{99m}Tc(CO)_3(H_2O)_3]^+$, obtained using an IsoLink kit, afforded in high radiochemical yield (>95%) cationic complexes of the type *fac*-$[^{99m}Tc(CO)_3(k^3\text{-L})]^+$ (**L** = $\mathbf{L}^1$, **1**; $\mathbf{L}^2$, **2**; $\mathbf{L}^3$, **3**; $\mathbf{L}^4$, **4**; $\mathbf{L}^5$, **5**) (Scheme 1).

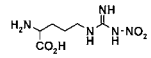
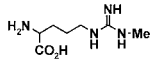
The hydro(lipo)philic nature of all ^{99m}Tc(I)-complexes was evaluated by determining the partition coefficient in physiological conditions (Supporting Information), and the results were expressed as log $P_{o/w}$. The radiocomplexes with a propyl spacer (log $P_{o/w}$ **1** = −2.19, log $P_{o/w}$ **2** = −1.41, and log $P_{o/w}$ **4** = −1.29) presented higher hydrophilic character than the ones with a hexyl spacer (log $P_{o/w}$ **3** = −0.29, and log $P_{o/w}$ **5** = −1.01).

The in vitro stability studies performed (incubation with solutions of amino acids with high affinity for Tc(I) such as histidine and cysteine, in phosphate-buffered saline pH 7.4, and human plasma at 37 °C for 24 h) have shown that all ^{99m}Tc(I)-complexes are stable, since no decomposition or reoxidation products were observed by RP-HPLC analysis (purity ≥95%).

The chemical identity of the ^{99m}Tc(I) complexes has been established by comparing their RP-HPLC analytical radioactive traces (γ-detection) with the UV/vis traces of the rhenium complex surrogates **1a**−**5a**, which have been prepared by reacting $\mathbf{L}^1$−$\mathbf{L}^5$ with the precursor $(NEt_4)_2[ReBr_3(CO)_3]$ in refluxing water, in the 1:1 molar ratio (Scheme 1). The complexes were obtained as air-stable colorless viscous oils in moderate yields (40−94%), after evaporation of the reaction solvent and washing of the residue obtained with $CHCl_3$ for NEt_4Br removal and further purification by preparative RP-HPLC (purity ≥95%). The novel complexes **3a**−**5a** were fully characterized (Supporting Information) by RP-HPLC, elemental analysis, ESI-MS, and NMR spectroscopy ($^1H/^{13}C$ NMR, ^1H-^1H COSY, and ^1H-^{13}C HSQC).

To assess the influence of the structural modifications introduced in **2a** in the enzymatic activity of NOS, the new bioconjugates $\mathbf{L}^3$−$\mathbf{L}^5$ and corresponding rhenium complexes **3a**−**5a** were tested as competitive inhibitors of purified mouse recombinant iNOS, and their activity compared to that of the previously described analogues (*22*). The iNOS activity was determined spectrophotometrically by monitoring the NO-mediated conversion of oxyhemoglobin to methemoglobin at two wavelengths (401 and 421 nm). The inhibition constants

Table 1. K_i Values for iNOS Competitive Inhibitors L^2−L^5 and 1a−5a

Entry	Inhibitor	K_i values[a] (μM)
1	 *N^{ω}-Nitro-L-arginine*	$3^{(22)}$ $8^{(24)}$
2	 *N^{ω}-Methyl-L-arginine*	$8^{(22)}$ $4^{(24)}$
3	*fac*-[Re(CO)$_3$(k^3-L^1)] (**1a**)	$36^{(22)}$
4	L^2	$178^{(22)}$
5	*fac*-[Re(CO)$_3$(k^3-L^2)] (**2a**)	$84^{(22)}$
6	L^3	36
7	*fac*-[Re(CO)$_3$(k^3-L^3)] (**3a**)	6
8	L^4	35
9	*fac*-[Re(CO)$_3$(k^3-L^4)] (**4a**)	103
10	L^5	137
11	*fac*-[Re(CO)$_3$(k^3-L^5)] (**5a**)	118

[a] Results are given as a mean of three or more independent experiments. Standard deviations of ±5−10% were observed.

(K_i), determined by the method of Eisenthal and Cornish-Bowden, are summarized in Table 1.

All bioconjugates showed decreased inhibitory potencies to iNOS (L^2−L^5) when compared with free, nonconjugated, N^{ω}-nitro-L-arginine. When the latter is coupled through its α-NH_2 group to the bifunctional chelator, a longer spacer length led to an increased affinity to the enzyme as can be concluded by comparing the K_i values of L^3 (36 μM) and L^2 (178 μM). An opposite effect has been observed when the α-CO_2H group of N^{ω}-nitro-L-arginine is involved in the attachment to the chelator. In this case, the longer spacer length led to a lower affinity for the enzyme (L^4, K_i = 35 μM; L^5, K_i = 137 μM). Unlike L^4, reaction of the analogue bioconjugates L^2 (K_i = 178 μM), L^3 (K_i = 36 μM), and L^5 (K_i = 137 μM) with the organometallic moiety *fac*-$[Re(CO)_3]^+$ gave complexes with increased inhibitory potencies (**2a**, K_i = 84 μM; **3a**, K_i = 6 μM; **5a**, K_i = 118 μM).

The increased inhibitory potency after metalation occurs independently of the functional group of the amino acid involved in the chemical bonding to the chelating unit (e.g., **3a** vs **5a**) and spacer length (e.g., **2a** vs **3a**). Such an effect has already been observed with other metal complexes that presented higher inhibitory potency than the corresponding metal-free inhibitors (*25*). Remarkably, in the case of **3a**, the inhibitory potency (K_i = 6 μM) is comparable to that of the free nonconjugated inhibitor N^{ω}-nitro-L-arginine (K_i = 3 μM).

These unprecedented results motivated us to evaluate the ability of the compounds to cross cellular membranes, a key feature for improving tracer uptake in vivo, and to interact intracellularly with their target (iNOS enzyme).

Both the ^{99m}Tc(I) complexes and their Re(I) surrogates were tested in RAW 264.7 macrophages, which present increased NO biosynthesis due to iNOS overexpression after treatment with endotoxins such as lipopolysaccharide (LPS) (*26*). LPS-induced iNOS overexpression was confirmed by Western blot analysis of protein extracts using an anti-iNOS antibody (Figure 1).

We began by evaluating the ability of bioconjugates L^2−L^5 and rhenium complexes **1a**−**5a** to inhibit intracellular iNOS by measuring nitrite accumulation using the Griess method (Figure 2). In order to assess the intrinsic cytotoxicity of the compounds at the concentration used in the NO assay (500 μM) and, consequently, its influence in nitrite accumulation, we have also performed a cell viability assay in parallel (MTT assay). The

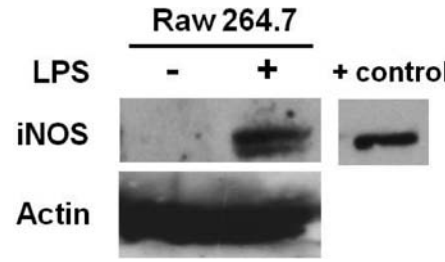


Figure 1. iNOS expression in RAW 264.7 macrophages after treatment with LPS for 24 h. Recombinant iNOS (6 μg) was used as a positive control and actin as an internal loading control.

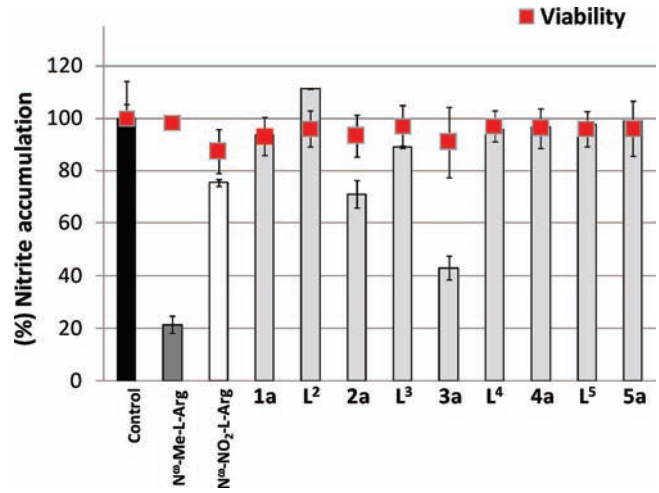


Figure 2. Effect of compounds L^2−L^5 and **1a**−**5a** in nitrite accumulation and cell viability in LPS-induced RAW 264.7 macrophages (mean ± S.D., n = 8). Cells were LPS-treated and cultured in the presence of the compounds. Final concentration of all compounds was 500 μM. NO production and viability in LPS-induced cells in the absence of any compound (control) was considered 100%. This experiment was repeated three times with comparable results.

assay has shown that all compounds tested are nontoxic for the cells under the described experimental conditions (Figure 2).

The rhenium complexes **2a** (ca. 30% inhibition) and **3a** (ca. 50% inhibition) appeared as the most potent inhibitors of NO production by LPS-activated macrophages. Remarkably, **3a** inhibited NO biosynthesis more effectively than the free inhibitor N^{ω}-nitro-L-arginine (N^{ω}-NO_2-L-Arg - ca. 25%). These results are in line with the in vitro enzymatic assays performed with purified iNOS, where complexes **2a** and **3a** also exhibited the highest inhibitory potency toward iNOS (**2a**, K_i = 84 μM; **3a**, K_i = 6 μM; Table 1). Since the inhibition of NO biosynthesis is being influenced not only by the intrinsic inhibitory capacity of the complexes as desired, but also by their ability to cross the cell membrane, we have performed internalization studies in the same cellular model with the radioactive ^{99m}Tc(I) analogues **2** and **3**, and compared their internalization levels with that of **1** (Figure 3).

These studies allowed us to conclude that the affinity of compound **3a** for the enzyme is strong enough to surpass the lower ability for crossing the cell membrane presented by the corresponding radioactive complex **3**, as demonstrated by its lower internalization level, when compared with compound **2** (0.43 ± 0.06% vs 0.83 ± 0.06% internalization/mg protein, respectively).

Despite presenting comparable ability for crossing cell membranes, as demonstrated by the similar internalization levels shown by **1** and **2** (0.76 ± 0.10% and 0.83 ± 0.06% internalization/mg protein, respectively), the surrogate compound **1a**, which presented a higher affinity for purified iNOS than

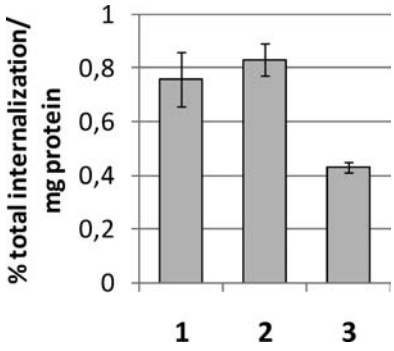


Figure 3. Internalization of the radioactive complexes **1**−**3** in LPS-induced RAW 264.7 macrophages (mean ± S.D., $n = 4$; 37 °C, 4 h post-incubation). The internalization level is expressed as a percentage of applied radioactivity per milligram of total protein.

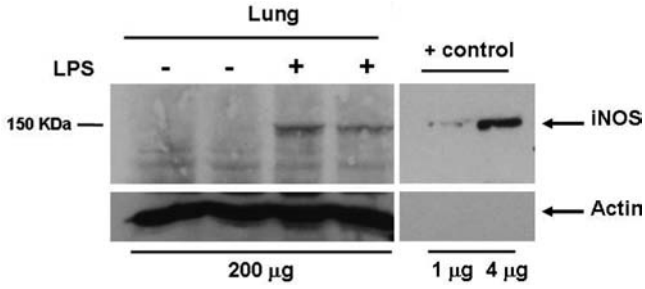


Figure 4. iNOS expression in the lungs of LPS-treated mice (10 mg/kg of LPS, 6 h). Recombinant iNOS (4 μg) was used as a positive control and actin as internal loading control.

compound **2a**, is not able to inhibit intracellular iNOS in the macrophages assay as is the case of **2a**.

As far as we are aware, the matched pairs **2/2a** and **3/3a** are rare examples of organometallic complexes able to cross cell membranes and interact specifically with a cytosolic enzyme. Encouraged by both the ability of **2a** and **3a** to interact with intracellular iNOS, inhibiting biosynthesis of NO in LPS-activated RAW 264.7 macrophages, and the moderate ability of **2** and **3** to cross cell membranes, the biodistribution of these ^{99m}Tc(I) complexes has been evaluated in LPS-pretreated mature female C57BL6 mice. Mice were treated with bacterial LPS (10 mg/kg, iv) to induce iNOS expression 6 h before the radioactive compounds were injected. The control group was injected with PBS. It has been demonstrated that iNOS mRNA and protein expression after LPS stimulation are increased in many organs, with the highest iNOS expression in the lungs (*27*). We have also confirmed increased levels of iNOS expression in lungs of LPS-treated mice by Western blot analysis of total protein (Figure 4).

The complexes **2** and **3** are stable in vivo as demonstrated by RP-HPLC analysis of urine and serum samples collected at sacrifice time. In fact, more than 98% of the radioactivity could be assigned to the complexes.

Compound **3** did not present any significant increase of radioactivity in the lungs of pretreated animals compared to the control group at 15 and 60 min postinjection. This result is in agreement with the cellular internalization data obtained for this compound and confirms the importance of crossing cell membranes for in vivo intracellular targeting and retention.

Compound **2** presented an overall higher uptake in most tissues of LPS-treated mice compared to the control group at 30 min postinjection (Figure 5). Unlike compound **3**, this increase is particularly relevant in lung (3.98 ± 0.76 vs 0.99 ± 0.13%ID/g), which is known to be the organ with the highest iNOS expression (*27*). This result suggests a direct correlation

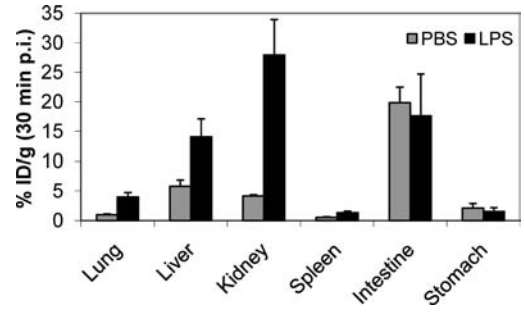


Figure 5. Biodistribution of **2** in LPS-treated mature female C57BL/6 mice (LPS) and control group (PBS) 30 min after intravenous injection (mean ± standard deviation, $n = 4$−5). ID: injected dose.

between lung uptake and iNOS upregulation. In contrast to intestine and stomach, the increased uptake in the excretory organs kidney and liver, as well as in the spleen, may also be partially related to iNOS overexpression in these tissues (*27*).

In conclusion, we have shown that complexes **2a** and **3a**, "inactive" surrogates of the ^{99m}Tc(I)-complexes **2** and **3**, presented remarkable affinity for purified iNOS, being similar to that of the free nonconjugated inhibitor in the case **3a**. Both complexes permeate through macrophage cell membranes and interact specifically with the cytosolic target enzyme, as confirmed by the inhibition of NO biosynthesis in LPS-treated macrophages. The ^{99m}Tc(I) complexes **2** and **3** are stable in vitro and present the ability to cross cell membranes. The biodistribution studies demonstrated that these complexes are stable in vivo and suggested that **2** is able to recognize iNOS in vivo. Therefore, the latter complex **2** presents a set of adequate features for potential targeting/imaging of NOS expression in vivo. These encouraging results brought together proved that metal complexes in general, and ^{99m}Tc(I)/Re(I) complexes in particular, can be "structurally tuned" to target intracellular low-capacity systems such as enzymes, paving the way to the design of innovative, more specific diagnostic or therapeutic agents.

ACKNOWLEDGMENT

This work has been partially supported by the Fundação para a Ciência e Tecnologia (FCT), Portugal (POCI/SAU-FCF/58855/2004). B. L. Oliveira thanks FCT for a PhD grant (SFRH/BD/38753/2007). Dr. J. Marçalo is acknowledged for performing the ESI-MS analyses. The QITMS instrument was acquired with the support of Contract REDE/1503/REM/2005 - ITN of FCT and is part of RNEM.

Supporting Information Available: Experimental Section. This material is available free of charge via the Internet at http://pubs.acs.org.

LITERATURE CITED

(1) Moncada, S., Palmer, R. M., and Higgs, E. A. (1991) Nitric oxide: physiology, pathophysiology, and pharmacology. *Pharmacol. Rev. 43*, 109–142.
(2) Kerwin, J. F., and Lancaster, J. R. (1995) Nitric oxide: a new paradigm for second messengers. *J. Med. Chem. 38*, 4343–4362.
(3) Marletta, M. A. (1993) Nitric oxide synthase structure and mechanism. *J. Biol. Chem. 268*, 12231–12234.
(4) Alderton, W. K., Cooper, C. E., and Knowles, R. G. (2001) Nitric oxide synthases: structure, function and inhibition. *Biochem. J. 357*, 593–615.
(5) Special Issue on Nitric Oxide in Cancer Biology and Treatment (Wink, D. A. , and Mitchell, J. B., Eds.) *Free Radic. Biol. Med.* 2003, *34*.

(6) Lechner, M., Lirk, P., and Rieder, J. (2005) Inducible nitric oxide synthase (iNOS) in tumor biology: the two sides of the same coin. *Sem. Cancer Biol. 15*, 277–289.
(7) Fukumura, D., Kashiwagi, S., and Jain, R. K. (2006) The role of nitric oxide in tumour progression. *Nat. Rev. Cancer 6*, 521–534.
(8) Duncan, A. J., and Heales, S. J. (2005) Nitric oxide and neurological disorders. *Mol. Aspects Med. 26*, 67–96.
(9) Hong, H., Sun, J., and Cai, W. (2009) Multimodality imaging of nitric oxide and nitric oxide synthases. *Free Radic. Biol. Med. 47*, 684–698.
(10) Nagano, T., and Yoshimura, T. (2002) Bioimaging of nitric oxide. *Chem. Rev. 102*, 1235–1270.
(11) Panda, K., Chawla-Sarkar, M., Santos, C., Koeck, T., Erzurum, S. C., Parkinson, J. F., and Stuehr, D. J. (2005) Visualizing inducible nitric-oxide synthase in living cells with a heme-binding fluorescent inhibitor. *Proc. Natl. Acad. Sci. U.S.A. 102*, 10117–10122.
(12) Dunn, A. R., Belliston-Bittner, W., Winkler, J. R., Getzoff, E. D., Stuehr, D. J., and Gray, H. B. (2005) Luminescent ruthenium(II)- and rhenium(I)-diimine wires bind nitric oxide synthase. *J. Am. Chem. Soc. 127*, 5169–5173.
(13) Moriyama, Y., Moriyama, E. H., Blackmore, K., Akens, M. K., and Lilge, L. (2005) In vivo study of the inflammatory modulating effects of low-level laser therapy on iNOS expression using bioluminescence imaging. *Photochem. Photobiol. 81*, 1351–1355.
(14) Zhang, J., Xu, M., Dence, C. S., Sherman, E. L. C., MacCarthy, T. J., and Welch, M. J. (1997) Synthesis, in vivo evaluation and PET study of a carbon-11-labeled neuronal nitric oxide synthase (nNOS) inhibitor 5-methyl-L-thiocitrulline. *J. Nucl. Med. 38*, 1273–1278.
(15) Zhou, D., Lee, H., Rothfuss, J. M., Chen, D. L., Ponde, D. E., Welch, M. J., and Mach, R. H. (2009) Design and synthesis of 2-amino-4-methylpyridine analogues as inhibitors for inducible nitric oxide synthase and in vivo evaluation of [^{18}F]6-(2-fluoropropyl)-4-methyl-pyridin-2-amine as a potential PET tracer for inducible nitric oxide synthase. *J. Med. Chem. 52*, 2443–2453.
(16) Ametamey, S. M., Honer, M., and Schubiger, P. A. (2008) Molecular imaging with PET. *Chem. Rev. 108*, 1501–1516.
(17) Jaffer, F. A., and Weissleder, R. (2005) Molecular imaging in the clinical arena. *JAMA 293*, 855–862.
(18) Wester, H.-J. (2007) Nuclear imaging probes: from bench to bedside. *Clin. Cancer Res. 13*, 3470–3481.
(19) Correia, J. D. G., Paulo, A., and Santos, I. (2009) Re and Tc complexes with pyrazolyl-containing chelators: from coordination chemistry to target-specific delivery of radioactivity. *Curr. Radiopharmaceuticals 2*, 277–294.
(20) Santos, I., Paulo, A., and Correia, J. D. G. (2005) Rhenium and technetium complexes anchored by phosphines and scorpionates for radiopharmaceutical applications. *Top. Curr. Chem. 252*, 45–84.
(21) Raposinho, P. D., Correia, J. D. G., Oliveira, M. C., and Santos, I. (2010) MC1 receptor-targeting with radiolabeled cyclic-melanocyte stimulating hormone analogs for melanoma imaging. *Biopolymers (Pept. Sci.)* Online Early Access. DOI: 10.1002/bip.21490.
(22) Oliveira, B. L., Correia, J. D. G., Raposinho, P. D., Santos, I., Ferreira, A., Cordeiro, C., and Freire, A. P. (2009) Re and 99mTc organometallic complexes containing pendant L-arginine derivatives as potential probes of inducible nitric oxide synthase. *Dalton Trans.* 152–162.
(23) Oliveira, B. L., Raposinho, P. D., Mendes, F., Santos, I. C., Santos, I., Ferreira, A., Cordeiro, C., Freire, A. P., and Correia, J. D.G. (2010) Targeting nitric oxide synthase with 99mTc/Re-tricarbonyl complexes containing pendant guanidino or isothiourea moieties. *J. Organomet. Chem.* Online Early Access. DOI: 10.1016/j.jorganchem. 2010.09.019.
(24) Reif, D. W., and McCreedy, S. A. (1995) N-Nitro-L-arginine and N-monomethyl-L-arginine exhibit a different pattern of inactivation toward the 3 Nitric-Oxide Synthases. *Arch. Biochem. Biophys. 320*, 170–176.
(25) Debreczeni, J. É., Bullock, A. N., Atilla, G. E., Williams, D. S., Bregman, H., Knapp, S., and Meggers, E. (2006) Ruthenium half-sandwich complexes bound to protein kinase Pim-1. *Angew. Chem., Int. Ed. 45*, 1580–1585.
(26) MacMicking, J., Xie, Q. W., and Nathan, C. (1997) Nitric oxide and macrophage function. *Annu. Rev. Immunol. 15*, 323–350.
(27) Kan, W., Zhao, Ke-S., Jiang, Y., Yan, W., Huang, Q., Wang, J., Qin, Q., Huang, X., and Wang, S. (2004) Lung, spleen, and kidney are the major places for inducible nitric oxide synthase expression in endotoxic shock: Role of P38 mitogen-activated protein kinase in signal transduction of inducible nitric oxide synthase expression. *Shock 21*, 281–287.

BC100291E

Supporting Information

Re and Tc Tricarbonyl Complexes: From the Suppression of NO Biosynthesis in Macrophages to *in vivo* Targeting of Inducible Nitric Oxide Synthase

Bruno L. Oliveira,[1] Paula D. Raposinho,[1] Filipa Mendes,[1] Flávio Figueira,[1] Isabel Santos,[1] António Ferreira,[2] Carlos Cordeiro,[2] Ana P. Freire,[2] João D. G. Correia[1,*]

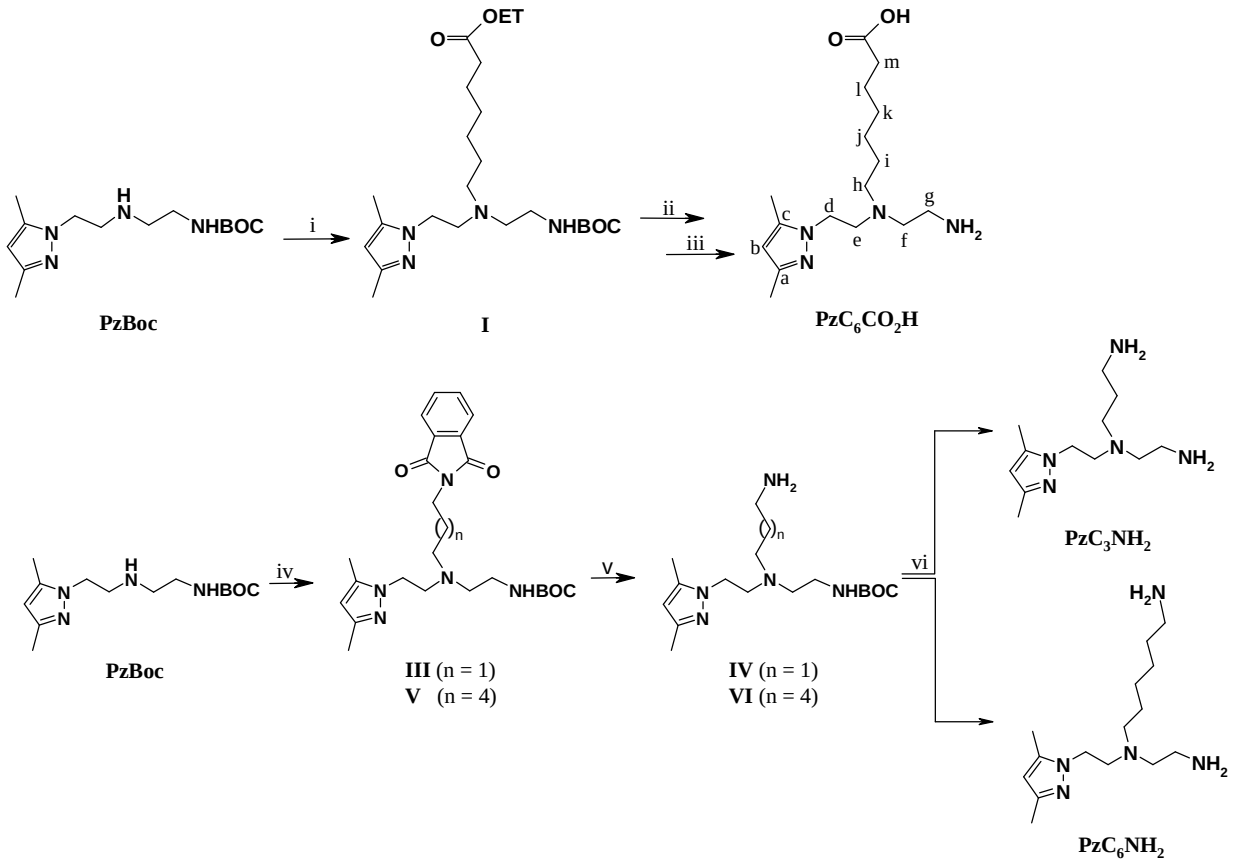
[1]Unidade de Ciências Químicas e Radiofarmacêuticas, ITN, Estrada Nacional 10, 2686-953 Sacavém, Portugal and [2]Centro de Química e Bioquímica, Departamento de Química e Bioquímica, Faculdade de Ciências da Universidade de Lisboa, Portugal

Bioconjugate Chemistry – Communication

General procedures and materials: All chemicals and solvents were of reagent grade and were used without purification unless stated otherwise. The precursor *tert*-butyl (2-{[2-(3,5-dimethyl-1*H*-pyrazol-1-yl)ethyl]amino}ethyl)carbamate (**PzBoc**), **L[1]**, **L[2]**, **1**/**1a**, **2**/**2a** and $(Et_4N)_2[Re(CO)_3Br_3]$ were prepared according to published methods (*1-3*). All other chemicals not specified above were purchased from Aldrich. $Na[^{99m}TcO_4]$ was eluted from a $^{99}Mo/^{99m}Tc$ generator using 0.9% saline. The radioactive precursor *fac*-$[^{99m}Tc(CO)_3(H_2O)_3]^+$ was prepared using a IsoLink® kit (Malinckrodt, Inc.). ^1H and ^{11}C NMR spectra were recorded at room temperature on a Varian Unity 300 MHz spectrometer. ^1H and ^{11}C chemical shifts were referenced with the residual solvent resonances relatively to tetramethylsilane. The spectra were assigned with the help of 2D experiments (^1H–^1H correlation spectroscopy, COSY and ^1H–^{13}C heteronuclear single quantum coherence, HSQC). Assignments of the ^1H and ^{13}C NMR resonances are given in accordance with the identification system shown in **Scheme S1**. Infrared spectra were recorded as KBr pellets on a Bruker Tensor 27 spectrometer. All compounds were characterized by electrospray ionization mass spectrometry (ESI-MS) using a Bruker model Esquire 3000 plus. Aliquots of ~ 5 mg of pure compounds (≥ 98 % ascertained by RP-HPLC) were lyophilized in eppendorf tubes and used for radioactive labelling and *in vitro* studies. HPLC analyses were performed on a Perkin Elmer LC pump 200 coupled to a Shimadzu SPD 10AV UV/Vis and to a Berthold-LB 509 radiometric detector, using an analytic Macherey-Nagel C18 reversed-phase column (Nucleosil 100-5, 250 x 3 mm) with a flow rate of 0.5 mL/min. Purification of the inactive compounds were achieved on a semi-preparative Macherey-Nagel C18 reversed-phase column (Nucleosil 100-7, 250 x 8 mm) or on a preparative Waters μ Bondapak C18 (150 x 19 mm) with a flow rate of 2.0 mL/min and 5.5 mL/min, respectively. UV detection: 220 or 254 nm. Eluents: aqueous 0.1% CF_3COOH/MeOH. Gradient: t = 0-5 min: 10%

MeOH; 5-30 min: 10→100% MeOH; 30-34 min: 100% MeOH; 34-35 min: 100→10% MeOH; 35-40 min: 10% MeOH.

NOS assays were recorded on an Agilent Technologies 8453 UV-Vis diode array spectrophotometer with a thermostated multicuvette holder with stirring. The iNOS (mouse recombinant enzyme), bovine hemoglobin, NADPH, BH_4 (Tetrahydrobiopterin), HEPES and DTT were purchased from Sigma Chemical Co.



Scheme S1. Synthesis of the precursor compounds **PzC_6CO_2H**, **PzC_3CNH_2** and **PzC_6NH_2** i) ethyl 7-bromoheptanoate or ethyl 4-bromobutanoate, K_2CO_3, KI, CH_3CN, reflux, ON; ii) NaOH, H_2O, THF, reflux, ON; iii) TFA, CH_2Cl_2, r.t.; iv) *N*-(3-bromopropyl)phthalimide or *N*-(6-bromohexyl)phthalimide, K_2CO_3, dioxane, reflux, overnight; v) MeOH, $NH_2NH_2 \cdot H_2O$, reflux;

vi) TFA, CH_2Cl_2, r.t. (*identification system for NMR assignments is displayed for PzC_6CO_2H as an example).*

- Synthesis of 7-{(2-aminoethyl)[2-(3,5-dimethyl-1H-pyrazol-1-yl)ethyl]amino}heptanoic acid (PzC_6CO_2H)

*Synthesis of ethyl 7-((2-(tert-butoxycarbonylamino)ethyl)(2-(3,5-dimethyl-1H-pyrazol-1-yl)ethyl)amino)heptanoate (**I**)*: The precursor **PzBoc** (0.40 g, 1.40 mmol) was dissolved in CH_3CN (60 mL) and ethyl 7-bromoheptanoate (0.67 g, 2.83 mmol), an excess of K_2CO_3 (0.39, 2.83 mmol), and a catalytic amount of KI were added. After refluxing for 18h, the solution was filtered, vacuum dried, and the residue was purified by column chromatography (hexane/EtOAc (50-100%). The intermediate compound **I** was obtained as a pale yellow oil upon removal of the solvents from the collected fractions. Yield: 79 % (0.50 g, 1.13 mmol). ^{1}H-NMR ($CDCl_3$): δ(ppm) 5.72 (s, CH^b, 1H), 5.05 (br s, NHBoc, 1H), 4.08 (q, OCH_2CH_3, 2H), 3.93 (t, CH_2^d, 2H), 3.02 (br m, 2H), 2.73 (t, 2H), 2.46 (t, 2H), 2.36 (t, 2H), 2.23 (t, 2H), 2.21 (s, CH_3pz, 3H), 2.17 (s, CH_3pz, 3H), 1.55 (m, 2H), 1.32 (s, CH_3, 9H), 1.27 (m, 2H), 1.21 (m, OCH_2CH_3 + CH_2, 5H), 1.16 (m, 2H). HPLC (R_t): 21.0 min (λ = 220 nm).

*Synthesis of 7-((2-(tert-butoxycarbonylamino)ethyl)(2-(3,5-dimethyl-1H-pyrazol-1-yl)ethyl)-amino)heptanoic acid (**II**)*: A solution of **I** (0.50 g, 1.13 mmol) and excess NaOH (0.45 g, 11.31 mmol) in H_2O/THF (3 mL/30mL) was refluxed overnight. The solution was carefully neutralized with HCl 1M at 0 ^oC and extracted with CH_2Cl_2. The organic phases were collected, dried over $MgSO_4$, filtered and the solvent evaporated. The crude product was purified by column chromatography ($CHCl_3$/MeOH (5-100%)) giving a yellow pale oil corresponding to **II**. Yield: 86 % (0.40 g, 0.97 mmol). ^{1}H-NMR ($CDCl_3$): δ(ppm) 5.70 (s, CH^b, 1H), 5.16 (br s, NHBoc, 1H),

3.91 (t, 2H), 2.97 (m, 2H), 2.72 (t, 2H), 2.43 (t, 2H), 2.35 (t, 2H), 2.16 (s, CH_3pz, 3H), 2.12 (s, CH_3pz, 3H), 1.45 – 1.20 (m, 10H), 1.37 (s, CH_3, 9H). HPLC (R_t): 20.0 min (λ = 220 nm).

*Synthesis of 7-((2-aminoethyl)(2-(3,5-dimethyl-1H-pyrazol-1-yl)ethyl)amino)heptanoic acid (**PzC_6CO_2H**)*: **PzC_6CO_2H** was obtained directly by dissolving **II** (0.17 g, 0.41 mmol) in a mixture of CH_2Cl_2/TFA (1 mL/3 mL) and allowed to react for 3 h at room temperature with stirring. The residue obtained after evaporation of the solvent was dissolved in H_2O, filtered through a 0.45 µm Millipore® filter, and purified by preparative RP-HPLC. The fractions containing $\mathbf{L^3}$ were collected and the solvent removed to provide a clear viscous colorless oil. Yield: 92 % (0.16 g, 0.38 mmol, calcd. for $C_{16}H_{30}N_4O_2$.TFA). IR (KBr, cm^{-1}): 3524m, 1694s, 1559m, 1442m and 1210m ^{1}H-NMR (D_2O): δ(ppm) 5.94 (s, CH^b, 1H), 4.35 (t, CH_2^d, 2H), 3.59 (t, CH_2^e, 2H), 3.44 (m, CH_2^f, 2H), 3.33 (m, CH_2^g, 2H), 3.09 (m, CH_2^m, 2H), 2.23 (m, CH_2^h, 2H), 2.20 (s, CH_3pz, 3H), 2.12 (s, CH_3pz, 3H), 1.52 (m, CH_2^l, 2H), 1.45 (m, CH_2^i, 2H), 1.18 (m, CH_2^j, CH_2^k, 4H). ^{13}C-NMR (D_2O): δ(ppm) 176.5 (CO), 165.3 (q, CF_3COO^-), 149.3 (pz), 145.4 (pz), 118.3 (q, CF_3COO^-), 106.4 (pz), 54.3 (CH_2), 53.4 (CH_2), 49.8 (CH_2), 42.2 (CH_2), 33.8 (CH_2), 33.5 (CH_2), 27.7 (CH_2), 25.3 (CH_2), 24.4 (CH_2), 22.9 (CH_2), 12.5 (CH_3pz), 9.8 (CH_3pz). HPLC (R_t): 18.6 min (λ = 220 nm). ESI-MS (+) (m/z): 311.1 $[M+H]^+$, calcd. for $C_{16}H_{30}N_4O_2$ = 310.2.

- *Synthesis of N^1-(2-aminoethyl)-N^1-(2-(3,5-dimethyl-1H-pyrazol-1-yl)ethyl)propane-1,3-diamine (PzC_3NH_2)*

*Synthesis of tert-butyl 2-((2-(3,5-dimethyl-1H-pyrazol-1-yl)ethyl)(3-(1,3-dioxo-2,3-dihydro-1H-inden-2-yl)propyl)amino)ethylcarbamate (**III**)*: A solution of **PzBoc** (1.11 g, 3.94 mmol), N-(3-bromopropyl)phthalimide (2.14 g, 8.05 mmol), and K_2CO_3 (1.10 g, 8.02 mmol) in dioxane (35 mL) was refluxed overnight. After reaction, the solution was filtered and the solvents evaporated

to give an oily residue which was purified by column chromatography (n-hexane to EtOAc). The fractions containing **III** were collected and the compound was obtained as an yellow oil after evaporation of the elution solvents. Yield: 78 % (1.45 g, 3.07 mmol). ^{1}H-NMR ($CDCl_3$): δ(ppm) 7.85 (m, phthalimide, 2H), 7.72 (m, phthalimide, 2H) 5.74 (s, CH^b, 1H), 5.15 (br s, NHBoc, 1H), 3.96 (t, CH_2^d, 2H), 3.61 (t, CH_2^e, 2H), 3.05 (m, CH_2^f, 2H), 2.78 (t, CH_2^h, 2H), 2.46 (m, CH_2^g/CH_2^j, 4H), 2.20 (s, CH_3pz, 3H), 2.15 (s, CH_3pz, 3H), 1.76-1.66 (m, CH_2^i, 2H), 1.39 (s, CH_3, 9H).

*Synthesis tert-butyl 2-((3-aminopropyl)(2-(3,5-dimethyl-1H-pyrazol-1-yl)ethyl)amino)-ethylcarbamate (**IV**)*: To a solution of **III** (1.45 g, 3.07 mmol) in MeOH (10 mL) was added hydrazine hydrate (3.01 mL, 63.20 mmol). After refluxing for 6 h, the solution was carefully acidified with HCl 1 M to pH 4 and a white precipitate was formed, which was removed by filtration. The obtained clear solution was neutralized with NaOH 1 M and extracted with $CHCl_3$. The organic layer was dried over $MgSO_4$. Removal of the solvent yielded an oily residue, which was purified by column chromatography ($CHCl_3$ to MeOH). After evaporation of the solvents, **IV** was obtained as a yellow oil. Yield: 86 % (0.90 g, 2.65 mmol). ^{1}H-NMR ($CDCl_3$): δ(ppm) 5.75 (s, CH^b, 1H), 5.28 (br s, NH_2, 2H), 5.10 (br s, NHBoc, 1H), 3.96 (t, CH_2^d, 2H), 3.07 (m, CH_2^e, 2H), 2.76 (t, CH_2^f, 2H), 2.60 (t, CH_2^g, 2H), 2.48 (m, CH_2^h/CH_2^j, 4H), 2.21 (s, CH_3pz, 3H), 2.19 (s, CH_3pz, 3H), 1.50-1.45 (m, CH_2^i, 2H), 1.42 (s, CH_3, 9H).

*Synthesis of N^1-(2-aminoethyl)-N^1-[2-(3,5-dimethyl-1H-pyrazol-1-yl)ethyl]propane-1,3-diamine (**PzC_3NH_2**):* **PzC_3NH_2** was obtained directly by dissolving **IV** (0.06 g, 0.17 mmol) in a mixture of CH_2Cl_2/TFA (1 mL/3 mL) and allowed to react for 3 h at room temperature with stirring. The residue obtained after evaporation of the solvent was dissolved in H_2O, filtered through a 0.45 µm Millipore® filter, and purified by preparative RP-HPLC. The fractions containing **PzC_3NH_2**

were collected and the solvent removed to provide a clear viscous colorless oil. Yield: 50 % (0.04 g, 0.086 mmol, calcd. for $C_{12}H_{25}N_5$.2TFA). IR (KBr, cm^{-1}): 1675s, 1190s and 1100m. ^{1}H-NMR (D_2O): δ(ppm) 5.83 (s, CH^b, 1H), 3.96 (t, CH_2^d, 2H), 2.85 (t, CH_2^e, 2H), 2.76 (m, CH_2^f/CH_2^g, 4H), 2.66 (m, CH_2^h, 2H), 2.51 (t, CH_2^j, 2H), 2.11 (s, CH_3pz, 3H), 2.01 (s, CH_3pz, 3H), 1.61 (m, CH_2^i, 2H). ^{13}C-NMR (D_2O): δ(ppm) 165.4 (q, CF_3COO^-), 151.2 (C^c), 144.1 (C^a), 118.7 (q, CF_3COO^-), 107.9 (C^b), 54.5 (C^e), 52.8 (C^f), 52.5 (C^d), 47.9 (C^h), 39.9 (C^j), 39.28 (C^g), 26.2 (C^i), 14.4 (CH_3pz), 12.5 (CH_3pz). HPLC (R_t): 16.8 min (λ = 220 nm). ESI-MS (+) (m/z): 240.2 $[M+H]^+$, calcd. for $C_{12}H_{25}N_5$ = 239.2.

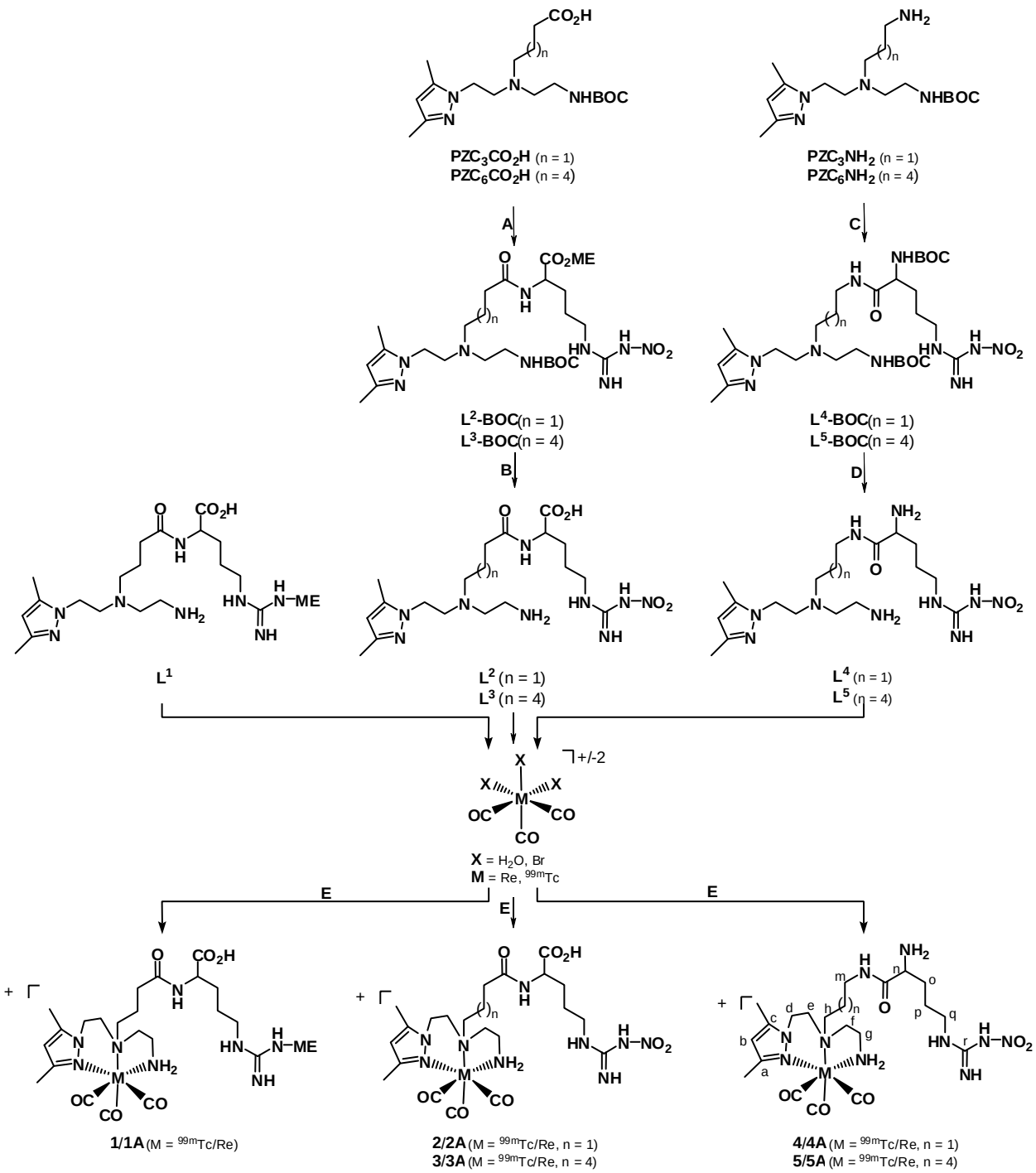
- Synthesis of *N*^{1}-(2-aminoethyl)-*N*^{1}-(2-(3,5-dimethyl-1*H*-pyrazol-1-yl)ethyl)hexane-1,6-diamine (PzC_6NH_2)

*Synthesis of tert-butyl 2-((2-(3,5-dimethyl-1H-pyrazol-1-yl)ethyl)(6-(1,3-dioxo-2,3-dihydro-1H-inden-2-yl)hexyl)amino)*ethylcarbamate (***V***): **V** was prepared as described for **III**. Starting with 0.49 g (1.74 mmol) of **PzBoc**, and 1.85 g (5.96 mmol) of N-(6-bromohexyl)phthalimide, a yellowish oil formulated as **V** was obtained after purification by column chromatography (n-hexane to EtOAc). Yield: 50 % (0.45 g, 0.87 mmol). ^{1}H-NMR ($CDCl_3$): δ(ppm) 7.81 (m, phthalimide, 2H), 7.68 (m, phthalimide, 2H), 5.73 (s, CH^b, 1H), 5.04 (br s, NHBoc, 1H), 3.93 (t, CH_2^d, 2H), 3.64 (t, CH_2^e, 2H), 3.03 (m, CH_2^f, 2H), 2.75 (t, CH_2^g, 2H) 2.46 (t, CH_2^h, 2H), 2.38 (t, CH_2^m, 2H), 2.20 (s, CH_3pz, 3H), 2.17 (s, CH_3pz, 3H), 1.67-1.57 (m, CH_2^i, CH_2^l, 4H), 1.30 (s, CH_3, 9H), 1.30-1.20 (m, CH_2^j, CH_2^k, 4H).

*Synthesis of tert-butyl 2-((6-aminohexyl)(2-(3,5-dimethyl-1H-pyrazol-1-yl)ethyl)amino)-ethylcarbamate (**VI**):* **VI** was prepared as described for **IV**. Starting with 0.46 g (0.89 mmol) of **V** and 0.86 mL (17.12 mmol) of hydrazine hydrate, a yellowish oil formulated as **VI** was

obtained after purification by column chromatography ($CHCl_3$ to MeOH). Yield: 90 % (0.33 g, 0.83 mmol). ^{1}H-NMR ($CDCl_3$): δ(ppm) 5.70 (s, CH^b, 1H), 5.02 (br s, NHBoc, 1H), 3.91 (t, CH_2^d, 2H), 3.00 (m, CH_2^e, 2H), 2.72 (t, CH_2^f, 2H), 2.62 (t, CH_2^g, 2H), 2.44 (t, CH_2^h, 2H), 2.35 (t, CH_2^m, 2H), 2.17 (s, CH_3pz, 3H), 2.15 (s, CH_3pz, 3H), 1.55 (m, CH_2^i, 2H), 1.32 (s, CH_3, 9H), 1.23 (m, CH_2^j + CH_2^k + CH_2^l, 6H).

Synthesis of N^1-(2-aminoethyl)-N^1-(2-(3,5-dimethyl-1H-pyrazol-1-yl)ethyl)hexane-1,6-diamine ***(PzC_6NH_2)***: Boc-deprotection of **VI** (0.080 g, 0,20 mmol) with CH_2Cl_2/TFA (1 mL/3 mL), as previously described, gave a colorless oil corresponding to **PzC_6NH_2** after purification by preparative RP-HPLC. Yield: 49 % (0.050 g, 0.098 mmol, calcd. for $C_{15}H_{31}N_5$.2TFA). IR (KBr, cm^{-1}): 1680s, 1200s and 1100m. ^{1}H-NMR (D_2O): δ(ppm) 6.03 (s, CH^b, 1H), 4.42 (t, CH_2^d, 2H), 3.59 (t, CH_2^e, 2H), 3.49 (m, CH_2^f, 2H), 3.34 (m, CH_2^g, 2H), 2.85 (t, CH_2^m, 2H), 2.15 (m, CH_2^h, 2H), 2.20 (s, CH_3pz, 3H), 2.12 (s, CH_3pz, 3H), 1.52 (m, CH_2^i, CH_2^l, 4H), 1.23 (m, CH_2^j, CH_2^k, 4H). ^{13}C-NMR (D_2O): δ(ppm) 165.4 (q, CF_3COO^-), 150.3 (C^c), 144.2 (C^a), 118.6 (q, CF_3COO^-), 107.1 (C^b), 54.0 (C^e), 51.9 (C^f), 49.8 (C^d), 42.2 (C^m), 39.3 (C^h), 33.8 (C^g), 26.7 (C^l), 25.4 (C^i), 25.3 (C^k), 22.9 (C^J), 11.8 (CH_3pz), 10.2 (CH_3pz). HPLC (R_t): 18.2 min (λ = 220nm). ESI-MS (+) (m/z): 282.2 $[M+H]^+$, calcd. for $C_{15}H_{31}N_5$ = 281.2.



Scheme S2. Synthesis of the intermediate bioconjugates $\mathbf{L^2}$ – $\mathbf{L^5}$ and organometallic complexes **1**/**1a** – **5**/**5a**. Numbering scheme for NMR assignment is presented for compound **4a**/**5a**.

- Synthesis of L^3

To a solution of **PzC_6CO_2H** (0.050 g, 0.12 mmol) in DMF were added triethylamine (0.036 g, 0.365 mmol) and *O*-benzotriazol-1-yl-*N*,*N*,*N*´,*N*´-tetramethyluronium hexafluorophosphate (HBTU, 0.054 g, 0.145 mmol). After 10 minutes N^{ω}-nitro-L-arginine methyl ester (0.039 g, 0.145 mmol) was added, and the reaction mixture stirred at room temperature under a nitrogen atmosphere for 2 h. The solvent was then removed under vacuum, and the residue purified by column chromatography ($CHCl_3$ to MeOH). The intermediate **L^3-Boc** was obtained as a yellowish oil. Yield: 66 % (0.050 g, 0.080 mmol). ^{1}H-NMR ($CDCl_3$): δ(ppm) 7.69 (br s, NH, 2H), 6.48 (br s, NH, 1H), 5.70 (s, CH^b, 1H), 5.10 (br s, NH, 1H), 4.57 (br s, NH, 1H), 3.91 (t, CH_2^d, 2H), 3.69 (s, OCH_3, 3H), 3.64 (br m, CH^n, 1H), 2.98 (m, CH_2, 2H), 2.72 (t, CH_2, 2H), 2.44 (t, CH_2, 2H), 2.36 (t, CH_2, 2H), 2.22 (m, CH_2, 2H) 2.19 (s, CH_3pz, 3H), 2.16 (s, CH_3pz, 3H), 1.89 (m, CH_2, 1H), 1.70 – 1.52 (m, CH_2, 7H), 1.40 (s, CH_3, 9H), 1.39 – 1.15 (m, CH_2, 6H). ^{13}C-NMR ($CDCl_3$): δ(ppm) 174.3 (CO), 172.6 (CO), 159.4 (C^r), 159.4 (CO), 147.3 (pz), 138.9 (pz), 104.9 (pz), 78.9 ($C(CH_3)_3$), 54.1, 53.7, 53.3, 52.7, 50.6, 47.0, 40.3, 38.4, 36.2, 30.8, 28.8, 28.4, 26.7, 25.4, 24.6, 13.4 (CH_3pz), 11.0 (CH_3pz).

L^3 was obtained directly by hydrolysis of the methyl ester group and Boc-deprotection of the intermediate **L^3-Boc** (0.090 g, 0.144 mmol) with a 3 N HCl solution (5 mL) at room temperature, for 72 h. After neutralization of the reaction mixture with a 1 M NaOH solution, the water was evaporated and the obtained residue extracted with MeOH. The solvent was evaporated, the residue dissolved in water and purified by RP-HPLC to give a colorless oil. Yield: 33 % (0.030 g, 0.048 mmol, calcd. for $C_{22}H_{41}N_9O_5$·TFA). IR (KBr, cm^{-1}): ~ 1650s, 1390m, 1265m (NO_2), 1200m and 1130m. ^{1}H-NMR (D_2O): δ(ppm) 5.76 (s, CH^b, 1H), 4.34 (br m, CH^n, 1H) 3.98 (t, CH_2^d, 2H), 3.87 (t, CH_2, 2H), 2.65 (m, CH_2, 4H), 2.31 (t, CH_2, 2H), 2.16 (s, CH_3pz, 3H), 2.14

(m, CH_2, 2H), 2.06 (s, CH_3pz, 3H), 1.79 (m, CH_2, 1H), 1.70 – 1.40 (m, CH_2, 7H), 1.39 – 1.00 (m, CH_2, 6H). ^{13}C-NMR ($CDCl_3$): δ(ppm) 175.3 (CO), 172.7 (CO), 162.2 (q, CF_3COO^-), 160.0 (C^r), 147.0 (pz), 139.7 (pz), 116.4 (q, CF_3COO^-), 105.1 (pz), 54.3, 53.1, 52.1, 51.1, 46.5, 40.5, 38.0, 35.4, 33.5, 28.9, 26.8, 26.6, 25.6, 24.7, 12.1 (CH_3pz), 9.7 (CH_3pz). ESI-MS (+) (*m/z*): 564.1 $[M+K]^+$; calcd for $C_{23}H_{43}N_9O_5$ = 525.3. Retention time (analytic RP-HPLC, 220 nm): 14.6 min. Elemental analysis calcd. for $C_{22}H_{41}N_9O_5$·TFA: C, 46.06; H, 6.76; N, 20.15. Found: C, 45.40; H, 6.20; N, 19.60 %.

- Synthesis of L^4

N^{α}-Boc-N^{ω}-nitro-L-arginine (0.11 g, 0.36 mmol), *N*,*N'*-Dicyclohexylcarbodiimide (DCC, 0.075 g, 0.36 mmol), and *N*-Hydroxybenzotriazole (HOBt, 0.050 g, 0.36 mmol) were dissolved in DMF (ca 5 mL) at room temperature under stirring. After 1 h, the reaction was cooled down with an ice bath, and *N*,*N*-Diisopropylethylamine (DIPEA, 125.4 µL, 0.72 mmol) and a solution of **PzC_3NH_2** (0.12 g, 0.36 mmol) in dichloromethane was added under stirring. After 18 h at room temperature the reaction was treated with water and the white precipitate corresponding to urea was removed by filtration. The aqueous phase was extracted with ethyl acetate, the organic phases were collected and dried over magnesium sulfate. Evaporation of the solvent afforded a yellowish oil which was chromatographed on an appropriate column of silica gel with methanol/dichloromethane/ammonia (10:89:1) to afford a colorless oil corresponding to **L^4-Boc**. This oil was dissolved in a dichloromethane/TFA solution (1 mL:3 mL) and stirred at room temperature for 3 h. The solvent was removed under vacuum, the residue dissolved in water and purified by semi-preparative RP-HPLC. Evaporation of the solvent from the collected fractions yielded compound **L^4·2TFA** as a colorless oil. Yield: 20 % (0.057 g, 0.073 mmol, calcd. for

$C_{18}H_{36}N_{10}O_3$·2TFA). IR (KBr, cm^{-1}): 3405m, ~1680s, 1427m, 1203m and 1134m. ^{1}H-NMR (D_2O): δ(ppm) 6.15 (s, H^b(4)pz, 1H), 4.53 (t, CH^d_2, 2H), 3.84 (t, CH^n, 1H), 3.57 (t, CH^e_2, 2H), 3.48 (m, CH^f_2, 2H) 3.34 (m, CH^g_2, 2H), 3.24 - 3.15 (t, CH^q_2/CH^h_2/CH^j_2) 2.22 (s, CH_3pz, 3H), 2.16 (s, CH_3pz, 3H), 1.77 (m, CH^o_2/CH^i_2, 4H), 1.52 (m, CH^p_2, 2H). ^{13}C-NMR (D_2O): δ(ppm) 169.9 (C=O), 162.3 (q, CF_3COO^-), 158.9 (C^r), 148.2 (C^c(3)pz), 146.7 (C^a(5)pz), 116.4 (q, CF_3COO^-), 108.2 (C^b(4)pz), 52.9 (C^n), 51.7 (C^h), 51.1 (C^e), 49.8 (C^f), 42.0 (C^d), 40.3 (C^q), 36.5 (C^j), 33.7 (C^g), 28.1 (C^i), 23.2 (C^p), 23.1 (C^o), 11.5 (CH_3pz), 10.1 (CH_3pz). ESI-MS (+) (*m/z*): 441.2 $[M+H]^+$; calcd for $C_{18}H_{36}N_{10}O_3$ = 440.3. Elemental analysis calcd. for $C_{18}H_{36}N_{10}O_3$·2TFA: C, 36.81; H, 5.02; N, 17.90. Found: C, 36.53; H, 5.32; N, 17.82 %. Retention time (analytic RP-HPLC, 220 nm): 21.1 min.

- Synthesis of L^5

N^{α}-Boc-N^{ω}-nitro-L-arginine (0.084 g, 0.262 mmol), *N*,*N'*-Dicyclohexylcarbodiimide (DCC, 0.064 g, 0.314 mmol), and *N*-Hydroxybenzotriazole (HOBt, 0.042 g, 0.314 mmol) were dissolved in DMF (ca 5 mL) at room temperature under stirring. After 1 h, the reaction was cooled down with an ice bath, and *N*,*N*-Diisopropylethylamine (DIPEA, 0.067 g, 0.524 mmol) and a solution of PzC_6NH_2 (0.100 g, 0.262 mmol) in DMF was added under stirring. After 18 h at room temperature the solvent was removed and the residue treated with water/ethyl acetate. The organic layer was dried over $MgSO_4$. Removal of the solvent yielded an oily residue, which was purified by column chromatography ($CHCl_3$ to MeOH). Yield: 70 % (0.125 g, 0.183 mmol). ^{1}H-NMR (CDCl3): δ(ppm) 7.69 (br s, NH, 2H), 6.92 (br s, NH, 1H), 5.79 (s, CH^b, 1H), 5.59 (br s, NH, 1H), 5.20 (br s, NH, 1H), 4.22 (br m, NH, 1H), 4.01 (t, CH_2^d, 2H), 3.71 (br m, CH^n, 1H), 3.50 – 3.20 (m, CH_2, 4H), 3.03 (m, CH_2, 2H), 2.76 (t, CH_2, 2H), 2.49 (t, CH_2, 2H), 2.42 (t, CH_2,

2H), 2.24 (s, CH_3pz, 3H), 2.20 (s, CH_3pz, 3H), 1.93 (m, CH_2, 3H), 1.70 (m, CH_2, 5H), 1.44 (s, CH_3, 9H), 1.43 (s, CH_3, 9H), 1.35 (m, CH_2, 2H), 1.25 (m, CH_2, 2H).

The Boc-deprotection of the intermediate **L^5-Boc** with CH_2Cl_2/TFA (1 mL/3 mL), as described above for **L^4**, gave a colorless oil after purification by preparative RP-HPLC corresponding to **L^5**. Yield: 92 % (0.120 g, 0.169 mmol, calcd. for $C_{21}H_{42}N_{10}O_3$·2TFA). IR (KBr, cm^{-1}): 3255m, ~1654s, 1396m, 1275m and 1203m. ^{1}H-NMR (D_2O): δ(ppm) 6.16 (s, H^b(4)pz, 1H), 4.55 (t , CH^d_2, 2H), 3.81 (t, CH^n, 1H), 3.59 (t, CH^e_2, 2H), 3.53 (m, CH^f_2, 2H) 3.35 (m, CH^g_2, 2H), 3.21-3.13 (m, CH^q_2/CH^h_2/CH^j_2) 2.24 (s, CH_3pz, 3H), 2.18 (s, CH_3pz, 3H), 1.75 (m, CH^o_2/ ´´, 2H), 1.54-1.50 (m, CH^p_2, CH^i_2, 4H) 1.34 (m, CH^l_2, 2H), 1.17 (m, CH^j_2/CH^k_2, 4H). ^{13}C-NMR (D_2O): δ(ppm) 169.2 (C=O), 158.7 (C^r), 147.9 (C^c(3/5)pz), 146.8 (C^a (3/5)pz), 108.4 (C^b), 53.9 (C^q), 53.0 (C^n), 50.8 (C^e), 49.7 (C^f), 42.0 (C^d), 40.3 (C^m), 39.5 (C^h), 33.7 (C^g), 28.1 (C^o), 28.0 (C^l), 25.8 (C^p), 25.3 (C^i), 23.3 (C^k), 22.8 (C^J), 10.6 (CH_3pz), 10.2 (CH_3pz). ESI-MS (+) (*m/z*): 242.0 $[M+H]^{2+}$; calcd for $C_{21}H_{42}N_{10}O_3$ = 482.3. Elemental analysis calcd. for $C_{21}H_{42}N_{10}O_3$·2TFA: C, 42.23; H, 6.24; N, 19.71. Found: C, 43.00; H, 6.50; N, 19.90 %. Retention time (analytic RP-HPLC, 220 nm): 23.1 min.

General procedure for the preparation of the Re complexes *fac*-[Re(CO)$_3$(k^3-L)] (3a, L = L^3; 4a, L = L^4; 5a, L = L^5)

$(NEt_4)_2[ReBr_3(CO)_3]$ was reacted with equimolar amounts of the compounds **L^3 – L^5** in refluxing water for 18h. After this time, the solvent was removed under vacuum, and the resulting residue washed with $CHCl_3$ to remove excess $[NEt_4]Br$. The resulting residue was dissolved in water, the precipitate formed eliminated by centrifugation and the supernatant purified by preparative RP-HPLC.

***Synthesis of fac-[Re(CO)$_3$(k^3-L^3)]$^+$* (3a)**

Starting from 0.035 g (0.055 mmol) of **L^3·TFA**, a colorless oil formulated as **3a** was obtained (0.020 g, 40 %, calcd. for $C_{25}H_{41}N_9O_8Re$·TFA). IR (KBr, cm^{-1}): 2024s and 1910s (C≡O), 1675s, 1290m, 1230m and 1135m. ^{1}H-NMR (CD3OD): δ(ppm) 6.20 (s, CH^b(4)pz, 1H), 5.50 (br s, NH, 1H), 4.55 – 4.49 (dd, CH_2, 1H), 4.45 (m, CH, 1H), 4.26 – 4.17 (dd, CH_2, 1H), 4.08 (m, NH, 1H), 3.66 (m, CH_2, 1H), 3.37 - 3.15 (m, overlapped with CD3OD, 7H), 2.82 (m, CH_2, 2H), 2.71 - 2.62 (m, CH_2, 1H), 2.57 - 2.43 (m, CH_2, 1H), 2.44 (s, CH_3pz, 3H), 2.36 (s, CH_3pz, 3H), 2.29 (t, CH_2, 2H), 1.93 (m, CH_2, 1H), 1.80 - 1.60 (m, CH_2, 5H), 1.42 (m, CH_2, 4H). ^{13}C-NMR (CD_3OD): δ(ppm) 197.0 (C≡O), 176.2 (C=O), 175.0 (C=O), 166.6 (C^r), 155.9 (C^c(3)pz), 145.6 (C^a(5)pz), 109.2 (C^b(4)pz), 68.7, 62.9, 53.4, 51.5, ~ 48.7 (2 signals overlapped with solvent CD_3OD), 43.7, 41.7, 37.8, 31.3, 31.0, 27.7, 26.5, 25.4, 16.0 (CH_3pz), 11.4 (CH_3pz). ESI-MS (+) (*m/z*): 782.0 [M]$^+$; calcd for $C_{25}H_{41}N_9O_8Re$ = 782.2. Elemental analysis calcd. for $C_{25}H_{41}N_9O_8Re$·TFA: C, 36.15; H, 4.72; N, 14.06. Found: C, 37.00; H, 4.90; N, 14.65 %. Retention time (analytic RP-HPLC, 220 nm): 24.0 min.

***Synthesis of fac-[Re(CO)$_3$(k^3-L^4)]$^+$* (4a)**

Starting from 0.040 g (0.060 mmol) of **L^4·2TFA**, a colorless oil formulated as **4a** was obtained (0.053 g, 94 %, calcd. for $C_{21}H_{36}N_{10}O_6Re$·2TFA). IR (KBr, cm^{-1}): 3410s, 2227s and 1903s (C≡O), 1674s, 1318m, 1201m and 1125m. ^{1}H-NMR (D_2O): δ(ppm) 6.05 (s, CH^b(4)pz, 1H), 5.05 (br s, NH, 1H), 4.31 (dd, CH$^{d'}$, 1H), 4.04 (m, CH$^{d''}$, H), 3.88 (t, CH^n, 1H), 3.66 (m, NH, 2H), 3.52 (m, CH$^{h'}$, 1H), 3.45-3.28 (m, CH$^{h''}$/CH$^{e'}$/CH$^j{}_2$, 4H), 3.20-3.06 (m, CH$^{g'}$/CH$^q{}_2$, 3H), 2.72 (m, CH$^f{}_2$, 2H), 2.55 (m, CH$^{e''}$, 1H), 2.39 (m, CH$^{g''}$, 1H), 2.27 (s, CH_3pz, 3H), 2.17 (s, CH_3pz, 3H), 2.10 (m, CH$^{i'}$, 1H), 1.81 (m, CH$^{i'}$/CH$^o{}_2$, 3H), 1.59 (m, CH$^p{}_2$, 2H). ^{13}C-NMR (D_2O):

δ(ppm) 197.2, 196.6, 195.2 (C≡O), 172.1 (C=O), 161.4 (C^{r}), 156.1 (C^{c}(3)pz), 146.7 (C^{a}(5)pz), 110.3 (C^{b}(4)pz), 67.1 (C^{h}), 64.2 (C^{f}), 55.5 (C^{n}), 55.4 (C^{e}), 49.5 (C^{d}), 44.6 (C^{g}), 39.8 (C^{j}), 39.7 (C^{q}), 30.7 (C^{o}), 26.7 (C^{i}), 26.5 (C^{p}), 17.7 (CH_3pz), 13.3 (CH_3pz). ESI-MS (+) (*m/z*): 711.1 $[M]^+$; calcd for $C_{21}H_{36}N_{10}O_6Re$ = 711.2. Elemental analysis calcd. for $C_{21}H_{36}N_{10}O_6Re$·2TFA: C, 31.94; H, 4.07; N, 14.90. Found: C, 31.50; H, 4.50; N, 14.70 %. Retention time (analytic RP-HPLC, 220 nm): 26.7 min.

***Synthesis of fac-[Re(CO)$_3$(k^3-L^5)]$^+$* (5a)**

Starting from 0.040 g (0.056 mmol) of **L^5·2TFA**, a colorless oil formulated as **5a** was obtained (0.041 g, 73 %, calcd. for $C_{24}H_{42}N_{10}O_6Re$·2TFA). IR (KBr, cm^{-1}): 3418m, 2026s and 1900s (C≡O), 1670s, 1289m, 1234m and 1135m. ^{1}H-NMR (D_2O): δ(ppm) 6.08 (s, CH^{b}(4)pz, 1H), 5.06 (br s, NH, 1H), 4.35 (dd, $CH^{d'}$, 1H), 4.12 (dd, $CH^{d''}$, 1H), 3.87 (t, CH^{n}, 1H), 3.66 (m, NH, 2H), 3.47 (m, $CH^{h'}$, 1H), 3.37-3.19 (m, $CH^{h''}$/CH^{m}_2, 3H), 3.01 (m, $CH^{e'}$/$CH^{g'}$/CH^{q}_2, 3H), 2.75 (m, CH^{f}_2, 2H), 2.66-2.55 (m, $CH^{e''}$, 1H), 2.47 - 2.38 (m, $CH^{g''}$, 1H), 2.31 (s, CH_3pz, 3H), 2.20 (s, CH_3pz, 3H), 1.87-1.79 (m, CH^{o}_2/$CH^{i'}$, 3H), 1.60 (m, $H^{i''}$, 1H), 1.45 (m, CH^{p}_2/ CH^{l}_2, 4H), 1.29 (m, CH^{j}_2/CH^{k}_2, 2H). ^{13}C-NMR (D_2O): δ(ppm) 194.7, 194.4, 193.0 (C≡O), 169.2 (C=O), 156.9 (C^{r}), 153.7 (C^{c}(3)pz), 144.2 (C^{a}(5)pz), 107.9 (C^{b}(4)pz), 67.6 (C^{h}), 61.9 (C^{f}) 53.3 (C^{e}), 53.3 (C^{n}), 47.0 (C^{d}), 42.2 (C^{g}), 40.5 (C^{m}), 39.6 (C^{q}), 28.2 (C^{l}), 28.2 (C^{o}), 25.9 (C^{j}/C^{K}), 24.4 (C^{l}), 24.4 (C^{i}), 23.8 (C^{p}), 15.3 (CH_3pz), 10.9 (CH_3pz). ESI-MS (+) (*m/z*): 753.1 $[M]^+$; calcd for $C_{24}H_{42}N_{10}O_6Re$ = 753.2. Elemental analysis calcd. for $C_{24}H_{41}N_{10}O_6Re$·2TFA: C, 34.24; H, 4.51; N, 14.27. Found: C, 34.18; H, 5.00; N, 14.60 %. Retention time (analytic RP-HPLC, 220 nm): 27.4 min.

Synthesis of the ^{99m}Tc(I) Complexes (1 - 5)

General Method. In a nitrogen-purged glass vial, 100 μL of a 10^{-3} or 10^{-4} M aqueous solution of the corresponding bioconjugate compounds (**L^2 – L^4**) were added to 900 μL of a solution of the organometallic precursor *fac*-[^{99m}Tc$(H_2O)_3(CO)_3]^+$ (1 - 2 mCi) in saline. The reaction mixture was then heated to 100 ºC for 30 - 60 min, cooled on an ice bath and the final solution analyzed by RP-HPLC. Retention times: 24.4 min (**3**), 27.4 min (**4**) and 28.1 min (**5**).

Plasma Stability *In Vitro*.

100 μl of **3**, **4** and **5** were added to 500 μl of human plasma and incubated at 37 ºC. After incubation (24h), aliquots (100 μl) were taken and the plasmatic proteins precipitated with ethanol (200 μl). The plasma was centrifuged at 3000 rpm for 15 min at 4ºC and the supernatant (protein free plasma) filtered trough a Millipore filter (0.22 μm), and analyzed by RP-HPLC.

Cysteine and Histidine Challenge

Aliquots of 100 μL of the ^{99m}TcI-complexes were added to 400 μL of 5 x 10^{-3} M cysteine or histidine solutions in PBS (pH 7.4). The solutions were incubated at 37 °C for 24 h and analyzed by analytical RP-HPLC.

Partition Coefficient

Was evaluated by the "shakeflask" method (*4*). The radioconjugate was added to a mixture of octanol (1 mL) and 0.1 M PBS pH = 7.4 (1 mL), previously saturated in each other by stirring the mixture. This mixture was vortexed and centrifuged (3000 rpm, 10 min, room temperature) to allow phase separation. Aliquots of both octanol and PBS were counted in a gamma counter.

The partition coefficient ($P_{o/w}$) was calculated by dividing the counts in the octanol phase by those in the buffer, and the results expressed as Log $P_{o/w}$.

Enzyme kinetic assays

The iNOS activity assay was based on the method of hemoglobin assay previously described by Hevel and Marletta with slight modifications (*5*,*6*). The kinetic parameters for iNOS were determined using initial rate analysis. Initial rate data were fitted to irreversible single substrate Michaelis-Menten models. The kinetic parameters were determined using the direct linear plot of Eisenthal and Cornish-Bowden and the Hyper software (J.S. Easterby, University of Liverpool, UK; http://www.liv.ac.uk/~jse/software.html) (*7*,*8*). The K_m and K_i values represent a mean of triplicate measurements. Standard deviations of ± 5 to 10 % were observed.

Hemoglobin capture assay

Preparation of Oxyhemoglobin

Oxyhemoglobin was prepared using a previously described protocol with some modifications (*9*). Briefly, bovine hemoglobin in 50 mM HEPES pH 7.4 was reduced to oxyhemoglobin with 10-fold molar excess of sodium dithionite. The sodium dithionite was later removed by dialysis against 50 volumes of HEPES buffer for 18 hours at 4°C. The buffer was replaced 3 times. The concentration of oxyhemoglobin was determined spectrophotometrically using $\varepsilon_{415\ nm}$ = 131 $mM^{-1}cm^{-1}$. Oxyhemoglobin was stored at -80°C before use.

Determination of kinetic parameters

Determination of K_m values

All initial velocity measurements were recorded at 37 ºC. Total reaction volumes were 1500 μL and contained 50 mM HEPES pH 7.4, 6 μM oxyhemoglobin, 200 μM NADPH, 10 μM BH_4, 100 μM DTT and at least three concentrations of the L-arginine (20 – 500 μM). Magnetic stirring in the spectrophotometer cuvette was essential to maintain isotropic conditions. Reactions were initiated by the addition of iNOS enzyme (~ 1 U) to the prewarmed cuvette (~ 5 min). The NO-mediated conversion of oxyhemoglobin to methemoglobin was followed by monitoring the increase in absorbance at dual wavelength (401 and 421 nm) for 10 min (*10*). Controls were performed in the some conditions without iNOS enzyme.

Determination of K_i Values.

The K_i values were obtained by measuring inhibition with at least three concentrations of L-arginine (20 – 150 μM) in the presence of 150 μM of the inhibitor, in the same conditions previously described. The formula used to calculate the K_i is: $K_i = [I]/((K_m^{app} / K_m) - 1)$ where [I] is the inhibitor concentration, K_m is the Michaelis-Menten constant of the substrate L-arginine and K_m^{app} is the apparent value of K_m for a substrate in the presence of the inhibitor (*7*). K_m value for L-arginine was determined as 6 μM.

Cell Culture

RAW 264.7 macrophages were grown in Dulbecco's Modified Eagle Medium (DMEM) with GlutaMax I supplemented with 10 % heat-inactivated foetal bovine serum and 1 % penicillin/streptomycin antibiotic solution (all from Gibco, Alfagene, Lisbon). Cells were

cultured in a humidified atmosphere of 95 % air and 5 % CO_2 at 37 ºC, with the medium changed every other day. The cells were adherent in monolayers and, when confluent, were harvested from the cell culture flasks, using a scrapper, and seeded farther apart.

Evaluation of the inhibitory effect of compounds L^1 - L^4 and 1a - 5a in NO biosynthesis in LPS-activated RAW 264.7 macrophages

Macrophages (in DMEM without phenol red and 10 % FBS) were plated at a density of 9 x 10^4 cells per well in 96-well plates. Cells were immediately induced with 10 μL of LPS (2 μg/mL in PBS) for 4 h, and then incubated for 24 h in the presence of various concentrations of compounds. At the end of the incubation period, the culture medium was collected and assayed for nitrite production using the commercially available Griess reagent method (Sigma-Aldrich) (*11*,*12*). Owing to solubility problems, compound **3** was dissolved in a 5 % MeOH/H_2O solution (10 mM solution) and further diluted with water, untill a final concentration of 1 mM was reached. Final MeOH concentrations were ≤ 0.25%, and were shown to not interfere neither with the nitrite assay nor with cell viability.

Western blot methodology

Western blot experiments were performed to demonstrate the overexpression of iNOS in LPS-induced RAW 264.7 macrophages and in the lungs of LPS-treated mice.

RAW 264.7 macrophages were treated with LPS (2 μg/mL) for 24 h and lysed in Cell Lytic-MT Extraction reagent (Sigma) supplemented with Complete protease inhibitor cocktail tablets (Roche Applied Science). After 15 miuntes on ice, lysates were centrifuged at 14000g for 10 min at 4 °C to pellet the cellular debris and the supernatants removed for further use.

Mature female C57BL/6 mice were induced with 10 mg/kg of LPS (or PBS) for 6h. Lungs from non-treated and LPS-treated mice were harvested and homogenized on a pre-chilled manual Poter-Elvehjem homogenizer. Homogenates were centrifuged at 14000g for 10 min at 4 °C and the supernatants removed for further use.

The total protein content was determined by using the DC Protein Assay Kit (Biorad) and aliquots of protein (200 micrograms) from each sample were analyzed using standard western blot procedures. Briefly, protein extracts were subjected to electrophoresis on a 7% SDS-polyacrylamide gel and transferred electrophoretically onto nitrocellulose membranes. The blots were blocked with PBS-T containing 5% nonfat dry milk for 1 h. Then, the blotting membranes were incubated with primary antibodies against iNOS (1:1000, Sigma) and actin (1:8000, Sigma) separately overnight. Membranes were washed with PBS-T and incubated for 1 h with secondary antibody (goat anti-mouse IgG-HRP, Biorad) diluted 1:3000. Finally, membranes were developed using the SuperSignal WetsPico Substrate kit (Pierce, Rockford, IL) according to the manufacturer's instructions.

Cellular Internalization of Radiocomplexes

Internalization assays of the radiocomplexes **1 - 3** were performed in RAW 264.7 macrophages seeded at a density of 0.3 million/well, in complete culture medium containing LPS 1 μg/mL, in a 24-well tissue culture plates and allowed to attach and to induce the expression of iNOS for 24 h at 37ºC. Then, the culture medium was removed and the cells were incubated with about 200000 cpm of the radiocomplexes **1** – **3** in 0.5 mL of assay medium (Modified Eagle's Medium with 25 mM HEPES and 0.2% BSA) for a period of 5 min to 4 h at 37 °C. Incubation was terminated by washing the cells with ice-cold assay medium. Cell-surface bound radioligand was

removed by two steps of acid wash (50 mM glycine.HCl/100 mM NaCl, pH 2.8) at room temperature for 5 min. The pH was neutralized with cold PBS with 0.2% BSA, and subsequently the cells were lysed by 10 min incubation with 0.5 N NaOH at 37ºC to determine internalized radioligand. Total macrophage protein has been determined using a commercially available BioRad® *DC* Protein Kit assay.

Biodistribution in LPS-treated mice

All animal experiments were performed in compliance with Portuguese regulations for animal treatment. The animals were housed in a temperature- and humidity-controlled room with a 12 h light/12 h dark schedule.

The biodistribution studies were performed in mature female C57BL/6 mice (10 – 14 weeks old) treated with bacterial lipopolysaccharide (LPS) (10 mg/kg, iv), to induce iNOS expression, 6h before the radioactive compounds were injected. The control group was injected with PBS instead of LPS. Animals were then intravenously injected into the retro-orbital sinus with the radiocomplexes 2 or 3 (60-90 μCi) diluted in 100 μL of PBS pH 7.2. Mice were killed by cervical dislocation at 15 and 30 min (complex 2), and at 60 min (complex 3) after injection. The dose administered and the radioactivity in the killed animals were measured using a dose calibrator (Curiemeter IGC-3, Aloka, Tokyo, Japan or Carpintec CRC-15W, Ramsey, USA). The difference between the radioactivity in the injected and that in the killed animals was assumed to be due to excretion. The tissues of interest were dissected, rinsed to remove excess blood, weighed, and their radioactivity was measured using a c-counter (LB2111, Berthold, Germany). Lungs from control and LPS-treated animals were harvested and analysed latter by Western Blot to demonstrate that 6h LPS-treatment was adequate to strongly increase iNOS expression in that

organ. Blood and urine were also collected and pooled together at the time the animals were killed to evaluate the stability *in vivo* of radiocomplexes. The uptake in the tissues of interest was calculated and expressed as a percentage of the injected radioactivity dose per gram of tissue. For blood, bone, muscle, and skin, total activity was estimated assuming that these organs constitute 6, 10, 40, and 15% of the total body weight, respectively.

LITERATURE CITED IN SUPP. INFORMATION

(1) S. Alves, A. Paulo, J. D. G Correia, L. Gano, C. J. Smith and I. Santos, *Bioconjugate Chem.* **2005**, *16*, 438.

(2) R. Alberto, R. Schibli, A. Egli, P. A. Schubiger, W. A. Herrmann, G. Artus, U. Abram and T. A. Kaden, *J. Organomet. Chem.* **1995**, *493*, 119.

(3) B. L. Oliveira, J. D. G. Correia, P. D. Raposinho, I. Santos, A. Ferreira, C. Cordeiro, A. P. Freire, *Dalton Trans.* **2009**, 152.

(*4*) D. E. Troutner, W. A. Volkert, T. J. Hoffman, R. A. Holmes, *Int. J. Appl. Rad. Isot.* **1984**, *35*, 467.

(5) J. M. Hevel, M. A. Marletta, *Meth. Enzymol.* **1994**, *233*, 250.

(*6*) S. Archer, *FASEB J.* **1993**, *7*, 349.

(*7*) R. Eisenthal, A. Cornish-Bowden, *Biochem. J.* **1974**¸ *139*, 715.

(*8*) A. Cornish-Bowden, *Fundamentals of Enzyme Kinetics*, Portland Press, revised edn**.**, 1995.

(*9*) D. J. Wolff, D. S. Gauld, M. J. Neulander and G. Southan, *J. Pharmacol. Exp. Ther*. **1997**, *283*, 265.

(10) R. G. Knowles, S. Moncada, *Biochem J.* **1994**, *298*, 249.

(11) L. C. Green, D. A.,Wagner, J. Glogowski, *Anal. Biochem.* **1982**, 126, 131.

(12) T. Mosmann, *J. Immun. Methods* **1983**, *65*, 55.

Matrix Metalloproteinase Sensitive Gold Nanorod for Simultaneous Bioimaging and Photothermal Therapy of Cancer

Dong Kee Yi,[†,‡] In-Cheol Sun,[†,§] Ju Hee Ryu,[§] Heebeom Koo,[§] Chul Wan Park,[||] In-Chan Youn,[§] Kuiwon Choi,[§] Ick Chan Kwon,[§] Kwangmeyung Kim,*[,§] and Cheol-Hee Ahn*[,⊥]

Division of Bionanotechnology, Gachon Bionano Institute, Kyungwon University, Geonggi-do 461-701, Korea, Biomedical Research Center, Korea Institute of Science and Technology, 39-1 Haweolgog-Dong, Sungbook-Gu, Seoul 136-791, South Korea, Mechanical Engineering and Mechanics, Drexel University, 3111-15 Chestnut Street, Philadelphia, Pennsylvania 19104, United States, and Research Institute of Advanced Materials (RIAM), Department of Materials Science and Engineering, Seoul National University, San 56-1 Sillim, Gwanak, Seoul, 151-744, Korea. Received July 12, 2010; Revised Manuscript Received October 19, 2010

Herein, we developed matrix metalloprotease (MMP) sensitive gold nanorods (MMP-AuNR) for cancer imaging and therapy. It was feasible to absorb NIR laser and convert into heat as well as visualize MMP activity. We showed the possibility of gold nanorods as a hyperthermal therapeutic agent and MMP sensitive imaging agent both in vitro and in vivo condition. The results suggested potential application of MMP-AuNR for simultaneous cancer diagnosis and therapy.

Simultaneous diagnosis and therapy contain in vivo real-time imaging of the diseased site and provide opportunities for rationally modulated clinical activities (*1*). It can be achieved by a combination of biotechnology, nanotechnology, and information technology. Especially, molecular bioimaging and nanomedicine allow not only noninvasive characterization of disease at the molecular level, but also optimized treatment with minimum toxicity (*2, 3*). In addition, they provide a synergistic method to visualize biodistibution of drug, determine the optimal therapeutic dosage or administration frequency, and monitor the process or cure of the disease. This strategy can assist in the discovery of various fundamentals in basic biological research or development of clinical applications for personalized medicine (*4*).

For many years, gold nanorods (AuNR) have been receiving much attention in applications of both imaging and therapy. AuNR have surface plasmon resonance (SPR), which is a common characteristic of gold materials and therefore has been applied as an imaging agent with various techniques like two-photon luminescence, optical coherence tomography, dark-field microscopy, photoacoustic tomography, Raman scattering, and computed tomography (CT) (*5*−*7*). In addition to its applications in imaging, AuNR have been used as a heat source for hyperthermia because AuNR are able to absorb laser irradiation strongly and convert it into heat efficiently (*8*−*11*). High temperatures over 43 °C are effective for selective destruction of cancer cells because of their lower heat tolerance caused by poor blood supply; therefore, hyperthermia is attractive for cancer therapy (*12, 13*). Especially, the wavelength of peak absorbance can be adjusted into the near-infrared (NIR) region by changing the aspect ratio of AuNR (*14*−*16*). For these properties, AuNR have great potential in both imaging and therapy. Therefore, in this report, we developed novel multifunctional agents for simultaneous diagnosis and therapy with AuNR.

Matrix metalloprotease (MMP) is a family of zinc-dependent proteins and the production of MMPs are distinctly involved in cancer metabolism (*17*). Therefore, in vivo imaging of MMPs could provide valuable information in cancer diagnosis, and various imaging modalities were developed for this purpose (*18, 19*). To develop a fluorescent probe for MMP with AuNR (MMP-AuNR), NIR fluorescent dye, Cy5.5, was conjugated to a peptide sequence (Gly-Pro-Leu-Gly-Val-Arg-Gly-Cys) known to be degraded by MMP (*20*), and the surfaces of AuNR were modified with the Cy5.5-conjugated MMP substrate. A schematic representation of the production of MMP-AuNR is shown in Scheme 1. For the quenching effect of AuNR, NIR fluorescence was quenched until the substrate was degraded by MMP enzymes which were secreted by cancer cells (*21*). By the recovery of quenched fluorescence, we could determine the expression of MMP and cancer progress as well as perform cancer therapy simultaneously based on photothermal effects of AuNR.

The morphology of AuNR was examined with TEM images after conjugation with MMP substrates and Cy5.5 NIR fluorescent dye (Figure 1A). It showed that the aspect ratio of MMP-AuNR was approximately 2 (length/width) and uniformly dispersed. The optical properties of MMP-AuNR were also confirmed with UV−vis absorption, in which two unique surface plasmon resonance (SPR) peaks were shown (Figure 1B). Between the two SPR peaks originating from the longitudinal and transverse oscillation of electrons on the AuNR surface, strong absorption was adjusted to the NIR (650−670 nm) region to minimize absorption by tissue and maximize AuNR absorption of laser (671 nm) irradiation by tuning their aspect ratio. The wavelength of SPR peaks was not changed after conjugation. On the basis of these data, it was proven that conjugated substrate did not affect the optical property and stability of AuNR. The optical changes after addition of 1,4-dithiothreitol (DTT) or MMP-2 were measured with a fluorescence spectrometer and also confirmed in NIR fluorescent images (Figure 1C,D). The fluorescence of Cy5.5 was quenched near the surface of AuNR due to surface energy transfer properties (*22*).

* To whom correspondence should be addressed. Phone: (+82) 2-958-5916, (+82) 2-880-5791. Fax: (+82) 2-958-5909, (+82) 2-883-8197. E-mail: (K.K.) kim@kist.re.kr; (C.-H.A.) chahn@snu.ac.kr.

† These authors contributed equally to this work.

‡ Kyungwon University.

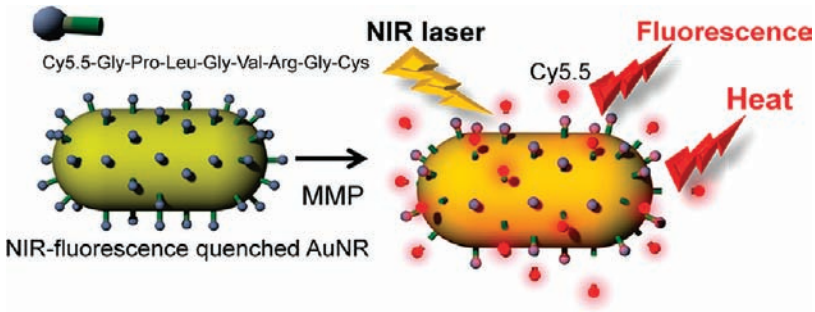
§ Korea Institute of Science and Technology.

|| Drexel University.

⊥ Seoul National University.

10.1021/bc100308p © 2010 American Chemical Society
Published on Web 11/09/2010

Scheme 1. Schematic Representation of Synthesis of MMP-AuNR for Simultaneous Imaging and Photothermal Therapy



However, the incubation of MMP-AuNR with activated MMP-2 (6.75 nM, 37 °C, 60 min) resulted in significant augmentation of the NIRF signal (7.8-fold) because the distance between AuNR and the fluorescence dye, Cy5.5, increased and the quenching effect was reduced by cleavage of the MMP substrate.

The NIRF recovery of Cy5.5 from the quenched state in MMP-AuNR was induced not from the nonspecific detachment of MMP substrate but from the specific decomposition, because recovery of the fluorescence was strongly disrupted in the presence of the MMP-2 inhibitor (2.6-fold). Also, the addition of DTT led to an enhanced NIRF-signal recovery because DTT caused a displacement of the MMP peptide from the AuNR surface (*18*). However, the aggregation of AuNR occurred 10 min after addition of DTT, because the displacement of substrate on the surface induced instability of AuNR. On the other hand, the decomposition of MMP substrate did not cause the aggregation of AuNR in the TCNB buffer. The unique color of AuNR was preserved throughout coating of MMP peptide and incubation with MMP-2.

As shown in Figure 1D, the peak intensity of DTT was 33% higher than that of MMP-2 because MMP peptide-Cy5.5 bound to AuNR was fully removed, maybe due to the smaller steric hindrance of DTT than that of the large MMP enzyme (*23*). This strong reducing property of DTT was employed to determine the amount of MMP substrates bound to AuNR. UV absorbance titration of Cy5.5 (675 nm) was performed by addition of DTT (10 mM) in MMP-AuNR colloid. The UV−vis absorption of detached free Cy-MMP substrate was calibrated with the standard curve of Cy5.5, and we estimated the amount of 1.34×10^2 molecules of Cy-MMP per AuNR. In addition, photothermal properties of MMP-AuNR were compared with those of cetyltrimethylammonium bromide (CTAB)-stabilized AuNR (Figure 1E). Laser was irradiated to AuNR and MMP-AuNR, respectively, and their temperature was measured with the needle probe of a T-type thermocouple. It was increased over 4 min up to 50 °C at which cancer cells could be selectively damaged (*14*). IR thermographic images of MMP-AuNR also demonstrated this result, and they showed that the temperature increment was not localized in the focal point of the laser (Figure 1F). Therefore, it was confirmed that Cy5.5-conjugated MMP substrate did not affect the photothermal properties or stability of MMP-AuNR.

The enzyme selectivity of MMP-AuNR was evaluated by incubation with various other MMP enzymes (MMP-3, -7, -9, -13), and their NIRF signals were measured by a fluorescence spectrometer (Figure 2A,B). After incubation with the respective enzymes and the inhibitor at 37 °C for 120 min, MMP-AuNR recovered its NIRF signal against various MMP enzymes (approximately 6.6-, 8.2-, and 6.6-fold for MMP-3, -9, and -13, respectively). However, when it comes to MMP-7, the NIRF signal was not recovered significantly (3.7-fold). It showed that MMP-AuNR has specificity against certain MMP enzymes. Furthermore, samples were moved to a 96-well plate and visualized with

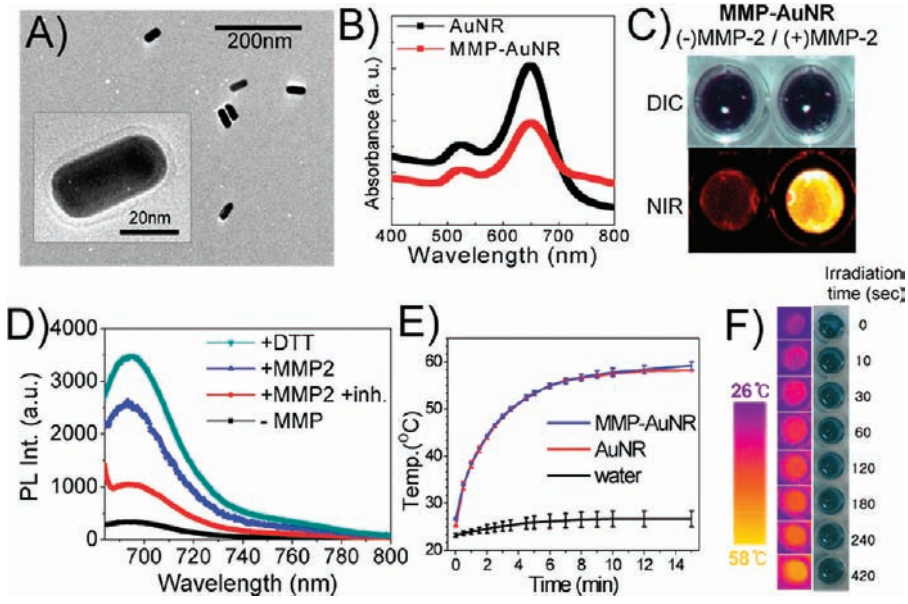


Figure 1. (A) TEM images of MMP-AuNR. (B) UV−vis spectroscopy of bare AuNR and Cy-MMP peptide conjugated AuNR (MMP-AuNR). (C) Bright and NIRF images of MMP-AuNP in 96-well plate before and after addition of MMP enzymes. (D) Fluorescence emission spectra of MMP-AuNR in the presence of MMP-2 enzyme (6.75 nM) and DTT (10 mM) after incubation at 37 °C for 60 min. (E) Optical and IR images of temperature increments of MMP-AuNR in 96-well plate as a function of laser irradiation time.

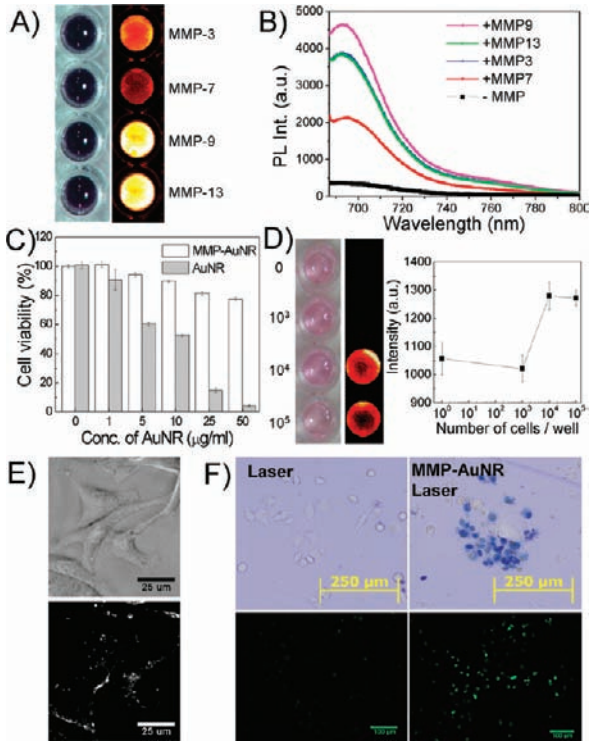


Figure 2. (A) Bright and NIRF images of MMP-AuNP in a 96-well plate containing various kinds of MMP enzymes. (B) Fluorescence emission spectra of MMP-AuNR in the presence of various MMP enzymes (MMP-3, -7, -9. and -13). (C) HeLa cell viability after 24 h of incubation with increasing concentration of AuNR and MMP-AuNR. (D) Optical and NIRF images of 96-well microplate containing MMP-AuNR and DMEM cell culture media extracted from different numbers of HeLa cells and their calculated ROI values. (E) Dark-field images of MMP-AuNR uptake of HeLa cells. (F) Microscopic images of HeLa cell after staining with trypan blue (upper) and annexin V-FITC assay (lower) at different treatment conditions.

a Kodak image station 4000MM equipped with filter systems for Cy5.5. The same results were able to be simply visualized through NIRF images, which could be applied for quantitative and visual analysis of the MMP enzyme activity.

In many areas of research, wide application of AuNR has been limited due to the existence of cytotoxic CTAB coated on its surface (*24*). We expected that the large portion of CTABs were exchanged with MMP peptide-Cy5.5, and this could reduce the cytotoxicity of our AuNR. To determine this, the cell viability test of AuNR and MMP-AuNR was performed without irradiation, before the photothermal therapeutic effect was investigated. MTT assay revealed that biocompatibility of MMP-AuNR was significantly improved because CTAB bilayers, which are noncovalently adsorbed onto the AuNR surface, were replaced by the MMP substrate (Figure 2C). To examine the feasibility of MMP-AuNR as an imaging and photothermal therapeutic agent, optical NIRF imaging of MMP enzymes in the cell culture media was performed. HeLa cells were cultured in a 96-well plate according to different numbers of cells (10^3, 10^4, 10^5 cell/well, respectively) using DMEM cell culture media (without FBS). After 24 h of incubation, cell culture media were extracted and mixed with the same volume of MMP-AuNR (8 mg/mL) at 37 °C for 90 min. The mixed culture media were centrifuged, and NIRF images of the supernatant were obtained. The activated MMP enzymes existing in the cell culture media were successfully visualized with MMP-AuNR by the NIR imaging technique (Figure 2D). Also, the calculated integrities from the NIRF images coincided with other previous results. Cellular uptake of MMP-AuNR was observed through a dark-field microscope (Figure 2E). It was confirmed that a large amount of MMP-AuNR was taken up within 1 h by HeLa cells, and no sign of cell damage was observed. A photothermal therapeutic effect of MMP-AuNR was also examined. After incubation of HeLa cells with MMP-AuNR (final conc.: 400 μg/mL) for 2 h and washing

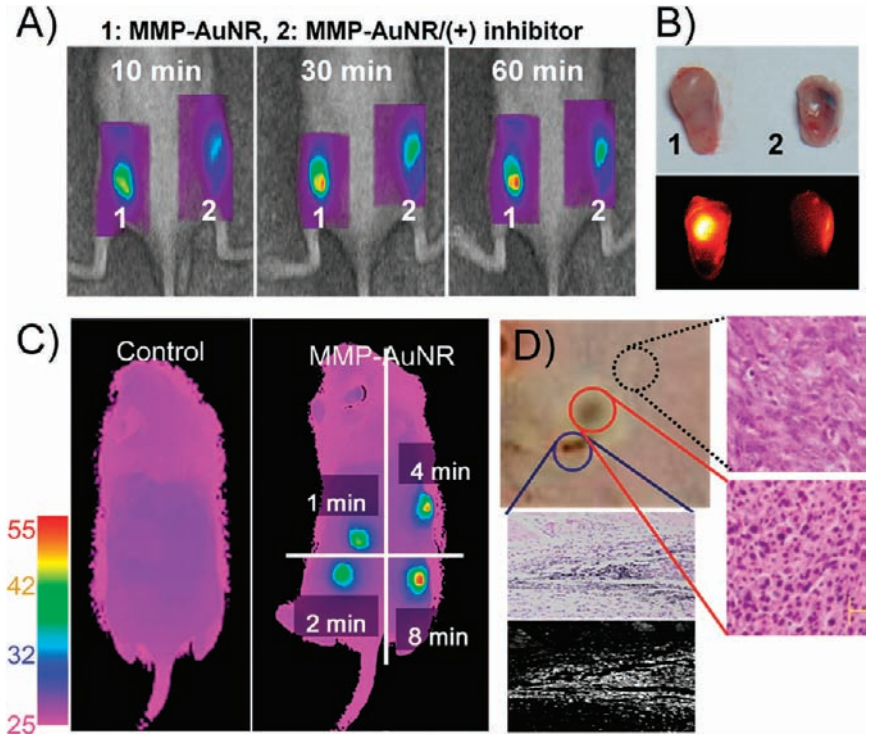


Figure 3. (A) NIRF tomographic images of SCC-7 tumor-bearing mice after intratumoral injection of the MMP-AuNR probe without (1) and with (2) inhibitor. (B) Optical and NIRF images of excised tumor after injection of MMP-AuNR without and with MMP-2 inhibitor. (C) Infrared thermal images of tumor-bearing mice according to different laser irradiation times. AuNR was injected intratumorally prior to laser irradiation. (D) Optical images of exterior of SCC-7 tumor irradiated by laser. Histology (right) and dark field image (lower) of tumor after treatment are also presented.

with DMEM, culture dishes were exposed to CW laser (671 nm, 200 W) for 10 min. After incubation for another 1 h, cells were stained with 0.4% trypan blue for 10 min to obtain distinct images of cell viability through a microscope. Dead cells were observed when the cells took up MMP-AuNR and were irradiated by a laser (Figure 2F, upper). However, cell viability was not affected when cells were exposed only to MMP-AuNR or laser. The same results were obtained when the samples were observed using annexin V-FITC assay through a microscope (Figure 2F, lower). The damaged cells were stained with FITC, which indicated apoptotic HeLa cells caused by photothermal therapy.

Finally, MMP-AuNR was tested for in vivo NIR imaging and photothermal therapy. In the back of an athymic nude mouse, two SCC-7 tumors were xenografted, and one of them was treated with MMP-2 inhibitor prior to 30 min of intratumoral injection of MMP-AuNR to both sites. As seen in the Figure 3A, enhanced NIR fluorescence was observed when the tumor was not treated with MMP inhibitor compared with that treated with inhibitor. Maximum NIRF intensity was observed 60 min after injection. These results were further confirmed with ex vivo NIR fluorescence imaging of tumors. They were excised after 4 h of MMP-AuNR injection, and their NIR fluorescence image was taken in the Kodak Image Station 4000MM. Intensive recovery of quenched fluorescence of Cy5.5 was revealed when the tumor was not treated with inhibitor (Figure 3B). In addition to optical imaging, hyperthermal therapy was facilitated with MMP-AuNR, which was able to absorb NIR laser and convert into heat. Four SCC-7 tumors were xenografted in the back of a nude mouse and MMP-AuNR was injected. The increased temperature after laser irradiation at different times was measured with a hypodermic thermocouple and visualized with an infrared thermal imaging device according to the irradiation time (Figure 3C). It was confirmed that the temperature was increased over 45 °C after about 4 min of irradiation, which was coincident with previous in vitro results. The hyperthermal treatment was assessed with histology stained with hematoxylin-eosin. The SCC-7 tumor tissue with MMP-AuNR showed internal damage when laser irradiation was given (Figure 3D). However, the sole irradiation did not cause any cell damage. The tissue damage was able to be verified with the naked eye because burning of the external skin of the SCC-7 tumor was observed. Also, the existence of MMP-AuNR in the tissue was further examined with dark-field microscopy, and the signal of MMP-AuNR was found in the damaged tissue.

In summary, MMP-AuNR was applied as an optical molecular imaging agent for visualization of MMP enzyme activity using its quenching property. Also, as a photothermal therapeutic agent, it was able to absorb NIR laser and convert into heat. We visualized enzymatic activity of MMP with optical NIRF imaging in vivo and successfully induced damage to cancer tissue by hyperthermia. The outstanding properties of MMP-AuNR suggested its potential application for simultaneous diagnosis and therapy.

ACKNOWLEDGMENT

This research was supported by Real-Time Molecular Imaging Project, GRL Program of MEST, M.D.-Ph.D. Program (2010-0019863, 2010-0019864) of MEST, the Intramural Research Program of KIST and the Kyungwon University Research Fund in 2010.

Supporting Information Available: Experimental procedures. This material is available free of charge via the Internet at http://pubs.acs.org.

LITERATURE CITED

(1) Haglund, E., Seale-Goldsmith, M. M., and Leary, J. (2009) Design of multifunctional nanomedical systems. *Ann. Biomed. Eng. 37*, 2048–2063.

(2) Kim, J. H., Park, K., Nam, H. Y., Lee, S., Kim, K., and Kwon, I. C. (2007) Polymers for bioimaging. *Prog. Polym. Sci. 32*, 1031–1053.

(3) Park, K. (2007) Nanotechnology: What it can do for drug delivery. *J. Controlled Release 120*, 1–3.

(4) Ozdemir, V., Williams-Jones, B., Glatt, S. J., Tsuang, M. T., Lohr, J. B., and Reist, C. (2006) Shifting emphasis from pharmacogenomics to theragnostics. *Nat. Biotechnol. 24*, 942–947.

(5) von Maltzahn, G., Park, J. H., Agrawal, A., Bandaru, N. K., Das, S. K., Sailor, M. J., and Bhatia, S. N. (2009) Computationally guided photothermal tumor therapy using long-circulating gold nanorod antennas. *Cancer Res. 69*, 3892–3900.

(6) Tong, L., Wei, Q. S., Wei, A., and Cheng, J. X. (2009) Gold nanorods as contrast agents for biological imaging: optical properties, surface conjugation and photothermal effects. *Photochem. Photobiol. 85*, 21–32.

(7) Maltzahn, G. v., Centrone, A., Park, J.-H., Ramanathan, R., Sailor, M. J., Hatton, T. A., and Bhatia, S. N. (2009) SERS-coded gold nanorods as a multifunctional platform for densely multiplexed near-infrared imaging and photothermal heating. *Adv. Mater. 21*, 3175–3180.

(8) Huang, X. H., El-Sayed, I. H., Qian, W., and El-Sayed, M. A. (2006) Cancer cell imaging and photothermal therapy in the near-infrared region by using gold nanorods. *J. Am. Chem. Soc. 128*, 2115–2120.

(9) Huff, T. B., Tong, L., Zhao, Y., Hansen, M. N., Cheng, J. X., and Wei, A. (2007) Hyperthermic effects of gold nanorods on tumor cells. *Nanomedicine 2*, 125–132.

(10) Tong, L., Zhao, Y., Huff, T. B., Hansen, M. N., Wei, A., and Cheng, J. X. (2007) Gold nanorods mediate tumor cell death by compromising membrane integrity. *Adv. Mater. 19*, 3136.

(11) Cheong, K. H., Yi, D. K., Lee, J.-G., Park, J.-M., Kim, M. J., Edel, J. B., and Ko, C. (2008) Gold nanoparticles for one step DNA extraction and real-time PCR of pathogens in a single chamber. *Lab Chip 8*, 810–813.

(12) Svaasand, L. O., Gomer, C. J., and Morinelli, E. (1990) On the Physical rationale of laser induced hyperthermia. *Lasers Med. Sci. 5*, 121–128.

(13) Dickerson, E. B., Dreaden, E. C., Huang, X. H., El-Sayed, I. H., Chu, H. H., Pushpanketh, S., McDonald, J. F., and El-Sayed, M. A. (2008) Gold nanorod assisted near-infrared plasmonic photothermal therapy (PPTT) of squamous cell carcinoma in mice. *Cancer Lett. 269*, 57–66.

(14) Huang, X. H., Jain, P. K., El-Sayed, I. H., and El-Sayed, M. A. (2008) Plasmonic photothermal therapy (PPTT) using gold nanoparticles. *Lasers Med. Sci. 23*, 217–228.

(15) Li, J. L., Day, D., and Gu, M. (2008) Ultra-low energy threshold for cancer photothermal therapy using transferrin-conjugated gold nanorods. *Adv. Mater. 20*, 3866–3871.

(16) Park, J.-H., Maltzahn, G. v., Ong, L. L., Centrone, A., Hatton, T. A., Ruoslahti, E., Bhatia, S. N., and Sailor, M. J. (2010) Cooperative nanoparticles for tumor detection and photothermally triggered drug delivery. *Adv. Mater. 22*, 880–885.

(17) Egeblad, M., and Werb, Z. (2002) New functions for the matrix metalloproteinases in cancer progression. *Nat. Rev. Cancer 2*, 161–174.

(18) Lee, S., Cha, E. J., Park, K., Lee, S. Y., Hong, J. K., Sun, I. C., Kim, S. Y., Choi, K., Kwon, I. C., Kim, K., and Ahn, C. H. (2008) A near-infrared-fluorescence-quenched gold-nanoparticle imaging probe for in vivo drug screening and protease activity determination. *Angew. Chem., Int. Ed. 47*, 2804–2807.

(19) Lee, S., Ryu, J. H., Park, K., Lee, A., Lee, S.-Y., Youn, I.-C., Ahn, C.-H., Yoon, S. M., Myung, S.-J., Moon, D. H.,

Chen, X., Choi, K., Kwon, I. C., and Kim, K. (2009) Polymeric nanoparticle-based activatable near-infrared nanosensor for protease determination in vivo. *Nano Lett. 9*, 4412–4416.

(20) Bremer, C., Tung, C. H., and Weissleder, R. (2001) In vivo molecular target assessment of matrix metalloproteinase inhibition. *Nat. Med. 7*, 743–748.

(21) Nikoobakht, B., Burda, C., Braun, M., Hun, M., and El-Sayed, M. A. (2002) The quenching of CdSe quantum dots photoluminescence by gold nanoparticles in solution. *Photochem. Photobiol. 75*, 591–597.

(22) Dubertret, B., Calame, M., and Libchaber, A. J. (2001) Single-mismatch detection using gold-quenched fluorescent oligonucleotides. *Nat. Biotechnol. 19*, 365–370.

(23) Rosi, N. L., Giljohann, D. A., Thaxton, C. S., Lytton-Jean, A. K. R., Han, M. S., and Mirkin, C. A. (2006) Oligonucleotide-modified gold nanoparticles for intracellular gene regulation. *Science 312*, 1027–1030.

(24) Singh, M., Briones, M., Ott, G., and O'Hagan, D. (2000) Cationic microparticles: A potent delivery system for DNA vaccines. *Proc. Natl. Acad. Sci. U.S.A. 97*, 811–816.

BC100308P

Matrix Metalloproteinase Sensitive Gold Nanorod for Simultaneous Bioimaging and Photothermal Therapy of Cancer

Dong Kee Yi,[†,⊥] *In-Cheol Sun,*[‡,⊿] *Ju Hee Ryu,*[‡] *Heebeom Koo,*[‡] *Chul Wan Park,*[§] *In-Chan Youn,*[‡] *Kuiwon Choi,*[‡] *Ick Chan Kwon*[‡], *Kwangmeyung Kim,*[*,‡] *and Cheol-Hee Ahn* [*,∥]

Supporting informations

Preparation of Cy5.5-MMP substrate conjugated gold nanorod (MMP-AuNR): Cy5.5 was conjugated to MMP substrate by same method in previous report.[18] AuNR was functionalized with Cy5.5-MMP by simple mixing method. First, cetyltrimethylammonium bromide (CTAB) stabilized AuNR was centrifuged (9000 rpm, 12 min) and washed twice to remove with TCNB buffer containing 100 mM of Tris, 5 mM of calcium chloride, 200 mM of NaCl, and 0.1% of Brij. Cy5.5-MMP (0.1 ml, 100 μg/ml) solution was added in AuNR colloid and it was kept in the absence of light at 25°C under stirring for 24 h. The solution was purified by repeated centrifugation (9000 rpm, 12 min) and washing 2 times in the presence of 20 % (v/v) of DMSO.

In vitro fluorescence recovery test: UV absorbance titration of Cy5.5 (675 nm) was performed to determine the amount of Cy5.5-MMP bound to the AuNR surface. The Cy5.5-MMP bound to AuNR was detached by addition of dithiothreitol (DTT, 10 mM) and its UV-

vis absorption was detected with UV-vis spectroscopy. The concentration of free Cy5.5-MMP was calibrated with a standard UV absorbance curve of Cy5.5 in aqueous solution and the amount of Cy5.5-MMP was calculated from known concentrations of DTT-treated AuNR. The NIRF recovery of MMP-AuNR was examined in terms of MMP enzyme specificity. MMP enzymes (MMP-2, 3, 7, 9 or 13) were activated by incubation at 37 ^{o}C for 1 h with 2.5 nM of 4-Aminophenylmercuric Acetate (APMA) in the TCNB buffer. Inhibitor of MMP-2 was co-incubated with MMP-2 enzyme before reaction with MMP-AuNR. The same amount of MMP-AuNR colloid was added to MMP enzyme solution and incubated additionally at 37 ^{o}C for 1 h. After incubation, samples were centrifuged and the fluorescence intensity of supernatant was monitored with F-7000 fluorescence spectrometer (Hitachi, Tokyo, Japan). The excitation wavelength was fixed at 675 nm and emission spectra were recorded from 680 to 800 nm using a 1 ml cuvette. In addition, NIRF images of MMP-AuNR was obtained from a 12-bit CCD (charge coupled device) camera (Kodak Image Station 4000MM, New Haven, CT, USA) equipped with the special C-mount lens and the Cy5.5 bandpass emission filter (680 nm to 720 nm; Omega Optical Inc., Brattlebore, VT, USA).

In vitro imaging and photothermal therapy: HeLa cells were cultured in DMEM medium at 37 °C in a humidified atmosphere of 5 % CO_2. Cells were seeded in 96-well flatbottomed plates at a density of 0, 10^2, 10^3, 10^4 and 10^5 cells/well respectively and allowed to adhere for 24 h. The cell media was extracted from 96-well plate and mixed with MMP-AuNR colloid (final concentration : 2 mg/ml) in Eppendorf tubes at 37 °C for 1 h. The mixture was moved to a 96-well plate and visualized with a Kodak image station 4000MM. For NIR photothermal therapy, NIR Diode Pumped Solid State (DPSS) laser (671 nm, 200 mW) was used. HeLa cells in 12-well plate (10 x 10^4 cell/ml) was exposed to 0.8 mg/ml of MMP-AuNR for 1 h and then washed with DPBS buffer and then exposed to the red laser light for

10 min. After treatment, cells were stained with 0.4% trypan blue (Gibco Invitrogen, Paisley, UK) for 10 min and observed through microscope and imaged under X10 in bright field.

Annexin V assay : annexin V-FITC fluorescence microscopy kit (BD Bioscience, San Jose, CA, USA) was used according to the protocol provided by manufacturer. Briefly, after the treatment of HeLa cells with laser, they were washed once with Annexin V Binding Buffer after fixation. Then, the cells were stained with annexin V-FITC solution for 10 min. The annexin V-FITC solution was removed and washed with Binding Buffer once for the observation under the microscopy. The cells were visualized using IX81 fluorescence microscope (Olympus, Tokyo, Japan) with excitation at 488 nm and emission at 530 nm.

In vivo imaging and photothermal therapy: Squamous cell carcinoma (SCC) - 7 cells cell line (1 X 10^6 cells/mouse) was cultured in RPMI 1640 medium containing 10% fetal bovine serum and xenografted subcutaneously into the backs of athymic nude mice (Crlj-nu, 5-6 weeks, male). When the size of tumors became 5 mm in diameter, 50 μl of MMP-AuNR (2 mg/ml) probe was injected intratumorally. For MMP inhibition experiment, MMP inhibitor was intratumorally administered into the other SCC-7 tumor, 30 min prior to injection of the MMP-AuNR. After injection of MMP-AuNR, the fluorescence recovery profiles of SCC-7 tumor-bearing mice were imaged using eXplore Optix system (ART advanced Research Technologies Inc., Montreal, Canada). A 670 nm pulsed laser diode was used and the laser power and count time settings were optimized to 15 μW and 0.3 per point, respectively. NIRF tomographic images were obtained by collecting NIR fluorescence emission at 700 nm with a fast photomultiplier tube (Hamamatsu, Japan) and time-correlated single photon counting system (Becker and Hickl GmbH, Berlin, Germany). After 4 hours of post-injection, tumors were dissected and ex vivo NIR fluorescence images were taken using Kodak Image Station 4000MM. For therapy, tumor-bearing mice were exposed to NIR laser after injection of MMP-AuNR under same condition and their infrared thermal images were obtained

according to irradiation time (1, 2, 4, 8 min, respectively). The exact temperature was measured with a 33 gauge T-type hypodermic thermocouple (Omega Engineering, Inc., Stamford, CT, USA). After irradiation, tumors were dissected, fixed and stained with hematoxylin-eosin for microscopic observation.

Facile Synthesis of Raman Active Phospholipid Gold Nanoparticles

Natalie C. M. Tam,[†,‡] Benjamin M. T. Scott,[‡,§] Danut Voicu,[‡,||] Brian C. Wilson,[‡,§] and Gang Zheng*[,†,‡,§,||]

Institute of Biomaterials and Biomedical Engineering, Department of Medical Biophysics, and Leslie Dan Faculty of Pharmacy, University of Toronto, and Ontario Cancer Institute & Campbell Family Cancer Research Institute, Toronto, Ontario, Canada.
Received August 27, 2010; Revised Manuscript Received October 18, 2010

Gold nanoparticle-based surface-enhanced Raman scattering (SERS) probes have shown promise for disease detection and diagnosis. To improve their structural and functional stability for in vivo applications, we synthesized a colloidal SERS gold nanoparticle that encapsulates Raman molecules adsorbed on 60 nm gold with a nonthiol phospholipid coating. Transmission electron microscopy and Raman and UV spectroscopy validated its reproducibility and stability. This novel lipid-based SERS probe provides a viable alternative to the PEGylation and silica coating strategies.

INTRODUCTION

Gold nanoparticles (AuNPs) have been extensively investigated for biological applications due to their inherent unique optical, chemical, and electrical properties. In particular, AuNPs exhibit surface-enhanced Raman scattering (SERS), which augment Raman scattering up to $10^{14}-10^{15}$ orders of magnitude upon illumination (*1, 2*). SERS AuNPs are ultrasensitive and photostable, and can be used for multiplexing due to the unique Raman scattering spectra of different molecules (*1, 3*). The inertness and low toxicity (*4, 5*) of AuNPs are attractive; however, AuNPs can be unstable especially in biological systems. Hence, to implement SERS AuNPs for in vitro and in vivo applications, increasing stability and biocompatibility are critical.

Currently, there are two classes of SERS colloidal AuNPs used in vivo (*2, 3*). They both utilize 60 nm AuNPs as their core and differ only by the surface coating where one has poly(ethylene glycol) (PEG) to confer biocompatibility, to prevent biofouling, and to prolong in vivo circulation times (*6*); the other SERS AuNP is covered with silica for long-term stability. Phospholipids are an appealing alternative, as they truly mimic cell membranes for maximum biocompatibility and have also been shown to stabilize AuNPs. In fact, a range of phospholipid-coated colloidal gold nanoparticles have been made, including gold-lipoprotein mimics using 6 nm AuNPs (*7,8*). Furthermore, phospholipid AuNPs from 1 to 70 nm (*9*−*11*) and gold nanorods (*12, 13*) have been found to stabilize and increase biocompatibility; however, none of these have included a Raman dye for SERS capability. To our knowledge, both PEG and phospholipid-stabilized gold nanoparticles have depended on either direct thiol PEG/lipid or templating agent such as dodecanethiol, which we found to have a detrimental effect on the stability of the Raman tag on the AuNP surface (Supporting Information Figure S1).

In the present study, we successfully designed and encapsulated Raman dye coated AuNPs with nonthiol containing phospholipid (Scheme 1) suitable for in vivo applications. The resulting Raman-active phospholipid AuNPs (RAP AuNPs) are rendered biocompatible by the lipid coating, while the presence of the Raman dye allows for SERS detection. Here, we used 60 nm colloidal gold particles to augment the Raman scattering signals, as this is the optimal size for maximum SERS enhancement in the biologically relevant red/near-infrared wavelength range (∼600−800 nm) (*2*).

RESULTS AND DISCUSSION

To synthesize RAP AuNPs, a 10 μM aqueous solution of Raman dye—in this instance, we used crystal violet—was first adsorbed onto the citrate-stabilized 60 nm AuNP also in aqueous solution. Since Raman dyes can easily aggregate AuNPs, the Raman tag was added gradually, while the Raman signals were monitored in real time from the stirring solution.

A 1:1 mix of double-chain and single-chain phospholipids (1,2-dimyristoyl-*sn*-glycero-3-phosphocholine, DMPC ($C_{36}H_{72}NO_8P$); 1-myristoyl-2-hydroxy-*sn*-glycero-3-phosphocholine, MHPC ($C_{22}H_{46}NO_7P$), respectively) was prepared in 19:1 chloroform/methanol as solvent. The Raman-coated AuNPs were stirred and gradually heated to 65 °C, while the phospholipid solution was added dropwise. Immediate evaporation of the organic solvents formed liposome-like structures that encapsulate the Raman-coated AuNPs. Since the phospholipid-encapsulated AuNPs were of much higher density than any free liposomes or free lipids in solution, purification was achieved through multiple rounds of centrifugation. The final product was redispersed in aqueous solution for further characterization. It is important to note that the presence of the single fatty acid chain phospholipid MHPC was imperative for the stable encapsulation of the AuNPs with a lipid bilayer. This is likely due to the tighter curvature that is possible with a mix of single- and double-chain phospholipids (*14, 15*), resulting in closer positively charged choline headgroup interaction with negatively charged citrate remaining on the Raman-coated gold surface (*16*). Negative phosphates on the lipid headgroup may also interact with AuNP surface by replacing any remaining citrate on AuNP surface, since Rhim et al. (2008) noted that the phosphate backbone of plasmid DNA has a stronger Au interaction than carboxylates (citrates). Nevertheless, dynamic light scattering (DLS) analyses demonstrated an increase in the hydrodynamic diameter throughout the synthesis steps. The

* Correspondance to Gang Zheng, TMDT 5-363, 101 College Street, Toronto, Ontario M5G 1L7, Canada. Tel: 416-581-7666; Fax: 416-581-7667; e-mail:gang.zheng@uhnres.utoronto.ca.

† Institute of Biomaterials and Biomedical Engineering, University of Toronto.

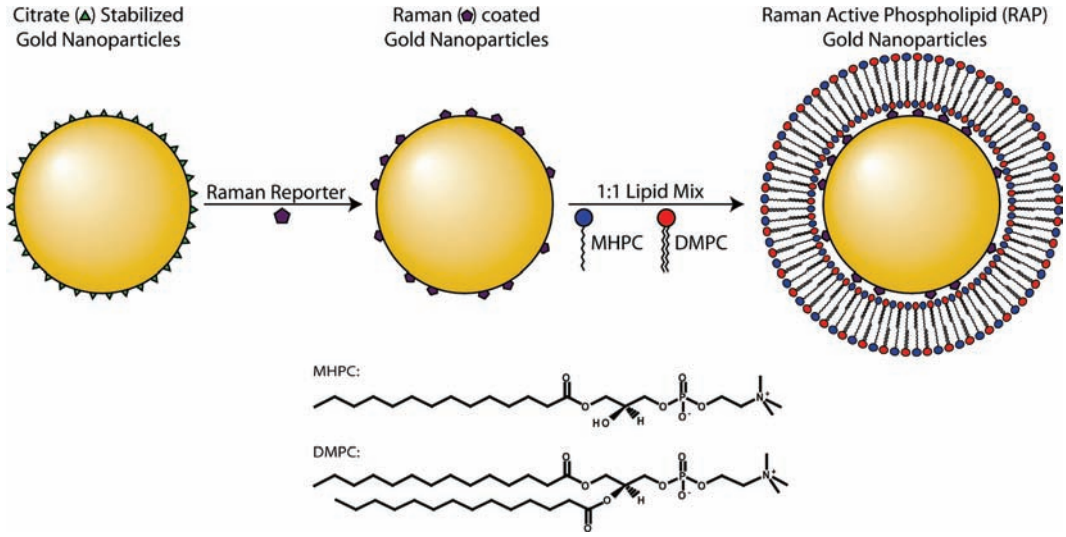
‡ Ontario Cancer Institute & Campbell Family Cancer Research Institute.

§ Department of Medical Biophysics, University of Toronto.

|| Leslie Dan Faculty of Pharmacy, University of Toronto.

10.1021/bc100386a © 2010 American Chemical Society
Published on Web 11/19/2010

Scheme 1. Synthesis of Raman-Active Phospholipid Gold Nanoparticles



starting citrate-stabilized AuNPs measured 54.4 ± 1.8 nm, while no increase in size was found after coating it with Raman dyes on the AuNP surface (53.8 ± 2.8 nm). After the final phospholipid addition, the hydrodynamic diameter of RAP AuNPs increased to 69.0 ± 1.4 nm.

The absorbance and Raman spectra of the starting, intermediate, and final AuNPs are shown in Figure 1a,b, respectively. Citrate-stabilized 60 nm AuNPs have λ_{max} of 538 nm, and no change was observed after addition of the Raman dye, confirming that the amount of crystal violet added maximized the SERS signal without causing aggregation. As expected from the hydrodynamic size increase, a small red shift of 4 nm was observed (λ_{max} = 542 nm) after addition of phospholipid to make RAP AuNPs. The Raman spectra of AuNPs measured during synthesis showed that the Raman dye is unperturbed on the AuNP surface. Further evidence of stable phospholipid coating is provided by transmission electron microscopy (TEM) analysis. TEM images of RAP AuNPs clearly show the presence of a encompassing lipid layer around the AuNPs (Figure 1c (4)) as opposed to the starting citrate AuNPs (Figure 1c (1)) and intermediate Raman coated AuNPs (Figure 1c (2)). This is especially obvious when particles are closely dried during sample preparation, where a fusion of lipid layers is observed (Supporting Information Figure S2).

The discrepancy between the size of RAP AuNPs between DLS and the TEM images is expected, as a thin layer of H_2O is known to exist at the zwitterionic phosphocholine headgroup in aqueous solutions of DMPC bilayers on metallic surfaces (*17*). Although there was an approximate 14 nm increase in diameter by DLS, the TEM images showed an approximate 6 nm increase (Supporting Information Figure S3). For the hydrodynamic size measurement, the 7 nm radius increase correlates well with an expected increase of 6−7 nm for DMPC bilayers in aqueous environment (*18*). Analysis of TEM images shows a 3-nm-thick phospholipid bilayer surrounding the AuNP, which is slightly lower than the expected 3.7−4.3 nm bilayer length of interdigitated DMPC leaflets (*19*−*22*). However, a gradual decrease in the thickness of the encapsulating bilayer

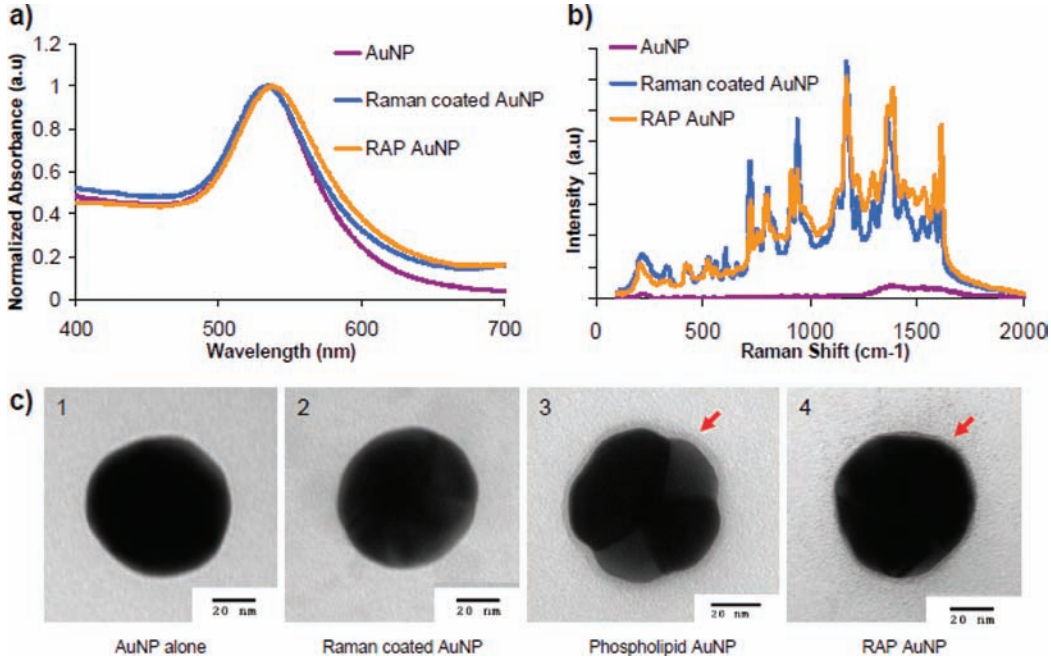


Figure 1. UV−vis spectroscopy (a) and Raman spectroscopy (b) of starting, intermediate, and final materials in RAP AuNP synthesis. (c) TEM images of AuNPs at each stage; red arrows indicate the phospholipid coating.

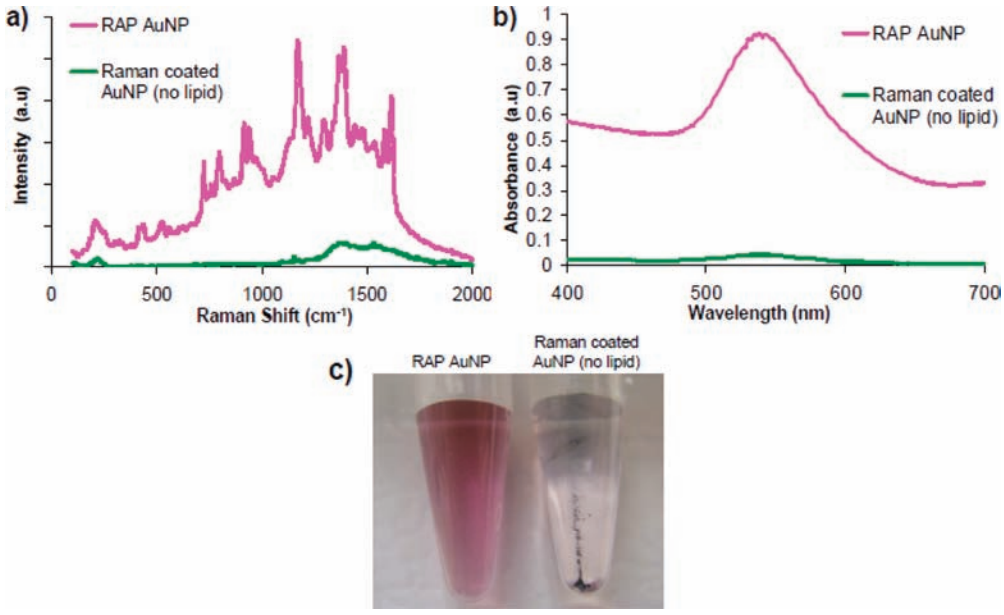


Figure 2. Raman (a) and UV−vis (b) spectra of Raman-coated AuNPs with (RAP AuNP) and without a phospholipid layer (only added organic solvents) after centrifugation. Photo of the RAP AuNP in aqueous solution compared with flocculated AuNPs without phospholipid protection (c).

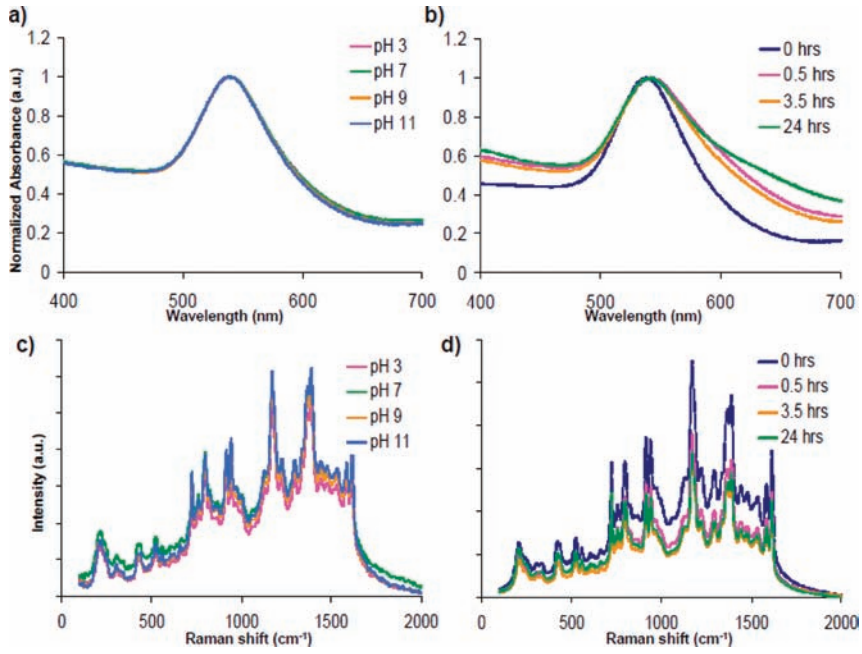


Figure 3. UV−vis spectra (a,b) and Raman spectra (c,d) to assess the RAP AuNP stability in various pHs (a,c) and in 10% serum in PBS at 37 °C for various time points (b,d).

was observed over time during TEM image acquisition. It is believed that the power of the electron beam caused a thinning of the bilayer surrounding the AuNPs, thereby accounting for a thinner coating than expected.

Raman spectra from RAP AuNPs and unprotected Raman dye-coated AuNPs reveal that the phospholipid layer not only retains and protects the Raman tag at the gold surface, but also stabilizes the entire nanoparticle. In Figure 2a, the presence of phospholipid on the surface preserved the Raman tag and thus the SERS enhancement on the metal nanoparticle surface even after purification through multiple rounds of centrifugation and resuspension. However, in the absence of the phospholipid encapsulation, the Raman signals are lost by centrifugation (Figure 2a). This is likely a result of the weakness of the Raman dye adsorption on the gold surface and lack of stabilizing interactions (*23*). Furthermore, the encompassing phospholipid coating also protects the AuNP in aqueous solution from aggregation (Figure 2c). Black precipitates (Figure 2c-right) show that there was flocculation of the Raman-coated AuNPs after two centrifugation steps following a mock lipid addition (containing only the organic solvent mixture). In contrast, RAP AuNPs easily redisperse into aqueous solutions after the same two centrifugations (Figure 2c left). This clearly indicates that this stabilization and retention of the Raman signals were not due to any procedures but only by the presence of phospholipids.

We further analyzed the stabilizing effect of the phospholipid layer in various pHs and in physiological buffer in order to test the biocompatibility of RAP AuNPs. Figure 3a,c shows the UV and Raman spectra of RAP AuNPs in a wide range of pH (3−11) after incubation for at least 30 min in phosphate buffer. Absence of any changes in the absorption maxima or Raman intensities indicated that RAP AuNPs did not aggregate and

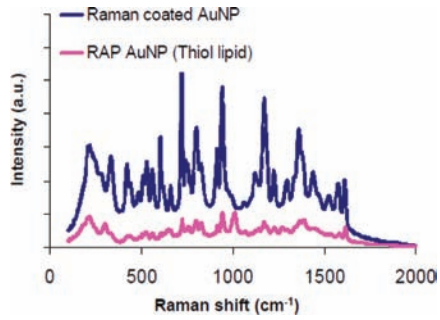


Figure 4. Raman spectra of RAP AuNPs made by thiol-containing phospholipid.

did not lose the phospholipid or the adsorbed Raman tag. For biocompatibility (Figure 3b,d), RAP AuNPs were subjected to 10% fetal bovine serum in phosphate buffered saline. There was a small 3 nm shift in the absorption maxima and a broadening of the absorption curve after 30 min incubation of RAP gold in 10% fetal bovine serum made up in phosphate buffer saline. This is likely due to protein adhesion on the particles, as there was an increase in absorption at 280 nm (Supporting Information Figure S4). However, this small absorption maxima shift did not increase with increasing incubation time in serum and thus is not indicative of induced aggregation. Further evidence of monomeric particles in solution is the lack of increasing Raman intensities. With aggregation of AuNPs, we expect a significant increase in the SERS signal due to the increased electromagnetic field by the close proximity of the oscillating plasmons on the metallic surface (*1, 24*). However, because our Raman measurements showed slightly lowered intensities, we ruled out any aggregation of RAP gold under physiological conditions. In fact, there was no time-dependent change in the SERS signal up to 24 h in serum. Moreover, the long-term stability of the RAP AuNPs was monitored, with no change in Raman intensities observed after 16 days at 4 °C storage in H_2O (Supporting Information Figure S5). This is likely attributed to the lack of competing interactions of the Raman tag and surrounding phospholipid on the AuNP surface. In fact, synthesis of RAP AuNPs with thiol-containing phospholipid (1,2-dipalmitoyl-*sn*-glycero-3-phosphothioethanol) resulted in a significant loss of Raman signals (Supporting Information Figure 4). This result showed that the strong interaction of thiol-containing molecules to AuNPs (*25*) can compete for sites on the AuNP surface and displace the adsorbed Raman tag—especially one without any thiol moieties such as crystal violet.

In summary, we have demonstrated the robust synthesis of Raman-active phospholipid gold nanoparticles with stable Raman signals. These lipid-coated nanoparticles are highly stable and are suitable for biological applications. By encapsulating AuNPs with a phospholipid coating after the adsorption of Raman dye, SERS signals are retained, while the nanoparticles become more water-soluble. The stable phospholipid coating renders the nanoparticle biologically compatible and highly versatile. This provides a nanoparticle platform from which targeted probes can be developed, since straightforward modifications to the coating, such as conjugating targeting ligands or incorporating targeting lipid/lipopeptide moieties, will allow for the construction of a range of targeting probes.

ACKNOWLEDGMENT

The authors thank Battista Calvieri and Jonathan Lovell for their assistance in acquiring TEM images. This research was supported by National Science and Engineering Research Council of Canada's Strategic Network for Bioplasmonic Systems (Biopsys) & Discovery Grant (#386613-10), and the Joey and Toby Tanenbaum/Brazilian Ball Chair in Prostate Cancer Research.

Supporting Information Available: Materials, methods, and additional data. This material is available free of charge via the Internet at http://pubs.acs.org.

LITERATURE CITED

(1) Kneipp, J., Kneipp, H., and Kneipp, K. (2008) SERS--a single-molecule and nanoscale tool for bioanalytics. *Chem. Soc. Rev. 37*, 1052–60.

(2) Qian, X., Peng, X. H., Ansari, D. O., Yin-Goen, Q., Chen, G. Z., Shin, D. M., Yang, L., Young, A. N., Wang, M. D., and Nie, S. (2008) In vivo tumor targeting and spectroscopic detection with surface-enhanced Raman nanoparticle tags. *Nat. Biotechnol. 26*, 83–90.

(3) Zavaleta, C. L., Smith, B. R., Walton, I., Doering, W., Davis, G., Shojaei, B., Natan, M. J., and Gambhir, S. S. (2009) Multiplexed imaging of surface enhanced Raman scattering nanotags in living mice using noninvasive Raman spectroscopy. *Proc. Natl. Acad. Sci. U.S.A. 106*, 13511–6.

(4) Kim, J. H., Kim, K. W., Kim, M. H., and Yu, Y. S. (2009) Intravenously administered gold nanoparticles pass through the blood-retinal barrier depending on the particle size, and induce no retinal toxicity. *Nanotechnology 20*, 505101.

(5) Lasagna-Reeves, C., Gonzalez-Romero, D., Barria, M. A., Olmedo, I., Clos, A., Sadagopa Ramanujam, V. M., Urayama, A., Vergara, L., Kogan, M. J., and Soto, C. (2010) Bioaccumulation and toxicity of gold nanoparticles after repeated administration in mice. *Biochem. Biophys. Res. Commun. 393*, 649–55.

(6) Liu, Y., Shipton, M. K., Ryan, J., Kaufman, E. D., Franzen, S., and Feldheim, D. L. (2007) Synthesis, stability, and cellular internalization of gold nanoparticles containing mixed peptide-poly(ethylene glycol) monolayers. *Anal. Chem. 79*, 2221–9.

(7) Thaxton, C. S., Daniel, W. L., Giljohann, D. A., Thomas, A. D., and Mirkin, C. A. (2009) Templated spherical high density lipoprotein nanoparticles. *J. Am. Chem. Soc. 131*, 1384–5.

(8) Cormode, D. P., Skajaa, T., van Schooneveld, M. M., Koole, R., Jarzyna, P., Lobatto, M. E., Calcagno, C., Barazza, A., Gordon, R. E., Zanzonico, P., Fisher, E. A., Fayad, Z. A., and Mulder, W. J. (2008) Nanocrystal core high-density lipoproteins: a multimodality contrast agent platform. *Nano Lett 8*, 3715–23.

(9) He, P., and Urban, M. W. (2005) Phospholipid-stabilized Au-nanoparticles. *Biomacromolecules 6*, 1224–5.

(10) Jin, Q., Xu, J. P., Ji, J., and Shen, J. C. (2008) Zwitterionic phosphorylcholine as a better ligand for stabilizing large biocompatible gold nanoparticles. *Chem. Commun. (Camb.)* 3058–60.

(11) Sitaula, S., Mackiewicz, M. R., and Reed, S. M. (2008) Gold nanoparticles become stable to cyanide etch when coated with hybrid lipid bilayers. *Chem. Commun. (Camb.)* 3013–5.

(12) Orendorff, C. J., Alam, T. M., Sasaki, D. Y., Bunker, B. C., and Voigt, J. A. (2009) Phospholipid-gold nanorod composites. *ACS Nano 3*, 971–83.

(13) Zhou, W., Shao, J., Jin, Q., Wei, Q., Tang, J., and Ji, J. (2010) Zwitterionic phosphorylcholine as a better ligand for gold nanorods cell uptake and selective photothermal ablation of cancer cells. *Chem. Commun. (Camb.) 46*, 1479–81.

(14) Han, H. S., and Kim, H. (1994) Spontaneous fragmentation of dimyristoylphosphatidylcholine vesicles into a discoidal form at low pH. *J. Biochem. 115*, 26–31.

(15) Kumar, V. V. (1991) Complementary molecular shapes and additivity of the packing parameter of lipids. *Proc. Natl. Acad. Sci. U.S.A. 88*, 444–8.

(16) Wang, P., Li, Y., Huang, X., and Wang, L. (2007) Fabrication of layer-by-layer modified multilayer films containing choline and gold nanoparticles and its sensing application for electrochemical determination of dopamine and uric acid. *Talanta 73*, 431–7.

(17) Brechling, A., Sundermann, M., Kleineberg, U., and Heinzmann, U. (2003) Characterization of DMPC bilayers and multilamellar islands on hydrophobic self-assembled monolayers of ODS/Si(100) and mixed ODS-DDS/Si(100). *Thin Solid Films 433*, 281–286.

(18) Kucerka, N., Liu, Y., Chu, N., Petrache, H. I., Tristram-Nagle, S., and Nagle, J. F. (2005) Structure of fully hydrated fluid phase DMPC and DLPC lipid bilayers using X-ray scattering from oriented multilamellar arrays and from unilamellar vesicles. *Biophys. J. 88*, 2626–37.

(19) Pencer, J., Nieh, M. P., Harroun, T. A., Krueger, S., Adams, C., and Katsaras, J. (2005) Bilayer thickness and thermal response of dimyristoylphosphatidylcholine unilamellar vesicles containing cholesterol, ergosterol and lanosterol: A small-angle neutron scattering study. *Biochim. Biophys. Acta 1720*, 84–91.

(20) Gallova, J., Uhrikova, D., Hanulova, M., Teixeira, J., and Balgavy, P. (2004) Bilayer thickness in unilamellar extruded 1,2-dimyristoleoyl and 1,2-dierucoyl phosphatidylcholine vesicles: SANS contrast variation study of cholesterol effect. *Colloids Surf., B 38*, 11–4.

(21) Lewis, B. A., and Engelman, D. M. (1983) Lipid bilayer thickness varies linearly with acyl chain length in fluid phosphatidylcholine vesicles. *J. Mol. Biol. 166*, 211–7.

(22) Howland, M. C., Szmodis, A. W., Sanii, B., and Parikh, A. N. (2007) Characterization of physical properties of supported phospholipid membranes using imaging ellipsometry at optical wavelengths. *Biophys. J. 92*, 1306–17.

(23) Lipkowski, J., Stolberg, L., Yang, D. F., Pettinger, B., Mirwald, S., Henglein, F., and Kolb, D. M. (1994) Molecular adsorption at metal-electrodes. *Electrochim. Acta 39*, 1045–1056.

(24) Schwartzberg, A. M., Grant, C. D., Wolcott, A., Talley, C. E., Huser, T. R., Bogomolni, R., and Zhang, J. Z. (2004) Unique gold nanoparticle aggregates as a highly active surface-enhanced Raman scattering substrate. *J. Phys. Chem. B 108*, 19191–19197.

(25) Gronbeck, H., Curioni, A., and Andreoni, W. (2000) Thiols and disulfides on the Au(111) surface: The headgroup-gold interaction. *J. Am. Chem. Soc. 122*, 3839–3842.

BC100386A

Supporting Information for:

Facile Synthesis of Raman Active Phospholipid Gold Nanoparticles

*Natalie C.M. Tam[1], Benjamin M. T. Scott[2], Danut Voicu[3], Brian C. Wilson[2], Gang Zheng[1,2,3]**

[1]Institute of Biomaterials and Biomedical Engineering, [2]Department of Medical Biophysics/Ontario Cancer Institute, [3]Leslie Dan Faculty of Pharmacy, University of Toronto

Materials.

60 nm gold nanoparticles were purchased from Ted Pella, Inc. Crystal violet was purchased from Sigma Aldrich. 1,2-dimyristoyl-*sn*-glycero-3-phosphocholine (DMPC), 1-myristoyl-2-hydroxy-*sn*-glycero-3-phosphocholine (MHPC), and 1,2-dipalmitoyl-*sn*-glycero-3-phosphothioethanol were purchased from Avanti Polar Lipids and used as received.

Methods.

Synthesis: A 10μM aqueous solution of crystal violet was prepared and kept stirring for at least 1 h for complete solubilization. 1.1 mL of 60 nm citrate stabilized AuNPs in aqueous solution were then stirred in a cuvette while being continuously monitored on a compact Raman system using 785nm excitation (Advantage Raman Series, Delta Nu). Fractions of crystal violet (11 μL) were added intermittently until a stable Raman intensity was reached on the highest scattering peak at 1173cm^{-1}. The Raman coated AuNPs were then transferred to 20 mL scintillation vials, diluted 1:3 with distilled de-ionized H_20 and heated to 65°C with stirring. Upon reaching 55°C, the phospholipid solution (DMPC (5mg) and MHPC (5mg)) in 500μL 19:1 chloroform to methanol was added dropwise slowly. The organic solvents were allowed to evaporate and the bubbles formed by evaporating organic solvents were allowed to settle between each addition. After the final addition, the vial was left to cool to room temperature and then aliquoted into microcentrifuge tubes. The resulting nanoparticles were purified by

two rounds of centrifugation for 15 min at 500xg. The supernatant was removed after each centrifugation step and re-dispersed in distilled de-ionized H_20

Characterization: RAP AuNPs were characterized by dynamic light scattering (Zetasizer Nano ZS90, Malvern Instruments), transmission electron microscopy (Hitachi H-7000 TEM) and UV-Vis Spectroscopy (Cary 50 UV-Vis Spectrophotometer, Varian).

Additional Data:

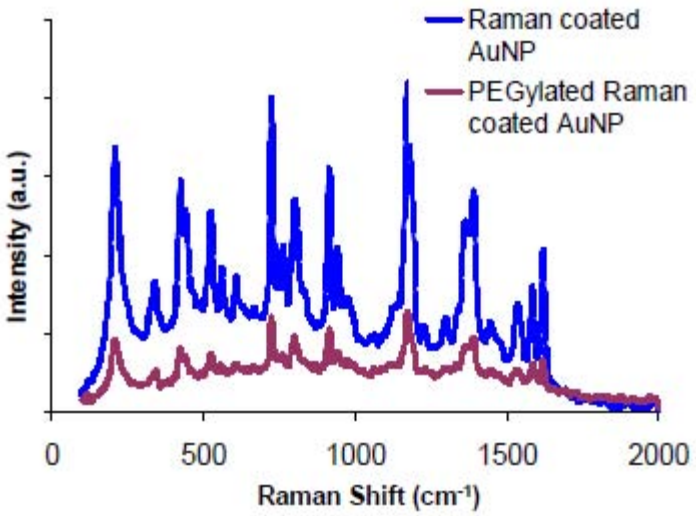


Figure S1. Raman spectra of AuNPs before and after being coated with thiol-PEG after multiple rounds of centrifugation.

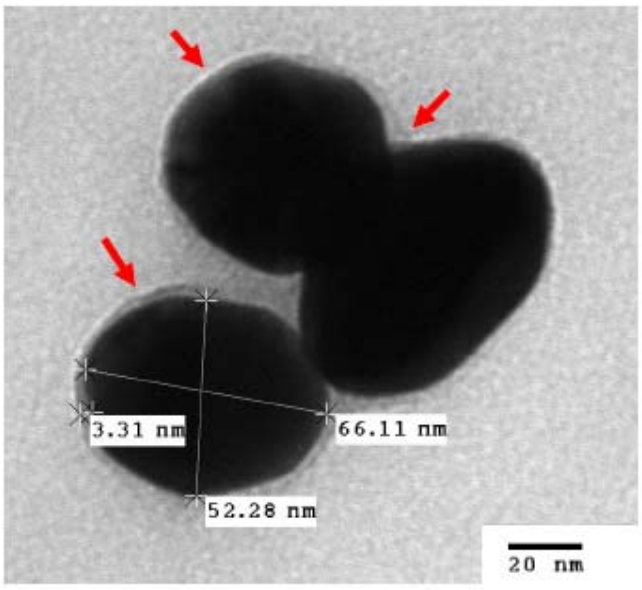


Figure S2. TEM images of RAP AuNPs clustered by TEM preparation clearly shows phospholipid coating (arrows) of approx. 3 nm surrounding the electron-dense AuNPs.

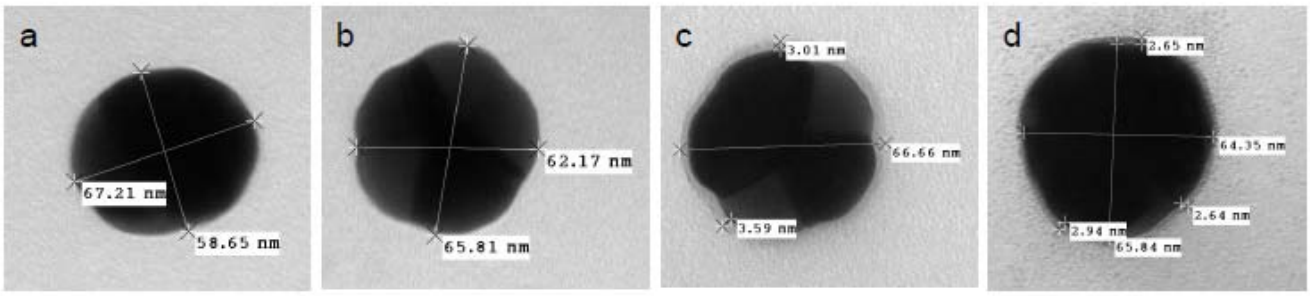


Figure S3. Analysis of TEM images showing citrate-stabilized AuNPs (a), Raman-coated AuNPs (b), phospholipid AuNPs (c) and RAP AuNPs (d), where the phospholipid coating on both (c) and (d) was approx. 3 nm.

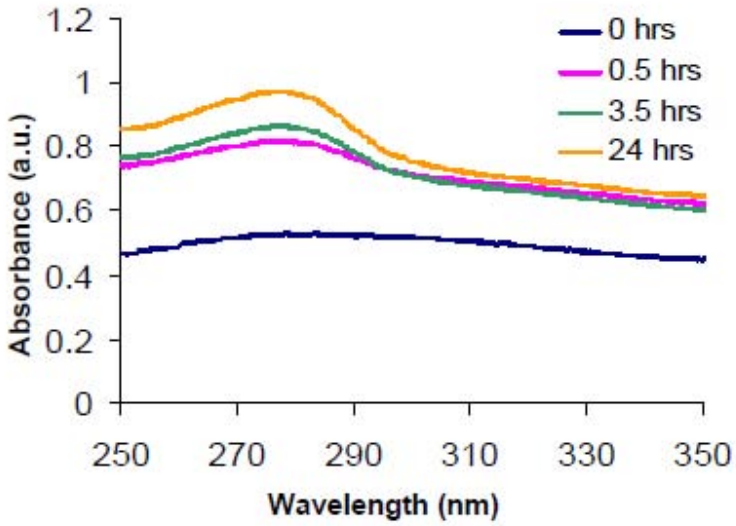


Figure S4. UV-Vis absorbance spectra showing possible protein adherence onto RAP gold after incubation in 10% fetal bovine serum in phosphate buffer saline.

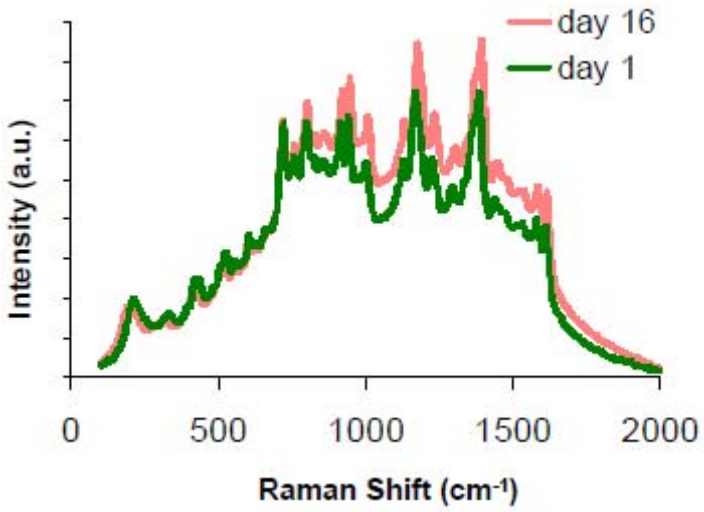


Figure S5. Raman spectra of RAP AuNPs before and after storage in distilled de-ionized water for 16 days at 4°C

Aptamer-Based Sensitive Detection of Target Molecules via RT-PCR Signal Amplification

Shiqi Liao,*[,†] Yuanqiang Liu,[†] Jiayu Zeng,[‡] Xiaoxu Li,[||] Ningsheng Shao,[§] Aihong Mao,[†] Li Wang,[†] Jin Ma,[†] Ha Cen,[†] Yunpu Wang,*[,‡] Xueli Zhang,[†] Ruitang Zhang,[†] Zhengli Wei,[†] and Xiaohui Wang[†]

Institute of Gansu Medical Science Research, Lanzhou, 730050, P. R. China, Key Laboratory of Polymer Material of Gansu Province, Institute of Polymer, Northwest Normal University, Lanzhou, 730070, P. R. China, Beijing Institute of Basic Medical Sciences, Beijing 100850, P. R. China, and Columbia Genome Center and Department of Chemical Engineering, Columbia University, New York, New York 10025. Received February 22, 2010; Revised Manuscript Received June 1, 2010

In the efforts to explore an aptamer-based approach for target sensing and detection with higher sensitivity and specificity, instead of directly labeling aptamer with fluorophores, we proposed a new strategy by attaching a polymerase chain reaction (PCR) template to an oligonucleotide aptamer selected by systematic evolution of ligands by exponential enrichment (SELEX), so that after aptamer target binding, the template moiety serves as the PCR template in real-time quantitative PCR (RT-PCR), and therefore, the binding event can be reported by the following RT-PCR signals. Using the subtractive SELEX method, the oligonucleotide aptamers specific for the Fc fragment of mouse IgG were selected and subjected to coupling with the PCR dsDNA template by using overlap and the asymmetric extension PCR method. The target binding affinity of the PCR template tethered aptamer has been proven by electrophoretic mobility shift assay (EMSA), and further template tethered aptamer mediated real-time quantitative PCR (A-PCR) was conducted to validate the application for such a template tethered aptamer to be a sensitive probe for IgG detection. The results show that the protocols of A-PCR can detect 10-fold serial dilutions of the target, demonstrating a new mechanism to convert aptamer target binding events to amplified RT-PCR signal, and the feasibility of the PCR template tethered aptamer as a facile, specific, and sensitive target probing and detection is established. This new approach also has potential applications in multiple parallel target detection and analysis in a wide range of research fields.

INTRODUCTION

In order to develop powerful biological probes which can provide insightful information on biological processes and mechanisms, highly sensitive, specific, and facile analytical machinery has been extensively exploited. Out of a variety of approaches, aptamers demonstrate high binding affinity and specificity to their non-nucleic acid target molecules, such as peptides, proteins, drugs, and organic and inorganic molecules, and are capable of distinguishing among homologous proteins (*1*−*3*) or nearly identical low molecular weight compounds (*4*−*11*). Their unique characteristics offer ideal recognition elements for use in analytical devices and techniques. Since the introduction of SELEX (systematic evolution of ligands by exponential enrichment) in 1990 (*12, 13*), design, screening, in vitro selection, and evolution of specific oligonucleotide aptamers has become routinely achievable. Moreover, advances in SELEX also make it possible for nucleic acid aptamers specific for almost every target to now be obtained (*14*−*21*). This opens up the door for aptamers to be feasible for a wide range of applications in multiple target detection and sensing (*22*−*24*). The key issue in the development of aptamer-based analytical methods and sensors is how to convert target recognition and binding into a measurable signal.

In aptamer-based electrochemical detection devices, aptamers are designed to be immobilized on the electrode allowing that the conformational transition of the aptamers upon binding to targets leads to the electron transfer switch "on or off" between the electrode and the electro-active molecules either labeled on or noncovalently trapped in aptamers (*24*−*26*). Quantum dots are also used to signal the aptamer−target binding because of its electronic and fluorescence properties. Aptamer-capped near-infrared PbS QD was constructed to detect target protein binding which can result in fluorescence quenching due to charge transfer from protein amino group to the QD (*27*). In another study, aptamer-functionalized QD 605 is capable of sensing the presence of small molecule targets through FRET signal switches (*28*).

More formats of signaling aptamer strategies based on mono- or dual- fluorophore labeling and measurement techniques have been abundantly demonstrated. In these approaches, target aptamer binding is transformed into changes of fluorescent signals (*22, 23, 29, 30*). The molecular beacon aptamer (MBA) approach is one of them and was proposed by combining the high binding specificity of the aptamer to its target with the sensitive signal transduction mechanism of the molecular beacon (*30, 31*), so that the aptamer target interaction event can be successfully reported by monitoring the changes in fluorescence intensity before and after aptamer−target binding. In a typical MBA assay, the aptamer is labeled with a fluorophore and a quencher. If the positions of the two labels are properly designed, upon binding to its target, the conformational change of the aptamer leads to the change in the distance between the fluorophore and the quencher; consequently, the significant change in fluorescence intensity before and after aptamer target binding can be measured. So far, beacon

* Corresponding authors. Present address: Gansu Academy of Medical Sciences, 2 Xiaoxihu E.S., Lanzhou, 730050, Gansu, P.R.China, Tel: +86-931-2607894, Fax: +86-931-2607894, E-mail addresses: liaoshiqi@nwnu.edu.cn, wangyp@nwnu.edu.cn.

[†] Institute of Gansu Medical Science Research.

[‡] Northwest Normal University.

[§] Beijing Institute of Basic Medical Sciences.

[||] Columbia University.

10.1021/bc100032v © 2010 American Chemical Society
Published on Web 11/10/2010

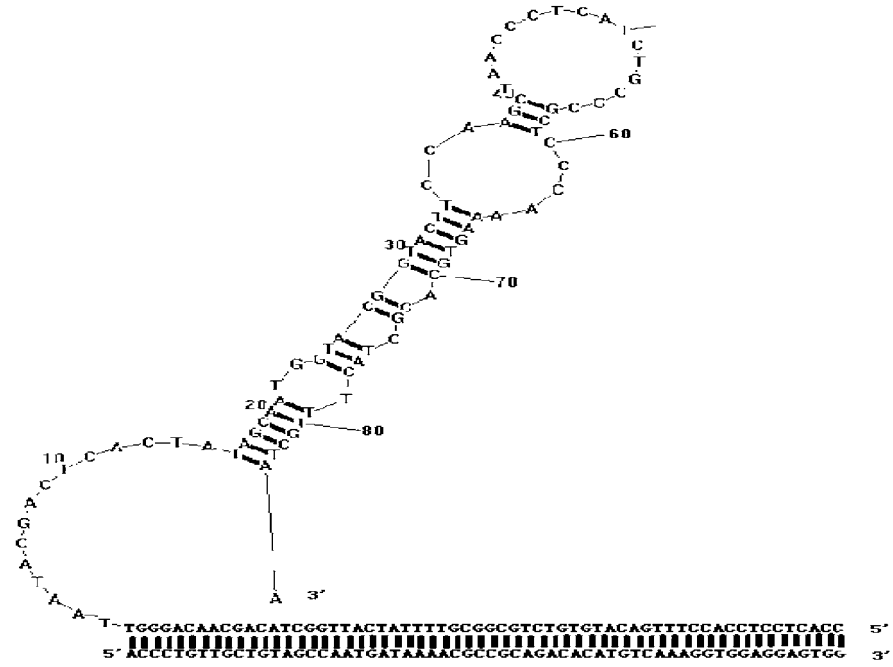


Figure 1. Secondary structure of constructed real-time quantitative-PCR template tethered aptamer targeting against IgG. The double-strand fragment (lower part) serves as PCR template and the loop-stem fragment functions as aptamer moiety.

aptamers for protein binding assay have been demonstrated well, such as that for detection of thrombin and Tat protein of HIV-1 (*32*−*35*). On the other hand, since the conformational change of aptamer has a negative effect on aptamer−target recognition and binding, in order to obtain a better beacon aptamer, usually more selection rounds are needed in the process of beacon aptamer construction. We also noticed that, in the existing aptamer-based assay methods, either the needs for electrode surface immobilization of aptamers or the needs for mono- or dual labeling of aptamers may increase the complexity and costs in real-world application. To overcome these remaining limitations, we are interested in searching more general strategies to couple the aptamer with an appropriate moiety or detection system, which could be used to signal the aptamer target binding with higher sensitivity and less complexity.

RT-PCR provides a precise and sensitive method for determination of specific DNA and RNA sequences in samples within a broad dynamic range (at least 5 orders of magnitude). The principle of RT-PCR is based on detecting the fluorescent signal produced proportionally during PCR amplification with the aid of computer analysis. The assays are easy to perform, capable of high throughput, and can combine high sensitivity with reliable specificity (*36*−*38*). So far, fluorescence-based RT-PCR is widely used for the quantification of steady-state DNA (and RNA) levels, and is becoming a standard tool box for biomedical researches (*39*). We further conceived that a dsDNA fragment which is linked at the terminal of the aptamer will be able to act as an amplification template in RT-PCR. The signal generated from RT-PCR therefore can be used as an indicator for aptamer−target binding after the bound aptamer is separated from the unbound one. In addition, the PCR signal can also be used to identify and quantitate target (such as protein) level in homogeneous solution. On the other hand, if properly designed, the dsDNA template would not interfere with aptamer target binding and vice versa due to high binding specificity of aptamers.

In this paper, we describe the design and construction of a new type of aptamer-based probe through which a target binding event can be reported by amplified RT-PCR signals. In such an aptamer (Figure 1), a ds DNA is coupled to the normal oligonucleotide aptamer selected by SELEX so that this attached dsDNA sequence can be used as a template in RT-PCR; upon target aptamer binding, the binding event could be easily monitored by conducting RT-PCR, and thus, the amplified PCR signal serves as an indicator of the target aptamer binding with high sensitivity (Figure 2). Using HBV antibodies as detection targets and dsDNA template tethered aptamer as probe, a proof-of-concept of the aptamer-mediated real-time quantitative PCR (A-PCR) assay for aptamer target binding is presented.

EXPERIMENTAL PROCEDURES

SELEX Selection. The polystyrene microtiter plate (Maxisorp96-wells, Nunc) was coated with mouse IgG (50 μL, 5 mg/mL) in 0.05 M carbonate buffer (pH 9.6) overnight at 4 °C. The negative control well was treated with carbonate buffer without IgG under the same conditions as above. Afterward, the wells were blocked with Tris-buffered saline (TBS) containing 5% (w/v) fat-free powdered milk (TBSM). A random library (5′-TAA TAC GAC TCA CTA TAG CAA TGG TAC GGT ACT TCC (N25) CA AAA GTG CAC GCT ACT TTG-3′; (N = A,C,T,G,)) was constructed as previously described (*12*) and was denatured by heating at 95 °C, maintained at that temperature for 5 min, and then cooled immediately to 0 °C in selection buffer (5 mM $MgCl_2$ in PBS). In order to reduce background interference, 1 mg/mL of yeast tRNA (Sigma) was added. Subtractive selection was performed by washing three times to elute IgG-aptamers with buffer (7 M urea, 0.5 M NH_4Ac, 1 mM EDTA, and 0.2% SDS) and extracting with phenol−chloroform. ssDNA was precipitated by 10 mM $MgCl_2$ and 0.3 M NaAc and a 2.5-fold volume of ethanol. Selected ssDNA was dissolved in PCR mixture containing 10 μL of 10 × PCR buffer, 8 μL of dNTP (10 mM each, Takara), 6 μL of 25 mM $MgCl_2$, 1 μL of 25 mM P7 long primer (5′-TAA TAC GAC TCA CTA TAG CAA TGG TAC GGT ACT TCC-3′), 1 μL of 25 mM P11 primer (5′-TTA GCA AAG TAG CGT GCA CTT TTG-3′), 73.5 μL of water, and 0.5 μL (2.5 U) of Taq DNA polymerase (Takara). The mixture was thermally cycled five times at 94 °C for 1 min, at 37 °C for 2 min, and at 72 °C for 2 min. The purified PCR products were used as templates to prepare ssDNA for the next round of SELEX.

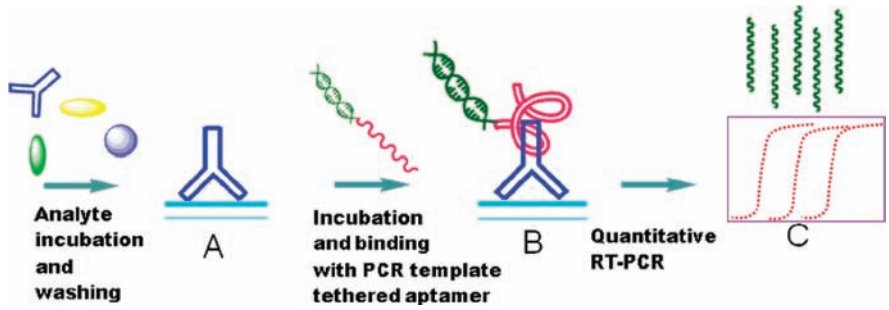


Figure 2. Aptamer-based sensitive detection of target molecules via real-time quantitative-PCR signal amplification. The target (mouse IgG) molecules are first captured on a surface (A); the following incubation with dsDNA PCR template-tethered aptamer specific to the target results in target aptamer binding and immobilization (B). Further real-time quantitative-PCR using attached DNA template generates amplified PCR signals that quantitate the target molecules (C).

Preparation of ssDNA Aptamer and Radioactive Labeling. The PCR mixture consisting of 5 μL of 1 pM dsDNA templates purified as described above, 2 μL of 25 mM P7 primer (5′-TAA TAC GAC TCA CTA TAG CAA TGG TAC GGT ACT TCC-3′), 0.2 μL of 25 mM P11 primer (3′-TTA GCA AAG TAG CGT GCA CTT TTG-5′), 8 μL of dNTP (10 mM each Takara), 6 μL of 25 mM $MgCI_2$, 10 μL of 10 × PCR buffer, 68.3 μL of water, and 0.5 μL (2.5 U) Taq DNA polymerase (Takara) was thermally cycled (94 °C for 30 s; 55 °C for 30 s; 72 °C for 30 s, 35 cycles). The PCR product was purified using 10% denatured polyacrylamide (0.5% bisacrylamide) gels containing 7 M urea. Radiolabeled ssDNA was prepared the same way as described above, except that ^{32}P-dATP was added to the PCR mixture instead of dATP.

Probing the Dot Blot with Radioactive Aptamer and Autoradiography. Radiolabeled ssDNA aptamers were denatured by heating to 95 °C and cooling immediately to 4 °C in selection buffer (5 mM $MgCl_2$ in PBS). 5 μL of serial dilutions of mouse IgG (0.5−25 μg) were dot-blotted on nitrocellulose membranes and blocked at 37 °C for 30 min in TBS containing 5% (w/v) of fat-free powdered milk (TBSM). A negative control membrane was treated with carbonate buffer without IgG. The membranes were then incubated with equal amounts of a mixture of radiolabeled ssDNA aptamers in 200 μL of selection buffer at 37 °C for 30 min. After washing three times with 3 mL of selection buffer, these nitrocellulose membranes were air-dried and autoradiographed.

Preparation of dsDNA Attached Aptamers. First, double-stranded DNA aptamers were prepared by overlap extension PCR. Typically, a PCR mixture containing 1 μL of a 25 μM negative strand of selected aptamer ssDNA(5′-TTA GCA AAG TAG CGT GCA CTT TTG GGA GCG CGC AGA TGA GGG TTA GCT TGG AAG TAC CGT ACC ATT GCT ATA GTG AGT CGT ATT A-3′) and 1 μL of 25 μM synthetic ssDNA (5′-CCA CTC CTC CAC CTT TGA CAT GTG TCT GCG GCG TTT TAT CAT TGG CTA CAG CAA CAG GGT TAA TAC GAC TCA CTA TAG CAA TGG TAC GGT ACT TCC-3′) as templates, 8 μL of dNTP (10 mM each, Takara), 6 μL of 25 mM $MgCl_2$, 10 μL of 10× PCR buffer, 0.5 μL (2.5 U) Taq DNA polymerase (Takara), and distilled H_2O in a final volume of 100 μL was thermally cycled (94 °C for 30 s; 55 °C for 30 s; 72 °C for 30 s, 5 cycles). Then, the single-stranded DNA attached aptamers were prepared by an asymmetric PCR method. A PCR mixture containing 10 μL overlap extension PCR product as templates, 2.2 μL of 25 μM P201 primer (5′-CCA CTC CTC CAC CTT TGA C-3′), 0.2 μL of 25 μM P11 primer (5′- TTA GCA AAG TAG CGT GCA CTT TTG-3′), 8 μL of dNTP (or ^{32}P-dATP was added into the PCR mixture instead of dATP for preparation of the radiolabeled one) (10 mM each, Takara), 6 μL of 25 mM $MgCl_2$, 10 μL of 10× PCR buffer, and 0.5 μL (2.5 U) Taq DNA polymerase (Takara), and distilled H_2O in a final volume of 100 μL was thermally cycled (94 °C for 30 s; 55 °C for 30 s; 72 °C for 30 s, 35 cycles). Meanwhile, the negative ssDNA was prepared by an asymmetric PCR method. A PCR mixture containing 10 μL overlap extension PCR product as template, 0.2 μL of 25 μM P201 primer (5′-CCA CTC CTC CAC CTT TGA C-3′), 2.2 μL of 25 μM P214 primer (5′-ACCCTGTTGCTGTAGCCA-3′), 8 μL of dNTP (or ^{32}P-dATP was added into the PCR mixture instead of dATP for preparation of the radiolabeled one) (10 mM each, Takara), 6 μL of 25 mM $MgCl_2$, 10 μL of 10× PCR buffer, and 0.5 μL (2.5 U) Taq DNA polymerase (Takara), and distilled H_2O in a final volume of 100 μL was thermally cycled (94 °C for 30 s; 55 °C for 30 s; 72 °C for 30 s, 35 cycles). Finally, the two asymmetric PCR products were combined and thermally cycled (95 °C for 5 min; 4 °C for 60 s) to afford the ssDNA aptamers attached with a dsDNA sequence. Further PAGE gel electrophoresis analysis (10% denatured PAGE gel at 100 V for 60 min) was conducted to characterize and separate the expected product.

Electrophoretic Mobility Shift Assay (EMSA). After the IgG-specific aptamers (5′-CCA CTC CTC CAC CTT TGA CAT GTG TCT GCG GCG TTT TAT CAT TGG CTA CAG CAA CAG GGT TAA TAC GAC TCA CTA TAG CAA TGG TAC GGT ACT TCC AAG CTA ACC CTC ATC TGC GCG CTC CCA AAA GTG CAC GCT ACT TTG CTA A-3′) were labeled by [α-^{32}P] ATP as described above, 100 pM ^{32}P-labeled DNA aptamers were incubated with serial dilutions of IgG (from 5 to 20 μg) in 20 μL binding buffer [10 mM HEPES (pH 7.6), 1 mM EDTA, 2 mM dithiothreitol, 50 mM KCl, 0.05% Triton X-100, and 5% glycerol] at 37 °C for 60 min. Bound and unbound DNA species were separated on 0.5% native agarose gel in 0.5× Tris-borate-EDTA (TBE) electrophoretic buffer at 80 V for 2 h. The gel was fixed with 10% acetic acid 50% methanol for 2 h, dried, and subjected to autoradiography. After autoradiography, the same gels were stained again with Coomassie brilliant blue, eluted, and photographed.

Real-Time Quantitative A-PCR. All RT-PCRs were carried out with a TaqMan probe on the Rotor-gene 3000 (Australian). The immuno-PCR microwells (Nunc TopYield) were coated with 20 μL of 10-fold serial dilutions of mouse anti-HBsAg IgG at 37 °C for 2 h 37 °C for 2 h or 4 °C overnight in 0.05 M carbonate buffer (pH 9.6). After blocking with TBSM (TBS buffer containing 5% (w/v) fat-free powdered milk), the microwells were washed with TBSET (TBS buffer containing 5 mM EDTA and 0.5% Tween-20) three times. Similarly, other specific or nonspecific IgG and protein samples were immobilized in microwells as described above. Then, 1 pg/mL dsDNA template tethered aptamers were added to the microwells and incubated in 20 μL binding buffer [10 mM HEPES (pH 7.6), 1 mM EDTA, 2 mM dithiothreitol, 50 mM KCl, 0.05% Triton X-100, and 5% glycerol] at 37 °C for 1 h, and then

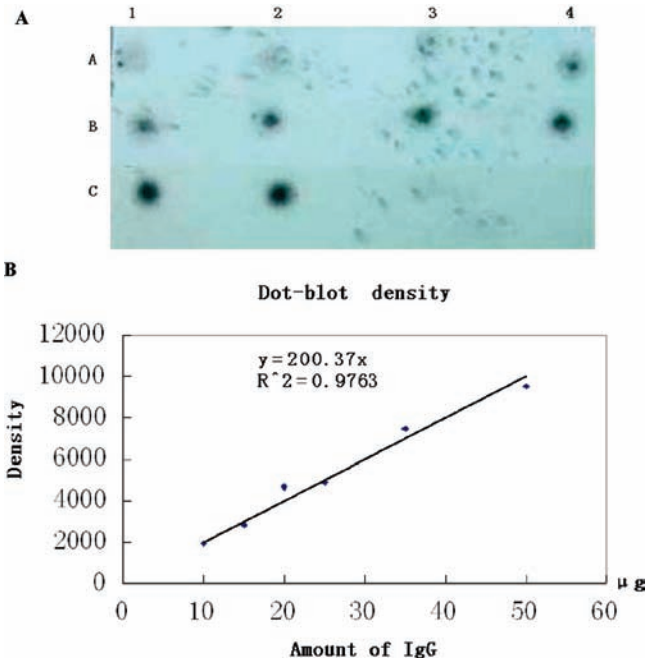


Figure 3. Dot-blot autoradiography assay for the binding of selected aptamer with IgG on nitrocellulose membranes. (A) Quantities of the target (IgG) dotted on the nitrocellulose membrane were as follows: A1, 0.25 μg; A2, 1 μg; A3, 2.5 μg; A4, 5 μg; B1, 10 μg; B2, 15 μg; B3, 20 μg; B4, 25 μg; C1, 35 μg; C2, 50 μg; C3, 0 μg. Images were taken after the nitrocellulose membrane was coincubated with ^{32}P-labeled aptamer. (B) The linear regression of dot-blot autoradiography was assayed by Melanie 3 - the 2-D Gel Image Analysis software package.

washed three times with binding buffer containing 0.5% Tween-20. The PCR mixture containing 1× PCR buffer (Takara), 4.5 mM $MgCl_2$, 0.25 mM of each primer, 0.8 mM of TaqMan probe, 0.25 mM of dNTP, 2.5 U Taq DNA polymerase (Takara), and distilled H_2O in a final volume of 20 μL was thermally cycled (94 °C for 5 min, followed by 40 cycles of 95 °C for 45 s, 55 °C for 60 s) by real-time PCR. Negative controls containing no template DNA were included in each batch of PCR tests. The threshold cycle (Cts) values were set as the cycle at which the measured fluorescence intersected the cycle threshold line.

RESULTS

Specific Binding Assay of the Selected Aptamers by Dot-Blot. Forty aptamers against the mouse IgG Fc fragment were selected after 16 rounds of SELEX. The selected aptamer with highest affinity was used for subsequent binding assay by dot-blot (Figure 3A). The blots were further analyzed by using the 2-D Gel Image Analysis software package (Melanie 3). The dot-blot autoradiography showed that the intensity of the dots had a linear relation with the IgG concentration (Figure 3B). The dot-blot binding assay of the aptamers with albumin, egg white protein, fat-free powdered milk, mouse IgG1, mouse IgG2a, and mouse anti-HBV IgG were conducted in parallel. The results showed that the selected aptamers specifically bind with mouse IgG1, mouse IgG2a, and mouse anti-HBV IgG, but not with albumin, egg white protein, or fat-free powdered milk. These results indicate the successful selection of oligonucleotide aptamers that can bind to the Fc fragment of mouse IgG with high affinity and specificity.

Construction and Electrophoresis Analysis of dsDNA Template Tethered Aptamer. The combination of overlap extension strategy and asymmetric PCR was carried out to generate expected dsDNA template tethered aptamer. Following denaturing, polyacrylamide gel electrophoresis (PAGE) (10% denatured PAGE gel at 200 V for 60 min) was carried out to analyze the dsDNA template−aptamer adduct (Figure 4). After consecutive PCRs and annealing process, lanes 1 and 2 show disappearance of both ssDNA template strand (band E) and ssPCR template DNA−aptamer adduct (band B) and appearance of ds DNA template tethered aptamer (band A). The band for dsDNA tethered aptamer is easily distinguishable from other oligo components in the PCR mixture showing a decent yield in preparation of the expected DNA tethered aptamer (Figure 4, band A).

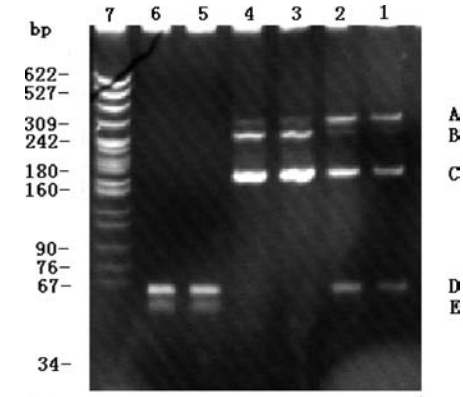


Figure 4. 10% denatured PAGE gel electrophoresis analysis of PCR template DNA attached aptamers. Lanes 1 and 2: A, dsDNA template tethered aptamer (positive strand only); C, dsDNA template tethered dsDNA aptamer; D, dsDNA template. Lanes 3 and 4: B, ssDNA template (positive strand) tethered aptamer (positive strand only); C, dsDNA template tethered dsDNA aptamer. Lanes 5 and 6: D, dsDNA template; E, ssDNA template (negative strand). Lane 7: M-pBR322DNA/MspI markers.

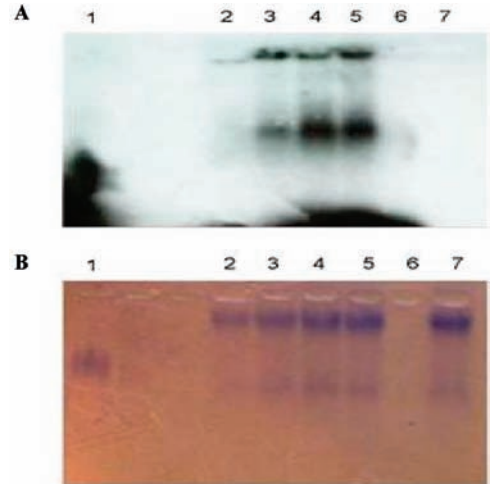


Figure 5. EMSA assay for specific binding of template tethered aptamers and target IgG. (A) EMSA autoradiography image of the binding complex of aptamer and IgG. Lane 1: mixture of boiled IgG (20 μg) and ^{32}P-template tethered aptamer (70 ng). Lanes 2−5: mixture of IgG (5 μg, 10 μg, 15 μg, 20 μg) and ^{32}P-template tethered aptamer (70 ng). Lane 6: ^{32}P-template tethered aptamer (70 ng) without IgG. Lane 7: IgG (20 μg) without ^{32}P-template tethered aptamer. (B) EMSA autoradiography gel stained with Coomassie brilliant blue.

EMSA Assay of the Binding Specificity of the PCR Template Tethered Aptamers. EMSA analyses were used to evaluate the binding affinity of the PCR template tethered aptamers with IgG (Figure 5A,B). The EMSA gels were subjected to autoradiography (Figure 5A), then were stained by Coomassie brilliant blue to quantify the bound IgG with DNA template tethered aptamer (Figure 5B). The color density of the electrophoretic bands corresponding to the aptamer-bound IgG increases with increasing concentration of IgG (Figure 5). On

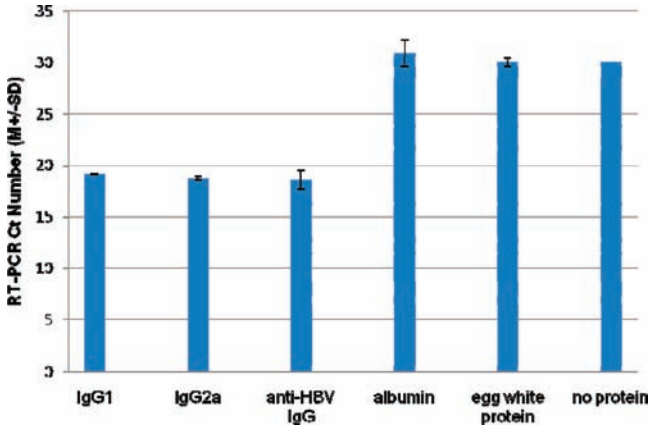


Figure 6. Ct values of the real-time quantitative A-PCR assay using specific and nonspecific protein as aptamer targets. RT-PCRs were carried out after sequential incubation of targets and PCR dsDNA template tethered aptamer in anti-HBV IgG, IgG1, IgG2a, albumin, egg white protein, and no protein precoated microwells. The Ct value results show very significant differences between specific and nonspecific targets ($p < 0.001$).

the contrary, the aptamer lost binding affinity to denatured IgG (Figure 5B) indicating that the PCR template tethered aptamers retain binding specificity and affinity to natural mouse IgG. The binding affinity of all three synthesized PCR tethered aptamers with IgG is shown to be the same, implying that the different template DNA-attached aptamers could bind with homologous Fc fragments of different mouse IgG subtypes.

Real-Time Quantitative A-PCR Assay for Target Detection. The capability of DNA template tethered aptamers as a novel probe to detect target molecules was further demonstrated using mouse IgG as the target and postbinding real-time quantitative-PCR as the signaling source. In the microwells coated with different target molecules including both specific and nonspecific proteins such as anti-HBsAg IgG, mouse IgG1, mouse IgG2a, albumin, egg white protein, and fat-free powdered milk and blocked with TBSM, further incubation with DNA template tethered aptamers leads to specific binding with immobilized mouse IgG in the microwells. After washing with TBSET to remove unbound ones, the following real-time quantitative A-PCR was carried out and Ct values of RT-PCR signals after aptamer incubation were recorded and summarized (Figure 6). A distinctive difference (40%) in RT-PCR Ct values is observed between RT-PCR runs after specific IgG target incubation and nonspecific protein incubation. The Ct values for nonspecific protein controls and for the "no protein" group were the same (as high as ~30) (Figure 6). This Ct level represents a background signal due to nonspecific immobilization of the dsDNA aptamer adduct. Further titration of the RT-PCR signal was conducted by using 10-fold serially diluted specific IgG ranging from 0.001 to 0.000 001 ng as a detection target. Within this range, the results show a linear relation with decreased Ct value versus increased IgG concentration (Figure 7).

DISCUSSION

The high affinity and specificity of aptamer make it an ideal probe in a variety of applications. The way to signal the aptamer target binding directly influences the feasibility of aptamer-based analysis and dominates the detection sensitivity. In this regard, the electron transfer switch, quantum dots, and FRET have been coupled with aptamer target binding as signaling methods (*22, 23*). Due to aptamer's nucleic acid nature, PCR amplification had been used to detect proteins with the aid of templates generated by postbinding ligation (*41, 42*). More recently, RT-PCR was

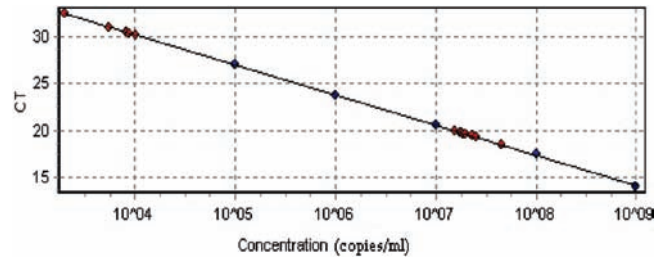


Figure 7. Real-time quantitative A-PCR shows a linear relation between decreased Ct values and increased specific target (IgG) concentration.

applied to aptamer-based protein detection using aptamer sequence as a template (*43*). In our earlier efforts to make use of aptamer fragments as PCR amplification template, we found, in a continuous workflow, that postbinding PCR could often be impaired, possibly due to existing target molecules which may compromise both polymerase template binding and hybridization between template and primer. More efficient and universal strategies are highly desirable.

In this study, we proposed a dsDNA template attached aptamer as a novel approach for sensing and detection of a specific target instead of using an aptamer fragment as PCR template. The dsDNA−aptamer adducts are composed of normal oligonucleotide aptamers selected by SELEX and dsDNA sequences which can be used as PCR template. Such a structure not only retains an aptamer's characteristic of specific binding to the target, but also endows the capacity to generate amplified PCR signal to report aptamer target binding. One advantage over beacon aptamer and electrochemical aptamer is that dsDNA attached aptamer probes do not need intrinsic fluorophore or electro-active molecular labels to produce observable signals. which may be more costly and may cause more complexity in aptamer design and selection. On the contrary, the dsDNA template attached aptamer is label-free, and the widely equipped RT-PCR tool box is used to transduce target aptamer binding into observable signal, providing PCR template tethered aptamer based assay, a more general and accessible method in wide range of applications. Moreover, the amplified signal produced by RT-PCR allows sensitive detection of target molecules at a similar low level at which a DNA sample could be detectable using RT-PCR. In comparison with other PCR-aided aptamer probing mechanisms mentioned above, attaching a DNA template to aptamer also allows more simple and straightforward detection. Thus, in a typical target detection, DNA template tethered aptamer mediated real-time quantitative PCR (A-PCR) can be fulfilled with a continuous workflow in a microwell: immobilize target molecules on surface, incubate with template tethered aptamers leading to formation of aptamer target binding complex, and wash to ensure that only the specific template tethered aptamer−target complex is retained on the surface. The following real-time quantitative PCR with on-aptamer dsDNA as template will generate an amplified signal to quantitate the existence of the target (Figure 2). These features enable dsDNA attached aptamer sensors to be more feasible for real-world analytical and biomedical research at low cost and ease.

Three DNA template tethered aptamer sensors were designed in this research, which are specific for IgG, all having the same primer but with different complementary sequences of TaqMan probes, respectively. The secondary structures of the template tethered aptamer sensors were analyzed using RNA structure 3.7 software. The ssDNA fragment contains a target binding sequence, and the dsDNA fragment serves as PCR template, including various Taqman probe complementary sequences flanked by defined primer binding sites (Figure 1). The conformations of the target binding fragment (aptamer moiety) and the PCR template fragment are very distinguishable (Figure

1). It is predictable that the recognition and binding of aptamer moiety and target molecule would not be interfered with, and neither would the following PCR be impaired by the target molecule. In construction of such a template tethered aptamer, the combined use of overlap extension strategy and asymmetric PCR supplied the expected conjugate containing both binding and signaling moieties in a simple and straightforward way. Parallel multiple target probing and detection of biological molecules will provide dynamic and insightful information on biomedical research and therefore are highly desirable. The simplicity and versatility of preparation of DNA template tethered aptamers has been shown. This method is adaptable, allowing us to attach DNA template onto different aptamers targeting a variety of analytes such as protein, peptide, nucleic acid, toxin, and ions. In combination with the routinely used RT-PCR tool box, this new approach may greatly expand its applications to target sensing and detection in a wide range of fields, and its extensive application would make multiplex target detection and sensing an achievable goal.

In this work, the proof-of-principle of A-PCR has been established using IgG as the target molecule. The sensitive detection of IgG within the range from 0.001 to 0.000 001 ng was realized. The higher quality of RT-PCR is dependent on the larger copy number of the dsDNA template attached with IgG bound aptamer and closely relevant to the lower cycle threshold (Ct) value in the RT-PCR amplification. When the other two different DNA template tethered aptamers were used, the same real-time quantitative A-PCR results in terms of Ct values were observed. As we expected, the results demonstrate that the aptamer retains its target binding specificity after an extra fragment of DNA template is attached. On the other hand, the extra DNA fragment does not interfere with the target-aptamer binding; this ensures an unambiguous detection of target using real-time quantitative A-PCR. In conclusion, a new mechanism to transduce the aptamer target binding event into a RT-PCR signal is fully validated by using the DNA template tethered aptamer as probe. Such an aptamer-based, RT-PCR-aided probing system shows potential as a universal tool to address the problem of parallel and multiple target detection and sensing and will greatly facilitate the systematic studies of biological processes and diagnosis. More efforts are underway by us focusing on multiplex detection of targets using A-PCR.

ACKNOWLEDGMENT

We thank Qunyan Lu, Zhongyu Song, Qingbin Han, and members of the Medical Molecular Lab of Medical Science Institute in Gansu and Ningsheng Shao's lab for their help in the Beijing Institute of Basic Medical Sciences. This work was supported by the National Natural Foundation of China (grants 30271219 and 30960104 to Shiqi Liao), the Innovation Foundation of China and Research Exploitation item (grants GKSOU-B06-10 and GKS031030), the Fund of Innovative Technology of Mini- or Medium-Sized Enterprises in China (06C26226200591), and the Capability Construction of Key Laboratory and Echelon of Talent of Gansu Provincial Science and Technology Department.

Supporting Information Available: DNA sequences of random library, 3 dsDNA template tethered aptamers, Taqman probes and primers used in this study; RT-PCR Ct values and the corresponding detectable copies of specific protein target per mL in real-time quantitative A-PCR assays using both specific and nonspecific proteins as aptamer targets. This material is available free of charge via the Internet at http://pubs.acs.org.

LITERATURE CITED

(1) Tuerk, C., MacDougal, S., and Gold, L. (1992) RNA pseudoknots that inhibit human immunodeficiency virus type 1 reverse transcriptase. *Proc. Natl. Acad. Sci. U.S.A. 89*, 6988–6992.

(2) Chen, H., and Gold, L. (1994) Selection of high-affinity RNA ligands to reverse transcriptase: inhibition of cDNA synthesis and RNase H activity. *Biochemistry 33*, 8746–8756.

(3) Jellinek, D., Lynott, C. K., Rifkin, D. B., and Janjic, N. (1993) High-affinity RNA ligands to basic fibroblast growth factor inhibit receptor binding. *Proc. Natl. Acad. Sci. U.S.A. 90*, 11227–11231.

(4) Ellington, A. D., and Szostak, J. W. (1990) In vitro selection of RNA molecules that bind specific ligands. *Nature 346*, 818–822.

(5) Sassanfar, M., and Szostak, J. W. (1993) An RNA motif that binds ATP. *Nature 364*, 550–553.

(6) Jension, R. D., Gill, S. C., Pardi, A., and Polisky, B. (1994) High resolution molecular discrimination by RNA. *Science 263*, 1425–1429.

(7) Connell, G. J., lllangesekare, M., and Yarus, M. (1993) Three small ribooligonucleotides with specific arginine sites. *Biochemistry 32*, 5497–5502.

(8) Lauhon, C. T., and Szostak, J. W. (1995) RNA aptamers that bind flavin and nicotinamide redox cofactors. *J. Am. Chem. Soc. 117*, 1246–1257.

(9) Jiang, F., Kumar, R. A., Jones, R. A., and Patel, D. J. (1996) Structural basis of RNA folding and recognition in an AMP-RNA aptamer complex. *Nature 382*, 183–186.

(10) Nolte, A., Klussmann, S., Bald, A., Erdmann, V. A., and Fürste, J. P. (1996) Mirror-design of L-oligonucleotide ligands binding to L-arginine. *Nat. Biotechnol. 14*, 1116–1119.

(11) Klussmann, S., Nolte, A., Bald, R., Erdmann, V. A., and Fürste, J. P. (1996) Mirror-image RNA that binds D-adenosine. *Nat. Biotechnol. 14*, 1112–1115.

(12) Tuerk, C., and Gold, L. (1990) Systematic evolution of ligands by exponential enrichment: RNA ligands to bacteriophage T4 DNA polymerase. *Science 249*, 505–510.

(13) Ellington, A. D., and Szostak, J. W. (1990) In vitro selection of RNA molecules that bind specific ligands. *Nature 346*, 818–822.

(14) Gold, L., Polisky, B., Unlenbeck, O., and Yarus, M. (1995) Diversity of oligonucleotide functions. *Annu. Rev. Biochem. 64*, 763–797.

(15) Gold, L., Brown, D., He, Y.-Y., Shtatland, T., Singer, B. S., and Wu, Y. (1997) From oligonucleotide shapes to genomic SELEX: Novel biological regulatory loops. *Proc. Natl. Acad. Sci. U.S.A. 94*, 59–64.

(16) Famulok, M., and Jeane, A. (1998) Oligonucleotide libraries-variatio delectat. *Curr. Opin. Chem. Biol. 2*, 320–327.

(17) Jayasena, S. D. (1999) Aptamers: an emerging class of molecules that rival antibodies in diagnostics. *Clin. Chem. 45*, 1628–1650.

(18) Hermann, T., and Patel, D. J. (2000) Adaptive recognition by nucleic acid aptamers. *Science 287*, 820–825.

(19) Shamah, S. M., Healy, J. M., and Cload, S. T. (2008) Complex target SELEX. *Acc. Chem. Res. 41*, 130–138.

(20) Gopinath, S. C. (2007) Methods developed for SELEX. *Anal. Bioanal. Chem. 387*, 171–82.

(21) Stoltenburg, R., Reinemann, C., and Strehlitz, B. (2007) SELEX— a revolutionary method to generate high-affinity nucleic acid. *Biomol. Eng. 24*, 381–403.

(22) Mairal, T., Ozalp, V. C., Lozano, Sánchez, P., Mir, M., Katakis, I., and O'Sullivan, C. K. (2008) Aptamers: molecular tools for analytical applications. *Anal. Bioanal. Chem. 390*, 989–1007.

(23) Tombelli, S., Minunni, M., and Mascini, M. (2005) Analytical applications of aptamers. *Biosens. Bioelectron. 20*, 2424–2434.

(24) Willner, I., and Zayats, M. (2007) Electronic aptamer-based sensors. *Angew. Chem., Int. Ed. 46*, 6408–6418.

(25) Zhang, S., Xia, J., and Li, X. (2008) Electrochemical biosensor for detection of adenosine based on structure-switching aptamer and amplification with reporter probe DNA modified Au nanoparticles. *Anal. Chem. 80*, 8382–8388.
(26) Centi, S., Tombelli, S., Minunni, M., and Mascini, M. (2007) Aptamer-based detection of plasma proteins by an electrochemical assay coupled to magnetic beads. *Anal. Chem. 79*, 1466–1473.
(27) Choi, J. H., Chen, K. H., and Strano, M. S. (2006) Aptamer-capped nanocrystal quantum dots: a new method for label-free protein detection. *J. Am. Chem. Soc. 128*, 15584–15585.
(28) Zhang, C. Z., and Johnson, L. W. (2009) Single quantum-dot-based aptameric nanosensor for cocaine. *Anal. Chem. 81*, 3051–3055.
(29) Nutiu, R., and Li, Y. (2005) Aptamers with fluorescence-signaling properties. *Methods 37*, 16–25.
(30) Li, J., Cao, Z. C., Tang, Z., Wang, K., and Tan, W. (2008) Molecular beacons for protein-DNA interaction studies. *Methods Mol. Biol. 429*, 209–224.
(31) Tyagi, S., and Kramer, F. R. (1996) Molecular beacons: probes that fluoresce upon hybridization. *Nat. Biotechnol. 14*, 303–308.
(32) Tan, W., Fang, X., Li, J., and Liu, X. (2000) Molecular beacons: a novel DNA probe for nucleic acid and protein studies. *Chemistry 6*, 1107–11.
(33) Yamamoto, R., Baba, T., and Kumar, P. K. (2000) Molecular beacon aptamer fluoresces in the presence of tat protein of HIV-1. *Genes Cells 5*, 389–396.
(34) Hamaguchi, N., Ellington, A., and Stanton, M. (2001) Aptamer beacons for the direct detection of proteins. *Anal. Biochem. 294*, 126–131.
(35) Li, J. J., Fang, X., and Tan, W. (2002) Molecular aptamer beacons for real-time protein recognition. *Biochem. Biophys. Res. Commun. 292*, 31–40.
(36) Heid, C. A., Stevens, J., Livak, K. J., and Williams, P. M. (1996) Real time quantitative PCR. *Genome Res. 6*, 986–994.
(37) Kim, D. W. (2001) Real time quantitative PCR. *Exp. Mol. Med. 33*, 101–109.
(38) Bustin, S. A. (2002) Quantifiction of mRNA using real-time reverse transcription PCR (RT-PCR): trends and problems. *J. Mol. Endocrinol. 29*, 23–9.
(39) VanGuilder, H. D., Vrana, K. E., and Freeman, W. M. (2008) Twenty-five years of quantitative PCR for gene expression analysis. *BioTechniques 44*, 619–626.
(40) Wang, C., Zhang, M., Yang, G., Zhang, D., Ding, H., Wang, H., Fan, M., Shen, B., and Shao, N. (2003) Single-stranded DNA aptamers that bind differentiated but not parental cells: subtractive systematic evolution of ligands by exponential enrichment. *J. Biotechnol. 102*, 15–22.
(41) Fredriksson, S., Gullberg, M., Jarvius, J., Olsson, C., Pietras, K., Gustafsdottir, S. M., Ostman, A., and Landegren, U. (2002) Protein detection using proximity-dependent DNA ligation assays. *Nat. Biotechnol. 20*, 473–477.
(42) Wang, X. L., Li, F., Su, Y. H., Sun, X., Li, X. B., Schluesener, H. J., Tang, F., and Xu, S. Q. (2004) Ultrasensitive detection of protein using an aptamer-based exonuclease protection assay. *Anal. Chem. 76*, 5605–5610.
(43) Yoshida, Y., Horii, K., Sakai, N., Masuda, H., Furuichi, M., and Waga, I. (2009) Antibody-specific aptamer-based PCR analysis for sensitive protein detection. *Anal. Bioanal. Chem. 395*, 1089–1096.

BC100032V

Aptamer Based Sensitive Detection of Target Molecules via RT-PCR Signal Amplification

Shiqi Liao[1,*], Yuanqiang Liu[1], Jiayu Zeng[2], Xiaoxu Li[4], Ningsheng Shao[3], Aihong Mao[1], Li Wang[1], Jin Ma[1], Ha Cen[1], Yunpu Wang[2*], Xueli Zhang[1], Ruitang Zhang[1], Zhengli Wei[1] and Xiaohui Wang[1]

[1]*Institute of Gansu Medical Science Research, Lanzhou, 730050, P.R. China*

[2]*Key Laboratory of Polymer Material of Gansu Province, Institute of Polymer, Northwest Normal University, Lanzhou, 730070, P. R. China*

[3]*Beijing Institute of Basic Medical Sciences, Beijing 100850, P. R. China*

[4] *Columbia Genome Center and Department of Chemical Engineering, Columbia University, New York, NY 10025, USA*

*Corresponding authors. Present address: Gansu Academy of Medical Sciences, 2 Xiaoxihu E.S., Lanzhou, 730050, Gansu, P.R.China

Tel: +86-931-2607894

Fax: +86-931-2607894

E-mail addresses: liaoshiqi@nwnu.edu.cn

wangyp@nwnu.edu.cn.

Supporting Information

Random library	5’-TAA TAC GAC TCA CTA TAG CAA TGG TAC GGT ACT TCC (N25)CA AAA GTG CAC GCT ACT TTG-3’ (N= A, C, T, G)
Aptamer sequencese	5’-TAATACGACTCACTATAGCAATGGTACGGTACTTCC AAGCTAACCCTCATCT GCGCGCTCC CAAAAGTGCACGCTACTTTGCTAA-3’
DNA template tethered aptamer	1. 5’-CCACTCCTCCACCTTTGACA TGTGTCTGCGGCGTTTTATCA TTGGCTACA GCAACAGGGT TAATACGACTCACTATAGCAATGGTACGGTACTTCC AAGC TAACCCTCATCTGCGCGCTCC CAAAAGTGCACGCTACTTTGCTAA-3’ 2. 5’-CCACTCCTCCACCTTTGACA TGTGTCTGATAGTAAGTGCCA TTGGCTACA GCAACAGGGT TAATACGACTCACTATAGCAATGGTACGGTACTTCC AAGC TAACCCTCATCTGCGCGCTCC CAAAAGTGCACGCTACTTTGCTAA-3’ 3. 5’-CCACTCCTCCACCTTTGACA TGCACGCAGGTCAAGATCAGA TTGGCTAC AGCAACAGGGT TAATACGACTCACTATAGCAATGGTACGGTACTTCC AAG CTAACCCTCATCTGCGCGCTCC CAAAAGTGCACGCTACTTTGCTAA-3’
Taqman probe	FAM-TGTGTCTGCGGCGTTTTATCA-TAMRA; FAM-TGTGTCTGATAGTAAGTGCCA-TAMRA; FAM-TGCACGCAGGTCAAGATCAGA-TAMRA
Forward primers 201	5′ -CCACTCCTCCACCTTTGAC-3′
Reverse primers 214	5′ -ACCCTGTTGCTGTAGCCA-3′

Table 1. DNA sequences of random library， aptamer， DNA template tethered aptamers, Taqman probes and primers.

Target Protein	Ct	Given Conc. (copies/ml)	Calc Conc. (copies/ml)	% Var.	Mean (copies/ml)
Standard 1	13.4	1,000,000,000	1,067,001,056	6.70%	
Standard 2	16.89	100,000,000	88,292,735	11.70%	
Standard 3	19.89	10,000,000	10,277,836	2.80%	
Standard 4	23.07	1,000,000	1,061,115	6.10%	
Standard 5	26.41	100,000	97,330	2.70%	
IgG1	19.16		17,317,180		
IgG1	19.11		17,962,663		17,732,234
IgG1	19.12		17,916,859		
IgG2a	18.75		23,207,351		
IgG2a	18.63		25,398,322		23,222,389
IgG2a	18.89		21,061,495		
anti-HBV IgG	19.35		15,189,941		
anti-HBV IgG	17.53		55,713,691		31,188,162
anti-HBV IgG	18.79		22,660,855		
albumin	29.95		7,732		
albumin	31.82		2,036		3,256
albumin			0		
fat free powder milk			0		
fat free powder milk			0		0
fat free powder milk			0		
egg white protein	30.52		5,156		
egg white protein	29.88		8,154		7,545
egg white protein	29.69		9,324		
No protein added	30.05				

Table 2. Summary of Ct values of real-time quantitative A-PCR assay using both specific and non specific proteins as aptamer targets. The detectable copies of specific protein target per ml are also concluded. RT-PCRs were carried out after sequential incubation of targets and ds template DNA tethered aptamer in microwells.

An Approach to Multiplexing an Immunosorbent Assay with Antibody−Oligonucleotide Conjugates

Ki-Cheol Han, Dae-Ro Ahn,* and Eun Gyeong Yang*

Life Sciences Research Division, Korea Institute of Science and Technology, P.O. Box 131, Cheongryang, Seoul 130-650, Republic of Korea. Received March 23, 2010; Revised Manuscript Received October 20, 2010

Early detection of cancer biomarkers provides clinically valuable information. While the conventional enzyme-linked immunosorbent assay (ELISA) has been routinely used for individual cancer markers, methods for simultaneous determination of multiple markers within a single sample are still in demand. Here, we present a novel oligonucleotide-linked immunosorbent assay (OLISA) with a multiplexing capability on the same microwell plate-based system as in ELISA. Employing a DNA oligonucleotide that is covalently conjugated to the detection antibody and a complementary RNA oligonucleotide which is appended with a fluorophore and a quencher, degradation of the RNA in the DNA-RNA duplex by RNase H is exploited for fluorescent signal generation. Iterative cycles of DNA-RNA duplexation and subsequent degradation of the RNA in the duplex by RNase H further lead to amplification of the detection signal in OLISA. Moreover, the use of antibody−oligonucleotide conjugates enables multiplexing of OLISA, which is successfully demonstrated by tethering DNA molecules to detection antibodies and by performing assays for three common cancer markers including α-fetoprotein, prostate-specific antigen, and carcinoembryonic antigen. With the simple procedure and reliable detection performance, the developed multiplex OLISA has a wide potential for use in analysis of a panel of biomarkers in clinical diagnostics.

INTRODUCTION

Enzyme-linked immunosorbent assay (ELISA) is the most widely used analytical technology to detect biologically informative molecules for disease diagnosis, as well as for biomedical research. The sandwich ELISA, in particular, permits accurate and sensitive detection of an antigen of interest, thereby providing highly quantitative and reproducible results in clinical laboratories. However, the traditional sandwich ELISA is unsuitable for simultaneous determination of multiple targets in a single assay.

In efforts made to remedy such drawbacks, a variety of platforms have been devised to meet the increased needs of multiplex immunoassays especially from the clinical area. Sticking to the principle of the sandwich ELISA, Q-Plex multiplex ELISA from Quansys Biosciences detects chemiluminescence signals from 96-well microplates in which each well contains multiple spots coated with specific capture antibodies (cAbs). On the other hand, flow cytometric multiplex assays such as the cytometric bead array (CBA) system from BD Biosciences and the multianalyte profiling (xMAP) technology from Luminex have been introduced by use of a proprietary set of beads, which are immobilized with fluorescent detection antibodies (dAbs), and thus readily analyzed by flow cytometry (*1*,*2*). Such multiplex bead assays have been successfully applied for the simultaneous quantitation of multianalytes including cytokines (*3*−*5*) and antibodies (*6*, *7*). In addition, more sophisticated technology developed by Meso Scale Discovery (MSD) has been incorporated into multiplex array kits, which comprise a microplate with electrodes integrated into its bottom and each electric wire coated with specific cAbs. Since the dAbs are conjugated to electrochemiluminescent labels, the assay detects emitted light by stimulation of the labels on the electrodes located in the bottom of microplates. In contrast, nucleic acids have been utilized for multiplex assays as in immuno-PCR coupled with gel electrophoresis (*8*). Multiple DNA-encoded antibody barcode arrays have also been patterned within the channels on a chip for in situ protein measurements (*9*). In improving performance of immunoassays, such exploitation of DNA−antibody conjugates has particularly been gaining more attention since the nucleic acid part presents various signal amplification strategies (*10, 11*). Although some methods require sophisticated instruments or delicately prebuilt array systems, the use of nucleic acids in general permits highly sensitive detection of different proteins across broad dynamic ranges and high-throughput analysis (*10, 11*).

In this study, we have attempted to develop a facile multiplex immunoassay compatible with the conventional sandwich assay in well plate format. Our novel oligonucleotide-linked immunosorbent assay (OLISA) is designed based on a dAb tethered with a DNA by incorporating the concept of RNase H-mediated signal amplification reported previously for an aptamer-based biosensor (*12*). Further, the use of DNA renders multiplexing ability of the assay, and thus, multi-RNA probes that are complementary to DNA sequences conjugated to dAbs and that contain different fluorophore/quencher pairs are utilized to recognize multitarget proteins. Proteins in a sample can be quantified by simply measuring fluorescence intensity at the relevant emission wavelengths of fluorophores, which is demonstrated by performing multiplex OLISA for simultaneous analysis of three cancer biomarkers.

EXPERIMENTAL PROCEDURES

Reagents. Biotinamidohexanoic acid *N*-hydroxysuccinimide ester and human serum were purchased from Sigma-Aldrich (St. Louis, MO, USA) and Streptavidin-HRP was from abcam (UK). *N*-[α-Maleimidoacetoxy]succinimide ester (AMAS), *N*-[ε-

* To whom correspondence should be addressed. Life Sciences Research Division, Korea Institute of Science and Technology, P.O. Box 131, Cheongryang, Seoul 130-650, Republic of Korea. Phone: +82-2-958-5178. Fax: +82-2-958-5909. E-mail addresses: eunyang@kist.re.kr, drahn@kist.re.kr.

10.1021/bc100147a © 2010 American Chemical Society
Published on Web 11/24/2010

Table 1. Sequences of DNA Labels and F-RNA-Q Probes

oligonucleotide	sequence	biomarker
DNA1	5′-AACCACAGTG-3′	AFP
F-RNA1-Q	FAM-5′-CACUGUGGUU-3′-BHQ1	
DNA2	5′-ACTCTATGGG-3′	PSA
F-RNA2-Q	ROX-5′-CCCAUAGAGU-3′-BHQ2	
DNA3	5′-AGCGTTGTAG-3′	CEA
F-RNA3-Q	Cy5−5′-CUACAACGCU-3′-BHQ2	

maleimidocaproyloxy]succinimide ester (EMCS), succinimidyl-6-[(β-maleimidopropionamido)hexanoate] (SMPH), and succinimidyl-4-[*N*-maleimidomethyl]cyclohexane-1-carboxy-[6-amidocaproate] (LC-SMCC) were obtained from Pierce (Rockford, IL, USA). Anti-α-fetoprotein (AFP) and anti-prostate-specific antigen (PSA) antibodies were from Fitzgerald (Acton, MA, USA), and anti-carcinoembryonic antigen (CEA) antibodies from Biodesign (Saco, Maine, USA). TMB substrate solution and stop solution were purchased from GenDepot (Barker, TX, USA), Protector RNase Inhibitor (PRI) was from Roche (Mannheim, Germany), and RNase H was from Takara (Japan). All other reagents were of highest grade commercially available.

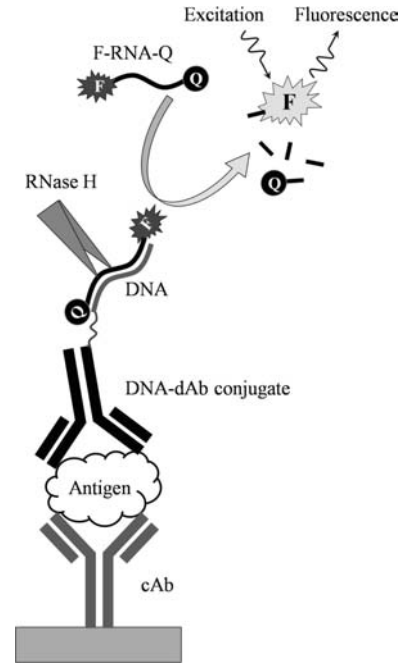
Preparation of Biotinylated dAbs for ELISA. One microliter of 20 mM biotinamidohexanoic acid *N*-hydroxysuccinimide ester was mixed with 50 μL of 2.5 mg/mL dAb and incubated for 30 min at room temperature. The biotinylated antibody was then purified using Amicon Ultra-15 centrifugal filter units (MWCO = 50 000, Millipore, Billerica, MA, USA).

ELISA Procedure. Each well of a transparent 96-well plate (Greiner bio-one, Germany) was coated with 100 μL of cAbs (2 μg/mL) by incubation overnight at 4 °C, followed by washes with PBS (3 × 300 μL). The cAb-coated wells were blocked with 200 μL of Blocking Buffer (3% BSA in PBS), incubated for 1 h at room temperature, and rinsed with PBST (0.05% Tween-20 in PBS, 3 × 300 μL). Protein solutions of varying concentrations (0, 0.625, 1.25, 2.5, 5, and 10 ng/mL) in 100 μL of Assay Buffer (1% BSA in PBST) were added to the wells, followed by incubation for 1 h at room temperature. The plate was then washed with PBST (3 × 300 μL) before addition of the biotinylated dAbs (100 μL, 3 μg/mL in Assay Buffer) and incubation for 1 h at room temperature. After rinsing with PBST (3 × 300 μL), streptavidin-HRP (2 μg/mL) in Assay Buffer (100 μL) was added and incubated for 1 h at room temperature. The plate was further washed with PBST (3 × 300 μL), and each well was incubated in TMB substrate solution (100 μL) for 20 min at 25 °C. After addition of TMB stop solution (100 μL) to the each well, optical density at 450 nm was immediately measured by means of a 96-well microplate reader (SpectraMax Plus, Molecular Devices, Sunnyvale, CA, USA).

Design and Preparation of DNA Labels and RNA Probes. DNA1, **DNA2**, and **DNA3** for conjugation with dAbs were designed to exhibit specificity and 50% of G + C content with the aid of *Vector NTI* software (Invitrogen, Carlsbad, CA, USA), and modified with a thiol group at the 5′-end for conjugation to dAbs. RNA probes whose sequences are complementary to the corresponding DNA labels were designed to contain fluorophores and their matching quenchers. All DNA labels and RNA probes whose sequences are presented in Table 1 were synthesized by Integrated DNA Technologies (Coralville, IA, USA).

Preparation of DNA-dAb Conjugates. DNA-dAb conjugates were prepared as shown in Scheme 2. A dAb (2.5 mg/mL) was incubated with AMAS, EMCS, SMPH, or LC-SMCC (2 mM) in PBS (50 μL) for 30 min at room temperature. After removal of unreacted linker molecules by using Amicon Ultra-15 centrifugal filter units (MWCO = 50 000), the solution of linker-modified dAb was added to the thiol-modified DNA (500 μM) in PBS (50 μL) and incubated for 30 min at room temperature and purified by using Amicon Ultra-15 centrifugal filter units (MWCO = 50 000).

Scheme 1. Working Principle of OLISA



OLISA Procedure. Black 96-well microplates (Greiner bio-one, Germany) were coated with cAbs (2 μg/mL) in PBS (100 μL/well) by incubation overnight at 4 °C. Each well was then washed with PBS (3 × 300 μL), blocked with Blocking Buffer (200 μL), and incubated for 1 h at room temperature. After rinses with PBST (3 × 300 μL), protein solutions of varying concentrations (0, 0.625, 1.25, 2.5, 5, and 10 ng/mL) in 100 μL of Assay Buffer were added to the wells, followed by incubation for 1 h at room temperature. The plate was washed with PBST (3 × 300 μL) before addition of DNA-dAb conjugates (100 μL, 3 μg/mL in Assay Buffer) and incubated for 1 h at room temperature. After rinsing with PBST (3 × 300 μL), the RNase H reaction solution (100 μL) containing 200 nM F-RNA-Q probe, 0.4 U of PRI, and 20 U of RNase H in RNase H buffer (40 mM Tris-HCl, 4 mM $MgCl_2$, 1 mM DTT, 0.003% BSA, pH 7.7) was added and incubated for 3 h at 25 °C. The reaction was then stopped by adding 10 mM EDTA (200 μL) and fluorescence intensities were measured by Appliskan (Thermoscientific, Waltham, MA, USA) with excitation/emission filter sets of 485/535 nm, 544/589 nm, and 633/700 nm for FAM, ROX, and Cy5, respectively. All assays were performed in duplicate.

Multiplex OLISA Procedure. Black 96-well microplates were coated with a mixture of cAbs for AFP, PSA, and CEA (2 μg/mL) in PBS (100 μL). Assays were carried out using mixed solutions of three marker proteins (AFP, PSA, and CEA) of varying concentrations, a mixed solution of three DNA-dAb conjugates (**DNA1**-dAb_{AFP}, **DNA2**-dAb_{PSA}, and**DNA3**-dAb_{CEA}) specific to the markers, and a mixed solution of three RNA probes (**F-RNA1-Q**, **F-RNA2-Q**, and **F-RNA3-Q**) in the same manner as described in the OLISA for a single analyte.

RESULTS

Our OLISA is based on the sandwich immunoassay, which can be performed on a conventional 96-well plate format. In terms of working principle (Scheme 1), OLISA is distinguished from the conventional ELISA in three aspects: (1) DNA, instead of protein, is conjugated with the dAb; (2) RNase H, instead of horseradish peroxidase (HRP), performs the enzymatic reaction; and (3) fluorescence signal, instead of chemiluminescence signal, is amplified as a result of antigen detection. The antigen bound

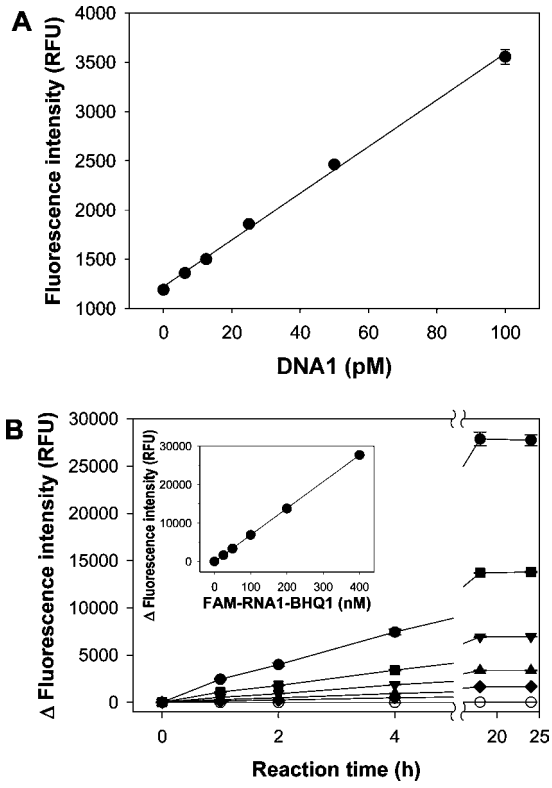


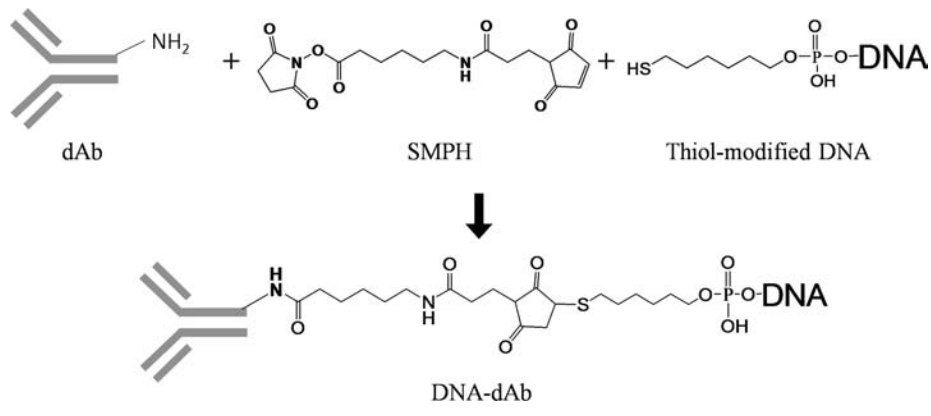
Figure 1. RNase H-mediated fluorescence signal amplification. (A) Mixtures containing **F-RNA1-Q** (200 nM) and RNase H (0.6 U) in RNase H buffer were incubated with varying concentrations of **DNA1** for 1 h at 25 °C, followed by fluorescence measurements. (B) Mixtures containing **DNA1** (300 pM) and RNase H (0.6 U) in RNase H buffer were incubated with varying concentrations of **F-RNA1-Q** (○, 0; ♦, 25; ▲, 50; ▼, 100; □, 200; ●, 400 nM) at 25 °C, followed by fluorescence measurements. The inset graph is a plot of the final fluorescence value as a function of the concentration of the RNA probe.

to the cAb on the plate is recognized by the dAb tethered with DNA, which then hybridizes with the complementary RNA probe, F-RNA-Q, which is appended with a fluorophore (F) at the 5′-end and a quencher (Q) at the 3′-end, respectively. The RNA in the RNA/DNA duplex, whose fluorescence is quenched by the quencher in proximity, is degraded with RNase H; this results in fluorescence recovery due to separation of the fluorophore from the quencher. Since F-RNA-Q degradation by RNase H leaves the DNA undamaged and thus available for duplex reformation with another F-RNA-Q molecule, the cycle of RNA/DNA duplexation followed by RNase H digestion leads to fluorescence signal amplification.

Since the signal amplification is directly dependent upon degradation of the RNA probe by RNase H, we first tested the level of fluorescence signal generation from **F-RNA1-Q** at a constant amount in the presence of increasing concentrations of **DNA1**. As shown in Figure 1A, the increased fluorescence intensity led by the reaction was linearly proportional to the concentration of **DNA1**. At a given reaction time, the limit of detection was as low as 5.4 pM. To confirm that the fluorescence signal is amplified by iterative cycles of RNA/DNA hybridization and subsequent degradation by RNase H, we measured fluorescence changes with varying concentrations **of F-RNA1-Q** in the presence of a small amount of **DNA1**. As predicted from the assay design, fluorescence signal increased with reaction time reached saturating values that were proportional to the concentration of the RNA probe (Figure 1B). We further reconfirmed signal amplification via iterative cycles of RNA/DNA duplexation by measuring the maximal fluorescence value upon degradation of the RNA probe by RNase, which was closely similar to the maximal signal obtained by OLISA (data not shown). To integrate such RNase H-mediated signal amplification into an immunoassay, we chose a well-known cancer marker AFP, and conjugated DNA to dAb_{AFP} (Scheme 2) using various cross-linker molecules including AMAS, EMCS, SMPH, and LC-SMCC, all of which contain an amine-reactive moiety at one end and a thiol-reactive moiety at the other end, respectively, but differ in their length. The conjugation reaction yielded products of approximately 0.9 **DNA1** per dAb of AFP (dAb_{AFP}) as determined based on the ratio of absorbance values at 260 and 280 nm. When these DNA-dAb conjugates mixed with **F-RNA1-Q** were subjected to RNase H treatment, similar increases in fluorescence intensity were observed irrespective of the linkers (data not shown). Therefore, the conjugate synthesized using SMPH was chosen to further evaluate the effects of the linker length. The linker length was varied by inserting thymidine-base linkers of T_{10}, T_{20}, and T_{30} between **DNA1** and SMPH, and fluorescence changes were monitored after incubation with **F-RNA1-Q** in the presence of RNase H. Interestingly, the longer the linker was inserted, the less fluorescence signal was generated by the RNase H reaction (Figure 2). Although the mechanism of such observations is not apparently clear, the linkers between DNA and antibody might hamper the formation of the duplex between DNA and the RNA probe.

On the basis of these results, the DNA-antibody conjugated directly with SMPH was utilized for setting up a sandwich immunoassay. The initial trial employed a conventional sandwich assay in well plate format for AFP on a 96-well plate precoated with cAb_{APF}, but establishment of a standard curve was unsuccessful due to unexpectedly high background. In attempts to resolve such background issue, we found that the

Scheme 2. Synthesis of DNA-dAb Conjugates: An Example with a Cross-Linker SMPH Is Shown



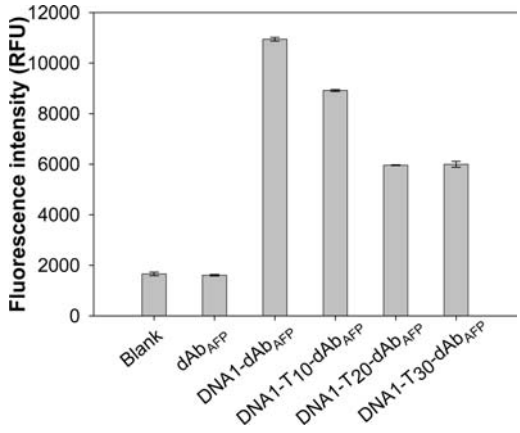


Figure 2. Effect of thymidine linkers between DNA and dAb on the RNase H reaction. Fluorescence intensities were measured for the mixtures containing **F-RNA1-Q** (200 nM) and RNase H (6.0 U) in RNase H buffer in the absence or presence of dAb$_{AFP}$, **DNA1**-dAb$_{AFP}$, **DNA1**-T$_{10}$-dAb$_{AFP}$, **DNA1**-T$_{20}$-dAb$_{AFP}$, or **DNA1**-T$_{30}$-dAb$_{AFP}$ (500 pM) after incubation for 1 h at 25 °C.

fluorescent signal increased considerably even in the absence of RNase H and **DNA1**-dAb$_{APF}$ when **F-RNA1-Q** alone was added to the well precoated with cAb$_{AFP}$. Since cAbs were purified from serum and thus its solution might still be contaminated with traces of ribonucleases, such a possibility was examined by inclusion of an RNase inhibitor PRI that is known to inhibit RNase A, RNase B, and RNase T2. When **F-RNA1-Q** was added to the cAb$_{AFP}$-coated wells in the presence of PRI, fluorescence signals generated by ribonuclease activity were diminished to the background level, and a small amount of PRI (0.125 U/well) was enough to inhibit the nonspecific degradation of the **F-RNA1-Q** probe (Figure 3A), confirming that the increased intensity was indeed due to ribonucleases remaining in antibody solutions. On the other hand, the RNase H reaction was not affected by PRI as demonstrated by fluorescence measurements of solutions containing **DNA1** and **F-RNA1-Q** (Figure 3B).

Using the assay buffer supplemented with PRI, we next performed sandwich immunoassays based on OLISA. As shown in Figure 4A (open circles), the fluorescence intensities at 535 nm generated as **F-RNA1-Q** was degraded in OLISA linearly increased with increasing concentrations of AFP. In addition, we analyzed two other cancer markers, PSA and CEA, using the same protocol. Microwell plates coated with cAb$_{PSA}$ or cAb$_{CEA}$ were prepared, and the corresponding detection antibodies, dAb$_{PSA}$ or dAb$_{CEA}$ conjugated with **DNA2** and **DNA3** (Table 1), were applied to detect PSA or CEA, respectively. As expected, fluorescence increases at 589 and 700 nm were found

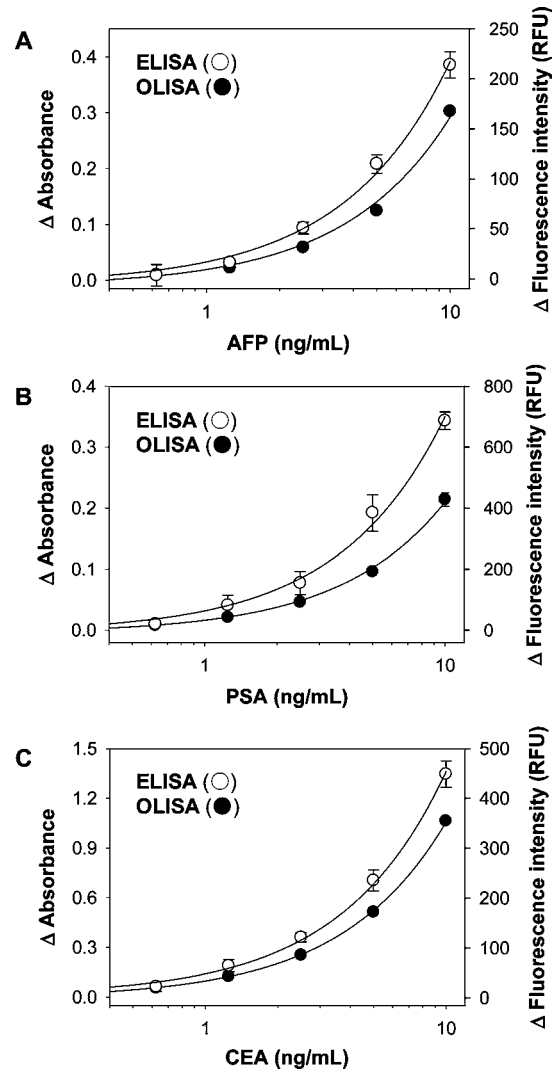


Figure 4. Comparison of OLISA with ELISA for (A) AFP, (B) PSA, and (C) CEA. ELISA results were obtained in changes of absorbance (○) while OLISA results were in changes of fluorescence intensity (●).

to be linearly proportional to the concentrations of PSA (Figure 4B, open circles) and CEA (Figure 4C, open circles), demonstrating general applicability of the developed assay to various analytes. To evaluate the performance of OLISA in comparison to ELISA, we also set up ELISA assays in parallel in which streptavidin-conjugated HRP was used to detect the bound biotinylated dAbs for the three markers. When absorbance changes in ELISA were compared with fluorescence changes

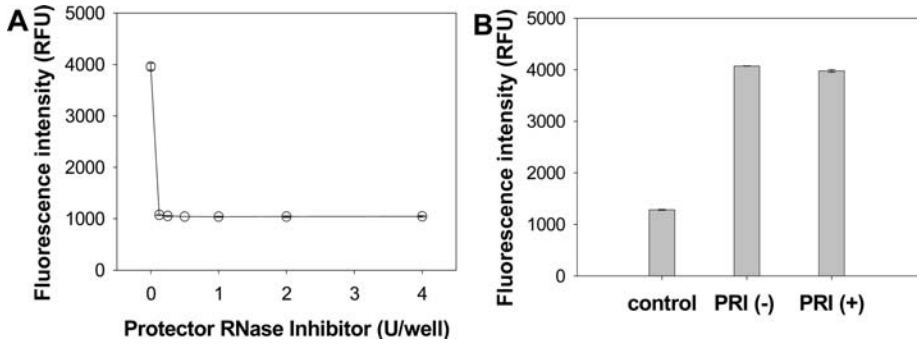


Figure 3. Blockade of nonspecific degradation of RNA probes by PRI treatment. (A) **F-RNA1-Q** (200 nM) in RNase H buffer was incubated with increasing concentrations of PRI on cAb$_{AFP}$-coated wells at 25 °C for 1 h, followed by fluorescence measurements. (B) Mixtures containing **DNA1** (500 pM) and **F-RNA1-Q** (200 nM) in RNase H buffer were incubated with or without PRI (2 U) in the presence of RNase H (6.0 U) for 1 h at 25 °C, followed by fluorescence measurements. A control sample was measured in the absence of RNase H.

Table 2. Detection Limits of ELISA and OLISA for Cancer Biomarkers

	limit of detection (ng/mL)		
biomarker	ELISA	single OLSIA	multiplex OLISA
AFP	1.05	1.07	0.74
PSA	0.60	0.99	0.43
CEA	0.48	1.03	1.29

in OLISA for these markers (Figure 4), the signal increases linearly depending on the concentration of the markers in OLISA appears as reliable as those in ELISA. To assess sensitivity of OLISA and ELISA, we also determined the limit of detection (LOD) for each marker by interpolating each concentration curve with the average value of the blank plus 3 times the standard deviation of the blank. The LOD values calculated for both ELISA and OLISA are summarized in Table 2. For all three cancer markers, OLISA showed sensitivity comparable to ELISA, and the LOD values in OLISA were estimated about 1 ng/mL for all three cancer markers. More specifically, AFP could be analyzed by OLISA with almost the same sensitivity as by ELISA, while ELISA assays for CEA and PSA were slightly more sensitive than OLISA assays.

After establishing single OLISA for the markers with successful performance, we finally attempted to quantitate all three markers in a single aliquot of sample by multiplex OLISA. Since all three markers need to be measured simultaneously, analytical specificity for each is imperative. Therefore, the possibility of cross duplexation between DNA labels and RNA probes was examined by performing RNase H reactions in solutions containing one of three DNA sequences in the presence of all three RNA probes. As shown in Figure 5, fluorescence signals were amplified only at the emission wavelength of the fluorophore attached to the complementary RNA probe, proving that each DNA binds to its complementary RNA but not to others. We also tested cross-reactivity of the detection antibodies. After addition of each biomarker onto the microwells plated with the cAb, followed by incubation with a mixture of three DNA-dAbs, a mixture of the RNA probes was added along with RNase H to generate fluorescence signal and found that the fluorescence signal increased in an antigen-concentration-dependent fashion only at the emission wavelength of the fluorophore corresponding to the biomarker present in the assay (Figure 6). As this result indicated that false positive signals would not be observed in a multiplex format, a mixture of cAb_{AFP}, cAb_{PSA}, and cAb_{CEA} was used to coat the microwell plate for multiplex OLISA. After a mixture of all three cancer markers was added to the wells of the plate, a mixture of three DNA-dAbs was allowed to bind to the corresponding proteins as illustrated in Scheme 3. When fluorescence measurements at 535, 589, and 700 nm were made to identify and quantitate cancer markers in the mixture, amplifications of fluorescence with increasing concentrations of AFP, PSA, and CEA exhibited linear curves at corresponding wavelengths (Figure 7). The LODs for AFP, PSA, and CEA in this multiplex OLISA were determined as 0.74, 1.06, and 1.29 ng/mL, respectively, which are comparable to the values obtained from the single assays (Table 2).

To further evaluate analytical performance of the multiplex OLISA, precision and accuracy were determined by preparing 35 serum samples spiked with a mixture of 3 cancer markers at 20, 40, and 80 ng/mL in human serum, followed by analyses via the developed multiplex OLISA and calculations of CV and recovery. As summarized in Table 3, analysis at low concentrations resulted in less precise data as presented by high %CV values, which were generally observed in other previous immunoassay formats (*13*). AFP was more precisely detected than the other two markers, showing the lowest %CV values at

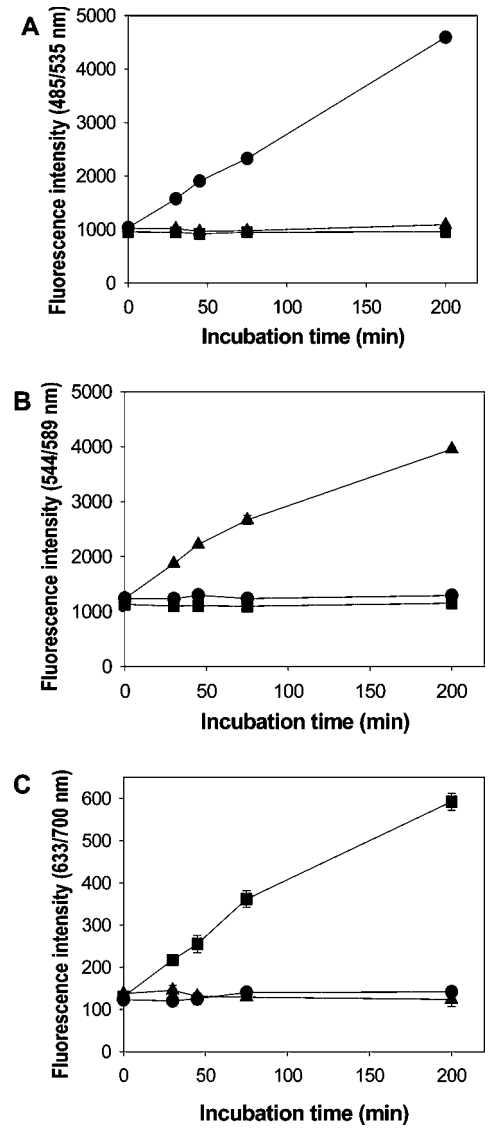


Figure 5. Specific degradation of RNA probes. RNA probe mixtures containing **F-RNA1-Q**, **F-RNA2-Q**, and **F-RNA3-Q** at 200 nM each in RNase H buffer were mixed with 500 pM of (A) **DNA1**, (B) **DNA2**, or (C) **DNA3** in the presence of RNase H (6 U), and incubated at 25 °C, followed by fluorescence measurements. Filled circles, triangles, and squares denote the fluorescence intensities obtained at 535, 589, and 700 nm upon excitation at 485, 544, and 633 nm, respectively.

all concentrations. While the level of precision in multiplex OLISA did not reach that routinely obtained by ELISA (less than 10%), the precision obtained in a multiplex format could be regarded as acceptable for clinical applications. Accuracy values of multiplex OLISA as expressed in %Recovery ranged from 91% to 116%, which were also not inferior to those shown by previously developed multiplex immunoassays (*13*).

DISCUSSION

Recent advances in cancer proteomics and other related research have promoted identification of tumor biomarkers. Thus, there is an urgent need to utilize a panel of biomarkers for detecting the presence of cancer accurately and faithfully. Although ELISA is a highly quantitative and reproducible method, it is limited to measurement of one analyte per assay in general. To enable the present sandwich assay in well plate format to perform multiplexed assays, a novel detection strategy was devised in the present study for quantifying multiple protein biomarkers simultaneously. Our new assay named OLISA

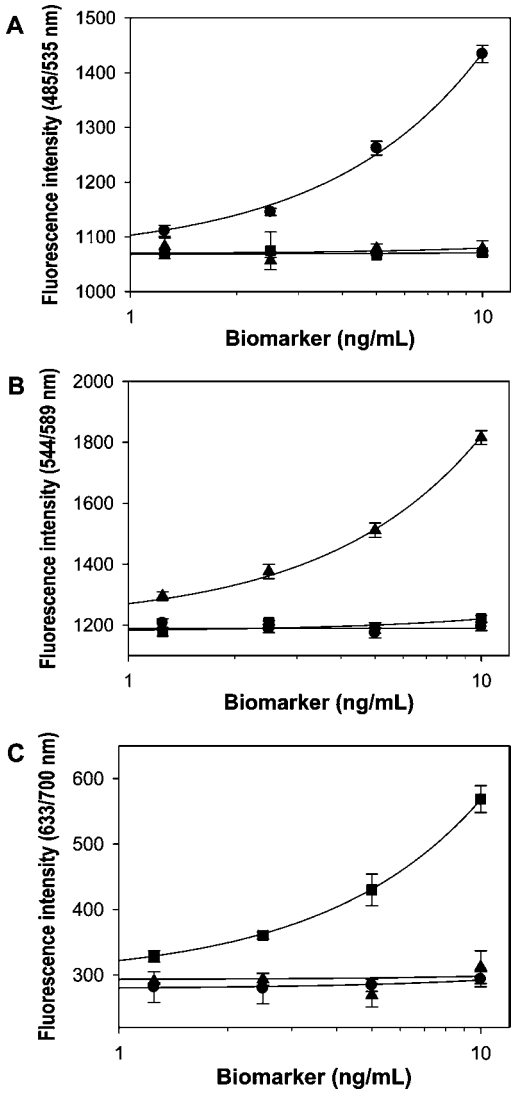
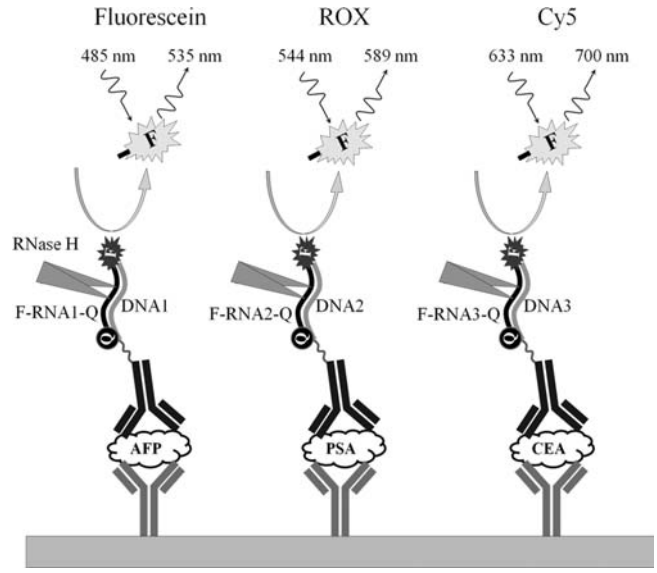


Figure 6. Specific fluorescence signal generation for biomarkers. Assays were performed as described in Experimental Procedures using a mixture of three DNA-dAb conjugates, followed by RNase H reaction in the presence of a mixture of **F-RNA1-Q**, **F-RNA2-Q**, and **F-RNA-3-Q** for (A) AFP, (B) PSA, or (C) CEA. Filled circles, triangles, and squares denote the fluorescence intensities obtained at 535, 589, and 700 nm upon excitation at 485, 544, and 633 nm, respectively.

employed DNA-conjugated dAbs, complementary RNA probes, and RNase H, which was optimized and validated using individual cancer biomarkers. In addition, simultaneous detection of three biomarkers was established to demonstrate the feasibility of the developed multiplex OLISA, which was facilitated by uniquely designed DNA labels that discriminate multiple analytes as intermediators of signal amplification.

Similarly to other multiplex immunoassays, multiplex OLISA is critically dependent on specificities of antibodies (*14*). Accordingly, a set of biomarkers including AFP, PSA, and CEA was chosen to demonstrate the feasibility of triplex OLISA since their monoclonal antibody pairs for the sandwich assays show no cross-reactivity to each other. As a result, successful performance of triplex OLISA has been attained, suggesting that OLISA could be applicable to reliable simultaneous detection of cancer biomarkers. The candidates include CA15-3 and CEA for breast cancer (*15*) or CA125, apolipoprotein, and α-chain of haptoglobin for ovarian cancer (*16, 17*) if appropriate antibodies are available. Because only a limited number of fluorophores can be selected to prevent spectral interference arising from excitation of a fluorophore by emission of another

Scheme 3. Design of Multiplex OLISA for Three Cancer Markers



fluorophore, less than 10 analytes can be practically assayed on multiplex OLISA. For the level of multiplexity, commercially available multiplex technologies such as Luminex xMAP technology and MSD system allow detection of up to 100 analytes in one sample. Despite its limited multiplexing capacity, our OLISA would be useful for clinical diagnosis based on a few biomarkers, since the cAb-coated microplates for multiplex OLISA can be readily prepared by simply mixing and incubating reagents similarly as for ELISA, and the operational procedures are analogous to those of ELISA.

Sensitivity, precision, accuracy, and linearity for OLISA have been characterized in a pre-study validation, which is mandatory before routine application of new analytical methods in order to ensure its fitness for purpose (*18*). AFP, PSA, and CEA are present in normal blood at less than 10, 4, and 5 ng/mL, respectively, whereas high levels of these markers are indicators

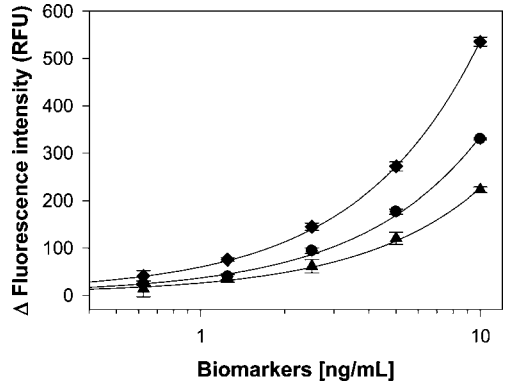


Figure 7. Multiplex OLISA for simultaneous detection of three cancer markers. Filled circles, triangles, and squares denote the data obtained for AFP, PSA, and CEA, respectively.

Table 3. Precision (%CV) and Accuracy (%Recovery) of Multiplex OLISA

	% CV/nominal concentration			% recovery/nominal concentration		
biomarker	20 ng/mL	40 ng/mL	80 ng/mL	20 ng/mL	40 ng/mL	80 ng/mL
AFP	7.9	3.1	3.3	91	98	96
PSA	8.7	12.8	7.0	113	105	99
CEA	20.8	16.8	11.6	116	96	102

of hepatocellular carcinoma, prostate cancer, and colorectal cancer, respectively, which are currently determined by ELISA as clinical tests. The LODs in multiplex OLISA as well as in OLISA for analysis of single markers are sensitive enough to cover the concentration ranges of the markers in clinical blood samples even after dilution. From the analyses of spiked serum samples, multiplex OLISA has been confirmed to satisfy the acceptance criteria of 20% for accuracy and precision to be adopted for immunoassay applications (*18*). Considering that other methods based on DNA−antibody conjugates including rolling circle amplification and immuno-PCR provide more sensitive immunoassays (*10, 11*), the sensitivity of OLISA needs to be improved by use of branched DNA or dendrimer molecules (*19, 20*) or by incorporating a rolling circle amplification reaction followed by RNase H reaction (*21*). Currently, we are working on modifying OLISA with a desire to create an ultrasensitive multiplex immunoassay.

In conclusion, we have devised an ELISA-based OLISA and demonstrated that OLISA is a convenient method to simultaneously detect multiple biomarkers in serum. OLISA exhibits comparable LODs to ELISA and reliable analytical performance. Moreover, OLISA could be multiplexed for simultaneous detection of three cancer markers in a sample solution with acceptable levels of precision and accuracy. Therefore, the developed multiplex OLISA would be well-suited for integrated analysis of individual ELISA-based methods for a few biomarkers.

ACKNOWLEDGMENT

This study was supported by the Functional Proteomics Research Center of the 21st Century Frontier Research Program and by the Pioneer Research Center Program through the National Research Foundation of Korea funded by the Ministry of Education, Science, and Technology.

LITERATURE CITED

(1) Morgan, E., Varro, R., Sepulveda, H., Ember, J. A., Apgar, J., Wilson, J., Lowe, L., Chen, R., Shivraj, L., Agadir, A., Campos, R., Ernst, D., and Gaur, A. (2004) Cytometric bead array: a multiplexed assay platform with applications in various areas of biology. *Clin. Immunol. 110*, 252–266.

(2) Fulton, R. J., McDade, R. L., Smith, P. L., Kienker, L. J., and Kettman, J. R., Jr. (1997) Advanced multiplexed analysis with the FlowMetrix system. *Clin. Chem. 43*, 1749–1756.

(3) Chen, R., Lowe, L., Wilson, J. D., Crowther, E., Tzeggai, K., Bishop, J. E., and Varro, R. (1999) Simultaneous quantification of six human cytokines in a single sample using microparticle-based flow cytometric technology. *Clin. Chem. 45*, 1693–1694.

(4) Oliver, K. G., Kettman, J. R., and Fulton, R. J. (1998) Multiplexed analysis of human cytokines by use of the FlowMetrix system. *Clin. Chem. 44*, 2057–2060.

(5) Carson, R. T., and Vignali, D. A. (1999) Simultaneous quantitation of 15 cytokines using a multiplexed flow cytometric assay. *J. Immunol. Methods 227*, 41–52.

(6) Pei, R., Lee, J., Chen, T., Rojo, S., and Terasaki, P. I. (1999) Flow cytometric detection of HLA antibodies using a spectrum of microbeads. *Hum. Immunol. 60*, 1293–1302.

(7) Lal, G., Balmer, P., Joseph, H., Dawson, M., and Borrow, R. (2004) Development and evaluation of a tetraplex flow cytometric assay for quantitation of serum antibodies to Neisseria meningitidis serogroups A, C, Y, and W-135. *Clin. Diagn. Lab. Immunol. 11*, 272–279.

(8) Hendrickson, E. R., Truby, T. M., Joerger, R. D., Majarian, W. R., and Ebersole, R. C. (1995) High sensitivity multianalyte immunoassay using covalent DNA-labeled antibodies and polymerase chain reaction. *Nucleic Acids Res. 23*, 522–529.

(9) Fan, R., Vermesh, O., Srivastava, A., Yen, B. K., Qin, L., Ahmad, H., Kwong, G. A., Liu, C. C., Gould, J., Hood, L., and Heath, J. R. (2008) Integrated barcode chips for rapid, multiplexed analysis of proteins in microliter quantities of blood. *Nat. Biotechnol. 26*, 1373–1378.

(10) Niemeyer, C. M. (2010) Semisynthetic DNA-protein conjugates for biosensing and nanofabrication. *Angew. Chem., Int. Ed. Engl. 49*, 1200–1216.

(11) Adler, M., Wacker, R., and Niemeyer, C. M. (2008) Sensitivity by combination: immuno-PCR and related technologies. *Analyst 133*, 702–718.

(12) Ahn, D. R., and Yang, E. G. (2007) An RNase H-assisted fluorescent biosensor for aptamers. *ChemBioChem 8*, 1347–1350.

(13) Ray, C. A., Bowsher, R. R., Smith, W. C., Devanarayan, V., Willey, M. B., Brandt, J. T., and Dean, R. A. (2005) Development, validation, and implementation of a multiplex immunoassay for the simultaneous determination of five cytokines in human serum. *J. Pharm. Biomed. Anal. 36*, 1037–1044.

(14) Leng, S. X., McElhaney, J. E., Walston, J. D., Xie, D., Fedarko, N. S., and Kuchel, G. A. (2008) ELISA and multiplex technologies for cytokine measurement in inflammation and aging research. *J. Gerontol., A: Biol. Sci. Med. Sci. 63*, 879–884.

(15) Coveney, E. C., Geraghty, J. G., Sherry, F., McDermott, E. W., Fennelly, J. J., O'Higgins, N. J., and Duffy, M. J. (1995) The clinical value of CEA and CA 15−3 in breast cancer management. *Int. J. Biol. Markers 10*, 35–41.

(16) Ye, B., Cramer, D. W., Skates, S. J., Gygi, S. P., Pratomo, V., Fu, L., Horick, N. K., Licklider, L. J., Schorge, J. O., Berkowitz, R. S., and Mok, S. C. (2003) Haptoglobin-alpha subunit as potential serum biomarker in ovarian cancer: identification and characterization using proteomic profiling and mass spectrometry. *Clin. Cancer Res. 9*, 2904–2911.

(17) Zhang, Z., Bast, R. C., Jr., Yu, Y., Li, J., Sokoll, L. J., Rai, A. J., Rosenzweig, J. M., Cameron, B., Wang, Y. Y., Meng, X. Y., Berchuck, A., Van Haaften-Day, C., Hacker, N. F., de Bruijn, H. W., van der Zee, A. G., Jacobs, I. J., Fung, E. T., and Chan, D. W. (2004) Three biomarkers identified from serum proteomic analysis for the detection of early stage ovarian cancer. *Cancer Res. 64*, 5882–5890.

(18) Findlay, J. W., Smith, W. C., Lee, J. W., Nordblom, G. D., Das, I., DeSilva, B. S., Khan, M. N., and Bowsher, R. R. (2000) Validation of immunoassays for bioanalysis: a pharmaceutical industry perspective. *J. Pharm. Biomed. Anal. 21*, 1249–1273.

(19) Collins, M. L., Irvine, B., Tyner, D., Fine, E., Zayati, C., Chang, C., Horn, T., Ahle, D., Detmer, J., Shen, L. P., Kolberg, J., Bushnell, S., Urdea, M. S., and Ho, D. D. (1997) A branched DNA signal amplification assay for quantification of nucleic acid targets below 100 molecules/ml. *Nucleic Acids Res. 25*, 2979–2984.

(20) Nilsen, T. W., Grayzel, J., and Prensky, W. (1997) Dendritic nucleic acid structures. *J. Theor. Biol. 187*, 273–284.

(21) Schweitzer, B., Roberts, S., Grimwade, B., Shao, W., Wang, M., Fu, Q., Shu, Q., Laroche, I., Zhou, Z., Tchernev, V. T., Christiansen, J., Velleca, M., and Kingsmore, S. F. (2002) Multiplexed protein profiling on microarrays by rolling-circle amplification. *Nat. Biotechnol. 20*, 359–365.

BC100147A

Mixed Stimuli-Responsive Magnetic and Gold Nanoparticle System for Rapid Purification, Enrichment, and Detection of Biomarkers

Michael A. Nash, Paul Yager, Allan S. Hoffman, and Patrick S. Stayton*

Department of Bioengineering, University of Washington, Seattle, Washington 98195, United States. Received April 23, 2010; Revised Manuscript Received October 5, 2010

A new diagnostic system for the enrichment and detection of protein biomarkers from human plasma is presented. Gold nanoparticles (AuNPs) were surface-modified with a diblock copolymer synthesized using reversible addition−fragmentation chain transfer (RAFT) polymerization. The diblock copolymer contained a thermally responsive poly(*N*-isopropylacrylamide) (pNIPAAm) block, a cationic amine-containing block, and a semi-telechelic PEG_2-biotin end group. When a mixed suspension of 23 nm pNIPAAm-modified AuNPs was heated with pNIPAAm-coated 10 nm iron oxide magnetic nanoparticles (mNPs) in human plasma, the thermally responsive pNIPAAm directed the formation of mixed AuNP/mNP aggregates that could be separated efficiently with a magnet. Model studies showed that this mixed nanoparticle system could efficiently purify and strongly enrich the model biomarker protein streptavidin in spiked human plasma. A 10 ng/mL streptavidin sample was mixed with the biotinylated pNIPAAm-modified AuNPs and magnetically separated in the mixed nanoparticle system with pNIPAAm mNPs. The aggregates were concentrated into a 50-fold smaller fluid volume at room temperature where the gold nanoparticle reagent redissolved with the streptavidin target still bound. The concentrated gold-labeled streptavidin could be subsequently analyzed directly using lateral flow immunochromatography. This rapid capture and enrichment module thus utilizes the mixed stimuli-responsive nanoparticle system to achieve concentration of a gold-labeled biomarker that can be directly analyzed using lateral flow or other rapid diagnostic strategies.

INTRODUCTION

Diagnostic testing is expanding from centralized hospital laboratories to more distributed settings in both the developed and developing worlds. A current dominant point-of-care diagnostic test format is the lateral flow immunoassay (LFIA) (*1*), which relies on capillary wicking of fluids through porous nitrocellulose strips. Such tests typically rely on the specific binding between gold-labeled biomarkers with capture antibodies immobilized at the test line of the solid phase. Current devices possess many desirable features, such as being rapid, inexpensive, portable, and easy to use. However, they suffer from a limitation in sensitivity related to the small sample volume (*2*) that limits the biomarker repertoire to those at relatively higher blood and plasma concentrations (*3*). These limitations have created a need for rapid and simple sample processing strategies for purifying and enriching biomarkers in a form that could then be applied directly to the existing lateral flow tests or other types of newly developed rapid tests.

Magnetic separation and enrichment strategies represent one of the most common methods for biomarker purification and separation. We have recently described a stimuli-responsive magnetic nanoparticle system (*4*, *5*) that circumvents one of the primary limitations of magnetic separations. This nanoparticle system allowed the use of very small magnetic nanoparticles that optimize biomarker binding, while still allowing rapid magnetophoretic separation of thermally aggregated nanoparticle−biomarker complexes. This system was useful for purification and concentration, but additional steps of biomarker release and gold labeling for optimized visual detection would be required in lateral flow or flow-through tests. AuNPs have a long history as optical labels in immunoassay and biodetection (*6*−*13*) due to their large extinction coefficients (>10^9 M^{-1} cm^{-1}) in the visible range and enhanced electric near-fields at the particle surface. While one potential solution to simplifying this system would be to use a stimuli-responsive core−shell Au/mNP system (*14*−*19*), we present here the finding that mixed stimuli-responsive AuNPs and mNPs coaggregate efficiently.

This system thus achieves rapid magnetic separation of the Au-labeled biomarker in a simple mixture of separate stimuli-responsive nanoparticles where each can be optimized independently. Stimuli-responsive polymers such as poly(*N*-isopropylacrylamide) (pNIPAAm) with "smart" phase-transition properties have been shown to enhance the capture/separation capabilities of immunoassays (*20*). The work presented herein shows that the pNIPAAm-mNPs can capture the pNIPAAm-AuNPs through a coaggregation mechanism, so that the thermally triggered and high-efficiency enrichment of the Au-labeled biomarker to be used in lateral flow is achieved in one step. To our knowledge, this is the first time the general strategy of stimuli-responsive phase separations has been applied to synergistically direct coaggregation of nanoparticles with different compositions and functions, i.e., magnetic nanoparticles aggregated with a gold nanoparticle labeling reagent. The coaggregates are large enough to rapidly magnetophorese toward the applied magnet. This strategy for purification and enrichment might also circumvent the high-dose "hook" effect that can occur when excess sample antigen occupies all of the binding sites on the solid phase, preventing the gold-labeled antigen from binding (*21*). This confounds LFIAs, because it results in lower signal strength at high antigen concentrations. Magnetic separation eliminates the high-dose "hook" effect because only antigen molecules bound to a label are separated and applied to the flow strip. Magnetic separation/enrichment of the gold-labeled

* Corresponding author. Patrick S. Stayton, Ph.D., University of Washington, Department of Bioengineering, Box 355061, Seattle, WA 98195, Tel: (206) 685-8148, Fax: (206) 685-8526, E-mail: stayton@u.washington.edu.

10.1021/bc100180q © 2010 American Chemical Society
Published on Web 11/11/2010

biomarkers from larger plasma volumes could therefore not only increase the sensitivity of LFIA, but also eliminate sample-matrix-derived interferences.

EXPERIMENTAL PROCEDURES

Materials and Suppliers. *N*,*N*-Dimethylaminoethylacrylamide (DMAEAm; Monomer, Polymer, & Dajac Laboratories) was twice-distilled through a short path prior to use. NIPAAm (Sigma, 97%) was recrystallized from hexanes prior to use. 2,2-Azobis(2-methylpropionitrile) (AIBN; Aldrich, 98%) was recrystallized from methanol. The RAFT chain transfer agent 4-cyano-4-(dodecylsulfanylthiocarbonyl)sulfanyl pentanoic acid (DCT) was synthesized as described in the literature (*22*). 2-(Dodecylsulfanylthiocarbonylsulfanyl)-2-methylpropionic acid (DMP) was a gift from Noveon. Dioxane (EMD, 99%), dimethylformamide (DMF; EMD, 99.8%), dichloromethane (DCM; EMD, 99.8%), pentane (J. T. Baker, 99%), tetraglyme (Aldrich, 99%), methanol (MeOH; EMD, 99.9%), tetrahydrofuran (THF; Mallinckrodt, 99.8%), *N*,*N*′-dicycohexylcarbodiimide (DCC; Fluka, 99%), *N*-hydroxysuccinimide (NHS; Fluka, 97%), $HAuCl_4$ (Aldrich, 99.99%), $Fe(CO)_5$ (Aldrich, 99.9%), and D-biotin (Aldrich, 99%) were used as received. Cellulose ultrafiltration membranes for AuNP purification were from Millipore (regenerated cellulose, 44.5 mm diameter, NMWL 100 000, cat no. 14422AM), and PD-10 desalting columns were from GE Healthcare. NH_2-PEG_2-biotin, HABA biotin quantitation kit, and dialysis membranes (7 and 20 kDa MWCO) were purchased from Pierce. Streptavidin labeled with Alexafluor 750 (SA-750 streptavidin) was purchased from Invitrogen. Purified rabbit polyclonal anti-streptavidin IgG was purchased from Abcam (product no. Ab6676). 1× phosphate buffered saline packets (1× PBS; 10 mM phosphate, 138 mM NaCl, 2.7 mM KCl, pH 7.4 at 25 °C) were purchased from Sigma. Human plasma in disodium EDTA (Valley Biomedical Inc., product no. HP1051) was centrifuged at 1000 × *g* for 30 min, and filtered through GDX graded syringe filters (Whatman) prior to use. Magnets were NdFeB, 1.27 cm × 0.63 cm, Br max = 12.1 kGauss (Force Field Magnets.com). Nitrocellulose LFIA membranes were Millipore HiFlow Plus 180. Zymed nonspecific membrane blocking solution was purchased from Invitrogen.

Polymer Synthesis. RAFT polymerization was carried out using previously published procedures with slight modification (*4*). A homo-pNIPAAm polymer with a target molecular weight of 15 kDa was polymerized by dissolving in a round-bottom flask 2 g (17.7 mmol) of NIPAAm, 54 mg (0.134 mmol) of DCT, and 2.2 mg (13.4 μmol) of AIBN in 4 g *p*-dioxane. The flask was purged with N_2 for 30 min and heated at 60 °C for 12 h, followed by precipitation into pentane. The product was dried under vacuum, dialyzed against DI water at 4 °C, and freeze−dried. A 5 kDa homo-pNIPAAm for use in mNP synthesis was prepared by polymerization in a round-bottom flask containing 2 g (17.7 mmol) of NIPAAm, 143.3 mg (0.4 mmol) of DMP, 6.66 mg (40.5 μmol) of AIBN, and 4 g of *p*-dioxane. Precipitation and purification was carried out identically as for the 15 kDa homo-pNIPAAm.

Diblock extension was performed by dissolving in a round-bottom flask 1.32 g (83 μmol) of the ∼15 kDa homo-pNIPAAm mCTA, 0.2258 g (1.59 mmol) of DMAEAm, 0.18 g (1.59 mmol) of NIPAAm, 1.4 mg (8.3 μmol) of AIBN in 8 mL of MeOH. This resulted in a [DMAEAm]:[NIPAAm]:[mCTA]:[initiator] ratio of 18:18:1:0.1. The flask was purged with N_2 for 30 min, followed by heating at 60 °C for 18 h. The MeOH was removed by rotary evaporation, and the product was dissolved in 5 mL of THF and precipitated thrice into pentane. The precipitate was dried under vacuum, dissolved in DI water, purified by PD-10 desalting column, and freeze−dried.

Polymer Analysis. Polymers were characterized using GPC performed on an Agilent 1200 series liquid chromatography system, equipped with TSKgel alpha 3000 and TSKgel alpha 4000 columns (TOSOH biosciences). The mobile phase was LiBr (0.01 M) in HPLC-grade DMF at a flow rate of 1 mL/min. MALS data were obtained on a miniDAWN TREOS (Wyatt Technologies Corp.) with 658 nm laser source and three detectors at 45.8°, 90.0°, and 134.2°. The instrument calibration constant was 5.746×10^{-5} V^{-1} cm^{-1}. Refractive index was measured using an Optilab Rex detector (Wyatt Technologies Corp.). The d*n*/d*c* value for the homo-pNIPAAm macro-chain-transfer agent (mCTA) was determined under the assumption of 100% mass recovery. The d*n*/d*c* value for the diblock copolymer was determined by injecting polymer samples at known concentrations into the RI detector postcolumn. The d*n*/d*c* value was then calculated using linear regression with the *Astra 5.3.4.14* data analysis software package (Wyatt Technologies Corp.). ^1H NMR (300 MHz.) spectroscopy in $CDCl_3$ was performed on a Bruker AV300. Nanoparticle absorption was measured on a Hewlett-Packard 8453 diode array extinction spectrophotometer with quartz cuvette sample holder. TEM was performed on a Technai G2 F20 200 kV microscope. Absorbance and fluorescence measurements were made using a 96-well microplate reader (Tecan).

Biotinylation of Diblock Copolymer. NHS activation of the diblock copolymer was performed by dissolution of 1.29 g (73 μmol) of polymer, 76 mg (372 μmol) of DCC, and 42 mg (365 μmol) of NHS in 7 mL of DCM. The reaction proceeded for 24 h at 22 °C, at which time an additional 76 mg of DCC and 42 mg of NHS were added. The reaction was allowed to proceed for an additional 24 h. The mixture was precipitated into pentane and dried under vacuum. The NHS-activated polymer was then mixed with 100 mg (266 μmol) of NH_2-PEG_2-biotin in 3 mL of DMF. The conjugation proceeded for 48 h at 22 °C and was precipitated into diethyl ether. The product was dried under vacuum, dissolved in DI water, filtered through a 0.2 μm filter, and obtained through PD-10 column purification and freeze−drying. Biotinylation efficiency was estimated using a commercially available HABA biotin quantification kit carried out according to manufacturer's instructions.

Nanoparticle Synthesis and Characterization. Citrate-stabilized colloidal gold was prepared according to the literature (*23*). All glassware was cleaned with aqua regia, thoroughly rinsed with DI water, and dried in an oven before use. 150 mL of 0.1 mg/mL $HAuCl_4$ was brought to a boil in a round-bottom flask. 1.76 mL of 10 mg/mL sodium citrate in DI water was added. The reaction was boiled under reflux for 30 min and cooled to room temperature. The pH was raised to 8 by addition of 0.1 M NaOH. Next, 1.2 mL of a 10 mg/mL solution of 17.7 kDa biotinylated diblock copolymer in DI water was added. The flask was purged with N_2 for 45 min. The gold sol was then sealed and stirred at 22 °C for 24 h in darkness, after which 1 g of NaCl was added, followed by an additional 24 h of stirring. The particles were then concentrated under 35 psi of N_2 using a membrane ultrafiltration system with a cellulose membrane (MWCO = 100 000 kDa). The polymer-modified gold nanoparticles (AuNPs) were washed off of the membrane with 3 mL of PBS buffer. The AuNPs were stored in PBS at 4 °C under N_2 for up to 4 months and used for further streptavidin binding/enrichment studies.

Magnetic nanoparticles (mNPs) coated with 5 kDa homo-pNIPAAm (without biotin) were synthesized as previously described (*4*, *5*), with slight modification. Briefly, the 5 kDa homo-pNIPAAm was dissolved in tetraglyme (3.6 mM) at 100 °C. Iron pentacarbonyl ($Fe(CO)_5$) was filtered through a 0.45 μm syringe filter prior to use. Four microliters of $Fe(CO)_5$ per mL of tetraglyme was added. After 10 min of stirring, the temperature was raised to 180 °C for 5 h. The reaction was cooled, and the mNPs obtained by precipitation into pentane,

drying under vacuum, dialysis against DI water at 4 °C, and freeze−drying. The mNPs were then dissolved in DI water at 50 mg/mL and stored at 4 °C for up to 3 months. TEM samples were prepared by dissolving particles in DI water (1 nM for the AuNPs, and 3 mg/mL for the mNPs). Particle solutions were aerosolized onto carbon-stabilized Formvar-coated copper grids (Ted Pella) using a spray bottle.

Magnetic Enrichment of Alexafluor-750-Labeled Streptavidin. Pooled human plasma was diluted with an equal volume of 2× PBS (20 mM phosphate, 276 mM NaCl, 5.4 mM KCl, pH 8.0). Alexafluor-750-labeled streptavidin (AF-750 streptavidin) was spiked into the 50% human plasma at a concentration of 5 nM. Stock solutions of the nanoparticle reagents were added to achieve final concentrations of 3 nM and 2 mg/mL for the AuNPs and mNPs, respectively. 8 kDa homo-pNIPAAm free polymer was added to a final concentration of 2 mg/mL. As a negative control, 1 μM free biotin was included in the plasma dilution buffer. 100, 250, or 500 μL of the 5 nM AF-750 streptavidin in 50% human plasma was added to Eppendorf tubes. Samples were incubated for 15 min with orbital shaking (400 rpm) inside an aluminum tube-holder equilibrated in an incubator set to 45 °C. This was followed by incubation of the sample tubes in close contact with neodymium iron boron magnets for 15 min at 45 °C using an in-house fabricated magnet holder. Next, the supernatant was discarded with a pipet, and the precipitate that had been captured along the side of the tube was resuspended into 10 μL of 1× PBS pH 6.0 buffer at 4 °C. Fluorescence of the AF-750 streptavidin (λ_{ex} = 752 nm, λ_{em} = 776 nm), and absorbance of the AuNPs at 520 nm was measured using a fluorescence/absorbance microwell plate reader (Tecan).

LFIA Device Fabrication. Rabbit polyclonal antistreptavidin IgG was deposited at 3 mg/mL onto HiFlow 180 nitrocellulose assay membranes using an in-house fabricated protein striping system (*23*). The membrane was diced into rectangles measuring 16 × 3 mm^2 using a CO_2 laser system (Universal Laser Systems). The strips were submerged in goat protein nonspecific blocking solution (Zymed) for 30 min, followed by drying in a vacuum desiccator overnight. The strips were then applied to adhesive-coated Mylar substrates measuring 48 × 3 mm^2. An absorbent pad (35 × 3 mm) was placed at the distal end of the flow strip to drive capillary wicking of the fluids. The length of the overlap between the assay membrane and the absorbent pad was 3 mm. LFIA strips were stored in a desiccator at 23 °C and used within one week.

Effect of Streptavidin Dose on LFIA Signal. 200 μL samples of 50% human plasma containing variable amounts of nonfluorescent streptavidin, from 50 ng/mL to 0 ng/mL, were prepared. The AuNPs, mNPs, and 8 kDa homo-pNIPAAm were added to achieve final concentrations of 3 nM, 2 mg/mL, and 2 mg/mL, respectively. Heating, magnetic separation, and removal of the supernatant were performed as described in the fluorescent capture study (see above). The magnetically captured particle aggregates were resuspended into 10 μL of 1× PBS pH 6.0 at 4 °C. Ten microliter droplets of the captured protein/particle mixture were deposited into wells of a 96-well plate. LFIA strips were placed into the droplets, which completely wicked into the strips within 5−6 min. The membranes were then transferred to wells containing PBS pH 6.0 rinse buffer. The buffer rinse was allowed to proceed for 20 min, or until the absorbent pad was saturated. Imaging of the developed strips was performed using a digital camera (Canon SD400) on digital macro setting. Strips were illuminated from behind at an oblique angle using a white light source, and the transmission images were quantified by image analysis. All samples were run in triplicate on three separate LFIA strips and imaged under identical lighting conditions.

Image analysis was performed using *Image J* software. The background-corrected mean pixel intensity of the green channel in the RGB images was measured from a region of interest encompassing the leading edge of the antibody binding patch.

Effect of Increasing Sample Volume on LFIA Signal. 10 ng/mL of streptavidin in 50% human plasma was prepared. Stock solutions of the nanoparticle/polymer reagents were added to achieve final concentrations of 3 nM, 2 mg/mL, and 2 mg/mL for the AuNPs, mNPs, and 8 kDa homo-pNIPAAm free polymer, respectively. The stock protein/particle solution at a fixed streptavidin concentration (10 ng/mL) was divided into aliquots of 100, 200, 300, 400, or 500 μL. Each sample tube was processed as described above. The captured aggregates were resuspended into 10 μL of 1× PBS pH 6.0 buffer at 4 °C. 10 μL droplets of the concentrated particle mixture were run on the LFIA strips following the protocol described for the dose−response experiment (see above).

RESULTS

System Design. The bioseparation/enrichment system consists of a mixture of magnetic and gold nanoparticles, each with a "smart" polymer coating. Gold nanoparticles (∼25 nm diameter) were modified with a biotinylated amine-containing diblock copolymer, and magnetic nanoparticles (∼10 nm diameter) were synthesized directly with a homo-pNIPAAm polymer surface coating. When mixtures of these two particle types were heated above the polymer LCST, the particles coaggregated, driven by hydrophobic interactions between the collapsed polymers. 8 kDa homo-pNIPAAm (2 mg/mL) was added to the particle mixture to facilitate mNP and AuNP cross-aggregation. The aggregates contained both magnetic (iron oxide) and gold aggregates with a strongly enhanced magnetophoretic mobility that allowed them to be rapidly coseparated in an applied magnetic field gradient. The separation mechanism is depicted in Figure 1. By resuspending the magnetically captured particle aggregates into a smaller volume of fluid, the gold-labeled model target biomarker streptavidin could be concentrated many-fold. The enriched gold-labeled target protein was then analyzed and visualized with an antistreptavidin immunochromatographic flow strip.

Polymer Synthesis and Characterization. Polymer synthesis was carried out using two thermally initiated RAFT polymerizations. The target molecular weight of the first RAFT polymerization was 15 kDa. A [NIPAAm]:[CTA]:[Initiator] ratio of 132:1:0.1 was used in *p*-dioxane. The homo-pNIPAAm product (**(1)** in Figure 2) was purified and analyzed. GPC showed the polymer had M_n = 15.7 kDa, polydispersity index (PDI) = 1.01, and d*n*/d*c* of 0.074. ^{1}H NMR analysis confirmed the NIPAAm chemical shifts, with peaks at δ (ppm) 1.15 (s, R-CO-NH-CH-($C\underline{H}_3$)$_2$) and at 4.00 (s, R-CO-NH-C$\underline{H}$-(CH_3)$_2$). These two peaks had an integrated peak area ratio of ∼6:1, consistent with the proton ratio in the NIPAAm monomer.

Diblock extension was performed using the 15.7 kDa homo-pNIPAAm as a macrochain transfer agent (mCTA). The mCTA was chain extended with a short random copolymer block of NIPAAm-co-DMAEAm. [NIPAAm]:[DMAEAm]:[mCTA]:[Initiator] ratios of 18:18:1:0.1 were used in MeOH. MeOH was chosen because the mCTA was highly soluble in MeOH. The diblock copolymer (**(2)** in Figure 2) was found to have a M_n = 17.7 by MALS, PDI = 1.25, and d*n*/d*c* = 0.071. GPC traces of the mCTA and the diblock copolymer can be found in the Supporting Information (Figure S1). ^{1}H NMR of the diblock copolymer can be found in the Supporting Information (Figure S2). ^{1}H NMR results from diblock copolymer preparations showed that the chemical shift of the DMAEAm methyl group protons was dependent on the protonation state of the tertiary amine. Diblock copolymers treated with 10 equiv of NaOH to

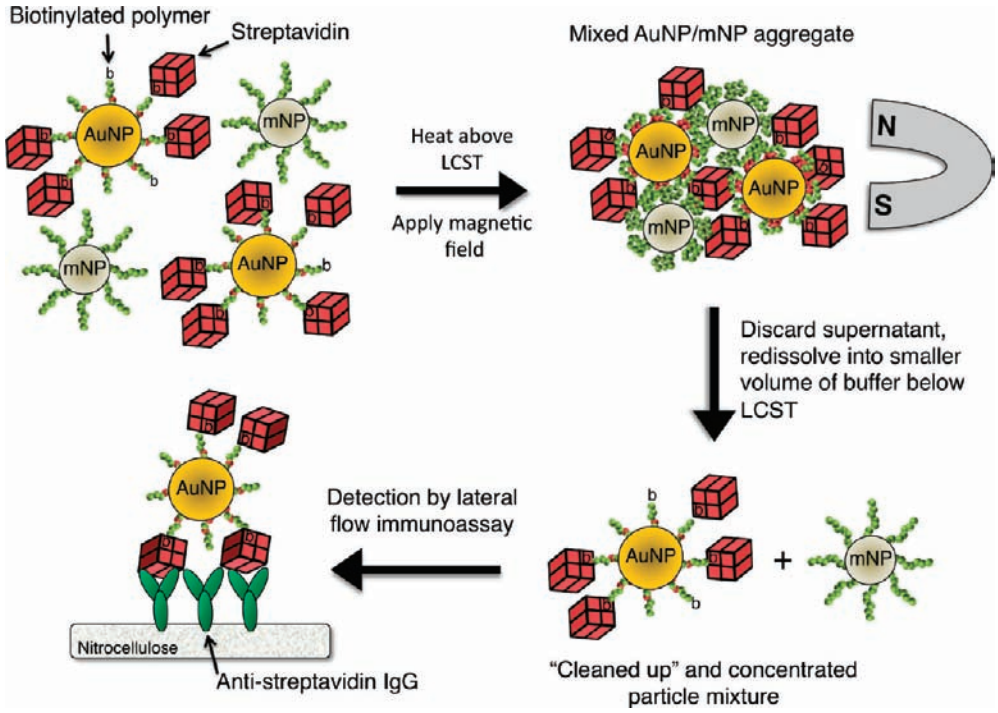


Figure 1. Dual nanoparticle magnetic separation scheme. AuNPs coated with biotinylated diblock copolymers bind to streptavidin spiked into 50% human plasma. mNPs coated with homo-pNIPAAm are added, and the temperature is raised above the polymer LCST. Mixed streptavidin−AuNP/mNP aggregates are separated by a magnet. The separated aggregates with gold-labeled target protein are resuspended into a smaller volume of buffer below the LCST and flowed through an LFIA strip with immobilized capture antibodies. Visualization of the target protein is achieved by AuNP light extinction at the capture line of the LFIA strip, while the non-biofunctional mNPs are rinsed away.

deprotonate the amines of DMAEAm were found to have DMAEAm methyl group shifts at δ (ppm) 2.26 (s, R-N(C$\underline{H}_3)_2$. Polymers treated with 10 equiv of HCl prior to NMR analysis, however, were found to have DMAEAm methyl group shifts at δ (ppm) = 3.1 (s, R-N(C$\underline{H}_3)_2$. Previous studies have reported the proton shift of the DMAEAm methyl group in monomeric form to be δ (ppm) 2.26 (*24*). In analyzing Supporting Information Figure S2, the four protons located between the amide and tertiary amine groups of DMAEAm were also assigned to the peak at δ (ppm) 3.1, which therefore represented 10 DMAEAm protons. The DPN of DMAEAm in the diblock was ∼15, based on the 1:1.15 integrated peak area ratio of the single NIPAAm hydrogen at δ (ppm) 4.0 to the 10 DMAEAm protons at δ (ppm) 3.1. The overall NIPAAm:DMAEAm ratio in the diblock copolymer was ∼9:1.

Biotinylation of Diblock Copolymer. The 17.7 kDa diblock copolymer was biotinylated via DCC/NHS ester activation and conjugation to NH_2-PEG_2-biotin. The dicyclohexylurea byproduct was removed using a 0.2 μm syringe filter. Biotinylation efficiency was measured by commercially available HABA dye-displacement assay (*25*). Known amounts of polymer were added to a solution of HABA-saturated avidin. The decrease in absorbance at 500 nm due to HABA dye displacement from the binding pocket was measured. A standard curve generated by addition of variable amounts of free biotin to the HABA-saturated avidin was used as a reference to quantify the number of available biotin moieties in the polymer preparations. The biotinylation efficiency was found to be 78% for the 17.7 kDa diblock copolymer. Results from the HABA dye displacement assay can be found in the Supporting Information (Figure S3).

Nanoparticle Synthesis and Characterization. Citrate-stabilized gold nanoparticles were synthesized using a protocol from the literature (*23*). Within 3 min of addition of sodium citrate to the boiling gold chloride solution, a rapid color change from yellow to deep red was observed. The positively charged diblock copolymer was allowed to interact with the negatively charged citrate-capped AuNPs overnight. In addition to electrostatics, chemisorption of the trithiocarbonate group from the RAFT CTA likely contributes to successful modification of the AuNPs (*26*). The polymer-modified AuNPs were then successfully transferred into 3 mL of 1× PBS buffer using membrane ultrafiltration. The AuNPs were washed off of the cellulose membrane and remained soluble for months stored in PBS buffer under N_2 at 4 °C. AuNPs were characterized by TEM imaging, particle sizing image analysis, and absorption spectrophotometry (Figure 3, top panel A−C). From TEM images, the AuNPs had pseudospherical morphology with diameter 23.5 ± 4.28 nm (mean ± standard deviation, no. of particles counted >200). The LSPR absorption peak (Figure 3, C) was observed at 530 nm. The extinction coefficient of the 23 nm AuNPs was estimated to be 2×10^9 M^{-1} cm^{-1} from sizing data and the literature (*27*). This molar extinction coefficient was used in further studies to estimate the concentration of the AuNPs.

Unlike citrate-stabilized AuNPs, the polymer-modified AuNPs were found to be colloidally stable in physiological buffers (e.g., PBS). The localized surface plasmon resonance (LSPR) wavelength did not red-shift after transfer of the particles into PBS buffer. The LSPR wavelength of the AuNPs was red-shifted upon raising the temperature above the LCST of the polymer (Figure 4C,D). Below the LCST, the gold colloid had an absorption peak at 530 nm, and transmitted white light appeared pink (Figure 4C). After raising the temperature above the LCST, the LSPR was red-shifted by ∼40 nm and the solution appeared purple (Figure 4D). The color change was due to dielectric coupling of LSPR oscillations between aggregated AuNPs in close proximity to each other (*28*). This behavior was similar to what has been previously reported on "smart" polymer−AuNP conjugates (*29*−*33*). Interestingly, the red shift of the LSPR was prevented upon addition of 0.2 mg/mL of homo-pNIPAAm free polymer. Addition of free polymer insulates the AuNPs from one another, preventing them from becoming sufficiently close in proximity to allow for coupling of the LSPR.

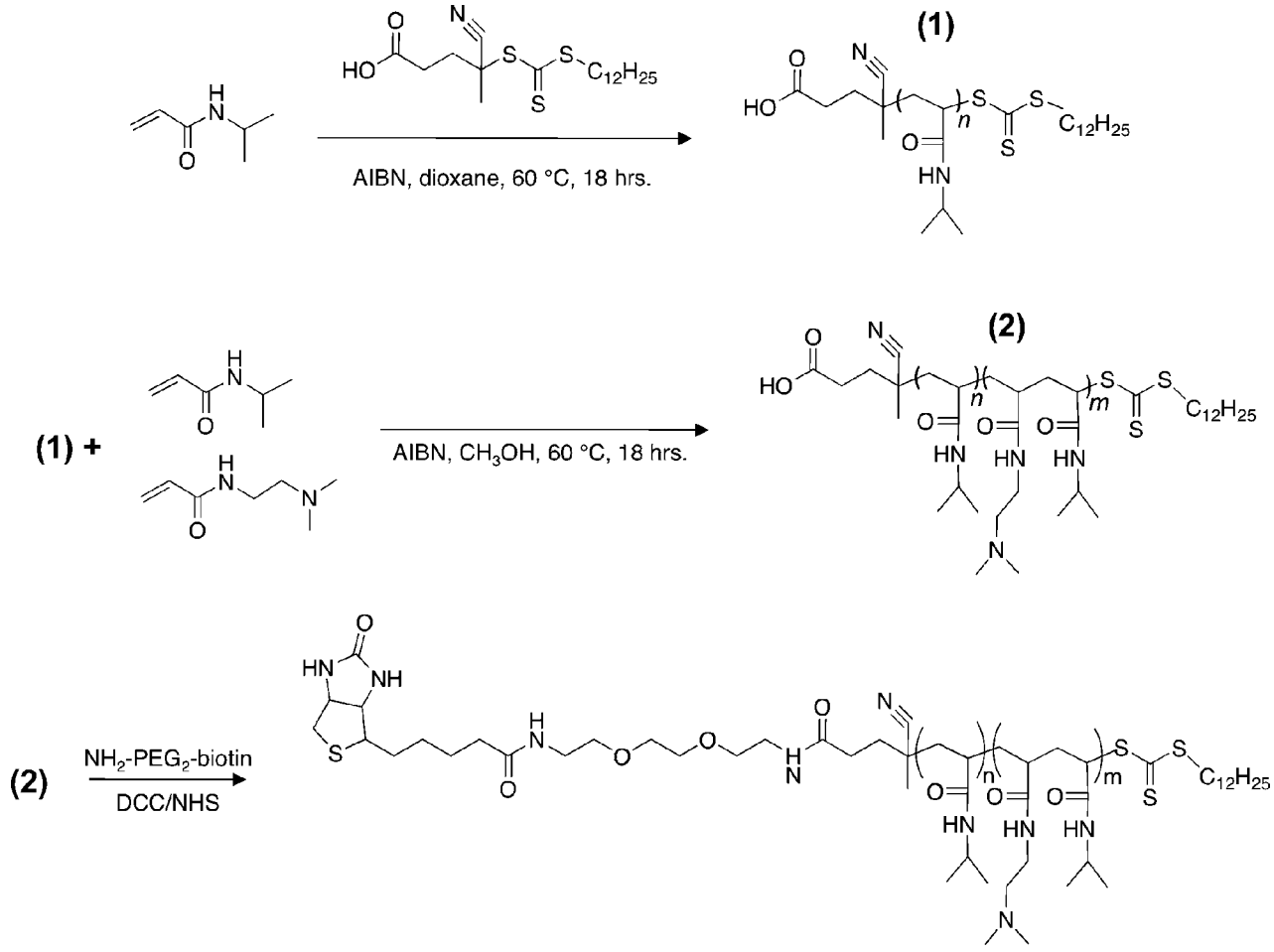


Figure 2. Diblock copolymerization scheme. The polymer contains a homo-pNIPAAm block ($n = 130$) for thermal responsiveness, a cationic DMAEAm-*co*-NIPAAm random copolymer block ($m = 15$) to drive adsorption onto anionic AuNPs, and a terminal biotin moiety.

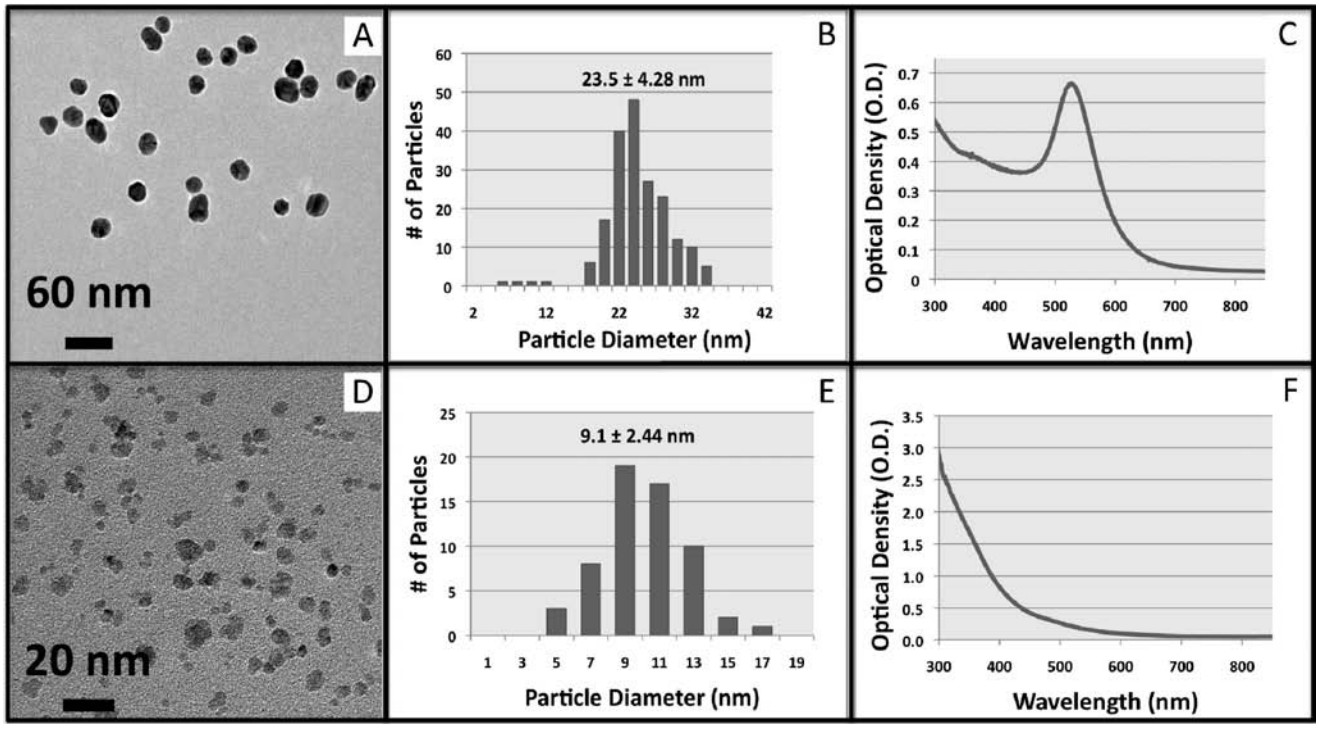


Figure 3. Characterization of magnetic and gold nanoparticles. TEM images, image analysis particle sizing histograms, and visible absorption spectra of AuNPs (top panel, A−C) and mNPs (bottom panel, D−F).

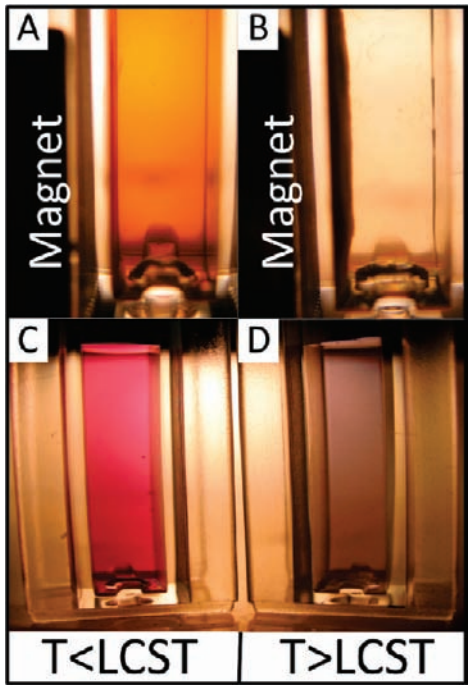


Figure 4. Photographs of white light transmittance through nanoparticle solutions. mNPs below the polymer LCST (A) do not respond to the magnet, but above the LCST (B) are aggregated and magnetically pulled against the cuvette wall. AuNPs below the LCST (C) appear pink, while above the LCST (D) appear purple due to aggregation and near-field plasmonic coupling.

The mNPs were synthesized using a 5 kDa homo-pNIPAAm, as previously described (*4*). This homo-pNIPAAm served as a stabilizer during mNP synthesis, resulting in pNIPAAm-coated mNPs. TEM and particle size analysis of the mNPs (Figure 3D,E) showed they have an average long-axis diameter of 9.1 ± 2.44 nm (mean ± standard deviation, no. of particles counted >60). The optical absorption spectrum of the mNPs showed a Rayleigh scattering profile, as seen in Figure 3F. The mNPs exhibited a thermally triggered increase in the magnetophoretic mobility, as has been previously described (*4, 5, 34, 35*). This behavior is demonstrated in Figure 4A,B. Below the LCST (Figure 4A), the mNPs did not rapidly respond to the magnet placed against the side of the cuvette, because they exist as <10 nm particles. When the temperature was raised above the polymer LCST (Figure 4B), the large aggregates had much larger magnetophoretic mobility and were rapidly separated against the cuvette side-wall by the magnet.

Both particle types (AuNPs and mNPs) therefore exhibit thermally triggered aggregation that modulates their magnetic and/or optical properties. It was found that mixtures of these two particle types possessed the magnetic separation behavior of the mNPs combined with the optical extinction properties of the AuNPs. AuNPs modified with the diblock copolymers could therefore be magnetically separated upon coaggregation with the pNIPAAm-coated mNPs and application of a magnetic field gradient. Video stills demonstrating magnetic separation of AuNPs can be found in the Supporting Information (Figure S4).

Magnetic Enrichment of Alexafluor-750-Labeled Streptavidin. As a validation of the bioseparation technique, we tested the ability of AuNPs to bind fluorescently labeled streptavidin, and concentrate the target protein via polymer-induced coaggregation and magnetic separation with mNPs. An advantage of this nanoparticle system is the ability to process large sample volumes as easily as microliter quantities. This capability was demonstrated by increasing the total processed sample volume at a fixed concentration of labeled streptavidin. AF-750 streptavidin (5 nM) spiked into 50% human plasma was used to mimic a clinical sample. Three nanomoles per liter of diblock-copolymer-modified AuNPs, 2 mg/mL mNPs, and 2 mg/mL of 8 kDa homo-pNPAAm were added sequentially. Each AuNP is expected to bind no more than 50 streptavidin molecules based on nanoparticle size and a theoretical streptavidin monolayer density of 2.8 ng/mm^2 (*36*).

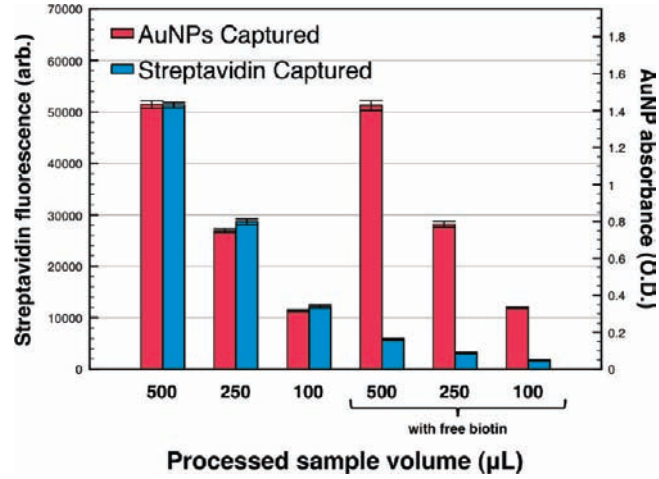


Figure 5. Magnetic enrichment of fluorescent streptavidin by AuNP/mNP mixtures. AF-750 labeled streptavidin fluorescence and AuNP absorbance were measured after processing variable volumes of 50% human plasma containing 5 nM fluorescent streptavidin. In all cases, the captured particles were redissolved into 10 μL of PBS 6.0 buffer, achieving a 50-fold, 25-fold, or 10-fold particle/protein enrichment factor for the 500, 250, and 100 μL samples, respectively. Samples spiked with 1 μM free biotin served as negative controls to block the streptavidin binding sites preventing fluorescence capture, while particle capture/absorbance remained high.

Samples of 100, 250, or 500 μL were heated to 45 °C causing polymer collapse and mixed AuNP/mNP aggregate self-assembly. A magnet was applied, and the aggregates were captured at the side of the carrying vessel. The supernatant was discarded, and the captured pellet was redissolved into a 10 μL volume of cool (<LCST) PBS 6.0 buffer. Figure 5 shows fluorescence and absorbance measurements taken on the redissolved aggregates below the LCST. Data bars in Figure 5 represent mean ± SD (n = 5) of labeled streptavidin fluorescent intensity at 776 nm or particle absorbance at 520 nm. Increasing the sample volume results in a corresponding linear increase in the AuNP absorbance and streptavidin fluorescence. In the presence of free biotin, the streptavidin binding sites are blocked and fluorescence capture is eliminated, demonstrating that capture is occurring via specific streptavidin−biotin binding. Only a small amount of fluorescence is captured due to nonspecific adsorption of the labeled streptavidin to the nanoparticle/polymer aggregates.

LFIA Device Fabrication. We further demonstrated the capabilities of the bioseparation/enrichment system by developing a quantitative lateral flow immunoassay of the model protein analyte streptavidin. LFIA strips were fabricated using an in-house protein striping system (*23*) capable of depositing the capture antibody (rabbit polyclonal antistreptavidin IgG) within the confines of a narrow line ~1.5 mm in width onto nitrocellulose substrates. The nitrocellulose strips and absorbent wicking pads were placed onto adhesive-coated Mylar. An image of the lateral flow strip can be seen in Figure 6, top.

Effect of Streptavidin Dose on LFIA Signal. Figure 6 shows the light extinction signal generated by processing varying amounts of streptavidin from 200 μL sample volumes and flowing the resuspended particle mixtures through the capture antibody line on the LFIA strips, followed by a rinse step. The curve is linear with a limit of detection of 6 ng/mL, determined

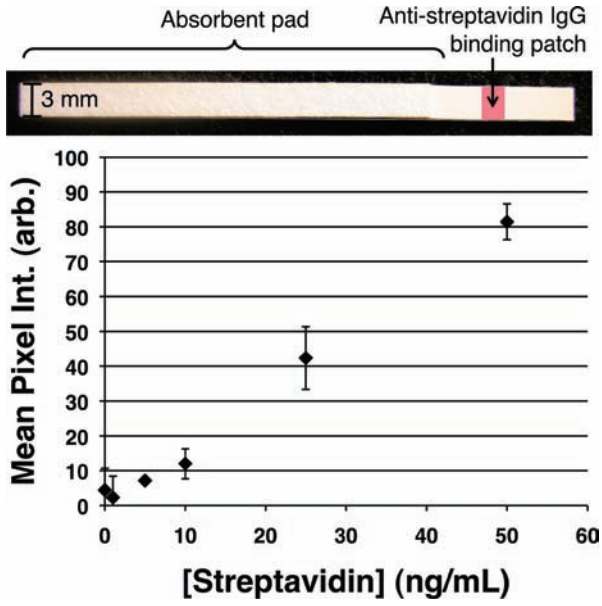


Figure 6. Lateral flow immunoassay standard curve. (Top) Image of the flow strip. (Bottom) Variable amounts of streptavidin spiked into 50% human plasma samples were captured at a fixed sample volume of 200 μL. The background-subtracted mean pixel intensity (mean $\pm$ SD, ($n = 3$)) at the leading edge of the antistreptavidin IgG binding patch on the nitrocellulose membrane was measured using *Image J*.

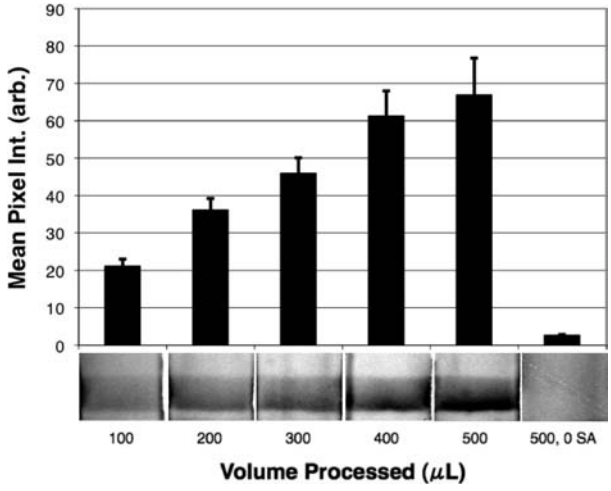


Figure 7. Effect of increasing sample volume on LFIA signal. Increasing sample volumes from 100 to 500 μL each with the same concentration of streptavidin (10 ng/mL) were processed using the AuNP/mNP bioseparaton method. 500 μL of 50% human plasma containing the nanoparticle reagents but no streptavidin (500, 0 SA) served as the negative control.

using 3 times the standard error of the zero antigen sample as the lower signal limit. The dual AuNP/mNP nanoparticle system is therefore able to generate specific signal proportional to the amount of diagnostic target in the sample, facilitating quantitative assays when combined with optical reader technologies.

Effect of Concentrating Model Biomarker from a Larger Sample Volume on LFIA Signal. By increasing the volume of the sample processed at a fixed concentration of streptavidin, we effectively capture more molecules of the target protein, which translates into increased light extinction at the test line of the LFIA strip. Figure 7 shows the increase in LFIA signal that was accomplished by increasing the sample volumes from 100 to 500 μL for a fixed 10 ng/mL of streptavidin. A 500 μL sample without streptavidin (500, 0 SA) served as the negative control. These results demonstrate that the smart nanoparticle system can increase the signal at a fixed analyte concentration by processing larger volumes of sample. Where larger samples can be obtained from the patient, this finding has implications for opening up new biomarkers to point-of-care testing that are currently too dilute to be detected by conventional nonconcentrating LFIA.

DISCUSSION

These results demonstrate the possibility of enhancing the performance of rapid tests using the dual AuNP/mNP system to achieve rapid and integrated biomarker labeling, purification, enrichment, and detection. Our key innovation was using stimuli-responsive coatings to direct coaggregation of two different types of nanoparticles, each with predesigned functionalities. The mNPs enable separation/enrichment of the diagnostic target bound to the AuNPs when the aggregate size is large enough to achieve rapid magnetophoretic separations, while the AuNPs provide a high-efficiency absorbing species by which the target molecule is visualized without the need for advanced optical instrumentation. A primary advantage of the mixed nanoparticle system compared to the core−shell nanoparticle approach is that it allows the direct purification of the gold-biomarker detection half-sandwich species. This half-sandwich is the active species that can be applied directly to lateral flow or flow-through diagnostic tests without the complications of having magnetic nanoparticles also bound to the biomarker. A second advantage of the dual particle system over a magnetic-core/gold-shell nanoparticle system is the ability to independently control the stoichiometric ratios of the magnetic and gold particles. This allows optimization of each particle type independent from one another and also facilitates tuning the magnetophoresis behavior. For example, when magnetophoresis is found to be slow, more magnetic particles can be added to improve the separation without changing the amount of detection gold nanoparticles in the mixture. This may allow more efficient optimization of signal to background noise in some assay systems. Future work will focus on transferring these proof-of-concept results to a real biomarker system by incorporating capture antibodies onto the AuNPs for disease-related and multiplexed antigen detection from clinical samples.

ACKNOWLEDGMENT

Michael A. Nash gratefully acknowledges funding from the National Science Foundation Graduate Research Fellowship Program (NSF-GRFP), and from the U.S. Department of Homeland Security (DHS) Scholarship and Fellowship Program, administered by the Oak Ridge Institute for Science and Education (ORISE) through an interagency agreement between the U.S. Department of Energy (DOE) and DHS. Dr. Selvi Srinivasan is acknowledged for helpful discussions on NMR. This work was supported in part by funding from the National Institutes of Health (Grant EB000252), and The Bill and Melinda Gates Foundation through the Grand Challenges Program.

Supporting Information Available: Figure S1: Refractive index GPC traces of mCTA and diblock copolymers. Figure S2: Proton NMR spectroscopy of the diblock copolymer. Figure S3: Quantitation of biotinylation efficiency by HABA assay. Figure S4: Time-lapse images of mNP/AuNP coaggregation and separation process. This material is available free of charge via the Internet at http://pubs.acs.org.

LITERATURE CITED

(1) Posthuma-Trumpie, G. A., Korf, J., and van Amerongen, A. (2009) Lateral flow (immuno) assay: its strengths, weaknesses,

opportunities and threats. A literature survey. *Anal. Bioanal. Chem. 393*, 569–582.
(2) Gordon, J., and Michel, G. (2008) Analytical sensitivity limits for lateral flow immunoassays. *Clin. Chem. 54*, 1250–1251.
(3) Anderson, N. L., Polanski, M., Pieper, R., Gatlin, T., Tirumalai, R. S., Conrads, T. P., Veenstra, T. D., Adkins, J. N., Pounds, J. G., Fagan, R., and Lobley, A. (2004) The human plasma proteome - A nonredundant list developed by combination of four separate sources. *Mol. Cell. Proteom. 3*, 311–326.
(4) Lai, J. J., Hoffman, J. M., Ebara, M., Hoffman, A. S., Estournes, C., Wattiaux, A., and Stayton, P. S. (2007) Dual magnetic-/temperature-responsive nanoparticles for microfluidic separations and assays. *Langmuir 23*, 7385–7391.
(5) Lai, J. J., Nelson, K. E., Nash, M. A., Hoffman, A. S., Yager, P., and Stayton, P. S. (2009) Dynamic bioprocessing and microfluidic transport control with smart magnetic nanoparticles in laminar-flow devices. *Lab Chip 9*, 1997–2002.
(6) Zhao, W., Brook, M. A., and Li, Y. F. (2008) Design of gold nanoparticle-based colorimetric biosensing assays. *ChemBioChem 9*, 2363–2371.
(7) Zhao, W., Ali, M. M., Aguirre, S. D., Brook, M. A., and Li, Y. (2008) Paper-based bioassays using gold nanoparticle colorimetric probes. *Anal. Chem. 80*, 8431–8437.
(8) Wilson, R. (2008) The use of gold nanoparticles in diagnostics and detection. *Chem. Soc. Rev. 37*, 2028–2045.
(9) Shyu, R. H., Shyu, H. F., Liu, H. W., and Tang, S. S. (2002) Colloidal gold-based immunochromatographic assay for detection of ricin. *Toxicon 40*, 255–258.
(10) Dar, V. S., Ghosh, S., and Broor, S. (1994) Rapid detection of rotavirus by using colloidal gold particles labeled with monoclonal-antibody. *J. Virol. Methods 47*, 51–58.
(11) Kunakorn, M., Petchclai, B., Khupulsup, K., and Naigowit, P. (1991) Gold blot for detection of immunoglobulin-M (IgM)-specific and IgG-specific antibodies for rapid serodiagnosis of melioidosis. *J. Clin. Microbiol. 29*, 2065–2067.
(12) Hsu, Y. H. (1984) Immunogold for detection of antigen on nitrocellulose paper. *Anal. Biochem. 142*, 221–225.
(13) Brada, D., and Roth, J. (1984) Golden blot-detection of polyclonal and monoclonal-antibodies bound to antigens on nitrocellulose by protein-A gold complexes. *Anal. Biochem. 142*, 79–83.
(14) Nash, M. A., Lai, J. J., Hoffman, A. S., Yager, P., and Stayton, P. S. (2010) Smart diblock copolymers as templates for magnetic-core gold-shell nanoparticle synthesis. *Nano Lett. 10*, 85–91.
(15) Bardhan, R., Chen, W. X., Perez-Torres, C., Bartels, M., Huschka, R. M., Zhao, L. L., Morosan, E., Pautler, R. G., Joshi, A., and Halas, N. J. (2009) Nanoshells with targeted simultaneous enhancement of magnetic and optical imaging and photothermal therapeutic response. *Adv. Funct. Mater. 19*, 3901–3909.
(16) Xu, Z. C., Hou, Y. L., and Sun, S. H. (2007) Magnetic core/shell Fe_3O_4/Au and Fe_3O_4/Au/Ag nanoparticles with tunable plasmonic properties. *J. Am. Chem. Soc. 129*, 8698.
(17) Lim, I. I. S., Njoki, P. N., Park, H. Y., Wang, X., Wang, L. Y., Mott, D., and Zhong, C. J. (2008) Gold and magnetic oxide/gold core/shell nanoparticles as bio-functional nanoprobes. *Nanotechnology 19*, 11.
(18) Park, H. Y., Schadt, M. J., Wang, L., Lim, I. I. S., Njoki, P. N., Kim, S. H., Jang, M. Y., Luo, J., and Zhong, C. J. (2007) Fabrication of magnetic core @ shell Fe oxide @ Au nanoparticles for interfacial bioactivity and bio-separation. *Langmuir 23*, 9050–9056.
(19) Lyon, J. L., Fleming, D. A., Stone, M. B., Schiffer, P., and Williams, M. E. (2004) Synthesis of Fe oxide core/Au shell nanoparticles by iterative hydroxylamine seeding. *Nano Lett. 4*, 719–723.
(20) Hoffman, A. S. (2000) Bioconjugates of intelligent polymers and recognition proteins for use in diagnostics and affinity separations. *Clin. Chem. 46*, 1478–1486.
(21) Jassam, N., Jones, C. M., Briscoe, T., and Horner, J. H. (2006) The hook effect: a need for constant vigilance. *Ann. Clin. Biochem. 43*, 314–317.
(22) Moad, G., Chong, Y. K., Postma, A., Rizzardo, E., and Thang, S. H. (2005) Advances in RAFT polymerization: the synthesis of polymers with defined end-groups. *Polymer 46*, 8458–8468.
(23) Nash, M. A., Hoffman, J. M., Stevens, D. Y., Hoffman, A. S., Stayton, P. S., and Yager, P. (2010) Laboratory scale protein striping system for patterning biomolecules onto paper based immunochromatographic test strips. *Lab Chip 10*, 2279−2282.
(24) Frens, G. (1973) Controlled nucleation for regulation of particle-size in monodisperse gold suspensions. *Nat. Phys. Sci. 241*, 20–22.
(25) Chen, T. M., Wang, Y. F., Kitamura, M., Nakaya, T., and Sakurai, I. (1996) Synthesis and properties of poly(acrylamide)s containing both long chain alkyl groups and phosphatidylcholine analogues in the side chains. *J. Polym. Sci., Part A: Polym. Chem. 34*, 1155–1164.
(26) Green, N. M. (1965) A spectrophotometric assay for avidin and biotin based on binding of dyes by avidin. *Biochem. J. 94*, C23.
(27) Fustin, C. A., and Duwez, A. S. (2009) Dithioesters and trithiocarbonates monolayers on gold. *J. Electron Spectrosc. Relat. Phenom. 172*, 104–106.
(28) Haiss, W., Thanh, N. T. K., Aveyard, J., and Fernig, D. G. (2007) Determination of size and concentration of gold nanoparticles from UV-vis spectra. *Anal. Chem. 79*, 4215–4221.
(29) Jain, P. K., Huang, W. Y., and El-Sayed, M. A. (2007) On the universal scaling behavior of the distance decay of plasmon coupling in metal nanoparticle pairs: A plasmon ruler equation. *Nano Lett. 7*, 2080–2088.
(30) Aqil, A., Qiu, H. J., Greisch, J. F., Jerome, R., De Pauw, E., and Jerome, C. (2008) Coating of gold nanoparticles by thermosensitive poly(N-isopropylacrylamide) end-capped by biotin. *Polymer 49*, 1145–1153.
(31) Boyer, C., Whittaker, M. R., Luzon, M., and Davis, T. P. (2009) Design and synthesis of dual thermoresponsive and antifouling hybrid polymer/gold nanoparticles. *Macromolecules 42*, 6917–6926.
(32) Raula, J., Shan, J., Nuopponen, M., Niskanen, A., Jiang, H., Kauppinen, E. I., and Tenhu, H. (2003) Synthesis of gold nanoparticles grafted with a thermoresponsive polymer by surface-induced reversible-addition-fragmentation chain-transfer polymerization. *Langmuir 19*, 3499–3504.
(33) Yusa, S. I., Fukuda, K., Yamamoto, T., Iwasaki, Y., Watanabe, A., Akiyoshi, K., and Morishima, Y. (2007) Salt effect on the heat-induced association Behavior of gold nanoparticles coated with Poly(N-isopropylacrylamide) prepared via reversible addition - Fragmentation chain transfer (RAFT) radical polymerization. *Langmuir 23*, 12842–12848.
(34) Zhu, M. Q., Wang, L. Q., Exarhos, G. J., and Li, A. D. Q. (2004) Thermosensitive gold nanoparticles. *J. Am. Chem. Soc. 126*, 2656–2657.
(35) Furukawa, H., Shimojyo, R., Ohnishi, N., Fukuda, H., and Kondo, A. (2003) Affinity selection of target cells from cell surface displayed libraries: a novel procedure using thermoresponsive magnetic nanoparticles. *Appl. Microbiol. Biotechnol. 62*, 478–483.
(36) Sun, Y. B., Ding, X. B., Zheng, Z. H., Cheng, X., Hu, X. H., and Peng, Y. X. (2006) Magnetic separation of polymer hybrid iron oxide nanoparticles triggered by temperature. *Chem. Commun.* 2765–2767.
(37) Gau, J. J., Lan, E. H., Dunn, B., Ho, C. M., and Woo, J. C. S. (2010) A MEMS-based amperometric detector for *E. coli* bacteria using self-assembled monolayers. *Biosensors and Bioelectronics 16*, 745–755.

BC100180Q

SUPPORTING INFORMATION

A Mixed Stimuli-Responsive Magnetic and Gold Nanoparticle System for Rapid Purification, Enrichment, and Detection of Biomarkers

*Michael A. Nash, Paul Yager, Allan S. Hoffman, Patrick S. Stayton**

Department of Bioengineering, University of Washington, Seattle, WA 98195

*Corresponding author.

Patrick S. Stayton, Ph.D.

University of Washington

Department of Bioengineering

Box 355061

Seattle, WA 98195

Tel: (206) 685-8148

Fax: (206) 685-8526

E-mail: stayton@u.washington.edu

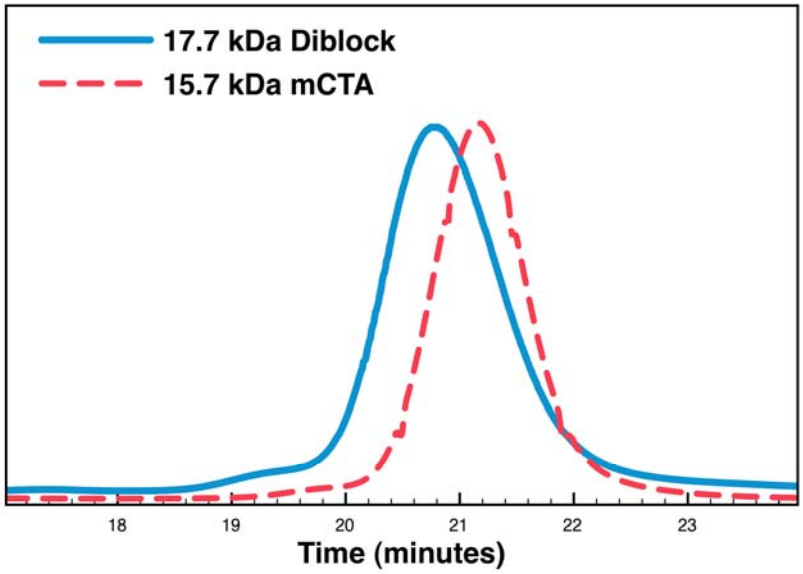
SUPPORTING INFORMATION CONTENTS

Figure S1. Refractive index GPC traces of mCTA and diblock copolymers.

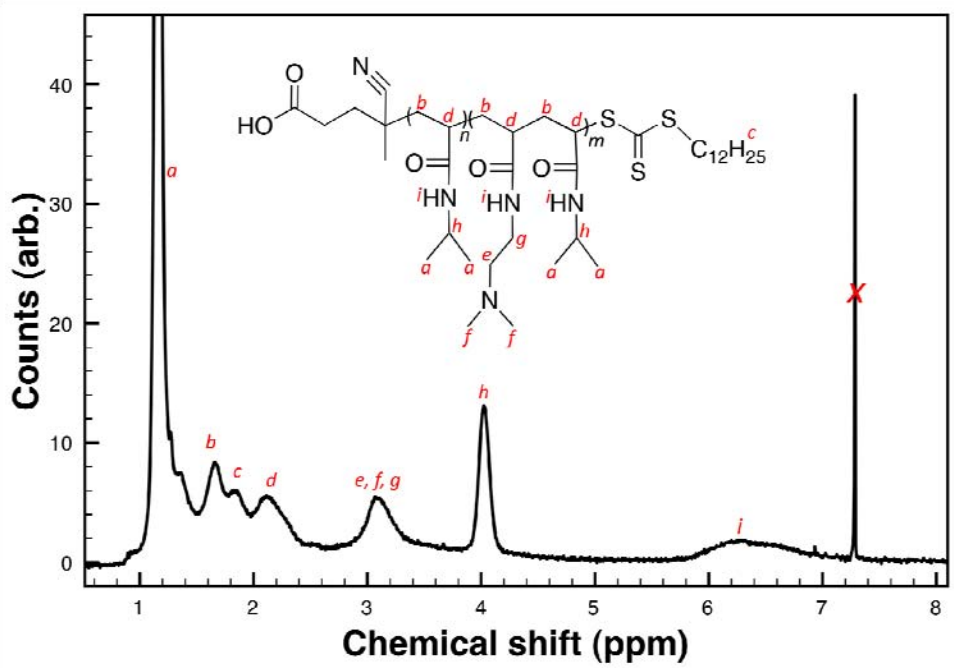
Figure S2. Proton NMR spectroscopy of the diblock copolymer.

Figure S3. Quantitation of biotinylation efficiency by HABA assay.

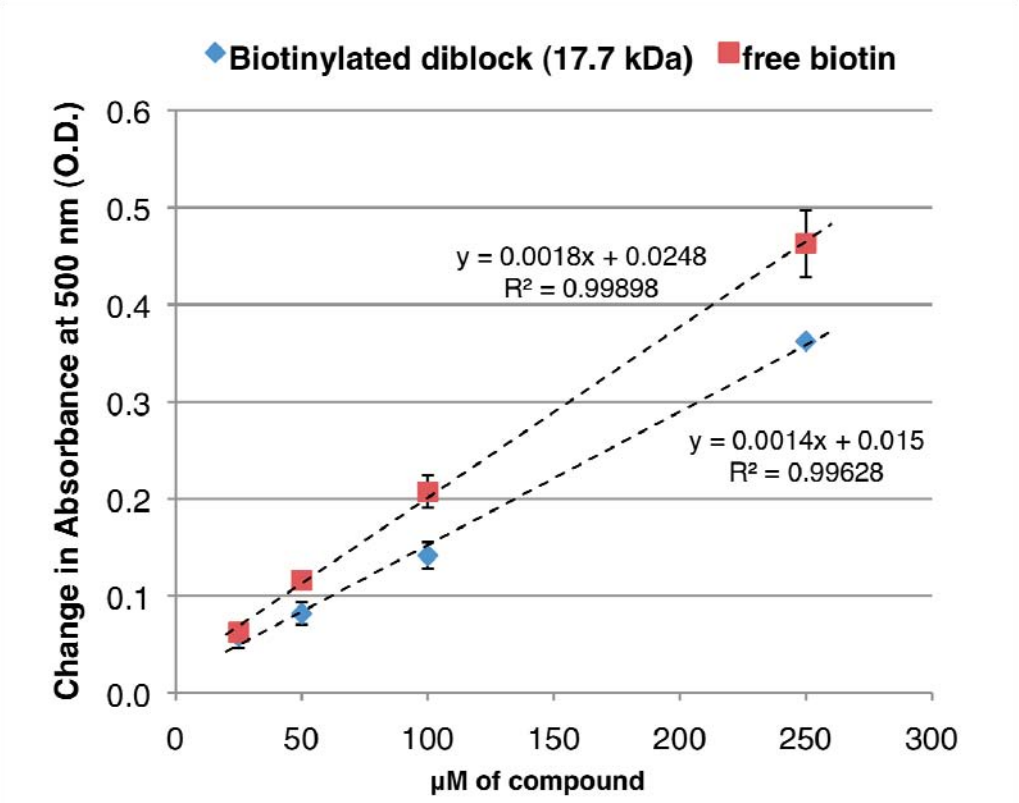
Figure S4. Time-lapse images of mNP/AuNP co-aggregation and separation process.



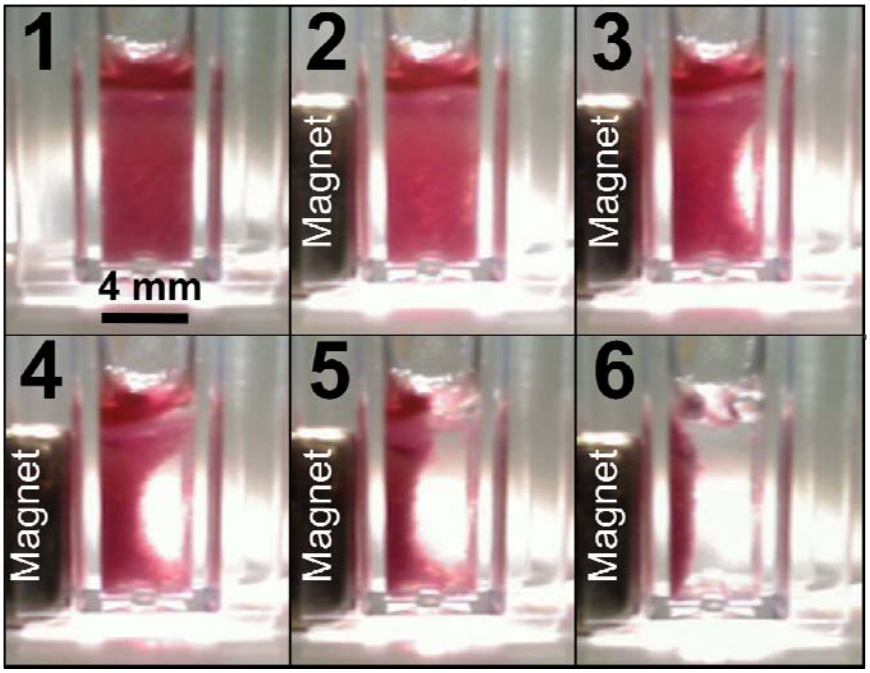
Supporting Figure S1. Refractive index GPC traces showing the molecular weight distributions of the 15.7 kDa mCTA (red, dashed), and the 17.7 kDa diblock copolymer (blue, solid).



Supporting Figure S2. ^{1}H-NMR (300 MHz in $CDCl_3$) of the 17.7 kDa diblock copolymer before biotinylation (compound (2) in Figure 2).



Supporting Figure S3. Quantitation of biotinylation efficiency. HABA dye-displacement assay on the 17.7 kDa biotinylated diblock copolymer was performed with free biotin as a standard reference. The biotinylation efficiency was found to be ~78%.



Supporting Figure S4. Video stills of dual AuNP/mNP co-aggregation and magnetic separation. For the purposes of the video, the sample comprised 250 μL of the AuNP/mNP/homo-pNIPAAm mixture in PBS buffer. 250 μL of 5M NaCl was used to trigger the pNIPAAm phase transition seconds before image 1 was acquired. The magnet was then applied for a total of 20 minutes. Comparable magnetic separation behavior was observed for mixtures that were co-aggregated using a thermal stimulus. The AuNP particle capture efficiency was evaluated by measuring the absorbance at 530 nm before and after magnetic capture and resuspension into an equal volume of fluid below the LCST. Typical nanoparticle capture efficiencies from 50% human plasma were found to be 75-85%.

Intracellular Delivery of a Protein Antigen with an Endosomal-Releasing Polymer Enhances CD8 T-Cell Production and Prophylactic Vaccine Efficacy

Suzanne Foster,† Craig L. Duvall,† Emily F. Crownover, Allan S. Hoffman, and Patrick S. Stayton*

Department of Bioengineering and Center for Intracellular Delivery of Biologics, University of Washington, Seattle Washington 98195, United States. Received April 27, 2010; Revised Manuscript Received September 2, 2010

Protein-based vaccines have significant potential as infectious disease and anticancer therapeutics, but clinical impact has been limited in some applications by their inability to generate a coordinated cellular immune response. Here, a pH-responsive carrier incorporating poly(propylacrylic acid) (PPAA) was evaluated to test whether improved cytosolic delivery of a protein antigen could enhance CD8+ cytotoxic lymphocyte generation and prophylactic tumor vaccine responses. PPAA was directly conjugated to the model ovalbumin antigen via reducible disulfide linkages and was also tested in a particulate formulation after condensation with cationic poly(dimethylaminoethyl methacrylate) (PDMAEMA). Intracellular trafficking studies revealed that both PPAA-containing formulations were stably internalized and evaded exocytotic pathways, leading to increased intracellular accumulation and potential access to the cytosolic MHC-1 antigen presentation pathway. In an EG.7-OVA mouse tumor protection model, both PPAA-containing carriers robustly inhibited tumor growth and led to an approximately 3.5-fold increase in the longevity of tumor-free survival relative to controls. Mechanistically, this response was attributed to the 8-fold increase in production of ovalbumin-specific CD8+ T-lymphocytes and an 11-fold increase in production of antiovalbumin IgG. Significantly, this is one of the first demonstrated examples of in vivo immunotherapeutic efficacy using soluble protein−polymer conjugates. These results suggest that carriers enhancing cytosolic delivery of protein antigens could lead to more robust CD8+ T-cell response and demonstrate the potential of pH-responsive PPAA-based carriers for therapeutic vaccine applications.

INTRODUCTION

There is continuing effort to develop more effective vaccines for infectious disease and as a therapeutic modality for cancer. For protein-based vaccines that represent an outside-in delivery paradigm, a considerable challenge is the intracellular delivery of antigens into the cytosol of antigen presenting cells (APCs) where the class I antigen presentation pathway may be more efficiently accessed. This pathway leads to generation of CD8+ cytotoxic T-lymphocytes (CTLs), which are capable of immunorecognition and direct apoptotic induction in cancer cells (*1, 2*). A diversity of approaches has been explored for delivering antigens to optimally stimulate CD8+ T-cell responses. Incorporation of MHC-1 adjuvants, such as CpG-DNA (*3*) or toll-like receptor (TLR) ligands (*4, 5*) into carrier formulations has been utilized to promote MHC-1 antigen presentation and induce production of antigen-specific CD8+ T-cells. Additionally, recombinant viral vectors have been employed as inside-out strategies for efficiently transfecting target cells (*6, 7*), and fusion with bacterial toxins (*8, 9*) has also been employed to enhance cytosolic delivery of vaccine antigens.

Synthetic carriers for protein antigen delivery have been intensively investigated to circumvent the safety concerns of viral vectors, but their efficiency is generally significantly lower. Liposomal systems (*10−13*), particles formed from poly(D,L-lactic-*co*-glycolic acid) (PLGA), and micelle carriers have been investigated for antigen delivery (*14−22*). There is substantial evidence from these studies that particle and micelle based systems yield a more efficient MHC-1 response relative to soluble conjugates due to uptake via phagocytotic pathways, as well as the possible adjuvancy of PLGA itself (*14, 15, 18, 23−25*).

The majority of synthetic vaccine delivery vehicles have been designed to explore or exploit the effects of particle size on immune response, but relatively little attention has been paid to other strategies for directing intracellular trafficking of antigens within APCs. Previous studies have employed pH-responsive degradable elements based on poly(L-glutamic acid)-poly(L-phenylalanine ethyl ester) (*26, 27*) and acid-labile particles and microgels that degrade at endosomal pH (*28−31*). However, pH-responsive polymeric carriers that actively alter vesicular trafficking pathways and promote endosomal escape of protein or peptide antigens have not been previously explored. This study aimed at testing whether an endosomal-releasing carrier would increase generation of antigen-specific CD8+ T-cells and provide a prophylactic effect in the ovalbumin vaccine model. Poly(propylacrylic acid) (PPAA)-based carriers have been investigated for intracellular delivery of biologic drugs including proteins, peptides, and siRNA (*32−40*). A PPAA carrier has previously been shown to enhance MHC-1 presentation and specific T-cell activation in an in vitro ovalbumin cell culture model (*41*). The present study further explored the mechanism of PPAA as a protein vaccine carrier and evaluated its efficacy in an in vivo mouse tumor protection model that allowed quantitation of the ovalbumin-specific CD8+ T-cell response. Both soluble conjugate and particulate PPAA-based formulations were tested, and importantly, both carriers were able to stimulate specific CD8+ T-cell development, antibody production, and significant tumor protection responses in vivo. These data show the potential of PPAA-based systems for

* Corresponding author/ Patrick S. Stayton, Ph.D.; University of Washington Department of Bioengineering; Box 355061; Seattle, WA 98195; Tel: (206) 685.8148; E-mail: stayton@u.washington.edu.

† Equally contributing co-first authors.

10.1021/bc100204m © 2010 American Chemical Society
Published on Web 11/02/2010

vaccine delivery and also suggest that modulating intracellular trafficking might enhance the effectiveness of induced immune responses.

EXPERIMENTAL PROCEDURES

Polymer Synthesis and Formulation with Ovalbumin. The synthesis and characterization of PPAA and poly(methacrylic acid) (PMAA) polymers and ovalbumin conjugates has been described previously (*41*). Briefly, PPAA was prepared by bulk free radical polymerization at 60 °C using the initiator azobisisobutyronitrile (AIBN). PMAA was prepared as a control polymer with similar structure to PPAA except that, due to its lower pK_a and decreased hydrophobicity, it does not enable effective endosomal escape (*41*). PMAA was prepared by reversible addition−fragmentation chain transfer (RAFT) polymerization at 40 °C using the chain transfer agent 4-cyanopentanoic acid dithiobenzoate (*41*) (CPAD) and the initiator 2,2′-azobis (2,4-dimethyl valeronitrile) (V65) in the absence of oxygen. A pyridyl disulfide functional acrylate monomer (PDSA) (*37*) was incorporated into these polymers at 3−5 mol % to provide protein conjugation sites. The polymers were purified by three rounds of precipitation from dimethyl formamide into diethyl ether. Characterization was performed by H^1 NMR and by spectrophotometric quantification of pyridine 2-thione release following reduction with dithiothreitol (DTT). Polymer molecular weight and polydispersity were determined by gel permeation chromatography (GPC) (Viscotek VE2001 sample module, VE3580 RI Detector, Waters Corp. Ultrahydrogel columns) in 0.1 M sodium phosphate buffer, pH 8, using poly(ethylene oxide) (PEO) standards (Polysciences, Inc., Warrington, PA).

Cationic poly(dimethylaminoethyl methacrylate) (PDMAEMA) was synthesized for nanoparticle formation driven by ionic complexation with anionic PPAA ovalbumin conjugates. DMAEMA monomer (Sigma-Aldrich) was distilled and polymerized using RAFT in the absence of oxygen at 33 wt % monomer in DMF at 30 °C for 16 h. 4-Cyano-4-(ethylsulfanylthiocarbonyl)sulfanyl pentanoic acid (ECT) served as the chain transfer agent (CTA) and 2,2′-azobis(4-methoxy-2,4-dimethylvaleronitrile) (V-70) was the radical initiator at an [ECT]/[V-70] molar ratio of 10. PDMAEMA was isolated by precipitation three times in 50% diethyl ether/50% pentane. Molecular weights were determined using GPC run with a DMF 0.1 wt % LiBr mobile phase at 60 °C and based on elution times of poly(methyl methacrylate) (PMMA) standards.

Ovalbumin (Ova) was conjugated to PPAA and PMAA via disulfide exchange reactions. Thiol groups were incorporated into ovalbumin using 2-iminothiolane (Traut's Reagent) as previously described (*41*). Thiolated proteins were subsequently reacted with the pendant pyridyl disulfide groups on the PPAA and PMAA polymers. Disulfide exchange reactions were carried out with a 2.5:1 molar ratio (polymer/ovalbumin) in 0.1 M phosphate buffer, pH 7.8, 0.15 M NaCl, 5 mM EDTA. Conjugation efficiency was quantified by measuring absorbance at 343 nm of the pyridine-2-thione, which is released upon disulfide exchange. PPAA−ovalbumin (PPAA-Ova) and PMAA−ovalbumin (PMAA-Ova) conjugates were purified using PD-10 desalting columns (GE Healthcare).

Particles containing PPAA-Ova soluble conjugates were formed by ionic complexation of cationic PDMAEMA with the anionic PPAA-Ova conjugate (PPAA-Ova/PDMAEMA). To form particles, PPAA-Ova conjugates were dissolved in PBS, pH 7.4, and PDMAEMA was added at ∓ charge ratios ranging from 1:1 to 60:1 The particle size and zeta potential were measured using a Brookhaven BI90Plus instrument, and particle sizes are reported as the number average. Particle size standard deviations were calculated from the reported polydispersity as previously described (*41*), and particle formation conditions were identified for subsequent testing based on production of nanoparticles in a desirable size range.

In Vitro Analyses of PPAA-Ova Conjugates and PPAA-Ova/PDMAEMA Particles. *Cytotoxicity of Polymer−Ovalbumin Conjugates and Particles.* The cytotoxicity of PPAA-Ova soluble conjugate and PPAA-Ova/PDMAEMA particulate delivery systems was tested in RAW macrophages using the Alamar Blue cytotoxicity assay. RAW macrophages were plated at 25 000 cells per well in 150 μL media (DMEM supplemented with 10% fetal bovine serum (FBS)) in a 96-well plate and incubated for 30 min at 37 °C. Alamar Blue reagent (20 μL) was added to each well, and PPAA-Ova conjugates or PPAA-Ova/PDMAEMA particles were added to the cells at polymer concentrations of 100 μg/mL, 200 μg/mL, 500 μg/mL, and 750 μg/mL. Samples were incubated for 24 h, and fluorescence was measured using a fluorescence plate reader. Percent viability compared to untreated cells was calculated for each sample.

Intracellular Uptake and Exocytotic Trafficking of PPAA-^{14}C-Ova and PPAA-^{14}C-Ova/PDMAEMA in Macrophages. Radiolabled conjugates were prepared for uptake and exocytosis studies as described previously (*41*). Briefly, Traut's reagent was reacted with ovalbumin at a 20-fold excess, followed by a 3-fold molar excess of ^{14}C-iodoacetamide (MP Biomedical). Polymer−Ova conjugation and particle formulation was subsequently completed as described above. To assess intracellular uptake, RAW macrophages were plated in a 48-well plate at 75 000 cells/well and allowed to grow overnight. Then, ^{14}C-Ova, PPAA-^{14}C-Ova, PMAA-^{14}C-Ova, or PPAA-^{14}C-Ova/PDMAEMA was added to the cells at a concentration of 50 μg/mL ovalbumin ($n \geq 3$ per treatment). Samples were incubated for 1 min and were then washed twice with PBS and lysed using 1% Triton X-100 in water. Radioactivity in the cell media, PBS wash, and cell lysate was measured using a liquid scintillation counter. Percent uptake of ^{14}C-ovalbumin was calculated based on the percent of the total radioactivity delivered that was present in the cell lysate.

Exocytosis studies were completed to gauge the ability of each of the Ova formulations to escape vesicular entrapment and endocytosis/exocytosis trafficking pathways in order to access the cytosolic MHC-1 presentation pathway. In these studies, ^{14}C-Ova, PMAA-^{14}C-Ova, PPAA-^{14}C-Ova, or PPAA-^{14}C-Ova/PDMAEMA was added to RAW cells at a concentration of 50 μg/mL ovalbumin ($n \geq 3$ per treatment). Samples were incubated for 15 min, media containing non-internalized ovalbumin was aspirated, and cells were washed twice with media. In a subset of samples, the percentage of the total ^{14}C-ovalbumin delivered that was internalized during the initial 15 min pulse was determined using cell lysates gathered in 1% Triton X. Parallel samples were then incubated with new media, which was then collected and replaced with fresh media at 5 min, 10 min, 20 min, 30 min, 1 h, 2 h, and 4 h. After 4 h, the cells were treated with 1% Triton X and the cell lysates were collected. ^{14}C-ovalbumin recycled into the extracellular media was quantified at each time point, and the quantity remaining in the cell lysates after 4 h was determined as a percentage of the quantity of ^{14}C-ovalbumin internalized during the initial 15 min pulse.

In Vivo Tumor Protection Against Ovalbumin Expressing Tumors. All animal studies were performed in compliance with the University of Washington Animal Care and Use Committee. Female C57Bl/6 mice 7−8 weeks old were purchased from Jackson Laboratories. E.G7-OVA thymoma cells stably transfected with the ovalbumin gene leading to cell surface expression of ovalbumin epitopes were obtained from ATCC and cultured per the supplier's instructions. Mice were anesthetized with isofluorane and injected subcutaneously on the dorsum with 150

μL of PBS, Ova, PMAA-Ova, PPAA-Ova, or PPAA-Ova/PDMAEMA, with an equivalent of 100 μg ovalbumin delivered to each mouse ($n \geq 4$ per group). Seven days after vaccination, mice were anesthetized and the hair on the left flank was removed using depilatory cream. The E.G7-OVA tumor cells (1×10^6 cells per mouse) were injected in a volume of 100 μL PBS subcutaneously on the left flank. Mice were monitored every 2−3 days, and tumor length and width were measured using digital calipers. Tumor volume was estimated using the commonly employed formula that is based on an ellipsoid geometry (*30, 42*).

Flow Cytometric Tetramer Detection of Ovalbumin-Specific CD8+ T-Cell Response in Vivo. In order to assess the ability of the PPAA carrier to induce CD8+ T-cell production, a flow cytometric assay using phycoerythrin (PE)-conjugated iTAg MHC-1 tetramers (Immunomics/Beckman Coulter) was used. MHC-1 tetramers have been employed to evaluate CD8+ responses in vaccine strategies using ovalbumin (*42*−*44*), as well as other antigens (*45, 46*). Here, the fluorescently labeled tetramers (PE-MHC-1/SIINFEKL) are complexes of MHC molecules and a specific ovalbumin epitope (SIINFEKL) that allows for the evaluation of the percentage of CD8+ T-cells from spleens of immunized mice that can recognize this specific ovalbumin fragment presented via an MHC-1 mechanism. For this experiment, 6−8-week-old female C57Bl/6 mice (4 per group) were immunized subcutaneously with 150 μL of PBS, Ova, PMAA-Ova, PPAA-Ova, or PPAA-Ova/PDMAEMA, with an equivalent of 100 μg ovalbumin delivered to each mouse. Seven days later, mice were euthanized and their spleens harvested. Spleens were forced through a 100 μm cell strainer into a Petri dish containing DMEM culture medium. Cells were counted and resuspended at 8×10^6 cells/mL. They were then stained according to the manufacturer's protocol, in addition to simultaneous staining with a FITC-labeled rat antimouse CD8a antibody to allow for identification of CD8+ T-cells within the heterogeneous cell population. The cells were analyzed using flow cytometry, and the percent of CD8 cells that stained positive for PE-MHC-1/SIINFEKL was determined.

ELISA Measurement of In Vivo Antibody Response. To evaluate the humoral immune response to the administered vaccines, the production of antiovalbumin IgG antibody was measured for the mice in the tumor study. Plasma was collected from blood harvested retro-orbitally and assayed for antiovalbumin IgG using a modification of the ELISA procedure described by Chung et al. (*47*). Nunc Maxisorp 96-well plates were coated overnight with 5 μg/mL ovalbumin at 4 °C and then blocked with 1% bovine serum albumin (BSA) solution in PBS for 1.5 h at room temperature. Plasma samples diluted 1:5000 in PBS and antiovalbumin standards (3−200 ng/mL clone OVA-14 IgG1, Sigma) were added in triplicate for 3 h at room temperature. The plate was washed 3 times with PBS−Tween and treated for 2 h with goat antimouse IgG conjugated to peroxidase (Sigma) at 1:3000 in 0.1% BSA PBS−Tween. The plate was washed 3 times with PBS−Tween, and SureBlue Reserve TMB peroxidase substrate (KPL Inc.) was used to quantify antiovalbumin antibody concentration in plasma samples relative to the standards by measuring absorbance at 450 nm.

Statistical Analysis. ANOVA was utilized to test for treatment effects, and Tukey's test was employed for posthoc comparisons. Significant differences were defined as $p < 0.05$.

RESULTS

Polymer Synthesis and Formulation with Ovalbumin. The PPAA copolymer had $M_n = 22$ kD and $M_w/M_n = 2.0$, with 3 mol % PDSA, and the PMAA copolymer had $M_n = 27$ kD and $M_w/M_n = 2.1$, with 2 mol % PDSA. The PDMAEMA used to form the PPAA-Ova/PDMAEMA ionic complexes had $M_n = 7.8$ kD and $M_w/M_n = 1.2$. The PPAA-Ova and PMAA-Ova conjugates used in this study were similar to those characterized in our previous in vitro experiments (*41*). Fifteen percent of the total available lysines in ovalbumin were thiolated, which equates to an average of three thiols per protein. The BCA assay revealed that both the PPAA-Ova and PMAA-Ova conjugates contained 38% ovalbumin by weight. GPC analysis revealed that $M_n = 43$ kD and $M_w/M_n = 2.9$ for the PPAA-Ova conjugate and $M_n = 54$ kD and $M_w/M_n = 2.4$ for the PMAA-Ova conjugate. The ^{14}C-labeled conjugates used for the cellular internalization studies were similar in size with $M_n = 40$ kD and $M_w/M_n = 3.5$ for the PPAA-^{14}C-Ova and $M_n = 50$ kD and $M_w/M_n = 2.4$ for the PMAA-^{14}C-Ova. The degree of thiolation of the ovalbumin used to form these radiolabeled conjugates was determined to be 30%, and the final conjugates were found to be 34% and 40% ovalbumin by weight for the PPAA-^{14}C-Ova and PMAA-^{14}C-Ova conjugates, respectively.

The particle formulation resulted in PPAA-Ova/PDMAEMA ionic particles that were characterized using dynamic light scattering (DLS) and zeta potential measurements (Supporting Information Table S1). For subsequent in vitro and in vivo experiments, the focus was the formulation with a ∓ charge ratio of 20:1 due to the formation of particles in a desirable size range using this composition. The 20:1 ∓ formulation had a hydrodynamic radius of 178 ± 45 nm (reported as number average), in PBS at pH 7.4, and the zeta potential was found to be −32 mV, which is consistent with the excess of negatively charged PPAA used in particle formation.

Mechanistic In Vitro Analyses of PPAA-Ova Conjugates and PPAA-Ova/PDMAEMA Particles. *Cytotoxicity of Polymer*−*Ovalbumin Conjugates and Particles.* After incubating RAW macrophages for 24 h with the polymer conjugates or PPAA-Ova/PDMAEMA particles, cell viability was evaluated using the Alamar Blue assay. Previous results (*41*) that found PPAA-Ova and PMAA-Ova conjugates to be nontoxic were corroborated, and it was confirmed that the particles also demonstrate cytocompatibility despite their larger size, different architecture, and inclusion of cationic PDMAEMA. For example, cells treated with PPAA-Ova/PDMAEMA particles maintained >98% viability at polymer concentrations up to 750 μg/mL, which is five times the concentration utilized for subsequent cellular uptake and exocytosis assays.

Intracellular Uptake, Cytosolic Accumulation, and Exocytotic Trafficking of PPAA-^{14}C-Ova and PPAA-^{14}C-Ova/2 > PDMAEMA in Macrophages. The uptake and intracellular accumulation was evaluated for ^{14}C-Ova, PMAA-^{14}C-Ova, PPAA-^{14}C-Ova, and PPAA-^{14}C-Ova/PDMAEMA in the RAW macrophages. The PMAA-^{14}C-Ova control is analogous in structure to PPAA-^{14}C-Ova, but PMAA has a shorter alkyl tail and its carboxylic acid has a lower pK_a relative to PPAA. PMAA serves as a control polymer with related chemistry to PPAA but with significantly reduced endosomolytic activity. Initial cellular uptake was found to be statistically equivalent for all groups at the 1 min time point (Figure 1A) indicating that significant early differences were not present among the different ^{14}C-Ova formulations. However, on longer time scales when intracellular quantities reflect a composite of uptake and exocytotic recycling, both the PPAA-^{14}C-Ova and PPAA-^{14}C-Ova/PDMAEMA formulations accumulated intracellularly to a significantly greater extent than the control ^{14}C-Ova and PMAA-^{14}C-Ova (Figure 1b, Supporting Information Figure S1). After normalizing to the quantity of ovalbumin initially internalized in a 15 min "pulse", exocytosis of PPAA-^{14}C-Ova and PPAA-^{14}C-Ova/PDMAEMA particles was significantly reduced compared to the protein and PMAA control conjugate (Figure 1B) as seen previously with the soluble conjugate (*41*). At the

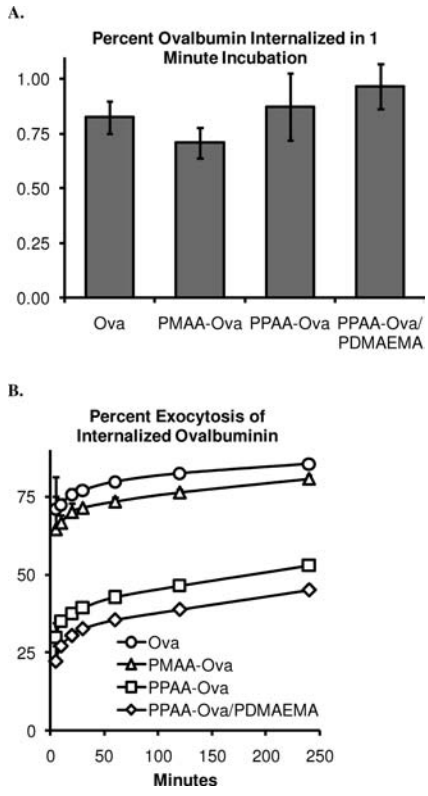


Figure 1. Enhanced ^{14}C-Ova intracellular accumulation and decreased exocytosis for PPAA-^{14}C-Ova conjugates and PPAA-Ova/PDMAEMA particles. (A) RAW macrophages incubated for 1 min with samples at a concentration of 50 μg/mL ^{14}C-ovalbumin showed that uptake of ^{14}C-ovalbumin was the same for all formulations during a time frame that precludes the effects of exocytosis (no significant differences between treatment groups). (B) Following a 15 min incubation with ^{14}C-ovalbumin formulations, the amount of ovalbumin exocytosed at each time point was determined. Significantly less exocytosis was seen with PPAA-containing carriers, indicating PPAA functionality in evading exocytotic fates. All experimental groups are statistically different in the exocytosis experiment.

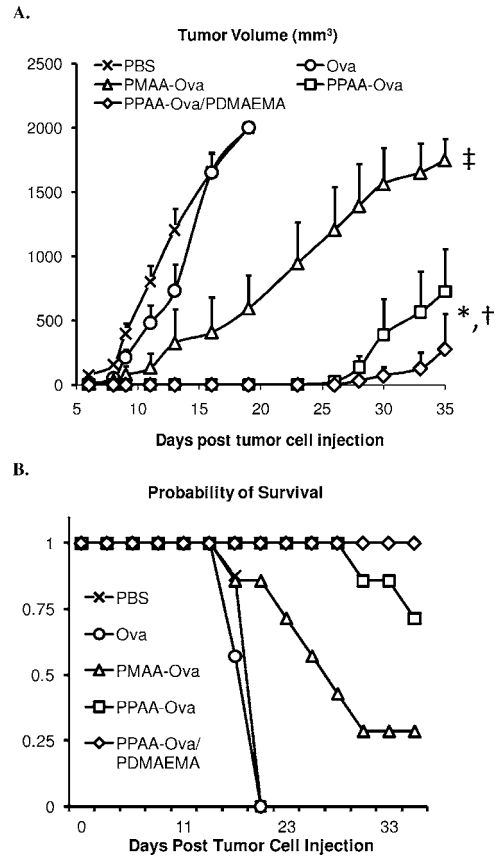


Figure 2. Enhanced tumor protection in mice immunized with PPAA-based vaccines. (A) C57Bl/6 mice were vaccinated with PBS, Ova, PMAA-Ova, PPAA−Ova, or PPAA-Ova/PDMAEMA at 100 μg ovalbumin per mouse. After 1 week, mice were injected with E.G7-OVA tumor cells, and tumor size was measured until it exceeded 2000 mm^3, at which point that animal was euthanized. The tumor size for euthanized mice was taken to be 2000 mm^3 for the calculation of mean tumor size at all subsequent time points until all mice in that treatment group were euthanized. PPAA-Ova and PPAA-Ova/PDMAEMA showed significant tumor protection relative to all other treatment groups, while PMAA-Ova had enhanced tumor protection relative to mice delivered the PBS control. Data are represented as mean ± standard error mean (SEM) and represent $n \geq 4$. *Significantly different from PBS and Ova. †Significantly different from PMAA-Ova. ‡Significantly different from PBS. (B) Kaplan−Meier survival plots for this study display the probability of survival as the fraction of mice whose tumors have not exceeded 2000 mm^3 on the indicated day. This plot illustrates the enhanced survival in mice vaccinated using PPAA-based carriers.

conclusion of the study at 4 h, less than 50% of the PPAA-containing formulations had been exocytosed. In contrast, ^{14}C-Ova and PMAA-^{14}C-Ova were rapidly exocytosed, with over 75% of the free Ova recycled back into the extracellular environment within 30 min. The rapid recycling rate observed for ^{14}C-Ova was in accordance with previous studies (*41*, *48*−*50*). The intracellular quantity of ^{14}C-labeled formulations was also evaluated and accurately complemented the exocytosis data, with the PPAA-containing formulations having significantly extended residence within the cells (Supporting Information Figure S1). Taken together, these data indicate that the pH-responsive, PPAA-containing formulations may be evading exocytosis pathways by aiding in endosomal escape and cytosolic delivery where protein cargo can potentially access the MHC-1 presentation pathway.

In Vivo Tumor Protection Against Ovalbumin Expressing Tumors. The in vivo efficacy of PPAA as a vaccine carrier was evaluated using a murine ovalbumin expressing tumor protection model. This model allows the characterization of prophylactic vaccine tumor protection, and additionally, it allows the quantitation of Ova-specific CD8+ induction to test whether the endosomal-releasing polymers enhance this presentation pathway. In this model, delivery of soluble PPAA-Ova and particulate PPAA-Ova/PDMAEMA vaccines dramatically prevented tumor growth compared to controls, as evidenced by the tumor growth curves (Figure 2A) and Kaplan−Meier survival plots (Figure 2B). Most PBS and Ova immunized control mice developed tumors within the 10 days of tumor cell injection and had to be euthanized by day 19 when tumors exceeded 2000 mm^3. PMAA-Ova delayed tumor growth to an extent compared to the saline controls, but statistical differences between tumor growth curves for free Ova and PMAA-Ova were not significant. Interestingly, PPAA-Ova conjugates and the PPAA-Ova/PDMAEMA particles both significantly delayed tumor growth, and there was no significant statistical difference between the soluble and particulate formulations in this study. As summarized in Table 1, PPAA-Ova and PPAA-Ova/PDMAEMA immunized mice averaged nearly 5 weeks before tumors developed following tumor cell inoculation. In terms of tumor-free survival following cell injection, PMAA-Ova immunized mice remained tumor-free significantly longer than the PBS and Ova controls but developed palpable tumors significantly earlier than mice immunized with PPAA-containing vaccines. The larger size of the PMAA-Ova conjugates compared to Ova alone and potential inflammatory stimulation could explain the small effects of this control formulation.

Table 1. Number of Days of Tumor Protection[a]

sample	avg. days tumor protection
PBS	9 ± 1
Ova	11 ± 3
PMAA-Ova	20 ± 7[b]
PPAA-Ova	33 ± 3[b,c]
PPAA-Ova/PDMAEMA	34 ± 3[b,c]

[a] Tumor protection is reported as the number of days post tumor challenge that each mouse developed a measurable tumor larger than 200 mm^3 For PPAA-Ova and PPAA-Ova/PDMAEMA groups, some mice were assigned a value of 35 days at the conclusion of the experiment even though they still did not present with tumors greater than 200 mm^3 at that time. [b] Significantly different from PBS and Ova. [c] Significantly different from PMAA-Ova.

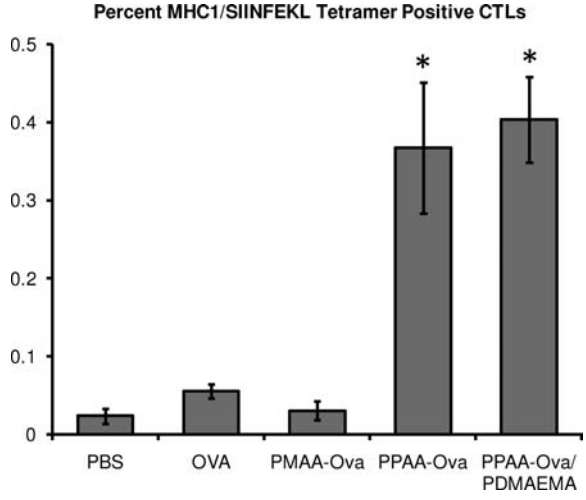


Figure 3. Enhanced CD8+ spleen-derived T-cell production in mice immunized with PPAA-based vaccines. C57Bl/6 mice were vaccinated with PBS, Ova, PMAA-ova, PPAA-Ova, and PPAA-Ova/PDMAEMA (100 μg ova per mouse). Seven days later, spleens were collected and splenocytes were stained with FITC-anti-CD8 and PE-MHC-1/SIINFEKL tetramers. Flow cytometric evaluation showed a significantly enhanced antiovalbumin MHC-1 driven CD8+ T-cell response induced by the PPAA-Ova soluble and PPAA-Ova/PDMAEMA particulate vaccines. Data are presented as mean $\pm$ SEM $n = 4$ per group, and * indicates significantly different from PBS, Ova, PMAA-Ova.

Flow Cytometric Tetramer Detection of Ovalbumin-Specific CD8+ T-Cell Response in Vivo. To investigate whether enhanced CTL generation played a role in the prophylactic immune response observed for the PPAA-Ova and PPAA-Ova/PDMAEMA groups, MHC-1/SIINFEKL tetramers were used to measure the number of Ova-reactive CD8+ T cells in the spleen using flow cytometry. In splenocytes harvested from mice 7 days postvaccination, delivery of free Ova or PMAA-Ova did not result in statistically significant CD8+ T-cell production compared to PBS. Vaccination with soluble PPAA-Ova and particulate PPAA-Ova/PDMAEMA resulted in enhanced CD8+ T-cell generation compared to all other treatment groups as evidenced by the increased number of CD8+/tetramer+ T-cells as depicted in Figure 3. Soluble and particulate PPAA-containing vehicles resulted in an approximately 8-fold increase in CD8+ T-cell development relative to delivery of free Ova. Surprisingly, the soluble PPAA-Ova conjugate was able to overcome any potential advantage of the PPAA-Ova/PDMAEMA particulate formulation in terms of increased uptake/presentation (*15, 18, 23*−*25*) and was found to lead to a similar level of ovalbumin SIINFEKL epitope recognition by CD8+ T-cells in vivo.

ELISA Measurement of In Vivo Antibody Response. To determine the role of the humoral component in the prophylactic immune response observed for PPAA-Ova and PPAA-Ova/PDMAEMA vaccinated mice, blood was drawn from all mice 20 days after vaccination and the antiovalbumin IgG titer was measured by ELISA. As show in Figure 4, no appreciable antibody production was observed for mice vaccinated with PBS, Ova, or PMAA-Ova. Conversely, a significant increase in antiovalbumin IgG was detected for PPAA-Ova and PPAA-Ova/PDMAEMA vaccinated mice, indicating that an antibody-mediated response also contributed to the tumor protection observed in these groups. No differences were detected, however, in PPAA-containing soluble conjugate and particulate forms.

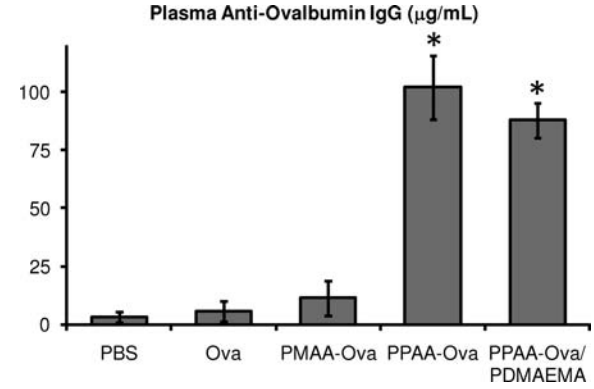


Figure 4. PPAA-based vaccine triggered antiovalbumin IgG antibody production. Mice were vaccinated with PBS, Ova, PMAA-Ova, PPAA-Ova, PPAA-Ova/PDMAEMA (100 μg ovalbumin per mouse). Twenty days after vaccine injection, blood was drawn and an ELISA was performed on plasma samples. The antiovalbumin antibody response induced by the PPAA soluble and particulate conjugates is significantly greater than that resulting from vaccination with Ova or PMAA-Ova. Data presented as mean $\pm$ SEM, and $n = 4$ per group. * indicates significantly different than PBS, Ova, PMAA-Ova.

DISCUSSION

In this study, PPAA-based protein vaccines effectively stimulated prophylactic immune responses with a single injection that led to a statistically significant delay in tumor development in the ovalbumin vaccine mouse model. Interestingly, both the soluble PPAA-Ova and particulate PPAA-Ova/PDMAEMA immunizations delayed tumor growth for nearly five weeks, while control mice injected with PBS and free ovalbumin developed tumors in less than 10 days. The robust antitumor response observed for both soluble and particulate PPAA-based carriers was mediated through an enhanced CD8+ T-cell response and a marked production of antiovalbumin antibodies. These data indicate that pH-responsive polymer protein conjugates may be able to access the MHC-1 pathway in the cytosol by triggering endosome escape, and this is, to our knowledge, the first reported account of soluble protein−polymer conjugates eliciting comparable antitumor activity to particulate platforms.

Mechanistically, both CD8+ T-cell generation and antibody production contributed to the robust antitumor response observed for the PPAA-based carriers. Enhanced CD8+ T-cell production of PPAA-based vaccines in vivo was in agreement with our previous in vitro observations that these carriers increase intracellular accumulation through pH-responsive endosomal escape and enhance MHC-1 presentation/T-cell activation (*41*). The antiovalbumin antibody production could be expected, and previous studies have found concomitant CD8+ T-cell generation and antibody response (*51*). Since the PPAA-based carriers increase accumulation in APCs, it is logical that these carriers would also enter the MHC-2 antigen presentation pathway, which can be accessed through specialized endosomal vesicles. This would lead to CD4+ T-helper cell activation and increased antibody production following treatment with the PPAA-containing vaccines.

Interestingly, the soluble and particulate PPAA-based carriers elicited comparable tumor protection and T-cell/antibody responses in vivo. As shown in Figure 1, both PPAA-Ova and PPAA-Ova/PDMAEMA had positive effects on protein evasion of exocytosis, but the particulate PPAA-Ova/PDMAEMA formulation resulted in slightly lower exocytosis in macrophages. The increase in stable internalization may be related to the presence of the cationic PDMAEMA component to neutralize a portion of the PPAA anionic charges and/or due to phagosomal uptake of particulate substances (*52*−*56*). It has not been clearly elucidated why the better in vitro performance of the PPAA-Ova/PDMAEMA particles relative to the PPAA-Ova conjugates was less evident in the in vivo studies. We hypothesize that diffusional limitations of the particles because of their larger size could hinder access to APCs and thus cell uptake in vivo. Unpackaging of the ionically complexed particles may also be a limiting step in antigen delivery to APCs for this formulation, and this step could lower this system's overall efficiency in vivo. Finally, it is possible that both the conjugate and the PPAA-Ova particles are saturating the in vivo response in this model, limiting our ability to discriminate differences due to the different formulations. It remains to be seen whether other types of particles incorporating PPAA may provide a better combination of particulate form and PPAA functionality.

It was also interesting to note that the PMAA-Ova conjugate provided an intermediate degree of tumor protection in vivo, although this formulation did not markedly decrease exocytotic fate in vitro or elicit measurable CD8+ T-cell or antibody production in vivo. This observation may be due to a CD4+ T-cell response, which is induced by MHC-2 presentation and does not require cytosolic entry of the antigen for activation. This pathway may have resulted in production of cytokines by CD4+ helper T-cells, leading to activation of cytotoxic macrophages and delayed tumor growth. Alternatively, there may have been a smaller or more transient effect from the PMAA-Ova treatment that was functionally significant for tumor protection although it was not detected at the specific time point analyzed in our CD8+ T-cell and antibody assays.

In the context of previous studies, the degree of tumor protection produced by the PPAA-based vaccines with a single dose and no adjuvant was substantial when compared to other vaccine formulations tested using the ovalbumin-based protein vaccine model. Discrepancies in the number of tumor cells injected, the number of rounds of immunization, and the inclusion of adjuvants hinder absolute comparison to previous studies, but some general comparisons demonstrate the effectiveness of the conjugate formulation. For example, the often-used PGA nanoparticle vaccine delivery strategy prevented tumor formation for approximately 16 days after tumor injection (*27*). Similarly, a particulate, acid-degradable carrier kept mice tumor-free for just over 2 weeks (*30*). Liposomes, another extensively tested vaccine delivery vehicle, have been shown to prevent tumor formation for 20−25 days when codelivered with the CpG-ODN adjuvant (*57*) and for 45 days when the carriers contain the cytokine IL-2 (*51*).

Relative to these previous studies, one can conclude that both soluble PPAA-Ova conjugates (33 ± 3 days tumor protection) and PPAA-Ova/PDAEMA particulate vaccine carriers (34 ± 3 days tumor protection) meet or exceed the precedent established in previous reports. Furthermore, the current results represent the first evidence of a soluble polymer−protein conjugate performing as well as a particulate carrier, which had been the previous standard. The promise of PPAA-based vaccines can be further expanded when one considers the potential improvements that may further enhance their efficacy such as multiple immunization protocols, codelivery with adjuvants, or inclusion of APC-specific targeting moieties. Examination of these avenues and evaluation of this technology against true therapeutic targets (human tumor xenografts, viral pathogens, etc.) are warranted for future investigation.

ACKNOWLEDGMENT

This project was supported by funding from the National Institutes of Health (grant R01EB2991) and the Washington State Life Sciences Discovery Fund through the Center for Intracellular Delivery of Biologics.

Supporting Information Available: Table S1: Particle sizing and zeta potential measurements on PPAA-Ova/PDMAEMA ionically complexed particles for a range of ∓ charge ratios. Figure S1: Increased intracellular persistence of PPAA-containing vaccine formulations. This material is available free of charge via the Internet at http://pubs.acs.org.

LITERATURE CITED

(1) Boon, T., Cerottini, J. C., Eynde, B. V., Bruggen, P., and Pel, A. V. (1994) Tumor antigens recognized by T lymphocytes. *Annu. Rev. Immunol. 12*, 337–365.

(2) Engers, H., Lahaye, T., Sorenson, G., Glasebrook, A., Horvath, C., and Brunner, K. (1984) Functional activity in vivo of effector T cell populations. II. Anti- tumor activity exhibited by syngeneic anti-MoMULV-specific cytolytic T cell clones. *J. Immunol. 133*, 1664–1670.

(3) Maurer, T., Heit, A., Hochrein, H., Ampenberger, F., O'Keeffe, M., Bauer, S., Lipford, G. B., Vabulas, R. M., and Wagner, H. (2002) CpG-DNA aided cross-presentation of soluble antigens by dendritic cells. *Eur. J. Immunol. 32*, 2356–2364.

(4) Hamdy, S., Elamanchili, P., Alshamsan, A., Molavi, O., Satou, T., and Samuel, J. (2007) Enhanced antigen-specific primary CD4+ and CD8+ responses by codelivery of ovalbumin and toll-like receptor ligand monophosphoryl lipid A in poly(D, L-lactic-co-glycolic acid) nanoparticles. *J. Biomed. Mater. Res. 81A*, 652–662.

(5) Heit, A., Schmitz, F., Haas, T., Busch, D. H., and Wagner, H. (2007) Antigen co-encapsulated with adjuvants efficiently drive protective T cell immunity. *Eur. J. Immunol. 37*, 2063–74.

(6) Bonnet, M. C., Tartaglia, J., Verdier, F., Kourilsky, P., Lindberg, A., Klein, M., and Moingeon, P. (2000) Recombinant viruses as a tool for therapeutic vaccination against human cancers. *Immunol. Lett. 74*, 11–25.

(7) Harrop, R., John, J., and Carroll, M. W. (2006) Recombinant viral vectors: Cancer vaccines. *Adv. Drug Delivery Rev. 58*, 931–947.

(8) Goletz, T. J., Klimpel, K. R., Leppla, S. H., Keith, J. M., and Berzofsky, J. A. (1997) Delivery of antigens to the MHC Class I pathway using bacterial toxins. *Hum. Immunol. 54*, 129–136.

(9) Shaw, C. A., and Starnbach, M. N. (2006) Stimulation of CD8+ T Cells following diphtheria toxin-mediated antigen delivery into dendritic cells. *Infect. Immunol.*

(10) Altin, J. G., and Parish, C. R. (2006) Liposomal vaccines - targeting the delivery of antigen. *Methods 40*, 39–52.

(11) Chikh, G., and Schutze-Redelmeier, M.-P. (2002) Liposomal delivery of CTL epitopes to dendritic cells. *Biosci. Rep. 22*, 339–353.

(12) Haining, W. N., Anderson, D. G., Little, S. R., von Berwelt-Baildon, M. S., Cardoso, A. A., Alves, P., Kosmatopoulos, K., Nadler, L. M., Langer, R., and Kohane, D. S. (2004) pH-Triggered microparticles for peptide vaccination. *J. Immunol. 173*, 2578–2585.

(13) Tacken, P. J., Torensma, R., and Figdor, C. G. (2006) Targeting antigens to dendritic cells in vivo. *Immunobiology 211*, 599–608.

(14) Maloy, K. J., Donachie, A. M., O'Hagan, D. T., and Mowat, A. M. (1994) Induction of mucosal and systemic immune responses by immunization with ovalbumin entrapped in poly-(lactide-co-glycolide) microparticles. *Immunology 81*, 661–667.

(15) Shen, H., Ackerman, A. L., Cody, V., Giodini, A., Hinson, E. R., Cresswell, P., Edelson, R. L., Saltzman, W. M., and Hanlon, D. J. (2006) Enhanced and prolonged cross-presentation following endosomal escape of exogenous antigens encapsulated in biodegradable nanoparticles. *Immunology 117*, 78–88.

(16) Panyam, J., Zhou, W.-z., Prabha, S., Sahoo, S. K., and Labhasetwar, V. (2002) Rapid endo-lysosomal escape of poly(DL-lactide-co-glycolide) nanoparticles: implications for drug and gene delivery. *FASEB J. 16*, 1217–1226.

(17) Newman, K. D., Kwon, G. S., Miller, G. G., Chlumecky, V., and Samuel, J. (2000) Cytoplasmic delivery of a macromolecular fluorescent probe by poly(d,l-lactic-co-glycolic acid) microspheres. *J. Biomed. Mater. Res. 50*, 591–597.

(18) Reddy, S. T., van der Vlies, A. J., Simeoni, E., Angeli, V., Randolph, G. J., O'Neil, C. P., Lee, L. K., Swartz, M. A., and Hubbell, J. A. (2007) Exploiting lymphatic transport and complement activation in nanoparticle vaccines. *Nat. Biotechnol. 25*, 1159–1164.

(19) Partidos, C. D., Vohra, P., Jones, D., Farrar, G., and Steward, M. W. (1997) CTL responses induced by a single immunization with peptide encapsulated in biodegradable microparticles. *J. Immunol. Methods 206*, 143–151.

(20) Bennewitz, N. L., and Babensee, J. E. (2005) The effect of the physical form of poly(lactic-co-glycolic acid) carriers on the humoral immune response to co-delivered antigen. *Biomaterials 26*, 2991–2999.

(21) Mundargi, R. C., Babu, V. R., Rangaswamy, V., Patel, P., and Aminabhavi, T. M. (2008) Nano/micro technologies for delivering macromolecular therapeutics using poly(D, L-lactide-go-glycolide) and its derivatives. *J. Controlled Release 125*, 193–209.

(22) Newman, K. D., Elamanchili, P., Kwon, G. S., and Samuel, J. (2002) Uptake of poly(D, L-lactic-co-glycolic acid) microspheres by antigen-presenting cells in vivo. *J. Biomed. Mater. Res. 60*, 480–486.

(23) Harding, C. V., and Song, R. (1994) Phagocytic processing of exogenous particulate antigens by macrophages for presentation by class I MHC molecules. *J. Immunol. 153*, 4925–4933.

(24) Kovacsovics-Bankowski, M., Clark, K., Benacerraf, B., and Rock, K. L. (1993) Efficient major histocompatibility complex class I presentation of exogenous antigen upon phagocytosis by macrophages. *Proc. Natl. Acad. Sci. U.S.A. 90*, 4942–4946.

(25) Thiele, L., Merkle, H. P., and Walter, E. (2003) Phagocytosis and phagosomal fate of surface-modified microparticles in dendritic cells and macrophages. *Pharm. Res. 20*, 221–228.

(26) Yoshikawa, T., Okada, N., Oda, A., Matsuo, K., Matsuo, K., Mukai, Y., Yoshioka, Y., Akagi, T., Akashi, M., and Nakagawa, S. (2008) Development of amphiphilic y-PGA-nanoparticle based tumor vaccine: potential of the nanoparticulate cytosolic protein delivery carrier. *Biochem. Biophys. Res. Commun. 366*, 408–413.

(27) Yoshikawa, T., Okada, N., Oda, A., Matsuo, K., Matsuo, K., Kayamuro, H., Ishii, Y., Yoshinaga, T., Akagi, T., Akashi, M., and Nakagawa, S. (2008) Nanoparticles built by self-assembly of amphiphilic y-PGA can deliver antigens to antigen-presenting cells with high efficiency: A new tumor-vaccine carrier for eliciting effector T cells. *Vaccine 26*, 1303–1313.

(28) Murthy, N., Xu, M., Schuck, S., Kunisawa, J., Shastri, N., and Frechet, J. M. J. (2003) A macromolecular delivery vehicle for protein-based vaccines: Acid-degradable protein-loaded microgels. *Proc. Natl. Acad. Sci. U.S.A. 100*, 4995–5000.

(29) Kwon, Y. J., Standley, S. M., Goh, S. L., and Frechet, J. M. J. (2005) Enhanced antigen presentation and immunostimulation of dendritic cells using acid-degradable cationic nanoparticles. *J. Controlled Release 105*, 199–212.

(30) Standley, S. M., Kwon, Y. J., Murthy, N., Kunisawa, J., Shastri, N., Guillaudeu, S. J., Lau, L., and Frechet, J. M. J. (2004) Acid-degradable particles for protein-based vaccines: enhanced survival rate for tumor-challenged mice using ovalbumin model. *Bioconjugate Chem. 15*, 1281–1288.

(31) Bachelder, E. M., Beaudette, T. T., Broaders, K. E., Paramonov, S. E., Dashe, J., and Frechet, J. M. (2008) Acid-degradable polyurethane particles for protein-based vaccines: biological evaluation and in vitro analysis of particle degradation products. *Mol. Pharm. 5*, 876–84.

(32) Murthy, N., Robichaud, J. R., Tirrell, D. S., Stayton, P. S., and Hoffman, A. S. (1999) The design and synthesis of polymers for eukaryotic membrane disruption. *J. Controlled Release 61*, 137–143.

(33) Murthy, N., Chang, I., Stayton, P. S., and Hoffman, A. S. (2001) pH-sensitive hemolysis by random copolymer of alkyl acrylates and acrylic acid. *Macromol. Symp. 172*, 49–55.

(34) Cheung, C. Y., Murthy, N., Stayton, P. S., and Hoffman, A. S. (2001) A pH-Sensitive polymer that enhances cationic lipid-mediated gene transfer. *Bioconjugate Chem. 12*, 906–910.

(35) Lackey, C. A., Press, O. W., Hoffman, A. S., and Stayton, P. S. (2002) A biomimetic pH-responsive polymer directs endosomal release and intracellular delivery of an endocytosed antibody complex. *Bioconjugate Chem. 13*, 996–1001.

(36) Murthy, N., Campbell, J., Fausto, N., Hoffman, A. S., and Stayton, P. S. (2003) Bioinspired pH-responsive polymers for the intracellular delivery of biomolecular drugs. *Bioconjugate Chem. 14*, 412–419.

(37) Bulmus, V., Woodward, M., Lin, L., Murthy, N., Stayton, P., and Hoffman, A. (2003) A new pH-responsive and glutathione-reactive, endosomal membrane-disruptive polymeric carrier for intracellular delivery of biomolecular drugs. *J. Controlled Release 93*, 105–120.

(38) El-Sayed, M. E., Hoffman, A. S., and Stayton, P. S. (2005) Rational design of composition and activity correlations for pH-responsive and glutathione-reactive polymer therapeutics. *J. Controlled Release 104*, 417–427.

(39) Convertine, A. J., Benoit, D. S., Duvall, C. L., Hoffman, A. S., and Stayton, P. S. (2009) Development of a novel endosomolytic diblock copolymer for siRNA delivery. *J. Controlled Release 133*, 221–9.

(40) Duvall, C. L., Convertine, A., Benoit, D. S., Hoffman, A. S., and Stayton, P. (2009) Intracellular delivery of a proapoptotic peptide via conjugation to a RAFT synthesized endosomolytic polymer. *Mol. Pharm. 7*, 468–76.

(41) Flanary, S., Hoffman, A. S., and Stayton, P. S. (2009) Antigen delivery with poly(propylacrylic acid) conjugation enhances MHC-1 presentation and T-cell activation. *Bioconjugate Chem. 20*, 241–8.

(42) Wakabayashi, A., Nakagawa, Y., Shimizu, M., Moriya, K., Nishiyama, Y., and Takahashi, H. (2008) Suppression of an already established tumor growing through activated mucosal CTLs induced by oral administration of tumor antigen with cholera toxin. *J. Immunol. 180*, 4000–4010.

(43) Llopiz, D., Dotor, J., Zabaleta, A., Lasarte, J. J., Prieto, J., Borras-Cuesta, F., and Sarobe, P. (2008) Combined immunization with adjuvant molecules poly(I:C) and anti-CD40 plus a tumor antigen has potent prophylactic and therapeutic antitumor effects. *Cancer Immunol. Immunother. 57*, 19–29.

(44) Schlosser, E., Mueller, M., Fischer, S., Basta, S., Busch, D. H., Gander, B., and Groettrup, M. (2008) TLR ligands and antigen need to be coencapsulated into the same biodegradable microsphere for the generation of potent cytotoxic T lymphocyte responses. *Vaccine 26*, 1626–1637.

(45) Bohnenkamp, H. R., Coleman, J., Burchell, J. M., Taylor-Papadimitriou, J., and Noll, T. (2004) Breast carcinoma cell lysate-pulsed dendritic cells cross-prime MUC1-specific CD8+ T cells identified by peptide-MHC-class-I tetramers. *Cellular Immunol. 231*, 112–125.

(46) Eo, S.-K., Yoon, H.-A., Lee, J.-H., Chae, J.-S., and Cho, J.-G. (2004) Mucosal CD8+ T cell-mediated immunity of vaccinized animals to genital infection of herpes simplex virus type 1. *J. Bacteriol. Virol. 34*, 39–46.

(47) Chung, Y., Choi, J., Chang, Y.-S., Cho, S.-H., and Kang, C.-Y. (2002) Preventative and therapeutic effects of oral tolerance in a murine model of asthma. *Immunobiology 2006*, 408–423.

(48) Besterman, J. M., Airhart, J. A., Woodworth, R. C., and Low, R. B. (1981) Exocytosis of pinocytosed fluid in cultured cells: Kinetic evidence for rapid turnover and compartmentation. *J. Cell Biol. 91*, 716–727.

(49) Weaver, D. J., Jr., and Voss, E. W., Jr. (1998) Analysis of rates of receptor-mediated endocytosis and exocytosis of a fluorescent hapten-protein conjugate in murine macrophage: implications for antigen processing. *Biol. Cell 90*, 169–181.

(50) Panyam, J., and Labhasetwar, V. (2003) Dynamics of endocytosis and exocytosis of poly(D, L-lactide-co-glycolide) nanoparticles in vascular smooth muscle cells. *Pharm. Res. 20*, 212–220.

(51) Johnston, D., Reynolds, S. R., and Bystryn, J.-C. (2006) Interleukin-2/liposomes potentiate immune responses to a soluble protein cancer vaccine in mice. *Cancer Immunol. Immunother. 55*, 412–419.

(52) Trombetta, E. S., and Mellman, I. (2005) Cell biology of antigen processing and in vitro and in vivo. *Annu. Rev. Immunol. 23*, 975–1028.

(53) Guermonprez, P., Valladeau, J., Zitvogel, L., Thery, C., and Amigorena, S. (2002) Antigen presentation and T cell stimulation by dendritic cells. *Annu. Rev. Immunol. 20*, 621–667.

(54) Kovacsovics-Bankowski, M., and Rock, K. L. (1995) A phagosome-to-cytosol pathway for exogenous antigens presented on MHC class I molecules. *Science 267*, 243–246.

(55) Brode, S., and Macary, P. A. (2004) Cross-presentation: dendritic cells and macrophages bite off more than they can chew. *Immunology 112*, 345–351.

(56) Houde, M., Bertholet, S., Gagnon, E., Brunet, S., Goyette, G., Laplante, A., Princiotta, M. F., Thibault, P., Sacks, D., and Desjardins, M. (2003) Phagosomes are competent organelles for antigen cross-presentation. *Nature 425*, 402–406.

(57) De Jong, S., Chikh, G., Sekirov, L., Raney, S., Semple, S., Klimuk, S., Yuan, N., Hope, M., Cullis, P., and Tam, Y. (2007) Encapsulation in liposomal nanoparticles enhances the immunostimulatory, adjuvant and anti-tumor activity of subcutaneiously administered CpG ODN. *Cancer Immunol. Immunother. 56*, 1251–1264.

BC100204M

SUPPORTING INFORMATION

Intracellular Delivery of a Protein Antigen with an Endosomal-Releasing Polymer Enhances CTL Production and Prophylactic Vaccine Efficacy

Suzanne Foster[†], Craig L. Duvall[†], Emily F. Crownover, Allan S. Hoffman, Patrick S. Stayton*

Department of Bioengineering, University of Washington, Seattle WA 98195

[†]Equally Contributing Co-First Authors

*Corresponding Author:

Patrick S. Stayton, Ph.D.

University of Washington

Department of Bioengineering

Box 355061

Seattle, WA 98195

Tel: (206) 685.8148

E-mail: stayton@u.washington.edu

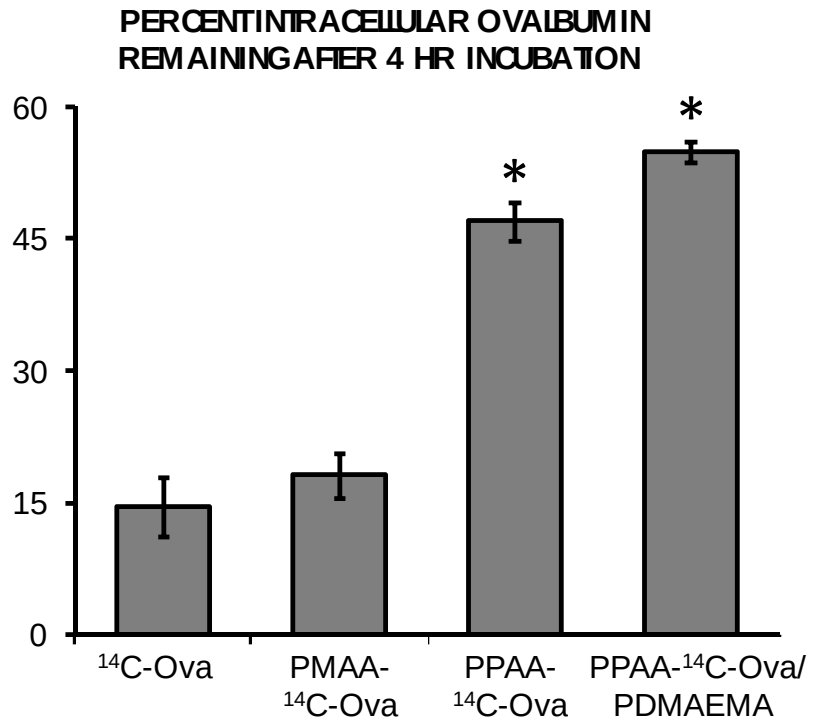
SUPPORTING INFORMATION CONTENTS

Table S1. Particle sizing and Zeta potential measurements on PPAA-^{14}C-Ova/PDMAEMA ionically complexed particles

Figure S1. Increased intracellular persistence of PPAA-containing vaccine formulations.

[-]/[+] Charge Ratio	Particle Size (nm)	Zeta Potential (mV)
60:1	72 ± 15	-39.8
40:1	125 ± 28	-35.4
20:1*	178 ± 45	-32.6
15:1	250 ± 65	-28.4
10:1	288 ± 67	-20.2
5:1	1990 ± 470	-21.3
≤2:1	large aggregates	NA

Supplementary Table S1. Particle sizing and Zeta potential measurements on PPAA-Ova/PDMAEMA ionically complexed particles for a range of -/+ charge ratios. Particle sizes are reported as the number average with standard deviations calculated from polydispersity as described previously (*44*). * indicates the charge ratio (20:1) used for the remainder of the cell and animal studies.



Supplementary Figure S1. Increased intracellular persistence of PPAA-containing vaccine formulations 4 hours after an initial 15 minute pulse with ^{14}C-ovalbumin formulations. Data illustrate significantly longer intracellular persistence by PPAA-^{14}C-Ova and PPAA-^{14}C-Ova/PDMAEMA, which was complementary to the decrease in exocytosis shown in Figure 1. Samples were evaluated with a minimum of n=3 and reported as mean ± standard deviation.* $p<0.05$ vs. ^{14}C-Ova and PMAA-^{14}C-Ova.

Carborane-Conjugated 2-Quinolinecarboxamide Ligands of the Translocator Protein for Boron Neutron Capture Therapy

Andrea Cappelli,*[,†] Salvatore Valenti,[†] Alessandra Mancini,[†] Germano Giuliani,[†] Maurizio Anzini,[†] Saverio Altieri,[‡,§] Silva Bortolussi,[‡,§] Cinzia Ferrari,[||] Anna Maria Clerici,[||] Cecilia Zonta,[||] Fabio Carraro,[⊥] Irene Filippi,[⊥] Gianluca Giorgi,[▽] Alessandro Donati,[†] Sandra Ristori,[○] Salvatore Vomero,[†] Alessandra Concas,[#] and Giovanni Biggio[#]

Dipartimento Farmaco Chimico Tecnologico and European Research Centre for Drug Discovery and Development, Università degli Studi di Siena, Via A. Moro, 53100 Siena, Italy, Dipartimento di Fisica Nucleare e Teorica, Università di Pavia, Via Ugo Bassi 6, 27100 Pavia, Italy, Istituto Nazionale di Fisica Nucleare (INFN), Sezione di Pavia, Via Ugo Bassi 6, 27100 Pavia, Italy, Dipartimento di Scienze Chirurgiche, Laboratorio di Chirurgia Sperimentale, Università di Pavia, Via Ferrata 9, 27100 Pavia, Italy, Dipartimento di Fisiologia, Università degli Studi di Siena, Via A. Moro, 53100 Siena, Italy, Dipartimento di Biologia Sperimentale "B. Loddo", Università degli Studi di Cagliari, Cittadella Universitaria, SS 554 (km 4.500), 09042 Monserrato (Cagliari), Italy, Dipartimento di Chimica, Università di Siena, Via A. Moro, 53100 Siena, Italy, and Dipartimento di Chimica and CSGI, Università di Firenze, Via della Lastruccia 7, 50019 Sesto Fiorentino, Italy. Received April 27, 2010; Revised Manuscript Received October 26, 2010

Potential boron neutron capture therapy (BNCT) agents have been designed on the basis of the evidence about translocator protein (TSPO) overexpression on the outer mitochondrial membrane of tumor cells. The structure of the first TSPO ligand bearing a carborane cage (compound **2d**) has been modified in order to find a suitable candidate for in vivo studies. The designed compounds were synthesized and evaluated for their potential interaction with TSPO and tumor cells. In vitro biological evaluation showed in the case of fluoromethyl derivative **4b** a nanomolar TSPO affinity very similar to that of **2d**, a significantly lower cytotoxicity, and a slightly superior performance as boron carrier toward breast cancer cells. Moreover, compound **4b** could be used as a ^{19}F magnetic resonance imaging (MRI) agent as well as labeled with ^{11}C or ^{18}F to obtain positron emission tomography (PET) radiotracers in order to apply the "see and treat" strategy in BNCT.

INTRODUCTION

BNCT (boron neutron capture therapy)[1] is a binary approach to cancer radiotherapy that establishes its potentialities on two distinct actions: enrichment of tumor cells with ^{10}B atoms and subsequent irradiation with a thermal neutron flux (*1*). The less abundant boron isotope ^{10}B (ca. 20% of total boron) has the interesting peculiarity of providing a large absorption cross section for thermal neutrons. The nuclear reaction of neutron capture produces high LET (linear energy transfer) particles such as ^{7}Li and α, which cause great damage in the range (less than 10 μm) of the cell diameter. The efficient energy transfer produces selective damage in the cells containing ^{10}B so that boron microdistribution plays a crucial role in BNCT selectivity. Provided that a ^{10}B concentration sufficient to produce cell death is reached in the tumor, and that a high concentration ratio between tumor and normal cells is obtained, uniform irradiation with thermal neutrons ensures the selective destruction of the tumor cells. With the neutron sources now available, in order to keep the irradiation times acceptable, the ^{10}B concentration in the tumor must be higher than 20−35 μg per gram of tissue.

BNCT has been used in the experimental treatment of a number of different tumors (e.g., glioblastoma (*2*−*4*), skin melanoma (*5*), head and neck cancer (*6*), mesothelioma (*7*), and diffuse liver metastases (*8*)) and could provide a useful option in the cases of tumors unaffected by conventional therapies or difficult to remove surgically (*9*). In fact, when metastases are spread through an entire organ, the use of a selective BNCT agent should allow the selective destruction of each single cell belonging to tumor nodules, without the necessity of their selective irradiation.

The selective ^{10}B incorporation inside cancer cells requires boron carrier molecules that show a particular tropism toward the target cells. A wide range of boron carriers have been designed, synthesized, and evaluated during the past decades (*10*), but only two compounds have been approved for clinical practice, namely, boronophenylalanine (BPA) (*11*) and sodium borocaptate (BSH) (*12*).

BPA is a derivative of the essential amino acid and is actively taken up by tumor cells. However, studies performed in animals and patients bearing liver metastases showed a maximum uptake ratio of about 6 between tumor and liver tissues (*2*, *13*). Research efforts are needed in order to develop new boron carriers capable of producing boron concentration ratios higher than those currently obtained with BPA and BSH. The use of boron clusters such as a carborane cage instead of single boron atoms allows to increase loading capability. Moreover, the carborane moiety is compatible with the biological environment (*14*, *15*) and carries 10 boron atoms per molecule.

* Corresponding author. Tel.: +39 0577 234320. Fax: +39 0577 234333. E-mail: cappelli@unisi.it.

[†] Dipartimento Farmaco Chimico Tecnologico and European Research Centre for Drug Discovery and Development, Università degli Studi di Siena.

[‡] Dipartimento di Fisica Nucleare e Teorica, Università di Pavia.

[§] Istituto Nazionale di Fisica Nucleare.

[||] Laboratorio di Chirurgia Sperimentale, Università di Pavia.

[⊥] Dipartimento di Fisiologia, Università degli Studi di Siena.

[#] Dipartimento di Biologia Sperimentale, Univerità di Cagliari.

[▽] Dipartimento di Chimica, Università di Siena.

[○] Università di Firenze.

[1] Abbreviations: BNCT, boron neutron capture therapy; LET, linear energy transfer; BPA, borophenylalanine; BSH, sodium borocaptate; DHD, DHD/K12/TRb; TSPO, translocator protein; PBR, periperal benzodiazepine receptor.

10.1021/bc100195s © 2010 American Chemical Society
Published on Web 11/18/2010

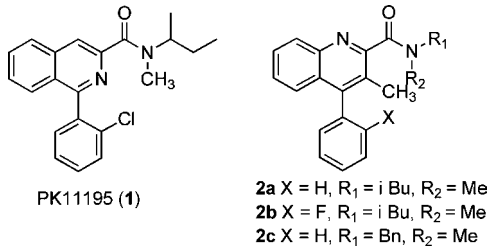


Figure 1. Structures of TSPO ligands **1** and **2a**−**c**.

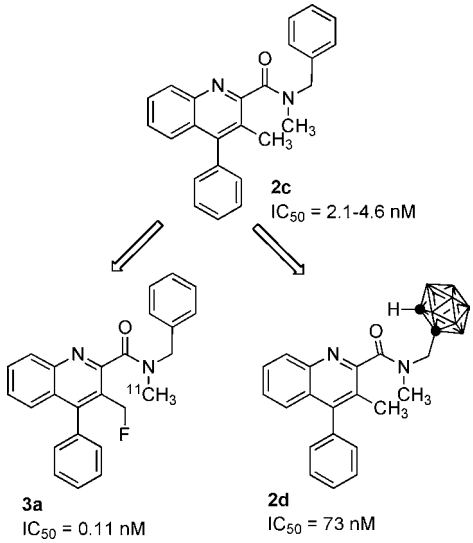


Figure 2. Development of PBR ligands **2d** and **3a**. In the icosahedral cage structure, closed circles represent carbon atoms and the vertices represent BH units.

The peripheral benzodiazepine receptor (PBR), recently renamed translocator protein (TSPO), is a 18 kDa protein showing five trans-membrane domains localized on the outer mitochondrial membrane (*16*−*18*). TSPO is linked to the voltage-dependent anion channel (VDAC) and to the adenine nucleotide translocase (ANT) and appears to be implicated in the regulation of the opening of the mitochondrial permeability transition pore (MPTP). Kidney, heart, testis, and adrenal gland are organs particularly rich in TSPO protein, while lower levels are found in the brain parenchyma, ependyma, choroid plexus, and olfactory neurons. Furthermore, high TSPO levels have been found in a variety of tumors (e.g., breast carcinoma, colorectal cancer, liver tumors, ovarian cancer, certain brain tumors, etc.), and its expression appears to be related to the degree of tumor malignancy (*19*−*26*). Isoquinolinecarboxamide derivative PK11195 (**1**, Figure 1) binds TSPO with nanomolar affinity and is largely used as a pharmacological tool for the study of the expression and the function of TSPO. Compound **1** was labeled with carbon-11 and used for the in vivo imaging of microglial/macrophage activation present in different brain disorders including tumors by means of positron emission tomography (PET) (*27*−*29*).

Our long-lasting interest in the synthesis of TSPO ligands has produced outstanding compounds in the class of PK11195 derivatives (*30*, *31*). For instance, potent quinoline carboxamide ligands **2a**−**c** were ^{11}C-labeled and the biodistribution studies indicated that these compounds are promising PET tracers for the in vivo imaging of PBR (*32*−*34*). Moreover, compound **2c** was used as a lead compound in the design of both the first PBR ligand bearing a carborane cage **2d** (Figure 2) (*35*) potentially useful in boron neutron capture therapy (BNCT) and fluoroderivative **3a**, which can be considered one of the most potent PET radiotracers for the in vivo imaging of the PBR so far described (*36*).

On the basis of the interesting results obtained, the program of the structural modification of compounds **2** was pursued in order to optimize the interaction of the 1,2-dicarba-*closo*-dodecaboranyl derivative **2d** with TSPO and with cancer cells, as well as to find a suitable candidate for the in vivo (e.g., biodistribution and efficacy) studies. Thus, this paper describes the results of a structure−activity relationship study focused on the selection of a candidate for in vivo studies endowed with nanomolar affinity for TSPO and low intrinsic cytotoxicity and capable of concentrating ^{10}B atoms into tumor cells.

EXPERIMENTAL PROCEDURES

Chemistry. All chemicals used were of reagent grade. Yields refer to purified products and are not optimized. Melting points were determined in open capillaries on a Gallenkamp apparatus and are uncorrected. Merck silica gel 60 (230−400 mesh) was used for column chromatography. Merck TLC plates with silica gel 60 F_{254} were used for TLC. ^{1}H NMR spectra were recorded by means of a Bruker AC 200 or a Bruker DRX 400 AVANCE spectrometer in the indicated solvents (TMS as internal standard); the values of the chemical shifts are expressed in parts per million, and the coupling constants (*J*) in hertz. Mass spectra were recorded on a ThermoFinnigan LCQ-Deca. The purity of compounds **4a**−**j** was assessed by RP-HPLC and was found to be higher than 95%. An Agilent 1100 Series system equipped with a Zorbax Eclipse XDB-C8 (4.6 × 150 mm) column was used in the HPLC analysis with acetonitrile−0.1% aqueous formic acid (95:5) as the mobile phase at a flow rate of 0.7 mL/min. UV detection was achieved at 220 nm.

***N*-[1,2-Dicarba-*closo*-dodecaboran(12)-1-ylmethyl]-3-methyl-4-phenylquinoline-2-carboxamide (4g).** A solution of carboxylic acid **5** (*30*) (0.13 g, 0.49 mmol) in $SOCl_2$ (3.0 mL) was refluxed for 2 h. Most of the $SOCl_2$ was distilled under reduced pressure, and the remainder was removed by azeotropic distillation with toluene. The residue was diluted with CH_2Cl_2 (6.0 mL), cooled at 0−5 °C, and treated in sequence with (aminomethyl)-*o*-carborane hydrochloride (*37*) (0.11 g, 0.52 mmol) and pyridine (0.10 mL, 1.2 mmol). The reaction mixture was stirred at room temperature for 30 min, washed with water, dried over sodium sulfate, and concentrated under reduced pressure. Purification of the residue by flash chromatography with $CHCl_3$ as the eluent gave **4g** as a white solid (0.14 g, yield 68%). An analytical sample was obtained by recrystallization from diethyl ether (mp 195−196 °C). HPLC: retention time = 3.8 min, purity = 96.3%.^{1}H NMR (200 MHz, $CDCl_3$): 0.75−3.75 (br m, 10BH), 2.54 (s, 3H), 4.06 (br s, 1H), 4.19 (d, J = 7.0, 2H), 7.21−7.55 (m, 7H), 7.70 (m, 1H), 8.10 (d, J = 8.4, 1H), 8.86 (t, J = 6.3, 1H). ^{1}H{^{11}B}-NMR (400 MHz, $CDCl_3$): 2.18 (br s, 5H), 2.29 (br s, 2H), 2.38 (br s, 1H), 2.47 (br s, 2H), 2.53 (s, 3H), 4.07 (br s, 1H), 4.19 (d, J = 6.9, 2H), 7.22 (m, 2H), 7.38 (m, 1H), 7.51 (m, 4H), 7.71 (m, 1H), 8.12 (d, J = 8.4, 1H), 8.89 (t, J = 6.8, 1H). MS (ESI): m/z 419 ($M + H^+$).

***N*-[1,2-Dicarba-*closo*-dodecaboran(12)-1-ylmethyl]-3-fluoromethyl-4-phenylquinoline-2-carboxamide (4h).** The title compound was synthesized starting from carboxylic acid **7** (*36*) (0.10 g, 0.35 mmol), (aminomethyl)-*o*-carborane hydrochloride (*37*) (73 mg, 0.35 mmol), and pyridine (0.10 mL, 1.2 mmol) following the same procedure used for compound **4g**. After purification by flash chromatography (dichloromethane as the eluent), compound **4h** (0.11 g, yield 72%) was recrystallized from diethyl ether to obtain colorless prisms melting at 173−174 °C. HPLC: retention time = 3.4 min, purity = 99.9%. ^{1}H NMR (200 MHz, $CDCl_3$): 0.75−3.75 (br m, 10BH), 4.08 (br s, 1H), 4.22 (d, J = 7.0, 2H), 5.77 (d, J = 46.6, 2H), 7.31 (m, 2H), 7.55 (m, 5H), 7.82 (m, 1H), 8.17 (d, J = 8.5, 1H), 8.76 (br t, 1H). MS (ESI): m/z 437 ($M + H^+$).

***N*-[1,2-Dicarba-*closo*-dodecaboran(12)-1-ylpropyl]-3-fluoromethyl-4-phenylquinoline-2-carboxamide (4i).** The title compound was synthesized starting from carboxylic acid **7** (*36*) (52 mg, 0.18 mmol), (aminopropyl)-*o*-carborane hydrochloride (*37*) (43 mg, 0.18 mmol), and pyridine (0.050 mL, 0.62 mmol) following the same procedure used for compound **4g**. Compound **4i** was purified by flash chromatography with dichloromethane as the eluent to obtain a white solid (60 mg, yield 72%) melting at 105−106 °C. HPLC: retention time = 3.2 min, purity = 95.2%. ^{1}H NMR (200 MHz, $CDCl_3$): 0.75−3.75 (br m, 10BH), 1.89 (m, 2H), 2.38 (m, 2H), 3.52 (q, J = 6.5, 2H), 3.67 (br s, 1H), 5.79 (d, J = 46.5, 2H), 7.31 (m, 2H), 7.52 (m, 5H), 7.77 (m, 1H), 8.11 (m, 2H). MS (ESI): *m*/*z* 465 ($M + H^+$).

***N*-[(1-Adamantyl)methyl]-3-methyl-4-phenylquinoline-2-carboxamide (4j).** The title compound was synthesized starting from carboxylic acid **5** (*30*) (0.50 g, 1.9 mmol), commercial 1-adamantanemethylamine (0.34 mL, 1.9 mmol), and TEA (1.0 mL) following the same procedure used for compound **4g**. Compound **4j** was purified by recrystallization from ethyl acetate−chloroform to obtain colorless needles melting at 169−170 °C (0.57 g, yield 73%). HPLC: retention time = 5.0 min, purity = 99.9%. ^{1}H NMR (200 MHz, $CDCl_3$): 1.56−1.77 (m, 12H), 2.01 (s, 3H), 2.54 (s, 3H), 3.22 (d, J = 6.7, 2H), 7.21−7.66 (m, 8H), 8.10 (m, 2H). MS(ESI): *m*/*z* 433 ($M + Na^+$).

***N*-[3,5-Bis(trifluoromethyl)benzyl]-*N*,3-dimethyl-4-phenylquinoline-2-carboxamide (4f).** The title compound was synthesized starting from carboxylic acid **5** (*30*) (0.13 g, 0.49 mmol), *N*-[3,5-bis(trifluoromethyl)benzyl]methylamine hydrochloride (0.15 g, 0.51 mmol), and pyridine (0.10 mL, 1.2 mmol) following the same procedure used for compound **4g**. Compound **4f** was purified by flash chromatography with dichloromethane-ethyl acetate (8:2) as the eluent to obtain a colorless glassy solid (0.13 g, yield 53%). HPLC: retention time = 3.2 min, purity = 99.0%. ^{1}H NMR (200 MHz, $CDCl_3$; the spectrum of this amide derivative shows the presence of two different rotamers in the ratio of about 55:45; for the sake of simplicity, the integral intensities have not been given): 2.22 (s), 2.23 (s), 2.92 (s), 3.14 (s), 4.56 (s), 4.97 (s), 7.21−7.27 (m), 7.35−7.71 (m), 7.83 (s), 7.93 (s), 7.99−8.13 (m). MS(ESI): *m*/*z* 503 ($M + H^+$).

***N*,3-Dimethyl-*N*-[2-methyl-1,2-dicarba-*closo*-dodecaboran(12)-1-ylmethyl]-4-phenylquinoline-2-carboxamide (4a).** *From Compound **4g**.* A solution of **4g** (50 mg, 0.12 mmol) in dry DMF (1.0 mL) was treated in sequence with methyl iodide (0.25 mL, 4 mmol) and NaH (3.0 mg, 0.13 mmol). After stirring at room temperature for 10 min, the reaction mixture was poured into ice−water, and the precipitate was extracted with dichloromethane. The organic layer was dried over sodium sulfate and concentrated under reduced pressure. The resulting residue was purified by flash chromatography with *n*-hexane−ethyl acetate (65:35) as eluent to obtain pure **4a** (20 mg, yield 37%) as a white solid melting at 146−147 °C. HPLC: retention time = 4.0 min, purity = 97.7%. ^{1}H NMR (200 MHz, $CDCl_3$; the spectrum of this amide derivative shows the presence of two different rotamers (*38*) in the ratio of about 9:1; for the sake of simplicity, the signals of the minor rotamer have been omitted): 0.75−3.75 (br m, 10BH), 2.26 (s, 3H), 2.34 (s, 3H), 3.07 (s, 3H), 4.37 (s, 2H), 7.27 (m, 2H), 7.42−7.71 (m, 6H), 8.09 (d, J = 8.5, 1H). MS(ESI) *m*/*z*: 447 ($M + H^+$).

*From Compound **2d**.* A solution of **2d** (60 mg, 0.14 mmol) in dry DMF (3.0 mL) was treated in sequence with methyl iodide (0.25 mL, 4 mmol) and NaH (4.0 mg, 0.17 mmol). After stirring at 45−50 °C for 1.5 h, the reaction mixture was poured into ice−water, and the precipitate was extracted with dichloromethane. The organic layer was dried over sodium sulfate and concentrated under reduced pressure. The resulting residue was purified by flash chromatography with *n*-hexane−ethyl acetate (65:35) as eluent to obtain 22 mg of unreacted **2d** and pure **4a** (13 mg, yield 21%) as a white solid.

***N*-[1,2-Dicarba-*closo*-dodecaboran(12)-1-ylmethyl]-3-fluoromethyl-*N*-methyl-4-phenylquinolin-2-carboxamide (4b).** A solution of **4h** (45 mg, 0.10 mmol) in dry DMF (1.0 mL) was treated in sequence with methyl iodide (0.32 mL, 5.1 mmol) and KOH (17 mg, 0.30 mmol). After stirring at room temperature for 30 min, the reaction mixture was poured into ice−water, and the precipitate was extracted with dichloromethane. The organic layer was dried over sodium sulfate and concentrated under reduced pressure. Purification of the resulting residue by flash chromatography with dichloromethane as eluent gave pure **4b** (11 mg, yield 24%) as a white solid melting at 189−190 °C. HPLC: retention time = 4.1 min, purity = 97.6%. ^{1}H NMR (200 MHz, $CDCl_3$; the spectrum of this amide derivative shows the presence of two different rotamers in the ratio of about 8:2 as in the case of **2d** (*38*); for the sake of simplicity, the integral intensities have not been given): 0.75−3.75 (br m), 3.11 (s), 3.26 (s), 3.99 (br s), 4.32 (br s), 5.37 (d, J = 47.4), 5.75 (br s), 7.32 (m), 7.54 (m), 7.79 (m), 7.99 (d, J = 8.1), 8.17 (d, J = 8.4). MS (ESI): *m*/*z* 451 ($M + H^+$).

3-Fluoromethyl-*N*-[2-methyl-1,2-dicarba-*closo*-dodecaboran(12)-1-ylmethyl]-*N*-methyl-4-phenylquinoline-2-carboxamide (4c). Compound **4c** was obtained as the more polar fraction of the flash chromatography purification of compound **4b** (32 mg, yield 69%, mp 181−182 °C). HPLC: retention time = 4.7 min, purity = 99.6%. The spectra of this amide derivative show the presence of two different rotamers (*38*) in the ratio of about 95:5; for the sake of simplicity, the signals of the minor rotamer have been omitted.^{1}H NMR (200 MHz, $CDCl_3$): 0.75−3.75 (br m, 10BH), 2.33 (s, 3H), 3.13 (s, 3H), 4.39 (s, 2H), 5.38 (d, J = 47.5, 2H), 7.32 (m, 2H), 7.54 (m, 5H), 7.79 (m, 1H), 8.18 (d, J = 8.5, 1H). ^{1}H{^{11}B}-NMR (400 MHz, $CDCl_3$): 2.20 (br s, 3H), 2.30 (br s, 2H), 2.33 (s, 3H), 2.37 (br s, 2H), 2.45 (br s, 3H), 3.13 (s, 3H), 4.40 (s, 2H), 5.38 (d, J = 47.6, 2H), 7.34 (m, 2H), 7.53 (m, 5H), 7.78 (m, 1H), 8.17 (d, J = 8.5, 1H). MS (ESI): *m*/*z* 465 ($M + H^+$).

3-Fluoromethyl-*N*-[2-methyl-1,2-dicarba-*closo*-dodecaboran(12)-1-ylpropyl]-*N*-methyl-4-phenylquinoline-2-carboxamide (4d). The title compound was synthesized starting from **4i** (43 mg, 0.093 mmol) following the same procedure used for compound **4b**. Compound **4d** was purified by flash chromatography with dichloromethane−ethyl acetate (9:1) as the eluent to obtain 20 mg of a pale yellow glassy solid (yield 44%). HPLC: retention time = 3.9 min, purity = 99.2%. ^{1}H NMR (200 MHz, $CDCl_3$; the spectrum of this amide derivative shows the presence of two different rotamers (*38*) in the ratio of about 6:4; for the sake of simplicity, the integral intensities have not been given): 0.75−3.75 (br m, 10BH), 2.04 (m), 2.41 (m), 2.95 (s), 3.19 (s), 3.31 (t, J = 6.8), 3.73 (t, J = 6.4), 5.39 (d, J = 47.6), 7.31 (m), 7.54 (m), 7.78 (m), 8.10 (m). MS (ESI): *m*/*z* 515 ($M + Na^+$).

***N*-[(1-Adamantyl)methyl]-*N*,3-dimetyl-4-phenylquinoline-2-carboxamide (4e).** The title compound was synthesized starting with **4j** (0.50 g, 1.2 mmol) following the same procedure used for the preparation of compound **4a.** Compound **4j** was purified by flash chromatography with chloroform−ethyl acetate (9:1) as the eluent to obtain 0.15 mg of white solid (yield 29%). An analytical sample was obtained by recrystallization from ethyl acetate−chloroform (mp 207−209 °C). HPLC: retention time = 4.2 min, purity = 97.9%. ^{1}H NMR (200 MHz, $CDCl_3$; the spectrum of this amide derivative shows the presence of two different rotamers in the ratio of about 8:2; for the sake of simplicity, the integral intensities have not been given):

1.38−2.01 (m), 2.21 (s), 2.25 (s), 2.96 (s), 3.21 (s), 3.26 (s), 3.34 (s), 7.21−7.68 (m), 8.09 (m). MS(ESI): *m*/*z* 447 ($M + Na^+$).

X-ray Crystallography. Single crystals of **4h** were submitted to X-ray data collection on an Oxford-Diffraction Xcalibur Sapphire 3 diffractometer with a graphite monochromated Mo−Kα radiation ($\lambda = 0.710\ 73$ Å) at 293 K. The structures were solved by direct methods implemented in *SHELXS-97* program (*39*). The refinements were carried out by full-matrix anisotropic least-squares on F2 for all reflections for non-H atoms by means of the *SHELXL-97* program (*40*). The structure shows a statistical disorder, and two different positions have been found for most of the atoms with site occupation factors refined to 0.51(1) and 0.49(1), respectively. Crystallographic data (excluding structure factors) for the structure in this paper have been deposited with the Cambridge Crystallographic Data Centre as supplementary publication no. CCDC 793508. Copies of the data can be obtained, free of charge, on application to CCDC, 12 Union Road, Cambridge CB2 1EZ, UK (fax: + 44 (0) 1223 336 033; or e-mail: deposit@ccdc.cam.ac.uk).

In Vitro Binding Assays. Male Sprague−Dawley CD rats (Charles River Italia, Calco, CO, Italy) with body masses of 200−250 g were used. Rats were acclimatized to the new housing conditions for at least one week. They were housed six per cage under an artificial 12-h-light, 12-h-dark cycle at a constant temperature of 22 ± 2 °C and a relative humidity of 65%. They had free access to water and standard laboratory food at all times. Animal care and handling throughout the experimental procedures were in accordance with the European Communities Council Directive of 24 November 1986 (86/609/EEC).

Rats were sacrificed by decapitation, and their brains were rapidly dissected into the various areas, which were stored at −80 °C until the day of the assay. The binding assays were performed as described in the literature (*41*). The cerebral cortex was subsequently thawed and then homogenized in 50 volumes of ice-cold Dulbecco's phosphate-buffered saline (PBS) pH 7.4 at 4 °C with a Polytron PT 10 disrupter (setting 5 for 20 s). The homogenate was centrifuged at 40 000*g* and 4 °C for 30 min, and the resulting pellet was resuspended in the same volume of fresh buffer and recentrifuged. The new pellet was resuspended in 10 volumes of the incubation buffer (PBS) and used for the binding assay.

[^{3}H]PK11195 binding was measured in a final volume of 500 μL, consisting of 50 μL of membrane suspension (0.15−0.20 mg of protein), 50 μL of [^{3}H]PK11195 (s.a. 85.5 Ci/mmol, New England Nuclear; final assay concentration of 1 nM), 5 μL of drug solution or solvent, and 395 μL of PBS. The binding reaction was performed at 25 °C for 90 min and began with the addition of membranes. The incubation was terminated by rapid filtration through glass-fiber filters (Whatman GF/B), which had been presoaked with 0.3% polyethyleneimine and placed in a cell harvester filtration manifold (Brandel). The filters were washed five times with 4 mL of ice-cold PBS, after which filter-bound radioactivity was quantified by liquid scintillation spectrometry. Nonspecific binding was defined as binding in the presence of 10 μM of unlabeled PK11195 (Sigma). Specific binding was determined by subtracting the nonspecific from the total binding and was about 80% of the total binding. The concentration of the test compounds that inhibited [^{3}H]ligand binding by 50% (IC_{50}) was determined by means of *Jandel Sigmaplot* (*42*) program with 6 to 10 concentrations of the displacers, each performed in triplicate.

MDAMB231 Cell Line. The highly invasive breast cancer cells MDAMB231 were grown in RPMI 1640 (Euroclone, Devon, UK) containing 10% fetal bovine serum (FBS, Euroclone), in the presence of L-glutamine (2 mM, Euroclone) and antibiotics (100 U/mL penicillin and 100 μg/mL streptomycin, Euroclone), at 37 °C, 95% humidity, in 5% CO_2. The cultures were free of mycoplasma.

DHD/K12/TRb Cell Line. DHD/K12/TRb (DHD) is an established cell line from colon adenocarcinoma, chemically induced in BD-IX rats by oral administration of 1,2-dimethylhydrazine (no. 90062901, ECACC, Salisbury, Wiltshire, U.K.) (*43, 44*). DHD cells were grown as a monolayer in a medium composed of a 1:1 (v/v) mixture of Ham's F10 and DMEM (Euroclone, Italy), with low glucose concentration (1 g/L), and containing 40 μg/mL gentamicin and 10% fetal bovine serum.

Cytotoxicity Evaluation. MDAMB231 cells were plated (5×10^4 cells/mL) in 100 μL RPMI 1640 with 10% FBS. After 4 h of incubation, the medium was changed to RPMI containing 0.5% FBS. After overnight incubation, the medium was changed to RPMI 1640 containing 10% FBS and the cells were treated with different concentrations (0−150 μM) of the studied compound for 72 h. The effect of the compounds was determined by ATP lite 1 step assay (Perkin-Elmer, Boston, MA). Briefly, cells were treated with 100 μL of luciferase and D-luciferin. The plates were placed in the dark for 10 min, and the luminescence was measured in a fluorescence microplate reader (FLUOstar Optima, BMG Labtech, Offenburg, Germany). Then, data analysis for IC_{50} calculations was performed with the LSW Data Analysis Package plug-in for *Excel* (Microsoft). The results are reported as mean ± SEM of three experiments, each performed in triplicate.

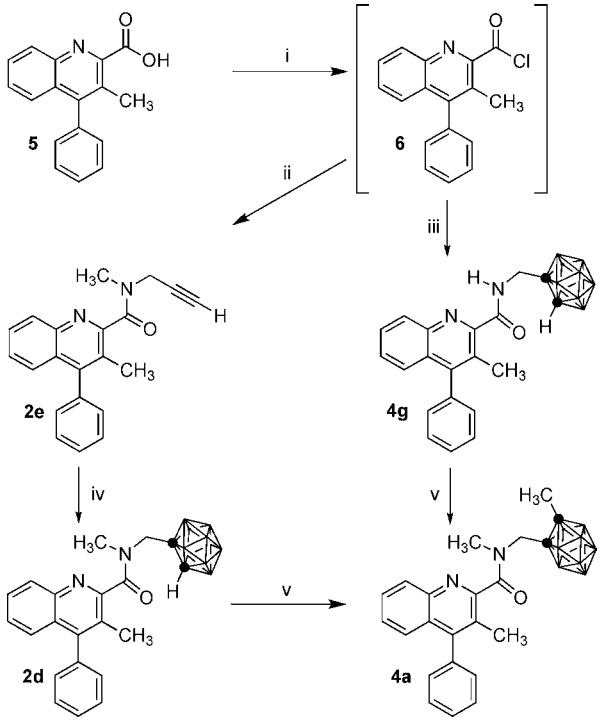
In DHD cells, the cytotoxicity of carborane derivative **2d** was evaluated by means of the plating efficiency test. Cells, after a 4 h incubation with **2d** (100 μM), were plated at three different dilutions (50, 100, 250 cells/plate) in five replicate Petri plates for each of them. They were allowed to grow at 37 °C for about 10 days. Colonies were fixed, stained, and counted. The ratio between the number of colonies with more than fifty cells and the number of seeded cells gives the value of the plating efficiency (PE). The cell survival is obtained by dividing the PE of the treated samples by the PE of the control sample.

Intracellular ^{10}B Uptake. MDAMB231 were seeded on a 6 well plate (Costar, Cambridge, MA) in RPMI 1640 containing 10% FBS at a concentration of 4.0×10^6 cells/well. After overnight starving, the medium was changed to RPMI 1640 containing 10% FBS, and the cells were treated with two different concentrations (50 μM and 100 μM) of the studied compound. From each well, 200 μL of supernatant was taken after 5 min, to allow diffusion. The compounds were incubated for 1 h at 37 °C. The cells were then washed and harvested with 200 μL of phosphate saline buffer (PBS). All the supernatant and cell suspensions were then added to Mylar disks.

For boron uptake measurements in DHD cells, these were cultured in a medium supplemented with carborane derivatives **2d** or BPA. After 4 h of treatment, the medium was removed and the cells were washed three times in PBS, trypsinized, and resuspended in boron-free medium. Control cells were processed in the same way as the boron-treated samples. Cells, enriched by centrifugation (10 min, 300 g), were finally layered on Mylar disks at a concentration of 4.0×10^6 cells/disk.

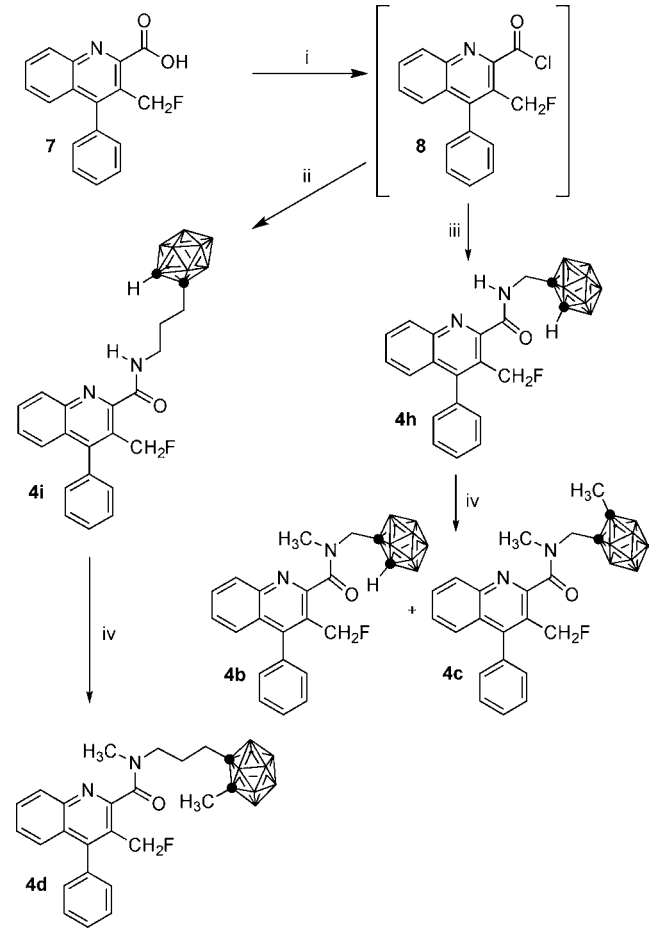
Boron Concentration Measurements. Boron concentration was measured by α spectroscopy, a method based on the ^{10}B(n, α)^{7}Li reaction induced by thermal neutrons (*45, 46*). Samples were prepared by depositing a known amount of cells on Mylar disks. The cells were left on the same support for the drying process. All samples were weighed before and after drying in order to determine the weighing factor necessary to correct for the concentration obtained in dry specimens. The Mylar supports covered by dry cells were positioned in a rotating holder, facing a thin silicon detector. The holder and the detector were placed

Scheme 1[a]



[a] Reagents: (i) $SOCl_2$, CH_2Cl_2; (ii) $CH_3-NH-CH_2C{\equiv}CH$, CH_2Cl_2, TEA; (iii) $NH_2-CH_2C(B_{10}H_{10})CH\cdot HCl$, CH_2Cl_2, pyridine; (iv) $B_{10}H_{14}$, CH_3CN, $CH_3C_6H_5$; (v) CH_3I, NaH, DMF.

Scheme 2[a]



[a] Reagents: (i) $SOCl_2$, CH_2Cl_2; (ii) $NH_2-CH_2CH_2CH_2C(B_{10}H_{10})CH\cdot HCl$, CH_2Cl_2, pyridine; (iii) $NH_2-CH_2C(B_{10}H_{10})CH\cdot HCl$, CH_2Cl_2, pyridine; (iv) CH_3I, KOH, DMF.

inside a vacuum chamber, and the entire system was irradiated inside the thermal column of the TRIGA Mark II reactor at the University of Pavia, Italy. At the irradiation position, the thermal neutron flux was about 2×10^9 cm^{-2} s^{-1}. The rotating device allowed irradiation and analysis of 10 samples without shutting down the reactor and opening the column. A scheme of this home-built apparatus is shown in ref *47*. Each sample was irradiated for 10 min. The spectra of all the charged particles emitted by the sample (i.e., α particles and ^7Li ions from the reaction of boron, and protons from the reaction of nitrogen) were collected electronically. The portion of spectra due to the α component only was used to calculate the boron concentration in the dry cells. The concentration of the original sample was then obtained by means of the correction factor measured before. This technique is innovative compared to the standard methods used in BNCT and offers a number of advantages. In particular, for tissues taken from a tumor zone, it allows the separation of the contributions coming from the tumor, the normal tissue, the necrotic tissue, and all other kinds of tissues that may coexist in a biopsy. Separation is accomplished by correcting the result of the spectroscopy with neutronographic images of a subsequent cut of the sample and with the histology of a third cut of the same sample. By means of this method, it is possible to determine the concentration of ^{10}B in the tumor cells with a higher precision compared to the conventional methods that provide only an average estimation of the concentration in the entire sample.

RESULTS AND DISCUSSION

Chemistry. First, 1,2-dicarba-*closo*-dodecaboranyl derivative **2d** was prepared following a linear procedure based on the reaction of propargyl derivative **2e** with a bis(acetonitrile)decaborane complex (Scheme 1) (*35*). As decaborane is a highly toxic compound, which forms impact-sensitive mixtures with several materials, the convergent synthesis shown in Schemes 1 and 2 was studied. The preparation of the required carborane synthons (e.g., (aminomethyl)-*o*-carborane hydrochloride and (aminopropyl)-*o*-carborane hydrochloride) was performed as reported in the literature (*37*) in order to reduce the exposure to the hazardous decaborane reagent to a minimum. In the convergent procedure, acid **5** (*30*) was activated to the corresponding acid chloride **6** and made to react with (aminomethyl)-*o*-carborane hydrochloride (*37*) in the presence of pyridine as the base to obtain secondary amide **4g**. Methylation of **4g** with methyl iodide in the presence of sodium hydride at room temperature gave the double-methylated compound **4a**. On the other hand, methylation of tertiary amide **2d** in the same conditions required a gentle warming to give compound **4a** (see the Experimental Procedures). These results suggest that a bidentate anion of **4g** is formed as a consequence of its NH deprotonation.

Interestingly, a similar reaction sequence performed on fluoro derivative **7** (*36*) (Scheme 2) allowed the required tertiary amide **4b** to be obtained in acceptable overall yield when methylation of the secondary amide **4h** was performed in the presence of potassium hydroxide. This result demonstrates that the labeling of **4b** with $[^{11}C]CH_3I$ is actually feasible. On the other hand, the use of the same experimental conditions in the methylation of secondary amide **4i** (obtained with (aminopropyl)-*o*-carborane hydrochloride (*37*)) led to the double-methylated amide **4d**. Although these results are quite functional to our medicinal chemistry work, their rationalization (e.g., the role of intramolecular H-bonding in the methylation reaction) requires further research work.

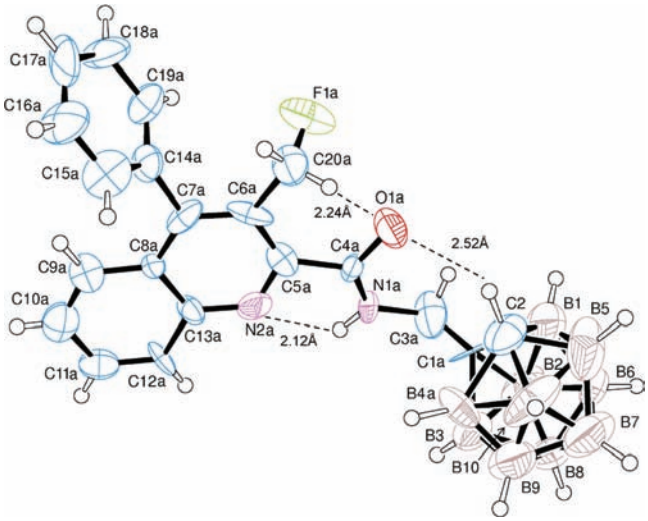
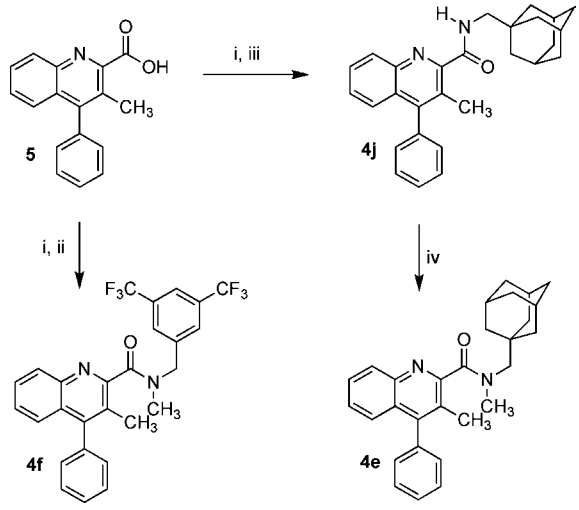


Figure 3. Crystal structure of a molecule (occupancy 0.51) of the secondary amide **4h**. Ellipsoids enclose 50% probability. Significant distances for hydrogen bonding interactions are also reported.

Scheme 3[a]



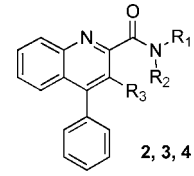
[a] Reagents: (i) $SOCl_2$, CH_2Cl_2; (ii) $(3,5\text{-}CF_3C_6H_3)CH_2NHCH_3$, TEA, CH_2Cl_2; (iii) 1-aminomethyladamantane, TEA, CH_2Cl_2; (iv) CH_3I, NaH, DMF.

Interestingly, the crystal structure of compound **4h** (Figure 3) shows the presence of an intramolecular hydrogen-bond network. The amide carbonyl oxygen atom behaves as an H-bond acceptor in two unconventional hydrogen bonding interactions with two polarized C−H groups: one belonging to the carborane cage (*38*) and the other belonging to the CH_2F group. Furthermore, the other potential H-bond acceptor present in the **4h** molecule, namely, the quinoline nitrogen atom, is involved in an H-bond interaction with amide N−H. Distances and angles of these interactions reflect the criteria for hydrogen bonds (*48*). They may play a key role in both conformational preferences and reactivity of compound **4h**.

Bulky tertiary amides **4e**,**f** were obtained by means of conventional amide chemistry from 2-quinolinecarboxylic acid **5** (*30*) (Scheme 3).

Binding Studies. Compounds **4a**−**h** were tested for their potential activity in inhibiting the specific binding of [^{3}H]**1** to TSPO in rat cortical membrane in comparison with reference compound **1**. The results of the binding studies are shown in Table 1, along with the previously published TSPO affinities of some selected 2-quinolinecarboxamide derivatives (**2c**,**d** and **3a**) that are included for comparison.

Table 1. TSPO Binding Affinities of Compounds 2c,d, 3a, and 4a−h



2, 3, 4

compd	R_1	R_2	R_3	IC_{50} (nM) ± SEM[a]
2c	$CH_2C_6H_5$	CH_3	CH_3	4.6[b]
2d	$CH_2C(B_{10}H_{10})CH$	CH_3	CH_3	73[b]
3a	$CH_2C_6H_5$	CH_3	CH_2F	0.11[c]
4a	$CH_2C(B_{10}H_{10})C-CH_3$	CH_3	CH_3	1750 ± 201
4b	$CH_2C(B_{10}H_{10})CH$	CH_3	CH_2F	93 ± 8.2
4c	$CH_2C(B_{10}H_{10})C-CH_3$	CH_3	CH_2F	1060 ± 132
4d	$CH_2CH_2CH_2C(B_{10}H_{10})C-CH_3$	CH_3	CH_2F	17 540 ± 2011
4e	CH_2(1-adamantyl)	CH_3	CH_3	2100 ± 196
4f	$CH_2(3,5\text{-}CF_3-C_6H_3)$	CH_3	CH_3	11 ± 1.4
4g	$CH_2C(B_{10}H_{10})CH$	H	CH_3	>10 000
4h	$CH_2C(B_{10}H_{10})CH$	H	CH_2F	>10 000
1				2.5 ± 0.4

[a] Each value is the mean ± SEM of 3 determinations and represents the concentration giving half the maximum inhibition of [^{3}H]**1** (final concentration 1nM) specific binding to rat cortical membranes. [b] See ref *35*. [c] See ref *36*.

The structure−affinity relationship analysis of the compounds included in Table 1 confirm the previously observed difference in affinity between secondary and tertiary amides (*30*). In fact, *o*-carboranylmethyl secondary amides **4g**,**h** show significantly lower TSPO affinities when compared to their *N*-methylated counterparts **2d**, **4b**.

The replacement of the benzyl group of compound **2c** and **3a** with the 1,2-dicarba-*closo*-dodecaboran-1-ylmethyl moiety of **2d** and **4b** appears to be tolerated by TSPO, but the comparison between the couples **2c**/**3a** and **2d**/**4b** shows that the positive effect of the fluorine atom observed for compound **3a** is not paralleled in the couple **2d**/**4b**. This result suggests that the replacement of the phenyl with an *o*-carboranyl moiety produces a change in the binding modalities of these 2-quinolinecarboxamide derivatives.

The nanomolar affinity of carboranylmethyl derivative **4b** attains a particular importance in consideration of the presence of a fluorine atom in its structure; thus, compound **4b** may be considered a potential ^{19}F magnetic resonance imaging agent or can be labeled either with C-11 or with F-18 in order to apply the "see and treat" concept in BNCT.

Methylation of the carborane C−H of **2d** and **4b** produces an affinity decrease of about 1 order of magnitude (compare **2d** with **4a** and **4b** with **4c**). This result suggests that carborane C−H plays a significant role in the interaction with TSPO. Reynolds and co-workers proposed that the carborane substituent sterically approximates a rotating phenyl ring and reported that the hydrogen attached to C2 of the carborane cage shows a pronounced positive partial charge (*49*). Thus, carborane C−H can behave as an H-bonding donor as suggested by the structural studies performed on compounds **4h** and **2d** (*38*). Moreover, the comparison of methylated carborane derivatives **4a**,**c** (IC_{50} = 1750, 1060 nM, respectively) with adamantyl derivative **4e** (IC_{50} = 2100 nM) supports the role of carborane C−H in the interaction with TSPO binding site and suggests that the methylated carborane moiety is recognized by the receptor in a similar manner as an adamantyl moiety. From this viewpoint, it is noteworthy that the introduction of bulky CF_3 substituents in the phenyl group of **2c** amide benzyl is tolerated by TSPO binding site better than its conversion into adamantane moiety (compare **4f** with **4e**). This result suggests that the micromolar affinities shown by adamantyl derivative **4e** and methylated

Table 2. ^{10}B Uptake Obtained by Exposition of Two Different Tumor Cell Lines to Compounds 2d, 4b, and BPA

compd	cell line	[^{10}B][a] medium (ppm)	time (h)	[^{10}B][b] tumor cell (ppm)	uptake ratio	ratio with respect to BPA
BPA	colon cancer	40	4	7.8	0.2	1
2d	colon cancer	8	4	56.5	7.1	35
2d	breast cancer	2	1	9.8	4.9	24
2d	breast cancer	1	1	5.6	5.6	28
4b	breast cancer	2	1	8.2	4.1	20
4b	breast cancer	1	1	7.8	7.8	39

[a] The ^{10}B concentration in the medium was calculated on the basis of the concentration of the boronated compound and ^{10}B abundance. [b] The experimental error associated to the boron concentration measurement by alpha spectrometry is in the order of 10%.

carboranyl derivatives **4a**,**c** can be rationalized in terms of specific interaction failure rather than of steric problems.

Finally, the elongation of the spacer between the amide nitrogen and the carborane moiety from one methylene unit (compound **4c**) to three methylene unities (**4d**) leads to an affinity decrease of about 1 order of magnitude, so that this transformation is unsuitable for optimizing the ligand−receptor interaction.

Cytotoxicity Studies. The structure−affinity relationship study performed with the carborane-conjugated 2-quinolinecarboxamide ligands described in the present paper consolidates the outstanding position of the *o*-carboranylmethyl tertiary amides **2d** and **4b** as nanomolar affinity TSPO ligands carrying 10 boron atoms per molecule. Therefore, these 2-quinolinecarbxamide derivatives can behave as boron carriers targeted toward the mitochondrial outer membrane of cells overexpressing TSPO and potentially capable of producing the ratios of boron concentration between tumor and normal tissues required to lead to tumor destruction with minimal side effects on the normal tissues. In order to minimize the side effects, the most important prerequisite for a boron carrier is the absence of intrinsic toxicity. Thus, the potential cytotoxicity of *o*-carboranylmethyl derivative **2d** was evaluated in DHD cells by means of the plating efficiency test, and no relevant toxic effect (21 ± 5.1%) was observed for treatments at a concentration of 100 μM for 4 h. Moreover, the potential cytotoxicity of **2d** and **4b** was evaluated in MDAMB231 cells in comparison with the nonboronated congener **2c**, which was included in order to obtain information on the structure−toxicity relationships. The ATP-based cell viability studies showed for *o*-carboranylmethyl derivatives **2d** and **4b** IC_{50} values (116 ± 4.1 and 195 ± 49 μM, respectively) higher with respect to the one shown by benzyl congener **2c** (IC_{50} = 66 ± 1.5 μM). This result suggests a low cytotoxicity for the potential boron carrier molecules **2d** and **4b**, even lower than that of nonboronated congener **2c**.

Intracellular ^{10}B Uptake. In order to assess the potential ability of compounds **2d** and **4b** to cross cellular membrane and accumulate into the tumor cells, the boron uptake was determined by means of α spectroscopy. After exposition to compounds **2d** and **4b** and placing on mylar disks, the cells were irradiated in the thermal column of the TRIGA Mark II reactor of Pavia University. The ^{10}B concentration was measured by analyzing the spectra of charged particles emitted in neutron capture reaction and recorded on a thin silicon detector. The results are summarized in Table 2, which includes the values of the uptake ratio obtained by normalizing the value of ^{10}B concentrations in the tumor cells as determined by neutron irradiation with respect to those present in the incubation medium.

The results reported in Table 2 demonstrate that *o*-carboranylmethyl derivatives **2d** and **4b** behave as effective boron carriers in vitro, since they are capable of concentrating boron atoms inside tumor cells. Interestingly, all the uptake values obtained with carborane derivatives **2d** and **4b** are higher than the corresponding values measured with BPA. A previous study (*50*) suggested that BPA is effectively incorporated by DHD cells through an active transport mechanism. The BPA uptake is thought to depend on the concentration used for the treatment, being only slightly dependent on the incubation period and showing a mild increase with increasing contact time. In our procedure, the ^{10}B concentration in the medium was optimized in order to obtain reliable measurements of the ^{10}B concentration in the cells. It is worth noting that, in the case of compound **2d**, a boron concentration of 1 ppm in the medium was sufficient to produce reliable boron concentrations (1 order of magnitude higher than the experimental error estimated in 0.5 ppm) in the cells, while in the case of BPA, a boron concentration in the medium of 40 ppm is required to obtain comparable results.

CONCLUSIONS

In the development of new BNCT agents, targeting mitochondria by means of a mitochondrial receptor such as TSPO can be considered an attractive concept because of the importance of these subcellular structures in the control of cell death. The irradiation with thermal neutrons can be assumed to induce damages to the mitochondria bearing carborane derivatives bound to TSPO. This could produce cytochrome c release in the cytosol with the activation of caspase cascades up to apoptosis. Therefore, carborane derivatives showing high TSPO binding affinity can be considered interesting tools to explore an alternative mechanism in BNCT in which tumor destruction should be obtained at boron concentrations lower than the usual ones. Thus, further exploration of the TSPO binding site by means of 2-quinolinecarboxamide derivatives **4a**−**h** produced the *o*-carboranylmethyl tertiary amide **4b**, which shows nanomolar affinity for TSPO very similar to that shown by previously published **2d**. Therefore, both these two carborane derivatives can be considered potential boron carriers targeted toward the mitochondrial outer membrane of tumor cells overexpressing TSPO. On the basis of these results, their interaction with cancer cells was evaluated in vitro in MDAMB231 breast cancer and DHD/K12/TRb colon adenocarcinoma cells. The cell viability studies suggests a low intrinsic toxicity for **2d** and **4b** and the boron uptake studies demonstrate that these *o*-carboranylmethyl derivatives behave in vitro as effective boron carriers, in that they are capable of concentrating boron atoms into the tumor cells investigated. Although fluoromethyl derivative **4b** is slightly less potent than **2d** in the TSPO binding studies, its significantly lower cytotoxicity, the good results obtained in boron uptake, and its potentialities as a ^{19}F magnetic resonance imaging (MRI) agent induce one to select it as a promising candidate for in vivo studies. Moreover, compound **4b** can be labeled either with C-11 or F-18 in order to monitor its in vivo pharmacokinetics, tumor extraction, and regional distribution by positron emission tomography (PET) in order to apply the "see and treat" strategy in BNCT.

ACKNOWLEDGMENT

The authors are grateful to Prof. Stefania D'Agata D'Ottavi for the careful reading of the manuscript and to Dr. Francesco Berrettini (CIADS, Università di Siena) for the X-ray data collection. G. Giorgi gratefully thanks Dr. Mark E. Light, School of Chemistry University of Southampton, for useful support for

X-ray data refinement. This work was financially supported by Ministero dell'Università e della Ricerca - PRIN (Programmi di ricerca di Rilevante Interesse Nazionale) and by Istituto Nazionale di Fisica Nucleare (INFN).

LITERATURE CITED

(1) Barth, R. F., Coderre, J. A., Vicente, M. G. H., and Blue, T. E. (2005) Boron neutron capture therapy of cancer: current status and future prospects. *Clin. Cancer Res. 11*, 3987–4002.

(2) Busse, P. M., Harling, O. K., Palmer, M. R., Kiger, W. S., Kaplan, J., Kaplan, I., Chuang, C. F., Goorley, J. T., Riley, K. J., Newton, T. H., Santa Cruz, G. A., Lu, X.-Q., and Zamenhof, R. G. (2003) A critical examination of the results from the Harvard-MIT NCT program phase I clinical trial of neutron capture therapy for intracranial disease. *J. Neurooncol. 62*, 111–121.

(3) Joensuu, H., Kankaanranta, L., Seppala, T., Auterinen, I., Kallio, M., Kulvik, M., Laakso, J., Vahatalo, J., Kortesniemi, M., Kotiluoto, P., Seren, T., Karila, J., Brander, A., Jarviluoma, E., Ryynanen, P., Paetau, A., Ruokonen, I., Minn, H., Tenhunen, M., Jaaskelainen, J., Farkkila, M., and Savolainen, S. (2003) Boron neutron capture therapy of brain tumors: clinical trials at the Finnish facility using boronophenylalanine. *J. Neurooncol. 62*, 123–134.

(4) Nakagawa, Y., Pooh, K., Kobayashi, T., Kageji, T., Uyama, S., Matsumura, A., and Kumada, H. (2003) Clinical review of the Japanese experience with boron neutron capture therapy and a proposed strategy using epithermal neutron beams. *J. Neurooncol. 62*, 87–99.

(5) Gonzales, S. J., Bonomi, M. R., Santa Cruz, G. A., Blaumann, H. R., Calzetta Larrieu, O. A., Menéndez, P., Jiménez Rebagliati, R., Longhino, J., Feld, D. B., Dagrosa, M. A., Argerich, C., Castiglia, S. G., Batistoni, D. A., Liberman, S. J., and Roth, B. M. C. (2004) First BNCT treatment of a skin melanoma in Argentina: dosimetric analysis and clinical outcome. *Appl. Radiat. Isot. 61*, 1101–1105.

(6) Kankaanranta, L., Seppala, T., Koivunoro, H., Saarhilati, K., Atula, T., Collan, J., Salli, E., Kortesniemi, M., Uusi-Simola, J., Makitie, A., Seppanen, M., Minn, H., Kotiluoto, H., Auterinen, I., Savolainen, S., Kouri, M., and Joensuu, H. (2007) Boron neutron capture therapy in the treatment of locally recurred head and neck cancer. *Int. J. Radiat. Oncol. Biol. Phys. 69*, 475–482.

(7) Suzuki, M., Sakurai, Y., Masunaga, S., Kinashi, Y., Nagata, K., Maruhashi, A., and Ono, K. (2006) Feasibility of boron neutron capture therapy (BNCT) for malignant pleural mesothelioma from a viewpoint of dose distribution analysis. *Int. J. Radiat. Oncol. Biol. Phys. 66*, 1584–1589.

(8) Zonta, A., Prati, U., Roveda, L., Ferrari, C., Zonta, S., Clerici, A. M., Zonta, C., Pinelli, T., Fossati, F., Altieri, S., Bortolussi, S., Bruschi, P., Nano, R., Barni, S., Chiari, P., and Mazzini, G. (2006) Clinical lessons from the first applications of BNCT on unresectable liver metastases. *J. Phys.: Conf. Ser. 41*, 484–495.

(9) Zonta, A., Pinelli, T., Prati, U., Roveda, L., Ferrari, C., Clerici, A. M., Zonta, C., Mazzini, G., Dionigi, P., Altieri, S., Bortolussi, S., Bruschi, P., and Fossati, F. (2009) Extra-corporeal liver BNCT for the treatment of diffuse metastases: What was learned and what is still to be learned. *Appl. Radiat. Isot. 67*, S67–S75.

(10) Soloway, A. H., Tjarks, W., Barnum, B. A., Rong, F. G., Barth, R. F., Codogni, I. M., and Wilson, J. G. (1998) The chemistry of neutron capture therapy. *Chem. Rev. 98*, 1515–1562.

(11) Coderre, J. A., Bergland, R., Chada, M., Chamana, A. D., Elowitz, E., Joel, D. D., Liu, H. B., Slatkin, D. N., Wielopolski, L. (1996) Boron neutron capture therapy of glioblastoma multiforme using the p-borophenylalanine-fructose complex and epithermal neutrons. *Neutron Capture Therapy for Cancer* (Mishima, Y., Ed.) pp 553−561, Plenum Press, New York.

(12) Yokoyama, K., Miyatake, S.-I., Kajimoto, Y., Kawabata, S., Doi, A., Yoshida, T., Asano, T., Kirihata, M., Ono, K., and Kuroiwa, T. (2006) Pharmacokinetic study of BSH and BPA in simultaneous use for BNCT. *J. Neurooncol. 78*, 227–232.

(13) Roveda, L., Prati, U., Bakeine, J., Trotta, F., Marotta, P., Valsecchi, P., Zonta, A., Nano, R., Facoetti, A., Chiari, P., Barni, S., Pinelli, T., Altieri, S., Braghieri, A., Bruschi, P., Fossati, F., and Pedroni, P. (2004) How to study boron biodistribution in liver metastases from colorectal cancer. *J. Chemother. 16* (Suppl. 5), 15–18.

(14) Fujii, S., Goto, T., Ohta, K., Hashimoto, Y., Suzuki, T., Ohta, S., and Endo, Y. (2005) Potent androgen antagonists based on carborane as a hydrophobic core structure. *J. Med. Chem. 48*, 4654–4662.

(15) Sivaev, I. B., and Bregadze, V. V. (2009) Polyhedral boranes for medical applications: current status and perspectives. *Eur. Inorg. Chem. 11*, 1433–1450.

(16) Papadopoulos, V., Baraldi, M., Guilarte, T. R., Knudsen, T. B., Lacapère, J.-J., Lindemann, P., Norenberg, M. D., Nutt, D., Weizman, A., Zhang, M.-R., and Gavish, M. (2006) Translocator protein (18 kDa): new nomenclature for the peripheral-type benzodiazepine receptor based on its structure and molecular function. *Trends Pharmacol. Sci. 27*, 402–409.

(17) Gavish, M., Katz, Y., Bar-Ami, S., and Weizman, R. (1992) Biochemical, physiological, and pathological aspects of the peripheral benzodiazepine receptor. *J. Neurochem. 58*, 1589–1601.

(18) Beurdeley-Thomas, A., Miccoli, L., Oudard, S., Dutrillaux, B., and Poupon, M. F. (2000) The peripheral benzodiazepine receptors: a review. *J. Neurooncol. 46*, 45–56.

(19) Starosta-Rubinstein, S., Ciliax, B. J., Penney, J. B., McKeever, P., and Young, A. B. (1987) Imaging of a glioma using peripheral benzodiazepine receptor ligands. *Proc. Natl. Acad. Sci. U.S.A. 84*, 891–895.

(20) Black, K. L., Ikezaki, K., and Toga, A. W. (1989) Imaging of brain tumors using peripheral benzodiazepine receptor ligands. *J. Neurosurg. 71*, 113–118.

(21) Black, K. L., Ikezaki, K., Santori, E., Becker, D. P., and Vinters, H. V. (1990) Specific high-affinity binding of peripheral benzodiazepine receptor ligands to brain tumors in rat and man. *Cancer 65*, 93–97.

(22) Miettinen, H., Kononen, J., Haapasalo, H., Helen, P., Sallinen, P., Harjuntausta, T., Helin, H., and Alho, H. (1995) Expression of peripheral-type benzodiazepine receptor and diazepam binding inhibitor in human astrocytomas: relationship to cell proliferation. *Cancer Res. 55*, 2691–2695.

(23) Batra, S., and Iosif, C. S. (1998) Elevated concentrations of mitochondrial peripheral benzodiazepine receptors in ovarian tumors. *Int. J. Oncol. 12*, 1295–1298.

(24) Venturini, I., Alho, H., Podkletnova, I., Corsi, L., Rybnikova, E., Pellicci, R., Baraldi, M., Pelto-Huikko, M., Helen, P., and Zeneroli, M. L. (1999) Increased expression of peripheral benzodiazepine receptors and diazepam binding inhibitor in human tumors sited in the liver. *Life Sci. 65*, 2223–2231.

(25) Hardwick, M., Fertikh, D., Culty, M., Li, H., Vidic, B., and Papadopoulos, V. (1999) Peripheral-type benzodiazepine receptor (PBR) in human breast cancer: correlation of breast cancer cell agressive phenotype with PBR expression, nuclear localization, and PBR-mediated cell proliferation and nuclear transport of cholesterol. *Cancer Res. 59*, 831–842.

(26) Maaser, K., Grabowski, P., Sutter, A. P., Hopfner, M., Foss, H. D., Stein, H., Berger, G., Gavish, M., Zeitz, M., and Scherubl, H. (2002) Overexpression of the peripheral benzodiazepine receptor is a relevant prognostic factor in stage III colorectal cancer. *Clin. Cancer Res. 8*, 3205–3209.

(27) Pike, V. W., Halldin, C., Crouzel, C., Barrè, L., Nutt, D. J., Osman, S., Shah, F., Turton, D. R., and Waters, S. L. (1993) Radioligands for PET studies of central benzodiazepine receptors and PK (peripheral benzodiazepine) binding sites - Current status. *Nucl. Med. Biol. 20*, 503–525.

(28) Junck, L., Olson, J. M., Ciliax, B. J., Koeppe, R. A., Watkins, G. L., Jewett, D. M., McKeever, P. E., Wieland, D. M., Kilbourn, M. R., Starosta-Rubinstein, S., Mancini, W. R., Kuhl, D. E., Greenberg, H. S., and Youngf, A. B. (1989) PET imaging of human gliomas with ligands for the peripheral benzodiazepine binding site. *Ann. Neurol. 26*, 752–758.

(29) Pappata, S., Cornu, P., Samson, Y., Prenant, C., Benavides, J., Scatton, B., Crouzel, C., Hauw, J. J., and Syrota, A. (1991) PET study of carbon-11-PK 11195 binding to peripheral type benzodiazepine sites in glioblastoma: a case report. *J. Nucl. Med. 32*, 1608–1610.

(30) Cappelli, A., Anzini, M., Vomero, S., De Benedetti, P. G., Menziani, M. C., Giorgi, G., and Manzoni, C. (1997) Mapping the peripheral benzodiazepine receptor binding site by conformationally restrained derivatives of 1-(2-chlorophenyl)-N-methyl-N-(1-methylpropyl)-3-isoquinolinecarboxamide (PK11195). *J. Med. Chem. 40*, 2910–2921.

(31) Anzini, M., Cappelli, A., Vomero, S., Seeber, M., Menziani, M. C., Langer, T., Hagen, B., Manzoni, C., and Bourguignon, J. J. (2001) Mapping and fitting the peripheral benzodiazepine receptor binding site by carboxamide derivatives. Comparison of different approaches to quantitative ligand-receptor interaction modeling. *J. Med. Chem. 44*, 1134–1150.

(32) Matarrese, M., Moresco, R. M., Cappelli, A., Anzini, M., Vomero, S., Simonelli, P., Verza, E., Magni, F., Sudati, F., Soloviev, D., Todde, S., Carpinelli, A., Galli Kienle, M., and Fazio, F. (2001) Labeling and evaluation of N-[^{11}C]methylated quinoline-2-carboxamides as potential radioligands for visualization of peripheral benzodiazepine receptors. *J. Med. Chem. 44*, 579–585.

(33) Matarrese, M., Soloviev, D., Cappelli, A., Todde, S., Moresco, R. M., Anzini, M., Vomero, S., Sudati, F., Carpinelli, A., Perugini, F., Galli Kienle, M., and Fazio, F. (1999) Synthesis of the novel [^{11}C]-labelled quinoline carboxamides: analogues of PK-11195 as putative radioligands for PET studies of peripheral type benzodiazepine receptors. *J. Labelled Cpd. Radiopharm. 42*, S397–S399.

(34) Belloli, S., Moresco, R. M., Matarrese, M., Biella, G., Sanvito, F., Simonelli, P., Turolla, E., Olivieri, S., Popoli, P., Cappelli, A., Vomero, S., Galli Kienle, M., and Fazio, F. (2004) Evaluation of three quinoline-2-carboxamide derivatives as potential radioligands for the in vivo PET imaging of neurodegeneration. *Neurochem. Int. 44*, 433–440.

(35) Cappelli, A., Pericot Mohr, G., Gallelli, A., Giuliani, G., Anzini, M., Vomero, S., Fresta, M., Porcu, P., Maciocco, E., Concas, A., Biggio, G., and Donati, A. (2003) Structure-activity relationships in carboxamide derivatives based on the targeted delivery of radionuclides and boron atoms by means of peripheral benzodiazepine receptor ligands. *J. Med. Chem. 46*, 3568–3571.

(36) Cappelli, A., Matarrese, M., Moresco, R. M., Valenti, S., Anzini, M., Vomero, S., Turolla, E., Belloli, S., Simonelli, P., Filannino, M. A., Lecchi, M., and Fazio, F. (2006) Synthesis, labeling, and biological evaluation of halogenated quinoline-2-carboxamides as potential radioligands for visualization of peripheral benzodiazepine receptors. *Bioorg. Med. Chem. 14*, 4055–4066.

(37) Wilson, J. G., Anisuzzaman, A. K. M., Alam, F., and Soloway, A. H. (1992) Development of carborane synthons: synthesis and chemistry of (aminoalkyl)carboranes. *Inorg. Chem. 31*, 1955–1958.

(38) Cappelli, A., Giorgi, G., Anzini, M., Vomero, S., Ristori, S., Rossi, C., and Donati, A. (2004) Characterization of persistent intramolecular C-H. .X(N, O) bonds in solid state and solution. *Chem.—Eur. J. 10*, 3177–3183.

(39) Sheldrick, G. M. *SHELXS-97, Rel. 97−2, A Program for Automatic Solution of Crystal Structures*, University of Göttingen, Göttingen, Germany, 1997.

(40) Sheldrick, G. M. *SHELXL-97, Rel. 97−2, A Program for Crystal Structure Refinement*, University of Göttingen, Göttingen, Germany, 1997.

(41) Cappelli, A., Giuliani, G., Valenti, S., Anzini, M., Vomero, S., Giorgi, G., Sogliano, C., Maciocco, E., Biggio, G., and Concas, A. (2008) Synthesis and structure-activity relationship studies in peripheral benzodiazepine receptor ligands related to alpidem. *Bioorg. Med. Chem. 16*, 3428–3437.

(42) Sigma Plot, Jandel Scientific Graphing Software for Windows, San Raphael, CA, USA, 1995.

(43) Martin, M. S., Bastien, H., Martin, F., Michiels, R., Martin, M. R., and Justrabo, E. (1973) Transplantation of intestinal carcinoma in inbred rats. *Biomedicine 12*, 555–558.

(44) Martin, F., Caignard, A., Jeannin, J. F., Leclerc, A., and Martin, M. (1983) Selection by trypsin of two sublines of rat colon cancer cells forming progressive or regressive tumors. *Int. J. Cancer 32*, 623–627.

(45) Wittig, A., Michel, J., Moss, R. L., Stecher-Rasmussen, F., Arlinghaus, H. F., Bendel, P., Mauri, P. L., Altieri, S., Hilger, R., Salvadori, P. A., Menichetti, L., Zamenhof, R., and Sauerwein, W. A. G. (2008) Boron analysis and boron imaging in biological materials for boron neutron capture therapy (BNCT). *Crit. Rev. Oncol. Hematol. 68*, 66–90.

(46) Chiaraviglio, D., De Grazia, F., Zonta, A., Altieri, S., Braghieri, A., Fossati, F., Pedroni, P., Pinelli, T., Perotti, A., Specchiarello, Perlini, G., and Rief, H. (1989) Evaluation of selective boron absorption in liver tumors. *Strahlenther. Onkol. 165*, 170–172.

(47) Altieri, S., Balzi, M., Bortolussi, S., Bruschi, P., Ciani, L., Clerici, A. M., Faraoni, P., Ferrari, C., Gadan, M. A., Panza, L., Pietrangeli, D., Ricciardi, G., and Ristori, S. (2009) Carborane derivatives loaded into liposomes as efficient delivery systems for boron neutron capture therapy. *J. Med. Chem. 52*, 7829–7835.

(48) Steiner, T. (1997) Unrolling the hydrogen bond properties of C-H···O interactions. *Chem. Commun.* 727–734.

(49) Reynolds, R. C., Campbell, S. R., Fairchild, R. G., Kisliuk, R. L., Micca, P. L., Queener, S. F., Riordan, J. M., Sedwick, W. D., Waud, W. R., Leung, A. K. W., Dixon, R. W., Suling, W. J., and Borhani, D. W. (2007) Novel boron-containing, nonclassical antifolates: synthesis and preliminary biological and structural evaluation. *J. Med. Chem. 50*, 3283–3289.

(50) Ferrari, C., Clerici, A. M., Zonta, C., Cansolino, L., Boninella, A., Altieri, S., Ballarini, F., Bortolussi, S., Bruschi, P., Stella, S., Bakeine, J., Dionigi, P., and Zonta, A. (2008) Boron neutron capture therapy of liver and lung coloncarcinoma metastases: an in vitro survival study. A New Option against Cancer, Proceedings of the 13th International Congress on Neutron Capture Therapy, Florence, Italy. (Zonta, A., Altieri, S., Roveda, L., and Barth, R., Eds.) pp 331−336, International Society for Neutron Capture Therapy.

BC100195S

Investigations on the Use of Fluorescence Dyes for Labeling Dendrimers: Cytotoxicity, Accumulation Kinetics, and Intracellular Distribution

A. M. Scutaru,[†] M. Krüger,[†] M. Wenzel,[†] J. Richter,[‡] and R. Gust*[,†,§]

Institute of Pharmacy, Freie Universität Berlin, Königin Luise Str. 2 + 4, 14195 Berlin, Germany, Charité Campus Benjamin Franklin, Institute of Clinical Physiology, Hindenburgdamm 30, 12203 Berlin, Germany, and Department of Pharmaceutical Chemistry, Institute of Pharmacy, University of Innsbruck, Innrain 52a, A-6020 Innsbruck, Austria. Received April 28, 2010

Fluorescent dyes (e.g., dansyl, fluoresceine isothiocyanate, or naphthalimide groups) are widely used as markers to study biological properties of drugs. In order to evaluate possible mediated cytotoxicity, we attached three molecules each to 1,3,5-tris(3-propylamino)benzene initially synthesized as core molecule for the design of dendrimers. Cytotoxic effects were only observed for the NO_2-substituted naphthalimide conjugate. The intracellular distribution was visualized via confocal fluorescence microscopy and pointed to an accumulation in the endosome or nucleus, dependent on the cell line used.

INTRODUCTION

Dendrimers have attracted considerable attention in the past two decades. The advantages of dendrimers, if compared with classical polymers, are their monodisperse geometry, the high terminal group density at their surface, as well as the possibility of a determined surface functionality.

The biological properties of dendrimers, including in vitro and in vivo toxicity and biodistribution, have gained more and more importance in the past few years. Their unique physical and chemical properties make them ideal candidates for drug delivery systems (*1*−*3*). Drugs can be covalently attached at the surface of the molecule, or in the case of larger dendrimers, they can be enclosed as guest molecules. Both concepts ensure targeted release (*4*−*11*).

For the use of macromolecular tumor therapy, it is important to control the accumulation of the carrier in the tumor tissue and the intercellular distribution. For this purpose, the carriers are miscellaneously labeled for detection through trace analysis. The most commonly used markers are radioactive elements such as ^{125}I (*12*−*16*), ^{51}Cr (*17*), and ^{111}In (*18*−*20*), which can easily be detected in vivo and in vitro, e.g., by methods in radioactive trace analysis. Alternatively, fluorescence analysis and high-resolution confocal fluorescence microscopy can be used to visualize the subcellular distribution if the molecule is labeled by fluorophors such as rhodamine (*21*), fluoresceine (*15, 22*−*24*), or Oregon Green (*25, 26*).

The use of dendrimers as drug delivery systems implies no cytotoxic properties of the macromolecule with and without labeling. In a previous study, we synthesized various dendrimers starting from the 1,3,5-tris(3-propylamino)benzene core molecule (**1**, Scheme 1) (*27*). This G0 molecule did not influence the growth of hormone-dependent MCF-7 or hormone-independent MDA-MB 231 cells. Therefore, we decided to use it to study the influence of macromolecular-bound fluoresceine isothiocyanate (FITC), naphthalimide, and nitronaphthalimide fluorophores on cytotoxicity, the accumulation kinetics, and the intracellular distribution in MCF-7 and MDA-MB-231 breast cancer cell lines.

* Corresponding author. Phone: +43 512 507 5245; Fax: +43 512 507 2940; E-mail: ronald.gust@uibk.ac.at.

[†] Freie Universität Berlin.

[‡] Institute of Clinical Physiology.

[§] University of Innsbruck.

MATERIALS AND METHODS

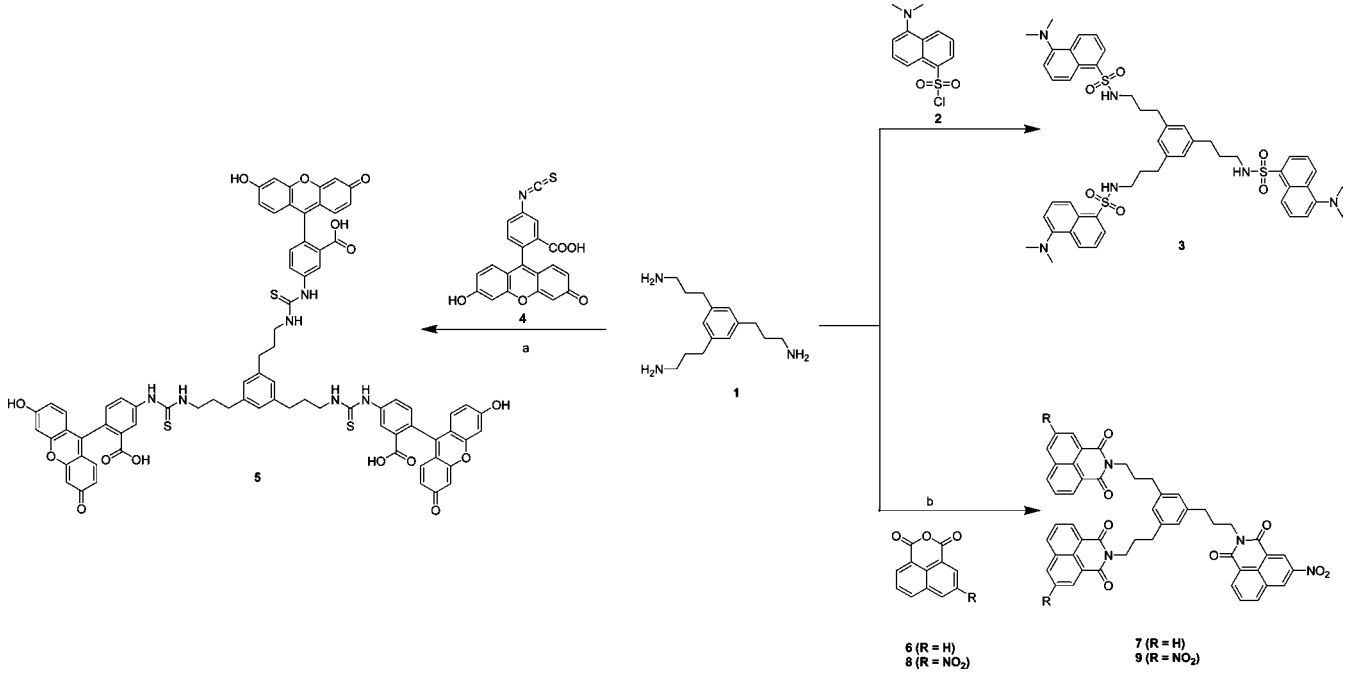
Synthesis. Compounds **1** and **3** were prepared according to the literature procedure (*27*). The other starting materials were purchased from commercial sources and were used without purification. Solvents were dried under standard conditions. ^{1}H NMR spectra were taken on a Bruker Avance/DPX 400 MHz with TMS as internal standard. Melting points (uncorrected) were measured with a Büchi Melting Point B-545. All column chromatography purifications were done by using silica gel 60 (0.063−0.1 mm, Merck). TLC was performed on silica gel 60 GF_{254} plates (Merck). Elemental analysis was carried out on a Vario EL (Hanau). EI spectra were recorded on a Thermo-Fisions VG Auto Spec (70 eV). The FAB spectra were measured on a CH-5, Varian MAT, Bremen. The ESI-TOF spectra were measured on an Agilent 6210 ESI-TOF, Agilent Technologies, Santa Clara, CA, USA. Solvent flow rate was adjusted to 4 μL/min; spray voltage set to 4 kV. Drying gas flow rate was set to 15 psi (1 bar). All other parameters were adjusted for a maximum abundance of the relative $[M+H]^+$.

1,3,5-Tris[*N*-(5-fluorescenyl)thiourea-propane-3,1-diyl]benzene (5). 1 × 3HCl (34.54 mg, 0.096 mmol) was dissolved in DMSO and treated with 0.16 mL of triethylamine (1.152 mmol). FITC was added to the solution, and the mixture was stirred for 24 h at room temperature in the dark. The solution was then poured in water and the pH value was adjusted to 4 with 5% hydrochloric acid. The color of the mixture changed from orange to yellow−green, and a solid precipitated. The compound was filtered off, washed with water, and then dried to afford an orange solid (100 mg, 73.4%); mp > 400 °C. ^{1}H NMR (400 MHz, CD_3OD): 1.98 (quin, ^3J(H,H) = 7.16 Hz, 6H, CH_2), 2.68 (t, ^3J(H,H) = 7.18 Hz, 6H, CH_2Ar), 3.61 (m, 6H, CH_2NH), 6.55 (dd, ^3J(H,H) = 2.34 Hz, 8.64 Hz, 6H, FITC), 6.69 (d, ^3J(H,H) = 1.94 Hz, 9H, FITC), 6.71 (s, 3H, FITC), 6.99 (s, 3H, Ar), 7.11 (d, ^3J(H,H) = 8.22 Hz, 3H, FITC), 7.69 (d, ^3J(H,H) = 7.31 Hz, 3H, FITC), 8.12 (s, 3H NH). MS (ESI): calcd. for $C_{78}H_{60}N_6O_{15}S_3Na^+$, 1439.3171; found 1439.3118. Anal. ($C_{78}H_{60}N_6O_{15}S_3$) C, H, N.

1,3,5-Tris{3-[1*H*-benzo[de]isoquinoline-1,3(2*H*)-dione]propylamino}benzene (7). 1 × 3HCl (359 mg, 1 mmol) was dissolved in 20 mL of dry ethanol and treated with 1.7 mL of dry

10.1021/bc1001906 © 2010 American Chemical Society
Published on Web 11/04/2010

Scheme 1. Synthesis of Labeled Conjugates 3, 5, 7, and 9[a]



[a] Reagents and conditions: (a) DMSO, TEA, RT; (b) EtOH, TEA, reflux.

triethylamine. 1,8-Naphtalic anhydride (654 mg, 3.3 mmol) was added and the mixture was refluxed for 3 h in the dark. The precipitated solid was vacuumed off, washed with ethanol, and dried over P_2O_5. Yield: 650 mg (82%) as a colorless solid; mp = 300 °C. ^{1}H NMR (400 MHz, $CDCl_3$): 1.97 (quin, ^3J(H,H) = 7.64 Hz, 6H, CH_2), 2.55 (t, ^3J(H,H) = 8.28 Hz, 6H, CH_2Ar), 4.20 (t, ^3J(H,H) = 7.38 Hz, 6H, CH_2N), 6.77 (s, 3H, Ar), 7.70 (t, ^3J(H,H) = 7.61 Hz, 6H, naphthalimide), 8.16 (d, ^3J(H,H) = 7.61 Hz, 6H, naphthalimide), 8.55 (d, ^3J(H,H) = 7.61 Hz, 6H, naphthalimide). MS (EI, 80 eV, 300 °C); *m*/*z* (%): 789.4 (1.74) [M^+], 398.9 (100.0) $C_{27}H_{28}NO_2$, 197.9 (49.95), $C_{12}H_7NO_2$. Anal. ($C_{51}H_{39}N_3O_6$) C, H, N.

1,3,5-Tris{3-[5-nitro-1*H*-benzo[de]isoquinoline-1,3(2*H*)-dione]propylamino}benzene (9). **1** × 3HCl (200 mg, 0.56 mmol) was dissolved in 10 mL of dry ethanol and treated with 940 μL of dry triethylamine. 3-Nitro-1,8-naphthalic anhydride (447.4 mg, 1.84 mmol) was added, and the mixture was refluxed for 3 h in the dark. The precipitated solid was vacuumed off, washed with ethanol, and dried over P_2O_5. Yield: 320 mg (61.8%) as a brown powder; mp = 272 °C. ^{1}H NMR (400 MHz, $CDCl_3$): 1.97 (quin, ^3J(H,H) = 7.41 Hz, 6H, CH_2), 2.53 (t, ^3J(H,H) = 7,93 Hz, 6H, CH_2Ar), 4.20 (t, ^3J(H,H) = 7.44 Hz, 6H, CH_2N), 6.74 (s, 3H, Ar), 7.92 (t, ^3J(H,H) = 7.67 Hz, 3H, naphthalimide), 8.40 (d, ^3J(H,H) = 8.14 Hz, 3H, naphthalimide), 8.75 (d, ^3J(H,H) = 6.46 Hz, 3H, naphthalimide), 9.10 (d, ^3J(H,H) = 2.10 Hz, 3H, naphthalimide), 9.24 (d, ^3J(H,H) = 2.13 Hz, 3H, naphthalimide). MS (FAB+, MNBA/DCM) *m*/*z* (%): 925.3 (30.23) [M+H]$^+$, 699.4 (65.70) [M-$C_{12}H_5N_2O_3$]$^+$. Anal. ($C_{51}H_{36}N_3O_6$) C, H, N.

Cell Culture. The human MCF-7 and MDA-MB 231 breast cancer cell lines were obtained from the American Type Culture Collection (ATCC). Cell line banking and quality control were performed according to the seed stock concept reviewed by Hay (*28*). The MCF-7 cells were maintained in Eagle's minimal essential medium (EMEM) containing L-glutamine supplemented with $NaHCO_3$ (2.2 g/L), sodium pyruvate (110 mg/L), gentamycin (50 mg/L), and 10% fetal calf serum (FCS, Gibco, Eggenheim, Germany) using culture flasks (75 cm^2, Nunc) in a water-saturated atmosphere (5% CO_2) at 37 °C. The MDA-MB-231 cells were maintained in McCoy's 5a Medium and 5% FCS. The cells were serially passaged weekly following trypsin treatment using a solution of trypsin (0.05%) and EDTA (0.02%).

In Vitro Chemosensitivity Assay. The in vitro testing of the compounds for cytotoxic activity was carried out on exponentially dividing cancer cells according to a previously published microtiter assay (*29*). Briefly, in 96-well microtiter assay plates (Nunc), 100 μL of a cell suspension was plated into each well and incubated at 37 °C for 3 days (MCF-7) and 2 days (MDA-MB-231) in a water-saturated atmosphere (5% CO_2). The desired test concentration was obtained by addition of an adequate volume of a stock solution of the respective compound to the medium. Sixteen wells were used for each test concentration and for the control, which contained the corresponding amount of solvent (0.1% v/v) respectively. After appropriate incubation periods, the medium was removed and the cells were fixed with a glutaraldehyde solution and stored at 4 °C. Cell biomass was determined by a crystal violet staining technique. The influence of the complexes on cell growth is expressed as the corrected *T*/*C* value according to the equation

$$\text{Cytostatic effect: } \%T/C_{\text{corr}} = [(T - C_0)/(C - C_0)] \times 100$$

in which *T* (test) and *C* (control) are the optical density values at 578 nm of the crystal violet extract of the cells in the wells (that is, the chromatin-bound crystal violet extracted with 70% ethanol), and C_0 is the density of the cell extract immediately before treatment. A microplate reader at 590 nm (Flashscan Analytik Jena AG) was used for the automatic estimation of the optical density of the crystal violet extract in the wells. The calculated %*T*/*C* values can be interpreted as follows:

$T/C > 80\%$: no antiproliferative effect
$80\% > T/C > 20\%$: antiproliferative effect
$20\% > T/C > 0\%$: cytostatic effect

Cellular Uptake Studies. The cells were seeded in 6-well plates (Nunc). When the cells reached 50−60% confluence (approximately after 5 days of incubation), the medium was exchanged for serum-free EMEM/Mc Coy's containing the compounds. The medium was removed after appropriate

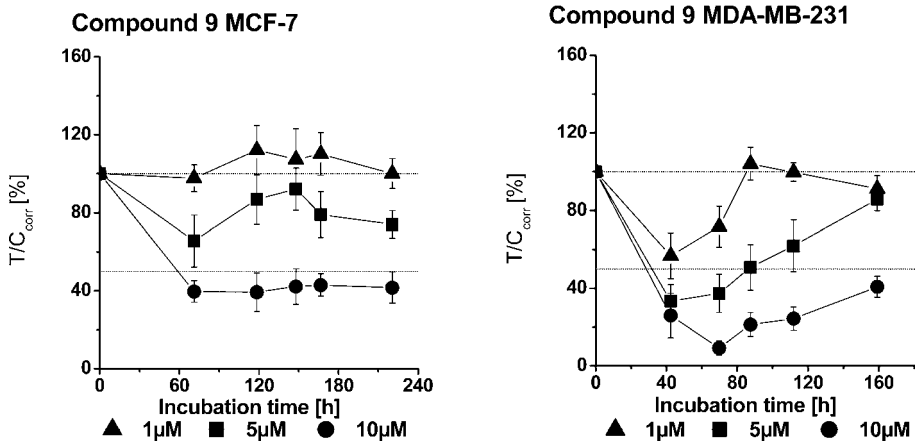


Figure 1. In vitro cytotoxicity of the nitronaphthalimide−conjugate **9**.

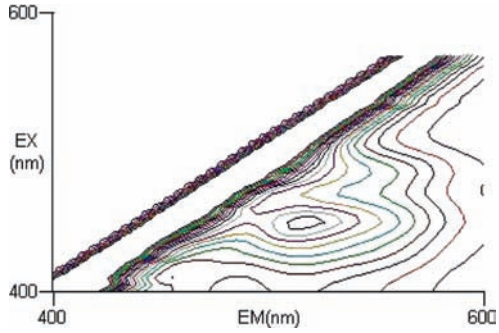


Figure 2. 3D spectrum of compound **5**; concentration: 1 μM in MeOH.

Table 1. Excitation and Emission Wavelengths of the Fluorescence-Labeled Conjugates

compound	fluorophor	λ_{max}ex (nm)	λ_{max}em (nm)
3	dansyl	340	535
5	fluoresceine isothiocyanate	450	519
7	naphthalimide	333	387
9	nitronaphthalimide	361	440

incubation periods, and the cells were washed with ice-cold PBS. After trypsination, the cells were harvested, washed two times with ice-cold PBS, and centrifuged (2000 *g*, 4 °C, 5 min) for storage at −18 °C until analysis. The cell pellet was homogenized by sonification in a Triton X-100 solution (1% (w/w)) and was adequately diluted for protein determination (*30*). The cellular concentrations of the compounds in the cells were determined as previously published (*31*).

RESULTS AND DISCUSSION

Synthesis. The synthesis of the dansyl derivative **3** (formulas of the conjugates; see Scheme 1) was already described in a previous paper (*27*). For the synthesis of the FITC-derivative **5**, the core molecule **1** × 3HCl was dissolved in DMSO and treated with triethylamine to provide the free base. Subsequently, FITC was added and the mixture was stirred in the dark at room temperature. The pure product **5** was obtained with 73% yield. To obtain **7** and **9**, **1** and the respective naphthalic anhydride (**6**, respectively, **8**) were refluxed for 3 h in ethanol under protection from light. The final products were precipitated from the reaction mixture.

In Vitro Cytotoxicity. The antiproliferative activity of the conjugates was determined in tests on the human MCF-7 and MDA-MB-231 breast cancer cell lines. Cisplatin used as a reference influenced the cell growth in a concentration-dependent manner and caused almost 100% inhibition in both cell lines at the highest concentration (5 μM).

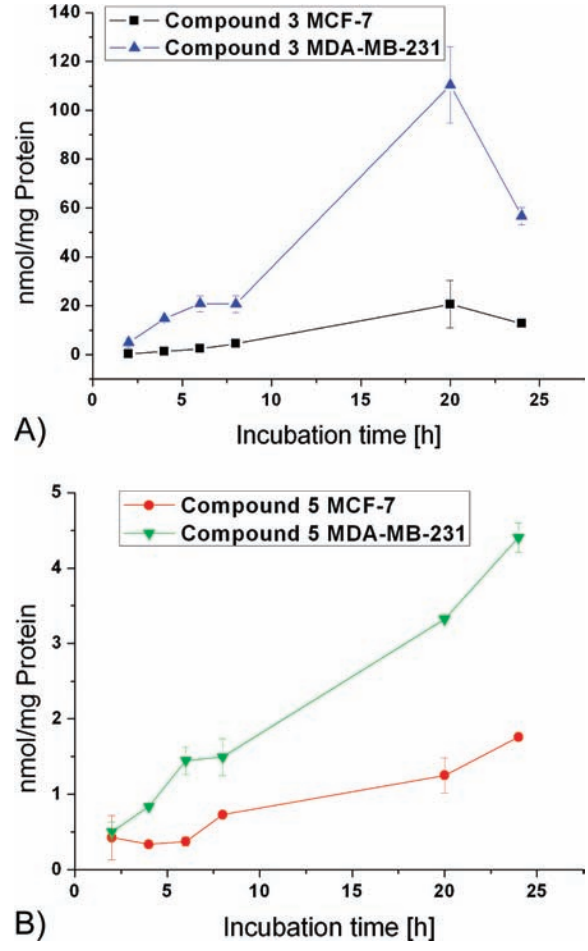


Figure 3. Accumulation kinetics of (A) dansyl conjugate **3** and (B) FITC conjugate **5**.

The antiproliferative effect (at concentrations of 1, 5, and 10 μM) expressed as T/C_{corr} values (T, treated group; C, control group) was correlated with the incubation time and documented for the free core molecule **1** (*27*) as well as the dansyl, fluoresceine isothiocyanate, and naphthalimide conjugates **3**, **5**, and **7**. No influence on the growth of MCF-7 and MDA-MB-231 cells could be observed (data not shown).

Interestingly, introduction of a nitro group to the naphthalimide in **7** strongly increased the cytotoxicity of the conjugate. As depicted in Figure 1, the effects of **9** were more pronounced

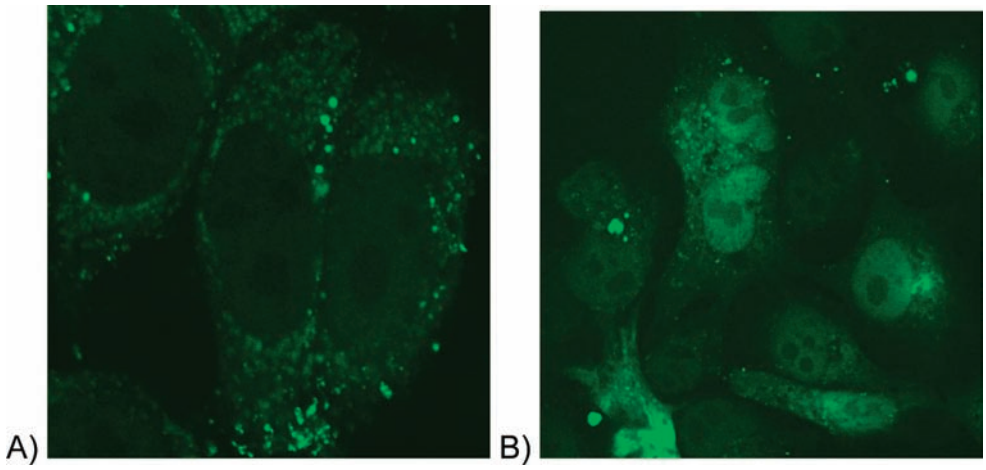


Figure 4. Fluorescence microscopy images of **5**: (A) MCF-7 cells; (B) MDA-MB-231 cells.

at the MDA-MB-231 cell line up to an incubation time of 72 h. The recuperation of the cells until the end of the test equals the effects at both cell lines. A possible explanation for these antitumor properties could be an involvement of the nitro group in intracellular redox reactions (*32*).

These findings documented the suitability of the dansyl, fluoresceine isothiocyanate, and the naphthalimide residue as fluorescence marker and require the determination of their spectroscopical properties after binding to **1**.

Fluorophor Characterization. The fluorescence of the synthesized conjugates was characterized by using a Hitachi F-4500 fluorescence spectrophotometer. All compounds showed only one excitation maximum. As an example, the 3D fluorescence spectrum of **5** is depicted in Figure 2.

The emission maximum of conjugates **3**, **5**, **7**, and **9** depended on the dye used (Table 1). Only **3** and **5** fulfill the requirement for accumulation studies (λ_{max} em > 500 nm) and can be used for accumulation studies.

Accumulation Kinetics. In order to quantify the cellular uptake, MCF-7 and MDA-MB-231 cells were incubated with 5 μM of the dye conjugates **3** and **5**, respectively, and the accumulation of the substance expressed as nmol/mg protein was fluorimetrically estimated. Possible inactivation reactions of the compounds due to protein binding were minimized by growing the cells in FCS-free EMEM. FCS is necessary for cell growth, but the short-term incubation did not change cell morphology and cell growth.

As depicted in Figure 3A, the dansylated conjugate **3** was accumulated to a higher degree in the tumor cells than **5** (Figure 3B). Furthermore, the kinetics differed significantly. In MDA-MB-231 cells, a fast accumulation of **3** occurred with saturation after 20 h. After 24 h, the intracellular content amounted to 56 nmol/mg protein. In the MCF-7 cells, the saturation was also reached after 20 h, but the intracellular amount of the dye was much lower (13 nmol/mg protein).

Exchange of the dansyl residue by fluoresceine isothiocyanate (**3** → **5**) reduced the accumulation kinetics. At both cell lines, no saturation was observed during the incubation time of 24 h. Furthermore, the intracellular amount of the conjugate **5** was considerably reduced.

Intracellular Localization. Conjugates **3**, **5**, **7** and **9** were incubated with either MCF-7 or MDA-MB-231 cells at a concentration of 10 μM for 24 h to visualize the intracellular distribution. Confocal fluorescence microscopy (Zeiss LSM 510) shots of the adnated cells clearly showed an accumulation of the fluorescence labeled conjugates in cell compartments. Surprisingly, the intracellular distribution differs depending on the cells used. The dye was mainly determined in the endosomes of MCF-7 cells, while the conjugates accumulated in MDA-MB-231 cells at the nucleus. Fluorescence microscopy images of **5** were depicted as examples in Figure 4.

CONCLUSION

Attachment of fluorescence dyes to the core molecule **1** did not increase the cytotoxicity but determined the intracellular distribution dependent on the cell type. Only the NO_2-bearing naphthalimide derivative **9** reduced the growth of MCF-7 and MDA-MB-231 cells, probably due to the interference in intracellular redox processes.

ACKNOWLEDGMENT

The presented study was supported by grants Gu285/4-1, Gu285/5-1, and Gu285/5-2, as well as the SFB 765 from the Deutsche Forschungsgemeinschaft.

Supporting Information Available: Elemental analyses of the new compounds. This material is available free of charge via the Internet at http://pubs.acs.org.

LITERATURE CITED

(1) Tomalia, D. A., Baker, H., Dewald, J., Hall, M., Kallos, G., Martin, S., Roeck, J., Ryder, J., and Smith, P. (1985) A new class of polymers - starburst-dendritic macromolecules. *Polym. J. 17*, 117–132.

(2) Newkome, G. R., Yao, Z. Q., Baker, G. R., and Gupta, V. K. (1985) Micelles part 1. Cascade molecules - a new approach to micelles - a (27)-arborol. *J. Org. Chem. 50*, 2003–2004.

(3) Hawker, C. J., and Frechet, J. M. J. (1990) Preparation of polymers with controlled molecular architecture - a new convergent approach to dendritic macromolecules. *J. Am. Chem. Soc. 112*, 7638–7647.

(4) Naylor, A. M., Goddard, W. A., Kiefer, G. E., and Tomalia, D. A. (1989) Starburst dendrimers part 5. Molecular shape control. *J. Am. Chem. Soc. 111*, 2339–2341.

(5) Jansen, J. F. G. A., De Brabander van den Berg, E. M. M., and Meijer, E. W. (1994) Encapsulation of guest molecules into a dendritic box. *Science 266*, 1226–1229.

(6) Hawker, C. J., Wooley, K. L., and Frechet, J. M. J. (1993) Unimolecular micelles and globular amphiphiles - dendritic macromolecules as novel recyclable solubilization agents. *J. Chem. Soc., Perkins Trans. 1*, 1287–1297.

(7) Jansen, J. F. G. A., Meijer, E. W., and De Brabander van den Berg, E. M. M. (1995) The dendritic box - shape-selective liberation of encapsulated guests. *J. Am. Chem. Soc. 117*, 4417–4418.

(8) Stevelmans, S., van Hest, J. C. M., Jansen, J. F. G. A., van Boxtel, D. A. F. J., de Brabander-van den Berg, E. M. M., and Meijer, E. W. (1996) Synthesis, characterization, and guest-host properties of inverted unimolecular dendritic micelles. *J. Am. Chem. Soc. 118*, 7398–7399.

(9) Baars, M. W. P. L., Froehling, P. E., and Meijer, E. W. (1997) Liquid-liquid extractions using poly(propylene imine) dendrimers with an apolar periphery. *Chem. Commun.* 1959–1960.

(10) Newkome, G. R., Young, J. K., Baker, G. R., Potter, R. L., Audoly, L., Cooper, D., Weis, C. D., Morris, K., and Johnson, C. S. (1993) Cascade polymers- pH-dependence of hydrodynamic radii of acid terminated dendrimers. *Macromolecules 26*, 2394–2396.

(11) Sideratou, Z., Tsiourvas, D., and Paleos, C. M. (2000) Quaternized poly(propylene imine) dendrimers as novel pH-sensitive controlled-release systems. *Langmuir 16*, 1766–1769.

(12) Malik, N., Wiwattanapatapee, R., Klopsch, R., Lorenz, K., Frey, H., Weener, J. W., Meijer, E. W., Paulus, W., and Duncan, R. (2000) Dendrimers: Relationship between structure and biocompatibility in vitro, and preliminary studies on the biodistribution of I-125-labelled polyamidoamine dendrimers in vivo. *J. Controlled Release 65*, 133–148.

(13) Noguchi, Y., Wu, J., Duncan, R., Strohalm, J., Ulbrich, K., Akaike, T., and Maeda, H. (1998) Early phase tumor accumulation of macromolecules: A great difference in clearance rate between tumor and normal tissues. *Jpn. J. Cancer Res. 89*, 307–314.

(14) Gillies, E. R., Dy, E., Frechet, J. M. J., and Szoka, F. C. (2005) Biological evaluation of polyester dendrimer: Poly(ethylene oxide) "bow-tie" hybrids with tunable molecular weight and architecture. *Mol. Pharmaceut. 2*, 129–138.

(15) Seymour, L. W., Ulbrich, K., Steyger, P. S., Brereton, M., Subr, V., Strohalm, J., and Duncan, R. (1994) Tumor tropism and anticancer efficacy of polymer-based doxorubicin prodrugs in the treatment of subcutaneous murine B16F10 melanoma. *Br. J. Cancer 70*, 636–641.

(16) De Jesus, O. L. P., Ihre, H. R., Gagne, L., Frechet, J. M. J., and Szoka, F. C. (2002) Polyester dendritic systems for drug delivery applications: In vitro and in vivo evaluation. *Bioconjugate Chem. 13*, 453–461.

(17) Matsumura, Y., and Maeda, H. (1986) A new concept for macromolecular therapeutics in cancer-chemotherapy - mechanism of tumoritropic accumulation of proteins and the antitumor agent smancs. *Cancer Res. 46*, 6387–6392.

(18) Bogdanov, A., Wright, S. C., Marecos, E. M., Bogdanova, A., Martin, C., Petherick, P., and Weissleder, R. (1997) A long-circulating co-polymer in "passive targeting" to solid tumors. *J. Drug Targeting 4*, 321–330.

(19) Bogdanov, A. A., Martin, C., Bogdanova, A. V., Brady, T. J., and Weissleder, R. (1996) An adduct of cis-diamminedichloroplatinum (II) and poly(ethylene glycol)poly(L-lysine)-succinate: Synthesis and cytotoxic properties. *Bioconjugate Chem. 7*, 144–149.

(20) Marecos, E., Weissleder, R., and Bogdanov, A. (1998) Antibody-mediated versus nontargeted delivery in a human small cell lung carcinoma model. *Bioconjugate Chem. 9*, 184–191.

(21) Cheng, J., Khin, K. T., and Davis, M. E. (2004) Antitumor activity of beta-cyclodextrin polymer - camptothecin conjugates. *Mol. Pharmaceut. 1*, 183–193.

(22) Crespo, L., Sanclimens, G., Montaner, B., Perez-Tomas, R., Royo, M., Pons, M., Albericio, F., and Giralt, E. (2002) Peptide dendrimers based on polyproline helices. *J. Am. Chem. Soc. 124*, 8876–8883.

(23) Tajarobi, F., El-Sayed, M., Rege, B. D., Polli, J. E., and Ghandehari, H. (2001) Transport of poly amidoamine dendrimers across madin-darby canine kidney cells. *Int. J. Pharm. 215*, 263–267.

(24) Wiener, E. C., Konda, S., Shadron, A., Brechbiel, M., and Gansow, O. (1997) Targeting dendrimer-chelates to tumors and tumor cells expressing the high-affinity folate receptor. *Invest. Radiol. 32*, 748–754.

(25) Godbey, W. T., Wu, K. K., and Mikos, A. G. (1999) Tracking the intracellular path of poly(ethylenimine)/DNA complexes for gene delivery. *Proc. Natl. Acad. Sci. U.S.A. 96*, 5177–5181.

(26) Yoo, H., and Juliano, R. L. (2000) Enhanced delivery of antisense oligonucleotides with fluorophore-conjugated PAMAM dendrimers. *Nucleic Acids Res. 28*, 4225–4231.

(27) Fuchs, S., Kapp, T., Otto, H., Schöneberg, T., Franke, P., Gust, R., and Schlüter, A. D. (2004) A surface-modified dendrimer set for potential application as drug delivery vehicles: Synthesis, in vitro toxicity, and intracellular localization. *Chem.—Eur. J. 10*, 1167–1192.

(28) Hay, R. J. (1988) The seed stock concept and quality-control for cell-lines. *Anal. Biochem. 171*, 225–237.

(29) Reile, H., Birnbock, H., Bernhardt, G., Spruss, T., and Schönenberger, H. (1990) Computerized determination of growth kinetic curves and doubling times from cells in microculture. *Anal. Biochem. 187*, 262–267.

(30) Bradford, M. M. (1976) Rapid and sensitive method for quantitation of microgram quantities of protein utilizing principle of protein-dye binding. *Anal. Biochem. 72*, 248–254.

(31) Gust, R., Schnurr, B., Krauser, R., Bernhardt, G., Koch, M., Schmid, B., Hummel, E., and Schönenberger, H. (1998) Stability and cellular studies of [rac-1,2-bis(4-fluorophenyl)ethylenediamine][cyclobutane-1,1-dicarboxylato]platinum(II), a novel, highly active carboplatin derivative. *J. Cancer Res. Clin. Oncol. 124*, 585–597.

(32) Arlt, V. M., Stiborova, M., Hewer, A., Schmeiser, H. H., and Phillips, D. H. (2003) Human enzymes involved in the metabolic activation of the environmental contaminant 3-nitrobenzanthrone: Evidence for reductive activation by human NADPH: cytochrome P450 reductase. *Cancer Res. 63*, 2752–2761.

BC1001906

Supporting information

Investigations on the Use of Fluorescence Dyes for Labeling Dendrimers: Cytotoxicity, Accumulation Kinetic and Intracellular Distribution

A.M. Scutaru[1], M. Krüger[1], M. Wenzel[1], J. Richter[2] and R. Gust[1,*]

1 Institute of Pharmacy, Freie Universität Berlin, Königin Luise Str. 2+4, 14195 Berlin, Germany

2 Charité Campus Benjamin Franklin, Institute of Clinical Physiology, Hindenburgdamm 30, 12203 Berlin, Germany

*Corresponding author. Phone: +49 (0)30 838 53272; Telefax: +49 (0)30 838 56906; E-mail: rgust@zedat.fu-berlin.de.

Content

Elemental analyses of new compounds

Elemental Analyses:

Compound 5:
calcd (%) for $C_{78}H_{60}N_6O_{15}S_3$: C 66.09, H 4.27, N 5.93; found: C 65.90, H 4.45, N 5.85

Compound 7:
calcd (%) for $C_{51}H_{39}N_3O_6$: C 77.55, H 4.98, N 5.32; found: C 77.57, H 5.50, N 4.95.

Compound 9:
calcd (%) for $C_{51}H_{36}N_3O_6$: C 66.23, H 3.92, N 9.09; found: C 65.90, H 4.01, N 9.32.

Enzyme-Mediated Site-Specific Antibody−Protein Modification Using a ZZ Domain as a Linker

Takayuki Sakamoto,[†] Shiori Sawamoto,[†] Tsutomu Tanaka,*[,‡] Hideki Fukuda,[‡] and Akihiko Kondo[†]

Department of Chemical Science and Engineering, Graduate School of Engineering, and Organization of Advanced Science and Technology, Kobe University, 1-1 Rokkodaicho, Nada, Kobe 657-8501, Japan. Received April 28, 2010; Revised Manuscript Received October 18, 2010

A ZZ domain (ZZ) and alkaline phosphatase (AP), luciferase (Luc), or glucose oxidase (GOD) were conjugated using Sortase A (SrtA) from *Staphylococcus aureus*. The specific peptidyl linker for SrtA was genetically fused to the C-terminus of ZZ, and the other linker was fused to the N-terminus of AP, Luc, or GOD, respectively. The resultant proteins were obtained separately by bacterial expression. The recombinant peptide-tagged ZZ and AP, Luc, or GOD were site-specifically conjugated by SrtA through the extra peptidyl linkers in vitro. The SrtA reaction had little influence on either the antibody-binding activity of the ZZ moiety or the enzymatic activity of AP, Luc, or GOD moieties of the conjugates. Additionally, antibody-ZZ-proteins were yielded easily by mixing antibody with ZZ-AP, ZZ-Luc, or ZZ-GOD, allowing their use in an enzyme-linked immunosorbent assay. These results suggest that the enzymatic approach with SrtA facilitates the construction of ZZ-proteins. Furthermore, mixing antibody and ZZ-proteins produces a wide variety of antibody-ZZ-proteins.

INTRODUCTION

Site-specific protein modification is a powerful strategy in biological research, because it enables protein manipulation without significant loss of function. Chemical modification is widely employed, although this strategy is not always "site-specific", but rather "residue-specific". If the target protein has a number of reactive residues, chemically modified products are often heterogeneous due to random modifications. Since cysteine (Cys) residues do not occur frequently in native proteins and a genetically introduced Cys may represent the only site to be modified, Cys-based protein modification with thiol-selective reagents has often been employed (*1*−*4*). Native chemical ligation, such as N-terminally introduced Cys-specific modification, is a more sophisticated strategy due to its being N-terminal-specific (*5, 6*). One obstacle is the difficulty associated with producing Cys-introduced proteins due to the formation of inclusion bodies or incorrect disulfide bridges.

Enzymatic approaches to site-specific protein modification have attracted much attention because the substrate specificity of an enzyme enables "site-specific" protein modification (*7, 8*). Several kinds of transglutaminases have been used for protein modification with primary amine-containing molecules such as fluorescence probes or PEG (*9*−*11*). Briefly, a short substrate sequence for transglutaminase is genetically introduced at the N- or C-terminus of the target protein. The expressed protein is modified with a small primary amine-containing molecule. Sortase has also been used for protein modification (*12*−*16*). The most studied one is Sortase A (SrtA), a transpeptidase from *Staphylococcus aureus*. Wild-type SrtA consists of 206 amino acids (23.5 kDa). N-Terminal 59-amino-acid truncated SrtA (17 kDa and pI = 6.8) has been used in many studies (*13*−*16*). SrtA recognizes the LPXTG sequence, cleaves between the Thr and Gly residues, and subsequently links the carboxyl group of Thr to an amino group of N-terminal glycine oligomers by a native peptide bond (*17, 18*). Recombinant soluble SrtA has been used for peptide−protein or protein−protein ligation in vitro because of its greater substrate specificity (*19*−*21*). The advantages of this enzymatic protein modification strategy are that it is highly selective and mild compared to conventional methods.

Antibody−protein conjugates have been widely used in various areas because of their remarkable molecular recognition properties. Generally, a Cys-based modification strategy is employed; however, site-specific modification of antibodies is not always achieved and the yield of modified antibody is not yet high enough. Although short peptide tag sequences should be introduced into antibodies in order to apply the enzymatic modification strategy, the establishment of a recombinant antibody production system is too difficult and is less versatile (*22*−*24*).

Here, we demonstrate site-specific antibody−protein conjugation using SrtA. We focused on an antibody-binding domain called the ZZ domain. The ZZ domain has high affinity to the Fc region of various kinds of antibodies, and its genetic manipulation and mass production is very easy (*25, 26*). The strategy of this study is shown in Figure 1A. ZZ domains were site-specifically conjugated with other proteins using sortase, and then the desired antibody−ZZ-protein conjugates were created by simply mixing the antibodies and ZZ−protein conjugates. We genetically introduced the LPETG sequence to the C-terminus of a ZZ domain (ZZ-LPETG). As model of partner proteins, alkaline phosphatase (*27*), luciferase (*28, 29*), and glucose oxidase (*30*) were used (Figure 1B). Pentaglycine appended alkaline phosphatase (Gly5-AP), luciferase (Gly5-Luc), and triglycine appended glucose oxidase (Gly3-GOD) were prepared (Figure 1B). ZZ-LPETG and Gly5-AP were site-specific conjugated by a SrtA-mediated reaction. In addition, Gly5-Luc and Gly3-GOD were also conjugated with ZZ-

* Corresponding author. Tsutomu Tanaka (T. Tanaka), E-mail: tanaka@kitty.kobe-u.ac.jp. Tel/Fax: +81-78-803-6202.

[†] Department of Chemical Science and Engineering, Graduate School of Engineering.

[‡] Organization of Advanced Science and Technology.

10.1021/bc100206z © 2010 American Chemical Society
Published on Web 11/11/2010

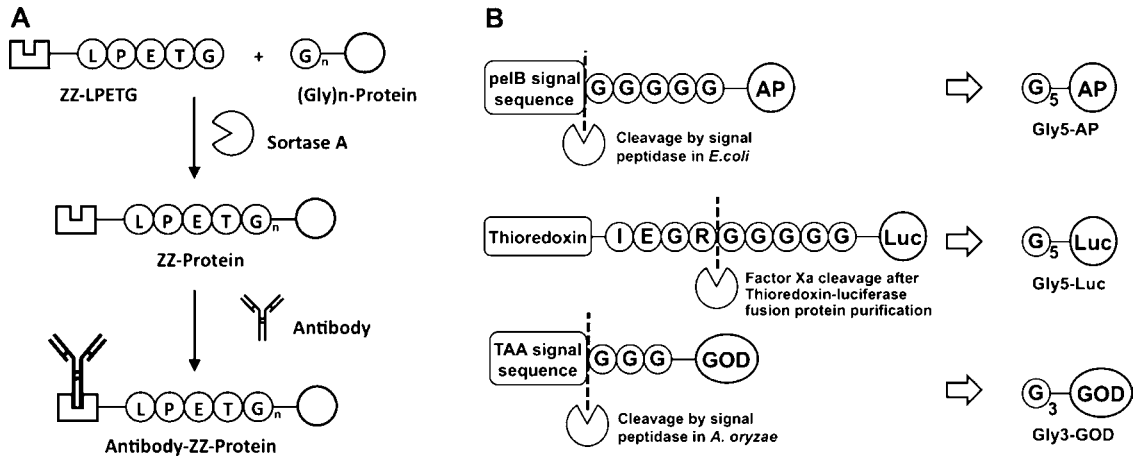


Figure 1. (A) Schematic illustration of antibody-ZZ-protein conjugation using Sortase A. ZZ-LPETG and (Gly)*n*-protein are site-specifically conjugated by Sortase A. The resultant ZZ−protein is simply mixed with whole antibody, and antibody-ZZ-protein is obtained due to the affinity between Fc region of ZZ and Fc region of antibody. (B) N-Terminal glycine appended proteins used in this study. Alkaline phosphatase and glucose oxidase were expressed with pelB signal sequence and Taka amylase (TAA) signal sequence, respectively. The moiety of signal sequence was cleaved by signal peptidase in each host cells; the N-terminal glycine exposed proteins were obtained. In the case of luciferase, Factor Xa cleavage between thioredoxin and luciferase could expose the N-terminal glycine of luciferase.

LPETG. Finally, we successfully demonstrated target molecule detection using antibody-ZZ-protein conjugates.

EXPERIMENTAL PROCEDURES

Plasmid Construction. The plasmid for pentaglycine appended alkaline phosphatase expression was constructed as follows. The gene encoding alkaline phosphatase (AP) from *E. coli* was amplified by PCR using *E. coli* genomic DNA as a template with the following primers: 5′-C CGT CAT ATG AAA TAC CTG CTG CCG ACC GCT GCT GCT GGT CTG CTG CTC CTC GCT GCC CAG CCG GCG ATG GCC GGC GGT GGA GGT GGA TCC ACA CCA GAA ATG CCT GTT CTG GAA AAC C-3′ and 5′-TTA ACT CGA GTG CGG CCG CTT TCA GCC CCA GAG CGG CTT TCA TGG-3′. (pelB leader sequence is underlined.) The amplified fragment was subcloned into the *Nde*I/*Xho*I sites of pET22b (Novagen). The resultant plasmid was named pET22b-Gly5-AP. The pelB leader sequences were cleaved during expression (*31*), and N-terminal glycine was exposed (Figure 1B).

The plasmid for LPETG sequence appended ZZ domain expression was constructed as follows. The gene encoding ZZ was amplified by PCR using pGLDLd33-ZZ (*32*) as a template using the following primers: 5′-GC GGT ACC GGA TCC GGT ATT GAG GGT CGC GGC GGT GGA GGT GGT GCG CAA CAC GAT GAA GCC GTA GAC-3′ and 5′-GC GAG CTC CTA GAA TTC ACC GCC AGT CTC AGG CAG GCC GCC GCC GGA GGA CTC TTT CGG CGC CTG AGC ATC ATT TAG C-3′. The amplified fragment was ligated into the *Kpn*I/*Sac*I sites of pBAD-Gly5-EGFP (*15*). The resultant plasmid was named pBAD-ZZ-LPETG. The plasmid for pentaglycine appended luciferase (Luc) expression was constructed as follows. The gene encoding Luc was amplified by PCR using pCBG68-Basic Vector (Promega) as a template using the following primers: 5′-GCG GTA CCG GAT CCG GTA TTGAGG GTC GCG GCG GTG GAG GTG GTG ACT ACA AGG ATG ACG ACG ACA AGA TGG TGA AAC GCG AAA AGA ACG TGA TCT ACG G-3′ and 5′-GCG AGC TCC TAG CCG CCA GCT TTT TCG AGG AGT TGC TTC AGC-3′. The amplified fragment was ligated into the *Kpn*I/*Sac*I sites of pBAD-Gly5-EGFP (*15*). The resultant plasmid was named pBAD-Gly5-Luc.

The plasmid for triglycine appended glucose oxidase (GOD) expression was constructed as follows. The gene encoding GOD was amplified by PCR using *Aspergillus niger* genomic DNA as a template using the following primers: 5′-GC CTC GAG AAA AGA GGC GGT GGA CAC CAC CAC CAC CAC CAC AGC AAT GGC ATT GAA GCC AGC CTG GTG ACT GAT CCC-3′ and 5′-G CAT AGC GGC CGC TCA CTG CAT GGA AGC ATA ATC TTC CAA-3′. The second PCR was carried out using the amplified fragment as a template using the following primers: 5′-G CAT ACT AGT AAA AGA GGC GGT GGA CAC CAC CAC CAC CAC CAC-3′ and 5′-G CAT AGC GGC CGC TCA CTG CAT GGA AGC ATA ATC TTC CAA-3′. The amplified fragment was ligated into the *Spe*I/*Not*I sites of pISI-EGFP (*33*). The resultant plasmid was named pISI-Gly3-GOD. In the case of Gly3-GOD, secretion signal sequence derived from taka amylase (*33*) were cleaved during secretion, and N-terminal glycine was exposed (Figure 1B).

The plasmid for myc sequence appended luciferase (Luc) expression was constructed as follows. The gene encoding Luc was amplified by quick change using the pBAD-Gly5-Luc Vector as a template using following primers: 5′-GAC TAC AAG GAT GAC GAC GAC AAG GAA CAA AAG TTG ATC AGC GAA GAG GAC CTC ATG GTG AAA CGC GAA AAG AAC GTG-3′ and 5′-CAC GTT CTT TTC GCG TTT CAC CAT GAG GTC CTC TTC GCT GAT CAA CTT TTG TTC CTT GTC GTC GTC ATC CTT GTA GTC-3′. The resultant plasmid was named pBAD-Gly5-myc-Luc.

The plasmid for pentaglycine and FLAG sequence appended red fluorescence protein (RFP) expression was constructed as follows. The gene encoding RFP was amplified by PCR using pmRFP-N1 (Clontech) as a template using the following primers: 5′-CGG GGT ACC ATT GAG GGT CGC GGC GGT GGA GGT GGT AGC GAT TAC AAG GAT GAC GAC GAT AAG AGC GAC AAC ACC GAG GAC GTC ATC AAG GAG TTC-3′ and 5′-GAG CTC CTA GCT AGC ATA ATC TGG AAC ATC ATA TGG ATA GCT GGA GCC GGA GTG GCG GGC CTC GGC GTG CTC-3′. The amplified fragment was ligated into the *Kpn*I/*Sac*I sites of pBAD-Gly5-EGFP (*15*). The resultant plasmid was named pBAD-Gly5-FLAG-RFP.

Protein Expression and Purification. SrtA and green fluorescence protein (GFP) were expressed and purified according to a previous report (*15*). The expression and purification of Gly5-AP was conducted as follows. Plasmid pET22b-Gly5-AP was transformed into *E. coli* BL21 (DE3) (Novagen). The cells were grown in LB medium to an OD (600 nm) value of 0.8, at which time expression of protein was induced by the addition of isopropyl-β-D-thiogalactopyranoside (IPTG) to a final concentration of 0.5 mM. After growth for an additional 16 h

at 25 °C, the cells were harvested by centrifugation. The cell pellets were resuspended in 50 mM Tris-HCl, 300 mM NaCl, pH 7.5, and lysed by sonication. Gly5-AP was purified from the soluble fraction of the lysate by TALON metal affinity resins (Clontech) according to the manufacturer's protocol and dialyzed against 50 mM Tris-HCl, 300 mM NaCl, pH 7.5. Protein concentration was determined using a BCA protein assay kit (Pierce).

Plasmids pBAD-ZZ-LPETG, pBAD-Gly5-Luc, pBAD-Gly5-myc-Luc, and pBAD-Gly5-FLAG-RFP were induced in *E. coli* Top10 (Invitrogen) by the addition of 0.1% L-arabinose and subsequent incubation for 16 h at 25 °C. ZZ-LPETG, Gly5-Luc, Gly5-myc-Luc, and Gly5-FLAG-RFP were purified using TALON metal affinity resin as described above. In the case of Gly5-Luc, Factor Xa (New England Biolabs) cleavage was carried out according to manufacturer's procedure to expose the N-terminal glycine (Figure 1B). After cleavage, Factor Xa was removed by Benzaimidine Sepharose 4 Fast Flow (GE Healthcare), and the cleaved thiredoxin moiety was also removed by TALON metal affinity resin.

The *Aspergillus oryzae* niaD mutant (strain IF4), derived from wild-type *A. oryzae*, OSI1031, was used as the GOD expression host. Czapek-Dox (CD) medium plates (2% glucose, 0.3% $NaNO_3$ (CD-NO_3), 0.2% KCl, 0.1% KH_2PO_4, 0.05% $MgSO_4 \cdot 7H_2O$, and 0.8 M NaCl, pH 6.0) containing 1.5% agar were used as the minimal medium to select the fungal transformants. GPY medium (3% glucose, 0.2% KCl, 0.1% KH_2PO_4, 0.05% $MgSO_4 \cdot 7H_2O$, 1% peptone, and 0.5% yeast extract, pH 6.0) was used for growing the transformants and for GOD expression. The transformation of *A. oryzae* was carried out according to the method described by Gomi et al. (1987). The resultant transformants were subcultured on a CD-NO_3 medium plate three times for obtaining the stable expression transformants. Then, the transformants were seeded on 250 mL of GPY medium and cultivated for 6 days at 30 °C. The culture supernatants were separated using Mira cloth (Millipore), and the secreted GOD was purified using TALON metal affinity resin according to the manufacturer's procedure.

SrtA Reaction between ZZ-LPETG and Pentaglycine Appended Proteins. The reaction between ZZ-LPETG (10 μM) and Gly5-AP (25 μM), Gly5-Luc (10 μM), and Gly3-GOD (10 μM) was initiated by the addition SrtA (35 μM). The reaction was carried out in 20 mM Tris-HCl, 150 mM NaCl, 0.5 mM $CaCl_2$, pH 7.5 at 24 °C. After incubation for 15 h, the reaction was terminated by mixing with SDS-PAGE sample buffer (50 mM Tris-Cl, 2% SDS, 6% 2-mercaptoethanol) and boiling. The samples were then subjected to SDS-PAGE, and the gels were stained with Coomassie brilliant blue R-250 (Nacalai Tesque).

AP Activity Analysis. In order to evaluate AP activity, luminescence was determined using CDP-Star (Applied Biosystems) after the SrtA reaction. Gly5-AP (25 μM), ZZ-LPETG (10 μM), and SrtA (35 μM), creating a ZZ-AP conjugate, were placed in each well of a 96-well microplate. After the addition of CDP-Star, the luminescence intensity in each well was measured at room temperature with a Wallac 1420 ARVOsx Multi Label Counter (Perkin-Elmer).

Luciferase Activity Analysis. In order to evaluate Luc activity, the luminescence was determined using Bright-Glo (Promega) after the SrtA reaction. Gly5-Luc (10 μM), ZZ-LPETG (10 μM), and SrtA (35 μM), creating a ZZ-Luc conjugate, were placed in each well of a 96-well microplate. After the addition of Bright-Glo, the luminescence intensity in each well was measured at room temperature with a Wallac 1420 ARVOsx Multi Label Counter.

GOD Activity Analysis. In order to evaluate GOD activity, the absorbance was determined using glucose and peroxidase and a coloring reagent (Nacalai Tesque) after the SrtA reaction. Gly3-GOD (10 μM), ZZ-LPETG (10 μM), and SrtA (35 μM), creating a ZZ-GOD conjugate, were placed in each well of a 96-well microplate. After the addition of glucose (0.5 M), peroxidase (1 mg/mL), and coloring reagent (100 μL), the absorbance at 450 nm in each well was measured at room temperature with a Wallac 1420 ARVOsx Multi Label Counter.

ELISA Using Antibody-ZZ-Protein Conjugates. BSA was Gly5-FLAG-RFP (10 μg/mL in PBS) were placed in each well of a 96-well microplate and incubated for 15 h at 4 °C to allow adsorption to the surface of the wells. At the same time, 15 μM ZZ-AP conjugate and 6 μM ZZ-Luc conjugate were added with anti-FLAG antibody 20 μg/mL (Sigma) and incubated for 1 h at 4 °C. Each well was washed three times with PBS. Then, anti-FLAG antibody-ZZ-AP conjugate and anti-FLAG antibody-ZZ-Luc conjugate were added to each well and incubated for 1 h at 4 °C, followed by washing three times with PBS. After the addition of CDP-Star (Applied Biosystems) and Bright-Glo (Promega), the luminescence intensity in each well was measured using a Wallac 1420 ARVOsx Multi Label Counter.

BSA or Gly5-myc-Luc (10 μg/mL in PBS) was placed in each well of a 96-well microplate and incubated for 15 h at 4 °C to allow adsorption to the surface of the wells. At the same time, 6 μM ZZ-GOD conjugate was added with antimyc antibody 20 μg/mL (Bethyl Laboratories) and incubated for 1 h at 4 °C. Each well was washed three times with PBS. Then, antimyc antibody-ZZ-GOD was added to each well and incubated for 1 h at 4 °C, followed by washing three times with PBS. After the addition of glucose, peroxidase, and coloring reagent (Nacalai Tesque), the absorbance at 450 nm in each well was measured using a Wallac 1420 ARVOsx Multi Label Counter.

In order to evaluate the applicability of the ZZ-Luc conjugate, ELISA for GFP was carried out. Different amounts of GFP (0, 0.25, 0.5, 2.5, 5, 6.25, 12.5, 25 nM in PBS) were placed in each well of a 96-well microplate and incubated for 15 h at 4 °C to allow adsorption to the surface of the wells. At the same time, 6 μM ZZ-Luc conjugate was added with anti-GFP antibody 20 μg/mL (Medical & Biological Laboratories) and incubated for 1 h at 4 °C. Each well was washed three times with PBS. Then, anti-GFP antibody-ZZ-Luc conjugate was added to each well and incubated for 1 h at 4 °C, followed by washing three times with PBS. After the addition of Bright-Glo, the luminescence intensity in each well was measured using a Wallac 1420 ARVOsx Multi Label Counter.

RESULTS AND DISCUSSION

Site-Specific Conjugation between ZZ-LPETG and Pentaglycine Appended Proteins Using SrtA. Figure 1A shows the effect of SrtA treatment on ZZ-LPETG and Gly5-AP. When Gly5-AP, ZZ-LPETG, and SrtA were mixed, a ZZ-AP conjugate (ca. 75 kDa) was clearly observed (Figure 2A, lane 7). ZZ-LPETG and Gly5-AP themselves were not susceptible to SrtA treatment (Figure 2A, lanes 5, 6), In addition, when ZZ-LPETG and AP without the pentaglycine tag at its N-terminus were mixed, the ZZ-AP conjugate was not observed, in spite of SrtA treatment (Figure 2B). These results suggest that site-specific ZZ-LPETG and Gly5-AP conjugation were carried out through the tag sequences. The yield of ZZ-AP was about 65% of the Gly5-AP, as evaluated by the ratio of the Gly5-AP band intensity before conjugation (Figure 2A, lane5) to that after conjugation (Figure 2A, lane 7). The ZZ-AP conjugates were also stable for more than one week even in the presence of the Sortase A, which is confirmed by SDS-PAGE (data not shown).

To expand the versatility of this strategy, we carried out site-specific protein conjugation between ZZ-LPETG and other proteins. Firefly luciferase and glucose oxidase were employed

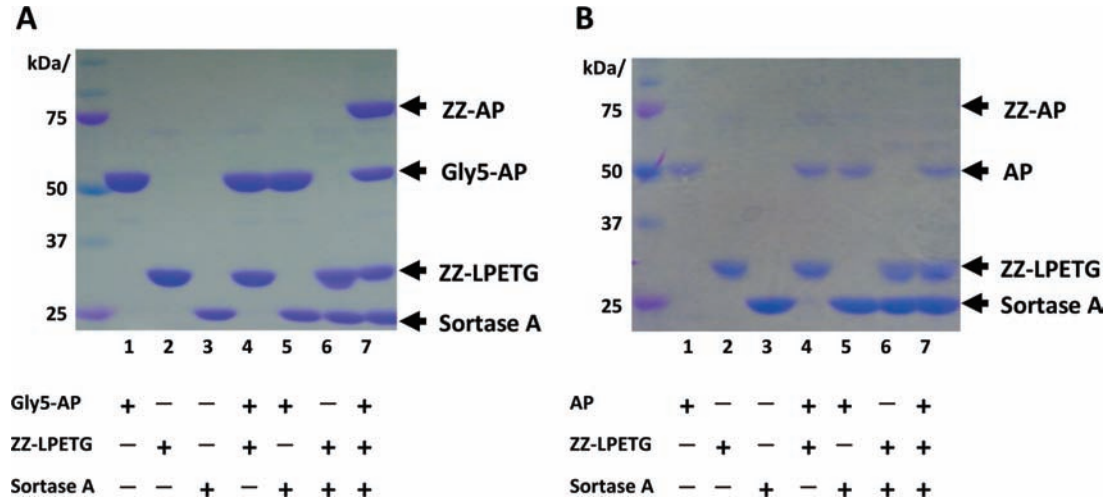


Figure 2. SDS-PAGE analysis of the site-specific reaction products after Sortase A treatment: (A) lane 1, Gly5-AP; lane 2, ZZ-LPETG; lane 3, Sortase A; lane 4, Gly5-AP; and ZZ-LPETG; lane 5, Gly5-AP and Sortase A; lane 6, ZZ-LPETG and Sortase A; lane 7, Gly5-AP and ZZ-LPETG and Sortase A. (B) lane 1, AP; lane 2, ZZ-LPETG; lane 3, Sortase A; lane 4, AP and ZZ-LPETG; lane 5, AP and Sortase A; lane 6, ZZ-LPETG and Sortase A; lane 7, AP and ZZ-LPETG and Sortase A.

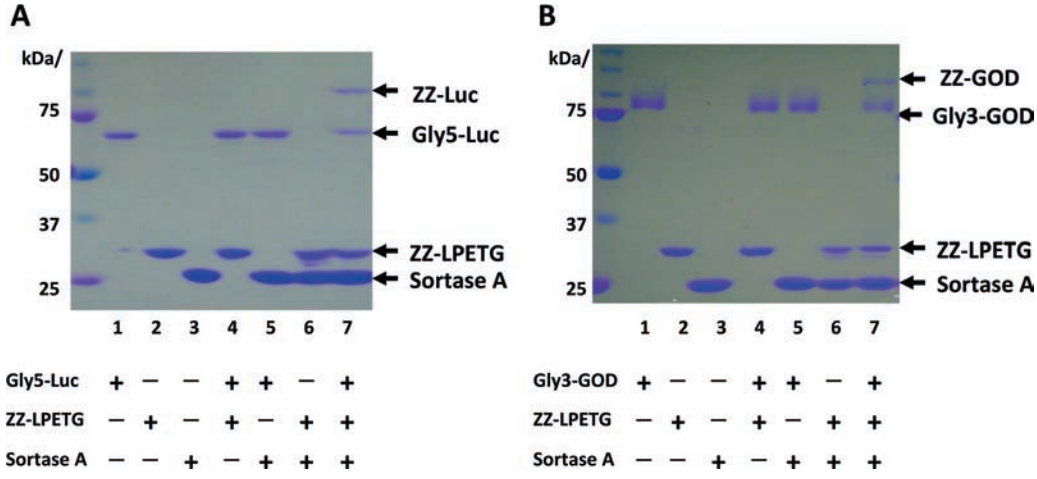


Figure 3. SDS-PAGE analysis of the reaction products after Sortase A treatment. (A) lane 1, Gly5-Luc; lane 2, ZZ-LPETG; lane 3, Sortase A; lane 4, Gly5-Luc and ZZ-LPETG; lane 5, Gly5-Luc and Sortase A; lane 6, ZZ-LPETG and Sortase A; lane 7, Gly5-Luc and ZZ-LPETG and Sortase A. (B) lane 1, Gly3-GOD; lane 2, ZZ-LPETG; lane 3, Sortase A; lane 4, Gly3-GOD and ZZ-LPETG; lane 5, Gly3-GOD and Sortase A; lane 6, ZZ-LPETG and Sortase A; lane 7, Gly3-GOD and ZZ-LPETG and Sortase A.

as reporter proteins. Firefly luciferase is widely used as a detection enzyme in ELISA, as well as in reporter gene assays. Luciferase was expressed as a thioredoxin-tag fusion protein using *E. coli* as a host. Then, N-terminal pentaglycine was exposed by protease (Factor Xa) digestion, and the thioredoxin tag was removed. Glucose oxidase is also widely used as a detection enzyme due to its high sensitivity against glucose. However, glycosylation is required for GOD activity, and hence, GOD cannot be expressed using *E. coli*. Other hosts such as *Aspergillus oryzae* or yeast are required.

Figure 3A shows the effect of SrtA treatment of ZZ-LPETG and Gly5-Luc. Gly5-Luc and Gly3-GOD were successfully expressed and purified using appropriate hosts. The smeared bands of GOD were caused by glycosylation. As expected, the ZZ-Luc conjugate (ca. 100 kDa) was successfully obtained after SrtA treatment (Figure 3A, lane 7). Figure 3B shows the effect of SrtA treatment of ZZ-LPETG and Gly3-GOD. The ZZ-GOD conjugate (ca. 110 kDa) was also successfully obtained after SrtA treatment (Figure 3B, lane 7). Neither Luc nor GOD was susceptible to SrtA because of its high substrate specificity. The yield of ZZ-GOD conjugates estimated with Gly3-GOD band intensity was about 65%, suggesting that the reactivity of SrtA was not affected by the target protein and/or protein modification such as glycosylation.

Evaluation of Enzymatic Activity after the Sortase Reaction. Figure 4 shows the enzymatic activity after SrtA treatment. The enzymatic activity of AP was almost the same when Gly5-AP was mixed with ZZ-LPETG or SrtA (Figure 4A, columns 1, 4, 5). This clearly shows that AP activity was not affected by other proteins. After SrtA treatment, the produced ZZ-AP conjugate retained its activity at almost the same level as Gly5-AP (Figure 4A, column 7). The other conjugates, ZZ-Luc and ZZ-GOD, both had enzymatic activity after SrtA treatment (Figure 4B,C, columns 1, 7). These data clearly show that SrtA enables conjugation of proteins without significant loss of their functions. Several previous reports have shown that protein activity after enzymatic conjugation is retained (*10*−*16*). Our results are consistent with these reports and demonstrate the superiority of the enzymatic protein conjugation method.

Detection of Target Molecules Using Antibody-ZZ-Protein Conjugates. Encouraged by these findings, we carried out the detection of target molecules using antibody-ZZ-protein conjugates. A moiety of the FLAG tag sequence in

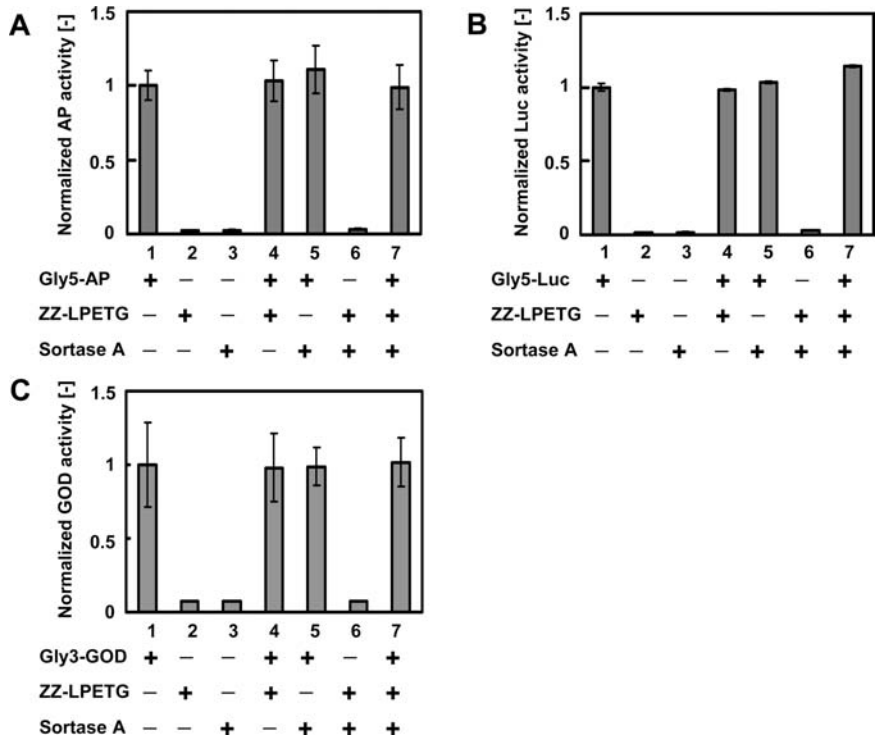


Figure 4. Evaluation of the enzymatic activity after Sortase treatment. (A) Alkaline phosphatase activity: column 1, Gly5-AP; column 2, ZZ-LPETG; column 3, Sortase A; column 4, Gly5-AP and ZZ-LPETG; column 5, Gly5-AP and Sortase A; column 6, ZZ-LPETG and Sortase A; column 7, Gly5-AP and ZZ-LPETG and Sortase A. (B) Luciferase activity: column 1, Gly5-Luc; column 2, ZZ-LPETG; column 3, Sortase A; column 4, Gly5-Luc and ZZ-LPETG; column 5, Gly5-Luc and Sortase A; column 6, ZZ-LPETG and Sortase A; column 7, Gly5-Luc and ZZ-LPETG and Sortase A.

Gly5-FLAG-RFP was employed as a model target molecule. ZZ-AP and anti-FLAG antibody (whole IgG) were simply mixed, and an anti-FLAG antibody-ZZ-AP conjugate was produced. As a negative control, BSA was employed. As shown

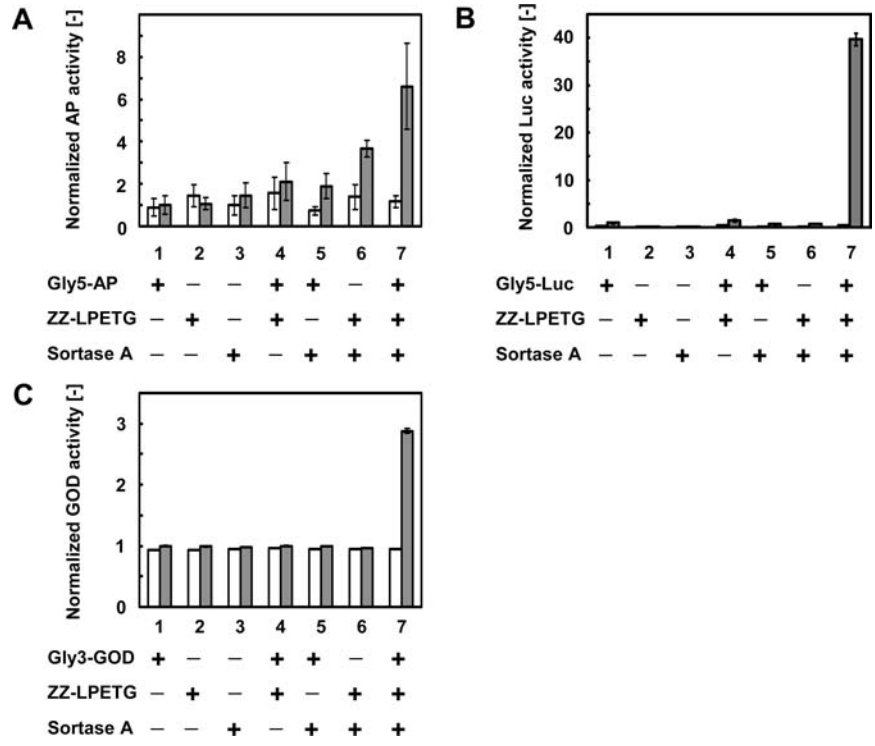


Figure 5. FLAG-tag detection using ZZ−enzyme conjugate. (A) ZZ-AP: column 1, Gly5-AP; column 2, ZZ-LPETG; column 3, Sortase A; column 4, Gly5-AP and ZZ-LPETG; column 5, Gly5-AP and Sortase A; column 6, ZZ-LPETG and Sortase A; column 7, Gly5-AP and ZZ-LPETG and Sortase A. (B) ZZ-Luc: column 1, Gly5-Luc; column 2, ZZ-LPETG; column 3, Sortase A; column 4, Gly5-Luc and ZZ-LPETG; column 5, Gly5-Luc and Sortase A; column 6, ZZ-LPETG and Sortase A; column 7, Gly5-Luc and ZZ-LPETG and Sortase A. myc-tag detection using ZZ-enzyme conjugate. (C) ZZ-GOD: column 1, Gly3-GOD; column 2, ZZ-LPETG; column 3, Sortase A; column 4, Gly3-GOD and ZZ-LPETG; column 5, Gly3-GOD and Sortase A; column 6, ZZ-LPETG and Sortase A; column 7, Gly3-GOD and ZZ-LPETG and Sortase A.

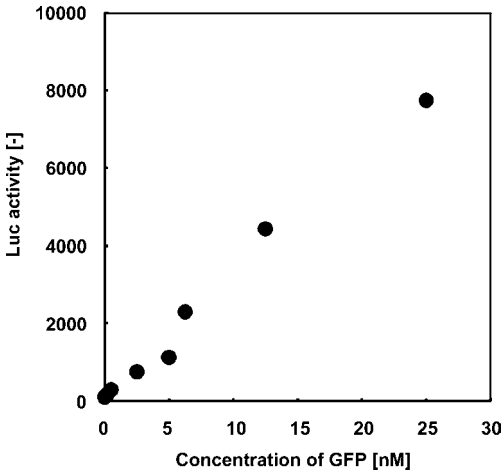


Figure 6. ELISA with anti-GFP antibody-ZZ-Luc conjugate. The signal intensities of wells containing varying concentrations of the antigen, GFP, were measured. Data are averages from three independent experiments and SD are indicated.

in Figure 5A, Gly5-FLAG-RFP was successfully detected using the anti-FLAG antibody-ZZ-AP conjugate (Figure 5A, column 7). No signal was observed against BSA, and no signal was observed without the ZZ-AP conjugate or by using a mixture of ZZ and AP (Figure 5A, columns 1−6). We also utilized the anti-FLAG antibody to ZZ-Luc conjugate. As shown in Figure 5B, Gly5-FLAG-RFP was successfully detected using the anti-FLAG antibody-ZZ-Luc conjugate (Figure 5B, column 7). No signal was observed against BSA, and no signal was observed without the ZZ-Luc conjugate (Figure 5B, columns 1−6).

The *S*/*N* (signal-to-noise) ratio was 40 in the presence or absence of Gly5-FLAG-RFP, which is 7-fold higher than that of ZZ-AP. This is due to the higher activity of luciferase compared to AP.

Additionally, Gly5-myc-Luc was employed as a model target molecule. ZZ-GOD and antimyc antibody (whole IgG) were simply mixed and antimyc antibody-ZZ-GOD conjugates were produced. As a negative control, BSA was employed. As shown in Figure 5C, Gly5-myc-Luc was successfully detected using the antimyc antibody-ZZ-GOD conjugate (Figure 5C, column 7). No signal was observed against BSA, and no signal was observed without the ZZ-GOD conjugate (Figure 5C, columns 1−6).

ELISA was also carried out to test the applicability of antibody-ZZ-Luc conjugate as immunoassay reagent. As shown in Figure 6, signal intensity was increased in response to the concentration of GFP administrated, and the detection limit of GFP with anti-GFP antibody-ZZ-Luc conjugates was found to be around 2.5−5 nM. In the case of using anti-HA antibody-ZZ-Luc conjugate, no signal observed against GFP and no signal was increased in response to the GFP concentration, as expected (data not shown). These results showed that antibody-ZZ-protein conjugate is able to be utilized for immunoassay because of its bifunctionality.

In conclusion, ZZ-LPETG and some enzymes were site-specifically conjugated by a SrtA-mediated reaction. These conjugates retained both the enzymatic activity of AP, Luc, or GOD and the IgG binding activity of ZZ after SrtA treatment. Because genetic engineering of the whole antibody is very difficult, ZZ−protein conjugate can be one of the ways to produce a bifunctional antibody by only mixing with whole antibody. Sortase A also can ligate between proteins and functional small molecules site-specifically (*13*−*16*), suggesting the extension of this ZZ-protein conjugate to ZZ-functional molecule conjugate, for example, fluorescent dyes and/or quantum dot (*14*−*16*). Also notable is that the additional short sequences (i.e., LPETG or GGGGG) may have little effect on the protein expression and refolding, which is possible to allow the ligation of ZZ-LPETG to tag-introduced proteins after refolding. Our strategy is highly useful and versatile for producing antibody−protein conjugates.

ACKNOWLEDGMENT

This work was supported in part by a Grant-in-Aid for Young Scientist B (21760638) of Japan Society for the Promotion of Science (JSPS) and Special Coordination Funds for Promoting Science and Technology, Creation of Innovation Centers for Advanced Interdisciplinary Research Areas (Innovative Bioproduction Kobe), MEXT, Japan.

LITERATURE CITED

(1) Hermanson, G. T. (1996) Functional targets. *Bioconjugate Techniques*, pp 3−23, Academic Press, San Diego, CA.
(2) Voynov, V., Chennamsetty, N., Kayser, V., Wallny, H. J., Helk, B., and Trout, B. L. (2010) Design and application of antibody cysteine variants. *Bioconjugate Chem. 21*, 385–92.
(3) Sirk, S. J., Olafsen, T., Barat, B., Bauer, K. B., and Wu, A. M. (2008) Site-specific, thiol-mediated conjugation of fluorescent probes to cysteine-modified diabodies targeting CD20 or HER2. *Bioconjugate Chem. 19*, 2527–34.
(4) Tolmachev, V., Xu, H., Wållberg, H., Ahlgren, S., Hjertman, M., Sjöberg, A., Sandström, M., Abrahmsén, L., Brechbiel, M. W., and Orlova, A. (2008) Evaluation of a maleimide derivative of CHX-A" DTPA for site-specific labeling of affibody molecules. *Bioconjugate Chem. 19*, 1579–87.
(5) Dawson, P. E., Muir, T. W., Clark-Lewis, I., and Kent, S. B. H. (1994) Synthesis of proteins by native chemical ligation. *Science 266*, 776–9.
(6) Muir, T. W., Sondhi, D., and Cole, P. A. (1998) Expressed protein ligation: A general method for protein engineering. *Proc. Natl. Acad. Sci. U.S.A. 95*, 6705–10.
(7) Johnsson, N., and Johnsson, K. (2003) A fusion of disciplines: chemical approaches to exploit fusion proteins for functional genomics. *ChemBioChem. 4*, 803–10.
(8) Lewandowski, A. T., Small, D. A., Chen, T., Payne, G. F., and Bentley, W. E. (2006) Tyrosine-based "activatable pro-tag": enzyme-catalyzed protein capture and release. *Biotechnol. Bioeng. 93*, 1207–15.
(9) Fontana, A., Spolaore, B., Mero, A., and Veronese, F. M. (2007) Site-specific modification and PEGylation of pharmaceutical proteins mediated by transglutaminase. *Adv. Drug Delivery Rev. 60*, 13–28.
(10) Sato, H., Yamamoto, K., Hayashi, E., and Takahara, Y. (2000) Transglutaminase-mediated dual and site-specific incorporation of poly(ethylene glycol) derivatives into a chimeric interleukin-2. *Bioconjugate Chem. 11*, 502–9.
(11) Lin, C. W., and Ting, A. Y. (2006) Transglutaminase-catalyzed site-specific conjugation of small-molecule probes to proteins in vitro and on the surface of living cells. *J. Am. Chem. Soc. 12*, 4542–3.
(12) Pritz, S., Wolf, Y., Kraetke, O., Klose, J., Bienert, M., and Beyermann, M. (2007) Synthesis of biologically active peptide nucleic acid-peptide conjugates by sortase-mediated ligation. *J. Org. Chem. 72*, 3909–12.
(13) Mao, H., Hart, S. A., Schink, A., and Pollok, B. A. (2004) Sortase-mediated protein ligation: a new method for protein engineering. *J. Am. Chem. Soc. 126*, 2670–1.
(14) Popp, M. W., Antos, J. M., Grotenbreg, G. M., Spooner, E., and Ploegh, H. L. (2007) Sortagging: a versatile method for protein labeling. *Nat. Chem. Biol. 11*, 707–8.
(15) Tanaka, T., Yamamoto, T., Tsukiji, S., and Nagamune, T. (2008) Site-specific protein modification on living cells catalyzed by sortase. *ChemBioChem 9*, 802–7.

(16) Parthasarathy, R., Subramanian, S., and Boder, E. T. (2007) Sortase A as a novel molecular "stapler" for sequence-specific protein conjugation. *Bioconjugate Chem. 18*, 469–76.

(17) Mazmanian, S. K., Liu, G., Ton-That, H., and Schneewind, O. (1999) *Staphylococcus aureus* Sortase, an enzyme that anchors surface proteins to the cell wall. *Science 285*, 760–3.

(18) Ilangovan, U., Ton-That, H., Iwahara, J., Schneewind, O., and Clubb, R. T. (2001) Structure of sortase, the transpeptidase that anchors proteins to the cell wall of *Staphylococcus aureus*. *Proc. Natl. Acad. Sci U.S.A. 98*, 6056–61.

(19) Mao, H. (2004) A self-cleavable sortase fusion for one-step purification of free recombinant proteins. *Protein Exp. Purif. 37*, 253–63.

(20) Zong, Y., Bice, T. W., Ton-That, H., Schneewind, O., and Narayana, S. V. (2004) Crystal structures of *Staphylococcus aureus* Sortase A and its substrate complex. *J. Biol. Chem. 279*, 31383–9.

(21) Kruger, R. G., Otvos, B., Frankel, B. A., Bentley, M., Dostal, P., and McCafferty, D. G. (2004) Analysis of the Substrate specificity of the *Staphylococcus aureus* sortase transpeptidase SrtA. *Biochemistry 43*, 1541–51.

(22) Abuknesha, R. A., Luk, C. Y., Griffith, H. H. M., Maragkou, A., and Iakovaki, D. (2005) Efficient labeling of antibodies with horseradish peroxidase using cyanuric chloride. *J. Immunol. Methods 306*, 211–7.

(23) Jain, M., Kamal, N., and Batra, S. K. (2007) Engineering antibodies for clinical applications. *Trends Biotechnol. 25*, 307–16.

(24) Constantinou, A., Epennetos, A. A., Hreczuk-Hirst, D., Jain, S., Wright, M., Chester, K. A., and Deonarain, M. P. (2009) Site-specific polysialylation of an antitumor single-chain Fv fragment. *Bioconjugate Chem. 20*, 924–31.

(25) Zhao, Y., Benita, Y., Lok, M., Kuipers, B., van der Ley, P., Jiskoot, W., Hennink, W. E., Crommelin, D. J., and Oosting, R. S. (2005) Multi-antigen immunization using IgG binding domain ZZ as carrier. *Vaccine 23*, 5082–90.

(26) Huang, Q., Chen, C., Chen, Y., Gong, C., Cao, L., Wang, J., and Hua, Z. (2006) Application to immunoassays of the fusion protein between protein ZZ and enhanced green fluorescent protein. *J. Immunol. Methods 309*, 130–8.

(27) Takazawa, T., Kamiya, N., Ueda, H., and Nagamune, T. (2004) Enzymatic labeling of a single chain variable fragment of an antibody with alkaline phosphatase by microbial transglutaminase. *Biotechnol. Bioeng. 86*, 399–404.

(28) Zhang, X., Kobatake, E., Kobayashi, K., Yanagida, Y., and Aizawa, M. (2000) Genetically fused protein A-luciferase for immunological blotting analyses. *Anal. Biochem. 282*, 65–9.

(29) Wu, C., Kawasaki, K., Ogawa, Y., Yoshida, Y., Ohgiya, S., and Ohmiya, Y. (2007) Preparation of biotinylated *Cypridina* luciferase and its use in bioluminescent enzyme immunoassay. *Anal. Chem. 79*, 1634–8.

(30) Frederick, K. R., Tung, J., Emerick, R. S., Masiarz, F. R., Chamberlain, S. H., Vasavada, A., and Rosenber, S. (1990) Glucose oxidase from *Aspergillus niger*. *J. Biol. Chem. 265*, 3793–802.

(31) Beck, R., and Burtscher, H. (1994) Expression of human placental alkaline phosphatase in *Escherichia coli*. *Protein Express. Purif. 5*, 192–197.

(32) Kurata, N., Shishido, T., Muraoka, M., Tanaka, T., Ogino, C., Fukuda, H., and Kondo, A. (2008) Specific protein delivery to target cells by antibody-displaying bionanocapsules. *J. Biochem. 144*, 701–7.

(33) Adachi, T., Ito, J., Kawata, K., Kaya, M., Ishida, H., Sahara, H., Hata, Y., Ogino, C., Fukuda, H., and Kondo, A. (2008) Construction of an Aspergillus oryzae cell-surface display system using a putative GPI-anchored protein. *Appl. Microbiol. Biotechnol. 81*, 711–9.

BC100206Z

Synthesis of Extended Nanoscale Optical Encoders

Charles E. Wickersham,[†] Daniel H. S. Kerr,[†,‡] and Everett A. Lipman*[,†,§]

Department of Physics, University of California, Santa Barbara, California 93106, United States, College of Creative Studies, University of California, Santa Barbara, California 93106, United States, and Biomolecular Science and Engineering Program, University of California, Santa Barbara, California 93106, United States. Received May 2, 2010; Revised Manuscript Received September 22, 2010

An optical encoder is a device that uses an interrupted light source−sensor pair to map linear or rotational motion onto a periodic signal. Simple, inexpensive optical encoders are used for precise positioning in machines such as desktop printers, disk drives, and astronomical telescopes. A strand of DNA labeled with a series of Förster resonance energy transfer acceptor dyes can perform the same function at the nanometer scale, producing a periodic fluorescence signal that encodes the movement of a single donor-labeled molecular motor with high spatial and temporal resolution. Previous measurements of this type have employed encoders limited to five acceptor dyes, and hence five signal periods, restricting the range of motion that could be followed. Here we describe two methods for synthesizing double-stranded DNA containing several to hundreds of regularly spaced dyes on one strand. Distinct functional groups incorporated at the encoder ends enable tethering for single-molecule measurements.

INTRODUCTION

Single-molecule Förster resonance energy transfer (FRET) (*1*, *2*) is a powerful technique for measuring nanoscale distances between two fluorophores. Its high sensitivity in the range of approximately 2−10 nanometers is ideal for the study of structural rearrangements in biological macromolecules (*3*−*5*). Until recently, single-molecule FRET measurements of processive motor proteins on DNA (*6*−*9*) have been limited by the presence of only one or a few dye pairs to examination of a restricted range of motion. Furthermore, it remains difficult to obtain accurate distances from measured FRET efficiencies (*10*−*13*).

Precise measurements of macroscopic motion are often made by mapping distance and velocity onto the phase and frequency of a periodic signal. This can be done using an optical encoder, in which a light source and sensor move with respect to a mask containing regularly spaced transparent windows. As the source and sensor move, the window pattern modulates the sensor output, producing the desired signal. We recently implemented a nanoscale encoder (*2*, *14*) using FRET between a moving donor fluorophore and a series of acceptors attached to one strand of a DNA molecule at 69 base pair (bp) intervals. As a donor-labeled helicase traveled along the FRET encoder, a periodic acceptor fluorescence signal was observed.

We synthesized the original five-period FRET encoders from 12 unique self-assembling DNA oligonucleotides. While this scheme has the advantage of producing a well-defined product, its cost and complexity both increase with the length of the encoder. To follow translocation over long distances, observe many cycles of the same molecular motor, and collect multiple periods of any signal modulation (*14*), it is desirable to have encoders many times longer than would be practical to synthesize using our original scheme. Here we demonstrate two methods that produce FRET encoders with lengths ranging from several to hundreds of periods.

The first method employs polymerization-driven self-assembly (*15*, *16*). We designed two synthetic oligonucleotides that, when annealed, form a double-stranded DNA monomer with two complementary cohesive ends. Upon annealing, the monomers undergo a step polymerization reaction that rapidly produces a wide distribution of encoder lengths.

The second method exploits rolling circle amplification (*17*) (RCA), a process used in the replication of many bacterial plasmids (*18*), in bacterial conjugation (*19*), and by many retroviruses (*20*) and bacteriophages (*21*). In RCA (Figure 4), a suitable polymerase binds to a primed single-stranded circular template. DNA synthesis begins from the 3′ terminus of the primer and proceeds around the circle, generating a linear complement to the circular template. After the polymerase completes one revolution around the template, the newly synthesized strand is removed by a cooperating helicase, or by the polymerase itself, so that the process can continue. Because of its extreme processivity and strand displacement ability, DNA polymerase from the ϕ29 bacteriophage is particularly suitable for RCA (*22*).

RCA has found many uses in nanotechnology (*23*), mutation detection (*24*), and immunoassays (*25*). Recently, two groups (*26*, *27*) used RCA to generate periodic double-stranded DNA templates, on which they assembled arrays of gold nanoparticles. We have adapted this technique to synthesize FRET encoders with more than 200 periods, terminated with biotin and digoxigenin groups for site-specific immobilization in single-molecule experiments.

EXPERIMENTAL PROCEDURES

Buffers and Reagents. All solutions were prepared in distilled deionized water (DDI). DNA was stored in 10 mM Tris-HCl (pH 8.0) with 1 mM EDTA (TE buffer). Gels were cast and run in 40 mM Tris-acetate and 1 mM EDTA. Fluorescence measurements were performed in a fluorescence buffer containing 50 mM Tris-HCl (pH 7.9), 1 mM EDTA, 10 mM NaCl, 10 mM $MgCl_2$, 4 mM dithiothreitol, and an enzymatic oxygen-scavenging system consisting of 35 μg/mL

* To whom correspondence should be addressed. E-mail: lipman@physics.ucsb.edu.

[†] Department of Physics, University of California.

[‡] College of Creative Studies, University of California.

[§] Biomolecular Science and Engineering Program, University of California.

10.1021/bc100215j © 2010 American Chemical Society
Published on Web 11/11/2010

Table 1. FRET Encoder Single-Stranded Oligonucleotide Sequences[a]

name	nucleotide sequence (5′ → 3′)
a-b	TTCTTGCACCAGTGTCCTCTCCGCGTCGTCCTACAG TGACTAGTCTGGAACGTATAGTATAAGC
A-B	GACACTGGTGCAAGAAGCTTATACTATACGTTCCA GACTAGTCACTGTAGGACGACGCGGAGAG
a-z-p	TTCTTGCACCAGTGTCCAATATGCAGAACGATCCAA GACGCAATAGCTCC
a-b10	TTCTTGCACCAGTGTCCTCTCCGCGT

[a] The primer−template complex (A-B−a-b10) melts at 74 °C in 100 mM NaCl.

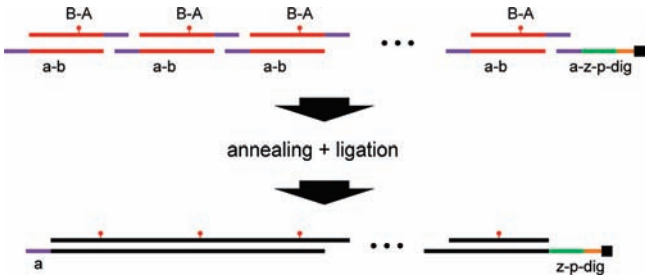


Figure 1. Schematic representation of the polymerizing FRET encoder. The fully assembled encoder consists of a series of regularly spaced FRET acceptor dyes on a double-stranded DNA scaffold. The acceptors are located between bases 32 and 33 of oligo A-B (read 5′ to 3′), and in the final product are spaced by 64 base pairs, approximately four times the Förster radius (R_0) when used with a typical donor dye. An increase in the amount of oligo a-z-p, which binds to unoccupied "A" sites and leaves an unmatched 34-nucleotide cohesive end, will limit the degree of polymerization.

catalase (Sigma-Aldrich C100), 0.2 mg/mL glucose oxidase (Sigma-Aldrich G2133), 0.8% (w/v) D-glucose (Sigma-Aldrich G8270), and 1.2 mM Trolox antioxidant (Sigma-Aldrich 238813) (*28*). Reaction buffers for T4 ligase, ϕ29 polymerase, and terminal transferase were supplied by the manufacturer (New England Biolabs, Ipswich, MA).

DNA Sequences. Sequences for the single-stranded oligonucleotides used in both synthesis schemes are listed in Table 1. All DNA was purchased from Integrated DNA Technologies (Coralville, IA). Oligos A-B and a-b were PAGE purified, and oligo A-B-Cy5, identical to oligo A-B except for a Cy5 fluorophore between bases 32 and 33, was purified by HPLC. All sequences other than a-z-p and a-b10 (the primer for rolling circle amplification reactions) have a 5′ phosphate to enable ligation. To allow for attachment of completed encoders in single-molecule experiments, oligo a-b10 has a 5′ biotin modification, and the terminating oligo a-z-p has a 3′ digoxigenin.

FRET Encoder Synthesis by Polymerization. For polymerization-driven self-assembly, we designed the two partially complementary 64-base oligonucleotides a-b and A-B listed in Table 1. Together they form a 48 bp double-stranded DNA monomer with two 16-base 5′ cohesive ends (Figure 1). The average molecular weight of the product was controlled by the terminator oligonucleotide a-z-p, which anneals at one end of the growing chain, preventing further polymerization from its binding site. The terminating oligo can be designed to incorporate a binding site for a particular motor protein at one end of the encoder, as well as a hapten or biotin for site-specific immobilization.

To synthesize the encoders, we annealed 50 pmol of oligo a-b, 100 pmol of oligo A-B, and a selected ratio of a-z-p to a-b (Figure 2) in a total volume of 8 μL of TE buffer containing

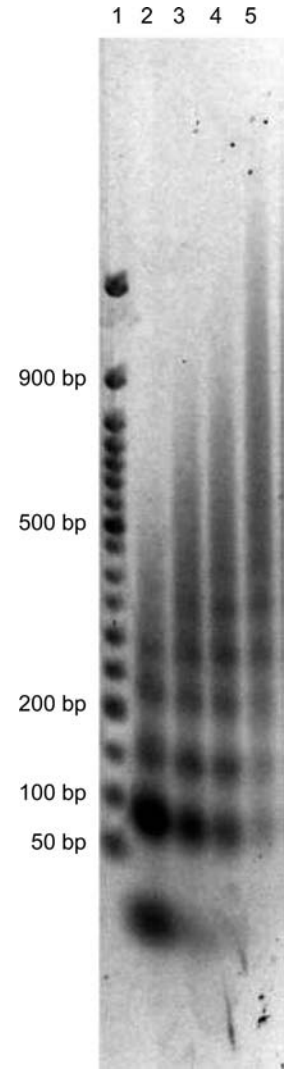


Figure 2. Tuning the molecular weight distribution with a terminator oligonucleotide. The left lane contained a 50 bp DNA marker ladder. The encoders in lanes 2, 3, 4, and 5 were annealed and ligated with 10:1, 2:1, 1:1, and 1:5 molar ratios of oligo a-z-p to monomers, respectively.

100 mM NaCl. When the ratio of a-b to A-B was varied (Figure 3), 50 pmol of a-b was used and the a-z-p terminator was omitted until after the encoders had been separated by size and purified. The mixtures were heated to 65 °C and then cooled to room temperature over the course of approximately 5 min. We connected discontinuous backbone strands in the resulting encoders by adding 1 μL (400 units) of T4 DNA ligase and 1 μL of 10× T4 ligase reaction buffer and incubating overnight at room temperature.

Polymerization results in a broad distribution of FRET encoder lengths. We separated the ligated polymer mixture on a 1.2% (w/v) agarose gel at 160 V for 4.5 h, alongside a 50 bp DNA marker ladder (New England Biolabs). The gel was poststained in a 0.5 μg/mL ethidium bromide solution for 30 min, destained for 30 min in DDI, and visualized using a UV transilluminator. Gel slices were purified using the Wizard Gel Clean-Up kit (Promega, Madison, WI) following the manufacturer's instructions, except that the gel slice was dissolved at room temperature. Heating of the ligated encoders was avoided to prevent melting. Because the DNA sequences are periodic, melting and subsequent reannealing could result in a relative frame shift between the two strands of some integral number of periods.

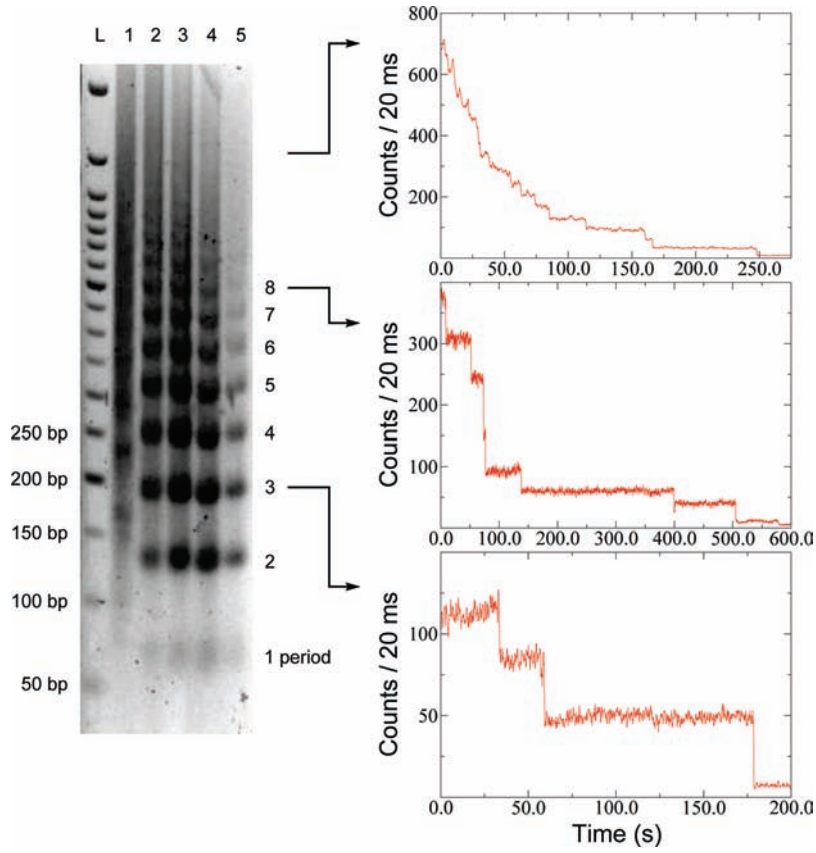


Figure 3. Characterization of polymerized FRET encoders. Agarose gel electrophoresis resolves discrete encoder lengths up to approximately 10 periods. Lane L contained a 50 bp DNA marker ladder. Encoders in lanes 1, 2, 3, 4, and 5 were synthesized with 1:1, 1:2, 1:3, 1:4, and 1:5 ratios of oligo A-B to a-b, respectively. An excess of one monomer oligo over the other improves resolution while preventing the growth of excessively long encoders. Photobleaching traces are shown for FRET encoder DNA extracted from the three- and eight-period bands, and from a position in the gel corresponding to approximately 15 periods. Random temporary drops in the signal are expected from dye blinking (*30*). In the eight-period event, two steps occur near 75 s, while the eighth, smaller step, occurs around 575 s.

FRET Encoder Synthesis by Rolling Circle Amplification. The procedure for RCA patterning is summarized in Figure 4. We formed rolling circle templates by combining 2 μL of 100 μM A-B oligo and 2 μL of 100 μM a-b10 primer in 200 μL of TE buffer containing 100 mM NaCl. We annealed the DNA by heating the solution to 65 °C and then cooling it to room temperature over the course of several hours. This step fully melts undesirable secondary structures in the component oligos, the most stable of which melts at 36.2 °C in 100 mM NaCl. We ligated nicks in the circular templates by adding 1 μL (400 units) of T4 DNA ligase and 21.2 μL of a 10× concentrate of the T4 DNA ligase reaction buffer.

After 3 h of ligation, 30 μL of 10× ϕ29 polymerase reaction buffer, 6 μL of 10 mg/mL bovine serum albumin, 30 μL of 10 mM dNTPs, 30 units of ϕ29 polymerase, and 9 μL of H_2O were added. The reaction mixture was incubated at 31 °C for 3 h, followed by a 10 min 65 °C heat inactivation of the polymerase. The single-stranded RCA product was separated from free nucleotides and the circular templates using a centrifugal filter device (Millipore Ultracel YM-100, 100 kDa NMWL cutoff, Fisher Scientific catalog no. 42412). The 300 μL reaction mixture was diluted to 500 μL with TE buffer and then concentrated to approximately 15 μL. This process was repeated twice more before the DNA was diluted to a final concentration of 75 μL. According to the filter manufacturer's specifications, encoder DNA recovery is expected to be greater than 95%, with more than 99% free nucleotide removal. Preparations for single-molecule measurements select for properly tethered molecules with significant fluorescence. Small residual impurities are either washed out of the flow cell prior to observations or remain undetected.

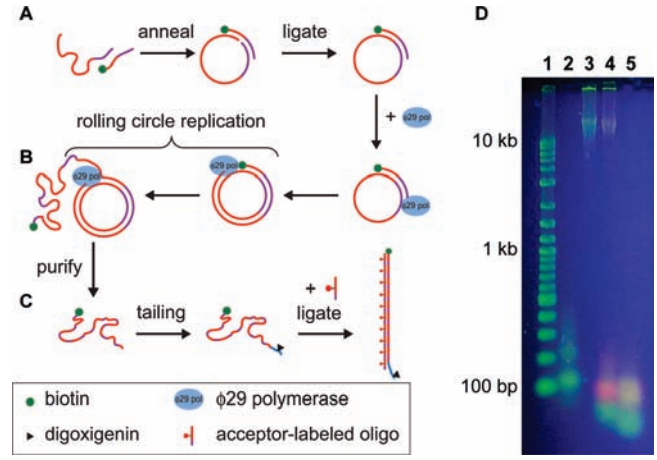


Figure 4. Rolling circle amplification for FRET encoder synthesis. After cyclization of the template by ligation in the presence of a primer (A), an RCA step (B) produces a long concatemer of the complement to the circular template. A tail is appended to the single-stranded product with terminal transferase using dTTP and digoxigenin-labeled dUTP, and subsequent annealing and ligation with the dye-labeled version of the circular template completes a long, bifunctionalized FRET encoder (C). (D) Lane 1 contained a 2 log DNA marker ladder. Lane 2 contained the circular template−primer complex, dimers and trimers of which are also visible. Lane 3 contained the single-stranded RCA product, while lane 4 contained the final annealed and ligated encoder. SpeI, a restriction enzyme that cuts the encoder DNA once per period, was added to the sample from lane 4, which was then run in lane 5. The disappearance of the ≈13 kb double-stranded DNA demonstrates that the encoder is periodic.

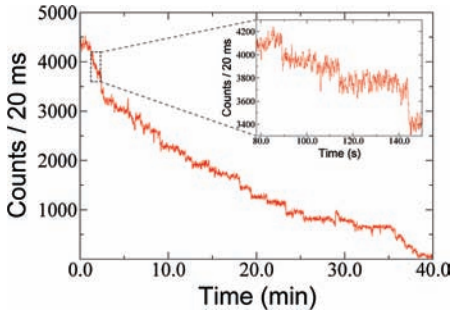


Figure 5. Photobleaching of an immobilized RCA FRET encoder. By eye, we can discern approximately 33 steps. Upward steps, such as those near 29 min and in the inset, are likely caused by the return of a single acceptor (Cy5) from a dark state (*30*). The horizontal position of the focus was adjusted manually in 10 nm increments every few minutes to correct for instrument drift, so that the encoder would remain centered during the 40 min measurement. A 10 nm displacement is only 2.7% of the measured beam waist at the sample plane (data not shown) and could not produce the observed steps.

We appended a digoxigenin-labeled tail to the RCA product by reacting it with terminal transferase in the presence of dTTP and digoxigenin-labeled dUTP. Terminal transferase is a template-independent polymerase that catalyzes the addition of nucleotides to the 3′ end of a strand of DNA. Supplying terminal transferase with a 5−10:1 mixture of dTTP and dig-dUTP produces a tail containing several digoxigenins spaced sufficiently far apart to allow multiple anti-digoxigenins to bind.

For the tailing reaction, 1.7 μg of the purified single-stranded RCA product was combined with 2.5 μL of 10× terminal transferase reaction buffer, 2.5 μL of 2.5 mM $CoCl_2$, 0.25 μL of 100 mM dTTP, 5 μL of 1 mM dig-dUTP, 100 units of terminal transferase (New England Biolabs), and sufficient DDI to yield a total solution volume of 25 μL. The reaction mixture was incubated at 37 °C for 2 h, then heated to 70 °C for a 10 min inactivation.

After the tailing reaction was complete, 12.5 μL of reacted solution was mixed with 10 μL of 100 μM A-B-Cy5 oligo, heated to 65 °C, and then cooled over several hours to room temperature so that dye-labeled oligos would anneal to the long single-stranded template. Once annealed, double-stranded DNA was purified using a PCR spin column (Invitrogen K3100-01) according to the manufacturer's instructions. Finally, nicks in the double-stranded DNA were closed with T4 ligase as described above, and the product was purified again with the same type of spin column.

Fluorescence Measurements. We characterized assembled and purified FRET encoders from both synthesis schemes with a single-molecule photobleaching assay described in detail previously (*14*). We tethered encoders sparsely to the inner surface of a fused-silica flow cell by incubating 50 pM encoder DNA and 1 nM anti-digoxigenin in fluorescence buffer in the cell for 20 min. Excess DNA was then flushed out with fluorescence buffer.

A 633 nm laser, reduced to 1 μW using absorptive neutral density filters, was focused at the fused-silica surface while a piezoelectric stage supporting the cell was scanned in a raster pattern to search for immobilized encoders. When the fluorescence intensity exceeded a designated threshold, indicating the presence of an encoder in the confocal detection volume, the scan was stopped, and the focal position was optimized using an automated centration algorithm (*29*). The encoder was then excited continuously while fluorescence intensity was measured by photon counting and recorded until all dye molecules had been photobleached. Data processed with a 420 ms (21-point) median filter are shown in Figures 3 and 5.

RESULTS AND DISCUSSION

As can be seen in Figure 2, the polymerization scheme produces a distribution of discrete encoder lengths that can be tuned by varying the amount of terminator oligo a-z-p. Figure 3 shows representative photobleaching measurements of polymerized encoders. Sudden, irreversible downward steps in the fluorescence data, each corresponding to the bleaching of a single dye molecule, are clearly evident, and the numbers of dyes counted in this manner correspond to the gel bands from which the encoders were extracted. It is difficult or impossible to identify discrete bands corresponding to lengths beyond 10 periods; however, photobleaching traces for encoders extracted from the high-molecular weight end of the gel indicate that lengths up to at least 15 periods are produced. The typical yield of purified five-period encoder DNA was approximately 1 pmol, making this reaction on the order of 10 times more efficient for this length alone than that described in ref *14*.

Figure 4 shows an agarose gel electrophoresis analysis of the RCA FRET encoders. Lane 2 contained the annealed primer−template complex. Monomeric and multimeric forms, which arise from primer-mediated cross-linking of the template DNA, are visible. The RCA product derived from any of these substrates will contain the same periodic sequence. The gel indicates that the RCA FRET encoders are approximately 13 kb (200 periods) long on average (lanes 3 and 4), and digestion with SpeI, a restriction enzyme that cuts the encoders once per period, demonstrates that they are periodic (lane 5). The red hue of the long DNA in lane 4 arises from annealing with the dye-labeled oligo, the vast excess of which is clearly visible at the bottom of the lane. In lane 5, the 64 bp DNA appears yellow because the stain more efficiently intercalates double-stranded DNA (the mixture of green stain fluorescence and red acceptor fluorescence produces yellow). In lanes 4 and 5, the lower-most band is an unlabeled truncation product left over from the synthesis of the dye-labeled oligo. As it is not fully complementary to oligo a-b, it does not interfere with assembly of the RCA encoder.

Photobleaching data from an RCA encoder are shown in Figure 5. The length of this encoder (approximately 4.4 μm) greatly exceeds the axial extent of the confocal volume. No refocusing was done during the measurement, so the ≈30 observed steps, corresponding to ≈650 nm of encoder contour length, match our expectation for the number of dyes within the region from which fluorescence was collected.

One could envision extending both of the synthesis schemes we have presented to create polymers with much longer repeat lengths. Several synthetic oligonucleotides could be annealed and ligated to form monomers hundreds of base pairs long, and these could be polymerized as described above. Alternatively, an extended substrate for the rolling circle amplification scheme could be fashioned from two or more single-stranded oligos, cyclized by an equal number of primers. Modification of all but one of the primers with 3′ terminal dideoxynucleotides would allow the origin of the RCA reaction to be specified. FRET encoders assembled in this manner could prove useful for measurements taking advantage of multiple acceptors with distinct spectra, or for studying the effects of specific sequences on transcription.

ACKNOWLEDGMENT

We thank Omar Saleh for discussions and advice. This work was supported by the Hellman Family Foundation and the California Nanosystems Institute. E.A.L. is an Alfred P. Sloan research fellow.

LITERATURE CITED

(1) Ha, T., Enderle, T., Ogletree, D. F., Chemla, D. S., Selvin, P. R., and Weiss, S. (1996) Probing the interaction between two single molecules: Fluorescence resonance energy transfer between a single donor and a single acceptor. *Proc. Natl. Acad. Sci. U.S.A. 93*, 6264–6268.

(2) Weiss, S. (1999) Fluorescence spectroscopy of single biomolecules. *Science 283*, 1676–1683.

(3) Deniz, A. A., Laurence, T. A., Dahan, M., Chemla, D. S., Schultz, P. G., and Weiss, S. (2001) Ratiometric single-molecule studies of freely diffusing biomolecules. *Annu. Rev. Phys. Chem. 52*, 233–253.

(4) Zhuang, X. W., and Rief, M. (2003) Single-molecule folding. *Curr. Opin. Struct. Biol. 13*, 88–97.

(5) Schuler, B., and Eaton, W. A. (2008) Protein folding studied by single-molecule FRET. *Curr. Opin. Struct. Biol. 18*, 16–26.

(6) Myong, S., Rasnik, I., Joo, C., Lohman, T. M., and Ha, T. (2005) Repetitive shuttling of a motor protein on DNA. *Nature 437*, 1321–1325.

(7) Myong, S., Bruno, M. M., Pyle, A. M., and Ha, T. (2007) Spring-loaded mechanism of DNA unwinding by hepatitis C virus NS3 helicase. *Science 317*, 513–516.

(8) Verbrugge, S., Lansky, Z., and Peterman, E. J. G. (2009) Kinesin's step dissected with single-motor FRET. *Proc. Natl. Acad. Sci. U.S.A. 106*, 17741–17746.

(9) Christian, T. D., Romano, L. J., and Rueda, D. (2009) Single-molecule measurements of synthesis by DNA polymerase with base-pair resolution. *Proc. Natl. Acad. Sci. U.S.A. 106*, 21109–21114.

(10) Sabanayagam, C. R., Eid, J. S., and Meller, A. (2005) Using fluorescence resonance energy transfer to measure distances along individual DNA molecules: Corrections due to nonideal transfer. *J. Chem. Phys. 122*, 061103.

(11) Braslavsky, S. E., Fron, E., Rodriguez, H. B., Roman, E. S., Scholes, G. D., Schweitzer, G., Valeur, B., and Wirz, J. (2008) Pitfalls and limitations in the practical use of Forster's theory of resonance energy transfer. *Photochem. Photobiol. Sci. 7*, 1444–1448.

(12) Beljonne, D., Curutchet, C., Scholes, G. D., and Silbey, R. J. (2009) Beyond Forster Resonance Energy Transfer in Biological and Nanoscale Systems. *J. Phys. Chem. B 113*, 6583–6599.

(13) Camley, B. A., Brown, F. L. H., and Lipman, E. A. (2009) Förster Transfer Outside the Weak-Excitation Limit. *J. Chem. Phys. 131*, 104509.

(14) Wickersham, C. E., Cash, K. J., Pfeil, S. H., Bruck, I., Kaplan, D. L., Plaxco, K. W., and Lipman, E. A. (2010) Tracking a Molecular Motor with a Nanoscale Optical Encoder. *Nano Lett. 10*, 1022–1027.

(15) Hartley, J. L., and Gregori, T. J. (1981) Cloning multiple copies of a DNA segment. *Gene 13*, 347–353.

(16) Winfree, E., Liu, F. R., Wenzler, L. A., and Seeman, N. C. (1998) Design and self-assembly of two-dimensional DNA crystals. *Nature 394*, 539–544.

(17) Fire, A., and Xu, S. Q. (1995) Rolling replication of short DNA circles. *Proc. Natl. Acad. Sci. U.S.A. 92*, 4641–4645.

(18) Khan, S. A. (1997) Rolling-circle replication of bacterial plasmids. *Microbiol. Mol. Biol. Rev. 61*, 442–455.

(19) Lanka, E., and Wilkins, B. M. (1995) DNA processing reactions in bacterial conjugation. *Annu. Rev. Biochem. 64*, 141–169.

(20) Branch, A. D., and Robertson, H. D. (1984) A replication cycle for viroids and other small infectious RNAs. *Science 223*, 450–455.

(21) Baas, P. D. (1985) DNA replication of single-stranded *Escherichia coli* DNA phages. *Biochim. Biophys. Acta 825*, 111–139.

(22) Blanco, L., Bernad, A., Lazaro, J. M., Martin, G., Garmendia, C., and Salas, M. (1989) Highly efficient DNA-synthesis by the phage ϕ-29 DNA-polymerase: Symmetrical mode of DNA-replication. *J. Biol. Chem. 264*, 8935–8940.

(23) Zhao, W. A., Ali, M. M., Brook, M. A., and Li, Y. F. (2008) Rolling circle amplification: Applications in nanotechnology and biodetection with functional nucleic acids. *Angew. Chem., Int. Ed. 47*, 6330–6337.

(24) Lizardi, P. M., Huang, X. H., Zhu, Z. R., Bray-Ward, P., Thomas, D. C., and Ward, D. C. (1998) Mutation detection and single-molecule counting using isothermal rolling-circle amplification. *Nat. Genet. 19*, 225–232.

(25) Schweitzer, B., Wiltshire, S., Lambert, J., O'Malley, S., Kukanskis, K., Zhu, Z. R., Kingsmore, S. F., Lizardi, P. M., and Ward, D. C. (2000) Immunoassays with rolling circle DNA amplification: A versatile platform for ultrasensitive antigen detection. *Proc. Natl. Acad. Sci. U.S.A. 97*, 10113–10119.

(26) Deng, Z. X., Tian, Y., Lee, S. H., Ribbe, A. E., and Mao, C. D. (2005) DNA-encoded self-assembly of gold nanoparticles into one-dimensional arrays. *Angew. Chem., Int. Ed. 44*, 3582–3585.

(27) Beyer, S., Nickels, P., and Simmel, F. C. (2005) Periodic DNA nanotemplates synthesized by rolling circle amplification. *Nano Lett. 5*, 719–722.

(28) Rasnik, I., McKinney, S. A., and Ha, T. (2006) Nonblinking and long-lasting single-molecule fluorescence imaging. *Nat. Methods 3*, 891–893.

(29) Ha, T., Chemla, D. S., Enderle, T., and Weiss, S. (1997) Single molecule spectroscopy with automated positioning. *Appl. Phys. Lett. 70*, 782–784.

(30) Bates, M., Blosser, T. R., and Zhuang, X. W. (2005) Short-range spectroscopic ruler based on a single-molecule optical switch. *Phys. Rev. Lett. 94*, 108101.

BC100215J

Chemoenzymatic Syntheses and Anti-HIV-1 Activity of Glucose−Nucleoside Conjugates as Prodrugs

Tatiana Rodríguez-Pérez,[†] Susana Fernández,[†] Yogesh S. Sanghvi,[‡] Mervi Detorio,[§] Raymond F. Schinazi,[§] Vicente Gotor,*[,†] and Miguel Ferrero*[,†]

Departamento de Química Orgánica e Inorgánica and Instituto Universitario de Biotecnología de Asturias, Universidad de Oviedo, 33006-Oviedo (Asturias), Spain, Rasayan Inc., 2802 Crystal Ridge Road, Encinitas, California 92024-6615, United States, and Center for AIDS Research, Department of Pediatrics, Emory University School of Medicine/Veterans Affair Medical Center, Decatur, Georgia 30033, United States. Received May 3, 2010; Revised Manuscript Received October 18, 2010

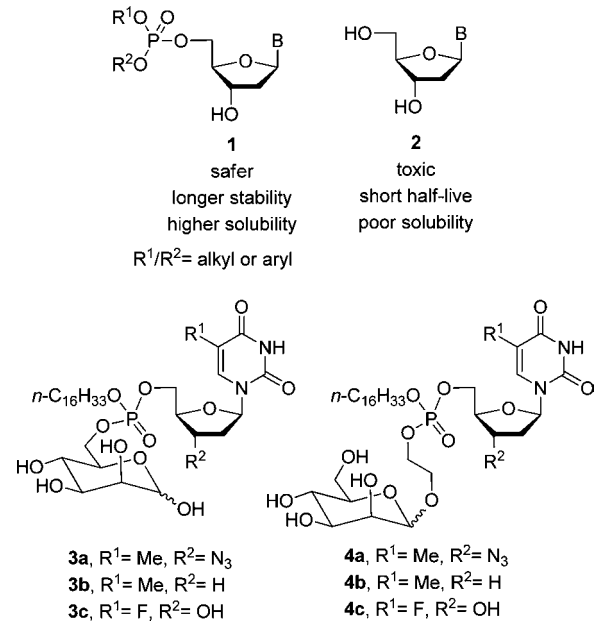
Phosphodiester linked conjugates of various nucleosides such as d4U, d4T, IdUrd, ddI, ddA, virazole, *ara*-A, and *ara*-C containing a glucosyl moiety have been described. These compounds were designed to act as prodrugs, where the corresponding 5′-monophosphates may be generated intracellularly. The synthesis of the glycoconjugates was achieved in good yields by condensation of a glucosyl phosphoramidite **7** with nucleosides in the presence of an activating agent. It was demonstrated that the glucose conjugates improve the water solubility of the nucleoside analogues, for example, up to 31-fold for the *ara*-A conjugate compared to that of *ara*-A alone. The new conjugates were tested for their anti-HIV-1 activity in human lymphocytes. These derivatives offer a convenient design for potential prodrug candidates with the possibility of improving the physicochemical properties and therapeutic activity of nucleoside analogues.

INTRODUCTION

Chemically modified nucleosides are widely used as therapeutic agents to treat cancer, fungal, bacterial, and viral infections (*1*−*5*). Similarly, carbohydrates are of paramount importance in intercellular recognition, bacterial and viral infection processes, and inflammation events making them an attractive target for drug development (*6*−*8*). Consequently, a conjugate of these two classes of molecules may offer an avenue to design and develop novel therapeutics with improved biological functions. The use of a phosphate ester linkage for conjugation is widely practiced because of its natural occurrence in cellular physiology and as a backbone for DNA and RNA molecules. The culmination of these attributes motivated us to use natural phosphate linkage to conjugate a biologically active nucleoside with a carbohydrate unit anticipating that we could modulate the therapeutic effects of known nucleosides in a favorable manner.

Several modified nucleosides (AZT, d4T, 3TC, ddI, ddC, and abacavir) have been approved by the US FDA as anti-HIV drugs. Although these drugs are effective for the treatment of HIV, some of the limitations such as toxicity, short half-life, and dependence on cellular enzymes preclude their wider use. In order to overcome these limitations and to improve the therapeutic potential of these nucleosides, several phosphate-based prodrug strategies have been developed (*9*−*16*). The prodrug approach appears to be a promising way to improve the anti-HIV activity of the approved nucleosides, reduce their cellular toxicity, enhance cellular uptake, and prevent viral resistance (*17*−*19*). The 5′-phosphate analogues of nucleosides have been extensively studied as prodrugs. For example, nucleoside glycoconjugate prodrugs (**1**, Chart 1) are able to penetrate cellular membranes as a result of their higher lipophilicity and are also able to improve the efficacy of antiviral and anticancer nucleoside analogues **2** (*20*). Phosphate derivatives of AZT (**3a**,**4a**), ddT (**3b**,**4b**), and FdUrd (**3c**,**4c**) with a D-mannose as a conjugating moiety were prepared as membrane soluble prodrugs directed toward cells carrying mannosyl receptors (*21*, *22*). Previously, glyco-conjugates of oligonucleotides have been reported to demonstrate improved anti-HIV activity (*23*).

Chart 1. Prodrugs of Phosphorylated Nucleosides



The main methods described in the literature for the preparation of nucleoside−carbohydrate phosphodiesters are the condensation of protected sugar monophosphates with nucleosides in the presence of an activating agent (*21*, *22*, *24*) or by coupling of a nucleoside phosphate with a protected glycosyl donor (*25*).

* Corresponding author. (V.G.) E-mail: vgs@uniovi.es. (M.F.) E-mail: mferrero@uniovi.es.
[†] Universidad de Oviedo.
[‡] Rasayan Inc.
[§] Emory University School of Medicine/Veterans Affair Medical Center.

10.1021/bc1002168 © 2010 American Chemical Society
Published on Web 11/15/2010

Among the various protocols available for conjugation, the phosphoramidite chemistry offers the best yields (*16*). Recently, it has been demonstrated that the solid-phase synthesis of a dinucleoside and a nucleoside−carbohydrate phosphodiester and thiophosphodiester using polymer-bound oxathiophospholanes as the phosphitylating agents is a viable way for the synthesis of conjugates (*14*).

As a part of our ongoing efforts in the discovery and design of therapeutic nucleoside analogues (*26*−*28*), we embarked on a path to synthesize nucleoside−carbohydrate conjugates linked via the phosphate backbone. We believe that these conjugates will act like prodrugs where the corresponding 5′-monophosphate could be liberated intracellularly by cellular phosphodiesterases. With this objective in sight, we elected to develop conjugation chemistry that will permit the convenient attachment of glucose 6-phosphate (*29*) to a nucleoside analogue of therapeutic value. For this study, we have utilized highly efficient phosphoramidite chemistry to create the conjugates of interest. Herein, we describe the synthesis, anti-HIV-1 activity, and cytotoxicity of novel glucose−nucleoside conjugates.

MATERIALS AND METHODS

Candida rugosa lipase (CRL, Type VII, 1410 U/mg) was purchased from Sigma. *Pseudomonas cepacia* lipase (PSL-C, Amano PS-C II, 1195 U/g) was purchased from Aldrich. *Candida antarctica* lipase B (CAL-B, Novozym 435, 7300 PLU/g) was a gift from Novo Nordisk Co. Synthesis of α-**5** and **6** have been previously described (*29*). Unless otherwise specified, flash chromatography was performed over silica 60 Å (230−400 mesh). 1*H*-Tetrazole was prepared according to the procedure previously described (*30*). The nucleosides **8c**, **8d**, **8f-i**, **14**, **15**, **17-19**, **21**, and **22** were isolated as amorphous solids upon concentration of the solutions. The melting range of these solid compounds was determined by the melting point Gallenkamp apparatus.

Synthesis of 2-Cyanoethyl-*N*,*N*-diisopropyl-(1,2,3,4-tetra-*O*-acetyl-α-D-glucopyranoside-6-yl)phosphoramidite (*7*). 2-Cyanoethyl-*N*,*N*,*N*′,*N*′-tetraisopropylphosphoramidite (1.1 mL, 3.45 mmol) and pyridinium trifluoroacetate (*31*) (673 mg, 3.45 mmol) was added to a stirred solution of **6** (1 g, 2.89 mmol) in anhydrous CH_2Cl_2 (7 mL) and the mixture stirred for 3 h at room temperature. Upon the complete consumption of the starting material (TLC), the solvent was evaporated and the residue purified by flash chromatography using silica 60 Å (32−63 μm). Elution with 33% EtOAc/hexane afforded **7** as a clear oil in 91% yield. For flash chromatography, silica was pretreated with 33% EtOAc/hexane containing 1% Et_3N (300 mL) and then with 33% EtOAc/hexane (300 mL). ^{1}H NMR ($CDCl_3$, 600 MHz): δ 1.13 (s, 3H, Me-^{i}Pr), 1.14 (s, 3H, Me-^{i}Pr), 1.15 (s, 6H, Me-^{i}Pr), 1.16 (s, 3H, Me-^{i}Pr), 1.17 (s, 6H, Me-^{i}Pr), 1.18 (s, 3H, Me-^{i}Pr), 1.99 (s, 3H, CH_3), 2.00 (s, 6H, CH_3), 2.02 (s, 3H, CH_3), 2.03 (s, 6H, CH_3), 2.14 (s, 3H, CH_3), 2.15 (s, 3H, CH_3), 2.62 (t, 4H, $H_{2'}$, $^3J_{HH}$ 6.4 Hz), 3.60 (m, 6H, H_6+ $H_{1''}$), 3.79 (m, 6H, $H_{1'}$ + H_6), 4.05 (m, 2H, H_5), 5.03 (m, 2H, H_2), 5.09 (t, 1H, H_4,$^3J_{HH}$ 10.1 Hz)), 5.15 (t, 1H, H_4,$^3J_{HH}$ 9.7 Hz), 5.44 (t, 2H, H_3,$^3J_{HH}$ 9.2 Hz), 6.31 (t, 2H, H_1,$^3J_{HH}$ 3.3 Hz). ^{31}P NMR ($CDCl_3$, 242.9 MHz): δ 149.64, 149.91. MS (ESI^+, *m*/*z*): 549 [$(M + H)^+$, 10%], 571 [$(M + Na)^+$, 100%].

Synthesis of 5-Iodo-3′-*O*-levulinyl-2′-deoxyuridine (8c). A suspension of **11** (200 mg, 0.56 mmol), *O*-levulinyl acetonoxime (*32*) (291 mg, 1.70 mmol), and PSL-C (600 mg) in anhydrous THF (5.7 mL) under nitrogen was stirred at 30 °C and 250 rpm for 24 h. The enzyme was filtered off and washed with CH_2Cl_2 and THF. The solvents were distilled under vacuum, and the residue was washed with Et_2O to afford **8c** as a white solid in 95% yield. Melting range: 164−166 °C. ^{1}H NMR (MeOH-d_4, 300 MHz): δ 2.36 (s, 3H, CH_3), 2.52 (m, 2H, $H_{2'}$), 2.77 (t, 2H, CH_2-Lev, $^3J_{HH}$ 6.7 Hz), 3.01 (t, 2H, CH_2-Lev, $^3J_{HH}$ 6.5 Hz), 3.99 (m, 2H, $H_{5'}$), 4.29 (m, 1H, $H_{4'}$), 5.50 (m, 1H, $H_{3'}$), 6.43 (apparent q, 1H, $H_{1'}$, $^3J_{HH}$ 5.8 Hz), 8.72 (s, 1H, H_6). MS (ESI^+, *m*/*z*): 475 [$(M + Na)^+$, 100%].

Synthesis of 5-Iodo-5′-*O*-levulinyl-2′-deoxyuridine (8d). A suspension of **11** (200 mg, 0.56 mmol), *O*-levulinyl acetonoxime (*32*) (291 mg, 1.70 mmol), and CAL-B (200 mg) in anhydrous THF (5.7 mL) under nitrogen was stirred at 30 °C and 250 rpm for 24 h. The enzyme was filtered off, washed with CH_2Cl_2 and THF, and the solvents distilled under vacuum. The residue was purified by flash chromatography using 5% ^{i}PrOH/CH_2Cl_2 and the resulting solid washed with Et_2O to afford **8d** as a white solid in 78% yield. Melting range: 140−143 °C. ^{1}H NMR (MeOH-d_4, 300 MHz): δ 2.37 (s, 3H, CH_3), 2.49 (m, 2H, $H_{2'}$), 2.87 (t, 2H, CH_2-Lev, $^3J_{HH}$ 6.3 Hz), 3.03 (t, 2H, CH_2-Lev, $^3J_{HH}$ 6.6 Hz), 4.28 (m, 1H, $H_{4'}$), 4.46 (m, 1H, $H_{5'}$), 4.55 (m, 2H, $H_{3'}$ + $H_{5'}$), 6.39 (apparent t, 1H, $H_{1'}$, $^3J_{HH}$ 6.5 Hz), 8.72 (s, 1H, H_6). MS (ESI^+, *m*/*z*): 475 [$(M + Na)^+$, 65%].

Synthesis of N^6-(Dimethylamino)methylene-2′,3′-dideoxyadenosine (8f). A mixture of **12** (149 mg, 0.63 mmol) and *N*,*N*-dimethylacetamide dimethyl acetal (824 μL, 6.3 mmol) in anhydrous DMF (3.2 mL) was stirred at room temperature for 4 h. The mixture was evaporated and the residue purified by flash chromatography using 8% MeOH/CH_2Cl_2 to afford **8f** as a white solid in 97% yield. Melting range: 61−64 °C (unstable compound, decomposes easily). ^{1}H NMR (MeOH-d_4, 300 MHz): δ 2.38 (m, 2H, $H_{2'}$ or $H_{3'}$), 2.72 (m, 2H, $H_{2'}$ or $H_{3'}$), 3.42 (s, 3H, Me), 3.43 (s, 3H, Me), 3.85 (dd, 1H, $H_{5'}$, $|^2J_{HH}|$ 12.2 Hz, $^3J_{HH}$ 3.9 Hz), 4.05 (dd, 1H, $H_{5'}$, $|^2J_{HH}|$ 12.2 Hz, $^3J_{HH}$ 3.1 Hz), 4.45 (m, 1H, $H_{4'}$), 6.51 (apparent t, 1H, $H_{1'}$, $^3J_{HH}$ 5.6 Hz), 8.59 (s, 1H, H_8), 8.70 (s, 1H, H_2), 9.07 (s, 1H, HC═N). MS (ESI^+, *m*/*z*): 291 [$(M + H)^+$, 100%].

Synthesis of 1-(2′,3′-Di-*O*-acetyl-β-D-ribofuranosyl)-1*H*-1,2,4-triazole-3-carboxamide (8g). To a solution of **15** (295 mg, 0.9 mmol) in chloroform (30 mL) was added formic acid (3−4 drops). After being stirred at room temperature for 18 h, the mixture was neutralized with 1 N KOH, and the solution was concentrated. The residue was purified by flash chromatography using 1−50% MeOH/CH_2Cl_2 as the elution gradient to yield **8g** as a white solid in quantitative yield. Melting range: 75−77 °C. ^{1}H NMR (MeOH-d_4, 300 MHz): δ 2.29 (s, 3H, CH_3), 2.31 (s, 3H, CH_3), 2.28 (s, 3H, CH_3), 3.92 (dd, 1H, $H_{5'}$, $|^2J_{HH}|$ 12.5 Hz, $^3J_{HH}$ 3.7 Hz), 4.03 (dd, 1H, $H_{5'}$, $|^2J_{HH}|$ 12.5 Hz, $^3J_{HH}$ 3.1 Hz), 4.52 (q, 1H, $H_{4'}$,$^3J_{HH}$ 5.1 Hz), 5.79 (t, 1H, $H_{3'}$, $^3J_{HH}$ 5.3 Hz), 5.96 (dd, 1H, $H_{2'}$, $^3J_{HH}$ 5.1, 3.9 Hz), 6.43 (d, 1H, $H_{1'}$, $^3J_{HH}$ 3.9 Hz), 8.73 (br s, 1H, NH), 9.02 (s, 1H, H_5). MS (ESI^+, *m*/*z*): 351 [$(M + Na)^+$, 90%].

Synthesis of N^6-Benzoyl-9-(2′,3′-di-*O*-acetyl-β-D-arabinofuranosyl)adenine (8h). A 4 M solution of hydrogen chloride in 1,4-dioxane (1.1 mL) was added to a stirred solution of **19** (330 mg, 0.44 mmol) in CH_2Cl_2 (8.8 mL) at −50 °C. After 15 min, the reaction was quenched by adding a solution of pyridine/MeOH (1:1, v/v) at −50 °C. The mixture was poured into saturated aqueous $NaHCO_3$ solution and extracted with CH_2Cl_2. The combined organic fractions were dried (Na_2SO_4) and concentrated under vacuum. The crude was purified by flash chromatography using 1−10% MeOH/CH_2Cl_2 as the elution gradient to yield **8h** as a white solid in 76% yield. Melting range: 165−167 °C. ^{1}H NMR (MeOH-d_4, 300 MHz): δ 1.96 (Me), 2.33 (Me), 4.09 (m, 2H, $H_{5'}$), 4.38 (m, 1H, $H_{4'}$), 5.79 (m, 2H, $H_{2'}$ + $H_{3'}$), 6.89 (d, 1H, $H_{1'}$, $^3J_{HH}$ 5.3 Hz), 7.69−7.85 (m, 3H, H_m + H_p), 8.26 (d, 2H, H_o, $^3J_{HH}$ 8.5 Hz), 8.86 (s, 1H, H_8), 8.89 (s, 1H, H_2). MS (ESI^+, *m*/*z*): 478 [$(M + Na)^+$, 100%] and 494 [$(M+K)^+$, 5].

Synthesis of N^4-acetyl-1-(2′,3′-di-*O*-acetyl-β-D-arabinofuranosyl)cytosine (8i). Acetic acid (57 μL, 1 mmol) and TBAF (2 mL, 1 M in THF, 2 mmol) were added to a solution of **22** (330

mg, 0.68 mmol) in anhydrous THF (6.8 mL), and the reaction was stirred at room temperature for 2 h. The mixture was concentrated and the residue purified by flash chromatography using 8% MeOH/CH_2Cl_2 for elution affording **8i** as a white solid in 82% yield. Melting range: 173−175 °C. ^{1}H NMR ($CDCl_3$, 300 MHz): δ 1.92 (s, 3H, Me), 2.14 (s, 3H, Me), 2.30 (s, 3H, Me), 3.88 (dd, 1H, $H_{5'}$, $|^2J_{HH}|$ 12.3 Hz, $^3J_{HH}$ 4.9 Hz), 3.96 (dd, 1H, $H_{5'}$, $|^2J_{HH}|$ 12.3 Hz, $^3J_{HH}$ 3.9 Hz), 4.83 (q, 1H, $H_{4'}$, $^3J_{HH}$ 4.8 Hz), 5.22 (m, 1H, $H_{3'}$), 5.58 (dd, 1H, $H_{2'}$, $^3J_{HH}$ 3.9, 2.2 Hz), 6.31 (d, 1H, $H_{1'}$, $^3J_{HH}$ 4.2 Hz), 7.58 (d, 1H, H_5, $^3J_{HH}$ 7.4 Hz), 8.26 (d, 1H, H_6, $^4J_{HH}$ 7.1 Hz), 9.9 (br s, 1H, NH). MS (ESI$^+$, *m*/*z*): 370 [(M + H)$^+$, 5%] and 392 [(M + Na)$^+$, 100].

General Procedure for the Synthesis of Phosphotriesters 9a−i. To a stirred solution of nucleoside **8** (1.07 mmol) and **7** (0.72 mmol) in anhydrous MeCN (8 mL) was added 1*H*-tetrazole (112.7 mg, 1.61 mmol). After the reaction was stirred at room temperature for 5 min, 5.1 mL of a 1 M solution of I_2 in Py/H_2O (9:1, v/v) was added to the mixture. After being stirred at room temperature for 5 min, the mixture was poured into $Na_2S_2O_3$ (5% aqueous solution) and extracted with CH_2Cl_2. The combined organic fractions were dried (Na_2SO_4) and concentrated under vacuum. The crude was purified by flash chromatography using 60 Å silica (32−63 μm) at pH 7 and 0−50% MeOH/EtOAc as the elution gradient to yield **9** as a white hygroscopic foam.

2-Cyanoethyl-(2′,3′-didehydro-2′,3′-dideoxyuridin-5′-yl)-1,2,3,4-tetra-*O*-acetyl-α-D-glucopyranos-6-yl phosphate (9a). 89% yield. ^{1}H NMR (MeOH-d_4, 600 MHz): δ 2.14 (s, 3H, Me), 2.15 (s, 3H, Me), 2.16 (s, 3H, Me), 2.17 (s, 3H, Me), 2.21 (s, 3H, Me), 2.22 (s, 3H, Me), 2.34 (s, 3H, Me), 2.35 (s, 3H, Me), 3.05 (t, 4H, $H_{2'''}$, $^3J_{HH}$ 6.1 Hz), 4.31−4.48 (m, 14H, $H_{5''}$ + $H_{6''}$ + $H_{5'}$ + $H_{1'''}$), 5.23 (m, 4H, $H_{2''}$ + $H_{4'}$), 5.34 (m, 2H, $H_{4''}$), 5.61 (m, 2H, $H_{3''}$), 5.88 (d, 1H, H_5, $^3J_{HH}$ 8.0 Hz), 5.91 (d, 1H, H_5, $^3J_{HH}$ 8.1 Hz), 6.18 (m, 2H, $H_{2'}$), 6.45 (d, 1H, $H_{1''}$, $^3J_{HH}$ 3.7 Hz), 6.47 (d, 1H, $H_{1''}$, $^3J_{HH}$ 3.7 Hz), 6.62 (m, 2H, $H_{3'}$), 7.12 (m, 2H, $H_{1'}$), 7.72 (d, 1H, H_6, $^3J_{HH}$ 8.1 Hz), 7.74 (d, 1H, H_6, $^3J_{HH}$ 8.1 Hz). ^{31}P NMR (MeOH-d_4, 242.9 MHz): δ −2.11, −2.19. MS (ESI$^+$, *m*/*z*): 696 [(M + Na)$^+$, 100%].

2-Cyanoethyl-(2′,3′-didehydro-2′,3′-dideoxythymidin-5′-yl)-1,2,3,4-tetra-*O*-acetyl-α-D-glucopyranos-6-yl phosphate (9b). 88% yield. ^{1}H NMR (MeOH-d_4, 600 MHz): δ 2.07 (d, 3H, H_7, $|^4J_{HH}|$ 1.1 Hz), 2.08 (d, 3H, H_7, $|^4J_{HH}|$ 1.1 Hz), 2.16 (s, 3H, Me), 2.17 (s, 3H, Me), 2.18 (s, 3H, Me), 2.19 (s, 3H, Me), 2.20 (s, 6H, Me), 2.37 (s, 3H, Me), 2.38 (s, 3H, Me), 3.08 (q, 4H, $H_{2'''}$, $^3J_{HH}$ 7.2 Hz), 4.36−4.53 (m, 14H, $H_{5''}$ + $H_{6''}$ + $H_{5'}$ + $H_{1'''}$), 5.25 (m, 4H, $H_{2''}$ + $H_{4'}$), 5.35 (m, 2H, $H_{4''}$), 5.65 (m, 2H, $H_{3''}$), 6.19 (d, 2H, $H_{2'}$, $^3J_{HH}$ 6.0 Hz), 6.46 (d, 1H, $H_{1''}$, $^3J_{HH}$ 3.8 Hz), 6.49 (d, 1H, $H_{1''}$, $^3J_{HH}$ 3.8 Hz), 6.64 (m, 2H, $H_{3'}$), 7.15 (m, 2H, $H_{1'}$), 7.58 (d, 1H, H_6, $|^4J_{HH}|$ 1.1 Hz), 7.60 (d, 1H, H_6, $|^4J_{HH}|$ 1.1 Hz). ^{31}P NMR (MeOH-d_4, 242.9 MHz): δ −1.99, −2.11. MS (ESI$^+$, *m*/*z*): 710 [(M + Na)$^+$, 100%].

2-Cyanoethyl-(3′-*O*-levulinyl-5-iodo-2′-deoxyuridin-5′-yl)-1,2,3,4-tetra-*O*-acetyl-α-D-glucopyranos-6-yl phosphate (9c). 80% yield. ^{1}H NMR (MeOH-d_4, 600 MHz): δ 2.18 (s, 6H, Me), 2.19 (s, 3H, Me), 2.20 (s, 6H, Me), 2.21 (s, 3H, Me), 2.26 (s, 3H, Me), 2.37 (s, 3H, Me), 2.38 (s, 6H, Me), 2.64 (m, 4H, $H_{2'}$), 2.79 (t, 4H, CH_2-Lev, $^3J_{HH}$ 6.2 Hz), 3.04 (t, 4H, CH_2-Lev, $^3J_{HH}$ 6.1 Hz), 3.14 (t, 4H, $H_{2'''}$, $^3J_{HH}$ 5.8 Hz), 4.40−4.61 (m, 16H, $H_{5''}$ + $H_{6''}$ + $H_{4'}$ + $H_{5'}$ + $H_{1'''}$), 5.27−5.50 (m, 4H, $H_{2''}$ + $H_{4''}$), 5.56 (m, 2H, $H_{3'}$), 5.65 (t, 2H, $H_{3''}$, $^3J_{HH}$ 9.8 Hz), 6.42 (m, 2H, $H_{1'}$), 6.48 (t, 2H, $H_{1''}$, $^3J_{HH}$ 4.1 Hz), 8.24 (s, 1H, H_6), 8.31 (s, 1H, H_6). ^{31}P NMR (MeOH-d_4, 242.9 MHz): δ −1.59, −1.95. MS (ESI$^+$, *m*/*z*): 938 [(M + Na)$^+$, 100%].

2-Cyanoethyl-(5′-*O*-levulinyl-5-iodo-2′-deoxyuridin-3′-yl)-1,2,3,4-tetra-*O*-acetyl-α-D-glucopyranos-6-yl phosphate (9d). 81% yield. ^{1}H NMR (MeOH-d_4, 600 MHz): δ 2.19 (s, 3H, Me), 2.20 (s, 6H, Me), 2.21 (s, 3H, Me), 2.22 (s, 3H, Me), 2.26 (s, 3H, Me), 2.37 (s, 3H, Me), 2.38 (s, 6H, Me), 2.39 (s, 3H, Me), 2.72 (m, 2H, $H_{2'}$), 2.88 (m, 6H, $H_{2'}$ + CH_2-Lev), 3.06 (m, 4H, CH_2-Lev), 3.12 (t, 4H, $H_{2'''}$, $^3J_{HH}$ 7.1 Hz), 4.40−4.67 (m, 16H, $H_{5''}$ + $H_{6''}$ + $H_{4'}$ + $H_{5'}$ + $H_{1'''}$), 5.32 (m, 4H, $H_{2''}$ + $H_{3'}$), 5.42 (m, 2H, $H_{4''}$), 5.65 (m, 2H, $H_{3''}$), 6.41 (m, 2H, $H_{1'}$), 6.50 (d, 1H, $H_{1''}$, $^3J_{HH}$ 3.6 Hz), 6.51 (d, 1H, $H_{1''}$, $^3J_{HH}$ 3.8 Hz), 8.28 (s, 1H, H_6), 8.29 (s, 1H, H_6). ^{31}P NMR (MeOH-d_4, 242.9 MHz): δ −2.76, −2.99. MS (ESI$^+$, *m*/*z*): 938 [(M + Na)$^+$, 100%].

2-Cyanoethyl-(2′,3′-dideoxyinosin-5′-yl)-1,2,3,4-tetra-*O*-acetyl-α-D-glucopyranos-6-yl phosphate (9e). 80% yield. ^{1}H NMR (MeOH-d_4, 600 MHz): δ 2.17 (s, 3H, Me), 2.18 (s, 3H, Me), 2.19 (s, 3H, Me), 2.20 (s, 3H, Me), 2.22 (s, 3H, Me), 2.23 (s, 3H, Me), 2.36 (s, 3H, Me), 2.37 (s, 3H, Me), 2.42 (m, 4H, $H_{3'}$), 2.80 (m, 4H, $H_{2'}$), 3.05 (t, 4H, $H_{2'''}$, $^3J_{HH}$ 6.1 Hz), 4.30−4.55 (m, 14H, $H_{5''}$ + $H_{6''}$ + $H_{5'}$ + $H_{1'''}$), 4.62 (m, 2H, $H_{4'}$), 5.24 (m, 2H, $H_{2''}$), 5.35 (t, 1H, $H_{4''}$, $^3J_{HH}$ 9.8 Hz), 5.37 (t, 1H, $H_{4''}$, $^3J_{HH}$ 8.0 Hz), 5.63 (m, 2H, $H_{3''}$), 6.44 (d, 1H, $H_{1''}$, $^3J_{HH}$ 3.7 Hz), 6.47 (d, 1H, $H_{1''}$, $^3J_{HH}$ 3.8 Hz), 6.52 (apparent t, 2H, $H_{1'}$, $^3J_{HH}$ 5.3 Hz), 8.26 (s, 2H, H_2), 8.44 (br s, 2H, H_8). ^{31}P NMR (MeOH-d_4, 242.9 MHz): δ −1.77, −1.79. MS (ESI$^+$, *m*/*z*): 700 [(M + H)$^+$, 100%].

2-Cyanoethyl-[N^6-(dimethylamino)methylen-2′,3′-dideoxyadenosin-5′-yl]-1,2,3,4-tetra-*O*-acetyl-α-D-glucopyranos-6-yl phosphate (9f). 60% yield. ^{1}H NMR (MeOH-d_4, 600 MHz): δ 2.17 (s, 3H, Me), 2.18 (s, 3H, Me), 2.19 (s, 3H, Me), 2.20 (s, 3H, Me), 2.22 (s, 3H, Me), 2.23 (s, 3H, Me), 2.36 (s, 3H, Me), 2.37 (s, 3H, Me), 2.45 (m, 4H, $H_{3'}$), 2.81 (m, 4H, $H_{2'}$), 3.05 (t, 4H, $H_{2'''}$, $^3J_{HH}$ 6.1 Hz), 3.45 (s, 6H, Me-N), 3.48 (s, 6H, Me-N), 4.26−4.72 (m, 16H, $H_{5''}$ + $H_{6''}$ + $H_{4'}$ + $H_{5'}$ + $H_{1'''}$), 5.21 (m, 2H, $H_{2''}$), 5.35 (q, 2H, $H_{4''}$, $^3J_{HH}$ 9.2 Hz), 5.61 (t, 2H, $H_{3''}$, $^3J_{HH}$ 10.2 Hz), 6.42 (d, 1H, $H_{1''}$, $^3J_{HH}$ 3.6 Hz), 6.44 (d, 1H, $H_{1''}$, $^3J_{HH}$ 3.8 Hz), 6.57 (apparent t, 2H, $H_{1'}$, $^3J_{HH}$ 5.9 Hz), 8.62 (s, 2H, H_8), 8.67 (s, 2H, H_2), 9.28 (s, 1H, HC=N), 9.30 (s, 1H, HC=N). ^{31}P NMR (MeOH-d_4, 242.9 MHz): δ −2.18, −2.21. MS (ESI$^+$, *m*/*z*): 754 [(M + H)$^+$, 100%].

2-Cyanoethyl-[2′,3′-di-*O*-acetyl-1′-(3-carbamoyl-1,2,4-triazoyl)-β-D-ribofuranos-5′-yl]-1,2,3,4-tetra-*O*-acetyl-α-D-glucopyranos-6-yl phosphate (9g). 89% yield. ^{1}H NMR (MeOH-d_4, 600 MHz): δ 2.17 (s, 3H, Me), 2.18 (s, 3H, Me), 2.19 (s, 3H, Me), 2.20 (s, 3H, Me), 2.23 (s, 3H, Me), 2.24 (s, 3H, Me), 2.29 (s, 3H, Me), 2.30 (s, 3H, Me), 2.31 (s, 3H, Me), 2.32 (s, 3H, Me), 2.37 (s, 3H, Me), 2.38 (s, 3H, Me), 3.09 (t, 4H, $H_{2'''}$, $^3J_{HH}$ 5.9 Hz), 4.36−4.63 (m, 14H, $H_{5''}$ + $H_{6''}$ + $H_{1'''}$ + $H_{5'}$), 4.71 (m, 2H, $H_{4'}$), 5.28 (m, 2H, $H_{2''}$), 5.37 (m, 2H, $H_{4''}$), 5.64 (m, 2H, $H_{3''}$), 5.91 (dd, 2H, $H_{3'}$, $^3J_{HH}$ 5.7 Hz), 5.97 (t, 1H, $H_{2'}$, $^3J_{HH}$ 9.4, 5.1 Hz), 6.49 (m, 4H, $H_{1''}$ + $H_{1'}$), 8.91 (s, 2H, H_5). ^{31}P NMR (MeOH-d_4, 242.9 MHz): δ −2.37, −2.60. MS (ESI$^+$, *m*/*z*): 792 [(M + H)$^+$, 90%].

2-Cyanoethyl-[2′,3′-di-*O*-acetyl-1′-(N^6-benzoyladeninyl)-β-D-arabinofuranos-5′-yl]-1,2,3,4-tetra-*O*-acetyl-α-D-glucopyranos-6-yl phosphate (9h). 70% yield. ^{1}H NMR (CD_3CN, 600 MHz): δ 1.86 (s, 3H, Me), 1.87 (s, 3H, Me), 1.97 (s, 3H, Me), 1.98 (s, 3H, Me), 2.01 (s, 3H, Me), 2.02 (s, 3H, Me), 2.06 (s, 3H, Me), 2.07 (s, 3H, Me), 2.17 (s, 3H, Me), 2.18 (s, 3H, Me), 2.19 (s, 3H, Me), 2.83 (q, 4H, $H_{2'''}$, $^3J_{HH}$ 5.8 Hz), 4.24 (m, 10H, $H_{5''}$ + $H_{6''}$ + $H_{1'''}$), 4.45 (m, 6H, $H_{4'}$ + $H_{5'}$), 5.12 (m, 2H, $H_{2''}$), 5.21 (q, 2H, $H_{4''}$, $^3J_{HH}$ 3.5 Hz), 5.47 (m, 2H, $H_{3''}$), 5.58 (m, 4H, $H_{3'}$ + $H_{2'}$), 6.32 (d, 1H, $H_{1''}$, $^3J_{HH}$ 3.6 Hz), 6.34 (d, 1H, $H_{1''}$, $^3J_{HH}$ 3.6 Hz), 6.74 (d, 2H, $H_{1'}$, $^3J_{HH}$ 4.6 Hz), 7.57 (t, 4H, H_m, $^3J_{HH}$ 7.7 Hz), 7.66 (t, 2H, H_p, $^3J_{HH}$ 7.3 Hz), 8.06 (d, 4H, H_o, $^3J_{HH}$ 6.6 Hz), 8.26 (s, 2H, H_8), 8.26 (s, 2H, H_2), 9.67 (br s, 2H, NH). ^{31}P NMR (CD_3CN, 242.9 MHz): δ −1.42, −1.55. MS (ESI$^+$, *m*/*z*): 919 [(M + H)$^+$, 100%].

2-Cyanoethyl-[2′,3′-di-*O*-acetyl-1′-(N^4-benzoylcytosinyl)-β-D-arabinofuranos-5′-yl]-1,2,3,4-tetra-*O*-acetyl-α-D-glucopyranos-6-yl phosphate (9i). 96% yield. ^{1}H NMR (CD_3CN, 600 MHz): δ 1.96 (s, 3H, Me), 1.97 (s, 6H, Me), 2.02 (s, 6H, Me), 2.03 (s,

6H, Me), 2.07 (s, 9H, Me), 2.15 (s, 3H, Me), 2.19 (s, 3H, Me), 2.20 (s, 6H, Me), 2.85 (q, 4H, $H_{2'''}$, $^3J_{HH}$ 5.7 Hz), 4.11−4.43 (m, 16H, $H_{5''} + H_{6''} + H_{4'} + H_{5'} + H_{1'''}$), 5.13 (m, 6H, $H_{2''} + H_{4''} + H_{3'}$), 5.45 (m, 4H, $H_{3''} + H_{2'}$), 6.27 (d, 1H, $H_{1''}$, $^3J_{HH}$ 3.8 Hz), 6.28 (d, 1H, $H_{1''}$, $^3J_{HH}$ 3.4 Hz), 6.34 (t, 2H, $H_{1'}$, $^3J_{HH}$ 3.4 Hz), 7.37 (d, 1H, H_5, $^3J_{HH}$ 7.5 Hz), 7.38 (d, 1H, H_5, $^3J_{HH}$ 7.5 Hz), 8.13 (d, 1H, H_6, $^3J_{HH}$ 7.5 Hz), 8.14 (s, 1H, H_6, $^3J_{HH}$ 7.5 Hz), 9.33 (br s, 2H, NH). ^{31}P NMR (MeOH-d_4, 242.9 MHz): δ −2.91, −3.17. MS (ESI$^+$, *m*/*z*): 833 [(M + H)$^+$, 100%].

General Procedure for the Synthesis of Phosphodiesters 10a−d. A solution of **9a−d** (0.30 mmol) in 6 mL of NH_4OH/MeOH (1:1, v/v) was stirred at room temperature overnight. The solution was concentrated in vacuum, and the residue was dissolved in water and treated with DOWEX 50WX8 (H^+ form). After stirring for 20 min, the resin was filtered, washed with water, and the filtrate concentrated. The residue was purified by reversed-phase HPLC with a Tracer Excel ODSA column (250 × 10 mm, 5 μm), flow rate 3 mL/min, 0.1% CF_3CO_2H/H_2O (1% MeCN) for elution, to afford **10a−d** as a hygroscopic white solid.

2′,3′-Didehydro-2′,3′-dideoxyuridine 5′-(α/β-D-glucopyranos-6-yl) phosphate (10a). 47% yield. ^{1}H NMR (D_2O, 400 MHz): δ 3.30 (t, 1H, $H_{2''}$ β anomer, $^3J_{HH}$ 8.1 Hz), 3.44−4.78 (m, 6H), 4.00 (m, 3H), 4.11 (m, 5H, $H_{5'}$), 4.68 (d, 1H, $H_{1''}$ β anomer, $^3J_{HH}$ 7.9 Hz), 5.16 (m, 2H, $H_{4'}$), 5.28 (d, 1H, $H_{1''}$ α anomer, $^3J_{HH}$ 3.8 Hz), 5.91 (d, 1H, H_5, $^3J_{HH}$ 8.1 Hz), 5.93 (d, 1H, H_5, $^3J_{HH}$ 8.1 Hz), 6.03 (m, 2H, $H_{2'}$), 6.56 (m, 2H, $H_{3'}$), 7.01 (m, 2H, $H_{1'}$), 7.85 (d, 1H, H_6, $^3J_{HH}$ 7.9 Hz), 7.88 (d, 1H, H_6, $^3J_{HH}$ 8.1 Hz). ^{31}P NMR (MeOH-d_4, 161.9 MHz): δ 0.64. MS (ESI$^-$, *m*/*z*): 451 [(M − H)$^-$, 100%].

2′,3′-Didehydro-2′,3′-dideoxythymidine 5′-(α/β-D-glucopyranos-6-yl) phosphate (10b). 45% yield. ^{1}H NMR (D_2O, 600 MHz): δ 1.89 (s, 6H, H_7), 3.23 (t, 1H, $H_{2''}$ β anomer, $^3J_{HH}$ 8.3 Hz), 3.37−4.52 (m, 5H), 3.68 (m, 1H, $^3J_{HH}$ 9.8 Hz), 3.87−4.07 (m, 8H), 4.60 (d, 1H, $H_{1''}$ β anomer, $^3J_{HH}$ 8.1 Hz), 5.09 (m, 2H, $H_{4'}$), 5.18 (d, 1H, $H_{1''}$ α anomer, $^3J_{HH}$ 3.5 Hz), 5.96 (d, 2H, $H_{2'}$, $^3J_{HH}$ 6.3 Hz), 6.48 (m, 2H, $H_{3'}$), 6.95 (m, 2H, $H_{1'}$), 7.60 (d, 1H, H_6, $|^4J_{HH}|$ 1.2 Hz), 7.61 (d, 1H, H_6, $|^4J_{HH}|$ 1.1 Hz). ^{31}P NMR (MeOH-d_4, 242.9 MHz): δ 0.38. MS (ESI$^-$, *m*/*z*): 465 [(M − H)$^-$, 100%].

2′-Deoxy-5-iodouridine 5′-(α/β-D-glucopyranos-6-yl) phosphate (10c). 40% yield. ^{1}H NMR (D_2O, 400 MHz): δ 2.41 (m, 4H, $H_{2'}$), 3.25 (t, 1H, $H_{2''}$ β anomer, $^3J_{HH}$ 8.8 Hz), 3.45−3.74 (m, 6H), 3.94 (m, 1H), 4.07−4.26 (m, 10H), 4.59 (m, 2H, $H_{3'}$), 4.64 (d, 1H, $H_{1''}$ β anomer, $^3J_{HH}$ 7.8 Hz), 5.19 (d, 1H, $H_{1''}$ α anomer, $^3J_{HH}$ 3.7 Hz), 6.29 (apparent t, 2H, $H_{1'}$, $^3J_{HH}$ 6.9 Hz), 8.27 (s, 1H, H_6), 8.28 (s, 1H, H_6). ^{31}P NMR (D_2O, 161.9 MHz): δ 0.46. MS (ESI$^-$, *m*/*z*): 595 [(M − H)$^-$, 100%].

2′-Deoxy-5-iodouridine 3′-(α/β-D-glucopyranos-6-yl) phosphate (10d). 43% yield. ^{1}H NMR (D_2O, 400 MHz): δ 2.48 (m, 2H, $H_{2'}$), 2.67 (m, 2H, $H_{2'}$), 3.29 (t, 1H, $H_{2''}$ β anomer, $^3J_{HH}$ 8.1 Hz), 3.34−4.27 (m, 15H), 4.30 (m, 2H, $H_{4'}$), 4.70 (d, 1H, $H_{1''}$ β anomer, $^3J_{HH}$ 7.9 Hz), 4.81 (m, 2H, $H_{3'}$), 5.28 (d, 1H, $H_{1''}$ α anomer, $^3J_{HH}$ 3.8 Hz), 6.32 (apparent t, 2H, $H_{1'}$, $^3J_{HH}$ 6.8 Hz), 8.38 (s, 1H, H_6), 8.39 (s, 1H, H_6). ^{31}P NMR (D_2O, 161.9 MHz): δ 0.42. MS (ESI$^-$, *m*/*z*): 595 [(M − H)$^-$, 100%].

General Procedure for the Synthesis of Phosphodiesters 10e−i. A solution of **9e−i** (0.30 mmol) in 6 mL of NH_4OH/MeOH (1:1, v/v) was stirred overnight at room temperature (at 50 °C for **10f** and **10h**). The solution was concentrated in vacuum, and the residue was purified by reversed-phase HPLC to afford the ammonium salt of **10e−i** as a hygroscopic white solid.

2′,3′-Dideoxyinosine 5′-(α/β-D-glucopyranos-6-yl) phosphate (10e). 39% yield. HPLC conditions: Waters XBridge C18 column (150 × 19 mm, 5 μm), flow rate 1.5 mL/min, and H_2O for elution. ^{1}H NMR (D_2O, 400 MHz): δ 2.29 (m, 4H, $H_{3'}$), 2.65 (m, 4H, $H_{2'}$), 3.27 (t, 1H, $H_{2''}$ β anomer, $^3J_{HH}$ 8.1 Hz), 3.40−3.61 (m, 6H), 3.74 (t, 1H, $^3J_{HH}$ 9.4 Hz), 3.85−4.44 (m, 8H), 4.54 (m, 2H), 4.65 (d, 1H, $H_{1''}$ β anomer, $^3J_{HH}$ 7.9 Hz), 5.22 (d, 1H, $H_{1''}$ α anomer, $^3J_{HH}$ 7.9 Hz), 6.43 (dd, 2H, $H_{1'}$, $^3J_{HH}$ 6.6, 3.4 Hz), 8.27 (s, 2H, H_2), 8.46 (br s, 2H, H_8). ^{31}P NMR (MeOH-d_4, 161.9 MHz): δ 0.71. MS (ESI$^-$, *m*/*z*): 477 [(M − H)$^-$, 100%].

2′,3′-Dideoxyadenosine 5′-(α/β-D-glucopyranos-6-yl) phosphate (10f). 37% yield. HPLC conditions: Waters XBridge C18 column (150 × 19 mm, 5 μm), flow rate 1.5 mL/min, and H_2O for elution. ^{1}H NMR (D_2O, 600 MHz): δ 2.25 (m, 4H, $H_{3'}$), 2.58 (m, 4H, $H_{2'}$), 3.23 (t, 1H, $H_{2''}$ β anomer, $^3J_{HH}$ 8.1 Hz), 3.40 (m, 6H), 3.73 (m, 4H), 3.95 (m, 3H), 4.1 (m, 2H), 4.49 (m, 2H, $H_{4'}$), 4.57 (d, 1H, $H_{1''}$ β anomer, $^3J_{HH}$ 7.7 Hz), 5.14 (d, 1H, $H_{1''}$ α anomer, $^3J_{HH}$ 3.7 Hz), 6.32 (dd, 2H, $H_{1'}$, $^3J_{HH}$ 6.6, 3.1 Hz), 8.20 (s, 2H, H_8), 8.39 (s, 2H, H_2). ^{31}P NMR (MeOH-d_4, 242.9 MHz): δ 0.35. MS (ESI$^-$, *m*/*z*): 476 [(M − H)$^-$, 100%].

1′-(3-Carbamoyl-1,2,4-triazoyl)-β-D-ribofuranose 5′-(α/β-D-glucopyranos-6-yl) phosphate (10g). 44% yield. HPLC conditions: Mediterránea Sea 18 column (250 × 10 mm, 5 μm), flow rate 1.1 mL/min, and H_2O for elution. ^{1}H NMR (D_2O, 600 MHz): δ 3.17 (t, 1H, $H_{2''}$ β anomer, $^3J_{HH}$ 8.1 Hz), 3.36−3.49 (m, 7H), 3.79−4.11 (m, 10H), 4.51 (m, 2H, $H_{3'}$), 4.55 (d, 1H, $H_{1''}$ β anomer, $^3J_{HH}$ 8.1 Hz), 4.62 (m, 2H, $H_{2'}$), 5.11 (d, 1H, $H_{1''}$ α anomer, $^3J_{HH}$ 3.5 Hz), 6.01 (d, 2H, $H_{1'}$, $^3J_{HH}$ 3.5 Hz), 8.73 (s, 2H, H_5). ^{31}P NMR (D_2O, 242.9 MHz): δ 0.50. MS (ESI$^-$, *m*/*z*): 485 [(M − H)$^-$, 100%].

1′-Adeninyl-β-D-arabinofuranose 5′-(α/β-D-glucopyranos-6-yl) phosphate (10h). 35% yield. HPLC conditions: Waters XBridge C18 column (150 × 19 mm, 5 μm), flow rate 1.5 mL/min, H_2O for elution. ^{1}H NMR (D_2O, 600 MHz): δ 3.29 (t, 1H, $H_{2''}$ β anomer, $^3J_{HH}$ 8.1 Hz), 3.42−3.65 (m, 6H), 3.90 (m, 1H), 4.04 (m, 2H), 4.13 (m, 1H), 4.25 (m, 6H), 4.52 (m, 2H, $H_{3'}$), 4.65 (d, 1H, $H_{1''}$ β anomer, $^3J_{HH}$ 8.4 Hz), 4.68 (m, 2H, $H_{2'}$), 5.22 (d, 1H, $H_{1''}$ α anomer, $^3J_{HH}$ 3.7 Hz), 6.49 (dd, 2H, $H_{1'}$, $^3J_{HH}$ 6.49 Hz, $|^4J_{HH}|$ 1.6 Hz), 8.31 (s, 2H, H_8), 8.48 (s, 2H, H_2). ^{31}P NMR (D_2O, 242.9 MHz): δ 0.23. MS (ESI$^-$, *m*/*z*): 508 [(M − H)$^-$, 100%].

1′-Cytosinyl-β-D-arabinofuranose 5′-(α/β-D-glucopyranos-6-yl) phosphate (10i). 49% yield. HPLC conditions: Mediterránea Sea 18 column (250 × 10 mm, 5 μm), flow rate 1.1 mL/min, and H_2O for elution. ^{1}H NMR (D_2O, 400 MHz): δ 3.28 (t, 1H, $H_{2''}$ β anomer, $^3J_{HH}$ 8.1 Hz), 3.49−3.61 (m, 5H), 3.74 (t, 1H, $^3J_{HH}$ 9.4 Hz), 4.05−4.29 (m, 12H), 4.53 (m, 2H, $H_{2'}$), 4.66 (d, 1H, $H_{1''}$ β anomer, $^3J_{HH}$ 8.0 Hz), 5.24 (d, 1H, $H_{1''}$ α anomer, $^3J_{HH}$ 3.7 Hz), 6.27 (d, 2H, $H_{1'}$, $^3J_{HH}$ 5.4 Hz), 6.30 (d, 1H, H_5, $^3J_{HH}$ 7.8 Hz), 6.32 (d, 1H, H_5, $^3J_{HH}$ 7.8 Hz), 8.17 (d, 1H, H_6, $^3J_{HH}$ 8.1 Hz), 8.18 (d, 1H, H_6, $^3J_{HH}$ 8.1 Hz). ^{31}P NMR (D_2O, 161.9 MHz): δ 0.41. MS (ESI$^-$, *m*/*z*): 484 [(M − H)$^-$, 100%].

Synthesis of 1-(5′-*O*-dimethoxytrityl-β-D-ribofuranosyl)-1,2,4-triazole-3-carboxamide (14). 4,4′-Dimethoxytrityl chloride (417 mg, 1,23 mmol), Et_3N (171 μL, 1.23 mmol), and DMAP (catalytic amount) are added to a solution of **13** (150 mg, 0.62 mmol) in anhydrous pyridine (3.1 mL), and the reaction is stirred at room temperature during 24 h. The mixture was poured into $NaHCO_3$ (5% aqueous solution) and extracted with EtOAc. The combined organic fractions was dried (Na_2SO_4) and concentrated under vacuum. The crude was purified by flash chromatography using 2% MeOH/CH_2Cl_2 for elution to yield **14** as a yellow solid in 83% yield. Melting range: 111−113 °C. ^{1}H NMR (MeOH-d_4, 300 MHz): δ 3.48 (m, 2H, $H_{5'}$), 3.86 (s, 6H, OMe), 4.39 (m, 1H, $H_{4'}$), 4.65 (t, 1H, $H_{2'}$ or $H_{3'}$, $^3J_{HH}$ 5.6 Hz), 4.85 (t, 1H, $H_{2'}$ or $H_{3'}$, $^3J_{HH}$ 3.4 Hz), 6.13 (d, 1H, $H_{1'}$, $^3J_{HH}$ 3.1 Hz), 6.91 (d, 4H, H_m, $^3J_{HH}$ 8.9 Hz), 7.35 (m, 7H, $H_m + H_o + H_p$), 7.53 (d, 2H, H_o, $^3J_{HH}$ 8.2 Hz), 8.82 (s, 1H, H_5). MS (ESI$^+$, *m*/*z*): 569 [(M + Na)$^+$, 100%].

Synthesis of 1-(2′,3′-di-*O*-acetyl-5′-*O*-dimethoxytrityl-β-D-ribofuranosyl)-1,2,4-triazole-3-carboxamide (15). To a solution of **14** (404 mg, 0.74 mmol) in anhydrous pyridine (5.2 mL) at 0 °C was added acetic anhydride (350 μL, 3.7 mmol). After being stirred at room temperature for 16 h, the mixture was poured into saturated aqueous $NaHCO_3$ solution and extracted with CH_2Cl_2. The combined organic fractions were dried (Na_2SO_4) and concentrated under vacuum. The crude was purified by flash chromatography using 1% MeOH/CH_2Cl_2 for elution to yield **15** as a white solid in 78% yield. Melting range: 99−101 °C. ^{1}H NMR (MeOH-d_4, 300 MHz): δ 2.24 (s, 3H, CH_3), 2.28 (s, 3H, CH_3), 3.48 (m, 1H, $H_{5'}$), 3.60 (dd, 1H, $H_{5'}$, $|^2J_{HH}|$ 11.9, $^3J_{HH}$ 3.2 Hz), 3.92 (s, 6H, OMe), 4.53 (q, 1H, $H_{4'}$, $^3J_{HH}$ 3.9 Hz), 5.89 (t, 1H, $H_{3'}$, $^3J_{HH}$ 5.3 Hz), 6.20 (dd, 1H, $H_{2'}$, $^3J_{HH}$ 5.1, 3.9 Hz), 6.43 (d, 1H, $H_{1'}$, $^3J_{HH}$ 3.8 Hz), 6.97 (d, 4H, H_m, $^3J_{HH}$ 8.8 Hz), 7.38 (m, 7H, $H_m + H_o + H_p$), 7.58 (d, 2H, H_o, $^3J_{HH}$ 8.3 Hz), 8.75 (br s, 1H, NH), 8.98 (s, 1H, H_5). MS (ESI$^+$, *m*/*z*): 653 [(M + Na)$^+$, 100%].

Synthesis of 9-(β-D-Arabinofuranosyl)-N^6-benzoyladenine (17). Compound **16** was evaporated with anhydrous pyridine (3 × 10 mL). To a solution of **16** (400 mg, 1.5 mmol) in anhydrous pyridine (7.5 mL) was added trimethylsilyl chloride (1.4 mL, 11.2 mmol). Upon the complete consumption of the starting material, benzoyl chloride (870 μL, 7.5 mmol) was added, and the reaction was stirred at room temperature for 2 h. The mixture was then cooled at 0 °C, and 2 mL of water was added. After 5 min, 3 mL of aqueous ammonia was added, and the mixture was stirred at this temperature for 30 min. The reaction was concentrated and the residue washed with water and EtOAc to give **17** as a white solid in 90% yield. Melting range: 185−187 °C. ^{1}H NMR (DMSO-d_6, 300 MHz): δ 3.68 (m, 2H, $H_{5'}$), 3.83 (q, 1H, $H_{4'}$, $^3J_{HH}$ 4.8 Hz), 4.23 (m, 2H, $H_{2'}$ + $H_{3'}$), 5.15 (s, 1H, OH), 5.61 (d, 1H, OH, $|^4J_{HH}|$ 3.9 Hz), 5.74 (d, 1H, OH, $|^4J_{HH}|$ 5.2 Hz), 6.42 (d, 1H, $H_{1'}$, $^3J_{HH}$ 5.1 Hz), 7.57 (m, 3H, $H_m + H_p$), 8.04 (d, 1H, H_o, $^3J_{HH}$ 8.4 Hz), 8.53 (s, 1H, H_8), 8.73 (s, 1H, H_2). MS (ESI$^+$, *m*/*z*): 372 [(M + H)$^+$, 100%].

Synthesis of N^6-Benzoyl-9-(5′-*O*-dimethoxytrityl-β-D-arabinofuranosyl)adenine (18). A procedure similar to that described for **14** afforded **18** as a yellow solid in 70% yield. Melting range: 147−149 °C. ^{1}H NMR (MeOH-d_4, 300 MHz): δ 3.68 (m, 2H, $H_{5'}$), 3.88 (s, 6H, MeO), 4.29 (m, 1H, $H_{4'}$), 4.57 (m, 2H, $H_{2'}$ + $H_{3'}$), 6.73 (d, 1H, $H_{1'}$, $^3J_{HH}$ 4.1 Hz), 6.96 (d, 4H, H_m, $^3J_{HH}$ 8.2 Hz), 7.33−7.77 (m, 12H, $H_m + H_o + H_p$), 8.21 (d, 2H, H_o, $^3J_{HH}$ 7.2 Hz), 8.67 (s, 1H, H_8), 8.82 (s, 1H, H_2). MS (ESI$^+$, *m*/*z*): 696 [(M + Na)$^+$, 100%].

Synthesis of N^6-Benzoyl-9-(2′,3′-di-*O*-acetyl-5′-*O*-dimethoxytrityl-β-D-arabinofuranosyl)-adenine (19). A procedure similar to that described for **15** afforded **19** as a white solid in 83% yield. Melting range: 88−90 °C. Flash chromatography was performed using 2% MeOH/CH_2Cl_2 for elution. ^{1}H NMR (MeOH-d_4, 300 MHz): δ 1.76 (s, 3H, Me), 2.27 (s, 3H, Me), 3.71 (m, 2H, $H_{5'}$), 3.94 (s, 6H, OMe), 4.49 (q, 1H, $H_{4'}$, $^3J_{HH}$ 4.1 Hz), 5.75 (dd, 1H, $H_{3'}$, $^3J_{HH}$ 5.4, 4.3 Hz), 5.91 (dd, 1H, $H_{2'}$, $^3J_{HH}$ 5.3, 4.2 Hz), 6.85 (d, 1H, $H_{1'}$, $^3J_{HH}$ 5.4 Hz), 7.03 (d, 4H, H_m, $^3J_{HH}$ 8.9 Hz), 7.37−7.65 (m, 12H, $H_m + H_p + H_o$), 7.82 (d, 2H, H_o, $^3J_{HH}$ 7.2 Hz), 8.62 (s, 1H, H_8), 8.77 (s, 1H, H_2). MS (ESI$^+$, *m*/*z*): 779 [(M + Na)$^+$, 100%].

Synthesis of 1-(5′-*O*-*tert*-Butyldimetylsilyl-β-D-arabinofuranosyl)cytosine (21). *tert*-Butyldimetylsilyl chloride (342 mg, 2.3 mmol), anhydrous Et_3N (287 μL, 2.2 mmol), and DMAP (38 mg, 0.15 mmol) were added to a solution of **20** (500 mg, 2.1 mmol) in anhydrous DMF (10.3 mL) and anhydrous CH_2Cl_2 (5.2 mL). The mixture was stirred at room temperature for 17 h. Next, the solvents were concentrated and the residue purified by flash chromatography using 10% MeOH/CH_2Cl_2 for elution affording **21** as a white solid in 82% yield. Melting range: 162−164 °C. ^{1}H NMR (MeOH-d_4, 300 MHz): δ 0.16 (s, 3H, Me-Si), 0.17 (s, 3H, Me-Si), 0.95 (s, 9H, Me_3C), 4.12 (m, 3H, $H_{4'}$ + $H_{5'}$), 4.33 (m, 1H, $H_{2'}$ or $H_{3'}$), 4.46 (m, 1H, $H_{2'}$ or $H_{3'}$), 5.93 (d, 1H, H_5, $^3J_{HH}$ 7.5 Hz), 6.16 (d, 1H, $H_{1'}$, $^3J_{HH}$ 3.7 Hz), 7.85 (d, 1H, H_6, $^4J_{HH}$ 7.5 Hz). MS (ESI$^+$, *m*/*z*): 358 [(M + H)$^+$, 100%].

Synthesis of N^4-Acetyl-1-(2′,3′-di-*O*-acetyl-5′-*O*-*tert*-butyldimetylsilyl-β-D-arabinofuranosyl)-cytosine (22). A procedure similar to that described for **15**, except that 10 equivalents of acetic anhydride were used, afforded **22** as a white solid in 85% yield. Melting range: 229−231 °C. Flash chromatography was performed using 50−100% EtOAc/hexane as the elution gradient. ^{1}H NMR ($CDCl_3$, 300 MHz): δ 0.12 (s, 3H, Me-Si), 0.13 (s, 3H, Me-Si), 0.94 (s, 9H, Me_3C), 1.93 (s, 3H, Me), 2.11 (s, 3H, Me), 2.30 (s, 3H, Me), 3.90 (dd, 1H, $H_{5'}$, $|^2J_{HH}|$ 10.7 Hz, $^3J_{HH}$ 4.1 Hz), 3.94 (dd, 1H, $H_{5'}$, $|^2J_{HH}|$ 11.3 Hz, $^3J_{HH}$ 3.9 Hz), 4.06 (q, 1H, $H_{4'}$, $^3J_{HH}$ 3.9 Hz), 5.28 (dd, 1H, $H_{3'}$, $^3J_{HH}$ 4.5, 3.4 Hz), 5.58 (dd, 1H, $H_{2'}$, $^3J_{HH}$ 4.5, 2.5 Hz), 6.35 (d, 1H, $H_{1'}$, $^3J_{HH}$ 4.7 Hz), 7.44 (d, 1H, H_5, $^3J_{HH}$ 7.5 Hz), 8.12 (d, 1H, H_6, $^4J_{HH}$ 7.5 Hz). MS (ESI$^+$, *m*/*z*): 484 [(M + H)$^+$, 100%].

Solubility Assays. The experiments were carried out taking 1 or 2 mg of the corresponding compound and then adding consecutive amounts of water with a micropipet. After each addition, a vigorous shaking of the solution was done. Then, the solution was checked for insoluble material with a magnifying glass.

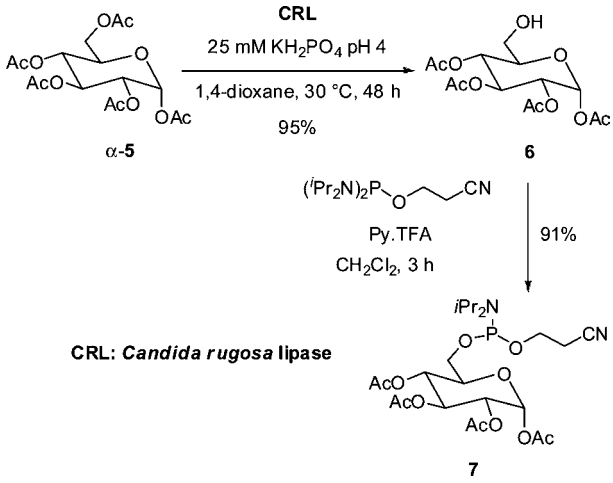
Antiviral Assays. The procedures for the antiviral assays in human peripheral blood mononuclear (PBM) cells were reported previously (*45*). Briefly, uninfected phytohemagglutinin (PHA)-stimulated human PBM cells were infected with HIV-1_{LAI} [about 63,000 disintegrations of reverse transcriptase (RT) activity per min per 10^7 cells per 10 mL of medium]. The nucleoside analogues or prodrugs were then added to duplicate or triplicate cultures. Uninfected and untreated PBM cells were grown in parallel at equivalent cell concentrations as controls. The cultures were maintained in a humidified 5% CO_2−95% air incubator at 37 °C for 6 days after infection, at which point all cultures were sampled for supernatant RT activity. The supernatant was clarified, and the viral particles were then pelleted at 40,000 rpm for 30 min by using a rotor and suspended in virus-disrupting buffer. The RT assay was performed in 96-well microdilution plates by using $(rA)_n \cdot (T)_{12-18}$ as the template primer. The RT results were expressed in disintegrations per minute per milliliter of originally clarified supernatant.

Cytotoxicity Assays. The nucleoside analogues and prodrugs were evaluated for their potential toxic effects on uninfected PHA-stimulated human PBM cells and also in CEM (lymphoblastoid) and Vero (African green monkey kidney) cells as described previously (*46*). PBM cells were obtained from whole blood of healthy HIV-1 and hepatitis B virus-seronegative volunteers and collected by single-step Ficoll-Hypaque discontinuous gradient centrifugation. CEM (CEM-CCRF) cells were a T-lymphoblastoid cell line that was obtained from the American Type Culture Collection, Rockville, MD. The CEM cells were maintained in RPMI 1640 medium supplemented with 20% heat-inactivated fetal bovine serum, penicillin (100 U/mL), and streptomycin (100 μg/mL). The PBM and CEM cells were cultured with and without drug for 6 days, at which time portions were counted for cell proliferation and viability by the trypan blue exclusion method. Only the effects on cell growth are reported since these correlated well with cell viability. The toxicity of the compounds in Vero cells was assessed after 3 days of treatment with a hemacytometer.

RESULTS AND DISCUSSION

We envisioned phosphoramidite **7** as the key building block for the synthesis of the target nucleoside−carbohydrate prodrugs for several reasons. First, phosphoramidite chemistry offers

Scheme 1. Synthesis of D-Glucose Phosphoramidite



excellent yield during solution-phase coupling of various nucleosides (*33*). Second, phosphoramidite compounds are reasonably stable and easy to handle during synthesis. Third, glucose−amidite **7** would be an ideal molecule offering a versatile conjugation unit for the attachment of glucose to a wide range of nucleosides.

A major challenge faced by carbohydrate or nucleoside chemists is to orchestrate selective transformation of hydroxyl groups with similar reactivity in a single molecule. Gratifyingly, enzyme-catalyzed reactions have provided selective modifications with high selectivity and efficiency (*34*). The synthesis of glucosyl phophoramidite **7** was accomplished in few steps via a regioselective enzymatic hydrolysis of 1,2,3,4,6-penta-*O*-acetyl-α-D-glucopyranose (**5**, Scheme 1).

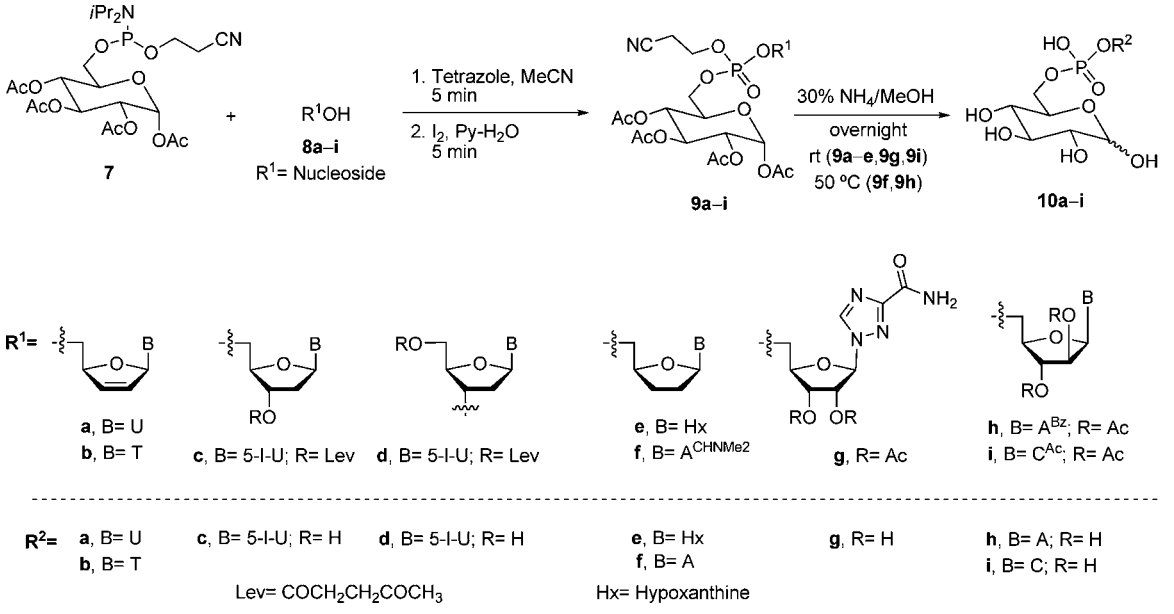
Commercial *Candida rugosa* lipase (CRL) was found to be an efficient catalyst for both regio- and chemoselective deacetylation of the primary hydroxyl group in the peracetylated α-D-glucose, furnishing the 6-OH derivative **6** in excellent yield after crystallization from diethyl ether/*n*-hexane (4:1) (*29*). The synthesis of phosphoramidite **7** was carried out by phosphitylation of **6** with 2-cyanoethyl-*N*,*N*,*N*′,*N*′-tetraisopropylphosphoramidite and pyridinium trifluoroacetate as the activator in high yield (*31*). The stability of phosphoramidite **7** was determined both in solution and as a neat product. A solution of **7** in $CDCl_3$ was found to be stable for six months (by ^{31}P NMR). Similarly, neat amidite **7** was stored for 18 months in the freezer (−24 °C) under nitrogen without any noticeable degradation.

The conjugation of glucosyl phosphoramidite **7** was practiced with a model nucleoside **8a** (d4U). Following standard amidite coupling conditions, **7** was first activated with 1*H*-tetrazole, and the resulting intermediate was oxidized *in situ* using an iodine/pyridine/water solution to give the phosphotriester derivative **9a** in 89% isolated yield after flash chromatography. As expected, the presence of P-diastereoisomers, due to the phosphorus stereocenter, was apparent from two signals at −2.11 and 2.19 ppm in the ^{31}P NMR spectrum. Next, the acetyl groups and the cyanoethyl group were removed simultaneously from **9a** by treatment with a 1:1 (v/v) mixture of aqueous ammonia and MeOH. The residue was purified on a DEAE Sephadex-A25 column with a linear gradient of triethylammonium hydrogen carbonate buffer (0.1−1.0 M) and the product lyophilized. However, this purification protocol resulted in a lower purity of the product with a significant amount of TEA salt. Alternatively, the crude residue was mixed with a Dowex 50WX8 hydrogen form exchange resin, and after filtration, the free acid was subjected to reverse-phase HPLC purification with a tracer excel 120 ODS-A column using H_2O (0.1% TFA, 1% MeCN) for elution. This technique allows for the isolation of phosphodiester **10a** in high purity and 47% yield. The two α/β-anomeric products corresponding to the glycosyl unit were observed in the ^1H NMR spectrum.

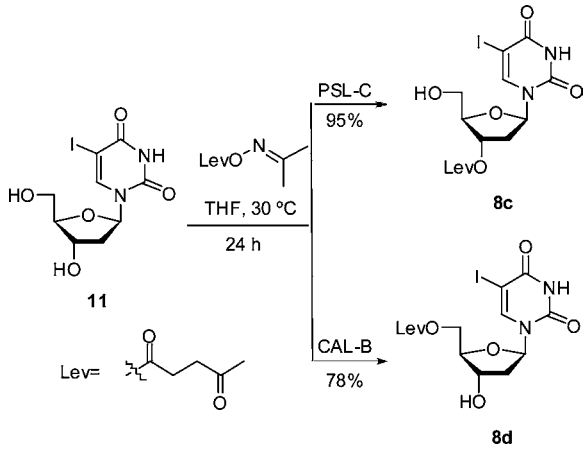
Having established an efficient protocol for the glucose−nucleoside conjugate, we were ready to synthesize the glucose conjugates of seven biologically active nucleosides (d4T, ddI, IdUrd, ddA, virazole, *ara*-A, and *ara*-C) that we selected for this study. Since d4T has only one reactive site, the synthesis of conjugate **10b** was easily accomplished from **8b** in two convenient steps (Scheme 2). Pronucleotide **10b** was purified by HPLC, and the structure was elucidated by NMR spectroscopy.

For the synthesis of the IdUrd-glucose phosphodiester derivative **10c**, coupling of sugar phosphoramidite **7** with the 5′-hydroxyl group of the parent nucleoside required the masking of the 3′-hydroxyl group. The selective protection of the 3′-secondary alcohol in **11** was accomplished with acetonoxime levulinate catalyzed by *Pseudomonas cepacia* lipase (PSL-C) in THF at 30 °C (Scheme 3). Under these conditions, facile

Scheme 2. Synthesis of Nucleosyl D-Glucopyranosyl Phosphodiesters



Scheme 3. Enzymatic Synthesis of 3′- and 5′-*O*-Lev-IdUrd



regioselective 3′-*O*-acylation of **11** was observed within 24 h, exclusively furnishing 3′-*O*-levulinyl derivative **8c** in 95% yield. Importantly, pure 3′-*O*-Lev-IdUrd **8c** was isolated via precipitation without a need for column chromatography.

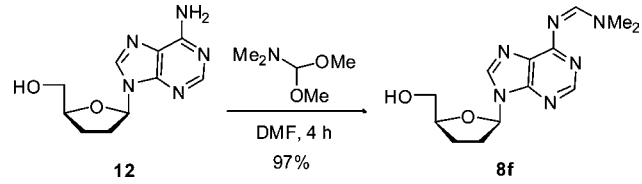
The protected nucleoside **8c** was coupled with phosphoramidite **7** according to the procedure summarized in Scheme 2. After oxidation, the coupled product was purified by column chromatography to afford the phosphotriester **9c** in 80% yield. Next, the 3′-*O*-levulinyl group was cleaved by treatment of **9c** with 1 M hydrazine hydrate in pyridine−acetic acid (3:2 v/v) at room temperature without affecting the phosphate protecting group, thereby establishing the orthogonality of these two protecting groups. However, this reaction resulted in a lower yield due to the troublesome purification of the final product. Therefore, **9c** was first deprotected at the phosphate group with Et_3N−MeCN (1:1, v/v) to furnish the free phosphate in 90% yield, and then the levulinyl group was removed, leading to compound **10c**. Nevertheless, the yield did not improve. Finally, the phosphodiester derivative **10c** was obtained in satisfactory yield by treatment of **9c** with a 1:1 (v/v) mixture of aqueous ammonia and MeOH (*35*). These conditions allowed for the deprotection of both the cyanoethyl and levulinyl groups simultaneously furnishing **10c** in 40% yield after HPLC purification.

In order to determine the relationship between biological activity and site of conjugation, we decided to synthesize a 3′-*O*-conjugate prodrug **10d** starting with IdUrd. Preparation of the 5′-*O*-protected IdUrd derivative **8d** was performed with acetonoxime levulinate catalyzed by *Candida antarctica* lipase (CAL-B) (Scheme 3). Acylation takes place with high selectivity at the 5′-hydroxyl group providing **8d** in 78% yield. Coupling of phosphoroamidite **7** and nucleoside **8d** followed by *in situ* oxidation and cleavage of the blocking groups yielded glucoconjugate **10d** with 43% overall yield.

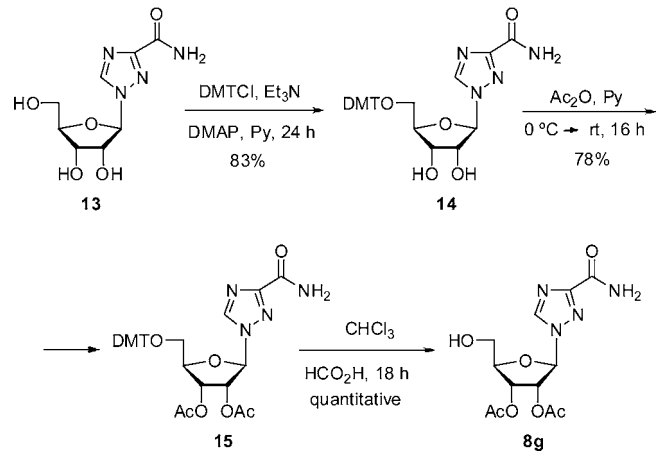
Next, glucoconjugates of nucleosides having purine bases were synthesized. Synthesis of glucosyl-ddI phosphodiester **10e** was accomplished in manner similar to that described above. Condensation of **7** and **8e** with 1*H*-tetrazole and iodine oxidation gave phosphotriester **9e** in 80% yield. To release the free phosphate, **9e** was treated with NH_4OH, and the crude product was purified by HPLC (see Materials and Methods) in 39% yield.

In order to synthesize the glucose conjugate of ddA (**12**, Scheme 4), it is essential that the N^6-amino group is masked appropriately, avoiding the interference with highly reactive amidite **7**. Conventional protection of the N^6-amino group in **12** following the Jones protocol (*36*) resulted in low yields, perhaps due to facile depurination of ddA. Therefore, formamidine was chosen as the protecting group for the amino group

Scheme 4. Synthesis of Formamidine Base Protected ddA



Scheme 5. Synthesis of the Virazole Nucleoside Precursor



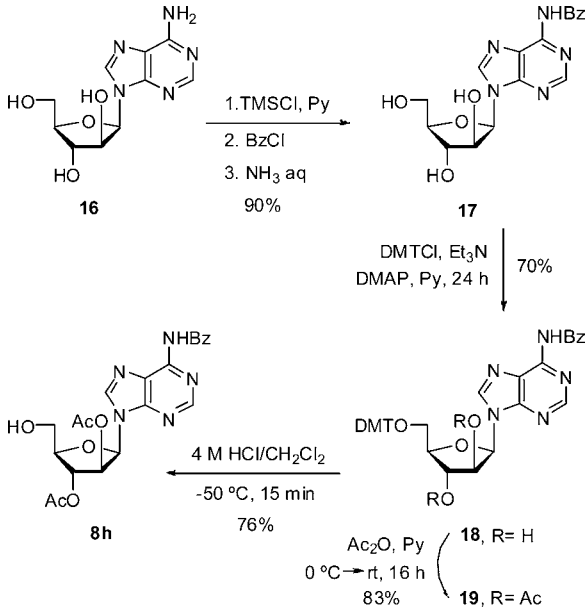
that is installed under neutral conditions following the protocol described by Minamoto (*37*).

Treatment of ddA (*12*) with DMF-dimethyl acetal generated the dimethylaminomethyleneamino compound **8f** in quantitative yield. Coupling of 1*H*-tetrazole activated phosphoramidite **7** with **8f**, followed by the oxidation of the resulting phosphite triester afforded the desired phosphotriester **9f** in 60% yield. The modest yield of the coupling and oxidation steps can be explained in terms of possible side reactions. The formamidine group is more labile than the benzoyl group, and degradation of the formamidine into formamide was observed (*37*). Subsequently, the phosphate moiety, the acetyl groups, and the formamidine group were simultaneously cleaved by aqueous ammonium at 50 °C, which gave the phosphodiester **10f** as its ammonium salt. Purification of **10f** was achieved by HPLC (see Materials and Methods).

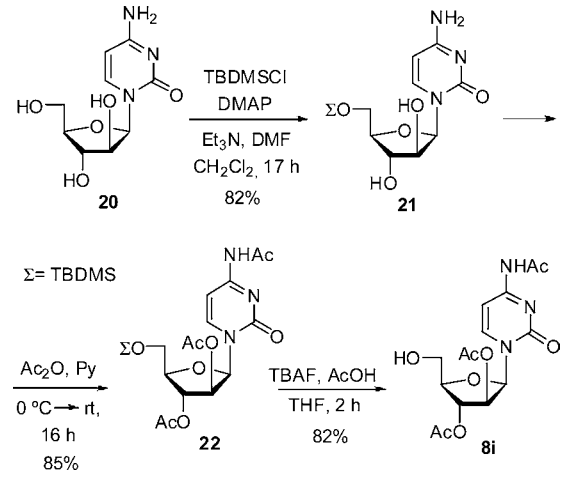
Prior to the conjugation of amidite **7** to the antiviral drug virazole **13**, masking of the 2′- and 3′-hydroxyl groups was essential. Our first attempt was based on the simultaneous protection of 2′- and 3′-hydroxyl groups of **13** as an acetal using acetone, copper(II) sulfate, and sulphuric acid resulted in less than 40% yield of the desired product. The yield could not be improved when **13** was treated with 2,2-dimethoxypropane in acetone. Next, we attempted the acylation of the secondary hydroxyl groups of **13** with acetonoxime levulinate in the presence of *Pseudomonas cepacia* (PSL-C) (*38*−*40*). Unfortunately, the mixture of acylated products and low conversions (<10%) were observed after 4 days at 50 °C. The conversion of **13** was improved by employing vinyl acetate as the acylating agent. However, 3′,5′-di-*O*-acetyl nucleoside was obtained as the major product, in addition to the 2′,5′-di-*O*-acetyl and the triacetyl derivatives. Additionally, we attempted the selective enzymatic hydrolysis of peracylated virazole anticipating the formation of **8g** (*41*). Multiple enzymes (*Candida antarctica* lipase B, porcine pancreas lipase, subtilisine) were employed, but we could not achieve the desired regioselectivity.

These failures directed our attention to a more traditional three-step approach described in Scheme 5. Selective protection of the primary hydroxyl group was easily achieved by the treatment of virazole (**13**) with dimethoxytrityl chloride, Et_3N,

Scheme 6. Synthesis of the *ara*-Adenosine Precursor



Scheme 7. Synthesis of the *ara*-Cytidine Precursor



and DMAP in pyridine. Product **14** was then subjected to acetylation with acetic anhydride in pyridine to provide 2′,3′-di-*O*-acetyl-5′-*O*-DMT nucleoside **15** in 78% yield. Deprotection of the 5′-hydroxyl group by formic acid in chloroform led to the desired precursor **8g** in quantitative yield. The protected nucleoside **8g** was coupled as described above, and the resulting phosphotriester **9g** was deprotected with a 1:1 (v/v) mixture of aqueous ammonia and MeOH. Phosphodiester **10g** was purified by reverse-phase HPLC on a C18 column.

Vidarabine is an *ara*-nucleoside drug with a wide range of antiviral activity. However, vidarabine is toxic and metabolically unstable (rapid deamination). Therefore, 5′-conjugates of vidarabine have been synthesized as prodrugs (*42*). In this vein, we decided to extend our study toward the synthesis of glycoconjugate **10h**. First, *ara*-adenosine (**16**) was *N*-benzoylated following the transient Jones protocol to furnish N^6-benzoyl-*ara*-adenosine (**17**) in 90% yield (Scheme 6). Transformation of **17** into **19** proceeded well yielding the corresponding 2′,3′-di-*O*-acetyl-5′-*O*-DMT derivative. Traditional deprotection of the dimethoxytrityl group of **19** with formic acid in $CHCl_3$ resulted in low yield and the formation of depurinated products. Milder deprotection of **19** was accomplished with 4 M HCl in CH_2Cl_2 at −50 °C furnishing a cleaner product, **8h**.

Coupling of phosphoramidite **7** with protected *ara*-adenosine **8h** and subsequent oxidation gave the compound **9h** in 70% yield after column chromatography. Deprotection of **9h** by aqueous ammonium at 50 °C and purification of the reaction product by reverse-phase HPLC led to phosphodiester **10h**.

Ara-cytidine is yet another drug that is poorly soluble in water, and prodrug approaches have been utilized to improve the oral bioavailability (*43*, *44*). We believe that the synthesis of a glucose conjugate **10i** would offer increased solubility for **20** in water. Preparation of the protected *ara*-cytidine precursor **8i** was accomplished as depicted in Scheme 7. The primary hydroxyl group in **20** was protected as silyl ether by reaction with *tert*-butyldimethylsilyl chloride, Et_3N, and DMAP in DMF and CH_2Cl_2 to afford **21** in 82% yield. Peracetylation was then performed using acetic anhydride in pyridine furnishing protected **22**. Subsequent treatment with tetrabutylammonium fluoride removed the TBDMS group and afforded the 2′,3′-protected nucleoside **8i** in 57% overall yield from *ara*-cytidine. Phosphotriester **9i** was prepared in 96% isolated yield by the coupling of **7** and **8i** followed by *in situ* oxidation. Finally, compound **10i** was purified by reverse-phase HPLC. On the basis of their NMR data, all conjugates **10a**−**i** were prepared in the furanose form.

In order to determine the impact of conjugating the glucose moiety onto the nucleosides, we compared the solubility of prodrugs **10a**−**i** with unprotected nucleosides (Figure 1). Solubility assays revealed that all conjugates **10a**−**i** prepared in this study were more soluble in water than the parent nucleosides. It is noteworthy that the phosphodiester of *ara*-adenosine **10h** was found to be 31 times more soluble in water than *ara*-adenosine. Also, the 3′-*O*- and 5′-*O*-conjugate derivatives of IdUrd **10c** and **10d** displayed markedly increased solubility in water (25 and 20 times more soluble, respectively). More importantly, poorly soluble nucleoside derivatives IdUrd and *ara*-A showed significant improvement in water solubility after conjugation with glucose. Clearly, such carbohydrate conjugates may lead to improved oral bioavailability of the drugs that lack water solubility.

Biological Evaluation. *Antiviral Assays.* Nine glucose conjugates **10a**−**i** were tested against HIV-1 with AZT (zidovudine) used as a positive control. All of the anti-HIV assays were performed in human PBM cells (*27*). We also included the unprotected starting materials used for the synthesis of conjugates and a representative commercial sample of the same product in the assay as additional controls. A stock solution (40 mM) of the conjugates **10a**−**i** and various controls were prepared in sterile DMSO and then diluted to the desired concentration in growth media.

An overall summary of the data expressed as the effective concentration required for the inhibition of viral replication by 50% (EC_{50}) and 90% (EC_{90}) is summarized in Table 1. The anti-HIV activity of the conjugates tested was in the order of **10b** > **10f** > **10i** > **10g** > **10e** > **10h** > **10c**. The traditional anti-HIV nucleosides d4T and ddI after conjugation showed moderate activity indicating that the potency of **10b** and **10e** could be attributed to the free nucleosides. A similar pattern of anti-HIV activity was observed with ddA before and after conjugation. The improved activity of the ddA conjugate **10f** compared to that of the conjugate of ddI **10e** may be due to the efficient deamination of **10f** to liberate ddI intracellularly. Furthermore, both virazole conjugate **10g** and *ara*-A conjugate **10h** exhibited better activity than their nucleoside counterpart, thus indicating that the glucose conjugates are possibly a good design for developing prodrugs. Most importantly, the conjugation of glucose to the nucleosides via a phosphate linkage did not abolish the antiviral activity of the parent nucleosides. The retention of modest anti-HIV activity exhibited by the new conjugates is encouraging and warrants further studies.

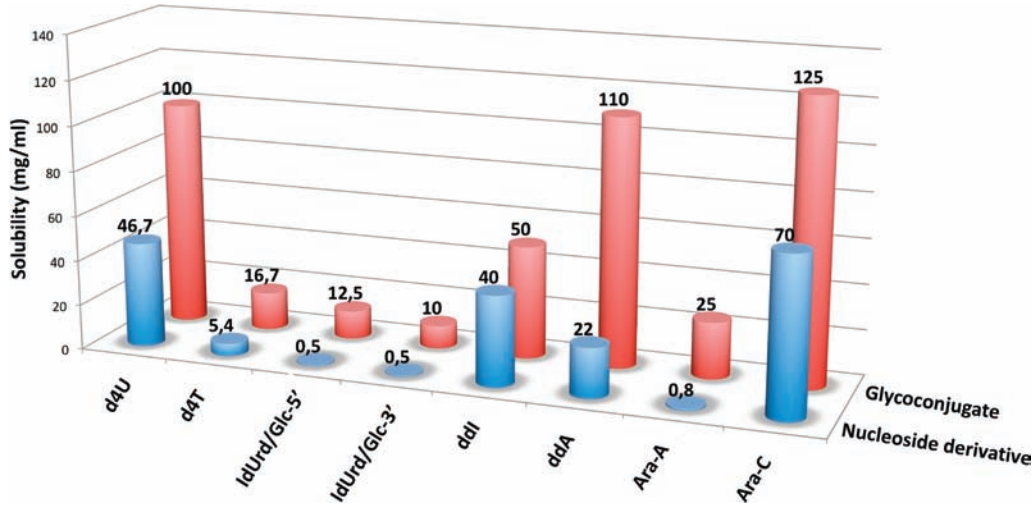


Figure 1. Comparative water solubility data of free nucleosides and prodrugs **10a**−**i**.

Table 1. Effects of Various Nucleosides and Their Conjugates 10a−**h against HIV-1 and Their Cytotoxicity Assays**

analogue	nucleoside/ conjugate (source)	Anti-HIV-1 activity in PBM cells[a]		cytotoxicity (IC_{50} [μM])[b]		
		EC_{50} [μM]	EC_{90} [μM]	PBM cells	CEM cells	VERO cells
AZT	(commercial)	0.0054	0.050	>100	14.3	56.0
d4U	(synthesized)	>100	>100	>100	55.9	>100
10a	Glc-d4U	>100	>100	>100	>100	>100
d4T	(commercial)	0.073	0.37			
d4T	(synthesized)	0.069	0.37	>100	>100	>100
10b	Glc-d4T	0.34	2.0	>100	76.8	>100
IdUrd	(commercial)	65.7	>100			
IdUrd	(synthesized)	86.5	>100	>100	2.7	>100
10c	Glc-5′-IdUrd	32.4	>100	>100	2.3	>100
10d	Glc-3′-IdUrd	>100	>100	>100	76.0	>100
ddI	(commercial)	0.32	2.8			
ddI	(synthesized)	0.06	0.76	>100	>100	>100
10e	Glc-ddI	15.5	>100	>100	22.7	>100
ddA	(synthesized)	0.59	3.8	>100	>100	>100
10f	Glc-ddA	1.1	9.9	87.6	13.2	73.2
virazole	(commercial)	77.5	>100			
virazole	(synthesized)	85.9	>100	>100	53.0	>100
10g	Glc-Virazole	12.8	39.1	>100	17.6	>100
ara-A	(commercial)	>100	>100			
ara-A	(synthesized)	>100	>100	26.0	26.2	>100
10h	Glc-Ara-A	19.5	>100	>100	18.9	>100
ara-C	(synthesized)	4.9	11.9	57.0	<0.1	ND
10i	Glc-Ara-C	5.8	14.0	17.5	<1.0	<1.0

[a] The HIV drug susceptibility assay was done as previously described in ref *45*. [b] The cytotoxicity assays in PBM, CEM, and Vero cells were done as previously described in ref *46*. ND = not determined.

Cytotoxicity Assays. The new conjugates were evaluated for their potential toxic effects using three different cell lines. First, the PBM cells were selected because of their slow growth and also being host cells for the anti-HIV assay. Second, we included lymphocytic CEM cells due to their quick replication and its common use for anti-HIV-1 assays. Third, Vero cells were utilized due to their rapid growth and because they were anchored on the surface. The screening of new conjugates in three cell types will enable us to distinguish the observed anti-HIV-1 activity from the toxicity. Among the various conjugates tested, the most potent anti-HIV-1 compound was **10b** with EC_{50} of 0.34 μM demonstrating no cytotoxicity in PBM and Vero cells and marginal IC_{50} of 76.8 μM in CEM cells. However, the ddA conjugate **10f** was found to be relatively more cytotoxic in all three cell lines. Overall, the new conjugates were found to be somewhat more cytotoxic in CEM cells compared to those in the PBM and Vero cells.

In summary, the anti-HIV-1 and cytotoxicity assays with conjugates **10a**−**i** reported herein confirm that the modification of various nucleosides with the glucose−phosphate conjugate did not completely abolish the original activity of the parent nucleosides. No significant toxicity was observed for the conjugates tested in this study with the exception of *ara*-C, which was found to be more cytotoxic when in the form of a glyco-conjugate than as a simple nucleoside.

CONCLUSIONS

Glycoconjugates of biologically active nucleoside analogues have been prepared as potential prodrugs since they can be cleaved intracellularly to the corresponding nucleosides and nucleotides. We have shown that the phosphoramidite approach is a convenient method that allows for the synthesis of stable glycosyl-nucleoside phosphodiester compounds. We demonstrated that glucosyl 6-phosphoramidite **7** is easily accessible in high yield through a regioselective chemoenzymatic strategy. Furthermore, we established that the phosphodiesters of d4T, IdUrd, ddI, ddA, virazole, *ara*-A, and *ara*-C exhibited higher solubility in water compared to their parent nucleosides. These water soluble conjugates of nucleosides may improve their oral bioavailability and increase the intestinal absorption as reported

for other carbohydrate conjugates (*47*, *48*). The anti-HIV-1 data is encouraging and expected to offer new opportunities in designing therapeutic nucleosides via a straightforward chemical conjugation approach. We anticipate that amidite **7** will find wider applications for other therapeutic agents that require enhanced water solubility.

ACKNOWLEDGMENT

This work is dedicated to Professor Francisco Palacios on the occasion of his 60th birthday. Financial support of this work by the Spanish Ministerio de Educación y Ciencia (MEC) (Project MEC-CTQ-2007-61126) is gratefully acknowledged. R.F.S. is supported in part by NIH grants 5P30-AI-50409 (CFAR), 5R37-AI-025899, and 5R37-AI-041980 and by the Department of Veterans Affairs.

Supporting Information Available: ^{1}H and ^{13}C NMR spectral data; the level of purity is indicated by the inclusion of copies of ^{1}H and ^{13}C NMR spectra; in addition, some 2D NMR experiments are shown, which were used to assign the peaks. This material is available free of charge via the Internet at http://pubs.acs.org.

LITERATURE CITED

(1) De Clercq, E. (2005) Recent highlights in the development of new antiviral drugs. *Curr. Opin. Microbiol. 8*, 552–560.
(2) Schinazi, R. F., and Liotta, D. C. (2004) *Frontiers in Nucleoside and Nucleic Acids*, IHL Press, Tucker, GA.
(3) Rachakonda, S., and Cartee, L. (2004) Challenges in antimicrobial drug discovery and the potential of nucleoside antibiotics. *Curr. Med. Chem. 11*, 775–793.
(4) De Clercq, E. (2004) Antiviral drugs in current clinical use. *J. Clin. Virol. 30*, 115–133.
(5) Chu, C. K. (2002) *Recent Advances in Nucleosides: Chemistry and Chemotherapy*, Elsevier Science, New York.
(6) Dove, A. (2001) The bittersweet promise of glycobiology. *Nat. Biotechnol. 19*, 913–917.
(7) Dwek, R. A. (1996) Glycobiology: toward understanding the function of sugars. *Chem. Rev. 96*, 683–720.
(8) Varki, A. (1993) Biological Roles of Oligosaccharides: all of the theories are correct. *Glycobiology 3*, 97–130.
(9) Peterson, L. W., and McKenna, C. E. (2009) Prodrug approaches to improving the oral absorption of antiviral nucleotide analogues. *Expert Opin. Drug Delivery 6*, 405–420.
(10) Jessen, H. J., Schulz, T., Balzarini, J., and Meier, C. (2008) Bioreversible protection of nucleoside diphosphates. *Angew. Chem., Int. Ed. 47*, 8719–8722.
(11) Wendicke, S., Warnecke, S., and Meier, C. (2008) Efficient synthesis of nucleoside diphosphate glycopyranoses. *Angew. Chem., Int. Ed. 47*, 1500–1502.
(12) Gold, H., van Delft, P., Meeuwenoord, N., Codée, J. D. C., Filippov, D. V., Eggink, G., Overkleeft, H. S., and van der Marel, G. A. (2008) Synthesis of sugar nucleotides by application of phosphoramidites. *J. Org. Chem. 73*, 9458–9469.
(13) Timmons, S. C., and Jakeman, D. L. (2007) Stereoselective chemical synthesis of sugar nucleotides via direct displacement of acylated glycosyl bromides. *Org. Lett. 9*, 1227–1230.
(14) Ahmadibeni, Y., and Parang, K. (2006) Solid-phase synthesis of dinucleoside and nucleoside−carbohydrate phosphodiesters and thiophosphodiesters. *J. Org. Chem. 71*, 6693–6696.
(15) Xiao, Q., Ju, Y., and Zhao, Y. (2003) A convenient route to symmetric phosphate, phosphorothioate, and phosphoroselenoate of AZT and d4T. *Synth. Commun. 33*, 4157–4162.
(16) Schlienger, N., Périgaud, C., Gosselin, G., and Imbach, J.-L. (1997) Synthesis and studies of mononucleoside glucosyl phosphotriester derivates. *J. Org. Chem. 62*, 7216–7221.
(17) Herdewijn, P. (2007) Nucleosiode Prodrugs and Delivery Strategies, *Current Protocols in Nucleic Acid Chemistry* (Beaucage, S. L., Bergstrom, D. E., Glick, G. D., and Jones, R. A., Eds.) pp 15.0.1−15.0.4, Chapter 15, John Wiley & Sons, New York.
(18) Meier, C., Renze, J., Ducho, C., and Balzarini, J. (2002) *Curr. Top. Med. Chem. 2*, 1111–1121.
(19) Wagner, C. R., Iyer, V. V., and McIntee, E. J. (2000) Pronucleotides: toward the in vivo delivery of antiviral and anticancer nucleotides. *Med. Res. Rev. 20*, 417–451.
(20) Parang, K., Wiebe, L. I., and Knaus, E. E. (2000) Novel approaches for designing 5′-*O*-ester prodrugs of 3′-azido-2′,3′-dideoxythymidine (AZT). *Curr. Med. Chem. 7*, 995–1039.
(21) Henin, Y., Gouyette, C., Schwartz, O., Debouzy, J.-C., Neumann, J.-M., and Huynh-Dinh, T. (1991) Lipophilic glycosyl phosphotriester derivatives of AZT: synthesis, NMR transmembrane transport study and antiviral activity. *J. Med. Chem. 34*, 1830–1837.
(22) Gouyette, C., Neumann, J. M., Fauve, R., and Huynh-Dinh, T. (1989) 6- and 1-substituted mannosyl phosphotriesters as lipophilic macrophage-targeted carriers of antiviral nucleosides. *Tetrahedron Lett. 30*, 6019–6022.
(23) D'Onofrio, J., Petraccone, L., Martino, L., Di Fabio, G., Iadonisi, A., Balzarini, J., Giancola, C., and Montesarchio, D. (2008) Synthesis, biophysical characterization, and anti-HIV activity of glyco-conjugated G-quadruplex-forming oligonucleotides. *Bioconjugate Chem. 19*, 607–616.
(24) Neumann, J. M., Herve, M., Debouzy, J.-C., Guerra, F. I., Gouyette, C., Dupraz, B., and Huynh-Dinh, T. (1989) Synthesis and transmembrane transport studies by NMR of a glucosyl phospholipid of thymidine. *J. Am. Chem. Soc. 111*, 4270–4277.
(25) Salam, M. A., and Behrman, E. J. (1982) Synthesis of nucleoside 5′-(β-D-glucopyranosyl monophosphates) by the sugar ortho ester route. *Carbohydr. Res. 102*, 139–146.
(26) Martínez-Montero, S., Fernández, S., Rodríguez-Pérez, T., Sanghvi, Y. S., Wen, K., Gotor, V., and Ferrero, M. (2009) Improved synthesis and isolation of 2′-*O*-methyladenosine: effective and scalable enzymatic separation of 2′/3′-*O*-methyladenosine regioisomers. *Eur. J. Org. Chem.* 3265–3271.
(27) Díaz-Rodríguez, A., Sanghvi, Y. S., Fernández, S., Schinazi, R. F., Theodorakis, E. A., Ferrero, M., and Gotor, V. (2009) Synthesis and anti-HIV activity of conformationally restricted bicyclic hexahydroisobenzofuran nucleoside analogues. *Org. Biomol. Chem. 7*, 1415–1423.
(28) Lavandera, I., Fernández, S., Magdalena, J., Ferrero, M., Kazlauskas, R. J., and Gotor, V. (2005) An inverse substrate orientation for the regioselective acylation of 3′,5′-diaminonucleosides catalyzed by *Candida antarctica* lipase B? *ChemBioChem 6*, 1381–1390.
(29) Rodríguez-Pérez, T., Lavandera, I., Fernández, S., Sanghvi, Y. S., Ferrero, M., and Gotor, V. (2007) Novel and efficient chemoenzymatic synthesis of D-glucose-6-phosphate and molecular modeling studies on the selective biocatalysis. *Eur. J. Org. Chem.* 2769–2778.
(30) Bronisz, R. (2002) Synthesis and structure of {[Zn(1,2-di(1,2,3,4-tetrazol-2-yl)ethane)$_3$](ClO_4)$_2$}$_n$. The first coordination polymer based on 2-substituted tetrazole. *Inorg. Chim. Acta 340*, 215–220.
(31) Sanghvi, Y. S., Guo, Z., Pfundheller, H. M., and Converso, A. (2000) Improved process for the preparation of nucleosidic phosphoramidites using a safer and cheaper activator. *Org. Process Res. Dev. 4*, 175–181.
(32) Lavandera, I., García, J., Fernández, S., Ferrero, M., Gotor, V., and Sanghvi, Y. S. (2005) Enzymatic Regioselective Levulinylation of 2′-Deoxyribonucleosides and 2′-*O*-Methylribonucleosides. *Current Protocols in Nucleic Acid Chemistry* (Beaucage, S. L., Bergstrom, D. E., Glick, G. D., and Jones, R. A., Eds.) pp 2.11.1−2.11.36, Chapter 2, John Wiley & Sons, New York. *O*-Levulinyl acetonoxime is now commercially available from Sai Life Sciences (www.sailifesciences.com).
(33) Beaucage, S. L., and Iyer, R. P. (1992) Advances in the synthesis of oligonucleotides by the phosphoramidite approach. *Tetrahedron 48*, 2223–2311.

(34) Ferrero, M., and Gotor, V. (2000) Biocatalytic selective modifications of conventional nucleosides, carbocyclic nucleosides, and *C*-nucleosides. *Chem. Rev. 100*, 4319–4348.

(35) Reese, C. B., and Yan, H. (2003) An approach to the desulfurization of oligonucleotide phosphorothioates. *Tetrahedron Lett. 44*, 2501–2504.

(36) Ti, G. S., Gaffney, B. L., and Jones, R. A. (1982) Transient protection: efficient one-flask synthesis of protected deoxynucleosides. *J. Am. Chem. Soc. 104*, 1316–1319.

(37) Minamoto, K., Fujiki, Y., Shiomi, N., Uda, Y., and Sasaki, T. (1985) Systematic general synthesis of purine 8,5′-imino and substituted imino cyclonucleosides. *J. Chem. Soc., Perkin Trans. 1*, 2337–2346.

(38) Lavandera, I., Fernández, S., Magdalena, J., Ferrero, M., Jarjap, H., Savile, C. K., Kazlauskas, R. J., and Gotor, V. (2006) Molecular basis for the unusual regioselectivity of lipase from *Pseudomonas cepacia* toward the secondary alcohol of 2′-deoxynucleosides. *ChemBioChem 7*, 693–698.

(39) García, J., Fernández, S., Ferrero, M., Sanghvi, Y. S., and Gotor, V. (2004) Study of regioselective enzymatic acylation of β-L-2′-deoxynucleosides: application to resolution of β-D/L-2′-deoxynucleoside racemic mixtures. *Org. Lett. 6*, 3759–3762.

(40) García, J., Fernández, S., Ferrero, M., Sanghvi, Y. S., and Gotor, V. (2003) Novel enzymatic synthesis of levulinyl protected nucleosides useful for solution phase synthesis of oligonucleotides. *Tetrahedron: Asymmetry 14*, 3533−3540.

(41) García, J., Fernández, S., Ferrero, M., Sanghvi, Y. S., and Gotor, V. (2002) Building-blocks for the solution phase synthesis of oligonucleotides: regioselective hydrolysis of 3′,5′-di-*O*-levulinylnucleosides using an enzymatic approach. *J. Org. Chem. 67*, 4513–4519.

(42) Shen, W., Kim, J.-S., Mitchell, S., Kish, P., Kijek, P., and Hilfinger, J. (2009) 5′-O-D-Valyl *Ara* A, a potential prodrug for improving oral bioavailability of the antiviral agent vidarabine. *Nucleosides Nucleotides Nucleic Acids 28*, 43–55.

(43) Wechter, W. J., Gish, D. T., Greig, M. E., Gray, G. D., Moxley, T. E., Kuentzel, S. L., Gray, L. G., Gibbons, A. J., Griffin, R. L., and Neil, G. L. (1976) Orally active derivatives of ara-cytidine. *J. Med. Chem. 19*, 1013–1017.

(44) Hong, C. I., Kirisits, A. J., Nechaev, A., Buchheit, D. J., and West, C. R. (1990) Synthesis and antitumor activity of 1-β-D-arabinofuranosylcytosine and cytidine conjugates of thioether lipids. *J. Med. Chem. 33*, 1380–1386.

(45) Schinazi, R. F., Sommadossi, J. P., Saalmann, V., Cannon, D. L., Xie, M.-W., Hart, G. C., Smith, G. A., and Hahn, E. F. (1990) Activity of 3′-azido-3′-deoxythymidine nucleotide dimers in primary lymphocytes infected with human immunodeficiency virus type 1. *Antimicrob. Agents Chemother. 34*, 1061–1067.

(46) Stuyver, L. J., Lostia, S., Adams, M., Mathew, J., Pai, B. S., Grier, J., Tharnish, P., Choi, Y., Chong, Y., Choo, H., Chu, C. K., Otto, M. J., and Schinazi, R. F. (2002) Antiviral activities and cellular toxicities of modified 2′,3′-dideoxy-2′,3′-didehydrocytidine analogues. *Antimicrob. Agents Chemother. 46*, 3854–3860.

(47) Hollman, P. C. H., van Trijp, J. M. P., Buysman, M. N. C. P., van der Gaag, M. S., Mengelers, M. J. B., de Vries, J. H. M., and Katan, M. B. (1997) Relative bioavailability of the antioxidant flavonoid quercetin from various foods in man. *FEBS Lett. 418*, 152–156.

(48) Kaminaga, Y., Nagatsu, A., Akiyama, T., Sugimoto, N., Yamazaki, T., Maitani, T., and Mizukami, H. (2003) Production of unnatural glucosides of curcumin with drastically enhanced water solubility by cell suspension cultures of *Catharanthus roseus*. *FEBS Lett. 555*, 311–316.

BC1002168

Chemoenzymatic Syntheses and Anti-HIV-1 Activity of Glucose-Nucleoside Conjugates as Prodrugs

Tatiana Rodríguez-Pérez,[†] Susana Fernández,[†] Yogesh S. Sanghvi,[‡] Raymond F. Schinazi,[§] Vicente Gotor[†,] and Miguel Ferrero[†,]**

[†]Departamento de Química Orgánica e Inorgánica and Instituto Universitario de Biotecnología de Asturias, Universidad de Oviedo, 33006-Oviedo (Asturias), Spain

[‡]Rasayan Inc., 2802 Crystal Ridge Road, Encinitas, CA 92024-6615, USA.

[§]Emory University School of Medicine/Veterans Affair Medical Center, Decatur, Georgia 30033, USA.

ELECTRONIC SUPPLEMENTARY INFORMATION (page 1 of 153 pages)

Contents:

Copies of ^{1}H, ^{13}C, DEPT, and some 2D NMR spectra of compounds **3**, **5**, **7**, **9**, and **10**:

- ^{1}H NMR of **7** (S4)
- ^{13}C NMR of **7** (S5)
- DEPT NMR of **7** (S6)
- ^{31}P NMR of **7** (S7)
- COSY of **7** (S8)
- HSQC of **7** (S9)
- HMBC of **7** (S10)
- NOESY of **7** (S11)
- ^{1}H NMR of **8c** (S12)
- ^{13}C NMR of **8c** (S13)
- DEPT NMR of **8c** (S14)
- COSY of **8c** (S15)
- ^{1}H NMR of **8d** (S16)
- ^{13}C NMR of **8d** (S17)
- DEPT NMR of **8d** (S18)
- ^{1}H NMR of **8f** (S19)
- ^{13}C NMR of **8f** (S20)
- DEPT NMR of **8f** (S21)
- ^{1}H NMR of **8g** (S22)
- ^{13}C NMR of **8g** (S23)
- DEPT NMR of **8g** (S24)
- ^{1}H NMR of **8h** (S25)
- ^{13}C NMR of **8h** (S26)
- DEPT NMR of **8h** (S27)

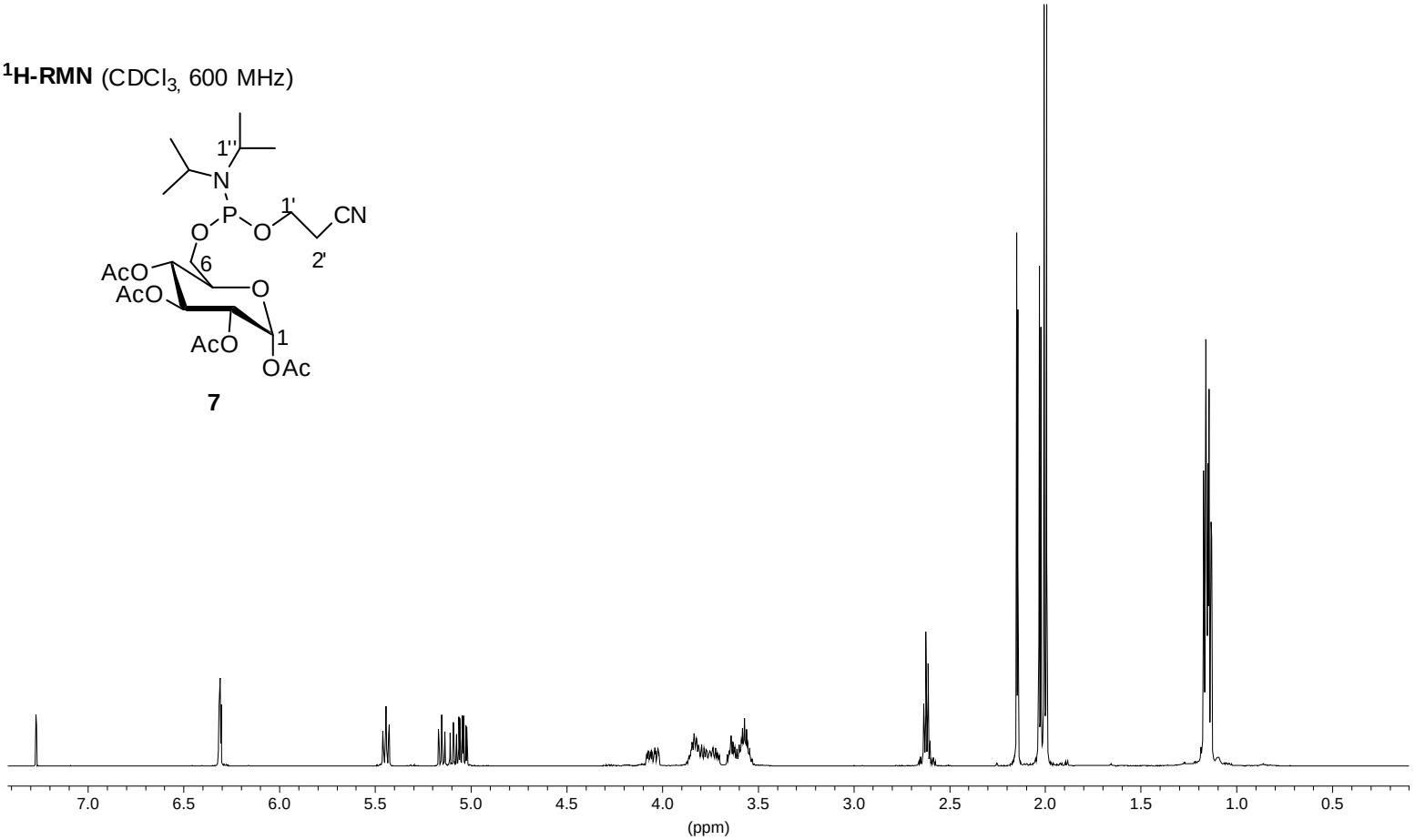
- ^{1}H NMR of **8i** (S28)
- ^{13}C NMR of **8i** (S29)
- DEPT NMR of **8i** (S30)
- ^{1}H NMR of **9a** (S31)
- ^{13}C NMR of **9a** (S31)
- DEPT NMR of **9a** (S33)
- ^{31}P NMR of **9a** (S34)
- ^{1}H NMR of **9b** (S35)
- ^{13}C NMR of **9b** (S36)
- DEPT NMR of **9b** (S37)
- ^{31}P NMR of **9b** (S38)
- COSY of **9b** (S39)
- HSQC of **9b** (S40)
- HMBC of **9b** (S41)
- ^{1}H NMR of **9c** (S42)
- ^{13}C NMR of **9c** (S43)
- DEPT NMR of **9c** (S44)
- ^{31}P NMR of **9c** (S45)
- COSY of **9c** (S46)
- HSQC of **9c** (S47)
- HMBC of **9c** (S48)
- ^{1}H NMR of **9d** (S49)
- ^{13}C NMR of **9d** (S50)
- DEPT NMR of **9d** (S51)
- ^{31}P NMR of **9d** (S52)
- COSY of **9d** (S53)
- HSQC of **9d** (S54)
- HMBC of **9d** (S55)
- ^{1}H NMR of **9e** (S56)
- ^{13}C NMR of **9e** (S57)
- DEPT NMR of **9e** (S58)
- ^{31}P NMR of **9e** (S59)
- COSY of **9e** (S60)
- HSQC of **9e** (S61)
- HMBC of **9e** (S62)
- ^{1}H NMR of **9f** (S63)
- ^{13}C NMR of **9f** (S64)
- DEPT NMR of **9f** (S65)
- ^{31}P NMR of **9f** (S66)
- ^{1}H NMR of **9g** (S67)
- ^{13}C NMR of **9g** (S68)
- DEPT NMR of **9g** (S69)
- ^{31}P NMR of **9g** (S70)
- COSY of **9g** (S71)
- HSQC of **9g** (S72)
- HMBC of **9g** (S73)
- ^{1}H NMR of **9h** (S74)
- ^{13}C NMR of **9h** (S75)
- DEPT NMR of **9h** (S76)
- ^{31}P NMR of **9h** (S77)
- COSY of **9h** (S78)
- HSQC of **9h** (S79)
- HMBC of **9h** (S80)
- ^{1}H NMR of **9i** (S81)
- ^{13}C NMR of **9i** (S82)
- DEPT NMR of **9i** (S83)
- ^{31}P NMR of **9i** (S84)
- HSQC of **9i** (S85)
- HMBC of **9i** (S86)
- NOESY of **9i** (S87)
- ^{1}H NMR of **10a** (S88)
- ^{13}C NMR of **10a** (S89)
- DEPT NMR of **10a** (S90)
- ^{31}P NMR of **10a** (S91)
- COSY of **10a** (S92)
- ^{1}H NMR of **10b** (S93)
- ^{13}C NMR of **10b** (S94)
- DEPT NMR of **10b** (S95)
- ^{31}P NMR of **10b** (S96)
- COSY of **10b** (S97)

- HSQC of **10b** (S98)
- ^{1}H NMR of **10c** (S99)
- ^{13}C NMR of **10c** (S100)
- DEPT NMR of **10c** (S101)
- ^{31}P NMR of **10c** (S102)
- COSY of **10c** (S103)
- ^{1}H NMR of **10d** (S104)
- ^{13}C NMR of **10d** (S105)
- DEPT NMR of **10d** (S106)
- ^{31}P NMR of **10d** (S107)
- COSY of **10d** (S108)
- ^{1}H NMR of **10e** (S109)
- ^{13}C NMR of **10e** (S110)
- DEPT NMR of **10e** (S111)
- ^{31}P NMR of **10e** (S112)
- COSY of **10e** (S113)
- ^{1}H NMR of **10f** (S114)
- ^{13}C NMR of **10f** (S115)
- DEPT NMR of **10f** (S116)
- ^{31}P NMR of **10e** (S117)
- COSY of **10f** (S118)
- ^{1}H NMR of **10g** (S119)
- ^{13}C NMR of **10g** (S120)
- DEPT NMR of **10g** (S121)
- ^{31}P NMR of **10g** (S122)
- ^{1}H NMR of **10h** (S123)
- ^{13}C NMR of **10h** (S124)
- DEPT NMR of **10h** (S125)
- ^{31}P NMR of **10h** (S126)
- COSY of **10h** (S127)
- ^{1}H NMR of **10i** (S128)
- ^{13}C NMR of **10i** (S129)
- DEPT NMR of **10i** (S130)
- ^{31}P NMR of **10i** (S131)
- COSY of **10i** (S132)
- ^{1}H NMR of **14** (S133)
- ^{13}C NMR of **14** (S134)
- DEPT NMR of **14** (S135)
- ^{1}H NMR of **15** (S136)
- ^{13}C NMR of **15** (S137)
- DEPT NMR of **15** (S138)
- ^{1}H NMR of **17** (S139)
- ^{13}C NMR of **17** (S140)
- DEPT NMR of **17** (S141)
- ^{1}H NMR of **18** (S142)
- ^{13}C NMR of **18** (S143)
- DEPT NMR of **18** (S144)
- ^{1}H NMR of **19** (S145)
- ^{13}C NMR of **19** (S146)
- DEPT NMR of **19** (S147)
- ^{1}H NMR of **21** (S148)
- ^{13}C NMR of **21** (S149)
- DEPT NMR of **21** (S150)
- ^{1}H NMR of **22** (S151)
- ^{13}C NMR of **22** (S152)
- DEPT NMR of **22** (S153)

2-Cyanoethyl-*N*,*N*-diisopropyl-(1,2,3,4-tetra-*O*-acetyl-α-D-glucopyranoside-6-yl)phosphoramidite (7)

^{1}H-RMN ($CDCl_3$, 600 MHz)

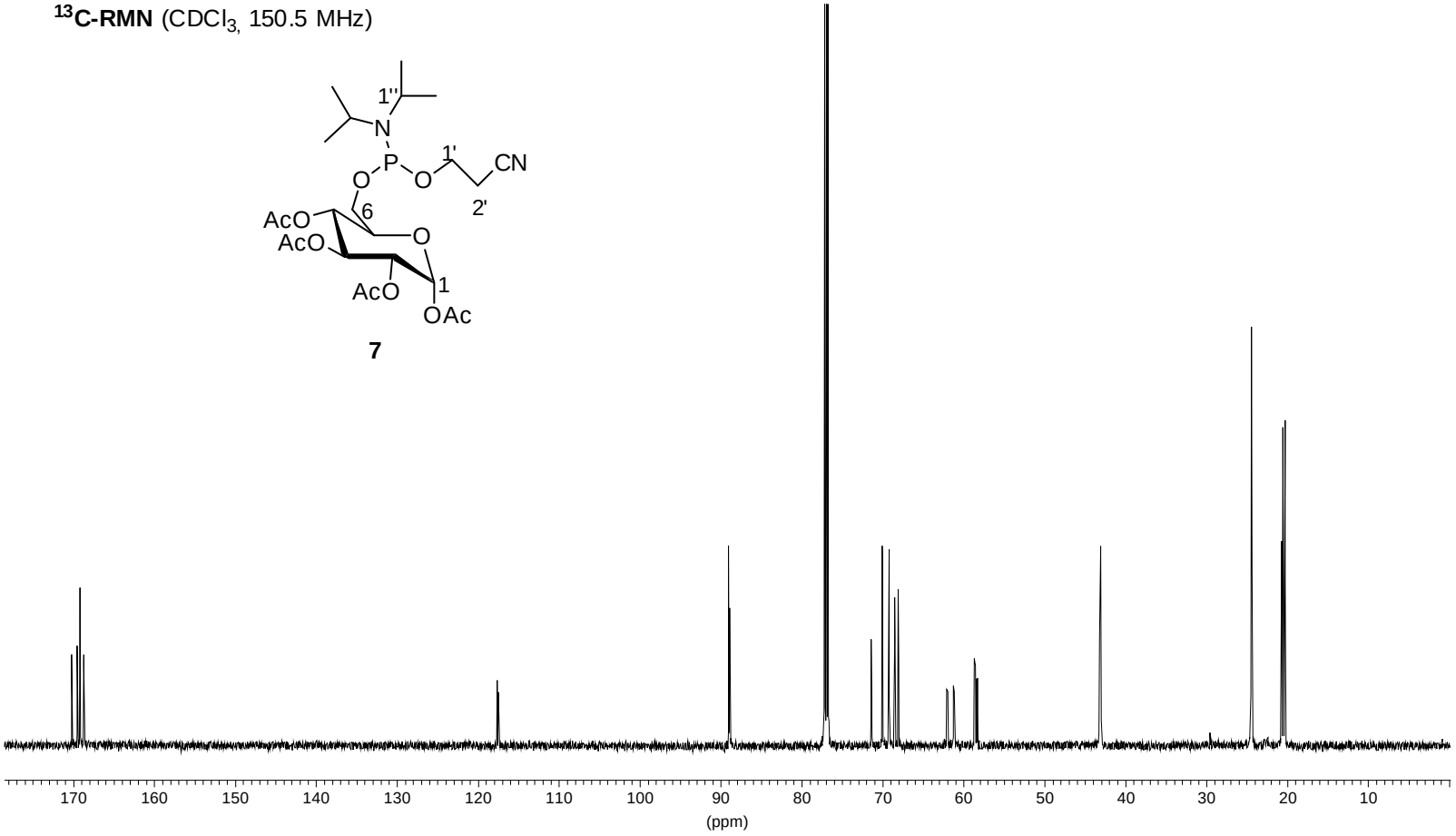
7



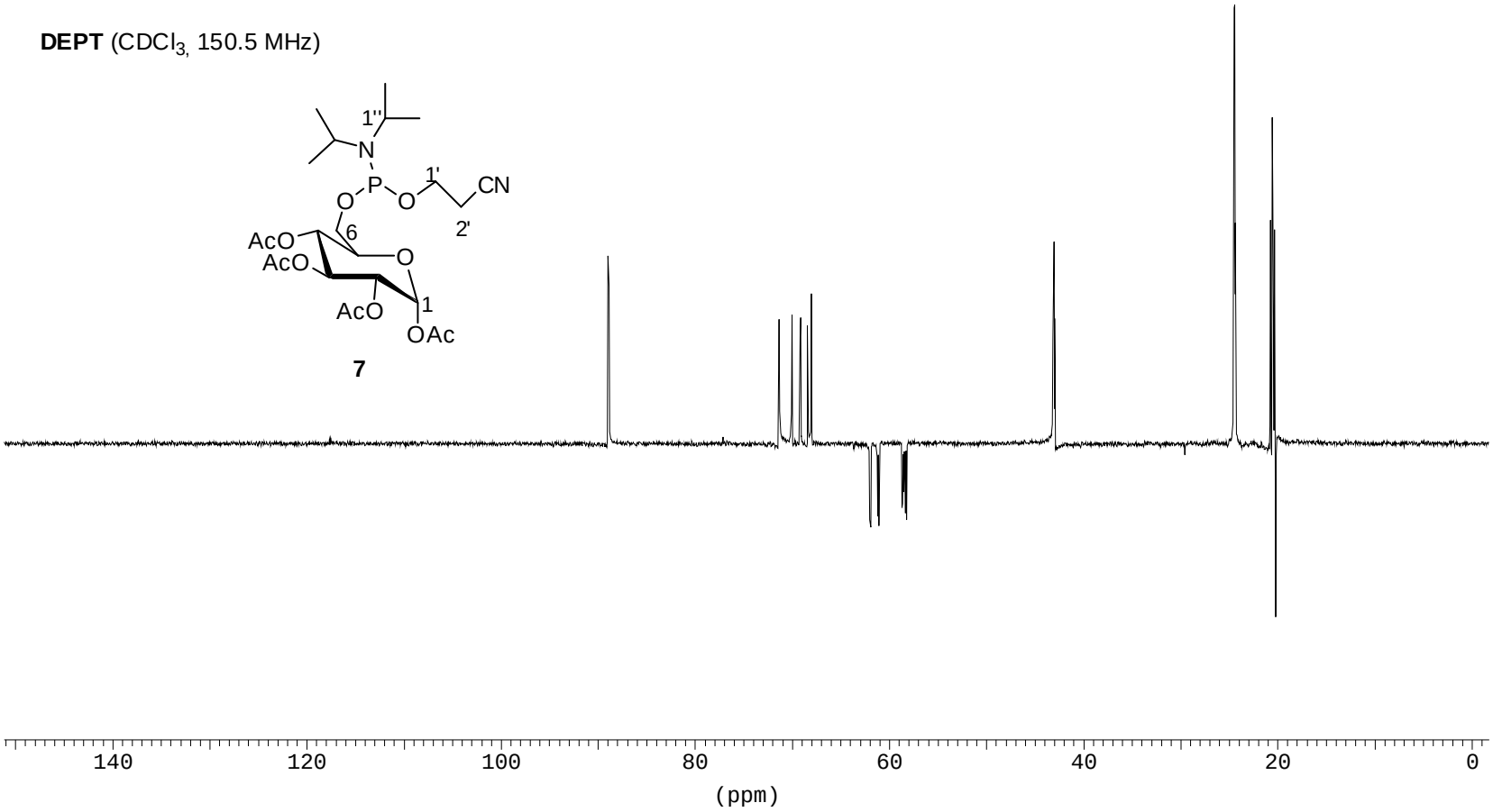
2-Cyanoethyl-*N*,*N*-diisopropyl-(1,2,3,4-tetra-*O*-acetyl-α-D-glucopyranoside-6-yl)phosphoramidite (7)

^{13}C-RMN ($CDCl_3$, 150.5 MHz)

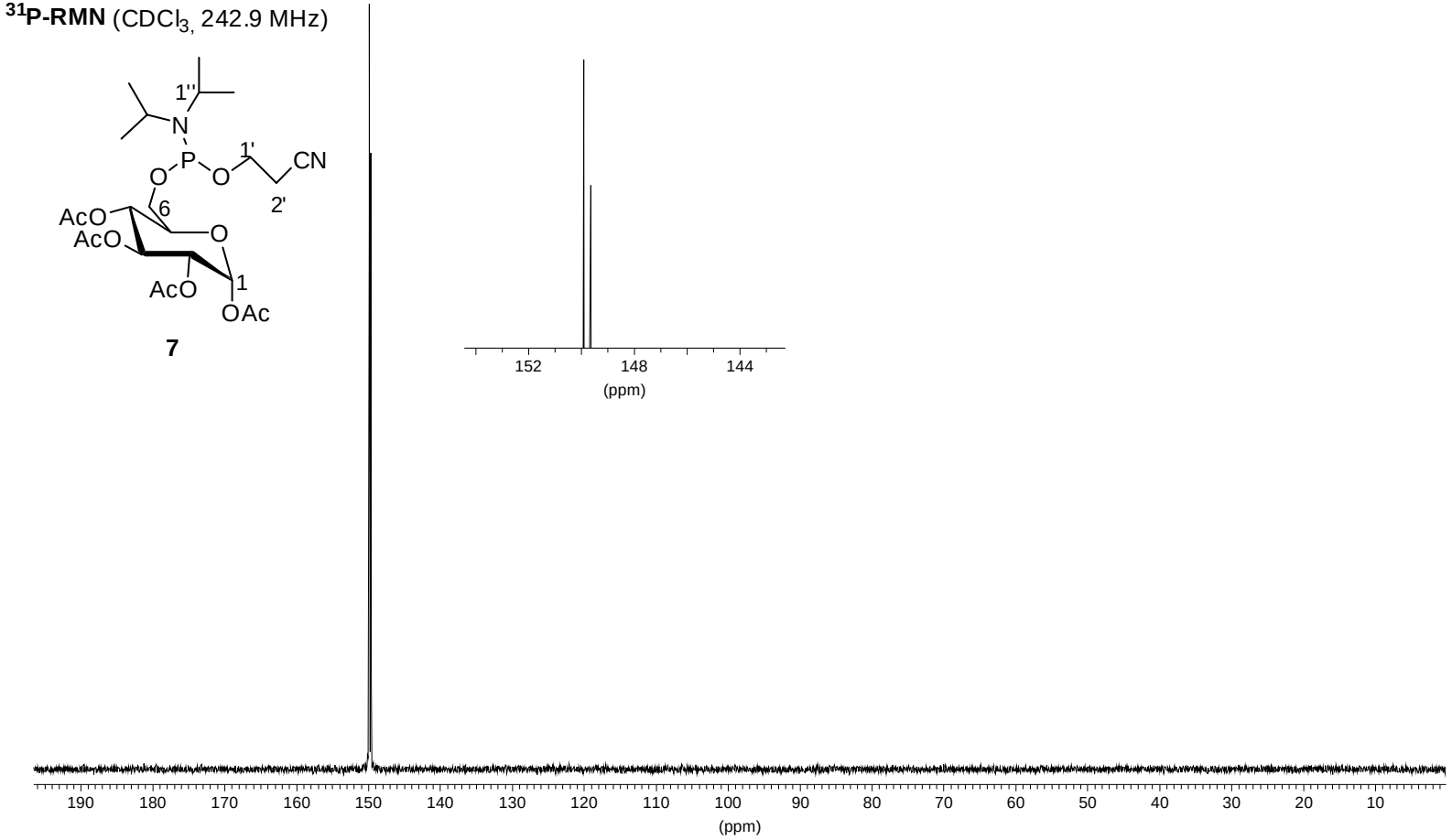
7



2-Cyanoethyl-*N*,*N*-diisopropyl-(1,2,3,4-tetra-*O*-acetyl-α-D-glucopyranoside-6-yl)phosphoramidite (7)

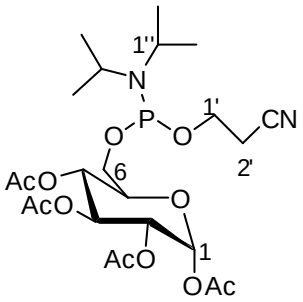


2-Cyanoethyl-*N*,*N*-diisopropyl-(1,2,3,4-tetra-*O*-acetyl-α-D-glucopyranoside-6-yl)phosphoramidite (7)

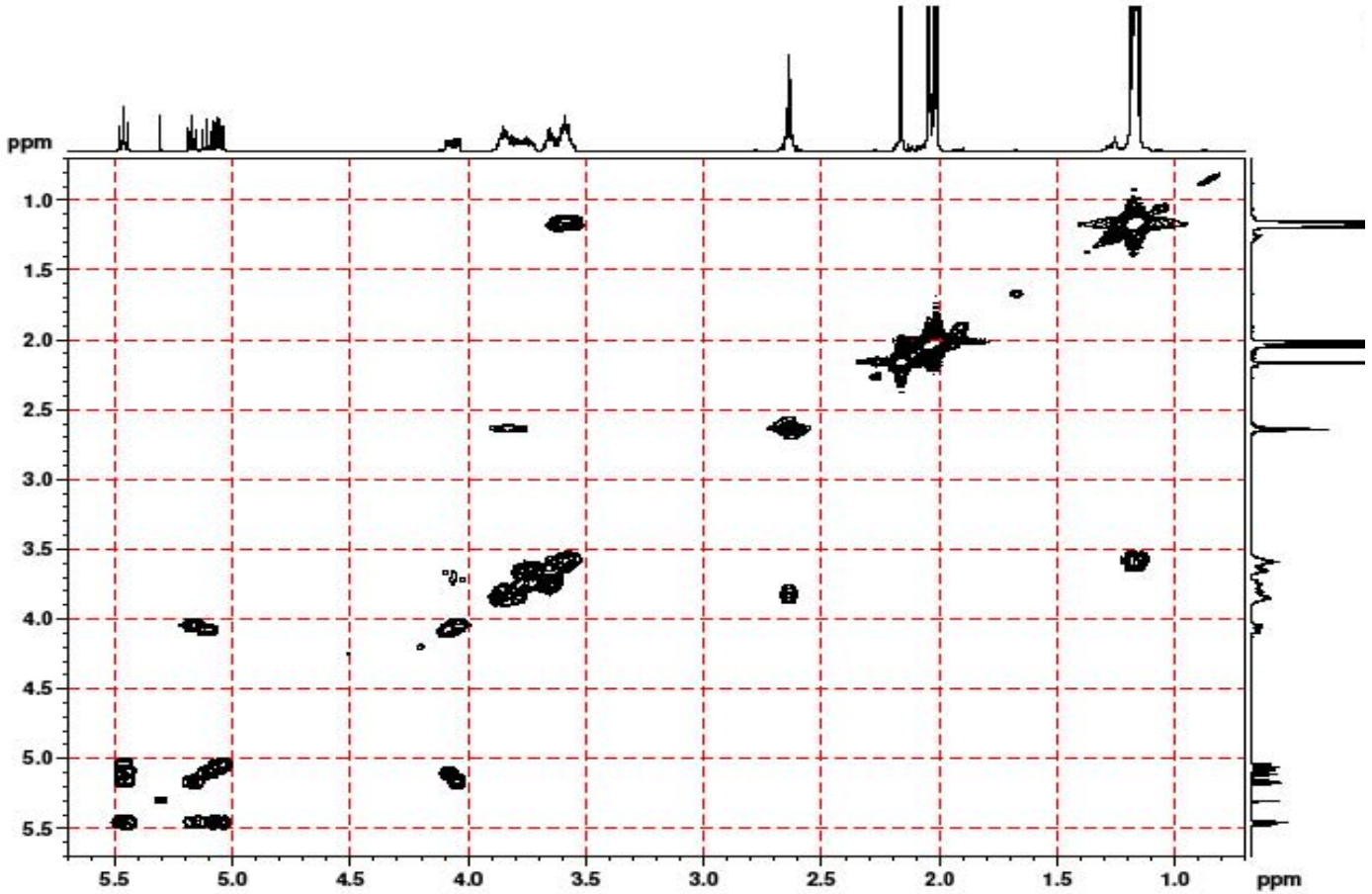


2-Cyanoethyl-*N*,*N*-diisopropyl-(1,2,3,4-tetra-*O*-acetyl-α-D-glucopyranoside-6-yl)phosphoramidite (7)

COSY ($CDCl_3$, 600 MHz)

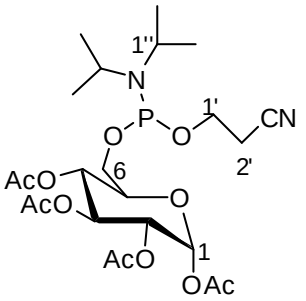


7

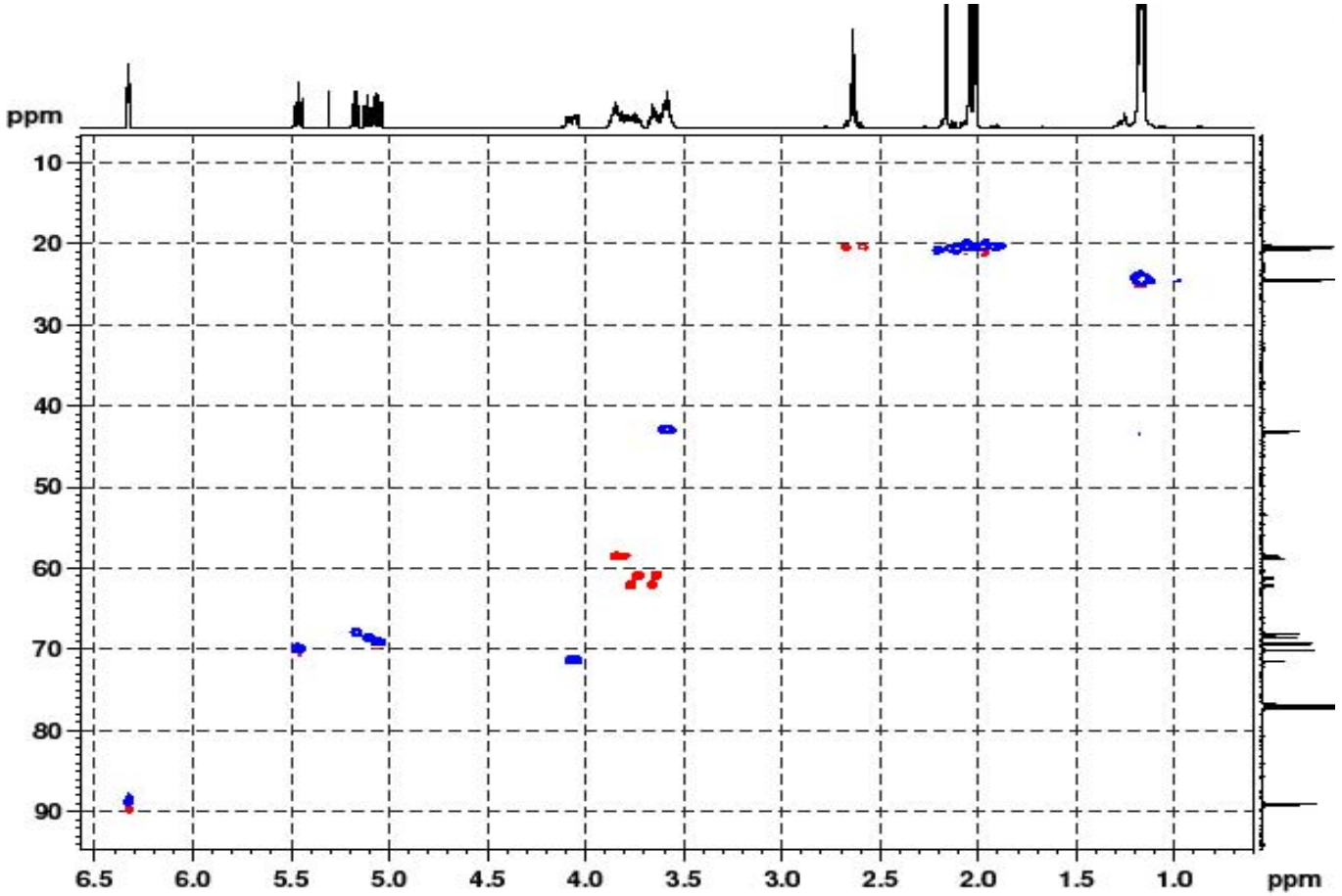


2-Cyanoethyl-*N*,*N*-diisopropyl-(1,2,3,4-tetra-*O*-acetyl-α-D-glucopyranoside-6-yl)phosphoramidite (7)

HSQC ($CDCl_3$, 600 MHz)

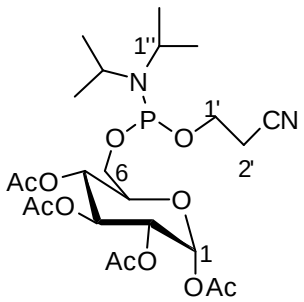


7

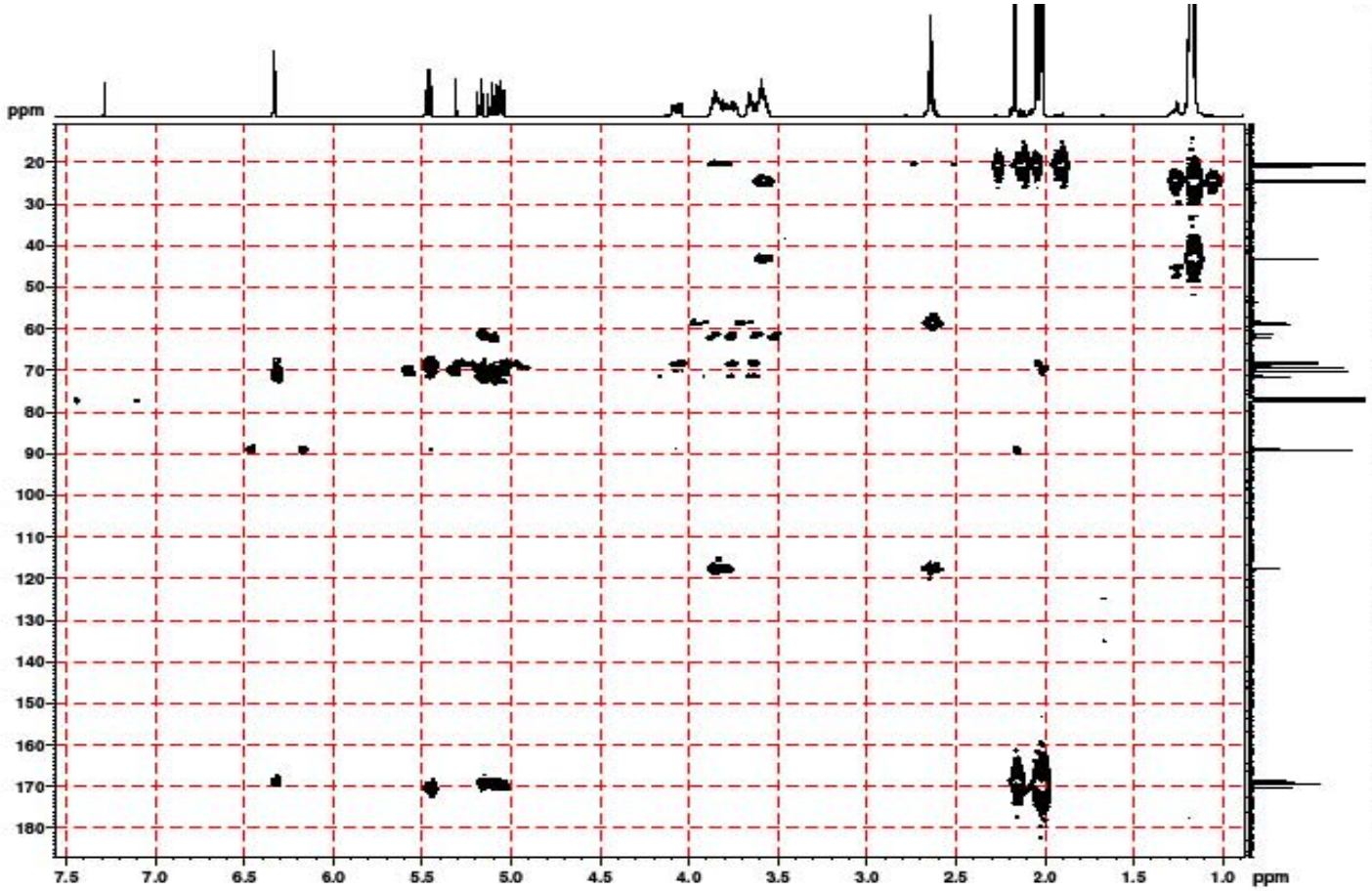


2-Cyanoethyl-*N*,*N*-diisopropyl-(1,2,3,4-tetra-*O*-acetyl-α-D-glucopyranoside-6-yl)phosphoramidite (7)

HMBC ($CDCl_3$, 600 MHz)

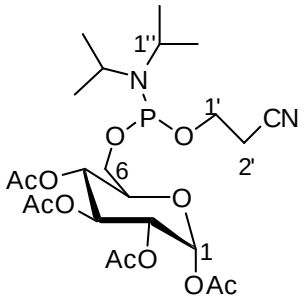


7

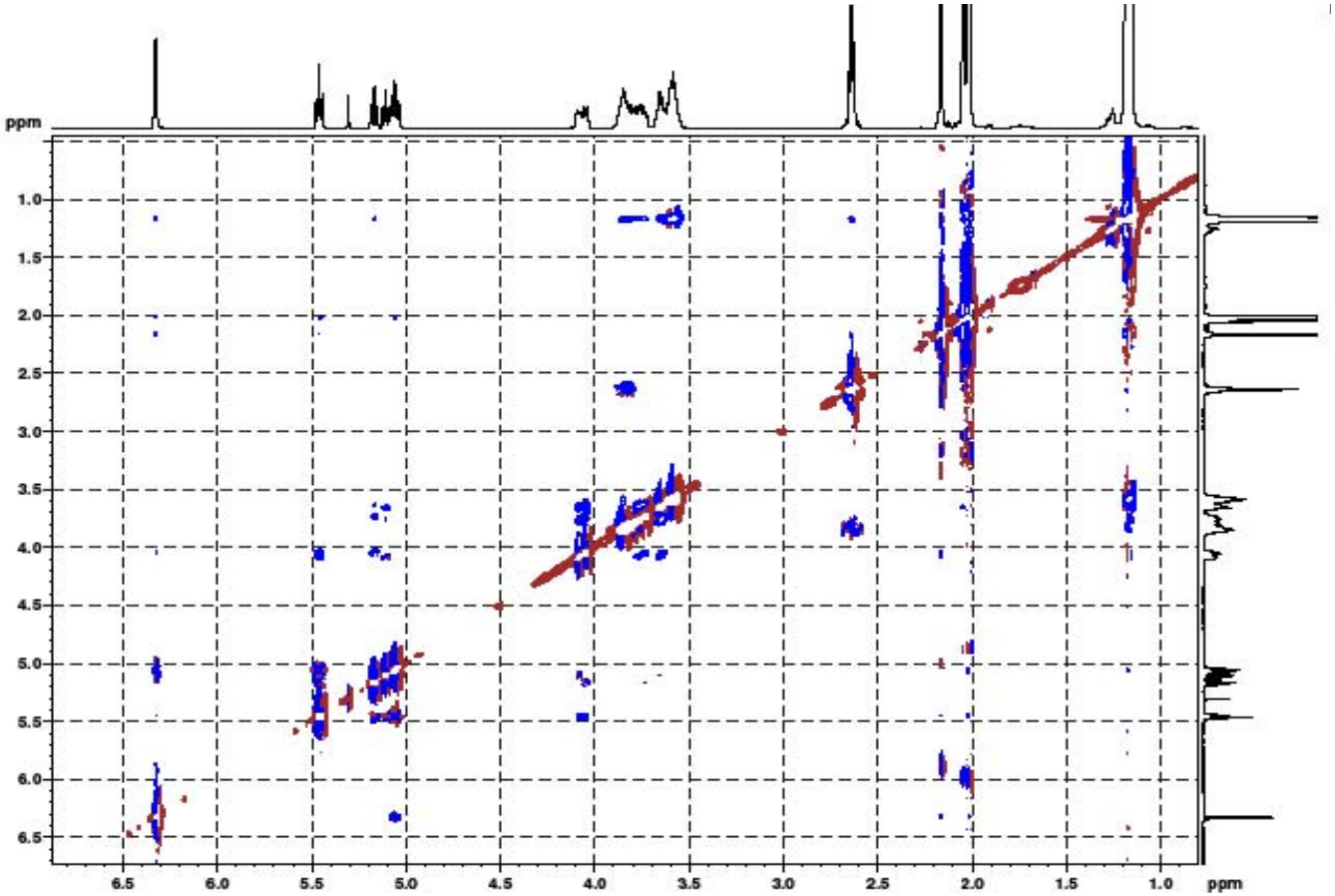


2-Cyanoethyl-*N*,*N*-diisopropyl-(1,2,3,4-tetra-*O*-acetyl-α-D-glucopyranoside-6-yl)phosphoramidite (7)

NOESY ($CDCl_3$, 600 MHz)



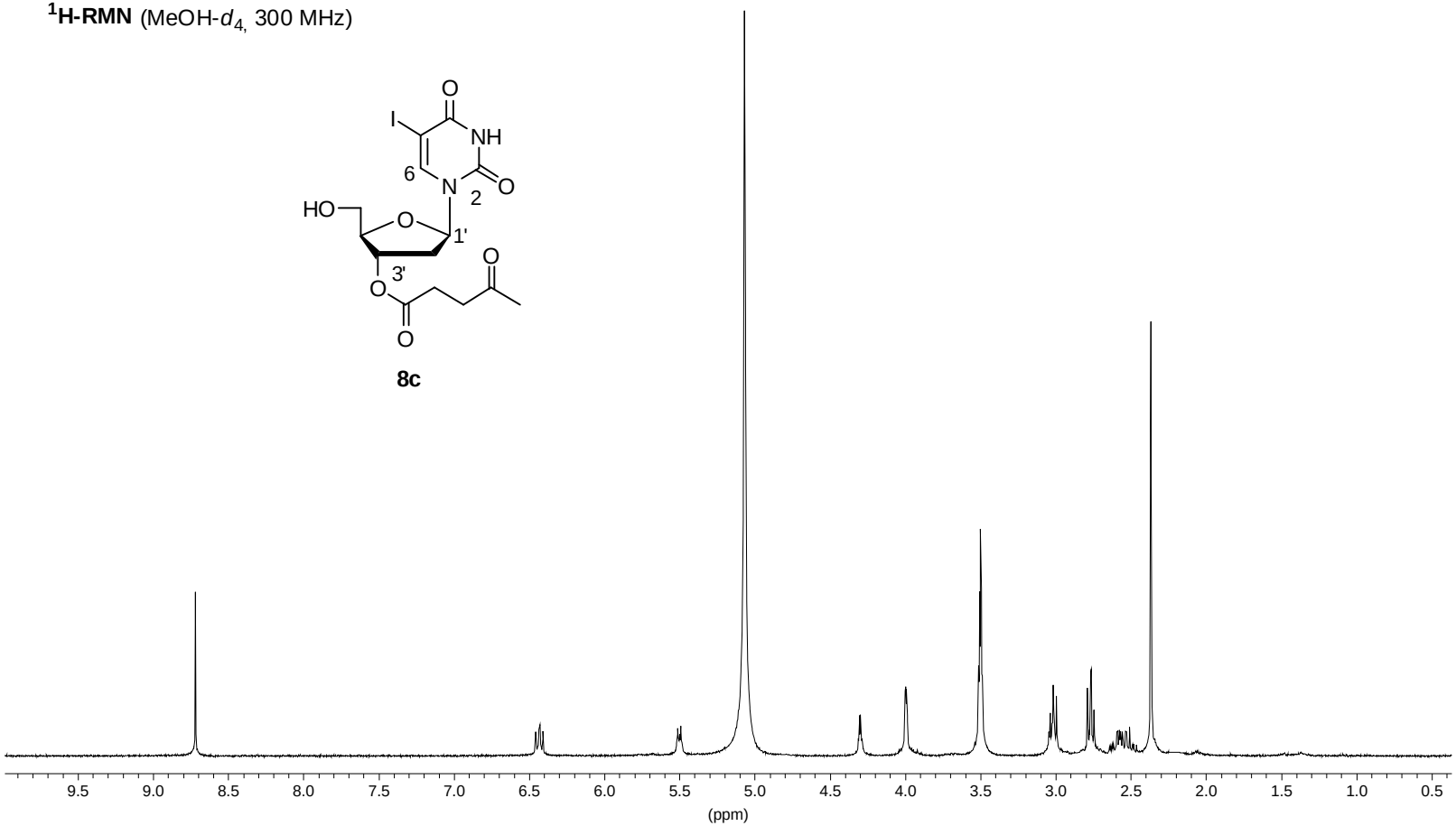
7



5-Iodo-3'-*O*-levulinyl-2'-deoxyuridine (8c)

^{1}H-RMN (MeOH-d_4, 300 MHz)

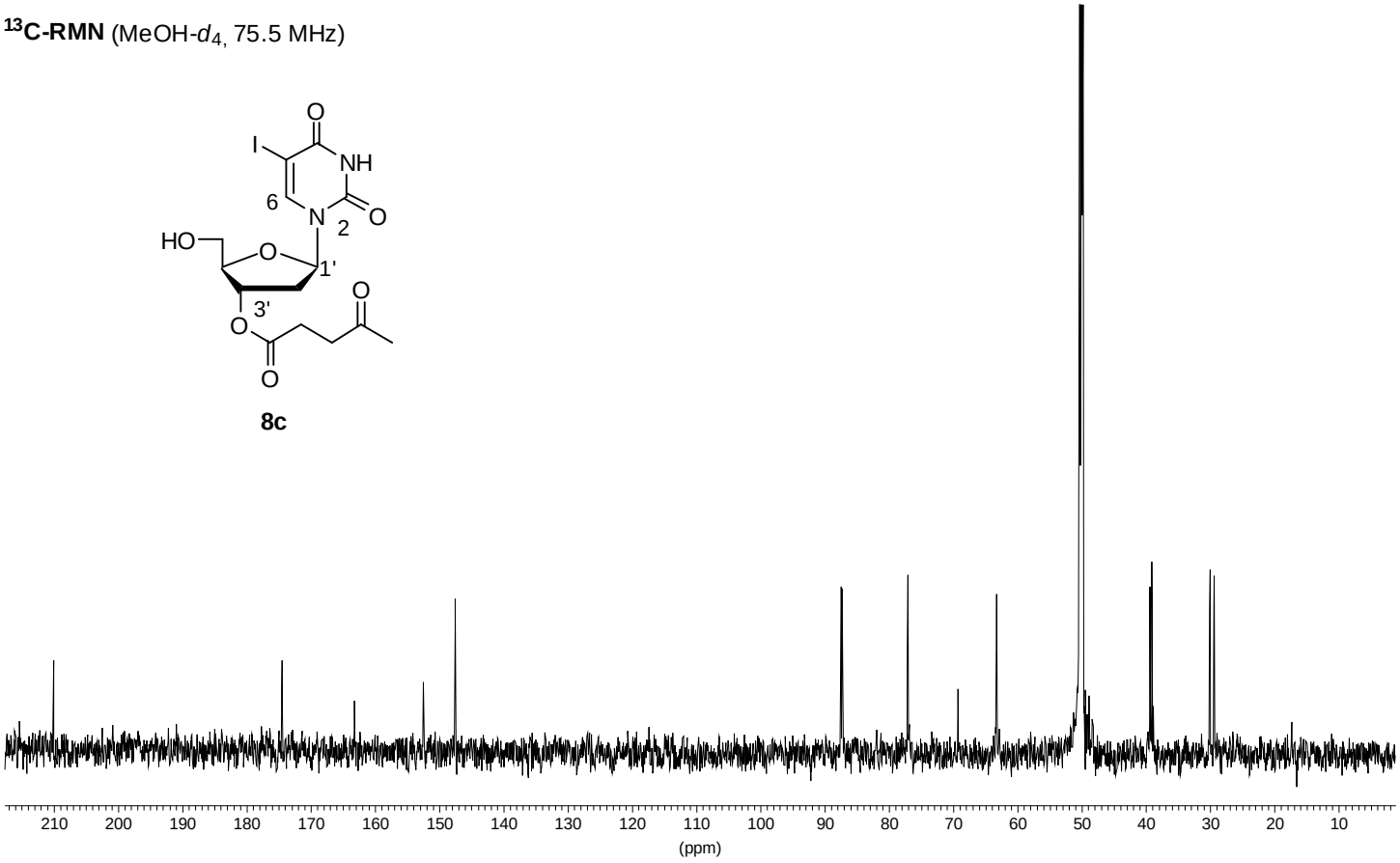
8c



5-Iodo-3'-*O*-levulinyl-2'-deoxyuridine (8c)

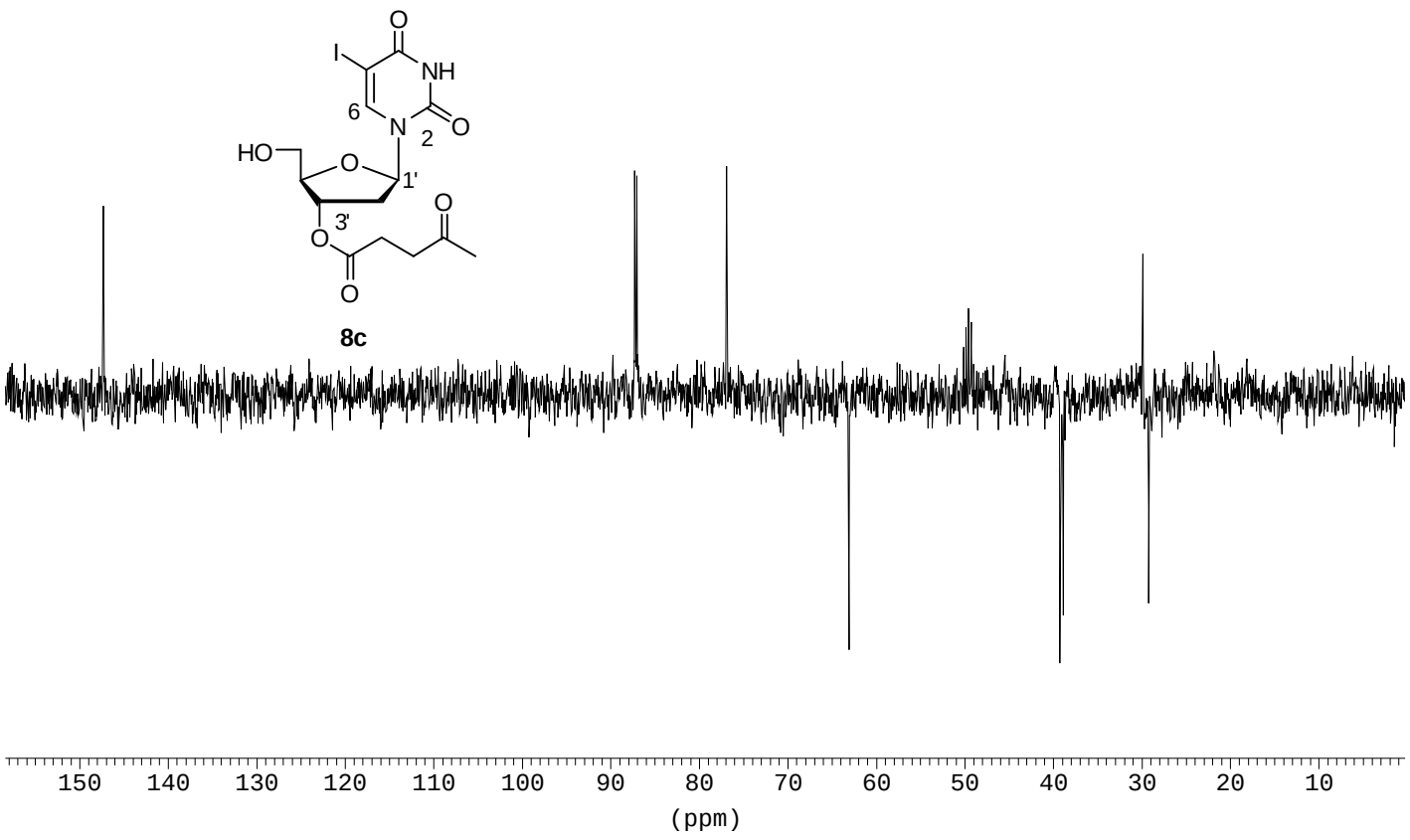
^{13}C-RMN (MeOH-d_4, 75.5 MHz)

8c



5-Iodo-3'-*O*-levulinyl-2'-deoxyuridine (8c)

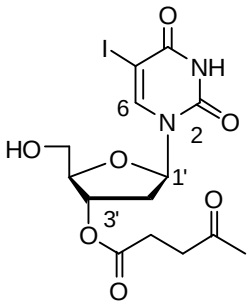
DEPT (MeOH-d_4, 75.5 MHz)



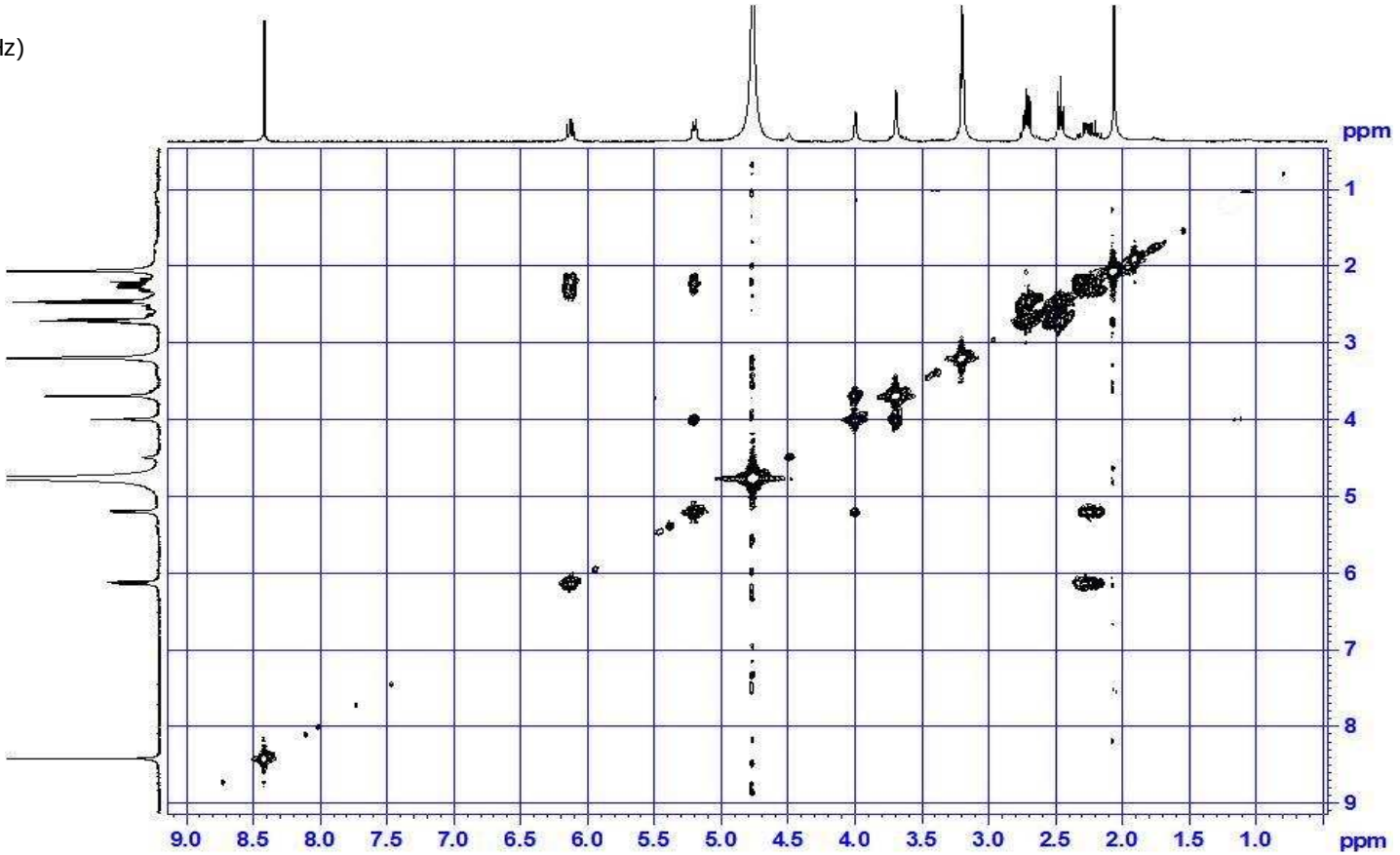
8c

5-Iodo-3'-*O*-levulinyl-2'-deoxyuridine (8c)

COSY (MeOH-d_4, 300 MHz)



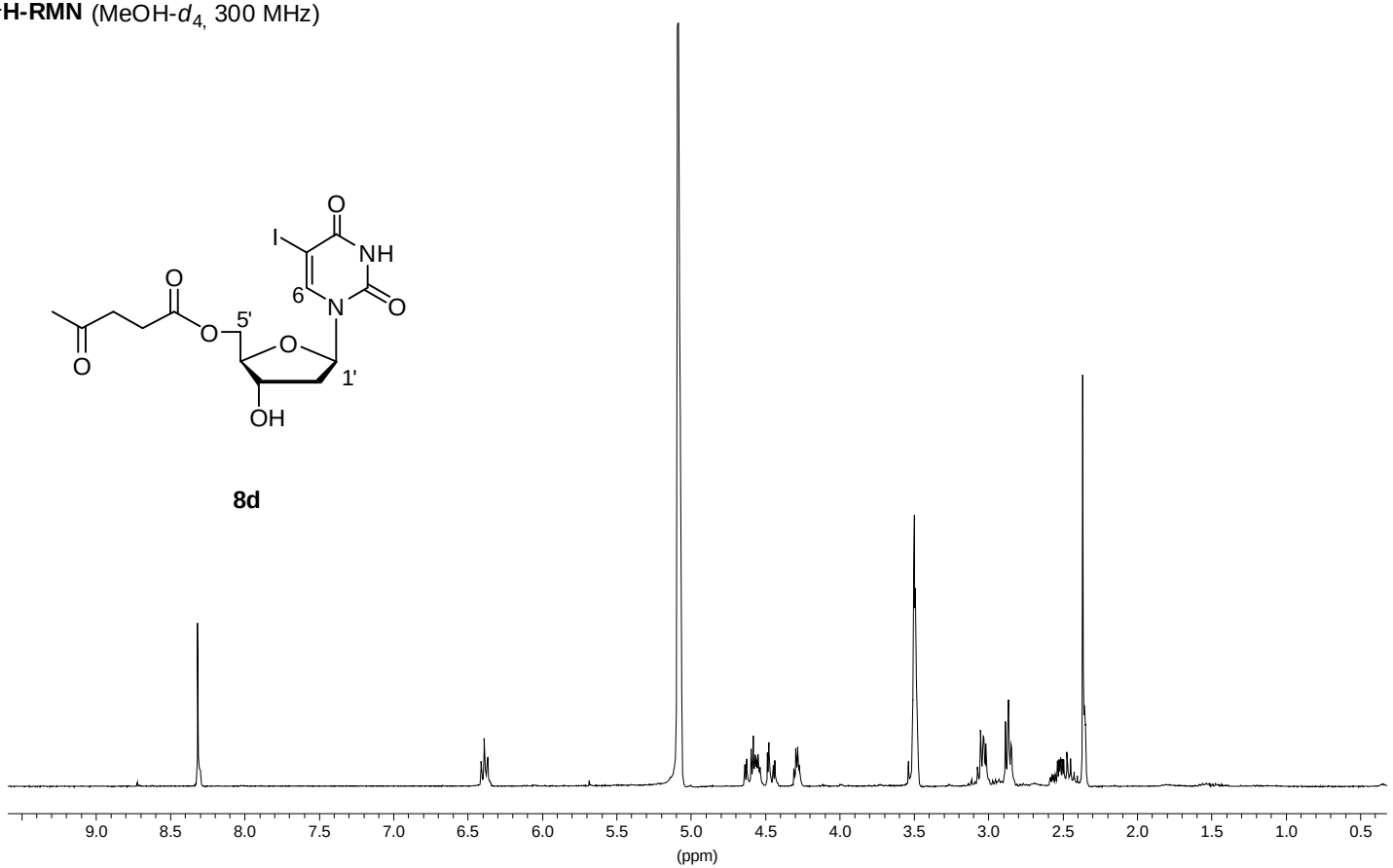
8c



5-Iodo-5'-*O*-levulinyl-2'-deoxyuridine (8d)

^{1}H-RMN (MeOH-d_4, 300 MHz)

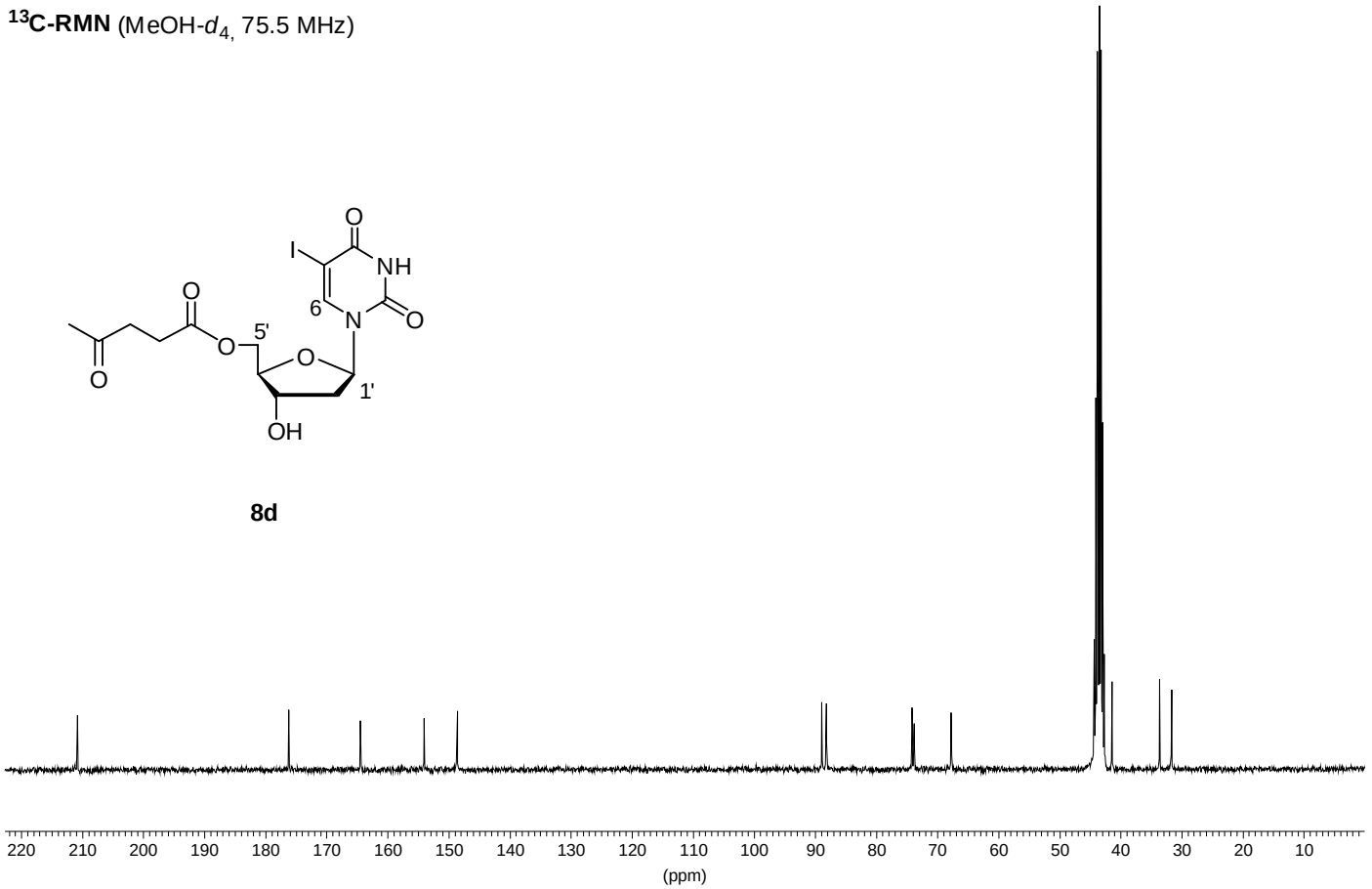
8d



5-Iodo-5'-*O*-levulinyl-2'-deoxyuridine (8d)

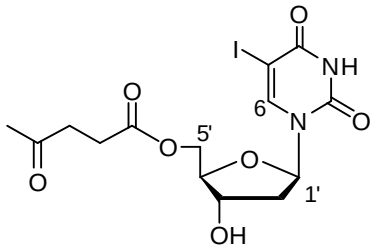
^{13}C-RMN (MeOH-d_4, 75.5 MHz)

8d

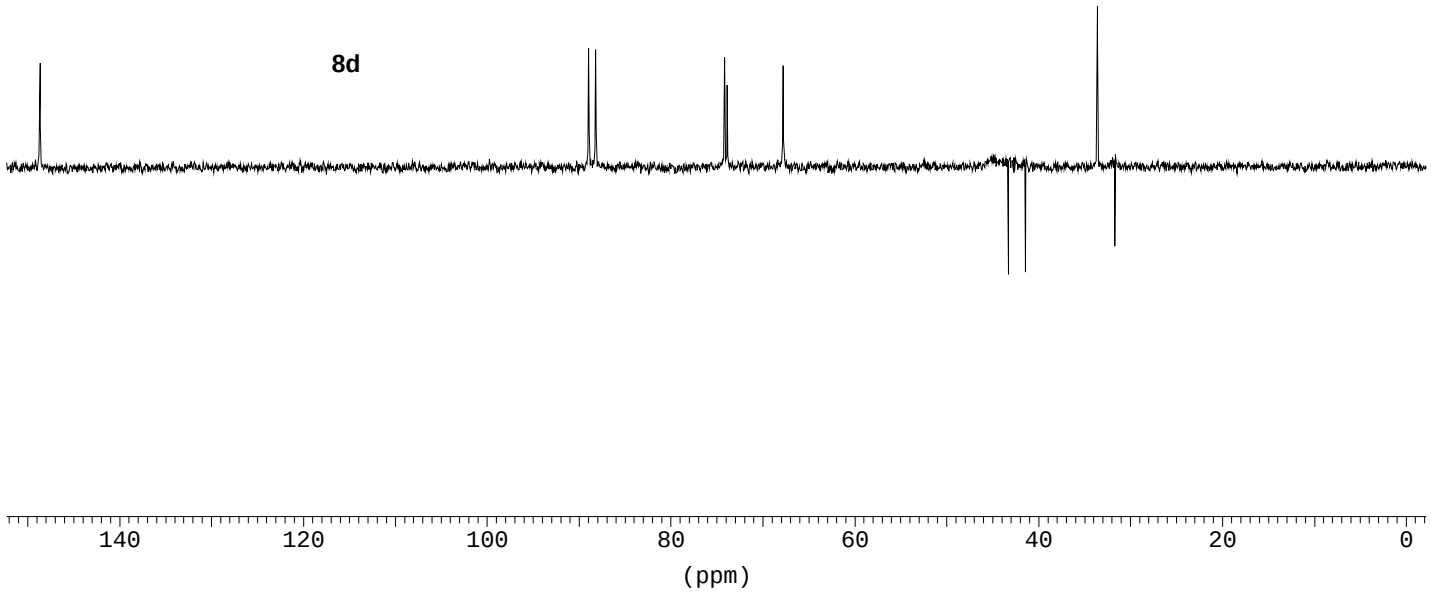


5-Iodo-5'-*O*-levulinyl-2'-deoxyuridine (8d)

DEPT (MeOH-d_4, 75.5 MHz)



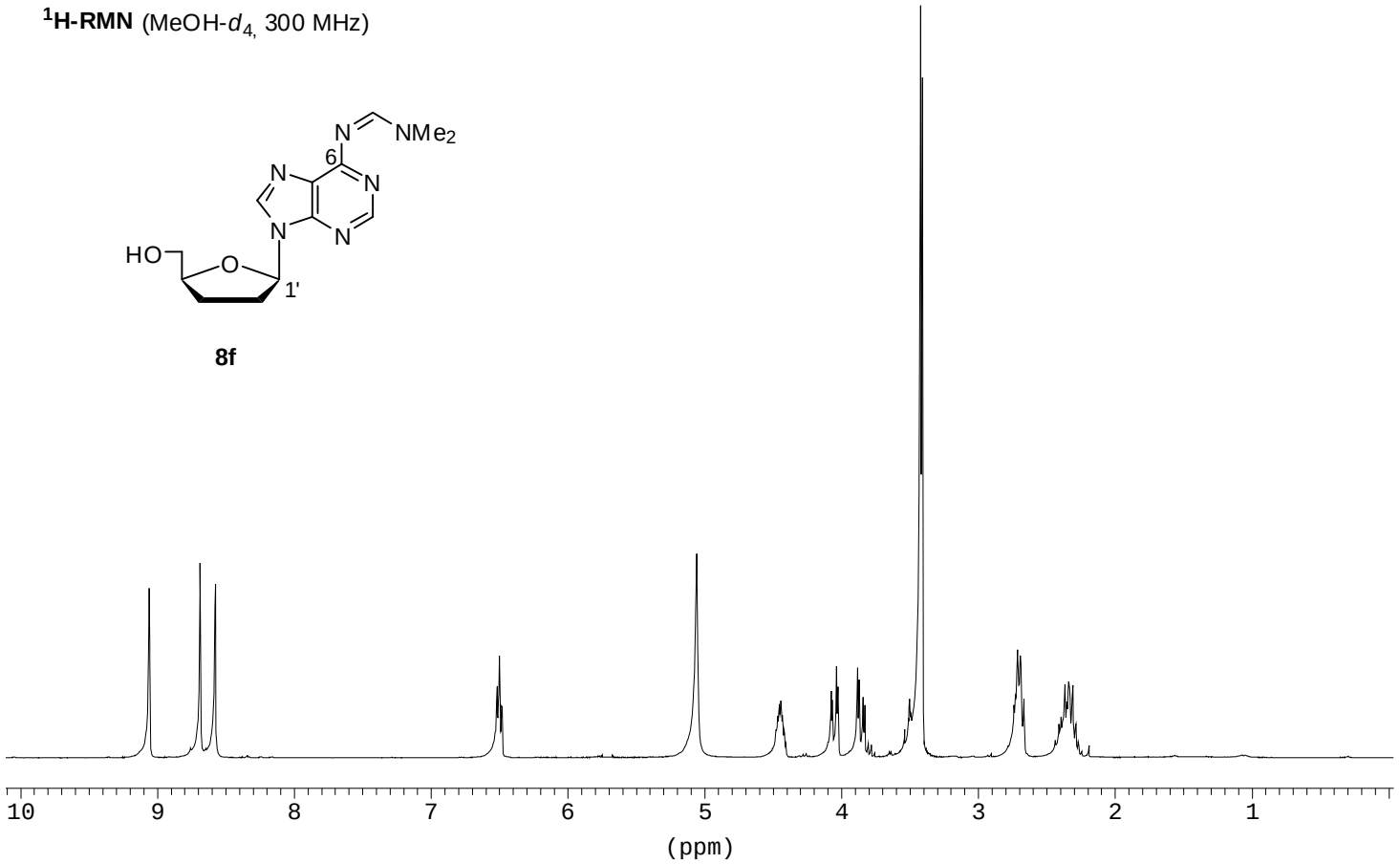
8d



N^6-(Dimethylamino)methylene-2',3'-dideoxyadenosine (8f)

^{1}H-RMN (MeOH-d_4, 300 MHz)

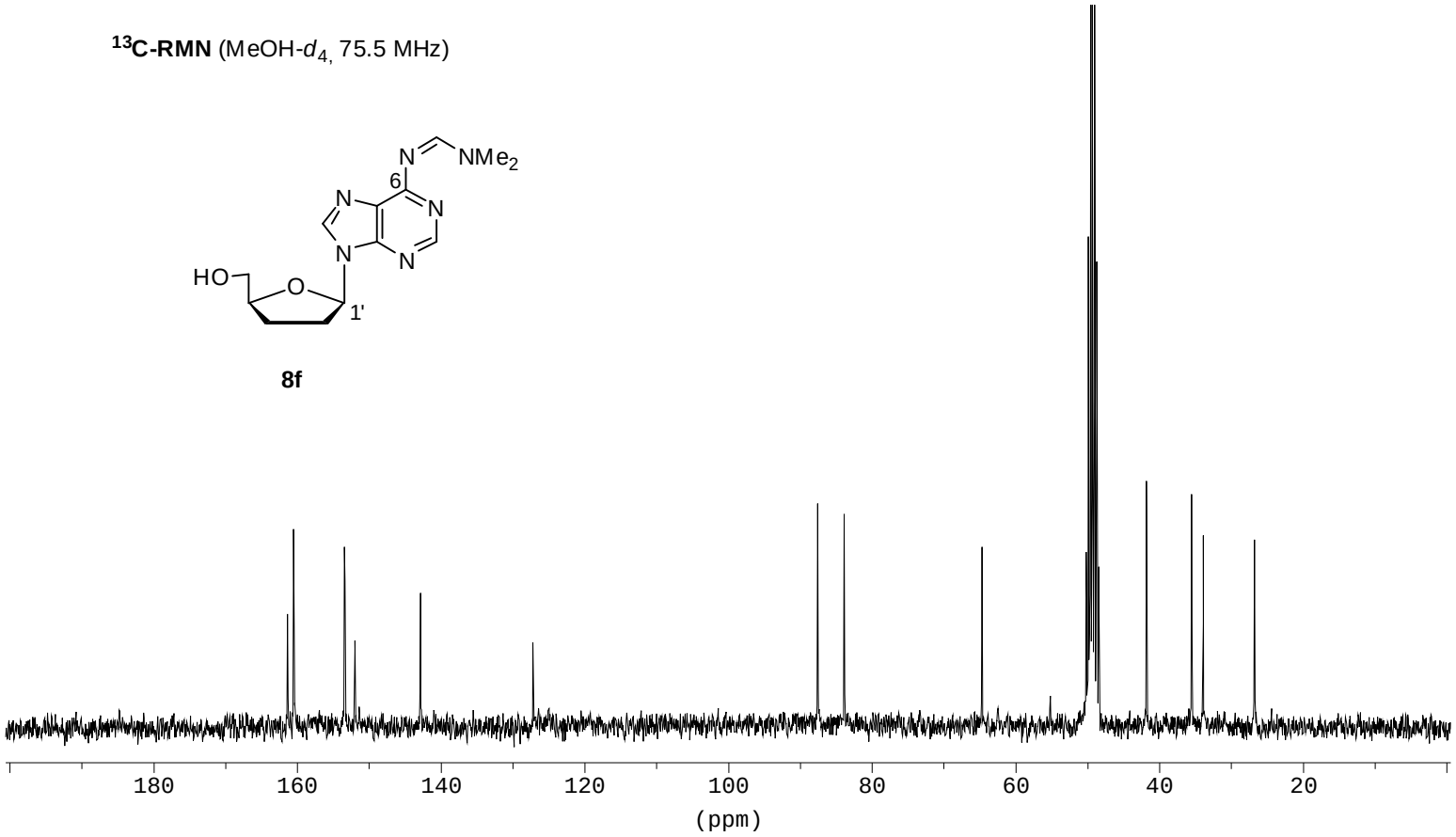
8f



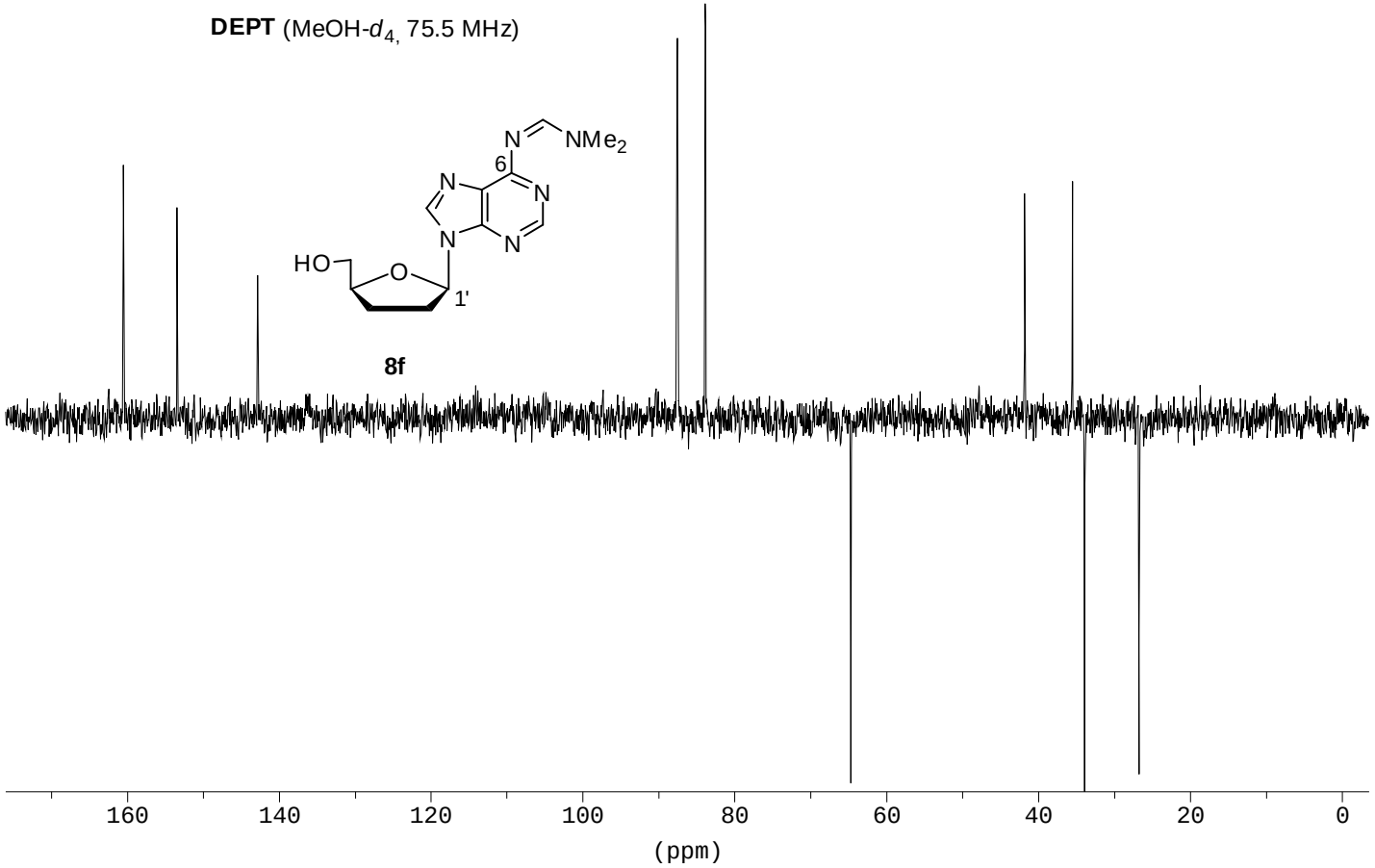
N^6-(Dimethylamino)methylene-2',3'-dideoxyadenosine (8f)

^{13}C-RMN (MeOH-d_4, 75.5 MHz)

8f



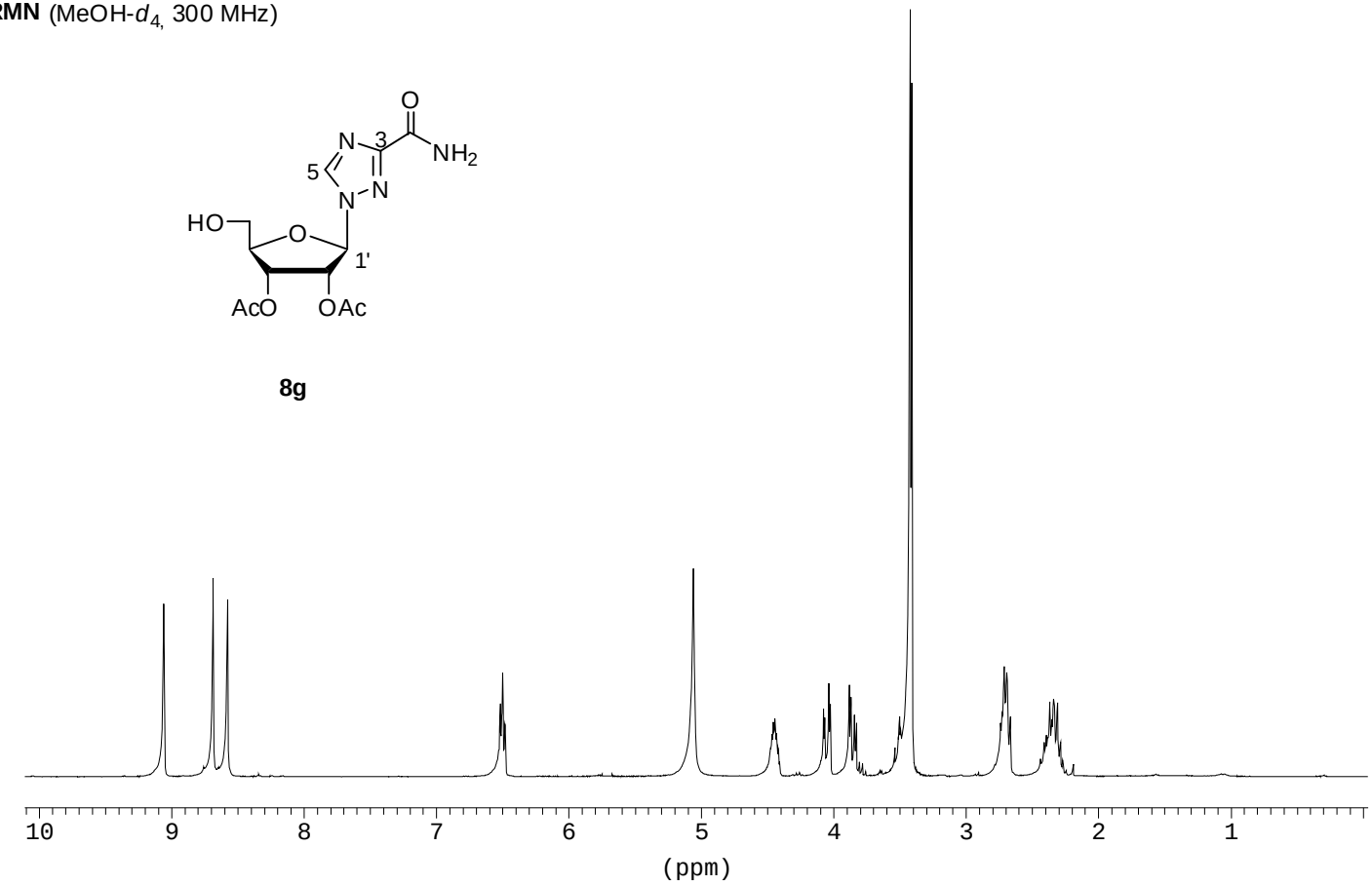
N^6-(Dimethylamino)methylene-2',3'-dideoxyadenosine (8f)



1-(2',3'-Di-*O*-acetyl-β-D-ribofuranosyl)-1*H*-1,2,4-triazole-3-carboxamide (8g)

^{1}H-RMN (MeOH-d_4, 300 MHz)

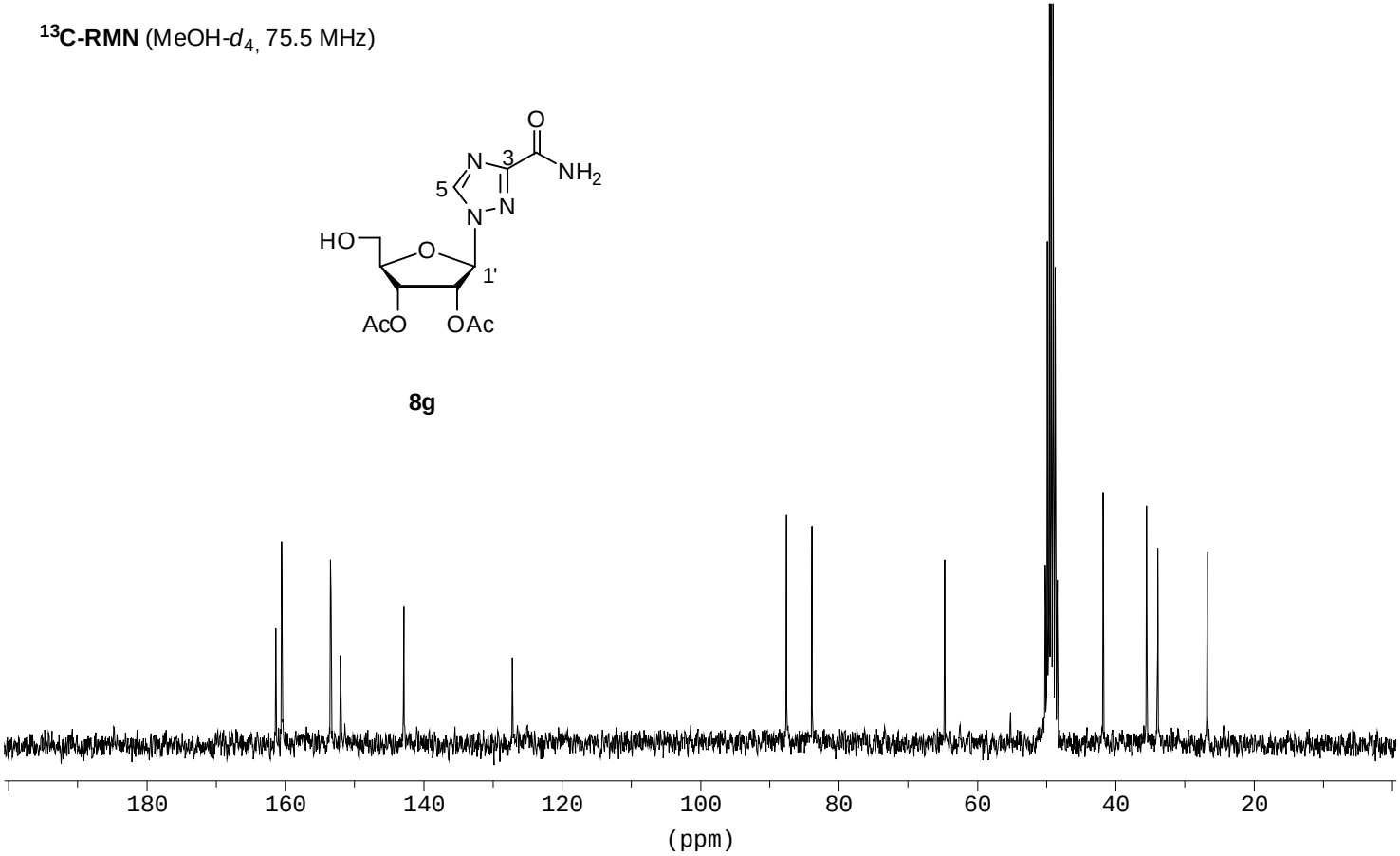
8g



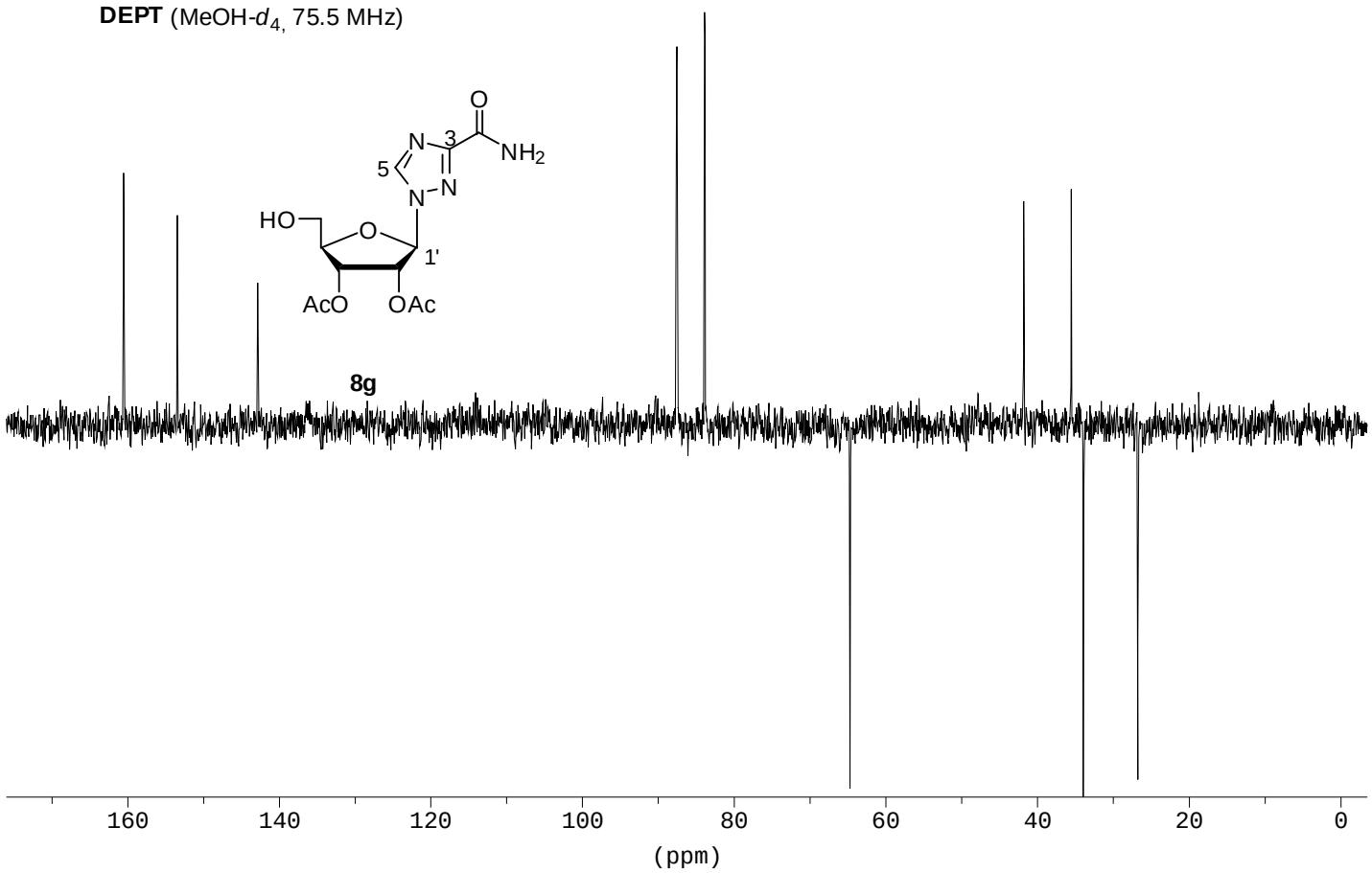
1-(2',3'-Di-*O*-acetyl-β-D-ribofuranosyl)-1*H*-1,2,4-triazole-3-carboxamide (8g)

^{13}C-RMN (MeOH-d_4, 75.5 MHz)

8g



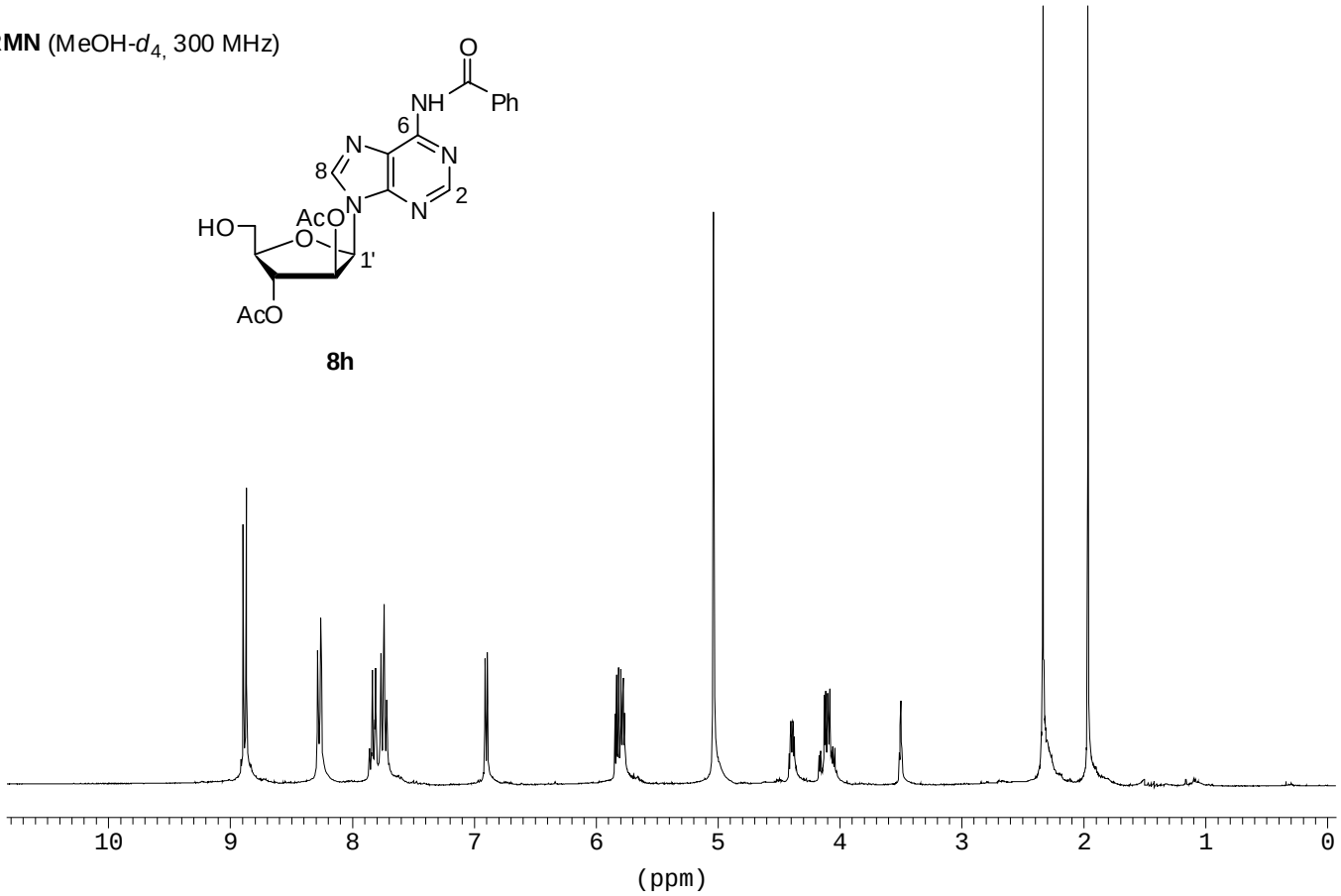
1-(2',3'-Di-*O*-acetyl-β-D-ribofuranosyl)-1*H*-1,2,4-triazole-3-carboxamide (8g)



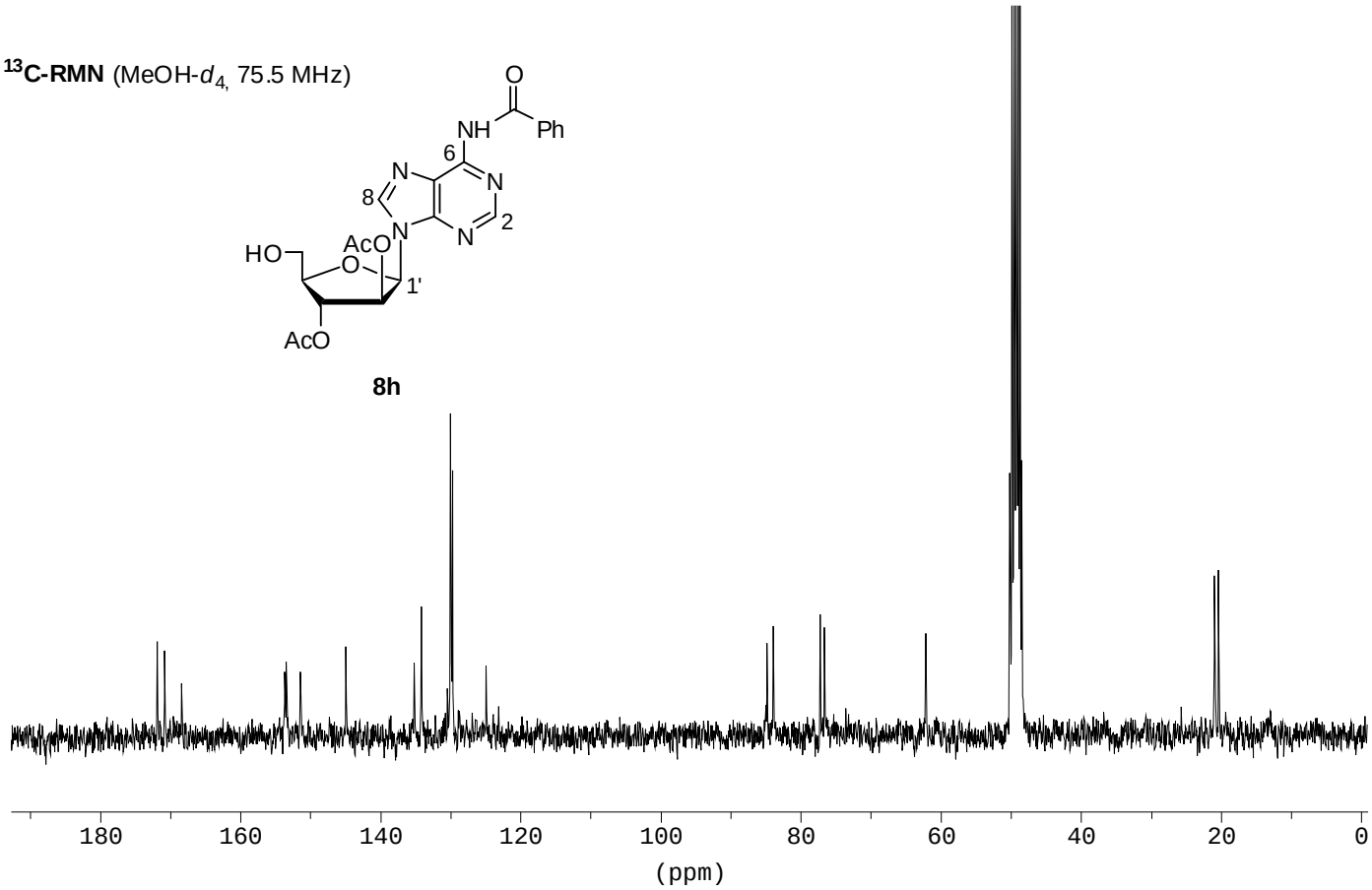
N^6-Benzoyl-9-(2',3'-di-*O*-acetyl-β-D-arabinofuranosyl)adenine (8h)

^{1}H-RMN (MeOH-d_4, 300 MHz)

8h

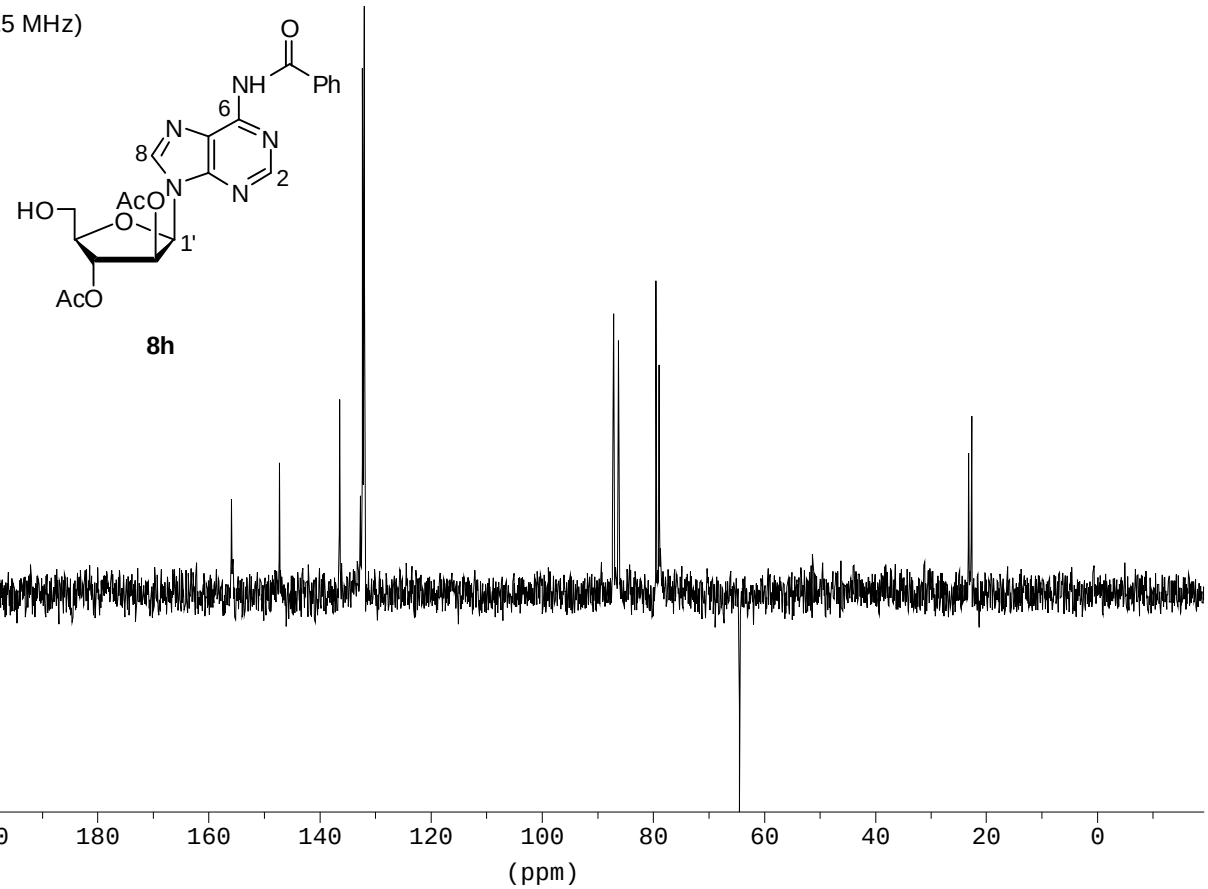


N^6-Benzoyl-9-(2',3'-di-*O*-acetyl-β-D-arabinofuranosyl)adenine (8h)



N^6-Benzoyl-9-(2',3'-di-*O*-acetyl-β-D-arabinofuranosyl)adenine (8h)

DEPT (MeOH-d_4, 75.5 MHz)

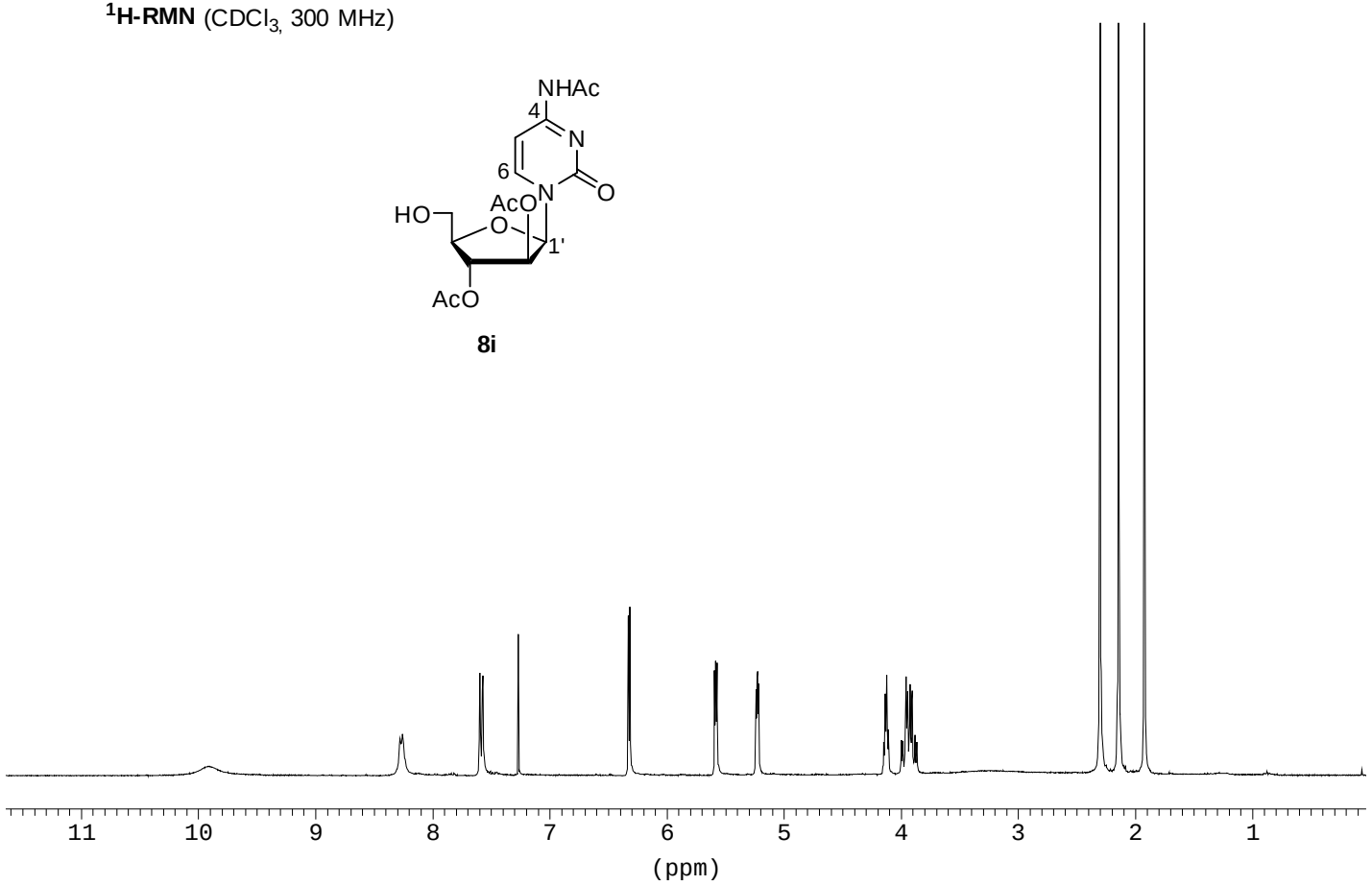


8h

N^4-Acetyl-1-(2',3'-di-*O*-acetyl-β-D-arabinofuranosyl)cytosine (8i)

^{1}H-RMN ($CDCl_3$, 300 MHz)

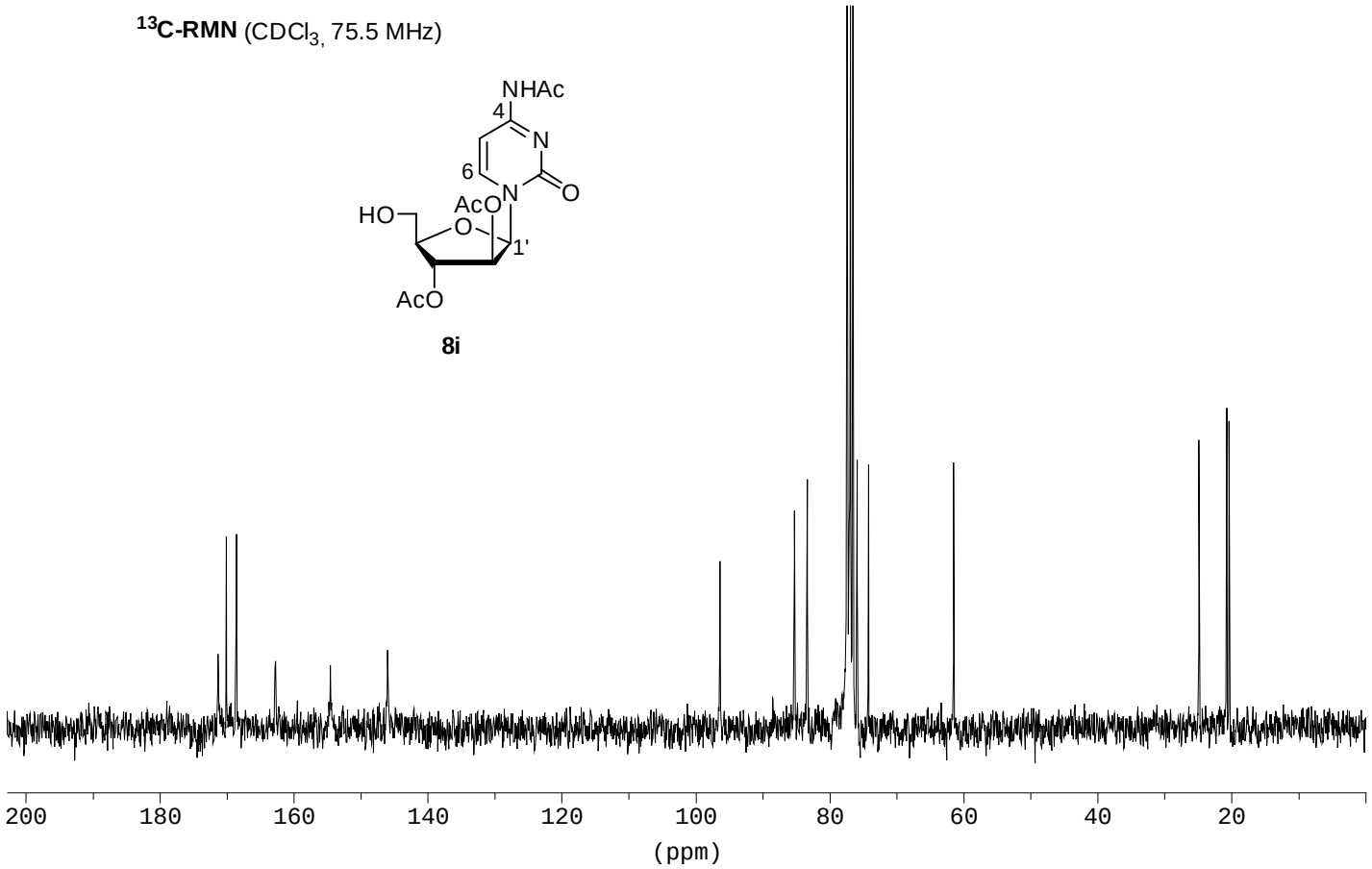
8i



N^4-Acetyl-1-(2',3'-di-*O*-acetyl-β-D-arabinofuranosyl)cytosine (8i)

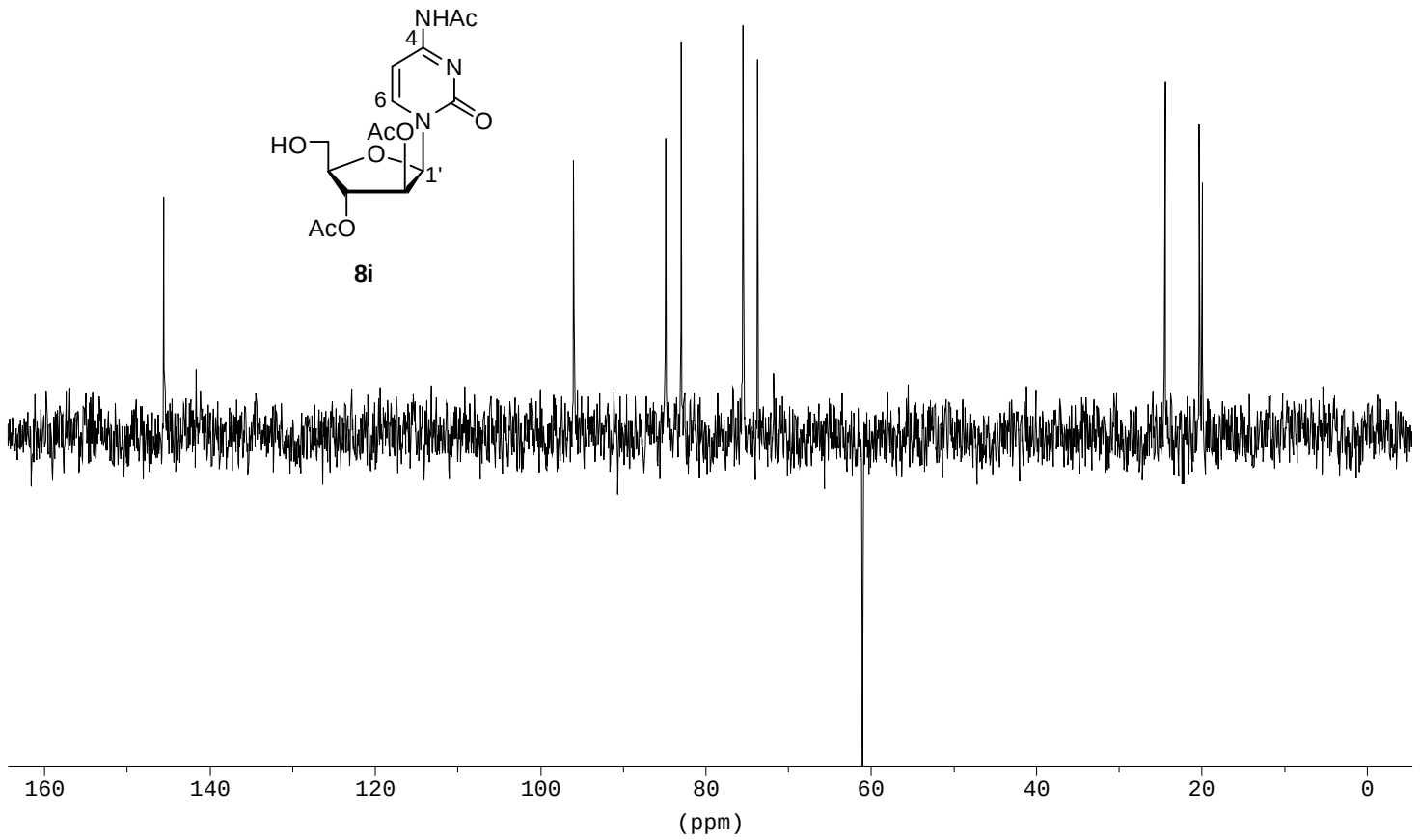
^{13}C-RMN ($CDCl_3$, 75.5 MHz)

8i



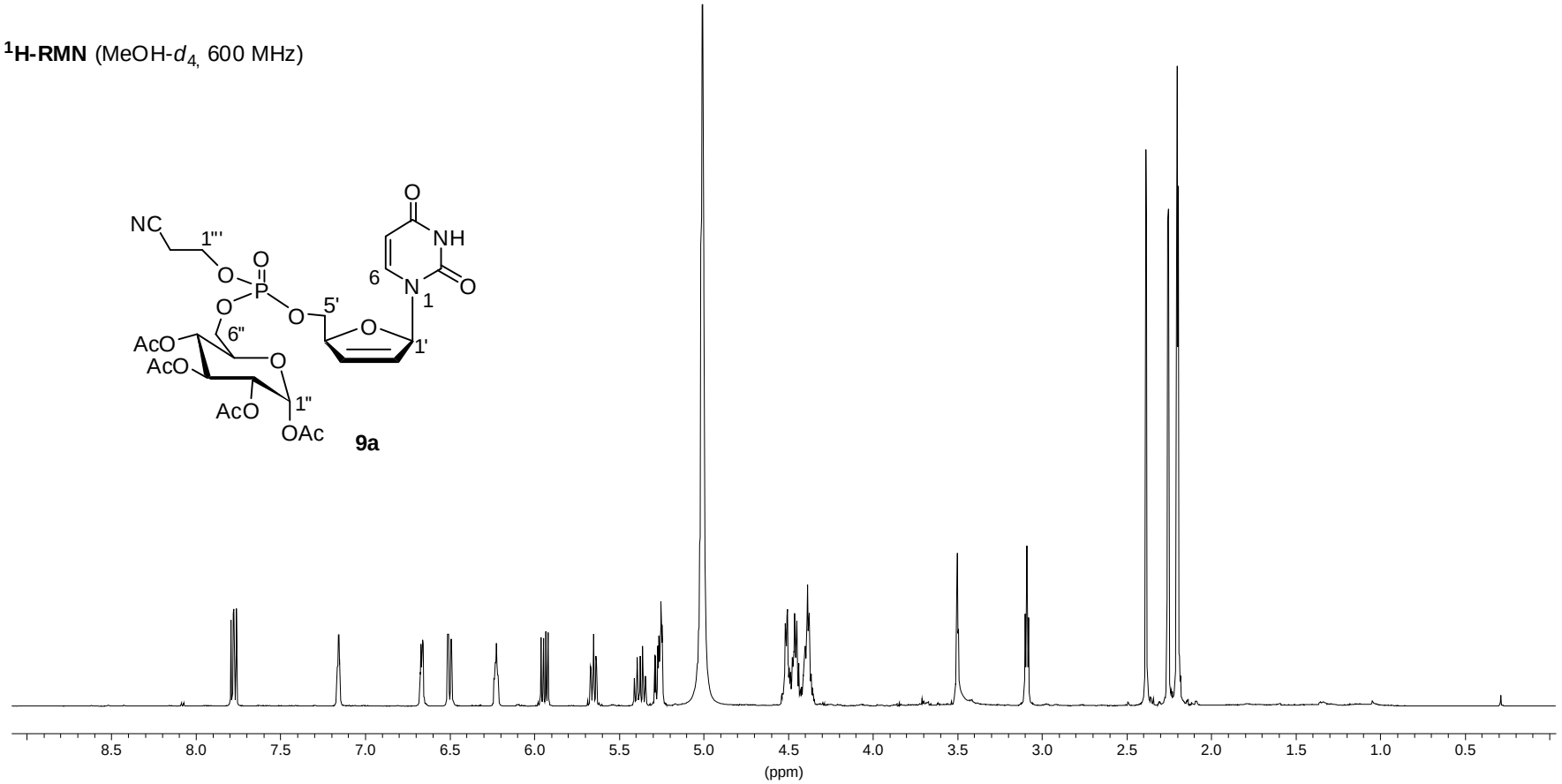
N^4-Acetyl-1-(2',3'-di-*O*-acetyl-β-D-arabinofuranosyl)cytosine (8i)

DEPT ($CDCl_3$, 75.5 MHz)



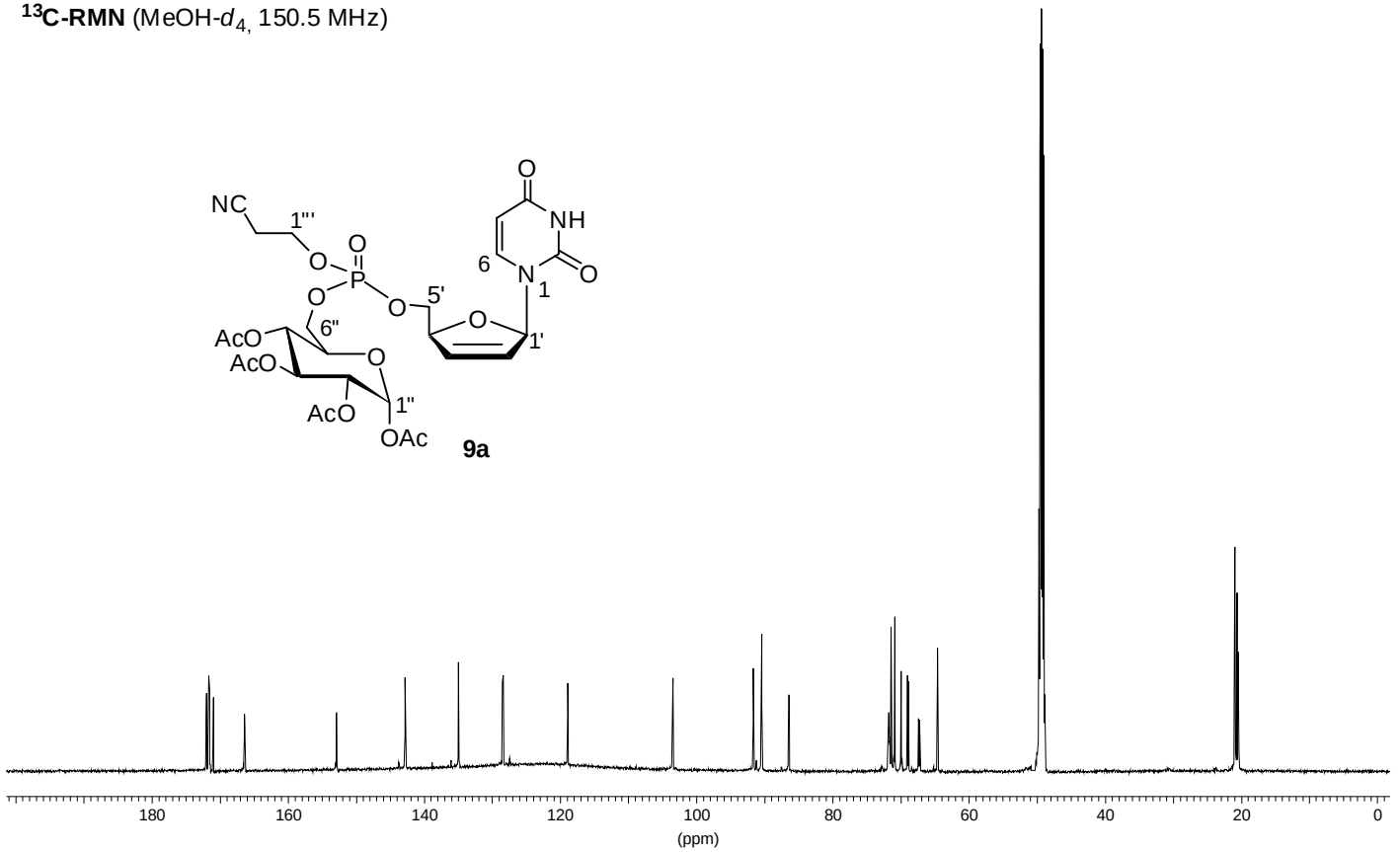
8i

2-Cyanoethyl-(2',3'-didehydro-2',3'-dideoxyuridin-5'-yl)-1,2,3,4-tetra-*O*-acetyl-α-D-glucopyranos-6-yl phosphate (9a)



2-Cyanoethyl-(2',3'-didehydro-2',3'-dideoxyuridin-5'-yl)-1,2,3,4-tetra-*O*-acetyl-α-D-glucopyranos-6-yl phosphate (9a)

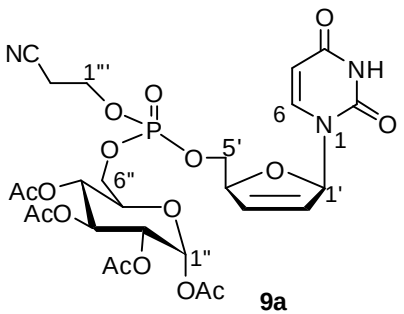
^{13}C-RMN (MeOH-d_4, 150.5 MHz)



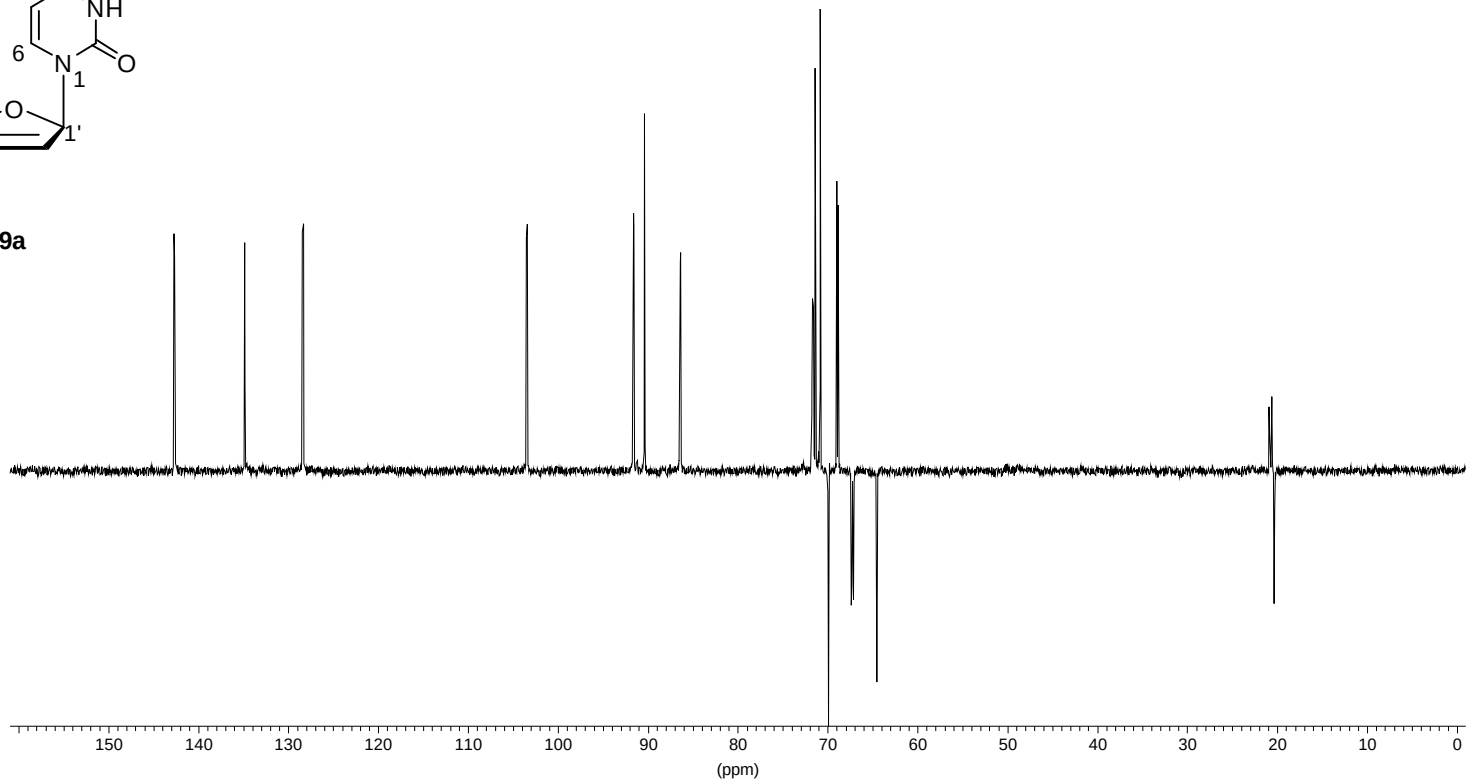
9a

2-Cyanoethyl-(2',3'-didehydro-2',3'-dideoxyuridin-5'-yl)-1,2,3,4-tetra-*O*-acetyl-α-D-glucopyranos-6-yl phosphate (9a)

DEPT (MeOH-d_4, 150.5 MHz)



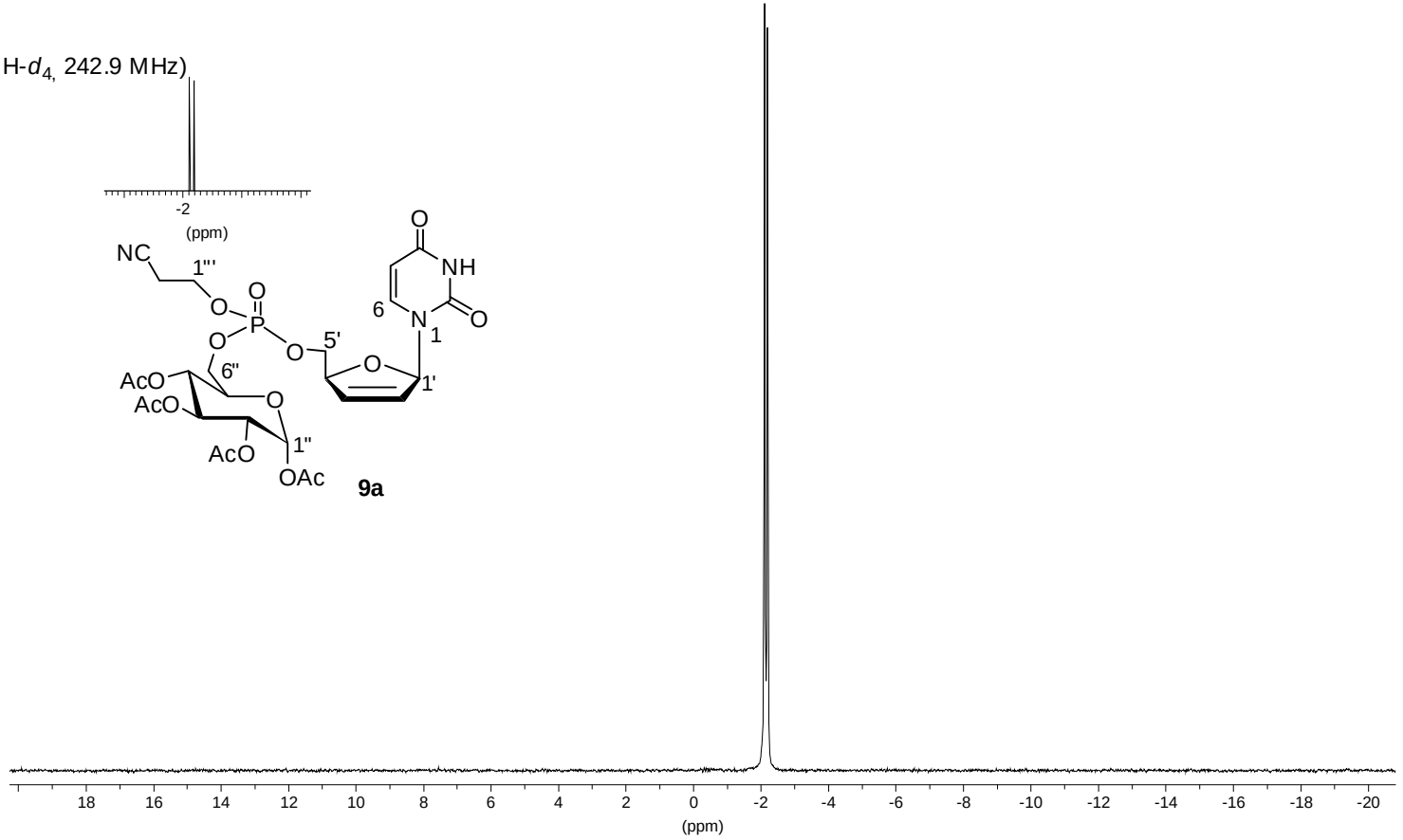
9a



2-Cyanoethyl-(2',3'-didehydro-2',3'-dideoxyuridin-5'-yl)-1,2,3,4-tetra-*O*-acetyl-α-D-glucopyranos-6-yl phosphate (9a)

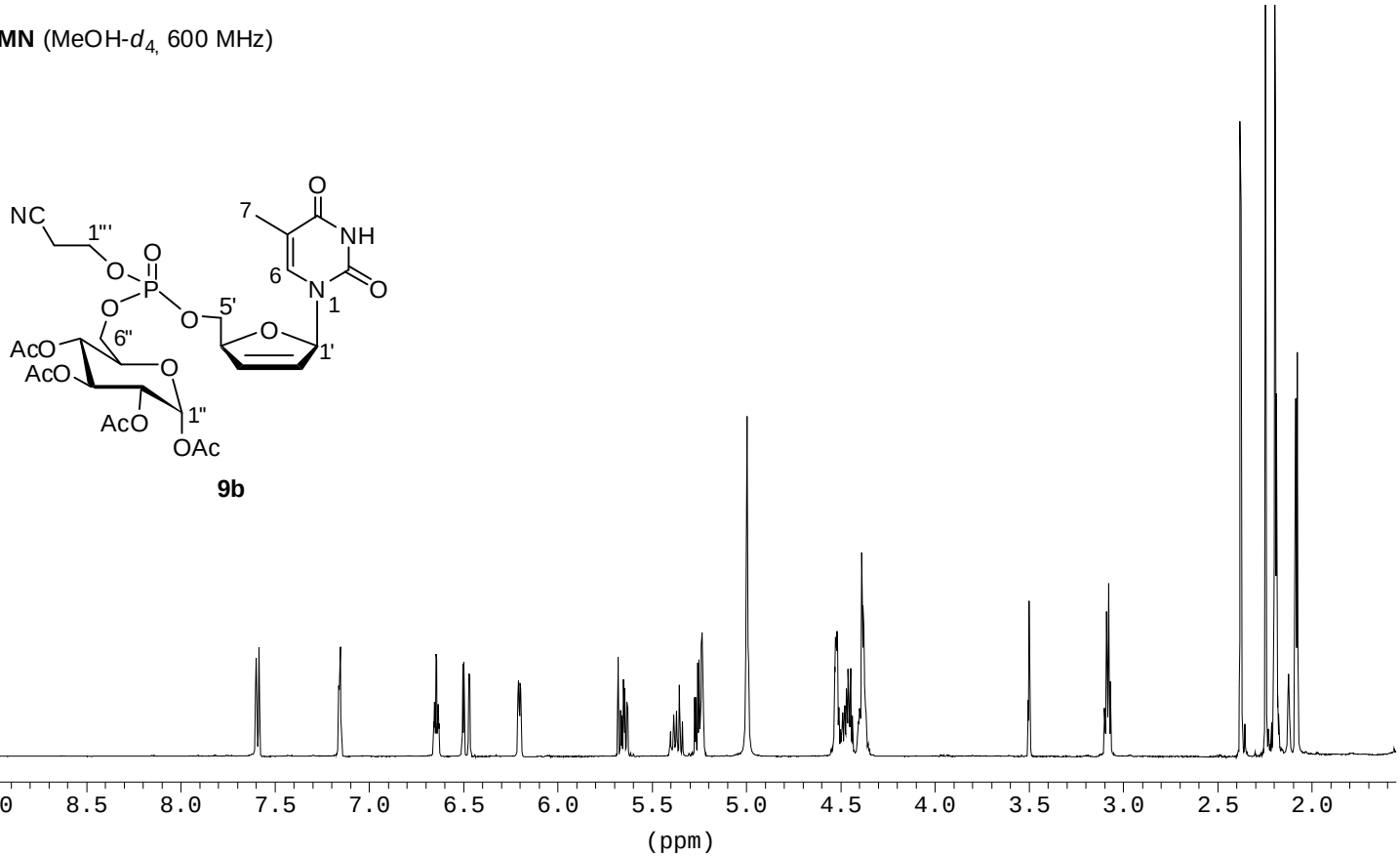
^{31}P-RMN (MeOH-d_4, 242.9 MHz)

9a



2-Cyanoethyl-(2',3'-didehydro-2',3'-dideoxythymidin-5'-yl)-1,2,3,4-tetra-*O*-acetyl-α-D-glucopyranos-6-yl phosphate (9b)

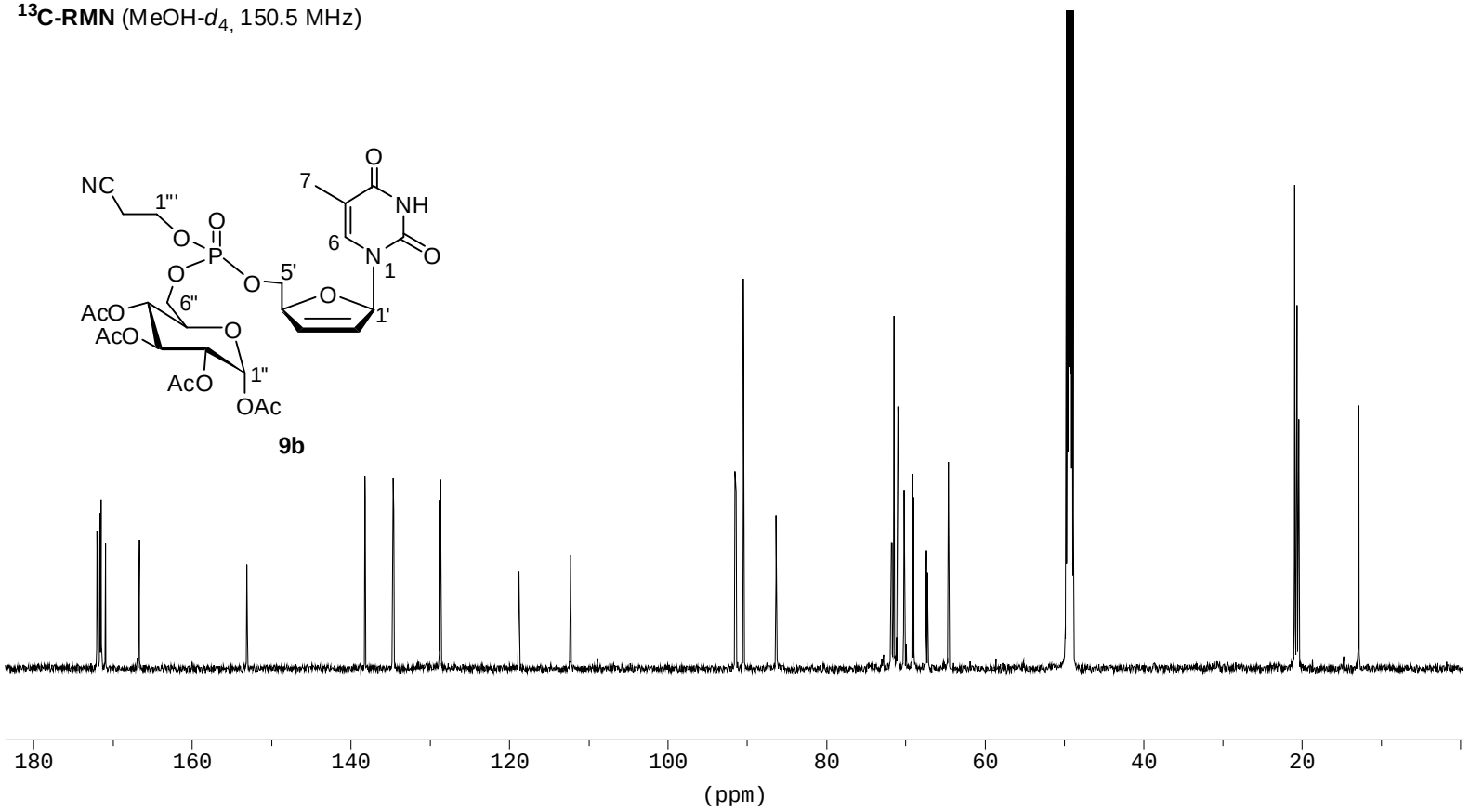
^{1}H-RMN (MeOH-d_4, 600 MHz)



9b

2-Cyanoethyl-(2',3'-didehydro-2',3'-dideoxythymidin-5'-yl)-1,2,3,4-tetra-*O*-acetyl-α-D-glucopyranos-6-yl phosphate (9b)

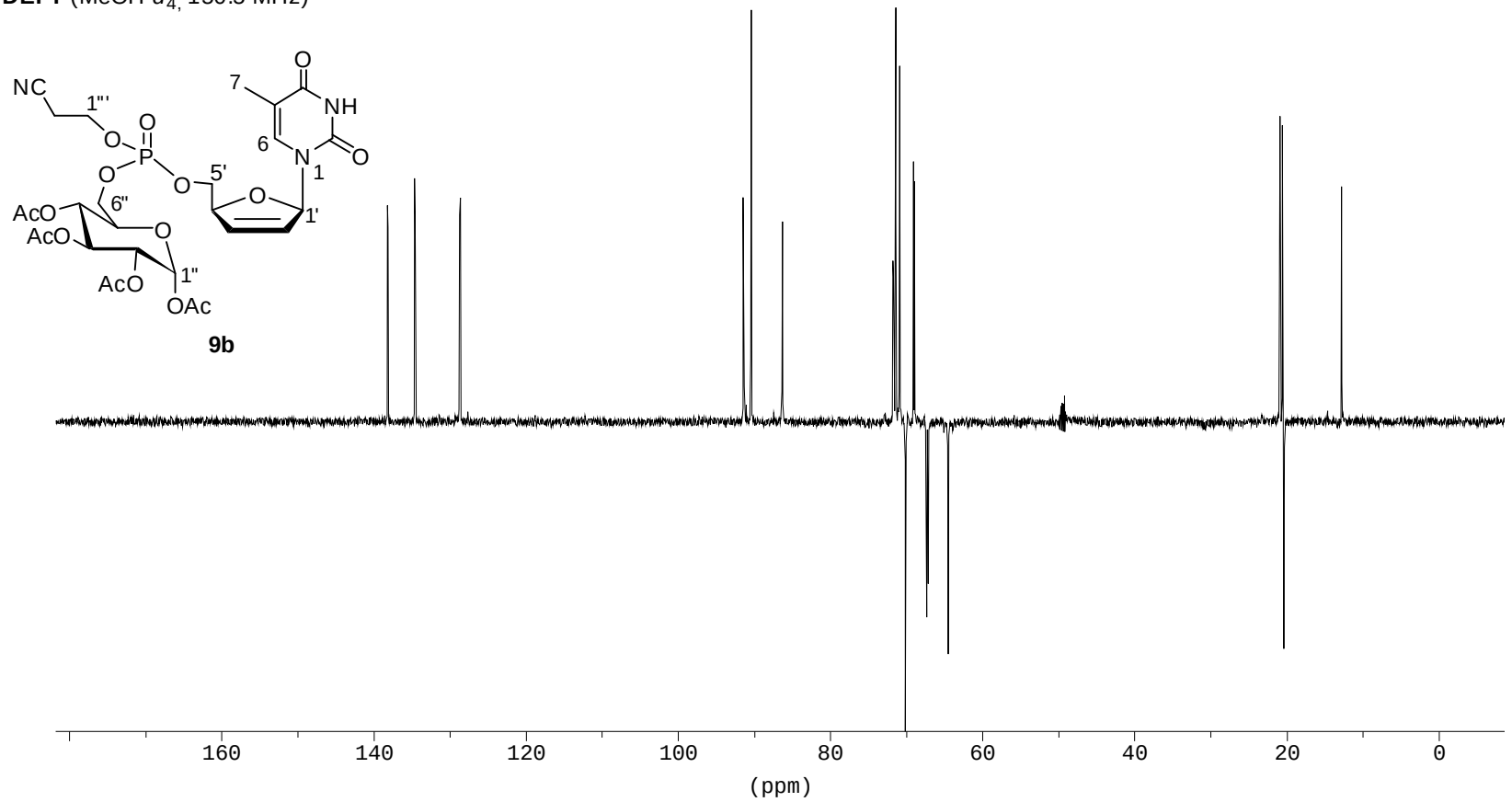
^{13}C-RMN (MeOH-d_4, 150.5 MHz)



9b

2-Cyanoethyl-(2',3'-didehydro-2',3'-dideoxythymidin-5'-yl)-1,2,3,4-tetra-*O*-acetyl-α-D-glucopyranos-6-yl phosphate (9b)

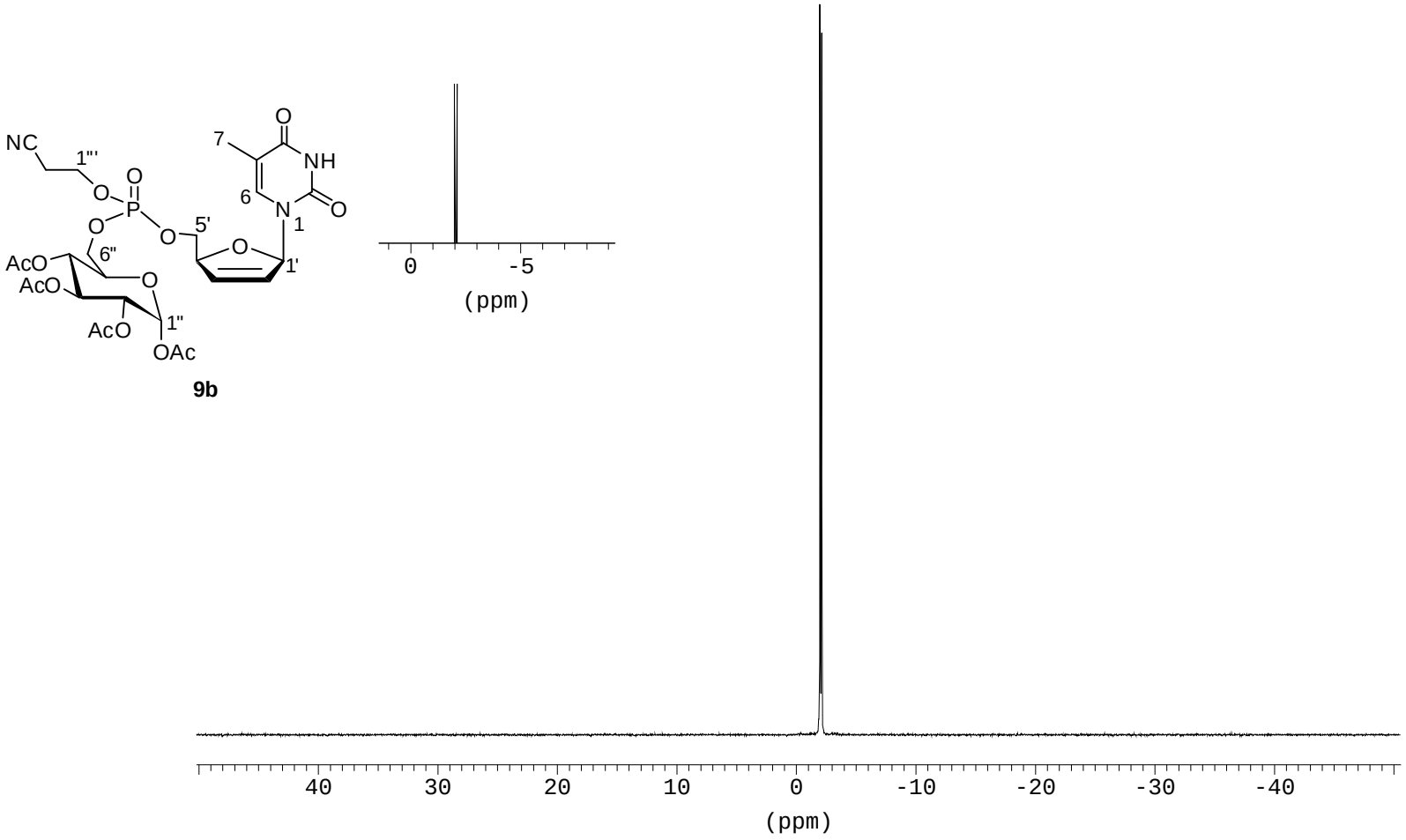
DEPT (MeOH-d_4, 150.5 MHz)



9b

2-Cyanoethyl-(2',3'-didehydro-2',3'-dideoxythymidin-5'-yl)-1,2,3,4-tetra-*O*-acetyl-α-D-glucopyranos-6-yl phosphate (9b)

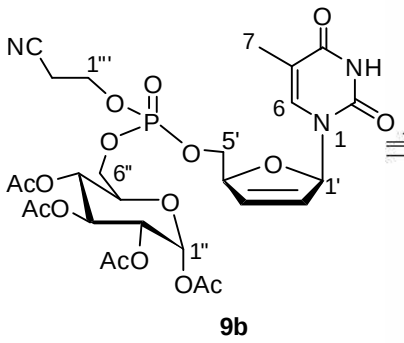
^{31}P-RMN (MeOH-d_4, 242.9 MHz)



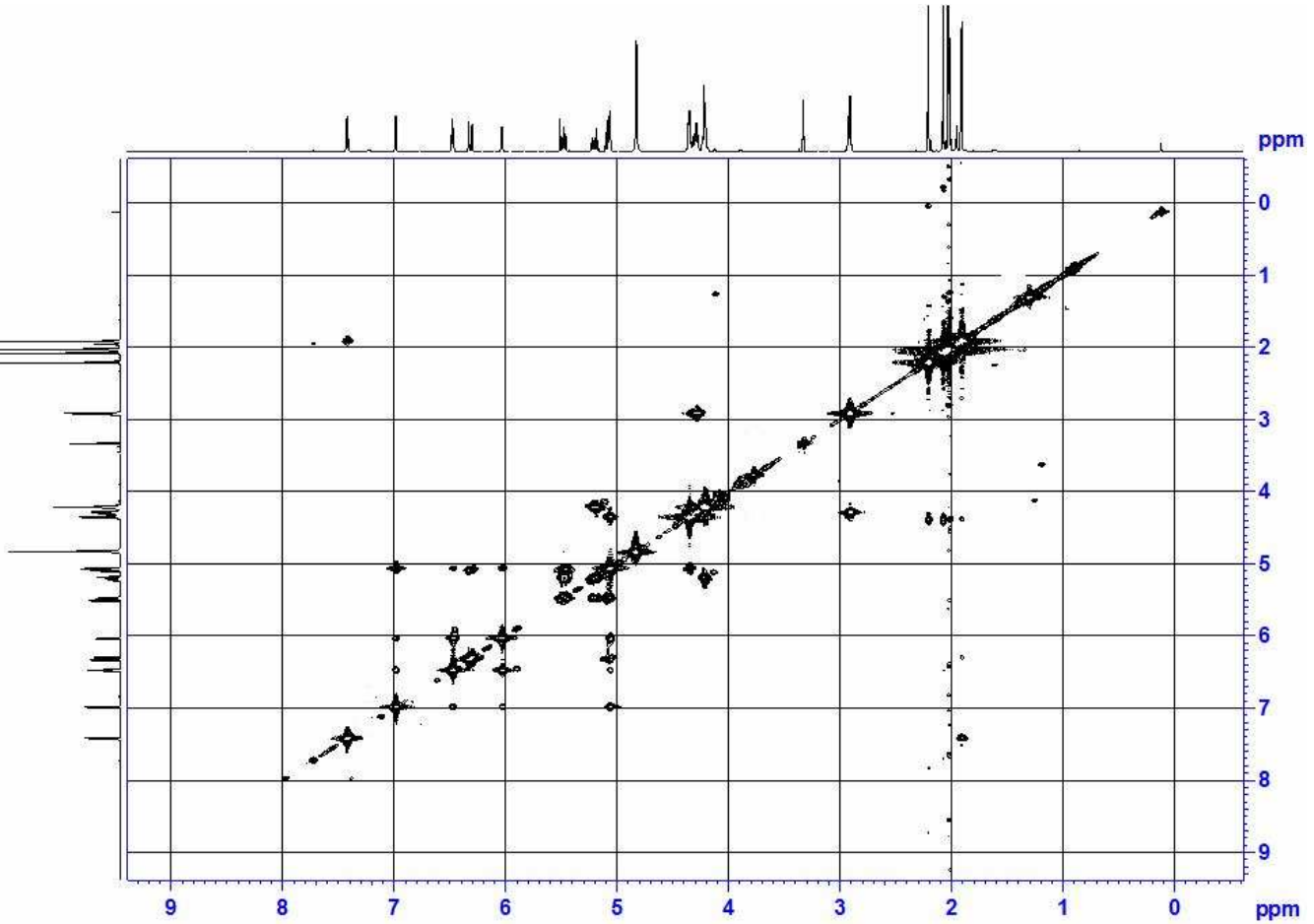
9b

2-Cyanoethyl-(2',3'-didehydro-2',3'-dideoxythymidin-5'-yl)-1,2,3,4-tetra-*O*-acetyl-α-D-glucopyranos-6-yl phosphate (9b)

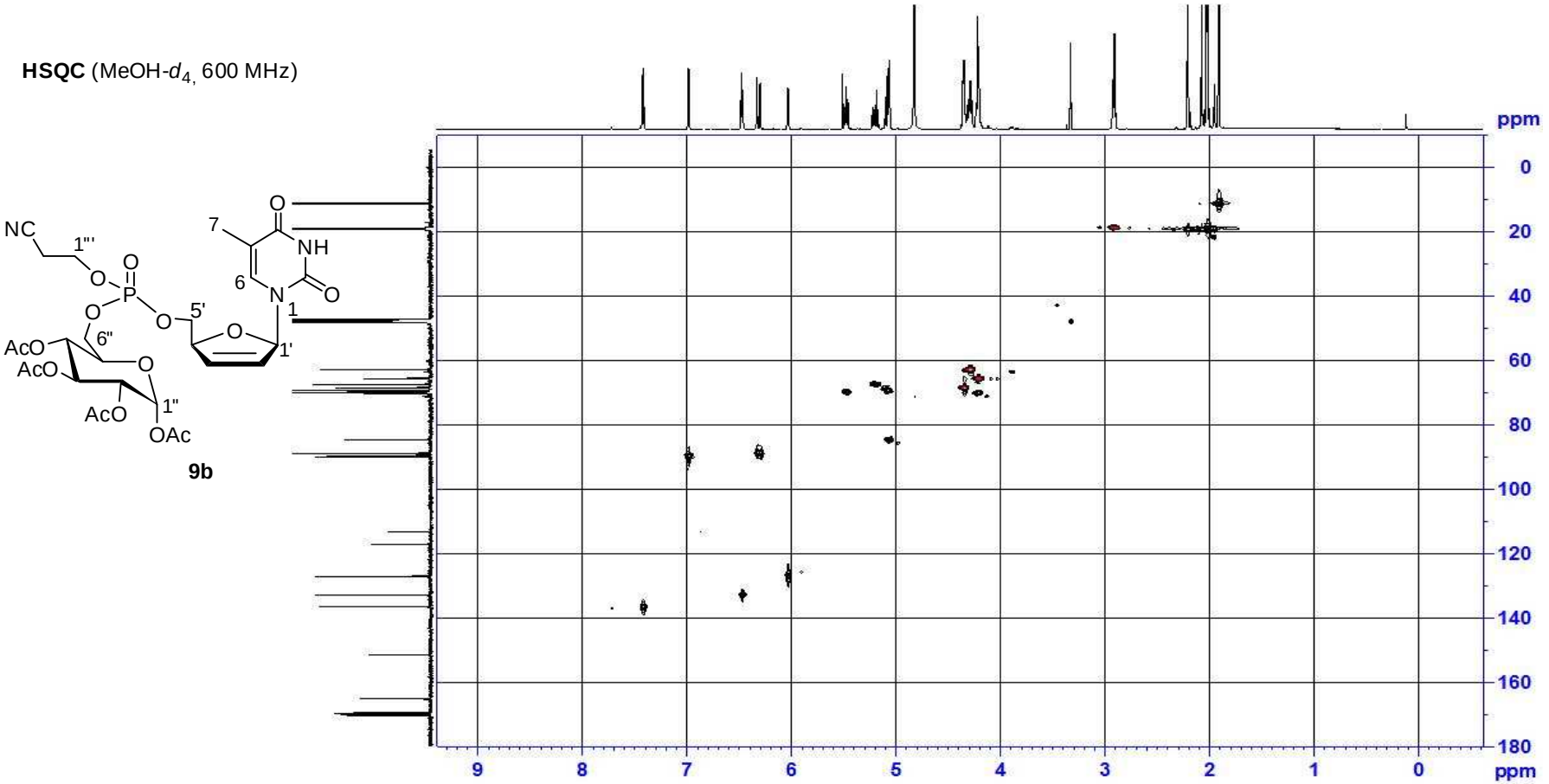
COSY (MeOH-d_4, 600 MHz)



9b

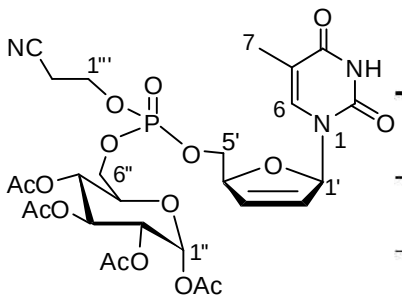


2-Cyanoethyl-(2',3'-didehydro-2',3'-dideoxythymidin-5'-yl)-1,2,3,4-tetra-*O*-acetyl-α-D-glucopyranos-6-yl phosphate (9b)

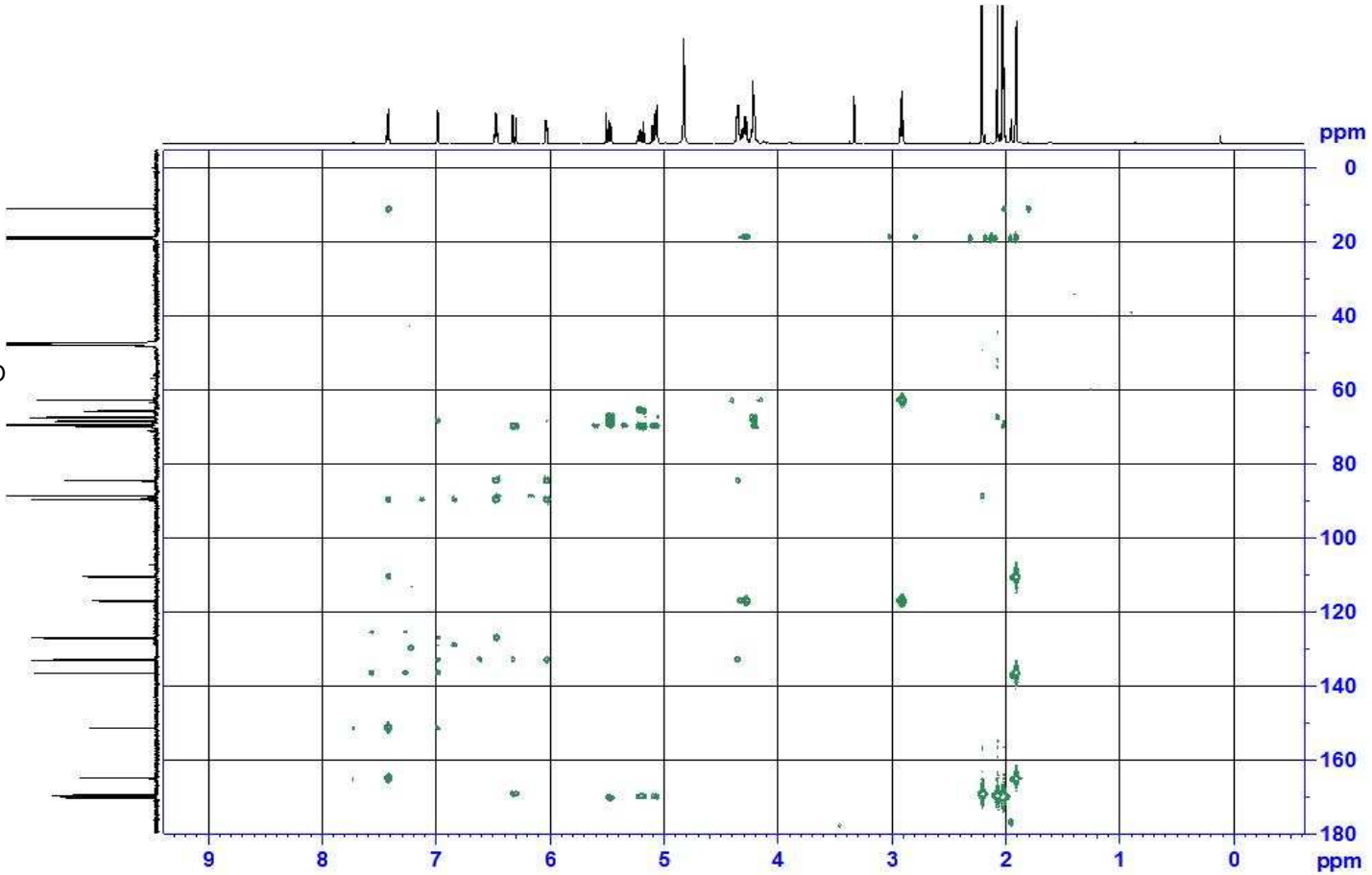


2-Cyanoethyl-(2',3'-didehydro-2',3'-dideoxythymidin-5'-yl)-1,2,3,4-tetra-*O*-acetyl-α-D-glucopyranos-6-yl phosphate (9b)

HMBC (MeOH-d_4, 600 MHz)



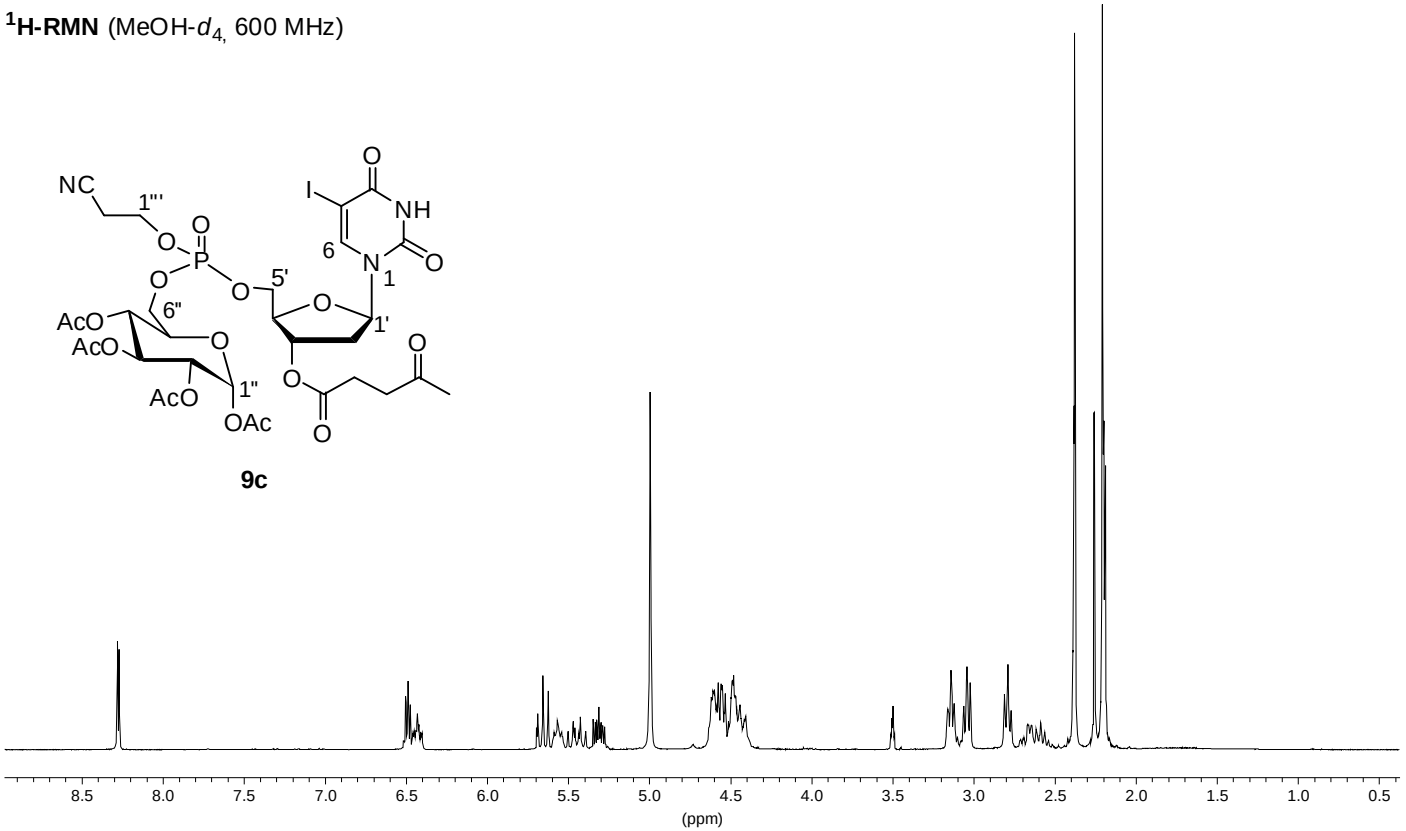
9b



2-Cyanoethyl-(3'-*O*-levulinyl-5-iodo-2'-deoxyuridin-5'-yl)-1,2,3,4-tetra-*O*-acetyl-α-D-glucopyranos-6-yl phosphate (9c)

^{1}H-RMN (MeOH-d_4, 600 MHz)

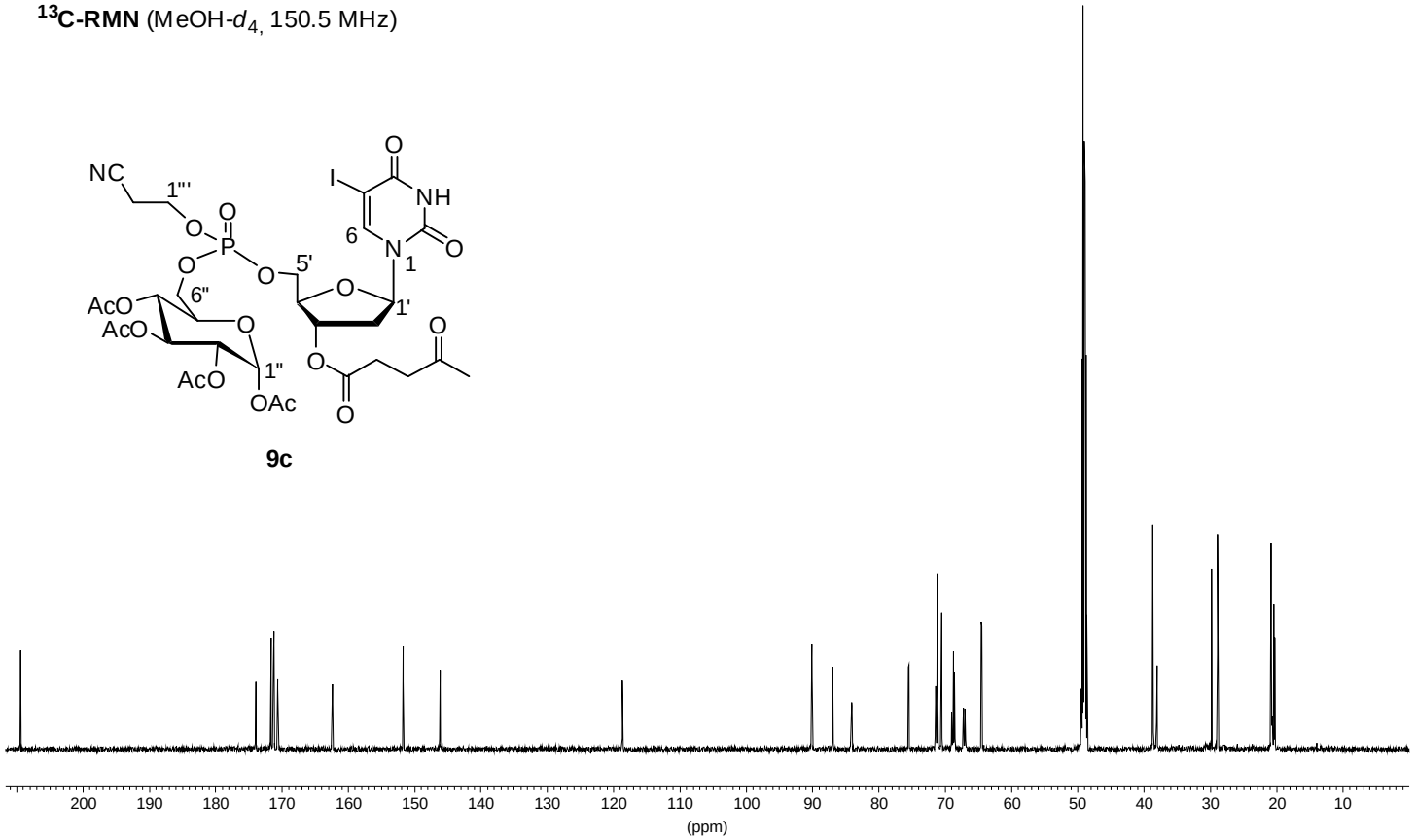
9c



2-Cyanoethyl-(3'-*O*-levulinyl-5-iodo-2'-deoxyuridin-5'-yl)-1,2,3,4-tetra-*O*-acetyl-α-D-glucopyranos-6-yl phosphate (9c)

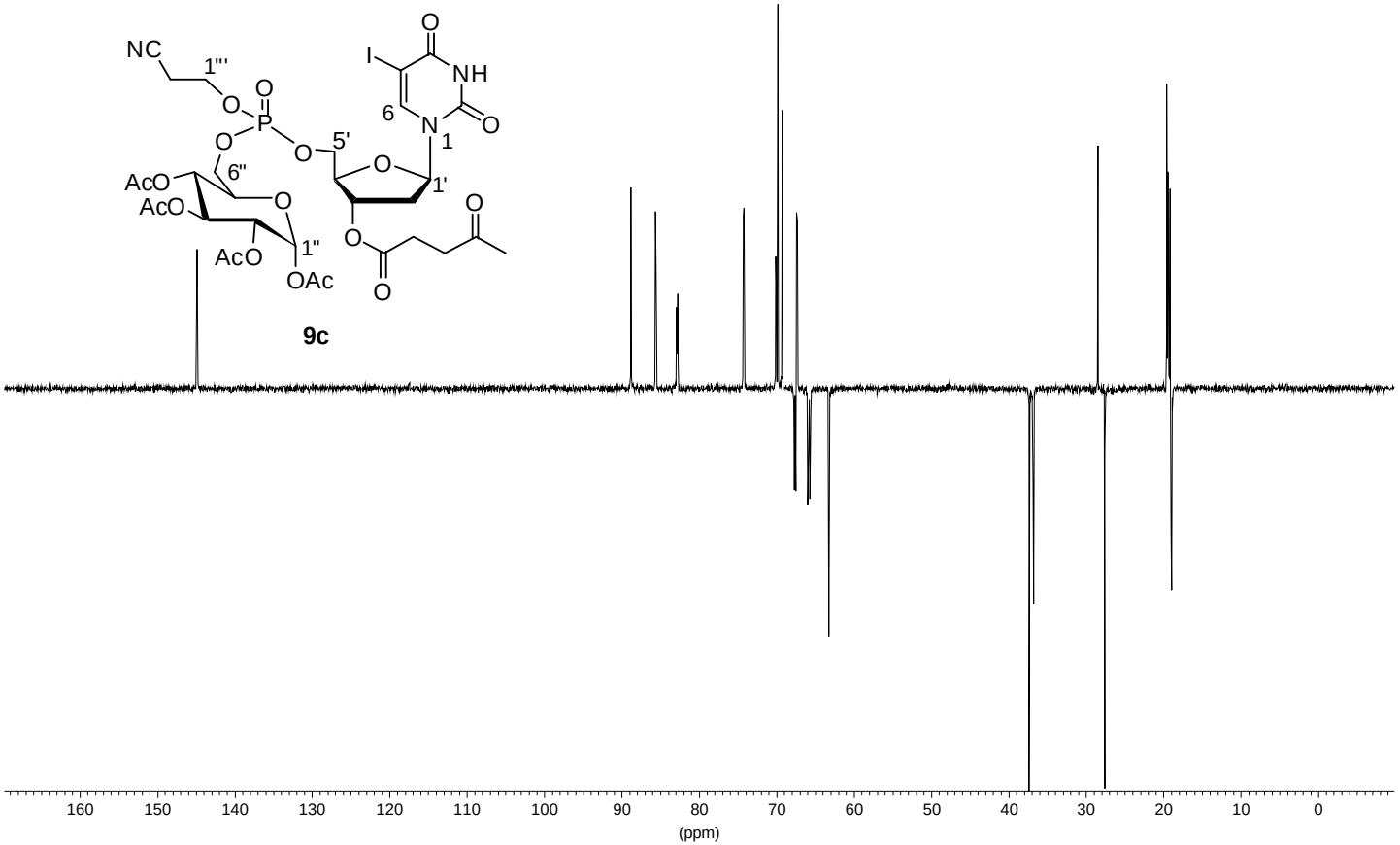
^{13}C-RMN (MeOH-d_4, 150.5 MHz)

9c



2-Cyanoethyl-(3'-*O*-levulinyl-5-iodo-2'-deoxyuridin-5'-yl)-1,2,3,4-tetra-*O*-acetyl-α-D-glucopyranos-6-yl phosphate (9c)

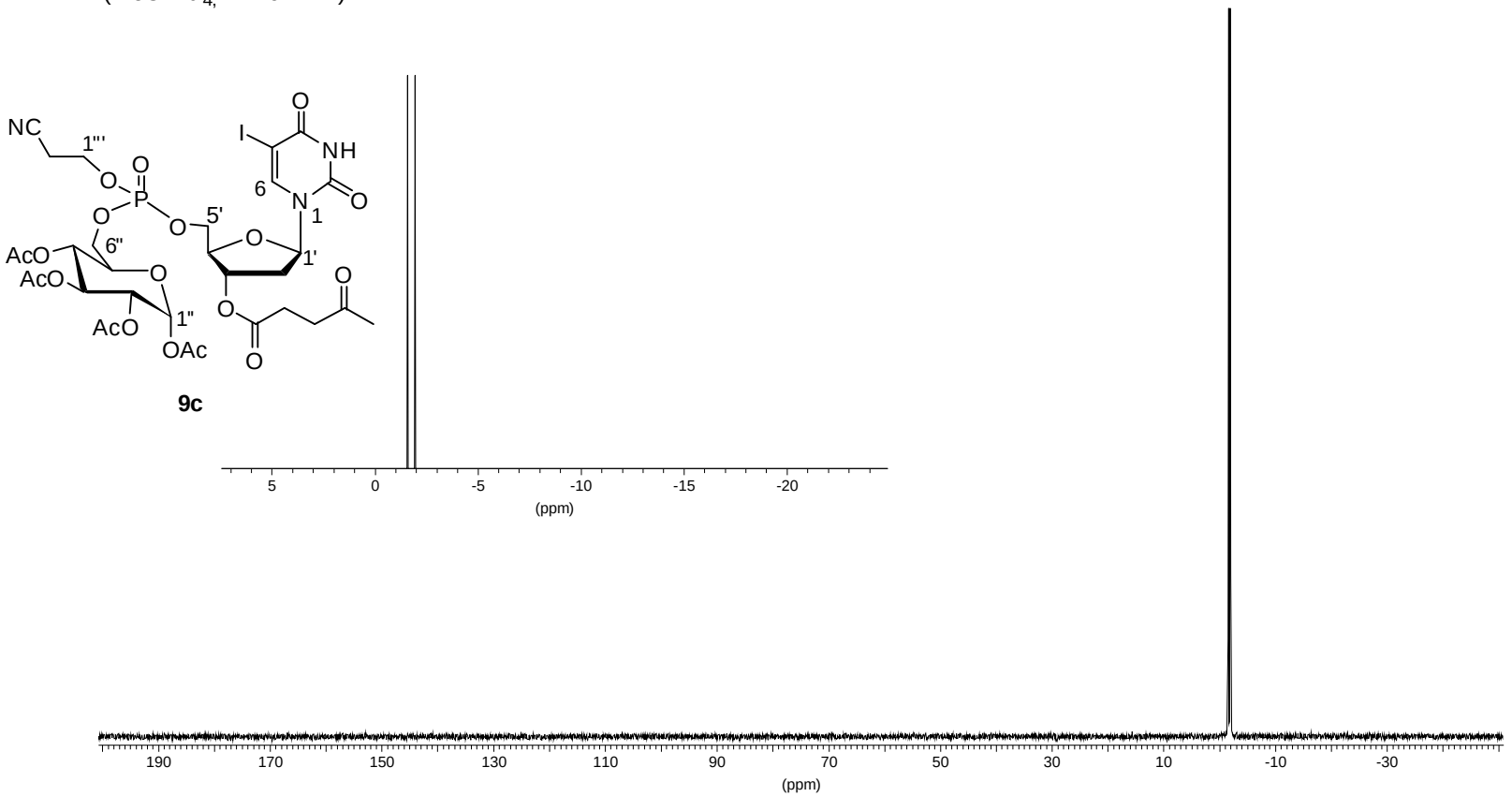
DEPT (MeOH-d_4, 150.5 MHz)



9c

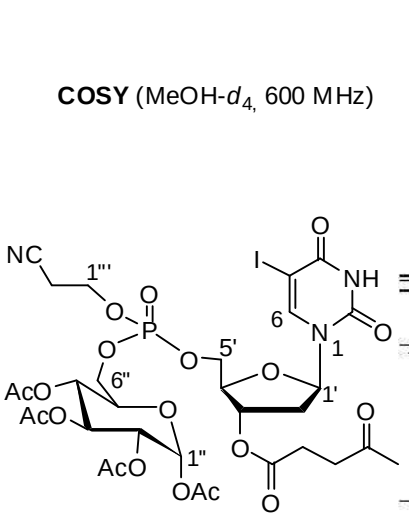
2-Cyanoethyl-(3'-*O*-levulinyl-5-iodo-2'-deoxyuridin-5'-yl)-1,2,3,4-tetra-*O*-acetyl-α-D-glucopyranos-6-yl phosphate (9c)

^{31}P-RMN (MeOH-d_4, 242.9 MHz)

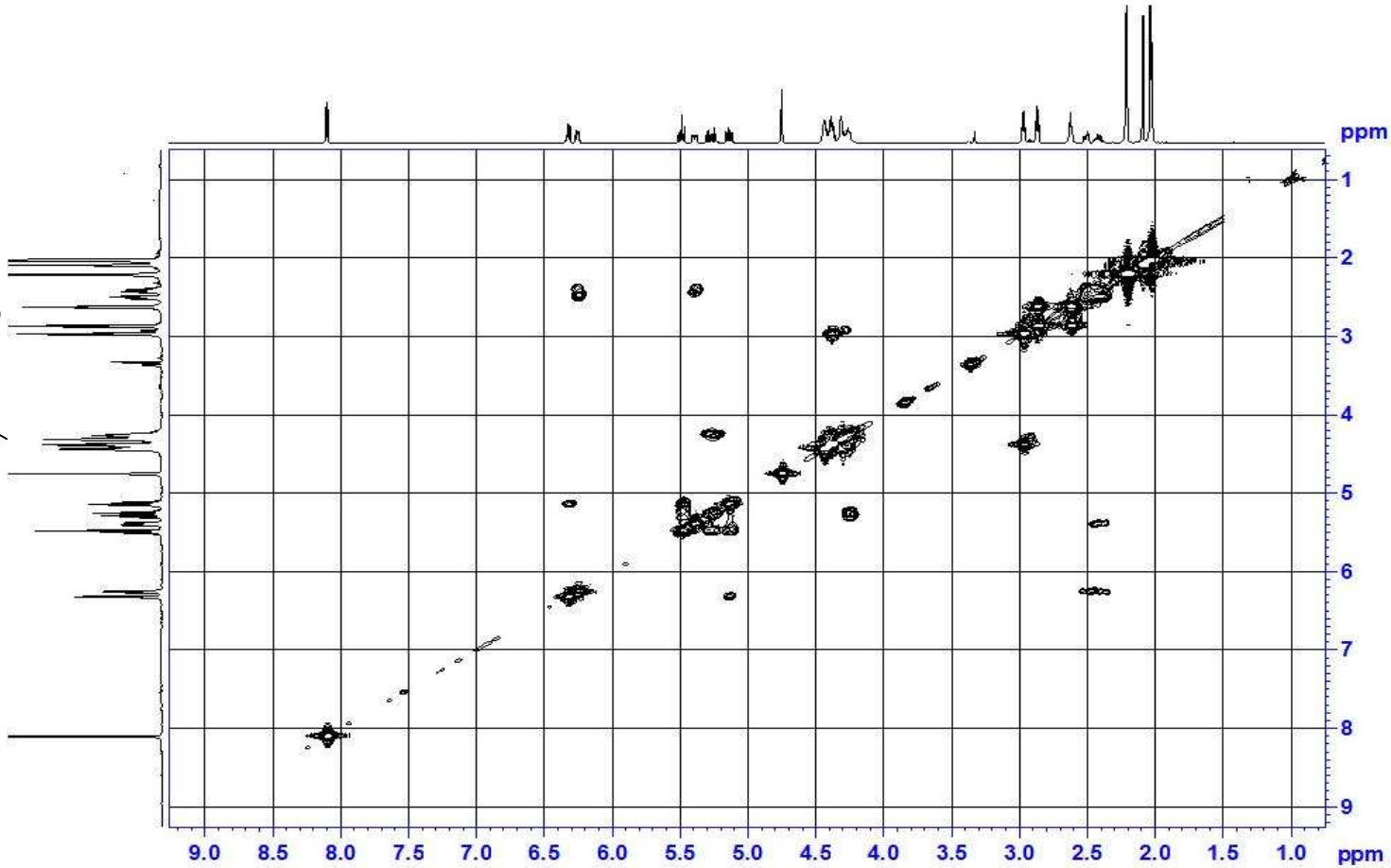


-Cyanoethyl-(3'-*O*-levulinyl-5-iodo-2'-deoxyuridin-5'-yl)-1,2,3,4-tetra-*O*-acetyl-α-D-glucopyranos-6-yl phosphate (9c)

COSY (MeOH-d_4, 600 MHz)

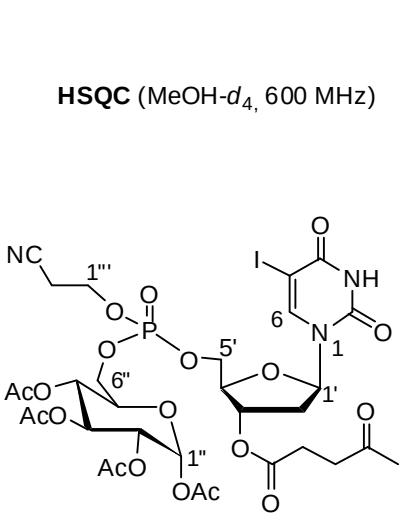


9c

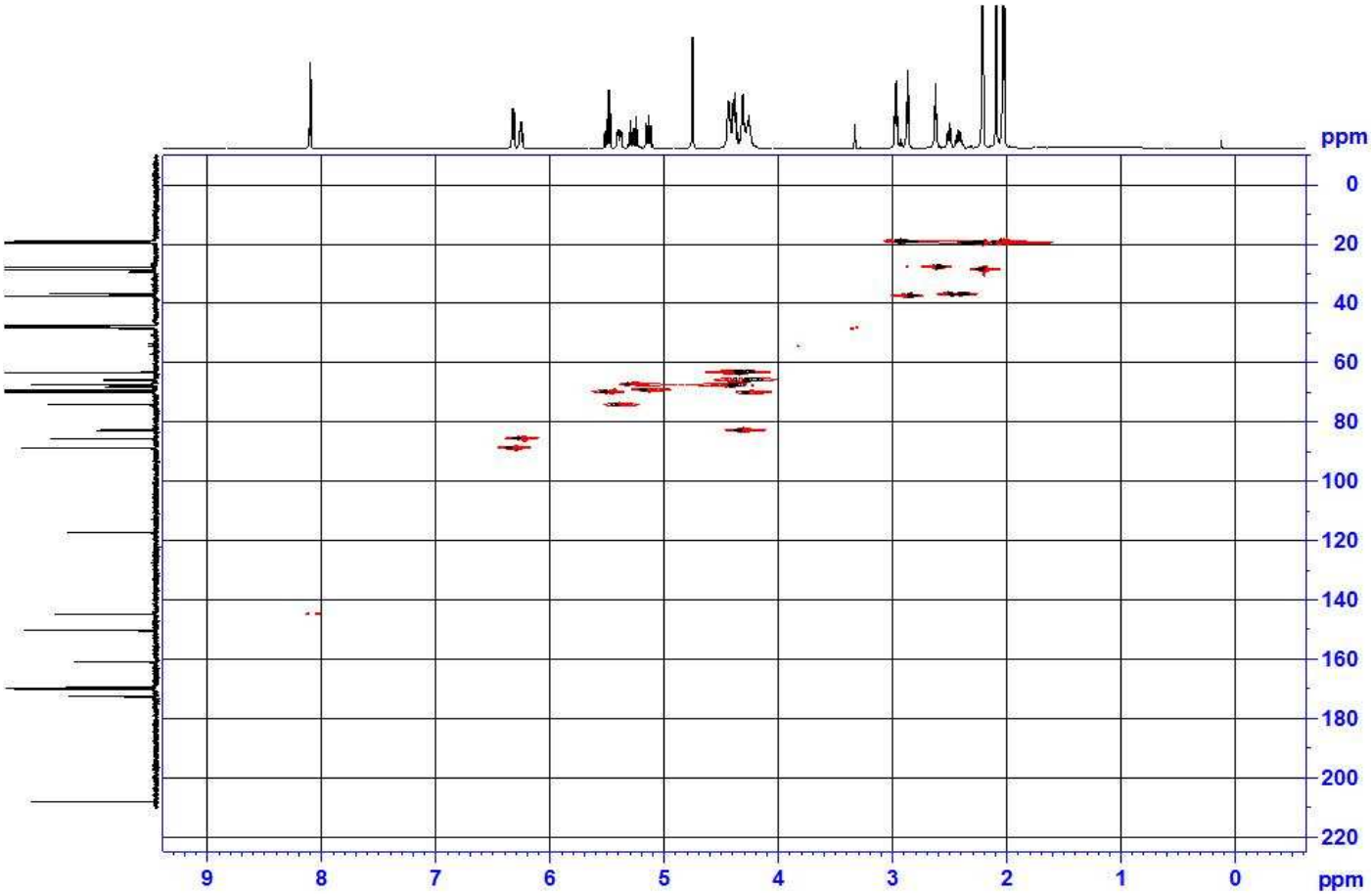


-Cyanoethyl-(3'-*O*-levulinyl-5-iodo-2'-deoxyuridin-5'-yl)-1,2,3,4-tetra-*O*-acetyl-α-D-glucopyranos-6-yl phosphate (9c)

HSQC (MeOH-d_4, 600 MHz)

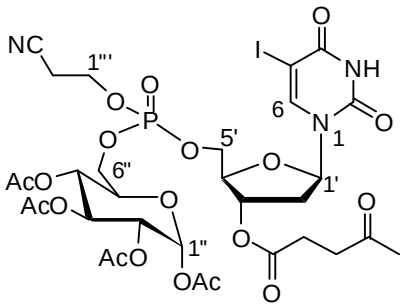


9c

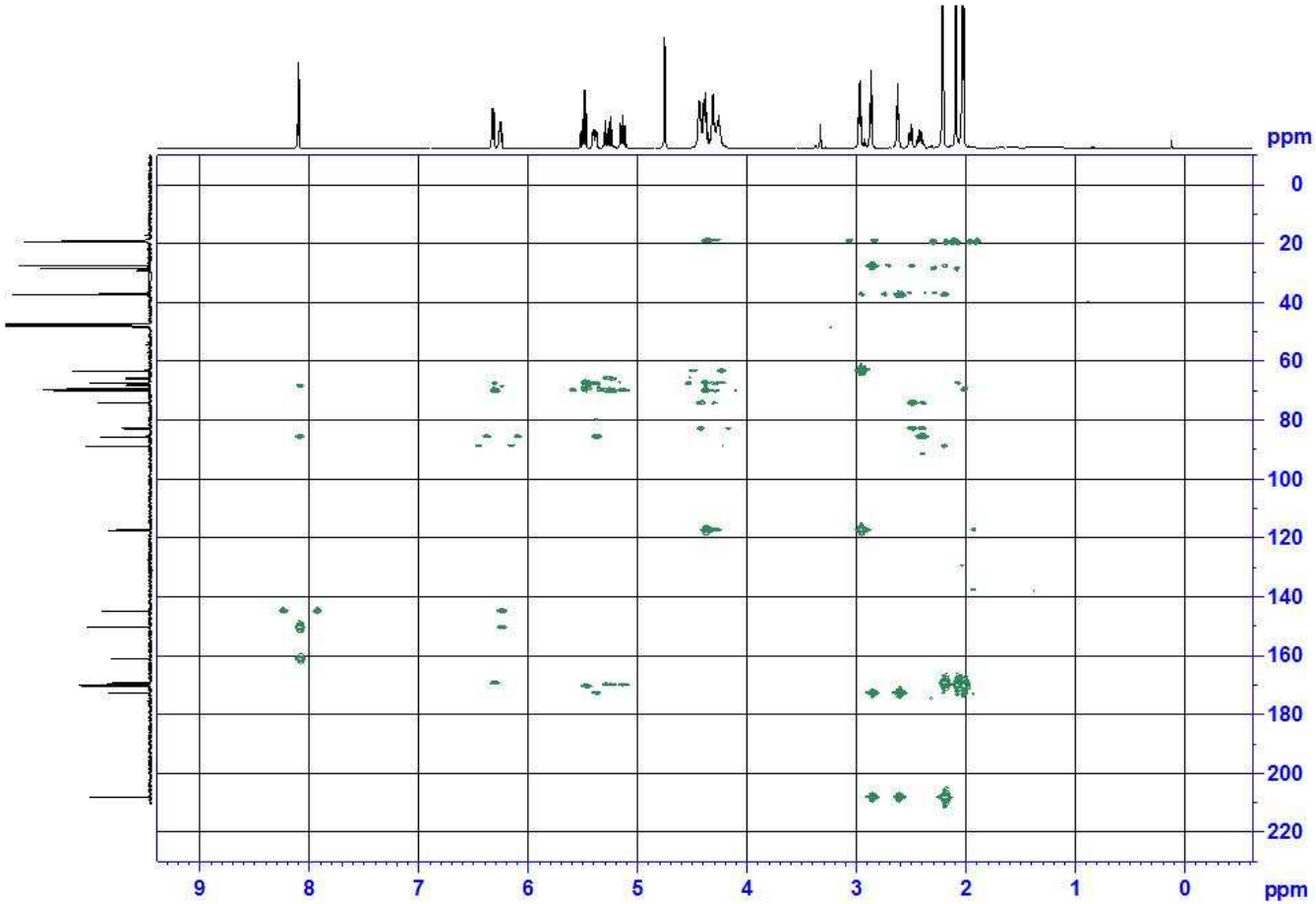


-Cyanoethyl-(3'-*O*-levulinyl-5-iodo-2'-deoxyuridin-5'-yl)-1,2,3,4-tetra-*O*-acetyl-α-D-glucopyranos-6-yl phosphate (9c)

HMBC (MeOH-d_4, 600 MHz)



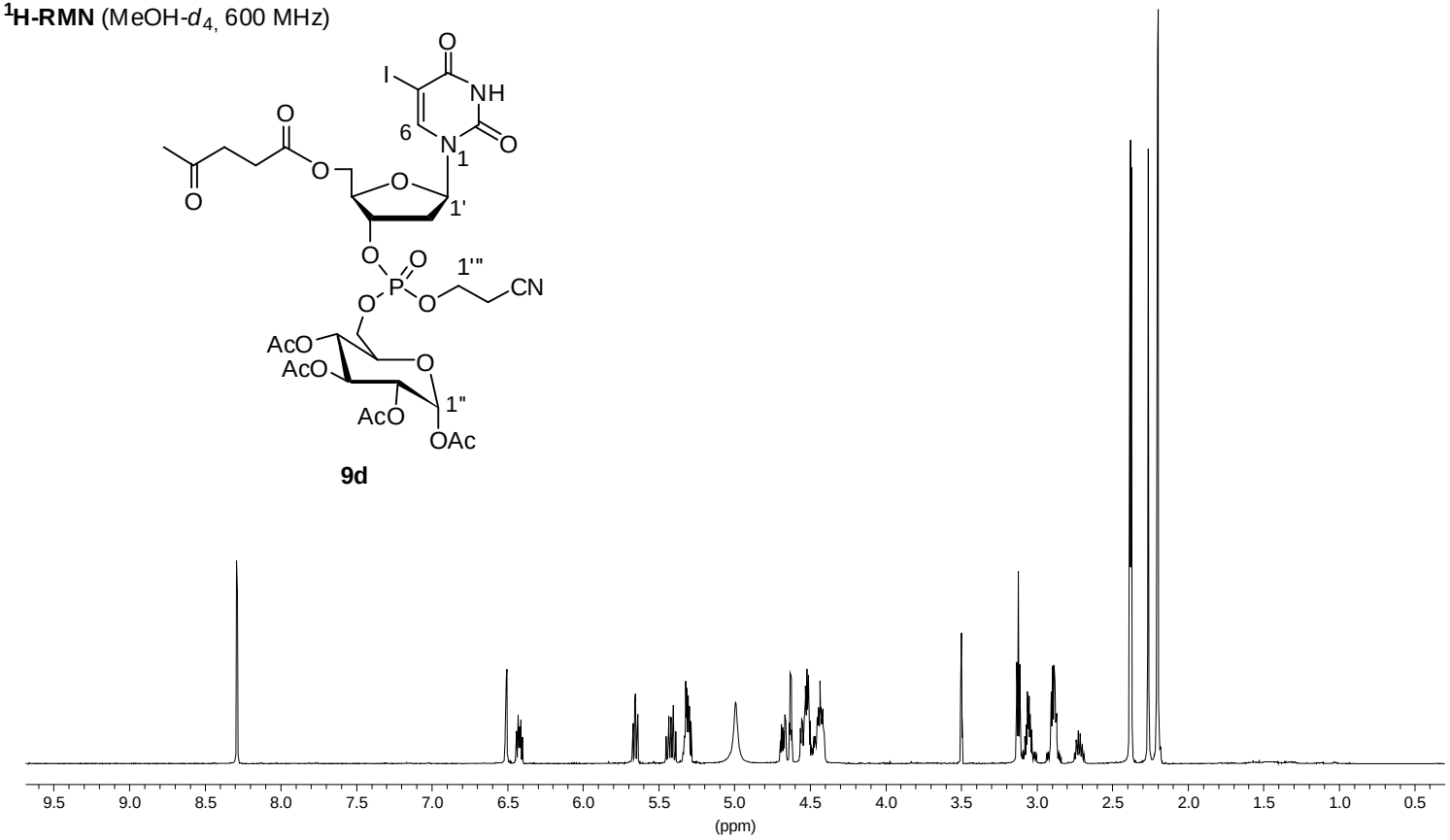
9c



2-Cyanoethyl-(5'-*O*-levulinyl-5-iodo-2'-deoxyuridin-3'-yl)-1,2,3,4-tetra-*O*-acetyl-α-D-glucopyranos-6-yl phosphate (9d)

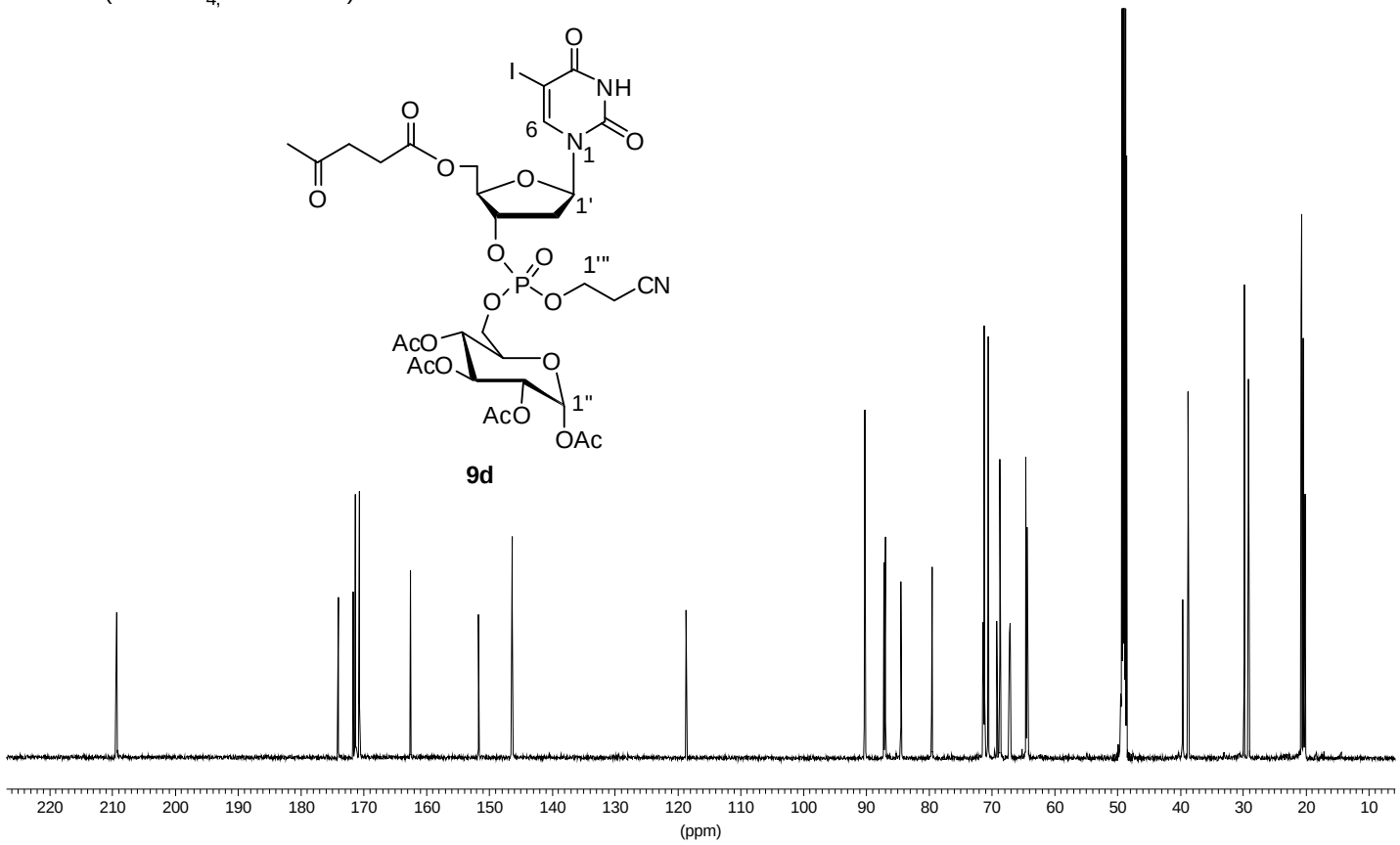
^{1}H-RMN (MeOH-d_4, 600 MHz)

9d

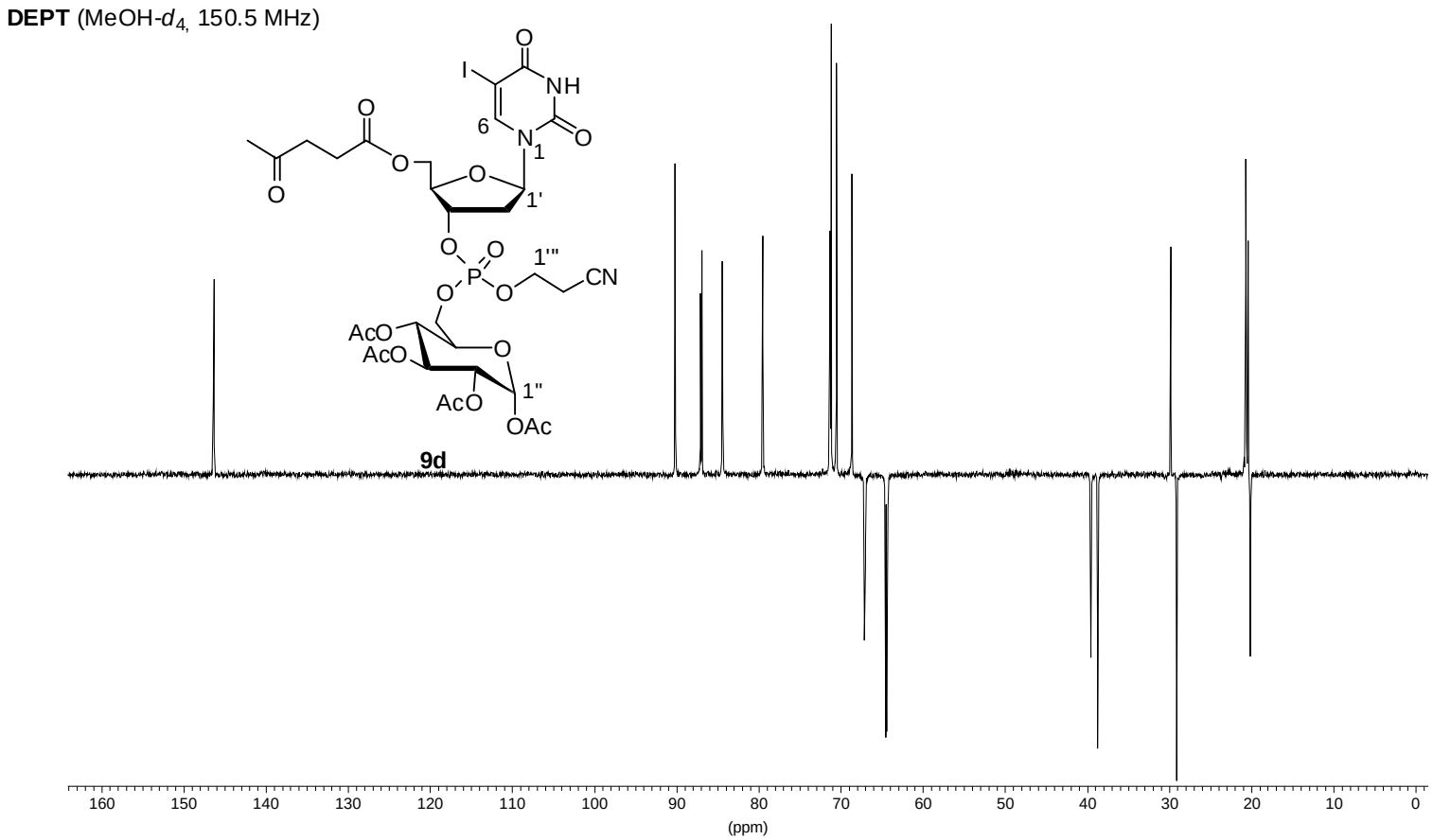


2-Cyanoethyl-(5'-*O*-levulinyl-5-iodo-2'-deoxyuridin-3'-yl)-1,2,3,4-tetra-*O*-acetyl-α-D-glucopyranos-6-yl phosphate (9d)

^{13}C-RMN (MeOH-d_4, 150.5 MHz)

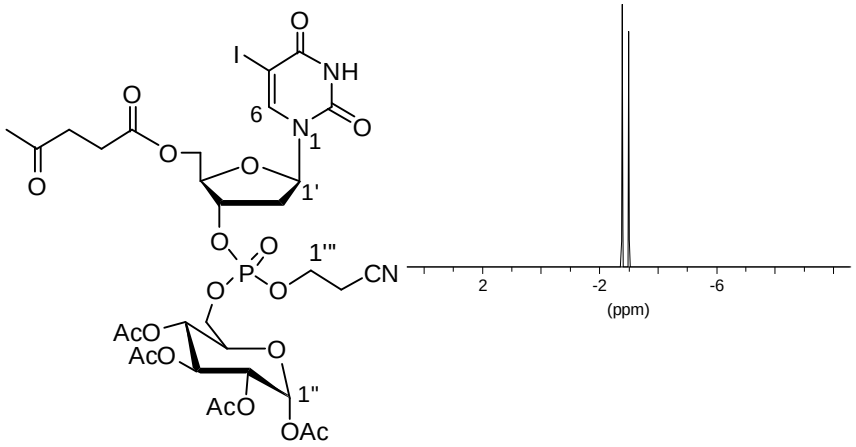


2-Cyanoethyl-(5'-*O*-levulinyl-5-iodo-2'-deoxyuridin-3'-yl)-1,2,3,4-tetra-*O*-acetyl-α-D-glucopyranos-6-yl phosphate (9d)

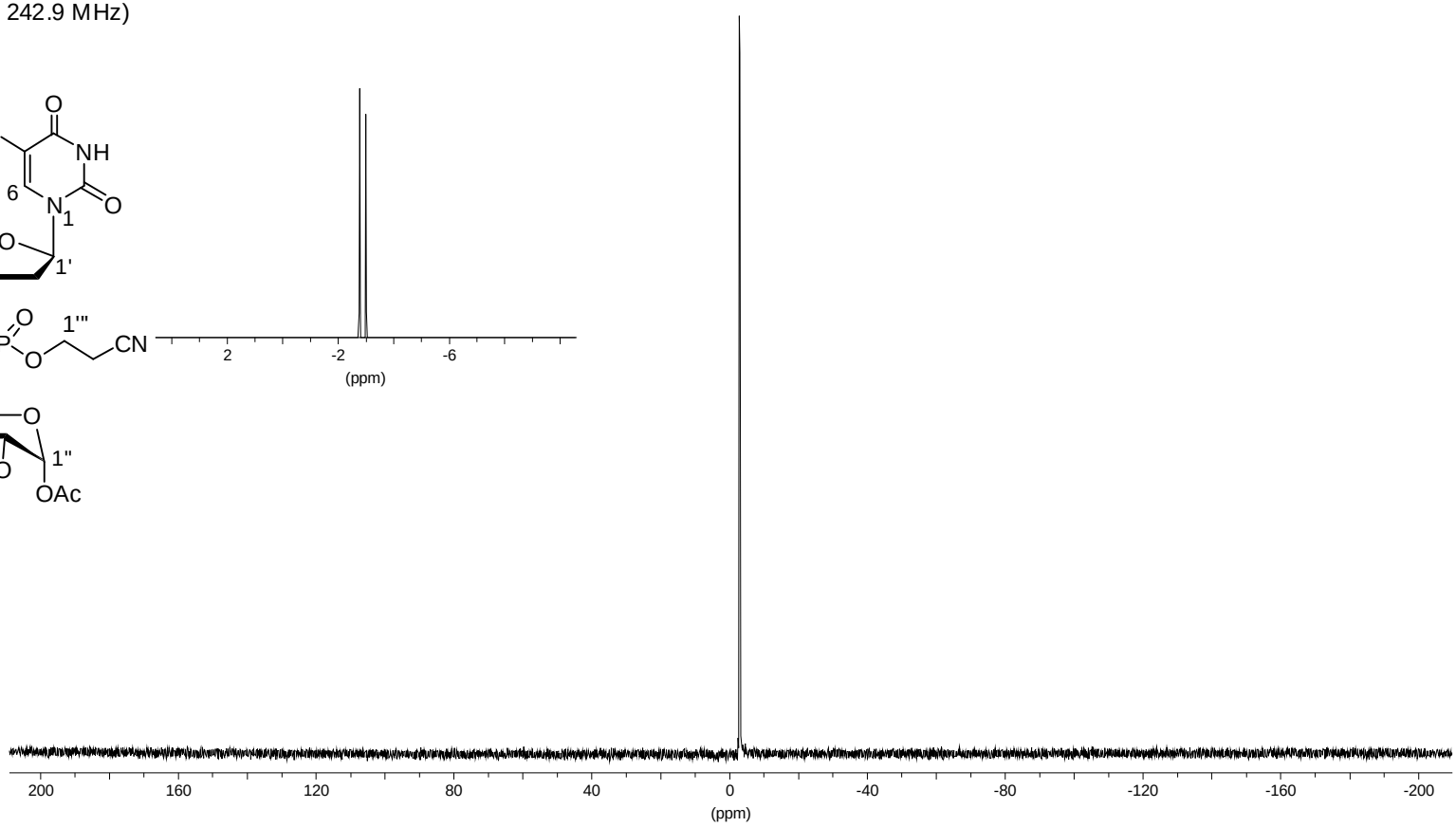


2-Cyanoethyl-(5'-*O*-levulinyl-5-iodo-2'-deoxyuridin-3'-yl)-1,2,3,4-tetra-*O*-acetyl-α-D-glucopyranos-6-yl phosphate (9d)

^{31}P-RMN (MeOH-d_4, 242.9 MHz)

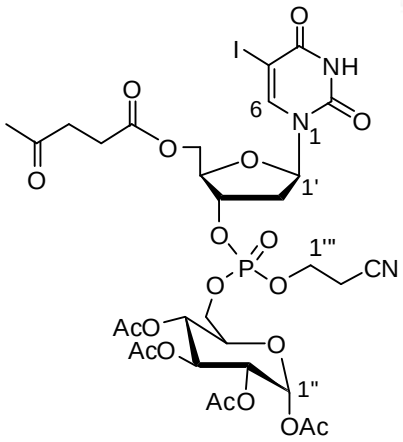


9d

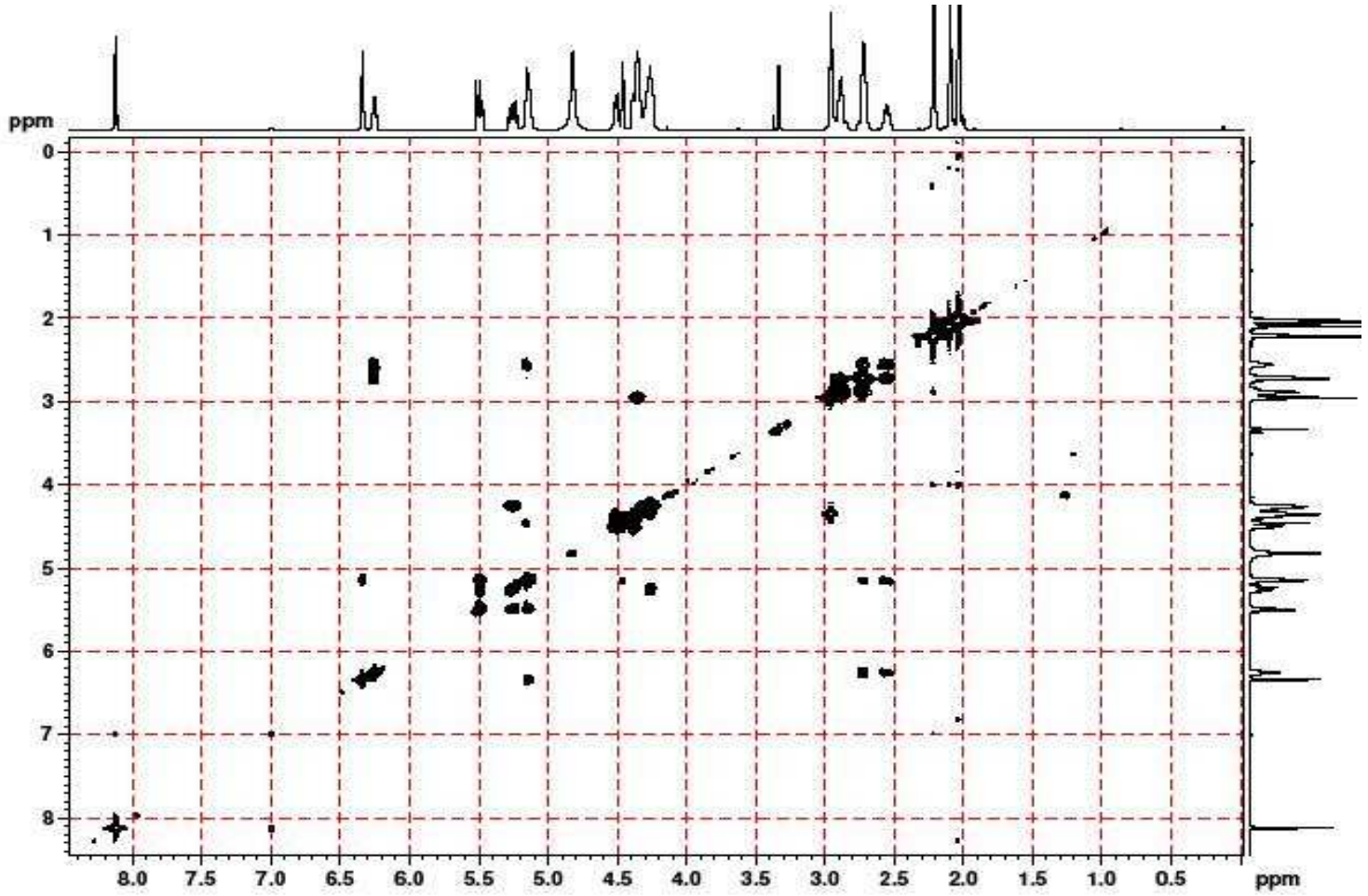


2-Cyanoethyl-(5'-*O*-levulinyl-5-iodo-2'-deoxyuridin-3'-yl)-1,2,3,4-tetra-*O*-acetyl-α-D-glucopyranos-6-yl phosphate (9d)

COSY (MeOH-d_4, 600 MHz)

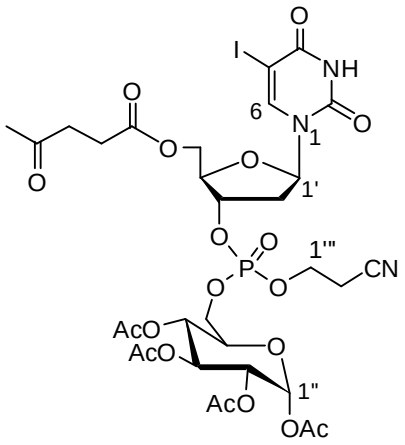


9d

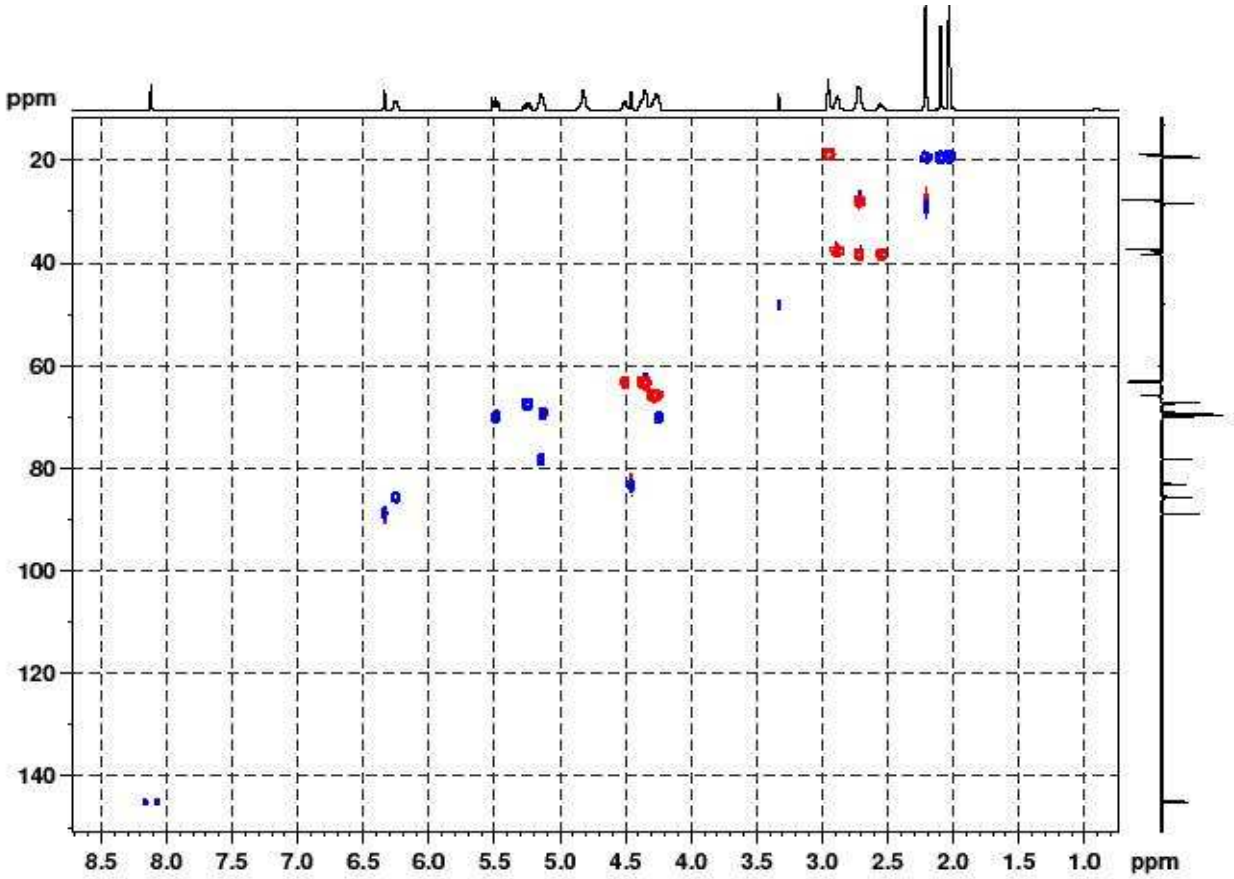


2-Cyanoethyl-(5'-*O*-levulinyl-5-iodo-2'-deoxyuridin-3'-yl)-1,2,3,4-tetra-*O*-acetyl-α-D-glucopyranos-6-yl phosphate (9d)

HSQC (MeOH-d_4, 600 MHz)

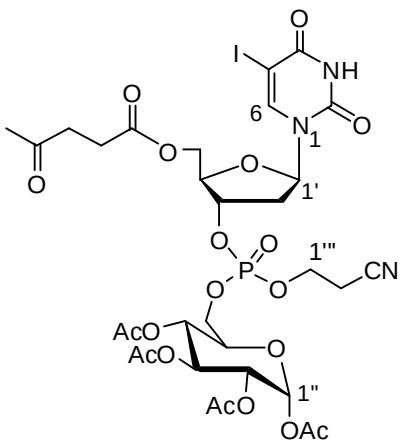


9d

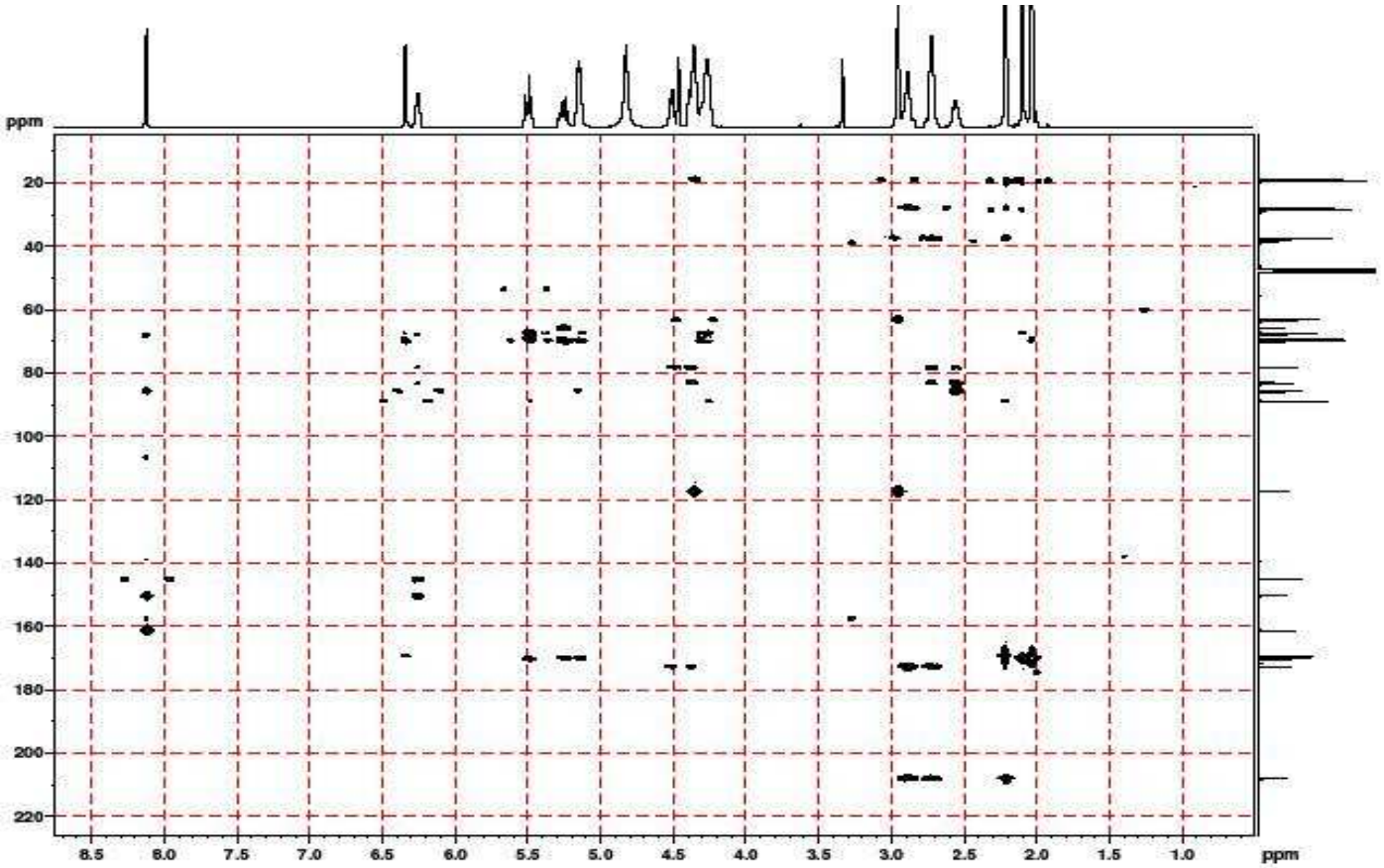


2-Cyanoethyl-(5'-*O*-levulinyl-5-iodo-2'-deoxyuridin-3'-yl)-1,2,3,4-tetra-*O*-acetyl-α-D-glucopyranos-6-yl phosphate (9d)

HMBC (MeOH-d_4, 600 MHz)



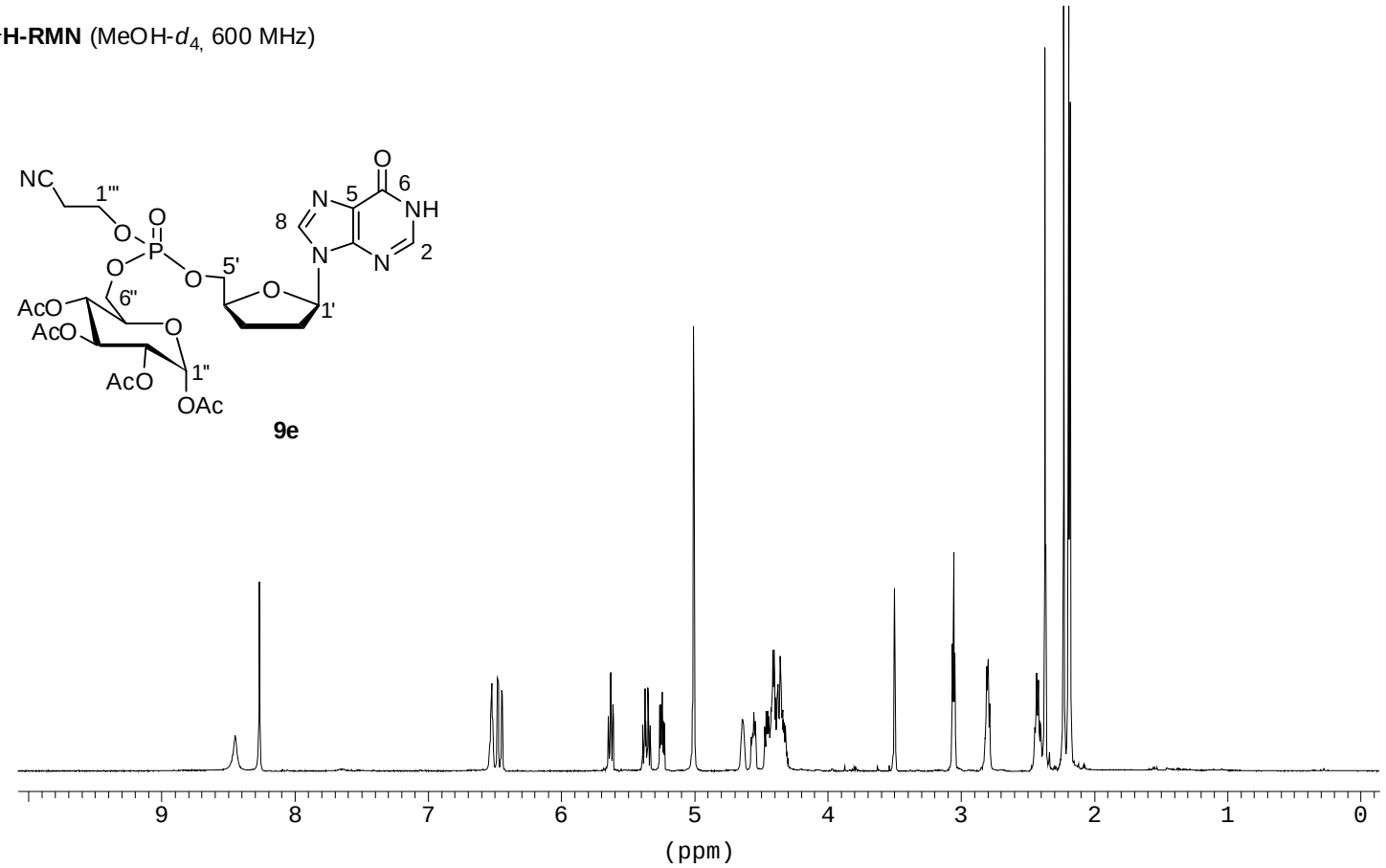
9d



2-Cyanoethyl-(2',3'-dideoxyinosin-5'-yl)-1,2,3,4-tetra-*O*-acetyl-α-D-glucopyranos-6-yl phosphate (9e)

^{1}H-RMN (MeOH-d_4, 600 MHz)

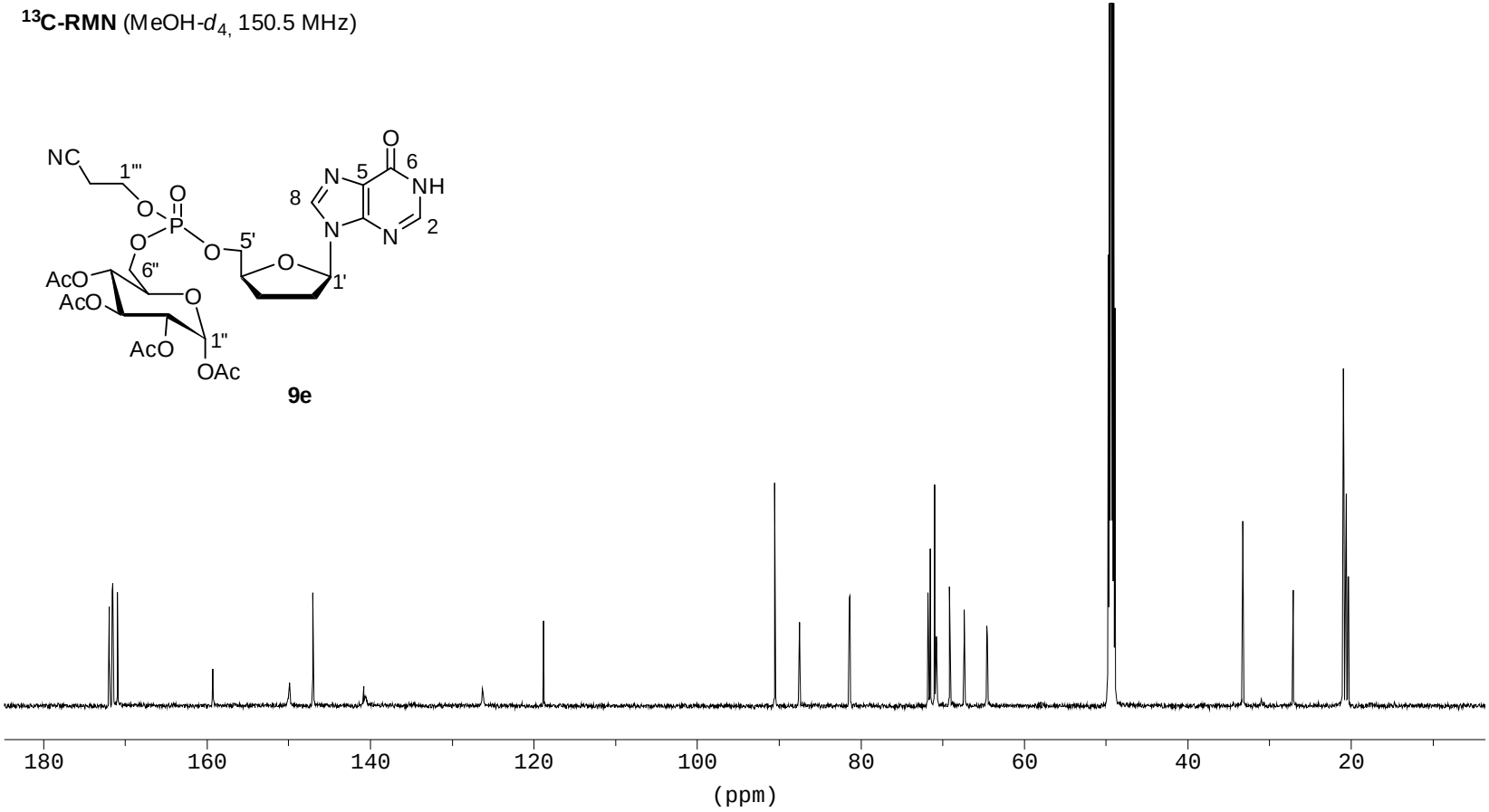
9e



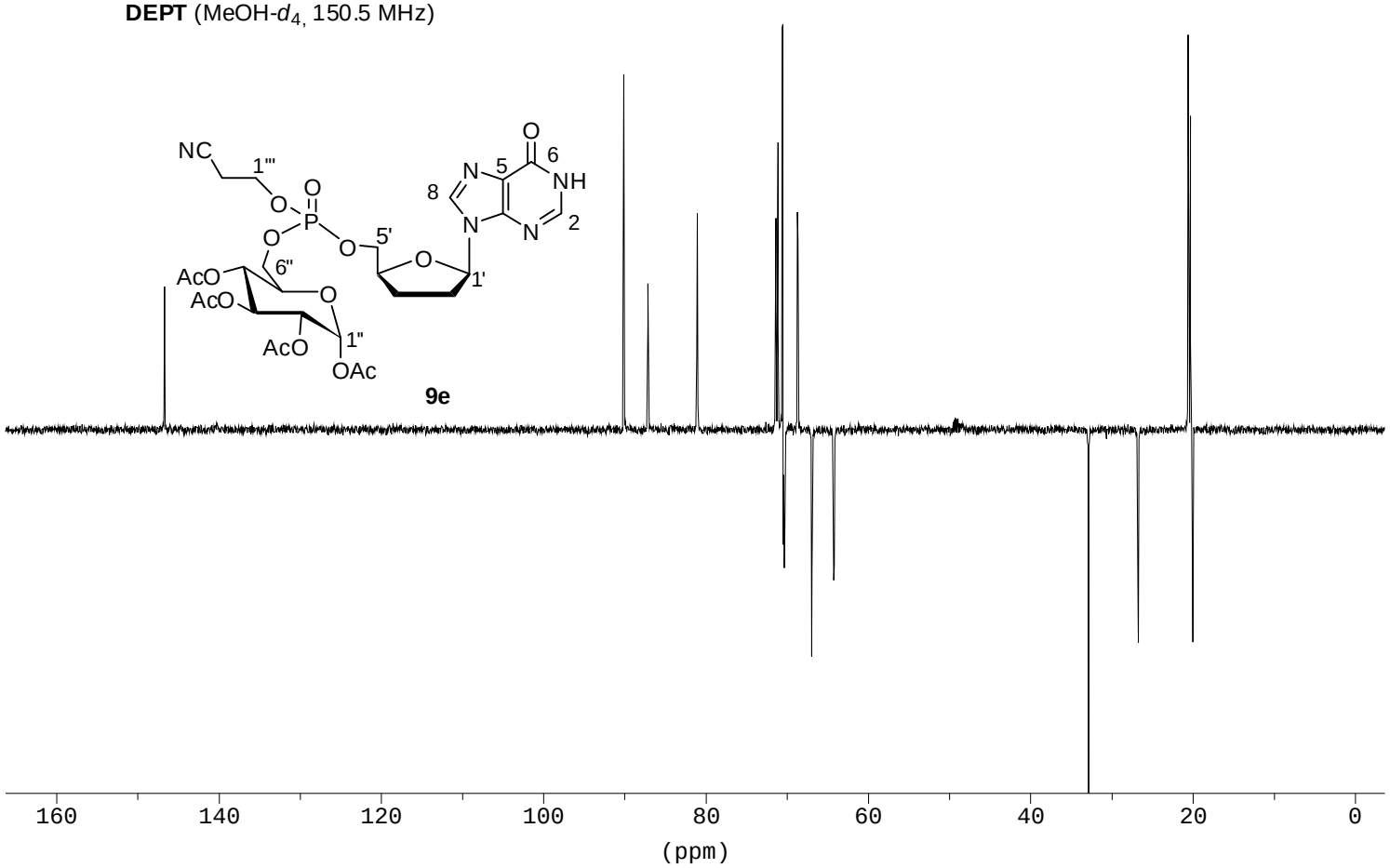
2-Cyanoethyl-(2',3'-dideoxyinosin-5'-yl)-1,2,3,4-tetra-*O*-acetyl-α-D-glucopyranos-6-yl phosphate (9e)

^{13}C-RMN (MeOH-d_4, 150.5 MHz)

9e

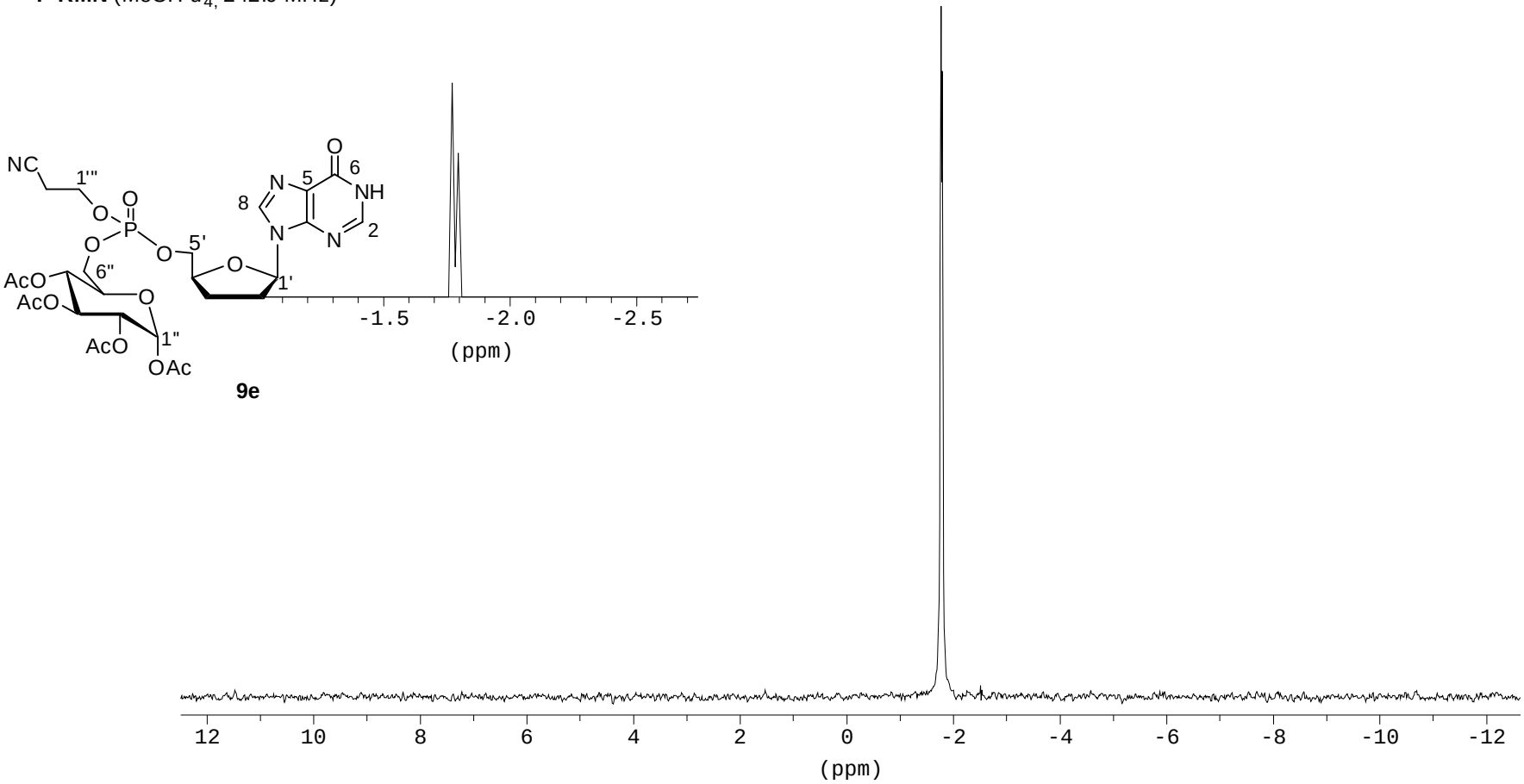


2-Cyanoethyl-(2',3'-dideoxyinosin-5'-yl)-1,2,3,4-tetra-*O*-acetyl-α-D-glucopyranos-6-yl phosphate (9e)



2-Cyanoethyl-(2',3'-dideoxyinosin-5'-yl)-1,2,3,4-tetra-*O*-acetyl-α-D-glucopyranos-6-yl phosphate (9e)

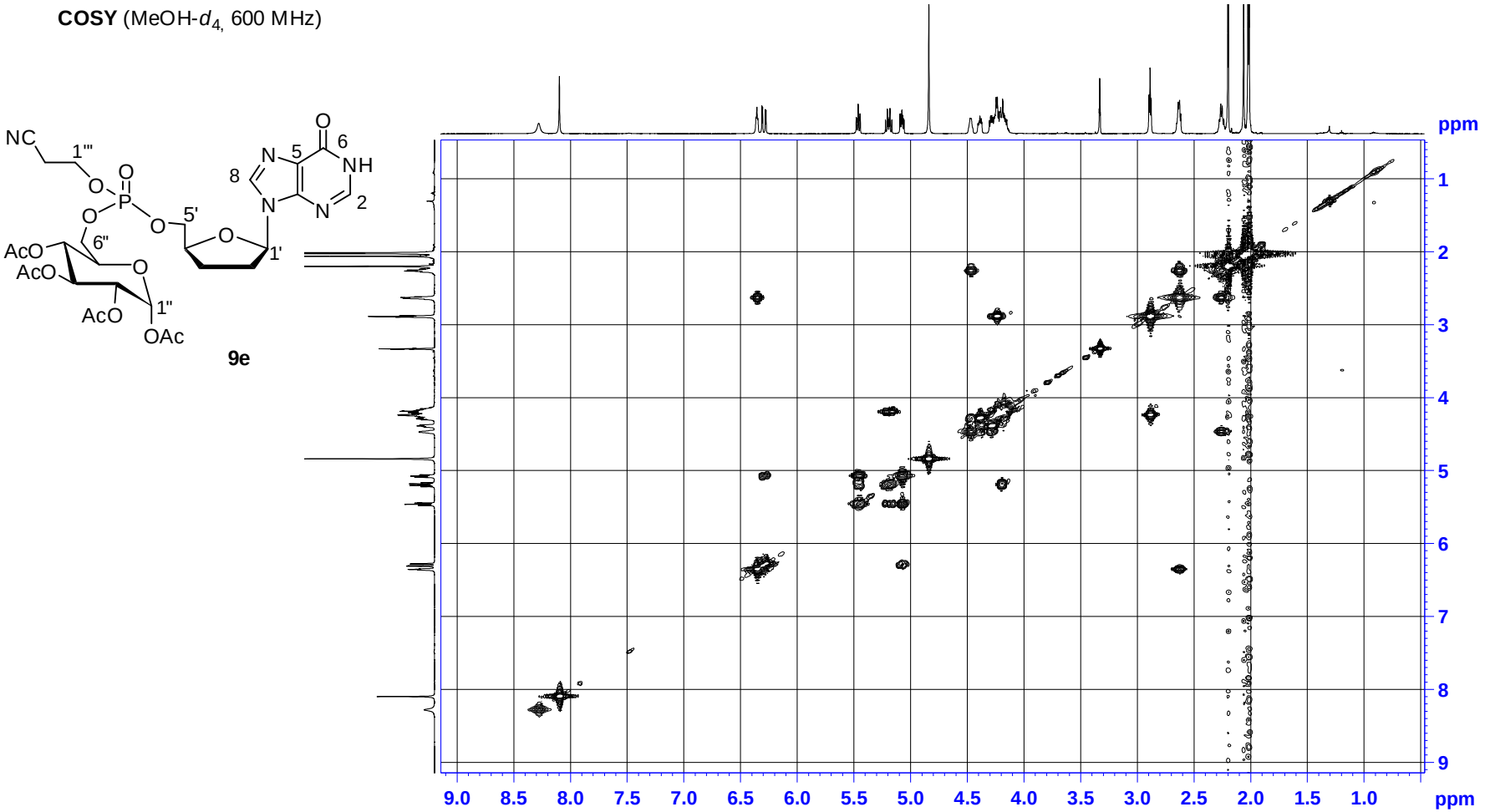
^{31}P-RMN (MeOH-d_4, 242.9 MHz)



9e

2-Cyanoethyl-(2',3'-dideoxyinosin-5'-yl)-1,2,3,4-tetra-*O*-acetyl-α-D-glucopyranos-6-yl phosphate (9e)

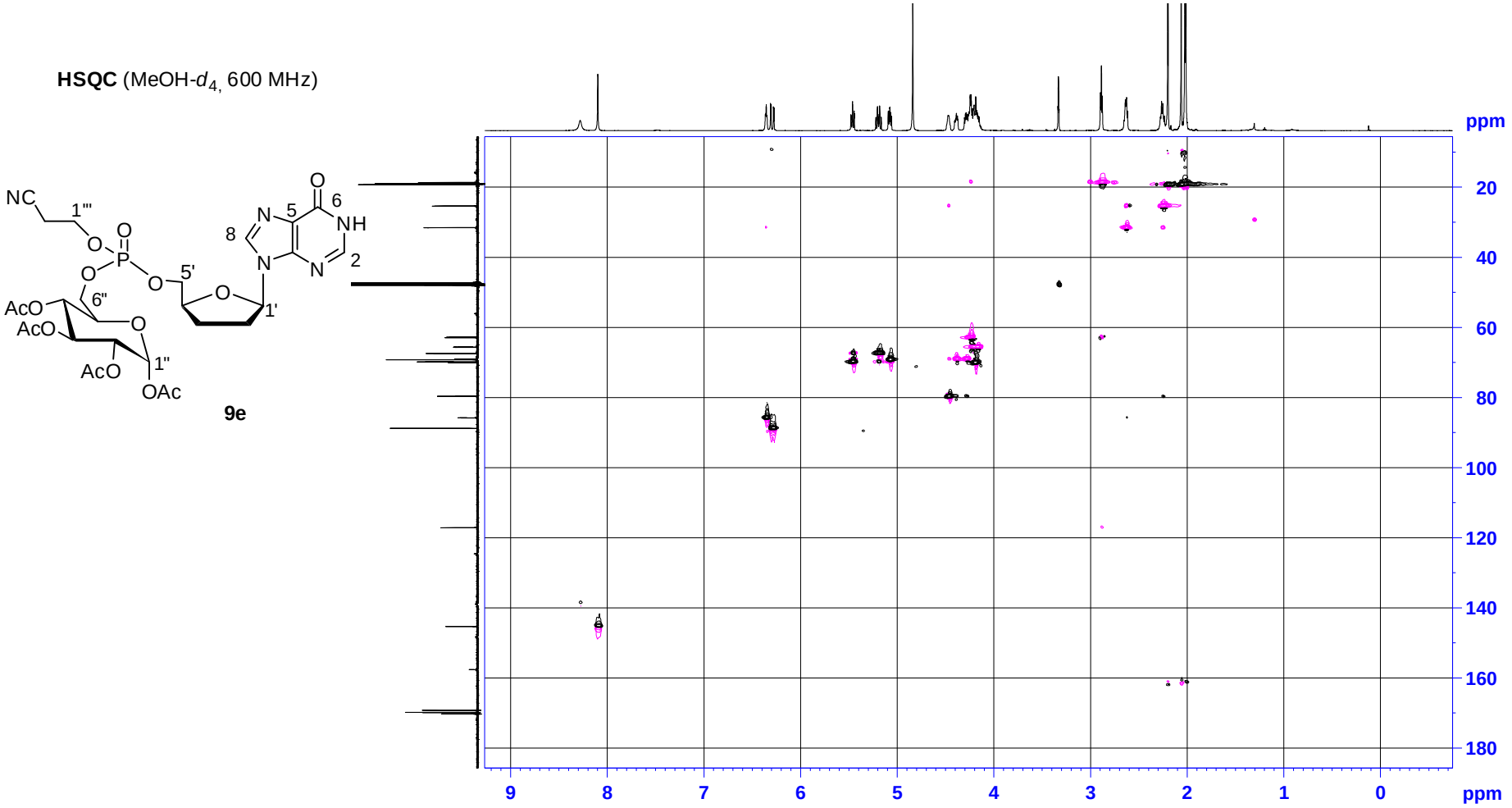
COSY (MeOH-d_4, 600 MHz)



9e

2-Cyanoethyl-(2',3'-dideoxyinosin-5'-yl)-1,2,3,4-tetra-*O*-acetyl-α-D-glucopyranos-6-yl phosphate (9e)

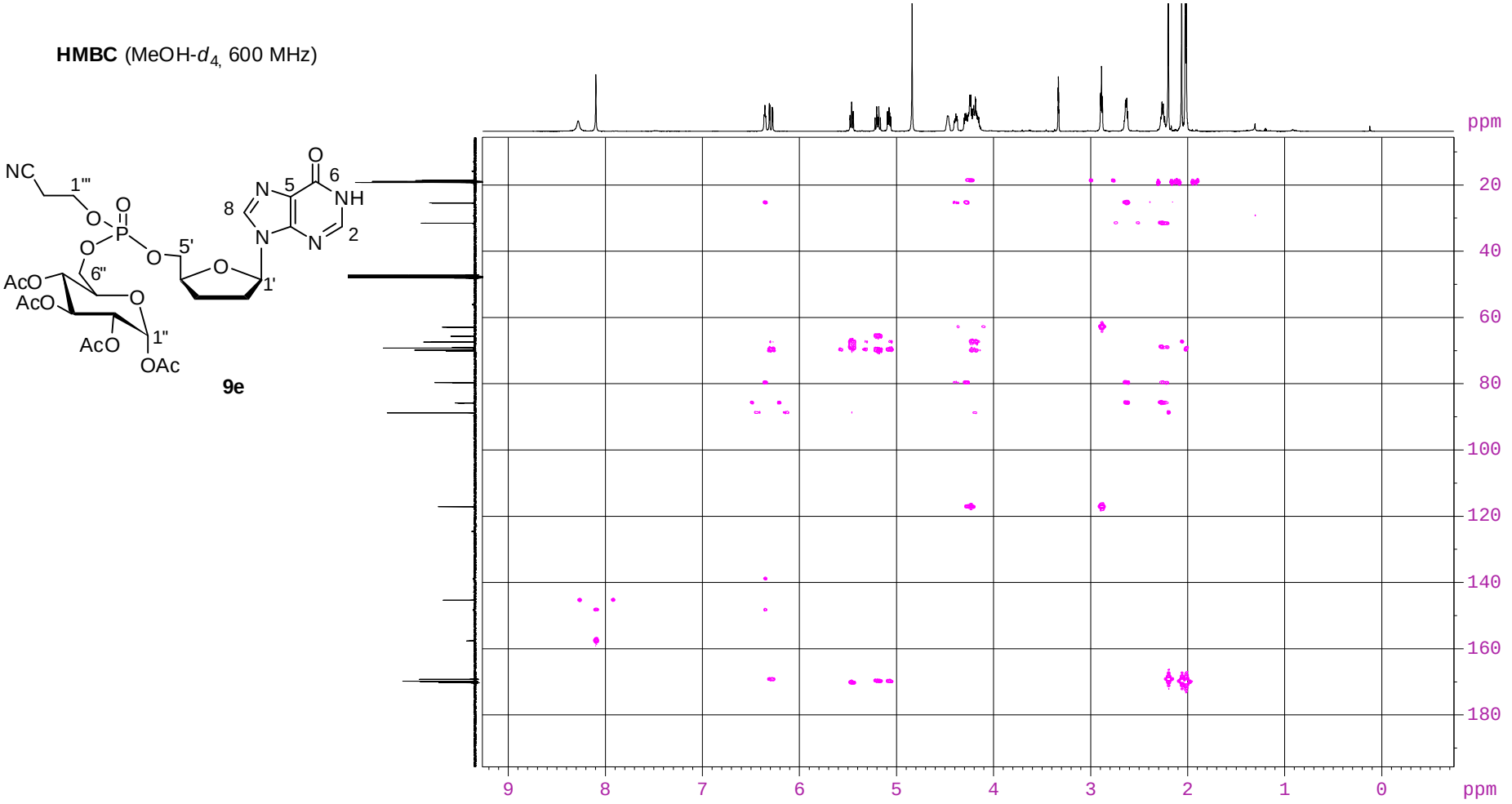
HSQC (MeOH-d_4, 600 MHz)



9e

2-Cyanoethyl-(2',3'-dideoxyinosin-5'-yl)-1,2,3,4-tetra-*O*-acetyl-α-D-glucopyranos-6-yl phosphate (9e)

HMBC (MeOH-d_4, 600 MHz)

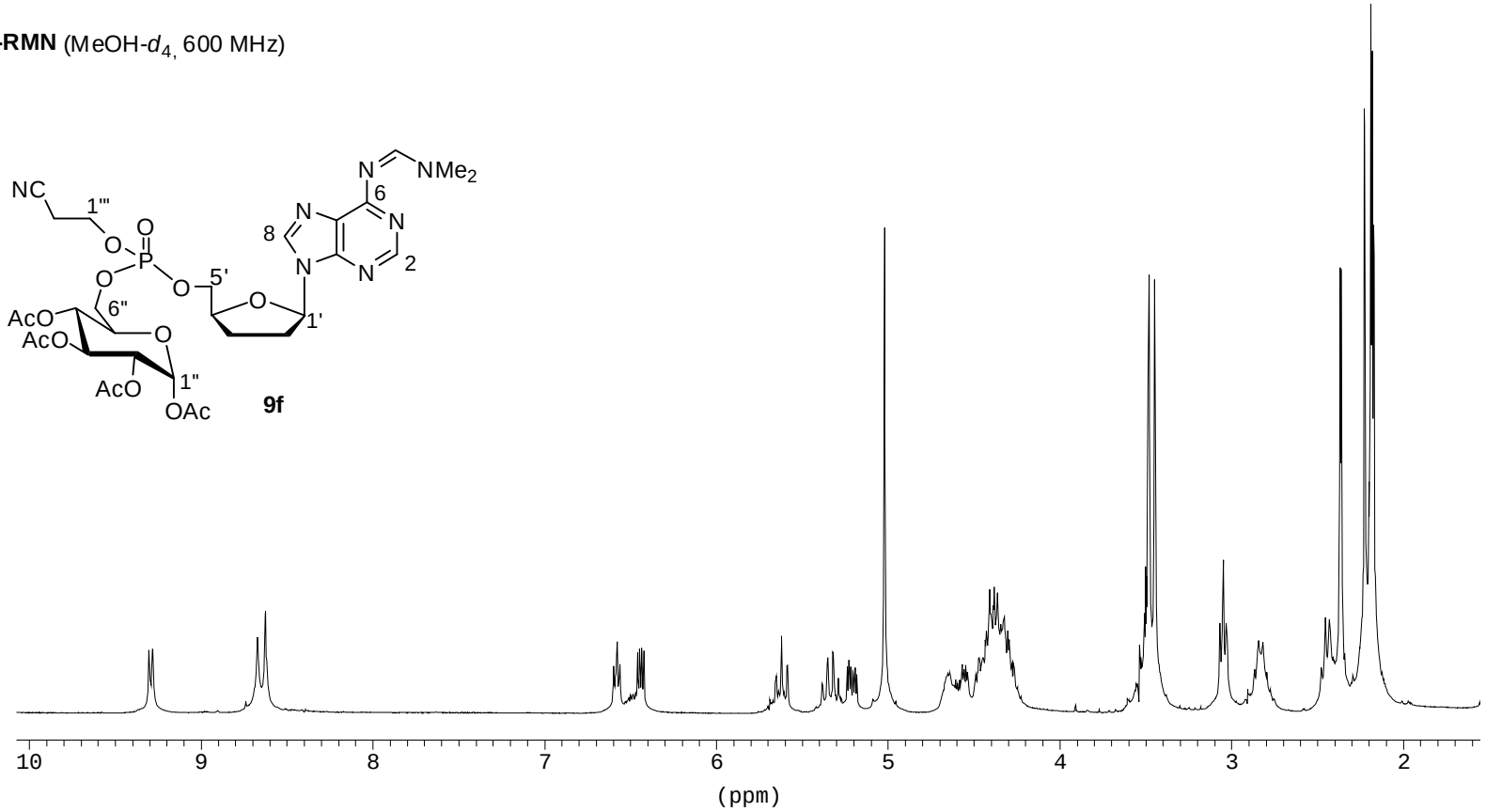


9e

2-Cyanoethyl-[N^6-(dimethylamino)methylen-2',3'-dideoxyadenosin-5'-yl]-1,2,3,4-tetra-*O*-acetyl-α-D-glucopyranos-6-yl phosphate (9f)

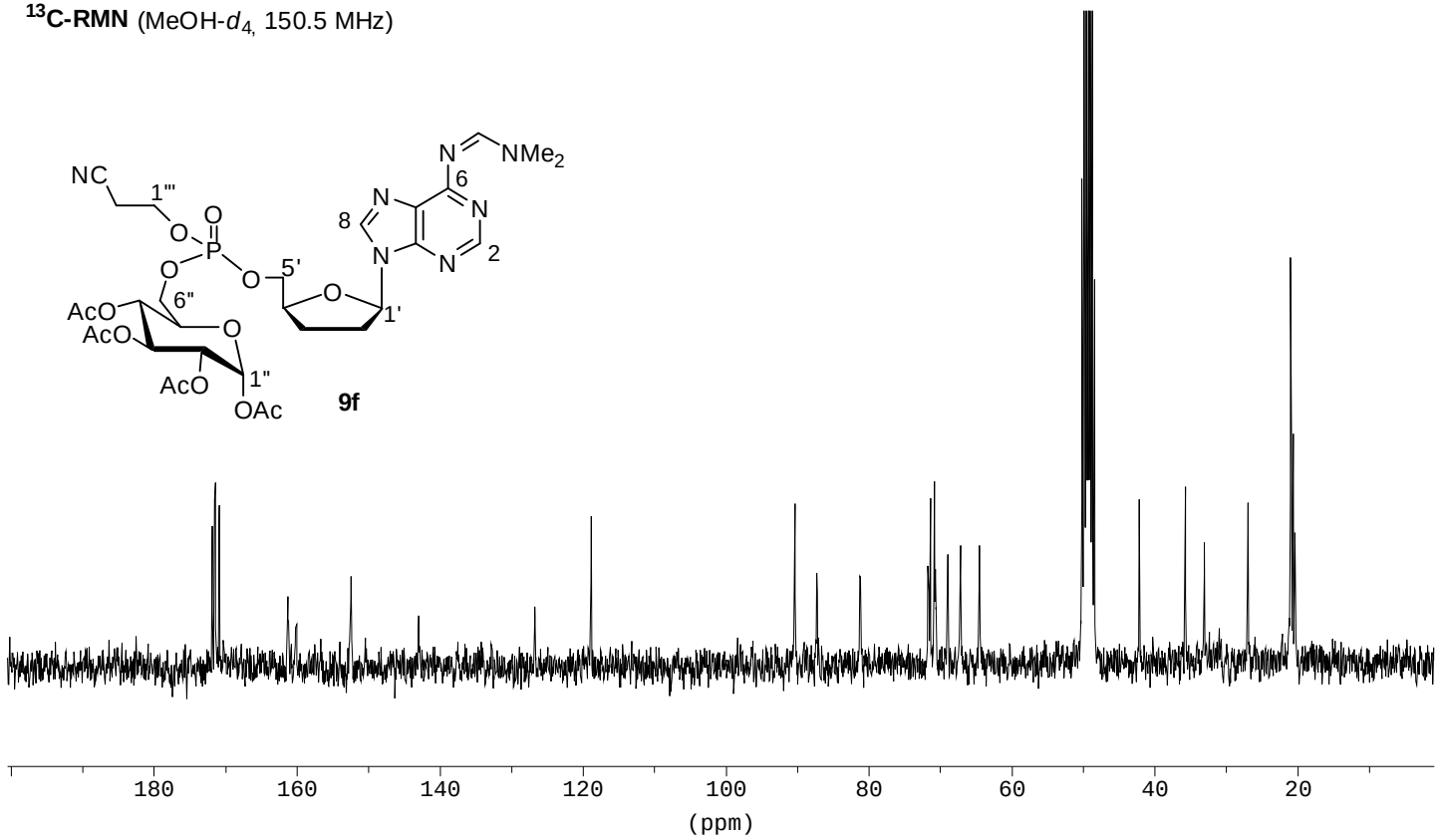
^{1}H-RMN (MeOH-d_4, 600 MHz)

9f



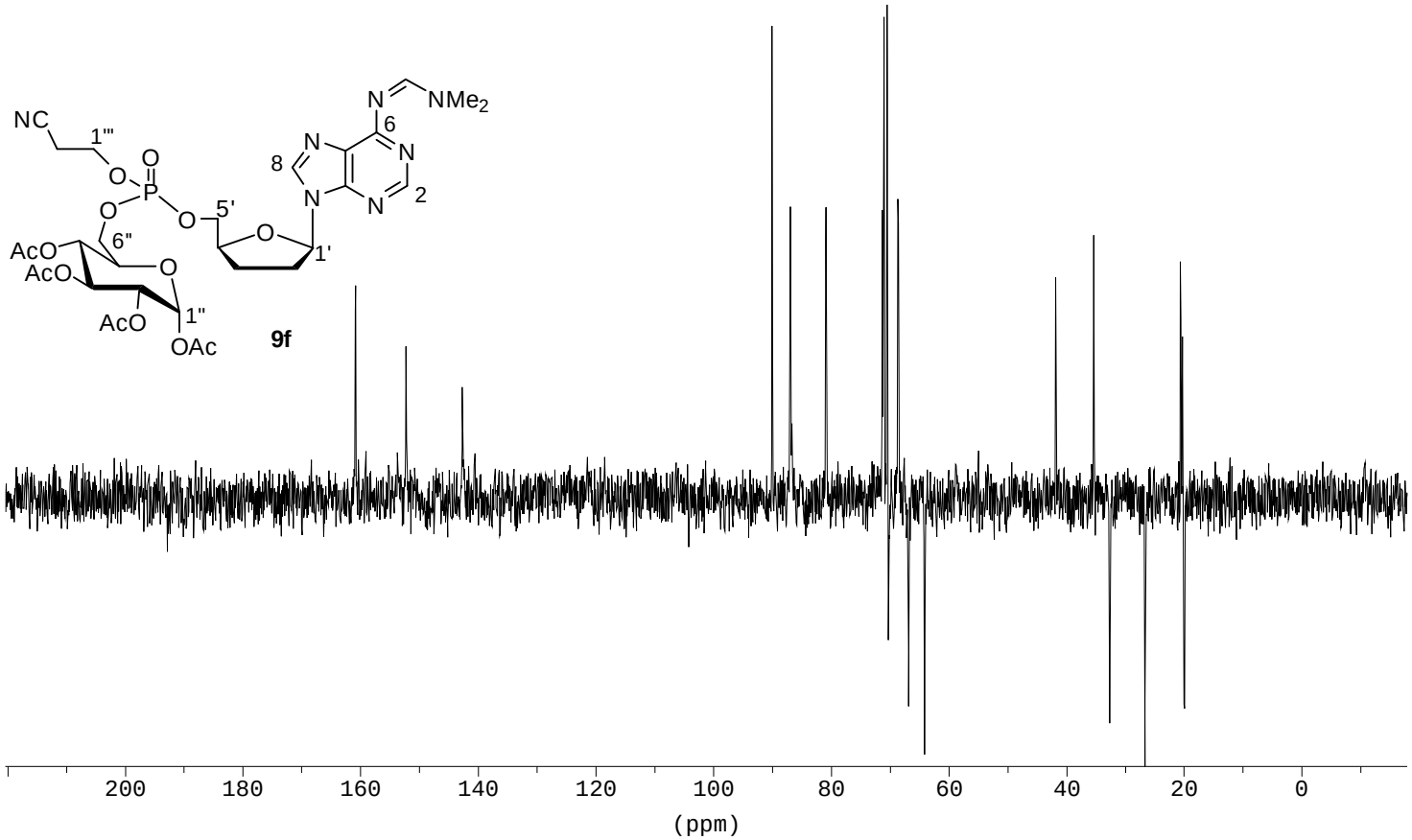
2-Cyanoethyl-[N^6-(dimethylamino)methylen-2',3'-dideoxyadenosin-5'-yl]-1,2,3,4-tetra-*O*-acetyl-α-D-glucopyranos-6-yl phosphate (9f)

^{13}C-RMN (MeOH-d_4, 150.5 MHz)



2-Cyanoethyl-[N^6-(dimethylamino)methylen-2',3'-dideoxyadenosin-5'-yl]-1,2,3,4-tetra-*O*-acetyl-α-D-glucopyranos-6-yl phosphate (9f)

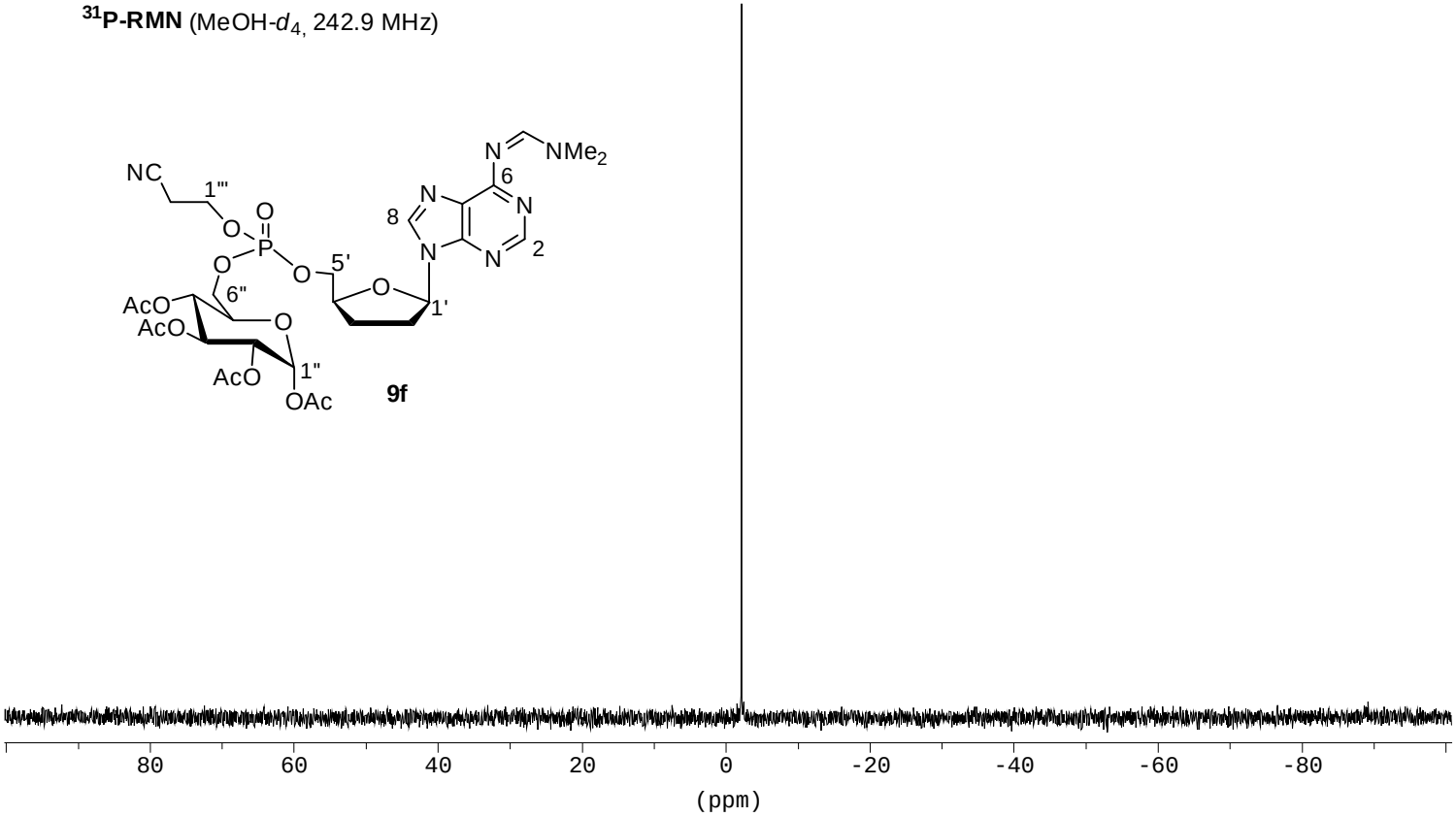
DEPT (MeOH-d_4, 150.5 MHz)



2-Cyanoethyl-[N^6-(dimethylamino)methylen-2',3'-dideoxyadenosin-5'-yl]-1,2,3,4-tetra-*O*-acetyl-α-D-glucopyranos-6-yl phosphate (9f)

^{31}P-RMN (MeOH-d_4, 242.9 MHz)

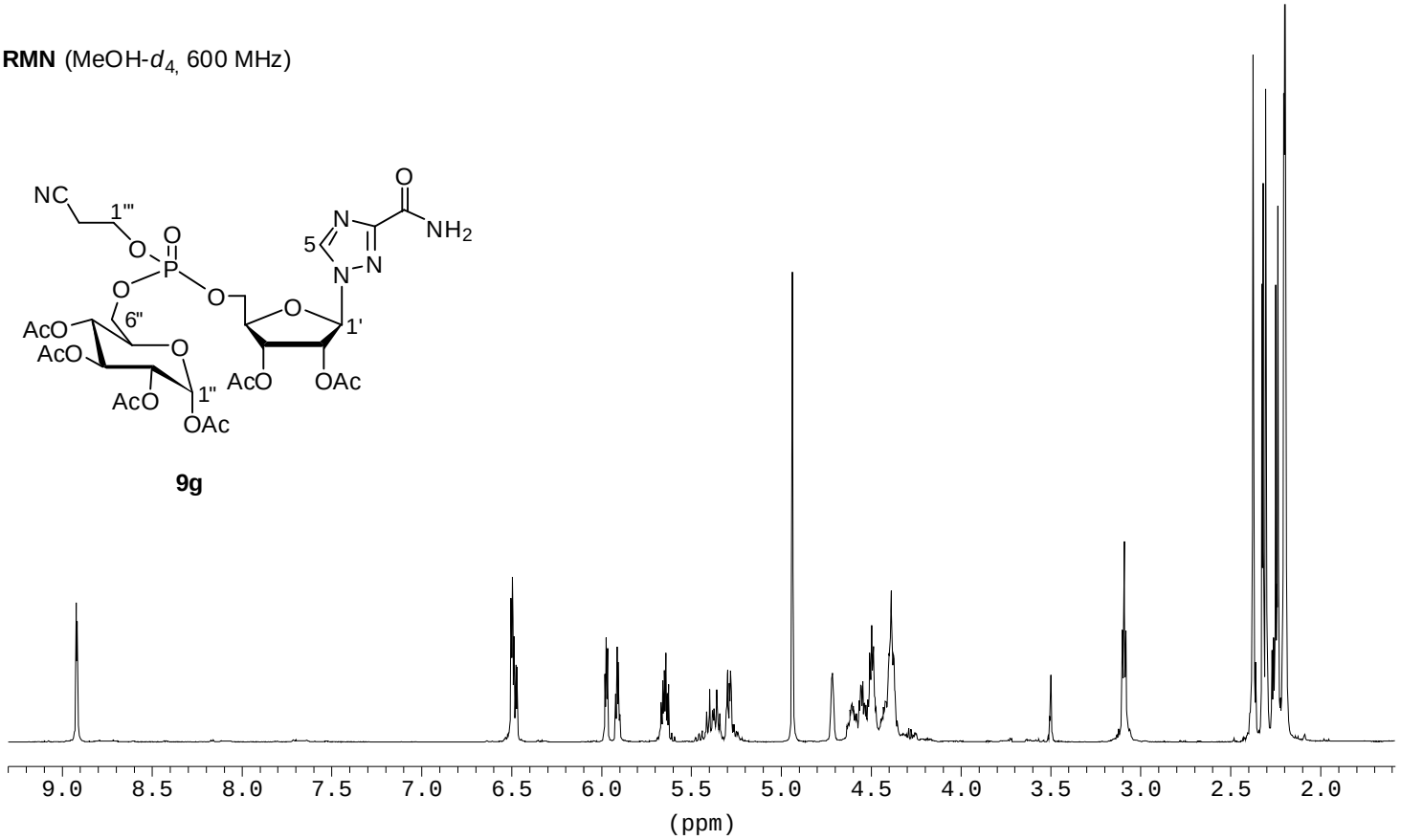
9f



2-Cyanoethyl-[2',3'-di-*O*-acetyl-1'-(3-carbamoyl-1,2,4-triazoyl)-β-D-ribofuranos-5'-yl]-1,2,3,4-tetra-*O*-acetyl-α-D-glucopyranos-6-yl phosphate (9g)

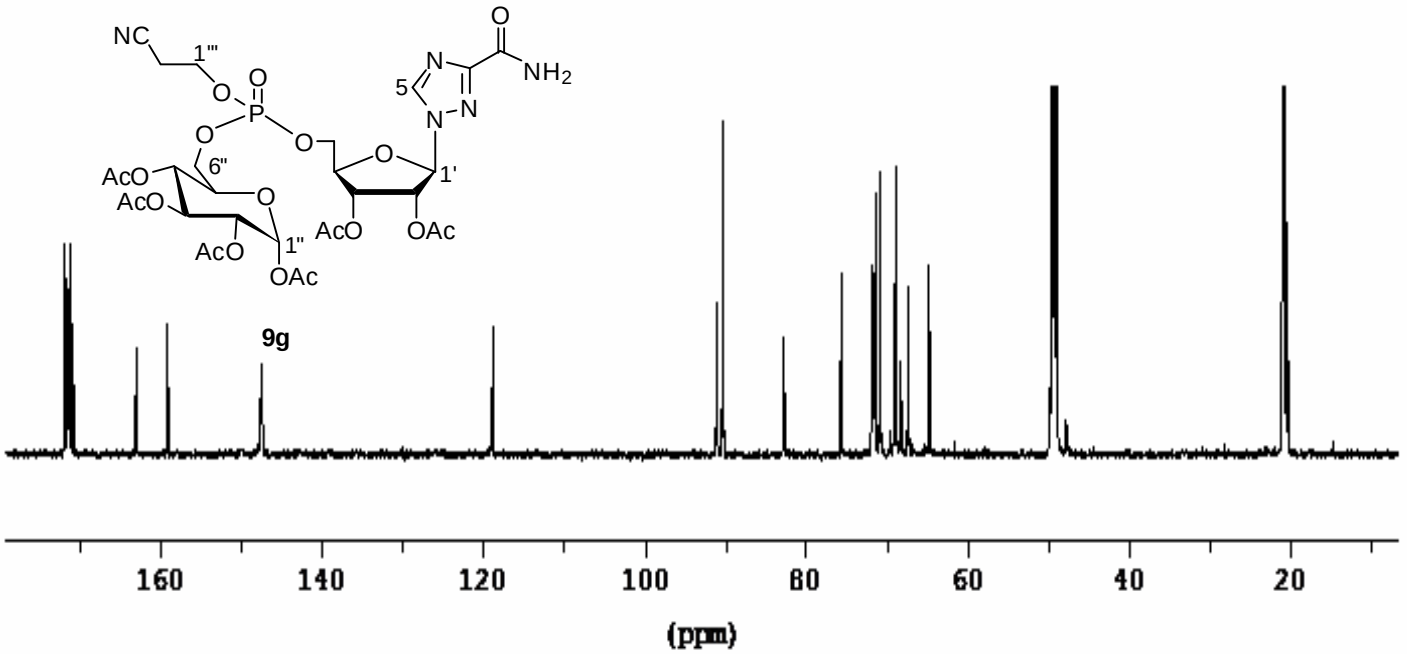
^{1}H-RMN (MeOH-d_4, 600 MHz)

9g



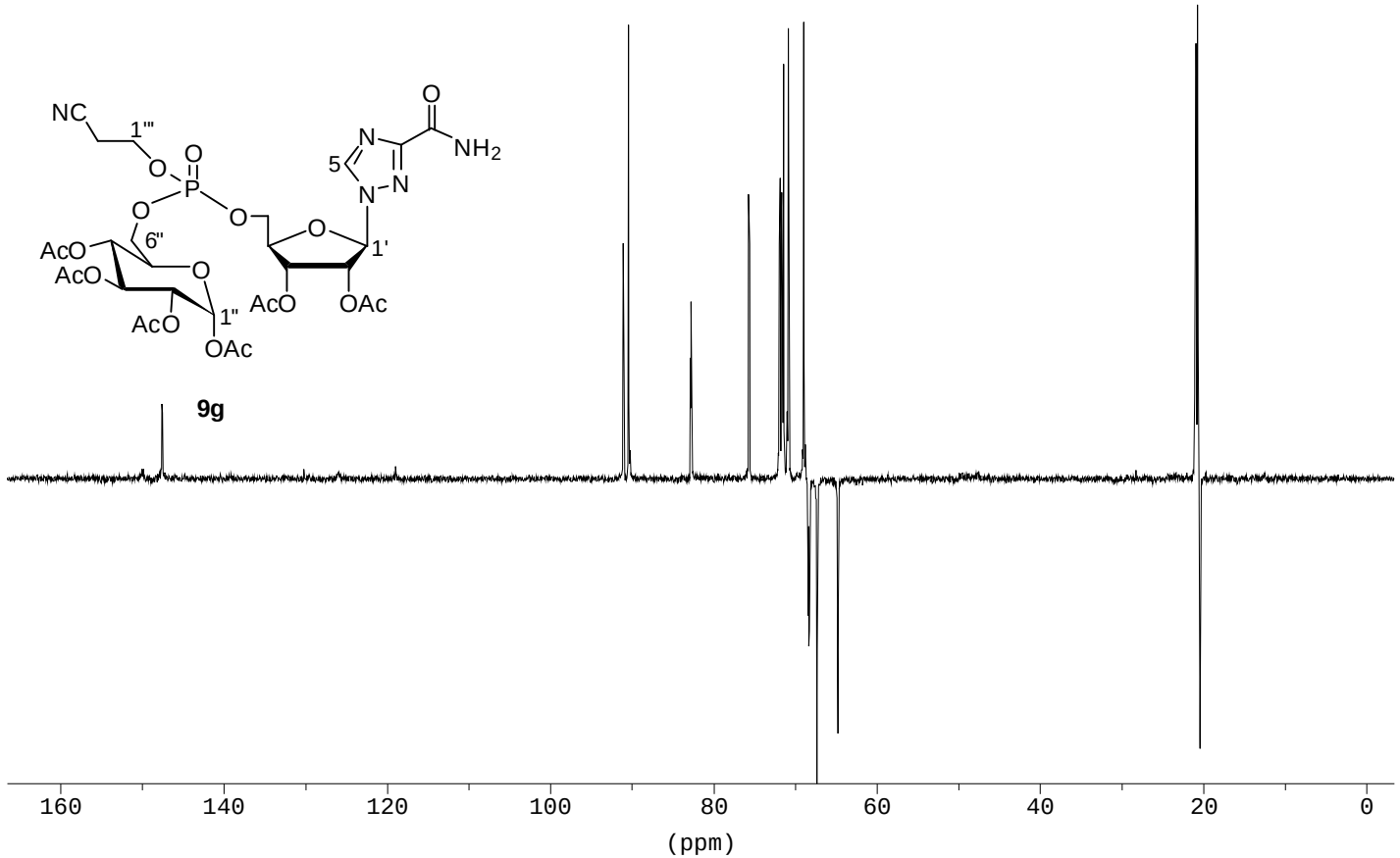
2-Cyanoethyl-[2',3'-di-*O*-acetyl-1'-(3-carbamoyl-1,2,4-triazoyl)-β-D-ribofuranos-5'-yl]-1,2,3,4-tetra-*O*-acetyl-α-D-glucopyranos-6-yl phosphate (9g)

^{13}C-RMN (MeOH-d_4, 150.5 MHz)



2-Cyanoethyl-[2',3'-di-*O*-acetyl-1'-(3-carbamoyl-1,2,4-triazoyl)-β-D-ribofuranos-5'-yl]-1,2,3,4-tetra-*O*-acetyl-α-D-glucopyranos-6-yl phosphate (9g)

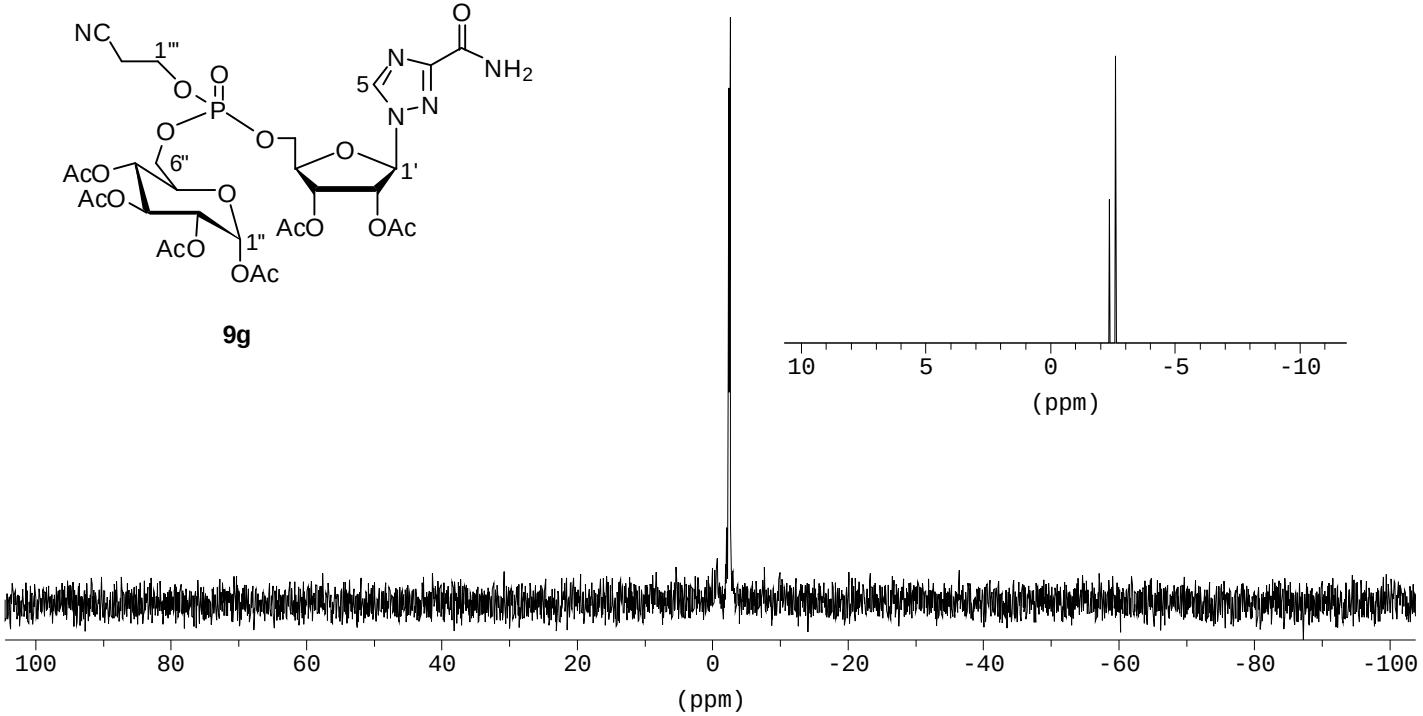
DEPT (MeOH-d_4, 150.5 MHz)



2-Cyanoethyl-[2',3'-di-*O*-acetyl-1'-(3-carbamoyl-1,2,4-triazoyl)-β-D-ribofuranos-5'-yl]-1,2,3,4-tetra-*O*-acetyl-α-D-glucopyranos-6-yl phosphate (9g)

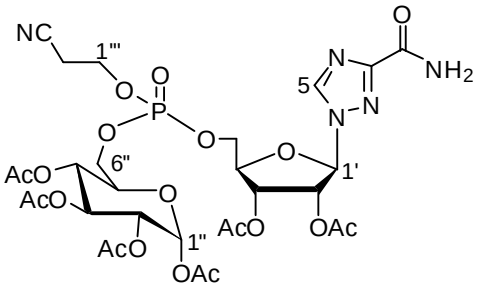
^{31}P-RMN (MeOH-d_4, 242.9 MHz)

9g

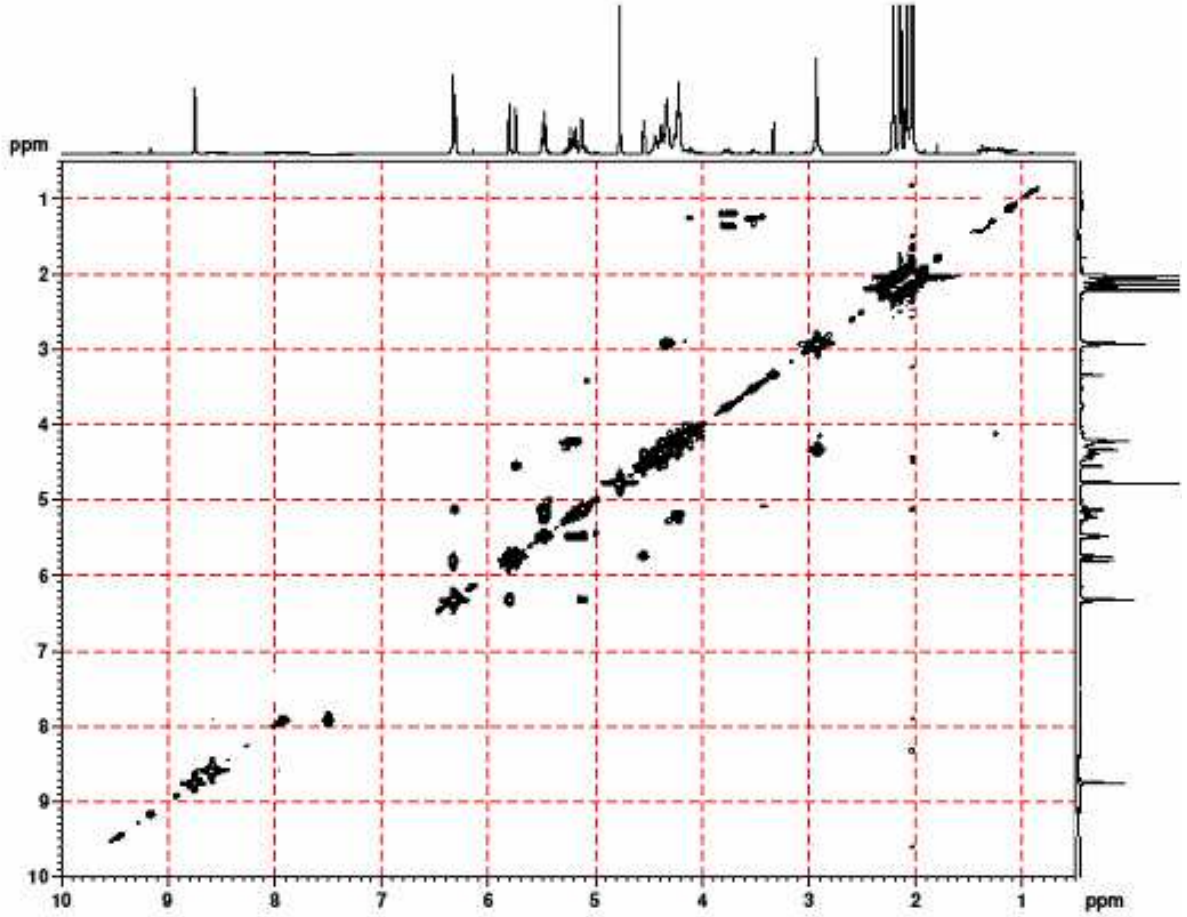


2-Cyanoethyl-[2',3'-di-*O*-acetyl-1'-(3-carbamoyl-1,2,4-triazoyl)-β-D-ribofuranos-5'-yl]-1,2,3,4-tetra-*O*-acetyl-α-D-glucopyranos-6-yl phosphate (9g)

COSY (MeOH-d_4, 600 MHz)

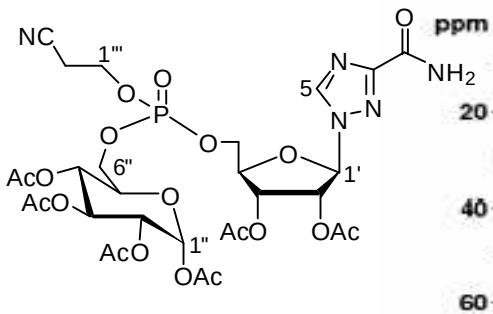


9g

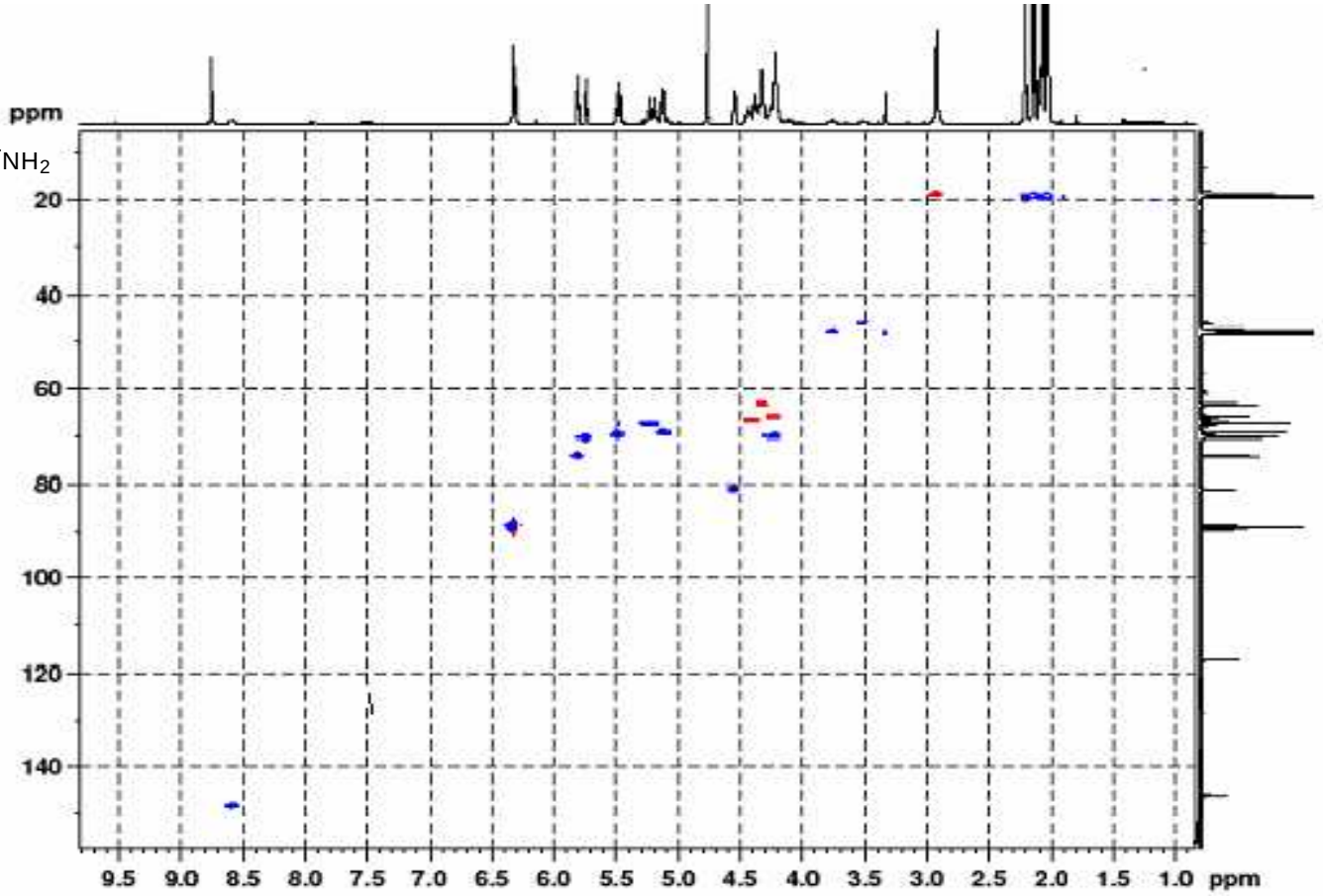


2-Cyanoethyl-[2',3'-di-*O*-acetyl-1'-(3-carbamoyl-1,2,4-triazoyl)-β-D-ribofuranos-5'-yl]-1,2,3,4-tetra-*O*-acetyl-α-D-glucopyranos-6-yl phosphate (9g)

HSQC (MeOH-d_4, 600 MHz)

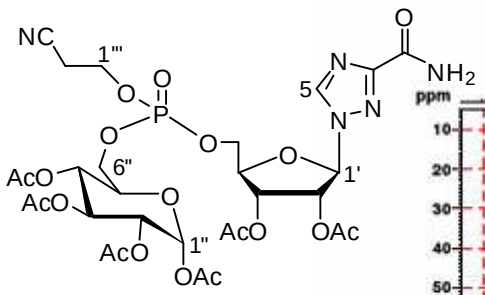


9g

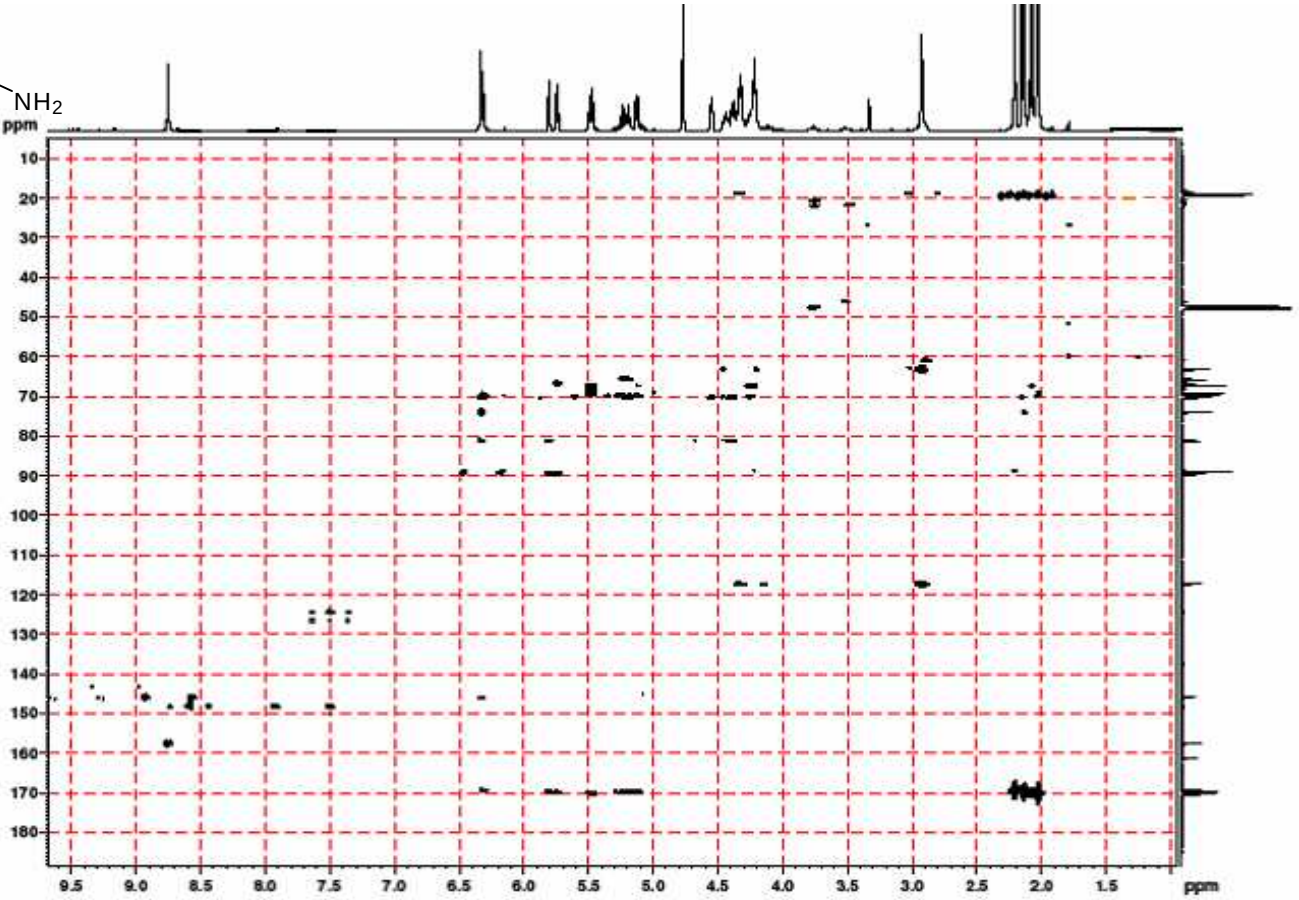


2-Cyanoethyl-[2',3'-di-*O*-acetyl-1'-(3-carbamoyl-1,2,4-triazoyl)-β-D-ribofuranos-5'-yl]-1,2,3,4-tetra-*O*-acetyl-α-D-glucopyranos-6-yl phosphate (9g)

HMBC (MeOH-d_4, 600 MHz)



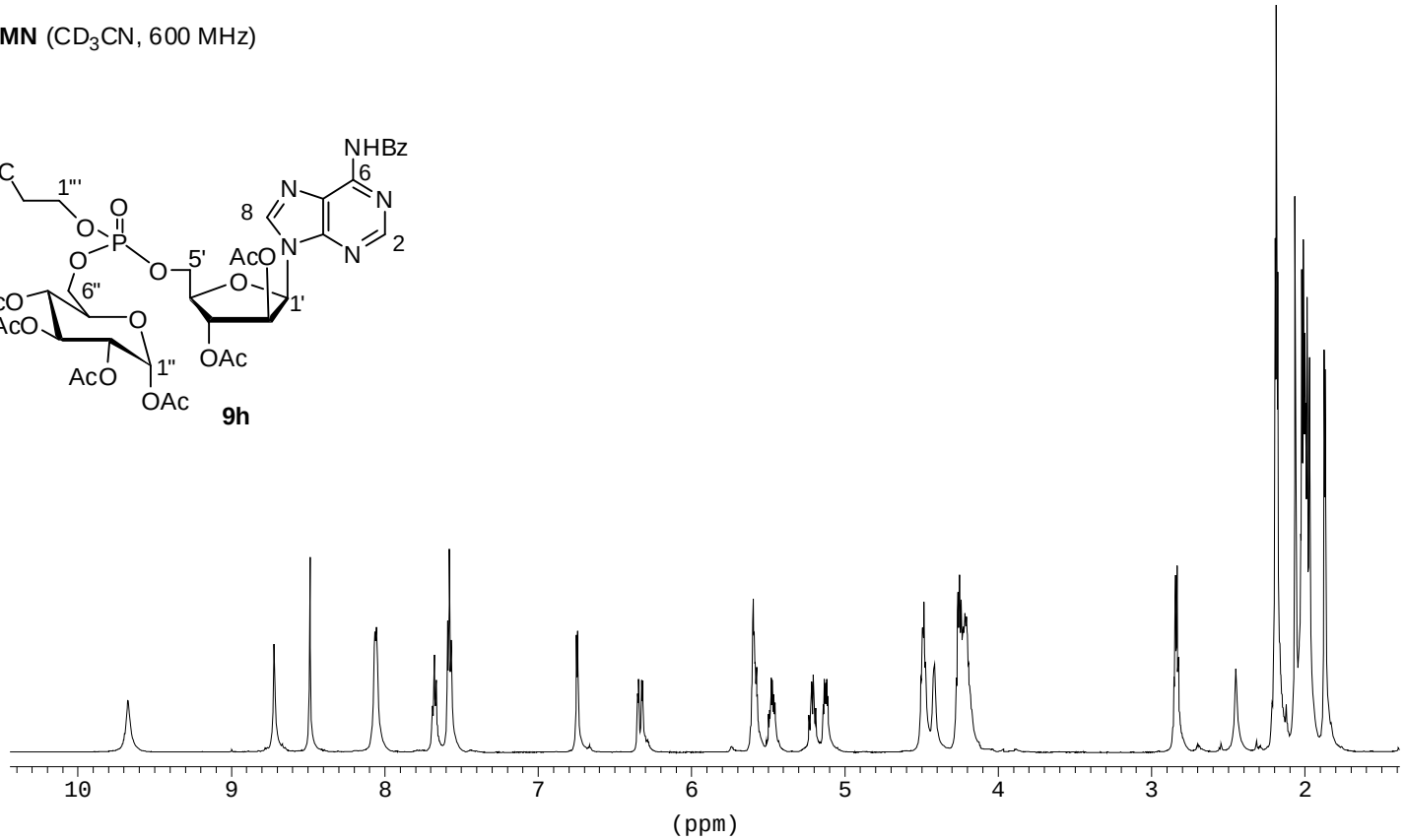
9g



2-Cyanoethyl-[2',3'-di-*O*-acetyl-1'-(*N*^{6}-benzoyladeninyl)-β-D-arabinofuranos-5'-yl]-1,2,3,4-tetra-*O*-acetyl-α-D-glucopyranos-6-yl phosphate (9h)

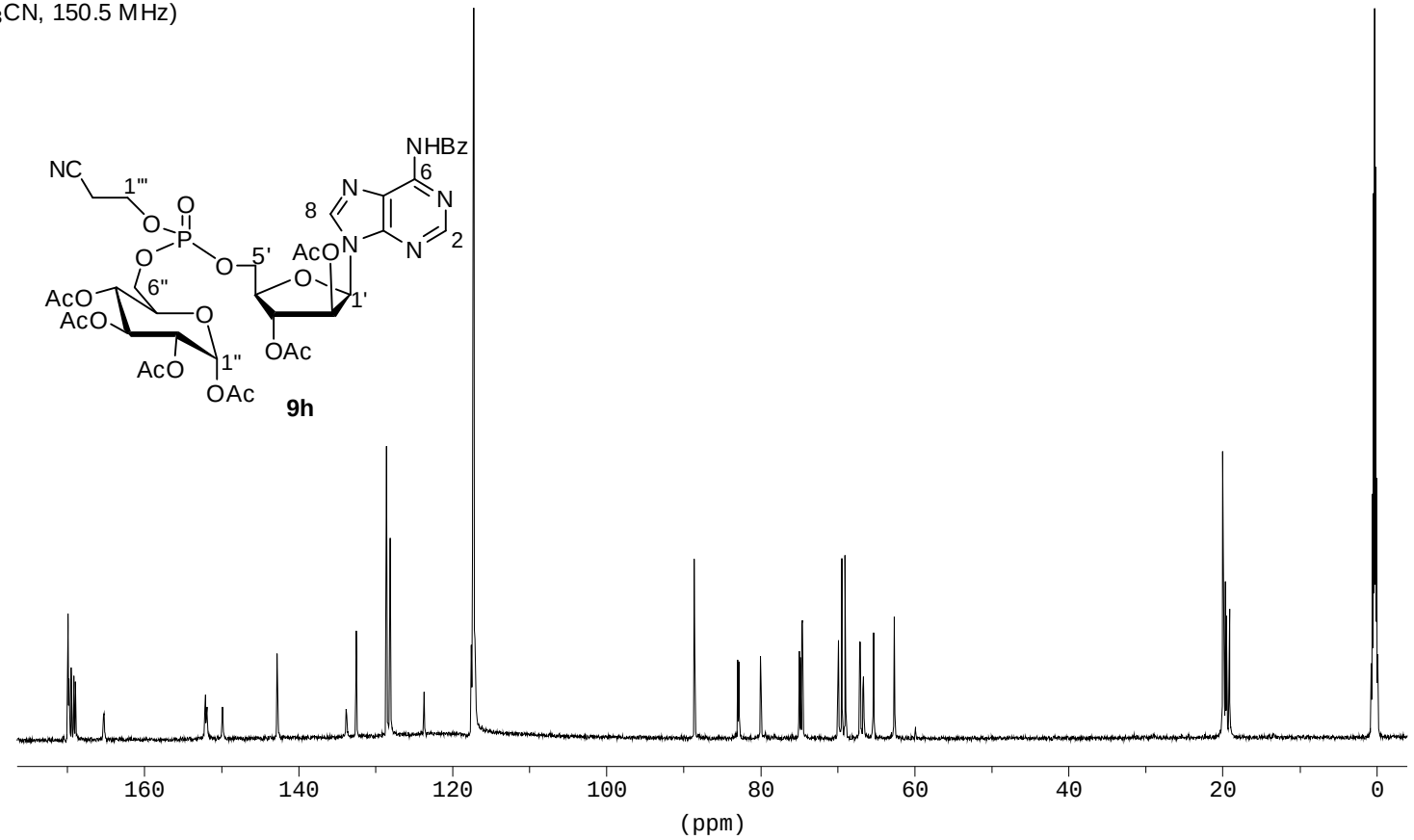
^{1}H-RMN (CD_3CN, 600 MHz)

9h



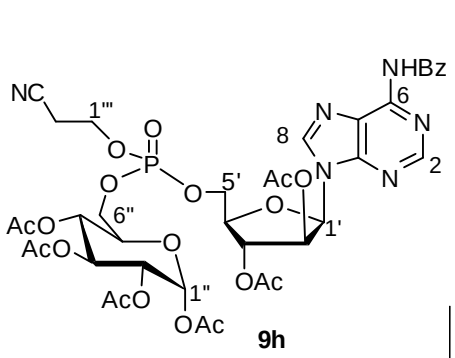
2-Cyanoethyl-[2',3'-di-*O*-acetyl-1'-(*N*^{6}-benzoyladeninyl)-β-D-arabinofuranos-5'-yl]-1,2,3,4-tetra-*O*-acetyl-α-D-glucopyranos-6-yl phosphate (9h)

^{13}C-RMN (CD_3CN, 150.5 MHz)

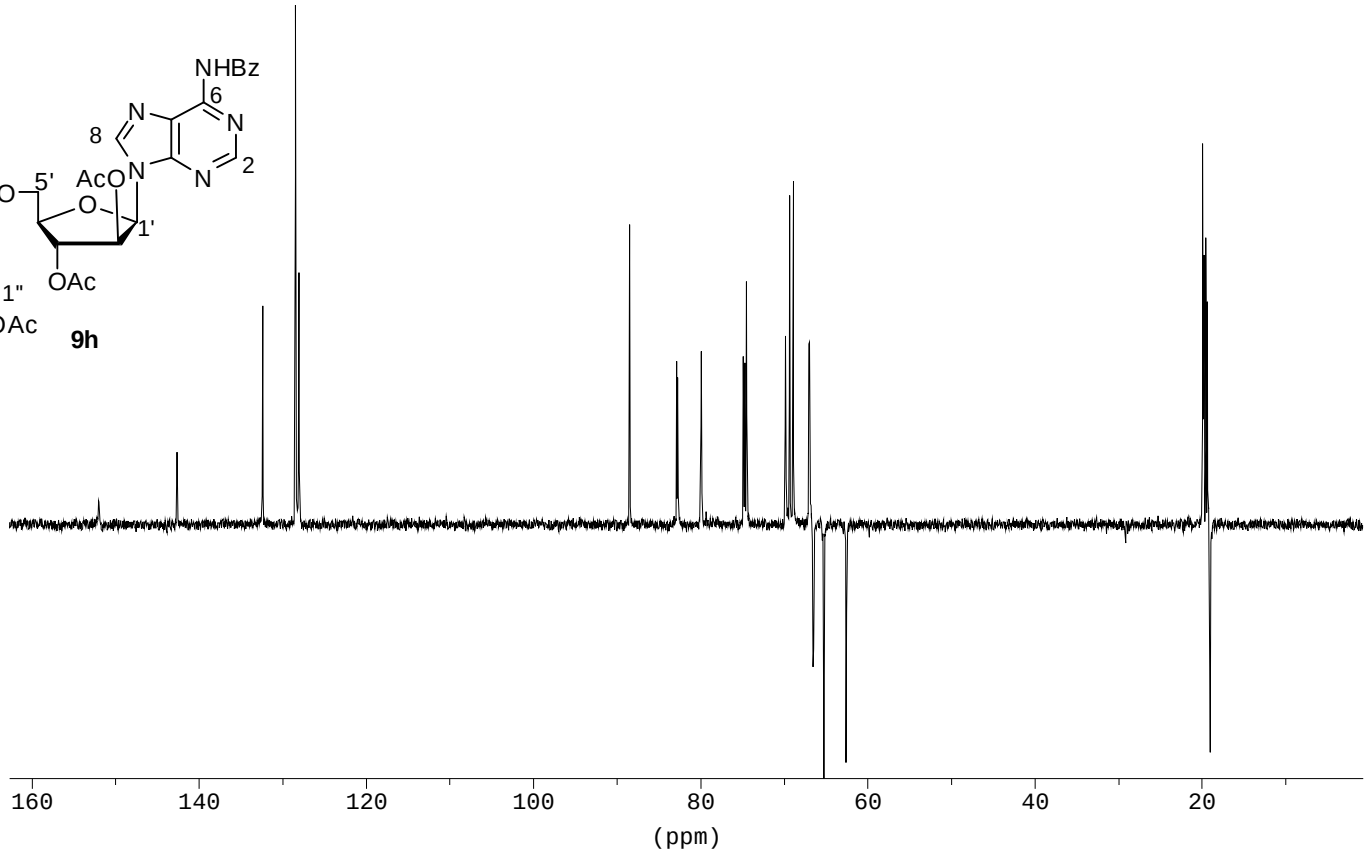


2-Cyanoethyl-[2',3'-di-*O*-acetyl-1'-(*N*^{6}-benzoyladeninyl)-β-D-arabinofuranos-5'-yl]-1,2,3,4-tetra-*O*-acetyl-α-D-glucopyranos-6-yl phosphate (9h)

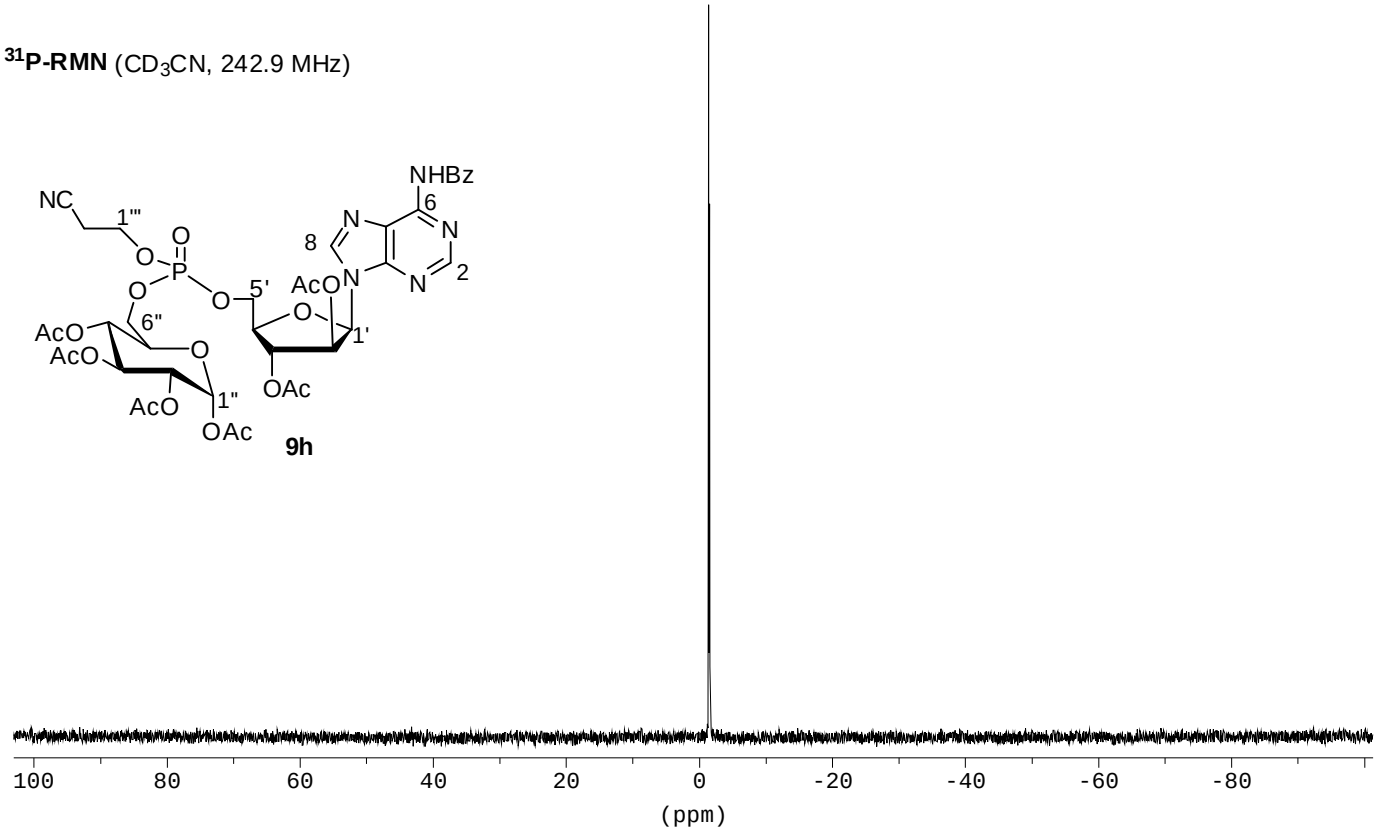
DEPT (CD_3CN, 150.5 MHz)



9h

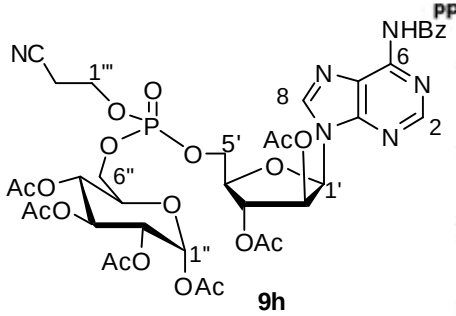


2-Cyanoethyl-[2',3'-di-*O*-acetyl-1'-(*N*^{6}-benzoyladeninyl)-β-D-arabinofuranos-5'-yl]-1,2,3,4-tetra-*O*-acetyl-α-D-glucopyranos-6-yl phosphate (9h)

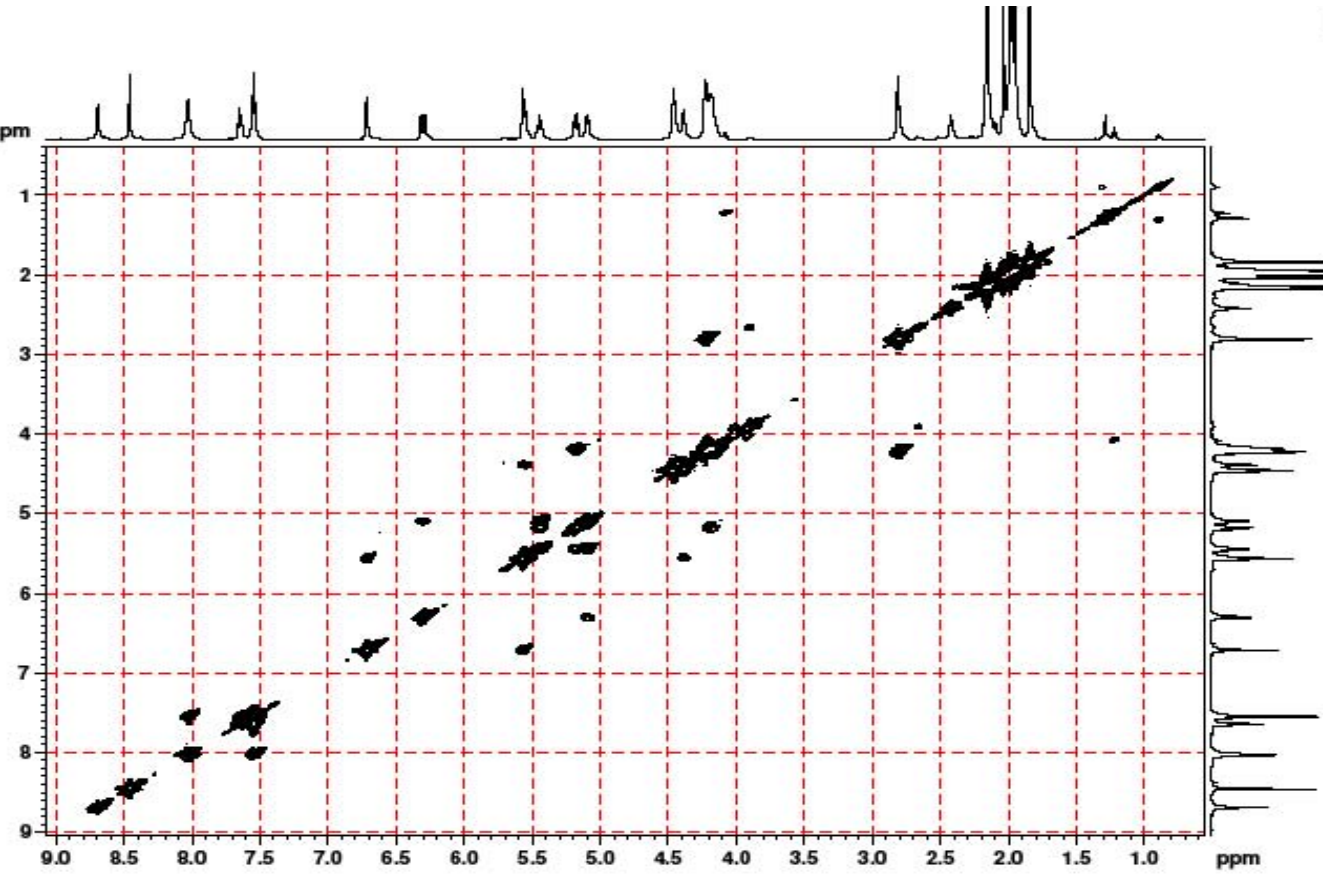


2-Cyanoethyl-[2',3'-di-*O*-acetyl-1'-(*N*^{6}-benzoyladeninyl)-β-D-arabinofuranos-5'-yl]-1,2,3,4-tetra-*O*-acetyl-α-D-glucopyranos-6-yl phosphate (9h)

COSY (CD_3CN, 600 MHz)

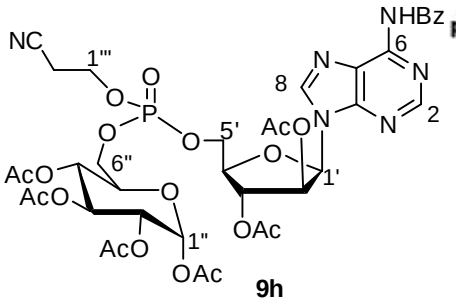


9h

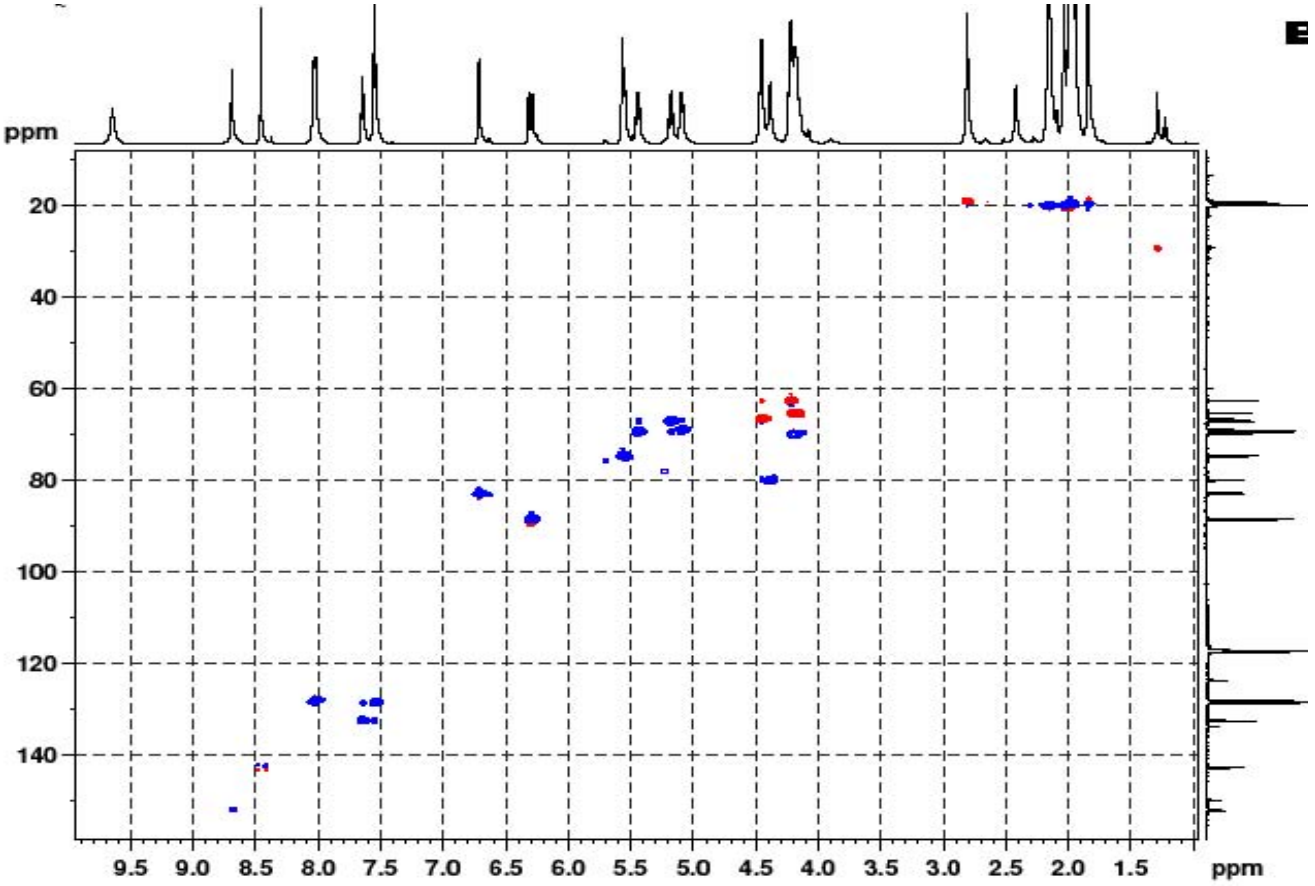


2-Cyanoethyl-[2',3'-di-*O*-acetyl-1'-(*N*^{6}-benzoyladeninyl)-β-D-arabinofuranos-5'-yl]-1,2,3,4-tetra-*O*-acetyl-α-D-glucopyranos-6-yl phosphate (9h)

HSQC (CD_3CN, 600 MHZ)

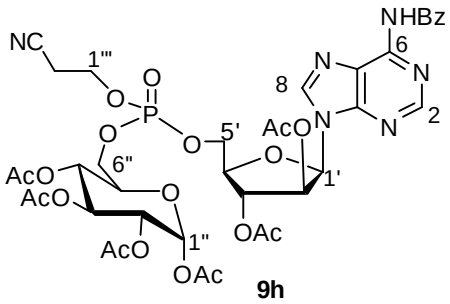


9h

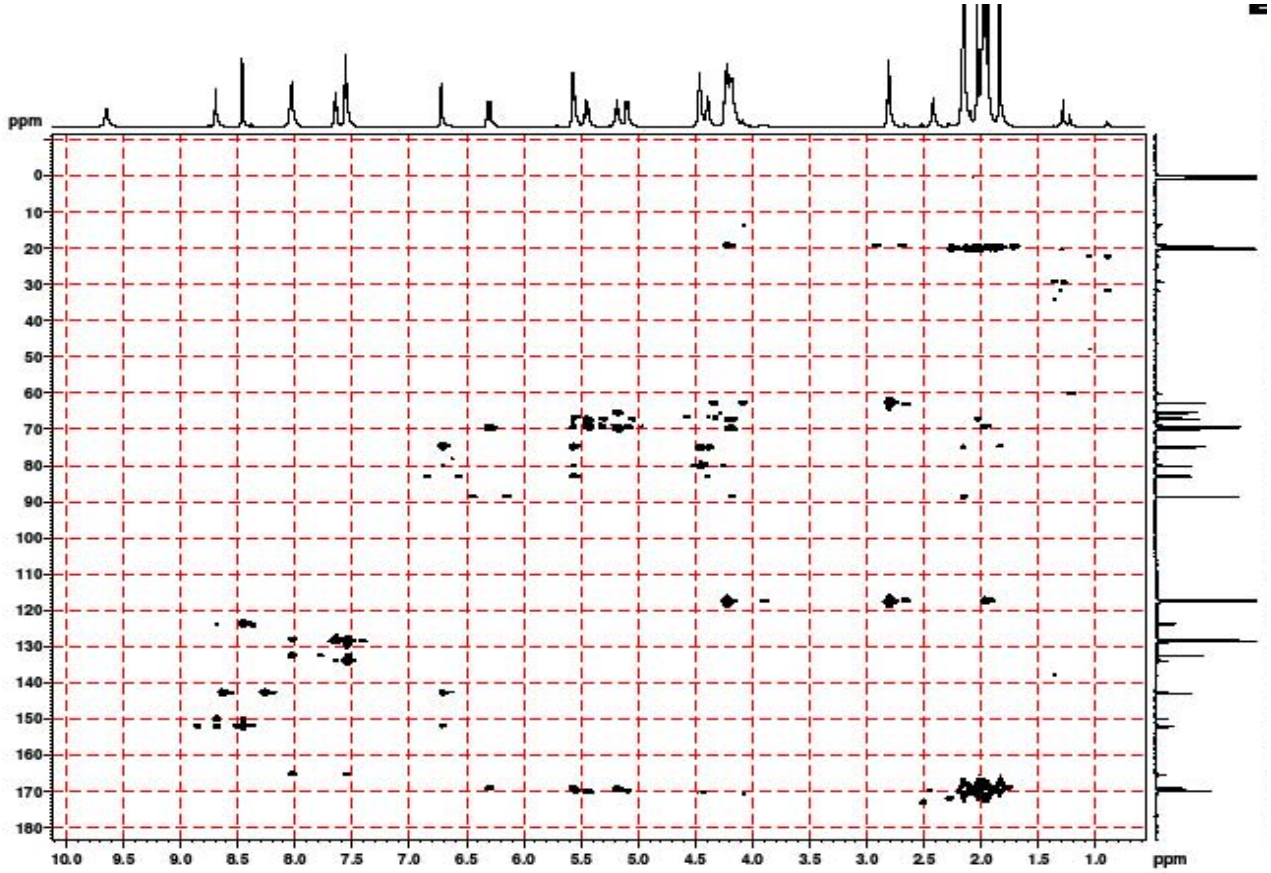


2-Cyanoethyl-[2',3'-di-*O*-acetyl-1'-(*N*^{6}-benzoyladeninyl)-β-D-arabinofuranos-5'-yl]-1,2,3,4-tetra-*O*-acetyl-α-D-glucopyranos-6-yl phosphate (9h)

HMBC (CD_3CN, 600 MHz)



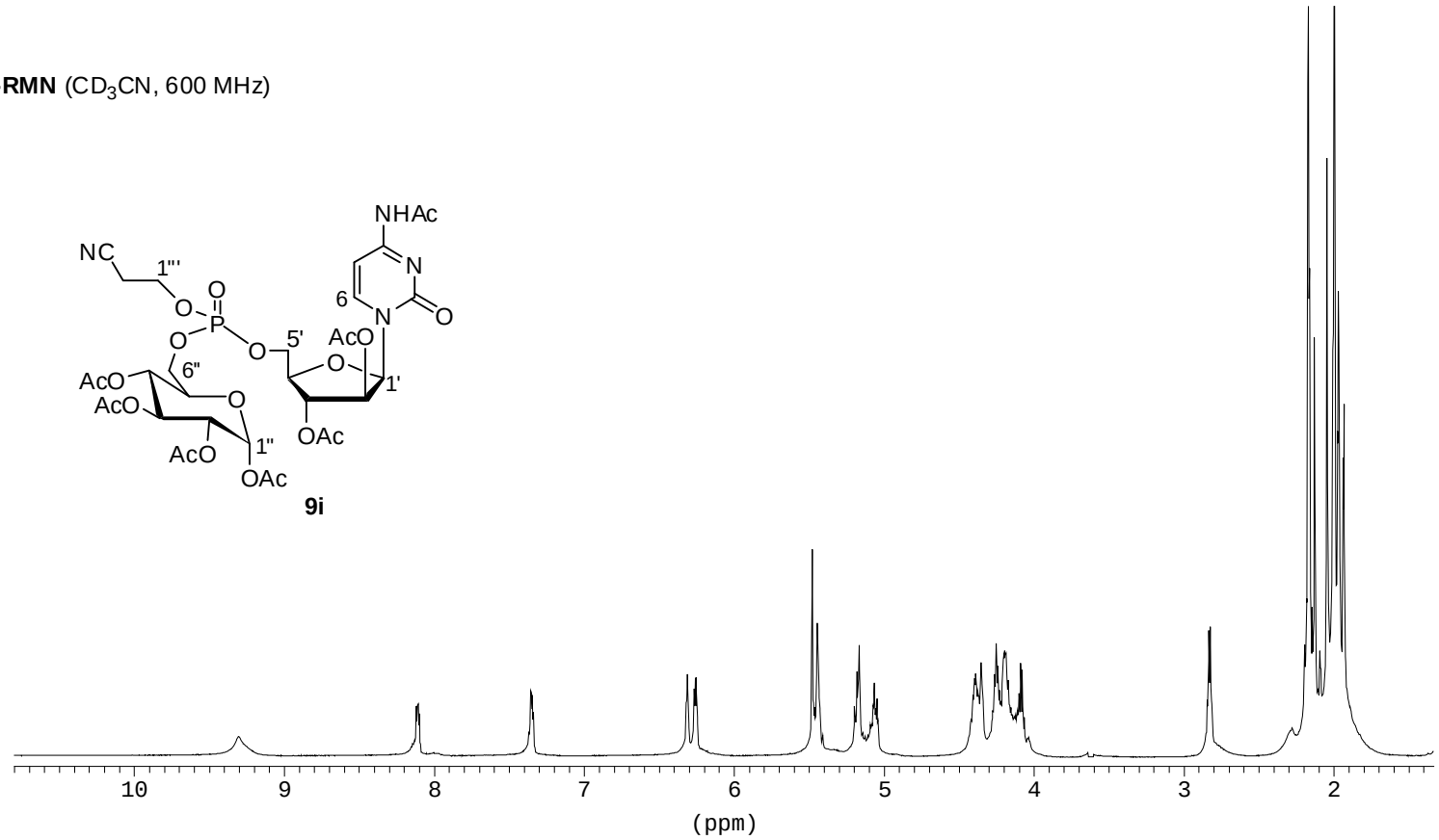
9h



2-Cyanoethyl-[2',3'-di-*O*-acetyl-1'-(N^4-benzoylcytosinyl)-β-D-arabinofuranos-5'-yl]-1,2,3,4-tetra-*O*-acetyl-α-D-glucopyranos-6-yl phosphate (9i)

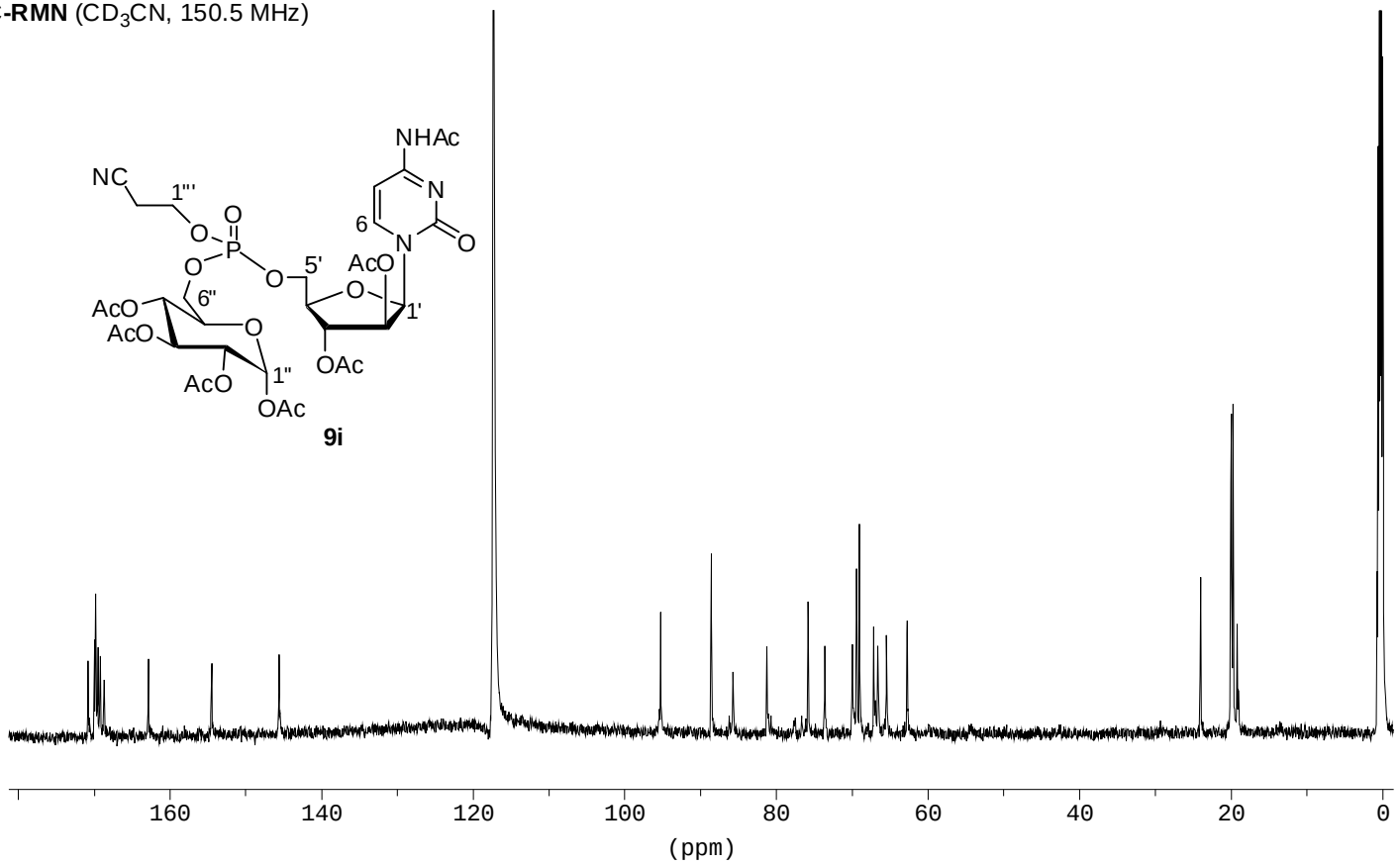
^{1}H-RMN (CD_3CN, 600 MHz)

9i



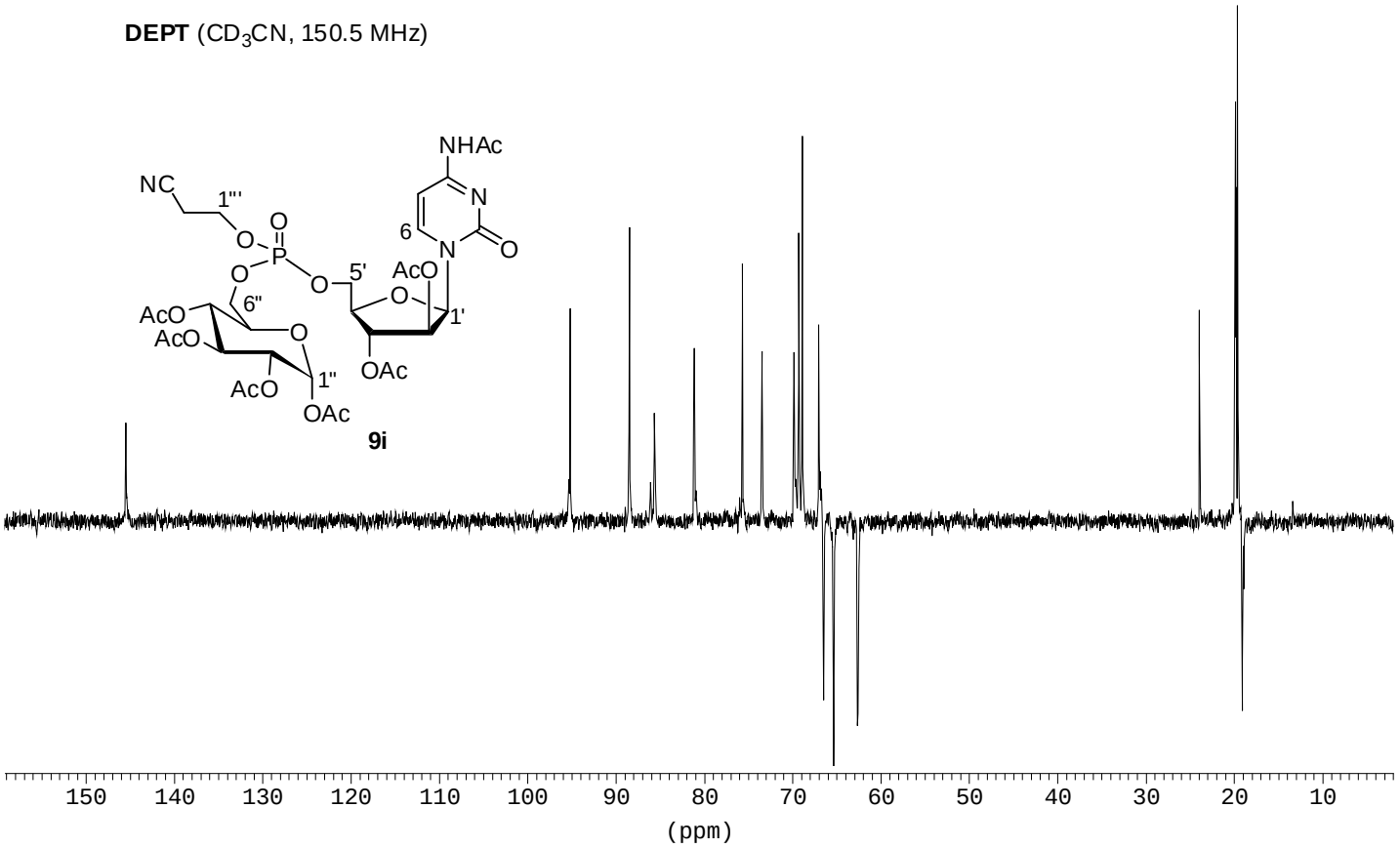
2-Cyanoethyl-[2',3'-di-*O*-acetyl-1'-(*N*^{4}-benzoylcytosinyl)-β-D-arabinofuranos-5'-yl]-1,2,3,4-tetra-*O*-acetyl-α-D-glucopyranos-6-yl phosphate (9i)

^{13}C-RMN (CD_3CN, 150.5 MHz)



9i

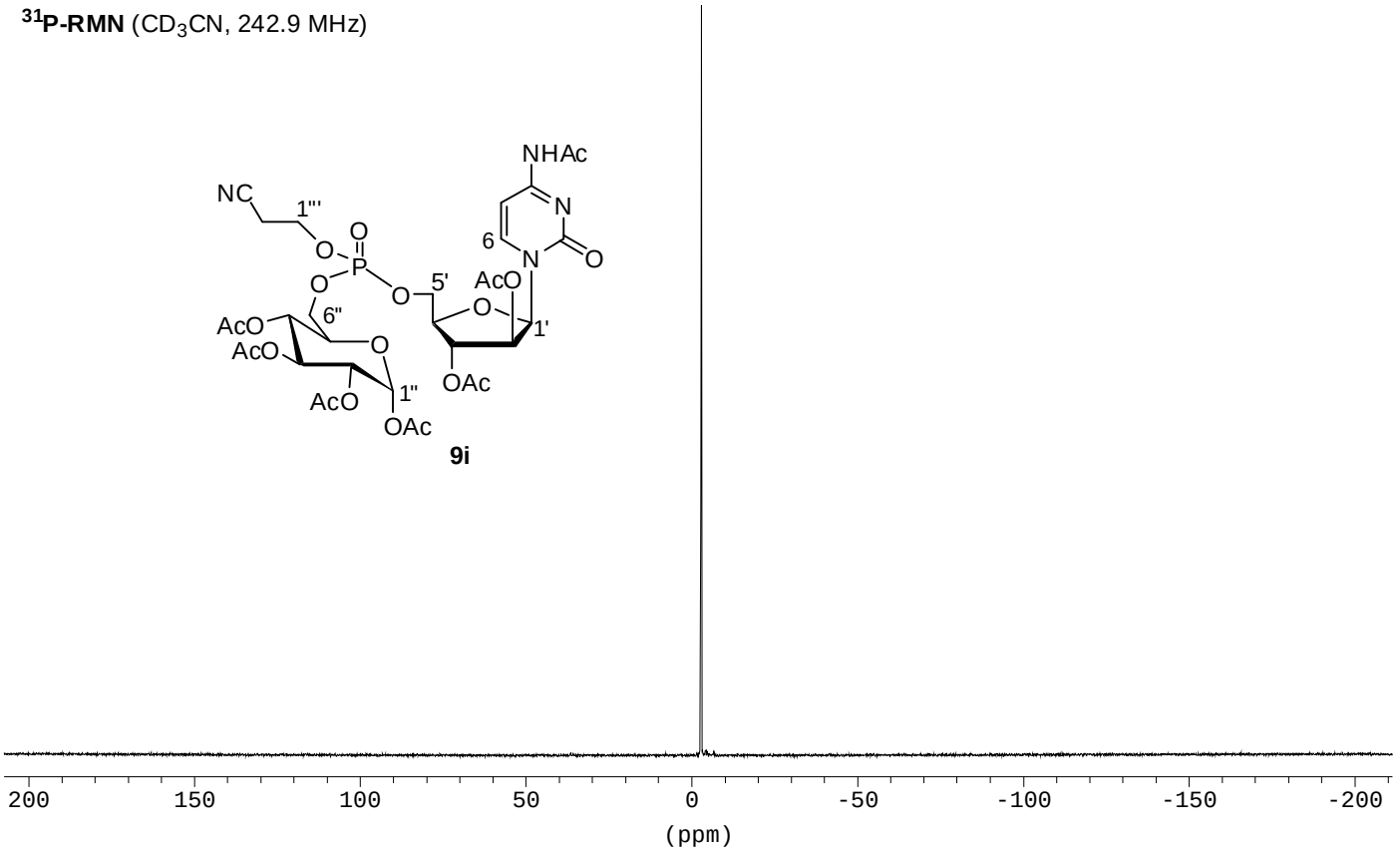
2-Cyanoethyl-[2',3'-di-*O*-acetyl-1'-(N^4-benzoylcytosinyl)-β-D-arabinofuranos-5'-yl]-1,2,3,4-tetra-*O*-acetyl-α-D-glucopyranos-6-yl phosphate (9i)



2-Cyanoethyl-[2',3'-di-*O*-acetyl-1'-(N^4-benzoylcytosinyl)-β-D-arabinofuranos-5'-yl]-1,2,3,4-tetra-*O*-acetyl-α-D-glucopyranos-6-yl phosphate (9i)

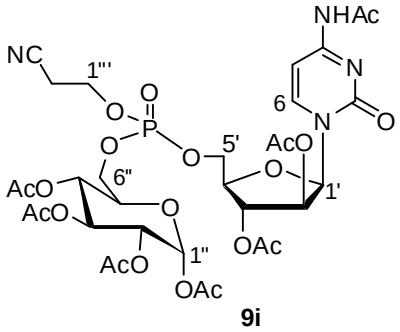
^{31}P-RMN (CD_3CN, 242.9 MHz)

9i

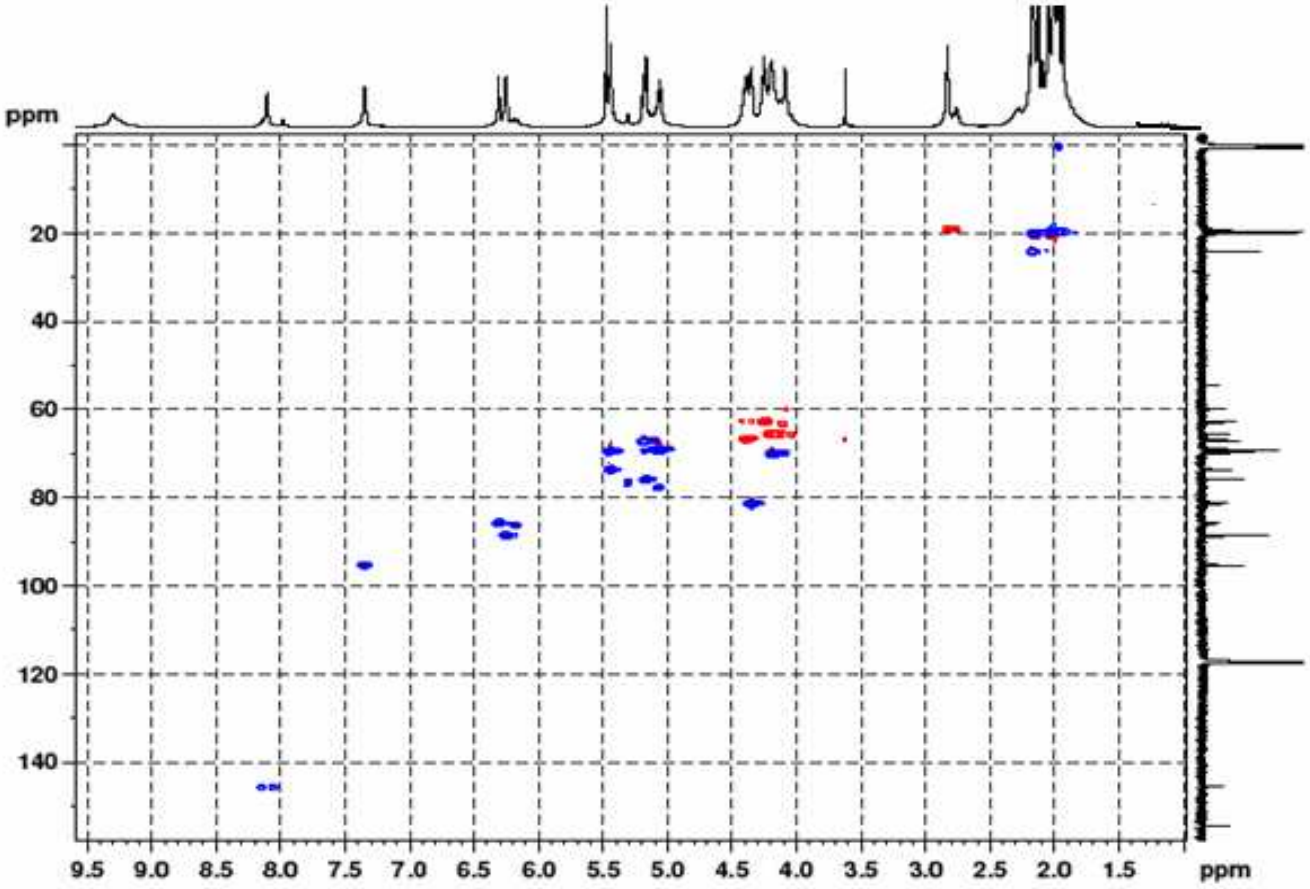


2-Cyanoethyl-[2',3'-di-*O*-acetyl-1'-(N^4-benzoylcytosinyl)-β-D-arabinofuranos-5'-yl]-1,2,3,4-tetra-*O*-acetyl-α-D-glucopyranos-6-yl phosphate (9i)

HSQC (CD_3CN, 600 MHz)

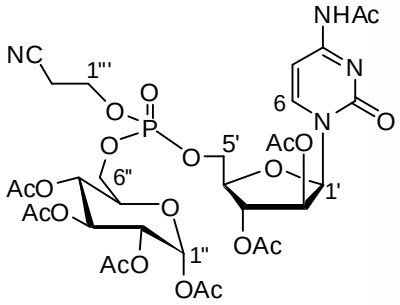


9i

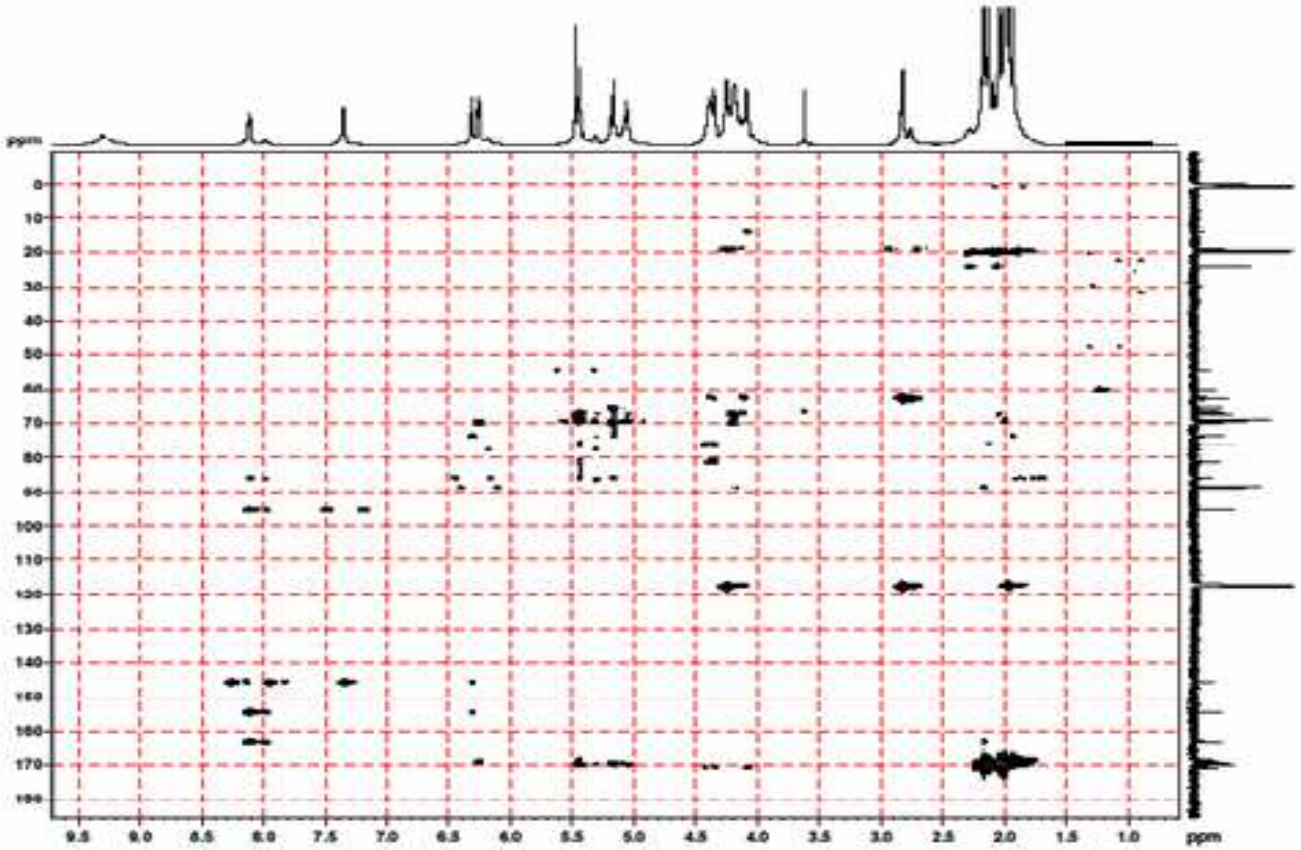


2-Cyanoethyl-[2',3'-di-*O*-acetyl-1'-(N^4-benzoylcytosinyl)-β-D-arabinofuranos-5'-yl]-1,2,3,4-tetra-*O*-acetyl-α-D-glucopyranos-6-yl phosphate (9i)

HMBC (CD_3CN, 600 MHz)

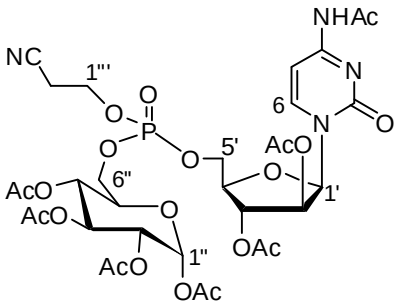


9i

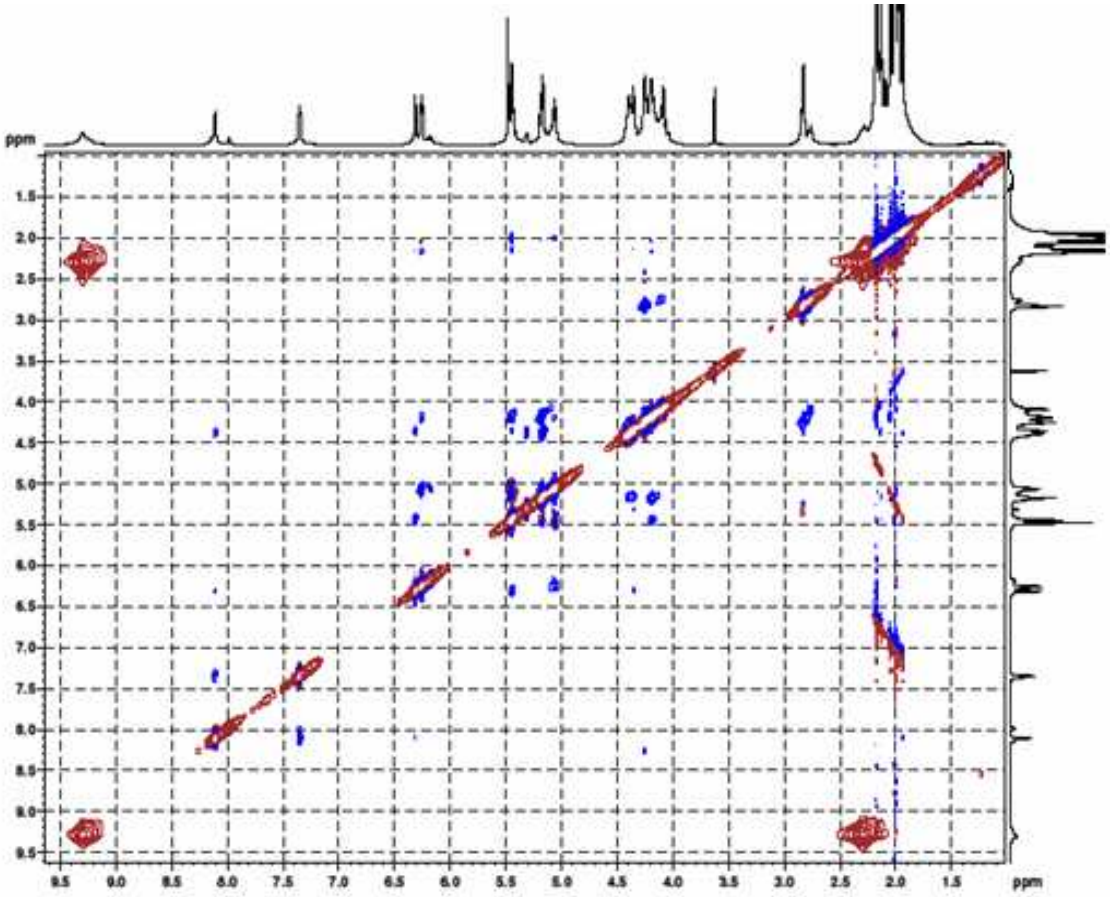


2-Cyanoethyl-[2',3'-di-*O*-acetyl-1'-(N^4-benzoylcytosinyl)-β-D-arabinofuranos-5'-yl]-1,2,3,4-tetra-*O*-acetyl-α-D-glucopyranos-6-yl phosphate (9i)

NOESY (CD_3CN, 600 MHz)

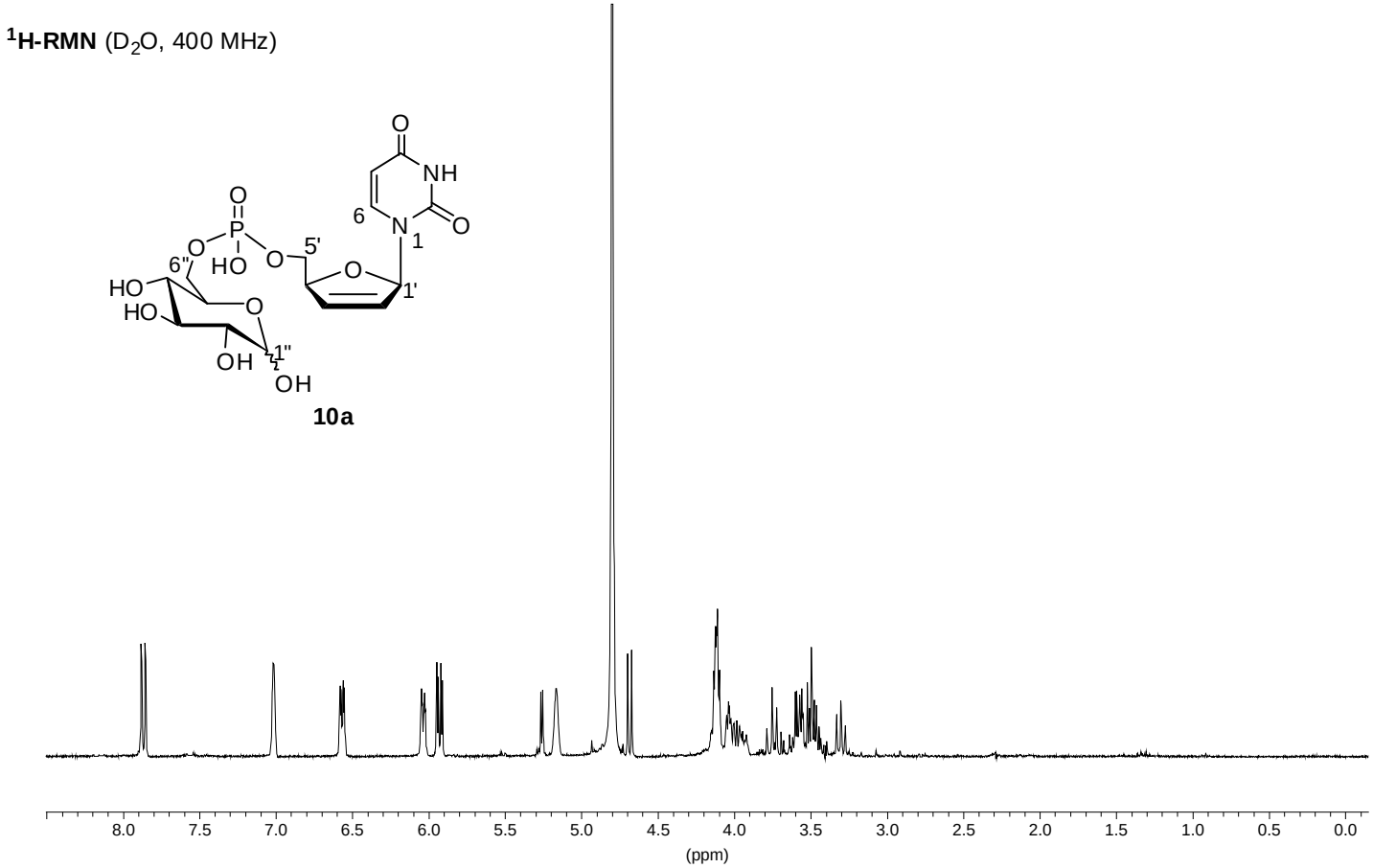


9i



2',3'-Didehydro-2',3'-dideoxyuridine 5'-(α/β-D-glucopyranos-6-yl) phosphate (10a)

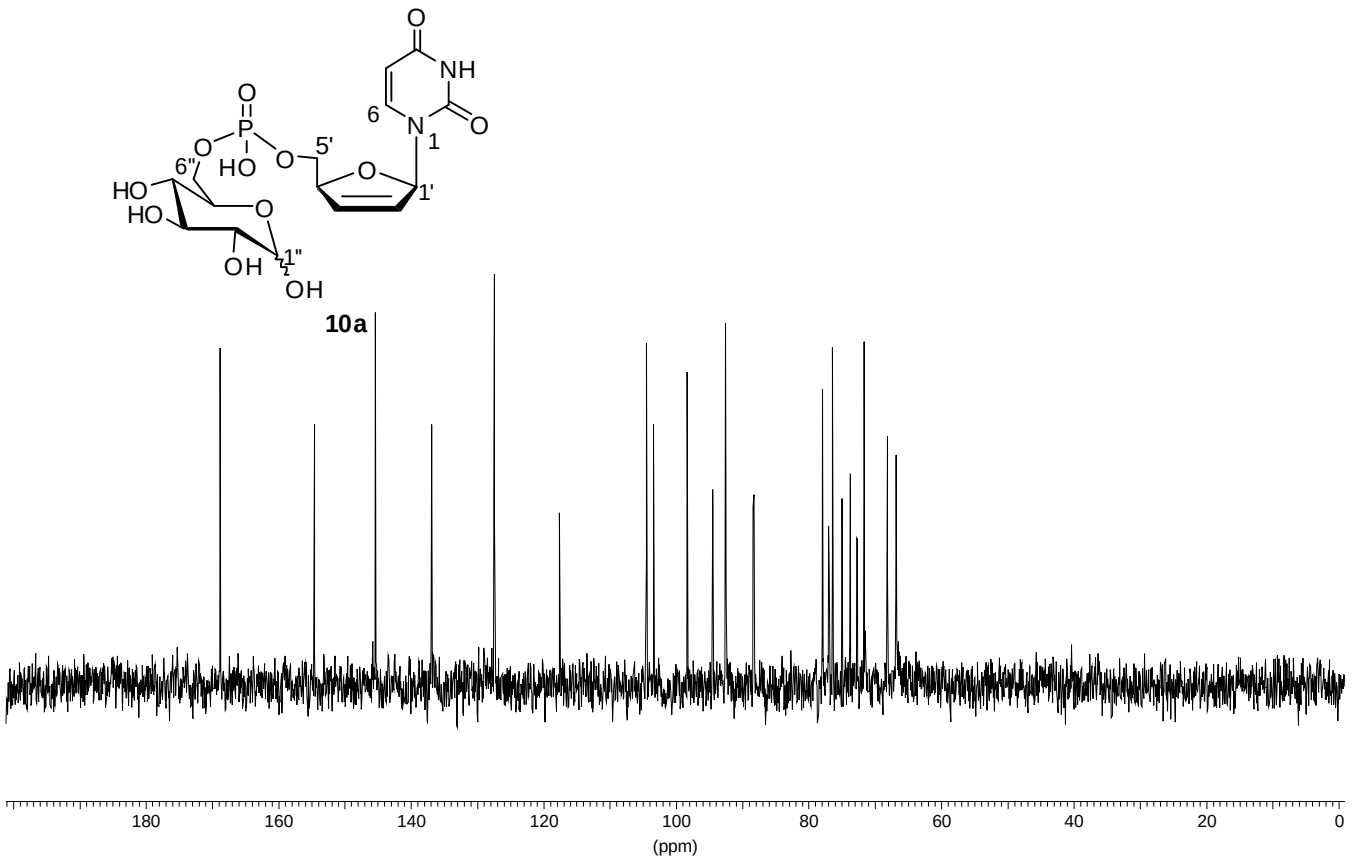
^{1}H-RMN (D_2O, 400 MHz)



10a

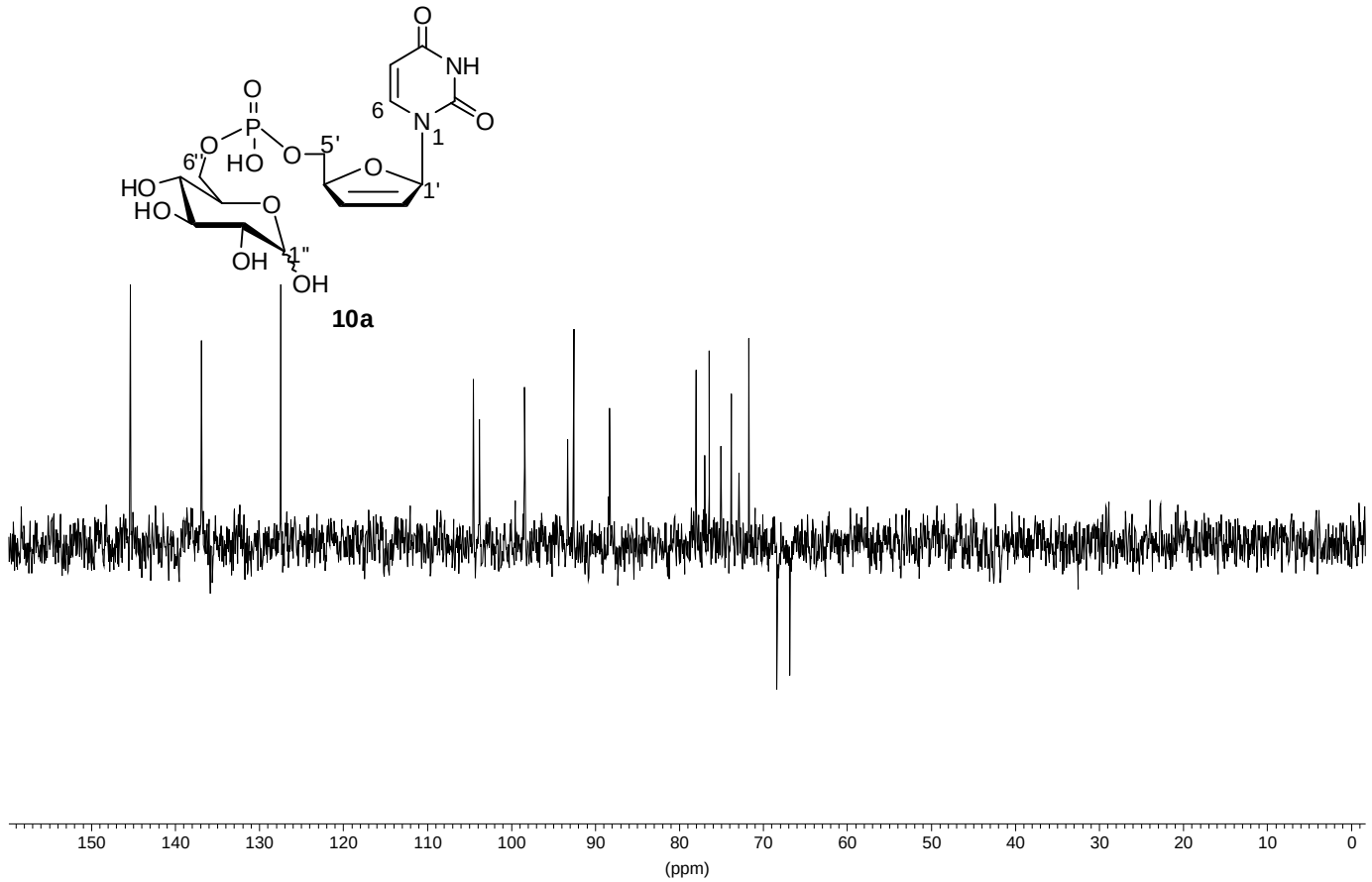
2’,3’-Didehydro-2’,3’-dideoxyuridine 5’-(α/β-D-glucopyranos-6-yl) phosphate (10a)

^{13}C-RMN (D_2O, 100.6 MHz)



2’,3’-Didehydro-2’,3’-dideoxyuridine 5’-(α/β-D-glucopyranos-6-yl) phosphate (10a)

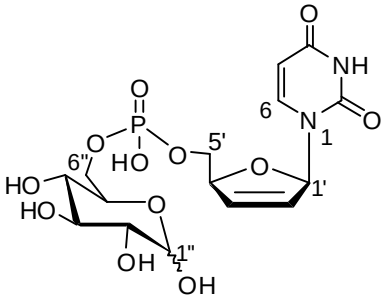
DEPT (D_2O, 100.6 MHz)



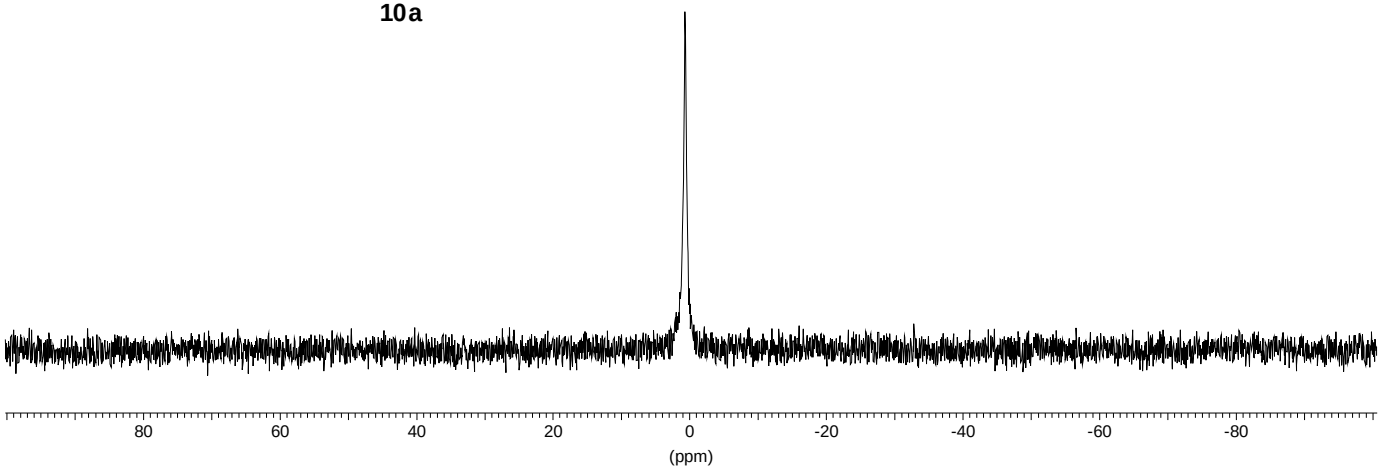
10a

2',3'-Didehydro-2',3'-dideoxyuridine 5'-(α/β-D-glucopyranos-6-yl) phosphate (10a)

^{31}P-RMN (D_2O, 161.9 MHz)

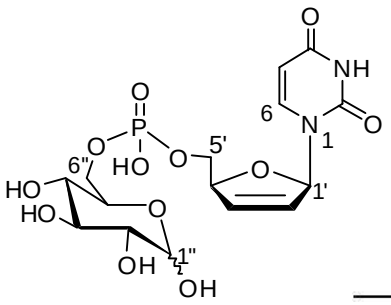


10a

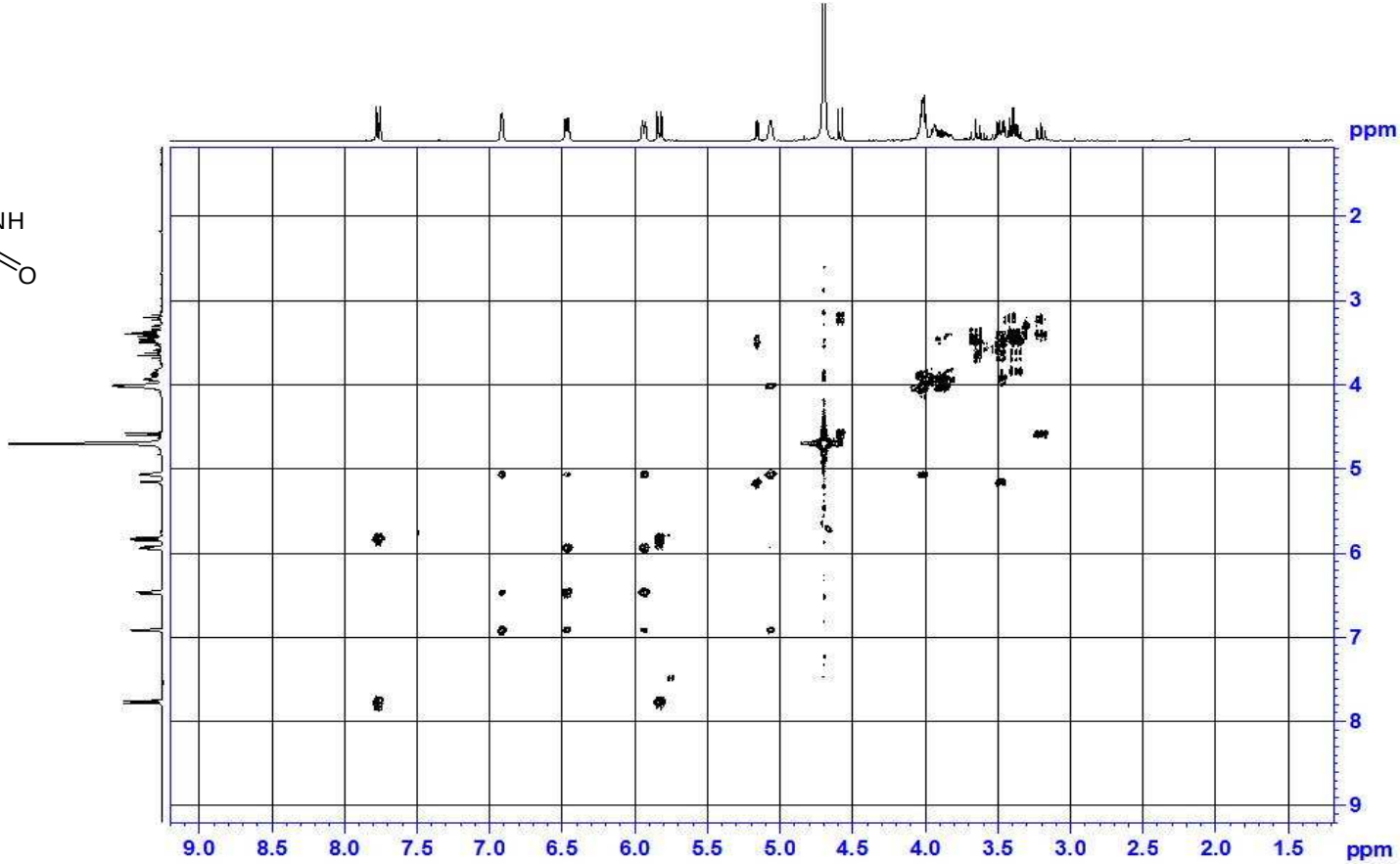


2',3'-Didehydro-2',3'-dideoxyuridine 5'-(α/β-D-glucopyranos-6-yl) phosphate (10a)

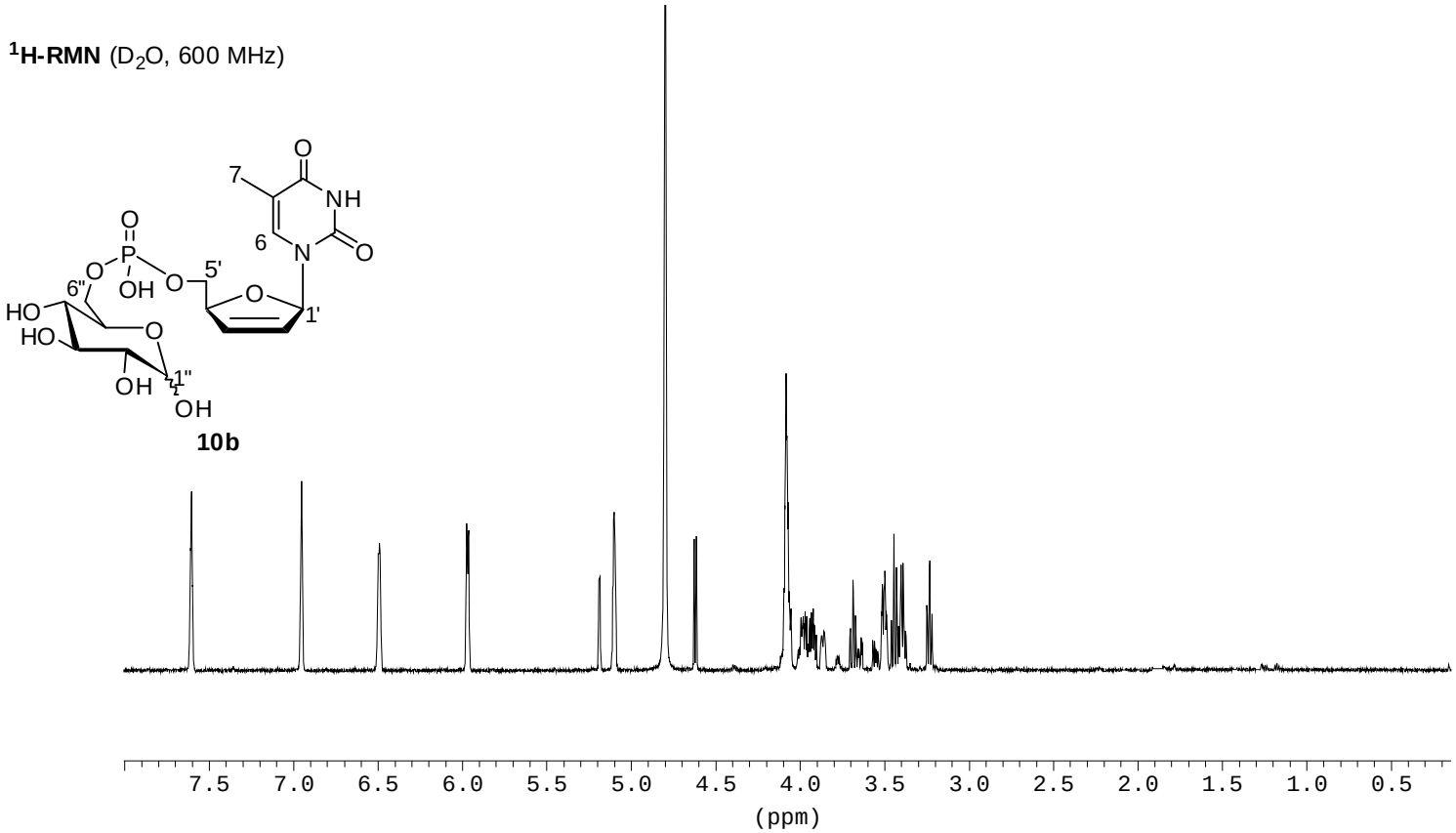
COSY (D_2O, 400 MHz)



10a

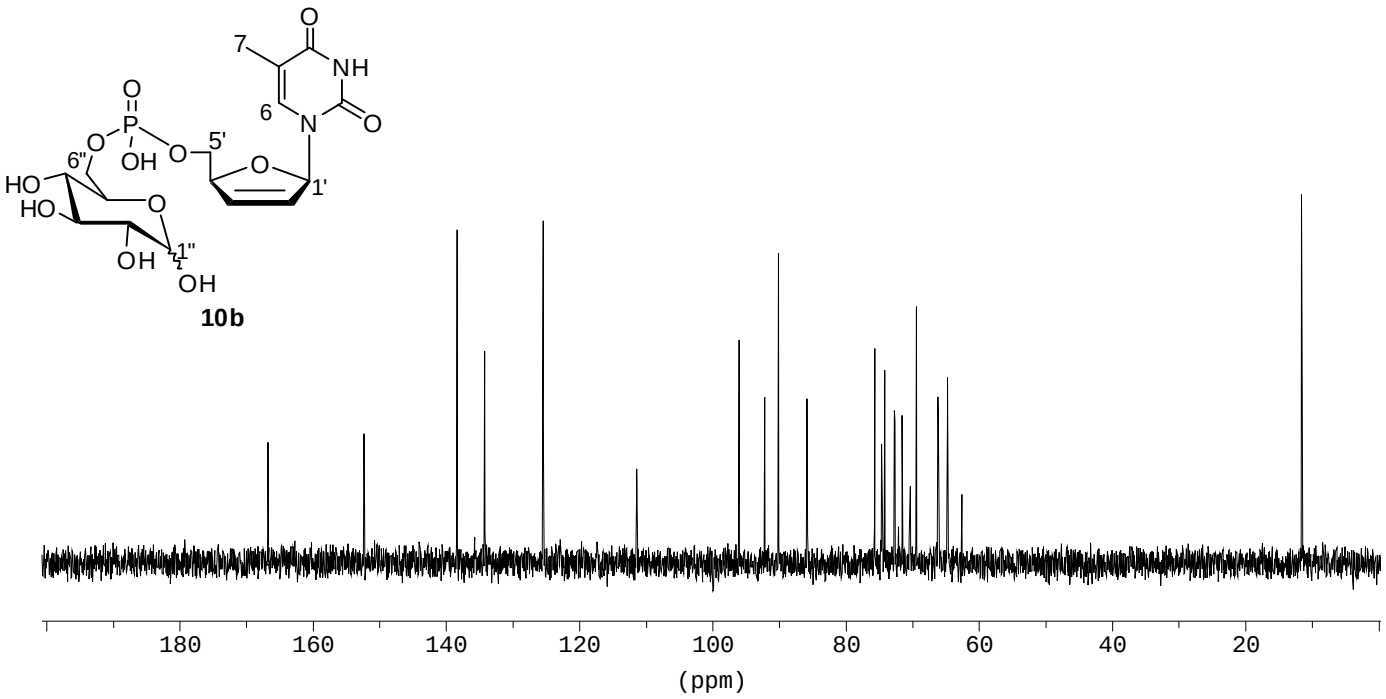


2',3'-Didehydro-2',3'-dideoxythymidine 5'-(α/β-D-glucopyranos-6-yl) phosphate (10b)



2',3'-Didehydro-2',3'-dideoxythymidine 5'-(α/β-D-glucopyranos-6-yl) phosphate (10b)

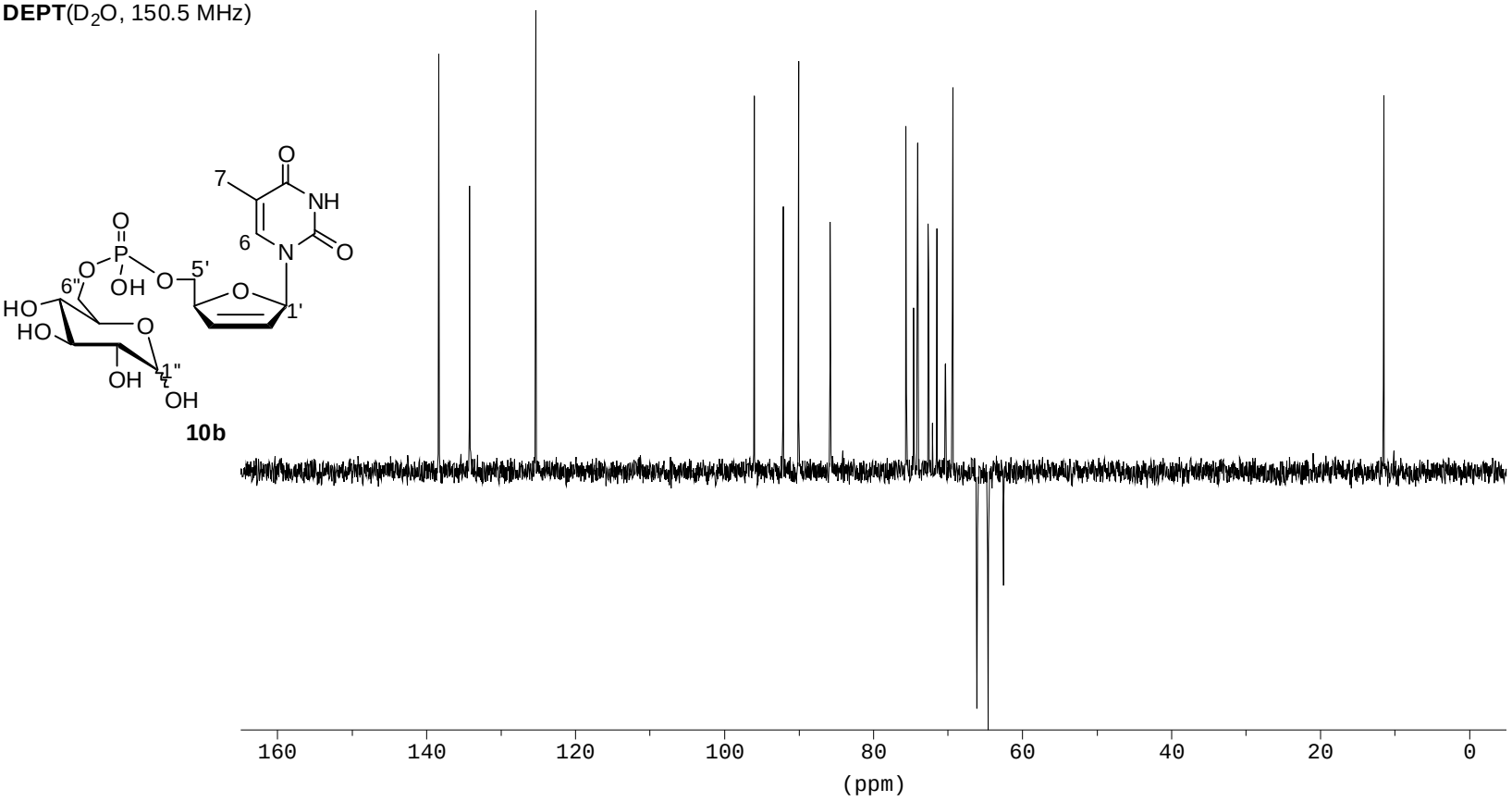
^{13}C-RMN (D_2O, 150.5 MHz)



10b

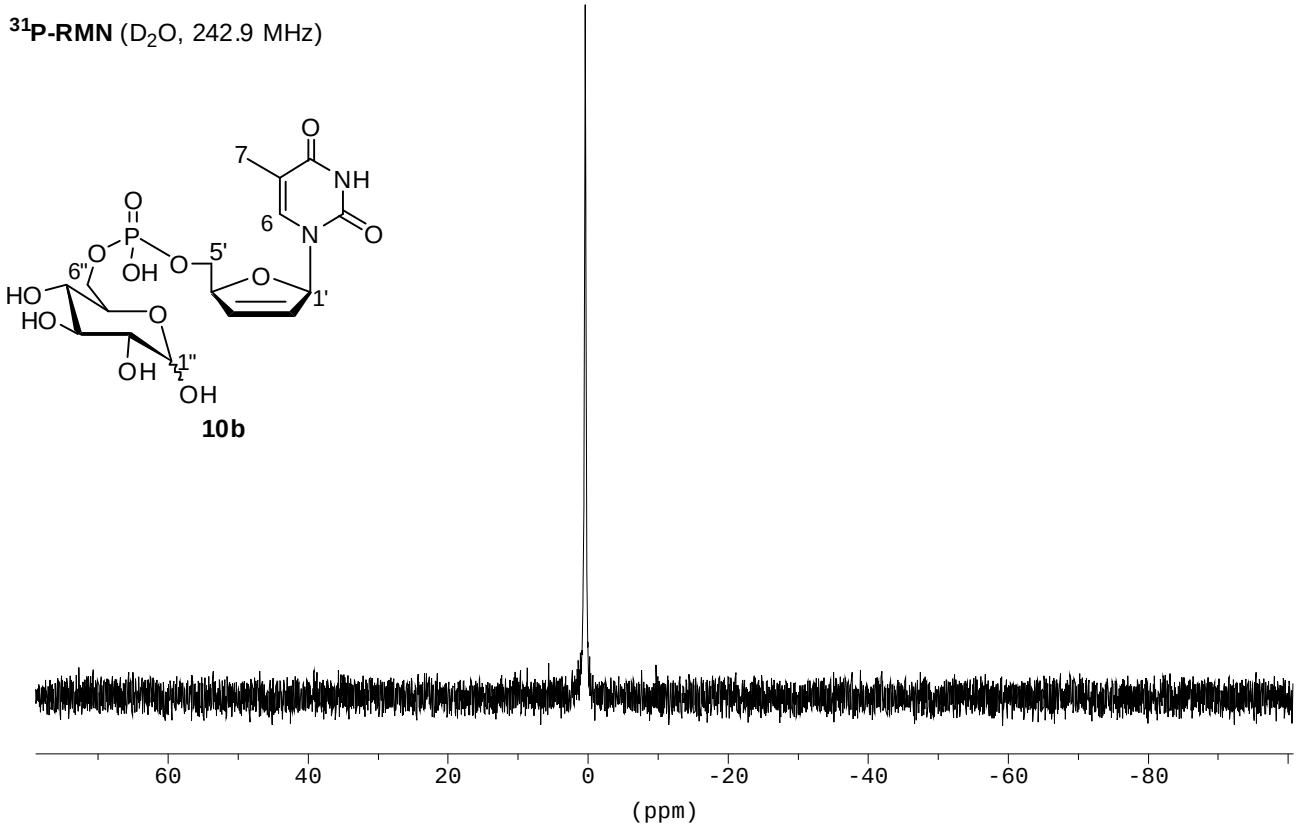
2',3'-Didehydro-2',3'-dideoxythymidine 5'-(α/β-D-glucopyranos-6-yl) phosphate (10b)

DEPT(D_2O, 150.5 MHz)



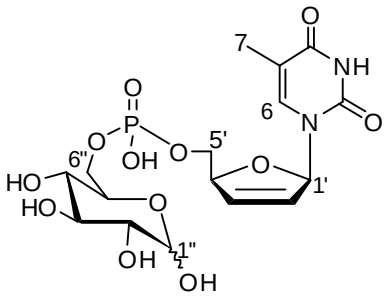
10b

2',3'-Didehydro-2',3'-dideoxythymidine 5'-(α/β-D-glucopyranos-6-yl) phosphate (10b)

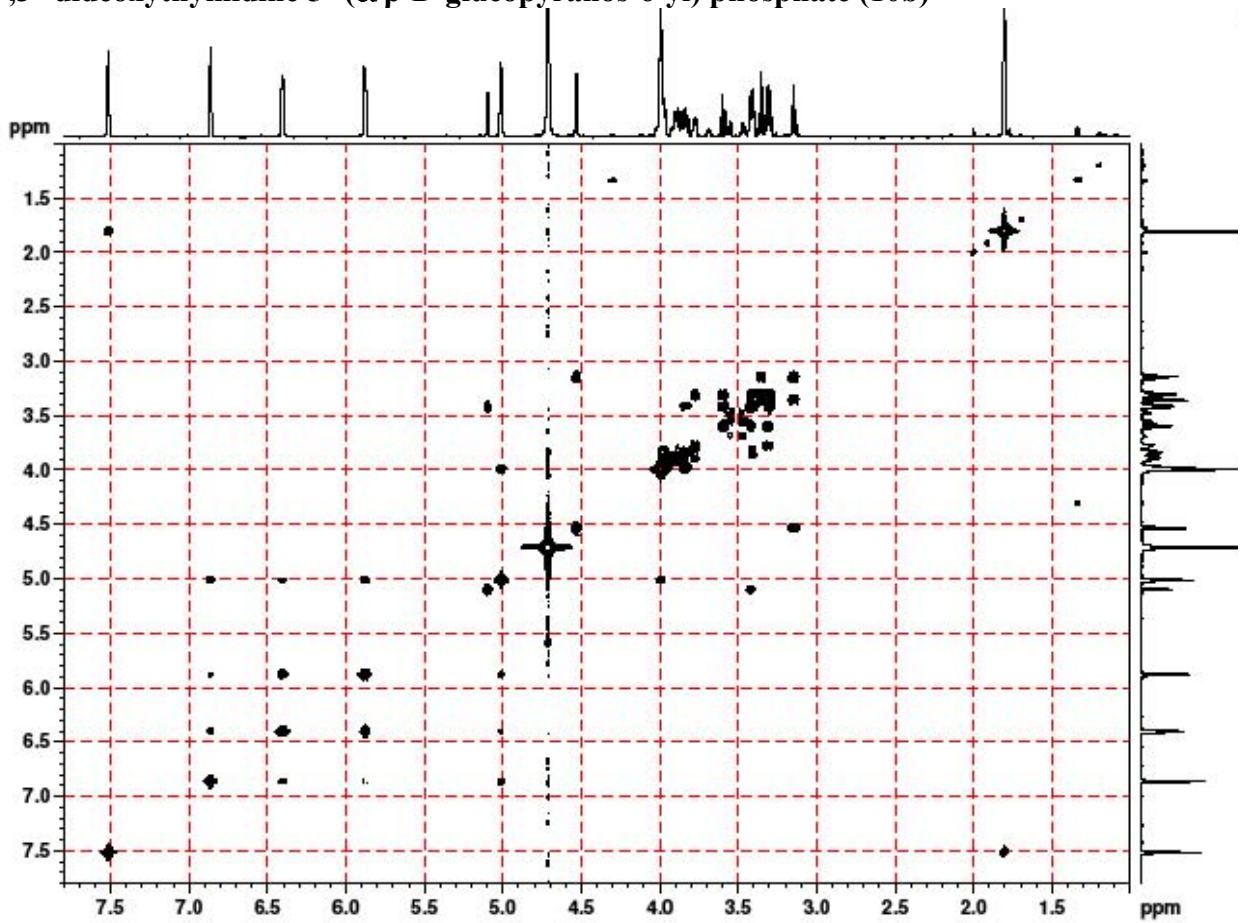


2',3'-Didehydro-2',3'-dideoxythymidine 5'-(α/β-D-glucopyranos-6-yl) phosphate (10b)

COSY (D_2O, 600 MHz)

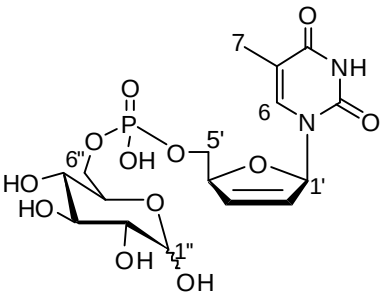


10b

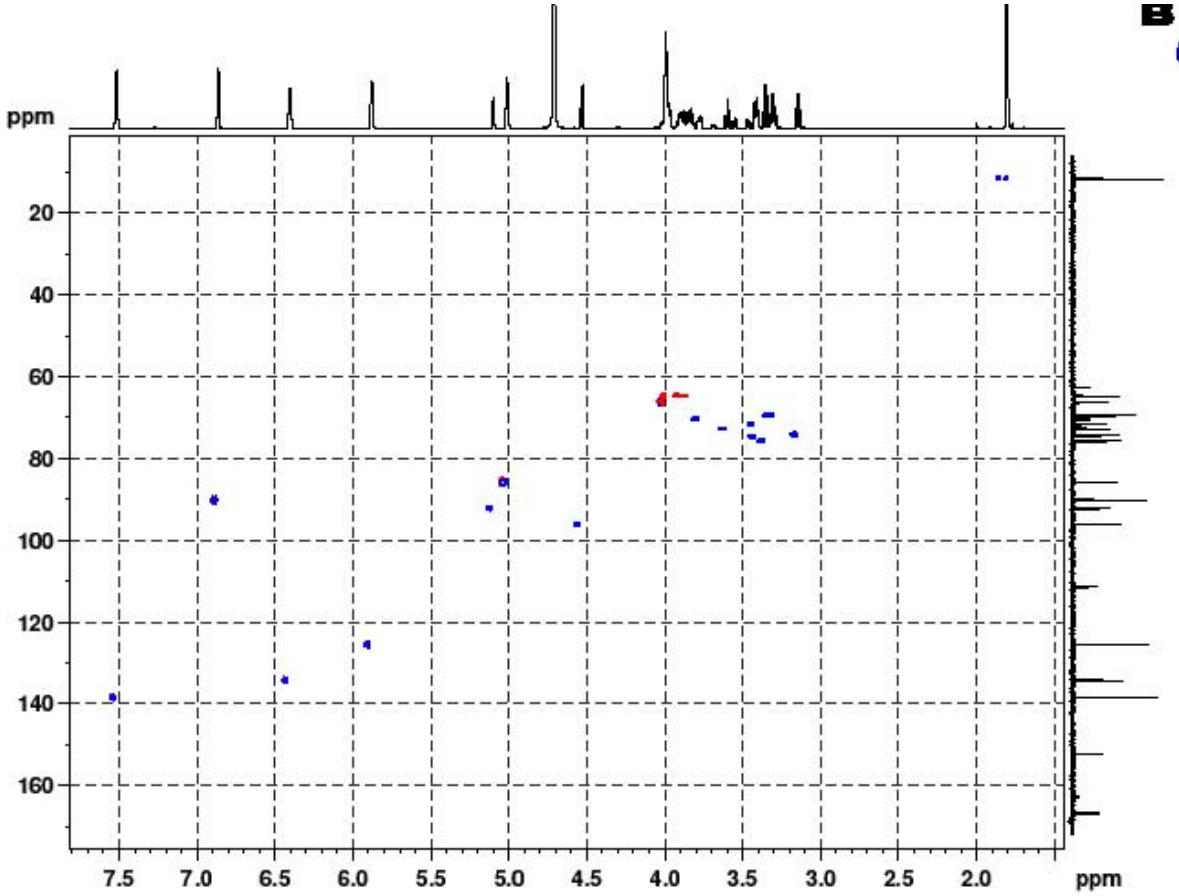


2’,3’-Didehydro-2’,3’-dideoxythymidine 5’-(α/β-D-glucopyranos-6-yl) phosphate (10b)

HSQC (D_2O, 600 MHz)



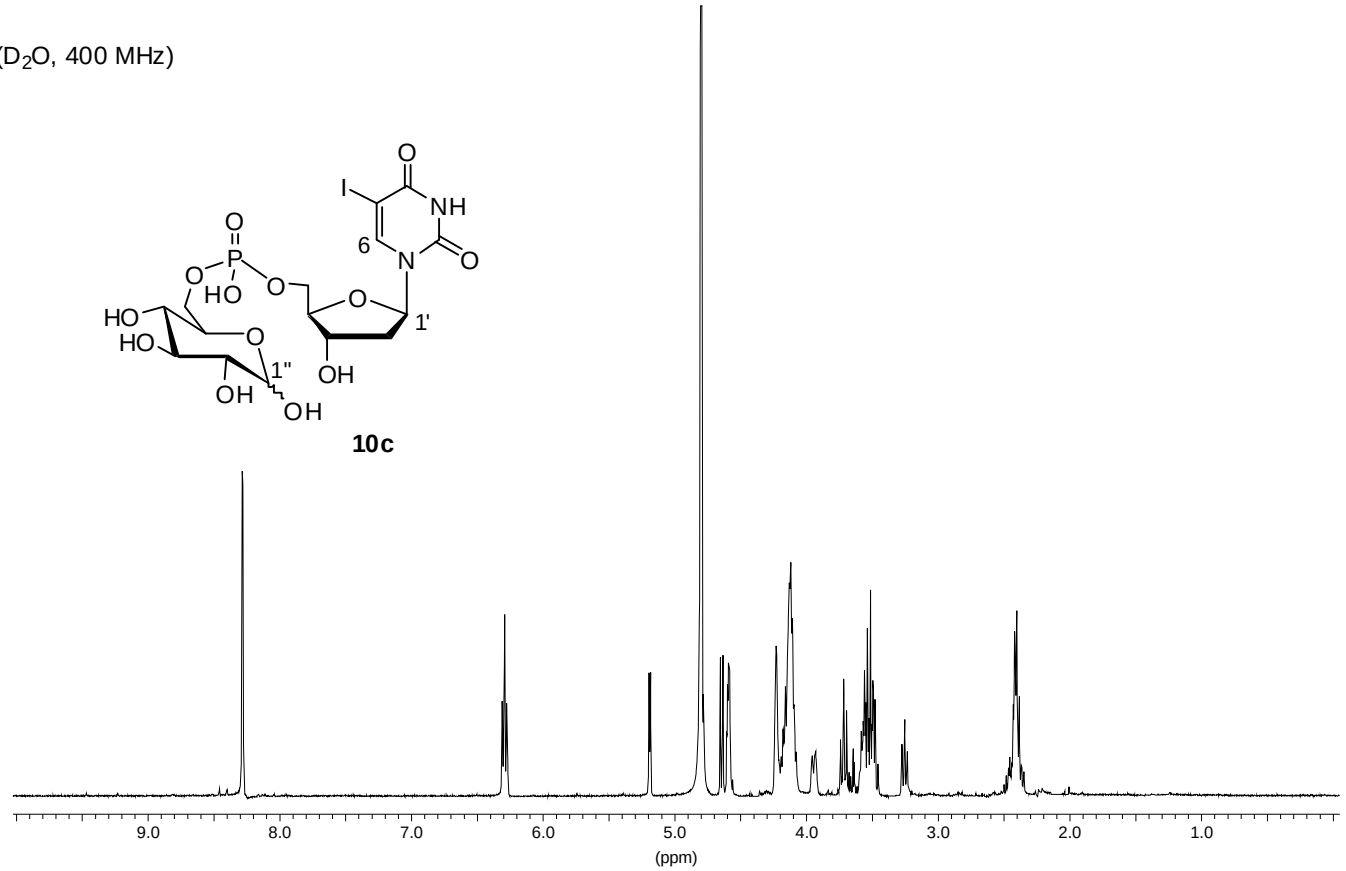
10b



2’-Deoxy-5-iodouridine 5’-(α/β-D-glucopyranos-6-yl) phosphate (10c)

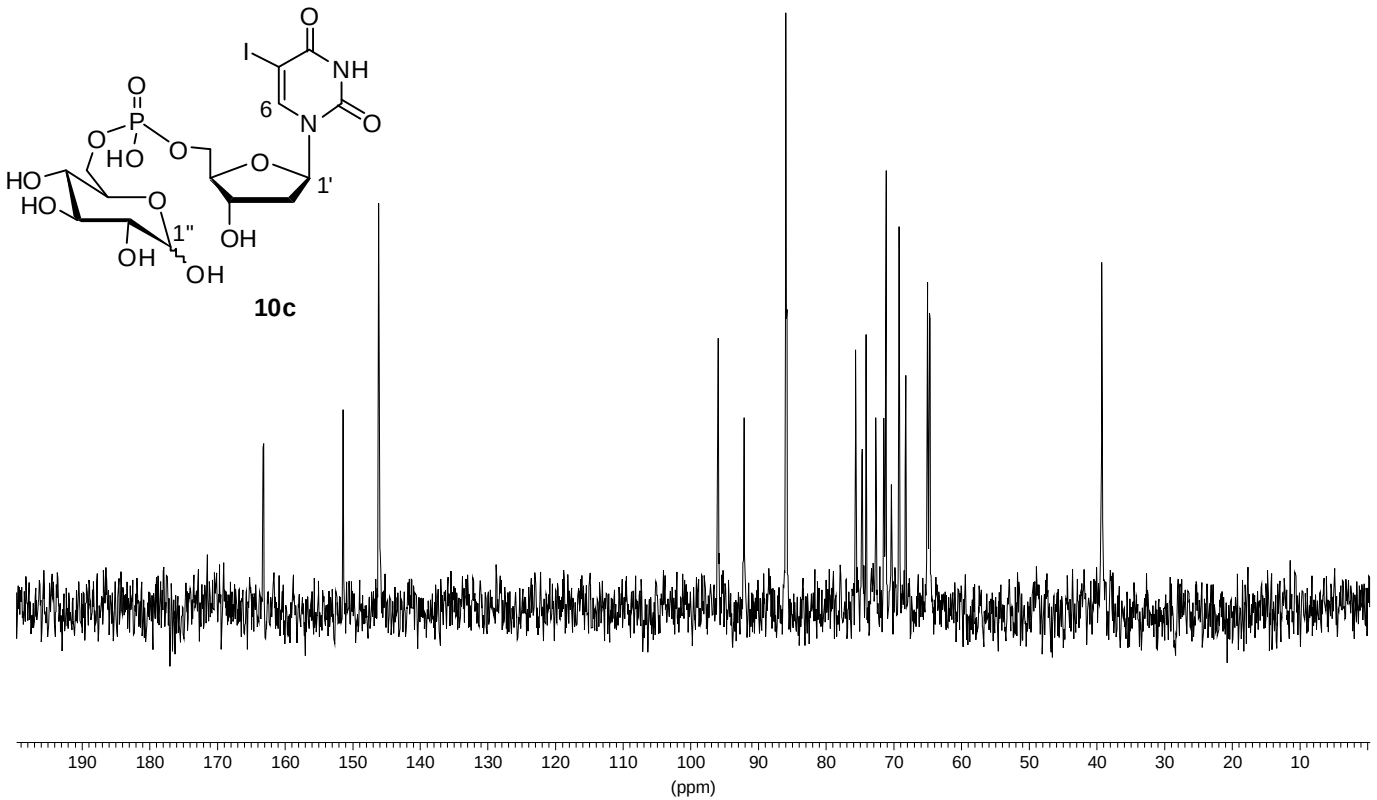
^{1}H-RMN (D_2O, 400 MHz)

10c



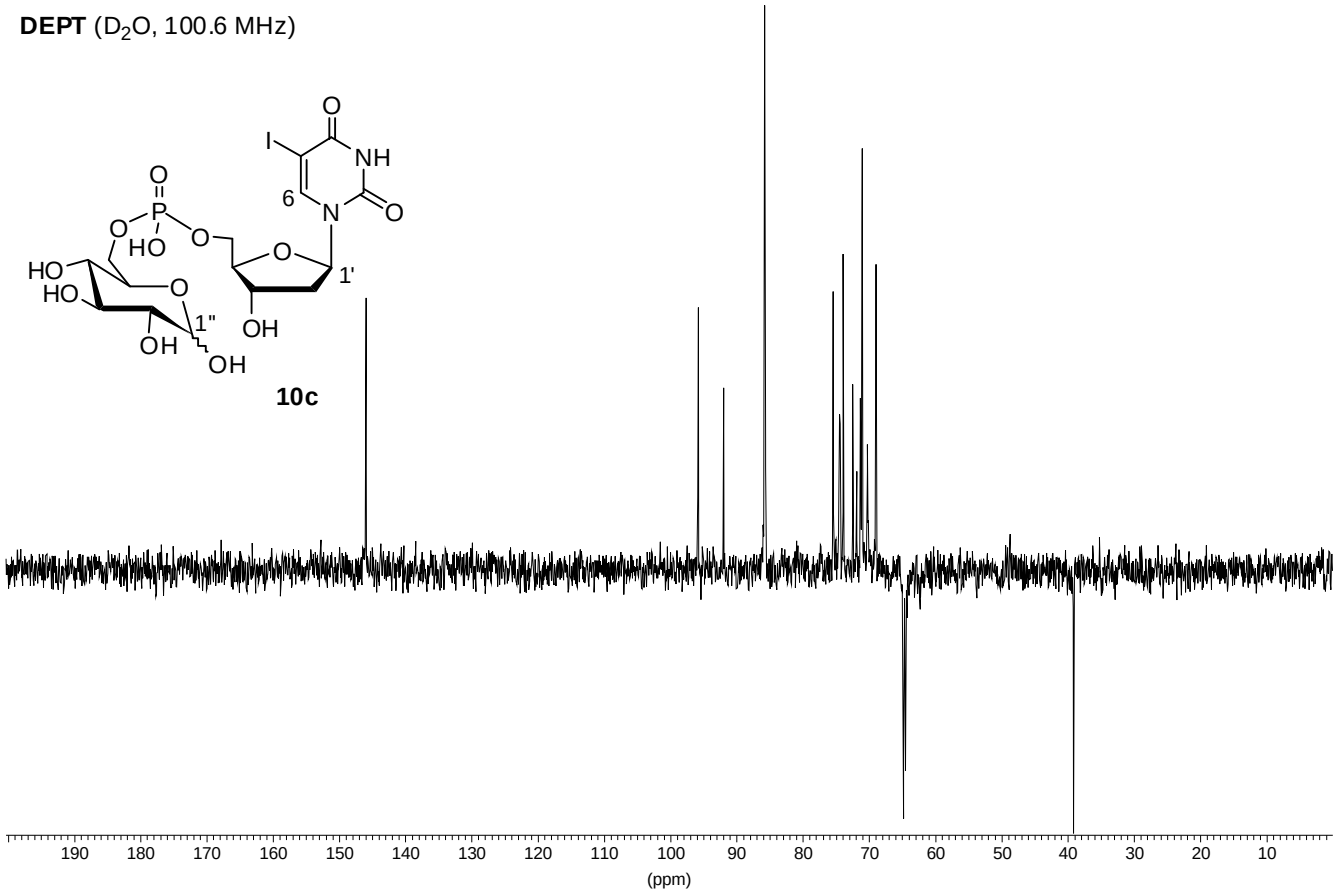
2’-Deoxy-5-iodouridine 5’-(α/β-D-glucopyranos-6-yl) phosphate (10c)

^{13}C-RMN (D_2O, 100.6 MHz)



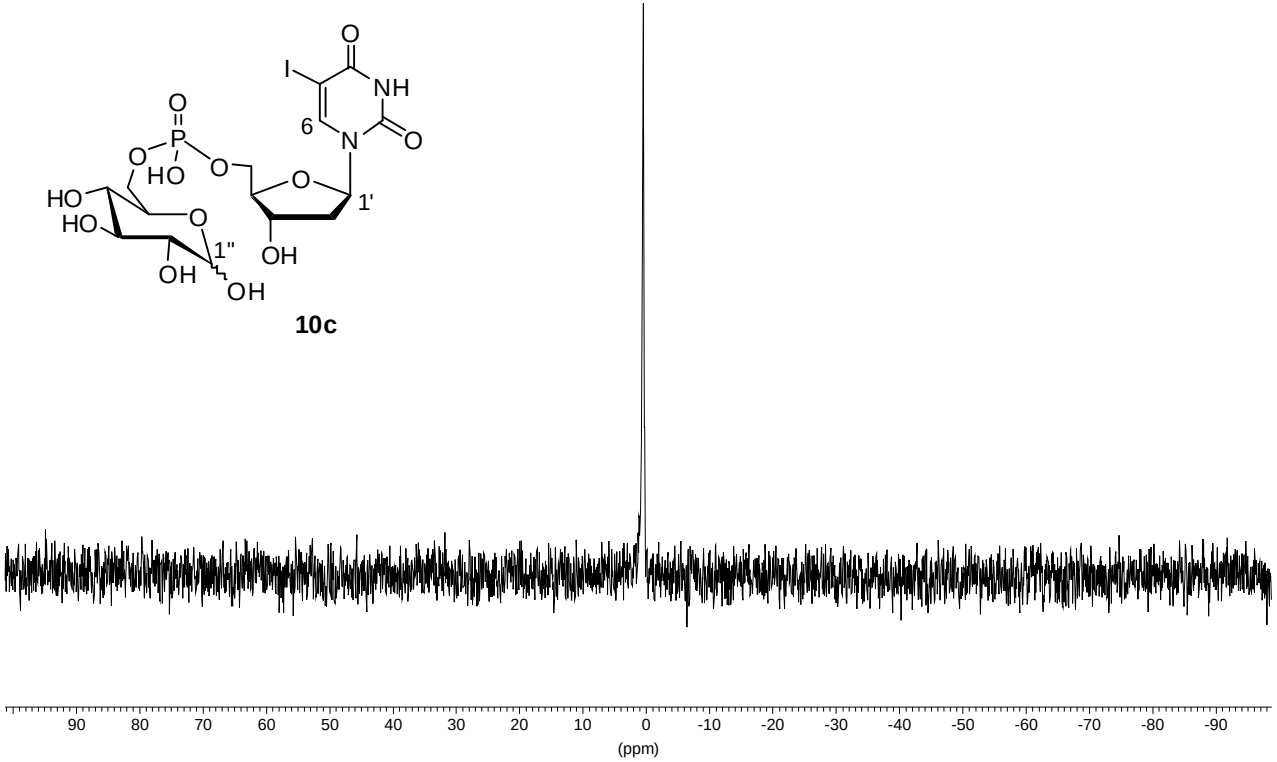
10c

2’-Deoxy-5-iodouridine 5’-(α/β-D-glucopyranos-6-yl) phosphate (10c)



2’-Deoxy-5-iodouridine 5’-(α/β-D-glucopyranos-6-yl) phosphate (10c)

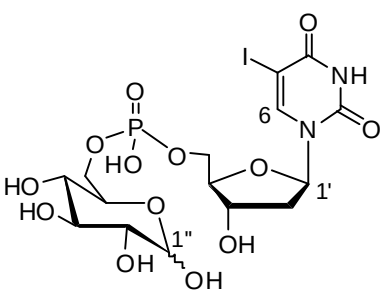
^{31}P-RMN (D_2O, 161.9 MHz)



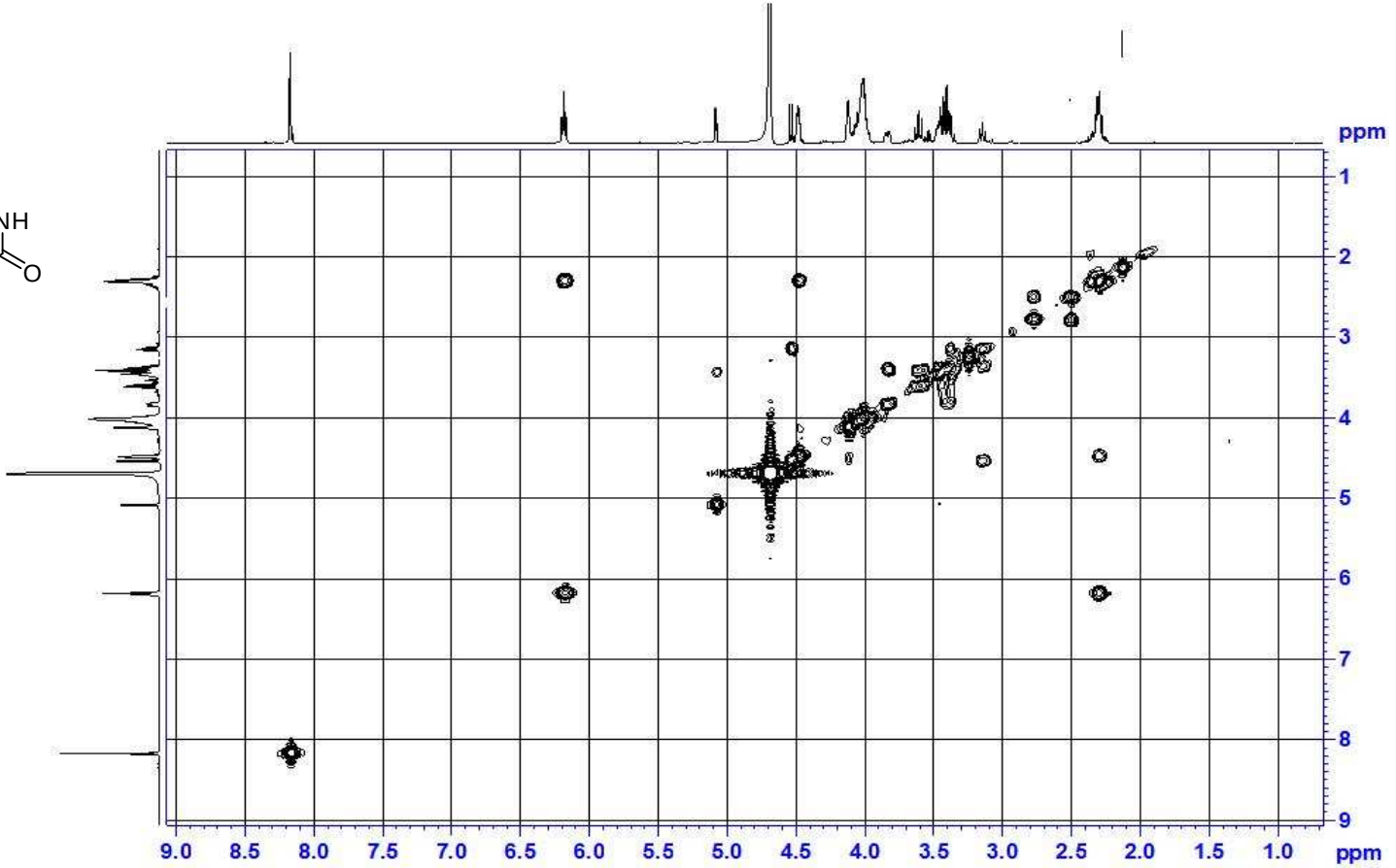
10c

2’-Deoxy-5-iodouridine 5’-(α/β-D-glucopyranos-6-yl) phosphate (10c)

COSY (D_2O, 400 MHz)

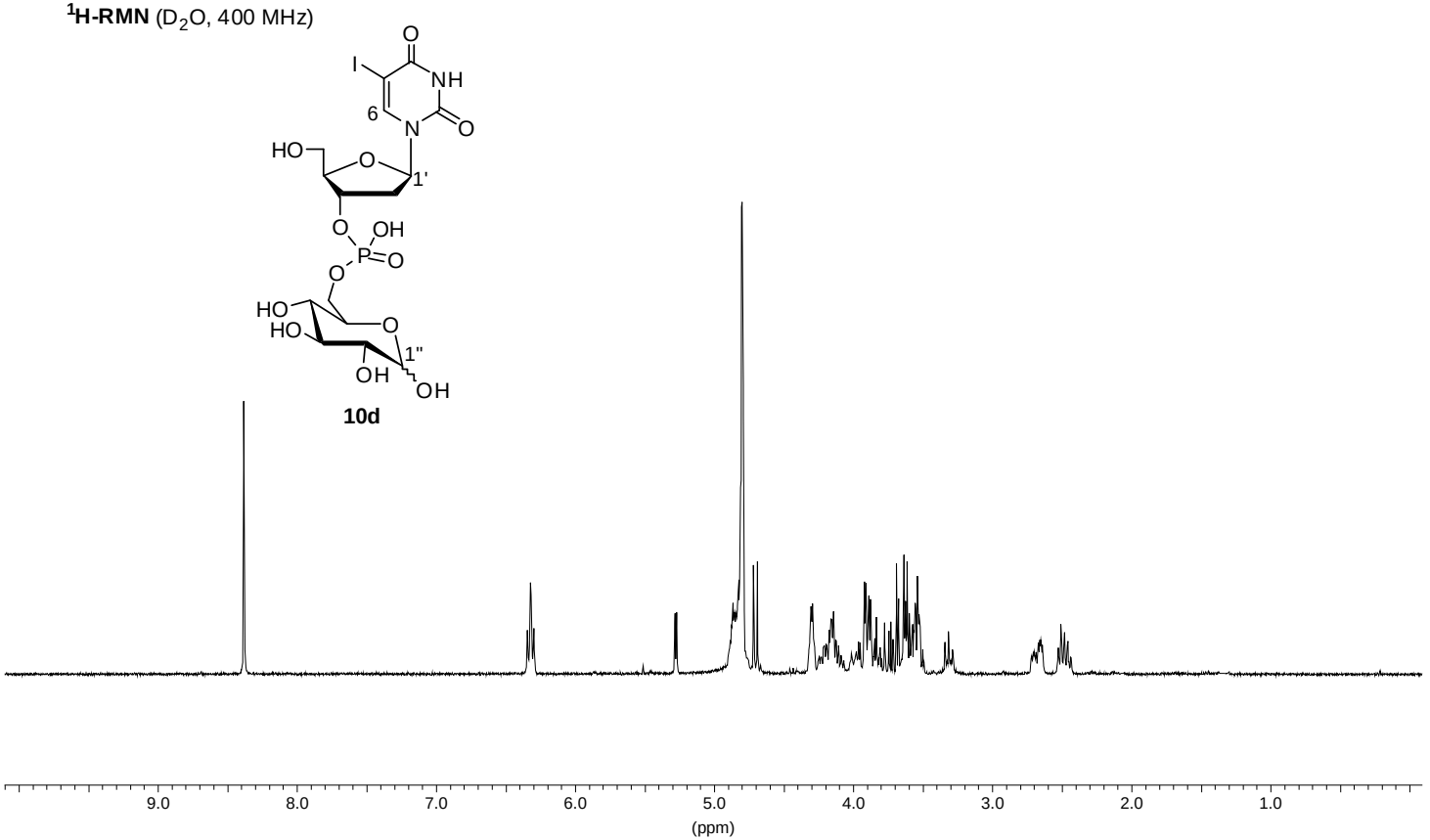


10c



2’-Deoxy-5-iodouridine 3’-(α/β-D-glucopyranos-6-yl) phosphate (10d)

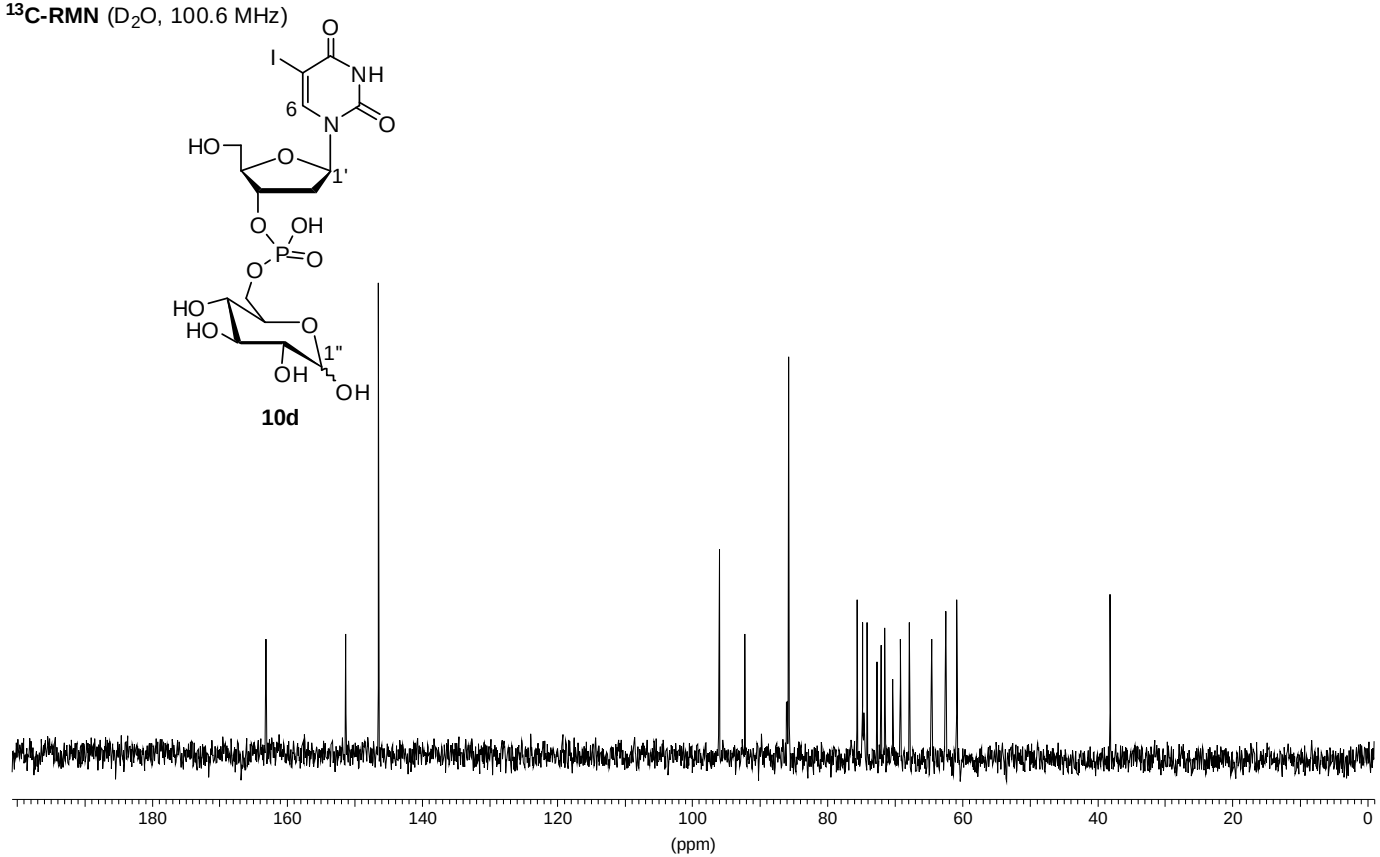
^{1}H-RMN (D_2O, 400 MHz)



10d

2’-Deoxy-5-iodouridine 3’-(α/β-D-glucopyranos-6-yl) phosphate (10d)

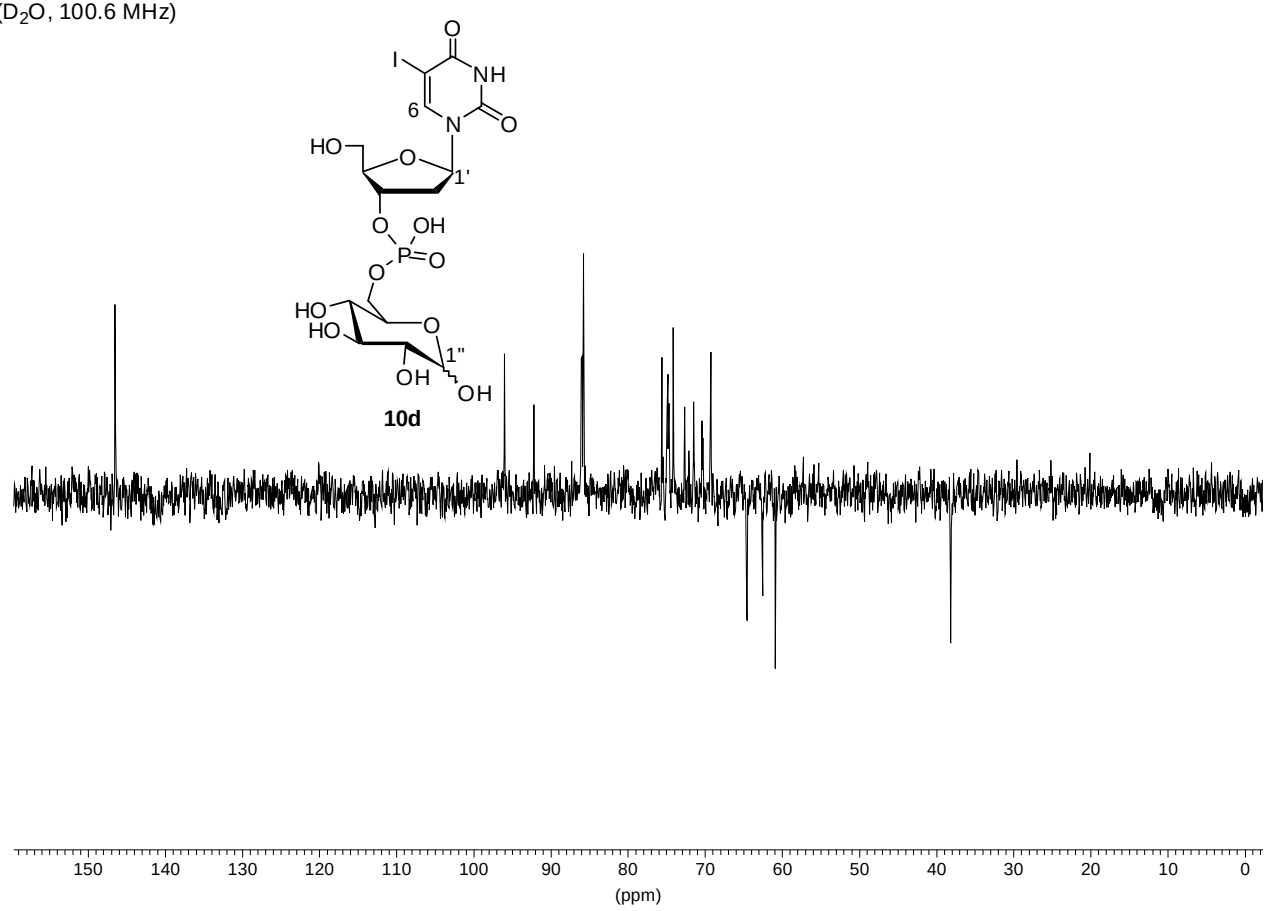
^{13}C-RMN (D_2O, 100.6 MHz)



10d

2’-Deoxy-5-iodouridine 3’-(α/β-D-glucopyranos-6-yl) phosphate (10d)

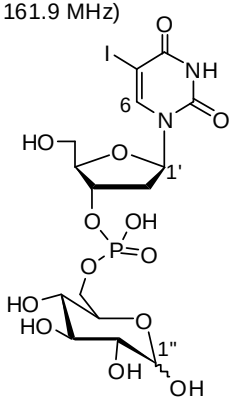
DEPT (D_2O, 100.6 MHz)



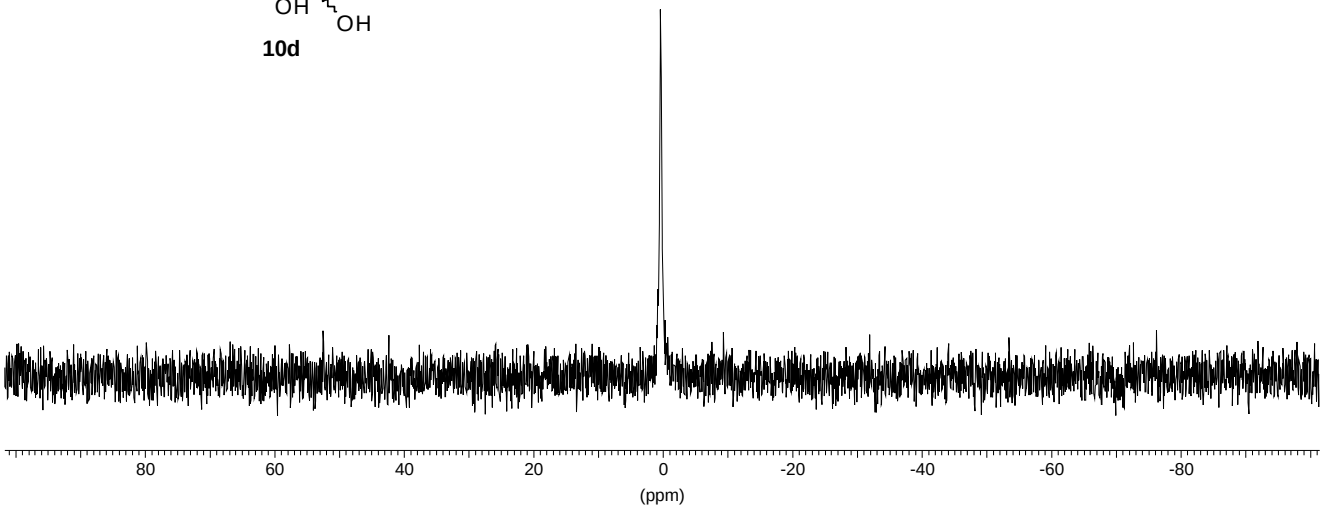
10d

2’-Deoxy-5-iodouridine 3’-(α/β-D-glucopyranos-6-yl) phosphate (10d)

^{31}P-RMN (D_2O, 161.9 MHz)

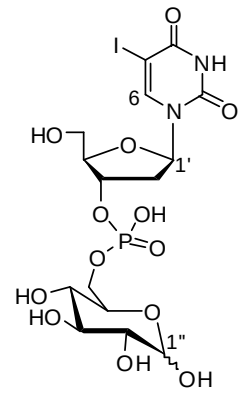


10d

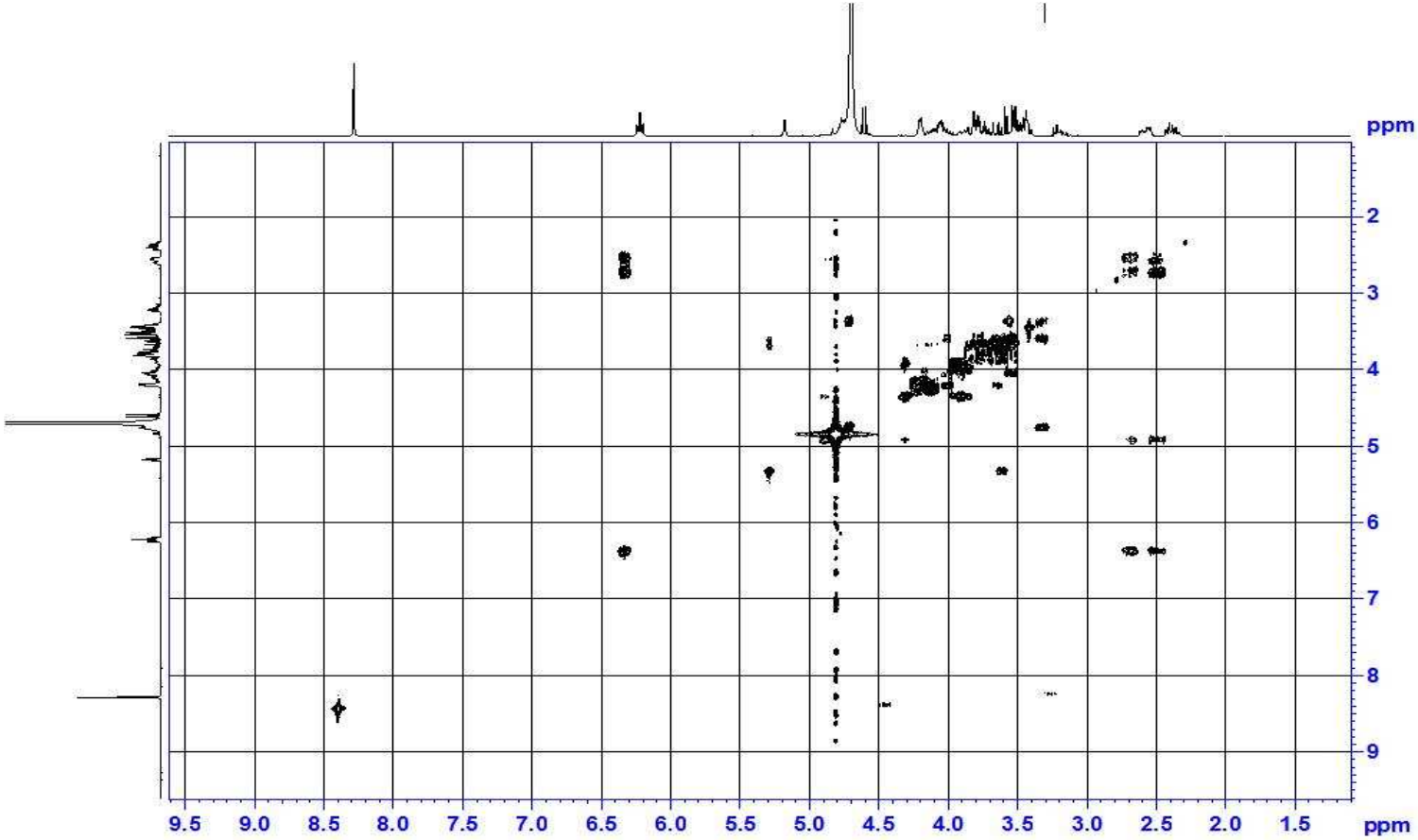


2’-Deoxy-5-iodouridine 3’-(α/β-D-glucopyranos-6-yl) phosphate (10d)

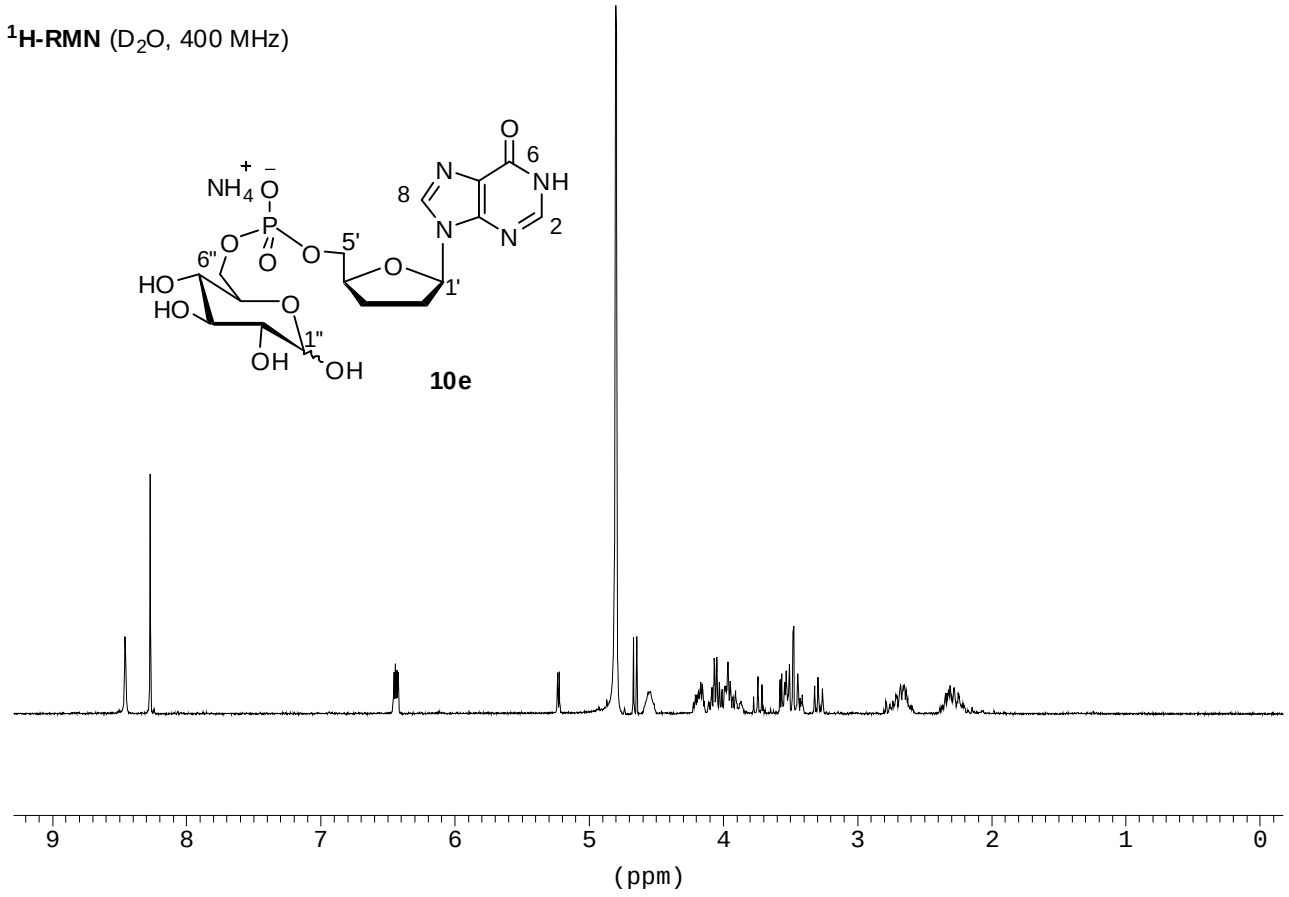
COSY (D_2O, 400 MHz)



10d

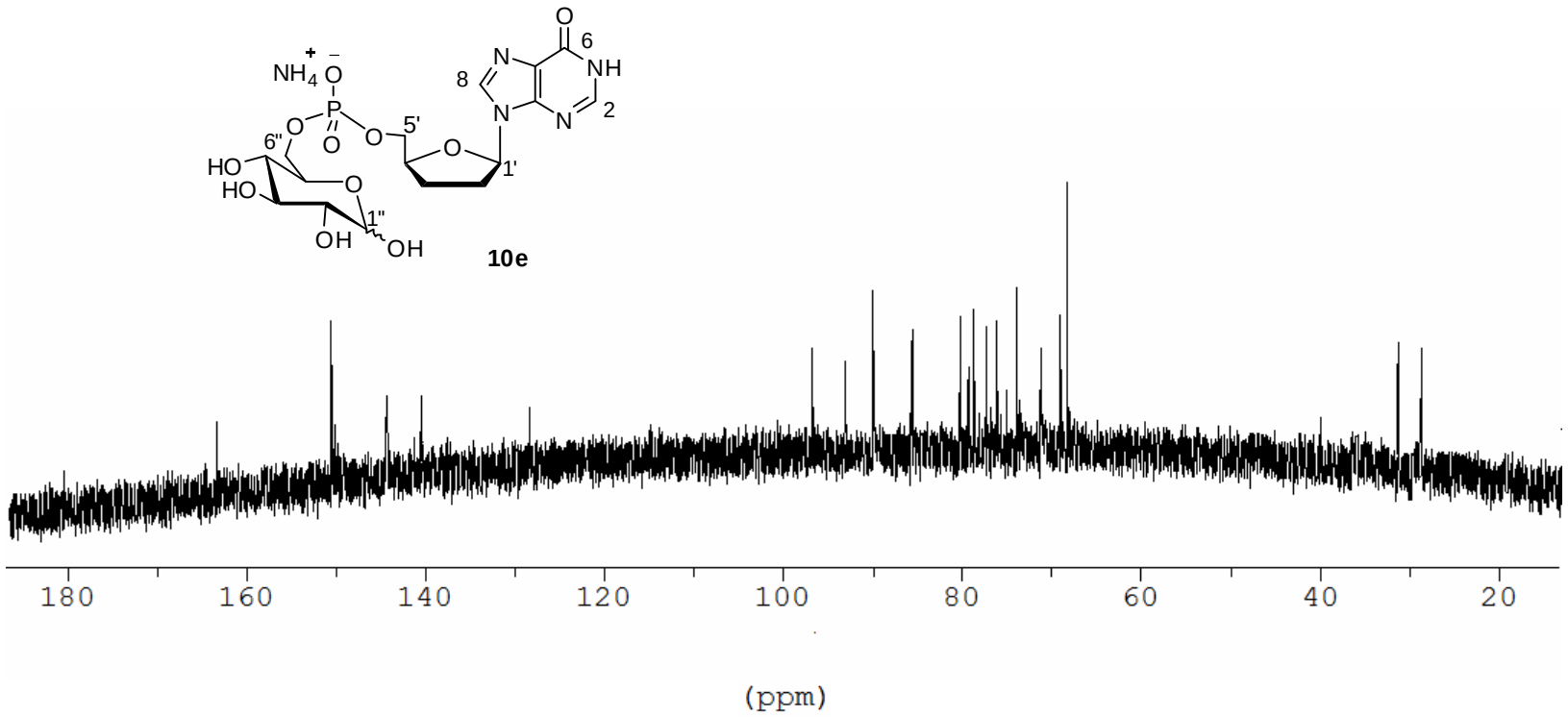


2',3'-Dideoxyinosine 5'-(α/β-D-glucopyranos-6-yl) phosphate (10e)



2',3'-Dideoxyinosine 5'-(α/β-D-glucopyranos-6-yl) phosphate (10e)

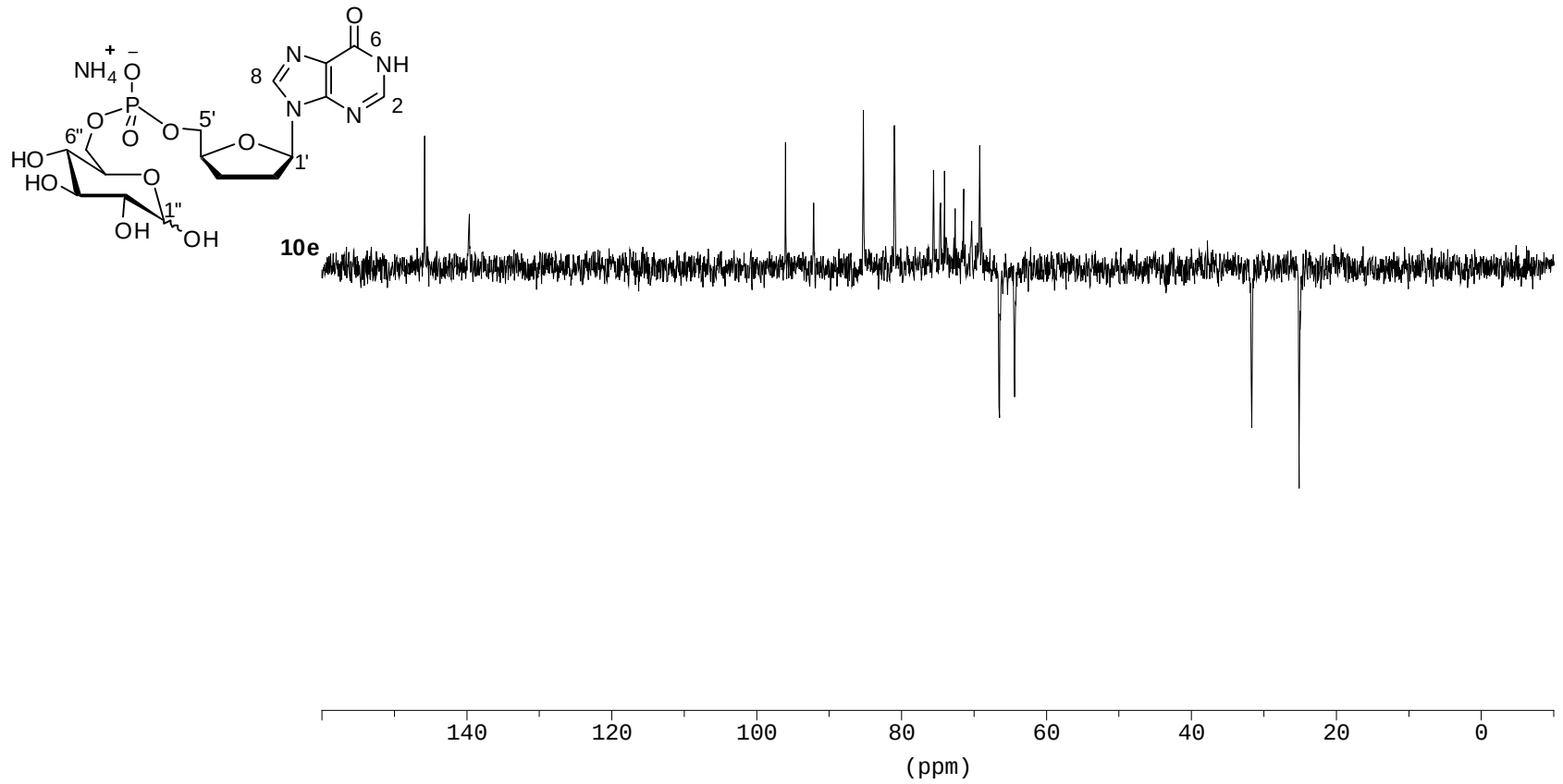
^{13}C-RMN (D_2O, 100.6 MHz)



10e

2',3'-Dideoxyinosine 5'-(α/β-D-glucopyranos-6-yl) phosphate (10e)

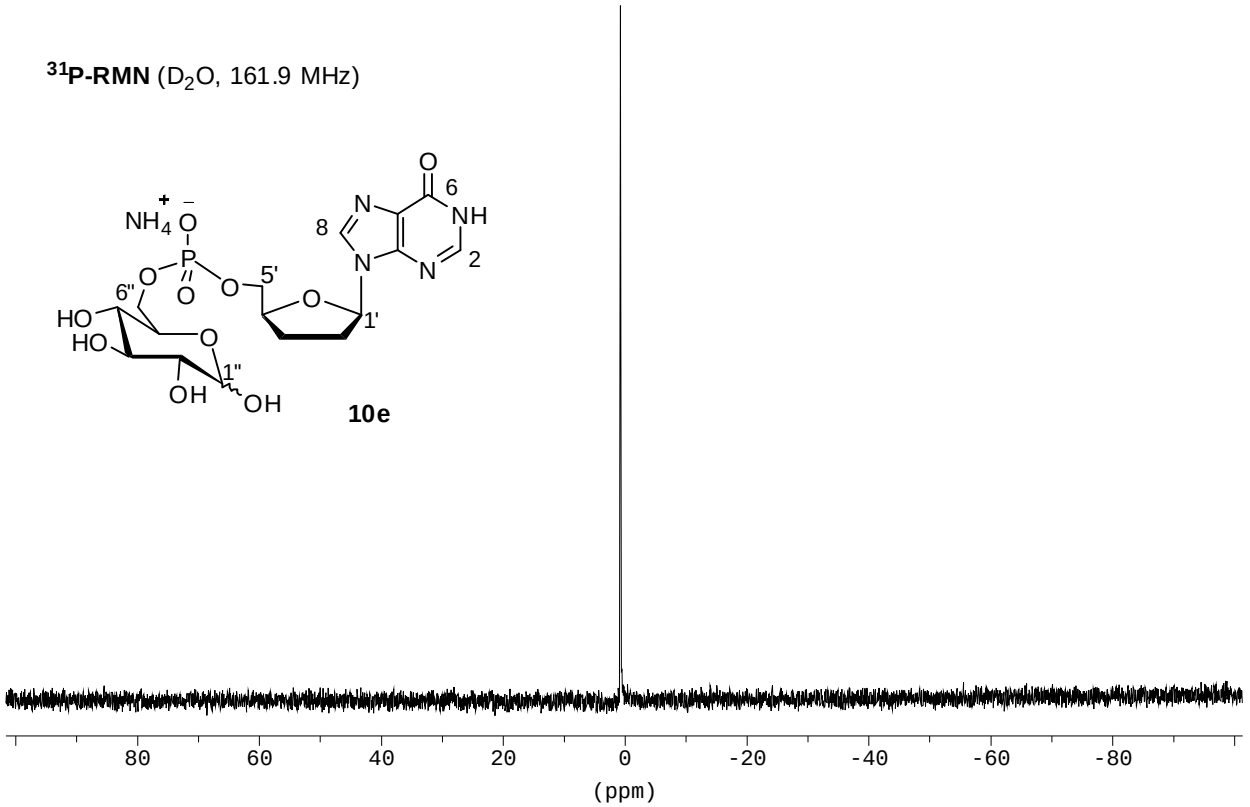
DEPT (D_2O, 100.6 MHz)



2',3'-Dideoxyinosine 5'-(α/β-D-glucopyranos-6-yl) phosphate (10e)

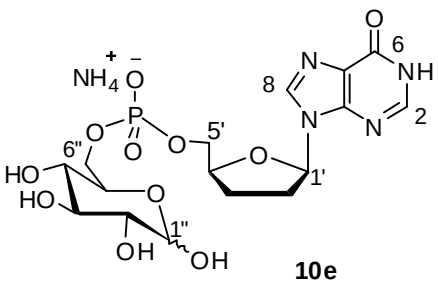
^{31}P-RMN (D_2O, 161.9 MHz)

10e

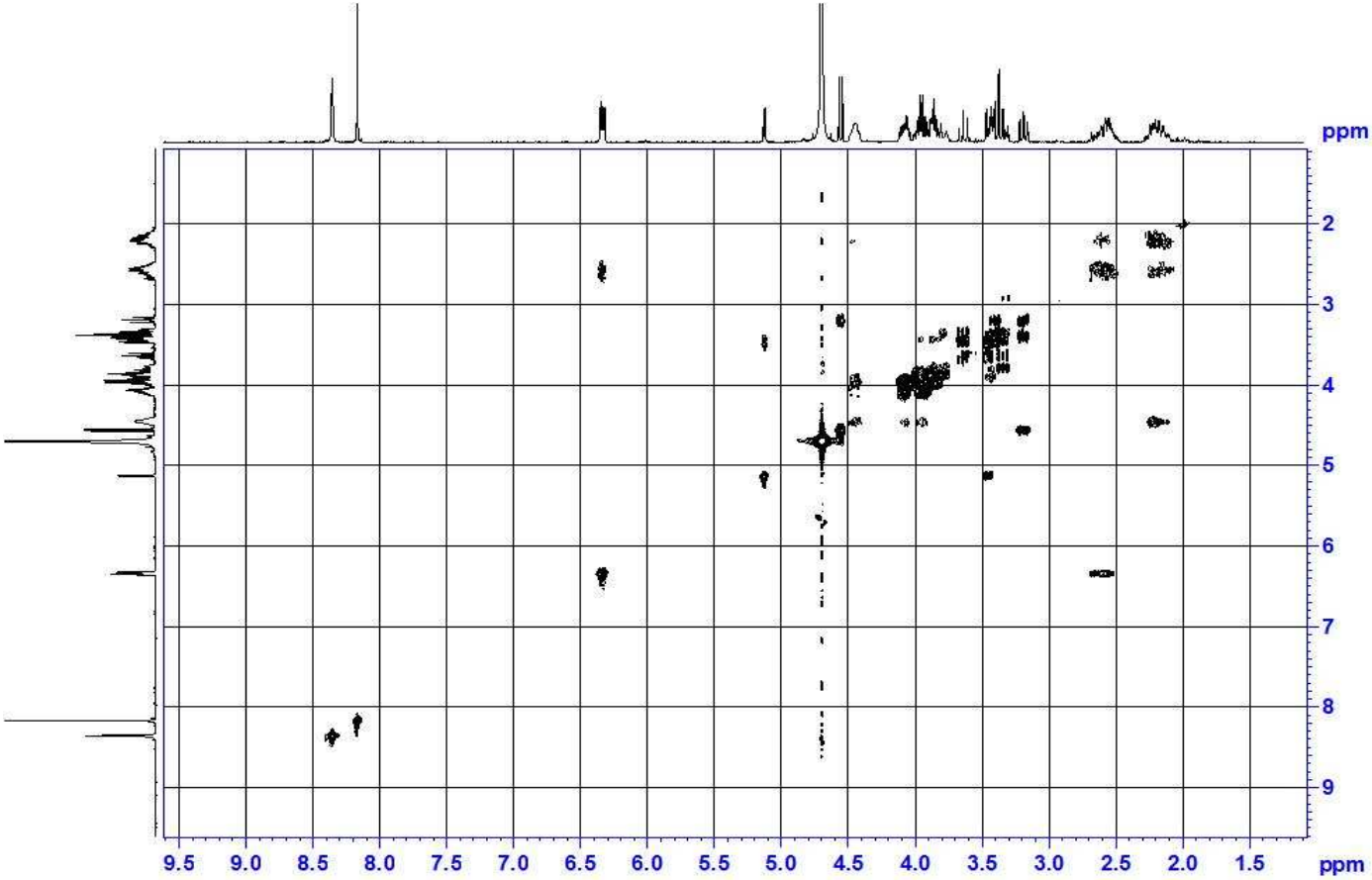


2’,3’-Dideoxyinosine 5’-(α/β-D-glucopyranos-6-yl) phosphate (10e)

COSY (D_2O, 400 MHz)



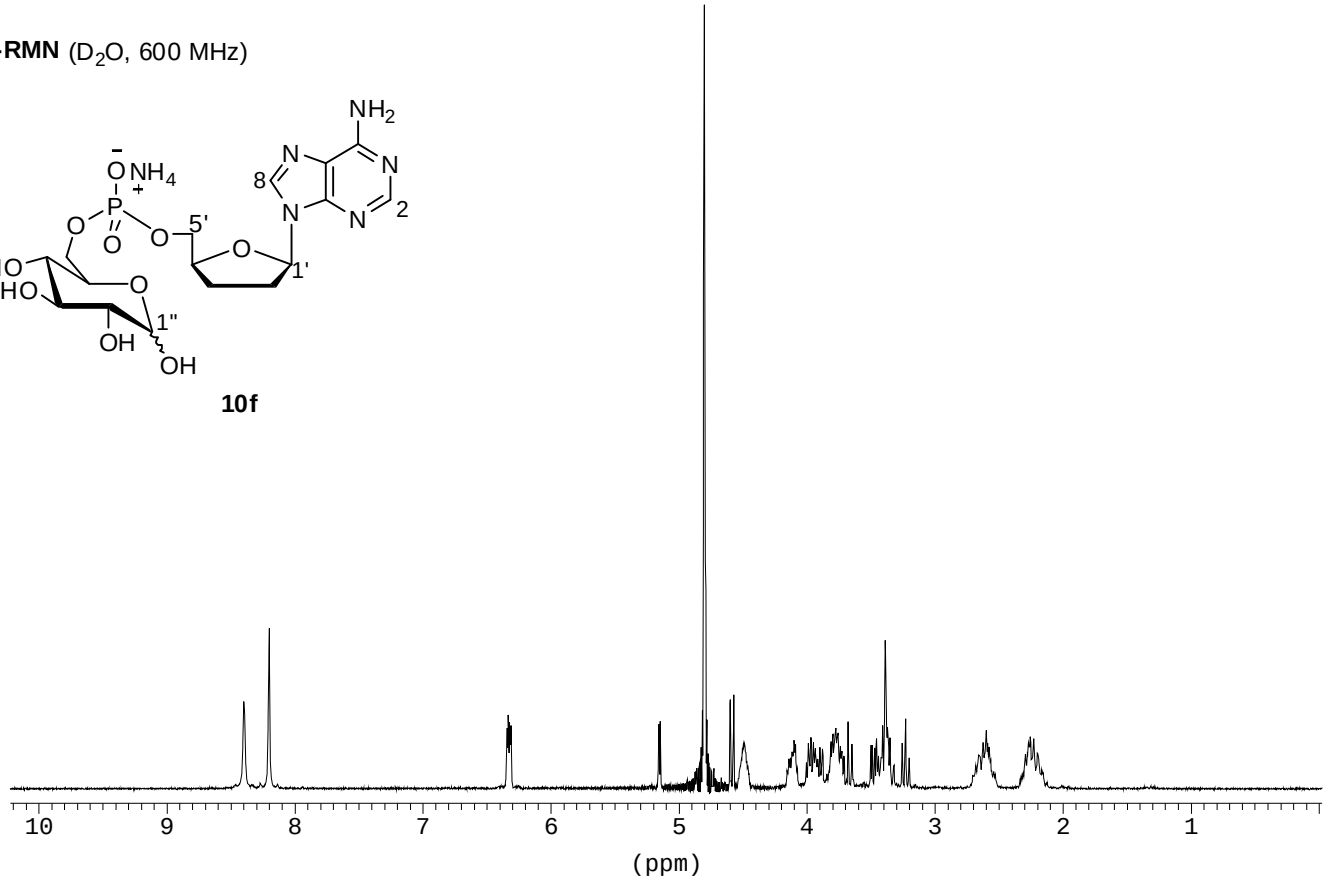
10e



2',3'-Dideoxyadenosine 5'-(α/β-D-glucopyranos-6-yl) phosphate (10f)

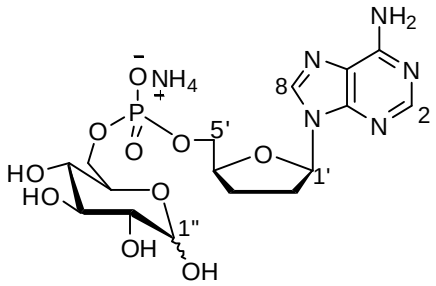
^{1}H-RMN (D_2O, 600 MHz)

10f

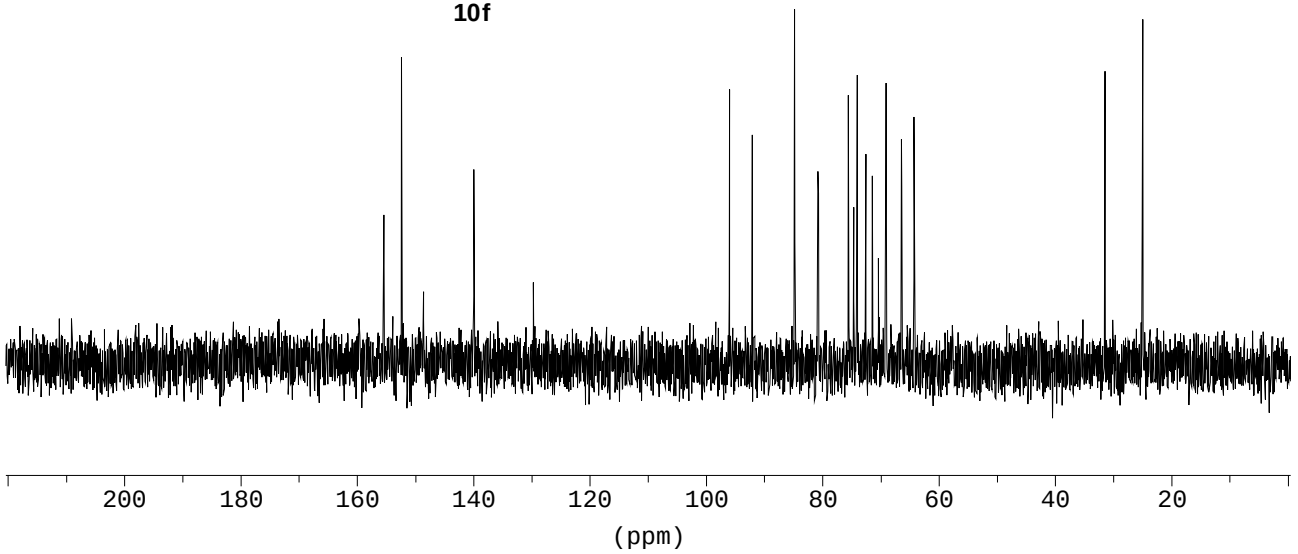


2',3'-Dideoxyadenosine 5'-(α/β-D-glucopyranos-6-yl) phosphate (10f)

^{13}C-RMN (D_2O, 150.5 MHz)

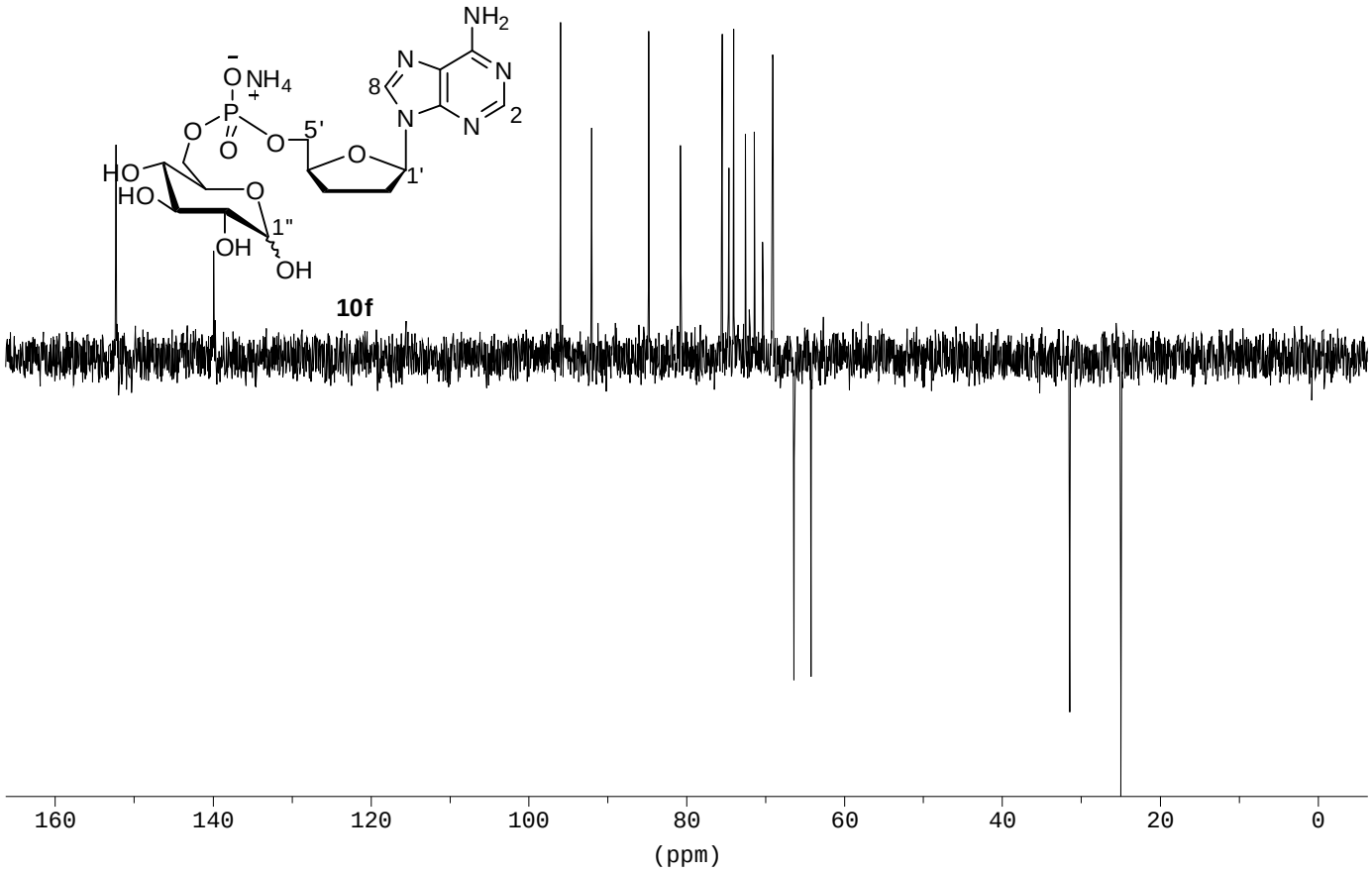


10f



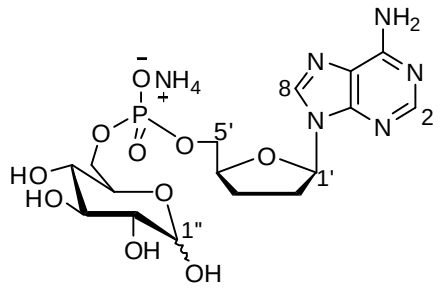
2',3'-Dideoxyadenosine 5'-(α/β-D-glucopyranos-6-yl) phosphate (10f)

DEPT (D_2O, 150.5 MHz)

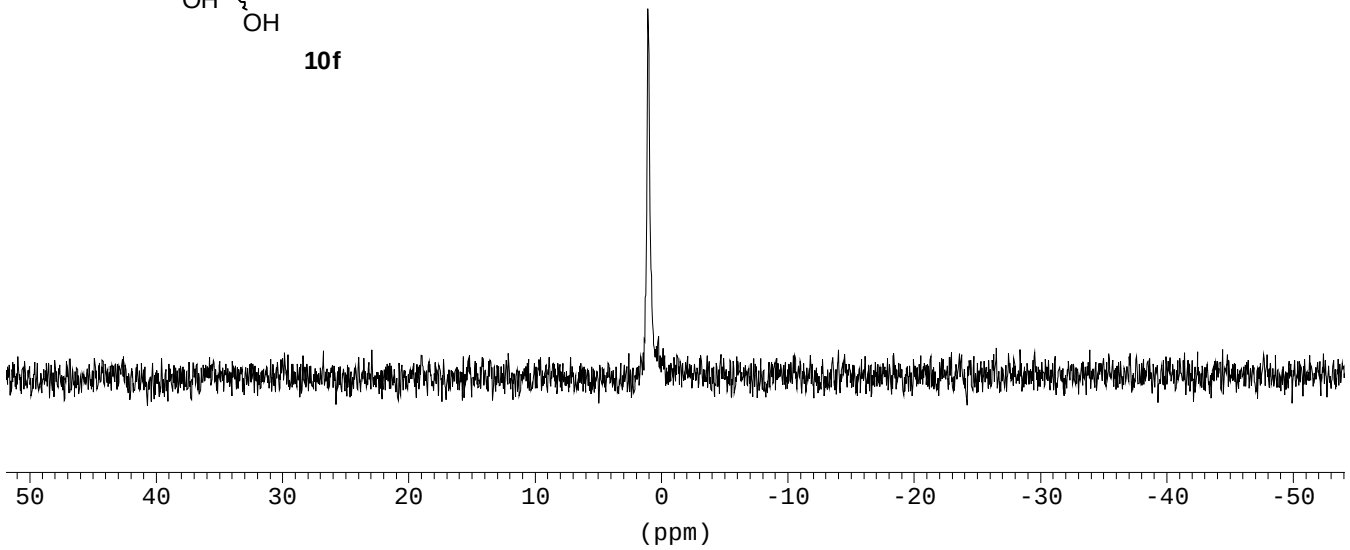


2',3'-Dideoxyadenosine 5'-(α/β-D-glucopyranos-6-yl) phosphate (10f)

^{31}P-RMN (D_2O, 242.9 MHz)

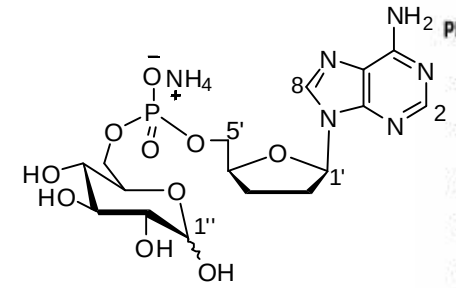


10f

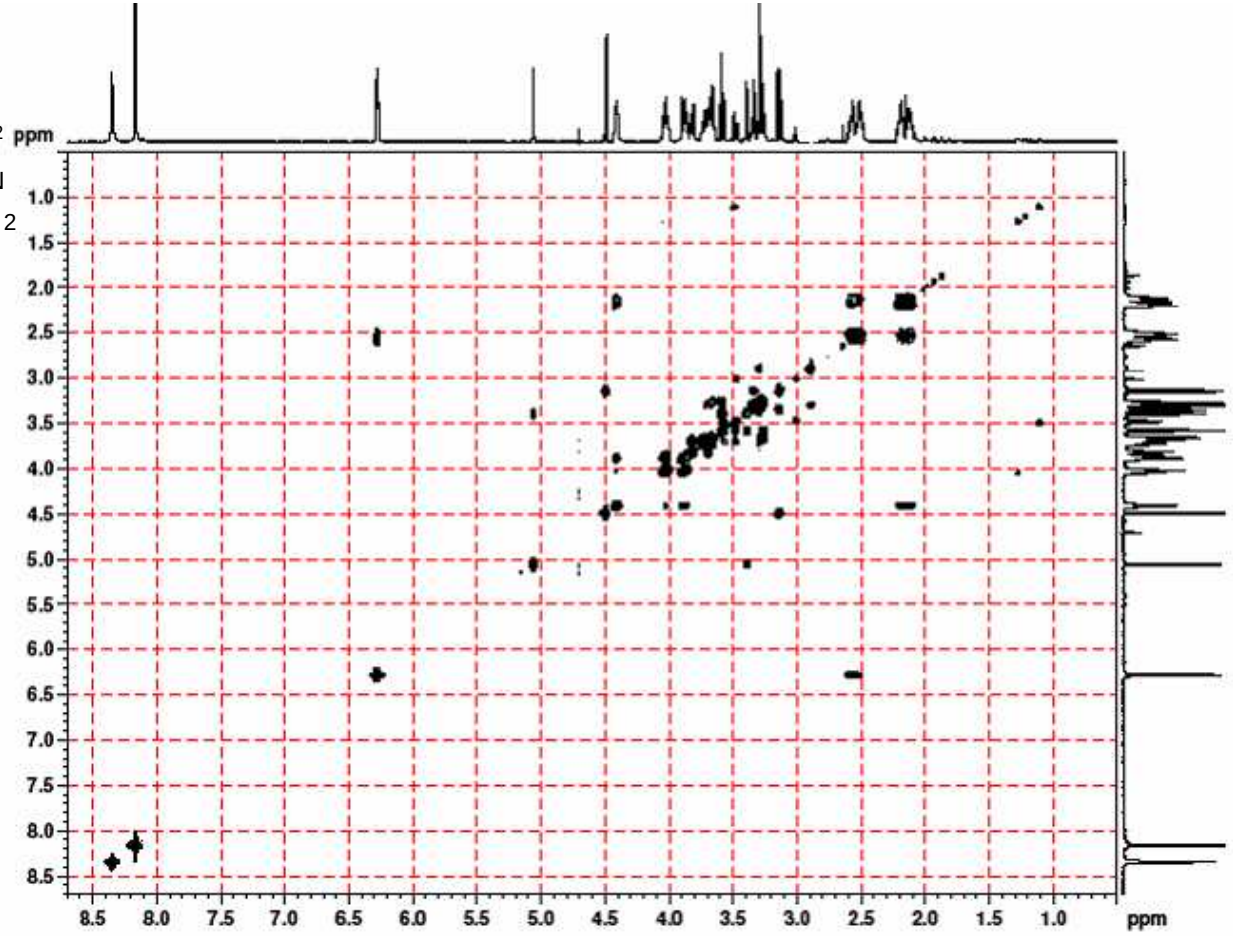


2’,3’-Dideoxyadenosine 5’-(α/β-D-glucopyranos-6-yl) phosphate (10f)

COSY (D_2O, 600 MHz)



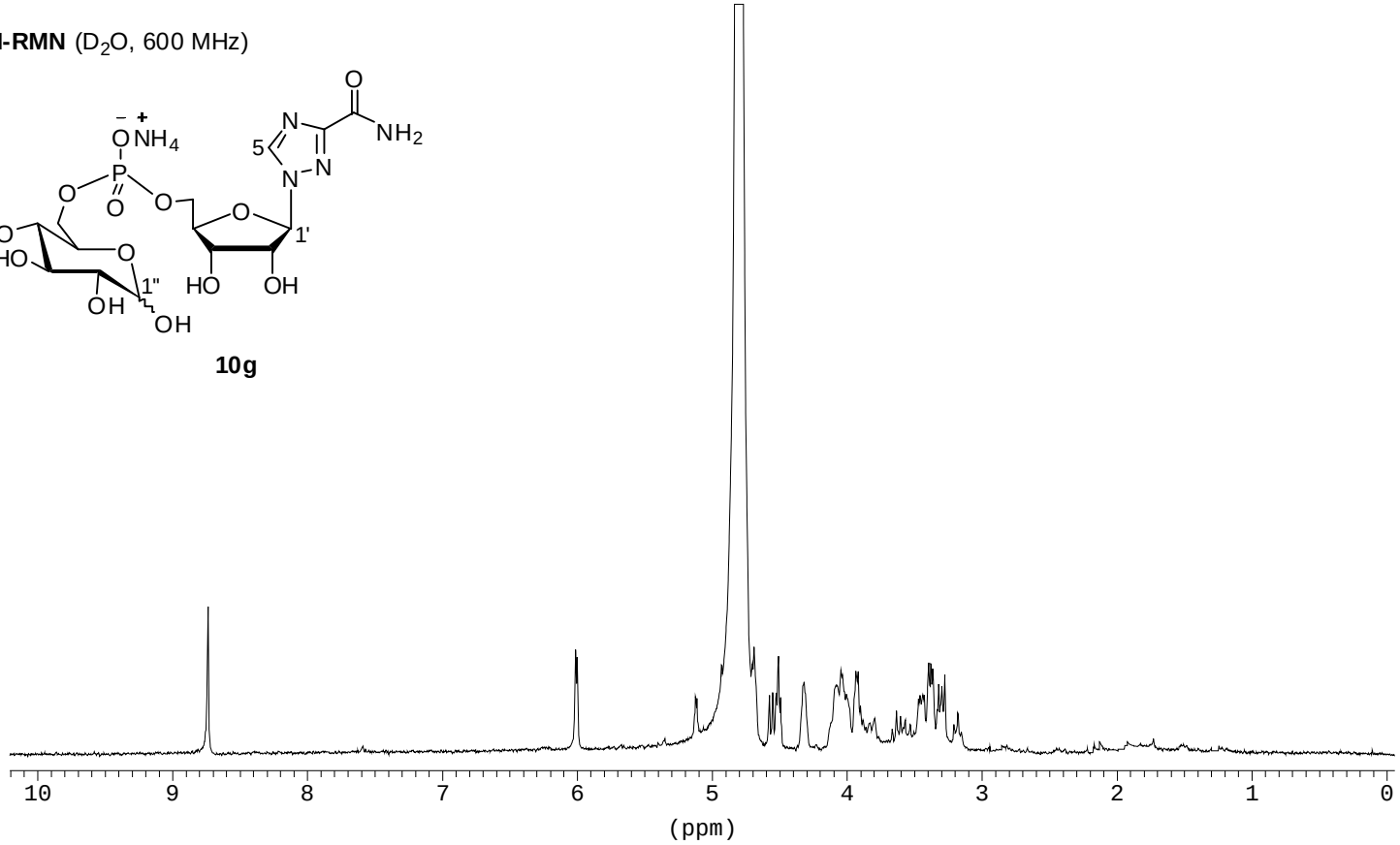
10f



1'-(3-Carbamoyl-1,2,4-triazoyl)-β-D-ribofuranose 5'-(α/β-D-glucopyranos-6-yl) phosphate (10g)

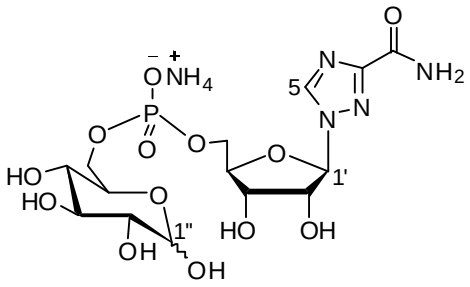
^{1}H-RMN (D_2O, 600 MHz)

10g

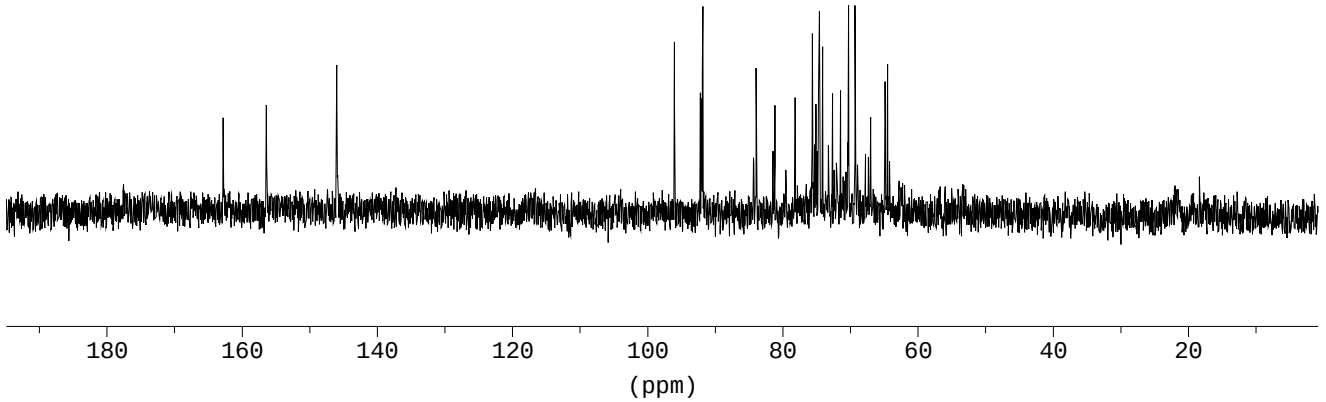


1'-(3-Carbamoyl-1,2,4-triazoyl)-β-D-ribofuranose 5'-(α/β-D-glucopyranos-6-yl) phosphate (10g)

^{13}C-RMN (D_2O, 150.5 MHz)

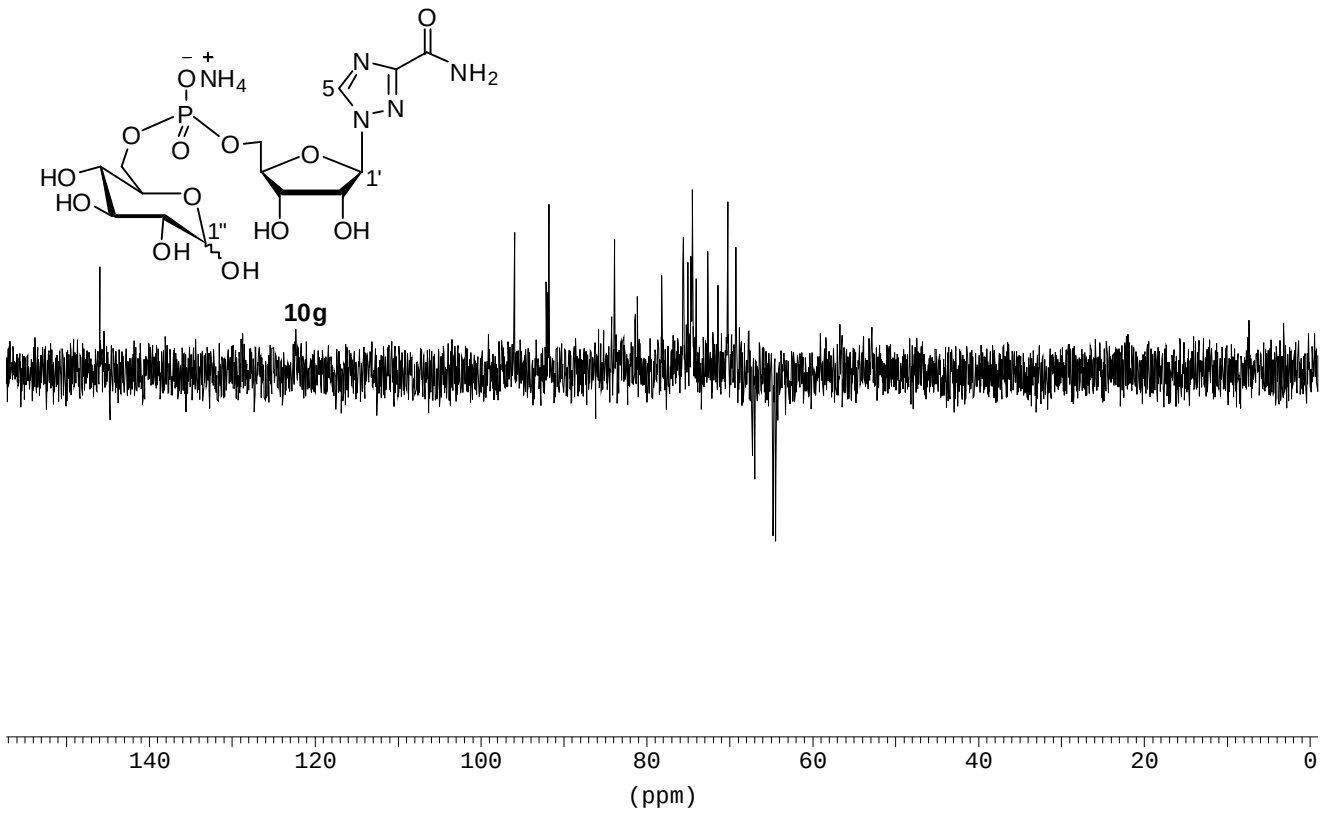


10g



1’-(3-Carbamoyl-1,2,4-triazoyl)-β-D-ribofuranose 5’-(α/β-D-glucopyranos-6-yl) phosphate (10g)

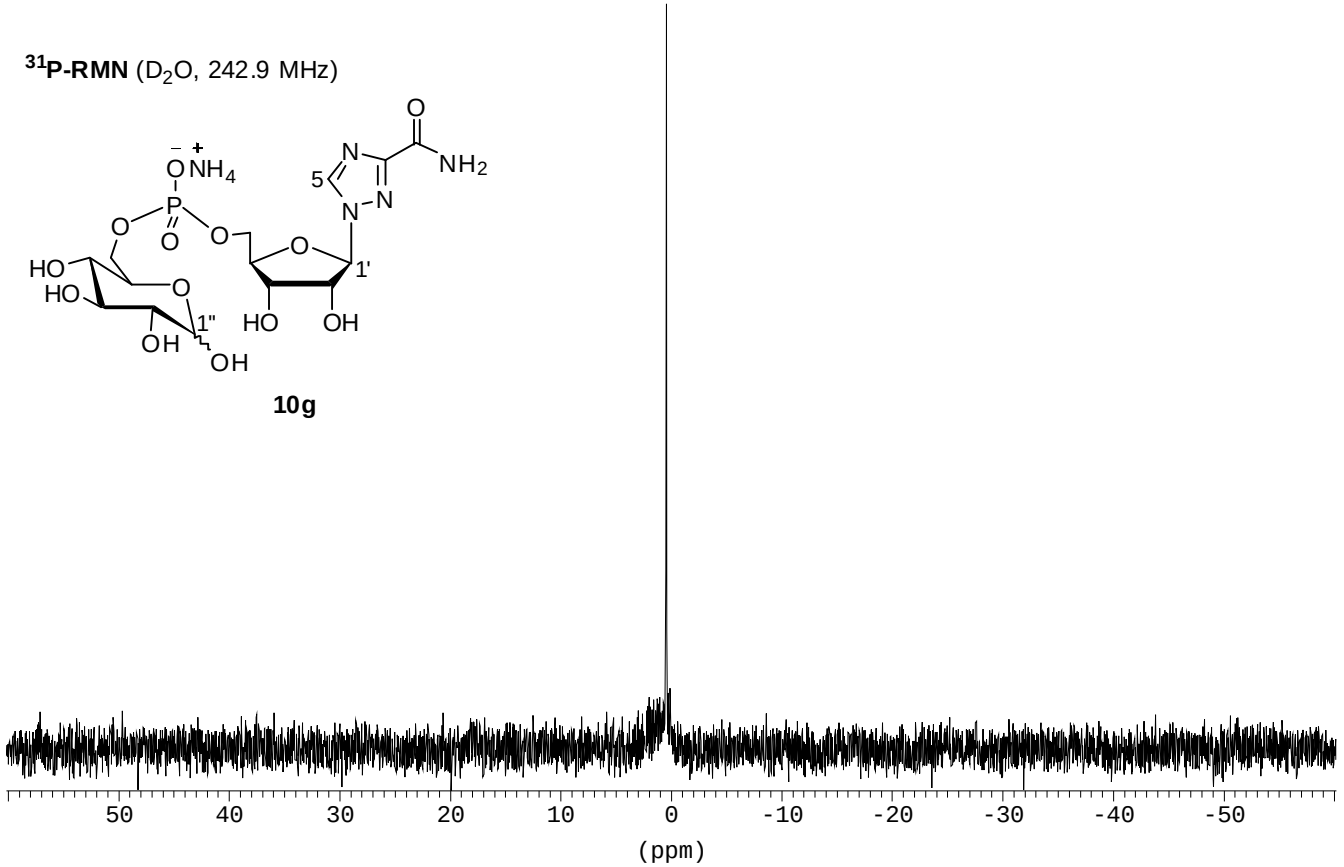
DEPT (D_2O, 150.5 MHz)



1'-(3-Carbamoyl-1,2,4-triazoyl)-β-D-ribofuranose 5'-(α/β-D-glucopyranos-6-yl) phosphate (10g)

^{31}P-RMN (D_2O, 242.9 MHz)

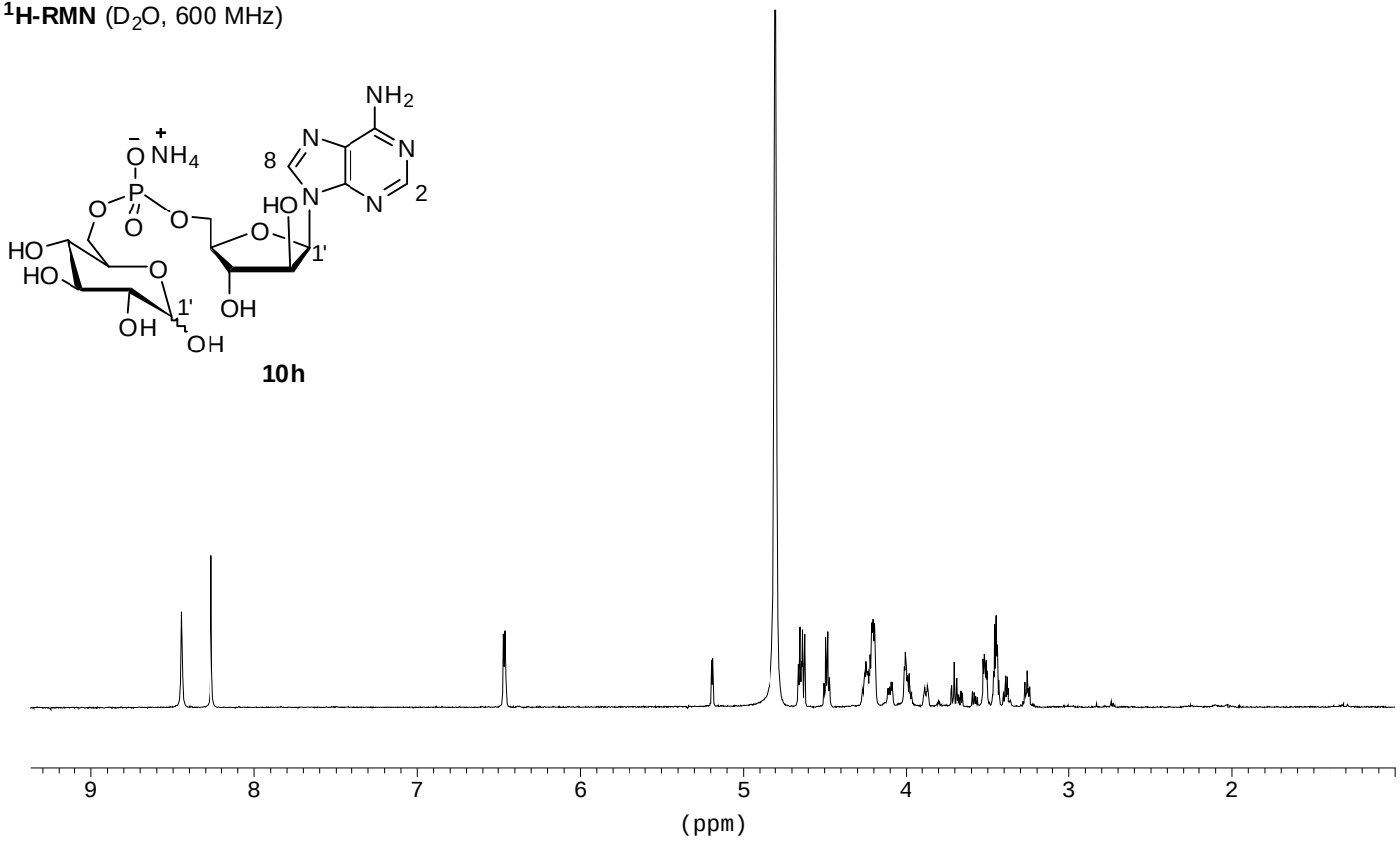
10g



1'-Adeninyl-β-D-arabinofuranose 5'-(α/β-D-glucopyranos-6-yl) phosphate (10h)

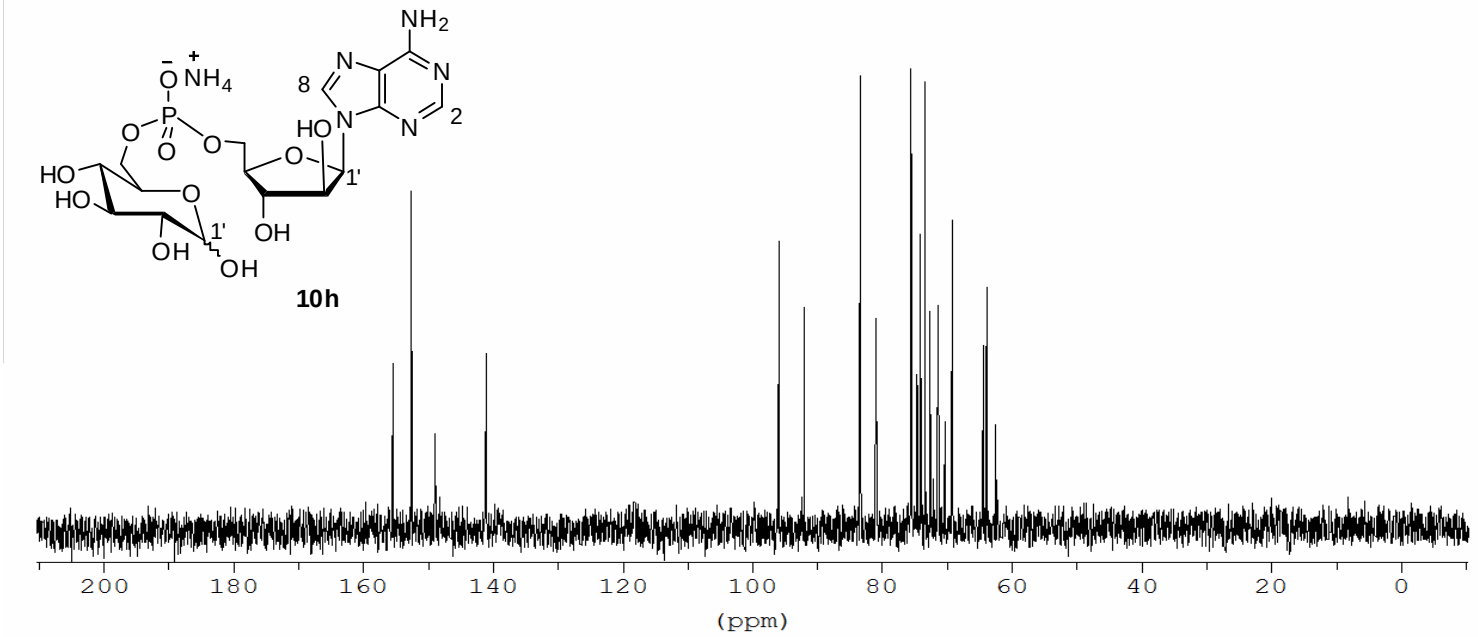
^{1}H-RMN (D_2O, 600 MHz)

10h

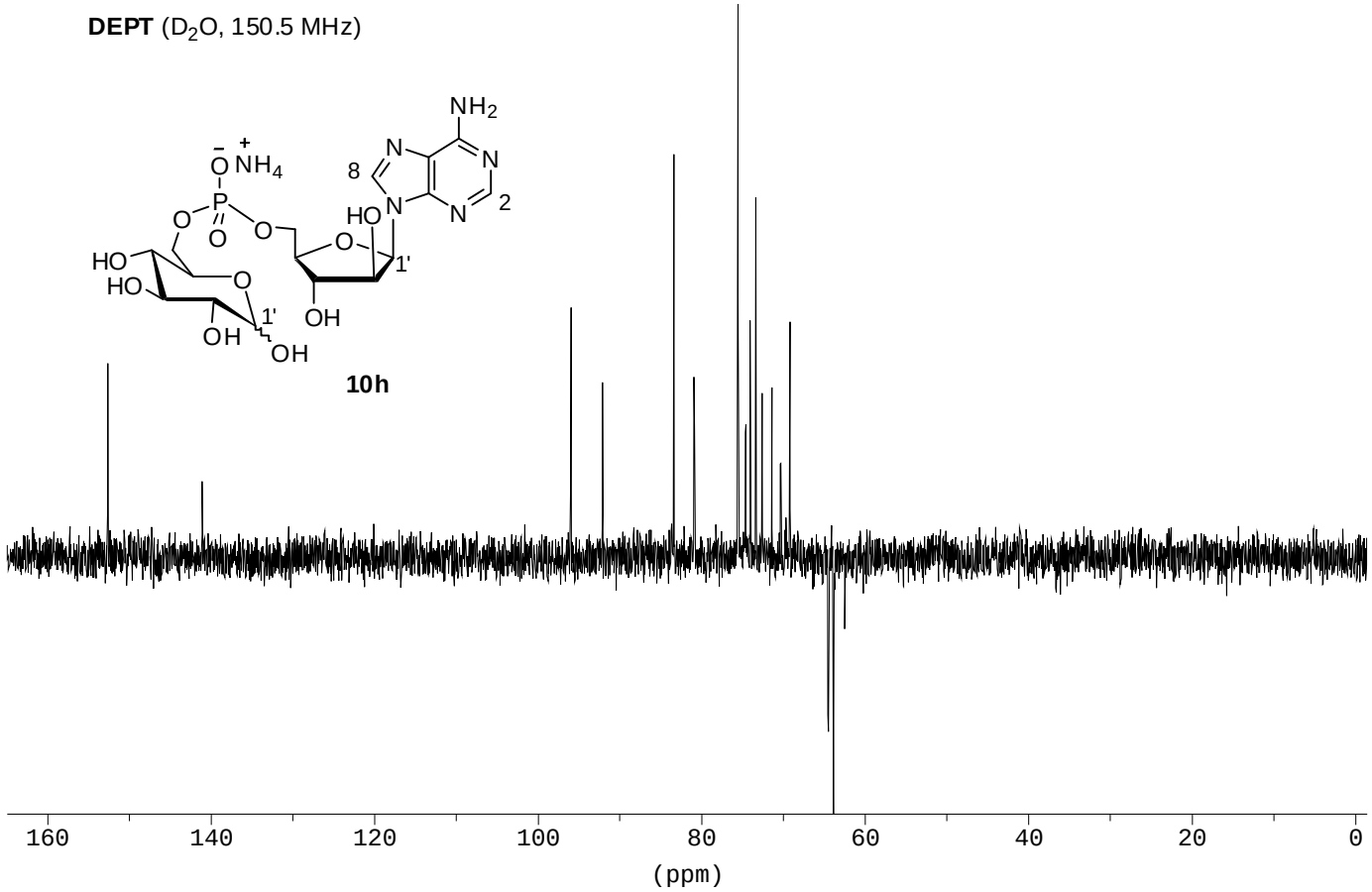


1’-Adeninyl-β-D-arabinofuranose 5’-(α/β-D-glucopyranos-6-yl) phosphate (10h)

^{13}C-RMN (D_2O, 150.5 MHz)

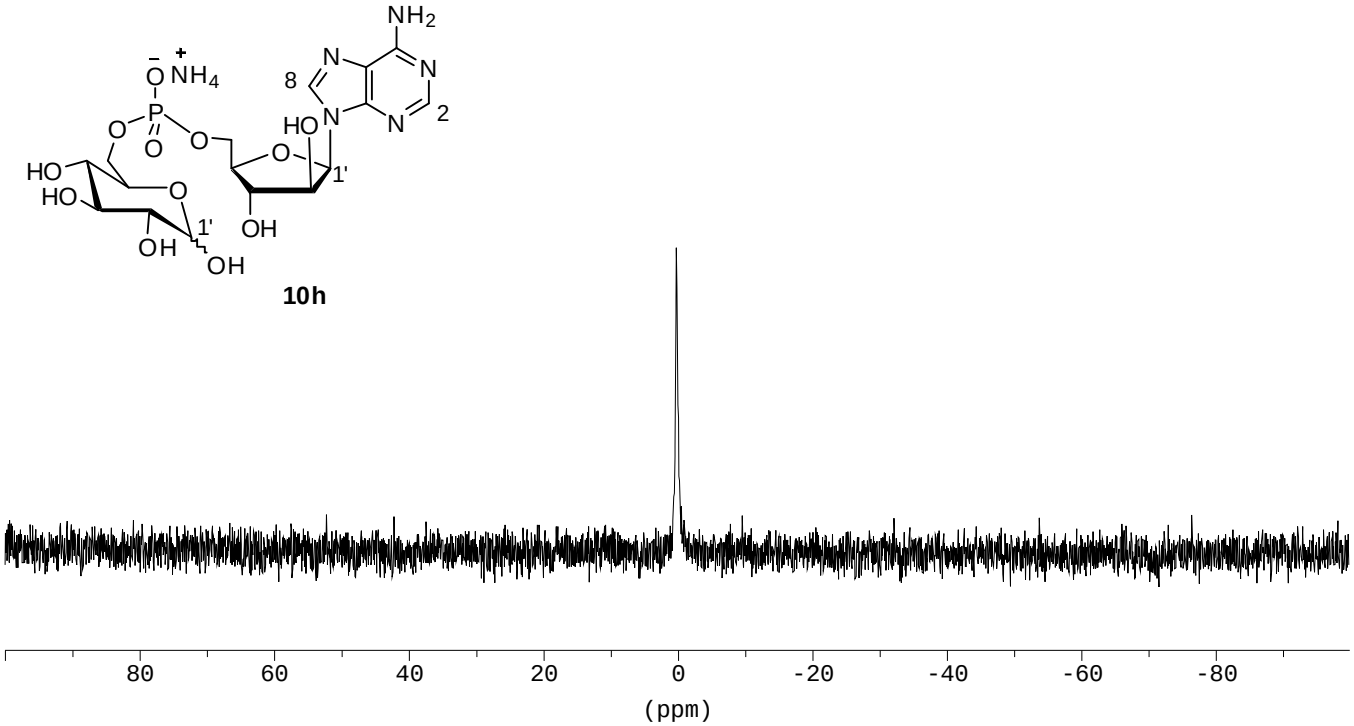


1'-Adeninyl-β-D-arabinofuranose 5'-(α/β-D-glucopyranos-6-yl) phosphate (10h)



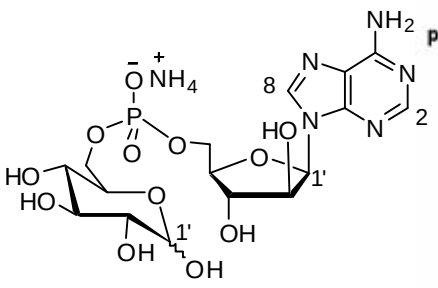
1'-Adeninyl-β-D-arabinofuranose 5'-(α/β-D-glucopyranos-6-yl) phosphate (10h)

^{31}P-RMN (D_2O, 242.9 MHz)

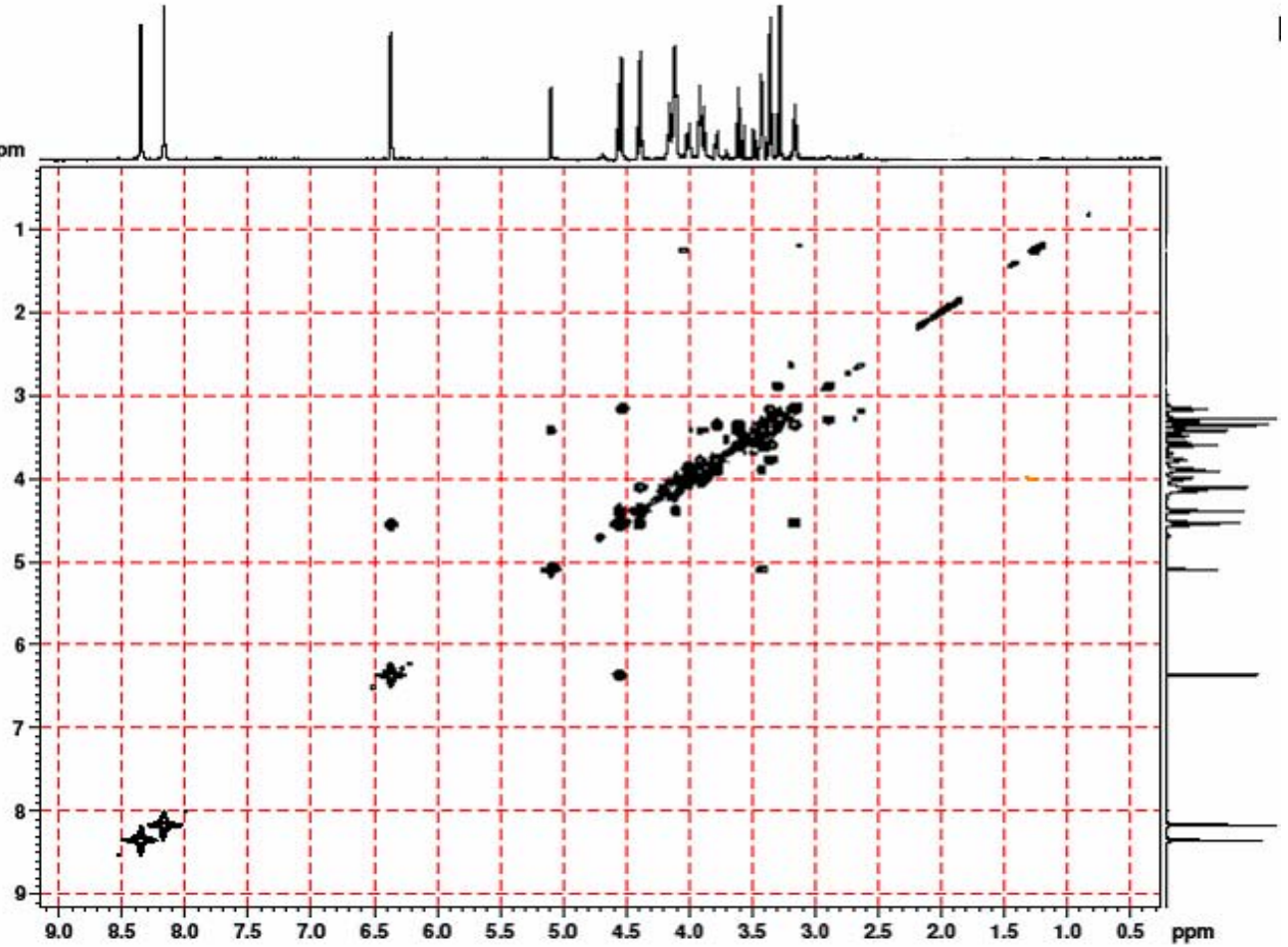


1'-Adeninyl-β-D-arabinofuranose 5'-(α/β-D-glucopyranos-6-yl) phosphate (10h)

COSY (D_2O, 600 MHz)

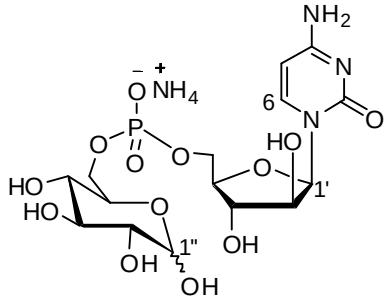


10h

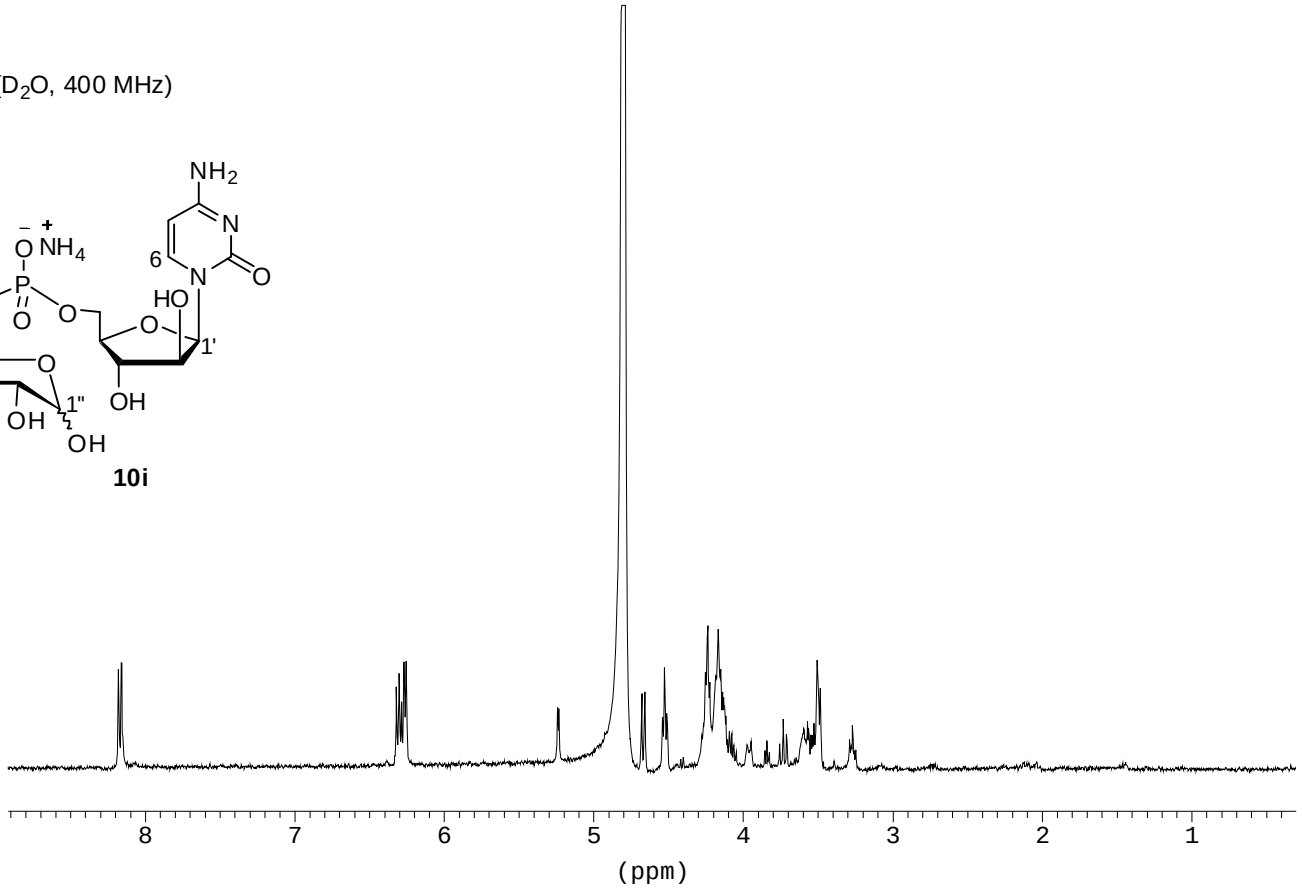


1'-Cytosinyl-β-D-arabinofuranose 5'-(α/β-D-glucopyranos-6-yl) phosphate (10i)

^{1}H-RMN (D_2O, 400 MHz)

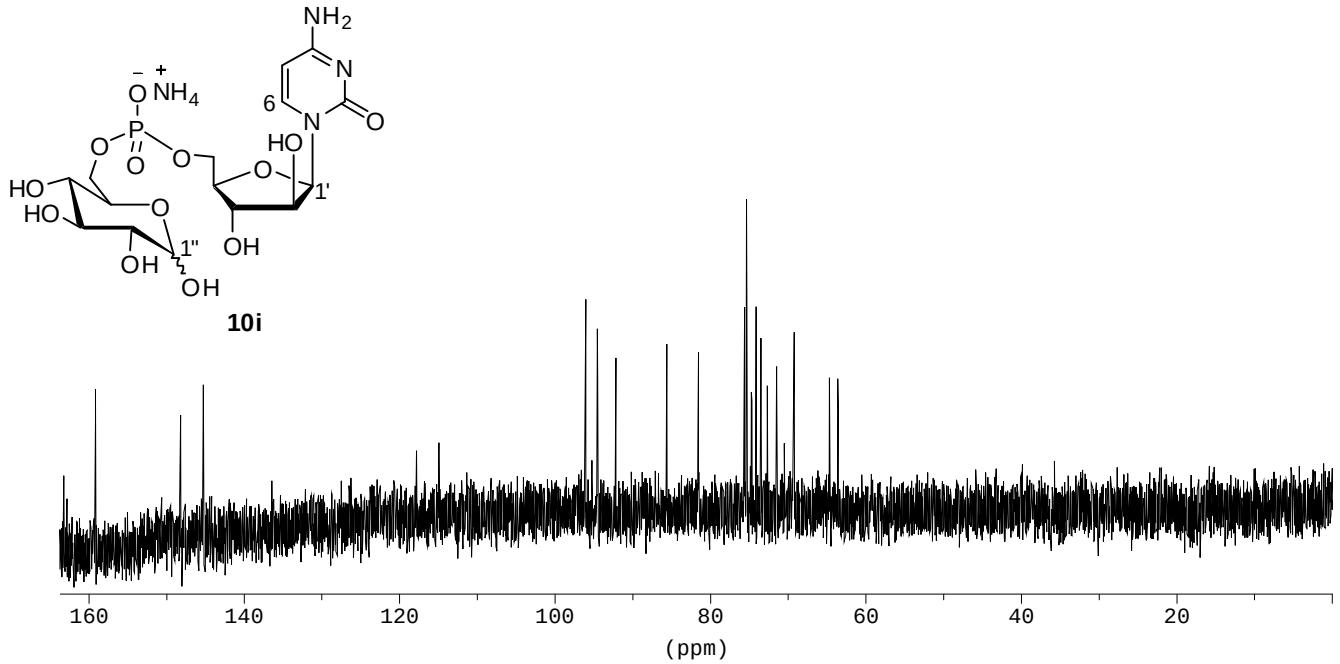


10i



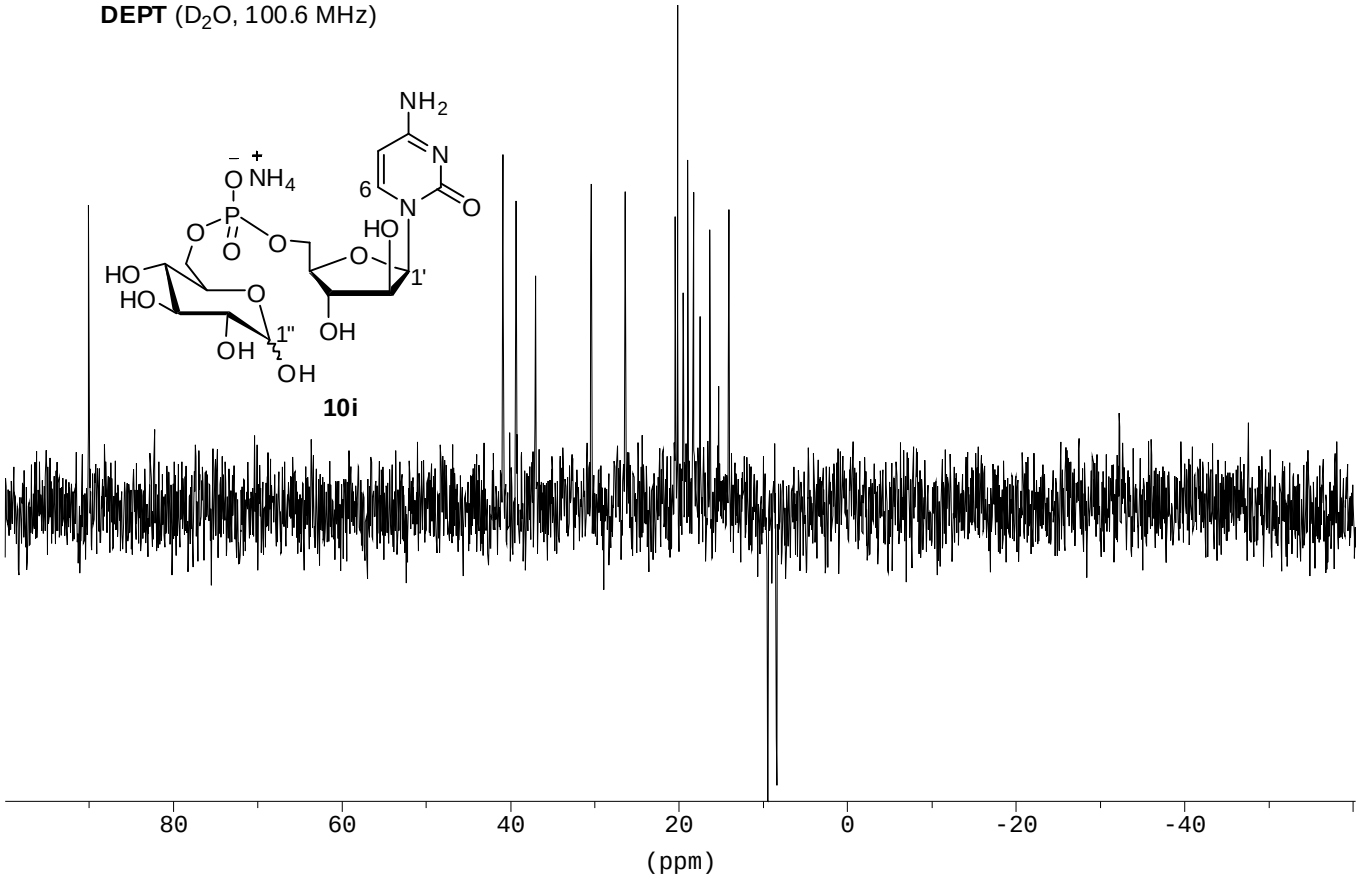
1’-Cytosinyl-β-D-arabinofuranose 5’-(α/β-D-glucopyranos-6-yl) phosphate (10i)

^{13}C-RMN (D_2O, 100.6 MHz)



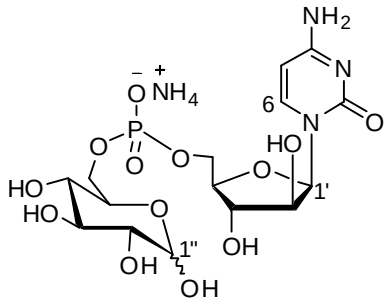
10i

1’-Cytosinyl-β-D-arabinofuranose 5’-(α/β-D-glucopyranos-6-yl) phosphate (10i)

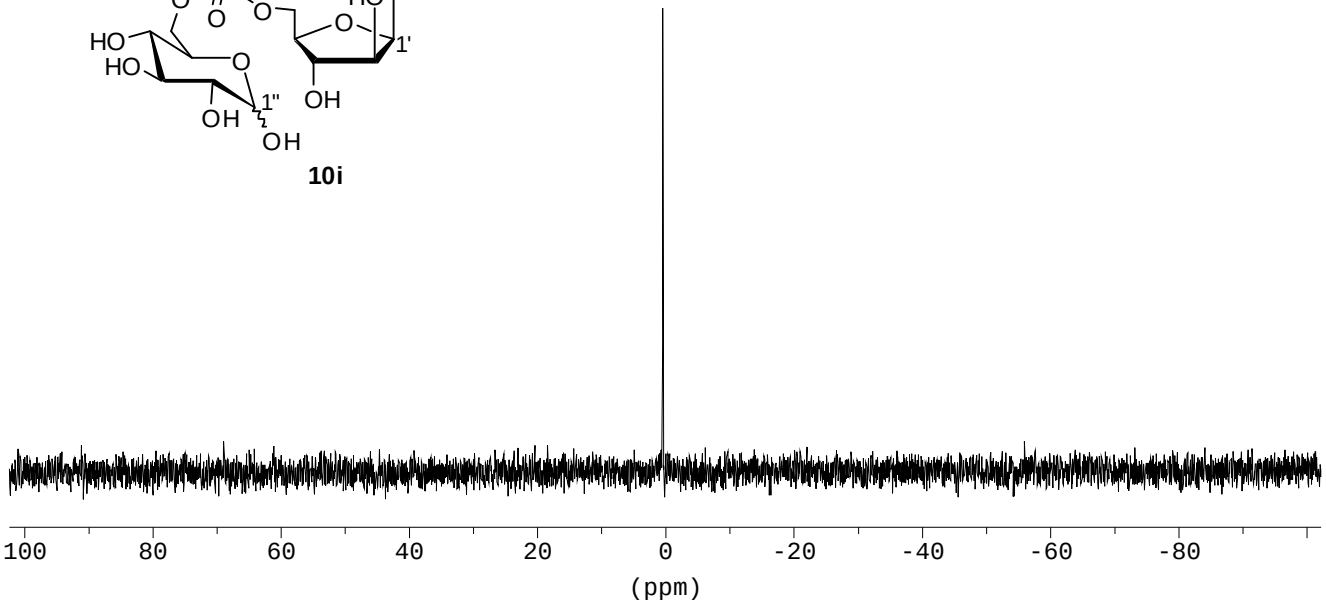


1’-Cytosinyl-β-D-arabinofuranose 5’-(α/β-D-glucopyranos-6-yl) phosphate (10i)

^{31}P-RMN (D_2O, 161.9 MHz)

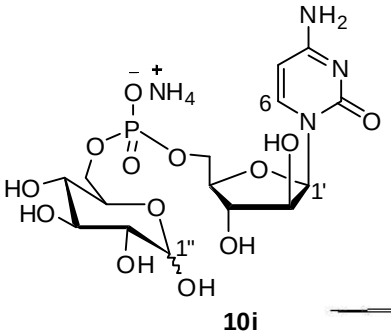


10i

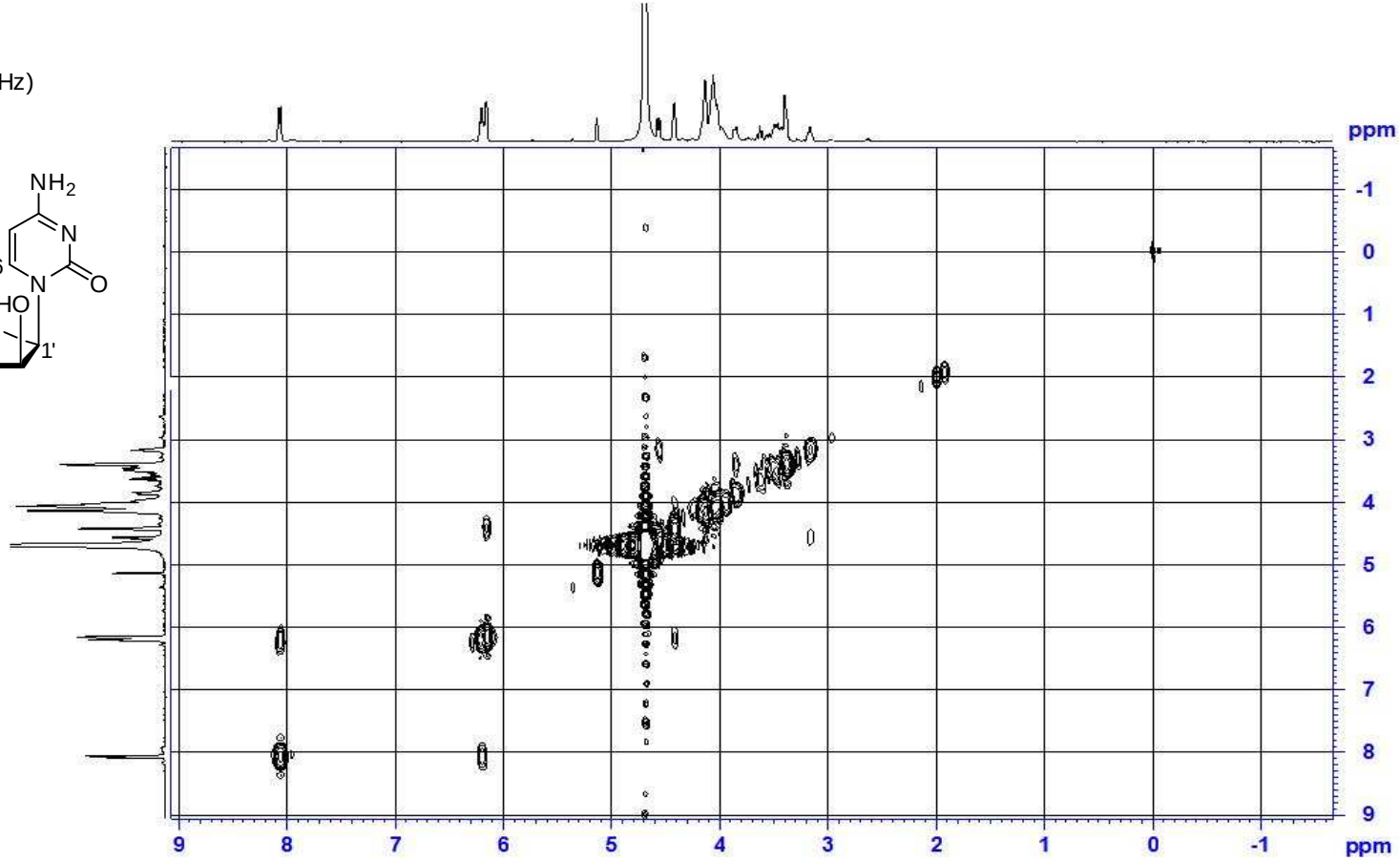


1'-Cytosinyl-β-D-arabinofuranose 5'-(α/β-D-glucopyranos-6-yl) phosphate (10i)

COSY (D_2O, 400 MHz)



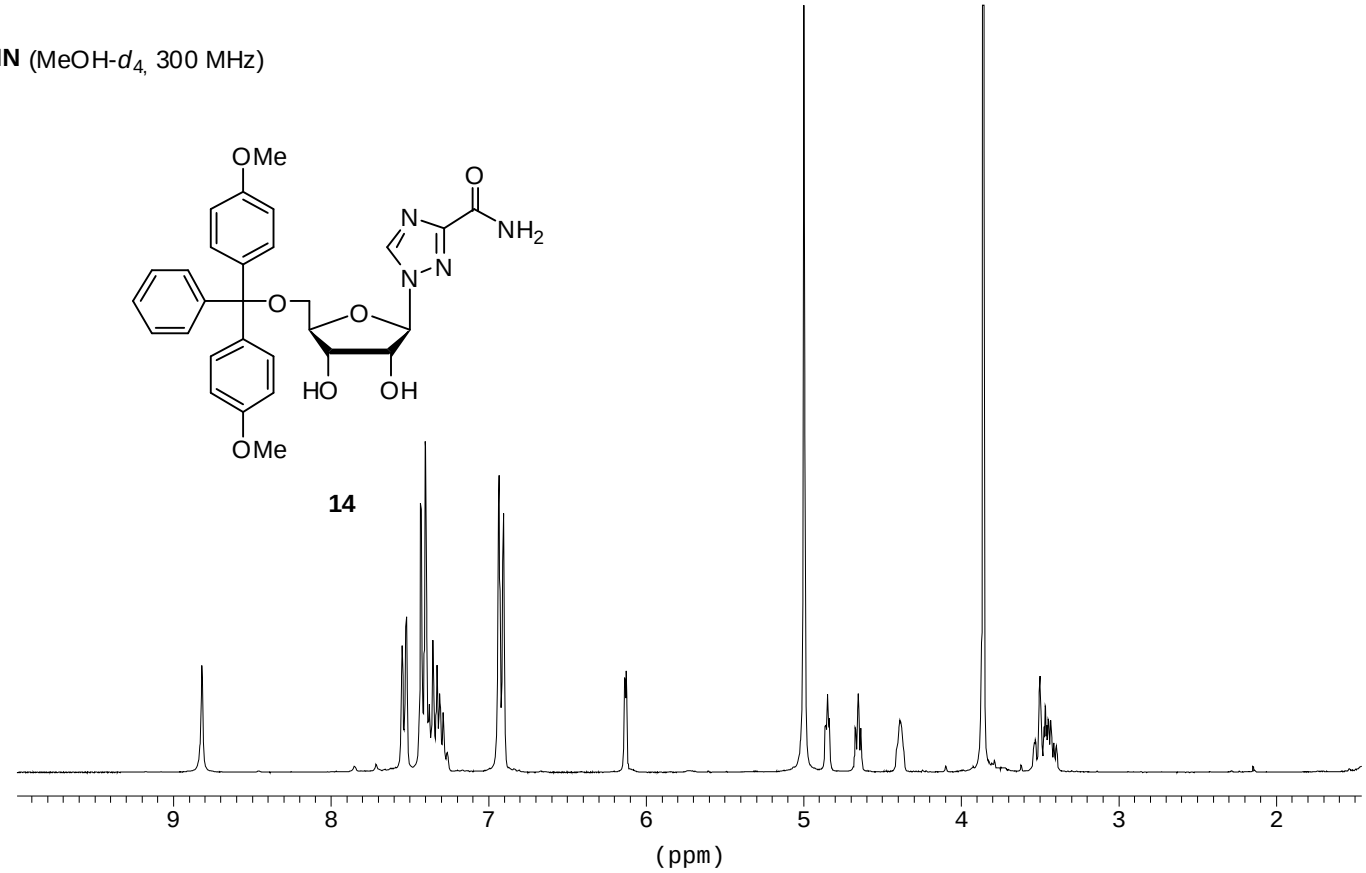
10i



1-(5'-*O*-dimethoxytrityl-β-D-ribofuranosyl)-1,2,4-triazole-3-carboxamide (14)

^{1}H-RMN (MeOH-d_4, 300 MHz)

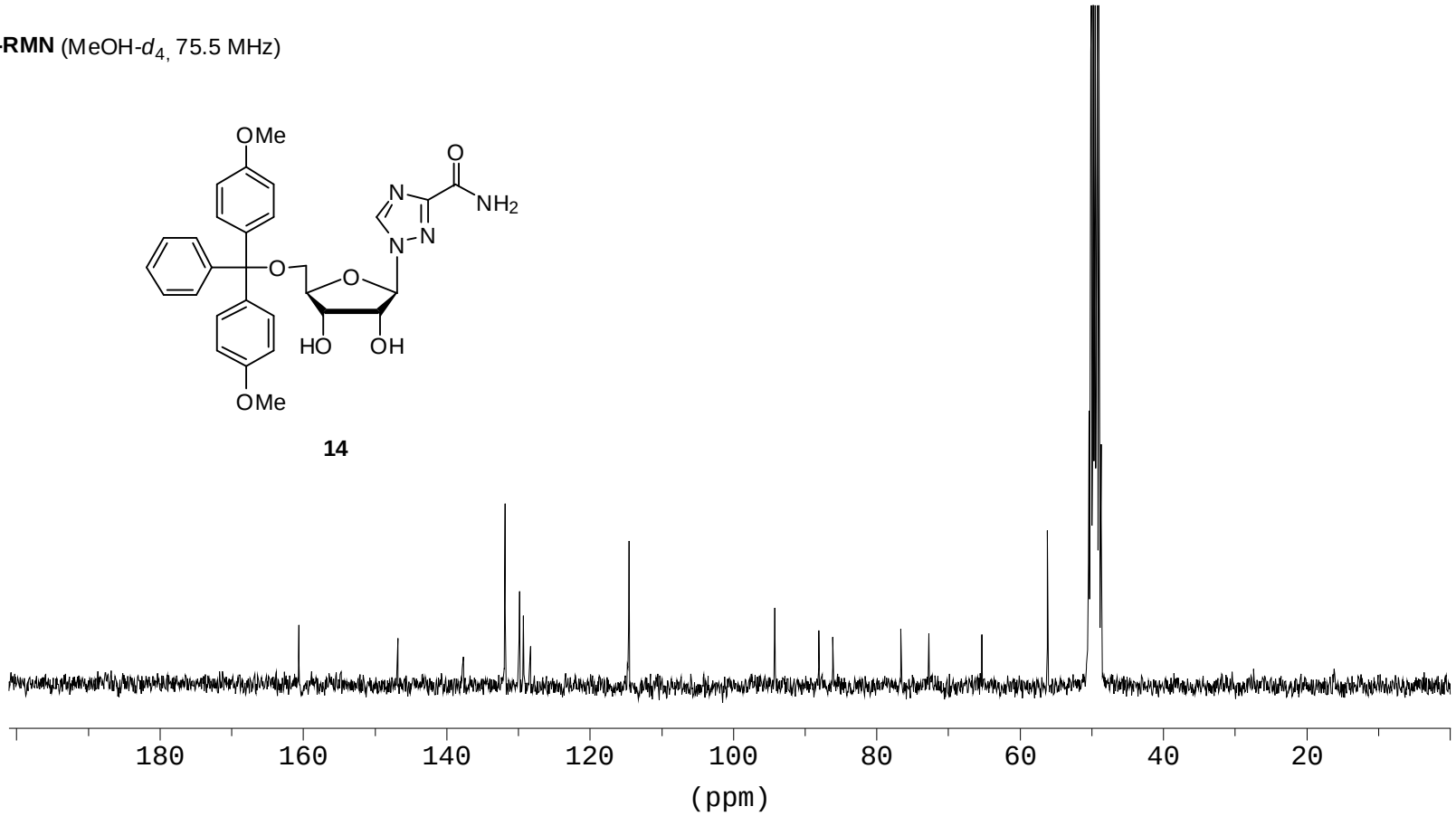
14



1-(5'-*O*-dimethoxytrityl-β-D-ribofuranosyl)-1,2,4-triazole-3-carboxamide (14)

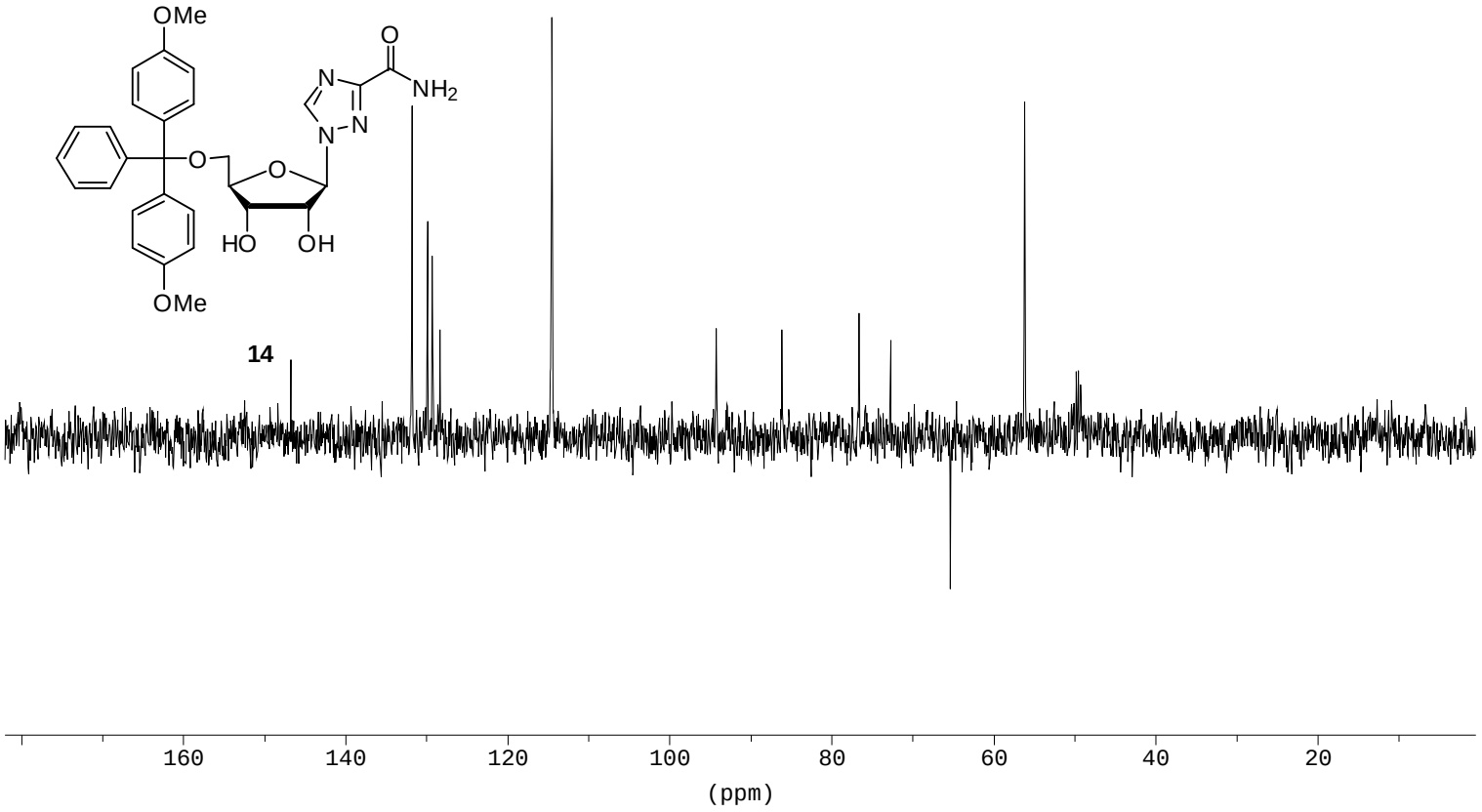
^{13}C-RMN (MeOH-d_4, 75.5 MHz)

14

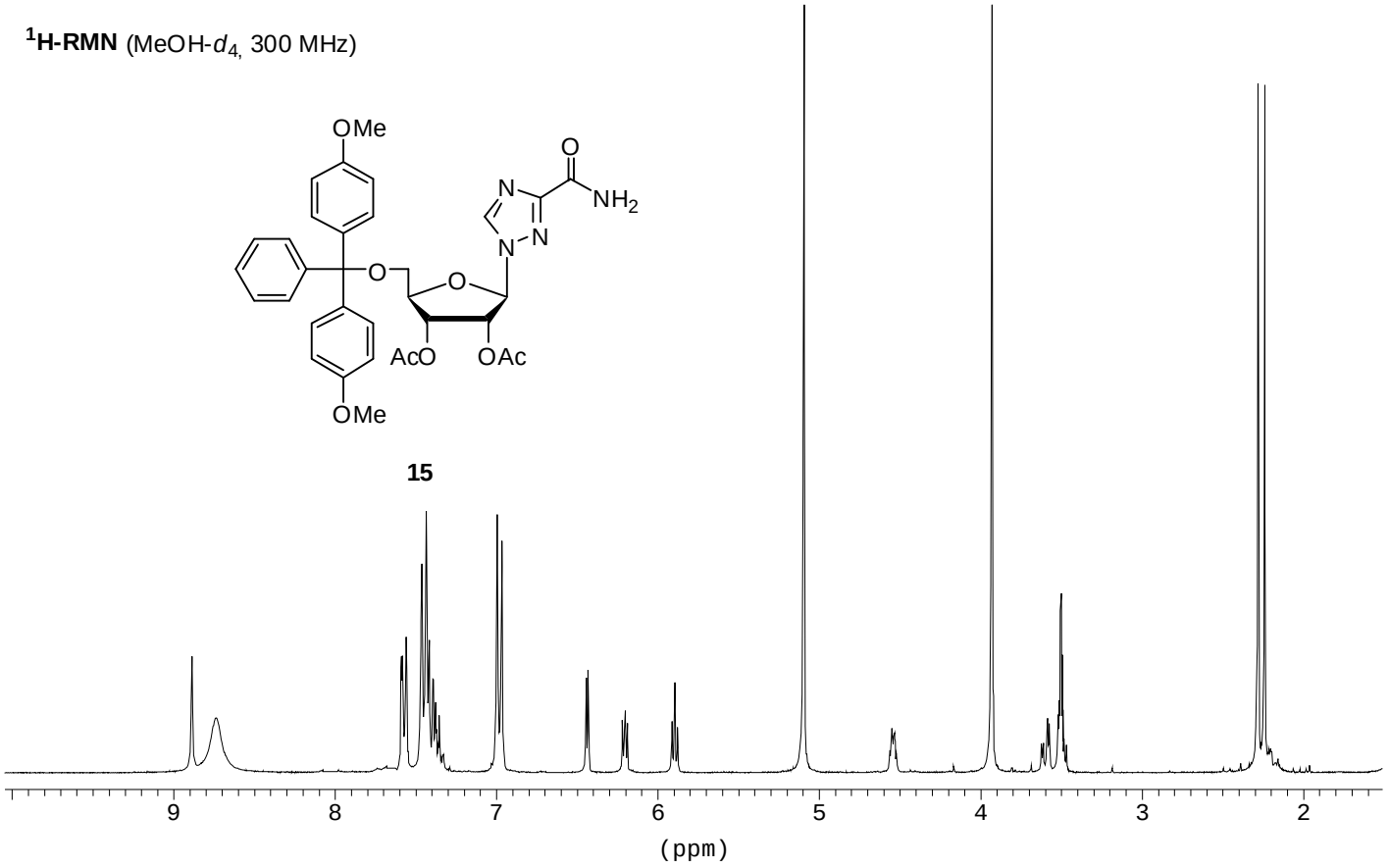


1-(5'-*O*-dimethoxytrityl-β-D-ribofuranosyl)-1,2,4-triazole-3-carboxamide (14)

DEPT (MeOH-d_4, 75.5 MHz)

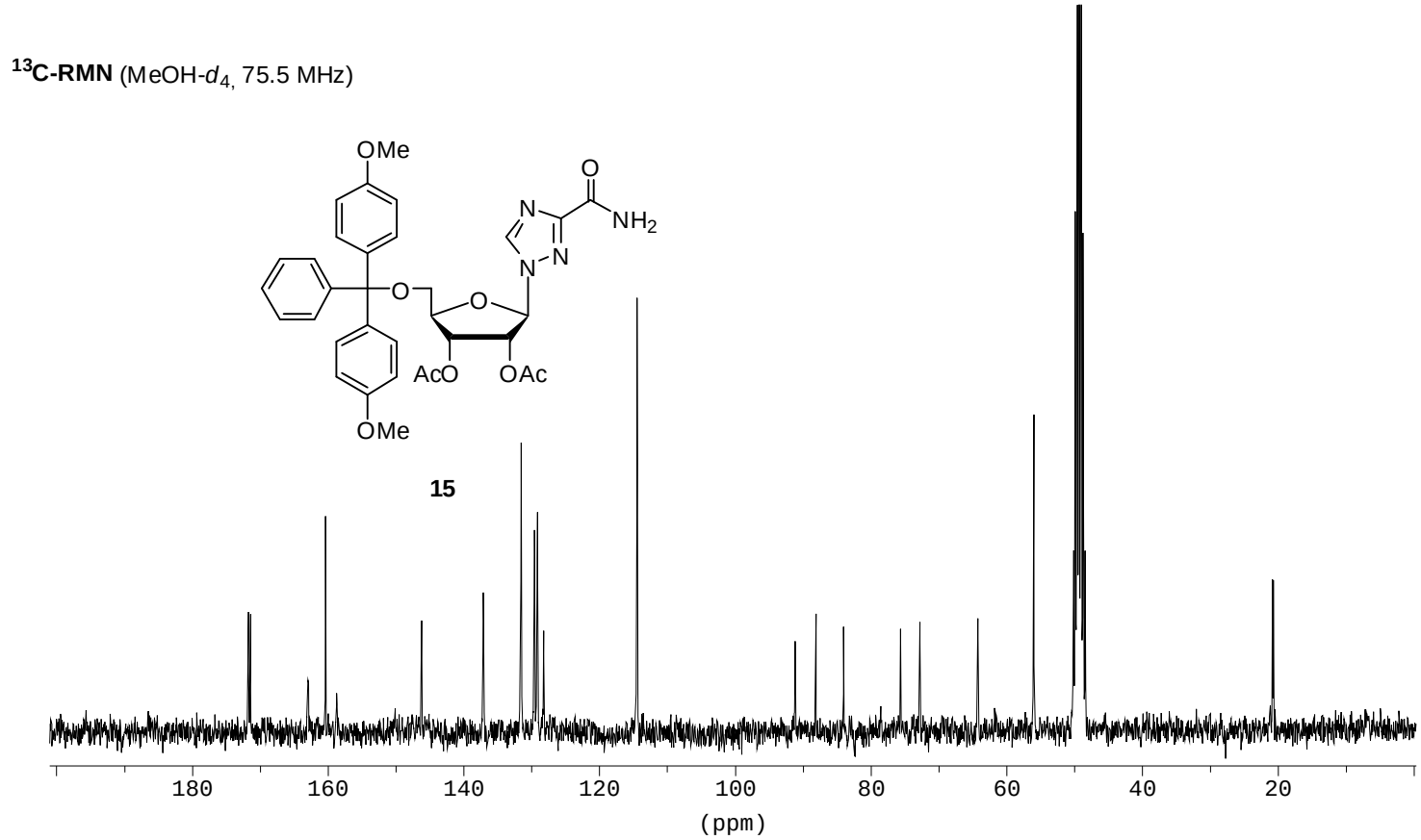


1-(2',3'-di-*O*-acetyl-5'-*O*-dimethoxytrityl-β-D-ribofuranosyl)-1,2,4-triazole-3-carboxamide (15).



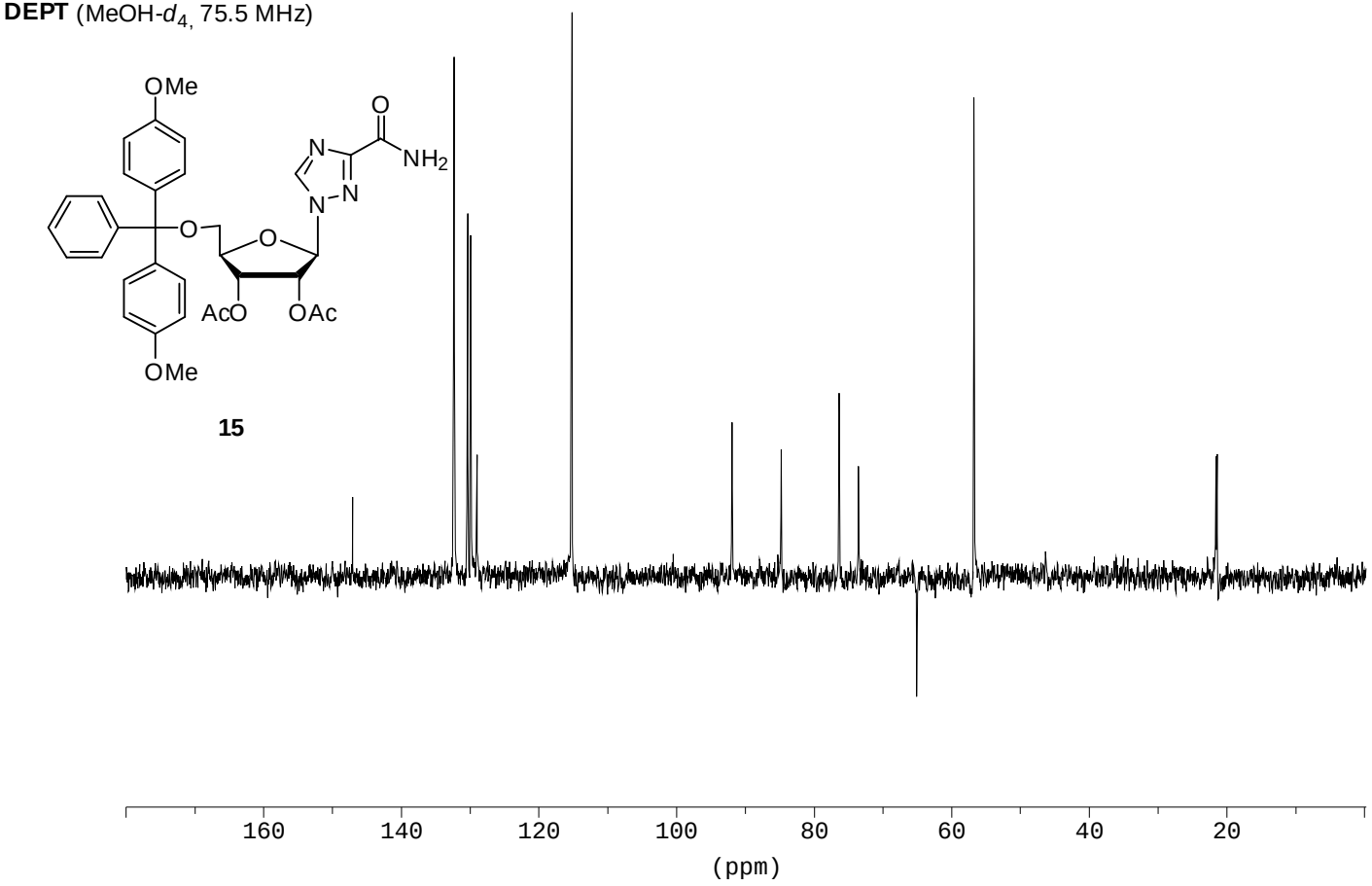
1-(2',3'-di-*O*-acetyl-5'-*O*-dimethoxytrityl-β-D-ribofuranosyl)-1,2,4-triazole-3-carboxamide (15).

^{13}C-RMN (MeOH-d_4, 75.5 MHz)



1-(2',3'-di-*O*-acetyl-5'-*O*-dimethoxytrityl-β-D-ribofuranosyl)-1,2,4-triazole-3-carboxamide (15).

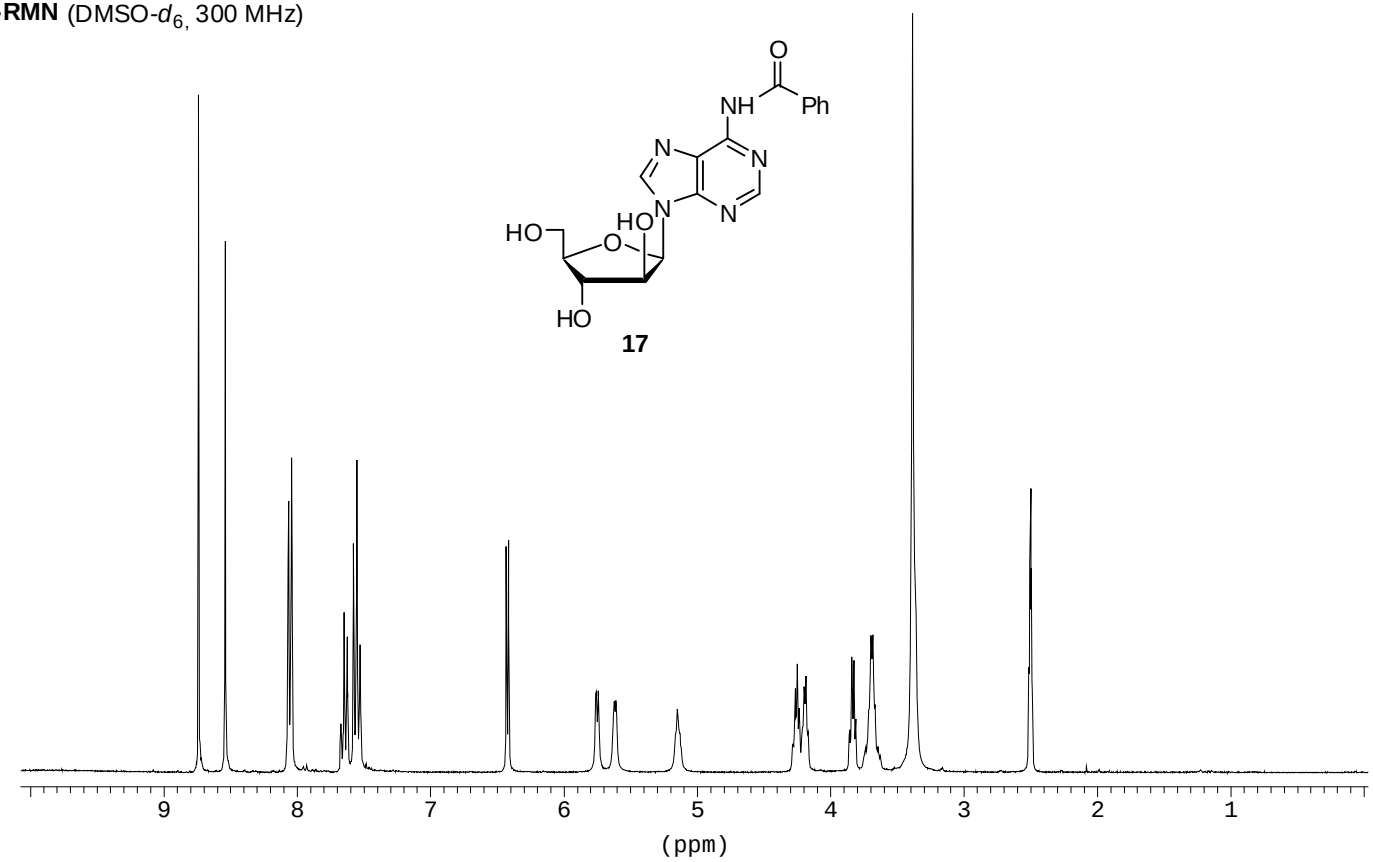
DEPT (MeOH-d_4, 75.5 MHz)



15

9-(β-D-arabinofuranosyl)-N^6-benzoyladenine (17)

^{1}H-RMN (DMSO-d_6, 300 MHz)

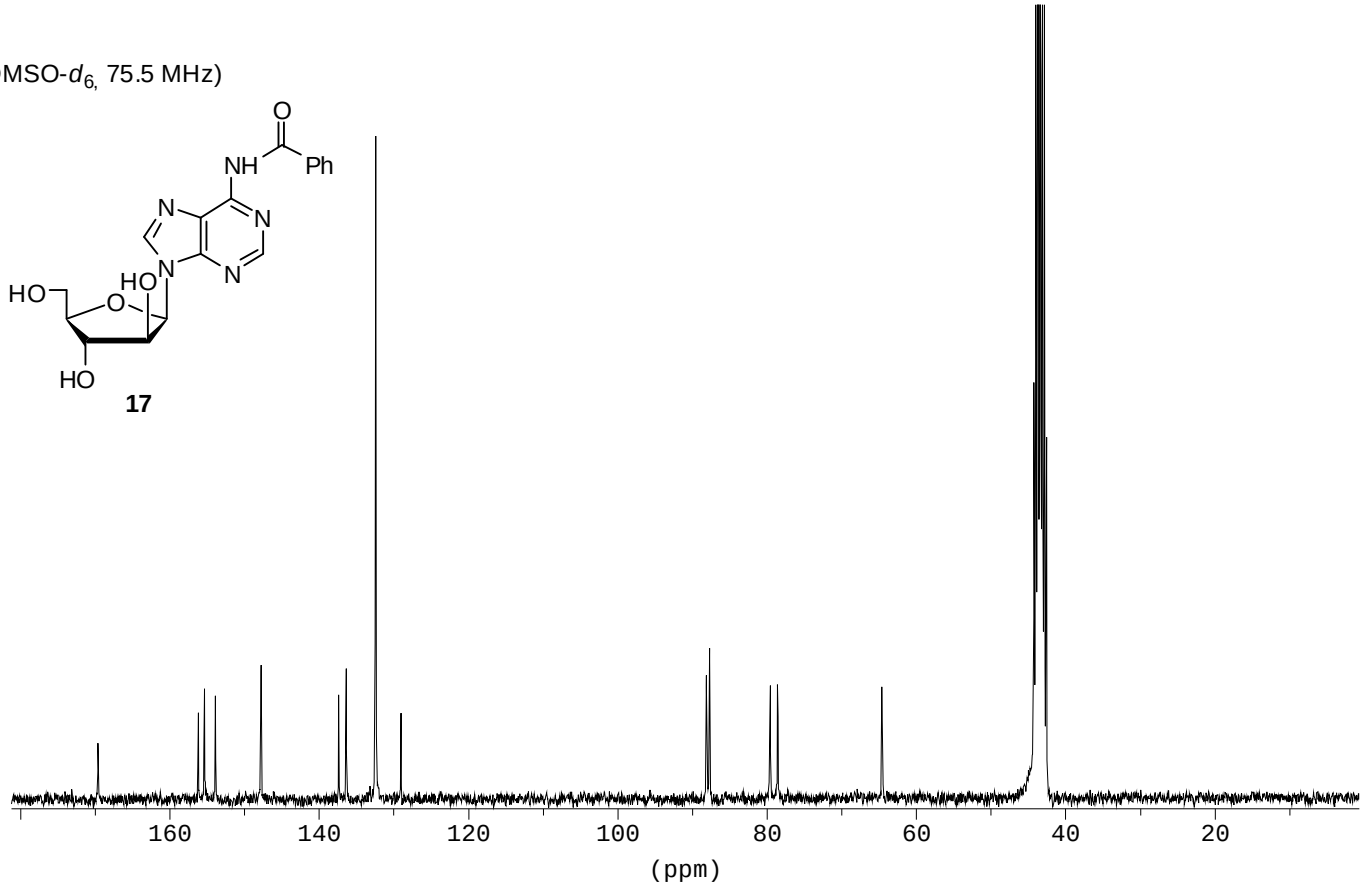


17

9-(β-D-arabinofuranosyl)-N^6-benzoyladenine (17)

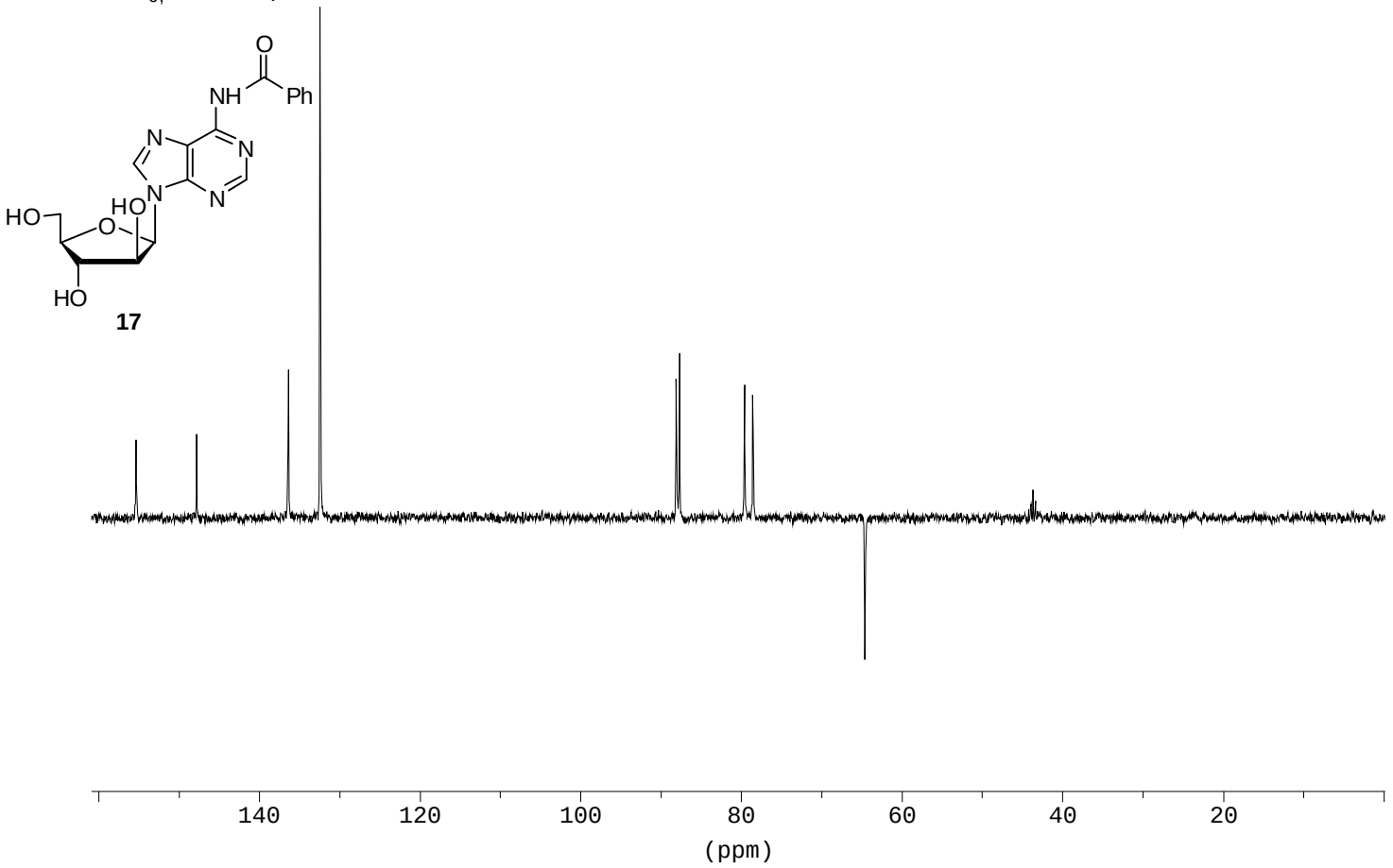
^{13}C-RMN (DMSO-d_6, 75.5 MHz)

17



9-(β-D-arabinofuranosyl)-N^6-benzoyladenine (17)

DEPT(DMSO-d_6, 75.5 MHz)

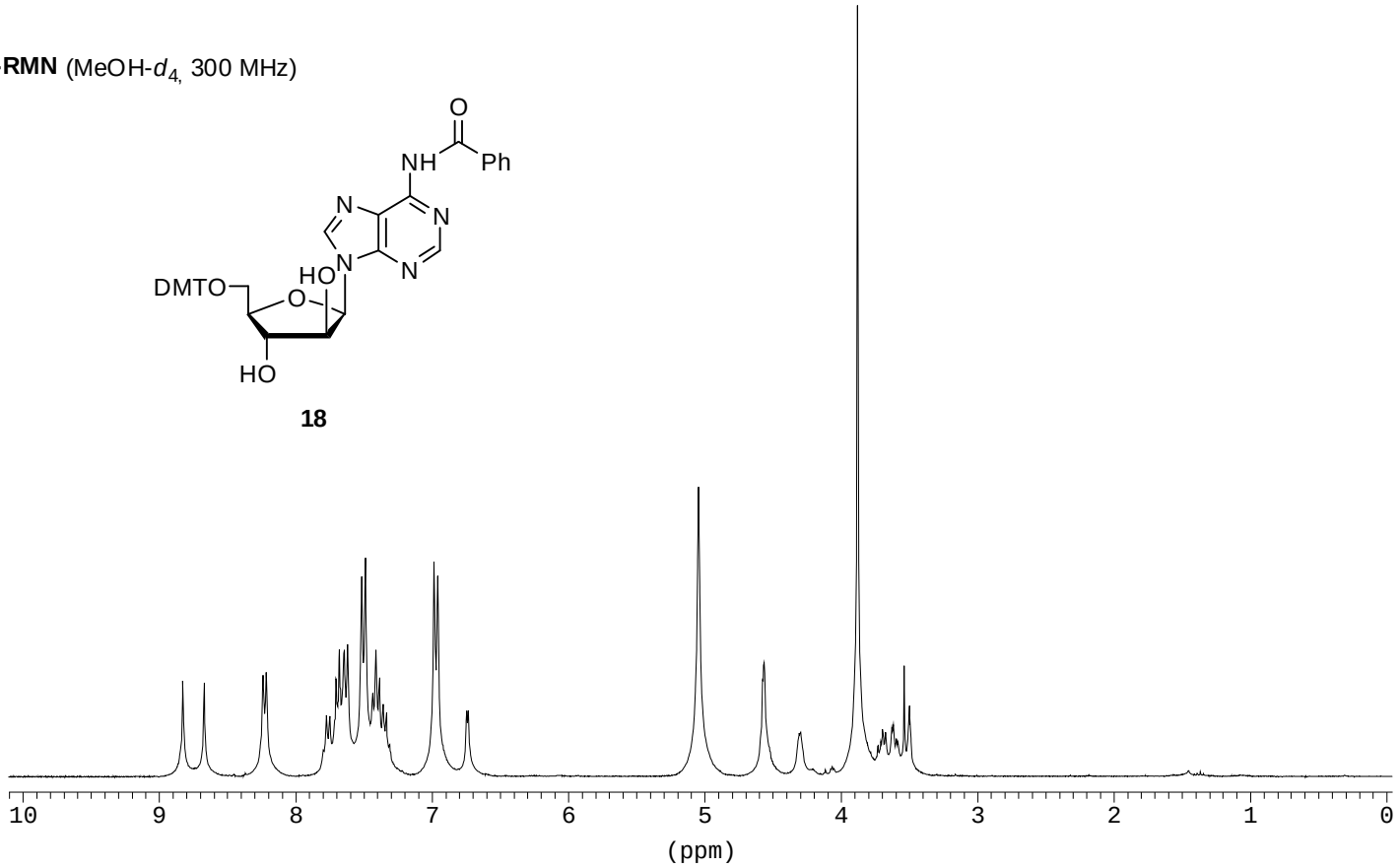


17

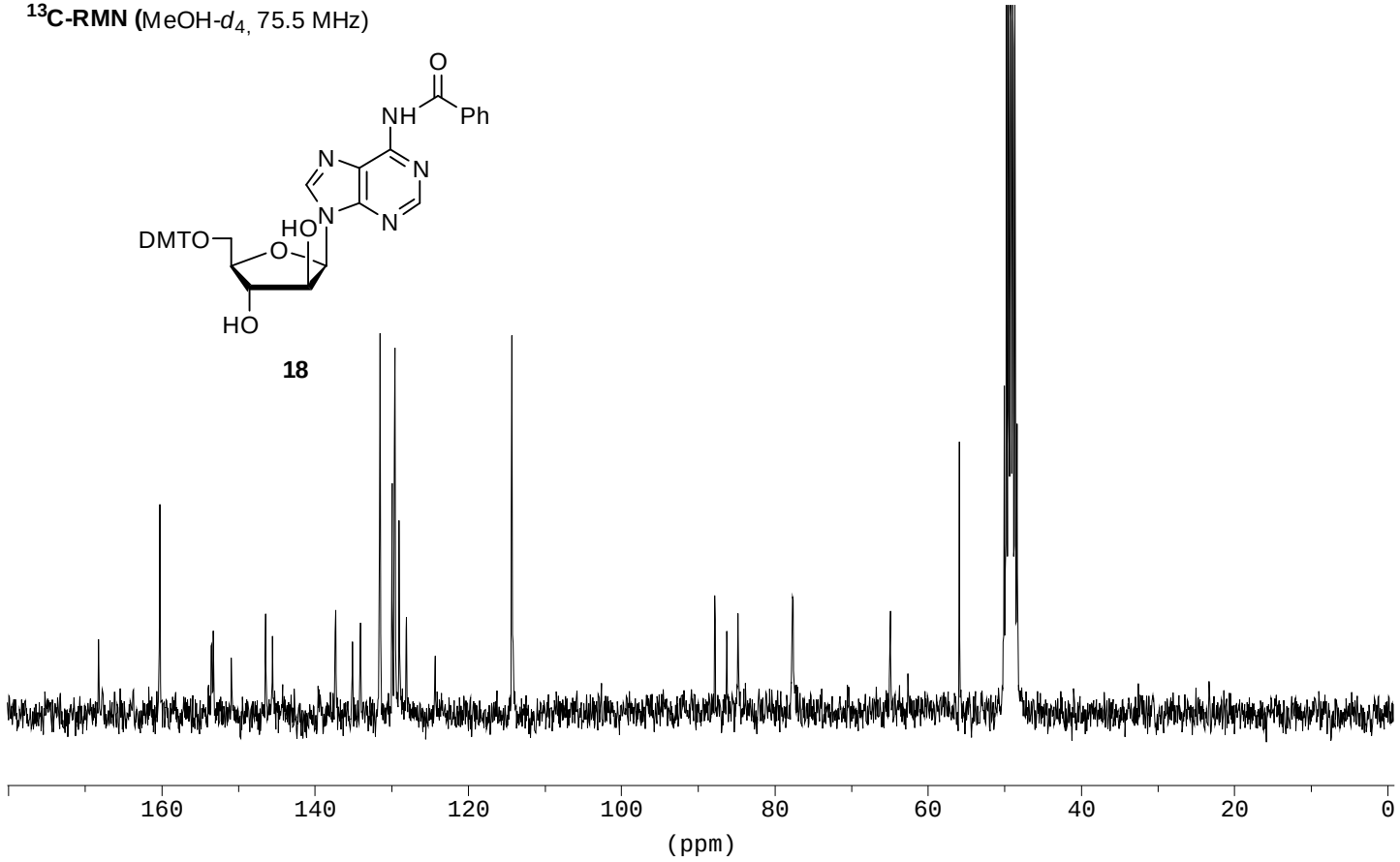
Synthesis of N^6-benzoyl-9-(5'-*O*-dimethoxytrityl-β-D-arabinofuranosyl)adenine (18)

^{1}H-RMN (MeOH-d_4, 300 MHz)

18

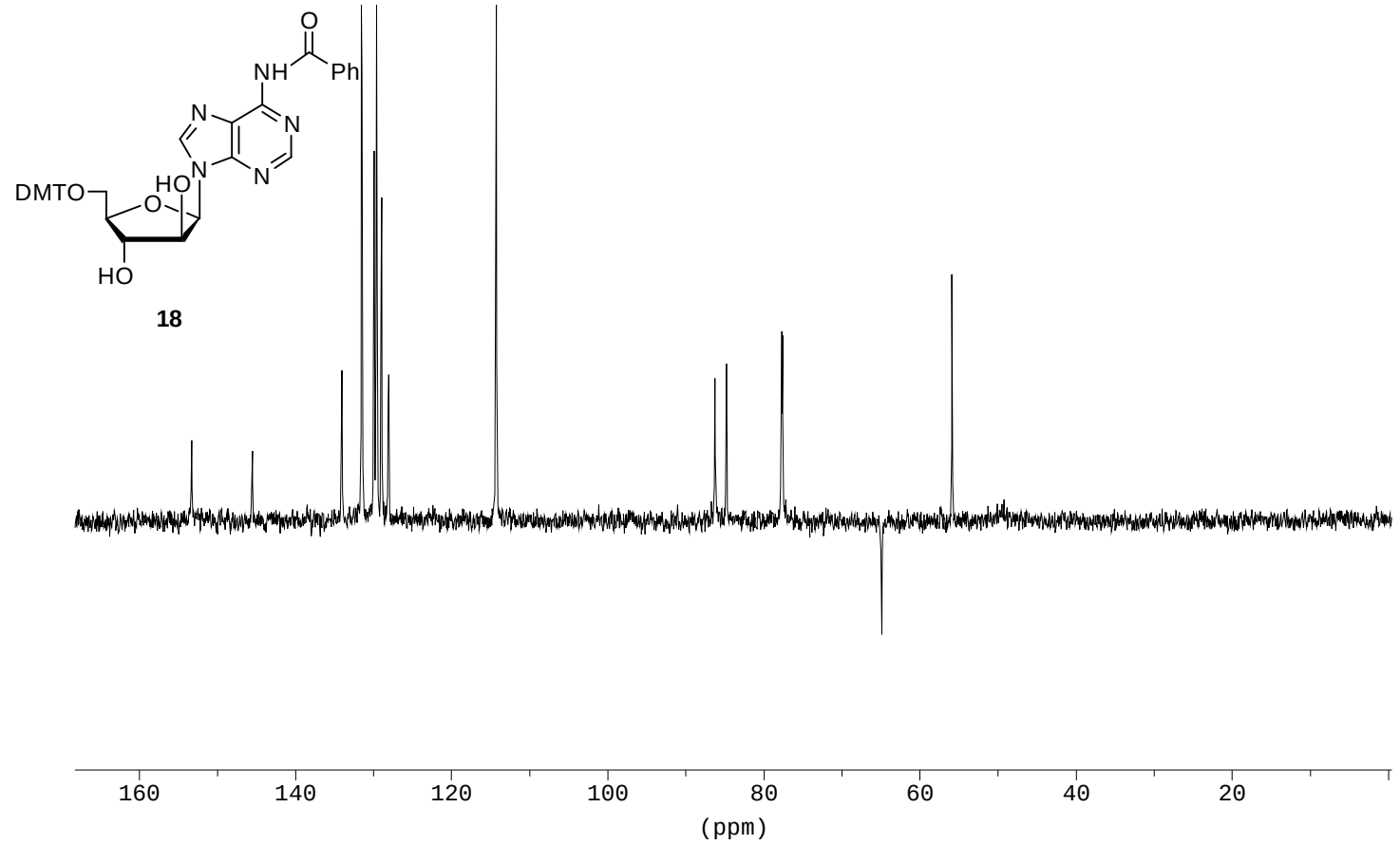


Synthesis of N^6-benzoyl-9-(5'-*O*-dimethoxytrityl-β-D-arabinofuranosyl)adenine (18)



Synthesis of N^6-benzoyl-9-(5'-*O*-dimethoxytrityl-β-D-arabinofuranosyl)adenine (18)

DEPT (MeOH-d_4, 75.5 MHz)

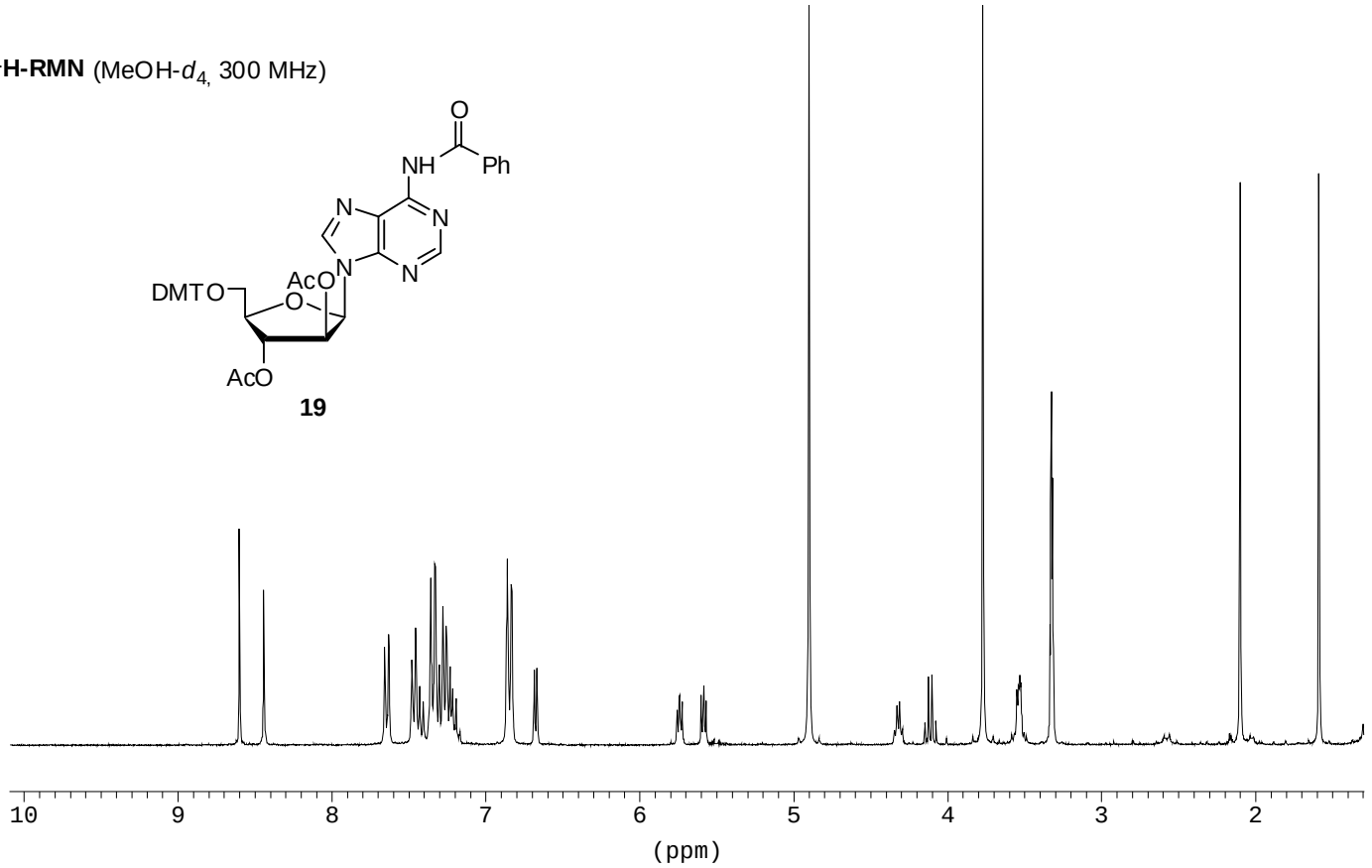


18

N^6-benzoyl-9-(2',3'-di-*O*-acetyl-5'-*O*-dimethoxytrityl-β-D-arabinofuranosyl)adenine (19)

^{1}H-RMN (MeOH-d_4, 300 MHz)

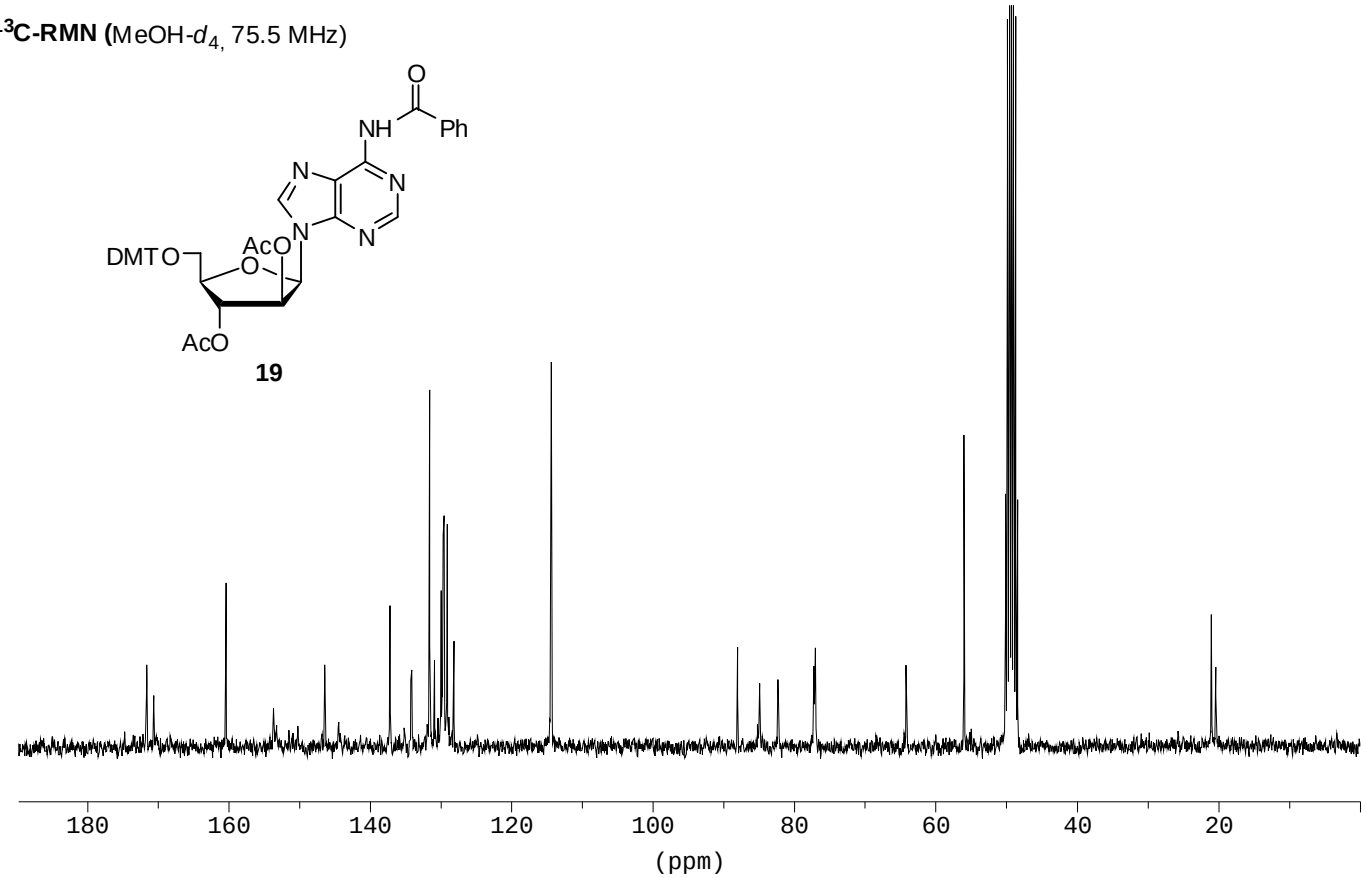
19



N^6-benzoyl-9-(2',3'-di-*O*-acetyl-5'-*O*-dimethoxytrityl-β-D-arabinofuranosyl)adenine (19)

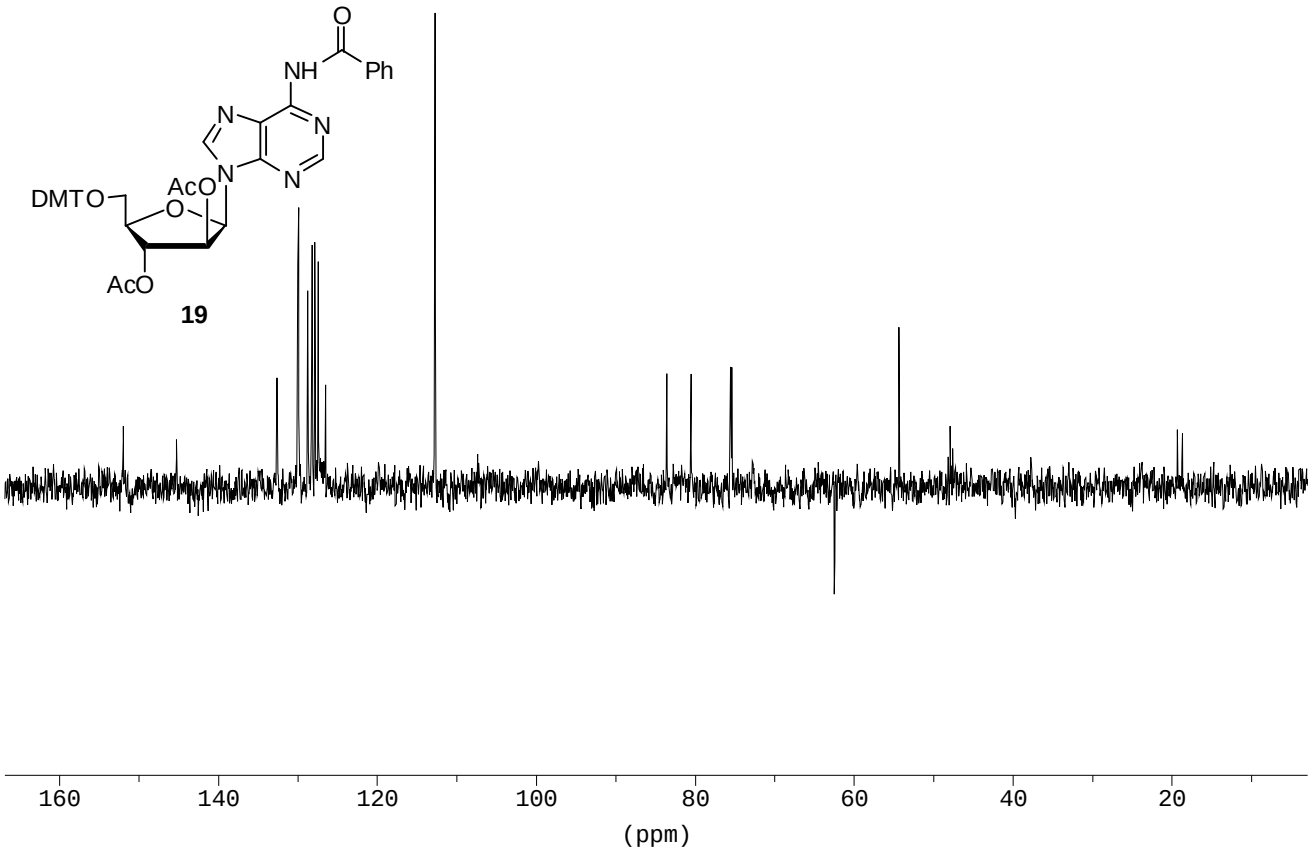
^{13}C-RMN (MeOH-d_4, 75.5 MHz)

19



N^6-benzoyl-9-(2',3'-di-*O*-acetyl-5'-*O*-dimethoxytrityl-β-D-arabinofuranosyl)adenine (19)

DEPT (MeOH-d_4, 75.5 MHz)

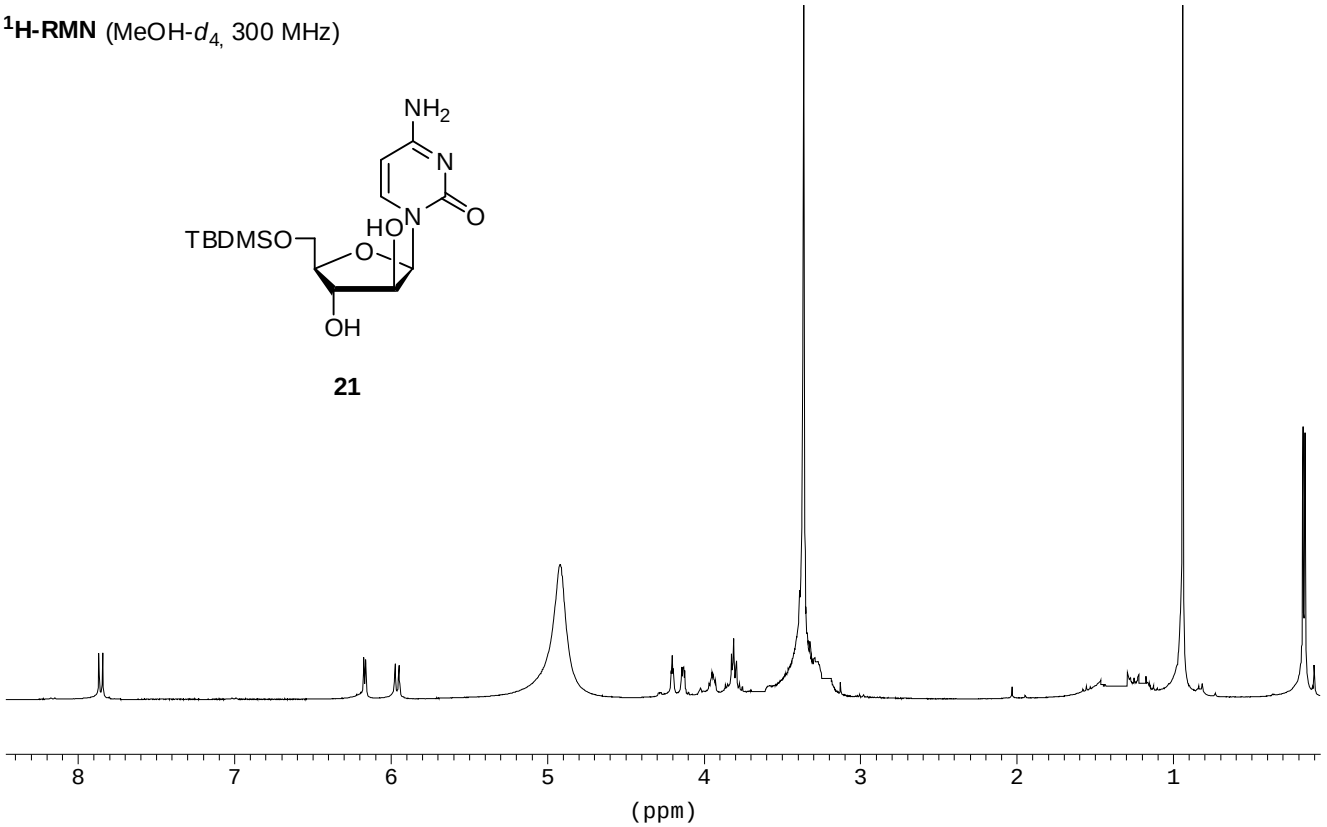


19

1-(5'-*O-tert*-butyldimetylsilyl-β-D-arabinofuranosyl)cytosine (21)

^{1}H-RMN (MeOH-d_4, 300 MHz)

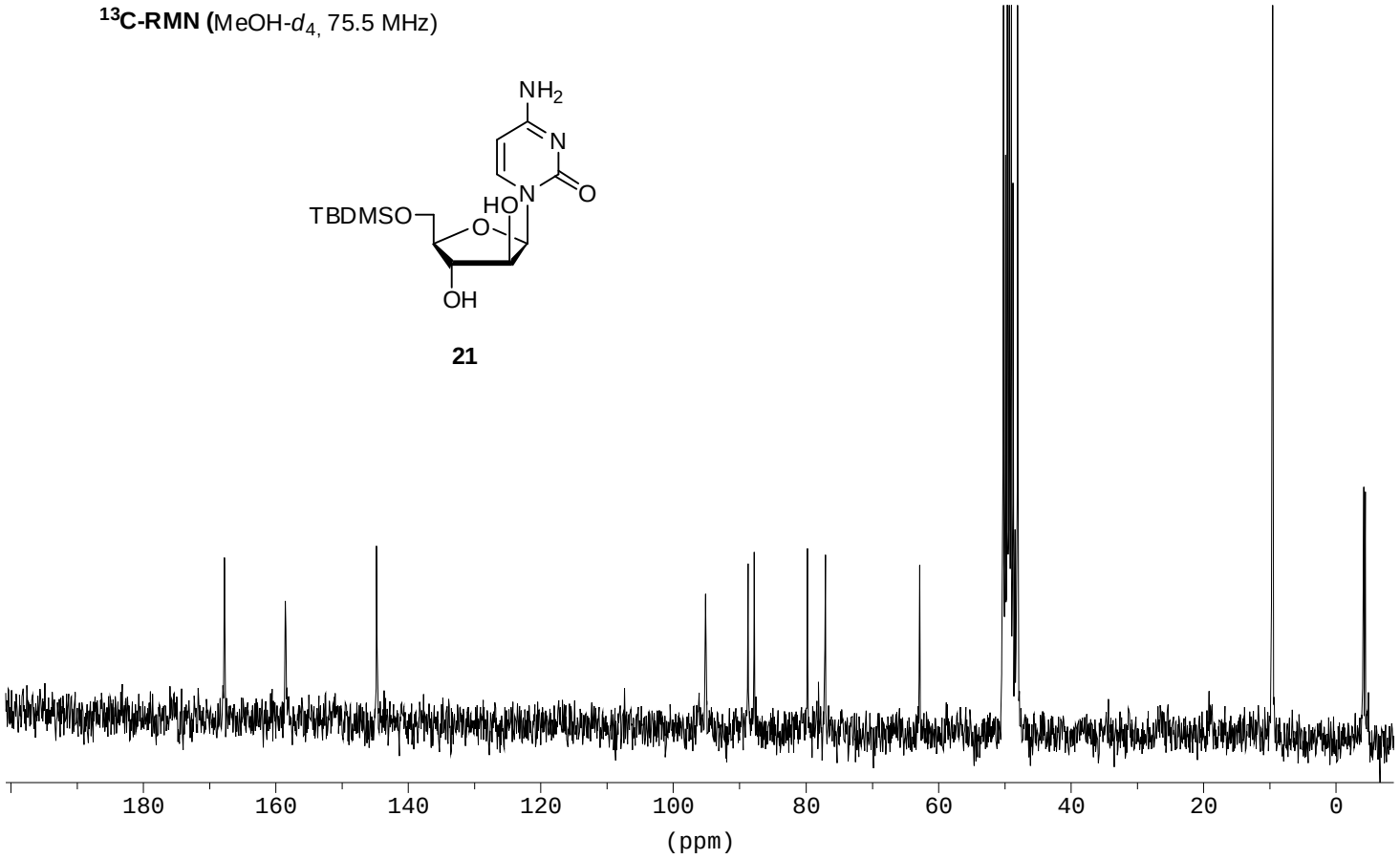
21



1-(5'-*O-tert*-butyldimetylsilyl-β-D-arabinofuranosyl)cytosine (21)

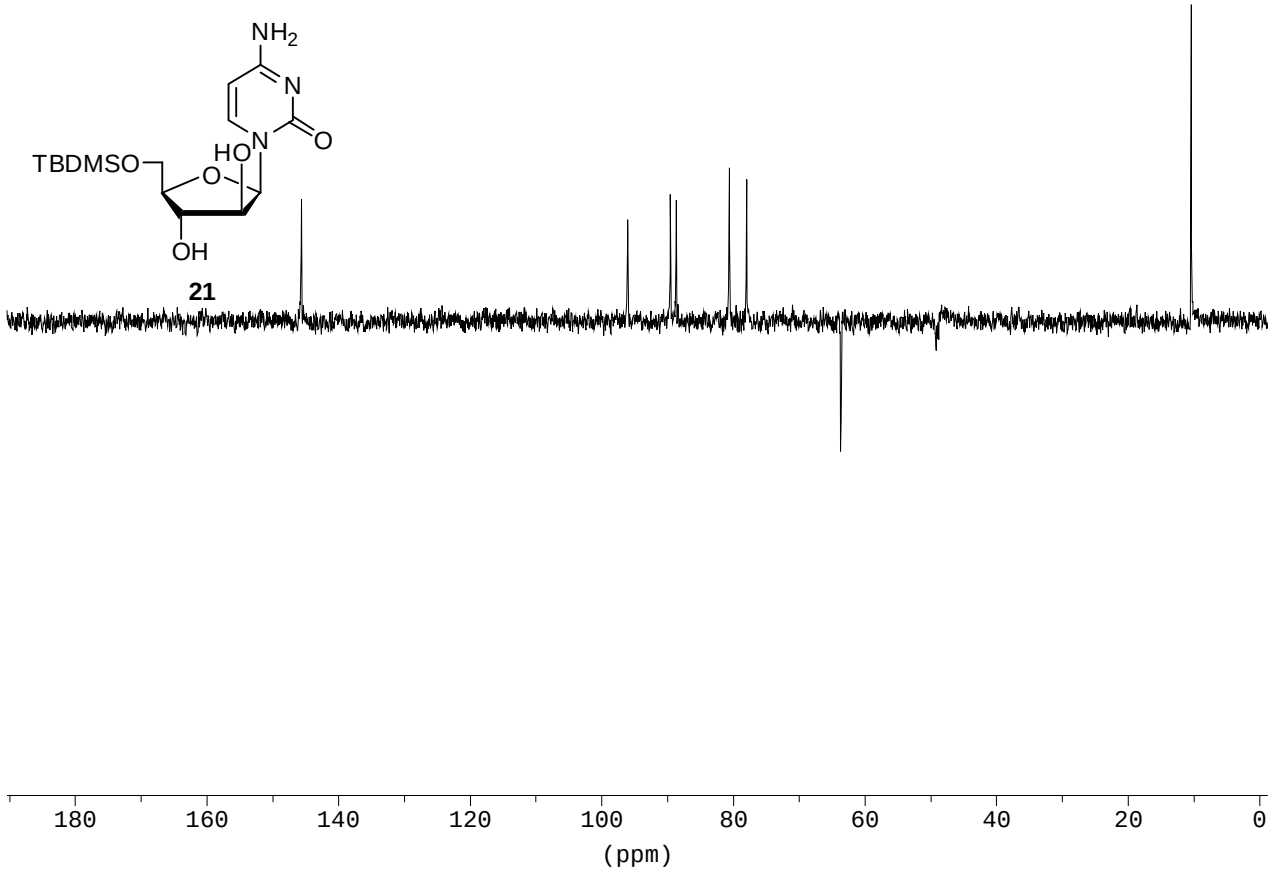
^{13}C-RMN (MeOH-d_4, 75.5 MHz)

21



1-(5'-*O*-*tert*-butyldimetylsilyl-β-D-arabinofuranosyl)cytosine (21)

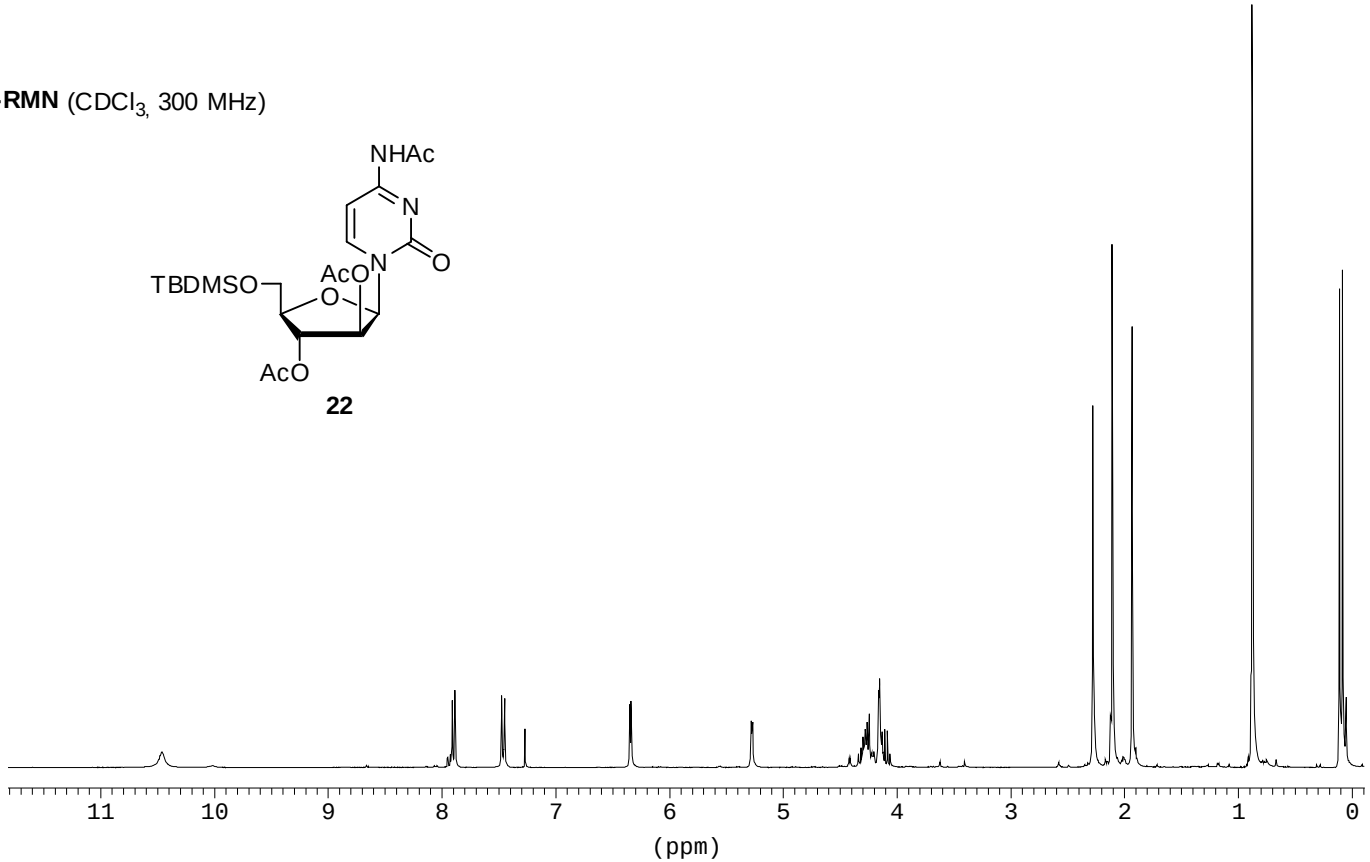
DEPT (MeOH-d_4, 75.5 MHz)



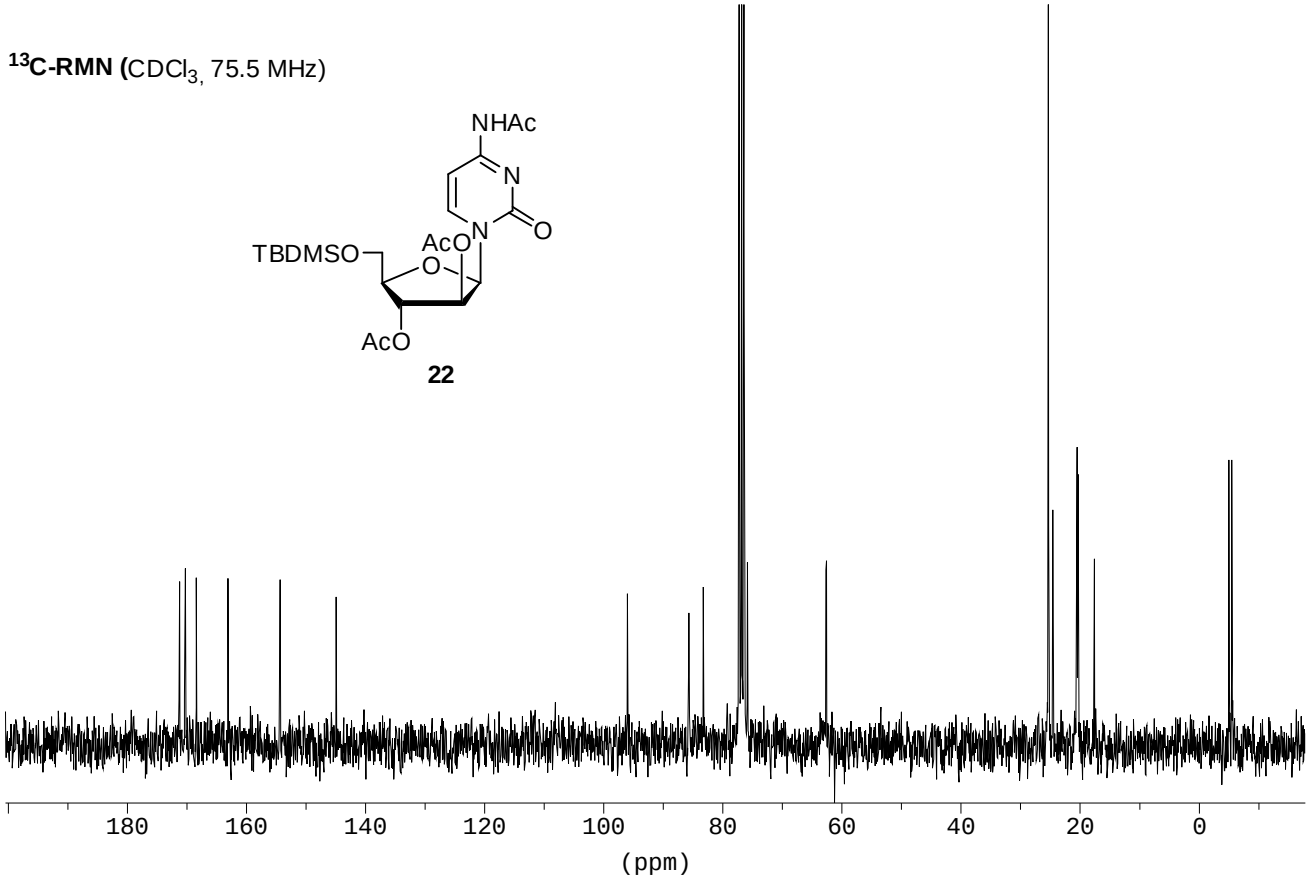
N^4-acetyl-1-(2',3'-di-*O*-acetyl-5'-*O*-*tert*-butyldimetylsilyl-β-D-arabinofuranosyl)cytosine (22)

^{1}H-RMN ($CDCl_3$, 300 MHz)

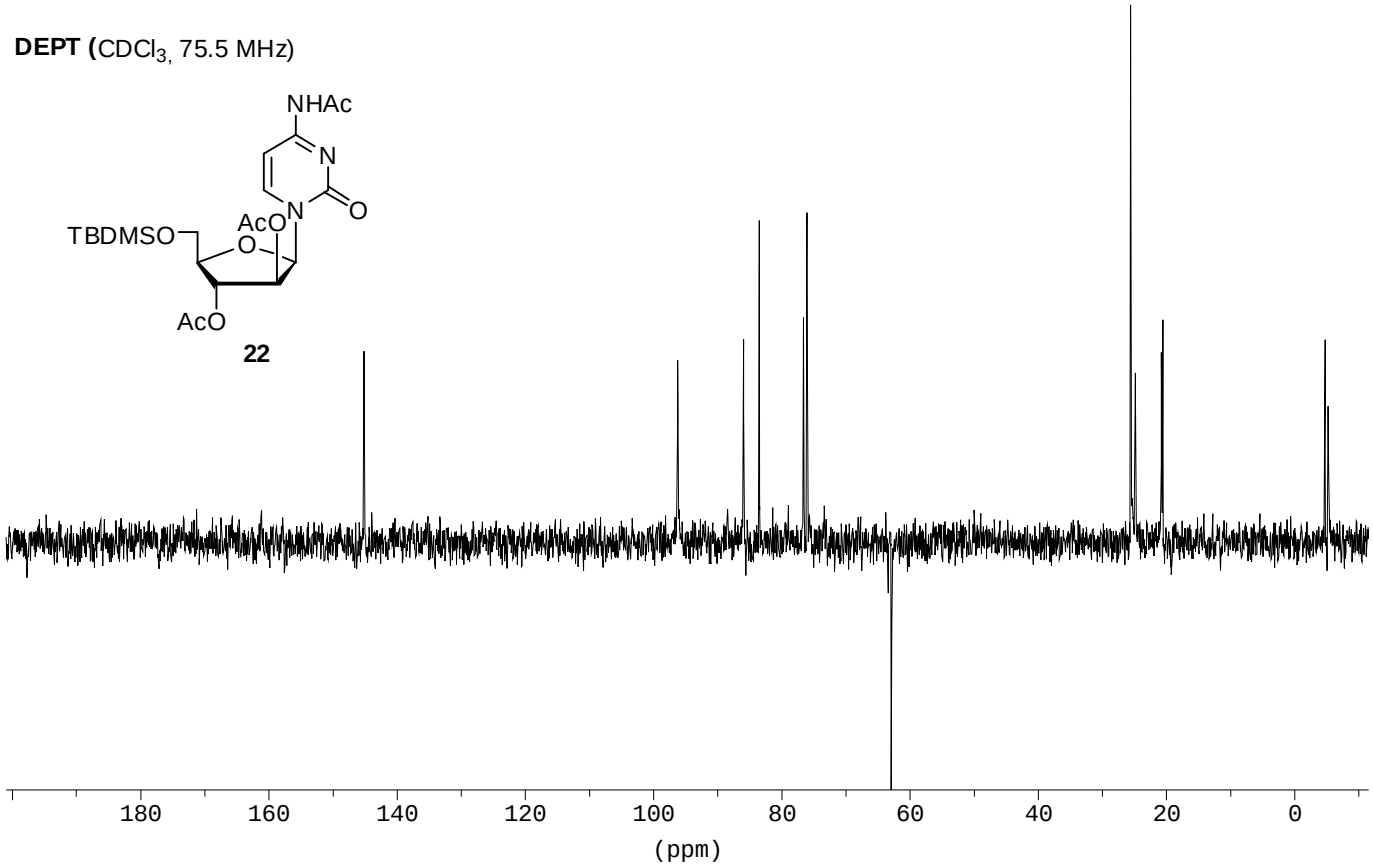
22



N^4-acetyl-1-(2',3'-di-*O*-acetyl-5'-*O*-*tert*-butyldimetylsilyl-β-D-arabinofuranosyl)cytosine (22)



N^4-acetyl-1-(2',3'-di-*O*-acetyl-5'-*O*-*tert*-butyldimetylsilyl-β-D-arabinofuranosyl)cytosine (22)



Scavenger Receptors Mediate Cellular Uptake of Polyvalent Oligonucleotide-Functionalized Gold Nanoparticles

Pinal C. Patel,[†,§] David A. Giljohann,[†,§] Weston L. Daniel,[‡,§] Dan Zheng,[†,§] Andrew E. Prigodich,[†,§] and Chad A. Mirkin*[,‡,§]

Interdepartmental Biological Sciences Program, Department of Chemistry, and International Institute for Nanotechnology, Northwestern University, Evanston, Illinois, United States. Received May 25, 2010; Revised Manuscript Received October 13, 2010

Mammalian cells have been shown to internalize oligonucleotide-functionalized gold nanoparticles (DNA-Au NPs or siRNA-Au NPs) without the aid of auxiliary transfection agents and use them to initiate an antisense or RNAi response. Previous studies have shown that the dense monolayer of oligonucleotides on the nanoparticle leads to the adsorption of serum proteins and facilitates cellular uptake. Here, we show that serum proteins generally act to inhibit cellular uptake of DNA-Au NPs. We identify the pathway for DNA-Au NP entry in HeLa cells. Biochemical analyses indicate that DNA-Au NPs are taken up by a process involving receptor-mediated endocytosis. Evidence shows that DNA-Au NP entry is primarily mediated by scavenger receptors, a class of pattern-recognition receptors. This uptake mechanism appears to be conserved across species, as blocking the same receptors in mouse cells also disrupted DNA-Au NP entry. Polyvalent nanoparticles functionalized with siRNA are shown to enter through the same pathway. Thus, scavenger receptors are required for cellular uptake of polyvalent oligonucleotide functionalized nanoparticles.

INTRODUCTION

Polyvalent DNA-functionalized gold nanoparticles (DNA-Au NP) are structures with a gold nanoparticle core and a high surface density of DNA ligands (*1*). As a result of this dense functionalization, these hybrid nanostructures have demonstrated applications in programmable materials crystallization (*2, 3*) and nonenzymatic biodiagnostic assays (*4*). Furthermore, the tailorable recognition properties of DNA and the catalytic and plasmonic properties of Au NPs have been used synergistically in a variety of highly sensitive and selective nucleic acid, small molecule, metal ion, and cancer cell detection strategies (*5*−*11*).

Recently, it was reported that DNA-Au NPs enter a wide variety of cell types (over 50 cell types examined to date) surprisingly readily without the aid of transfection agents (*12, 13*). These structures have properties that make them particularly attractive as intracellular gene regulation agents. They resist nuclease degradation (*12, 14*), exhibit enhanced target binding (*15*), show minimal interferon β response (*16*), and enter cells rapidly and efficiently (*17*). Consequently, they have been used for antisense (*12, 18*) and siRNA (*19*−*21*) based post-transcriptional gene regulation, intracellular detection of biologically relevant molecules (*22, 23*), and intracellular delivery of MRI contrast agents (*24*), as well as chemotherapeutic agents (*25*). Given the fundamental ability of these nanomaterials to readily enter cultured cells, the mechanism of cellular uptake is of significant interest. It has shown that subtle changes in surface functionalities can lead to drastic changes in cellular internalization ability of nanoparticles (*26, 27*). We have shown that the densely functionalized shell of polyanionic DNA (19 pmol/cm^2 for 13 nm gold particle) is a primary contributor to the cellular uptake of DNA-Au NPs (*17*), despite the conventional wisdom that negatively charged materials will not enter cells efficiently.

When material surfaces are exposed to biological environments, they are often modified by the adsorption of biomolecules, such as proteins (*28*). It has been shown that adsorption of proteins to a surface causes conformational changes in the proteins. These changes may expose hidden epitopes that cause unpredictable behavior and result in unusual properties (*29*). Protein adsorption on a nanoparticle surface has been implicated in facilitating uptake of various nanomaterials, including single-walled nanotubes, nanosized amorphous silica, and citrate capped gold nanoparticles (*30*−*32*). Indeed, we have previously shown that serum proteins are adsorbed to the dense monolayer of DNA on the Au NP surface, and that increasing the density of DNA on the Au NP surface increased the number of proteins adsorbed to DNA-Au NPs (*17*), as well as intracellular concentration of DNA-Au NPs.

In this paper, we explore the role of certain adsorbed serum proteins (BSA and transferrin) in the cellular internalization of the highly negatively charged DNA-Au NPs. We show that the adsorbed serum proteins reduce the cellular uptake of DNA-Au NPs, and that DNA-Au NP uptake is highest in serum-free conditions. Furthermore, using pharmacological methods, we identify scavenger receptors as the membrane proteins primarily responsible for facilitating the cellular uptake of DNA-Au NPs. We show that other oligonucleotide-functionalized nanoparticles, such as siRNA-Au NPs, also follow the same pathway of internalization. For DNA-Au NPs, the density of DNA on nanoparticles determines the extent of their cellular uptake. This entry pathway is conserved in mouse cells and may be a general mechanism of cellular entry of nanomaterials displaying dense monolayers of oligonucleotides.

EXPERIMENTAL PROCEDURES

Synthesis of Gold Nanoparticles, DNA, and RNA. Citrate-stabilized gold nanoparticles (13 ± 1 nm diameter) were prepared as described previously (*33*). DNA oligonucleotides were synthesized on an Expedite 8909 Nucleotide Synthesis

* Author to whom correspondence should be addressed. E-mail: chadnano@northwestern.edu, Northwestern University, 2145 Sheridan Road, Evanston, IL 60208-3113, USA.

† Interdepartmental Biological Sciences Program.

§ International Institute for Nanotechnology.

‡ Department of Chemistry.

10.1021/bc1002423 © 2010 American Chemical Society
Published on Web 11/11/2010

System (ABI) using standard solid-phase phosphoramidite synthesis techniques. RNA oligonucleotides were synthesized using TOM-RNA reagents (Glen Research) on a MerMade 6 system (Bioautomation) using manufacturer-recommended cleavage and deprotection stategy. All oligonucleotides were purified using reverse-phase high-performance liquid chromatography (RP-HPLC) on a Varian Microsorb C_{18} column (10 μm, 300 $\times$ 10 mm) with 0.03 M triethylammonium acetate (TEAA), pH 7, and a 1%/min gradient of 95% CH_3CN/5% 0.03 M TEAA at a flow rate of 3 mL/min, while monitoring the UV signal of the nucleic acids at 254 nm. After purification, the oligonucleotides were lyophilized and stored at −80 °C until use. The following oligonucleotide sequences were synthesized: RNA sequences: 5′-ACC CUG AAG UUC AUC UGC ACC ACC G-(hexa(ethylene glycol))$_2$-propylthiol-3′,5′-CGG UGG UGC AGA UGA ACU UCA GGG UCA-3′. DNA sequences: 5′-AGT AGA GGC AGG GAT GAT G AAA AAA AAA A-propylthiol-3′,5′-Fluorescein-AGT AGA GGC AGG GAT GAT G AAA AAA AAA A-propylthiol-3′,5′-TTT TGG GGT TTT GGG GTT TTG GGG TTT TGG GG-propylthiol-3′,5′-TTT TGG GGT TTT GGG GTT TTG GGG TTT TGG GG-3′,5′ (DTPA) AAA AAA AAA AGT AGT AGG GAC GGA GAT GA 3′ and 5′ (Tosyl-T)-AAA AAA AAA A (S−S) TCA TCT CCG TCC CTA CTA CG 3′. Tosyl-modified thymidine phosphoramidite was synthesized as described previously (*34*) and added to the oligonucleotide manually as described previously (*35*). DNA or RNA functionalized gold nanoparticles were prepared following published methods (*12*, *19*). Mixed monolayer nanoparticles with variable DNA density were prepared following a published protocol (*17*) but with following modified oligonucleotide as diluent strand: 5′ (Propyl Spacer)$_{19}$-AAA AAA AAA A-propylthiol-3′. DNA loading onto mixed monolayer nanoparticles was determined using a fluorescein-modified DNA strand.

Preparation of Protein−DNA Conjugates. All proteins used in this study were purchased from Sigma Aldrich and/or Fisher Scientific. The protein was mixed with the tosyl-modified oligonucleotide at a 3-fold molar excess in 0.1 M borate buffer, pH 8.5. The mixture was shaken at room temperature overnight. Unreacted oligonucleotides were separated from protein−DNA conjugates using 30 000 MWCO spin columns (Chemicon).

Preparation of Gold Nanoparticle Conjugates with Variable Protein Loading. Oligonucleotide-modified gold nanoparticle conjugates were made as described previously (*1*). DNA-Au NPs were loaded with various amounts of proteins by mixing with variable volumes of protein−DNA conjugates in phosphate buffered saline (PBS) (Hyclone), heating the mixture to 65 °C, and cooling it to room temperature. The conjugates were centrifuged at 4 °C and redispersed in 1× PBS three times to remove excess protein−DNA conjugate. The average number of protein molecules per gold nanoparticle was determined using previously published methods (*17*). Briefly, the protein-loaded Au NPs were dissolved with potassium cyanide (KCN, 2 mM final concentration). The KCN-digested samples were treated with a Quant-iT fluorescent reagent (Invitrogen) as described by the manufacturer. The resulting fluorescence was measured at room temperature using a fluorescence microplate reader (Fluo Dia T70, Photal) with excitation at 486 nm and recording emission at 570 nm. Estimation of the number of proteins in solution was calculated by comparing the fluorescence values of these unknowns to those obtained from a standard curve of known protein concentrations under the same assay conditions. Finally, the average number of proteins per nanoparticle was calculated by dividing this number by the initial nanoparticle concentration prior to KCN digestion.

Cell Culture. The uptake of gold nanoparticles (DNA-Au NPs or siRNA-Au NPs) was studied using a model cell line. HeLa (human cervical carcinoma) cells were obtained from American Type Culture Collection (ATCC) and maintained in minimum essential medium (EMEM) supplemented with 10% heat-inactivated FBS and 1% penicillin/streptomycin at 5% CO_2 and 37 °C. In the serum-free conditions, FBS was omitted from the EMEM formulation. HeLa cells were acclimated to serum-free culture by slowly reducing serum concentration from 10% to 0%. Mouse C166 cells (ATCC) were cultured in DMEM with 10% FBS at 5% CO_2 and 37 °C.

Serum Preincubation of DNA-Au NPs. DNA-Au NPs were prepared as described above. The nanoparticle conjugates were added to MEM buffer containing 10% FBS and incubated at 37 °C for at least 12 h. Following the incubation, excess serum was removed by three centrifugation, supernatant removal, and redispersion steps. The nanoparticle conjugates were added to HeLa cells in serum-containing and serum-free MEM to measure cellular uptake.

Cellular Uptake Studies and Nanoparticle Calculations. Hela cells were added to 96-well plates (25 000 cells/well) 24 h prior to nanoparticle addition. Filter sterilized nanoparticle conjugates were added directly to the cell culture media of adherent cells in 5 and 10 nM concentrations. 48 hours after nanoparticle addition, the cells were washed twice with PBS, collected, counted, and their viability measured using the Guava Viacount reagent on an EasyCyte flow cytometer (Millipore). The gold content of the cell digest was determined by inductively coupled plasma mass spectrometry (ICP-MS) (Thermo-Fisher). To prepare samples for ICP-MS, the cells were dissolved with nitric acid at 60 °C overnight, diluted in a matrix consisting of 2% HNO_3, 2% HCl, and 1 ppb indium (internal standard). The number of nanoparticles in each sample was calculated based on the concentration of Au found in the sample.

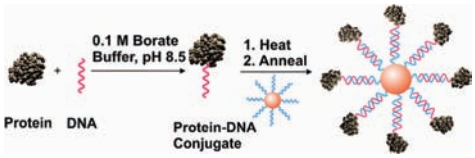
Treatments with Chemical Inhibitors. All chemicals were purchased from Sigma-Aldrich. HeLa cells were treated with different concentrations of methyl-β-cyclodextrin (MβCD), cytochalasin D (CytoD), or bafilomycin A (Baf A) for 60 min. DNA-Au NPs were then added in the presence of these chemicals. Controls include incubations of DNA-Au NPs in the presence of the solvent dimethylsulfoxide (DMSO) and in the absence of any chemicals. To probe the role of scavenger receptors, cells were similarly incubated in the presence of known ligands of scavenger receptors, polyinosinic acid (Poly I) and Fucoidan. Compounds that are not known to inhibit scavenger receptors, polyadenosinic acid (Poly A), galactose, lipopolysacchride (LPS), and untreated cells were used as controls. 24 hours after the addition of nanoparticles, cells were washed with phosphate buffered saline, trypsinized, counted using Viacount (Millipore) reagent, and prepared for ICP-MS.

Knockdown of Scavenger Receptors. HeLa cells were plated in 48-well plates at 50 000 cells/well. The cells were transfected with commercially bought siRNA (100 nM, 50 nM, and 25 nM) against scavenger receptors A and scavenger receptors B1 (Santa Cruz) with Dharmafect (Dharmacon) following the manufacturer's protocol. After 48 h, the media was replaced with DNA-Au NP containing media (10 nM) for 24 h. An equal volume of lipofectamine was used as delivery agent control. The cells were prepared for ICP-MS to determine the cellular gold content as described above.

RESULTS AND DISCUSSION

Serum Proteins Reduce Cellular Uptake of DNA-Au NPs. Previous work has shown that the cellular uptake of DNA-Au NPs correlates positively with the density of oligonucleotides on the nanoparticles and that, when DNA-Au NPs are added to serum containing media, they are coated with serum proteins (*17*). We hypothesized that, if adsorption of serum protein promotes cellular uptake, then covalent attachment of serum

Scheme 1. Stable Loading of Proteins on DNA Functionalized Gold Nanoparticles[a]



[a] The proteins are covalently attached to tosyl-modified oligonucleotides, which are then hybridized to nanoparticles functionalized with a complementary sequence. The variable loading of proteins is achieved by using different ratios of protein−DNA conjugate to DNA-Au NPs.

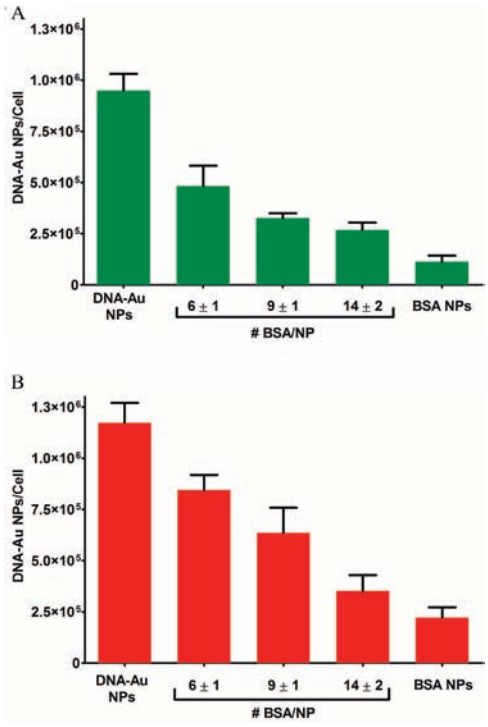


Figure 1. Cellular internalization of DNA-Au NPs when coated with increasing amounts of BSA. The method for loading a variable number of proteins on DNA-Au NPs is shown in Scheme 1. Cells were grown in media containing 10% FBS with 5 nM (A) and 10 nM (B) of DNA-Au NPs.

proteins may increase uptake even further. To test this hypothesis, we attached bovine serum albumin (BSA) and transferrin, two highly abundant serum proteins, through DNA hybridization on DNA-Au NPs. BSA is also the most abundant protein in serum and is known to coat polymer nanoparticles in complex media (*36*). Protein−DNA conjugates were made by covalently linking a tosyl-terminated oligonucleotide to amine groups on BSA or transferrin. These conjugates were then mixed at different ratios with DNA-Au NPs functionalized with the complementary oligonucleotide sequence to load variable numbers of proteins around the nanoparticles (Scheme 1). These nanoconjugates loaded with the same number of oligonucleotides but different numbers of proteins were then added to HeLa cells, and their cellular internalization was measured by ICP-MS (see Experimental Procedures).

The results show that, as BSA loading onto DNA-Au NPs increases, the number of nanoparticles taken up by cells decreases (Figure 1 and Supporting Information). For example, as the number of BSA molecules per DNA-Au NP increased from 0 to 14 ± 2, the number of DNA-Au NPs internalized by cells in serum-containing conditions decreased by up to 80%, from $1.0 \times 10^6 \pm 0.1 \times 10^6$ to $2.5 \times 10^5 \pm 0.7 \times 10^5$ Au NPs per cell. A 70% decrease was observed when transferrin was used to coat DNA-Au NPs instead of BSA (Supporting Information, Figure 1). These results suggest that the most abundant components of serum reduce uptake when they are bound strongly to DNA-Au NPs. These results are surprising, since previously we observed that the high density of DNA on nanoparticles resulted in increased adsorption of proteins, as well as cellular uptake, and when DNA density was reduced with oligo(ethylene glycol) (OEG) passivation, protein adsorption and cellular uptake were reduced (*17*). One explanation of this apparent discrepancy is that the dense monolayer of DNA on nanoparticles may generally promote both cellular uptake and protein adsorption. However, adsorbed serum proteins do not necessarily promote cellular uptake and may be displaced by some cellular proteins that affect nanoparticle uptake. When nanoparticles are functionalized with lower density of DNA, their binding to all proteins is reduced, as is their cellular uptake. In this experiment, since serum proteins are strongly bound to nanoparticles, they cannot be easily displaced by cellular proteins that affect nanoparticle uptake. Furthermore, preincubation of DNA-Au NPs in serum and subsequent addition to cell culture also reduced cellular uptake by a similar amount (Supporting Information, Figure 2a). Thus, it is unlikely that the binding of other less abundant serum proteins promotes cellular uptake of nanoparticles. Overall, these results suggest that serum protein generally reduce cellular uptake of DNA-Au NPs and point to other factors as positive regulators of cellular entry.

DNA-Au NP Uptake Is Highest in Serum-Free Culture. To confirm that serum proteins generally reduce nanoparticle uptake, we performed previously described experiments in serum-free media and compared the results to the results from normal serum-containing cultures. In all cases, the number of DNA-Au NPs internalized by cells in serum-free conditions was significantly higher than in serum-containing conditions. For example, at a 5 nM DNA-Au NP solution concentration, $2.5 \times 10^6 \pm 0.02 \times 10^6$ DNA-Au NPs/cell were internalized in serum-free conditions, while $1.0 \times 10^6 \pm 0.1 \times 10^6$ DNA-Au NPs/cell were internalized when the media contained 10% serum, a 150% increase (Supporting Information, Figure 2b). Furthermore, this increase was observed for DNA-Au NPs that were preincubated with serum or DNA-Au NPs loaded with covalently immobilized BSA (Figure 2) or transferrin (Supporting Information, Figure 3).

While the number of DNA-Au NPs internalized is still high in serum-containing media, a 150% or higher uptake is observed in serum-free cultures for all of the particles tested, with the exception of fully BSA- or transferrin-coated nanoparticles that contained no oligonucleotides, which did not exhibit such an increase. These results are consistent with the conclusion that serum proteins are responsible for decreasing the uptake of DNA-Au NPs. Since it was shown previously that serum proteins adsorb to DNA-Au NPs (*17*), it is likely that the adsorbed proteins compete with the binding interactions required for nanoparticles to be internalized by cells. These binding interactions between oligonucleotides on the DNA-Au NPs and cellular proteins may promote internalization through receptor-mediated endocytosis.

Pharmacological Inhibitors of DNA-Au NP Uptake Machinery. DNA-Au NP entry was explored using a pharmacological approach that tested the effect of inhibitors of cellular uptake mechanisms on nanoparticle uptake. Bafilomycin A (Baf A) can inhibit the acidification of endosomes, thus preventing their maturation and fusion into lysosomes (*33*). Baf A treatment did not inhibit nanoparticle uptake (Figure 3C). Therefore, the endosomal−lysosomal acidification process is not critical for nanoparticle entry in HeLa cells. Similarly, methyl-β-cyclodextrin (MβCD) and cytochalasin-D, inhibitors of caveolae-

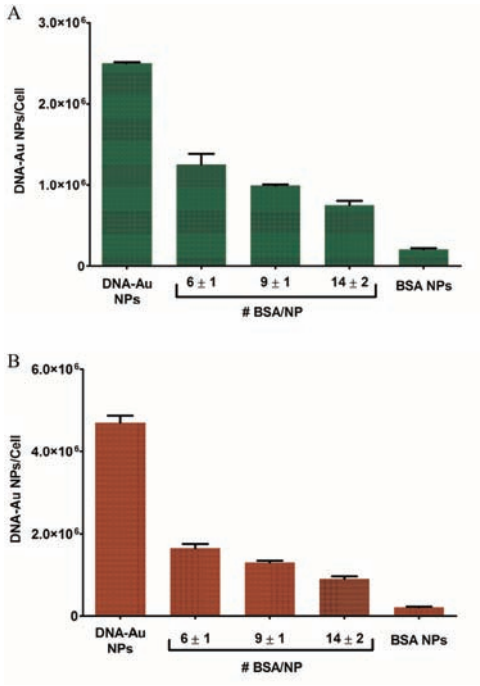


Figure 2. (A) Cellular uptake of DNA-Au NPs loaded with varying numbers of BSA molecules at 5 nM (A) and 10 nM (B) solution concentrations of DNA-Au NPs in serum-free conditions. Serum-free conditions yield a significantly higher number of nanoparticles per cell (150% increase) compared with normal 10% serum cultures (shown in Figure 1).

mediated endocytosis and phagocytosis, respectively, largely did not affect nanoparticle entry into cells (Figure 3D; Supporting Information Figure 4A). Cytochalasins cause the depolymerization of the actin cytoskeleton and inhibit uptake through the caveolae and macropinocytosis without affecting clathrin-mediated endocytosis, whereas MβCD inhibits phagocytosis by the disruption of lipid rafts (*32*). These experiments suggest that the broader classes of endocytotic process such as caveolae-mediated endocytosis, macropinocytosis, or phagocytosis are not the primary modes of entry of DNA-Au NPs into HeLa cells.

DNA-Au NP Uptake is Blocked by Agonists of Pattern-Recognition Receptors. The role of pattern-recognition receptors in DNA-Au NP uptake was evaluated using a chemical approach. Scavenger receptors are a group of structurally unrelated molecules known to mediate the endocytosis of certain polyanionic ligands, including nucleic acids (*37*), and are implicated in uptake of phosphorothioate-modified oligonucleotides in animals (*38*). We examined whether molecules known to interact with scavenger receptors competed for binding of the DNA-Au NPs, and thus inhibited cellular uptake. Poly I and fucoidan, well-known ligands of the scavenger-receptor family, inhibited nanoparticle uptake by >60% as measured by ICP-MS (Figure 3A,B). In contrast, chemically related molecules that interact with other receptors, but do not inhibit scavenger receptors (such as lipopolysacchrides (LPS), polyadenylic acid (poly A), ssDNA, or the monosaccharide galactose), did not affect DNA-Au NP uptake (Supporting Information, Figure 4). There was a slight decrease in viability of cells when treated with the highest concentrations of poly I and fucoidan. However, this decrease in viability was not correlated with decrease in cellular uptake as treatments with related chemicals that cause similar drop in viability, poly A and lipopolysaccharides, did not lead to a decrease in uptake (Supporting Information, Table 1). Thus, the decrease in cellular uptake of nanoparticles is most likely caused by binding of poly I and fucoidan to scavenger receptors, which prevents DNA-Au NPs from binding to the same receptors. We also measured the stability of DNA-Au NPs in poly I and fucoidan solutions to rule out any possibility of drop in stability of nanoparticles causing the decrease in uptake (Supporting Information, Figure 9).

While RNAi down-regulation of class A (SR-A) or class B (SR-B1) scavenger receptors (Supporting Information, Figure 10) did not result in inhibition of nanoparticle uptake (Supporting Information, Figure 5), the inhibition observed by the pharmacological treatments suggests that multiple types of scavenger receptors with overlapping functions participate in DNA-Au NP uptake. To explore this possibility, mixed siRNAs targeting

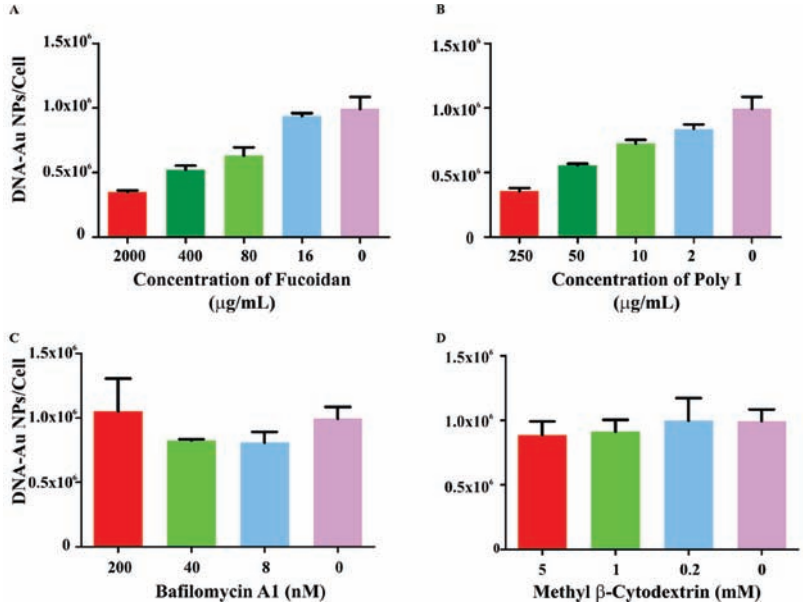


Figure 3. Endocytotic uptake of DNA-Au NPs in HeLa cells is mediated by scavenger receptors. Treatment with agonists of scavenger receptors, fucoidan (A) and polyinosinic acid (poly I, B), prior to nanoparticle addition results in up to 60% inhibition of the cellular uptake of DNA-Au NPs. Pharmacological agents that inhibit other modes of cellular entry, such as bafilomycin A1 and methyl β-cytodextrin, did not inhibit nanoparticle uptake (C, D, Supporting Information, Figure 4).

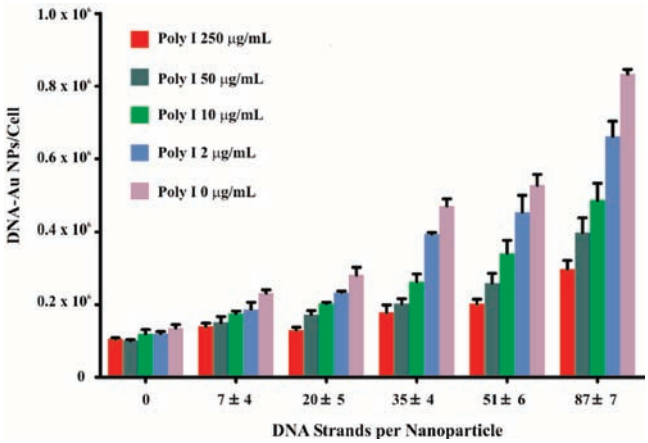


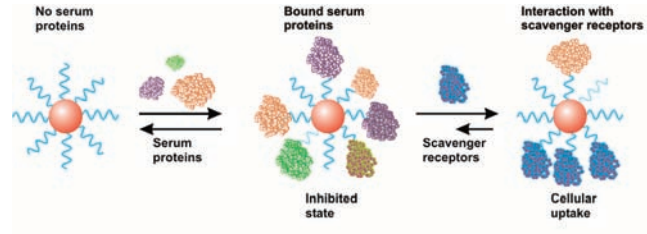
Figure 4. Polyinosinic acid dependent inhibition of DNA-Au NPs is dependent on the density of DNA on nanoparticles. When the cellular uptake of DNA-Au NPs is lowered with decreasing DNA density, the ability of Poly I to inhibit cellular internalization of DNA-Au NPs is lowered as well.

SR-A and SR-B1 were transfected into HeLa cells. This mixture did not result in a significant reduction in nanoparticle uptake. Recent reports have shown that long dsRNA is internalized by scavenger receptor-mediated endocytosis in S2 cells (*39*, *40*). However, these reports were also unable to show that down-regulation of individual scavenger receptors significantly reduced dsRNA uptake or resultant RNAi. It is possible that simultaneously targeting the two classes of receptors by RNAi is not effective enough to impair the DNA-Au NP binding to the remaining receptors. It is also possible that unidentified members of this family of transporter proteins are responsible for this uptake function.

DNA Density on Nanoparticles Determines the Extent of Inhibition. We next sought to understand the molecular basis of binding of DNA-Au NPs to scavenger receptors. It has been shown that poly I forms complex quadraplex-like structures at physiologic temperatures and that the binding of polynucleotides to scavenger receptors depends on the formation of stable four-stranded structures (*41*, *42*). Thus, it is likely that other polynucleotide sequences predicted to fold into a structure that can bind scavenger receptors would lower cellular uptake of nanoparticles. Indeed, treatment with telomere-like DNA sequences (which are predicted to fold into quadraplex-like structures) prior to addition of DNA-Au NPs reduced cellular uptake of nanoparticles (Supporting Information, Figure 6). Higher concentrations of this synthetic ligand were necessary to inhibit nanoparticle entry, which is likely due to the weaker binding of the synthetic DNA strand to scavenger receptors compared to Poly I or fucoidan.

Thus, we hypothesized that the dense monolayer of DNA on the nanoparticle surface mimics the complex structure that Poly I forms in order to bind to scavenger receptors. Indeed, reducing the density of DNA on nanoparticles decreased the Poly I dependent inhibition of nanoparticle uptake (Figure 4). However, since we also reduced the ability of nanoparticles to bind scavenger receptors, the total nanoparticles internalized by the cell decreased as well. Interestingly, the extent of inhibition was greater for nanoparticles with higher surface density of DNA. For nanoparticles with 87 ± 7 DNA per nanoparticle, the cellular uptake decreased 64% (from 8.33×10^5 to 2.98×10^5 DNA-Au NPs per cell) as Poly I concentration increased from 0 to 250 μg/mL. By contrast, for the nanoparticles with 7 ± 4 DNA per nanoparticle, the cellular uptake decreased 38% (from 2.32×10^5 to 1.42×10^5 DNA-Au NPs per cell) with the same Poly I treatment. This difference suggests that the nanoparticles with higher density of oligonucleotides are more dependent on scavenger receptors and thus show more inhibition over the range of concentrations of Poly I that competes for binding to the same receptors.

Scheme 2. Proposed Mechanism of Cellular uptake of DNA-Au NPs[a]



[a] In serum-containing media, DNA-Au NPs are coated with proteins which reduce nanoparticle interactions with scavenger receptors. Cellular uptake is mediated by the displacement of serum proteins by these receptors. In the absence of serum proteins, these interactions are more easily facilitated, resulting in greater uptake as a result of high DNA density. If the binding to scavenger receptors is inhibited by addition of competitive ligands, then the cellular uptake of nanoparticles is also reduced.

These experiments strongly suggest that the dense monolayer of DNA on nanoparticles mimics the complex structures of other polynucleotides, such as Poly I or long dsRNA, and serves as a ligand for scavenger receptors. This hypothesis is further strengthened by experiments showing that the cellular uptake of siRNA-Au NPs is inhibited by fucoidan and Poly I but not by the other pharmacological treatments (Supporting Information, Figure 7). For siRNA-Au NPs, the inhibition was >85% versus that of the untreated samples at highest concentrations of the agonists, suggesting that these nanomaterials depend on scavenger receptor binding for cellular entry. Identical experiments in a mouse cell line also yielded the same results suggesting that the entry pathway in mouse cells is conserved (Supporting Information, Figure 8). Recently, our group has shown that iron oxide nanoparticles also enter cells with high efficiency when functionalized with a dense monolayer of oligonucleotides (*43*). Therefore, it is likely that nanomaterials displaying a dense monolayer of oligonucleotides can engage these receptors and be internalized by mammalian cells using the scavenger receptor pathway.

CONCLUSIONS

We have shown that serum proteins act to reduce the cellular uptake of oligonucleotide-functionalized nanoparticles and that highest nanoparticle uptake is observed in serum-free cultures. Using a pharmacological approach, we demonstrated that scavenger receptors mediate the cellular entry of oligonucleotide-functionalized gold nanoparticles. We have shown that the interaction of DNA-Au NPs and scavenger receptors is dependent on the density of oligonucleotides on nanoparticles. This interaction can be partially blocked by synthetic polynucleotides that mimic the structures of other ligands of scavenger receptors. Thus, our results show that a determining factor for cellular uptake of DNA-Au NPs is the polyvalent interaction of DNA-Au NPs with scavenger receptors on the cell surface (Scheme 2) suggesting a general mechanism by which nanostructures with dense monolayers of oligonucleotides can be internalized by cells.

ACKNOWLEDGMENT

C.A.M. acknowledges a Cancer Center for Nanotechnology Excellence (NCI-CCNE) award for support of this research.

P.C.P. was supported by a Ryan Fellowship and Malkin Foundation Fellowship. A.E.P. was supported by a Ryan Fellowship. W.L.D. is grateful for support from the Chicago Biomedical Consortium.

Supporting Information Available: Experimental procedures, nanoparticle characterization data, and results from additional experiments. This material is available free of charge via the Internet at http://pubs.acs.org.

LITERATURE CITED

(1) Mirkin, C. A., Letsinger, R. L., Mucic, R. C., and Storhoff, J. J. (1996) A DNA-based method for rationally assembling nanoparticles into macroscopic materials. *Nature 382*, 607–609.

(2) Park, S. Y., Lytton-Jean, A. K., Lee, B., Weigand, S., Schatz, G. C., and Mirkin, C. A. (2008) DNA-programmable nanoparticle crystallization. *Nature 451*, 553–556.

(3) Nykypanchuk, D., Maye, M. M., van der Lelie, D., and Gang, O. (2008) DNA-guided crystallization of colloidal nanoparticles. *Nature 451*, 549–552.

(4) Nam, J.-M., Thaxton, C. S., and Mirkin, C. A. (2003) Nanoparticle-based bio-bar codes for the ultrasensitive detection of proteins. *Science 301*, 1884–1886.

(5) Elghanian, R., Storhoff, J. J., Mucic, R. C., Letsinger, R. L., and Mirkin, C. A. (1997) Selective colorimetric detection of polynucleotides based on the distance-dependent optical properties of gold nanoparticles. *Science 277*, 1078–1081.

(6) Park, S. J., Taton, T. A., and Mirkin, C. A. (2002) Array-based electrical detection of DNA with nanoparticle probes. *Science 295*, 1503–1506.

(7) Taton, T. A., Mirkin, C. A., and Letsinger, R. L. (2000) Scanometric DNA array detection with nanoparticle probes. *Science 289*, 1757–1760.

(8) Liu, J., and Lu, Y. (2005) Fast colorimetric sensing of adenosine and cocaine based on a general sensor design involving aptamers and nanoparticles. *Angew. Chem., Int. Ed. 45*, 90–94.

(9) Liu, J., and Lu, Y. (2003) A colorimetric lead biosensor using DNAzyme-directed assembly of gold nanoparticles. *J. Am. Chem. Soc. 125*, 6642–6643.

(10) Liu, J., and Lu, Y. (2007) Colorimetric Cu2+ detection with a ligation DNAzyme and nanopairticles. *Chem. Commun.* 4872–4874.

(11) Medley, C. D., Smith, J. E., Tang, Z., Wu, Y., Bamrungsap, S., and Tan, W. (2008) Gold nanoparticle-based colorimetric assay for the direct detection of cancerous cells. *Anal. Chem. 80*, 1067–1072.

(12) Rosi, N. L., Giljohann, D. A., Thaxton, C. S., Lytton-Jean, A. K. R., Han, M. S., and Mirkin, C. A. (2006) Oligonucleotide-modified gold nanoparticles for intracellular gene regulation. *Science 312*, 1027–1030.

(13) Giljohann, D. A., Seferos, D. S., Daniel, W. L., Massich, M. D., Patel, P. C., and Mirkin, C. A. (2010) Gold nanoparticles for biology and medicine. *Angew. Chem., Int. Ed. 49*, 3280–3294.

(14) Seferos, D. S., Prigodich, A. E., Giljohann, D. A., Patel, P. C., and Mirkin, C. A. (2009) Polyvalent DNA nanoparticle conjugates stabilize nucleic acids. *Nano Lett. 9*, 308–311.

(15) Lytton-Jean, A. K., and Mirkin, C. A. (2005) A thermodynamic investigation into the binding properties of DNA functionalized gold nanoparticle probes and molecular fluorophore probes. *J. Am. Chem. Soc. 127*, 12754–12755.

(16) Massich, M. D., Giljohann, D. A., Seferos, D. S., Ludlow, L. E., Horvath, C. M., and Mirkin, C. A. (2009) Regulating immune response using polyvalent nucleic acid-gold nanoparticle conjugates. *Mol. Pharmaceutics 6*, 1934–1940.

(17) Giljohann, D. A., Seferos, D. S., Patel, P. C., Millstone, J. E., Rosi, N. L., and Mirkin, C. A. (2007) Oligonucleotide loading determines cellular uptake of DNA-modified gold nanoparticles. *Nano Lett. 7*, 3818–3821.

(18) Patel, P. C., Giljohann, D. A., Seferos, D. S., and Mirkin, C. A. (2008) Peptide antisense nanoparticles. *Proc. Natl. Acad. Sci. U.S.A. 105*, 17222–17226.

(19) Giljohann, D. A., Seferos, D. S., Prigodich, A. E., Patel, P. C., and Mirkin, C. A. (2009) Gene regulation with polyvalent siRNA-nanoparticle conjugates. *J. Am. Chem. Soc. 131*, 2072–2073.

(20) Lee, J. S., Green, J. J., Love, K. T., Sunshine, J., Langer, R., and Anderson, D. G. (2009) Gold, poly(beta-amino ester) nanoparticles for small interfering RNA delivery. *Nano Lett. 9*, 2402–2406.

(21) Lee, S. H., Bae, K. H., Kim, S. H., Lee, K. R., and Park, T. G. (2008) Amine-functionalized gold nanoparticles as non-cytotoxic and efficient intracellular siRNA delivery carriers. *Int. J. Pharm. 364*, 94–101.

(22) Seferos, D. S., Giljohann, D. A., Hill, H. D., Prigodich, A. E., and Mirkin, C. A. (2007) Nano-flares: probes for transfection and mRNA detection in living cells. *J. Am. Chem. Soc. 129*, 15477–15479.

(23) Zheng, D., Seferos, D. S., Giljohann, D. A., Patel, P. C., and Mirkin, C. A. (2009) Aptamer nano-flares for molecular detection in living cells. *Nano Lett. 9*, 3258–3261.

(24) Song, Y., Xu, X., MacRenaris, K. W., Zhang, X.-Q., Mirkin, C. A., and Meade, T. J. (2009) Multimodal gadolinium-enriched DNA-gold nanoparticle conjugates for cellular imaging. *Angew. Chem., Int. Ed. 48*, 9143–9147.

(25) Dhar, S., Daniel, W. L., Giljohann, D. A., Mirkin, C. A., and Lippard, S. J. (2009) Polyvalent oligonucleotide gold nanoparticle conjugates as delivery vehicles for platinum(IV) warheads. *J. Am. Chem. Soc. 131*, 14652–14653.

(26) Zhu, Z. J., Ghosh, P. S., Miranda, O. R., Vachet, R. W., and Rotello, V. M. (2008) Multiplexed screening of cellular uptake of gold nanoparticles using laser desorption/ionization mass spectrometry. *J. Am. Chem. Soc. 130*, 14139–14143.

(27) Verma, A., Uzun, O., Hu, Y. H., Hu, Y., Han, H. S., Watson, N., Chen, S. L., Irvine, D. J., and Stellacci, F. (2008) Surface-structure-regulated cell-membrane penetration by monolayer-protected nanoparticles. *Nat. Mater. 7*, 588–595.

(28) Dobrovolskaia, M. A., Patri, A. K., Zheng, J., Clogston, J. D., Ayub, N., Aggarwal, P., Neun, B. W., Hall, J. B., and McNeil, S. E. (2009) Interaction of colloidal gold nanoparticles with human blood: effects on particle size and analysis of plasma protein binding profiles. *Nanomed.: Nanotechnol. 5*, 106–117.

(29) Linse, S., Cabaleiro-Lago, C., Xue, W. F., Lynch, I., Lindman, S., Thulin, E., Radford, S. E., and Dawson, K. A. (2007) Nucleation of protein fibrillation by nanoparticles. *Proc. Natl. Acad. Sci. U.S.A. 104*, 8691–8696.

(30) Chithrani, B. D., Ghazani, A. A., and Chan, W. C. W. (2006) Determining the size and shape dependence of gold nanoparticle uptake into mammalian cells. *Nano Lett. 6*, 662–668.

(31) Dutta, D., Sundaram, S. K., Teeguarden, J. G., Riley, B. J., Fifield, L. S., Jacobs, J. M., Addleman, S. R., Kaysen, G. A., Moudgil, B. M., and Weber, T. J. (2007) Adsorbed proteins influence the biological activity and molecular targeting of nanomaterials. *Toxicol. Sci. 100*, 303–315.

(32) Bajaj, A., Samanta, B., Yan, H. H., Jerry, D. J., and Rotello, V. M. (2009) Stability, toxicity and differential cellular uptake of protein passivated-Fe_3O_4 nanoparticles. *J. Mater. Chem. 19*, 6328–6331.

(33) Frens, G. (1973) Controlled nucleation for the regulation of the particle size in monodisperse gold solutions. *Nat. Phys. Sci. 241*, 20–22.

(34) Herrlein, M. K., Nelson, J. S., and Letsinger, R. L. (1995) A covalent lock for self-assembled oligonucleotide conjugates. *J. Am. Chem. Soc. 117*, 10151–10152.

(35) Storhoff, J. J., Elghanian, R., Mucic, R. C., Mirkin, C. A., and Letsinger, R. L. (1998) One-pot colorimetric differentiation of polynucleotides with single base imperfections using gold nanoparticle probes. *J. Am. Chem. Soc. 120*, 1959–1964.

(36) Cedervall, T., Lynch, I., Foy, M., Berggad, T., Donnelly, S. C., Cagney, G., Linse, S., and Dawson, K. A. (2007) Detailed identification of plasma proteins adsorbed on copolymer nanoparticles. *Angew. Chem., Int. Ed. 46*, 5754–5756.

(37) Greaves, D. R., and Gordon, S. (2005) Recent insights into the biology of macrophage scavenger receptors. *J. Lipid Res. 46*, 11–20.

(38) Bijsterbosch, M. K., Manoharan, M., Rump, E. T., DeVrueh, R. L. A., vanVeghel, R., Tivel, K. L., Biessen, E. A. L., Bennett, C. F., Cook, P. D., and vanBerkel, T. J. C. (1997) In vivo fate of phosphorothioate antisense oligodeoxynucleotides: Predominant uptake by scavenger receptors on endothelial liver cells. *Nucleic Acids Res. 25*, 3290–3296.

(39) Saleh, M. C., van Rij, R. P., Hekele, A., Gillis, A., Foley, E., O'Farrell, P. H., and Andino, R. (2006) The endocytic pathway mediates cell entry of dsRNA to induce RNAi silencing. *Nat. Cell Biol. 8*, 793–802.

(40) Ulvila, J., Parikka, M., Kleino, A., Sormunen, R., Ezekowitz, R. A., Kocks, C., and Ramet, M. (2006) Double-stranded RNA is internalized by scavenger receptor-mediated endocytosis in Drosophila S2 cells. *J. Biol. Chem. 281*, 14370–14375.

(41) Arnott, S., Chandras., R., and Marttila, C. M. (1974) Structures for polyinosinic acid and polyguanylic acid. *Biochem. J. 141*, 537–543.

(42) Pearson, A. M., Rich, A., and Krieger, M. (1993) Polynucleotide binding to macrophage scavenger receptors depends on the formation of base-quartet-stabilized 4-stranded helices. *J. Biol. Chem. 268*, 3546–3554.

(43) Cutler, J. I., Zheng, D., Xu, X. Y., Giljohann, D. A., and Mirkin, C. A. (2010) Polyvalent oligonucleotide iron oxide nanoparticle "click" conjugates. *Nano Lett. 10*, 1477–1480.

BC1002423

(Supporting Information)

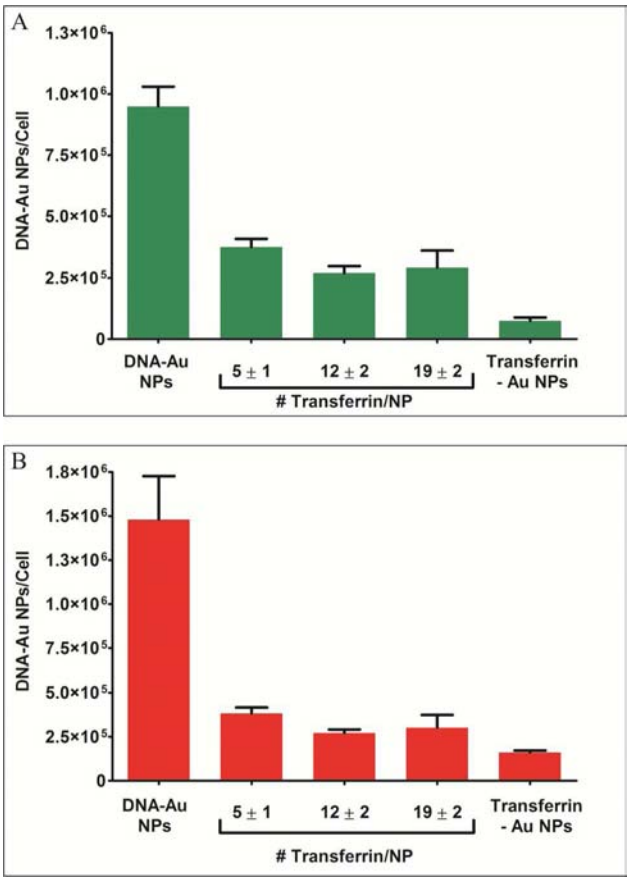
Scavenger Receptors Mediate Cellular Uptake of Polyvalent Oligonucleotide-Functionalized Gold Nanoparticles

Pinal C. Patel[†,§], David A. Giljohann[†,§], Weston L. Daniel[‡,§], Dan Zheng[†,§], Andrew E. Prigodich[†,§] and Chad A. Mirkin[‡,§,*]
† Interdepartmental Biological Sciences Program ‡ Department of Chemistry § International Institute for Nanotechnology
* Author to whom correspondence should be addressed. E-mail: chadnano@northwestern.edu, Northwestern University, 2145 Sheridan Road, Evanston, IL 60208-3113 USA

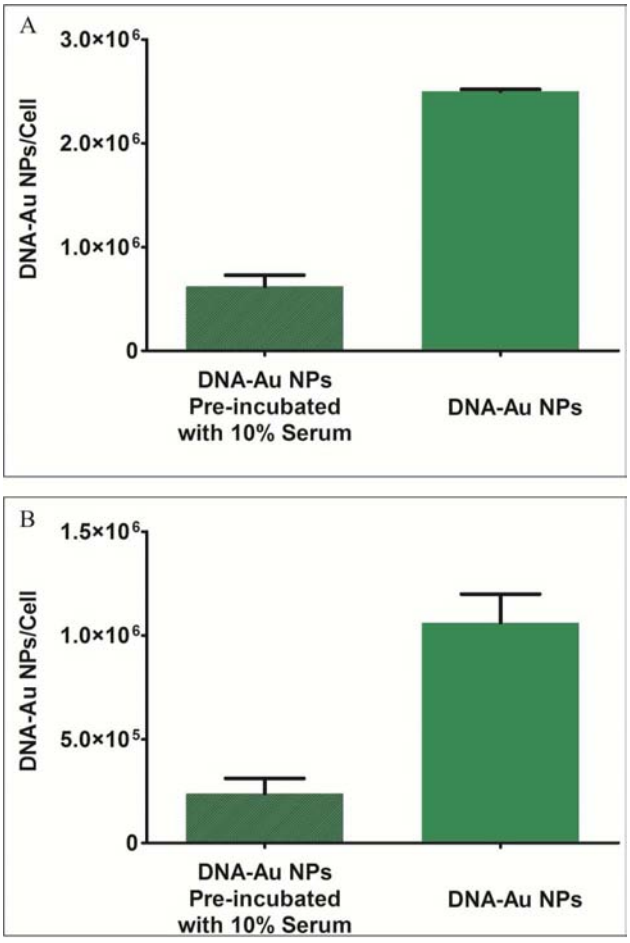
EXPERIMENTAL PROCEDURES

Nanoparticle stability in poly I and fucoidan solutions. DNA and siRNA functionalized gold nanoparticles were prepared as described in experimental procedures. Poly I and fucoidan solutions were prepared in phosphate buffered saline. DNA-Au NPs and siRNA-Au NPs were incubated with poly I and fucoidan at solution concentration of 10nM for 24 hours at 37°C. Nanoparticles without any additional chemicals were used as controls. Following the incubation, the stability of nanoparticles was measured using Cary 5000 UV-VIS-NIR instrument, scanning between 400-700nm wavelengths. The resultant spectra were normalized to the gold SPR peak.

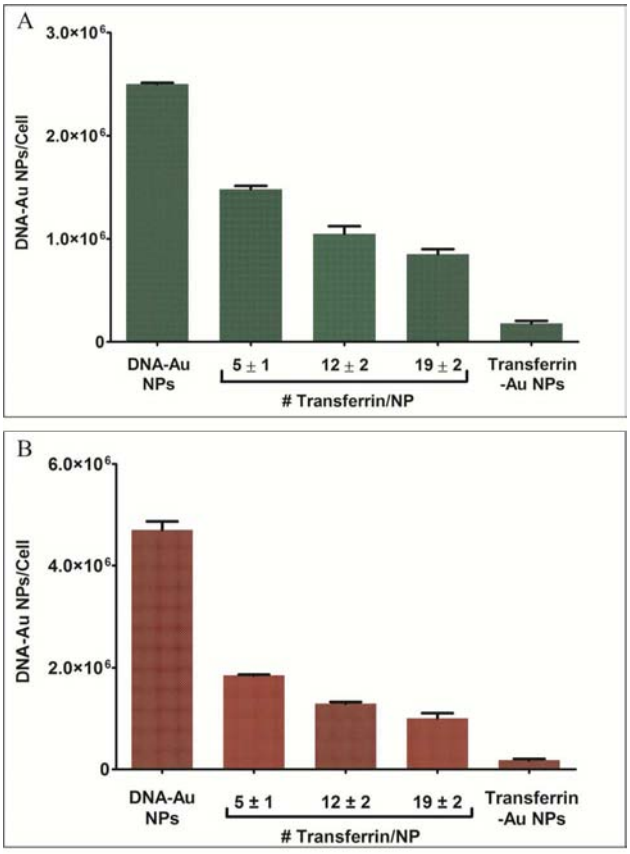
Quantitative real-time polymerase chain reaction. HeLa cells were plated in 48-well plate at density of 25000 cells/well. Following overnight incubation, the cells were treated with 25nM and 50nM of siRNAs targeting scavenger receptors A and B1 (Santa Cruz) using lipofectamine transfection reagent. After 24 hours, the siRNA containing medium was replaced with regular growth medium, EMEM with 10% FBS. The cells were allowed to grow for another 24 hours after which the experiment was terminated. Total RNA was extracted using TRIzol (Invitrogen) following manufacturer's recommended protocol. One μg of this RNA was used for cDNA synthesis using Taqman Gold RT-PCR kit (Applied Biosystems). Real-time PCR was performed on a Roche 480 Lightcycler. Hydrolysis probes (Roche) were used to measure the relative abundance of each target mRNA. These values were normalized to actin expression and compared to cells treated with lipofectamine alone to determine the change in mRNA levels. The primers used in these experiments were, SR-A left, 5' -TTT GAT GCT CGC TCA ATG AC- 3', SR-A right, 5' -TGA AGG GAA GGG CTG TTT TT- 3', SR-B1 left, 5' -CAT CAA GCA GCA GGT CCT TA- 3', SR-B1 right, 5' – CGG AGA GAT AGA AGG GGA TAG G- 3'. Actin primers are probes were purchased as single reagent from Roche.



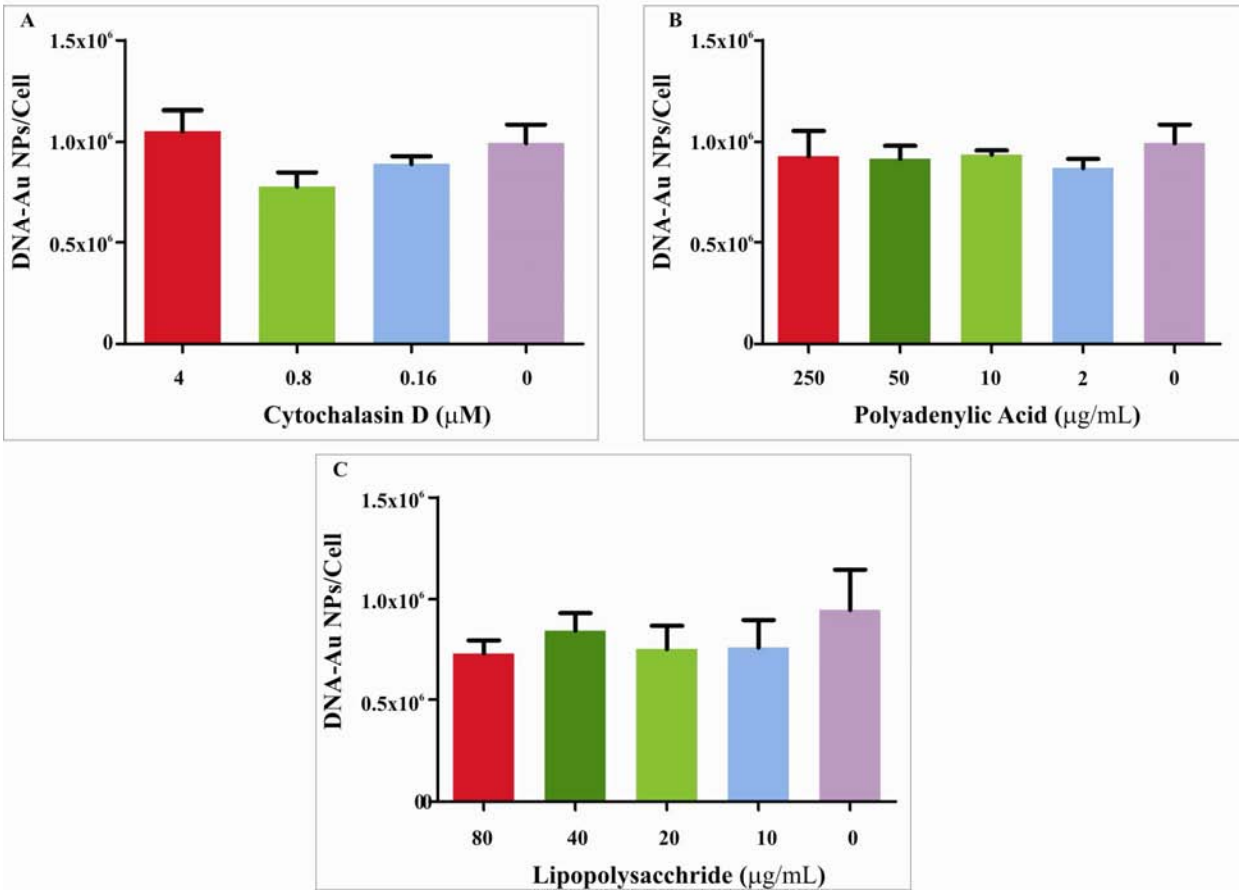
Supporting Figure 1. Cellular uptake of DNA-Au NPs coated with varying numbers of transferrin molecules. The method for loading a variable number of proteins on DNA-Au NPs is shown in Scheme 1. Cells were grown in media containing 10% FBS with 5 nM (green) or 10 nM (red) concentration of nanoparticles.



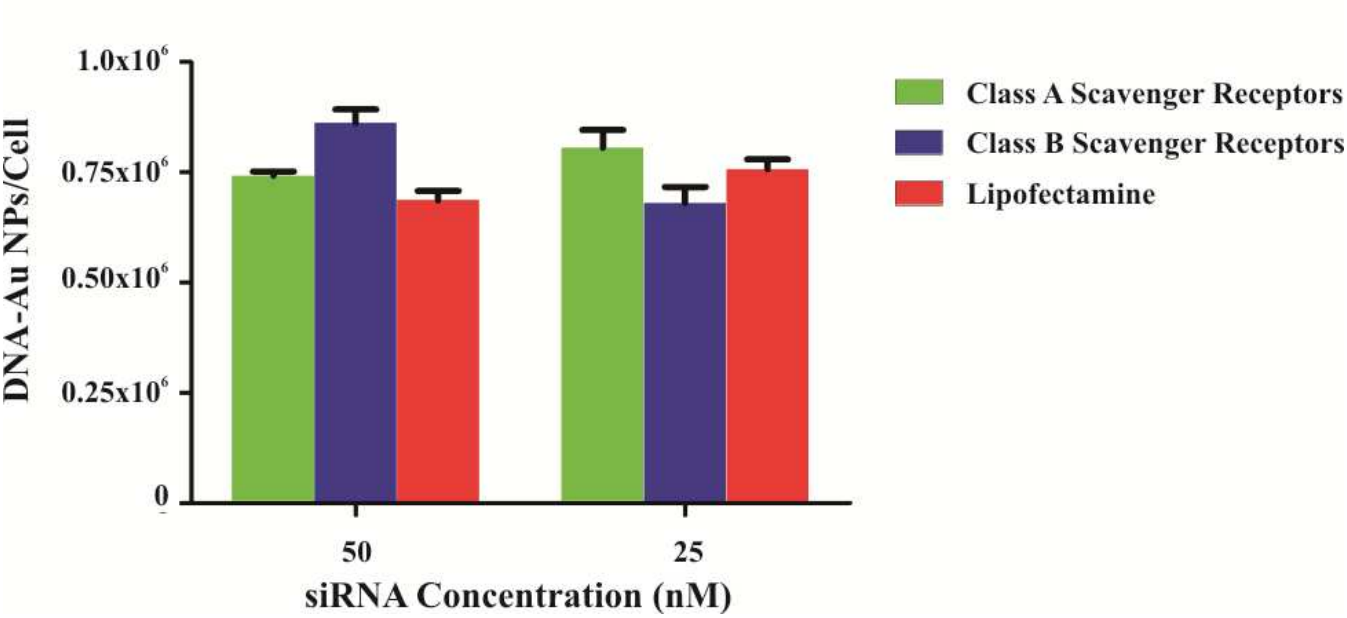
Supporting Figure 2. (A) Cellular uptake of DNA-Au NPs (5nM) with or without serum pre-incubation in normal culturing conditions (EMEM+10% FBS). Pre-incubation of DNA-Au NPs with serum reduces cellular uptake by 76% when compared direct addition without pre-incubation. (B) Comparison of cellular uptake of DNA-Au NPs in serum-free and normal 10% FBS cultures. The serum-free conditions yield 150% higher nanoparticle uptake.



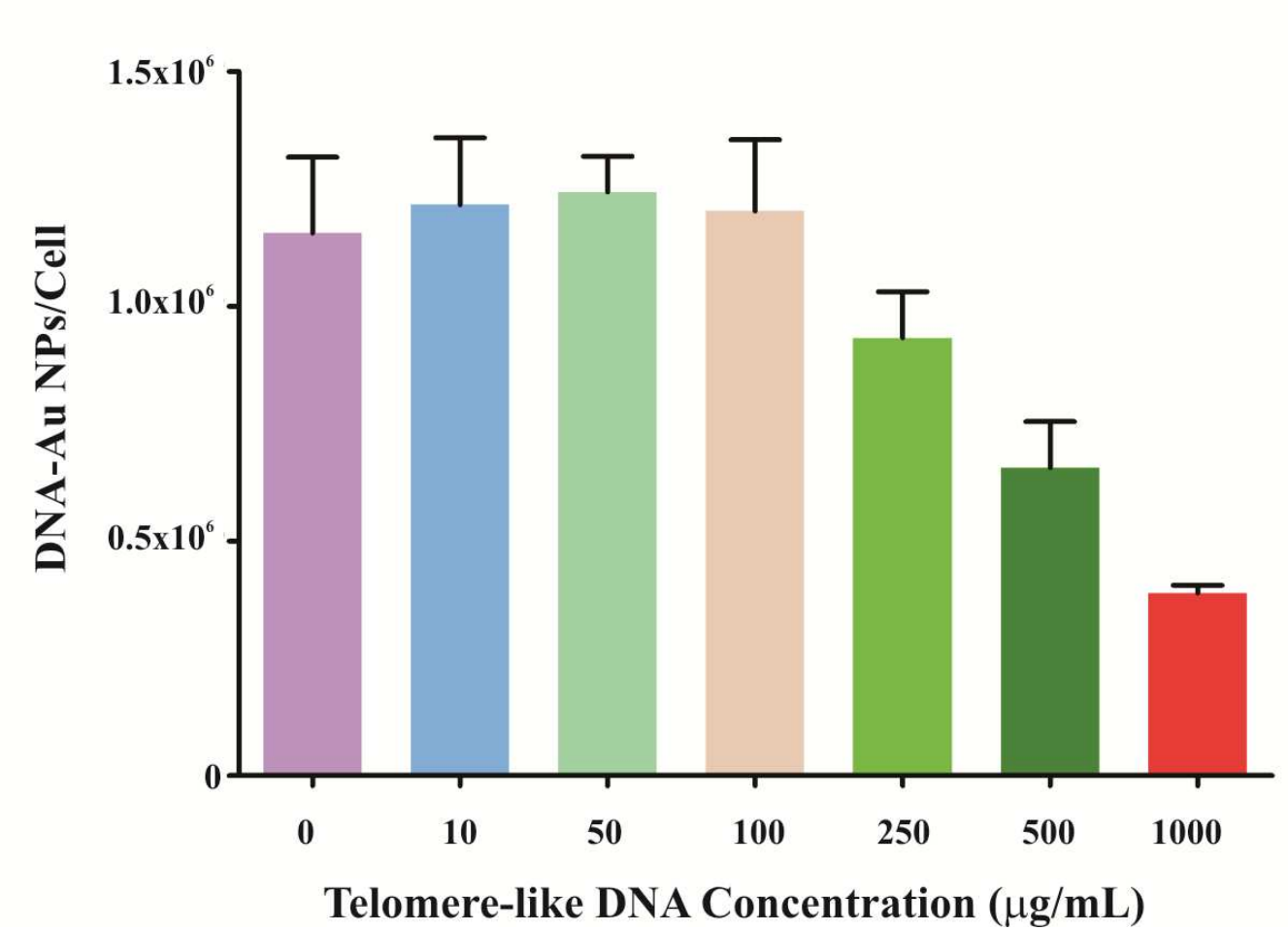
Supporting Figure 3. Cellular uptake of DNA-Au NPs when coated with varying numbers of transferrin molecules. The method for loading variable number of proteins on DNA-Au NPs is shown in Scheme 1. Cells were grown in serum-free conditions with 5 nM (green) or 10 nM (red) concentration of nanoparticles. Nanoparticle uptake is significantly higher than in normal serum culturing conditions (Supp. Figure 1).



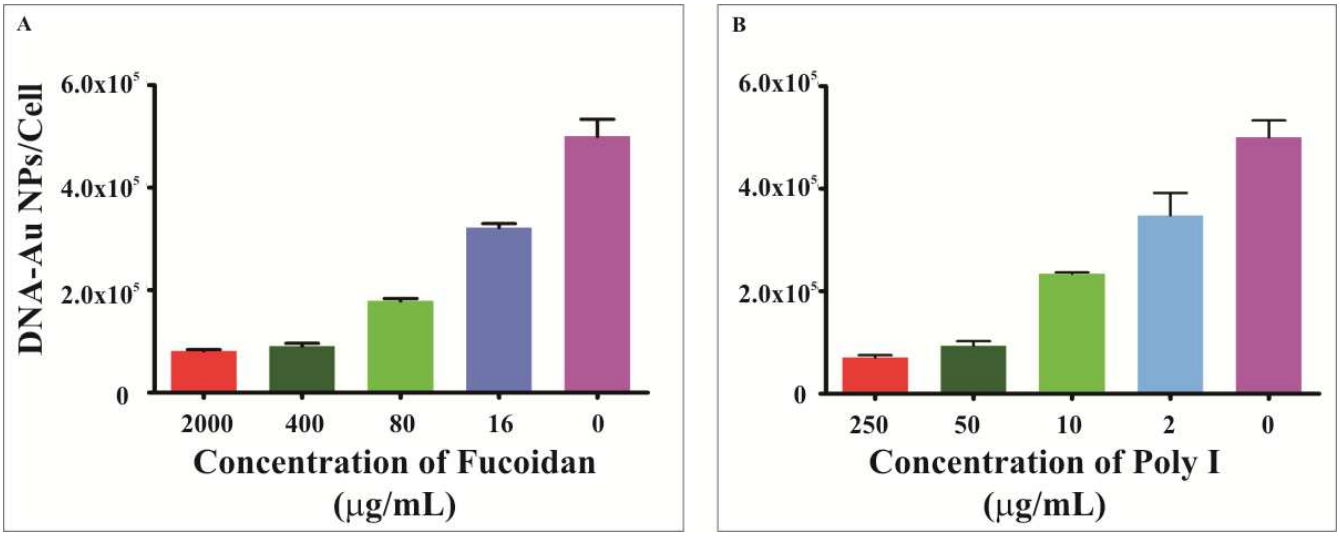
Supporting Figure 4. Cellular uptake of DNA-Au NPs in HeLa cells treated with inhibitors of endocytotic pathways. High cellular uptake in the presence of Cytochalasin D (A) suggests that DNA-Au NPs do not depend on phagocytosis as the primary mode of cellular entry. The cellular entry is inhibited in the presence of agonists of scavenger receptors, such as fucoidan and polyinosinic acid but not in the presence of chemically related molecules that do not bind scavenger receptors, such as polyadenylic acid (B) and lipopolysacchrides (C).



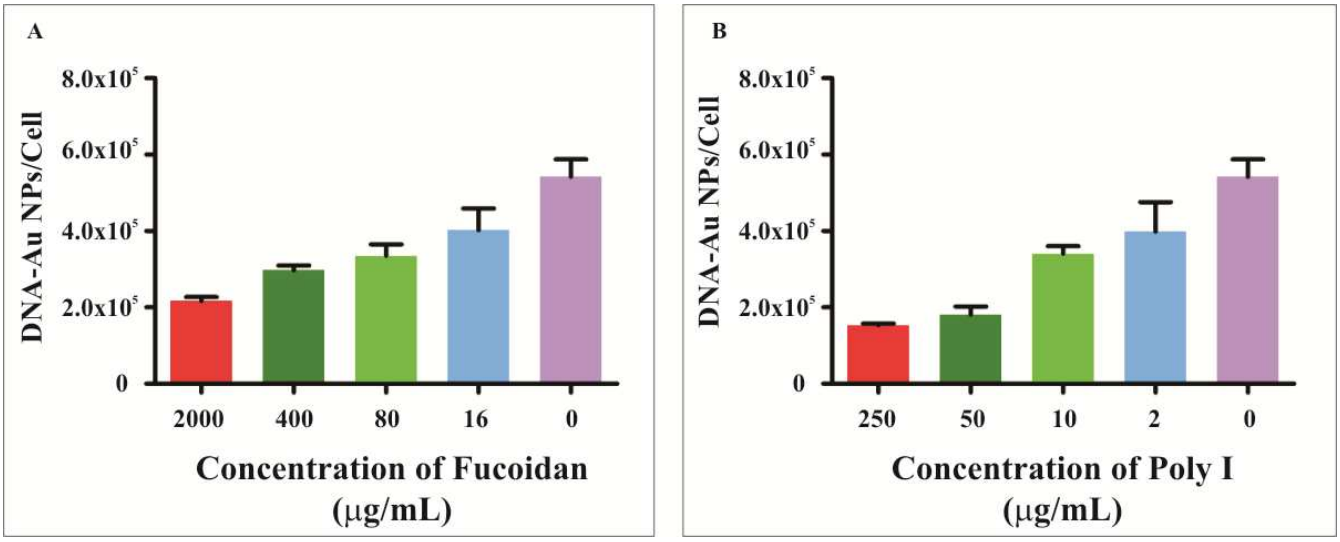
Supporting Figure 5. RNAi mediated knockdown of class A and class B scavenger receptors have no significant effect on cellular entry of DNA-Au NPs. Identical volumes of lipofectamine were used as control for each siRNA concentration. Equal volume of the two siRNA pools had no significant effect on nanoparticle uptake (data not shown).



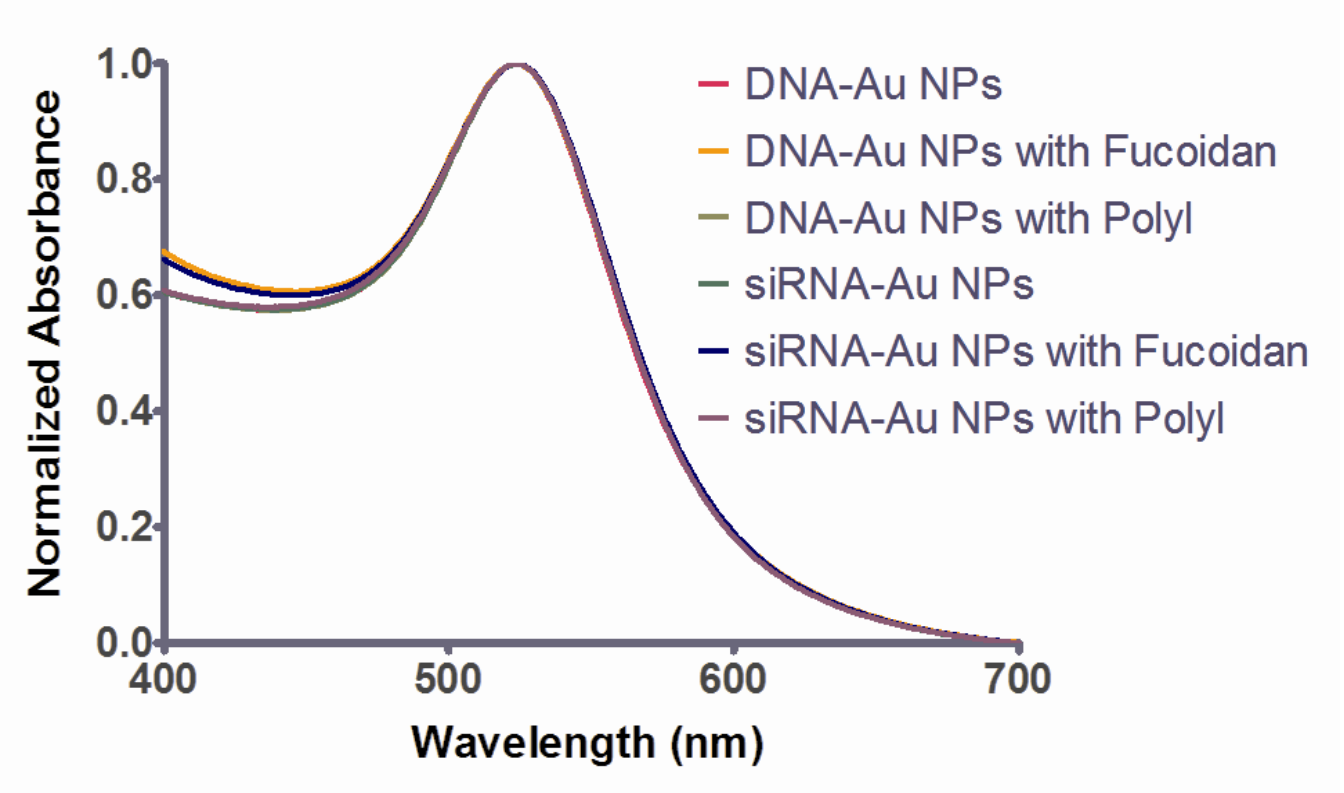
Supporting Figure 6. Synthetic ligands of scavenger receptors inhibit cellular entry of DNA-Au NPs in HeLa cells. Telomere-like DNA is theorized to form complex quadraplex-like structure that may mimic solution structure of polyinosinic acid. Higher concentration of telomere-like DNA is needed to inhibit nanoparticle entry into HeLa cells.



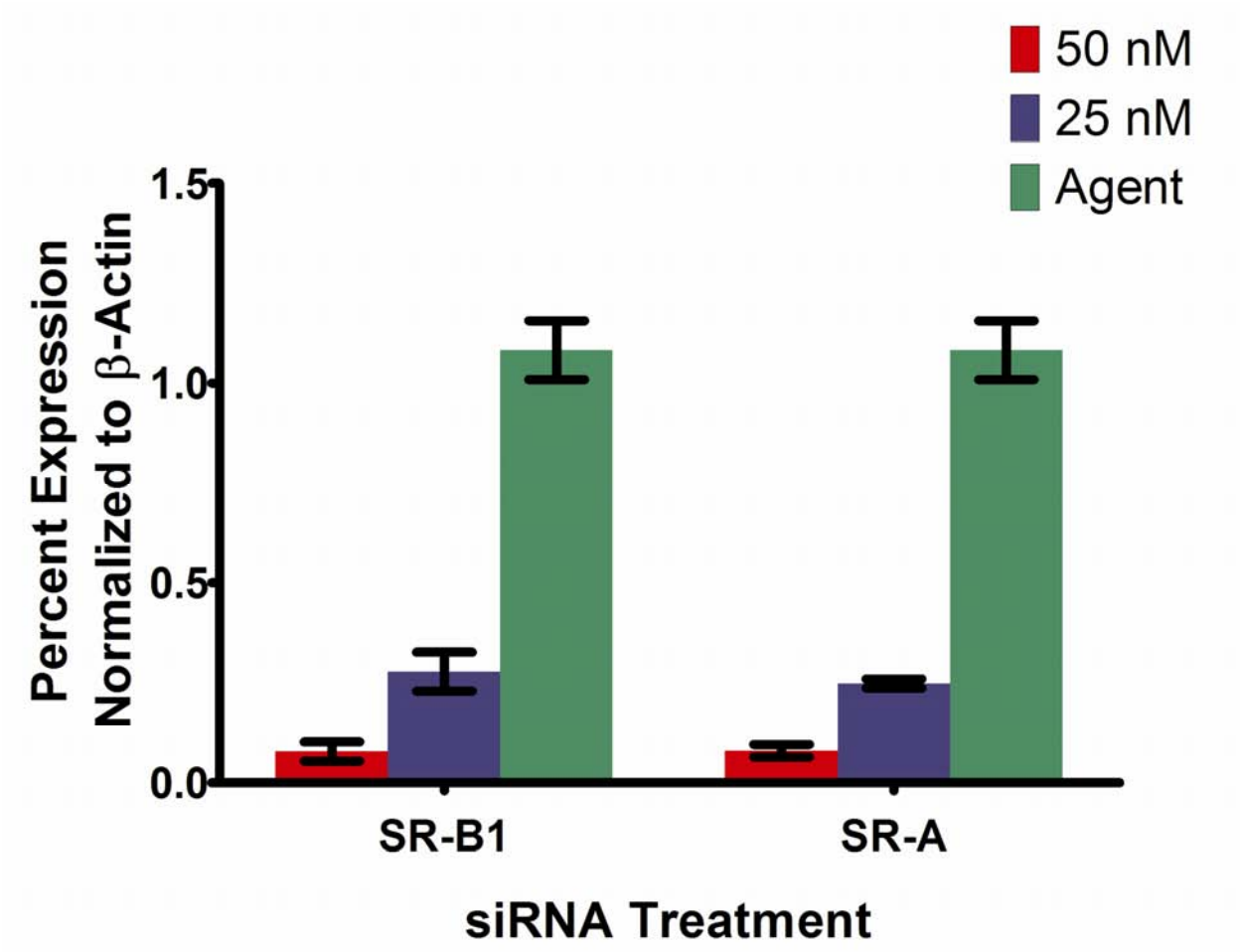
Supporting Figure 7. Cellular uptake of siRNA-functionalized nanoparticles (siRNA-Au NPs) is strongly inhibited by ligands of scavenger receptors. Both polyinosinic acid and fucoidan reduced siRNA-Au NPs entry into HeLa cells. The extent of inhibition was greater for siRNA-Au NPs than for DNA-Au NPs.



Supporting Figure 8. Cellular uptake of DNA-Au NPs in mouse cells (C166) is inhibited by ligands of scavenger receptors.



Supporting Figure 9. Stability of DNA and siRNA functionalized gold nanoparticles in the presence of Fucoidan (2000μg/mL) and Poly I (250μg/mL). The nanoparticles were incubated with the chemicals at 37°C for 24 hours. The spectra are normalized to the SPR peak at 522nm.



Supporting Figure 10. RNAi mediated knockdown of class A and class B scavenger receptors as measured by quantitative real-time PCR. Beta actin is used as an internal control and the results are normalized to cell treated with lipofectamine treatment.

CHEMICAL TREATMENT	% CELLVIABILITY
Lipopolysacchrides (80 μg/mL)	91.7 ± 0.42
Fucoidan (2000 μg/mL)	91.9 ± 2.9
Poly I (250 μg/mL)	93.2 ± 1.3
Poly A (250 μg/mL)	93.5 ± 1.1
Untreated Cells	99.2 ± 0.85

Supporting Table 1. Cell viability as a result of treatment with highest concentration of various chemicals. Untreated cells were not given any chemicals or nanoparticles. Poly I and Poly A are similar polymers and show comparable effects on cell viability as do LPS and Fucoidan. Poly A and LPS treatments do not inhibit cellular uptake of DNA-Au NPs whereas Poly I and Fucoidan treatments inhibit internalization of DNA-Au NPs.

Impact of Epidermal Growth Factor Tethering Strategy on Cellular Response

Benoît Liberelle,[†] Cyril Boucher,[†,‡] Jingkui Chen,[†] Mario Jolicoeur,[†] Yves Durocher,[‡] and Gregory De Crescenzo*[,†]

Department of Chemical Engineering, Groupe de Recherche en Sciences et Technologies Biomédicales, Bio-P^2 Research Unit, École Polytechnique de Montréal, P.O. Box 6079, succ. Centre-Ville, Montréal (Qc), Canada H3C 3A7, and Animal Cell Technology Group, Bioprocess Sector, Biotechnology Research Institute, National Research Council Canada, Montréal (Qc), Canada H4P 2R2. Received June 8, 2010; Revised Manuscript Received October 15, 2010

In an effort to evaluate the impact of various epidermal growth factor (EGF) grafting strategies upon cell surface receptor activation and cell adhesion, we generated low-fouling surfaces by homogeneously grafting carboxymethylated dextran (CMD) on amino-coated glass substrate. By preventing nonspecific cell adhesion while providing reactive groups facilitating subsequent protein grafting, CMD allowed achieving specific cell/tethered EGF interactions and therefore deriving unambiguous conclusions about various EGF grafting strategies. We demonstrate here that A-431 cell response to immobilized EGF is highly dependent on the bioactivity of the tagged protein being tethered, its proper orientation, and its surface density. Among all the approaches we tested, the oriented tethering of fully bioactive EGF via a *de novo*-designed coiled-coil capture system was shown to be the most efficient. That is, it led to the most intense and sustained phosphorylation of EGF receptors as well as to strong A-431 cell adhesion, the latter being comparable to that observed with amino-coated surfaces in the absence of CMD.

INTRODUCTION

Bioengineered implants are becoming extremely promising with respect to the development of biocompatible surfaces aiming at promoting and sustaining tissue regeneration. Within the last three decades, in an effort to mimic nature's mechanisms that are involved in tissue development and healing processes, the immobilization of growth factors on various substrates has been extensively studied by several groups (*1–3*). Such an interest from the scientific community may be ascribed to the direct implication of growth factors in almost all fundamental cellular processes, including cell survival, proliferation, migration, differentiation, and apoptosis. Furthermore, growth factor immobilization is believed to limit their clearance through endocytosis/degradation pathways and their diffusive mobility, thus restraining delivery to the local implant region (*4*). In that context, the epidermal growth factor (EGF), a soluble 6 kDa polypeptide that mediates its biological function by promoting the oligomerization (*5, 6*) and the phosphorylation (*7–9*) of cell surface EGF receptors (EGFRs), has attracted a lot of attention and has already shown great promises for the generation of smart corneal implants promoting re-epithelialization (*10, 11*) as well as for *ex vivo* stem cell expansion (*12–15*).

Nonspecific adsorption of EGF on substrate has been demonstrated to drastically diminish EGF bioactivity, most likely due to the occurrence of adsorption-induced conformational changes or inappropriate orientation of EGF (*4*). In contrast, covalent immobilization strategies via photoimmobilization or wet chemistry route resulted in unambiguous effects upon cell adhesion, phenotypic changes, and DNA synthesis (*4, 16*). However, for human EGF (hEGF), amine chemistry has been acknowledged to be suboptimal since the lysine side chains of hEGF extensively contribute to receptor binding; their involvement in the generation of an amide bound during EGF immobilization has been shown to greatly decrease its bioactivity (*4, 17, 18*). To counteract this caveat, oriented and stable tethering of hEGF has been successfully achieved through the use of recombinant EGF chimeras. That is, EGF has been fused to various tags or domains including the Fc region of immunoglobulin G (*19*), poly histidine (*12*), or coil peptide tags (*18*), in order to subsequently tether these chimeras on surfaces on which Protein A/G, nitrilotriacetate (NTA), or complementary coil peptide had been immobilized in a covalent fashion, respectively. Although the noncovalent but stable capture of EGF via tags hold great promise, this strategy should be examined with caution. We indeed recently demonstrated that the nature and the position of the tags both influence EGF bioactivity (*20*). More specifically, an Fc tag was shown to have a deleterious effect on EGF bioactivity when fused at its N- or C-terminus, as deduced from the ability of these constructs to induce A-431 cell receptor phosphorylation *in vitro*. In this assay, EGFR phosphorylation was not detected when the cells were treated with soluble Fc-EGF, while EC_{50} values of 17 nM versus 4.3 nM for EGF-Fc and EGF, respectively, were determined when these ligands were provided to the cells in their soluble forms. In stark contrast, EGF being N-terminally tagged with a short (i.e., 35 amino-acid-long) peptide (the Ecoil) was found to be as active as untagged EGF (EC_{50} of 5.5 nM). The effect of these various tags upon EGF signaling, when captured in an oriented fashion, has never been rigorously compared, although several independent studies have demonstrated that the EGF moiety of these chimeric proteins was able to promote a cellular response.

Another point to be considered with great care in growth factor immobilization resides in the choice of the spacer arm ensuring proper display and attachment of the growth factor of interest. So far, homo- (*21*) and heterobifunctional (*22*) polyethylene glycol (PEG) chains have been extensively used. However, as outlined by Kuhl et al. (*4*) and Klenkler et al. (*21*),

* To whom correspondence should be addressed. E-mail: gregory.decrescenzo@polymtl.ca. Tel: (514) 340-4711 (#7428). Fax: (514) 340-2990.

[†] École Polytechnique de Montréal.

[‡] National Research Council Canada.

10.1021/bc1002604 © 2010 American Chemical Society
Published on Web 11/08/2010

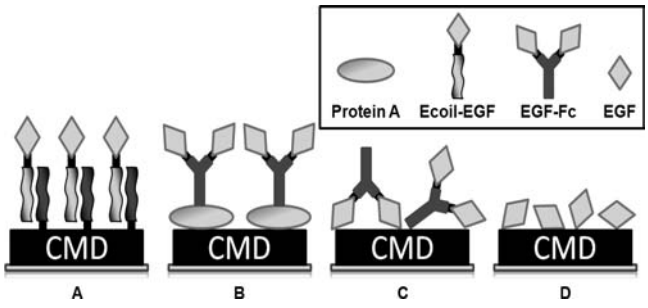


Figure 1. Strategies for EGF immobilization on CMD. (A) Ecoil−EGF capture on a covalently attached Kcoil peptide layer, (B) EGF−Fc capture on a covalently attached Protein A layer, and random covalent attachment of (C) EGF−Fc and (D) untagged EGF on CMD layer.

PEG grafting often results in heterogeneous surface coverage that does not totally block nonspecific adsorption of the growth factor under investigation or of other proteins present in the medium. Furthermore, as already mentioned, subsequent hEGF chemical linkage to activated PEG also leads to heterogeneous EGF display. Hence, results from *in vitro* cell culture experiments performed on PEG surfaces being derivatized with growth factors may not only reflect the effect of the tethered protein but may also be attributed to more complex phenomena being triggered by the combination of suboptimally immobilized and adsorbed species.

As an alternative to PEG, synthetic or natural polymers presenting functionalities such as amine (e.g., chitosan and polyvinylamine), or carboxyl (e.g., carboxymethylated dextran (CMD)) groups distributed homogeneously along their chains are often used as a linker to facilitate the attachment of specific proteins and thus further tailor material surface properties (*1*). In addition to introducing desired reactive groups at the material surface for subsequent protein grafting, the added polymeric layer *per se* can also affect the macroscopic surface properties (hydrophilicity, roughness) and modulate cell and protein affinity for the engineered material surface (*22–24*).

The aim of this work was to compare various controlled constructions of EGF-coated surfaces within the same study (Figure 1) in order to further investigate the impact of the tags (nature and size), the immobilization strategy (i.e., random immobilization versus oriented tethering) upon EGFR activation, and cell adhesion. A-431 cells were cultured on various EGF-derivatized surfaces to correlate the type of EGF display with cell adhesion and EGFR activation. In that effort, a homogeneous polymeric layer of CMD was selected as a polymeric spacer for its ability to provide sufficient reactive groups homogeneously distributed on the surface and because of its low-fouling properties (*25–27*). By preventing nonspecific cell adhesion, CMD allowed us to achieve specific cell interactions with immobilized EGF and therefore derive unambiguous conclusions about the impact of our various EGF grafting strategies upon receptor activation and cell adhesion.

MATERIALS AND METHODS

Chemicals and Reagents. Native silicon wafers (Prime Si P/Boron) were obtained from University Wafer (South Boston, MA), and amino-coated glass slides (10 × 10 mm) were from Erie Scientific Co. (Portsmouth, NH). Anhydrous 3-aminopropyltriethoxysilane (APTES, 99% purity), cysteine (99+% purity), monochloroacetic acid (99+% purity), sodium hydroxide (98+% purity), sodium monobasic phosphate (99+% purity), and sodium chloride (99.99% purity) were purchased from Sigma-Aldrich Canada, Ltd. (Oakville, ON). Hydrogen peroxide (30% v/v), chlorhydric acid (37% v/v), chloroform (99.8% purity), sulfuric acid (98% purity), dimethyl sulfoxide (DMSO, 99+% purity) and toluene (99.5% purity) were purchased from VWR International, Inc. (Mont-Royal, Qc, Canada). All solvents were distilled under strict anhydrous conditions prior to use. Milli-Q quality water (18.2 MΩ·cm; total organic compounds (TOC) = 4 ppb) was generated with a Millipore Gradient A 10 purification system. Cysteine-tagged Kcoil peptides were synthesized by the peptide facility at the University of Colorado (Denver, CO) (*28*). Untagged hEGF and EGFRED-Fc (artificially dimerized EGFR ectodomain through the Fc portion of an IgG_1) was purchased from R&D Systems (Minneapolis, MN). All the surface plasmon resonance (SPR) experiments were performed using a Biacore T100 instrument (GE Healthcare, Baie d'Urfé, Qc, Canada). CM4 sensor chips, *N*-hydroxysuccinimide (NHS), ethyl-*N*′-(3-dimethylaminopropyl) carbodiimide hydrochloride (EDC), ethanolamine, 2-(2-pyridinyldithio)ethaneamine hydrochloride (PDEA), and borate buffer (pH 8.5) were also purchased from GE Healthcare. Dextran (70 kDa) was obtained from Pharmacosmos A/S (Holbaek, Denmark).

Dextran Carboxymethylation and Characterization. Dextran carboxymethylation and characterization was performed by adapting previously reported protocols (*29*). Briefly, 400 mg of dextran was dissolved in 10 mL of 3 M NaOH containing 1 M monochloroacetic acid. The solution was stirred for 2 h at room temperature (RT). The reaction was stopped by the addition of 40 mg of NaH_2PO_4 followed by pH adjustment to neutral using 18 M H_2SO_4. The solution was then filtered through a 0.2 μm PTFE filter, dialyzed five times against Milli-Q water for 1 h in order to remove reagents and salts, and finally lyophilized. CMD powder was stored at 4 °C until use.

The carboxymethylation degree of our product was assessed using ^{1}H NMR spectroscopy. Spectra for CMD were recorded with a Varian Unity Inova 400 MHz NMR spectrometer equipped with a 5-mm indirect probe, operating at a frequency of 399.95 MHz. Samples were examined as solutions in D_2O at 323.1 K. Water signal was suppressed by pulse sequences (72.4°). Chemical shifts are given relative to external tetramethylsilane (TMS = 0 ppm).

Ecoil-Tagged and Fc-Tagged EGF Production. Ecoil−EGF, EGF−Fc, and Fc−EGF were produced in HEK293-6E cells, purified, and quantified as previously described (*20*). Purified recombinant proteins were then aliquoted and stored at −80 °C until use.

Surface Preparation. Glassware was carefully cleansed by overnight immersion in a bath of KOH-saturated isopropyl alcohol followed by intensive rinsing with Milli-Q water. Prior to layer grafting, silicon and amino-coated glass surfaces were washed to remove any adsorbed organic compounds. The silicon surfaces (10 × 10 mm) were cleansed according to the Piranha method, i.e., the surfaces were immersed in a 3:1 mixture of sulfuric acid and hydrogen peroxide for 10 min at 100 °C. After intensive rinsing with Milli-Q water, the surfaces were dried in air at RT and then introduced in a dried Schlenk. To ensure anhydrous conditions, two cycles of vacuum/dry argon were performed in the Schlenk. The amino-coated glass surfaces (10 × 10 mm) were cleansed in an ultrasonic bath for 1 min in distilled chloroform and then dried in air at RT.

Grafting Procedures. *APTES Grafting on Silicon Surfaces.* Amino groups were generated on silicon surfaces using a silanization procedure as previously reported (*18, 30*). Briefly, APTES was first dissolved in anhydrous toluene at a concentration of 10 mM. The solution was injected through a 0.2 μm PTFE filter in dry Schlenk tubes each containing one silicon surface. After a reaction time of 3 h at RT, the surfaces were taken out from the Schlenk tubes, dried in air for 1 min, and placed in an oven at 120 °C for 30 min. The surfaces were then rinsed by soaking them in freshly distilled toluene for 5 min.

CMD Grafting on Amino-Coated Silicon and Glass Surfaces. CMD was covalently attached onto amino-coated surfaces using water-soluble carbodiimide chemistry. CMD solutions (2 mg/mL) were prepared in Milli-Q water. Once dissolved, NHS-activation of CMD was performed by adding 150 μL of 0.4 M EDC in Milli-Q water and 150 μL of 0.1 M NHS in Milli-Q water to the CMD solutions. The amino-coated surfaces were covered with 150 μL of NHS-activated CMD solution for 2 h at RT. The surfaces were finally washed in a 10 mM phosphate buffer solution (pH 7.4) in ultrasonic bath for 2 min, rinsed by soaking them in 10 mM phosphate buffer (pH 7.4) and rinsing three times in fresh Milli-Q water.

Kcoil Peptide Grafting on CMD-Coated Surfaces. Kcoil peptides were immobilized on CMD-coated surfaces using PDEA cross-linker. CMD-coated surfaces were first activated with 100 μL of 0.2 M EDC and 0.05 M NHS in Milli-Q water for 15 min at RT and rinsed in fresh Milli-Q water for 5 min. One hundred microliters of 10 mg/mL PDEA in borate buffer (10 mM disodium tetraborate, 1 M NaCl, pH 8.5) was deposited on each surface for 15 min at RT. The surfaces were rinsed by soaking them in Milli-Q water for 5 min. The thiol-reactive surfaces were then reacted with 100 μL of 10 μM cysteine-tagged Kcoil (5 heptad repeats (*28*)) in 10 mM acetate buffer (pH 5.5) for 2 h at RT. The surfaces were finally rinsed by soaking them in 5 M guanidium hydrochloride solution, 10 mM phosphate buffer, and in Milli-Q water for 5 min each. Unreacted PDEA sites were blocked using 100 μL of 50 mM cysteine solution (1 M NaCl in 0.1 M sodium acetate, pH 4.0) followed by rinsing with Milli-Q water for 5 min.

Kcoil Peptide Grafting on Amino-Coated Glass Surfaces. Kcoil peptides were immobilized onto amino-coated surfaces via *N*-succinimidyl-6-(3'-(2-pyridyldithio)-propionamido)-hexanoate (LC-SPDP) linker, as previously described (*18*). Briefly, the surfaces were covered with 150 mL of 2 mM LC-SPDP in 100 mM phosphate buffer (10% DMSO) for 2 h at RT. The surfaces were rinsed by soaking them in Milli-Q water for 5 min. Then, the LC-SPDP-coated surfaces were covered with 150 mL of 10 mM cysteine-tagged Kcoil peptides in 10 mM phosphate buffer for 2 h at RT. The surfaces were rinsed in 10 mM phosphate buffer (pH 7.4) and in Milli-Q water. One hundred fifty microliters of 50 mM cysteine solution (1 M NaCl in 0.1 M sodium acetate, pH 4.0) was used to block unreacted LC-SPDP sites. The surfaces were rinsed by soaking them in Milli-Q water for 5 min.

Ecoil-Tagged EGF Tethering and Removal. Surfaces harboring covalently bound Kcoil were covered with 150 μL of 600 nM Ecoil-EGF in 10 mM phosphate buffer (pH 7.4) for 2 h at RT. The surfaces were rinsed in 10 mM phosphate buffer and Milli-Q water for 5 min. When necessary, removal of the Ecoil-tagged EGF was performed by soaking the surfaces in a 5 M guanidium hydrochloride solution, followed by rinsing in 10 mM phosphate buffer and Milli-Q water for 5 min each.

Nonoriented EGF Covalent Immobilization on CMD-Coated Surfaces. CMD-coated surfaces were treated with 100 μL of 0.2 M EDC and 0.05 M NHS in Milli-Q water for 15 min at RT and rinsed in fresh Milli-Q water for 5 min. 100 μL of 600 nM untagged hEGF or Fc-tagged EGF in 10 mM acetate buffer (pH 4.5) were deposited on NHS-activated CMD surfaces for 2 h at RT. The surfaces were then rinsed by soaking them in 10 mM phosphate buffer and Milli-Q water for 5 min each.

Fc-Tagged EGF Capture via Immobilized Protein A. CMD-coated surfaces were activated with 100 μL of 0.2 M EDC and 0.05 M NHS in Milli-Q water for 15 min at RT and rinsed in fresh Milli-Q water for 5 min. 100 μL of 10 μM Protein A in 10 mM acetate buffer (pH 4.5) were reacted with NHS-activated CMD surfaces for 1 h at RT. The surfaces were rinsed in 10 mM phosphate buffer and Milli-Q water for 5 min each. The surfaces were then covered with 100 μL of 1 μM Fc-tagged EGF in 10 mM phosphate buffer (pH 7.4) for 2 h at RT. The surfaces were finally rinsed by soaking them in 10 mM phosphate buffer and Milli-Q water for 5 min each.

Contact Angle and Ellipsometric Measurements. Contact angle and ellipsometric measurements were performed as previously described (*18*).

SPR Assays. SPR experiments were conducted at 25 °C using HBS-T (10 mM HEPES pH 7.4, 150 mM NaCl, 3.4 mM EDTA, 0.05% Tween 20) as running buffer.

Kcoil Immobilization on CMD Sensorchip. All the covalent immobilization steps were carried out at a flow rate of 10 μL/min. The carboxylic groups of the CMD matrix of biosensor chips were first activated by injecting 0.05 M NHS mixed with 0.2 M EDC (7 min). The NHS-activated carboxylic groups were then reacted with PDEA cross-linker (10 mg/mL in borate buffer, 7-min injection) to end-graft cysteine-labeled Kcoil (10 μM Kcoil in 10 mM acetate buffer (pH 5.5), 20-s injection). Finally, freshly prepared cysteine solution (50 mM in 0.1 M acetate buffer, 1 M NaCl, pH 4.0) was injected (7 min) to block all unreacted PDEA-activated sites. For each Kcoil-functionalized surface, a mock surface was also generated by applying the same procedure but replacing Kcoil peptide injection by buffer injection.

Ecoil-EGF Capture and Subsequent Injections of EGFRED-Fc. Ecoil-EGF capture and subsequent injections of EGFRED-Fc to test Ecoil-EGF bioactivity were performed at a flow rate of 50 μL/min. Regeneration of the sensorchip (i.e., removal of Ecoil-EGF) was accomplished by two pulses of guanidium hydrochloride (50 μL, 100 μL/min, 5M).

Immobilized EGF Quantification. Commercially available DuoSet ELISA kit (DY-236, R&D Systems, Minneapolis, MN) was used to quantify EGF and Ecoil-EGF concentrations in solution before and after immobilization/capture on surfaces according to the manufacturer recommendations and using a Victor (*3*) V ELISA plate reader (PerkinElmer Inc., Woodbridge, ON). Standard curves were generated with tagged and untagged EGF proteins depending on the protein to be quantified.

Cellular Assays. *Cell Culture.* A-431 cells were maintained in 175 cm^2 flasks in Dulbecco's modified Eagle's medium (DMEM, GIBCO/BRL, Burlington, ON) supplemented with 10% fetal bovine serum (Invitrogen, Burlington, ON) at 37 °C with 5% CO_2 until 85−90% confluence was reached.

A-431 Seeding. Prior inoculations onto our various surfaces, A-431 cells were washed with phosphate buffered saline (PBS) and incubated overnight in DMEM medium without serum. After trypsinization (5 min, 37 °C), A-431 cells were washed by centrifugation and resuspended in DMEM (no serum). Then, A-431 cells were distributed at 1×10^6 cells/mL, 1 mL/well, in 24-well plates containing aminated glass surfaces, Kcoil functionalized glass surfaces where Ecoil−EGF had previously been immobilized via coiled-coil interactions, CMD-coated glass surfaces in the presence or absence of soluble EGF (4 nM), CMD-coated glass surfaces where Ecoil−EGF had been previously immobilized via coiled-coil interactions, CMD-coated glass surfaces where EGF−Fc had been previously captured via Fc/protein A interactions, and CMD-coated glass surfaces where EGF and EGF−Fc had been covalently immobilized via amine chemistry (nonoriented immobilization).

Cell Adhesion. DMEM medium was removed 4 h after inoculation and adhered cells were washed three times with DMEM (serum-free). Cells were observed using inverted microscope Axiovert S100TV (Carl Zeiss Canada, North York, ON). Images were processed with a QICAM Fast 1394 camera (QImaging) and cell count was achieved using Northern Eclipse image acquisition software (Empix imaging).

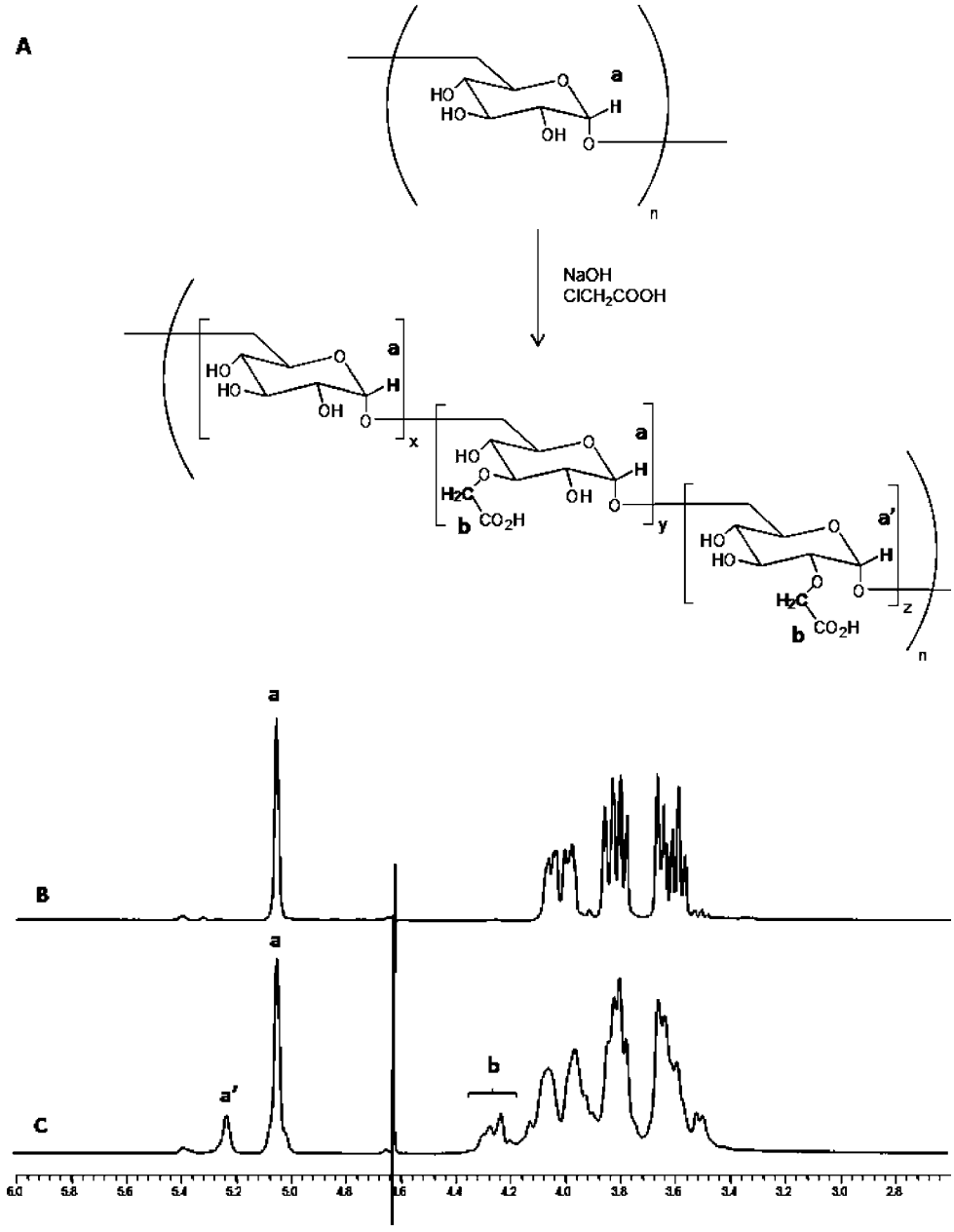


Figure 2. 70 kDa dextran carboxymethylation. Chemical reaction scheme (A) and ^{1}H NMR spectra of dextran (B) and product of dextran carboxymethylation (C). Letters in bold correspond to the protons borne by the anomeric carbons (**a** and **a′**) or by the methyl groups (**b**) added by the chemical reaction.

Phosphorylation Assays and Cell Lysis. DMEM medium was removed 2, 3, 4, and 5 h after inoculation, and A-431 cells were washed three times with PBS supplemented with sodium-orthovanadate (1 mM, Sigma) and extracted with lysis buffer (50 mM HEPES pH 7.4), 150 mM NaCl, 1% Thesit, 0.5% Na Deoxycholate, Complete protease inhibitor cocktails (Roche, Laval, Qc)) supplemented with 0.1 mM Na_3VO_4, 20 mM β-glycerophosphate, 10 mM $Na_4P_2O_7 \cdot 10\ H_2O$ and 0.5 μM microcystin). Insoluble material was removed by centrifugation at 10 000 *g* for 5 min at 4 °C. Protein phosphorylation was then analyzed by Western blotting as previously described (*18*).

RESULTS AND DISCUSSION

Dextran Carboxymethylation and Grafting on Amino-Coated Glass Surfaces. To introduce carboxylic groups, 70-kDa dextran chains were first transformed into negatively charged CMD (Figure 2A). $-CH_2-COOH$ groups were introduced in the chain by reaction of monochloroacetic acid with the hydroxyl groups held by the glucopyranose rings of dextran without degrading the polysaccharidic backbone (as opposed to methods relying on periodate oxidation) (*25*). Although the carboxymethylation protocol we used is known to kinetically favor the modification of hydroxyl groups held by the C_2 carbon, modifications may also occur on all the $-OH$ groups of the glucopyranose cycle (*25*). Dextran modification was confirmed by ^{1}H NMR spectroscopy. As shown in Figure 2, the product of the carboxymethylation reaction exhibited two distinct peaks within the spectral region corresponding to an anomeric proton signal (Figure 2C). By comparing this spectrum to that of unmodified dextran (Figure 2B), peaks at $\delta = 5.04$ ppm and $\delta = 5.23$ ppm were attributed to the anomeric protons of glucopyranose units being unsubstituted (**a**) or bearing a carboxymethyl group (**a′**) at their C_2 position, respectively. Also, the spectrum corresponding to the carboxymethylation product was characterized by the presence of new peaks within the 4.17−4.35 ppm δ region (denoted **b** within Figure 2C). These

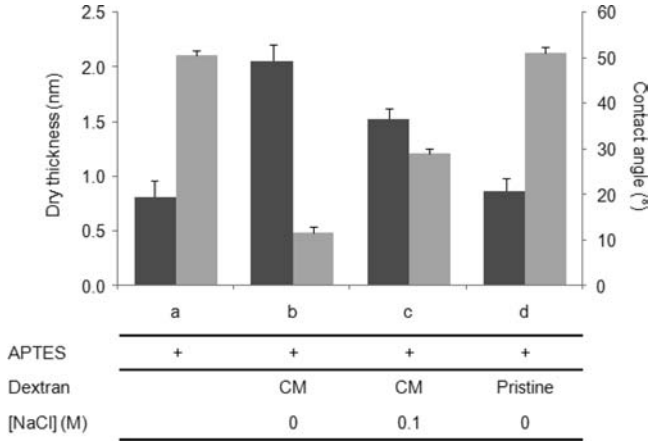


Figure 3. Ellipsometric and water contact angle characterization of CMD grafting on aminated silicon surfaces. APTES layer grafted on silicon surfaces (a) and subsequent grafting of carboxymethylated (CM) dextran in the absence of salt (b) or dissolved in 0.1 M NaCl solution (c). As a comparison, the characterization of pristine (unmodified) dextran incubation on APTES-coated surfaces is also presented. The dark and light gray bars correspond to dry thickness and contact angle measurements, respectively. The reference was set as (0 nm, 0°) for a cleaned silicon surface. The successive grafting reactions were performed as described in the Materials and Methods section and summarized in the table below the graph. Values are given as mean value ± standard deviation ($n = 5$).

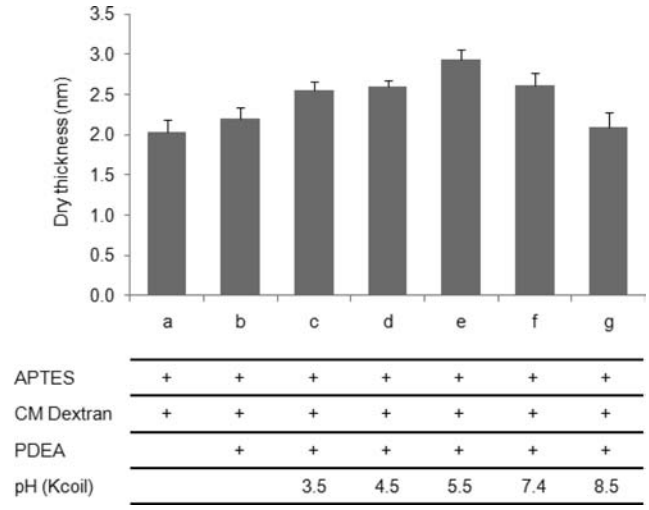


Figure 4. Ellipsometric characterization of Kcoil peptide covalent immobilization on CMD surfaces. PDEA grafting (b) and subsequent immobilization of cysteine-tagged Kcoil peptide (c−g) on CMD-coated silicon surfaces (a). Cysteine-tagged Kcoil was reacted on PDEA-covered surfaces at pH 3.5 (c), pH 4.5 (d), pH 5.5 (e), pH 7.4 (f) and pH 8.5 (g). The reference was set as 0 nm for a cleaned silicon surface. The grafting reactions were performed as described in the Materials and Methods section and summarized in the table below the graph. Values are given as mean value ± standard deviation ($n = 5$).

peaks corresponded to the $-CH_2$ protons of the added carboxymethyl group. The degree of carboxymethylation was thus determined from the ratio of the areas corresponding to the $-CH_2$ signals of the CH_2-COOH groups (**b** region within Figure 2C) to the areas corresponding to the anomeric proton signals (**a** and **a′** peaks within Figure 2C). Under our experimental conditions, the carboxymethylation degree of our 70-kDa dextran was estimated to be 22%.

In a second step, silicon surfaces were chosen as substrate to investigate CMD grafting to aminated substrate. Ellipsometric and water contact angle measurements were performed to evaluate the effect of salt upon our grafting protocol. In that endeavor, amine groups were first generated on silicon surfaces via a silanization reaction occurring between APTES and silanol groups that are naturally exposed on the surfaces (*18*). As illustrated in Figure 3 (condition a), the layer of deposited APTES appeared to be thin and homogeneous as deduced from ellipsometric thickness (0.8 ± 0.15 nm) and water contact angle (51 ± 2°) measurements, both in excellent agreement with those we determined in a previous study (*18*). CMD chains were then grafted on these amino-functionalized surfaces using EDC and NHS as coupling agents. In this way, NHS-activated carboxyl groups of CMD chains were reacted with free amine groups on the surface to create a stable amide bound. In an effort to maximize CMD grafting on amino-coated surfaces, the coupling reaction was carried out both in the absence and presence of salt (0.1 M NaCl) in the CMD solution (Figure 3, conditions b and c). We reasoned that salt addition would decrease the electrostatic repulsions that may occur within and between the charged CMD chains. We thus expected to obtain more compact individual CMD chains in solution and therefore denser grafted CMD layers. Whereas a dense and hydrophilic polymeric layer was grafted (net dry thickness of 1.3 nm and water contact angle of 11 ± 2°) in the absence of salt, the addition of 0.1 M NaCl resulted in a 53% lower net dry thickness (0.7 nm). As a negative control, when the same reaction was performed with pristine dextran, only minor variations in surface characteristics were observed when compared to APTES-coated silicon surfaces (+ 0.05 nm and +0.5° for dry thickness and contact angle values, respectively). The negative impact of salt upon CMD grafting has previously been reported by others (*31*). This effect is most likely related to a drastic loss of NHS-activated carboxyl groups via hydrolysis, the latter being promoted by high salt concentrations (*32*).

EGF Grafting. The covalent immobilization as well as the stable tethering of several EGF variants were then studied on optimized CMD-grafted surfaces by applying the oriented and nonoriented strategies described in Figure 1. That is, two distinct tag systems were independently evaluated (coil and Fc tags) and compared to the nonoriented but covalent immobilization of EGF or EGF−Fc onto CMD.

Coiled-Coil-Mediated EGF Tethering. The first tethering strategy consisted in covalently grafting cysteine-tagged Kcoil peptides on CMD-covered surfaces, followed by the capture of Ecoil-tagged proteins via E/K coiled-coil interactions. Cysteine-tagged Kcoil peptides were first grafted on CMD using PDEA as a bifunctional linker (*28*). NHS-activated CMD chains were reacted with the free amine group of PDEA linker to form an amide bond. The resulting film showed an ellipsometric thickness of 2.2 ± 0.2 nm (Figure 4, condition b). The other extremity of PDEA linker, terminated by a pyridyl disulfide group, was then reacted with the thiol group of cysteine-terminated Kcoil peptide to create a covalent disulfide bond. In an effort to maximize Kcoil grafting density, the coupling reaction was studied at various pHs ranging from 3.5 to 8.5 (Figure 4, conditions c−g). Maximal effective thickness, i.e., 0.7 ± 0.1 nm (Figure 4, condition e), was obtained for Kcoil peptides reacted at pH 5.5. Cysteine was then used to block unreacted pyridyl disulfide group of PDEA linkers and therefore prevent the undesired attachment of other molecules containing thiol groups. No significant changes in surface characteristics were observed before (Figure 4, conditions b and e) and after (Figure 5, conditions a and d) cysteine-mediated PDEA deactivation. The ability of our CMD surfaces, when functionalized with Kcoil peptides, to recruit N-terminally Ecoil-tagged EGF chimera was then tested. As can be seen in Figure 5, the incubation of Ecoil−EGF on Kcoil peptides previously bound to CMD surfaces, followed by extensive rinsing to elute unbound material, led to a net increase in dry thickness of 0.8 ± 0.2 nm. Further treatment of surfaces on which Ecoil−EGF

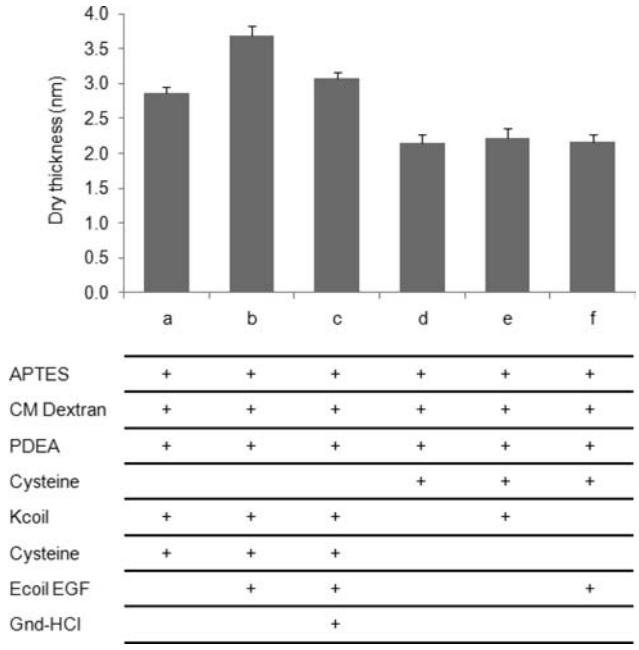


Figure 5. Ellipsometric characterization of Ecoil-tagged EGF tethering on Kcoil-coated CMD surfaces. Dry thickness measurements corresponding to silicon surfaces sequentially treated with APTES, CMD, PDEA, Kcoil (pH 5.5) and cysteine solutions (a) that were incubated with Ecoil−EGF (b) and then exposed to a 5 M guanidium hydrochloride (Gnd-HCl) solution (c). As negative control, the incubation of Kcoil peptides (e) and Ecoil−EGF proteins (f) on cysteine-blocked PDEA layers (d) are presented. The reference was set as 0 nm for a cleaned silicon surface. The successive grafting reactions were performed as described in the Materials and Methods section and summarized in the table below the graph. Values are given as mean value ± standard deviation ($n = 5$).

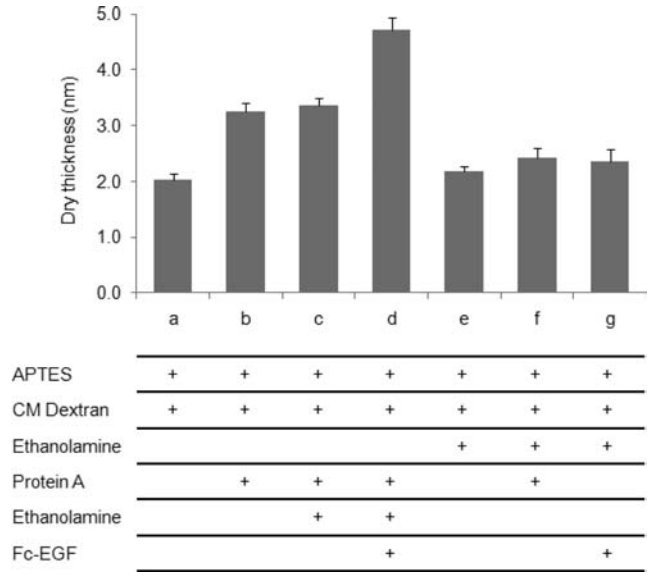


Figure 6. Ellipsometric characterization of EGF−Fc tethering on Protein A-coated surfaces. Dry thickness measurements corresponding to silicon surfaces sequentially treated with APTES and CMD (a) on which covalent coupling of Protein A had been achieved by amine chemistry (b), and for whom remaining activated group had been blocked by ethanolamine (c). EGF−Fc capture on (c) is shown as (d). As negative control, the incubation of Protein A (f) and EGF−Fc (g) on ethanolamine-blocked CMD layers (e) are presented. The reference was set as 0 nm for a cleaned silicon surface. The successive grafting reactions were performed as described in the Materials and Methods section and summarized in the table below the graph. Values are given as mean value ± standard deviation ($n = 5$).

had been captured, with 5 M guanidium hydrochloride, a strong chaotropic agent known to disrupt coiled-coil interactions (*28*), induced a decrease in dry thickness of 0.6 nm, which confirmed the reversibility of the coiled-coil interaction. Finally, when Ecoil−EGF or cysteine-tagged Kcoil were incubated on cysteine-deactivated PDEA/CMD layers (Figure 5, conditions e and f, respectively), no significant changes in dry thickness values were observed when compared to those measured prior incubation (Figure 5, condition d), hence demonstrating that nonspecific adsorption of Ecoil−EGF and Kcoil peptides on dextran-coated surfaces was negligible.

Fc-Mediated EGF Tethering. The second EGF capture strategy was based on the covalent attachment of Protein A to CMD, followed by the oriented capture of C-terminally Fc-tagged EGF proteins (EGF−Fc) via Protein A/Fc interactions (*33*). To do so, NHS/EDC coupling agents were used to activate grafted CMD surfaces. Ten micromolar Protein A diluted in 10 mM acetate buffer (pH 4.5) was found to be the best condition among those we tested for Protein A covalent grafting on NHS-activated CMD (data not shown). The resulting film displayed a dry thickness of 3.3 ± 0.1 nm (Figure 6, conditions b). After Protein A grafting, the remaining NHS-reactive groups were deactivated using ethanolamine as blocking agent in order to prevent any undesired attachment of amine-containing molecules. The ethanolamine-mediated NHS deactivation did not induce any significant change in the layer thickness (Figure 6, compare conditions b and c). Fc-tagged EGF proteins were then tethered on the Protein A layer, giving rise to final dry thickness of 4.7 ± 0.2 nm after extensive rinsing to remove any unbound material. As negative control, Protein A and EGF−Fc were incubated on ethanolamine-deactivated CMD (Figure 6, conditions f and g, respectively). Minor variations in dry thickness values were noticed when compared to that of deactivated dextran layer (Figure 6, condition e). This observation suggested that Protein A was mainly attached via covalent amide bonds to CMD-coated surfaces while Fc−EGF nonspecific adsorption on CMD was negligible.

Altogether, the negative controls shown in Figures 5 and 6 demonstrated that the experimental protocol we optimized to generate our low-fouling CMD layer was successful. This conclusion is in total agreement with those drawn by Monchaux and Vermette who reported very low levels of serum protein adsorption on similar CMD surfaces (*31*).

EGF Covalent Immobilization. For the sake of comparison, covalent immobilization of EGF was also performed on CMD surfaces using untagged hEGF and EGF−Fc proteins. In that approach, available amine groups of EGF or Fc tag (displayed on lysine residue side chains or at the N-terminus of the proteins) were used to create amide bonds with NHS-activated CMD layer. One micromolar of hEGF or EGF−Fc dissolved at pH 4.5 (10 mM acetate buffer) was found to be the optimal condition to obtain thick and homogeneous grafted layers on CMD surfaces (data not shown) that were characterized by effective dry thicknesses of 1.1 and 0.9 nm, respectively. In contrast to both oriented capture approaches we described earlier, our EGF covalent immobilization protocol required the use of acetate buffer at acidic pH far from physiological values. In order to assess if such a pH difference might have induced EGF unfolding, additional SPR biosensing experiments were performed as follows. Kcoil peptide was first immobilized at the surface of commercially available biosensor chips harboring a CMD layer, using the same chemistry protocol as the one we previously described for Kcoil covalent grafting on CMD-coated silicon surfaces (650 RU of immobilized Kcoil peptide). Ecoil−EGF (43 μM) was either freshly diluted in biosensor running buffer (HBS, pH 7.4, 1/430 dilution) or diluted in acetate buffer (pH 4.5, 1/12 dilution), let for 2 h at RT then further

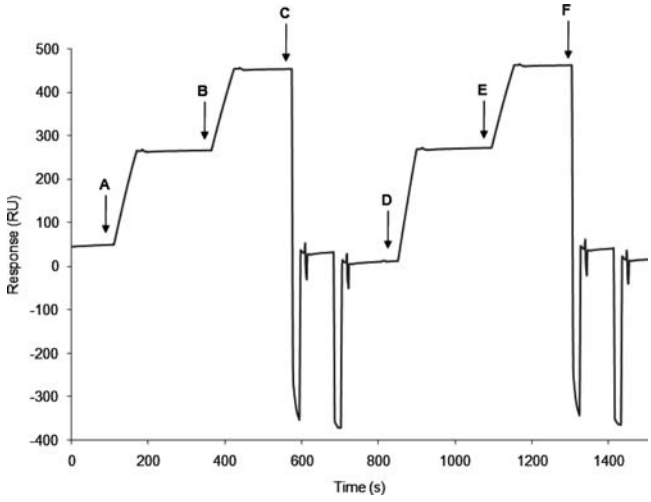


Figure 7. Acidic pH does not affect EGF bioactivity during immobilization procedure. Control-corrected sensorgrams corresponding to the sequential capture of Ecoil−EGF chimera that has been directly diluted in running buffer (A, pH 7.4), followed by EGFR−Fc injection (B) and 5 M Gnd-HCl pulses (C) to remove coil-tagged EGF. In order to evaluate the impact of acidic pH upon EGF bioactivity, Ecoil−EGF that had been kept for 2 h at pH 4.5, was diluted in running buffer prior biosensor surface capture (D), EGFR−Fc injection (E, same as B) and regeneration (F). Note that EGFR−Fc binding to captured Ecoil−EGFs (B and E) gave identical responses.

diluted in HBS buffer (pH 7.4, 1/36 dilution to get a final 1/432 dilution of EGF stock solution). The bioactivity of both Ecoil−EGF preparations was then assessed by capturing Ecoil−EGF onto Kcoil-functionalized biosensor surface and then injecting the soluble extracellular domain of EGFR being artificially dimerized through the Fc portion of an antibody (namely, EGFR−Fc). As can be seen in Figure 7, a 2-h incubation of Ecoil−EGF in acidic buffer did not alter its ability to bind to its receptor ectodomain since similar SPR responses were obtained when injecting EGFR−Fc over the same amount of coiled-coil captured EGF that had been either incubated in acetate or freshly dissolved at physiological pH prior to capture. It is thus most likely that the use of acetate buffer at acidic pH in our immobilization protocol does not alter *per se* EGF or EGF−Fc bioactivity.

Quantification of EGF Surface Densities. EGF surface densities were evaluated by ELISA for all our immobilization/capture strategies. Ecoil−EGF (600 nM) incubated on Kcoil layers previously generated on amino-coated (no dextran) and on CMD-coated silicon surfaces resulted in EGF densities of 30.7 ± 3.6 and 31.5 ± 3.5 pmol/cm^2, respectively. When EGF−Fc had been incubated at 600 nM on Protein A layers (previously grafted on CMD), an EGF density of 13.4 ± 2.3 pmol/cm^2 was obtained. In parallel, covalent coupling of EGF proteins (i.e., untagged EGF and EGF−Fc, 600 nM) on NHS-activated CMD layers resulted in EGF grafting densities of 37.5 ± 1.6 and 9.3 ± 2.4 pmol/cm^2, respectively. Dry thickness measurements were also performed to evaluate the impact of soluble tagged EGF concentration upon resulting amount of captured EGF. As shown in Figure 8, EGF surface density could be easily controlled over a wide range by varying soluble concentrations during incubation. Similar apparent thermodynamic dissociation constant (K_D) of 15 and 30 nM were deduced for Ecoil−EGF binding to immobilized Kcoil peptide and EGF−Fc binding to immobilized Protein A, respectively, assuming that Ecoil−EGF/Kcoil and EGF−Fc/Protein A interactions are well-depicted by a Langmuirian isotherm. These results thus indicate that the compact coil tag is an interesting alternative to bulkier Fc tag since the former allowed higher EGF surface density to be reached without any compromise on affinity.

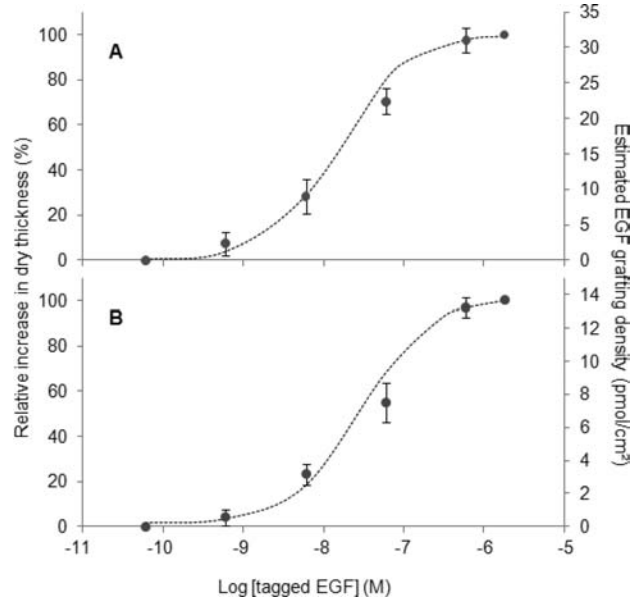


Figure 8. The amount of tagged EGF being captured on CMD layers via coiled-coil or Fc−Protein A interactions is controllable. Variation of the effective dry thickness as a function of tagged EGF concentration when Ecoil−EGF was incubated on Kcoil layers grafted on CMD (A) or when EGF−Fc was incubated on Protein A layers grafted on CMD (B). Surface density (pmol/cm^2) was deduced by ELISA assay for the maximal Ecoil−EGF or EGF−Fc concentrations. Each dot corresponds to values obtained for three independent measurements while the dotted line corresponds to data fitting using a simple Langmuirian isotherm (K_D = 15 and 30 nM for panels A and B, respectively).

EGFR Phosphorylation Assays. EGF-dependent cellular response is mediated through EGF binding to its cell surface receptors, which in turn lead to receptor intracellular kinase activation via a trans-autophosphorylation mechanism (*6*). Phosphorylation levels of A-431 cell EGFR were thus assayed at different time points by Western blot analysis (Figure 9). As expected, no phosphorylation of EGFR was observed for aminated glass surfaces that were coated or not with CMD. Also, Fc−EGF (a chimeric protein in which EGF is fused to the C-terminus of the Fc portion of an IgG), when captured onto Protein A surfaces did not lead to any significant EGFR phosphorylation. This result was expected since this chimeric construct was shown to poorly interact with EGFR ectodomain (*20*). When the cells were treated with soluble EGF, EGFR phosphorylation was found to be transient (maximal phosphorylation levels occurred after 2 h and no more phosphorylation could be observed after 4 h). These results sharply contrasted with those related to covalently immobilized or stably captured EGF conditions, for which sustained phosphorylation (i.e., at least 5 h after cell seeding) was always observed.

Of interest, the stable capture of EGF in an oriented fashion (via Fc−Protein A or coiled-coil interactions) resulted in increased EGFR activation when compared to all the nonoriented immobilization strategies we tested. That is, phosphorylation signals were found to be more intense for surfaces where Ecoil−EGF or EGF−Fc had been captured via coiled-coil or Fc−Protein A interactions than for surfaces where EGF or EGF−Fc had been covalently immobilized in a random fashion (compare "nonoriented immobilization" to "oriented capture" panels in Figure 9). Since comparable levels of coil-tagged EGF (31.5 ± 3.5 pmol/cm^2) or untagged EGF (37.5 ± 1.6 pmol/cm^2) had been captured or covalently immobilized, respectively, these results unambiguously confirmed that hEGF grafting strategies relying on covalent coupling through amine chemistry negatively impact its bioactivity, as previously reported (*17, 18*). This loss of bioactivity cannot be attributed to the acidic

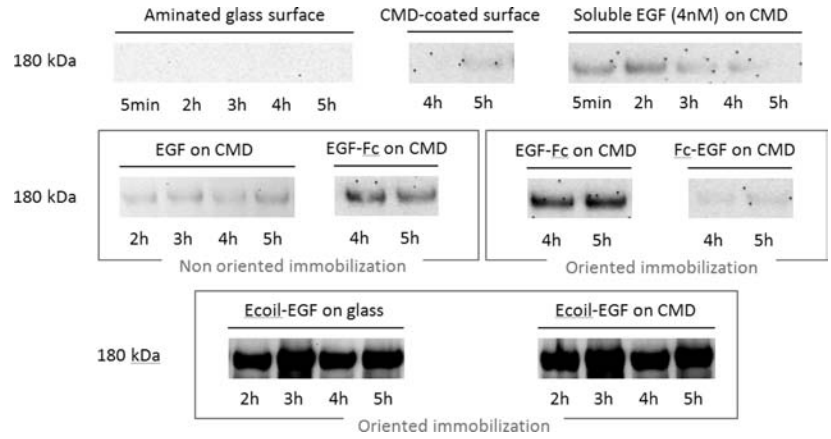


Figure 9. Phosphorylation of A-431 cell surface EGFRs. The phosphorylation of EGFRs on A-431 cells was monitored at different times by Western blot. The 180 kDa band immunoreactive to anti-pTyr antibody (corresponding to EGFR) was captured using a Kodak 440cf imager. Surface type and mode of EGF supply is indicated for each panel.

conditions that were used for covalent grafting (see previous SPR results, Figure 7), but most likely results from the involvement of the EGF lysine side-chains in the grafting reaction. This conclusion holds true when examining the phosphorylation levels (Figure 9) for EGF−Fc that was captured via Protein A/Fc interactions (13.4 ± 2.3 pmol/cm^2) to those related to randomly immobilized EGF−Fc (9.3 ± 2.4 pmol/cm^2).

Finally, Ecoil−EGF tethering via coiled-coil interactions on surfaces previously coated with CMD was the approach that induced the most intense activation of EGFR. In that specific case, phosphorylation levels were comparable to those obtained when Ecoil−EGF was directly tethered on amino-coated surfaces via coiled-coil interactions (Figure 9). This maximal response can be attributed to the fact that (i) the EGF moiety within the Ecoil−EGF chimera is fully bioactive, as opposed to EGF−Fc (*20*), (ii) that the coiled-coil strategy allowed capturing almost 3-fold more EGF when compared to strategies relying on Protein A/Fc interactions (most likely due to the compactness of the coiled-coil structure), and (iii) that the use of a coil tag linked to the EGF moiety thanks to a glycine linker, enhanced EGF mobility when compared to that of untagged EGF being directly coupled.

Tethered EGF Increases A-431 Cell Adhesion on Low-Fouling CMD. The effect of CMD layer, combined to our various strategies aiming at immobilizing/tethering EGF, upon A-431 cell adhesion was then investigated. For this purpose, A-431 cells were directly seeded on aminated glass surfaces (control), on Kcoil functionalized glass surfaces to which Ecoil−EGF had been captured via coiled-coil interactions, on CMD-coated glass surfaces in the presence or absence of soluble EGF (4 nM), on CMD-coated glass surfaces on which Ecoil−EGF had been immobilized via coiled-coil interactions or via Fc-Protein A interactions and on CMD-coated glass surfaces where EGF and EGF−Fc were covalently immobilized via amine chemistry (nonoriented immobilization) (Figure 10). As expected from the low-fouling properties of dextran (*26*), CMD layers drastically limited A-431 cell adhesion when compared to aminated surfaces (110 versus 2177 cells/mm^2). The nonoriented immobilization of EGF (native EGF or EGF−Fc) on CMD only resulted in a less than 3-fold increase of A-431 cell adhesion (299 and 277 cells/mm^2, respectively) and to levels comparable to those determined when signaling-incompetent Fc-EGF had been tethered via its interaction with Protein A (283 cells/mm^2). In stark contrast, a marked increase of A-431 cell adhesion was observed for Ecoil−EGF being tethered via coiled-coil interaction on CMD-coated surfaces (2182 cells/mm^2). In that specific case, adhesion was determined

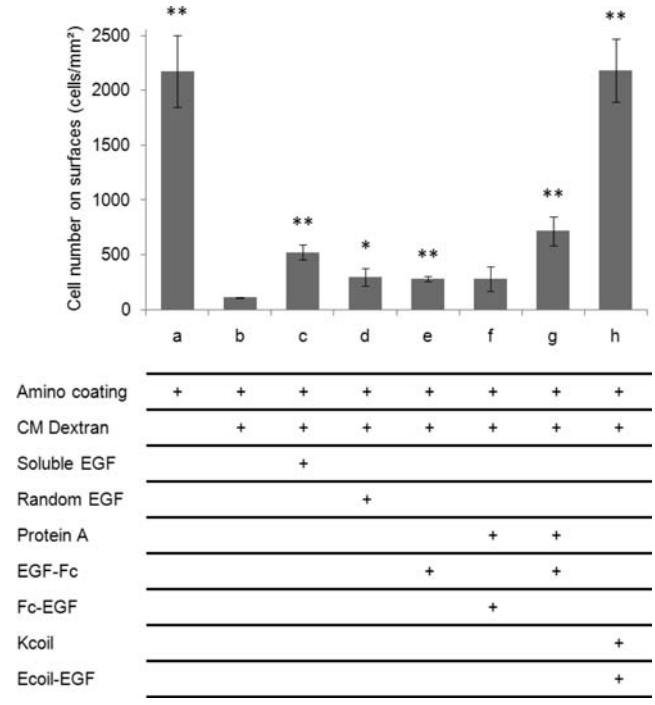


Figure 10. Cell adhesion assays. A-431 cells were incubated for 4 h on glass surfaces being amino-coated only (a), or coated with CMD both in the absence (b) or presence of soluble EGF (c). Conditions (d−h) correspond to approaches leading to EGF covalent immobilization (d,e) or to its tag-driven capture (g,h). Condition f corresponds to the negative control for condition g. The successive grafting reactions were performed as described in the Materials and Methods section and summarized in the table below the graph. Values are given as mean value ± standard deviation ($n = 5$). In order to compare each condition to condition b, statistical analysis was performed by independent two-sample t test with equal variances. Values of $p < 0.05$ and $p < 0.001$ were considered to be statistically significant and are identified by * and **, respectively.

to be as strong as for amino-coated surfaces (no CMD, Figure 10). Statistically significant but lower increases of cell adhesion were also observed for EGF−Fc being tethered via Fc/Protein A interactions (716 cells/mm^2) or with soluble EGF supply (522 cells/mm^2). These results are in excellent agreements with those from Kempiak et al. demonstrating that local activation of EGFR with EGF-coated beads caused a rapid actin polymerization response and lamellipod extrusion (*34*), two traits of A-431 cellular adhesion. Additionally, EGF grafting has also been shown to increase 3T3 Swiss (*19*) and human corneal epithelial

(*35*) cell adhesion, most likely due to the sustained activation of various downstream signaling pathways (e.g., ERK 1/2 and Akt), in turn leading to increased production of extracellular matrix proteins.

Altogether, the results presented in Figures 9 and 10 demonstrate that a strong EGF-induced A-431 cell adhesion on CMD surfaces can only be achieved when EGF is presented to the cells in a nondiffusible way, while preserving its biological activity. Indeed, EGF tethering on CMD surfaces via coiled-coil interactions (which corresponded to the most intense and sustained phosphorylation of A-431 cell surface receptors on CMD coating; Figure 9), was the only experimental condition that lead to adhesion levels similar to those obtained on control aminated surfaces (Figure 10). In stark contrast, only limited, but yet significant, increase in cell adhesion was observed (Figure 10, conditions c-g) when the grafting strategies altered EGF bioactivity (as demonstrated by low levels of EGFR phosphorylation, Figure 9) or when only transient phosphorylation of EGFR was triggered by diffusible EGF (Figure 9).

CONCLUSION

In the context of tissue engineering and regenerative medicine, EGF immobilization at the surface of implants has attracted a lot of attention. Here we show that fully bioactive EGF being tethered on carefully engineered surfaces may play, *per se*, a significant role in promoting cell adhesion, in addition to cell survival and proliferation as already demonstrated by several research groups. Among all the approaches we tested, the oriented tethering of EGF via coiled-coil interactions was shown to be the most efficient on low-fouling CMD surfaces. This most likely resulted from the many advantages of this capture system. First, it permitted the adequate display of captured EGF, and in turn the maximal biological effect as opposed to random covalent coupling. While we previously showed that the Ecoil peptide had no impact on EGF bioactivity (in contrast to the Fc tag), the relatively small size of the coiled-coil structure allowed achieving levels of captured EGF 3-fold higher than those obtained with a bulkier Fc/Protein A capture system. Altogether, coiled-coil tethered EGF led to the most intense and sustained phosphorylation of A-431 cell EGFRs as well as to strong cell adhesion. Of interest, the latter was comparable to that observed with an amino-coated surface. Our results thus highly suggest that CMD may be an interesting alternative to PEG for the generation of surfaces limiting nonspecific adhesion, and that these surfaces could be further tailored through growth factor capture via coiled-coil interactions.

ACKNOWLEDGMENT

This work was supported by the Canada Research Chair on Protein-Enhanced Biomaterials (G.D.C.), the Canada Research Chair in Applied Metabolic Engineering (M.J.), by the Natural Sciences and Engineering Research Council of Canada (G.D.C., M.J.) and by GRSTB (postdoctoral fellowship to B.L. and financial help to J.C.).

LITERATURE CITED

(1) Goddard, J. M., and Hotchkiss, J. H. (2007) Polymer surface modification for the attachment of bioactive compounds. *Prog. Polym. Sci. 32*, 698–725.

(2) Ito, Y. (2008) Covalently immobilized biosignal molecule materials for tissue engineering. *Soft Matter 4*, 46–56.

(3) Ma, Z. W., Mao, Z. W., and Gao, C. Y. (2007) Surface modification and property analysis of biomedical polymers used for tissue engineering. *Colloids Surf. B: Biointerfaces 60*, 137–157.

(4) Kuhl, P. R., and Griffith-Cima, L. G. (1996) Tethered epidermal growth factor as a paradigm for growth factor-induced stimulation from the solid phase. *Nat. Med. 2*, 1022–1027.

(5) Ogiso, H., Ishitani, R., Nureki, O., Fukai, S., Yamanaka, M., Kim, J. H., Saito, K., Sakamoto, A., Inoue, M., Shirouzu, M., and Yokoyama, S. (2002) Crystal structure of the complex of human epidermal growth factor and receptor extracellular domains. *Cell 110*, 775–787.

(6) Schlessinger, J. (2002) Ligand-induced, receptor-mediated dimerization and activation of EGF receptor. *Cell 110*, 669–672.

(7) Yarden, Y., and Sliwkowski, M. X. (2001) Untangling the ErbB signalling network. *Nat. Rev. Mol. Cell Biol. 2*, 127–137.

(8) Zhang, X., Gureasko, J., Shen, K., Cole, P. A., and Kuriyan, J. (2006) An allosteric mechanism for activation of the kinase domain of epidermal growth factor receptor. *Cell 125*, 1137–1149.

(9) Hubbard, S. R., and Miller, W. T. (2007) Receptor tyrosine kinases: mechanisms of activation and signaling. *Curr. Opin. Cell Biol. 19*, 117–123.

(10) Klenkler, B. J., Dwivedi, D., West-Mays, J. A., and Sheardown, H. (2009) Corneal epithelial cell adhesion and growth on EGF-modified aminated PDMS. *J. Biomed. Mater. Res. A 93*, 1043–1049.

(11) Klenkler, B. J., Griffith, M., Becerril, C., West-Mays, J. A., and Sheardown, H. (2005) EGF-grafted PDMS surfaces in artificial cornea applications. *Biomaterials 26*, 7286–7296.

(12) Kato, K., Sato, H., and Iwata, H. (2005) Immobilization of histidine-tagged recombinant proteins onto micropatterned surfaces for cell-based functional assays. *Langmuir 21*, 7071–7075.

(13) Fan, V. H., Tamama, K., Au, A., Littrell, R., Richardson, L. B., Wright, J. W., Wells, A., and Griffith, L. G. (2007) Tethered epidermal growth factor provides a survival advantage to mesenchymal stem cells. *Stem Cells 25*, 1241–1251.

(14) Nakaji-Hirabayashi, T., Kato, K., Arima, Y., and Iwata, H. (2007) Oriented immobilization of epidermal growth factor onto culture substrates for the selective expansion of neural stem cells. *Biomaterials 28*, 3517–3529.

(15) Nakaji-Hirabayashi, T., Kato, K., and Iwata, H. (2009) Surface-anchoring of spontaneously dimerized epidermal growth factor for highly selective expansion of neural stem cells. *Bioconj. Chem. 20*, 102–110.

(16) Ogiwara, K., Nagaoka, M., Cho, C. S., and Akaike, T. (2006) Effect of photo-immobilization of epidermal growth factor on the cellular behaviors. *Biochem. Biophys. Res. Commun. 345*, 255–259.

(17) O'Connor-McCourt, M. D., De Crescenzo, G., Lortie, R., Lenferink, A., Grothe, S. (1998) The analysis of surface plasmon resonance-based biosensor data using numerical integration: The epidermal growth factor receptor-ligand interaction as an example. In *Quantitative Analysis of Biospecific Interactions* (Lundahl, P., Lundqvist, A., Greiger, E., Eds.), pp 175−190, Harwood Academic Publishers, Australia.

(18) Boucher, C., Liberelle, B., Jolicoeur, M., Durocher, Y., and De Crescenzo, G. (2009) Epidermal growth factor tethered through coiled-coil interactions induces cell surface receptor phosphorylation. *Bioconj. Chem. 20*, 1569–1577.

(19) Ogiwara, K., Nagaoka, M., Cho, C.-S., and Akaike, T. (2005) Construction of a novel extracellular matrix using a new genetically engineered epidermal growth factor fused to IgG-Fc. *Biotechnol. Lett. 27*, 1633–1637.

(20) Boucher, C., St-Laurent, G., Loignon, M., Jolicoeur, M., De Crescenzo, G., and Durocher, Y. (2008) The bioactivity and receptor affinity of recombinant tagged EGF designed for tissue engineering applications is defined by the nature and position of the tags. *Tissue Eng. Part A 14*, 2069–2077.

(21) Klenkler, B. J., and Sheardown, H. (2006) Characterization of EGF coupling to aminated silicone rubber surfaces. *Biotechnol. Bioeng. 95*, 1158–1166.

(22) Klenkler, B. J., Chen, H., Chen, Y., Brook, M. A., and Sheardown, H. (2008) A high-density PEG interfacial layer alters the response to an EGF tethered polydimethylsiloxane surface. *J. Biomater. Sci. Polym. Ed. 19*, 1411–1424.

(23) Jo, S., and Park, K. (2000) Surface modification using silanated poly(ethylene glycol)s. *Biomaterials 21*, 605–616.

(24) Massia, S. P., Stark, J., and Letbetter, D. S. (2000) Surface-immobilized dextran limits cell adhesion and spreading. *Biomaterials 21*, 2253–2261.

(25) Heinze, T., Liebert, T., Heublein, B., and Hornig, S. (2006) Functional polymers based on dextran. *Polysaccharides II 205*, 199–291.

(26) Monchaux, E., and Vermette, P. (2007) Bioactive microarrays immobilized on low-fouling surfaces to study specific endothelial cell adhesion. *Biomacromolecules 8*, 3668–3673.

(27) Monchaux, E., and Vermette, P. (2008) Cell adhesion resistance mechanisms using arrays of dextran-derivative layers. *J. Biomed. Mater. Res. A 85A*, 1052–1063.

(28) De Crescenzo, G., Litowski, J. R., Hodges, R. S., and O'Connor-McCourt, M. D. (2003) Real-time monitoring of the interactions of two-stranded *de novo* designed coiled-coils: Effect of chain length on the kinetic and thermodynamic constants of binding. *Biochemistry 42*, 1754–1763.

(29) Surugiu, L., Dey, E. S., Svitel, J., Pirvutoiu, S., and Danielsson, B. (2001) Dextran-modified surface for highly sensitive chemiluminescent ELISA. *Analyst 126*, 1633–1635.

(30) Liberelle, B., Banquy, X., and Giasson, S. (2008) Stability of silanols and grafted alkylsilane monolayers on plasma-activated mica surfaces. *Langmuir 24*, 3280–3288.

(31) Monchaux, E., and Vermette, P. (2007) Development of dextran-derivative arrays to identify physicochemical properties involved in biofouling from serum. *Langmuir 23*, 3290–3297.

(32) Tobiesen, F. A., and Michielsen, S. (2002) Method for grafting poly(acrylic acid) onto nylon 6,6 using amine end groups on nylon surface. *J. Polym. Sci., Part A1: Polym. Chem. 40*, 719–728.

(33) Saha, K., Bender, F., and Gizeli, E. (2003) Comparative study of IgG binding to proteins G and A: Nonequilibrium kinetic and binding constant determination with the acoustic waveguide device. *Anal. Chem. 75*, 835–842.

(34) Kempiak, S. J., Yip, S. C., Backer, J. M., and Segall, J. E. (2003) Local signaling by the EGF receptor. *J. Cell. Biol. 162*, 781–787.

(35) Boucher, C., Ruiz, J.-C., Thibault, M., Buschmann, M. D., Wertheimer, M., Jolicoeur, M., Durocher, Y., and De Crescenzo, G. (2010) Human corneal epithelial cell response to epidermal growth factor tethered via coiled-coil interactions. *Biomaterials 31*, 7021–7031.

BC1002604

Synthesis and Characterization of New Porphyrazine-Gd(III) Conjugates as Multimodal MR Contrast Agents

Ying Song,[†] Hong Zong,[†] Evan R. Trivedi,[†] Benjamin J. Vesper,[‡,§] Emily A. Waters,[†] Anthony G. M. Barrett,[||] James A. Radosevich,[‡,§] Brian M. Hoffman,*[,†] and Thomas J. Meade*[,†,⊥]

Departments of Chemistry, Biochemistry, Molecular Biology, and Cell Biology, Northwestern University, Evanston, Illinois, Center for Molecular Biology of Oral Diseases, College of Dentistry, University of Illinois at Chicago, Chicago, Illinois, Jesse Brown VA Medical Center, Chicago, Illinois, Department of Chemistry, Imperial College of Science, Technology and Medicine, South Kensington, London, England, and Departments of Neurobiology, Physiology, and Radiology, Northwestern University, Evanston, lllinois, United States. Received June 22, 2010; Revised Manuscript Received October 1, 2010

Magnetic resonance imaging (MRI) has long been used clinically and experimentally as a diagnostic tool to obtain three-dimensional, high-resolution images of deep tissues. These images are enhanced by the administration of contrast agents such as paramagnetic Gd(III) complexes. Herein, we describe the preparation of a series of multimodal imaging agents in which paramagnetic Gd(III) complexes are conjugated to a fluorescent tetrapyrrole, namely, a porphyrazine (pz). Zinc metalated pzs conjugated to one, four, or eight paramagnetic Gd(III) complexes are reported. Among these conjugates, Zn-Pz-8Gd(III) exhibits an ionic relaxivity four times that of the monomeric Gd(III) agent, presumably because of increased molecular weight and a molecular relaxivity that is approximately thirty times larger, while retaining the intense electronic absorption and emission of the unmodified pz. Unlike current clinical MR agents, Zn-Pz-1Gd(III) is taken up by cells. This probe demonstrates intracellular fluorescence by confocal microscopy and provides significant contrast enhancement in MR images, as well as marked phototoxicity in assays of cellular viability. These results suggest that pz agents possess a new potential for use in cancer imaging by both MRI and near-infrared (NIR) fluorescence, while acting as a platform for photodynamic therapy.

INTRODUCTION

In the past decade, magnetic resonance imaging (MRI) has become a powerful diagnostic tool in clinical uses such as brain imaging, angiography, and tumor detection. The strength of MRI lies in its ability to produce 3-D anatomical information of human structures noninvasively with exceptional soft tissue contrast (*1*–*3*). Typically, MR contrast agents are applied to enhance the image contrast. Clinical MR contrast agents are primarily Gd(III) complexes that can effectively reduce the relaxation time of water protons, rendering a locally brighter region in an MR image (T_1 weighted). Low sensitivity and the lack of cell specificity, however, remain as barriers to realizing the potential of MR probes.

One approach to improve MR agents is through co-registration of cells and tissues by creating a multimodal agent. Exploiting the strengths of two different imaging modalities, such as MRI and near-infrared (NIR) fluorescence imaging, can increase the accuracy of analysis (*4*–*8*). Conjugating probes that are detectable by different techniques creates agents of multimodality. For example, covalent attachment of a fluorescent probe to an MR agent results in a conjugate that reports cellular and subcellular localization via fluorescence while providing deep anatomical information by MRI (*9*, *10*). In this report, we focus on employing a class of NIR molecules known as the porphyrazines (pzs) to serve as the platform for the attachment of Gd(III) MR contrast agents.

Porphyrazines, or tetraazaporphyrins, resemble the porphyrins in structure, but the *meso*-CH groups linking the pyrrole rings are replaced by nitrogen atoms. The pzs are prepared via a different synthetic route than the porphyrins; this synthetic pathway enables the pzs to be more easily functionalized than the porphyrins (*11*). Pzs exhibit intense optical absorption ($\varepsilon > 10^5$) and fluorescence at short wavelengths (~300−400 nm) and NIR wavelengths (~700−900 nm) (*12*). The NIR emission bands of pzs appear beyond the absorption of hemoglobin ($\lambda \approx 700$ nm) and before the onset of absorption by water ($\lambda \approx 900$ nm), minimizing interference in the imaging of tissues (*13*). In addition, certain pzs accumulate preferentially in tumor tissues and show marked phototoxicity due to their excellent quantum yield of singlet oxygen generation. These properties make pzs extremely attractive as potential tumor optical imaging and photodynamic therapy (PDT) agents (*14*–*17*).

Herein, we exploit the structural flexibility of pzs and apply click chemistry to covalently attach a specific number of Gd(III) complexes to the periphery of zinc metalated pzs. The photophysical properties that make pzs advantageous for biological applications are preserved upon the attachment of Gd(III) complexes, and the resulting Zn-Pz-Gd(III) conjugates have improved magnetic relaxivities relative to current clinical MR contrast agents. Furthermore, these modified Zn-Pz-Gd(III) complexes exhibit enhanced water solubility compared to previously studied pz agents and can be tailored to exhibit selective cellular uptake. Thus, they represent a promising new

* Corresponding author. Thomas J. Meade; Brian M. Hoffman, 2145 Sheridan Rd, Department of Chemistry, Northwestern University, Evanston, IL 60208, Tel: 847-491-2481, Fax: 847-491-3832, E-mail: tmeade@northwestern.edu; bmh@northwestern.edu.

[†] Departments of Chemistry, Biochemistry, Molecular Biology, and Cell Biology, Northwestern University.

[‡] College of Dentistry, University of Illinois at Chicago.

[§] Jesse Brown VAMC.

[||] Imperial College of Science, Technology and Medicine.

[⊥] Departments of Neurobiology, Physiology, and Radiology, Northwestern University.

10.1021/bc1002828 © 2010 American Chemical Society
Published on Web 11/09/2010

class of multimodal and multifunctional diagnostic agents for tumor imaging and therapy.

EXPERIMENTAL PROCEDURES

Materials. All solvents and chemicals were of reagent-grade quality, purchased from Sigma-Aldrich Chemical Co., and used without further purification unless otherwise noted. Thin-layer chromatography (TLC) and column chromatography were performed with 25 DC-Plastikfolien Kieselgel 60 F254 (Merck), and Baxter silica gel 60 Å (230−400 mesh), respectively.

Instrumentation. Nuclear magnetic resonance (NMR) spectra were obtained using a Varian Inova 500 MHz spectrometer. Matrix-assisted laser desorption ionization time-of-flight mass spectra (MALDI-TOF-MS) were recorded on a PE Biosystems Voyager System 6050, using 2,5-dihydroxybenzoic acid as the matrix. High-performance liquid chromatography (HPLC) analyses and preparation were performed on a Varian Prepstar system (Varian Instruments Inc., USA) using a reverse-phase HPLC column (Atlantis C18, Waters, USA). Electrospray ionization mass spectra (ESI-MS) were recorded using a Micromass Quattro II Electronic HPLC/MS/MS mass spectrometer. UV−vis spectra were recorded on an Agilent 8453 UV−vis spectrometer. Fluorescence measurements were conducted on a Hitachi F-4500 fluorescence spectrophotometer. Relaxivity was measured on a Bruker 60 MHz, at 37 °C. Doubly distilled deionized water was obtained from a Millipore-Q system to 18 MΩ·cm resistivity.

Synthesis. 1-Azido-3-aminopropane, Gd(III)-DOTA derivative (MW = 595 g/mol, **Gd595**), and Pzs **1** and **11** were prepared according to literature (*18–20*).

Pz-1acid. *H_2[Pz(A_2); (SC_4O_2Pr)$_3$(SC_4O_2H)$_1$], A = 3,6 Bis(isopropyloxy)-1,2-benzo (***5***).* Thirty milliliters of 0.4 M LiOH aqueous solution was added to a solution of pz **1** (260 mg, 0.20 mmol) in 20 mL THF and stirred at room temperature for 1.5 h. THF was removed by rotary evaporation, and 0.1 M HCl(aq) was added dropwise until the solution was acidic, followed by extraction with CH_2Cl_2. The organic phase was dried with Na_2SO_4 and evaporated under reduced pressure. The resulting residue was purified by column chromatography on silica gel (eluent AcOEt/CH_2Cl_2 = 5:95, MeOH/CH_2Cl_2 = 1/99) to give **5** as a green solid (50 mg, 20%). 145 mg starting material **1** was recovered from the column chromatography. ^{1}H NMR (400 MHz, $CDCl_3$) δ −0.52 (br s, 2H), 0.73 (m, 9H), 1.40 (m, 6H), 1.79 (m, 24H), 1.98 (m, 8H), 2.57 (m, 8H), 3.83 (m, 6H), 4.21 (m, 8H), 5.26 (sept, J = 5.6 Hz, 4H), 7.71 (d, J = 5.6 Hz, 4H); APCI-MS m/z 1245.5 (M + H$^+$) calcd for $C_{61}H_{81}N_8O_{12}S_4$ 1245.5.

Pz-1azide. *H_2[Pz(A_2); (SC_4O_2Pr)$_3$($SC_4ONHC_3N_3$)$_1$], A = 3,6 Bis(isopropyloxy)-1,2-benzo.* Pz-1acid **5** (40 mg, 0.032 mmol), *N*-hydroxysuccinimide (NHS) (18 mg, 0.16 mmol), and *N,N′*-dicyclohexylcarbodiimide (DCC) (33 mg, 0.16 mmol) were dissolved in 5 mL of THF and stirred at room temperature overnight. The mixture was concentrated to dryness and redissolved in CH_2Cl_2. The mixture was filtered, and the solid was washed with CH_2Cl_2. The filtrate and washings were combined, evaporated to dryness under reduced pressure, and dissolved in 4 mL of THF. 1-Azido-3-aminopropane (16 mg, 0.16 mmol), dissolved in 1 mL of THF, was added, and the mixture was stirred at room temperature for 2 h. The final mixture was concentrated and purified by TLC on silica gel (eluent CH_3OH/CH_2Cl_2 = 5/95) to give **Pz-1azide** as a green solid (34 mg, 80%). ^{1}H NMR (500 MHz, $CDCl_3$) δ −0.52 (br s, 2H), 0.75 (m, 9H), 1.45 (m, 8H), 1.81 (m, 24H), 2.00 (sept, J = 7.0 Hz, 8H), 2.57 (t, J = 7.5 Hz, 6H), 2.61 (t, J = 7.5 Hz, 2H), 3.01 (m, 4H), 3.85 (m, 6H), 4.01 (t, J = 6.5 Hz, 2H), 4.22 (t, J = 7.0 Hz, 4H), 4.29 (t, J = 7.0 Hz, 2H), 5.30 (m, 4H), 6.35 (t, J = 6.0 Hz, 1H), 7.59 (m, 4H); ^{13}C NMR (500 MHz, $CDCl_3$) δ 10.5, 22.0, 23.01, 23.03, 23.1, 25.8, 28.9, 30.0, 33.0, 33.2, 34.9, 35.0, 36.9, 49.2, 66.1, 66.3, 72.5, 72.6, 73.6, 118.8, 118.6, 118.4, 120.1, 128.7, 137.6, 139.2, 140.0, 149.4, 149.9, 150.4, 173.0, 173.3, 173.5; MALDI-MS m/z 1327.6 (M + H$^+$) calcd for $C_{64}H_{87}N_{12}O_{11}S_4$ 1327.5.

Zn-Pz-1acid. *Zn[Pz(A_2); (SC_4O_2Pr)$_3$($SC_4ONHC_3N_3$)$_1$], A = 3,6 Bis(isopropyloxy)-1,2-benzo (***6***).* **Pz-1azide** (34 mg, 0.026 mmol) and 10 equiv of zinc chloride were dissolved in 5 mL of DMF. The solution was stirred at room temperature under nitrogen. The metalation procedure was monitored by UV−vis spectroscopy (24−36 h). The mixture was evaporated to dryness under reduced pressure, dissolved in CH_2Cl_2, and twice washed with H_2O. The organic phase was concentrated and purified by TLC on silica gel (eluent CH_3OH/CH_2Cl_2 = 5/95) to give **6** as a green solid (28 mg, 86%). ^{1}H NMR (500 MHz, $CDCl_3$) 0.71 (m, 9H), 1.40 (m, 8H), 1.82 (m, 24H), 1.98 (m, 8H), 2.51 (m, 8H), 3.34 (m, 4H), 3.67 (m, 6H), 4.16 (m, 8H), 5.31 (m, 4H), 6.15 (s, 1H), 7.79 (d, J = 5.0 Hz, 2H), 7.56 (s, 2H); ^{13}C NMR (500 MHz, $CDCl_3$) δ 10.4, 10.5, 22.0, 22.96, 23.04, 23.1, 25.8, 25.9, 30.0, 33.1, 35.0, 36.3, 48.5, 66.1, 66.2, 72.2, 72.4, 73.6, 128.9, 130.0, 140.9, 149.7, 149.9, 150.6, 172.7, 173.55, 173.61; ESI-MS m/z 1389.8 (M + H$^+$) calcd for $C_{64}H_{85}N_{12}O_{11}S_4Zn$ 1389.5.

Zn-Pz-1Gd(III). *Zn[Pz(A_2); (SC_4O_2Pr)$_3$(SC_4ONHC_3Gd)$_1$], A = 3,6 Bis(isopropyloxy)-1,2-benzo.* Gd595 (17.0 mg, 0.029 mmol), copper sulfate (1.9 mg, 0.012 mmol), sodium ascorbate (3.4 mg, 0.044 mmol), and pz **6** (13.0 mg, 0.009 mmol) were dissolved in 4 mL of water/DMF (v/v = 1:1). The reaction mixture was heated in an oil bath at 70 °C overnight. After cooling, the reaction mixture was loaded into a dialysis bag with MWCO 100 and dialyzed for 48 h against Millipore water. The final reaction mixture was reconcentrated and passed through a sephadex LH20 column using MeOH as the eluent to give **Zn-Pz-1Gd(III)** as a green solid (86.1%). MALDI-MS m/z 1985.8 (M + H$^+$) calcd for $C_{83}H_{113}GdN_{17}O_{18}S_4Zn$ 1985.6.

Pz-4azide. *H_2[Pz(A_2); ($SC_4ONHC_3N_3$)$_4$], A = 3,6 Bis(isopropyloxy)-1,2-benzo.* Pz **2** (44 mg, 0.039 mmol), *N*-hydroxysuccinimide (NHS) (90 mg, 0.79 mmol), and *N,N′*-dicyclohexylcarbodiimide (DCC) (55 mg, 0.79 mmol) were dissolved in 10 mL of THF and stirred at room temperature overnight. The mixture was concentrated to dryness and redissolved in CH_2Cl_2. The resulting suspension was filtered, and the solid was washed with CH_2Cl_2. The filtrate and washings were combined, evaporated to dryness under reduced pressure, and redissolved in 5 mL of THF. 1-Azido-3-aminopropane (53 mg, 0.79 mmol) in 5 mL of THF was added, and the mixture was stirred at room temperature for 2 h. The mixture was concentrated and purified by column chromatography on silica gel (eluent CH_3OH/CH_2Cl_2 = 2/98) to give **Pz-4azide** as a green solid (31 mg, 54%). ^{1}H NMR (500 MHz, $CDCl_3$) δ −0.54 (br s, 2H), 1.49 (m, 8H), 1.79 (d, J = 6.5 Hz, 24H), 1.96 (m, 8H), 2.53 (t, J = 7.5 Hz, 8H), 3.01 (m, 16H), 4.15 (m, 8H), 5.26 (sept, J = 6.0 Hz, 4H), 6.36 (s, 4H), 7.57 (s, 4H); ^{13}C NMR (500 MHz, $CDCl_3$) δ 22.1, 23.1, 26.2, 28.8, 30.0, 35.0, 35.5, 37.0, 49.3, 73.2, 119.5, 129.0, 139.1, 149.9, 172.9; ESI-MS m/z 1447.9 (M + H$^+$) calcd for $C_{64}H_{87}N_{24}O_8S_4$ 1447.6.

Zn-Pz-4azide. *Zn[Pz(A_2); ($SC_4ONHC_3N_3$)$_4$], A = 3,6 Bis(isopropyloxy)-1,2-benzo, (***3***).* **Pz-4azide** (29 mg, 0.019 mmol) and 10 equiv of zinc chloride were dissolved in 5 mL of DMF. The resulting solution was heated to 70 °C under nitrogen. The metalation procedure was monitored by UV−vis spectroscopy (24−36 h). The mixture was evaporated to dryness under reduced pressure and redissolved in CH_2Cl_2. The solution was washed with equal volumes of brine twice. The organic phase was dried over Na_2SO_4, concentrated under reduced pressure, and purified by TLC on silica gel (eluent CH_3OH/CH_2Cl_2 = 5/95) to give **3** as a green solid (26 mg, 86%). ^{1}H NMR (500 MHz, $CDCl_3$) δ 1.12 (m, 8H), 1.37 (m, 8H), 1.71 (d, J = 6.0

Hz, 24H), 2.00 (m, 8H), 2.51 (m, 8H), 2.83 (t, $J = 6.0$ Hz, 8H), 3.75 (m, 8H), 5.27 (sept, $J = 6.0$ Hz, 4H), 6.29 (t, $J = 5.5$ Hz, 4H), 7.52 (s, 4H); ^{13}C NMR (500 MHz, $CDCl_3$) δ 23.0, 25.7, 28.4, 34.4, 35.2, 36.8, 49.0, 73.3, 119.1, 129.2, 149.7, 154.6, 156.1, 172.8; ESI-MS *m/z* 1509.3 ($M + H^+$) calcd for $C_{64}H_{85}N_{24}O_8S_4Zn$ 1509.5.

Zn-Pz-4Gd(III). *Zn[Pz(A$_2$); (SC$_4$ONHC$_3$Gd)$_4$], A = 3,6 Bis-(isopropyloxy)-1,2-benzo.* Gd595 (44 mg, 0.074 mmol), copper sulfate (3.8 mg, 0.024 mmol), sodium ascorbate (8.7 mg, 0.044 mmol). and Zn-Pz-4azide **3** (25.0 mg, 0.017 mmol) were dissolved in 8 mL of a water/DMF (v/v = 1:1) mixture. The reaction mixture was heated in an oil bath at 70 °C overnight. After cooling, the reaction mixture was loaded into a dialysis bag with MWCO 100 and dialyzed for 48 h against Millipore water. The resulting solution was reconcentrated and run through a Chelax column to ensure the complete removal of copper ions. Finally, the product was purified with reverse-phase HPLC using a water/acetonitrile gradient to give **Zn-Pz-4Gd** as a green solid (40 mg, 62%). MALDI-TOF-MS *m/z* 3893.1 ($M + H^+$) calcd for $C_{140}H_{197}Gd_4N_{44}O_{36}S_4Zn$ 3894.0.

Bis(2-azidoethyl) Amine. A solution of bis(2-chloroethyl) amine hydrochloride (3.57 g, 20.0 mmol) and sodium azide (7.80 g, 120 mmol) in 20 mL H_2O was heated to 80 °C for 15 h. After removing the water by distillation, the reaction mixture was cooled in an ice bath. Diethyl ether (20 mL) and KOH (pellets 1.6 g) were added in small portions. The solution was stirred at room temperature for 2 h. After separation of the organic phase, the aqueous layer was extracted with diethyl ether. The combined organic layers were dried over Na_2SO_4, concentrated, and purified by column chromatography (eluent AcOEt/CH_2Cl_2 = 5/95) to give **6** as a pale yellow liquid (2.05 g, 66%). ^{1}H NMR (500 MHz, $CDCl_3$) δ 1.56 (s, 1H), 2.81 (t, $J = 6.0$ Hz, 4H), 3.42 (t, $J = 6.0$ Hz, 4H); ^{13}C NMR (500 MHz, $CDCl_3$) δ 48.4, 51.6, 53.7; ESI-MS *m/z* 156.2 ($M + H^+$) calcd for $C_4H_9N_7$ 156.1.

Pz-8azide. *H$_2$[Pz(A$_2$); (SC$_4$ON(C$_2$N$_3$)$_2$)$_4$], A = 3,6 Bis(isopropyloxy)-1,2-benzo.* Pz **2** (64 mg, 0.057 mmol), 1-hydroxybenzotriazol hydrate (HOBT) (62 mg, 0.46 mmol), dicyclohexylcarbodiimide (DCC) (94 mg, 0.46 mmol), and **6** (178 mg, 1.15 mmol) were dissolved in 10 mL of THF and stirred at room temperature for 2 days. The suspension was filtered and washed with cold THF. The combined filtrates were evaporated to dryness and purified by column chromatography on silica gel (eluent CH_3OH/CH_2Cl_2 = 2/98) followed by TLC (eluent CH_3OH/CH_2Cl_2 = 2/98) to give **Pz-8azide** as a green solid (53 mg, 56%). ^{1}H NMR (500 MHz, $CDCl_3$) δ 0.53 (br s, 2H), 1.80 (d, $J = 6.0$ Hz, 24H), 1.97 (m, 8H), 2.66 (t, $J = 7.0$ Hz, 8H), 3.33 (m, 32H), 4.28 (t, $J = 6.5$ Hz, 8H), 5.27 (sept, $J = 6.0$ Hz, 4H), 7.58 (s, 4H); ^{13}C NMR (500 MHz, $CDCl_3$) δ 23.1, 25.6, 31.5, 35.2, 46.4, 48.2, 49.5, 50.1, 72.8, 128.8, 129.9, 138.9, 149.9, 173.0; ESI-MS *m/z* 1667.5 ($M + H^+$) calcd for $C_{68}H_{91}N_{36}O_8S_4$ 1667.7.

Zn-Pz-8azide. *Zn[Pz(A$_2$); (SC$_4$ON(C$_2$N$_3$)$_2$)$_4$], A = 3,6 Bis(isopropyloxy)-1,2-benzo, (**4**).* **Pz-8azide** (37 mg, 0.022 mmol) and 10 equiv of zinc chloride were dissolved in 5 mL DMF. The solution was heated to 70 °C under nitrogen protection. The metalation procedure was monitored by UV−vis spectroscopy (24−36 h). The mixture was evaporated to dryness under reduced pressure and redissolved in CH_2Cl_2. The solution was washed with equal volumes of H_2O twice. The organic phase was concentrated and purified by thin-layer chromatography on silica gel (eluent CH_3OH/CH_2Cl_2 = 5/95) to give **4** as a green solid (33 mg, 86%). ^{1}H NMR (500 MHz, $CDCl_3$) δ 1.71 (m, 8H), 1.79 (d, $J = 6.5$ Hz, 24H), 2.44 (m, 8H), 2.95 (m, 16H), 3.10 (m, 16H), 4.10 (m, 8H), 5.33 (sept, $J = 6.0$ Hz, 4H), 7.58 (s, 4H); ^{13}C NMR (500 MHz, $CDCl_3$) δ 23.0, 25.5, 31.3, 35.2, 46.2, 48.1, 49.2, 49.8, 72.5, 128.9, 149.8, 154.6, 155.8, 173.0; ESI-MS *m/z* 1729.8 ($M + H^+$) calcd for $C_{68}H_{89}N_{36}O_8S_4Zn$ 1729.6.

Zn-Pz-8Gd(III). *Zn[Pz(A$_2$); (SC$_4$ON(C$_2$Gd)$_2$)$_4$], A = 3,6 Bis-(isopropyloxy)-1,2-benzo.* Gd595 (97 mg, 0.16 mmol), copper sulfate (5.6 mg, 0.035 mmol), sodium ascorbate (19 mg, 0.098 mmol), and Zn-Pz-8azide **5** (31.0 mg, 0.019 mmol) were dissolved in 10 mL of water/DMF (1:1) mixture. The reaction mixture was heated in an oil bath at 70 °C overnight. After cooling, the reaction mixture was loaded into a dialysis bag with MWCO 100 and dialyzed for 48 h against Millipore water. The resulting solution was reconcentrated and run through a Chelex column to ensure the complete removal of copper ions. The product was purified with reverse-phase HPLC using water/acetonitrile gradient to give **Zn-Pz-8Gd** as a green solid (60 mg, 50%). MALDI-TOF-MS *m/z* 6496.5 ($M + H^+$) calcd for $C_{220}H_{313}Gd_8N_{76}O_{64}S_4Zn$ 6498.6.

Relaxivity (r_1). Solutions of Zn-Pz-*n*Gd(III) conjugates were prepared in 500 μL of Millipore water for T_1 acquisition. T_1 (spin−lattice relaxation time) was determined at 60 MHz (1.41 T) and 37 °C using an inversion recovery pulse sequence on a Bruker mq60 minispec NMR spectrometer with 4 averages, 15 s repetition time, and 10 data points (Bruker Canada; Milton, Ontario, Canada). The starting and final Gd(III) concentrations of the solutions were determined using inductively coupled plasma-mass spectrometer (ICP-MS). The inverse of the longitudinal relaxation time ($1/T_1$, s^{-1}) was plotted against Gd(III) concentration (mM) and fitted to a straight line with $R^2 > 0.99$. The slope of the fitted line was recorded as the relaxivity, r_1.

General Cell Culture. Cell lines were obtained from American Type Culture Collection (Manassas, VA, USA), and all media, Dulbecco's phosphate buffered saline (DPBS), and 0.25% trypsin/EDTA solutions were purchased from Invitrogen (Carlsbad, CA, USA). Human pulmonary adenocarcinoma cell line (A549) and a SV40 transformed embryonic cell line (WI-38 VA13) were used in this study. The A549 cell line was grown in RPMI 1640 media supplemented with 10% fetal calf serum heat inactivated at 56 °C for 30 min, 2 mM L-glutamine, 100 μg/mL streptomycin, 100 U/mL penicillin, and 2.5 μg/mL Amphotericin B solution. The WI-38 VA13 cell line was grown in Minimum Essential Medium (MEM) with Earle's salts supplemented with 10% fetal calf serum heat-inactivated at 56 °C for 30 min, 2 mM L-glutamine, 100 μg/mL streptomycin, 100 U/mL penicillin, and 2.5 μg/mL Amphotericin B solution, as well as 100 μM MEM nonessential amino acids and 1 mM sodium pyruvate. All experiments were performed in the aforementioned cell-specific media in a 5.0% CO_2 incubator operating at 37 °C.

Confocal Laser Scanning Microscopy (CLSM). Cells were seeded on glass coverslips in round 10 cm^2 plates and allowed to grow to 60−80% confluency. Media solutions for staining cells were prepared from a 5 mM solution in water for Zn-Pz-4Gd(III) and Zn-Pz-8Gd(III), in DMSO for Zn-Pz-1Gd(III). After 24 h incubation with pz-Gd(III) complexes, coverslips were rinsed twice with PBS and placed onto microscope slides with imaging buffer for live cell imaging. The imaging buffer used for live-cell imaging was prepared using a literature procedure (*21*). Images were acquired on a Zeiss LSM 510 inverted microscope (computer controlled using Zeiss Zen software) equipped with a mode-locked Mai Tai DeepSee Ti: sapphire two-photon laser (Spectra Physics, Mountain View, CA, USA). Specifically, pz-Gd(III) conjugates were excited using the 750 nm wavelength of the two-photon laser and imaged with a PMT through a band-pass 390−465 nm emission filter. Images of cells stained with pz-Gd(III)s and associated vehicle controls were taken at the same gain and amplitude settings.

MR Imaging. For cell phantoms, ~1.5 × 10^6 cells were incubated with 50 or 100 μM [Gd(III)] concentrations of Pz-Gd(III) conjugates for 18 h at 37 °C, rinsed three times with DPBS buffer, and harvested with trypsin. After the addition of complete media (1.0 mL total volume), cells were added to flame-sealed 53/4″ Pasteur pipettes and centrifuged at 4.0 °C and 100 × *g* for 5 min to form pellets with a diameter of approximately 1 mm.

Cell pellets were arranged around a tube of water and imaged on a 4.7 T (200 MHz) Bruker Biospec 4740 MR imager (Bruker Corporation, Billerica, MA). The radiofrequency coil used was a volume coil with 38 mm internal diameter (Rapid MR International, Columbus, OH). Images were acquired by a standard T_2-weighted multislice multiecho sequence with TR = 750 ms, TE ranging from 15−60 ms, matrix size 128 × 128, FOV = 25 × 25 × 1 mm^3.

Inductively Coupled Plasma−Mass Spectrometry (ICP-MS). ICP-MS was performed on either a computer-controlled (*Plasmalab* software) Thermo PQ ExCell ICP-MS (Thermo Fisher Scientific, Waltham, MA) equipped with a CETAC 500 autosampler or a computer-controlled (*Plasmalab* software) Thermo X series II ICP-MS equipped with an ESI SC-2 autosampler (Omaha, NE, USA). Each sample was acquired using 1 survey run (10 sweeps) and 3 main (peak jumping) runs (100 sweeps). The isotopes selected were ^{156,157}Gd for acquisition, with ^{115}In, ^{165}Ho, and ^{209}Bi as internal standards for data interpolation and machine stability.

Cell Viability Assays. Zn-Pz-*n*Gd(III) solutions were prepared as 5 mM stock solutions in either DMSO [Zn-Pz-1Gd(III)] or H_2O [Zn-Pz-4Gd(III), Zn-Pz-8Gd(III)]. A549 and WI-38 VA13 cells were seeded into 96-well microtiter plates and grown until they were approximately 70% confluent. The plates were treated in the dark with 50, 25, or 12.5 μM pz-Gd(III) or a volume of DMSO or H_2O equivalent to the volume of compound added at these concentrations. The plates were incubated for 72 h, after which the media was removed and replaced with 100 μL of a 2 g/L solution of 3-[4,5-dimethylthiazol-2-yl]-2,5-diphenyltetrazolium bromide (MTT) in DPBS. The plates were then incubated for 5 h. During this incubation, purple formazan crystals formed because of the cleaving of the tetrazolium ring of the MTT molecules by the mitochondrial dehydrogenases of viable cells. Following the 5 h incubation, the supernatant was removed and 100 μL of DMSO was added to each well to dissolve the remaining formazan crystals. A SpectraMax Plus 384 spectrophotometer (Molecular Devices, Sunnyvale, CA, USA) was used to record the absorbance at 540 nm for each well. Each data point represents the average of at least four microtiter wells for each plate, and a minimum of two independent trials were carried out for each experiment. Data was normalized and averaged such that the final reported values represent at least eight independent values for each reported condition, for each cell line. Data points lying outside of two standard deviations from the mean were removed.

Phototoxicity Assays. Zn-Pz-*n*Gd(III) solutions were prepared as 5 mM stock solutions in either DMSO [Zn-Pz-1Gd(III)] or H_2O [Zn-Pz-4Gd(III) and Zn-Pz-8Gd(III)]. Two identical 96-well microtiter plates were seeded with A549 and WI-38 VA13 cells; the cells were established to ~70% confluency. The cells were treated with 50 μM Pz-Gd(III), and the plates were incubated for an additional 24 h. A volume of DMSO or H_2O equivalent to 50 μM were used as negative controls, and Photofrin (HpD, 50 μM) was used as a positive control. Following the 24 h incubation, aluminum foil was wrapped around the sides and top of the first plate, leaving the bottom of the plate uncovered for illumination. The second plate was completely wrapped in aluminum foil to inhibit light from reaching the cells and served as the dark control. The two plates were then placed on top of a standard X-ray illuminator (consisting of four 15 W bulbs, ~3600 total lumens) and exposed to 10 min of white light. The plates were placed back into the incubator for an additional 24 h, after which time MTT cytotoxicity assays were performed as described above. Each data point represents the average of at least four microtiter wells for each plate. Data was normalized and averaged such that the final reported values represent at least four independent values for each reported condition and for each cell line. Data points lying outside 2 standard deviations from the mean were removed.

RESULTS AND DISCUSSION

Synthesis. Since the synthesis of the first optical/MRI contrast agent, a monomeric Gd(III) complex conjugated with tetramethylrhodamine (*22*), polymeric MR-optical agents were developed based on polylysine and dextran to increase the sensitivity of the agents (*10, 23*). Conjugation of Gd(III) complexes with polymer backbones was carried out under peptide coupling conditions in most cases (*24*). These methods, however, normally resulted in a polydispersed mixture with poor batch-to-batch reproducibility, rendering the determination of the Gd(III)-to-fluorophore ratio difficult. In the present work, the coupling procedure adopts click chemistry where multiple Gd(III)-alkyne complexes are simultaneously attached to a pz-azide in high yield to produce monodispersed MR-optical agents (*19, 25, 26*). This click chemistry approach provides a facile means to generate new MRI contrast agents with high relaxivities and discrete molecular weights.

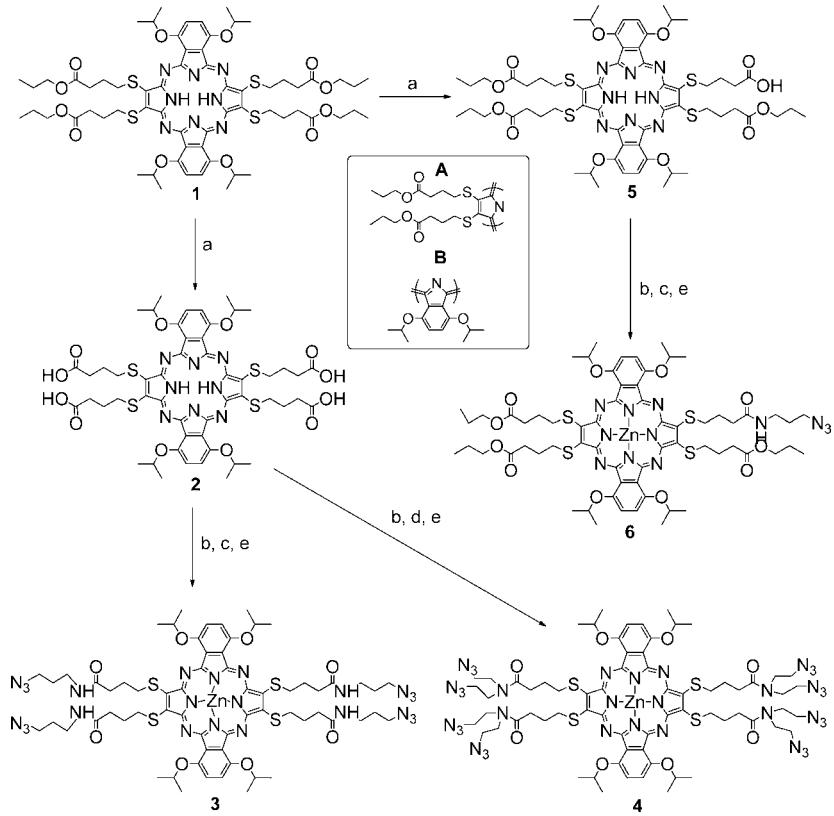
The synthesis starts with A_2B_2 pz **1**, prepared following literature procedures, where A has an appended sulfide moiety and B is a fused benzo group (Scheme 1) (*20*). Hydrolysis with excess LiOH(aq) affords **2** with four terminal acids, while sub-stoichiometric hydrolysis produces **5** with one terminal acid. Peptide coupling of **2** and **5** with 1-azido-3-aminopropane followed by metalation with zinc chloride yields Zn-Pz-4azide **3** and Zn-Pz-1azide **6**, respectively. In a similar fashion, coupling of **2** with bis(2-azido ethyl)amine yields Zn-Pz-8azide **4**.

Initial attempts to apply click chemistry to metal-free azido-pzs showed that pzs would sequester copper ions, resulting in a mixture of metalated and nonmetalated products. Therefore, the pz azides were metalated with zinc(II) prior to conjugation with Gd(III) complexes via click chemistry. Trans-metalation of Zn-Pzs in the presence of catalytic copper salts was not observed. In later attempts, stoichiometric copper salt was used to ensure that pzs were fully metalated and Cu-Pz-*n*Gd(III) (*n* = 4, 8) conjugates were characterized. Cu-Pz and Zn-Pz possess different optical properties, but their Gd(III) conjugates exhibit similarities in relaxivity (Table 2 and Supporting Information, Table SI-1).

Click chemistry between the Gd(III) alkyne analogue, Gd595, and pz substrates **3**, **4**, and **6** was carried out in a DMF/water (v/v = 1:1) mixture (Scheme 2). The reaction was highly efficient in conjugating one, four, and eight Gd595 molecules at the pz periphery in 50−60% yield. The resulting Zn-Pz-4Gd(III) and Zn-Pz-8Gd(III) complexes are freely water-soluble suggesting that the conjugates could be administered intravenously without the addition of a co-solvent. Zn-Pz-1Gd(III) exhibited limited water solubility but could be dissolved in a water/DMSO mixture.

UV Absorption and Fluorescence. The electronic absorption and emission features of Zn-Pz-*n*Gd(III) (*n* = 1, 4, 8) are summarized in Table 1. Similar to previously reported pzs, Zn-Pz-*n*Gd(III) conjugates display an intense Soret band (340 nm) and a pair of Q-bands (~670 nm, ~780 nm). Both Zn-Pz-

Scheme 1. Synthetic Scheme for the Preparation of Pz Azide Substrates[a]



[a] Conditions: (a) LiOH, H_2O, THF; (b) DCC, NHS, THF; (c) 1-azido-3-aminopropane, THF; (d) bis(2-azidoethyl) amine, THF; (e) $ZnCl_2$, DMF. (The inserted figure shows the building blocks of A_2B_2 pz.)

4Gd(III) and Zn-Pz-8Gd(III) exhibit dual fluorescence in water (Table 1 and Supporting Information Figure SI-5). Short-wavelength fluorescence was observed at $\lambda \approx 440$ nm, and long-wavelength near-infrared (NIR) fluorescence occurred at $\lambda \approx 815$ nm. With Zn-Pz-1Gd(III), both emission peaks were present in DMSO solution, but the 813 nm emission peak was quenched in aqueous solution (Figure 1 and Supporting Information Figure SI-6).

The NIR emission from a hydrophobic pz such as **1** is typically sensitive to the local polar environment and is quenched by water due to a combination of hydrogen bonding and aggregation (*27*). The observation of NIR fluorescence in water from Zn-Pz-*n*Gd(III) ($n = 4, 8$) compounds suggests that the hydrophilic Gd(III) complexes tethered to the pz periphery protect the pz core from interaction with water and consequent quenching. According to the Lippert-Mataga relationship, a fluorophore's stokes shift increases with the polarity of its local environment (*28*). The stokes shift of the pz-Gd(III) conjugates decrease with added Gd(III)-chelates to the periphery with Zn-Pz-8Gd(III) exhibiting the smallest effective stokes shift (in H_2O). This is in agreement with the notion that appended Gd(III) complexes protect the pz core from nonradiative de-excitation in aqueous solutions. Cu-Pz-*n*Gd(III) ($n = 4, 8$) conjugates showed weak, if any, NIR fluorescence, presumably due to enhanced spin−orbit coupling to the triplet state by the paramagnetic Cu(II). This characteristic of Cu-Pz-Gd(III) limits application in fluorescence imaging (see Supporting Information Table SI-2, Figure SI-5). However, Cu-Pz-Gd(III) conjugates can serve as model compounds for the preparation of MR-PET (positron emission topography) agents, that use ^{64}Cu as the radionuclide.

Relaxivity Properties. The efficiency of a contrast agent in reducing the longitudinal relaxation time of water protons is measured by the property known as relaxivity ($mM^{-1}\ s^{-1}$). Several major parameters influence the relaxivity, including the number of coordinated water molecules, *q*; rotational correlation time, τ_R; and mean water residence time, τ_m. Solomon-Bloembergen-Morgan theory predicts that an increase in rotational correlation time, τ_r, by slowing down the molecular tumbling of an agent in solution will result in an increase in relaxivity (*29*). A common approach to reduce molecular tumbling is by attaching small Gd(III) complexes to a macromolecule through rigid linkages (*19*, *25*, *30*).

The relaxivities of Zn-Pz-*n*Gd(III) ($n = 1, 4, 8$) at 60 MHz, 37 °C, are summarized in Table 2. As expected, the molecular relaxivities of these conjugates increase nonlinearly with the number of appended Gd(III) complexes, presumably because of increased molecular weights. Zn-Pz-1Gd(III) showed an ionic relaxivity of 4.2 $mM^{-1}\ s^{-1}$ per Gd(III), which is slightly higher than the monomeric Gd595. Zn-Pz-4Gd(III) and Zn-Pz-8Gd(III) exhibited enhanced ionic relaxivities of 10.5 $mM^{-1}\ s^{-1}$ and 12.8 $mM^{-1}\ s^{-1}$, respectively. These ionic relaxivities are ∼3−4 times higher than that of the clinically employed agent DOTA-Gd(III) at the same magnetic field strength (Dotarem, $r_1 = 2.7-3.1$ $mM^{-1}\ s^{-1}$ at 60 MHz, 37 °C; DOTA = 1,4,7,10-tetraazacyclododecane-*N*,*N*′,*N*″,*N*‴-tetraacetic acid), while the molecular relaxivities range up to more than 30-fold greater (*30*). A slight difference in relaxivities was observed between Cu-Pz-*n*Gd(III) and Zn-Pz-*n*Gd(III) ($n = 4, 8$) which is likely due to the paramagnetism of Cu(II) (Supporting Information Table SI-1). Overall, these conjugates exhibit similar relaxivities to the polymer-Gd(III) conjugates reported in the literature (*32*–*34*).

Confocal Fluorescence Microscopy. Initial cellular localization and uptake studies of Zn-Pz-*n*Gd(III) conjugates were performed using confocal fluorescence microscopy in WI-38

Scheme 2. Synthetic Scheme for the Preparation of Zn-Pz-*n*Gd(III) ($n = 1, 4, 8$) via Click Chemistry

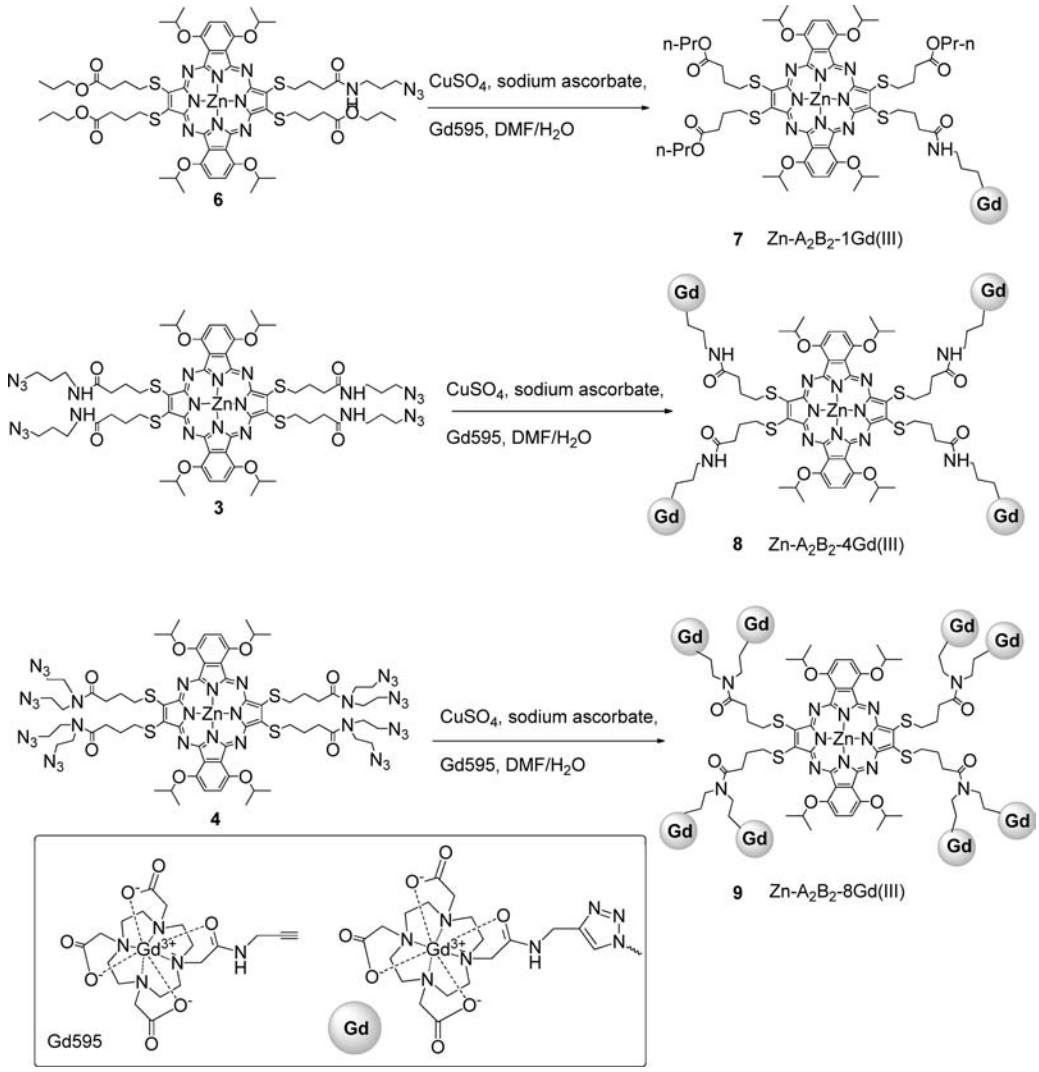


Table 1. Summary of UV−vis/NIR Absorption and Emission Peaks of Zn-Pz-*n*Gd(III) Complexes ($n = 4, 8$, in water; $n = 1$, in DMSO)

compounds	absorption/nm	emission/nm	$\nu_a - \nu_f$ (cm^{-1})
Zn-Pz-1Gd(III)	348, 668, 765	432, 813	772
Zn-Pz-4Gd(III)	346, 678, 783	460, 813	471
Zn-Pz-8Gd(III)	347, 683, 790	458, 816	403
*Free Pz (**1**)	340, 654, 794	444, 826	489

* Measured in CH_2Cl_2.

VA13 cells, a non-tumorigenic, embryonic fibroblast-like human cell line. Cells were incubated with 50 μM Zn-Pz-*n*Gd(III) ($n = 1, 4, 8$) for 24 h and imaged for both short-wavelength (390−465 nm) and NIR (>700 nm) fluorescence. Cells that were stained with Zn-Pz-1Gd(III) displayed the short-wavelength pz fluorescence but very little NIR emission (Figure 2). This result revealed that Zn-Pz-1Gd(III) is incorporated inside the cells. Intracellular pz fluorescence is not observed from Zn-Pz-*n*Gd(III) ($n = 4, 8$) under the same condition, suggesting no cellular uptake of these two conjugates (see Supporting Information Figure SI-7).

Although the mechanism for cellular uptake and subcellular localization of the pz-Gd(III) conjugates has not been investigated, evidence has shown that low-density lipoprotein (LDL) can facilitate cellular uptake of pz analogues (*17*). In these previous studies, the hydrophobic portions of pzs were found to interact with LDL, leading to receptor-mediated cellular uptake. It is likely that Zn-Pz-1Gd(III) follows a similar uptake mechanism, involving the hydrophobic pz core of the compound. The fact that Zn-Pz-*n*Gd(III) ($n = 4, 8$) showed no observable cellular uptake further indicates that introducing a higher number of Gd(III) complexes can prohibit cellular uptake, because of either the hindered interaction of the pz with LDL or the

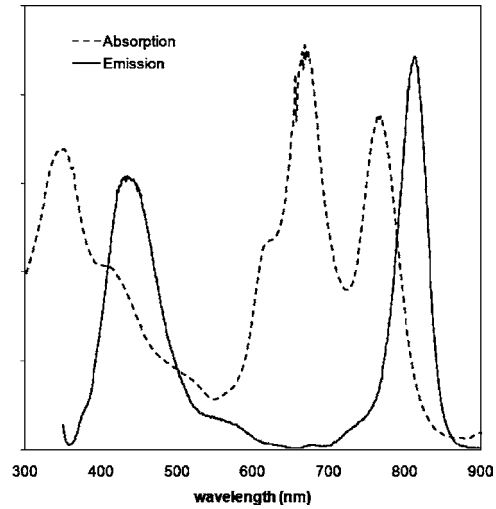


Figure 1. UV−vis/NIR absorption and emission spectrum of Zn-Pz-1Gd(III) in DMSO. (dotted line, absorption; continuous line, fluorescence emission; excited at 340 nm.)

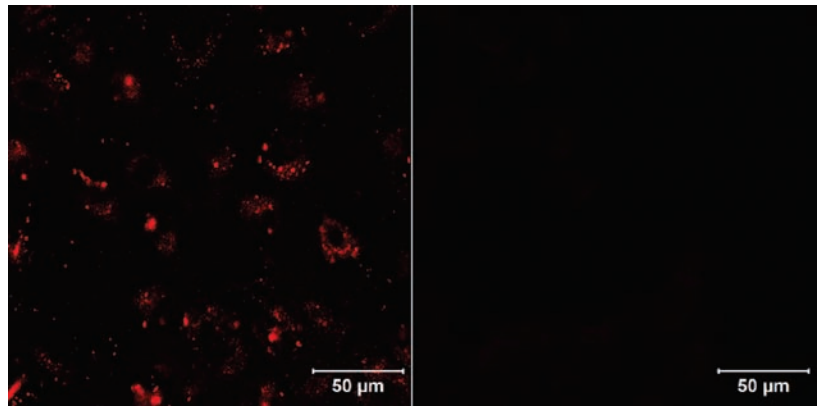


Figure 2. False-red images taken with confocal fluorescence microscopy of WI38-VA13 human embryonic fibroblast-like cells treated with 50 μM Zn-Pz-1Gd(III) for 24 h (left) versus control (right) (750 nm two-photon excitation, 390−465 nm emission).

Table 2. Molecular and Gd(III) Ionic Relaxivity of Zn-Pz-*n*Gd(III) (n = 1, 4, 8) Complexes in Water at 37 °C, 60 MHz

compounds	MW (g/mol)	Gd(III) ionic r_1(mM^{-1} s^{-1})	No. of Gd(III)	molecular r_1(mM^{-1} s^{-1})
Gd595	595.7	3.21	1	3.21
Zn-Pz-1Gd(III)	1985.6	4.2[a]	1	4.2[a]
Zn- Pz-4Gd(III)	3893.9	10.5	4	42
Zn- Pz-8Gd(III)	6496.9	12.8	8	102.4

[a] Measured in DMSO/water, v/v = 1:5.

increased hydrophilicity. Therefore, MR imaging of cell pellets was carried out with Zn-Pz-1Gd(III).

MR Imaging and Cell Uptake. Cell pellets labeled with the Zn-Pz-1Gd(III) over a range of concentrations were imaged on a Bruker Biospec 4.7 T MR imager. Each cell pellet imaged was ~1 mm in diameter and contained ~1.5 × 10^6 cells. Image contrast was highly dependent on the incubation concentration (Figure 3A), with cells incubated at 100 μM of Zn-Pz-1Gd(III) producing a more pronounced contrast enhancement than those incubated at 50 μM in the T_1 weighted image.

To quantify the Gd(III) content in each cell pellet, ICP-MS was employed to determine the amount of Gd(III) per cell. As shown in Figure 3B, Gd(III) per cell increases linearly with the increase in cell incubation concentration. In addition, we have compared the cellular uptake between Zn-Pz-1Gd(III) and DOTA-Gd(III), which is known to be exogenous (Supporting Information Figure SI-8). The result shows that WI-38 VA13 cell uptake was 10-fold greater for Zn-Pz-1Gd(III) than for DOTA-Gd(III) when treated under the same conditions. This finding is consistent with cellular incorporation of Zn-Pz-1Gd(III).

Cellular Viability. MTT assays were performed with WI-38 VA13 cells exposed to varying concentrations of Zn-Pz-*n*Gd(III) (n = 1, 4, 8) over a 72 h period (Figure 4). Control cells were exposed to water or DMSO according to the solvent of the pz-Gd(III) stock solutions. Zn-Pz-*n*Gd(III) (n = 4, 8) showed little effect on cell viability at all three concentrations, namely, 12.5, 25, 50 μM, over 72 h (~90% viable vs control). Zn-Pz-1Gd(III) exhibited dose-dependent toxicity where only 60% of cells remained viable upon 50 μM exposure for 72 h.

Phototoxicity was measured by exposing cells to the conjugates followed by irradiation with white light for 10 min (Figure 5). Given that the Zn-Pz-*n*Gd(III) all contain the same core structure, it would be expected that all three compounds would generate similar levels of singlet oxygen and therefore exhibit similar phototoxicity effects when incorporated into cells. However, only Zn-Pz-1Gd(III) was found to show phototoxicity. Approximately 50% of the cells were killed upon treatment of Zn-Pz-1Gd(III) for 24 h and white light for 10 min. In contrast, nearly all of the cells were killed upon exposure to Photofrin under the same

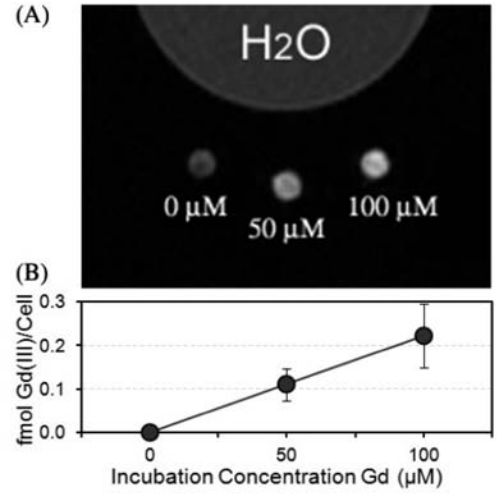


Figure 3. (A) T_1 weighted MR image of WI-38 VA13 cells incubated with 0, 50, and 100 μM of Zn-Pz-1Gd(III) for 24 h at 4.7 T. (B) Cellular uptake of Zn-Pz-1Gd(III) measured by ICP-MS corresponding to the cell pellets in the MR image of (A).

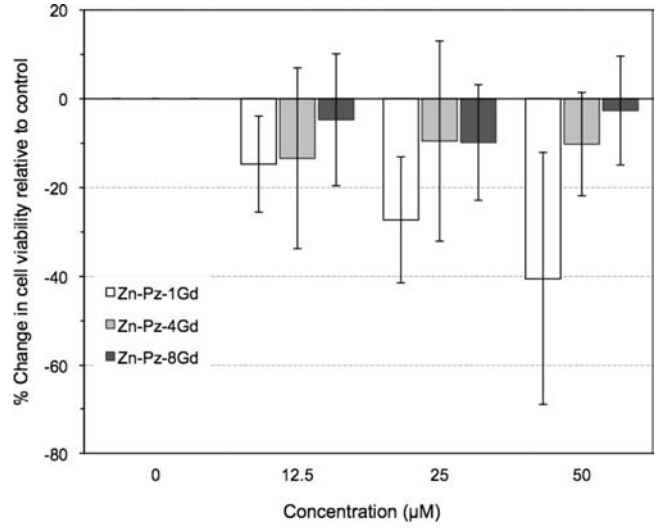


Figure 4. Concentration-dependent dark toxicity of Zn-Pz-*n*Gd(III) (n = 1, 4, 8) in WI-38 VA13 cells. Cells were incubated for 72 h for all three agents.

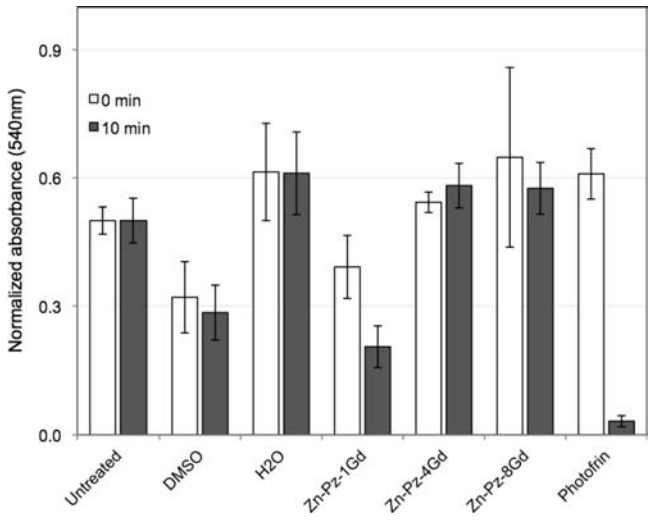


Figure 5. Phototoxicity of Zn-Pz-*n*Gd(III) ($n = 1, 4, 8$) in WI-38 VA13 cells upon 50 μM pz exposure for 24 h, followed by 0 or 10 min of white light exposure. Photofrin was used as a positive control. It is notable that Zn-Pz-1Gd(III) is the only pz-Gd(III) conjugate showing significant phototoxicity.

conditions. The lack of phototoxicity observed for Zn-Pz-4Gd(III) and Zn-Pz-8Gd(III) corresponds to our observation with confocal microscopy and MR contrast that these two conjugates are not taken up by cells, whereas Zn-Pz-1Gd(III) is.

CONCLUSION

The measurements of Pz-based-MRI multimodal probes described herein highlight numerous properties of this unique class of complexes that make them superior to Gd(III)-based MR contrast agents and optical probes. Unlike previously developed polymeric MR-optical multimodal agents, the pzs can be characterized and possess strict batch-to-batch consistency. Furthermore, the photophysical properties that make the pz class of molecules attractive for biological applications are preserved upon addition of the Gd(III) complexes, and the water solubility properties of these compounds are enhanced by the addition of the hydrophilic Gd(III) moieties. The Pz-Gd(III) conjugates possess improved ionic and molecular relaxitivites relative to well-known single-molecule MRI agents. Perhaps most importantly, we show that the biological properties of the conjugates can be tailored to achieve cellular uptake of an MR agent, as exhibited by Zn-Pz-1Gd(III).

These studies show that we have the potential to create a single pz [containing Gd(III) complexes] that can not only function as an MRI agent, but also possess a second moiety that can be used to target specific cell types (i.e., tumors). Furthermore, changing the core pz structure and/or metal ion allows us to control the antitumor functionality of the compound, suggesting that these compounds could be used as PDT agents. Thus, multimodal and multifunctional pzs, such as those described herein, have the potential to serve as dual MRI-NIR/antitumor therapeutic agents capable of targeting specific tumor types.

ACKNOWLEDGMENT

We thank Ellen K. Kohlmeir and Allison S. Harney for helpful discussions. This work was supported by National Institutes of Health Grant 2R01EB005866-05A1and 5 U54 CA1193 41-02 and by the Baxter Healthcare Corporation through the Baxter-Northwestern Alliance (BMH).

Supporting Information Available: Information on Zn-Pz-Gd(III) conjugates in terms of characterization, cell uptake, toxicity details. This material is available free of charge via the Internet at http://pubs.acs.org.

LITERATURE CITED

(1) Mulder, W. J. M., Strijkers, G. J., Griffioen, A. W., van Bloois, L., Molema, G., Storm, G., Koning, G. A., and Nicolay, K. (2004) A Liposomal system for contrast-enhanced magnetic resonance imaging of molecular targets. *Bioconjugate Chem. 15*, 799–860.

(2) Josephson, L., Tung, C. H., Moore, A., and Weissleder, R. (1999) High-efficiency intracellular magnetic labeling with novel superparamagnetic-Tat peptide conjugates. *Bioconjugate Chem. 10*, 186–191.

(3) Mazooz, G., Mehlman, T., Lai, T.-S., Greenberg Charles, S., Dewhirst Mark, W., and Neeman, M. (2005) Development of magnetic resonance imaging contrast material for in vivo mapping of tissue transglutaminase activity. *Cancer Res. 65*, 1369–75.

(4) Ntziachristos, V., Ripoll, J., Wang, L. V., and Weissleder, R. (2005) Looking and listening to light: the evolution of whole-body photonic imaging. *Nat. Biotechnol. 23*, 313–320.

(5) Bremer, C., Ntziachristos, V., and Weissleder, R. (2003) Optical-based molecular imaging: contrast agents and potential medical applications. *Eur. Radiol. 13*, 231–43.

(6) Caravan, P., Cloutier, N. J., Greenfield, M. T., McDermid, S. A., Dunham, S. U., Bulte, J. W. M., Amedio, J. C., Looby, R. J., Supkowski, R. M., Horrocks, W. D., McMurry, T. J., and Lauffer, R. B. (2002) The interaction of MS-325 with human serum albumin and its effect on proton relaxation rates. *J. Am. Chem. Soc. 124*, 3152–62.

(7) Allen, M. J., and Meade, T. J. (2004) Magnetic resonance contrast agents for medical and molecular imaging. *Metal Ions Biol. Syst. 42*, 1–38.

(8) Allen, M. J., MacRenaris, K. W., Venkatasubramanian, P. N., and Meade, T. J. (2004) Cellular delivery of MRI contrast agents. *Chem. Biol. 11*, 301–7.

(9) Modo, M. M., and Bulte, J. W. W., Eds. (2007) *Molecular and Cellular MR Imaging*, CRC Press, Boca Raton, FL.

(10) Frullano, L., and Meade, T. J. (2007) Multimodal MRI contrast agents. *J. Biol. Inorg. Chem. 12*, 939–49.

(11) Rodriguez-Morgade, M. S., and Stuzhin, P. A. (2004) The chemistry of porphyrazines: an overview. J. *Porphyrins Phthalocyanines 8*, 1129–65.

(12) Michel, S. L. J., Hoffman, B. M., Baum, S. M., and Barrett, A. G. M. (2001) Peripherally functionalized porphyrazines: novel metallomacrocycles with broad, untapped potential. *Prog. Inorg. Chem. 50*, 473.

(13) Fuchter, M. J., Zhong, C., Zong, H., Hoffman, B. M., and Barrett, A. G. M. (2008) Porphyrazines: designer macrocycles by peripheral substituent change. *Aust. J. Chem. 61*, 235–55.

(14) Trivedi, E. R., Vesper, B. J., Weitman, H., Ehrenberg, B., Radosevich, J. A., Barrett, A. G. M., and Hoffman, B. M. (2010) Chiral bis-acetal porphyrazines as near-infrared optical agents for detection and treatment of cancer. *Photochem. Photobiol. 86*, 410–417.

(15) Vesper, B. J., Lee, S., Hammer, N. D., Elseth, K. M., Barrett, A. G. M., Hoffman, B. M., and Radosevich, J. A. (2006) Developing a structure-function relationship for anionic porphyrazines exhibiting selective anti-tumor activity. *J. Photochem. Photobiol., B 82*, 180–6.

(16) Hammer, N. D., Lee, S., Vesper, B. J., Elseth, K. M., Hoffman, B. M., Barrett, A. G. M., and Radosevich, J. A. (2005) Charge dependence of cellular uptake and selective antitumor activity of porphyrazines. *J. Med. Chem. 48*, 8125–33.

(17) Trivedi, E. R., Harney, A. S., Olive, M. B., Podgorski, I., Moin, K., Sloane, B. F., Barrett, A. G. M., Meade, T. J., and Hoffman, B. M. (2010) Chiral porphyrazine near-IR optical

imaging agent exhibiting preferential tumor accumulation. *Proc. Natl. Acad. Sci. U.S.A. 107*, 1284–88.
(18) Carboni, B., Benalil, A., and Vaultier, M. (1993) Aliphatic amino azides as key building-blocks for efficient polyamine syntheses. *J. Org. Chem. 58*, 3736–41.
(19) Song, Y., Kohlmeir, E. K., and Meade, T. J. (2008) Synthesis of multimeric MR contrast agents for cellular imaging. *J. Am. Chem. Soc. 130*, 6662–63.
(20) Lee, S., White, A. J. P., Williams, D. J., Barrett, A. G. M., and Hoffman, B. M. (2001) Synthesis of near-IR absorbing/emitting porphyrazine derivatives with tunable solubility. *J. Org. Chem. 66*, 461–5.
(21) Brown, P. S., Wang, E., Aroeti, B., Chapin, S. J., Mostov, K. E., and Dunn, K. W. (2000) Definition of distinct compartments in polarized Madin-Darby canine kidney (MDCK) cells for membrane-volume sorting, polarized sorting and apical recycling. *Traffic (Copenhagen) 1*, 124–40.
(22) Hueber, M. M., Staubli, A. B., Kustedjo, K., Gray, M. H. B., Shih, J., Fraser, S. E., Jacobs, R. E., and Meade, T. J. (1998) Fluorescently detectable magnetic resonance imaging agents. *Bioconjugate Chem. 9*, 242–49.
(23) Modo, M., Cash, D., Mellodew, K., Williams Steven, C. R., Fraser Scott, E., Meade Thomas, J., Price, J., and Hodges, H. (2002) Tracking transplanted stem cell migration using bifunctional, contrast agent-enhanced, magnetic resonance imaging. *Neuroimage 17*, 803–11.
(24) Modo, M., Mellodew, K., Cash, D., Fraser Scott, E., Meade Thomas, J., Price, J., and Williams Steven, C. R. (2004) Mapping transplanted stem cell migration after a stroke: a serial, in vivo magnetic resonance imaging study. *Neuroimage 21*, 311–7.
(25) Prasuhn, D. E., Jr., Yeh, R. M., Obenaus, A., Manchester, M., and Finn, M. G. (2007) Viral MRI contrast agents: coordination of Gd by native virions and attachment of Gd complexes by azide-alkyne cycloaddition. *Chem. Commun. 28*, 1269–1271.
(26) Bryson, J. M., Chu, W.-J., Lee, J.-H., and Reineke, T. M. (2008) A β-cyclodextrin "click cluster" decorated with seven paramagnetic chelates containing two water exchange sites. *Bioconjugate Chem. 19*, 1505–1509.
(27) Maiti, N. C., Mazumdar, S., and Periasamy, N. (1998) J- and H-aggregates of porphyrin-surfactant complexes: time-resolved fluorescence and other spectroscopic studies. *J. Phys. Chem. B 102* (9), 1528–1538.
(28) Mataga, N., Kaifu, Y., and Koizumi, M. (1956) Solvent effects upon fluorescence spectra and the dipole moments of excited molecules. *Bull. Chem. Soc. Jpn. 29*, 465–70.
(29) Toth, E., Helm, L., and Merbach, A. E. (2002) Relaxivity of MRI contrast agents. *Top. Curr. Chem. 221*, 6–101.
(30) Datta, A., Hooker, J. M., Botta, M., Francis, M. B., Aime, S., and Raymond, K. N. (2008) High relaxivity gadolinium hydroxypyridonate-viral capsid conjugates: Nanosized MRI contrast agents. *J. Am. Chem. Soc. 130*, 2546–52.
(31) Rohrer, M., Bauer, H., Mintorovitch, J., Requardt, M., and Weinmann, H. J. (2005) Comparison of magnetic properties of MRI contrast media solutions at different magnetic field strengths. *Invest. Radiol. 40*, 715–24.
(32) Kiessling, F., Heilmann, M., Lammers, T., Ulbrich, K., Subr, V., Peschke, P., Waengler, B., Mier, W., Schrenk, H.-H., Bock, M., Schad, L., and Semmler, W. (2006) Synthesis and characterization of HE-24.8: a polymeric contrast agent for magnetic resonance angiography. *Bioconjugate Chem. 17*, 42–51.
(33) Kaneshiro Todd, L., Ke, T., Jeong, E.-K., Parker Dennis, L., and Lu, Z.-R. (2006) Gd-DTPA L-cystine bisamide copolymers as novel biodegradable macromolecular contrast agents for MR blood pool imaging. *Pharm. Res. 23*, 1285–94.
(34) Lu, Z.-R., Ye, F., and Vaidya, A. (2007) Polymer platforms for drug delivery and biomedical imaging. *J. Controlled Release 122*, 269–277.

BC1002828

Supporting Information

Synthesis and Characterization of New Porphyrazine-Gd(III) Conjugates as Multimodal MR Contrast Agents

Ying Song[†], Hong Zong [†], Evan R. Trivedi[†], Benjamin J. Vesper[‖,§], Emily A. Waters[†], Anthony G.M. Barrett[¶], James A. Radosevich[‖,§], Brian M. Hoffman[†,*], and Thomas J. Meade[†,‡,*]

[†]Departments of Chemistry, and Biochemistry, Molecular Biology and Cell Biology, Northwestern University, Evanston, IL.
[‖]Center for Molecular Biology of Oral Diseases, College of Dentistry, University of Illinois at Chicago, Chicago, IL.
[§]Jesse Brown VAMC, Chicago, IL.
[¶]Department of Chemistry, Imperial College of Science, Technology and Medicine, South Kensington, London, England.
[‡]Departments of Neurobiology and Physiology and Radiology, Northwestern University, Evanston, IL.

Corresponding Author:
Thomas J. Meade; Brian M. Hoffman
2145 Sheridan Rd
Department of Chemistry, Northwestern University
Evanston, IL 60208
Tel: 847-491-2481
Fax: 847-491-3832
Email: tmeade@northwestern.edu; bmh@northwestern.edu

Experimental Procedure:..... 4

Figure SI-1. MALDI-MS spectrum of Zn-Pz-nGd (n=1, 4, 8). 5

Figure SI-2 MALDI-MS spectrum of Cu-Pz-nGd(III) (n=4, 8). 6

Figure SI-3 Relaxivity measurement of Zn-Pz-nGd(III) (n=1, 4, 8). 7

Figure SI-4 Relaxivity measurement of Cu-Pz-nGd(III) (n=4, 8). 8

Table SI-1. Molecular and Gd(III) ionic relaxivity Cu-Pz-nGd(III) (n= 4, 8) complexes in water at 37 ^{o}C, 60 MHz..... 9

Table SI-2. Summary of UV-Vis/NIR absorption and emission peaks of Cu-Pz-nGd(III) complexes (n= 4, 8). *measured in CH_2Cl_2. 9

Figure SI-5. UV-Vis and fluorescence spectra of Zn-Pz-nGd(III) and Cu-Pz-nGd(III) (n =4, 8). Green line is the UV-Vis absorption spectra; blue line is the emission in the UV region and red line is the emission in the NIR region..... 10

Figure SI-6. False-red images taken with confocal fluorescence microscopy of WI38-VA13 human embryonic fibroblast cells treated with 50 μM Zn-Pz-4Gd(III) (left) and Zn-Pz-8Gd(III) (middle) for 24 hrs versus vehicle control (right) (750 nm 2-photon excitation, 390-465 nm emission)..... 11

Figure SI-7. Comparison between Zn-Pz-1Gd(III) and DOTA-Gd(III) in cell uptake studies by ICP-MS. Cells were incubated in 50 μM Zn-Pz-1Gd(III) or DOTA-Gd(III) for 24 hours..... 12

Figure SI-8. MR images of WI-38 VA13cell pellets (top) and A549 cell pellets (bottom) incubated with 0 (a), 50 (b), and 100 μM (c) of Zn-Pz-1Gd(III). 13

Figure SI-9. Cellular uptake of Zn-Pz-1Gd(III) measured by ICP-MS in WI-38 VA13 cells and A549 cells corresponding to the MR images in Figure SI-7. (A) Total Gd(III) content per cell pellet. (B) Gd(III) content per cell in the cell pellets. 14

Figure SI-10. Concentration dependent dark toxicity of Zn-Pz-nGd(III) in A549 cells (n=1,4,8). Cells were incubated for 24 hours for all three agents. Control for Zn-Pz-1Gd(III): cells + DMSO; control for all other pz-Gd(III): cells + H_2O. 16

Figure SI-11. Phototoxicity of Zn-Pz-nGd(III) conjugates (n=1, 4, 8) with A549 cells at 50 μM incubation concentration. Photofrin was used as a positive control. Control for Zn-Pz-1Gd(III): cells + DMSO; control for all other pz-Gd(III): cells + H_2O..... 17

Experimental Procedure:

Cu-Pz-8Gd(III). Cu[Pz(A_2); ($SC_4ON(C_2Gd)_2)_4$], A = 3,6 Bis(isopropyloxy)-1,2-benzo. Gd595 (22 mg, 0.037 mmol), copper sulfate (1.3 mg, 0.008 mmol), sodium ascorbate (4.4 mg, 0.022 mmol) and Pz-8azide (7.0 mg, 0.004 mmol) were dissolved in 3 ml of water/DMF (1:1) mixture. The reaction mixture was heated in an oil bath at 70 ºC overnight. After cooling, the reaction mixture was loaded into a dialysis bag with MWCO 100 and dialyzed for 48 hrs against Millipore water. The resulting solution was re-concentrated and run through a Chelex column to ensure the complete removal of copper ions. Finally the product was purified with reverse phase HPLC using water/acetonitrile gradient to give **Cu-Pz-8Gd(III)** as a green solid (16 mg, 59%). MALDI-TOF-MS *m/z* 6497.6 ($M + H^+$) calcd for $C_{220}H_{313}CuGd_8N_{76}O_{64}S_4$: 6497.3.

Cu-Pz-4Gd(III). Cu[Pz(A_2); ($SC_4ONHC_3Gd)_4$], A = 3,6 Bis(isopropyloxy)-1,2-benzo (7). Gd595 (9.1 mg, 0.015 mmol), copper sulfate (0.8 mg, 0.005 mmol), sodium ascorbate (1.8 mg, 0.009 mmol) and PZ-4 azide (5.0 mg, 0.004 mmol) were dissolved in 2 ml water/DMF (1:1). The reaction mixture was heated in an oil bath at 70 ºC overnight. After cooling down, the reaction mixture was loaded into a dialysis bag with MWCO 100 and dialyzed for 48 hrs against Millipore water. The resulting solution was re-concentrated and run through a Chelex column to ensure the complete removal of copper ions. Finally the product was purified with reverse phase HPLC using water/acetonitrile gradient to give **Cu-Pz-4Gd(III)** as a green solid (9 mg, 67%). MALDI-TOF-MS *m/z* 3894.9 ($M + H^+$) calcd for $C_{140}H_{197}CuGd_4N_{44}O_{36}S_4$ 3893.0.

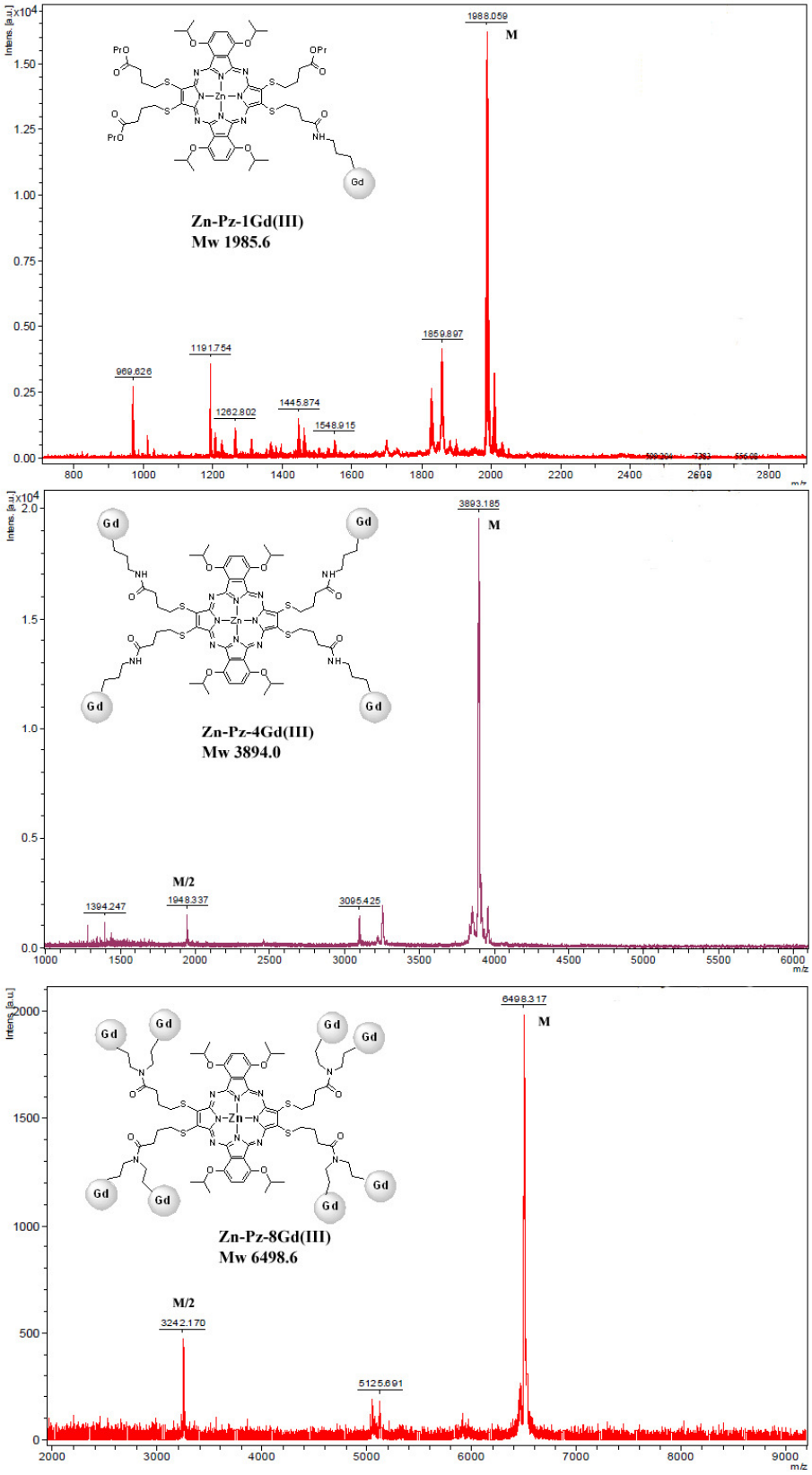


Figure SI-1. MALDI-MS spectrum of Zn-Pz-nGd (n=1, 4, 8).

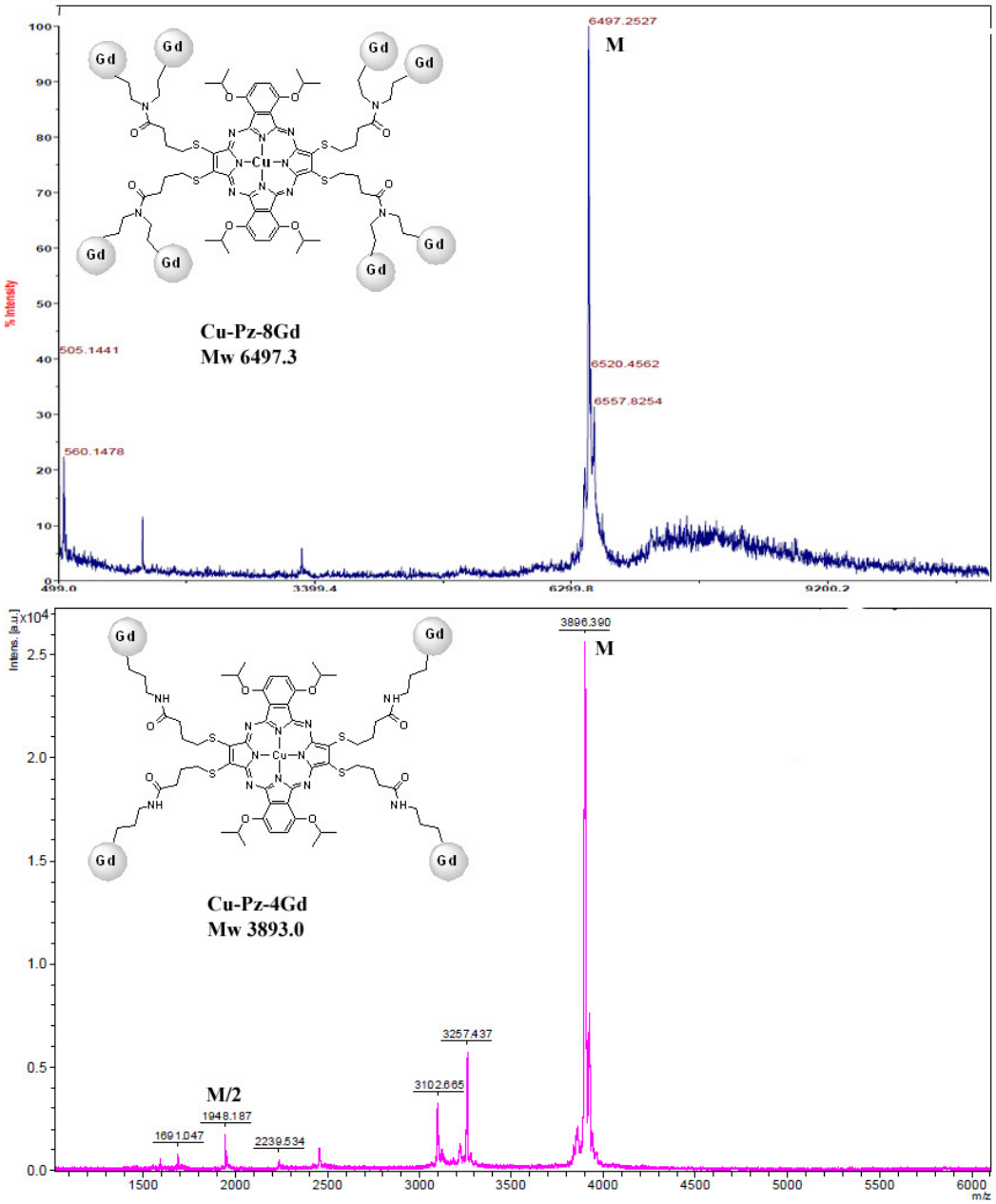


Figure SI-2 MALDI-MS spectrum of Cu-Pz-nGd (n=4, 8).

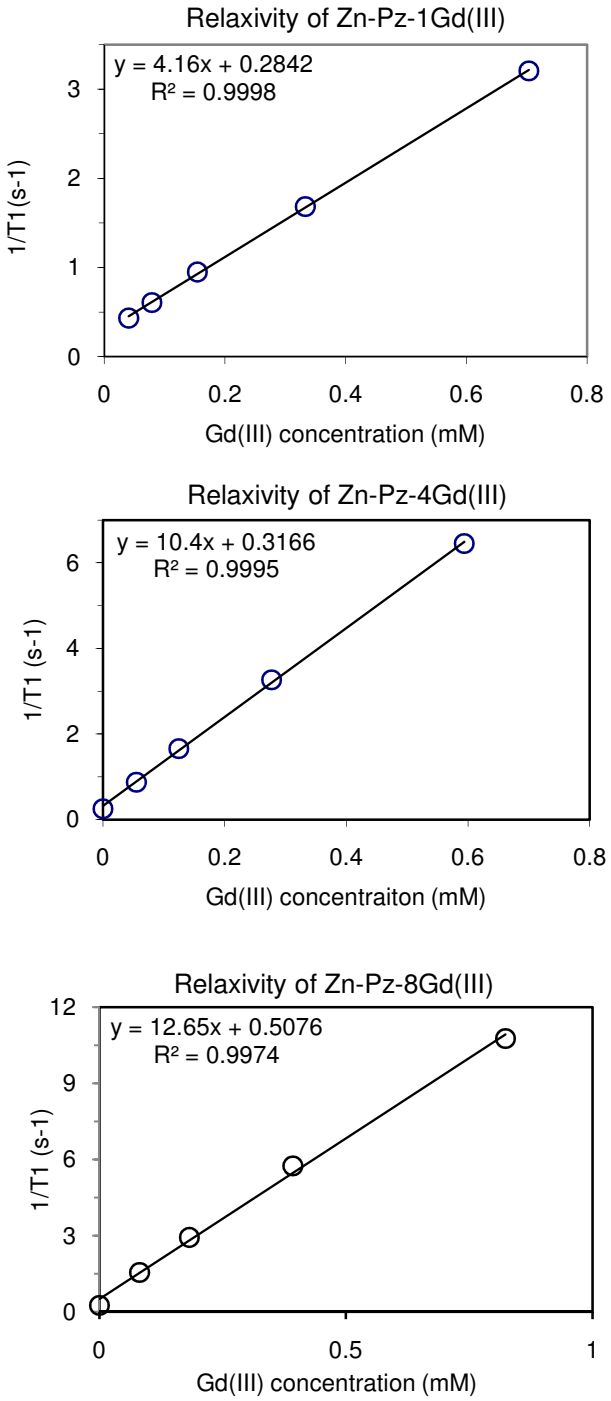


Figure SI-3 Relaxivity measurements of Zn-Pz-nGd(III) (n=1, 4, 8).

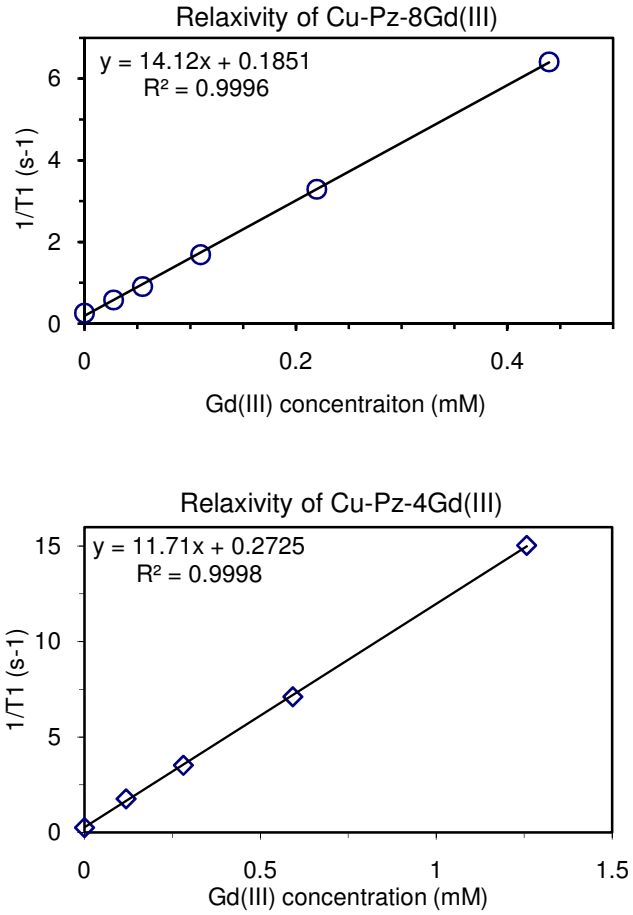


Figure SI-4 Relaxivity measurement of Cu-Pz-nGd(III) (n=4, 8).

Table SI-1. Molecular and Gd(III) ionic relaxivity Cu-Pz-nGd(III) (n= 4, 8) complexes in water at 37 ^{o}C, 60 MHz.

Compounds	MW (g/mol)	Gd(III) ionic $r_1(mM^{-1}\ s^{-1})$	No. of Gd(III)	Molecular $r_1(mM^{-1}\ s^{-1})$
Gd595	595.7	3.21	1	3.21
Cu-Pz-4Gd(III)	3892.1	11.7	4	46.8
Cu- Pz-8Gd(III)	6495.1	14.1	8	112

Table SI-2. Summary of UV-Vis/NIR absorption and emission peaks of Cu-Pz-nGd(III) complexes (n= 4, 8). *measured in CH_2Cl_2.

Compounds	Absorption peaks/nm	Emission peaks/nm
Cu-Pz-8Gd(III)	342, 683, 789	497
Cu-Pz-4Gd(III)	339, 677, 783	468
*Free Pz (**1**)	340, 654, 794	444, 826

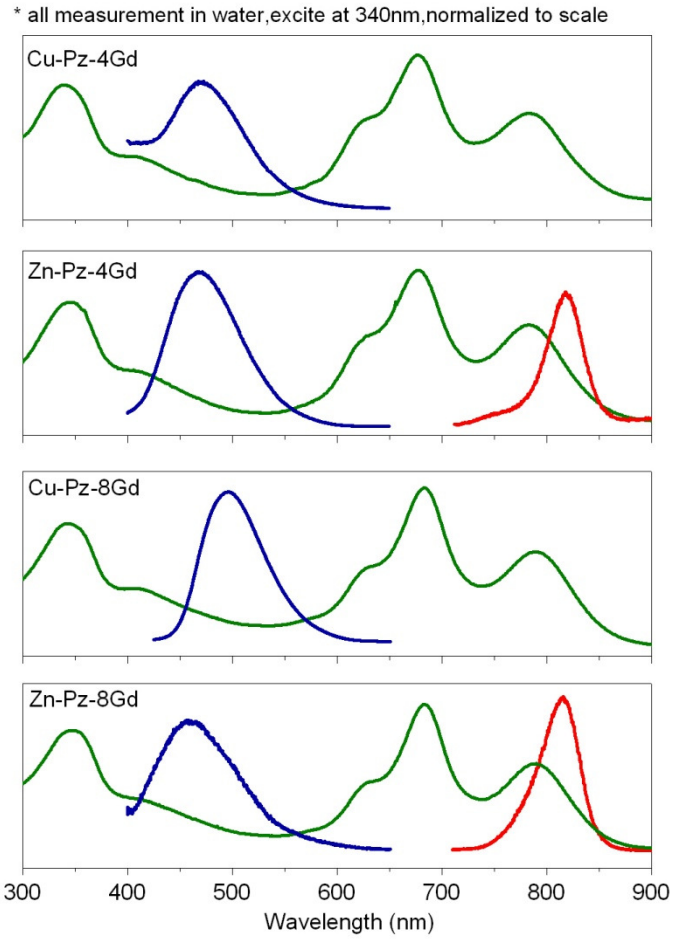


Figure SI-5. UV-Vis and fluorescence spectra of Zn-Pz-nGd(III) and Cu-Pz-nGd(III) (n =4, 8). Green line is the UV-Vis absorption spectra; blue line is the emission in the UV region and red line is the emission in the NIR region.

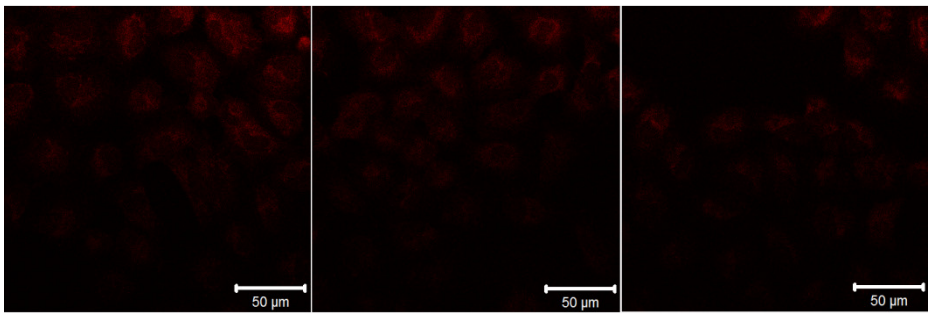


Figure SI-6. False-red images taken with confocal fluorescence microscopy of WI38-VA13 human embryonic fibroblast cells treated with 50 µM Zn-Pz-4Gd(III) (left) and Zn-Pz-8Gd(III) (middle) for 24 hrs versus vehicle control (right) (750 nm two-photon excitation, 390-465 nm emission).

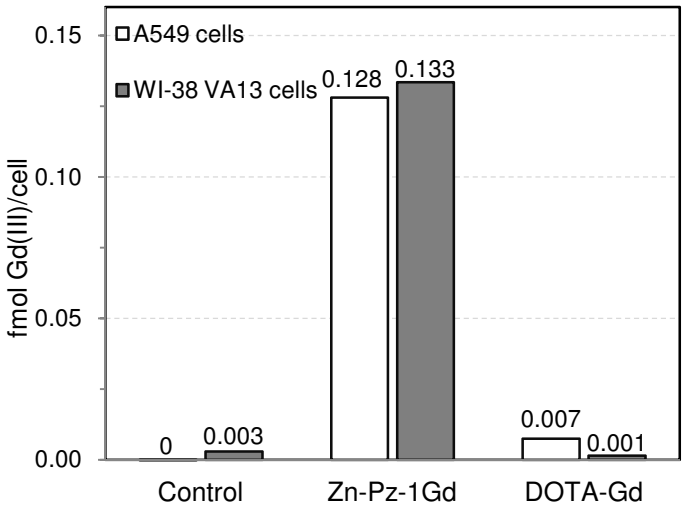


Figure SI-7. Comparison between Zn-Pz-1Gd(III) and DOTA-Gd(III) in cell uptake studies by ICP-MS. Cells were incubated in 50 μM Zn-Pz-1Gd(III) or DOTA-Gd(III) for 24 hours.

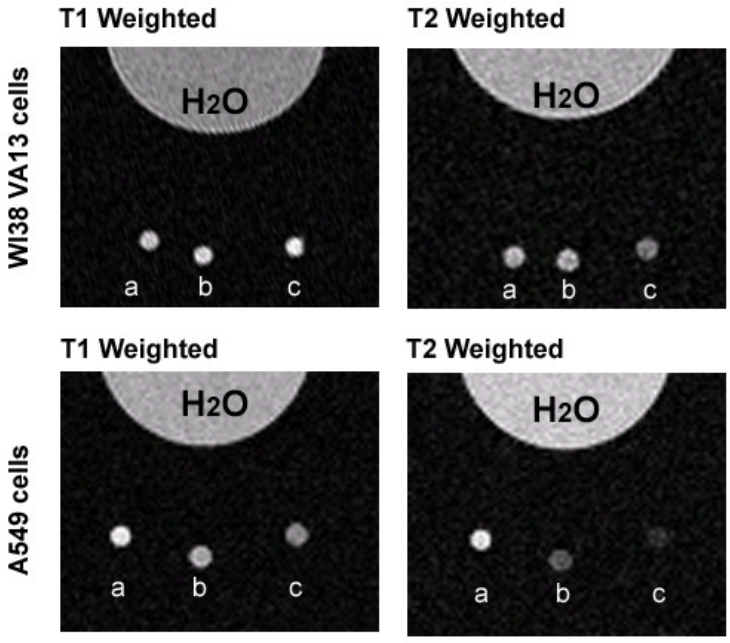
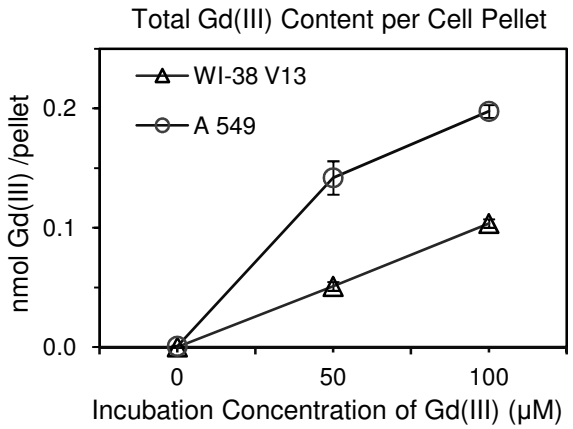


Figure SI-8. MR images of WI-38 VA13cell pellets (top) and A549 cell pellets (bottom) incubated with 0 (a), 50 (b), and 100 μM (c) of Zn-Pz-1Gd(III).

(A)



(B)

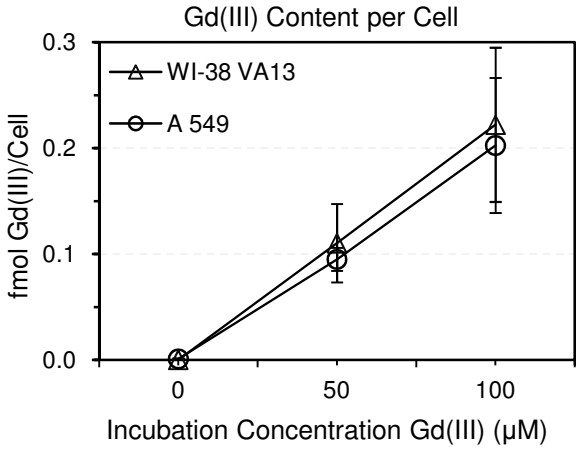


Figure SI-9. Cellular uptake of Zn-Pz-1Gd(III) measured by ICP-MS in WI-38 VA13 cells and A549 cells corresponding to the MR images in Figure SI-7. (A) Total Gd(III) content per cell pellet. (B) Gd(III) content per cell in the cell pellets.

Explanation for Figure SI-8 and Figure SI-9:

In Figure SI-8, images on the left are T_1-weighted images which were acquired with short TE (15 ms) for minimal T_2-weighting, and images on the right are T_2-weighted images which were acquired with a long TE (40 ms) to demonstrate the signal dropout due to the presence of Gd(III).

Generally in a T_1-weighted image, a higher local concentration of Gd(III) will induce higher brightness, which was observed in the T_1-weighted images of WI-38 VA13 cell pellets. However, the result with A549 cells was counter-intuitive, as the T_1 weighted images appeared darker in pellets prepared with increasing incubation concentration of Gd(III). This was due to a strong T_2-shortening effect caused by an overwhelming amount of Gd(III) in the given volume under these imaging conditions. Therefore, the high concentration of local Gd(III) caused dark images for the A549 cell pellets and the bright images for the WI-38 VA13 pellets.

Interestingly, ICP-MS studies showed that the Gd(III) count per cell was similar for both cell lines when subjected to the same incubation concentration. This result indicated that both cell lines were taking up similar amounts of Gd(III) per cell (see Figure SI-9B). Further study showed that the A549 cell pellets contained twice the amount of Gd(III) per pellet than the W-I38 VA13 cell (Figure SI-9A). Based on this evidence, we concluded that in the A549 cell pellets, twice the number of cells was packed into approximately the same volume as that of the WI-38 VA13 cells during the spin-down cell pellet preparation. Therefore, the local Gd(III) concentration was higher in A549 cell pellets and induced the T_2 effect.

The T_2-weighted image is more straightforward in Figure SI-8. Because of the increasing concentration of Gd(III), the labeled cells appeared markedly darker compared to the control cells pellets. The higher the incubation concentration of Gd(III), the darker

the pellets appeared in the image. The maximum signal dropout occurred with the A549 cells incubated at 100 μM of Zn-Pz-1Gd(III), which is consistent with the ICP-MS data showing the highest Gd(III) content in the sample (see Figure SI-7B).

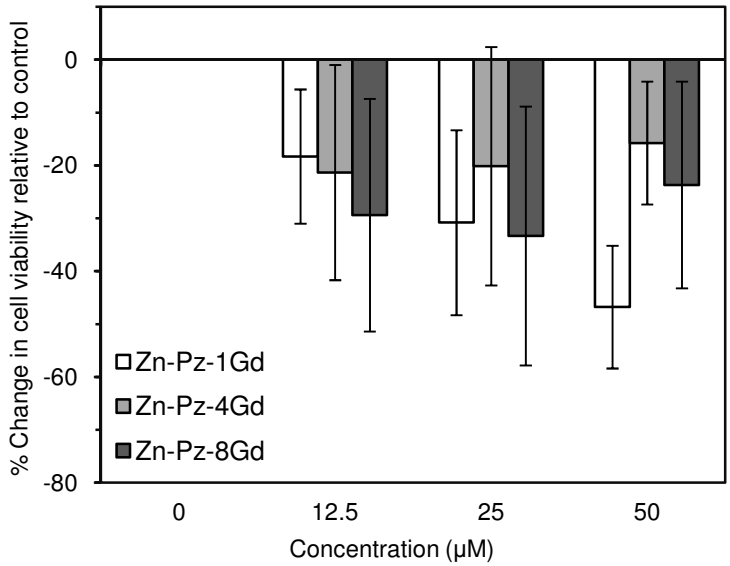


Figure SI-10. Concentration dependent dark toxicity of Zn-Pz-nGd(III) in A549 cells (n=1,4,8). Cells were incubated for 24 h for all three agents. Control for Zn-Pz-1Gd(III): cells + DMSO; control for Zn-pz-4Gd(III) or Zn-Pz-8Gd(III): cells + H_2O.

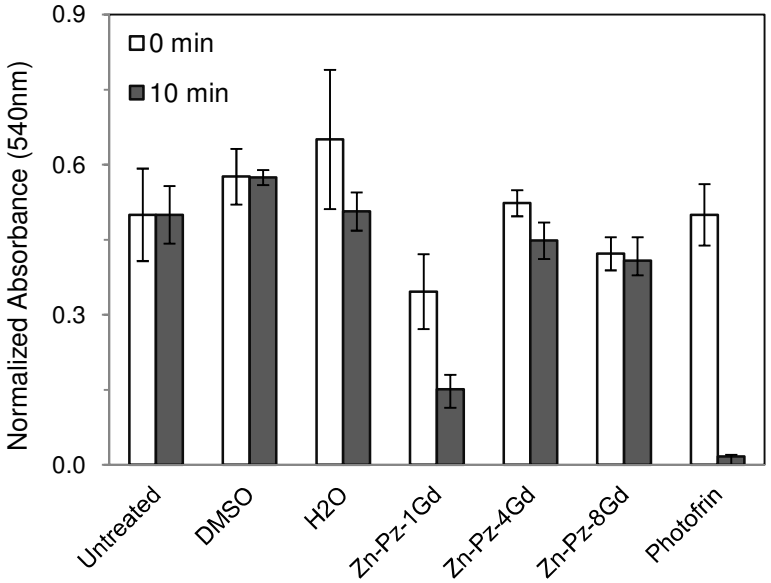


Figure SI-11. Phototoxicity of Zn-Pz-nGd(III) conjugates (n=1, 4, 8) with A549 cells at 50 μM incubation concentration. Photofrin was used as a positive control. Control for Zn-Pz-1Gd(III): cells + DMSO; control for Zn-pz-4Gd(III) or Zn-Pz-8Gd(III): cells + H_2O.

ECHO-LNA Conjugates: Hybridization-Sensitive Fluorescence and Its Application to Fluorescent Detection of Various RNA Strands

Kaori Sugizaki[†] and Akimitsu Okamoto*[,‡]

RIKEN Advanced Science Institute, 2-1 Hirosawa, Wako, Saitama 351-0198, Japan, and PRESTO, Japan Science and Technology Agency, 4-1-8 Honcho, Kawaguchi, Saitama 332-0012, Japan. Received June 30, 2010; Revised Manuscript Received August 23, 2010

Hybridization-sensitive fluorescent DNA probes containing the nucleotide units of locked nucleic acid (LNA) have been developed. Exciton-controlled hybridization-sensitive fluorescent oligonucleotide (ECHO) probes that incorporated LNA nucleotides achieved high thermostability of the hybrid with target RNA strands. The appropriately designed ECHO-LNA chimeric probes exhibited an effective on−off switching property of fluorescence depending on hybridization with RNA and facilitated fluorescent detection of the TAR RNA strand forming a hairpin structure and distinction of one base difference in PLAC4 RNA sequence.

INTRODUCTION

Ribonucleic acid (RNA) is one of many essential biomolecules responsible for the expression, maintenance, and control of cell functions. RNA is highly diverse in terms of size, structure, mass, function, location, and expression timing, as well as in sequences (*1*). In particular, the structural and sequential diversity of RNA, such as higher-ordered structure formation and one-base mutations, plays an important role in characterizing the function of RNA. Therefore, effective detection of such RNA strands is very important for understanding the cell functions.

Many fluorescent nucleic acid probes have been developed for observation of the functions of target nucleic acids (*2*−*4*). In particular, much effort has been invested in the rational design of hybridization-sensitive fluorescent probes to detect effectively the target nucleic acid using on−off switching of fluorescence depending on hybridization (*5*−*9*). However, the functions of these probes are insufficient for effective detection of a variety of RNA molecules, because accessing the RNA sequence that forms a higher-ordered structure and distinguishing the target RNA sequence from the one-base mutants are often thermodynamically difficult for fluorescent nucleic acid probes.

Incorporation of the nucleotide units of locked nucleic acid (LNA) into hybridization-sensitive probes may provide one of the more effective methods for solving such problems (*10*). Chimeric probes having select positions modified with LNA nucleotides have been reported to enhance duplex stability (*11*). In addition, LNA trinucleotides enhance the thermostability of the duplex formed with the complementary sequences, whereas the duplex stability with mismatched sequences is much lower (*12*−*14*). Incorporation of LNA nucleotides into hybridization-sensitive fluorescent DNA probes would make fluorometric detection of a variety of RNA molecules more effective. However, the bridged sugar structure of LNA nucleotides may diminish the function of hybridization-sensitive on−off switching of fluorescence. To choose the correct course for design of the fluorescent probe sequence including LNA nucleotides, the effect of LNA incorporation on the fluorescence intensity of probes needs to be estimated through several model experiments.

In this paper, we report fluorescence properties of hybridization-sensitive fluorescent probes possessing LNA nucleotides. Incorporation of LNA nucleotides into hybridization-sensitive fluorescent DNA probes provided higher thermostability with the complementary RNA strand compared with probes consisting of only 2′-deoxyribonucleotides. In addition, fluorescent detection of the RNA strand forming a hairpin structure and distinction of a one-base difference in an RNA sequence were facilitated by LNA-incorporated fluorescent probes.

EXPERIMENTAL PROCEDURES

General. Reverse-phase HPLC was performed on Chemcobond 5-ODS-H columns (10 × 150 mm) with a Gilson Chromatograph, model 305, using a Jasco multiwavelength detector, MD-2015Plus. MALDI-TOF mass spectra were measured with a Bruker Daltonics Reflex apparatus. Absorption and fluorescence spectra were recorded on a Shimadzu UV-2550 spectrophotometer and RF-5300PC spectrofluorophotometer, respectively.

Probe Synthesis. Oligonucleotides containing both LNA nucleotides and a diamino-modified nucleotide, which is a precursor of the D_{514} nucleotide, were synthesized by Gene Design (Osaka, Japan). RNA was synthesized by Japan Bio Service. DNA oligomers were synthesized by a conventional phosphoramidite method on a DNA/RNA synthesizer. Oligonucleotides containing a diamino-modified nucleotide and a 2′-*O*-methyl RNA nucleotide were synthesized through a conventional phosphoramidite method by using an H-8 DNA/RNA autosynthesizer (Nihon Techno Service). The diamino-modified nucleoside phosphoramidite was synthesized according to our previous report (*15*). The synthesized oligonucleotides were cleaved from the support with 28% aqueous ammonia and deprotected at 25 °C for 16 h. After removal of ammonia from the solution under reduced pressure, the DNA was purified by reverse-phase HPLC, followed by elution with a solvent mixture of 0.1 M triethylammonium acetate (TEAA) (pH = 7.0) and linear gradient over 20 min from 5% to 30% acetonitrile at a flow rate of 3.0 mL/min. The concentration of the oligonucleotides was determined by absorption at 260 nm.

A solution of the *N*-hydroxysuccinimidyl ester of thiazole orange pentanoic acid (*15*) (40 mM, 22 equiv to an active amino

* Phone: +81-48-467-9238. Fax: +81-48-467-9205. E-mail: aki-okamoto@riken.jp.

[†] RIKEN Advanced Science Institute.

[‡] PRESTO.

10.1021/bc1002949 © 2010 American Chemical Society
Published on Web 11/19/2010

group of an oligonucleotide) in DMF was added to a deprotected oligonucleotide solution (164 μM) in 100 mM sodium carbonate buffer (pH = 9.0) and incubated at 25 °C for 30 min. The reaction mixture was diluted with ethanol. After centrifuging at 4 °C for 20 min, the supernatant liquid was removed. The residue was dissolved in a small amount of water, and then the solution was passed through a 0.45 μm filter. The product was purified by reverse-phase HPLC on a 5-ODS-H column, elution with a solvent mixture of 0.1 M TEAA (pH = 7.0) and linear gradient over 30 min from 5% to 30% acetonitrile at a flow rate of 3.0 mL/min. The product was subsequently desalted by reverse-phase HPLC on a 5-ODS-H column, elution with a solvent mixture of deionized water, and linear gradient over 20 min from 0% to 100% acetonitrile at a flow rate of 3.0 mL/min. The concentration of the oligonucleotides was determined by absorption at 260 nm. The oligonucleotides were identified by MALDI-TOF mass spectrometry. (Here, the molecular weight of the counteranions of dyes was not included in the value of *M*, and D_{514} denotes a doubly thiazole orange-labeled deoxynucleotide. Lower-case and lower-case italic characters represent LNA and 2′-*O*-methyl RNA nucleotides, respectively. The LNA nucleotide "c" denotes a 5-methylcytosine LNA nucleotide, and the 2′-*O*-methyl RNA nucleotide "*u*" denotes a uracil 2′-*O*-methyl RNA nucleotide.): **DNA(0)**, CGCAATD$_{514}$TAACGC, calcd for $C_{180}H_{217}N_{56}O_{78}P_{12}S_2$ ([M − H]$^+$) 4848.8, found 4851.4; **LNA(−4)**, CGcAATD$_{514}$TAACGC, calcd for $C_{182}H_{220}N_{56}O_{79}P_{12}S_2$ ([M − H]$^+$) 4891.8, found 4891.3; **LNA(−3)**, CGCaATD$_{514}$TAACGC, calcd for $C_{181}H_{218}N_{56}O_{79}P_{12}S_2$ ([M − H]$^+$) 4877.8, found 4878.9; **LNA(−2)**, CGCAaTD$_{514}$TAACGC, calcd for $C_{181}H_{218}N_{56}O_{79}P_{12}S_2$ ([M − H]$^+$) 4877.8, found 4878.0; **LNA(−1)**, CGCAAtD$_{514}$TAACGC, calcd for $C_{181}H_{218}N_{56}O_{79}P_{12}S_2$ ([M − H]$^+$) 4877.8, found 4880.0; **LNA(+1)**, CGCAATD$_{514}$tAACGC, calcd for $C_{181}H_{218}N_{56}O_{79}P_{12}S_2$ ([M − H]$^+$) 4877.8, found 4879.8; **LNA(+2)**, CGCAATD$_{514}$TaACGC, calcd for $C_{181}H_{218}N_{56}O_{79}P_{12}S_2$ ([M − H]$^+$) 4877.8, found 4878.9; **LNA(+3)**, CGCAATD$_{514}$TAaCGC, calcd for $C_{181}H_{218}N_{56}O_{79}P_{12}S_2$ ([M − H]$^+$) 4877.8, found 4878.3; **LNA(+4)**, CGCAATD$_{514}$TAAcGC, calcd for $C_{182}H_{220}N_{56}O_{79}P_{12}S_2$ ([M − H]$^+$) 4891.8, found 4893.9; **OMe(−4)**, CG*c*AATD$_{514}$TAACGC, calcd for $C_{181}H_{220}N_{56}O_{79}P_{12}S_2$ ([M − H]$^+$) 4879.8, found 4879.1; **OMe(−3)**, CGC*a*ATD$_{514}$TAACGC, calcd for $C_{181}H_{220}N_{56}O_{79}P_{12}S_2$ ([M − H]$^+$) 4879.8, found 4879.2; **OMe(−2)**, CGCA*a*TD$_{514}$TAACGC, calcd for $C_{181}H_{220}N_{56}O_{79}P_{12}S_2$ ([M − H]$^+$) 4879.8, found 4879.6; **OMe(−1)**, CGCAA*u*D$_{514}$TAACGC, calcd for $C_{180}H_{218}N_{56}O_{79}P_{12}S_2$ ([M − H]$^+$) 4865.8, found 4865.5; **OMe(+1)**, CGCAATD$_{514}$*u*AACGC, calcd for $C_{180}H_{218}N_{56}O_{79}P_{12}S_2$ ([M − H]$^+$) 4865.8, found 4865.3; **OMe(+2)**, CGCAATD$_{514}$T*a*ACGC, calcd for $C_{181}H_{220}N_{56}O_{79}P_{12}S_2$ ([M − H]$^+$) 4879.8, found 4880.6; **OMe(+3)**, CGCAATD$_{514}$TA*a*CGC, calcd for $C_{181}H_{220}N_{56}O_{79}P_{12}S_2$ ([M − H]$^+$) 4879.8, found 4879.9; **OMe(+4)**, CGCAATD$_{514}$TAA*c*GC, calcd for $C_{181}H_{220}N_{56}O_{79}P_{12}S_2$ ([M − H]$^+$) 4879.8, found 4879.5; **LNA(anti-TAR)**, GCtCcCaGGCD$_{514}$CAGaT, calcd for $C_{213}H_{256}N_{67}O_{101}P_{15}S_2$ ([M − H]$^+$) 5899.4, found 5902.0; **DNA(anti-TAR)**, GCTCCCAGGCD$_{514}$CAGAT, calcd for $C_{208}H_{254}N_{67}O_{97}P_{15}S_2$ ([M − H]$^+$) 5773.4, found 5771.4; **LNA(anti-PLAC4-C)**, AGD$_{514}$TAGacgA, calcd for $C_{157}H_{183}N_{50}O_{62}P_9S_2$ ([M − H]$^+$) 4105.3, found 4107.3; **DNA(anti-PLAC4-C)**, AGD$_{514}$TAGACGA, calcd for $C_{153}H_{181}N_{50}O_{59}P_9S_2$ ([M − H]$^+$) 4007.3, found 4008.5; **LNA(anti-PLAC4-T)**, AGD$_{514}$TAGatgA, calcd for $C_{157}H_{182}N_{49}O_{63}P_9S_2$ ([M − H]$^+$) 4106.3, found 4106.8; **DNA(anti-PLAC4-T)**, AGD$_{514}$TAGATGA, calcd for $C_{154}H_{182}N_{49}O_{60}P_9S_2$ ([M − H]$^+$) 4022.3, found 4022.8.

Melting Temperature. The melting temperature (T_m) values of duplexes (1.0 μM) were measured in 50 mM sodium phosphate (pH = 7.0) containing 100 mM sodium chloride. The absorbance of the samples was monitored at 260 nm from 10 to 90 °C with a heating rate of 0.5 °C min^{-1}. From these profiles, first derivatives were calculated to determine the value of T_m.

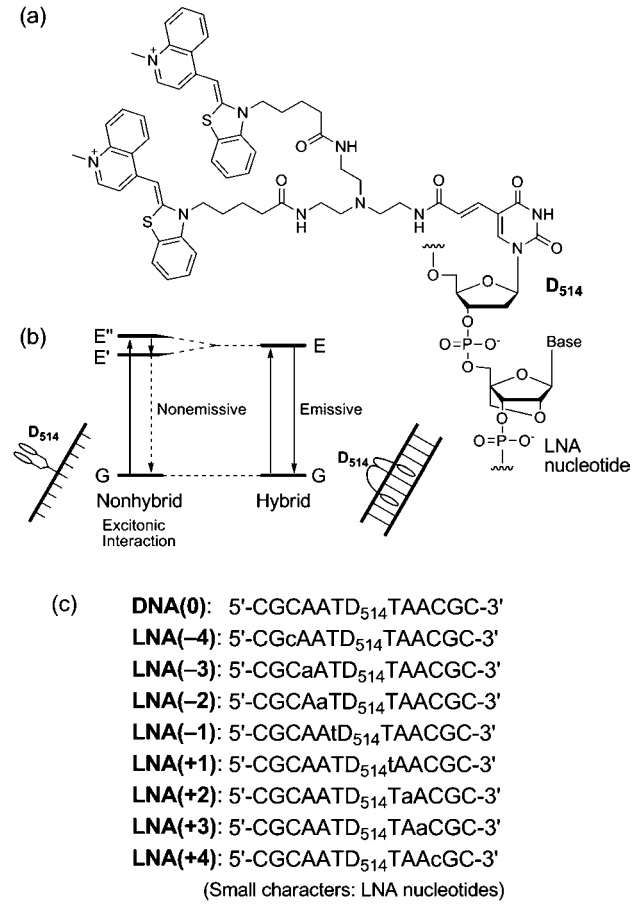


Figure 1. Structures and functions of the fluorescent probes. (a) A hybridization-sensitive fluorescent nucleotide D_{514} and an LNA nucleotide. (b) Schematic representation of the energy levels of the single- and double-stranded states of the hybridization-sensitive fluorescent DNA probe controlled by excitonic interaction between the fluorescent dyes of D_{514}. (c) Probe sequences in this study.

Absorption and Fluorescence Spectra. Absorption and fluorescence spectra of the fluorescent probes (0.4 μM) in the absence or presence of the target RNA (0.4 μM) were measured in 50 mM sodium phosphate (pH = 7.0) containing 100 mM sodium chloride using a cell with a 1 cm path length. The excitation and emission bandwidths were 1.5 nm. A water circulator EYELA NCB-1200 was connected to the spectrofluorophotometer for programmed temperature control in Figures 5 and 6.

CD Spectra. CD spectra of the fluorescent probes (2.5 μM) in the absence or presence of the target RNA (2.5 μM) were measured in 50 mM sodium phosphate (pH = 7.0) containing 100 mM sodium chloride using a cell with a 0.1 cm path length.

RESULTS AND DISCUSSION

ECHO-LNA Chimeric Probe. We prepared a hybridization-sensitive fluorescent probe including an LNA nucleotide. Exciton-controlled hybridization-sensitive fluorescent oligonucleotide (ECHO) probes have been developed for the function of hybridization-sensitive on−off switching of fluorescence (Figure 1) (*15*, *16*). This DNA probe is a new type of hybridization-sensitive probe, which has a doubly fluorescence-labeled nucleotide to achieve high fluorescence intensity for a hybrid with the target nucleic acid and effective quenching of a single-stranded probe (*17*−*22*). An excitonic interaction between the fluorescence dyes linked covalently to a single

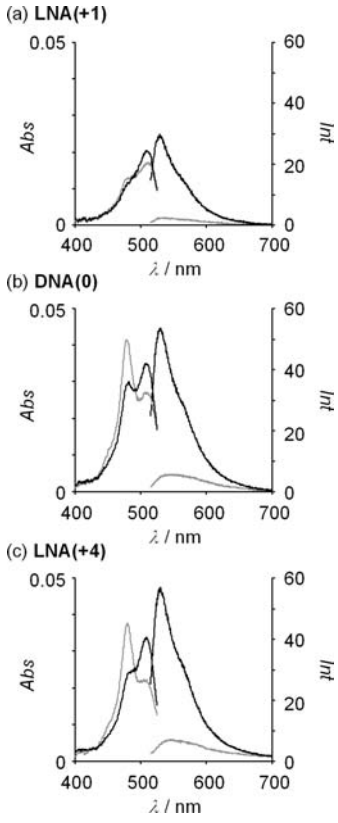


Figure 2. Absorption and emission spectra of ECHO probes. Gray lines, probes before hybridization; black lines, probes hybridized with the corresponding complementary RNA. Emission spectra were recorded with excitation at 488 nm.

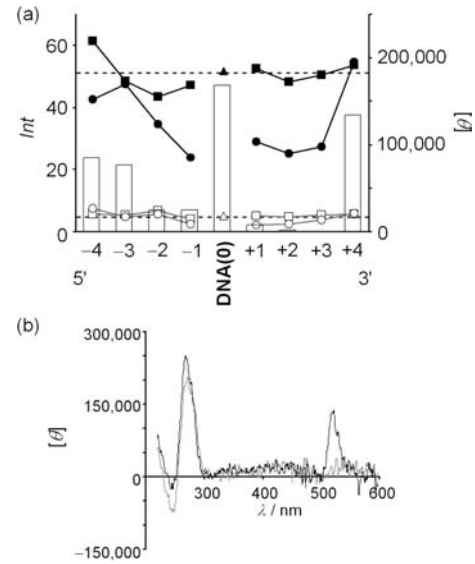


Figure 3. Effect of site incorporating LNA on the intensity of fluorescence emission and induced CD. (a) Intensity of fluorescence emission at 532 nm and induced CD at 520 nm. The fluorescence intensities of LNA-incorporated probes (open circles), and their hybrids with complementary RNA (closed circles), 2′-*O*-methyl RNA-incorporated probes (open squares), and their hybrids with complementary RNA (closed squares) are presented, together with the fluorescence intensity of the probe with an unmodified DNA backbone, **DNA(0)** (an open triangle and an accompanying dot line), and its hybrid with the complementary RNA (a closed triangle and an accompanying dotted line). The intensities of the induced CD of LNA-incorporated probes are shown by the height of the bars at each LNA incorporation site. (b) Typical CD spectra showing a strong or negligible induced CD signal. Gray and black lines are CD spectra of **LNA(+1)** and **LNA(+4)** hybridized with the complementary RNA, respectively.

nucleotide in a probe was produced by the formation of an H-aggregate between dyes, and as a result, emission from the probe was suppressed through splitting of the excited state (*23*). Dissociation of dye aggregates by hybridization with the complementary RNA resulted in disruption of the excitonic interaction and a strong emission from the hybrid.

We initially synthesized a probe with an LNA nucleotide incorporated next to the thiazole orange dye-labeled nucleotide (D_{514}). The chimeric probe **LNA(+1)** showed hybridization-sensitive fluorescence emission at 531 nm when hybridized with the complementary RNA, but the fluorescence emission of the probe itself was much weaker (Figure 2a). A shift in the absorption band, which is characteristic for H-aggregation of dyes, was also observed. The absorption shift and fluorescence switching suggest that the fluorescence emission of ECHO probes modified by an LNA nucleotide was controlled by excitonic interaction between fluorescence dyes. However, the fluorescence intensity of the **LNA(+1)**-RNA hybrid at 531 nm was only about half that of the **DNA(0)**-RNA hybrid, which includes no LNA nucleotides (Figure 2b), although the T_m of the **LNA(+1)**-RNA hybrid (52 °C) was 5 °C higher than that of the **DNA(0)**-RNA hybrid. In addition, the absorbance of **LNA(+1)** was lower than that of **DNA(0)**. These weak photophysical signals of **LNA(+1)** may suggest that the intercalation or aggregation of thiazole orange dyes linked to **LNA(+1)** was incomplete, as reported in the studies on the photophysics of free thiazole orange dye (*24, 25*). The reason for these photophysical behaviors of **LNA(+1)** was not the existence of an LNA nucleotide in the probe, but the location of LNA incorporation. Another LNA probe **LNA(+4)** showed high fluorescence intensity after hybridization with RNA (Figure 2c), as well as formation of a highly thermostable hybrid (58 °C). The photophysical behavior of **LNA(+4)** was close to that of the **DNA(0)**. Incorporation of an LNA nucleotide into a different site in the probe resulted in different absorption and fluorescence spectra.

Effect of Location of the Incorporated LNA Nucleotide. In the case of **LNA(+1)**, incorporation of an LNA nucleotide into ECHO probes induced a decrease in the fluorescence intensity of the hybrid with complementary RNA, although the hybrid showed higher stability and maintained its hybridization-sensitive emission property. The design of the probe containing LNA nucleotides, i.e., determination of where we should insert LNA nucleotides, is a key point for obtaining an effective fluorescent probe. We next prepared several chimeric probes with LNA nucleotides incorporated at different sites in the probe sequence (Figure 1c). The T_m values of the hybrids formed by the ECHO-LNA probes and the complementary RNA were 4−11 °C higher than that of the **DNA(0)**-RNA hybrid. The incorporation of an LNA nucleotide made the duplex with the complementary RNA more stable, regardless of the incorporation site. In contrast, the fluorescence intensities of the hybrids of chimeric probes and complementary RNA strongly depended on the LNA insertion site. The fluorescence intensities of the hybrid with RNA by **LNA(−2)**, **LNA(−1)**, **LNA(+2)**, and **LNA(+3)** were low, and likewise for the **LNA(+1)**-RNA hybrid (Figure 3a). On the other hand, **LNA(−4)**, **LNA(−3)**, and **LNA(+4)**, where an LNA nucleotide was located at the site far from the dye nucleotide D_{514}, showed high fluorescence intensity after hybridization with RNA, close to the fluorescence intensity of the **DNA(0)**-RNA hybrid. Fluorescence of ECHO probes has been reported to be induced by dissociation of H-aggregation and intercalation of dyes into stacking base pairs (*15, 16*). Incorporation of LNA nucleotides into the sites close to D_{514} may be unfavorable for the binding of two dyes of D_{514} to the hybrid structure.

LNA would slightly change the duplex structure from the structure of the **DNA(0)**-RNA hybrid, because the fixed puckering of LNA bridged ribose (C3′-*endo*) is close to that of RNA ribose but not DNA 2′-deoxyribose (C2′-*endo*) (*26*). However, sugar puckering may be unimportant for fluorescence intensity in the present case. The chimeric probes in which LNA nucleotides were replaced with a 2′-*O*-methyl RNA nucleoside (C3′-*endo*) kept the high fluorescence intensity of the hybrid with complementary RNA regardless of the site of 2′-*O*-methyl RNA nucleoside incorporation. Therefore, the effect of partial conformational change by sugar puckering on the fluorescence intensity in an ECHO probe was not large.

The CD spectra of LNA-containing probes provided us with key information on the intercalation of D_{514} thiazole orange dyes. The CD spectra of the hybrid of **LNA(+4)** with RNA showed a strong positive Cotton effect at 520 nm (Figure 3b), which was also observed for the **DNA(0)**-RNA hybrid. On the other hand, the hybrid formed by RNA and **LNA(+1)**, containing an LNA nucleotide located close to a D_{514} nucleotide, showed a very weak induced CD signal. These weak signals indicated that binding of D_{514} thiazole orange dyes was unsuccessful in the hybrid, suggesting that incorporation of an LNA nucleoside made the dye intercalation from the major groove side inefficient. The rigidity of the LNA sugar unit is disadvantageous for dye intercalation because dye intercalation requires the flexibility of sugar−phosphate backbones to extend the distance between base pairs (*27*). Actually, hybrids of the probes containing a lowly rigid 2′-*O*-methyl RNA nucleoside and complementary RNA showed an induced CD at 520 nm regardless of incorporation sites. Intercalation of D_{514} dyes into the hybrid structure is a key factor for dissociation of the dye aggregate and fluorescence emission. As shown in Figure 3a, the LNA incorporation sites of the probes showing a weak CD signal were consistent with the LNA incorporation sites of the probes showing low fluorescence intensity. Therefore, the rigidity of the LNA sugar unit resulted in a decrease in the fluorescence intensity of the probe through intercalation inhibition. The LNA incorporation sites where the fluorescence intensity of the hybrid decreased were not distributed symmetrically around D_{514} (two nucleotides of 5′ side of D_{514} and three of 3′ side) (Figure 4). This asymmetry can be explained by considering the distance that the dyes can reach through a linker in the right-handed double helical structure of the hybrid. To obtain an effective ECHO-LNA conjugate with high fluorescence intensity, LNA nucleotides should be incorporated into the probe, avoiding the positions marked with closed triangles in Figure 4.

Fluorescence Detection of RNA with Higher-Ordered Structure: The Example of HIV-1 TAR RNA. Insertion of LNA nucleotides into the hybridization-sensitive fluorescent probes would facilitate analysis of higher-ordered structures (*28*). HIV-1 TAR RNA, which is the transactivation responsive element located at the 5′-end of HIV-1 mRNA (*29*), is a small RNA hairpin consisting of a stem-loop structure with a three-nucleotide bulge, which is essential for Tat protein recognition and activity (*30, 31*). We designed the 16-mer ECHO probe (**LNA(anti-TAR)**) for fluorescent detection of the TAR RNA stem-loop structure (T_m = 57 °C) (Figure 5). Four LNA nucleotides were incorporated into the probe to gain high binding affinity to TAR RNA. These LNA nucleotides lay at least three nucleotides apart from D_{514} to not lose the strong fluorescence of hybrid by LNA incorporation as described above. **LNA(anti-TAR)** before hybridization showed low fluorescence intensity, which was at the same level as that of a DNA probe **DNA(anti-TAR)**. On the other hand, **LNA(anti-TAR)** showed more effective on−off switching of fluorescence emission, and the fluorescence intensity of **LNA(anti-TAR)** was higher after

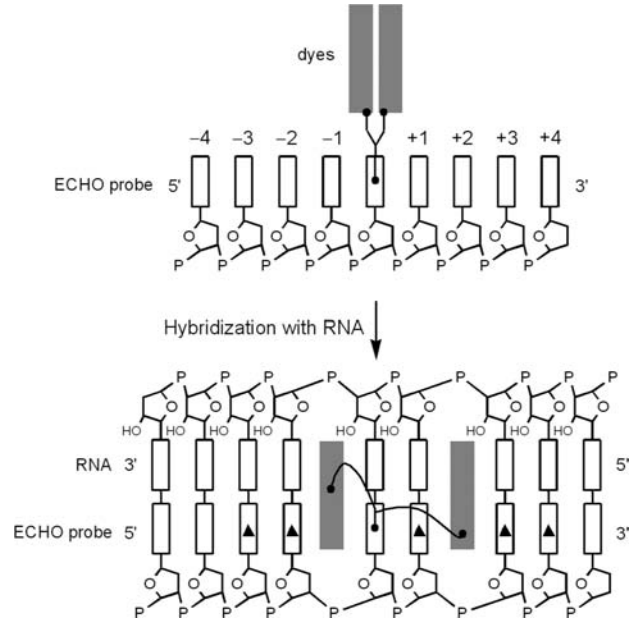


Figure 4. Binding site of D_{514} thiazole orange dyes proposed from fluorescence intensities and induced CD spectra of the hybrid with RNA. Thiazole oranges are represented by gray rectangles. The replacement by LNA nucleotides in the positions indicated with closed triangles resulted in hybrids with low fluorescence intensity and low induced CD signals.

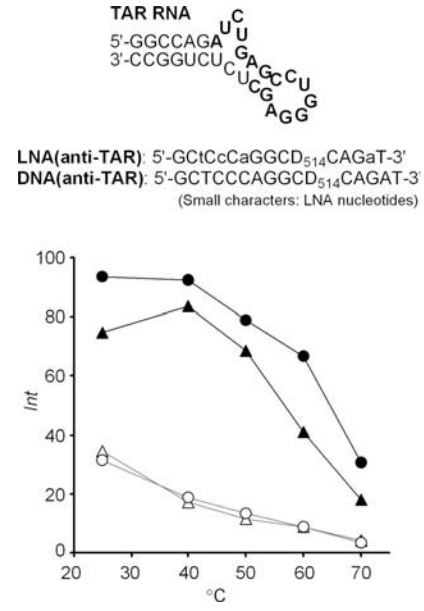


Figure 5. Fluorescence intensities of ECHO probes binding to TAR RNA. The fluorescence intensities at 531 nm at different temperatures are plotted with open circles for **LNA(anti-TAR)**, closed circles for its hybrid with TAR RNA, open triangles for **DNA(anti-TAR)**, and closed triangles for its hybrid with TAR RNA.

hybridization with TAR RNA than that of **DNA(anti-TAR)**. The T_m of the hybrid of **LNA(anti-TAR)** and TAR RNA was 56 °C, i.e., 11 °C higher than that of the hybrid of **DNA(anti-TAR)** and TAR RNA (45 °C). Thus, the largest difference in their fluorescence intensities was observed for the fluorescence measurement at 60 °C, which was close to the T_m values observed for a stem-loop TAR RNA and an **LNA(anti-TAR)**-TAR hybrid. The higher fluorescence intensity of the hybrid formed by a well-designed LNA-incorporating probe suggested that use of LNA nucleotides and temperature control was

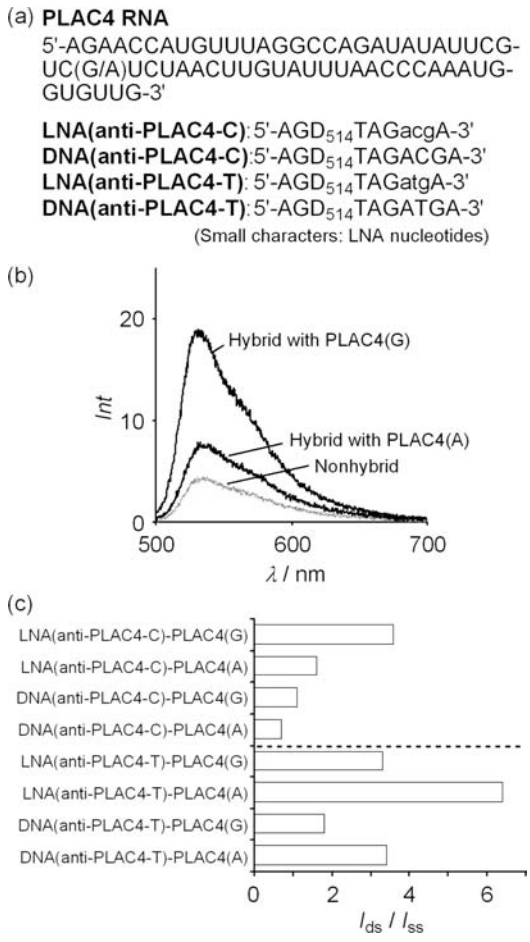


Figure 6. Fluorometric detection of the single nucleotide polymorphism (SNP) of PLAC4 RNA. (a) Sequences of a PLAC4 RNA fragment including a G/A SNP site and ECHO probes for detection of PLAC4 RNA. (b) Fluorescence spectra of **LNA(anti-PLAC4-C)**. The temperature was 50 °C, and excitation wavelength was 488 nm. (c) Ratio of the fluorescence intensities of hybrids (I_{ds}) to that of probe alone (I_{ss}). The temperature was 50 °C for LNA probes and 25 °C for DNA probes.

effective for clearer on−off fluorescence observation of an RNA strand with a higher-ordered structure.

Fluorescence Detection of Single Nucleotide Alteration of RNA: The Example of PLAC4 RNA. LNA is also effective for mismatch discrimination. A one-base difference in a genome sequence is well-known as a single-nucleotide polymorphism (SNP), and this sequence variation is among the very important research targets for progress of gene diagnosis and personalized medicine. LNA trinucleotides have been reported as being useful for recognition of one-base alteration (*32*). We next designed the ECHO probe for fluorescent SNP detection. The target SNP was placenta-specific 4 (PLAC4) rs130833, which is an SNP located in the transcribed regions of placental-expressed mRNA in maternal plasma (*33*, *34*). We designed ECHO-LNA conjugates, in which the LNA trinucleotide recognizes the target SNP site of PLAC4 RNA, and compared the SNP selectivity of fluorescence emission with DNA probes. ECHO-LNA conjugate probes, **LNA(anti-PLAC4-C)** and **LNA(anti-PLAC4-T)**, showed high T_m values for hybridization with matched PLAC4 RNA sequences (61 and 55 °C, respectively) but much lower T_m values with mismatched sequences (34 and 44 °C, respectively). On the other hand, the gap in T_m values of DNA probes for hybridization with matched and mismatched RNA was less than 3 °C, although the matched hybrid was only slightly more thermostable. The large gap between T_m values of matched and mismatched hybrids observed for LNA-incorporating probes meant that appropriate temperature control was effective for clear fluorescence detection of SNP. When the fluorescence intensity was measured at 50 °C, i.e., between the T_m values of the matched and mismatched hybrids of LNA-containing probes and PLAC4 RNA, the emission at 531 nm was selective for matched hybrids (Figure 6). LNA-containing probes distinguished a one-nucleotide difference of the target RNA more sensitively compared with DNA probes. Combination of a hybridization-sensitive fluorescent probe and an SNP-recognizing LNA trinucleotide was effective for mix-and-read fluorescent SNP typing.

In conclusion, we have designed ECHO probes showing sequence-selective fluorescence for higher-ordered RNA and RNA SNPs through the incorporation of LNA nucleotides into appropriate sites of the probes. This probe achieved high thermostability of the hybrid with target RNA strands and fluorescence detection of higher-ordered RNA and single base alteration. Although further aspects remain to be examined toward an easier-to-use intracellular RNA analysis, such as molecular design for higher sensitivity and selectivity of a small amount of the target RNA, we anticipate that this new concept of the hybridization-sensitive fluorescent probe supported by the nucleic acid chemistry and photochemical basis will be the starting point for the development of a practical assay for detection of RNAs in vivo.

ACKNOWLEDGMENT

We thank Dr. Takehiro Suzuki (RIKEN) for the MALDI-TOF mass spectrometry and Dr. Shuji Ikeda (RIKEN) for valuable discussions on the present study.

Supporting Information Available: Photophysical data (three tables). This material is available free of charge via the Internet at http://pubs.acs.org.

LITERATURE CITED

(1) Bloomfield, V. A., Crothers, D. M., and Tinoco, I., Jr. (2000) *Nucleic Acids: Structures, Properties, and Functions*, University Science Books, Sausalito, CA.
(2) Paillasson, S., Van De Corput, M., Dirks, R. W., Tanke, H. J., Robert-Nicoud, M., and Ronot, X. (1997) *In situ* hybridization in living cells: detection of RNA molecules. *Exp. Cell Res. 231*, 226–233.
(3) Asseline, U. (2006) Development and applications of fluorescent oligonucleotides. *Curr. Org. Chem. 10*, 491–518.
(4) Marti, A. A., Jockusch, S., Stevens, N., Ju, J., and Turro, N. J. (2007) Fluorescent hybridization probes for sensitive and selective DNA and RNA detection. *Acc. Chem. Res. 40*, 402–409.
(5) Tyagi, S., and Kramer, F. R. (1996) Molecular beacons: probes that fluoresce upon hybridization. *Nat. Biotechnol. 14*, 303–308.
(6) Lartia, R., and Asseline, U. (2006) New cyanine-oligonucleotide conjugates: relationships between chemical structures and properties. *Chem.—Eur. J. 12*, 2270–2281.
(7) Jarikote, D. V., Köhler, O., Socher, E., and Seitz, O. (2005) Divergent and linear solid-phase synthesis of PNA containing thiazole orange as artificial base. *Eur. J. Org. Chem. 15*, 3187–3195.
(8) Marin, V. L., and Armitage, B. A. (2006) Hybridization of complementary and homologous peptide nucleic acid oligomers to a guanine quadruplex-forming RNA. *Biochemistry 45*, 1745–1754.
(9) Kerr, C. E., Mitchell, C. D., Ying, Y. M., Eaton, B. E., and Netzel, T. L. (2000) Synthesis and photophysics of a 1-pyrenylmethyl-substituted 2′-deoxyuridine-5-carboxamide nucleoside: electron-transfer product lifetimes and energies. *J. Phys. Chem. B 104*, 2166–2175.
(10) Petersen, M., and Wengel, J. (2003) LNA: a versatile tool for therapeutics and genomics. *Trends Biotechnol. 21*, 74–81.

(11) Koshkin, A. A., Singh, S. K., Nielsen, P., Rajwanshi, V. K., Kumar, R., Meldgaard, M., Olsen, C. E., and Wengel, J. (1998) LNA (locked nucleic acids): synthesis of the adenine, cytosine, guanine, 5-methylcytosine, thymine and uracil bicyclonucleoside monomers, oligomerisation, and unprecedented nucleic acid recognition. *Tetrahedron 54*, 3607–3630.

(12) Chou, L.-S., Meadows, C., Wittwer, C. T., and Lyon, E. (2005) Unlabeled oligonucleotide probes modified with locked nucleic acids for improved mismatch discrimination in genotyping by melting analysis. *BioTechniques 39*, 644–647.

(13) Tolstrup, N., Nielsen, P. S., Kolberg, J. G., Frankel, A. M., Vissing, H., and Kauppinen, S. (2003) OligoDesign: optimal design of LNA (locked nucleic acid) oligonucleotide capture probes for gene expression profiling. *Nucleic Acids Res. 31*, 3758–3762.

(14) Simeonov, A., and Nikiforov, T. T. (2002) Single nucleotide polymorphism genotyping using short, fluorescently labeled locked nucleic acid (LNA) probes and fluorescence polarization detection. *Nucleic Acids Res. 30*, e91.

(15) Ikeda, S., and Okamoto, A. (2008) Hybridization-sensitive on-off DNA probe: application of the exciton coupling effect to effective fluorescence quenching. *Chem. Asian J. 3*, 958–968.

(16) Okamoto, A. (2010) Excitonic interaction: Another photophysical process for fluorescence-controlled nucleic acid sensing. *Chem. Rec. 10*, 188–196.

(17) Ikeda, S., Kubota, T., Kino, K., and Okamoto, A. (2008) Sequence dependence of fluorescence emission and quenching of doubly thiazole orange-labeled DNA: effective design of a hybridization-sensitive probe. *Bioconjugate Chem. 19*, 1719–1725.

(18) Kubota, T., Ikeda, S., and Okamoto, A. (2009) Doubly thiazole orange-labeled DNA for live cell RNA imaging. *Bull. Chem. Soc. Jpn. 82*, 110–117.

(19) Kubota, T., Ikeda, S., Yanagisawa, H., Yuki, M., and Okamoto, A. (2009) Hybridization-sensitive fluorescent probe for long-term monitoring of intracellular RNA. *Bioconjugate Chem. 20*, 1256–1261.

(20) Ikeda, S., Kubota, T., Yuki, M., and Okamoto, A. (2009) Exciton-controlled hybridization-sensitive fluorescent probes: multicolor detection of nucleic acids. *Angew. Chem., Int. Ed. 48*, 6480–6484.

(21) Ikeda, S., Yuki, M., Yanagisawa, H., and Okamoto, A. (2009) Doubly thiazole orange-labeled cytidine for functional expansion of a hybridization-sensitive probe. *Tetrahedron Lett. 50*, 7191–7195.

(22) Ikeda, S., Kubota, T., Yuki, M., Yanagisawa, H., Tsuruma, S., and Okamoto, A. (2010) Hybridization-sensitive fluorescent DNA probe with self-avoidance ability. *Org. Biomol. Chem. 8*, 546–551.

(23) Kasha, M. (1963) Energy transfer mechanisms and molecular exciton model for molecular aggregates. *Radiat. Res. 20*, 55–71.

(24) Rye, H. S., Yue, S., Wemmer, D. E., Quesada, M. A., Haugland, R. P., Mathies, R. A., and Glazer, A. N. (1992) Stable fluorescent complexes of double-stranded DNA with bis-intercalating asymmetric cyanine dyes: properties and applications. *Nucleic Acids Res. 20*, 2803–2812.

(25) Nygren, J., Svanvik, N., and Kubista, M. (1998) The interactions between fluorescent dye thiazole orange and DNA. *Biopolymer 46*, 39–51.

(26) Obika, S., Nanbu, D., Hari, Y., Morio, K.-i.; In, Y., Ishida, T., and, and Imanishi, T. (1997) Synthesis of 2′-*O*,4′-*C*-methyleneuridine and -cytidine. Novel bicyclic nucleosides having a fixed $C_{3'}$-*endo* sugar puckering. *Tetrahedron Lett. 38*, 8735–8738.

(27) Nielsen, C. B., Singh, S. K., Wengel, J., and Jacobsen, J. P. (1999) The solution structure of a locked nucleic acid (LNA) hybridized to DNA. *J. Biomol. Struct. Dyn. 17*, 175–191.

(28) Sannes-Lowery, K. A., Hu, P., Mack, D. P., Mei, H.-Y., and Loo, J. A. (1997) HIV-1 Tat peptide binding to TAR RNA by electrospray ionization mass spectrometry. *Anal. Chem. 69*, 5130–5135.

(29) Dingwall, C., Ernberg, I., Gait, M. J., Green, S. M., Heaphy, S., Karn, J., Lowe, A. D., Singh, M., and Skinner, M. A. (1990) HIV-1 Tat protein stimulates transcription by binding to a U-rich bulge in the stem of the TAR RNA structure. *EMBO J. 9*, 4145–4153.

(30) Roy, S., Delling, U., Chen, C.-H., Rosen, C. A., and Sonenberg, N. (1990) A bulge structure in HIV-I TAR RNA is required for Tat binding and Tat mediated *trans*-activation. *Genes Dev. 4*, 1365–1373.

(31) Cordingley, M. G., LaFemina, R. L., Callahan, P. L., Condra, J. H., Gotlib, L., Schlabach, A. J., and Colonno, R. J. (1990) Sequence-specific interaction of Tat protein and Tat peptides with the transactivation-responsive sequence element of human-immunodeficiency-virus type-1 in vitro. *Proc. Natl. Acad. Sci. U.S.A. 87*, 8985–8989.

(32) You, Y., Moreira, B. G., Behlke, M. A., and Owczarzy, R. (2006) Design of LNA probes that improve mismatch discrimination. *Nucleic Acids Res. 34*, e60.

(33) Lo, Y. M. D., Tsui, N. B. Y., Chiu, R. W. K., Lau, T. K., Leung, T. N., Heung, M. M. S., Gerovassili, A., Jin, Y., Nicolaides, K. H., Cantor, C. R., and Ding, C. (2007) Plasma placental RNA allelic ratio permits noninvasive prenatal chromosomal aneuploidy detection. *Nat. Med. 13*, 218–223.

(34) Go, A. T. J. I., Visser, A., Mulders, M. A. M., Blankenstein, M. A., van Vugt, J. M. G., and Oudejans, C. B. M. (2007) 44 single-nucleotide polymorphisms expressed by placental RNA: assessment for use in noninvasive prenatal diagnosis of trisomy 21. *Clin. Chem. 53*, 2223–2224.

BC1002949

ECHO–LNA Conjugates: Hybridization-sensitive Fluorescence and its Application to Fluorescent Detection of Various RNA Strands

Supporting Information

Kaori Sugizaki[†] and Akimitsu Okamoto*[,†,‡]

[†]RIKEN Advanced Science Institute, 2-1 Hirosawa, Wako, Saitama 351-0198, Japan

[‡]PRESTO, Japan Science and Technology Agency, 4-1-8 Honcho, Kawaguchi, Saitama 332-0012, Japan

*Phone: +81-48-467-9238; Fax: +81-48-467-9205; E-mail: aki-okamoto@riken.jp

Contents

Table S1. ECHO probes hybridized with RNA 5'-GCGUUAAAUUGCG-3'.

Table S2. ECHO probes for TAR RNA.

Table S3. ECHO probes for PLAC4 RNA.

Table S1. ECHO probes hybridized with RNA 5'-GCGUUAAAUUGCG-3'.

Probe sequences [a]			T_m / °C [b]	Φ_f [c]	I_{ds} / I_{ss} [d]
DNA(0)	5'-CGCAATD$_{514}$TAACGC-3'	ss	-	0.037	-
		ds	47	0.17	11
LNA(−4)	5'-CGcAATD$_{514}$TAACGC-3'	ss	-	0.052	-
		ds	56	0.17	6
LNA(−3)	5'-CGCaATD$_{514}$TAACGC-3'	ss	-	0.037	-
		ds	54	0.16	10
LNA(−2)	5'-CGCAaTD$_{514}$TAACGC-3'	ss	-	0.037	-
		ds	53	0.15	6
LNA(−1)	5'-CGCAAtD$_{514}$TAACGC-3'	ss	-	0.022	-
		ds	51	0.12	10
LNA(+1)	5'-CGCAATD$_{514}$tAACGC-3'	ss	-	0.022	-
		ds	52	0.16	13
LNA(+2)	5'-CGCAATD$_{514}$TaACGC-3'	ss	-	0.023	-
		ds	52	0.14	11
LNA(+3)	5'-CGCAATD$_{514}$TAaCGC-3'	ss	-	0.036	-
		ds	52	0.14	7
LNA(+4)	5'-CGCAATD$_{514}$TAAcGC-3'	ss	-	0.043	-
		ds	58	0.16	10
OMe(−4)	5'-CG*c*AATD$_{514}$TAACGC-3'	ss	-	0.040	-
		ds	49	0.17	12
OMe(−3)	5'-CGC*a*ATD$_{514}$TAACGC-3'	ss	-	0.035	-
		ds	48	0.15	10
OMe(−2)	5'-CGCA*a*TD$_{514}$TAACGC-3'	ss	-	0.052	-
		ds	45	0.16	7
OMe(−1)	5'-CGCAA*u*D$_{514}$TAACGC-3'	ss	-	0.035	-
		ds	46	0.15	11
OMe(+1)	5'-CGCAATD$_{514}$*u*AACGC-3'	ss	-	0.036	-
		ds	46	0.16	11
OMe(+2)	5'-CGCAATD$_{514}$T*a*ACGC-3'	ss	-	0.034	-
		ds	46	0.16	11
OMe(+3)	5'-CGCAATD$_{514}$TA*a*CGC-3'	ss	-	0.033	-
		ds	48	0.15	10
OMe(+4)	5'-CGCAATD$_{514}$TAA*c*GC-3'	ss	-	0.044	-
		ds	49	0.16	11

[a] Small and small italic characters present LNA and 2'-*O*-methyl RNA nucleotides, respectively. The LNA nucleotide "c" denotes a 5-methylcytosine LNA nucleotide, and the 2'-*O*-methyl RNA nucleotide "*u*" denotes a uracil 2'-*O*-methyl RNA nucleotide. [b] All T_m values of probe-RNA duplexes (1.0 μM) were taken in in 50 mM sodium phosphate (pH = 7.0) containing 100 mM sodium chloride. [c] Fluorescent quantum yield measured using 0.4 μM probe solution in 50 mM sodium phosphate (pH = 7.0) containing 100 mM sodium chloride excited at 488 nm. [d] Ratio of the fluorescence intensities of hybrids (ds) and nonhybridized probes (ss) at λ_{em} 531 nm.

Table S2. ECHO probes for TAR RNA.

Probe sequences [a]		T_m / °C [b]	Φ_f [c]	I_{ds} / I_{ss} [d]
LNA(anti-TAR)	5'-GCtCcCaGGCD$_{514}$CAGaT-3'	-	0.12	-
	+ TAR RNA	56	0.26	3
DNA(anti-TAR)	5'-GCTCCCAGGCD$_{514}$CAGAT-3'	-	0.13	-
	+ TAR RNA	45	0.25	2

[a] Small characters present LNA. The LNA nucleotide "c" denotes a 5-methylcytosine LNA nucleotide. [b] All T_m values of probe-RNA duplexes (1.0 μM) were taken in in 50 mM sodium phosphate (pH = 7.0) containing 100 mM sodium chloride. [c] Fluorescent quantum yield measured using 0.4 μM probe solution in 50 mM sodium phosphate (pH = 7.0) containing 100 mM sodium chloride excited at 488 nm. [d] Ratio of the fluorescence intensities of hybrids (ds) and nonhybridized probes (ss) at λ_{em} 531 nm.

Table S3. ECHO probes for PLAC4 RNA.

Probe sequences [a]		T_m / °C [b]	Φ_f [c,d]	I_{ds} / I_{ss} [c,e]
LNA(anti-PLAC4-C)	5'-AGD$_{514}$TAGacgA-3'	-	0.073	-
	+ **PLAC4(A)** (mismatched)	34	0.12	1.6
	+ **PLAC4(G)** (matched)	61	0.13	3.6
LNA(anti-PLAC4-T)	5'-AGD$_{514}$TAGatgA-3'	-	0.059	-
	+ **PLAC4(A)** (matched)	55	0.16	6.4
	+ **PLAC4(G)** (mismatched)	44	0.13	3.4
DNA(anti-PLAC4-C)	5'-AGD$_{514}$TAGACGA-3'	-	0.072	-
	+ **PLAC4(A)** (mismatched)	26	0.068	0.69
	+ **PLAC4(G)** (matched)	29	0.064	1.1
DNA(anti-PLAC4-T)	5'-AGD$_{514}$TAGATGA-3'	-	0.032	-
	+ **PLAC4(A)** (matched)	33	0.069	3.4
	+ **PLAC4(G)** (mismatched)	31	0.061	1.8

[a] Small characters present LNA nucleotides. The LNA nucleotide "c" denotes a 5-methylcytosine LNA nucleotide. [b] All T_m values of probe-RNA duplexes (1.0 μM) were taken in in 50 mM sodium phosphate (pH = 7.0) containing 100 mM sodium chloride. Short complementary RNAs, 5'-UCAUCUAACU-3' for **PLAC4(A)**, 5'-UCGUCUAACU-3' for **PLAC4(G)**, were used in only the T_m measurements. [c] Photophysical data were collected at 50 °C for LNA probes and 25 °C for DNA probes. [d] Fluorescent quantum yield measured using 0.4 μM probe solution in 50 mM sodium phosphate (pH = 7.0) containing 100 mM sodium chloride excited at 488 nm. [e] Ratio of the fluorescence intensities of hybrids (ds) and nonhybridized probes (ss) at λ_{em} 531 nm.

Synthesis of N_4'-[^{18}F]Fluoroalkylated Ciprofloxacin as a Potential Bacterial Infection Imaging Agent for PET Study

Kalme Sachin, Eun-Mi Kim, Su-Jin Cheong, Hwan-Jeong Jeong, Seok Tae Lim, Myung-Hee Sohn, and Dong Wook Kim*

Department of Nuclear Medicine, Cyclotron Research Center, Research Institute of Clinical Medicine, Chonbuk National University Medical School, Jeonju, Jeonbuk 561-712, Korea. Received July 2, 2010; Revised Manuscript Received October 3, 2010

Syntheses and evaluation of fluoroalkylated ciprofloxacin analogues are described. Among these analogues, N_4'-3-fluoropropylciprofloxacin (**16**) showed the most efficient antibacterial activity against *E. coli* strains (DH5α and TOP10) and a high binding affinity for DNA gyrase of bacteria. To develop bacteria-specific infection imaging agents for positron emission tomography (PET), no-carrier-added N_4'-3-[^{18}F]fluoropropylciprofloxacin ([^{18}F]**16**) was prepared in two steps from N_4'-3-methanesufonyloxypropylciprofloxacin, resulting in a 40% radiochemical yield (decay corrected for 100 min) via the *tert*-alcohol media radiofluorination protocol with high radiochemical purity (>99%) as well as high specific activity (149 ± 75 GBq/μmol). The agent was stable (>90%), as shown by an in vitro human serum stability assay. A bacterial uptake and blocking study of [^{18}F]**16** using authentic compound **16** in TOP10 cells demonstrated its high specific bacterial uptake. The results suggest that this radiotracer holds promise as a useful bacterial infection radiopharmaceutical for PET imaging.

INTRODUCTION

Fluoroquinolones, such as ciprofloxacin (**1**) and enrofloxacin (**2**), as an important class of antibiotics are commonly prescribed because of their broad spectrum of activity against Gram-negative and Gram-positive bacteria (*1*). It is known that their effect is due to the interaction of fluoroquinolones with bacterial DNA gyrase, thus inhibiting DNA uncoiling and subsequent DNA synthesis (*2, 3*).

Radiolabeled fluoroquinolones are used as radiotracers for single-photon emission computed tomography (SPECT) or positron emission tomography (PET) and have been developed as shown in Figure 1. They have received much attention in the clinical field because they can differentiate between bacterial infection and nonbacterial infection or sterile inflammation (*4*−*9*). ^{99m}Tc-ciprofloxacin as a SPECT imaging agent has been widely used for this purpose in clinical studies (*4, 5*). However, the chemical structure of ^{99m}Tc-ciprofloxacin has been not determined, and it has been shown to have very low specific activity (*6*−*9*). Since the use of PET as a noninvasive nuclear imaging approach allows the measurement of nano- or picomolar-level concentrations of molecules in the tissues of virtually all organs with higher spatial and temporal resolutions than SPECT (*10*−*12*), many researchers have shown an interest in ciprofloxacin analogues labeled with a positron emitter for PET such as [^{18}F]ciprofloxacin (*13*), [^{18}F]COPCA (*14*), and N_4'-[^{11}C]methylciprofloxacin (*15*). However, [^{18}F]ciprofloxacin also has low specific activity (which can decrease PET imaging quality), because it is [^{18}F]radiolabeled via an ^{18}F- by ^{19}F-exchange reaction from ciprofloxacin in nature; consequently, it is difficult to prepare and results in poor radiochemical yield (*13, 16*). [^{18}F]COPCA was developed to increase specific activity, and this radiotracer has no specific binding to bacteria and is difficult to purify (*14*). Due to short imaging time (the short half-life of carbon-11; $t_{1/2}$ = 20.4 min), N_4'-[^{11}C]methylciprofloxacin is not preferred as a PET radiotracer for pharmacokinetics analysis (*15, 10*). It is widely accepted that fluorine-18 is the most desirable PET radionuclide due to its ideal physical properties ($t_{1/2}$ = 110 min) (*17*).

According to previous structure−activity relationship (SAR) studies, an introduction of short alkyl chains such as ethyl and *n*-propyl groups at the N-4′ position of ciprofloxacin could maintain or increase the antibacterial potency of the ciprofloxacin analogues (*18*−*22*). On the basis of this knowledge, we designed N_4'-[^{18}F]fluoroalkylated ciprofloxacin analogues, which have a high specific activity, for the development of a promising bacteria-specific infection imaging agent for PET. In this report, we describe the preparation and evaluation of N_4'-[^{18}F]fluoroalkylciprofloxacins.

EXPERIMENTAL SECTION

General. Unless otherwise noted, all reagent and solvents were commercially available from Sigma-Aldrich. Reaction progress was followed by TLC on 0.25 mm silica gel glass plates containing F-254 indicator. Visualization on TLC was monitored by UV light or radio-TLC scanner. Flash chromatography was performed using a 230−400 mesh silica gel (Merck KGaA). ^{1}H NMR spectra were recorded on a 600 MHz spectrometer (JEOL, Japan). Chemical shifts were reported in δ units (ppm) relative to tetramethylsilane, and coupling constants were reported in hertz. ^{13}C NMR spectra were acquired at 125 MHz. Low- and high-resolution electron impact (EI, 70 eV) spectra were obtained. [^{18}F]Fluoride ion was produced from a cyclotron (KIRAMS 13 MeV, South Korea) using the ^{18}O(p,n)^{18}F nuclear reaction with 19 MeV proton irradiation of an enriched [^{18}O]H_2O target. High-performance liquid chromatography (HPLC) was performed with spectra system (Thermo Scientific, Waltham, MA) using semipreparative column (C18 silica gel, 10 μm, 10 × 250 mm, Hypersil gold) and analytic column (C18 silica gel, 5 μm, 4.6 × 250 mm, Hypersil gold, 10 mM aqueous phosphoric acid/ethanol = 88:12). The eluant was simultaneously monitored by a UV detector (215 nm) and a NaI(Tl) radioactivity detector. Radioactivity was measured in a dose calibrator.

* Corresponding author. Assist. Prof. Dong Wook Kim, Department of Nuclear Medicine, Research Institute of Clinical Medicine, Chonbuk National University Medical School, Jeonju, Jeonbuk 561-712, Korea. Telephone: +82-63-250-2396, FAX: +82-63-255-1172, e-mail: kimdw@chonbuk.ac.kr.

10.1021/bc1002983 © 2010 American Chemical Society
Published on Web 11/04/2010

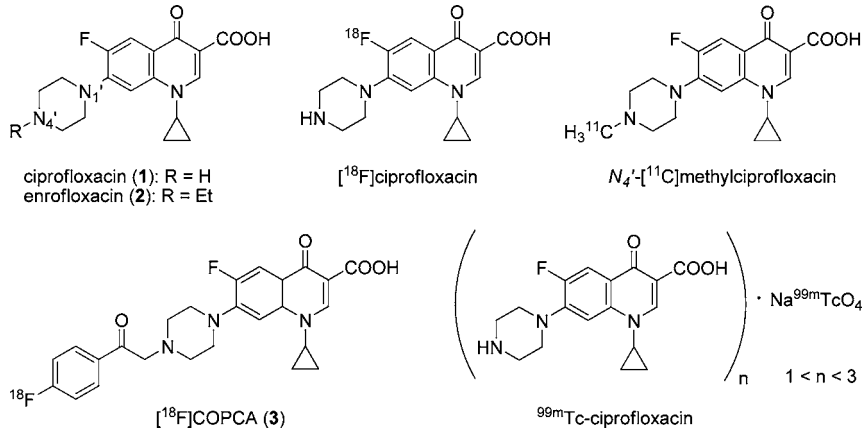


Figure 1. Structure of the radiolabeled ciprofloxacin derivatives.

Ciprofloxacin Methyl Ester (4). To a stirred solution of ciprofloxacin (Fluka, >98.0%, 200 mg, 0.60 mmol) in methanol (20 mL) was added *p*-toluenesulfonic acid (172 mg, 0.89 mmol). The mixture was refluxed for 16 h at 100 °C and then cooled to room temperature. The reaction mixture was dissolved in a $NaHCO_3$ solution (100 mL) and extracted from the aqueous phase with CH_2Cl_2 (100 mL × 3). The organic layer was dried over sodium sulfate and evaporated under reduced pressure. The residue was purified by flash column chromatography (5% MeOH/CH_2Cl_2) to obtain 166 mg (81%) of ciprofloxacin methyl ester (**4**) as a white solid; ^{1}H NMR (600 MHz, $CDCl_3$) δ 1.13−1.15 (m, 2H), 1.30−1.34 (m, 2H), 3.0−3.1 (m, 4H), 3.22−3.24 (m, 4H), 3.41−3.45 (m, 1H), 3.91 (s, 3H), 7.26 (d, J = 7.0 Hz, 1H), 8.04 (d, J = 13.7 Hz, 1H), 8.55 (s, 1H); ^{13}C NMR (150 MHz, $CDCl_3$) δ 8.20, 34.59, 46.06, 51.25 (d, J = 4.0 Hz), 52.11, 104.80 (d, J = 2.9 Hz), 110.09, 113.30 (d, J = 23.0 Hz), 123.00 (d, J = 7.2 Hz), 138.10, 145.10 (d, J = 11.4 Hz), 148.40, 153.53 (d, J = 247.0 Hz), 166.51, 173.17; MS (EI) *m*/*z* 345 (M^+), 303 (100); HRMS (EI) *m*/*z* calcd for $C_{18}H_{20}N_3O_3F$ (M^+) 345.1489, found 345.1486.

General Procedure for *N*-Alkylation Reaction. To a mixture of **4** (1.44 mmol) and potassium carbonate (4.32 mmol) in acetonitrile (20 mL) was added each $Br(CH_2)_nOH$ (2.88 mmol). The mixture was stirred at 100 °C for 12 h. The reaction mixture was dissolved in water (100 mL) and extracted from the aqueous phase with CH_2Cl_2 (100 mL × 3). The organic layer was dried over sodium sulfate and evaporated under reduced pressure. Flash column chromatography (5% MeOH/CH_2Cl_2) gave each N_4'-hydroxyalkyl ciprofloxacin methyl ester compound.

N_4'-2-Hydroxyethylciprofloxacin Methyl Ester (5). According to the general procedure for *N*-alkylation reaction with **4** (500 mg, 1.44 mmol), potassium carbonate (600 mg, 4.32 mmol), and 2-bromoethanol (360 mg, 2.88 mmol), **5** (390 mg, 69%) was obtained as a white solid; ^{1}H NMR (600 MHz, $CDCl_3$) δ 1.13−1.16 (m, 2H), 1.31−1.34 (m, 2H), 2.66 (t, J = 10.3 Hz, 2H), 2.74−2.76 (m, 4H), 3.29−3.30 (m, 4H), 3.41−3.45 (m, 1H), 3.68 (t, J = 19.0 Hz, 2H), 3.91 (s, 3H), 7.27 (d, J = 9.0 Hz, 1H), 8.05 (d, J = 14.8 Hz, 1H), 8.55 (s, 1H); ^{13}C NMR (150 MHz, $CDCl_3$) δ 7.16, 34.92, 49.35 (d, J = 4.4 Hz), 50.74, 53.06, 58.54, 59.95, 105.55 (d, J = 2.9 Hz), 108.68, 111.57 (d, J = 24.4 Hz), 121.73 (d, J = 5.7 Hz), 138.40, 144.77 (d, J = 10.0 Hz), 153.40 (d, J = 247.0 Hz), 165.23, 173.73; MS (EI) *m*/*z* 389 (M^+), 358 (100); HRMS (EI) *m*/*z* calcd for $C_{20}H_{24}N_3O_4F$ (M^+) 389.1751, found 389.1753.

N_4'-3-Hydroxypropylciprofloxacin Methyl Ester (6). According to the general procedure for *N*-alkylation reaction with **4** (275 mg, 0.80 mmol), potassium carbonate (550 mg, 3.98 mmol), and 3-bromopropanol (221 mg, 1.59 mmol), **6** (300 mg, 93%) was obtained as a white solid; ^{1}H NMR (600 MHz, $CDCl_3$) δ 1.12−1.15 (m, 2H), 1.30−1.33 (m, 2H), 1.77−1.81 (m, 2H), 2.73 (t, J = 11.0 Hz, 2H), 2.76 (m, 4H), 3.27 (m, 4H), 3.40−3.43 (m, 1H), 3.85 (t, J = 10.3 Hz, 2H), 3.91 (s, 3H), 7.26 (d, J = 6.8 Hz, 1H), 8.05 (d, J = 13.0 Hz, 1H), 8.55 (s, 1H); ^{13}C NMR (150 MHz, $CDCl_3$) δ 8.24, 27.18, 34.61, 50.08 (d, J = 4.3 Hz), 52.15, 53.14, 58.80, 64.67, 104.97 (d, J = 2.9 Hz), 110.20, 113.42 (d, J = 23.0 Hz), 123.33 (d, J = 5.7 Hz), 138.07, 144.54 (d, J = 10.0 Hz), 148.48, 153.53 (d, J = 247.0 Hz), 166.54, 173.15; MS (EI) *m*/*z* 403 (M^+), 358 (100); HRMS (EI) *m*/*z* calcd for $C_{21}H_{26}N_3O_4F$ (M^+) 403.1907, found 403.1912.

N_4'-4-Hydroxybutylciprofloxacin Methyl Ester (7). According to the general procedure for *N*-alkylation reaction with **4** (600 mg, 1.74 mmol), potassium carbonate (720 mg, 5.21 mmol), and 4-bromobutanol (530 mg, 3.47 mmol), **7** (475 mg, 63%) was obtained as a white solid; ^{1}H NMR (600 MHz, $CDCl_3$) δ 1.12−1.14 (m, 2H), 1.30−1.33 (m, 2H), 1.74 (m, 4H), 2.51 (t, J = 7.0 Hz, 2H), 2.76 (m, 4H), 3.31 (m, 4H), 3.38−3.42 (m, 1H), 3.62 (t, J = 5.5 Hz, 2H), 3.91 (s, 3H), 7.27 (d, J = 8.8 Hz, 1H), 8.05 (d, J = 13.0 Hz, 1H), 8.55 (s, 1H); ^{13}C NMR (150 MHz, $CDCl_3$) δ 8.26, 25.39, 32.61, 34.63, 49.60 (d, J = 4.3 Hz), 52.14, 52.68, 58.63, 62.84, 105.11 (d, J = 2.9 Hz), 110.19, 113.39 (d, J = 23.0 Hz), 123.38 (d, J = 7.2 Hz), 138.06, 144.43 (d, J = 10.0 Hz), 148.48, 153.57 (d, J = 247.0 Hz), 166.54, 173.16; MS (EI) *m*/*z* 417 (M^+), 358 (100); HRMS (EI) *m*/*z* calcd for $C_{22}H_{28}N_3O_4F$ (M^+) 417.2064, found 417.2063.

General Procedure for Hydrolysis. To a solution of each methyl ester compound (0.41 mmol) in methanol/water (4:1, 50 mL) was added LiOH (2.04 mmol). The mixture was stirred at room temperature for 8 h. The reaction solution was acidified (pH 5−6) with acetic acid and dissolved in water (100 mL). The reaction mixture was extracted from the aqueous phase with CH_2Cl_2 (100 mL × 3). The organic layer was dried over sodium sulfate and evaporated under reduced pressure. Flash column chromatography (10% MeOH/CH_2Cl_2) gave each acid compound.

N_4'-2-Hydroxyethylciprofloxacin (8). According to the general procedure for hydrolysis reaction with **5** (100 mg, 0.26 mmol), LiOH (30 mg, 1.28 mmol), **8** (80 mg, 83%) was obtained as a white solid; ^{1}H NMR (600 MHz, $CDCl_3$) δ 1.19−1.22 (m, 2H), 1.38−1.41 (m, 2H), 2.67 (t, J = 10.3 Hz, 2H), 2.76−2.78 (m, 4H), 3.36−3.38 (m, 4H), 3.52−3.56 (m, 1H), 3.70 (t, J = 8.3 Hz, 2H), 7.36 (d, J = 7.0 Hz, 1H), 8.04 (d, J = 13.1 Hz, 1H), 8.78 (s, 1H); ^{13}C NMR (150 MHz, $CDCl_3$) δ 8.37, 35.37, 49.95 (d, J = 5.7 Hz), 52.63, 57.92, 59.38, 104.86 (d, J = 1.8 Hz), 108.19, 112.44 (d, J = 23.0 Hz), 120.05 (d, J = 7.2 Hz), 139.15, 145.90 (d, J = 11.5 Hz), 147.49, 153.57 (d, J = 247.0 Hz), 167.08, 177.13; MS (EI) *m*/*z* 375 (M^+), 344 (100); HRMS (EI) *m*/*z* calcd for $C_{19}H_{22}N_3O_4F$ (M^+) 375.1594, found 375.1592.

***N*$_4$′-3-Hydroxypropylciprofloxacin (9).** According to the general procedure for hydrolysis reaction with **6** (135 mg, 0.33 mmol), LiOH (40 mg, 1.67 mmol), **9** (125 mg, 96%) was obtained as a white solid; ^{1}H NMR (600 MHz, $CDCl_3$) δ 1.19−1.22 (m, 2H), 1.37−1.41 (m, 2H), 1.78−1.81 (m, 2H), 2.73 (t, J = 11.0 Hz, 2H), 2.78 (m, 4H), 3.34 (m, 4H), 3.51−3.54 (m, 1H), 3.85 (t, J = 10.3 Hz, 2H), 7.36 (d, J = 6.8 Hz, 1H), 8.02 (d, J = 13.0 Hz, 1H), 8.78 (s, 1H); ^{13}C NMR (150 MHz, $CDCl_3$) δ 8.34, 27.22, 35.37, 49.91 (d, J = 4.3 Hz), 53.00, 58.71, 64.59, 105.02 (d, J = 2.8 Hz), 108.31, 112.57 (d, J = 23.0 Hz), 120.21 (d, J = 7.2 Hz), 139.31, 145.86 (d, J = 10.0 Hz), 147.57, 152.81 (d, J = 247.0 Hz), 167.06, 177.22; MS (EI) *m/z* 389 (M^+), 344 (100); HRMS (EI) *m/z* calcd for $C_{20}H_{24}N_3O_4F$ (M^+) 389.1751, found 389.1755.

***N*$_4$′-4-Hydroxybutylciprofloxacin (10).** According to the general procedure for hydrolysis reaction with **7** (170 mg, 0.41 mmol), LiOH (50 mg, 2.04 mmol), **10** (125 mg, 96%) was obtained as a white solid. ^{1}H NMR (600 MHz, $CDCl_3$) δ 1.18−1.21 (m, 2H), 1.37−1.410 (m, 2H), 1.74 (m, 4H), 2.52 (t, J = 7.0 Hz, 2H), 2.76−2.78 (m, 4H), 3.37−3.38 (m, 4H), 3.50−3.53 (m, 1H), 3.62 (t, J = 5.5 Hz, 2H), 7.37 (d, J = 7.5 Hz, 1H), 8.04 (d, J = 13.0 Hz, 1H), 8.78 (s, 1H); ^{13}C NMR (150 MHz, $CDCl_3$) δ 8.35, 25.33, 32.55, 35.41, 49.47 (d, J = 4.3 Hz), 52.73, 58.58, 62.85, 105.17 (d, J = 2.5 Hz), 108.24, 112.45 (d, J = 23.0 Hz), 120.16 (d, J = 7.2 Hz), 139.10, 145.82 (d, J = 10.1 Hz), 147.54, 153.82 (d, J = 247.0 Hz), 167.05, 177.19; MS (EI) *m/z* 403 (M^+), 344 (100); HRMS (EI) *m/z* calcd for $C_{21}H_{26}N_3O_4F$ (M^+) 403.1907, found 403.1909.

***N*$_4$′-2-Chloroethylciprofloxacin Methyl Ester (11).** To a mixture of **5** (300 mg, 0.77 mmol) and *p*-toluenesulfonylchloride (293 mg, 1.54 mmol) in CH_2Cl_2 (15 mL) was added triethylamine (0.32 mL, 2.31 mmol). The mixture was stirred at 25 °C for 30 h. The reaction mixture was dissolved in water (50 mL) and extracted from the aqueous phase with CH_2Cl_2 (50 mL × 3). The organic layer was dried over sodium sulfate and evaporated under reduced pressure. The residue was purified by flash column chromatography (5% MeOH/CH_2Cl_2) to obtain 235 mg (74%) of N_4′-2-chloroethylciprofloxacin methyl ester (**11**) as a white solid; ^{1}H NMR (600 MHz, $CDCl_3$) δ 1.12−1.15 (m, 2H), 1.30−1.35 (m, 2H), 2.74−2.76 (m, 4H), 2.38 (t, J = 13.7 Hz, 2H), 3.29−3.30 (m, 4H), 3.40−3.44 (m, 1H), 3.46 (t, J = 13.1 Hz, 2H), 3.91 (s, 3H), 7.27 (d, J = 10.0 Hz, 1H), 8.05 (d, J = 13.1 Hz, 1H), 8.55 (s, 1H); ^{13}C NMR (150 MHz, $CDCl_3$) δ 8.22, 34.58, 41.00, 49.95 (d, J = 4.3 Hz), 52.15, 52.94, 55.71, 104.92 (d, J = 3.2 Hz), 110.18, 113.39 (d, J = 23.0 Hz), 123.21 (d, J = 5.7 Hz), 138.08, 144.65 (d, J = 10.0 Hz), 153.52 (d, J = 247.0 Hz), 165.55, 173.13; MS (EI) *m/z* 407 (M^+), 149 (100); HRMS (EI) *m/z* calcd for $C_{20}H_{23}N_3O_3FCl$ (M^+) 407.1412, found 407.1411.

***N*$_4$′-3-Methanesulfonylpropylciprofloxacin Methyl Ester (12).** To a mixture of **6** (0.39 g, 0.97 mmol) and methane sulfonylchloride (0.09 mL, 1.16 mmol) in CH_2Cl_2 (10 mL) was added triethylamine (0.174 mL, 1.16 mmol) at 0 °C. The mixture was stirred at 25 °C for 2 h. The reaction mixture was dissolved in water (25 mL) and extracted from the aqueous phase with CH_2Cl_2 (25 mL × 3). The organic layer was dried over sodium sulfate and evaporated under reduced pressure. The residue was purified by flash column chromatography (5% MeOH/CH_2Cl_2) to obtain 310 mg (66%) of N_4′-3-methanesulfonylpropylciprofloxacin methyl ester (**12**) as a white solid; ^{1}H NMR (600 MHz, $CDCl_3$) δ 1.12−1.15 (m, 2H), 1.30−1.34 (m, 2H), 1.95−2.00 (m, 2H), 2.56 (t, J = 13.7 Hz, 2H), 2.65−2.67 (m, 4H), 3.03 (s, 3H), 3.26−3.28 (m, 4H), 3.40−3.44 (m, 1H), 3.91 (s, 3H), 4.35 (t, J = 13..0 Hz, 2H), 7.26 (d, J = 7.0 Hz, 1H), 8.04 (d, J = 13.1 Hz, 1H), 8.54 (s, 1H); ^{13}C NMR (150 MHz, $CDCl_3$) δ 8.24, 27.18, 34.61, 49.95, 51.97 (d, J = 4.4 Hz), 59.14, 62.62, 104.97 (d, J = 3.3 Hz), 110.20, 113.42 (d, J = 23.0 Hz), 123.74 (d, J = 5.7 Hz), 138.07, 142.21 (d, J = 11.5 Hz), 148.48, 153.78 (d, J = 247.0 Hz), 166.54, 173.15; MS (FAB) *m/z* 482 (M + H), 386 (100); HRMS (FAB) *m/z* calcd for $C_{22}H_{29}N_3O_6F$ (M + H) 482.1758, found 482.1761.

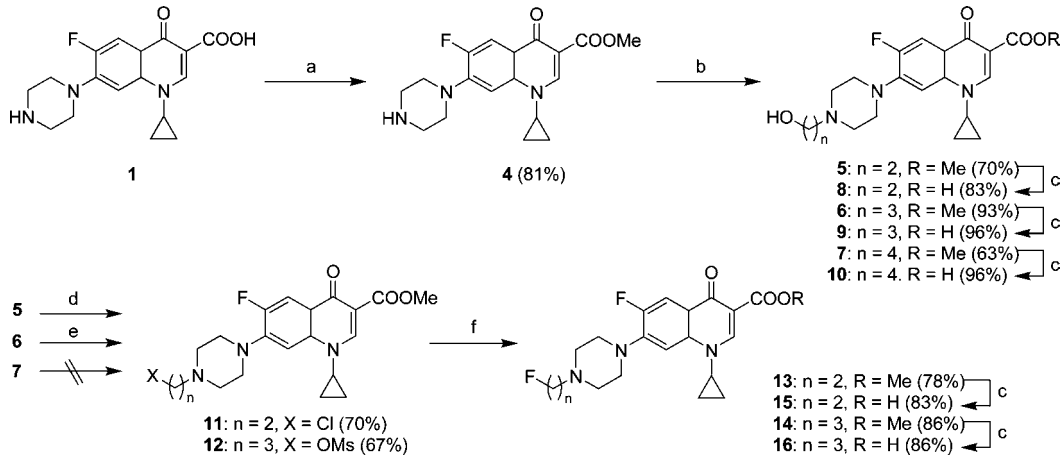
***N*$_4$′-2-Fluoroethylciprofloxacin Methyl Ester (13).** To a solution of **11** (135 mg, 0.25 mmol) in *t*-amyl alcohol (5 mL) was added TBAF (130 mg, 0.50 mmol). The mixture was stirred at 80 °C for 6 h. The reaction mixture was dissolved in water (10 mL) and extracted from the aqueous phase with ethyl acetate (10 mL × 3). The organic layer was dried over sodium sulfate and evaporated under reduced pressure. The residue was purified by flash column chromatography (5% MeOH/CH_2Cl_2) to obtain 76 mg (78%) of N_4′-2-fluoroethylciprofloxacin methyl ester (**13**) as a white solid; ^{1}H NMR (600 MHz, $CDCl_3$) δ 1.12−1.15 (m, 2H), 1.30−1.35 (m, 2H), 2.77−2.78 (m, 4H), 2.82 (t, J = 9.6 Hz, 2H), 3.30−3.32 (m, 4H), 3.41−3.44 (m, 1H), 3.91 (s, 3H), 4.62 (dt, J = 47.4, 4.7 Hz, 2H), 7.27 (d, J = 7.0 Hz, 1H), 8.05 (d, J = 13.1 Hz, 1H), 8.55 (s, 1H); ^{13}C NMR (150 MHz, $CDCl_3$) δ 8.20, 34.57, 49.98 (d, J = 4.3 Hz), 52.11, 53.32, 58.21 (d, J = 20.1 Hz), 81.96 (d, J = 166.6 Hz), 104.89 (d, J = 3.2 Hz), 110.16, 113.36 (d, J = 23.0 Hz), 123.15 (d, J = 7.2 Hz), 138.08, 144.65 (d, J = 10.0 Hz), 153.51 (d, J = 248.0 Hz), 165.54, 173.13; MS (EI) *m/z* 391 (M^+), 315 (100), 358; HRMS (EI) *m/z* calcd for $C_{20}H_{23}N_3O_3F_2$ (M^+) 391.1707, found 391.1711.

***N*$_4$′-3-Fluoropropylciprofloxacin Methyl Ester (14).** Prepared from mesylate precursor **12** by the method used to prepare the fluorocompound **13**, 200 mg (86%) of N_4′-3-fluoropropylciprofloxacin methyl ester (**14**) was obtained as a white solid; ^{1}H NMR (600 MHz, $CDCl_3$) δ 1.12−1.15 (m, 2H), 1.30−1.33 (m, 2H), 1.89−1.98 (m, 2H), 2.57 (t, J = 14.4 Hz, 2H), 2.67−2.69 (m, 4H), 3.28−3.29 (m, 4H), 3.40−3.44 (m, 1H), 3.91 (s, 3H), 4.55 (dt, J = 46.7, 5.8 Hz, 2H), 7.27 (d, J = 7.5 Hz, 1H), 8.04 (d, J = 13.1 Hz, 1H), 8.55 (s, 1H); ^{13}C NMR (150 MHz, $CDCl_3$) δ 8.20, 27.96 (d, J = 20.1 Hz), 34.57, 50.05 (d, J = 4.3 Hz), 52.12, 53.04, 54.25 (d, J = 5.7 Hz), 84.41 (d, J = 163.7 Hz), 104.80 (d, J = 3.8 Hz), 110.17, 113.37 (d, J = 23.0 Hz), 123.08 (d, J = 7.2 Hz), 138.10, 144.65 (d, J = 11.5 Hz), 148.41, 153.51 (d, J = 248.0 Hz), 166.57, 173.15; MS (EI) *m/z* 405 (M^+), 358 (100); HRMS (EI) *m/z* calcd for $C_{21}H_{25}N_3O_3F_2$ (M^+) 405.1864, found 405.1868.

***N*$_4$′-2-Fluoroethylciprofloxacin (15).** According to the general procedure for hydrolysis reaction with **13** (100 mg, 0.26 mmol), LiOH (30 mg, 1.28 mmol), 80 mg (83%) of N_4′-2-fluoroethylciprofloxacin (**15**) was obtained as a white solid; ^{1}H NMR (600 MHz, $CDCl_3$) δ 1.19−1.21 (m, 2H), 1.37−1.41 (m, 2H), 2.77−2.80 (m, 4H), 2.83 (t, J = 10.0 Hz, 2H), 3.37−3.39 (m, 4H), 3.53−3.57 (m, 1H), 4.63 (dt, J = 48.1, 4.8 Hz, 2H), 7.3 (d, J = 7.0 Hz, 1H), 8.02 (d, J = 13.1 Hz, 1H), 8.77 (s, 1H); ^{13}C NMR (150 MHz, $CDCl_3$) δ 8.30, 35.37, 49.08 (d, J = 4.3 Hz), 53.17, 58.15 (d, J = 20.1 Hz), 81.97 (d, J = 168.0 Hz), 104.89 (d, J = 2.9 Hz), 108.18, 112.54 (d, J = 23.0 Hz), 119.89 (d, J = 7.2 Hz), 139.17, 145.96 (d, J = 10.0 Hz), 147.58, 153.78 (d, J = 249.0 Hz), 167.10, 177.16; MS (EI) *m/z* 377 (M^+), 333 (100); HRMS (EI) *m/z* calcd for $C_{19}H_{21}N_3O_3F_2$ (M^+) 377.1549, found 391.1546.

***N*$_4$′-3-Fluoropropylciprofloxacin (16).** According to the general procedure for hydrolysis reaction with **14** (110 mg, 0.27 mmol), LiOH (32 mg, 1.36 mmol), 81 mg (76%) of N_4′-3-Fluoropropylciprofloxacin (**16**) was obtained as a white solid. ^{1}H NMR (600 MHz, $CDCl_3$) δ 1.19−1.21 (m, 2H), 1.37−1.40 (m, 2H), 1.89−1.98 (m, 2H), 2.58 (t, J = 15.1 Hz, 2H), 2.68−2.70 (m, 4H), 3.35−3.36 (m, 4H), 3.52−3.55 (m, 1H), 4.55 (dt, J = 46.7, 5.8 Hz, 2H), 7.36 (d, J = 7.5 Hz, 1H), 8.01 (d, J = 13.1 Hz, 1H), 8.77 (s, 1H); ^{13}C NMR (150 MHz, $CDCl_3$) δ 8.53, 27.94 (d, J = 20.1 Hz), 35.34, 49.88 (d, J = 4.3 Hz), 52.91, 54.18 (d, J = 5.3 Hz), 82.33 (d, J = 168.0 Hz), 104.82 (d, J = 2.9 Hz), 108.14, 112.40 (d, J = 26.0 Hz), 119.81 (d, J

Scheme 1. Synthesis of N_4'-Substituted Ciprofloxacin Derivatives[a]



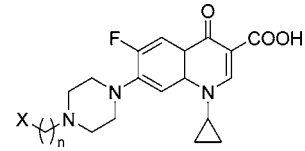
[a] Reagents and conditions: (a) TsOH, MeOH, reflux, 24 h; (b) Br(CH$_2$)$_n$OH, CH$_3$CN, K$_2$CO$_3$, 100 °C, 16 h; (c) LiOH, MeOH/H$_2$O (4:1), room temp, 16 h; (d) *p*-toluenesulfonylchloride, TEA, CH$_2$Cl$_2$, room temp, 20 h; (e) methanesulfonylchloride, TEA, CH$_2$Cl$_2$, room temp, 2 h; (f) TBAF, *t*-amyl alcohol, 80 °C, 6 h.

= 7.2 Hz), 139.41, 146.01 (d, J = 10.0 Hz), 147.74, 153.77 (d, J = 249.0 Hz), 167.10, 177.15; MS (EI) *m*/*z* 391 (M^+), 344 (100); HRMS (EI) *m*/*z* calcd for $C_{20}H_{23}N_3O_3F_2$ (M^+) 391.1707, found 391.1704.

Procedure for Labeling [^{18}F]16. [^{18}F]fluoride was produced in a cyclotron by the ^{18}O(p, n)^{18}F reaction. A volume of 200−400 μL of [^{18}F]fluoride (370−666 MBq) in water was added to a vacutainer containing *n*-Bu$_4$NHCO$_3$ (40% aq, 15 μL, 20.3 μmol). The azeotropic distillations were conducted with 200 μL aliquots of CH$_3$CN at 75 °C under a stream of nitrogen. A [^{18}F]fluoride displacement reaction of **12** (10 mg, 20.8 μmol) with *n*-Bu$_4$N[^{18}F]F in *tert*-amyl alcohol (500 μL) was carried out in a reaction vial at 100 °C for 20 min. After the reaction, the vial was cooled in an ice bath. The solvent was removed under a gentle stream of nitrogen at room temperature. For hydrolysis of the ester group, the residue was treated with LiOH (5 mg, 217 μmol) in 3 mL of MeOH/H$_2$O (4:1) at 100−110 °C for 20 min. After cooling the reaction mixture, the reaction mixture was acidified with acetic acid (pH = 5−6). The solvent was removed with a gentle stream of nitrogen. The crude compound was injected onto reverse-phase HPLC with 10 mM aqueous phosphoric acid (1 mL, pH 2.2) and purified. The desired compound was collected from HPLC (t_R = 10.6 min; C18 silica gel, 10 μm, 10 × 250 mm; 10 mM aqueous phosphoric acid/ethanol = 88:12 (v/v); pH 2.3; 215 nm; 4 mL/min). After the HPLC solvent was removed (70−75 °C) using a gentle stream of nitrogen, N_4'-3-[^{18}F]fluoropropylciprofloxacin ([^{18}F]**16**) was obtained for biological study. For the identification of the radioproduct, the collected HPLC fraction was coinjected with the cold compound **16**. The total reaction time of [^{18}F]**16** was 100 min, and the overall decay-corrected radiochemical yield was approximately 40%. Specific activity at the end of synthesis was calculated by relating radioactivity to the mass associated with the UV absorbance (215 nm) peak of cold compound. Specific radioactivity of [^{18}F]**16** (149 ± 75 GBq/μmol, n = 3) was obtained on an HPLC column.

In Vitro Antibacterial Activity Analysis Studies. The antibacterial activity analysis was determined from the lowest concentration to the high concentration of test compounds that resulted in a complete inhibition of visible growth in the medium. In vitro antibacterial activity analysis was studied according to previously published procedures (*23*). Ciprofloxacin and tested compounds were dissolved (mg/mL) in 10 mM phosphoric acid, and the mixture was adjusted to pH 7. Serial dilutions (ranging from 0 μg/mL to 500 μg/mL of test compounds) were made using LB broth (BD Bioscience, San Jose, CA). *E. coli* DH5α or TOP10 (5 × 10^6/mL) (Invitrogen, Carlsbad, CA) was added to tubes containing the diluted test compounds. Each tube was incubated in a shaking incubator at 37 °C for 18 h, and optical density was measured at 600 nm (Amersham biosciences, Ultraspec 2100 pro, Piscataway, NJ). Antibacterial activities were carried out in quintuple. The MIC$_{50}$ (ng/mL) of the test compounds and ciprofloxacin were determined. The MIC$_{50}$ was defined as the 50% concentration of an antibacterial agent that inhibited visible growth after incubation at 37 °C for 18 h.

Table 1. In Vitro Antibacterial Activity and Inhibitory Activity against DNA Gyrase of N_4'-Substituted Ciprofloxacin Derivatives[a]



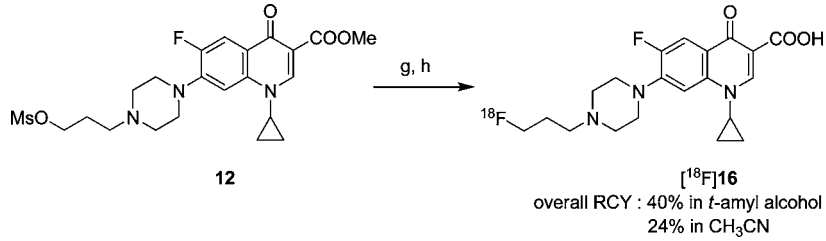
			MIC$_{50}$ (ng/mL)[b]		IC$_{50}$ (μg/mL)
compound	*n*	X	DH5α	TOP10	DNA gyrase
ciprofloxacin	-	-	13.9 ± 2.7	0.40 ± 0.06	3.20 ± 0.8
8	2	OH	6.76 ± 0.55	3.80 ± 0.96	16.8 ± 3.4
9	3	OH	35.7 ± 0.58	6.66 ± 1.0	ND
10	4	OH	40.0 ± 2.1	21.3 ± 3.5	ND
15	2	F	346 ± 18	3.16 ± 0.23	12.6 ± 4.4
16	3	F	157 ± 4.0	3.13 ± 0.20	9.63 ± 3.6

[a] Data are expressed as mean ± SD. ND = not determined. [b] MIC$_{50}$ for 50% of strains tested.

DNA Gyrase Inhibition Studies. Measurement of minimum inhibitory concentration (MIC) was done as described previously (*24*). DNA supercoiling activity was assayed with relaxed pHOT-1 DNA as a substrate (TopoGEN, Inc., FL, USA) according to the manufacturer's protocol. The standard reaction mixture (20 μL) contained 35 mM Tris-Cl, pH 7.5, 24 mM KCl, 4 mM MgCl$_2$, 2 mM dithiothreitol, 1.8 mM spermidine, 1 mM ATP, 6.5% glycerol, 0.1 mg/mL BSA, 167 ng/μL relaxed pHOT-1, and *E. coli* DNA gyrase. The reaction mixture was incubated at 37 °C for 1 h and was terminated by addition of a stop buffer (5% Sarkosyl, 0.125% bromophenol blue, 25% glycerol) and a chloroform/isoamyl alcohol (24:1) mixture. After a brief vortex, the blue aqua phase was analyzed by electrophoresis in 0.8% agarose. The IC$_{50}$ was defined as the drug concentration that reduced the enzymatic activity observed with drug-free controls by 50%.

In Vitro Stability Study of [^{18}F]16. For the labeling stability test, [^{18}F]**16** (0.74 MBq/100 μL) was incubated with human

Scheme 2. Radiosynthesis of N_4'-[^{18}F]Fluoropropylciprofloxacin in tert-Alcohol Medium[a]



[a] Reagents and conditions: (g) [^{18}F]TBAF, *t*-amyl alcohol or CH_3CN, 100 °C, 20 min; (h) LiOH, MeOH:H_2O (4:1), 100 °C, 30 min.

serum (0.5 mL) at 37 °C water bath for 5 h and then analyzed by chromatography on ITLC-sg strips eluted with 5% methanol/methylene chloride ([^{18}F]**16**, $R_f = 0.79$; serum bound [^{18}F]**16**, $R_f = 0$). After they were developed, the chromatographic strips were scanned on an automatic TLC scanner (Bioscan, Washington, DC, USA). TLC was performed at various time points. All the experiments were done in triplicate.

Competitive Bacteria Uptake Experiments of [^{18}F]16 and Cold Authentic Compound. Bacterial uptake test was performed with TOP10. TOP10 (5×10^7) was incubated with [^{18}F]**16** (2.96 MBq) for 30 min at 37 °C. For the blocking studies, [^{18}F]**16** was co-treated with **16** (25 nmol) as a blocker to the TOP10 (5×10^7) sample for 30 min at 37 °C. These blocker concentrations did not affect TOP10 survival. This was verified at 400 nm before starting the test. After incubation, TOP10 was washed with PBS buffer twice and counted on a γ-counter (Packard, Meriden, CT). The experiment was carried out in triplicate. The values were expressed as mean ± SD.

RESULTS AND DISCUSSION

The synthesis of non-radiolabeled N_4'-fluoroalkylated and hydroxyl ciprofloxacin derivatives were achieved via a versatile and efficient synthetic route from commercially available ciprofloxacin (**1**), as shown in Scheme 1. According to structure−activity relationship (SAR) studies, it should be noted that variation at the N-4′ substituent of fluoroquinolones with alkyl groups plays an important role in antibacterial activity (*6*). On the basis of this information, we introduced various fluoroalkyl groups at the terminal nitrogen of the piperazine of ciprofloxacin (N-4′ position). After the esterification of **1** to the methyl ester **4** for the protection of the acid group (*19*), the alkylation of **4** with 2-bromoethanol, 3-bromopropanol, and 4-bromobutanol under reflux conditions in CH_3CN yielded the N_4'-2-hydroxyethyl, 3-hydroxyproyl, and 4-hydroxybutyl ciprofloxacin methyl esters (**5**−**7**), respectively, in reasonable yields (63−93%). Hydrolysis of **5**−**7** with LiOH in methanol/water produced N_4'-hydroxyalkyl ciprofloxacin derivatives **8**−**10**. The chloride precursor **11** was prepared by the chlorination of the alcohol compound **5** with *p*-toluenesulfonyl chloride and triethylamine (TEA) in CH_2Cl_2 at 70% yield. Similarly, the mesylate precursor **12** was prepared by treating the alcohol compound **6** with methanesulfonylchloride and TEA. Unfortunately, the precursor produced by the methanesulfonylation or chlorination reaction of N_4'-3-hydroxybutyl ciprofloxacin methyl ester (**7**) could not be obtained because the precursor product immediately converted to its five-membered intracyclization salt compound during the reaction process. The *tert*-alcohol media nucleophilic fluorination (*25*−*27*) of precursors **11** and **12** using tetrabutylammonium fluoride (TBAF) proceeded selectively producing the desired fluoro-products in high yields (**13**, 78%; and **14**, 86%, respectively) without intracyclic or alkene byproducts (*20, 21*). N_4'-2-Fluoroethyl ciprofloxacin (**15**) and N_4'-3-fluoropropylciprofloxacin (**16**) were produced by hydrolysis of methyl esters **13** and **14**, respectively.

To investigate the antibacterial potency of the N_4'-substituted ciprofloxacin derivatives, including the N_4'-fluoroalkylated ciprofloxacin derivatives (**15** and **16**), we measured the EC_{50} values of these derivatives (**8**, **9**, **10**, **15**, and **16**) for their in vitro antibacterial activity against two *E. coli* DH5α and TOP10 strains, as shown in Table 1. Whereas N_4'-fluoroalkylated ciprofloxacin derivatives **15** and **16** exhibited less potent in vitro antibacterial activity against the DH5α strain than did the N_4'-hydroxyalkylated ciprofloxacin derivatives (**8**−**9**), they showed good antibacterial activity against the TOP10 strain compared with these N_4'-hydroxyalkylated compounds **8** and **9**. Next, we evaluated the inhibition potencies of the three selected derivatives (**8**, **15**, and **16**) and the inhibition potentials of ciprofloxacin in the presence of DNA gyrase of *S. aureus*. Among the compounds tested, N_4'-3-fluoropropylciprofloxacin (**16**) exhibited the best ability to inhibit the target enzyme, DNA gyrase, as well as the greatest antibacterial activity against the TOP10 strains. In this in vitro study, the introduction of a 3-fluoropropyl group onto the N-terminal of the piperazinyl moiety in ciprofloxacin maintained both high binding affinity for the enzyme and a antibacterial potency comparable to that of the parent compound, ciprofloxacin. On the basis of the in vitro study results, we selected **16** as the compound of choice for further investigation and prepared N_4'-3-[^{18}F]fluoropropylciprofloxacin ([^{18}F]**16**) as a potential bacterial infection imaging agent for PET study.

N_4'-3-[^{18}F]fluoropropylciprofloxacin ([^{18}F]**16**) was generated by a two-step procedure consisting of *tert*-alcohol media [^{18}F]radiofluorination (*27*) and subsequent hydrolysis of the methyl ester compound [^{18}F]**14**, as shown in Scheme 2. The first radiolabeling step, [^{18}F]radiofluorination reaction of the mesylate precursor **12** with [^{18}F]TBAF in *tert*-amyl alcohol at 100 °C, produced the labeled compound [^{18}F]**14** at high radiochemical yield (RCY) compared with [^{18}F]radiofluorination reaction in conventional solvent—CH_3CN. After the basic hydrolysis of [^{18}F]**14**, the final product compound, [^{18}F]**16**, was isolated by reverse-phase HPLC purification, as described in the Experimental Section. Figure 2A shows a representative semipreparative HPLC chromatogram of the crude reaction mixture, which indicates that [^{18}F]**16** could be obtained with high specific activity (an average specific activity of 149 ± 75 GBq/μmol when starting from a relatively low amount (370−666 MBq) of [^{18}F]fluoride) compared to that of the previous radiolabeled ciprofloxacins (0.43 ± 0.2 GBq/μmol) (*13*). The radiochemical purity of [^{18}F]**16**, which coeluted on analytical HPLC with an authentic sample of unlabeled **16** (Figure 2B), was >99%. The overall radiosynthesis of [^{18}F]**16** resulted in a decay-corrected RCY of approximately 40% with a total synthesis time (including the HPLC purification) of 100 min from the end of bombardment in two steps; the RCY of overall radiosynthesis of [^{18}F]**16** using the radiofluorination reaction in CH_3CN showed 24%.

The radiotracer (0.74 MBq) was incubated, and the percentage of the remaining [^{18}F]**16** ($R_f = 0.79$) was greater than 90% after 5 h when incubated in human serum at 37 °C, indicating the relatively high in vitro stability of the radiotracer as shown in Figure 3. On the other hand, serum-bound [^{18}F]**16** ($R_f = 0$) was less than 10% after 5 h postlabeling. This result demonstrated

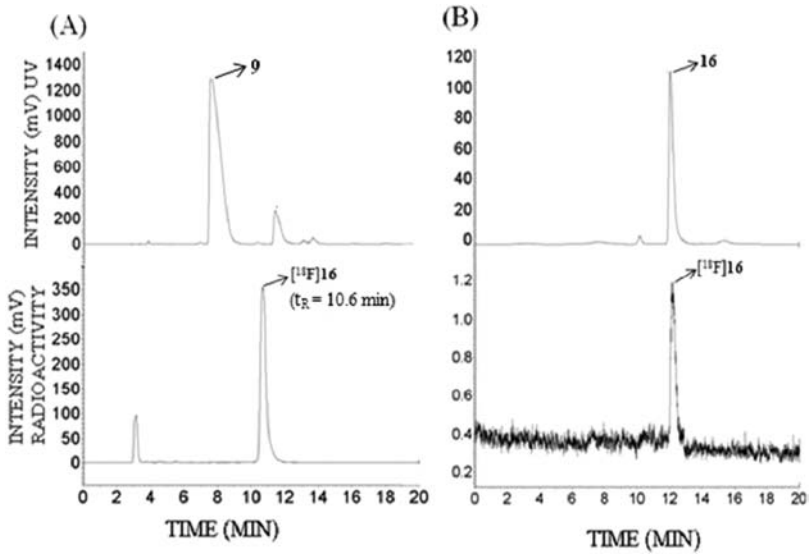


Figure 2. (A) Purification of [^{18}F]**16** on HPLC. The reaction mixture was injected on a semipreparative C18 column and was eluted with 10 mM aqueous phosphoric acid/EtOH (88:12) at a flow rate of 4.0 mL/min. (B) Representative analytical HPLC chromatogram of [^{18}F]**16** coinjected with its non-radioactive analogue **16**.

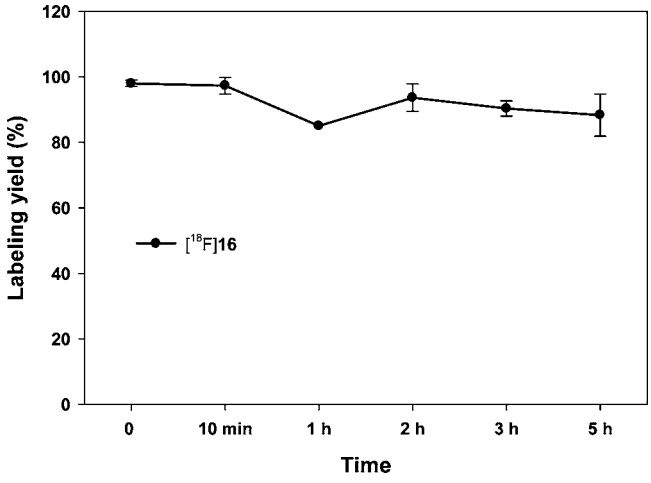


Figure 3. In vitro human serum stability of [^{18}F]**16**.

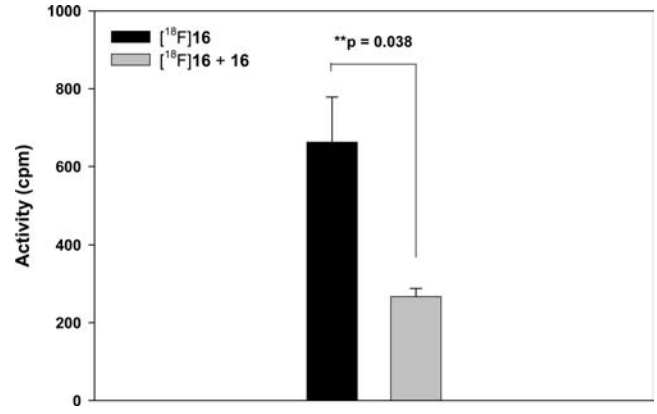


Figure 4. Bacterial uptake and blocking of [^{18}F]**16** in TOP10 ($n = 3$). TOP10 was incubated with [^{18}F]**16** and the authentic compound **16** (25 nmol) as inhibitor. The data are presented as the mean ± SD ($P < 0.05$).

that the [^{18}F]fluoropropyl moiety in the radiotracer is quite stable in human serum.

Competitive bacterial binding assays were carried out on the TOP10 with a cold authentic compound **16**, as shown in Figure 4. Bacterially bound levels decreased by 59% of control levels in the presence of 25 nmol of cold authentic compound **16**. This inhibition study demonstrated high specificity of [^{18}F]**16** binding to the DNA gyrase of TOP10; these results illustrate that this radiotracer has great potential as an imaging agent to detect bacterial infections or to evaluate pharmacokinetics of quinolone antibacterial drugs through its high specific bacterial uptake.

CONCLUSION

In summary, we present syntheses and evaluation of fluoroalkylated ciprofloxacin derivatives to investigate bacterial infection radiopharmaceuticals for PET. The SAR study suggests that the introduction of a 3-fluoropropyl group onto the N-4′ position in ciprofloxacin should have little influence on either high binding affinity to the DNA gyrase of bacteria or antibacterial potency; we prepared no-carrier-added N_4'-3-[^{18}F]fluoropropylciprofloxacin ([^{18}F]**16**) in two steps starting from its mesylate precursor using the *tert*-alcohol media radiofluorination method with good radiochemical yield. The competition bacterial binding study and high specific activity of [^{18}F]**16** suggest that it may have potential as a useful PET radiopharmaceutical agent for the differentiation between bacterial infection and nonbacterial infection or sterile inflammation. Further studies to evaluate the utilities of this radiotracer for PET bacterial infection in vivo imaging are in progress in our laboratories.

ACKNOWLEDGMENT

This work was supported by the Nuclear Research & Development Program of the Korea Science and Engineering Foundation (KOSEF) grant funded by the Korean government (MEST) (grant code: 2010-0017509) and the Conversing Research Center Program through the National Research Foundation of Korea (NRF) funded by the MEST (grant code: 2010K001050).

Supporting Information Available: ^{1}H and ^{13}C NMR spectra of all compounds. This material is available free of charge via the Internet at http://pubs.acs.org.

LITERATURE CITED

(1) Hoopper, D. C. (1998) Clinical application of quinolones. *Biochim. Biophys. Acta 1400*, 45–61.

(2) Drlica, K. (1999) Mechanism of fluoroquinolone action. *Curr. Opin. Microbiol. 2*, 504–508.
(3) Levine, C., Hiasa, H., and Marians, K. J. (1998) DNA gyrase and topoisomerase IV: biochemical activities, physiological roles during chromosome replication, and drug sensitivities. *Biochim. Biophys. Acta 1400*, 29–43.
(4) Vinjamuri, S., Hall, A. V., Solanki, K. K., Bomanji, J., Siraj, Q., O'Shaughnessy, E., Das, S. S., and Britton, K. E. (1996) Comparision of 99mTc infecton imaging with radiolabelled white-cell imaging in the evaluation of bacterial infection. *Lancet 347*, 233–235.
(5) Boerman, O. C., Rennen, H., Wim, J. G., and Frans, H. M. (2001) Radiopharmaecuticals to image infection and inflammation. *Semin. Nucl. Med. 4*, 286–295.
(6) Sarda, L., Cremieux, A. C., Lebellec, Y., Meulemans, A., Rachida, L., Hayem, G., Genin, R., Delahaye, N., Huten, D., and Guludec, D. L. (2003) Inability of 99mTc-ciprofloxacin scintigraphy to discriminate between septic and sterile osteoarticular diseases. *J. Nucl. Med. 44*, 920–926.
(7) Welling, M. M., Lupetti, A., Balter, H. S., Lanzzeri, S., Souto, B., Rey, A. M., Savio, E. O., Annema, A. P., Pauwels, E. K. J., and Nibbering, P. H. (2001) 99mTc-labeled antimicrobial peptides for detection of bacterial and candida albicans infection. *J. Nucl. Med. 42*, 788–794.
(8) Brunner, M., Langer, O., Dobrozemsky, G., Muller, U., Zeitlinger, M., Mitterhauser, M., Wadsak, W., Dudczak, R., Kletter, K., and Muller, M. (2004) [^{18}F]Ciprofloxacin, a new positron emission tomography tracer for noninvasive assessment of the tissue distribution and pharmacokinetics of ciprofloxacin in humans. *Antimicrob. Agents Chemother. 48*, 3850–3857.
(9) Oyen, W. J. G., Corstens, F. H. M., and Boerman, O. C. (2005) Discriminating infection from sterile inflammation: can radiolabelled antibiotic solve the problem? *Eur. J. Nucl. Med. Mol. Imaging 32*, 151–152.
(10) Phelps, M. E. (2000) Positron emission tomography provides molecular imaging of biological processes. *Proc. Natl. Acad. Sci. U.S.A. 97*, 9226–9233.
(11) Rowland, D. J., and Cherry, S. R. (2008) Small animal preclinical nuclear medicine instrumentation and methodology. *Semin. Nucl. Med. 38*, 209–222.
(12) Rahmim, A., and Zaidi, A. (2008) PET versus SPECT: strength, limitations and challenges. *Nucl. Med. Commun. 29*, 193–207.
(13) Langer, O., Mitterhauser, M., Brunner, M., Zeitlinger, M., Ziegler, S., Wadsak, W., Mayer, B. X., Kletter, K., and Muller, M. (2003) Synthesis of fluorine-18-labeled ciprofloxacin for PET studies in humans. *Nucl. Med. Biol. 30*, 285–291.
(14) Zijlstra, S., Gunawan, J., Freytag, C., and Burchert, W. (2006) Synthesis and evaluation of fluorine-18 labelled compounds for imaging of bacterial infections with pet. *Appl. Radiat. Isot. 64*, 802–807.
(15) Goethals, P., and Volkaert, A. (2002) Preparation of N'_4-[^{11}C]methyl-ciprofloxacin for positron emission tomography studies. *J. Label. Compd. Radipharm. 45*, 213–216.
(16) Langer, O., Brunner, M., Zeitlinger, M., Ziegler, S., Muller, U., Dobrozemsky, G., Lackner, E., Dudczak, R., Kletter, K., and Muller, M. (2005) In vitro and in vivo evaluation of [^{18}F]ciprofloxacin for the imaging of bacterial infections with PET. *Eur. J. Nucl. Med. Mol. Imaging 32*, 143–150.
(17) Kilbourn, M. R., Jarabek, P. A., and Welch, M. J. (1985) An improved [^{18}O]water target for [^{18}F]fluoride production. *Int. J. Appl. Radiat. Isot. 36*, 327–328.
(18) Haemers, A., Leysen, D., Bollaert, W., Zhang, M., and Pattyn, S. (1990) Influence of N substitution on antimycobacterial activity of ciprofloxacin. *Antimicrob. Agents Chemother. 34*, 496–497.
(19) Chu, D. T. W., and Fernandes, P. B. (1989) Structure-activity relationship of the fluoroquinolones. *Antimicrob. Agents Chemother. 33*, 131–135.
(20) Asahina, Y., Iwase, K., Iinuma, F., Hosaka, M., and Ishizaki, T. (2005) Synthesis and antibacterial activity of 1-(2-fluorovinyl)-7-substituted-4-quinolone-3-carboxylic acid derivatives, conformationally restricted analogues of fleroxacin. *J. Med. Chem. 48*, 3194–3202.
(21) Zhi, C., Long, Z., Manikowski, A., Comstock, J., Xu, W. C., Brown, N. C., Tarantino, P. M., Jr., Holm, K. A., Dix, E. J., Wright, G. E., Barnes, M. H., Butler, M. M., Foster, K. A., Lamarr, W. A., Bachand, B., Bethell, R., Cadilhac, C., Charron, S., Lamothe, S., Motorina, I., and Storer, R. (2006) Hybrid antibacterials. DNA polymerase-topoisomerase inhibitors. *J. Med. Chem. 49*, 1455–1465.
(22) Sriram, D., Yogeeswari, P., Basha, J. S., Deshpande, R. R., and Nagaraja, V. (2005) Synthesis and antimycobacterial evaluation of various 7-substituted ciprofloxacin derivatives. *Bioorg. Med. Chem. 13*, 5774–5778.
(23) Meca, G., Sospedra, I., Soriano, J. M., Ritieni, A., Valero, M. A., and Mañes, J. (2009) Isolation, purification and antibacterial effects of fusaproliferin produced by Fusariumsubglutinans in submerged culture. *Food Chem. Toxicol. 47*, 2539–2543.
(24) Pokrovskaya, V., Belakhov, V., Hainrichson, M., Yaron, S., and Baasov, T. (2009) Design, synthesis, and evaluation of novel fluoroquinolone-aminoglycoside hybrid antibiotics. *J. Med. Chem. 52*, 2243–2254.
(25) Kim, D. W., Jeong, H.-J., Lim, S. T., Sohn, M.-H., Katzenellenbogen, J. A., and Chi, D. Y. (2008) Facile nucleophilic fluorination reactions using *tert*-alcohols of alkali metal fluorides and improved selectivity. *J. Org. Chem. 73*, 957–962.
(26) Kim, D. W., Jeong, H.-J., Lim, S. T., and Sohn, M.-H. (2008) Tetrabutylammonium tetra (tert-butyl alcohol)-coordinated fluoride as a facile fluoride source. *Angew. Chem., Int. Ed. 47*, 8404–8406.
(27) Kim, D. W., Ahn, D.-S., Oh, Y.-H., Lee, S., Kil, H. S., Oh, S. J., Lee, S. J., Kim, J. S., Ryu, J. S., Moon, D. H., and Chi, D. Y. (2006) A new class of S_N2 reaction catalyzed by protic solvents: facile fluorination for isotopic labeling of diagnostic molecules. *J. Am. Chem. Soc. 128*, 16394–16397.

BC1002983

Supporting Informations

Synthesis of N_4'-[^{18}F]Fluoroalkylated Ciprofloxacin as a Potential Bacterial Infection Imaging Agent for PET Study

*Kalme Sachin, Eun-Mi Kim, Su-Jin Cheong, Hwan-Jeong Jeong, Seok Tae Lim, Myung-Hee Sohn and Dong Wook Kim**

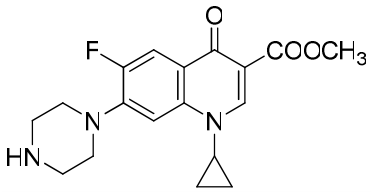
Department of Nuclear Medicine, Cyclotron Research Center, Research Institute of Clinical Medicine, Chonbuk National University Medical School, Jeonju, Jeonbuk 561-712, Korea
E-mail: kimdw@chonbuk.ac.kr

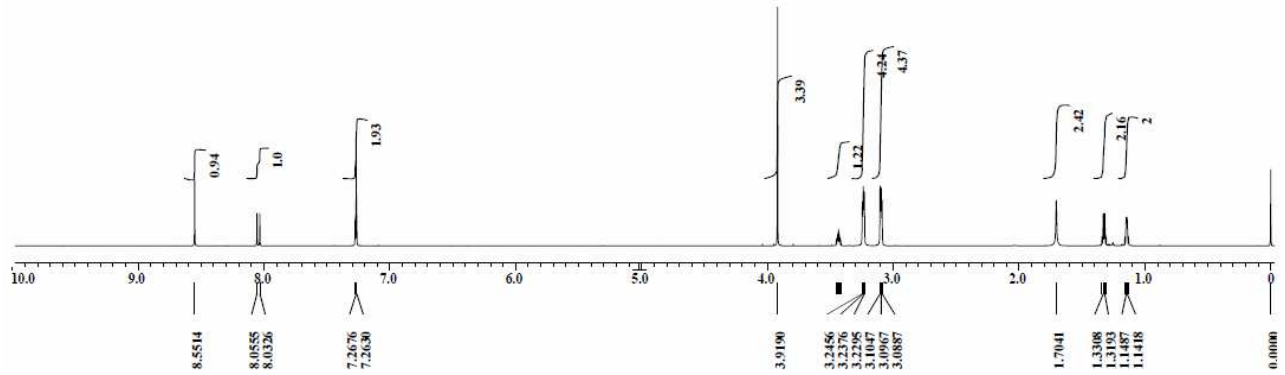
Table of Contents

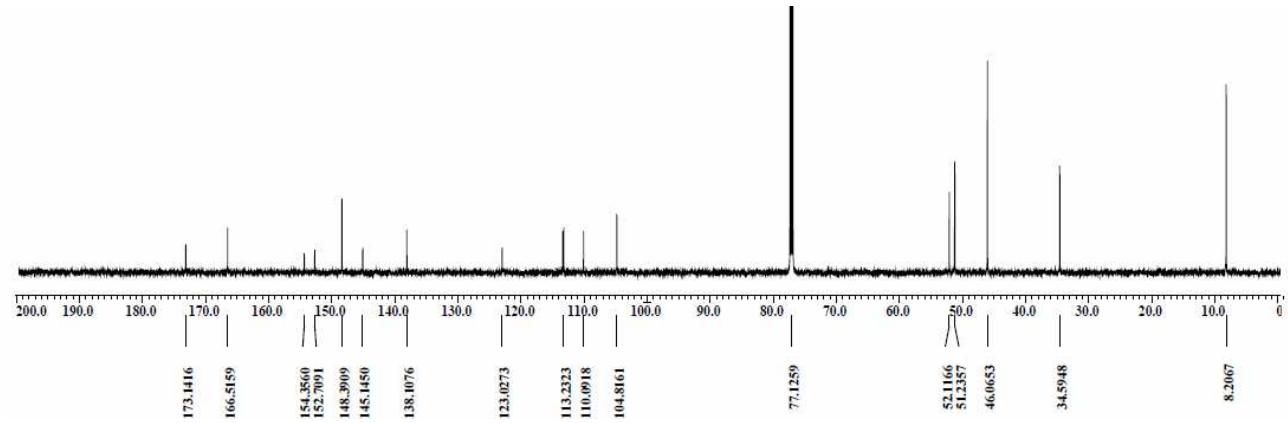
Information	Page
^{1}H and ^{13}C NMR Spectra of all compounds	
Ciprofloxacin methyl ester (**4**)	S2
N_4'-2-Hydroxyethylciprofloxacin Methyl Ester (**5**)	S3
N_4'-3-Hydroxypropylciprofloxacin Methyl Ester (**6**)	S4
N_4'-4-Hydroxybutylciprofloxacin Methyl Ester (**7**)	S5
N_4'-2-Hydroxyethylciprofloxacin (**8**)	S6
N_4'-3-Hydroxypropylciprofloxacin (**9**)	S7
N_4'-4-Hydroxybutylciprofloxacin (**10**)	S8
N_4'-2-Chloroethylciprofloxacin Methyl Ester (**11**)	S9
N_4'-3-Methanesulfonylpropylciprofloxacin Methyl Ester (**12**)	S10
N_4'-2-Fluoroethylciprofloxacin Methyl Ester (**13**)	S11
N_4'-3-Fluoropropylciprofloxacin Methyl Ester (**14**)	S12
N_4'-2-Fluoroethylciprofloxacin (**15**)	S13
N_4'-3-Fluoropropylciprofloxacin (**16**)	S14

^{1}H and ^{13}C NMR Spectra of all compounds

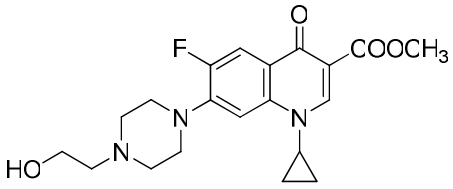
Ciprofloxacin methyl ester (4).

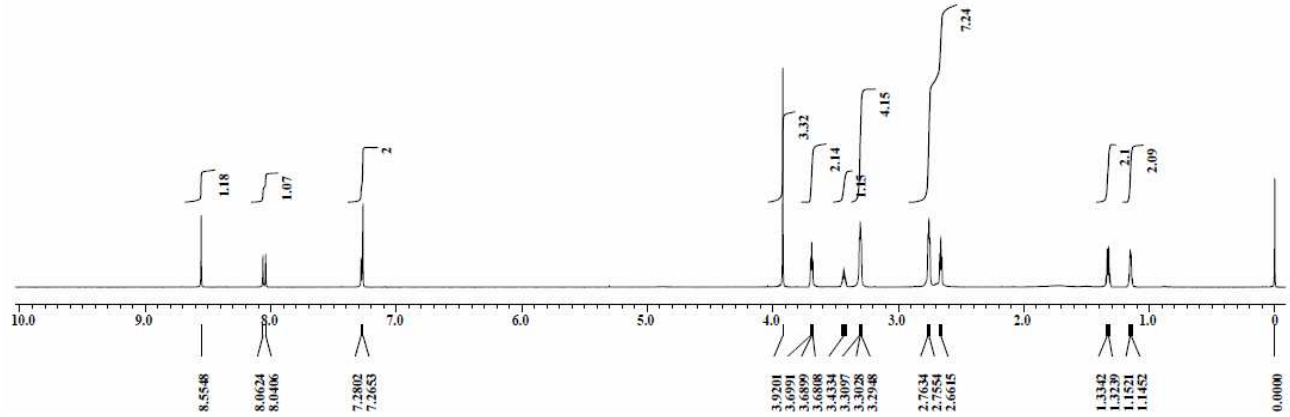


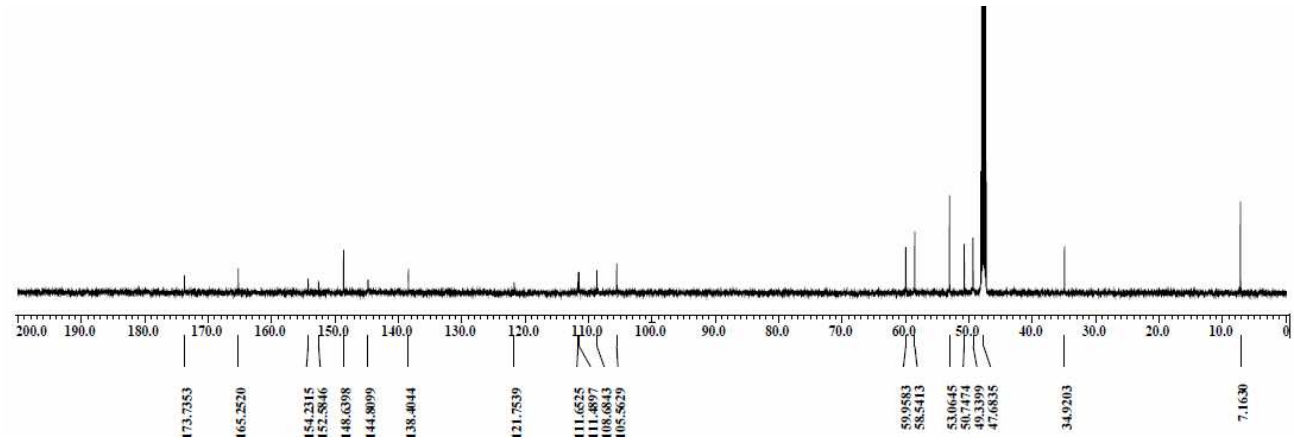




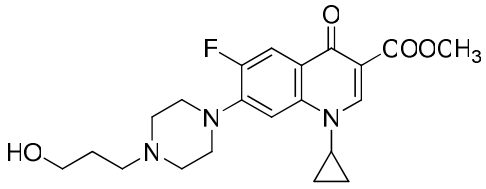
***N_4'*-2-Hydroxyethylciprofloxacin Methyl Ester (5).**

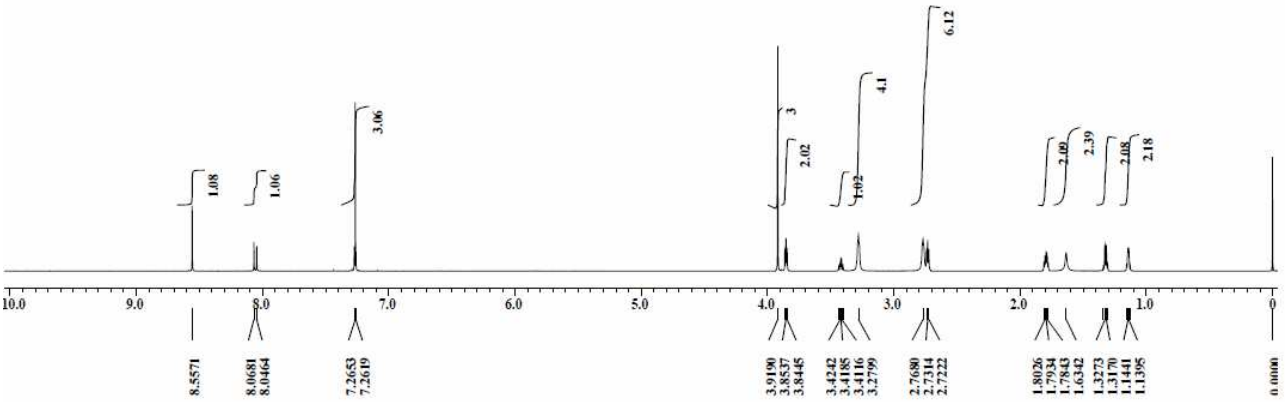


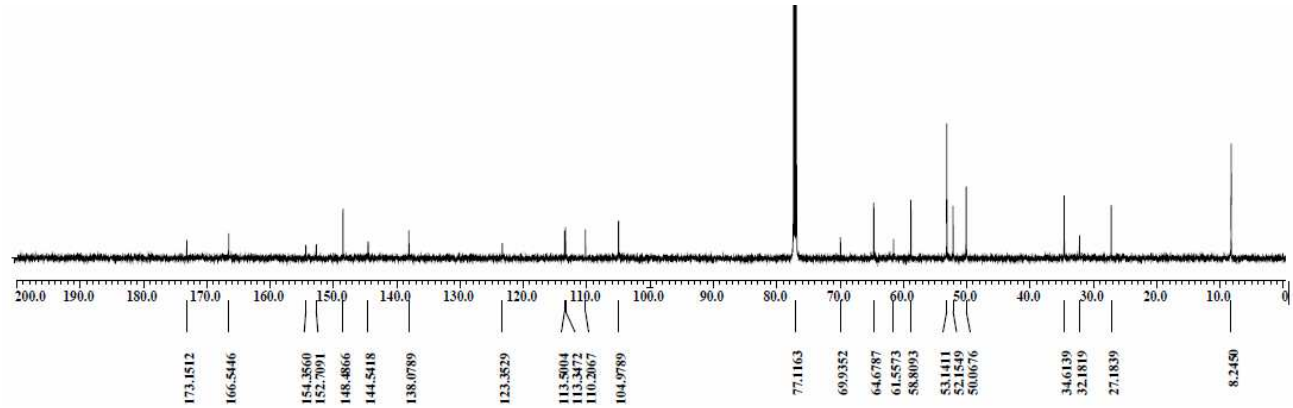




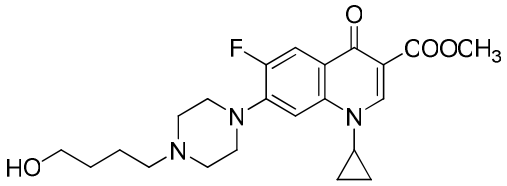
***N*$_4$'-3-Hydroxypropylciprofloxacin Methyl Ester (6).**

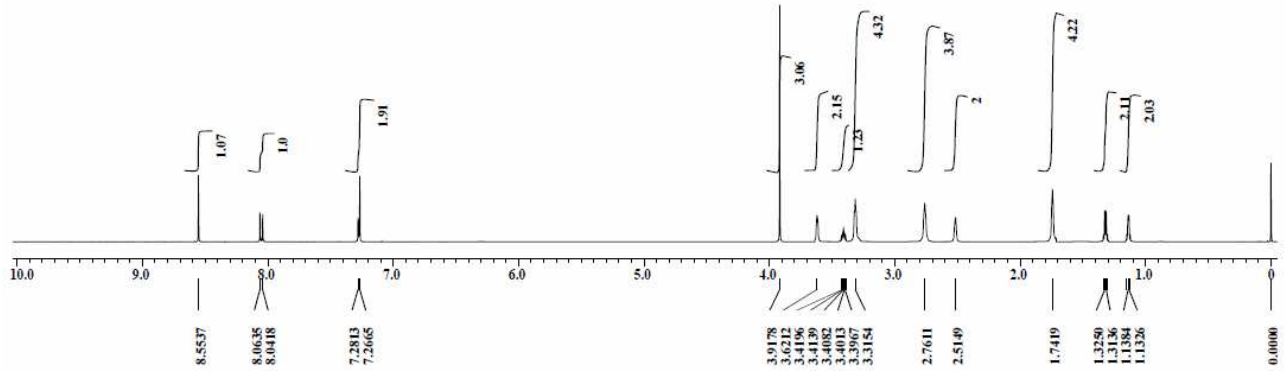


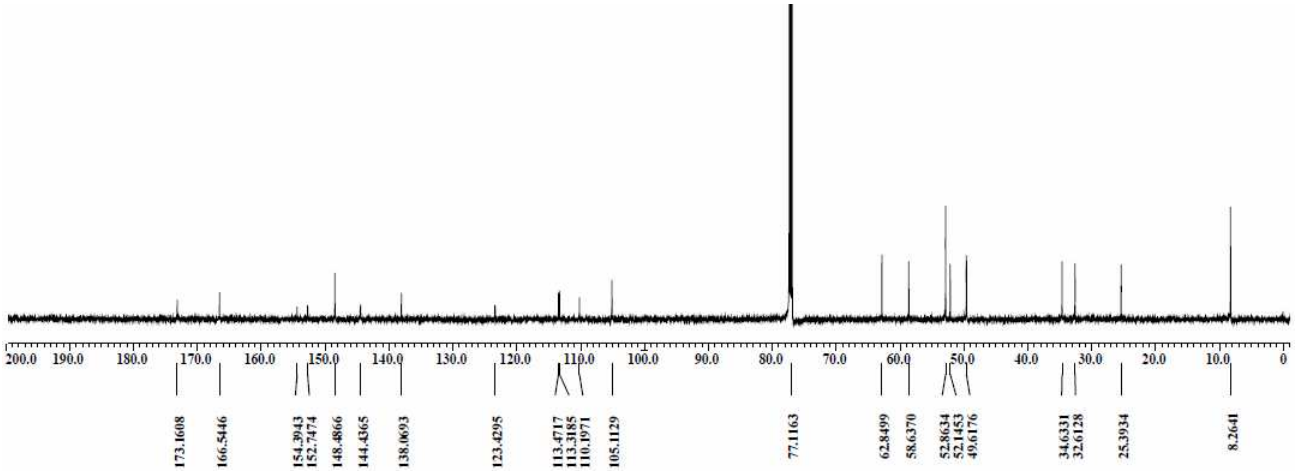




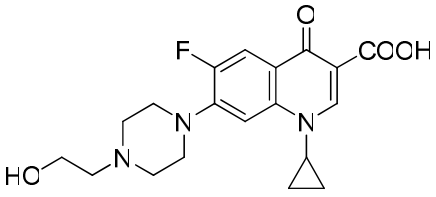
***N_4'*-4-Hydroxybutylciprofloxacin Methyl Ester (7).**

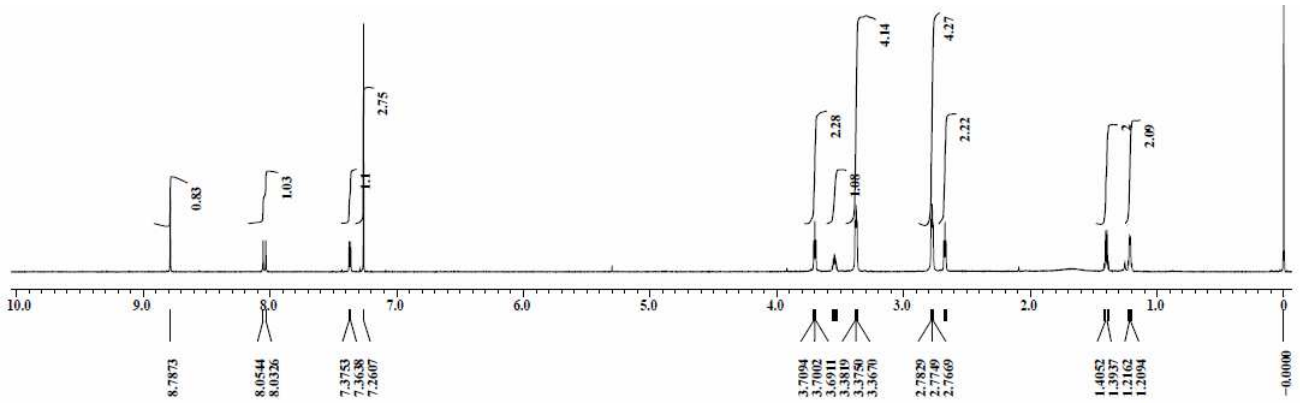


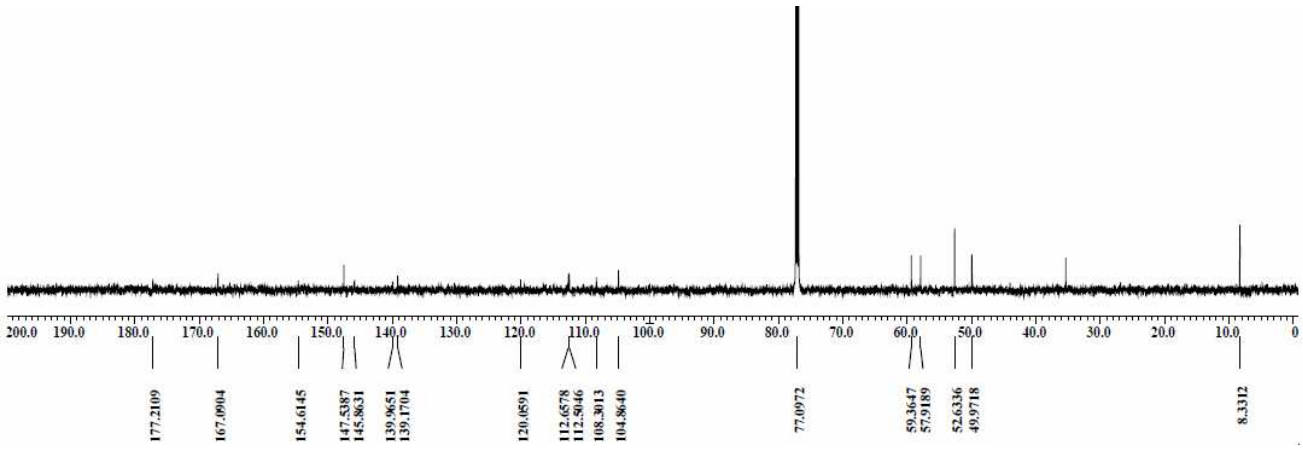




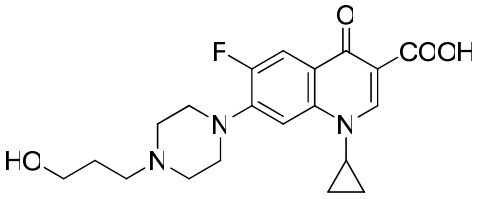
N_4'-2-Hydroxyethylciprofloxacin (8).

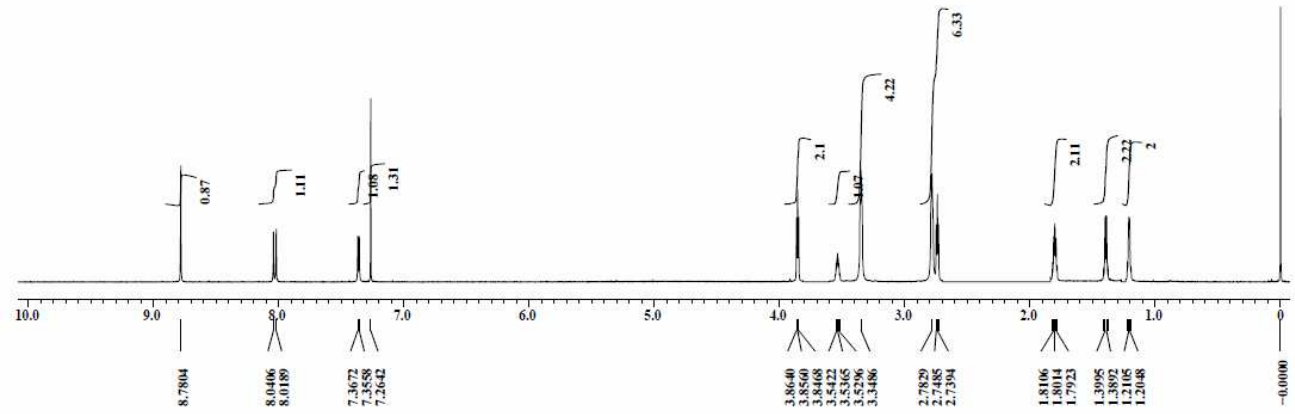


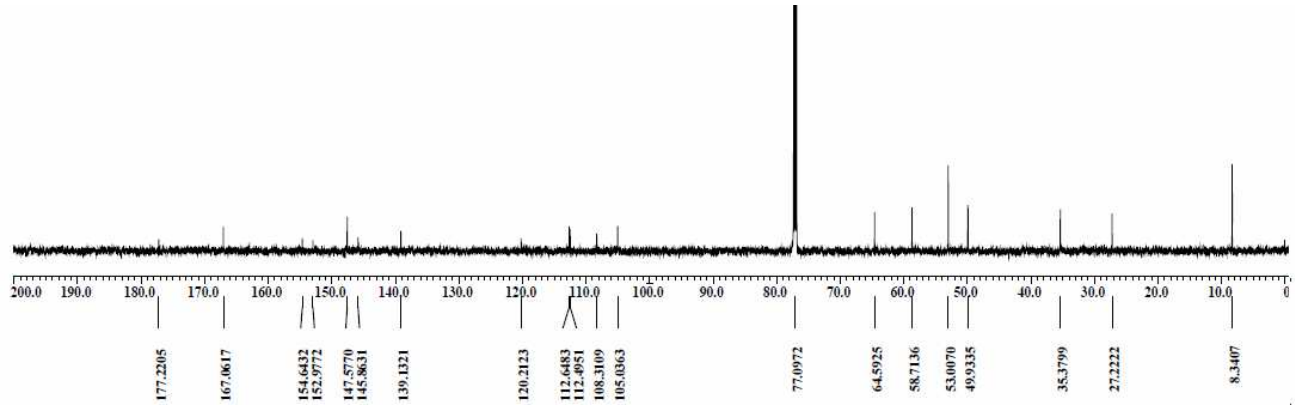




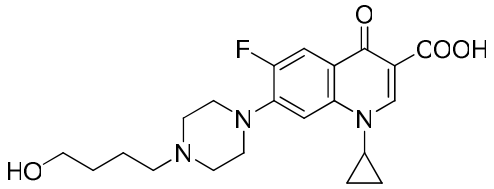
***N*$_4$′-3-Hydroxypropylciprofloxacin (9).**

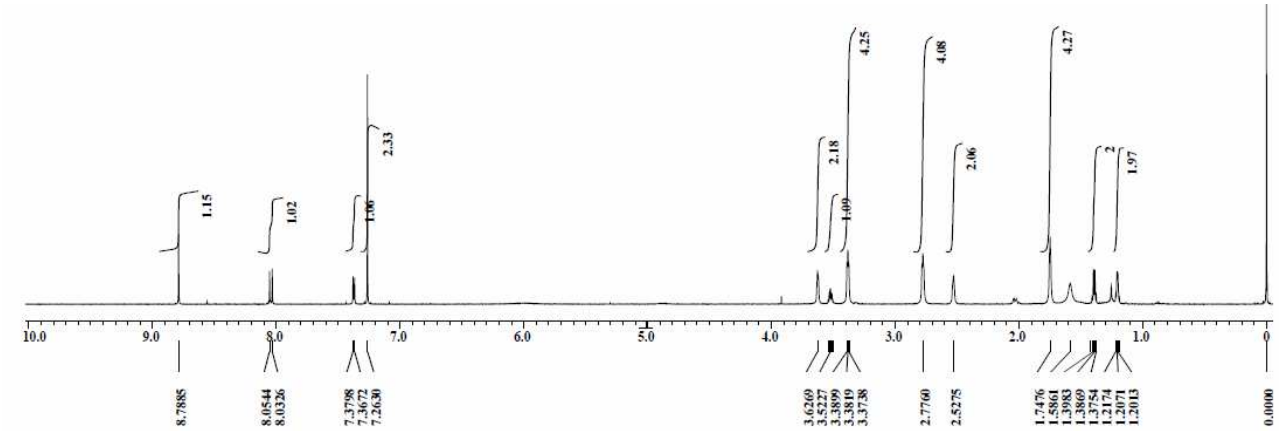


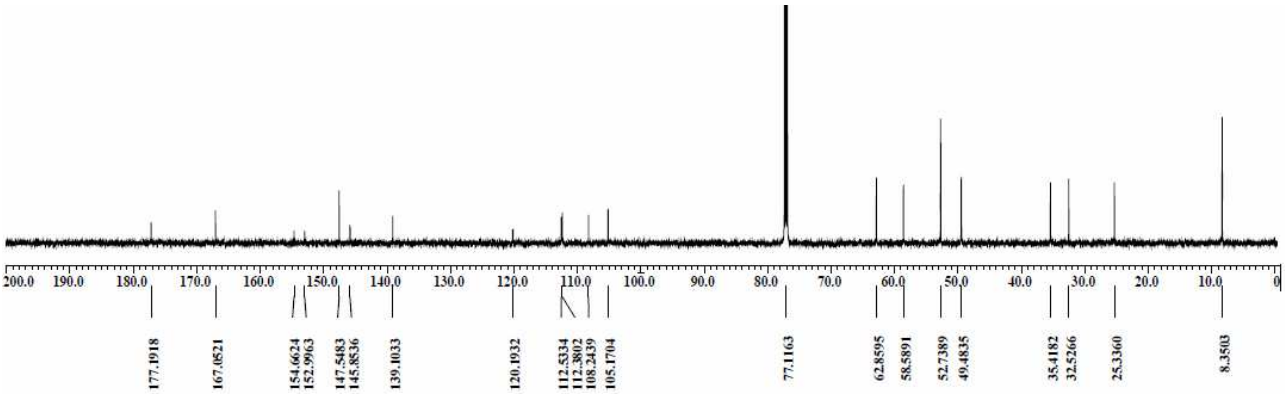




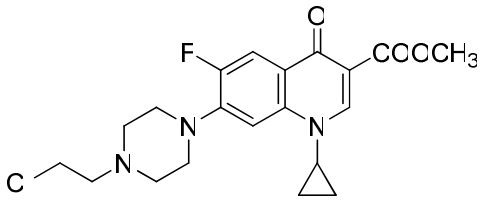
***N_4'*-4-Hydroxybutylciprofloxacin (10).**

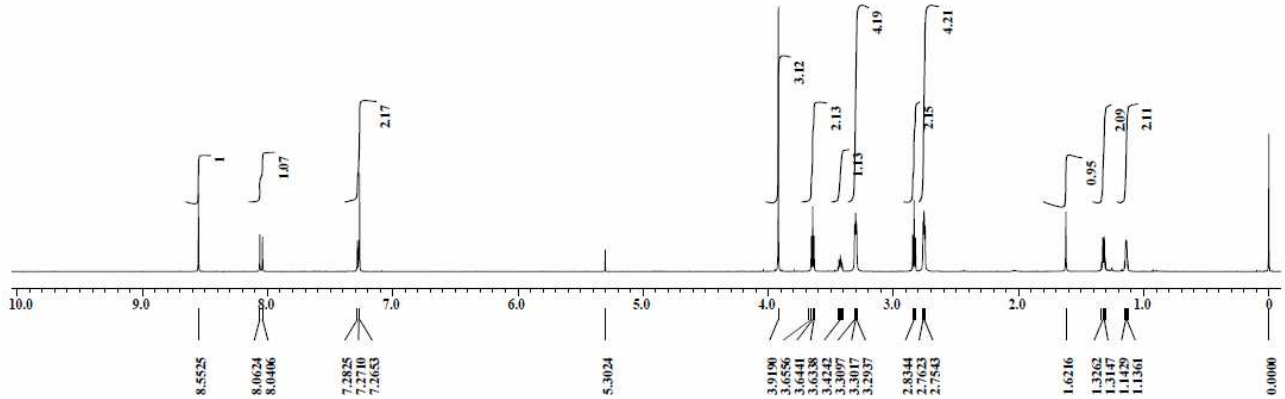


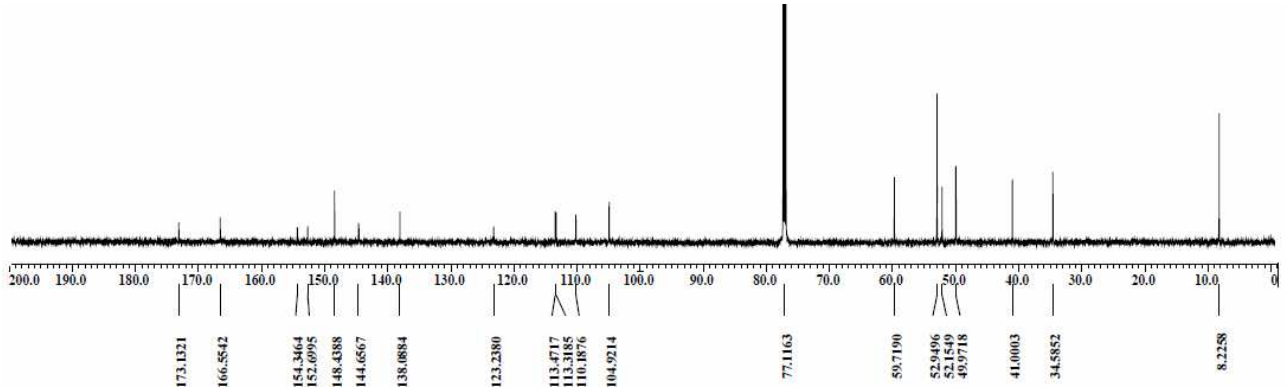




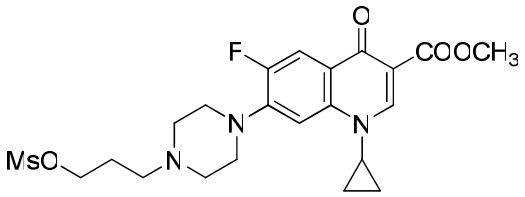
***N_4'*-2-Chloroethylciprofloxacin Methyl Ester (11).**

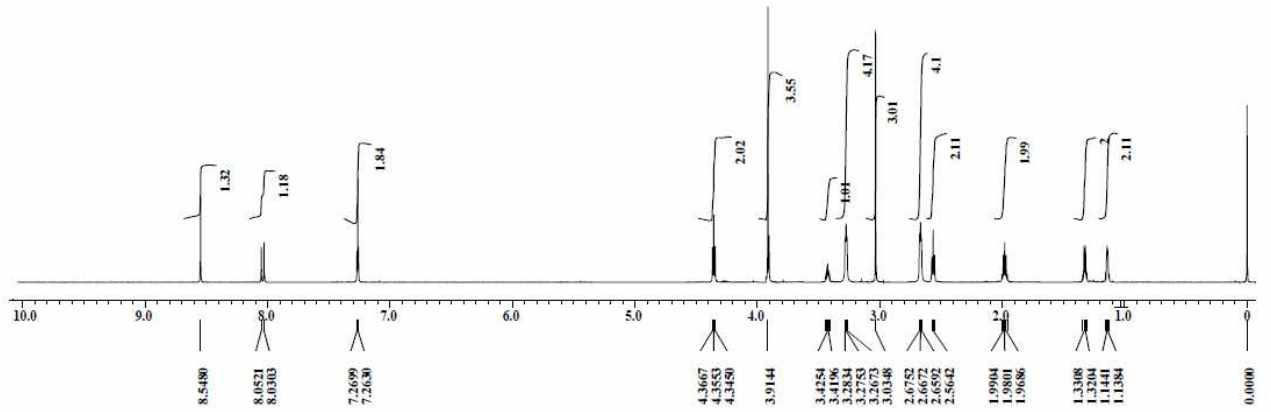


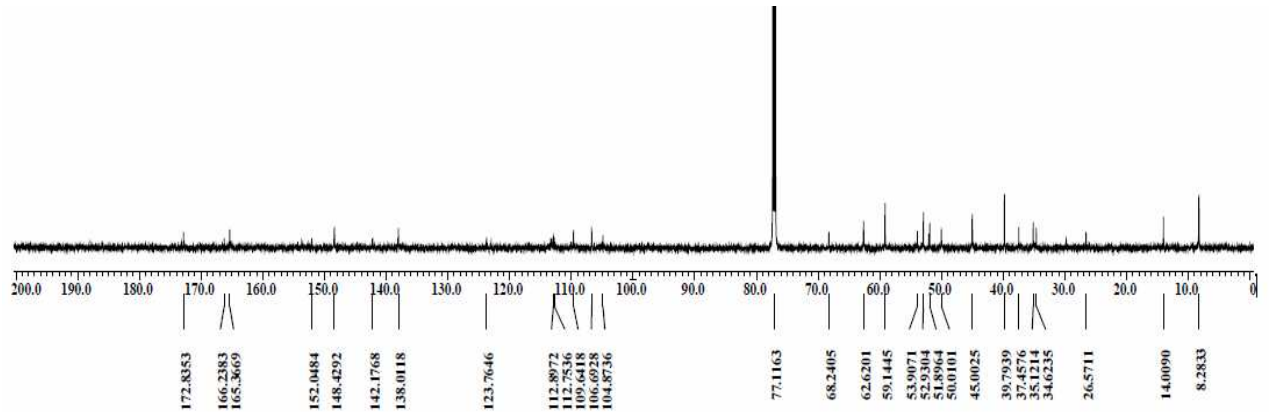




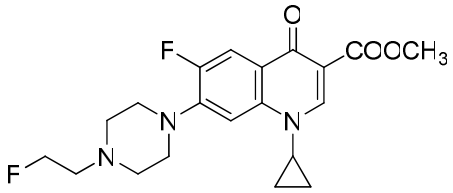
***N*$_4$'-3-Methanesulfonylpropylciprofloxacin Methyl Ester (12).**

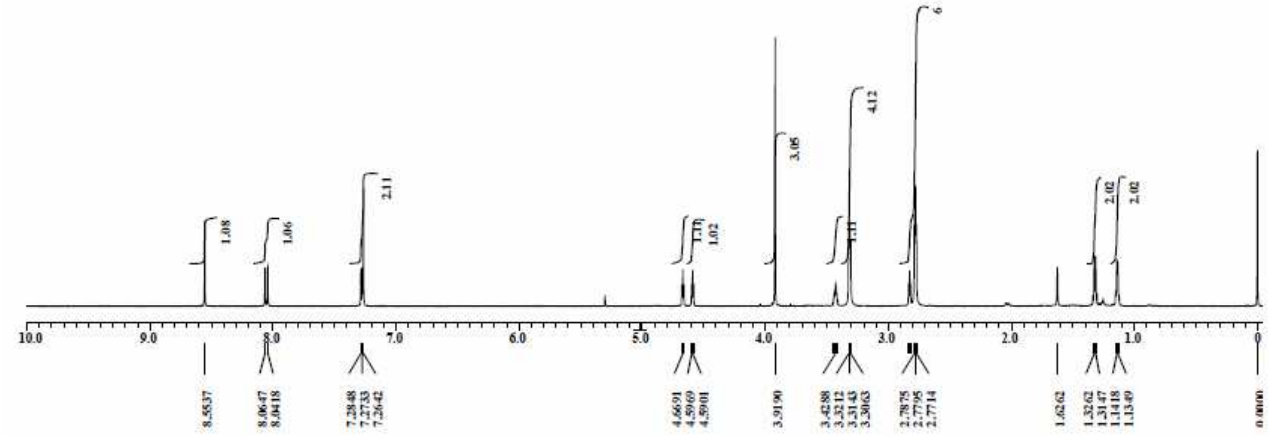


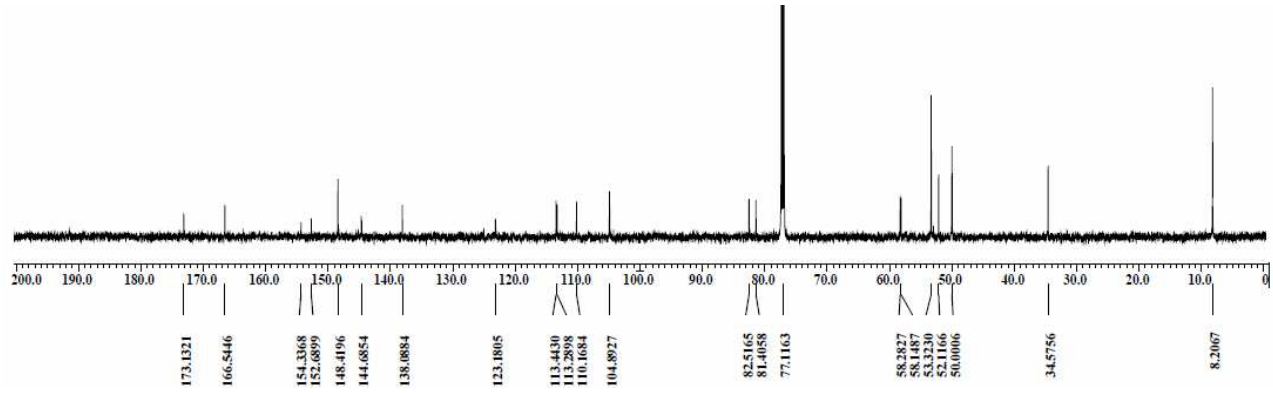




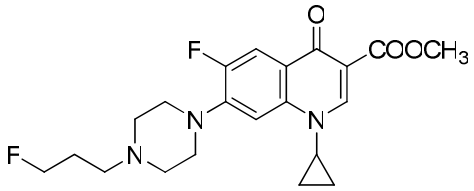
***N_4'*-2-Fluoroethylciprofloxacin Methyl Ester (13).**

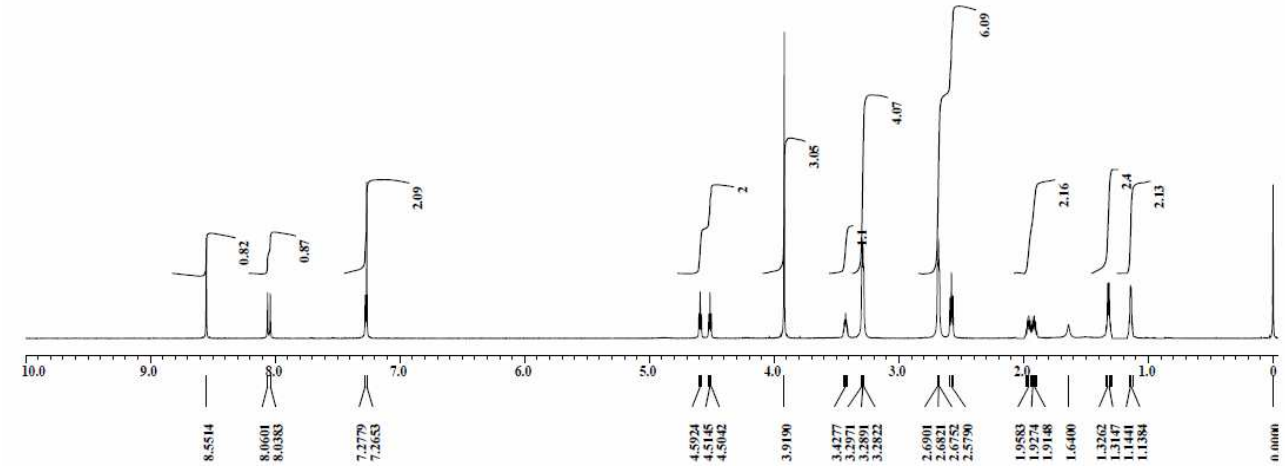


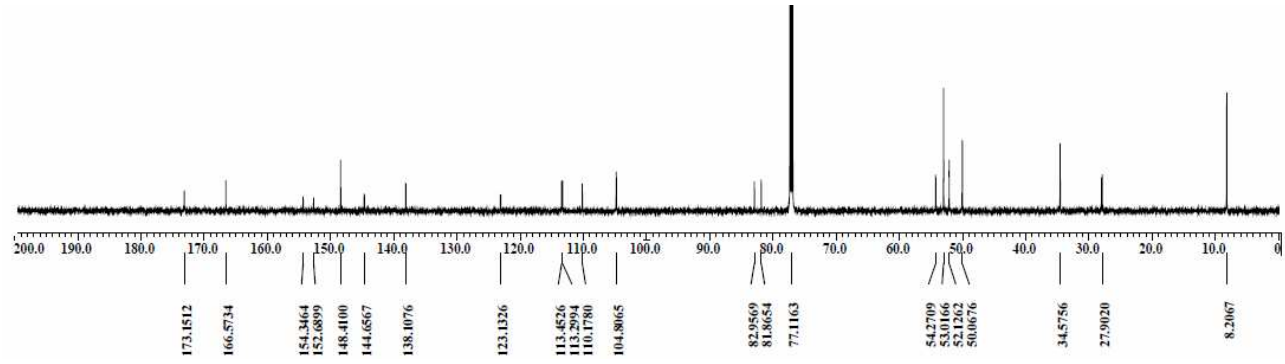




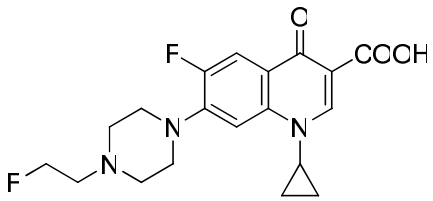
***N_4'*-3-Fluoropropylciprofloxacin Methyl Ester (14).**

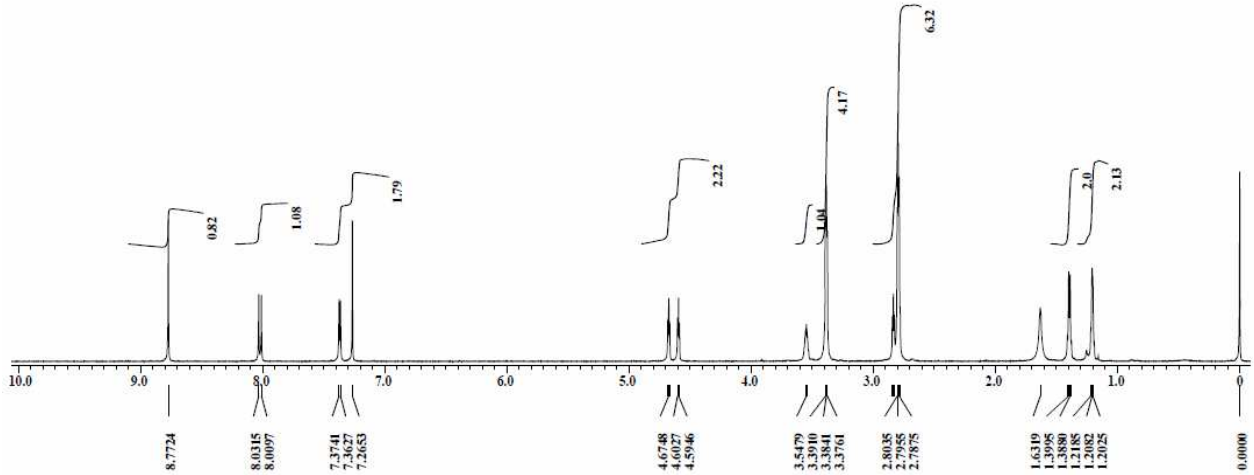


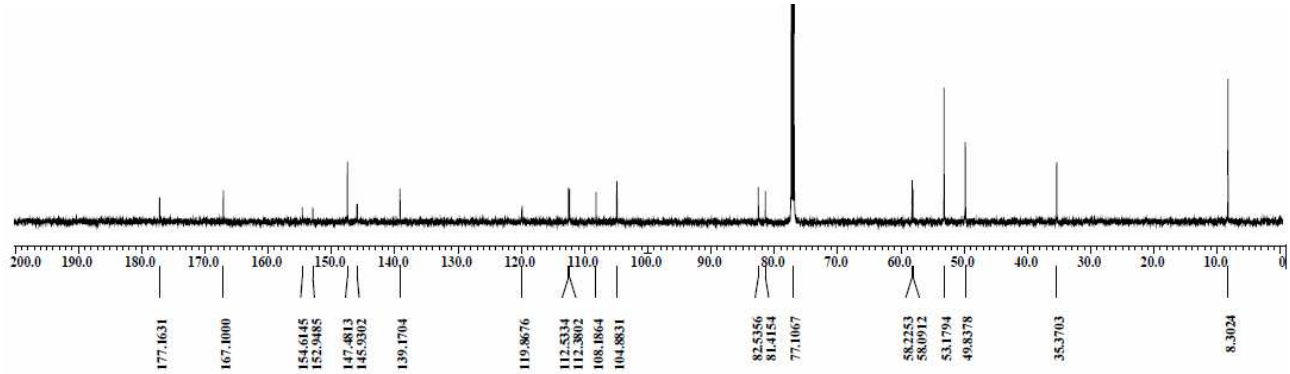




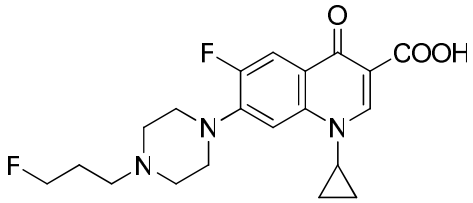
***N_4'*-2-Fluoroethylciprofloxacin (15).**

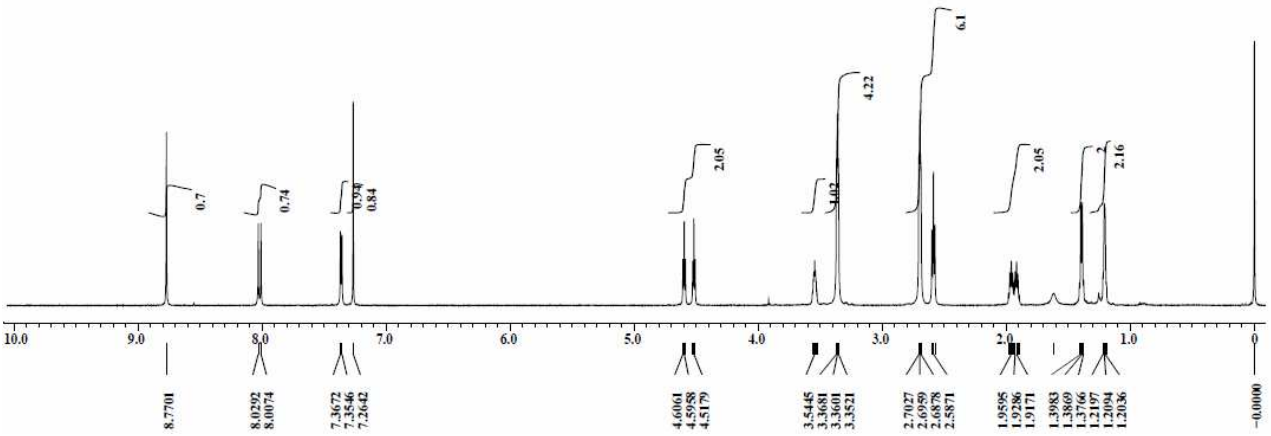


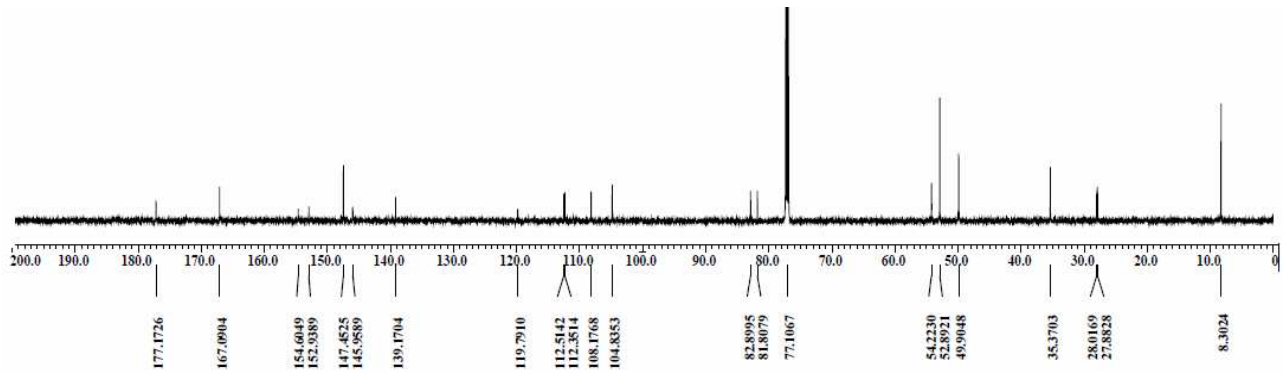




***N*$_4$'-3-Fluoropropylciprofloxacin (16).**







One-Step ^{18}F-Labeling of Carbohydrate-Conjugated Octreotate-Derivatives Containing a Silicon-Fluoride-Acceptor (SiFA): In Vitro and in Vivo Evaluation as Tumor Imaging Agents for Positron Emission Tomography (PET)

Carmen Wängler,[†] Beatrice Waser,[‡] Andrea Alke,[§] Ljuba Iovkova,[||] Hans-Georg Buchholz,[⊥] Sabrina Niedermoser,[†] Klaus Jurkschat,[||] Christian Fottner,[#] Peter Bartenstein,[†] Ralf Schirrmacher,[▽] Jean-Claude Reubi,[‡] Hans-Jürgen Wester,[§] and Björn Wängler*

Department of Nuclear Medicine, Hospital of the Ludwig-Maximilians-University, Munich, Germany, Institute of Pathology, University of Berne, Berne, Switzerland, Department of Nuclear Medicine, Technical University Munich, Munich, Germany, Department of Inorganic Chemistry II, University of Dortmund, Dortmund, Germany, Department of Nuclear Medicine and I. Medical Clinic, University of Mainz, Germany, and McConnell Brain Imaging Centre, Montreal Neurological Institute, McGill University, Montreal, Canada. Received July 13, 2010; Revised Manuscript Received October 18, 2010

The synthesis, radiolabeling, and initial evaluation of new silicon-fluoride acceptor (SiFA) derivatized octreotate derivatives is reported. So far, the main drawback of the SiFA technology for the synthesis of PET-radiotracers is the high lipophilicity of the resulting radiopharmaceutical. Consequently, we synthesized new SiFA-octreotate analogues derivatized with Fmoc-NH-PEG-COOH, Fmoc-Asn(Ac_3AcNH-β-Glc)-OH, and SiFA-aldehyde (SIFA-A). The substances could be labeled in high yields (38 ± 4%) and specific activities between 29 and 56 GBq/μmol in short synthesis times of less than 30 min (e.o.b.). The in vitro evaluation of the synthesized conjugates displayed a sst2 receptor affinity (IC_{50} = 3.3 ± 0.3 nM) comparable to that of somatostatin-28. As a measure of lipophilicity of the conjugates, the log P_{ow} was determined and found to be 0.96 for SiFA-Asn(AcNH-β-Glc)-PEG-Tyr^3-octreotate and 1.23 for SiFA-Asn(AcNH-β-Glc)-Tyr^3-octreotate, which is considerably lower than for SiFA-Tyr^3-octreotate (log P_{ow} = 1.59). The initial in vivo evaluation of [^{18}F]SiFA-Asn(AcNH-β-Glc)-PEG-Tyr^3-octreotate revealed a significant uptake of radiotracer in the tumor tissue of AR42J tumor-bearing nude mice of 7.7% ID/g tissue weight. These results show that the high lipophilicity of the SiFA moiety can be compensated by applying hydrophilic moieties. Using this approach, a tumor-affine SiFA-containing peptide could successfully be used for receptor imaging for the first time in this proof of concept study.

INTRODUCTION

Fluorine-18 (^{18}F, $t_{1/2}$ = 109.7 min) is the most important radionuclide for imaging by means of positron emission tomography (PET), a noninvasive imaging modality which found its way into human diagnostic imaging more than 30 years ago. The introduction of 2-[^{18}F]FDG, a ^{18}F-labeled sugar derivative, has pushed nuclear medicine forward, and 2-[^{18}F]FDG today accounts for the majority of human PET scans in a variety of human afflictions such as cancer and neurological diseases. Further stimulated by the introduction of PET/CT, it is very likely that the number of PET-scans will continue to rise within the next years particularly as the single-photon-emission-tomography (SPECT) technology has recently suffered from radioisotope shortages and thus impaired reliability (*1, 2*). One apparent drawback of the PET technology is the often complicated synthesis of the respective imaging agents, a circumstance which, despite best efforts, has not yet been alleviated. Especially for larger molecules, such as peptides and proteins, simple one-step labeling procedures have been evasive despite several advancements in the field (*3*−*7*). Although direct labeling via nucleophilic substitution has recently been shown to be a possible route for the ^{18}F-labeling of some selected peptides with nonacidic side chain functionalities (*8*), this path lacks general applicability to more complex and temperature-sensitive peptides. A further drawback of all the described methods for the radiolabeling of peptides and proteins based on the formation of a carbon-^{18}F bond is the necessity for intricate purification methods (e.g., HPLC) (*9*). Recently, our group and Ametamey et al. independently described the synthesis of sterically hindered silicon-^{18}F building blocks used as prosthetic groups in the synthesis of radiolabeled peptides and proteins (*10*−*13*). Our method was coined SiFA chemistry (SiFA: Silicon-Fluoride-Acceptor), whose concept is based on a simple isotopic exchange reaction, yet yielding compounds of high specific activity. Single-step labeling as well as two-step labeling procedures were described, and the first true ^{18}F-kit labeling procedure for proteins emerged from these efforts (*14*−*16*). Despite this success for protein labeling, the initial application of silicon-^{18}F derivatized peptides for tumor imaging unambiguously revealed a pronounced lipophilicity imparted by the Si−F building blocks, leading to a high unspecific liver and low tumor uptake (*17, 13*). In order to circumvent this problem, we report here the application of our SiFA chemistry together with hydrophilic PEG spacers and carbohydrates in the syntheses of octreotate derivatives in order

* To whom correspondence should be addressed. Björn Wängler: Tel: +49 89 7095 7543, fax: +49 89 7095 4648, bjoern.waengler@med.uni-muenchen.de.

[†] Hospital of the Ludwig-Maximilians-University.

[‡] University of Berne.

[§] Technical University Munich.

[||] University of Dortmund.

[⊥] Department of Nuclear Medicine, University of Mainz.

[#] I. Medical Clinic, University of Mainz.

[▽] McGill University.

10.1021/bc100316c © 2010 American Chemical Society
Published on Web 11/17/2010

to obtain compounds with improved properties for the in vivo imaging of somatostatin receptor positive tumors (*18*−*20*). The peptides Tyr^3-octreotate as well as Tyr^3-octreotide (an alcohol derivative of Tyr^3-octreotate) are analogues of the peptide hormone somatostatin and have a preferentially high affinity to the somatostatin receptor subtype 2, which is highly overexpressed on the cell surface of several neuroendocrine tumors. Thus, these peptides represent ideal compounds for receptor-mediated tumor targeting and imaging (*21*−*23*). As of now, the radiolabeling of somatostatin analogues with ^{18}F is complicated and time-consuming, as it necessitates a two-step procedure for (i) the synthesis of a secondary labeling precursor (which has in most cases to be purified by HPLC) and (ii) the subsequent reaction with the peptidic compound. Thus, a more simple and efficient method for the introduction of ^{18}F into peptides is highly desirable. A promising approach is the use of the SiFA technology, as this would allow the introduction of ^{18}F into peptides in a one-step reaction. Thus, the aim of this work was to demonstrate that (i) the introduction of hydrophilic groups in combination with the SiFA moiety into peptides yields radiofluorinated products retaining their binding affinity to the target receptor while (ii) simultaneously displaying improved in vivo behavior for PET imaging compared to radiofluorinated peptides using silicon-fluoride building blocks alone, and that furthermore (iii) one-step synthesis of these radiotracers is feasible.

EXPERIMENTAL SECTION

Materials. Commercially available chemical compounds were purchased in highest purity and used without further purification. The resin for peptide synthesis (Fmoc-Thr(tBu)-Wang resin), Fmoc-protected amino acids, Fmoc-8-amino-3,6-dioxaoctanoic acid (Fmoc-NH-PEG-COOH), *N*-α-Fmoc-*N*-*β*-[3,4,6-tri-*O*-acetyl-2-(acetylamino)-deoxy-2-*β*-glucopyranosyl]-L-asparagine (Fmoc-Asn(Ac_3AcNH-*β*-Glc)-OH), and bis-Boc-aminooxy acetic acid (Bis-boc-Ao-OH) were purchased from NovaBiochem (Nottingham, UK). 4-(Di-*tert*-butylfluorosilyl) benzaldehyde (silicon-fluoride-acceptor aldehyde, SiFA-A) (**1**) as well as [^{18}F]-SiFA-Tyr^3-octreotate (**[^{18}F]-2**) were synthesized according to a published procedure (*11*). SepPak C-18 cartridges were obtained from Waters Corporation (Milford, MA, USA), Chromafix PS-HCO_3 cartridges from GE-Healthcare Europe (Freiburg, Germany).

Instruments. The analytical and semipreparative HPLC system used was an Agilent 1200 system equipped with a Raytest Gabi Star radioactivity detector together with an analytical Chromolith Performance column (RP-18e, 100 × 4.6 mm, Merck, Germany) at a flow rate of 4 mL/min and a semipreparative Chromolith column (RP-18e, 100 × 10 mm, Merck, Germany) at a flow rate of 8 mL/min, respectively. ESI mass spectra were obtained by using a Finnigan MAT95Q. The PET scans were performed using a Siemens Inveon 120 small animal PET system (Siemens Preclinical Imaging, Knoxville, TN, USA) or a Philips MOSAIC small animal scanner (Philips Healthcare, Eindhoven, The Netherlands). Gamma counting was performed using a Packard Canberra apparatus.

*Peptide Synthesis. Synthesis of Aoa-Asn(AcNH-β-Glc)-PEG-Tyr^3-octreotate (**3**).* Tyr^3-octreotate was synthesized on solid support applying standard Fmoc solid-phase peptide synthesis as described by Wellings et al. (*24*) on a Fmoc-Thr(tBu)-Wang resin (standard coupling procedure: 4 equiv amino acid, 3.9 equiv HBTU, 4 equiv DIPEA in DMF; Fmoc-cleavage: 50% piperidine in DMF). After cyclization of the Tyr^3-octreotate peptide sequence (Fmoc-D-Phe-Cys(Acm)-Tyr-D-Trp-Lys-Thr-Cys(Acm)-Thr-Wang) by incubating the resin with Tl(III)-trifluoroacetate in DMF for 45 min, the terminal Fmoc protecting group was removed. Subsequently, Fmoc-NH-PEG-COOH, Fmoc-Asn(Ac_3AcNH-*β*-Glc)-OH, and Bis-boc-Aoa-OH were successively coupled using standard coupling conditions. The peptide was cleaved from the resin by incubation with a mixture of TFA (trifluoroacetic acid)/TIS (triisopropylsilane)/H_2O (95:2.5:2.5, 1.5 mL) for 45 min, precipitated in diethyl ether, washed twice with diethyl ether, and dried. For cleavage of the carbohydrate acetyl protecting groups, the dried crude peptide was dissolved in methanol (1 mL), and a sodium methanolate solution in methanol (0.5M) was added until the pH of the mixture reached 12−13 (approximately 0.6 mL; pH determined on moistened pH indicator strips). After 30 min reaction at room temperature, the mixture was acidified with neat TFA (approximately 50 μL) and purified by semipreparative HPLC using a gradient of 15−40% MeCN + 0.1% TFA over 5 min. The product was isolated as white solid after lyophilization (23.2 mg, 14.6 μmol, 19% yield).

HR-ESI-MS (*m*/*z*) for $[M+H]^+$ (calculated) 1584.63 (1584.64); (*m*/*z*) for $[M+2H]^{2+}$ (calculated) 792.82 (792.82).

*Synthesis of SiFA-Asn(AcNH-β-Glc)-Tyr^3-octreotate (**4**).* The intermediate Aoa-Asn(AcNH-*β*-Glc)-Tyr^3-octreotate was synthesized by reacting fully protected Tyr^3-octreotate on resin with Fmoc-Asn(Ac_3AcNH-*β*-Glc)-OH and Bisboc-Aoa-OH and cleaved from the resin as described before for the synthesis of **3**. The deprotection of the O-acetyl protecting groups was also performed analogously to **3** by reacting the peptide for 30 min with sodium methanolate solution in methanol. When the reaction was finished, the volatile components of the mixture were evaporated, the obtained solid was dissolved in phosphate buffer (0.5 M, pH = 4.0, 400 μL) and reacted with SiFA-A (**1**) dissolved in acetonitrile by adding SiFA-A in small amounts until an excess of SiFA-A could be detected by analytical HPLC (gradient of 0−100% MeCN + 0.1% TFA over 5 min) after reaction times of 5 min. The crude product was purified by semipreparative HPLC using a gradient of 10−50% MeCN + 0.1% TFA over 5 min. The product was isolated as white solid after lyophilization (5.5 mg, 3.3 μmol, 13.3%).

HR-ESI-MS (*m*/*z*) for $[M+H]^+$ (calculated): 1686.70 (1686.69).

*Synthesis of SiFA-Asn(AcNH-β-Glc)-PEG-Tyr^3-octreotate (**5**).* For the oxime formation, a modified protocol from that described by Poethko et al. was used (*25*). A solution of Aoa-Asn(AcNH-*β*-Glc)-PEG-Tyr^3-octreotate (**3**, 10 mg, 6.3 μmol) in phosphate buffer (0.25 M, pH = 4.0, 400 μL) was added to a solution of SiFA-A (**1**, 2.1 mg, 7.9 μmol, 1.25 equiv) in acetonitrile (500 μL). The pH was adjusted to 4.0 by adding phosphate buffer (0.5 M, pH = 4.0, ∼50 μL). The mixture was incubated for 5 min at ambient temperature, and subsequently, the product was purified by semipreparative HPLC using a gradient of 40−80% MeCN + 0.1% TFA over 4 min. The product was isolated as a white solid after lyophilization (9.3 mg, 5.1 μmol, 80%).

HR-ESI-MS (*m*/*z*) for $[M+H]^+$ (calculated) 1832.02 (1832.77); (*m*/*z*) for $[M+2H]^{2+}$ (calculated) 917.39 (917.88).

*Radiolabeling. Preparation of a Stock Solution Containing [^{18}F]F$^-$/Kryptofix 2.2.2/K$^+$ Complex for the Labeling of SiFA-Asn(AcNH-β-Glc)-Tyr^3-octreotate (**4**) and SiFA-Asn(AcNH-β-Glc)-PEG-Tyr^3-octreotate (**5**).* Aqueous [^{18}F]fluoride (4000−7500 MBq) that had been produced by the ^{18}O(p,n)^{18}F nuclear reaction on an enriched [^{18}O]water (95%) target was loaded onto a Chromafix PS-HCO_3 cartridge and eluted with a mixture of acetonitrile (800 μL), water (200 μL), potassium oxalate solution (1 M, 10 μL), and Kryptofix 2.2.2 (12.5 mg). The solvents were removed by coevaporation to dryness under reduced pressure (650 mbar) using a stream of helium at 87 °C for 4 min. The drying step was repeated twice with CH_3CN (0.8 mL) (3 min) and full vacuum (∼10 mbar) was applied in the final drying step (4 min). The dried [^{18}F]F$^-$/Kryptofix 2.2.2/K$^+$ complex was

dissolved in dry DMSO (500−1000 μL) and used as stock solution for labeling.

*Radiosynthesis of [^{18}F]SiFA-Asn(AcNH-β-Glc)-Tyr^3-octreotate (**[^{18}F]-4**) and [^{18}F]SiFA-Asn(AcNH-β-Glc)-PEG-Tyr^3-octreotate (**[^{18}F]-5**).* The SiFA containing peptides **4** and **5** (10−25 nmol, 10−25 μL of a 1 mmol/L stock solution in dry DMSO) were added to 450−500 μL of the stock solution containing [^{18}F]F$^-$/Kryptofix 2.2.2/K$^+$ complex (2−3 GBq) in dry DMSO and reacted at ambient temperature for 5 min without stirring. Subsequently, the reaction mixture was added to HEPES buffer (0.1 M, pH 4, 9 mL) and loaded on a Waters SepPak C-18 light cartridge, previously conditioned by subsequent rinsing with ethanol (5 mL) and water for injection (10 mL). The trapped [^{18}F]SiFA-peptides were washed with water for injection (5 mL), eluted from the cartridge with ethanol (200 μL), and diluted with isotonic saline solution (2 mL). The solution was filtered sterile for further use. The overall synthesis time was 15 min. Reverse-phase HPLC revealed radiochemical purities ranging from 92% to 96%. ^{18}F-fluoride impurities were in all cases <1%. The syntheses yielded 0.7 to 1.4 GBq of **[^{18}F]-4** and **[^{18}F]-5** starting from 2−3 GBq of the [^{18}F]F$^-$/Kryptofix 2.2.2/K$^+$ complex of the used stock solution. The products could be obtained in specific activities between 29 and 56 GBq/μmol and radiochemical yields (RCY) of 38 ± 4%.

Plasma Stability. [^{18}F]SiFA-Asn(AcNH-β-Glc)-PEG-Tyr^3-octreotate **[^{18}F]-5** (100 MBq) in injectable solution obtained as described before) was added to human plasma (500 μL) at 37 °C. At certain time points (5, 10, 40, 60, and 120 min), 75 μL of this mixture were taken and added to acetonitrile (250 μL). The samples were stored on ice for 5 min for complete precipitation of plasma proteins. The precipitate was removed by centrifugation, and the supernatants were analyzed by radio-HPLC. Radioactivity in precipitate and supernatant was measured.

Lipophilicity. 1−2 MBq of [^{18}F]SiFA-Asn(AcNH-β-Glc)-Tyr^3-octreotate (**[^{18}F]-4**) or [^{18}F]SiFA-Asn(AcNH-β-Glc)-PEG-Tyr^3-octreotate (**[^{18}F]-5**) was added to a mixture of 1-octanol (900 μL) and phosphate buffer (0.05 M, pH = 7.4, 900 μL) and the mixtures were vigorously vortexed for 5 min. After subsequent centrifugation at 14 000 rpm for 2 min, aliquots of 100 μL were taken from each phase and measured in a gamma-counter. As a control, the experiment was repeated by partinioning the organic layer from the aqueous layer. The organic layer was added to the same amount of fresh phosphate buffer and again treated as described before.

In Vitro Evaluation. Receptor subtype affinity of the synthesized peptides to the somatostatin receptor subtypes 1−5 (sst1−5) was determined as described in detail previously (*26*). In brief, sections of cell membrane pellets on microscopic slides were used. These cell membrane pellets were prepared from different cell types expressing the somatostatin receptor as described before (*27*). Displacement experiments were performed by incubating the sections for 2 h at room temperature using the somatostatin radioligand [Leu^8, D-Trp^{22}, [^{125}I]-Tyr^{25}]somatostatin-28 and increasing concentrations of the unlabeled peptides ranging from 0.1 to 1000 nM. After 2 washing steps, the sections were dried quickly and exposed to a radiosensitive film (Biomax MR; Kodak) for 7 days. IC$_{50}$ values were calculated after quantification of the data using a computer-assisted image processing system as described previously (*27*). Tissue standards (Autoradiographic [^{125}I] and/or [^{14}C] microscales, GE Healthcare, Little Chalfont, UK) that contain known amounts of isotope, cross-calibrated to tissue-equivalent ligand concentrations, were used for quantification (*28*).

In Vivo Biodistribution of [^{18}F]SiFA-PEG-Asn(AcNH-β-Glc)-PEG-Tyr^3-Octreotate **[^{18}F]-5** *in AR42J Tumor-Bearing Nude Mice (CD 1 nu/nu).* Mice were housed according to German animal protection laws and protocols of the local committee. To establish a tumor model with high expression of sst2, the rat pancreatic tumor cell line AR42J was utilized (*29*). In brief, nude mice (CD 1 nu/nu, female, 6−8 weeks) were injected with 100 μL of a cell suspension (containing (2.5−5) × 10^6 cells) of AR42J cells s.c. into the right flank (*30, 31*). The biodistribution experiments were performed 10 to 14 days after tumor inoculation under inhalation anesthesia (oxygen 1.2 L/min, isofluran 1.5 vol %) and appropriate warming to prevent hypothermia. For in vivo biodistribution experiments, 4−5 animals per group bearing AR42J tumors (200−900 mg) on the right flank were used. 1.0−1.8 MBq of [^{18}F]SiFA-PEG-Asn(AcNH-β-Glc)-PEG-Tyr^3-octreotate (**[^{18}F]-5**) were administered i.v. The animals were sacrificed after 10 and 60 min. The tissues of interest were dissected and weighed, and the incorporated radioactivity was measured using a gamma counter. For the small animal PET imaging experiment evaluating **[^{18}F]-5**, 7.86 MBq of the radiotracer was injected i.v. List mode data were acquired over 90 min using the Siemens Inveon 120 small animal PET system (Siemens Preclinical Imaging, Knoxville, TN, USA) and divided into temporal frames of increasing length varying from 20 s to 20 min for the assessment of temporal changes in regional tracer accumulation. For the small animal PET imaging experiment evaluating **[^{18}F]-2**, 35 MBq of the radiotracer were injected i.v. List mode data were acquired over 90 min using the Philips Mosaic III small animal PET Scanner (Philips Healthcare, Amsterdam, The Netherlands) and divided into 18 frames of 5 min for the assessment of temporal changes in regional tracer accumulation.

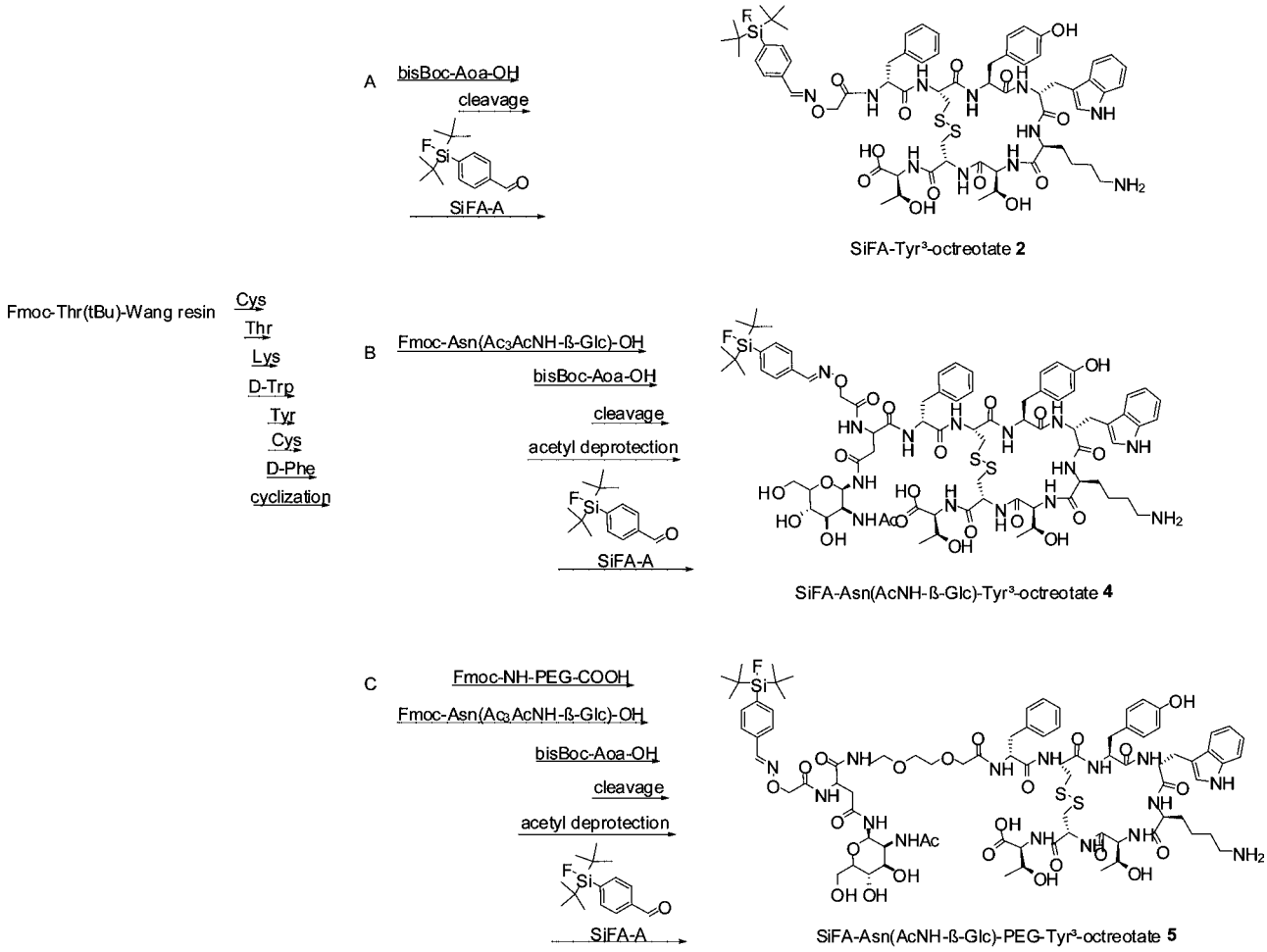
RESULTS AND DISCUSSION

Synthesis of PEG and Glucose Derivatized Octreotate Derivatives 4 and 5. In order to obtain Tyr^3-octreotate derivatives showing a lower lipophilicity and therefore a more favorable in vivo biodistribution, our synthesis strategy was to introduce groups of high hydrophilicity such as carbohydrates and polyethylene glycols (PEGs) into the peptide sequence compensating the high lipophilicity of the SiFA building block (Scheme 1). This approach was shown to result in peptide derivatives with improved in vivo behavior by Schottelius et al. (*18, 19*) and Antunes et al. (*32*).

The synthesis of the less lipophilic peptide derivatives started with of Tyr^3-octreotate obtained by standard Fmoc solid-phase peptide synthesis methods (*24*). In the synthesis of SiFA-Asn(AcNH-β-Glc)-Tyr^3-octreotate (**4**) and SiFA-Asn(AcNH-β-Glc)-PEG-Tyr^3-octreotate (**5**), Tyr^3-octreoate was synthesized on solid support and further reacted with the PEG spacer Fmoc-NH-PEG-COOH (in case of **5**), the glucose-derivative Fmoc-Asn(Ac$_3$-Ac-NH-βGlc)-OH and bis-Boc-aminooxyacetic acid (Bis-boc-Aoa) (Scheme 1). After cleaving the peptides from solid support and purification via semipreparative HPLC, the acetyl-protecting groups of the glucose-hydroxyl functions were cleaved by incubating the intermediates with sodium methanolate in methanol at pH 12−13. Analytical HPLC revealed the maximum achievable yields after 30 min at ambient temperature to be around 40%. Longer deprotection times resulted in a significant decomposition of the peptides complicating the subsequent HPLC-purification. Aoa-Asn(AcNH-β-Glc)-PEG-Tyr^3-octreotate **3** could be isolated after semipreparative HPLC purification and lyophilization in ∼20% yield. The corresponding Tyr^3-octreoate derivative Aoa-Asn(AcNH-β-Glc)-Tyr^3-octreotate could not be purified by means of HPLC due to the side-products which were formed in the acetyl-deprotection step and was therefore used without further purification for the subsequent coupling of the SiFA moiety via oxime formation reaction.

For further derivatization of the peptides with the SiFA ^{18}F-acceptor moiety, both peptides were reacted with SiFA-A (**1**)

Scheme 1[a]



Synthesis of the SiFA-conjugated octreotate-derivatives SiFA-Tyr^3-octreotate **2** (route A), SiFA-Asn(AcNH-β-Glc)-Tyr^3-octreotate **4** (route B), and SiFA-Asn(AcNH-β-Glc)-PEG-Tyr^3-octreotate **5** (route C).

[a] After a standard Fmoc solid-phase synthesis of Fmoc-Tyr^3-octreotate, the on resin cyclization was carried out using Tl(III)trifluoroacetate. For the synthesis of the SiFA-derivatized peptides, Tyr^3-octreotate was further reacted on resin with Fmoc-NH-PEG-COOH (C), Fmoc-Asn(Ac_3AcNH-*β*-Glc)-OH (B, C), and bis-boc-aminooxyacetic acid (A, B, C) prior to the cleavage from resin and semipreparative HPLC-purification. After the acetyl deprotection of the carbohydrated intermediates using sodium methanolate (B, C), the oxime formation (A, B, C) was carried out in an acetonitrile buffer mixture reacting the intermediates with SiFA-A (**1**) at pH 4 for 5 min following a strategy described by Poethko et al (*25*).

in a mixture of phosphate buffer and acetonitrile via oxime formation (Scheme 1) (*25*). The coupling reaction was carried out at pH 4.0 giving the desired products in high yields after reaction times of only 5 min at room temperature. The overall yields for **4** and **5** were 13.3% and 15.2% after final HPLC purification, respectively. These two compounds represent the direct, unprotected labeling precursors for the one-step ^{18}F-labeling reaction.

Radiolabeling. In general, a drawback of the isotopic exchange reaction for radiolabeling is the limited specific activity (SA) because the precursor cannot be separated from the final product. As a result of its overall inefficiency, the precursor amount used for isotopic ^{19}F−^{18}F exchange is in the micromolar range. In order to achieve higher SA, the amount of labeling precursor used must be minimized. A high SA of the radiotracer for in vivo receptor imaging with PET is a prerequisite, as imaging probes being of low SA insufficiently delineate the target tissue as a result of direct binding competition of nonradioactive ^{19}F-compound. For SiFA-Tyr^3-Octreotate (**2**), we found 75 nmol to be the smallest possible amount for a direct labeling procedure to introduce 350−400 MBq (∼10 mCi) of ^{18}F, resulting in specific activities of 3−5 GBq/μmol (*10*). This SA would normally not be sufficient for PET-imaging. To obtain labeled peptides with much higher specific activities, we developed a two-step labeling procedure. The first step using this approach was the radiolabeling reaction in amounts of down to 3.75 nmol of SiFA-aldehyde (SIFA-A) and the subsequent reaction with an aminooxy-derivatized Tyr^3-octreotate, resulting in specific activities of up to 680 GBq/μmol (*11*). However, using this synthesis route, a HPLC-purification step was required to separate the final products from the precursors and intermediates, extending the synthesis time and diminishing the benefits of the fast reaction kinetics of the SiFA approach.

To circumvent a two-step labeling approach and HPLC-purification steps, we intended to find radiolabeling conditions resulting in the formation of the desired peptidic products **[^{18}F]-4** and **[^{18}F]-5**, even when small amounts of the new and more hydrophilic precursors SiFA-Asn(AcNH-*β*-Glc)-Tyr^3-octreotate (**4**) and **5** of ≤25 nmol were used. The resulting octreotate derivatives should then be obtained in high specific activities allowing their use in animal PET imaging applications.

When starting from stock solutions of dried [^{18}F]F$^-$/Kryptofix 2.2.2/K$^+$ complex in DMSO, the labeling experiments with both **4** and **5** displayed a ^{18}F-incorporation of about 40% and 60%

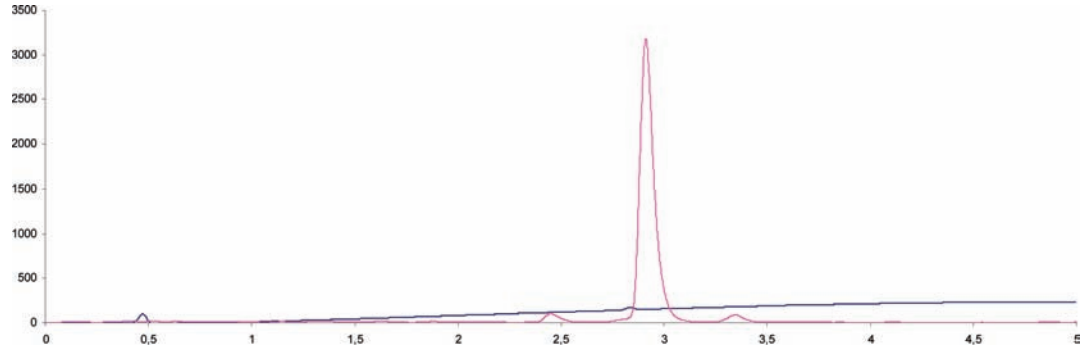


Figure 1. Typical UV/Radio-HPLC chromatogram of [^{18}F]SiFA-Asn(AcNH-β-Glc)-PEG-Tyr^3-octreotate **[^{18}F]-5** purified by solid-phase extraction, blue = UV trace at 214 nm, magenta = radioactivity trace (R_t (**[^{18}F]-5**) = 2.9 min).

when 10 nmol and 25 nmol of precursor were used, respectively. As the SiFA-modified peptides are labeling precursors and labeled products at the same time, the advantage of the SiFA-labeling technique is the absence of a labeling precursor chemically different from the product requiring a HPLC-purification. The SiFA-isotopic exchange labeling is performed under very mild conditions preventing the occurrence of radioactive side products. Only unreacted ^{18}F has to be removed using a reversed-phase (RP) cartridge. The cartridge purification also removes DMSO and Kryptofix 2.2.2 after a final washing step with water, retaining the respective peptides. Final elution of the cartridge with ethanol and dilution with sterile buffer yielded compound **[^{18}F]-5** in 38 ± 4% RCY as an injectable solution after sterile filtration. After this simple RP-cartridge purification step, analytical HPLC revealed a radiochemical purity of the products of 92−96% (Figure 1). The chemical purity of **[^{18}F]-5** was determined by HPLC at 214 nm and showed no side products.

The resulting specific activities of **[^{18}F]-4** and **[^{18}F]-5** ranged between 29 and 56 GBq/μmol—assessed from the precursor amount used for the synthesis—thus being in a suitable range for imaging sst-positive tumors. The labeling reaction and cartridge purification of [^{18}F]SiFA-Asn(AcNH-β-Glc)-Tyr^3-octreotate (**[^{18}F]-4**) and [^{18}F]SiFA-Asn(AcNH-β-Glc)-PEG-Tyr^3-octreotate (**[^{18}F]-5**) were completed in less than 15 min (30 min overall synthesis time, including the preparation of the [^{18}F]F$^-$/Kryptofix 2.2.2/K$^+$ complex).

Thus, this labeling method is highly efficient, proceeding in very short time spans in only one reaction step and requiring only one final cartridge purification.

Stability Studies. The chemical batch stability of **[^{18}F]-5** was determined over 4 h at room temperature by analytical radio-HPLC. Within this time span, compound **[^{18}F]-5** displayed no observable decomposition. In addition, the plasma stability was determined over 2 h displaying no degradation of the product as well. In this experiment, more than 86% of the radioactivity was found in the supernatant. These findings are in accordance with the data published for several silicon-derivatized peptides comprising huge, sterically hindered substituents (*10, 33*).

Lipophilicity. We and other groups found bulky, lipophilic substituents are a prerequisite to stabilize the Si−F bond against hydrolysis. The resulting high lipophilicity represents, however, a problem for in vivo application of SiFA-containing peptides. To determine whether our concept of introducing hydrophilic moieties such as carbohydrates and PEG spacers has a positive effect on the lipophilicity of the obtained Tyr^3-octreotate derivatives, making them ultimately better-suited for in vivo application, we determined the lipophilicity of the radiolabeled compounds [^{18}F]SiFA-Tyr^3-octreotate (**2**), [^{18}F]SiFA-Asn(AcNH-β-Glc)-Tyr^3-octreotate (**4**), and [^{18}F]SiFA-Asn(AcNH-β-Glc)-PEG-Tyr^3-octreotate (**5**). By determining the 1-octanol/phosphate buffered saline (PBS) partition coefficient P_{ow} and the lipophilicity log P_{ow}, we found for SiFA-TATE (**2**), (**4**), and (**5**) log P_{ow} values of 1.59, 1.23, and 0.96, respectively (Table 1). This displays a significant increase in hydrophilicity of the derivatized peptides **4** and **5** compared to SiFA-TATE (**2**) (*10*).

Table 1. Lipophilicity of SiFA-Derivatized Octreotate Derivatives (n = 3, values are mean ± SD)

peptide	log P_{ow}
SIFA-Tyr^3-octreotate (**2**)	1.59 ± 0.01
SiFA-Asn(AcNH-β-Glc)-Tyr^3-octreotate (**4**)	1.23 ± 0.05
SiFA-Asn(AcNH-β-Glc)-PEG-Tyr^3-octreotate (**5**)	0.96 ± 0.07
[^{125}I]-Tyr^3-octreotide[a]	0.18 ± 0.03[a]

[a] Data from ref *18*.

In Vitro Evaluation. The new compounds SiFA-Asn(AcNH-β-Glc)-Tyr^3-octreotate (**4**) and SiFA-Asn(AcNH-β-Glc)-PEG-Tyr^3-octreotate (**5**) were tested for their affinity toward the human somatostatin receptor subtypes (sst1−sst5) (Table 2). Both display affinities to the sst2—the most important receptor subtype for imaging—which are comparable to the affinity of Tyr^3-octreotide, a physiologically stabilized derivative of the natural ligand somatostatin-28. Tyr^3-octreotide was the lead compound for the development of several SPECT and PET radiotracers for receptor scintigraphy of sst-postive tumors in human studies. Comparing the PEGylated (**5**) and the non-PEGylated derivative (**4**), we found an increased affinity of the former compound to the somatostatin receptor subtype 2 (sst2), being in the same range as for Tyr^3-octreotide, which might be explained by the higher distance of the peptide to the highly lipophilic SiFA moiety using a PEG spacer in addition to the carbohydrated asparagine derivative. In comparison to Tyr^3-octreotide, compound **5** displayed the same binding affinity to sst2. Antunes and co-workers (*32*) used different hydrophilic spacers to derivatize the somatostatin-binding peptide NOC (Nal^3-octreotide) and found only marginal changes in the binding affinities to sst2, which is in contrast to our own findings. We assume that, for the compounds presented here, the observed larger variations in specific binding affinities that are achieved by using different spacers can be attributed to the more substantial decrease in the overall lipophilicity (Table 1).

In Vivo Biodistribution. In our initial in vivo experiment which was done using [^{18}F]SiFA-Tyr^3-octreotate (**[^{18}F]-2**) in a tumor model published by Fottner et al. (*31*), the animal PET images revealed no tumor uptake after 90 min but a significant radioactivity accumulation in liver and intestines. This experimental outcome is in accordance with data published for the biodistribution of ^{18}F-labeled silicon-modified bombesin derivatives suffering from the same shortcomings (*13*). Since affinity data for this compound are not available, we speculate that the faint tumor uptake can be attributed to an unfavorably high lipophilicity resulting in fast blood clearance, high liver uptake, and high unspecific binding.

Table 2. Affinity Profiles (IC_{50}) to the Human sst1−sst5 Receptors, Determined for Compounds 4 and 5 Using [Leu^8, D-Trp^{22}, ^{125}I-Tyr^{25}]somatostatin-28 as the Radioligand[a]

peptide	sst1	sst2	sst3	sst4	sst5
Somatostatin-28	3.6 ± 0.3[b]	2.1 ± 0.3[b]	3.2 ± 0.2[b]	3.0 ± 0.3[b]	2.5 ± 0.2[b]
Tyr^3-octreotide[b]	>1000[b]	3.1 ± 1.8[b]	330 ± 146[b]	346 ± 114[b]	10.8 ± 1.8[b]
[^{125}I]-Tyr^3-octreotide[c]	>10 000[c]	1.3 ± 0.3[c]	128 ± 22[c]	867 ± 33[c]	50 ± 12[c]
SiFA-Asn(AcNH-β-Glc)-Tyr^3-octreotate (**4**)	>1000 (2)	4.4 ± 0.2 (2)	756 ± 176 (2)	444 ± 96 (2)	302 ± 25 (2)
SiFA-Asn(AcNH-β-Glc)-PEG-Tyr^3-octreotate (**5**)	>1000 (2)	3.3 ± 0.3 (2)	184 ± 66 (2)	93 ± 26 (2)	126 ± 10 (2)

[a] Values are given as mean ± SD. [b] Data from ref *34*. [c] Data from ref *18*.

Table 3. Tissue Distribution [ID/g] of ^{18}F-SiFA-Asn(AcNH-β-Glc)-PEG-Tyr^3-Octreotate ([^{18}F]-5) in AR42J Tumor-Bearing Mice

tissue	10 min p.i.[a]	60 min p.i.[b]
blood	13.43 ± 2.58	5.92 ± 1.52
lung	8.30 ± 2.96	5.82 ± 1.59
liver	29.55 ± 7.04	16.11 ± 3.80
pancreas	5.64 ± 1.22	11.99 ± 2.89
spleen	3.94 ± 0.87	2.72 ± 0.48
stomach	4.36 ± 0.85	14.46 ± 2.14
large intestine	1.59 ± 1.16	2.14 ± 1.15
small intestine	2.93 ± 0.45	6.90 ± 1.10
kidney	6.67 ± 1.11	6.35 ± 0.98
adrenals	6.14 ± 2.46	3.92 ± 1.13
muscle	0.89 ± 0.19	0.59 ± 0.21
femur	1.88 ± 1.15	3.79 ± 1.24
tumor	3.25 ± 1.06	7.73 ± 1.90

[a] Group of 4 mice. [b] Group of 5 mice. Values are mean ± SD injected dose per gram tissue (% ID/g).

As ^{18}F-SiFA-Asn(AcNH-β-Glc)-PEG-Tyr^3-Octreotate (**[^{18}F]-5**) showed the most promising in vitro evaluation profile and the most favorable properties with regard to hydrophilicity, we evaluated the compound in vivo in AR42J tumor-bearing nude mice. The tissue distribution after 10 and 60 min postinjection is shown in Table 3.

As expected, and despite the hydrophilic derivatization, the lipophilicity of **[^{18}F]-5** leads to a high accumulation of 30% and 16% ID/g tissue in the liver after 10 and 60 min, respectively. The radioactivity concentration in the blood decreases from ~13.4% (10 min p.i.) to 6% (60 min p.i.), displaying a relatively high plasma half-life of the derivative. The accumulation in pancreas, stomach, and intestines increases by the factor 2−3 over time.

In Vivo Animal PET Data for a Silicon-^{18}F Derivatized [^{18}F]SiFA-Octreotate of High Lipophilicity Lacking PEG and/or Glucose Moieties. Initial laboratory results for the in vivo evaluation of the SiFA-derivatized octreotate derivative [^{18}F]SiFA-Tyr^3-octreotate (**[^{18}F]-2**), the radiosynthesis of which was published by our group in 2007 (*11*) as well as the results published by Höhne et al. (*13*) for the in vivo evaluation of an ^{18}F−Si derivatized bombesin derivative revealed only a negligible uptake in the tumor tissue of the corresponding mouse model (Figure 2A).

These findings can most probably be attributed to the high lipophilicity of the evaluated compounds which lead to an extraordinarily high uptake of the radiolabeled peptides in the liver and gallbladder. This high lipophilicity is a result of the *tert*-butyl substituents of the SiFA-moiety, which are necessary to stabilize the silicon-based fluoride acceptor systems against hydrolysis.

In contrast to these preliminary data found for the small animal PET study of ^{18}F-SiFA-Tyr^3-octreotate **[^{18}F]-2**, we found an uptake of 7.7% ID/g of ^{18}F-SiFA-Asn(AcNH-β-Glc)-PEG-Tyr^3-octreotate (**[^{18}F]-5**) in the tumor after 60 min p.i.. Compared to the uptake of radioiodinated octreotide and octreotate derivatives in tumor tissue, these findings are comparable to the uptake of a radioiodinated octreotide derivative already used for in vivo imaging, but display significantly lower uptake than the respective radioiodinated octreotate derivative (*18, 35*).

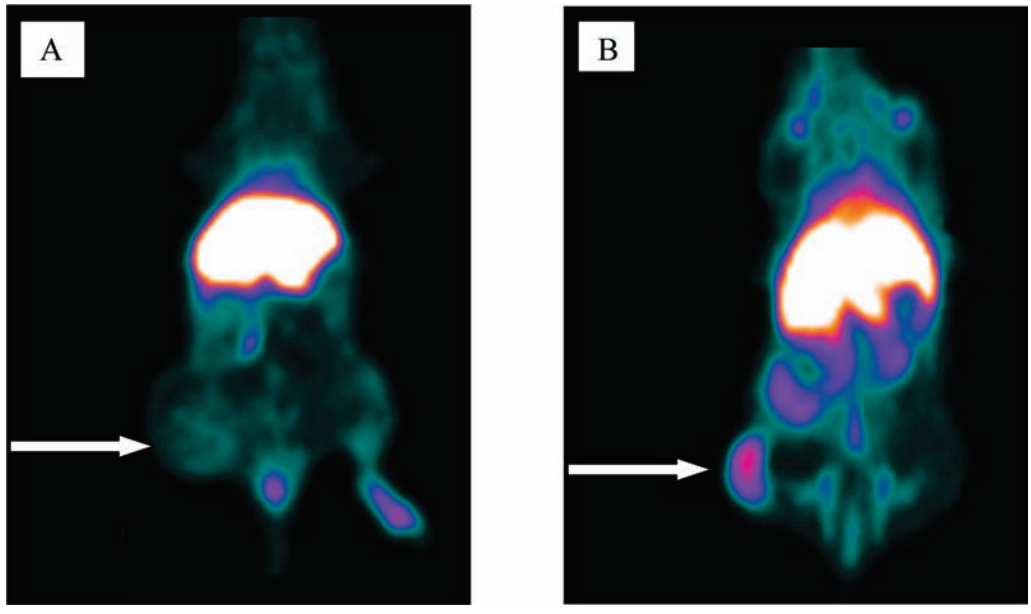


Figure 2. Small animal PET evaluation of nonmodified **[^{18}F]-2** (A) and modified **[^{18}F]-5** (B) in AR42J tumor-bearing nude mice (CD1 nu/nu). Both images show coronal slices (sum from 50 to 90 min p.i.). (A) In vivo small animal PET evaluation of ^{18}F-SiFA-Tyr^3-Octreotate (**[^{18}F]-2**) in a tumor bearing nude mouse model was carried out using a Philips Mosaic small animal scanner. The site of the tumor is indicated by an arrow. (B) In vivo evaluation of ^{18}F-SiFA-Asn(AcNH-β-Glc)-PEG-Tyr^3-octreotate **([^{18}F]-5)** was carried out using a Siemens Inveon small animal PET-scanner in the same tumor model showing the uptake of the radiotracer in the tumor tissue (arrow).

Though giving no optimal results, this is the first approach demonstrating the applicability of silicon-based building blocks (SiFAs) for the one-step ^{18}F-radiolabeling of a receptor-affine peptide for PET and a successful in vivo imaging of a receptor-positive tumor (Figure 2 B). According to these encouraging findings, one part of further developments will now focus on the remaining challenge of the SiFA-approach, namely, the still intrinsically high lipophilicity deriving from the SiFA-building blocks developed so far. Even the introduction of a small PEG-spacer and a carbohydrate as presented in this work could not fully compensate the high lipophilicity of the SiFA building block. In order to further reduce the lipophilicity of SiFA-derivatized peptides, we intend to introduce larger sugar moieties, such as maltotriose or cellobiose (*19*), or charged chemical groups, such as phosphates and quarternary ammonia groups, into the peptides or to use more hydrophilic silicon building blocks stable against hydrolysis.

CONCLUSION

This study demonstrates the feasibility of silicon-fluoride building blocks for the labeling of glucose and glucose/PEG derivatized octreotate derivatives. The SiFA moiety can easily be introduced via chemoselective oxime formation between the aminooxy-derivatized octreotate derivatives and the aldehyde group of SiFA-A (**1**). The conjugates can be radiolabeled with $^{18}F^-$ in a simple one-step isotopic exchange reaction at ambient temperature within 5 min, yielding radiofluorinated octreotate derivatives with reduced lipophilicity suitable for in vivo PET-imaging of sst-positive tumors in mice.

We further demonstrated that the PEG- and carbohydrate-derivatized SiFA-octreotate derivatives can be radiolabeled in high specific activities of 29−56 GBq/μmol. In contrast to other studies using Si−F building blocks, no HPLC purification was required for the isolation of ^{18}F-SiFA-Asn(AcNH-β-Glc)-Tyr^3-octreotate (**[^{18}F]-4**) and ^{18}F-SiFA-Asn(AcNH-β-Glc)-Tyr^3- PEG-octreotate (**[^{18}F]-5**) from the reaction mixture. Although substantial chemical modifications have been made to the original octreotate, both derivatized octreotate conjugates display preserved binding affinities to the sst2 subtype. Compound **[^{18}F]-5** could be used for a successful visualization of a sst2-positive tumor in vivo in an AR42J tumor mouse model with a high tumor uptake of 7% after 60 min.

In conclusion, we progressed significantly toward a feasible application of the SiFA labeling technique for PET tracer development demonstrating that a reduction of the inherent high lipophilicity of the SiFA building block is the key to successful in vivo imaging.

ACKNOWLEDGMENT

Parts of this work were funded from the Deutsche Forschungsgemeinschaft (DFG grant number WA 2132/3-1) to B.W. C.W. would like to thank the Fonds der Chemischen Industrie for financial support.

LITERATURE CITED

(1) Steinbrook, R. (2009) Drug shortages and public health. *N. Engl. J. Med. 362*, 1525–1527.

(2) Ballinger, J. R. (2010) 99Mo shortage in nuclear medicine: crisis or challenge? *J. Label. Compd Radiopharm. 53*, 167–168.

(3) Laverman, P., McBride, W. J., Sharkey, R. M., Eek, A., Joosten, L., Oyen, W. J. G., Goldenberg, D. M., and Boerman, O. C. (2010) A novel facile method of labeling octreotide with 18F-fluorine. *J. Nucl. Med. 51*, 454–460.

(4) Studenov, A. R., Adam, M. J., Wilson, J. S., and Ruth, T. J. (2005) New radiolabelling chemistry: synthesis of phosphorus-[18F]fluorine compounds. *J. Label. Compd. Radiopharm. 48*, 497–500.

(5) Ting, R., Adam, M. J., Ruth, T. J., and Perrin, D. M. (2005) Arylfluoroborates and alkylfluorosilicates as potential PET imaging agents: high-yielding aqueous biomolecular 18F-labeling. *J. Am. Chem. Soc. 127*, 13094–13095.

(6) Martarello, L., Schaffrath, C., Deng, H., Gee, A. D., Lockhart, A., and O'Hagan, D. (2003) The first enzymatic method for C-18F bond formation: the synthesis of 5′-[18F]-fluoro-5′-deoxyadenosine for imaging with PET. *J. Label. Compd. Radiopharm. 46*, 1181–1189.

(7) Wängler, C., Schirrmacher, R., Bartenstein, P., and Wängler, B. (2010) Click-chemistry reactions in radiopharmaceutical chemistry: fast & easy introduction of radiolabels into biomolecules for in vivo imaging. *Curr. Med. Chem. 17*, 1092–1116.

(8) Becaud, J., Mu, L., Karramkam, M., Schubiger, P. A., Ametamey, S. M., Graham, K., Stellfeld, T., Lehmann, L., Borkowski, S., Berndorff, D., Dinkelborg, L., Srinivasan, A., Smits, R., and Koksch, B. (2009) Direct one-step 18F-labeling of peptides via nucleophilic aromatic substitution. *Bioconjugate Chem. 20*, 2254–2261.

(9) Schirrmacher, R., Wängler, C., and Schirrmacher, E. (2007) Recent developments and trends in 18F-radiochemistry: syntheses and applications. *Mini-Rev. Org. Chem. 4*, 317–329.

(10) Schirrmacher, R., Bradtmöller, G., Schirrmacher, E., Thews, O., Tillmanns, J., Siessmeier, T., Buchholz, H. G., Bartenstein, P., Wängler, B., Niemeyer, C. M., and Jurkschat, K. (2006) 18F-labeling of peptides by means of an organosilicon-based fluoride acceptor. *Angew. Chem., Int. Ed. 45*, 6047–6050.

(11) Schirrmacher, E., Wängler, B., Cypryk, M., Bradtmöller, G., Schäfer, M., Eisenhut, M., Jurkschat, K., and Schirrmacher, R. (2007) Synthesis of p-(di-tert-butyl[(18)F]fluorosilyl)benzaldehyde ([(18)F]SiFA-A) with high specific activity by isotopic exchange: a convenient labeling synthon for the (18)F-labeling of N-aminooxy derivatized peptides. *Bioconjugate Chem. 18*, 2085–2089.

(12) Mu, L., Höhne, A., Schubiger, P. A., Ametamey, S. M., Graham, K., Cyr, J. E., Dinkelborg, L., Stellfeld, T., Srinivasan, A., Voigtmann, U., and Klar, U. (2008) Silicon-based building blocks for one-step 18F-radiolabeling of peptides for PET imaging. *Angew. Chem., Int. Ed. 47*, 4922–4925.

(13) Höhne, A., Mu, L., Honer, M., Schubiger, P. A., Ametamey, S. M., Graham, K., Stellfeld, T., Borkowski, S., Berndorff, D., Klar, U., Voigtmann, U., Cyr, J. E., Friebe, M., Dinkelborg, L., and Srinivasan, A. (2008) Synthesis, 18F-labeling, and in vitro and in vivo studies of bombesin peptides modified with silicon-based building blocks. *Bioconjugate Chem. 19*, 1871–1879.

(14) Wängler, B., Quandt, G., Iovkova, L., Schirrmacher, E., Wängler, C., Boening, G., Hacker, M., Schmoeckel, M., Jurkschat, K., Bartenstein, P., and Schirrmacher, R. (2009) Kit-like 18F-labeling of proteins: synthesis of 4-(di-tert-butyl[^{18}F]-fluorosilyl)benzenethiol (Si[^{18}F]FA-SH) labeled rat serum albumin for blood pool imaging with PET. *Bioconjugate Chem. 20*, 317–321.

(15) Rosa-Neto, P., Wängler, B., Iovkova, L., Boening, G., Reader, A., Jurkschat, K., and Schirrmacher, E. (2009) [^{18}F]SiFA-isothiocyanate: a new highly effective radioactive labeling agent for lysine-containing proteins. *ChemBioChem 10*, 1321–1324.

(16) Iovkova, L., Wängler, B., Schirrmacher, E., Schirrmacher, R., Quandt, G., Boening, G., Schürmann, M., and Jurkschat, K. (2009) para-Functionalized aryl-di-tert-butylfluorosilanes as potential labeling synthons for (18)F radiopharmaceuticals. *Chem.—Eur. J. 15*, 2140–2147.

(17) Schirrmacher, R. Unpublished results.

(18) Schottelius, M., Wester, H. J., Reubi, J. C., Senekowitsch-Schmidtke, R., and Schwaiger, M. (2002) Improvement of pharmacokinetics of radioiodinated Tyr(3)-octreotide by conjugation with carbohydrates. *Bioconjugate Chem. 13*, 1021–1030.

(19) Schottelius, M., Rau, F., Reubi, J. C., Schwaiger, M., and Wester, H. J. (2005) Modulation of pharmacokinetics of radioiodinated sugar-conjugated somatostatin analogues by variation

of peptide net charge and carbohydration chemistry. *Bioconjugate Chem. 16*, 429–437.
(20) Antunes, P., Ginj, M., Walter, M. A., Chen, J., Reubi, J. C., and Maecke, H. R. (2007) Influence of different spacers on the biological profile of a DOTA-somatostatin analogue. *Bioconjugate Chem. 18*, 84–92.
(21) Reubi, J. C., Waser, B., Schaer, J. C., and Laissue, J. A. (2001) Somatostatin receptor sst1-sst5 expression in normal and neoplastic human tissues using receptor autoradiography with subtype-selective ligands. *Eur. J. Nucl. Med. 28*, 836–846.
(22) Hofland, L. J., and Lamberts, S. W. J. (1999) *Octreotide: The Next Decade* (Lamberts, S. W. J., Ed.) pp 27−38, BioScientifica, Bristol, U.K.
(23) Jaïs, P., Terris, B., Ruszniewski, P., LeRomancer, P., Rey-Desmars, F., Vissuzaine, C., Cadiot, G., Mignon, M., and Lewin, M. J. (1997) Somatostatin receptor subtype gene expression in human endocrine gastroentero-pancreatic tumours. *Eur. J. Clin. Invest. 27*, 639–644.
(24) Wellings, D. A., and Atherton, E. (1997) Standard Fmoc protocols. *Methods Enzymol. 289*, 44–67.
(25) Poethko, T., Schottelius, M., Thumshirn, G., Hersel, U., Herz, M., Henriksen, G., Kessler, H., Schwaiger, M., and Wester, H. J. (2004) Two-step methodology for high-yield routine radiohalogenation of peptides: (18)F-labeled RGD and octreotide analogs. *J. Nucl. Med. 45*, 892–902.
(26) Cescato, R., Erchegyi, J., Waser, B., Piccand, V., Maecke, H. R., Rivier, J. E., and Reubi, J. C. (2008) Design and in vitro characterization of highly sst2-selective somatostatin antagonists suitable for radiotargeting. *J. Med. Chem. 51*, 4030–4037.
(27) Reubi, J. C., Schaer, J. C., Waser, B., Wenger, S., Heppeler, A., Schmitt, J. S., and Mäcke, H. R. (2000) Affinity profiles for human somatostatin receptor sst1-sst5 of somatostatin radiotracers selected for scintigraphic and radiotherapeutic use. *Eur. J. Nucl. Med. 27*, 273–282.
(28) Erchegyi, J., Cescato, R., Grace, C. R., Waser, B., Piccand, V., Hoyer, D., Riek, R., Rivier, J. E., and Reubi, J. C. (2009) Novel, potent, and radio-iodinatable somatostatin receptor 1 (sst1) selective analogues. *J. Med. Chem. 52*, 2733–2746.
(29) Viguerie, N., Tahiri-Jouti, N., Esteve, J. P., Clerc, P., Logsdon, C., Svoboda, M., Susini, C., Vaysse, N., and Ribet, A. (1988) Functional somatostatin receptors on a rat pancreatic acinar cell line. *Am. J. Physiol. 255*, G113–G120.
(30) Schottelius, M., Poethko, T., Herz, M., Reubi, J. C., Kessler, H., Schwaiger, M., and Wester, H. J. (2004) First (18)F-labeled tracer suitable for routine clinical imaging of sst receptor-expressing tumors using positron emission tomography. *Clin. Cancer Res. 10*, 3593–3606.
(31) Fottner, C., Mettler, E., Goetz, M., Schirrmacher, E., Anlauf, M., Strand, D., Schirrmacher, R., Klöppel, G., Delaney, P., Schreckenberger, M., Galle, P. R., Neurath, M. F., Kiesslich, R., and Weber, M. M. (2010) *In vivo* molecular imaging of somatostatin receptors in pancreatic islet cells and neuroendocrine tumors by miniaturized confocal laser-scanning fluorescence microscopy. *Endocrinology 151*, 2179–2188.
(32) Antunes, P., Ginj, M., Walter, M. A., Chen, J., Reubi, J. C., and Maecke, H. R. (2007) Influence of different spacers on the biological profile of a DOTA-somatostatin analogue. *Bioconjugate Chem. 18*, 84–92.
(33) Höhne, A., Yu, L., Mu, L., Reiher, M., Voigtmann, U., Klar, U., Graham, K., Schubiger, P. A., and Ametamey, S. M. (2009) Organofluorosilanes as model compounds for 18F-labeled silicon-based PET tracers and their hydrolytic stability: experimental data and theoretical calculations (PET = positron emission tomography). *Chem.—Eur. J. 15*, 3736–3743.
(34) Reubi, J. C., Kvols, L. K., Waser, B., Nagorney, D., Heitz, P. U., Charboneau, J. W., Reading, C. C., and Moertel, C. (1990) Detection of somatosatin receptors in surgical and percutaneous needle biopsy samples of carcinoids and islet cell carcinomas. *Cancer Res. 50*, 5969–5977.
(35) Wester, H. J., Schottelius, M., Scheidhauer, K., Reubi, J. C., Wolf, I., and Schwaiger, M. (2002) Comparison of radioiodinated TOC, TOCA and Mtr-TOCA: the effect of carbohydration on the pharmacokinetics. *Eur. J. Nucl. Med. Mol. Imaging 29*, 28–38.

BC100316C

Radiosynthesis and Biodistribution of a Prosthetic Group (^{18}F-FENMA) Conjugated to Cyclic RGD Peptides

Dag Erlend Olberg,*[,†] Alan Cuthbertson,[‡] Magne Solbakken,[‡] Joseph M. Arukwe,[‡] Hong Qu,[§] Alexandr Kristian,[||] Skjalg Bruheim,[||] and Ole Kristian Hjelstuen[†,‡]

Department of Pharmaceutics & Biopharmaceutics, University of Tromsø, Norway, GE Healthcare Medical Diagnostics R&D, Oslo, Norway, Centre for Molecular Biology and Neuroscience (CMBN), University of Oslo, Norway, and Department of Tumour Biology, Institute of Cancer Research, Rikshospitalet, Oslo, Norway. Received July 16, 2010; Revised Manuscript Received October 21, 2010

We have recently reported a new *N*-methylaminooxy-based prosthetic group for the site-selective introduction of ^{18}F-fluorine under mild acidic aqueous conditions into model peptides functionalized with a Michael acceptor moiety. To further investigate the utility of this methodology, the radiosynthesis of two cyclic RGD peptides was carried out, and in vivo biodistribution and microPET studies were performed in tumor-bearing mice. A cyclic RGD peptide was functionalized with the Michael acceptors *trans*-β-nitrostyrene carboxylic acid and 3-vinylsulfonylpropionic acid. Radiolabeling was then performed with the prosthetic group *O*-(2-(2-[^{18}F]fluoroethoxy)-ethyl)-*N*-methylhydroxylamine (^{18}F-FENMA) yielding the ^{18}F-conjugates in moderate yields (8.5−12%). Biodistribution, blocking, and microPET imaging studies were performed in a mouse xenograft model. The vinylsulfonyl-modified conjugate demonstrated good in vitro plasma stability. Biodistribution and microPET studies revealed excellent tumor uptake with low background in key organs and renal elimination as the predominant route of excretion. Blocking studies with coinjected nonlabeled RGD peptide confirmed the in vivo specificity for the integrin $\alpha_v\beta_3$. On the other hand, ^{18}F-FENMA-nitrostyrene-RGD, although stable at conjugation pH 5, was found to rapidly degrade at physiological pH through loss of the ^{18}F-prosthetic group.

INTRODUCTION

Positron emission tomography (PET) has become an important functional imaging modality in diagnostic medicine due to the high sensitivity, high resolution, and ability to quantify the radioactive concentration in tissues (*1*). Fluorine-18 is a particularly attractive radionuclide due to the favorable nuclear and chemical properties (*2*), as well as its availability from medical cyclotrons in high specific activity (*3, 4*). The low positron energy of 0.64 MeV results in low radiation doses and short tissue range, and the relatively long 109.7 min half-life allows both multistep radiosynthesis and extended scanning protocols (*5*).

Although numerous drug-like molecules have been successfully labeled with fluorine-18, optimization of the radiolabeling route to complex molecules such as peptides and proteins still offers significant challenges to the radiochemist. Direct incorporation of [^{18}F]fluoride at high specific radioactivity into macromolecules is hampered by the harsh reaction conditions, and as a consequence, peptide and protein labeling is usually carried out by adopting a prosthetic group strategy (*6*). This methodology, also referred to as radiolabeling using bifunctional labeling agents, involves first ^{18}F incorporation into a small organic molecule, which is then conjugated to the macromolecule under mild conditions in a second step. The variety of chemistries exploited for the conjugations includes acylation, Huisgen 1,3-dipolar cycloaddition (click chemistry), alkylation, and oxime or hydrazone forming reactions (*7*−*10*). Each approach has its own advantages and limitations affecting the radiolabeling yields and biodistribution profile of the tracer. For example, increasing the lipophilicity of the prosthetic group changes the physicochemical properties of the drug product leading to increased hepatobiliary excretion (*11*). In order to control excretion routes, peptides are often modified with poly(ethylene glycol) (PEG) units or other pharmacokinetic modifiers (PKMs) (*12, 13*) to counteract the lipophilic nature of the prosthetic group. As an alternative, hydrophilic prosthetic groups are therefore considered desirable.

Recently, we reported a novel prosthetic group *O*-(2-(2-[^{18}F]fluoroethoxy)ethyl)-*N*-methylhydroxylamine (^{18}F-FENMA) utilizing the site-selective reactivity of the *N*-methylaminooxy functionality with peptides modified with a Michael acceptor (*14, 15*). Further extension of this approach is reported in this study using the RGD peptide **1** modified with either 4-[(*E*)-2-nitrovinyl-]benzoic acid or a 3-vinylsulfonylpropionyl group. The nitrostyrene−peptide **2** showed rapid reaction kinetics with ^{18}F-FENMA forming a more hydrophobic peptide as evidenced by radio-HPLC. The 3-vinylsulfonylpropionyl−peptide **3** formed the more hydrophilic conjugate [^{18}F]**5** but with slower reaction kinetics. The ultimate aim of this study was to determine the radiochemical yields, in vitro stability, biodistribution, and tumor targeting properties of the peptide conjugates in osteosarcoma xenograft bearing mice.

EXPERIMENTAL PROCEDURES

Materials. All chemicals were of analytical grade and obtained commercially. No carrier added [^{18}F]F^- was produced via the ^{18}O(p,n)^{18}F reaction by bombardment of an isotopically enriched [^{18}O]water target with 16.5 MeV protons using a GE PETtrace 6 cyclotron (Uppsala, Sweden). NMR spectra were run on a Bruker Avance III 400 spectrometer (Fällanden, Switzerland) equipped with a 5 mm BBFO PFG probe.

* Corresponding author. Dag Erlend Olberg; e-mail: dag.erlend.olberg@petsenteret.no. Phone: + 47 230 76327. Fax: +47 230 76310.
† University of Tromsø.
‡ GE Healthcare Medical Diagnostics R&D.
§ University of Oslo.
|| Institute of Cancer Research.

10.1021/bc1003229 © 2010 American Chemical Society
Published on Web 11/11/2010

Preparative reversed-phase HPLC was performed on a Shimadzu LC-8A (Bergman, Oslo, Norway) system using a Phenomenex Luna C18(2) column (Teknolab, Oslo, Norway) (250 mm × 21.2 mm, 5 μm), flow rate 10 mL/min, with gradients 0−30% solvent B (Preparative Method 1) or 0−40% solvent B (Preparative Method 2) over 60 min (solvent A, water/0.1% TFA; solvent B, acetonitrile/0.1% TFA). LC-MS spectra were recorded on a LCQ DECA XP MAX instrument using electrospray ionization (ESI) or a Waters LCT-TOF (Instrument teknikk AS, Oslo, Norway) instrument (for high-resolution mass spectrometry (HRMS)) using a Phenomenex Luna (Teknolab) C18(2) column (20 mm × 2 mm, 3 μm), flow rate 0.6 mL/min with gradient 0−30% B. UV detection was in all instances at 214 and 254 nm. Synthesis of the tosylate precursor and labeling with [^{18}F]fluoride yielding *O*-(2-(2-[^{18}F]fluoroethoxy)ethyl)-*N*-methylhydroxylamine (abbreviated ^{18}F-FENMA) was carried out as described previously (*14*). The cyclic RGD peptide NC100717, was supplied by GE Healthcare (Oslo, Norway) (*16*). Boc-protected cysteic acid (*N*-Boc-L-cysteic acid) was prepared according to Jia et al. (*17*).

Chemistry and Radiochemistry. *Synthesis of Peptide (**1**).* To a stirred solution of NC100717 (100 mg, 97 μmol) in DMF (3 mL) was added Boc-L-cysteic acid (32 mg, 115 μmol) preactivated with tetramethylfluoroformamidiniun hexafluorophosphate (TFFH) (31 mg, 115 μmol) and *N*,*N*-diisopropylethylamine (DIPEA) (101 μL, 0.58 mmol). After 2 h, solvent was removed in vacuo, and the crude residue was treated with trifluoroacetic acid (TFA) (5 mL) for 5 min. TFA was removed under reduced pressure. The two-step cycle described above was repeated to introduce and deprotect the second cysteic acid residue. The crude mixture was then subjected to purification by preparative HPLC (Method 1), and after removal of the organic solvents under reduced pressure, the pure product (>95%) was isolated by lyophilization. Yield: 26 mg (17% based on NC100717). LC-MS found $m/z = 1560.5$ $[M+H]^+$ calculated for $C_{56}H_{89}N_{17}O_{25}S_5$ 1559.48.

Synthesis of 3-(Vinylsulfonyl)propionic Acid. To a stirred solution of 3-(2-chloro-ethanesulfonyl)propionic acid methyl ester (100 mg) in dichloromethane (5 mL) was added 3 equiv of triethylamine at room temperature, and the reaction mixture was allowed to stand overnight. After removal of solvents under reduced pressure, the residue was purified by normal-phase flash chromatography (gradient 0−50% ethyl acetate in hexane). Purified intermediate was dissolved in 0.1 M HCl (20 mL) and refluxed overnight. The aqueous phase was evaporated off, and the residue was dissolved in dichloromethane and dried over Na_2SO_4 for 1 h. After filtration and removal of solvents, 3-(vinylsulfonyl)propionic acid was obtained as a white powder (59 mg, 77%). ^{1}H NMR (400 MHz, $CDCl_3$): δ (ppm) 6.65 (dd, $J_1 = 9.7$ Hz, $J_2 = 16.7$ Hz, 1H), δ 6.49 (d, $J = 16.7$ Hz, 1H), δ 6.22 (d, $J = 9.7$ Hz, 1H), δ 3.34 (t, $J = 7.4$ Hz, 2H), δ 2.87 (t, $J = 7.4$ Hz, 2H). ^{13}C NMR (100 MHz, $CDCl_3$): δ (ppm) 173.8, 135.8, 131.5, 49.2, 27.0.

*Synthesis of Nitrostyrene-RGD (**2**) and Sulfonyl-RGD (**3**).* 4-[(*E*)-2-Nitrovinyl]benzoic acid was synthesized as previously described (*18*). To a stirred solution of **1** (13 mg, 7.9 μmol) in DMF (3 mL) was added either 4-[(*E*)-2-nitrovinyl]benzoic acid or 3-vinylsulfonylpropionic acid (12 μmol) preactivated with TFFH (3.2 mg, 12 μmol) and DIPEA (10 μL, 0.60 μmol). The reaction mixtures were placed in a sonication bath for 1 h and product formation was monitored by LC-MS. If necessary, the above procedure was repeated until complete conversion was achieved. Reaction mixtures were subjected to purification by preparative HPLC (method 2 compound **2**, method 1 compound **3**), and products were isolated from fractions by lyophilization. Nitrostyrene-RGD (**2**): Yield 8.2 mg (60%), LC-MS found $m/z = 1735.7$, $[M+H]^+$ calculated for $C_{65}H_{94}N_{18}O_{28}S_5$ was 1734.5. Sulfonyl-RGD (**3**): Yield 7.4 mg (55%), LC-MS found $m/z = 1706.7$, $[M+H]^+$ calculated for $C_{61}H_{95}N_{17}O_{28}S_6$ was 1705.5.

*Synthesis of Nonradioactive Reference Standard FENMA Conjugates **4** and **5**.* To a solution of *O*-(2-(2-fluoroethoxy)-ethyl)-*N*-methylhydroxylamine (1 mg, 4 μmol) in acetate buffer 0.4 M pH 5 (1 mL) was added either **2** or **3** (0.9 μmol). Conversion to **4** was completed after only 15 min at room temperature, whereas **5** was formed in >90% yield with heating to 60 °C for 60 min. Reaction mixtures were subjected to purification by preparative HPLC (method 2), and the pure products were isolated from fractions by lyophilization. (**4**): Yield 1.4 mg (85%), LC-HRMS found $m/z = 1870.5868$, $[M-H]^-$ calculated for $C_{70}H_{106}FN_{19}O_{30}S_5$ was 1871.5941. (**5**): Yield 1.3 mg (80%), LC-HRMS found $m/z = 1841.5627$, $[M-H]^-$ calculated for $C_{66}H_{107}FN_{18}O_{30}S_6$ was 1842.5709.

*Radiosyntheses of [^{18}F]**4** and [^{18}F]**5**.* Peptide precursors **2** and **3** were radiolabeled by reaction with ^{18}F-FENMA in acetate buffer pH 5 with a specific activity of 40−50 GBq/μmol (after formulation) as determined by comparison of the radiochromatogram with a calibration curve of authentic reference standards. The radiosynthesis and purification of ^{18}F-FENMA was carried out as previously described (*14*). In short, a solution of **2** or **3** (1.2 μmol) in acetate buffer 0.4 M pH 5 (0.8 mL) was added to the reaction vial containing purified ^{18}F-FENMA. Conjugation conditions were 40 °C for 15 min and 70 °C for 60 min for [^{18}F]**4** and [^{18}F]**5**, respectively. Postconjugation, the reaction mixture was diluted with water (4 mL) before purification by C18 reversed-phase liquid chromatography using both radiometric detection and UV detection at 214 nm. The HPLC fraction containing the radioactive material was diluted with water and passed through a Waters C18 Sep-Pak light cartridge preactivated with ethanol (2 mL) and water (5 mL). The cartridge with bound drug product was washed with water (5 mL), and the product was eluted into a sealed sterile vial with 1 mL absolute ethanol. The ethanol was removed under a stream of nitrogen at 70 °C. The radioactive residue was reconstituted in isotonic saline (adjusted to pH 4 for compound [^{18}F]**4**) for use in the animal experiments. The identities of [^{18}F]**4** and [^{18}F]**5** were confirmed by coelution with the corresponding nonradioactive reference compounds.

Integrin Receptor-Binding Assay. The binding affinity and specificity of **4** and **5** for $\alpha_v\beta_3$ integrin were assessed in a competitive cell binding assay using ^{125}I-echistatin and membrane preparations from the human endothelial adenocarcinoma cell line EA-Hy926 as previously described (*16*). K_i values were calculated from the binding curves using *Graphpad Prism* software.

In Vitro Stability in Mice Plasma. Approximately 2 MBq each of either [^{18}F]**4** and [^{18}F]**5** in saline (50 μL) was added to freshly collected mouse plasma (0.5 mL total volume) and the samples incubated at 37 °C. After 30 min, 1 and 2 h aliquots (100 μL) were collected, diluted 1:1 with phosphate buffered saline (PBS), and the mixtures filtered (Ultrafree filter unit 5000 NMWL, Millipore) at 14 000 rpm for 15 min. The resulting filtrate was diluted with water/0.1% TFA and analyzed by C18 reversed-phase radio-HPLC.

Octanol/Water Partition Coefficient. Approximately 50 kBq of [^{18}F]**5** in 30 μL PBS was diluted with 470 μL of PBS and added to 500 μL of *n*-octanol in an Eppendorf cup ($n = 4$). After vortexing for 3 min, the cups were centrifuged (10 300 rpm; 6 min), and the radioactivity of 100 μL aliquots of the PBS and *n*-octanol phases was counted in a gamma counter.

Animals and Tumor Model. Housing and handling of animals were performed according to protocols approved by the Animal Care and Use Committee, in compliance with the National Committee for Animal Experiments guidelines on animal welfare. Female Balb/c nu/nu mice, bred at the

nude rodent facility at the Norwegian Radium Hospital, were maintained under specific pathogen-free conditions with food and water supplied ad libitum. The xenografts have previously been established by direct implantation of patient tumor specimens in nude mice (*19*). The xenografts were established by subcutaneous injection of human osteosarcoma cells (3×10^6) in 100 μL of PBS solution into distal part of mouse right flank when animals were 4−6 weeks of age. When the average tumor diameter was about 5−10 mm (14−21 days after implant), the mice underwent biodistribution and microPET imaging experiments. Visualization of neovascularization in the tumor tissue was performed by immunohistochemistry with a rat antimouse-CD31 monoclonal antibody (clone MEC 13.3; BD Pharmigen).

Biodistribution and MicroPET Studies. *Biodistribution.* Nude mice bearing subcutaneously xenografted human OHS tumors were injected intravenously with approximately 1 MBq of [^{18}F]**5**. Animals were euthanized and sacrificed at 5 min and 2 h post-injection (3 or 4 per time point). Blood, tumor, and the major organs and tissues were collected, wet-weighed, and their radioactivity counted in a gamma counter (MINAXI 5000 series, United Technologies Packard, Zurich, Switzerland). The percentage of injected dose per gram (%ID/g) was calculated for each sample. For each mouse, the amount of radioactivity present in the tissue samples was calibrated against a calibration curve of the injectate. Values are expressed as mean ± standard deviation (SD) for a group of 3−4 animals. For the receptor blocking experiment, [^{18}F]**5** was coinjected with 10 mg/kg of NC100717 in tumor bearing mice. Biodistribution was determined as described above at 2 h post-injection.

MicroPET. PET scans and image analysis were performed using a microPET F120 scanner (Siemens Medical Solutions). Tumor-bearing mice were injected via a tail vein with 4−7 MBq of [^{18}F]**5**. Static PET images were acquired for 15 min in mice under isoflurane anesthesia 105 min post-injection. For dynamic PET scans, mice were prepositioned in the microPET scanner under isoflurane anesthesia, injected with tracers, and imaged continuously from time 0 to 120 min.

The images were reconstructed using a three-dimensional ordered subsets expectation maximization/maximum a posteriori/(OSEM3D/MAP) algorithm, and no correction was applied for attenuation and scatter.

Statistical Analysis. The data are expressed as means ± SD. One-way analysis of variance (ANOVA) was used for statistical evaluation. A *P*-value of <0.05 was considered significant.

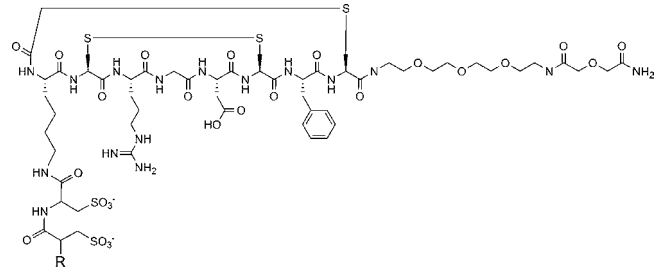
RESULTS

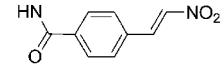
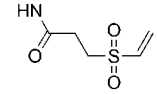
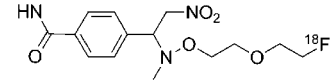
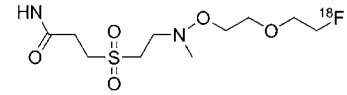
The structures of **1**, **2**, **3**, [^{18}F]**4**, and [^{18}F]**5** are shown in Table 1. Synthesis of tosyl precursor and radiosynthesis of the prosthetic group *O*-(2-(2-[^{18}F]fluoroethoxy)ethyl)-*N*-methylhydroxylamine (^{18}F-FENMA) and its site-selective ligation in aqueous buffer with model peptides has been described previously (*14*, *15*).

In order to provide good solubility of the peptide precursors in the relatively concentrated aqueous acetate buffer (0.4 M) which was required for conjugation reaction with ^{18}F-FENMA, the core peptide NC100717 was modified with two cysteic acids.

The modification of NC100717 was accomplished by reacting *N*-Boc-protected L-cysteic acid activated with TFFH to the free ε-amine of lysine in two synthetic steps. TFFH was used in this reaction, as it generally gave cleaner reaction mixtures and higher yields compared to more traditional coupling reagents *N*,*N*,*N*′,*N*′-tetramethyl-*O*-(7-azabenzotriazol-1-yl)uronium hexafluorophosphate (HATU) and (7-azabenzotriazol-1-yloxy)tripyrrolidinophosphonium hexafluorophosphate (PyAOP). After HPLC purification and isolation by lyophilization, peptide **1** was obtained in moderate yield (17%) calculated from starting peptide NC100117. Reaction of the Michael acceptor moieties, 4-[(*E*)-2-nitrovinyl]benzoic acid or 3-vinylsulfonylpropionic acid, with the amino terminus using TFFH gave the peptide precursors **2** and **3** in good yields. The conjugation reaction of FENMA with **2** and **3** proceeded smoothly in acetate buffer pH 5. Differences in the reaction kinetics between the two systems were clearly observed. After addition of FENMA to the nitrostyrene peptide **2**, the reaction was essentially complete in 15 min at room temperature. In contrast, the vinylsulfone **3** required heating at 60 °C for 1 h with FENMA to achieve yields above 90% as analyzed by HPLC.

Table 1. Structures of Peptide 1, Peptide Precursors 2 and 3, and ^{18}F-Labeled Peptides [^{18}F]4 and [^{18}F]5



compound	R
1	NH_2
2	
3	
[^{18}F]**4**	
[^{18}F]**5**	

The radiosynthesis time for ^{18}F-FENMA-nitrostyrene-RGD ([^{18}F]**4**) after formulation was about 2 h with a decay-corrected yield of 6−7% ($n = 3$) based on [^{18}F]fluoride. Extended reaction times were required for the radiosynthesis of ^{18}F-FENMA-sulfonyl-RGD ([^{18}F]**5**), being produced in 2−4% ($n = 5$) radiochemical yield (decay-corrected postformulation) with 165 min reaction time using 2 mg of precursor peptide. Experiments using higher peptide concentrations, however, clearly demonstrated the dependence of synthesis yield on peptide quantity. Using 5 mg of peptide precursor, the overall yields increased, ranging from to 8.5% to 12% (decay-corrected postformulation). Importantly, unreacted peptide precursor could readily be separated from ^{18}F-labeled peptides to yield both [^{18}F]**4** and [^{18}F]**5** with a radiochemical purity >98% based on analytical HPLC and a specific activity of 40−50 GBq/μmol. As expected, the retention time for [^{18}F]**4** (11.1 min) was significantly higher than for [^{18}F]**5** (9.75 min), reflecting the higher lipophilicity of [^{18}F]**4** compared to that of [^{18}F]**5**.

The stability of [^{18}F]**4** and [^{18}F]**5** was determined following incubation in mouse plasma at 37 °C over 2 h with samples collected for analysis by radio-HPLC at 30 min, 1 h, and

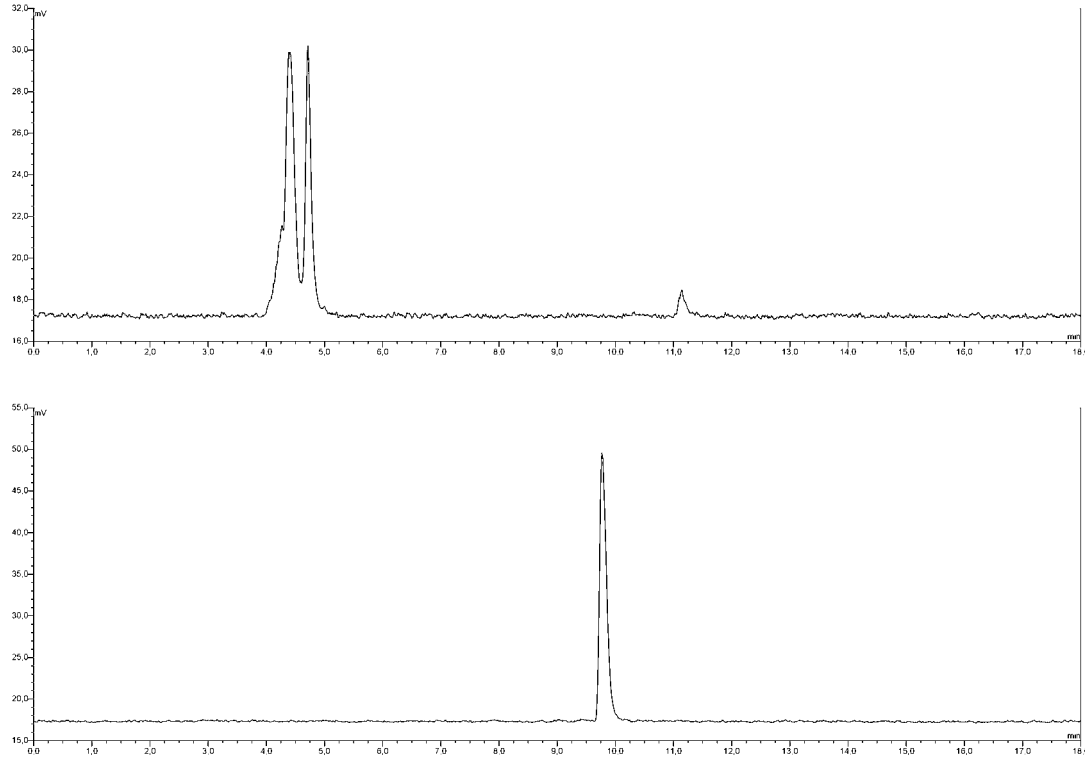


Figure 1. Above chromatogram: [^{18} F]**4** following incubation in mouse plasma after 1 h. Right peak at t_R = 11 min is intact [^{18} F]**4**. Lower chromatogram: [^{18} F]**5** incubation in mouse plasma after 1 h. Main peak is intact [^{18} F]**5**.

2 h. Plasma studies with [^{18}F]**5** revealed no detectable degradation over 2 h. On the other hand, conjugate [^{18}F]**4** demonstrated poor stability in plasma with only 5% of the intact tracer remaining after 2 h (Figure 1). Subsequent studies of **4** in phosphate buffer at different pH values revealed that the stability was pH-dependent. At pH 7.3, 17% of **4** remained intact after 60 min, while at pH 6, 50% remained intact after 60 min. At pH 4, no degradation of **4** was observed within the time frame of the study (2 h). The observed degradation was attributed to the retro-Michael addition of the prosthetic group favored at higher pH. LC-MS studies supported this assumption with reappearance of peptide precursor **2** being confirmed in a stock solution of **4** stored at pH 7 (data not shown) (*20*). Since [^{18}F]**4** proved to be unstable in mice plasma, log *P* experiments were conducted only for [^{18}F]**5**. The log *P* (octanol/water) for [^{18}F]**5** was -2.61 ± 0.01 confirming the hydrophilic nature of the compound.

The affinity of compound **5** for $\alpha_v\beta_3$ integrin was determined in a competitive binding assay with ^{125}I-echistatin. Binding of ^{125}I-echistatin to $\alpha_v\beta_3$ was competed out by **5** in a concentration-dependent manner with a measured K_i value of 3.0 nM as shown in Figure 2. This suggests that attachment of the prosthetic group to the peptide had no effect on receptor binding, with the reported K_i for NC100717 being 6.8 nM (*16*). The unstable nature of **4** precluded an accurate interpretation of the K_i for this compound.

Despite its poor plasma stability, dynamic microPET scans were performed with [^{18}F]**4** in three tumor-bearing mice. We rationalized that, due to low interstitial pH caused by hypoxia and metabolic activity in the lesion, any intact [^{18}F]**4** distributed to the local tumor environment would display greater stability (*21*−*23*). The more rapid degradation of background [^{18}F]**4** at normal physiological conditions would result in a more rapid excretion of the prosthetic group improving the signal-to-noise ratios. Lewis et al. have also

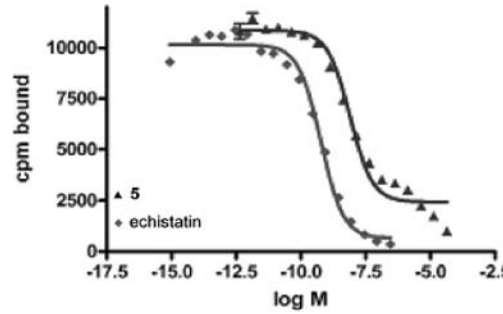


Figure 2. Competition of ^{125}I-echistatin by **5** (K_i = 3 nM) on EA-Hy926 cell membranes (▲). Echistatin for reference (♦).

conducted similar studies with a labile maleimidocysteineamido-DOTA side chain (*24*, *25*). However, this hypothesis proved to be incorrect with the rapid degradation in blood preventing tumor accumulation, and thus, [^{18}F]**4** was not evaluated further.

The results of the biodistribution of [^{18}F]**5** in mice with subcutaneously implanted OHS tumors are shown in Figure 3. The tracer cleared rapidly from the blood (0.18% ID/g, 2 h post-injection) and had good tumor uptake (3.48% ID/g) 2 h post-injection, low bone uptake indicating little or no defluorination, and a favorable biodistribution profile. At 120 min post-injection, the tumor to blood and tumor to muscle ratios were 19 and 5, respectively. The systemic clearance was predominately by renal excretion.

In a separate experiment addressing specificity, mice were coinjected with [^{18}F]**5** and 10 mg/kg of nonradioactive RGD peptide NC100717. The blocking study demonstrated a >10-fold reduction in tumor uptake at 120 min post-injection (3.48% ID/g vs 0.25% ID/g, $P < 0.05$) indicating $\alpha_v\beta_3$-mediated tumor binding. Uptake in nontarget organs was also reduced in the presence of excess unlabeled RGD peptide, indicating that the uptake in these tissues was at least partly $\alpha_v\beta_3$-mediated;

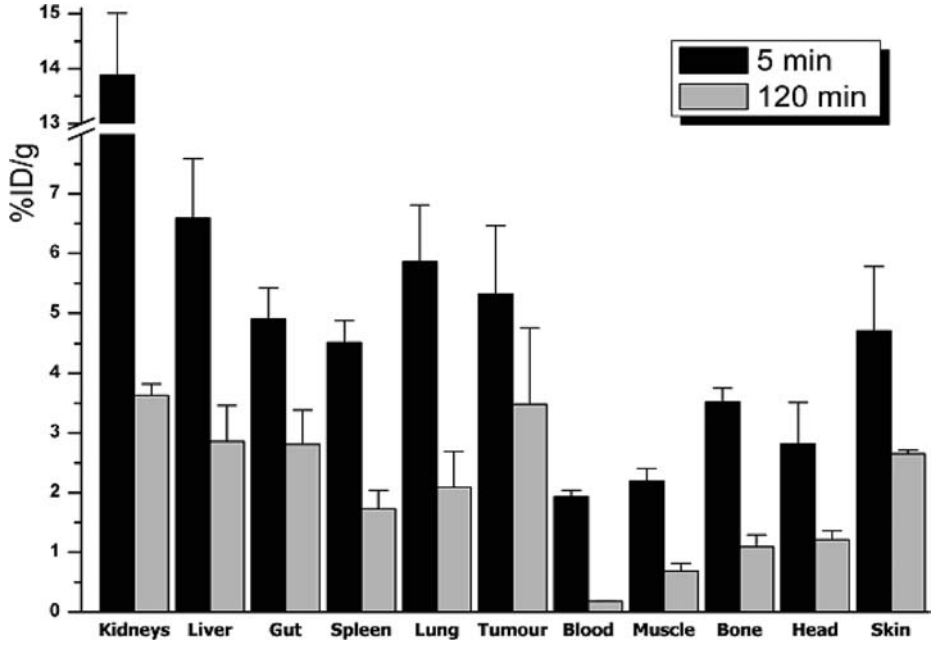


Figure 3. Radioactivity expressed as percentage injected dose per gram tissue in the tumor and key organs of the subcutaneous human OHS xenograft mouse model 5 and 120 min after intravenous injection of approximately 1 MBq [^{18}F]**5** at. ($n = 4$ for each time point).

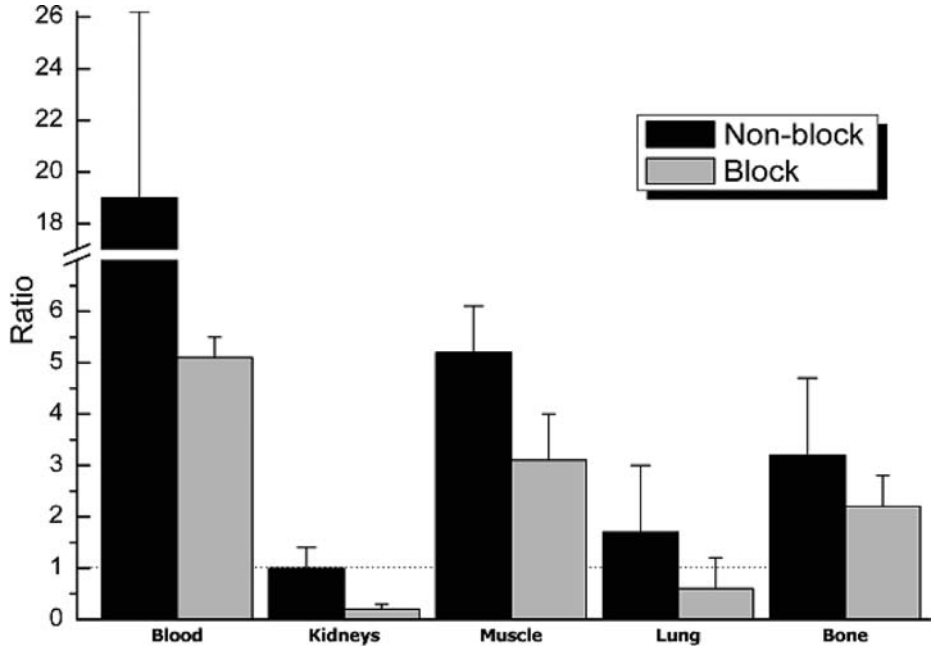


Figure 4. Tumour to nontarget ratios of key organs for [^{18}F]**5** without and in the presence of coinjected excess NC100717.

however, tumor uptake was reduced most markedly (Figure 4). Similar observations have been reported with other radiolabeled RGD peptides (*26*−*29*).

MicroPET images (15 min static single frame) were taken at 105 min of one mouse bearing an OHS tumor injected with 5.2 MBq [^{18}F]**5** as shown in Figure 5. The tumor was clearly visible with high tumor to background activity ratio. Highest uptake of radioactivity was seen in the kidneys and to a lesser extent in the liver/GI region, which is in agreement with the data obtained from direct tissue sampling. In a similar study, the specificity of [^{18}F]**5** for the $\alpha_v\beta_3$ integrin in vivo was confirmed by a blocking experiment where the tracer was coinjected with nonlabeled cyclic RGD peptide (10 mg/kg). As can be seen from Figure 6, uptake in OHS tumor in the presence of nonradiolabeled RGD peptide was clearly lower than without RGD blocking, which is in good agreement with the biodistribution studies.

DISCUSSION

There have been several reports on the use of various ^{18}F-prosthetic groups for labeling of peptides for in vivo PET studies (*30*, *31*). However, many of these strategies are dependent on acylation reactions (*32*−*34*) which, for peptide sequences containing more than one free amino group, lead to the formation of a multitude of products. Site-selective chemistries are available using, for example, click chemistry, oxime bond formation, and alkylation reactions with thiols (^{18}F-maleimide, ^{18}F-thiols), which produce a single radiolabeled product (*35*, *36*). However, all the above approaches have their limitations. The click chemistry requires a copper catalyst and

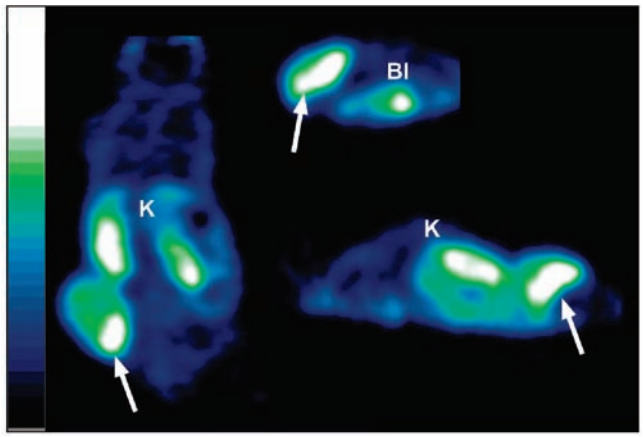


Figure 5. Coronal (left), transaxial (upper right), and sagittal (lower right) microPET images (15 min static single frame) at 105 min post-injection of an OHS tumor-bearing mouse injected with 5.2 MBq [^{18}F]**5**. K = kidneys. Bl = bladder. White arrow indicates tumor.

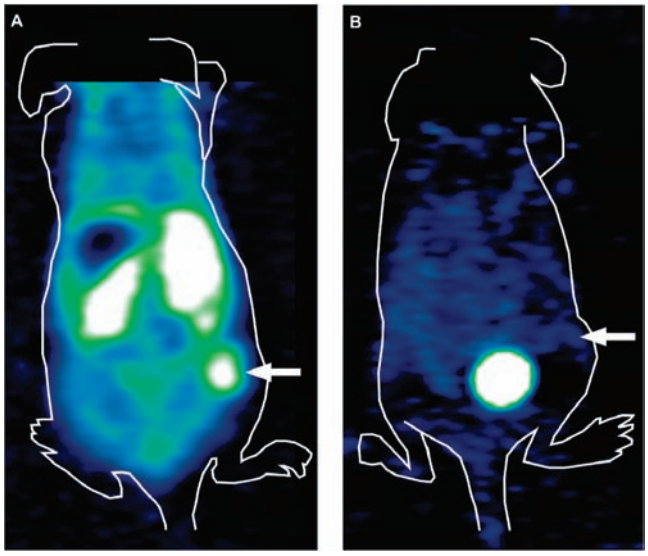


Figure 6. Coronal microPET images of OHS tumor-bearing mice at 105 min post-injection of [^{18}F]**5** without (A) and with (B) coinjection of nonradioactive RGD peptide (10 mg/kg). Tumors are indicated by white arrows.

is complicated by a distillation step which is nontrivial with respect to automation. Free sulfhydryl groups are relatively uncommon in most peptides and are furthermore susceptible to oxidation and disulfide formation.

In this study, the site-selective introduction of an ^{18}F-*N*-methylaminooxy prosthetic group into an RGD peptide was explored, with the peptide component bearing two different types of Michael acceptor moiety. The ^{18}F-FENMA-nitrostyrene-RGD ([^{18}F]**4**) conjugate displayed pH-dependent degradation with poor stability in the physiological to alkaline pH range. Improved stability was observed at lower pH values with no observable degradation of the conjugate at pH 4. The hypothesis of enhanced product stability in the tumor interstitia combined with rapid clearance from the background was tested (vide supra), but no tumor uptake was observed. The reason for this was likely a rapid retro-Michael addition of the ^{18}F-FENMA from the nitrostyrene in vivo. It remains to be explored whether substituents other than the nitro group on the styrene moiety can render sufficient stability to the conjugates.

The conjugation kinetics of ^{18}F-FENMA with the vinylsulfone peptide **3** were slower than for the nitrostyrene derivative, requiring a 60 min reaction time; however, using 5 mg of precursor **3** a yield of 8.5−12% (decay-corrected postformulation) of the drug product [^{18}F]**5** was obtained. In contrast to [^{18}F]**4**, [^{18}F]**5** demonstrated excellent stability in mouse plasma over two hours, and was more hydrophilic as reflected by a shorter HPLC retention time. However, for clinical utility of this methodology, further optimization with respect to synthesis yield and shorter synthesis time is a prerequisite.

The two cysteic acid residues in the peptide precursor contribute to the high hydrophilicity of the conjugate as the side-chains remain deprotonated at physiological pH. Biodistribution studies with [^{18}F]**5** demonstrated that the tracer was excreted mainly through the renal system reflecting its hydrophilic nature. As a further demonstration of in vivo stability, the initial low uptake and subsequent wash-out of radioactivity over time in the femurs of the mice suggested that no significant defluoridation of [^{18}F]**5** was taking place. Uptake in nontarget organs was most pronounced in kidney, followed by liver, gut, and skin. The high kidney uptake may be $\alpha_v\beta_3$ mediated, as rodent kidneys have been found to express integrin in the endothelial cells of the small vessels in the glomerulus (*37*). The data presented herein are similar to those published for the ^{18}F-galacto-RGD studied in osteosarcoma-bearing mice with higher uptake values for organ and tumor for [^{18}F]**5**. The slight differences in biodistribution may be a result of the higher log *P* of [^{18}F]**5** compared to that of ^{18}F-galacto-RGD (−2.61 and −3.17, respectively), which increases the relative retention of this peptide in vivo (*38*).

The xenograft model used in this study was an osteosarcoma model derived from human tissue. Direct immunohistochemical staining of $\alpha_v\beta_3$-integrin expression was not possible due to the absence of a suitable antibody specific for mice (*39*). Staining with CD31 demonstrated vascularization of the tumors. The assumption that [^{18}F]**5** was able to target the neovasculature via the $\alpha_v\beta_3$ receptors expressed on endothelial cells was supported by the work of Pasqualini et al. who demonstrated that tumor vessels are the structural elements predominantly targeted by the RGD sequence (*40*).

Tracer uptake was significantly higher in nonblocked animals than those coinjected with 10 μg/g nonradioactive RGD peptide, suggesting a specificity for $\alpha_v\beta_3$ expression in the human OHS osteosarcoma. This was in accordance with published data from other groups working with alternative osteosarcoma mouse model where the tumors were induced using ^{90}Sr (*38*, *27*).

The relatively large standard deviations in tumor uptake observed at 2 h post-injection (±1.27% ID/g) compared to nontarget organs (±0.28% ID/g) may reflect the difference in tumor sizes among the mice (0.1−0.4 g) used in the study. Tumor size is likely to impact the degree of neovascularization and $\alpha_v\beta_3$ expression, as new blood vessels are required to supply oxygen and nutrients when the lesion reaches a diameter of around 1−2 mm (*41*). Although the data set was not large enough to reach full statistical significance, plots of tumor uptake (%ID/g) of the tracer against tumor weight indicated a sufficient correlation ($R = 0.79$). Similar observations have been reported previously in the literature with $\alpha_v\beta_3$ specific radioligands (*28*).

CONCLUSION

In conclusion, the prosthetic group *O*-(2-(2-[^{18}F]fluoroethoxy)ethyl)-*N*-methylhydroxylamine (^{18}F-FENMA) was found to have promising characteristics for in vivo use in combination with a vinylsulfonyl modified RGD peptide in human OHS xenograft bearing mice. In vitro studies demonstrated high integrin $\alpha_v\beta_3$ binding affinity and good in vitro plasma stability. MicroPET showed good visualization of tumor along with good tumor-to-background ratios. The excretion of ^{18}F[**5**] was predominately by the renal route.

ACKNOWLEDGMENT

Many thanks to Prof. Erik Dissen and Ph.D. student Per Christian Sæther (Dept of Anatomy, University of Oslo) for giving us access to the gamma counter and the included excellent technical support.

LITERATURE CITED

(1) Volkow, N. D., Mullani, N. A., and Bendriem, B. (1988) Positron emission tomography instrumentation: an overview. *Am. J. Physiol. Imaging 3*, 142–53.

(2) Cai, L., Lu, S., and Pike, V. W. (2008) Chemistry with [^{18}F]fluoride ion. *Eur. J. Org. Chem. 17*, 2853–73.

(3) Helus, F., Maier-Borst, W., Sahm, U., and Wiebe, L. I. (1979) The fluorine-18 cyclotron production methods. *Radiochem. Radioanal. Lett. 38*, 395–410.

(4) Guillaume, M., Luxen, A., Nebeling, B., Argentini, M., Clark, J. C., and Pike, V. W. (1991) Recommendations for fluorine-18 production. *Appl. Radiat. Isot. 42*, 749–62.

(5) Lasne, M. C., Perrio, C., Rouden, J., Barre, L., Roeda, D., Dolle, F., and Crouzel, C. (2002) Chemistry of β^+-emitting compounds based on fluorine-18. *Top. Curr. Chem. 222*, 201–258.

(6) Okarvi, S. M. (2001) Recent progress in fluorine-18 labelled peptide radiopharmaceuticals. *Eur. J. Nucl. Med. 28*, 929–938.

(7) Poethko, T., Schottelius, M., Thumshirn, G., Herz, M., Haubner, R., Henriksen, G., Kessler, H., Schwaiger, M., and Welter, H. J. (2004) Chemoselective pre-conjugate radiohalogenation of unprotected mono- and multimeric peptides via oxime formation. *Radiochim. Acta 92*, 317–327.

(8) Glaser, M., and Robins, E. G. (2009) Click labelling in PET radiochemistry. *J. Labelled. Compd. Radiopharm. 52*, 407–414.

(9) Kilbourn, M. R., Dence, C. S., Welch, M. J., and Mathias, C. J. (1987) Fluorine-18 labeling of proteins. *J. Nucl. Med. 28*, 462–470.

(10) Bruus-Jensen, K., Poethko, T., Schottelius, M., Hauser, A., Schwaiger, M., and Wester, H. J. (2006) Chemoselective hydrazone formation between HYNIC-functionalized peptides and 18F-fluorinated aldehydes. *Nucl. Med. Biol. 33*, 173–183.

(11) Glaser, M., Morrison, M., Solbakken, M., Arukwe, J., Karlsen, H., Wiggen, U., Champion, S., Kindberg, G. M., and Cuthbertstson, A. (2008) Radiosynthesis and biodistribution of cyclic RGD peptides conjugated with novel [^{18}F]fluorinated aldehyde-containing prosthetic groups. *Bioconjugate Chem. 19*, 951–957.

(12) Wu, Z., Li, Z. B., Cai, W., He, L., Chin, F. T., Li, F., and Chen, X. (2007) 18F-labeled mini-PEG spacered RGD dimer (18F-FPRGD2): synthesis and microPET imaging of $\alpha_v\beta_3$ integrin expression. *Eur. J. Nucl. Med. Mol. Imaging 34*, 1823–1831.

(13) Wu, Z., Li, Z. B., Chen, K., Cai, W., He, L., Chin, F. T., Li, F., and Chen, X. (2007) MicroPET of tumor integrin $\alpha_v\beta_3$ expression using 18F-labeled PEGylated tetrameric RGD peptide (18F-FPRGD4). *J. Nucl. Med. 48*, 1536–1544.

(14) Olberg, D. E., Hjelstuen, O. K., Solbakken, M., Arukwe, J., Karlsen, H., and Cuthbertson, A. (2008) A novel prosthetic group for site-selective labeling of peptides for positron emission tomography. *Bioconjugate Chem. 19*, 1301–1308.

(15) Olberg, D. E., Hjelstuen, O. K., Solbakken, M., Arukwe, J. M., Dyrstad, K., and Cuthbertson, A. (2009) Site-specific addition of an 18F-N-methylaminooxy-containing prosthetic group to a vinylsulfone modified peptide. *J. Labelled Compd. Radiopharm. 52*, 571–575.

(16) Indrevoll, B., Kindberg, G. M., Solbakken, M., Bjurgert, E., Johansen, J. H., Karlsen, H., Mendizabal, M., and Cuthbertson, A. (2006) NC-100717: A versatile RGD peptide scaffold for angiogenesis imaging. *Bioorg. Med. Chem. Lett. 16*, 6190–6193.

(17) Jia, B., Liu, Z., Shi, J., Yu, Z., Yang, Z., Zhao, H., He, Z., Liu, S., and Wang, F. (2008) Linker effects on biological properties of 111In-labeled DTPA conjugates of a cyclic RGDfK dimer. *Bioconjugate Chem. 19*, 201–210.

(18) Park, J., and Pei, D. (2004) Trans-β-nitrostyrene derivatives as slow-binding inhibitors of protein tyrosine phosphatases. *Biochemistry 43*, 15014–1521.

(19) Fodstad, O., Brogger, A., Bruland, O., Solheim, O. P., Nesland, J. M., and Pihl, A. (1986) Characteristics of a cell line established from a patient with multiple osteosarcoma, appearing 13 years after treatment for bilateral retinoblastoma. *Int. J. Cancer 38*, 33–40.

(20) Bernasconi, C. F., Renfrow, R. A., and Tia, P. R. (1986) Nucleophilic addition to olefins. 16. Unusual substituent effects in the reaction of amines with beta-nitrostyrenes. Solvent effect on intrinsic rate constants. *J. Am. Chem. Soc. 108*, 4541–4549.

(21) Helmlinger, G., Yuan, F., Dellian, M., and Jain, R. K. (1997) Interstitial pH and pO_2 gradients in solid tumors in vivo: High-resolution measurements reveal a lack of correlation. *Nat. Med. 3*, 177–182.

(22) Stubbs, M., McSheehy, P. M. J., and Griffiths, J. R. (1999) Causes and consequences of acidic pH in tumors: a magnetic resonance study. *Adv. Enzyme Regul. 39*, 13–30.

(23) Horiuchi, K., Saji, H., and Yokoyama, A. (1998) Tc(V)-DMS tumor localization mechanism: a pH-sensitive Tc(V)-DMS-enhanced target/nontarget ratio by glucose-mediated acidosis - Preparation and labeling condition studies. *J. Nucl. Biol. Med. 25*, 549–555.

(24) Lewis, M. R., and Shively, J. E. (1998) Maleimidocysteineamido-DOTA derivatives: New reagents for radiometal chelate conjugation to antibody sulfhydryl groups undergo pH-dependent cleavage reactions. *Bioconjugate Chem. 9*, 72–86.

(25) Williams, L. E., Lewis, M. R., Bebb, G. G., Clarke, K. G., Odom-Maryon, T. L., Shively, J. E., and Raubitschek, A. A. (1998) Biodistribution of 111In- and 90Y-Labeled DOTA and maleimidocysteineamido-DOTA conjugated to chimeric anticarcinoembryonic antigen antibody in xenograft-bearing nude mice: Comparison of stable and chemically labile linker systems. *Bioconjugate Chem. 9*, 87–93.

(26) Dijkgraaf, I., Beer, A. J., and Wester, H. J. (2009) Application of RGD-containing peptides as imaging probes for alphavbeta3 expression. *Front. Biosci. 14*, 887–899.

(27) Haubner, R., Wester, H. J., Reuning, U., Senekowitsch-Schmidtke, R., Diefenbach, B., Kessler, H., Stöcklin, G., and Schwaiger, M. (1999) Radiolabeled $\alpha_v\beta_3$ integrin antagonists: a new class of tracers for tumor targeting. *J. Nucl. Med. 40*, 1061–1071.

(28) Shi, J., Wang, L., Kim, Y. S., Zhai, S., Jia, B., Wang, F., and Liu, S. (2009) 99mTcO(MAG2−3G3-dimer): a new integrin $\alpha_v\beta_3$-targeted SPECT radiotracer with high tumor uptake and favorable pharmacokinetics. *Eur. J. Nucl. Med. Mol. Imaging 36*, 1874–1884.

(29) Dijkgraaf, I., Kruijtzer, J. A., Liu, S., Soede, A. C., Oyen, W. J., Corstens, F. H., Liskamp, R. M., and Boerman, O. C. (2007) Improved targeting of the $\alpha_v\beta_3$ integrin by multimerisation of RGD peptides. *Eur. J. Nucl. Med. Mol. Imaging 34*, 267–273.

(30) Li, Z. B., Wu, Z., Chen, K., Chin, F. T., and Chen, X. (2009) Click chemistry for 18F-labeling of RGD peptides and microPET imaging of tumor integrin $\alpha_v\beta_3$ expression. *Bioconjugate Chem. 18*, 1987–1994.

(31) Liu, Z., Liu, S., Wang, F., Liu, S., and Chen, X. (2009) Noninvasive imaging of tumor integrin expression using 18F-labeled RGD dimer peptide with PEG4 linkers. *Eur. J. Nucl. Med. Mol. Imaging 36*, 1296–1307.

(32) Wust, F., Hultsch, C., Bergmann, R., Johannsen, B., and Henle, T. (2003) Radiolabelling of isopeptide N^{ϵ}-(γ-glutamyl)-L-lysine by conjugation with *N*-succinimidyl-4-[^{18}F]fluorobenzoate. *Appl. Radiat. Isot. 59*, 43–48.

(33) Liu, Z., Liu, S., Wang, F., Liu, S., and Chen, X. (2009) Noninvasive imaging of tumor integrin expression using 18F-labeled RGD dimer peptide with PEG4 linkers. *Eur. J. Nucl. Med. Mol. Imaging 36*, 1296–1307.

(34) Wester, H. J., and Schottelius, M. (2007) Fluorine-18 labeling of peptides and proteins. *PET Chemistry - The driving force in*

molecular imaging (Schubiger, A. P., Lehmann, L., and Friebe, M., Eds.) pp 80−104, Chapter 4, Springer, Berlin.

(35) Glaser, M., Solbakken, M., Turton, D. R., Pettitt, R., Barnett, J., Arukwe, J., Karlsen, H., Cuthbertson, A., Luthra, S. K., and Arstad, E. (2009) Methods for 18F-labeling of RGD peptides: comparison of aminooxy [^{18}F]fluorobenzaldehyde condensation with 'click labeling' using 2-[^{18}F]fluoroethylazide, and S-alkylation with [^{18}F]fluoropropanethiol. *Amino Acids 37*, 717–724.

(36) Cai, W., Zhang, X., Wu, Y., and Chen, Z. (2006) A thiol-reactive 18F-labeling agent, N-[2(4-^{18}F-fluorobenzamido)ethyl-]maleimide, and synthesis of RGD peptide-based tracer for PET imaging of $\alpha_v\beta_3$ integrin expression. *J. Nucl. Med. 47*, 1172–1180.

(37) Li, Z. B., Chen, K., and Chen, X. (2008) 68Ga-labeled multimeric RGD peptides for microPET imaging of integrin $\alpha_v\beta_3$ expression. *Eur. J. Nucl. Med. Mol. Imaging 35*, 1100–1108.

(38) Haubner, R., Westerm, H. J., Weber, W. A., Mang, C., Ziegler, S. I., Goodman, S. L., Senekowitsch-Schmidtke, R., Kessler, H., and Schwaiger, M. (2001) Noninvasive imaging of $\alpha_v\beta_3$ integrin expression using18F-labeled RGD-containing glycopeptide and positron emission tomography. *Cancer Res. 61*, 1781–1785.

(39) Mulder, W., Castermans, K., van Beijnum, J., oude Egbrink, M. G., Chin, P. T., Fayad, Z. A., Löwik, C. W., Kaijzel, E. L., Que, I., Storm, G., Strijkers, G. J., Griffioen, A. W., and Nicolay, K. (2009) Molecular imaging of tumor angiogenesis using $\alpha v\beta 3$-integrin targeted multimodal quantum dots. *Angiogenesis 12*, 17–24.

(40) Pasqualini, R., Koivunen, E., and Ruoslahti, E. (1997) αv integrins as receptors for tumor targeting by circulating ligands. *Nat. Biotechnol. 15*, 542–546.

(41) Folkman, J. (1971) Tumor angiogenesis: therapeutic implications. *N. Engl. J. Med. 285*, 1182–1186.

BC1003229

Improved Speciation Characteristics of PEGylated Indocyanine Green-Labeled Panitumumab: Revisiting the Solution and Spectroscopic Properties of a Near-Infrared Emitting anti-HER1 Antibody for Optical Imaging of Cancer

Aaron Joseph L. Villaraza, Diane E. Milenic, and Martin W. Brechbiel*

Radioimmune and Inorganic Chemistry Section, Radiation Oncology Branch, National Cancer Institute, National Institutes of Health, 10 Center Drive, Bethesda, Maryland 20892-1002, United States. Received July 23, 2010; Revised Manuscript Received October 26, 2010

A water-soluble amine-reactive PEGylated analogue of near-infrared emitting dye indocyanine green (**5**) was synthesized and used to label the anti-HER1 antibody panitumumab (Vectibix) at various equivalents. These conjugates were compared with non-PEGylated analogue conjugate products and the solution speciation analyzed with UV−vis spectrophotometry, size exclusion HPLC, and SDS-PAGE. PEGylation of the bioconjugates was successful in preventing aggregation in solution, a phenomenon observed with the non-PEGylated bioconjugates presumably due to the hydrophobicity of indocyanine green. Competitive radioimmunoassay demonstrated that the targeting moiety of the PEGylated bioconjugates was conserved. Fluorescence microscopy also demonstrated membrane binding of the bioconjugate to HER1-expressing A431 cells. Hence, these bioconjugates are suitable candidates for the in vivo optical imaging of HER1-expressing tumors.

INTRODUCTION

There has been a great amount of interest in near-infrared (NIR) dyes as reporter groups for bioconjugate probes as NIR light (700−1000 nm) is relatively transparent to tissue (*1*). The many applications of NIR dyes for in vivo fluorescence biological imaging has been reviewed in detail elsewhere (*2, 3*). Chief among this class of reporter groups are the water-soluble cyanine (Cy) dyes designed to react selectively with either sulfhydryl or amine groups present on biomolecules (*4*−*8*).

However, excessive loading of Cy dye on proteins results in quenching of fluorescence, a phenomenon more pronounced in the longer-chain cyanine dyes, such as Cy5 and Cy7 (*9*). Indeed, dye−dye-mediated self-quenching was found to be more evident in the Cy dyes than in other commercially available NIR dyes, such as the AlexaFluor dyes (*10*). This phenomenon has led to the development of particular applications such as enzyme-responsive NIR-protein bioconjugates which fluoresce upon enzymatic cleavage of the bioconjugate (*11*−*13*). Cy dyes have also been used to label monoclonal antibodies (mAbs) targeting tumor-associated antigens (*14*−*17*), with Cy7 demonstrating a fluorescence response with the deepest tissue penetration (*14*). More recently, mAbs labeled with both a Cy dye and a radioactive reporter have been described toward the development of multimodal diagnostic agents (*18, 19*).

Indocyanine green (ICG) (**1**) is an FDA-approved cyanine dye first described in the construction of dilution curves for cardiovascular physiological studies (*20*). The absorption and emission characteristics of this dye at the near-infrared end of the spectrum further extended its application to fluorescence angiography (*21*), necessitating a thorough investigation of the effects of solvent on the absorption and emission spectra of ICG in blood plasma in comparison with ICG dissolved in commonly used laboratory solvents (*22, 23*). In general, it has been observed that dye-aggregation, whether due to the nature of the solvent, the concentration of the dye, or combinations of both, results in the quenching of ICG fluorescence.

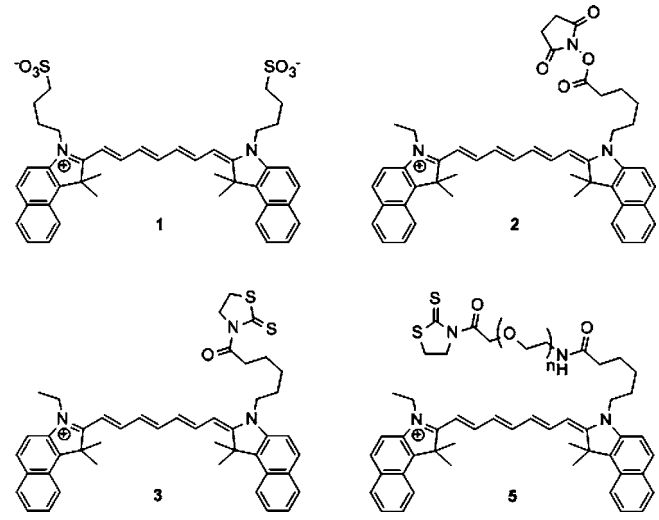


Figure 1. (**1**) ICG, (**2**) ICG-OSu, (**3**) ICG-ATT, (**5**) ICG-PEG-ATT.

Monoclonal antibody conjugates with amine-reactive ICG (*24, 25*) (**2** and **3**) (Figure 1) have been used in immunohistochemical staining of gastric microcancers (*26*−*29*) and as an in vivo probe for tumor imaging (*30*−*32*). Interestingly, some examples of these ICG-mAb bioconjugates were found to be nonfluorescent in PBS, but became fluorescent either in vitro when in the presence of denaturing agents such as 5% SDS and β-mercaptoethanol (β-ME), or upon internalization in tumor cells (*31, 32*). The exact mechanism for this observed fluorescence activation was not elucidated, though the authors suggest aggregation as the cause of fluorescence quenching. Further-

* To whom correspondence should be addressed. Martin W. Brechbiel, Ph.D. Radioimmune and Inorganic Chemistry Section, Radiation Oncology Branch, NCI, NIH, 10 Center Drive, Building 10, Room B3B69, Bethesda, Maryland 20892-1002, United States. Phone: (301) 496-0591. Fax: (301) 402-1923. E-mail: martinwb@mail.nih.gov.

10.1021/bc100336b This article not subject to U.S. Copyright. Published 2010 by the American Chemical Society
Published on Web 11/12/2010

more, these conjugates also exhibited significant uptake and retention in the liver.

The studies herein describe an amine-reactive PEGylated ICG analogue (**5**) and its conjugation to the mAb panitumumab. Panitumumab (Vectibix) is an FDA-approved mAb which binds to HER1 (*33*), a surface antigen which is overexpressed in a variety of cancers. These conjugates were compared with mAb conjugates of non-PEGylated analogues **2** and **3**, and their solution speciation characterized spectroscopically and chromatographically. The immunoreactivity of the mAb postmodification was evaluated by radioimmunoassay using purified antigen and by fluorescence microscopy. PEGylation was found to render ICG water-soluble, thereby obviating the need for intermediary solvents such as DMSO or DMF in the conjugation reaction. The PEGylated ICG-mAb was hypothesized to exhibit improved solubility and pharmacokinetic characteristics and to minimize or eliminate aggregation of the conjugation product in comparison with the non-PEGylated analogue. Furthermore, PEGylation of biologically active molecules, antibodies, and antibody fragments has been found to reduce their immunogenicity and improve in vivo clearance (*34*, *35*).

MATERIALS AND METHODS

Compounds **2** and **3** were synthesized as previously described (*24*, *25*). NH_2-PEG-CM-3400 (average molecular weight 3250) was purchased from Laysan Bio Inc. (Arab, AL). 1-Ethyl-3-(3-dimethylaminopropyl)carbodiimide hydrochloride (EDC) and 2-mercaptothiazoline (ATT) were obtained from TCI America (Portland, OR) and 4-dimethylaminopyridine (DMAP) was purchased from Sigma-Aldrich Chemical Co. (St. Louis, MO). Sephadex G-25 Medium was purchased from GE Healthcare (Piscataway, NJ). Panitumumab (AMGEN Inc., Thousand Oaks, CA) was purchased through the Veterinary Resources Pharmacy, NIH.

^{1}H and ^{13}C NMR spectra were obtained using a Bruker Avance 300 MHz instrument, and chemical shifts are reported in ppm on the δ scale relative to TMS or residual solvent. Proton chemical shifts are annotated as follows: ppm (multiplicity, coupling constant (Hz), integration). Reaction progress was also monitored by Silica Gel 60 thin layer chromatography (Merck, Germany).

Absorbance spectra were recorded on an Agilent 8453 spectrophotometer (Santa Clara, CA). Size exclusion HPLC (SE-HPLC) was performed on a Waters HPLC system (Milford, MA) using a TOSOH TSK4000SW column (Tokyo, Japan) with 67 mM Na_3PO_4/100 mM KCl buffer (pH 6.8) as eluent (flow rate 0.5 mL/min). Radioactivity was measured using a Wizard One Perkin-Elmer γ-scintillation counter (Shelton, CT).

ICG-PEG-COOH (4). NH_2-PEG-CM-3400 (1.0 g, 0.31 mmol) was dissolved in MeCN (50 mL) and stirred in the presence of Et_3N (50 μL, 0.36 mmol) over ice. Compound **3** (0.24 g, 0.34 mmol) was added, and the solution stirred over ice for 1 and 18 h at room temperature. The reaction mixture was diluted with $CHCl_3$ (50 mL) and washed with 0.1 M HCl (50 mL). The aqueous layer was extracted further with $CHCl_3$ (2 × 50 mL). The organic portions were pooled together and dried over anhydrous $MgSO_4$. The mixture was filtered and the filtrate evaporated under reduced pressure. The dye−polymer conjugate was purified by passing through a Sephadex G-25 size exclusion column previously equilibrated with water. The volume of the pure fraction was brought up to ~50 mL with water, acidified with 0.1 M HCl, and extracted into $CHCl_3$ (3 × 50 mL). The organic portions were pooled together, dried over anhydrous $MgSO_4$, filtered, and the filtrate evaporated under reduced pressure. The dark green oily residue was triturated with diethyl ether, the supernatant decanted, the resulting solid washed with more diethyl ether, and the residue dried under reduced pressure to yield a dark green powder (0.91 g, 77%). R_f = 0.5 ($CHCl_3$/MeOH 9:1); ^{1}H NMR ($CDCl_3$, 300 MHz) δ 1.5 (t, J = 7.2 Hz, 3H), 1.6−2.4 (m, 6H), 2.0 (s, 12H), 3.4−3.5 (m, 5H), 3.6−3.8 (m, 307H), 3.9 (t, J = 6.2 Hz, 3H), 4.1−4.4 (m, 4H), 4.2 (s, 2H), 6.3 (d, J = 13.1 Hz, 1H), 6.4 (d, J = 12.9 Hz, 1H), 6.8 (m, 2H), 7.3−8.2 (m, 15H); ^{13}C NMR ($CDCl_3$, 300 MHz) δ 12.74, 25.22, 26.50, 27.58, 36.15, 39.08, 44.66, 50.90, 59.53, 68.97, 69.72, 70.23, 71.27, 81.61, 110.09, 110.56, 122.18, 124.81, 124.99, 127.70, 128.20, 128.33, 130.00, 130.55, 130.66, 131.63, 131.78, 133.54, 133.75, 139.25, 139.53, 171.42, 173.08; λ_{max} = 783 nm (PBS).

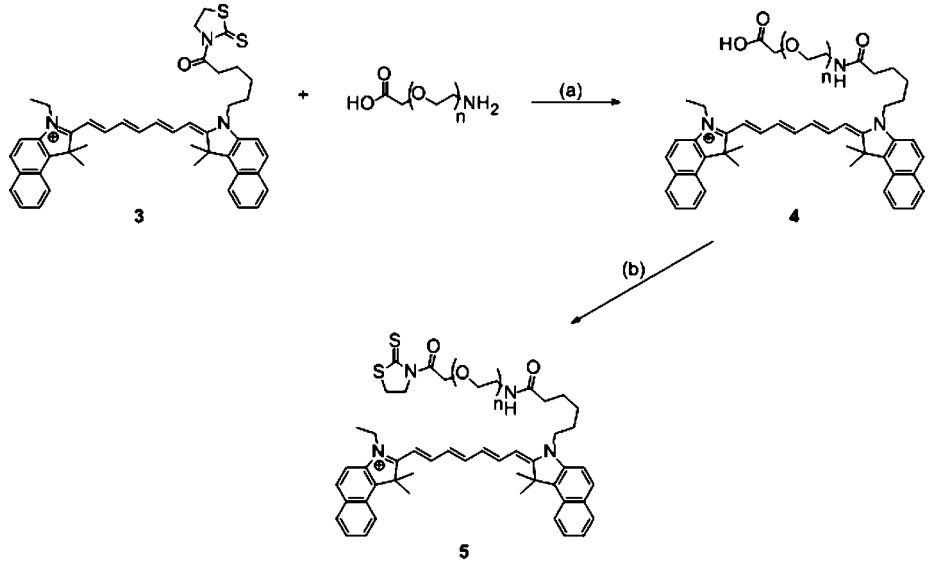
ICG-PEG-ATT (5). Compound **4** (0.76 g, 0.20 mmol) was dissolved in DCM (20 mL) and cooled over ice. EDC (45 mg, 0.22 mmol) and DMAP (27 mg, 0.22 mmol) were added and the solution stirred for 30 min. Afterward, ATT (26 mg, 0.22 mmol) was added, and the reaction was stirred over ice for 1 h and at room temperature for 18 h. The reaction mixture was then washed successively with 0.1 M $NaHCO_3$ (1 × 50 mL) and 0.1 M HCl (2 × 50 mL). The organic portions were pooled together, dried over anhydrous $MgSO_4$, filtered, and the filtrate evaporated under reduced pressure. In a similar manner as with **4**, the residue was triturated with diethyl ether and then dried under reduced pressure to yield a dark green powder (0.64 g, 84%). R_f = 0.8 ($CHCl_3$/MeOH 9:1); ^{1}H NMR ($CDCl_3$, 300 MHz) δ 1.5 (t, J = 7.0 Hz, 3H), 1.6−2.4 (m, 6H), 2.0 (s, 12H), 3.4−3.5 (m, 5H), 3.6−3.8 (m, 295H), 3.9 (m, 3H), 4.0 (t, J = 7.8 Hz, 2H), 4.1−4.4 (m, 4H), 4.6 (t, J = 7.2 Hz, 2H), 5.1 (s, 2H), 6.3 (d, J = 13.1 Hz, 1H), 6.4 (d, J = 12.9 Hz, 1H), 6.8 (m, 2H), 7.3−8.2 (m, 15H); ^{13}C NMR ($CDCl_3$, 300 MHz) δ 12.78, 25.27, 26.44, 27.61, 29.56, 33.75, 36.19, 39.12, 44.68, 50.92, 51.60, 55.48, 59.50, 60.00, 70.54, 74.00. 81.58, 110.16, 110.67, 122.22, 125.07, 127.77, 128.21, 130.03, 130.62, 131.64, 133.48, 133.71, 139.22, 139.51, 171.97, 173.12, 201.13; λ_{max} = 783 nm (PBS).

Conjugation of Antibodies. Solutions of mAb (typically 10 mg, 66.7 nmol) were incubated with 2, 4, or 8 equiv of **2**, **3**, or **5** in 0.1 M $NaHCO_3$ (pH 8.5) buffer for 1 h at 37 °C with stirring at 750 rpm. The mAb solution was vortexed as the amine-reactive dye was added dropwise to ensure homogeneity of the reaction. All conjugation reactions were made up to a total volume of 1 mL. In particular, **5** was added as a 200 μL aliquot in buffer, while **2** and **3** were added as a 200 μL aliquot in DMSO. After incubation, the reaction was transferred to a 3 mL Slide-A-Lyzer Dialysis Cassette G2 (Thermo Fisher Scientific, Rockford, IL) and dialyzed against PBS buffer at 4 °C for three days with nine buffer changes (9 L total). Protein recovery during conjugation was determined by measuring the UV absorption at 280 nm.

Absorbance Measurements. The extinction coefficient of **3** was determined in DMF and in 9:1 PBS/DMF solution, while the extinction coefficient of **5** was determined in DMF, in 9:1 PBS/DMF solution, and in PBS. The absorbance spectra of 50 μg/mL samples of the bioconjugates were measured in PBS and in 9:1 PBS/DMF. On the basis of a previously described procedure (*22*), the changes in the shape of the spectra as a function of concentration were monitored by preparing 500, 100, 50, and 10 μg/mL samples of bioconjugate. The absorbance spectra of 500 μg/mL and 50 μg/mL samples were measured in a 2 mm cuvette, while 100 μg/mL and 10 μg/mL samples were measured in a 10 mm cuvette. The spectra of samples whose product of concentration c and path length b were the same (i.e., $A = \epsilon bc$ where bc = constant) where superimposed. These measurements were performed in PBS and in 8:2 PBS/DMSO.

Competition Radioimmunoassay (General Procedure). The immunoreactivities of immunoconjugates were evaluated using a competition radioimmunoassay. Fifty nanograms of

Scheme 1[a]



[a] Synthesis of **5**: (a) Et_3N, MeCN, 0 °C, (b) DCM, EDC, DMAP, ATT, 0 °C.

human epidermal growth factor receptor (hEGFR) (Sigma-Aldrich, St. Louis, MO) in 50 μL of PBS containing Mg^{2+} and Ca^{2+} was added to each well of a 96-well plate and incubated overnight at 4 °C. The excess antigen was removed, 150 μL of 1% bovine serum albumin in PBS (BSA/PBS) was added to each well, and the plate allowed to sit at ambient temperature for 1 h. The wells were then aspirated and serial dilutions (1000−0.02 ng in 50 μL BSA/PBS) of the immunoconjugates were added to the wells in triplicate (leaving one set of wells as a blank, i.e., no competitor), followed by ^{125}I-panitumumab (*36*) (~50 000 cpm in 50 μL BSA/PBS). The plate was then incubated at 37 °C for 4 h. Afterward, the wells were emptied and washed with BSA/PBS (3 × 200 μL), the bound radioactivity removed with 100 μL 0.2 M NaOH, absorbed into cotton filters, placed in 12 × 75 mm tubes, and counted in a γ-scintillation counter. The percent inhibition was calculated and plotted. Unconjugated panitumumab was included in the assay as well as a negative mAb HuM195 (kindly provided by M. McDevitt, Memorial Sloan Kettering Cancer Center), which reacts with human CD33.

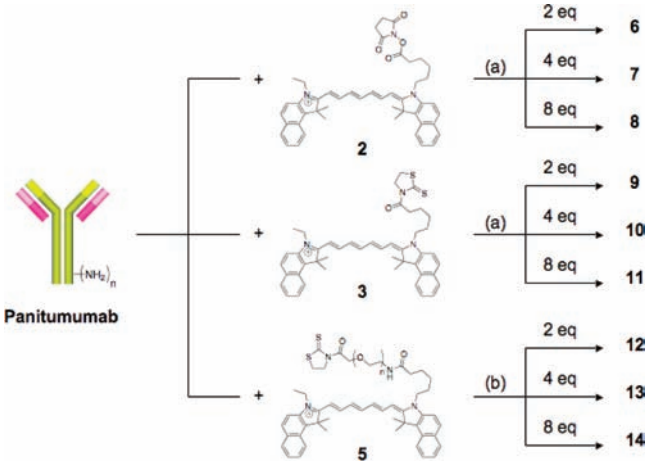
SDS-Polyacrylamide Gel Electrophoresis. The immunoconjugates were analyzed by SDS-polyacrylamide gel electrophoresis (SDS-PAGE) both with and without reduction by β-ME using 4−20% precast Tris-Glycine polyacrylamide gels, respectively (Invitrogen, Carlsbad, CA). Five micrograms of the immunoconjugates was added to each lane, and the gels were run according to the method of Laemmli (*37*). Lanes containing 5 μg of panitumumab were included as a comparison.

Fluoresence Microscopy. HER1-positive A431 cells were utilized for fluorescence microscopy to demonstrate tumor targeting and specificity of the PEGylated panitumumab−ICG conjugate. The cells were obtained from ATCC (Manasass, VA) and grown in RPMI 1640 media (Lonza, Walkersville, MD) supplemented with 10% FetalPlex (Gemini Bioproducts, Woodland, CA), 1 mM nonessential amino acids, and 2 mM glutamine. The fluorescence microscopy study was performed by adding A431 cells (2.5×10^4) to each chamber of an 8 chamber slide and incubated for 72 h. The chambers were washed 3 times with phosphate-buffered saline (PBS, pH 7.2) and fixed for 10 min at room temperature with 4% paraformaldehyde. After 3 more washes with PBS, 0.5 mL of PBS containing 1% bovine serum albumin was added to each chamber. Following 1 h incubation at ambient temperature, the 1% BSA/PBS was removed and 1 μg of **12** or **15** (negative control) was added to a chamber and incubated for 1 h at 37 °C. The chambers were then washed 3 times with PBS, the chambers removed, and the slide mounted with a coverslip using FluorSave (Calbiochem, La Jolla, CA). Fluorescence microscopy was performed using an Olympus BX61 microscope (Olympus America, Inc., Center Valley, PA) equipped with the following filters: excitation wavelength 672.5 to 747.5 nm, emission wavelength 765 to 855 nm. Transmitted differential interference contrast (DIC) images were also collected.

RESULTS AND DISCUSSION

Amine-reactive ICG dyes **2** and **3** were synthesized in good yields. To produce ICG-PEG conjugate **4**, compound **3** was chosen to react with NH_2-PEG-CM-3400 as the aminolysis of 3-acylthiazolidine-2-thione activated esters to form amides has been thoroughly demonstrated to be efficient (*38*, *39*). Furthermore, the reactivity of **3** itself has been tested with a variety of amino acids and primary amines under different conditions and found to be efficient (*25*). The benefits of PEGylating ICG were expected to be threefold: first, the dye−polymer conjugate **4** would be dramatically more water-soluble than **3**; second, the increase in molecular weight would promote simplified purification of the resulting dye−polymer conjugate **4** by size-exclusion chromatography (indeed, due to the differences in molecular weight and solubility between the starting materials and product, unreacted dye was retained at the top of the Sephadex column while the dye−polymer eluted); third, since the molecular weight of the polymer is significantly greater than that of the dye, the resulting mass of **4** is much higher relative to the amount of **3** used in the reaction, which again facilitates handling. This bodes well if the same reaction scheme is to be applied to the synthesis of dye−polymer conjugates using commercially available Cy dyes, which are relatively expensive and sold only in small amounts. Interestingly, **4** could, in fact, be extracted back into chloroform upon slight acidification of the purified fraction. Synthesis of activated ester **5** was chosen over a succinimidyl ester analogue in order to be able to compare mAb labeling efficiencies with **3** (Scheme 1). The formation of the activated ester was easily monitored by thin layer chromatography. Finally, both PEGylated and non-PEGylated amine-reactive dyes were found to "stick" to the flask, but trituration in diethyl ether dislodged both products, thereby maximizing reaction yields.

Scheme 2[a]



[a] Conjugation of **2**, **3**, and **5** with panitumumab: (a) 25% DMSO in 0.1 M $NaHCO_3$ buffer, (b) 0.1 M $NaHCO_3$ buffer.

Amine-reactive dyes **2**, **3**, and **5** were added to panitumumab in increasing equivalents of 2, 4, and 8 per mAb to (1) compare their respective labeling efficiencies and (2) determine the effect of increased labeling on the immunoreactivity of the resulting conjugates (Scheme 2). As **5** proved to be water-soluble, the conjugation reaction was performed solely in buffered aqueous solutions as described above. However, the insolubility of **2** and **3** in aqueous solutions required dissolution in DMSO before addition to the buffered protein solution. Prior to the conjugation reactions with the ICG compounds, the maximum percentage of DMSO in buffer that panitumumab could tolerate without loss of immunoreactivity was determined to be 25% DMSO in reaction buffer (data not shown). Hence, the conjugation reactions involving **2** and **3** were performed with the desired equivalents being added as a 200 μL DMSO solution to 800 μL buffered protein solution, resulting in a final reaction volume of 1 mL. All conjugates were purified via extensive dialysis against PBS and recovered in good yield on a protein basis.

A previous study on the UV−vis absorption properties of ICG noted the following: (1) the characteristics of the absorbance spectrum of ICG are dependent upon its concentration in solution and the nature of the solvent; (2) at relatively low concentrations, the absorbance maximum of the dye is red-shifted when comparing spectra taken in water versus plasma; and (3) a continuous increase in ICG concentration results in a collapse of the absorbance maximum at ~780 nm accompanied by simultaneous growth of a peak within the range 700−720 nm (*22*). The presence of this peak is a clear indication of the formation of dye aggregates in aqueous solvent due to the hydrophobicity of ICG (*40*). Indeed, analogous solvent- and concentration-dependent formation of dye aggregates has been observed for other cyanine dyes as well (*41*). The formation of aggregates alters the optical density of the dye, and correspondingly, the extinction coefficient ε. This change has profound implications on the use of ICG as a fluorescent probe in biological applications, as the optical density determines the fluorescence intensity. This occurrence is underlined by the inconsistency of reported ICG quantum yields in the literature, which were also found to be both solvent- and concentration-dependent (*23, 42*).

The extinction coefficients of **3** and **5** were determined in different solvents at micromolar concentrations. Compounds **3** was insoluble in PBS, but soluble in a 10% DMF in PBS solution and in DMF alone. The calculated extinction coefficients were drastically different, being a fifth lower in PBS/DMF than in just DMF. On the other hand, the calculated extinction coefficients of **5** were independent of the three solvents used (Table 1). However, a slight red-shift from 783 to 790 nm was observed when comparing the absorbance maxima ranging from aqueous to organic solvent (Figure 2).

Table 1. Comparison of Optical Properties of 3 and 5 in Different Solvents

	compound			
	3		**5**	
solvent	λ_{max}	ε (μM^{-1} cm^{-1})	λ_{max}	ε (μM^{-1} cm^{-1})
PBS	---	---	783	0.155
9:1 PBS/DMF	800	0.034	785	0.154
DMF	790	0.170	790	0.158

More critically, the effect of solvent on the extinction coefficient of the dye has important implications in the determination of the dye-to-protein (D/P) ratio of resulting ICG-labeled proteins. D/P ratios can be determined spectrophotometrically by calculating the concentration of dye based on its absorbance at its λ_{max}, and likewise the protein concentration from its absorbance at 280 nm. These calculations require the construction of a calibration curve for each separate component (i.e., dye and protein) measured in an ideal aqueous solvent such as PBS. As both **2** and **3** are insoluble in PBS, no such calibration curve could be constructed, and therefore D/P ratios for proteins labeled with them cannot be determined. On the other hand, a protein calibration curve in 9:1 PBS/DMF is meaningless, as this solvent combination does not mimic physiological conditions. Indeed, in previous reports (*31, 32*) the D/P ratios of a variety of ICG-labeled mAbs were determined under denaturing conditions, i.e., in the presence of 5% SDS and β-mercaptoethanol. Applying the same argument, such results and measurement are at best questionable, as these solvent conditions do not reflect the physiological state of the antibody conjugates under study.

However, as the extinction coefficient of **5** is consistent throughout the range of solvents described, the concentrations of panitumumab and ICG can be accurately determined from the absorbances of the conjugates at 280 and 783 nm (Figure 3a) in PBS. Using this method, the D/P ratios for the PEGylated dye−protein conjugates **12**, **13**, and **14** were calculated to be 0.73, 1.74, and 3.38, respectively. HuM195 was also reacted with **5** to form conjugate **15**, and its D/P ratio was determined to be 1.05. The challenge of determining D/P ratios in dye-labeled proteins is not limited to ICG conjugates; for example, it has been addressed previously in antibody conjugates of rhodamine B, a relatively hydrophobic dye (*43, 44*). The importance of accurately establishing the D/P ratio of a fluorescently labeled antibody cannot be overstated, as high loading of dye molecules onto a single antibody has been shown to result in fluorescence quenching rather than fluorescence enhancement, observed especially in the longer-chain Cy dyes due to their relative hydrophobicity (*9, 10*).

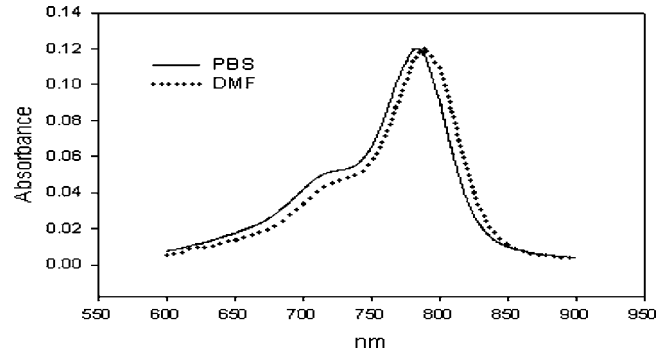


Figure 2. A slight red shift in the λ_{max} of **5** is observed when in aqueous solvent (PBS) vs organic solvent (DMF).

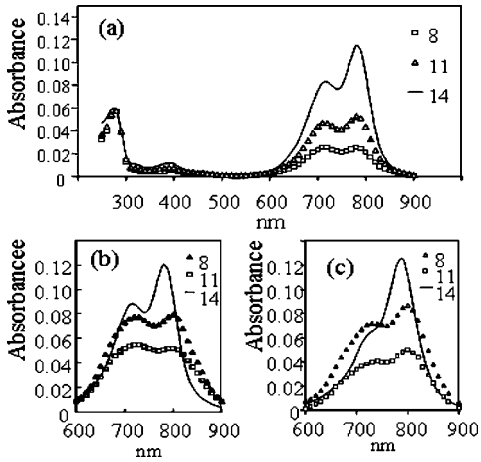


Figure 3. (a) ICG-PEG-mAbs **12**, **13**, **14** in PBS; (b) **8**, **11**, **14** in PBS; (c) **8**, **11**, **14** in 9:1 PBS/DMF (50 μg samples).

Table 2. SE-HPLC Data of Conjugates[a]

sample	% HMW	% IgG
6	9.2	90.8
7	15.7	84.3
8	26.0	74.0
9	5.3	94.7
10	12.2	87.9
11	19.9	74.0
12	0	100
13	0	100
14	0	100

[a] IgG (Panitumumab): t_R = 19.9 min. HMW species (**6**−**8**): t_R = 11.2 and 16.9−18.4 min. HMW (**9**−**11**): t_R = 11.2. Molecular weight standards: 158 kDa (20.5 min), 232 kDa (19.3 min), 440 kDa (16.5 min), Blue Dextran (11.2 min).

Absorption spectra of 50 μg/mL samples of all bioconjugates were measured; for brevity, the spectral range corresponding to dye absorption of **8**, **11**, and **14** are presented (Figure 3b,c). As discussed earlier, the depression of the absorbance peak at 790 nm, the shift and broadening of the λ_{max} to around 800 nm, and the increase of the absorbance within the 700−720 nm range in the spectra of **8** and **11** in PBS are all indicators of dye aggregation in these conjugates, characteristics which are much less pronounced in the spectrum of the PEGylated conjugate **14** (Figure 3b). Similar to previously published absorption spectra of ICG-mAb bioconjugates (*27*), the spectra of **8**, **11**, and **14** when measured in 9:1 PBS/DMF show suppression of the 720 peak and growth in the 790 nm peak (Figure 3c) relative to that measured in PBS alone, suggesting that the presence of DMF prevents or reduces dye aggregation. Again, however, this solvent combination is not representative of physiological conditions, and therefore, absorbance measurements performed in it do not reflect the true absorption properties of these conjugates, particularly when translated to an in vivo environment. On the other hand, the absorption spectra of the PEGylated conjugates suggest that they are more stable against dye aggregation, a result of the increased hydrophilicity of **5** due to the water-soluble PEG polymer.

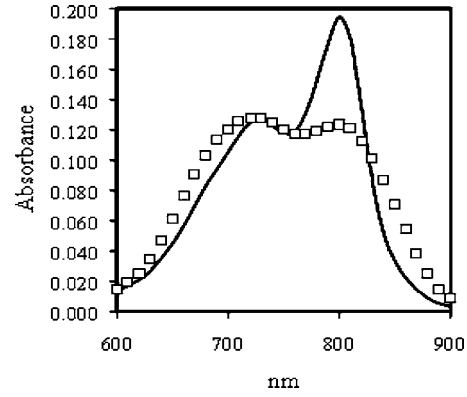


Figure 5. Absorption spectra of (□) aggregate HMW fraction and (−) pure IgG fraction.

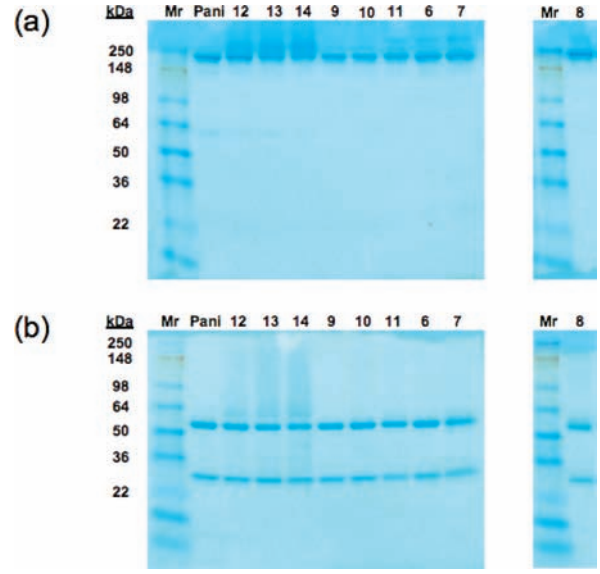


Figure 6. SDS-PAGE of ICG-labeled panitumumab bioconjugates under (a) nondenaturing and (b) denaturing conditions with β-ME.

To determine if aggregation is an effect of concentration, the absorption spectrum of **11** was measured at different concentrations (ranging from10 to 500 ng/mL) in PBS (Figure 4a,b). Furthermore, to determine if the solvent also had an effect, the same measurements were performed in 20% DMSO in PBS

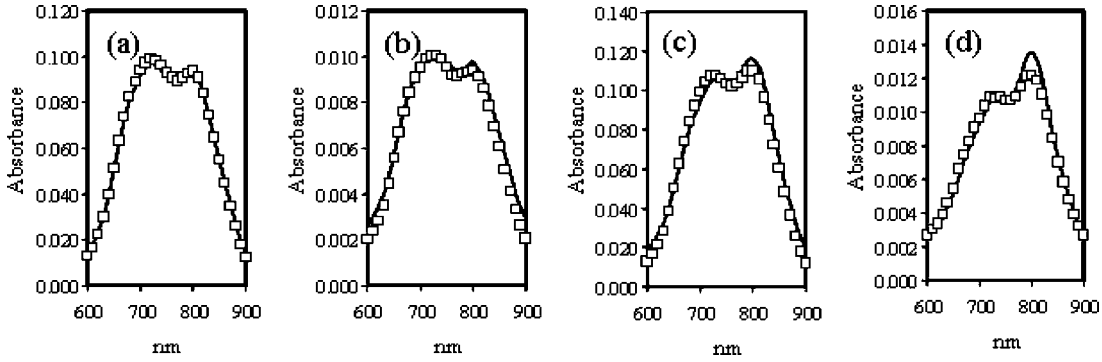


Figure 4. (a) and (b) **11** in PBS, (c) and (d) **11** in 2:8 DMSO:PBS at (□) 0.5 mg/mL and (−) 0.1 mg/mL.

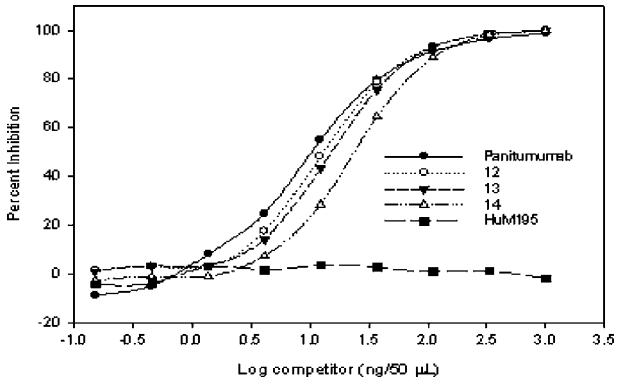


Figure 7. Competition RIA of **12**, **13**, and **14** with ^{125}I-Panitumumab.

(Figure 4c,d). No change was observed in the spectra measured in PBS regardless of the sample concentration. However, for the samples measured in 2:8 DMSO/PBS, the data suggest that aggregation is reduced upon dilution of the sample in the presence of an organic cosolvent, indicated once again by the suppression of the peak at 720 nm and the growth of the peak at 790 nm.

The SE-HPLC data demonstrated that the aggregation occurs on a macromolecular level, as evidenced by the formation of high molecular weight (HMW) species with conjugates **8**−**11** which were clearly observable by chromatography (Table 2). Aggregates were formed only in those conjugates which were labeled with non-PEGylated dye. Furthermore, the degree of aggregation is directly related to the amount of dye loaded onto the protein. Interestingly, previous studies which describe the synthesis of ICG-mAb conjugates fail to report any SE-HPLC data, stating only that purification of the conjugation reaction mixture involved elution through a desalting PD-10 column (*24*,*26*−*32*) to remove any excess or unreacted dye. However, this method is incapable of discriminating between the labeled mAb and any aggregates. The assumptions were that the eluted fraction was a pure product. The SE-HPLC analysis presented in this study demonstrates that this assumption cannot be made. The SE-HPLC data clearly demonstrates that the PEGylated conjugates (**12**−**14**) were void of aggregate formation. Indeed, it has been reported many times in the literature that PEGylation of mAbs and mAb fragments is useful in preventing their aggregation in solution (*35*).

To determine if aggregation was an equilibrium-based process, conjugate **8** was purified by SE-HPLC, the aggregate was separated from the IgG fraction, and the corresponding fractions pooled together and concentrated. Measurement of absorption spectra in PBS confirmed their identities (Figure 5). These repurified products were allowed to sit at 4 °C for three weeks, after which time an aliquot was taken and characterized by SE-HPLC. No formation of aggregates was observed, suggesting that the bioconjugate is stable and therefore the observed aggregation is not an equilibrium-based process but a result of the amount of dye loaded in the conjugation reaction.

All bioconjugates under study were analyzed by SDS-PAGE under both nondenaturing (Figure 6a) and denaturing (Figure 6b) conditions. Under nondenaturing conditions, the band patterns for conjugates **6**−**11** suggest that the presence of SDS was sufficient to disassociate any aggregates present. Furthermore, since all samples under study exhibit the same band pattern as that of native panitumumab in the presence of β-ME, it can be inferred that the aggregates observed in SE-HPLC are associated purely by supramolecular forces; i.e., no covalent cross-linking between antibody molecules during the conjugation reaction occurred. A slight smearing of bands is observed for the PEGylated compounds **12**−**14** under both conditions, a

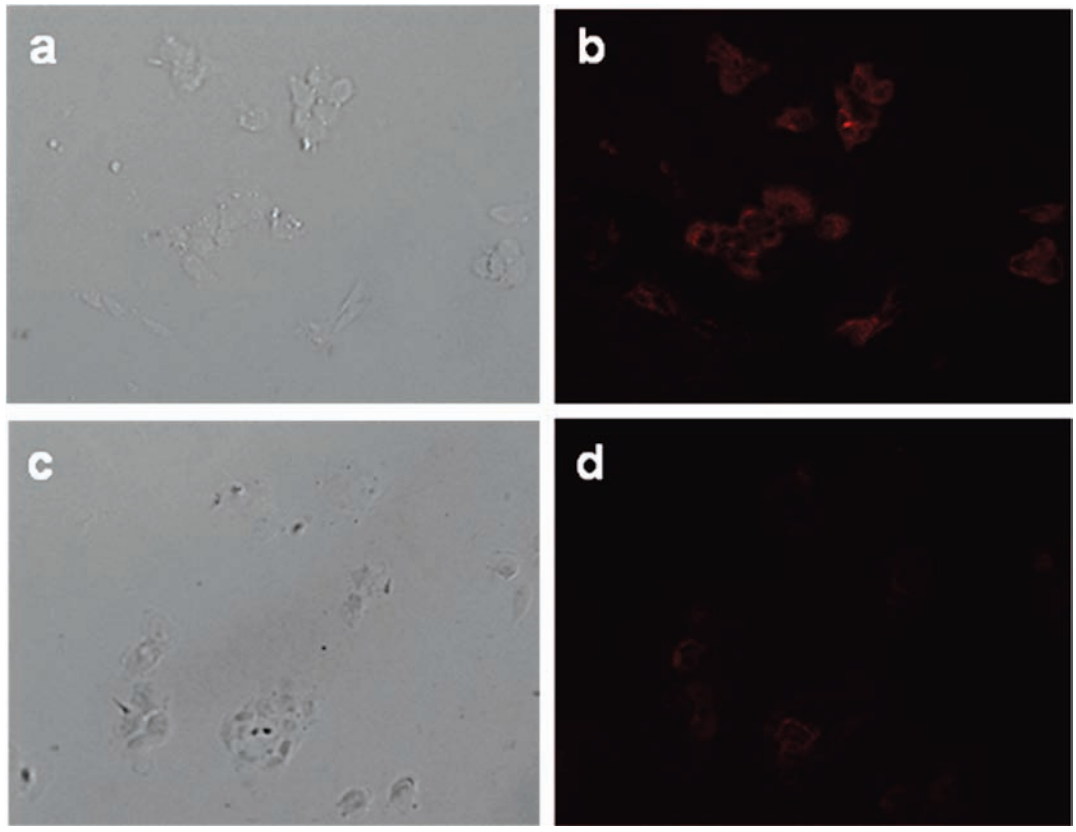


Figure 8. HER1-positive A431 fixed cells incubated with 1 μg of test antibody for 1 h at 37 °C. (a) DIC and (b) fluorescence image of cells stained with **12**. (c) DIC and (d) fluorescence image of cells stained with **15** (negative control).

behavior observed previously in other PEGylated antibodies and antibody fragments (*35*).

The SDS-PAGE data suggest that the mechanism of fluorescence activation previously described for other ICG-labeled mAbs in vitro in the presence of 5% SDS and β-ME or upon cell internalization, and in vivo with mouse cancer xenografts (*31*, *32*), could actually be the result of dye disaggregation of the dye−mAb conjugate. On the other hand, no such problem is anticipated for PEGylated compounds **12**−**14**, as they form no aggregates; furthermore, the linear polymer can serve as an effective spacer to minimize dye−dye interactions.

PEGylated mAbs **12**−**14** were analyzed by competition radioimmunoassay against ^{125}I-labeled panitumumab (Figure 7). The amount of bioconjugate required for 50% inhibition increased with the degree of labeling: 14 ng (**12**), 15 ng (**13**), 23 ng (**14**) vs 10 ng (native panitumumab). Though **12** and **13** exhibit comparable affinities, **14** showed the least amount of affinity among the samples under study, indicating a threshold value had been reached. Therefore, modification of panitumumab with **5** with a resulting D/P ratio less than 3 did not significantly compromise the immunoreactivity of the mAb.

Finally, **12** and **15** (negative control) were used to stain HER-1 expressing A431 cells and their fluorescence monitored by confocal microscopy. The images taken of fixed cells show that the panitumumab-based bioconjugate binds to the cell membranes (Figure 8). Fluorescence of the probe is observed even without internalization into the cell. This reinforces the previously described mechanism of fluorescence activation upon internalization into cells to be one of disaggregation of the dye−mAb conjugate. Fluorescence images of viable cells were also taken and showed similar binding of the fluorescent probe to the cell membranes (Supporting Information Figure 5).

In summary, a PEGylated amine-reactive derivative of NIR-emitting cyanine dye ICG has been successfully synthesized. This was used to label the anti-HER1 antibody panitumumab, and the resulting bioconjugate was characterized alongside previously reported non-PEGylated analogues. UV−vis spectrophotometry and SE-HPLC demonstrate that PEGylation prevents aggregation of the bioconjugate from occurring, in comparison with the non-PEGylated analogues. SDS-PAGE analysis of the bioconjugates show that the presence of SDS is sufficient to disassociate any aggregates formed, and denaturation with β-ME also shows that aggregation is not the result of covalent cross-linkage. These results suggest that the previously reported mechanism of fluorescence activation in ICG-labeled mAbs probably occurs via dye disaggregation. Competitive radioimmunoassay demonstrated that PEGylation of panitumumab with 2 equiv of **5** did not significantly reduce immunoreactivity of the mAb. This result was demonstrated further by fluorescence microscopy of HER1-expressing A431 cells stained with the PEGylated mAb, showing fluorescence on the cell membrane without internalization. This study highlights the fact that, though many protocols for the purification of bioconjugates are well-established and tools for these are commercially available as kits, the need to thoroughly characterize novel bioconjugates using classical methods is necessary to have a proper understanding of their solution properties and speciation.

It is hoped that the PEGylated bioconjugates described here would exhibit not only improved fluorescence properties in vivo but also better pharmacokinetic behavior in visualizing HER1-expressing tumor lesions. Indeed, the benefits of PEGylating proteins for therapeutic purposes have been described thoroughly in the literature, namely, that PEGylation increases the in vivo circulation half-life of the protein thereby enhancing its bioavailability, and that the modified protein exhibits a reduced immunogenicity and antigenicity coupled with increased plasma stability as the steric hindrance introduced by the water-soluble polymer masks it from proteolytic enzymes and other degrading agents (*45*−*47*). Hence, future work involving these single-modality imaging agents will include in vivo testing in animal models to determine their biodistribution and other pharmacokinetic characteristics. Futhermore, it is of immediate interest to this group to assess if PEGylation will improve the solution and in vivo biodistribution properties of our previously reported dual-modality optical/SPECT imaging agents (*18*, *19*), as PEGylation of a radiolabeled protein for SPECT imaging has previously been shown to possess improved pharmacokinetic behavior in the noninvasive monitoring of tumor response to applied therapy (*48*).

ACKNOWLEDGMENT

This research was supported by the Intramural Research Program of the NIH, National Cancer Institute, Center for Cancer Research. We would like to acknowledge the assistance of Dr. Kwamena Baidoo for supplying the ^{125}I-labeled panitumumab for the radioimmunoassay and Dr. Hisataka Kobayashi for the use of the confocal fluorescence microscope.

Supporting Information Available: NMR spectra of compounds **4** and **5**, and in vitro confocal microscopy images of compounds **12** and **15** with viable A431 cells. This material is available free of charge via the Internet at http://pubs.acs.org.

LITERATURE CITED

(1) Weisledder, R., and Ntziachristos, V. (2003) Shedding light onto live molecular targets. *Nat. Med. 9*, 123–128.
(2) Frangioni, J. V. (2003) In vivo near-infrared fluorescence imaging. *Curr. Opin. Chem. Biol. 7*, 626–634.
(3) Hilderbrand, S. A., and Weisledder, R. (2010) Near-infrared fluorescence: application to *in vivo* molecular imaging. *Curr. Opin. Chem. Biol. 14*, 71–79.
(4) Ernst, L. A., Gupta, R. K., Mujumdar, R. B., and Waggoner, A. S. (1989) Cyanine dye labeling reagents for sulfhydryl groups. *Cytometry 10*, 3–10.
(5) Mujumdar, R. B., Ernst, L. A., Mujumdar, S. R., and Waggoner, A. S. (1989) Cyanine dye labeling reagents containing isothiocyanate groups. *Cytometry 10*, 11–19.
(6) Southwick, P. L., Ernst, L. A., Tauriello, E. W., Parker, S. R., Mujumdar, R. B., Mujumdar, S. R., Clever, H. A., and Waggoner, A. S. (1990) Cyanine dye labeling reagents - carboxymethylindocyanine succinimidyl esters. *Cytometry 11*, 418–430.
(7) Mujumdar, R. B., Ernst, L. A., Mujumdar, S. R., Lewis, C. J., and Waggoner, A. S. (1993) Cyanine dye labeling reagents: sulfoindocyanine succinimidyl esters. *Bioconjugate Chem. 4*, 105–111.
(8) Mujumdar, S. R., Mujumdar, R. B., Grant, C. M., and Waggoner, A. S. (1996) Cyanine-labeling reagents: sulfobenzindocyanine succinimidyl esters. *Bioconjugate Chem. 7*, 356–362.
(9) Gruber, H. J., Hahn, C. D., Kada, G., Riner, C. K., Harms, G. S., Ahrer, W., Dax, T. G., and Knaus, H.-G. (2000) Anomalous fluorescence enhancement of Cy3 and Cy3.5 versus anomalous fluorescence loss of Cy5 and Cy7 upon colvaent linking to IgG and noncovalent binding to avidin. *Bioconjugate Chem. 11*, 696–704.
(10) Berlier, J. E., Rothe, A., Buller, G., Bradford, J., Gray, D. R., Filanoski, B. J., Telford, W. G., Yue, S., Liu, J., Cheung, C.-Y., Chang, W., Hirsch, J. D., Beechem, J. M., Haugland, R. P., and Haugland, R. P. (2003) Quantitative comparison of long-wavelength Alexa Fluor dyes to Cy dyes: fluorescence of the dyes and their bioconjugates. *J. Histochem. Cytochem. 51*, 1699–1712.
(11) Lin, Y., Weisledder, R., and Tung, C.-H. (2002) Novel near-infrared cyanine fluorochromes: synthesis, properties and bioconjugation. *Bioconjugate Chem. 13*, 605–610.
(12) Hilderbrand, S. A., Kelly, K. A., Weisledder, R., and Tung, C.-H. (2005) Monofunctional near-infrared fluorochromes for imaging applications. *Bioconjugate Chem. 16*, 1275–1281.

(13) Bouteiller, C., Clave, G., Bernardin, A., Chipon, B., Massonneau, M., Renard, P. Y., and Romieu, A. (2007) Novel water-soluble near-infrared cyanine dyes: synthesis, spectral properties and use in the preparation of internally-quenched fluorescent probes. *Bioconjugate Chem. 18*, 1303–1317.

(14) Ballou, B., Fisher, G. W., Deng, J.-S., Hakala, T. R., Srivastava, M., and Farkas, D. L. (1998) Cyanine fluorochrome-labeled antibodies *in vivo*: assessment of tumor imaging using Cy3, Cy5, Cy5.5 and Cy7. *Cancer Detect. Prev. 22*, 251–257.

(15) Zou, P., Xu, S., Povoski, S. P., Wang, A., Johnson, M. A., Martin, E. W., Subramaniam, V., Xu, R., and Sun, D. (2009) Near-infrared fluorescence labeled anti-TAG-72 monoclonal antibodies for tumor imaging in colorectal cancer xenograft mice. *Mol. Pharm. 6*, 428–440.

(16) Ogawa, M., Regino, C. A. S., Choyke, P. L., and Kobayashi, H. (2009) In vivo target-specific activatable near-infrared optical labeling of humanized monoclonal antibodies. *Mol. Cancer Ther. 8*, 232–239.

(17) Rosenthal, E. L., Kulbersh, B. D., Duncan, R. D., Zhang, W., Magnuson, J. S., Carroll, W. R., and Zinn, K. (2006) In vivo detection of head and neck cancer orthotopic xenografts by immunofluorescence. *Laryngoscope 116*, 1636–1641.

(18) Xu, H., Baidoo, K., Gunn, A. J., Boswell, A., Milenic, D. E., Choyke, P. L., and Brechbiel, M. W. (2007) Design, synthesis and characterization of a dual modality positron emission tomography and fluorescence imaging agent for monoclonal antibody tumor-targeted imaging. *J. Med. Chem. 50*, 4759–4765.

(19) Xu, H., Eck, P. K., Baidoo, K. E., Choyke, P. L., and Brechbiel, M. W. (2009) Toward preparation of antibody-based imaging probe libraries for dual modality positron emission tomography and fluorescence imaging. *Bioorg. Med. Chem. 17*, 5176–5181.

(20) Fox, I. J., Brooker, L. G. S., Heseltine, D. W., Essez, H. E., and Wood, E. H. (1957) A tricarbocyanine dye for continuous recording of dilution curves in whole blood independent of variations in blood oxygen saturation. *Proc. Staff Meet. Mayo Clin. 32*, 478–484.

(21) Fox, I. J., and Wood, E. H. (1960) Indocyanine green: physical and physiologic properties. *Proc. Staff Meet. Mayo Clin. 35*, 732–744.

(22) Landsman, M. L. J., Kwant, G., Mook, G. A., and Zijlstra, W. G. (1976) Light-absorbing properties, stability and spectral stabilization of indocyanine green. *J. Appl. Physiol. 40*, 575–583.

(23) Philip, R., Penzkofer, A., Baumler, W., Szeimies, R. M., and Abels, C. (1996) Absorption and fluorescence spectroscopic investigation of indocyanine green. *J. Photochem. Photobiol., A 96*, 137–148.

(24) Ito, S., Muguruma, N., Kakehashi, Y., Hayashi, S., Okamura, S., Shibata, H., Okahisa, T., Kanamori, M., Takesako, K., Nozawa, M., Ishida, K., and Shiga, M. (1995) Development of fluorescence-emitting antibody labeling substance by near-infrared ray excitation. *Bioorg. Med. Chem. Lett. 5*, 2689–2694.

(25) Hirata, T., Kogiso, H., Morimoto, K., Miyamoto, S., Taue, H., Sano, S., Muguruma, N., Ito, S., and Nagao, Y. (1998) Synthesis and reactivities of 3-indocyanine-green-acyl-1,3-thiazolidine-2-thione (ICG-ATT) as a new near-infrared fluorescent-labeling reagent. *Bioorg. Med. Chem. 6*, 2179–2184.

(26) Muguruma, N., Ito, S., Hayashi, S., Taoka, S., Kakehashi, Y., Ii, K., Shibamura, S., and Takesako, K. (1998) Antibodies labeled with fluorescence-agent excitable by infrared rays. *J. Gastroenterol. 33*, 467–471.

(27) Tadatsu, M., Ito, S., Muguruma, N., Kusaka, Y., Inayama, K., Bando, T., Tadatsu, Y., Okamoto, K., Ii, K., Nagao, Y., Sano, S., and Taue, H. (2003) A new infrared fluorescent-labeling agent and labeled antibody for diagnosis microcancers. *Bioorg. Med. Chem. 11*, 3289–3294.

(28) Tadatsu, Y., Muguruma, N., Ito, S., Tadatsu, M., Kusaka, Y., Okamoto, K., Imoto, Y., Taue, H., Sano, S., and Nagao, Y. (2006) Optimal labeling condition of antibodies available for immunofluorescence endoscopy. *J. Med. Invest. 53*, 52–60.

(29) Yano, H., Muguruma, N., Ito, S., Aoyagi, E., Kimura, T., Imoto, Y., Cao, J., Inoue, S., Sano, S., Nagao, Y., and Kido, H. (2006) Fab fragment labeled with ICG-derivative for detecting digestive tract cancer. *Photodiagnosis Photodyn. Ther. 3*, 177–183.

(30) Withrow, K. P., Gleysteen, J. P., Safavy, A., Skipper, J., Desmond, R. A., Zinn, K., and Rosenthal, E. L. (2007) Assessment of indocyanine green-labeled cetuximab to detect xenografted head and neck cancer cell lines. *Otolaryngol. Head Neck Surg. 137*, 729–734.

(31) Ogawa, M., Kosaka, N., Choyke, P. L., and Kobayashi, H. (2009) In vivo molecular imaging of cancer with a quenching near-inrared fluorescent probe using conjugates of monoclinal antibodies and indocyanine green. *Cancer Res. 69*, 1268–1272.

(32) Ogawa, M., Regino, C. A. S., Seidel, J., Green, M. V., Xi, W., Williams, M., Kosaka, N., Choyke, P. L., and Kobayashi, H. (2009) Dual-modality molecular imaging using antibodies labeled with activatable fluorescence and a radionuclide for specific and quantitative targeted cancer detection. *Bioconjugate Chem. 20*, 2177–2184.

(33) Yarden, Y., and Sliwkowski, M. X. (2001) Untangling the ErbB signalling network. *Nat. Rev. Mol. Cell Biol. 2*, 127–137.

(34) Zalipsky, S. (1995) Chemistry of polyethylene glycol conjugates with biologically active molecules. *Adv. Drug Delivery Rev. 16*, 157–182.

(35) Chapman, A. P. (2002) PEGylated antibodies and antibody fragments for improved therapy: a review. *Adv. Drug Delivery Rev. 54*, 531–545.

(36) Millar, W. T., and Smith, J. F. B. (1983) Protein iodination using Iodogen®. *Int. J. Appl. Radiat. Isot. 34*, 639–641.

(37) Laemmli, U. K. (1970) Cleavage of structural proteins during the assembly of the head of Bacteriophage T4. *Nature 227*, 680–685.

(38) Nagao, Y., Seno, K., Kawabata, K., Miyasaka, T., Takao, S., and Fujita, E. (1980) Monitored aminolysis of 3-acylthiazolidine-2-thione: a new convenient synthesis of amide. *Tetrahedron Lett. 21*, 841–844.

(39) Nagao, Y., Seno, K., Miyasaka, T., and Fujita, E. (1980) Monitored aminolysis of 3-acylthiazolidine-2-thione: a new synthesis of macrocyclic amides. *Chem. Lett. 9*, 159–162.

(40) Baker, K. J. (1962) Binding of sulfobromophthalein (BSP) sodium and indocyanine green (ICG) by plasma α_1 lipoproteins. *Proc. Soc. Exp. Biol. Med. 122*, 957–963.

(41) West, W., and Pearce, S. (1965) The dimeric state of cyanine dyes. *J. Phys. Chem. 69*, 1894–1903.

(42) Benson, R. C., and Kues, H. A. (1978) Fluorescence properties of indocyanine green as related to angiography. *Phys. Med. Biol. 23*, 159–163.

(43) McKinney, R. M., and Spillane, J. T. (1975) An approach to quantitation in rhodamine isothiocyanate labeling. *Ann. N.Y. Acad. Sci. 254*, 55–64.

(44) Chen, R. F. (1969) Fluorescent protein-dye conjugates II. Gamma globulin conjugated with various dyes. *Arch. Bioch. Biophys. 133*, 263–276.

(45) Fuertges, F., and Abuchowski, A. (1990) The clinical efficacy of poly(ethylene glycol)-modified proteins. *J. Controlled Release 11*, 139–148.

(46) Chapman, A. P., Antoniw, P., Spitali, M., West, S., Stephens, S., and King, D. J. (1999) Therapeutic antibody fragments with prolonged in vivo half-lives. *Nat. Biotechnol. 17*, 780–783.

(47) Veronese, F. M., and Pasut, G. (2005) PEGylation, successful approach to drug delivery. *Drug Discovery Today 10*, 1451–1458.

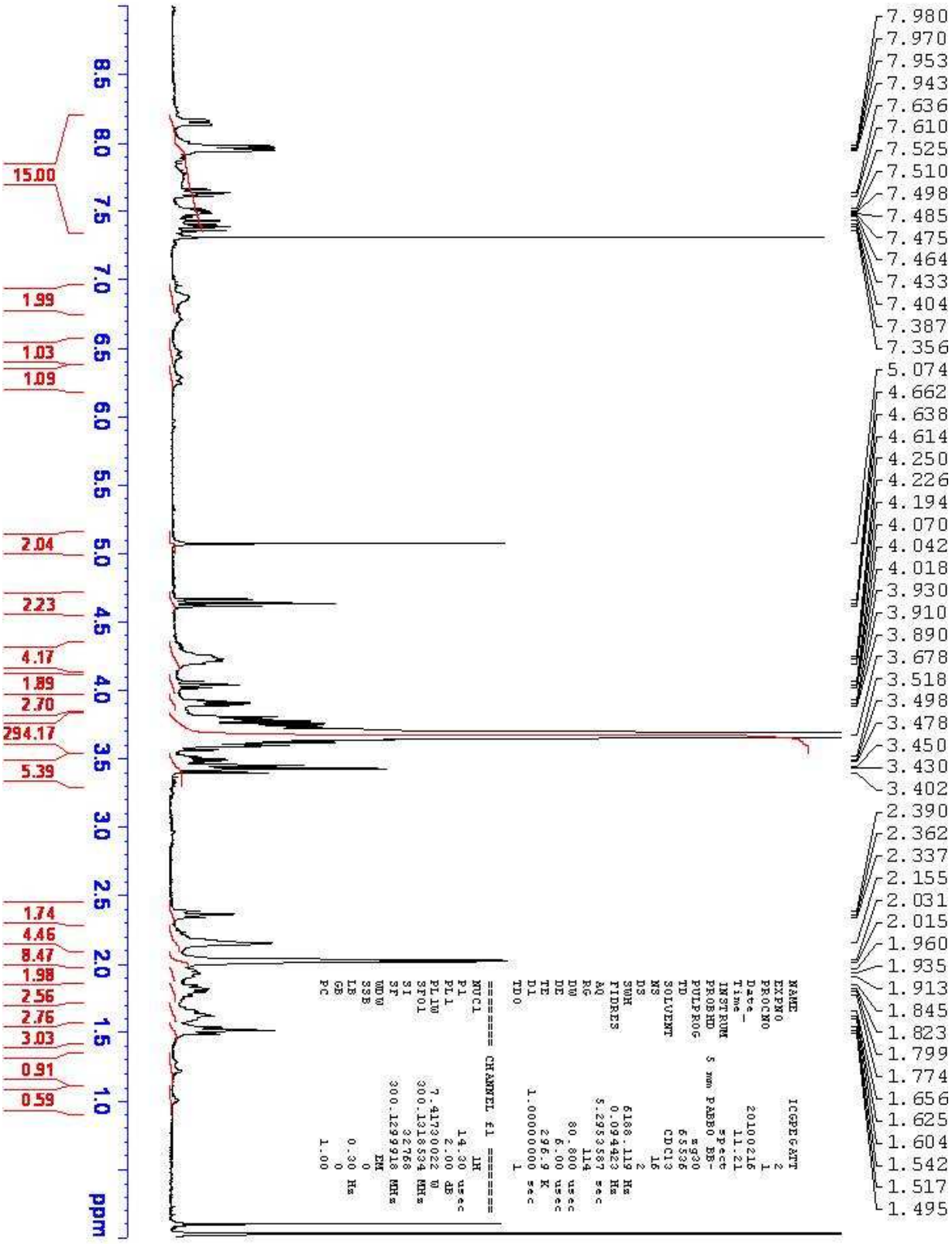
(48) Wen, X., Wu, Q.-P., Ke, S., Wallace, S., Charnsangavej, C., Huang, P., Liang, D., Chow, D., and Li, C. (2003) Improved radiolabeling of PEGylated protein: PEGylated annexin V for non-invasive imaging of tumor apoptosis. *Cancer Biother. Radiopharm. 18*, 819–827.

BC100336B

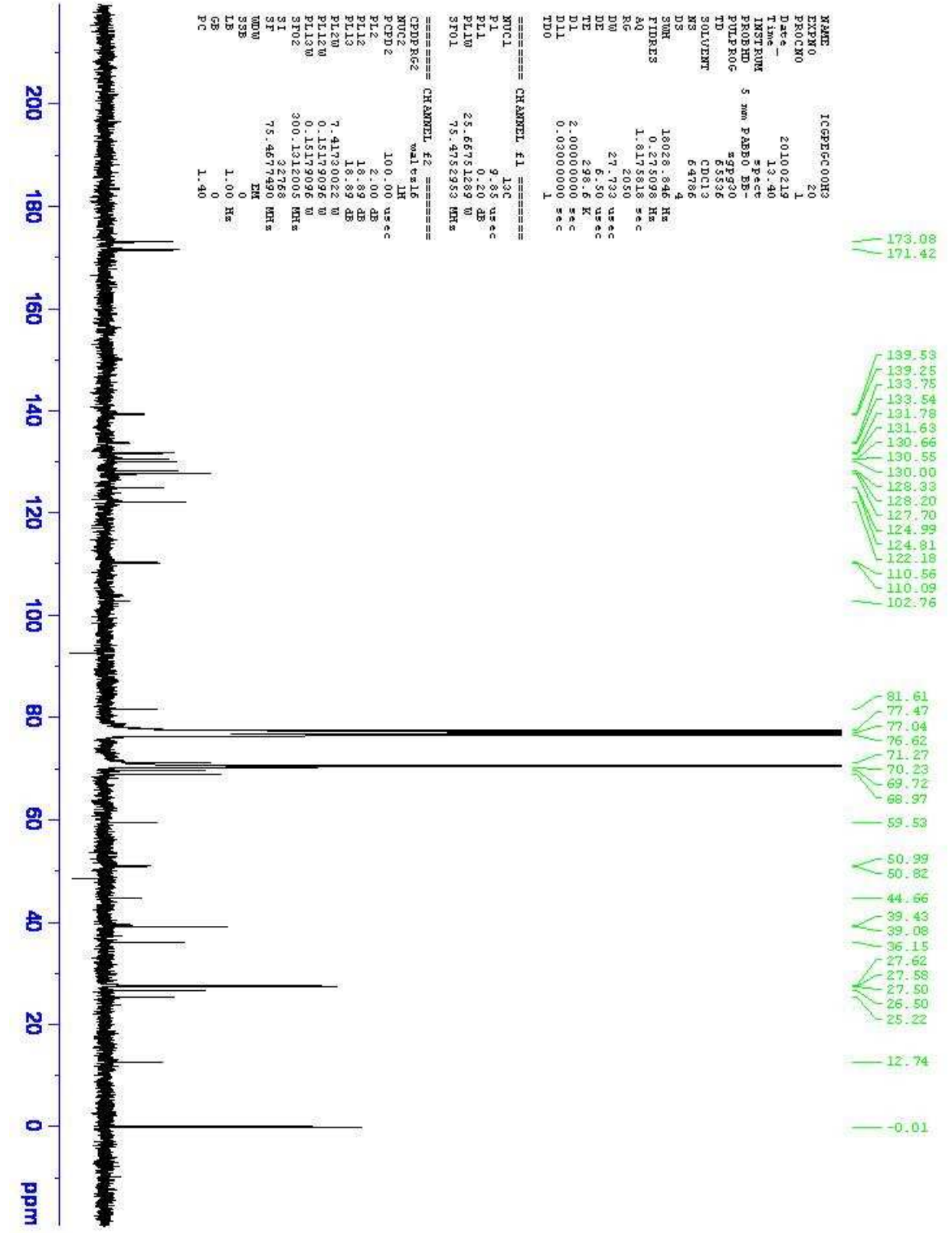
Supplementary Information

Improved Speciation Characteristics of PEGylated Indocyanine Green-Labeled Panitumumab: Revisiting the Solution and Spectroscopic Properties of a Near-Infrared Emitting anti-HER1 Antibody for Optical Imaging of Cancer

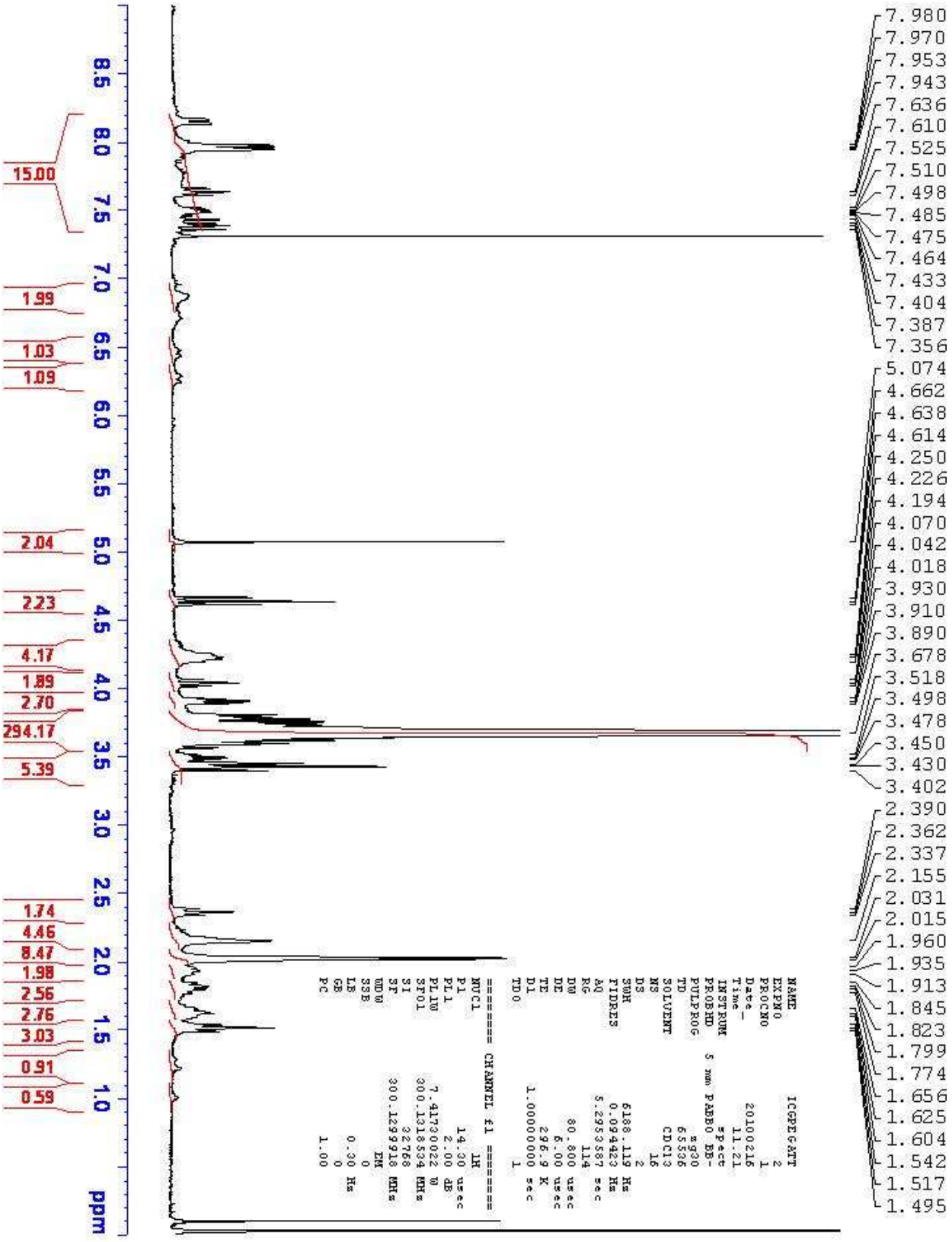
Aaron Joseph L. Villaraza, Diane E. Milenic, and Martin W. Brechbiel



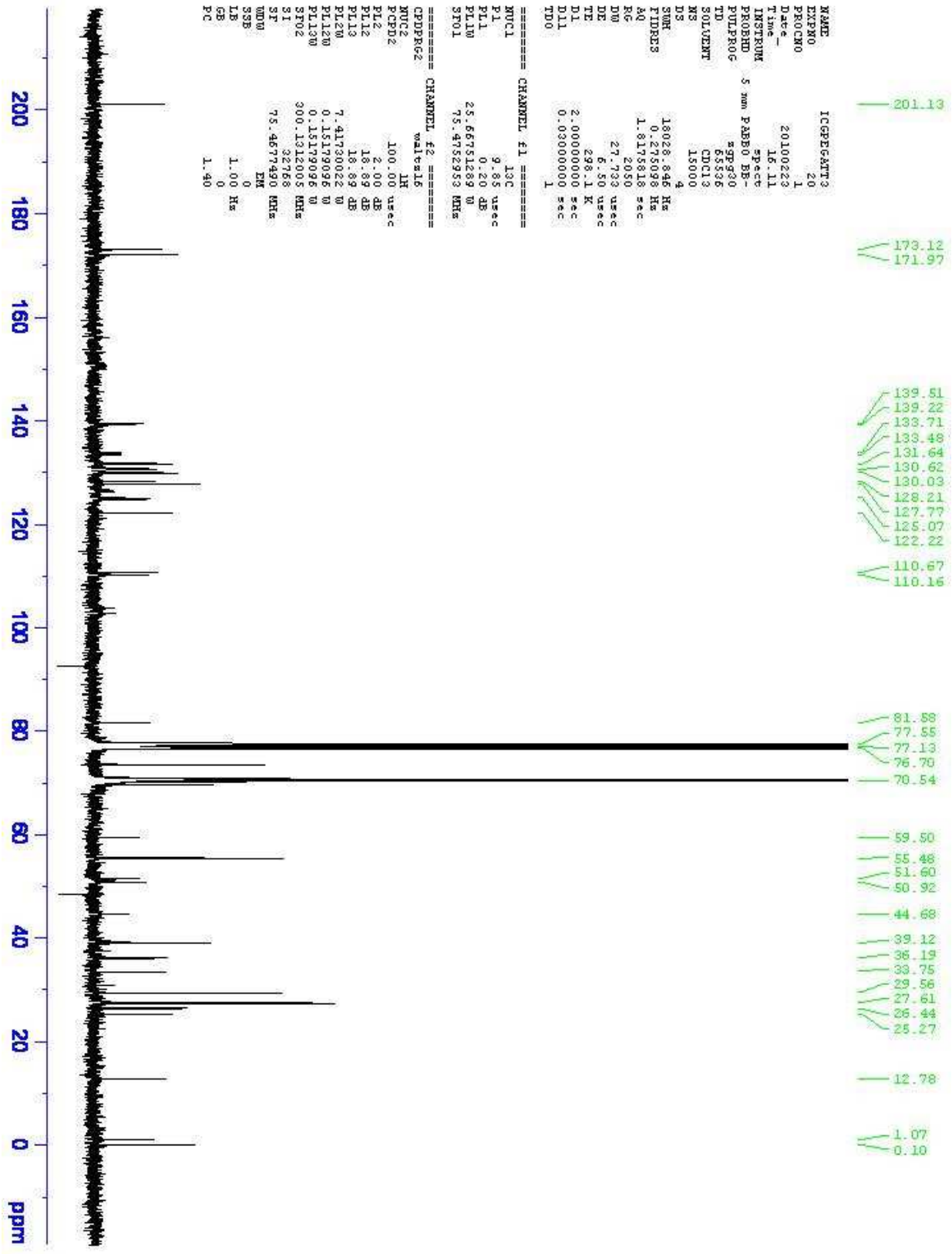
Supplementary Figure 1. ^{1}H NMR spectrum of PEGylated ICG (**4**).



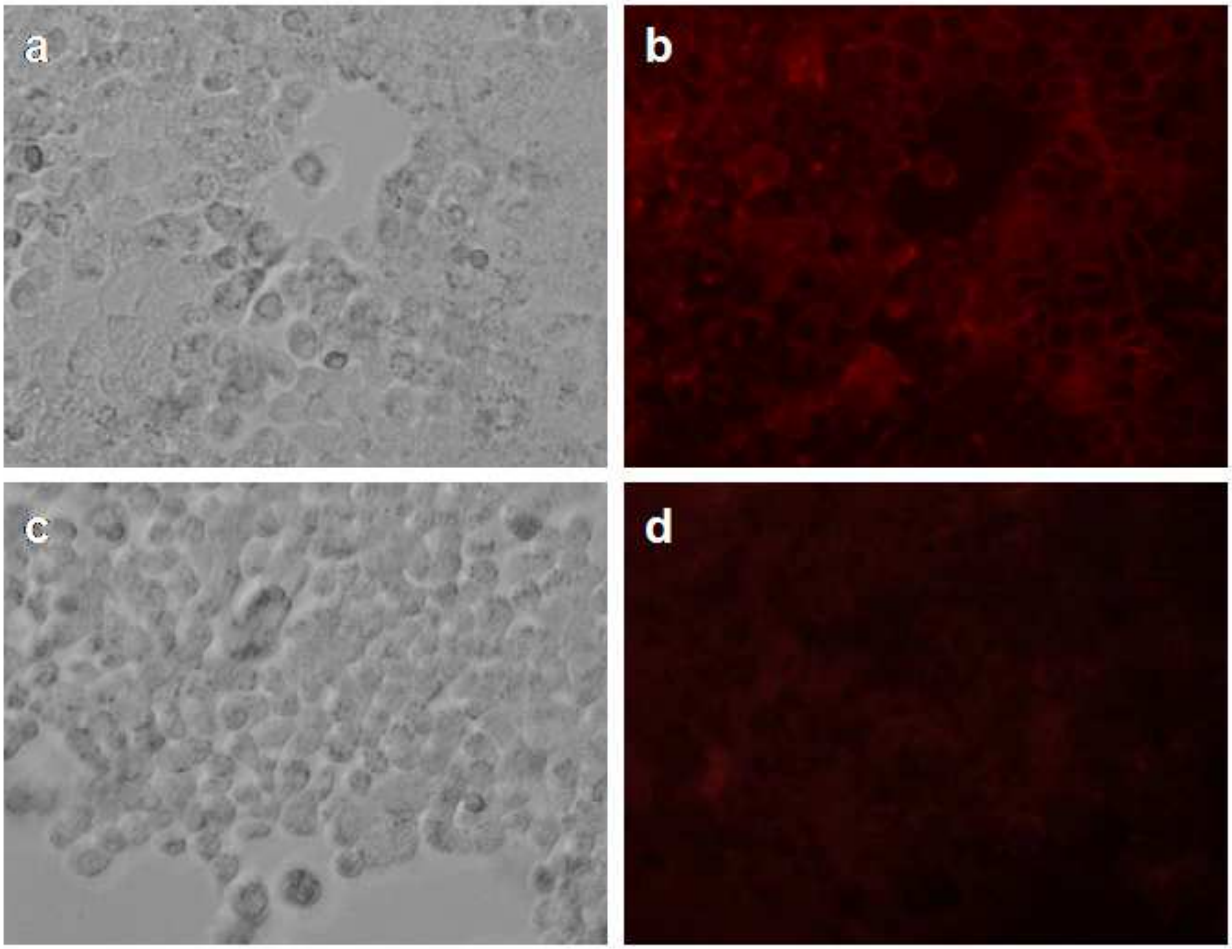
Supplementary Figure 2. ^{13}C NMR spectrum of PEGylated ICG (**4**).



Supplementary Figure 3. ^{1}H NMR spectrum of amine-reactive PEGylated ICG (**5**).



Supplementary Figure 4. ^{13}C NMR spectrum of PEGylated ICG (**5**).



Supplementary Figure 5. HER1-positive A431 viable cells incubated with 1μg of test antibody for 2 h at 4 ºC. (**a**) DIC and (**b**) fluorescence image of cells stained with **12**. (**c**) DIC and (**d**) fluorescence image of cells stained with **15** (negative control).

Synthesis and Evaluation of 15-(4-(2-[^{18}F]Fluoroethoxy)phenyl)pentadecanoic Acid: A Potential PET Tracer for Studying Myocardial Fatty Acid Metabolism

Zhude Tu, Shihong Li, Terry L. Sharp, Pilar Herrero, Carmen S. Dence, Robert J. Gropler, and Robert H. Mach*

Division of Radiological Sciences, Washington University School of Medicine, 510 South Kingshighway Blvd. St. Louis, Missouri 63110, United States. Received July 27, 2010; Revised Manuscript Received October 12, 2010

15-(4-(2-[^{18}F]fluoroethoxy)phenyl)pentadecanoic acid ([^{18}F]**7**) was synthesized as a PET probe for assessing myocardial fatty acid metabolism. The radiosynthesis of [^{18}F]**7** was accomplished using a two-step reaction, starting with the corresponding tosylate ester, methyl 15-(4-(2-(tosyloxy)ethoxy)phenyl)pentadecanoate (**5**), and gave the radiolabeled fatty acid, [^{18}F]**7** in a radiolabeling yield of 55−60% and a specific activity of >2000 Ci/mmol (decay corrected to EOB). The biological evaluation of [^{18}F]**7** in rats displayed high uptake in heart (1.94%ID/g at 5 min), which was higher than the uptake (%ID/g) in blood, lung, muscle, pancreas, and brain. MicroPET studies of [^{18}F]**7** in Sprague−Dawley rats demonstrated excellent images of the myocardium when compared with [^{11}C]palmitate images in the same animal. Moreover, the tracer kinetics of [^{18}F]**7** paralleled those seen with [^{11}C]palmitate, with an early peak followed by biphasic washout. When compared to [^{11}C]palmitate, [^{18}F]**7** exhibited a slower early clearance (0.17 ± 0.01 vs 0.30 ± 0.02, $P < 0.0001$) and a significantly higher late clearance (0.0030 ± 0.0005 vs 0.0006 ± 0.00013, $P < 0.01$). These initial studies suggest that [^{18}F]**7** could be a potentially useful clinical PET tracer to assess abnormal myocardial fatty acid metabolism.

INTRODUCTION

Fatty acid metabolism is the major source of energy production in the normal myocardium contributing 90% of aerobic metabolism through the β-oxidation pathway (*1*−*3*). Abnormalities in myocardial fatty acid metabolism play a central role in a variety of cardiac diseases such as obesity, diabetes mellitus, dilated cardiomyopathy, and myocardial ischemia (*1*, *4*). An overdependence on fatty acid metabolism typifies obesity and diabetes mellitus. This increase in fatty acid use can initiate a cascade of events such as worsening myocardial insulin resistance, impaired energetics, and an increase in oxidative stress and lipid accumulation, all of which have detrimental effects on myocellular health and can lead to reduced cardiac function (*5*−*7*). In contrast, a reduction in fatty acid metabolism leading to an overdependence on glucose use occurs in left ventricular hypertrophy, dilated cardiomyopathy, and myocardial ischemia. This metabolic pattern can impair cardiac function through a variety of mechanisms including reduced energy production, increased oxidative stress, and accelerated cell death (*8*, *9*). The importance of altered fatty acid metabolism in these various cardiac disease processes is highlighted by the robust development of new therapeutics designed to favorably manipulate myocardial fatty acid use such as the peroxisome proliferator-activated receptor alpha (PPARα) agents and partial fatty acid oxidation inhibitors (*10*−*12*).

Detection of these different patterns in myocardial fatty acid metabolism may have important diagnostic, prognostic, and therapeutic implications in the management of the cardiac patient. However, to achieve this goal requires the availability of an accurate and widely applicable noninvasive method to image myocardial fatty acid metabolism. To this end, investigators have focused on optimizing the structures of the fatty acids to identify radioligands that have extended retention time in heart and suitable pharmacokinetic properties for use as positron emission tomography (PET) or single photon emission computed tomography (SPECT) imaging probes (Figure 1) (*13*−*16*). However, because PET has higher sensitivity and higher spatial and temporal resolution compared to SPECT, developing a suitable PET probe which is capable of accurately quantifying myocardial fatty acid metabolism is highly desirable. Currently, [^{11}C]palmitate (Figure 1) is the most accurate PET radiotracer for measuring myocardial fatty acid metabolism. However, the short half-life of carbon-11 ($t_{1/2} = 20$ min) limits the use of [^{11}C]palmitate in the study of cardiovascular disease to imaging centers having the capability to produce the radiotracer onsite. Therefore, a number of groups have focused on developing fluorine-18 labeled PET tracers which are capable of imaging fatty acid uptake in the heart.

In this regard, two different strategies have been pursued: (1) developing radiotracers such as [^{11}C]palmitate whose kinetics closely track those of unlabeled fatty acids and thus reflect all aspects of myocardial fatty acid oxidation and storage (*7*, *16*−*19*); and (2) developing radiolabeled tracers that will be trapped within the myocardium and can thus reflect a specific aspect of fatty acid metabolism such as cellular uptake (*16*, *20*−*28*). For the first strategy, the advantages are the assessment of various aspects of myocardial fatty acid metabolism, such as uptake, oxidation, and storage, with appropriate mathematical modeling techniques capable of quantifying fatty acid metabolism in each pathway. In contrast, trapped fatty acid tracers offer the potential of higher image quality, but are not capable of discriminating between the oxidation and storage pathways. A prime example of the latter approach is the radiotracer, 14-(*R*,*S*)-[^{18}F]fluoro-6-thia-heptadecanoic acid ([^{18}F]FTHA) (Figure 1) (*20*, *21*). Imaging studies of [^{18}F]FTHA showed high uptake and retention in the myocardium in various diseases (*23*−*25*), but this radiotracer lacked sensitivity to measure the inhibition of β-oxidation by myocardium under conditions of hypoxia (*14*).

* Address correspondence to Robert H. Mach, Ph.D., Division of Radiological Sciences, Washington University School of Medicine, Campus Box 8225, 510 S. Kingshighway Blvd., St. Louis, MO 63110. Tel: 314-362-8538. Fax: 314-362-8555. E-mail: rhmach@mir.wustl.edu.

10.1021/bc100343h © 2010 American Chemical Society
Published on Web 11/11/2010

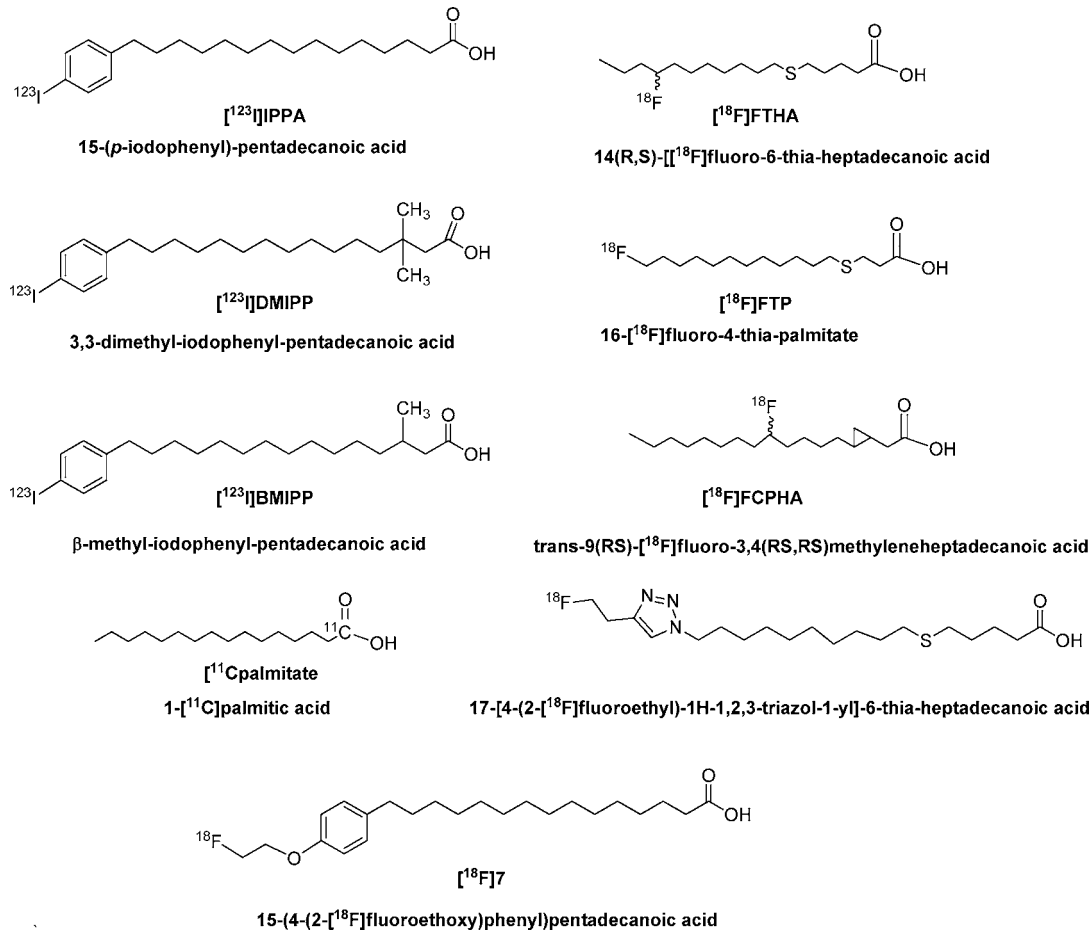


Figure 1. Radiolabeled fatty acid analogues used in PET and SPECT imaging studies.

Subsequently, 16-[^{18}F]fluoro-4-thia-palmitate ([^{18}F]FTP) (Figure 1) was developed, and its metabolic trapping function was proportional to β-oxidation under normal oxygenation and hypoxic conditions (*22*). However, it is not clear if [^{18}F]FTP can accurately differentiate between fatty acid oxidation and esterification (*27*).

Recently, trans-9-(*RS*)-[^{18}F]fluoro-3,4-(*RS*,*RS*) methylene heptadecanoic acid ([^{18}F]FCPHA) (Figure 1), which incorporates a cyclopropyl group at C3−C4 to block β-oxidation, was reported as a radiolabeled fatty acid analogue (*26*). The uptake of [^{18}F]FCPHA in rat myocardium reached approximately 1.5%ID/gram tissue at 5 min and displayed little change over a period of 60 min. However, the impact of altered plasma substrate levels, cardiac workload, and myocardial blood flow on the pharmacokinetics of [^{18}F]FCPHA is not known. It is also not clear if the kinetics of [^{18}F]FCPHA will be able to differentiate among fatty acid uptake, oxidation, and esterification. Currently, both [^{18}F]FTP and [^{18}F]FCPHA are being evaluated in phase 1 clinical trials (*4*). In 2009, 17-[4-(2-[^{18}F]fluoroethyl)-1*H*-1,2,3-triazol-1-yl]-6-thia-heptadecanoic acid, a "click-labeling" analogue of [^{18}F]FTHA, was reported as a potential PET agent for visualizing fatty acid metabolism in myocardium (*28*). However, the same issues apply to this radiotracer regarding the ability to differentiate between fatty acid oxidation and storage mechanisms in the heart.

The goal of our research was to identify an ^{18}F-labeled fatty acid analogue which is capable of mimicking [^{11}C]palmitate with regard to its ability to measure fatty acid uptake, β-oxidation, and storage as triglycerides. The lead compound for our studies was 15-(*para*-iodophenyl)-pentadecanoic acid (IPPA) (Figure 1), which was developed over twenty years ago as a SPECT myocardial imaging agent. In this case, the *p*-iodine atom of IPPA was replaced with a 2-fluoroethoxy group to make 15-(4-(2-fluoroethoxy)phenyl)pentadecanoic acid (**7**) (Figure 1). IPPA was chosen as the lead compound for developing a PET radiotracer because its kinetics closely match those of [^{11}C]palmitate but are too rapid to be imaged with clinical SPECT scanners.

In this article, we report the synthesis and radiosynthesis of [^{18}F]**7**, and our initial results measuring myocardial uptake in rats. MicroPET imaging studies of [^{18}F]**7** were also performed in Sprague−Dawley rats and its pharmacokinetics were compared with that of [^{11}C]palmitate.

EXPERIMENTAL PROCEDURES

General Chemistry. All analytical-grade chemicals and reagents were purchased from Sigma-Aldrich (Milwaukee, WI) and were used without further purification unless otherwise specified. Flash column chromatography was conducted using Scientific Adsorbents, Inc., silica gel, 60 Å, "40 Micron Flash" (32−63 μm). Melting points were determined using MEL-TEMP 3.0 apparatus and uncorrected. ^{1}H NMR spectra were recorded at 300 MHz on a Varian Mercury-VX spectrometer with $CDCl_3$ as solvent and tetramethylsilane (TMS) as the internal standard. All chemical shift values are reported in ppm (δ). Elemental analyses (C, H) were determined by Atlantic Microlab, Inc. (Norcross, GA).

Methyl 15-Bromopentadecanoate (2). A 2.0 M solution of trimethylsilyl diazomethane in hexane (3.4 mL, 6.8 mmol) was added to the solution of 15-bromopentadecanoic acid **1** (1 g, 3 mmol) in THF/MeOH (v/v, 7/2) (18 mL), and the reaction mixture was stirred at room temperature for 2 h. The solvent was removed under reduced pressure. Chloroform (80 mL) was

used to dissolve the residue, and the solution was washed with water (2 × 30 mL) and brine (2 × 30 mL). The organic solution was dried over sodium sulfate. After the solvent was removed under reduced pressure, it afforded **2** as colorless syrup (0.99 g, 99%). ^{1}H NMR (300 MHz, $CDCl_3$): δ 1.2−1.36 (m, 20H); 1.36−1.48 (2H, m); 1.58−1.78 (m, 2H); 1.79−1.92 (m, 2H); 2.26−2.34 (t, 2H); 3.36−3.48 (t, 2H); 3.67 (s, 3H).

Methyl 15-(4-(Benzyloxy)phenyl)pentadecanoate (3). A solution of compound **2** (400 mg, 1.2 mmol) in 2-methyl-2-butanol (5 mL) was added to a round-bottom flask (25 mL) that contained 4-benzyloxyphenylboronic acid methyl ester (408 mg, 1.79 mmol), $Pd(OAc)_2$ (26.8 mg,12 mmol), [HP(t-Bu)$_2$Me]BF_4 (62.7 mg, 0.25 mmol), and potassium *tert*-butoxide (KO-t-Bu) (53.5 mg, 0.48 mmol), and the reaction mixture was stirred overnight at ambient temperature. The reaction was quenched with ethyl acetate (60 mL), water (13 mL), and glacial acetic acid (2 mL). The organic layer was separated and washed with brine (3 × 10 mL). The organic solution was dried over sodium sulfate, and the solvent was removed under reduced pressure. The product was purified by silica gel column chromatography using ethyl acetate/hexane (1/10, v/v) as the eluent to afford the intermediate compound, 15-(4-(benzyloxy)-phenyl)pentadecanoic acid, as a white solid (240 mg, 45%), mp: 95−96 °C. ^{1}H NMR (300 MHz, $CDCl_3$): δ 1.38−1.18 (m, 20H), 1.70−1.50 (m, 2H), 2.34 (t, 2H), 5.04 (s, 2H), 2.54 (t, 2H), 6.93−6.87 (m, 2H), 7.12−7.05 (m, 2H), 7.50−7.30 (m, 5H). 0.5 mL of concentrated sulfuric acid was added into a solution of 15-(4-(benzyloxy)phenyl)pentadecanoic acid (230 mg, 0.54 mmol) in 30 mL methanol. The reaction mixture was stirred at reflux overnight and quenched with a saturated aqueous solution of sodium bicarbonate. After removing the methanol under reduced pressure, the residue was partitioned between dichloromethane and brine. The organic layer was dried over sodium sulfate, filtered, and concentrated under reduced pressure. The crude product was purified by silica gel column chromatography using ethyl acetate/hexane (v/v, 1/10) as the eluent to afford **3** (185 mg, 78%) as a white solid: mp 56−57 °C. ^{1}H NMR (300 MHz, $CDCl_3$): δ 1.18−1.40 (m, 20H); 1.50−1.68 (4H, m); 2.26−2.36 (t, 2H); 2.48−2.58 (t, 2H); 3.66 (s, 3H); 5.04 (s, 2H); 6.86−6.94 (m, 2H); 7.06−7.13 (m, 2H); 7.28−7.46 (m, 5H). Elemental analysis $C_{29}H_{42}O_3$ calcd: C, 79.41; H, 9.65. Found: C, 79.14; H, 9.81.

Methyl 15-(4-Hydroxyphenyl)pentadecanoate (4). Palladium (10 wt % on activated carbon; 50 mg) was added under a nitrogen atmosphere to a solution of compound **3** (185 mg, 0.42 mmol) in ethyl acetate (10 mL). Hydrogen was added into the system to reach 6 pounds per square inch (psi) pressure, and the mixture was stirred for over 5 h. The reaction mixture was filtered through Celite and washed with ethyl acetate (5 mL). After removing excess solvent, the product was purified by silica gel column chromatography using ethyl acetate/hexane (v/v, 1/5) as the eluent to afford **4** as a white solid (111 mg, 75%): mp 75−76 °C. ^{1}H NMR (300 MHz, $CDCl_3$): δ 1.30−1.47 (m, 20H); 1.50−1.68 (m, 4H); 2.26−2.36 (t, 2H); 2.49−2.58 (t, 2H); 3.67 (s, 3H); 6.72−6.78 (m, 2H); 7.04−7.09 (m, 2H). Elemental analysis $C_{22}H_{36}O_3$ calcd: C, 75.82; H, 10.41. Found: C, 75.71; H, 10.46.

Methyl 15-(4-(2-(Tosyloxy)ethoxy)phenyl)pentadecanoate (5). Compound **4** (106 mg, 0.30 mmol) and ethylene glycol-1,2-bistosylate (338 mg, 0.91 mmol) were dissolved into anhydrous acetonitrile (20 mL), and then potassium carbonate (42 mg, 0.30 mmol) was added into the reaction mixture. The reaction mixture was stirred at reflux under a nitrogen atmosphere for 18 h until thin layer chromatography (TLC) indicated the reaction was complete. After removing the solvent, dichloromethane (10 mL) was used to dissolve the residue. The organic layer was washed with brine (10 mL), dried over sodium sulfate, filtered, and concentrated under reduced pressure. The residue was purified by silica gel column chromatography using ether/hexane (v/v, 1/2) as the eluent to afford compound **5** as a white solid (145 mg, 87%): mp 44−45 °C. ^{1}H NMR (300 MHz, $CDCl_3$): δ 1.18−1.40 (m, 20H); 1.46−1.68 (4H, m); 2.26−2.36 (t, 2H); 2.45 (s, 3H); 2.48−2.56 (t, 2H); 3.66 (s, 3H); 4.09−4.15 (2H); 4.32−4.38; 6.66−6.74 (m, 2H); 7.01−7.08 (m 2H); 7.30−7.37 (m, 2H); 7.78−7.853 (m, 2H). Elemental analysis $C_{31}H_{46}O_6S \cdot 4H_2O$ calcd: C, 60.17; H, 8.80. Found: C, 60.03; H, 8.44.

Methyl 15-(4-(2-Fluoroethoxy)phenyl)pentadecanoate (6). Compound **4** (104 mg, 0.3 mmol), 1-bromo-2-fluoroethane (227 mg, 1.8 mmol), and potassium carbonate (246 mg, 1.8 mmol) were added into a flask containing acetone (40 mL). The reaction mixture was stirred at reflux under a nitrogen atmosphere for 18 h. Volatiles were removed under reduced pressure, and the residue was partitioned between ethyl acetate (60 mL) and water (20 mL). The organic layer was washed with brine, dried over sodium sulfate, filtered, and concentrated under reduced pressure. The residue was purified by silica gel column chromatography using ethyl acetate/hexane (v/v, 1/10) as the eluent to afford compound **6** as a white solid (115 mg, 98%): mp 66−67 °C. ^{1}H NMR (300 MHz, $CDCl_3$): δ 1.18−1.40 (m, 20H); 1.50−1.68 (m, 4H); 2.26−2.37 (t, 2H); 2.49−2.58 (t, 2H); 3.67 (s, 3H); 4.12−4.18 (t, 1H), 4.22−4.27 (t, 3H); 4.64−4.70 (t, 1H); 4.80−4.85 (t, 1H); 6.82−6.88 (m, 2H); 7.06−7.13 (m, 2H). Elemental analysis $C_{24}H_{39}FO_3$ calcd: C, 73.06; H, 9.96. Found: C, 73.30, H, 10.14.

5-(4-(2-Fluoroethoxy)phenyl)pentadecanoic Acid (7). Compound **6** (110 mg, 0.28 mmol) and NaOH (180 mg, 4.5 mmol) were dissolved into 11 mL of dichloromethane/methanol/water (5/5/1), and the reaction mixture was stirred at ambient temperature for 18 h. Solvents were removed under reduced pressure; the residue was acidified to pH 2.0 with 1 N aqueous HCl and extracted into ethyl acetate (3 × 20 mL). The organic layer was dried over sodium sulfate, filtered, and concentrated under reduced pressure to afford compound **7** as a white solid (95 mg, 89%): mp 84−85 °C. ^{1}H NMR (300 MHz, $CDCl_3$): δ 1.18−1.40 (m, 20H); 1.50−1.708 (m,4H); 2.30−2.39 (t, 2H); 2.49−2.58 (t, 2H); 4.12−4.17 (t, 1H), 4.21−4.37 (t, 3H); 4.64−4.70 (t, 1H); 4.80−4.85 (t, 1H); 6.81−6.88 (m, 2H); 7.06−7.13 (m, 2H). Elemental analysis $C_{23}H_{37}FO_3$ calcd: C, 75.29; H, 9.80. Found: C, 72.77; H, 9.82.

Radiochemistry. *Production of [^{18}F]Fluoride.* $H_2{}^{18}O$ was purchased from Rotem Industries (Israel). [^{18}F]Fluoride was produced in our institution by proton irradiation of enriched ^{18}O water (95%) [reaction: ^{18}O(p, n)^{18}F] using a Siemens Eclipse Cyclotron (Siemens Medical Systems, Inc., Knoxville, TN). ^{18}F-enriched $H_2{}^{18}O$ (up to 1500 mCi) was delivered from the Eclipse Cyclotron and transferred to the reaction vial through an anion-exchange column, Sep-Pak Light QMA. [^{18}F]fluoride was eluted from the Sep-Pak by addition of an aqueous solution of potassium carbonate (2 mg of K_2CO_3 in 0.5 mL of water) into the reactor vessel.

15-(4-(2-[^{18}F]fluoroethoxy)phenyl)pentadecanoic Acid ([^{18}F]7). [^{18}F]Fluoride (100−150 mCi) was added to a 10 mL Pyrex screw cap tube containing 5−6 mg of Kryptofix 2.2.2 and 1−2 mg of K_2CO_3. HPLC-grade acetonitrile (3 × 1.0 mL) was used to remove the water by azeotropic evaporation from this reaction vessel at 110 °C under a stream of nitrogen. After all the water was removed, a solution of precursor **11** (1−2 mg) in 0.25−0.30 mL acetonitrile was added. The tube was capped and heated at 110−115 °C for 5−10 min. This solution was diluted with 1.0 mL acetonitrile and passed through a silica gel Sep-Pak (Alltech Associates, Inc., Deerfield, IL) into a collection vial. An additional 2 mL of acetonitrile was used to rinse out the remaining radioactive product from the Sep-Pak into the above collection vial. Radio-thin-layer chromatography (radio-TLC) showed that the

Table 1. Distribution of [^{18}F]7 in Male Sprague−Dawley Rats (%ID/gram)[a]

	5 min	30 min	60 min	120 min
blood	0.76 ± 0.05	0.75 ± 0.06	0.56 ± 0.06	0.26 ± 0.06
lung	1.26 ± 0.32	0.87 ± 0.06	0.95 ± 0.27	0.52 ± 0.06
liver	2.71 ± 0.37	1.39 ± 0.09	0.81 ± 0.10	0.49 ± 0.07
spleen	0.94 ± 0.05	0.63 ± 0.07	0.57 ± 0.11	0.40 ± 0.06
kidney	1.30 ± 0.09	1.26 ± 0.08	1.02 ± 0.15	0.52 ± 0.07
muscle	0.23 ± 0.03	0.24 ± 0.04	0.21 ± 0.02	0.12 ± 0.01
fat[b]	0.14 ± 0.02	ND	0.17 ± 0.01	ND
heart	2.00 ± 0.44	0.72 ± 0.10	0.86 ± 0.28	0.34 ± 0.04
pancreas	0.73 ± 0.07	0.50 ± 0.03	0.42 ± 0.04	0.28 ± 0.02
brain	0.11 ± 0.01	0.13 ± 0.01	0.10 ± 0.01	0.06 ± 0.01
bone[b]	0.28 ± 0.01	ND	0.33 ± 0.06	ND

[a] Data are shown as mean ± std dev. [b] Results not determined (ND) for fat and bone at 30 and 60 min.

radiochemical purity was >95% on a Bioscan System 2000 system (Bioscan, Inc., Washington, DC). The acetonitrile was removed by a stream of nitrogen gas at 80−85 °C. [^{18}F]**6** was used directly in the next step, without further purification. 0.5 mL of ethanol and 0.2 mL of a 2 N NaOH aqueous solution were added into the above collection vessel containing dried [^{18}F]**6**. The vessel was heated at 80 °C for 2 min, and then 0.4 mL of 1 N aqueous HCl was added into the reaction mixture to neutralize the mixture to pH = 7.0. Acetonitrile (2 mL) was added, and the reaction mixture was loaded through a 0.45 μm filter into a high-performance liquid chromatography (HPLC) system equipped with an Alltech Econosil C18 reverse-phase column (10 × 250 mm) and eluted with acetonitrile/0.1 M ammonium formate buffer (v/v, 85/15) at a flow rate of 4.0 mL/min. A vial was used to collect the radioactive product from 24 to 25.5 min. The HPLC mobile-phase solution was concentrated under reduced pressure, and the residue was azeotroped with ethanol (2 × 1 mL) to remove the residual mobile phase. The labeled fatty acid [^{18}F]**7** was formulated in 6 mL of 3% human serum albumin (HSA) preincubated at 45 °C for 3 min and passed through 0.22 μm Millex-GP sterile syringe filter (cat no. SLMP025SS, Millipore, Billerica, MA) into a final dose vial. The dose sample was authenticated by coinjection with the corresponding cold standard onto an analytical HPLC system, which included an Alltech Econosil C18 column (10 μm, 250 mm × 4.6 mm), using acetonitrile/0.1 M ammonium formate buffer (v/v, 90/10) as mobile phase, 1.5 mL/min flow rate, and 274 nm UV wavelength. Under these conditions, the retention time of the product [^{18}F]**7** was 7.4 min. The total radiosynthesis took ~2 h; the labeling yield ranged 50−60% (decay corrected to EOB), radiochemical purity >95%, and specific activity >2000 Ci/mmol (decay corrected to EOB).

Biodistribution Studies. All animal experiments were conducted in compliance with the NIH Guidelines for the Care and Use of Research Animals under IACUC approved protocols reviewed by the Washington University School of Medicine Animal Studies Committee. The biodistribution of [^{18}F]**7** was performed in adult male Sprague−Dawley rats (170−250 g). Rats were anesthetized with 2−3% isoflurane/O_2, and [^{18}F]**7** (approximately 20−25 μCi/100 μL) was injected via the lateral tail vein. Rats were euthanized under anesthesia at 5, 30, 60, and 120 min post-injection, 4−8 rats for each time point. Samples of blood, lung, liver, kidney, spleen, muscle, heart, brain, and pancreas were removed from each rat, weighed, and counted in a Beckman Gamma 8000 counter. Bone and fat were taken only for the 5 and 60 min time points from 4 rats. A standard dilution of the injectate was counted with the samples from each animal. The biodistribution results were calculated as percent injected dose per gram of tissue (%ID/g) and are presented in Table 1.

MicroPET Studies. MicroPET imaging studies were performed in fasted male Sprague−Dawley rats using a microPET Focus 220 scanner. The rats were secured using a custom-designed acrylic restraining device, and placed inside the field of the window of the microPET Focus 220 scanner (*29, 30*). After a bolus injection of radiotracer via the right jugular catheter, microPET imaging studies of each rat were performed using 1 h dynamic data acquisition. The microPET studies were first conducted with [^{11}C]palmitate (0.30−0.40 mCi/150 μL). After a 1 h period for biological clearance and radioactive decay, [^{18}F]**7** (0.30−0.40 mCi/150 μL) was administered into the same rat, and a second microPET dynamic imaging scan was acquired. [^{11}C]Palmitate and [^{18}F]**7** blood time−activity curves were generated from dynamic PET images by placing one 3 × 3 voxel region of interest (ROI) on the left ventricle. Myocardial ROIs encompassing the anteriolateral myocardium were drawn on three consecutive PET slices as shown in Figure 2C,D.

RESULTS AND DISCUSSION

Chemistry. The synthesis of compound **7** is shown in Scheme 1. The ester **2** was made via O-alkylation of 15-bromopentadecanoic acid, **1**, with trimethylsilyl diazomethane in tetrahydrofuran as described in the literature (*31*). The Suzuki cross-coupling of **2** with 4-benzyloxyphenyboronic acid gave 15-(4-(benzyloxy)phenyl)pentadecanoic acid in modest yield (45%). The methyl group was removed from the ester **3**, because potassium *tert*-butoxide (KO-t-Bu) is a strong Lewis base that led to the hydrolysis of intermediate ester, methyl 15-(4-(benzyloxy)phenyl)pentadecanoate. It is of interest to note that, when the Suzuki cross-coupling reaction was directly performed between 15-bromopentadecanoic acid and 4-benzyloxyphenyboronic acid, no product was obtained. Esterification of 15-(4-(benzyloxy)phenyl)pentadecanoic acid in methanol with concentrated sulfuric acid as a catalyst afforded compound **3** in 78% yield. Removal of the benzyl group of **3** was accomplished by hydrogenolysis over 10% palladium-activated carbon to afford **4** in 75% yield. O-alkylation of the phenol group of **4** with 1-bromo-2-fluoroethane in acetone using potassium carbonate as the base afforded the fluoroethoxy ester **6** in high yield (98%). Hydrolysis of the ester group afforded the target compound **7** in 89% yield. Compound **5**, the precursor for making [^{18}F]**7**, was prepared via O-alkylation of **4** with ethylene glycol-1,2-bistosylate in acetonitrile using potassium carbonate as the base (87% yield) as shown in Scheme 1.

Radiochemistry. The radiosynthesis of the target compound [^{18}F]**7** was made using the two-step reaction sequence shown in Scheme 2. First, nucleophilic displacement of the tosylate group of ester **5** with [^{18}F]KF/Kryptofix 2.2.2 in acetonitrile afforded [^{18}F]**6**. Hydrolysis of the ester with aqueous sodium hydroxide followed by neutralization with aqueous hydrochloric acid and semipreparative HPLC gave the target fatty acid analogue, [^{18}F]**7**. The identity of the target compound was confirmed by coinjection with the cold standard **7** using an analytical HPLC system. Radiosynthesis and formulation of [^{18}F]**7** took approximately 2 h, with the yield ranging from 50% to 60%, the specific activity was >2000 mCi/μmol (decay corrected to the end of synthesis), and the radiochemical and chemical purities were >95% (n = 10). The radiosynthesis is straightforward and can be easily adapted to an automated synthesis module.

Radiosynthesis of [^{11}C]palmitate was performed as previously described (*32*).

Biodistribution Studies. The tissue distribution of [^{18}F]**7** in adult male Sprague−Dawley rats is shown in Table 1. At 5 min post-i.v. injection, the uptake of [^{18}F]**7** in the heart (2.00 ± 0.44%ID/g) and liver (2.71 ± 0.37%ID/g) was higher than that of any other tissues sampled. The ratio of activity in heart/nontarget tissues was 2.55:1 for blood and 8.3:1 for skeletal muscle. The brain had the lowest initial uptake of [^{18}F]**7**, 0.11 ± 0.01%ID/g; tracer uptake in fat activity was also very low, 0.14 ±

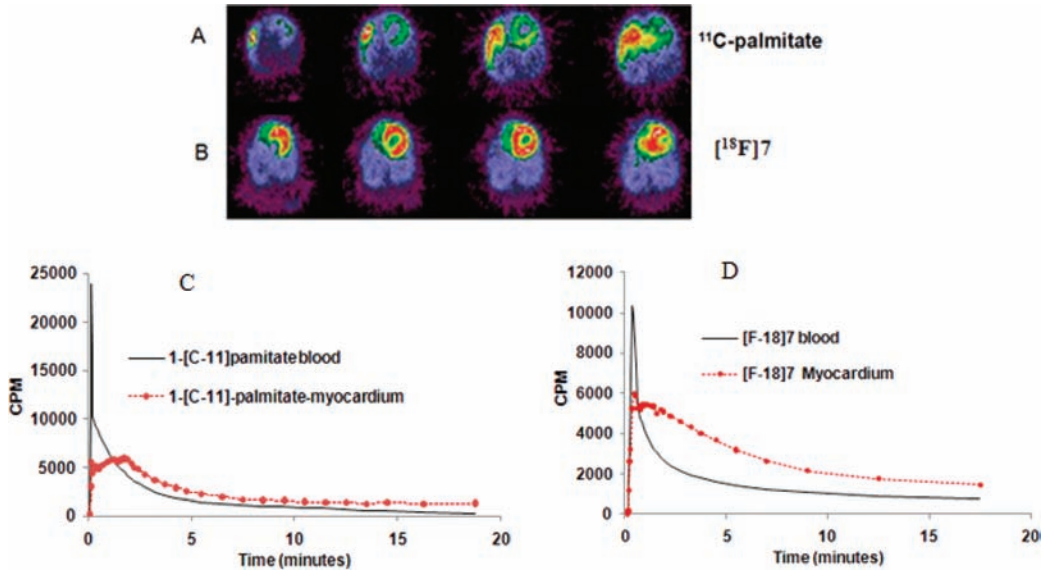
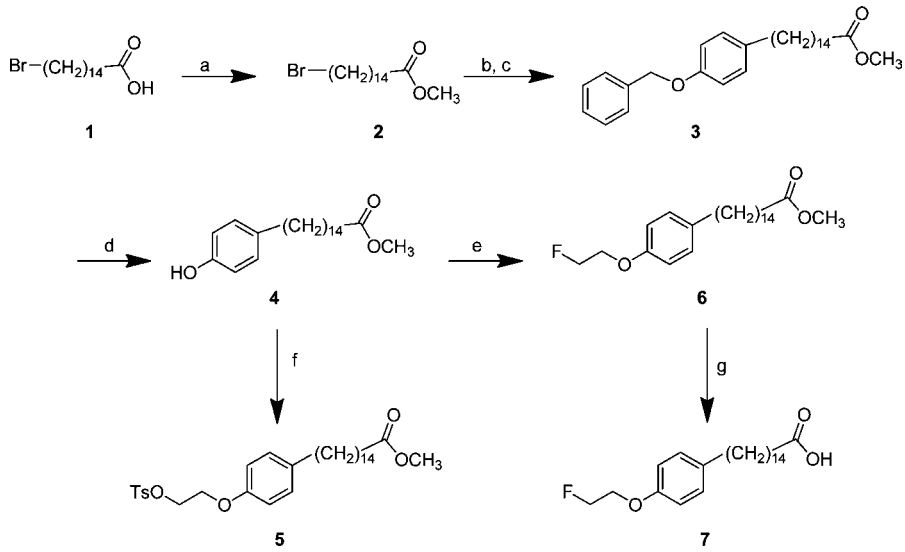


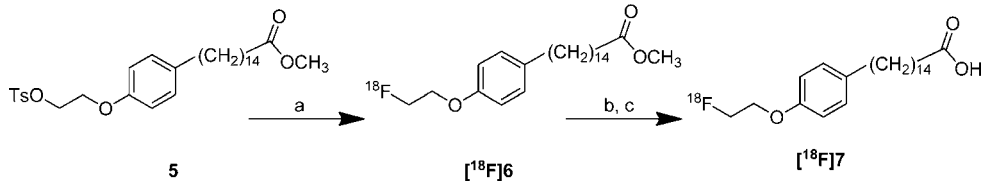
Figure 2. MicroPET imaging studies of [^{11}C]palmitate (panel A) and [^{18}F]**7** (panel B) in male Sprague−Dawley rats. Images are displayed on the transaxial axis and represent data acquired 20−30 min postinjection of the radiotracer. [^{18}F]**7** images display excellent quality and higher tracer accumulation than the [^{11}C]palmitate images. Tissue time−activity curve are shown in panel C for [^{11}C]palmitate and panel D for [^{18}F]**7**. Both radiotracers display biphasic washout kinetics, but some differences are noted. For example, when compared to [^{11}C]palmitate, [^{18}F]**7** exhibited an early plateau followed by a slower early tracer clearance (0.17 ± 0.01 vs 0.30 ± 0.02, $P < 0.0001$) and a significantly higher late clearance (0.0030 ± 0.0005 vs 0.0006 ± 0.00013, $P < 0.01$).

Scheme 1[a]



[a] Reagents and conditions: (a) trimethylsilyl diazomethane, THF, hexane, 2 h; (b) 4-benzyloxyphenylboronic acid, $Pd(OAc)_2$, $[HP(t\text{-}Bu)_2Me]BF_4$, KO-t-Bu, *t*-amyl alcohol, argon, RT; (c) 98% sulfuric acid, methanol; (d) Pd/c, EtOAc, H_2; (e) $BrCH_2CH_2F$, K_2CO_3, acetone; (f) $TsOCH_2CH_2OTs$, K_2CO_3, CH_3CN, reflux; (g) 2 N NaOH, aqueous MeOH. Synthesis of the precursor for radiolabeling and the HPLC standard.

Scheme 2[a]



[a] Reagents and conditions: (a) [^{18}F]F-, Kryptofix 2.2.2, K_2CO_3, CH_3CN, 80 °C; (b) 2 N NaOH/MeOH, H_2O; (c) 1 N HCl Radiosynthesis of [^{18}F]**7**.

0.02%ID/g. [^{18}F]**7** has a calculated log *P* value of 5.56 (ACD, Log D/suite 7.0). Consequently, this high lipophilicity will make it difficult to passively cross the blood−brain barrier, which explains the low uptake of [^{18}F]**7** in the brain. The 5 min uptake of [^{18}F]**7** in liver was 2.71 ± 0.37%ID/g, the only organ with higher uptake than that seen in heart. By 30 min post-injection, the uptake of [^{18}F]**7** in heart had decreased to 35% of the 5 min activity and remained stable between 30 and 60 min (0.72 ± 0.10 and 0.86 ± 0.28%ID/g, respectively). At 120 min, the uptake of [^{18}F]**7** in the heart remained 0.34 ± 0.04%ID/g, which

was approximately 1.4-fold higher than that in blood (0.26 ± 0.06% ID/g) at 120 min. Between 30 and 60 min, activity in blood, liver, and kidney continued to decrease, while activity levels in lung, heart, spleen, muscle, pancreas, and brain remained fairly stable. The increase in mean uptake of [^{18}F]**7** in lung and heart from 30 to 60 min was within experimental error and was not significant (*P* values comparing the 30 and 60 min time points using the Students *t* test were 0.56 for lung and 0.66 for heart). Bone and fat were taken only at the 5 and 60 min time points. Although the activity in fat increased 20% (from 0.14 ± 0.02 to 0.17 ± 0.01%ID/g, Student's *t* test *P* value = 0.04), there was no significant accumulation of [^{18}F]**7** activity in bone between 5 and 60 min (from 0.28 ± 0.01 to 0.33 ± 0.06%ID/g, Student's *t* test *P* value = 0.14). These data indicate that there was no significant metabolic defluorination during the period of time needed for PET data acquisition.

MicroPET Studies. MicroPET imaging studies in adult male Sprague−Dawley rats ($N = 3$) were also conducted in order to compare the myocardial uptake of [^{18}F]**7** with that of [^{11}C]palmitate. Representative myocardial microPET images obtained from same rat are displayed in Figure 2A when using [^{11}C]palmitate and Figure 2B when using [^{18}F]**7**. Images are displayed on the transaxial axis and represent data acquired 20−30 min postinjection. [^{18}F]**7** images displayed excellent quality and higher tracer activity than the corresponding [^{11}C]palmitate images. PET images were consistent with the biodistribution data and showed no evidence of accumulation in bone. Because the biological half-life of [^{11}C]palmitate in human heart is short, a tissue time−activity curve for 0−20 min provides sufficient information for measuring the kinetics of fatty acid metabolism (*33*). To be consistent, Figure 2C,D displays 0−20 min tissue time−activity curves for both radiotracers. [^{18}F]**7** exhibited significant tracer uptake in the heart and a rapid biphasic washout. However, some differences were noted when the data were compared with the time−activity curves of [^{11}C]palmitate. For example, [^{18}F]**7** exhibited an early plateau followed by a slower early tracer clearance (0.17 ± 0.01 vs 0.30 ± 0.02, $P < 0.0001$) and a significantly higher late clearance (0.0030 ± 0.0005 vs 0.0006 ± 0.00013, $P < 0.01$). Studies to determine if the differences in washout kinetics of [^{18}F]**7** versus [^{11}C]palmitate reflect a difference in fatty acid metabolism or are due to the position of the radiolabel (C-1 position in [^{11}C]palmitate vs *p*-position of the benzene ring in [^{18}F]**7**) are currently ongoing in our group.

CONCLUSION

We have successfully synthesized the fatty acid analogue [^{18}F]**7** with good yield, high radiochemical purity, and high specific activity. The initial biodistribution and microPET imaging studies of [^{18}F]**7** in rats indicate that [^{18}F]**7** displays a high uptake in heart and good contrast vs blood and other tissues. The initial microPET studies of [^{18}F]**7** in male Sprague−Dawley rats indicated that the tissue time−activity of [^{18}F]**7** displays rapid biphasic washout kinetics similar to that of [^{11}C]palmitate.

There is a compelling need for widely applicable radiotracer method that provides accurate and comprehensive measurements of myocardial fatty acid metabolism in humans. Current radiotracers are limited by their lack of quantitative capability (e.g., [^{123}I]BMIPP),[1] inability to track various aspects of fatty acid metabolism (e.g., ([^{18}F]FTHA or [^{18}F]FTP) or widespread applicability (e.g., [^{11}C]palmitate). The availability of [^{18}F]**7** combined with appropriate image analysis tools should overcome these limits. The availability of these methods will facilitate the identification of relevant fatty acid metabolic biomarkers predictive of the presence and/or progression of cardiac disease and to evaluate specific therapeutic strategies. Once these data are obtained, the usefulness of this radiotracer technique in the clinical management of patients could be determined. Moreover, PET studies with [^{18}F]**7** could be used to measure fatty acid metabolism in other organs such as skeletal muscle and liver. Thus, the impact on human health of an ^{18}F-labeled radiotracer for measuring fatty acid metabolism could be further expanded by enabling the study of other common diseases where alterations in cellular fatty acid metabolism are central to disease pathophysiology, such as insulin resistance syndrome and nonalcoholic fatty liver disease.

[1]Abbreviations: BMIPP, [^{123}I]β-methyl iodophenylpentadecanoic acid; [^{11}C]palmitate, [^{11}C]palmitic acid; [^{18}F]FCPHA, trans-9(*RS*)-[^{18}F]fluoro-3,4(*RS,RS*) methyleneheptadecanoic acid; [^{18}F]FTHA, 14(*R,S*)-[^{18}F]fluoro-6-thia-heptadecanoic acid; [^{18}F]FTP, 16-[^{18}F]fluoro-4-thia-palmitate; HPLC, high-performance liquid chromatography; %ID/g, percent injected dose per gram; IPPA, 15-(*para*-iodophenyl)-pentadecanoic acid; MP, melting point; ND, not determined; PPARα, peroxisome proliferator-activated receptor alpha; PET, positron emission tomography; SPECT, single photon emission computed tomography; TLC, thin layer chromatography; TMS, tetramethylsilane.

ACKNOWLEDGMENT

This research was supported by NIH grant HL69100 (RJG). The authors gratefully thank the staff of the Washington University Cyclotron Facility and the Washington University Small Animal Imaging Facility for their excellent technical assistance.

LITERATURE CITED

(1) Yoshinaga, K., and Tamaki, N. (2007) Imaging myocardial metabolism. *Curr. Opin. Biotechnol. 18*, 52–59.
(2) Wisneski, J. A., Gertz, E. W., Neese, R. A., and Mayr, M. (1987) Myocardial metabolism of free fatty acids. Studies with ^{14}C-labeled substrates in humans. *J. Clin. Invest. 79*, 359–366.
(3) Mathur, A., Subramanian, S., Mallia, M. B., Banerjee, S., Samuel, G., Sarma, H. D., and Venkatesh, M. (2008) Synthesis and bio-evaluation of a new fatty acid derivative for myocardial imaging. *Bioorg. Med. Chem. 16*, 7927–7931.
(4) Gropler, R. J. (2009) PET radiotracers of the cardiovascular system. *PET Clinics 4*, 69–87.
(5) Shi, C. Q., Young, L. H., Daher, E., DiBella, E. V. R., Liu, Y.-H., Heller, E. N., Zoghbi, S., Wackers, F. J. T., Soufer, R., and Sinusas, A. J. (2002) Correlation of myocardial p-^{123}I-iodophenylpentadecanoic acid retention with ^{18}F-FDG accumulation during experimental low-flow ischemia. *J. Nucl. Med. 43*, 421–431.
(6) Behnam Azad, B., Rota, V. A., Breadner, D., Dhanvantari, S., and Luyt, L. G. (2010) Design, synthesis and in vitro characterization of Glucagon-Like Peptide-1 derivatives for pancreatic beta cell imaging by SPECT. *Bioorg. Med. Chem. 18*, 1265–1272.
(7) Peterson, L. R., Herrero, P., Schechtman, K. B., Racette, S. B., Waggoner, A. D., Kisrieva-Ware, Z., Dence, C., Klein, S., Marsala, J., Meyer, T., and Gropler, R. J. (2004) Effect of obesity and insulin resistance on myocardial substrate metabolism and efficiency in young women. *Circulation 109*, 2191–2196.
(8) Peterson, L. R., and Gropler, R. J. (2010) Radionuclide imaging of myocardial metabolism. *Circ. Cardiovasc. Imaging 3*, 211–222.
(9) Bashir, A., and Gropler, R. J. (2009) Translation of myocardial metabolic imaging concepts into the clinics. *Cardiol. Clin. 27*, 291–310.
(10) Holness, M. J., Samsuddin, S., and Sugden, M. C. (2009) The role of PPARs in modulating cardiac metabolism in diabetes. *Pharmacol. Res. 60*, 185–194.
(11) Burkart, E. M., Sambandam, N., Han, X., Gross, R. W., Courtois, M., Gierasch, C. M., Shoghi, K., Welch, M. J., and Kelly, D. P. (2007) Nuclear receptors PPARβ/δ and PPARα direct distinct metabolic regulatory programs in the mouse heart. *J. Clin. Invest. 117*, 3930–3939.
(12) Shoghi, K. I., Gropler, R. J., Sharp, T., Herrero, P., Fettig, N., Su, Y., Mitra, M. S., Kovacs, A., Finck, B. N., and Welch,

M. J. (2008) Time course of alterations in myocardial glucose utilization in the Zucker diabetic fatty rat with correlation to gene expression of glucose transporters: a small-animal PET investigation. *J. Nucl. Med. 49*, 1320–1327.

(13) Otto, C. A., Brown, L. E., Wieland, D. M., and Beierwaltes, W. H. (1981) Radioiodinated fatty acids for myocardial imagine: effects on chain length. *J. Nucl. Med. 22*, 613–618.

(14) Renstrom, B., Rommelfanger, S., Stone, C. K., DeGrado, T. R., Carlson, K. J., Scarbrough, E., Nickles, R. J., Liedtke, A. J., and Holden, J. E. (1998) Comparison of fatty acid tracers FTHA and BMIPP during myocardial ischemia and hypoxia. *J. Nucl. Med. 39*, 1684–1689.

(15) Kudoh, T., Tadamura, E., Tamaki, N., Hattori, N., Inubushi, M., Kubo, S., Magata, Y., Nishimura, K., Matsuda, K., and Konishi, J. (2000) Iodinated free fatty acid and ^{201}Tl uptake in chronically hypoperfused myocardium: histologic correlation study. *J. Nucl. Med. 41*, 293–296.

(16) Eckelman, W., and Babich, J. (2007) Synthesis and validation of fatty acid analogs radiolabeled by nonisotopic substitution. *J. Nucl. Cardiol. 14*, S100–S109.

(17) Bergmann, S. R., Weinheimer, C. J., Markham, J., and Herrero, P. (1996) Quantitation of myocardial fatty acid metabolism using PET. *J. Nucl. Med. 37*, 1723–1730.

(18) Davila-Roman, V. G., Vedala, G., Herrero, P., de las Fuentes, L., Rogers, J. G., Kelly, D. P., and Gropler, R. J. (2002) Altered myocardial fatty acid and glucose metabolism in idiopathic dilated cardiomyopathy. *J. Am. Coll. Cardiol. 40*, 271–277.

(19) Herrero, P., Peterson, L. R., McGill, J. B., Matthew, S., Lesniak, D., Dence, C., and Gropler, R. J. (2006) Increased myocardial fatty acid metabolism in patients with type 1 diabetes mellitus. *J. Am. Coll. Cardiol. 47*, 598–604.

(20) Stone, C. K., Pooley, R. A., DeGrado, T. R., Renstrom, B., Nickles, R. J., Nellis, S. H., Liedtke, A. J., and Holden, J. E. (1998) Myocardial uptake of the fatty acid analog 14-fluorine-18-fluoro-6- thia-heptadecanoic acid in comparison to beta-oxidation rates by tritiated palmitate. *J. Nucl. Med. 39*, 1690–1696.

(21) Takala, T. O., Nuutila, P., Katoh, C., Luotolahti, M., Bergman, J., Maki, M., Oikonen, V., Ruotsalainen, U., Gronroos, T., Haaparanta, M., Kapanen, J., and Knuuti, J. (1999) Myocardial blood flow, oxygen consumption, and fatty acid uptake in endurance athletes during insulin stimulation. *Am. J. Physiol. Endocrinol. Metab. 277*, E585−E590.

(22) Degrado, T. R., Wang, S., Holden, J. E., Nickles, R. J., Taylor, M., and Stone, C. K. (2000) Synthesis and preliminary evaluation of ^{18}F-labeled 4-thia palmitate as a PET tracer of myocardial fatty acid oxidation. *Nucl. Med. Biol. 27*, 221–231.

(23) Taylor, M., Wallhaus, T. R., Degrado, T. R., Russell, D. C., Stanko, P., Nickles, R. J., and Stone, C. K. (2001) An evaluation of myocardial fatty acid and glucose uptake using PET with [^{18}F]fluoro-6-thia-heptadecanoic acid and [^{18}F]FDG in patients with congestive heart failure. *J. Nucl. Med. 42*, 55–62.

(24) Wallhaus, T. R., Taylor, M., DeGrado, T. R., Russell, D. C., Stanko, P., Nickles, R. J., and Stone, C. K. (2001) Myocardial free fatty acid and glucose use after carvedilol treatment in patients with congestive heart failure. *Circulation 103*, 2441–2446.

(25) Takala, T. O., Nuutila, P., Pulkki, K., Oikonen, V., Gronroos, T., Savunen, T., Vahasilta, T., Luotolahti, M., Kallajoki, M., Bergman, J., Forsback, S., and Knuuti, J. (2002) 14(R, S)-[^{18}F]Fluoro-6-thia-heptadecanoic acid as a tracer of free fatty acid uptake and oxidation in myocardium and skeletal muscle. *Eur. J. Nucl. Med. Mol. Imaging 29*, 1617–1622.

(26) Shoup, T. M., Elmaleh, D. R., Bonab, A. A., and Fischman, A. J. (2005) Evaluation of trans-9−^{18}F-fluoro-3,4-methylene-heptadecanoic acid as a PET tracer for myocardial fatty acid imaging. *J. Nucl. Med. 46*, 297–304.

(27) DeGrado, T. R., Kitapci, M. T., Wang, S., Ying, J., and Lopaschuk, G. D. (2006) Validation of ^{18}F-fluoro-4-thia-palmitate as a PET probe for myocardial fatty acid oxidation: effects of hypoxia and composition of exogenous fatty acids. *J. Nucl. Med. 47*, 173–181.

(28) Kim, D. H., Choe, Y. S., Choi, J. Y., Choi, Y., Lee, K. H., and Kim, B. T. (2009) 17-[4-(2-[^{18}F]fluoroethyl)-1H-1,2,3-triazol-1-yl]-6-thia-heptadecanoic acid: a potential radiotracer for the evaluation of myocardial fatty acid metabolism. *Bioconjugate Chem. 20*, 1139–1145.

(29) Welch, M. J., Lewis, J. S., Kim, J., Sharp, T. L., Dence, C. S., Gropler, R. J., and Herrero, P. (2006) Assessment of myocardial metabolism in diabetic rats using small-animal PET: A feasibility study. *J. Nucl. Med. 47*, 689–697.

(30) Shoghi, K. I., Gropler, R. J., Sharp, T., Herrero, P., Fettig, N., Su, Y., Mitra, M. S., Kovacs, A., Finck, B. N., and Welch, M. J. (2008) Time course of alterations in myocardial glucose utilization in the Zucker diabetic fatty rat with correlation to gene expression of glucose transporters: a small-animal PET investigation. *J. Nucl. Med. 49*, 1320–1327.

(31) Salomon, A., Arad-Yellin, R., Shanzer, A., Karton, A., and Cahen, D. (2004) Stable room-temperature molecular negative differential resistance based on molecule-electrode interface chemistry. *J. Am. Chem. Soc. 126*, 11648–11657.

(32) Welch, M. J., Dence, C. S., Marshall, D. R., and Kilbourn, M. R. (1983) Remote system for production of carbon-11 labeled palmitic acid. *J. Label. Compd. Radiopharm. 20*, 1087–1095.

(33) Knuuti, J., Takala, T. O., Nagren, K., Sipila, H., Turpeinen, A. K., Uusitupa, M. I., and Nuutila, P. (2001) Myocardial fatty acid oxidation in patients with impaired glucose tolerance. *Diabetologia 44*, 184–187.

BC100343H

Multicolor Protein Labeling in Living Cells Using Mutant β-Lactamase-Tag Technology

Shuji Watanabe,[†] Shin Mizukami,[†,‡] Yuichiro Hori,[†] and Kazuya Kikuchi*[,†,‡]

Division of Advanced Science and Biotechnology, Graduate School of Engineering, and Immunology Frontier Research Center, Osaka University, 2-1 Yamadaoka, Suita, Osaka, 565-0871, Japan. Received July 29, 2010; Revised Manuscript Received September 21, 2010

Protein labeling techniques using small molecule probes have become important as practical alternatives to the use of fluorescent proteins (FPs) in live cell imaging. These labeling techniques can be applied to more sophisticated fluorescence imaging studies such as pulse-chase imaging. Previously, we reported a novel protein labeling system based on the combination of a mutant β-lactamase (BL-tag) with coumarin-derivatized probes and its application to specific protein labeling on cell membranes. In this paper, we demonstrated the broad applicability of our BL-tag technology to live cell imaging by the development of a series of fluorescence labeling probes for this technology, and the examination of the functions of target proteins. These new probes have a fluorescein or rhodamine chromophore, each of which provides enhanced photophysical properties relative to coumarins for the purpose of cellular imaging. These probes were used to specifically label the BL-tag protein and could be used with other small molecule fluorescent probes. Simultaneous labeling using our new probes with another protein labeling technology was found to be effective. In addition, it was also confirmed that this technology has a low interference with respect to the functions of target proteins in comparison to GFP. Highly specific and fast covalent labeling properties of this labeling technology is expected to provide robust tools for investigating protein functions in living cells, and future applications can be improved by combining the BL-tag technology with conventional imaging techniques. The combination of probe synthesis and molecular biology techniques provides the advantages of both techniques and can enable the design of experiments that cannot currently be performed using existing tools.

INTRODUCTION

Recent prominent advances in fluorescence imaging techniques enabled investigations of direct localization and trafficking of biomolecules in living cells. Genetic engineering has also been progressing dramatically and provides methods for expressing various proteins in specific organelles in cells. Fusion proteins prepared by linkage of fluorescent proteins (FPs) can be used to obtain tools for imaging any protein of interest (POI) (*1*). However, it is difficult to use FPs in pulse-chase imaging studies for investigating protein function over time within the space inside a living cell and to optimize fluorescence properties such as emission and excitation wavelengths, extinction coefficients, and photostability for various experiments. Moreover, certain FPs tend to form protein aggregates that affect the function and/or localization of the target POIs (*2, 3*).

Protein labeling methods using small molecule probes have attracted great attention because they may have the ability to overcome the limitations of FPs. Several methods for labeling proteins with small molecules have been commercialized, including Lumio-tag (*4*−*6*), HaloTag (*7*), SNAP-tag (*8*−*10*), and DHFR-based tag (*11*). Lumio-tag, using FlAsH or ReAsH, is based upon a fluorescent biarsenical dye that reacts with tetracysteine peptide and generates strong fluorescence. HaloTag is a modified haloalkane dehalogenase designed to covalently react with synthetic haloalkyl ligands. SNAP-tag utilizes human O^6-alkylguanine-DNA-alkyltransferase (hAGT) as the protein tagged with synthetic benzylguanine derivatives. DHFR-based tag employs the noncovalent interaction between *Escherichia coli* dihydrofolate reductase and fluorescently labeled methotrexate. Other protein labeling methods based on biotin ligase (*12*), transglutaminase (*13*), hexahistidine (*14*), and tetraaspartic acid (*15*) have also been reported.

The advantages of synthetic fluorescent probes are tunable switches for changes in fluorescence characteristics. These probes have intense fluorescence properties and provide a wide range of choices in fluorophores. Meanwhile, the advantages of using protein expression systems are provided by specific expression in cellular components and tissues, convenient experimental procedures, and the potential for in vivo studies using transgenic mice. Combining the advantages of both techniques is expected to provide enhanced methods for exploring molecular functions in biological systems.

For incorporation of the tunable switches in expressed protein tags, we previously reported a specific protein labeling system with an off/on fluorescence switch that employs a mutant enzyme and its specific substrate. The system involves covalent modification of a mutant β-lactamase (BL-tag) with a rationally designed fluorogenic probe based on fluorescence resonance energy transfer (FRET) (*16*). β-Lactamases are members of a family of bacterial enzymes that efficiently cleave β-lactam moieties within compounds such as penicillins and cephalosporins (*17*). Since the activity of β-lactamases is not observed in eukaryotic cells, these proteins have been widely exploited as reporter enzymes in living mammalian cells (*18*−*20*). Furthermore, their three-dimensional structures, catalytic mechanism, and inhibitors have been widely studied because of their clinical importance (*21*). A well-characterized isoform is the 29 kDa TEM-1 β-lactamase from *Escherichia coli* categorized as a class A β-lactamase (*22*).

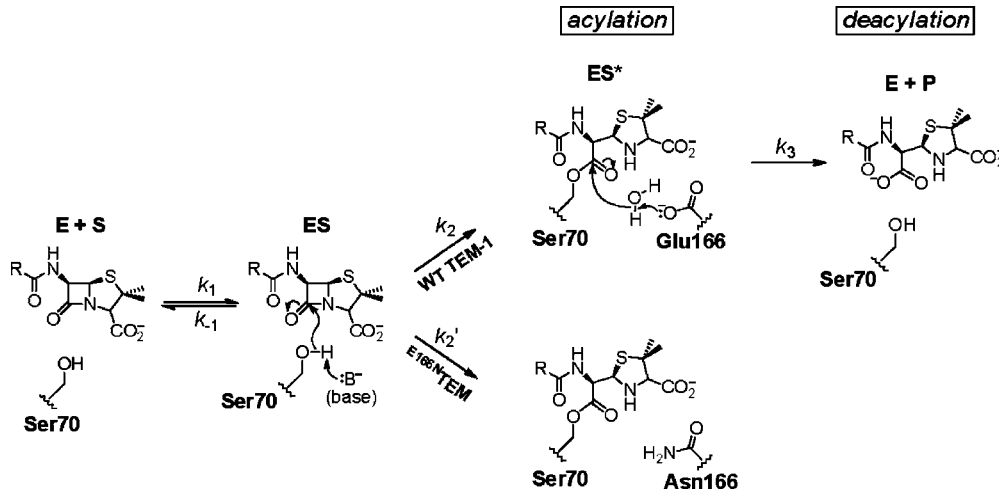
* E-mail: kkikuchi@mls.eng.osaka-u.ac.jp. Phone: +81-6-6879-7924. Fax: +81-6-6879-7875.

[†] Division of Advanced Science and Biotechnology.

[‡] Immunology Frontier Research Center.

10.1021/bc100333k © 2010 American Chemical Society
Published on Web 10/20/2010

Scheme 1. Reaction Mechanism of Wild-Type (WT) and Mutant (E166N) TEM-1 β-Lactamase



The reaction of wild-type (WT) TEM-1 with β-lactams involves acylation and deacylation steps (Scheme 1). Nucleophilic attack on the β-lactam ring by Ser70 leads to the covalent acyl-enzyme intermediate. In WT TEM-1, Glu166 acts as a base to catalyze hydrolysis of the intermediate (*23*), resulting in release of the product and regeneration of WT TEM-1. In ^{E166N}TEM, Asn166 is ineffective as a base; hence, the intermediate accumulates as a stable covalent adduct (*24*).

According to the above-mentioned mechanism, we have reported a novel protein labeling system with an off−on fluorescence switch based on a combination of a mutant β-lactamase (BL-tag) and coumarin-based substrates. Owing to the rational design of both the tag protein and the labeling probes, this system enabled us to simultaneously achieve specific and fluorogenic labeling of the target protein on living cells (*16*). In our previous report, we designed and synthesized both a simple fluorescent labeling probe, designated CA, and a fluorogenic probe, designated CCD. CA is a 7-hydroxycoumarin−ampicillin conjugate and CCD includes three main components; 7-hydroxycoumarin, cephalosporin, and DABCYL. The fluorescence of CCD is largely quenched by intramolecular FRET from coumarin to DABCYL. Cleavage of the cephalosporin β-lactam ring produces a free amino group, which triggers spontaneous elimination of any leaving group previously attached to the 3′ position (*25*). Consequently, fluorogenic labeling with CCD of fusion proteins of ^{E166N}TEM (BL-tag) was successfully performed in vitro and on the surfaces of living cells.

In this paper, we demonstrated the broad applicability of this labeling technology for live cell imaging experiments by developing a series of labeling probes with various fluorophores. We also show that this technology has a low interference with respect to the functions of EGFR and is orthogonal to another currently used protein labeling method.

EXPERIMENTAL PROCEDURES

Fluorometric Analysis. The slit width was 2.5 nm for both excitation and emission, and the photomultiplier voltage was 700 V. All fluorescent probes were dissolved in DMSO to obtain 10 mM stock solutions, and these solutions were diluted to the desired final concentrations with an appropriate aqueous buffer solution. Relative fluorescence quantum yields of the compounds were obtained by comparing the area under the emission spectrum of the sample with that of an EtOH solution of rhodamine B, which has a quantum efficiency of 0.97 when excited at 545 nm (*26*), and with that of a 100 mM NaOH solution of fluorescein, which has a quantum efficiency of 0.85 when excited at 492 nm (*27*).

Calculation of Förster Distance (R_0) and Energy Transfer Efficiency (E). For evaluation of R_0 and E, a revised version of the Förster formula was used (*28*)

$$R_0 = 9.78 \times 10^3(\Phi_D \kappa^2 n^{-4} J)^{1/6} \quad \left(J = \int_0^\infty f_D(\lambda)\varepsilon_A\lambda^4\, d\lambda\right)$$

$$E = R_0^6/(R_0^6 + R^6)$$

where R_0 is expressed in Å units, κ^2 is the orientation factor, Φ_D is the donor quantum yield in the absence of acceptor, n is the refractive index of the medium, $f_D(\lambda)$ is the normalized donor emission spectrum, $\varepsilon_A(\lambda)$ is the acceptor molar absorption coefficient in M^{-1} cm^{-1} units, and R is the donor−acceptor distance. The wavelength is expressed in nanometer units. The value $\kappa^2 = 2/3$, which corresponds to a dynamic isotropic regime, was assumed and $n = 1.33$ was applied. The molar absorption coefficient (ε) of DABCYL was 25 500 ($\lambda = 462$ nm) in 100 mM HEPES buffer (pH 7.4). R_0 values were calculated for the CA-DABCYL pair for CCD, the FA-DABCYL pair for FCD, and the RA-DABCYL pair for RCD. The quantum yields (Φ_D) of the compounds were 0.40 for CA, 0.71 for FA, and 0.49 for RA. The donor−acceptor distance (R) was evaluated by using the integrated molecular modeling packages *Maestro* v 8.5 and *MacroModel* v 9.6.

HPLC Analysis. HPLC analyses were performed with an Inertsil ODS-3 (4.6 × 250 mm) column (GL Sciences Inc.) using an HPLC system that comprises a pump (PU-2080, JASCO) and a detector (MD-2010 or FP-2020, JASCO). Preparative HPLC was performed with an Inertsil ODS-3 (10.0 × 250 mm) column (GL Sciences Inc.) using an HPLC system that comprises a pump (PU-2087, JASCO) and a detector (UV-2075, JASCO).

Fluorescence Microscopy. Fluorescence microscopic images were recorded using a IX71 fluorescence microscope (Olympus), a Cool Snap HQ cooled CCD camera (Roper Scientific), and a USH-103OL mercury lamp (Olympus). The filter sets used were Olympus BP330-385, DM455, and BA455 for Hoechst 33342 and coumarin derivatives; BP470-495, DM505, and BA510-550 for fluorescein derivatives; and BP510-550, DM575, and BA575-625 for rhodamine derivatives. *MetaMorph* imaging software (Universal Imaging Corporation) was used for imaging and data analysis.

Detection of Protein Labeling by SDS-PAGE. WT TEM-1 or ^{E166N}TEM (*16*) (20 μM) was added to a solution of probes (30 μM) in 100 mM HEPES buffer (pH 7.4) at 25 °C. After 30 min, the labeled protein was denatured in 2 × SDS gel loading buffer (100 mM Tris−HCl buffer (pH 6.8), 2.5% SDS, 20%

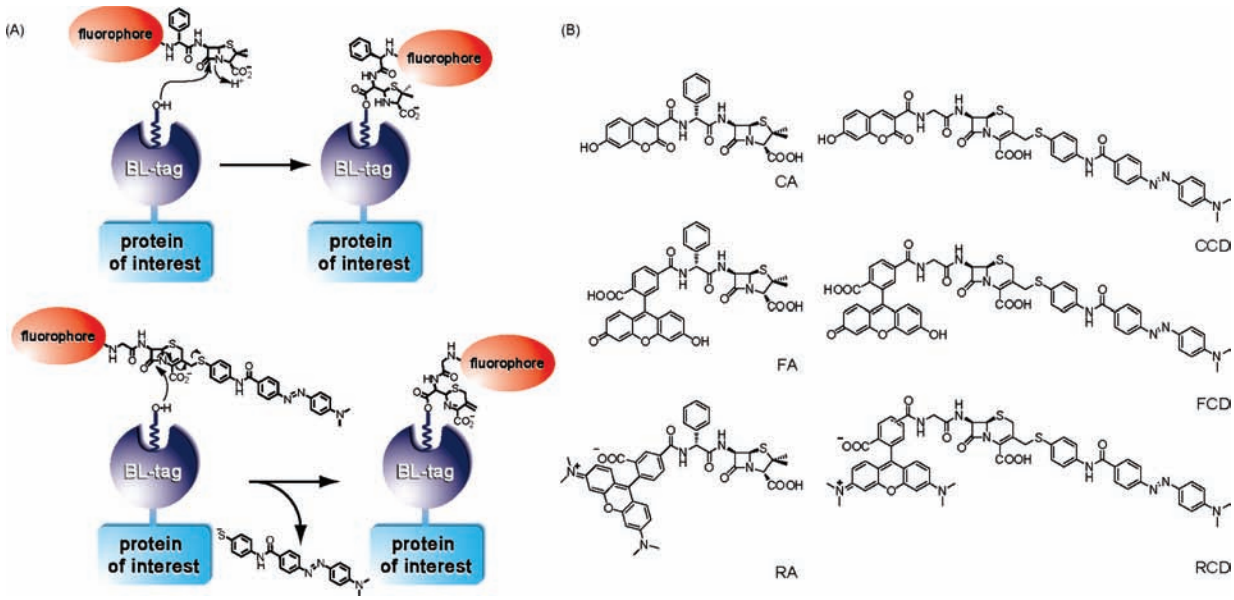


Figure 1. (A) General labeling mechanisms of the ampicillin- and cephalosporin-based probes. (B) Structures of β-lactam derivatives used for fluorescence labeling of BL-tag fusion proteins.

glycerol, and 10% mercaptoethanol) and resolved by NuPAGE (12% bis-Tris gel, Invitrogen). The fluorescence images of the gels were captured using a digital camera (Nikon COOLPIX P6000). The gels were stained with Coomassie Brilliant Blue prior to the capture of images.

Labeling of Cell Surface pcDNA3.1(+)-^{E166N}TEM-EGFR (BL-EGFR) with Various Probes. HEK293T cells maintained in 10% FBS in DMEM (Invitrogen) at 37 °C under 5% CO_2 were transfected with a plasmid coding for BL-EGFR, which was prepared as described previously (*16*), using Lipofectamine 2000 (Invitrogen). After 5−6 h, the culture medium was replaced with DMEM (without phenol red), and the cells were incubated at 37 °C for 24 h. The cells were then washed three times with DMEM (without phenol red) and incubated with 10 μM labeling probes in a CO_2 incubator for 30 min for CA, FA, and RA, or for 2 h for CCD and FCD. The cell nuclei were co-stained with Hoechst 33342 (100 ng mL^{-1}). After washing with DMEM containing 10% FBS, cells were incubated with HBSS, and the fluorescence images were captured with appropriate filter sets for each of the fluorophores.

Analysis of Fluorescence Images. Labeled cell images with CA, CCD, FA, and RA were acquired according to the above-mentioned procedure. 256 × 256 pixels area, where cells were confluently cultured, was selected at random from the acquired fluorescence images. The average fluorescence intensity of different colors per pixel was computed from the selected area using *MetaMorph* imaging software.

Multilabeling of Cells with BL-tag and SNAP-tag. Plasmids coding for BL-EGFR and COX8-2-SNAP were co-transfected into HEK293T cells. The cells were then incubated with FA, SNAP-Cell TMR Star, and Hoechst 33342 in a CO_2 incubator for 30 min (final concn of FA, 10 μM; SNAP-Cell TMR Star, 0.8 μM; Hoechst 33342, 100 ng mL^{-1}), and the fluorescence images were captured. The detailed procedure was the same as the procedure followed for the single protein labeling.

Western Blot Analysis of EGFR and BL-EGFR Expressed in HEK293T Cells after EGF Stimulation. HEK293T cells were transfected with BL-EGFR or pcDNA3.1(+)-EGFR using Lipofectamine 2000. After 5−6 h, the culture medium was replaced with DMEM, and the cells were incubated at 37 °C for 24 h. Prior to EGF addition, the cells were incubated overnight in the medium containing 0.5% serum. The cells were then washed once with PBS (−) and treated with EGF (100 ng mL^{-1}, Sigma, E9644) for 10 min at 25 °C. After one rinse with PBS (−), the cells were lysed with 200 μL of 1× SDS gel loading buffer (50 mM Tris−HCl buffer (pH 6.8), 1.3% SDS, 10% glycerol, and 5% mercaptoethanol). After scraping, the lysates were boiled at 95 °C for 3 min. Subsequently, samples were electrophoresed in a 7.5% or 10% SDS-polyacrylamide gel and transferred to PVDF membranes for Western blot. Membranes were blocked by 1 h incubation with TBST buffer (0.01% Tween 20, 138 mM NaCl, 20 mM Tris, pH 7.6) containing 5% skim milk (for anti-EGFR, anti-β-lactamase, and anti-β-actin antibodies) or 3% BSA (for anti-EGFR-pY1197 antibody) at room temperature. Then, anti-EGFR (1:500 dilution), anti-β-lactamase (1:5000 dilution), anti-EGFR-pY1197 (1:500 dilution), or anti-β-actin (1:5000 dilution) antibodies were added to each membrane. After incubation for 16 h at 4 °C with shaking, the membranes were washed three times with TBST buffer, incubated with horseradish peroxidase-linked secondary antibody, washed with TBST buffer, and visualized using ECL Western blotting detection reagents.

Immunofluorescence Detection of the Tyrosine Phosphorylation on BL-EGFR after EGF Stimulation. Transfected HEK293T cells were prepared and treated with EGF according to the above-mentioned procedure. After one rinse with PBS(−), the cells were fixed with 3.7% formaldehyde/PBS(−) at 25 °C for 20 min. After two rinses with PBS(−), the cells were blocked with blocking buffer (PBS containing 5% Goat Serum (Invitrogen) and 0.05% NaN_3) at 25 °C for 1 h. Anti-EGFR-pY1197 antibody, followed by fluorescein-conjugated goat antimouse antibody, was used to stain BL-EGFR or EGFR. After mounting, microscopic images were acquired using a filter set for fluorescein.

RESULTS AND DISCUSSION

Design and Synthesis of Fluorophores for the Labeling of BL-tag Fusion Proteins. Although it was previously shown that BL-tag fusion proteins can be specifically labeled with 7-hydroxycoumarin-conjugated β-lactam probes (Figure 1), the fluorescence was found to be dim and the excitation wavelength was short and hindered by the intrinsic autofluorescence of mammalian cells. The use of brighter and longer-excitation wavelength fluorophores is advantageous for various functional

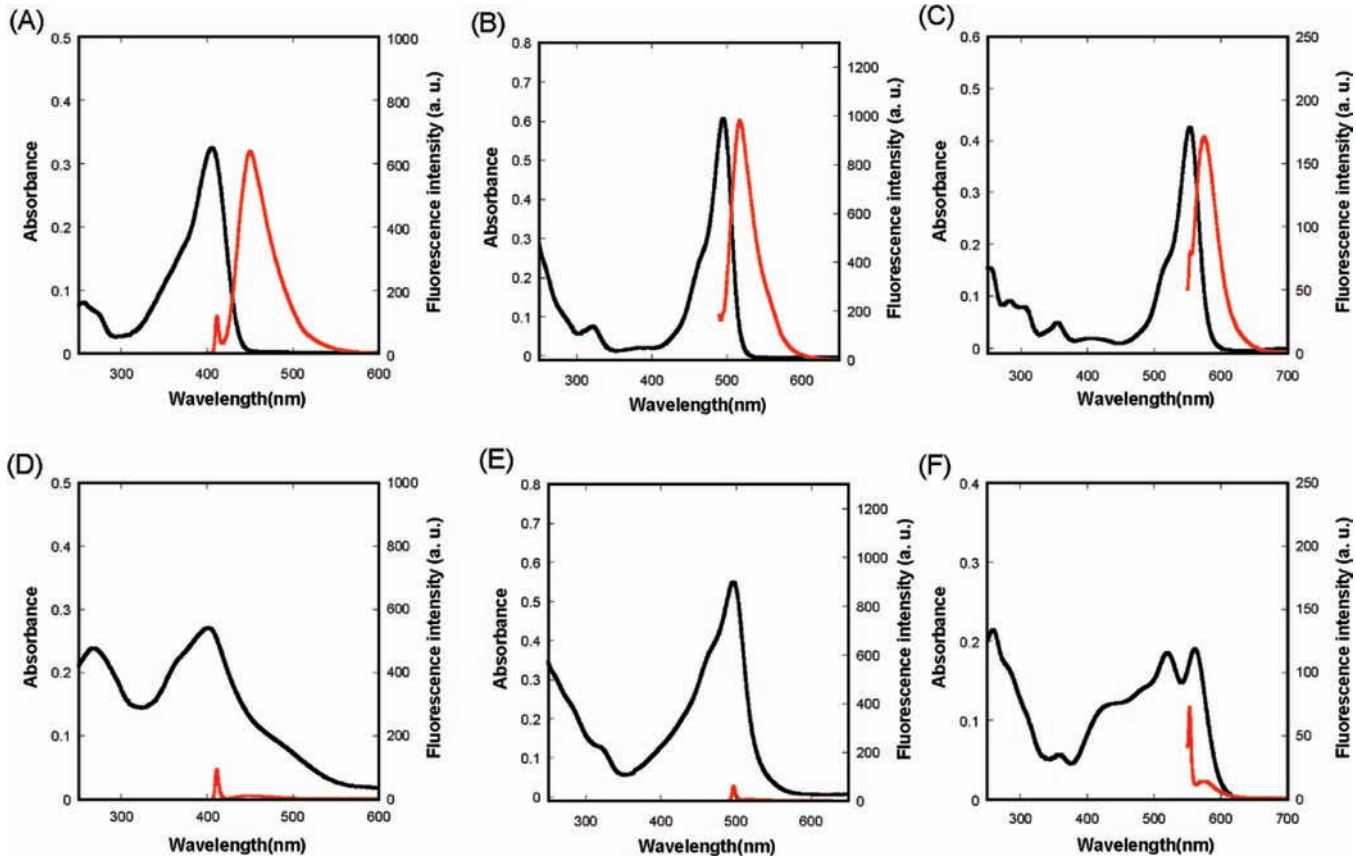


Figure 2. Absorption (black line) and emission spectra (red line) of (A) CA, (B) FA, (C) RA, (D) CCD, (E) FCD, and (F) RCD in 100 mM HEPES buffer (pH 7.4). In the absorption measurements, the probe concentrations were 5 μM for FA, FCD, RA, and RCD and 10 μM for CA and CCD. In the absorption measurements, the probe concentrations were 0.5 μM for FA, FCD, RA, and RCD and 1 μM for CA and CCD. Excitation wavelengths were 405 nm for CA and CCD, 492 nm for FA, 496 nm for FCD, and 553 nm for RA and RCD.

Table 1. Spectroscopic Properties and Calculated Values for FRET of Labeling Probes in 100 mM HEPES Buffer (pH 7.4)

compound	$\lambda_{abs,\ max}$/nm	$\lambda_{em,\ max}$/nm	fluorescence quantum efficiency (Φ)	Förester distance[a] (R_0)/Å	donor−acceptor distance[b] (R)/Å	energy transfer efficiency[c] (E)
CA	405	453	0.40	–	–	–
CCD	400	450	0.006	44.2	26.3	0.96
FA	492	517	0.71	–	–	–
FCD	496	520	0.005	43.4	27.8	0.93
RA	553	575	0.49	–	–	–
RCD	525, 565	573	0.07	19.6	27.7	0.12

[a] R_0 values were derived from the overlap integral between the absorption spectrum of DABCYL and the fluorescence spectrum of CA for CCD, FA for FCD, and RA for RCD. [b] R values were evaluated from the farthest distance between the fluorophore and DABCYL by using the molecular modeling software. [c] Energy transfer efficiencies were calculated from the equation $E = R_0^6/(R_0^6 + R^6)$.

studies using living cells. Therefore, β-lactam probes conjugated to fluorescein or tetramethylrhodamine (TAMRA) were designed and synthesized (Figure 1B). The fluorescence labeling probes FA and RA were synthesized in one step from ampicillin and activated esters of the corresponding fluorophores. FCD and RCD, which were designed to be fluorogenic as well as CCD, were also synthesized. RCD was synthesized from the activated ester of the 5(6)-TAMRA isomers and used for the experiments without separation of the 5(6)-isomers (see Figure S1 in Supporting Information).

Absorption and emission spectra of all β-lactam labeling probes are shown in Figure 2, and the spectroscopic properties are summarized in Table 1. FA and RA exhibited similar spectroscopic properties to fluorescein and TAMRA, respectively. From the Förster radii caluculated from their spectra and the simulated donor−acceptor distances, the FRET efficiency was estimated (Table 1). We predicted that FCD fluorescence would be quenched sufficiently from the FRET efficiency value. Indeed, FCD was largely quenched by intramolecular FRET from coumarin to DABCYL ($\Phi = 0.005$). In contrast, RCD fluorescence would theoretically not be quenched because of the limited overlap between the absorption spectrum of DABCYL and the emission spectrum of TAMRA. Nevertheless, RCD fluorescence was considerably quenched ($\Phi = 0.07$). This quenching of RCD fluorescence can be ascribed to the intramolecular association between TAMRA and DABCYL moieties. We previously reported that, if two hydrophobic dyes are located in close proximity, self-quenching occurs due to the close contact of the two dyes in aqueous solution (*29*). The fluorescence intensities of FCD and RCD were recovered by the addition of WT TEM-1 and BL-tag in a time-dependent manner (see Figure S2 in Supporting Information). These results indicate that elimination of the DABCYL moieties occurs by the enzymatic cleavage of the β-lactam in both cases. The labeling capabilities of all compounds with BL-tag were confirmed by SDS-PAGE (see Figure S3 in Supporting Information).

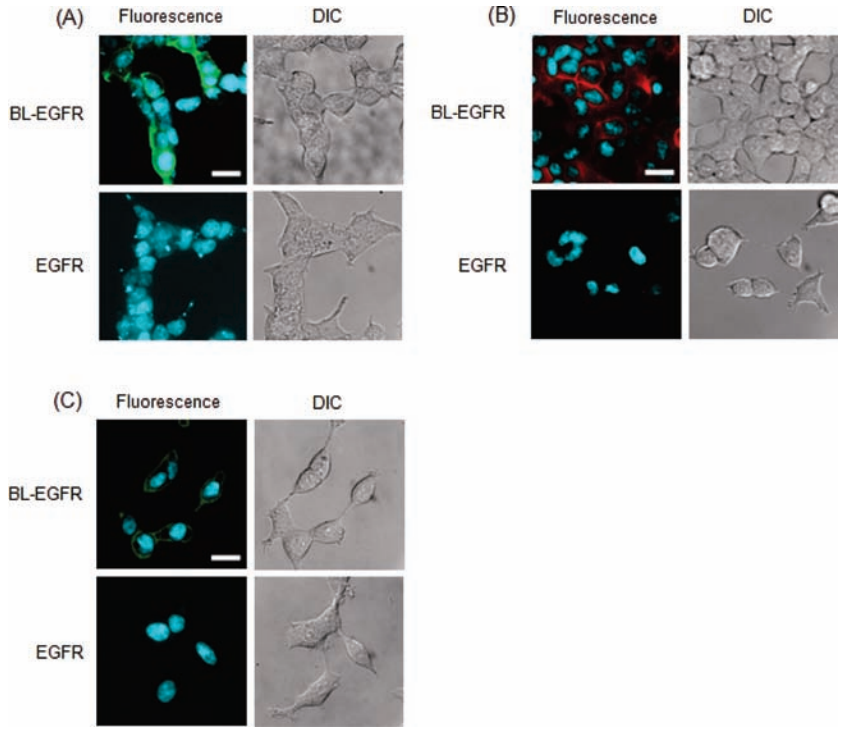


Figure 3. Labeling of BL-tag fusion proteins with (A) FA, (B) RA, and (C) FCD. HEK293T cells were transfected with a plasmid encoding BL-EGFR or EGFR. The cell nuclei were costained with Hoechst 33342. For fluorescence microscopic images, the cells were excited at 330−385 nm for Hoechst 33342, 460−490 nm for FA, and 510−550 nm for RA. Scale bar: 20 μm.

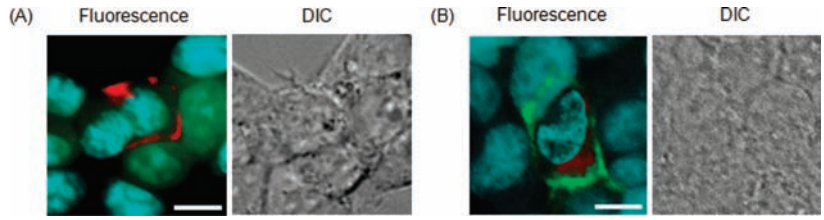


Figure 4. (A) Multicolor imaging of HEK293T cells expressing BL-EGFR. BL-EGFR, nuclei, and cytosol were labeled with RA (red), Hoechst 33342 (cyan), and CellTracker Green (green), respectively. (B) Multiprobe labeling of HEK293T cells expressing BL-EGFR and COX8-2-SNAP. BL-EGFR was labeled with FA, COX-8-2-SNAP with SNAP-Cell TMR-STAR, and nuclei with Hoechst 33342. Fluorescence microscopic images were excited at 330−385 nm, 460−490 nm, and 510−550 nm. Scale bar: 10 μm.

Fluorescence Labeling of BL-tag Fusion Proteins by the Synthesized Probes. BL-tag was fused to the N-terminus of epidermal growth factor receptor (EGFR), and the fusion protein BL-EGFR was expressed on cell surfaces of HEK293T cells by transfection with a plasmid encoding BL-EGFR. The cells were incubated with FA or RA, washed three times, and observed using a fluorescence microscope. The cells generating BL-EGFR clearly emitted green or red fluorescence at the plasma membrane (Figure 3A,B). We calculated the average fluorescence intensity per pixel from BL-EGFR expressing cells and negative control cells, and compared with each other (see Figure S4 in Supporting Information). As a result, the fluorescence signal from labeled cells by FA or RA was clearly enhanced compared with the background signal (about 1.8 times), while the fluorescence signal of cells labeled by CA or CCD was about 10% higher than the background signal. Therefore, the signal-to-background ratio was largely improved by FA and RA relative to CA and CCD. Subsequently, the labeling properties of FCD were investigated. The cells generating BL-EGFR were labeled by FCD in a labeling procedure similar to the procedure used for FA and RA (Figure 3C).

Multicolor Imaging by Simultaneous Labeling with BL-tag and SNAP-tag. We applied BL-tag technology to multicolor imaging of cells in order to demonstrate its wide versatility. After transfection of HEK293T cells with a plasmid encoding BL-EGFR, Hoechst 33342, CellTracker Green, and RA were incubated. Cells were then imaged using different fluorophores with appropriate filter sets. Each organelle was confirmed by multicolor fluorescence imaging (Figure 4A). In addition, BL-tag fusion proteins were found to be labeled with different color fluorophores (Figure 3). This property is beneficial for pulse-chase fluorescence imaging experiments used for tracing protein trafficking after various stimulations (*30, 31*).

Next, multicolor fluorescence labeling of two different target proteins was performed with another specific protein labeling system known as SNAP-tag technology. In this experiment, SNAP-tag was applied as a COX8-2-SNAP fusion plasmid encoding COX8-2 (subunit 8-2 protein of cytochrome c oxidase) cloned upstream of SNAP-tag. Cytochrome c oxidase is a terminal enzyme of the respiratory transport chain and localized at the inner mitochondrial membrane (*32*). The COX8-2-SNAP fusion proteins provide fluorescence in mitochondria when labeled with SNAP-Cell TMR-Star.

HEK293T cells were co-transfected with BL-EGFR and COX8-2-SNAP plasmids. The cells were incubated with FA, SNAP-Cell TMR-Star, and Hoechst 33342, and then washed three times with DMEM containing 10% FBS prior to imaging with a fluorescence microscope. Though the co-expression

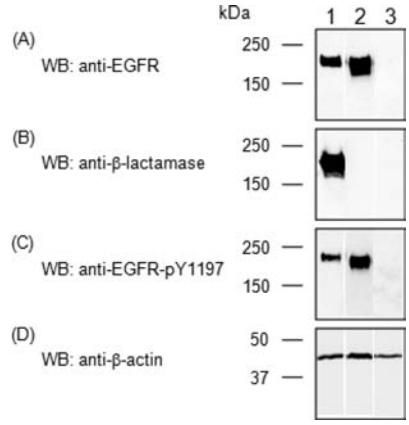


Figure 5. Western blot analysis of the EGFR and BL- EGFR expressed in transfected HEK293T cells after EGF stimulation. (A) Detection of EGFR with polyclonal anti-EGFR antibody. (B) Detection of TEM-1 with polyclonal anti-β-lactamase antibody. (C) Detection of phosphorylated tyrosine at 1197 position with monoclonal anti-EGFR-pY1197 antibody. (D) Detection of β-actin cytoskeleton with monoclonal anti-β-actin antibody. Lane 1: BL-EGFR-expressing cells. Lane 2: EGFR-expressing cells. Lane 3: Cells transfected with an empty plasmid vector.

efficiencies were not very good in this experiment, green fluorescence derived from FA was observed along the plasma membrane and red fluorescence from SNAP-Cell substrates in mitochondria was observed in the same cells (Figure 4B). This result distinctly indicates that BL-tag and SNAP-tag have nonoverlapping substrate specificity and can be used simultaneously in single cells.

Ligand-Induced Activation of the BL-tag Fusion Protein. Finally, we demonstrate the low interference of BL-tag with the function of the target protein EGFR. EGFR is a 170 kDa transmembrane glycoprotein that belongs to a tyrosine kinase receptor family comprising four members. The intracellular trafficking behavior and ligand-dependent dimerization of EGFR has attracted great attention (*33*). It was, however, reported that the expression and trafficking of EGFR was greatly disrupted as a result of extracellular GFP fusion and appropriate expression of the fusion protein was not detected by Western blot analysis with anti-GFP antibody (*34*) due to the fact that the fluorophore formation of GFP strongly depends upon the structural integrity of the protein (*3*). The identity of the BL-EGFR fusion protein was characterized by Western blot analysis with anti-β-lactamase, anti-EGFR, and anti-EGFR-pY1197 phosphorylation site-specific antibodies. Specific ligand binding on the extracellular domain of EGFR results in dimerization of the receptor and subsequent autophosphorylation of the tyrosine residues, the most predominant of which is pY1197 (*35*).

HEK293T cells were transfected with fusion proteins or EGFR plasmids, followed by incubation under serum-starved conditions. The cells were then stimulated with EGF and analyzed by Western blot. Naive (nontransfected) HEK293T cells express extremely low levels of endogenous EGFR as demonstrated in cells transfected with a control plasmid vector probed with an anti-EGFR antibody (lane 3 in Figure 5A) (*36*). When lysates of the cells transfected with EGFR plasmids were probed with an anti-EGFR antibody, one major band was visible with a molecular weight of about 170 kDa, corresponding to EGFR (lane 2 in Figure 5A). A single band was also detected from cells transfected with BL-EGFR. This band appeared in the slightly upper position of that of EGFR. This is consistent with the increase of the molecular weight as a result of fusion of BL-tag to EGFR (lane 1 in Figure 5A). On the other hand, when the membrane was probed with an anti-β-lactamase antibody, the immunoblotted band was observed only in the lane of the lysate containing BL-EGFR fusion protein (Figure 5B). These results suggest that the BL-EGFR fusion protein was properly expressed in HEK293T cells.

After stimulation by EGF, phosphorylation of Y1197 was confirmed using an anti-EGFR-pY1197 antibody. A single band shows that phosphorylation was observed in the lanes of cell lysates containing BL-EGFR or EGFR (lanes 1 and 2 in Figure 5C). In addition, we compared the distribution of BL-EGFR and EGFR after EGF stimulation by immunofluorescence staining with anti-EGFR-pY1197 antibody. Cells expressing BL-EGFR and EGFR gave the same distribution pattern of fluorescence responses that demonstrate phosphorylation in the cells (see Figure S5 in Supporting Information). From these results, it is evident that the phosphorylation function of EGFR can be preserved after introduction of the BL-tag to the extracellular domain of EGFR. All of the results discussed herein suggest that BL-tag has lower interference than GFP with respect to the function of EGFR.

In conclusion, we have designed and synthesized various labeling probes for BL-tag. These new probes have superior spectroscopic properties relative to the previously reported probes, CA and CCD. FA and RA can specifically label BL-tag in living cells, while FCD and RCD possess fluorogenic properties based on FRET or intramolecular stacking interaction which provides a useful switching mechanism for protein labeling probes, as we recently reported (*37*). The function of EGFR was found to be considerably preserved after the fusion of BL-tag to the extracellular domain. This low interference with the function of the target protein can provide a great advantage relative to fusion to GFP and should be suitable for studying the function or trafficking of POIs. Furthermore, BL-tag technology can be simultaneously used with other protein labeling methods such as SNAP-tag technology. Orthogonality of the substrate specificity between BL-tag and SNAP-tag was also shown.

In the future, a series of labeling probes with various fluorophores for BL-tag can be applied to a pulse-chase experiment that can distinguish between young and old copies of proteins by labeling at different time points with different fluorophores. Moreover, protein labeling techniques can be used not only for fluorescence imaging, but also for inducers of protein−protein interactions. Techniques based on multiple protein labeling methods are quite useful for studying and controlling protein−protein interactions (*38, 39*). Thus, we have provided a potential tool for practical biological applications. BL-tag technology can be exploited with conventional protein labeling methods for the specific labeling of two or more different proteins within a single cell. Furthermore, combinations of BL-tag technology with other imaging methods such as MRI or NIR are expected to contribute to the clarification of various protein−protein interactions.

ACKNOWLEDGMENT

This work was supported in part by the Grant-in-Aid for Scientific Research from the Ministry of Education, Culture, Sports, Science and Technology (MEXT) of Japan, by the Grant-in-Aid from the Ministry of Health, Labour and Welfare (MHLW) of Japan, and by the New Energy and Industrial Technology Development Organization (NEDO) of Japan. K.K. expresses his special thanks for support from the Takeda Science Foundation. S.W. acknowledges support from a Global COE Fellowship of Osaka University and a JSPS Research Fellowship.

Supporting Information Available: Materials and Instruments; synthetic details and characterization of FA, FCD, RA and RCD; supplementary figures. This material is available free of charge via the Internet at http://pubs.acs.org.

LITERATURE CITED

(1) Giepmans, B. N. G., Adams, S. R., Ellisman, M. H., and Tsien, R. Y. (2006) The fluorescent toolbox for assessing protein location and function. *Science 312*, 217–224.

(2) Phillips, G. N., Jr. (1997) Structure and dynamics of green fluorescent protein. *Curr. Opin. Struct. Biol. 7*, 821–827.

(3) Lisenbee, C. S., Karnic, S. K., and Trelease, R. T. (2003) Overexpression and mislocalization of a tail-anchored GFP redefines the identity of peroxisomal ER. *Traffic 4*, 491–501.

(4) Griffin, B. A., Adams, S. R., and Tsien, R. Y. (1998) Specific covalent labeling of recombinant protein molecules inside live cells. *Science 281*, 269–272.

(5) Griffin, B. A., Adams, S. R., Jones, J., and Tsien, R. Y. (2000) Fluorescent labeling of recombinant proteins in living cells with FLAsH. *Methods Enzymol. 327*, 565–578.

(6) Adams, S. R., Campbell, R. E., Gross, L. A., Martin, B. R., Walkup, G. K., Yao, Y., Llopis, J., and Tsien, R. Y. (2002) New biarsenical ligands and tetracystein motif for protein labeling *in vitro* and *in vivo*. Synthesis and biological applications. *J. Am. Chem. Soc. 124*, 6063–6076.

(7) Los, G. V., et al. (2008) Halotag: A novel protein labeling technology for cell imaging and protein analysis. *ACS Chem. Biol. 3*, 373–382.

(8) Keppler, A., Gendreizig, S., Pick, H., Vogel, H., and Johnsson, K. (2003) A general method for the covalent labeling of fusion proteins with small molecules *in vivo*. *Nat. Biotechnol. 21*, 86–89.

(9) Kindermann, M., Sielaff, I., and Johnsson, K. (2004) Synthesis and characterization of bifunctional probes for the specific labeling of fusion proteins. *Bioorg. Med. Chem. Lett. 14*, 2725–2728.

(10) Keppler, A., Pick, H., Arrivoli, C., Vogel, H., and Johnsson, K. (2004) Labeling of fusion proteins with synthetic fluorophores in live cells. *Proc. Natl. Acad. Sci. U.S.A. 101*, 9955–9959.

(11) Miller, L. W., Sable, J., Goelet, P., Sheetz, M. P., and Cornish, V. W. (2004) Methotrexate conjugates: A molecular *in vivo* protein tag. *Angew. Chem., Int. Ed. 43*, 1672–1675.

(12) Chen, I., Howarth, M., Lin, W., and Ting, A. Y. (2005) Site-specific labeling of cell surface proteins with biophysical probes using biotin ligase. *Nat. Methods 2*, 99–104.

(13) Lin, C.-W., and Ting, A. Y. (2006) Transglutaminase-catalyzed site-specific conjugation of small molecule probes to proteins *in vitro* and on the surface of living cells. *J. Am. Chem. Soc. 128*, 4542–4543.

(14) Hauser, C. T., and Tsien, R. Y. (2007) A hexahistidine-Zn^{2+}-dye label reveals STIM1 surface exposure. *Proc. Natl. Acad. Sci. U.S.A. 104*, 3693–3697.

(15) Ojida, A., Honda, K., Shinmi, D., Kiyonaka, S., Mori, Y., and Hamachi, I. (2006) Oligo-Asp tag/Zn(II) complex probe as a new pair for labeling and fluorescence imaging of proteins. *J. Am. Chem. Soc. 128*, 10452–10459.

(16) Mizukami, S., Watanabe, S., Hori, Y., and Kikuchi, K. (2009) Covalent protein labeling based on non-catalytic β-lactamase and a designed FRET substrate. *J. Am. Chem. Soc. 131*, 5016–5017.

(17) Christensen, H., Martin, T. M., and Waley, S. G. (1990) β-lactamase as fully efficient enzymes. *Biochem. J. 266*, 853–861.

(18) Moore, J. T., Davis, S. T., and Dev, K. I. (1997) The development of β-lactamase as a highly versatile genetic reporter for eukaryotic cells. *Anal. Biochem. 247*, 203–209.

(19) Zlokarnik, G., Negulescu, P. A., Knapp, T. E., Mere, L., Burres, N., Feng, L., Whitney, M., Roemer, K., and Tsien, R. Y. (1998) Quantitation of transcription and clonal selection of single living cells with β-lactamase as reporter. *Science 279*, 84–88.

(20) Gao, W., Xing, B., Tsien, R. Y., and Rao, J. (2003) Novel fluorogenic substrates for imaging β-lactamase gene expression. *J. Am. Chem. Soc. 125*, 11146–11147.

(21) Fisher, F. J., Meroueh, S. O., and Mobashery, S. (2005) Bacterial resistance to β-lactam antibiotics: Compelling opportunism, compelling opportunity. *Chem. Rev. 105*, 395–424.

(22) Matagne, A., Lamotte-Blasseur, J., and Frére, J.-M. (1998) Catalytic properties of class A β-lactamases: efficiency and diversity. *Biochem. J. 330*, 581–598.

(23) Guillaume, G., Vanhove, M., Lamotte-Brasseur, J., Ledent, P., Jamin, M., Joris, B., and Frére, J.-M. (1997) Site-directed mutagenesis of glutamate 166 in two β-lactamases. *J. Biol. Chem. 272*, 5438–5444.

(24) Adachi, H., Ohta, T., and Matsuzawa, H. (1991) Site-directed mutants, at position 166, of RTEM-1 β-lactamase that form a stable acyl-enzyme intermediate with penicillin. *J. Biol. Chem. 266*, 3186–3191.

(25) Page, M. I., and Proctor, P. (1984) Mechanism of β-lactam ring opening in cephalosporins. *J. Am. Chem. Soc. 106*, 3820–3825.

(26) Nishikawa, Y., and Hiraki, K. (1984) Calculation of quantum efficiency of rhodamine derivatives. *Analytical Methods of Fluorescence and Phosphorescence*, p 76, Kyoritsu Publishing Company, Tokyo

(27) Parker, C. A., and Rees, W. T. (1960) Correction of fluorescence spectra and measurement of fluorescence quantum efficiency. *Analyst 85*, 587–600.

(28) Lakowicz, J. R. (2006) Calculation of Förster distance and Energy transfer efficiency. *Principle of Fluorescence Spectroscopy*, 3rd ed., pp 443−475, Chapter 13, Springer Science+Business Media, LLV, New York.

(29) Mizukami, S., Kikuchi, K., Higuchi, T., Urano, Y., Mashima, T., Tsuruo, T., and Nagano, T. (1999) Imaging of caspase-3 activation in HeLa cells stimulated with etoposide using a novel fluorescent probe. *FEBS Lett. 453*, 356–360.

(30) Gaietta, G., Deerinck, T. J., Adams, S. R., Bouwer, J., Tour, O., Laird, D. W., Sosinsky, G. E., Tsien, R. Y., and Ellisman, M. H. (2002) Multicolor and electron microscopic imaging of connexin trafficking. *Science 296*, 503–507.

(31) Vivero-Pol, L., George, N., Krumm, H., Johnsson, K., and Johnsson, N. (2005) Multicolor imaging of cell surface proteins. *J. Am. Chem. Soc. 127*, 12770–12771.

(32) Malmström, B. G. (1990) Cytochrome c oxidase as a redox-linked proton pump. *Chem. Rev. 90*, 1247–1260.

(33) Sorkin, A., and Goh, L. K. (2009) Endocytosis and intracellular trafficking of ErbBs. *Exp. Cell Res. 315*, 683–696.

(34) Brock, R., Hamelers, I. H. L., and Jovin, T. M. (1999) Comparison of fixation protocols for adherent cultured cells applied to a GFP fusion protein of the epidermal growth factor receptor. *Cytometry 35*, 353–362.

(35) Chattopadhyay, A., Vecchi, M., Ji, Q., Memaugh, R., and Carpenter, G. (1999) The role of individual SH2 domain in mediating association of phospholipase C-γ1 with the activated EGF receptor. *J. Biol. Chem. 274*, 26091–26097.

(36) Jones, S. M., Foreman, S. K., Shank, B. B., and Kurten, R. C. (2002) EGF receptor downregulation depends on a trafficking motif in the distal tyrosine kinase domain. *Am. J. Physiol. Cell Physiol. 282*, C420–C433.

(37) Hori, Y., Ueno, H., Mizukami, S., and Kikuchi, K. (2009) Photoactive yellow protein-based protein labeling system with turn-on fluorescence intensity. *J. Am. Chem. Soc. 131*, 16610–16611.

(38) Gendreizig, S., Kindermann, M., and Johnsson, K. (2003) Induced protein dimerization *in vivo* through covalent labeling. *J. Am. Chem. Soc. 125*, 14970–14971.

(39) Chidley, C., Mosiewicz, K., and Johnsson, K. (2008) A designed protein for the specific and covalent heteroconjugation of biomolecules. *Bioconjugate Chem. 19*, 1753–1756.

BC100333K

Supporting Information

Multicolor Protein Labeling in Living Cells Using Mutant β-Lactamase-tag Technology

Shuji Watanabe,[†] Shin Mizukami,[†,‡] Yuichiro Hori,[†] and Kazuya Kikuchi[†,‡,]*

[†]Division of Advanced Science and Biotechnology, Graduate School of Engineering, and [‡]Immunology Frontier Research Center, Osaka University, 2-1 Yamadaoka, Suita, Osaka 565-0871, Japan

* To whom correspondence should be addressed: kkikuchi@mls.eng.osaka-u.ac.jp

CONTENTS:

1. Materials and Instruments

2. Syntheses of Compounds

3. Supporting Figures

4. Reference

1. Materials and Instruments

Materials. General chemicals for organic synthesis were of the highest grade available supplied by Tokyo Chemical Industries, Wako Pure Chemical, and Aldrich Chemical Co, and were used without further purification. 7-Amino-3-chloromethyl-3-cephem-4-carboxylic acid *p*-methoxybenzyl ester hydrochloride (ACLE·HCl) was obtained from Otsuka Chemical Co. Ltd. COX8-2-SNAP plasmid and SNAP-Cell^{TM} TMR-Star were purchased from New England Biolabs Inc. (E9100S). Anti-EGFR antibody was purchased from Abcam (ab2430), anti-β-lactamase antibody was purchased from Millipore (ab3738), anti-β-actin antibody was purchased from Sigma (A5441) and anti-EGFR-pY1197 antibody was purchased from DACO (M7299). Horseradish peroxidase-linked secondary antibody was purchased from GE Healthcare (anti-rabbit NA934, anti-mouse NA931). ECL Western Blotting Detection Reagents were purchased from GE Healthcare (RPN2109). Fluorescein-conjugated goat anti-mouse antibody was purchased from Bethyl Laboratories (A90-116F). 5 (6)-Carboxytetramethylrhodamine succinimidyl ester was purchased from Invitrogen (C1171). All probes were dissolved in DMSO (biochemical grade, Wako) before fluorescence measurements in order to facilitate solubilization in aqueous solvents. Silica gel column chromatography was performed using BW-300 (Fuji Silysia Chemical Ltd.).

Instruments. NMR spectra were recorded on a JEOL JNM-AL400 instrument at 400 MHz for ^{1}H and at 100.4 MHz for ^{13}C NMR, using tetramethylsilane as an internal standard. Mass spectra were measured on a JEOL JMS-700 mass spectrometer for FAB and on a Waters LCT-Premier XE mass

spectrometer for ESI. Fluorescence spectra were measured using a Hitachi F4500 spectrometer. UV-visible absorbance spectra were measured using a Shimadzu UV1650PC spectrometer. Fluorescence images of SDS-PAGE were visualized using an AE-6935B VISIRAYS-B (ATTO) for fluorescein derivatives, or BSPEBV001 EtBr viewer (Biospeed) for rhodamine derivatives.

2. Syntheses of Compounds

Syntheses of compounds 1–4

Syntheses of these compounds were reported in our previous paper (*S1*).

Synthesis of FA.

Ampicillin (44 mg, 127 μmol) was dissolved in DMF (500 μL), then TEA (13 mg, 127 μmol) and 6-carboxyfluorescein-succinimidyl ester (20 mg, 42 μmol) were added at 0 °C. The mixture was stirred for 12 h, and AcOEt was then added to the reaction mixture. The organic phase was washed with 10% citric acid aq. and water, and then dried with brine and sodium sulfate. After removal of the solvent, the residue was purified with reversed-phase HPLC and eluted with H_2O/acetonitrile containing 0.1% formic acid to yield FA (13 mg, y. 32%). ^{1}H NMR (400 MHz, DMSO-d_6) δ 1.37 (s, 3H), 1.43 (s, 3H), 4.17 (s, 1H), 5.30 (d, 1H, J = 4.0 Hz), 5.50 (dd, 1H, J = 3.9 Hz, 7.3 Hz), 5.87 (d, 1H, J = 7.3 Hz), 6.54–6.68 (m, 4H), 6.90 (s, 2H), 7.27–7.43 (m, 5H), 7.84 (s, 1H), 8.07 (d, 1H), 8.23 (dd, 1H, J = 1.0, 7.6 Hz), 9.04 (d, 1H, J = 7.3 Hz), 9.22 (d, 1H, J = 7.6 Hz), 10.1 (brs, 1H); ^{13}C NMR (100 MHz, DMSO-d_6) δ 26.5, 30.4, 56.7, 58.3, 63.6, 67.2, 70.2, 83.5 102.2, 109.1, 109.2, 112.7, 122.8,

124.7, 127.6, 127.7, 128.2, 128.6, 129.2, 130.1, 137.1, 140.1, 151.8, 152.3, 159.6, 164.8, 168.0, 168.8, 169.8, 173.1; HRMS (FAB^+) *m*/*z*: 708.1649 (Calcd for $[M+H]^+$: 708.1652).

Synthesis of RA.

Ampicillin (30 mg, 85 μmol) was dissolved in DMF (500 μL). TEA (8.6 mg, 85 μmol) and 5 (6)-carboxytetramethylrhodamine-succinimidyl ester (15 mg, 28 μmol) were then added at 0 °C. The mixture was stirred for 12 h, and the solvent was lyophilized. The residue was purified with reversed-phase HPLC and eluted with H_2O/acetonitrile containing 0.1% formic acid to yield RA (6 mg, y. 28%). ^1H NMR (400 MHz, DMSO-d_6) δ 1.37 (s, 3H.), 1.43 (s, 3H), 2.95 (s, 12H), 4.22 (s, 1H), 5.44 (d, 1H, *J* = 4.0 Hz), 5.57 (dd, 1H, *J* = 3.9, 7.8 Hz), 5.95 (d, 1H, *J* = 8.3 Hz), 6.51 (m, 6H), 7.30–7.55 (m, 6H), 8.26 (d, 1H, *J* = 7.8 Hz), 8.57 (s, 1H), 9.12 (d, 1H, *J* = 7.8 Hz), 9.34 (d, 1H, *J* = 7.8 Hz); ^{13}C NMR (100 MHz, DMSO-d_6) δ 26.6, 30.4, 56.8, 58.3, 63.7, 67.3, 70.3, 84.7, 98.0, 105.6, 109.0, 124.1, 126.7, 127.7, 128.2, 128.4, 129.0, 135.0, 135.5, 137.4, 152.0, 152.2, 155.0, 163.1, 165.1, 168.3, 168.9, 169.9, 173.3; HRMS (FAB^+) *m*/*z*: 762.2595 (Calcd for $[M+H]^+$: 762.2598).

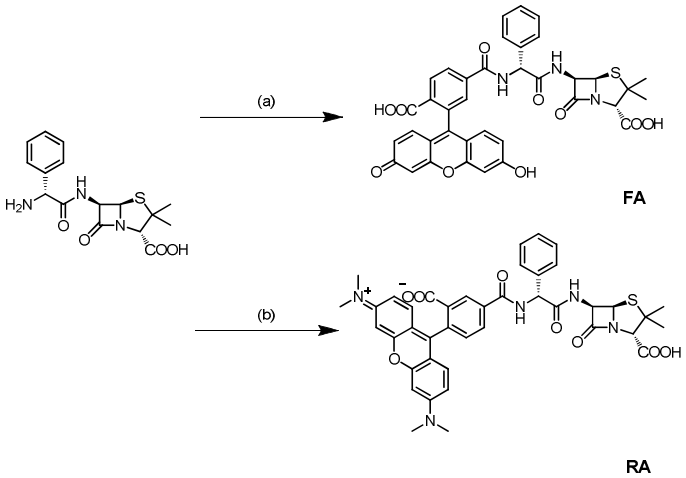
Synthesis of FCD.

Compound **4** (30 mg, 47 μmol) was dissolved in DMF (500 μL), then DIEA (30 mg, 230 μmol) and 6-carboxyfluorescein-succinimidyl ester (26 mg, 56 μmol) were added at -20 °C. The mixture was stirred for 16 h, and the solvent was evaporated followed by the addition of 100 mM ammonium formate aq. (15 mL). The precipitate was collected and washed thoroughly with 100 mM ammonium formate aq. and water to afford pure FCD (18 mg, y. 39%). ^1H NMR (400 MHz, DMSO-d_6) δ 3.07 (s,

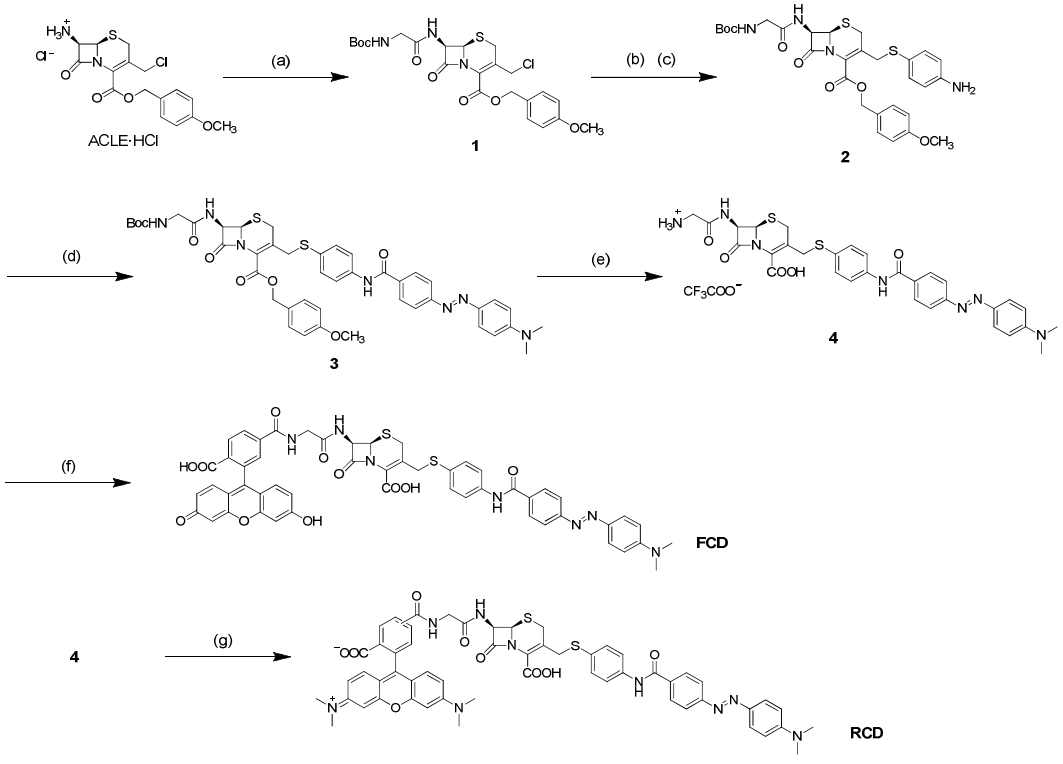
6H), 3.29 (d, 1H, *J* = 17.1 Hz), 3.57 (d, 1H, *J* = 17.1 Hz), 3.88 (m, 2H), 3.98 (d, 1H, *J* = 12.7 Hz), 4.24 (d, 1H, *J* = 12.7 Hz), 4.91 (d, 1H, *J* = 4.4 Hz), 5.48 (dd, 1H, *J* = 4.4 Hz, 8.8 Hz), 6.56 (m, 4H), 6.69 (d, 2H, *J* = 1.9 Hz), 6.85 (d, 1H, *J* =9.3 Hz), 7.47 (d, 2H, *J* = 8.8 Hz), 7.70 (s. 1H), 7.73 (d, 2H, *J* = 8.8 Hz), 8.84 (m, 4H), 8.07 (m, 3H), 8.17 (d, 1H, *J* = 7.8 Hz), 9.01 (d, 1H, *J* = 8.8 Hz), 9.18 (t, 1H, *J* = 5.9 Hz), 10.5 (s, 1H); ^{13}C NMR (100 MHz, DMSO-d_6) δ 26.6, 36.9, 39.9, 42.2, 57.3, 58.3, 102.3, 109.0, 109.1, 111.6, 112.9 , 120.9, 121.6, 122.5, 124.9, 125.2, 128.4, 128.8, 128.9, 129.0, 129.2, 129.5 129.6, 134.5, 137.4, 140.2, 142.7,151.9, 152.7, 152.9,154.2, 159.9, 162.9, 164.1, 164.8, 164.9, 168.1, 169.4; HRMS (FAB$^+$) *m*/*z*: 1004.2371 (Calcd for [M+H]$^+$: 1004.2384).

Synthesis of RCD.

Compound **4** (14 mg, 19 μmol) was dissolved in DMF (500 μL). TEA (5.8 mg, 57 μmol) and 5 (6)-carboxytetramethylrhodamine-succinimidyl ester (10 mg, 19 μmol) were then added at 0 °C. The mixture was stirred for 7 h, and the solvent was evaporated followed by the addition of 100 mM ammonium formate aq. (15 mL). The precipitate was collected and thoroughly washed with 100 mM ammonium formate aq. and 100 mM HEPES buffer (pH 7.4) to afford pure RCD as mixed 5- and 6-isomers (2 mg, y. 10%). The purity was confirmed by reversed-phase HPLC (Figure. S1). HRMS (FAB$^+$) *m*/*z*: 1058.3322 (Calcd for [M+H]$^+$: 1058.3329).



Scheme S1. Synthetic route to FA and RA. (a) 6-Carboxyfluorescein succinimidyl ester, TEA, DMF, 0 °C. (b) 5(6)-Carboxytetramethylrhodamine succinimidyl ester, TEA, DMF, 0 °C.



Scheme S2. Synthetic route to FCD and RCD. (a) Boc-glycine, HOBt/H_2O, WSCD·HCl, TEA, DMF, 0 °C. (b) NaI, acetone, RT. (c) 4-Aminothiophenol, $NaHCO_3$, DMF, RT. (d) 4-Dimethylaminoazobenzene-4'-carboxylic acid, $POCl_3$, pyridine, -20 °C. (e) TFA, thioanisole, CH_2Cl_2, 0 °C. (f) 6-Carboxyfluorescein succinimidyl ester, TEA, DMF, 0 °C. (g) 5(6)-Carboxytetramethylrhodamine succinimidyl ester, TEA, DMF, 0 °C.

3. Supporting Figures

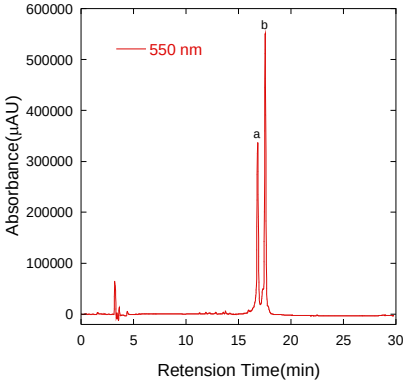


Figure S1. Reversed-phase HPLC with absorbance detection of RCD as mixed 5- and 6-isomers. Eluent: H_2O/acetonitrile containing 0.1% formic acid (gradient mode). The product mass (ESI-TOF $[M+H]^+$ 1058.3) was observed from each of the two peaks (a and b).

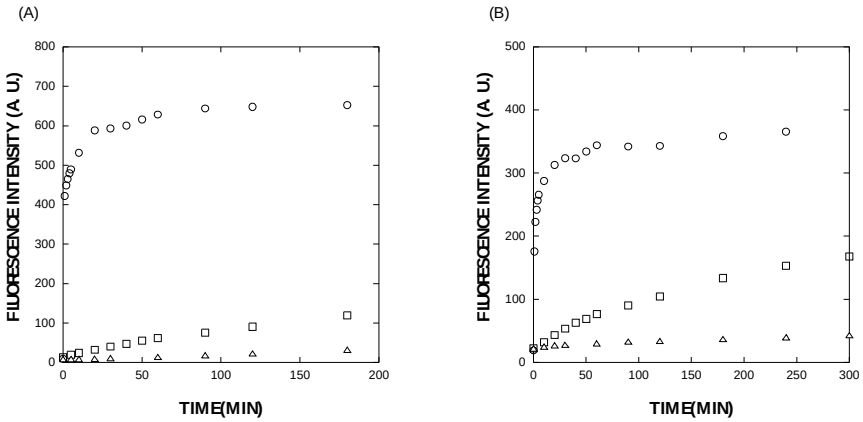


Figure S2. Time-dependent fluorescence intensity of (A) FCD and (B) RCD in the presence of ^{E166N}TEM (BL-tag, square), WT TEM-1 (circle), and in the absence of them (triangle)

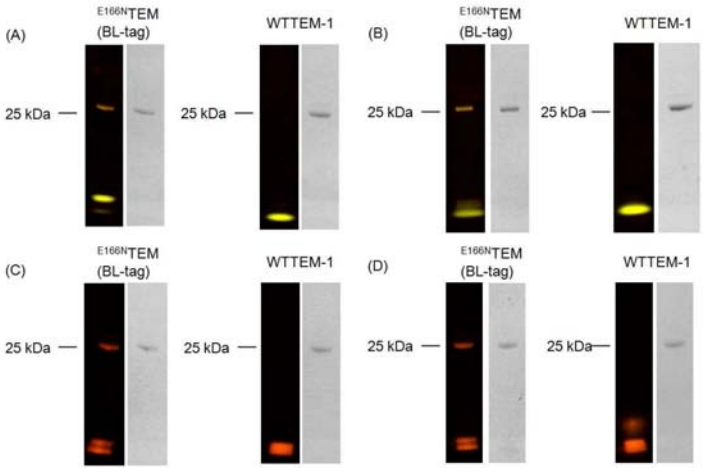


Figure S3. Fluorescence (left) and CBB-stained (right) gel images of ^{E166N}TEM (BL-tag) and WT TEM-1 with (A) FA, (B) FCD, (C) RA, and (D) RCD

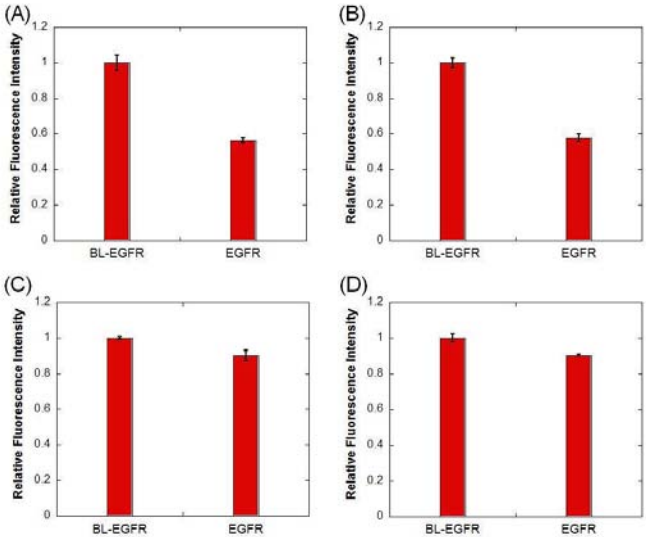


Figure S4. Relative fluorescence intensities of labeled HEK293T cells transfected with BL-EGFR or EGFR plasmids. Transfected HEK293T cells were labeled with (A) FA, (B) RA, (C) CA, and (D) CCD. Average fluorescence intensity per pixel of labeled cells was analyzed by MetaMorph imaging software. Data are means ± S.E.M. of triplicate determinations from fluorescence images.

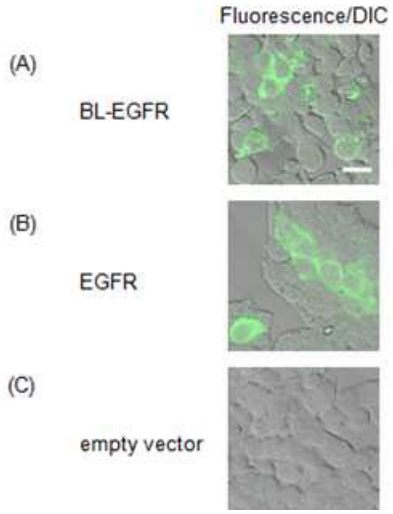


Figure S5. Analysis of the effect of the BL-tag on EGFR function after EGF stimulation. HEK293T cells expressing (A) BL-EGFR, (B) EGFR, and (C) transfected with the empty vector, which were immunostained with the primary antibody; anti-EGFR-pY1197 and the fluorescein-conjugated secondary antibody. Fluorescence microscopic images were excited at 460–490 nm and merged with DIC images. Scale bar: 20 μm.

4. Reference

S1. Mizukami, S., Watanabe, S., Hori, Y., and Kikuchi, K. (2009) Covalent protein labeling based on non-catalytic β-lactamase and a designed FRET substrate. *J. Am. Chem. Soc. 131*, 5016–5017.

Multiplexed and Reiterative Fluorescence Labeling via DNA Circuitry

Dzifa Y. Duose,[†] Ryan M. Schweller,[†] Walter N. Hittelman,[§] and Michael R. Diehl*[,†,‡]

Department of Bioengineering and Department of Chemistry, Rice University, 6100 Main Street, Houston, Texas 77005, United States, and Department of Experimental Therapeutics, M. D. Anderson Cancer Center, Houston, Texas 77030, United States. Received July 30, 2010; Revised Manuscript Received October 12, 2010

A class of reactive DNA circuits was adapted as erasable molecular imaging probes that allow fluorescent reporting complexes to be assembled and disassembled on a biological specimen. Circuit reactions are sequence-dependent and therefore facilitate multiplexed (multicolor) detection. Yet, the ability to disassemble reporting complexes also allows fluorophores to be removed and new circuit complexes to be used to label additional markers. Thus, these probes present opportunities to increase the total number of molecular targets that can be visualized on a biological sample by allowing multiple rounds of fluorescence microscopy to be performed.

INTRODUCTION

In situ imaging of molecular markers has become increasingly important to advancements in the biological and biomedical sciences (*1*−*5*). These approaches offer advantages over bulk analyses, since they allow spatially dependent expression patterns of RNA and proteins to be delineated in cells and tissues. Several antibody and nucleic acid-based fluorescent probe technologies have been developed for marker imaging, and the sensitivity of these probes has been continually improved (*5*−*8*). Yet, many contemporary cytological studies now require increasingly comprehensive molecular pathway analyses to characterize the network-level properties of cells and resolve functional relationships between cell phenotypes and their tissue distribution (*9*−*11*). In such cases, the number of markers one seeks to examine can easily exceed the number of probes that can be used simultaneously for detection due to the spectral overlap of the reporting dye molecules. Thus, various biological studies stand to benefit from methods that allow a greater number of molecular markers to be visualized.

The number of markers that can be evaluated on an individual biological sample could be increased if it were possible to remove fluorescent probes from cells such that new markers could be labeled and detected using the same fluorescent reporting molecules. However, dye molecules are typically attached covalently to probes that are engineered specifically to bind their targets with high affinity. Probe removal therefore requires the use of harsh chemical and/or physical treatments that can disrupt cell and tissue morphology and compromise subsequent marker analyses.

To overcome these limitations, we adapted a new class of DNA circuit technologies as molecular imaging probes that allow fluorophores to be sequentially coupled to, and removed from, molecular markers using exceptionally mild processing conditions. Derived from "entropically driven" circuits developed by Zhang et al. (*12*), these probes operate using principles distinct from those of fluorescence in situ hybridization (FISH) probes and molecular beacons. Whereas these latter technologies rely on more classical, sequence-dependent hybridization reaction mechanisms for target recognition, the different complexes that make up the entropically driven circuits are designed to react with one another via a process called strand-displacement: the selective exchange of individual oligonucleotides between different complexes of DNA (*13*−*16*). These reactions proceed in a sequence-dependent fashion, and hence, multiple circuits can be employed simultaneously to label different targets. Yet, the total number of matched base pairs that are formed through these reactions does not necessarily have to increase for them to proceed efficiently (i.e., reactant and product complexes can be isoenergetic). As a result, strand displacement reactions can be used to assemble, isolate, and disassemble stable intermediate-state complexes of multistep reaction cycles. Herein, we show that such capabilities can be harnessed to create erasable molecular imaging probes that can function at ambient temperatures and in mild, nondenaturing buffers (e.g., Tris-based buffers). Thus, while the circuit-based probes facilitate multiplexed (simultaneous multicolor) detection, they should also allow the same-colored dye molecules to be used reiteratively to label different markers on an individual sample of fixed cells.

EXPERIMENTAL PROCEDURES

General Methods. Oligonucleotides were purchased from Integrated DNA Technologies (IDT). The recombinant target protein GFP-Z_E, was designed with C-terminal leucine zipper (Z_E) and 6× Histidine tag (6xHis) for purification using standard cloning procedures. Artificial proteins were labeled with catalyst DNA as described in ref *17*.

DNA Circuit Design and Characterization. The DNA circuit sequences were designed as previously described (*12*). Fluorophores and quenchers were incorporated into substrate complexes as shown in Supporting Information Table S1. Strands outfitted with fluorophores or quenchers were purchased HPLC-purified. DNA complexes were formed via a thermal annealing procedure: strands were mixed together at a 1:1 stoichiometry in TAE/Mg^{2+} buffer at a final concentration of 3 μM. The temperature of this solution was then raised to 95 °C and reduced to 25 °C over 90 min. DNA complex formation was verified by 12% nondenaturing PAGE gel analyses using SYBR-Gold staining (Invitrogen).

Microarray Procedures. The DNA microarrays were printed on Vantage silyated aldehyde slides (CEL Associates) using SMP3 pins (ArrayIt) and a custom fabricated microcontact

* To whom correspondence should be addressed. Michael R. Diehl, E-mail: diehl@rice.edu, Department of Bioengineering, 6500 Main Street, ms-142, Houston, Texas 77030.

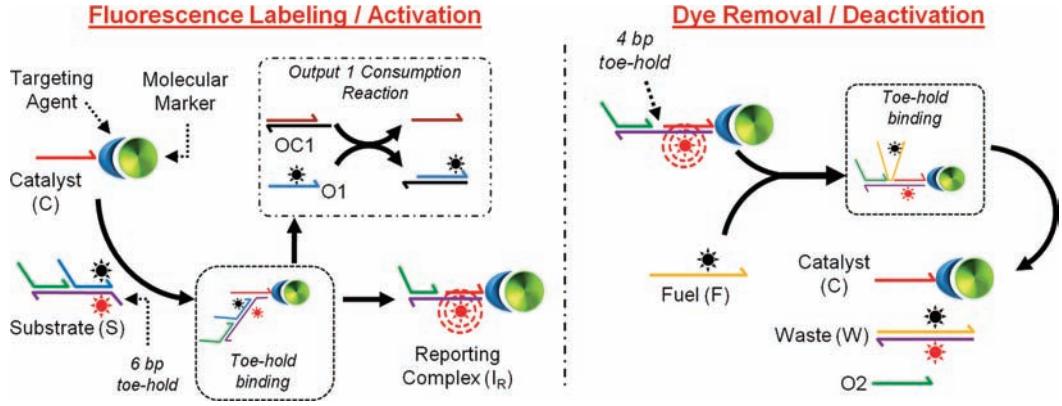
[†] Department of Bioengineering, Rice University.

[‡] Department of Chemistry, Rice University.

[§] M. D. Anderson Cancer Center.

10.1021/bc100348q © 2010 American Chemical Society
Published on Web 11/16/2010

Scheme 1. DNA Circuit-Based Marker Labeling and Dye Removal Reactions



printer. Arrays were fabricated by spotting solutions of 3′-amine labeled C strands (10, 5, 1, 0.5, 0.1, and 0.05 μM stocks for gradient experiments and 2 μM stocks for all others) in PBS (pH 6.6) containing 30% glycerol. Afterward, the slides were incubated in a humidity chamber for 6 h. Free aldehyde groups on the slides were then quenched for 5 min in a sodium borohydride solution (3:1 PBS/EtOH 2.5% $NaBH_4$). Slides were blocked for 2 h in 4× SSPE buffer (600 mM NaCl, 40 mM NaH_2PO_4, and 5 mM EDTA) containing 0.1% BSA, washed 3 times with 4× SSPE buffer with 0.1% SDS, rinsed with milli-H_2O, and dried under nitrogen.

Microarray labeling/activation and dye removal/deactivation reactions were performed using a static incubation procedure or with a hybridization station (TrayMix2: ArrayIt) that provides active mixing of reagents over the slide. For static incubation, Gene frames (AbGene) were affixed over the arrays to create a reaction chamber containing 5 pmol substrate and OC1 consumption complex in TAE w/Mg^{2+}. The arrays were incubated overnight. The Gene frames were then removed and slides were washed 3 times in 4× SSPE buffer, rinsed again in milli-H_2O, and dried under a nitrogen stream. Deactivation and reiterative labeling experiments were performed similarly by affixing new Gene frames to the slides and repeating the incubation procedure. Microarray analysis was performed using *ImageJ* (http://rsbweb.nih.gov/ij/).

Cell Culture and Labeling. HeLa cells were cultured in an 8-chambered coverslips (Lab-Tek) for 24 h in DMEM supplemented with 10% FBS, 50 μg/mL penicillin, and 50 μg/mL of streptomycin. For GFP labeling experiments, the media was replaced and the cells were transfected with GFP-Z_E DNA using Fugene (Roche) transfection reagent under the manufacturer's protocol.

To label cells, coverslips were washed once with PBS and fixed with freshly prepared 4% paraformaldehyde (PFA) solution for 30 min. The cells were then washed twice for 2 min with PBS, permeabilized for 5 min with 0.2% Triton X-100, washed twice again with PBS, and stored overnight at 4 °C. Prior to circuit labeling experiments, the cells were washed again with PBS and then incubated for 2 h with a blocking solution (1% BSA, 1 mg/mL denatured Herring sperm DNA, and 0.5 μM polyT DNA in PBS). For GFP labeling experiments, the cells were also incubated with 400 nM of Z_R-ELS_6-Cat1 in PBS for 2 h. Excess polymer was then removed by washing twice with PBS prior to circuit-based labeling.

Circuit labeling reactions were carried out by incubating the cells for 1.5 h with 100 nM substrate complex and then washing twice with PBS for 2 min. Dye removal was performed similarly using 1 μM fuel. Before imaging experiments, slides were washed twice with PBS and then mounted on a glass slide using rubber cement.

Fluorescence Imaging and Analyses. All images were collected using a Zeiss Axioplan epifluorescence microscope and are contrasted identically in each figure. Correlations between GFP and Cy5-circuit signals and Cy5 signals produced during sequential labeling of cells (ON_1 and ON_2) were analyzed using a custom program written in *Matlab*.

RESULTS AND DISCUSSION

An illustration depicting our use of entropically driven circuits as imaging probes is shown in Scheme 1. Adopting the nomenclature of Zhang et al. (*12*), these circuits are composed of three main components: a single-stranded "catalyst" strand (C), a three-strand DNA complex called the "substrate" (S), and a "fuel" strand (F). In the circuit reaction cycle, the binding of C to a 6 nucleotide "toehold" domain at one end of S initiates a strand displacement reaction that releases an "output" strand (O1) and produces an intermediate-state complex (I_R) that possesses a new, internal 4 bp toehold domain. The binding of F to this toehold then initiates a second strand displacement reaction that releases C from the I_R complex and produces a "waste" product (W). To convert these complexes into imaging probes, catalyst strands can be appended to targeting agents that bind to specific molecular markers. The circuit substrates are modified by incorporating fluorescent dye (Cy3 or Cy5) and quencher (Iowa Black) molecules that are positioned such that the reaction of S with C results in an I_R complex that contains an unquenched fluorophore. The dye-bearing strand within I_R can then be removed from the marker and rendered inactive in the waste product by incubation with a modified F strand that carries a second quencher molecule. Overall, the use of quenched substrates and waste products should reduce background fluorescence resulting from potential nonspecific binding of either complex to a sample. Finally, we note that, in contrast to prior work where C truly functioned as a catalyst (*12*), marker labeling and removal in the present application is achieved by performing partial circuit reactions while using C for targeting. We therefore use the term catalyst only for continuity with previous reports.

To evaluate the efficiency of the circuit-based labeling and dye removal reactions, we first examined distributions of product complexes that were formed upon incubations of S and C, as well as S, C, and F via native PAGE-gel analyses (Figure 1a). After a partial circuit reaction of S with C, the catalyst strand is bound to the I_R complex through a total of 22 matched base pairs. This complex is therefore stable at room temperature and can be isolated on a gel. Yet, the free energy difference between S and I_R is small (ΔG ~0.4 kcal/mol). As a result, the reaction of S and C, when performed using equimolar concentrations, results in an equilibrium distribution of circuit components possessing near-equivalent concentrations of S, I_R, and free,

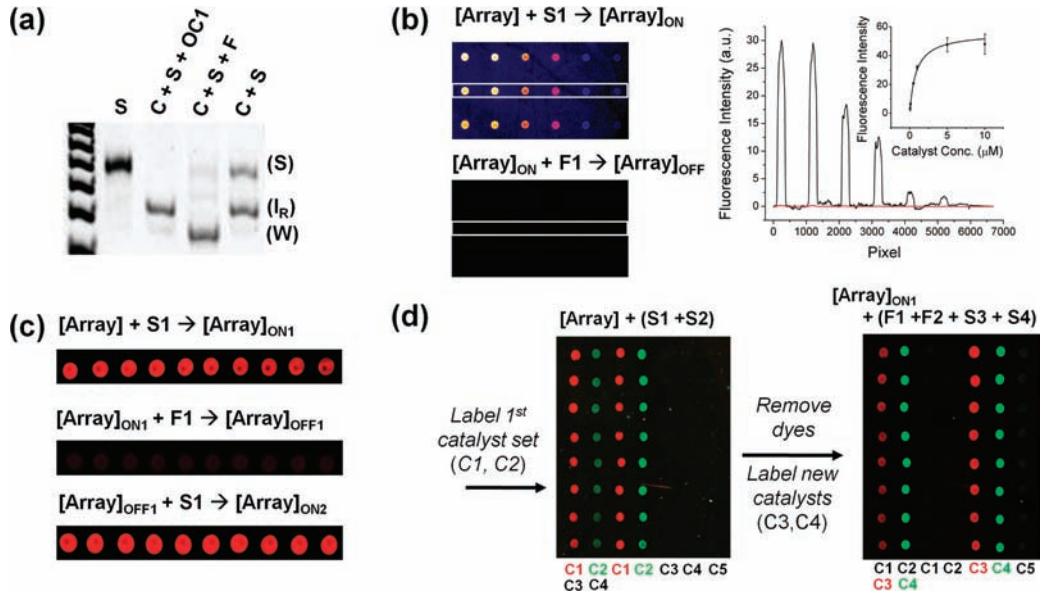


Figure 1. Multiplexed and reiterative fluorescence labeling of ssDNA catalyst. (a) Native PAGE-gel displaying DNA circuit reaction products: all components were reacted at a concentration of 200 nM. (b) A catalyst microarray possessing a gradient of spot concentrations (using 10, 5, 1, 0.5, 0.1, and 0.05 μM stock solutions) that was first labeled and then erased via the sequential addition of S (top image) and a fuel strand (bottom image). Images are rendered as heat maps. Plots of the averaged intensity profile of the boxed regions for the labeling (black line) and dye removal (red line) reactions are shown. Average spot intensities can be approximated by the Langmuir equation (inset). (c and d) Reiterative labeling of an individual (c) and multiple (d) arrayed catalysts. The reactions performed on the arrays are indicated above each image.

"unlabeled" catalyst (Figure 1a, lane 5). While this result is not optimal for marker labeling, this reaction can be driven forward by adding a second complex (OC1) that consumes (O1) once it is liberated from S (boxed reaction in Scheme 1). As demonstrated in other strand displacement systems (*18*), the sequestration of O1 shifts the equilibrium distribution of the reaction significantly toward the I_R state (Figure 1a, lane 3). Alternatively, this distribution can also be shifted using an excess of S relative to C, which should often be the case when labeling catalysts (markers) that are immobilized on a specimen. Nevertheless, the ability to drive strand displacement reactions forward through output sequestration will likely be useful for optimizing dye-labeling kinetics or when local target concentrations within a sample are high.

The removal of dyes from a sample via the reaction of I_R and F constitutes an equally important step in our marker imaging procedure. Here, the use of three-strand S and I_R complexes, as opposed to somewhat simpler two-strand complexes, allows dye-bearing strands to be displaced from the reporting I_R complex without output sequestration (Figure 1a, lane 4), since two strands (C and O2) must react simultaneously with final circuit product W for the reverse reaction W + O2 + C → I_R + F to occur. Hence, the dye removal reaction is effectively irreversible.

We next performed a series of DNA microarray experiments that were designed to evaluate the use of DNA circuit complexes as molecular imaging probes (Figure 1). In these experiments, amine-modified C strands are arrayed on the surfaces of glass slides, and the reaction of S with C produces a fluorescent I_R complex that is anchored to the slide surface and can be detected using a fluorescence microarray scanner. Analyses of arrays where a catalyst was printed at variable spot concentrations confirm that the I_R complex of the circuit can function as a reliable reporter of the levels of immobilized catalyst (Figure 1b, top). Here, spot intensity profiles can be approximated by the Langmuir adsorption equation, as is commonly found with DNA microarrays (*19*, *20*). Furthermore, after the same slide is incubated with a fuel strand, each spot disappears and cannot be detected over background autofluorescence signals of the slide (Figure 1b, bottom).

Our microarray experiments also allowed us to demonstrate the use of DNA circuit probes for both multiplexed and reiterative marker labeling. We found that immobilized C strands can be labeled with dyes multiple times via sequential reactions of arrays with S, F, and then a second solution of S complexes (Figure 1c). Each labeling reaction produced arrays possessing near identical spot intensities. We also demonstrated that multiple C targets could be labeled and/or erased simultaneously using multiple S and F complexes in a single reaction step (Figure 1d). In these experiments, five different C strands were printed both as mixtures of two strands and individually on the surface of the slide. The array was then reacted with two different substrate complexes (S1-Cy5 and S2-Cy3), yielding a spot pattern that corresponded directly to the positions of the printed catalysts (C1 and C2). Subsequently, in a single incubation step, this pattern was erased with F1 and F2, and a new spot pattern was generated through a reaction with a second set of substrates (S3-Cy5 and S4-Cy3); spotted lanes where C3 and C4 were printed appear in the scanned image. Throughout this procedure, the fifth printed catalyst strand of the array (C5) remains unlabeled in both scanned images. Thus, these experiments confirm that DNA circuitry can be used for multiplexed and reiterative imaging: two fluorescent dye molecules and two spectral channels of an imaging system are used to detect four distinct markers on the same sample. Importantly, all labeling and removal reactions in these assays were performed using mild processing conditions (room temperature and Tris buffer supplemented with 12.5 mM Mg^{2+}).

We next performed a series of imaging experiments that show DNA circuit complexes can be used to selectively label molecular markers on fixed and permeablized HeLa cells. Background circuit reactivity was first tested by incubating cell samples with a quenched S complex (100 nM) for 1.5 h. The resulting images show no discernible fluorescence signals and possess signal to background ratios of 1 (Figure 2a), implying that the substrate complexes have exceptionally low background reactivity with cells. We attribute this property to the high stability of the duplexed substrate complex, the enhanced sequence specificity of strand exchange over a classical hybridization mechanism (*21*), and the ability to place dye and

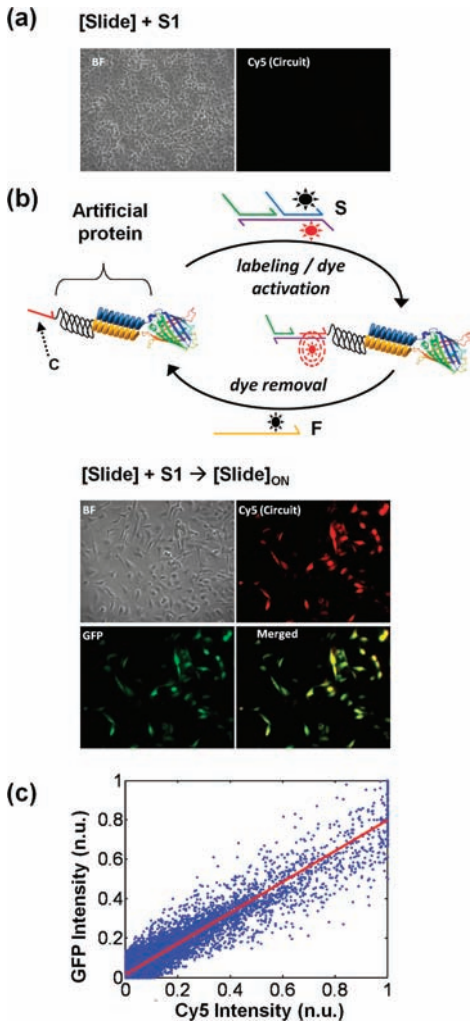


Figure 2. Selective targeting of an exogenously expressed GFP protein marker. (a) Bright field (BF) and fluorescence images of paraformaldehyde-fixed and permeablized HeLa cells reacted with a substrate complex that incorporates a Cy5 and a quencher (Iowa Black). (b) Circuit-based labeling of GFP-Z_E transfected HeLa cells. The catalyst is attached to the GFP marker via a DNA-conjugated artificial protein (Z_R-ELS_6-ssCat) that is introduced postfixation. (c) Intensity correlation analyses of GFP-Z_E and DNA circuit (Cy5) signals. The correlation coefficient, *r*, for the fitted line is 0.95.

quencher molecules in close proximity to one another within the substrate complex.

To label markers on cells, we chose to target the DNA circuit complexes to a transfected and expressed green fluorescent protein construct (GFP-Z_E) so that circuit labeling and dye removal efficiencies could be benchmarked directly against an internal standard (Figure 2b). The catalyst strand was coupled to the GFP using DNA-conjugated artificial-protein-based polymers (Z_R-ELS_6-ssCat) that we have previously developed for protein−DNA labeling (*17*). These polymers associate with the GFP-Z_E via a heterodimeric leucine zipper complex (Z_E/Z_R: $K_D \sim 10^{-15}$ M). Thus, after incubating GFP-Z_E transfected HeLa cells with Z_R-ELS_6-ssCat and then washing the samples to remove unbound polymer, GFP-Z_E transfected cells can be labeled by a reaction of a circuit substrate complex that carries a Cy5 dye and a quencher. As seen in Figure 2b, cells that were successfully transfected with GFP-Z_E reacted with S to produce fluorescent signals in the Cy5 channel of the microscope. While cells that were not transfected did not exhibit fluorescence, clear linear correlations are observed between GFP-Z_E and circuit labeling intensities, yielding a correlation coefficient $r = 0.95$.

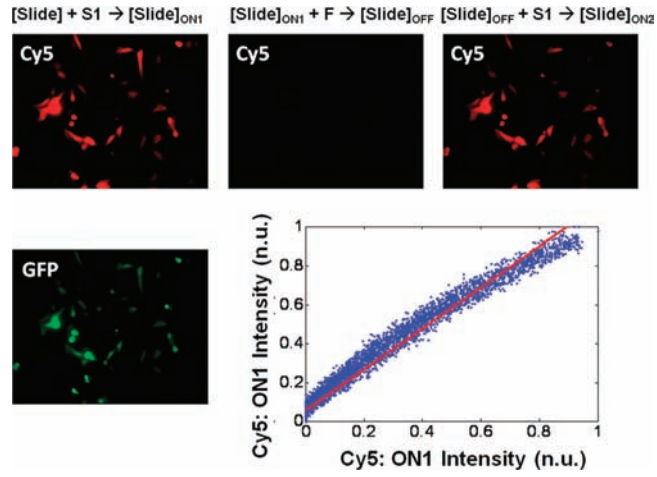


Figure 3. Reiterative circuit labeling of GFP-Z_E transfected cells. Sequential images of GFP-Z_E transfected cells where circuit complexes were used to label (ON1), erase (OFF), and relabel (ON2) the same sample of HeLa cells are shown. The pixel intensities in both Cy5 images (Cy5/ON1 and Cy5/ON2) are linearly correlated; fitted slope = 1.1, $r = 0.92$.

We also tested whether molecular markers could be labeled multiple times on a single sample of cells without loss of fluorescence signal intensities (Figure 3). After a first round of circuit labeling and imaging, fuel strands were added to remove Cy5 dyes from a sample of GFP-Z_E transfected cells. As in our microarray experiments, dye removal reactions are found to be efficient and yield signal to background ratios of 1. In addition, the transfected cells could be labeled and imaged a second time by incubating the sample with a fresh solution of substrate. Bright field imaging showed that a small portion of the cells detached from the slide surface during our manual washing and coverslip mounting procedures. Nevertheless, GFP and Cy5 signals remain highly correlated on a pixel-by-pixel basis after both rounds of fluorescence labeling ($r > 0.95$). Furthermore, strong correlations were found between cell images collected after the first and second dye labeling reactions are performed (i.e., between the ON1 and ON2 images in Figure 3 bottom). The Cy5 intensities of both images are linearly correlated and can be approximated by a line possessing a slope of 1.1. We therefore conclude that the Cy5 dyes can be coupled to the GFP-Z_E markers with near-identical efficiencies through sequential rounds of circuit-based labeling.

CONCLUSION

In summary, we have demonstrated that DNA circuit complexes can be used as erasable molecular imaging probes. Here, the sequence-dependent specificity of the DNA circuit reactions facilitates multiplexed marker detection. The use of strand displacement mechanisms also allows fluorescence reporting complexes to be disassembled, and hence, new reporting complexes can be created and used to image additional sets of molecular markers. Importantly, these reactions can be carried out at ambient temperature and in mild buffering conditions to minimize potential perturbations to a biological specimen. While such capabilities should offer opportunities to increase the number of molecular markers that one can examine on a single biological sample via fluorescence microscopy by at least a factor of 2 or 3, the next challenge will also be to develop diverse sets of molecular targeting agents (e.g., monovalent DNA-conjugated antibodies) that can facilitate efficient molecular marker recognition and react with the DNA circuitry reliably. Efforts to optimize syntheses of such agents are currently underway.

ACKNOWLEDGMENT

We thank P. Constantinou, P. Rothemund, and D. Zhang for helpful discussions. D.Y.D. and R.M.S. contributed equally to this manuscript. This work was supported by grants from the National Science Foundation (MCB-0643832), the NIH (1R21CA147912), the Welch Foundation (C-1625), and the Army Medical Research and Material Command (BAA08-1). R.M.S. is supported by the Nanobiology Interdisciplinary Graduate Training Program of the W. M. Keck Center for Interdisciplinary Bioscience Training of the Gulf Coast Consortia (NIH grant no. T32 EB009379).

Supporting Information Available: A listing of DNA sequences and their modifications are provided in Table S1. This material is available free of charge via the Internet at http://pubs.acs.org.

LITERATURE CITED

(1) Mitchell, P. (2001) Turning the spotlight on cellular imaging. *Nat. Biotechnol. 19*, 1013–1017.

(2) Femino, A. M., Fay, F. S., Fogarty, K., and Singer, R. H. (1998) Visualization of single RNA transcripts in situ. *Science 280*, 585–590.

(3) Pinkel, D., Straume, T., and Gray, J. W. (1986) Cytogenetic analysis using quantitative, high-sensitivity, fluorescence hybridization. *Proc. Natl. Acad. Sci. U.S.A. 83*, 2934–2938.

(4) Nakakuki, T., Birtwistle, M. R., Saeki, Y., Yumoto, N., Ide, K., Nagashima, T., Brusch, L., Ogunnaike, B. A., Okada-Hatakeyama, M., and Kholodenko, B. N. (2010) Ligand-specific c-Fos expression emerges from the spatiotemporal control of ErbB network dynamics. *Cell 141*, 884–896.

(5) Wu, X., Liu, H., Liu, J., Haley, K. N., Treadway, J. A., Larson, J. P., Ge, N., Peale, F., and Bruchez, M. P. (2003) Immunofluorescent labeling of cancer marker Her2 and other cellular targets with semiconductor quantum dots. *Nat. Biotechnol. 21*, 41–46.

(6) Santangelo, P. J., Nix, B., Tsourkas, A., and Bao, G. (2004) Dual FRET molecular beacons for mRNA detection in living cells. *Nucleic Acids Res. 32*, e57.

(7) Soderberg, O., Gullberg, M., Jarvius, M., Ridderstrale, K., Leuchowius, K.-J., Jarvius, J., Wester, K., Hydbring, P., Bahram, F., Larsson, L.-G., and Landegren, U. (2006) Direct observation of individual endogenous protein complexes in situ by proximity ligation. *Nat. Methods 3*, 995–1000.

(8) Rhee, W. J., Santangelo, P. J., Jo, H., and Bao, G. (2008) Target accessibility and signal specificity in live-cell detection of BMP-4 mRNA using molecular beacons. *Nucleic Acids Res. 36*, e30.

(9) Hoos, A., Stojadinovic, A., Singh, B., Dudas, M. E., Leung, D. H. Y., Shaha, A. R., Shah, J. P., Brennan, M. F., Cordon-Cardo, C., and Ghossein, R. (2002) Clinical significance of molecular expression profiles of hurthle cell tumors of the thyroid gland analyzed via tissue microarrays. *Am. J. Pathol. 160*, 175–183.

(10) Gao, X., and Nie, S. (2003) Molecular profiling of single cells and tissue specimens with quantum dots. *Trends Biotechnol. 21*, 371–373.

(11) Roederer, M., Brenchley, J. M., Betts, M. R., and De Rosa, S. C. (2004) Flow cytometric analysis of vaccine responses: how many colors are enough? *Clin. Immunol. 110*, 199–205.

(12) Zhang, D. Y., Turberfield, A. J., Yurke, B., and Winfree, E. (2007) Engineering entropy-driven reactions and networks catalyzed by DNA. *Science 318*, 1121–1125.

(13) Macdonald, J., Li, Y., Sutovic, M., Lederman, H., Pendri, K., Lu, W., Andrews, B. L., Stefanovic, D., and Stojanovic, M. N. (2006) Medium scale integration of molecular logic gates in an automaton. *Nano Lett. 6*, 2598–2603.

(14) Turberfield, A. J., Mitchell, J. C., Yurke, B., Mills, A. P., Blakey, M. I., and Simmel, F. C. (2003) DNA fuel for free-running nanomachines. *Phys. Rev. Lett. 90*, 118102.

(15) Yurke, B., Turberfield, A. J., Mills, A. P., Simmel, F. C., and Neumann, J. L. (2000) A DNA-fuelled molecular machine made of DNA. *Nature 406*, 605–608.

(16) Yin, P., Choi, H. M. T., Calvert, C. R., and Pierce, N. A. (2008) Programming biomolecular self-assembly pathways. *Nature 451*, 318–322.

(17) Schweller, R. M., Constantinou, P. E., Frankel, N. W., Narayan, P., and Diehl, M. R. (2008) Design of DNA-conjugated polypeptide-based capture probes for the anchoring of proteins to DNA matrices. *Bioconjugate Chem. 19*, 2304–2307.

(18) Zhang, D. Y., and Winfree, E. (2006) Control of DNA strand displacement kinetics using toehold exchange. *J. Am. Chem. Soc. 131*, 17303–17314.

(19) Carlon, E., and Heim, T. (2006) Thermodynamics of RNA/DNA hybridization in high-density oligonucleotide microarrays. *Physica A 362*, 433–449.

(20) Peterson, A. W., Wolf, L. K., and Georgiadis, R. M. (2002) Hybridization of mismatched or partially matched DNA at surfaces. *J. Am. Chem. Soc. 124*, 14601–14607.

(21) Zhang, D. Y., and Winfree, E. (2010) Robustness and modularity properties of a non-covalent DNA catalytic reaction. *Nucleic Acids Res. 38*, 4182–4197.

BC100348Q

(Supporting Information)

MULTIPLEXED AND REITERATIVE FLUORESCENCE LABELING VIA DNA CIRCUITRY

Dzifa Duose,[†] Ryan M. Schweller,[†] Walter N. Hittelman,[§] and

Michael R. Diehl[†, ‡,*]

[*] Michael R. Diehl

Departments of Bioengineering[†] and Chemistry[‡], Rice University, 6100

Main Street, Houston, Texas 77005

Department of Experimental Therapeutics[§], M.D. Anderson Cancer Center[§],

Houston, Texas 77030

E-mail: diehl@rice.edu

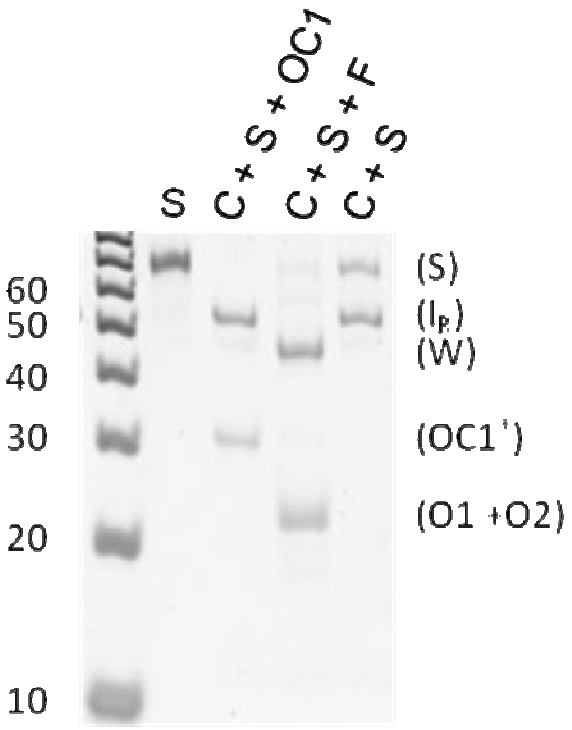


Figure S1. Complete native PAGE-gel illustrating the influence of the output sequestration reaction (O1 + OC1 → OC1*) on equilibrium distributions produced by partial circuit reactions. While efficient conversion of S to I_R requires output sequestration when S and C are present at similar concentrations, the I_R complex can be disassembled near quantitatively by simply adding a fuel strand to the reaction, without the use of output sequestration components.

TABLE S1. List of oligonucleotide sequences used in design of DNA-circuits. Underlined oligonucleotides denote toehold domains. All strands are listed in 5' to 3' direction. /3AmMC6/ denotes a 3' amino modifier on carbon 6; /5Cy5/ denotes 5' Cy5 fluorophore; /5Cy3/ denotes 5' Cy3 fluorophore and /3IAbRQSp/ denotes 3'Iowa black quencher.



SEQUENCE NAME	NUCLEIC ACID SEQUENCE
Circuit1_O1	CCA CAT ACA TCA TAT TCC CTC ATT CAA TAC CCT ACG/3IAbRQSp/
Circuit1_O2	CTT TCC TAC A CC TAC GTC TCC AAC TAA CTT ACG G
Circuit1_LB	TGG AGA /iCy5/CGT AGG GTA TTG AAT GAG GGC CGT AAG TTA GTT GGA GAC GTA GG
Circuit1_C	CAT TCA ATA CCC TAC GTC TCC ATT TTT TTT TT /3AmMC6/
Circuit1_Fuel	CCT ACG TCT CCA ACT AAC TTA CGG CCC TCA TTC AAT ACC CTA CG/3IAbRQSp/
Circuit1_O1 comp	GTA TTG AAT GAG GGA ATA TGA TGT ATG TGG
Circuit1_O1short	CCA CAT ACA TCA TAT TCC CTC ATT
Circuit2_O1	ACC TCT TCA CGA ACA TTT CA/3IAbRQSp/
Circuit2_O2	ACC TAA TAG C AC CAC ATC AAT CTC GAT CCA GTA C
Circuit2_LB	TGG CTA /iCy3/TGA AAT GTT CGT GAA GAG GTG TAC TGG ATC GAG ATT GAT GTG GT
Circuit2_C	CTT CAC GAA CAT TTC ATA GCC ATT TTT TTT TT /3AmMC6/
Circuit2_Fuel	ACC ACA TCA ATC TCG ATC CAG TAC ACC TCT TCA CGA ACA TTT CA
Circuit2_O1comp	TGT TCG TGA AGA GGT
Circuit2_O1short	ACC TCT TCA
Circuit3_O1	TCA CAC ATC AAC CTC T TCTT T CTC TCG ACA CAT CAC
Circuit3_O2	CTT TCC TAC A CT TAT TCA TCC TTT CAC TCA CTT C
Circuit3_LB	GAA GTG AGT GAA AGG ATG AAT AAG AAG AGTG ATG TGT CGA GAG AAAG TAA
Circuit3_C	TCT CTC GAC ACA TCA C TTA CTT TT TTT TTT TT /3AmMC6/

Circuit3_Fuel	CT TAT TCA TCC TTT CAC TCA CTT CTCTT TCT CTC GAC ACA TCA C
Circuit3_O1comp	TGT CGA GAG AAA GAA GAG GTT GAT GTG TGA
Circuit3_O1short	TCA CAC ATC AAC CTC TTC TTT CTC
Circuit4_SB	CAC CAA CCC AAT TCT C CCTA C CCA TTC CTG TAT CAT
Circuit4_OB	ACC TAA TAG C TAC CTT CCC TCT ATT CAT GTC CAC
Circuit4_LB	GTG GAC ATG AAT AGA GGG AAG GTATAG GATG ATA CAG GAA TGG GTGG AGT
Circuit4_C	CCC ATT CCT GTA TCA T AC TCC A TT TTT TTT TT /3AmMC6/
Circuit4_Fuel	TAC CTT CCC TCT ATT CAT GTC CAC CCT ACC CAT TCC TGT ATC AT
Circuit4_O1comp	CAG GAA TGG GTA GGG AGA ATT GGG TTG GTG
Circuit4_O1short	CAC CAA CCC AAT TCT C CCTA C CCA
Circuit5_O1	CAT ACC ACA ACA ATT TAC TTC ACC AAC CCA TCC ACT
Circuit5_O2	CTT TCC TAC AAA TCG CCA AAC TAC AAA CTC AAT C
Circuit5_LB	GAG GTG AGT GGA TGG GTT GGT GAA GTG ATT GAG TTT GTA GTT TGG CGA TT
Circuit5_C	CAC CAA CCC ATC CAC TCA CCT C TT TTT TTT TT /3AmMC6/
Circuit5_Fuel	AAT CGC CAA ACT ACA AAC TCA ATC ACTT CAC CAA CCC ATC CAC T
Circuit5_O1comp	TGG GTT GGT GAA GTA AAT TGT TGT GGT ATG
Circuit5_O1short	CAT ACC ACA ACA ATT TAC TTC ACC
1compcy5	/5Cy5/TGT AGG AAA G
1compcy3	/5Cy3/GCT ATT AGG T

Time-Dependent Enzyme Activity Dominated by Dissociation of J-Aggregates Bound to Protein Surface

Kenji Watanabe and Koji Kano*

Department of Molecular Chemistry and Biochemistry, Doshisha University, Kyotanabe, Kyoto, 610-0321, Japan. Received August 3, 2010; Revised Manuscript Received October 18, 2010

J-Aggregates of diprotonated 5,10,15,20-tetrakis(4-sulfonatopheny)porphyrin (H_4TPPS^{2-}) were stabilized even in a neutral aqueous solution (pH 7.0) containing per-*O*-methylated β-cyclodextrin by binding to the surface of α-chymotrypsin (ChT). The large J-aggregates covered the active site of ChT and completely inhibited the hydrolysis of the peptides. However, enzyme activity was gradually restored with the dissociation of the J-aggregates attached to the protein surface to monomers. After the completion of dissociation of the aggregates, the enzyme activity was almost completely restored, though the structure of ChT significantly changed. Circular dichroism spectroscopy suggested that the microscopic structure at the active site of ChT was scarcely affected by the J-aggregates, but the binding of J-aggregates to ChT increased the content of the random coils in the enzyme. The present study showed a new type of effector for controlling the function of ChT.

INTRODUCTION

Modulation of protein functions by artificial means is an important challenge in the fields of biochemistry, chemical biology, medicinal chemistry, and medical chemistry. Pseudosubstrates that selectively bind to the enzyme active sites have been used as strong inhibitors and can be used to suppress the propagation of viruses (*1*−*3*). Artificial receptors that recognize protein surfaces might also be useful for the inhibition of protein−protein and/or protein−substrate interactions. Hamilton et al. designed and prepared several artificial receptors based on calixarene, porphyrin, and G-quartet scaffolds, which recognize the surfaces of proteins such as α-chymotrypsin (ChT) and cytochrome c (cyt c) (*4*−*14*). Rotello et al. used functionalized gold nanoparticles to regulate the function of ChT (*15*−*25*). These artificial receptors of proteins have larger molecular size than that of pseudosubstrates and, therefore, cover a wider area on the protein surface. Most of these protein receptors are anionic and can nonspecifically recognize the surfaces of basic proteins such as ChT and cyt c. An artificial protein receptor primarily binds to the surface of the protein. If the receptor covers the active site of the protein, it inhibits the activity of the protein. If the receptor causes alteration in protein structure, such receptors act as the denaturant. In the former case, detachment of the receptor from the protein surface restores the protein function. Kano et al. used 5,10,15,20-tetrakis(4-sulfonatophenyl)porphyrinato iron(III) ($Fe^{III}TPPS^{3-}$) as a receptor of ChT that resulted in inhibition of the hydrolysis of an amide substrate (*26*). They found that the ChT function is recovered by detaching $Fe^{III}TPPS^{3-}$ from ChT using heptakis(2,3,6-(tri-*O*-methyl)-β-cyclodextrin (TMe-β-CD), which forms a very stable inclusion complex with the porphyrin. In the latter case, refolding of the denatured protein is so difficult that, in most cases, the function of the protein is permanently lost.

In the present study, we have introduced a concept of spontaneous restoration of enzyme activity, whose function is initially inhibited by a protein receptor. Recently, we found that J-aggregates of diprotonated H_2TPPS^{4-} (H_4TPPS^{2-}) are stabilized by ferric myoglobin (metMb) in aqueous solution at pH 7.0 and 25 °C (*27*). The average half-life of the J-aggregates bound to metMb is approximately 3 h. The J-aggregates gradually dissociate to monomers and the native metMb structure was restored. The results of our previous study prompted us to investigate the time-dependent recovery of ChT activity that is initially inhibited due to covering of the ChT active site by H_4TPPS^{2-} J-aggregates. There have been very few studies on time-dependent changes in enzyme activity. Hamilton's group reported time-dependent inhibition of ChT activity by 4 peptide loops attached to the upper rimes of calix[4]arene and G-quartet scaffolds (*4*−*6*). Similar time-dependent inhibition of ChT activity by functionalized gold nanoparticles has also been reported (*15*). These phenomena were attributed to the slow binding of receptors to ChT. Meanwhile, we explained the similar inhibition by $Fe^{III}TPPS^{3-}$ as time-dependent irreversible denaturation of ChT (*26*). At any rate, the enzyme activity lowered by the protein receptors is hardly restored. In the present study, we examined the self-restoration of ChT activity that is initially inhibited by the J-aggregates of H_4TPPS^{2-}.

EXPERIMENTAL PROCEDURES

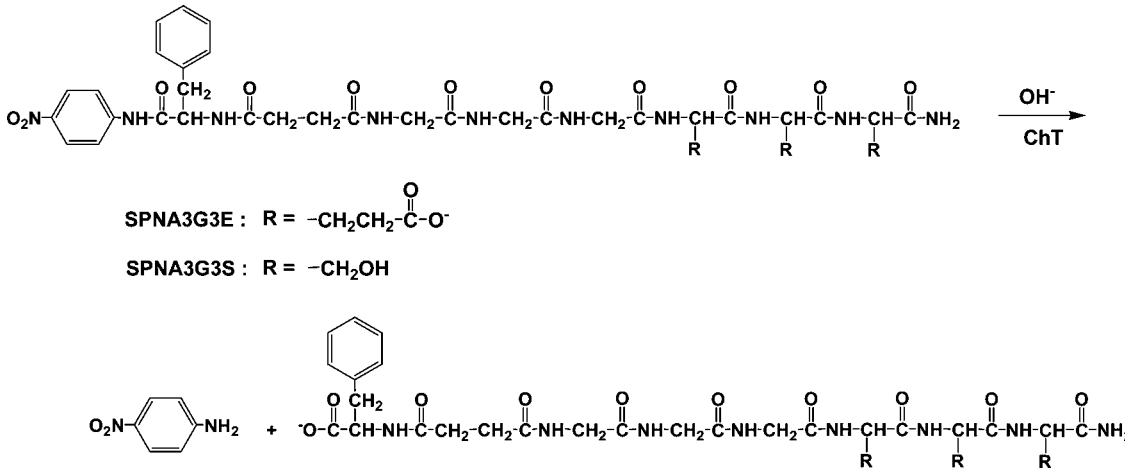
Materials. $H_2TPPS \cdot nH_2O$ (acidic form, >98%, Tokyo Chem. Ind. Co.) was purchased and used without further purification. The concentration of H_2TPPS^{4-} was determined by measuring the absorbance at 414 nm in aqueous NaOH (6 mM) solution using the molar extinction coefficient of $\varepsilon_{414} = 5.33 \times 10^5\ M^{-1}\ cm^{-1}$ (*28*). ChT from bovine pancreas (Sigma-Aldrich Japan) was used as received. The concentration of ChT was determined by measuring the absorbance at 280 nm using the molar extinction coefficient of $\varepsilon_{280} = 5.06 \times 10^4\ M^{-1}cm^{-1}$ (*29*). The building blocks of the substrates, Fmoc-Gly-OH, Fmoc-Glu(^{t}Bu)-OH, and Fmoc-Ser(^{t}Bu)-OH, were purchased from Peptide Institute Inc. (Osaka, Japan). *N*-Succinyl-L-phenylalanine *p*-nitroanilide (SPNA) was obtained from Sigma-Aldrich Jap. Other reagents and solvents were commercially available and used without further purification. Water was purified using a Millipore Simpack 1 (Nihon Millipore, Tokyo, Japan).

Instruments. Absorption and fluorescence spectra were recorded on a Shimadzu UV-2100 spectrophotometer and a Shimadzu RF-5300PC spectrofluorometer, respectively. Circular

* E-mail: kkano@mail.doshisha.ac.jp. Fax: 81-774-65-6845. Phone: 774-65-6624.

10.1021/bc100355v © 2010 American Chemical Society
Published on Web 11/12/2010

Scheme 1. Substrates and ChT-Catalyzed Hydrolysis



dichroism (CD) spectra were measured using a Jasco J820 spectropolarimeter. MALDI-TOF MS measurements were performed by using an Shimadzu AXIMA-CFRplus system. A Horiba F-52 pH meter was used to adjust the pH values of the solutions.

Synthesis. SPNA3G3E (p-NA-Phe-Suc-Gly-Gly-Gly-Glu-Glu-Glu-$CONH_2$): The SPNA3G3E peptide (Scheme 1) was prepared by Fmoc solid-phase peptide synthesis on the TGS-RAM resin (Shimadzu, Kyoto, Japan). Fmoc deprotection was achieved by treatment with 30% (v/v) piperidine in DMF. Each coupling reaction involved the reaction of the NH_2 group on the resin with a carboxy group of Fmoc-amino acid (10 equiv) in DMF containing HBTU (1.2 equiv), HOBt (1.2 equiv), and DIEA (2.4 equiv). The N-terminus of the peptide was conjugated with SPNA (4 equiv) using the coupling agents HBTU (4 equiv), HOBt (4 equiv), and DIEA (4 equiv) in DMF. After the reaction, the peptide was cut off from the resin using a mixture of trifluoroacetic acid/1,2-ethandiol/thioanisole/triisopropylsilane/water (86:5:5:1.5:2.5, v/v) and precipitated with diethyl ether. The crude peptide was purified using an ÄKTApurifier FPLC system (GE Healthcare Jpn. Co., Tokyo, Japan) equipped with a Wakosil-II 5C18 AR reverse phase column (Wako Pure Chem. Ind., Osaka, Japan). The purity of the peptide was confirmed by the FPLC analysis (Supporting Information, Figure S1). Yield 21 mg (76%). MS (MALDI-TOF, α-cyano-4-hydroxycinnamic acid) *m/z*: calcd for $[M - H]^-$ 940.8; found 941.3.

SPNA3G3S (p-NA-Phe-Suc-Gly-Gly-Gly-Ser-Ser-Ser-$CONH_2$): The SPNA3G3S peptide (Scheme 1) was synthesized according to the procedure similar to that followed for SPNA3G3E synthesis. The purity of the peptide was confirmed by FPLC analysis (Supporting Information, Figure S2). Yield 19 mg (79%). MS (MALDI-TOF, α-cyano-4-hydroxycinnamic acid) *m/z*: Calcd for $[M + Na]^+$ 839.3; found 838.6. Calcd for $[M + K]^+$ 855.3; found 855.6.

Sample Preparation. A stock solution of the J-aggregates of H_4TPPS^{2-} (2.0×10^{-3} M as the monomer) was prepared by dissolving $H_2TPPS \cdot nH_2O$ (acidic form) into phosphate buffer (pH 7.0, 5.0×10^{-3} M) and the solution was allowed to stand for a night in dark. Because the buffering effect of the system was not enough, the pH value of the resulting solution decreased to 2.8 due to dissociation of the acidic SO_3H groups of the porphyrin. The main species in this solution were the J-aggregates of H_4TPPS^{2-} (>80%) as confirmed by the UV−visible absorption spectrum (Supporting Information, Figure S3).

RESULTS AND DISCUSSION

Stabilization of J-Aggregates by ChT. Since the pH of the stock solution of H_4TPPS^{2-} ($pK_a = 4.8$) (*30*) was 2.8, the J-aggregates were formed through electrostatic interactions between the SO_3^- groups in the periphery and diprotonated tetrapyrroles of H_4TPPS^{2-} (*31*−*35*). The aggregation numbers of the J-aggregates have been estimated to be tens to hundreds thousands by resonance light scattering (RLS) (*36, 37*). When a stock solution of H_4TPPS^{2-} (2.0×10^{-3} M of H_2TPPS^{4-} monomer) was injected into a neutral phosphate buffer solution (pH 7.0, 1.0×10^{-2} M) to achieve the apparent porphyrin concentration of 1×10^{-6} M, the J-aggregates of H_4TPPS^{2-} immediately dissociated to H_2TPPS^{4-} monomers. In the presence of ChT (1.0×10^{-6} M), however, the dissociation of the J-aggregates was strongly slowed down even in a neutral aqueous solution. Figure 1 (in black) shows the UV−visible spectrum of the resulting solution measured immediately after sample preparation. The characteristic narrow and strong absorption bands at 491 and 706 nm were ascribed to the J-aggregates of H_4TPPS^{2-}, and the coexisting band at 413 nm was due to the monomer of H_2TPPS^{4-} (*31*−*35*). These results indicate that ChT stabilizes the J-aggregates of H_4TPPS^{2-} in neutral aqueous solution. Similar stabilization of the J-aggregates was observed in the H_4TPPS^{2-}/metMb system (*27*). An image of the H_4TPPS^{2-}J-aggregate/ChT complex is shown in Figure

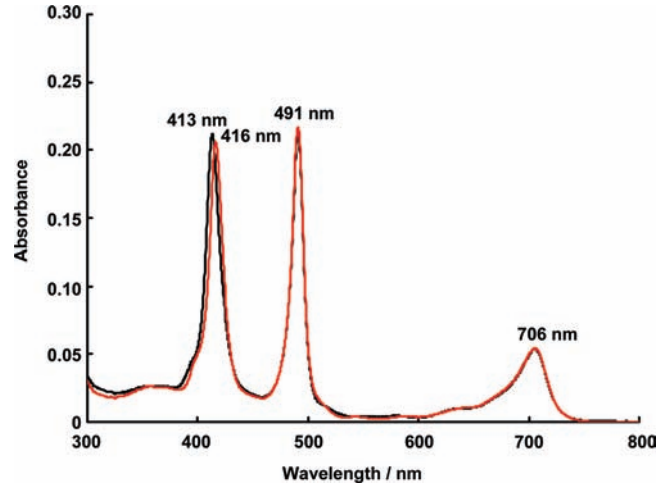


Figure 1. UV−visible spectrum of a sample (sample A) prepared by injecting a stock solution of the J-aggregates of H_4TPPS^{2-} (2.0×10^{-3} M as monomer) into 4 mL of phosphate buffer (pH 7.0, 1.0×10^{-2} M) containing ChT (1.0×10^{-6} M) at 25 °C (black solid line) and the spectrum of a sample (spectrum B) prepared by subsequent addition of TMe-β-CD (8.0×10^{-6} M) to sample A (red solid line).

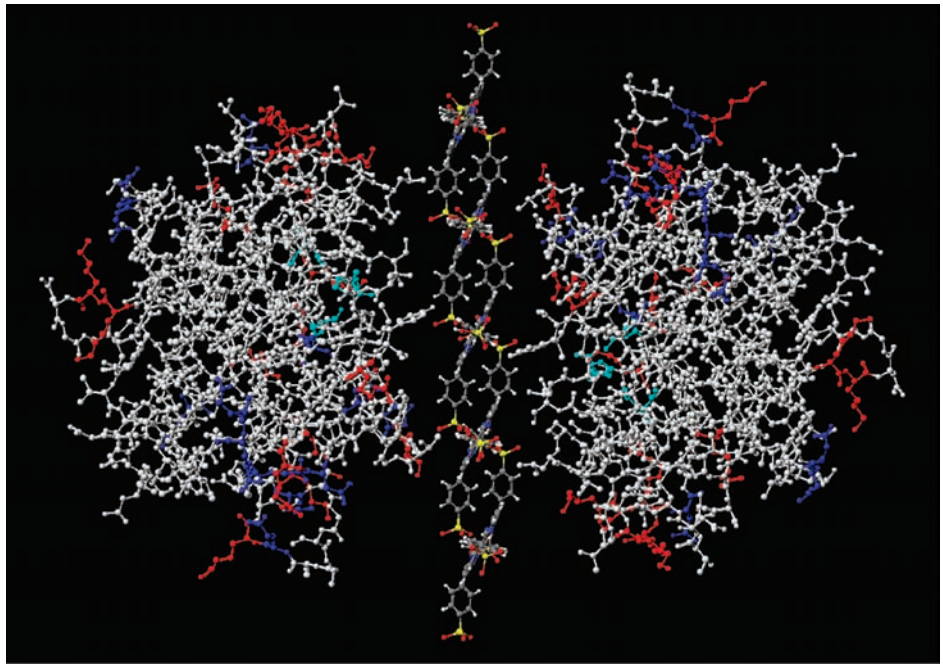


Figure 2. Image of the complex of J-aggregate of H_4TPPS^{2-} with ChT (PDB code 4CHA) drawn by using BioMed CAChe V6. The cationic and anionic amino acid residues of ChT are shown in the red and blue colors, respectively. The light blue color represents the active site of ChT.

2. The J-aggregates stabilized by ChT gradually dissociated to monomers with a $t_{1/2}$ of 27.2 ± 5.5 min (Supporting Information, Figure S4).

We previously found that the $Fe^{III}TPPS^{3-}$ monomer strongly binds with ChT ($K = (4.8 \pm 0.3) \times 10^5\ M^{-1}$) and inhibits its activity (*26*). The H_2TPPS^{4-} monomer also formed a fairly stable complex with ChT ($K = (1.8 \pm 0.4) \times 10^5\ M^{-1}$) (Supporting Information, Figure S5). To prevent the interaction between the H_2TPPS^{4-} monomer and ChT, we externally added TMe-*β*-CD, which forms an extremely stable 2:1 inclusion complex with H_2TPPS^{4-} (*38*), to the system. In the presence of TMe-*β*-CD (8.0×10^{-6} M), the absorption maximum of the monomer band ($\lambda_{max} = 413$ nm) shifted to 416 nm due to the formation of the 2:1 TMe-*β*-CD and H_2TPPS^{4-} complex (Figure 1, in red), but the absorption band of the J-aggregates was not affected at all. The dissociation of the J-aggregates in the presence of TMe-*β*-CD was analyzed by UV−visible spectroscopy (Figure 3). The $t_{1/2}$ in the presence of TMe-*β*-CD was 26.1 ± 2.9 min, which was similar to that in the absence of TMe-*β*-CD, indicating that the dissociation of the J-aggregates was not accelerated by TMe-*β*-CD. Pasternack et al. extensively studied the formation of self-aggregates (not J-aggregates) of a cationic porphyrin (5,10-diphenyl-15,20-bis(*N*-methylpyridinium)porphyrin) (t-$H_2P_{agg}^{2+}$) on a polyanionic DNA double strand (*39*−*41*). They reported that the cationic porphyrin molecules are detached from the DNA after the addition of *β*-cyclodextrin (*41*). The inconsistency in the effects of cyclodextrins between the J-aggregates on ChT and the self-aggregates on DNA might be due to the difference in the regularity of the arrangements of these aggregates. In the case of the J-aggregates, the H_4TPPS^{2-} molecules are highly ordered so that the insertion of a cyclodextrin molecule into the aggregate is difficult. However, the t-$H_2P_{agg}^{2+}$ molecules on DNA are arranged in a relatively disordered manner, and therefore, a cyclodextrin molecule can include the phenyl group of the porphyrin (*41*).

Effect of J-Aggregates on Enzyme Activity. ChT is a proteolytic enzyme that catalyzes the hydrolysis of an amide linkage at the C-terminus of a protein. Because ChT recognizes the aromatic moieties of amino acid residues such as Phe, Tyr, and Trp, we introduced a Phe residue into the substrates

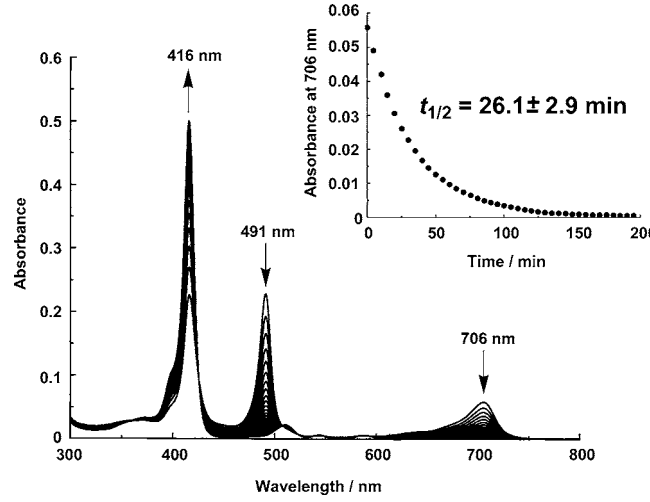


Figure 3. Decomposition of the J-aggregates of H_4TPPS^{2-} bound to ChT into the TPPS/TMe-*β*-CD inclusion complex. The spectra were collected with 5 min intervals. Inset: Progressive change in absorbance at 706 nm due to the J-aggregates. The total concentration of the porphyrin in the system was 1.0×10^{-6} M.

(SPNA3G3E and SPNA3G3S, Scheme 1) used in this study. SPNA3G3E and SPNA3G3S are the anionic and nonionic substrates, respectively. SPNA3G3E with a GluGluGlu sequence was designed to allow recognition of the Phe residue by ChT at the C-terminus and to enhance electrostatic repulsion with the J-aggregates. The hydrolysis of the substrate was monitored by following the changes in the absorbance of released *p*-nitroaniline at 355 nm that correspond to the isosbestic point in the UV−visible spectral changes of the H_4TPPS^{2-} J-aggregates to the H_2TPPS^{4-}/TMe-*β*-CD inclusion complex (Supporting Information, Figure S6).

Figure 4a (in black) shows the progressive changes in the absorbance at 355 nm in the hydrolysis of SPNA3G3E (3.0×10^{-4} M) catalyzed by ChT (1.0×10^{-6} M) in phosphate buffer (pH 7.0, 1.0×10^{-2} M) at 25 °C. The result at the initial stage of hydrolysis, where less than 16% of the substrate molecules were hydrolyzed, is shown in Figure 4. The absorbance at 355

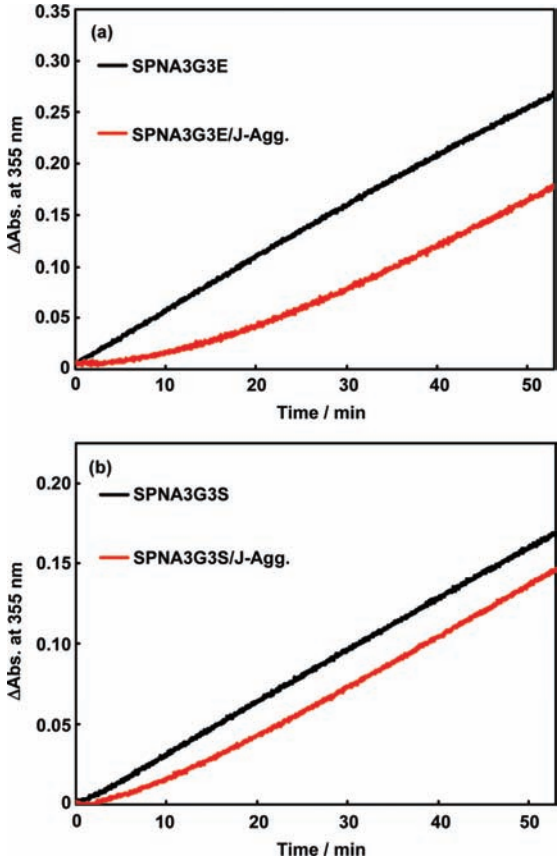


Figure 4. Hydrolysis profiles of SPNA3G3E (3.0×10^{-4} M) (a) and SPNA3G3S (3.0×10^{-4} M) (b) catalyzed by ChT (1.0×10^{-6} M) in the absence (black) and the presence (red) of both the J-aggregates of H_4TPPS^{2-} ($[H_2TPPS^{4-}] = 1.5 \times 10^{-5}$ M) and TMe-β-CD (1.2×10^{-4} M) in phosphate buffer (pH 7.0, 1.0×10^{-2} M) at 25 °C.

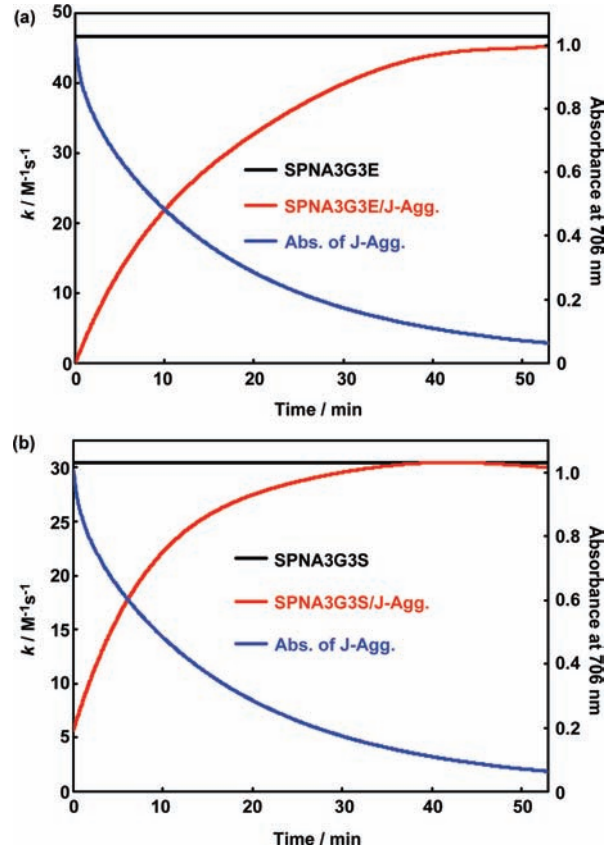


Figure 5. Progressive changes in the rate constants for the ChT-catalyzed hydrolyses of SPNA3G3E (a) and SPNA3G3S (b) in the absence (black) and the presence (red) of both the J-aggregates and TMe-β-CD. The progressive change in the absorbance at 706 nm due to the J-aggregates of H_4TPPS^{2-} (blue) is also shown.

nm appeared to increase linearly in the case of ChT-catalyzed hydrolysis of SPNA3G3E in the absence of the J aggregates. Meanwhile, the ChT-catalyzed hydrolysis of SPNA3G3E in the presence of both H_4TPPS^{2-} J-aggregates (1.5×10^{-5} M as the monomer) and TMe-β-CD (1.2×10^{-4} M) showed a characteristic reaction profile which suggested that the hydrolysis was completely inhibited by the J-aggregates during initial 2 min and the reaction rate gradually increased until 50 min from the start. The inhibition effect depended on the amount of H_4TPPS^{2-} added to the system (Supporting Information, Figure S7). TMe-β-CD itself as well as the 2:1 complex of TMe-β-CD and H_2TPPS^{4-} did not affect the hydrolysis at all. These results clearly indicate that the J-aggregates of H_4TPPS^{2-} play a role in the time-dependent inhibition of ChT-catalyzed hydrolysis of SPNA3G3E.

The results in Figure 4a were analyzed by the following equations. The change in the absorbance at 355 nm (ΔA) is represented as

$$\Delta A = (\varepsilon_S C_S l + \varepsilon_P C_P l) - \varepsilon_S C_{S0} l \quad (1)$$

where ε_S and ε_P are the extinction coefficients of the substrate and the product, respectively, at 355 nm, C_{S0} is the initial concentration of the substrate, C_S and C_P are the concentrations of the substrate and the product, respectively, at time t, and l is the optical length. Since $C_P = (C_{S0} - C_S)$, the C_P can be expressed as

$$C_P = \Delta A/(\varepsilon_P - \varepsilon_S)l \quad (2)$$

The C_P−time profiles obtained for the systems in the absence and the presence of both the J-aggregates and TMe-β-CD fitted well with the linear and six-order polynomial equations (eq 3) using the least-squares method. We arbitrarily selected the six-order polynomial equation. The degrees of fittings were evaluated from the R^2 values that were over 0.999.

$$C_P = f(t) = \sum_{m=0}^{n} a_m t^m \quad (n = 1 \text{ or } 6) \quad (3)$$

Equation 3 was differentiated with time (t) to obtain velocity ($v(t)$) at time t.

$$v(t) = \frac{df(t)}{dt} = \sum_{m=1}^{n} a_m m t^{m-1} \quad (4)$$

The second-order rate constant at t was obtained from eq 5 where the enzyme and substrate concentrations were assumed

$$k(t) = v(t)/[E][S] \quad (5)$$

to be the same as their respective initial concentrations.

Figure 5a shows the rate constants as a function of time for the ChT-catalyzed hydrolyses of SPNA3G3E in the absence and the presence of both the J-aggregates and TMe-β-CD. In the absence of the J-aggregates, the $k(t)$ value was constant until 50 min from the start (Figure 5a, in black). In the presence of a large excess of the substrate, ChT-catalyzed hydrolysis appeared to proceed linearly at the initial stage. Meanwhile, the $k(t)$ value in the presence of the J-aggregates and TMe-β-CD gradually increased and reached the value obtained in the absence of the J-aggregates (Figure 5a, in red). The progressive change in the $k(t)$ was in good agreement with the decrease in

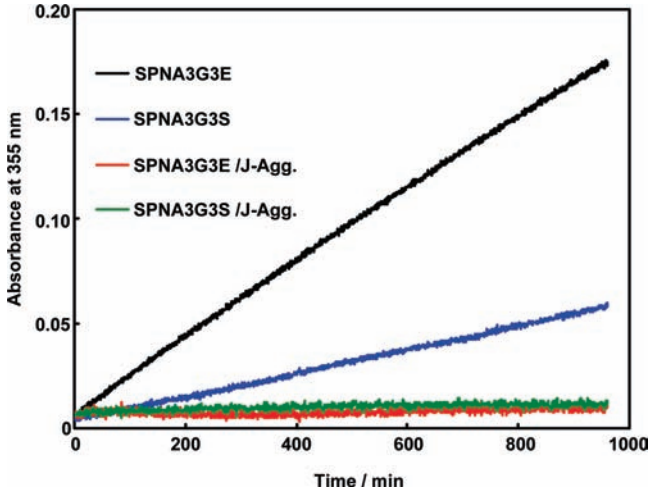


Figure 6. Hydrolysis profiles of SPNA3G3E (3.0×10^{-4} M; black and red) and SPNA3G3S (3.0×10^{-4} M; blue and green) catalyzed by ChT (1.0×10^{-6} M) in the absence and the presence of both the J-aggregates of H_4TPPS^{2-} ($[H_2TPPS^{4-}] = 1.5 \times 10^{-5}$ M) and TMe-β-CD (1.2×10^{-4} M) in succinic acid buffer (pH 4.0, 1.0×10^{-2} M) at 25 °C.

the absorbance at 706 nm due to the dissociation of the J-aggregates (Figure 5a, in blue). These results clearly indicate that the enzyme activity of ChT was inhibited by the J-aggregates and that it gradually recovered to the original value with the progressive dissociation of the J-aggregates. The restoration of the enzyme activity was 98% at 50 min from the start of the dissociation of the J-aggregates.

Inhibition Mechanism. The following three mechanisms are proposed for the inhibition of ChT activity by the J-aggregates of H_4HPPS^{2-}: (1) electrostatic repulsion between the anionic groups of SPNA3G3E and the J-aggregates, (2) covering of the active site of ChT by the J-aggregates, and (3) structural changes in ChT caused by the J-aggregate.

To study the contribution of electrostatic interaction to the inhibition of the hydrolysis of anionic SPNA3G3E, we used a neutral SPNA3G3S (Scheme 1) as the substrate. The reaction profile is shown in Figure 4b, which exhibits that the J-aggregates inhibit the hydrolysis of the neutral substrate in the manner similar to that of the anionic substrate, though the inhibitory effect in the case of neutral SPNA3G3S is not as remarkable as that in the case of SPNA3G3E. The degrees of inhibition by the J-aggregates at 500 s from the start were 83% and 35% for SPNA3G3E and SPNA3G3S, respectively. It can be concluded, therefore, that electrostatic repulsion between the polyanionic J-aggregates and anionic SPNA3G3E is one of the important factors that reduces the hydrolysis of this anionic substrate.

Since the hydrolysis of the neutral substrate was inhibited by the J-aggregates, the covering effect might also influence the hydrolysis. To this end, we evaluated the inhibition effect of the J-aggregates in aqueous solution at pH 4.0, wherein the J-aggregates do not dissociate to a marked extent. The results are shown in Figure 6. Since the optimum pH range of ChT activity is 8−9, the rates of the hydrolyses of both SPNA3G3E and SPNA3G3S at pH 4.0 were much less than those at pH 7.0. The hydrolyses of both the substrates were completely suppressed in the presence of the J-aggregates. The results clearly show that the J-aggregates of H_4TPPS^{2-} cover the active site of the enzyme and block the binding of the substrate leading to complete inhibition of the hydrolysis. At pH 7.0, the partial dissociation of the J-aggregates occurs from the start of the reaction, freeing the active site to interact with the substrate. In this stage, electrostatic interactions influence the approach of the substrate to the open active site of ChT.

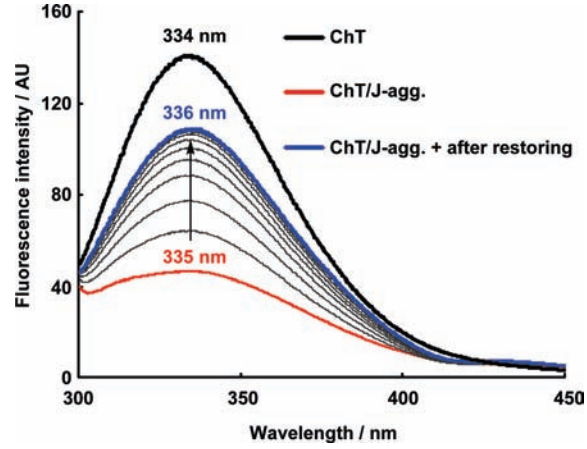


Figure 7. Fluorescence spectra of ChT (1.0×10^{-7} M) before (black) and after (red) the addition of both J-aggregates of H_4TPPS^{2-} ($[H_2TPPS^{4-}] = 1.5 \times 10^{-6}$ M) and TMe-β-CD (1.2×10^{-5} M) (red solid line) in phosphate buffer (pH 7.0, 1.0×10^{-2} M) at 25 °C. The fluorescence intensity gradually recovered to the spectrum indicated in a blue line. The spectra were recorded with 5 min intervals.

Finally, we studied the effect of the J-aggregates on changes in the protein structure of ChT. ChT possesses eight Trp residues, which are located in the core and the surface of the protein (*42*). The Trp residues exhibit fluorescence and are useful to probe changes in the protein structure, because the fluorescence of these residues greatly depends on the microenvironment (*43, 44*). Figure 7 shows the fluorescence spectral changes of ChT after the addition of J-aggregates. The fluorescence intensity at 334 nm markedly decreased immediately after the addition of the J-aggregates and gradually recovered with the dissociation of the J-aggregates from the protein surface. The fluorescence maximum of ChT scarcely shifted though the fluorescence intensity markedly diminished, suggesting that the Trp residues in the interior of the protein are not exposed on the protein surface upon binding with the J-aggregates. ChT appears to change its conformation upon binding with J-aggregates without undergoing distinct denaturation. The change in the conformation of ChT might cause enhanced fluorescence quenching of the Trp fluorescence by other amino acid residues (*44*). The fluorescence was not completely recovered, meaning occurrence of permanent change in the structure of ChT, although the enzyme activity was almost completely restored after the complete dissociation of the J-aggregates (see Figure 5).

CD spectra also revealed structural changes in ChT after the addition of J-aggregates (Figure 8). Since the CD measurement required about 10 min, the observed spectrum did not reflect the structure of ChT immediately after binding with the J-aggregates. Upon addition of the J-aggregates, the negative CD bands of ChT at 203 nm shifted to 201 nm along with enhancement of the negative Cotton effect. Meanwhile, the band at 230 nm scarcely changed. The CD spectrum of ChT further changed during the dissociation of the J-aggregates and the CD band finally shifted to 198 nm. The negative CD signal at 198 nm indicates the formation of a random coil structure. The negative band at 230 nm was retained in the final CD spectrum. The negative CD band at 230 nm is characteristic of the Trp 141 that is located close to the His 57 and Ser 195 at the active site of ChT (*18, 45*). This band has been used as a probe for predicting the enzyme activity of ChT (*18, 45*). Reduction in the band at 230 nm indicates lowering of the enzyme activity. If the band is not affected by any perturbation, the enzyme activity will be maintained (*46*). The CD spectral data is

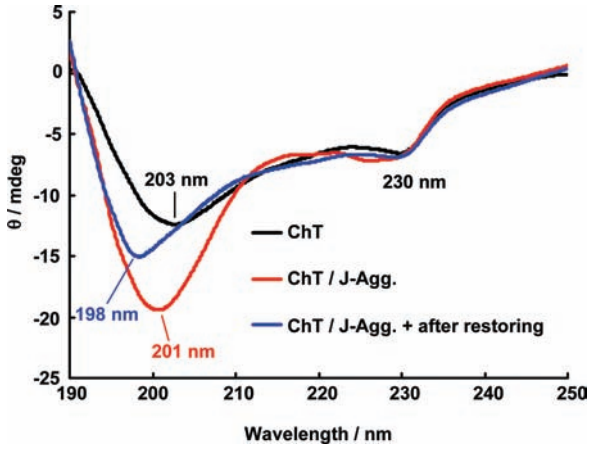


Figure 8. CD spectra of ChT (1.0×10^{-6} M) before (black) and after the addition (red) of the J-aggregates of H_4TPPS^{2-} ($[H_2TPPS^{4-}] = 1.5 \times 10^{-5}$ M) and TMe-β-CD (1.2×10^{-4} M) in phosphate buffer (pH 7.0, 1.0×10^{-2} M) at 25 °C. A spectrum in blue was recorded after complete dissociation of the J-aggregates.

consistent with the fact that the enzyme activity is restored after complete dissociation of the J-aggregates from the surface of ChT.

CONCLUSION

The J-aggregates of H_4TPPS^{2-} are stabilized by ChT even in neutral aqueous solution. These aggregates cover the active site of the enzyme and completely inhibit the enzyme activity. However, the enzyme activity is restored almost completely with the dissociation of the J-aggregates. The J-aggregates induce a progressive change in enzyme activity from complete inhibition to complete restoration without the aid of a secondary additive.

On the basis of the findings of this study, it is possible to develop a "dream drug" with the following features: (1) The drug specifically binds to a target protein. (2) The drug inhibits protein function for a desired time period. (3) The function of the protein is completely restored after the drug has performed its work. (4) The used drug is removed from the body.

The present study shows that J-aggregates of H_4TPPS^{2-} partially fulfill these requirements. The polyanionic J-aggregates selectively bind with a basic protein and do not interact with polyanionic DNA and RNA. The large J-aggregates cover the protein surface and inhibit substrate binding or protein−protein interaction. The J-aggregates spontaneously dissociate to monomers, gradually restoring the protein function. The monomer of H_2TPPS^{4-} forms an extremely stable 2:1 inclusion complex with TMe-β-CD that is easily excreted in urine (*47*). The J-aggregates of H_4TPPS^{2-} cannot be actually used as drugs because of difficulty in administration to a living body. However, the present study introduces the concept of preparing a dream drug in the future.

ACKNOWLEDGMENT

This study was supported by Grants-in-Aid on Construction of Research Base in Private University from Ministry of Education, Culture, Sports, Science and Technology.

Supporting Information Available: Additional experimental data. This material is available free of charge via the Internet at http://pubs.acs.org.

LITERATURE CITED

(1) Mitsuya, H., and Erickson, J. (1999) Drug Development. *Textbook of AIDS medicine* (Merigan, T. C., Jr., Bartlett, J. G., and Bolognesi, D., Eds.) pp 751−780, Chapter 45, Lippincott, Williams & Wilkins, Baltimore.

(2) Clercq, E. D. (2007) The design of drugs for HIV and HCV. *Nat. Rev. Drug Discovery 6*, 1001–1018.

(3) Magano, J. (2009) Synthetic approaches to the neuraminidase inhibitors zanamivir (Relenza) and oseltamivir phosphate (Tamiflu) for the treatment of influenza. *Chem. Rev. 109*, 4398–4438.

(4) Park, H. S., Lin, Q., and Hamilton, A. D. (1999) Protein surface recognition by synthetic receptors: a route to novel submicromolar inhibitors for α-chymotrypsin. *J. Am. Chem. Soc. 121*, 8–13.

(5) Park, H. S., Lin, Q., and Hamilton, A. D. (2002) Modulation of protein-protein interactions by synthetic receptors: design of molecules that disrupt serine protease-proteinaceous inhibitor interaction. *Proc. Natl. Acad. Sci. U.S.A 99*, 5105–5109.

(6) Cai, J., Rosenzwig, B. A., and Hamilton, A. D. (2009) Inhibition of chymotrypsin by a self-assembled DNA quadruplex functionalized with cyclic peptide binding fragments. *Chem.—Eur. J. 15*, 328–332.

(7) Hamuro, Y., Calama, M. C., Park, H. S., and Hamilton, A. D. (1997) A calixarene with four peptide loops: An antibody mimic for recognition of protein surface. *Angew. Chem., Int. Ed. 36*, 2680–2683.

(8) Jain, R. K., and Hamilton, A. D. (2000) Protein surface recognition by synthetic receptors based on a tetraphenylporphyrin scaffold. *Org. Lett. 2*, 1721–1723.

(9) Wei, Y., Mclendon, G. L., Hamilton, A. D., Case, M. A., Purring, C. B., Lin, Q., Park, H. S., Lee, C.-S., and Yu, T. (2001) Disruption of protein-protein interactions: design of a synthetic receptor that blocks the binding of cytochrome c to cytochrome c peroxidase. *Chem. Commun.* 1580–1581.

(10) Jain, R. K., and Hamilton, A. D. (2002) Designing protein denaturants: synthetic agents induce cytochrome c unfolding at low concentration and stoichiometries. *Angew. Chem., Int. Ed. 41*, 641–643.

(11) Wilson, A. J., Groves, K., Jain, R. K., Park, H. S., and Hamilton, A. D. (2003) Directed denaturation: room temperature and stoichiometric unfolding of cytochrome c by a metalloporphyrin dimer. *J. Am. Chem. Soc. 125*, 4420–4421.

(12) Aya, T., and Hamilton, A. D. (2003) Tetraphenylporphyrin-based receptors for protein surfaces show sub-nanomolar affinity and enhance unfolding. *Biorg. Med. Chem. Lett. 13*, 2651–2654.

(13) Groves, K., Wilson, A. J., and Hamilton, A. D. (2004) Catalytic unfolding and proteolysis of cytochrome c induced by synthetic binding agents. *J. Am. Chem. Soc. 126*, 12833–12842.

(14) Tagore, D. M., Sprinz, K. I., Fletcher, S., Jayawickramarajah, J., and Hamilton, A. D. (2007) Protein recognition and denaturation by self-assembling fragments on a DNA quadruplex scaffold. *Angew. Chem., Int. Ed. 46*, 223–225.

(15) Fischer, N. O., McIntosh, C. M., Simard, J. M., and Rotello, V. M. (2002) Inhibition of chymotrypsin through surface binding using nanoparticle-based receptors. *Proc. Natl. Acad. Sci. U.S.A. 99*, 5018–5023.

(16) Hong, R., Fischer, N. O., Verma, A., Goodman, C. M., Emrick, T., and Rotello, V. M. (2004) Control of protein structure and function through surface recognition by tailored nanoparticle scaffold. *J. Am. Chem. Soc. 126*, 739–743.

(17) Hong, R., Emrick, T., and Rotello, V. M. (2004) Monolayer-controlled substrate selectivity using noncovalent enzyme-nanoparticle conjugates. *J. Am. Chem. Soc. 126*, 13572–13573.

(18) Verma, A., Simard, J. M., and Rotello, V. M. (2004) Effect of ionic strength on the binding of α-chymotrypsin to nanoparticle receptors. *Langmuir 20*, 4178–4181.

(19) You, C.-C., De, M., Han, G., and Rotello, V. M. (2005) Tunable inhibition and denaturation of α-chymotrypsin with amino acid-functionalized gold nanoparticles. *J. Am. Chem. Soc. 127*, 12873–12881.

(20) You, C.-C., De, M., and Rotello, V. M. (2005) Contrasting effects of exterior and interior hydrophobic moieties in the complexation of amino acid functionalized gold clusters with α-chymotrypsin. *Org. Lett. 7*, 5685–5688.

(21) You, C.-C., Agasti, S. S., De, M., Knapp, M. J., and Rotello, V. M. (2006) Modulation of the catalytic behavior of α-chymotrypsin at monolayer-protected nanoparticle surfaces. *J. Am. Chem. Soc. 128*, 14612–14618.

(22) De, M., You, C.-C., Srivastava, S., and Rotello, V. M. (2007) Biomimetic interactions of proteins with functionalized nanoparticles; a thermodynamic study. *J. Am. Chem. Soc. 129*, 10747–10753.

(23) De, M., and Rotello, V. M. (2008) Synthetic "chaperones": nanoparticle-mediated refolding of thermally denaturated proteins. *Chem. Commun* 3504–3506.

(24) You, C.-C., Agasti, S. S., and Rotello, V. M. (2008) Isomeric control of protein recognition with amino acid- and dipeptide-functionalized gold nanoparticle. *Chem.—Eur. J. 14*, 143–150.

(25) Jordan, B. J., Hong, R., Han, G., Rama, S., and Rotello, V. M. (2009) Modulation of enzyme-substrate selectivity using tetraethylene glycol functionalized gold nanoparticles. *Nanotechnology 20*, 434004.

(26) Kano, K., and Ishida, Y. (2008) Regulation of α-chymotrypsin catalysis by ferric porphyrins and cyclodextrins. *Chem. Asian J. 3*, 678–686.

(27) Kano, K., Watanabe, K., and Ishida, Y. (2008) Porphyrin J-aggregates stabilized by ferric myoglobin in neutral aqueous solution. *J. Phys. Chem. B 112*, 14402–14408.

(28) Fleischer, E. B., Palmer, J. M., Srivastava, T. S., and Chatterjee, A. (1971) Thermodynamic and kinetic properties of an iron-porphyrin system. *J. Am. Chem. Soc. 93*, 3162–3167.

(29) Pace, C. N., Vajdos, F., Fee, L., Grimsley, G., and Gray, T. (1995) How to measure and predict the molar absorption coefficient of a protein. *Protein Sci. 4*, 2411–2423.

(30) Kalyanasundaram, K. (1983) Photochemistry and sensitized evolution of hydrogen from water using water-soluble cationic porphyrins. Tetrakis(trimethylaminophenyl)porphyrinatozinc and its free base. *J. Chem. Soc. Faraday Trans. 2 79*, 1365–1374.

(31) Pasternack, R. F., Huber, P. R., Boyd, P., Engasser, G., Francesconi, L., Gibbs, E., Fasella, P., Venturo, G. C., and Hinds, L. de C. (1972) Aggregation of meso-substituted water-soluble porphyrins. *J. Am. Chem. Soc. 94*, 4511–4517.

(32) Ohno, O., Kaizu, Y., and Kobayashi, H. (1993) J-aggregate formation of a water-soluble porphyrin in acidic aqueous media. *J. Chem. Phys. 99*, 4128–4139.

(33) Sutter, T. P. G., Rahimi, R., Hambright, P., Bommer, J. C., Kumar, M., and Neta, P. (1993) Steric and inductive effects on the basicity of porphyrins and on the site of protonation of porphyrin dianions: radiolytic reduction of porphyrin and metalloporphryins to chlorines or phlorins. *J. Chem. Soc., Faraday Trans. 89*, 495–502.

(34) Ribó, J. M., Crusats, J., Farrera, J.-A., and Valero, M. L. (1994) Aggregation in water solutions of tetrasodium diprotonated meso-tetrakis(4-sulfonatophenyl)porphyrin. *J. Chem. Soc., Chem. Commun.* 681–682.

(35) Akins, D. L., Zhu, H.-R., and Guo, C. (1994) Absorption and Raman scattering by aggregated meso-tetrakis(p-sulronatophenyl)porphine. *J. Phys. Chem. 98*, 3612–3618.

(36) Pasternack, R. F., Schaefer, K. F., and Hambright, P. (1994) Resonance light-scattering studies of porphyrin diacid aggregates. *Inorg. Chem. 33*, 2062–2065.

(37) Collings, P. J., Gibbs, E. J., Starr, T. E., Vafek, O., Yee, C., Pomerance, L., and Pasternack, R. F. (1999) Resonance light scattering and its application in determining the size shape and aggregation number for supramolecular assemblies of chromophores. *J. Phys. Chem. B 103*, 8474–8481.

(38) Kano, K., Nishiyabu, R., Asada, T., and Kuroda, Y. (2002) Static and dynamic behavior of 2:1 inclusion complexes of cyclodextrin and charged porphyrins in aqueous organic media. *J. Am. Chem. Soc. 124*, 9937–9944.

(39) Pasternack, R. F., Gibbs, E. J., Collings, P. J., de Paula, J. C., Turzo, L. C., and Terracina, A. (1998) A nonconventional approach to supramolecular formation dynamics. The kinetics of assembly of DNA-bound porphyrins. *J. Am. Chem. Soc. 120*, 5873–5878.

(40) Pasternack, R. F., Ewen, S., Rao, A., Meyer, A. S., Freedam, M. A., Collings, P. J., Frey, S. L., Ranen, M. C., and de Paula, J. C. (2001) Interactions of copper(II) porphyrins with DNA. *Inorg. Chem. Acta 317*, 59–71.

(41) Pasternack, R. F., Gibbs, E. J., Bruzewicz, D., Stewart, D., and Engstrom, K. S. (2002) Kinetics of disassembly of a DNA-bound porphyrin supramolecular array. *J. Am. Chem. Soc. 124*, 3533–3539.

(42) Tsukada, H., and Blow, D. M. (1985) Structure of α-chymotrypsin refined at 1.68 Å resolution. *J. Mol. Biol. 184*, 703–711.

(43) Ladokhin, A. S. (2000) Fluorescence Spectroscopy in Peptide and Protein Analysis. *Encyclopedia of Analytical Chemistry* (Meyers, R. A., Ed.) pp 5762−5779, John Wiley & Sons Ltd., Chichester.

(44) Chen, Y., and Barkley, H. D. (1998) Toward understanding tryptophan fluorescence in proteins. *Biochemistry 37*, 9976–9982.

(45) Schechter, N. M., Eng, G. Y., Selwood, T., and McCaslin, D. R. (1995) Structural changes associated with the spontaneous inactivation of the serine proteinase human tryptase. *Biochemistry 34*, 10628–10638.

(46) McConn, J., Fasman, G. D., and Hess, G. P. (1969) Conformation of the high pH form of chymotrypsin. *J. Mol. Biol. 39*, 551–562.

(47) Kitagishi, H., Negi, S., Kiriyama, A., Honbo, A., Sugiura, Y., Kawaguchi, A. T., and Kano, K. (2010) A diatomic molecular receptor that removes CO in a living organism. *Angew. Chem., Int. Ed. 49*, 1312–1315.

BC100355V

Supporting Information

Time-Dependent Enzyme Activity Dominated by Dissociation of J-Aggregates Bound to Protein Surface

Kenji Watanabe and Koji Kano*

Department of Molecular Chemistry and Biochemistry, Doshisha University, Kyotanabe, Kyoto, 610-0321, Japan

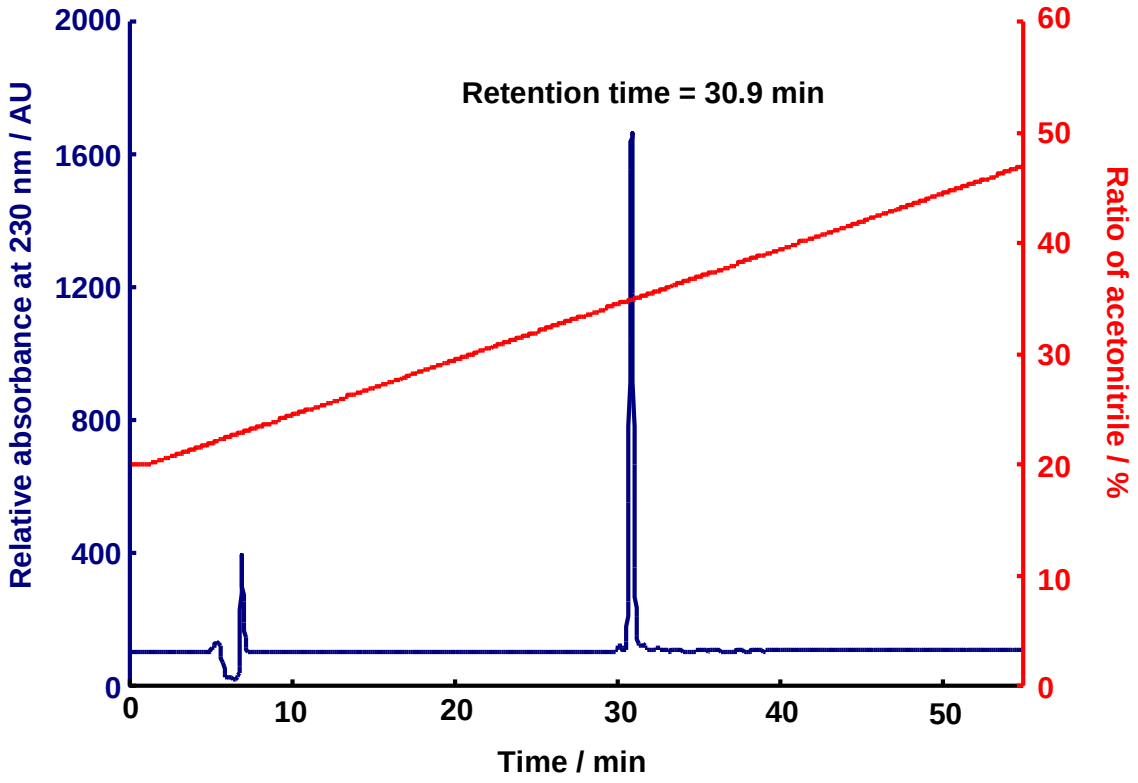


Figure S1. FPLC profile of SPNA3G3E recorded at 230 nm. Red solid line represents the ratio of acetonitrile in the eluent (acetonitrile/water containing 0.1 v/v% TFA). A COSMOSIL 5C18-AR-II (4.6 mm x 250 mm) column (Nacalai Tesque, Kyoto Japan) was used for the analysis. Flow rate of the eluent was 0.5 mL/min.

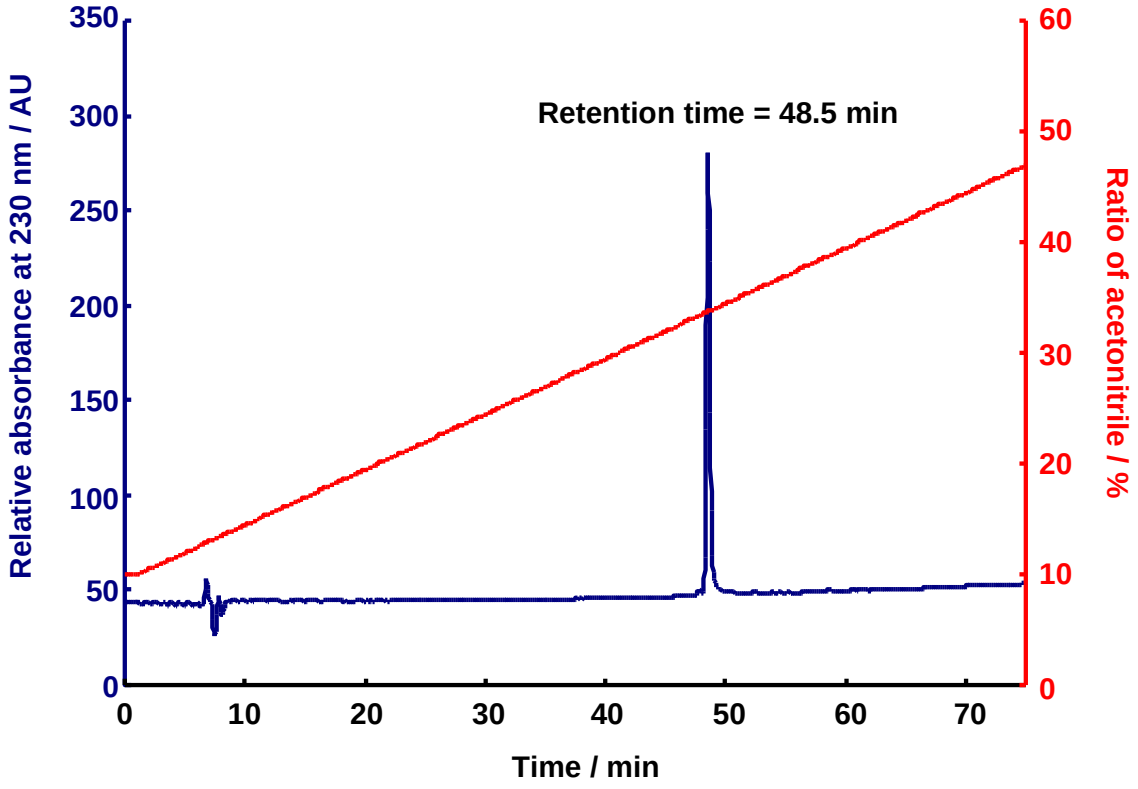


Figure S2. FPLC profile of SPNA3G3S recorded at 230 nm. Red solid line represents the ratio of acetonitrile in the eluent (acetonitrile/water containing 0.1 v/v% TFA). A COSMOSIL 5C18-AR-II (4.6 mm x 250 mm) column (Nacalai Tesque, Kyoto Japan) was used for the analysis. Flow rate of the eluent was 0.5 mL/min.

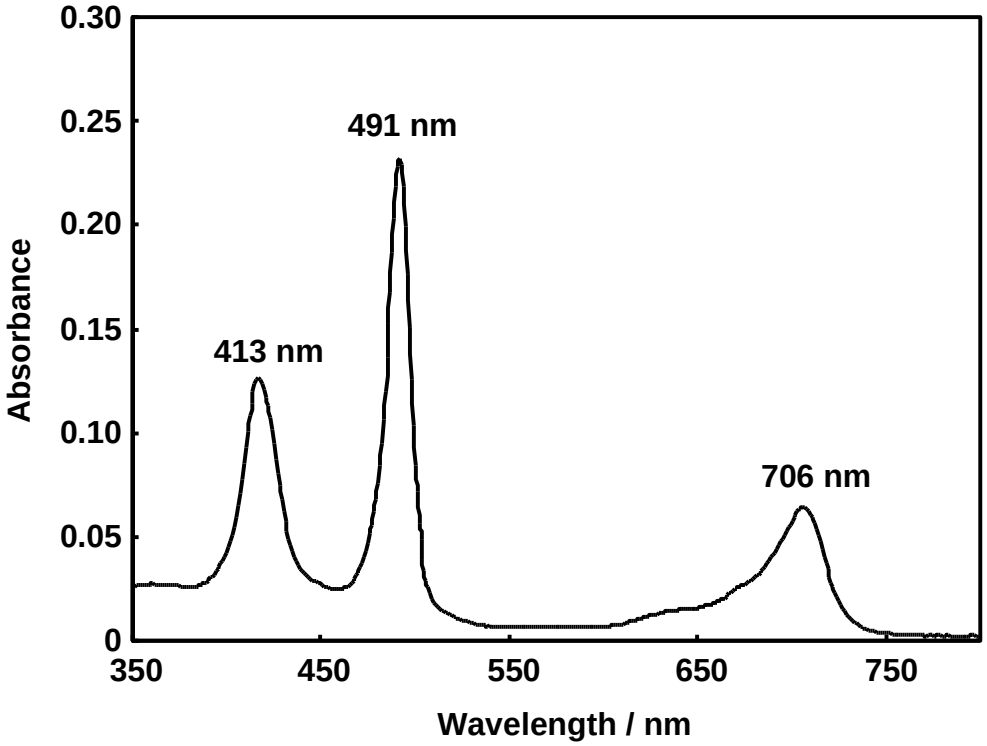


Figure S3. UV-visible spectrum of a sample prepared by injecting a stock solution of J-aggregates of H_4TPPS^{2-} (2.0 μL, 2.0 x 10^{-3} M) into 4 mL of phosphate buffer (pH 7.0, 1.0 x 10^{-2} M) containing ChT (1.0 x 10^{-4} M) at 25 ^{o}C. The total concentration of the porphyrin in the system was 1.0 x 10^{-6} M.

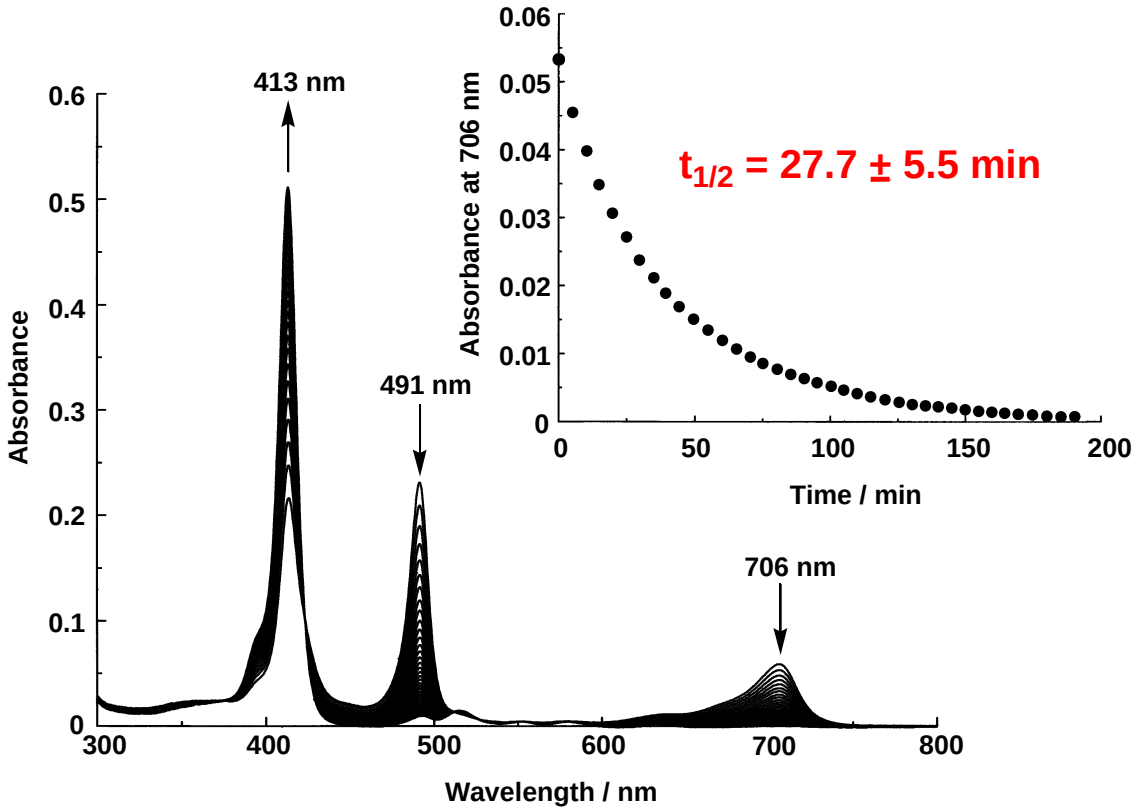


Figure S4. Progressive absorption spectral change for decomposition of J-aggregates of H_4TPPS^{2-} bound to ChT (1.0 x 10^{-6} M) into the monomers of H_2TPPS^{4-} in phosphate buffer (pH 7.0, 1.0 x 10^{-2} M) at 25 ^{o}C. Inset: Time-course of the absorbance of the J-aggregates at 706 nm. The total concentration of the porphyrin in the system was 1.0 x 10^{-6} M.

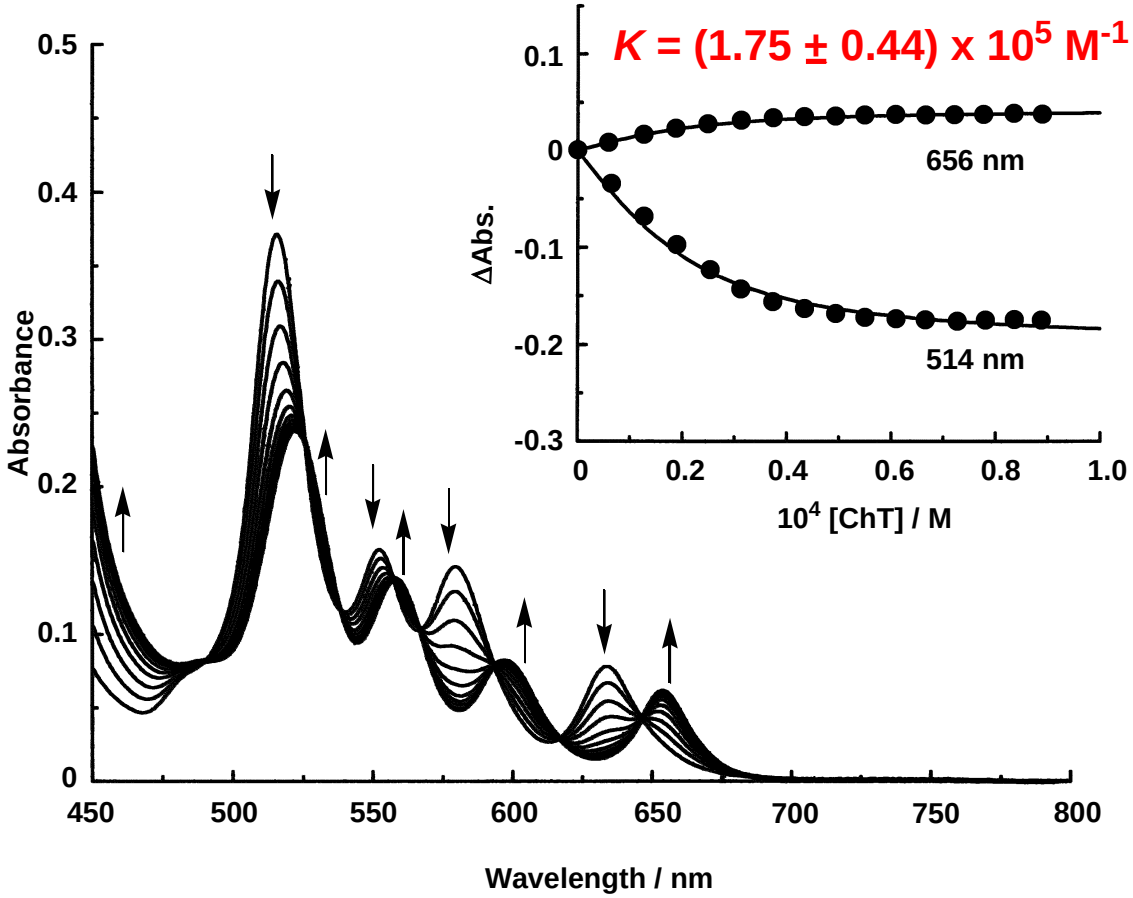


Figure S5. UV-visible spectral change of H_2TPPS^{4-} (2.0×10^{-5} M) upon addition of ChT in phosphate buffer (pH 7.0, 1.0×10^{-2} M) at 25 ^{o}C. Inset: Plots of absorbance changes as a function of [ChT] at 514 nm and 656 nm. The solid lines represent the best fits of the data to an equation for 1:1 complexation for determining *K* value.

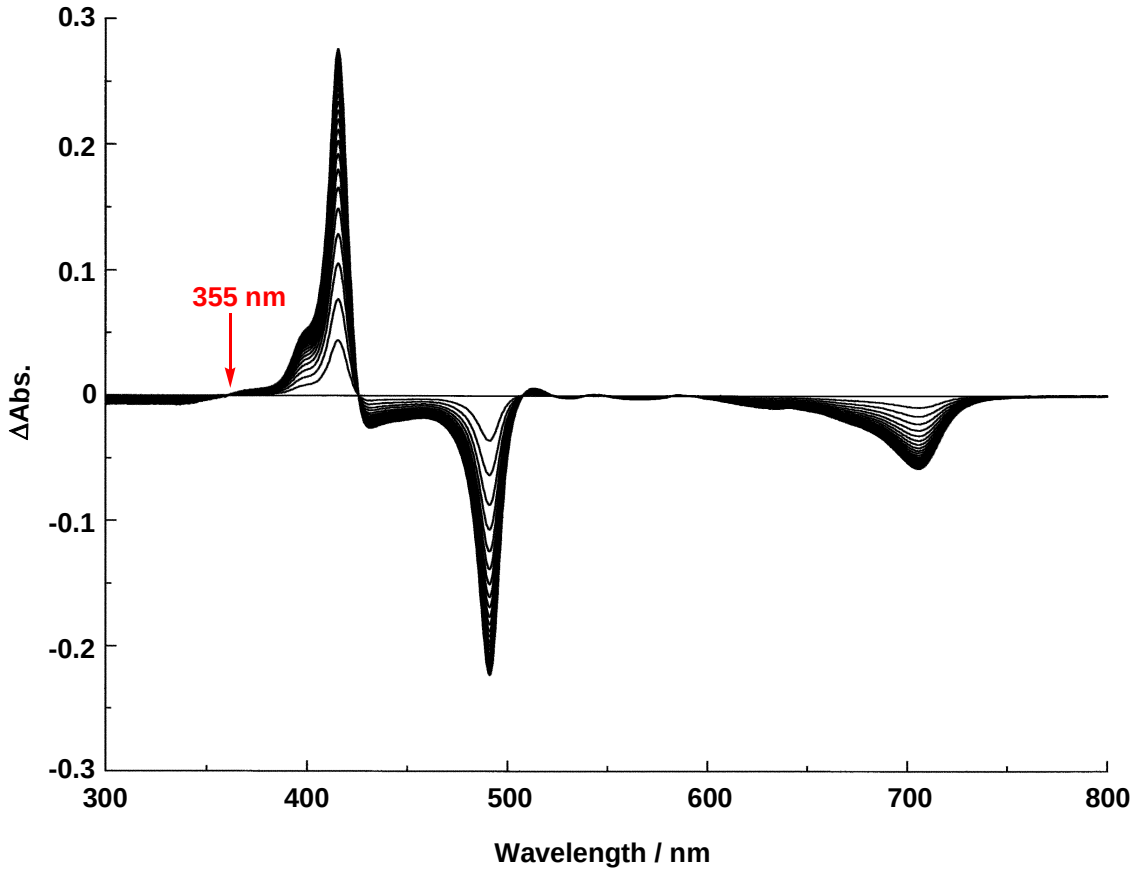


Figure S6. Differential spectral change for decomposition of J-aggregates of H_4TPPS^{2-} bound to ChT (1.0 x 10^{-6} M) into the H_2TPPS^{4-}/TMe-β-CD inclusion complex in phosphate buffer (pH 7.0 and 1.0 x 10^{-2} M) containing TMe-β-CD (8.0 x 10^{-6} M) at 25 ^{o}C. The total concentration of the porphyrin in the system was 1.0 x 10^{-6} M.

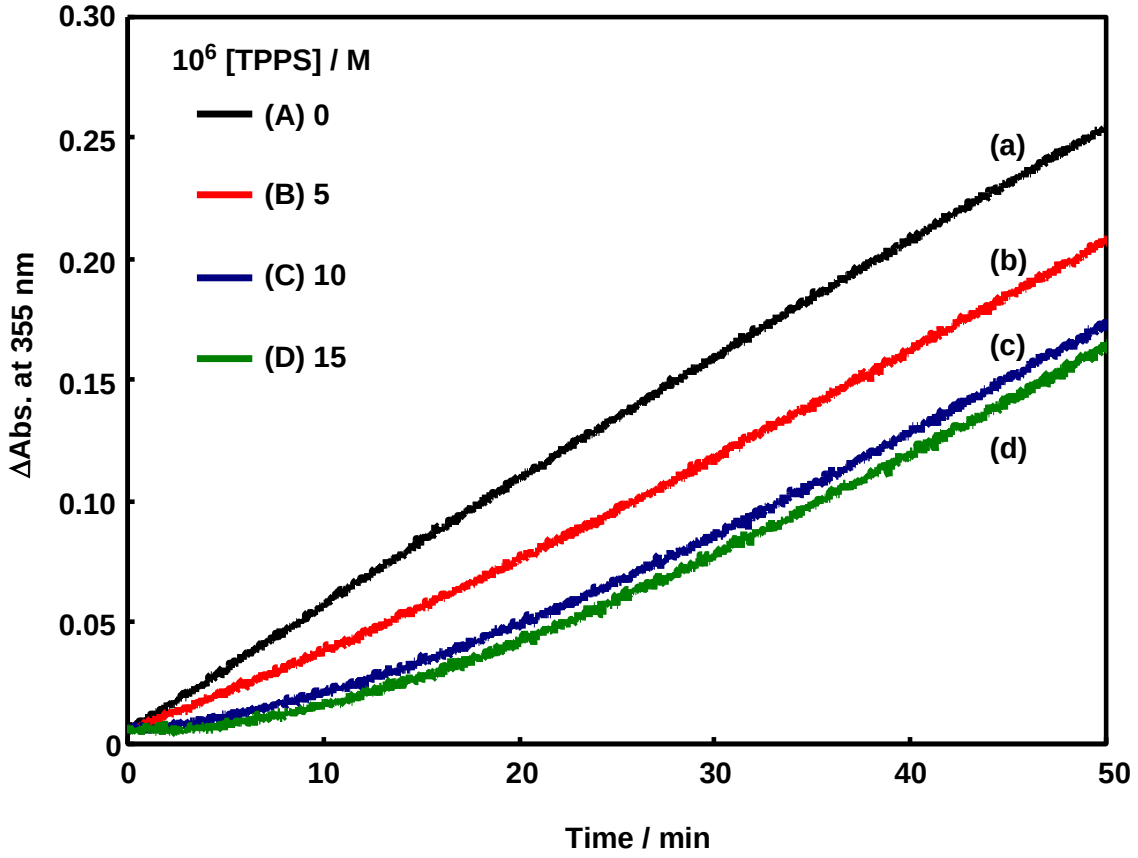


Figure S7. Effects of the amount of J-aggregates on hydrolysis of SPNA3G3E (3.0 x 10^{-4} M) catalyzed by ChT (1.0 x 10^{-6} M) in phosphate buffer (pH 7.0, 1.0 x 10^{-2} M) containing TMe-β-CD (1.2 x 10^{-4} M) at 25 ^{o}C. [TPPS] = 0 M (A); 5.0 x 10^{-6} M (B); 1.0 x 10^{-5} M (C); 1.5 x 10^{-5} M (D.

Gene Silencing Activity of siRNA Polyplexes Based on Thiolated *N,N,N*-Trimethylated Chitosan

Amir K. Varkouhi,[†] Rolf J. Verheul,[†] Raymond M. Schiffelers,[†] Twan Lammers,[†,‡] Gert Storm,[†] and Wim. E. Hennink*[,†]

Department of Pharmaceutics, Utrecht Institute for Pharmaceutical Sciences, Faculty of Science, Utrecht University, Sorbonnelaan 16, 3584 CA Utrecht, The Netherlands, and Department of Experimental Molecular Imaging, RWTH - Aachen University, Pauwelsstrasse 30, 52074 Aachen, Germany. Received August 20, 2010; Revised Manuscript Received October 10, 2010

N,N,N-Trimethylated chitosan (TMC) is a biodegradable polymer emerging as a promising nonviral vector for nucleic acid and protein delivery. In the present study, we investigated whether the introduction of thiol groups in TMC enhances the extracellular stability of the complexes based on this polymer and promotes the intracellular release of siRNA. The gene silencing activity and the cellular cytotoxicity of polyplexes based on thiolated TMC were compared with those based on the nonthiolated counterpart and the regularly used lipidic transfection agent Lipofectamine. Incubation of H1299 human lung cancer cells expressing firefly luciferase with siRNA/thiolated TMC polyplexes resulted in 60−80% gene silencing activity, whereas complexes based on nonthiolated TMC showed less silencing (40%). The silencing activity of the complexes based on Lipofectamine 2000 was about 60−70%. Importantly, the TMC-SH polyplexes retained their silencing activity in the presence of hyaluronic acid, while nonthiolated TMC polyplexes hardly showed any silencing activity, demonstrating their stability against competing anionic macromolecules. Under the experimental conditions tested, the cytotoxicity of the thiolated and nonthiolated siRNA complexes was lower than those based on Lipofectamine. Given the good extracellular stability and good silencing activity, it is concluded that polyplexes based on TMC-SH are attractive systems for further in vivo evaluations.

INTRODUCTION

Cationic polymers have been studied for nucleic acid delivery both in vitro and in vivo (*1*−*4*). Due to their positive charge, these polymers are able to complex with anionic nucleic acid molecules to form polyplexes which are able to cross cellular barriers and reach their intracellular targets (*5*−*8*). However, the complexes based on many of these cationic polymers are insufficiently stable in biological fluids and consequently do not protect the DNA/siRNA molecules against enzymatic degradation by nucleases (*9, 10*). Moreover, insufficient uptake by target cells, poor intracellular release properties, and considerable cellular toxicity are other limiting factors for pharmaceutical and therapeutic application of these polymers. Therefore, the search for effective and nontoxic vectors is currently of prime interest (*11*−*13*).

N,N,N-Trimethylated chitosan (TMC) is a biodegradable polymer emerging as a promising nonviral vector for nucleic acid and protein delivery (*14*−*16*). This polymer is a partially quaternized chitosan derivative which, as compared to chitosan, has improved solubility in aqueous solution at neutral pH, safety, and effectiveness (*17, 18*). The beneficial ability of TMC to reversibly open tight junctions between epithelial cells, which facilitates the uptake of therapeutics, its muco-adhesive properties, and relatively low toxicity, make TMC a valuable polymer for several drug delivery applications (*19, 20*).

Introduction of thiol groups into several carrier systems has been shown to enhance their delivery properties. This is due to the formation of reducible disulfide bonds between thiol groups, leading to increased extracellular stability and improved intracellular release properties (*21*−*23*). Therefore, introduction of thiol groups in TMC likely enhances the stability of its complexes with nucleic acids and also allows further chemical derivatization with targeting ligands and PEG making use of unreacted SH groups (*24*−*26*). Moreover, the thiol groups in TMC-SH can promote its muco-adhesive potential due to formation of disulfide bonds between the polymer and mucin glycoproteins on the cell membrane, which might lead to enhanced cellular uptake (*27, 28*).

Recently, considerable research effort has been dedicated to the use of small interfering RNAs (siRNA) as novel biotherapeutics (*29*). These double-stranded RNA molecules are rapidly degraded by nucleases present in biological fluids and are not able to enter the cytoplasm, where the RNA interference (RNAi) machinery is located (*30, 31*). Therefore, a key challenge to the effective and widespread use of this new class of biotherapeutics is their cytosolic delivery (*32*−*34*).

Our group recently reported on thiolated TMC and the formation of nanoparticles based on this polymer (*24*). In the present study, thiolated and nonthiolated TMC (Figure 1) were investigated for siRNA delivery and gene silencing. The silencing activity and the cellular toxicity of polyplexes based on these biodegradable polymers were compared with those based on the regularly used lipidic transfection agent Lipofectamine (*35*).

EXPERIMENTAL PROCEDURES

Materials. The double-stranded siRNA which specifically targets firefly luciferase (used against mRNA from pGL3; structure below), was obtained from Dharmacon Bioscience (Lafayette, LA, USA), and anti-EGFP siRNA as nonspecific

* Corresponding author. Mailing address: Department of Pharmaceutics, Utrecht Institute for Pharmaceutical Sciences, Faculty of Science, Utrecht University, Sorbonnelaan 16, 3584 CA Utrecht, The Netherlands. Tel: +31-30.2537388. Fax: +31-30.2517839. E-mail address: W.E.Hennink@uu.nl.

[†] Utrecht University.

[‡] RWTH - Aachen University.

10.1021/bc1003789 © 2010 American Chemical Society
Published on Web 11/04/2010

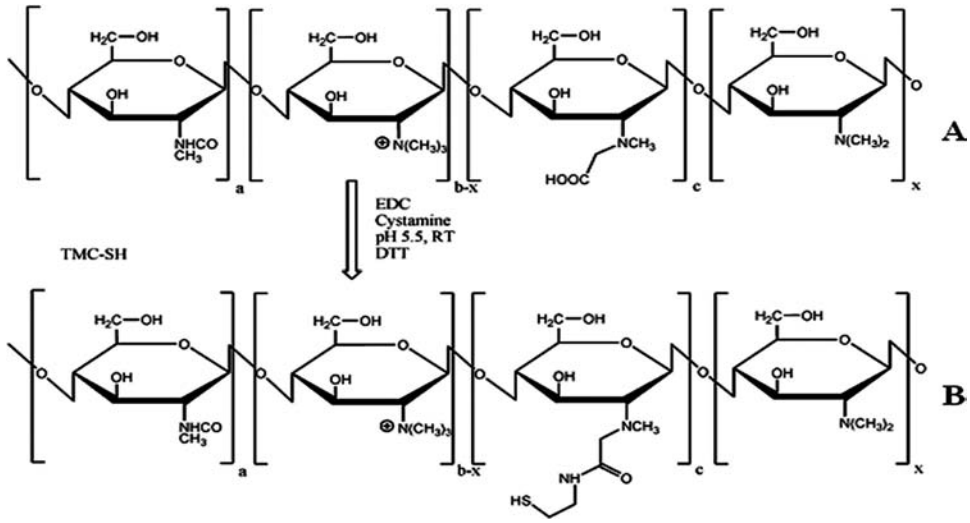


Figure 1. Structure of nonthiolated (A) and thiolated *N,N,N*-trimethylated chitosan (TMC) (B).

siRNA and Fluc-TYE563- labeled siRNA were obtained from Integrated DNA Technologies BVBA (Leuven, Belgium).

Sense strand: 5′- GAU UAU GUC CGG UUA UGU A UU. Antisense strand: UU CUA AUA CAG GCC AAU ACA U P-5′.

Thiolated TMC (TMC-SH) with different extents of thiol modification of 2%, 5%, and 7% and molecular weights of 180, 215, and 144 kDa, respectively, and nonthiolated TMC (MW = 100 kDa) and thiolated HA (HA-SH, 40 kDa) with 21% thiol modification were synthesized and purified as described previously (*24*). The degree of quaternization and acetylation of the studied TMCs were 25% and 17%, respectively. Sodium heparin was obtained from Sigma Aldrich (Zwijndrecht, The Netherlands); and Lipofectamine 2000 and LysoTrackerR Green DND-26 were obtained from Invitrogen (Breda, The Netherlands). Luciferase assay reagent and reporter lysis buffer were obtained from Promega (Leiden, The Netherlands). DRAQ5 was obtained from Biostatus Limited (Leicestershire, UK).

Physicochemical Characterization of Polyplexes. Polyplexes were prepared at different polymer to siRNA ratios (expressed as *N*/*P* ratios, where *N* is the moles of cationic nitrogens in the polymer and *P* is moles of phosphate in siRNA) between 0.5 and 14 by adding a siRNA solution (200 μL, 40 μg/mL) in HEPES (5 mM, pH 7.4) to polymer solutions (200 μL, various concentrations) in the same buffer. The resulting solutions were vortexed for 10 s. After 3 h incubation at room temperature, *Z*-average diameters were measured with dynamic light scattering at 25 °C with a Malvern 4700 system using an argon-ion laser (488 nm) operating at 10.4 mW (Uniphase) and *PCS* (photon correlation spectrometry) software for Windows v 1.34 (Malvern, UK). Viscosity and refractive index of water at 25 °C were used. Calibration was done with an aqueous dispersion of polystyrene particles with a diameter of 100 nm. Particle size distribution is characterized by the polydispersity index (PDI), ranging from 0 for a monodisperse to 1 for a heterodisperse preparation. The zeta potential of the polyplexes prepared in HEPES (5 mM, pH 7.4) was determined at 25 °C in a DTS5001 cell using a Zetasizer 2000 unit (Malvern). The instrument was calibrated with a polystyrene dispersion with known zeta potential. To study the formation of covalent disulfide bonds in the polyplexes based on TMC-SH and their effect in the stability of the complexes, in some experiments after adding the siRNA solution (200 μL, 40 μg/mL) in HEPES (5 mM, pH 7.4) to polymer solutions (200 μL, various concentrations) in the same buffer, immediately 50 μL of either thiolated (*24*) or nonthiolated hyaluronic acid (1 mg/mL) solution in HEPES (5 mM, pH 7.4) was added to the complex and incubated for 3 h at room temperature.

Agarose Gel Electrophoresis. The complexation of siRNA with the thiolated and nonthiolated TMC as well as the L-glutathione/heparin-induced destabilization of the polyplexes was investigated using agarose gel electrophoresis. The agarose gels (NuSieve GTG Agarose, Lonza, Rockland, ME, USA) were made at a concentration of 4% (w/v) in Tris-acetate-EDTA (TAE) running buffer and contained 0.5 μg/mL ethidium bromide. Polyplexes of TMC's with the siRNA and thiolated or nonthiolated HA made at *N*/*P* ratio of 8 were prepared as described above. Naked siRNA was used as a control. Polyplex dispersions with or without heparin (1.5 USP/μg siRNA; molar ratio of amine groups of the polymer and sulfate groups of heparin was 0.5 (N/S)) were incubated for 5 min at room temperature. In another experiment, polyplex dispersions were incubated for 30 min at 37 °C with L-glutathione (5 mM) and subsequently incubated with or without heparin (N/S: 0.5) for 5 min at room temperature. Polyplexes (15 μL, corresponding to 15 pmol siRNA) were applied in the starting slot of the gel and electrophoresis was performed at 60 V for 50 min. The siRNA bands, stained with ethidium bromide, were detected on a UV transilluminator (ImaGo compact imaging system, B&L Systems, The Netherlands).

Gene Silencing and Cytotoxicity Experiments. The human lung cancer cell line H1299 which expresses firefly luciferase was used to study the gene silencing activity of the TMC formulations. The cell line was maintained in RPMI 1640 medium with HEPES and L-glutamine (PAA laboratories GmbH, Pasching, Austria, catalog no. E15-842) completed with fetal bovine serum (FBS) (final concentration 10% v/v) and cultured at 37 °C at 5% CO_2 humidified atmosphere. The cells (8×10^3 cells/well) were seeded into 96-well plates and cultured overnight. The anti-Luciferase siRNA polyplexes were added to the cells in the presence or absence of serum in the medium and incubated at 37 °C for 24 h. Then, the medium was removed, and fresh medium was added. Subsequently, the cells were incubated at 37 °C for 1 day, after which the luciferase protein expression was analyzed using Luciferase reporter gene assay (Promega). The cytotoxicity of the polyplexes was measured using the XTT colorimetric viability assay as previously described (*36*). Complexes of either specific or nonspecific siRNA with Lipofectamine 2000 were prepared by gently mixing 50 μL siRNA (20 μg/mL) in HEPES (5 mM, pH 7.4) with 3.7 μL Lipofectamine 2000 in 50 μL HEPES (5 mM, pH

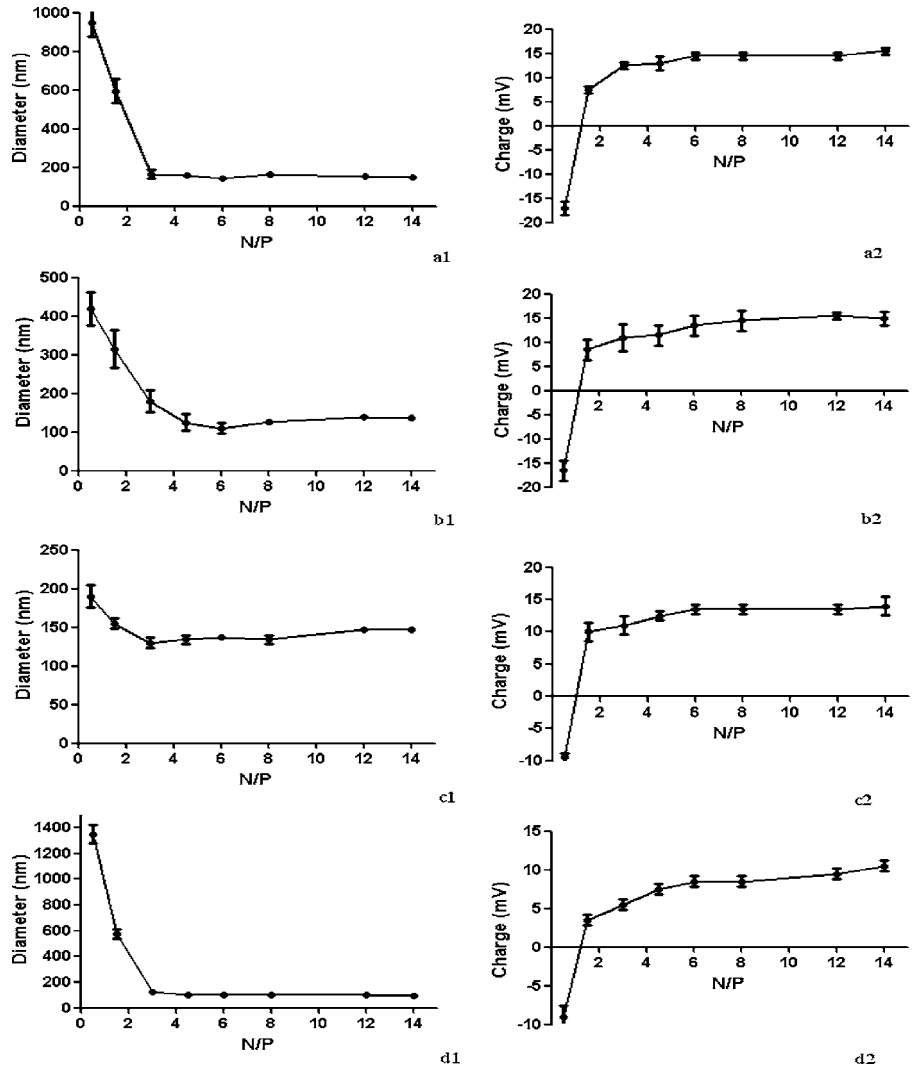


Figure 2. Average diameter and zeta potential of polyplexes prepared at different *N*/*P* ratios. (a1, a2) TMC-SH 2%. (b1, b2) TMC-SH 5%. (c1, c2) TMC-SH 7%. (d1, d2) Nonthiolated TMC (mean ± standard deviation ($n = 3$)).

7.4) followed by 30 min incubation at room temperature and then were incubated with cells.

Determination of Luciferase Activity. Luciferase activity was measured after removal of the growth medium and lysis of the cells by the addition of 100 μL reporter gene lysis buffer. After a freeze/thaw cycle at −80 °C/room temperature, 50 μL of luciferase assay reagent was added to 50 μL of the cell lysate, and relative light units (RLU) were measured for 10 s at room temperature using a FLUOstar OPTIMA microplate-based multidetection reader with a microinjector.

Confocal Laser Scanning Microscopy (CLSM). The cellular uptake of polyplexes was investigated with CLSM. In short, 8×10^3 cells were seeded in Fluorodish cell culture dish (WPI, Sarasota, NY, USA). The cells were cultured for 24 h at 37 °C and subsequently incubated with Fluc TYE563-labeled siRNA lipo/polyplexes for 4 h. Then, the cells were washed with PBS and incubated for 5 min with medium containing 40 μM DRAQ5 for nuclear staining and 75 nM LysoTracker Green DND-26 for endosomal/lysosomal staining. The cells were subsequently analyzed on a Leica TCS-SP confocal laser scanning microscope (Leica, Heidelberg, Germany) equipped with three lasers: 488 nm argon, 568 nm krypton, and 647 nm HeNe laser.

RESULTS AND DISCUSSION

Physicochemical Characterization of Polyplexes. The average diameter of the polyplexes prepared at different *N*/*P* ratios was measured by dynamic light scattering (Figure 2). Both thiolated and nonthiolated TMC were capable of forming complexes with siRNA over the whole *N*/*P* range 0.5−14. The average size of the particles decreased with increasing *N*/*P* ratio, with small-sized nanoparticles of ≤200 nm being formed at *N*/*P* ratio of ≥3. This can probably be ascribed to an increased polymer amount in the formulations which leads to tighter complexes. There was no significant difference in size of the nanoparticles based on thiolated and nonthiolated TMCs. Furthermore, a polydispersity index (PDI) of ≤0.3 was observed for all polyplex formulations made at *N*/*P* ratio of ≥3, which indicates a rather narrow size distribution.

At *N*/*P* of 0.5, the polyplexes had a negative zeta potential (about −10 to −25 mV), which can be explained by the excess of siRNA present in the complexes. At *N*/*P* ≥ 1.5, positively charged particles for the different TMC-SH based formulations (zeta potential +5 to +15 mV) and nonthiolated TMC (+5 to +10 mV) were formed (Figure 2). The average diameter and zeta potential of the particles based on TMC-SH and nonthiolated TMC (*N*/*P*: 8) in combination with thiolated hyaluronic acid (HA-SH) and the nonthiolated one (HA) were measured. The particles based on TMC-SH/siRNA/HA-SH had an average diameter of 170 ± 10 nm and an average zeta potential of 10 ± 2 mV, whereas the other formulations (with nonthiolated TMC instead of TMC-SH) led to formation of particles of ≥1000 nm.

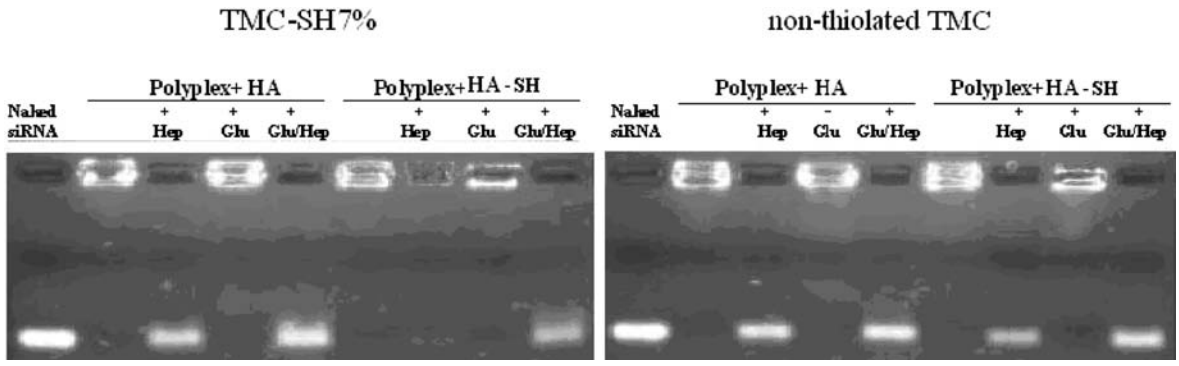


Figure 3. Agarose gel electrophoresis. Polyplexes of TMC-SH and nonthiolated TMC with siRNA made in 5 mM HEPES buffer (pH 7.4) at *N*/*P* ratio 8, containing either nonthiolated hyaluronic acid (HA) or HA-SH were applied on a 4% agarose gel. By adding heparin (*N*/*S* = 0.5, *N* is the moles of cationic nitrogens in the polymer and *S* is moles of sulfate in siRNA) release of siRNA was observed for all complexes, except for those based on TMC-SH/siRNA/HA-SH, which is probably due to disulfide bond formation in the complex. Incubation of the complexes with L-glutathione (5 mM) for 30 min at 37 °C did not lead to release of the siRNA Complexes based on TMC-SH/siRNA/HA-SH only showed release of the siRNA after incubation with L-glutathione and heparin sequentially.

Agarose Gel Electrophoresis. Binding of TMC-SH to siRNA molecules and subsequent complex formation are essential for protection of siRNA against degradation by nucleases. Moreover, formation of covalent disulfide bonds between thiolated molecules likely increases the stability of the particles which avoids the dissociation of the siRNA from the complex in the extracellular matrix by anionic macromolecules such as proteins and polysaccharides (*37, 38*). On the other hand, polyplex destabilization still needs to occur in the cytosol to achieve gene silencing due to released siRNA.

TMC-SH and HA-SH as another thiolated polymer were formulated with siRNA and the stability of the formed particles was studied. As control formulations, polyplexes based on TMC-SH and nonthiolated HA and additionally polyplexes based on nonthiolated TMC in combination with HA-SH were prepared.

Figure 3 shows that siRNA remains in the starting slots of the gel for all the polyplexes prepared at *N*/*P* = 8, indicating that siRNA is stably associated with the cationic TMC. To monitor the sensitivity of these complexes for dissociation and release of siRNA, complexes were incubated with heparin, which is commonly used as a model anionic polyelectrolyte able to dissociate siRNA (*39, 40*). Figure 3 shows that, after incubation of the complexes with heparin, siRNA is released from all complexes, except from those based on TMC-SH/siRNA/HA-SH, demonstrating that siRNA is stably encapsulated in these particles. SiRNA is released from these particles only after incubation with L-glutathione and heparin, which indicates that siRNA can only be released after the disulfide bonds in the particles are cleaved by L-glutathione. These observations indicate an enhanced stability of the polyplexes based on TMC-SH/HA-SH likely due to formation of disulfide bonds between TMC-SH and HA-SH molecules. As a result, release of the siRNA from these complexes is expected to occur in two steps: (1) after cellular internalization of the particles, cleavage of the disulfide bonds between thiolated molecules inside the complex occurs, due to the relatively high concentrations of reducing agenst in the cytosol, and subsequently followed by (2) dissociation of the complexes and release of siRNA is likely due to competition with the negatively charged macromolecules such as proteins and mRNA (*41*) present in the cytosol.

Silencing Activity and Cell Viability. Human lung cancer cells (H1299) expressing luciferase were used for gene silencing studies. SiRNA polyplexes based on thiolated and nonthiolated TMC polymers prepared at *N*/*P* ratios of 8 were selected for silencing studies, because these particles showed binding to the siRNA (Figure 3), and upon complexation had a positive mean zeta potential and small average size (Figure 2). TMC-SH with highest degree of thiolation (7%) was selected for the silencing/

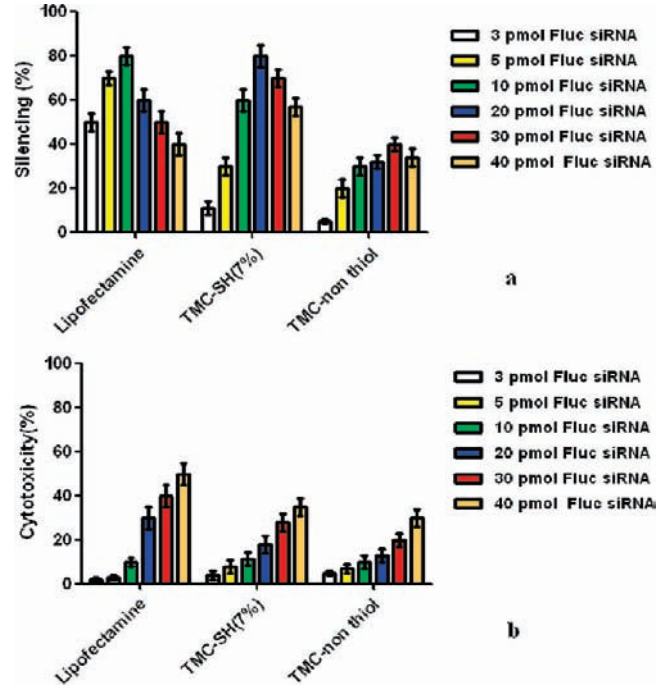


Figure 4. (a) Dose response effect of the siRNA complexes in Luciferase gene silencing after incubation with H1299 cells for 24 h in serum-free medium. (b) Cell viability as measured by XTT assay after incubation of H1299 cells for 24 h with siRNA complexes in serum-free medium (mean ± standard deviation (n = 3)).

cytotoxicity experiments, because the most stable particles can be expected using this polymer. The silencing activity and cytotoxicity of these complexes were compared to those based on Lipofectamine 2000, and in all cases, the silencing results were corrected for cytotoxicity.

Figure 4a shows that increasing the dose of the TMC-SH polyplexes from 3 to 20 pmol siRNA content per well resulted in a significant enhancement of the silencing activity from 10% to above 80%, whereas doses higher than 20 pmol siRNA led to a gradual decrease in silencing activity of the complexes due to the increased cytotoxicity (Figure 4b). In case of the nonthiolated TMC, by increasing the dose of the siRNA, a gradual increase in silencing activity from 5% up to 40% was observed. In terms of silencing activity and cytotoxicity, the efficiency of TMC-SH polyplexes in gene silencing is substantially higher than those based on Lipofectamine 2000 (approximately 60% at a dose of 20 pmol siRNA) and nonthiolated TMC (approximately 30% at a dose of 20 pmol).

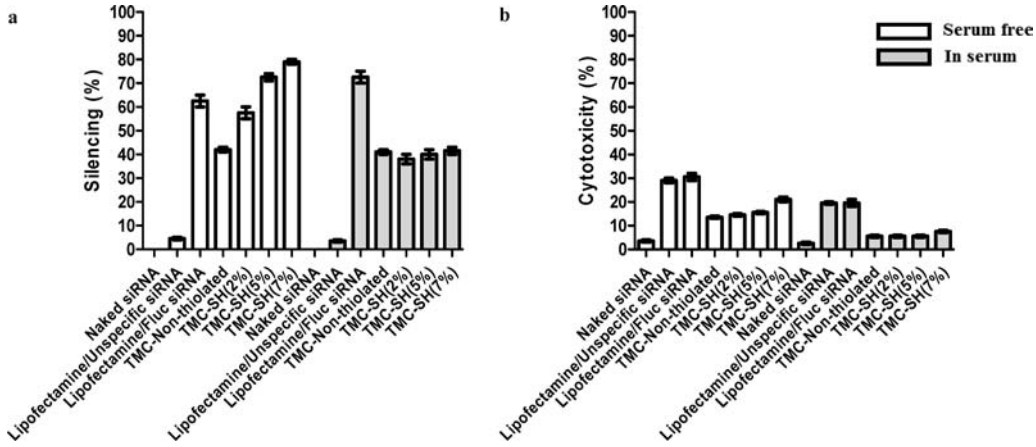


Figure 5. (a) Luciferase gene silencing after incubation of H1299 cells with siRNA complexes in serum-free medium and in the presence of serum. (b) Cell viability as measured by XTT assay after incubation of H1299 cells with siRNA complexes in serum-free medium and in the presence of serum (mean ± standard deviation ($n = 3$)).

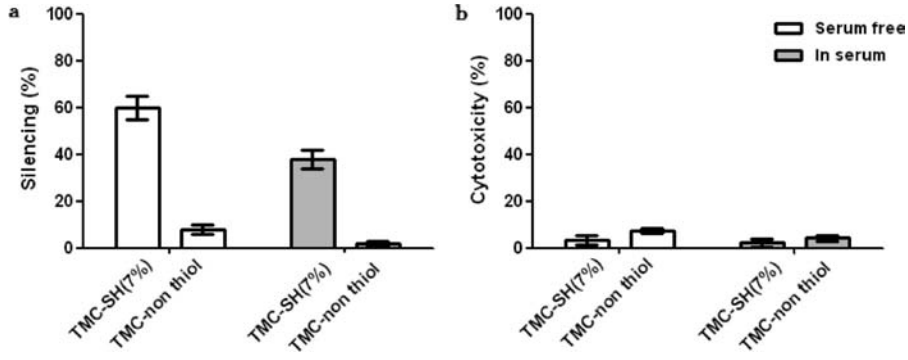


Figure 6. (a) Effect of hyaluronic acid (HA) (0.5 mg/mL) on Luciferase gene silencing activity of siRNA complexes based on TMC-SH (7%) and nonthiolated TMC. (b) Effect of HA on cell viability as measured by XTT assay after incubation of H1299 cells with siRNA complexes (mean ± standard deviation ($n = 3$)).

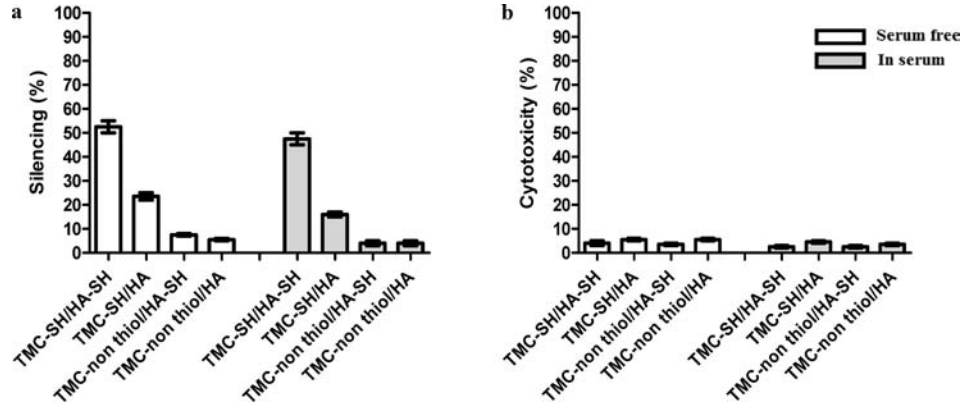


Figure 7. (a) Luciferase gene silencing after incubation of H1299 cells for 24 h with siRNA complexes in serum-free medium and in the presence of serum. (b) Cell viability as measured by XTT assay after incubation of H1299 cells with siRNA complexes in serum-free media and in the presence of serum (mean ± standard deviation ($n = 3$)).

Figure 4b shows that the cytotoxicity of TMC-SH/siRNA formulation is lower than that of the standard transfection system Lipofectamine 2000. In addition, TMCs have substantially lower cytotoxicity than other cationic polymers (*42, 43*). On the basis of these results, a dose of 20 pmol siRNA per well was selected as the dose for further gene silencing studies.

Figure 5a shows that, in the absence of serum, incubation of cells with polyplexes based on TMC-SH polymers containing 2%, 5%, and 7% thiol groups resulted in 60−80% silencing activity, whereas incubation with nonthiolated TMC complexes showed about 40% gene silencing. These results show that, by introduction of thiol groups in TMC structure, the gene silencing activity of the polyplexes is substantially increased. This might be due to the increased stability of the polyplexes of thiolated TMC.

The differences in gene silencing activity of the lipofectamine formulations in the absence and presence of serum are small (~60% and ~70%, respectively). It has been reported that the in vitro transfection activity of complexes increases once they aggregate in serum, due to more intense contact with cells (*44*). In the presence of 10% FBS, gene silencing activity of the siRNA polyplexes based on TMC-SH polymers decreased to 45%, whereas the gene silencing activity of the nonthiolated TMC remained the same as in serum-free conditions. This

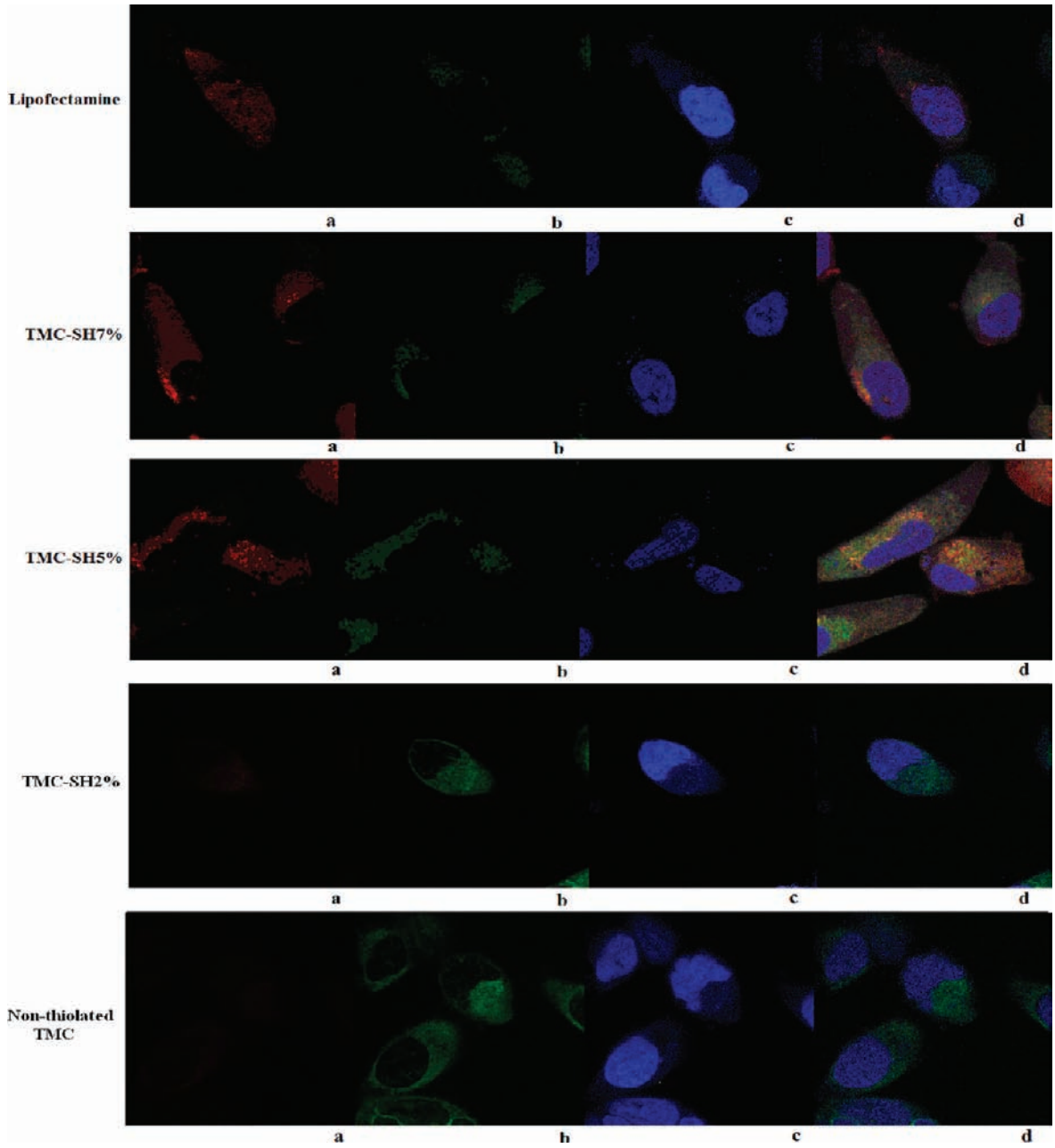


Figure 8. Confocal laser scanning microscopy images of H1299 cells incubated with complexes prepared with TYE563-labeled siRNA. Images (a): Pattern of intracellular TYE563-labeled siRNA. Images (b): Endosomes/lysosomes stained with LysoTracker Green DND-26. Images (c): Nuclei of cells stained with DRAQ5. Images (d): Blue, nuclei of cells; green, endosomes/lysosomes; red, free or complexed siRNA inside the cytoplasm; yellow, free or complexed siRNA entrapped inside the endosomes/lysosomes.

reduction in silencing effect might be partly explained by the inhibitory effect of serum proteins on the uptake of nanoparticles (Figure 5a) (*45*).

Figure 5b shows low cytotoxicity of both thiolated and nonthiolated TMC/siRNA formulations made at an *N*/*P* ratio of 8 (<20%) compared to Lipofectamine with a cytotoxicity about 30%. Moreover, in the presence of serum, the cytotoxicity of the polyplexes was slightly lower than that of the complexes incubated with the cells in medium without serum. This effect is in line with the literature suggesting that serum proteins can mask the cytotoxicity of cationic polyplexes (*46, 47*). No significant differences in cytotoxicity of thiolated and nonthiolated TMCs were observed (Figures 4b and 5b).

The gene silencing efficiency of the polyplexes based on thiolated and nonthiolated TMC polymers was further investigated in the presence of hyaluronic acid (HA), which is an polyanionic macromolecule present in biological fluids that has been shown to inhibit the transfection activity of pDNA/cationic polymer nanoparticles (*48*, *49*).

In the presence of 0.5 mg/mL HA, TMC-SH/siRNA complexes showed up to 60% silencing activity, whereas the silencing activity of nonthiolated TMC polyplexes was less than 10%. In the presence of both HA and serum in the growth medium, the silencing activity of the TMC-SH polyplexes was decreased to 40%, whereas nonthiolated TMC polyplexes hardly showed any silencing (Figure 6a). These results illustrate the key role of disulfide bonds present in the TMC-SH polyplexes which enhance the stability of the complexes against competitor macromolecules present in biological fluids.

Furthermore, the silencing activity of the polyplexes based on TMC-SH and nonthiolated TMC in combination with either HA-SH or nonthiolated HA was studied. In the absence and presence of serum in the growth medium, siRNA complexes based on TMC-SH/HA-SH showed >50% gene silencing activity

(Figure 7a), whereas the gene silencing activity of the other formulations is ≤20% (Figure 7a). These results are in line with Figure 3, indicating better stability of the polyplexes based on TMC-SH/HA-SH due to formation of disulfide bonds between TMC-SH and HA-SH molecules, which consequently results in a higher gene silencing activity of this formulation compared to the other formulations. The XTT cell viability assay showed low cytotoxicity of the studied complexes (Figure 7b).

Confocal Laser Scanning Microscopy (CLSM). Confocal laser scanning microscopy (CLSM) was used to study the cellular uptake and internalization of siRNA complexes using fluorescently labeled siRNA. Figure 8 shows that red spots originating from the labeled siRNA (images a and d) were intracellularly observed after incubation of the cells with the various siRNA formulations investigated in this study, demonstrating that the complexes were internalized. The images of cells treated with Lipofectamine/siRNA complexes do visualize the presence of siRNA into both the cytosol and the nucleus, in agreement with previous observations (*23, 50*). In the case of TMC-SH 7% and TMC-SH 5% based complex-treated cells, the intensity of the internalized siRNA (images a and d) is considerably higher than in the case of the other groups, which is in agreement with the gene silencing results (Figure 5a). Furthermore, in the case of TMC-SH 7%, a diffuse pattern of the siRNA inside the cytosol is observed, while the lipofectamine and TMC-SH 5% treated cells mostly show a punctuated pattern of the siRNA. The yellow dots in panel d represent the colocalization of the siRNA with fluoresecent markers for endosomes/lysosomes. We speculate that these observations reflect the enhanced level of cellular uptake for the complexes based on TMC-SH with higher extent of thiol modification (5% and 7%), which might be related to their enhanced muco-adhesive properties (*27, 28*) and stability in the extracellular environment.

CONCLUSION

This study reports on TMC-SH as a promising vector for siRNA delivery. As compared to the nonthiolated TMC and Lipofectamine-based complexes, the gene silencing activity of the siRNA complexes based on thiolated TMC was substantially higher. Importantly, the polyplexes based on TMC-SH retained their silencing activity in the presence of hyaluronic acid, while nonthiolated TMC polyplexes hardly showed any silencing activity. Furthermore, the cytotoxicity profiles of TMC-SH and nonthiolated TMC were the same and more favorable compared to that of Lipofectamine. The results of this study suggest enhanced stability of the TMC-SH polyplexes, which is likely due to formation of the reducible disulfide bonds in the complex. These features make TMC-SH an attractive candidate for further development and evaluation in animal studies.

ACKNOWLEDGMENT

This project was funded by MEDITRANS, an Integrated Project funded by the European Commission under the "Nanotechnologies and Nano-sciences, Knowledge-based Multifunctional Materials and New Production Processes and Devices" (NMP), thematic priority of the Sixth Framework Program. We would like to thank Miss Esther van't Veld from the Centre for Cell Imaging (Faculty of Veterinary Medicine, Utrecht University) for technical assistance with the CLSM and Prof. Thomas Kissel and Dr Olivia Merkel from Marbourg University, Germany, for provding the H1299 cell line.

LITERATURE CITED

(1) Yu, H., and Wagner, E. (2009) Bioresponsive polymers for nonviral gene delivery. *Curr. Opin. Mol. Ther. 11*, 165–178.

(2) Luten, J., van Nostrum, C. F., De Smedt, S. C., and Hennink, W. E. (2008) Biodegradable polymers as non-viral carriers for plasmid DNA delivery. *J. Controlled Release 126*, 97–110.

(3) De Smedt, S. C., Demeester, J., and Hennink, W. E. (2000) Cationic polymer based gene delivery systems. *Pharm. Res. 17*, 113–126.

(4) Mintzer, M. A., and Simanek, E. E. (2009) Nonviral vectors for gene delivery. *Chem. Rev. 109*, 259–302.

(5) Thomas, M., and Klibanov, A. M. (2003) Non-viral gene therapy: polycation-mediated DNA delivery. *Appl. Microbiol. Biotechnol. 62*, 27–34.

(6) Jere, D. J., and Cho, C. S. (2010) Biodegradable polymer-mediated sh/siRNA delivery for cancer studies. *Methods Mol. Biol. (Clifton, N.J.) 623*, 243–269.

(7) Patil, M. L., Zhang., M., Betigeri, S., Taratula, O., He, H., and Minko, T. (2008) Surface-modified and internally cationic polyamidoamine dendrimers for efficient siRNA delivery. *Bioconjugate Chem. 19*, 1396–1403.

(8) Zintchenko, A., Philipp, A., Dehshahri, A., and Wagner, E. (2008) Simple modifications of branched PEI lead to highly efficient siRNA carriers with low toxicity. *Bioconjugate Chem. 19*, 1448–1455.

(9) Kuo, J. H. S., Jan, M. S., and Sung, K. C. (2003) Evaluation of the stability of polymer-based plasmid DNA delivery systems after ultrasound exposure. *Int. J. Pharm. 257*, 75–84.

(10) Gary, D. J., Puri, N., and Won, Y. Y. (2007) Polymer-based siRNA delivery: Perspectives on the fundamental and phenomenological distinctions from polymer-based DNA delivery. *J. Controlled Release 121*, 64–73.

(11) Xia, T., Kovochich, M., Liong, M., Meng, H., Kabehie, S., George, S., Zink, J. I., and Nel, A. E. (2009) Polyethyleneimine coating enhances the cellular uptake of mesoporous silica nanoparticles and allows safe delivery of siRNA and DNA constructs. *ACS Nano 3*, 3273–3286.

(12) Grigsby, C. L., and Leong, K. W. (2010) Balancing protection and release of DNA: tools to address a bottleneck of non-viral gene delivery. *J. R. Soc. Interface 7 Suppl 1*, S67–82.

(13) Putnam, D., Gentry, C. A., Pack, D. W., and Langer, R. (2001) Polymer-based gene delivery with low cytotoxicity by a unique balance of side-chain termini. *Proc. Natl. Acad. Sci. U.S.A. 98*, 1200–1205.

(14) Mao, S., Sun, W., and Kissel, T. (2010) Chitosan-based formulations for delivery of DNA and siRNA. *Adv. Drug Delivery Rev. 62*, 12–27.

(15) Mishra, N., Goyal, A. K., Tiwari, S., Paliwal, R., Paliwal, S. R., Vaidya, B., Mangal, S., Gupta, M., Dube, D., Mehta, A., and Vyas, S. P. (2010) Recent advances in mucosal delivery of vaccines: Role of mucoadhesive/biodegradable polymeric carriers. *Expert Opin. Ther. Pat. 20*, 661–679.

(16) Amidi, M., Mastrobattista, E., Jiskoot, W., and Hennink, W. E. Chitosan-based delivery systems for protein therapeutics and antigens. *Adv. Drug Delivery Rev. 62*, 59–82.

(17) Verheul, R. J., Amidi, M., van der Wal, S., van Riet, E., Jiskoot, W., and Hennink, W. E. (2008) Synthesis, characterization and in vitro biological properties of O-methyl free N, N, N-trimethylated chitosan. *Biomaterials 29*, 3642–3649.

(18) Sahni, J. K., Chopra, S., Ahmad, F. J., and Khar, R. K. (2008) Potential prospects of chitosan derivative trimethyl chitosan chloride (TMC) as a polymeric absorption enhancer: Synthesis, characterization and applications. *J Pharm. Pharmacol. 60*, 1111–1119.

(19) Thanou, M., Florea, B. I., Langemeÿer, M. W. E., Verhoef, J. C., and Junginger, H. E. (2000) N-trimethylated chitosan chloride (TMC) improves the intestinal permeation of the peptide drug buserelin in vitro (caco-2 cells) and in vivo (rats). *Pharm. Res. 17*, 27–31.

(20) Thanou, M., Verhoef, J. C., and Junginger, H. E. (2001) Chitosan and its derivatives as intestinal absorption enhancers. *Adv. Drug Delivery Rev. 50*, 91–101.

(21) Meng, F., Hennink, W. E., and Zhong, Z. (2009) Reduction-sensitive polymers and bioconjugates for biomedical applications. *Biomaterials 30*, 2180–2198.

(22) Loretz, B., Thaler, M., and Bernkop-Schnurch, A. (2007) Role of sulfhydryl groups in transfection? A case study with chitosan-NAC nanoparticles. *Bioconjugate Chem. 18*, 1028–1035.

(23) Breunig, M., Hozsa, C., Lungwitz, U., Watanabe, K., Umeda, I., Kato, H., and Goepferich, A. (2008) Mechanistic investigation of poly(ethylene imine)-based siRNA delivery: Disulfide bonds boost intracellular release of the cargo. *J. Controlled Release 130*, 57–63.

(24) Verheul, R. J., van der Wal, S., and Hennink, W. E. (2010) Tailorable thiolated trimethyl chitosans for covalently stabilized nanoparticles. *Biomacromolecules 11*, 1965–1971.

(25) Lee, D., Zhang, W., Shirley, S. A., Kong, X., Hellermann, G. R., Lockey, R. F., and Mohapatra, S. S. (2007) Thiolated chitosan/DNA nanocomplexes exhibit enhanced and sustained gene delivery. *Pharm. Res. 24*, 157–167.

(26) Slutter, B., Soema, P. C., Ding, Z., Verheul, R., Hennink, W., and Jiskoot, W. Conjugation of ovalbumin to trimethyl chitosan improves immunogenicity of the antigen. *J. Controlled Release 143*, 207–214.

(27) Yin, L., Ding, J., He, C., Cui, L., Tang, C., and Yin, C. (2009) Drug permeability and mucoadhesion properties of thiolated trimethyl chitosan nanoparticles in oral insulin delivery. *Biomaterials 30*, 5691–5700.

(28) Langoth, N., Kahlbacher, H., Schöffmann, G., Schmerold, I., Schuh, M., Franz, S., Kurka, P., and Bernkop-Schnürch, A. (2006) Thiolated chitosans: Design and in vivo evaluation of a mucoadhesive buccal peptide drug delivery system. *Pharm. Res. 23*, 573–579.

(29) Kim, D. H., and Rossi, J. J. (2007) Strategies for silencing human disease using RNA interference. *Nat. Rev. Genet. 8*, 173–184.

(30) Elbashir, S. M., Harborth, J., Lendeckel, W., Yalcin, A., Weber, K., and Tuschl, T. (2001) Duplexes of 21-nucleotide RNAs mediate RNA interference in cultured mammalian cells. *Nature 411*, 494–498.

(31) Kurreck, J. (2009) RNA interference: From basic research to therapeutic applications. *Angew. Chem., Int. Ed. 48*, 1378–1398.

(32) Gilmore, I. R., Fox, S. P., Hollins, A. J., Sohail, M., and Akhtar, S. (2004) The design and exogenous delivery of siRNA for post-transcriptional gene silencing. *J. Drug Targeting 12*, 315–340.

(33) Jeong, J. H., Mok, H., Oh, Y. K., and Park, T. G. (2009) SiRNA conjugate delivery systems. *Bioconjugate Chem. 20*, 5–14.

(34) Blackburn, W. H., Dickerson, E. B., Smith, M. H., McDonald, J. F., and Lyon, L. A. (2009) Peptide-functionalized nanogels for targeted siRNA delivery. *Bioconjugate Chem. 20*, 960–968.

(35) Lesko, E., Miekus, K., Grabowska, A., Gładys, A., and Majka, M. (2008) Optimization of a synthetic siRNA delivery for the treatment of rhabdomyosarcoma. *Cen. Eur. J. Biol. 3*, 371–379.

(36) Scudiero, D. A., Shoemaker, R. H., Paull, K. D., Monks, A., Tierney, S., Nofziger, T. H., Currens, M. J., Seniff, D., and Boyd, M. R. (1988) Evaluation of a soluble tetrazolium/formazan assay for cell growth and drug sensitivity in culture using human and other tumor cell lines. *Cancer Res. 48*, 4827–4833.

(37) Ruponen, M., Honkakoski, P., Tammi, M., and Urtti, A. (2004) Cell-surface glycosaminoglycans inhibit cation-mediated gene transfer. *J. Gene Med. 6*, 405–414.

(38) Ruponen, M., Arkko, S., Reinisalo, M., Urtti, A., and Ranta, V. P. (2008) Intracellular elimination and unpacking kinetics of DNA mediated with various non-viral gene delivery systems. *Hum. Gene Ther. 19*, 1094–1095.

(39) Neu, M., Sitterberg, J., Bakowsky, U., and Kissel, T. (2006) Stabilized nanocarriers for plasmids based upon cross-linked poly(ethylene imine). *Biomacromolecules 7*, 3428–3438.

(40) Chen, T. H. H., Bae, Y., and Furgeson, D. Y. (2008) Intelligent biosynthetic nanobiomaterials (IBNs) for hyperthermic gene delivery. *Pharm. Res. 25*, 683–691.

(41) Ellis, R. J. (2001) Macromolecular crowding: obvious but underappreciated. *Trends Biochem. Sci. 26*, 597–604.

(42) Amidi, M., Romeijn, S. G., Borchard., G., Junginger, H. E., Hennink, W. E., and Jiskoot, W. (2006) Preparation and characterization of protein-loaded N-trimethyl chitosan nanoparticles as nasal delivery system. *J. Controlled Release 111*, 107–116.

(43) Kean, T., and Thanou, M. (2009) Biodegradation, biodistribution and toxicity of chitosan. *Adv. Drug Delivery Rev. 62*, 3–11.

(44) Wightman, L., Kircheis, R., Rössler, V., Carotta, S., Ruzicka, R., Kursa, M., and Wagner, E. (2001) Different behavior of branched and linear polyethylenimine for gene delivery in vitro and in vivo. *J. Gene Med. 3*, 362–72.

(45) Elouahabi, A., and Ruysschaert, J. M. (2005) Formation and intracellular trafficking of lipoplexes and polyplexes. *Mol. Ther. 11*, 336–347.

(46) Höbel, S., Prinz, R., Malek, A., Urban-Klein, B., Sitterberg, J., Bakowsky, U., Czubayko, F., and Aigner, A. (2008) Polyethylenimine PEI F25-LMW allows the long-term storage of frozen complexes as fully active reagents in siRNA-mediated gene targeting and DNA delivery. *Eur. J. Pharm. Biopharm. 70*, 29–41.

(47) Hill, I. R. C., Garnett, M. C., Bignotti, F., and Davis, S. S. (1999) In vitro cytotoxicity of poly(amidoamine)s: Relevance to DNA delivery. *Biochim. Biophys. Acta 1427*, 161–174.

(48) De Wolf, H. K., Luten, J., Snel, C. J., Storm, G., and Hennink, W. E. (2008) Biodegradable, cationic methacrylamide-based polymers for gene delivery to ovarian cancer cells in mice. *Mol. Pharm. 5*, 349–357.

(49) Van De Wetering, P., Schuurmans-Nieuwenbroek, N. M. E., Hennink, W. E., and Storm, G. (1999) Comparative transfection studies of human ovarian carcinoma cells in vitro, ex vivo and in vivo with poly(2-(dimethylamino)ethyl methacrylate)-based polyplexes. *J. Gene Med. 1*, 156–165.

(50) Inoue, Y., Kurihara, R., Tsuchida, A., Hasegawa, M., Nagashima, T., Mori, T., Niidome, T., Katayama, Y., and Okitsu, O. (2008) Efficient delivery of siRNA using dendritic poly-(l-lysine) for loss-of-function analysis. *J. Controlled Release 126*, 59–66.

BC1003789

Photophysical Characterization of a FRET System Using Tailor-Made DNA Oligonucleotide Sequences

Roman Flehr,[†] Andrea Kienzler,[‡] Willi Bannwarth,[‡] and Michael U. Kumke*[,†]

University of Potsdam, Institute of Chemistry (Physical Chemistry), Karl-Liebknecht-Str. 24-25, 14476 Potsdam-Golm, Germany, and Albert-Ludwigs University of Freiburg, Institute of Organic Chemistry and Biochemistry, Albertstr. 21, 79104 Freiburg, Germany. Received August 31, 2010; Revised Manuscript Received October 19, 2010

We have carried out a detailed photophysical study of the FRET D/A pair consisting of a carbostyril donor and a Ru(II)bathophenanthroline complex acceptor in double-stranded synthetic DNA. Altogether 13 different double-stranded 30 base pair DNAs showing small incremental differences in the distances between donor and acceptor were synthesized. Using the fluorescence of the donor as well as of the acceptor, D/A separations were determined and compared to those derived from a well-established model for DNA distance calculations. The model calculations and anisotropy studies revealed that the donor can nearly be seen as a free rotator allowing the application of the established FRET data evaluation.

INTRODUCTION

In life sciences, the fundamental principle of fluorescence resonance energy transfer (FRET) is widely applied to study macromolecules, especially with respect to their intra- and intermolecular interactions (*1*−*4*). In clinical diagnostics, FRET-based immunoassays successfully compete with radio immunoassays, and moreover, biochemical processes can even be investigated on a single molecule level making use of this principle (*5*−*8*). Due to increasing demand and the growing number of applications in life sciences and medical application, there is an ongoing search for novel dyes with tailor-made spectroscopic properties to create FRET systems with special characteristics (e.g., making use of dyes absorbing and emitting in the far-red to NIR spectral range in order to minimize disturbances arising from biological samples) (*9*−*13*). Depending on the analytical problem to be solved, different FRET systems are required (*14*). In order to use FRET-based analysis as a "molecular ruler", well-characterized reference systems are needed showing under "working conditions" a clear relationship between the distance of donor−acceptor and the resulting FRET efficiencies.

For a specific donor−acceptor (D/A) pair, the Förster radius R_0 determines the working range with respect to analytically accessible distances between donor (D) and acceptor (A). As a rule of thumb, a specific D/A pair can be used for distance determinations within a range of $R_0/2 < R < 2R_0$. Therefore, for a powerful tailor-made FRET system two aspects are of major importance: (i) The spectroscopic properties of the D and A dye molecules need to be matched in order to adjust R_0 to the required needs, and (ii) from a synthetic point of view, an easy and robust labeling protocol should allow an exact (strategic) positioning of the dye molecules in the macromolecular system under investigation. With respect to (i), major prerequisites are a high donor fluorescence quantum yield Φ_D, a large molar extinction coefficient ε_A of A and an intensive spectral overlap between the emission spectrum of D and the absorption spectrum of A (*15*). In addition to matching the spectroscopic properties, an important factor is the relative orientation of the transition dipole moments of D and A (*16*−*18*). Coupling to a macromolecule may influence the overall performance of a D/A pair due to changes in the spectroscopic properties and/or due to limitations in the rotational freedom of the dyes. The latter may arise from specific interactions between the dye molecules and the macromolecule (e.g., H-bonding) and has to be considered by adapting the orientation factor κ in the calculations properly. In addition, at short D/A distances additional dye−dye quenching may occur, which needs to be accounted for (*19*).

In the past, polyprolines with different numbers of proline units as well as DNA fragments with a variable number of base pairs were used as scaffold. Double-stranded DNA fragments show a clear relationship between the number of base pairs (bp) and overall length with a large persistence length of about 50 nm (*16*, *17*, *19*−*23*). In contrast, polypeptides may build secondary and even ternary structures depending on the peptide sequence making their use as reference systems, in which a systematic variation of the separation between donor and acceptor is desired, more demanding, e.g., additional information from complementary analytical techniques such as X-ray structure analysis may be needed to determine the molecular distances. It turned out that in solution model systems based on polyproline spacers are not completely rigid, leading to deviations between calculated and measured values for R_0 (*24*). Subsequently, the observed distance distribution of D and A may limit the overall spatial resolution of the FRET system, and proper calibration factors such as for the sequence-dependent bending of the DNA sequence are needed to correctly estimate D/A distances (*16*−*18*).

For dyes attached to DNA, intercalation of the dye molecule or other specific binding interactions (such as H-bonding) between dye and DNA are of major concern (*18*, *25*). In order to minimize limitations due to rotational hindrance of the donor and acceptor dyes, flexible linker entities were suggested (*26*, *27*). FRET pairs consisting of dyes like tetramethylrhodamine, Cy3, or R6G have already been applied in DNA as donors in combination with Cy5 or JA133 as acceptor (*19*, *28*, *29*).

In the present paper, a FRET system based on a carbostyril (quinolin-2(1*H*)-one) chromophore as donor and a (bathophenanthroline)ruthenium(II)-complex as acceptor (Figure 1) bound to double-stranded DNA was systematically character-

* E-mail: kumke@uni-potsdam.de. Tel.: +49 331 9775209. Fax: +49 331 9775058.

[†] University of Potsdam.

[‡] Albert-Ludwigs University of Freiburg.

10.1021/bc100389k © 2010 American Chemical Society
Published on Web 11/29/2010

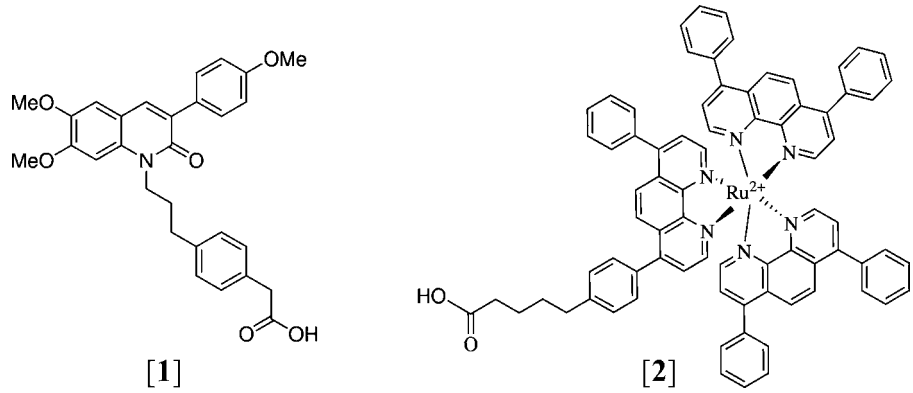


Figure 1. Carbostyril (quinolin-2(1H)-one) **1** and (bathophenanthroline)ruthenium(II)-complex.

ized. Feasibility studies for the FRET system were first carried out in peptides (*30*, *31*) and later also in synthetic DNA (*32*, *33*). In comparison to other FRET systems, this D/A pair has several benefits. The donor is very robust with respect to its chemical stability and can be directly incorporated as a building block into DNA during its automated assembly on solid support allowing exact positioning within any desired DNA sequence.

The acceptor (**2**) can be coupled to the donor-labeled DNA on solid support directly after synthesis via an amide bond formation (*33*). The Ru-complex (**2**) outmatches other reported acceptors due to its thermodynamic stability, its chemical inertness, its straightforward synthetic accessibility (*34*), and the possibility of time-gated detection as a result of the long luminescence decay time (*34*−*38*).

The unique combination of chemically robust dye-labeled building blocks and remarkable spectroscopic properties of the FRET system prompted us to perform a detailed study concerning synthetic DNA, in which the distance between donor and acceptor was systematically varied by the number of separating base pairs. On the basis of the evaluation of the donor as well as acceptor related emission, the energy transfer efficiencies (D/A separations) were determined and compared to a well-established model for DNA distance calculations evaluating under "working conditions" the "molecular ruler" properties.

MATERIALS AND METHODS

In the present study, 13 different DNA fragments **3**−**15** all bearing the Ru-complex (A) at the 5′-end and the carbostyril donor (D) at different distance intervals defined by the number of separating base pairs (Δbp) between donor and acceptor were prepared (Figure 2). In addition, we have also prepared the complementary sequences **16**−**21**. Due to the attachment of A at the 5′-position of 2′-deoxyuridine, the hybridization to the complementary strand is not hampered.

General. Oligonucleotide syntheses were carried out on an Expedite 8909 Nucleic Acid Synthesis system on a 1 μmol scale using phosphoramidite chemistry and standard protocols. Phosphoramidites as well as nucleosides coupled to solid support (CPG) were obtained from Proligo/Sigma Aldrich. Cleavage of the modified and unmodified oligonucleotides from the solid support and deprotection was performed by a 25% NH-solution followed by vortexing overnight at room temperature. After exchanging NH_4^+ with K^+, the oligonucleotide samples were desalted by size exclusion chromatography using NAP-10 columns. Purification of the modified oligonucleotides was performed by preparative polyacrylamide gel electrophoresis (PAGE). The oligonucleotides were visualized at 366 nm, and bands containing the desired DNA were isolated and extracted with water. The resulting oligonucleotide samples were again desalted on NAP-10 columns. All oligonucleotides were analyzed by analytical PAGE after staining with Stains-All (Fluka). Quantification was done by UV-measurements on a Perkin-Elmer-Lambda-35-UV/Vis spectrometer. H, C, and P NMR spectra were measured on AC 250, AM 400, and DRX 500 from Bruker, as well as a Mercury VX 300 from Varian using $CDCl_3$, CD_3CN, or d-DMSO as solvent. Column chromatography was performed on silica gel type 60 ACC 35−70 μm.

Compounds **22** and **23** were synthesized according to ref *33*. Spectroscopic data were in accordance to literature data (*32*, *33*).

Synthesis of Modified Oligonucleotides 3−**15.** The two modified building blocks **22** and **23** (67 μmol/mL in MeCN) were incorporated during automated synthesis using standard cycles. For the attachment of the Ru-complex **2**, the MMT-protecting group was cleaved after complete assembly on the synthesizer using standard detritylation conditions. Then, a mixture of HBTU (54.6 mg, 143 μmol), HOBT (24.5 mg, 181 μmol), and Ru-complex **2** (50.8 mg, 42.4 μmol) was dissolved in DMF (960 μL) followed by the addition of DIEA (65.6 μL). After vortexing for 10 min, it was added to the DNA attached to the solid support (16 mg, ∼0.4 μmol) in an Eppendorf reaction vessel (*39*). The slurry was slowly shaken at room temperature overnight. After removal of the supernatant, the solid support was washed with DMF (2 × 1 mL) and MeCN (2 × 1 mL). Cleavage from solid support and deprotection was performed according to standard protocols. Purification was done by preparative gel.

Hybridization (Preparation of FRET Constructs). To the donor and acceptor-labeled DNA (0.1 OD in 1 μL H_2O), 1.3 equiv. of the corresponding unmodified DNA-strand (0.1 OD in 1 μL H_2O) were added and the solvent removed in vacuum. The precipitate was dissolved in phosphate buffer (5 mM, pH 7) and thermal hybridization was performed by heating the sample to 90 °C for 2 min and then cooling it slowly to room temperature yielding dye-labeled double-stranded DNA (FRET constructs).

Photophysical Characterization. The absorption and fluorescence spectra were recorded on a Lambda 750 UV/Vis spectrometer (Perkin-Elmer) and a Fluoromax3 spectrometer (Jobin Yvon). In the time-resolved emission measurements, the frequency doubled output (second harmonic generation, SHG) with a vertical polarization plane of a Titan sapphire laser (Tsunami 3960; Spectra Physics; $\lambda_{TiSa} = 720$ nm, $\lambda_{SHG} = 360$ nm, pulse width (fwhm) 120 fs) was used for excitation. The repetition rate of 80.2 MHz was reduced to 4 MHz to 50 kHz with a Pulse Picker (Pulse Select; APE). The luminescence was detected in a right angle configuration to the incoming beam. The emission polarizer was set to 0°, 90°, and 55° with respect to the polarization plane of the laser. For the detection, a multichannel plate (ELDI EM1−132/300; Europhoton GmbH) coupled to a FL920 fluorescence lifetime spectrophotometer (Edinburgh Instruments) was used. The time-resolved emission was recorded in the time-correlated single photon counting

Bis-labeled DNA strands:

DNA 3 $^{5'}$T^{A}TG CTC ATC CTG CTA CTT TTG CTC CTA CT^{D}T$^{3'}$

DNA 4 $^{5'}$T^{A}TG CTC ATC CTG CTA CTT TTG CTC CT^{D}A CTT$^{3'}$

DNA 5 $^{5'}$T^{A}TG CTC ATC CTG CTA CTT TTG CT^{D}C CTA CTT$^{3'}$

DNA 6 $^{5'}$T^{A}TG CTC ATC CTG CTA CTT TT^{D}G CTC CTA CTT$^{3'}$

DNA 7 $^{5'}$T^{A}TG CTC ATC CTG CTA CT^{D}T TTG CTC CTA CTT$^{3'}$

DNA 8 $^{5'}$T^{A}TG CTC ATC CTG CT^{D}A CTT TTG CTC CTA CTT$^{3'}$

DNA 9 $^{5'}$T^{A}TG CTC ATC CT^{D}G CTA CTT TTG CTC CTA CTT$^{3'}$

DNA 10 $^{5'}$T^{A}TG CTC ATC T^{D}TG CTA CTT TTG CTC CTA CTT$^{3'}$

DNA 11 $^{5'}$T^{A}TG CTC ATT^{D} CTG CTA CTT TTG CTC CTA CTT$^{3'}$

DNA 12 $^{5'}$T^{A}TG CTC T^{D}TC CTG CTA CTT TTG CTC CTA CTT$^{3'}$

DNA 13 $^{5'}$T^{A}TG CTT^{D} ATC CTG CTA CTT TTG CTC CTA CTT$^{3'}$

DNA 14 $^{5'}$T^{A}TG T^{D} TC ATC CTG CTA CTT TTG CTC CTA CTT$^{3'}$

DNA 15 $^{5'}$T$^{A}T^{D}$G CTC ATC CTG CTA CTT TTG CTC CTA CTT$^{3'}$

Complementary DNA strands:

Complementary strand for DNA 3-9, DNA 15:

DNA 16: $^{5'}$AAG TAG GAG CAA AAG TAG CAG GAT GAG CAA$^{3'}$

Complementary strand for DNA 10:

DNA 17: $^{5'}$AAG TAG GAG CAA AAG TAG CAA GAT GAG CAA$^{3'}$

Complementary stand for DNA 11:

DNA 18: $^{5'}$AAG TAG GAG CAA AAG TAG CAG AAT GAG CAA$^{3'}$

Complementary stand for DNA 12:

DNA 19: $^{5'}$AAG TAG GAG CAA AAG TAG CAG GAA GAG CAA$^{3'}$

Complementary strand for DNA 13:

DNA 20: $^{5'}$AAG TAG GAG CAA AAG TAG CAG GAT AAG CAA$^{3'}$

Complementary strand for DNA 14:

DNA 21: $^{5'}$AAG TAG GAG CAA AAG TAG CAG GAT GAA CAA$^{3'}$

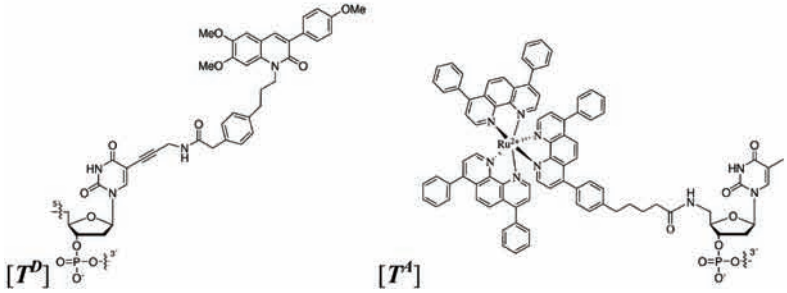


Figure 2. Modified DNA strands and their complementary sequences.

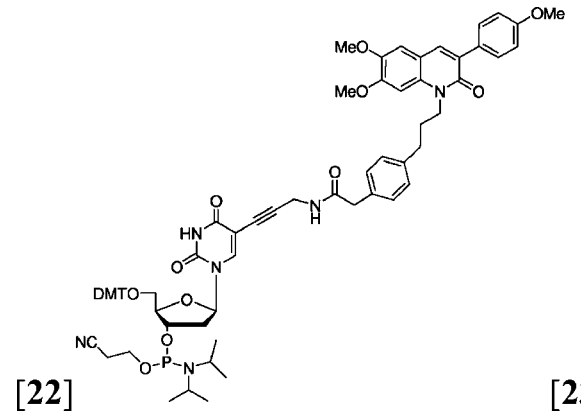


Figure 3. Modified phosphoramidites for DNA synthesis.

mode. The fluorescence quantum yields were measured on a PL Quantum Yield measurement system C9920−02 with an integrating sphere (Hamamatsu, Japan).

Data Analysis. For the energy transfer efficiency E, the distance R_{DA} between D and A is of fundamental importance. For DNA, the distance R_{DA} at different Δbp can be calculated according to eq 1 (*40*). In this model, the geometrical parameters of a B-form double-stranded (ds) DNA helix in solution are applied (diameter 20 Å, 3.4 Å rise, and 36° turn per base pair) to calculate R_{DA}.

$$Q = L_D^2 + L_A^2 - 2L_D L_A \cos(\Omega + 36\Delta\text{bp})$$

$$R_{DA} = \sqrt{(K + 2.4\Delta\text{bp})^2 + Q} \tag{1}$$

In eq 1, Δbp represents the number of base pairs separating D and A, K is the theoretical relative distance of D and A in the case in which both dyes are attached to the same base (Δbp = 0). L_D and L_A are the distances between the dyes and the helical axis for D and A, respectively. Ω is the interdye angle for Δbp = 0.

On the basis of eqs 2 and 3, the critical Förster distance R_0 [Å] was calculated from experimental spectroscopic data.

$$R_0^6 = \frac{(9000 \ln 10)\kappa^2 \Phi_D}{128\pi^5 n^4 N_A} J(\lambda) \tag{2}$$

$$J(\lambda) = \int_0^\infty F_D(\lambda)\varepsilon_A(\lambda)\lambda^4 \, d\lambda \tag{3}$$

In eq 2, Φ_D is the fluorescence quantum efficiency of D, and κ^2 represents the orientation factor describing the relative orientation of the transition dipole moments of emission and absorption for D and A, respectively. The refractive index of the solvent is taken into account by n. $J(\lambda)$ is the spectral overlap integral calculated from the area-normalized fluorescence spectrum of D and the absorption spectrum of A (see eq 3).

Using eq 1, the mean distance R_{DA} of D and A for each FRET construct can be calculated. In addition, theoretical energy transfer efficiencies E_{theo} were calculated using eqs 4 and 1 to fit experimentally obtained E_{exp} based on the measured emission data (vide infra).

$$E_{theo} = \frac{1}{1 - \left(\frac{R_{DA}}{R_0}\right)^6} \tag{4}$$

The experimental energy transfer efficiencies E_{exp} were determined from the following equations.

(i). Donor Fluorescence Signal. On the basis of eq 5:

$$E_{exp,D} = 1 - \frac{I_{DA}}{I_D} \tag{5}$$

In eq 5, I_{DA} is the fluorescence signal of D in the presence of A and I_D in the absence of A.

(ii). Ratio Method. According to eq 6 introduced and applied by Clegg et al. from the fluorescence excitation spectra (*20, 40−43*)

$$E_{exp,D} = 1 - \frac{F_{ex,D}(\lambda_{em,D})}{F_{ex,A}(\lambda_{em,A})} \cdot \frac{\varepsilon_A(\lambda_A)}{\varepsilon_D(\lambda_D)} \tag{6}$$

where $F_{ex,D}$ and $F_{ex,A}$ are the emission signals in the excitation spectrum (for D in the spectral range of 325 nm < λ_{ex} < 415 nm at λ_{em} = 435 nm and for A in the spectral range of 410 nm < λ_{ex} < 600 nm at λ_{em} = 620 nm), ε_D and ε_A are the molar extinction coefficients of D and A at their respective absorption maxima.

(iii). Increased Acceptor and Decreased Donor Emission (44).

$$E_{exp,A} = \frac{I_A}{I_D + \frac{\Phi_A}{\Phi_D} I_A} \tag{7}$$

In eq 7, I_A is the fluorescence of the acceptor corrected for contribution from direct excitation, I_D the fluorescence of the donor (I_D, 375 nm < λ_{em} < 550 nm; I_A, 560 nm < λ_{em} < 690 nm), and Φ_D and Φ_A are the quantum yields of the donor and acceptor, respectively. $E_{exp,A}$ is often used to calculate the energy transfer efficiencies in single molecule experiments, but it has also been successfully applied to data of batch emission measurements (*28*).

Time-dependent fluorescence anisotropy measurements $r(t)$ were carried out to determine the rotational mobility of the donor dye in the FRET constructs. The anisotropy decay was calculated according to eq 8 by measuring the fluorescence decay with the emission polarizer set in a vertical ($I_{VV}(t)$) and horizontal ($I_{VH}(t)$) position relative to the excitation polarization (*45*).

$$r(t) = \frac{I_{VV} - I_{VH}G}{I_{VV} + 2I_{VH}G} \tag{8}$$

In eq 8, G is the instrumental correction factor and the subscipts V and H refer to the vertical or horizontal orientation of the polarizers for the excitation and emission. The G-value was determined according to ref *46*.

$$r(t) = \sum_n r_{0n}\, e^{-t/\varphi_n} \quad \text{with } n \leq 2 \tag{9}$$

The obtained anisotropy decay curves were fitted using eq 9, where r_{0n} and φ_n are the limiting anisotropy and decay times associated with the rotations of the dye (*27*). For the free donor, n was set to 1, and for donor−DNA construct, n was set to 2.

RESULTS AND DISCUSSION

Basic Spectroscopic Properties: Absorption, Emission, and Anisotropy. In the absorption spectra of the FRET constructs, the absorption maximum of the donor was found at $\lambda = 360$ nm, that of the acceptor at $\lambda = 450$ nm, and that of the oligonucleotides at $\lambda = 260$ nm, respectively. Compared to the parent compounds, the absorption spectra of D and A were not altered due to the covalent binding to DNA.

An advantage of this D/A pair is the complementary donor and acceptor absorption characteristics. The absorption maximum of D is located at the minimum of the acceptor absorption, resulting in a desired low direct excitation of A. Therefore, all samples were excited at $\lambda_{ex} = 355$ nm, corresponding to the absorption minimum of the Ru-complex (A).

The fluorescence spectra of the FRET constructs containing D and A show a "dual" fluorescence corresponding to the emission of the donor and acceptor part at $\lambda_{em} = 430$ nm and at $\lambda_{em} = 620$ nm, respectively. Figure 4 shows the fluorescence emission spectra of the FRET constructs with Δbp = 5, 9, 13, 19, and 28. Spectral shifts of neither the donor- nor the acceptor-related emission were observed for the FRET constructs. Especially, the fact that at small D−A distances (low Δbp) the emission spectra are free of spectral changes indicates that no strong electronic coupling between the electronic systems of D and A is operative. Weak electronic coupling is a prerequisite for the application of the FRET formalism. The emission curves intersect at a single point, which indicates a direct correlation between the decrease of donor fluorescence and the increase of acceptor fluorescence. This is also expected for FRET.

In contrast to the spectral characteristics, the emission intensities of the donor and acceptor fluorescence were strongly correlated with Δbp. With decreasing Δbp, the donor emission was decreased, and at the same time, for the corresponding acceptor fluorescence an increase was observed.

The fluorescence excitation spectra recorded at the emission wavelength of the acceptor ($\lambda_{em} = 620$ nm) show a distinct increase under indirect excitation at $\lambda_{ex} = 365$ nm of the Ru-complex (A) with decreasing Δbp (see Figure 5). It clearly shows that energy is transferred from the carbostyril (D) to the Ru-complex (A) and emphasizes the occurrence of FRET in the DNA constructs.

From time-resolved anisotropy measurements of the free donor dye, a rotational correlation time φ_1 of about 0.5 ns was determined. For the corresponding DNA constructs, the donor anisotropy showed two rotational correlation times: $\varphi_1 \approx 0.5$ ns and $\varphi_2 \approx 7$ ns (see Table 1). φ_1 and φ_2 can be tentatively attributed to the rotation of the donor itself and to the overall rotation of the donor-DNA strand (*47*). For the acceptor, anisotropy measurements were not performed because of its very long luminescence decay time (τ_A in degassed aqueous solution was determined to be 5 μs (*48*)) rendering anisotropy measurements meaningless, since the rotation of A as well as the DNA strands occurs on a much shorter time scale (few nanoseconds or less; see Table 1).

Determination of FRET Parameters. An important parameter for the evaluation of a D/A FRET pair is the critical Förster distance R_0 (see eqs 2 and 3). The fluorescence spectrum of the carbostyril (D) and the absorption spectrum of the Ru-complex (A) show a large spectral overlap, which is a prerequisite for a large R_0. In Figure 6, the absorption spectrum $\varepsilon_A(\lambda)$ and the area normalized (area = 1) fluorescence spectrum F_D are shown. On the basis of the experimental spectral data, a spectral overlap integral $J = 1.05 \times 10^{15}$ l·mol^{-1}·cm^{-1}·nm^4 was calculated. Using a value of $\Phi_D = 0.17$ for the donor fluorescence quantum efficiency, the refractive index of water ($n = 1.4$), and setting the orientation factor $\kappa^2 = 2/3$, the $R_{0,spec} = (37 \pm 3)$ Å was calculated according to eq 2.

From the fluorescence emission and excitation spectra the FRET efficiencies $E_{exp,D}$ and $E_{exp,A}$ were determined according to methods (i)−(iii) (vide supra). The data sets of the donor-based $E_{exp,D}$ and acceptor-based $E_{exp,A}$ show the same dependency on Δbp (see Figure 7). After a first increase of the experimentally observed energy transfer efficiency upon increasing Δbp up to 7, E_{exp} decreases at larger Δbp. The comparison between $E_{exp,D}$ and $E_{exp,A}$ shows a small difference with respect to the corresponding uncertainties of the data. Especially at larger Δbp, an increase in the experimental error of the determined energy transfer efficiencies is found and can be attributed to the increasing relative contribution of noise for

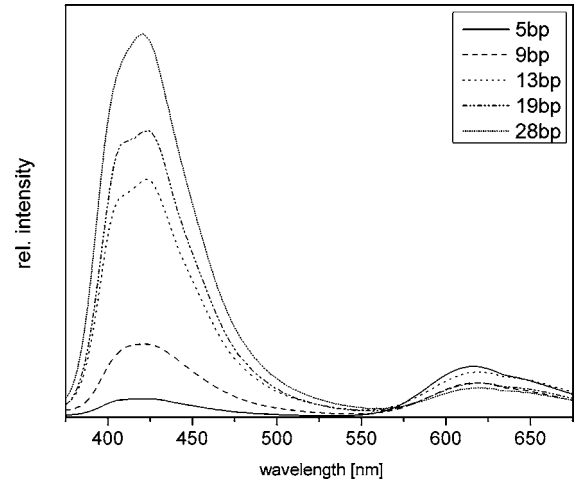


Figure 4. Fluorescence emission spectra of FRET constructs ($\lambda_{ex} = 355$ nm) with different Δbp.

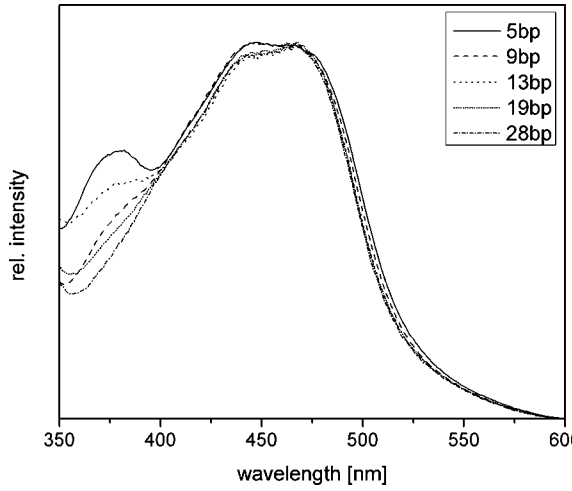


Figure 5. Normalized fluorescence excitation spectra of FRET constructs with different base pair separation between D and A ($\lambda_{em} = 620$ nm).

Table 1. Anisotropy Decay Parameters ($\lambda_{ex} = 360$ nm)

	λ_{em} [nm]	φ_1 [ns]	φ_2 [ns]	r_{01}	r_{02}
donor	430	0.51 ± 0.01	-	0.23 ± 0.05	-
donor-DNA	430	0.48 ± 0.01	7.3 ± 0.5	0.06 ± 0.002	0.24 ± 0.05

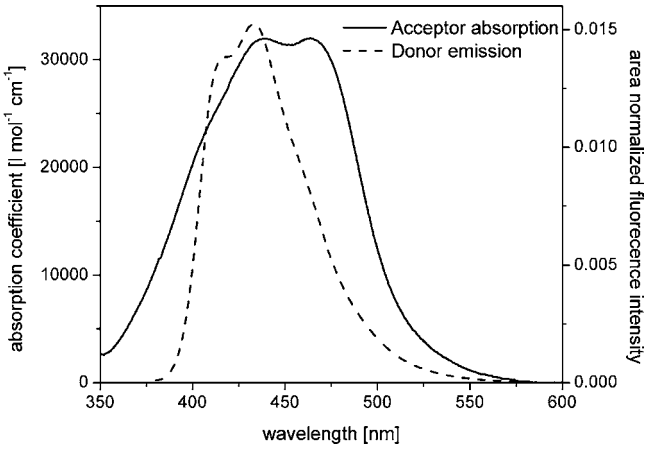


Figure 6. Spectral overlap between fluorescence emission of D and absorption of A.

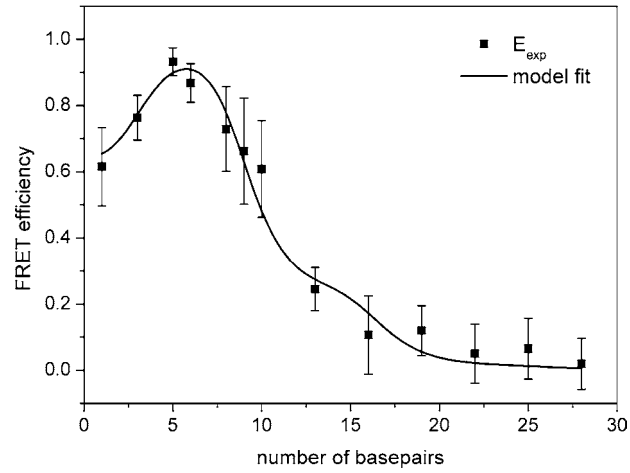


Figure 8. Experimental and theoretical FRET efficiencies (according to eq 4 with $R_{DA,cal}$ from eq 1). From the data analysis, the following parameters were obtained: $L_A = (4 \pm 1)$ Å, $L_D = (28 \pm 1)$ Å, $K = (-13 \pm 2)$ Å, and $\Omega = (134 \pm 15)$, respectively.

decreasing signals. For the acceptor signal, this is more effective because of a lower absolute signal and also because of smaller absolute changes in the signal intensity.

From eq 1, the absolute distances between D and A (see Figure 7, top *x*-scale) can be determined. It can be seen that the observed energy transfer efficiency depends on the absolute number of base pairs between D and A (Δbp) as well as the relative orientation between D and A in space (same or opposite side of the DNA helix), which can be concluded from the comparison of the experimentally determined and calculated data based on the model. In Figure 8, experimentally determined FRET efficiency E_{exp} calculated as an average of all $E_{exp,X}$ (X = A, D) and theoretically expected efficiencies E_{theo} are compared. The latter were calculated using eq 1 for the determination of the theoretical distance between D and A assuming an ideal DNA helix and transforming those distances subsequently into an energy transfer efficiency based on eq 4. In the calculation, the Förster distance R_0 determined from the spectral data was used and the parameters K, L_D, L_A, and Ω were varied to fit the model to the experimental FRET efficiencies. It can be seen that the experimental data can be nicely fitted with the model, especially at distances $R_{DA} \leq R_0$ ($\Delta bp \leq 10$). At larger R_{DA} (Δbp), the differences between experimentally determined and model-based FRET efficiencies become larger.

It is striking that in the beginning—with increasing numbers of separating base pairs—an increase of the energy transfer efficiency is observed, which—after passing a maximum at around $\Delta bp = 7$—is decreasing again for larger Δbp. This trend, which is also predicted by the model, can be attributed to the turn of the DNA helix. The "in-space" distance between D and A is dependent on their relative position with respect to each other. In the case in which D and A are on the same side of the DNA helix, a shorter overall distance is expected compared to a situation in which D and A are located at opposite sides. Hence, due to the turn of the DNA helix a damped sinusoidal oscillation of the energy transfer efficiency with a maximum every $\Delta bp = 10$ (for a full turn of the DNA helix, ten base pairs are required) is predicted by the model.

From the fitted parameters, Ω is especially intriguing, as it represents an interdye angle. From the data fitting, a Ω-value of $(134 \pm 15)°$ was obtained. This interdye angle may explain that for the FRET constructs the maximum energy transfer efficiency is observed around $\Delta bp \approx 5$, which corresponds to a situation of D and A aligned on the same side of the DNA strand.

The applied model also predicts a small second maximum for E at $\Delta bp \approx 16$ (next full turn of DNA helix), which is not

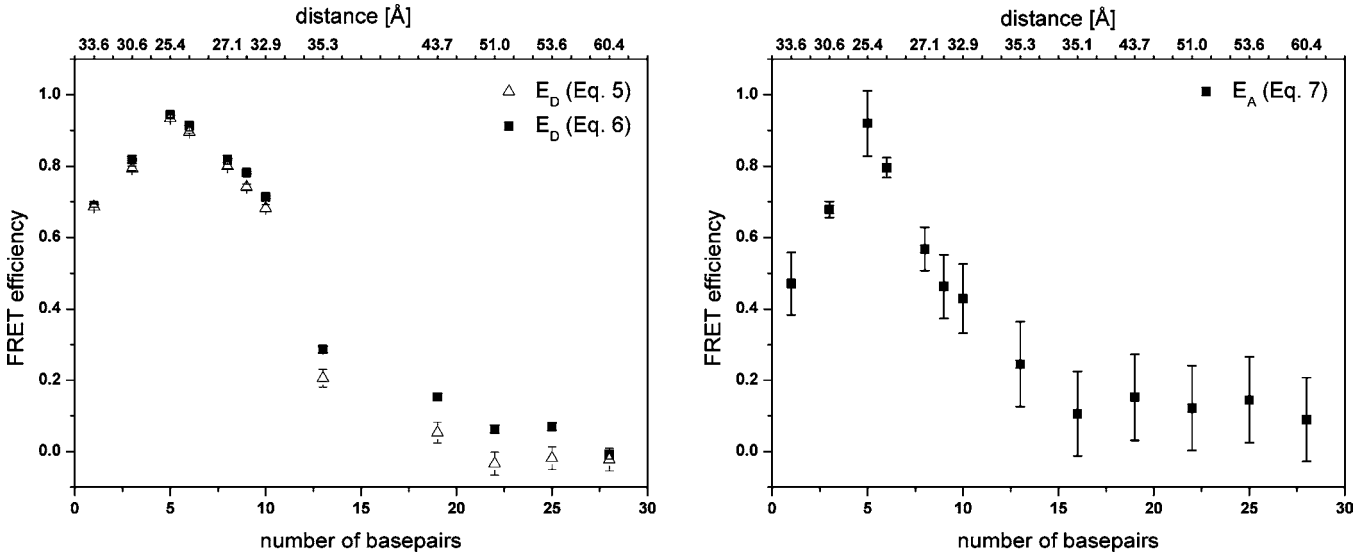


Figure 7. Experimental FRET efficiencies for donor (left) and acceptor (right) at increasing numbers of separating base pairs (Δbp).

found in the experimental data. Here, the increasing uncertainty of the determined energy efficiencies at large distances ($R \geq 2R_0$) may be seen as an explanation. For such large distances between D and A, only minor changes in the donor fluorescence due to very low FRET efficiencies are expected, making the exact determination of E rather challenging.

The setting of the orientation factor $\kappa^2 = 2/3$ is often used in distance calculations, but has been questioned especially for dyes bound to macromolecules, since in this case, the rotational motion of D and/or A can be hindered due to interactions such as H-bonding between the dye and the macromolecule. In these cases, κ^2 may differ from 2/3. As a consequence, the expected and measured energy transfer efficiencies (and subsequently the distances) can be significantly different. For the FRET constructs, setting κ^2 to 2/3 seems to be a good approximation judged by the fit according to eq 4 (see Figure 8) and by the results of the time-resolved anisotropy measurements (see Table 1). Both results strongly suggest that the donor when attached to the DNA is free to rotate and is not hindered due to specific dye−DNA interactions. The acceptor is attached to the 5′-end of the DNA, and due to the excellent agreement between model and experimental data, it seems reasonable to assume that it is also not hindered in its rotational motion.

CONCLUSION

The FRET system, based on a carbostyril (quinolin-2(1*H*)-one) chromophore as donor and the (bathophenanthroline)ruthenium(II) complex as FRET acceptor attached to double-stranded DNA fragments with different separating base pairs between D and A, was characterized with respect to its photophysical properties. The distance dependency of the energy transfer efficiencies for different Δbp was experimentally determined and could be well-described by a model, which considers the turn of the DNA helix as well as the relative orientation of D and A. It was shown that, for small numbers of separating base pairs (Δbp < 5), a decrease in the experimental energy transfer efficiency was observed. Such a phenomenon was described in earlier publications, and additional quenching of the donor emission for short D/A distances due to specific interactions was suggested (*28*), e.g., the dyes are hindering each other at short D−A distances, thereby limiting the free rotation (which may result in $\kappa^2 \neq 2/3$). However, in the present work it is shown that for the FRET constructs the distance dependence of FRET is well-described by taking into account Δbp as well as the relative positions of D and A in space (by the angle Ω between D and A). Moreover, anisotropy measurements support the assumption that no hindrance of the free rotation for the donor is present for the FRET constructs. Our results show that such FRET constructs are well-suited to serve as a construction kit in the design and characterization of novel FRET pairs. Distances between D and A can be tailor-made by adjusting Δbp and taking the operative in-space distance into account. The latter can be predicted and calculated using eq 1.

The difference between model and experimental data especially at large D/A distances ($R_{DA} < 2R_0$) also demonstrate the need for advanced FRET systems. The "simple" approach of maximizing R_0 will make the system "blind" at shorter distances. In more sophisticated concepts, two FRET systems are coupled; here, an acceptor serves as the donor for the second (triple-color FRET). In such systems, the potential of high spatial resolution at short and medium distances is retained, while the sensing of larger distances is improved. Work is in progress to implement such a multichromophor FRET system for DNA analysis using the carbostyril and the (bathophenanthroline)ruthenium(II)-unit as central building blocks.

ACKNOWLEDGMENT

Parts of this work were funded by the German Federal Department for Science and Education BMBF (IP 03/517).

LITERATURE CITED

(1) Sapsford, K. E., Berti, L., and Menditz, I. L. (2006) Materials for fluorescence resonance energy transfer analysis: beyond traditional donor-acceptor combinations. *Angew. Chem. Int. 45*, 4562–4589.

(2) Endoh, T., Shintani, R., Mie, M., Kobatake, E., Ohtsuki, T., and Sisdo, M. (2009) Detection of bioactive small molecules by fluorescence resonance energy transfer (FRET) in RNA-protein conjugates. *Bioconjugate Chem. 20*, 2242–2246.

(3) Li, X., and Kohli, P. (2010) Investigating molecular interactions in biosensors based on fluorescence resonance energy transfer. *J. Phys. Chem. C 114*, 6255–6264.

(4) Chung, H. S., Gopich, I. V., McHale, K., Cellmer, T., Louis, J. M., and Eaton, W. A. (2010) Extracting rate coefficients from single-molecule photon trajectories and FRET efficiency histograms for a fast-folding protein. *J. Phys. Chem. A* ASAP.

(5) Tinnefeld, P., and Sauer, M. (2005) Neue Wege in der Einzelmolekül-Fluoreszenzspektroskopie: Herausforderungen für die Chemie und Einfluss auf die Biologie. *Angew. Chem. 117*, 2698–2728.

(6) Ha, T., Enderle, Th., Ogletree, D. F., Chemla, D. S., Selvin, P. R., and Weiss, S. (1996) Probing the interaction between two single molecules: fluorescence resonance energy transfer between a single donor and a single acceptor. *Proc. Natl. Acad. Sci. U.S.A. 93*, 6264–6268.

(7) Selvin, P. R. (2000) The renaissance of fluorescence resonance energy transfer. *Nat. Struct. Biol. 7*, 730–734.

(8) Sharma, B., Deo, S. K., Bachas, L. G., and Daunert, S. (2005) Competitive binding assay using fluorescence resonance energy transfer for the identification of calmodulin antagonists. *Bioconjugate Chem. 16*, 1257–1263.

(9) Maliwal, B. P., Gryczynski, Z., and Lakowicz, J. R. (2001) Long-wavelength long-lifetime luminophores. *Anal. Chem. 73*, 4277–4285.

(10) Lakowicz, J. R., Piszczek, G., and Kang, J. S. (2001) On the possibility of long-wavelength long-lifetime high-quantum-yiels luminophores. *Anal. Biochem. 288*, 62–75.

(11) Kang, J. S., Lakowicz, J. R., and Piszczek, G. (2002) DNA Dynamics: a fluorescence resonance energy transfer study using a long-lifetime metal-ligand complex. *Arch. Pharm. Res. 25*, 143–150.

(12) Buschmann, V., Weston, K. D., and Sauer, M. (2003) Spectroscopic study and evaluation of red-absorbing fluorescent dyes. *Bioconjugate Chem. 14*, 195–204.

(13) Bouteiller, C., Clave, G., Bernadin, A., Chipon, B., Massonneau, M., Renard, P.-Y., and Romieu, A. (2007) Novel water-soluble near-infrared cyanine dyes: synthesis, spectral properties, and use in the preparation of internally quenched fluorescent probes. *Bioconjugate Chem. 18*, 1303–1317.

(14) Sahoo, H., Roccatano, D., Hennig, A., and Nau, W. M. (2007) A 10Å spectroscopic ruler applied to short polyprolines. *J. Am. Chem. Soc. 129*, 9762–9772.

(15) Förster, T. (1948) Zwischenmolekulare Energiewanderung und Fluoreszenz. *Ann. Phys. 2*, 55–75.

(16) Iqbal, A., Arsian, S., Okumus, B., Wilson, T. J., Giraud, G., Norman, D. G., Ha, T., and Lilley, D. M. J. (2008) Orientation dependence in fluorescent energy transfer between Cy3 and Cy5 terminally attached to double-stranded nucleic acids. *Proc. Natl. Acad. Sci. U.S.A. 105*, 11176–11181.

(17) Woznaik, A. K., Schröder, G. F., Grubmüller, H., Seidel, C. A. M., and Oesterhelt, F. (2008) Single-molecule FRET measures bends and kinks in DNA. *Proc. Natl. Acad. Sci. U.S.A. 105*, 18337–18342.

(18) Börjesson, K., Preus, S., El-Sagheer, A. H., Brown, T., Albinsson, B., and Wilhelmsson, L. M. (2009) Nucleic acid base analog FRET-pair facilitating detailed structural measurements in nucleic acid containing systems. *J. Am. Chem. Soc. 131*, 4288–4293.

(19) Di Fiori, N., and Meller, A. (2010) The effect of dye-dye interactions on the spatial resolution of single-molecule FRET measurements in nucleid acids. *Biophys. J. 98*, 2265–2272.

(20) Clegg, R., Murchie, A., Zechel, A., and Lilley, D. (1993) Observing the helical geometry of double-stranded DNA in solution by fluorescence resonance energy transfer. *Proc. Natl. Acad. Sci. U.S.A. 90*, 2994–2998.

(21) Deniz, A., Dahan, M., Grunwell, J., Ha, T., Faulhaber, A., Chemla, D., Weiss, S., and Schultz, P. (1999) Single-pair fluorescence resonance energy transfer on freely diffusing molecules: observation of Förster distance dependence and subpopulations. *Proc. Natl. Acad. Sci. U.S.A. 96*, 3670–3675.

(22) Hagerman, P. J. (1988) Flexibility of DNA. *Annu. Rev. Biophys. Biophys. Chem. 17*, 265–286.

(23) Zheng, G., Czapla, L., Srinivasan, A., and Olson, W. (2009) How stiff is DNA? *Phys. Chem. Chem. Phys. 12*, 1399–1406.

(24) Schuler, B., Lipman, E. A., Steinbach, P. J., Kumke, M., and Eaton, W. A. (2005) Polyproline and the "spectroscopic ruler" revisited with single-molecule fluorescence. *Proc. Natl. Acad. Sci. U.S.A. 102*, 2754–2759.

(25) Eggerling, C., Fries, J., Brand, L., Günther, R., and Seidel, C. (1998) Monitoring conformational dynamics of a single molecule by selective fluorescence spectroscopy. *Proc. Natl. Acad. Sci. U.S.A. 95*, 1556–1561.

(26) Stryer, L. (1978) Fluorescence energy transfer as a spectroscopic ruler. *Annu. Rev. Biochem. 47*, 819–846.

(27) Lakowicz, J. R. (2006) Fluorescence Anisotropy, In *Principles of fluorescence spectroscopy*, 3rd ed., pp 353−382, Kluwer Academic, Plenum Publishers, New York.

(28) Dietrich, A., Buschmann, V., Müller, C., and Sauer, M. (2002) Fluorescence resonance energy transfer (FRET) and competing processes in donor-acceptor substituted DNA strands: a comparative study of ensemble and single-molecule data. *Rev. Mol. Biotechnol. 82*, 211.

(29) Tinnefeld, P., Heilmann, M., and Sauer, M. (2005) Design of molecular photonic wires based on multistep electronic excitation transfer. *Chem. Phys. Phys. Chem. 6*, 217–222.

(30) Kainmüller, E., and Bannwarth, W. (2006) A new robust and highly sensitive FRET donor-acceptor pair: synthesis, characterization, and application in a thrombin assay. *Helv. Chim. Acta 89*, 3056–3070.

(31) Kainmüller, E. K., Olle, E. P., and Bannwarth, W. (2005) Synthesis of a new pair of fluorescence resonance energy transfer donor and acceptor dyes and its use in a protease assay. *Chem. Commun. 43*, 5459–5461.

(32) Clima, L., Hirtz-Haag, C., Kienzler, A., and Bannwarth, W. (2007) Application of a highly robust and efficient fluorescence-resonance-energy-transfer (FRET) system in DNA. *Helv. Chim. Acta 90*, 1082–1098.

(33) Clima, L., and Bannwarth, W. (2008) Building-block approach for the straightforward incorporation of a new FRET (fluorescence-resonance-energy transfer) system into synthetic DNA. *Helv. Chim. Acta 91*, 165–175.

(34) Kramer, R. A., Kainmüller, E. K., Flehr, R., Kumke, M. U., and Bannwarth, W. (2008) Quenching of the long-lived Ru(II)bathophenanthroline luminescence for the detection of supramolecular interactions. *Org. Biomol. Chem. 6*, 2355−2360.

(35) Bannwarth, W., Schmidt, D., Stallard, R. L., Hornung, C., Knorr, R., and Müller, F. (2085) (1988) Bathophenanthroline-ruthenium(II) complexes as non-radioactive labels for oligonucleotides which can be measured by time-resolved fluorescence techniques. *Helv. Chim. Acta 71*, 2099.

(36) Ju Youn, H., Terpetschnig, E., Szmacinski, H., and Lakowicz, J. R. (1995) Fluorescence energy transfer immunoassay based on a long-lifetime luminescent metal-ligand complex. *Anal. Biochem. 232*, 24–30.

(37) Marti, A. A., Puckett, C. A., Dyer, J., Stevens, N., Jockusch, S., Ju, J., Barton, J. K., and Turro, N. J. (2007) Inorganic-organic hybrid luminescent binary probe for DNA detection based on spin-forbidden resonance energy transfer. *J. Am. Chem. Soc. 129*, 8680–868.

(38) Altevogt, D., Hrenn, A., Kern, C., Clima, L., Bannwarth, W., and Merfort, I. (2009) A new assay format for NF-κB based on a DNA triple helix and a fluorescence resonance energy transfer. *Org. Biomol. Chem. 7*, 3934–3939.

(39) Narayanan, S., Gall, J., and Richert, C. (2004) Clamping down on weak terminal base pairs: oligonucleotides with molecular caps as fidelity-enhancing elements at the 5′- and 3′-terminal residues. *Nucleic Acids Res. 32*, 2901–2911.

(40) Clegg, R. M. (1992) Fluorescence resonance energy transfer and nucleic acids DNA structures part A: Synthesis and physical analysis of DNA. *Methods Enzymol. 211*, 353–388.

(41) Clegg, R. M., Murchie, A. I. H., Zechel, A., Carlberg, C., Diekmann, S., and Lilley, D. M. J. (1992) Fluorescence resonance energy transfer analysis of the structure of the four-way DNA junction. *Biochemistry 31*, 4846–4856.

(42) Stühmeier, F., Welch, J. B., Murchie, A. I. H., Lilley, D. M. J., and Clegg, R. M. (1997) Global structure of three-way DNA junctions with and without additional unpaired bases: a fluorescence resonance energy transfer analysis. *Biochemistry 36*, 13530–13538.

(43) Vámosi, G., and Clegg, R. M. (2008) Helix-coil transition of a four-way DNA junction observed by multiple fluorescence parameters. *J. Phys. Chem. B 112*, 13136–13148.

(44) Ying, L., Wallace, M. I., Balasubramanian, S., and Klenerman, D. (2000) Ratiometric analysis of single-molecule fluorescence resonance energy transfer using logical combinations of threshold criteria: a study of 12-mer DNA. *J. Phys. Chem. B 104*, 5171–5178.

(45) Luschtinetz, F., Dosche, C., and Kumke, M. U. (2009) Influence of streptavidin on the absorption and fluorescence properties of cyanine dyes. *Bioconjugate Chem. 20*, 576–582.

(46) O'Connor, D. V. Phillips, D. (1984) Time Dependence of Fluorescence Anisotropy, In *Time-correlated single photon counting*, pp 252−283, Academic Press Harcourt Brace Jovanovich Publishers, London.

(47) Hochstrasser, R., Chen, S.-M., and Millar, D. (1992) Distance distribution in a dye-linked oligonucleotide determined by time-resolved fluorescence energy transfer. *Biophys. Chem. 45*, 133–145.

(48) Kramer, R., Flehr, R., Lay, M., Kumke, M., and Bannwarth, W. (2009) Comparative studies of different quinolinone derivatives as donors in fluorescence-resonance-energy transfer (FRET) - systems in combination with a (bathophenanthroline)ruthenium(II) complex as acceptor. *Helv. Chim. Acta 92*, 1933–1943.

BC100389K

Radiofluorinated Rhenium Cyclized α-MSH Analogues for PET Imaging of Melanocortin Receptor 1

Gang Ren, Shuanlong Liu, Hongguang Liu, Zheng Miao, and Zhen Cheng*

Molecular Imaging Program at Stanford (MIPS), Department of Radiology and Bio-X Program, Canary Center at Stanford for Cancer Early Detection, Stanford University, Stanford, California, 94305-5344, United States. Received September 1, 2010; Revised Manuscript Received October 18, 2010

In order to accomplish *in vivo* molecular imaging of melanoma biomarker melanocortin 1 receptor (MC1R), several α-melanocyte-stimulating hormone (α-MSH) analogues have been labeled with *N*-succinimidyl-4-^{18}*F*-fluorobenzoate (^{18}F-SFB) and studied as positron emission tomography (PET) probes in our recent studies. To further pursue a radiofluorinated α-MSH peptide with high clinical translation potential, we utilized 4-nitrophenyl 2-^{18}*F*-fluoropropionate (^{18}F-NFP) to radiofluorinate the transition metal rhenium cyclized α-MSH metallopeptides for PET imaging of MC1R positive malignant melanoma. Metallopeptides Ac-d,Lys-ReCCMSH(Arg^{11}) (two isomers, namely **RMSH-1** and **RMSH-2**) were synthesized using conventional solid phase peptide synthesis chemistry and rhenium cyclization reaction. The two isomers were then conjugated with ^{19}F-NFP or ^{18}F-NFP. The resulting cold or radiofluorinated metallopeptides, **$^{18/19}$F-FP-RMSH-1** and **$^{18/19}$F-FP-RMSH-2**, were further evaluated for their *in vitro* receptor binding affinities, *in vivo* biodistribution, and small-animal PET imaging properties. The binding affinities of **^{19}F-FP-RMSH-1** and **^{19}F-FP-RMSH-2** were determined to be within low nanomolar range. *In vivo* studies revealed that both ^{18}F-labeled metallopeptides possessed good tumor uptake in the B16F10 murine model with high MC1R expression, while possessing much lower uptake in A375M human melanoma xenografts. Moreover, **^{18}F-FP-RMSH-1** displayed more favorable *in vivo* performance in terms of higher tumor uptake and much lower accumulation in the kidney and liver, when compared to that of **^{18}F-FP-RMSH-2** at 2 h postinjection (p.i.). **^{18}F-FP-RMSH-1** also displayed lower liver and lung uptake when compared with that of the same peptide labeled with ^{18}F-SFB (named as **^{18}F-FB-RMSH-1**). Small animal PET imaging of **^{18}F-FP-RMSH-1** in mice bearing B16F10 tumors at 1 and 2 h showed good tumor imaging quality. As expected, much lower tumor uptake and poorer tumor/normal organ contrast were observed for A375M model compared to those of the B16F10 model. **^{18}F-FP-RMSH-1** also exhibited higher tumor uptake and better tumor retention when compared with **^{18}F-FB-RMSH-1**. **^{18}F-FP-RMSH-1** demonstrates significant advantages over **^{18}F-FB-RMSH-1** and **^{18}F-FP-RMSH-2**. It is a promising PET probe for imaging MC1R positive melanoma and MC1R expression *in vivo*.

INTRODUCTION

The incidence of malignant melanoma in western countries has kept increasing in the last two decades. According to the National Cancer Institute, there will be an estimated 68,000 new cases and 8,650 deaths in the United States in 2010. Although melanoma represents only 5% of all skin cancer subtypes, it contributes to more than 50% of deaths related to skin cancer (*1, 2*). Melanoma is an aggressive disease with high metastatic potential and resistance to cytotoxic agents. Currently, early diagnosis and accurate staging of melanoma remain crucial for the improvement of management of melanoma patients (*3, 4*).

Melanocortin type 1 receptor (MC1R[1]) is a G-protein coupled receptor and has been found to be overexpressed in many types of murine and human melanomas, making it an attractive target for receptor based melanoma imaging and therapy (*5, 6*). Over the last two decades, a wide variety of alpha-melanocyte-stimulating hormone (α-MSH) peptides have been developed and extensively studied for MC1R targeted melanoma imaging and treatment (*7, 8*). To date, two classes of α-MSH analogues have shown the most promising results for *in vivo* targeting of MC1R positive melanoma. One class is the linear α-MSH, Ac-Nle-Asp-His-d,Phe-Arg-Trp-Gly-Lys-NH_2 (referred to as NAPamide) and its analogues (*9*−*12*); the other is transition metal rhenium cyclized α-MSH, ReO[Cys^{3,4,10}, d,Phe^{7}, Arg^{11}]α-MSH_{3-13} [referred to as ReCCMSH(Arg^{11})] based metallopeptides (*13*−*18*).

In our previous research, both NAPamide and ReCCMSH(Arg^{11}) analogues had been synthesized and radiolabeled with a well-established radiofluorination synthon, *N*-succinimidyl-4-^{18}F-fluorobenzoate (^{18}F-SFB), for positron emission tomography (PET) imaging of melanoma (*12, 19*). The resulting ^{18}F-probes exhibited good tumor imaging contrast as early as 1 h postinjection (p.i.) in B16F10 tumor mouse models. Compared with ^{18}F-SFB labeled NAPamide, ^{18}F-SFB conjugated ReCCMSH(Arg^{11}) peptides displayed higher tumor uptake and retention, suggesting the advantages of rhenium cyclized CCMSH(Arg^{11}) as a scaffold for developing MC1R PET imaging agents (*19*). Overall, these pioneer studies highlight that ^{18}F-SFB labeled α-MSH peptides can efficiently target malignant melanoma with overexpression of

* To whom correspondence should be addressed. Molecular Imaging Program at Stanford, Department of Radiology and Bio-X Program, Canary Center at Stanford for Cancer Early Detection, 1201 Welch Road, Lucas Expansion, P095, Stanford University, Stanford, CA, USA. Phone: 94305-5484, 650-723-7866. Fax: 650-736-7925. E-mail: zcheng@stanford.edu.

[1]Abbreviations: α-MSH, alpha-melanocyte stimulating hormone; MC1R, melanocortin type 1 receptor; PET, positron emission tomography; SPECT, single photon emission spectroscopy; HPLC, high-performance liquid chromatography; ^{18}F-NFP, 4-nitrophenyl 2-^{18}*F*-fluoropropionate; ^{18}F-SFB, *N*-succinimidyl-4-^{18}*F*-fluorobenzoate; [^{18}F]-FDG, 2-deoxy-2-[^{18}*F*]fluoro-D-glucose; p.i., postinjection.

10.1021/bc100391a © 2010 American Chemical Society
Published on Web 11/12/2010

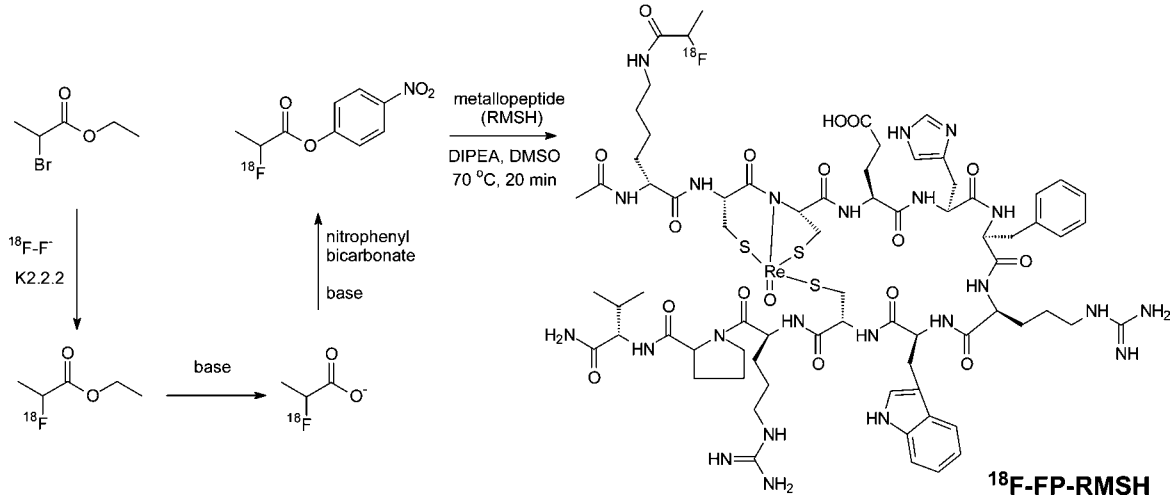


Figure 1. Scheme of the radiosynthesis of **^{18}F-FP-RMSH**.

MC1R in mice and that they can be promising candidates for MC1R targeted melanoma PET imaging.

However, ^{18}F-SFB conjugated ReCCMSH (Arg^{11}) peptides also show moderate liver and lung uptake and relatively high uptake in the gallbladder, which is unfavorable for clinical translation (*19*). In this research, we aimed to further optimize the *in vivo* behavior of ^{18}F labeled α-MSH metallopeptides for melanoma PET imaging. 4-Nitrophenyl-2-[^{18}F]fluoropropionate (^{18}F-NFP) is a small prosthetic group with less hydrophobicity and has been widely used for the radiofluorination of many peptides (*20*). The ^{18}F-NFP conjugated galacto-RGD peptide has even been evaluated in patients of different solid tumors for tumor angiogenesis imaging (*21*−*23*). The promising results suggested NFP as an attractive labeling moiety. Herein, we report the radiosynthesis of ^{18}F-NFP labeled Ac-d,Lys-ReCCMSH(Arg^{11}) peptides (two isomers, abbreviated as **RMSH-1** and **RMSH-2**, respectively) (Figure 1). The resulting probes **^{18}F-FP-RMSH-1** and **^{18}F-FP-RMSH-2** were then evaluated in C57BL/6 mice bearing subcutaneous murine B16F10 melanoma tumors with high levels of the MC1R and Foxn1 nude mice bearing human A375M melanoma with low levels of the MC1R.

MATERIALS AND METHODS

General. ^{125}I-(Tyr^2)-[Nle^4,D-Phe^7]-α-MSH [^{125}I-(Tyr^2)-NDP] was purchased from Perkin-Elmer (Waltham, MA). All N-α-Fmoc-protected amino acids were purchased from Advanced Chemtech (Louisville, KY). Dimethylformamide (DMF) and methylene chloride were from Fisher Scientific (Fair Lawn, NJ). Piperidine (20%) in DMF and 0.4 M *N*-methylmorpholine in DMF were from Protein Technologies Inc. (Tucson, AZ). Trifluoroacetic acid (TFA), *O*-benzotriazole-*N*,*N*,*N*′,*N*′-tetramethyluronium hexafluoro-phosphate (HBTU), and 4-(2′,4′-dimethoxyphenyl-Fmoc-aminomethyl)-phenoxy resin **(**Rink amide resin LS, 100−200 mesh, 1% DVB, 0.2 mmol/g) were from Advanced Chemtech. Pyridine, acetic anhydride, acetic acid, and anhydrous ether were from J.T.Baker (Phillipsburg, NJ). Triisopropylsilane (TIPS), *N*,*N*′-diisopropylethylamine (DIPEA), and 1,2-ethanedithiol (EDT) were purchased from Sigma-Aldrich (Milwaukee, WI). High performance liquid chromatography (HPLC) grade acetonitrile (CH_3CN) and Millipore 18 mΩ water were used for peptide purifications. 4-Nitrophenyl 2-fluoropropionate (^{19}F-NFP) was synthesized as previously reported (*24*). All other standard synthesis reagents were purchased from Sigma-Aldrich Chemical Co. (St. Louis, MO). All the other general materials (cell lines, mice, etc.) and instruments [reverse phase HPLC, radioactive dose calibrator, and electrospray ionization mass spectrometry (ESI-MS), or matrix-assisted laser desorption/ionization time-of-flight mass spectrometry (MALDI-TOF-MS)] are the same as previously reported (*12*). The A375M cell line was a generous gift from Dr. M. Kolodny, University of California, Los Angeles, CA, and B16/F10 murine melanoma cells were obtained from American Type Tissue Culture Collection (Manassas, VA). C57BL/6 and Fox Chase SCID mice were purchased from Charles River Laboratories (Boston, MA).

Synthesis of RMSH and ^{19}F-FP-RMSH. The rhenium cyclized metallopeptide, RMSH, was synthesized as previously reported using the Ac-d,Lys-CCMSH(Arg^{11}) peptide (amino acid sequence: Ac-kCCEHdFRWCRPV-NH_2) and rhenium-gluco-heptonate transchelation reaction (*19*). Two major products (isomers **RMSH-1** and **RMSH-2**) with identical molecular weights (MW) but different HPLC retention times were obtained. The reference standards **^{19}F-FP-RMSH-1** and **-2** were then prepared by a reaction of the metallopeptides with ^{19}F-NFP (*24*). Briefly, **RMSH-1** or **-2** (1 μmol) in DMSO (100 μL) was added to ^{19}F-NFP (5 μmol) in DMSO (100 μL), followed by the addition of DIPEA (5 μL). The mixture was heated at 60 °C for 2 h. After it cooled down to room temperature, the reaction solution was quenched by adding TFA (50 μL) and injected into a semipreparative HPLC for purification. The flow rate was 3 mL/min, with the mobile phase starting at 95% solvent A and 5% solvent B (0−3 min), going to 35% solvent A and 65% solvent B at 33 min, then going to 15% solvent A and 85% solvent B and maintaining this solvent composition for another 3 min (36−39 min), and returning to initial solvent composition after 42 min had elapsed. Fractions containing the product were collected, lyophilized, and characterized by ESI-MS or MALDI-TOF-MS.

Radiosynthesis of ^{18}F-FP-RMSH-1 and -2. The radiofluorination synthon, ^{18}F-NFP, was prepared on the basis of the procedure reported previously (*23*, *25*). ^{18}F-NFP (specific activity of 0.4−1.0 Ci/μmol or 14.7−37 GBq/μmol) dissolved in acetonitrile (100 μL) was then added to the peptide (**RMSH-1** or **-2**; 100 μg) dissolved in DMSO and reacted for 20 min at 60 °C. After adding TFA (50 μL) to quench the reaction, the reaction solution was injected into a semipreparative HPLC using the same elution gradient as the one used in the synthesis of cold **^{19}F-FP-RMSH** (**1** or **2**). The HPLC fractions containing the radiolabeled product were subsequently collected, combined, and evaporated with a rotary evaporator to dryness. The radiolabeled peptide was reconstituted in phosphate-buffered saline (PBS, 0.01 M, pH 7.4) and passed through a 0.22 μm Millipore filter into a sterile vial for *in vitro* and animal experiments.

***In Vitro* Cell Binding Assay.** B16F10 murine melanoma cells were cultured in Dulbecco's modified Eagle's high-glucose medium (DMEM) supplemented with 10% fetal bovine serum (FBS) and penicillin and streptomycin. The cells were maintained at 37 °C in a 5% CO_2 humidified incubator. The receptor binding affinity studies of **^{19}F-FP-RMSH-1** and **-2** for the MC1R were performed using B16F10 cells. Briefly, 0.5×10^6 cells were resuspended in Dulbecco's modified Eagle's medium containing 25 mM HEPES, 0.2% BSA, and 0.3 mM 1,10-phenanthroline. The cells were then incubated at 37 °C for 90 min with either **^{19}F-FP-RMSH-1** or **-2** (peptide concentration varying from $10^{-12}-10^{-6}$ M) and approximately 40,000 counts per minute (cpm) of ^{125}I-(Tyr^2)-NDP. Cells were washed three times with ice-cold PBS, and the radioactivity of the cells was measured. Data was analyzed by Graphpad Prism 5.0 (Northampton, MA). The IC_{50} values, the concentration of competitor required to inhibit 50% of the radioligand binding, of the peptides were calculated.

Biodistribution Studies. All animal experiments were performed in compliance with a protocol approved by Stanford University Institutional Animal Care and Use Committee. Five- to six-week old male C57BL/6 mice were implanted with 1×10^6 B16F10 murine melanoma cells, and Foxn1 nude mice were inoculated with 3×10^6 A375M human melanoma cells in the right flank. When the diameters of the tumors reached around 8 mm, approximately 110−130 μCi (4.07−4.81 MBq) of **^{18}F-FP-RMSH-1** or **-2** was injected into each mouse through the tail vein. After injection of the radiotracer, the B16F10 mice ($n = 3$) were sacrificed at 1, 2, and 4 h p.i., while A375M ($n = 3$) mice were sacrificed at 2 h p.i. by carbon dioxide. Tumors, blood, and major organs of interest were harvested, weighed, and counted in a Wallac 1480 automated γ-counter (Perkin-Elmer, Waltham, MA). The radioactivity uptake in tumors and normal tissues was expressed as a percentage of the injected radioactive dose per gram of tissue (% ID/g).

Small-Animal PET Imaging Studies. PET imaging of tumor bearing mice was performed on a small-animal PET R4 rodent model scanner (Siemens Medical Solutions USA, Inc., Knoxville, TN). The mice bearing B16F10 or A375M tumors were injected with 110−130 μCi (4.07−4.81 MBq) of **^{18}F-FP-RMSH-1** or **-2** through the tail vein. At 1 and 2 h p.i., the mice were anesthetized with 2% isofluorane and placed in the prone position near the central field of view in the small-animal PET. Five-minute static scans were obtained, and images were reconstructed by a two-dimensional ordered subsets expectation maximum (OSEM) algorithm. Regions of interest (ROIs) were then drawn over the tumor or organ of interest on decay-corrected whole-body coronal images. The mean counts per pixel per minute were obtained from the ROI and converted to counts per milliliter per minute by using a calibration constant. By assuming a tissue density of 1 g/mL, the ROIs were converted to counts$\cdot g^{-1}\cdot min^{-1}$. An image ROI-derived % ID/g of tissue was then determined by dividing counts per gram per minute with injected dose (ID). No attenuation correction was performed.

Statistical Methods. Statistical analysis was performed using the Student's *t*-test for unpaired data. A 95% confidence level was chosen to determine the significance between groups, with $P < 0.05$ being significantly different.

RESULTS

Chemistry, Radiochemistry, and IC_{50}. The linear peptide, Ac-d,Lys-CCMSH(Arg^{11}), could react with rhenium-glucoheptonate to produce two major products (**RMSH-1** and **RMSH-2**) with same molecular weight (MW) and similar binding affinities to MC1R, which was reported previously (*19*). The nonradioactive fluorinated metallopeptides were then prepared by conjugation with cold ^{19}F-NFP to allow for characterization of the ^{18}F labeled counterparts. Under the HPLC gradient (5−65% over 30 min) used in the study, the retention times for **^{19}F-FP-RMSH-1** and **-2** were found to be 16.6 and 18.1 min, respectively (Figure 2). The desired products were purified by semipreparative HPLC (>90% yield and >95% purity) and characterized by MALDI-TOF-MS. For all of the metallopeptides prepared above, the measured MW was consistent with the expected MW: $m/z = 1878.1$ for $[M + H]^+$ ($C_{73}H_{104}FN_{23}O_{17}ReS_3$, calculated MW = 1878.2). The receptor binding assay showed that the IC_{50} values of **^{19}F-FP-RMSH-1** and **-2** were 6.1 and 33.7 nM, respectively (Table 1).

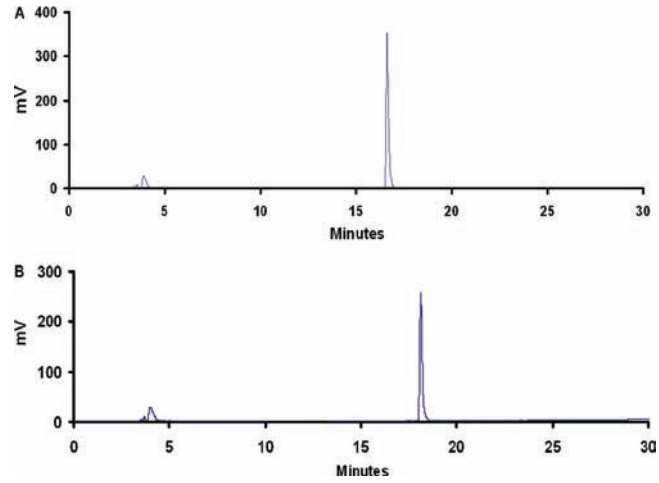


Figure 2. HPLC profiles of **^{19}F-FP-RMSH-1** (A) and **2** (B).

Table 1. IC_{50} Values of the Fluorinated α-MSH Analogues and Their Expected and Measured Molecular Weights (M.W.) for $[M + H]^+$ by ESI-MS or MALDI-TOF-MS

peptides	expected M.W.	measured M.W.	IC_{50} (nM)
^{19}F-FP-RMSH-1	1878.2	1878.1	6.1 ± 0.6
^{19}F-FP-RMSH-2	1878.2	1878.1	33.7 ± 3.0

Similarly, **^{18}F-FP-RMSH-1** and **-2** were prepared by the conjugation of **RMSH-1** or **-2** with the radioactive ^{18}F-NFP. On the basis of the retention times acquired from the nonradioactive fluorinated peptides, the radiofluorinated products were identified and collected using the same HPLC gradient. The total radiosynthesis time for making the radiopeptide took about 100 min. The decay-corrected radiochemical yields of **^{18}F-FP-RMSH-1** and **-2** were based on ^{18}F-NFP and were 12.0% ± 2.7% and 10.5% ± 1.8% ($n = 4$), respectively, at the end of synthesis (EOS). The radiochemical purities of the labeled peptides were over 95%, as verified by analytical radio-HPLC. Since the difference in retention times of radiolabeled and unlabeled peptide was greater than 1.5 min, the radiofluorinated **RMSH-1** and **-2** were easily separated from their nonradiolabeled counterparts by HPLC. The specific activity of the two **^{18}F-FP-RMSH-1** and **-2** were estimated to be ~20 GBq/μmol (decay corrected) on the basis of the labeling agent ^{18}F-NFP.

***In Vivo* Biodistribution of ^{18}F-FP-RMSH-1 and -2.** The *in vivo* biodistribution studies of both **^{18}F-FP-RMSH-1** and **-2** were examined in B16F10 murine allograft and A375M human xenograft melanoma bearing mice. As shown in Table 2, for **^{18}F-FP-RMSH-1**, the uptake in the B16F10 tumor with high expression of MC1R was 1.80 ± 0.18, 2.12 ± 1.08, and 1.09 ± 0.23% ID/g at 1, 2, and 4 h p.i., respectively, suggesting good tumor uptake and retention of this PET probe. **^{18}F-FP-RMSH-1** also displayed rapid blood clearance and low uptake in muscle, resulting in decent tumor/blood and tumor/muscle ratios (3.80 ± 0.89 and 9.36 ± 3.98, respectively) at 2 h p.i. It was also noted that **^{18}F-FP-RMSH-1** displayed a much lower

Table 2. Biodistribution Data for ^{18}F-FP-MSH-1 and -2 in C57BL/6 Mice Bearing Subcutaneously Xenotransplanted B16F10 Murine Melanoma and Foxn1 Nude Mice Bearing A375M Human Melanoma[a]

	^{18}F-FP-RMSH-1				^{18}F-FP-RMSH-2	
	B16F10			A 375M	B16F10	A 375M
organ (% ID/g)	1h	2h	4h	2h	2h	2h
tumor	1.80 ± 0.18	2.12 ± 1.08	1.09 ± 0.23	*0.84 ± 0.39	*0.78 ± 0.10	*0.63 ± 0.19
blood	0.90 ± 0.10	0.42 ± 0.06	0.15 ± 0.04	0.33 ± 0.22	0.31 ± 0.11	0.20 ± 0.09
heart	0.55 ± 0.03	0.31 ± 0.06	0.14 ± 0.06	0.41 ± 0.19	0.21 ± 0.06	0.18 ± 0.07
liver	1.36 ± 0.22	0.78 ± 0.05	0.44 ± 0.11	0.69 ± 0.21	*1.97 ± 0.17	1.66 ± 0.08
lung	1.72 ± 0.16	0.80 ± 0.03	0.31 ± 0.07	0.68 ± 0.10	0.64 ± 0.15	0.47 ± 0.21
muscle	0.33 ± 0.11	0.17 ± 0.03	0.06 ± 0.01	0.19 ± 0.08	0.20 ± 0.05	0.10 ± 0.02
spleen	0.61 ± 0.05	0.34 ± 0.07	0.20 ± 0.04	0.34 ± 0.19	0.53 ± 0.03	0.27 ± 0.03
brain	0.11 ± 0.04	0.11 ± 0.04	0.04 ± 0.01	0.05 ± 0.01	0.04 ± 0.01	0.04 ± 0.01
intestine	0.99 ± 0.45	1.14 ± 0.80	0.29 ± 0.18	0.40 ± 0.19	0.91 ± 0.33	0.17 ± 0.00
stomach	0.67 ± 0.31	0.47 ± 0.24	0.31 ± 0.07	0.44 ± 0.02	0.42 ± 0.14	0.52 ± 0.50
pancreas	0.32 ± 0.08	0.18 ± 0.03	0.06 ± 0.01	0.78 ± 0.49	0.10 ± 0.03	0.09 ± 0.01
bone	0.69 ± 0.18	0.68 ± 0.37	0.17 ± 0.09	0.23 ± 0.11	0.52 ± 0.08	0.25 ± 0.12
kidney	8.82 ± 0.76	6.76 ± 0.82	4.41 ± 0.78	6.59 ± 1.53	*15.13 ± 0.88	*13.45 ± 0.91
			Uptake Ratio			
tumor/blood	2.03 ± 0.33	3.80 ± 0.89	7.45 ± 0.69	3.11 ± 1.30	2.74 ± 0.80	2.90 ± 0.04
tumor/muscle	5.78 ± 1.35	9.36 ± 3.98	16.97 ± 1.73	4.49 ± 0.17	3.98 ± 1.09	6.40 ± 2.66

[a] Data were expressed as the mean ± SD, indicating the percentage administered activity (injected dose) per gram of tissue (%ID/g) after intravenous injection of 110−130 μCi (4.01−4.87 MBq) tracers ($n = 3$). $P < 0.05$ when compared with **^{18}F-FP-RMSH-1** at 2 h.

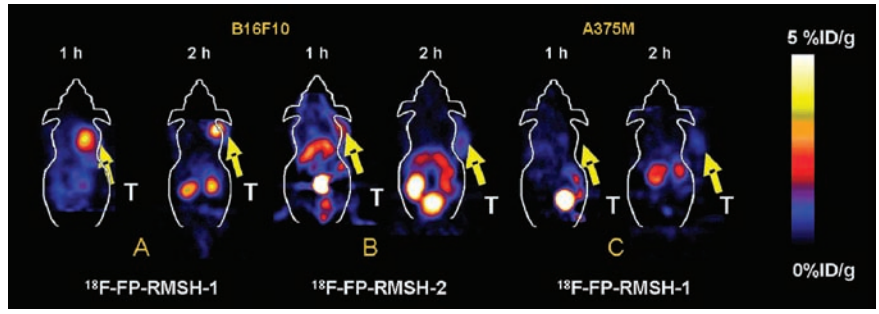


Figure 3. Representative decay-corrected coronal small-animal PET images of mice bearing B16F10 tumors on the right shoulder at 1 and 2 h after tail vein injections of **^{18}F-FP-RMSH-1** (A) and **-2** (B) ($n = 3$ for each group). T stands for tumor. (**C**) Representative decay-corrected coronal small-animal PET images of A375M tumor bearing mice at indicated time points after a tail vein injection of **^{18}F-FP-RMSH-1**.

uptake in the lung and liver (0.80 ± 0.03 and 0.78 ± 0.05, respectively) compared with **^{18}F-FB-RMSH-1** (*19*). Also compared with **^{18}F-FB-RMSH-1**, **^{18}F-FP-RMSH-1** showed lower kidney uptake in B16F10 tumor bearing mice ($P < 0.05$). The level of accumulation in the kidney was 8.82 ± 0.76 and 6.76 ± 0.82% ID/g at 1 and 2 h p.i., respectively, for **^{18}F-FP-RMSH-1**. For the A375M model, tumor uptake of **^{18}F-FP-RMSH-1** was only 0.84 ± 0.39% ID/g at 2 h p.i., which was significantly lower than that in B16F10 tumors ($P < 0.01$).

For **^{18}F-FP-RMSH-2**, the uptake in the B16F10 tumor model was 0.78 ± 0.10% ID/g at 2 h p.i., which was much lower than that of **^{18}F-FP-RMSH-1** ($P < 0.05$). Meanwhile, **^{18}F-FP-RMSH-2** showed much higher kidney uptake of 15.13 ± 0.88% ID/g at 2 h p.i. ($P < 0.05$). In addition, **^{18}F-FP-RMSH-2** demonstrated a higher uptake in the liver when compared to that of **^{18}F-FP-RMSH-1**. For other major organs including the lung, spleen, pancreas, and stomach, **^{18}F-FP-RMSH-2** exhibited an uptake similar to that of **^{18}F-FP-RMSH-1** ($P > 0.05$). Lastly, **^{18}F-FP-RMSH-2** revealed very low tumor uptake (0.63 ± 0.19% ID/g), but high uptake (13.45 ± 0.91% ID/g) was observed in the kidneys at 2 h p.i in the A375M tumor model.

Small-Animal PET Imaging. Small-animal PET imaging of mice bearing B16F10 using **^{18}F-FP-RMSH-1** and **-2** was performed, and the imaging results were compared (Figure 3A,B). Visual examination showed that **^{18}F-FP-RMSH-1** uptake in the tumor was higher than that of **^{18}F-FP-RMSH-2** at both 1 and 2 h p.i. Both probes showed moderate to high uptake in the liver and kidney. Further quantification analysis of small-animal PET images demonstrated that **^{18}F-FP-RMSH-2** had a much higher uptake in the kidney than that of **^{18}F-FP-RMSH-1** ($P < 0.01$) at 1 and 2 h p.i. (Figure 4). Improved quality of PET images was also observed at 2 h p.i. for **^{18}F-FP-RMSH-1**. On the basis of the above findings, **^{18}F-FP-RMSH-1** was selected as a PET probe for further evaluation.

^{18}F-FP-RMSH-1 was then imaged in the nude mice bearing A375M melanoma with low MC1R expression at 1 and 2 h (Figure 3C). Compared with B16F10 tumor bearing mice, much lower tumor uptake and poor tumor-to-background ratio were observed in A375M tumors at both time points. The A375M tumor was barely discernible, while high activity accumulation in kidneys was still observed.

DISCUSSION

It has been reported that overexpression of MC1R may correlate with the prognosis of malignant melanoma (*26*, *27*). Peptide based radioactive probes have been extensively studied for tumor receptor targeted imaging and therapy (*28*−*30*). Recently, a number of studies have also been performed to develop molecular probes that specifically target MC1R in melanoma (*12*, *19*). However, ^{18}F-SFB labeled **RMSH** has its own limitations such as suboptimal tumor uptakes and relatively high uptakes in the liver and lung. Thus, the major goal of this research is to study whether we can further optimize the *in vivo* profile of ^{18}F-labeled **RMSH** analogues by using a different

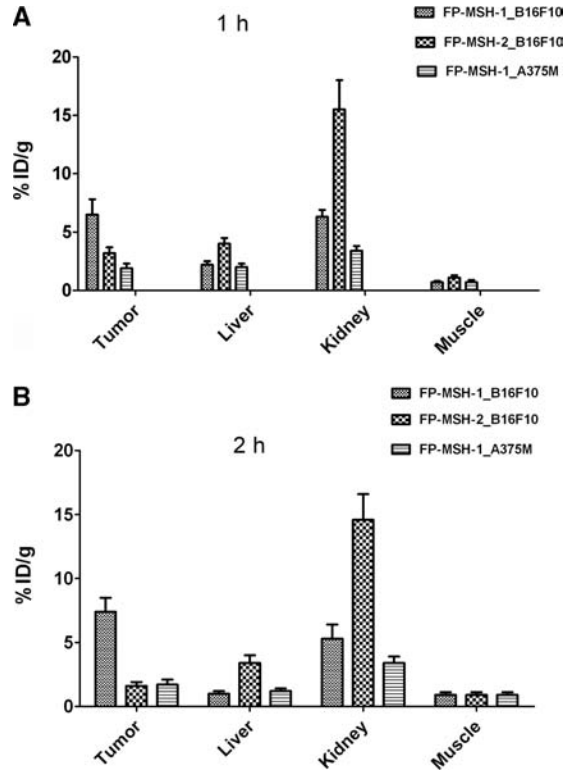


Figure 4. PET quantification of the tumor and other major organ uptakes derived from 1 (**A**) and 2 h (**B**) after tail vein injections of **^{18}F-FP-RMSH-1** or **-2**. Data are shown as the mean ± SD % ID/g ($n = 3$).

radiofluorination synthon, ^{18}F-NFP. The resulting PET probe, **^{18}F-FP-RMSH**, was also studied for its ability to image melanoma and differential MC1R expression in tumor mice models.

The two isomers of rhenium cyclized Ac-d,Lys-CCMSH-(Arg^{11}), **RMSH-1** and **-2**, were reproducibly formed in previous studies and proved to possess high MC1R binding affinity in the nanomolar (nM) range. Further modification of **RMSH** with the small prosthetic group ^{19}F-NFP only slightly reduced their affinities, as evidenced by *in vitro* cell binding assays (Table 1). The NFP conjugation to **RMSH** did not change the binding capability to B16F10 cells which overexpress MC1R. In addition, **^{19}F-FP-RMSH-1** displays much higher MC1R binding affinity than **^{19}F-FP-RMSH-2** (6.1 vs 33.7 nM), which is consistent with the study of the ^{19}F-SFB conjugated **RMSH** peptides (*19*). Since the affinities of both compounds are in the low nanomolar range and thus very encouraging, further *in vivo* evaluation of the ^{18}F-NFP labeled metallopeptides is warranted.

In biodistribution studies in the B16F10 tumor mice model, a higher tumor uptake of **^{18}F-FP-RMSH-1** can be observed compared to that of **^{18}F-FP-RMSH-2** along with much lower kidney and liver uptake for **^{18}F-FP-RMSH-1** at 2 h ($P < 0.05$). The higher tumor uptake with lower kidney uptake was further evidenced by small-animal PET imaging as well as quantification analysis of PET images. For **^{18}F-FP-RMSH-1**, B16F10 tumors are clearly delineated over the background at 1 and 2 h p.i., while **^{18}F-FP-RMSH-2** shows a much less prominent tumor uptake (Figure 3A,B). The quantification analysis of small-animal PET images further reveals significant differences in the tumor, liver, and kidney uptake between the two probes ($P < 0.01$) (Figure 4). **^{18}F-FP-RMSH-2** exhibits a much lower tumor uptake but higher kidney uptake than those of **^{18}F-FP-RMSH-1** at both 1 and 2 h in B16F10 tumor bearing mice. In the A375M model, the tumor uptake is low for both **^{18}F-FP-RMSH-1** and **-2**. Interestingly, the higher uptake in the liver and kidney for **^{18}F-FP-RMSH-2** compared with that of **^{18}F-FP-RMSH-1** ($P < 0.05$) may further suggest the different clearance time of these two isomers. Overall, **^{18}F-FP-RMSH-1** clearly displays more favorable *in vivo* properties, which suggests that it could be a better candidate for imaging MC1R *in vivo*.

^{18}F-FP-RMSH-1 exhibits longer retention times in the B16F10 tumor than all other normal organs but the kidney (Table 2). The tumor-to-blood and tumor-to-muscle ratios reach the highest levels at 4 h. More importantly, it is noticed that **^{18}F-FP-RMSH-1** displays high tumor-to-background ratios, for example, tumor-to-blood and tumor-to-muscle ratios at 4 h are 7.45 ± 0.69 and 16.97 ± 1.73, respectively. While for another two radiofluorinated α-MSH peptides reported previously, **^{18}F-FB-NAPamide** and **^{18}F-FB-RMSH-1**, their tumor-to-blood ratios at 4 h are only 3.60 ± 0.37 and 1.65 ± 0.11, respectively, and their tumor-to-muscle ratios at 4 h are 7.46 ± 2.68 and 5.24 ± 1.43, respectively (*12*, *19*). These increased tumor-to-background ratios as well as tumor residence time would make longitudinal observation of the malignant melanoma with overexpression of MC1R more feasible when using NFP conjugated **RMSH-1** as PET probes. For the A375M tumor model, the tumors are barely noticeable and show background uptake at 1 and 2 h p.i., when the mice were injected with **^{18}F-FP-RMSH-1** (Figure 3C). This low uptake is likely caused by nonspecific uptake. The better PET imaging quality in the B16F10 tumor compared to that in the A375M suggests that **^{18}F-FP-RMSH-1** could differentiate melanoma with different MC1R expression in living subjects.

More importantly, compared with previous ^{18}F-SFB conjugated **RMSH-1** (**^{18}F-FB-RMSH-1**) that possesses moderate lung and liver uptake in the B16F10 tumor model (*19*), **^{18}F-FP-RMSH-1** shows similar tumor uptake at 1 and 2 h, but the uptake gets significantly higher than that of **^{18}F-FB-RMSH-1** at 4 h ($P < 0.05$). The background uptake, particularly in the liver and lung, is much lower for **^{18}F-FP-RMSH-1**. Much higher tumor-to-blood and tumor-to-muscle ratios are also observed for **^{18}F-FP-RMSH-1** than that of **^{18}F-FB-RMSH-1**. Furthermore, the liver and lung uptakes are lower for **^{18}F-FP-RMSH-2** when compared with that of **^{18}F-FB-RMSH-2** in both models ($P < 0.05$). All of these observations highlight that different radiofluorination methods have significant impact in this metallopeptide's *in vivo* properties. Additionally, these observations further suggest that the uptake in the liver and lung are due to nonspecific accumulation.

Taken together, ^{18}F-NFP shows advantages over ^{18}F-SFB for labeling of **RMSH** peptides. Compared to **^{18}F-FB-RMSH-1**, **^{18}F-FP-RMSH-1** is more promising for translation into melanoma MC1R PET imaging in clinics. The relatively low liver and lung uptakes of **^{18}F-FP-RMSH-1** also validate the possibility of using it as a potential PET probe for the early detection of malignant melanoma metastasis in these regions. **^{18}F-FP-RMSH-1** seems by far the best radiofluorinated probe reported for imaging MC1R expression *in vivo*.

CONCLUSIONS

In summary, radiofluorinated rhenium cyclized α-MSH analogue, **^{18}F-FP-RMSH-1** and **-2**, were successfully synthesized. Their characteristics including binding affinities and *in vivo* profiles were investigated in this study. **^{18}F-FP-RMSH-1** demonstrates significant advantages over **^{18}F-FB-RMSH-1** and **^{18}F-FP-RMSH-2**. **^{18}F-FP-RMSH-1** displays favorable *in vivo* pharmacokinetics in MC1R overexpressing tumor mice models. It is a promising PET probe for imaging MC1R positive melanoma and MC1R expression *in vivo*.

ACKNOWLEDGMENT

This work was supported, in part, by National Cancer Institute (NCI) *In Vivo* Cellular Molecular Imaging Center (ICMIC) grant P50 CA114747 and Melanoma Research Alliance. We also thank the Radiochemistry Facility at Stanford for ^{18}F production and Dr. Zhe Liu for his help on peptides synthesis.

LITERATURE CITED

(1) Gray-Schopfer, V., Wellbrock, C., and Marais, R. (2007) Melanoma biology and new targeted therapy. *Nature 445*, 851–857.

(2) Jemal, A., Siegel, R., Xu, J., and Ward, E. (2010) Cancer statistics. *CA Cancer J. Clin. 60*, 277–300.

(3) Rohren, E. M., Turkington, T. G., and Coleman, R. E. (2004) Clinical applications of PET in oncology. *Radiology 231*, 305–32.

(4) Belhocine, T. Z., Scott, A. M., Even-Sapir, E., Urbain, J. L., and Essner, R. (2006) Role of nuclear medicine in the management of cutaneous malignant melanoma. *J. Nucl. Med. 47*, 957–967.

(5) Siegrist, W., Solca, F., Stutz, S., Giuffre, L., Carrel, S., Girard, J., and Eberle, A. N. (1989) Characterization of receptors for alpha-melanocyte-stimulating hormone on human melanoma cells. *Cancer Res. 49*, 6352–6358.

(6) Siegrist, W., Stutz, S., and Eberle, A. N. (1994) Homologous and heterologous regulation of alpha-melanocyte-stimulating hormone receptors in human and mouse melanoma cell lines. *Cancer Res. 54*, 2604–2610.

(7) Ren, G., Pan, Y., and Cheng, Z. (2010) Molecular probes for malignant melanoma imaging. *Curr. Pharm. Biotechnol. 11*, 590–602.

(8) Miao, Y., and Quinn, T. (2008) Peptide-targeted radionuclide therapy for melanoma. *Crit. Rev. Oncol. Hematol. 67*, 213–228.

(9) Froidevaux, S., Calame-Christe, M., Tanner, H., and Eberle, A. N. (2005) Melanoma targeting with DOTA-alpha-melanocyte-stimulating hormone analogs: structural parameters affecting tumor uptake and kidney uptake. *J. Nucl. Med. 46*, 887–895.

(10) Froidevaux, S., Calame-Christe, M., Tanner, H., Sumanovski, L., and Eberle, A. N. (2002) A novel DOTA-alpha-melanocyte-stimulating hormone analog for metastatic melanoma diagnosis. *J. Nucl. Med. 43*, 1699–1706.

(11) Cheng, Z., Xiong, Z., Subbarayan, M., Chen, X., and Gambhir, S. S. (2007) ^{64}Cu-labeled alpha-melanocyte-stimulating hormone analog for microPET imaging of melanocortin 1 receptor expression. *Bioconjugate Chem. 18*, 765–772.

(12) Cheng, Z., Zhang, L., Graves, E., Xiong, Z., Dandekar, M., Chen, X., and Gambhir, S. S. (2007) Small-animal PET of melanocortin 1 receptor expression using a 18F-labeled alpha-melanocyte-stimulating hormone analog. *J. Nucl. Med. 48*, 987–994.

(13) Chen, J., Cheng, Z., Hoffman, T. J., Jurisson, S. S., and Quinn, T. P. (2000) Melanoma-targeting properties of 99mtechnetium-labeled cyclic alpha-melanocyte-stimulating hormone peptide analogues. *Cancer Res. 60*, 5649–5658.

(14) Chen, J., Cheng, Z., Owen, N. K., Hoffman, T. J., Miao, Y., Jurisson, S. S., and Quinn, T. P. (2001) Evaluation of an 111In-DOTA-rhenium cyclized alpha-MSH analog: a novel cyclic-peptide analog with improved tumor-targeting properties. *J. Nucl. Med. 42*, 1847–1855.

(15) Cheng, Z., Chen, J., Miao, Y., Owen, N. K., Quinn, T. P., and Jurisson, S. S. (2002) Modification of the structure of a metallopeptide: synthesis and biological evaluation of 111In-labeled DOTA-conjugated rhenium-cyclized alpha-MSH analogues. *J. Med. Chem. 45*, 3048–3056.

(16) Cheng, Z., Chen, J., Quinn, T. P., and Jurisson, S. S. (2004) Radioiodination of rhenium cyclized alpha-melanocyte-stimulating hormone resulting in enhanced radioactivity localization and retention in melanoma. *Cancer Res. 64*, 1411–1418.

(17) McQuade, P., Miao, Y., Yoo, J., Quinn, T. P., Welch, M. J., and Lewis, J. S. (2005) Imaging of melanoma using ^{64}Cu- and 86Y-DOTA-ReCCMSH(Arg^{11}), a cyclized peptide analogue of alpha-MSH. *J. Med. Chem. 48*, 2985–2992.

(18) Giblin, M. F., Wang, N., Hoffman, T. J., Jurisson, S. S., and Quinn, T. P. (1998) Design and characterization of alpha-melanotropin peptide analogs cyclized through rhenium and technetium metal coordination. *Proc. Natl. Acad. Sci. U.S.A. 95*, 12814–12818.

(19) Ren, G., Liu, Z., Miao, Z., Liu, H., Subbarayan, M., Chin, F. T., Zhang, L., Gambhir, S. S., and Cheng, Z. (2009) PET of malignant melanoma using 18F-labeled metallopeptides. *J. Nucl. Med. 50*, 1865–1872.

(20) Liu, S., Shen, B., Chin, F., and Cheng Z. (2010) Recent progress in radiofluorination of peptides for PET molecular imaging. *Curr. Org. Synth.*, in press.

(21) Guhlke, S., Coenen, H. H., and Stöcklin, G. (1994) Fluoroacylation agents based on small n.c.a. 18F-fluorocarboxylic acids. *Appl. Radiat. Isot. 45*, 715–727.

(22) Haubner, R., Kuhnast, B., Mang, C., Weber, W. A., Kessler, H., Wester, H. J., and Schwaiger, M. (2004) 18F-Galacto-RGD: synthesis, radiolabeling, metabolic stability, and radiation dose estimates. *Bioconjugate Chem. 15*, 61–69.

(23) Beer, A. J., Haubner, R., Sarbia, M., Goebel, M., Luderschmidt, S., Grosu, A. L., Schnell, O., Niemeyer, M., Kessler, H., Wester, H. J., Weber, W. A., and Schwaiger, M. (2006) Positron emission tomography using 18F-Galacto-RGD identifies the level of integrin alpha(v)beta3 expression in man. *Clin. Cancer Res. 12*, 3942–3949.

(24) Liu, S., Liu, Z., Chen, K., Yan, Y., Watzlowik, P., Wester, H. J., Chin, F. T., Chen, X. (2010) 18F-labeled galacto and PEGylated RGD dimers for PET imaging of $\alpha(v)\beta$ (3) integrin expression. *Mol Imaging Biol. 12*, 530−538.

(25) Haubner, R., Kuhnast, B., Mang, C., Weber, W. A., Kessler, H., Wester, H. J., and Schwaiger, M. (2004) 18F-Galacto-RGD: synthesis, radiolabeling, metabolic stability, and radiation dose estimates. *Bioconjugate Chem. 15*, 61–69.

(26) Benjamin, C. L., Melnikova, V. O., and Ananthaswamy, H. N. (2007) Models and mechanisms in malignant melanoma. *Mol. Carcinog. 46*, 671–678.

(27) Bohm, M., Luger, T. A., Tobin, D. J., and Garcia-Borron, J. C. (2006) Melanocortin receptor ligands: new horizons for skin biology and clinical dermatology. *J. Invest. Dermatol. 126*, 1966–1975.

(28) Liu, S. (2009) Radiolabeled cyclic RGD peptides as integrin alpha(v)beta(3)-targeted radiotracers: maximizing binding affinity via bivalency. *Bioconjugate Chem. 20*, 2199–2213.

(29) Lee, S., Xie, J., and Chen, X. (2010) Peptides and peptide hormones for molecular imaging and disease diagnosis. *Chem. Rev. 110*, 3087–3111.

(30) Lewis, J. S., and Anderson, C. J. (2007) Radiometal-labeled somatostatin analogs for applications in cancer imaging and therapy. *Methods Mol. Biol. 386*, 227–240.

BC100391A

Volume 21, Number 8, 2010.

Insoo Kim, Tae Hyung Kim, Kyungwan Ma, Eun Seong Lee, Dongin Kim, Kyung Taek Oh, Don Haeng Lee, Kang Choon Lee, and Yu Seok Youn*

Synthesis and Evaluation of Human Serum Albumin-Modified Exendin-4 Conjugate via Heterobifunctional Polyethylene Glycol Linkage with Protracted Hypoglycemic Efficacy

The affiliation of the first author, Insoo Kim, was erroneously labeled. The correct affiliation for Insoo Kim is Pusan National University.

BC100456U

10.1021/bc100456u
Published on Web 11/12/2010